ΔΙΟΡΓΑΝΩΣΗ:

ΠΑΝΕΠΙΣΤΗΜΙΟ ΑΙΓΑΙΟΥ

www.ege2025lesvos.gr

ΜΟΥΣΕΙΟ ΦΥΣΙΚΗΣ ΙΣΤΟΡΙΑΣ ΑΠΟΛΙΘΩΜΕΝΟΥ ΔΑΣΟΥΣ ΛΕΣΒΟΥ

Book of Extended Abstracts

Special Publication No. 15, 2025

17th International Congress of the Geological Society of Greece

University of the Aegean

www.ege2025lesvos.gr

28-31 May, 2025
Mytilene, Lesvos island, Greece

Bulletin of the Geological Society
Special Publication No. 15, 2025
Publisher: Geological Society of Greece
ISBN (print) 978-618-86841-6-4
ISBN (e-book) 978-618-86841-7-1

17th INTERNATIONAL CONGRESS of the Geological Society of Greece

Book of Extended Abstracts Contents

		Volume A: Papers 001-050	
A/A	**EC**	**AUTHORS and TITLE**	**PAGE**
1	93	Athanasios Agrafiotis, George Papathanassiou and Sotiris Valkaniotis **Monitoring the evolution of landslide phenomena using new technologies location: Pyrra Trikala**	**1**
2	268	Dimitra Amanatidou, Konstantinos Soukis, Christina Stouraiti and Klea Dimitri **Structural study of the Theodorion meta-migmatitic complex (Serbomacedonian massif, northern Greece)**	**3**
3	44	Vasilis Anagnostou, Pavlos Bonatis, Vasileios Karakostas, Christos Kourouklas, Eleftheria Papadimitriou, Angeliki Adamaki, Stefania Alexandra Andriopoulou Mounteanou, George Bathrellos, Stylianos Bitharis, Michalis Foumelis, Ion-Anastasios Karolos, George Kaviris, Elena Papageorgiou, Christos Pikridas, Vassilis Sakkas, Hariklia Skilodimou, Ioannis Spingos and Angelos Zymvragakis **Fostering FAIR approaches to the seismological data life cycle**	**6**
4	43	Vasilis Anagnostou, Eleftheria Papadimitriou, Vasileios Karakostas and Torbjörn Bäck **Detailing the stress pattern in the area of central Ionian Islands**	**12**
5	30	Stefania Alexandra Andriopoulou Mounteanou, George Bathrellos and Hariklia Skilodimou **Flood events over the past 115 years in the Municipality of Patras, southern Greece**	**17**
6	31	Stefania Alexandra Andriopoulou Mounteanou, George Bathrellos, Hariklia Skilodimou, Angeliki Adamaki, Vassilis Anagnostou, Stylianos Bitharis, Pavlos Bonatis, Michalis Foumelis, Vassilis Karakostas, Ion-Anastasios Karolos, George Kaviris, Christos Kourouklas, Eleftheria Papadimitriou, Elena Papageorgiou, Christos Pikridas, Vassilis Sakkas, Ioannis Spingos and Angelos Zymvragakis **HOMEROS project for natural hazards: An example from northern Peloponnese, Greece**	**23**
7	202	Emmanouil Antonakis and Nickolas Zouros **Digital Visualization of Geological Heritage at Lesvos UNESCO Global Geopark: The Role of 3D Animations in** Educational Experiences	**29**
8	82	Nikolaos Antoniadis and Constantinos Loupasakis **Land Subsidence and Flooding in the East Thessaly Plain: A Historical Overview**	**34**

9	205	Alkistis Antonopoulou, Nikolaos Depountis and Sotirios Kokkalas **Geological suitability in remote mountainous settlements using the AHP method. The case study of the settlement of Klepa in Greece**	**38**
10	16	George Apostolopoulos, Alireza Malehmir, Ioannis Vakalas, Haralambos Kranis, Konstantinos Leontarakis, Christos Orfanos, Emmanouil Konstantinidis, Magdalena Markovic, Myrto Papadopoulou, Stylianos Chailas, Emmanouil Skourtsos, Andreas Tzanis and Evaggelos Spyridonos **Legacy data analysis combined with an integrated geological and geophysical survey for geothermal site exploration at Petra-Lesvos, Greece**	**44**
11	256	Konstantina Apostolopoulou, Efthimios Karymbalis, Maria Salomidi and Evangelia G. Drakou **Modelling Coastal Protection as an ecosystem service in the Greek coastal zone**	**50**
12	305	Konstantina Maria Apostolou, Elissavet Feloni and Anastasia Stergiadou **Simulation of Domestic Rainwater Harvesting Systems on Fourni Island, Aegean Sea: Assessing Efficiency Under Historic and Climate Change Scenarios.**	**55**
13	28	Foteini Aravani, Lambrini Papadopoulou, Antonios Koroneos and Alexandros Chatzipetros **Metapelitic assemblages in the contact metamorphic zone of the Varnous plutonite (NW Macedonia, Greece): preliminary results.**	**63**
14	135	Ariadne Argyraki, Artemis Kontomichalou, Zacharenia Kypritidou and Alexandros Liakopoulos **Balancing Precision and Resources: The Effect of Sampling Density in Regional Soil Geochemical Mapping**	**69**
15	318	Stella Arnaouti and Olga-Joan Ktenidou **Seismic resilience of primary water transfer network at Lagadas municipality, North Greece**	**74**
16	23	Nikolaos Arvanitidis, Konstantinos Laskaridis and Christos Christidis **Implementing the Critical Raw Materials Act to explore strategic minerals potential in Greece**	**81**
17	173	Pavlos Asteriou, Dimitrios Sotiriadis, Eleni Petala, Labros Kazelis and Nikolaos Klimis **Assessing the effect of 2023 Evros Wildfire: a new Post-Fire Rockfall Hazard System**	**89**
18	331	Ioannis Athinelis, Eleftheria Basiou, Triantafyllos Falaras and Issaak Parcharidis **Estimation of the displacement components in South Aegean islands as a response to the early 2025 seismicity of the Anydros Islet using Sentinel-1 imagery.**	**96**

19	332	Ioannis Athinelis, Ignacio Castro Melgar, Theodoros Gatsios, Pavlos Krassakis and Issaak Parcharidis **Employing Sentinel-1 imagery to monitor the deformation rate over the caldera of the Santorini Volcanic Island Complex using multitemporal InSAR from January 2023 up to February 2025.**	**104**
20	321	Efstratios Avgerinos, Efthymia Kostopoulou, Ioannis Tegoulias and Christos Giannakopoulos **Impacts of Climate Change on Maritime Conditions and Medicane Formation: Analyzing SST Changes in the Eastern Mediterranean (1940–2023) using Thematic Maps**	**111**
21	128	Pavlos Avramidis, Alexis Ramfos, Ioannis Sarris, Dionisios Christodoulopoulos, Marinos Alexandridis, Maria Michalopoulou, Nikolaos Depountis and Stefanos Papazisimou **Seasonal Water Column Stratification and Heavy Metal Distribution in the Pinios Dam Reservoir: A Comprehensive Environmental Monitoring Study**	**117**
22	158	Antonios Isidoros Avrithis, Efterpi Koskeridou, Evangelia Rentoumi, Evangelos Vlachos and Davit Vasilyan **A Preliminary Review of Microvertebrate and Invertebrate Fauna from the Early Pleistocene of Koukos region (Kos Island, Dodecanese, Greece)**	**119**
23	125	Mohammad Mahdi Badami, Yashar Aghaei and Constantinos Sioutas **Impact of Emission Regulations on the Temporal Trends of Toxicity of PM2.5 in Los Angeles**	**123**
24	235	Athanasia Bakopoulou, Chrysi Dousiaki, Michalis Diakakis, Emmanouil Andreadakis, Spyridon Mavroulis, Maria-Evangelia Gogou, Haralambos Kranis, Assimina Antonarakou and Efthymios Lekkas **Teachers' experience, attitudes and skills on flood events: The case of Daniel storm 2023, Thessaly, Greece**	**127**
25	203	Eftychia-Christina Bardi, Paraskevi Lampropoulou, Alexandros Sergoulopoulos, Aikaterini Rogkala, Panagiota P. Giannakopoulou, Fotis Margaritis, Dimitrios Papoulis, Anastasios Tsinidis, Islam Ihtisham and Petros Petrounias **A (preliminary) comparative gemmological-mineralogical study of quartz crystals derived from Greece and Brazil**	**130**
26	77	Vasiliki Barsaki, Irene Michailidou, Filio Peppa, Georgia Kerdela and Eugenia Moraiti **The UNESCO Global Geopark of Lavreotiki: a pillar for climate change adaptation & the example of sustainable water use, Greece**	**136**
27	96	Vasiliki Barsaki, Panagiotis Voudouris and Eugenia Moraiti **The world class geodiversity of the Lavreotiki UNESCO Global Geopark's minerals, Lavreotiki Municipality, Greece**	**140**
28	261	Vasiliki Barsaki, Irene Zananiri and Eugenia Moraiti **Highlighting the Geological Heritage of the Island of Kythira, Greece**	**143**

29	151	Davide Bartolozzi, Sotiria Kothri, Maria Filomena Loreto, Nomikou, Ganas, Valentina Ferrante, Kei, Fabrizio Balsamo, Lampridou, Ranero and Nikoli **Mapping the geo-hazard elements offshore the Ionian Islands (Western Greece)**	**149**
30	362	Dimitrios-Vasileios Batzakis, Efthimios Karymbalis and Konstantinos Tsanakas **Assessing earthquake-triggered tsunami hazard in Santorini-Amorgos Tectonic Zone: A deterministic simulation-based approach**	**155**
31	161	Konstantina Bejelou, Paraskevi Nomikou, Solveig Bühring, Dimitrios Papanikolaou, Stephanos Kilias, Andrea Koschinsky-Fritsche, Wolfgang Bach, Karsten Haase, Christian Ferreira, Evgenia Bazhenova, Alissa Bach, Yukari Azakura, Danai Lampridou, Areti Belka, Eirini Anagnostou, Effrosyni Varotsou and Sotiria Kothri **Oceanographic survey M192 off Milos reveals tectonic controls on hydrothermal vent distribution in a complex volcanic-tectonic system of the South Aegean**	**162**
32	262	Alexandros Belesis, Ioannis Tsentzos, Maria Belesis and Ioannis Koukouvelas **Storm Daniel flooding of Larissa City: embankments failure the aftermath**	**166**
33	149	Areti Belka, Paraskevi Nomikou, Solveig Bühring, Konstantina Bejelou, Danai Lampridou, Alissa Bach, Sotiria Kothri, Effrosyni Varotsou and Dimitrios Papanikolaou **Morphotectonic analysis of Antimilos volcanic Group**	**173**
34	357	Konstantina Bentana and Nickolaos Zouros **Geoheritage as a tool to engage children with the Sustainable Development Goals in UNESCO Global Geoparks: Best practices in educational activities from Lesvos Island UNESCO Global Geopark**	**180**
35	55	Evangelia Besiou, George Kontakiotis, Iuliana Vasiliev and Assimina Antonarakou **Environmental controls on Globorotalia menardii size variability preceding the Tortonian/Messinian boundary**	**184**
36	61	Pavlos Bonatis, Vasileios Anagnostou, Vasileios Karakostas, Christos Kourouklas, Eleftheria Papadimitriou, Angeliki Adamaki, Stefania-Alexandra Andriopoulou-Mounteanou, George Bathrellos, Stylianos Bitharis, Michael Foumelis, Ion-Anastasios Karolos, George Kaviris, Elena Papageorgiou, Christos Pikridas, Vassilis Sakkas, Hariklia Skilodimou, Ioannis Spingos and Angelos Zymvragakis **Cultivating FAIR principles for multi-hazard assessment**	**188**
37	86	Vasileios Boumpoulis, Maria Michalopoulou, Anastasios Kazolias, Maria Geraga, Nikolaos Depountis and George Papatheodorou **Development of an index-based methodology for assessing coastal vulnerability at a national scale and preliminary results**	**193**
38	207	Evangelia Bouranta and Ioannis Hatzopoulos **Development of a Geographic Information System for the Near-Real-Time Management of the seismic risk. Case study: The city of Mytilene, Lesvos (Greece)**	**197**

39	59	Nicolina Bourli, Chrysanthos Botziolis, Penelope Papadopoulou, Panagiotis Zelilidis, Elena Zoumpouli, George Iliopoulos, Angelos G Maravelis, Efthymios Tripsanas, Ioannis Oikonomopoulos, Aristotelis Pagoulatos and Avraam Zelilidis **Facies and depositional architecture of Upper Miocene tidal flat sedimentation in Kefalonia and Corfu Islands, West Greece**	**203**
40	330	Simon Bufféral, Pierre Briole, Aurélien Dupont, Javier Escartin and Philippe Heinrich **Tsunami Modelling for a Potential Earthquake between Santorini and Amorgos (Greece)**	**204**
41	312	Riccardo Caputo, Iannis Koukouvelas, Giorgos Papathanassiou, Davide Russo, Maria Taftsoglou, Gabriele Tarabusi and Sotiris Valkaniotis **The Greek Database of Seismogenic Sources (GreDaSS) version 3.0. A compilation of potential seismogenic sources (Mw> 5.5) in the Aegean Region**	**211**
42	2	Ismar S. Carvalho, Maria Helena P. Henriques and Giuseppe Leonardi **Sousa Dinosaur Valley, Brazil: The largest record of Lower Cretaceous dinosaur footprints in South America and its influence in local communities**	**217**
43	279	Stylianos Chailas and Andreas Tzanis **A Preliminary 3D Gravity Model for the pre-Volcanic Basement of Lesvos Island, Greece**	**223**
44	296	Paraskevi Chantzi, Sofia Doani and Konstantinos Albanakis **Sediment dynamics in the Sperchios river basin and their influence on stevia cultivation**	**229**
45	299	Angelos Chasiotis, Elissavet Feloni and Panagiotis Nastos **Sustainable Practices for Resilient Hydrosystems at a Municipal Level: Insights from the Greek Island of Chios**	**232**
46	271	Theodora Chatzakou, Aikaterini Tsiri, Antonios Koroneos, Ioanna Gerontidou and Alexandros Drakoulis **Kentavros plutonite (Thrace, Greece): Geochemistry and Petrogenesis**	**237**
47	51	Efstratia Chatzi, Evangelia-Theodora Derdemezi and Georgios Tsilimigkas **The Impact of Urban Sprawl on Areas of Natural and Cultural Heritage and Geoheritage. Evidence of Lemnos island, Greece**	**243**
48	255	Emmanouil Chatziangelis, Vasileios Boumpoulis and Nikolaos Depountis **Slope failures of friable sandstone in coastal areas. A Case study from Western Greece.**	**248**
49	248	Nikolaos Panagiotis Chatzigogos, Agisilaos Poulios and Thomas Makedon **Settlements in residual soils**	**254**
50	253	Alexandros Chatzipetros and Vassiliki Samantzi **Geotopes of Thessaly (central Greece) and their educational approach**	**259**

Volume B: Papers 051-100

A/A	EC	AUTHORS and TITLE	PAGE
51	350	Dimitrios Chatzistratis, Isavela Monioudi, Theodoros Chalazas, Olympos Andreadis, Konstantinos Moschopoulos, Antonis Chatzipavlis, Fotis Psarros and Adonis Velegrakis **Flood risk of a touristic island beach under Climate Change: Komi beach Chios**	**265**
52	182	Themistoklis Chatzitheodosiou, Ioannis Farmakis, Dimitra Papouli, George Stoumpos, George Prountzopoulos and Vassilis Marinos **Three Years of Progress in Digital Applications and Monitoring Utilizing 3D Reality Capture Technologies for Landslide Hazard Mitigation, the Case in Evritania, Central Greece**	**269**
53	314	Eleftheria Christodoulopoulou, Olga Ktenidou and Grigorios Tsinidis **Mapping and Categorization of damage on the built and natural environment caused by the 2023 Daniel and Elias storms in Mount Pelion, Greece**	**274**
54	7	Demerios Constantinides **ERBE SYMPOSIUM 2027– LAVRION GREECE: Honouring the Values of Geo-Mining Heritage**	**278**
55	11	Salomé C. Custódio, Maria Helena Henriques and Artur A. Sá **The Geoheritage of the "Atlantic Geopark" Project (Central Portugal) at a Glance**	**284**
56	70	Panagiota Dalgkitsi, Alfred Uchman, Chrysanthos Botziolis, Panagiotis Zelilidis, Nicolina Bourli and Avraam Zelilidis **The transitional deposits from carbonates to clastic in the Pindos foreland basin: an example from the Mazia village, Ioannina region, Greece**	**290**
57	210	Maria Georgia Dasoula, Zafeiria Roumelioti, Efthimios Sokos and Sotirios Kokkalas **Statistics on seismic moment tensors for the Aegean Sea and surrounding area: preliminary results**	**291**
58	206	Stamatia Deligianni and Alexandros Chatzipetros **Environmental Seismic Intensity Scale (ESI 2007)**	**297**
59	223	Klea Dimitri, Christina Stouraiti, Dimitra Amanatidou and Konstantinos Soukis **The Triassic post-collisional high-K alkali-calcic granites in the Vertiskos Unit, Serbo-Macedonian Massif: insights from Miriofito granite, Kerkini complex, Greece**	**303**
60	146	Evangelia Dimou, Angeliki Papoutsa, Vasilios Pletsas, Nikolaos Zegkinoglou, Stephanos Kilias, Paraskevi Nomikou and Paraskevi Polymenakou **Biogenicity of Arsenic Sulfide Biomorphous Structures in Deep-Sea Hydrothermal Vents, Kolumbo Arc Volcano: Morphological, Mineralogical and Geochemical Evidence**	**307**
61	143	Vasiliki Grigoria Dimou, Olga Koukousioura, Gyorgy Less, Maria Triantaphyllou, Margarita Dimiza, Georgios Syrides and Martin Langer **Microfacies and species richness analyses of middle-late Eocene western Thrace Basin (Neotethys Ocean, Greece): Paleoenvironmental evolution and species-richness hotspot revealed**	**314**

62	242	Panagiotis Sotirios Dittopoulos and Alexandros Chatzipetros **Using alternative methods to promote geoheritage: the Koziakas Mt., central Greece, case study.**	**317**
63	54	Antonia Dretaki and Alexandros Chatzipetros **Assessment of fault hazard in the broader area of Sitia, Eastern Crete**	**323**
64	264	Antonia Dretaki, Panagiotis Sotirios Dittopoulos, Alexandros Chatzipetros, Vasilios Papavasiliou, Nikolaos Paspaliaris, Georgios Tsirakakis and Evangelos Perakis **Formation of Sitia's Geopark (Crete Island, Greece) caves in correlation with the structural setting of the area**	**329**
65	27	Hara Drinia and George Zafeiropoulos **Enhancing Geoheritage through GEOAM: A Case Study of Tinos Island, central Aegean Sea, Greece**	**336**
66	244	Hara Drinia and Georgios Zafeiropoulos **Tinos Island, Aegean Sea, Greece, Geopark: A Pioneering Initiative in Climate Change Resilience and Geoconservation**	**339**
67	13	Christos Drougas, Efstratios Kelepertzis, Zacharenia Kypritidou, Evangelia Sigala, Christos Roumpos, Georgios Louloudis, Eleni Mertiri and Evangelos Oikonomopoulos **Hydrogeochemical Characteristics of Alfeios River and the wider hydrographic Network in the Lignite Basin Area of Megalopolis**	**342**
68	71	Panagiotis Elias, Gaetano Festa, Lauro Chiaraluce, Pascal Bernard, George Kaviris, Christos Evangelidis, Efthimios Sokos, John Clinton, Alexandru Marmureanu, Simona Colombelli, Mariano Supino, Dimitris Paronis, Vassilis Karastathis, Men-Andrin Meier, Semih Ergintav, Alessandro Vuan, Tomas Fischer, Stanka Sebela, Dimitris Paliatsas, Anna Serpetsidaki and Andreas Karakonstantis **EU funding to integrate cutting-edge methodological and technological solutions, enabling the development of a next-generation network of Near Fault Observatories across Europe (project TRANSFORM²)**	**348**
69	315	Martin Engi, Andreas Gialoglou, Panayiotis Koutsabasis, Valentin Laurent and Constantinos G. Mavrogonatos **The Syros GeoPark Project**	**351**
70	342	Christos Evangelidis and Ioannis Fountoulakis **The 2024–2025 Seismic Sequence in the Santorini-Amorgos Region: High-Resolution Seismological Insights into a Volcano-Tectonic Crisis**	**356**
71	250	Dionysia Fasoli and Elizabeth Stathopoulou **Tooth enamel meso- and microstructure of fossilized Hipparionine horses of Pikermi (Attica, Greece)**	**359**
72	208	Charalampos Fassoulas, Spyridon Staridas and Emmanouel Nikolakakis **Local driven protection of a tectonic geosite, in Crete, Greece: The Paligremnos Protected Landscape**	**363**

73	354	Charalampos Fassoulas, R. Tamborrino, P. Bolca, G. Marra, G. Mezzalama, V. Tackacs, N. Leonhardmair and M.E. Demir **Assessing the management of Arkalochori EQ crisis in Crete, Greece under the implementation of RESILIAGE project in order to strengthen community resilience**	**368**
74	136	Eugenia Fatourou, Aikaterini Kafetzidou, Fabienne Marret, Konstantinos Panagiotopoulos and Katerina Kouli **Quaternary eustatic cycles and their impact on the Paleoceanography of the Gulf of Corinth (NE Mediterranean Sea)**	**374**
75	227	Kyriaki Fellachidou and Georgios Lazaridis **Underground rivers in Greece**	**377**
76	292	Christos Filis, Emmanuel Skourtsos, Armela Korovesai, Emmanuel Andreadakis, Eleni Kapourani, Nikolaos Karalemas and Apostolos Alexopoulos **Preliminary estimation of the recession coefficient of the "Kefalari Agios Ioannis" spring, Dimitsana, Peloponnesus, Greece**	**381**
77	336	Michael Foumelis, Elena Papageorgiou, Elisa Trasatti, Deodato Tapete, Stylianos Bitharis, Christos Pikridas and Costas Papazachos **Role of Earth Observation in Monitoring Santorini–Anydros Volcano-Tectonic Crisis**	**386**
78	204	Kalliopi Elli Fragkouli, Georgios Drakatos, Spyridon Pavlides and Sotirios Sboras **Seismotectonic Features of the 2023 Strong Earthquake Sequence in Southeast Turkey.**	**389**
79	62	Dimitris Galanakis, Dimitris Sakellariou, Sotiris Sboras, Spyros Pavlides, Kyriaki Iordanidou, Charalambos Georgiou, Athanasios Ganas, Yiannis Koukouvelas, Charalampos Kranis, Spiros Lalexos, Theodora Rondoyanni and Efthymios Lekkas **The Hellenic DataBase of Active Faults (HeDBAF): a new national geodatabase**	**393**
80	120	Odysseus Galanis and Areti Panou **An investigation of the use of deep-neural-network-based seismic arrival time picking methods for the automatization of earthquake sequence monitoring: The case of the November 3, 2024 MW 5.3 Kassandra earthquake**	**397**
81	37	Erasmia Galazoudi, George Bathrellos, Hariklia Skilodimou, Ioannis Koukouvelas and Konstantinos Nikolakopoulos **Evolution of map-making from prehistoric times to the Middle Ages**	**403**
82	22	Athanassios Ganas, Dimitrios Anastasiou, Georgios Mavropoulos, Ioannis Karamitros, Konstantinos Nikolakopoulos and Varvara Tsironi **Ground motion monitoring with low-cost multi-GNSS installations in Achaia, western Greece**	**408**
83	343	Athanassios Ganas, Pierre Briole, Varvara Tsironi, Georgios Goutsos, Nicolaos Madonis, Eustratios Liadopoulos and Ioannis Mintourakis **Geodetic monitoring of the 2024–2025 Santorini volcanic unrest using GNSS and InSAR data: preliminary results**	**413**

84	21	Athanassios Ganas, Francesco Carnemolla, Ioannis Karamitros, Nikolaos Madonis and Vasileios Georgakopoulos **Geodetic monitoring of the Methana volcano (central Greece) using campaign GNSS data: preliminary results**	**417**
85	254	Athanassios Ganas, Vasilis Kapetanidis, Varvara Tsironi, Andreas Karakonstantis and Ioannis Karamitros **Integrated monitoring of the Milos geothermal site (Cyclades, Greece) using InSAR, GNSS and local seismic network data**	**422**
86	102	Athanassios Ganas, Varvara Tsironi, Georgios Goutsos, Eirini Efstathiou, Christina Tsimi, Nikolaos Madonis and Vasileios Georgakopoulos **NOAFAULTs: 12-yrs of studies and investigations towards building a geospatial database for active faults in Greece and surrounding areas**	**427**
87	307	Amalia Gasteratou and Effie Kostopoulou **Climatological analysis and Trend Assessment of Climate Indices in two forest areas of Greece experienced extreme fire events in 2023.**	**430**
88	33	Alexandra Gemitzi, Odysseas Kopsidas, Foteini Stefani, Apostolos Polymeros, Vasilis Bellos and George Falalakis **A flood hazard assessment tool using satellite based high resolution land cover dataset within Google Earth Engine**	**436**
89	358	Gonca Gençalioğlu Kuşcu and Göksu Uslular **How medial tephra records contribute to proximal tephrochronology: Case study of Nisyros Volcano**	**441**
90	169	Maria Georgaki, Hrissi Karapanagioti, Małgorzata Wojtaszek-Kalaitzidi and Stavros Kalaitzidis **Evaluation of PAHs sorption behavior in coals and cokes**	**444**
91	138	Maria Nefeli Georgaki, Athanasios Georgakis, Dimosthenis Sarigiannis and Nerantzis Kazakis **Groundwater Quality Evaluation of Thessaly and Peloponnese: Data Analysis of 2019 year and Evidence of Degradation**	**448**
92	309	Georgios P. Georgalas, Polychronis Kolokoussis, Sofia Laskari and Konstantinos Soukis **Automatic Detection and Extraction of Geological Lineaments on Amorgos Island Using Satellite Data and Open-Source Software**	**454**
93	87	Ioanna Gerontidou and Antonios Koroneos **Major and trace element analysis on geological samples using WD-XRF on pressed pellets**	**458**
94	142	Dina Ghikas and Anna Batsi **The Art of Stone in Grevena-Kozani UGGp: Community-led Conservation Efforts**	**465**

95	63	Christina Giamali, George Kontakiotis and Assimina Antonarakou **Paleoecological imprints of pteropod assemblages and their response to sapropel S1 conditions in the eastern Mediterranean Sea**	**468**
96	212	Panagiota P. Giannakopoulou, Aikaterini Rogkala, Paraskevi Lampropoulou, Petros Koutsovitis, Maria Kalpogiannaki, Vasileios Giamas, Odyseas Seikatis, Ihtisham Islam and Petros Petrounias **Correlation study of overland and marine aggregates capable to be used in various construction applications**	**472**
97	69	Anna Giannakou, Nikolaos Soulakellis, Nikolaos Zouros and Dimitrios Kavroudakis **Estimation of an empirical relationship for calculating quantities of demolished materials through three-dimensional visualization of buildings affected by the earthquake of June 12, 2017, in Vrisa, Lesvos.**	**477**
98	282	Katerina Giouri, Christos L. Stergiou, Vasilios Melfos, Lambrini Papadopoulou, Nikolaos Kantiranis, Irena Peytcheva and Elitsa Stefanova **Preliminary results on the toxic elemental accumulation in the Fe-oxides of the stream sediments from Palea Kavala, Northern Greece**	**482**
99	311	Salvatore Giuffrida, Letizia Anderlini, Shannon Graham, Francesco Carnemolla, Fabio Brighenti, Giorgio de Guidi, Flavio Cannavò and Riccardo Caputo **Investigating the interseismic coupling degree of the northern Apennines external Arc in Emilia Romagna region, (northern Italy).**	**488**
100	117	Antonela Gjika, Christina Stouraiti, Panagiotis Voudouris, Konstantinos Laskaridis, Marianthi Anastasatou, Constantinos Mavrogonatos and Harald Strauss **Geochemical and Mineralogical Study of the Antimony (Sb)-mineralization at the north Pelion region, Magnesia, Greece**	**491**

Volume C: Papers 100-150

A/A	EC	AUTHORS and TITLE	PAGE
101	355	Konstantinos Gkogkas, Costas Papazachos, Nikolaos Chatzis, Dominikos Vamvakaris, Eleni Karagianni, Chrisa Ventouzi, Alexandros Vellis, Nikolaos Anterriotis-Kalpakidis, Dimitrios Madelis, Parthena Paradisopoulou, Eleni Aidona and Christos Pikridas **SantoArray: Densifying station coverage in Santorini amidst the Amorgos-Anydros earthquake swarm crisis**	**494**
102	337	Marilia Gogou, Nafsika Ioanna Spyrou, Spyridon Mavroulis, Niki Evelpidou, Maria Mavrouli, Efthimis Lekkas and Assimina Antonarakou **Assessment of assembly point suitability in tsunami-prone South Aegean coasts after the 2025 Santorini-Amorgos earthquake swarm and related risk reduction measures**	**498**
103	165	Vasilis Golfinopoulos, David J. W. Piper, Avraam Zelilidis, Georgia Pe-Piper, Penelope Papadopoulou, Nicolina Bourli and George Iliopoulos **Palaeoenvironmental Interpretation and Soft Sediment Deformation of the Ionian Basin Lower Jurassic Formations in Astakos (Western Greece)**	**504**
104	234	Georgios Goutsos, Vasiliki Kouskouna, Georgios Sakkas and Nikolaos Sakellariou **A decade of data: Updating the Hellenic Macroseismic Database for historical earthquakes**	**508**
105	18	Ioannis Grendas and Zafeiria Roumelioti **Seeking for dependencies of the high frequency "kappa" parameter of earthquake spectrum on weather/climate conditions**	**514**
106	326	Georgios Grimpylakos **Digital model of Hydrological components, Mean annual Temperature, Precipitation and Evapotranspiration in Macedonia, Greece**	**521**
107	75	Maria Groumpou, Ioannis Koukouvelas, Konstantinos Nikolakopoulos, Josep Sanjuan, Penelope Papadopoulou and George Iliopoulos **The Pheneos palaeolake in N. Peloponnese, Greece**	**527**
108	131	Maria Grylionaki, Nikolaos Theodoulidis, Areti Panou and Panagiotis Chatzidimitriou **Estimation of soil vulnerability index in the metropolitan area of Thessaloniki (Greece)**	**530**
109	9	Levent Gülen **Seismotectonics of the NE Aegean region: The Lesvos Island and the Gulf of Edremit**	**531**
110	366	Erdal Gumus, Nikolas Zouros **The rocks connect us: Volcanic geoheritage of Lesvos Geopark (Greece) and Ida Madra Geopark (Türkiye)**	**537**
111	324	Petros Hadjicostas and Evi Kazamia **Assessing Climate Change Impacts on Troodos Mountain (Troodos UNESCO Global Geopark area) Through Methodological Approaches and Community Engagement in the ClimEmpower Project**	**542**

112	4	Maria Helena Henriques, Salomé C. Custódio and Ismar S. Carvalho **Geoconservation in Portugal: an overview**	**543**
113	247	Iatrou Alexandra, Karakostas Dimitrios, Fragkiskos Markozanes, Aikaterini Karditsa and Serafeim Poulos **Beach retreat due to sea level rise induced by climate Change: The case of the Korasida, Heromylos and Limnionas beaches of south Evia facing the Aegean Sea.**	**549**
114	294	George Iliopoulos, Penelope Papadopoulou, Ilias Valiakos and Nickolas Zouros **Contribution to the stratigraphic study of the pyroclastic Formations of the Lesvos Petrified Forest, Lesvos Island, Greece.**	**552**
115	209	Dimitrios Ioannidis, Emmanouil Katrivanos and Alexandros Chatzipetros **Geological study of the basement structure in the wider area of Filiro (Circum-Rhodope Belt, Central Macedonia, Greece)**	**558**
116	313	Despoina Ioannidou and Olga-Joan Ktenidou **Integrating Geotechnical Data and Site Response Analyses in the Municipality of Chalandri, Athens, Greece**	**564**
117	319	Angelos Kannelos Irakleidis and Olga Joan Ktenidou **Seismic vulnerability of cultural heritage. The case of the archaeological museum of Rhodes: building performance, safety of the public and exhibits**	**570**
118	157	Alexandros Wilfred Irakliotis and George Papathanassiou **Rock slope stability analysis on the road axis of Kleisoura – Kastoria, Greece**	**576**
119	140	Aikaterini Kafetzidou, Eugenia Fatourou, Konstantinos Panagiotopoulos, Fabienne Marret, Olga Koukousioura and Katerina Kouli **Relict Taxa and Refugial Dynamics in the Corinth Gulf: Insights from the Pollen Record**	**579**
120	94	Aikaterini Kafetzidou, Olga Koukousioura, Vassilis Zotiadis and Katerina Kouli **Rare Insights in the Oligocene flora of Thrace (Greece): Preliminary results from the Rhodopi Petrified Forest**	**581**
121	1	Maria Kaimakami **Mapping the geological landscape of NW bay of Navarino through time**	**583**
122	50	Maria Kakavas, Aggeliki Kyriou, Konstantinos Nikolakopoulos and Ioannis Koukouvelas **The influence of DSMs spatial resolution on rockfall simulation.**	**587**
123	8	Christina Kalaitzi and Dimitris Kostopoulos **The late Ruscinian leporid Trischizolagus (Leporidae, Lagomorpha) from Megalo Emvolon (Thessaloniki, Greece)**	**594**
124	171	Panagiotis Kalaitzis, Michael Foumelis, Antonios Mouratidis and Nikolaos Soulakellis **Multiscale Geo-visualization Dashboard of Persistent Scatterer Interferometry SAR Data, Lesvos Island, Greece**	**596**

125	221	Iraklis Kalogeropoulos, Georgios Lazaridis and A. Tsekoura **Methodology of cave mapping: comparison of surveys**	**601**
126	174	Kalpogiannaki Maria, Aikaterini Rogkala, Panagiota P. Giannakopoulou, Petros Koutsovitis, Paraskevi Lampropoulou, Petros Petrounias, Dimitrios Papoulis, Nikolaos C. Koukouzas and Panagiotis Pomonis **Geoeducational and Geotourism values of geological resources as novel path for Geosciences Education**	**605**
127	111	Isidoros Kampolis, Panagiotis Voudouris and Evgenia Moraiti **The pseudokarst at the Kaki Thalassa Bay reveals unknown ancient mining activities (Lavreotiki UNESCO Global Geopark)**	**610**
128	258	Christos Kanellopoulos, Vasiliki Aggelatou and Christos Papatrechas **Preliminary results of black sands in Corfu Island (Ionian Sea, Greece).**	**614**
129	220	Christos Kanellopoulos, Dimitrios Galanakis, Leonidas Moforis, Sotiris Sboras, Olga Chalkiadaki, Nikolaos Xirokostas and George Vougioukalakis **Preliminary results on Agios Efstratios island (NE Aegean Sea, Greece) geology.**	**617**
130	214	Christos Kanellopoulos, Dimitrios Galanakis, Sotiris Sboras, Kyriaki Iordanidou, Leonidas Moforis, Nikolaos Xirokostas, Olga Chalkiadaki and George Vougioukalakis **Pagasitikos volcanism (Lichades-Kamena Vourla-Achillio-Mikrothives-Porfyrio-Psathoura): Preliminary results on a Quaternary tectonically related volcanism.**	**620**
131	35	Konstantina Kantareli and Vassilis Sakkas **Investigating crustal deformation of Zakynthos Island using Satellite Interferometry (InSAR): pre- and post- seismic analysis of the October 25, 2018 earthquake**	**623**
132	80	Vasilis Kapetanidis, Ioannis Spingos, Christofer Kaltsas and George Kaviris **Application of a machine-learning model for the determination of focal mechanisms in the area of the Corinth Rift Laboratory Near-Fault Observatory (CRL NFO), Central Greece**	**629**
133	58	Athanasia Theodora Karachaliou, Dimitrios Vogiatzis and Nikolaos Kantiranis **Preliminary results of physicomechanical properties of lightweight mortars using palygorskite as sand replacement**	**636**
134	172	Özlem Karagöz and Onur Tan **Microtremor array explorations and the importance of local site effect in Western Türkiye**	**642**
135	335	Vasileios Karakostas, Anthony Lomax, Vasilis Anagnostou, Eleftheria Papadimitriou, Valerio Acocella, Stephen Hicks and Pierre Henry **The 2025 seismicity burst in the Santorini – Amorgos seismovolcanic zone**	**646**
136	367	P. Karanis **Climate changes, neglected and emerging diseases**	**651**

137	167	Efstratios Karantanellis, Vassilios Marinos and Anika Braun **AI-Driven Approaches for Landslide Modeling: Challenges and Opportunities**	**653**
138	226	Georgia Karountzou, Maria-Roi Panagiotaki, Dionisis Semitekolos and Costas Charitidis **Evaluation of Greek clay for pottery applications**	**656**
139	361	Jens Karstens, Paraskevi Nomikou, Marius Isken, Michelle Maree Parks, Vincent Drouin, Emilie E.E. Hooft, Thomas R. Walter, Mahmud Haghshenas Haghighi and Dimitris Anastasiou **The 2025 seismic crisis reveals a coupled magma feeding system at Santorini and Kolumbo**	**657**
140	280	Theodora Karympali **The role of painting as a historical indicator of relative sea-level change: a review**	**659**
141	154	Marianthi Katheri, Olga Koumoutsakou and Assimina Antonarakou **Challenges and Opportunities in the AI Era: Promoting Earth Science Education for Deaf and Hard of Hearing Students**	**666**
142	347	Ioannis Katsafados, Dimitrios Anastasiou, Melissinos Paraskevas, Maria Tsakiri, Paraskevi Nomikou and Costas Synolakis **Preliminary results of displacements from the recent seismic and volcanic crisis in the Santorini Island complex, Greece**	**668**
143	90	Anna Katsigera, Paraskevi Nomikou, Paraskevi Polymenakou, Sergio Sciré Scappuzzo, Gianluca Lazzaro, Aggelos Mallios, Valsamis Ntouskos, Sotiris Spanos, Christos Antoniou, Andrea Luca Rizzo, Manfredi Longo, Javier Escartin, Konstantinos Karantzalos, Walter D Alessandro, Lars-Eric Heimburger, Stephanos Kilias, Theodoros Mertzimekis, Fausto Grassa, Danai Lampridou, Eirini Anagnostou and Vasiliki Papadimitriou **SANTORY shallow seafloor observatory: First time series data from an active submarine volcano**	**674**
144	176	Chrysoula Katsora, Evaggelos Levadiotis, Ourania Tzoraki and Nektaria Papadopoulou **Flash drought assessment: insights from Lesvos island, Greece**	**677**
145	251	Katerina Kavoura, Garyfalia Konstantopoulou and Panagiotis Paschos **Rainfall-induced landslides in Corfu island: effectiveness of the regional scale landslide susceptibility map**	**681**
146	201	Nerantzis Kazakis, Ioanna Sideri, Maria Margarita Ntona, Vasiliki Stavropoulou, Dimitra Lampropoulou, Eleni Zagana and Konstantinos Voudouris **Origin of nitrate pollution in groundwater of Mygdonia Plain, Greece**	**685**
147	104	Shoaib Ahmed Khan, Theodora Tsourou, Emmanuel Skourtsos, Konstantinos Soukis, Ioannis Michailidis, Elisavet Skampa and Maria Triantaphyllou **Micropaleontological and paleoenvironmental study of carbonate intercalations within Boeotia (Greece) clastic formations**	**691**

148	79	Georgia Kitsaki, Christos L. Stergiou and Haritakis Papaioannou **"Vikos-Aoos Geopark: Toponyms as a Link Between Geological Heritage and Culture"**	**693**
149	241	Charalampos Kkallas, Costas Papazachos and Basil Margaris **A Duration Model for Strong Seismic Motions of Intermediate-Depth Earthquakes in the Southern Aegean and its implication for stochastic simulations**	**695**
150	49	Foivos Klimis, Olga Sykioti, Efthimios Karymbalis and Isaak Parcharidis **Lunar Pits: Statistical Analysis of Morphometric and Geophysical Properties**	**700**
151	92	Aliki Kokkala, Vassilis Marinos and George Papathanassiou **Utilizing engineering geological database for urban geohazard assessment: a case study from Thessaloniki, Greece**	**706**
152	276	Sotirios Kokkalas, Vasileios Psarros and Petros Koutsovitis **Diapiric structures in evaporites of Western Greece as potential geoenergy storage areas.**	**709**

Volume D: Papers 151-200

A/A	EC	AUTHORS and TITLE	PAGE
153	281	Eleni Kolaiti, Nikolaos Soulakellis, Georgios Tataris and Nikos Mourtzas **The Argo-Beachrock Project: web mapping and geovisualisation of beachrocks using UAS along the coast of the Argolic Gulf, Greece**	**715**
154	353	Eleni Kolaiti, Nikolaos Zouros and Nikos Mourtzas **The Corinth Canal (Greece): monumentality and protection**	**721**
155	179	Maria Kolendrianou, Zacharenia Kefalogianni, Agapi Kalomoiri and Charalampos Fassoulas **Synergies for geo- education: materials and initiatives from Psiloritis UNESCO Global Geopark and the Center for Environmental Education and Sustainability of Anogia, (Crete) Greece.**	**728**
156	156	Pavlina Kolyva, Olga Koumoutsakou and Assimina Antonarakou **The Role of Fairy Tales in Fostering Geoscience Understanding in Early Childhood**	**735**
157	119	Georgios Kontokostas and Assimina Antonarakou **Application of the educational proposal for Geoscience: Geology in secondary education through educational geopaths in the urban environment.**	**737**
158	260	Orestis Kontopidis, Alexandros Theocharis, Nikolaos Koukouzas, Jan Burda and Ioannis Zevgolis **Interpretation of CPTu data for mining slope stability assessment in reclamation projects: The case of pit Lake Most, Czech Republic**	**740**
159	259	Orestis Kontopidis, Alexandros Theocharis and Ioannis Zevgolis **A semi-quantitative multi-hazard approach for Tailings Storage Facilities**	**745**
160	124	Efterpi Koskeridou, Christos Psarras, Evangelia Rentoumi, Ioannis Giaourtsakis and Marija Bošnjak **The role of the museums in the geoscience education– examples from the Museum of Paleontology and Geology of the National and Kapodistrian University of Athens, Greece and the Croatian Natural History Museum, Croatia**	**750**
161	17	Panagiotis Kosmas, Constantinos Loupasakis, Vasiliki Eleftheriou, Rozalia Christodoulopoulou and Antigoni Vrouva **Ultrasonic analysis of the structural stones of the Parthenon at the Acropolis of Athens – Investigation of the physical / mechanical properties and integrity control of the grouted Joints**	**753**
162	180	Georgia Kostaki, Hans-Juergen Gawlick, Adamantios Kilias, Sigrid Missoni, George Ghon and Emmanouil Katrivanos **The Koziakas Mélange Unit: New perspectives on Its Mesozoic paleogeographic and geotectonic evolution (Central Greece)**	**757**

163	308	Effie Kostopoulou, Christos Giannakopoulos, Constantinos Nefros and Constantinos Loupasakis **Assessing Climate Extremes as Drivers of Geohazards in Greece**	**763**
164	122	Sotiria Kothri, Paraskevi Nomikou, Maria Filomena Loreto, César Rodríguez Ranero, Danai Lampridou, Elisavet Nikoli, Irene Merino, Valentina Ferrante, Serafeim Poulos and Athanassios Ganas **Submarine geomorphological structures in the Ionian Sea, Greece**	**769**
165	66	Christina Kotsakostoudi, Anna Bourliva, Christina Mytiglaki, Lambrini Papadopoulou and Nikolaos Kantiranis **Heavy metal concentrations in indoor house dusts from the city of Thessaloniki, N. Greece: a small-scale study**	**773**
166	103	Artemis Kotsomitopoulou, Nikolaos Tsaparas and Galazoudi Erasmia **New Clypeaster fossils from South Crete (Rodakino, Rethymno)**	**778**
167	310	Athanasios Koukoulis and Markos Xenakis **Measurements of soil gas emissions (Radon and Thoron) in the municipality of west Lesbos, Stypsis – Petras, and correlation with tectonic structures (Rift Zone) of the subsidence coast of Petra**	**782**
168	152	Olga Koukousioura, Paraskevi Nomikou, Adam Woodhouse, Shun Chiyonobu, Paraskevi Polymenakou, Tim Druitt, Steffen Kutterolf, Thomas Ronge, Sarah Beethe, Alexis Bernard, Carole Berthod, Hehe Chen, Acacia Clark, Susan DeBari, Sofia Della Sala, Tatiana Fernandez-Perez, Ralf Gertisser, Christian Hübscher, Raymond Johnston, Christopher Jones, Kumar Batuk Joshi, Anna Katsigera, Stephanos Kilias, Gunther Kletetschka, Xiaohui Li, Michael Manga, Molly McCanta, Iona McIntosh, Abigail Metcalfe, Antony Morris, Katharina Pank, Vasiliki Papadimitriou, Ally Peccia, Jonas Preine, Masako Tominaga, Yuzuru Yamamoto, Takeru Yoshimoto and Dimitrios Papanikolaou **Foraminiferal response to a giant shallow-marine pyroclastic-flow-eruption from ancestral Santorini discovered by IODP Expedition 398 – Objectives, challenges and results of deep drilling into Christiana-Santorini-Kolumbo volcanic field**	**789**
169	139	Olga Koukousioura, Konstantinos Panagiotopoulos, Eugenia Fatourou, Aikaterini Kafetzidou, Paula Diz, Katerina Kouli and Patrick Grunert **Late Quaternary dynamics of paleoenvironments and ecosystems in the Gulf of Corinth (eastern Mediterranean): IODP Expedition 381**	**792**
170	100	Nikolaos Koukouzas, Pavlos Tyrologou, Christos L. Stergiou, Julio Carneiro, Paula Fernández-Canteli, Christina Karatrantou and Stamatina Asimakopoulou **Characterization of Sandstone Formations in the Mesohellenic Trough for CO2 Storage: Insights from the Integration of Optical Mineralogy, Geochemistry, and Automated Imaging Techniques**	**794**
171	153	Olga Koumoutsakou and Assimina Antonarakou **Unveiling the Potential of AI in Geoscience Education: A Student-Centered Perspective**	**800**

172	245	Vasiliki Koumpou, Serafeim Poulos, Aikaterini Karditsa, Stylianos Petrakis and Vasileios Kapsimalis **An insight to grain size composition of the beach sediment along the north coast of the Messiniakos Gulf (Greek Mainland).**	**803**
173	105	Alexandros Aristotelis Koupatsiaris and Hara Drinia **A systematic review of grey literature in Greek universities repositories to uncover Greek UNESCO Global Geoparks**	**805**
174	98	Alexandros Aristotelis Koupatsiaris and Hara Drinia **Assessing Educators' Sense of Place and Geoethical Awareness at the 4th Summer School of Sitia UNESCO Global Geopark**	**810**
175	41	Christos Kourouklas, Pavlos Bonatis, Eleftheria Papadimitriou and Vasileios Karakostas **Fault–based recurrence models and occurrence probabilities of large earthquakes (M≥6.0) in the Corinth Rift, Greece**	**817**
176	191	Petros Koutsovitis, Gerasimina Pahaki, Vasileios Giamas and Lemonia Kalantzi **A preliminary petrographic approach to the pyroclastic tuffs in the island of Tilos**	**824**
177	187	Petros Koutsovitis and Aikaterini Papaioannou **A preliminary petrographic approach of the altered Triassic volcanic lavas in Argolis, Greece**	**828**
178	183	Petros Koutsovitis, Konstantinos Tetisis and Georgia Kolovadi **Petrographic evidence for the metamorphic conditions in ultramafic rocks at Makrymalli – Evia Island**	**830**
179	36	Petros Koutsovitis, Michiel van der Meulen, Tirza van Daalen, Pavlos Tyrologou, Nikolaos Koukouzas, Alkiviadis Sideridis, Christos Karkalis, Michel Grégoire, Petros Petrounias, Theodoros Ntaflos and Konstantinos Lentas **An outline on some of the recently reported granitoids from St. Martin Island**	**831**
180	64	Evlampia Kouzeli, Olga Sykioti, Konstantinos Nikolakopoulos, Saeid Asadzadeh, Friederike Koerting and Daniel Schläpfer **Mineral mapping using satellite multispectral and hyperspectral data for a pyrite mine in the frame of the m4mining project**	**833**
181	298	Kalliopi Kravari and Dimitrios Emmanouloudis **A Novel Approach to Flood and Drought Management in Arid Regions using Multi-Agent Systems**	**840**
182	218	Phaedra Kravvariti, Andreas Tzanis, Vasileios Sakkas and Haralambos Kranis **Contemporary distributed block deformation in the South Aegean Sea (Greece), deduced by the analysis of continuous GNSS measurements**	**846**
183	291	Konstantina Krotka, Fikos Ilias and Papathanassiou George **Geophysical investigation of landslide phenomena in the Perivoli area, Grevena, using the electrical resistivity tomography method**	**852**

184	325	Olga-Joan Ktenidou, Antonia Papageorgiou, Fevronia Gkika, Erion-Vasilis Pikoulis, Kalliopi Fragouli, Fanis Chalaris, Spyros Liakopoulos, Ziya Cekinmez, Panagiotis Savvaidis and Christos Evangelidis **A holistic proposition for assessing reference station conditions**	**858**
185	6	Erwin Kunz **The Xerias Window near Argos (Peloponnesus)**	**863**
186	290	Anastasios Kyriakos, Grigorios Aarne Sakellaris, Vasilios Melfos, Christos L Stergiou, Lambrini Papadopoulou and Nikolaos Kantiranis **Mineralogy and Geochemistry of the Non-Sulfide Zinc-Lead Deposits, Thasos Island, North Aegean, Greece**	**864**
187	175	Anastasios Ladas, Vasileios Melfos, Lamprini Papadopoulou and Nikolaos Kantiranis **Study of the geochemical distribution of uranium and thorium in the soils of the Sarigiol Basin, Kozani, and their environmental significance.**	**870**
188	285	Lida Lakidi, Nafsika Ioanna Spyrou, Michalis Diakakis, Christos Filis, Evelina Kotsi, Spyridon Mavroulis, Emmanuel Skourtsos, Haralambos Kranis and Efthymios Lekkas **Flood Dredge Spoils Mapping with the Use of UAS and GIS: The Case of 2020 Evia Flood**	**876**
189	322	Aggelos Lamprakopoulos and Nikolaos Zouros **Contribution to the neotectonic study of West Lesvos**	**882**
190	213	Georgios Lazaridis, Bogdan Onac, Jo De Waele, Konstantinos Vouvalidis, Spyridon Gkelis, Vasilis Gerovasileiou, Konstantinos Trimmis, Kimon Papadimitriou, Panagiotis Georgiakakis, Kaloust Paragamian, Despina Dora, Savvas Paragkamian, Markos Digenis, Foteini Sdraka, C. Alexandropoulou, T. Alikakou, C. Arvaniti, N. Chatzinikolaou, K. Chavanidis, X. Georgopoulou, A. Giannopoulou, D. Koumparelou, C. Lytra and I. Simoglou **Field-Work Methods in Speleology: A Multidisciplinary Training Approach**	**888**
191	219	Georgios Lazaridis, Foteini Sdraka, M. E. Georgiadou, A. Batsi, D. Gkikas, Despina Dora and Konstantinos Trimmis **Evaluation of karst geosites in Grevena-Kozani UNESCO Global Geopark**	**892**
192	217	Georgios Lazaridis, Christos L. Stergiou, Alexandros Chatzipetros, Konstantinos Stamoulis, Despina Dora, Xenia Georgopoulou, Konstantinos Vouvalidis, Evangelos Nikolaou, Panagiotis Paschos, Georgia Kitsaki and Haritakis Papaioannou **Utilizing Information and Communication Technology for geosite development: The case of sulfuric acid caves in the Vikos-Aoos UNESCO Global Geopark**	**898**
193	148	Vasiliki Lianou and Petros Tsakiridis **Management of solid wastes from offshore oil drilling, based on their geochemical properties: A case study from the Prinos facilities in the Northern Aegean Sea.**	**903**
194	215	Eleni M. Liapi, George Iliopoulos and Nikolaos Zouros **Palaeobotanical study of the Vrisaki flora from the Lesvos Petrified Forest**	**906**

195	364	Marco Liuzzo, Cinzia Federico, Fausto Grassa, Christos Kanellopoulos, Kostas Kyriakopoulos, Spyros Lalechos, Maria Manousaki, Barbara Nisi, Giancarlo Tamburello, Franco Tassi, Orlando Vaselli, George Vougioukalakis, Antonio Paonita, Francesca Bianco and Walter D'Alessandro **Preliminary results of the fluid geochemistry surveillance campaigns on Santorini island (Greece) after the 2025 Anydros seismic sequence**	**912**
196	25	Athanasios Lois, Dimitrios Giannopoulos and Efthimios Sokos **Automated Seismic signals' identification: A statistical criterion for decreasing the false alarm rate; Implementation on synthetic data.**	**913**
197	123	Maria Filomena Loreto, Valentina Ferrante, Marco Ligi, Filippo Muccini, Camilla Palmiotto, Lorenzo Petracchini, Stefania Romano, Athanassios Ganas, Andrea Argnani, Alessia Conti, Marco Cuffaro, Alenssandra Pensa, Sotiria Kothri, Danai Lampridou, Irene Merino, Cesar R. Ranero and Paraskevi Nomikou **Mapping the active Faults affecting Ionians Islands, Western Hellenic Arc**	**917**
198	101	Georgios Lyras, Athanassios Athanassiou, Alexandra van der Geer, George Kontakiotis, Evangelia Besiou and Assimina Antonarakou **The Early Pleistocene vertebrate fauna of Vatera, Lesbos, Greece**	**922**
199	317	Parina Machaira, Effie Kostopoulou, Christos Giannakopoulos, Myrto Gratsea and Gianna Kitsara **Assessing the impact of climate change on olive cultivation in the Peloponnese, Greece: A long-term analysis using climate indices**	**925**
200	144	Efthymios Magkoufis, Athanassios Ganas, Konstantinos Nikolakopoulos and Betty Charalampopoulou **A WebGIS platform for the multiparametric monitoring of ground deformation and critical infrastructures under the name PROION**	**931**
201	246	Mangifesta M., Scalella G., Sciarra N. **An example of DsGSDs in Abruzzo Region (Central Italy): the complex case of Civitella del Tronto**	**935**
202	38	Emmanouil Manoutsoglou **The 'treasure' of aeolianites on the coastal front of Marathopoli Dialiskari, Messinia, Western Coast of the Peloponnese: rhizoliths petrified forest and historical abandoned quarries**	**939**
203	47	Emmanouil Manoutsoglou, Nikolaos Andronikidis, Ilias Lazos, Georgios Kritikakis, Nikolaos Economou, Emmanouil Steiakakis, Georgios Xiroudakis and Antonios Vafeidis **Monitoring sea water intrusion at Samaria Gorge National Park**	**945**

Volume E: Papers 201-250

A/A	EC	AUTHORS and TITLE	PAGE
204	26	Kyriaki Manta, Grigoris Rousakis, Maria Geraga, George Papatheodorou, Dimitris Sakellariou and Aristomenis Karageorgis **Preliminary results on sedimentological characteristics of Mass Transport Deposits (MTDs) during the Amorgos tsunami 1956: sediment provenance and geochemical elements.**	**949**
205	341	Spyridon Mavroulis, Andromachi Sarantopoulou, Maria Mavrouli, Assimina Antonarakou and Efthymios Lekkas **Increased preparedness in anticipation of an imminent disaster: actions during the early 2025 Santorini – Amorgos (Aegean Sea, Greece) earthquake crisis and lessons learned**	**955**
206	277	Vasileios Mazarakis, Konstantinos Tsanakas, Noam Greenbaum, Dimitrios Vasileios Batzakis, Alessia Sorrentino, Ioannis Tsodoulos, Kanella Valkanou and Efthimios Karymbalis **Application of GIS-Based Multicriteria Decision Analysis and Analytic Hierarchy Process for Flood-Hazard Mapping in the Messapios River Basin, Central Evia Island, Greece**	**962**
207	287	Margarita Melfou, Panagiotis Voudouris, Reiner Klemd, Manuel Keith, Alexandre Tarantola, Vasilios Melfos, Lambrini Papadopoulou and Nikolaos Kantiranis **Indium and tellurium enrichment in sulfides and sulfosalts at the Pefka high- to intermediate-sulfidation epithermal deposit, Rhodope, Greece**	**969**
208	84	Ioannis Michalakis, Adonis Photiades and Spyros Staridas **An Overview of Geological Map Sheets of Crete by HSGME**	**975**
209	20	Ioannis Michalakis and Eleni Tsolaki **Water Wells in Crete: Distribution by Municipality, Use, and Ownership—Results of a Systematic Inventory in Greece**	**981**
210	12	Ioannis Michalakis, Eleni Tsolaki, Constantinos Loupasakis, Konstantinos Voudouris and Charalampos Kontoes **Preliminary Results on Land Subsidence Induced by Groundwater Overexploitation Using Copernicus Sentinel Data: Insights from the Messara Basin, Crete**	**987**
211	118	Maria Michalopoulou, Nikolaos Depountis, Eleni Zagana and Pavlos Avramidis **Application of geochemical indices for heavy metal evaluation in the Pinios Dam, Greece**	**993**
212	127	Sofia Michalopoulou, Sara Faulwetter, Dionisios Christodoulopoulos, Alexis Ramfos and Pavlos Avramidis **The impact of aquaculture units on Copper (Cu) concentrations in marine sediments**	**999**
213	196	Georgios Michas **Spatiotemporal diffusion variability in seismic swarms**	**1004**
214	137	Zoe Misiri, Spyridon Lainas and Nikolaos Depountis **Hellenic Landslide Platform (He.L.P.): A Geospatial Landslide Inventory for Western Greece**	**1009**

215	78	Leonidas Moforis, George Kontakiotis, Assimina Antonarakou, Alexandra Zambetakis-Lekkas, Ahmad Sajjad, Panagiotis Paschos, Dimitrios Galanakis, Christos Kanellopoulos, Sotiris Sboras, Hammad Tariq Janjuhah, Ilias Lazos and Vasileios Karakitsios **Biostratigraphy, Sedimentary Microfacies, and Depositional Environment of the Paleocene-Early Eocene Calciturbidites in Gardiki Section (Epirus, Western Greece)**	**1014**
216	349	Isavela Monioudi, Dimitrios Chatzistratis, Adonis Velegrakis, Anastasios Risgos, Antonis Chatzipavlis, Antigoni Nikolaou and Olympos Andreadis **The geospatial characteristics of an island beach: the case of Kos, Greece**	**1018**
217	29	Eugenia Moraiti, Panagiotis Voudouris and Vassiliki Barsaki **Innovative educational programs at the Lavreotiki UNESCO Global Geopark: the ERASMUS+ "ARTeMIS" Program Action for Research and Teaching Mineral exploration Inclusive School, Greece**	**1023**
218	53	Hara Moshou and Hara Drinia **Empowering Future Generations: Incorporating Geo – Environmental Education on Climate Change into Greek Compulsory Education**	**1025**
219	19	Nikos Mourtzas, Antonis Gkiolas, George Papacharalambous, Anastassios Tsakonas and Eleni Kolaiti **Slope stability rehabilitation in the traditional settlement of Chora, Andros Island, Greece**	**1030**
220	32	Harry Moustakas, Zafeiria Roumelioti, Efthimios Sokos and Christos Evangelidis **The Horizontal-to-Vertical Spectral Ratio Method for Underground Voids Detection: Testing Over Mycenaean Tombs**	**1036**
221	194	Lemonia Moysidou, Ermioni Eirini Papadopoulou, Stavros Proestakis, Nikolaos Zouros and Nikolaos Soulakellis **Multiscale 3D mapping and Geovisualization of a Petrified Forest Park in Lesvos, Greece, using UAV.**	**1042**
222	301	Ch. Mpakopoulou, D. Tsesmelis, K. Kalogeropoulos, K. Vasilakou, E. Feloni, E. Zervas and A. Tsatsaris **Investigating Drought Dynamics in Greece Using Climate and Meteorological Indicators**	**1048**
223	40	Jan Mrlina **Density modeling based on gravity survey at faulted area around Aigion, Gulf of Corinth, Greece**	**1054**
224	39	Jan Mrlina **Gravity monitoring at Santorini volcanic island, Greece**	**1060**
225	147	Valentini Navrozidou, Olga Koukousioura, Sofia Doani, Peter Frenzel, Maria Triantaphyllou, Konstantinos Albanakis and Georgios Syrides **Ostracod-based environmental reconstruction of Lake Koronia, (Central Macedonia-Greece) during the Holocene**	**1066**

226	14	Constantinos Nefros, Gianna Kitsara, Constantinos Loupasakis and Christos Giannakopoulos **Rapid Detection of Landslides Triggered by Mediterranean Cyclones Using Google Earth Engine and Open-Access Data**	**1068**
227	112	Elisavet Nikoli, Paraskevi Nomikou, Evangelos Tasioulas, Christophis Koroneos, Kalliopi Sakkali, Georgios Koukourakis, Panagiotis Nastos, Varvara Antoniou, Dimitrios Emmanouloudis, George Pehlivanides and Aristidis Batis **Integrating Volcanic Geoheritage and Community Engagement: The Case of Nisyros aspiring UNESCO Global Geopark**	**1073**
228	293	Ioanna Nikolopoulou, Gian Maria Bocchini, Marco Roth, David Essing, Rebecca Harrington, Anna Serpetsidaki, Ioannis Fountoulakis, Christos Evangelidis and Efthimios Sokos **The 2024 March 29, 5.9 ML Strofades Earthquake (Greece) and its Seismic Sequence: Relocation, Focal Mechanism Solutions and Stress Inversion**	**1075**
229	141	Stefania Nisio, Sergio Madonna, Giancarlo Ciotoli, Gentili Francesco and Livio Ruggieri **Sinkholes, roads and exceptional transports, a risk to be assessed**	**1079**
230	108	Paraskevi Nomikou, Elisavet Nikoli, Evangelos Tasioulas, Christophis Koroneos, Kalliopi Sakkali, Georgios Koukourakis, Panagiotis Nastos, Varvara Antoniou, Dimitrios Emmanouloudis, George Pehlivanides and Aristidis Batis **Nisyros Geopark: A Living Laboratory of Volcanic Geoheritage in the South Aegean**	**1085**
231	129	Maria Margarita Ntona, Vasiliki Stavropoulou, Dimitra Lampropoulou, Eleni Zagana, Christos Pouliaris and Nerantzis Kazakis **Assessment of groundwater quality and seasonal dynamics in Chortiatis, northern Greece: Insights for sustainable resource management**	**1088**
232	24	Panos Ntontos **Evaluation of National Groundwater Monitoring Network at the Peloponnese, Greece**	**1094**
233	189	Efthymios Ntouros, Nikolaos Sofis, Maria Ellie Damoulianou, Margarita Iatrou, Tassos Grammatikopoulos, George Papaptheodorou and Stavros Kalaitzidis **Characteristics of REE mineralization in bauxite strata and in bauxite residue deposited into the Corinth Gulf, Greece**	**1100**
234	231	Grace Paez, Karla Vizuete, Alexis Debut, Mario Cruz-D'Howitt, Juan José Ortiz and Theofilos Toulkeridis **Characterization and timing of charcoal in geoheritage sites preserved by major volcanic destructions – Geoarcheological and paleo-environmental considerations in Ecuador**	**1103**
235	346	Gerasimos Papadopoulos, Ioanna Triantafyllou, Constantinos Siettos and Konstantinos Spiliotis **Foreshock-aftershock discrimination in real-time during the 2025 seismic cluster near Santorini volcano, Greece, based on earthquake statistics and complex networks theory**	**1108**

236	65	Theodoros Papadopoulos, Sofia Pechlivanidou, Michael Foumelis and Christos Pennos **Image-based grain size analysis of coastal sediments**	**1110**
237	85	Ermioni Eirini Papadopoulou, Stavros Proestakis, Christos Nikolaos Anagnostopoulos and Nikolaos Soulakellis **Development of a cartographic web application for monitoring the Corinth Canal using UAV data**	**1113**
238	236	Evdokia Papadopoulou and Alexandros Chatzipetros **An integrated approach using Remote Sensing and the Environmental Seismic Intensity Scale ESI 2007 for three major earthquakes in the Aegean region**	**1118**
239	185	Penelope Papadopoulou, Charalampos Fassoulas, George Iliopoulos, Georgia Kitsaki, Maria Kolendrianou, Elina Mikroulea, Charitakis Papaioannou, Dimitris Pattakos, Vaggelis Perakis, Maria Tsoni and Iro Tsimpri **Expertise on Specifications – Evaluation Criteria and Design of a Special Label for Local Agrotourism Products and Services: a cooperation for the benefit of four Greek UNESCO Global Geoparks!**	**1123**
240	232	Penelope Papadopoulou, George Iliopoulos, James Bendle, Kimon Christanis, Stavros Kalaitzidis, Eleni Liapi, Konstantinos Perleros, Nikolaos Soulakelis, Marianthi Tzortzi and Nikolaos Zouros **West Akrocheiras section: a pilot multi-proxy palaeoenvironmental analysis**	**1126**
241	238	Antonia Papageorgiou, Olga-Joan Ktenidou, Vasilis-Erion Pikoulis and Efthimios Sokos **Comparing broadband and strong-motion data using collocated sensors in the HP network, Greece**	**1132**
242	200	Elena Papageorgiou, Michael Foumelis, Pascal Dominique, Pavlos Bonatis, Daniele Raucoules, Marcello De Michele and Eleftheria Papadimitriou **Groundwater changes and induced seismicity influencing surface deformation in post-mining landscapes**	**1134**
243	134	Maria Papailiopoulou, Paraskevi Apostolopoulou, Vasiliki Stavropoulou, Christos Pouliaris, Nerantzis Kazakis and Eleni Zagana **Hydrochemical characterization of multi-layer porous aquifer of Larissos system, Peloponnese**	**1136**
244	288	Maria Papailiopoulou, Krystalia Chrisanthakopoulou, Vasiliki Stavropoulou, Christos Pouliaris, Nerantzis Kazakis and Eleni Zagana **Assessment of the groundwater vulnerability using DRASTIC method in Larissos watershed, Greece**	**1142**
245	132	Chara Papailiou, Maria Kolendrianou and Charalampos Fassoulas **RescueME, a Research Action that focuses on the enhancement of the resilience of coastal cultural landscapes in Europe. The case study of Psiloritis UGGp, Crete, Greece**	**1147**

246	89	Haritakis Papaioannou, Christos L. Stergiou, Spiros Staridas, Aristotelis Stagkikas and Georgia Kitsaki **Innovative Efforts in Geotourism: The Vikos-Aoos UNESCO Global Geopark**	**1152**
247	113	Dimitrios Papanikolaou, Paraskevi Nomikou and Danai Lambridou **Volcanism and the metamorphic core complexes of Rhodope and Cyclades**	**1157**
248	150	George Papathanassiou, Sotiris Valkaniotis and Maria Taftsoglou **The influence of stratigraphy for the generation of surface evidence of liquefaction phenomena; case study Piniada, Greece**	**1160**
249	365	Costas Papazachos, George Vougioukalakis, Stylianos Bitharis, Christos Pikridas, Michael Foumelis, Chrysanthi Ventouzi, Charalambos Kkallas, Eleni Karagianni, Domenikos Vamvakaris and Elena Papageorgiou **Monitoring the Santorini Volcano for 3 decades (1995–2025) by ISMOSAV and its role for the early detection of the 2011–2012 and 2024–2025 intra-caldera unrests**	**1162**
250	168	Angeliki Papoutsa, Stephanos Kilias, Nikolaos Zegkinoglou, Vasilios Pletsas, Rebecca Avoukatou, Paraskevi Nomikou, Paraskevi Polymenakou, Andrea Somogyi and Qasid Ahmad **Effects of boiling and seawater mixing on hyper-enrichment of antimony in active polymetallic seafloor massive sulfide hydrothermal diffusers at the Aegean Kolumbo volcano**	**1168**
251	116	Evaggelia Pappa, Costas Papazachos and Nikolaos Chatzis **VS30 Estimation from P-Wave Seismograms: Exploring a Frequency-Domain Approach for Stations Located in Sedimentary Basins**	**1174**
252	348	Melissinos Paraskevas, Ioannis Katsafados, Dimitrios Anastasiou, Maria Tsakiri, Paraskevi Nomikou and Costas Synolakis **Preliminary results of High-Resolution Microgravity Monitoring During the 2025 Santorini Unrest**	**1180**
253	3	Panagiotis Paschos **Stone bridges. Resilience to catastrophic phenomena**	**1184**

Volume F: Papers 251-300

A/A	EC	AUTHORS and TITLE	PAGE
254	266	Nikoleta Passali, Grigorios Aarne Sakellaris, Margarita Melfou, Lamprini Papadopoulou and Nikolaos Kantiranis **Mineralogy and Geochemistry of the polymetallic nodules of the Clarion Clipperton Zone, NE Pacific.**	**1187**
255	197	Adamantia Paschali Patouchi, Ioannis Panagiotopoulos and Dimitrios Vandarakis **A Pilot Study of Erosion in the Mavro Lithari Beach, part of the Highly Urbanized Coastal Zone of the Eastern Saronic Gulf, through the use of drone technology**	**1193**
256	352	Spyros Pavlides, Vassilis Karastathis, Evangelos Mouzakiotis, Sotiris Sboras, Alexandros Chatzipetros and Ilias Lazos **Active Faulting in Santorini and the recent intra-caldera (2024–2025) seismic activity along the Kameni-Fira Fault line**	**1197**
257	95	Spyros Pavlides, Sotirios Sboras, Ilias Lazos, Evaggelos Mouzakiotis and Vassilios Karastathis **The Fira fault, Santorini (Thera): morphotectonic, geomorphological and seismological evidence of fault activity**	**1199**
258	252	Eleni Pegioudi and Alexandros Chatzipetros **Geological routes on Ammouliani Island, northern Greece**	**1205**
259	286	Christos Pennos, Maria Perraki, Sofia Pechlivanidou, Rannveig Øvrevik Skoglund, Christos Salmas, Eleni Vasileiou, Yorgos Sotiriadis and Markos Vaxevanopoulos **Assessing Microplastic Pollution in Atzinolakas caves, Crete: Implications for Remote Karst Aquifers**	**1210**
260	97	Dimitris Pepas, Vassilios Marinos, Pavlos Nomikos and Charalampos Saroglou **Investigating the failure characteristics of several rock types using the Acoustic Emission technique**	**1216**
261	106	Argyrios Periferakis, Lamprini Troumpata, Aristodemos-Theodoros Periferakis and Konstantinos Periferakis **Coal and Asbestos Mining-Induced Pulmonary Pathologies: Radiological Diagnosis and Associated Challenges**	**1222**
262	295	Eftychia Peristeridou, Vasilios Melfos, Panagiotis Voudouris, Lambrini Papadopoulou, Jaroslav Pršek and Nikolaos Kantiranis **Mineralogical composition and mineral chemistry of the listvenite-hosted mineralization in Kato Vyrsini area, Thrace, Greece**	**1228**
263	107	Adonis Photiades, Isidoros Kampolis, Ioannis Vakalas and George Deligiannakis **The geological structure of the Myrtoan Sea islets**	**1234**

264	243	Serafeim Poulos, George Alexandrakis, Aikaterini Karditsa, Stamatina Lesioti, Markozanes Markozanes, Ioannis Katritsis and Nikolaos Kampanis **Assessment of the exposure of coastal sectors of the Greek Mainland to hazards induced by climate change, using the Coastal Hazard Wheel**	**1238**
265	88	Dimitrios Pyrgakis, Vasiliki Stavropoulou, Eleni Kaskani, Maria Papailiopoulou, Christos Pouliaris, Dimitra Lampropoulou, Eleni Zagana, Konstantinos Chalikakis and Nerantzis Kazakis **Hydrogeological and hydrochemical investigations of Selinous basin region**	**1242**
266	188	Dimitra Rapti **Assessment of natural and anthropogenic contamination of the sediments in the Sacca di Goro lagoon (Po river delta, northern Italy)**	**1248**
267	184	Dimitra Rapti **The role of hydrogeology in the sustainable exploration of shallow geothermal resources**	**1250**
268	192	Dimitra Rapti, George Papathanassiou, Sotiris Valkaniotis, Maria Taftsoglou and Riccardo Caputo **Liquefaction susceptibility in delta environments: the case of the Po delta area (northern Italy)**	**1252**
269	351	Georgia Rapti and Ourania Tzoraki **Investigation of legislation and tools for coastline demarcation: the coastline along the Kalamas delta in Thesprotia as a case study**	**1254**
270	109	Aikaterini Rogkala, Petros Petrounias, Panagiota P. Giannakopoulou, Petros Koutsovitis, Maria Kalpogiannaki, Paraskevi Lampropoulou and Harilaos Tsikos **Remnants of oceanic crust of Edessa ophiolite (North Greece): Petrographic and geochemical characteristics**	**1260**
271	283	Zafeiria Roumelioti and Nikitas Katsaitis **Shallow Depth P-wave Velocity Profiling Using Seismic Interferometry: The CORSSA Site**	**1265**
272	76	Artemios Roussos, Efstratios Kelepertzis, Zacharenia Kypritidou, Epameinondas Aivatzidis, Christos Drougas, Emmanouil Vassilakis, Panagiotis Voudouris and Nikolaos Zouros **Soil Geochemical Mapping on Lesvos Island, Greece**	**1271**
273	199	Aikaterini Maria Rozi and Zafeiria Papadimitriou **Pluto is lost!**	**1275**
274	198	Davide Russo and Riccardo Caputo **Rheological behaviour along the Hellenic Subduction Zone and the Adria-Eurasia continental collision**	**1277**

275	345	Dimitris Sakellariou, Ioannis Morfis, Isidoros Livanos, Alexandros Varesis, Stylianos Petrakis and Vasilis Kapsimalis **Marine geological-geophysical data may contribute to the understanding of the early 2025 seismic activity in the Santorini-Amorgos Zone**	**1285**
276	15	Dimitris Sakellariou, Ioannis Morfis, Dimitris Vandarakis, Isidoros Livanos and Ioannis Kourliaftis **Airborne and marine survey of the 8th June 2023 earthquake-triggered coastal collapse at Mylos Gialtron, North Evia: Contribution to the understanding of coastal zone vulnerability**	**1287**
277	339	Vassilis Sakkas, Christos Pikridas, Athanasios Ganas, Dimitrios Anastasiou, Panagiotis Elias, Stylianos Bitharis, Konstantinos Chousianitis, Konstantinos Raptakis, Vasilis Kapetanidis, George Kaviris, Stratos Liadopoulos, Nikolaos Voulgaris, John D. Alexopoulos and Evangelos Lagios **Continuous GNSS Geodetic Networks. A Powerful Tool for Monitoring and Understanding Complex Volcanic Environments: The Case of Santorini Volcano During the Seismic Crisis of 2024–2025**	**1293**
278	164	Vassilis Sakkas, Andreas Tzanis and Evangelos Lagios **Ground Deformation in Nisyros Volcano (Greece) Determined by GPS and SAR Interferometric Techniques**	**1295**
279	91	Myrsini-Ifigeneia Samothraki, Zacharenia Kypritidou and Ariadne Argyraki **Comparison of dermal bioaccessibility of potentially toxic elements contained in modern and ancient cosmetics**	**1300**
280	130	Panagiotis Sampatakakis, Marietta Theodoropoulou, Maria Tzima and Christos Christidis **Result of an inventory program (SAMY) of boreholes of various uses and their contribution to the water balances of groundwater systems.**	**1305**
281	334	Eirini Sardeli, Kyriaki Pavlou, Andreas Karakonstantis, Alexandros Athanasopoulos, Sokratis Pappas and Filippos Vallianatos **The 2025 Santorini Swarm: Spatiotemporal Distribution and Coulomb Stress Changes. Preliminary Results**	**1310**
282	363	Charalampos Saroglou, Vasileios Kallimogiannis, Athina Tsirogianni and Georgia Klironomou Stabilisation of volcanic rock slopes in traditional settlements. The case of Petra, Lesvos Island	**1315**
283	327	Loukas Savvelos and Nikolaos Zouros **Mapping pyroclastic formations at the Lesvos Petrified Forest, Greece the Akrocheiras hill pyroclastic sequence**	**1320**
284	359	Loukas Savvelos and Nikolaos Zouros **Mapping pyroclastic formations at the Lesvos Petrified Forest, Greece the Bali Alonia area pyroclastic sequence**	**1326**

285	133	Vanessa Schifano, Lorenza Li Vigni, Luciana Randazzo, Lorenzo Brusca, Sergio Bellomo, Sergio Calabrese and Walter D'Alessandro **Travertine deposits of Greece, a mineralogical and geochemical study**	**1332**
286	229	Vahram Serobyan, Taniel Danelian and Araiyk Grigoryan **The Upper Devonian sequence of the Noravank and Ertych geosites in Armenia: stratigraphy and geotouristic potential**	**1337**
287	74	Alkiviadis Sideridis, Evangelos Koutsoumpis, Katerina Mytakidou, Maria Boumpouka, Vasiliki Anevlavi and Paraskevas Rousopoulos **Marble as an educational fabric interweaving cultural and geological heritage, the case study of ancient Philippi site rock art, Kavala, Greece**	**1342**
288	42	Paraskevi Sklavounaki, Vasiliki Tzafaridi, Thomas Hasiotis, Stefanos Missias and Aristeidis Paleokrassas **First record of pockmarks in the North Aegean Trough**	**1344**
289	115	Loukia Skontovolou, Paraskevi Lampropoulou, Ioannis Baskoutas, Christina Raptopoulou, Panagiota P. Giannakopoulou, Aikaterini Rogkala, Aggeliki Kareli, Prokopis Savvatis and Petros Petrounias **Mineralogical and petrographic characterization of different limestones used as raw materials in the cement production**	**1347**
290	270	Emmanuel Skourtsos, Christos Filis, Emmanuel Vassilakis, Aliki Konsolaki, Evangelia Kotsi and Efthimios Lekkas **The role of the epikarst zone in the influx of water and the manifestation of humidity at the Holy Monastery of Kleiston, Mount Parnitha, Attica, Greece**	**1352**
291	52	Emilia Sofianska, Konstantinos Athanassoulis, Dimitrios Tarenides and Maria Gkagka **Composition and physicochemical properties of muds from the Evros river delta, Thrace district (Northern Greece) and their potential use in pelotherapy**	**1358**
292	222	Nikolaos Sofis, Efthymios Ntouros and Stavros Kalaitzidis **REE distribution in the b1 bauxite strata of the Parnassos–Giona Unit, Greece**	**1364**
293	225	Sophia Sotiropoulou, Michail Kalaitzis, Emmanuel Skourtsos, Dimitris Sakellariou and Haralambos Kranis **Plio-Quaternary tectonics and evolution of Southwestern Lesvos Island and Lesvos Basin, Greece: Transtensional deformation and relationship with the July 2017 earthquake activity**	**1367**
294	275	Kimon Soultanis, Konstantinos Soukis and Maria V. Triantaphyllou **Discovering the geoheritage of Skiathos Island (Northern Sporades, Greece)**	**1373**
295	5	Natalia Spanou **Cyclone Daniel's Impact: A Study of Geohazards in Meteora, Greece**	**1375**

296	284	Nafsika Ioanna Spyrou, Michalis Diakakis, Spyridon Mavroulis, Georgios Deligiannakis, Emmanuel Andreadakis, Christos Filis, Evelina Kotsi, Zacharias Antoniadis, Maria Melaki, Marilia Gogou, Katerina-Navsika Katsetsiadou, Eirini-Spyridoula Stanota, Emmanuel Skourtsos, Emmanuel Vassilakis and Efthymios Lekkas **Combining Ground and UAV Mapping for GIS-Based Assessment of Flash Flood Impact Severity: Application of the FFISS to the 2009 and 2020 Evia (Greece) Floods**	**1378**
297	163	Panagiotis Stamatis, Michaela Doukari and Kostas Topouzelis **Evaluating Airborne LiDAR and RGB Imagery for Accurate Shoreline Detection**	**1384**
298	303	Thomas Stavropoulos and Elissavet Feloni **Domestic Rainwater Harvesting Tanks˙ Sizing under Climate Change Conditions in Nisyros Island**	**1391**
299	340	Maria Stavropoulou, Konstantinos Soukis, Haralambos Kranis, Emmanuel Skourtsos and George Exadaktylos **Numerical modeling of fault genesis in the Santorini-Amorgos basin: an interplay of tectonic forces and magmatism**	**1396**
300	263	Christos L. Stergiou, Haritakis Papaioannou, Grigoria-Vasiliki Dimou, Eftychia Peristeridou, Margarita Melfou, Aristeidis G. Stamatiadis, Vasilios Melfos, Olga Koukousioura and Georgia Kitsaki **Sedimentary, Metamorphic, and Igneous Rocks in Harmony: Unveiling the rocky microcosm of the Vikos-Aoos UNESCO Global Geopark**	**1401**
301	240	Christos L. Stergiou, Grigorios-Aarne Sakellaris, Margarita Melfou, Vasilios Melfos, Lambrini Papadopoulou and Christos Stefanou **Insights from the mineralogy and mineral chemistry of the antimony mineralization at Philadelphio, Vertiskos Unit, Northern Greece**	**1407**
302	265	Spyridon Strongylis, Grigorios Aarne Sakellaris, Nikolaos Kantiranis and Alexandros Chatzipetros **Threshold Value Analysis in Geochemical Mapping for Gold-Only Vein-Type Mineralization**	**1413**
303	160	Maria Taftsoglou, Sotiris Valkaniotis, George Papathanassiou and Sotirios Argyroudis **Liquefaction risk assessment of airport infrastructure using geological data and remote sensing techniques**	**1419**

Volume G: Papers 301-358

A/A	EC	AUTHORS and TITLE	PAGE
304	159	Maria Taftsoglou, Sotiris Valkaniotis, George Papathanassiou, Vassilis Ntouvartzis, Dimitra Rapti and Riccardo Caputo **A correlation of liquefaction phenomena with the surficial geology of point bar deposits; case studies 2021 Damasi, Greece, 2023 Kahramanmaraş, Türkiye and 2010–2011 Christchurch, New Zealand**	**1423**
305	110	Onur Tan and Özlem Karagöz **Earthquake hazard implications for Lesvos (Midilli) and the surrounding region**	**1427**
306	60	Despoina Tektonidou, Panagiotis Voudouris, Constantinos Mavrogonatos, Federica Zaccarini, Vassilios Melfos, George Soulamidis, Ariadni Afroditi Georgatou, Evgenia Serfa, Degao Zhai, Manuel Keith, Alexandre Tarantola, Stylianos Tombros, Dimitrios Alifieris, Margarita Melfou, Evangelia Zygouri and Christos Kanellopoulos **The Megala Therma-Katsilemonas gold-silver mineralization, Lesvos island, Greece: a new alkalic-type epithermal deposit in Greece?**	**1430**
307	45	Dimosthenis Telemenis, Spyridon Bellas, Evangelos Vavouranakis and Emmanouil Manoutsoglou **Source rock potentiality of the late Miocene sapropelic layers of Gavdos island, Greece, based on geochemical and stratigraphic data**	**1436**
308	297	Alexia Theocharaki, Maria Nikopoulou, Stefanos Karampelas, Kantiranis Nikolaos, Stavros Oikonomidis and Lambrini Papadopoulou **Study of "Corundum" Samples from the Collection of the Mineralogical – Petrological Museum at Aristotle University of Thessaloniki, Greece**	**1441**
309	368	Tonbol K.M. **Climatic Variability and Wind Pattern Shifts in Alexandria: Twenty Years of Data to Guide Coastal Resilience in Northern Egypt**	**1447**
310	306	Aris Toska and Elizabeth Stathopoulou **The effect of microorganisms in the fossilization of skeletal material**	**1448**
311	224	Theofilos Toulkeridis, Aaron Addison, Silviu Constantin and Grace Tatiana Páez-Barrera **Ecuadorian candidates for the World Natural Heritage List – The Triple Volcano and Tayos caves**	**1451**
312	99	Maria Triantaphyllou, Elisavet Skampa and Vasiliki-Grigoria Dimou **A review of calcareous nannofossil biostratigraphic studies in the Hellenic territory (Greece): the contribution of the Micropaleontology Collection of the Laboratory of Historical Geology and Biogeosciences (NKUA)**	**1456**
313	181	Efstathia Tringa and Konstantia Tolika **Assessing Future Climate Change Risk to Cultural Heritage of Greece: A Case Study of Mycenae and Delos**	**1460**

314	228	Francesco Tripodi **Preliminary results of GEM (Gaseous elemental mercury) concentration in interstitial soil and free gases from Mt. Etna, Sicily**	**1462**
315	145	Fani Tripolitsiotou, Ariadne Argyraki and Hara Drinia **"Unfolding the Fold"- An Introduction to the Geology of Greece Through a Museum Kit by the Natural History Museum of Arsakeia Schools**	**1465**
316	249	Fani Tripolitsiotou, Hara Drinia and Ariadne Argyraki **Exploring Urban Geotourism Through Geomythology: A Geotrail from Faliro Bay to Vouliagmeni Peninsula, Attiki Region, Greece**	**1468**
317	304	Alexandros Troupakis, Elissavet Feloni, Kleomenis Kalogeropoulos and Andreas Tsatsaris **Exploring Social Perceptions of Water Scarcity and Local Water Resource Management in Greece: Insights from a National Survey**	**1471**
318	289	Dimitrios Tsagkas, Foteini Chalkiopoulou, Giorgos Kanakidis and Alexia Charmalia **Contribution of Engineering Geology to the rescuing and enhancing of cultural works and constructions. Case study: The fountain at the Antaeus and Gennaios Kolokotronis streets' junction in the Amalia Merkouri Square in Petralona.**	**1475**
319	274	Konstantinos Tsanakas, Alessia Sorrentino, Gaia Mattei, Pietro Patrizio Ciro Aucelli and Efthimios Karymbalis **Preliminary results on the mapping of uplifted marine terraces in the Laconic Peninsula, SE Peloponnese, Greece**	**1481**
320	272	Panagiota-Elpida Tsekoura, Marianthi Stefouli, Ioannis Vakalas, Eleni Vasileiou and Maria Perraki **Applications of satellite data analysis in the exploration of geothermal systems: The case of the Methana Peninsula, Greece**	**1487**
321	193	Anastasios Tsikrikis, Vassilis Marinos and Theodosis Papaliangas **The influence of mineralogy on the nondilatant friction angle of rock fractures**	**1493**
322	73	Dora Tsipra and Hara Drinia **Exploring Participant Experiences in a Geoconservation Program in Apano Meria, Syros island, Greece**	**1499**
323	56	Varvara Tsironi, Jean-Mathieu Nocquet, Athanassios Ganas, Efthimios Sokos and Ioannis Koukouvelas **Crustal Block Kinematics in Western Greece using geodetic data**	**1502**
324	278	Ioannis Tsodoulos, Efthimios Karymbalis, Maria Ferentinou, Andrew Green, Konstantinos Stamoulis and Christina Gallousi **Optically Stimulated Luminescence (OSL) dating of a shell midden layer at Umhlanga Rocks, Natal North Coast, South Africa**	**1505**

325	162	Maria Tsoni, Eleni Koumoutsou and George Iliopoulos **Chelmos- Vouraikos Unesco Global Geopark 2024: Advancing Conservation, Education, and Community Engagement**	**1511**
326	267	Theodora Tsourou, Eleni Anastasia Markoglou, Taniel Danelian, Constantine Parinos, Alexandra Gogou and Maria Triantaphyllou **Deep sea agglutinated foraminifera from the surface sediments of NE Mediterranean Sea**	**1514**
327	257	Theodora Tsourou, Nikolaos Sakoulas, Aggeliki Paraskevopoulou, Ifigeneia Perraki and Maria Triantaphyllou **Stratigraphic assignment of the Mesozoic shallow carbonate succession of Epos Mountain, Chios Island, Greece**	**1517**
328	269	Andreas Tzanis, Stylianos Chailas and Evaggelos Spyridonos **The geothermal prospect of the NW Lesvos Island, Greece: Three-dimensional magnetotelluric and gravity exploration**	**1519**
329	126	Marianthi Tzortzi, Federico Lugli, Thomas Tütken, Vasilis Golfinopoulos, George Iliopoulos and Andreas Darlas **Tracking mobility of Late Pleistocene ruminants using enamel strontium isotope analysis of teeth from Melitzia Cave, Mani Peninsula (Greece)**	**1525**
330	114	Nikolas Vagionakis, Konstantinos Diamantis, Maria Stavropoulou and Emmanouil Andreadakis **Application of UAVs in Rockfall Hazard Assessment and Mitigation Measures in the Vrachon Theatre, Byron Area, Greece**	**1528**
331	186	Dimitra Valavani, Penelope Papadopoulou, Peter Frenzel, Mauro Alivernini, Maria Tsoni, Maria Groumpou, Theodora Tsourou, Silvia Kolomaznik, Magdalena Kreuzheck and George Iliopoulos **Boosting Cave Ostracods Biodiversity: A case study from the Cave of the Lakes (Chelmos Vouraikos UNESCO Global Geopark, Peloponnese, Greece) with report of a new species of Trapezicandona**	**1534**
332	369	Valavani Eleni, Siarkos Ilias, Tzoraki Ourania **Overview of Legislation and Tools for Stram Flood Risk Assessment**	**1538**
333	328	Ilias Valiakos, Konstantina Bentana and Nikolaos Zouros **Conservation and Interpretation of Fossiliferous Sites in the Lesvos Island UNESCO Global Geopark**	**1539**
334	155	Sotiris Valkaniotis, Dimitra Rapti, Maria Taftsoglou, George Papathanassiou and Riccardo Caputo **Geomorphological mapping and lithological heterogeneity as tools for the assessment of liquefaction likelihood: Piniada Valley case study (central Greece)**	**1544**

335	211	Sotiris Valkaniotis, Maria Taftsoglou, Domna Samara, George Papathanassiou, Konstantia Tolika, Caterina Zei and Themistoklis Chatzitheodosiou **Development of a Medicane-induced landslide inventory with field and remote sensing data; 2023 Storm Daniel, central Greece**	**1547**
336	230	Kanella Valkanou, Efthimios Karymbalis and Konstantinos Tsanakas **Investigating the interaction between Flood Hazard and Soil Erosion in Northern Evia Island, Greece, using GIS Morphometric Analysis**	**1550**
337	216	Aikaterini Vardava, Vasilios Kyriakopoulos, Emmanuel Skourtsos and Christos Filis **Preliminary results on geological and hydrogeological conditions in Vilia, Attica, Greece**	**1555**
338	300	George Vargemezis, Panayiotis Tsourlos, Ilias Fikos, Eytychia Amanatidou, Prodromos Louvaris and Eleni Tzima **Contribution of Electrical Resistivity Tomography to the investigation of landslide conditions on slopes**	**1559**
339	233	Athanasios Varotsos, Konstantinos Filis, Vayia Xanthopoulou and Ioannis Iliopoulos **Mineralogical and Petrographic study of Hellenistic stamped transport amphorae from the area of Aigion, NW Peloponnese.**	**1563**
340	121	Effrosyni Varotsou, Paraskevi Nomikou, Dimitrios Papanikolaou, Serafeim Poulos, Ioannis Asteriou, Nikolaos Tsernotopoulos, Yannis Tsaparas, Ilias Koliopanos and Maria Petroulia **Morphotectonic Analysis and Geohazard Implications of the Messiniakos Gulf**	**1568**
341	34	Charalampos Vasilatos, Ifigeneia Megremi, Zoi Gkioka, Neofyta Theori, Erika Yessenia Cuida Lopez, Anca-Iulia Stoica and Athena Economou-Amilli **Assessment of Geo-environmental Status of Trichonis Lake, Greece: Mineralogy, Sedimentology, and Chemistry**	**1573**
342	333	Emmanuel Vassilakis, Efthymios Lekkas, Assimina Antonarakou, Panagiotis Nastos, Aliki Konsolaki, Evelina Kotsi, John Lialiaris and Michael Foumelis **Rockfall Source Identification and Risk Assessment at the Caldera of Santorini Island, Greece, based on Aerial LiDAR Data**	**1579**
343	190	Nikos Vavlas and Anastasia Kiratzi **Scaling Relations Between Earthquake Magnitude and Source Duration with Applications to Greece**	**1585**
344	83	Chrisanthi Ventouzi, Costas Papazachos, Charalambos Kkallas and Evaggelos Spyridonos **Microseismicity Monitoring of the Broader Stypsi Geothermal Field Area (Northern Lesvos Island, Greece) Using a Local Seismological Network**	**1591**
345	170	Amélie Viger, Haralambos Kranis, Athanassios Ganas and Alex Whittaker **Preliminary results on the interseismic deformation of the Argolis Peninsula, Greece**	**1597**

346	237	Paris Xypolias, Nikolaos Gerogiannis, Eirini Aravadinou and Konstantinos Apostolos Tsourtis **Spatial distribution and deformation of columnar calcite occurred in the high-pressure marbles of Cycladic Massif (Hellenides)**	**1603**
347	344	Isobel Yeo, Paraskevi Nomikou, Michael Clare, John Jamieson, Gaye Bayrakci, Anna Lichtschlag, Emma Gregory, Gemma Portlock, Sofia Della Sala, Alice Hopkins, Jacob Nash, Jaycee Favela, Katlin Adamczyk, Erin Bethell, Jennifer Spalding, Anna Katsigera, Sebastian Hölz, Konstantin Reeck, Martin Wollatz-Vogt, Hannah Zimmer, Jieyu Tan and Tom Kwasnitchka **Preliminary findings from expedition DY190 to the Christiana-Santorini-Kolumbo volcanic field in March 2025**	**1607**
348	320	Jiří Zahradník, Efthimios Sokos, Zafeiria Roumelioti and Fatih Turhan **Non-shear faulting of the 2025 Santorini-Amorgos (Anydros) earthquakes**	**1610**
349	177	Faedra-Tzesi Zanai, Penelope Papadopoulou, Nikolaos Depountis, Panagiotis Pelekis and George Iliopoulos **Integrating micropalaeontological, geotechnical and sedimentological data to reconstruct the palaeoenvironmental evolution of Mesolongi Lagoon**	**1616**
350	57	Avraam Zelilidis, George Iliopoulos, Angelos G Maravelis and Nicolina Bourli **The presence of nappes, in SW Peloponnesus peninsula, and the strongly metamorphic Plattenkalk series, in central south Peloponnesus and Crete Island, change the dynamic evolution of west and south Greece**	**1620**
351	67	Panagiotis Zelilidis, Alfred Uchman, George Iliopoulos, Panagiota Dalgkitsi and Nicolina Bourli **The trace fossil Zoophycos as an indicator for the Apulian Platform Margins evolution during Eocene in Lefkas Island.**	**1626**
352	302	Yanbin Zhu, Yongdong Wang and Nikolaos Zouros **New results on the Miocene gymnosperm fossil wood of Lesvos Petrified Forest, Lesvos Island, Greece, and its palaeoenvironment significance**	**1627**
353	48	Kerasia Ziazopoulou, Constantinos Loupasakis, Konstantinos Laskaridis, Michael Patronis, Angeliki Arapakou and Ioannis Kouseris **Utilizing ultrasound velocity measurements to estimate physicomechanical properties of carbonate ornamental rocks**	**1633**
354	178	Vasilis Zorapas and Olga Chalkiadaki **Spatial distribution of trace elements in four water districts of Greece during the period 2018–2023. Results from National Groundwater Monitoring Network Program of Greece**	**1637**
355	72	Elena Zoumpouli, Nicolina Bourli, Penelope Papadopoulou, Avraam Zelilidis, George Iliopoulos and Michalis Xanthakis **The actions of Kefalonia and Ithaca UGGp aiming at the promotion of the area through sustainable development**	**1644**

356	316	Nikolaos Zouros, Ilias Valiakos, Konstantina Bentana, George Grimpilakos, Eystratios Zgournios, Nikolaos Tsoukalas, Michail Georgitsis, Loukas Savvelos, Maria Agiasoti, Nikolaos Grammenopoulos, Ioannis Chorafas and Nikolaos Salamparchos **Excavations in the Lesvos Petrified Forest – A significant geo-conservation project alomg the Kalloni-Sigri road, in the Lesvos island UNESCO Global Geopark, Greece**	**1649**
357	356	Nikolaos Zouros **UNESCO Global Geoparks and Global Geoparks Network: Protecting, promoting and managing Earth heritage – Building Sustainable Communities**	**1655**
358	360	Nikolaos Zouros, Nikolaos Soulakellis, Ilias Valiakos, Konstantina Bentana, Giorgos Grimpylakos, Aggelos Lamprakopoulos, Parthenopi Panidou, Ermioni-Eirini Papadopoulou and Georgios Tataris **Lemnos Island Geosites and their Geotourism and Education Potential**	**1662**

17th INTERNATIONAL CONGRESS of the Geological Society of Greece

GEOLOGICAL SOCIETY OF GREECE • 1951 •

Mytilene, Lesvos Greece
28-31 May 2025
GSG2025

Book of Abstracts

ORGANIZED BY:

UNIVERSITY OF THE AEGEAN

www.ege2025lesvos.gr

NATURAL HISTORY MUSEUM OF THE LESVOS PETRIFIED FOREST

17th INTERNATIONAL CONGRESS of the Geological Society of Greece

MYTILENE, LESVOS GREECE
28–31 MAY 2025
GSG2025

Book of Abstracts

17th INTERNATIONAL CONGRESS of the Geological Society of Greece

BULLETIN OF THE GEOLOGICAL SOCIETY OF GREECE, SP. PUBL.

EXTENDED ABSTRACT 001

Monitoring the evolution of landslide phenomena in Pyrra, Trikala, using advanced geospatial technologies

Agrafiotis Athanasios.[1], Papathanassiou Georgios.[1], Valkaniotis Sotirios.[2]
1 Aristotle University of Thessaloniki, Thessaloniki, Greece, aagrafia@geo.auth.gr
1 Aristotle University of Thessaloniki, Thessaloniki, Greece, gpapatha@geo.auth.gr
2 Aristotle University of Thessaloniki, Thessaloniki, Greece, valkaniotis@yahoo.com

Abstract

This study utilizes Unmanned Aerial Vehicles (UAVs) and advanced 3D modeling techniques to monitor and analyze the evolution of a significant landslide in Pyrra, Trikala, following the severe weather event known as Daniel in 2023. Specifically**,** In September 2023, Greece was impacted by the severe weather event known as Daniel, which led to intense rainfall and caused widespread natural disasters in Thessaly, including extensive landslides and floods (Dimitriou et al.,2024). The village of Pyrra in Trikala was notably affected, experiencing a large-scale landslide. This study focuses on documenting and monitoring this landslide to understand its progression over time.

Objectives: The primary objectives of this study was to employ advanced geospatial technologies to capture detailed data on the landslide and to use this data to monitor its evolution. (Highland & Bobrowsky, 2008). By doing so, the study aims to contribute to a better understanding of landslide dynamics and inform future mitigation strategies.

Geological setting: The landslide in Pyrra, occurred in an area consisting mainly of Pindus flysch. The failure mechanism of the landslide is a translational slide influenced by pre – existing cracks, the geometry of the slope and dye to the continuous rainfall.

Methods: The methodology involves multiple steps. Initially, high-resolution aerial imagery of the landslide area was captured using UAVs. These images were processed using photogrammetric methods, specifically the Structure from Motion (SfM) technique, to create detailed 3D models of the terrain. CloudCompare software was employed to analyze the changes in the landscape by comparing datasets collected at two different times: October 2023 and June 2024. The software's C2C (Cloud-to-Cloud) and M3C2 (Multiscale Model-to-Model Cloud Comparison) methods were used to quantify the displacement of materials and provide a comprehensive assessment of the landslide's evolution.

Results: The analysis revealed substantial material displacement and changes in the morphology of the landslide. The generated 3D models offer a detailed visualization of the impacted region, showing significant shifts in terrain and volume changes. Quantitative analysis revealed the extent of material movement and highlighted critical areas of instability.

Figure 1 Point cloud representation of the landslide, generated from UAV imagery using SfM techniques.

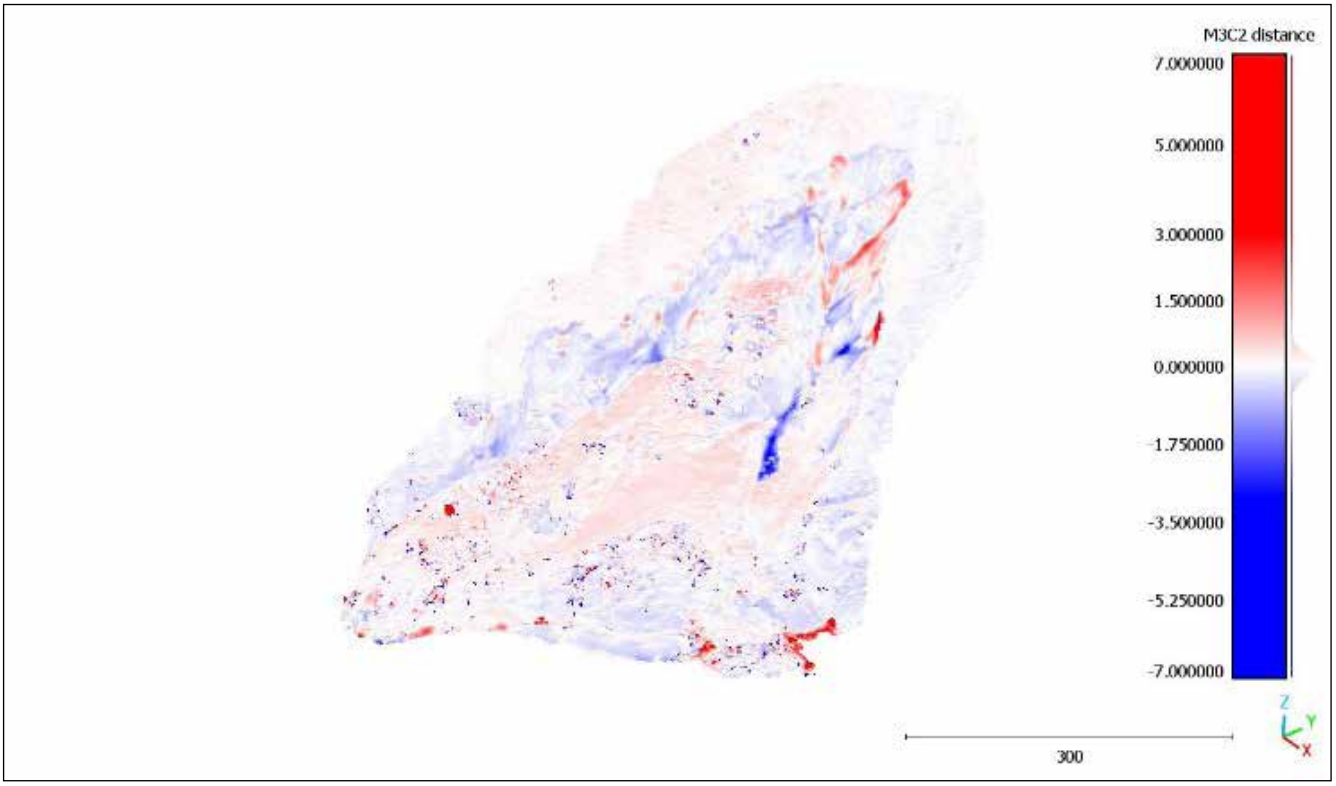

Figure 2 Detection of surficial displacement based on the M3C2 method. With red color depicts the areas where we have removal material and in blue the locations where we have deposited material.

Conclusions

The use of UAVs combined with advanced software tools like CloudCompare proved highly effective in monitoring and analyzing the landslide phenomena. This approach enables detailed observation and documentation of the landslide over time and provides valuable information for developing risk assessment and mitigation strategies. These findings of this study emphasize the potential of modern geospatial technologies in enhancing our understanding of landslide behavior and improving disaster response planning (Lacroix, 2020).

References

Dimitriou, E., et al. (2024). “Post-Analysis of Daniel Extreme Flood Event in Thessaly.” Water, 16(7): 980. **[Journal Article]**

Highland, L.M., & Bobrowsky, P. (2008). “The Landslide Handbook.” U.S. Geological Survey Circular 1325. **[Book]**

Lacroix, P. (2020) “Life and death of slow-moving landslides. “ Nat Rev Earth Environ 1, 404–419. **[Journal Article]**

17th INTERNATIONAL CONGRESS of the Geological Society of Greece

BULLETIN OF THE GEOLOGICAL SOCIETY OF GREECE, SP. PUBL.

EXTENDED ABSTRACT 002

Structural study of the Theodorion meta-migmatitic complex (Serbomacedonian massif, northern Greece)

Amanatidou Dimitra[1], Soukis Konstantinos[1], Dimitri Klea[1], Stouraiti Christina[1]
(1) National and Kapodistrian University of Athens, dimitraam@gmail.com

Introduction

This paper presents the results of detailed mapping (1:10.000 scale) tectonostratigraphic and structural study on the high-grade metamorphic rocks of Vertiskos Unit, exposed in the Theodorion area (Northern Greece), which shows that they form an east-dipping sequence affected by at least three ductile deformation events.

Geological Setting

The high-grade SerboMacedonian Massif (SMM), exposed in northern Greece, represents the structurally highest crustal block of the Hellenides. It is bounded to the west by the low-grade Circum Rhodope metasediments and the Vardar ophiolitic rocks (Peonias Unit) and to the east by the high-grade rocks of the Rhodope Massif (Kockel et al., 1977; Kilias et al., 1999; Papanikolaou 2021). The SMM is subdivided into two main units: the overlying Vertiskos Unit and the underlying Kerdylia Unit. The contact is decorated by lenses of metamorphosed basic to ultrabasic rocks comprising the Volvi-Therma-Gomati complex, and it has been characterized as a top-SW Cenozoic detachment (Sokoutis et al., 1993). Geochronological data revealed that Vertiskos Unit includes late Proterozoic Pan-African rocks intruded by early (Silurian) and late (Carboniferous) Paleozoic granites and pegmatites and later on by Triassic A-type Arnea-Kerkini granites (Christofides et al., 1999, 2007; Himmerkus et al., 2007, 2009; Poli et al., 2009; Abbo et al., 2020). During the Mesozoic - Cenozoic period, the SMM was involved in the prolonged closing of the Neotethyan Vardar oceanic basin (Pe-Piper and Piper 2002; Papanikolaou 2021).

Tectonostratigraphy - Structural data

Detailed mapping along an NE transect revealed that the Theodorion area comprises three formations (Figure 1a-d): a lower migmatitic gneiss, an overlying biotite gneiss, and the uppermost garnet-mica schists. The overall structural thickness of the sequence reaches 1000m. The lowermost migmatitic gneiss shows a coarse-grained granitic core surrounded by typical gneissic layers with typical mineral assemblage, including feldspars + quartz ± biotite ± muscovite + opaque. It has to be noted that the granitic core is also foliated but not as strongly as the gneissic cover. At the transition zone between the two lithologies, high-grade structures such as ptygmatic folding are often observed (Figure 2a). The overlying biotite gneiss is lithologically quite heterogeneous and includes alternating biotite-rich schistose and gneissic layers, with a typical mineral assemblage of feldspars + quartz + biotite ± muscovite + opaque. Amphibolitic lenses are intercalated in places with mineral assemblage hornblende + epidote + plagioclase ± pyroxene + opaque. The uppermost garnet-mica schists include more aluminum-rich lithologies such as muscovite and garnet porphyroblasts and typical mineral assemblage muscovite + quartz + garnet ± biotite ± feldspars + opaque.

All the rocks present a roughly east-northeast-dipping gneissic layering with a coarse-grained foliation Sn and an east-north-east plunging stretching lineation Ln. In the microscopic scale, Sn is formed by alternating layers of quartz, felspar and quartz+biotite+white mica aggregates. Isoclinally folded quartz veins reveal that Sn is an axial planar foliation to Bn isoclinal folds, which have folded an older Sn-1 foliation, now observed as inclusion traces in feldspar porphyroblasts. Kinematic indicators such as S-C fabrics and garnet porphyroblasts show a consistent top-to-E or NE sense of shear. The entire sequence and the Sn are further folded by macro-to-mesoscale asymmetric SW-verging NW-SE open to tight folds, producing a fine-grained Sn+1 foliation associated with an Ln+1 intersection/stretching lineation trending NW-SE. Locally, Sn is reworked by a mylonitic Sn+1 foliation. On a microscopic scale, Sn+1 is formed by quartz+biotite aggregates (Figure 2b). The fold vergence indicates a top-SW tectonic transport for this event. Finally, distributed top-to-SW shear bands crosscut all previous structures.

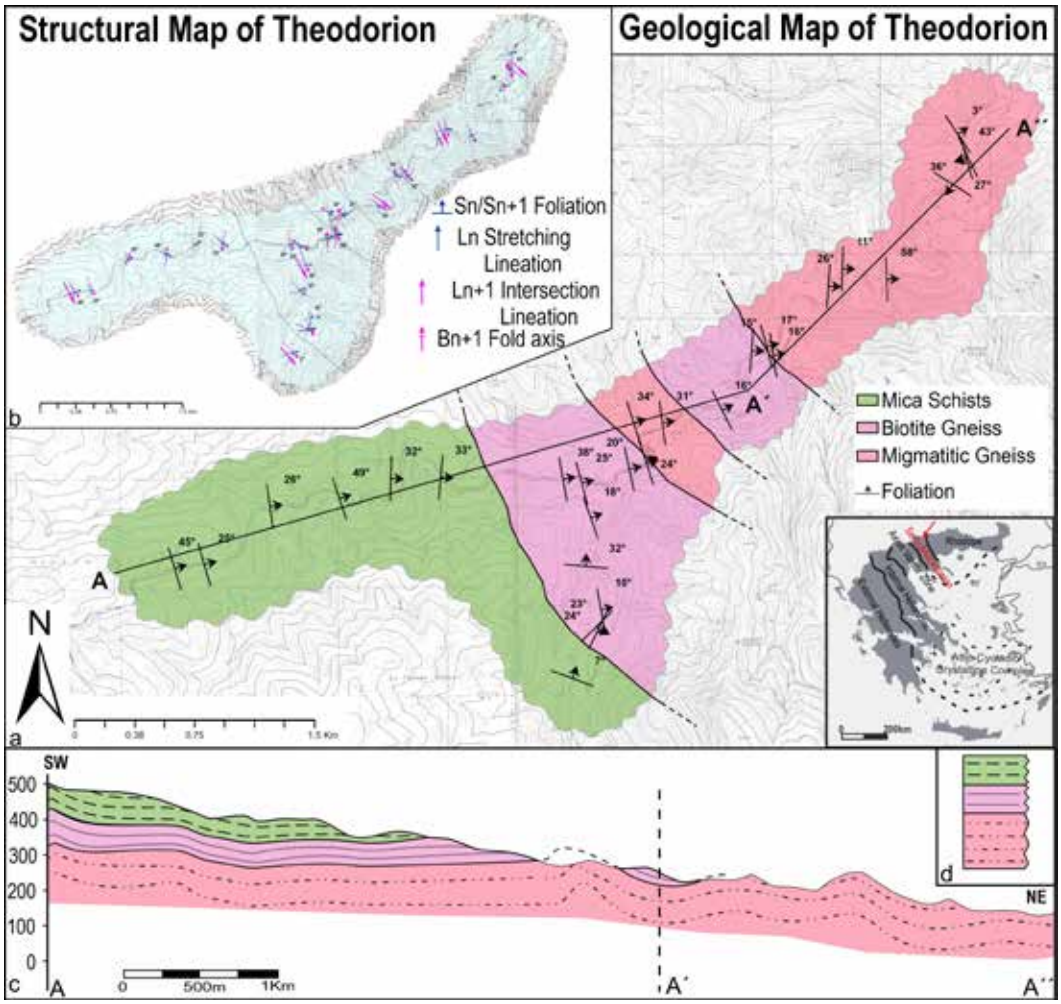

Figure 1a-d. a-b) Geological and structural map of the Theodorion area. Inlet shows the location of the study area. c-d) SW-NE crosssection A-A´-A´´ showing the structure of the Theodorion area and tectonostratigraphic column.

Figure 2a-b a) Close view of the lowermost migmatitic gneiss, red arrow indicating ptygmatic folds. b) Photomicrograph of the biotite gneiss showing the oblique Sn foliation folded by a greenschist-facies Sn+1 foliation (XZ section +polars).

Discussion - Conclusions

Our detailed mapping showed that a northeast-dipping sequence of high-grade rocks exists in the Theodorion area. The lowermost migmatitic gneiss and biotite gneiss represent prealpine basement lithologies of granitic or migmatitic protoliths that underwent high-grade metamorphism through multiple tectonometamorphic events as reported by previous researchers (Pe-Piper and Piper 2002 and references therein; Himmerkus et al., 2007, 2009; Abbo et al., 2020). The origin of the uppermost mica schist is less straightforward to conclude. It could represent a metasedimentary cover, in which case, based on existing geochronological data for the Vertiskos Unit basement rocks, it could be the late Proterozoic to early Paleozoic cover of the granitic precursors. On the other hand, given that these rocks have participated in several orogenic events, a meta-migmatitic origin cannot be excluded.

As for the structural history of these rocks, the early Dn-1 and Dn events could be associated with the Mesozoic (late Jurassic-Cretaceous) history related to the Vardar closure and subsequent deformation. The Dn+1 event could correspond to the Eocene thrusting of the Serbomacedonian Massif on the Circum Rhodope and the Vardar ophiolites. The late-stage top-SW shear bands probably accompanied the late Eocene-Oligocene exhumation of the underlying Kerdylia Unit.

References

Abbo, A., Avigad, D., Gerdes, A., 2020. Crustal evolution of peri-Gondwana crust into present day Europe: the Serbo-Macedonian and Rhodope massifs as a case study. Lithos 356–357, 105295. doi: 10.1016/j. lithos.2019.105295.

Christofides G., Koroneos A., Pe-Piper G., Katirtzoglou K., Chatzikirkou A., 1999. Pre-Tertiary A-Type magmatism in the Serbomacedonian massif (N. Greece): Kerkini granitic complex. Bull. Geol. Soc. Greece, xxxiii, 131-148.

Christofides G., Koroneos A., Liati A., Kral J., 2007. The A-Type Kerkini granitic complex in North Greece: geochronology and geodynamic implications. Bull. Geol. Soc. Greece, xl, 700-711.

Himmerkus, F., Anders, B., Reischmann, T., Kostopoulos, D., 2007. Gondwana-derived terranes in the northern Hellenides. In 4-D Framework of Continental Crust (eds RD Hatcher, MP Carlson, JH McBride and JR Martinez Catalán), pp. 379–90. Geological Society of America, Memoirs no. 200.

Himmerkus, F., Reischmann, T., Kostopoulos, D., 2009. Serbo-Macedonian revisited: a Silurian basement terrane from northern Gondwana in the Internal Hellenides, Greece. Tectonophysics 473, 20–35. doi: 10.1016/j. tecto.2008.10.016.

Kilias, A., Falalakis, G., Mountrakis, D., 1999. Cretaceous–Tertiary structures and kinematics of the Serbomacedonian metamorphic rocks and their relation to the exhumation of the Hellenic hinterland (Macedonia, Greece). International Journal of Earth Sciences 88, 513–31. doi: 10.1007/ s005310050282.

Kockel, F., Mollat, H., Walther, H. W., 1977. *Erlauterungen zur geologicschen karte der Chalkidiki und angrenzender Gebiete 1/100.000 (Nord Griechenland)*. Hanover: Bundesanstalt für Geowissenschaften und Rohstoffe, 119 pp.

Papanikolaou, D.I., 2021. Regional Geology Reviews The geology of Greece. Springer Nature.

Pe-Piper, G. and Piper, D.J.W., 2002. The igneous rocks of Greece. The anatomy of an orogen.–Gebrüder Borntraeger, Berlin, Stuttgart.

Poli, G., Christofides, G., Koroneos, A., Soldatos, T., Perugini, D., Langone, A., 2009. An Early Triassic granitic magmatism—Arnea Kerkini granitic complexes—In the Vertiskos unit (Serbo-macedonian massif, north-eastern Greece) and its significance in the geodynamic evolution of the area. *Acta Vulcanologica*, *21*, 47–70.

Sokoutis D, Brun JP, Van den Driessche J, Pavlides S (1993) A major Oligocene–Miocene detachment in southern Rhodope controlling north Aegean extension. J Geol Soc Lond 150(2), pp.243-246.

17th INTERNATIONAL CONGRESS of the Geological Society of Greece

BULLETIN OF THE GEOLOGICAL SOCIETY OF GREECE, SP. PUBL.

EXTENDED ABSTRACT 003

Fostering FAIR approaches to the seismological data life cycle

Anagnostou V.[1], Bonatis P.[1], Karakostas V.[1], Kourouklas C.[1], Papadimitriou E.[1], Adamaki A.[2], Andriopoulou-Mounteanou S-A.[3], Bathrellos G.D[3], Bitharis S.[1], Foumelis M.[1], Karolos I-A.[1], Kaviris G.[4], Papageorgiou E.[1], Pikridas C.[1], Sakkas V.[1], Skilodimou H.D.[32], Spingos I.[4], Zymvragakis A.[4]
(1) Aristotle University of Thessaloniki, Thessaloniki, Greece, vanagno@geo.auth.gr (2) Lund University, Lund, Sweden (3) University of Patras, Rio, Greece (4) Section of Geophysics – Geothermics, Department of Geology and Geoenvironment, National and Kapodistrian University of Athens, Athens, Greece

Introduction

Natural disasters such as earthquakes floods and landslides expose communities living within hazard-prone areas to significant risks, particularly in today's increasingly interconnected world, making the need for advancement in multi-hazard assessment techniques critical. The HOMEROS project seeks to tackle the challenges presented by those advancements, focusing on seismology, geodesy and geology and leveraging cutting-edge technical solutions tailored to the big data era. HOMEROS makes strides in standardizing research methods, fostering collaboration, and improving the ability to understand and foresee natural hazards through Open Science practices. The project focuses on assessing hazard in high-risk areas in Greece, known for their significant seismic activity, major earthquake occurrence, floods, and landslides, through its transparent, reproducible and widely accessible research products. Data and tools developed by the project will strictly adhere to the FAIR principles (Findable, Accessible, Interoperable, Reusable), thereby maximizing their value for the scientific community, policy makers and stakeholders. HOMEROS will compile earthquake catalogues and assess ground deformation products to provide a comprehensive evaluation of seismic hazard. Furthermore, it will enhance knowledge of flood and landslide hazards, contributing to more effective mitigation efforts.

Project objectives

The HOMEROS project seeks to fulfill the critical need for reliable and standardized methods to assess multiple hazards in an increasingly dynamic risk environment. Harnessing the potential of Open Science and interdisciplinary collaboration, the project strives to expand scientific understanding, support data-informed decision-making, and strengthen community resilience. Its goals are centered around three core pillars:

- Utilization of platforms, such as the European Open Science Cloud (EOSC) and the Environmental Research Infrastructure (ENVRI) (Adamaki & Vermeulen, 2023) for the creation of accessible and efficient ecosystems for interdisciplinary data sharing. This effort builds on prior integration efforts in ENVRI projects and promotes FAIR principles, ensuring usability and reproducibility of research outputs.
- Development of methodologies and workflows for integrating and utilising diverse datasets, including geodetic, seismic and geological data to create detailed physical models, visualization products, such as maps, and data inventories. These efforts seek to aid in the advancement and enhancement of multi-hazard assessment.
- Fostering collaboration and communication among research institutions, infrastructures, and projects. Scientific results will be shared through Open Access publications, workshops, and educational resources.

This paper presents data, workflows and results from the HOMEROS project, related to a specific swarm-like seismic excitation that occurred during the 2024 February – April period in the offshore area to the west of Asos village, Kefalonia island. This work includes preliminary findings from the project, highlighting the collaboration between the participating institutions and the potential for clear and reproducible scientific results by the adherence of available seismic datasets to FAIR principles.

Study area

The areas chosen as case studies for the HOMEROS project are the central Ionian Islands, along with the western Gulf of Corinth. These areas exhibit high deformation rates (Pikridas et al., 2016, Bitharis

et al., 2024), frequent occurrences of strong earthquakes (e.g., Papadimitriou et al., 2017; Kaviris et al., 2021; Sakkas et al., 2022) and destructive floods and landslides (Bathrellos et al., 2017, Skilodimou et al., 2018). More than 50% of the seismic energy in Europe is released in Greece, placing earthquakes among the most impactful geohazards in the country, highlighting the need for a reliable seismic hazard model. A comprehensive evaluation of seismic hazard for such areas can be achieved by Peak Ground Acceleration (PGA) and Peak Ground Velocity (PGV) calculations, alongside site-specific analysis (Uniform Hazard Spectra – UHS and hazard curves) in towns that exhibit the highest population in the study areas (e.g., Kaviris et al., 2022, 2024).

The preliminary results presented in this paper concern the rigorous swarm taking place in 2024 in the offshore area west of Asos village of Kefalonia island. The study area is part of the Kefalonia Transform Fault Zone (KTFZ), which dominates the central Ionian Islands, which is the most seismically active area in the Mediterranean (Figure 1). Specifically, the swarm–like activity that lasted more than two months is located in a thoroughly studied part of the KTFZ, that is recognized as an extensional duplex transfer zone that links the northern (Lefkada) with the southern (Kefalonia) branches of the KTFZ (Karakostas et al., 2015). This stepover zone consists of small sub–parallel fault segments, striking roughly WSW–ENE, deflecting the azimuth of the main fault branches. Since only moderate magnitude earthquakes are known to have occurred in this area, this swarm–like excitation raises scientific concern for the exploitation of the large amount of seismological data that were collected during the activity and the exploitation of the collected data for deciphering the dynamic and kinematic properties of the activated structures. Advancing knowledge of the seismotectonic properties will provide valuable insight in assessing seismic hazard in the broader central Ionian Islands region.

Methods and data

High quality seismic data from regional networks are essential for the compilation of earthquake catalogue and the production of efficient data pipelines ready for multidisciplinary utilization. HOMEROS aims to exploit a benchmark seismic dataset for the February – April 2024 Central Ionian Islands swarm – like activity –among others–, containing more than 2000 earthquakes to explore integration opportunities for enhanced data exchange e.g., data pipelines between research groups of various disciplines, interested in leveraging seismic data for their research. This will be achieved by taking advantage of the resources provided by the EOSC and the ENVRI cluster. This effort also seeks to demonstrate the added value of these services, integrating their tools and services for multi–disciplinary research. Availability of both the relocated benchmark seismic catalogue and the raw waveform dataset will be enhanced following FAIR principles and Open Science practices, ensuring the ease of access to the data. To facilitate interoperability, the relocated catalogue will be provided in the QuakeML schema, a widely used form of seismological data representation, in a modular XML form, able to contain a variety of information, including moment tensors. The waveform dataset will be provided in miniSEED format, accompanied by the corresponding metadata for each station used to collect the data.

Along with providing ease of access to the benchmark data, HOMEROS aims to provide open–source tools for managing, obtaining, processing and visualizing seismic data. To this end, interactive coding platforms such as Jupyter Labs, will be utilized for better dissemination of the developed workflows and tools to scientists from different disciplines (e.g., in the form of Jupyter Notebooks), since an essential component of the project is to ensure the reproducibility, interoperability and ease of access of all research outputs of HOMEROS.

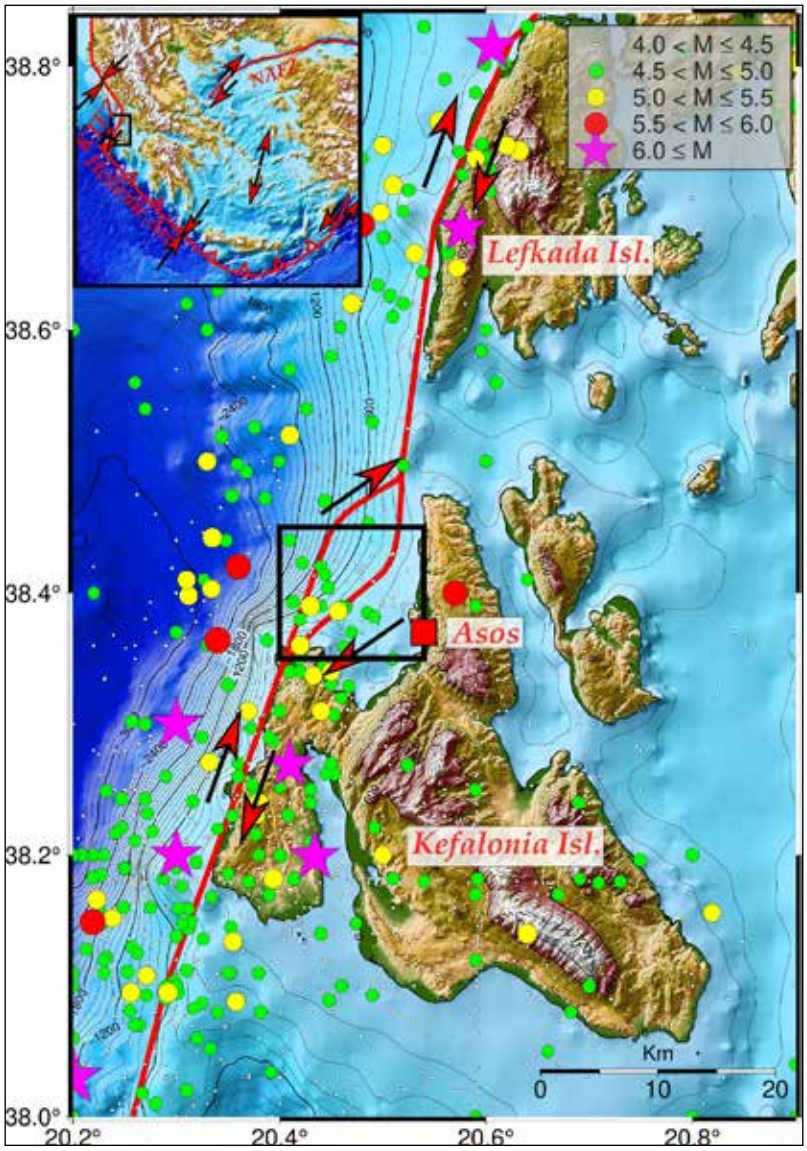

Figure 1: Map of the study area of the central Ionian islands. Circles and stars of different colors and sizes denote seismicity in the region since 1970, according to the legend. The area is placed within the context of the seismotectonics of the Aegean in the map inset, along with major structures of the region, marked with red lines. The main fault segments of the KTFZ, along with the extensional stepover area are denoted with red lines on the map of the study area. Arrows show the relative movement of the faults. The black rectangle encloses the region where the February – April 2024 seismic swarm took place, whereas the red rectangle denotes the location of Asos village

Exploitable results

The primary output for the seismology part of the HOMEROS project multi–hazard outputs, will be open–access datasets, including earthquake catalogues and waveform inventories. It is essential that these datasets will adhere to FAIR principles and be publicly available through platforms such as EPOS ERIC, ENVRI repositories, and other widely used repositories (e.g., GitHub, Zenodo). The benchmark seismic dataset for the February–April 2024 central Ionian Islands swarm-like activity contains over 2000 earthquakes with information on their relocated epicenters, depths, origin time, along with focal

mechanisms for a number of them (Figure 2). The waveform dataset of the swarm contains raw data along with station metadata for 14 seismic stations of the central Ionian Islands. Another key outcome is the development of clear and reproducible research workflows documented through interactive tools such as Jupyter Notebooks. These workflows will showcase the integration of seismic data with various datasets and methodologies, allowing researchers to replicate and tailor the processes for comparable studies, while also providing means of preliminary visualization of the data without the need of prior knowledge of complex tools developed for specific scientific disciplines. In our case, Jupyter notebooks containing complete workflows, along with instructions for waveform data homogenization and earthquake magnitude estimation will be provided.

Type	**Description**	**Format**
Raw data	Seismic Waveforms	miniSEED
Metadata	Station Metadata	StationXML (.xml)
Raw data	Earthquake Catalogues	QuakeML (.xml)
Raw data	Focal mechanisms	QuakeMl (.xml)
Interactive notebook	Waveform dataset homogenization and Magnitude Estimation	Jupyter Notebook
Interactive notebook	Seismic data fetching and simple visualization	Jupyter Notebook

Table 1. Summary of expected data products for the February–April 2024 central Ionian Islands swarm-like activity case study of the HOMEROS project.

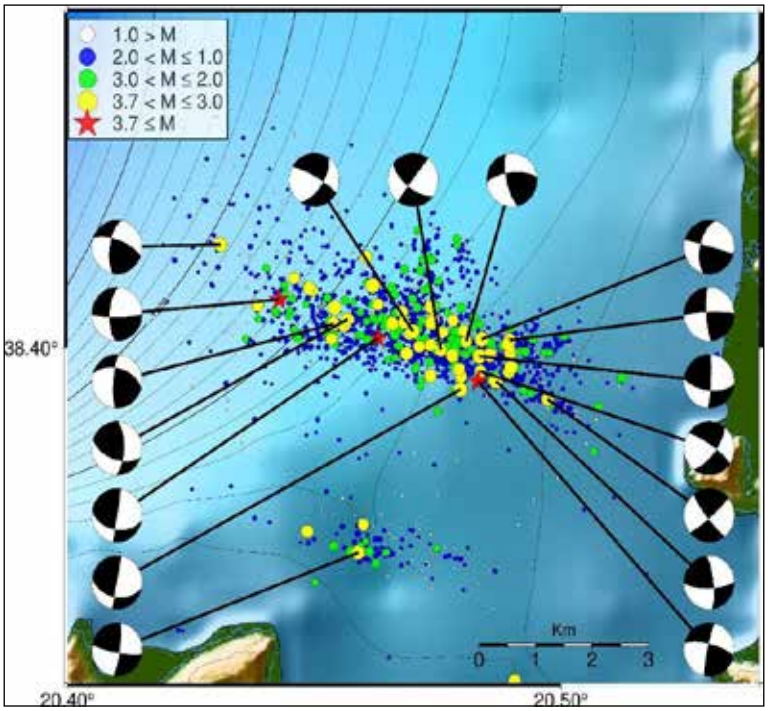

Figure 2: Relocated epicenters of earthquakes that occurred in the study area during the 24/02/2024 – 24/04/2024. Colored dots denote earthquakes with 0.1 ≤ M ≤ 3.7, according to legend. The focal mechanisms of the 17 strongest earthquakes of the excitation are also presented, shown as equal area lower hemisphere projections. The excitation catalog, along with focal mechanisms, is currently available as a preliminary dataset (Anagnostou, 2025) and will be enhanced and finalized with clear metadata and reproducibility information, adhering to FAIR principles through the HOMEROS project.

A workflow along with instructions on obtaining seismic data from open access databases for specific temporal and spatial restrictions and visualizing them on simple maps (Figure 3) will be provided. These workflows will illustrate the combination of diverse datasets and methodologies, empowering researchers to replicate and modify the processes for related studies. Comprehensive documentation for each workflow, presented through interactive notebooks, will act as a best-practice reference for future multidisciplinary research endeavors.

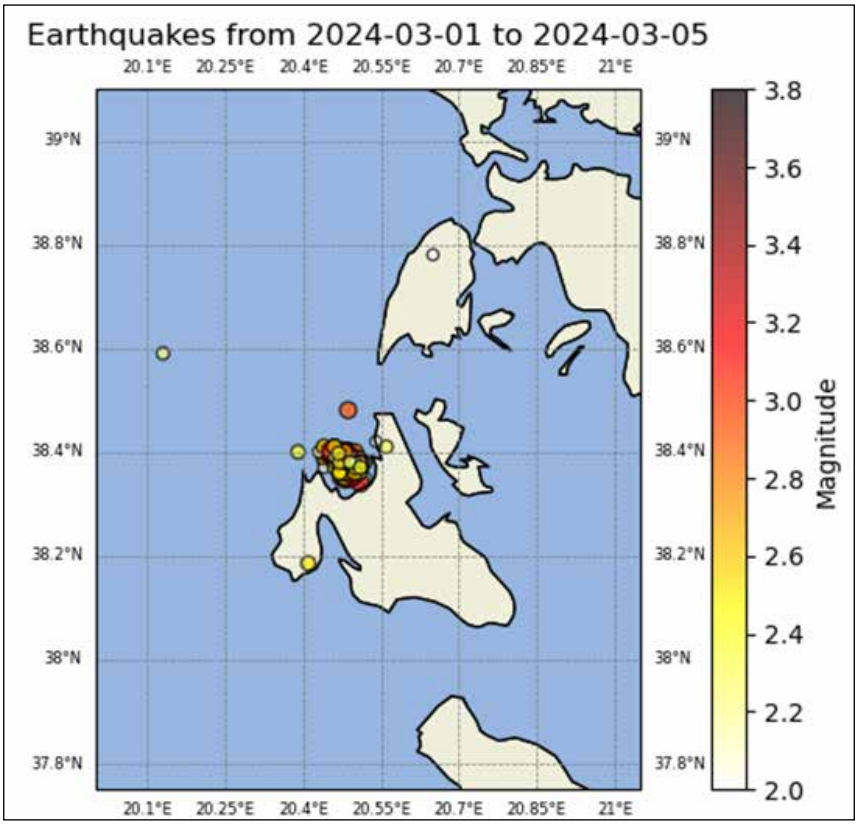

Figure 3: Simple map created using the Seismic data fetching and visualization notebook, presenting earthquakes for the study area during the first 5 days of March 2024, when the excitation activity was peaking. Colored epicenters correspond to the magnitude color bar on the right side of the figure. Data obtained from public EMSC catalogues.

Conclusions

HOMEROS represents an important step forward in addressing the rapidly growing ramifications of multi-hazard assessment. Through unifying data from various scientific fields and embracing Open Science principles, the project addresses critical challenges in making hazard assessment thorough and accessible. By providing seismic datasets and developed workflows following FAIR principles, HOMEROS seeks to propel forward multidisciplinary collaboration and provide clear, reproducible scientific results. The project lays the foundation for scalable and interoperable tools and approaches to understanding natural hazards and their complex interactions. By focusing on a specific case study in a high–risk area such as the central Ionian Islands, we seek to demonstrate the practicality of our developed workflows, the accessibility of our seismic datasets and their potential for further utilization and application from researchers beyond the Earth sciences disciplines. Finally, the outputs comprising open–access data, scientific publications, and training modules, will provide valuable resources for policy–making and disaster management, contributing to a safer and more resilient society.

Acknowledgements

The authors acknowledge the OSCARS project, which has received funding from the European Commission's Horizon Europe Research and Innovation programme under grant agreement No. 10112975.

References

Adamaki, A., & Vermeulen, A. (2023). ENVRI-FAIR D5.7: ENVRI-Hub design study, Zenodo. https://doi.org/10.5281/zenodo.8119522

Anagnostou, V. (2025). February - April 2024 Ionian islands Swarm-like exciation seismic catalog [Data set]. Zenodo. https://doi.org/10.5281/zenodo.14652121

Bathrellos, G. D., Skilodimou, H. D., Chousianitis, K., Youssef, A. M., & Pradhan, B. (2017). Suitability estimation for urban development using multi-hazard assessment map. *Science of the total environment*, *575*, 119-134. https://doi.org/10.1016/j.scitotenv.2016.10.025

Bitharis, S., Pikridas, C., Fotiou, A., Rossikopoulos D., 2024. GPS data analysis and geodetic velocity field investigation in Greece, 2001–2016. *GPS Solutions 28*, 16. https://doi.org/10.1007/s10291-023-01549-8

Karakostas, V., Papadimitriou, E., Mesimeri, M., Gkarlaouni, Ch., Paradisopoulou, P., 2015. The 2014 Kefalonia doublet (Mw6.1 and Mw6.0) central Ionian Islands, Greece: Seismotectonic implications along the Kefalonia Transform Fault Zone. *Acta Geophysica 63*, 1-16. https://doi.org/10.2478/s11600-014-0227-4

Kaviris, G., Elias, P., Kapetanidis, V., Serpetsidaki, A., Karakonstantis, A., Plicka, V., De Barros, L., Sokos, E., Kassaras, I., Sakkas, V., Spingos, I., Lambotte, S., Duverger, C., Lengline, O., Evangelidis, C.P., Fountoulakis, I., Ktenidou, O.-J., Gallovic, F., Bufferal, S., Klein, E., Aissaoui, E.M., Scotti, O., Lyon-Caen, H., Rigo, A., Papadimitriou, P., Voulgaris, N., Zahradnik, J., Deschamps, A., Briole, P., & Bernard, P. (2021). The Western Gulf of Corinth (Greece) 2020–2021 Seismic Crisis and Cascading events: first results from the Corinth Rift Laboratory Network. Seism. Rec., 1, 85–95. https://doi.org/10.1785/0320210021.

Kaviris, G., Zymvragakis, A., Bonatis, P., Kapetanidis, V., & Voulgaris, N. (2022). Probabilistic and Scenario-Based Seismic Hazard Assessment on the Western Gulf of Corinth (Central Greece). *Applied Sciences*, *12*(21), 11152. https://doi.org/10.3390/app122111152

Kaviris, G., Zymvragakis, A., Kapetanidis, V., Kouskouna, V., Spingos, I., Sakellariou, N., & Voulgaris, N. (2024). A logic-tree based probabilistic seismic hazard assessment for the central ionian islands of cephalonia and ithaca (Western Greece). *Journal of Seismology*, *28*(5), 1087-1103. https://doi.org/10.1007/s10950-024-10242-3

Papadimitriou, E., Karakostas, V., Mesimeri, M., Chouliaras, G., & Kourouklas, Ch. (2017). The Mw6.5 17 November 2015 Lefkada (Greece) Earthquake: Structural Interpretation by Means of the Aftershock Analysis. *Pure and Applied Geophysics*, 174(10), 3869–3888. https://doi.org/10.1007/s00024-017-1601-3

Pikridas C., Bitharis S., Fotiou A., Rossikopoulos D., Katsougiannopoulos S., Spanakaki K, Karolos I., 2016. Monitoring seismic displacements using GNSS data with PPP method. *Bulletin of the Geological Society of Greece 50* (3), 1563-1569. https://doi.org/10.12681/bgsg.11870

Sakkas, V., Kapetanidis, V., Kaviris, G., Spingos, I., Mavroulis, S., Diakakis, M., Alexopoulos, J.D., Kazantzidou-Firtinidou D., Kassaras, I., Dilalos, S., Vassilakis, E., Kotsi, E., Tselentis, G., Lekkas, E. & Voulgaris, N. (2022). Seismological and ground deformation study of the Ionian Islands (W. Greece) during 2014–2018, a period of intense seismic activity. *Applied Sciences, 12*(5), 2331. https://doi.org/10.3390/app12052331

Skilodimou, H. D., Bathrellos, G. D., Koskeridou, E., Soukis, K., & Rozos, D. (2018). Physical and anthropogenic factors related to landslide activity in the Northern Peloponnese, Greece. *Land*, *7*(3), 85. https://doi.org/10.3390/land7030085

17th INTERNATIONAL CONGRESS of the Geological Society of Greece

BULLETIN OF THE GEOLOGICAL SOCIETY OF GREECE, SP. PUBL.

EXTENDED ABSTRACT 004

Detailing the stress pattern in the area of central Ionian Islands

Anagnostou V.[1], Papadimitriou E.[1], Karakostas V.[1], Bäck T.[2]
Department of Geophysics, Aristotle University of Thessaloniki, Thessaloniki, Greece, vkarak@geo.auth.gr
Nuclear Science and Engineering department, KTH Royal Institute of Technology, Stockholm

Background

The Kefalonia Transform Fault Zone (KTFZ) is the most seismically active area in the Mediterranean and consists of two major branches, the Lefkada fault segment to the north and the Kefalonia fault segment to the south. KTFZ acts as an active boundary between the subduction zone of the remnants of the oceanic lithosphere of the Eastern Mediterranean that subducts under the Aegean microplate to the south and the continental collision between the Eurasian plate and the Adriatic Microplate to the north. The tectonic activity in the region is reflected in the rapid crustal deformation rates of the region and subsequently the frequent occurrence of strong earthquakes ($M_w \geq 6.0$) that occurred during both the historical and instrumental era of seismology. Those strong earthquakes and their temporal distribution can be explained due to stress transfer between closely located fault segments (Papadimitriou, 2002) and as such, studying those stress interactions is an integral part of understanding the long-term tectonic loading in the region.

For better understanding of the kinematics and the distribution of continental deformation that is occurring within the brittle crustal layer in the study area, we assess the regional stress field by inverting focal mechanisms. Contemporary stress field in an area is a result of processes that operate at significantly different spatial scales (Zoback, 1992). Forces that are linked to major tectonic movements such as ridge push and slab pull affect the stress field at large wavelengths, beyond 2000 km and are considered first–order sources of stress field perturbation. At intermediate wavelengths (between 2000 and 500 km) the crustal stress field is affected by processes such as orogenic lithospheric flexure (Zoback, 1992) with those processes representing second order sources of stress field disturbances. Third order patterns of crustal stress field are linked to small–scale variations (<100km) that are produced by processes such as active faulting and at times these variations may lead to the nucleation of potentially destructive earthquakes (Hergert and Heidbach, 2011). Detailed knowledge of the contemporary stress field characteristics of high–risk areas, such the central Ionian Islands region is valuable for possible investigations of stress triggering sensitivity due to the coseismic slip of strong earthquakes.

Objectives

The main objective of this paper is to present crustal stress data for the area of central Ionian Islands, inferred from the inversion of 485 focal mechanisms using the SATSI inversion method of Hardebeck and Michael (2006) and specifically the MSATSI implementation of the method (Martinez–Garzon et al., 2014). We seek to better detail the stress field by binning the focal mechanism dataset according to known structures in the area and producing a representative focal mechanism for each subarea based on the stress inversion results. Previous work in defining the stress pattern has been done for the Greek region (e.g., Kapetanidis & Kassaras, 2019) including our study area. We focus on detailing the stress pattern around the main branches of the KTFZ along with the transfer zone that connects them and has been identified as an extensional stepover zone (Karakostas et al., 2015).

Data and Method

Our dataset contains 485 focal mechanisms and was compiled from data obtained from a variety of sources, mainly published works (Hatzfeld et al., 1995; Louvari et al., 1999; Benetatos et al., 2004, 2005; Pondrelli et al., 2004, 2007, 2011; Karakostas & Papadimitriou, 2010; Karakostas et al., 2015; Papadimitriou et al., 2017; Kostoglou et al., 2020) along with routine solutions from various observatories (GCMT, ETH, HUSN, GEOFON). In cases of duplicate solutions, we prioritized the focal mechanism computed by published works over routine solutions. MSATSI deals with the ambiguity of the fault-plane solution by allowing the user to explicitly specify the probability that each input fault plane solution is thought to be the real one. We used the typical 50% value for our inversions. Focal mechanisms that correspond to seismicity occurring below crustal depths (>30km) were discarded in order to constrain the stress patterns to crustal, third order levels. The KTFZ comprises five major fault segments with striking from 12° to 40°, with fault lengths between 12–40km and rake values that exhibit right–lateral strike–slip faulting (Kourouklas et al., 2023). Four out of the five segments bound the western coastlines of the Lefkada and Kefalonia Islands and were identified

as the causative faults of four of the strongest earthquakes that occurred in the study area during the 21st century (Karakostas et al., 2004, 2015; Papadimitriou et al., 2017). The fifth segment is located offshore, south of Kefalonia and was associated with the 1983 M_w=7.0 earthquake (Scordilis et al., 1985). The gridding scheme for our focal mechanism dataset follows the segmentation of the KTFZ for its five segments, with an additional grid point located in the stepover zone that connects the northern Kefalonia segment with the southern Lefkada segment (Figure 1).

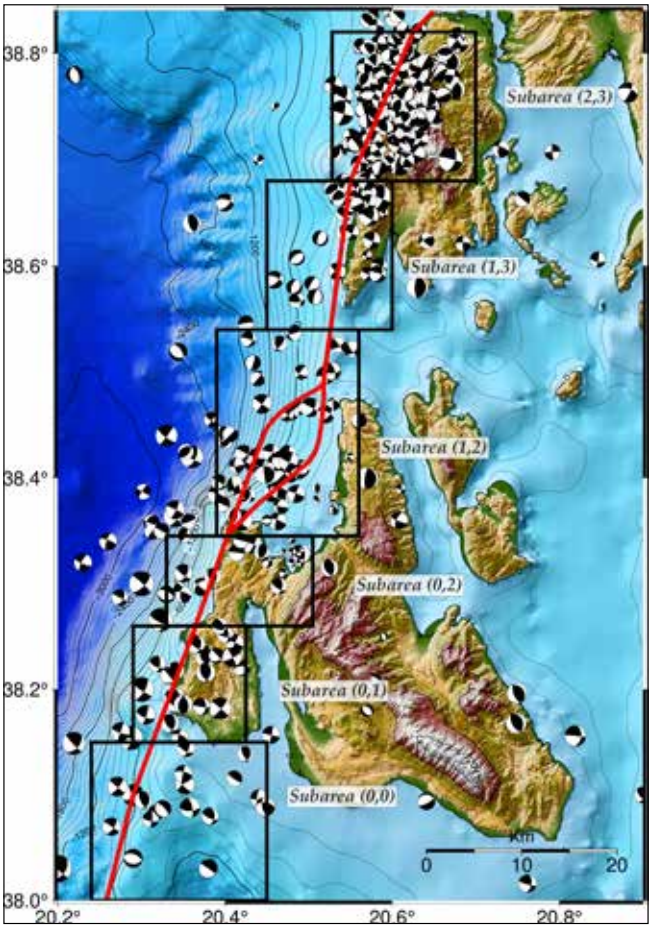

Figure 1: Map of the study area of the central Ionian Islands along with the major fault segments of the KTFZ and the extensional stepover area, denoted with red lines and enclosed by rectangles that correspond to the subareas or grid points containing the focal mechanisms used in the inversion. The focal mechanisms are shown as equal area lower hemisphere projections.

After compiling and subdividing our dataset to their corresponding subareas, securing that each one comprises at least 20 focal mechanisms to ensure robustness of results, we perform stress inversion for each subset, by applying the SATSI inversion algorithm. The algorithm inverts focal mechanism data for spatially and/or temporally variable stress field, using a damped least–squares inversion method to obtain a smoothed solution (stress tensor) for each subarea while avoiding data singularities. MSATSI provides the orientation of the three principal axes, as well as a relative stress magnitude quantity (R):

$$R = \frac{\sigma_1 - \sigma_2}{\sigma_1 - \sigma_3} R = \frac{\sigma_1 - \sigma_2}{\sigma_1 - \sigma_3} \qquad (1)$$

where σ_1, σ_2, σ_3 are the magnitudes of the principal stress axes obtained from the deviatoric stress tensor. This way, the R value quantifies whether the magnitude of the intermediate principal stress σ_2 is closer to the magnitude of the most compressive or the least compressive principal stress. MSATSI calculates the optimal damping parameter by performing a series of inversions with varying values and comparing the resulting data misfit to the degree of

heterogeneity of the solution (model length). The chosen damping parameter is found on the trade–off curve of the two values, corresponding to the point that minimizes both the data misfit and the model length. Finally, we assess the uncertainties of our results using a bootstrap resampling method. We perform resamplings at least 20 times the number of our data for each grid point, specifying the confidence interval of the uncertainties at 95%. Finally, we construct a representative focal mechanism for each grid point, according to the best stress tensor derived from our methodology.

Exploitable Results

The results of the damped stress inversion are presented in Figure 2 and Table 1. We observe that in all grid points, the plunge and azimuth of the principal stress axes agree as expected with a strike–slip faulting regime, with low plunge values of both the σ_1 and σ_3 principal stress components. Our data constrain the plunge and azimuth of the principal stress axes adequately for the Kefalonia branch of the KTFZ, the stepover zone north of Kefalonia and the southern Lefkada grid point. In the case of the northern Lefkada (grid point 2, 3) subarea, we observe higher uncertainties in the plunges of both the σ_3 and the σ_2 principal stress components. Assessing these uncertainties through bootstrap resamplings, we find that they are mainly concerned with the plunges of the σ_3 axis. This, along with the value of the relative stress ratio R, indicate a stronger normal faulting component in this subarea and thus extensional characteristics. R values for the southern Lefkada (grid point 1, 3) and the stepover zone (grid point 1, 2) are found to be 0.45 and 0.41, respectively. Values of R closer to 0.0 evidence extensional component of the prevailing regional stress field, whereas values approaching to 1.0 are indicative of rather transpressional regimes. This is present in the north Kefalonia (grid point 0, 2) south Kefalonia (grid point 0, 1) and offshore Kefalonia (0,0) subareas, where the relative stress magnitude values increase, evidencing a stronger compressive stress component as we move towards the southern edge of the KTFZ. Nevertheless, the R values for all subareas under study remain relatively close to the 0.5 value, meaning the dominant faulting that characterize the regional stress regime is strike–slip. Following the World Stress Map project guidelines (Zoback, 1992) we calculate the azimuth of the maximum horizontal stress axis for every grid point. We observe as expected, that the maximum compression axis σ_1 corresponds to the S_{Hmax} and strikes SW–NE. Using the calculated best solutions for the P and T axes geometrical characteristics, we produced six representative focal mechanisms, one for each grid point. All are pointing towards a strike–slip stress regime, with the one nodal plane striking NNE–SSW and the second (conjugate) WNW–ESE.

Grid point (X,Y)	Optimal σ_1 Trend and Plunge	Optimal σ_2 Trend and Plunge	Optimal σ_3 Trend and Plunge	Relative Stress Magnitude	Representative Focal Mechanism					
					Nodal Plane 1			Nodal Plane 2		
					Strike	Dip	Rake	Strike	Dip	Rake
(0,0)	249°/10°	130°/62°	341°/11°	0.76	25°	75°	179°	115°	89°	15°
(0,1)	248°/11°	132°/63°	343°/23°	0.75	21°	68°	171°	114°	82°	21°
(0,2)	246°/11°	123°/70°	340°/16°	0.71	22°	73°	176°	112°	86°	17°
(1,2)	244°/5°	99°/78°	337°/6°	0.41	20°	80°	-177°	290°	87°	-9°
(1,3)	242°/13°	82°/84°	335°/1°	0.45	19°	86°	-177°	289°	87°	-4°
(2,3)	248°/13°	10°/67°	152°/18°	0.47	290°	67°	4°	198°	86°	157°

Table 1: Stress inversion results and representative focal mechanisms corresponding to the optimal principal stress axes for each grid point of our study area.

Summary and Conclusions

An effort has been exerted to detail the third–order stress field patterns that dominate the area of central Ionian Islands, the most seismically active part of the broader Aegean area drawing significant interest for its seismotectonic properties. Taking advantage of the wealth of data provided by the rigorous scientific work done on the region, we find consistent stress field characteristics, typical of dextral strike – slip stress regime. Relative stress magnitude

values for each subarea, point towards a notable extensional component to the northern parts of our study area, corresponding to the Lefkada KTFZ fault segments and the extensional duplex zone that connects the southern and northern KTFZ branches, whereas evidencing a transition towards a more transpressional regime towards the Kefalonia branch to the south. Nevertheless, the study area is dominated by the strike–slip fault motions of the KTFZ, indicated by the maximum compression axis being equal to the SH_{max} while the intermediate stress axis plunging steeply in every grid point.

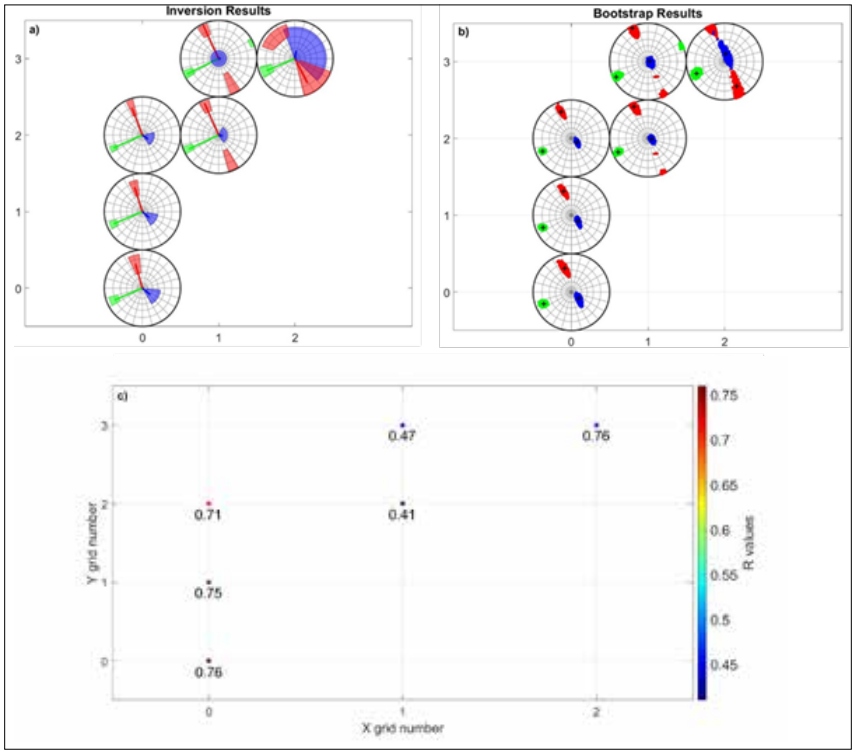

Figure 2: a) Inversion results for the 6 grid points of our study area. Optimal solutions for trend and plunge of the principal stress components σ_1, σ_2, σ_3 (colored green, blue and red, respectively) plotted on Wulff stereographic projection plots, each corresponding to a numbered subarea, according to Table 1. The respective colored areas denote the axes uncertainties in plunge and trend. b) Same as a, but presenting the trend and plunge scatter of the principal stress axes, after 2000 bootstrap resamplings for 95% confidence interval. Black crosses denote the optimal solution for each axis. c) Relative Stress Magnitudes for each of the 6 grid points

Acknowledgements

This research is partially financially supported by the artEmis Project funded by the European Union, under Grant Agreement nr 101061712. The views and opinions expressed are, however, those of the author(s) only and do not necessarily reflect those of the European Union or European Commission–Euratom. Neither the European Union nor the granting authority can be held responsible for them.

References

Hardebeck, J. L., & Michael, A. J. (2006). Damped regional scale stress inversions: Methodology and examples for southern California and the Coalinga aftershock sequence. *Journal of Geophysical Research: Solid Earth*, *111*(B11). https://doi.org/10.1029/2005JB004144

Hergert, T., & Heidbach, O. (2011). Geomechanical model of the Marmara Sea region—II. 3-D contemporary background stress field. *Geophysical Journal International*, *185*(3), 1090-1102. https://doi.org/10.1111/j.1365-246X.2011.04992.x

Kapetanidis, V., & Kassaras, I. (2019). Contemporary crustal stress of the Greek region deduced from earthquake focal mechanisms. *Journal of Geodynamics*, *123*, 55-82. https://doi.org/10.1016/j.jog.2018.11.004

Karakostas, V. (2004). Properties of the 2003 Lefkada, Ionian Islands, Greece, Earthquake Seismic Sequence and Seismicity Triggering. *Bulletin of the Seismological Society of America*, 94(5), 1976–1981. https://doi.org/10.1785/012003254

Karakostas, V., Papadimitriou, E., Mesimeri, M., Gkarlaouni, C., & Paradisopoulou, P. (2015). The 2014 Kefalonia doublet (Mw 6.1 and Mw 6.0), central Ionian Islands, Greece: Seismotectonic implications along the Kefalonia transform fault zone. *Acta Geophysica*, *63*, 1-16. https://doi.org/10.2478/s11600-014-0227-4

Kourouklas, C., Papadimitriou, E., & Karakostas, V. (2023). Long-Term Recurrence Pattern and Stress Transfer along the Kefalonia Transform Fault Zone (KTFZ), Greece: Implications in Seismic Hazard Evaluation. *Geosciences*, *13*(10), 295. https://doi.org/10.3390/geosciences13100295

Martínez-Garzón, P., Kwiatek, G., Ickrath, M., & Bohnhoff, M. (2014). MSATSI: A MATLAB package for stress inversion combining solid classic methodology, a new simplified user□handling, and a visualization tool. *Seismological Research Letters*, *85*(4), 896-904. https://doi.org/10.1785/0220130189

Papadimitriou, E. E. (2002). Mode of Strong Earthquake Recurrence in the Central Ionian Islands (Greece): Possible Triggering due to Coulomb Stress Changes Generated by the Occurrence of Previous Strong Shocks. *Bulletin of the Seismological Society of America*, 92(8), 3293–3308. https://doi.org/10.1785/0120000290

Scordilis, E. M., Karakaisis, G. F., Karacostas, B. G., Panagiotopoulos, D. G., Comninakis, P. E., & Papazachos, B. C. (1985). Evidence for transform faulting in the Ionian Sea: The Cephalonia Island earthquake sequence of 1983. *Pure and Applied Geophysics*, 123(3), 388–397. https://doi.org/10.1007/BF00880738

Zoback, M. L. (1992), First- and second-order patterns of stress in the lithosphere: The World Stress Map Project, *J. Geophys. Res.*, 97(B8), 11703–11728, doi:10.1029/92JB00132

Data Sources

Benetatos, C., Kiratzi, A., Papazachos, C., & Karakaisis, G. (2004). Focal mechanisms of shallow and intermediate depth earthquakes along the Hellenic Arc. *Journal of Geodynamics*, *37*(2), 253–296. https://doi.org/10.1016/j.jog.2004.02.002

Benetatos, C., Kiratzi, A., Roumelioti, Z., Stavrakakis, G., Drakatos, G., & Latoussakis, I. (2005). The 14 August 2003 Lefkada Island (Greece) earthquake: Focal mechanisms of the mainshock and of the aftershock sequence. *Journal of Seismology*, *9*(2), 171–190. https://doi.org/10.1007/s10950-005-7092-1

Ekström, G., Nettles, M., & Dziewoński, A. M. (2012). The global CMT project 2004–2010: Centroid-moment tensors for 13,017 earthquakes. *Physics of the Earth and Planetary Interiors*, *200–201*, 1–9. https://doi.org/10.1016/j.pepi.2012.04.002

ETH Zurich. (1986). Swiss Seismological Service (SED). In *National Seismic Networks of Switzerland, ETH Zürich*. https://doi.org/10.12686/sed/networks/ch

GEOFON Data Centre. (1993). GEOFON Seismic Network [Data set]. GFZ Data Services. https://doi.org/10.14470/TR560404

Hatzfeld, D., Kassaras, I., Panagiotopoulos, D., Amorese, D., Makropoulos, K., Karakaisis, G., & Coutant, O. (1995). Microseimicity and strain pattern in northwestern Greece. *Tectonics*, *14*(4), 773–785. https://doi.org/10.1029/95TC00839

National Observatory of Athens, Institute of Geodynamics, Athens. (1975). *National Observatory of Athens Seismic Network* [Data set]. International Federation of Digital Seismograph Networks. https://doi.org/10.7914/SN/HL

Karakostas, V., & Papadimitriou, E. (2010). Fault complexity associated with the 14 August 2003 Mw6.2 Lefkada, Greece, aftershock sequence. *Acta Geophysica*, *58*(5), 838–854. https://doi.org/10.2478/s11600-010-0009-6

Kostoglou, A., Karakostas, V., Bountzis, P., & Papadimitriou, E. (2020). The February-March 2019 seismic swarm offshore north Lefkada Island, Greece: Microseismicity analysis and geodynamic implications. *Applied Sciences (Switzerland)*, *10*(13). https://doi.org/10.3390/app10134491

Louvari, E., Kiratzi, A. A., & Papazachos, B. C. (1999). The Cephalonia transform fault and its extension to western Lefkada Island (Greece). *Tectonophysics*, *308*(1-2), 223-236. https://doi.org/10.1016/S0040-1951(99)00078-5

Papadimitriou, E., Karakostas, V., Mesimeri, M., Chouliaras, G., & Kourouklas, C. (2017). The Mw6.5 17 November 2015 Lefkada (Greece) Earthquake: Structural Interpretation by Means of the Aftershock Analysis. *Pure and Applied Geophysics*, *174*(10), 3869–3888. https://doi.org/10.1007/s00024-017-1601-3

Pondrelli, S., Morelli, A., & Ekström, G. (2004). European-Mediterranean regional centroid-moment tensor catalog: solutions for years 2001 and 2002. *Physics of the Earth and Planetary Interiors*, *145*(1–4), 127–147. https://doi.org/10.1016/J.PEPI.2004.03.008

Pondrelli, S., Salimbeni, S., Morelli, A., Ekström, G., & Boschi, E. (2007). European–Mediterranean Regional Centroid Moment Tensor catalog: Solutions for years 2003 and 2004. *Physics of the Earth and Planetary Interiors*, *164*(1–2), 90–112. https://doi.org/10.1016/J.PEPI.2007.05.004

Pondrelli, S., Salimbeni, S., Morelli, A., Ekström, G., Postpischl, L., Vannucci, G., & Boschi, E. (2011). European–Mediterranean Regional Centroid Moment Tensor catalog: Solutions for 2005–2008. *Physics of the Earth and Planetary Interiors*, *185*(3–4), 74–81. https://doi.org/10.1016/J.PEPI.2011.01.007

17th INTERNATIONAL CONGRESS of the Geological Society of Greece

BULLETIN OF THE GEOLOGICAL SOCIETY OF GREECE, SP. PUBL.

EXTENDED ABSTRACT 005

Flood events over the past 115 years in the Municipality of Patras, southern Greece

Andriopoulou Mounteanou S.A.[1], Bathrellos G.D.[1], Skilodimou H.D.[1]
(1) University of Patras, Greece, geo13014@ac.upatras.gr

Introduction

Natural hazards are physical phenomena that can cause substantial harm to both the natural world and human environments. These hazards arise from endogenic or exogenic processes, such as tectonic activity or climate change, which can alter landforms and influence natural hazards, often directly affecting human activities (Migiros *et al.,* 2011, Kamberis *et al.,* 2012, Skilodimou *et al.,* 2014, Kokinou *et al.,* 2015, Bathrellos *et al.,* 2017, Bathrellos *et al.,* 2018).

Floods are natural events that have occurred throughout geological history, resulting from excessive surface runoff. Floodplains are formed through sediment deposition when rivers overflow their banks. They are considered favorable locations for human settlement due to their fertile soils, flat terrain, ease of excavation, and proximity to water sources. These advantages have encouraged the development and urbanization of floodplains, leading to an increase in flood-related disasters. Despite efforts to mitigate flooding through structures like dams, levees, and river channeling, the damage caused by floods continues to rise (Bathrellos and Skilodimou, 2006, Bathrellos, 2007, Skilodimou *et al.,* 2024).

Floods are a common occurrence in certain regions of the world. In urban settings floods are among the most hazardous natural events. The impacts of flooding extend beyond environmental damage, encompassing social and economic consequences as well. Floods can harm urban infrastructure and agricultural lands, and in severe cases, they can even result in the loss of human lives (Bathrellos *et al.,* 2016).

Between 2000 and 2024, there have been more than 400 major floods, including several catastrophic events floods that affected over 1.9 million people in Europe, claiming more than 2,000 lives and causing economic losses estimated at over 70 billion Euros (EM-DAT, 2024). Flooding is a frequent natural hazard in Greece, with numerous severe events occurring over the 25 years. These floods have led to the tragic loss of over 72 lives and caused extensive damage to properties, buildings, infrastructure, and the environment. Their effects have significantly disrupted both the national and rural economies with the financial impact surpassing 1 billion (Skilodimou *et al.,* 2021, EEA, 2024).

Objectives

This study highlights the flood events and their impacts in the Municipality of Patras from 1909 to 2024. In detail, the study explores the hydrological basins of the rivers within the study area, the occurrences of flooding, the regions impacted, and the damage inflicted on the urban infrastructure, particularly focusing on buildings. Furthermore, the study analyzes the occurrence of floods in particular areas and establishes a correlation between the impacted regions and the damaged structures.

Study area

The study area (Fig. 1A) includes the drainage basins of the Glafkos, Diakoniaris, Meilichos, Haradros and Selemnos river located in the northern Peloponnese region of southern Greece (Fig. 1B). These rivers discharge into the Gulf of Patras. The areas of the drainage basins are as follows: Glafkos River covers 108.5 km², Diakoniaris River spans 26.5 km², Meilichos River encompasses 22 km², Haradros River covers 25 km², and Selemnos River occupies 17.8 km², resulting in a total combined area of 199.8 km².

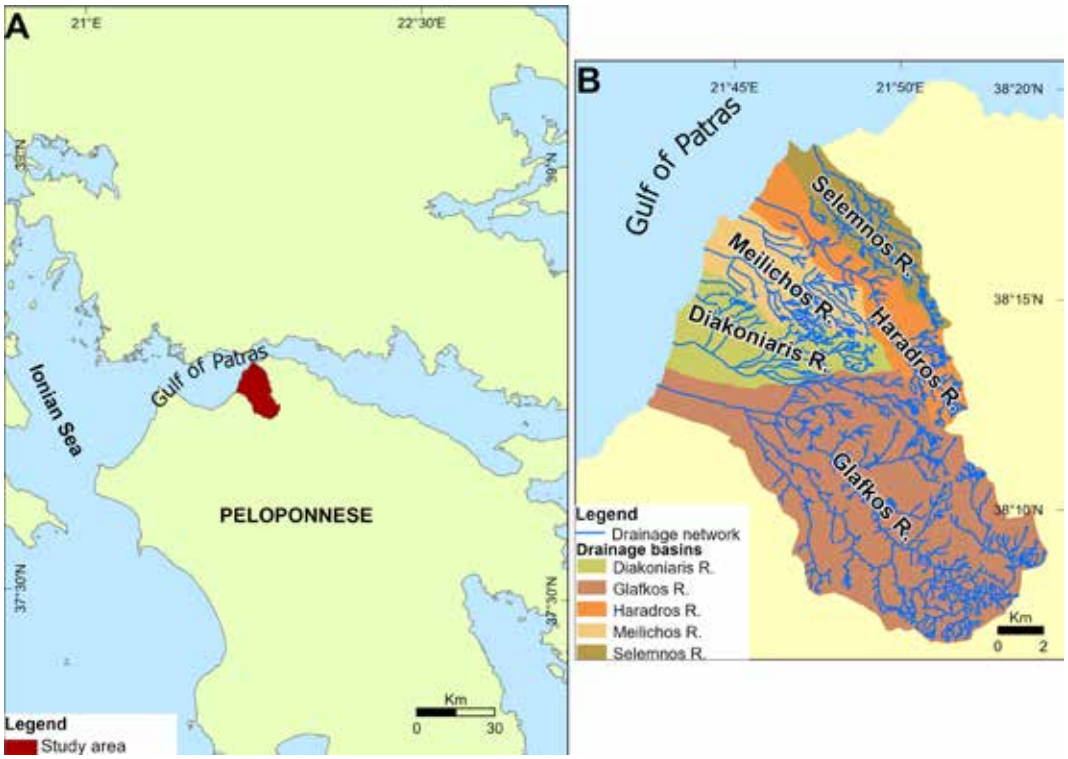

Figure 1. (A) Location map of the study area, (B) a map of the drainage networks and basins of the study area.

Methodology - Data

The data collected in the context of the current research were:

- Collection data from online sources (Ministry of Environment and Energy, 2017, METEO, 2024).
- Fact-checking the provided information and gathering additional details (UEDNPEI, 2014).

This study focused on key elements such as the flood locations, dates of occurrence, extent of the flooded area, types of damages, and the total damage caused by each flood event.

The data collection was initially carried out by consulting meteo.gr, which provides material on floods that have occurred between 2000 and 2024. Additional information, like the number of flooded buildings and the districts that these events occurred, was gathered from local newspapers. Following this, a search was performed on the official Press Museum website using filters and keyword searches to identify older flood events. The affected areas were determined from this data, and Google Earth was utilized for detailed calculations of the impacted regions. Thematic maps were then generated using ArcGIS Pro.

A temporal statistical analysis was performed to determine the number of events, the flooded area (in km²), the number of affected buildings, and human casualties impacted by floods throughout the 115-year period. The frequency of flood occurrences in each district of Patras during this period was analyzed. Furthermore, data from Urban Atlas 2018 (Copernicus, Urban Atlas 2018, 2021) were used to evaluate the extent of the urban structure and to calculate the Building Cover Ratio (BCR) impacted by flooding.

Results

A total number of 20 flood events were recorded in the drainage basins of the Glafkos, Diakoniaris, Meilichos, Haradros and Selemnos rivers. Table 1 outlines the year in which floods occurred and the corresponding river, the affected area and the specific districts, the number of impacted buildings, and the human casualties. Over the 115-year period, there was only one instance of human casualties, occurring in 2001, which resulted in the loss of two lives.

Table 1. Classes of the year of the flood event, river that contributed for the phenomenon, flooded area, number of buildings that were casualties and people that lost their life

YEAR	RIVER	AREA (km2)	AFFECTED DISTRICTS	FLOODED BUILDINGS
1909	DIAKONIARIS	0.28	PSAROFAI, GIROKOMIO	40
1917	GLAFKOS	0.12	LEFKA	0
1927	GLAFKOS-HARADROS	1.12	MPOZAITIKA, KASTELOKAMPOS, MPEGOULAKI, ITIES	80
1931	GLAFKOS	0.24	ITIES, KRIA ITEON	25
1935	GLAFKOS	0.13	ITIES, KRIA ITEON	20
1940	DIAKONIARIS	0.62	AG. AIKATERINI, AG. PARASKEVI, TASI, GIROKOMIO, VILLA LADOPOULOU, AG. IOANNIS PRATSIKA	100
1956	DIAKONIARIS - GLAFKOS	2.03	MPEGOULAKI, PSAROFAI, AG. GEORGIOS LAGOURA, ZAROUCHLEIKA, AG. IOANNIS PRATSIKA, LAGOURA, AG. AIKATERINI, ITIES, KRIA ITEON	250
1959	HARADROS	0.22	SKAGIOPOULIO	100
1960	GLAFKOS	0.03	ITIES	0
1962	DIAKONIARIS - GLAFKOS-MEILICHOS - HARADROS-SELEMNOS	3.25	EGLIKADA, AG. AIKATERINI, AG. IOANNIS PRATSIKA, ITIES, AGYIA, AG. GEORGIOS LAGOURA, PSAROFAI, PROASTIO, SKAGIOPOULIO	4,000
1965	GLAFKOS	0.06	ITIES, KRIA ITEON	25
1997	DIAKONIARIS	3.01	EGLIKADA, AG. AIKATERINI, AG. IOANNIS PRATSIKA, AG. GEORGIOS, LAGOURA, PSAROFAI, GIROKOMIO	1,500
2001	DIAKONIARIS	0.28	ZAROUCHLEIKA	150
2002	DIAKONIARIS	0.01	CENTER	2
2013	MEILICHOS	0.05	AGYIA	0
2021	MEILICHOS	0.21	VOUTENI, KOTRONI	40
2024	GLAFKOS	0.01	ITIES	0

The Municipality of Patras consists of just over 50 districts, with this study focusing on the main districts, including and those that have experienced flooding.

Figure 2 depicts the drainage basins of the Glafkos, Diakoniaris, Meilichos, Haradros, and Selemnos rivers, along with the spatial distribution of flooded areas across each district and drainage basin. Notably, in the Diakoniaris River basin, the flooded area results from multiple flood events over different years. This basin has the largest flooded area, covering approximately 3 km². It also exhibits the highest level of urban development among the studied hydrological basins and has experienced a significant number of flood events. In contrast, the Selemnos River basin has the smallest flooded area.

Figure 3 illustrates the number of flood events across various districts in Patras. Ities has the highest frequency, with six flooding events, making it the most affected district in Patras, other significantly affected districts include Psarofai (4 flooding events), Ag. Aikaterini, Girokomio, Kria Iteon and several others with 3 events each. Many regions, including Ketes and Anthoupoli recorded only one flooding event. Some, appear to have no significant recorded flooding frequency, indicated by the absence of bars. Notably, 40% of the districts have been affected by flooding multiple times emphasizing the recurrent nature of the issue.

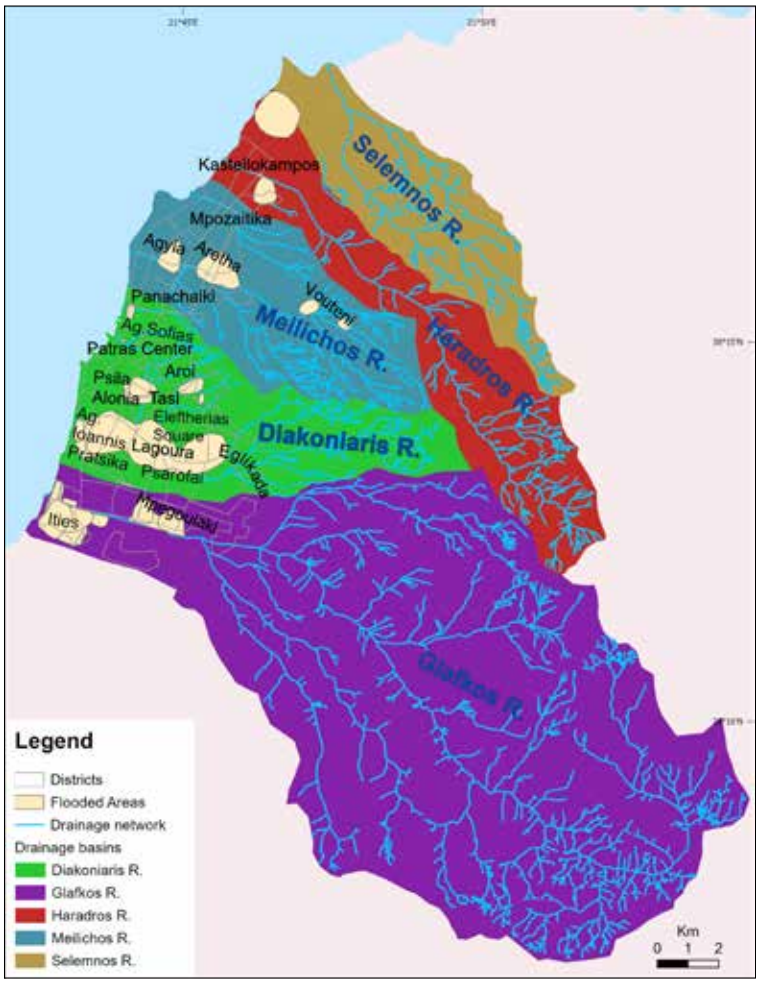

Figure 2. Map of Patras with districts, drainage basins and networks as well as flooded areas.

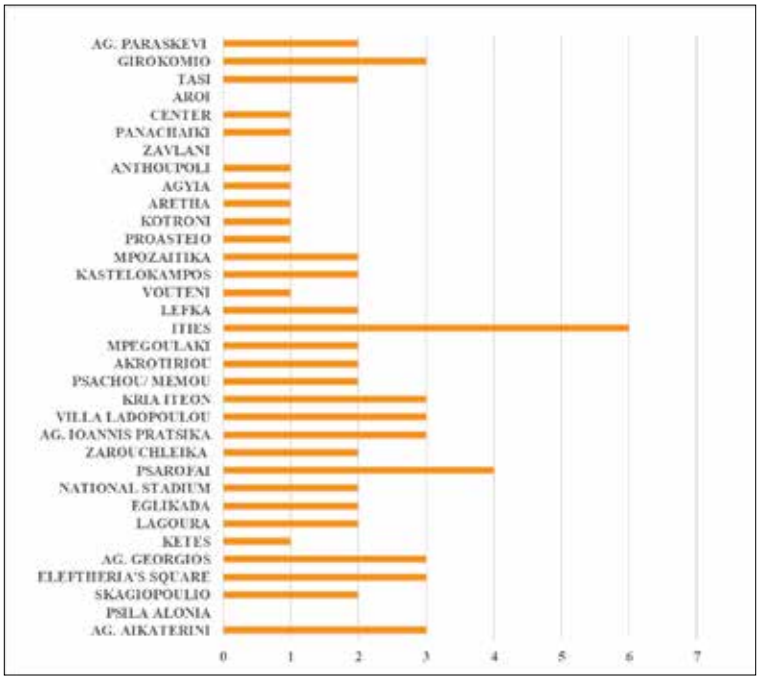

Figure 3. The number of flood events in the districts of Patras.

Figure 4 illustrates the impact of flooding on the Building Cover Ratio (BCR) over the past 115 years. When analyzed alongside the data in Table 1, a clear correlation emerges between the BCR, the extent of the flooded area, and the number of affected buildings in specific years.

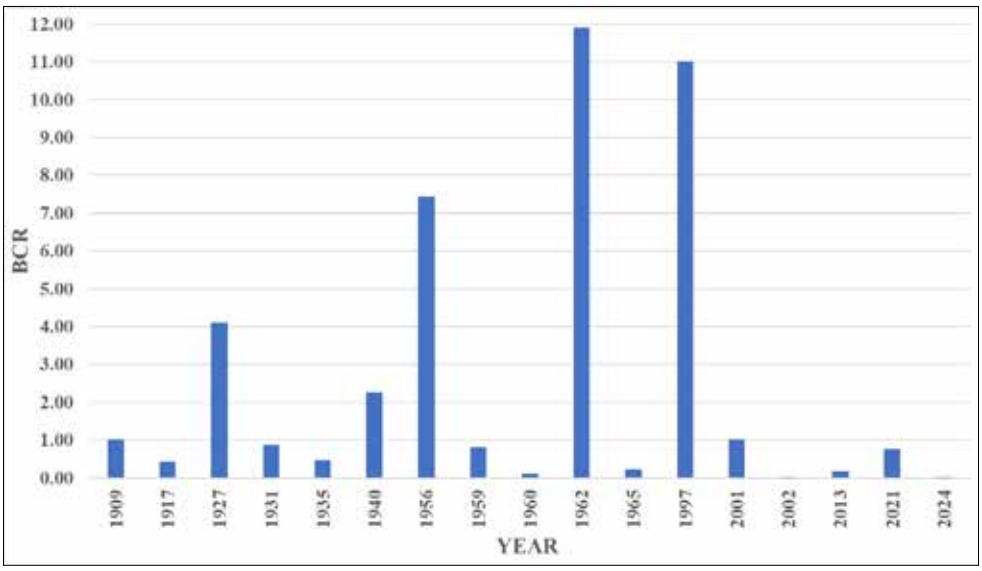

Figure 4. The Building Cover Ratio (BCR) affected by flood over the past 115 years.

Notably, in 1927, the BCR reached a high value of 4.1, which coincided with a significant flooded area of 1.12 km² and a large number of flooded buildings (80). Moreover, in 1956, the BCR was recorded at 7.43, indicating a significant flooding event, with the flooded area extending to 2.03 km² and the number of affected buildings reaching 250, both at considerable levels. In 1962, the BCR reached its peak value of 11.90, corresponding to the largest flooded area of 3.25 km² and the highest number of affected buildings (4,000), marking one of the most catastrophic floods recorded._Similarly, in 1997, the BCR (11.09) was nearly at its peak, corresponding to the flooded area of 3.01 km² and a significant number of affected buildings (1,500). The buildings affected by floods mainly involve basements and ground-floor structures.

Conclusions and discussion

The study of flood events in Patras reveals significant insights into the frequency, impact, and trends over the past 115 years. A total of 20 flooding events were recorded within the drainage basins of Glafkos, Diakoniaris, Meilichos, Haradros, and Selemnos rivers, affecting various districts of Patras.

The year 1962 stands out as the most catastrophic flooding event, followed by 1956 and 1997, with both the flooded area and the number of affected buildings reaching their highest levels. These years highlight the direct relationship between the extent of the flooded area and the resulting damage to infrastructure. While 2001 is the only recorded year with human casualties, emphasizing the severity of the event despite a subsequent reduction in flooded areas.

Ities is identified as the most flood-prone district in Patras, with six recorded flooding events, making it the most severely impacted area. It is worth mentioning, 40% of the regions have experienced flooding more than once, emphasizing the widespread and recurrent nature of the issue.

A distinct relationship is observed between the BCR, the size of the flooded area, and the number of flooded buildings in particular years. The peak BCR of 11.90 was recorded in 1962, coinciding with the largest flooded area of 3.25 km² and the highest number of flooded buildings (4,000).

References

Bathrellos, G., Skilodimou, H., 2006. Geomorphic Hazards and Disasters. Bull. Geol. Soc. Greece, 39 (3), 96–103.

Bathrellos, G.D., 2007. An overview in Urban Geology and Urban Geomorphology. Bull. Geol. Soc. Greece, 40 (3), 1354–1364.

Bathrellos, G.D.; Karymbalis, E.; Skilodimou, H.D.; Gaki-Papanastassiou, K.; Baltas, E.A., 2016. Urban flood hazard assessment in the basin of Athens Metropolitan city, Greece. Environ Earth Sciences, 75(4), 319.

Bathrellos, G.D.; Skilodimou, H.D.; Maroukian, H.; Gaki Papanastassiou, K.; Kouli, K.; Tsourou, T.; Tsaparas, N., 2017. Pleistocene glacial and lacustrine activity in the southern part of Mount Olympus (central Greece). Area, 49 (2), 137-147.

Bathrellos, G. D., Skilodimou, H. D., Soukis, K., Koskeridou, E., 2018. Temporal and spatial analysis of flood occurrences in the drainage basin of pinios river (thessaly, central greece). Land, 7(3), 106.

Copernicus. Urban Atlas 2018. Copernicus Land Monitoring Service, 2021 Available at https://land.copernicus.eu/local/urban-atlas/urban-atlas-2018.

EEA (European Environment Agency), 2024. Economic losses from weather- and climate-related extremes in Europe. Available online: https://www.eea.europa.eu/en.

EM-DAT, 2024. The International Disaster Database. Center for Research on Epidemiology of Disasters. Available online: https://www.emdat.be/ (accessed on 02 December 2024).

Kamberis, E., Bathrellos, G., Kokinou, E., & Skilodimou, H., 2012. Correlation between the structural pattern and the development of the hydrographic network in a portion of the Western Thessaly Basin (Greece). Open Geosciences, 4(3), 416-424.

Kokinou, E.; Skilodimou, H.D.; Bathrellos, G.D.; Antonarakou, A.; Kamberis, E., 2015. Morphotectonic analysis, structural evolution/pattern of a contractional ridge: Giouchtas Mt., Central Crete, Greece. Journal of Earth System Science, 124(3), 587-602.

METEO, 2024. All about weather. Available online: https://www.meteo.gr/weather_cases.cfm (accessed on 22 January 2024).

Migiros, G., Bathrellos, G. D., Skilodimou, H. D., Karamousalis, T. 2011. Pinios (Peneus) River (Central Greece): hydrological—geomorphological elements and changes during the quaternary. Central European Journal of Geosciences, 3, 215-228.

Ministry of Environment and Energy, 2017. Special secretariat for water. Floods, Historic floods., Available online: http://www.ypeka.gr/Default.aspx?tabid=252&language=el-GR (accessed on 03 January 2024).

UEDNPEI, 2014. Press Museum of the Union of Editors of Daily Newspapers of the Peloponnese, Epirus, and the Islands (UEDNPEI). Available online: http://www.mouseiotipou.gr/ (accessed on 10 January 2024).

Skilodimou, H.D.; Bathrellos, G.D.; Maroukian, H.; Gaki-Papanastassiou K., 2014. Late Quaternary evolution of the lower reaches of Ziliana stream in south Mt. Olympus (Greece). Geogr. Fis. Din. Quat. 2014, 37 (1), 43-50.

Skilodimou, H.D., Bathrellos, G.D., Alexakis, D.E., 2021. Flood Hazard Assessment Mapping in Burned and Urban Areas, Sustainability, 13 (8), 4455.

Skilodimou, H. D., Bathrellos, G. D., Pappa, M. I., Youssef, A. M., Kontakiotis, G., Karymbalis, E., 2024. Assessing flood hazard mapping using AHP and GIS in a tectonically active region. Zeitschrift für Geomorphologie. Published online.

17th INTERNATIONAL CONGRESS of the Geological Society of Greece

BULLETIN OF THE GEOLOGICAL SOCIETY OF GREECE, SP. PUBL.

EXTENDED ABSTRACT 006

HOMEROS project for natural hazards: An example from northern Peloponnese, Greece

Andriopoulou-Mounteanou S.A.[1], Bathrellos G.D.[1], Skilodimou H.D.[1], Adamaki A.[2], Anagnostou V.[3], Bitharis S.[3], Bonatis P.[3], Foumelis M.[3], Karakostas V.[3], Karolos I. A.[3], Kaviris G.[4], Kourouklas C.[3], Papadimitriou E.[3], Papageorgiou E.[3], Pikridas C.[3], Sakkas V.[4], Spingos I.[4], Zymvragakis A.[3]

(1) University of Patras, Patras, Greece, geo13014@ac.upatras.gr (2) Lund University, Lund, Sweden, (3) Aristotle University of Thessaloniki, Thessaloniki, Greece, (4) National & Kapodistrian University of Athens, Athens, Greece.

Background

Natural phenomena such as earthquakes, floods, and landslides, which appear throughout geological history, are now classified as natural hazards. These events pose significant risk to human safety on a global scale (Bathrellos and Skilodimou, 2006). Effective planning is essential for minimizing loss of life and reducing the economic impact of these hazards (Bathrellos *et al.,* 2024). Accurate information on the spatial distribution of natural hazards serves as a crucial resource for environmental planners and engineers, helping them identify suitable sites for land use and development (Bathrellos and Skilodimou, 2019).

Natural hazards are complex phenomena, and most published studies have focused on in-depth analyses of individual hazard types (Bathrellos *et al.,* 2016, Karpouza *et al.,* 2021, Skilodimou *et al.,* 2021, Youssef *et al.,* 2024). However, a particular area is rarely affected by only one hazard; instead, multiple hazards may occur simultaneously or consecutively. In such cases, managing separate hazard zones for each type of disaster becomes impractical, especially when multiple hazards must be considered (Bathrellos *et al.,* 2021, Karpouza *et al.,* 2023). The solution to this challenge lies in adopting a multi-hazard analysis, which allows for a comprehensive assessment of various hazard types. Multi-hazard analysis is an essential tool for selecting appropriate land uses and evaluating the vulnerability and risk of urban areas. It plays a critical role in mitigating natural hazards and managing urban disasters (Karpouza *et al.,* 2024).

Objectives

In this context, the HOMEROS project focuses on enhancing multi-hazard assessment approaches within the fields of seismology, geodesy, geology, geomorphology and engineering geology. It utilizes technical solutions tailored to the big data era, marking a major step forward in standardizing research methodologies, fostering collaboration, and improving the understanding and forecasting of natural hazards through Open Science practices. HOMEROS concentrates on high-hazard regions in Greece, characterized by intense seismic activity, floods, and landslides. It consolidates earthquake, ground deformation, flood, and landslide data to offer a comprehensive assessment of these hazards.

This paper provides data and results from the program related to flood events and the production of flood hazard assessment maps in the northern Peloponnese. This work represents an early example of the findings from the HOMEROS project, stemming from the collaboration between the University of Patras, Lund University, Aristotle University of Thessaloniki, and the National and Kapodistrian University of Athens.

Study area

The study area includes the drainage basins of the Xerias, Phoenix, and Peneus rivers, located in the northern Peloponnese region of southern Greece (Fig. 1). The Xerias drainage basin spans 170 km² with a predominantly north-south elongated shape. Similarly, the Phoenix River basin covers around 94 km² and exhibits a southwest-to-northeast elongated orientation. Both river systems drain into the Gulf of Corinth. In contrast, the Peneus River drainage basin, occupying an area of approximately 900 km², extends in an east-west direction. It flows westward and discharges into the Ionian Sea (Fig. 1).

Methods

HOMEROS adopts an innovative approach by leveraging existing data and services from e-science gateways and platforms at multiple levels (national, research infrastructures, or scientific clusters), as well as external resources like Copernicus. It emphasizes the application of FAIR principles in research to deliver new open-access data products.

In this context, data from existing scientific publications were utilized to implement the project. Specifically, HOMEROS incorporated documented flood events that occurred for the period from 1920 to 2021, in the drainage basins of the Xerias, Phoenix, and Peneus rivers (Fig. 2), as reported by Bathrellos *et al.* (2017), Skilodimou *et al.* (2024) and Skilodimou *et al.* (2019), respectively. Additionally, it utilized information from these works concerning the applied methodologies and flood hazard assessment maps.

Figure 1. The study area comprises the drainage basins of the Xerias, Phoenix, and Peneus rivers.

Five key factors have been identified as the most significant in influencing flood events. These factors include slope, elevation, hydro-lithology, distance to streams, and land use. The Analytical Hierarchy Process (AHP) was integrated with Geographic Information System (GIS) to facilitate the assessment of the chosen factors employed in the production of the flood hazard assessment maps.

Figure 2. Flood events in the drainage basins of the Xerias, Phoenix, and Peneus rivers.

Results

The recorded number of past flood events for each drainage basin is as follows: ten for the Xerias River, eleven for the Phoenix River, and eight for the Peneus River.

The flood hazard assessment maps for the three drainage basins were categorized into five levels of flood hazard: very low, low, moderate, high, and very high (Bathrellos et al., 2016, Skilodimou et al., 2021). As stated by Bathrellos *et al.* (2017), the northern and central regions of the Xerias drainage basin have the most extensive coverage of very high and high flood hazard zones. The moderate hazard zone is primarily located in the northeastern and central parts of the basin, whereas the low and very low hazard zones are concentrated in the southern region (Fig. 3).

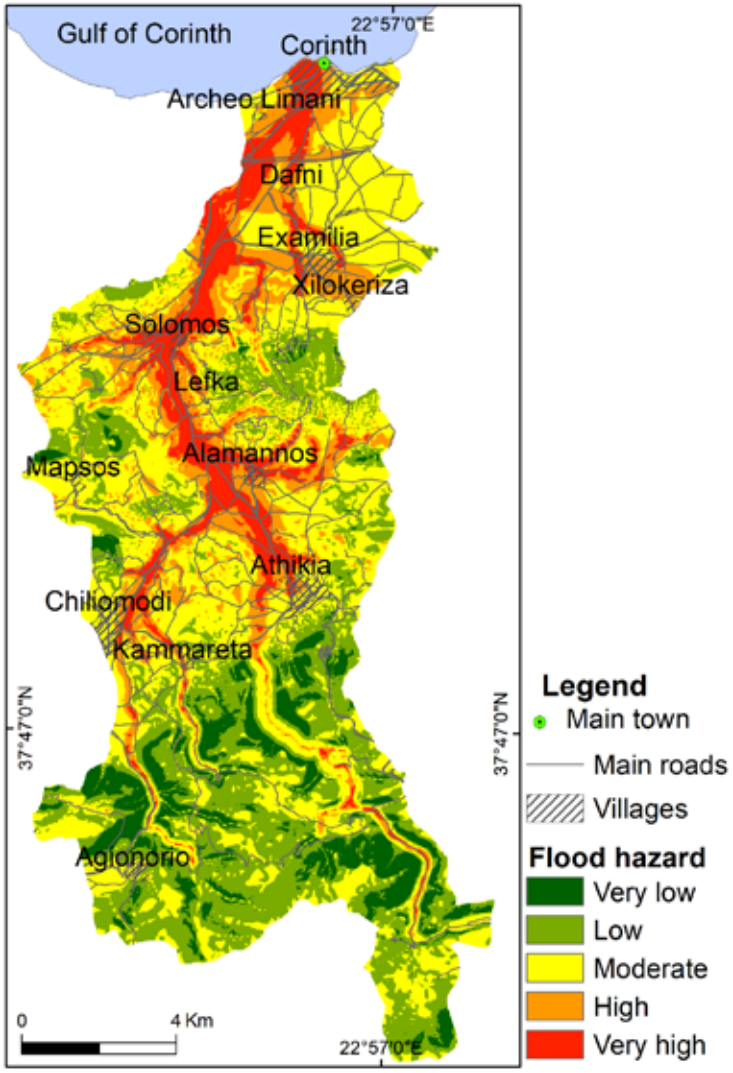

Figure 3. The flood hazard assessment map in the drainage basin of the Xerias River.

The high and very high hazard zones are mainly located along the mainstream of the Xerias drainage network and at the points where it intersects with major tributaries. Notably, most of the recorded flood events in the study area occur within the very high and high flood hazard zones. The lowland terrain, gentle slopes, presence of impermeable formations, and urbanization of these areas contribute to increased surface runoff, creating conditions that are more prone to flooding.

According to Skilodimou *et al.* (2024), the very high and high flood hazard zones are mainly found in the northern and central parts of the Phoenix drainage basin, along the mainstream channel of the drainage network. The moderate hazard zone is largely concentrated in the central area, extending into the northern, western, and southern areas. In contrast, the southern, western, and eastern parts of the study area include many locations within the low and very low hazard zones (Fig. 4).

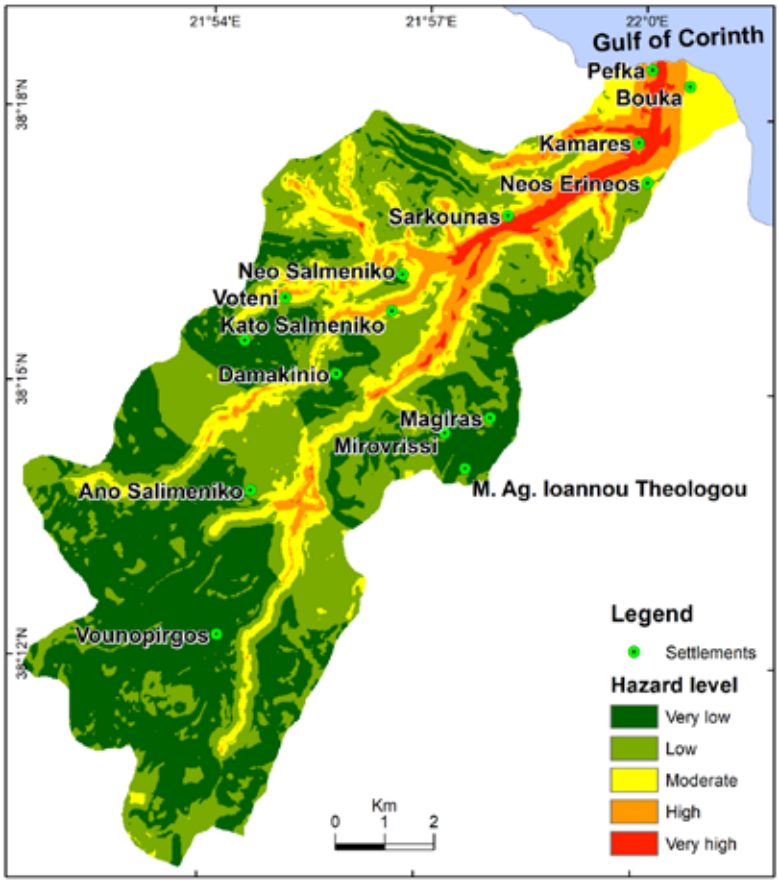

Figure 4. The flood hazard assessment map in the drainage basin of the Phoenix River.

The relatively small size of the Phoenix River drainage basin, along with its ephemeral streams, plays a key role in influencing flood events within the study area. Furthermore, the constricted artificial riverbed in the river's downstream sections, caused by agricultural and urban activities, disrupts the river's natural flow patterns and contributes to flooding incidents.

As reported by Skilodimou et al. (2019), the western, northern, and southwestern parts of the Peneus drainage basin include areas most susceptible to flooding, primarily along the mainstream of the Peneus drainage network. The moderate hazard zone is situated in the western and northern sections of the basin, while the low and very low hazard zones are found in the southern and eastern parts of the area (Fig. 5).

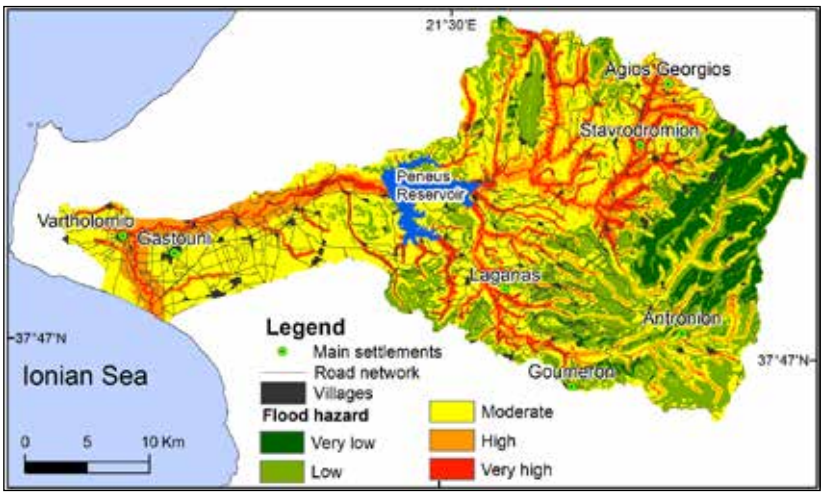

Figure 5. The flood hazard assessment map in the drainage basin of the Peneus River.

Land use changes in areas impacted by extensive fires have contributed to an increase in flood events. Additionally, the constricted artificial riverbed in the lower reaches of the Peneus River, resulting from agricultural land use and urban development, significantly disrupts the natural flow dynamics and exacerbates flooding.

Table 1 displays the percentage of area covered by each flood hazard zone for the Xerias, Phoenix, and Peneus drainage basins.

Table 1. The percentage of area for each flood hazard zone for the Xerias, Phoenix, and Peneus drainage basins.

	Xerias drainage basin	Phoenix drainage basin	Peneus drainage basin
Flood hazard zone	**Area (%)**		
Very low	9	38	8
Low	27	36	24
Moderate	40	16	39
High	15	8	20
Very high	9	2	9

In the Xerias drainage basin, the very high and high flood hazard zones cover a significant portion, making up about one-quarter of the basin. In comparison, the Phoenix drainage basin has a much smaller coverage, with these two zones spanning only 10% of the area. The Peneus drainage basin, however, has the largest extent, with the very high and high hazard zones covering approximately one-third of the basin.

Conclusions

The total number of past flood events across the drainage basins of the Xerias, Phoenix, and Peneus rivers amounts to twenty-nine. The northern and central areas of the Xerias and Phoenix drainage basins are the most flood-prone, while the western, northern, and southwestern regions of the Peneus drainage basin are particularly vulnerable to flooding. Among the three drainage basins, the Peneus drainage basin has the largest areas classified as very high and high flood hazard zones.

The gentle slopes and widespread urban development of the lowland areas in the Xerias drainage basin play a role in flooding. In the downstream sections of the Phoenix River drainage basin, the narrow artificial riverbed, shaped by agricultural and urban activities, also contributes to flooding. Changes in land use in regions affected by extensive fires have led to an increase in flooding events in the Peneus drainage basin.

Acknowledgements

The authors acknowledge the OSCARS project, which has received funding from the European Commission's Horizon Europe Research and Innovation programme under grant agreement No. 10112975.

References

Bathrellos, G., Skilodimou, H., 2006. Geomorphological Hazards and Disasters. Bulletin of the Geological Society of Greece, 39(3), 96-103.

Bathrellos, G.D., Skilodimou, H.D., 2019. Land Use Planning for Natural Hazards. Land, 8(9), 128.

Bathrellos, G.D., Karymbalis, E., Skilodimou, H.D., Gaki-Papanastassiou, K., Baltas, E.A., 2016. Urban flood hazard assessment in the basin of Athens Metropolitan city, Greece. Environmental Earth Sciences, 75(4), 319.

Bathrellos, G. D., Skilodimou, H. D., Chousianitis, K., Youssef, A. M., Pradhan, B., 2017. Suitability estimation for urban development using multi-hazard assessment map. Science of the Total Environment, 575, 119-134.

Bathrellos, G. D., Skilodimou, H. D., Zygouri, V., Koukouvelas, I. K., 2021. Landslide: A recurrent phenomenon? Landslide hazard assessment in mountainous areas of central Greece. Zeitschrift für Geomorphologie, 63, 95-114.

Bathrellos, G. D., Koukouvelas, I. K., Skilodimou, H. D., Nikolakopoulos, K. G., Vgenopoulos, A. L., 2024. Landslide causative factors evaluation using GIS in the tectonically active Glafkos River area, northwestern Peloponnese, Greece. Geomorphology, 109285.

Karpouza, M., Chousianitis, K., Bathrellos, G.D., Skilodimou, H.D., Kaviris, G., Antonarakou, A., 2021. Hazard zonation mapping of earthquake-induced secondary effects using spatial multi-criteria analysis. Natural Hazards, 109, 637-669.

Karpouza, M., Bathrellos, G. D., Kaviris, G., Antonarakou, A., Skilodimou, H. D., 2023. How could students be safe during flood and tsunami events? International Journal of Disaster Risk Reduction, 95, 103830.

Karpouza, M., Skilodimou, H. D., Kaviris, G., Zymvragakis, A., Antonarakou, A., Bathrellos, G. D., 2024. Escape routes and safe points in natural hazards. A case study for soil. Engineering Geology, 340, 107683.

Skilodimou, H.D., Bathrellos, G.D., Chousianitis, K., Youssef, A.M., Pradhan, B., 2019. Multi-hazard assessment modeling via multi-criteria analysis and GIS: A case study. Environmental Earth Sciences, 78(2), 47.

Skilodimou, H. D., Bathrellos, G. D., Alexakis, D. E., 2021. Flood hazard assessment mapping in burned and urban areas. Sustainability, 13(8), 4455.

Skilodimou, H. D., Bathrellos, G. D., Pappa, M. I., Youssef, A. M., Kontakiotis, G., Karymbalis, E., 2024. Assessing flood hazard mapping using AHP and GIS in a tectonically active region. Zeitschrift für Geomorphologie. Published online.

Youssef, A.M., El-Haddad, B.A., Skilodimou, H.D. Bathrellos, G. D., Golkar, F., Pourghasemi, H. R., 2024. Landslide susceptibility, ensemble machine learning, and accuracy methods in the southern Sinai Peninsula, Egypt: Assessment and Mapping. Natural Hazards 120, 14227–14258.

17th INTERNATIONAL CONGRESS of the Geological Society of Greece

BULLETIN OF THE GEOLOGICAL SOCIETY OF GREECE, SP. PUBL.

EXTENDED ABSTRACT 007

Digital Visualization of Geological Heritage at Lesvos UNESCO Global Geopark: The Role of 3D Animations in Educational Experiences

Antonakis Emmanouil 1, Nicholas Zouros 2
(1) University of the Aegean, Mytilene, Greece, manolis.antonakis@rocketmail.com (2) University of the Aegean, Mytilene, Greece

Introduction / Background

In this paper, we use 3D animation technologies to visualize, interpret and communicate geological heritage in Lesvos UNESCO Global Geopark. Our objective is to make geological heritage more accessible to the general public. 3D animations have been utilized as a means to periodically monitor and document changes in geological sites over time, supporting conservation initiatives. Additionally, they can replicate geological events, describe the formation and evolution of landscapes, simulate how we believe paleoenvironments looked for a holistic learning experience. Their interactive and dynamic nature can boost engagement and facilitate learning in an educational context, while it can also engage tourists by offering previews, virtual tours of inaccessible or fragile sites. In this paper, we select 21 case studies of geosites or monuments of geological heritage to 3D geo-visualize. The selection method is based on three criteria: accessibility, supervision and relief of the geosite out of the total number of 151 designated geosites of the Geopark. The results were verified with a pilot study to participants of environment educational programs in the Natural History Museum of Lesvos Petrified Forest in 2024. . Overall, the approach promotes visitor democracy, as all groups have access to the visualized geosites and can be used to further improve the visibility of the geosites and that of the Geopark.

Objectives

In this paper, we use 3D animation technologies to visualize, interpret and communicate geological heritage of Lesvos UNESCO Global Geopark. Our objective is to make geological heritage more accessible to the general public.

Methodology

This research included the creation of 3D animation in Google Earth Studio to introduce the most important geosites within Lesvos UNESCO Global Geopark, it was divided into four topics: geosite selection, data collection and preparation, animation creation and visualizations evaluation. The main goal is to use these 3D animations in educational activities for students and non-experts.

Selection of Geosites:

The first phase involved identifying key geosites within the Lesvos UNESCO Global Geopark that would benefit from enhanced visual representation. Criteria for selection included accessibility of Geosite, Supervision of the location of the geosite,, and The topography of a geosite's location. Key sites, such as volcanic formations, petrified parks, and notable tectonic features, were chosen to highlight the geological diversity of the region.

Data Collection and Preparation:

for each selected geosite, topographic and geological data were gathered to accurately represent the site in 3D animation. Sources included geological maps, high-resolution satellite imagery, and geospatial data accessible through Google Earth. Historical and interpretive information on each site was also collected to provide context for the animations.

Animation Development with Google Earth Studio:

Using Google Earth Studio, each geosite was visualized in a sequence of animations. The development process included defining camera paths to capture distinct perspectives, zooming into details of geological formations, and incorporating dynamic movements to simulate real-world exploration. Attention was given to camera angles and framing to ensure that animations were both engaging and informative.

For added educational value, labels, annotations, and shapes were embedded directly in the animations, highlighting significant geological features and processes relevant to each site. This interactive approach aimed to increase viewer comprehension of the complex geological structures and their historical importance.

Evaluation of Visualizations:

The educational activities focus on presenting complex geosites with one more easy and interactive way. After completing the educational activity, we made it for students and educators. The users give us feedback through questionaries. was collected to assess the animations' comprehensive, engaging, and educational impact, The responses guided further refinements, with adjustments made to optimize the balance between scientific accuracy and accessibility for a non-specialist audience.

Dissemination and Public Engagement:

The finalized 3d animation were presented to students and public due to guided tour in fieldtrips in Lesvos UNESCO Global Geopark and in educational trips at Natural History Museum of the Petrified Forrest of Lesvos, also were shared through the official Lesvos UNESCO Global Geopark website and social media platforms to reach a wider audience. By incorporating Google Earth Studio's animations, the project aimed to make complex geological phenomena more comprehensive and engaging for the public, fostering a broader appreciation of Lesvos's geological heritage.

This methodology demonstrates a structured approach to utilizing 3D animation as a powerful tool for geosite interpretation and education, highlighting the potential of Google Earth Studio to enhance public understanding of geological heritage sites.

Table 1 Methodology Flowchart

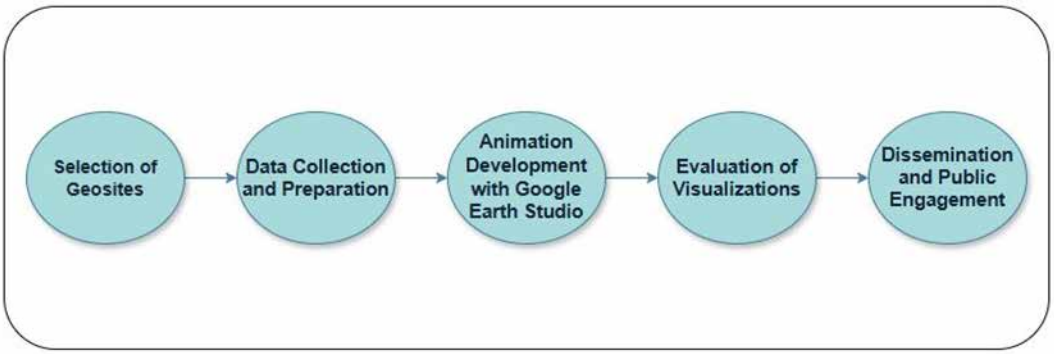

The study area

Lesvos UNESCO Global Geopark has a unique wealth of geological monuments and landscapes of natural beauty, habitats and cultural monuments which have contributed to its recognition and inclusion in the Global Geoparks Network of UNESCO.

In its western part, the Petrified Forest dominates, a unique piece of geological history, which has been declared a "Preservable Monument of Nature". Lesvos is scattered with a multitude of geological monuments and landforms of unique value and importance. Some of them are impressive volcanoes, hot springs, important fossil sites, large geological faults, waterfalls, coastal landforms that are important evidence of geological history that testify to the evolution of the Aegean basin.

The geosites: selection process

In this paper, we select 21 case studies of geosites or monuments of geological heritage to 3D geo-visualize. The selection method is based on three criteria: accessibility, supervision and relief of the geosite out of the total number of 151 designated geosites of the Geopark.

Geological Heritage, Education, and Geotourism

Geological heritage encompasses the unique geological formations, landscapes, and features that hold scientific, educational, and cultural significance. The integration of geological heritage into education fosters a deeper understanding of Earth's processes, history, and conservation needs. Geotourism, which focuses on showcasing geological attractions, bridges education and sustainable tourism by engaging visitors in immersive, place-based learning experiences. By blending science with storytelling, geotourism not only raises awareness about geological phenomena but also supports the local economy and conservation efforts, creating a holistic approach to promoting and preserving geosites like the Lesvos UNESCO Global Geopark.

3D Tools and Geoheritage

Digital tools, particularly 3D technologies, have revolutionized the way geological heritage is presented and understood. Otherwise, 3D animations, virtual reconstructions, and interactive visualizations, it is possible to bring to life geological features and processes that are otherwise inaccessible or difficult to comprehend. In the context of Lesvos UNESCO Global Geopark, these tools offer a dynamic platform for engaging educational experiences, allowing students and visitors to explore virtual landscapes, simulate volcanic activity, or visualize tectonic faults. This innovative approach not only enhances learning but also deepens appreciation for geoheritage by making abstract or hidden processes tangible and memorable.

Results

In this study, a total of 225 students and educators from Greece and other EU countries were surveyed during their visit to the Natural History Museum of the Lesvos Petrified Forest and various geosites within the Lesvos UNESCO Global Geopark. These participants were provided with scientific information regarding the geological heritage of the area, with the consideration of 3D geosite animations incorporated into the presentations to facilitate enhanced comprehension of the geosites. After the educational activity the users asked questionnaires, the findings of the study indicated the following:

To the question "On a scale of 1 to 5, how understandable was the concept of a geosite » 54% of respondents reported that the use of 3D animations made geosites highly comprehensive, while 33% found them very comprehensive.

Table 3 Methodology Flowchart

Discussion

The implementation of 3D animations through Google Earth Studio as educational tool for geosites within the Lesvos UNESCO Global Geopark has provided significant insights into the potential of digital tools for geoheritage promotion and education in other geoparks. This discussion addresses the benefits, challenges, and future implications of using this approach in geoscientific communication.

Enhanced Public Engagement and Education

Mixing geoeducation with the tours is an optimal way to keep tourism interesting. the tour guide and educational boards play an important role (Wang et al., 2023) The results demonstrate that 3D animations can serve as an effective tool for increasing public interest and comprehension of complex geological processes and formations. By offering an immersive, interactive view of geosites, animations make the scientific details of the landscape accessible to a broader audience, including those with limited geoscientific knowledge. Enhanced engagement aligns with findings in prior studies, where 3D visualization has been shown to effectively support educational initiatives in geoparks and geoscience education more generally.

Accessibility and Preservation of Geoheritage

The virtual nature of 3D animations also addresses key challenges in geoheritage conservation. By providing virtual access to sensitive or inaccessible areas, these animations help minimize the environmental impact of tourism, reduce the risk of physical degradation, and allow continuous public engagement without compromising the integrity of the geosites. This approach aligns with current geoheritage conservation goals, which advocate for minimal environmental impact while promoting public awareness and educational

outreach. Virtual flights over larger territories, supported by relevant commentaries highlighting relationships between nature and humans, may in turn be an attractive means to become acquainted with areas which lack singular spectacular sites (Migoń and Pijet-Migoń, 2024)

Technical and Methodological Limitations

Despite the successes observed, google earth is not perfect there exist several limitations, that is the inconsistent quality of images, insufficient capability for quantitative measurement (Yu and Gong, 2012),

lack of analytical functionalities, the study faced limitations in terms of data resolution and platform capabilities. Google Earth Studio, while powerful, has constraints regarding data detail and may not fully capture subtle geological features. Future studies could explore supplementary tools like high-resolution GIS mapping software or custom 3D modeling to complement Google Earth Studio, thus enhancing the accuracy of the representations. Additionally, labeling and annotation tools within Google Earth Studio could be expanded to improve the educational value of animations.

Future Research and Practical Applications

The use of 3D animation for geoheritage could be expanded in future research to include more comprehensive datasets, interdisciplinary collaborations. Also, it can be a useful tool for geoparks with hard accessible and fragile geosites.highlighting the role of 3D animations in geoheritage education and conservation.

However, it could further elaborate on the specific technical constraints of Google Earth Studio. For example, while the paper mentions data resolution issues, a deeper analysis of how these limitations affect the accuracy of geological feature representations such as fine-scale in different variations or subtle geomorphological changes—would be beneficial. Additionally, a comparison with alternative 3D modeling tools, such as GIS-integrated software or photogrammetry-based reconstructions, could provide a more comprehensive perspective on the advantages and trade-offs of the chosen methodology.

Furthermore, expanding the future research directions section to explore AI-driven enhancements, such as machine-learning-assisted geosite identification or automated annotation features, could significantly enhance the study's impact. Integrating AI could help refine data visualization, allowing for real-time user interaction and adaptive learning experiences tailored to different audiences. These aspects would not only strengthen the study's contribution to digital geoheritage visualization but also position it within the broader context of emerging technologies in geoscience education.

Conclusion

This study highlights the strong potential of using 3D animations as educational tools for geoheritage promotion, offering a way to communicate advanced geological science contents in an effective and enjoyable manner that can effectively engage the public in learning about culturally complex geological knowledge. Considering these benefits, while digital solutions will remain a powerful asset in the future of geoscience education and conservation, both technical innovations and methodological optimizations are necessary to enhance the impact of such visualizations. The combinations of Guided tour with 3D animation it can be an educational approach, and it can contribute to geological heritage management for fragile and inaccessible geosites.

Overall, the approach promotes visitor democracy, as all groups have access to the visualized geosites and can be used to further improve the visibility of the geosites and that of the Geopark

References

Migoń, P. and Pijet-Migoń, E. (2024) 'Non-Uniform Distribution of Geoheritage Resources in Geoparks—Problems, Challenges and Opportunities', Resources, 13(2). doi: 10.3390/resources13020023.

Wang, Y. et al. (2023) 'From Geoparks to Regional Sustainable Development: Geoheritage Protection and Geotourism Promotion of Geoparks in Hebei Province, China', Geoheritage. Springer Berlin Heidelberg, 15(3). doi: 10.1007/s12371-023-00870-5.

Fassoulas, C., Nikolakakis, E. and Staridas, S. (2022) 'Digital Tools to Serve Geotourism and Sustainable Development at Psiloritis UNESCO Global Geopark in COVID Times and Beyond', pp. 1–22.

Wang, J. and Zouros, N. (2021) 'Educational Activities in Fangshan UNESCO Global Geopark and Lesvos Island UNESCO Global Geopark', Geoheritage. Springer Berlin Heidelberg, 13(3), pp. 1–16. doi: 10.1007/s12371-021-00570-y.

Yu, L. and Gong, P. (2012) 'Google Earth as a virtual globe tool for Earth science applications at the global scale: progress and perspectives', International Journal of Remote Sensing, 33(12), pp. 3966–3986. doi: 10.1080/01431161.2011.636081.

Pringle, H. (2010) 'Google earth shows Clandestine worlds', Science, 329(5995), pp. 1008–1009. doi: 10.1126/science.329.5995.1008.

Zouros N and Valiakos I (2010) 'Geoparks management and assessment', Bulletin of the Geological Society of Greece, XLIII(2), pp. 965–975. Available at: www.europeangeoparks.org.

SHARPLES, C. (2007) 'Geoconservation in forest management-principles and procedures.', Research Gate, 62(December 1995), pp. 37–50.

17th INTERNATIONAL CONGRESS of the Geological Society of Greece

BULLETIN OF THE GEOLOGICAL SOCIETY OF GREECE, SP. PUBL.

EXTENDED ABSTRACT 008

Land Subsidence and Flooding in the East Thessaly Plain: A Historical Overview

Antoniadis N.1, Loupasakis C.1
(1) School of Mining & Metallurgical Engineering, National Technical University of Athens, nikolaosantoniadis@metal.ntua.gr

Background

The East Thessaly Plain, a critical region for agricultural production in Greece, has a rich and complex geological and hydrological history that has shaped its current environmental and socio-economic landscape. Prehistorically, Lake Voivida, a vast body of water, covered the Plain and influenced early human settlements (Thermou, 2023). Over centuries, the lake experienced fluctuating water levels, with humans adapting to the changing environment. The region's evolution saw a transition from lake-based ecosystems to large-scale agricultural land use, particularly as drainage and flood management projects were implemented in the late 19th and early 20th centuries. In the 1960s and 1970s, rapid agricultural expansion, combined with intensive groundwater extraction for irrigation, led to significant hydrological changes. As a result, the East Thessaly Plain became one of the most important agricultural areas in Greece, contributing significantly to the country's grain production. However, this transformation came at a significant environmental cost, including land subsidence, water shortages, and vulnerability to flooding (Arapostathis et al., 2024). In recent decades, the Plain has experienced recurring land subsidence, particularly in areas that rely heavily on groundwater for irrigation. These subsidence phenomena, linked by the overexploitation of the aquifers, have been influenced by extreme weather events, including the 2023 Daniel storm, which caused widespread flooding and infrastructural damage. The interaction between land subsidence, flooding, and land use changes, compounded by climate change, has created a complex set of challenges for the region's future.

Objectives

This paper aims to provide a comprehensive historical overview of the evolution of the East Thessaly Plain emphasizing on the land subsidence, as well as explore its interaction with flooding events, land use changes, and extreme storms, particularly in the context of the intensification of agricultural practices over the past century. The study draws upon existing research, reports, satellite-based InSAR data, and historical accounts.

Methods

A detailed review of historical documents, archaeological excavations, and scientific literature has been conducted to track the region's evolution from prehistoric lake systems to modern agricultural landscapes. Key sources include studies of early human settlements in Thessaly, geological, geotechnical and geophysical surveys, and flood records. The study incorporates data from geological surveys, such as reports conducted by the Hellenic Survey of Geology and Mineral Exploration (HSGME), Central Laboratory Public Works (KEDE), as well as reports from the Ministry of Environment and Energy of Greece.

Open-access InSAR (Interferometric Synthetic Aperture Radar) products, such as Copernicus European Ground Motion Service have been used to track land subsidence over the last decade, providing a unique opportunity to assess the long-term impacts of groundwater extraction and flooding phenomena on the region's land stability.

Field surveys and ground-based observations have been combined with remote sensing data to assess the physical and hydrological changes in the East Thessaly Plain, focusing on key areas such as Larissa, Tyrnavos, and Velestino. This multi-method approach allows for a more comprehensive understanding of the historical and ongoing processes affecting the region.

Results

The results of the study reveal a clear relationship between land subsidence, changes in land use, and extreme weather events. Historical records suggest that the area has long been subject to fluctuating surface water levels, with periods of lake expansion and contraction. The draining of Lake Karla in 1962, which transformed large parts of the Thessaly Plain into cultivated land, marked a significant turning point in the region's hydrological history. This, along with the intensification of irrigation practices, created a situation where groundwater extraction reached unsustainable levels, leading to the onset of land subsidence.

Satellite-based InSAR data has shown that subsidence is most pronounced in areas that experienced intensive groundwater extraction, with significant subsidence recorded in the regions of Larissa and Tyrnavos. The rate of subsidence has increased since the 1990s, coinciding with the period of progressive intensification of agricultural practices in the region. InSAR data also highlights that the subsidence is not uniform, with certain areas showing localized shifts in the ground level that correspond with faults and tectonic zones (Fakhri & Kalliola, 2015; Parcharidis et al., 2011; Vassilopoulou et al., 2013). Land subsidence phenomena are still ongoing as shown by the European Ground Motion Service's products (Figure 1).

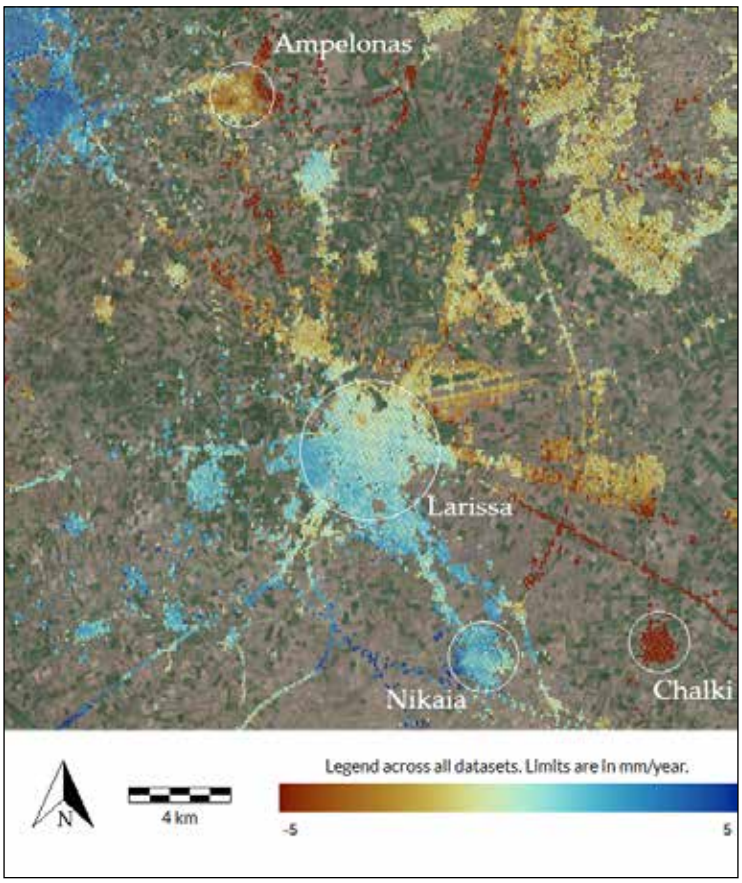

Figure 1. Ground deformation phenomena in the greater area around Larissa from EGMS Copernicus

Field surveys and studies reported land subsidence phenomena in several villages such as Rizomylos, Stefanovikeio, Kastrio, Melia, and Niki, where the drop in the water table reached up to 35 meters by the early 1990s (Soulios, 1997), while similar patterns have been identified in the villages of Halki and Magoula (Kaplanides A. & Fountoulis D., 1997). Land subsidence has also been observed in the Karla area, where excessive groundwater extraction took place. Marginal fractures appeared as the thickness of

the Quaternary sediments diminished (Rozos, 2007). These findings were aligned with tectonic patterns in the region, where subsidence appeared more pronounced along fault zones, suggesting a combination of natural tectonic activity and human-induced groundwater extraction as primary contributors to subsidence in the region.

On the other hand, flooding events, particularly those caused by extreme storms like the Daniel storm in 2023, have further affected the impact of subsidence on the region. These floods have caused widespread inundation, damaging infrastructure and agricultural land. The interaction between land subsidence and flooding is particularly problematic in areas with poor drainage systems, such as the Lake Karla area, where water remains stagnant for extended periods after heavy rainfall.

Conclusions

The East Thessaly Plain's evolution has been shaped by a complex interaction between geological processes, human activity, and climate change. The expansion of irrigation systems and exploitation of the underground water have transformed the Plain into one of the most productive agricultural regions in Greece. However, this transformation has come at the cost of land subsidence, which has been exacerbated by groundwater overexploitation. The review underscores the need for more sustainable water management practices to mitigate further subsidence and flooding risks. The integration of satellite-based monitoring techniques like InSAR offers a powerful tool for tracking ground deformation and assessing the long-term impacts of land use changes.

The findings highlight the importance of continued monitoring of groundwater levels and the implementation of flood control measures to protect the agricultural productivity of the East Thessaly Plain. Furthermore, the ongoing challenges posed by land subsidence and extreme weather events underscore the need for adaptive strategies to address the evolving risks associated with climate change and urbanization in the region. The study also calls for further research into the interactions between groundwater extraction, land subsidence, and storm-related flooding to develop more comprehensive and effective risk management strategies for the future.

Acknowledgements

This publication has been prepared using the European Union's Copernicus Land Monitoring Service information (https://egms.land.copernicus.eu/). The key elements of the European Ground Motion Service (EGMS) are stated in the White Paper, available online at https://land.copernicus.eu/user-corner/technical-library/egms-white-paper (EU-GMS Task force, 2017).

References

EU-GMS Taskforce. (2017). *EGMS White Paper*. https://land.copernicus.eu/en/products/european-ground-motion-service/egms-white-paper

Fakhri, F., & Kalliola, R. (2015). Monitoring ground deformation in the settlement of Larissa in Central Greece by implementing SAR interferometry. *Natural Hazards*, *78*(2), 1429–1445. https://doi.org/10.1007/s11069-015-1779-6

Kaplanides A., & Fountoulis D. (1997). Subsidence phenomena and ground fissures in Larissa, Karla basin, Greece: their results in urban and rural environment. In P. Marinos, G. Koukis, G. Tsiambaos, & G. Sambatakakis (Eds.), *Eng Geol Environ* (pp. 729–735). Balkema.

Parcharidis, I., Foumelis, M., & Katsafados, P. (2011). Seasonal ground deformation monitoring over Southern Larissa Plain (Central Greece) by SAR interferometry. In *Advances in the Research of Aquatic Environment* (pp. 497–504). Springer Berlin Heidelberg. https://doi.org/10.1007/978-3-642-24076-8_58

Soulios, G. (1997). Subsidence de terrains alluviaux dans le sud-est de la plaine de Thessalie. *International Symposium on Engineering Geology and the Environment*, 1067–1072.

Vassilopoulou, S., Sakkas, V., Wegmuller, U., & Capes, R. (2013). Long term and seasonal ground deformation monitoring of Larissa Plain (Central Greece) by persistent scattering interferometry. *Open Geosciences*, *5*(1). https://doi.org/10.2478/s13533-012-0115-x

Arapostathis, E., Vlachos, G., Gousios, D., Danalatos, N., Hliou, N., & Tsimpoukas, K. (2024). *AGRICULTURAL DEVELOPMENT PLAN OF THESSALY*. (in Greek) https://www.thessaly.gov.gr/images/right/sxedio.pdf

Thermou, M. (2023, September 15). *Same picture: The Thessaly plain today, as it was 10,000 years ago*. (in Greek) Mononews. https://www.mononews.gr/politismos/idia-ikona-o-thessalikos-kampos-simera-opos-prin-apo-10-000-chronia

Rozos, D. (2007). *Engineering Geology I - Manual, Landslides - Land subsidence - Settlements*. Department of Geological Sciences, Laboratory of Engineering Geology and Hydrogeology, School of Mining and Metallurgical Engineering, NTUA.

17th INTERNATIONAL CONGRESS of the Geological Society of Greece

BULLETIN OF THE GEOLOGICAL SOCIETY OF GREECE, SP. PUBL.

EXTENDED ABSTRACT 009

Geological suitability in remote mountainous settlements using the AHP method. The case study of the settlement of Klepa in Greece

Antonopoulou A.[1], Depountis N.[1], Kokkalas S.[1]*
*(1) Department of Geology, University of Patras, 26504 Patras, Greece. *up1065387@ac.upatras.gr*

Research Highlights: **GIS-based Analytical Hierarchy Process (AHP) for geological suitability evaluation in remote mountainous settlements**

Introduction

The evaluation of geological suitability is crucial in managing and planning residential development in settlements, where geological conditions are harsh, and accessibility is limited. This becomes even more critical in areas affected by geohazards, such as landslides that primarily occur in remote mountainous regions due to their complex terrain, geological characteristics, and human activities. These studies are compulsory in every case of urban planning or demarcation of a settlement and aim to safeguard the built environment from natural hazards or hazards resulting from human intervention and activities (Depountis, 2023).

Focusing on mountainous remote settlements influenced by landslide events, this study employs a GIS-based multicriteria analysis using the Analytical Hierarchy Process (AHP) to evaluate geological suitability. This methodology incorporates various geological factors affecting the study area to produce a suitability map and categorize existing settlement conditions into safe or unsafe building zones. The Analytical Hierarchy Process (AHP) assigns certain weights to the chosen criteria and spatial datasets are produced within a GIS environment to create a geological suitability map that identifies optimal areas for development; thus, categorizing them as suitable, unsuitable, or suitable under specific conditions.

Background

The settlement of Klepa, located in the Central Western Greece, belongs to the regional unit of Aitoloakarnania. The geology of the study area is characterized by the presence of Alpine bedrock, specifically the Pindos unit. The formations in the study area are primarily comprised of flysch, limestone and cherts. In addition, Quaternary deposits are present, including fluvial deposits, scree and landslide materials.

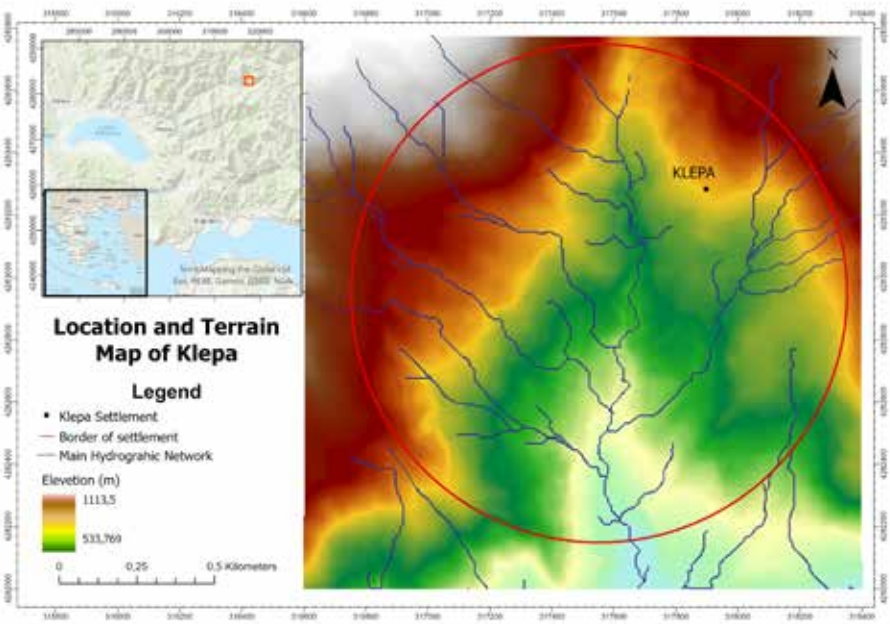

Figure 1. Location and terrain map of the study area.

The landslide problem in the wider area of Klepa is well-known and has been repeatedly examined by the Hellenic Survey of Geology and Mineral Exploration. In particular, the area has recorded activations of old or recent landslides at least four times in the last 35 years, with the most recent and severe occurred in 2015. The impact of landslides was severe, destroying several houses and a section of the provincial road about 120 meters long.

Methodology

The methodology of this study is divided into four key phases: a) criteria selection, b) AHP application, c) spatial analysis and standardization, and d) suitability assessment. The criteria were selected from the study by Depountis (2023), which proposes an outline for the application of various parameters for MCE suitability related to different land uses. The selected criteria are (1) Geohazards/Landslides, (2) Geomorphology/ Slope, (3) Geology/Lithology, (4) Hydrology/Rivers, (5) Ground Seismicity Hazard and (6) Tectonics/Faults. The current study employs the Analytic Hierarchy Process by Saaty (1980), a multicriteria decision method that uses eigenvalue theory to compute weights and maintain consistency in pairwise comparisons. The AHP is a comprehensive measurement theory, which allows the creation of ratio scales through comparison of discrete and continuous variables (Hajar, 2017) and is a globally recognized technique aiding in risk assessment and mitigation planning (Mokhtari et al., 2023).

The pairwise comparison of the chosen criteria was performed to assess their relative importance to a defined objective, using Saaty's weighting scale 1-9. After the process of the matrix's normalization to ensure logical consistency, the Consistency Ratio (CR) is calculated, which includes the following indices:

- Random Index (RI): A constant derived from Saaty's random index scale, based on the number of criteria.
- Maximum Eigenvalue (λmax): The mean obtained by multiplying elements of the normalized comparison matrix by the priority vector (weights).
- Consistency Index (CI): A measure of matrix consistency, using the number (n) of criteria and calculated as:

$$CI = \frac{\lambda_{max} - n}{n - 1} \quad (1)$$

The CR is computed by dividing the CI by the RI, with values ≤0.10 deemed acceptable; higher values suggest the need for revised comparisons (Saaty, 1980).

The main purpose of the application of the analytical hierarchy process is to determine the weight values of the criteria discussed to solve the problem and their place in the hierarchical structure at the solution stage (Topuz & Deniz, 2023).

The criteria (or factors) used in this study and their calculated weights are presented in Table 1. In Table 2 the criteria used are presented as data layers imported in the GIS framework and divided into four classes (1-4) for proper suitability assessment.

Table 1. Pairwise matrix of the criteria and produced weightage W_i.

Criteria	Geohazards/ Landslides	Geomorphology/ Slope	Geology/ Lithology	Hydrology/ Rivers	Ground Seismicity Hazard	Tectonics/ Faults	Weight W_i.
Geohazards/ Landslides	1	2	3	4	4	4	0.368
Geomorphology/ Slope		1	2	3	3	3	0.236
Geology/ Lithology			1	2	2	2	0.144
Hydrology/ Rivers				1	2	2	0.106
Ground Seismicity Hazard					1	1	0.073
Tectonics/Faults						1	0.073

Table 2. Division of criteria into classes and Suitability assessment.

Data Layer	Class	SC	Data Layer	Class	SC	Data Layer	Class	SC
Landslides	Active/ recent	4	Slope (%)	<10	1	Lithology	Recent loose Landslide materials	4
	Inactive/ older	3		10-20	2		Paleo & Older semi-compacted Landslide materials	3
	Absence	1		20-35	3			
				>35	4			
Distance from Streams (m)	<10	4	Ground Seismicity Hazard	A	1		River bed deposits	3
	10-50	3		B	2		River terrace	1
	50-100	2		C	3		Scree	3
	>100	1		D, X	4		Sandstone/ Flysch Pindos Unit	2
Distance from Faults (m)	0-20	4					Siltstone/ Flysch Pindos Unit	2
	>20	1					Limestone/ Pindos Unit	1
							Cherts/ Pindos Unit	2
CR= 0.0192 ≤ 0.10								

1: Suitability Class (SC) refer as; (1) Highly Suitable, (2) Moderately suitable, (3) Marginally suitable and (4) Unsuitable.

The spatial analysis was conducted in ArcGIS Pro 3.1 software. To illustrate the spatial distribution of the relevant criteria, six thematic maps were developed based on the data layers and classification categories specified in Table 2. These maps provide a detailed spatial representation, contributing to a more thorough understanding of the patterns and relationships within the study area (Figure 2, 3). The data necessary for the creation of the aforementioned layers were sourced from various references, which are detailed subsequently. Moreover, a modification and validation of vector data was performed, specifically for the limits of the area of active landslides. Figure 2A depicts the landslide inventory, classifying areas into three distinct classes: (i) absence, (ii) inactive/older landslides, and (iii) active/recent landslides. This classification is crucial for identifying regions with historical or ongoing instability. Slope plays a pivotal role in affecting the occurrence of landslide events. Steeper slopes are more prone to instability due to the greater gravitational force acting along the slope surface, which increases the probability of failure. A slope map was generated by processing the Digital Elevation Model (DEM) of the area, which has a grid size of 5x5m. The layer was classified into four distinctive categories that are: (i) less than 10, (ii) 10 to 20, (iii) 20 to 35 and (iv) greater than 35, each representing different slope percentages (Figure 2B).

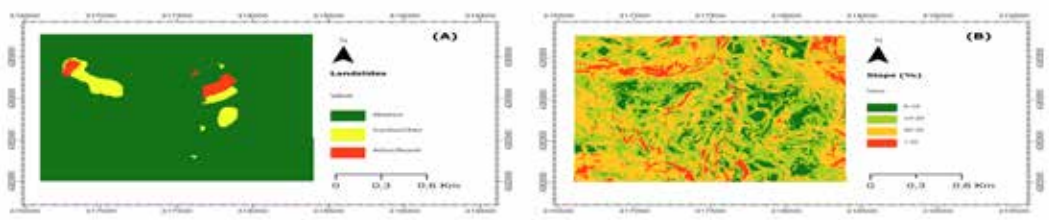

Figure 2. Thematic layer maps: (A) Landslides, (B) Slope.

Figure 3C presents the lithological classification, detailing various geological formations. The geological and lithology features were digitized from a large-scale (1:2.000) Engineering Geological map produced by the Hellenic Survey of Geological and Mineral Exploration (T-2855/2016) and an update was made after an on-site geological surveying.
The distance from streams portrays a critical hydrological factor influencing slope stability. The drainage network was derived from the Digital Elevation Model (DEM) and subsequently verified against the Engineering Geological map. The vector data was modified to define the boundaries of the river banks, and buffer zones were established around the streams, categorized as follows: (i) less than 10 meters, (ii) 10 to 50 meters, (iii) 50 to 100 meters, and (iv) greater than 100 meters. These buffer zones are represented as a layer in Figure 3D.
Furthermore, Figure 3E illustrates the proximity to fault lines, categorizing the study area into two classes: (i) areas within 0 to 20 meters from faults and (ii) areas beyond 20 meters, based on the provided data of the Engineering Geological map. Figure 3F represents the ground seismicity hazard of the geological formations, with the layer classified into four categories: (i) A, (ii) B, (iii) C, (iv) D, X, corresponding to the Engineering Geological map of the area and the Greek Code for Seismic Resistant Structures (EAK 2000). It is important to note that the third class is not represented in the thematic map, as no geological formations were classified within this category.

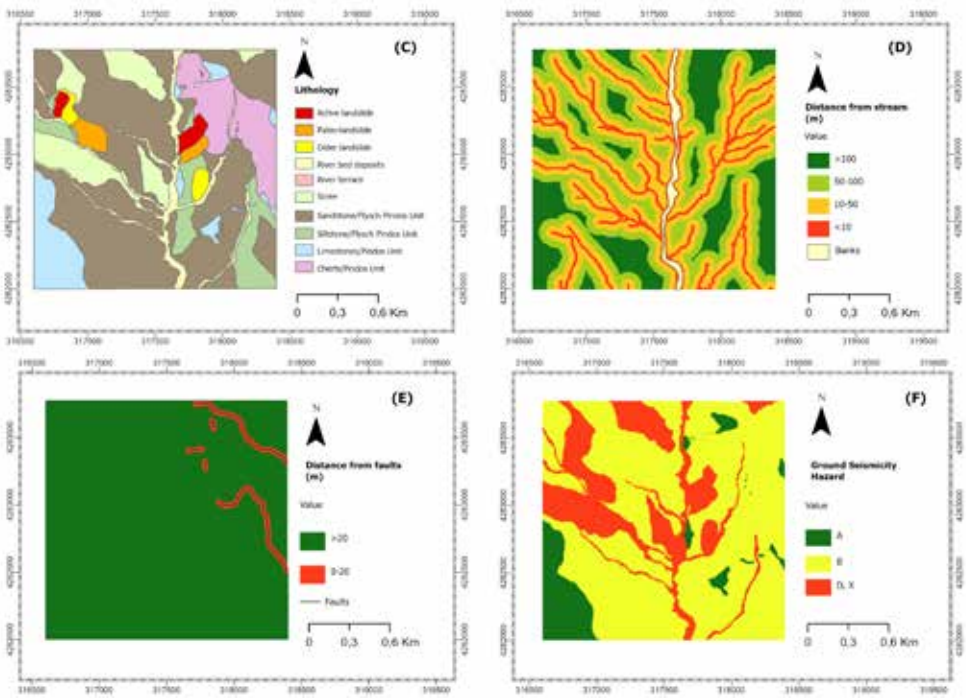

Figure 3. Thematic layer maps: (C) Lithology, (D) Distance from stream, (E) Distance from faults and (F) Ground Seismicity Hazard.

The raster layers were exported and then a scale of 1-4 was applied for the process of reclassification, following the scale of suitability values mentioned in Table 2. The levels of suitability were evaluated based on the relative significance of the contribution made by each criterion as has been suggested by Feizizadeh (2012). The reclassification of the spatial layers was made in order to eliminate the units of measurement and transform the data into a unitless format as has been suggested by Mansour et al. (2019). This process enhances compatibility, allowing for smoother integration with other datasets, regardless of their measurement system.
Following spatial analysis, a geological suitability map was obtained by the Weight Linear Combination

(WLC) method, then reclassified with Jenks natural break, categorizing the study area into four suitability categories (Figure 4). The WLC approach is one of the most frequently used in GIS-MCDA (Malczewski, 2000). The criteria and their individual weights are summed up in WLC, and the combined sum presents the final suitability map using the equation:

$$\sum_{i=1}^{n} = w_i \cdot c_{ij} \quad (2)$$

Where Wi: weights of selected criterion i, Cij: Reclassified criteria and n denotes total number of criteria.

Results

Each individual category of the final map corresponds to a unique geological suitability level with a specific color (Figure 4). For example, the lowest suitability level, represented by the highest weighted score, is highlighted in red. In this study, the suitability map shows four suitability categories as follows: (a) Unsuitable, (b) Marginally suitable, (c) Moderately suitable and (d) Highly suitable.

The analysis reveals that 38.58% of the total area is classified as highly suitable for residential development. The largest share of the land, 44.85%, falls under the “Moderately suitable” category, making it the most dominant classification in the analysis. While considering the land area that is not suitable, it is seen that a small area of the field consists of the Marginally suitable class 12.77%, whereas 3.80% of the study area is considered unsuitable for residential development.

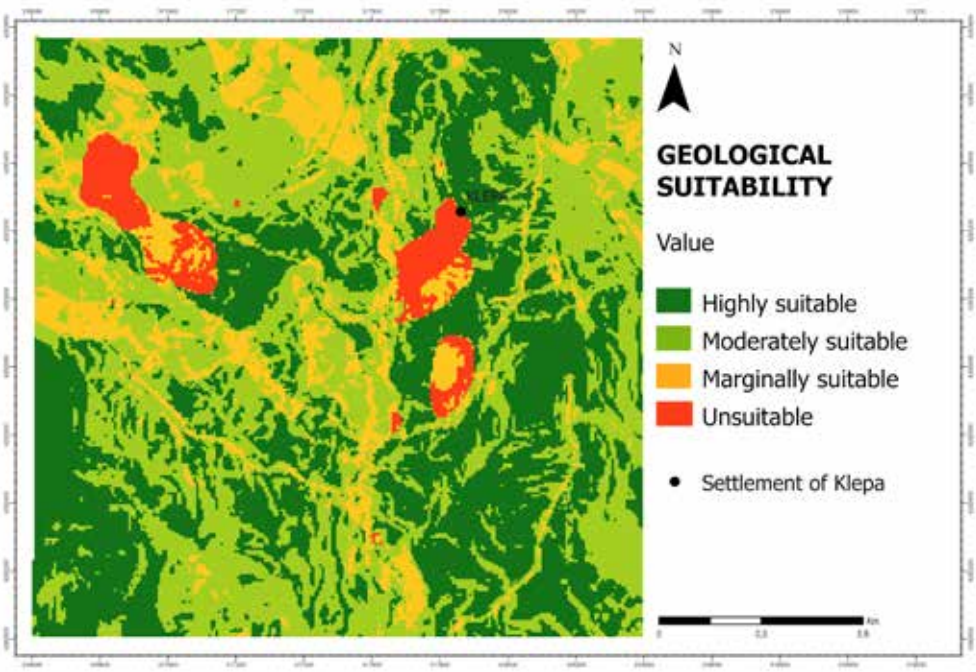

Figure 4. Geological Suitability map of the study area with color classification for each suitability category.

Conclusions

This study effectively combines Geographic Information Systems (GIS) and the Analytic Hierarchy Process (AHP) to assess geological suitability and residential development in mountainous settlements impacted by landslide events. By prioritizing key criteria through AHP and via GIS for spatial analysis, a geological suitability map is obtained. The produced map presents four levels of suitability: Unsuitable, Marginally Suitable, Moderately Suitable, and Highly Suitable. The analysis reveals that 38.58% of the investigated area is highly suitable for development, whereas 44.85%, of the total area falls under the Moderately

Suitable category. A smaller portion, 12.77%, is Marginally Suitable and 3.80% is classified as Unsuitable. This comprehensive approach provides a valuable decision-making tool for sustainable residential development and planning, particularly in remote settlements and geohazard-prone areas, that can be adapted to diverse cases and assess the influence of multiple factors in a region.

References

Depountis, N. (2023). Geological studies for regional and urban planning in Greece. European Geologist, 56.

Elhadj Mokhtari, Farouk Mezali, Brahim Abdelkebir, Bernard Engel, (2023). Flood risk assessment using analytical hierarchy process: A case study from the Cheliff-Ghrib watershed, Algeria. Journal of Water and Climate Change 14 (3): 694–711.

Feizizadeh, B., & Blaschke, T. (2012). Land suitability analysis for Tabriz County, Iran: a multi-criteria evaluation approach using GIS. Journal of Environmental Planning and Management, 56(1), 1–23. https://doi.org/10.1080/09640568.2011.646964

Hajar YAA, (2017). Using Analytical Hierarchy Process (AHP) to build suppliers' selection model. Int J Acad Res Bus Soc Sci. Pages 772-787. ISSN: 2222-6990. http://dx.doi.org/10.6007/IJARBSS/v6-i12/2552

Hellenic Survey of Geology and Mineral Exploration (2016). Engineering Geological study of the Kato Klepa settlement, Municipality of Nafpaktia, Regional Unit of Etoloakarnania (T-2855).

Malczewski J (2000) On the use of weighted linear combination method in GIS: common and best practice approaches. Trans GIS 4(1):5–22

Mansour, Shawky & Al-Awadhi, Talal & Al-Hatrushi, Salim. (2019). Geospatial based multi-criteria analysis for ecotourism land suitability using GIS & AHP: a case study of Masirah Island, Oman. Journal of Ecotourism. 19. 1-20. 10.1080/14724049.2019.1663202.

Saaty, Thomas. (1980). The Analytic Hierarchy Process. McGraw-Hill, New York.

Topuz, M., Deniz, M. (2023). Application of GIS and AHP for land use suitability analysis: case of Demirci district (Turkey). Humanit Soc Sci Commun 10, 115. https://doi.org/10.1057/s41599-023-01609-x

17th INTERNATIONAL CONGRESS of the Geological Society of Greece

BULLETIN OF THE GEOLOGICAL SOCIETY OF GREECE, SP. PUBL.

EXTENDED ABSTRACT 010

Legacy data analysis combined with an integrated geological and geophysical survey for geothermal site exploration at Petra-Lesvos, Greece

Apostolopoulos G.[1], Malehmir A.[2], Vakalas I.[1], Kranis C.[3], Leontarakis K.[1], Orfanos C.[1], Konstantinidis E.[2], Markovic M.[2], Papadopoulou M.[2], Chailas S.[3], Skourtsos E.[3], Tzanis A.[3], Spyridonos E.[4]

(1) National Technical University of Athens, Athens, Greece, gapo@metal.ntua.gr
(2) Uppsala University, Uppsala, Sweden
(3) National and Kapodistrian University of Athens, Athens, Greece
(4) Public Power Corporation Renewables S.A., Athens, Greece

Introduction / Background

Geothermal source of energy has become a priority in the energy sector providing a precious transition from hydrocarbons. Geothermal energy has the great advantage to be used when it is needed especially in islands when there is a boost in consumption in the summer period. Public Power Corporation Renewables SA (PPCR) has sponsored geological and geophysical surveys for many years now for geothermal exploration leading to important results through geophysical surveys (Tzanis et al., 1991, Lagios et al., 1994, Lagios and Apostolopoulos, 1995, Apostolopoulos et al., 1997, Tzanis et al., 2018, Tzanis et al., 2020) in various sites of geothermal fields of interests. In the Lesvos Island, faults that may act as thermal circulation zones have been speculated through geothermal springs and through geophysical studies (Thanassoulas and Xanthopoulos, 1991, Apostolopoulos et al., 1997). A good correlation between geology, seismicity and geothermics has been found using remote sensing data and GIS in the island (Voulgaris et al., 2004)

Kontis et al. (1994) state that the active geothermal system in the Megala Therma (Northern Lesvos) is probably a late evolutionary stage in the formation of mineralization with different types of alterations from silicification, propylitization, argillic alteration and potassic to phyllic. This is important because in the gravity Bouguer anomaly map of Lesvos Island (Figure 1) this area is part of a low gravity anomaly trending in south-westwards towards Stipsi and extending to the south with relatively low gravity values where Kalloni and Polychnitos area are also of geothermal interest.

Figure 1. Northern Central part of the Bouguer gravity anomaly map (in mGals) of Lesvos Island over Google Earth map.

Geothermal exploration today involves geophysical method such as magnetotellurics (MT), a method of great detection depth, which is sensitive to zones of conductivity and possibly associated with geothermal circulation or reservoir but also with saline water presence. In the case of Lesvos, 3D interpretation of legacy magnetotelluric data (Tzanis, 2024) provide resistivity distributions at various depths with one particular at depth of approximately 1.25 km below mean sea level (Figure 2) showing great correlation between low resistivity values and low gravity regions previously inferred.

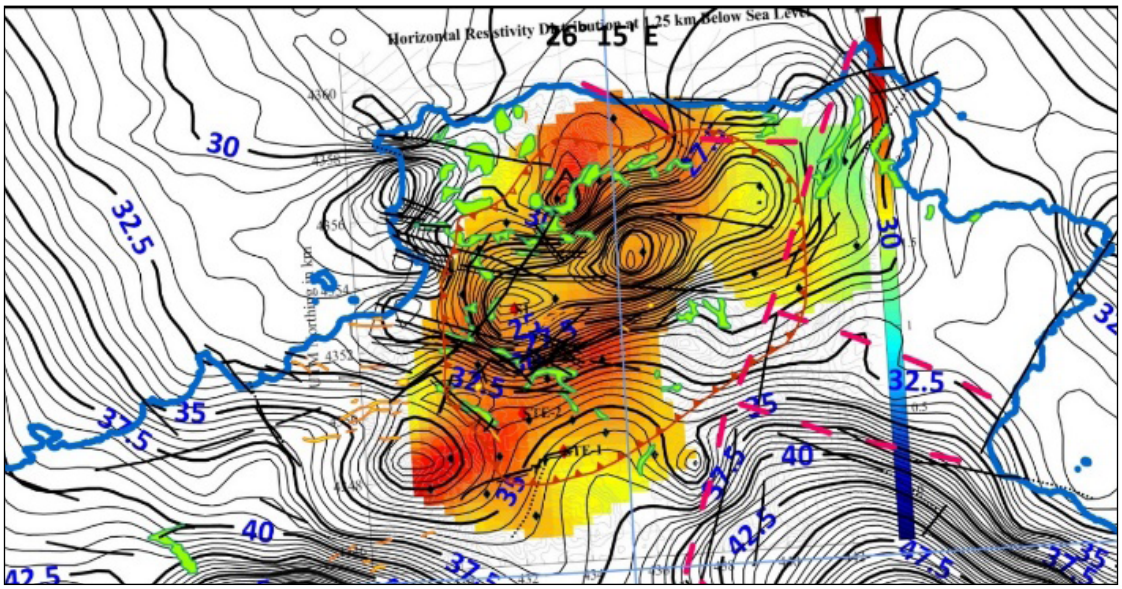

Figure 2. Northern Central part of Lesvos Island with horizontal electrical resistivity slice at the depth of 1.25km below mean sea level over the Bouguer gravity anomaly map (in mGals). The resistivity slice among others was extracted from the 3-D model elaborated by Tzanis (2024) on legacy magnetotelluric data.

PPCR has sponsored a renewed geothermal project under the coordination of National Technical University of Athens (NTUA, School of Mining and Metallurgical Engineering, Laboratory of Hydrocarbon's Exploitation & Applied Geophysics) in collaboration with Uppsala University (UU, Department of Earth Sciences) and National and Kapodistrian University of Athens (NKUA, Faculty of Geology and Geoenvironment) that consists a geological-tectonic and geophysical study in an integrated mode that will provide a better understanding of the geothermal field through the positioning of faults that act as geothermal circulation zones and areas of geothermal alteration. The project goal is to propose the best position for a new deep borehole in the area for geothermal exploration. The project involves the evaluation of all available geological and geophysical data, new geological field survey including the use of UAV imaging for remote sensing in areas of interest such as fault zones, new gravity, and magnetic data along with an active seismic survey.

Geology of the Petra area

The geological formations (Figure 3) presented in Mythimna and Ayia Paraskevi work (Hecht, 1973, 1974), were verified macroscopically in the field. The main lithological types are the following: i) entirely silicified lava, ii) Dykes (rhyodacitic or dacitic), iii) Upper lava unit (dacitic, latitic, latitandesitic and quartz-andesitic; minor rhyodacitic lavas), iv) Lowermost parts of the upper lava unit (mostly latitic to latitandesitic), v) Pyroclastic layer (lapilli tuff and tuff breccia containing increasing amounts of volcanic bombs towards the west region of Scalochori), vi) Lower lava unit of the Stipsi and Vatoussa areas (mostly latitandesitic, partly andesitic or latitic, lavas; kaolinized zones of the lower lava unit, locally silicified. Basic lapilli tuff, magmatic breccia, or agglomerate within the lower lava unit).

Figure 3. Geological map of Lesvos Island Northern Central part (geographical coordinates UTM 35N) (Hecht 1973, 1974).

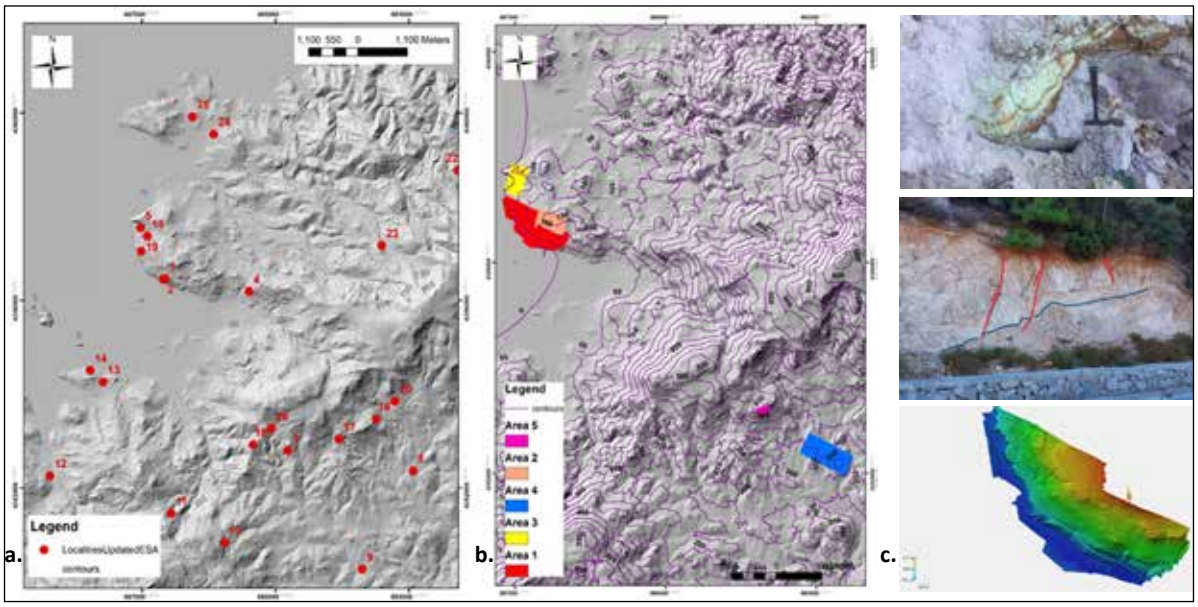

Figure 4. a) Geological data acquisition map in Petra study area, b) areas were drone surveyed (geographical coordinates Greek Grid), c) Hydrothermal alterations in the contact of pyroclastic sediments with the lower part of the Upper Lava Unit, faults affecting the silicified lavas (East of Stipsi), digital elevation model of Area 1.

The field geological survey (Figure 4a) focused on the following objectives:

- Identifying the rock units in the study area, using the geological map sheets of Mythimna and Ayia Paraskevi (HSGME, scale 1:50000) as reference.
- Conducting structural measurements, including faults and joints.

Additionally, in areas of interest, such as fault zones, data collection was enhanced using UAV imaging for remote sensing (Figure 4b).

Macroscopical identification of the lithological units in the study area, identification and measurement of potential fault zones and remote sensing data acquisition in 5 areas utilizing a set of 1373 aerial images were accomplished (Figure 4c) with the next step to be the construction of the structural model of the area in collaboration of the geophysical team.

Geophysical surveys

After considering all legacy data, geological and geophysical, in parallel with the geological survey, an integrated geophysical survey was designed in such a way to cover all interesting geological and tectonic features around the Petra area and the areas with low gravity and resistivity values the extended gravity map and magnetotelluric results.

The gravity and magnetic measurements designed and operated by NTUA-NKUA teams as well as the seismic profiles designed and operated by UU groups covered areas from Molyvos to Anaxos and Lafionas and from Petra to Petri and Stipsi (Figure 5). The gravity measurements were acquired from two groups with the Lacoste Romberg gravity meters and the magnetic measurements with the magnetometers Scintrex Envipro and Geometrics 852 (Figure 5). Differential RTK LEICA GPS instruments and Metrica Network were used for the positioning of the measurements. Four seismic profiles were positioned for a total of 24 km long across several suspected geological structures. UU subcontracted the Geological Survey of Denmark and Greenland (GEUS) in order to provide their new vibro-truck (Innova UV2 weighs approximately 17 tons, operates at a peak force equal to 115.6 kN and configured to produce a time-synchronised and phase-locked linear sweep signal from 10-140 Hz over 18 seconds) and its operation, while coordinated the survey and design with its own recording instrumentations (1000 wireless or nodal recorders connected with 10 Hz geophones for autonomous data recording). Receiver and shot points had a spacing of 10 m, except for P4 which was 20 m. At every shot point, 3 sweeps were generated to improve signal-to-noise ratio by vertical stacking of the repeated shot records. The recording time was set to 25 s with a sampling rate of 2 ms. Aiming for upper 2-3 km subsurface imaging and capitalizing from the large number of nodal recorders, long offset data were aimed for during the acquisition, reaching sometimes to up to 7.2 km.

Bouguer gravity and magnetic anomaly, reduced to the pole, maps show in the eastern region lower values something that was expected from the Bouguer gravity map of the Island (part of it in Figure 1). These lower values are very well associated with the Upper Lava Unit and possibly with geothermal alteration of the underground formations.

The unmigrated seismic section of P1 (Figure 6) shows an interesting cross-section of the subsurface with various characters appearing to suggest fault systems. Noteworthy the Bouguer gravity values show similar general behavior as the reflection seismic section (Figure 6). A gravity low correlates well with a seismic depression zone in the Petra area.

Figure 5. Gravity and magnetic measurements along with seismic profiles in the survey area on Google Earth map. Photos from gravity and magnetic measurements (left) and seismic survey (right).

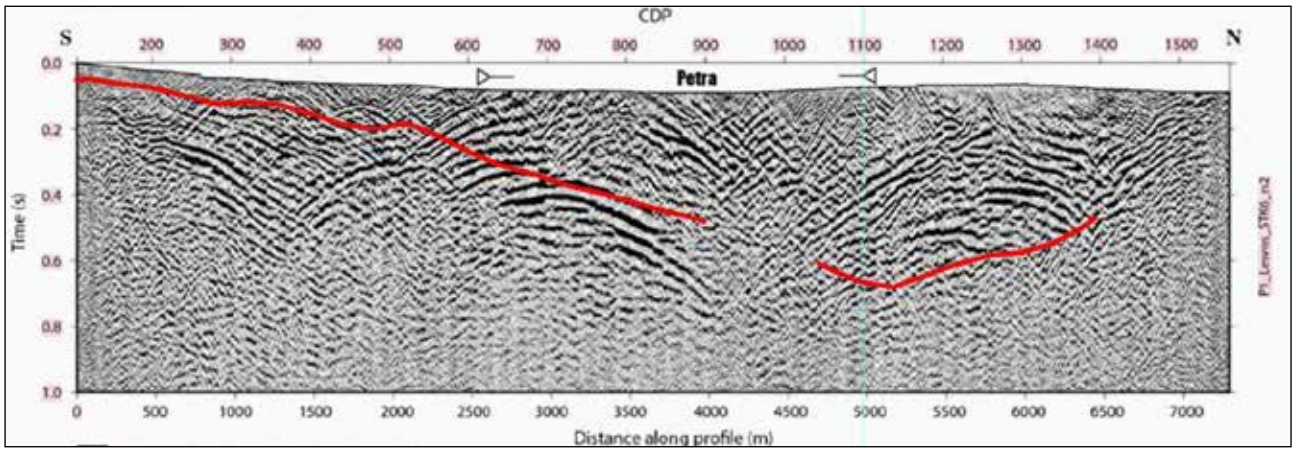

Figure 6. Unmigrated reflection seismic section of "P1" profile with the red line showing the of Bouguer gravity anomaly values extracted along the same profile.

First comments

According to the legacy data analysis, the geophysical and geological data coverage that was followed in the field with the final survey area extended as much to the east reaching Stipsi village to include in a substantial way the area of gravity low (Figure 1) as well as the resistivity low (Figure 2), the boreholes "S1" and "STE-2" (Figure 5) and most of the proposed faults. All data as expressed in maps or sections look of great quality and very good coincidence of what previous data were suggesting. The geophysical maps (Bouguer gravity anomaly map, magnetic anomaly reduced to the pole) which are considered reference map as uniquely represent the underground response already give interesting areas for geothermal activity. It is expected that further processing and data interpretation will lead to 3D models of the underground. The seismic shot gathers and unmigrated CDP sections show useful information of subsurface structures. This information will be useful both for density models as well as to refine the geological model suggested by surface geological observations. The fact that many of the features to be interpreted in the gravity maps as well as the surveyed geological and tectonic features are in seismic profiles gives the benefit of the integrated interpretation this project has as a target.

Acknowledgements

The authors wish to thank firstly Public Power Corporation Renewables for sponsoring the project. We also thank the Geological Survey of Denmark and Greenland (GEUS), which provided their new vibro-truck and their geoscientists Dr. G. Donoso and Mr. L. Solheim who operated it. Thanks to the important contribution in the field survey of Ms. K. Polychronopoulou (M.Sc.), Mr. S. Karizonis, Mr. D. Karaiskos, Mr. T. Ntagiantas, mining engineers, Ms. A. Dromiadi, Ms. T. Tzovara, Mr. A. Tsiftsidis NTUA students, Ms. K. Kantareli, Ms. N. Kranidioti, NKUA students, Mr. E. Konstantinidis, Mr. S. Zappala, Ms. J. Putnaite, Mr. V. Stender, Ms. K. Kucinskaite, PhD students of UU.

References

Apostolopoulos, G., Louis, I. and Lagios, E., 1997. The self-potential method in the geothermal exploration of Greece. Geophysics v.62, No. 6, pp.1715-1723. **[Journal Article].**

Hecht, J., 1973. Geological Map of Greece (Scale 1:50,000), Lesbos Island, Ayia Paraskevi Sheet, (N.I.G.M.R. publisher).

Hecht, J., 1974. Geological Map of Greece (Scale 1:50,000), Lesbos Island, Mithimna Sheet, (N.I.G.M.R. publisher).

Kontis, E., Kelepertsis, E. and Skounakis, S., 1994. Geochemistry and alteration facies associated with epithermal precious metal mineralization in an active geothermal system, northern Lesvos, Greece. Mineral Deposita 29,

430-433. **[Journal Article]**

Lagios, E., Tzanis, A., Delibasis, N., Drakopoulos, J. and Dawes, G.K.J., 1994. The geothermal exploration of Kos Island, Greece: Magnetotelluric and microseismicity studies. Geothermics, 23 (3), 267-281. **[Journal Article]**

Lagios, E. and Apostolopoulos, G., 1995. Integrated geophysical study of the geothermal system in the Southern Part of Nisyros Island, Greece. Journal of Applied Geophysics v.34, pp.55-61. **[Journal Article]**

Thanassoulas, C. and Xanthopoulos, N., 1991. Location of possibly productive geothermal fracture zones/faults using integrated geophysical methods over Lesvos Island geothermal field, Greece. Geothermics 20, 5/6, 355-368. **[Journal Article]**

Tzanis, A. and Lagios, E. 1991. Magnetotelluric Exploration of Geothermal Potential in Greece. Pro-ceedings, 1st Gen. Conf. of Balkan Phys. Union, Thessaloniki, Greece, September 26-28 1991, v 1, 520-522. **[Conference Proceedings]**

Tzanis, A., Sakkas, V. and Lagios, E., 2018, Magnetotelluric Reconnaissance of the Nisyros Caldera and Geothermal Resource (Greece). In: Dietrich, V.J. and Lagios, E. (eds), "Nisyros Volcano: The Kos - Yali - Nisyros Volcanic Field", Springer Verlag, 203-225; doi: 10.1007/978-3-319-55460-0_6. **[Book]**

Tzanis, A., Efstathiou, A., Chailas, S., Lagios, E. and Stamatakis, M., 2020b. The Methana Volcano – Geothermal Resource, Greece, and its relationship to regional tectonics, Journal of Volcanology and Geothermal Research, 404, 107035; doi: 10.1016/j.jvolgeores.2020.107035. **[Journal Article]**

Tzanis, A., 2024. Investigation of the geothermal potential of the wider area of Stıpsi, Lesvos: 3D inversion of digitized old (year 2000) magnetotelluric measurements. Technical Report to Public Power Corporation Renewables under the contract PO77000646.

Voulgaris, N., Parcharidis, I., Pahoula, M., and Pirlis, E., 2004. Correlation of tectonics, seismicity and geothermics of Lesvos Island using remote sensing data and geographical information systems. Bulleting of the Geological Society of Greece vol. XXXVI, Proceedings of the 10th International Congress, Thessaloniki. **[Conference Proceedings]**

17th INTERNATIONAL CONGRESS of the Geological Society of Greece

BULLETIN OF THE GEOLOGICAL SOCIETY OF GREECE, SP. PUBL.

EXTENDED ABSTRACT 011

Modelling Coastal Protection as an ecosystem service in the Greek coastal zone

Konstantina Apostolopoulou[1], Efthimios Karymbalis[1], Maria Salomidi[2], Evangelia G. Drakou[1]

(1) Department of Geography, Harokopio University, El. Venizelou 70, 176 76 Kallithea, Attica, Greece (2) Institute of Oceanography, Hellenic Centre for Marine Research, 46.7 km Athens Sounio Ave., 19013, Anavyssos, Greece

Research Highlights

Structural connectivity within seagrass meadows can enhance the ecosystem service of coastal protection capacity. This work provides an integrated modelling approach of biotic and abiotic seascape features while incorporating the role of structural connectivity to existing coastal protection ES models.

Background

Coastal areas are known to contribute to human well-being through the supply of ecosystem services (ES) (Liquete et al., 2013) or nature's contributions to people (NCP) (Díaz et al., 2018). Among these ES, coastal protection is of particular importance , especially in the face of increasing climate change impacts. Coastal protection is defined as the ecosystem service which provides natural defense of the coastal zone against inundation and erosion from waves, storms and sea level rise (Liquete et al., 2013). Coastal habitats, such as mangroves, saltmarshes, seagrasses, coral reefs and dunes, can act as natural defense against coastal flooding and erosion through wave attenuation, storm surge reduction and seabed elevation, thereby enhancing the resilience of coastal communities against these hazards (Trégarot et al., 2021). This is very timely, as climate change is expected to increase the frequency and magnitude of extreme weather events, such as storms and hurricanes, as well as lead to accelerated sea level rise. This increasing frequency and intensity of extreme events, along with anthropogenic activities such as coastal development, which degrade the coastal zone, pose a great threat to coastal populations and economies through increased erosion, flooding, and damage to infrastructure.

Greece has a diverse array of coastal habitats that are crucial for coastal protection. Sandy beaches act as dynamic buffers, absorbing wave energy and dissipating storm surge. Rocky shores provide refuge for marine life and offer resistance to erosion. Wetlands, such as salt marshes and lagoons, absorb floodwater. Seagrass meadows, stabilize sediments, and reduce wave energy. Among them, *Posidonia oceanica* meadows, endemic to the Mediterranean, as well as *Cymodocea nodosa*, are particularly important for coastal protection in Greece. *Posidonia oceanica* is identified as the most abundant seagrass species in Greece, being present in almost 70% of the Greek coastline (Panayotidis et al., 2022). In more shallow, brackish and sheltered areas, especially in the northern Aegean latitudes, *Cymodocea nodosa* also forms extensive meadows, playing a respective key role in coastal dynamics. Other seagrass species namely *Zostera noltei* and *Halophila stipulacea* also have a restricted presence in the Greek coastal zone (Panayotidis et al., 2022). Greece's complex coastal geomorphology with numerous bays, gulfs, peninsulas and islands, influences wave patterns, currents, and sediment transport, which in turn affect the distribution and resilience of coastal habitats. For instance, the steep slopes and narrow coastal plains characteristic of Greece's coastline, influence the vulnerability of coastal communities to sea-level rise and extreme weather events. Understanding the complex relationship between geomorphology, coastal habitats and their distribution, and biophysical processes is essential for developing effective coastal management strategies in Greece (Hasan et al., 2022).

In Greece, there have been many studies focusing on different aspects of coastal protection. Anastasiou and Sylaios (2016) investigated shoreline dynamics and evaluated coastal protection approaches in an erosion-vulnerable deltaic region of Northern Greece. Tragaki et al. (2018) assessed the physical and social vulnerability of Peloponnese to coastal hazards through variables like geomorphology, shoreline change rate, coastal slope, relative sea-level rise, mean wave height, and mean tide range. Hasan et al. (2022) adapted a regional coastal protection model proposed by Liquete et al. (2013) to Greece by mapping three

indicators, coastal protection capacity, exposure, and societal demand.

Objectives

The aim of this work is to assess and map the ecosystem service of coastal protection in Greece with a more holistic and integrated manner. The work presented uses existing knowledge and modelling approaches on coastal protection as an ES and enhances it with estimates of structural connectivity and fragmentation within coastal habitat types. The paper focuses on seagrass meadows, particularly *Posidonia oceanica* and *Cymodocea nodosa*, being the most abundant along the Greek coasts, and assess their distribution and connectivity patterns, in order to assess the role of seascape patterns in coastal protection.

Methods

The paper focuses on the role of the connectivity of seagrass meadows in enhancing coastal protection. The dataset developed by Panayotidis et al (2022) was used to account for the spatial distribution of seagrass meadows in the Greek coastal zone (Figure 1). Extra emphasis is given on *Posidonia oceanica*, a seagrass species endemic to the Mediterranean Sea, considered a priority habitat under the European Union's Habitats Directive (92/43/EEC). Seagrass beds form extensive underwater meadows up to 40 meters depth that provide essential ES, such as coastal protection. Coastal protection provided by seagrasses is based on their capacity to mitigate flooding and erosion, which are the primary natural threats to coastlines (Ondiviela et al., 2013). Seagrass beds and even more, *Posidonia oceanica* are well known for their ability to provide coastal protection through mechanisms such as wave attenuation and sediment stabilization (Campagne et al., 2015). They reduce wave energy, thereby mitigating the hydrodynamic force impacting the shoreline. The effectiveness of wave attenuation is influenced by factors such as meadow extent, density, blade length, and the overall health of the seagrass ecosystem. Beyond direct habitat effects, seagrass banquettes— formed on the shoreline by beach-cast dead leaves and rhizomes from the meadows— also absorb wave energy, acting as natural barriers that further enhance coastal resilience against erosion and storm surges. (Boudouresque et al., 2016; Ottero et al., 2018).

While there is little research on the contribution of *Cymodocea nodosa* on coastal protection, it has been shown that the species' meadows in combination with *Posidonia oceanica* meadows could significantly reduce the average annual wave height, reducing the amount of energy reaching the beach and enhancing the defense against flooding and erosion. Also, the largest wave damping can be observed in water depths between 1 and 5 meters, because of the greater submergence ratio (canopy height over water depth) (Sierra et al., 2023). In the Greek coastal zone, *C. nodosa* replaces *P. oceanica* at these depths in almost every semi-enclosed gulf where muddy-sand substrata prevail (Panayotidis et al., 2022).

Continuous and dense meadows provide a larger surface area for interaction with water flow, enhancing their capacity to reduce wave and current energy. Fragmented meadows, however, may not offer the same level of protection due to reduced biomass and connectivity. Also, fragmented meadows may lead to increased coastal erosion as the protective barrier they provide is compromised (Ondiviela et al., 2013). In addition, fragmentation can lead to increased sediment resuspension and transport, as the cohesive structure of the meadow is disrupted, reducing its ability to trap and stabilize sediments effectively (Montefalcone et al., 2010).

Incorporating this information within existing models of coastal protection is achieved through the identification and quantification of biophysical and socioeconomic variables. An adaptation of the model developed by Liquete et al. (2013) and downscaled by Hasan et al. (2022), is used. They assessed coastal protection through three indicators: coastal protection capacity, exposure and demand. Through these indicators they calculated the flow of the ES and eventually the benefit of coastal protection. Data on 20 biophysical and socio-economic variables were collected. For coastal protection capacity, slope, geomorphology, seabed and emerged habitat and sediment accretion rate were considered. Within the seabed and emerged habitat variables, an additional to the original model variable to capture the connectivity impact on coastal protection, was included. To assess the structural connectivity and fragmentation patterns

of the meadows, spatial pattern metrics using the FRAGSTATS software were calculated. Metrics and indicators that describe density and shape of the habitat patches, but also those which are dedicated connectivity measures, such as Splitting and Aggregation Indices were selected. For coastal protection exposure, wave height, storm surge height, sea level rise and tidal range, as well as wind speed and eastward and northward current were considered. Coastal protection demand was calculated based on population density, transportation network, artificial surface and cultural sites density, with the addition of port area density, ecologically important site density and mineral extraction site density.

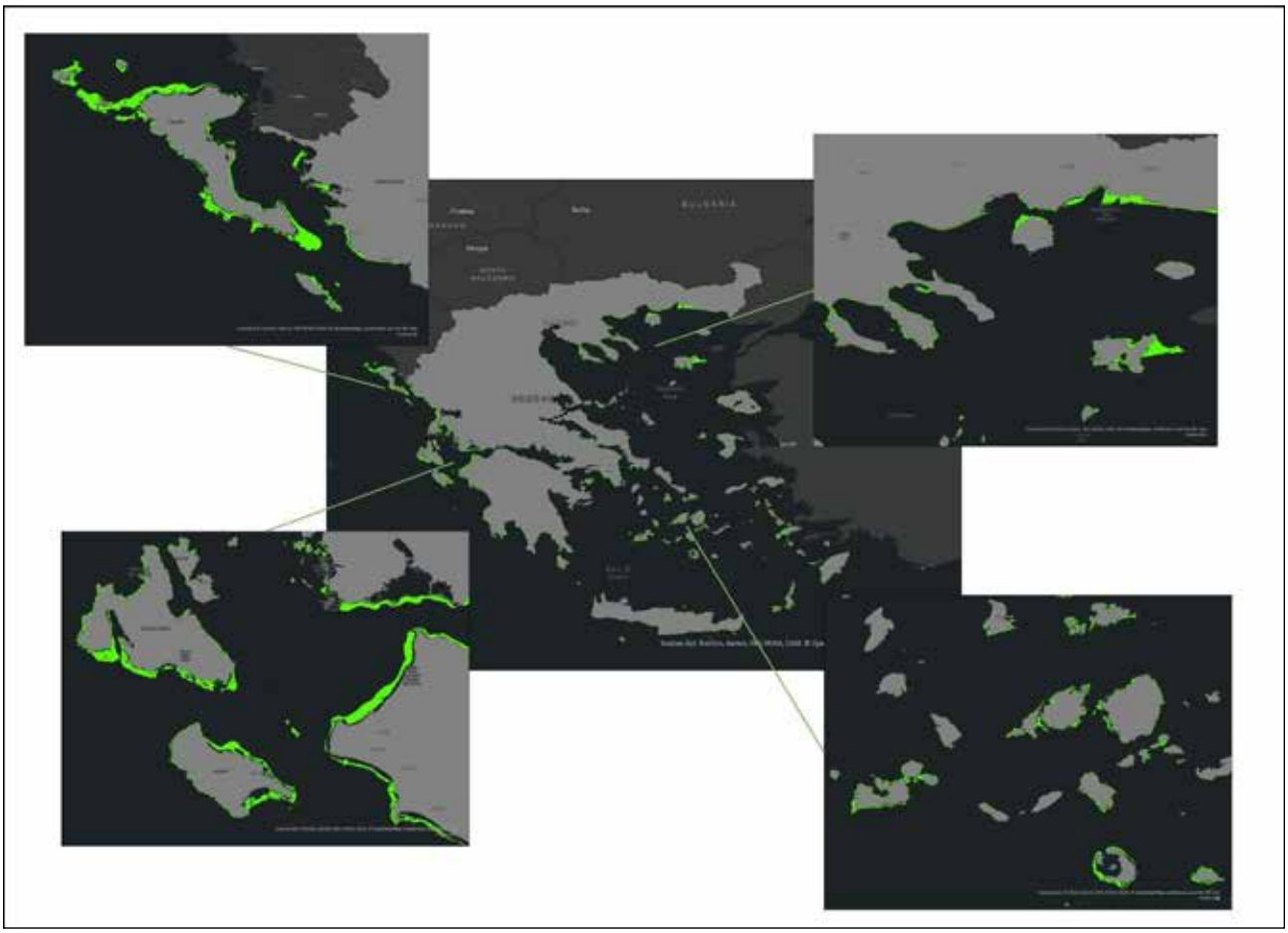

Figure 1. Seagrass meadows in the Greek coastal zone adapted from Panayotidis et al., 2022.

Results

The results are analyzed at two levels: i) the understanding of the spatial patterns emerging across the seascape and ii) the coastal protection ES across the coastal zone of Greece, and its linkage with the spatial patterns of seagrass meadows. For the connectivity assessment, a series of landscape metrics were applied on the locations of seagrass meadows across the coastal seascape. The indicators used were analyzed statistically to identify those that can better describe the variability in structure of submerged coastal vegetation. The results indicated that Shape and Aggregation metrics were able to reveal differences across locations. For instance, the islands of the north Aegean Sea such as Lemnos, or the Western part of the country such as Peloponnese and Corfu (in the Ionian Sea), had largely connected habitats, while the coastline of the mainland or Crete had a quite patchy and dispersed habitat.

Connectivity indicators were then included in the modelling of coastal protection and the results indicate

that there might be a shared pattern across the two. The largest cities in Greece, particularly Athens and Thessaloniki, seem to have low natural protection capacity since seagrass meadows are absent or at low density. Many of the islands show a pattern of high demand and exposure to coastal threats, yet only those with presence of seagrasses have medium natural capacity for protection. Also, certain regions within Peloponnese, particularly in the northern and eastern parts, experience high exposure and demand for coastal protection while simultaneously having low protection capacity. Only areas that have high density of seagrass meadows, such as the southern west and east part of Attica, coasts of Western Greece and north Aegean islands have a relatively high coastal protection capacity. The results indicate a positive correlation between well-connected seagrass vegetation with areas that show higher coastal protection capacity.

Conclusions

This research highlights the critical role of seagrass meadows and particularly *Posidonia oceanica* and *Cymodocea nodosa* in enhancing coastal protection within the Greek coastal zone, particularly in the context of increasing climate change impacts. By integrating biotic and abiotic factors to assess structural connectivity, the study underscores the importance of understanding the spatial dynamics of seagrass meadows and their contribution to mitigating coastal erosion and flooding. The findings indicate that while urban areas such as Athens and Thessaloniki face high demand for coastal protection, they simultaneously exhibit low natural protection capacity due to the natural absence or decline of seagrass meadows. Conversely, regions with dense seagrass coverage demonstrate a greater ability to withstand coastal threats. The research emphasizes the need for comprehensive coastal management strategies that prioritize the protection and restoration of these important ecosystems, particularly in areas most vulnerable to extreme weather events.

References

Anastasiou, S., & Sylaios, G. (2016). Assessment of Shoreline Changes and Evaluation of Coastal Protection Methods to Mitigate Erosion. Coastal Engineering Journal, 58(2), 1650006-1-1650006–1650024. https://doi.org/10.1142/S0578563416500066

Boudouresque, C. F., Pergent, G., Pergent-Martini, C., Ruitton, S., Thibaut, T., & Verlaque, M. (2016). The necromass of the Posidonia oceanica seagrass meadow: Fate, role, ecosystem services and vulnerability. Hydrobiologia, 781(1), 25–42. https://doi.org/10.1007/s10750-015-2333-y

Campagne, C. S., Salles, J.-M., Boissery, P., & Deter, J. (2015). The seagrass Posidonia oceanica: Ecosystem services identification and economic evaluation of goods and benefits. Marine Pollution Bulletin, 97(1–2), 391–400. https://doi.org/10.1016/j.marpolbul.2015.05.061

Díaz, S., Pascual, U., Stenseke, M., Martín-López, B., Watson, R. T., Molnár, Z., Hill, R., Chan, K. M. A., Baste, I. A., Brauman, K. A., Polasky, S., Church, A., Lonsdale, M., Larigauderie, A., Leadley, P. W., Van Oudenhoven, A. P. E., Van Der Plaat, F., Schröter, M., Lavorel, S., … Shirayama, Y. (2018). Assessing nature's contributions to people. Science, 359(6373), 270–272. https://doi.org/10.1126/science.aap8826

Hasan, M. U., Drakou, E. G., Karymbalis, E., Tragaki, A., Gallousi, C., & Liquete, C. (2022). Modelling and Mapping Coastal Protection: Adapting an EU-Wide Model to National Specificities. Sustainability, 15(1), 260. https://doi.org/10.3390/su15010260

Liquete, C., Zulian, G., Delgado, I., Stips, A., & Maes, J. (2013). Assessment of coastal protection as an ecosystem service in Europe. Ecological Indicators, 30, 205–217. https://doi.org/10.1016/j.ecolind.2013.02.013

Montefalcone, M., Parravicini, V., Vacchi, M., Albertelli, G., Ferrari, M., Morri, C., & Bianchi, C. N. (2010). Human influence on seagrass habitat fragmentation in NW Mediterranean Sea. Estuarine, Coastal and Shelf Science, 86(2), 292–298. https://doi.org/10.1016/j.ecss.2009.11.018

Ondiviela, B., Losada, I. J., Lara, J. L., Maza, M., Galván, C., Bouma, T. J., & Van Belzen, J. (2013). The role of seagrasses in coastal protection in a changing climate. Coastal Engineering, 87, 158–168. https://doi.org/10.1016/j.coastaleng.2013.11.005

Otero M.M., Simeone S., Aljinovic B., Salomidi M., Mossone P., Giunta Fornasin M.E., Gerakaris V., Guala I., Milano P., Heurtefeux H., Issaris Y., Guido M., Adamopoulou M. (2018). POSBEMED: Governance and management of the Posidonia beach/dune systems. Final Report. 66pp & Annexes.

Panayotidis, P., Papathanasiou, V., Gerakaris, V., Fakiris, E., Orfanidis, S., Papatheodorou, G., Kosmidou, M.,

Georgiou, N., Drakopoulou, V., & Loukaidi, V. (2022). Seagrass meadows in the Greek Seas: Presence, abundance and spatial distribution. Botanica Marina, 65(4), 289–299. https://doi.org/10.1515/bot-2022-0011

Sierra, J. P., Gracia, V., Castell, X., García-León, M., Mösso, C., & Lin-Ye, J. (2023). Potential of Transplanted Seagrass Meadows on Wave Attenuation in a Fetch-Limited Environment. Journal of Marine Science and Engineering, 11(6), 1186. https://doi.org/10.3390/jmse11061186

Tragaki, A., Gallousi, C., & Karymbalis, E. (2018). Coastal Hazard Vulnerability Assessment Based on Geomorphic, Oceanographic and Demographic Parameters: The Case of the Peloponnese (Southern Greece). Land, 7(2), 56. https://doi.org/10.3390/land7020056

Trégarot, E., Catry, T., Pottier, A., El Hacen, E. M., Sidi Cheikh, M. A., Cornet, C. C., Maréchal, J., & Failler, P. (2021). Coastal protection assessment: A tradeoff between ecological, social, and economic issues. Ecosphere, 12(2), e03364. https://doi.org/10.1002/ecs2.3364

17th INTERNATIONAL CONGRESS of the Geological Society of Greece

BULLETIN OF THE GEOLOGICAL SOCIETY OF GREECE, SP. PUBL.

EXTENDED ABSTRACT 012

Simulation of Domestic Rainwater Harvesting Systems on Fourni Island, Aegean Sea: Assessing Efficiency Under Historic and Climate Change Scenarios.

Apostolou K.-M.[1] ,Feloni E.[2] ,Stergiadou A.[1]
1. Department of Forestry and Natural Environment, Faculty of Agriculture, Forestry and Natural Environment, Aristotle University of Thessaloniki, 54124 Thessaloniki, Greece; nanty@for.auth.gr
2. Department of Surveying and Geoinformatics Engineering, University of West Attica, 28 Ag. Spiridonos, 12243 Egaleo, Athens, Greece; efeloni@uniwa.gr

Introduction and scope

Rainwater harvesting (RWH) has long been an essential practice for ensuring water availability, especially in regions with limited freshwater resources. With increasing global concerns about climate change, the demand for sustainable water management systems has grown (EEA, 2009). Climate change is exacerbating existing water scarcity problems, contributing to prolonged droughts, extreme heat events, and shifting precipitation patterns (Eckstein, 2009). The Greek islands, particularly small islands like Fourni, face significant challenges in water security due to their limited natural water sources (Feloni and Nastos, 2024). This underscores the potential of rainwater harvesting systems to provide an efficient alternative for in-house water needs, such as toilet and laundry use, while enhancing the sustainability of both the island's water resources and the agricultural sector (Essendi, 2014; Koumoura et al., 2018; Londra et al., 2015, 2022).

Fourni Island, located in the Aegean Sea, is characterized by its small population, limited freshwater supply, and vulnerable water resources. This makes it an ideal case study for assessing the potential role of rainwater harvesting systems in addressing local water scarcity.

This study focuses on evaluating various domestic RWH scenarios to simulate the system's efficiency under both historical climatic conditions and projected future scenarios based on the Representative Concentration Pathways (RCP) 4.5 and 8.5 models. These scenarios allow for an exploration of how climate change might influence the feasibility of RWH systems for domestic use, with specific attention given to factors such as household size, tank volume, and rooftop collection area. In this work, we simulate a range of scenarios involving different household sizes (2, 3, and 4 residents), rooftop areas (40-140 m²), and tank volumes (5-30 m³) to assess their impact on the efficiency of RWH systems in achieving coverage targets of 30%, 40%, and 50% of daily water consumption needs. We also consider how these systems would perform under both current climate conditions and the future projections of the RCP 4.5 and RCP 8.5 models, using available timeseries of the EURO-CORDEX regional climate downscaling (Jacob et al., 2020) provided by the DEAR-Clima web application (DEAR-Clima, 2023). While rainwater harvesting systems have the potential to offer significant benefits in arid regions (e.g., Preka et al., 2017), this study highlights the challenges faced by Fourni Island in meeting the desired coverage targets, especially considering future climate projections.

Methods

To evaluate the performance of the rainwater harvesting (RWH) system and compare different scenarios, a water balance simulation model was employed (Tsihrintzis and Baltas, 2013). This model simulates the daily operation of the RWH system, focusing on the collection, storage, and utilization of rainwater. The system collects rainwater from rooftops and other available surfaces and stores it in tanks, which vary in material and size.

To implement the model, it is crucial to have accurate rainfall data for the region. This data serves as input to the simulation model, determining the volume of rainwater that can be captured. Additionally, the volume of rainfall influences the sizing of the storage tank and helps assess the percentage of demand that the system can meet.

The amount of stored water is calculated using a daily water balance equation:

$$St = St-1 + Rt - Dt \ , \ 0 \leq St-1 \leq Vtank$$

Where: St the volume of water that can be stored in the tank on t days (m^3), $St-1$ the volume of water that can be stored in the tank on the previous day (m^3), Rt the volume of the rainwater that runoff from the collection water and enters the tank on t days (m^3), Dt the demands on water on day t (m^3) και $Vtank$ the capacity of the water tank (m^3).

The efficiency of the rainwater harvesting system is determined for the simulation period using the efficiency factor Re. To calculate the efficiency factor Re, several equations are used in the simulation model (Rosas et al., 2024). These equations account for daily storage, runoff, and demand, and allow for the determination of the system's performance across different scenarios, including variations in household size, collection area, and tank volume. In this analysis, this factor is the ratio of the number of days in which the tank water meets the household's full water needs to the total number of days over which the rainfall data is recorded and used in the model.

$$Re = \frac{D_{eff}}{D_{total}}$$

Where: Re is the Efficiency factor, as the ratio of effective days (D_{eff}) to the total number of simulation days (D_{total}).

In this study, daily rainfall data for the area of Fourni were used to simulate the performance of the rainwater harvesting system. The data covered a period from 2012 to 2023, encompassing a total of 10 hydrological years. This data was used as input for the simulation model to determine the volume of rainwater that could be harvested over the specified period.

Several different scenarios were analyzed to assess the impact of various factors on the efficiency of the rainwater harvesting system. The scenarios considered the following parameters:

- Household Size: Two different household sizes were modeled: one with 2 members and another with 4 members. These values were represented as N_{cap}, reflecting the number of people in the household and their corresponding water demands.
- Rooftop Area: The area of the rooftop used for rainwater collection was varied between 40 m² and 140 m². This range covers typical household roof sizes, affecting the volume of rainwater that can be harvested each day.
- Rainwater Tank Volume: The capacity of the rainwater storage tank was varied between 5 m³ and 30 m³. Larger tank volumes allow for more significant storage and provide greater flexibility to manage periods of lower rainfall.
- Coverage Target: The primary objective of the study was to meet a coverage target of 30% of the household's total daily water demand that is about the water amount required for toilet demand (Domènech and Saurí, 2011, after Domene et al., 2004). Further analysis also provided regarding the target of meeting the 40% and 50% of the total daily water demand. The daily water demand was set at 180 L per person, a standard value based on typical household usage for non-potable needs, such as toilet flushing and laundry. Each of these factors was simulated across a range of possible configurations, with the efficiency of the system being evaluated based on the ability to meet the target coverage. The simulations allowed for the comparison of different scenarios and helped to identify which combinations of household size, collection area, and tank volume provide the most efficient solutions for rainwater harvesting on Fourni Island.

The efficiency of the rainwater harvesting system was further examined under future climate change scenarios. To simulate the potential impacts of climate change on the system's performance, EURO-CORDEX climate projections were used, focusing on two representative concentration pathways (RCPs): RCP4.5 (moderate scenario) and RCP8.5 (adverse scenario). These climate scenarios provide projections of future climate conditions, offering insights into how temperature, precipitation, and other climate variables may evolve over time. The time series for future estimates was set to cover 30 hydrological years, from October 1st, 2030 to September 30th, 2060. It is important to note that these projections are not forecasts but tools used to simulate potential climate conditions based on current climate models.

For the future climate scenarios, the following parameters were considered:

- Household Size: The simulations included household sizes of 2 and 3 members (N_{cap} =2,3), reflecting

different household configurations and their corresponding water needs.

- Rooftop Area: The rainwater collection area was adjusted to a range of 60 m² to 100 m². This represents a slightly larger minimum collection area compared to the historical scenarios, accommodating potential increases in demand or larger household sizes in the future.
- Rainwater Tank Volume: The tank volume was limited to a smaller range, between 5 m³ and 10 m³, reflecting the more conservative storage capacity designed for future needs, potentially due to anticipated changes in rainfall patterns and storage efficiency under climate change. These sizes are also available in the market.
- Coverage Target: As with the historical scenarios, the coverage target was set at 30% of the household's total daily water demand. This target was chosen to match non-potable water usage such as toilet flushing, with the daily demand still set at 180 L per person.

The climate scenarios were used to simulate the effect of changing precipitation patterns and other climate variables on the efficiency of the rainwater harvesting system. The simulations aimed to determine how the system's ability to meet the daily water demand would be affected under the moderate scenario (RCP4.5) and high emissions scenario (RCP8.5). This analysis helps to assess the potential future performance of the system and identify how climate change may influence the viability and effectiveness of rainwater harvesting as a sustainable water supply solution for Fourni Island.

To better illustrate the system's performance under varying scenarios, the daily fluctuation of water storage in the domestic tank is presented for cases involving two (2) household members and tank volumes ranging from 5 to 20 m³ (Figure 1). Calculations are based on the daily water balance method. Additionally, for the smallest tank volume, changes in water storage are shown for several rooftop areas (60–100 m²). As observed, rooftop area is the most critical parameter influencing model efficiency. Under the first scenario, overall performance reaches 89%; when rooftop area increases, the system fully satisfies the target demand coverage.

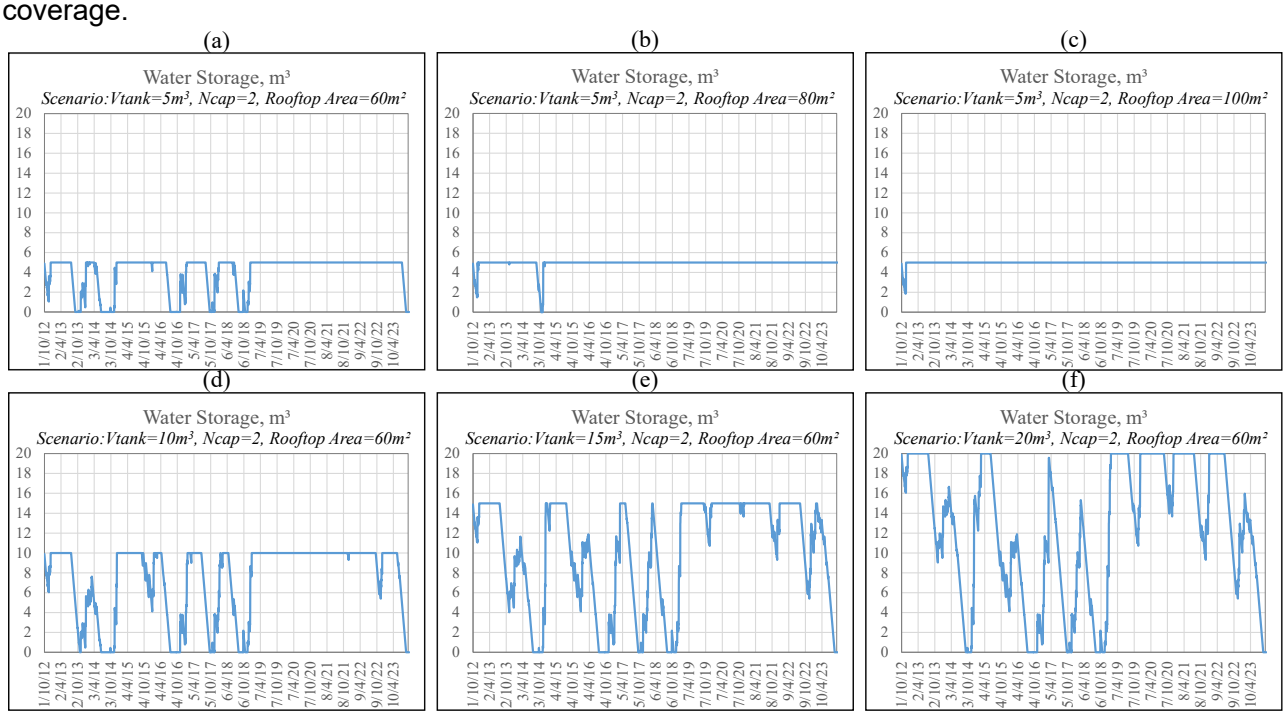

Figure 1. Daily water storage fluctuation in the domestic tank under different combinations of tank volume and rooftop area for two household members, using the water balance method. Sub-figures represent: (a) V = 5 m³, rooftop area = 60 m²; (b) V = 5 m³, rooftop area = 80 m²; (c) V = 5 m³, rooftop area = 100 m²; (d) V = 10 m³, rooftop area = 60 m²; (e) V = 15 m³, rooftop area = 60 m²; (f) V = 20 m³, rooftop area = 60 m².

Results

Initial simulations (historic timeseries of a ten-year period)

The results of the rainwater harvesting system simulation highlight the impact of rooftop collection area and tank volume on system efficiency, expressed through the reliability factor Re. The system's performance was assessed for different household sizes and water demand coverage targets.

- Household with 2 Members (N_{cap}=2): As shown in Figure 2, for a rooftop area of 80 m² or larger, the system meets the 30% water demand coverage target. The efficiency of the system increases with larger rooftop areas, reaching near 100% for collection areas of 120 m² regardless of the size of the tank. In other words, tank volume has a lesser impact on efficiency compared to the rooftop area, as even smaller tanks (5-10 m³) provide sufficient storage when combined with a large collection surface.
- Household with 3 Members (N_{cap}=3): As seen in Figure 2 (right panel), when the household size increases, the system struggles to meet the 30% coverage target for most scenarios. The target is only achieved for collection areas of 140 m² with large tank volumes. For smaller rooftop areas (≤100 m²), the system remains inefficient, indicating that a larger roof area is essential for sustaining a 3-member household.
- Higher Coverage Targets (40% and 50%): When the target coverage is increased to 40% and 50% of total water demand, the system's reliability significantly drops for smaller collection areas. The system is only effective ($Re \geq 90\%$) when the collection area is at least 100 m². Tank volume remains a less sensitive parameter, meaning that increasing storage capacity does not significantly improve efficiency unless the collection area is also sufficiently large.

The graphical results provide valuable insights into selecting the optimal tank size based on individual household conditions. By examining the figures, it becomes evident that the coverage target is more frequently achieved in the 2-member household compared to larger households.

- For 2-member households , the system successfully meets the 30% coverage target for collection areas starting from 80 m².
- For 3-member households, achieving the 30% target is significantly more challenging and is only possible for the largest rooftop area (140 m²) with maximum tank volumes.
- For 4-member households, the system fails to meet the 30% coverage target in all cases, indicating that rainwater harvesting alone cannot be a reliable solution for larger families under current conditions.

When the coverage target increases beyond 30%, the system's performance declines, as seen in Figure 3.

The key observations are:

- Only collection areas of 100 m² or larger provide acceptable efficiency ($Re \geq 90\%$) for 40% and 50% demand coverage.
- Tank size has a limited impact compared to rooftop area, reinforcing the importance of maximizing the collection surface rather than solely increasing storage capacity.
- The system's reliability remains low overall, as it rarely meets higher demand coverage targets, emphasizing the need for supplementary water sources on Fourni Island.

These findings underline the limitations of RWH systems in semi-arid environments and suggest that their effectiveness is highly dependent on household size, available rooftop area, and target water demand levels.

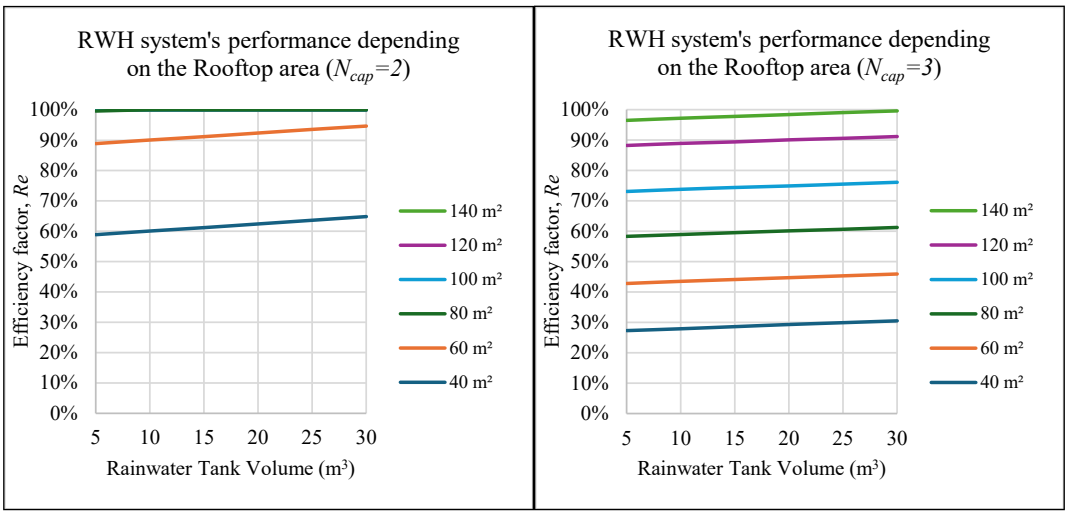

Figure 2. RWHS' performance for two-member (left panel) and three-member household (right panel), and for a 30% coverage target, using the historic timeseries.

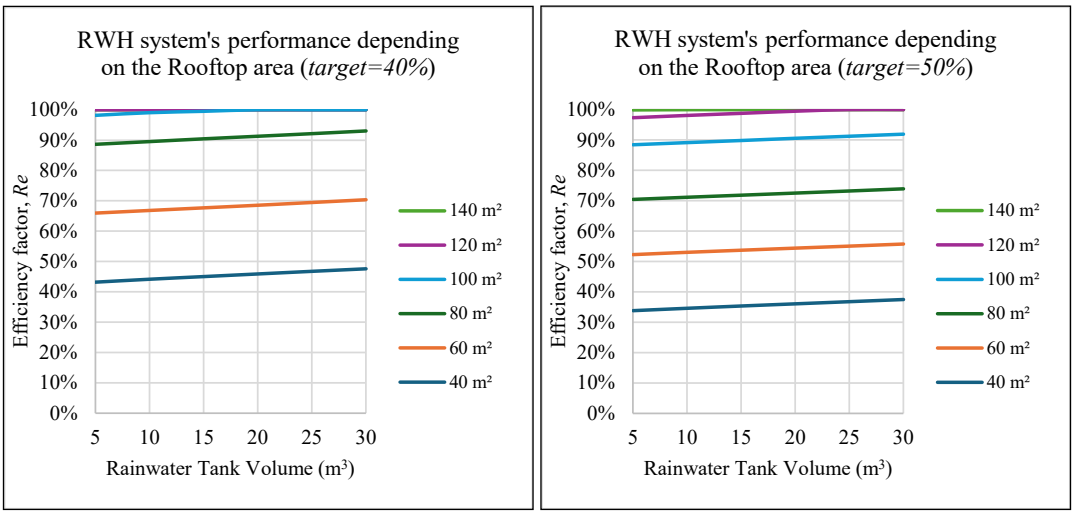

Figure 3. RWHS' performance for a two-member household, and for a coverage target of 40% and 50% (historic period).

B. Impact of Climate Change on System Performance

The results of the rainwater harvesting system simulations (Table 1; codes 1-8) under climate change conditions (RCP 4.5 and RCP 8.5) reveal notable variations compared to the historical timeseries (Table 1; code = 0). The system's efficiency, represented by the reliability factor, Re, is particularly affected for the cases of smaller collection areas, demonstrating the potential impact of altered precipitation patterns in future scenarios.

Key observations from Climate Change (CC) simulations and for a two-member household are presented in Figures 4-5, for RCP4.5 and RCP8.5, respectively. The performance of the rainwater harvesting system under climate change scenarios exhibits significant variability across models. The CC6 scenario (SMHI-RCA4_IPSL-IPSL-CM5A-MR) consistently results in the lowest system performance for both RCP 4.5 and RCP 8.5, irrespective of tank size (5 m³ or 10 m³), indicating that rainfall projections under this model predict less favorable conditions for rainwater harvesting efficiency. In contrast, CC3 and CC4 slightly overestimate system efficiency, yielding performance levels marginally higher than those observed in the historical period; however, these improvements are negligible and do not significantly alter the overall conclusions regarding RWH feasibility. A general decline in system reliability is evident, as most climate

change simulations indicate a decrease in the Re factor, with system effectiveness projected to deteriorate under future climate conditions. On average, the Re factor under climate change scenarios is approximately 15% lower than in the historical period for a rooftop area of 60 m², suggesting that reduced precipitation and increased variability may challenge the reliability of RWH systems on Fourni Island. These findings underscore the vulnerability of rainwater harvesting systems to climate change, particularly for smaller collection areas, with potential consequences for households reliant on rainwater as a primary source of water. To ensure long-term water security, additional water management strategies may be necessary. Meanwhile, larger collection areas (≥100 m²) remain the most effective approach to maintaining system efficiency despite changing climatic conditions. Overall, the results highlight the need for adaptive planning in water resource management to mitigate the adverse effects of climate change on domestic rainwater harvesting, especially in small island environments.

Table 1. Summary of Climate Change Scenario Simulations for Precipitation Inputs

code	Timeseries/ EURO-CORDEX Models Used for Future Rainfall Projections
0	historic period daily precipitation timeseries
1	CLMcom-CCLM4-8-17_CNRM-CERFACS-CNRM-CM5
2	CLMcom-CCLM4-8-17_MPI-M-MPI-ESM-LR
3	IPSL-INERIS-WRF331F_IPSL-IPSL-CM5A-MR
4	KNMI-RACMO22E_ICHEC-EC-EARTH
5	SMHI-RCA4_CNRM-CERFACS-CNRM-CM5
6	SMHI-RCA4_IPSL-IPSL-CM5A-MR
7	SMHI-RCA4_MOHC-HadGEM2-ES
8	SMHI-RCA4_MOHC-HadGEM2-ES

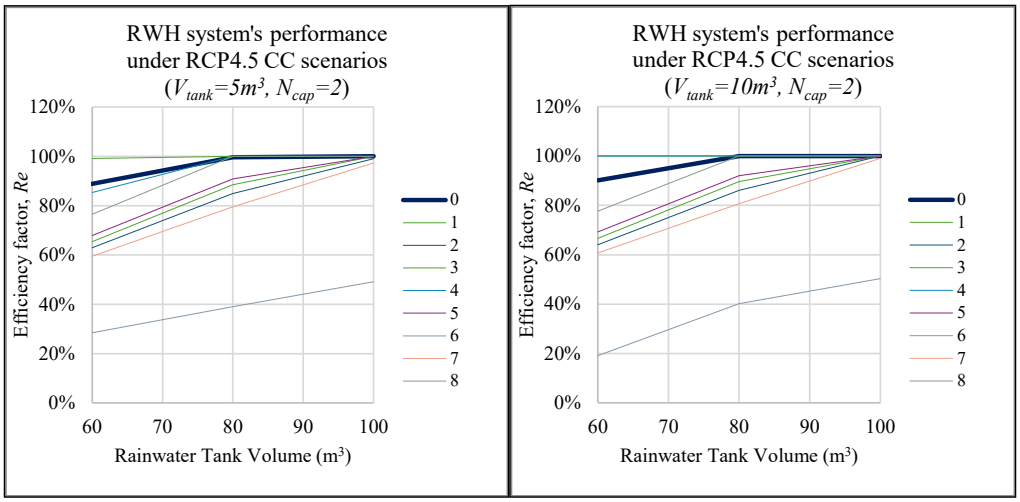

Figure 4. Performance of the Rainwater Harvesting System (RWHS) under Various Climate Change Scenarios (RCP 4.5).

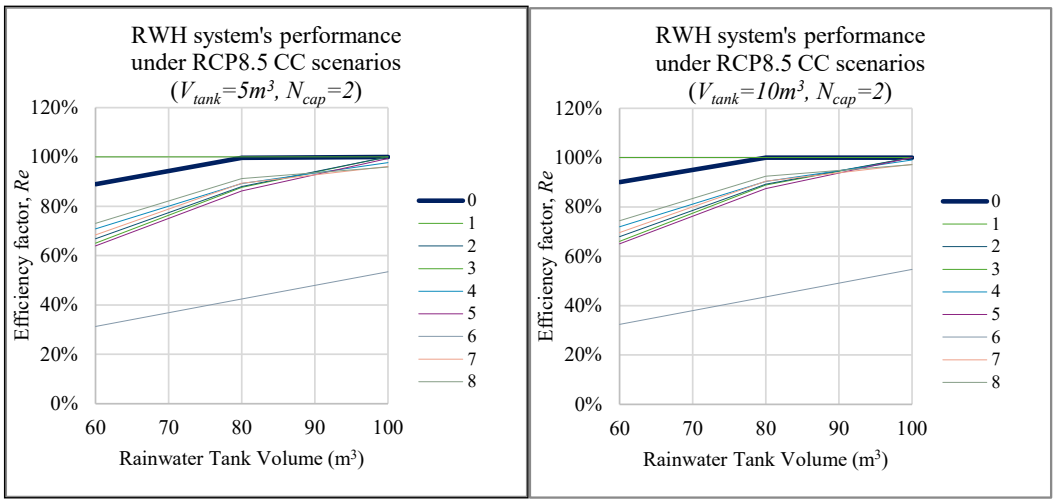

Figure 5. Performance of the Rainwater Harvesting System (RWHS) under Various Climate Change Scenarios (RCP 8.5).

Conclusions

This study assessed the efficiency of domestic rainwater harvesting (RWH) systems on Fourni Island, Greece, under various household and climate change scenarios. The findings highlight the potential and limitations of RWH as a supplementary water source in an arid island environment with limited freshwater resources.

The results demonstrated that rooftop collection area is the most significant factor influencing the system's performance. Larger collection surfaces (≥100 m²) improve system efficiency, ensuring higher rainwater availability. Tank volume plays a secondary role; once a sufficient storage capacity is reached (10-30 m³), additional increases in volume provide diminishing returns in performance.

For two-member households, the system achieved the 30% coverage target in several scenarios, particularly when collection areas exceeded 80 m². However, for three- and four-member households, meeting the coverage target proved significantly more challenging. The four-member household scenario failed to reach the target under any conditions, highlighting the system's limitations in larger households. Higher coverage targets (40% and 50%) further reduced the system's efficiency, requiring rooftop areas of at least 100 m² to maintain reliability (Re ≥ 90%).

When assessing the impact of climate change (RCP 4.5 & RCP 8.5) on system reliability, most scenarios projected a decline in efficiency. Most climate models indicated an average 15% reduction in Re compared to historical conditions, particularly for smaller collection areas (60 m²). The CC6 scenario (SMHI-RCA4_IPSL-IPSL-CM5A-MR) consistently showed the lowest efficiency across both climate pathways, indicating that future rainfall projections under this model predict less favorable conditions for RWH. In contrast, CC3 and CC4 models slightly overestimated system performance but did not significantly alter overall conclusions.

Despite these challenges, RWH remains a viable water management strategy, particularly during peak demand periods such as the tourist season, when water needs increase sharply. While it may not fully replace conventional water sources, RWH can serve as a reliable supplementary resource, reducing dependence on external water supply systems.

Future research should focus on cost-benefit analysis, assessing whether the implementation of RWH systems is economically viable for households in the short and long term. Additionally, exploring hybrid solutions, such as integrating RWH with desalination or greywater reuse, could enhance water security on small islands like Fourni.

In conclusion, while RWH offers potential benefits, its effectiveness depends on site-specific factors such as rooftop area, storage capacity, and climate conditions. Policymakers and local authorities should consider

adaptive planning strategies, including financial incentives for larger collection areas and optimized tank sizing, to improve the feasibility and long-term sustainability of RWH in water-scarce island regions.

References

DEAR-Clima, Data Extraction Application for Regional Climate (2023). Web Application Tool. Available online: http://meteo3.geo.auth.gr:3838/ (accessed on October 12, 2023).

Domene, E., Saurí, D., Martí, X., Huelin, S., Boada, M., Garriga, N. and Molina, J., 2004. Estudi del consum d'aigua als edificis de la Regió Metropolitana de Barcelona. Situació actual i possibilitats d'estalvi. Fundació Abertis, Universitat Autònoma de Barcelona, Departament de Medi Ambient i Habitatge and Fudació Agbar [online]

Domènech, L. and Saurí, D., 2011. A comparative appraisal of the use of rainwater harvesting in single and multi-family buildings of the Metropolitan Area of Barcelona (Spain): social experience, drinking water savings and economic costs. Journal of Cleaner production, 19(6-7), pp.598-608.

Eckstein, G.E., (2009). Water scarcity, conflict, and security in a climate change world: challenges and opportunities for international law and policy. Wis. Int'l LJ, 27, p.409.

EEA, European Environment Agency (2009). Water resources across Europe – confronting water scarcity and drought, Copenhagen. Retrieved in January 2011 from http://www.eea.europa.eu/publications/water-resources-across-europe/at_download/file (Last accessed on December 30, 2024).

Essendi, S.M., (2014). Enhancing household water use efficiency and domestic rainwater harvesting potential in Nairobi county (Doctoral dissertation, University of Nairobi).

Feloni, E. & Nastos, P.T., (2024). Evaluating Rainwater Harvesting Systems for Water Scarcity Mitigation in Small Greek Islands under Climate Change. Sustainability, 16(6), p.2592.

Jacob, D., Teichmann, C., Sobolowski, S., Katragkou, E., Anders, I., Belda, M., Benestad, R., Boberg, F., Buonomo, E., Cardoso, R.M. & Casanueva, A., (2020). Regional climate downscaling over Europe: perspectives from the EURO-CORDEX community. Regional environmental change, 20, pp.1-20.

Koumoura, K.A., Feloni, E.G., Londra, P.A., Baltas, E.A. and Tsihrintzis, V.A., 2018. Uncertainty analysis in sizing rainwater harvesting tanks in an isolated island with limited water resources. Glob. NEST Int. J, 20, pp.534-540.

Londra, P.A., Theocharis, A.T., Baltas, E. & Tsihrintzis, V.A., (2015). Optimal sizing of rainwater harvesting tanks for domestic use in Greece. Water resources management, 29, pp.4357-4377.

Londra, P.A., Gkolfinopoulou, P., Mponou, A. & Theocharis, A.T., (2022). Effect of Rainfall Regime on Rainwater Harvesting Tank Sizing for Greenhouse Irrigation Use. Hydrology, 9(7), p.122.

Preka, M., Feloni, E., Londra, P., Kotsifakis, K. & Baltas, E. (2017). Rainwater harvesting tanks' efficiency in Thera Island. 15th International Conference on Environmental Science and Technology, Rhodes, Greece, 31 August to 2 September 2017.

Rosas, D.F., de Oliveira, F.G., de Castilho Carvalho, L., de Almeida, J.C.A., Souza, A.B., de Souza Lemos, J., Júnior, A.A.O. & Obraczka, M., (2024). Method of Calculation the Efficiency and Economic Viability of Rainwater Harvesting Systems. Revista De Gestão Social E Ambiental, 18(2), pp.e04471-e04471.

Tsihrintzis, V. and Baltas, E., (2013). Sizing of rainwater harvesting tank for in-house water supply. In 13th International Conference on Environmental Science and Technology, Athens, Greece (pp. 5-7).

17th INTERNATIONAL CONGRESS of the Geological Society of Greece

BULLETIN OF THE GEOLOGICAL SOCIETY OF GREECE, SP. PUBL.

EXTENDED ABSTRACT 013

Metapelitic assemblages in the contact metamorphic zone of the Varnous plutonite (NW Macedonia, Greece): preliminary results.

Aravani F.[1], Papadopoulou L.[1], Koroneos A.[1], Chatzipetros A.[2]

(1) Department of Mineralogy-Petrology-Economic Geology, School of Geology, Aristotle University of Thessaloniki, 54124 Thessaloniki, Greece, faravani@geo.auth.gr. (2) Department of Structural, Historical & Applied Geology, School of Geology, Aristotle University of Thessaloniki, 54124 Thessaloniki, Greece

Introduction

The area of the Varnous plutonite is located in northwestern Macedonia, Greece. It lies west of the town of Florina, east of Mikri Prespa Lake, and extends northward across the border between Greece and North Macedonia. The southern boundary extends to the foothills of Mount Vernon (Fig. 1). The plutonite is differentiated, comprising various petrological types ranging from leucogranite to monzodiorite (Katerinopoulos, 1983; Koroneos & Christofides, 1990; Koroneos, 1991; Koroneos et al., 1991; Koroneos 1993, Koroneos et al., 1994). It intruded the basement of the Pelagonian Nappe in 297 Ma (Koroneos et al., 1993).

Although several studies have mentioned the existence of thermally metamorphosed rocks in contact with plutonite, this aspect has not been thoroughly investigated (Kilias, 1980; Katerinopoulos, 1983; Kilias & Mountrakis 1989; Koroneos, 1991). There is ongoing debate regarding whether these rocks are thermally or regionally metamorphosed (Mposkos et al., 2001). The aim of this study is to identify the different metamorphic assemblages and clarify the presence or absence of a thermal aureole.

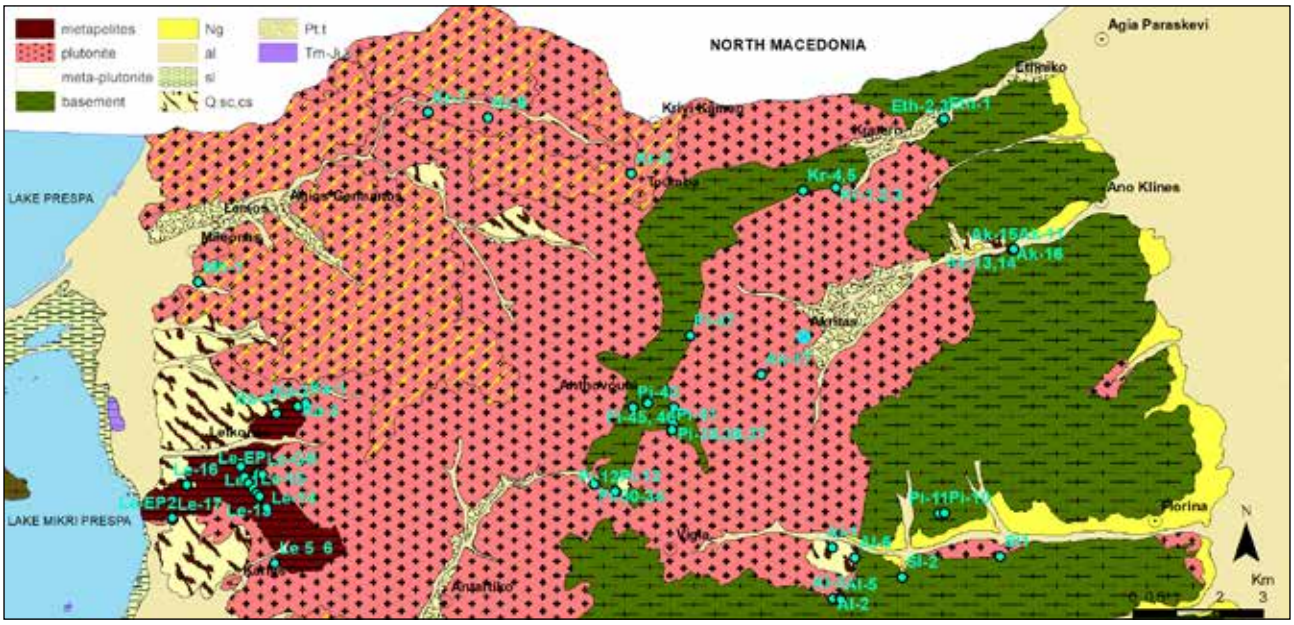

Figure 1. Geological map of the study area., Ng=Neogene sands, clays and conglomerates, al=alluvial deposits, sl=marshy areas, Q.sc,cs=old and recent scree and talus cones, Pt.t=old terrestrial terraces, Tm-Ji.k= Middle Triassic-Lower Jurassic limestones and dolomitic limestones. With cyan sampling locations

Materials and Methods

Seventy-eight polished-thin sections of the rocks surrounding the plutonite were studied by optical and scanning electron microscope for the determination of their mineralogical composition and their textures (see Figure 1 for sampling locations). The scanning electron microscope used was a JEOL JSM-6390LV type equipped with an energy dispersive spectrometer INCA 300, at the Laboratory of Scanning Electron Microscopy at Aristotle

University of Thessaloniki. Analytical conditions were 20 kV operating voltage, 0.4 mA beam current, 80 s analysis time and ≈1 μm beam diameter.

Results

For better data management, the study area has been subdivided into three regions: the eastern part, parallel to the Florina-Agia Paraskevi Road; the western part, parallel to the Andartiko-Mileonas road; and the southern part, parallel to the Florina-Pissoderi-Andartiko road. The southern and eastern parts exhibit the most similarities, while the western part is considerably different.

The eastern part contains the most complex assemblages within the study area. In the same thin section, minerals from a wide range of temperatures and pressures can be observed. The samples can be divided into those that contain sillimanite and those that do not. The main assemblages are as follows (abbreviations after Whitney and Evans 2010)

- Qtz + Mica (Ms-Ph+Pg) + Bt + Grt + St + Sil ± Chl ± Ilm ± Pl ± Ap, and
- Qtz + Mica (Ms-Ph+Pg) + Chl + Grt + Cld ± Bt ± Ilm

Analyses of the minerals are presented in Table 1.

Similar assemblages are found in the southern part; however, in some cases, St occurs alongside Cld. Evidence of overprinting in the samples (Figs. 2 and 3) suggests that the minerals formed as a result of polymetamorphism. Large garnet crystals contain inclusions of sillimanite and appear broken and deformed. A new generation of garnet is observed, characterized by small euhedral crystals. Staurolite and chloritoid occur in some locations, forming euhedral crystals that do not conform to the rock's overall texture. In some samples, sillimanite appears broken and/or replaced by mica, while in other cases, it occurs in the form of fibrolite.

In contrast, the main assemblage in the western part is Qtz + Mica (Ph + Par + Mrg) + And + Crd + Bt ± Pl ± Kfs ± Chl ± Ilm ± Rt ± Sil ± Cld. Crd is, in some cases, almost completely replaced by Ms, Mrg, Bt, and Chl (Fig a,b). In other cases, Crd rim is altered to pinite (Fig. 2 c,d).

Table 1. Representative compositions of minerals from the samples of the area. The structural formulae were calculated on the basis of fixed oxygens. FeOt=total.

	Ms-Ph	Mrg	Pg	Bt	Chl	And	Sil	Crd	Cld	Grt	Pl	Kfs
	Le-1a	Ka-2	Le-2	Le-2	Le-4a	Le-17	Le-10	Le-14	Ka-2	Ka-4a	Le-11	Le-13
SiO_2	45.57	32.04	46.87	39.40	29.66	37.00	37.06	46.90	23.83	38.67	63.16	64.22
TiO_2	0.31	-	0.25	3.28	0.18	0.09	0.04	-	-	0.25	-	18.78
Al_2O_3	34.67	49.77	39.02	20.11	21.20	62.55	61.51	32.67	40.94	20.36	23.01	-
FeOt	1.75	0.30	0.29	18.23	24.29	0.03	0.14	11.25	24.23	30.9	0.1	0.12
MnO	0.08	0.25	-	0.88	1.01	-	0.4	0.11	2.12	6.74	-	-
MgO	0.48	0.03	0.10	6.00	8.44	-	-	5.62	1.48	2.77	-	-
CaO	0.12	11.27	0.53	0.17	-	0.16	0.49	0.43	0.16	1.23	4.02	0.22
Na_2O	0.29	1.35	6.19	-	0.75	-	-	0.38	0.22	-	9.09	0.91
K_2O	9.84	0.06	1.75	8.58	0.26	-	0.23	0.64	0.30	-	0.46	15.43
Total	95.1	95.06	95.03	96.66	85.72	99.84	99.65	98.01	93.29	100.92	99.83	99.68
O	22	22	22	22	28	20	20	18	14	12	8	8
Si	6.31	4.25	6.02	5.78	6.17	4.00	4.027	4.95	1.97	3.00	2.80	2.97
Al^{IV}	1.69	3.75	1.98	2.22	-	-	-	1.05	3.00	-	1.20	1.02
Al^{VI}	3.73	4.02	3.93	1.26	5.20	7.97	7.88	3.01	1.00	1.92	-	-
Ti	0.03	-	0.02	0.36	0.03	0.01	-	-	-	0.02	-	-
Fe^{2+}	0.19	0.03	0.03	2.24	3.45	-	0.01	0.99	1.68	2.07	-	-
Mn	0.01	0.03	-	0.11	0.18	-	0.04	0.01	0.18	0.46	-	-
Mg	0.09	0.01	0.02	1.31	2.62	-	-	0.88	0.15	0.33	-	-
Ca	0.02	1.60	0.07	0.03	-	0.02	0.06	0.05	0.01	0.11	0.19	0.01
Na	0.07	0.35	1.54	-	0.60	-	-	0.08	0.04	-	0.78	0.08
K	1.67	0.01	0.29	1.61	0.14	-	0.03	0.09	0.03	-	0.03	0.91

All minerals that form solid-solution series with Fe-Mg are iron rich. Chl is classified as brunsvigite, a type of chamosite, with Fe/Fe+Mg ratio of 0.62, while in Bt the same ratio is 0.63. In Cld the ratio Fe/Fe+Mg ratio is 0.8, whereas in Crd it is 0.53. As shown by the representative analyses, micas exhibit a wide range of compositions. The underlying causes of these variations in mica composition are still under investigation. Garnet, where present, is almost always represented by the following composition: $Alm_{66}Sps_{14}Py_{9}Grs_{4}Adr_{2}$. Plagioclase is classified as albite in some samples, while in others it is identified as oligoclase.

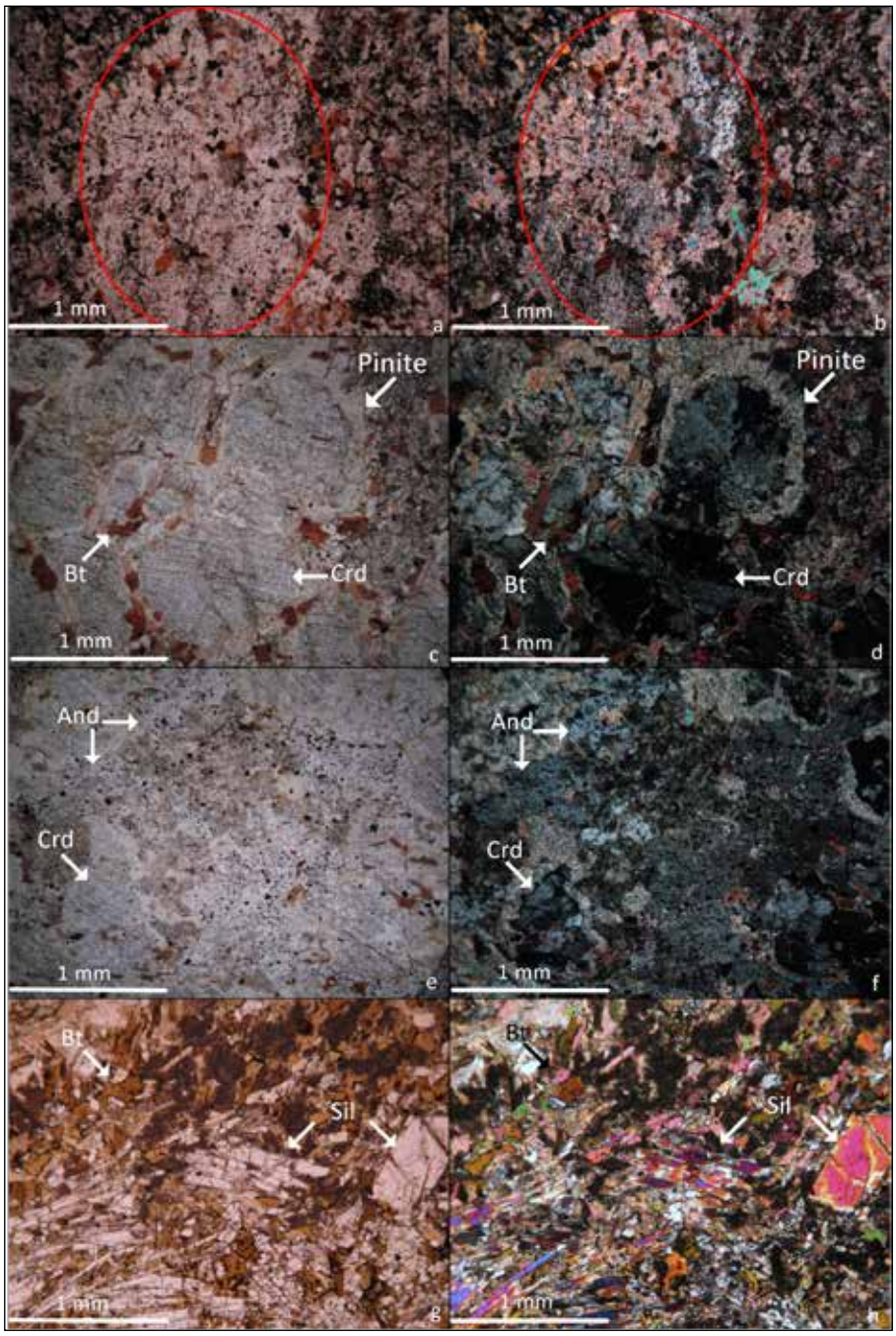

Figure 2. Microscopic images of metapelitic samples of the area. On the left are images with //N and on the right images with +N. Pictures a) and b) show pseudomorphs of mica, biotite and chlorite after cordierite from the western part. Pictures c) and d) show cordierite crystals with pinitic alteration and biotite from the western part. Pictures e) and f) show andalusite and cordierite from the western part. Pictures g) and h) show prismatic sillimanite and biotite with diablastic texture from the eastern part.

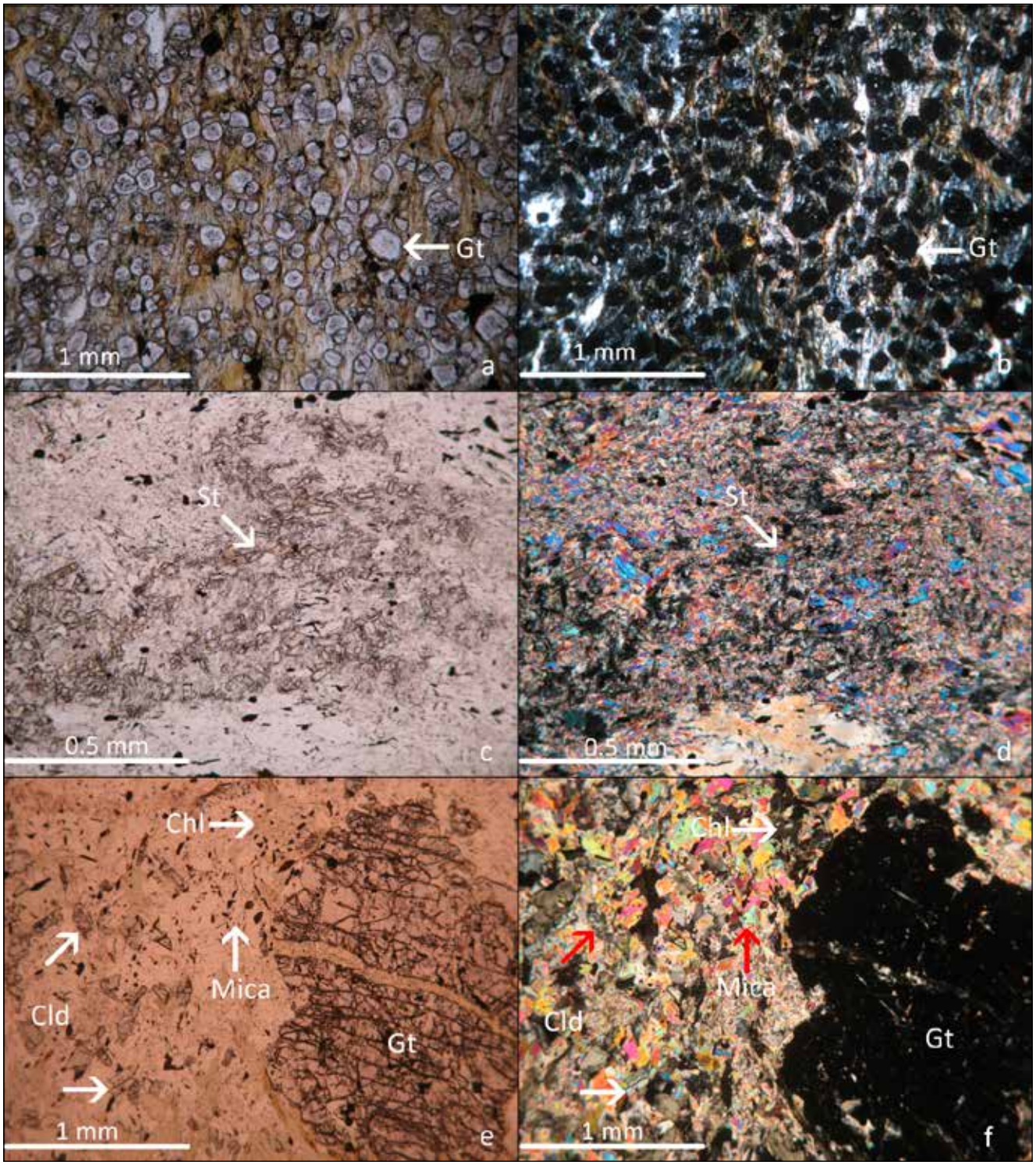

Figure 3. Microscopic images of Alpine metamorphosed rocks of the area. On the left are images with //N and on the right images with +N. Pictures a) and b) show newly formed small garnets in a biotite, chlorite, mica lepidoblastic mass from the eastern part. Pictures c) and d) show staurolite crystals with sericite mass from the eastern part. Pictures e) and f) show prismatic crystals of chloritoid with chlorite and mica and an old garnet with sillimanite inclusions, partially altered to chlorite

Discussion and Conclusions

The eastern and southern parts of the study area exhibit significant similarities, whereas the western part is distinctly different. It is important to note that the basement of the Pelagonian Nappe is considered to represent a continental fragment of Gondwana. Having been formed before the Alpine orogenesis, it has undergone all the tectonic and metamorphic stages associated with this event. Since the plutonite intruded the basement, the surrounding rocks must predate the intrusive rock, with some studies estimating their age at approximately 700 Ma (Anders, 2005; Zlatkin et al., 2014). Consequently, the tectonic history of the area supports the evidence of polymetamorphism observed in the samples.

The Alpine metamorphism in the study area has been well-documented (Avgerinas, 2014; Kilias et al., 2010). According to these studies, a metamorphic event occurred between 150 and 130 Ma, resulting in the formation of an assemblage comprising Cld + Mica + Chl + Kfs + Pl + Qtz + Grt. Another metamorphic event, dated to 110–90 Ma, overprinted the previous assemblage, as evidenced by the alteration of mica to sericite and garnet to chlorite, along with quartz and plagioclase. Finally, a mylonitic event occurred between 90 and 70 Ma.

Based on these studies, it can be inferred that the samples collected from the eastern and southern parts demonstrate these Alpine assemblages, as well as older ones. The older assemblages include Sil-Bt-Grt, characterized by a diablastic texture with large prismatic crystals of sillimanite (Fig. 2 g, h). In some samples, sillimanite occurs as small fibrolite crystals forming an ino-lepidoblastic texture together with chlorite and chloritoid. Samples from the western part also exhibit a diablastic texture, which strongly suggests that these rocks formed under low-pressure/high-temperature conditions.

The assemblages Sil-Bt-Grt in the eastern part and And-Crd-Bt-Ms in the western part are older than the Alpine metamorphic events. These assemblages are attributed to thermal contact metamorphism associated with the intrusion of the Varnous plutonite. This conclusion is further supported by the overprinting of Alpine metamorphic events onto these earlier assemblages.

The sequence of metamorphic events in the area can be summarized as follows:

1. Formation of Sil + Bt + Grt and And + Crd + Bt + Ms at approximately 297 Ma.
2. Development of Cld + Mica + Chl + Kfs + Pl + Qtz + Grt ± St during the Alpine event at 150–130 Ma.
3. Alteration of these assemblages by sericite, chlorite, and margarite at 110–90 Ma.
4. Mylonitization of all previous assemblages at 90–70 Ma.

Further research is ongoing to determine the factors responsible for the formation of different assemblages in the eastern and western parts of the contact aureole.

References

Anders, B. 2005. The pre-Alpine evolution of the basement of the Pelagonian Zone and the Vardar Zone, Greece (Doctoral dissertation, Mainz, Univ., Diss., 2005).

Avgerinas, A. 2014. Deformation and kinematics analysis of the pelagonian zone in Northern Greece. Faculty of Sciences, School of Geology. PhD Thesis, Aristotle University of Thessaloniki

Katerinopoulos, A. 1983. Contribution in the study of plutonic rocks from Western Varnountas, School of Geology. PhD Thesis, University of Athens.

Kilias, A. 1980. Geologische und tectonische Untersuchung des Gebietes von östlichen Varnous (NW Makedonien). Thesis, Univ. of Thessaloniki, Greece

Kilias, A., Mountrakis, D., 1989. The Pelagonian nappe: tectonics, metamorphism and magmatism. Δελτίον της Ελληνικής Γεωλογικής Εταιρίας, 23(1), 29-46.

Kilias, A., Frisch, W., Avgerinas, A., Dunkl, I., Falalakis, G., & Gawlick, H. J. 2010. Alpine architecture and kinematics of deformation of the northern Pelagonian nappe pile in the Hellenides. Austrian Journal of Earth Sciences, 103(1), 4-28.

Koroneos, A., 1991. Mineralogy, Petrology and Geochemistry of Eastern Varnountas plutonite (NW Macedonia), Faculty of Sciences, School of Geology. PhD Thesis, Aristotle University of Thessaloniki

Koroneos, A., 1993a. Study of the coexisting biotites and amphiboles from the eastern Varvountas plutonite (NW Macedonia). Ορυκτός Πλούτος, 1993(085), 31-46.

Koroneos, A., 1993. Comparative, mineralogical-petrological and geochemical study of the plutonic and gneissic

rocks of eastern Varnountas (NW Macedonia) Annales Géologiques des pays helléniques, Athènes, Départment des sciences de la terre de l'université.

Koroneos, A., Christofides, G., 1990 Petrology and geochemistry of the Eastern Varnountas plutonite (NW. Macedonia): preliminary presentation. Δελτίον της Ελληνικής Γεωλογικής Εταιρίας, 22, 97-113.

Koroneos, A., Christofides, G., Eleftheriadis, G., 1991. Evolution of Eastern Varnountas plutonite (NW. Macedonia): major and trace element fractional crystallization models. Δελτίον της Ελληνικής Γεωλογικής Εταιρίας, 25(2), 81-99.

Koroneos, A., Christofides, G., Del Moro, A., & Kilias, A., 1993. Rb-Sr geochronology and geochemical aspects of the Eastern Varnountas plutonite (NW Macedonia, Greece). Neues Jahrbuch für Mineralogie. Abhandlungen, 165(3), 297-315.

Koroneos, A., Soldatos, T., Christofides, G., Eleftheriadis, G., 1994. Origin of eastern Varnountas plutonite (NW Macedonia). Δελτίον της Ελληνικής Γεωλογικής Εταιρίας, 30(1), 193-204.

Mposkos, E., Kostopoulos, D., Krohe, A. 2001. Low-P/High-T pre Alpine metamorphism and medium-P Alpine overprint of the Pelagonian z;one documented in high-alumina metapelites from the Vernon massif, western Macedonia, Northern Greece. Bulletin of the Geological Society of Greece, 34, 3-949

Whitney, D. L., & Evans, B. W. (2010). Abbreviations for names of rock-forming minerals. American mineralogist, 95(1), 185-187.

Zlatkin, O., Avigad, D., & Gerdes, A., 2014. Peri-Amazonian provenance of the Proto-Pelagonian basement (Greece), from zircon U–Pb geochronology and Lu–Hf isotopic geochemistry. *Lithos*, *184*, 379-392.

17th INTERNATIONAL CONGRESS of the Geological Society of Greece

BULLETIN OF THE GEOLOGICAL SOCIETY OF GREECE, SP. PUBL.

EXTENDED ABSTRACT 014

Balancing Precision and Resources: The Effect of Sampling Density in Regional Soil Geochemical Mapping

Argyraki A.[1], Kontomichalou A.[1], Kypritidou, Z.[1], Liakopoulos, A.[2]
(1) Department of Geology and Geoenvironment, National and Kapodistrian University of Athens, Athens, Greece, argyraki@geol.uoa.gr (2) Hellenic Survey for Geology and Mineral Exploration, Athens, Greece

Research Highlights

This study investigates the impact of field sampling density on the quality and reliability of regional geochemical maps using chromium (Cr) and lead (Pb) as case studies due to their contrasting geochemical behaviour within the mapped area. Two data sets, comprising 117 and 24 evenly distributed sampling locations within the same study area of 2500 km^2, were used to produce geochemical maps for each element. Key statistical metrics, including the mean, median, and standard deviation were compared to assess the impact of varying sampling densities. The Inverse Distance Weighting (IDW) interpolation method was then applied to generate maps, enabling visualisation of spatial variability.

Introduction

Geochemical mapping is a method of "revealing the invisible", initially involving systematic sampling, followed by sample preparation, chemical analysis, interpretation of the results, and the plotting of geochemical maps. This valuable tool is used today in various fields, including mineral resource exploration, development planning, contaminated site inventory, epidemiology, agriculture, and forestry.

The work presented here is part of a preliminary study on establishing the soil geochemical baselines of a pilot area (Attiki-Voiotia region), with the ultimate aim of publishing the first Soil Geochemical Atlas of Hellas. The project is implemented by the Hellenic Survey for Geology and Mineral Exploration, Department of Geochemistry and Environment, through the National Funds Programme in collaboration with the Laboratory of Economic Geology and Geochemistry of the University of Athens. The dominant lithological types identified across the entire extent of the pilot area can be categorised into three groups: (a) Carbonate rocks of the Alpine orogeny (limestones, dolomites, and marbles), (b) Argillaceous-siliceous rocks of the Alpine orogeny (schists and schist-chert sequences) in stratigraphic or tectonic contact with the carbonates, and (c) Post-Alpine sedimentary rocks (marls, conglomerates, sandstones, etc.) and looser sediments (colluvium, alluvial clastic material), which occupy the lower topographic areas and plains. Mineralogical analysis by semi-quantitative powder X-Ray Diffraction of selected soil samples from the study area assisted in their classification into two major groups depending on the proportion of carbonate minerals, related to the underlying lithology. Specifically, samples of significantly lower carbonate mineral content are associated with the alpine rocks (Kypritidou et al., 2024).

The objective of the present study is to investigate the impact of field sampling density on the quality and reliability of regional geochemical maps using chromium (Cr) and lead (Pb); they are used as case studies due to their contrasting geochemical behaviour within the mapped area. Chromium is a primarily lithogenic element enriched in mafic-ultramafic rocks and their weathering products, and Pb is an element typically associated with diffuse anthropogenic contamination as well as areas of enrichment, related to massive sulphide ore bodies.

Methods

Top-soil (0-20 cm) samples were collected from 117 locations on a 5 x 5 km grid within an area of about 2500 km^2 by following and appropriately adjusting the guidance of the International Union of Geological Sciences Manual of Standard Methods for Establishing the Global Geochemical Reference Network (Demetriades et al., 2022). Dried and sieved (<2 mm) soil samples were analysed by ICP-AES / ICP-MS following hot aqua regia dissolution. The present study is focused on the analytical results of Cr and Pb.

To prepare the geospatial database for the pilot project, which incorporated the results of laboratory determinations and chemical analyses, a corresponding file was compiled in ArcGIS Pro. Sampling locations were integrated into the file by importing the complete KML format file exported from the GPS. The eastern coastline boundary, along with the

boundaries of HNHS (Hellenic National Mapping Agency) maps, or the municipal and community boundaries of the pilot area, were used to isolate and clip thematic layers to the extent of the pilot project area from broader national data sets. For the purposes of this study, a subset of 24 sampling points out of the total 117 locations, was used, i.e., by reducing the number of samples by 80%. The selection of the samples was based on their uniform spatial distribution, the different land uses, and litho-geological types of the area. It is noted that since the overall objective of the project is to establish the geochemical baselines, this thinned-out sample distribution did not include any samples within the urban area of Athens, in line with the prescribed methodology by the Manual of Standard Methods for Establishing the Global Geochemical Reference Network to "sample natural residual soil, meaning soil that is not affected by any anthropogenic activities" (Batista et al., 2022). The resulted sampling scheme is equivalent to a sampling density of approximately 1 sample per 10 x 10 km grid. This thinning-out of the grid would correspond to saving a great deal of resources during sampling, sample preparation and analysis.

The statistical treatment of the concentrations of Cr and Pb at the two sampling densities included the calculation of the basic statistical parameters, and the plotting of probability curves in order to test normality and calculate appropriate percentiles for defining the concentration classes in the produced colour-surface geochemical maps. Notched box-and-whisker plots were constructed to allow pairwise comparison of the medians to be performed at the 95% confidence level by examining whether the two notches overlap. One-way analysis of variance (ANOVA) was used to indicate the statistical significance of the differences between results by the two sampling densities. The subsequent geochemical mapping procedure followed the typical steps of spatial data posting and interpolation by using the deterministic IDW technique with output cell size set at 200, power of 2 and search radius variable with 12 points in ArcGIS Pro. Error analysis, by applying exploratory interpolation in ArcGIS Pro, was used to calculate mean error enabling comparison of interpolated results between the datasets.

Results and discussion

The descriptive statistics for the two elements at the two sampling densities, and their probability plots are presented in Table 1 and Figure 1, respectively.

Table 1. Summary statistics for Cr and Pb (mg/kg) in soil for the two sampling densities.

Element	N	Mean	Median	Standard Deviation	Minimum	Maximum
Cr	117	134	86	190	2	1273
Cr	24	185	89	225	2	990
Pb	117	213	29	969	5	10000
Pb	24	238	31	558	8	2138

The statistical parameters of the raw data (Table 1) indicate that both elements display non-normal, right skewed statistical distributions with mean values significantly higher than their corresponding medians and several outlying values. A comparison of the median values for the two sampling densities demonstrates nearly similar results for both elements. One-way ANOVA (95% confidence level) on log-transformed data indicated no statistically significant differences in mean Cr and Pb concentrations between the two sampling densities. Particularly for Pb, the median values of 29 mg/kg for the dense and 31 mg/kg for the sparse sampling locations are comparable with the values of 26 and 45 mg/kg measured for rural and suburban soil within the area in a previous study by Argyraki et al. (2018).

Although Cr data approach a log-normal distribution, Pb data after log-transformation are not normalised, probably due to the presence of multiple populations within the study area. Indeed, the effect of elevated Pb concentrations in soil samples from the sulphide-ore bearing Lavreotiki peninsula is profound as a separate geochemical domain within the study area. Following these observations, and the number of samples classified in each interval, concentrations corresponding to the 25th, 50th, 75th, 90th, and 95th percentiles of the data were selected to define the class limits for mapping both elements at the two sampling densities.

The boxplot comparison (Figure 1) shows that the notches at the 95%-confidence interval about the medians overlap, indicating that there is no significant difference between the median values of Cr and Pb at the two sampling

densities. However, the folding-in behaviour of the Cr low sampling density boxplot is caused by the notch extending beyond the first quartile, suggesting that more samples are needed to define the background population.

For plotting the interpolated surfaces, the deterministic IDW technique was used. The resulting maps are displayed in Figure 2. Graduated size symbol layers are superimposed on the colour surface maps to provide the exact concentration measured at each sampling site. Visual inspection of the maps indicates that although the spatial variability is better captured by the dense sampling data set, anomalous areas can still be delineated even when using the 24 sampling locations. This observation highlights that careful selection of sampling sites in conjunction with a thorough study of the underlying lithology plays a crucial role in regional geochemical mapping, and that a 10 x 10 km sampling grid would still be fit-for-purpose for the delineation of regional geochemical trends.

Within the study area, elevated Cr concentrations correspond to areas of laterite occurrences in the north-west part of the map, serpentinised rocks in Hymettus Mt., and greenstones in the south-east part of the map. A gradual increase in Pb concentration is observed from north-west towards south-east areas on the map, peaking in the Lavreotiki area, which hosts the well-known galena ore deposits. These trends are captured by both the dense and the sparse sampling data sets. However, error analysis on the interpolated results indicated a 6-fold and a 3-fold increase of mean error for Pb and Cr respectively when the number of samples is reduced to 24.

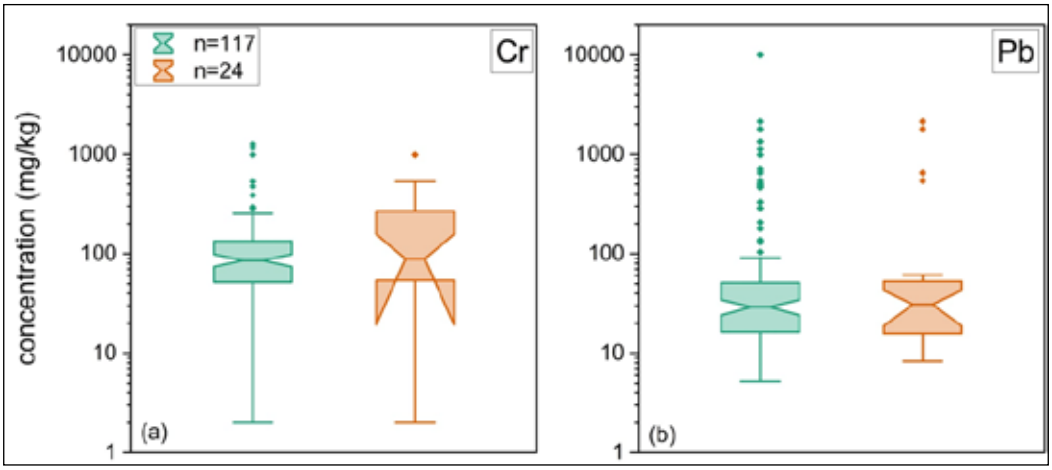

Figure 1. Notched box-and-whisker plots of Cr (a) and Pb (b) for comparison at different sampling densities.

Conclusions

The main findings of the comparison presented between the two sampling densities and the Cr and Pb spatial distribution are as follows:

- The geochemical patterns of both elements in soil are explained by bedrock lithology.
- No significant differences were identified between the descriptive statistics for both elements and sampling densities; the overall trend of the statistical distribution was captured with sufficient precision by the lower sampling density data set.
- The interpolated surfaces in the geochemical maps show anomalous concentrations in the same areas. The lower sampling density captured most of the anomalous areas. However, the spatial variability is better attained by the dense sampling data set for both elements.

Overall, the results of this study suggest that soil sampling locations for mapping the geochemical baseline of chemical elements at the regional scale should be selected by adopting a combination of statistical and judgmental approaches with careful consideration of the local conditions at each sampling site. In this way the balance between effort and final map precision can be achieved.

Further work should focus on testing the results for additional elements of interest and for different sampling densities. The current sampling data set on the 5 x 5 km sampling grid provides the opportunity for such trials, which

could be of paramount importance for optimising available resources for sampling, sample preparation and analysis when expanding the project to the national scale.

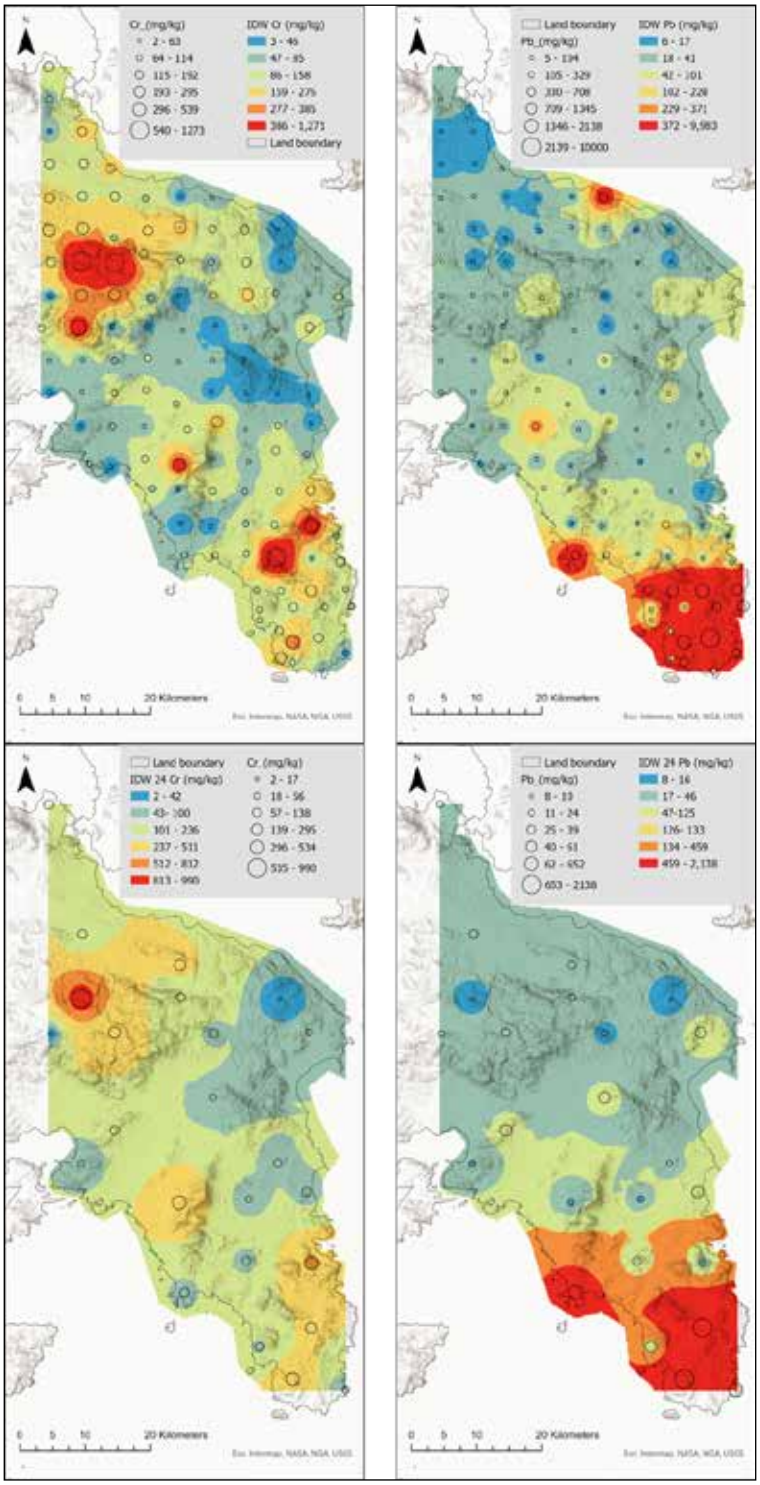

Figure 2. IDW interpolated colour surfaces of Cr and Pb based on 117 samples (top) and 24 samples (bottom).

Acknowledgements

We acknowledge financial support by HSGME through the National Funds Programme, project no. 2020ΣΕ06100004 (HSGME no 22204). We thank Dr. Alexandros Demetriades and an anonymous reviewer for the thorough review of this extended abstract.

References

Argyraki, A., Kelepertzis, E., Botsou, F., Paraskevopoulou, V., Katsikis, I., Trigoni, M., 2018. Environmental availability of trace elements (Pb, Cd, Zn, Cu) in soil from urban, suburban, rural and mining areas of Attica, Hellas. In: Demetriades, A., Johnson, C. and Birke, M. (Eds.), Urban Geochemical Mapping: The EuroGeoSurveys Geochemistry Expert Group's URGE Project, Journal of Geochemical Exploration, 187, 201−213; https://doi.org/10.1016/j.gexplo.2017.09.004

Batista, M.J., Demetriades, A., Johnson, C.C., Tarvainen, T., Savin, I., Smith, D.B., Haslinger, E., Salminen, R., Gregorauskienė, V., Zomeni, Z., Lacassie Reyes, J.P., Astudillo, F. & Oliva Vicentelo, P.S, 2022. *Residual Soil and Humus Sampling*. Chapter 3.2 In: Demetriades, A., Johnson, C.C., Smith, D.B., Ladenberger, A., Adánez Sanjuan, P., Argyraki, A., Stouraiti, C., Caritat, P. de, Knights, K.V., Prieto Rincón, G. & Simubali, G.N. (Editors), International Union of Geological Sciences Manual of Standard Methods for Establishing the Global Geochemical Reference Network. IUGS Commission on Global Geochemical Baselines, Athens, Hellenic Republic, Special Publication, **2**, 91−119.

Demetriades, A., Johnson, C.C., Smith, D.B., Ladenberger, A., Adánez Sanjuan, P.A., Argyraki, A., Stouraiti, C., Caritat, P. de, Knights, K.V., Prieto Rincón, G., Simubali, G.N. (Eds.), 2022. International Union of Geological Sciences. Manual of Standard Methods for Establishing the Global Geochemical Reference Network. IUGS Commission on Global Geochemical Baselines, Athens, Hellenic Republic, Special Publication, 2, 515 pp.; https://doi.org/10.5281/zenodo.7307696..

Kypritidou, Z., Kontomichalou, A., Botsou, F., Argyraki, A., Liakopoulos, A., 2024. Soil mineralogy in support of a regional geochemical baseline study in Greece. Joint Conference of ISEH ICEPH & ISEG, Galway, Ireland, Book of Abstracts p. 410; https://www.universityofgalway.ie/media/ineh/files/ISEH-ICEPH-ISEG-Book-of-Abstracts.pdf.

17th INTERNATIONAL CONGRESS of the Geological Society of Greece

BULLETIN OF THE GEOLOGICAL SOCIETY OF GREECE, SP. PUBL.

EXTENDED ABSTRACT 015

Seismic resilience of primary water transfer network at Lagadas municipality, North Greece

Arnaouti, S.[1], Ktenidou O.-J.[2]

(1) Civil Engineer at Municipal Water Supply and Sewerage Company of Lagadas, Greece

(2) Senior Researcher at National Observatory of Athens, Greece

Introduction

Among natural disasters, earthquakes have the most destructive potential to water pipe networks. The induced damages to the water supply can be the main reason for post seismic economical disruptions. Thus, it is of utmost importance to recognize the most vulnerable elements of the water pipe network under seismic load, in order to manage effectively prevention and post seismic actions.

At the present work, we estimate the seismic resilience of the external water network - based on Balaei et al (2020) methodology - at Lagadas municipality, one of the ten largest area municipality in Greece, as a measure of the system's ability to absord a shock when occurs and to recover quickly after that (Bruneau, 2003). The results can be used to rank the prevention actions necessary to reduce earthquake consequences to water network performance.

Background

The term 'resilience' was first introduced by Holling (1973) at ecology field, as a measure of the system capacity to absorb parameter changes. The term was imported to engineering by Klein et al. (2003), that study the characteristics of mega-cities resilience to natural hazards. The conceptual work of Bruneau et al. (2003) defines seismic resilience as 'the ability of social units to mitigate hazards, contain the effects of disasters when they occur and carry out recovery activities in ways that minimize social disruption and mitigate the effects of future earthquakes.' As such, a resilient system entails the properties of robustness, redundancy, resourcefulness and rapidity to recovery.

Focusing at the water pipe networks, the works of Menoni et al. (2002) and Borzi (2023) estimate the network's vulnerability. In respect of the 'resilience' term, Arcadis company (2016) ranks fifty cities worldwide regarding their ability to secure constant water supply. Cimellaro et al. (2015) propose a resilience index for the water distribution network (WDN) as a product of three parameters: the number of users that lose their access to water, the water level in the tank and the water quality. The same year, Matthews analyses the water and sewage network resilience during natural hazards. In his study, the key parameters of the water infrastructure are quantified, based on Katrina and Rita hurricane events. Farahmandfar et al. (2016) propose a metric for seismic resilience of WDNs dependent on hazard intensity, estimated pipeline response and network topology in order to prioritise pipeline replacement works. Makropoulos et al. (2018) recognize three failure states for the WDNs, namely insufficient water quantity, insufficient water quality and infrastructure failure and suggest a toolbox to assess network resilience. Mo'Tamad et al. (2022) applied 27 different earthquake senarios to the WDN of an M-city in Ontario and examined how the expected failures affect its hydraulic resilience, in terms of pressure, water serviceability and population impacted. The analysis showed that for medium to large earthquakes, water supply can be lost for days and affect more than 90% of the city population.

Balaei et al. (2020) propose an index-based methodology to estimate WDN resilience under seismic load; the technical factors that affect WDN resilience are established through literature review and expert interviews and then quantified through expert judgement. The study showed that vulnerability, redundancy and criticality are the major technical factors affecting system resilience.

Methodology

The methodology used to estimate water system resilience is based on the work of Balaei et al. (2020) and is described in detail at Arnaouti, 2020. Balaei et al. (2020) initially state that system resilience consists of two principal terms: the residual functionality of the system after shock (robustness) and the swiftness of the system to return to its initial functionality (recovery rapidity). For the first part, the authors consider

that it mainly depends on the physical characteristics of the system rather than in social, economic and organizational parameters. For the latter part, the authors assume that the recovery time depends on the same parameters as the robustness, in the sense that an organization that creates a robust system usually develops quick time responses as well. By taking those simplified assumptions under consideration, Balaet et al. (2020) convert the resilience estimation problem to a robustness estimation problem. Literature review and field expert interviews resulted in the selection of three technical factors that define water system robustness under seismic load: vulnerability, redundancy and criticality. The authors suggest index values for those three factors through provided tables. For the vulnerability index assessment, the authors take account of the three main seismic hazards to the water network, namely fault rupture, slope failure and liquefaction. Once the vulnerability index (V_i), the redundancy index (ρ_i) and the criticality index (C_i) are determined for each pipeline section i, the robustness index R_i is given by the following equation:

$$R_i = 1 - \frac{V_i \cdot C_i}{\rho_i} \quad (1)$$

If L_i is the length of pipe section i and N is the number of the network pipe sections of the settlement water network, then the total robustness of the network is:

$$R = \frac{\sum_i^N L_i \cdot R_i}{\sum_i^N L_i} \quad (2)$$

Study area

The Municipality of Lagadas is located about 20 klm northeast of Thessaloniki and is the 10th larger municipality in Greece in terms of area (1220.3 km^2). It consists of seven municipality units, namely Assiros, Vertiskos, Kallindia, Koronia, Lagadas, Lahanas and Sohos) and its total population is 37.022 inhabitants (ELSTAT data, 2021).

The present study focuses on to the primary transfer water network of the total 37 housing areas/ settlements of Lagadas municipality, since there are scarce data for their water distribution network.

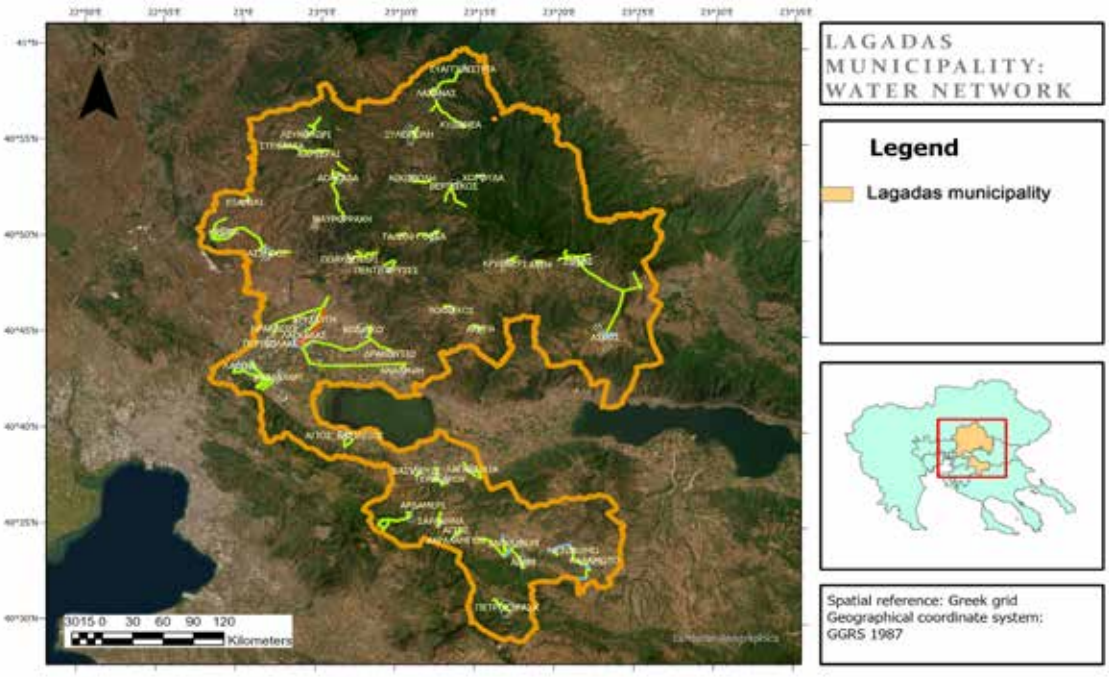

Figure 1: Primary water transfer network of the 37 settlements of Lagadas municipality

- **Fault ruptures at Lagadas**

Caputo et al. (2012) report two main fault ruptures in Lagadas area, the Sohos-Mavrouda fault and the Mygdonia fault. The Sohos-Mavrouda fault has a W-E direction, its length is about 41 km and it is an antithetic fault, since it is the only one with south-dipping structure. The Mygdonia fault with a total length of 69 km, is divided in three parts, that follow the borders of the homonymous basin: from west to east, there is Lagadas segment, Gerakarou segment and Apollonia segment. The Gerakarou segment with a W-E direction dips to the North and was the causative fault of the 1978 Mw=6.5 Thessaloniki earthquake, while the Lagadas segment strikes NW-SE and caused the M6.5 Assiros earthquake in 1902. The authors state that some researchers consider that Lagadas segment is not related to the current stress field, though oblique-slip kinematics show evidence of reactivation. On the other hand, some researchers believe that the seismic activity has abandoned Lagadas segment and been transferred to the south, towards Asvestohori fault. In addition, Chatzipetros et al. (2006) have detected a fault in Lagyna region with a NW-SE strike that was not included to the IGME geological map. This fault is parallel to the rest of the active faults of the area and is considered to be caused by recent over pumping activity. The map with the aforementioned fault ruptures available at Chatzipetros et al. (2006) was digitized through ArcGIS Pro program.

- **Landslides at Lagadas**

Koukis et al. (2005) recorded landslide occurrences in Greece for the time period 1950-2004 and provide a landslide hazard zonation map of Greece. According to this map, the Lagadas area exhibit a number of 0-1 landslides per 100 km^2 area. In addition, Wilde et al. (2018) and Günther et al. (2014) created a landslide susceptibility map of Europe with a 200x200m resolution based on a semi-quantitative method that relates the number of landslide occurrences to slope angle, lithology and land cover. The map was received in a raster form through the ESDAC Dataset Access service, after digital request.

- **Liquefaction at Lagadas**

As stated by Papathanassiou (2006), the 1902 Assiros earthquake caused liquefaction phenomena in Assiros and at the Thermal Springs of Lagadas, as written descriptions of mud puddles in dry tributary reveal. Papathanassiou et al. (2010) created a liquefaction susceptibility map of Greece by correlating liquefaction occurrences with geological, geomorphological and seismological data. Though a susceptibility map in a regional scale instead of national scale would have been more appropriate for the present study, the lack of such data led to the use of the data available.

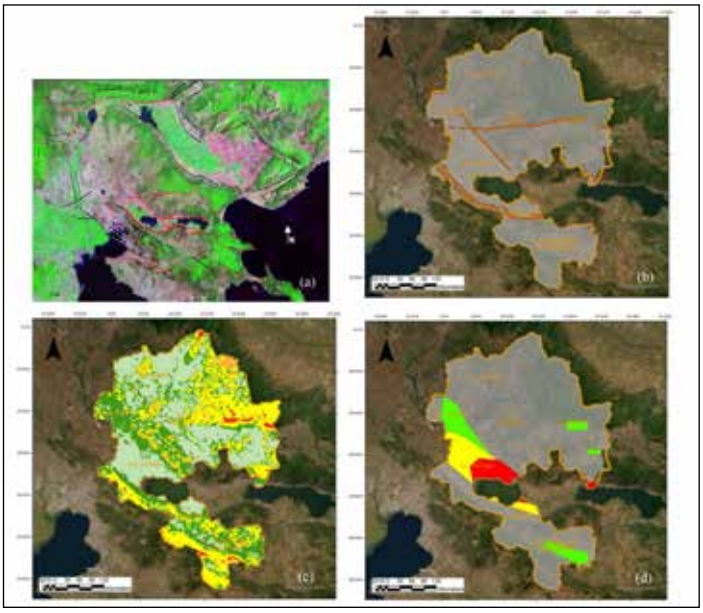

Figure 2: (a) Fault rupture maps at Lagadas area, taken from Chatzipetros et al. (2006), (b) Active faults of Lagadas municipality used for the present study, based on Chatzipetros et al. (2006) map, (c) Landslide susceptibility map of Lagadas municipality used for the present study (based on ESDAC data) and (d) Liquefaction susceptibility map of Lagadas municipality used for the present study (based on Papathanassiou et. Al, 2010 susceptibility map)

Calculations

- **Vulnerability index Vi**

According to the literature, vulnerability index Vi of the pipelines can be estimated based on their technical characteristics. For example, Menoni et al. (2002) propose a method for estimating Vi based on pipe age, pipe depth, construction material and pipe diameter. However, Menoni's methodology results in an almost uniform vulnerability index throughout Lagadas municipality, since the primary water transfer network share common characteristics (their diameter is usually below 300 mm, their material is PVC besides a few cases made of asbestos and the majority of the networks was constructed at the decade 1999-2009, just before the beginning of economic crisis in Greece).

According to the technicians of Municipal Water Supply and Sewerage Company of Lagadas, this is not the case in practice; transfer water pipe networks exhibit a considerable different performance under regular conditions, with damages ranging from almost none to too many damages per year. This different performance is attributed to three main reasons: (a) the asbestos pipelines that haven't been replaced yet (as Commission Directive 1999/77/EC defines), exhibit leaks at their joints, because the rubber joints have been worn with time. In addition, their repair is demanding due to the lack of special joints for large diameters, (b) inadequate initial design, since in practice the need to serve houses outside the settlement boundaries (in greater elevations and/or great distances from the settlement) lead to water pressures greater than initially designed and (c) inadequate compliance with technical specifications during construction; for example, non-appropriate pipe depth, no use of pipe sand-enacased or concrete-encased techniques when appropriate.

In order to import our technical staff knowledge about pipe actual vulnerability into our analysis, we have introduced five vulnerability categories (categories 0 to 4, where category 0 is for a pipe that is not in use, and categories 1 to 4 for pipes that exhibit damages 0, 1-2, 3-4 and more than 4 per year respectively) and set the vulnerability index according to the actual pipe performance under standard conditions. The most vulnerable sections of the transfer water pipe network are located at the municipal unit of Lagadas and more specifically at Lagadas, at Lagynas and at Irakleion – Perivolaki asbestos networks. At the rest of the municipal units, vulnerable sections can be found where elongated pipelines are used to transfer water to adjacent settlements, like in Stefania and Ossa.

- **Criticality index C_i**

Following Balaei et al. (2020) study, we used five categories for the criticality index (categories 1 to 5, when the population served was 0-50, 51-200, 201-500, 501-1000 and more than 1000 inhabitants respectively).

- **Redundancy index ρ_i**

Balaei et al. (2020) set five categories for the redundancy index (categories 1 to 5, for very high, high, some, low and no redundancy respectively). Since the redundancy description of Di Nardo et al (2016) is applied to water distribution networks and not to transfer water networks, we defined new categories and definitions for the redundancy index, shown at Table 1 below:

Table 1. Redundancy index categories for standpipes and downpipes, used in the present study

Redundancy index (ρ)	Standpipe (water transfer from drilling to the tank)	Downpipe (water transfer from tank to the settlement)
1	-	>2 downpipes
2	>5 functioning standpipes OR >2 standpipes with at least one spare	-
3	4-5 functioning standpipes OR 2 standpipes with at least one spare	2 downpipes
4	2-3 functioning standpipes	-
5	one functioning standpipes	One downpipe

- Rupture impact index $I_{RP,i}$, landslide impact index $I_{LD,i}$ and liquefaction impact index $I_{LQ,i}$

The impact indexes are estimated based on the tables provided by Balaei et al. (2020).

- **Robustness index**

The robustness index of pipe section i for seismic hazard j is:

$$R_{j,i} = \frac{1}{(V_i \cdot C_i \cdot \rho_i \cdot I_{j,i})}$$

Five categories were selected for the robustness index (index values: 1 for high robustness to 5 for very limited robustness), when robustness is 15-100%, 5-15%, 1-5%, 0.5-1% and 0-0.5% respectively. The robustness index in total, by taking account all three seismic hazards, is considerer to be the robustness of the worst-case scenario, thus it is the max robustness index: . $R_i = \max_{j=1\ldots3} R_{j,i}$. Through Eq.2, the robustness category per settlement network can be estimated.

All the calculations and maps of the present study were performed using ArcGIS Pro software, v.3.3.0, @ ESRI Inc 2024 (free license was available to MSc students of University of Aegean).

Results

Figure 4 shows the robustness of the water transfer network per pipeline section and per settlement.

The study reveals the very limited robustness of the water transfer pipelines at Lagadas, Lagyna, Perivolaki, Gerakarou and Lagadikia due to its proximity to faults. Liquefaction phenomena affect the water network at Lagadas, Xrisavgi and Irakleion. Regarding landslides, pipelines at Lagadas, Xrisavgi and Lagyna exhibit very limited robustness.

In terms of settlement networks, the only settlement with high robustness is Galini. Indeed, Galini is relatively protected by the seismic hazards and it has small population. Settlements at Lagadas municipality unit show very limited robustness due to the network's high vulnerability, the large population relative to the other municipality units, the proximity to fault ruptures and the liquefaction susceptibility. Very limited robustness can also be met at settlements of Koronia municipality unit, mostly because these networks lack redundancy and they are close to fault ruptures.

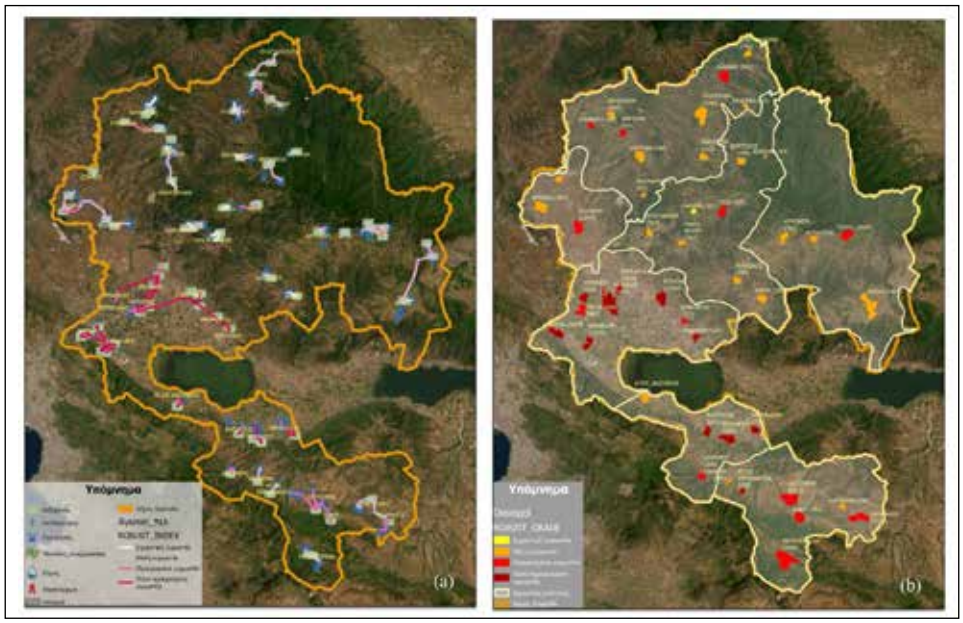

Figure 4: Water transfer network robustness. (a) Robustness per pipeline (white: high robustness, light pink: medium robustness, pink: limited robustness, magenta: very limited robustness. (b) Robustness per settlement of Lagadas municipality (yellow: high robustness, orange: medium robustness, red: limited robustness, brown: very limited robustness)

Conclusions

According to literature, the basic reason of failure of the water pipelines after earthquake is soil displacement, that can be caused by fault rupture displacements, landslide effects and liquefaction phenomena. The methodology proposed by Balaeti et al. (2020) takes account of all three seismic hazards.

Although literature review offers many approaches for estimating pipe vulnerability based on their physical characteristics, the use of our technical staff knowledge seems more appropriate, since it integrates critical aspects of the network, like inadequate initial design and not compliance with technical specifications during construction.

The results reveal that the majority of settlements in Lagadas municipality are not that robust and severe disruptions to water supply is expected after earthquake. Increasing pipeline vulnerability and enhancing network's redundance are prevention works for the least robust systems. Settlement robustness offers a valuable indicator to prioritize the prevention measures.

Acknowledgements

I would like to express my sincere appreciation to Municipal Water Supply and Sewerage Company of Lagadas and to its technical staff for providing all the necessary data for the water network providing and sharing their experience on its performance.

References

Holling, C., 1973. Resilience and stability of ecological systems. Annual Review of Ecology and Systematics, 4, 1-23.

Klein, R., Nicholls, R., & Thomalla, F., 2003. Resilience to natural hazards: How useful is this concept? Environmental Hazards, 5, 35-45.

Bruneau, M., Chang, S., Eguchi, R., Lee, G., O'Rourke, T., Reinhorn, A., Shinozuka, M., Tierney, K., von Winterfield, D., 2003. A Framework to Quantitatively Assess and Enhance the Seismic Resilience of Communities. Earthquake Spectra, 19(4), 733-752.

Menoni, S., Pergalani, F., Boni, M., & Petrini, V., 2002. Lifelines earthquake vulnerability assessment: a systemic approach. Soil Dynamics and Earthquake Engineering, 22, 1199-1208.

Borzi, I., 2023. Vulnerability assessment of water supply infrastructures through multiple indicator methodology. Journal of Water and Climate Change. doi:10.2166/wcc.2023.148

Arcadis Company, 2016. Sustainable cities water index. Amsterdam: Arcadis-Design and Consultancy for Natural and Built Assets. https://www.arcadis.com/media.

Cimellaro, G., Tinebra, A., Renschler, C., & Fragiadakis, M., 2015. New resilience index for urban water distribution networks. Journal of Structural Engineering, C4015014-1-13. https://doi.org/10.1061/(ASCE)ST.1943-541X.0001433.

Matthews, J., 2015. Disaster resilience of critical water infrastructure systems. Journal of of Structural Engineering, 142(8), C6015001.

Farahmandfar, Z., Piratla, K., & Andrus, R., 2016. Resilience evaluation of water supply networks against seismic hazards. Journal of Pipeline Systems Engineering and Practice, 8(1), 04016014. doi:10.1061/(ASCE)PS.1949-1204.0000251.

Makropoulos, C., Nikolopoulos, D., Palmen, L., Kools, S., Segrave, A., Vries, D., Koop, S., von Alphen, H.J., Vonk, E., van Thienen, P., Rozos, E. & Medema, G. 2018. A resilience assessment method for urban water systems. Urban Water Journal. https://doi.org/10.1080/1573062X.2018.1457166.

Mo'Tamad, H., Carriveau, R., & Ting, D.-K., 2022. Urban water supply systems' resilience under earthquake scenario. Scientific Reports, 12: 20555. https://doi.org/10.1038/s41598-022-23126.

Balaei, B. W., 2020. Investigating the technical dimension of water supply resilience to disasters. Sustainable Cities and Society, 56(102077). https://doi.org/10.1016/j.scs.2020.102077.

Arnaouti, S., 2024. Resilience of the external water supply network of Lagadas municipality (Northern Greece) to earthquake-related hazards. Dissertation of the Inter-Institutional Master Course 'Natural Hazards and Disaster Mitigation'. University of the Aegean, June 2024 (in Greek).

Caputo, R., Chatzipetros, A., Pavlides, S., & Sboras, S., 2012. The Greek Database of Seismogenic Sources (GreDaSS): state-of-the-art for northern Greece. Annals of Geophysics, 55(5), 859-894. doi:10.4401/ag-5168.

Chatzipetros, A., Tsapanos, Th. & Pavlidis, S. 2006. Geological-seismological investigation for the fault of the

Lagynas area in Lagadas Municipalitu. Thessaloni: Geology departhment of A.U.Th..

Koukis, G., Sabatakakis, N., Nikolaou, N., & Loupasakis, C., 2005. Landslide hazard zonation in Greece. Proceedings of open symposium on landslide risk analysis and sustainable disaster management in the First General Assembly of International Consortium on Landslides, pp. 291-296.

Wilde, M., Günther, A., Reichenbach, P., Malet, J.-P., & Hervás, J., 2018. Pan-European landslide susceptibility mapping: ELSUS Version 2. Journal of Maps, 14(2), 97-104. doi:10.1080/17445647.2018.1432511.

Günther, A., Van Den Eeckhaut, M., Malet, J.-P., Reichenbach, P., & Hervás, J., 2014. Climatephysiographically differentiated Pan-European landslide susceptibility assessment using spatial multi-criteria evaluation and transnational landslide information. Geomorphology, 224, 69-85.

ESDAC dataset, 2024. European Soil Data Centre, Joint Research Centre, European Commission. https://esdac.jrc.ec.europa.eu/resource-type/datasets.

Papathanassiou, G., 2006. Soil liquefaction phenomena in Hellenic region. Ph.D. thesis. Aristotle University of Thessaloniki.

Papathanassiou, G., Valkaniotis, S., Chaztipetros, A., & Pavlides, S., 2010. Liquefaction susceptibility map of Greece. Bulletin of the Geological Society of Greece, 43(3), 1383–1392. https://doi.org/10.12681/bgsg.11314.

Di Nardo, A., Di Natale, M., Giudicianni, C., Musmarra, D., Rodriguez Varela, J., Sntnastaso, G., . . . Tzatchkov, V. (2017). Redundancy features of water distribution systems. XVIII International Conference on Water Distribution Systems Analysis, WDSA2016. 186, pp. 412 – 419. Elsevier.

17th INTERNATIONAL CONGRESS of the Geological Society of Greece

BULLETIN OF THE GEOLOGICAL SOCIETY OF GREECE, SP. PUBL.

EXTENDED ABSTRACT 016

Implementing the Critical Raw Materials Act to explore strategic minerals potential in Greece

Arvanitidis N.[1], Laskaridis K.[2], Christidis C.[2]

(1) President of the Mineral Raw Materials Committee of the Association of Greek Geologists, nikolaos.arvanitidis@gmail.com (2) Hellenic Survey of Geology and Mineral Exploration, Greece, klaskaridis@eagme.gr, christidisc@hotmail.com

Introduction / Background

Vast amounts of raw materials from minerals will be needed to meet the demand for a global economy free of hydrocarbons. Some are categorised as Critical and Strategic Minerals (CSMs) due to their high economic significance and supply risk. Of the 34 minerals and metals on the current EU list of CSMs, established in 2023, 16—such as copper, nickel, and aluminium—are strategically significant (Grohol et al., 2023). The CSMs are the foundation on which modern technology is built. From photovoltaics to semiconductors, wind turbines, and lithium batteries, to transport and store the produced renewable energy. In addition to lithium, battery value chains need cobalt, graphite, nickel, and manganese (Rachovides, et al., 2024). The electrification of cars requires permanent magnets, whose value chains use rare earth elements (REE) such as neodymium, dysprosium, and praseodymium, but also increase the use of nickel, copper, zinc, and lead. The CSMs are also essential in digital technology. Without CSMs, there cannot be an energy and digital shift. As a result, the resilience and sustainability of the CSM value chains that deal with technology facilitating the energy transition are highly valued by the EU. The EU would need up to 18 times more lithium and 5 times more cobalt by 2030 and almost 60 times more lithium and 15 times more cobalt by 2050 to cope with the increase in the production of electric vehicle batteries. By 2030, the demand for graphite is expected to reach 4 million tons per year, with 75% going to lithium battery anodes (Rachovides, et al., 2024). A shortfall of around 780,000 tons per year is estimated by 2030. Given that several of the Green Deal's goals, such as reducing greenhouse gas emissions by at least 55%, must be addressed and achieved by 2030, the growing need for CSMs becomes even more urgent.

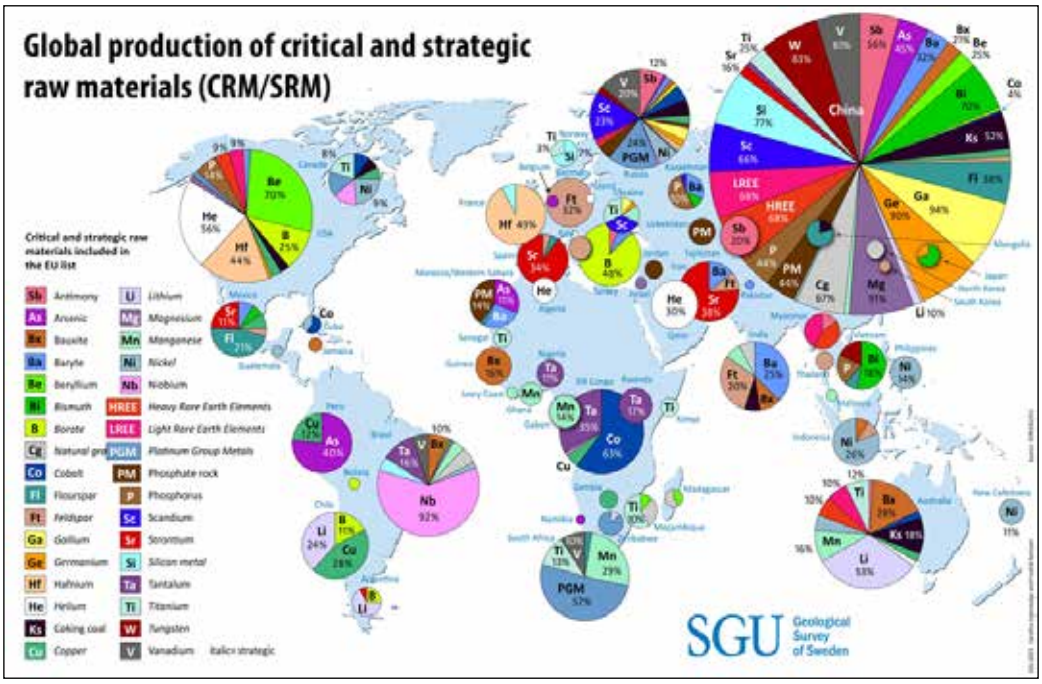

Figure 1. Map of world production of CSMs according to the current European list. Source: Geological Survey of Sweden.

The above forecasts seem "scary" considering that the EU depends on 75 to 100% of imports for most CSMs. It also happens that the production and processing of many CSMs are geographically controlled, making their geopolitical access and disposal vulnerable, accompanied by a series of social, economic, environmental, and other risks. So, some CSMs, but also their related value chains, tend to a large extent to be productively monopolized by specific regions of the planet, sometimes by essentially one country. For example, about 60% of the world's cobalt comes from the Democratic Republic of Congo (Fig. 1). China mines around 60% of the world's REE production, produces 85% of associated processed and metallurgical products, and consumes 70% (Arvanitidis, 2024). The urgent need for a global hydrocarbon-free economy will require therefore increasing quantities of raw materials. Therefore, it is important to know which and how many raw materials are needed to understand and assess the implications of their scarce access or scarcity for the European, and hence the Greek, economy. This article views why and how strategic and criticality in mineral resources arises, the geopolitical dominance of China, the European Regulation on Strategic and Critical Mineral Resources Act(CRMA), the key deposit of strategic and critical mineral raw materials resources, the need for increased investment in mineral exploration, new methodological approaches to mineral exploration, dynamic CRM systems in Europe and Greece and proposals for projects in mineral bearing areas of Greece.

The European Critical Raw Materials Act (CRMA)

The CRMA (European Commission, 2024) has become the political and strategic tool, but also the operational platform seeking to promote the implementation of the Green Deal, the new industrial strategy, the European partnership for innovation, the circular economy, and the integrated intra-European mining production, with the primary objective of making Europe climate neutral. This regulatory initiative is timely and necessary in formulating a policy for exploiting the European CSMs.

The main targets of the CRMA are until 2030

- At least 10% of CSM's annual consumption comes from European mineral deposits.

Europe's geology and metallogenetic evolution considerably favour its capability to capitalise on domestic CSM resources and become self-sufficient, resilient, and sustainable. Mineral exploration technologies for CSM deposits must be further developed to provide reliable resource estimates and feasibility studies. The national Geological Surveys of the member states must review the economic geology of their potential CSM systems, with the aim of a more documented and systematic assessment, to identify any exploitable targets.

- At least 40% of processed minerals are produced within the EU.

The integrated operation of resilient strategic value chains for the energy transition requires developing sustainable processing and refining technologies.

- At least 25% of the annual need in CSMs should come from recycling.

Most CSMs are mainly found as minor components in sulfide and oxide deposits of base metals (e.g. copper, lead, zinc, nickel, iron, aluminum). With mining and processing focused on base metal minerals, any accompanying CSM concentrations end up in various mining wastes, such as waste rocks and beneficiation tailings. Historical mining waste makes up the secondary resources that through their recycling and reuse, can potentially lead to the recovery of the CSMs they contain.

- Less than 65% dependence of each CSM on one country.

Minerals have been the missing link in the climate debate for many years. It is now clear that the EU's climate targets cannot be achieved without them. More specifically, any disruptions to the access and adequacy of CSMs, have implications for ensuring the energy transition and achieving the climate goals.

- Strengthening the resilience of strategic value chains for more effective implementation of energy and digital transition.

The value chains for CSMs include upstream mineral exploration and extraction, midstream processing (concentration, metallurgy), and downstream industrial processing and recycling. Unfortunately, in Europe today there are limited possibilities for the sustainable and integrated operation of CSM-based technology value chains

- Simplifying and speeding up licensing procedures.

The rapidly growing demand for mineral raw materials has also increased the need to update mining policy and research and innovation projects. The CRMA aims to reduce licensing time, and Member States will ensure that the overall permitting process related to such projects becomes faster. The governments of the EU Member States

agreed, in cooperation with the European Commission, the European Council, and the European Parliament, to highlight and implement strategic projects that would benefit from shorter and more efficient authorization procedures and easier access to finance.

- Development of environmentally friendly mining and production methods.

A common European understanding of best practices in the responsible mining of mineral resources, concerning social, environmental, and economic commitments and applications, set a trajectory toward the UN Sustainable Development Goals (SDGs).

- Channeling strategic partnerships between the EU and third countries to ensure sustainable and resilient CSM supply chains.

The CRMA aims to pave the way for long-term partnerships, with knowledge and technology transfer, training, and skills development for new jobs with better working conditions and income, as well as sustainable/ESG compliant extraction and processing in the partner countries from where Europe will be able to access and import some of the CSMs.

Metallogenetic settings sourcing CSMs

Most of the CSMs are minor accompanying components of important sulfides, oxides, and other metallic mineral systems. In nickel ore exploration, cobalt should also be a complementary target. Examples of CSMs found in subordinate concentrations along with known metallogenetic systems are,

- cobalt (Co) with nickel (Ni) and copper (Cu) deposits
- gallium (Ga), germanium (Ge), indium (In), antimony (Sb) with mixed sulfides
- gallium (Ga), rare earths (REE), scandium (Sc) with aluminum (Al) deposits
- platinum-based (PGM) with chromium (Cr), nickel (Ni) and copper (Cu)
- tungsten (W), niobium (Nb), indium (In), tantalum (Ta) with tin (Sn) deposits
- rare earth (REE) with phosphate (P) deposits.

"Critical" need for increased investment in mineral exploration.

Increasing the degree of self-sufficiency from 2-3% to 10% in 2030 means a 300-400% increase in intra-European production in 7 years. Huge efforts are therefore required for an increase in investment in mineral exploration to at least an equivalent degree to make the 10% degree of self-sufficiency possible. In this direction, innovative and sustainable approaches must be applied, using innovative prospecting technologies, thus improving economic performance and obtaining information that could not be obtained with conventional methods. The CRMA requests the member states to implement national CSM exploration projects through systematic economic geology approaches.

CSM potential mineral systems in Greece

Europe's geological environment and metallogenetic evolution substantially favour its ability to become self-sufficient, resilient, and sustainable in CSMs from domestic deposits.

In Greece (Fig. 2), potential CSM systems (Melfos and Voudouris, 2012; Stergiou, et al., 2023) relate to:

- active areas of mining base metal, magnesite, laterite, and aluminum bauxite mineral deposits (Fig. 2). Elevated geochemical values to higher grades of arsenic and antimony have been determined in the polymetallic ores in northern Greece. Along with nickel, the potential of exploitable cobalt contents in the laterites is a challenging target. A current project addresses the recovery of gallium, scandium, and REE with bauxite extraction and aluminium production.
- systems of metallic minerals in mainly Northern Greece (Figure 2, where mining activity (brownfields) or various scales (regional scale, deposit scale) of mineral exploration have been conducted in the past. The epithermal gold system in the Thrace region is connected to Tertiary volcanic basins and rocks with typical examples being the exploitable deposits of Sappes (Shaw and Constantinides, 2001; Border et al., 1999; Bridges et al., 1998; Cheliotis et al., 1999; Voudouris et al. 2006, Voudouris 1993), Agios Dimitrios (Michael, 1993; 2004; 2005; Michael et al., 1988), and Perama (Voudouris and Skarpelis, 1998; Lescuyer et al., 2003; McAlister et al., 1999; Michael C., 2002; Voudouris et al., 2011). In the case of this system, bismuth might be a potential target, as well as the challenging

target of locating deeper-seated copper mineralisation (Melfos et al., 2002). In the metamorphic basement of the Thrace region, there is a CSM exploration potential for antimony, with typical examples of mineralisation in Kallintiri (Michael, et al., 2012; Michael, et al., 2013; Kanellopoulos, et al., 2014), A prominent antimony prospect is found in Chios (Tsamantouridis and Chorianopoulou, 1977; Dimou et al., 1986).

- potential CSM exploration targets in central Macedonia are associated with the carbonate-replacement polymetallic mineral systems in the Serbo-Macedonian and Rhodope zones. In the lead-zinc-silver-gold ore deposits of Olympias and Mavres Petres in NE of Halkidiki arsenic and antimony, are mineralogically and geochemically also determined. The mineralisation in Thermes belongs to the same system (Arvanitidis et al., 1987) and the volcanogenic massive base-metal sulfide deposit (VMS) in Polykastro, where germanium and indium could also be of potential exploration interest. The VMS Molai base metal deposit in Peloponnese having a similar mineralogical composition, shows feasible germanium exploration results. While exploitable resources are mostly associated with the palladium-containing porphyry copper-gold mineral systems in the central Macedonian regions of Skouries and Kilkis, copper is the focus of exploration attention in the Kimmeria skarn mineralisation. The pyrolusitic manganese ores of the Varvara area in NE Halkidiki, which was explored in the past, probably needs a new review. Regarding antimony, the historical mining in the central Macedonia Lahanas area should not be ignored.
- to the mineral system of magmatic mineralisations, which is largely genetically linked to the ophiolite zones in mainly western Macedonia, with the predominant occurrence of Vourinos chromite deposits and the hydrothermally formed and ultrabasic rock-hosted magnesite in Halkidiki and Evia. Bauxites and laterites, formed by alteration, weathering and re-working of ophiolite-related ultramafic rocks and associated rocks (Valeton, et al, 1987), are exploratory placed in this system, with particularly increased contents of CSMs of gallium, scandium, REE, and cobalt, as mentioned with the respective active bauxite and laterite mines (Fig. 2). As far as nickel and cobalt are concerned, the mineral deposits in the western and eastern Vermio (e.g., Flamouria area), an exploration project previously implemented, concluded that an economic geology re-evaluation is highly recommended.
- the resource dimension and perspective of historical mining waste (mining tailings, beneficiation tailings, metallurgical residues), as part of the circular economy practices promoted and recommended by the CRMA, with exploring the potential of contained CSM resources, based on the UNFC classification system.

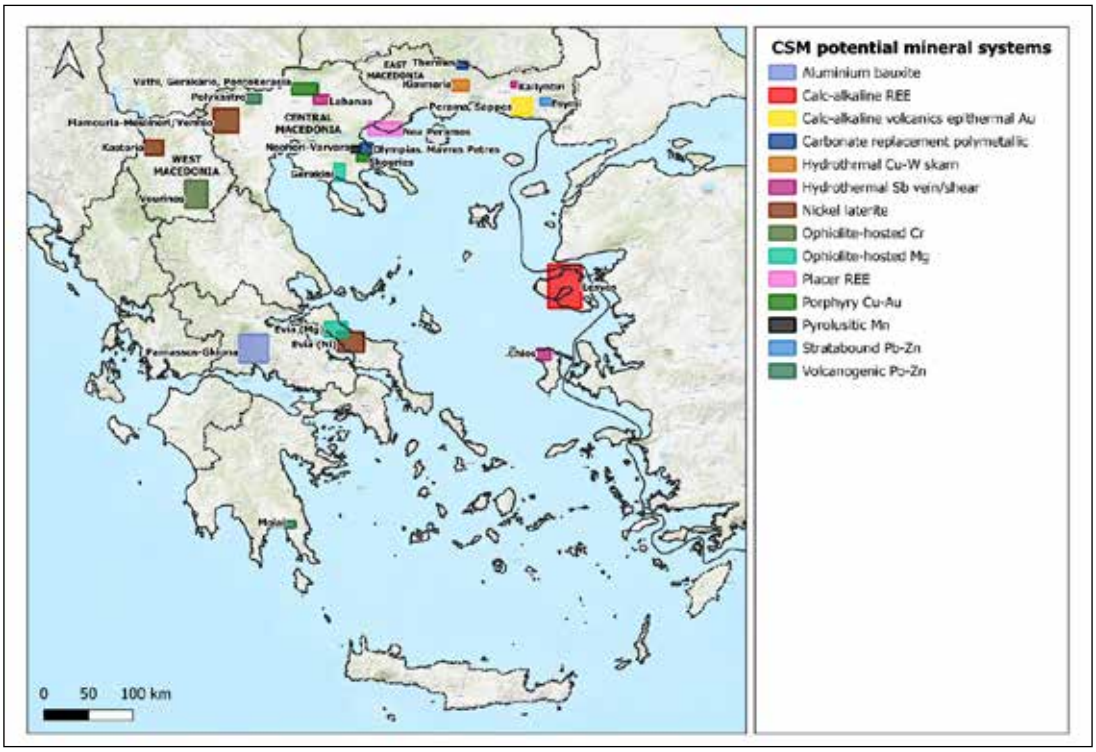

Figure 2. Map showing CSM potential mineral systems in Greece.

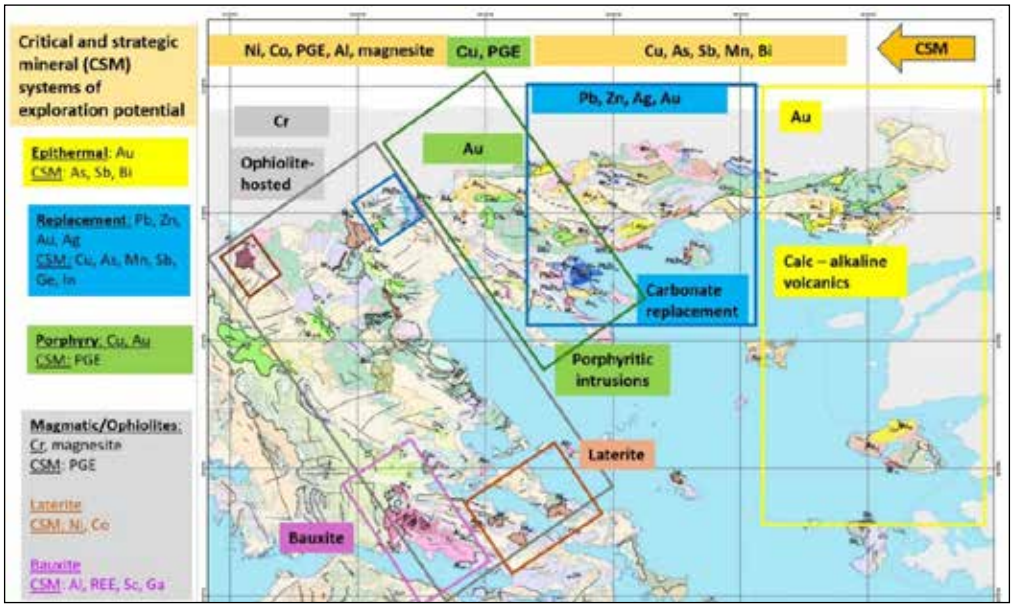

Figure 3. Mineral systems of CSM exploration potential in central and northern Greece.

- greenfields where the regional geology and lithological features justify conducting further economic geology approaches and exploration to target CSMs. For example, monazitic concentrations of REE have been identified in the coastal area of Nea Peramos. Exploring the granitic country rocks is necessary since they may be the sources of the REE found in the monazitic sands. The volcanic rocks in the NW part of Lesvos are found in the western extension of the Mesozoic-Cenozoic REE belt (Goodenough, et al., 2016) where a Turkish REE mineralisation was also made known. The REE geochemistry of these alkaline volcanics needs to be further explored. As far as lithium is concerned, several European Geological Surveys are exploring its potential in pegmatites. That could also be the case for the Greek pegmatites, particularly the ones of magmatic origin.

High-priority CSM exploration projects in Greece

Porphyry copper mineral systems. The project aims to explore economic geology and the feasibility of exploiting the porphyry copper mineralisations in Kilkis County's Pontokerasia, Vathi, Gerakario, and Mylohori areas (Apostolou and Stefanidis, 1987; Tsamadouridis, 1982; Drougas et al., 1981; Arvanitidis, 2010; Kelepertsis et al., 1986). The demand for strategic copper will increase rapidly and its price will follow the same upward trend, due to its use in energy transition technologies. Important copper resources can be found in Greece, such as Skouries, where mining is about to start. These developments are a motivation and an opportunity to highlight the CSM value of other porphyry copper-gold mineral systems, as they are in Pontokerasia, Vathi, Gerakario, and Mylohori. The resource potential is estimated at over 80 million tons, with typical grades of 0.30% copper and 0.8 grams/ton of gold. Porphyry copper systems typically develop a cylindrical structure, sometimes in the form of an inverted cone, and extend to an average depth of 2000 meters, with 1000 meters being a feasible exploration target.

Carbonate-replacement and VMS polymetallic sulfide minerals systems. The project addresses the economic geology and ore feasibility of Polykastro, Mavro Dendro, and Thermes base metal deposits, focused on the CSMs of copper, tungsten, germanium, and indium. The Polykastro mineral deposit, in Kilkis County, has an estimated resource of 4.7 million tons with about 6 % zinc and lead together, while the corresponding potential resources were estimated at 12 million tons. New exploration efforts will target deeper-seated copper mineralisation. In the neighboring area, the porphyry style Mavro Dendro deposit, amounts 4.8 million tons with 0.25% molybdenum and increased contents of copper and tungsten were

identified. In Thermes, in the County of Xanthi, there are confirmed 5.1 million tons with 6.9% zinc and lead, and 28 grams/ton of silver. In the same area, a graphite reserve of 400,000 tons with a content of 6% is found.

Manganese mineral systems. Previous exploration in Neohori and Varvara, including drilling, resulted in an estimated 1.5 million tons with 25-30% of pyrolusitic manganese, suitable for batteries. These mineralisations are found in the western part of the Stratoni fault, a regional structure known for its polymetallic sulfide minerals underlying iron-manganese oxidations. Characteristic examples of the Stratoni fault-controlled structural link between manganese oxides and base metal sulfides, as they move from shallower to deeper levels, are the Mavres Petres sulfide ore deposit in the eastern part of the fault and the Piavitsa sulfide mineralisation in the middle part.

Base and precious mineral sulfide systems. This project will target further exploration of several prospects of the County of Evros, in the Thrace region, which have been studied for lead, zinc, molybdenum, silver, and gold, including beneficiation testing. The potential occurrence of the CSMs of copper and bismuth will be in focus. Characteristic examples are the Esymi base metal deposit with 14 million tons of 6% zinc, and the adjacent Myli copper mineralisation. Excellent examples of feasible epithermal gold mineral systems are the ore deposits at Perama and Sappes.

Lateritic nickel mineral systems. The project will address the economic geology and exploitation potential of the lateritic nickel mineralisation in the Flamouria and Mesimeri areas of the prefecture of Pella. According to recent estimates (Source: Raw Materials Group, Future Mine & Mineral), global demand for stainless steel will continue to grow, with a projected increase of over 90% during the period 2021-2050. This is predicted to increase demand for nickel over the same period, by over 115%. Electric vehicles, which weren't on investors' radars in the early 2000s, are the new price engine for the anticipated nickel booms this time. Greece has a long-standing relationship with nickel mining production in LARCO's mining centers in Evia, Viotia, and Kastoria. Strategic nickel exploration was carried out in the Flamouria and Mesimeri areas, estimating a resource potential of over 1.5 million tons with approximately 0.9% Ni and 0.04% Co. Since cobalt and nickel are both now CSMs and the mineralisations are open downward geologically, more exploration is required. It should be noted that the need for deposits with high nickel grades has been greatly lowered by using hydrometallurgy rather than pyrometallurgy.

These selected exploration projects will contribute to access to increase the CSMs resource potential in Greece and the EU, as the CRMA targets, and to enable shortening the current timelines, to take no more than 27 months for mining licenses and 15 months for processing and recycling licenses.

References

Apostolou N. and Stefanidis P., 1987. Report on the geological and mineralogical mapping in the Gerakario area – Central – Gavras N. Kilkis. Report in Greek by I.G.M.E. **[Report]**

Arvanitidis N., Constantinides D., Dimadis E., Favas N., Nikolaou S., Romaidis Y., Iliev I., Katzkov N., Manev D., Milev V., Yanev V. 1987. Greek - Bulgarian joint project on the Geology, Metallogeny and prospecting of the Thermes ore-field, Northern Greece - Special volume I.G.M.E. Xanthi. **[Report]**

Arvanitidis N., 2010. New metallogenetic concepts and sustainability perspectives for non-energy metallic minerals in Greece. - 12th International Congress of The Geological Society of Greece. Bulletin of the Geological Society of Greece Volume XLIII, No 5. 2010. **[Conference Proceedings]**

Arvanitidis, N. 2024. Europe's economic geology generates exploitable critical mineral resources enabling to reduce its geopolitical dependence- Progress beyond state-of-the-art. Technical Annals. 1. 10.12681/ta.36119. **[Journal Article]**

Border A. J.M., Constantinides D. C., Michael C., Abatzioglou M., 1999. Discovery and Evaluation of the Sappes gold deposits, North-eastern Greece. - New Generation gold mines 99. Conference proceedings, 22-23, November, Perth, Western Australia, 1999. **[Conference Proceedings]**

Bridges P. S., Gordon M. J., Michael C., Abazioglou M., 1998. Gold mineralization at Sappes, Northern Greece. - In: Europe's major gold deposits, Irish Association for Econ. Geol., Abstracts volume, IAEG, Geological survey of Ireland, 95-107, 1998. **[Conference Proceedings]**

Cheliotis I., Naden J., Michael C., Shepherd T., Bitzios D., Leng M., Eliopoulos D., Spyro B., Dimitroula M., Kilias

S., Constantinidou E., 1999. Creation of models of Epithermal systems in the Rhodope and Aegean areas. - Final report (In Greek) **[Report]**

Dimou E., Papastavrou St., Serment R., 1986. The Sb in Greece (Part Two) - Study of occurrences and deposits of antimony in South Chios and Pelion (Metallic Paragenesis - Metallogenesis), Report in Greek by I.G.M.E. **[Report]**

Drougas I., Pantazis M., Papaioannou K. Polychronakis I., Spanos N., Tsamadouridis P., Charalambidis P., 1981. Economic and technical study on the feasibility of exploiting the mixed sulfide deposit in the Polykastro-Skra area, I.G.M.E. Unpublished Report in Greek No. 5, p. 111. **[Report]**

European Commission, 2024. Critical Raw Material Act https://single-market-economy.ec.europa.eu/sectors/raw-materials/areas-specific-interest/critical-raw-materials/critical-raw-materials-act_en **[Report]**

Geological Survey of Sweden, 2024. Critical and strategic raw materials. https://www.sgu.se/en/mineral-resources/critical-raw-materials/ **[Report]**

Grohol, M. and Veeh, C., 2023. Study on the critical raw materials for the EU – Final report. European Commission: Directorate-General for Internal Market, Industry, Entrepreneurship and SMEs, Publications Office of the European Union, 2023, https://data.europa.eu/doi/10.2873/725585. **[Report]**

Goodenough, K.M., Schilling, J., Jonsson, E., Kalvig, P., Charles, N., Tuduri, J., Deady, E.A., Sadeghi, M., Schiellerup, H., Müller, A., Bertrand, G., Arvanitidis, N., Eliopoulos, D.G., Shaw, R.A., Thrane, K., Keulen, N. (2016). Europe's rare earth element resource potential: An overview of REE metallogenetic provinces and their geodynamic setting, Ore Geology Reviews, Volume 72, Part 1, 2016, Pages 838-856, ISSN 0169-1368, https://doi.org/10.1016/j.oregeorev.2015.09.019. **[Journal Article]**

Kanellopoulos, Christos & Voudouris, Panagiotis & Moritz, Robert., 2014. Detachment-related Sb-Pb-Zn-Ag-Au-Te mineralization in Kallintiri area, northeastern Greece: Mineralogical and Geochemical constraints. Bul. Shk. Gjeol. 1/2014 - Special Issue Proceedings of XX CBGA Congress, Tirana, Albania, 24-26 September 2014. **[Conference Proceedings]**

Kelepertsis, A. E., Reeves, R., and Androulakis, J., 1986. Geochemical studies of porphyry type mineralization at Gerakario-Vathi of Kilkis area, northern Greece. Mineral Wealth, 42, pp. 43-48. **[Journal Article]**

Lescuyer J. L., Baily L., Cassard D., Lips A.L. W., Piantone P., Mc Alister M. 2003. Sediment-hosted gold in South-eastern Europe: the epithermal deposits of Perama, Thrace Greece: - Mineral Exploration and Sustainable Development. **[Conference Proceedings]**

McAlister M., Hammond J.M., Normand D. & Kampasakakis M., 1999. Discovery case history for the Perama Hill gold deposit, Greece - New Generation Gold Mines Conference in Perth, p. 10, West Aust., 22-23rd Nov. 1999**[Conference Proceedings]**

Melfos V., Voudouris P. (2012) Geological, mineralogical and geochemical aspects for critical and rare metals in Greece. Minerals 2, 300-317, https://doi.org/10.3390/min2040300

Melfos, V., Vavelidis, M., Christofides, G., Seidel, E., 2002. Origin and evolution of the Tertiary Maronia porphyry copper-molybdenum deposit, Thrace, Greece. Mineralium Deposita 37, 648-668. **[Journal Article]**

Michael C, Arvanitidis N., Iliadis, A., Papavasiliou, K., Christidis C., 2013. Orogenic mineralisations – A new exploration target for gold-polymetallic ore deposits in Greece. Proceed. 6th Conf. Sustain. Devel. Min. Industry, Milos Island, Greece, pp. 139-145. **[Conference Proceedings]**

Michael C., 1993. Geology and Geochemistry of epithermal gold deposit in Konos area. - Internal report of I.G.M.E. (In Greek). **[Report]**

Michael C., 2002. Exploration - valuation study of primary gold - IGME, internal report (In Greek). **[Report]**

Michael C., 2004. Epithermal systems and gold mineralization in western Thrace (North Greece). - Bulletin of the Geological Societies of Greece, vol. xxxvi. Proceedings of the 10th International Congress, Thessaloniki, April 2004. **[Conference Proceedings]**

Michael C., 2005. Mineralogical and Geochemical characteristics of Sappes epithermal system in western Thrace (Northen Greece). - In: Comptes rendus de l'Academie bulgare des sciences. Vol. 58, No 6, p. 691-698, 2005. **[Conference Proceedings]**

Michael C., Arvanitidis N., Gaál G., Papavasileiou K., Iliadis A., Christidis C., 2012. Orogenic mineralisations – A new exploration target for gold-polymetallic ore deposits in Greece. 34th International Geological Congress (IGC): Australia. **[Conference Proceedings]**

Michael C., Papadopoulos P., Marantos I., Evagelou E., 1988. Epithermal mineralization of gold in the Konos area (Eastern Rhodope). - Internal report of I.G.M.E. (in Greek), 1988. **[Report]**

Rachovides M., Arvanitidis N., Constantinides D., Anderhuber F., 2024. Critical minerals and rare earth elements: Ethical and societal considerations. Chapter 19. Editor(s): Silvia Peppoloni, Giuseppe Di Capua, Geoethics for

the Future, Elsevier, 2024, Pages 249-267, ISBN 9780443156540. **[Book chapter]**

Shaw A., Constantinides D., 2001. The Sappes gold project. - Bulletin of the Geological Society of Greece vol. 34,3, 1073 - 1080. Proceedings of the 9th International Congress, Athens, September 2001. **[Conference Proceedings]**

Stergiou, C.L.; Sakellaris, G.A.; Melfos, V.; Voudouris, P. 2023. A Review of the Distribution of Critical and Strategic Mineral Raw Materials in the Vein-Type Mineralisations of Vertiskos Unit, Northern Greece. Mater. Proc. 2023, 15, 51. https://doi.org/10.3390/materproc2023015051. **[Conference Proceedings]**

Tsamadouridis P., 1982. The polymetallic deposit Pb-Zn-Cu of Polykastro – Skra N. Kilkis, Report in Greek by I.G.M.E. **[Report]**

Tsamantouridis P., Chorianopoulou P., 1977. Report on the mineralogical assessment of the island of Chios (Occurrences of Antimony – Mixed Sulfides). Report in Greek by I.G.M.E. **[Report]**

Valeton I., Biermann M., Reche R., Rosenberg F., 1987.Genesis of nickel laterites and bauxites in Greece during the Jurassic and Cretaceous, and their relation to ultrabasic parent rocks, Ore Geology Reviews, Volume 2, Issue 4, Pages 359-404,

Voudouris P (1993): Mineralogical, geochemical and microthermometric studies of epithermal Au-Ag mineralization at Kassiteres/Sappes area (northeastern Greece) University of Hamburg, Germany, 218p (in German).

Voudouris P. and Skarpelis, N. 1998. Mineralisations of Epithermal gold-silver in Perama (Thrace) and Limnos. - Bulletin in Greek Geological Society. 32 (3) 1998, pages 125-135, 19 ref. 1998. **[Conference Proceedings]**

Voudouris P, Tarkian M, Arikas K 2006 Mineralogy of telluride-bearing epithermal ores in Kassiteres-Sappes area, western Thrace, Creece. Mineralogy and Petrology, 87, 31-52

Voudouris, P., Melfos, V., Spry, P.G., Moritz, R., Papavassiliou, C., Falalakis, G., 2011. Mineralogy and geochemical environment of formation of the Perama Hill high-sulfidation epithermal Au-Ag-Te-Se deposit, Petrota Graben, NE Greece. Mineralogy and Petrology 103, 79-100. **[Journal Article]**

17th INTERNATIONAL CONGRESS of the Geological Society of Greece

BULLETIN OF THE GEOLOGICAL SOCIETY OF GREECE, SP. PUBL.

EXTENDED ABSTRACT 017

Assessing the effect of 2023 Evros Wildfire: a new Post-Fire Rockfall Hazard System

Asteriou P.[1], Sotiriadis D.[1], Petala E.[1], Kazelis L.[1], Klimis N.[1]

(1) Democritus University of Thrace, Civil Engineering Dpt. Xanthi, Greece, pasterio@civil.duth.gr

This paper proposes a risk and hazard assessment system for rockfalls in fire-affected areas. The system has the ability to efficiently prioritize hazardous sites and evaluate post-fire rockfall risks, supporting rapid decision-making for mitigation actions.

Introduction

The Evros forest fire in August 2023 burned more than 90,000 hectares, making it the largest wildfire ever recorded on European soil since 2000. During the two-day period of August 21–23, the fire spread at an explosive rate, growing from approximately 8,500 hectares on August 21 to over 65,000 hectares by August 23, accounting for 60% of the total burned area. The explosive growth of the wildfire was driven by extremely dry atmospheric conditions during the incident and the prolonged drought that had affected the broader region in the preceding months. These factors led to exceptionally low moisture levels in the forest material, significantly facilitating the rapid spread of the fire.

Wildfires cause significant economic and social impacts, as they result in severe damage to infrastructure, area evacuations, livestock and wild animals, crops, farmlands, human lives and are associated with serious ecological consequences (Cunningham et al., 2024). Beyond the immediate effects of a wildfire, other natural phenomena and extreme events may arise. Wildfires can increase the susceptibility, frequency, magnitude, and area of influence of geohazards such as shallow landslides, rockfalls, debris flows, and soil erosion, triggering a destructive chain reaction with adverse consequences (Vahedifard et al., 2024). The occurrence of rockfalls depends on various factors related both to the slope, such as its gradient, geology, weathering, and vegetation, as well as, external factors, including climate, seismic activity, and exposure to human activities (Scheidl et al., 2020).

When a block detaches above a forested area, its movement will be constrained due to the impacts with the tree trunks. However, the destruction of vegetation, following a wildfire, cancels out this benefit. As a result, the block's travel distance is extended, and the severity of the impact increases. Consequently, the effects of a rockfall become more pronounced, posing a hidden threat to the safety of the exposed activities. The presence of vegetation makes the implementation of protective measures more cost-effective or even unnecessary (Scheidl et al., 2020). According to Moos et al. (2017), it has been found that protective forests can reduce the occurrence of rockfalls by up to 90% and their intensity by up to 70%, depending on variations in parameters such as the forest coverage, tree density and diameter, trunk arrangement, and the volume of the falling blocks. An overview of the current scientific knowledge and practical methods for addressing rockfall hazards in forested slopes can be found in Stoffel et al. (2006), Dorren et al. (2007), and others.

Recent studies report an increase in rockfall activity during and after wildfires (e.g., DeGraff et al., 2015; Perez-Rey et al., 2023). A combination of factors affects both the detachment areas and the propagation zones. Such factors include changes in the mechanical properties of the rocks and their fragmentation due to the high temperatures, the loss of vegetation's protective capacity, the impact of firefighting activities, and/or the destruction of existing protective measures (Sarro et al., 2021; Perez-Rey et al., 2023).

Objectives

The impacts of climate change, including rising temperatures and severe droughts, have intensified the occurrence of wildfires globally, leading to increased frequency, severity, and extent (Liu et al., 2010). Consequently, higher rockfall activity in burnt areas is expected, even in locations previously deemed safe due to vegetation. Thus, the objectives of this study are:

- Develop a user-friendly rockfall risk assessment system that accounts for the effects of wildfires. The system is designed to serve as a quick and efficient decision-support tool for identifying vulnerable locations.
- Apply the system to the area affected by the 2023 Evros wildfire, with the goal of identifying prone areas

and prioritizing them to facilitate decision-making regarding the restoration strategy, contributing to the area's restoration process.

Rockfall risk-hazard rating system

Ferrari et al. (2016) highlight the need for effective risk management by conducting a comprehensive review of existing methodologies for rockfall hazard and risk assessment. These methodologies are categorized into two main types: qualitative and quantitative. Qualitative methods rely on descriptive or classified criteria, requiring fewer data and allowing for quicker application, making them suitable for preliminary assessments or areas with limited data. In contrast, quantitative approaches involve numerical calculations and probability estimates, offering higher accuracy but demanding extensive data, complex models, and higher costs. When sufficient data are available, quantitative methods are preferred for detailed analyses of specific locations.

Classification Systems are widely used qualitative methods, that classify slopes based on their characteristic parameters. They have proven particularly effective for road networks, where slopes are evaluated to prioritize mitigation measures. The primary advantages of qualitative methods over quantitative ones are their cost-effectiveness and flexibility, enabling rapid hazard assessments across large areas. Their value lies in identifying high-risk zones that require further analysis. However, their main drawbacks are subjectivity and lack of precision.

The most popular hazard assessment system is the Rockfall Hazard Rating System (RHRS), developed in the late 1980s by the Oregon Department of Transportation (Pierson, 1992) as a standardized tool for assessing and prioritizing rockfall risks along roadways. Each slope section is rated based on factors influencing rockfall risk, such as slope height, ditch effectiveness, average traffic exposure, sight distance, road width, geological conditions, and rock fragment size. These parameters are rated on an exponential scale ranging from 3 to 81 points, depending on the severity of the risk. The original RHRS has been adapted to various regions to address local geological, climatic conditions, and infrastructure needs. These adaptations often involve modifications to rating criteria and the inclusion of additional parameters to enhance accuracy under specific site conditions. Examples include customized systems tailored to regional requirements, such as mRHRs (Budetta, 2004), the proposition of Saroglou et al. (2012) for Monemvasia, Greece, and others.

The precise assessment of rockfall hazard involves evaluating: a) susceptibility; b) magnitude; c) intensity; d) potential runout area; and e) frequency of rockfalls. Susceptibility is determined by the rock mass properties and possible factors that may weaken it. Magnitude refers to the size (volume) of the detached rock blocks, while intensity relates to the kinetic energy of the trajectory. Although precise intensity is typically calculated through simulations, it can be estimated indirectly in a hazard-risk assessment system by considering the maximum height from which a block can detach. Similarly, the potential runout area is often determined via trajectory simulation, but simpler parameters such as slope height and angle can also be used for estimation. Finally, frequency is rarely based on detailed data; instead, it is typically inferred from general information and field observations that indicate recent activity, such as rock block at the slope base, impact marks on the slope face, or damage to the roadway.

For the development of the rockfall hazard-risk assessment system (Figure 1) for the area affected by 2023 Evros wildfire, the aim was to include the essential parameters without requiring time-consuming procedures during field surveys. Following this approach and after reviewing existing systems in the literature, seven parameters were selected, all of which can be measured or estimated through on-site observations. Five of these parameters are related to the hazard (H) of the slope, while the remaining two are related to exposure and vulnerability (R).

Rating for all parameters follows an exponential scale, consistent with the original system proposed by Pierson (1992), but have been modified to have a maximum value of 100. The parameters H1 (slope height), H2 (block size), and H3 (rainfall height) are derived from the original RHRS, while the parameters H4 (rock mass condition) and H5 (rockfall frequency) are based on the proposal by Eggers et al. (2021). To calculate the total rockfall hazard (E), the scores of each H parameter are summed.

To assess risk, in addition to hazard, it is essential to determine and rate exposure and vulnerability. Parameter R1 is determined from measurements made during the field survey along with a correlation of reach angle that considers the influencing parameters and was developed for this study. It is worth noting that for calculating the score of the R1 parameter, vulnerability factors of the infrastructure are considered, such as road width, and exposure is also assessed using the reach angle concept. Therefore, the R1 parameter is a combination of both vulnerability and

exposure.

Reach angle (r) is defined as the angle formed by the horizon and the line that connects the detachment position and the furthest trajectory endpoint. As demonstrated from a detailed site-specific study in Avantas settlement, that was severely affected by the 2023 Evros wildfire (Asteriou et al., 2024), the parameters influencing reach angle are: a) slope height; b) slope angle; c) vegetation density; and d) block size. To estimate the potential area affected by rockfalls, parametric analyses were conducted using RocFall2 by varying those parameters within their typical range for the broader study area. Table 1 presents the values used in the analyses, which combined result to a total of 216 analyses.

Table 1. Parameters and their discrete values used in parametric analysis.

Parameter	Discrete values
Slope height, H [m]	15, 30, 45
Slope angle, θ [°]	45, 60, 75
Vegetation density, ρ [m²/m²]	0, 0.01, 0.03, 0.05
Block volume, V [m³]	0.01, 0.05, 0.1, 0.25, 0.5, 1.0

Figure 1. The proposed Post-fire Rockfall Hazard-Risk Assessment System, FiRo-RiS.

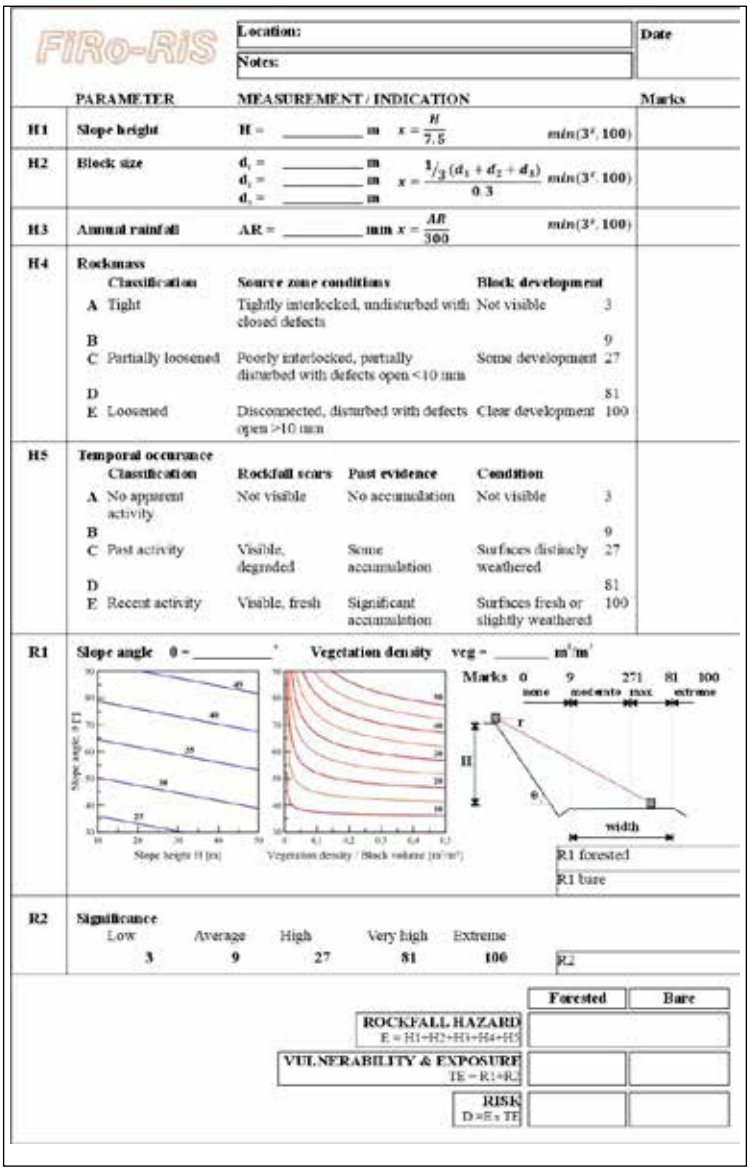

Reach angle (r) was divided into two components: a) the basic reach angle (r_{bas}), which depends on the slope height and slope angle (without vegetation), and b) the surplus reach angle (r_{sur}), which depends on the block size and vegetation density. This allows for directly identifying the impact of vegetation loss due to a wildfire on the trajectory length, which affects the exposure. Before a wildfire, the reach angle (r) is the sum of these components. After the wildfire, the reach angle equals the basic reach angle, since the vegetation has been destroyed.

Utilizing the results of the parametric analyses conducted without the vegetation (bare slope), the basic reach angle (r_{bas}) is correlated with the slope height (H) and the slope angle (θ). The additional effect of vegetation on reach angle is correlated with the vegetation density (ρ), expressed as the total area of stems at breast height per square meter, the block volume (V), and the slope angle (θ). These correlations are embedded in the developed hazard-risk system (Figure 1) as nomographs.

Through the reach angle and the slope height, the runout distance or exposure is calculated. Parameter R1 is rated depending on the position that is influenced by the incident. In case that a road is affected, the following cases are discerned: a) the falling block does not reach the road, so no consequences are expected (R1 = 0); b) the falling block reaches the road but leaves a free width of 3 m width, allowing vehicle movement, thus the road maintains serviceability (R= 9 to 27, depending on the unaffected width); c) the falling block affects the entire road cross-section, resulting in maximum consequences (R1 = 81); and d) .the falling block exceeds the road area and threatens additional infrastructure, having extreme consequences (R1 = 100). The consequences are considered extreme (R1=100) when a resident or a facility is located within the rockfall propagation zone.

The R2 parameter refers to the significance of the potential impacts. It has a subjective nature and is based on the importance of exposed elements from a socio-economic perspective. For example, when the main infrastructure affected is the road network, criteria for assessing its importance could include daily traffic volume, the presence of alternative routes, or others.

The sum of the individual scores for the R1 and R2 parameters gives the total score for the combination of vulnerability and exposure, according to TE = R1 + R2. The final risk score is calculated as the product of the total hazard score and the total vulnerability-exposure score, according to D = E × TE. To avoid excessively large values, the total scores of E and TE are normalized by dividing them to their maximum possible scores, which are 500 and 200, respectively. The proposed system is named FiRo-RiS, derived from the initials of the words Fire Rockfall Risk System.

Application to the area affected by the 2023 Evros Wildfire

The developed Rockfall Hazard-Risk System FiRo-RiS was applied to the area of Evros that was severely affected by the devastating wildfire (see Figures 2 to 4), during an on-site inspection carried out between September 16–18, 2024. The surveyed routes included the mountainous road network and settlements that were impacted by the wildfire. Along these routes, 36 slopes were identified and examined.

Figure 2 presents the hazard map of the examined locations, as derived from the normalized score, E_{norm}. The five classes of the E_{norm} were obtained by applying the Jenks algorithm (Jenks, 1968), according to which the classes are designed to minimize the standard deviation of the scores within the same class, while maximizing the distances between the central values of the classes. Since the system has a comparative character between the slopes examined, each class is given a qualitative description as follows: a) Low; b) Moderate; c) High; d) Very High; and e) Extreme, respectively.

The impact of vegetation loss is highlighted through the comparison of the maps in Figures 3 and 4, which show the distribution of the total risk score before and after the wildfire. It is noteworthy that before the fire, the majority of the locations (61%) were characterized by ‘Low’ risk, with the remaining classes occupying 6%, 14%, 5%, and 14% of the examined slopes, respectively. After the loss of vegetation, there is a significant decrease in the number of locations classified as ‘Low’ risk (19%), and a notable increase in the number of locations categorized as ‘Moderate’ risk (39%). For the ‘High’, ‘Very High’, and ‘Extreme’ risk classes, there is a slight increase, reaching percentages of 17%, 8%, and 17%, respectively.

Figure 2. Normalized hazard map of the investigated area.

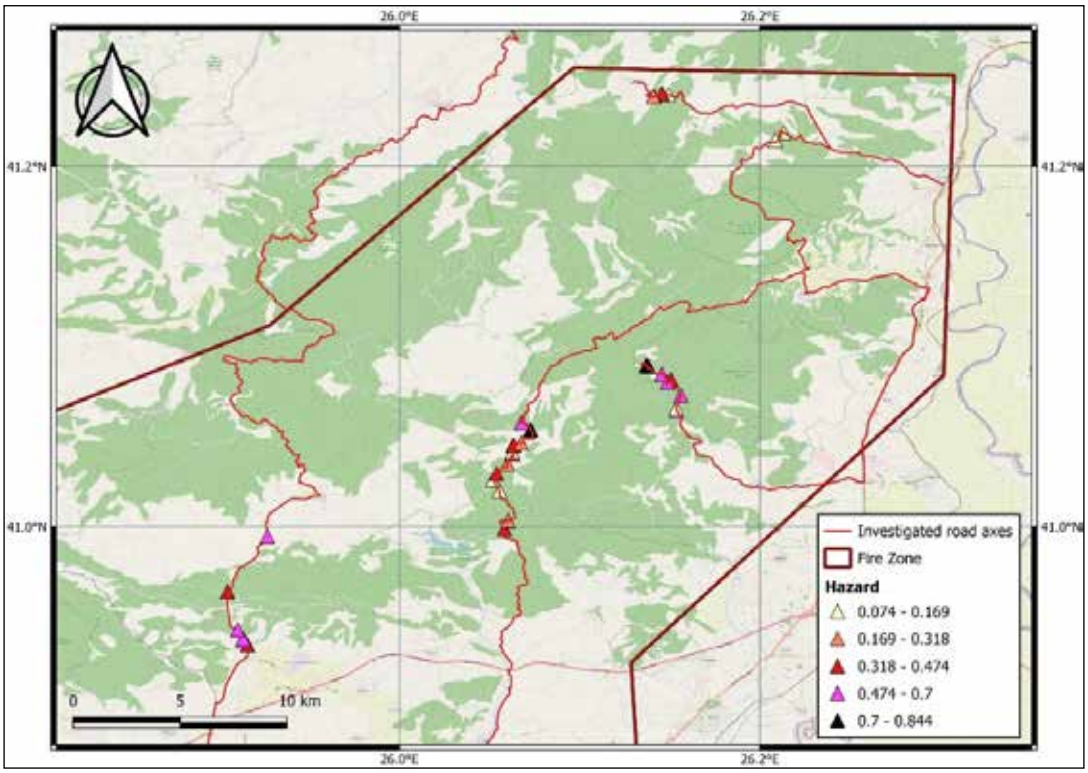

Figure 3. Normalized risk map before the wildfire of the investigated area.

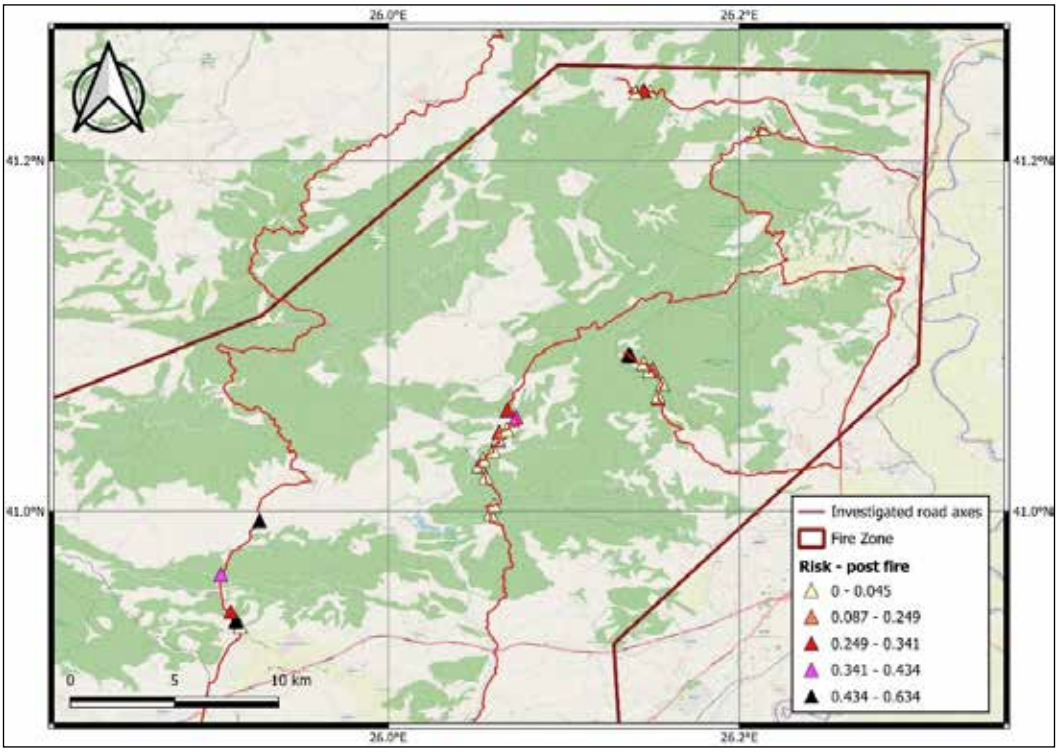

Figure 4. Normalized risk map after the wildfire of the investigated area..

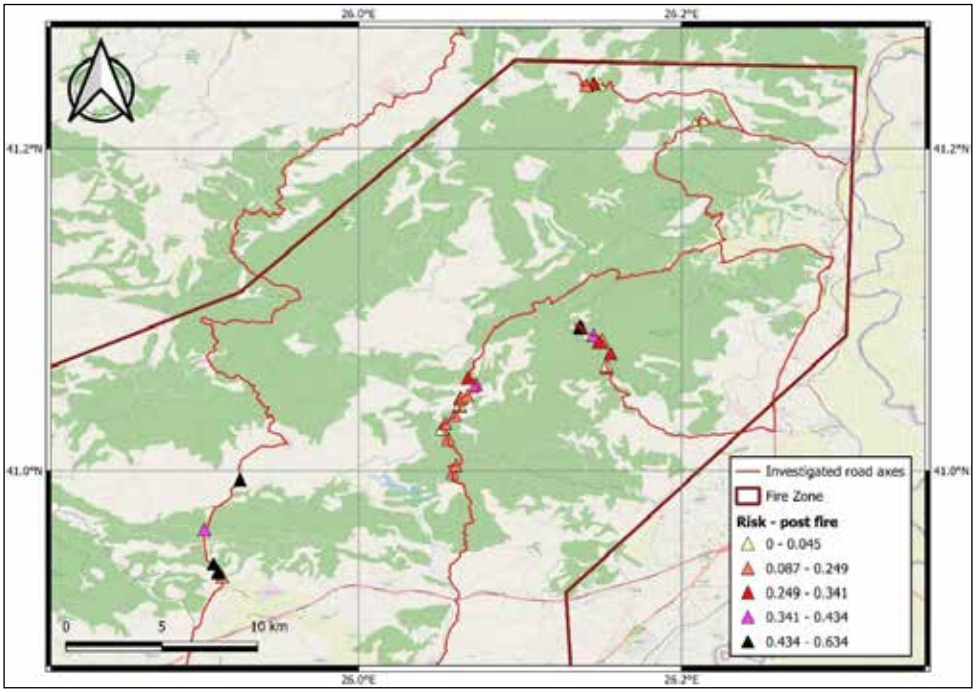

Conclusions and Discussion

The FiRo-RiS (Fire Rockfall Risk System) was developed and successfully applied to the wildfire-affected region of Evros. By incorporating critical parameters from existing international methodologies and introducing modifications to account for the impacts of vegetation loss, the system provides an efficient and systematic approach for assessing rockfall hazard and risk. The system includes factors that consider susceptibility (via geological characterization of the rockmass), magnitude, intensity (through parameters such as block size and slope height), frequency of occurrence, and potential extent (through the calculation of the reach angle). The results demonstrate the system's utility in identifying high-risk sites and prioritizing them for mitigation actions, offering a practical decision-support tool for infrastructure managers and local authorities.

A key innovation of FiRo-RiS lies in its ability to quantify the impact of wildfire-induced vegetation loss on exposure and risk, a feature that addresses a growing concern in regions increasingly affected by climate change. By combining quantitative and qualitative evaluations, the system is both robust and user-friendly. Furthermore, the system can be adapted to diverse geomorphological and environmental conditions.

Despite its strengths, the proposed system has limitations, as is the case with any such system. It relies on predefined parameters that may not fully capture complex geological settings. Some criteria are based on empirical formulas derived from site-specific data. Additionally, the inclusion of subjective parameters, such as the socio-economic impact assessment, introduces variability in risk evaluations depending on the user's perspective. However, when the system is implemented by the same user, ensuring consistency and comparative evaluation of the sites, the ranking of locations remains reliable.

Acknowledgements

This project (KE83226) was funded by Democritus University of Thrace under the initiative "DUTh To The People: Actions to Mitigate the Effects of the Devastating Fires in Thrace."

References

Asteriou, P., Sotiriadis, D., Petala, E., Kazelis, L., Evaggelou, E., Tzevelekis, T., Klimis, N. 2024. Assessing rockfall hazards post-wildfires: a case study in Evros, Greece. EURONGEO 2024. 4th European Regional Conference

of IAEG. Dubrovnik, Croatia.
Budetta, P., 2004. Assessment of rockfall risk along roads. Nat Hazards Earth Syst Sci 4, 71–81.
Cunningham, C.X., Williamson, G.J., Bowman, D.M.J.S., 2024. Increasing frequency and intensity of the most extreme wildfires on earth. Nat Ecol Evol 8, 1420–1425.
De Graff, J.V., Shelmerdine, B., Gallegos, A., Annis, D. 2015. Uncertainty associated with evaluating rockfall hazard to roads in burned areas. Env Eng Geosc 21(1), 21–33.
Dorren, L.K.A., Berger, F., Le Hir, C., Mermin, E., Tardif, P. 2007. Mechanisms, effects and management implications of rockfall in forests. For Ecol Manage 215, 183–195.
Eggers, M.J., Nash, T., Dwumfour, D., Turbitt, S., Dixon, J. 2021. Natural slope hazard management and integration with mining operations, in PM Dight (ed.), SSIM 2021: Second International Slope Stability in Mining, Australian Centre for Geomechanics, Perth, pp. 261-276.
Ferrari, F., Giacomini, A., Thoeni, K. 2016. Qualitative Rockfall Hazard Assessment: A Comprehensive Review of Current Practices. Rock Mech Rock Eng 49, 2865–2922.
Jenks, G.F. 1967. The Data Model Concept in Statistical Mapping. International Yearbook of Cartography 7, 186–190.
Liu, Y., Stanturf, J., Goodrick, S. 2010. Trends in global wildfire potential in a changing climate. For. Ecol. Manag. 259, 685–697.
Moos, C., Dorren, L.K.A., Stoffel, M. 2017. Quantifying the effect of forests on frequency and intensity of rockfalls. Nat Hazards Earth Syst Sci 17, 291–304.
Pierson, L.A., Davis, S.A., Van Vickle, R. 1990. Rockfall hazard rating system implementation manual, federal highway administration (FHWA), report FHWA-OR-EG-90–01, FHWA. US Department of Transporation, Oregon.
Perez-Rey, I., Sarro, R., Tomás, R., Alejano, L.A., Hernández Gutiérrez, L.E., Mateos, R.M., Riquelme, A.2023. A brief review of the effect of wildfires on rockfall occurrence. IOP Conf. Ser.: Earth Environ. Sci. 1124. September 11-15, Helsinki, Finland
Saroglou, H., Marinos, V., Marinos, P., Tsiambaos, G. 2012. Rockfall hazard and risk assessment: an example from a high promontory at the historical site of Monemvasia, Greece- Natural Hazards and Earth System Sciences 12(6), 1823-1836
Sarro, R, Pérez-Rey, I., Tomás, R., Alejano, L.R., Hernández-Gutiérrez, L.E., Mateos, R.M. 2021. Effects of wildfire on rockfall occurrence: A review through actual cases in Spain. Appl Sci 11, 2545.
Scheidl, C., Heiser, M., Vospernik, S., Lauss, E., Perzl, F., Kofler, A., Kleemayr, K., Bettella, F., Lingua, E., Garbarino, M, Skudnik M, Trappmann, D., Berger, F., 2020. Assessing the protective role of alpine forests against rockfall at regional scale. European J For Res 139, 969–980.
Stoffel, M., Wehrli, A., Kühne, R., Dorren, L.K.A., Perret, S., Kienholz, H. 2006. Assessing the protective effect of mountain forests against rockfall using a 3D simulation model. For Ecol Manag 225, 113–122.
Vahedifard, F., Abdollahi, M., Leshchinsky, B., Stark, T., Sadegh, M., AghaKouchak, A. 2024. Interdependencies between wildfire□induced alterations in soil properties, near□surface processes, and geohazards. Earth and Space Science 11(2)

17th INTERNATIONAL CONGRESS of the Geological Society of Greece

BULLETIN OF THE GEOLOGICAL SOCIETY OF GREECE, SP. PUBL.

EXTENDED ABSTRACT 018

Estimation of the displacement components in South Aegean islands as a response to the early 2025 seismicity of the Anydros Islet using Sentinel-1 imagery.

Athinelis I.[1], Basiou E.[2], Falaras, T.[1, 3] and Parcharidis I.[1]

(1) Department of Geography, Harokopio University of Athens, 176 76 Athens, Greece, gp222301@hua.gr (A.I.), falaras@hua.gr (F.T.), parchar@hua.gr (P.I.)

(2) Department of Geology and Geoenvironment, National and Kapodistrian University of Athens, 15771 Athens, Greece, eleutheriaba@geol.uoa.gr (B.E.)

(3) SUPCO - sustainable urban planning consultants, Thessalonikis 121, 18346 Moschato, Attica, Greece.

Research Highlights

- DInSAR analysis of Sentinel-1 data reveals significant coseismic deformation between Santorini and Amorgos, with uplift in South Thira (+2.1 cm) and subsidence near Oia (-2.8 cm), paired with a horizontal distancing trend between Thirasia (-2.7 cm), Nea Kameni (-1.5 cm) and Oia (+4.0).
- Amorgos and Anafi show westward displacement (-4.0 cm, -2.3 cm), indicating active faulting.

Abstract

The region between Santorini and Amorgos is seismically active and recently has seen a noticeable increase in earthquake frequency, causing significant tectonic deformation linked to active faulting and, potentially, magmatic processes. This extended abstract focuses on the analysis of the coseismic displacement components of Santorini, South Ios, Anafi and Amorgos islands, using Sentinel-1 satellite data and the DInSAR (Differential Interferometric Synthetic Aperture Radar) method, which revealed noteworthy vertical (up-down) and horizontal (E-W) ground displacement. Results indicate uplift in South Thira (+2.1 cm), subsidence near Oia (-2.8 cm), and significant east-west displacement in Santorini, where Thirasia, Nea Kameni and Oia seem to move away from each other. SW and NE Amorgos show a significant westward motion (-4.0 cm in Kalofana, -3.5 cm in Aigiali), while Anafi and Ios exhibit localized subsidence and uplift. These findings seem to reference ongoing fault activity and strain accumulation, presenting the need for continued monitoring of the seismically active area.

Key words: Santorini, Amorgos, earthquake, coseismic displacement, DInSAR, Sentinel-1.

Introduction / Background

Greece and the islands of the South Aegean sea particularly are no strangers to seismic activity, due to their proximity to the Hellenic subduction zone of the African plate moving at a pace of ~ 0.9 cm/year under the Aegean plate (Reilinger et al., 2006; McClusky et al., 2000; Andinisari et al., 2021; Krassakis, 2024). For a long time, the South Aegean Islands, such as Santorini, Amorgos, Anafi, and Ios have been the focus of seismological studies, due to the complex tectonic setting and frequent seismic activity in the region between Santorini and Amorgos. More specifically, in the shear zone found NE of Santorini and NW of Amorgos, known as the Santorini-Amorgos Fault Zone (Tsampouraki-Kraounaki et al., 2021), a large number of significant earthquakes has been recorded, some reaching Mw > 5.0 (Nomikou et al., 2016; Andinisari et al., 2021). Such a seismic occurrence, arguably one of the most important events in the region were the twin earthquakes, M 7.8 and 7.2, of 1956, which caused a lethal tsunami 20 m in height (Nomikou et al., 2016; Andinisari et al., 2021).

In recent weeks, Santorini Island and the surrounding region (Figure 1) have experienced a series of earthquakes, with magnitudes reaching up to M 5.3 (10/2/2025). Most of the seismic activity is occurring approximately 25 km northeast of the Santorini complex, near Anydros, at an average depth of about 7 km beneath the seabed. Seismic activity has been gradually increasing since June 2024, with a notable surge in the first weeks of February. Initially, the earthquakes were centered around the Santorini caldera,

but their epicenters have gradually migrated northeast toward Amorgos, specifically around the small, uninhabited islet of Anydros.

The threat that earthquakes and other natural disasters pose have led to significant advancements in the field of remote sensing throughout the years, in an effort to study these events and their deformation effects more effectively. Specifically, techniques utilizing Synthetic Aperture Radar (SAR) satellite images, such as those of the Sentinel-1 mission of the European Space Agency's (ESA) Copernicus program, have been extremely reliable in the study of earthquake-induced deformation (Wright et al., 2004; Suresh & Yarrakula, 2019; Li et al., 2021). More particularly, the method of Differential SAR Interferometry (DInSAR) has been extensively utilized to estimate ground displacement due to earthquakes, using the phase difference between pre and post event images (Wright et al., 2004; Suresh & Yarrakula, 2019; Li et al., 2021).

In this research, the impact of the early 2025 earthquake swarm on the islands of Santorini, Amorgos, Anafi and South Ios was studied using Sentinel-1 SAR data and the DInSAR method. Via differential interferometry, the Line-of-Sight (LOS) displacement of the four islands was estimated and then analyzed into vertical (up-down) and horizontal (E-W) displacement components.

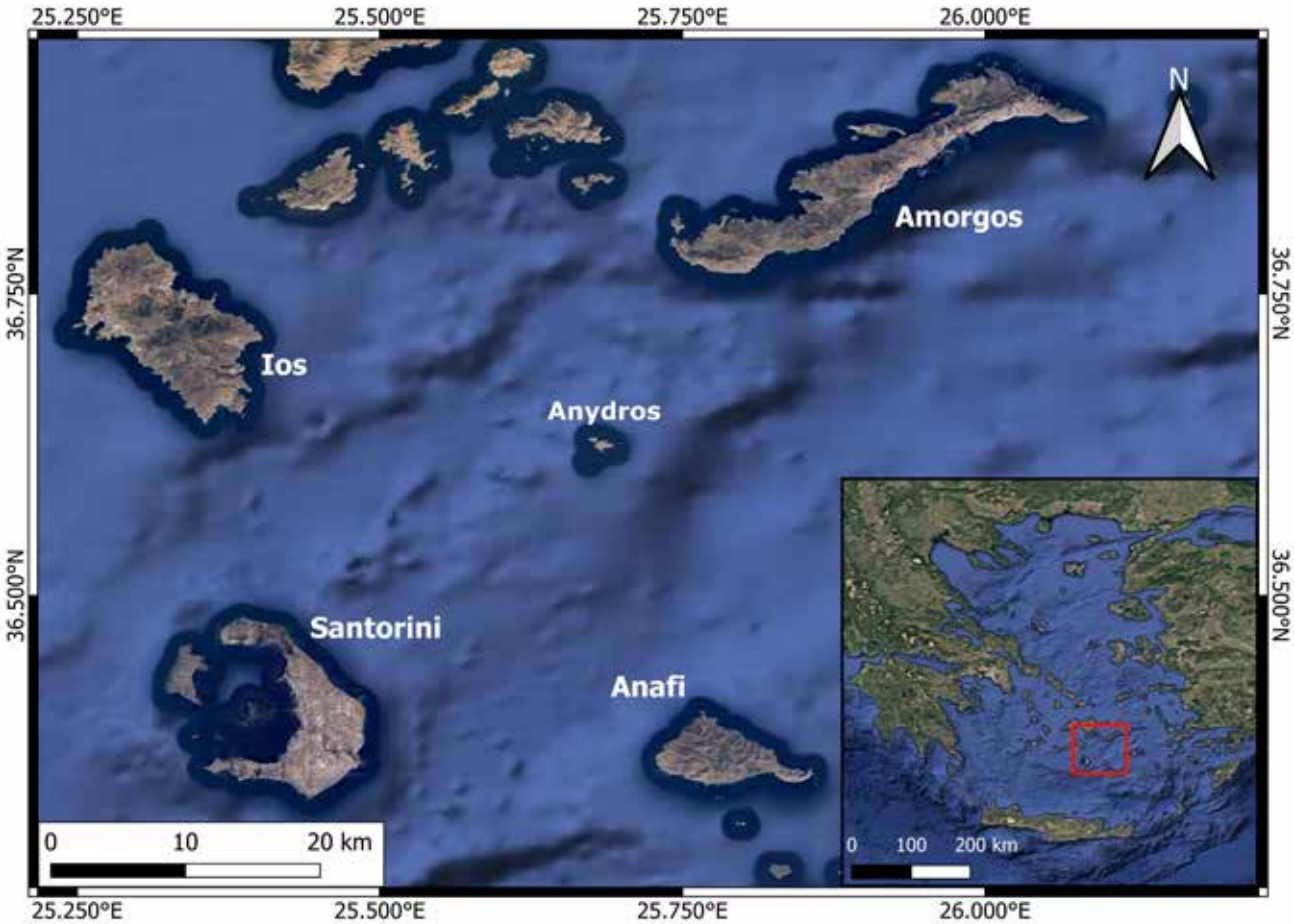

Figure 1. Study area map in QGIS v3.28.1 using the Google Satellite basemap based on Google Earth Pro. Projection: WGS84. (After Athinelis).

Data & Methodology

To study the deformation caused by the recent earthquake in the area around Anydros Island and its effects on the close islands, D-InSAR (Differential Interferometric Synthetic Aperture Radar) was utilized.

InSAR has gained widespread recognition for monitoring surface deformation, due to its many benefits (Calvet et al., 2023). SAR images were utilized for this study, obtained from the Copernicus Data Space Ecosystem browser (Copernicus Data Space Ecosystem). The time-frame studied in this research was of the seismicity during the transitional period from January 2025 to early February 2025, especially between 30/01/2025 and 05/02/2025. As such, the SAR images selected were covering this time-period while having the least time-difference possible. Specifically, a pre-event image on 30/01/2025 and a post-event image on 11/02/2025 were used for the ascending orbit pass and a pre-event image on 24/01/2025 and a post-event image on 05/02/2025 were acquired for the descending orbit pass. The Level-1 Single Look Complex (SLC) Interferometric Wide Swath (IW) data products from the Sentinel-1 are derived from the satellite's C-band SAR C-SAR instrument with a wavelength of approximately 5.5 cm (Kotzerke et al. 2022). The ESA STEP Sentinel Application Platform (SNAP v11.0) software was utilized for the process (ESA). Two pairs of Sentinel-1 IW SLC images were used in this research, for ascending and descending orbits respectively.

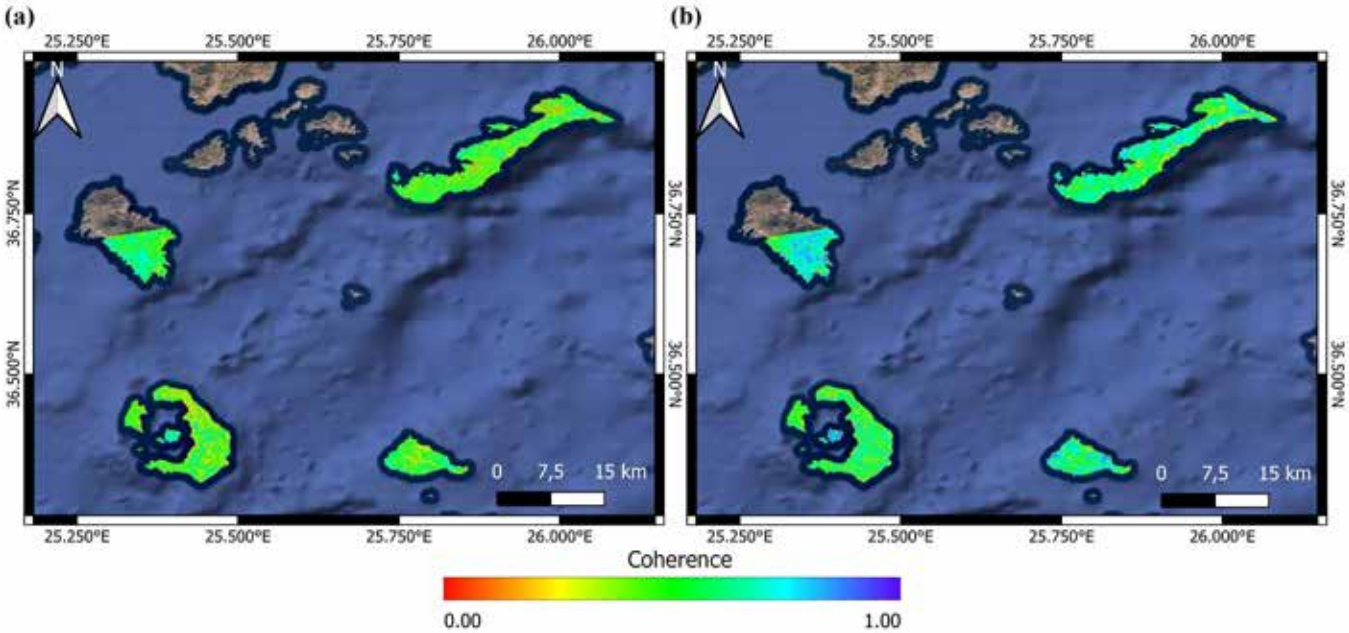

Figure 2. Coherence maps of the studied islands in ascending (a) and descending (b) pass geometry. Made in QGIS v3.28.1 using the Google Satellite basemap based on Google Earth Pro. Projection: WGS84.

The first step is to align two SAR images—a master image and a "slave" image—into a single stack, the pixels in the "slave" image are adjusted to match those in the master image. During this process, orbit correction is applied, and a DEM is utilized with back-geocoding co-registration. In this case the SRTM 1Sec HGT DEM was used, automatically downloaded by the software. The next step involves interferogram generation and coherence estimation, where the interferometric phase and coherence (Figure 2) are computed. This was accomplished through the Interferogram Formation tool, which, unlike other software, does not require the use of a specific reference point and automatically utilizes an area of multiple points for the creation of the interferograms but has been known to provide reliable results (Mavroulis et al., 2021). The interferograms were generated by pairing the aforementioned images as seen in Table 1.

Table 1. List of the interferometric image pairs used for each island.

	Interferometric image pairs		Orbit / Frame	Baseline	
Santorini	S1A	S1A		**Perpendicular**	**Temporal**
Ascending pair	30/01/2025	11/02/2025	29 / 113	49m	12d
Descending pair	24/01/2025	05/02/2025	109 / 471	39m	12d
Amorgos					
Ascending pair	30/01/2025	11/02/2025	29 / 113	49m	12d
Descending pair	24/01/2025	05/02/2025	109 / 471	39m	12d
Anafi					
Ascending pair	30/01/2025	11/02/2025	29 / 113	49m	12d
Descending pair	24/01/2025	05/02/2025	109 / 471	39m	12d
South Ios					
Ascending pair	30/01/2025	11/02/2025	29 / 113	49m	12d
Descending pair	24/01/2025	05/02/2025	109 / 471	39m	12d

Additionally, applying TOPSAR deburst eliminates the boundary areas between consecutive bursts (Marbuti et al. 2017). Before unwrapping, the SRTM 1Sec HGT was used again to remove the topographic phase and the images were multi-looked at 6 range pixels and 2 azimuth pixels. The SNAPHU software plugin (Stanford University) was utilized for the phase unwrapping. Phase unwrapping is essential for eliminating the ambiguity associated with the multiple-wavelength factor in the interferometric phase, allowing for the determination of motion (Goldstein et al. 1998). In this stage it important to specify that no tropospheric phase delay removal was applied to these results. The unwrapped phase is converted into displacement, which is geocoded, resulting in the LOS displacement (Monterroso et al. 2018). Finally, the LOS displacement (D) of the study areas is split into two components, vertical (dz) and horizontal (de), using the incidence angle (θ) of ascending (a) and descending (d) geometries, calculated in radians and the following formulas (Manzo et al., 2006; Dalla Via et al., 2012):

$$dz = \frac{Dd * sin(\theta a) + Da * sin(\theta d)}{sin(\theta d + \theta d)} \quad (1)$$

$$de = \frac{Dd * cos(\theta a) - Da * cos(\theta d)}{sin(\theta d + \theta d)} \quad (2)$$

The positive values of dz signify uplifting, while the negatives are attributed to subsidence. Similarly, negative de values suggest westward displacement, while positive are of an eastward displacement. The decomposition of the deformation into vertical and horizontal displacement was performed in QGIS v.3.28.1, through Raster Calculator tool, by inserting the raster layers of the incidence angles and the LOS displacement into the formulas (1) and (2) respectively (Mavroulis et al., 2021).

Results

Analyzing the resultant vertical (up-down) deformation component (Figure 3) of the four islands a few observations can be made. Santorini (fig. 3-a) shows an upward displacement trend in the southern part of Thira island, reaching up to ~ +2.1 cm (+0.021 m). Most of the rest of the island complex seems relatively stable, while the northwestern part of the island, ESE of Oia, shows an abrupt subsidence reaching up to ~ -2.8 cm (-0.028 m). This subsidence could be related to the SW - NE trending active fault found in the same region. Despite this, the uplifting in South Thira is relatively unexpected. Uplifting can be noticed in the western edge of Anafi island (fig. 3-b), as well as the southeastern coastal areas between the Katsouni

and Roukounas beaches, reaching +0.7 - +1.0 cm. The areas of Agios Nikolaos (Saint Nikolaos) northeast of Klisidi, the area southeast of Agios Nikolaos and the easternmost part of the island present subsidence, with the first two zones reaching ~ -2.2 cm, while eastern Anafi reached ~ -2.4 cm. Amorgos (fig. 3-c) shows subsidence mainly in the northeastern edge of the island reaching up to ~ -2.7 cm. While most of the island seems stable in terms of vertical up-down displacement, a zone of ~ +1.0 cm uplifting can be seen southwest of the Amorgos settlement. In the case of South Ios (fig. 3-d), northward, near the center of the island a subsidence zone of up to ~ -2.0 cm can be seen. East of that zone, a slight uplifting trend can be viewed of about ~ +1.0 cm, while uplifting of ~ +0.5 cm is presented in Petalidi. A maximum of ~ +1.7 cm is seen in the islet of Varvaronisi, southeast of the Magganari settlement off the coast.

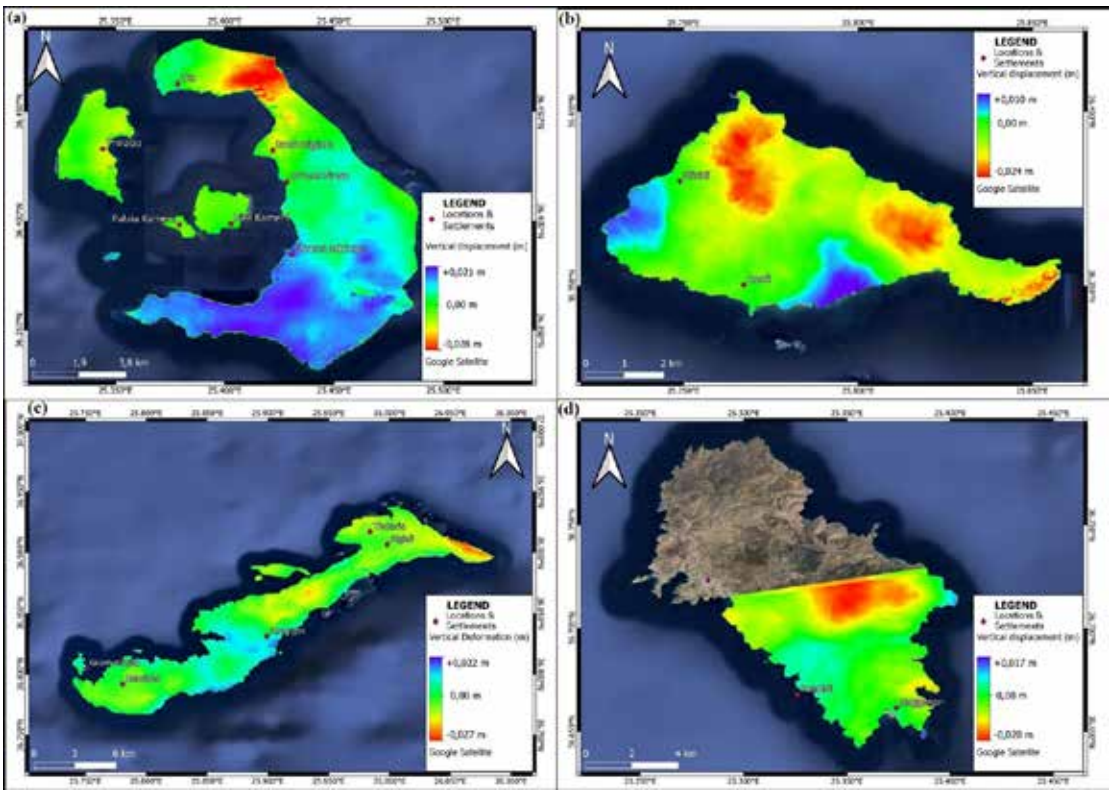

Figure 3. Interferograms showing the vertical displacement taking into account the images before and after the seismic events which happened between 24/01/2025 and 11/02/2025. The layers were overlayed on a Google Satellite basemap in QGIS v3.28.1.

The horizontal, E-W displacement of these islands (Figures 4 & 5) can also highlight some intriguing information, especially in the case of Santorini (fig 4-a). Specifically, the Thirasia island of the Santorini complex showed displacement westward at ~ -2.7 cm, while the eastern Thira island, in the Oia region, saw a significant eastward displacement of up to ~ +4.0 cm. The Nea Kameni island was displaced westward to a smaller degree of ~ -1.5 cm. In Anafi island (fig. 4-b), between the Klisidi and Anafi settlements there's a region presenting westward displacement of up to ~ -2.3 cm. The East-Southeast edge of the island presents eastward displacement of ~ +1.0 cm. Amorgos island (fig. 4-c) is particularly interesting as the entire island seems to have a mild trend westward with the SW part, in Kalofana and the NE part, east of Aigiali, presenting a more significant westward displacement of ~ -4.0 cm and ~ -3.5 cm respectively. The Gramvoussa islet shows an eastward displacement of ~ +1.3 cm. Lastly, South Ios (fig. 4-d) seems fairly stable in the E-W direction with a westward ~ -3.6 cm displacement southeast of Magganari and an eastward displacement zone of ~ +0.4 cm in the coast southeast of Ios settlement.

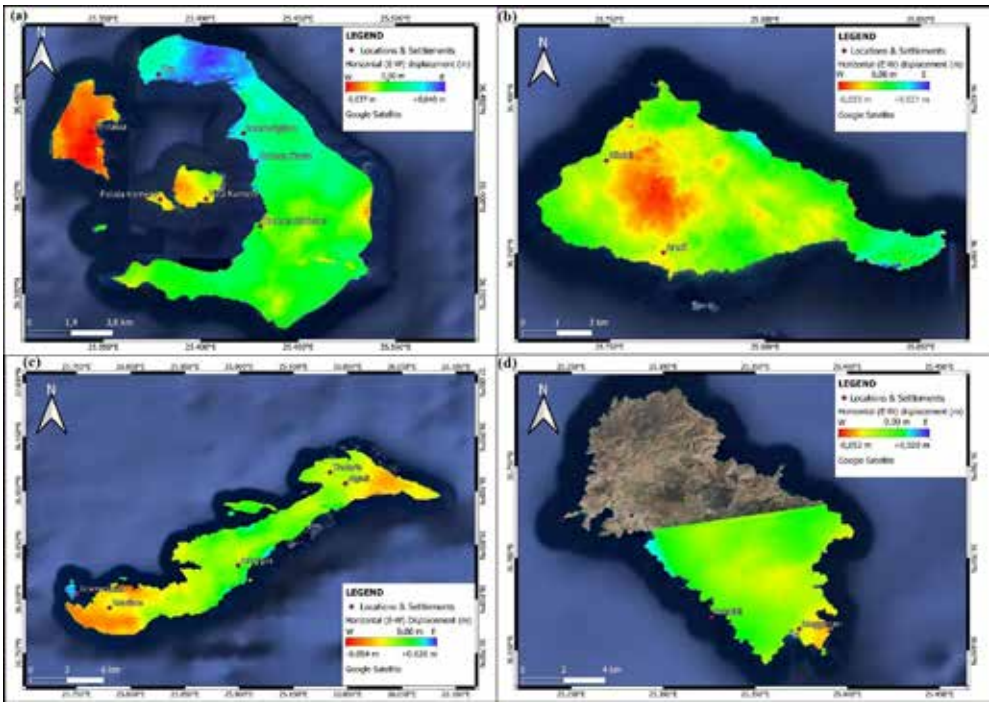

Figure 4. Interferograms showing the horizontal displacement taking into account the images before and after the seismic events which happened between 24/01/2025 and 11/02/2025. The layers were overlayed on a Google Satellite basemap in QGIS v3.28.1.

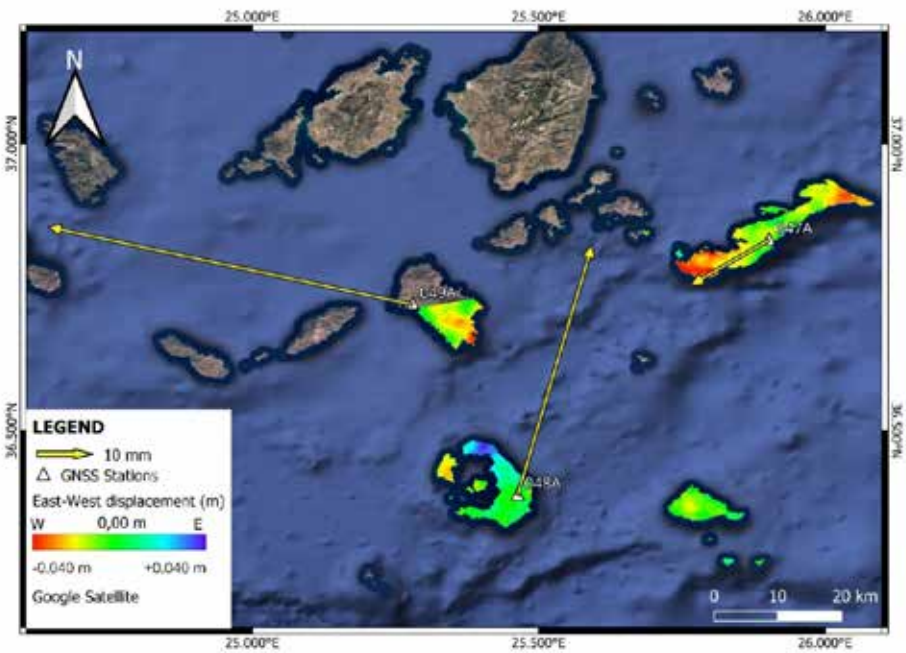

Figure 5. Horizontal shift of the South Aegean Islands shown through GNSS station data, for the period between 28/01/2025 and 20/02/2025, compared to the horizontal displacement trends of the current study. The vectors were created by the Dionysos Satellite Observatory of the National Technical University of Athens (NTUA) using data from the HEPOS GNSS station network. The layers were overlayed on a Google Satellite basemap in QGIS v3.28.1.

Conclusions

Santorini showed a spreading trend in-between the islands of Thirasia, Nea Kameni and North Thira, which were moving away from, seemingly, an underwater center. This might be caused by active tectonic and/or magmatic processes within the submerged caldera found in that region. Despite this, the uplifting trend observed in South Santorini does not seem to fit with that hypothesis and might be the result of residual atmospheric disturbances. Both Anafi and Amorgos showed significant westward displacement where, in Anafi's case, this horizontal shift seems to be due to internal stress. Moreover, uplift was noticed in western and southeastern Anafi, along with subsidence in Agios Nikolaos and the eastern island, possibly connected to similar tectonic processes. In Amorgos there was northeastern subsidence and minor uplift southwest. In the case of South Ios, the island was characterized by localized subsidence and minor uplift. The displacement in these islands does not seem to be related, necessarily, to the seismicity in Anydros, due to their geographic distribution. Overall, these trends found in the four islands studied in this research, seem to indicate ongoing fault activity and, possibly, magmatic processes, though concrete conclusions may require further research and investigation.

Acknowledgements

We would like acknowledge the contribution of Andreas Karavias (NTUA) in his support and advice during the processing phase. We also acknowledge Dionysos Satellite Observatory of NTUA for their displacement vector analysis using HEPOS GNSS data. Acknowledgements should be given to the Hellenic Cadastre, for their ownership of the HEPOS GNSS network. Moreover, we would like to thank Dr A. Ganas (National Observatory of Athens) and Prof. M. Foumelis (Aristotle University of Thessaloniki) for their help in the GNSS explanation as well as during all the crisis. Last but not least, we acknowledge ESA for openly and freely providing the Sentinel-1 satellite data of the Copernicus program through the Copernicus Data Space Ecosystem platform.

References

Andinisari, R., Konstantinou, K.I., Ranjan, P., 2021. Seismicity along the Santorini-Amorgos zone and its relationship with active tectonics and fluid distribution. Phys. Earth Planet. Inter. 312, 106660. https://doi.org/10.1016/j.pepi.2021.106660

Calvet, A., Balbarani, S., Gende, M., 2023. DinSAR coseismic deformation measurements of the Mw 8.3 Illapel earthquake (Chile). Journal of Geodetic Science 13(1), 20220154. https://doi.org/10.1515/jogs-2022-0154.

Copernicus Data Space Ecosystem. Copernicus Browser. Available at: https://browser.dataspace.copernicus.eu/ [Accessed 12 February 2025].

Dalla Via, G., Crosetto, M., Crippa, B., 2012. Resolving vertical and east-west horizontal motion from differential interferometric synthetic aperture radar: The L'Aquila earthquake. J. Geophys. Res. Solid Earth 117(B2). https://doi.org/10.1029/2011JB008689

Dionysos Satellite Observatory. *Santorini Volcano*. National Technical University of Athens. Available at: https://dionysos.survey.ntua.gr/dsoportal/_projects/supersites/santorini/ [Accessed 12 February 2025].

European Space Agency (ESA). Sentinel Application Platform (SNAP). Available at: https://step.esa.int/main/toolboxes/snap/ [Accessed 12 Feb. 2025].

Goldstein, R.M., Werner, C.L., 1998. Radar interferogram filtering for geophysical applications. Geophys. Res. Lett. 25, 4035–4038.

Krassakis, P. 2024. Geospatial intelligence for multi-hazard assessment in coastal areas of the Hellenic volcanic arc. Ph.D. Thesis, Harokopio University, Athens, Greece, 283 p. https://doi.org/10.12681/eadd/56709

Kotzerke, P., Siegmund, R., Langenwalter, J., Andersen, H.S., 2022. End-to-End Implementation and Operation of the European Ground Motion Service (EGMS) Product User Manual. European Environment Agency, Copenhagen, Denmark. [Google Scholar]

Marbouti, M., Praks, J., Antropov, O., Rinne, E., Leppäranta, M., 2017. A study of landfast ice with Sentinel-1 repeat-pass interferometry over the Baltic Sea. Remote Sens. 9, 833. https://doi.org/10.3390/rs9080833

Manzo, M., Ricciardi, G.P., Casu, F., Ventura, G., Zeni, G., Borgström, S., Berardino, P., Del Gaudio, C., Lanari, R., 2006. Surface deformation analysis in the Ischia Island (Italy) based on spaceborne radar interferometry. J. Volcanol. Geotherm. Res. 151(4), 399–416. https://doi.org/10.1016/j.jvolgeores.2005.09.010

McClusky, S., Balassanian, S., Barka, A., Demir, C., Ergintav, S., Georgiev, I., Gurkan, O., Hamburger, M., Hurst, K., Kahle, H., Kastens, K., Kekelidze, G., King, R., Kotzev, V., Lenk, O., Mahmoud, S., Mishin, A., Nadariya, M., Ouzounis, A., Paradissis, D., Peter, Y., Prilepin, M., Reilinger, R., Sanli, I., Seeger, H., Tealeb, A., Toksoz, M.N., Veis, G., 2000. Global positioning system constraints on plate kinematics and dynamics in the eastern Mediterranean and Caucasus. J. Geophys. Res. 105, 5695–5719. https://doi.org/10.1029/1999JB900351

Monterroso, F., de Luca, C., Bonano, M., Lanari, R., Manunta, M., Manzo, M., Zinno, I., Casu, F., 2018. Automatic generation of co-seismic displacement maps by using Sentinel-1 interferometric SAR data. Procedia Comput. Sci. 138, 332–337. https://doi.org/10.1016/j.procs.2018.10.047

Mavroulis, S., Triantafyllou, I., Karavias, A., Gogou, M., Katsetsiadou, K.-N., Lekkas, E., Papadopoulos, G.A., Parcharidis, I., 2021. Primary and secondary environmental effects triggered by the 30 October 2020, Mw = 7.0, Samos (Eastern Aegean Sea, Greece) earthquake based on post-event field surveys and InSAR analysis. Appl. Sci. 11, 3281. https://doi.org/10.3390/app11073281

Nomikou, P., Hübscher, C., Ruhnau, M., Bejelou, K., 2016. Tectono-stratigraphic evolution through successive extensional events of the Anydros Basin, hosting Kolumbo volcanic field at the Aegean Sea, Greece. Tectonophysics 671, 202–217. https://doi.org/10.1016/j.tecto.2016.01.021

QGIS Development Team. QGIS v.3.28.1. Available at: https://qgis.org/ [Accessed 12 Feb. 2025]

Reilinger, R., McClusky, S., Vernant, P., Lawrence, S., Ergintav, S., Cakmak, R., Ozener, H., Kadirov, F., Guliev, I., Stepanyan, R., Nadariya, M., Hahubia, G., Mahmoud, S., Sakr, K., ArRajehi, A., Paradissis, D., Al-Aydrus, A., Prilepin, M., Guseva, T., Evren, E., Dmitrotsa, A., Filikov, S.V., Gomez, F., Al-Ghazzi, R., Karam, G., 2006. GPS constraints on continental deformation in the Africa–Arabia–Eurasia continental collision zone and implications for the dynamics of plate interactions. J. Geophys. Res. 111. https://doi.org/10.1029/2005JB004051

Stanford University. *SNAPHU: Statistical-Cost, Network-Flow Algorithm for Phase Unwrapping*. Stanford University. Available at: https://web.stanford.edu/group/radar/softwareandlinks/sw/snaphu/ [Accessed 12 February 2025]

Tsampouraki-Kraounaki, K., Sakellariou, D., Rousakis, G., Morfis, I., Panagiotopoulos, I., Livanos, I., Manta, K., Paraschos, F., Papatheodorou, G., 2021. The Santorini-Amorgos shear zone: Evidence for dextral transtension in the south Aegean back-arc region, Greece. Geosciences 11(5), 216. https://doi.org/10.3390/geosciences11050216

17th INTERNATIONAL CONGRESS of the Geological Society of Greece

BULLETIN OF THE GEOLOGICAL SOCIETY OF GREECE, SP. PUBL.

EXTENDED ABSTRACT 019

Employing Sentinel-1 imagery to monitor the deformation rate over the caldera of the Santorini Volcanic Island Complex using multitemporal InSAR from January 2023 up to February 2025.

Athinelis I.[1], Castro-Melgar I.[1,2], Gatsios T.[1], Krassakis P.[1] and Parcharidis I[1].
(1) Department of Geography, Harokopio University of Athens, 176 76 Athens, Greece, gp222301@hua.gr (A.I.) icastromelgar@ig.cas.cz (C.-M.I.), gatsios@hua.gr (G.T.), pkrassakis@hua.gr (K.P.), parchar@hua.gr (P.I.)
(2) Institute of Geophysics, Czech Academy of Sciences, 141 00 Prague, Czech Republic

Research Highlights

- MT-InSAR processing of Sentinel-1 data unveiled significant uplifting deformation velocity in the northwestern part of the caldera, focusing in Nea Kameni, Thirasia, Imerovigli & Oia, possibly connected to swelling of the magmatic chamber due to magma accumulation.
- Increased deformation velocity was noticed past June 2024, suggesting increasing volcano-tectonic activity relating to the increased seismicity in Anydros.

Abstract

Santorini is one of the most significant islands in the South Aegean Sea and a well-known volcanic center in the South Aegean Volcanic Arc. It is known for its seismicity, caused by active volcanic and tectonic processes, such as the occurrences of 2011-2012 and 2024-2025. This study focuses on estimating the ground deformation velocity of Santorini's caldera by utilizing Multitemporal InSAR method of SBAS (Small Baseline Subset) and Sentinel-1 satellite imagery. The research found increased uplifting deformation rate in northwestern Nea Kameni and Imerovigli, up to ~ +17.6 mm/yr and ~ +17 mm/yr respectively. A lesser uplifting trend was recorded in Northwestern Thira (Oia) and Thirasia. Significant horizontal westward deformation was seen in south Thirasia and west Oia (up to -20 mm/yr) and Palaia Kameni (~ -39 mm/yr), while an eastward pattern was representing Imerovigli (up to ~ +21 mm/yr), which might signify swelling of the caldera due to magmatic and tectonic processes in the volcanic chamber. Time-series vertical and horizontal deformation diagrams attribute a more impactful effect after June of 2024.
Key words: Santorini, caldera, seismicity, ground deformation, SBAS, Sentinel-1.

Introduction / Background

Santorini (fig. 1), a prominent volcanic island complex in the Aegean Sea, is part of the South Aegean Volcanic Arc, which extends from Methana to Nisyros (Greece) (Krassakis, 2024). This arc is associated with the subduction of the African plate beneath the Eurasian plate, a process that has driven volcanic activity in the region for at least 4.7 million years (Vougioukalakis et al., 2019). The Santorini Volcanic Complex (SVC) consists of five main islands—Thira, Thirasia, Aspronisi, Palea Kameni and Nea Kameni—formed through successive eruptions, the most significant being the Minoan eruption (~1600 BCE). This event shaped the current morphology of the caldera and deposited widespread tephra layers (Vougioukalakis et al., 2019). Since then, the volcanic activity has been concentrated in the central part of the caldera, mainly at Nea Kameni, with the last eruption occurring in 1950.

The island remains an active volcanic system, experiencing recurrent unrest episodes. The most recent significant period of activity occurred between 2011 and 2012, marked by increased seismicity, ground deformation, and magmatic inflation at shallow depths (Vougioukalakis et al., 2016). During this episode, uplift reached up to 14 cm at Cape Skaros and 9 cm at Nea Kameni, as detected by geodetic techniques such as GPS and Interferometric Synthetic Aperture Radar (InSAR) (Foumelis et al., 2013). Seismicity was concentrated along the Kameni and Kolumbo fault zones, indicating a strong structural control on magma emplacement (Vougioukalakis et al., 2016). Despite these significant signals, no eruption followed, and subsequent geodetic studies from 2015 to 2021 confirmed a return to quiescence (Castro-Melgar et al., 2025).

Since June 2024, a new seismic sequence has been developing in the region, reaching its peak in a Mw 5.3 earthquake on 10 February 2025, located approximately 25 km northeast of the Santorini caldera, near the islet of Anydros, at an average depth of ~7 km. Over 7,000 earthquakes have been recorded in the broader Santorini-Amorgos area, suggesting a gradual reactivation of the regional stress field. Given the complex interplay between magmatic processes, tectonic stresses, and hydrothermal activity in Santorini, continuous geodetic monitoring is essential for understanding the current unrest. Remote sensing techniques, particularly multitemporal InSAR (MT-InSAR), offer a valuable tool for detecting and quantifying ground deformation, enabling the identification of subtle precursory signals.

Objectives

In this study, we employ Sentinel-1 imagery and the MT-InSAR method of Small BAseline Subset (SBAS) to monitor progression of the deformation rate in vertical (up-down) and horizontal (east-west) direction around the Santorini caldera from January 2023 up until February of 2025. More specifically, we aim on studying the entire development of non-linear deformation from the early 2023 rest period going into the unrest phase of late 2024 to early 2025, through the use of time-series diagrams. This approach allows for precise quantification of surface displacement patterns, offering valuable insights into the ongoing deformation dynamics of the Santorini caldera.

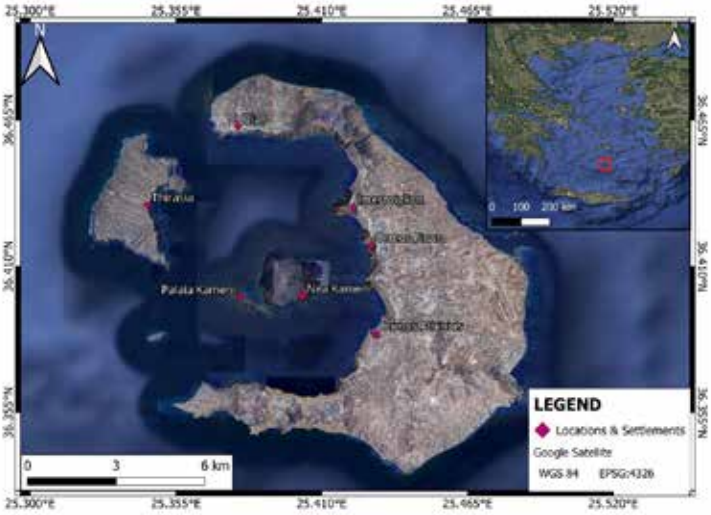

Figure 1. Study area map in QGIS v3.28.1 using the Google Satellite basemap based on Google Earth Pro. Projection: WGS84. (After Athinelis)

Methods

In recent years, MultiTemporal Interferometric Synthetic Aperture Radar (MT-InSAR) has emerged as the most effective method for detecting ground deformations and mapping potential landslides on a regional scale. This is primarily due to its cost efficiency, extensive spatial coverage, and capability to provide high-frequency and high-precision measurements of surface displacement (Zhang,2020). The interferometric processing was performed, using the GAMMA software (GAMMA Remote Sensing AG, Gümligen, Switzerland) and the SBAS technique (Berardino et al., 2002). The SBAS method is an MT-InSAR technique based on the use of multiple SAR images to estimate phase differences in time between image pairs and convert them into a pixel-based deformation time-series (Chen et al., 2024). The basis for the method is that the baseline of the interferometric pairs is smaller than the critical, thus reducing the decorrelation (Ferretti, 2014).

The study area can be characterized as peri-urban. Certain towns exhibit a high density of buildings, whereas some villages contain a comparatively lower number of structures. In the areas that the buildings

are absent, there are some objects that scatter radar signal stronger and more coherent than their surroundings. In this case, the pixel-based SBAS method was selected, which is based on DS, due to its better coverage of natural areas with less dense urban structures (Ferretti, 2014), such as the Santorini Island Complex. Moreover, this method has been found to provide more reliable results when estimated non-linear deformation (Gheorghe & Armaş, 2016; Chen et al., 2021), such as this case where both rest and unrest periods are studied in a singular dataset. The processing can be distinguished into two sub-processing stages: the pre-processing and the main processing.

The methodology for this research utilized 127 Sentinel-1 Interferometric Wide (IW) Single Look Complex (SLC) images from the Copernicus program of the European Space Agency (ESA with an orbital tube less than 100m), which were collected from the Vertex platform of the Alaska Satellite Facility Distributed Active Archive Centers (ASF DAAC).

The generation of parametric files for the 64 SLC images of ascending orbit took place during pre-processing and also the orbital refinement using precise orbits. The stack of ascending SLC images were co-registered using as reference image the scene of 12/03/2024, resulting in a stack of 186 differential interferograms. Similarly, 63 SLC descending orbit images were coregistered with the reference image of 18/03/2024 and 183 differential interferometric pairs were formed. The Shuttle Radar Topography Mission (SRTM) 1-arcsec (i.e., 30 m/pixel) Digital Elevation Model (DEM) (Farr, 2007) was used for the elimination of the topographical contribution from the interferograms. A minimum coherence threshold of 0.8 was used in this phase.

The first step in the primary SBAS processing involved the generation of a multi-reference stack, incorporating both single-look and multi-look differential interferometric phases. The differential interferograms were constructed by comparing each scene to the three consecutive scenes. The reference point was chosen near the airport area, which is regarded as the most stable on the island. After estimating height corrections and atmospheric phase delays, they were subtracted from the interferometric phase and a deformation model was produced. By repeating the final step several times, this model was improved. Ultimately, the ground deformation phases were masked based on a maximum standard deviation threshold of 1.2 for ascending and 1.3 for descending orbit and were then converted into LOS deformation time-series.

The Line-of-Sight (LOS) deformation velocity (D) of Santorini was estimated using the SBAS method. This velocity is then decomposed into vertical (dz) and horizontal (de) components by incorporating the incidence angle (θ), expressed in radians, from both ascending (a) and descending (d) acquisition geometries, following the approach of Manzo et al. (2006) and Dalla Via et al. (2012):

$$dz = \frac{Dd * \sin(\theta a) + Da * \sin(\theta d)}{\sin(\theta d + \theta d)} \quad (1)$$

$$de = \frac{Dd * \cos(\theta a) - Da * \cos(\theta d)}{\sin(\theta d + \theta d)} \quad (2)$$

The negative de values signify a westward displacement, while the positives are attributed to an eastward displacement. Similarly, negative dz values suggest subsidence, while positive are indicative of an uplifting trend. The corresponding results were visualized in a QGIS environment.

Results

The results of the SBAS method showed a smooth deformation pattern throughout the area, especially in the Thirasia and Oia. Particularly, the vertical (up-down) deformation component (fig. 2) suggested that Thirasia is relatively stable in this direction, with the deformation rate in the eastern part being around ~ +6 mm/yr and increasing up to ~ +9 mm/yr towards the northeastern area. Similarly, a vertical deformation rate of about +3 to +5 mm/yr was observed in the Oia region in northwestern Thira island. The most significant vertical deformation velocity was estimated in the Nea Kameni and Palaia Kameni islands, with the latter showing deformation rates in the range of ~ +6 to +8 mm/yr. Most importantly, however, Nea Kameni was represented by velocities > +10.00 mm/yr with an increasing pattern towards the northern and northwestern parts, reaching up to ~ +17.6 mm/yr. Similar deformation rates were noticed in Imerovigli with velocities exceeding +10 mm/yr up to ~ +17 mm/yr.

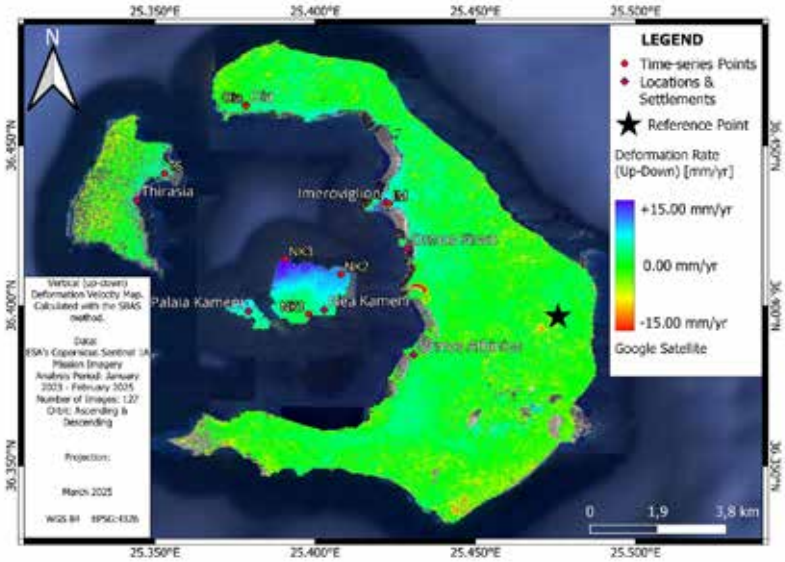

Figure 2. Vertical deformation map of Santorini using the SBAS method. Time period: January 2023 – February 2025. The layers were overlayed on a Google Satellite basemap in QGIS v3.28.1.

Analyzing the horizontal (East - West) deformation rate component (fig. 3), southern Thirasia and the northwestern edge of Thira, west of Oia, suggests a westward movement mostly between -12 to -15 mm/yr while reaching up to ~ -20 mm/yr. The remaining Thira island is dominated by a general eastward deformation, peaking in Imerovigli with velocities near ~ +7 mm/yr and even exceeding +15, up to a maximum of ~ +21 mm/yr. Palaia Kameni represents the highest horizontal deformation rate, showing significant westward displacement, mostly between -15 to -18 mm/yr, with the northern part reaching up to ~ -39. mm/yr. Juxtaposed to this, Nea Kameni seems to be rather stable in the horizontal direction with a slight westward movement of ~ -2 mm/yr.

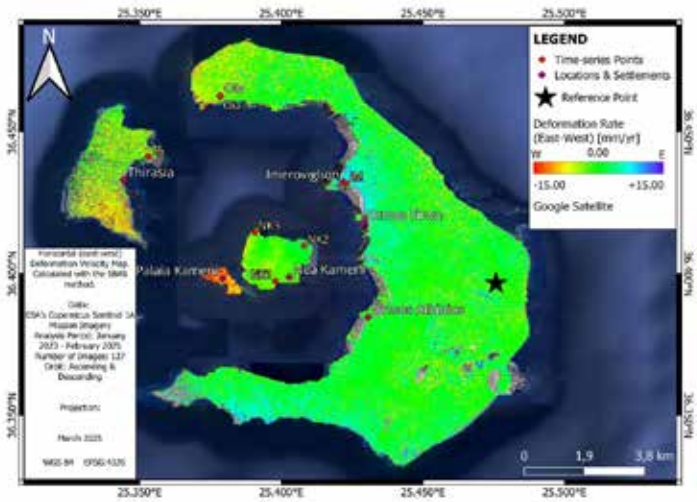

Figure 3. Vertical deformation map of Santorini using the SBAS method. Time period: January 2023 – February 2025. The layers were overlayed on a Google Satellite basemap in QGIS v3.28.1.

It is important to mention that, due to both rest and unrest phases being included in this analysis, the deformation rates calculated may be rather underestimated, as the deformation of both periods is averaged. As such, in order to better comprehend the progression of the deformation in the caldera, it is required that the deformation trend is thoroughly observed through the multitemporal time-series diagrams. The

time-series diagrams show that the multitemporal vertical deformation in Imerovigli (fig. 4-c), Nea Kameni (fig.4-a) and Thirasia (fig. 4-g) has increased significantly since June 2024,continuing climbing up until the end of the study period. More specifically, all three points in Nea Kameni (NK1, NK2 & NK3) suggest a pronounced increase in vertical deformation since June 2024, with NK3 representing a higher deformation rate in northwestern Nea Kameni compared to the eastern (NK2) and southern (NK1) parts. By the end of the study period, uplift values at NK1, NK2, and NK3 reached approximately +10mm, +25mm and 48mm, respectively, relative to the stable reference position. Thirasia presents a more anomalous increase in vertical deformation after June 2024, reaching ~ +12 mm in February 2025. Similarly, Imerovigli, located in western Thira, experienced progressive deformation beginning slightly earlier, near the end of April 2024, with a marked acceleration from June 2024 onward. This deformation reached up to ~ +16 mm by the end of the studyperiod. In contrast, the vertical deformation trend in Oia is less clear (fig. 4-e). Specifically, the time-series diagram of the vertical deformation shows an uplifting trend beginning in December of 2023, declining in June 2024 but increasing again from October 2024 onward. January 2025 presented the highest uplift in Oia at +8mm, dropping to ~ +5.5 mm by February 2025. Regarding horizontal deformation, Nea Kameni (fig. 4-b) shows a clear eastward movement beginning in June 2024 onwards in the northwestern island (NK2) up to ~ +17 mm. A similar but more significant eastward trend is observed in Imerovigli (fig. 4-d), culminating in a deformation of +40 mm east. Oia (fig. 4-f) and Thirasia (fig, 4-h) show westward deformation beginning in October 2024 which appears to reverse after January 2025, stabilizing around-6 mm in both cases.

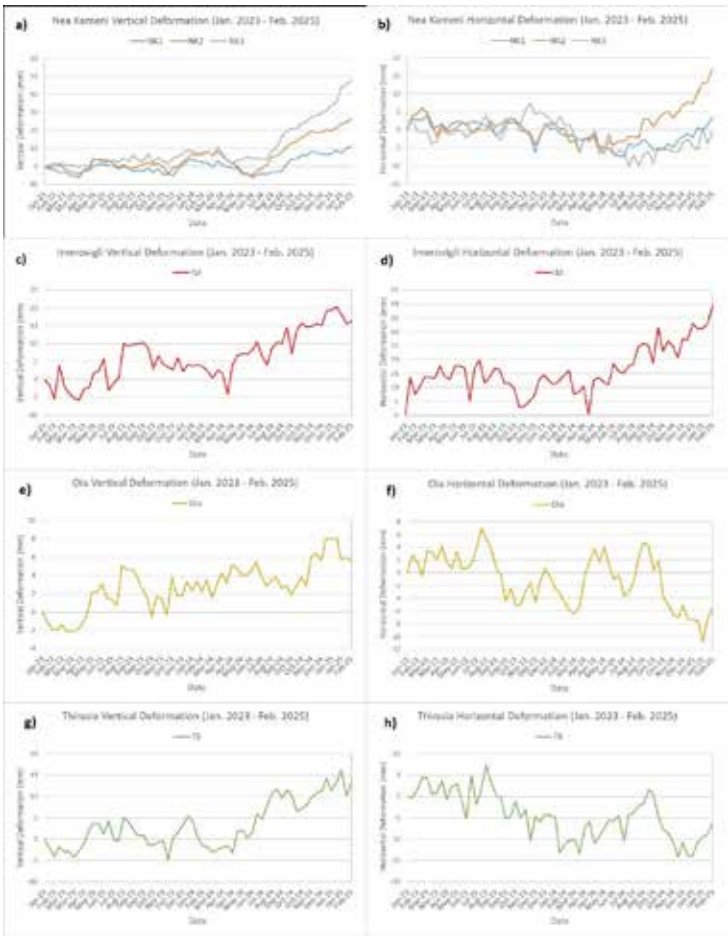

Figure 4. Time-series diagrams showing the vertical (a, c, e, g) and horizontal (b, d, f, h) deformation of Nea Kameni, Imerovigli, Oia & Thirasia respectively.

Conclusions

This research concerned the study of the deformation rate in the caldera of the Santorini volcanic island complex through the MT-InSAR technique SBAS. Using multiple satellite images throughout the studied time period (January 2023 to February 2025) several observations were made concerning the vertical and horizontal deformation velocity. Specifically, the deformation velocity was most significant in the zones closest to the interior of Santorini's Caldera, where Nea Kameni is situated. The area of mainly deformation accumulation lies northwest of Nea Kameni, directly above the submerged caldera and the magmatic reservoir beneath it. The uplifting pattern in that region could suggest swelling within the caldera due to magma accumulation in the magmatic chamber. The notable positive vertical deformation values in northwestern Thira may be the result of increased magmatic processes in the caldera due to the significant and frequent seismicity in the Anydros islet in recent months. This can also be explained by the vertical deformation time-series diagrams, showing a continuous significant increase in deformation velocity past June 2024, suggesting that the notable deformation is related to the beginning of the earthquake swarm event in Anydros. Moreover, the horizontal deformation rate component of the depicted a westward movement trend for both Thirasia, Palaia Kameni and Oia (northwestern Thira), while the remaining Thira area moves eastward, with Nea Kameni being mostly stable with a slight westward trend. These contrasting deformation vectors support the hypothesis of caldera inflation, as the islands of the volcanic complex appear to be moving away from the central caldera, suggesting radial expansion associated with magma intrusion.

Acknowledgements

We acknowledge the contribution of Andreas Karavias (National Technical University of Athens) for his consultation and support during the processing phase of the study. We would also like to acknowledge Dr. Urs Wegmüller, President of Executive Board, director, and Senior project scientist in GAMMA Remote Sensing AG for his ownership of the GAMMA software and his advice during processing. Acknowledgements should be given ESA their ownership of the Sentinel-1 satellite data of the Copernicus program which are provided through open and free sources. Last but not least, we acknowledge the University of Alaska Fairbanks, owners of the ASF DAAC Vertex platform through which the research data were acquired.

References

Alaska Satellite Facility. ASF SAR DAAC Vertex Data Search. Available at: https://search.asf.alaska.edu/ [Accessed 12 Feb. 2025]

Berardino, P., Fornaro, G., Lanari, R., & Sansosti, E., 2002. A new algorithm for surface deformation monitoring based on small baseline differential SAR interferograms. IEEE Transactions on Geoscience and Remote Sensing, 40(11), 2375–2383. https://doi.org/10.1109/TGRS.2002.803792

Castro-Melgar, I., Gatsios, T., Prudencio, J., Ibanez, J. M., Lekkas, E., Parcharidis, I., 2025. Volcano Monitoring: Using SAR Interferometry for the Pre-Unrest of La Palma and the Post-Unrest of Santorini. Remote Sensing for Geophysicists, CRC Press, 440-459. https://doi.org/10.1201/9781003485278.

Chen, X., Tessari, G., Fabris, M., Achilli, V., & Floris, M., 2021. Comparison between PS and SBAS InSAR techniques in monitoring shallow landslides. Understanding and Reducing Landslide Disaster Risk: Volume 3 Monitoring and Early Warning 5th, 155-161. http://dx.doi.org/10.1007/978-3-030-60311-3_17

Chen, Y., Ding, C., Huang, P., Yin, B., Tan, W., Qi, Y., Xu, W. & Du, S., 2024. Research on time series monitoring of surface deformation in Tongliao urban area based on SBAS-PS-DS-InSAR. Sensors, 24(4), 1169. https://doi.org/10.3390/s24041169

Dalla Via, G., Crosetto, M., Crippa, B., 2012. Resolving vertical and east-west horizontal motion from differential interferometric synthetic aperture radar: The L'Aquila earthquake. J. Geophys. Res. Solid Earth 117(B02310). https://doi.org/10.1029/2011JB008689

Farr, T. G., Rosen, P. A., Caro, E., Crippen, R., Duren, R., Hensley, S., Kobrick, M., Paller, M., Rodriguez, E., Roth, L., Seal, D., Shaffer, S., Shimada, J., Umland, J., Werner, M., Oskin, M., Burbank, D. & Alsdorf, D., 2007. The shuttle radar topography mission. Reviews of geophysics, 45(2). https://doi.org/10.1029/2005RG000183

Ferretti, A., 2014. Satellite InSAR data: reservoir monitoring from space. EAGE publications. ISBN: 978-90-73834-

71-2. http://dx.doi.org/10.3997/9789073834712

Foumelis, M., Trasatti, E., Papageorgiou, E., Stramondo, S., Parcharidis, I., 2013. Monitoring Santorini volcano (Greece) breathing from space. Geophysical Journal International 193, 161-170. https://doi.org/10.1093/gji/ggs135.

GAMMA Remote Sensing AG. GAMMA Remote Sensing AG. Available at: https://www.gamma-rs.ch/ [Accessed 12 Feb. 2025]

Gheorghe, M., & Armaş, I., 2016. Comparison of multi-temporal differential interferometry techniques applied to the measurement of Bucharest City Subsidence. Procedia Environmental Sciences, 32, 221-229. http://dx.doi.org/10.1016/j.proenv.2016.03.027

Krassakis, P., 2024. Geospatial intelligence for multi-hazard assessment in coastal areas of the Hellenic volcanic arc. Ph.D. Thesis, Harokopio University, Athens, Greece, 283 p. https://doi.org/10.12681/eadd/56709

Manzo, M., Ricciardi, G.P., Casu, F., Ventura, G., Zeni, G., Borgström, S., Berardino, P., Del Gaudio, C., Lanari, R., 2006. Surface deformation analysis in the Ischia Island (Italy) based on spaceborne radar interferometry. J. Volcanol. Geotherm. Res. 151(4), 399–416. https://doi.org/10.1016/j.jvolgeores.2005.09.010

QGIS Development Team, QGIS. Available at: https://qgis.org/ [Accessed 12 Feb. 2025]

Vougioukalakis, G., Sparks, R. S., Druitt, T., Pyle, D., Papazachos, C., & Fytikas, M., 2016. Volcanic Hazard Assessment at Santorini Volcano: A review and a synthesis in the light of the 2011-2012 Santorini unrest. Bulletin of the Geological Society of Greece, 50(1), 274-283. https://doi.org/10.12681/bgsg.11728

Vougioukalakis, G. E., Satow, C. G., & Druitt, T. H., 2019. Volcanism of the South Aegean volcanic arc. Elements: An International Magazine of Mineralogy, Geochemistry, and Petrology, 15(3), 159-164. https://doi.org/10.2138/gselements.15.3.159

Zhang, Y., Meng, X., Dijkstra, T.A., Jordan, C.J., Chen, G., Zeng, R., & Novellino, A., 2020. Forecasting the magnitude of potential landslides based on InSAR techniques. Remote Sensing of Environment, 241, 111738. ISSN 0034-4257 https://doi.org/10.1016/j.rse.2020.111738

17th INTERNATIONAL CONGRESS of the Geological Society of Greece

BULLETIN OF THE GEOLOGICAL SOCIETY OF GREECE, SP. PUBL.

EXTENDED ABSTRACT 020

Impacts of Climate Change on Medicane Formation: Analyzing SST Changes in the Eastern Mediterranean (1940–2023) using Thematic Maps

Avgerinos E[1]., Kostopoulou E[1]., Tegoulias I[2]., Giannakopoulos C[3].
(1) Department of Geography, University of Aegean, Greece, stratos.avgs@gmail.com (2) Department of Geology, Aristotle University of Thessaloniki, Greece (3) Institute for environmental Research and Sustainable Development, National Observatory of Athens, Greece

Introduction

Rising sea levels, increasing frequency of extreme weather events, and transformations in marine ecosystems present significant challenges for the Eastern Mediterranean region. These changes directly affect maritime routes, port infrastructure, and the broader environment. In this context, understanding the relationship between sea surface temperature (SST) fluctuations and their effects on the environment has become a matter of increasing importance. This paper focuses on an in-depth analysis of SST trends in the Eastern Mediterranean from 1940 to 2023, examining both annual and monthly scales. By analyzing these temperature trends, the study aims to assess their potential environmental impacts, considering both operational and ecological perspectives.

In addition to SST trends, this study includes a detailed examination of extreme weather events, specifically Mediterranean cyclones, also known as Medicanes. A case study of the Mediterranean Cyclone Zorba, which significantly impacted the Eastern Mediterranean in late September and early October 2018, is included. Furthermore, the study references the average monthly SST values for September and October of 2018. Through this integrated approach, the research aims to provide valuable insights into the challenges and risks faced by the region and to offer guidance for future strategies to address these emerging environmental shifts.

Data and Methodology

This study utilized ERA5 Reanalysis data on Sea Surface Temperature (SST) to analyze the Eastern Mediterranean region, from January 1940 to December 2023. The data were examined at multiple temporal resolutions, including annual, monthly, and daily intervals, to capture both long-term trends and short-term variability in SST. The ERA5 dataset, which provides high-resolution, accurate climate data, is publicly available to the scientific community through the Copernicus Climate Change Service, in collaboration with the European Centre for Medium-Range Weather Forecasts (ECMWF). This dataset offers an invaluable resource for researchers and decision-makers involved in climate studies and environmental assessments.

To facilitate the interpretation of SST patterns over time, a series of thematic maps were generated, illustrating spatial and temporal variations of SST across different periods. These maps highlight significant trends, anomalies, and fluctuations in SST within the study area. The maps were created using Python programming, employing data visualization libraries such as Matplotlib and Plotly, in combination with ArcGIS software for spatial analysis and cartographic rendering. This methodological approach allowed for a detailed and comprehensive representation of the SST data, offering insights into both regional and temporal dynamics.

The integration of Python code and ArcGIS software enabled the efficient processing, analysis, and visualization of large datasets, ensuring that the results are both scientifically rigorous and easily interpretable. These visualizations not only serve to illustrate the trends in SST over the decades but also provide a tool for identifying areas of concern, such as regions experiencing rapid warming or significant deviations from historical patterns. The availability of this data to the broader scientific community, alongside the advanced mapping techniques employed in this work, provides a valuable contribution to the ongoing research on climate change and its effects on the Mediterranean region.

Results

The analysis of Sea Surface Temperature (SST) trends in the Eastern Mediterranean region from 1940 to 2023 reveals significant spatiotemporal variations, which are essential for understanding regional climate dynamics and their potential impacts on marine ecosystems and maritime activities.

The average annual SST for the Eastern Mediterranean during the study period is presented in Figure 1, with the red

trend line indicating a clear upward trend from 1940 to 2023. Over this period, SST has increased by approximately 1.5°C, despite notable interannual variability—particularly between 1940 and 2000. Relatively low temperatures are evident between 1975 and 1992, while higher values observed from 2005 to 2023. Post-2000, SSTs rise more consistently and sharply. It is important to note that the rate of increase in sea surface temperature (SST) is directly correlated with the rate of increase in air temperature. However, due to the distinct heat capacity of the ocean as a fluid, compared to atmospheric air, these rates are not equal. Additionally, the acceleration of the warming trend in recent decades is noteworthy, with SST consistently exceeding 20°C from 2010 onwards.

Although fluctuations with unusually cold or warm years are expected, the overall pattern reveals a steady long-term increase.

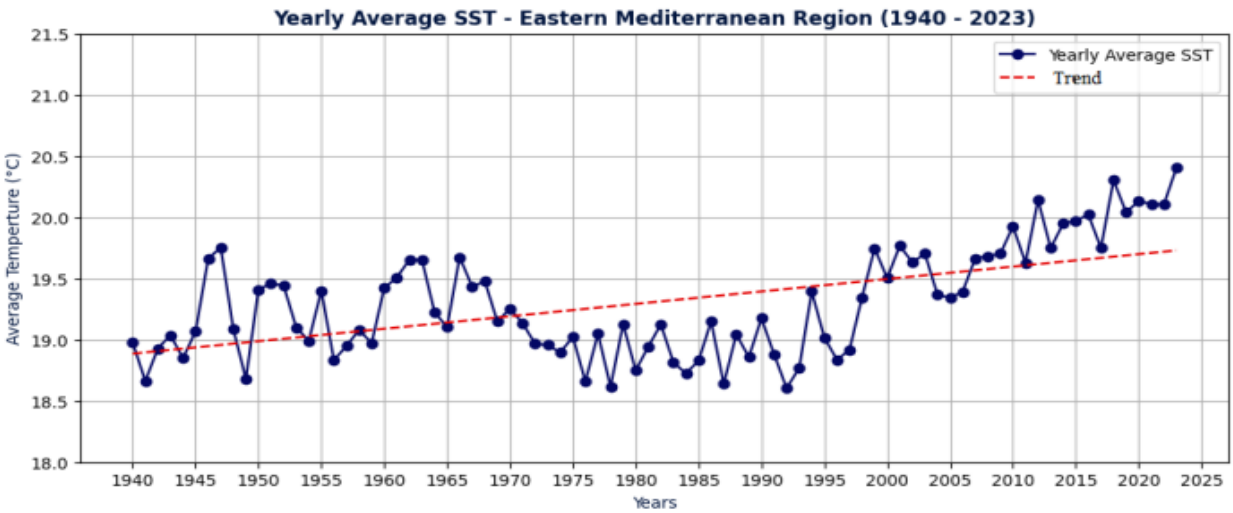

Figure 1. Annual Average Sea Surface Temperature from 1940 to 2023 for the Eastern Mediterranean region, with trend line

The spatial distribution of the average annual SST across the Eastern Mediterranean basin for the period 1940 to 2023 is shown in Figure 2. The spatial analysis of SST reveals several key areas of variability. The warmest waters are in the Gulf of Sirte, south of Crete, around Cyprus, and along the northern coasts of Africa, particularly in the southern and southeastern parts of the basin. In these areas, the average annual SST consistently exceeds 21°C. Previous studies (e.g., Ozer et al., 2022) suggest that the Eastern Mediterranean, due to its relatively small size and limited connection to the Atlantic Ocean, reflects and intensifies global warming trends. Notably, the southeastern part of the basin, bordering Israel, shows the highest temperatures, as water from the Atlantic Ocean has ample time to warm as it moves toward the region.

In contrast, the central and southern Aegean Sea, the Ionian Sea, and the southwestern parts of the Eastern Mediterranean exhibit average annual SSTs ranging from 19°C to 20°C. These regions show a more gradual but consistent warming trend compared to the period prior to 1940 (Bruno, M., 2019 & Lough, J. M., & Coughlan, L. M., 2015).

The coldest SSTs in the Eastern Mediterranean are found in the Adriatic Sea, with average temperatures ranging from 16°C to 18°C, particularly in the northern sections. This area experiences a significant influx of cold, fresh water from rivers in the Italian Alps. Similarly, the northern Aegean Sea is affected by the inflow of water masses from the Black Sea through the Bosporus Strait and the Dardanelles. This water, known as the Black Sea Water (BSW) current, has a lower temperature and salinity, further reducing the average SST in this region (Poulos et al., 1997; Zodiatis, 1996). Moreover, the northern Aegean Sea also receives freshwater contributions from the Evros, Strymon, and Nesto's rivers, as well as from rivers in the Turkish mainland, which further influence the temperature and salinity of the surface waters (Therianos, 1974).

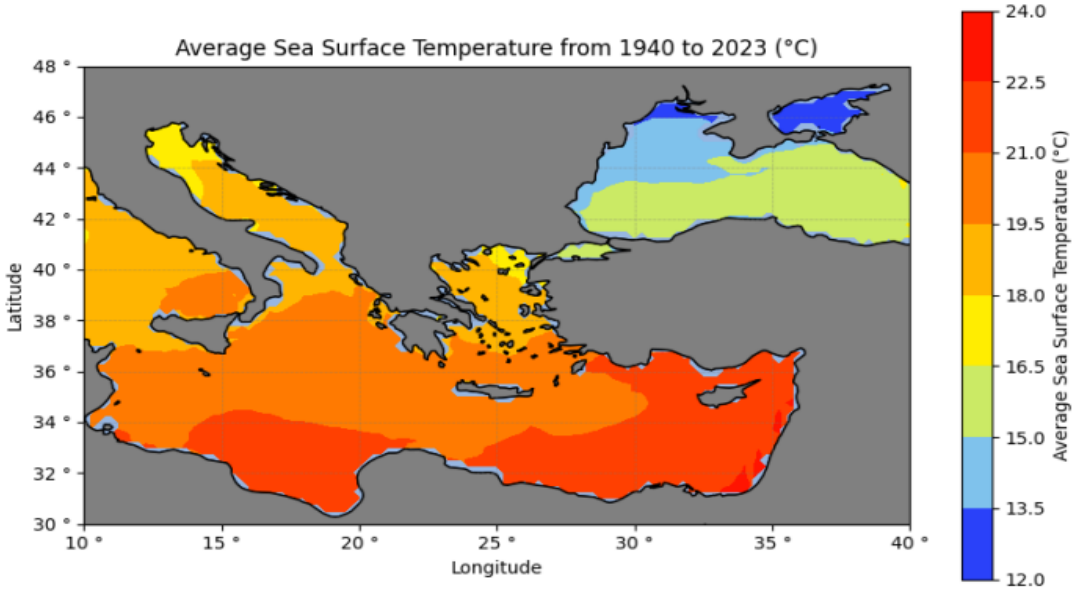

Figure 2. Spatial distribution of the annual average SST in the Eastern Mediterranean from 1940 to 2023

Figure 3 illustrates the average sea surface temperature (SST) in the Eastern Mediterranean for September during the period from 2000 to 2023. The SST range for this period varies from 19°C to 23°C, with the coldest waters located in the Adriatic Sea and the northern Aegean, while the warmest waters are found along the northern African coasts and around Cyprus. This represents a warm period compared to other times, as previously mentioned, with the average SST exceeding 20°C in many locations. The climatic average SST in the Eastern Mediterranean depends on the season, geographical location, and local climatic conditions.

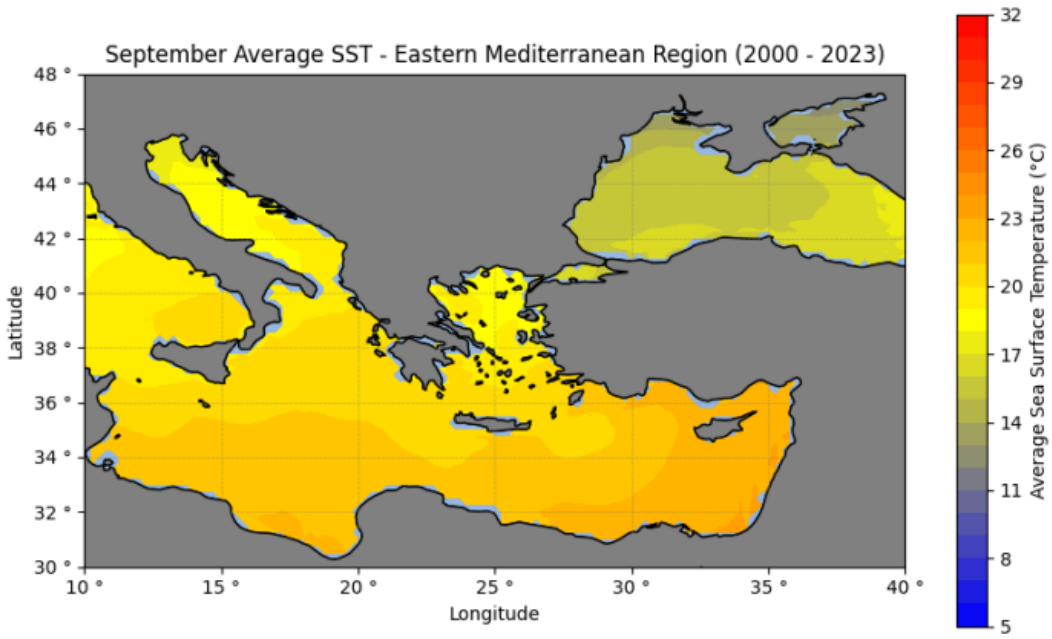

Figure 3. Average SST for September – Period 2000–2023, Eastern Mediterranean

The Mediterranean Cyclone "Zorbas," which occurred in September 2018, is a significant event that serves as an illustrative case study of the relationship between sea surface temperature (SST) and cyclone formation in the Eastern Mediterranean.

September 2018 was characterized by notably high temperatures, both in terms of air temperature and SST. As depicted in Figure 4, the average SST for several locations across the Eastern Mediterranean basin exceeded 25°C, with temperatures reaching up to 29°C near the Gulf of Sirte and to the east of Cyprus. These elevated sea surface temperatures provided a conducive environment for the development and intensification of a Mediterranean cyclone.

The warm SSTs in the Gulf of Sirte played a crucial role in the cyclogenesis that occurred south of Italy. The energy from the warm waters contributed to the further strengthening of a low-pressure system, transforming it into a Mediterranean Cyclone with tropical characteristics (Tsikoudi, I., et al. 2019). The dynamics of this cyclone underscore the significant influence of SST on the formation and development of such systems in the Mediterranean region.

As the cyclone moved northward toward the Aegean Sea, and with October already underway, the system began to weaken. The decreasing SSTs in the northern regions of the basin no longer provided sufficient energy to sustain the cyclone. Consequently, the system lost strength, and its intensity diminished (Ziv, B., et al., 2018 & Papageorgiou, A., et al., 2020). To illustrate this, Figure 5 presents the average SST for October 2018, highlighting the contrast in sea surface temperatures compared to those in September 2018, as depicted in the preceding figure.

This case study reinforces the critical role that SST plays in the development, intensification, and eventual weakening of Mediterranean cyclones. The warm waters in the southern parts of the Eastern Mediterranean can significantly enhance cyclonic activity, while lower SSTs in the northern regions lead to the dissipation of these systems. Understanding these SST dynamics is essential for improving forecasting and risk assessment of Mediterranean cyclones, which have considerable implications for coastal areas and maritime operations in the region.

The Mediterranean Cyclone Zorbas (Medicane Zorbas) also struck Greece. Specifically, on September 29, 2018, it reached the Peloponnese with maximum winds of 120 km/h and a central pressure of 987 hPa, classifying it as a Category 1 Cyclone. It then moved through the Aegean Sea before weakening in Turkey on October 2. In its path, it caused extensive damage, particularly in the Peloponnese and central Greece. Heavy rainfall, flooding, and strong winds (up to 10-12 Beaufort) affected areas such as Argos, Corinth, and Attica. Rivers overflowed, roads were blocked, and many homes were flooded. In several areas, such as the Municipality of Argos - Mycenae, a state of emergency was declared due to the widespread damage. Zorbas highlighted the increasing risks from such extreme weather events in the Mediterranean, confirming concerns about the impacts of climate change in the region.

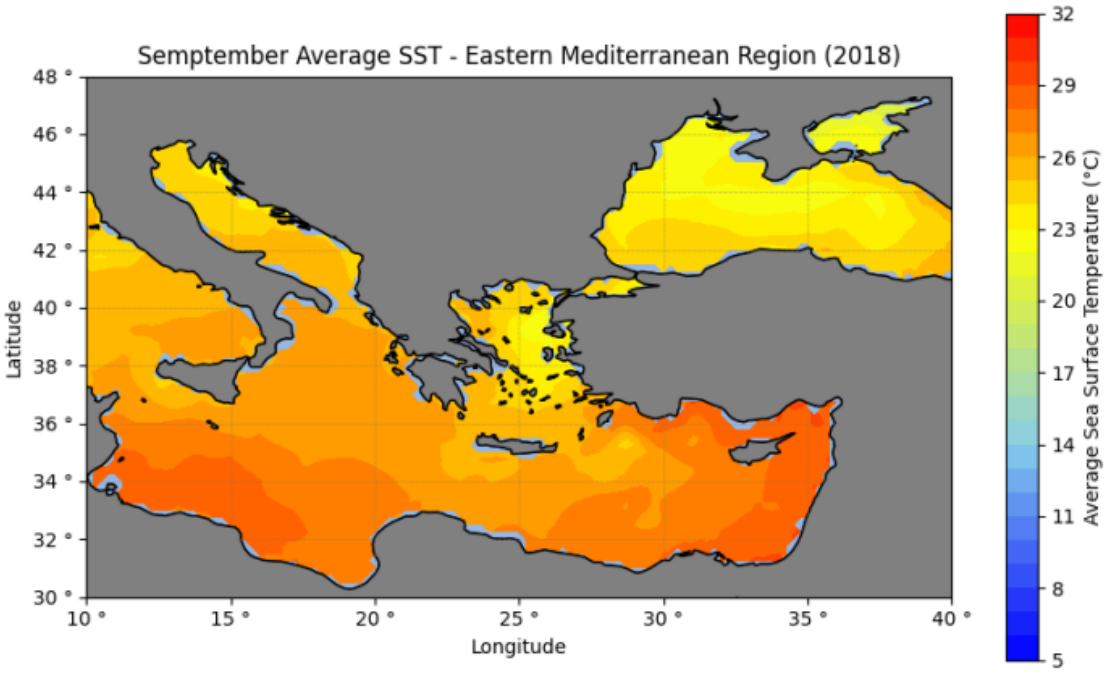

Figure 4. Average SST for September 2018, Eastern Mediterranean

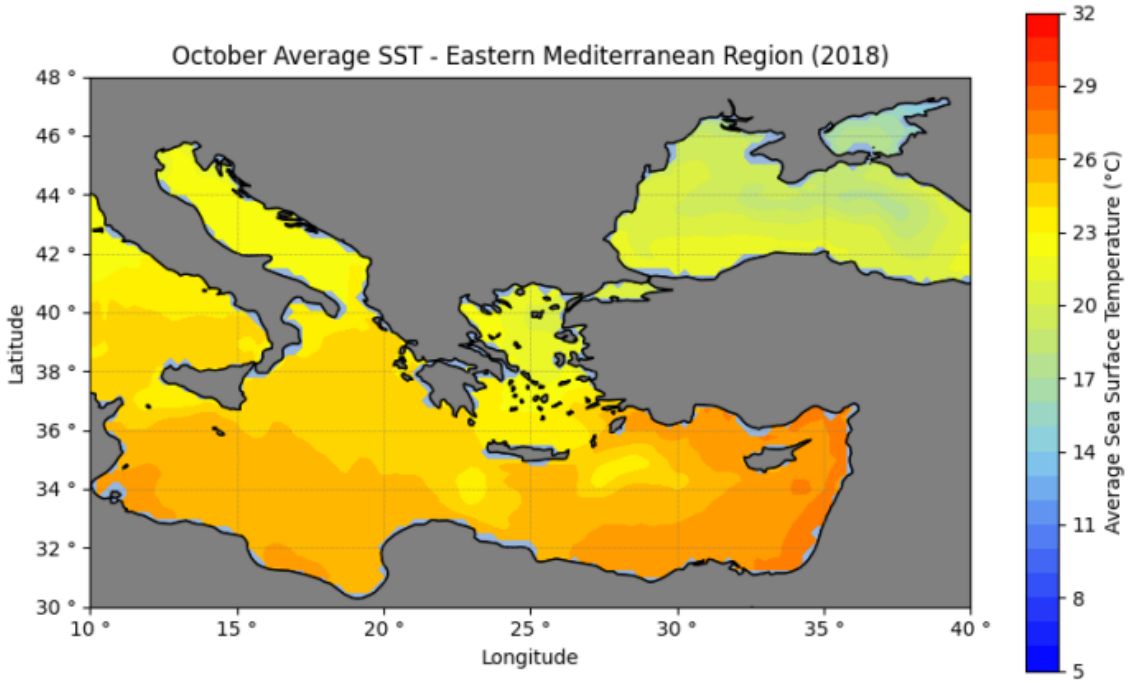

Figure 5. Average SST for October 2018, Eastern Mediterranean

Discussion and Conclusion

The results of this analysis demonstrate a clear warming trend in the Eastern Mediterranean, particularly over the past few decades, with significant regional variability. The southern and southeastern parts of the basin are experiencing the highest SSTs, while the northern Aegean and Adriatic Sea remain cooler due to the influence of freshwater inflows and the BSW current. These findings underscore the importance of continued monitoring of SST in the region.

This study has examined the rising Sea Surface Temperature (SST) in the Eastern Mediterranean from 1940 to 2023, highlighting the significant trends, contributing factors, and implications for the region's environment and maritime industry. The Eastern Mediterranean was selected for this research due to its unique characteristics, such as its semi-closed nature, which results in an accelerated increase in sea temperatures compared to other global seas, as well as its crucial role in linking three continents directly influenced by the weather phenomena that originate here.

Over the past eighty-three years, the SST in the Eastern Mediterranean has consistently risen, with a noticeable acceleration of this warming since the 2010s. The region has experienced an increase of approximately +0.4°C to +0.6°C per decade since the 1980s. During the summer months, SSTs often exceed 26°C, with September being the warmest month. This warming trend, driven by factors such as rising greenhouse gas emissions, alterations in atmospheric circulation, and the reduction of polar ice, has led to a marked increase in the frequency and severity of Mediterranean cyclones (Giorgi, F., et al., 2019 & Gaertner, M. A., et al., 2017). These cyclones, which combine characteristics of both tropical and extratropical systems, have become more prevalent, with notable events including Cyclones "Zorbas" (2018).

The increased SST and the intensification of extreme weather events, such as Medicanes, have profound implications for maritime operations. The impact of Cyclone "Zorbas" on the ports of Peloponnese serves as a clear example of how such events can severely affect the maritime sector.

Considering these findings, it is evident that the rising SST and the increasing frequency of extreme weather events pose substantial challenges to the coastal communities in the Eastern Mediterranean. Therefore, it is crucial to implement strategies to adapt to these changing conditions. Advanced weather forecasting

systems should be developed to improve preparedness, while the resilience of port infrastructure must be strengthened to withstand the impact of these extreme events. Additionally, international cooperation is essential to address the underlying drivers of climate change, such as CO_2 emissions, and to mitigate further environmental impacts.

This research underscores the urgent need for further studies to monitor the ongoing changes in SST and to better understand their long-term effects on marine ecosystems, biodiversity, and global trade routes. Ultimately, proactive measures and informed decision-making will be critical to managing the evolving challenges posed by climate change in the Eastern Mediterranean and beyond.

Acknowledgements

We would like to express our sincere gratitude to the European Centre for Medium-Range Weather Forecasts (ECMWF) and the Copernicus program for providing the essential data used in this study. Their invaluable resources and support have significantly contributed to the success of our research. Without the access to ECMWF's advanced weather and climate data and the Copernicus Earth Observation program's rich datasets, this work would not have been possible. We also appreciate the efforts of all teams involved in data collection, maintenance, and dissemination.

References

Balling Jr, R. C., Vose, R. S., and Weber, G. 1998. "Analysis of Long-Term European Temperature Records: 1751–1995." Climate Research 10: 193–200.

Bruno, M. (2019). *Long-term Sea Surface Temperature Variability in the Mediterranean Sea*. Climate Dynamics, 52(11-12), 7239-7250. https://doi.org/10.1007/s00382-018-4586-9

Carlson, T. N. 1980. "Airflow through Mid-Latitude Cyclones and the Comma Cloud Pattern." Monthly Weather Review 108: 1498–1509.

Cavicchia, L., von Storch, H., & Gualdi, S. (2014). Mediterranean Tropical-Like Cyclones (Medicanes). Atmosphere, 10(4), 206.

Climate Copernicus. 2023. "Climate Indicators – Sea Surface Temperature." April 20. https://climate.copernicus.eu/climate-indicators/sea-surface-temperature.

Copernicus Marine Service. "Ocean Warming." Copernicus Marine Service, https://marine.copernicus.eu/el/explainers/phenomena-threats/ocean-warming.

Copernicus Climate Change Service. "ERA5: Reanalysis Data on Single Levels." Copernicus Climate Data Store (CDS), https://cds.climate.copernicus.eu/datasets/reanalysis-era5-single-levels

Donlon, C. J., Martin, M., Stark, J. D., Roberts-Jones, J., Fiedler, E., and Wimmer, W. 2011. "The Operational Sea Surface Temperature and Sea Ice Analysis (OSTIA)." Remote Sensing of the Environment. https://doi.org/10.1016/j.rse.2010.10.017.

Gaertner, M. A., et al. (2017). "Sea surface temperature and cyclogenesis in the Mediterranean: A comprehensive review." *Atmospheric Research*, 191, 68-83.

Giorgi, F., et al. (2019). "Climate change and Mediterranean cyclones: A new trend." *Environmental Research Letters*, 14(7), 074002.

Leone Cavicchia, Hans von Storch, & Silvio Gualdi (2014). Mediterranean Tropical-Like Cyclones in Present and Future Climate. Journal of Climate. DOI: 10.1175/JCLI-D-14-00339.1

Lionello, P., et al. 2006. "Cyclones in the Mediterranean Region: Climatology and Effects on the Environment."

Noyelle, R., Ulbrich, U., Becker, N., & Meredith, E. P. (2019). Assessing the impact of sea surface temperatures on a simulated Medicane using ensemble simulations. Natural Hazards and Earth System Sciences, 19, 941–955. DOI: 10.5194/nhess-19-941-2019

Lough, J. M., & Coughlan, L. M. (2015). *Warming of the Mediterranean Sea and its Impacts on Marine Ecosystems*. Environmental Research Letters, 10(11), 114003. https://doi.org/10.1088/1748-9326/10/11/114003

Papageorgiou, A., et al. (2020). "The role of sea surface temperature in the intensification of Mediterranean cyclones." *Atmospheric Science Letters*, 21(2), e952.

Tsikoudi, I., et al. 2019, University of Athens. "Dynamic Analysis of a Medicane." https://www.openarchives.gr/aggregator-openarchives/edm/pergamos/000005-_uoa_dl_object_uoadl%3A2878611

Ziv, B., et al. (2018). "The weakening of Mediterranean tropical-like cyclones: A case study of Cyclone Zorba (2018)." *Geophysical Research Letters*, 45(6), 2997-3005.

17th INTERNATIONAL CONGRESS of the Geological Society of Greece

BULLETIN OF THE GEOLOGICAL SOCIETY OF GREECE, SP. PUBL.

EXTENDED ABSTRACT 021

Seasonal Water Column Stratification and Heavy Metal Distribution in the Pinios Dam Reservoir: A Comprehensive Environmental Monitoring Study

Avramidis P.,[1] Ramfos A.[2], Sarris I.[1], Cristodoulopoulos, D.[1], Alexandridis M.[1], Michalopoulou M.[1], Depountis N.[1] Papazisimou S.[3]
(1) Department of Geology, University of Patras, Patra, Greece,
(2) Department of Biology University of Patras, Greece
3) Region of Western Greece, Patras, Greece

Research Highlights: **water stratification and anoxic condition as important environmental parameters for the dam's life cycle**

Introduction

Reservoirs are artificial lakes that play a critical role in water resource management worldwide, providing essential services such as water supply for drinking and irrigation, flood control, and hydroelectric power generation (Directive EU 2020/2184). However, reservoirs, like natural lakes, are susceptible to environmental and anthropogenic influences that can alter their ecological balance. The stratification of water bodies is a key physical process that affects the distribution of temperature, dissolved oxygen, and other physicochemical properties, which in turn impacts water quality and aquatic life. Thermal stratification, particularly in monomictic and dimictic lakes, causes the development of distinct layers in the water column that can become isolated from atmospheric oxygen, leading to hypoxic or anoxic conditions in the deeper layers. These conditions, often exacerbated by nutrient inputs and organic matter decomposition, can significantly affect water chemistry, particularly the solubilization and mobility of heavy metals from sediments. This creates potential environmental hazards, particularly in drinking water reservoirs where water quality is a priority.

The study area is Pinios Dam which is located at northwest Peloponnese which has already recorded as reservoir with high concentrations of Mn and Fe (Michalopoulou et al, 2024). For this study, a detailed bathymetric survey was conducted, four monitoring stations were installed, and seasonal water column profiles were recorded. Additionally, physicochemical parameters, including pH, temperature, conductivity, redox potential, and heavy metal concentrations of Mn and Fe, were measured and analyzed".

Methods

Water samples were collected from the artificial reservoir of the Pinios Dam at four pre-determined stations (SPA1–SPA4), strategically selected to provide comprehensive coverage of the study area. These stations were located along the reservoir's main axis, with depths ranging from 9 m to 35 m. Sampling occurred seasonally, between February 2023 and October 2023, and utilized a multi-depth water sampler equipped with valves suitable for depths up to 100 m. Samples were collected at 4 m intervals from the surface to the bottom, yielding a total of 74 samples.

Physical and chemical parameters, including pH, temperature, dissolved oxygen, and conductivity, were measured using a portable multi-parameter probe (IN-SITU AQUA TROLL 6000). Measurements were taken along the vertical profile of the water column at 10 cm intervals.

Collected samples were analyzed for various chemical parameters, such as chloride (Cl^-), nitrate (NO_3^-), nitrite (NO_2^-), ammonium (NH_4^+), phosphate (PO_4^{3-}), sulfate (SO_4^{2-}), total organic carbon (TOC), total nitrogen (TN), manganese (Mn), and iron (Fe). Analyses were conducted using an ion chromatograph (Dionex ICS-1100) and a spectrophotometer (HACH-LANGE), with quality assurance adhering to ISO 17025 standards.

Results

Seasonal Variations

The study identified notable seasonal variations in the reservoir's physical and chemical parameters.

Temperature stratification was evident during the summer, with surface temperatures peaking at 25°C and bottom temperatures remaining around 15°C. Dissolved oxygen levels decreased with depth, particularly during summer and autumn, indicating thermal stratification and oxygen depletion at deeper layers.

Chemical Composition

Chloride concentrations ranged between 10.12 mg/L and 20.96 mg/L, showing minimal seasonal fluctuation. Nutrient concentrations, particularly nitrates (0.11–1.43 mg/L) and ammonium (0.02–0.36 mg/L), varied with depth and season, reflecting biological activity and nutrient cycling within the reservoir. Phosphate levels were generally below detection limits, except for occasional peaks (up to 0.06 mg/L).

Heavy Metals

Manganese and iron concentrations exhibited significant depth-dependent trends. Mn concentrations ranged from 0.01 mg/L to 0.198 mg/L, while Fe varied from 0.01 mg/L to 0.204 mg/L. Both metals showed elevated concentrations in bottom layers during late summer and autumn, coinciding with reduced oxygen levels.

Conclusions

Thermal stratification played a significant role in shaping the reservoir's chemical profile. The development of distinct temperature layers during summer inhibited vertical mixing, leading to oxygen depletion in deeper layers. This, in turn, facilitated the release of Mn and Fe from sediments into the water column, as indicated by their elevated concentrations at depth.

The distribution of nitrates and ammonium highlighted the complex interplay between biological uptake, decomposition, and nutrient cycling. Elevated nitrate levels near the surface during spring suggest enhanced productivity, while higher ammonium concentrations at depth during late summer point to decomposition processes under low-oxygen conditions.

The observed seasonal and depth-dependent variations in key parameters underline the reservoir's susceptibility to eutrophication and metal mobilization, particularly during stratified periods. These findings are critical for designing management strategies to mitigate potential water quality issues.

Acknowledgements

The authors are grateful for the financial and administrative support of the research by the Region of Western Greece and the Municipality of Ilida.

References

Directive (EU) 2020/2184 of the European Parliament and of the Council of 16 December 2020 on the quality of water intended for human consumption. Available online: https://eur-lex.europa.eu/eli/dir/2020/2184/oj. (accessed on 11 November 2024).

Michalopoulou, M., Depountis, N., Zagana, E., Avramidis, P., 2024. Investigation of the Origin of Elevated Amounts of Iron and Manganese in a Dam Reservoir. Geosciences, 14, 336.

17th INTERNATIONAL CONGRESS of the Geological Society of Greece

BULLETIN OF THE GEOLOGICAL SOCIETY OF GREECE, SP. PUBL.

EXTENDED ABSTRACT 022

A Preliminary Study of Microvertebrate and Invertebrate Fauna from the Early Pleistocene of Koukos region (Kos Island, Dodecanese, Greece)

Authors : Antonios Isidoros Avrithis [1], Efterpi Koskeridou [2], Evangelia Rentoumi [2], Evangelos Vlachos [3], Davit Vasilyan [4, 5]

(1) The Open University, Milton Keynes, United Kingdom, tonyavrithis@gmail.com, (2) Department of Historical Geology and Palaeontology, Faculty of Geology and Geoenvironment, National and Kapodistrian University of Athens, 15774 Athens, Greece, (3) CONICET and Museo Paleontológico Egidio Feruglio, Av. Fontana 140, 9100 Trelew, Chubut, Argentina, (4) JURASSICA Museum, Route de Fontenais 21, 2900 Porrentruy, Switzerland, (5) University Fribourg, Chemin de Musée 6, 1700 Fribourg, Switzerland

Research Highlights

A new locality with amphibians, reptiles, fishes, gastropods, and ostracods is described from the Early Pleistocene of Koukos region in Kos Island. These findings are valuable for palaeoecosystem reconstruction and biogeographical interpretations and represent a rare assemblage of that age in Greece.

Introduction

The island of Kos in the southeastern Aegean Sea was part of the Anatolian peninsula during the Pleistocene and maintained a connection to the mainland till the Last Glacial Maximum (Rohling *et al.* 2014). During the Early Pleistocene, several extinct mammals inhabited the area such as *Anancus* sp., *Homotherium* sp., *Leptobos* sp. (Desio, 1928). During the Late Pleistocene, fossils show a shift towards shallow marine environments (Drinia *et al.* 2010). The area of Koukos has been studied by Charrier and Giglio (1969) who refer to the locality as 'Iliopeia' where some large mammal fossils have been found. The presence of microvertebrates had never been reported before the discovery of the site of Koukos, in Kardamena village of the island. The newly discovered site contains a rich assemblage of amphibians, reptiles and fishes, also described as ectothermic fauna. The co-occurrence of fossil gastropods and ostracods is valuable for palaeoecological interpretations. Further analysis on the biogeographical affinities of these findings will be valuable for deciphering the origins of modern-day distributions of several extant taxa. Finally, this locality is the only site in Greece from the Early Pleistocene which bears both ichthyological and herpetofaunal remains (Argyriou 2022, Delfino & Georgalis 2022, Vlachos, 2022).

Geological Setting

The site is located in the Koukos area of Kardamena village of Kos Island, in Southeastern Mediterranean (fig.1). According to Willmann (1983), the site belongs to the lowermost Tafi formation, which is dated as Lower Pleistocene. Additionally, Magrograssi (1928) has described a gastropod species *Melanopsis pseudopigmea* from the same outcrop.

The section of Koukos consists of claystones, siltstones and sandstones, with the latter dominating. The first layer (fig.2) consists of fossil-free grey claystone, the second layer (fig. 2) is a 25cm green claystone layer with amphibians, reptiles, fishes, ostracods, and gastropods (Table 1). The third layer is yellowish siltstone. The last (fourth) layer, consisting mostly of fossil free sandstones and conglomerates, overlies the previous beds with an erosive base suggesting high energy river deposition (fig. 2).

Materials and methods

Test samples of 2 kg have been obtained from each layer, which have been treated with a solution with 0.1% perhydrol. They have been washed using a series of four sieves of 1 cm, 500 μm, 250 μm and 125 μm mesh sizes. After the discovery of the fossiliferous layer of green clay, another sample of 20 kg was washed.

For the taxonomy of the gastropods, we used Neumayr (1880), Magrograssi (1928), Willmann (1981), Bouchet *et al.* (2005), as well as numerous other studies focusing on the classification of lacustrine

gastropods from the Pleistocene. The ecoregions concept Barbieri et al. (2015) has been applied for the interpretation of fish forms.

Figure 1. Map of Greece, indicating Koukos locality with a yellow star. Maps modified from Wikimedia Commons (https://upload.wikimedia.org/wikipedia/commons/8/87/MapZ.png, https://upload.wikimedia.org/wikipedia/commons/2/24/Kos_location_map.svg)

Figure 2. A. Stratigraphic log of the section, asterisk indicating the sampled fossiliferous bed. B. Field photo of the section with numbers corresponding to the stratigraphic units, red lines indicate the border between strata

Results

The fauna consists of 22 taxa. The vertebrate taxa are 14, of which 6 belong to ray-finned fish, 4 to amphibians, 3 to reptilians and 1 to mammals. The invertebrates are represented by 5 gastropod species and 3 ostracod species.

Class	Family	**Taxon**
Actinopterygii	Cyprinidae	? *Barbus* sp.
		Leuciscus sp.
		Luciobarbus sp.
		Chondrostoma sp.
	Cobitidae	Cobitidae indet.
	Gobiidae	Gobiidae indet.
Amphibia	Salamandridae	Salamandridae indet. (small-sized)
	Ranidae	*Pelophylax* sp.
	Hylidae	*Hyla* sp.
		Bufonidae / Pelobatidae indet.
Reptilia	Geoemydidae	*Mauremys* sp.
	Colubridae	Colubridae indet.
		Colubrinae indet.
Mammalia	Cricetidae	Cricetidae indet.
Gastropoda	Melanopsidae	*Melanopsis pseudopigmea* Magrograssi, 1928
	Valvatidae	*Valvata hellenica* Tournouer, 1877
	Melanopsidae	*Melanopsis gorceixi polyptycha* Tournouer, 1875
	Neritidae	*Theodoxus doricus doricus* (Neumayr, 1880)
	Hydrobiidae	*Iraklimelania coa* Willmann, 1981
Ostracoda	Candonidae	*Fabaeformiscandona* cf. *brevicornis* (Klie, 1925)
		Candona sp.
	Cyprididae	*Ilyocypris gibba* (Ramdohr, 1808)

Table 1. Fauna of Koukos locality

Discussion-Conclusions

The ectothermic vertebrate fauna suggests the presence of running freshwater water body (rivers) with very (*Leuciscus* sp., *Luciobarbus* sp., *Chondrostoma* sp., Cobitidae indet.) slowly flowing or stagnant parts (Gobiidae indet., *Pelophylax* sp., *Mauremys* sp.). The water body was surrounded by hedgerows and meadows with higher vegetation (Salamandridae indet. (small-sized), *Hyla* sp.).

The herpetofauna of the Koukos site contains forms which are broadly present also in present-day Kos and other nearby islands (Valakos et al., 2008). From the perspective of the fossil fauna, Koukos contributes so far to the scarcely studied record of ectothermic vertebrates. *Mauremys rivulata* found previously in Kos but the exact location was missing (Vlachos, 2022) and another freshwater turtle that was discovered in the broader area belonged to the family Trionychidae (Avrithis and Georgalis, 2024). For the amphibians, only 4 sites of that age are found in Greece mainland (Delfino & Georgalis, 2022).

The mollusk fossil assemblage from the Koukos region indicates deposition in a low-energy aquatic system, such as a shallow lacustrine or slow-flowing riverine environment. The investigation of the gastropod species that were found suggest warm, temperate climatic conditions and abundant vegetation with large aquatic plants. Forms like *Melanopsis pseudopigmea*, *Valvata hellenica*, *Iraklimelania coa*, and *Theodoxus doricus doricus* appear to have been adapted to these freshwater habitats. The presence of

Iraklimelania coa in fine-grained lacustrine and riverine deposits suggests the species inhabited low-energy environments, where fine sediments like muds and silts accumulated in areas of reduced flow. These depositional environments are characteristic of slow-moving waters with high sedimentation rates.

Ostracod findings of *Ilyocypris gibba* and *Candona* species are indicative of freshwater bodies like lakes or ponds. Those two genera of freshwater ostracods are often found together in sedimentary deposits. *Ilyocypris gibba* may suggest more stable and warmer freshwater habitats while *Candona* species are adapted to a wider range of temperatures, salinities and dissolved oxygen. Thus, the co-occurrence of these two ostracods may indicate fluctuations between warmer and cooler phases.

The fish fauna contains a remarkable complex, suggesting a link between the Koukos fauna with Asia Minor. This fits with a further fact that the recent freshwater fish fauna of the Island of Kos, being in the ecoregion 7 (the Eastern Aegean), according to Barbieri et al. (2015), which have Asia Minor affinities.

References

Argyriou, T., 2022. The Fossil Record of Ray-Finned Fishes (Actinopterygii) in Greece. In: Vlachos, E. (Eds.) Fossil Vertebrates of Greece 1, Springer Nature, 92-142 https://doi.org/10.1007/978-3-030-68398-6_4

Avrithis, A. I., Georgalis, G. L., 2024. One of the last shelters of soft-shelled turtles (Testudines, Trionychidae) in Europe – first fossil occurrence of a trionychid from the Plio-Pleistocene of Kos Island, Greece. Historical Biology, 1–6. https://doi.org/10.1080/08912963.2024.2302575

Barbieri, R., Zogaris, S., Kalogianni, E., Stoumboudi, M., Chatzinikolaou, Y. Giakoumi S., Kapakos, Y., Kommatas, D., Koutsikos, N., Tachos, V., Vardakas L., Economou, A.N., 2015. Freshwater fishes and lampreys of Greece: An annotated checklist. Monographs on Marine Sciences No. 8. Hellenic Centre for Marine Research: Athens, Greece, 128 p.

Bouchet P., Rocroi J.-P., Frýda J., Hausdorf B., Ponder W., Valdés Á., Warén A. 2005. Classification and nomenclator of gastropod families. Malacologia: International Journal of Malacology, 47, (1–2). Hackenheim, Germany: ConchBooks: 1–397. ISBN 3925919724. ISSN 0076-2997.

Charrier, G., Giglio, A., 1969. Primi risultati di una campagna di rilevamento geologico nell'isola di Coo (Sporadi meridionali – Mare Egeo). Bollettino Associazione Mineraria Subalpina, 6, 482-516.

Delfino, M., Georgalis, G.L., 2022. The Fossil Record of Amphibians (Amphibia: Urodela and Anura) in Greece. In: Vlachos, E. (Eds.) Fossil Vertebrates of Greece 1, Springer Nature, 185-203.

Desio, A., 1924. Appunti geologici sull'isola di Cos (Dodecaneso). Bollettino della Società Geografica Italiana 43, 151-160.

Drinia, H, Koskeridou,E., Antonarakou, A., Tzortzaki, E. 2010. Benthic foraminifera associated with the zooxanthellate coral *Cladocora* in the Pleistocene of the Kos island (Aegean Sea, Greece): Sea level changes and paleoenvironmental conditions. Bulletin of the Geological Society of Greece 43:613–619.

Magrograssi, A., 1928. La fauna levantina di Coo e di Rodi. Atti della Società Italiana di Scienze Naturali e del Museo Civico di Storia Naturale in Milano, 67, 260-264.

Neubauer, T.A., Harzhauser, M., Kroh, A., Georgopoulou, E., Mandic, O., 2014. Freshwater Gastropods of the European Neogene database (FreshGEN). Accessed at http://www.marinespecies.org/freshgen on 2021-01-05. doi:10.14284/363

Neumayr, M., 1880. Über den geologischen Bau der Insel Kos und über die Gliederung der jungtertiären Binnenablagerungen des Archipels. Denkschriften der Kaiserlichen. Akademie der Wissenschaften, Mathematisch Naturwissenschaftliche Classe, 40, 213-314.

Rohling, E., Foster, G., Grant, K., Marino, G., Roberts, A.P., Tamisiea, M.E., Williams, F., 2014. Sea-level and deep-sea-temperature variability over the past 5.3 million years. Nature 508:477-482.

Valakos, E. D., Pafilis, P., Sotiropoulos, K. Lymerakis, P., Maragou, P., Foufopoulos, J., 2008. The Amphibians and Reptiles of Greece. Edition Chimaira, Frankfurt, 463.

Vlachos, E., 2022. The Fossil Record of Turtles and Tortoises (Reptilia: Testudines) in Greece. In: Vlachos, E. (Eds) Fossil Vertebrates of Greece, 1, Springer Nature, 245-282. https://doi.org/10.1007/978-3-030-68398-6_9

Willmann, R. 1983. Neogen und jungtertiäre Entwicklung der Insel Kos (Ägäis,Griechenland). Geologische Rundschau, 72, 815-860 https://doi.org/10.1007/BF01848345

17th INTERNATIONAL CONGRESS of the Geological Society of Greece

BULLETIN OF THE GEOLOGICAL SOCIETY OF GREECE, SP. PUBL.

EXTENDED ABSTRACT 023

Impact of Emission Regulations on the Temporal Trends of Toxicity of Fine Particulate Matter in Los Angeles

Authors: Mohammad Mahdi Badami[1], Yashar Aghaei[1], and Constantinos Sioutas[1]
Affiliation: (1) University of Southern California, Department of Civil and Environmental Engineering, Los Angeles, California, USA

Research Highlights

- Initial reductions in $PM_{2.5}$ mass due to emission controls were followed by increased toxicity from non-tailpipe sources.
- The oxidative potential of $PM_{2.5}$ has risen since 2012, indicating a shift towards more harmful aerosol constituents.

Background

Ambient particulate matter (PM) is a major environmental health challenge worldwide, associated with a variety of serious health issues, including respiratory and cardiovascular diseases, lung cancer, and increased mortality rates. PM is classified based on its size into coarse particles, fine particles ($PM_{2.5}$), and ultrafine particles (UFPs). Among these, $PM_{2.5}$ is particularly hazardous because its small size allows it to penetrate deep into the lungs and enter the bloodstream, leading to systemic inflammation and affecting multiple organs. In densely populated urban areas like Los Angeles, vehicular emissions are the primary source of $PM_{2.5}$, resulting in higher incidences of asthma, heart disease, and other health problems compared to less polluted regions. The frequent air quality alerts in the early 2000s raised significant public health concerns, especially for vulnerable groups such as children and the elderly, prompting urgent regulatory actions aimed at reducing PM emissions from both vehicles and industrial sources.

Over the past few decades, extensive regulatory measures at both federal and state levels have substantially improved air quality in Los Angeles and throughout California. Programs initiated by the U.S. Environmental Protection Agency and the California Air Resources Board have successfully lowered the mass concentrations of primary combustion-related pollutants like organic carbon and elemental carbon. These efforts have led to significant reductions in $PM_{2.5}$ levels and associated health risks. However, despite these successes, the number of ultrafine particles has not decreased proportionally and has even plateaued in recent years. This indicates that current regulations may not fully address all sources of PM, particularly non-tailpipe emissions such as brake and tire wear, as well as the formation of secondary aerosols from volatile organic compounds. Additionally, the chemical composition of $PM_{2.5}$ has become more complex, incorporating a diverse range of toxic substances, including metals and organic compounds, which contribute to its overall oxidative potential and health impacts. These developments highlight the need for regulatory frameworks to evolve, incorporating strategies targeting particulate matter's most harmful components to further enhance air quality and protect public health.

Objectives

The primary aim of this study is to analyze the temporal trends in both the chemical composition and oxidative potential of $PM_{2.5}$ in Los Angeles over the past two decades. Specifically, the research seeks to determine the effectiveness of emission regulations in reducing $PM_{2.5}$ toxicity and to identify emerging sources contributing to any observed changes in oxidative potential. By understanding these dynamics, the study aims to provide insights that can inform more comprehensive and effective air quality management strategies.

Methods

Data on $PM_{2.5}$ oxidative potential were compiled through an extensive review of studies conducted over the past two decades (Badami et al. 2023; Cho et al. 2005; Farahani et al. 2022; Hu et al. 2008; Li et al. 2003; Ntziachristos et al. 2007; Saffari et al. 2014; 2016; Shirmohammadi et al. 2016; 2017; Verma et al. 2009; 2011). The dithiothreitol (DTT) assay data were originally reported in various units (activity per mass or per volume) and were standardized using corresponding PM mass and sampling duration measurements to ensure comparability. Detailed information

on measurement methods, equipment calibration, instrument specifications, and uncertainties can be found in the original publications (Badami et al. 2023; Cho et al. 2005; Farahani et al. 2022; Hu et al. 2008; Li et al. 2003; 2009; Ntziachristos et al. 2007; Saffari et al. 2014; 2016; Shirmohammadi et al. 2016; 2017; Verma et al. 2009; 2011; Zhang et al. 2016). The majority of DTT data were obtained from the Particle Instrumentation Unit (PIU) at the University of Southern California (USC), located in an urban area near downtown Los Angeles, 150 meters from a major freeway (I-110) that is generally situated in the downwind direction of this freeway. Additionally, trends of various chemical species such as metals (e.g., Barium [Ba], Copper [Cu], Manganese [Mn], Zinc [Zn], Chromium [Cr], Nickel [Ni], Cadmium [Cd], Iron [Fe]) and inorganic ions (sulfate [SO_4^{2-}] and nitrate [NO_3^-]) were sourced from the North Main Street monitoring station, operated by the U.S. Environmental Protection Agency (EPA) as part of the Air Quality System (AQS) and Chemical Speciation Network (CSN). These trends correspond to the sampling periods of the reviewed DTT studies, noting that data were only available from 2005 to 2024 due to the absence of CSN data prior to 2005 and the lack of metals data in 2005.

Additional sampling was conducted in January and February 2024 at the PIU of USC to assess contemporary conditions under the latest regulatory environment. $PM_{2.5}$ was collected using pre-baked quartz filters in Sioutas Personal Cascade Impactor Samplers (PCISs, SKC Inc., Eighty-Four, PA, USA) with a flow rate of 9 liters per minute to ensure accurate mass measurements. The oxidative potential of collected $PM_{2.5}$ samples was assessed using the DTT assay, adhering to established protocols.

Results

The long-term analysis of $PM_{2.5}$ oxidative potential in Los Angeles from 2001 to 2024 identified two distinct phases corresponding to different regulatory periods. Between 2001 and 2008, there was a significant decline in DTT activity per volume, decreasing from approximately 0.84 to 0.37 nmol/min/m³. This reduction coincided with stringent tailpipe emission regulations that effectively lowered primary combustion-related pollutants such as organic carbon (OC) and elemental carbon (EC). However, starting in 2012, despite a continued slight decrease in overall $PM_{2.5}$ mass, the oxidative potential began to rise, reaching around 0.97 nmol/min/m³ by 2024. This increase is primarily driven by the stabilization and slight rise in concentrations of metals like Fe and Zn, which are associated with non-tailpipe emissions such as brake and tire wear, as well as the formation of secondary organic aerosols. These changes indicate a shift in the toxicological profile of $PM_{2.5}$, where non-tailpipe sources are increasingly contributing to its oxidative potential consistent with the increase in the vehicle miles traveled (VMT) in this period (Badami, Tohidi, and Sioutas 2024).

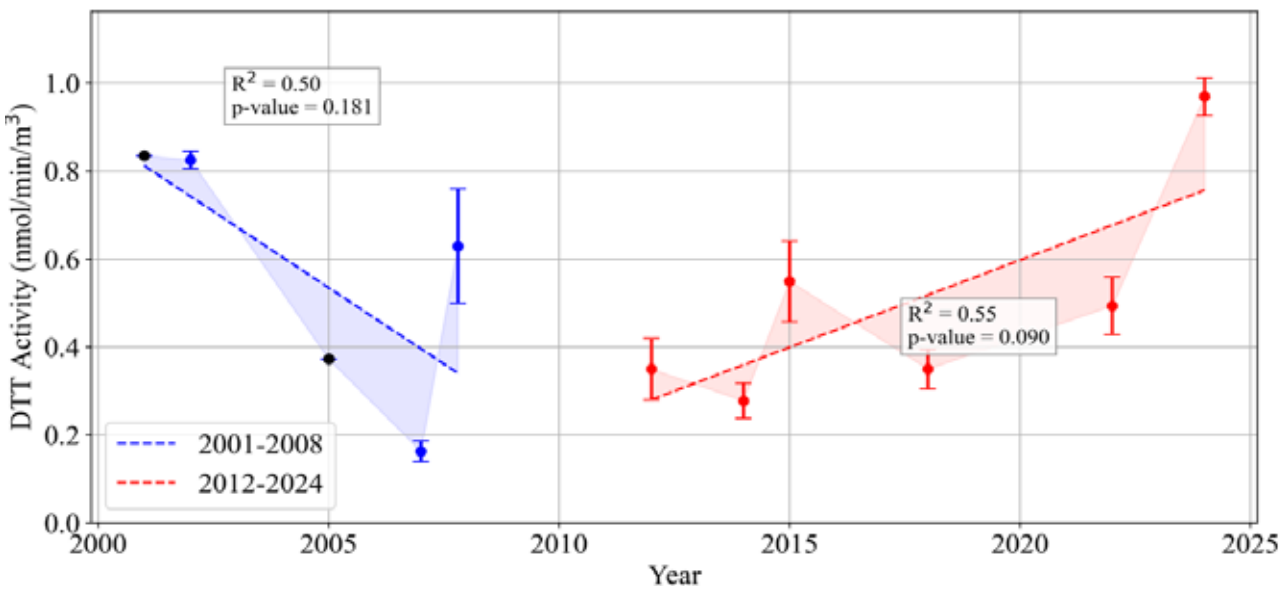

Figure1. $PM_{2.5}$ DTT activity Long-term trends (2001–2024).

Additionally, the correlations between DTT activity and specific $PM_{2.5}$ components have evolved over the study period. Metals including Fe, Zn, Cu, Mn, and Pb demonstrated strengthening correlations with DTT activity, highlighting their growing role in driving the oxidative potential of fine particulate matter. In contrast, the correlation between OC and DTT activity showed a slight decreasing trend, suggesting a reduced influence of tailpipe emissions on oxidative potential over time. EC exhibited a modest increase in its correlation with DTT activity, potentially reflecting its association with non-tailpipe sources rather than its inherent toxicity. These findings underscore the importance of addressing non-tailpipe and secondary emission sources in regulatory frameworks to effectively mitigate the oxidative toxicity of $PM_{2.5}$ and improve public health outcomes.

Conclusions

This study investigated the long-term trends in both the chemical composition and oxidative potential of $PM_{2.5}$ in Los Angeles over the past two decades, utilizing the DTT assay as a measure of particle-induced oxidative stress. The findings reveal that while regulatory measures effectively reduced mass concentrations of primary combustion markers such as OC and EC, notably before 2016, a significant shift has occurred in the composition of $PM_{2.5}$ towards non-tailpipe emission tracers. These unregulated species, including stable or proportionally increasing metals Fe, Cu, and Zn, have contributed to a partial resurgence and stabilization of DTT activity per mass from 2012 to 2024. Additionally, the oxidative potential per volume of fine $PM_{2.5}$ has continued to rise, underscoring the growing impact of non-tailpipe sources and secondary aerosol formation on $PM_{2.5}$ toxicity.

Acknowledgments

This research was supported by the National Institutes of Health (NIH) under grant numbers 5R01ES033660-03, 1RF1NS130681-01, and 5R01AI065617-23. The authors are grateful for the support from the Viterbi School of Engineering at the University of Southern California through the Ph.D. fellowship award.

References

Badami, Mohammad Mahdi, Ramin Tohidi, Mohammad Aldekheel, Vahid Jalali Farahani, Vishal Verma, and Constantinos Sioutas. 2023. “Design, Optimization, and Evaluation of a Wet Electrostatic Precipitator (ESP) for Aerosol Collection.” *Atmospheric Environment* 308 (September):119858. https://doi.org/10.1016/J.ATMOSENV.2023.119858.

Badami, Mohammad Mahdi, Ramin Tohidi, and Constantinos Sioutas. 2024. “Los Angeles Basin’s Air Quality Transformation: A Long-Term Investigation on the Impacts of PM Regulations on the Trends of Ultrafine Particles and Co-Pollutants.” *Journal of Aerosol Science* 176 (February):106316. https://doi.org/10.1016/j.jaerosci.2023.106316.

Cho, A. K., C. Sioutas, A. H. Miguel, Y. Kumagai, and J. R. Froines. 2005. “Redox Activity of Airborne Particulate Matter (PM) at Different Sites in the Los Angeles Basin.” *Environ. Res.* 99:40–47.

Farahani, Vahid Jalali, Abdulmalik Altuwayjiri, Milad Pirhadi, Vishal Verma, Ario Alberto Ruprecht, Evangelia Diapouli, Konstantinos Eleftheriadis, and Constantinos Sioutas. 2022. “The Oxidative Potential of Particulate Matter (PM) in Different Regions around the World and Its Relation to Air Pollution Sources.” *Environmental Science: Atmospheres* 2 (5): 1076–86. https://doi.org/10.1039/d2ea00043a.

Hu, S., A. Polidori, M. Arhami, M. M. Shafer, J. J. Schauer, A. Cho, and C. Sioutas. 2008. “Redox Activity and Chemical Speciation of Size Fractioned PM in the Communities of the Los Angeles-Long Beach Harbor.” *Atmospheric Chemistry and Physics* 8 (21): 6439–51. https://doi.org/10.5194/acp-8-6439-2008.

Li, Ning, Constantinos Sioutas, Arthur Cho, Debra Schmitz, Chandan Misra, Joan Sempf, Meiying Wang, Terry Oberley, John Froines, and Andre Nel. 2003. “Ultrafine Particulate Pollutants Induce Oxidative Stress and Mitochondrial Damage.” *Environmental Health Perspectives* 111 (4): 455–60. https://doi.org/10.1289/ehp.6000.

Li, Ning, Meiying Wang, Lori A. Bramble, Debra A. Schmitz, James J. Schauer, Constantinos Sioutas, Jack R. Harkema, and Andre E. Nel. 2009. “The Adjuvant Effect of Ambient Particulate Matter Is Closely Reflected by the Particulate Oxidant Potential.” *Environmental Health Perspectives* 117 (7): 1116–23. https://doi.org/10.1289/

EHP.0800319.

Ntziachristos, Leonidas, John R. Froines, Arthur K. Cho, and Constantinos Sioutas. 2007. "Relationship between Redox Activity and Chemical Speciation of Size-Fractionated Particulate Matter." *Particle and Fibre Toxicology* 4 (June). https://doi.org/10.1186/1743-8977-4-5.

Saffari, Arian, Nancy Daher, Martin M. Shafer, James J. Schauer, and Constantinos Sioutas. 2014. "Seasonal and Spatial Variation in Dithiothreitol (DTT) Activity of Quasi-Ultrafine Particles in the Los Angeles Basin and Its Association with Chemical Species." *Journal of Environmental Science and Health - Part A Toxic/Hazardous Substances and Environmental Engineering* 49 (4): 441–51. https://doi.org/10.1080/10934529.2014.854677.

Saffari, Arian, Sina Hasheminassab, Martin M. Shafer, James J. Schauer, Talal A. Chatila, and Constantinos Sioutas. 2016. "Nighttime Aqueous-Phase Secondary Organic Aerosols in Los Angeles and Its Implication for Fine Particulate Matter Composition and Oxidative Potential." *Atmospheric Environment* 133 (May):112–22. https://doi.org/10.1016/j.atmosenv.2016.03.022.

Shirmohammadi, Farimah, Sina Hasheminassab, Dongbin Wang, James J. Schauer, Martin M. Shafer, Ralph J. Delfino, and Constantinos Sioutas. 2016. "The Relative Importance of Tailpipe and Non-Tailpipe Emissions on the Oxidative Potential of Ambient Particles in Los Angeles, CA." *Faraday Discussions* 189:361–80. https://doi.org/10.1039/c5fd00166h.

Shirmohammadi, Farimah, Dongbin Wang, Sina Hasheminassab, Vishal Verma, James J. Schauer, Martin M. Shafer, and Constantinos Sioutas. 2017. "Oxidative Potential of On-Road Fine Particulate Matter (PM2.5) Measured on Major Freeways of Los Angeles, CA, and a 10-Year Comparison with Earlier Roadside Studies." *Atmospheric Environment* 148 (January):102–14. https://doi.org/10.1016/j.atmosenv.2016.10.042.

Verma, Vishal, Payam Pakbin, Ka Lam Cheung, Arthur K. Cho, James J. Schauer, Martin M. Shafer, Michael T. Kleinman, and Constantinos Sioutas. 2011. "Physicochemical and Oxidative Characteristics of Semi-Volatile Components of Quasi-Ultrafine Particles in an Urban Atmosphere." *Atmospheric Environment* 45 (4): 1025–33. https://doi.org/10.1016/j.atmosenv.2010.10.044.

Verma, Vishal, Andrea Polidori, James J. Schauer, Martin M. Shafer, Flemming R. Cassee, and Constantinos Sioutas. 2009. "Physicochemical and Toxicological Profiles of Particulate Matter in Los Angeles during the October 2007 Southern California Wildfires." *Environmental Science and Technology* 43 (3): 954–60. https://doi.org/10.1021/es8021667.

Zhang, Xian, Norbert Staimer, Daniel L. Gillen, Tomas Tjoa, James J. Schauer, Martin M. Shafer, Sina Hasheminassab, et al. 2016. "Associations of Oxidative Stress and Inflammatory Biomarkers with Chemically-Characterized Air Pollutant Exposures in an Elderly Cohort." *Environmental Research* 150 (October):306–19. https://doi.org/10.1016/j.envres.2016.06.019.

17th INTERNATIONAL CONGRESS of the Geological Society of Greece

BULLETIN OF THE GEOLOGICAL SOCIETY OF GREECE, SP. PUBL.

EXTENDED ABSTRACT 024

Teachers' experience, attitudes and skills on flood events: The case of Daniel storm 2023, Thessaly, Greece

Bakopoulou A.[1], Dousiaki C.[1], Diakakis M.[1], Andreadakis E.[1], Mavroulis S.[1], Gogou M.[1], Kranis, H., Antonarakou A.[1], Lekkas E.[1]

(1) National and Kapodistrian University of Athens, Department of Geology and Geoenvironment, Athens, Greece, abakopoulou@geol.uoa.gr

Extended Abstract

School environment poses a challenge for the protection against the increasing occurrences of natural disasters (Lekkas & Andreadakis, 2015), and the education of teachers and students alike should be a first-order priority. This pilot study is a first step to reveal teachers' attitudes and skills after the Daniel storm 2023 (Thessaly, Greece) in order to record awareness level in terms of flood risk reduction toward the development of an educated resilient and adaptable school community to decrease flood vulnerability and susceptibility.

Within the scope of this quasi-experimental research, semi-structured interviews were conducted in October and November 2023, focusing on teachers at local primary schools that suffered from the Daniel flood. Questions of the research tool were cross-checked by two educators and responses were qualitatively elaborated by two geoscientists to keep internal validity.

After the qualitative elaboration of interview responses and in terms of teachers' attitude about Daniel flood and their flood background knowledge, it comes out in general that a) there is a diversity in the pre-existing knowledge of teachers regarding floods usually exhibiting low scores of awareness, which is in line with other research (Bakopoulou et al, 2022), and b) the real-life experience of Daniel events has significantly contributed to the raising of awareness within the local school community. The majority of teachers: (i) point out the importance of targeted educational initiatives; (ii) recognize the increased risk in the local flood-affected areas; (iii) highlight the severe interrelation between personal and professional challenges during natural disasters, emphasizing the need for broad and systemic support; (iv) assure that the flood impact on the school environment extends beyond the immediate effects on the classroom, affecting infrastructure and the overall functionality of the school; and (v) acknowledge the importance of preparedness and resilience and the need for further training.

Regarding the emergency management cycle, all teachers are partially aware of it, which means that they either are not aware of the different cycle phases, or are unable to accurately discriminate among each management phase. At the same time, all teachers point out that it was not possible to implement emergency management measures immediately, due to the timing of the storm occurrence. Therefore, they recognize the importance of student and teacher education and skill development on prevention and protection measures, even in cases that students have not been directly affected. Some teachers emphasized the critical role of collaboration and mutual support among school authorities, colleagues, parents and the wider community, while the involvement of school counsellors, psychologists, and social workers is recognized as essential for providing emotional support to students and addressing the psychological impacts of the flood beyond the school environment. External support from other schools and volunteerism are also identified as valuable resources. Donations are claimed to have fostered a positive and inclusive atmosphere within the school community. The use of various communication channels, including social media platforms, has been emphasized as a necessary contribution and seminars and guidelines from educational authorities after the storm provided teachers with valuable insights for addressing the consequences of the floods, highlighting the importance of professional development and guidance.

As far as the flood consequences on school community and school environment are concerned, the storm had a significant impact on students and teachers demolishing their living and learning environment (Lekkas et al 2024). Additionally, the disruption of students' routine, the potential relocation of home or school, and exposure to abundant challenges disturbed their emotional balance and required careful

management and support. Students experienced increased anxiety and fear, with some facing stress and depression. Relocation and adjustment to new environments are recorded as the main factors that contributed to increased emotional stress; while students exhibited violent behaviour after the disaster emphasizing that they should be treated with more compassion, care, patience and tenacity in the post-flood schooling. Additionally, failures in living and learning environment caused concentration disorders to students, which in turn led to low learning abilities in the post-flood period. Besides, teachers expressed emotions of depression, stress and mental and bodily exhaustion; and suffered from severe stress of how to achieve the annual learning goals within such adverse circumstances after the disaster. Despite curriculum rigidity, teachers transformed their teaching goals to emotional ones, addressing the emotional impact and adopting measures, such as engaging in therapeutic activities in classrooms with collaboration with counsellors, psychologists, and parents, where students shared their stories focused on emotional expression and resilience. This goal transition created extra stress on teachers as they had doubts about whether they would succeed in their new goals or not, while the demand to keep in line with educational curriculum goals increased teachers' stress. Another stress factor is the fact that despite their using their own means and resources voluntarily to help especially poor students to overcome difficulties, they often felt inadequate to contribute. Finally, the need for emotional support, relocation and the adaptation of teaching methods emerges as recurring patterns that all teachers faced after the occurrence of the event.

In terms of skill development school programmes, ensuring the safety of students and teachers is an utmost priority, as reflected in the multifaceted approaches adopted by schools; therefore, all teachers claimed that the whole local school community should be trained and educated on flood risk reduction, according to the age of each target-team. Teachers should be trained to effectively support the mitigation of symptoms of post-traumatic stress among student population individually. Berger, Abu-Raiya & Benatov (2016) emphasize the long-term strong benefits and effectiveness in minimizing the symptoms of post-traumatic stress of individual education by trained teachers. However, no teacher had participated in a flood risk reduction programme in the past, even though it is a flood-prone area. Nonetheless, all teachers claimed that skill development school programmes should be engaged and enriched with flood risk reduction, protection and management activities. In addition, teachers insisted that training school community towards making quick, immediate and appropriate decisions in emotionally stressed and adverse during the flood and post-flood periods is of major importance. This could be achieved through skill development school workshops. In this sense, teachers proposed that these skill programmes or workshops should definitely include: (a) concrete simulations, (b) drills organized by local authorities, (c) digital simulations and (d) expert lectures.

Concluding, the implications of the aforementioned data are manifold: the importance of education, training and skill development on flood risk reduction and emergency management before the occurrence of severe weather events and floods constitutes a necessity, while continuous education, adapted to local needs and based on local experiences and local flooded-area history, is crucial for building resilience and preparedness for local schools and local community. Skill development school programmes or workshops can serve as a means to address flood risk reduction and protection education. Addressing these challenges can forward the development of effective support systems, ensuring the mental well-being of school community and fostering an environment that promotes effective post-disaster education. Authorities should consider the aforementioned data so that they establish educational policies aimed at enhancing the preparedness and resilience of school community in the face of flood vulnerability and risk reduction, flood mitigation, resilience and adaptability.

References

Bakopoulou A., Katsetsiadou N.A., Kyriazis E., Alexoudi V., Grambas A., Kotsi E., Stamati E., Antonarakou A., Lekkas E. (2022). Disaster and crisis management awareness level of local authorities in the District of Attica Municipalities before and after training courses. Proc. 16th Int. Congr. Geol. Soc. Greece, 17-19 October 2022, Patras, Greece, Bul. Geol. Soc. Greece, Sp. Pub. 10, Ext. Abs. GSG2022-283. **[Conference Proceedings]**

Berger, R., Abu-Raiya, H., & Benatov, J. (2016). Reducing primary and secondary traumatic stress symptoms

among educators by training them to deliver a resiliency program (ERASE-Stress) following the Christchurch earthquake in New Zealand. *American Journal of Orthopsychiatry*, *86*(2), 236. **[Journal Article]**

Lekkas E. & Andreadakis E., (2015). Introduction to the theory of crisis and disaster management, Department of Geology and Geoenvironment, NKUA, 178p. **[Book]**

Lekkas E, Diakakis M., Mavroulis S., Filis Ch., Bantekas Y., Gogou M., Katsetsiadou K-N., Mavrouli M., Giannopoulos V., Sarantopoulou A., Nastos P., Vassilakis E., Konsolaki A., Kotsi E., Carydis P., Parcharidis I., Tounta S., Falaras T., Skourtsos E., Bakopoulou A., Korkovelos A., Ronzi L., Speis P-D., Lekka Ch., Stamati E., Moraitis S. (2024). The early September 2023 Daniel storm in Thessaly Region (Central Greece). Newsletter of Environmental, Disaster and Crises Management Strategies, NKUA, Issue No 30, January 2024. **[Journal Article]**

17th INTERNATIONAL CONGRESS of the Geological Society of Greece

BULLETIN OF THE GEOLOGICAL SOCIETY OF GREECE, SP. PUBL.

EXTENDED ABSTRACT 025

A (preliminary) comparative gemological-mineralogical study of quartz crystals derived from Greece and Brazil

Bardi E.[1], Lampropoulou P.[1], Sergoulopoulos A.[2], Rogkala A.[1], Giannakopoulou P.P.[1], Margaritis F.[1], Papoulis D.[1], Tsinidis A.[3], Islam I.[4], Petrounias P.[1]

(1) Department of Geology, University of Patras, 265 04 Patras, Greece, eftibardi@gmail.com (2) Department of Geology, University of Patras, 265 04 Patras, Greece (2) Gem Testing Laboratory Athens, Gem-A Athens ATC, 10562 Athens, Greece (3) Field collector, Thessaloniki (4) Department of Geology, Shaheed Benazir Bhutto University Sheringal, Dir Upper, 18030, Pakistan

Introduction

In this study, quartz crystals from Greece and Brazil are studied and characterized regarding their macroscopic and microscopic characteristics, emphasizing on their inclusions. Generally, quartz crystals present a tremendous variety of crystal and fluid inclusions (liquid and gas). So many mineral varieties have been identified in quartz that it would be impossible to mention them all. Specifically, this study focuses on samples originating from Internal Hellenides, namely Serbo-Macedonian and Rhodope Massifs (Greece), and Espinhaço Range (Brazil). Solid and liquid inclusions can provide information about the formation processes, the specific environment and the age that quartz crystals were formed, while they also characterize the quality of these as gemstones (Brace-Thompson, 2023; Deer, Howie, & Zussman, 1992; Roedder, 1984). The results presented in this publication are preliminary as our study is in progress. Different techniques are used in order to investigate the mineral inclusions of the studied samples such as X-ray diffraction (XRD), Scanning Electron Microscope (SEM), Raman spectroscopy (Raman) and the results of their full characterization will be presented in the future.

Geological setting-Geologic Background

Based on recent publications quartz found in Greece is distinguished in two main groups in respect to its formation environment (Maneta & Voudouris, 2010; Voudouris et al., 2004, 2019). The first group involves quartz that is formed in alpine fissures hosted in lithologies such as ortho- and paragneisses (in the Rhodope Massif: Drama, Thassos Island and the Attico-Cycladic Massif: Penteli Mt, Evia, Ios Islands), as well as in amphibolites (Evros, Thassos, Evia and Andros Islands), phyllites (Lesvos Island) and meta-quartzites (Crete Island). The second group, providing gem quality quartz, is related to Tertiary and Mesozoic magmatic-hydrothermal environments and associated rocks (e.g. granitoids, pegmatites, skarns, non-skarn carbonate-replacement deposits, hydrothermal-altered volcanic rocks) found across Greece (Voudouris *et al.*, 2019).

Quartz in Brazil is also found in two main geological settings (Favacho-Silva, 2000). The first includes the hydrothermal vein system of the Serra do Espinhaço, where quartz is of hydrothermal origin and is embedded in rocks of the super-group Espinhaço. Rocks observed are mainly quartzites, followed by phyllites and to a lesser extent meta-conglomerates and carbonate rocks. The second geological setting is the pegmatitic province of Eastern Brazil, where quartz is part of the core of pegmatite veins, associated with granites that have penetrated the synorogenetic turbidities of Salinas formation or its basement (Macauba Group) (Favacho-Silva, 2000).

Materials and Methods

Quartz from Greece was collected from multiple places in the Serbo-Macedonian and Rhodope Massifs, northern Greece. In detail, Greek samples were derived from outcrops found near Lefkopetra in Xanthi, Koinira in Thassos Island, Dassoto, Kato Vrontou, Panorama in Drama and Madem Lakkos in Chalkidiki. The samples from Brazil comprised of colorless and light brown quartz and there is no precise evidence of origin beyond the state where they were sourced from.

Quartz samples from both Greece (19) and Brazil (19) were polished and observed under a Proapex gemological microscope with x10 and x30 magnification. Their selection was based on whether the samples were free of inclusions or presented inclusions for further investigation. This was the reason why seventeen (17) and two (2) samples were

selected from group one and two respectively of the Brazilian quartzes. Most of the samples of the second group were inclusion free. All the studied quartz samples had their refractive indexes and specific gravity calculated. Following, based on previous observations, fifteen samples were chosen and thin sections of these samples were produced. Thin sections were examined under a Leitz Ortholux polarizing petrographic microscope and photographed using a Jenoptik ProgRes C3 digital camera.

Results and discussion

The quartz samples from Greece consist of multiple varieties and derived from the geological environments that are mentioned above. According to their macroscopic characteristics they are classified in four (4) different groups of varieties and they have further been characterized. Representative results of studied samples derived from Greece are presented below.

Amethyst

Five (5) amethyst samples (DAS01A, DAS01B, DAS01C, DAS01E, DAS01F) from the area of Dassoto, Drama were macroscopically and gemologically analyzed and their refractive indices values are 1.543 ± 0.003 and 1.552 ± 0.003 and the specific gravity showed values of 2.62 ± 0.01. These specimens are scepter-shaped and have a light purple color on the crown. In the three crystals where the body of the scepter is preserved, light to dark smoky quartz is observed (Figure 1a).

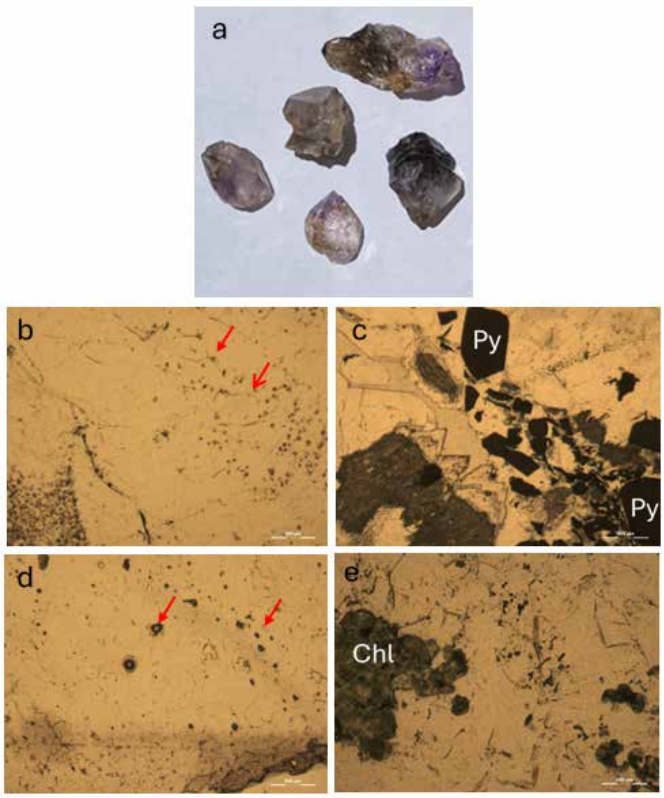

Figure 1. (a) Photo of scepter-shaped amethyst samples from the area of Dassoto, Drama. (b) Photomicrograph of zebra-like inclusions in DAS01B taken in parallel Nicols in transmitted light with magnification x25.(c) Photomicrograph of pyrite included in quartz in MAN01D taken in parallel Nicols in transmitted light with magnification x25. (d)Photomicrograph of two-phase fluid inclusions in KOI01 taken in parallel Nicols in transmitted light with magnification x25. (e) Photomicrograph of chlorite in LEY01A taken in parallel Nicols in transmitted light with magnification x4.

Regarding their microscopic observation, DAS01B sample was selected. Zebra-like inclusions, alternating dark and light parallel color bands related to twinning in the crystal (Gem-A, 2022), iron oxides, negative crystals and feldspars were observed in the DAS01B sample (Figure 1b). In this context, “negative crystals” will refer to hollow, crystal-shaped cavities, particularly exhibiting trigon-like geometry.

Rock crystal

This group includes six (6) samples (DAS01D, PAN01, MAN01A, MAN01B, MAN01C, MAN01D) from the areas of Dassoto, Panorama in Drama and Madem Lakkos in Chalkidiki. Along with amethyst samples from the Dassoto area of Drama, a prismatic crystal of colorless quartz with a few chlorite inclusions was collected and analyzed. This crystal gave values of 1.544 and 1.533 for refractive indices and for specific gravity 2.62. The crystal from Panorama has several inclusions of chlorite, rutile and possibly actinolite. The values of the refractive indices are 1.548 and 1.557 and the specific gravity 2.60. Three of the four samples from the Madem Lakkos deposit in Chalkidiki had their refractive indices measured, while the fourth sample (MAN01D) was excluded due to measurement constraints. Therefore, the refractive index values for Madem Lakkos are1.547±0.002 and 1.556±0.002 and the specific gravity was determined to be 2.65±0.02.

DAS01C and MAN01D samples were analyzed using microscope. Iron oxides in cracks, negative crystals, feldspar, muscovite and chlorite were identified in the DAS01C sample. In the sample MAN01D, pyrite, chlorite, iron oxides in cracks, negative crystals, feldspars and fluid inclusions were identified (Figure 1c).

Table 1. Summary of the refractive indexes of Greece’s quartz.

Samples	**Refractive Indexes**	
Amethyst		
DAS01A	1.540	1549
DAS01B	1.543	1.552
DAS01C	1.545	1.554
DAS01E	1.544	1.553
DAS01F	1.546	1.555
Rock crystal		
DAS01D	1.544	1.553
PAN01	1.548	1.557
MAN01A	1.549	1.558
MAN01B	1.548	1.557
MAN01C	1.545	1.554
MAN01D		
Smoky quartz		
KOI01	1.540	1.549
DAS02A	1.530	1.539
DAS02B	1.548	1.557
DAS03A	1.542	1.551
DAS03B	1.550	1.559
Milky quartz		
LEY01A	1.544	1.553
LEY01B	1.548	1.557
KAT01	1.540	1.549

Smoky quartz

Refractive index measurements were taken from five (5) samples (KOI01, DAS02A, DAS02B, DAS03A, DAS03B), with colors ranging from light to dark, from the areas Koinira in Thassos and Dassoto in Drama. For Koinira, measured values were 1.544 and 1.553. However, they varied significantly between light quartz samples or between light and dark. Specifically, the refractive indices were 1.539 ± 0.009 and 1.548 ± 0.009 for light smoky quartz and 1.546 ± 0.004and 1.555 ± 0.004 for dark smoky quartz from Dassoto. The specific gravity measured for all samples gave values limited to 2.66 ± 0.03.

Samples KOI01, DAS02B, and DAS03C (equivalent to DAS03A and DAS03B) were selected for microscopic observation. Iron oxides in cracks, negative crystals, muscovite and fluid inclusions (one and two-phase) were identified in the KOI01 sample (Figure 1d). In DAS02B iron oxides, fluid inclusions (both one- and two-phase), negative crystals, muscovite and possibly metallic minerals were recognized, while in DAS03C iron oxides in cracks, muscovite and liquid inclusions (both one- and two-phase) occur.

Milky quartz

Three (3) samples were analyzed (LEY01A, LEY01B, KAT01) from Lefkopetra in Xanthi and from Kato Vrontou in Drama. The refractive indices are 1.546 ± 0.002 and 1.535 ± 0.002 for Lefkopetra of Xanthi and for Kato Vrontou 1.540 and 1.459. The specific gravity for all samples is 2.62 ± 0.01.

Samples LEY01A and KAT01 were examined under the microscope. Chlorite and muscovite were the main mineral inclusions found in sample LEY01A (Figure 1f). Iron oxides were detected in cracks, while fluid inclusions and negative crystals are common. In sample KAT01, feldspar, muscovite, clinopyroxene, iron oxides in cracks, fluid inclusions (both one- and two-phase) and chlorite (near the margin) were observed.

Most of the samples from Brazil are consisted of colorless quartz, with two exceptions. They are likely of hydrothermal origin, as the majority predominantly contain two-phase fluid inclusions. The studied samples of Brazil are divided in two varieties and representative results of their characterization presented as follows:

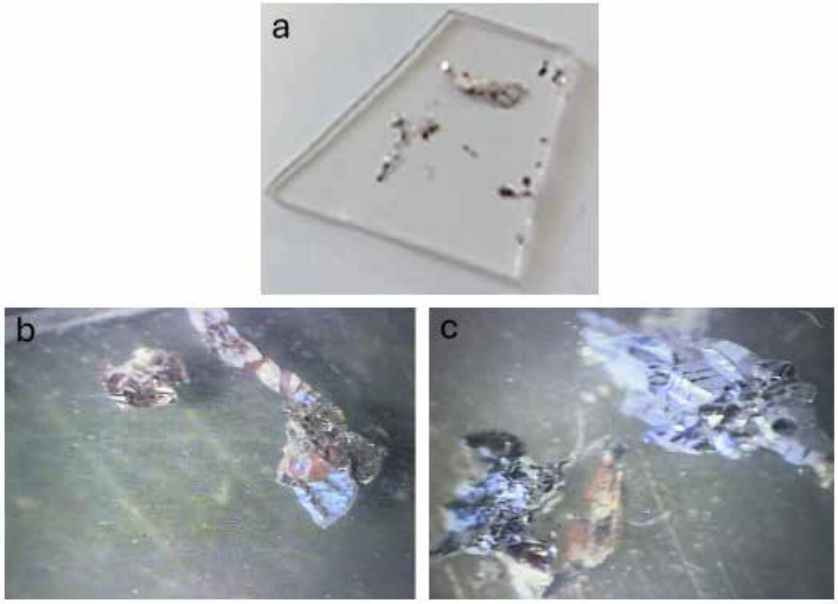

Figure 2. (a) Photo of red and black inclusions showing dendritic form in sample MIN04 from Minas Gerais, Brazil. (b, c) Photomicrographs of red and black inclusions in sample MIN04 as shown in a gemological microscope with magnification x 30.

Rock crystal

In total, seventeen (17) samples were analyzed. Based on macroscopic observation, eleven (MIN03,

MIN05, MIN06, MIN09, MIN10, MIN11, MIN13, MIN14, MIN15, MIN16, MIN17) appear clear and vitreous, containing little to no inclusions. Their refractive indices range from 1.543 to 1.550 and from 1.552 to 1.599with specific gravity of 2.60 ± 0.05. Samples MIN01 and MIN19 exhibit high concentration of liquid inclusions, with measured values1.549+ 0.001 and1.558 + 0.001for refractive indices and 2.63 + 0.01 for specific gravity. In MIN04 and MIN08, red and black inclusions that in localized spots are showing dendritic form were macroscopically visible (Figure 2a), while MIN12 contained orange-colored iron oxides. The refractive indices are limited to 1.543+ 0.007 and 1.552 + 0.007and the specific gravity is 2.59 + 0.05. Finally, although MIN07 appeared mostly transparent, chlorite was observed macroscopically. Its refractive index values are 1.539 and 1.548 and its specific gravity is 2.64.

For their microscopic observation, samples MIN01, MIN03, MIN07, MIN08, MIN12 and MIN15 were selected. Plagioclase, muscovite and fluid inclusions (both one- and two-phase) were observed in MIN01 sample. In MIN03 and MIN07 samples, iron oxides in cracks, fluid inclusions (both one- and two-phase), muscovite, negative crystals and chlorite were distinguished, while in MIN15 negative crystals, iron oxides, muscovite and chlorite were distinguished (Figure 2b). Also, iron oxides, negative crystals, muscovite and hematite were identified in MIN08.

Table 2. Summary of the refractive indexes of Brazil's quartz.

Samples	**Refractive Indexes**	
Rock crystal		
MIN01	1.550	1.559
MIN03	1.550	1.559
MIN04	1.543	1.552
MIN05	1.543	1.552
MIN06	1.550	1.559
MIN07	1.539	1.548
MIN08	1.550	1.559
MIN09	1.549	1.558
MIN10	1.548	1.557
MIN11	1.544	1.553
MIN12	1.550	1.559
MIN13	1.550	1.543
MIN14	1.543	1.552
MIN15	1.543	1.552
MIN16	1.550	1.559
MIN17	1.550	1.559
MIN19	1.549	1.558
Smoky quartz		
MIN02	1.543	1.552
MIN18	1.550	1.559

Smoky quartz

The color of MIN02 and MIN18 samples is presented as light brown color. The refractive indices obtained from the measurement of the two (2) samples are 1.543 + 0.007 and 1.552 + 0.007 and the specific gravity showed values 2.62 + 0.03.

Sample MIN02 was chosen for microscopic observation. Iron oxides in cracks, negative crystals and fluid inclusions (both one- and two-phase) were identified in the sampleMIN02.

Conclusions

Samples from Greece include mineral varieties such as: amethyst, rock crystal, smoky quartz and milky

quartz, while those derived from Brazil mainly include smoky quartz. So far, the following conclusions can be drawn:

- The difference between refractive indices of the same variety or the same country or the two countries is random and no correlation can be concluded.
- As for the specific gravity (SG) in Greek samples, is observed that amethysts, rock crystal from Drama and milky quartz have SG < 2.65 but rock crystal from Chalkidiki and smoky quartz have SG > 2.65. On the other hand, in Brazilian samples, all except two have SG < 2.65. However, they are exceptions in their variety because one is a rock crystal and the other is smoky quartz.
- Even though Brazilian amethyst was not included in this study, it was observed that amethyst from Greece contains zebra-like inclusions. Zebra-like" inclusions are typical of amethyst, but there are not always present in a sample. The observation of this type of inclusion in a Greek sample is worth mentioning.
- Inclusions that were present in every sample were iron oxides in cracks, negative crystals and fluid inclusions. Both muscovite and chlorite were frequently found in both Greek and Brazilian samples.

As this study is still evolving, the evaluation of XRD data of some samples is not completed while their characterization via other analytic techniques (e.g. SEM, FTIR and Raman) is in progress. The results of a fully characterization in macro-micro-nano scale of quartz gem crystals with combined methods will be presented in the future in order to be used as a new data base of gems from Greece and/ or other areas. It is considered that it will be enriched by new research in the future, providing significant geological, gemological information in a more systematic mode.

Acknowledgements

Thanks to the postgraduates student Pahaki M. and graduate student Skontovolou L. for their help, the cutting workshop Michael Hatzimihail that polished the samples and the EAGME laboratories for preparing the thin sections of samples.

References

Brace-Thompson, J. (2023). 9 Types of Inclusions in Quartz. Retrieved from Rockngem.com website: https://www.rockngem.com/9-types-of-inclusions-in-quartz/

Deer, W. A., Howie, R. A., & Zussman, J. (1992). An Introduction to the Rock-forming Minerals (2nd ed., p. 467). Prentice Hall.

Favacho- Silva, M.D. (2000). Variedadesgemológicas de quartzoem Minas Gerais: geologia, mineralogia, causas de cor, técnicas de tratamento e aspectosmercadológicos (Dissertação de Mestrado). Universidade Federal de Minas Gerais.

GIA (2022). Top 5 Most Recognisable Gemstone Inclusions For Gemmologists. Retrieved from The Gemmological Association of Great Britain | Gem-A website: https://gem-a.com/gem-hub/top-5-most-recognisable-gemstone-inclusions-for-gemmologists/

Maneta, V., & Voudouris, P. (2010). QUARTZ MEGACRYSTS IN GREECE: MINERALOGY AND ENVIRONMENT OF FORMATION. Bulletin of the Geological Society of Greece, 43(2), pp.685-696. https://doi.org/10.12681/bgsg.11231

Voudouris P, Katerinopoulos A, Melfos V (2004) Alpine-type fissure minerals in Greece. Documenta Naturae 151, pp.23-45

Voudouris, P., Mavrogonatos, C., Graham, I., Giuliani, G., Tarantola, A., Melfos, V., Karampelas, S., Katerinopoulos, A.,Magganas, A. (2019). Gemstones of Greece: Geology and Crystallizing Environments. Minerals 9(8), p.461, https://doi.org/10.3390/min9080461

Roedder, E. (1984). Fluid inclusions. Reviews in Mineralogy (Vol. 12, p. 644; P. H. Ribbe, Ed.). Mineralogical Society of America.

17th INTERNATIONAL CONGRESS of the Geological Society of Greece

BULLETIN OF THE GEOLOGICAL SOCIETY OF GREECE, SP. PUBL.

EXTENDED ABSTRACT 026

The UNESCO Global Geopark of Lavreotiki: a pillar for climate change adaptation & the example of sustainable water use, Greece

Barsaki V.[1], Michailidou Ir.2, Peppa F.[2], Kerdela G.[2] & Moraiti E.[1]
(1) Lavreotiki UNESCO Geopark, 1 Koundouriotou Str., 19500 Lavrion, Attica, Greece. e-mail: vasilikibarsaki@gmail.com
(2) Lavrion Environmental Center, L.T.C.P., 19500, Lavrion.

Introduction

UNESCO Global Geoparks are geographically defined areas that combine monuments of significant geological value with elements of ecological, cultural, and aesthetic importance. They are managed with a holistic approach to protection, education, and sustainable development. They are ideal destinations that support local communities and serve the 17 goals of the United Nations' Green Agenda in various ways.

Education in the frame of a UNESCO Global Geopark

One of the main axes of action for geoparks is Education. UNESCO Global Geoparks implement educational programs based on the geodiversity and biodiversity they host. Through collaborative partnerships, they educate and prepare societies for new, modern challenges. Geosites function as experiential laboratories, welcoming students, educators, and visitors to offer them unique experiences.

A good practice of such actions, aimed at preparing societies to tackle the climate crisis and adapt to new conditions, are the workshops for educators organized by the Lavreotiki UGGp in collaboration with the Lavrion Environmental Center (KEPEA) and/or other educational institutions active in the area. These workshops are often organized in the frame of the celebration of an established World Day.

Figure 1. Workshops for teachers and educators within the Lavreotiki UGGp.

The geosites of the Lavreotiki Geopark play a leading role during the workshops, offering stimuli and many opportunities for exploration and interaction with the environment, engaging and inspiring teachers and educators. In the field, the participant does not remain a mere spectator but experiences a rich learning experience. The Lavreotiki Geopark boasts numerous geosites that demonstrate the different environments (terrestrial, lacustrine, marine) that have developed in the territory and record climate changes over geological time, along with the impact on the palaeoenvironment, the societies and the living organisms. Among the notable geosites, are the lacustrine deposits of the "Alogari" hill, the submerged paleo-coasts along the geopark's coastline (such as the submerged port of Thorikos) and the karstic geomorphs of Kaki Thalassa.

Figure 2. Lavreotiki UGGp's geosites: Left: the lacustrine deposits of Alogari hill. Middle: karstic geomorphs of Kaki Thalassa. Right: submerged port of Thorikos.

However, the monuments that make Lavreotiki UNESCO Global Geopark unique in the world, except for its geological heritage and geodiversity, are the sites of mining heritage. The installations of the ancient Greeks for mining and metallurgy represent a perfectly designed infrastructure, harmonized with the climatic conditions of the time.

In antiquity, similar to the present time, Lavreotiki was an arid area with limited water resources but significant water needs. In ancient societies, water covered the biological needs of people, the needs for cultivating the land and raising animals, while large quantities were needed in mining and metallurgy. Given the large industrial zones that had developed in Lavreotiki (for the collection and processing of the ore deposits), the presence of water was of crucial importance. The ancient Greeks had addressed the high demand with innovative methods of water recycling and reuse for the time.

A characteristic example of such a mining heritage monument is the geosite named *"Souriza valley,"* located in the National Park of Sounion. It is the most representative site of ancient mining and metallurgical activity in the geopark, which gave birth to an unparalleled civilization. The entire area (now a declared archaeological site) hosts numerous mining galleries and metallurgical workshops, as well as other facilities for housing miners. Mining and metallurgical work followed a specific practical process, related to the type of extracted product, the depth of the deposits, and the necessary processing and subsequent smelting for the extraction of argentiferous lead. With the development of technology, mining and metallurgical practices improved relatively, and more productive technological installations were invented (Morin, D. *et al*., 2021). As a result, the entire ore-bearing land of Souriza became a vast working area. Today, many of the ore enrichment workshops are very well preserved. The working areas included ore crushing and grinding areas, a washing plant, storage areas for processed ore and concentrate, and one or more water tanks for the operation of the washing plants (Konofagos *et al*., 1970; Papadimitriou, 2017).

Figure 3. Aerial photo of the "Souriza valley" – mining and metallurgy center.

Water management was very well studied. The washing plant installations were developed within the valleys to utilize rainwater runoff from the slopes. Given the lack of atmospheric precipitation, the main concern of the ancient metallurgists was to prevent water loss, which was essential for the operation of the washing plants. For this reason, the internal surfaces of the rainwater tanks, as well as the washing plants and pipelines, were lined with a special hydraulic mortar (Meimaroglou *et al*., 2023).

Case study: World Water Day - sustainable water use

In the context of celebrating World Water Day (on 22nd March each year), the Lavrion Environmental Center, with the participation of the Lavreotiki Geopark, organizes a workshop for all educators, including a 3hours visit to the "Souriza valley" geosite. The main thematic units of the workshop are:

- The importance and use of water in modern societies.
- The importance and use of water in antiquity.
- The journey of water through geological time in the Lavreotiki UNESCO Global Geopark.
- Sustainable management of water, the example of water recycling – the ancient mining center of "Souriza valley".
- Modern challenges in the era of the climate crisis.

The role of the Lavreotiki UGGp

The Lavreotiki geopark hosts geosites that narrate impressive changes related to the distribution of water on the Earth's surface over geological time. From sea-level changes during the Quaternary period to the ancient lakes that existed during the Miocene era and the changes in the hydrological basins of its streams (Pavlopoulos, 1992 & Vasileiou, 2010), the participants of the workshop can understand how significant changes occur on the land we inhabit, cultivate, and exploit. A characteristic example is the ancient Greeks and their efficient water management, as evidenced by the archaeological/mining findings in the Souriza Valley. During the seminar, the aforementioned data are presented, emphasizing the importance of adapting to climate changes and the sustainable management of Earth's resources.

Results

The participation of educators is always high, and they fulfil the program with great interest. Upon completion of the workshop, an evaluation process follows. The table below presents the statistical results of the last workshop (year 2024).

Table 1. Indicative statistical results of the workshop's evaluation form.

No of applications	Hosting capability (No of participants)	No of participants	gender		Evaluation of the workshop		Comments for improvement
			male	female	Satisfied	Not satisfied	
95	20-60	62	19	43	62	-	Longer duration / recurrence

Workshops, such as the latter study case, that offer educators modern scientific knowledge, new perspectives in fundamental issues, such as the sustainable use of water and present free educational tools, enhance school communities and the next generations. Meaningful partnerships, such as the example between the Lavrion Environmental Center and the Lavreotiki UGGp, represent good practices for the adaptation and sustainability of local communities in the era of the climate crisis. They cultivate interdisciplinarity and communicate science and universal values, such as cooperation, respect, inclusion, and quality education, to the general public. These values are included and promoted by the United Nations Sustainable Development Goals (such as SDG 4, SDG 11, SDG 12, SDG 13, and SDG 17).

Figure 1. The SDG's promoted through this educational action of the Lavreotiki UGGp and the Lavrion Environmental Center.

References

Papadimitriou, G., 2017. Ore washeries and water cisterns in the mines of Laurion-Attica. In: Wellbrock, K. (ed.): Schriften der Deutschen Wasserhistorischen Gesell-schaft, Band 27-2, Siegburg, 2017, 395-416.

Konofagos, K., Musshe H., 1970. The helical ore washeries of the ancient Greeks in Lavrion. A lost ancient Greek invention. Transactions of the Academy of Athens, 29.

Meimaroglou, N., Mouzakis, Ch., Kalagri, A. & Kapetanios, A., 2023. Earthen and hydraulic mortars used at Lavrion during classical antiquity (5th-4th century B.C.). A fundamental relationship between earthen building tradition and sophisticated hydraulic binders and concrete. 10.46586/DBM.264.

Morin, D., Herbach, R. & Rosenthal, P. 2021. The Laurion shafts, Greece: ventilation systems and mining technology in antiquity. Historical Metallurgy, 46(1), pp. 9–18.

Pavlopoulos, K., 1992. The geomorphological evolution of South Attica. Athens: PhD Thesis. National and Kapodistrian University of Athens.

Vasileiou, A., 2010. Relief analysis and geotectonic structure of Eastern Attica. Athens: PhD Thesis. Agricultural University of Athens.

17th INTERNATIONAL CONGRESS of the Geological Society of Greece

BULLETIN OF THE GEOLOGICAL SOCIETY OF GREECE, SP. PUBL.

EXTENDED ABSTRACT 027

The world class geodiversity of the Lavreotiki UNESCO Global Geopark's minerals, Lavreotiki Municipality, Greece

Barsaki V.[1], Voudouris P.[2] & Moraiti E.[1]
(1) Lavreotiki UNESCO Geopark, 1 Koundouriotou str., 19500 Lavrion, Attica, Greece. e-mail: vasilikibarsaki@gmail.com
(2) Faculty of Geology and Geoenvironment NKUA, University Campus, Zografou, 15784 Attica, Greece.

Lavreotiki UGGp mineralization

The Lavreotiki Geopark occupies the area where both hypogene and supergene processes created an amazing underground world, decorated with an exquisite variety of minerals of international recognition and value. Its mineralization is unique and of high geodiversity, as the territory contains 748 naturally occurring mineral species, the most of any other district in the world (Rieck, 2024; https://www.mindat.org/loc-1942.html). From about 10 to 7 million years ago, massive tectonic movements along the so-called "Western Cycladic Detachment System", accommodated magma emplacement, and facilitated hydrothermal fluid circulation and ore deposition within permeable lithologies. These processes in combination with subsequent supergene oxidation of the ores, gave birth to one of the most important, historically and economically, polymetallic deposits in the world exploited by the Ancient Greeks and during the modern times (Voudouris *et al.*, 2008; Boshall *et al.*, 2011; Ross *et al.*, 2021).

The mining and metallurgical industry, developed in antiquity -which triggered the cultural and economic development of the city-state of Athens, as well as its hegemonic role in classical times- has gained worldwide scientific interest. Essential questions concerning the mining of ores and their processing remain unresolved (Conophagos, 1980).

Geodiversity

- 5 different types of mineralization are present in the geopark's ore deposits.
- The Lavreotiki UGGp hosts some of the best mineral specimens in the world.
- It hosts the biggest collection of the most impressive pseudomorphs.
- 60 chemical elements of the periodic table are presented in the geopark's ore deposits.
- The extended and ongoing oxidation of the primary ore resulted in the formation of one of the best developed oxidation zones on Earth (up to 270 m thick).
- 25 Type Locality (TL) minerals.
- Slag minerals (150 valid mineral species and 7 Type Locality Minerals).
- The Lavreotiki UGGp is included in the top ten areas, worldwide, with the highest variety in minerals.

Figure 1. Left: Hilarionite FOV: 3mm, right: Agardite-[Nd] FOV: 3mm, (copyright Toth Lazlo).

The TL mineral list of the Lavreotiki UGGp

The geopark hosts ten geosites (ancient and modern mining galleries), where 25 minerals have been identified for the first time worldwide and are included in the International Mineralogical Association's list of Type-locality minerals (IMA list) (Pekov *et al*., 2011; Voudouris *et al.*, 2021; Rieck, 2024). The localities belong to the most impressive and probably the most unique labyrinth mining centers in the world.

Table 1. List of the Type – locality minerals from the Lavreotiki UGGp.

Mineral	Formula	Mining gallery
Agardite – (Nd)	$NdCu(AsO_4)_3(OH)_6 . 3H_2O$	Hilarion 50
Attikaite	$Ca_3Cu_2Al_2(AsO_4)_4(OH)_4 . 2H_2O$	Christiana 132
Drobecite	$CdSO_4 . 4H_2O$	Esperanza
Fabrizite	$Zn_9(SO_4)(OH)_{12}Cl_2 . 6H_2O$	Hilarion
Glaucocerinite	$(Zn_{1-x}Al_x)(OH)_2(SO_4)_{x/2} . nH_2O$	Serpieri
Hilarionite	$Fe^{3+}{}_2(SO_4)AsO_4)(OH) . 6H_2O$	Hilarion 50
Kamarizaite	$Fe^{3+}{}_3(AsO_4)_2(OH)_3 . 3H_2O$	Kamariza
Kapellasite	$Cu_3Zn(OH)_6Cl_2$	Sounion 19
Katerinopoulosite	$(NH_4)Zn(SO_4)_2 . 6H_2O$	Esperanza
Katsarosite	$Zn(C_2O_4) . 2H_2O$	Esperanza
Ktenasite	$ZnCu_4(SO_4)_2(OH)_6 . 6H_2O$	Jean Baptiste
Laurionite	$PbCl(OH)$	Kamariza
Lazaridisite	$Cd_3(SO_4)_3 . 8H_2O$	Esperanza
Mereiterite	$K_2Fe(SO_4)_2 . 4H_2O$	Hilarion 50
Natroglaucocerinite	$[Zn_5Al_3(OH)_{16}][(SO_4)_{1.5}Na_{1.5}(SO_4)_{0.75}(H_2O)_9]$	Hilarion
Nickeltsumcorite	$Pb(Ni,Fe^{3+})_2(AsO_4)_2(H_2O,OH)_2$	"km3"
Niedermayrite	$CdCu(SO_4)_2(OH)_6 . 4H_2O$	Esperanza
Pracharite	$CaSb^{5+}{}_2(As^{3+}{}_2O_5)_2O_2 . 10H_2O$	Plaka 80
Serpierite	$Ca(Cu,Zn)_4(SO_4)_2(OH)_6 . 3H_2O$	Serpieri
Stergiouite	$CaZn_2(AsO_4)_2 . 4H_2O$	Plaka 80
Voudourisite	$Cd(SO_4) . H_2O$	Esperanza
Tzeferisite	$CaZn_8(SO_4)_2(OH)_{12}Cl_2(H_2O)_9$	Damianos
Zincaluminite	$Zn_6Al_6(SO_4)_2(OH)_{16} . 5H_2O$	Hilarion
Zincolivenite	$CuZn(AsO_4)(OH)$	Kamariza
Zincowoodwardite	$[Zn_{1-x}Al_x(OH_2][(SO_4)_{x/2} . n(H_2O)]$	Christiana

Lavreotiki Geopark's geological heritage contains geosites of international value, most of them representing its amazing underground world. In particular, the geopark hosts ten ancient and modern mining galleries, all branches of the following three mining centers, Plaka, Agios Konstantinos (Kamariza) and Sounion center. The geopark maintains a geodatabase concerning its minerals of international value and the labyrinth mining centers, constantly enriched with the latest scientific discoveries and the corresponding localities.

Acknowledgements

Special thanks to Dr. Karl Heinz Fabritz, Dr Uwe Kolitch and Dr Branko Rieck for their research and offer to the Lavreotiki UGGp.

References

Bonsall, T.A., Spry, P.G., Voudouris, P., Tombros, S., Seymour, K., Melfos, V. 2011. The Geochemistry of Carbonate-Replacement Pb-Zn-Ag Mineralization in the Lavrion District, Attica, Greece: Fluid Inclusion, Stable Isotope, and Rare Earth Element Studies. Economic Geology, 106, 619–651.

Conophagos C. (1980). The Lavrion and the ancient Greek techniques for silver production. Athens, Ekdotiki Athinion, 458 p.

Pekov, I.V., Chukanov, N.V., Zadov, A.E., Voudouris, P., Magganas, A., Katerinopoulos, A., 2011. Agardite-(Nd) NdCu6(AsO4)3(OH)6.3H2O from the Hilarion Mine, Lavrion, Greece: Mineral description and chemical

relations with other members of the agardite-zálesiite solid-solution system. Journal of GEOsciences 57, 249-255.

Rieck B. (2024) Lavrion Mining District, Lavreotiki, East Attica, Attica, Greece, https://www.mindat.org/loc-1942.html

Ross, J., Voudouris, P., Melfos, V., Vaxevanopoulos, M., Soukis, K., Merigot, K. 2021. The Lavrion silver district: Reassessing its ancient mining history. Geoarchaeology, 36(4), 617-642.

Voudouris, P., Melfos, V., Spry, P.G., Bonsall, T.A., Tarkian, M., Solomos, Ch., 2008. Carbonate-replacement Pb-Zn-Ag±Au mineralization in the Kamariza area, Lavrion, Greece: Mineralogy and thermochemical conditions of formation. Mineralogy and Petrology, 94, 85-106.

Voudouris, P., Melfos, M., Mavrogonatos, C., Photiades, A., Moraiti, E., Rieck, B., Kolitsch, U., Tarantola, A., Scheffer, C., Morin, D., Vanderhaeghe, O., Spry, P.G., Ross, J., Soukis, K., Vaxevanopoulos, M., Pekov, I.V., Chukanov, N.V., Magganas, A., Kati, M., Katerinopoulos, A., Zaimis, S., 2021. The Lavrion mines: a unique site of geological and mineralogical heritage, Minerals, 11, 76, https://doi.org/10.3390/min11010076

17th INTERNATIONAL CONGRESS of the Geological Society of Greece

BULLETIN OF THE GEOLOGICAL SOCIETY OF GREECE, SP. PUBL.

EXTENDED ABSTRACT 028

Highlighting the Geological Heritage of the Island of Kythira, Greece

Barsaki V.[1], PhD. Zananiri I.[1]& Moraiti E.[1]
(1) Hellenic Survey of Geology and Mineral Exploration (HSGME), Acharnes, Greece, email: vmparsaki@eagme.gr, vasilikibarsaki@gmail.com

Introduction

The geological heritage of a country consists of sites that reflect its geological history. Geosites are locations where the historical record of the Earth is preserved and testify to its long-term evolution, as well as areas where contemporary planetary processes are recorded. Geological heritage combined with biodiversity constitutes the natural heritage of a territory, describes its unique identity and should be protected for the benefit of present and future generations.

To achieve these goals, in the frame of the "GEOINFRA" project ("Geological Mapping of Greece for the support of innovation and entrepreneurship"), Work package 5 "Documentation of Geosites and Geotrails, Geopark studies" (NSRF 2014-2020/2023), the Hellenic Survey of Geology and Mineral Exploration selected Kythira Island for recording and promoting its geological heritage. Due to its geographical and geotectonic setting, lying in the convergence of two tectonic plates in the southwestern part of the South Aegean Hellenic Arc and between the Ionian and the Aegean Sea, Kythira boasts significant geological, geomorphological and paleontological wealth. Tectonic structures, fossils, gorges, caves, coastal geoforms and rocks await visitors to narrate their own stories and myths.

Geography – geomorphology

Kythira island, located between Peloponnese and Crete along the Hellenic island arc, spans over an area of 280 km^2. The climate is characterized as "Mediterranean", with high relative humidity and strong winds mainly in winter. The dominant relief is semi-mountainous with deep valleys and a maximum altitude of 507 meters (Mermigaris Mount). A smooth plateau exists along the central part of the territory with a few arable zones. The coastline has a length of approximately 52 km and forms many pocket beaches, while the rugged coastal terrain is the combined result of tectonics and lithology along with the significant wave energy, shaping its shores into steep rocky cliffs with deep bays (Gaki *et al*., 2011).

Geology

The geological structure of the island of Kythira constitutes post-Alpine formations, the Pindos Unit overlying the Tripolis Unit and a metamorphic crystalline basement. The latter is highly folded and occupies the northern part of the island. Tripolis Unit and its carbonate rocks form the elongated mountain masses in the eastern and western part of the island; especially in the west limestones reach sea level, creating abrupt cliffs due to offshore faults. Pindos Unit domains are mainly located in the central and southern part of the island. The Neogene sediments extend mainly in the south and are primarily marine with intercalations of fluvial and lacustrine deposits. The latter are composed of sandstones, marls, marly limestones and conglomerates of transgressive (at the top) and regressive (at the bottom) origin. Concerning the tectonics of Kythira, an older pre-Alpine phase of ENE-WSW direction can be distinguished, which folded the metamorphic crystalline basement, followed by an Alpine phase responsible for the folding and faulting of the Tripolis and Pindos Units. Post-Alpine tectonism with NNW-SSE trending faults formed the modern terrain of grabens and horsts. Today, extensional tectonism has resulted in the ongoing uplift of the island and the recording of many catastrophic earthquakes (Lyberis *et al*., 1982).

The geological heritage of Kythira Island

The island of Kythira hosts a geological heritage of national significance. Lying in the convergence of two tectonic plates, next to the orogenic arc of East Mediterranean Sea, the island has been uplifted for millions of years. Kythira rise from the sea and the elements of this movement are reflected in its rocks, relief, and coastlines; ancient Greeks associated these movements with the birth of goddess Aphrodite and her emergence from the sea foam. During the Alpine Orogeny the rocks comprising Kythira's surface, were deformed, folded, and displaced due to the presence of

large-scale fault surfaces (Danamos, 1992 & Marsellos, 2008). Complex processes, accompanied by intense seismic activity, caused significant changes in the paleoenvironment, forming lakes or shallow seas, which are evidenced by the palaeontological findings across the island, e.g. the Mitata settlement (Bartsokas, 1998). The contemporary processes of the Earth sculpt the surface of Kythira and create landscapes of natural beauty and rarity that enrich the nine (9) thematic geotrails designated in the framework of the GEOINFRA project. More than one hundred geosites were recorded and classified in 14 different main categories (fig.1), according to their predominant geological features (Drandaki, 2009 & Moraiti, 2016).

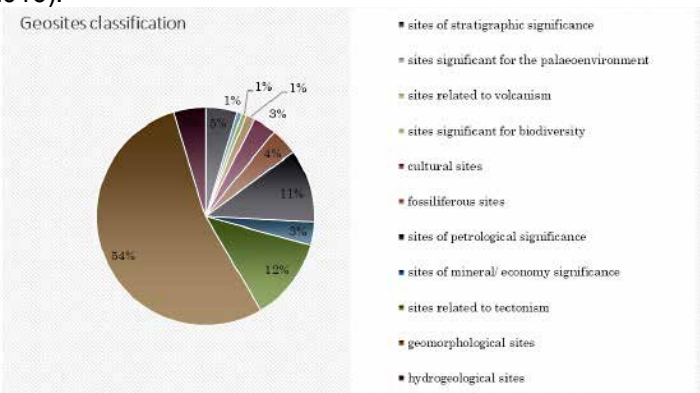

Figure 1. Classification diagram of the geosites recorded at Kythira Island, in the framework of GEOINFRA project.

The marine terraces of Platia Ammos, the oldest rocks of Kythira forming the pre-alpine basement (fig.2), the gorge of Kakia Lagada, Lykodimos beach, the cave of Agia Sophia in Mylopotamos hosting fossils of rudists and fault mirrors forming an impressive steep cliffed coast (fig.3), Kaladi beach, the marine cave on Chytra islet and the thanatocoenosis of lamellibranchia at Mitata (fig.4) are some examples of the most representative sites defining the core of Kythira's geodiversity.

Figure 2. Left: marine terraces at Platia Ammos beach, middle: regressive conglomerates at Platia Ammos beach and right: the oldest rocks of Kythira Island (pre-alpine basement).

Figure 3. Left: Kaki Lagada gorge, middle: Lykodimos beach, a cliffy coast of high aesthetic value depicting, in the left photo, the earth's modern processes and a record of tens of millions of years, while hosting the most impressive isoclinal folded limestones on Kythira Island as shown in the next photoand right: rudist limestones at Agia Sophia cave of Mylopotamos settlement.

Figure 4. Left: Kaladi beach hosting a tombolo/ coastal geoform, middle: marine cave of Chytra islet and right: thanatocoenosis of lamellibranchia at the Mitata suburbs.

Geotourism of Kythira

Geotourism is a mild form of tourism that has been rising during the last decades, especially in Europe (Ólafsdóttir, 2019). In the scope of promoting the geoheritage of Kythira, nine (9) geotrails were designated, connecting attractions of geological, archaeological, historical, cultural, environmental, and religious significance, as well as sites important for biodiversity, aiming to narrate the story of a destination in a holistic way. They were designed either to follow geographical boundaries or to support specific themes and have varying levels of difficulty, while one is a marine route visited solely by boat. During the designation of the trails specific safety specifications for travellers were followed, based on international and national standards

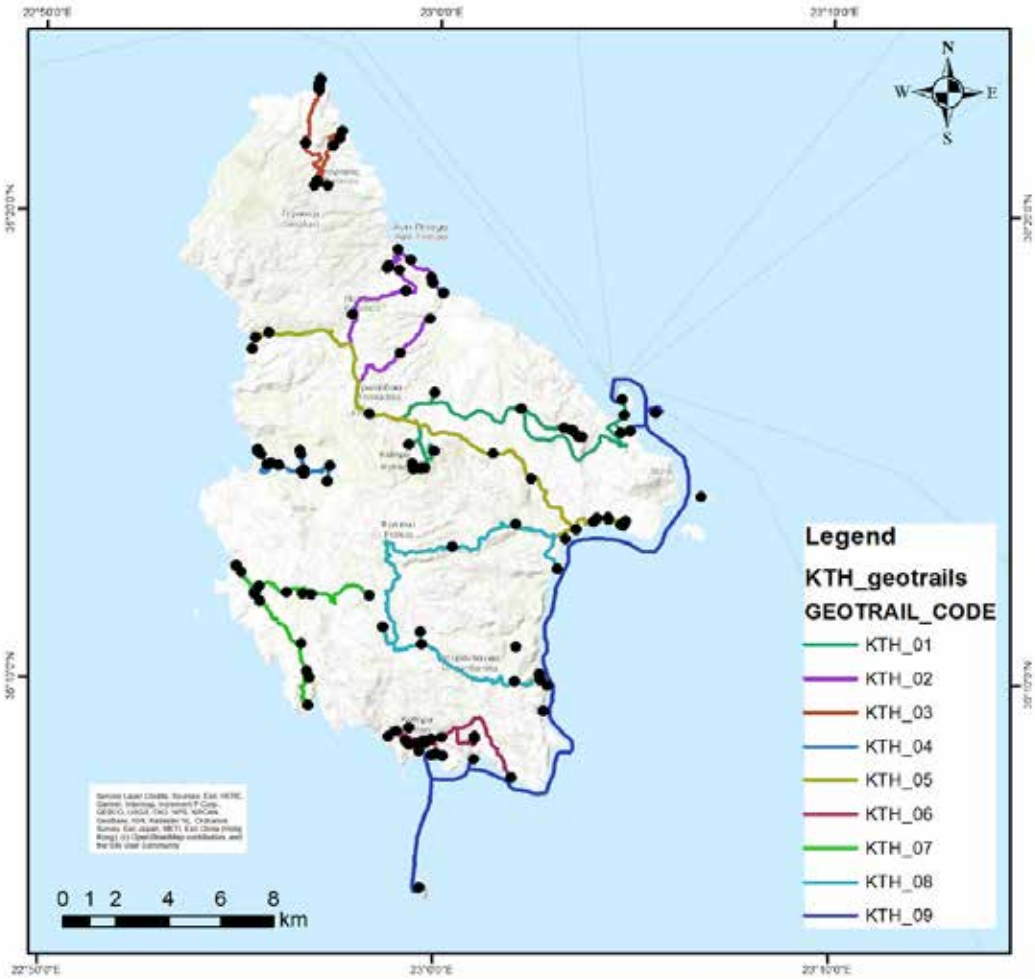

Figure 5. Mapped geotrails of Kythira Island.

Table 1. Presentation of the designed geotrails of Kythira Island.

Code	Name	Descriptive name	Short description	Nr of sites
KTH_01	Diakofti - Mitata	Discovering Kythira	This pleasant and scenic trail starts from the port of Kythira in Diakofti, where visitors first arrive, and ends inland, in the settlement of Mitata. From the first stops, the unique character of Kythira and the main geological features that have contributed to the creation of the island's identity are revealed. At the same time, one observes the dynamic relationship between humans and their natural environment over time and meets the living world of both the modern era and the geological past.	20
KTH_02	Palaiochora - Kaki Lagada	The gorge of the pirates	Linked to the raid of the pirate Barbarossa and the destruction of the Palaiochora Castle, this trail travels us through landscapes of exceptional natural beauty and picturesque settlements of another era, highlighting both modern processes of nature, as well as processes of millions of years that are still active and shape the unique biodiversity and geodiversity of Kythira.	14
KTH_03	Moudari - Karavas - Platia Ammos	Kythira from a different viewpoint	The geotrail starts from Cape Spathi, the northernmost point of Kythira, with its imposing monuments, the geological formations and landforms that compose a familiar landscape for the visitor. Soon the scenery changes and the trail lead us through rocks that do not resemble any other rock of the territory, narrating their own story. These are the most ancient rocks on the island, which today, 350 million years later, lie on the surface.	16
KTH_04	Arei - Mylopotamos - St. Sofia Cave	Unique landscapes	This geotrail of unique natural beauty starts from the traditional settlements of Arei and Mylopotamos, with its picturesque alleys and churches and elaborate bell towers. The valley of the watermills is an important attraction of the island, where nature and man mix in a unique way. The geotrail leads to the castle of Kato Chora and its amazing panoramic view and ends at the cave of Agia Sophia Mylopotamos. The cave hosts impressive speleothems and ecclesiastical elements of high value, while outdoors the scenery is comprised of fossilized limestones, hosting numerous marine organisms, such as rudists (~65 million years old).	16
KTH_05	Avlemonas - Paleopoli - Fratsia - Aroniadika - Lykodimos beach	Contrasts	Starting from the eastern shore of the island and its diverse beaches, the geotrail crosses the Paleopolis basin with its significant archaeological and palaeontological findings and through small, traditional settlements, ends up at the western coastline of the island. Lykodimos beach combines a landscape of wild and rare beauty, hosting steep cliffs, the most impressive isoclinal folds and unique coastal geoforms, remnants of the timeless struggle between the exogenous and endogenous forces of nature.	19
KTH_06	Agia Elessa - Chora (Kythira) - Kalamos - Chalkos beach	Geology and culture	This geotrail highlights the geological and cultural attractions of the capital city of Kythira. Over the centuries, the island has been a crossroad of cultures, mainly due to its geographical location and the many conquerors who controlled the territory during different eras. Visits to the museums of Chora provide reach information on the long history and the identity of the island. Along the geotrail the geology intertwining with man offers beautiful geosites, revealing interesting stories.	16

KTH_07	Keramoti - Kalokerines - Limnaria - Melidoni	Wild nature	This geotrail crosses the western part of Kythira, offering visitors the possibility to wander around rocky landscapes, next to the highest mountain peaks of the territory. The mountainous mass of Agia Elessa, with the homonymous monastery, at an altitude of 476m, owes its formation to a large tectonic structure, perhaps the largest mapped on the island, extending for several kilometres. Heading to Limnaria beach, the type locality of the wildflower *Limonium aphrodita sp.*, the trail crosses "Tyros layers", a geological formation only seen here. The tour ends at Melidoni beach, with an amazing view of the Chytra islet.	15
KTH_08	Kaladi - Agios Ilias - Livadi - Fyri Ammos	Landscapes and colours	The geotrail connects two enchanting destinations on the eastern coasts of the island, Kaladi beach and Fyri Ammos Livadi beach. These are the two most famous beaches of Kythira, where visitors can enjoy the sun and sea in a riot of colours. The geological formations create unique landscapes, with impressive coastal geoforms, alternating with white, red, and yellow rocks, giving the waters turquoise and deep blue hues. Modern earth processes sculpt the relief, and landslide phenomena dominate. Almost the entire trail passes through rocks that formed millions of years ago in a deep ocean, and many Byzantine chapels. Fields with shrub vegetation, and olive groves dominate.	17
KTH_09	Kapsali - Diakofti	...from the sea	This marine geotrail starts from the port of Kapsali. After visiting the islet of Chytra, with the impressive sea cave and its unique biodiversity, hosting the *Sempreviva sp.*, the flower of Paris and beautiful Helen, traverses the coastline of Kythira back to the port. It offers alternative, memorable experiences, allowing visitors either to reach some inaccessible beaches or admire the island's most famous ones by sea. The last attraction is the "Nordland" shipwreck at Diakofti beach, an ideal destination for divers.	20

Geotouristic products designed for Kythira Island in the frame of GEOINFRA project

A total of 150 sites of geological interest were recorded, processed and evaluated, while data concerning the island's biodiversity, cultural heritage and history were collected and enriched the HSGME's geodatabase. The project's outcomes concerning Kythira included:

- 9 mapped geotrails
- 18 interpretation panels for 9 different areas of geological interest, in Greek and English
- 1 mobile application
- 1 geotouristic guide entitled "Kythira"
- 1 ESRI story map entitled "Geotourism in Kythira Island".

Figure 6. Examples of the interpretation panels designed by the HSGME for the promotion of geotourism in Kythira Island.

Acknowledgements

This project was funded by the National Strategic Reference Framework (NSRF), 2014-2020/2023, grant number 5030010 ("Geological Mapping of Greece for the support of innovation and entrepreneurship—GEOINFRA").

References

Bartsokas A., 1998. Palaeontology of Kythira. Kythira Society of Studies Publications.

Danamos G., 1992. Contribution to the geology and hydrogeology of Kythira Island (Greece). Faculty of Geology, School of Science. Ph.D. Thesis, National and Kapodistrian University of Athens, 355p.

Drandaki I., 2009. 3rd C.S.F. Project: Geosites – Geoparks, contribution to sustainable development. IGME Publications (in Greek), pp 40.

Gaki-Papanastassiou K., Maroukian H. & Kourmpanian V., 2011. The morphotectonic evolution of southern half of Kythira Island (Ionian Sea, Greece) during the Quaternary. "Prace Geograficzne", volume 127, p. 49–60.

Lyberis N., Angelier J., and Lallemant S., 1982, Active deformation of a segment of arc: The strait of Kythira, Hellenic arc, Greece, Journal of Structural Geology, 4(3), 299−311.

Marsellos A., 2008. Extension and Exhumation of the Hellenic Forearc Ridge in Kythera. E.S.F. Kidd, The Journal of Geology, volume 116, p. 640–651.

Moraiti E., 2016. A thorough report on the IGME database of geosites – geoparks. IGME Publications (in Greek), pp. 166.

Ólafsdóttir R., 2019. Geotourism. Geosciences, 9(1), 48.

17th INTERNATIONAL CONGRESS of the Geological Society of Greece

BULLETIN OF THE GEOLOGICAL SOCIETY OF GREECE, SP. PUBL.

EXTENDED ABSTRACT 029

Mapping the geo-hazard elements offshore the Ionian Islands (Western Greece)

D. Bartolozzi[1], S. Kothri[2], P. Nomikou[2], M.F. Loreto[3], A. Ganas[4], V. Ferrante[3], O. Kei[5], F. Balsamo[6], D. Lampridou[2], E. Nikoli[2], C. Ranero[7,8]

(1) Università degli Studi di Bologna – Facoltà di Geografia e processi territoriali, Italy
(2) Department of Geography and Climatology - National and Kapodistrian University of Athens (NKUA), Greece
(3) CNR, Istituto di Scienze Marine (ISMAR), Bologna, Italy
(4) Institute of Geodynamics - National Observatory of Athens (NOA), Greece
(5) Università degli Studi di Genova, Dipartimento di scienze della terra, dell'ambiente e della Vita (DISTAV), Italy
(6) University of Parma – Dip. di Scienze Chimiche, della Vita, e della Sostenibilità Ambientale
(7) Institució Catalana de Recerca i Estudis Avançats (ICREA), Barcelona, Spain
(8) Barcelona Center for Subsurface Imaging, ICM, CSIC, Barcelona, Spain

Introduction and objectives

The area offshore the central Ionian Islands (Cephalonia, Lefkada, Zakynthos, and Ithaca), western Greece, is considered as one with the highest seismic activity and tsunamigenic potential among the seismogenic Mediterranean regions. A series of destructive earthquakes, such as the 1953 events (Mw > 6.6; Stiros et al. 1994) that destroyed the island of Cephalonia and Zakynthos, or more recent events such as the 28 October 2018 Mw 6.8 Zakynthos (Ganas et al., 2020) affect the area and most of these have the epicentre located in the offshore. The earthquakes are due to plate convergence across the Ionian Sea, as Africa (Nubia) subducts beneath Peloponnese while a major right-lateral fault (the Cephalonia Transform Fault) transfers horizontal motion towards North where Adria (Apulia) subducts beneath Northwest Greece (Epirus) and Albania (Fig.1). However, a complete mapping and understanding of the all-geological risk elements affecting the offshore of the islands has not yet been produced to date. During recent surveys, carried out in June 2023 on board of the R/V Laura Bassi - the POSEIDON project supported by the Eurofleet+ program and in May 2022 on board of the R/V G. Dallaporta supported by the Italian CNR - IONIANS cruise carried out, a multiscale geophysical dataset has been collected together with sediment samples. The collection of such data was fundamental for our seabed interpretation and for the production of an accurate map of submarine geohazards in this area.

Method

The morphological interpretation is based on TOPAS seismic profiles, EMODNET bathymetry and higher resolution bathymetric data collected in the frame of the POSEIDON 2023 project.

First, we geolocated and uploaded all seismic data on Kingdom software, which we used to view georeferenced seismic profiles and annotate visible morphologies of interest, such as faults, landslide bodies, gas and fluids trapped within sediments (Fig.2).

We then proceeded with the bathymetric interpretation of the seabed in Global Mapper software, which provides tools such as 3D models and 2D bathymetric profiles, through which we were able to locate and recognize several elements of interest (canyons, canyon heads, landslide scars, tectonic deformations etc.).

Finally, merging the seismic interpretation with the bathymetric one, we produced a map of all the morphologies that represent geohazards in the Ionian Island area (Fig. 3). The map was graphically refined using Adobe Illustrator.

The map of geohazards, produced using geophysical data, will be in a second step integrated with geological data obtained by sediments sampled with a gravity corer in a very deep basin (4220 m below sea level) offshore Zakynthos.

Results

The analysis of all available data, following the method above shortly described, allow us to map a series of morphological scarps bounding the western slope of Cephalonia and Lefkada. These scarps correspond with the shallow expression of the Cephalonia Transform Fault, which to the south is organized into a system of horseshoe-shaped faults that to the north merge into a single fault boarding the area off northern Cephalonia and the coast of Lefkada. The entire fault system results more than 120 km-long and, in the southern part, more than 20 km-wide (Fig. 3). We were also able to identify and map in high detail the seafloor displacement and the fault plane north of Lefkada by using Topas data.

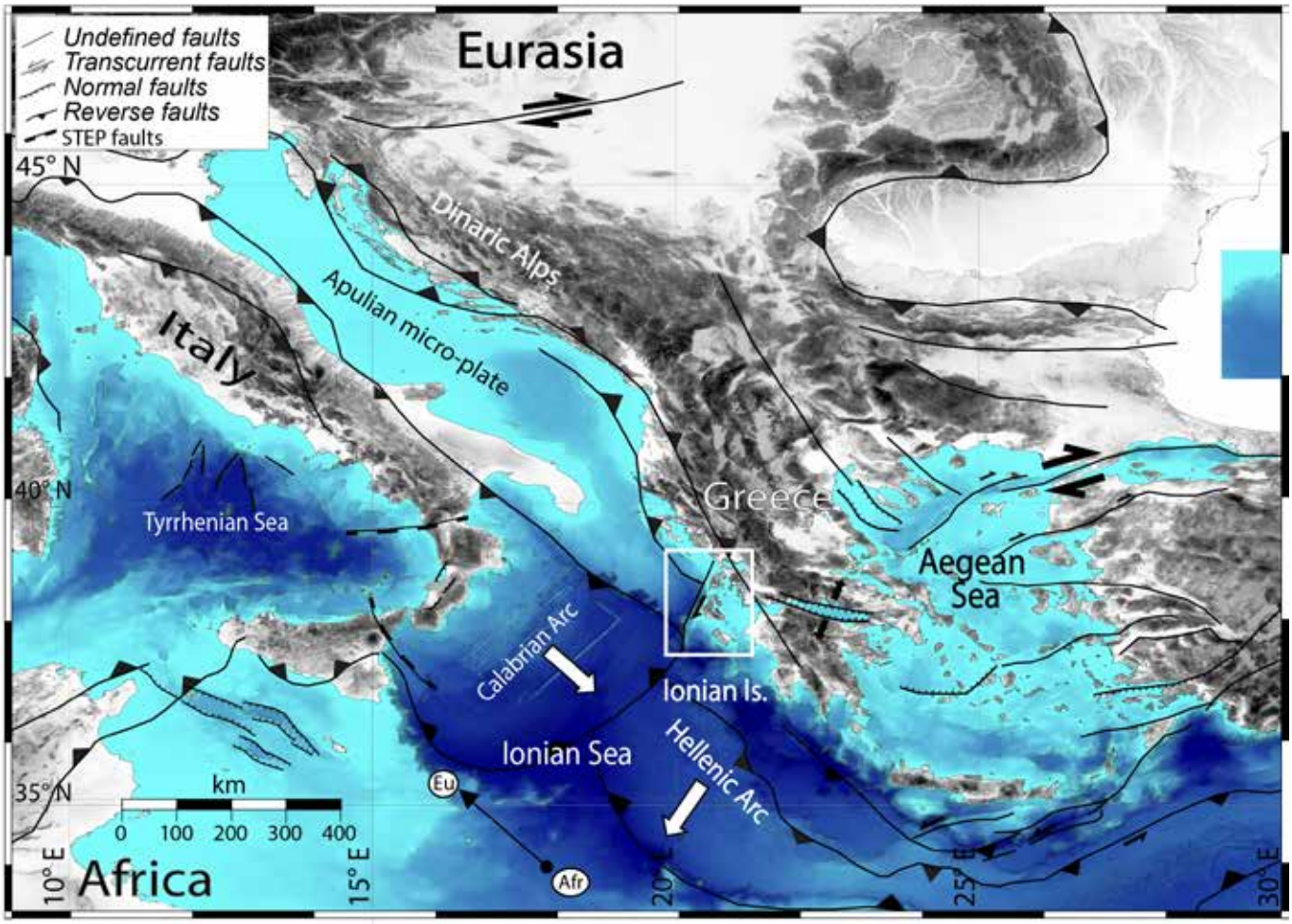

Figure 1. Tectonic map of the central Mediterranean with location of the study area (white box). Bathymetry data download from EMODnet portal https://emodnet.ec.europa.eu/en/bathymetry#bathymetryapproach) and gridded using GMT software (Wessel et al., 2019). Mediterranean structural sketch modified after an online Tectonic Map (Woudloper - Own work, CC BY-SA 1.0) and by Loreto et al., 2020. The Thick white arrows mark the migration of the active accretionary prisms; Black thick arrows mark the main cinematic of faults. Thin black arrow marks the convergence of Africa toward Eurasia. The map is represented in geographic coordinates on Mercator Projection.

A series of submarine channels and canyons have been mapped, most of them located off Lefkada and others along the slope of the elongated N-S ridge south of Cephalonia. Some of these channels

are interrupted or dislocated by the morphological scarp associated with the Cephalonia Fault System. Other canyons, but in smaller quantities, are found along the slope south of Zakynthos and west of the Peloponnese. Here, the numerous landslide scars that have been mapped show a regressive/erosive character. While south of Zakynthos there is a giant landslide with a scar more than 10 km-wide responsible for the intense erosion affecting the slope, which is further shaped by the presence of NE-SW oriented morphological scarps.

The internal basin, bounded by the Ionian Islands and Western Greece (Fig. 3), shows a few small randomly distributed ridges sometimes associated with evaporite upwelling other times associated with tectonic activity. However, the most interesting finding in this basin are the several huge landslides or body collapses buried under recent, Holocene, sediments. These landslide bodies are characterized by great internal chaos and intense gas/fluid release capable of deforming the overlying well-stratified sediments. Several gas/fluid upwellings have also been recorded in the sea strip between Cephalonia and Ithaca (Fig. 2), where they remain trapped under a well-identifiable layer, probably characterized by a lithology with low permeability.

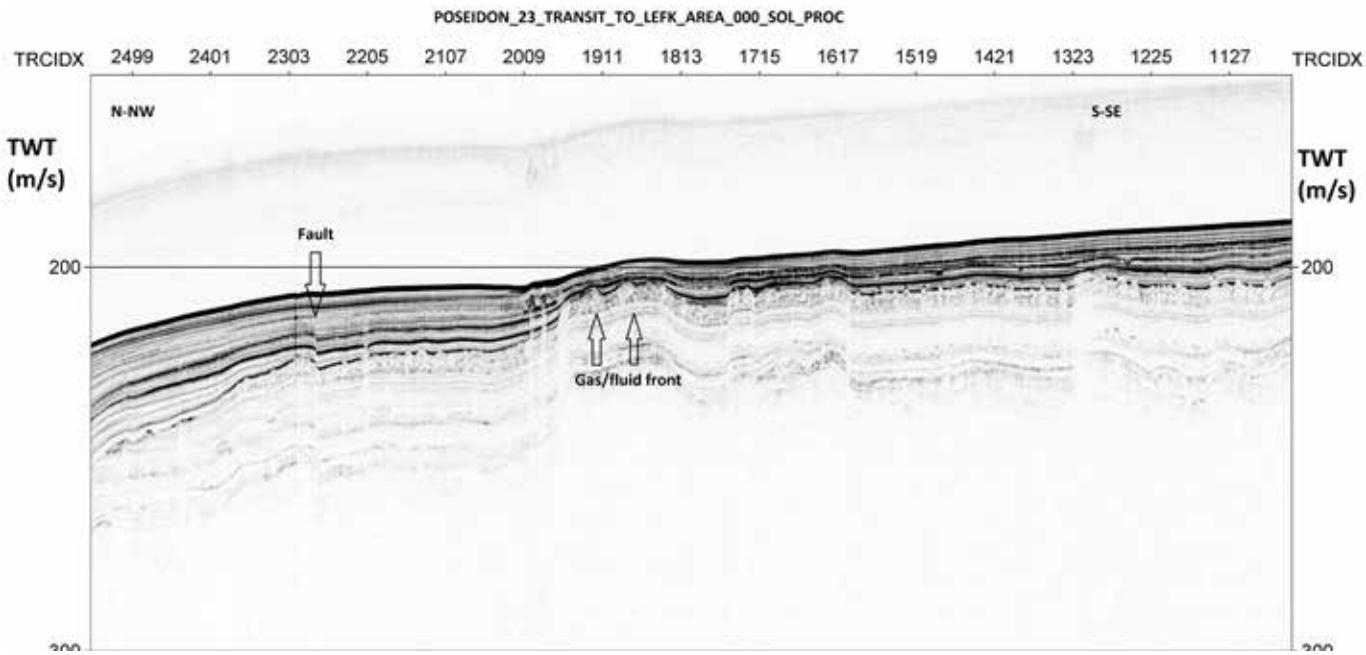

Figure 2. Section of a Chirp profile from data collected during POSEIDON 2023 oceanographic cruise. The fault highlighted on the left is recognizable because of the horizons' offset, while the gas/fluid bubbles can be identified because of whitening effect and of deformation they cause on the host layer.

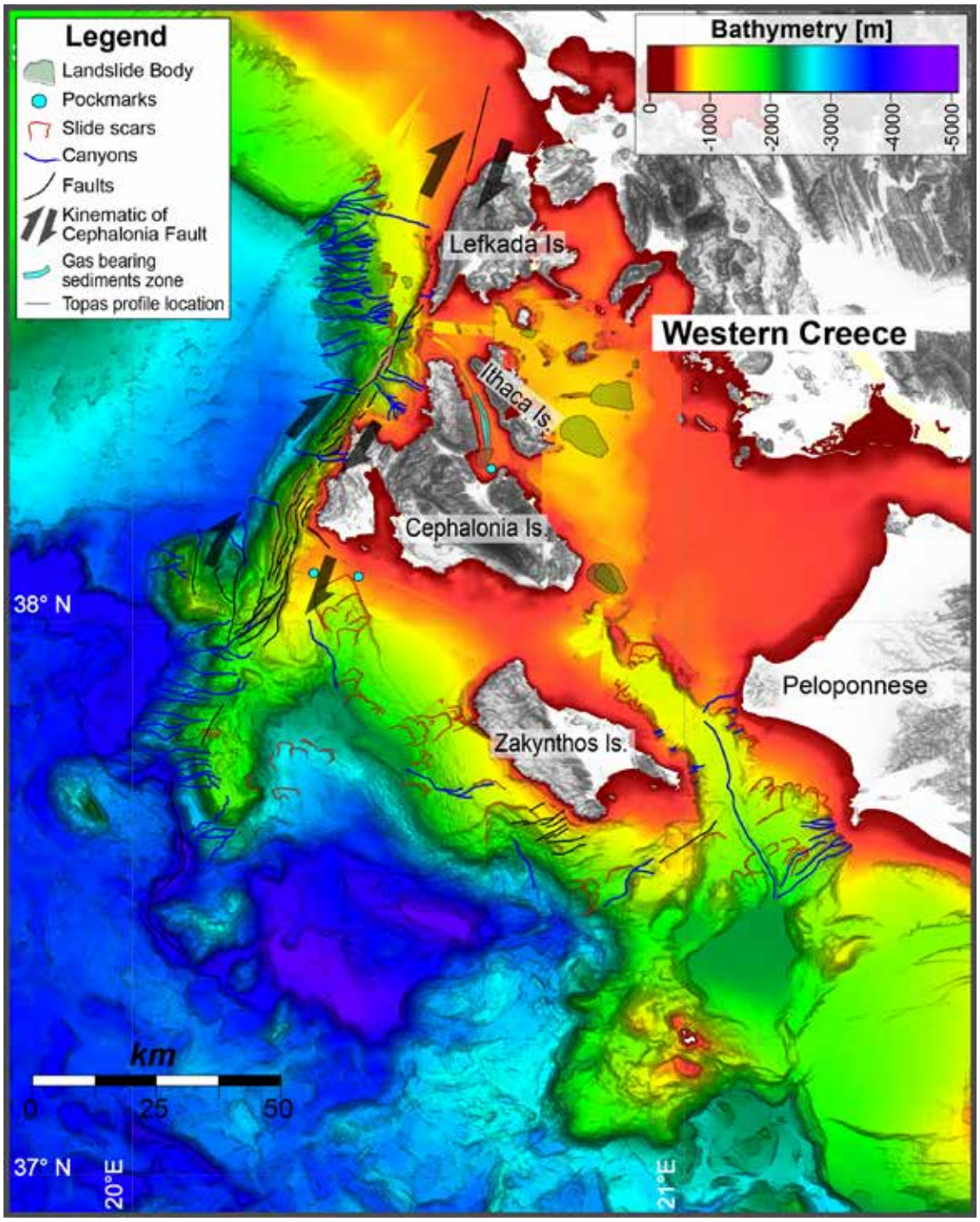

Figure 3. Morpho-bathymetric map of the Ionian Islands (Western Greece) showing the mapped morphological elements that can be associated with the geological hazard of the area. The most relevant hazard elements are represented by the Cephalonia Fault System, which delimits the western side of the islands of Cephalonia and Lefkada, and by the numerous locally large landslides that erode mainly the southern margin of Zakynthos and the Peloponnese. Furthermore, some canyon heads erode sediments very close the coastal line. Some pockmarks have also been mapped, witnessing the abundant gas that fills the shallow sediments. The bathymetry is a combination between EMODnet data (https://emodnet.ec.europa.eu /en/ bathymetry#bathymetry-approach) and the newly collected data during the Poseidon cruise.

Discussion

Based on the method described above, a map of the morphological features associated with geohazards in the offshore area of the Ionian Islands has been produced (Fig. 3). Based on this map, the area can be divided into two main zones: 1) the Kefalonia Transform Fault (CTF) zone and 2) the zone surrounding the island of Zakynthos.

The CTF zone is characterized by a steep slope (with maximum inclination of ca. 44° or 97%) shaped by a series of incisions that delimit small sigmoidal ridges, area south of Cephalonia (Fig. 3). The sigmoidal morphology has been associated with a series of positive flower-like structures bounded by strike-slip faults with a reverse component (Loreto et al., under review). The Cephalonia system becomes very broad to the south and deforms both sediments and rocks (Pre-Apulian unit), resulting in a 25 km-wide deformed area. West of Lefkada, the fault system changes its behavior becoming a single incision associated with a very well-defined morphological scarp (Fig. 3). Furthermore, this area is strongly incised by numerous channels and canyons, some of which are interrupted against the CTF system, others less evident are displaced by the CTF and where it has been possible to do the measurements the dislocation is approximately 500 m. The group of channels and canyons that are located to the north are set along a slope that delimits an anomalously deep plateau. This anomalous tendency of the plateau could be due to the tectonic activity of the Cephalonia fault. At the present stage the analyses carried out are not sufficient to provide the complete correlation between morphologies and tectonics, a step that will be developed in the future.

The surroundings of Zakynthos (zone 2; Fig. 3) are mainly affected by landslides with variable sizes ranging from hundreds of metres to tens of kilometres in scar width. The largest landslide, a giant landslide, located south of Zakynthos (Fig. 3) is in close correlation with the NE-SW oriented morphological steps mapped next to one its flank. These morphological steps have been associated with normal faults displacing sediments towards the southeast. The gravitational control on tectonics has been best explored in Loreto et al. (under review). Since this area is dominated by compressional tectonics, the gravitational instability here must be of enormous magnitude since it has also been recorded on land with earthquakes with normal kinematics (Kassars et al., 2016). Most of the faults inferred from morphological features on the seabed are active. The assessment of the seismogenic potential of these faults will be investigated at a later stage; here we want to drive the attention on the offshore morphological elements that have been mapped in this area for the first time.

Finally, the presence of gas-bearing sediments (Fig. 2) represents a significant risk for the surrounding areas. It has been observed along several margins that when gas accumulates in the sediments the shear strength is greatly reduced predisposing the slope to gravitational instability (Sultan et al., 2004). When the gas accumulated in the sediments is released into the water column it results in the formation of pockmarks (Hovland, 1989) which are frequently related to submarine landslides that can be triggered even in conditions of slope inclination lower than 1° (Kvalstad et al., 2005). Consequently, all the infrastructures installed offshore are exposed to high risk from landslides, sediment subsidence and gas explosion on the seabed (Hovland et al., 2002).

Summary

By combining bathymetric data from Emodnet with the new high-resolution swath bathymetry and comparing this map with the Topas profiles and high-resolution seismic profiles, we have mapped all geohazard elements affecting the area. From the northern part of Lefkada up to the southern part of Cephalonia, the 120 km-long Cephalonia transform fault has been completely mapped. A series of channels, channel heads, landslide scars and multiple slide deposits have been mapped all around the islands, at the continental slope and in the narrow inner basin between the island of Ithaca and the Peloponnese. This new dataset has revealed a seabed extremely shaped by faults, gravitational instabilities, channels and often tectonically-controlled channels, and adds a further step forward in the geological risk assessment of Western Greece.

Acknowledgements

Interpretation of all seismic data combined with morpho-bathymetry has been done using the Kingdom Suite software (S&P Global), freely available under the S&P Global University Grant Program. Geophysical data were collected during the IONIANS cruise supported by internal CNR funding (https://www.ismar.cnr.it/web-content/rapporto-tecnico-n-11/) and aboard of the R/V L. Bassi – INOGS during the POSEIDON cruise supported by the Eurofleet program (http://eurofleet.maris2.nl/cds-report/25). A thanks the the ISMAR-CNR institute of Bologna for hosting my internship.

References

Ganas, A., Briole, P., Bozionelos, G., Barberopoulou, A., Elias, P., Tsironi, V., ... & Mintourakis, I.; 2020: The 25 October 2018 Mw= 6.7 Zakynthos earthquake (Ionian Sea, Greece): A low-angle fault model based on GNSS data, relocated seismicity, small tsunami and implications for the seismic hazard in the west Hellenic Arc. Journal of Geodynamics, 137, 101731.

Hovland, M. (1989). The formation of pockmarks and their potential influence on offshore construction. *Quarterly Journal of Engineering Geology and Hydrogeology*, *22*(2), 131-138.

Hovland, M., Gardner, J. V., & Judd, A. G. (2002). The significance of pockmarks to understanding fluid flow processes and geohazards. *Geofluids*, *2*(2), 127-136.

Kvalstad, T. J., Andresen, L., Forsberg, C. F., Berg, K., Bryn, P., & Wangen, M. (2005). The Storegga slide: evaluation of triggering sources and slide mechanics. In *Ormen Lange–an integrated study for Safe Field development in the Storegga submarine area* (pp. 245-256). Elsevier.

Loreto, M. F., Zitellini, N., Ranero, C. R., Palmiotto, C., & Prada, M. (2021). Extensional tectonics during the Tyrrhenian back□arc basin formation and a new morpho□tectonic map. *Basin Research*, *33*(1), 138-158.

Loreto, M.F., Ferrante, V., Ligi, M., Muccini, F., Palmiotto, C., Petracchini, L., Romano, S., Ganas, A., Argnani, A., Conti, A., Cuffaro, M., Kothri, S., Lampridou, D., Merino, I., Ranero, R.C. and Nomikou, P. Anatomy of the Right-Lateral Strike-Slip Cephalonia Fault to the Western Hellenic Arc Frontal Thrust. *Under review in Tectonics*.

Stiros, S. C., P. A. Pirazzoli, J. Laborel, F. Laborel-Deguen, 1994. The 1953 earthquake in Cephalonia (Western Hellenic Arc): coastal uplift and halotectonic faulting, Geophysical Journal International, Volume 117, Issue 3, Pages 834–849, https://doi.org/10.1111/j.1365-246X.1994.tb02474.x

Wessel, P., Luis, J. F., Uieda, L., Scharroo, R., Wobbe, F., Smith, W. H. F., & Tian, D. (2019), The Generic Mapping Tools Version 6, *Geochemistry, Geophysics, Geosystems*, 20(11), 5556–5564. https://doi.org/10.1029/2019GC008515

17th INTERNATIONAL CONGRESS of the Geological Society of Greece

BULLETIN OF THE GEOLOGICAL SOCIETY OF GREECE, SP. PUBL.

EXTENDED ABSTRACT 030

Assessing earthquake-triggered tsunami hazard in Santorini-Amorgos Tectonic Zone: A deterministic simulation-based approach

Batzakis D.-V.[1], Karymbalis E.[1], Tsanakas K.[1]
(1) Department of Geography, Harokopio University, Athens, Greece, mpatzakis@hua.gr

Introduction

The Aegean region is shaped by the dynamic interactions caused by tectonic plate kinematics. To the north, the Aegean is bounded by the North Anatolian Fault (NAF), the major strike-slip fault that accommodates the westward motion of the Anatolian microplate at a rate of about 2.4 cm/year (Taymaz *et al.*, 2007). The Hellenic subduction zone defines the southern boundary, where the African plate subducts beneath the Aegean microplate at a rate of 0.9 cm/year (Andinisari *et al.*, 2021, and references therein). This process, combined with the westward extrusion of Anatolian microplate, drives the southward retreat of the Aegean microplate at an estimated rate of around 3.5 cm/year (Andinisari *et al.*, 2021, and references therein), resulting in extensive crustal deformation, the development of diverse tectonic and volcanic structures, and various faulting mechanisms in the broader region (Papazachos & Kiratzi, 1996). The south Aegean is characterized by an extensional deformation environment driven by the rollback of the subducting slab (Sachpazi *et al.*, 2016), where crustal stretching leads to the formation of numerous normal faults (Papazachos *et al.*, 1999). This ongoing extensional regime is associated with the presence of active tectonic zones with high seismicity accompanied by the evolution of volcanic centers (Hooft *et al.*, 2017). One of the most distinctive zones is the Santorini-Amorgos Tectonic Zone (SATZ), a geodynamically complex area influenced by subduction processes and extensional tectonics. It is characterized by active faulting, significant seismic activity, and the presence of volcanic centers (Nomikou *et al.*, 2018).

In the early months of 2025, a notable seismic activity was recorded in the area between the islands of Santorini and Amorgos. From January 25 to March 6, more than 4,000 earthquakes were documented, with the largest event reaching a magnitude of 5.3 (IG-NOA, 2025). The high frequency and the magnitude of these earthquakes raised concerns regarding the potential for a stronger earthquake, particularly given the region's complex tectonic setting and its history of significant seismic events. Furthermore, the possibility of a tsunami generated by a major earthquake heightened these concerns, considering the region's experience with such events. This study aims to assess the tsunami hazard in the SATZ by simulating earthquake-triggered tsunami waves. A deterministic approach is adopted, developing worst-case earthquake scenarios based on the dimensions and characteristics of the major active faults within the tectonic zone. Using simulation techniques, the propagation and inundation extent of earthquake-triggered tsunamis are calculated, providing insights into the potential impact of the waves on specific coastal areas of the surrounding islands.

Study Area

The SATZ is located in the South Aegean Sea, bordered by the islands of Santorini, Ios, Amorgos, Astypalaea, and Anafi. It is a seismically active structure that marks the transition from the relatively quiescent western part of South Aegean to the highly active eastern part (Bohnhoff *et al.*, 2006). Recent seismic reflection and bathymetric data revealed that the SATZ is a structural feature composed of tectonic grabens and horsts, formed by the presence of several major and minor faults oriented in a NE-SW direction (Nomikou *et al.*, 2018; Tsampouraki-Kraounaki *et al.*, 2021). Crustal deformation in the zone is mainly dominated by several major faults which control the development of graben-horst structures (Nomikou *et al.*, 2018). These faults exhibit varying dip angles and are characterized by significant fault throws, indicating normal faulting (Nomikou *et al.*, 2016; Nomikou *et al.*, 2018; Preine *et al.*, 2020). However, a right-lateral strike-slip component has been observed, suggesting a trans-tensional stress in the area (Heath *et al.*, 2019; Tsampouraki-Kraounaki *et al.*, 2021, and references therein).

In recent times, the SATZ experienced significant seismic activity, including the M_w ~6 events in 1911 and 1919 (Andinisari *et al.*, 2021). The most prominent event was the 1956 M_w 7.8 earthquake along the Amorgos Fault (AmF), which triggered a tsunami that caused significant run-up along the coasts of the surrounding islands, although the exact source mechanism remains debated (Okal *et al.*, 2009). The major faults within the SATZ include the Ios Fault

Zone (IF) and Amorgos Fault (AmF), which extend across the northern part; the Santorini-Anafi Fault (SAF) and Anydros Fault (AF) located in the central part; and the Anafi-Astypalaea Fault Zone (AnF-AsF), across the southern margin of the SATZ (Figure 1). AmF and SAF exhibit southeastward dipping, IF exhibits southwestward dipping, while AF and AnF-AsF show opposite polarity with northwestward dipping motion (Tsampouraki-Kraounaki *et al.*, 2021). Apart from the AF, these faults are sufficiently long to generate earthquakes of $M_w \geq 7$ (Leclerc *et al.*, 2024).

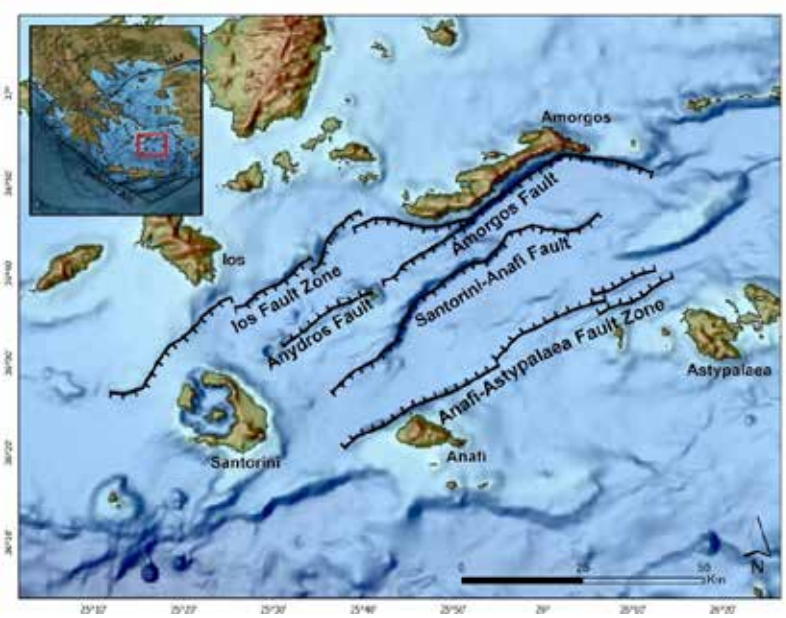

Figure 1. Map of the major active faults in the Santorini-Amorgos Tectonic Zone (modified after Leclerc *et al.*, 2024; Nomikou *et al.*, 2018; Tsampouraki-Kraounaki *et al.*, 2021).

Methodology

Seismic events along the major faults were considered, to analyze the propagation patterns and the potential impact of earthquake-triggered tsunamis within the SATZ. Moreover, five coastal areas hosting settlements—Kamari and Perissa in Santorini, Katapola in Amorgos, Gialos in Ios, and Chora in Astypalaea—were selected for hazard assessment due to their touristic development, extensive human activities, and the presence of critical infrastructure, that make them particularly exposed to tsunami.

The MOST (Method of Splitting Tsunami) numerical model, implemented through ComMIT (Community Model Interface for Tsunamis) modelling framework developed by NOAA, is employed to simulate tsunami generation, propagation, and onshore inundation (Titov *et al.*, 2011). ComMIT utilizes three nested computational topo-bathymetric grids for tsunami simulation. Two coarser grids, which cover broader areas, are used to calculate the initial conditions and the wave propagation in the open sea. A third finer grid, which covers the coastal area, is used to perform the inland penetration calculations. For the coarser grids, topo-bathymetric data from the General Bathymetric Chart of the Oceans (GEBCO-2024), with a resolution of approximately 375 m, were utilized. For the finer grid, a detailed elevation dataset with a resolution of 5 m was used. This dataset was created by combining the 5 m resolution topographic data provided by the Hellenic Cadastre with the bathymetric data from Navionics nautical charts, which have a resolution ranging from 10 m in the nearshore zone to 50 m in deeper offshore areas. The data processing was conducted using GIS software to generate a seamless elevation model for the coastal areas of interest. Adjustments to the coarser grids were performed based on the finer grid to improve their accuracy in the coastal areas under study, where the tsunami impact will be assessed, utilizing the Map Algebra tools in GIS software.

The seismic source mechanism parameters required for the initial phase of tsunami generation were obtained from studies conducted in the SATZ, where bathymetric and seismic data have been presented and analyzed (Nomikou *et al.*, 2016; Nomikou *et al.*, 2018; Tsampouraki-Kraounaki *et al.*, 2021). The fault length and strike used in the simulation were derived from the fault trace as mapped in the study area. The fault width (W) was calculated as W

= H / sinδ, where H is the thickness of the seismogenic layer, assigned a value of 12.5 km according to Andinisari *et al*. (2021), and δ is the average fault dip angle, estimated from the values provided in the aforementioned studies. The magnitude of the potential earthquake was estimated using the regression equation correlating the M_w with the rupture area (S) of the fault, while the mean displacement (u) was calculated using the regression equation that correlates M_w with u, as proposed for dip-slip continental faults by Papazachos *et al.* (2004). Furthermore, it was assumed that the faults would rupture along their entire length, with IF and AnF-AsF considered as a single fault. These estimations were obtained by applying Equations (1) and (2), respectively.

$$\log(S)=0.78M_w-2.56 \quad (1)$$

$$\log(u)=0.72M_w-2.28 \quad (2)$$

A depth of 10 km was assigned to the potential earthquake for all the faults, based on observations of recent seismicity in the SATZ (IG-NOA, 2025). The epicenter of the earthquake was defined as the midpoint of the fault length, and the distance (d) from the fault trace was calculated as d = D / tanδ, where D is the earthquake depth. A rake value of -135° was used, consistent with the NOA fault catalog for the AmF (Ganas *et al.*, 2013), adopting a normal right-lateral oblique slip for the faults. All the parameters used in the simulations are listed in Table 1 and the fault planes are represented in Figure 2. The results were overlaid on a satellite imagery basemap using GIS to visualize the extent of inundation and calculate the run-up.

Table 1. Seismic source parameters used for tsunami simulation calculations.

Seismic source	Earthquake epicenter (°)		Length (km)	Width (km)	Rupture area (km²)	M_w	Depth (km)	Mean displacement (m)	Strike (°)	Dip (°)	Rake (°)
	Latitude	Longitude									
Ios Fault Zone	36.54925	25.50823	55	17.7	973	7.11	10	2.00	48	45	-135
Amorgos Fault	36.77155	25.93779	40	16.3	652	6.89	10	1.38	48	50	-135
Anydros Fault	36.64383	25.51760	20	17.7	354	6.55	10	0.79	235	45	-135
Santorini-Anafi Fault	36.64002	25.90768	60	15.2	912	7.08	10	1.89	45	55	-135
Anafi-Astypalaea Fault Zone	36.57636	25.90581	65	15.2	988	7.12	10	2.03	237	55	-135

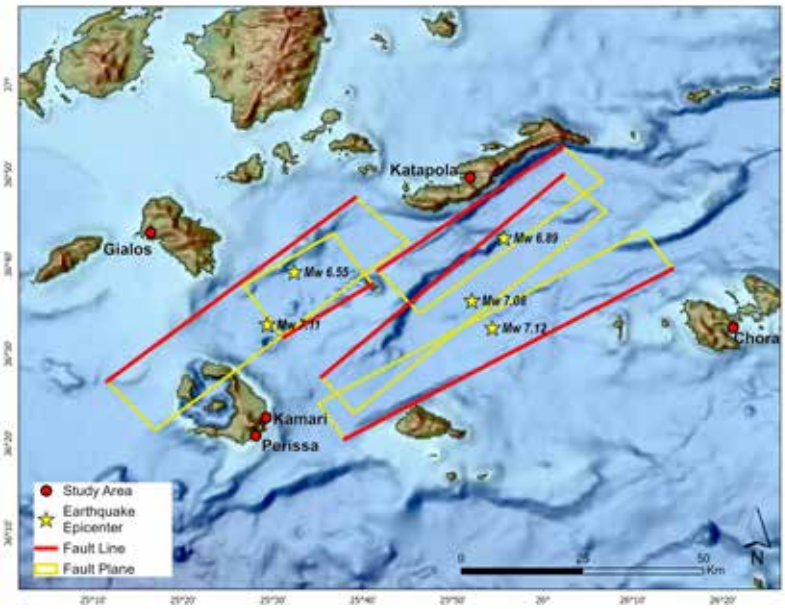

Figure 2. Map of the selected tsunamigenic earthquake sources and study areas. The rectangles represent the surface projection of the fault planes used in this study for tsunami simulations.

Results

The numerical simulations illustrated the generation and propagation of tsunami waves triggered by the five selected earthquake scenarios (Figure 3). The computed initial wave amplitude fields revealed the sea surface displacement, which corresponds to the uplift and subsidence associated with each seismic event. The main wave direction and the maximum observed amplitudes were aligned with the fault strike, primarily propagating toward the northwest and southeast. The wavefront time frames also captured the interactions with underwater features which create bathymetric variations, influencing tsunami propagation. Notably, the Anydros horst, which hosts Anydros Islet in the central-western part of the SATZ, plays a significant role in wave diffraction. These bathymetric variations, along with coastal morphology, impact the wave refraction and amplification, especially in the nearshore zone. The highest wave heights, reaching up to 2.5–3 m, were observed near the southern coasts of Ios and the western coasts of Astypalaea, generated by the largest earthquake scenarios of IF, SAF and AnF-AsF.

Table 2 summarizes the estimated tsunami arrival times at the study areas for each tsunamigenic source, measured in minutes after the earthquake. The arrival times range from several minutes to tens of minutes, with variations due to the proximity of each study area to the respective fault. Among the study areas, Perissa and Chora experienced the fastest tsunami arrival following an earthquake along the AnF-AsF, and Kamari after an earthquake along the AF, with waves reaching the coast in just 10 minutes. In contrast, the longest arrival time of 40 minutes was observed in Chora following an earthquake along the IF.

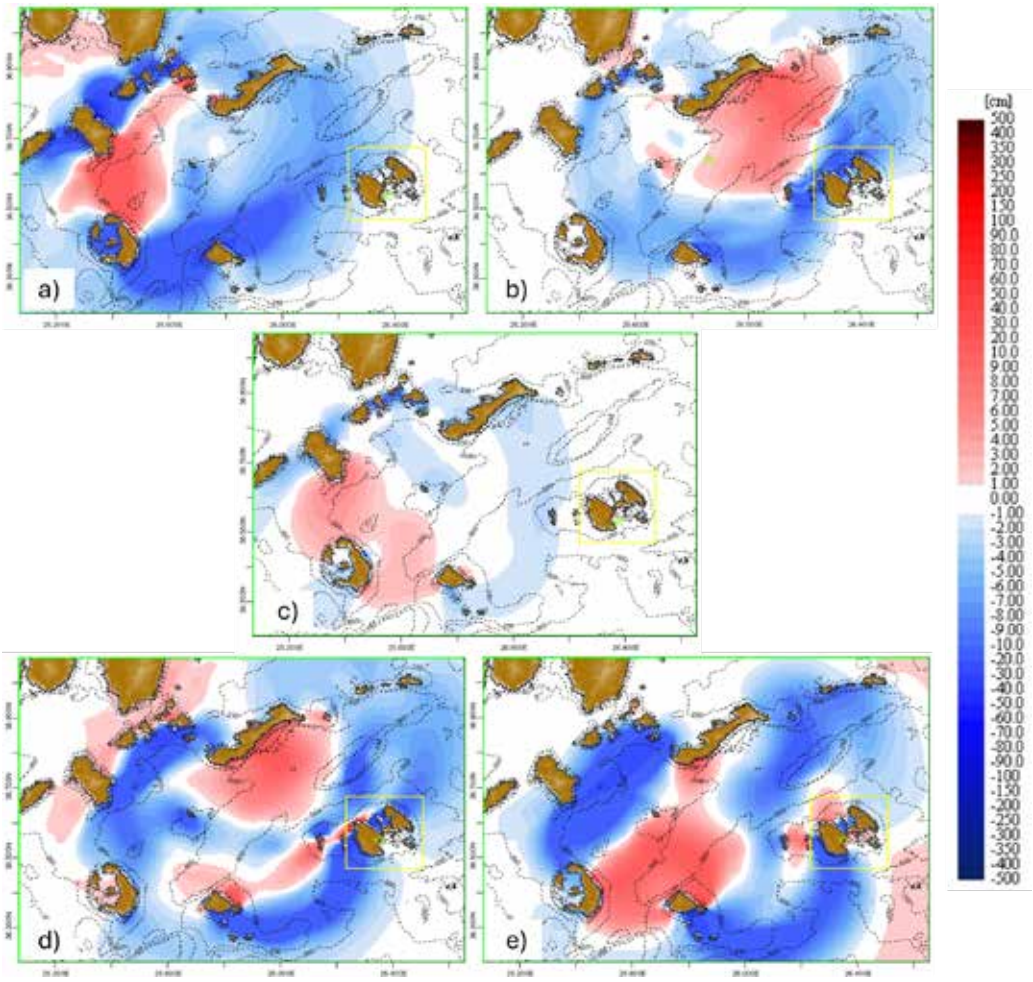

Figure 3. Wave propagation and amplitude distribution for the seismic sources along: a) IF, b) AmF, c) AF, d) SAF, and e) AnF-AsF, shown as snapshots approximately 10 minutes after the seismic events.

Table 2. Tsunami arrival times for each seismic source at the study areas, measured in minutes following the seismic events.

Seismic source	Calculated arrival times (in minutes after the seismic event)				
	Gialos	Katapola	Kamari	Perissa	Chora
Ios Fault Zone	15	25	20	25	40
Amorgos Fault	30	15	20	25	30
Anydros Fault	25	25	10	15	35
Santorini-Anafi Fault	30	35	20	25	30
Anafi-Astypalaea Fault Zone	30	35	15	10	10

The tsunami simulations also provided insights into the extent of coastal inundation and the run-up in the studied coastal areas. The run-up values varied across the five coastal areas, reflecting both the magnitude of the seismic events and the coastal morphology (Table 3). The IF, SAF and AnF-AsF scenarios consistently produced higher run-up values in most study areas. Specifically, IF resulted in the highest run-up value in Gialos, while AnF-AsF produced the highest run-up in Ghora, with both areas experiencing a maximum run-up of 2.8 m. The SAF and AnF-AsF also exhibited high run-up values along the eastern coast of Santorini, with maximum run-ups of 2.4 m observed in Kamari and 2.2 m in Perissa. High run-up values of 2.3 m were observed in Gialos, resulting from the AnF-AsF scenario, and 2.1 m in Gialos and Chora from the SAF. The highest run-up from the AmF was recorded in Perissa, with a value of 1.8 m, followed by 1.5 m in Gialos. The AF appeared to generate the smallest run-up, with values of 0.4–0.6 m observed in Kamari, Perissa, and Gialos. This suggests that the fault may not produce large tsunamis due to its smaller size. Figure 4 illustrates the maximum inundation extent and corresponding flow depth values in the study areas for the various seismic scenarios.

Overall, the observed tsunami inundation extent and run-up values in the selected study areas are not substantial enough to cause a major disaster. However, in Gialos (Ios), Katapola (Amorgos), and Chora (Astypalaea), the inundation flows extend into the coastal zone, affecting the residential zone. Notably, these coastal settlements also host the main ports of the islands, meaning that a potential tsunami could exacerbate a seismic crisis by disrupting critical infrastructure used for emergency response efforts. In Kamari and Perissa, Santorini, the inundation does not appear to extend beyond the coastal front, possibly resulting in large waves along the shoreline without extensive inland penetration.

Table 3. Observed run-up values (in meters) in the study areas for the various seismic sources. N/A indicates no observed run-up.

Seismic source	Observed run-up values (in meters)				
	Gialos	Katapola	Kamari	Perissa	Chora
Ios Fault Zone	2.8	2.3	1.6	1.4	0.8
Amorgos Fault	1.5	1.3	1.4	1.8	0.6
Anydros Fault	0.4	N/A	0.6	0.5	N/A
Santorini-Anafi Fault	2.1	1.9	2.4	2.2	2.1
Anafi-Astypalaea Fault Zone	2.3	1.4	2.4	2.2	2.8

Figure 4. Maximum observed inundation extent in the study areas for the various seismic sources considered in the simulation scenarios: a) Gialos, Ios b) Katapola, Amorgos c) Kamari and d) Perissa, Santorini and e) Chora, Astypalaea. The associated fault is indicated in the map legends.

Concluding Remarks

The study assessed the earthquake-triggered tsunami hazard within the Santorini-Amorgos Tectonic Zone by examining worst-case scenarios. Through simulations of tsunami wave generation, propagation, and inundation from various well-documented seismic sources, the results demonstrated significant variations in tsunami arrival times across the study areas, ranging from just a few minutes to over 40 minutes, depending on proximity to the seismic sources. The observed inundation extent and run-up values indicated localized impact, with a maximum run-up of 2.8 m recorded at Gialos (Ios) and Chora (Astypalaea), and 2.3 m at

Katapola (Amorgos) potentially affecting residential zones and the main ports of these islands. In contrast, Kamari and Perissa (Santorini) experienced a maximum observed run-up of 2.4 and 2.2 m, respectively, with the inundation extending only slightly beyond the coastline. Although earthquake-triggered tsunamis pose a potential hazard, the results suggested that these events are unlikely to lead to a disaster in the study areas.

References

Andinisari, R., Konstantinou, K. I., Ranjan, P., 2021. Seismicity along the Santorini-Amorgos zone and its relationship with active tectonics and fluid distribution. Physics of the Earth and Planetary Interiors, 312, 106660.

Bohnhoff, M., Rische, M., Meier, T., Becker, D., Stavrakakis, G., Harjes, H. P., 2006. Microseismic activity in the Hellenic Volcanic Arc, Greece, with emphasis on the seismotectonic setting of the Santorini-Amorgos zone. Tectonophysics, 423(1–4), 17–33.

Ganas, A., Oikonomou, I. A., Tsimi, C., 2013. Noafaults: a digital database for active faults in Greece. Bulletin of Geological Society of Greece, 47(2), Chania, Greece, p. 518.

General bathymetric Chart of the Oceans (GEBCO), Gridded Bathymetry Data-2024, available at: https:// https://download.gebco.net/

Heath, B. A., Hooft, E. E. E., Toomey, D. R., Papazachos, C. B., Nomikou, P., Paulatto, M., Morgan, J. V., Warner, M. R., 2019. Tectonism and Its Relation to Magmatism Around Santorini Volcano From Upper Crustal P Wave Velocity. Journal of Geophysical Research: Solid Earth, 124(10), 10610–10629.

Hooft, E. E., Nomikou, P., Toomey, D. R., Lampridou, D., Getz, C., Christopoulou, M. E., O'Hara, D., Arnoux, G. M., Bodmer, M., Gray, M., Heath, B. A., VanderBeek, B. P., 2017. Backarc tectonism, volcanism, and mass wasting shape seafloor morphology in the Santorini-Christiana-Amorgos region of the Hellenic Volcanic Arc. Tectonophysics, 712, 396–414.

Institute of Geodynamics-National Observatory of Athens, 2025. Observations and preliminary results on the seismic sequence between Santorini and Amorgos, available at: https://www.emsc.eu/Special_reports/?id=351

Leclerc, F., Palagonia, S., Feuillet, N., Nomikou, P., Lampridou, D., Barrière, P., Dano, A., Ochoa, E., Gracias, N., Escartin, J., 2024. Large seafloor rupture caused by the 1956 Amorgos tsunamigenic earthquake, Greece. Communications Earth and Environment, 5(1), 663.

Nomikou, P., Hübscher, C., Papanikolaou, D., Farangitakis, G. P., Ruhnau, M., Lampridou, D., 2018. Expanding extension, subsidence and lateral segmentation within the Santorini-Amorgos basins during Quaternary: Implications for the 1956 Amorgos events, central - south Aegean Sea, Greece. Tectonophysics, 722, 138–153.

Nomikou, P., Hübscher, C., Ruhnau, M., Bejelou, K., 2016. Tectono-stratigraphic evolution through successive extensional events of the Anydros Basin, hosting Kolumbo volcanic field at the Aegean Sea, Greece. Tectonophysics, 671, 202–217.

Okal, E. A., Synolakis, C. E., Uslu, B., Kalligeris, N., Voukouvalas, E., 2009. The 1956 earthquake and tsunami in Amorgos, Greece. Geophysical Journal International, 178(3), 1533–1554.

Papazachos, B. C., Papaioannou, C. A., Papazachos, C. B., Savvaidis, A. S., 1999. Rupture zones in the Aegean region. Tectonophysics 308(1-2), 205–221.

Papazachos, B. C., Scordilis, E. M., Panagiotopoulos, D. G., Papazachos, C. B., Karakaisis, G. F., 2004. Global relations between seismic fault parameters and moment magnitude of earthquakes. Bulletin of the geological society of Greece, 36(3), Thessaloniki, Greece, p. 1482.

Papazachos, C. B., Kiratzi, A. A., 1996. A detailed study of the active crustal deformation in the Aegean and surrounding area. Tectonophysics 253(1-2), 129–153.

Preine, J., Schwarz, B., Bauer, A., Hübscher, C., 2020. When There Is No Offset: A Demonstration of Seismic Diffraction Imaging and Depth-Velocity Model Building in the Southern Aegean Sea. Journal of Geophysical Research: Solid Earth, 125(9), 1–19.

Sachpazi, M., Laigle, M., Charalampakis, M., Diaz, J., Kissling, E., Gesret, A., Becel, A., Flueh, E., Miles, P., Hirn, A., 2016. Segmented Hellenic slab rollback driving Aegean deformation and seismicity. Geophysical Research Letters, 43(2), 651–658.

Taymaz, T., Yilmaz, Y., Dilek, Y., 2007. The geodynamics of the Aegean and Anatolia: Introduction. In Taymaz, T., Yilmaz, Y., Dilek, Y. (Eds), The Geodynamics of the Aegean and Anatolia. Geological Society Special Publication 291, 1–16.

Titov, V. V., Moore, C. W., Greenslade, D. J. M., Pattiaratchi, C., Badal, R., Synolakis, C. E., Kânoğlu, U., 2011. A New Tool for Inundation Modeling: Community Modeling Interface for Tsunamis (ComMIT). Pure and Applied Geophysics, 168(11), 2121–2131.

Tsampouraki-Kraounaki, K., Sakellariou, D., Rousakis, G., Morfis, I., Panagiotopoulos, I., Livanos, I., Manta, K., Paraschos, F., Papatheodorou, G., 2021. The Santorini-Amorgos shear zone: Evidence for dextral transtension in the south Aegean back-arc region, Greece. Geosciences, 11, 126, 1–36.

17th INTERNATIONAL CONGRESS of the Geological Society of Greece

BULLETIN OF THE GEOLOGICAL SOCIETY OF GREECE, SP. PUBL.

EXTENDED ABSTRACT 031

Oceanographic survey M192 off Milos reveals tectonic controls on hydrothermal vent distribution in a complex volcanic-tectonic system of the South Aegean

Bejelou K.[1], Nomikou P.[1], Bühring S.[2], Papanikolaou D.[1], Kilias S.[1], Koschinsky A.[3], Bach W.[2], Haase K.[4], Ferreira C.[2], Bazhenova E.[2], Bach A.[2], Azakura Y[2], Lampridou D.[1], Belka A.[1], Anagnostou E.[3], Varotsou E.[1], Kothri S.[1]

(1) National and Kapodistrian University of Athens, Athens, Greece (2) MARUM – Center for Marine Environmental Sciences, University of Bremen (3) Constructor University, Bremen, Germany (4) Friedrich-Alexander-Universität Erlangen-Nürnberg

Introduction

Milos is located at the southwestern edge of the Cyclades islands in the Aegean Sea, Greece, and is part of the South Aegean Volcanic Arc (Pe-Piper, et al., 2005). The island's geological history includes volcanic activity from the Late Pliocene to the Early Pleistocene, with the last subaerial eruption occurring around 80,000 years ago (Sonder, 1924; Fytikas, 1977; Fytikas, et al., 1986). Its tectonic background is characterized by alternating phases of extension and compression related to volcanic activity during the Pliocene-Pleistocene (Angelier, et al., 1977). The neotectonic and active faults of Milos have produced a block structure, characterized by the occurrence of specific stratigraphic formations in each block (Papanikolaou, et al., 1990). These faults have served as conduits for geothermal fluids, resulting in hydrothermal alteration of the adjacent volcano-sedimentary formations and giving birth to several exploitable ore deposits (Fytikas, 1989). The most active onshore vent fields are located in the Aghia Kiriaki area, along the eastern edge of the Fyriplaka Volcano, near the intersection of the NW-SE and ENE-WSW active faults. As for the offshore domain, extensive hydrothermal venting has been documented in Paleochori, Adamas Bay and Voudia Bay (Dando, et al., 1995; Dando, et al., 2000). Specifically, in Paleochori area, from shore up to depths of almost 500 m, hydrothermal venting is manifested through emissions of gases and high-temperature fluids, often associated with bacterial mats and/or hydrothermal mineral precipitates (Puzenat, et al., 2021).

Highly dominant tectonic features are two major fault zones bounding the central block of the Milos – Fyriplaka tectonic graben, which hosts the Fyriplaka volcanic crater and numerous vent fields both onshore and offshore (Papanikolaou, et al., 1990). Seismic activity, such as the earthquake of 5.2 ML on March 20, 1992, in the southeastern part of the graben, caused extended impacts, including structural damage on buildings, seismic fractures, variations in intensity and temperature of gas emissions, landslides, rockfalls and liquefaction phenomena (Papanikolaou et al., 1993). A recent study has confirmed ongoing seismic and ground deformation along a NW-SE, east-dipping fault on Milos Island, through microseismicity recordings, and InSAR data, showing a significant ground motion of up to 1 cm/yr across the fault (Ganas et al., 2022).

This study combines geodynamic constraints with high-resolution geophysical data to determine the influence of tectonic processes over the distribution of hydrothermal vent fields on the continental shelf around Milos as well as their evolution in relation to sea-level changes particularly since Middle Pleistocene, with the most recent lowstand averaging around 130 m in depth (Seibold & Berger, 1993), thus documenting the interconnection of hydrothermal activity associated with volcanism, tectonics and climatic fluctuations both onshore and offshore.

Data collection and Methodology

The cruise M192, conducted in August 2023 on board the RV Meteor investigated the area offshore Milos in terms of the geomorphology, geology, geochemistry and microbiology of marine hydrothermal systems in a transect from the shallow continental shelf, photic zone off Milos to the deep, offshore, aphotic zone (Bühring et al, 2024, Nomikou et al., 2025 under review). The mission was separated into 2 legs. The major aim of Leg 1 was the systematic mapping using the multibeam echosounder system of RV Meteor, the parasound system and the AUV (Autonomous Underwater Vehicle) MARUM-SEAL in expansive areas around Milos was performed during cruise M192 of R/V Meteor, 08 August – 05 September 2023. On the second leg (M192_2) the hydrothermal vent areas targeted during the first leg were systematically sampled by multicorer and identified with the ROV MARUM-SQUID.

Results and Discussion

Processing of the acquired bathymetric data revealed that the coastal zone around Milos features a distinct shelf and slope area separated by a shelf break, which varies in depth around the island (130-220m), being deeper and disrupted on the eastern side (Fig. 1). The shelf break depth varies due to tectonic deformation, from 130-150 m on the western block (consistent with pre-Holocene sea levels) to 170-220 m in the southeastern tectonic graben, reflecting active faulting. This survey also provided us with the first documentation of Hydrothermal Vent Fields (HVFs), related to volcanism in the modern Milos geothermal system, up to depths of about 220 m and confined within the continental shelf. The distribution of the discovered vent fields around Milos Island is highly selective at the SE and NW coastal zone covering a small percentage of the Milos offshore domain. The present study reveals that these vent fields illustrate a strong correlation between hydrothermal vent fields and active faults, highlighting the interplay between tectonics and geothermal activity. Some of the discovered vent fields are associated with the NW-SE Milos Gulf–Fyriplaka tectonic graben, which hosted the last volcanic eruption 80,000 years ago. Others align with E-W and WNW-ESE faults in southeastern Milos.

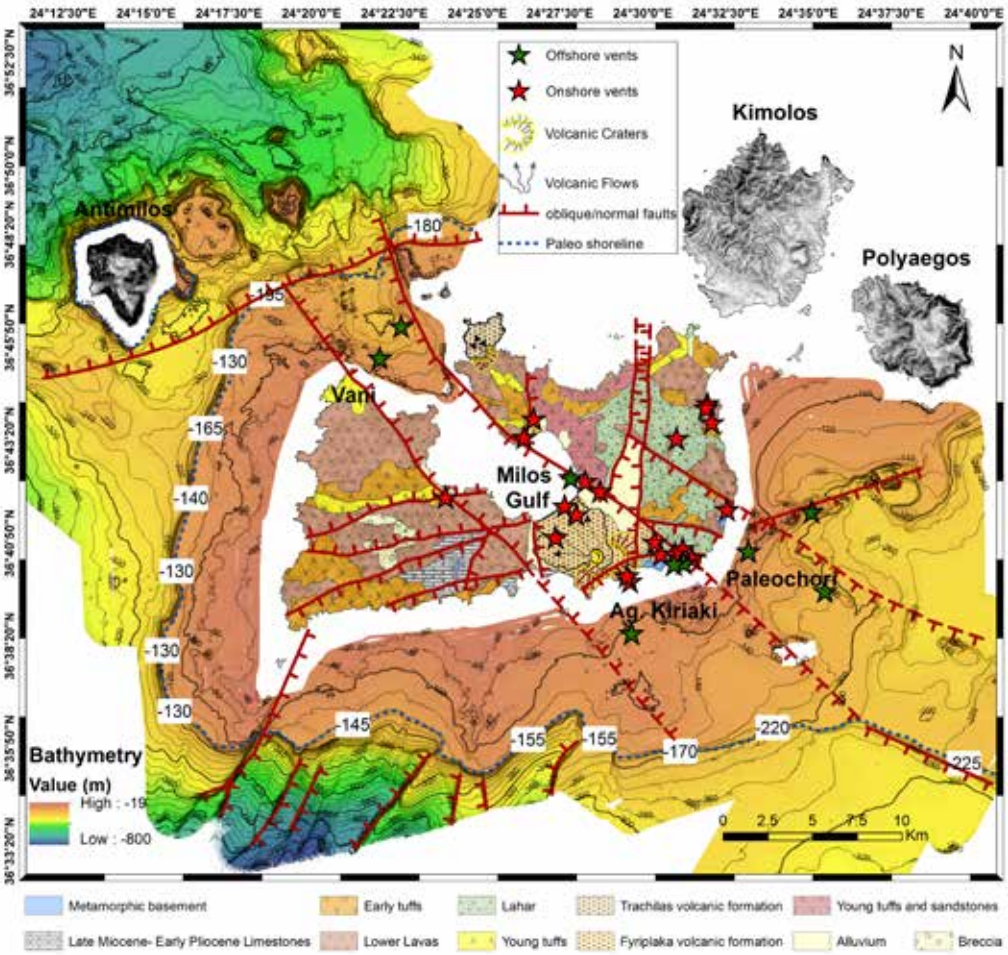

Figure 1. Synthetic tectonic map based on the swath data, the parasound seismic profiles acquired during the M192 expedition and the produced morphologic slope map. Onshore geologic map modified after Papanikolaou et al., 1990.

Two key tectonic features, the NW-SE Milos Gulf–Fyriplaka graben and the ENE-WSW fault system near Fyriplaka Volcano, separate the island's geothermal activity. The most active offshore vent fields occur at Paleochori (Puzenat, et al., 2021) along the southern coast, while Aghia Kiriaki (Fig. 1) hosts the primary onshore vent field at the intersection of active faults.

Depths of detected hydrothermal activity reveal distinct distributions varying in depth from 130 to 220 m. Despite this variation, the prevailing depth is around 110 m, with fewer hydrothermal manifestations beyond

150 m. The shelf break subsidence due to tectonic processes thus seem to strongly influence the location, depth, and activity of geothermal vent fields, with faults acting as conduits for hydrothermal fluids while leaving other regions inactive.

Notably, the E-W neotectonic faults of SW Milos and NE-SW trending faults on the SE slope do not extend onto the shelf and lack associated hydrothermal activity creating geothermal activity gaps.

Conclusions

The oceanographic research M192 around Milos, a young volcanic island in the South Aegean, revealed the offshore prolongation of the Milos major tectonic zones and their interconnection to high-temperature hydrothermal vents and continental shelf volcanism.

Hydrothermal activity has persisted beneath the Milos shelf since the Late Pleistocene, independent of active faulting, and continues today. This evolution reflects a combination of tectonic processes and climatic shifts, alternating between subaerial erosion during sea-level lowstands and submarine venting during highstands. These findings may apply to similar volcanic and geothermal systems in island arcs at convergent plate boundaries.

Acknowledgements

We are thankful to the METEOR-Berichte, Cruise M192, Pireus – Limassol, 08 August – 05 September 2023, the technical staff of the R/V METEOR, and all of the shipboard personnel for a great expedition. We also thank the member organizations of this cruise University of Bremen and MARUM for the financial aid and the supply of all the necessary equipment for preparing and completing the expedition. We would also like to acknowledge the contribution of the program IKYDA 2024: Bridging the Gap between hydrothermal biogeochemistry and Volcano-Tectonics: Exploring Synergies Along the Hellenic Arc off Milos (BITECHELL), for the promotion of the exchange and scientific cooperation between Greece and Germany.

References

Angelier, J, Cantagrel, J-M and Vilminot, J-C. 1977. Neotectonique cassante et volcanisme plio-quaternaire dans l'arc egeen interne; l'ile de Milos (Grece). *Bulletin de la Société Géologique de France.* 1977, Vols. S7-XIX, 1, pp. 119-124.

Bühring, S., Koschinsky, A., Bach, W., Elvert, M., Kleint, C., Kumawat, P., Maak, J., Meckel, E.-M., Nomikou, P., Röttgen, C., and Schefuß, E.: Discovery of a unique submarine hydrothermal system between shallow photic and deep dark sites around the Greek island of Milos (Aegean Sea, Greece), EGU General Assembly 2024, Vienna, Austria, 14–19 Apr 2024, EGU24-17022, https://doi.org/10.5194/egusphere-egu24-17022, 2024.

Dando, P.R., et al. 1995. Gas venting rates from submarine hydrothermal areas around the island of Milos, Hellenic Volcanic Arc. *Continental Shelf Research.* 1995, Vol. 15, 8.

Dando, P.R., et al. 2000. Hydrothermal studies in the Aegean Sea. *Physics and Chemistry of the Earth, Part B: Hydrology, Oceans and Atmosphere.* 2000, Vol. 25, 1, pp. 1-8.

Fytikas, Michael. 1977. Geological and Geothermal Study of Milos Island. 1977, Vol. XVIII, 1, p. 228.

Fytikas, Michael. 1989. Updating of the geological and geothermal research on Milos island. *Geothermics.* 1989, Vol. 18, 4, pp. 485-496.

Fytikas, Michael, et al. 1986. Volcanology and petrology of volcanic products from the island of Milos and neighbouring islets. *Volcanology and Geothermal Research.* 1986, Vol. 28, 3-4, pp. 297-317.

Ganas, Athanassios, Karakonstantis, Andreas, Kapetanidis, Vasilis, Tsironi, Varvara, Karamitros, Ioannis, Efstathiou, Eirini, Karasante, Ilektra and Kassaras, Ioannis. 2022. Ground deformation and microseismicity patterns onshore Milos, Cyclades, Greece. *Bull. Geol. Soc. Greece.* 2022, Sp. Publ. 10, pp. 663-664, ISBN: 978-960-98709-8-6.

Nomikou, P., Bejelou, K., Koschinsky, A, Ferreira, C., Papanikolaou, D., Lampridou, D., Kilias, S., Anagnostou, E., Elvert, Röttgen, Maak, Bach, A., Bach, Belka, A., Bazhenova, E., Haase, K., Kleint, Kothri, S., Kurahashi, Liao, Meckel, Pedre, Schäfer, Schefuss, Seidel, Varotsou, E., & Bühring S. 2025. Bimodal distribution of hydrothermal vent fields on the shelf platform reveals tectonic and sea-level controls. *Nature Geoscience.* Under review.

Papanikolaou, Dimitrios, Lekkas, Efthymis and Syskakis, D. 1990. Tectonic analysis of Milos geothermal field. *Bull. Geol. Soc. Greece.* 1990, Vol. 24, pp. 27-46.

Papanikolaou, D., Lekkas, E., Syskakis, D., & Adamopoulou, E. (1993). Correlation of neotectonic structures with the geodynamic activity in Milos during the earthquakes of March 1992. Bull. Geol. Soc. Greece, XXVIII/3, pp. 413-428.

Pe-Piper, Georgia and Piper, David. 2005. *The South Aegean active volcanic arc: Relationships between magmatism and tectonics.* [ed.] Michael Fytikas and Georges E. Vougioukalakis. s.l. : Elsevier Science, 2005. pp. 113-133. Vol. Developments in Volcanology. ISSN 1871-644X.

Puzenat, V., Escartín, J., Martelat, J., Barreyre , T., Le Moine Bauer, S., Nomikou, P., Gracias, N., Allemand, P., Antoniou, V., Coskun, O., Garcia, R., Grandjean, P., Polymenakou, P., Schouw, A., Vallicrosa, G., Vlasopoulos, O. 2021. Shallow-water hydrothermalism at Milos (Greece): Nature, distribution, heat fluxes and impact on ecosystems. *Marine Geology.* 2021, Vol. 438, p. 106521.

Seibold, E., & Berger, W. H. (1993). Sea Level Processes and Effects of Sea Level Changes. In The Sea Floor: An Introduction to Marine Geology (2nd edition ed., pp. 127--155). Berlin, Heidelberg: Springer Berlin Heidelberg. doi:10.1007/978-3-662-22519-6_6

Sonder, Richard August. 1924. Zur Geologie und Petrographie der Inselgruppe von Milos. *Zeitschrift für Vulkanologie.* 1924, 8, pp. 181-237. 29.

17th INTERNATIONAL CONGRESS of the Geological Society of Greece

BULLETIN OF THE GEOLOGICAL SOCIETY OF GREECE, SP. PUBL.

EXTENDED ABSTRACT 032

Storm Daniel flooding of Larissa City: embankments failure the aftermath

Belesis A.[1], Tsentzos I.[1] , Belesis M.[1], Koukouvelas I.K.[2]
1.Ermogenous 6, 41447 Larissa, Greece; abelesis1960@gmail.com
2 Department of Geology, University of Patras, 26504 Patras, Greece

Introduction

Storm Daniel was a catastrophic cyclone that became the costliest cyclone outside the North Atlantic Basin. The storm caused extensive flooding in Greece, Bulgaria, Turkey, and Libya. It was initiated on September 3rd, 2023, and on September 5th, the village of Zagora received 759 millimeters of rain (Kolios and Papavasileiou 2024). The storm flooded many villages in the low-lying area of Karditsa, in the Thessaly Plain, and towns and villages were blocked by water (Dimitriou *et al.* 2024; Kalafatis *et al.* 2024; Mavroulis *et al.* 2024).

In Larissa, after rains ended on 8th of September 2023, the water continued to rise as the Pineios River overflowed to reach 9.5 m, more than twice the typical level of 4 m. The Pineios River Basin in Thessaly occupies an area of about 11,000 km2 (Kalafatis *et al.* 2024). Its hydrologic basin is drained by the Pineios River, the third longest river in Greece at 213 km. Major tributaries of the river are the Malakassiotiko, Mourgkanis, Portaikos, Lithaios, Pamissos, Enipeas, and Titarisios, which all drain extensive meteorologically and geologically heterogeneous areas (Bathrellos *et al.* 2018).

Historical data shows that the Pineios River flooding at Larissa happens approximately every 25 years, primarily during winter (i.e. Bathrellos 2005; Bathrellos *et al.* 2018). These data indicate building damage and casualties in Larissa over the last centuries. Two of the most severe flooding events devastated the city in 1883 and 1901. Thus, to prevent the town from flooding in the 1930s, the BOOT company was entrusted to construct a riverbed for water diversion outside the city. Finally, this riverbed was finished by the Ministry of Public Works sometime after 1935. After WWII, in the 1950s, part of the Pineios water was returned to the old riverbed, with a controlled flow from a dam located west of Larissa City. The reactivation of the old riverbed was related to the city's craft economy during this period. The old riverbed remains active for aesthetic reasons and as a recreational area. In previous years, the Larissa area was included in the epicentral area of the Damasi 2021 earthquake. Two strong earthquakes of magnitudes 6.3 and 6.1, on March 3rd and 4th, respectively, happened during this earthquake while a long aftershock activity was also noticed (Koukouvelas *et al.* 2021; 2023 Sarchosis *et al.* 2022). During this seismic activity, the peak ground acceleration in Larissa was 0.16 g (Sarchosis *et al.* 2022). The study area is about 20-30 km SE of the two epicenters, respectively.

This work describes the embankments during the three days of flooding in Larissa City. For this reason, we provide field examples and descriptions to understand the embankments' problems and propose some improvements to their network along the Pineios River in Larissa's territory.

Material and methods

Immediately after the Daniel storm, on the 8th of September 2023, a sector of Larissa City came under the pressure of flooding due to the river overflow reaching 9.5 m. A series of embankments along the river came under pressure. We executed repeated fieldwork in an area characterized by meanders and two riverbeds, the old one flowing through the city and the post-1935 riverbed flowing a few hundred meters north of the old one (Figure 1). During the fieldwork, we mapped overtopping, piping, seepage, and foundation defects. Furthermore, we used Google Earth scenes after the flooding to define the results of embankment failure and to measure the dimensions of the embankments approximately.

Figure 1. Google Earth scene showing the study area, showing localities of embankment problems in close proximity with the Larissa City. Inset shows the location of the study area in Greece.

Data

Five embankment sites were analyzed in detail because these localities caused severe flooding (Figure 1). Embankments, or levees or dykes, are constructed mainly from earth materials and are used to confine stream flow preventing flooding events. Five major embankment sites failed during the storm Daniel from west to east called hereinafter DEYAL, Kioski, Alkazar Stadium I and II, and Alsos (Fig. 1 and Table 1).

Table 1. Embankment dimensions and configurations

	DEYAL	Kioski	Alsos	Alkazar Stadium I and II
Embankment crest width (m)	7,00	7,00	7,00	20,00
Embankment height (m)	5,00-6,00	4,00-5,00	5,00	5,00
Embankment slope (inner and outer)	2:3	1:1,20	2:3	2:3

In the first site, the embankment problems start as seepage. However, this seepage stopped due to the immediate reaction by local authorities during the flooding accumulating earth material and the final repair of the site just after the flood (Fig. 2).

Figure 2. (a) Google Earth scene showing two failed low-height embankments. (b) Field photo of the two failed embankments. (c) The embankment at the DEYAL site was repaired immediately after the flooding. All the localities are at the west entrance of Larissa City, near DEYAL facilities.

The second site at Kioski locality is related to a severe embankment destruction that caused the flooding of large cultivated area and a block of buildings. After the flooding, a 100 m long by 50 m wide and 7 m deep erosional basin was created. This basin is probably the result of extensive water pipping before the embankment collapsed due to overtopping (Fig. 3). At present the embankment is fully restored (Fig. 3). In the same site, we also noticed the existence of small-scale slides across the embankment suggesting that the flooding caused significant problems across the Kioski embankment and the whole area needs analytic inspection. Of particular importance in the Kioski failure is a basin developed on both sites of the embankment that is interpreted as the result of flow along the structural interface of the embankment and the diffused flow through granular media below its foundation.

Figure 3. Google Earth scene showing the Kioski failure on October 2023 note on the satellite view the produced basin due to the embankment failure and the deposited material over cultivated lands. The lower left photo shows the restored embankment a few days after the flooding the photograph was taken looking west. The photograph to the right shows the basin at the south of the embankment.

The Alkazar Stadium sites I and II are two cases where initial piping was stopped by the immediate response by the authorities with the use of earth materials to stop seepage successfully (Fig. 4).

Figure 4. Google Earth scene (left) and field photo (right) of piping failure at locality Stadium just after the Pineios River flooding. The white rectangle in satellite scene show the area of field photo.

Flooding results at the Alsos embankment (Fig. 5) show its destruction for a length of 55 m. In this particular area, at the junction of old and new riverbeds, the flow of the river rise attained a maximum level. As a result, the embankment failed, and the water moved in the river's floodplain over cultivated lands to the northeast. The failure of the embankment in this area was the result of water overtopping. Overtopping phenomena were noticed for 100 m in total beyond the point of the embankment collapse. Concomitantly, the embankment destruction caused the deposition of significant thickness mud over cultivated lands (Fig. 5 blue arrow). The failure at Kioski and Alsos caused the flooding of a large area to the north.

Figure 5. Google Earth scene of the repaired embankment at Alsos locality. The blue arrow shows the flow direction and mud deposition on the cultivated lands. This embankment failure caused by extensive overtopping of the Pineios River.

In addition, second-order failures on the embankments during flooding are noticed in several places ruptures on top of the embankments (Fig. 6a). We interpret these cracks as the result of lateral spreading processes. Except for the along-strike cracks, they are mapped at several places circular to elliptical holes resulting from piping (Fig. 6b). The circular ruptures are interpreted as small-scale landslides commonly developed at the embankments.

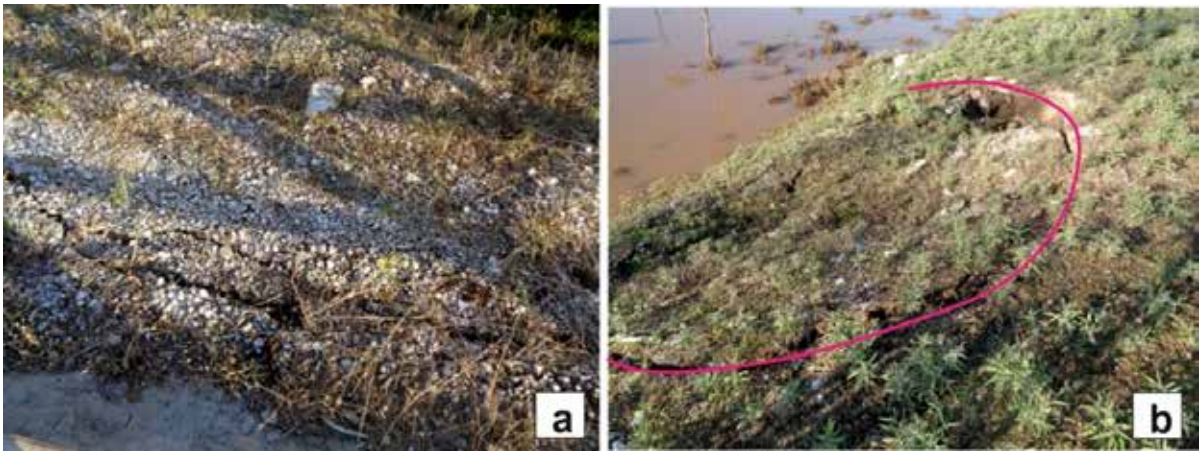

Figure 6 Second order failures of embankments.

In summary, the embankments in the study area are constructed with fine-grained materials were failed for two main reasons: the piping and overtopping. These embankments are categorized as hydrologically or seismically deficient. Notably, in 2021, the area of flooding was rocked by a strong seismic sequence that caused significant ground acceleration in the area of Larissa and their surroundings.

Overtopping manifests when the level of water is higher than the embankment crest elevation, as was the case of Kioski and Alsos. Piping failure of the embankment is caused in DEYAL, probably by the removal of soil particles through the intergranular flow within the soil mass of the embankment.

Discussion

In Greece, Daniel's severe rainfall led to flooding that caused more than two billion euros in damage, making it the costliest recorded storm for the country. Typical embankments in the study area are 80 m at their base and a height of up to 10 m. However, it has to be noticed that these dimensions vary along the entire length of the embankments. Their construction age is from 1930-1970, and their age of construction is ranging from 55-100 years old. The risk of failure of embankments that channelize a river is produced due to seepage induced by temporary and occasional impoundments taking place on the upstream side as a consequence of exceptional rainfalls is frequently underestimated. Commonly the failure of embankments results from the following factors: the flooding event, the hydraulic weakness and the embankment's geotechnical weakness or any combination of these three factors. However, the failure of embankments due to seepage and other water-related issues is often underestimated. In addition, considering climate change will have impacts on flood magnitudes and frequency in the same area we propose that the protection of the villages and cities has to be revised. In particular, for the case of Larissa and its flood hazard, the embankments need inspection after the 2021 earthquake and the 2023 flooding. However, as the area where these embankments are constructed is the Pineios floodplain it is also important to consider the processes related to the stratigraphy of the floodplain.

Conclusions

In five cases, close to Larissa City we mapped almost catastrophic types of failure by sudden, rapid, and uncontrolled release of impounded water. In three cases the emergency action of the local authorities prevents the failure.

Based on the severity of the flooding we considered the failures of the embankments in the territory of Larissa as of low hazard potential. However, given that the area was inflicted by a strong earthquake in 2021 and the flooding in 2023 we consider that a program of careful embankment inspection has to be considered as urgent.

References

Bathrellos G. 2005. Geological, Geomorphological and Geographic Study of Urban Areas in Trikala Prefecture—Western Thessaly. Ph.D. Thesis, National & Kapodistrian University of Athens, Athens, 561 p.

Bathrellos G.D., Skilodimou, H.D., Soukis K., Koskeridou E. 2018. Temporal and Spatial Analysis of Flood Occurrences in the Drainage Basin of Pinios River (Thessaly, Central Greece). Land 7, 106; doi:10.3390/land7030106. **[Journal Article]**

Dimitriou, E.; Efstratiadis, A.; Zotou, I.; Papadopoulos, A.; Iliopoulou, T.; Sakki, G.-K.; Mazi, K.; Rozos, E.; Koukouvinos, A.; Koussis, A.D.; et al. 2024. Post-Analysis of Daniel Extreme Flood Event in Thessaly, Central Greece: Practical Lessons and the Value of State-of-the-Art Water-Monitoring Networks. Water, 16, 980. https://doi.org/10.3390/w16070980. **[Journal Article]**

Kalafatis, A., Kyriou A., Nikolakopoulos K. 2024. Mapping of large-scale flooding in Thessaly region using Sentinel data. Earth Resources and Environmental Remote Sensing/GIS Applications XV, edited by Karsten Schulz, Ulrich Michel, Konstantinos G. Nikolakopoulos, Proc. of SPIE Vol. 13197, 131970F.

Kolios, S.; Papavasileiou, N. 2024. Daily Rainfall Patterns During Storm "Daniel" Based on Different Satellite Data. Atmosphere, 15, 1277. https://doi.org/10.3390/ atmos15111277 **[Journal Article]**

Koukouvelas, IK, Nikolakopoulos, KG, Kyriou, A, Caputo, R, Belesis, A, Zygouri, V, Verroios, S, Apostolopoulos,

D, Tsentzos, I, 2021. The March 2021 Damasi Earthquake Sequence, Central Greece: Reactivation Evidence across the Westward Propagating Tyrnavos Graben. Geosciences, 11, 328. doi.org/10.3390/geosciences11080328. **[Journal Article]**

Koukouvelas, I.K., Caputo, R., Nikolakopoulos, K.G., Kyriou, A., Famiglietti, N.A. 2023. Is the Mesochori Fault a Key Structure for Understanding the Earthquake Activity during the 2021 Damasi Earthquakes in Northern Thessaly, Greece? Geosciences, 13, 331. https://doi.org/10.3390/geosciences13110331 **[Journal Article]**

Mavroulis, S.; Mavrouli, M.; Lekkas, E.; Tsakris, A. 2024. Impact of the September 2023 Storm Daniel and Subsequent Flooding in Thessaly (Greece) on the Natural and Built Environment and on Infectious Disease Emergence. Environments, 11, 163. https://doi.org/ 10.3390/environments11080163 **[Journal Article]**

Sarhosis V., Giarlelis C. Karakostas·C., Smyrou E., Bal I.E., Valkaniotis S., Ganas A. 2022. Observations from the March 2021 Thessaly Earthquakes: an earthquake engineering perspective for masonry structures. Bulletin of Earthquake Engineering, 20, 5483–5515. **[Journal Article]**

17th INTERNATIONAL CONGRESS of the Geological Society of Greece

BULLETIN OF THE GEOLOGICAL SOCIETY OF GREECE, SP. PUBL.

EXTENDED ABSTRACT 033

Morphotectonic analysis of Antimilos volcanic Group

Belka A.[1], Nomikou P.[1], Bühring S.I.[2], Bejelou K.[1], Lampridou D.[1], Kothri S.[1], Varotsou E.[1], Bach A.[3], Papanikolaou D.[1]

(1) Department of Geology and Geoenvironment, National and Kapodistrian University of Athens, Athens, Greece, aretibelka@gmail.com (2) MARUM- Center for Marine Environmental Sciences, University of Bremen, Bremen, Germany (3) Faculty of Geosciences, University of Bremen, Bremen, Germany

Introduction

The Aegean Volcanic Arc, a crucial part of the Hellenic Arc and Trench System, is situated along the convergent boundary of the northward-subducting African Plate beneath the European Plate and since the Late Miocene beneath the Aegean Plate This volcanic arc has demonstrated continuous activity for at least the last 45 million years, as evidenced by various geological studies (McKenzie, 1972; Le Pichon et al., 1979; Papanikolaou, 1993; Royden & Papanikolaou, 2011). The current geodynamic structure includes the Hellenic Trench, a 1500-km-long arcuate trough extending from the Ionian Sea to the Libyan Sea, with the South Aegean volcanic arc developed parallel to it.

The Milos volcanic center comprises a cluster of islands located at the junction between the Myrtoon Basin, Cretan Basin, and southwestern border of the Cycladic plateau. This region includes Milos, Kimolos, Antimilos, Poliaigos, and smaller islets such as Akrathi and Arkadi. Antimilos is positioned 8.9 km northwest of Milos Island and is entirely composed of volcanic rocks with its highest elevation reaching 686 m (Sonder, 1924; Marinos, 1961). The volcanic deposits on Antimilos have been dated to approximately 0.32 million years ago (Fytikas et al., 1986), though this only represents a portion of its volcanic history.

Antimilos Onshore Geology

The island of Antimilos serves as the subaerial manifestation of the only composite volcano within the Milos Volcanic Field, as established by Fytikas et al. (1986) and Vougioukalakis et al. (2019). This roughly triangular island features two prominent topographic elevations: the rounded northern peak reaching approximately 686 meters, and a smaller southern peak at 435 meters. The simplified stratigraphy of Antimilos, as shown in the modified by Marinos (1961) geological map (Fig. 1a, 1b), consists of several distinct layers. Multiple dacitic domes overlying lower pyroclastic formations, with one major dome forming northern peak Sterna and other minor domes comprising Agiokastro peak and Alonia crater. Distinct eruptions have followed with new dacitic products emerging at Agiokastro peak alongside two neighboring craters and new andesitic products at Sterna peak, where thin volcanic flows extend toward eastern and western slopes from previous dacitic domes in a relatively smooth relief compared to earlier steep slopes.

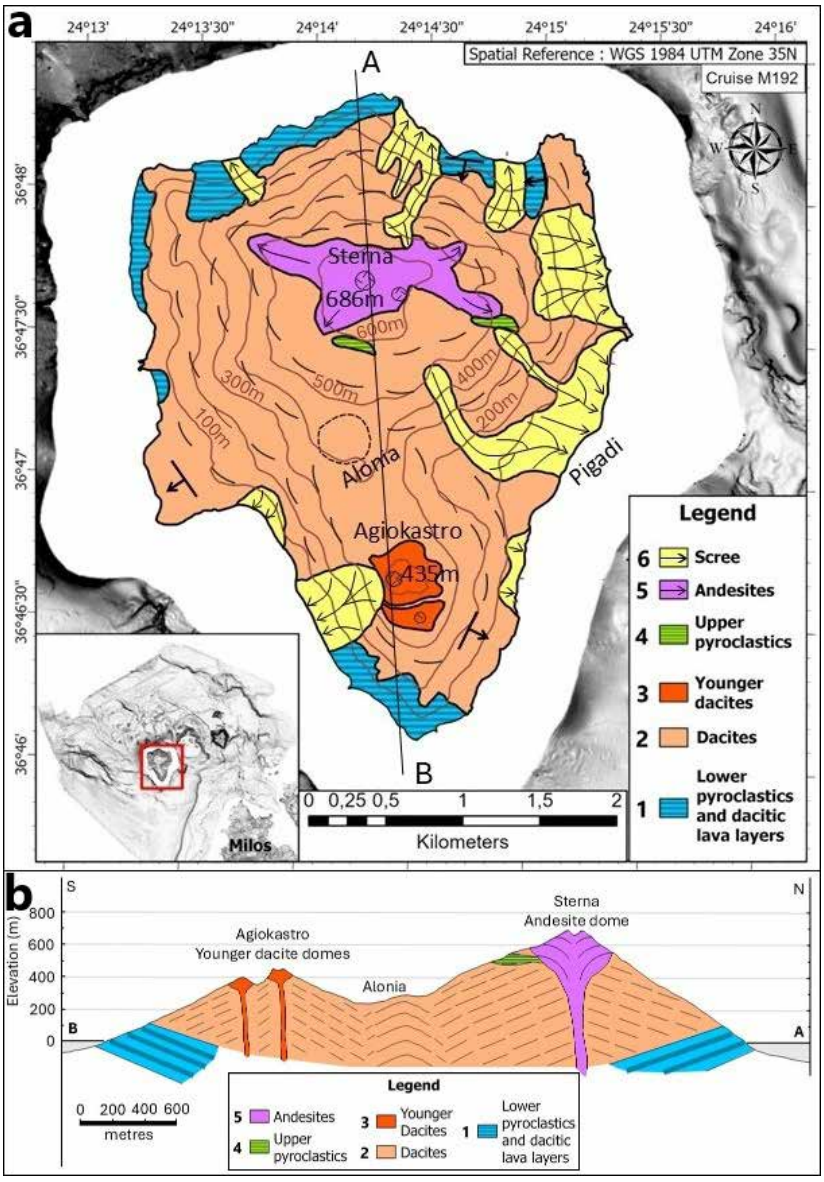

Figure. 1. (a) Geological map of Antimilos Island, modified after the geological sketch of Marinos (1961). (b) N-S Geological Profile across the Antimilos volcano.

Materials and Methods

The survey aboard R/V METEOR during cruise M192 (August 8 – September 5, 2023) utilized the EM710 multibeam echosounder for high-resolution seabed mapping. The system, operating effectively at depths of 3–2000 meters with a swath width up to 5.5 times water depth, covered areas from northern Milos southeastward. Data acquisition, managed via SIS software, integrated sound speed profiles and collected bathymetric (.all) and water column data (.wci), excluding AUV deployment/recovery phases.

Bathymetric data were processed in Qimera QPS, with manual corrections using Slice Editor and 3D Editor, resulting in a 5-meter resolution CUBE surface. Seismic profiles from the ATLAS PARASOUND P70 system provided morphological and sub-bottom data via high- and low-frequency parametric sonar.

Results

The constructed bathymetric map of the seafloor morphology around Antimilos Island reveals intricate features and distinct geological formations (Fig. 2). The analysis indicates that the seafloor morphology

transitions from the shelf zone, which extends up to approximately 140 meters in depth, down to the deeper regions of the southern Myrtoon Basin at around 1000 meters. Notably, in the transect from NW Milos to Antimilos, the Milos shelf exhibits a width of about 5 km, while that of Antimilos is significantly narrower, measuring less than 1 km. Between these two regions lies a small basin with depths ranging from 300 to 320 meters.

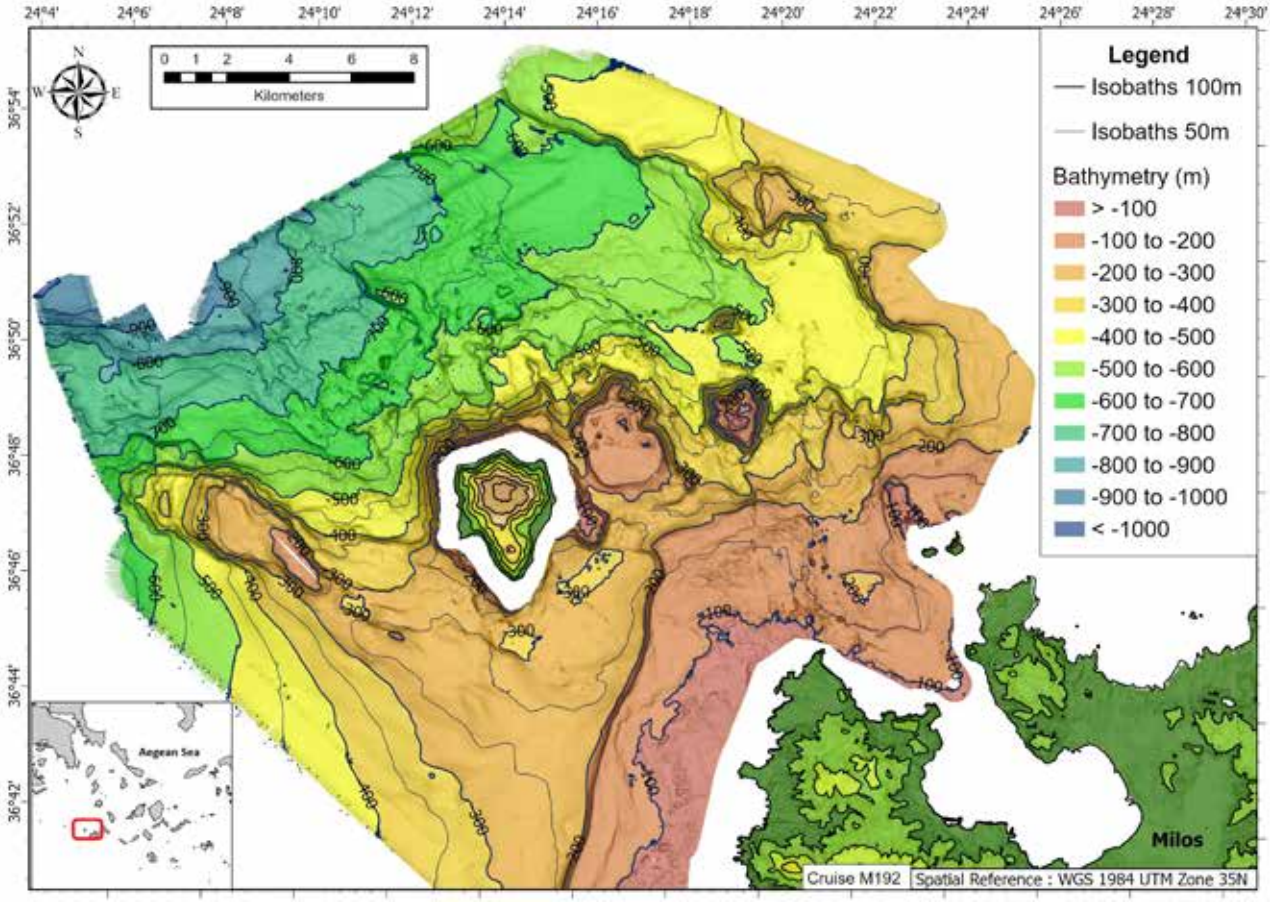

Fig. 2. Detailed swath bathymetry map of the Milos-Antimilos volcanic field (resolution 5 meters). The onshore DEM is obtained from SRTM and has a pixel size of about 30 meters resolution. The location of Antimilos is given in the inset map.

Three prominent submarine volcanic domes are identified to the east of Antimilos (Fig. 3) : Bangos cone, Shallow cone, and Deep cone. The largest of these is Bangos cone, followed by the medium-sized Shallow cone and the smaller Deep cone located further north. The NW slope hosting Antimilos and these three sea mounts is bordered by two significant NW-SE trending cliffs: one from the northeast at depths between 300 and 600 meters, marking the boundary with the Cycladic plateau, and another from the southwest at similar depths forming what is referred to as the Western Ridge. Bangos Dome stands at 349 meters tall and the summit has a flat top with a mean water depth of 140–145 meters. This flat area likely resulted from wave erosion during periods of low sea level. Shallow Cone reaches a total height of 417 meters with its summit at a depth of 58 meters. Although wave activity during the Last Glacial Maximum eroded its summit, it remains the shallowest cone among the three. A shelf has developed at depths between 130-140 meters. Deep Cone has with a total height of 226 meters and a conical shape that narrows significantly towards the summit with its peak at 293 meters below sea level. Due to its depth, it has remained unaffected by low sea level fluctuations that have impacted the other two domes.

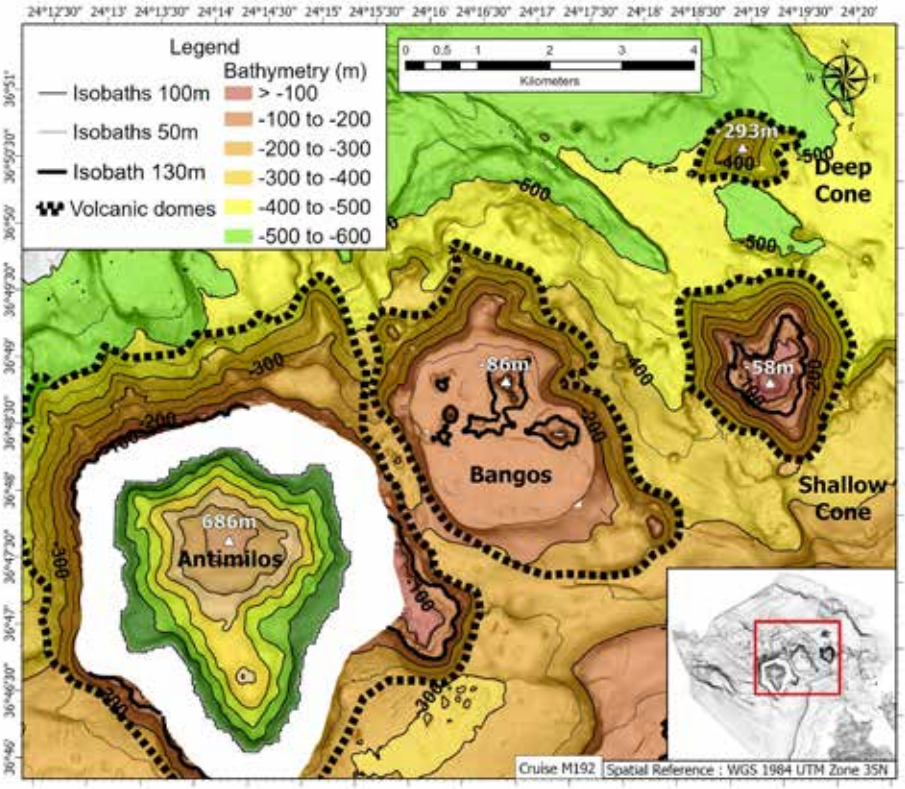

Figure. 3. Bathymetric map showing the boundaries of the volcanic domes NE of Antimilos island.

The hummocky area (Fig. 4) located offshore northwestern Antimilos is characterized by a rough, blocky terrain and has been identified as a significant Volcanic Debris Avalanche (VDA) deposit, which plays an essential role in understanding the geological processes that have shaped the area. The VDA covers approximately 72 km² and consists of numerous blocks that vary widely in size, shape, and orientation (Fig. 4). A detailed morphometric analysis was conducted on them, focusing on several key parameters such as height, area, distance from the coastline, and volume. The vertical drop-to-run-out ratio (H/L) was calculated to assess the mobility of the displaced material. The analysis revealed a total of 88 individual blocks distributed along the foot slope, extending up to 8.3 km from the coastline. Their orientation generally aligns with the slope's direction but also displays a discernible trend along a SE-NW axis.

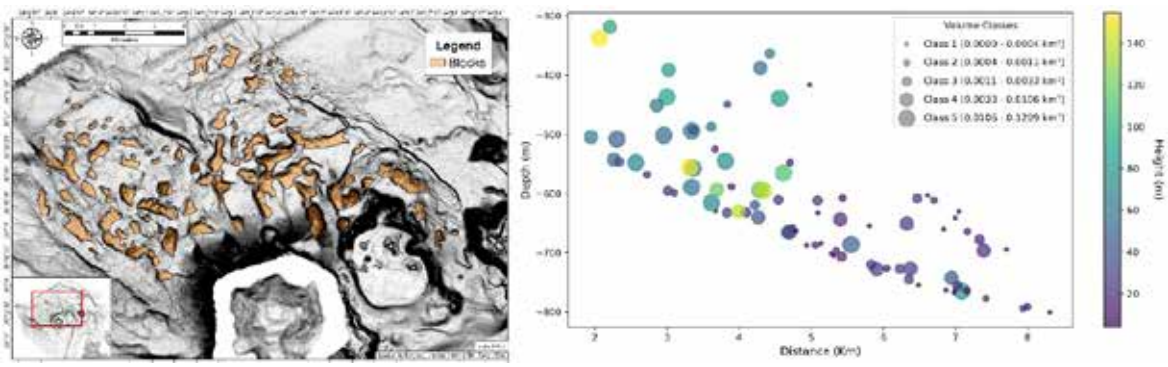

Figure. 4. VDA Blocks. (a) Gray-shaded map showing the identified blocks. (b) Scatter plot depth vs distance from the coastline of the block. The color scale indicates the height of each block.

Conclusions

The morphotectonic analysis of the Antimilos volcanic field, northwest of Milos Island, reveals four volcanic structures: the subaerial Antimilos volcano and three submarine volcanoes. The volcanic relief is 1180 m for Antimilos, 350 m for Bangos, 420 m for the Shallow and 200 m for the Deep Cone. Except for the Deep Cone the other three domes are highly affected by the climatic fluctuations, which have peneplained the Bangos dome at 140 m depth and have created a broad shelf zone at 100-140 m depth in Antimilos Island and the Shallow Cone. The available Middle Pleistocene age of 0.32 Ma indicates a pre-Holocene volcanic activity including the development of the shelf at least during the last three low stands. On the contrary, all three submarine volcanic cones are rather geometric, indicating one major volcanic phase, probably also of Middle Pleistocene age, judging from the development of the shelf in the two shallow cones.

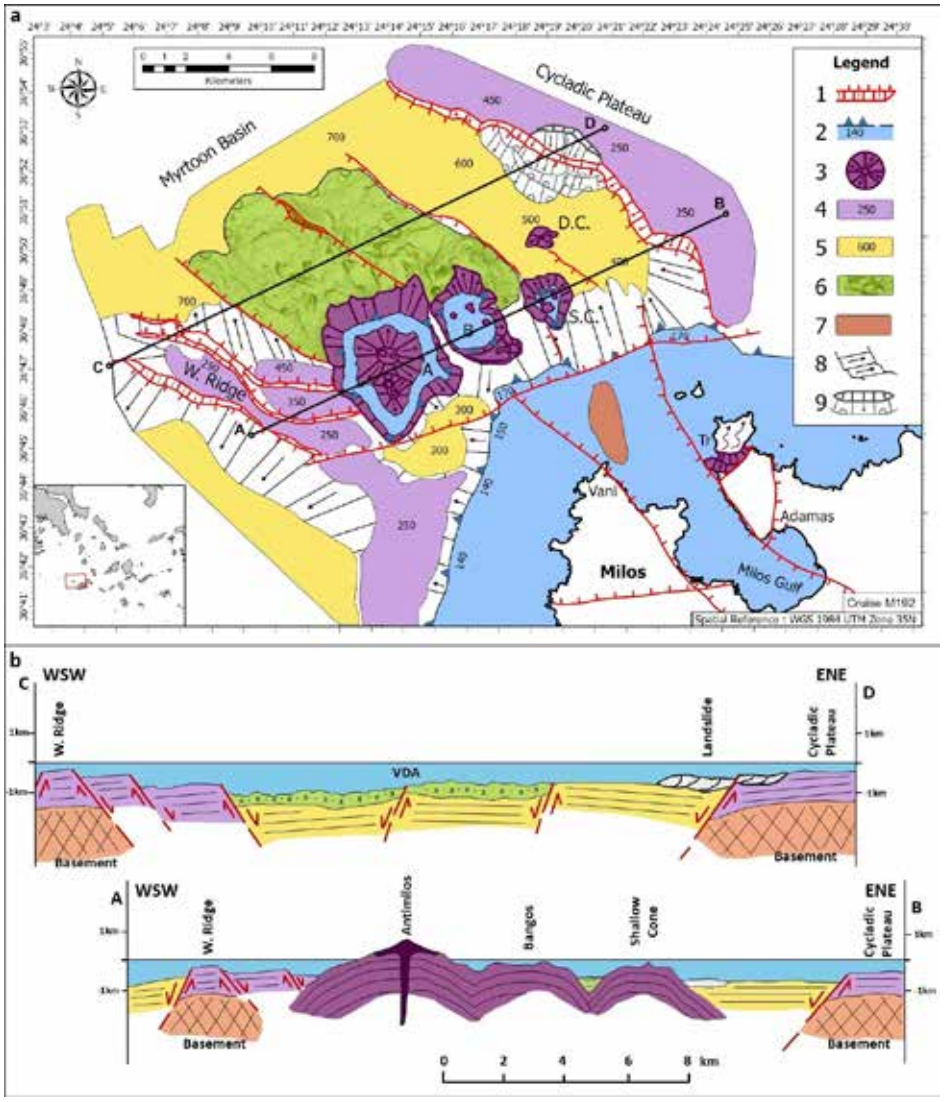

Figure 5. Morphotectonic map of the Milos-Antimilos volcanic field. Tr : Trachilas volcano, A : Antimilos Island, B : Bangos Cone, S.C. : Shallow cone, D.C. : Deep cone, 1 : Normal fault, 2 : Shelf and shelf break, 3 : Volcanic dome, 4 : Submarine Plateau, 5 : Basin, 6 : VDA – Flow direction, 7 : Distribution of flairs, 8 : Moderate morphological slope, 9 : Landslide and related fans. b) Subparallel tectonic profiles through the shallow (A-B profile at 300-500 m depth) and the deep (C-D profile at 500-800 m depth) parts of the Antimilos tectonic graben. The main elements are the three volcanic domes along the shallow profile and the VDA deposits along the deep profile.

The Antimilos group lies at the 7 km wide shallow zone extending between 250 m and 500 m depth within the 17 km long depression/tectonic graben formed to the NW of Milos, bounded by two prominent NW-SE normal faults one towards the NE from the Cycladic plateau and another from the SW from the Western Ridge (Fig. 5). Three additional NW-SE faults traverse the graben's central zone at depths of 600–900 m, confining extensive VDA deposits originating from the Antimilos and Bangos domes. This hummocky area contains volcanic blocks transported several kilometers northwest from their sources. The volcanic domes of Antimilos are located at depths of 500–250 m within the graben's shallow zone, while deeper profiles feature VDA deposits bordered by intra-basin faults. An intermediate zone (200–300 m depth) separates Antimilos from the NW Milos shelf, delineated by an ENE-WSW fault zone over 20 km long. This fault disrupts the NW Milos shelf, causing displacements of up to 30 m and delimiting the Vani hydrothermal vent field. Despite the shared NW-SE fault trend in both areas, there is no structural continuity across the ENE-WSW fault zone. The fault's 20 m Holocene displacement over 14 ka corresponds to a slip rate of 1.43 mm/year. The volcanic domes' development reflects climatic fluctuations, with low-stand periods (~100 ka) causing subaerial erosion and high-stand periods (10–20 ka) promoting marine deposition. Antimilos exhibits dacite and andesite domes with minor pyroclastic deposits, while Bangos, Shallow, and Deep Cones consist solely of volcanic domes, the Bangos Cone accompanied by two minor domes.

A vast hummocky area of VDA deposits with sliding blocks of volcanics occurs to the NW of Antimilos and Bangos domes, reaching 5-7 km distance down to 700-800 m depth, bounded by NW-SE normal faults at the central zone of the Antimilos tectonic graben. Their distribution aligns with the SE-NW trend of debris flows (Alexandri et al., 2001; Nomikou et al., 2013, 2014). The Antimilos VDA deposits shows several similarities to the VDA deposits reported from Santorini and Nisyros along the eastern part of the Aegean volcanic arc.

Acknowledgements

We are thankful to the the Dept. of Geology & Geoenvironment of the University of Athens (NKUA-GREECE), the University of Hamburg, and the collaborative project from the DFG Emmy Noether Group Hydrothermal Geomicrobiology, led by chief scientist S.I. Bühring, titled "Bridging Hydrothermal Sites Along the Hellenic Arc off Milos from Shallow to Deep". We also thank the Programme for the promotion of the exchange and scientific cooperation between Greece and Germany IKYDA 2024 "Bridging the Gap between hydrothermal biogeochemistry and Volcano-Tectonics: Exploring Synergies Along the Hellenic Arc off Milos (BITECHELL)", and all the shipboard personnel for a great expedition.

References

Alexandri, M, Papanikolaou, D., Nomikou, P. and Ballas, D. (2001) 'Geological Structure of the Myrtoon Basin (Aegean Sea) Based on Swath Bathymetry', Rapport Commission International Pour lexplorationscientifique de La MerMediterranee, 36 (3).

Fytikas, M. et al. (1986) 'Volcanology and petrology of volcanic products from the island of Milos and neighbouring islets', Journal of Volcanology and Geothermal Research, 28(3–4), pp. 297–317.

Le Pichon, X.L. and Angelier, J. (1979) 'The hellenic arc and trench system: A key to the neotectonic evolution of the eastern mediterranean area', Tectonophysics, 60(1–2), pp. 1–42.

Marinos, G. (1961) 'The Antimilos volcano in Aegean Sea', Bull Geol Soc Greece IV (1), pp. 38–50.

McKenzie, D. (1972) 'Active tectonics of the Mediterranean region', Geophysical Journal International, 30(2), pp. 109–185.

Nomikou, P., Papanikolaou, D., Tibaldi, A., Carey, S., Livanos, I., Bell, K.L.C., Pasquarè, F.A., Rousakis, G. (2014) 'The Detection of Volcanic Debris Avalanches (VDAs) Along the Hellenic Volcanic Arc, Through Marine Geophysical Techniques.', In Submarine Mass Movements and Their Consequences: 6th International Symposium, edited by Sebastian Krastel, Jan-Hinrich Behrmann, David Völker, Michael Stipp, Christian Berndt, Roger Urgeles, Jason Chaytor, Katrin Huhn, Michael Strasser, and Carl Bonnevie Harbitz, 339–49. Cham: Springer International Publishing.

Nomikou, P., Papanikolaou, D., Alexandri, M., Sakellariou, D. and Rousakis, G. (2013) 'Submarine Volcanoes along the Aegean Volcanic Arc', Tectonophysics, 597–598:123–46.

Papanikolaou, D. (1993) 'Geotectonic evolution of the Aegean', Bull. Geol. Soc. Greece, 28(1), 33-48.
Royden, L.H. and Papanikolaou, D.J. (2011) 'Slab segmentation and late Cenozoic disruption of the Hellenic arc', Geochemistry, Geophysics, Geosystems, 12(3), p. 2010GC003280.
Sonder, R. (1924) 'Zur Geologie and Petrographie der Inselgruppe yon Milos', Zeitschr. Volc, 8, pp. 11–231.
Vougioukalakis, G. E., Satow, C. G., & Druitt, T. H. (2019) 'Volcanism of the South Aegean Volcanic Arc. Elements', 15(3), 159–164.

17th INTERNATIONAL CONGRESS of the Geological Society of Greece

BULLETIN OF THE GEOLOGICAL SOCIETY OF GREECE, SP. PUBL.

EXTENDED ABSTRACT 034

The Geoheritage as a tool to engage children with the Sustainable Development Goals in UNESCO Global Geoparks: Best practices of educational activities from Lesvos Island UNESCO Global Geopark

Konstantina Bentana[1,2], Nikolaos Zouros[1,2]
(1) UNESCO Chair on Geoparks and Sustainable Development of Insular and Coastal Areas, Department of Geography, University of the Aegean, Greece, k.bentana@aegean.gr, (2) Natural History Museum of the Lesvos Petrified Forest

Introduction

Geoheritage constitutes an excellent tool for UNESCO Global Geoparks for the teaching of many cognitive subjects as well as the education of school students of all educational levels in a series of fundamental local or global problems that our society faces (Bentana and Zouros, 2020).

At the same time, UNESCO and other international organizations have been urging educators to seek out and utilize new learning environments outside the classroom, as well as pedagogical tools such as geological heritage in UNESCO Global Geoparks, in order to engage students with issues of sustainability and environmental protection (UNESCO, 2019).

UNESCO Global Geoparks utilize all aspects of their geological heritage in combination with natural and cultural heritage to enhance the education of children and their understanding of contemporary local or global problems (UNESCO, 2016).

However, for the next generation to be able to address contemporary problems, they must know what these problems are. A good way to ensure this is by engaging children to the subjects of the Sustainable Development Goals (SDGs). At the same time, the Sustainable Development Goals help children to understand our impact on the planet, to see the bigger picture and what role we can all play in taking responsibility.

By integrating geological heritage and processes with broader environmental, cultural, and social narratives, UNESCO Global Geoparks offer immersive, hands-on learning experiences among young learners. These natural learning environments not only highlight Earth's dynamic history but also provide a unique platform to illustrate the interconnectedness of geological and natural systems with human activities. In this context, geological heritage becomes a compelling pedagogical tool for introducing children to the Sustainable Development Goals.

This paper aims to explore how geological heritage, when combined with educational infrastructure and active engagement, can effectively involve school students in learning about the UN Sustainable Development Goals. Drawing on best practices from educational activities successfully implemented by the Natural History Museum of the Lesvos Petrified Forest, management body of the Lesvos Island UNESCO Global Geopark, this paper highlights how such initiatives provide meaningful learning experiences beyond the traditional classroom setting. By using local examples and fostering international collaborations, these programs offer students a rich context for understanding global challenges and contribute to the development of informed and active citizens.

Methods

The methodology used for this paper involved a qualitative case study, focusing on the educational activities implemented by the Natural History Museum of the Lesvos Petrified Forest within the Lesvos Island UNESCO Global Geopark. This methodology included an analysis of the educational programmes, focusing on their content, target school student groups, and connections to the Sustainable Development Goals. In addition, the study included the documentation of these educational activities to demonstrate how geoheritage education is applied in alignment with the Sustainable Development Goals in practice. In this paper, we analyzed three educational programmes based on the age of the children: 5-8, 9-12 and 13-17 years old.

Results

Lesvos Island UNESCO Global Geopark offers a wealth of geosites such as the Petrified Forest, which has

been designated a Protected Natural Monument, volcanoes, hot springs, important fossiliferous sites, faults, waterfalls, coastal landforms, which constitute significant evidence of the geological history of the Aegean area and contributed to the island's recognition as UNESCO Global Geopark (Zouros *et al.*, 2015).

Geosites and the rich geoheritage of the island are the main tools that are used for educational purposes by the Natural History Museum of the Lesvos Petrified Forest, the management body of the Lesvos UNESCO Global Geopark. The Museum actively utilizes the island's unique geoheritage in its educational programmes to engage children with the subjects of the Sustainable Development Goals. The educational activities analysed demonstrate a strong connection between geological heritage and the Sustainable Development Goals, and cultivate active citizens.

The first educational programme analysed is entitled "The Deinotherium and the Animals of the Petrified Forest" and is dedicated to school students 7-9 years old.

The programme aims to help children acquire values for the protection of biodiversity and geological heritage. The educational programme focuses on the paleoenvironment of the Petrified Forest, allowing students to identify different fossilized plant species and learn about the animals that coexisted 20 million years ago. Children get to know the animals through the replica of the Lesvos Deinotherium and the Liota crocodile. A theatrical play has been designed for younger children, and the pupils embody roles from the dramatized story of the Petrified Forest (Figure 1).

Geoheritage link: The diverse fossilized flora and fauna within the Petrified Forest showcase the rich biodiversity of the past ecosystems of Lesvos. This provides a baseline for understanding current biodiversity and the impact of habitat loss and environmental change.

Connecting Geoheritage to SDG: 15 "Life on Land"

Preparing active citizens: Students participate in discussions about the need for protecting present-day biodiversity, engaging in activities like creating their school and home gardens, and returning to the Museum petrified tree trunks that they identify by accident.

Figure 1. Children embody roles from the dramatized story of the Petrified Forest.

The second educational programme analysed is entitled "Climate change: learning about the impacts by observing the Lesvos Petrified Forest" and is dedicated to school students 9-12 years old.

The aim of the educational programme is students to understand the consequences of climate change on biodiversity. At the Petrified Forest Park and at the exhibition room of the Natural History Museum of the Lesvos Petrified Forest, children analyze fossilized leaves and tree rings to understand the past climate of Lesvos (Figure 2). Children continue their research at the botanical garden of the museum and are asked to look for evidence about the climate in the modern ecosystem of the Lesvos Petrified Forest area. By observing the vegetation at the time the Petrified Forest lived and the current vegetation, they record the data they collected, process it, and draw their conclusions about the consequences of climate change in the biodiversity of the region over the last 18Ma. Children then compare their results about past climate with the current climate crisis,

discussing the accelerated rate of change and the human impact.

Geoheritage link: The Petrified Forest itself is a direct record of past climate and environmental change during the early Miocene. Fossilized plants provide evidence of a subtropical forest ecosystem and the subsequent environmental shifts caused by volcanic activity and changing climate conditions.

Connecting geoheritage to SDG: 13 “Climate Action”

The Petrified Forest of Lesvos provides invaluable records of past climate change, aiding in the scientific understanding of current and future climate trends.

Preparing active citizens: International collaborations between schools from Lesvos and schools from other UNESCO Global Geoparks around the globe are implemented, encouraging children to participate in common activities. One such activity was implemented in collaboration with Maiella UNESCO Global Geopark (Italy). School students were encouraged to join the educational action “I LOWER THE LIGHTS, LIGHT UP THE FUTURE!” where school students were encouraged to turn off the lights in their school on a specific day and to discover what they can do themselves to save energy in their everyday life at school and at home and how they can become active citizens (Figure 3).

Figure 2. Children participate in research activities at Lesvos Petrified Forest for past climate records.

Figure 3. Children from Vatousa Elementary school joined the educational action “I LOWER THE LIGHTS, LIGHT UP THE FUTURE!” and turned off the lights in their school.

The third educational programme analysed is entitled “Natural Processes on our planet. All about the earthquakes” and is dedicated to school students 13-17 years old.

The main part of the educational programme is the experiential activity of earthquake simulation on the museum's seismic simulator. The seismic simulator has been shaped like a school classroom, and children experience devastating earthquakes from Greece and around the globe. On the seismic simulator the children are trained on how to respond to earthquakes and learn about preparedness measures (Figure 4).

Geoheritage link: Lesvos is located in a seismically active region. Understanding the geological processes that lead to earthquakes is crucial for building resilient communities.

Connecting geoheritage to SDGs: 11 "Sustainable cities and communities"

Knowledge of geological hazards, such as earthquakes, is critical for developing resilient and sustainable urban and rural communities.

Preparing Active Citizens: Students become more informed about earthquake hazards and are empowered to take proactive steps for their safety and contribute to community resilience efforts.

Figure 4. Children participate in the experiential activity of earthquake simulation on the museum's seismic table and are implementing the preparedness measures in case of an earthquake.

Conclusions

Geoheritage serves as an exceptionally powerful and effective pedagogical tool for engaging children with the Sustainable Development Goals. The comprehensive educational activities developed and implemented by the Natural History Museum of the Lesvos Petrified Forest in the Lesvos Island UNESCO Global Geopark provide a robust model for how to leverage geological heritage to foster environmental awareness, promote sustainable practices, and empower young generations. By offering hands-on activities, interdisciplinary approaches and age-appropriate learning experiences, these programs aim to foster a deeper understanding of sustainability challenges and empower students to become informed, responsible, and active citizens committed to a sustainable future. The best practices and valuable lessons learned from the Lesvos Island UNESCO Global Geopark are highly adaptable and can be effectively applied in other UNESCO Global Geoparks and diverse educational settings worldwide, contributing significantly to global sustainability efforts.

References

Bentana, K., Zouros, N., 2020. Educational activities to enhance geomorphological heritage sites in Lesvos UNESCO Global Geopark.

UNESCO, 2016. UNESCO Global Geoparks contributing to the Sustainable Development Goals. Celebrating Earth heritage, Sustaining local Communities.

UNESCO, 2019. Framework for the implementation of Education for Sustainable Development (ESD) beyond 2019, 40 C/23.

Zouros, N., Bentana, K., Valiakos, I., Vasilieadou, K., Thomaidou, E., 2015. Guide of the Lesvos Geopark.

17th INTERNATIONAL CONGRESS of the Geological Society of Greece

BULLETIN OF THE GEOLOGICAL SOCIETY OF GREECE, SP. PUBL.

EXTENDED ABSTRACT 035

Environmental controls on *Globorotalia menardii* size variability preceding the Tortonian/Messinian boundary

Besiou E.[1], Kontakiotis G.[1], Vasiliev I.[2], Antonarakou A.[1]

(1) Department of Historical Geology-Paleontology, Faculty of Geology and Geoenvironment, School of Earth Sciences, National and Kapodistrian University of Atheμ ns, Panepistimiopolis, Zografou, 15784 Athens, Greece (2) Senckenberg Biodiversity and Climate Research Centre, Senckenberganlage 25, D-60325 Frankfurt am Main, Germany

Research Highlights

Analyzing the potential drivers of *Globorotalia menardii* size variability in the eastern Mediterranean, we compare the *G. menardii* maximum diameter with the most significant regional environmental parameters during the Late Miocene. Among the examined abiotic factors, the strongest correlations were found to be with oxygen isotopic composition ($\delta^{18}O$) and sea surface salinity (SSS), while the correlations with sea surface temperature (SST) and carbon isotopic composition ($\delta^{13}C$) of planktonic foraminifera were relatively weak, suggesting that salinity had a greater impact on *G. menardii* size than sea surface temperature or primary productivity.

Introduction

Morphological changes in marine microorganisms have been of increasing interest to more and more researchers over the last decades. The size variability of species, a significant morphological parameter, can be altered by paleoceanographic changes reflecting global environmental events and/or local hydrographic changes (Schmidt *et al.*, 2004; Metcalfe *et al.*, 2015). Particularly, planktonic foraminifera are commonly preferred for morphological investigations, as they capture the abiotic environmental parameters in water masses, such as temperature, salinity, stratification and productivity (Adebayo *et al.*, 2023), but also for their abundance and global distribution (Schmidt *et al.*, 2004). Moreover, it has been observed that planktonic foraminifera can reach their maximum size under favorable conditions in the water column, while away from these areas occurred the opposite (Hecht, 1976), indicating their adaptive responses to the modified water mass structure (Friesenhagen, 2022; Besiou *et al.*, 2023). For the documentation of test size alterations, several studies have been carried out on illustration of the morphological variability of both Neogene and modern planktonic foraminifera. Particularly for the studies dealing with *G. menardii*, most of them have been performed in the Pacific, Atlantic, and Indian Oceans (Bhonsale and Saraswat, 2012; Knappertsbusch, 2016, 2022; Friesenhagen, 2022), showing that its size varies significantly over the different oceanic basins. Nevertheless, there is a gap in the morphometric study applied to the sedimentary archive of Mediterranean basin, without any evidence of size distribution patterns of *G. menardii* from this marginal subtropical setting.

Objectives

In our effort to examine how the environmental factors interplay with the observed morphological variability, we mainly attempt to investigate which environmental factor had the greatest influence on the size alterations of *G. menardii* specimens picked up from Potamida section (Crete Island, eastern Mediterranean; Fig. 1).

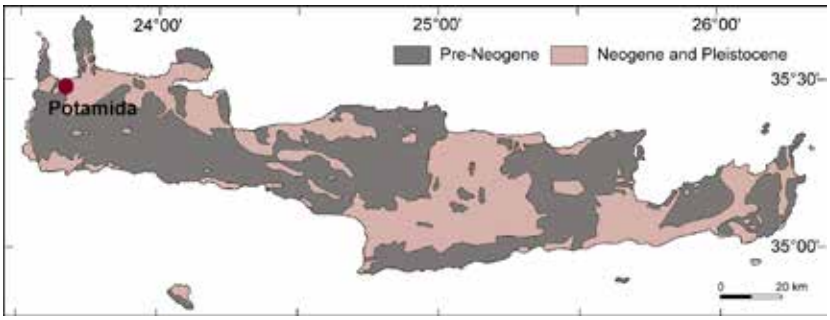

Figure 1. Geological sketch map of Crete Island, showing the Potamida section position (red circle).

On this context, the size variations of the analyzed species correlated to TEX_{86}-derived SST and SSS reconstructed values (Besiou *et al.*, 2024). Additional indices such the coiling direction and the species abundance were also evaluated as biotic measures of the foraminiferal ecological optimum conditions.

Material and Methods

The studied samples were collected from Potamida section in western Crete during the Thalys Project in 2017. Potamida section consists of blue-grey marls in the Tortonian and white-beige pelagic marls to clay limestones towards the Messinian (Agiadi *et al.*, 2017; Moissette *et al.*, 2018). The chronostratigraphic framework of the study section resulted from the combination of planktonic foraminiferal biostratigraphy, magnetostratigraphy and cyclostratigraphy published in Besiou *et al.* (2024) (Fig. 2). For size analysis, 10 specimens of *G. menardii* form 5 were handpicked from the >250 μm size fraction split per sample for the 7.36–7.24 Ma time interval. Then, the foraminiferal shells were positioned to capture the maximum diameter of each individual in the umbilical side and were photographed by a LEICA MZ16 stereo-zoom microscope supplemented by a digital camera connected to a computer. For testing the potential relationship to environmental perturbations, $\delta^{18}O$ and $\delta^{13}C$ isotopes measured on the shallow-dweller *Globigerinoides obliquus*. Moreover, SST estimates were calculated based on TEX_{86} biomarker proxy and SSS through the combined stable isotope and biomarker-based SST data.

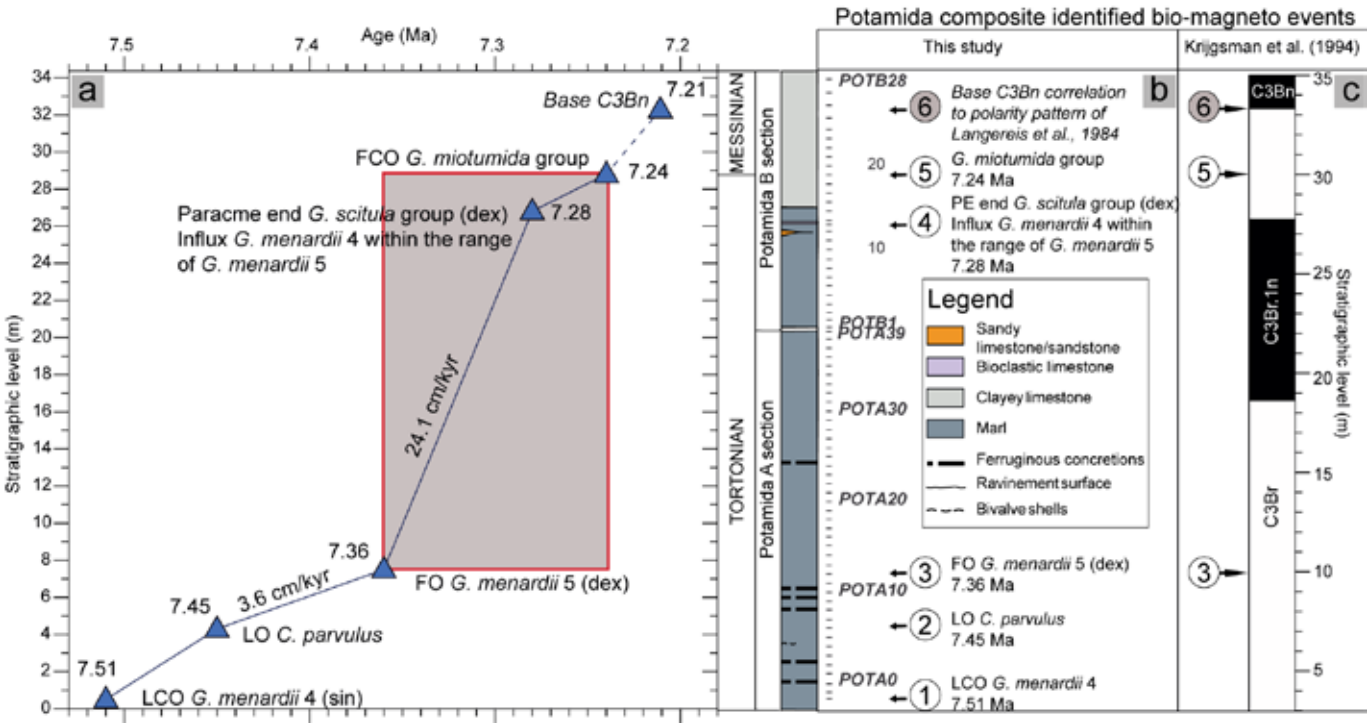

Figure 2. a) Age model of the composite Potamida section (modified by Besiou et al. 2024) with marked the studied time interval (represented by the red frame). b) The lithostratigraphy of the section along with five astronomically calibrated planktonic foraminiferal bio-events (labelled from 1 to 5) and the base of C3Bn magnetic polarity zone labeled in grey circle as event 6. c) The composite magnetostratigraphy based on Krijgsman et al. (1994).

Results

The evaluation of the existing dataset of Late Miocene Potamida section showed that optimum conditions in *G. menardii* are better inferred from its preferred environmental conditions rather than its relative abundance.

Therefore, the relative abundance may not the best descriptor of optimum growth conditions in planktonic foraminifera as the observed pattern is possibly attributed to adaptation strategies of the targeted species as a response to regional environmental forcings (Besiou *et al.*, 2023). Moreover, the coiling direction of this species within the study time interval remained constant (dextral) and not environmentally controlled. Size analysis further highlighted a quite large range of sizes between 330-450 μm (Fig. 3), consisting of small, intermediate and large specimens. These three groups of test sizes clearly reflect a biological adaptation to the significant environmental changes that took place in the Mediterranean Sea during the latest Tortonian. The distribution pattern of the average size of *G. menardii* varies significantly over the 7.36-7.24 Ma time interval. Size fluctuations are better correlated with the oxygen isotopic signal and more explicitly with the SSS reconstructions, indicating that the morphological characteristics are mostly influenced by the vertical changes of upper water column stratification in terms of salinity variations within the thermocline. This relationship is inversely proportional, with higher salinity conditions leading to smaller sizes in *G. menardii*.

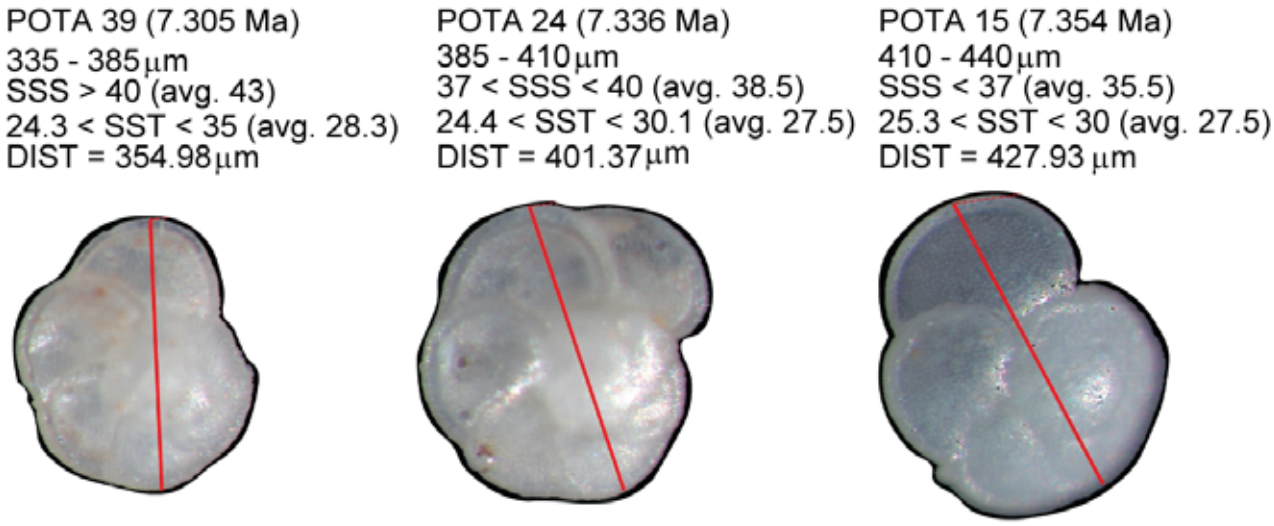

Figure 3. Images of *G. menardii* specimens separated in three maximum size groups (from the left to the right small, intermediate and large specimens).

Conclusions

The linear correlation analyses among the environmental parameters indicated that the dependence of test size on the temperature is not primary as initially thought to be, but secondary. Within such a highly evaporative stressed environment, salinity exerts a stronger influence on the size of *G. menardii* compared to sea surface temperature. Moreover, primary productivity seems to have only a minimized effect in such an ultra-oligotrophic setting as the Late Miocene eastern Mediterranean. The large size variability observed in Potamida samples corresponds to both small and large specimens of *G. menardii* (including intermediates) that were produced during colder/saltier and warmer/fresher sea water events in the lower and upper thermocline, respectively. Overall, our findings highlight the importance of analyzing species-specific paleoceanographic records around the globe by evaluating the shell size response to different environmental drivers in a regional context.

Acknowledgements

The authors would like to acknowledge the Goethe Universität–Senckenberg BiK-F and the Department of Historical Geology–Paleontology of the National and Kapodistrian University of Athens (NKUA) for providing laboratory facilities.

References

Adebayo, M.B., Bolton, C.T., Marchant, R., Bassinot, F., Conrod, S., de Garidel-Thoron, T., 2023. Environmental Controls of Size Distribution of Modern Planktonic Foraminifera in the Tropical Indian Ocean. Geochemistry 24, e2022GC010586. **[Journal Article]**

Agiadi, K., Antonarakou, A., Kontakiotis, G., Kafousia, N., Moissette, P., Cornée, J.J., Manoutsoglou, E., Karakitsios, V., 2017. Connectivity controls on the late Miocene eastern Mediterranean fish fauna. International Journal of Earth Sciences 106, 1147–1159. **[Journal Article]**

Besiou, E., Kontakiotis, G., Vasiliev, I., Moissette, P., Cornée, J.-J., Antonarakou, A., 2023. Evolutionary Palaeoecological and Morphological Response of *Globorotalia menardii* to Environmental Stress Conditions Preceding the Tortonian-Messinian Boundary in the Mediterranean Basin, Journal of Marine Science and Engineering 11(6), 1228. **[Journal Article]**

Besiou, E., Vasiliev, I., Kontakiotis, G., Agiadi, K., Methner, K., Mulch, A., Krijgsman, W., Antonarakou, A., 2024. Large and rapid salinity fluctuations affected the eastern Mediterranean at the Tortonian–Messinian transition. Palaeogeography, Palaeoclimatology, Palaeoecology 656, 112568. **[Journal Article]**

Bhonsale, S., Saraswat, R., 2012. Abundance and size variation of *Globorotalia menardii* in the Northeastern Indian Ocean during the late quaternary. Journal of the Geological Society of India 80, 771-782. **[Journal Article]**

Friesenhagen, T., 2022. Test-size evolution of the planktonic foraminifer *Globorotalia menardii* in the eastern tropical Atlantic since the Late Miocene. Biogeosciences 19, 777-805. **[Journal Article]**

Hecht, A.D., 1976. An ecologic model for test size variation in Recent planktonic foraminifera; applications to the fossil record. Journal of Foraminiferal Research 6, 295-311. **[Journal Article]**

Knappertsbusch, M., 2016. Evolutionary prospection in the Neogene planktic foraminifer *Globorotalia menardii* and related forms from ODP Hole 925B (Ceara Rise, western tropical Atlantic): evidence for gradual evolution superimposed by long distance dispersal? Swiss Journal of Palaeontology 135, 205-248. **[Journal Article]**

Knappertsbusch, M., 2022. Morphological evolution of menardiform globorotalids at Western Pacific Warm Pool ODP Hole 806C (Ontong-Java Plateau) Evolution morphologique du groupe de *Globorotalia menardii* au Site ODP 806C (Ontong-Java Plateau, Pacifique tropical occidental). Revue de Micropaléontologie 74, 100608. **[Journal Article]**

Krijgsman, W., Hilgen, F., Langereis, C.G., Zachariasse, W.J., 1994. The age of the Tortonian/Messinian boundary. Earth and Planetary Science Letters 121, 533–547. **[Journal Article]**

Metcalfe, B., Feldmeijer, W., de Vringer-Picon, M., Brummer, G.J.A., Peeters, F.J.C., Ganssen, G.M., 2015. Late Pleistocene glacial–interglacial shell-size–isotope variability in planktonic foraminifera as a function of local hydrography. Biogeosciences 12, 4781-4807. **[Journal Article]**

Moissette, P., Cornée, J.J., Antonarakou, A., Kontakiotis, G., Drinia, H., Koskeridou, E., Tsourou, T., Agiadi, K., Karakitsios, V., 2018. Palaeoenvironmental changes at the Tortonian/Messinian boundary: A deep-sea sedimentary record of the eastern Mediterranean Sea. Palaeogeography, Palaeoclimatology, Palaeoecology 505, 217–233. **[Journal Article]**

Schmidt, D.N., Renaud, S., Bollmann, J., Schiebel, R., Thierstein, H.R., 2004. Size distribution of Holocene planktic foraminifer assemblages: biogeography, ecology and adaptation. Marine Micropaleontology 50, 319-338. **[Journal Article]**

17th INTERNATIONAL CONGRESS of the Geological Society of Greece

BULLETIN OF THE GEOLOGICAL SOCIETY OF GREECE, SP. PUBL.

EXTENDED ABSTRACT 036

Cultivating FAIR principles for multi-hazard assessment

Bonatis P.[1], Anagnostou V.[1], Karakostas V.[1], Kourouklas C.[1], Papadimitriou E.[1], Adamaki A.[2], Andriopoulou-Mounteanou S-A.[3], Bathrellos G.D.[3], Bitharis S.[1], Foumelis M.[1], Karolos I-A.[1], Kaviris G.[4], Papageorgiou E.[1], Pikridas C.[1], Sakkas V.[1], Skilodimou H.D.[3], Spingos I.[4], Zymvragakis A.[4]

(1) Aristotle University of Thessaloniki, Thessaloniki, Greece, mponatis@geo.auth.gr (2) Lund University, Lund, Sweden (3) University of Patras, Rio, Greece (4) National and Kapodistrian University of Athens, Athens, Greece

Research Highlights

- HOMEROS stands for "Harmonising Observations from Multi-hazard Environments in Research for Open Science".
- The project aims to deliver FAIR-compliant tools and datasets to enhance disaster preparedness and resilience in high-risk regions through transparent and collaborative research.

Introduction

In today's interconnected world, communities face a diverse range of hazards, including natural disasters like earthquakes, floods, and landslides, as well as human-induced events. To address these challenges, the HOMEROS project aims to strengthen multi-hazard assessment methodologies in seismology, geodesy, and geology (Figure 1). Leveraging technical solutions suited to the big data era, HOMEROS represents a significant advancement in standardizing research processes, promoting collaboration, and enhancing understanding and prediction capabilities for natural hazards through Open Science practices. By adhering to FAIR principles (Findable, Accessible, Interoperable, Reusable), HOMEROS ensures that its research outputs are transparent, reproducible, and universally accessible, maximizing their value for the scientific community and stakeholders. Focusing on high-risk areas in Greece with significant seismic activity, strong earthquakes, floods, and landslides, HOMEROS will compile earthquake catalogues and assess ground deformation products to provide a comprehensive evaluation of seismic hazards. Additionally, it will enhance the understanding of flood and landslide risks, vital for effective mitigation strategies.

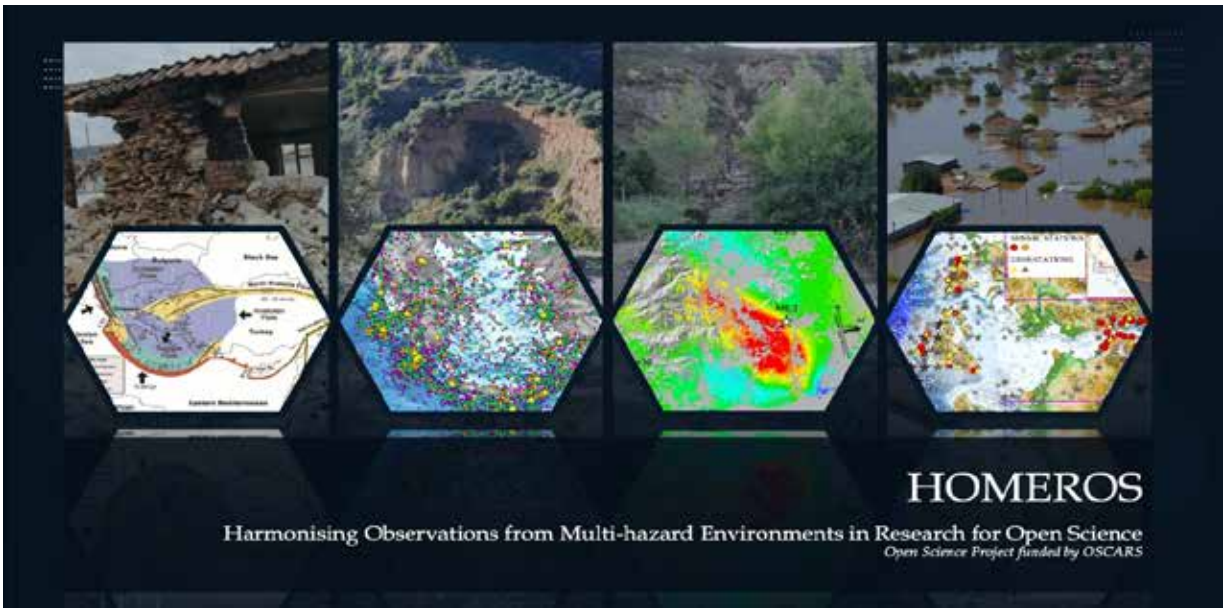

Figure 1. Official logo of the HOMEROS project, highlighting its multi-hazard focus

Objectives

The HOMEROS project addresses the critical need for robust and standardized multi-hazard assessment methodologies in a rapidly evolving risk landscape. By leveraging the power of Open Science and interdisciplinary collaboration, the project aims to advance scientific knowledge, foster data-driven decision-making, and enhance community resilience. Its objectives focus on three key pillars:

- Integration with Open Science environments: HOMEROS aims to utilize platforms such as the European Open Science Cloud (EOSC) and the Environmental Research Infrastructure (ENVRI) Hub (Adamaki & Vermeulen, 2023) to create accessible ecosystems for data sharing. This builds on prior integration efforts in ENVRI projects and promotes FAIR principles to ensure the usability and reproducibility of research outputs.
- Enhancing multi-hazard assessment: The project seeks to develop methodologies for integrating diverse datasets, including seismic, geodetic, and geological data. It will advance the understanding of earthquakes, floods, and landslides through the creation of detailed models, maps, and inventories.
- Fostering collaboration and communication: HOMEROS aspires to strengthen partnerships among research institutions, infrastructures, and projects. Results will be shared through Open Access publications, workshops, and training resources.

Multi-hazard environments - Pilot areas

The HOMEROS project focuses on two high-risk pilot areas in Greece, the central Ionian Islands and the western Gulf of Corinth (Figure 2), which represent diverse and complex multi-hazard environments. These regions have been selected due to their significant seismic activity and susceptibility to other natural hazards, such as floods and landslides. By studying these areas, HOMEROS aims to develop and demonstrate innovative methodologies for multi-hazard assessment.

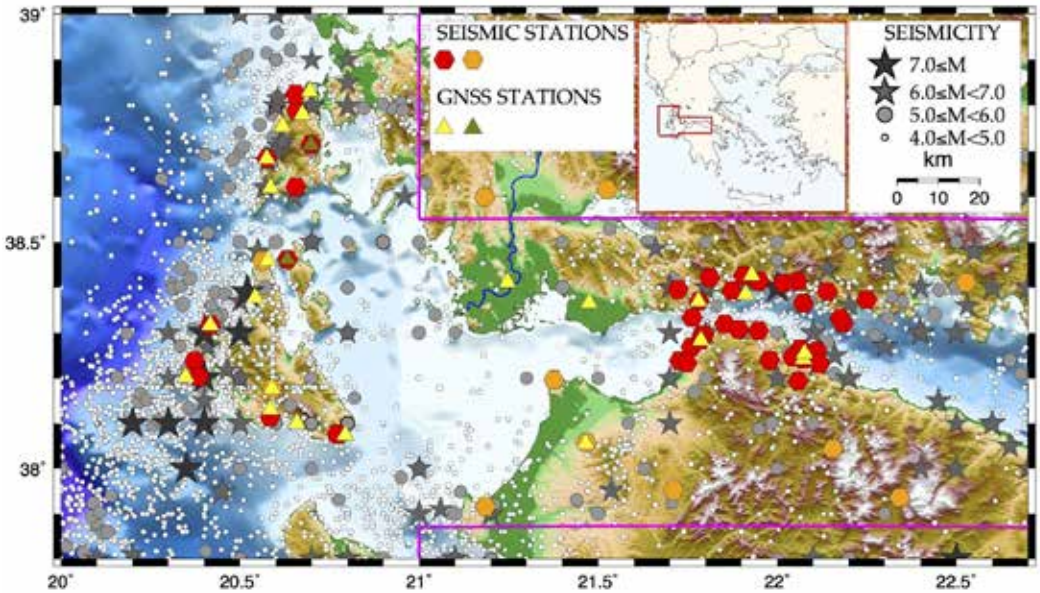

Figure 2. Map of the pilot areas encompassing the central Ionian Islands and western Corinth gulf. Different symbols denote the epicenters of all known earthquakes in the study area with magnitudes M>4.0 as shown in the upper right inset. The central inset shows the territory of Greece with the study area enclosed in the red polygon. Hexagons illustrate the positions of the seismological stations providing online access to their recordings. Yellow triangles depict the installation sites of GNSS stations in operation, whereas the olive triangles the positions where additional GNSS stations are planned to be installed in the framework of the project, collocated with already existing and operated seismological stations.

The central Ionian Islands, along with the western Gulf of Corinth, accommodate the highest seismicity in the eastern Mediterranean, exhibiting high deformation rates (Pikridas et al., 2016; Bitharis et al., 2024) and frequent occurrences of strong earthquakes (e.g., Karakostas et al., 2015; Sakkas et al., 2022). The compilation of earthquake catalogues (e.g. from the Euro-Mediterranean Seismological Centre - EMSC, the European Plate Observing System - EPOS providers as the ORFEUS infrastructure, the database of the Aristotle University of Thessaloniki - AUTh seismological center, and others), comprising historical, instrumental, and recent events, along with focal mechanism and stress field data, represent a significant contribution to the understanding of seismic hazard. Earthquakes are among the most impactful geohazards in Greece given that more than 50% of seismic energy in Europe is released in the country. A reliable seismic hazard model can contribute to seismic risk mitigation. To that end, Peak Ground Acceleration (PGA) and Peak Ground Velocity (PGV) together with a site-specific analysis (Uniform Hazard Spectra - UHS and hazard curves) in the most populated towns can provide a holistic evaluation of seismic hazard (e.g., Kaviris et al., 2022; 2024). Besides strong earthquakes, the aforementioned areas along with parts of the northern Peloponnese have experienced severe floods and landslides that resulted in loss of life and substantial loss of property, along with extensive damage to the natural and built environment and key infrastructure (Bathrellos et al., 2017; Skilodimou et al., 2018). Maps displaying the spatial distribution of flood and landslide hazards are invaluable at identifying areas at risk (Skilodimou et al., 2019; Bathrellos et al., 2024). The project will enhance the understanding of the spatial distribution of historical and recently recorded floods, along with the identification of flood – prone areas, which constitute critical input information on effective flood-risk mitigation. Regarding landslides, they are mostly observed in the mountainous part of the Gulf of Corinth, the Ionian Islands, and parts of western Peloponnese, where serious damage has been repeatedly caused to sections of urban areas and the road network. Landslide hazard assessment maps are important tools for prediction and mitigation of natural disasters. In this context, the project will work on an inventory map that includes recorded landslide events, crucial for understanding the landslide hazard.

Data and Methods

Comprehensive multi-hazard assessment requires diverse data sources and advanced methodologies to address the complexity of natural hazards. HOMEROS will integrate high-quality datasets from seismology, geodesy, and geological monitoring to provide robust and reproducible insights. Seismic data from regional networks form the basis for compiling earthquake catalogues, analyzing focal mechanisms, and studying ground deformation, all of which are critical inputs for seismic hazard assessment. Geodetic observations, including GNSS and InSAR, enhance the understanding of tectonic deformation (Bonatis et al., 2024) and enable the integration of precise ground deformation monitoring with broader hazard assessments. Flood and landslide hazards can be assessed using historical records and remote sensing data. Spatial analyses and advanced techniques, such as InSAR, help to identify flood and landslide prone areas (Aslan et al., 2020). These methods are complemented by the development of inventories that catalog historical events. A key component of the project is the harmonization of data and the application of Open Science principles to ensure all research outputs are transparent, reproducible, and widely accessible. Collaborative platforms and tools will be utilized to integrate datasets from diverse sources, fostering interdisciplinary research and promoting knowledge sharing. Reproducible workflows will enable the seamless combination of datasets and methodologies to deliver actionable insights into natural hazards.

Exploitable results

The HOMEROS project aims to deliver a range of results that will significantly advance multi-hazard assessment and enhance disaster resilience (Table 1). A primary output will be open-access datasets, including earthquake catalogues, ground deformation products, flood hazard maps, and landslide inventories. These datasets will adhere to FAIR principles and will be shared through platforms such as EPOS ERIC, ENVRI repositories, and other open repositories (e.g., GitHub, Zenodo). These data products will provide valuable resources for advancing research and fostering interdisciplinary collaboration.

Another key outcome is the development of transparent and reproducible research workflows documented through tools like Jupyter Notebooks. These workflows will demonstrate the integration of diverse datasets and methodologies, enabling researchers to replicate and adapt the processes for similar studies. This documentation will serve as a best-practice guide for future multi-disciplinary research projects.

Table 1. Summary of the key outcomes of HOMEROS

Output	Description	Impact
Open-access datasets	Comprehensive datasets including earthquake catalogues, ground deformation products (GNSS and InSAR), flood hazard maps, and landslide inventories.	Enabling improved hazard modeling, interdisciplinary research, and data-driven policy-making.
Scientific publications	Peer-reviewed articles published in Open Access journals, showcasing HOMEROS methodologies and findings.	Advancing scientific knowledge.
Training modules	Educational resources designed to teach Open Science principles, data sharing practices, and the utilization of research tools like Jupyter Notebooks and ENVRI/EOSC services.	Capacity building among researchers, students, and professionals, fostering widespread adoption of Open Science practices.
Integration demonstrators	Showcase of pathways to integrate data pipelines from diverse sources, including ENVRI and EOSC infrastructures, to highlight interoperability and scalability.	Improved data interoperability.
Policy recommendations support tools	Practical outputs such as hazard maps and risk models suited for policymakers and disaster management stakeholders.	Enhancing disaster preparedness and resilience.

Conclusions

HOMEROS represents a vital step forward in addressing the growing complexity of multi-hazard environments. By harmonizing data from diverse scientific domains and adhering to Open Science principles, the project tackles key challenges in making hazard assessment both comprehensive and accessible. It lays the foundation for more integrated and scalable approaches to understand natural hazards, from earthquakes to floods and landslides, in high-risk regions. The emphasis on FAIR principles ensures that HOMEROS outputs not only benefit current research but also provide a robust framework for future innovations in hazard modeling. The project's focus on high-risk areas, such as the Ionian Islands and the Gulf of Corinth, will demonstrate its applicability, while offering scalable solutions that can be adapted to other geohazardous regions worldwide. Lastly, the outputs including open-access data, scientific publications, and training modules, will serve as valuable resources for academia, policy-making, and disaster management, fostering a safer and more resilient society.

Acknowledgements

The authors acknowledge the OSCARS project, which has received funding from the European Commission's Horizon Europe Research and Innovation programme under grant agreement No. 10112975.

References

Adamaki, A., Vermeulen, A., 2023. ENVRI-FAIR D5.7: ENVRI-Hub design study, Zenodo. https://doi.org/10.5281/zenodo.8119522.

Aslan, G., Foumelis, M., Raucoules, D., De Michele, M., Bernardie, S., Cakir, Z., 2020. Landslide Inventory Mapping and Monitoring Using Persistent Scatterer Interferometry (PSI) Technique in the French Alps. Remote Sensing 12(8), 1305.

Bathrellos, G. D., Skilodimou, H. D., Chousianitis, K., Youssef, A. M., Pradhan, B., 2017. Suitability estimation for urban development using multi-hazard assessment map. Science of the Total Environment 575, 119-134.

Bathrellos, G.D., Koukouvelas, I.K., Skilodimou, H.D., Nikolakopoulos, K.G., Vgenopoulos, A.L., 2024. Landslide causative factors evaluation using GIS in the tectonically active Glafkos River area, northwestern Peloponnese, Greece. Geomorphology 461, 109285.

Bitharis, S., Pikridas, C., Fotiou, A., Rossikopoulos D., 2024. GPS data analysis and geodetic velocity field

investigation in Greece, 2001–2016. GPS Solutions 28, 16.

Bonatis, P., Karakostas, V., Kaplon, J., Papadimitriou, E., Kaviris, G., Ilieva, M., Foumelis, M., Pikridas, C., 2024. Co-seismic and post-seismic slip associated with the 2021 M_w5.9 Arkalochori, Central Crete (Greece) earthquake constrained by geodetic data and aftershocks. Tectonophysics 889, 230481.

Karakostas, V., Papadimitriou, E., Mesimeri, M., Gkarlaouni, Ch., Paradisopoulou, P., 2015. The 2014 Kefalonia doublet (Mw6.1 and Mw6.0) central Ionian Islands, Greece: Seismotectonic implications along the Kefalonia Transform Fault Zone. Acta Geophysica 63, 1-16.

Kaviris, G., Zymvragakis, A., Bonatis, P., Kapetanidis, V., Voulgaris, N., 2022. Probabilistic and Scenario-Based Seismic Hazard Assessment on the Western Gulf of Corinth (Central Greece). Applied Sciences 12(21), 11152.

Kaviris, G., Zymvragakis, A., Kapetanidis, V., Kouskouna, V., Spingos, I., Sakellariou, N., Voulgaris, N., 2024. A Logic-Tree Based Probabilistic Seismic Hazard Assessment for the Central Ionian Islands of Cephalonia and Ithaca (Western Greece). Journal of Seismology 28, 1087-1103.

Pikridas C., Bitharis S., Fotiou A., Rossikopoulos D., Katsougiannopoulos S., Spanakaki K, Karolos I., 2016. Monitoring seismic displacements using GNSS data with PPP method. Bulletin of the Geological Society of Greece 50 (3), 1563-1569.

Sakkas, V., Kapetanidis, V., Kaviris, G., Spingos, I., Mavroulis, S., Diakakis, M., Alexopoulos, J., Kazantzidou-Firtinidou, D., Kassaras, I., Dilalos, S., Vassilakis, E., Kotsi, E., Tselentis, G.-A., Lekkas, E., Voulgaris, N., 2022. Seismological and Ground Deformation Study of the Ionian Islands (W. Greece) During 2014-2018, a Period of Intense Seismic Activity. Applied Sciences 12, 2331.

Skilodimou, H. D., Bathrellos, G. D., Koskeridou, E., Soukis, K., Rozos, D., 2018. Physical and anthropogenic factors related to landslide activity in the Northern Peloponnese, Greece. Land 7(3), 85.

Skilodimou, H.D., Bathrellos, G.D., Chousianitis, K., Youssef, A.M., Pradhan, B., 2019. Multi-hazard assessment modeling via multi-criteria analysis and GIS: a case study. Environmental Earth Sciences 78, 47.

17th INTERNATIONAL CONGRESS of the Geological Society of Greece

BULLETIN OF THE GEOLOGICAL SOCIETY OF GREECE, SP. PUBL.

EXTENDED ABSTRACT 037

Development of an index-based methodology for assessing coastal vulnerability at a national scale and preliminary results

Boumpoulis V.[1], Michalopoulou M.[1], Kazolias A.[3], Geraga M.[2], Depountis N.,[1] Papatheodorou G.[2]

(1) University of Patras, Department of Geology, Laboratory of Engineering Geology, Greece, vasileios_boumpoulis@ac.upatras.gr

(2) University of Patras, Department of Geology, Laboratory of Marine Geology and Physical Oceanography, Greece

(3) University of Peloponnese, Department of Digital Systems, Sparti, Greece.

Research Highlights: **Development of an index-based equation and methodology for assessing coastal vulnerability in Greece at a national scale**

Introduction

Coastal areas are one of the most vulnerable environments and due to their continuously growing population, their protection is of great importance for society and economy. Moreover, climate change can increase the intensity of climate related coastal hazards, especially coastal erosion and sea level rise, whose adverse impacts on coastal zones are expected to be significant even under the most optimistic emission scenario (IPCC 2022). Against these rising threats, different risk and vulnerability assessment methodologies have been developed to understand the processes underpinning coastal hazards. More specifically, the assessment and calculation of coastal vulnerability, focusing on coastal erosion processes, is accomplished with the following methods: (a) methods based on a specific vulnerability index, (b) methods based on a sequence of indicators, (c) methods based on geographical information system (GIS)-based decision-making systems and (d) methods based on dynamic computational model (Ramieri et al. 2011).

In the present study, the use of a method based on a specific vulnerability index, and more specifically the Coastal Vulnerability Index (CVI) approach was chosen to assess vulnerability along the Hellenic coastlines and for this reason it was named HCVI. The CVI is a very productive, low-cost and effective tool for mapping and managing coastal risks. In this way, it provides an initial identification of coastal vulnerability to facilitate local and regional authorities in preparing coastal management and protection plans, coastal zone regulation and adaptation strategies against erosion.

However, despite the effective application of the CVI index, there are limited publications in the literature addressing its use at the national scale. Furlan et al. (2021), developed a modified CVI index (MDim-CVI) for Italy, incorporating four different sub-indices: a) Coastal Forcing, b) Environmental, c) Social and d) Economic. In addition, López Royo et al. (2016), estimated coastal vulnerability for the entire coastal zone of Spain again using a modified CVI index, which was calculated for 4 different future climate models (RCPs) of sea level rise, based on IPCC future projections.

The aim of this project is the creation, implementation and presentation of the Hellenic Coastal Vulnerability Index (HCVI) for the assessment of vulnerability along the Hellenic coastlines and the creation of a national scale vulnerability map.

Methodology

For the calculation of coastal vulnerability at a national scale, the classic vulnerability index CVI (Coastal Vulnerability Index) was chosen, with the following variables: 1) Geological resilience, 2) Coastal Slope, 3) Historical shoreline change, 4) Significant wave height, 5) Sea level rise and 6) Tidal range.

The calculation of CVI for the Hellenic coastlines was carried out using the equation proposed by (Gornitz (1991) according to which the result is equal to the square root of the product of the variables divided by the number of variables. For the calculation of the CVI, the coastline of Greece was divided into coastal segments of 100 meters, precisely at the same locations where transects were created for calculating

the historical shoreline change using the DSAS software (Digital Shoreline Analysis System version 6) (Himmelstoss et al., 2024).

The equation for calculating HCVI is presented below:

$$HCVI = \sqrt{\frac{a * b * c * d * e * f}{6}}$$

where a: Geological resilience, b: Significant average wave height, c: Coastal slope, d: Historical shoreline change, e: Average tidal range, f: Sea level rise (SLR).

The initial step before calculating the Coastal Vulnerability Index is to determine the range values of each variable to classify them with a specific vulnerability value, for example, from very low to very high vulnerability. The five (5) ranges of vulnerability classification values used in this project are presented in Table 1.

Table 1. Vulnerability classification ranges for each of the variables used in the HCVI calculations.

Variables	Very Low (1)	Low (2)	Moderate (3)	High (4)	Very High (5)
Geological resilience	Limestones, plutonic and metamorphic rocks	Flysch, evaporites, igneous and semi-metamorphic rocks	Neogene deposits (hard soils- soft rocks)	Quaternary loose materials with a higher percentage of coarse-grained materials (sand, gravel and pebbles)	Quaternary loose materials with a higher percentage of fine or mixed phase deposits (silts and sands)
Significant Wave Height (m)	<0.3	0.3–0.6	0.6–0.9	0.9–1.2	>1.2
Coastal Slope (%)	>12	12- 9	9 – 6	6 – 3	<3
Historical Shoreline Change (m/y)	>(+1.5)	(+1.5)–(+0.5)	(+0.5)–(-0.5)	(-0.5)–(-1.5)	<(-1.5)
Average Tidal Range (m)	<0.2	0.2–0.4	0.4–0.6	0.6–0.8	<0,8
Sea Level Rise (mm/y)	<1.8	1.8 - 2.5	2.5 – 3.0	3.0 – 3.4	>3.4

Geological resilience is one of the most important variables in the equation of HCVI as it assesses the resistance of any geological formation to erosion. The more resistant the formation is to erosion, the lower the vulnerability class corresponds to. Based on this principle, the data of the geotechnical map of Greece, published by EAGE, which includes 28 engineering-geological units at a scale of 1:500,000, were used. Subsequently, the units were grouped into five vulnerability classes, according to the guidelines for the European coastal zone of the EUROSION programme (EC 2004), as presented in Table 1.

Wave height is the main hydrodynamic force, which causes sediment transport leading to erosion. Therefore, vulnerability is higher as wave height increases, while it decreases with lower wave height. Therefore, in CVI applications, wave height is included as an indicator of wave energy, influencing the coastal sediment balance. For the calculation of the significant wave height, data produced through ERA5 reanalysis from 2001 to 2017 (Copernicus database) were used (https://cds.climate.copernicus.eu/datasets/sis-ocean-wave-indicators?tab=overview).

A coast characterized by a gentle slope is considered more vulnerable to erosion than a coast with a steeper slope during an inundation event (Boumboulis et al. 2021). As a result, the coastline is classified as low vulnerability on steep coasts and as high vulnerability in gentle coasts. The coastal slope variable for Greece was determined by processing the Digital Elevation Model (DEM) (5X5 m) of Greece for a range of 8 km from coast to land. More specifically, after the creation of the DEM, it was processed to calculate the coastal slope, expressed as a percentage,

based on the distance between the 10m elevation contour and the coastline of Greece.

For the calculation of the historical shoreline change, multi-spectral satellite images of Greece from 1984 to 2024 as derived from the satellite system of Landsat and processed with ArcGIS Pro were used in order to extract the shoreline in various time periods. The evolution or rate of change of the shoreline is an important variable that indicates the deposition/erosion regime in an area. In this work, the extracted shorelines of 1984 and 2024 were used for the calculation of the rate of change from 1984 to 2024, while the DSAS software was used for the statistical visualization and estimation of the rate of change of the shoreline by calculating the end point rates (EPR). The EPR is calculated by dividing the distance of coastlines (between the oldest and more recent coastlines) by the number of years between their captured dates.

According to Gornitz (1991), macro-tidal environments (high tidal range) are vulnerable to erosion, because they can create stronger currents and cause larger sediment transportation in comparison with the micro-tidal environments. The Greek coastline has low vulnerability to erosion due to the prevailing micro-tidal regime so in the present study, this hypothesis was adopted. The data used for the calculation of tidal range was retrieved from Copernicus and confirmed Greece's low tidal range (https://cds.climate.copernicus.eu/datasets/sis-water-level-change-indicators-cmip6?tab=overview).

SLR is the annual mean increase or decrease of water elevation measured at tide gauges, and is the sum of eustatic, hydro-isostatic and tectonic factors. In this specific research, sea level rise data derived by the Copernicus platform are used, which are attributed to time series based on historical records of sea level changes (https://cds.climate.copernicus.eu/datasets/sis-water-level-change-timeseries-cmip6?tab=overview).

Results

The spatial distribution of the HCVI along the Hellenic coastlines, calculated using the equation proposed in the methodology, is illustrated in the map in Figure 1, highlighting two specific areas identified as having high and very high vulnerability. In particular, the Northwestern Peloponnese and a significant part of Northern Greece were identified under the regime of high and very high vulnerability.

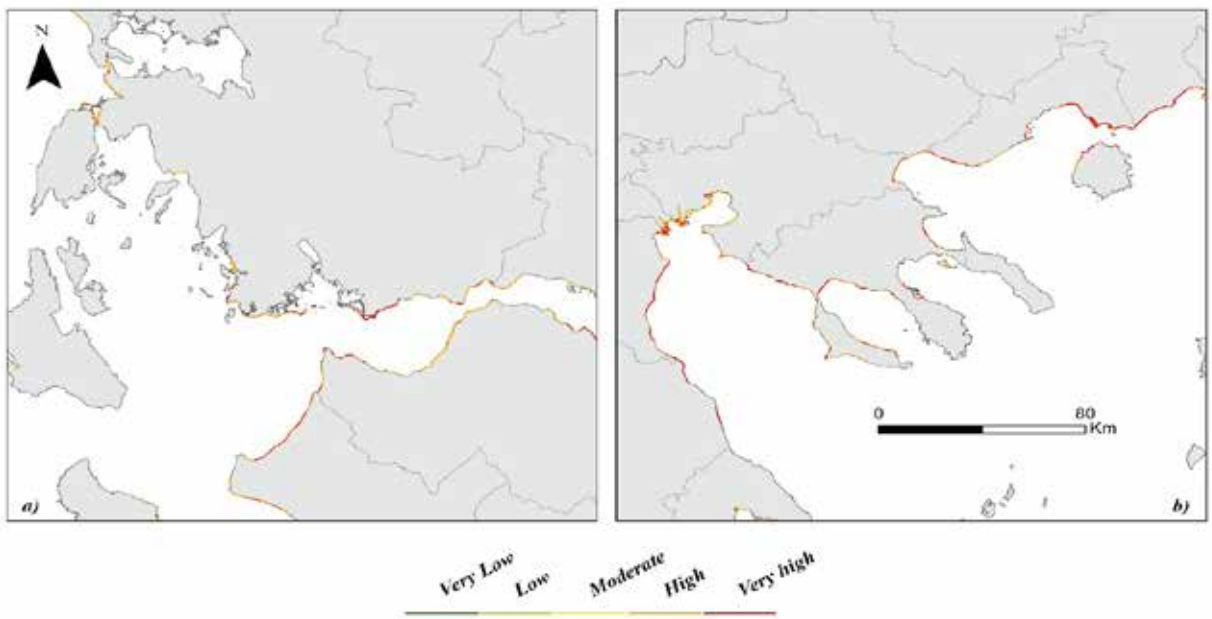

Figure 1. Spatial distribution of high and very high vulnerability classes in a) Northwestern Peloponbese and b) Northern Greece.

More specifically, a large part of the northern Peloponnese (northern and southern part of the Gulf of Patras, southern part of the Gulf of Corinth) is under a high and very high vulnerability regime. Similarly, under the regime of high to very high vulnerability is also the western part of the Peloponnese (Gulf of Kyparissia

and the shoreline from Kalogria to Kyllini) (Figure 1a). The rest of the Peloponnese is characterized by low and moderate vulnerability, with only small areas exhibiting high to very high vulnerability, notably in the Messenian and Laconian Gulfs.

A significant part of the coastline extending from the Regional Unit of Larissa to the Kassandra Peninsula is characterized by high to very high vulnerability due to the presence of gentle slopes and geological formations of low resistance to erosion (Figure 1b). Similarly, a significant part of the coastline of the Regional Unit of Kavala, as well as the entire coastline of the Regional Units of Xanthi and Evros, are characterized by high to very high vulnerability.

Most of the country's islands are in a very low to low vulnerability regime, as they are composed of rocky geological formations and steep slopes. Exceptions are the islands of Rhodes, Limnos, Lesvos, Corfu and Crete, where a large part of their coasts are in a high and very high vulnerability regime.

Conclusion

Among a variety of other indexes and methodologies, the Coastal Vulnerability Index (CVI) was chosen as a method for the estimation and calculation of vulnerability as low-cost and effective tool for mapping and managing coastal risks at a national scale. It is important to note that the coastal vulnerability assessment methodology used in this study was implemented for the first time on a national scale in Greece. Therefore, the application and the produced results can inform national strategic decisions regarding the impacts of climate related hazards on coastal zones.

However, the HCVI results presented in this study are preliminary and are expected to be further improved by incorporating additional variables into the final model, drawing on indicators identified in existing methodologies from literature. This could lead to adjustments of the index and improvements of the findings on the vulnerability of the Greek coasts.

Despite the presence of high percentage of High and Very High vulnerability classes in the study area potential future climate projection was not included in the model, which means that the vulnerability regime could be increased in the future with severe impacts for the entire coastline of Greece.

Acknowledgements

The current research was funded by the Onasis Foundation in the framework of the project "Vulnerabilty of Greek coasts due to climate change" ("Initiative 1821-2021" - Protovoulia 21).

References

Boumboulis, V., Apostolopoulos, D., Depountis N., Nikolakopoulos, K., 2021. The Importance of Geotechnical Evaluation and Shoreline Evolution in Coastal Vulnerability Index Calculations. J Mar Sci Eng 9:423. https://doi.org/10.3390/jmse9040423

EC [European Commission] 2004. Living with Coastal Erosion in Europe – Sediment and Space for Sustainability. OPOCE, Luxembourg. http://www.eurosion.org/project/eurosion_en.pdf.

Furlan, E., Pozza, PD., Michetti, M., et al., 2021. Development of a Multi-Dimensional Coastal Vulnerability Index: Assessing vulnerability to inundation scenarios in the Italian coast. Sci Total Environ 772:144650. https://doi.org/10.1016/j.scitotenv.2020.144650

Gornitz, V., 1991. Global coastal hazards from future sea level rise. Palaeogeogr Palaeoclimatol Palaeoecol 89:379–398. https://doi.org/10.1016/0031-0182(91)90173-O

Himmelstoss, E.A., Henderson, R.E., Farris, A.S., Kratzmann, M.G., Bartlett, M.K., Ergul, A., McAndrews, J., Cibaj, R., Zichichi, J.L., and Thieler, E.R., 2024. Digital Shoreline Analysis System version 6.0: U.S. Geological Survey software release, https://doi.org/10.5066/P13WIZ8M.

IPCC 2022. Impacts of 1.5°C Global Warming on Natural and Human Systems

López Royo, M., Ranasinghe R., Jiménez J.A., 2016. A Rapid, Low-Cost Approach to Coastal Vulnerability Assessment at a National Level. J Coast Res 32:932–945. https://doi.org/10.2112/JCOASTRES-D-14-00217.1

Ramieri, E., Hartley, A.J., Barbanti, A., et al., 2011. Methods for assessing coastal vulnerability to climate change. Eur Environ Agency, Eur Top Cent Clim Chang impacts, vulnerability Adapt 1–93

17th INTERNATIONAL CONGRESS of the Geological Society of Greece

BULLETIN OF THE GEOLOGICAL SOCIETY OF GREECE, SP. PUBL.

EXTENDED ABSTRACT 038

Development of a Geographic Information System for the Near-Real-Time Management of the seismic risk. Case study: The city of Mytilene, Lesvos (Greece)

E. Bouranta[1], J.N. Hatzopoulos[1]
[1]University of Aegean, Department of the Environment, University Hill, 81100 Mytilene, Greece.

[*]Corresponding author:
E-mail: bourant_e@yahoo.gr , bouranta@webmail.aegean.gr tel:6973855260

ABSTRACT

Mytilene is the capital of Lesvos, the largest island in the North Aegean. The region of North Aegean is a geotectonically complex area because its geodynamic status is directly affected by the North Anatolian Fault Zone. The seismic activity negatively impacts the material and technical infrastructure and, by extension, social and economic life. This fact makes mitigation of negative impacts of seismic events imperative. This paper describes the development of a web-based GIS for disaster response in Mytilene, Lesvos (Greece), urban area through the ArcGIS Online application (https://www.esri.com). WebGIS technologies provide a wide range of solutions for fault mapping, data analysis, and publication of results. The completion of this project contributes to the improvement of methodologies and applied technologies and the proposal and development of new ones, indicating the direction for the implementation of similar research projects and the introduction of new geographic information technologies in seismic risk management.

Keywords: Earthquakes, emergency management, GIS, Web-based

1. Introduction

An earthquake is a highly challenging natural phenomenon to forecast, making each occurrence essential for advancing research (Darzi et al., 2022). Geographic Information System (GIS) can support disaster management as a powerful tool for collecting, storing, analyzing, modeling, and displaying large amounts of data. Online GIS combines the advantages of both GIS and the Internet. The WebGIS is addressed to a broad target of end users and supports the implementation of seismic risk mitigation strategies. Web GIS is one of the most widely used technologies for the propagation of open data for multiple purposes. WebGIS technologies have also been widespread for natural risk assessment and communication (*Daud et al., 2024; Vinueza-Martinez et al., 2024*). Web GIS and geodatabase technologies have been used to advance interactive tools for defining seismic hazard scenarios and risk analysis (Pessina & Meroni, 2009; *Aye et al., 2015*). The ArcGIS Online application (https://www.esri.com) helps create interactive maps.

An Earthquake Information Management System (EIMS) is a system that records, collects, keeps, retrieves, and analyzes inputs, produces reports and required information for earthquakes, and informs the responsible stakeholders. The information does not comprise an end but contributes to better decisions in policy design, disaster planning, management, monitoring, and evaluation of disaster plans and damage reduction (*Ajami & Fattahi, 2009; Kirschenbaum et al., 2017).*

Earthquake Information Management Systems (EIMS) use ArcGIS (Geographic Information System) to map and visualize ground vibration, the pattern of damaged buildings, and demographic information about a community (*Cao et al., 2023)*. Once the location and magnitude of an earthquake have been determined, the EIMS will assess the distribution of ground vibrations, building failures, casualties, transmission system failures, power, and water outages, population displacement, and the cost of repairing potential faults (Ajami et al., 2008; Cao et al., 2023). In this study, we developed a Web GIS for earthquake management and monitoring in the urban area of Mytilene, Lesvos (Greece). Decision-makers and the general public can use our Web-based GIS model.

2. Materials and methods

2.1. General description of the analyzed area

Lesvos is the third largest island of the Greek Islands, with 1.632 square kilometers in extent. It is located in the northeastern Aegean Sea. Mytilene is the capital of the island of Lesvos and the Prefecture of Lesvos. The geology can be summarized as a basement composed of Alpidic and pre-Alpidic metamorphic rocks, which were covered later by post-Alpine formations, mainly Miocene volcanic rocks and Neogene marine and lacustrine deposits (Soulakellis et al., 2006). The island was characterized by high seismicity hazards and had been affected many times by powerful, devastating earthquakes. Mytilene is the capital of Lesvos and is located in the eastern part of the island. The altitude fluctuates from 0 to 100 m, and it is a smooth relief.

2.2. Methodology

The steps of the methodology include:

1. Microtremor measurements and processing

Microtremor measurements have been conducted to study the site effect and the site ground response in case of an earthquake in the urban area of Mytilene. The Horizontal-to-Vertical Spectral Ratio (HVSR) technique has been applied to ambient noise measurements (Nakamura's technique). The Nakamura technique is helpful for subsurface soil structure and site response studies (*Araque-Pérez, 2024*). The microtremor HVSR method has been widely used in seismic micro-zonation and site effect studies.

Ambient noise measurements have been performed in Mytilene from May 2012 to February 2013. One hundred measurements of ambient noise have been conducted throughout the city. The measurements were carried out from Monday to Friday from 23:00-02:30. A global Positioning System (GPS) module localizes the spatial position of each measurement point (Hatzopoulos & Hatzopoulos, 2024). The sampling rate was 200Hz, and the recording duration was 30 minutes. These data are acquired according to guidelines proposed by Duval et al. (2004). The sites of microtremor recordings were selected to cover all the different geological formations of the area. Figure 1 shows the locations of measured points in the urban town of Mytilene.

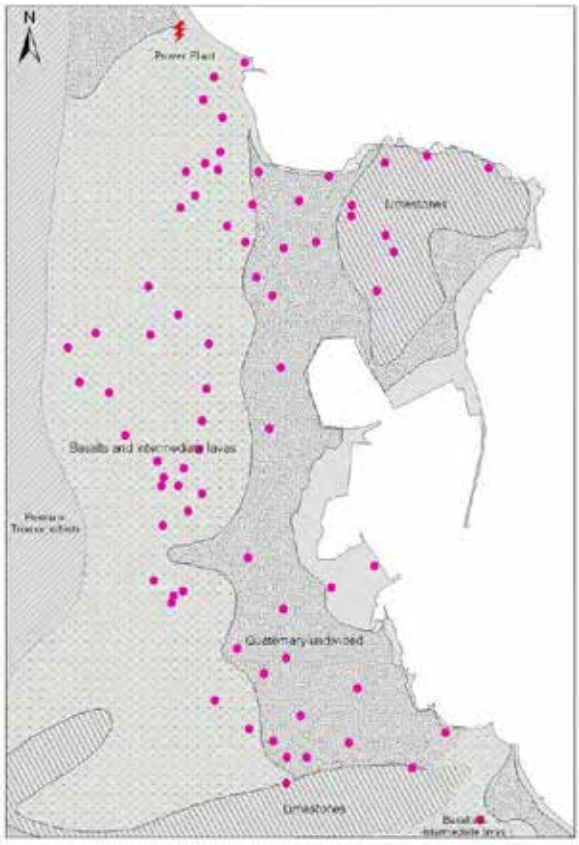

Figure 1. Position map of microtremor measurements in the urban area of Mytilene

2. Deployment of temporary strong motion network

A strong motion sensor network was deployed in the three different geological formations to provide valuable information for the region (Fig. 2). A total of 198 seismic events were recorded from December 15, 2014, to July 20, 2015, for the study area.

Figure 2. One of the three stations. The accelerograph is on the left, and the GPS is on the right.

The spatial distribution of the strong motion parameters, such as the Peak Ground Acceleration (PGA), Peak Ground Velocity (PGV), and Peak Ground Displacement (PGD) observed at the urban area of Mytilene are presented with the use of a Geographic Information System (GIS) environment (Figures 3, 4, 5). The results provide valuable information on earthquake hazards before and after detrimental seismic events to supply systems supporting civil protection decisions for prevention and emergency response.

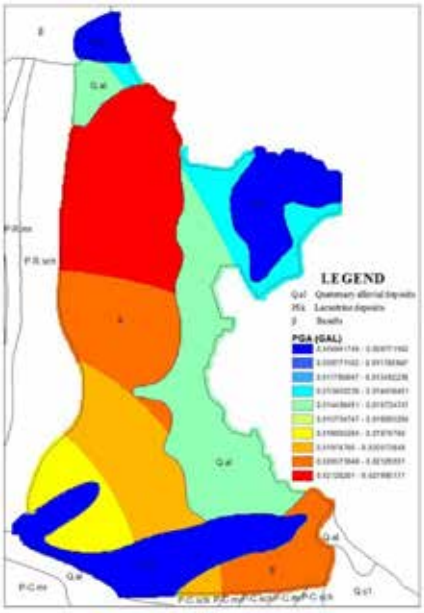

Figure 3. Spatial Distribution of PGA

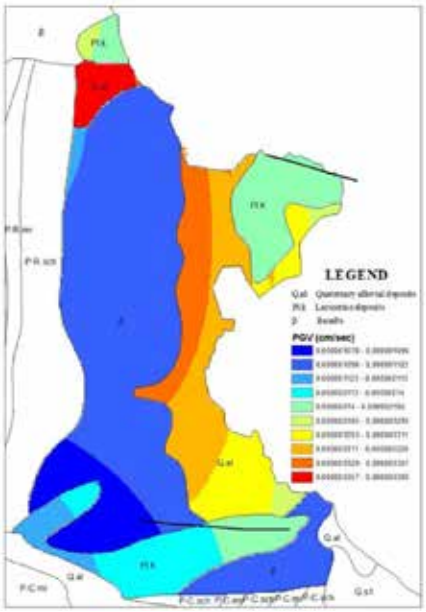

Figure 4. Spatial Distribution of PGV

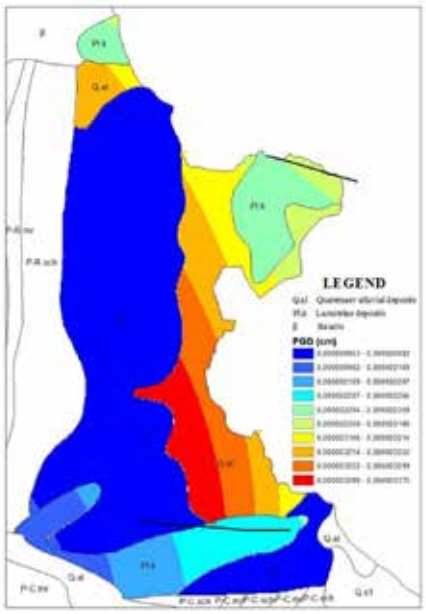

Figure 5. Spatial Distribution of PGD

3.

3. Development of a Web-based interface for earthquake management and monitoring

Finally, dynamic seismic hazard maps were created for the urban complex of Mytilene. Dynamic maps enable the user to manage geoinformation via the Internet. Creating a dynamic map requires the use of a network GIS. (web GIS). This is a GSP that can work and be used on the Internet. Using the ArcGIS Online application (https://www.arcgis.com/home/), the corresponding dynamic maps of maximum ground acceleration (PGA), maximum ground speed (PGV), and maximum ground shift (PGD) were created. The application allows the creation of custom cartographic compositions with user data and the ability to select a background.

3. Results and Discussion

The pilot strong-motion network comprises three stations, which were, however, strategically positioned to represent distinct geological formations. The objective was not to achieve full spatial coverage, but rather to evaluate the potential for site-specific, geology-dependent ground response. This approach serves as a foundation for the future expansion of the network. The correlation of recorded motion data with subsurface characteristics provides valuable insights into the spatial variability of seismic site effects.

WebGIS is constantly gaining ground in decision-making and spatial planning applications, as it enables researchers and stakeholders to benefit from the visualization, exchange, and evaluation of geospatial data with minimal effort and cost. Both scientific staff and stakeholders having access to the correct data at the right time can make the right decisions to mitigate the effects and address the risks of an impending earthquake. Thus, an online GIS can be a powerful tool in all phases of a disaster management cycle. The proposed platform distinguishes itself through its focused application at the local scale, effectively integrating in-situ microtremor measurements with real-time strong-motion data. A key innovation lies in its capacity to generate dynamic seismic hazard maps and offer interactive tools designed to serve both technical experts and the broader public, thereby enhancing accessibility and practical utility in risk communication.

The generated maps of maximum ground acceleration (PGA), maximum ground velocity (PGV), and maximum ground displacement (PGD) can give an idea of the magnitude of the damage that an earthquake can cause depending on the existing local soil conditions. Assessing the effects of an earthquake enables preparedness and immediate response to the crisis in the event of an earthquake. The dynamic maps that are created can be shared via a link. Following the link below gives the user direct access to dynamic maps: http://arcg.is/1QIlj1X (Fig.6).

Figure 6 is a screenshot of the application and illustrates the interface of the WebGIS application, showing the PGA map, where users can interactively explore areas of maximum ground acceleration based on different parameters. The map highlights the spatial variation of PGA across the region, helping stakeholders prioritize high-risk zones.

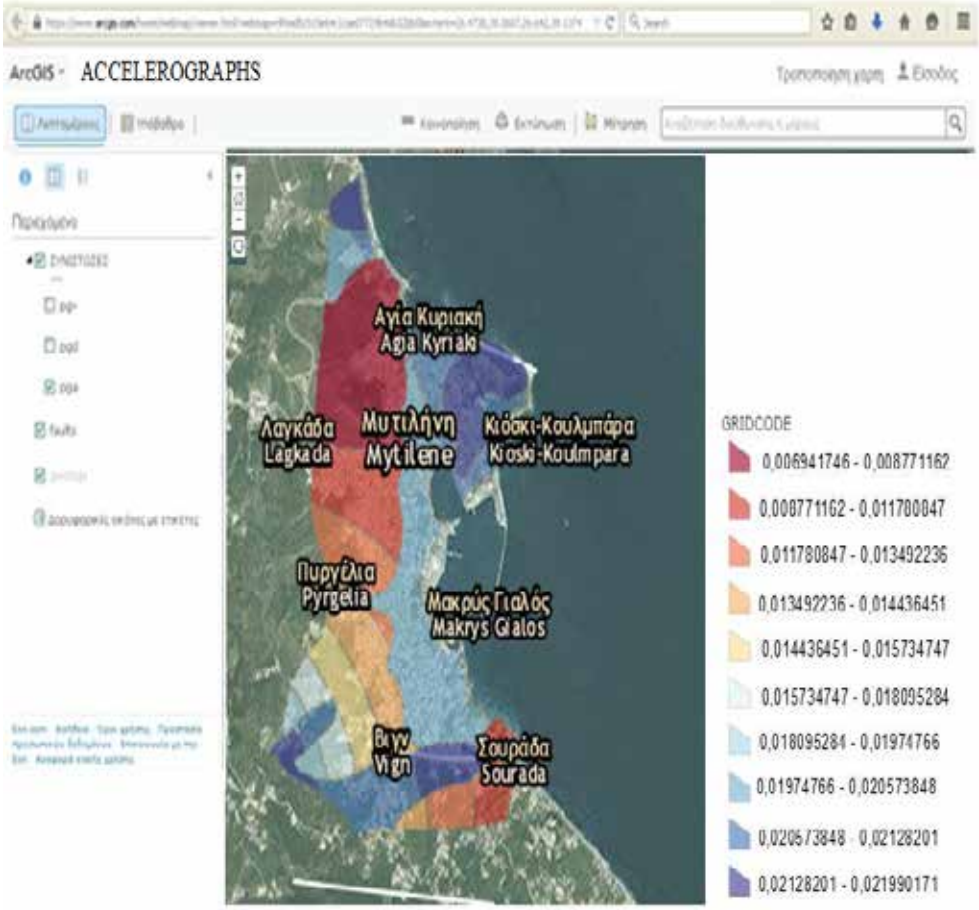

Figure 6. Screenshot of application

The analysis conducted in this study highlights the criticality of using WebGIS tools for earthquake preparedness and disaster management. For the city of Mytilene, the generated maps indicate specific areas that are more vulnerable to seismic activities due to local soil conditions. In particular, zones with high PGA and PGV values should be given priority in terms of preventive measures and resource allocation. These high-risk areas can guide city planners and emergency response teams to implement targeted interventions that mitigate potential damages.

Moreover, the findings suggest that immediate attention should be focused on zones with critical infrastructure and dense populations in an earthquake. Prioritizing these areas ensures residents' safety and essential services' functionality. The application of WebGIS in identifying and visualizing such zones proves invaluable for proactive planning and efficient disaster response. By integrating real-time data and dynamic maps, stakeholders can make informed decisions that enhance the resilience of Mytilene to seismic hazards.

The obtained results can be a valuable tool for the rational management of seismic risk as they can be applied at any stage of disaster management (mitigation, preparedness, response, rehabilitation). In the future, as far as the online GIS is concerned, this will mainly be addressed to experts and the general public. For this reason, a mechanism could be created to offer solutions to non-skilled people, such as making a discussion forum. Developing an application using open-source or free software could also be addressed to any user, enabling the general public to participate in decision-making processes.

The developed WebGIS system demonstrates strong potential for future scalability and functional

expansion. One of its most promising directions lies in the integration of additional datasets, such as detailed building inventory information—including structural typology, construction year, and height—as well as socio-economic indicators like population density, age distribution, and social vulnerability indices. Incorporating such multidimensional data would enable the generation of more sophisticated and realistic seismic risk scenarios, tailored to both the physical and human dimensions of urban environments. Furthermore, the integration of Building Information Modeling (BIM) technologies with the WebGIS framework could pave the way for a unified risk management platform, combining geospatial intelligence with structural-level detail. This holistic approach would significantly enhance the capacity for pre-event planning, impact assessment, and post-event response in earthquake-prone areas. Finally, registering building stock data in an electronic database would make it possible to create seismic risk scenarios, which would be a helpful guide for the relevant services.

Acknowledgement.

Bouranta Evangelia was supported by the Greek State Scholarships Foundation (IKY). The authors would like to express sincere thanks and appreciation to **Professor Filippos Vallianatos** for his invaluable guidance, insightful feedback, and continuous support throughout the development of this work.

References

Ajami, S., & Fatahi, M. (2008). Reduce destroys and rule of Earthquake Information Systems: The comparative study in Turkey, Afghanistan and Iran. In *Proceedings of the International Disaster and Risk Conference (IDRC)* (August 25–29). Davos, Switzerland.

Ajami, S., & Fattahi, M. (2009). The role of earthquake information management systems (EIMSs) in reducing destruction: A comparative study of Japan, Turkey, and Iran. *Disaster Prevention and Management, 18,* 150–161.

Araque-Pérez, C. (2024). Reevaluating soil amplification using multi-spectral HVSR technique in La Chana neighborhood, Granada, Spain. *Journal of Seismology.*

Aye, Z. C., Jaboyedoff, M., Derron, M., Westen, C. J., Hussin, H., Ciurean, R. L., Frigerio, S., & Pasuto, A. (2015). An interactive web-GIS tool for risk analysis: A case study in the Fella River basin, Italy. *Natural Hazards and Earth System Sciences, 16,* 85–101.

Cao, Y., Xu, C., Aziz, N.M., & Kamaruzzaman, S.N. (2023). BIM-GIS Integrated Utilization in Urban Disaster Management: The Contributions, Challenges, and Future Directions. Remote. Sens., 15, 1331.

*Darzi, A., Bessason, B., Halldorsson, B., Molina, S., Kharazian, A., & Moosapoor, M. (2022). High spatial-resolution loss estimation using dense array strong-motion near-fault records. Case study for Hveragerði and the Mw 6.3 Ölfus earthquake, South Iceland. International Journal of Disaster Risk Reduction, 73***, 102894.**

Daud, M., Ugliotti, F. M., & Osello, A. (2024). Comprehensive analysis of the use of Web-GIS for natural hazard management: A systematic review. *Sustainability.*

Hatzopoulos, J., D. J. Hatzopoulos (2024). *Topographic Mapping.* Second Edition. Boca Raton, FL: Universal Publishers.

Kirschenbaum, A.A., Rapaport, C., & Canetti, D. (2017). The impact of information sources on earthquake preparedness. International journal of disaster risk reduction, 21, 99-109.

Pessina, V., & Meroni, F. (2009). A WebGIS tool for seismic hazard scenarios and risk analysis. *Soil Dynamics and Earthquake Engineering, 29,* 1274–1281. https://doi.org/10.1016/j.soildyn.2009.03.001

Soulakellis, N., Novak, I., Zouros, N., Lowman, P., & Yates, J. (2006). Fusing Landsat-5/TM imagery and shaded relief maps in tectonic and geomorphic mapping: Lesvos Island, Greece. *Photogrammetric Engineering & Remote Sensing, 72*(6), 693–700.

Vinueza-Martinez, J., Correa-Peralta, M., Ramírez-Anormaliza, R., Franco Arias, O., & Vera Paredes, D. (2024). Geographic information systems (GISs) based on WebGIS architecture: Bibliometric analysis of the current status and research trends. *Sustainability.*

17th INTERNATIONAL CONGRESS of the Geological Society of Greece

BULLETIN OF THE GEOLOGICAL SOCIETY OF GREECE, SP. PUBL.

EXTENDED ABSTRACT 039

Facies and depositional architecture of Upper Miocene tidal flat sedimentation in Kefalonia and Corfu Islands, West Greece

Bourli N.[1], Botziolis Ch.[1], Papadopoulou P.[2], Zelilidis P.[2], Zoumpouli E.[1], Iliopoulos G.[2], Maravelis A.G.[3], Tripsanas E.[4], Oikonomopoulos I.[4], Pagoulatos A.[4], Zelilidis A.[1]

1 University of Patras, Department of Geology, Laboratory of Sedimentology, 26504, Patras, Greece, n_bourli@ac.upatras.gr

2 University of Patras, Department of Geology, Laboratory of Paleontology and Stratigraphy 26504, Patras, Greece.

3 Department of Geology, Aristotle University of Thessaloniki 54124 Thessaloniki, Greece

4. HELPE Upstream S.A., Hellenic Energy Holdings S.A., 8ª Chimaras str., 15125 Marousi Athens, Greece.

This research involves the integrated sedimentological and paleontological analysis of the Neogene tidal deposits in the eastern parts of the Hellenic Fold and Thrust Belt, in South Kefalonia (Paliolinos - Avithos coast) and in NW Corfu (Arillas coast) islands. The study of tidal is supported by illustrative outcrop photographs, with a particular emphasis on two synthetic outcrops. Sedimentary logs were generated to document detailed bed-by-bed measurements, descriptions, and identification of sedimentary structures. Additionally, over 75 samples were chosen for age determination and paleoenvironmental analysis. Micropaleontological analysis encompassed 52 samples from South Kefalonia and 23 samples from NW Corfu and the results point to an Upper Miocene time interval. The sedimentological examination revealed sixteen distinct sedimentary structures within the studied deposits. The study results indicate for NW Corfu that the deposition displays fluctuations between low and high energy episodes, predominantly representing a tidally-influenced continental shelf (Figure 1a); whereas in the South Kefalonia deposition took place in a back-barrier restricted basin and highly active margins (Figure 1b). The different tidal environments, in the two studied regions, were related with the different tectonic conditions. When the tidal environment in a basin mostly controlled either by transfer or strike-slip faults, open shelf tidal environment could be formed; whereas when the major influence is the normal or the thrust faults then a tidal back-barrier environment could be formed.

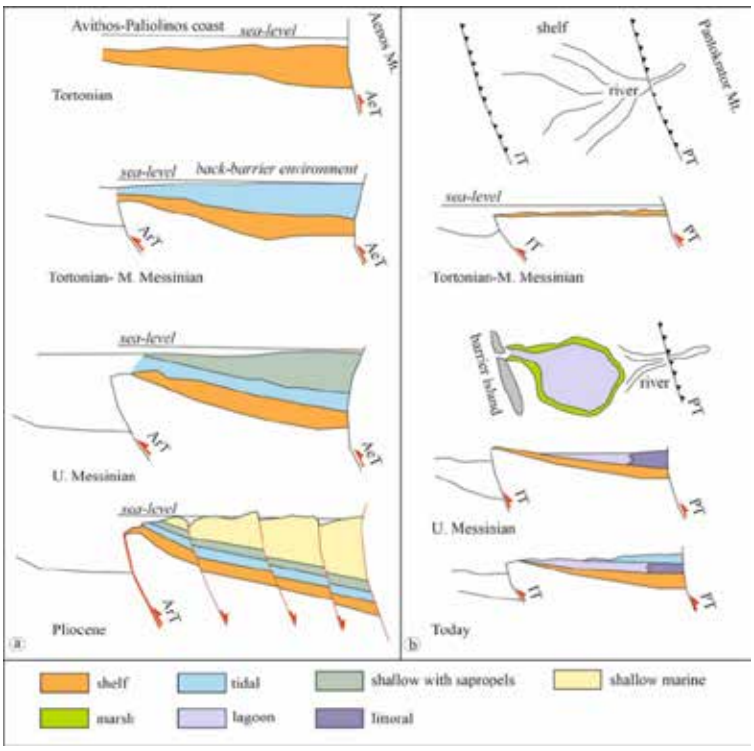

Figure 1. Evolutionary models for two studied areas.

Key words: Kefalonia Island, Corfu Island, shallow-marine tidal deposits, open coast tidal flats, Greece.

17th INTERNATIONAL CONGRESS of the Geological Society of Greece

BULLETIN OF THE GEOLOGICAL SOCIETY OF GREECE, SP. PUBL.

EXTENDED ABSTRACT 040

Tsunami modelling for a potential earthquake between Santorini and Amorgos (Greece)

Bufféral S.[1], Briole P.[1], Dupont A.[2], Escartin J.[1], Heinrich P.[2]
(1) Laboratoire de Géologie, ENS-CNRS, UMR3538, PSL University, Paris, France - simon.bufferal@ens.fr
(2) CEA, DAM, DIF, F-91297 Arpajon, France

Highlights

The seismic swarm that struck northeast of Santorini Island (Greece) in February 2025 highlights the critical need to assess tsunami hazards in this historically vulnerable region. Using Okada's model for seafloor displacement and subsequent tsunami simulations, we discuss hypothetical tsunami scenarios from shallow normal faults identified around the recent swarm. Our simulations suggest that a potential tsunami could impact the eastern coast of Santorini in as little as 6 minutes and reach the surrounding islands within 25 minutes. For a magnitude Mω = 6.3–6.5 earthquake, heights along nearby coastlines could range from 0.1 to 0.6 meters, with localized amplification possible in closed bays. Based on these scenarios, we propose a strategic placing of tide gauges at Agios Nikolaos Port (Anafi) and Agios Andreas (Astypalaia) to enhance tsunami detection and improve regional early warning capabilities.

Context

A volcano-tectonic unrest has been active since late 2024 in the surrounding area of the Santorini volcano, in the Aegean Sea (Greece), peaking with a significant seismic swarm during the first half of February 2025, along a fault zone that ranges between Santorini and Amorgos islands. This region is characterized by both significant volcanic and seismic hazards, as it lies along the volcanic arc associated with the Hellenic subduction zone and an active rift likely related to the Anatolian extrusion. Historically, the area has experienced destructive tsunamis, notably a volcanic-induced event after the Minoan eruption at Santorini around 1600 BC (McCoy and Heiken, 2000; Friedrich *et al.*, 2006; Manning *et al.*, 2006; Goodman-Tchernov *et al.*, 2009) and an earthquake-triggered tsunami after the 9 July 1956 earthquake along the eastern coast of Amorgos (Galanopoulos, 1957; Ambraseys, 1960; Okal *et al.*, 2009; Leclerc *et al.*, 2024). The 2025 seismic crisis has been occurring in the southwestern continuity of the 1956 earthquake zone, underlining the need for a reevaluation of the seismic and tsunamigenic hazards in the area.

Potential for seismic rupture

The seismic crisis began in September 2024 within the Santorini caldera, then migrated northeast of the island starting on 27 January 2025. During February 2025, approximately 200 earthquakes with magnitudes Mω ≥ 4.0 and 8 events with Mω ≥ 5.0 were recorded[1]. At the time of writing (March 2025), seismic activity has been slowing down, although earthquakes exceeding Mω ≥ 4.0 continue to occur intermittently. With geodetic modelling indicating a total slip in the middle to lower crust of an equivalent seismic moment of $2 \cdot 10^{19}$ N·m, i.e., over an order of magnitude greater than the cumulative moment released seismically, the possibility of a stronger earthquake triggered by elastic loading of the upper crust cannot be ruled out. Independent studies have found that the observed surface deformation is consistent with a slow-slip event occurring on a low-angle, southeast-dipping plane initiating below 7 km depth (Briole *et al.*, *in review*). Assuming a listric geometry, this segment would intersect the surface at the mapped location of the West Ios Fault, according to the NOAfaults database (Ganas, 2024; see Table 1 and Figure 1). The present study explores the possibility of rupture on the shallow, locked portion of that fault, and the tsunami that would follow. We model such a scenario by simulating a shallow earthquake producing 0.8 m of slip on a fault measuring 22 km in length and 11 km in width, with an average dip of 50°, consistent with a moment magnitude of Mω = 6.5. This scenario is compared with two additional candidate faults from the NOAfaults database (see Table 1), each approximately 14 km long and 9 km wide, with a dip of 60°. A slip of 0.8 m on such a fault would correspond to a moment magnitude of Mω = 6.3. The focal mechanism for a hypothetical rupture on the Ios West Fault (GR2691) is presented in Figure 1.

1 https://bbnet.gein.noa.gr/HL/databases/database

Table 1. Characteristics of the two candidate faults considered.

Fault Code	Name	Length	Width	Centroid (°E, °N, Depth)	Azimuth	Dip	Slip Type
GR2691	Ios West fault	22.0 km	11 km	25.51, 36.72, 5 km	N054°	50° SE	Pure normal
GR3219	Anhydros Fault	14.6 km	9 km	25.71, 36.52, 7 km	N045°	60° NW	Pure normal
GR3222	SAF-SW Branch	13.5 km	9 km	25.55, 36.58, 7 km	N222°	60° SE	Pure normal

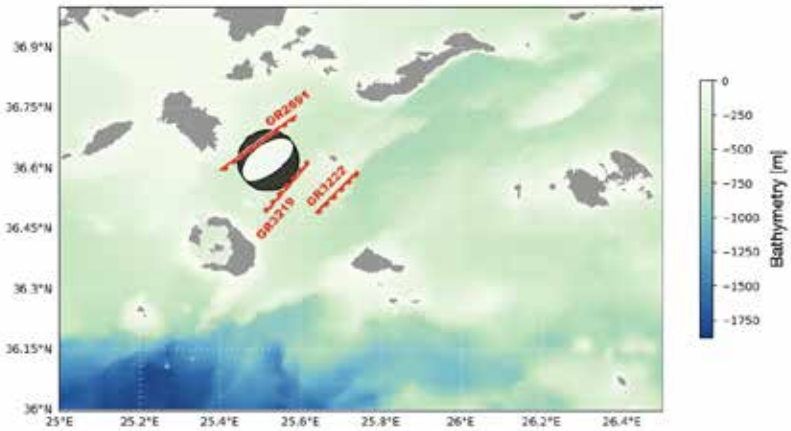

Figure 1. Focal mechanism of a hypothetical rupture on Ios West Fault (GR2691): N054°, 50°SE, pure normal slip.
Simplified surface traces of faults GR3219 and GR3222 are also represented.

Tsunami simulations

We use Okada's equations (Okada, 1985) to calculate the seafloor displacement induced by potential ruptures on the main faults surrounding the 2025 seismic zone (see Table 1 and Figure 1). The Glimsdal transfer equation (Glimsdal *et al.*, 2013) is then applied to evaluate the initial water surface deformation (Figure 2). Finally, tsunami propagation is modelled using the Taitoko code, developed by the Commissariat à l'Énergie Atomique (CEA, France), based on shallow-water wave equations (Heinrich *et al.*, 2021; Heinrich *et al.*, 2024). These calculations use bathymetric data from the European Marine Observation and Data Network (EMODnet[2]), with a grid resolution of 110 meters.
Figure 2 illustrates the initial water surface displacement for an instantaneous and homogeneous normal slip of 80 cm on fault GR2691, with its upper edge located at 1 km depth.

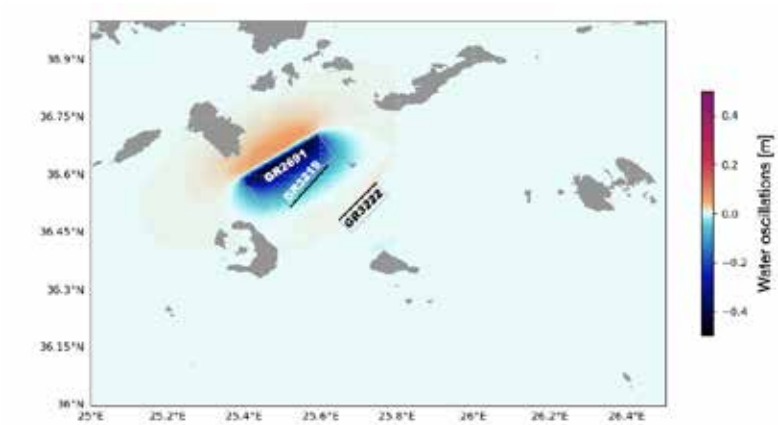

Figure 2. Initial water displacement for 80 cm homogenous normal slip stopping at 1 km depth on Ios West Fault (GR2691). Surface projection of the rupture patch is represented with a rectangle. Potential rupture areas on faults GR3222 and GR3219 are also drawn.

2 https://emodnet.ec.europa.eu/en

Figure 3 shows the wave position after 10 minutes of propagation for the same model. One of the key results of our simulations is that, if an earthquake were to occur in the zone of unrest, the first wave would reach:

- the eastern coast of Santorini in 6 to 15 minutes, depending on the fault location and dip direction;
- Agios Nikolaos Port (Anafi Island) in 11 to 16 minutes;
- Katapola Port (Amorgos Island) in 20 to 25 minutes;
- Chora Port (Ios Island) in 20 to 27 minutes.

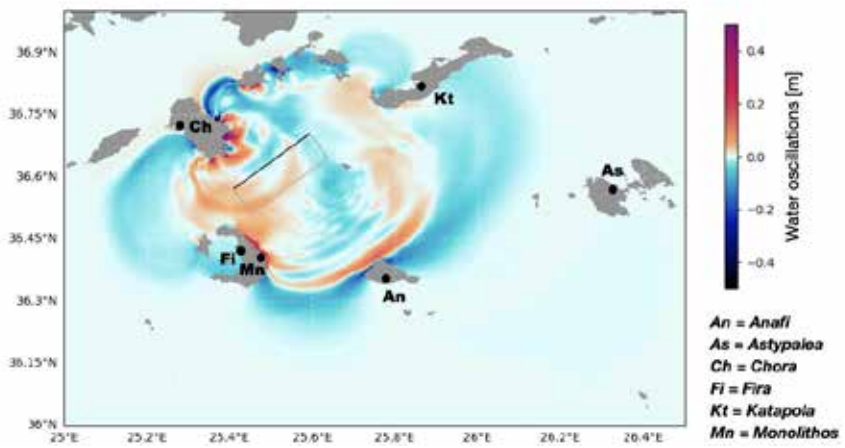

Figure 3. Location of the wave after 10 minutes of propagation for the scenario of a rupture with an 80 cm normal slip stopping at 1 km depth on fault GR2691. The locations of the main harbors are indicated.

Figure 4 presents these arrival times for key ports and coastal areas for a rupture on fault GR3222. These short arrival times emphasize the critical need for early anticipation to ensure an effective response for at-risk populations.

According to our simulations, a tsunami generated by such ruptures would produce wave heights between 0.2 and 0.5 m along the coastlines of nearby islands (Figure 5). The precise wave height depends on the depth and location of the rupture. While these heights may seem moderate, they represent a significant volume of displaced water and high wave energy upon coastal impact, as observed in Samos in 2020 (Kalligeris *et al.*, 2022), with potential risks to people and infrastructure. Due to their geomorphological configuration, bays and inlets are particularly vulnerable to wave amplification, making coastal flooding highly likely in the most pessimistic scenarios.

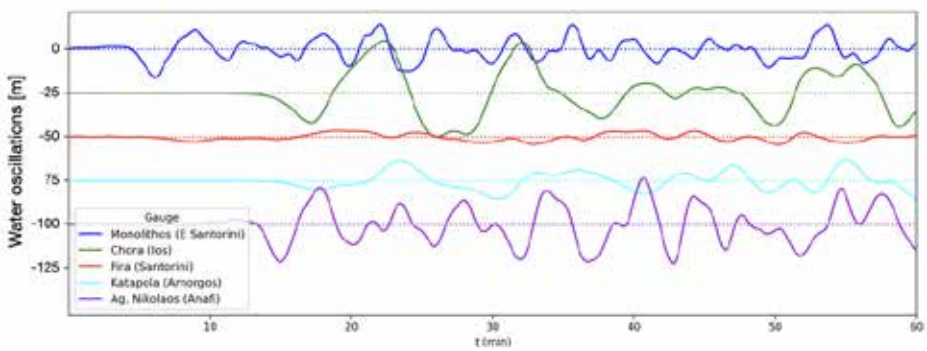

Figure 4. Arrival times at nearby harbors relative to the earthquake origin time for 80 cm normal slip stopping at 3 km depth on fault GR3222.

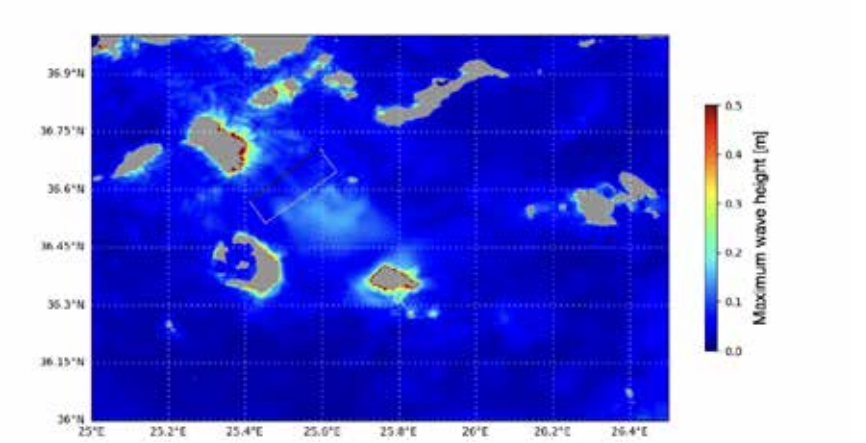

Figure 5. Maximum wave height for 80 cm normal slip stopping at 1 km depth on fault GR2691. These large-scale results do not take into account further local wave amplification phenomena in bays and inlets.

Figure 6 shows the water movement in Chora Bay (Ios Island) for two fault locations:

- GR3219: northwest dip, southwest of Anhydros Island.
- GR3222: southeast dip, south of Anhydros Island.

The upper edge of the rupture is tested at 1 km, 3 km, and 5 km depth.

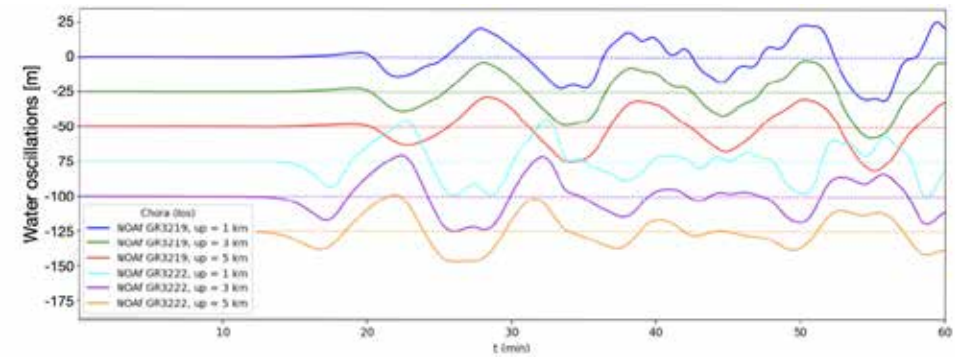

Figure 6: 1-hour water oscillations in Chora Bay (Ios) for two faults and three upper rupture depths.

Our simulations indicate that, in this configuration with several closely spaced islands, the rupture location is the primary factor influencing both wave arrival times and wave attenuation or amplification, depending on interactions with headlands, islands, or underwater obstacles. For instance, shifting the hypocenter 15 km north significantly reduces the wave amplitude reaching Chora Bay (Figure 6). Unlike lower-magnitude earthquakes, whose effects are quickly dampened by upper-crustal layers, the depth of the upper fault edge appears to play a secondary role, provided it remains within realistic values for the region. As shown in Figure 6, variations in depth have a negligible impact on tsunami amplitude, with a maximum discrepancy of only a few centimeters. The azimuth and dip angle of the fault also have limited influence on tsunami morphology, as any normal fault generates an initial water surface depression with a relatively consistent shape. This is confirmed by tests made using the same fault location but opposite fault dips.

Comparison with the 1956 Amorgos Tsunami

On 9 July 1956, a magnitude Mω = 7.1–7.8 earthquake struck south of Amorgos Island, just a few dozen

kilometers north of the current seismic swarm. This event generated an exceptionally large tsunami, with waves reaching up to 20 meters in height in Astypalaia, causing three direct fatalities on Kalimnos Island and several injuries and severe coastal damage in the nearby islands (Ambraseys, 1960).
For a long time, the unusual size of this tsunami was attributed to a submarine landslide (Galanopoulos, 1957; Okal *et al.*, 2009), which was believed to have displaced a large volume of water, producing a wave of exceptional intensity. However, recent studies have failed to find clear evidence of such a landslide, shifting the focus to the hypothesis of a co-seismic displacement of approximately 10 meters as the primary cause (Leclerc *et al.*, 2024).
Given the steep submarine slopes in the region, which show evidence of past landslides, a similar scenario cannot be ruled out for the ongoing seismic crisis, potentially leading to a much stronger tsunami. This study does not specifically address this less likely hypothesis.

Implications for a useful monitoring of future tsunamis

In response to recent tsunami events, studies that used local high-resolution bathymetric data digitized from nautical charts demonstrated that incorporating finer (e.g., ~10 m pixel resolution) bathymetric grids into models significantly modifies tsunami waveforms, potentially doubling wave amplitudes at the coastline (Zahradník *et al*., 2022; Alfonsi *et al*., 2024). It is therefore highly problematic that, despite the existence of numerous high-resolution bathymetric datasets in the Aegean Sea, none are freely accessible. This situation introduces significant reliability issues for tsunami modelling and poses a critical risk to civil safety, as emergency preparedness scenarios may be underestimated, leading to inadequate hazard assessment.
It should also be noted that environmental factors, such as tidal conditions and atmospheric pressure, can intensify the impact of tsunamis. These key parameters call for continuous monitoring of sea level heights and coastal subsidence in the region. In this framework, as part of the ongoing GNSS deployment aimed at monitoring, among others, the Santorini magma chamber inflation, a priority should be given to co-located GNSS and tide gauge stations.
Based on our simulations, closed bays such as the Santorini Caldera, where sub-meter amplitude waves either do not arrive or arrive with a significant delay, should be avoided. Instead, we recommend the maintenance and continuity of instruments on the east coast of Santorini (e.g., NOA-99[3]), where waves arrive quickly with minimal interference or attenuation.
Our results highlight the need for more tide gauges in the region, to monitor water movements in the event of a tsunami, to better constrain climate-change-induced sea level rise, and, ideally, to provide early warning if the gauges are positioned at strategic locations along possible wave paths. High-frequency sampling (~1 Hz) is advised to ensure a rapid and accurate tsunami alert. In the framework of the current instrumentation of the Santorini region, we suggest two more locations for additional tide gauge installation:
● Port of Agios Nikolaos, on the island of Anafi. This harbor appears to be a strategic location for early warning. Simulations show that waves always reach it quickly due to the deep waters offshore. It is not located in an enclosed bay, and the coastline is relatively smooth, minimizing the effects of wave interference. From a broader regional perspective, southern Anafi is an optimal monitoring site as it would be among the first coasts to be hit by a tsunami arriving from the south, particularly likely given the seismic hazard in Crete, which hosts both the Hellenic subduction zone and active normal faults.
● Port of Agios Andreas, on the north coast of the island of Astypalaia. Given the high amplitude of the waves that reached this coast after the 1956 earthquake (Ambraseys, 1960), the harbor of Agios Andreas, on the north coast of Astypalaia, appears as a suitable location for studying large-scale wave propagation in the region.

Conclusions

● The possibility of a tsunami triggered by volcanic or seismic events in the highly active southern Aegean

3 http://antares.gein.noa.gr/TAD_Server/SensorData.aspx?id=53

Sea is significant and must be taken into account. Local populations and tourists should be adequately prepared, particularly by being informed about potential wave propagation scenarios resulting from such events. Civil protection authorities should also be ready to issue tsunami alerts rapidly.

● Accurate knowledge of wave trajectories and arrival times is crucial for enhancing preparedness and improving tsunami early warning protocols. Tsunami wave modelling allows for identifying the most suitable observation sites, whether for post-event analysis to understand tsunami processes or for real-time monitoring to support early warning systems. It also helps distinguish less strategic locations, such as enclosed harbors, where waves tend to be delayed and are less representative of regional tsunami impacts.

● Additional tide gauges are needed to better constrain tsunami models and support the development of early warning capabilities. Moreover, sea-level sensors serve as valuable tools for monitoring broader phenomena, such as climate change-induced sea-level rise, underscoring the need for long-term installations capable of producing reliable time series with minimal influence from local effects like coastal subsidence.

● The critical lack of publicly available coastal bathymetric data introduces significant uncertainties into tsunami modelling, putting people's lives at risk. Addressing this urgent issue by ensuring the existence of comprehensive and accessible coastal bathymetric datasets is, therefore, of paramount importance.

References

Alfonsi, L., Cesaroni, C., Hernandez-Pajares, M., Astafyeva, E., Bufféral, S., Elias, P., Belehaki, A., Tsagouri, I., Yang, H., & Guerran M., 2024. Ionospheric response to the 2020 Samos earthquake and tsunami. Earth Planets Space 76, 13. https://doi.org/10.1186/s40623-023-01940-2

Ambraseys, N., 1960. The seismic sea wave of July 1956 in the Greek Archipelago: J. Geophys. Res., v. 65, p. 1257–1265.

Briole, P., Ganas, A., Serpetsidaki, A., Beauducel, F., Sakkas, V., Tsironi, V., & Elias, P., Volcano-tectonic interaction at Santorini. The crisis of February 2025. Constraints from geodesy. Geophysical Journal International.

Friedrich, W.L., Kromer, B., Friedrich, M., Heinemeier, J., Pfeiffer, T., & Talamo, S., 2006. Santorini eruption radiocarbon dated to 1627–1600 B.C. Science, 312, 548, doi: 10.1126/science.1125087.

Galanopoulos, A.G., 1957. The seismic sea wave of 9 July 1956. Prakt. Akad. Athens, 32, 90–101 (in Greek).

Ganas, A., 2024. NOAFAULTS KMZ layer Version 6.0 (version 6.0) [Data set]. Zenodo. https://doi.org/10.5281/zenodo.13168947

Glimsdal, S., Pedersen, G.K., Harbitz, C.B., & Løvholt, F., 2013. Dispersion of tsunamis: does it really matter? Natural Hazards and Earth System Sciences, 13(6), 1507–1526.

Goodman-Tchernov, B.N., Dey, H.W., Reinhardt, E.G., McCoy, F., & Mart, Y., 2009. Tsunami waves generated by the Santorini eruption reached Eastern Mediterranean shores. Geology, 37(10), 943–946.

Heinrich, P., Dupont, A., Menager, M., Trilla, A., Gailler, A., Delouis, B., & Hébert, H., 2024. Simulation of the Mediterranean tsunami generated by the Mw 6.0 event offshore Bejaia (Algeria) on 18 March 2021. Geophysical Journal International, 237(3), 1400–1413.

Heinrich, P., Jamelot, A., Cauquis, A., & Gailler, A., 2021. Taitoko, an advanced code for tsunami propagation, developed at the French Tsunami Warning Centers. European Journal of Mechanics-B/Fluids, 88, 72–88.

Kalligeris, N., Skanavis, V., Charalampakis, M. et al., Field survey of the 30 October 2020 Samos (Aegean Sea) tsunami in the Greek islands, 2022. Bull Earthquake Eng 20, 7873–7905. https://doi.org/10.1007/s10518-021-01250-6

Leclerc, F., Palagonia, S., Feuillet, N., et al., 2024. Large seafloor rupture caused by the 1956 Amorgos tsunamigenic earthquake, Greece. Commun Earth Environ, 5, 663, doi: 10.1038/s43247-024-01839-0.

Manning, S.W., Ramsey, C.B., Kutschera, W., Higham, T., Kromer, B., Steier, P., & Wild, E.M., 2006. Chronology for the Aegean Late Bronze Age 1700–1400 B.C. Science, 312, 565–569, doi: 10.1126/science.1125682.

McCoy, F., & Heiken, G., 2000. Tsunami generated by the Late Bronze Age eruption of Thera (Santorini), Greece. Pure and Applied Geophysics, 157, 1227–1256, doi: 10.1007/s000240050024.

Okada, Y., 1985. Surface deformation due to shear and tensile faults in a half-space. Bulletin of the Seismological Society of America, 75(4), 1135–1154.

Okal, E.A., Synolakis, C.E., Uslu, B., Kalligeris, N., & Voukouvalas, E., 2009. The 1956 earthquake and tsunami in Amorgos, Greece: Geophys. J. Int., 178, 1533–1554.

Zahradník, J., Aissaoui, E. M., Bernard, P., Briole, P., Bufféral, S., De Barros, L., et al., 2022. An atypical shallow Mw 5.3, 2021 earthquake in the western Corinth rift (Greece). Journal of Geophysical Research: Solid Earth, 127, e2022JB024221. https://doi.org/10.1029/2022JB024221

17th INTERNATIONAL CONGRESS of the Geological Society of Greece

BULLETIN OF THE GEOLOGICAL SOCIETY OF GREECE, SP. PUBL.

EXTENDED ABSTRACT 041

The Greek Database of Seismogenic Sources (GreDaSS) version 3.0. A compilation of potential seismogenic sources (Mw> 5.5) in the Aegean Region

Caputo R.[1], Koukouvelas I.[2], Papathanassiou G.[3], Russo D.[1], Taftsoglou M.[1,2], Tarabusi G.[4], Valkaniotis S.[3]

(1) University of Ferrara, Department of Earth Sciences, 44122 Ferrara, Italy
(2) University of Patras, School of Geology, Patras, Greece
(3) Aristotle University of Thessaloniki, Department of Geology, Thessaloniki, Greece
(4) Istituto Nazionale di Geofisica e Vulcanologia, Rome, Italy

The broader Aegean Region, including the Southern Balkans, is among the most tectonically active areas of the Mediterranean realm and has the highest seismicity both in terms of frequency of events and magnitudes. The principal aim of this note is to present the new release of the Greek Database of Seismogenic Sources (GreDaSS) corresponding to version 3.0 systematically revised in terms of sources and seismotectonic parameters and largely improved both qualitatively and quantitatively (Figure 1).

Background

The importance of a complete repository for active faults in the Aegean Region became clear since the late 1990's; however, the first efforts were primarily focused on tectonic structures associated to pre-instrumental and instrumental seismicity (e.g. Ambraseys and Jackson, 1998; Papazachos et al., 1999) and thus based almost entirely on historical and seismological data. This approach can be successful in studying recently activated seismogenic sources, but becomes inappropriate for sources without any seismological record (neither pre-instrumental nor instrumental) and characterized by a long recurrence period. The 13 May 1995 Kozani earthquake (Ms = 6.5; e.g. Pavlides et al., 1995; Meyer et al., 1996; 1998a; 1998b; Chiarabba and Selvaggi, 1997; Clarke et al., 1997, 1998; Hatzfeld et al., 1997; 1998) and the 7 September 1999 Athens earthquake (Mw = 6.0; e.g. Kontoes et al., 2000; Voulgaris et al., 2001; Ganas et al., 2004; Atzori et al., 2008; Foumelis et al., 2009) are emblematic examples of ruptures occurred in areas considered till that moment as aseismic or associated with low seismic activity. Although the subsequent works managed to include the geological records in the source identification process, most of them resulted to be too much descriptive, lacking in quantitative parameters information (e.g. Mountrakis et al., 2006; Pavlides et al., 2007; Karakaisis et al., 2010).

For these reasons, in the late '90ies on the track of the European FAUST Project and the Italian DISS, the GreDaSS Project was thus launched initially at the University of Basilicata and then permanently developed at the University of Ferrara (copyright owner) with an international working group. The financial support of this initiative was primarily provided by the Italian Ministry of University and the University of Ferrara.

The principal aim of the GreDaSS Project was indeed i) to overcome the above described critical issues , ii) to provide a complete and accurate repository of fully parametrized seismogenic sources and not simply, for example, a 2D map of (active) fault traces (Papazachos et al., 2001; Pavlides et al., 2008) and iii) to contribute to better and more realistic Seismic Hazard Assessment (SHA) analyses.

Since its beginning, GreDaSS was obviously populated by seismicity-related sources, but the preferred approach was intrinsically multidisciplinary (e.g. Caputo and Helly, 2008; Caputo et al., 2015) giving emphasis and exploiting as many as possible different sources of information digging any geological, structural, morphotectonic, geodetic, palaeoseismological, historical, archaeoseismological, geophysical, etc. data available in the literature or specifically collecting new data by the research group.

During the years and becoming a reference database for SHA analyses, the products of GreDaSS were included in several European projects, like the European Seismic Hazard Model (ESHM13; Woessner et al., 2015) and more recently the European Fault-Source Model 2020 (EFSM20; Basili et al., 2024).

Since its almost 30 years of research activity, the working group of the GreDaSS Project evolved in time and saw the collaboration and contribution of several PhD students, like Valkaniotis (2009), Sboras (2012), Maggini (2020) and Russo (2025) and colleagues. The authorship of this note is limited to the contributors of the new entirely revised and updated version 3.0 of GreDaSS, which is the object of the present note.

Method

For our purposes we used the well tested, time-proof, worldwide acknowledged database structure and method proposed by the Istituto Nazionale di Geofisica e Volcanologia (INGV) for the Italian Database of Individual Seismogenic Sources (DISS), which represents the result of almost twenty years research experience of its Working Group (Valensise and Pantosti, 2001). The DISS uses many basic levels of data that can be either independent or directly related. Among the most important ones are the Individual Seismogenic Sources (ISS), the Composite Seismogenic Sources (CSS) and the Subduction Sources (SDS); see also Basili et al. (2008) for a more detailed description of the informatic framework.

- "Individual Seismogenic Sources" (ISS) are obtained from geological and geophysical data and are characterized by a full set of geometric (strike, dip, length, width and depth), kinematic (rake) and seismological-palaeoseismological parameters (average displacement per event, magnitude, slip rate, return period) and by a rating of the associated uncertainties. ISSs are assumed to exhibit "characteristic" behaviour with respect to rupture length/width and expected mean and maximum magnitude. They are tested against worldwide databases for internal consistency in terms of length, width, average displacement and magnitude. This category of sources favours accuracy of the information supplied over completeness of the sources themselves. As such, they can be used for deterministic assessment of seismic hazard, for calculating earthquake and tsunami scenarios, and for tectonic and geodynamic investigations.

- "Composite Seismogenic Sources" (CSS) are still obtained from geological and geophysical data and characterized by geometric (strike, dip, width, depth) and kinematic (rake) parameters, but their length is more loosely defined and spans two or more Individual Sources. They are not assumed to be capable of a specific earthquake, but their potential can be derived from existing earthquake catalogues. A CSS is essentially inferred on the basis of regional surface and subsurface geological data, that are exploited well beyond the simple identification of active faults or youthful tectonic features. Opposite to the previous case, this category of sources favours completeness of the record of potential earthquake sources over accuracy of source description. In conjunction with seismicity and modern strain data, CSSs can thus be used for regional probabilistic seismic hazard assessment and for investigating large-scale geodynamic processes.

- "Subduction Sources" (SDS) are designed to include a simplified model of this complex tectonic environment. They represent the dipping slab at mantle depth, the interface between the two plates at crustal depth, and the detachment at the base of the accretionary wedge. In map view, a set of depth contour lines depicts the geometry of the subducted slab. At the upper end of the slab, a fault trace marks the boundary of the two plates. A set of basic parameters relative to the tectonic behavior, the possible segmentation of the Wadati-Benioff surface and the net convergence direction and rate are also added in the corresponding layers of information. This type of reconstruction is typically performed using data from geology, exploration geophysics, seismicity distribution, and seismic tomography.
The details about how faults are graphically represented in the database and what are the attributes of every information field can be found in the paper of Basili et al. (2008).

Informatic platform

Different from version 2.0 that is available as a Google Maps version or a downloadable KMZ version, Gredass 3.0 is hosted on "SEISMOFAULTS.EU" IT infrastructure (Basili et al, 2022) that provides access through standard web services protocols such as the Web Map Service (WMS), Web Feature Service (WFS), or Web Coverage Service (WCS), developed by the Open Geospatial Consortium (OGC; https://ogc.org). Through the OGC web services, data can also be downloaded as CSV (Comma-Separated Values), SHP (Esri shapefile), KML (Keyhole Markup Language), GeoJson, and many others.
The last release of GreDaSS (version 3.0) is also publicly available through a web GIS interface (Figure 1). Since the database structure remains consistent, we have chosen to adopt the same web interface designed and developed by DISS Working Group of INGV for the most recent version of Italian Database of Individual Seismogenic Sources (DISS Working Group, 2021). This interface is developed in JavaScript language, using the open-source library OpenLayers for mapping data directly querying the web services made available by the "SEISMOFAULTS.EU" infrastructure.

Results

Within the investigated area, we have already recognized, characterized and parametrized numerous CSSs and

ISSs. All ISSs show evidence of Late Pleistocene-Holocene activity and sometimes also the occurrence of past 'linear morphogenic earthquakes' (sensu Caputo, 2005) as inferred, for example, from palaeoseismological trenches, archaeoseismological investigations or detailed morphotectonic mapping. In some cases, a moderate to strong earthquake has occurred in the last few decades, therefore allowing us to investigate the re-activated fault with a great detail, based on a modern scientific approach, and especially exploiting a rich seismological information associated with the mainshock. In particular, available instrumental data commonly provide crucial constraints about focal depth, magnitude, focal mechanism (i.e. strike, dip and rake) and aftershock distribution. This additional 'co-seismic' information is obviously not available for all the other geologically-derived seismogenic sources (ISSs) where no historical or instrumental earthquakes have been recorded. Accordingly, these faults represent a crucial test for the database and especially for its possible applications in seismic hazard assessment analyses. They have been independently investigated according to the two approaches, in one case the available 'co-seismic' constraints of the principal seismotectonic parameters have been ignored and mainly the cumulative effects of Late Quaternary morphogenic events have been considered; in the other case this additional co-seismic information has been included (Caputo et al., 2015).

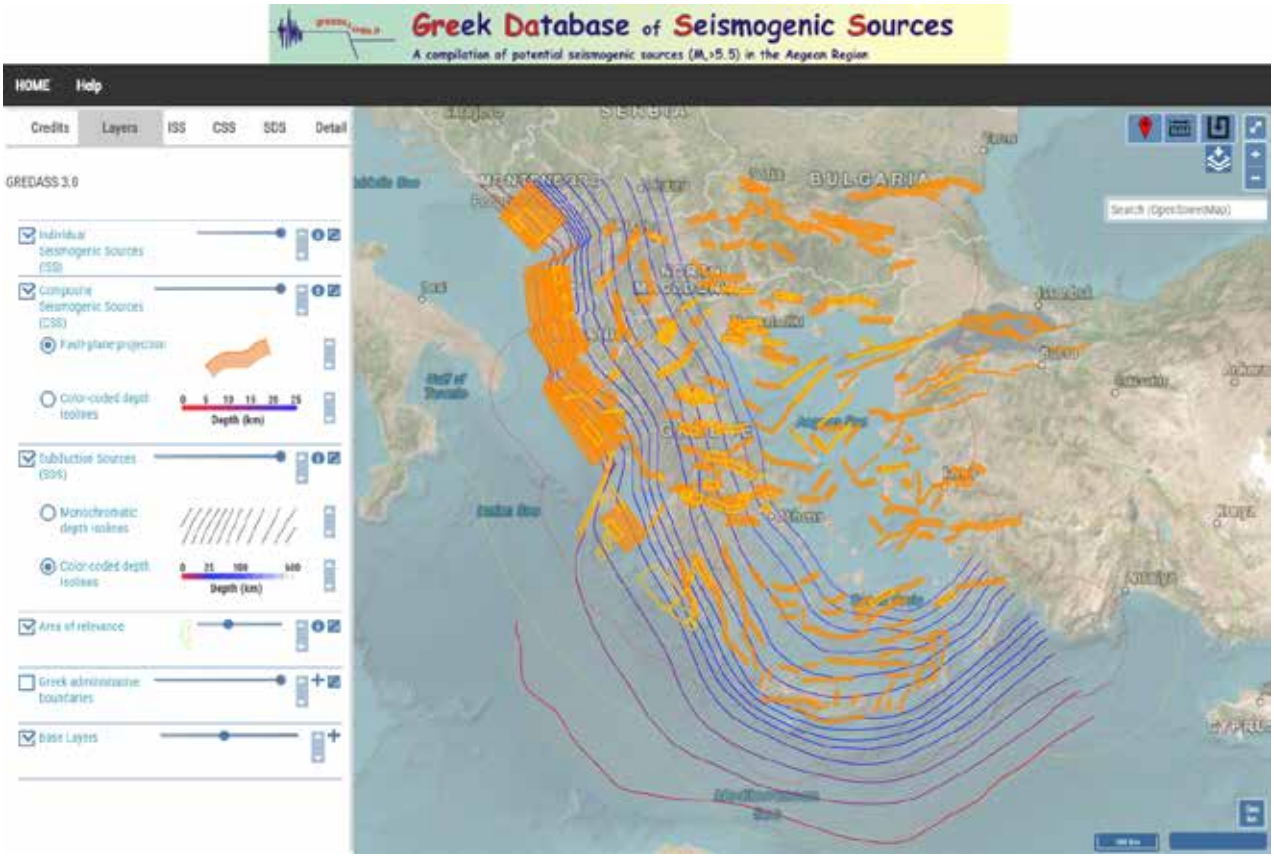

Figure 1. Screen capture of the last release of GreDaSS (version 3.0) available through the new web GIS interface.

It is worth noting that relative to the previous one (release 2.0; Caputo and Pavlides, 2013) the new version of GreDaSS (release 3.0) has been largely improved both qualitatively and quantitatively. In particular, all seismotectonic parameters have been systematically revised and most of the numerical fields have been completed and/or compiled where missing. This work produced an overall rough increase in the order of +70% of the information contained. It is worth noting the significant improvement that was achieved in better constraining the seismogenic layer all over the investigated area by applying the results of the 3D thermo-rheological model recently produced for the broader Aegean Region (Maggini, 2020; Maggini and Caputo, 2020; 2021; Maggini et al., 2023). Based on this model, a set of crucial seismotectonic parameters, like maximum depth, width, dip-angle and maximum credible magnitude of the seismogenic sources, have been systematically revised and/or better quantified.

Crustal faults (i.e. CSSs and ISSs) included in the database are at present 277 (instead of 267) and 117 (108), respectively. As concerns the other two informative layers (the graphical one and the relevant literature), the number

of figures associated with the sources are now 1667 (916) and references 853 (679), showing in both cases an important step forward the completeness and improvement of the database especially if compared to version 2.0.
When a seismogenic source is associated with secondary effects, especially liquefaction features, because of a recent or historical event, this information taken from DALO (Papathanassiou et al., 2010) has been systematically included in the descriptive layer of the new GreDaSS release.
A further major difference of the last release is represented by the reconstructed and modelled Wadati-Benioff zones that were not included in the previous version of GreDaSS. In version 3.0, they are actually two, the Hellenic Subduction Zone and the Adriatic Continental Collision (Figure 1), therefore better defining the seismotectonics of the active accretionary wedges surrounding the southern Balkan peninsula.
As a final comment, we want to stress the fundamental and intrinsic difference of GreDaSS with respect to other apparently similar catalogues and/or databases available or under construction for the broader Aegean Region. Indeed, GreDaSS with its philosophical approach, its informatic structure and especially the choice of including some crucial parameters is the only one that could be directly exported and easily used for performing seismic hazard assessment analyses, like for example, in the Seismic Hazard Harmonization in Europe Project (SHARE; http://www.share-eu.org/) or the TAP Project between the Greece-Turkey border and southern Italy (Slejko et al., 2021; Moratto et al., 2021).

Acknowledgements
We acknowledge the financial contribution provided by INGV and the EPOS Italia Project and the multi-decennial support of the University of Ferrara. We also thank R. Basili for the continuous discussions and exchanges of ideas and the contributors to the previous release of the database.

References

Ambraseys, N.N., Jackson J.A., 1998. Faulting associated with historical and recent earthquakes in the Eastern Mediterranean region. Geophys. J. Int., 133, 390-406.
Atzori, S., Manunta, M., Fornaro, G., Ganas, A., Salvi, S., 2008. Postseismic displacement of the 1999 Athens earthquake retrieved by the Differential Interferometry by Synthetic Aperture Radar time series. J. Geophys. Res., 113, B09309.
Basili, R., Valensise, G., Vannoli, P., Burrato, P., Fracassi, U., Mariano, S., Tiberti, M.M., Boschi, E., 2008. The database of individual seismogenic sources (DISS), version 3: summarizing 20 years of research on Italy's Earthquake Geology. Tectonophys., 453(1-4), 20-43.
Basili R., Danciu L., Beauval C., Sesetyan K., Vilanova S., Adamia S., Arroucau P., Atanackov J., Baize S., Canora C., Caputo R., Carafa M., Cushing M., Custódio S., Demircioglu Tumsa M., Duarte J., Ganas A., García-Mayordomo J., Gómez de la Peña L., Gràcia E., Jamšek Rupnik P., Jomard H., Kastelic V., Maesano F. E., Martín-Banda R., Martínez-Loriente S., Neres M., Perea H., Sket-Motnikar B., Tiberti M. M., Tsereteli N., Tsironi V., Vallone R., Vanneste K., Zupančič P. (2022). European Fault-Source Model 2020 (EFSM20): online data on fault geometry and activity parameters [Data set]. Istituto Nazionale di Geofisica e Vulcanologia (INGV), https://doi.org/10.13127/efsm20.
Basili R., Danciu L., Beauval C., Sesetyan K., Vilanova S.P., Adamia S., Arroucau P., Atanackov J., Baize S., Canora C., Caputo R., Carafa M.M.C., Cushing E.M., Custódio S., Demircioglu Tumsa M.B., Duarte J.C., Ganas A., García-Mayordomo J., Gómez de la Peña L., Gràcia E., Jamšek Rupnik P., Jomard H., Kastelic V., Maesano F.E., Martín-Banda R., Martínez-Loriente, S., Neres M., Perea H., Šket Motnikar B., Tiberti M.M., Tsereteli N., Tsironi V., Vallone R., Vanneste K., Zupančič P. and Giardini D., 2024. The European Fault-Source Model 2020 (EFSM20): geologic input data for the European Seismic Hazard Model 2020. Nat. Haz. Earth Syst. Sci. 24., 3945-3976, doi: 10.5194/nhess-24-3945-2024.
Caputo, R., 2005. Ground effects of large morphogenic earthquakes. J. Geodyn., 40(2-3), 113-118.
Caputo R. and Helly B., 2008. The use of distinct disciplines to investigate past earthquakes. Tectonophys., 453(1-4), 7-19, doi: 10.1016/j.tecto.2007.05.00.
Caputo, R., Pavlides, S., 2013. The Greek Database of Seismogenic Sources (GreDaSS), version 2.0.0: A compilation of potential seismogenic sources (Mw > 5.5) in the Aegean Region. https://gredass.unife.it/, doi: 10.15160/unife/gredass/0200.
Caputo, R., Sboras, S., Pavlides, S., Chatzipetros, A., 2015. Comparison between *single-event effects* and *cumulative effects* for the purpose of seismic hazard assessment. A review from Greece. Earth-Science Reviews 148, 94-120.
Chiarabba, C., Selvaggi, G., 1997. Structural central on fault geometry: example of the Grevena Ms 6.6, normal

faulting earthquake. J. Geophys. Res., 102, 22445-22457.
Clarke, P., Paradisis, D., Briole, P., England, P., Parson, B., Billiris, H., Veis, G., Ruegg, J-C., 1997. Geodetic investigation of the 13 May 1995 Kozani-Grevena (Greece) earthquake. Geophysical J Int., 135, 195-214.
Clarke, P.J., Paradisis, D., Briole, P., England, P.C., Parson, B.E., Billiris, H., Veis, G., Ruegg, J-C., 1998. Geodetic investigation of the 13 May 1995 Kozani-Grevena (Greece) earthquake. Geophys. Res. Letts., 24(6), 707-710.
DISS Working Group, 2021. Database of Individual Seismogenic Sources (DISS), Version 3.3.0: A compilation of potential sources for earthquakes larger than M 5.5 in Italy and surrounding areas. Istituto Nazionale di Geofisica e Vulcanologia (INGV), https://doi.org/10.13127/diss3.3.0.
Foumelis, M., Parcharidis, Is., Lagios, E., Voulgaris, N., 2009. Evolution of post-seismic ground deformation of the Athens 1999 earthquake observed by SAR interferometry. Journal of Applied Geophysics, 69(1), 16-23.
Ganas, A., Pavlides, S.B., Sboras, S., Valkaniotis, S., Papaioannou, S., Alexandris, G.A., Plessa, A., Papadopoulos, G.A., 2004. Active fault geometry and kinematics in Parnitha Mountain, Attica, Greece. J. Struct. Geol., 26, 2103-2118.
Hatzfeld, D., Karakostas, V., Ziazia, M., Selvaggi, G., Lebogne, S., Berge, C., Makropoulos K., 1998. The Kozani-Grevena (Greece) earthquake of May 13, 1995, a seismological study. J. Geodyn., 26(2-4), 245-254.
Hatzfeld, D., Karakostas, V., Ziazia, M., Selvaggi, G., Leborgne, S., Berge, C., Guiguet, R., Paul, A., Voidomatis, P., Diagourtas, D., Kassaras, I., Koutsikos, I., Makroulos, K., Azzara, R.., Di Bona, M., Baccheschi, S., Bernard, P., Papaioannou, C., 1997. The Kozani-Grevena (Greece) earthquake of 13 May 1995 revisited from a detailed seismological study. Bull. Seism. Soc. Am., 87(2), 463-473.
Karakaisis, G.F., Papazachos, C.B., Scordilis, E.M., 2010. Seismic sources and main seismic faults in the Aegean and surrounding area. Bull. Geol. Soc. Greece, 43(4), 2026-2042.
Kontoes, C., Elias, P., Sykioti, O., Briole, P., Remy, D., Sachpazi, M., Veis, G., Kotsis, I., 2000. Displacement field and fault modelling for the September 7, 1999 Athens Earthquake inferred from Ers-2 Satellite Radar Interferometry. Geophys. Res. Lett., 27(24), 3989-3992.
Maggini M., 2020. 3D rheological modelling in the Aegean Region and its importance for the seismotectonics of the area. PhD Thesis, University of Ferrara, Italy, 268 pp.
Maggini M. and Caputo R., 2020. Sensitivity analysis for crustal rheological profiles: examples from the Aegean Region. Ann. Geophys., 63(3), SE334, doi: 10.4401/ag-8244.
Maggini M. and Caputo R., 2021. Seismological data versus rheological modelling: comparisons across the Aegean Region for improving the seismic hazard assessment. J. Struct. Geol., 145, 104312, doi: 10.1016/j.jsg.2021.104312.
Maggini M., Russo D. and Caputo R., 2023. A 3D rheological model for the Aegean Region: mechanical layering and seismotectonic implications. J. Struct. Geol., 175, 104956, doi: 10.1016/j.jsg.2023.104956.
Meyer, B., Armijo, R., De Chabalier, J., Delacourt, C., Ruegg, J., Acache, J., Brioke, P., Papanastassiou, D., 1996. The 1995 Grevena (Northern Greece) earthquake: fault model constrained with tectonic observations and SAR interferometry. Geophys. Res. Lett., 23(19), 2,677-2,680.
Meyer, B., Armijo, R., Massonnet, D., de Chabalier, J.B., Delacourt, C., Ruegg, J.C., Achache, J., Papanastassiou, D., 1998. Results from combining tectonic observations and SAR interferometry for the 1995 Grevena earthquake: a summary. J. Geodyn., 26(2-4), 255-259.
Meyer, B., Armijo, R., Massonnet, D., de Chabalier, J.B., Delacourt, C., Ruegg, J.C., Achache, J., Papanastassiou, D., 1998. Comment on “Geodetic investigation of the 13 May Kozani-Grevena (Greece) earthquake” by Clarke et al., Geophys. Res. Lett., 25, 129-l30.
Moratto L., Vuan A., Saraò A., Slejko D., Papazachos C., Caputo R., Civile D., Volpi V., Ceramicola S., Chatzipetros A., Daja S., Fabris P., Garcia-Pelaez J., Geletti R., Karvelis P., Pavlides S., Rapti D., Rebez A., Rossi G., Sandron D., Santulin M., Sboras S., Tamaro A., Zecchin M., Zgur F. and Zuliani D., 2021. Seismic hazard for the Trans Adriatic Pipeline (TAP) (Part2): broadband scenarios at the Fier Compressor Station (Albania). Bull. Earthq. Eng., 19, 3389-3143, doi: 10.1007/s10518-021-01122-z.
Mountrakis, D., Tranos, M., Papazachos, C., Thomaidou, E., Karagianni, E., Vamvakaris, D., 2006. Neotectonic and seismological data concerning major active faults, and the stress regimes of Northern Greece. In: Robertson, A.H.F., Mountrakis D. (Eds.), Tectonic Development of the Eastern Mediterranean Region. Geol. Soc. London Spec. Publ., 260, 649-670.
Papathanassiou, G., Valkaniotis, S., Chaztipetros, A., Pavlides, S., 2010. Liquefaction susceptibility map of Greece. Bull. Geol. Soc. Greece, 43, 1383-1392.
Papazachos, B.C., Papaioannou, C.A., Papazachos, C.B., Savvaidis, A.S., 1999). Rupture zones in the Aegean region. Tectonophys., 308, 205-221.

Pavlides, S.B, Zouros, N.C, Chatzipetros, A.A., Kostopoulos, D.S., Mountrakis, D.M., 1995. The 13 May 1995 western Macedonia, Greece (Kozani Grevena) earthquake; preliminary results, Terra Nova, 7, 544-549.

Pavlides S.B., Valkaniotis S. and Chatzipetros A. (2007): Seismically capable faults in Greece and their use in seismic hazard assessment. 4th Int. Conf. Earthq. Geotech. Eng., Thessaloniki, Greece, p. 1609.

Pavlides, S., Chatzipetros, A., Valkaniotis, S., 2008. Active faults of Greece and surroundings. 33rd Int. Geol. Congr., August 6-14, 2008, Oslo, Norway.

Russo D., 2025. Seismotectonic characterization of the South-Western Balkans seismogenic sources and 3D modelling of the uppermost part of the Hellenic Subduction Zone. PhD Thesis, University of Ferrara, Italy, 214 pp.

Sboras S., 2012. The Greek Database of Seismogenic Sources: seismotectonic implications for North Greece. PhD Thesis, University of Ferrara, Italy, 252 pp.

Slejko D., Rebez A., Santulin M., Garcia-Pelaez J., Sandron D., Tamaro A., Civile D., Volpi V., Caputo R., Ceramicola S., Chatzipetros A., Daja S., Fabris P., Geletti R., Karvelis P., Moratto L., Papazachos C., Pavlides S., Rapti D., Rossi G., Saraò A., Sboras S., Vuan A., Zecchin M., Zgur F. and Zuliani D., 2021. Seismic hazard for the Trans Adriatic Pipeline (TAP). Part 1: probabilistic seismic hazard analysis along the pipeline. Bull. Earthq. Eng., 19, 3349-3388, doi: 10.1007/s10518-021-01111-2.

Valensise, G., Pantosti, D. (Eds), 2001. Database of potential sources for earthquakes larger than M 5.5 in Italy. Ann. Geofisica, 44(4), 797-807.

Valkaniotis S., 2009. Συσχέτιση Νεοτεκτονικών ομών και Σεισμικότητας στην Ευρύτερη Περιοχή του Κορινθιακού Κόλπου (Κεντρική Ελλάδα). PhD Thesis, Aristotle University of Thessaloniki, 240 pp.

Vallone R., Basili R., 2023. Technical documentation of SEISMOFAULTS.EU: the IT infrastructure employed by the European Databases of Seismogenic Faults (EDSF) installation. Rapp. Tec. INGV, 474: 134, doi: 10.13127/rpt/474.

Voulgaris, N., Pirli, M., Papadimitriou, P., Kassaras, J., Makropoulos K., 2001. Seismotectonic characteristics of the area of western Attica derived from the study of the September 7, 1999 Athens earthquake aftershock sequence. Bull. Geol. Soc. Greece, 34(4), 1645-1651.

Woessner, J., Danciu, L., Giardini, D., Crowley, H., Cotton, F., Grünthal, G., Valensise, G., Arvidsson, R., Basili, R., Demircioglu, M. B., Hiemer, S., Meletti, C., Musson, R. W., Rovida, A. N., Sesetyan, K., Stucchi, M., and the SHARE Consortium: The 2013 European Seismic Hazard Model: key components and results, Bull. Earthq. Eng., 13, 3553–3596, doi: 10.1007/s10518-015-9795-1, 2015.

17th INTERNATIONAL CONGRESS of the Geological Society of Greece

BULLETIN OF THE GEOLOGICAL SOCIETY OF GREECE, SP. PUBL.

EXTENDED ABSTRACT 042

Sousa Dinosaur Valley, Brazil: The largest record of Lower Cretaceous dinosaur footprints in South America and its influence in local communities

Carvalho I.S.[1,2], Henriques M.H.[2], Leonardi G.[3]

(1) Department of Geology, Federal University of Rio de Janeiro, Cidade Universitária - Ilha do Fundão, CCMN/ IGEO 21.949-900, Rio de Janeiro, Brazil, ismar@geologia.ufrj.br, Geosciences Centre, (2) Department of Earth Sciences, Faculty of Sciences and Technology, University of Coimbra (Polo II), Rua Sílvio Lima 3030-790, Coimbra, Portugal, (3) Istituto Cavanis, Venice, Italy

Introduction

The "Rio do Peixe Dinosaur Valley" comprises four sedimentary basins: Sousa, Triunfo (also called the Uiraúna-Brejo das Freiras basin), Pombal, and Vertentes. Located in the western part of the Brazilian Paraíba State, these areas are intracratonic basins that developed along preexisting structural trends of the basement during the origin of the South Atlantic Ocean. The age of these basins, based on microfossils, is characteristic of the Rio da Serra (Berriasian to Hauterivian) and Aratu (early Barremian) local stages (Lima and Coelho, 1987; Regali, 1990; Sousa *et al.*, 2019). Deposition is the result of tectonic activity, and it is represented by alluvial fans at the faulted borders, changing to an anastomosing fluvial system more distally, and by meandering fluvial system with a wide floodplain, where perennial and temporary lakes developed, in the central region of the basins (Carvalho, 2000; Fig. 1).

Especially in the Sousa Basin footprints and trackways, mainly of large theropods, sauropods, and ornithopods are common, as well as invertebrate ichnofossils, such as traces and burrows (Fernandes and Carvalho, 2001). Body fossils are represented by ostracods, conchostracans, plant fragments, palynomorphs, fish scales, and bones of crocodylomorph and dinosaurs. The abundance of dinosaurian ichnofaunas represents an extensive Lower Cretaceous megatracksite (Viana *et al.,* 1993; Carvalho, 2000; Leonardi and Carvalho, 2000, 2002) established during the early stages of the South Atlantic opening. In this area, 42 sites and approximately 96 individual stratigraphic levels preserve occurrences of more than 636 individual dinosaur trackways and isolated footprints, as well as rare tracks and traces of the vertebrate mesofauna (Leonardi and Carvalho, 2021). To date, the four basins of "Rio do Peixe Dinosaur Valley" show together the following dinosaur trackmakers for the corresponding trackways or isolated footprints: 38 graviportal ornithopods (Fig. 2A); one ankylosaur; one small quadrupedal thyreophoran; two small ornithopods (altogether, 42 ornithischians). Then, 447 individual theropods (Fig. 2B-C) and 90 sauropods (altogether, 537 saurischians) were identified. In total, the number of classifiable individual dinosaur tracks is 579; and the total number of dinosaur footprints and trackways, including the indeterminate tracks, is 636. This last number includes also four possible dinosaur tail impressions.

The meso-ichnofauna, very rare in these basins, is represented by just one set of batrachopodid prints, some crocodilian traces and tracks, one lacertoid footprint, perhaps a poor specimen of mammal tracks, and a very large number of small chelonian swimming tracks (Leonardi, 1989, 2021; Leonardi and Carvalho, 2021, 2024).

It is noteworthy that the large number of theropods represented is impressive, compared to the number of herbivores, which is quite common in the whole world. This phenomenon seems to be contrary to the biomass pyramid theory. It can be explained, however, considering that carnivores probably had a higher level of mobility and therefore printed more tracks and footprints daily. It is also quite remarkable that the ankylosaur hand-foot set (specimen SOES 7, from the Serrote do Pimenta, Sousa), discovered in 1979 (Leonardi, 1984, 1989, 1994), represents the first record of the presence of this clade of Thyreophora in the South American continent.

The diversity of dinosaur tracks: an insight into the Early Cretaceous ecosystems

The dinosaur footprints in the Sousa Basin occur in at least 42 localities, in clastic deposits within all the formations of the Rio do Peixe Group (Antenor Navarro, Sousa and Rio Piranhas formations). At least 636 individual trackmakers are recorded in the Rio do Peixe basins (Carvalho and Leonardi 1992; Leonardi, 1984, 1994; Leonardi and Carvalho, 2021, 2024), and many others in a widely distributed set of track localities named the Borborema Megatracksite (Viana *et al.*, 1993). This megatracksite expands to the neighboring basins of Icó, Iguatu, Malhada Vermelha, Lima Campos (Leonardi, 1989; Leonardi and Spezzamonte, 1994), Cedro (Carvalho *et al.*, 1993), Araripe (Carvalho *et al.*, 1994, 2019, 2024; Carvalho and Leonardi, 2021, 2024), and can also be extended to encompass the region of the Cameroon Basin (Africa) as suggested by Jacobs *et al.* (2024).

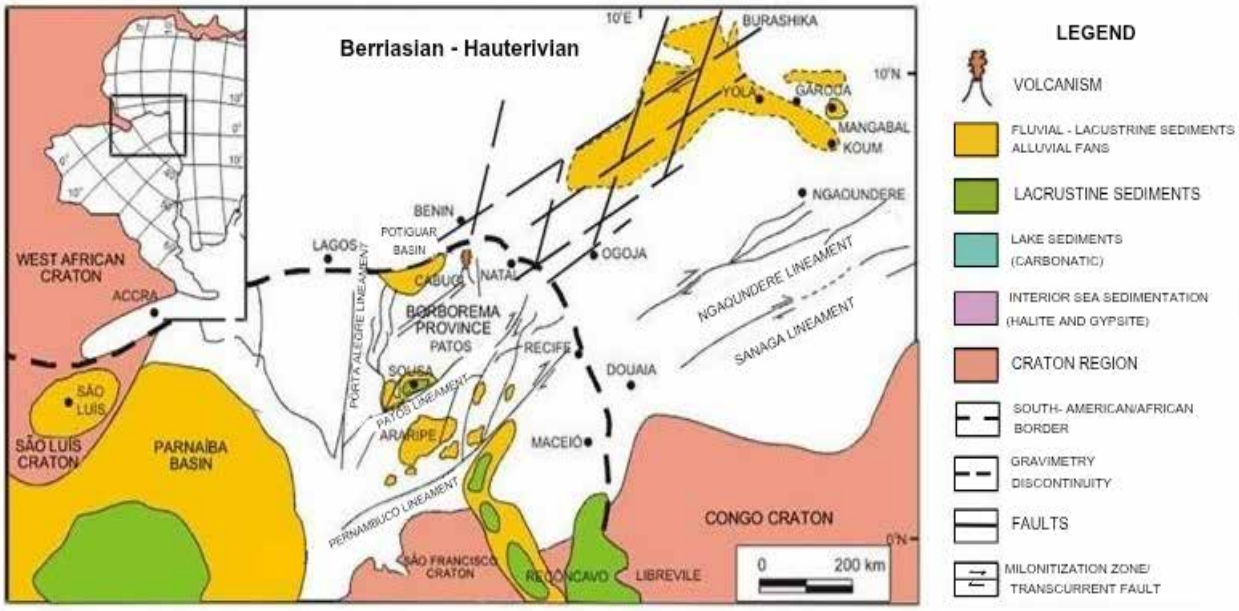

Figure 1. Geological context of Sousa Basin, northeastern Brazil during the Barremian-Hauterivian. The dinosaur footprints from the Sousa Basin were formed in the environments established during the first stages of South America – Africa drifting (modified from Popoff, 1988).

The set of footprints is indicative of the high diversity of dinosaurs in the terrestrial ecosystems, despite the few osteological remains. Footprints are rare in the Antenor Navarro and Rio Piranhas formations as they are preserved only in fine sediments that accumulated as subaerial sandy bars in alluvial fans and anastomosing rivers close to the basin margins. In the Sousa Formation, the sediments of finer grain sizes are more suitable for track preservation. This last unit is interpreted as deposited in lacustrine, swampy, and meandering braided fluvial environments (Leonardi and Carvalho, 2024; Fig. 2).

The Dinosaur Valley and its Influence in the Sousa Community

The town of Sousa is undeniably the "capital" of the "valley of the dinosaurs" of western Paraíba. The Sousa municipality has a territory of 842 km² located in the region of the Alto Sertão da Paraíba, in the semi-arid belt of Paraíba State. The municipality of Sousa has 67,259 inhabitants (IBGE, 2022).

The influence of the scientific studies concerning dinosaur tracks in the region allowed new economic perspectives. After one hundred years of research (beginning with Moraes, 1924), dinosaur footprints became a popular aspect of the local culture. The main occurrence and most accessible ichnosite is located at Passagem das Pedras (Ilha Farm) in the Sousa municipality. In December 1992 (Diário Oficial do Estado da Paraíba, Decree nº 14.833, December 20th, 1992), through a state act, the area was defined as a natural monument and named "Dinosaur Valley Natural Monument" (Monumento Natural Vale dos Dinossauros). Since then, the influence of the dinosaur theme on a variety of community activities has been incontestable, reflecting the improvement of science knowledge in the municipality.

Over the last fifty years, the region, previously known mainly for its cotton agriculture, acquired a new identity as a result of the regular presence of researchers, undergraduate and graduate students, and the media's diffusion about the dinosaur tracks in Sousa County. In the downtown area of Sousa city references to dinosaurs progressively invaded different aspects of community life, from sports to commercial and social activities, which shows the way that the people of Sousa connect to the dinosaur tracks recorded in their municipality, considered to be a heritage that deserves to be preserved (Fig. 3).

It is possible to preserve any geological heritage through public policies, but the main way to preserve it is the reconnaissance by the community about their importance and economic relevance. The tourism in the Sousa region, the local museum, a national identity based on the soccer team (Green Dinosaurs from Sertão, Sousa Futebol Clube), and the continuous support of scientific research allowed the engagement of the local population to the preservation of their ichnofossils. They are recognized as important objects to the economy and social development (Carvalho and Leonardi, 2007; Fernandes and Carvalho, 2007; Santos *et al.*, 2016, 2019), a fundamental condition for safeguarding their physical integrity.

But the ichnofossils of Sousa are exposed to risks of non-anthropic origin that call for new approaches to the issue of in-situ preservation of this type of heritage. Although the best way for educational and economic purposes is the preservation of the footprints in the natural outcrops, the environmental conditions to which they are currently subject can destroy them. Many of the

track-bearing surfaces will be worn out by natural erosion, especially where the tracks occur in surfaces nearside the temporary rivers. Besides the traditional methodology of documentation, it is also necessary to digitally reconstruct the ichnosites and their footprints (Falkingham *et al.*, 2014, 2018) as they are subject to destruction by erosion and in some rare cases to vandalism. In these cases, the removal and subsequent storage in museums, universities and research centers is the best solution to an ex-situ preservation of the paleontological heritage. Given the relevance of these ichnofossils to the population of Sousa, it would be necessary to consider replacing the original footprints with replicas, as happened within prehistoric cave paintings like Lascaux and Chauvet in France, or Altamira in Spain, a non-consensual management strategy but generally well accepted by tourists (Hughes *et al*., 2021). Other geoconservation issues of technical nature include expanding signage and improving accessibility to ichnosites, and enlargement of the Visitor Center with upgrade of the exhibition space on the theme of fossil footprints and dinosaurs of Sousa. Tormey (2019) refers to several ways of communicating geoheritage with people who are visiting protected areas or who are looking at a distance from the traditional to the most innovative social media platforms around the world which may inspire local authorities (Sousa municipality) and state authorities (Pernambuco State).

Figure 2. The great diversity of dinosaur tracks in the region of the Sousa Basin allows the reconstruction of terrestrial Cretaceous ecosystems. A. Iguanodontid footprints, the longest trackway (57 m) found in Sousa Basin, Passagem das Pedras ichnosite; B. Theropod footprints after excavation on mudstones with mudcracks, Passagem das Pedras ichnosite; C. Theropod footprint on coarse sandstones from Serrote do Letreiro ichnosite.

Figure 3. References to dinosaurs and their tracks in the emergence of a new identity for the region: A. Sousa Radio (Progresso AM); B. Sousa Sport Club, the main soccer game from the Sousa city, Paraíba State; C. A small inn located in the downtown; D. A market and bakery; E. A veterinary drugstore.

Geoconservation practitioners, researchers, and all the geoscience community need to enhance the engagement of the Sousa community with its geoheritage. This requires communication strategies targeted to different publics, such as local communities, local entrepreneurs and stakeholders, media, scientific community, tourists, politicians and policymakers around an ambitious geotourism plan to boost economic activity in the region and improve the social

conditions of the population, without jeopardizing the conservation of the paleontological heritage.
Future actions to promote the economy and social development of Sousa should include establishing guidelines by the State of Paraíba to stimulate private initiative aimed at tertiary sector activities geared towards employability around scientific tourism. At the same time, it is necessary to establish education programs that focus on the geoheritage value of Sousa ichnosites, which play a major role in raising people's awareness of their territory's paleontological heritage (Santos *et al*., 2019). On the part of the academic community, it will be important to maintain a continuous program of excavations and prospecting for new localities with fossil footprints, to guarantee a continuous flow of scientific publications and dissemination about Sousa's paleontological heritage.

Acknowledgements
The authors acknowledge the support from Conselho Nacional de Desenvolvimento Científico e Tecnológico (303596/2016-3) and Fundação Carlos Chagas Filho de Amparo à Pesquisa do Estado do Rio de Janeiro (E-26/200.998/2024). This study was supported by Portuguese funds of Fundação para a Ciência e a Tecnologia in the frame of the UIDB/00073/2025 (https://doi.org/10.54499/UIDB/00073/2020) and the UIDP/00073/2025 (https://doi.org/10.54499/UIDP/00073/2020) projects.

References

Carvalho, I.S., 2000. Geological Environments of Dinosaur Footprints in the Intracratonic Basins of Northeast Brazil during the Early Cretaceous Opening of the South Atlantic. Cretaceous Research 21, 255–267.
Carvalho, I.S., Leonardi, G., 1992. Geologia das bacias de Pombal, Sousa, Uiraúna-Brejo das Freiras e Vertentes (Nordeste do Brasil). Anais da Academia Brasileira de Ciências 64, 231–52.
Carvalho, I.S., Leonardi, G., 2007. The Dinosaur Valley Natural Monument: Dinosaur Tracks from Rio do Peixe Basins (Lower Cretaceous, Brazil). Reunión Argentina de Icnología, 5, Y Reunión de Icnología del Mercosur, 3. Ushuaia, Argentina, Marzo, Ushuaia, Argentina, p. 28–30.
Carvalho, I.S., Leonardi, G., 2021. Fossil footprints as biosedimentary structures for paleoenvironmental interpretation: Examples from Gondwana. Journal of South American Earth Sciences 106, 102936.
Carvalho, I.S., Leonardi, G. (Eds.), 2024. Dinosaur Tracks of Mesozoic Basins in Brazil Impact of Paleoenvironmental and Paleoclimatic Changes. 1st. ed. Switzerland: Springer Nature.
Carvalho, I.S., Viana, M.S.S., Lima Filho, M.F., 1993. Bacia de Cedro: a icnofauna cretácica de vertebrados. Anais da Academia Brasileira de Ciências 65, 459–460.
Carvalho, I.S., Viana, M.S.S., Lima Filho, M.F., 1994. Dinossauros do Siluriano: um anacronismo crono-geológico nas bacias interiores do Nordeste? 38º Congresso Brasileiro de Geologia, Camboriú. Boletim de Resumos Expandidos, Camboriú, Santa Catarina, Sociedade Brasileira de Geologia 3, 213-214.
Carvalho, I.S., Rios-Netto, A.M., Borghi, L., Freitas, A.P., Leonardi, G., Andrade, J.A., Freitas, F.I., 2019. Dinosaur Trampling from the Rio da Batateira Formation–Lower Cretaceous of Araripe Basin, Brazil, in: Fialho, P., Silva, R. (Eds.), Livro de Resumos. Paleo Fall Meeting 2019. Universidade de Évora, Portugal, p. 21.
Carvalho, I.S., Leonardi, G., Dias, J.J., 2024. The Cretaceous Araripe Basin Dinosaur Tracks and Their Paleoenvironmental Meaning. Dinosaur Tracks of Mesozoic Basins in Brazil, in: Carvalho, I.S., Leonardi, G. (Eds.), 1st. ed. Switzerland: Springer Nature Switzerland, 147-177.
Falkingham, P.L., Bates, K.T., Farlow, J.O., 2014. Historical Photogrammetry: Bird's Paluxy River Dinosaur Chase Sequence Digitally Reconstructed as It Was Prior to Excavation 70 Years Ago. Public Library of Science ONE 9(4): e93247. https://doi.org/10.1371/journal.pone.0093247.
Falkingham, P.L., Bates, K.T., Avanzini, M., Bennett, M., Bordy, E.M, Breithaupt, B.H., Castanera, D., Citton, P., Diaz-Martinez, I., Farlow, J.O. *et al.*, 2018. A Standard Protocol for Documenting Modern and Fossil Ichnological Data. Palaeontology, Frontiers In Palaeontology 61(4), 469-480.
Fernandes, A.C.S., Carvalho, I.S., 2001. Icnofósseis de invertebrados da Bacia de Sousa (Estado da Paraíba, Brasil): a localidade de Serrote do Letreiro. Simpósios Sobre a Bacia do Araripe e Bacias Interiores do Nordeste, 1 e 2. Novembro de 1997. Crato—Ceará. Comunicações 2001. Coleção Chapada do Araripe, Brazil, 1, p. 147–155.
Fernandes, A.C.S., Carvalho, I.S., 2007. As pegadas de dinossauros da Bacia do Rio do Peixe: elementos de transformação cultural em Sousa, Paraíba—Brasil, in: 5 Reunión Argentina de Icnologia, Y 3 Reunión de Icnología del Mercosur, Resúmenes, Laboratório de Geología Andina CADIC—CONICET, Argentina, p. 57.
Hughes, K., Mkono, M., Myers, D., Echentille, S., 2021. Are you for real?! Tourists' reactions to four replica cave sites in Europe. Tourism Management Perspectives 37, 100780.
IBGE (2022) Instituto Brasileiro de Geografia e Estatística. *censos.ibge.gov.br*. Access December 15th 2024.
Jacobs, L.L., Flynn, L.J., Scotese, C.R., Vineyard, D.P., Carvalho, I.S., 2024. The Early Cretaceous Borborema-Cameroon dinosaur dispersal corridor, in: Taylor, L.H., Raynolds, R.G., Lucas, S.G. (Eds.), Vertebrate

Paleoichnology: A Tribute to Martin Lockley. New Mexico Museum of Natural History and Science Bulletin 95, 199-212.

Leonardi, G., 1984. Le impronte fossili di dinosauri, in: Bonaparte, J. F., Colbert, E.H., Currie, P.J., Ricqlès, A.J de, Keilan-Jaworowska, Z., Leonardi, G., Morello, F., Taquet, P. (Eds.), Sulle orme dei dinosauri. Venezia-Mestre, Erizzo, 1984. (Esplorazioni e ricerche, IX) 335, 161–186.

Leonardi, G., 1989. Inventory and Statistics of the South American Dinosaurian Ichnofauna and its Paleobiological Interpretation, in: Gillette, D.D., Lockley, M.G. (Eds.), Dinosaur Tracks and Traces. Cambridge, Cambridge University Press, 165-178.

Leonardi, G., 1994. Annotated Atlas of South America Tetrapod Footprints (Devonian to Holocene) with an appendix on Mexico and Central America. Companhia de Pesquisa de Recursos Minerais, Brasília, Brasil. 248 p., 35 plates

Leonardi, G., 2021. Main results of 45 years of ichnological research on the dinosaur tracks of the Rio do Peixe basins (Paraíba, Brazil, Early Cretaceous). Annali del Museo Civico di Rovereto, Sez. Archeologia, Storia, Scienze Naturali 37, 159-182.

Leonardi, G., Carvalho, I.S., 2000. As pegadas de dinossauros das bacias Rio do Peixe, PB. [The Dinosaur Footprints from Rio do Peixe Basins, Paraíba State, Northeastern Brazil]; 15 pp., in: Schobbenhaus, C., Campos, D.A., Queiroz, E.T., Winge, M., Berbert-Born, M. (Eds.), Sítios Geológicos e Paleontológicos do Brasil. http://sigep.cprm.gov.br/sitio079/sitio079english.htm.

Leonardi, G., Carvalho, I.S., 2002. Icnofósseis da Bacia do Rio do Peixe, PB. O mais marcante registro de pegadas de dinossauros do Brasil, in: Schobbenhaus, C., Campos, D.A., Queiroz, E.T., Winge, M., Berbert-Born, M. (Eds.), Sítios geológicos e paleontológicos do Brasil. Brasília. Brasil, Departamento Nacional de Produção Mineral, 2002, Brazil, 101–111.

Leonardi, G., Carvalho, I.S., 2021. Dinosaur Tracks from Brazil: A Lost World of Gondwana. 1st. ed. Indiana: Indiana University Press.

Leonardi, G., Carvalho, I.S., 2024. Walking in the Gondwanic Floodplains of Rio do Peixe Basins, in: Carvalho, I.S., Leonardi, G. (Eds.), Dinosaur Tracks of Mesozoic Basins in Brazil. 1st. ed. Switzerland: Springer Nature Switzerland, 179-214.

Leonardi, G., Spezzamonte, M., 1994. New Tracksites (Dinosauria: Theropoda and Ornithopoda) from the Lower Cretaceous of the Ceará, Brasil. Studi Trentini di Scienze Naturali. Acta Geologica 69(1992), 61–70.

Lima, M.R., Coelho, M.P.C.A., 1987. Estudo palinológico da sondagem estratigráfica de Lagoa do Forno, Bacia do Rio do Peixe, Cretáceo do Nordeste do Brasil. Boletim do Instituto de Geociências–USP, Série Científica 18, 67–83.

Moraes, L.J., 1924. Serras e montanhas do Nordeste; pp. 43–58, in: Inspectoria de Obras Contra As Seccas. Geologia. Rio de Janeiro. Ministério da Viação e Obras Publicas. (Série I. D. Publ. 58). 2nd ed. Coleção Mossoroense 35(1). Fundação Guimarães Duque, Rio Grande do Norte, Brasil.

Popoff, M., 1988. Du Gondwana à l'Atlantique sud: les conexions du fossé de la Bénoué avec bassins du Nord-Est brésilien jusqu'à l'ouverture du golfe de Guinée au Crétacé inférieur. Journal of African Earth Sciences 7, 409–431.

Regali, M.S.P., 1990. Biocronoestratigrafia e paleoambiente do Eocretáceo das bacias do Araripe (CE) e Rio do Peixe (PB), NE-Brasil, in: Simpósio Sobre a Bacia do Araripe e Bacias Interiores do Nordeste, 1, Atas, Crato, Ceará, Brazil, p. 163–72.

Santos, W.F.S., Carvalho, I.S., Brilha, J.B., 2019. Public Understanding on Geoconservation Strategies at the Passagem das Pedras Geosite, Paraíba (Brazil): Contribution to the Rio do Peixe Geopark Proposal. Geoheritage 11, 2065–2077.

Santos, W.F.S., Carvalho, I.S., Brilha, J.B., Leonardi, G., 2016. Inventory and Assessment of Palaeontological Sites in the Sousa Basin (Paraíba, Brazil): Preliminary Study to Evaluate the Potential of the Area to Become a Geopark. Geoheritage 8(4), 315–32.

Sousa, A.J., Carvalho, I.S., Ferreira, E.P., 2019. Non-marine Ostracod Biostratigraphy of Cretaceous Rift Lake Deposits (Sousa Basin, Brazil): Paleogeographical Implications and Correlation with Gondwanic Basins. Journal of South American Earth Sciences 96, 102345.

Tormey, D., 2019. New approaches to communication and education through geoheritage. International Journal of Geoheritage and Parks 7, 192–198.

Viana, M.S.S., Lima Filho, M.F., Carvalho, I.S., 1993. Borborema Megatracksite: uma base para correlação dos "arenitos inferiores" das bacias intracontinentais do Nordeste do Brasil, in: Simpósio de Geologia do Nordeste, Sociedade Brasileira de Geologia/Núcleo Nordeste, Boletim 13, 23–25.

17th INTERNATIONAL CONGRESS of the Geological Society of Greece

BULLETIN OF THE GEOLOGICAL SOCIETY OF GREECE, SP. PUBL.

EXTENDED ABSTRACT 043

A Preliminary 3D Gravity Model for the Pre-volcanic Basement of Lesvos Island, Greece

S. Chailas[1], A. Tzanis[1]

(1) Section of Geophysics – Geothermy, National and Kapodistrian University of Athens, Athens, Greece; schailas@geol.uoa.gr.

Introduction / Background

The present work focuses on mapping the relief of the pre-volcanic basement on the Island of Lesvos, by interpreting the Bouguer gravity anomalies map using a 3D inversion scheme. Although the resulting model is not yet optimal, it nevertheless reveals the magnitude of the volcanic activity experienced by the area, as well as its relationship with the observed tectonic grain.

Lesvos, along with the region of the north-central Aegean, is part of a wider area that extends to northwestern Turkey, which has exhibited shoshonitic-type volcanism as part of the volcanic arc that has operated since during the Upper Oligocene – Middle Miocene periods. The volcanic rocks occupy almost the entire central and western part of Lesvos. (Hecht, 1972-1976; Pe-Piper et *al*., 2019).

Outcrops of the pre-alpine and alpine basement through which the volcanic formations were emplaced are mainly seen in the southeast part of the island; only minor occurrences exist at the western extremity of the island. In terms of age, the lithological formations of the basement cover the period from the Carboniferous to the upper Triassic, while there are also post-alpine formations of the Oligocene epoch.

The volcanic activity on Lesvos lasted for almost 6.0 Ma. Volcanic rocks are mainly shoshonitic in composition. A few calcareous andesites are placed at the beginning (Eressos area, 21.5Ma) and the end (Mytilene area, 16.5Ma) of volcanic activity.

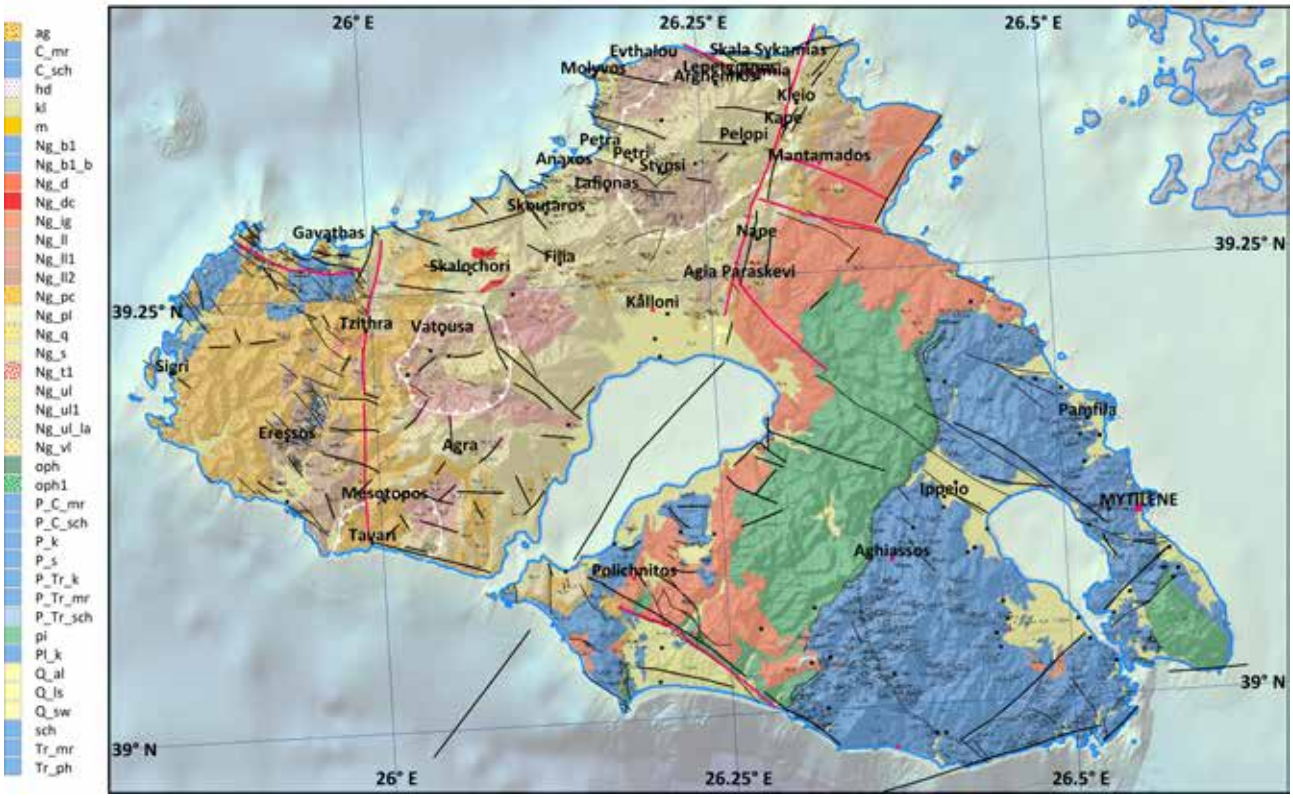

Figure 1. Geological map of Lesvos digitized from Hecht (1972-1976). The tectonic lines are from various sources

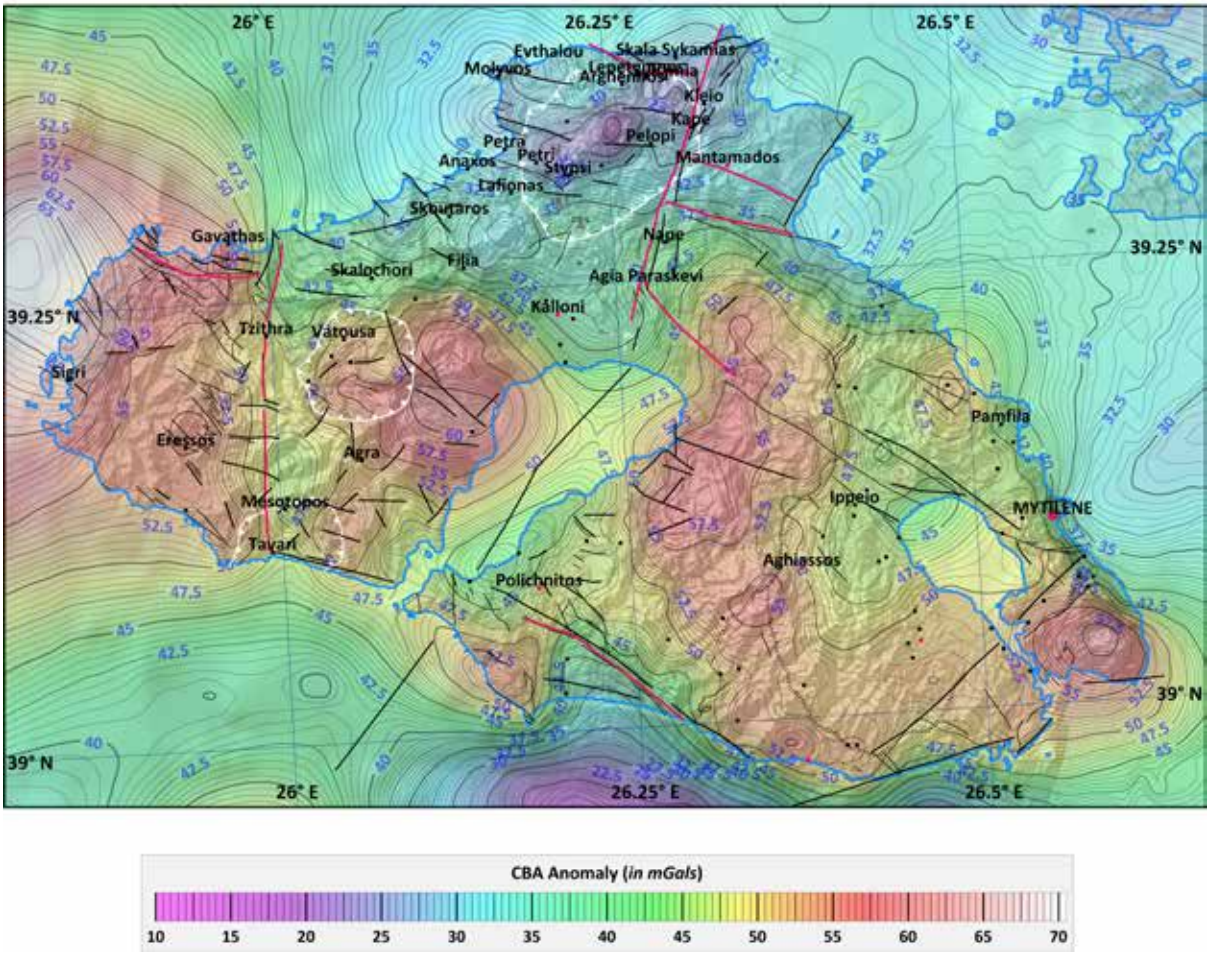

Figure 2. Bouguer Gravity Anomaly Map

The stratigraphy of the volcanic formations presented below is summarized from the work of Pe-Piper et *al*. (2019) and was based on the 1:50,000 geological maps of Hecht (1972–1976) and paleomagnetic and radiometric datings by Pe-Piper (1980) and Pe-Piper and Piper (1993). At 21.6 ± 0.5 Ma (new radiometric dating from Nissiopi Island is giving 23.3 ± 0.5 Ma) for the first andesitic-dacitic domes to break through and cover the basement at the Eressos area of western Lesbos (*Eressos Formation*). This, together with the Gavathas formation, was overlaid by the *Sigri Pyroclastic Formation* of several hundreds of meters thickness in western Lesbos and comprises principally tuffs. A prominent welded ignimbrite approx. 25 m thick is interbedded in the upper Sigri Pyroclastic Formation to the west of Antissa. In turn, the Sigri Pyroclastic Formation is covered by the *Skoutaros Formation* consisting of basaltic and andesitic flows. Some younger andesites and dacites are also included in the formation. The *Polychnitos Ignimbrite Formation* in eastern Lesbos comprises seven widespread welded ignimbrite units, each 30–50 m thick (Pe-Piper, 1980b). They appear to be contemporary with the upper part of the Skoutaros Formation. Pe-Piper (1977) suggests two different centers for its origin: a caldera near Lepetymnos for the older units and the caldera at Vatoussa for the younger (deposited in the southeast of the Gulf of Kalloni). The *Skalohorion* (eastern Lesvos) *and Sykaminea* (northern Lesvos) formations, consisting of younger andesitic and dacitic lavas, were paleomagnetically dated to between 17.0 – 17.6 Ma; these were followed by younger (16.8 Ma) minor basalts and andesites of the *Mytilene Formation* (Pe-Piper and Piper, 2002). Several sets of dykes run in different directions through the above formations. A significant stage of the geological evolution of the western Lesvos is the main volcanic phase, dated to around 17 Ma; in this, an increase in the tempo of volcanism is observed in the central volcanic chain, resulting apart from the eruption of the Polichnitos ignimbrites to the formation of the Lepetymnos and Vatoussa calderas.

As remnants of the volcanic activity, significant surface hydrothermal alterations have been mapped. These are distributed in two major groups, each collocated with one of the two calderas. The alteration ranges from argillic to pyritic and to silicic and is associated with veins whose length varies from several meters to a few kilometers and whose formation was controlled by the then active faulting.

The gravity anomaly map

The Bouguer Gravity Anomalies Map

A complete Bouguer Gravity (CBA) anomaly map of Lesvos was compiled on the basis of the Gravity Data Bank of the Department of Geophysics of NKUA (Lagios et *al.* 1995,1996). Gravity measurements (stations) are evenly distributed over the island, with a spatial density of approximately two stations per 5 km^2. The data has been referred to the IGSN71 datum and has been subject to complete Bouguer correction up to a radius of 166 km around each station. This allows the generation of gravity anomaly grids with 1km spacing. In the offshore area, the sparsity of gravity measurements, together with the absence of data from the gulfs of Kalloni, Gera and Edermit (Turkey), do not allow for any reliable representation of gravity anomalies in these areas; the contours shown in Fig. 2, 3 and 4 are only results of extrapolation.

The final CBA (Fig. 2) allows for the analysis of the gravitational signatures, not only of the volcanics as a whole, but also of individual volcanic formations with sizes comparable to the distances between stations, and of the main fault zones. Gravity anomaly amplitudes range between 10 and 70 mGal; they generally trend to the North with the highest values observed over areas of outcropping alpine and pre-alpine basement, while the lowest values are observed at the northernmost parts of the island.

Regional – Residual Anomalies Separation

To isolate gravity anomalies due to the geological structure of the area, we proceeded with the determination and reduction of the long wavelength anomalies from the Bouguer anomaly map. The resulting long wavelength (regional) anomaly map is presented in Fig. 3 and the residual Bouguer anomaly map, after subtracting it from the CBA, is presented in Fig. 4 (on top of the Geological map).

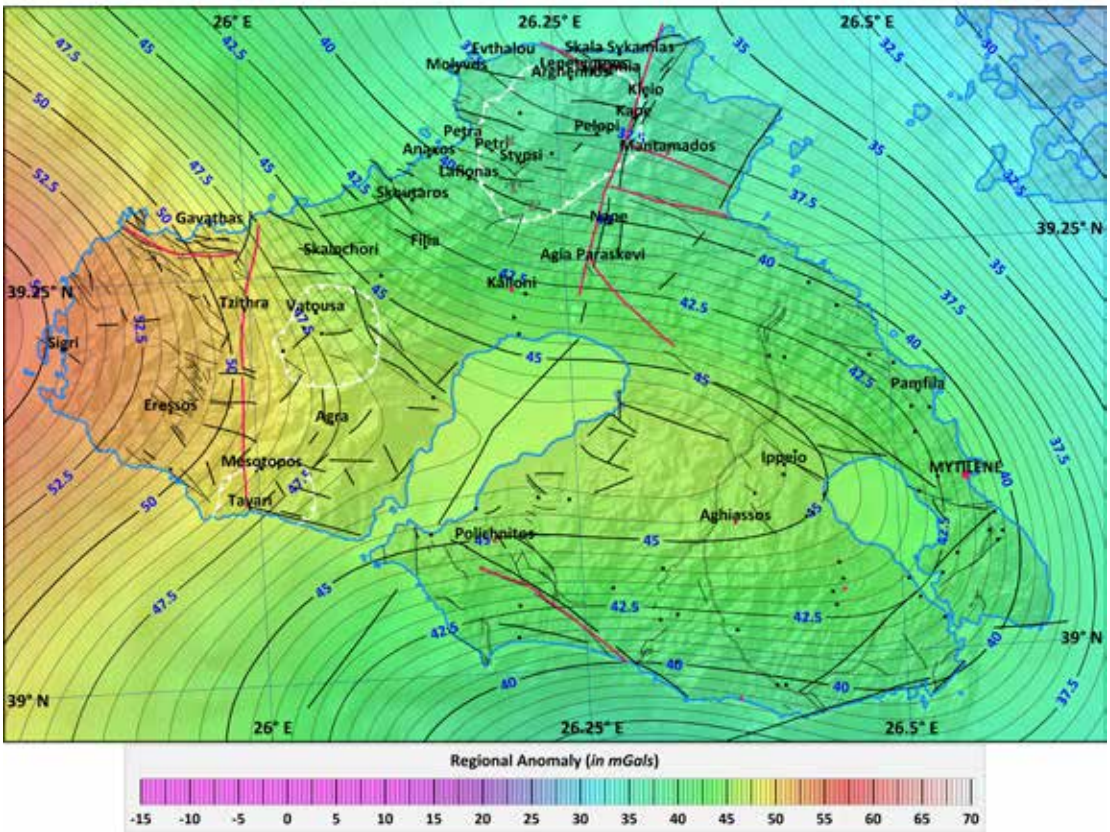

Figure 3. Regional Gravity Anomaly Map.

In the western part of Lesvos, the morphology of the residual anomalies correlates with the geology of the area. It displays a high over the area where the allochthonous basement is exposed on the surface, which is attributed to the high densities of the peridotitic rocks and the metamorphic sole. In the eastern and central parts of the Island, the presence of volcanics is evident in the comparatively lower anomaly amplitudes. Since the only extensive formations with unambiguously “low” density appearing in the area are the Sigri pyroclastics in the west, and the ignimbrites surrounding the ophiolites in the east, the low values in the rest of the area should probably be attributed to volcanic structures that extend in depth. A pronounced positive local anomaly between Vatoussa and Kalloni, not related to the exposure of an apparent high-density geological formation, requires further investigation. The presence of the

lower lavas in the area, east of Agra at an altitude of 500 meters (Fig. 1), in combination with the anomaly, points to the possibility of the generally small thickness of the volcanics in that area. Considering also the amplitude and width of this anomaly, we tentatively conclude that it could be attributed to the presence of the allochthonous basement.

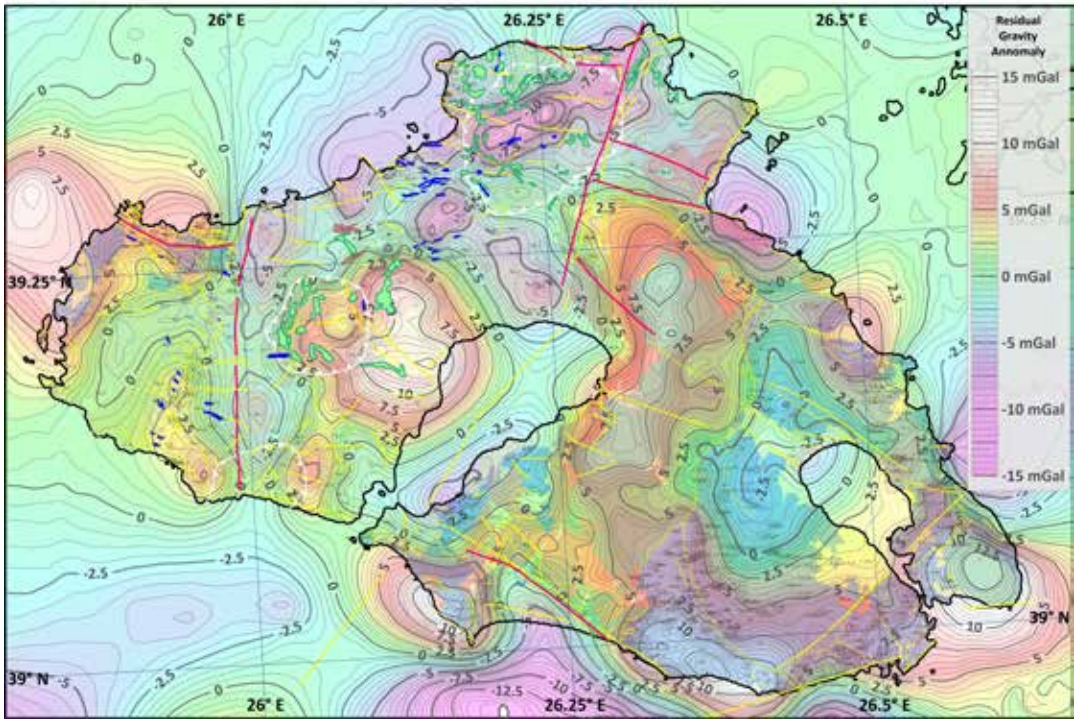

Figure 4. Residual Gravity Anomaly Map (overlaid on the geological map)

The gravity signals of Lepetymnos and Vatoussa calderas (expected to present low anomalies) seem to exist but neither of them is as clear as they were expected to be. The Lepetymnos caldera shows a significant elongate gravity low, delimited though in the area covered by the upper lavas (*Ng_ul* in the geological map). The gravity effect of the lower lavas (*Ng_ll2*) that are in contact with Ng_ll and extend to the north of the caldera, and to the south up to the trace of the caldera, seems to be unaffected by the formation of the caldera. The caldera of Vatoussa shows a more complicated figure. The caldera itself is located at the top of the topography. The gravity anomalies within the boundary of the caldera exhibit lower amplitudes with respect to the adjacent gravity high.

Inversion and Modeling

The modelling was performed with an unpublished algorithm developed by S. Chailas. In this approach, buried three-dimensional geological bodies are approximated by polyhedra of polygonal cross-section and their gravity effect is calculated by the method of Radhakrishna Murthy et *al*., (1989, 1990). Because any polyhedron can be defined by an upper and a lower boundary surface, the shape of any geological body can be determined by using prior information to fix one of the surfaces while adjusting the other. Surface topography, boreholes, other geophysical surveys and surface geology are some obvious sources of prior information.

The adjustment of the boundary surface(s) is automated by an iterative procedure derived from Bott (1960). Letting $\hat{\mathbf{g}}$ denote the matrix of observed gravity anomalies, $\mathbf{g}(k)$ the matrix of calculated gravity anomalies at the kth iteration and $\Delta\mathbf{g}(k) = \hat{\mathbf{g}} - \mathbf{g}(k-1)$ the corresponding residual anomalies, the adjusted boundary surface $\mathbf{Z}(k)$ is modified according to the scheme

$$\mathbf{Z}(k) = \mathbf{Z}(k-1) - \frac{\Delta\mathbf{g}(k)}{2\pi G \Delta\rho} \circ \mathbf{W}_Z, \qquad k = 2,3,\ldots ,$$

where G is the universal gravitational constant, $D\rho$ is the density contrast across $\mathbf{Z}(k)$, $\mathbf{W}_Z$ is a matrix of weights and $\circ$ denotes the Hadamard product. The iterative procedure aims at minimizing the objective function

$$\sum\sum\left(\hat{\mathbf{g}} - \mathbf{g}\right)^2 \circ \mathbf{W}_G ,$$

where $\mathbf{W}_G$ is a matrix of weights. The elements of $\mathbf{W}_Z$ and $\mathbf{W}_G$ are either 0 or 1. Thus it is possible to keep $\mathbf{Z}(k)$ fixed wherever prior information exists and to isolate and study specific gravity anomalies.

In the present analysis and based on the data of Section 3.2.1 and Table 1, we have assumed that the volcanic rocks and Quaternary sediments on one hand, and the pre-alpine basement on the other, have a uniform density contrast of -0.25gr/cm^3. Accordingly, the analysis entailed the stripping of the gravity effect of the volcanic layer from the residual Bouguer anomaly. The upper boundary surface $\mathbf{Z}_U^{(1)}$ represents the actual topography and bathymetry (elevation) and was therefore fixed, while the lower boundary surface $\mathbf{Z}_L^{(1)}$ was allowed to vary. The thickness of the volcanic layer is $\mathbf{Z}_U^{(1)} - \mathbf{Z}_L^{(1)}$ and was kept fixed and equal to zero at the outcrops of the pre-volcanic basement. The final surface $\mathbf{Z}_L^{(2)}$ was taken to represent the topography of the pre-volcanic basement.

The adopted density contrast of -0.25 gr/cm^3 is plausible, as it represents the average value of lava densities. Note though that using a common average density for all the volcanic formations may introduce a degree of upward or downward bias to the thickness of the volcanics in localities where local densities deviate significantly from the average. For example, this may occur in areas where the cross-section of the low-density Sigri Pyroclastics is very thick. Nevertheless, it is expected that the resulting model of the volcanics layer is sufficiently representative of geological reality.

The elevation of the lower surface of the volcanic layer, i.e. the topography of the basement, is shown in Fig. 7 in both shaded relief and contour map forms. It exhibits an intricate pattern of structural features. An explanation of the more significant of these features is attempted below.

Discussion and Conclusions

The pre-volcanic basement exhibits a relief that appears to correlate with the older tectonism of the region and is only partly modulated by contemporary active tectonics. In western Lesvos, the basement is relatively shallow (-500 to –900 m) to the west of the currently active tectonic zone of Antissa, but plunges abruptly to the east, reaching elevations of -900 to -1250 m.

The Sigri formation, which extends to the orange dashed line, appears to have covered a preexisting basin (**B$_1$**) and an elongated morphological trough (**B$_2$**), possibly related to past tectonism. Along the orange line, which passes through the center of the Vatousa caldera, a sharp morphological change is observed in the basement, running from coast to coast subparallel to the Antissa fault and parallel to the active zone of Agia Paraskevi. On either side of the southern part of the Gulf of Kalloni, the morphology of the basement indicates the possible existence of an older basin (**B$_3$**). Further north, the area of Kalloni appears to be the southern end of basin **B$_4$**, which has a NW-SE oriented axis at the deepest point of which the Agia Paraskevi fault terminates.

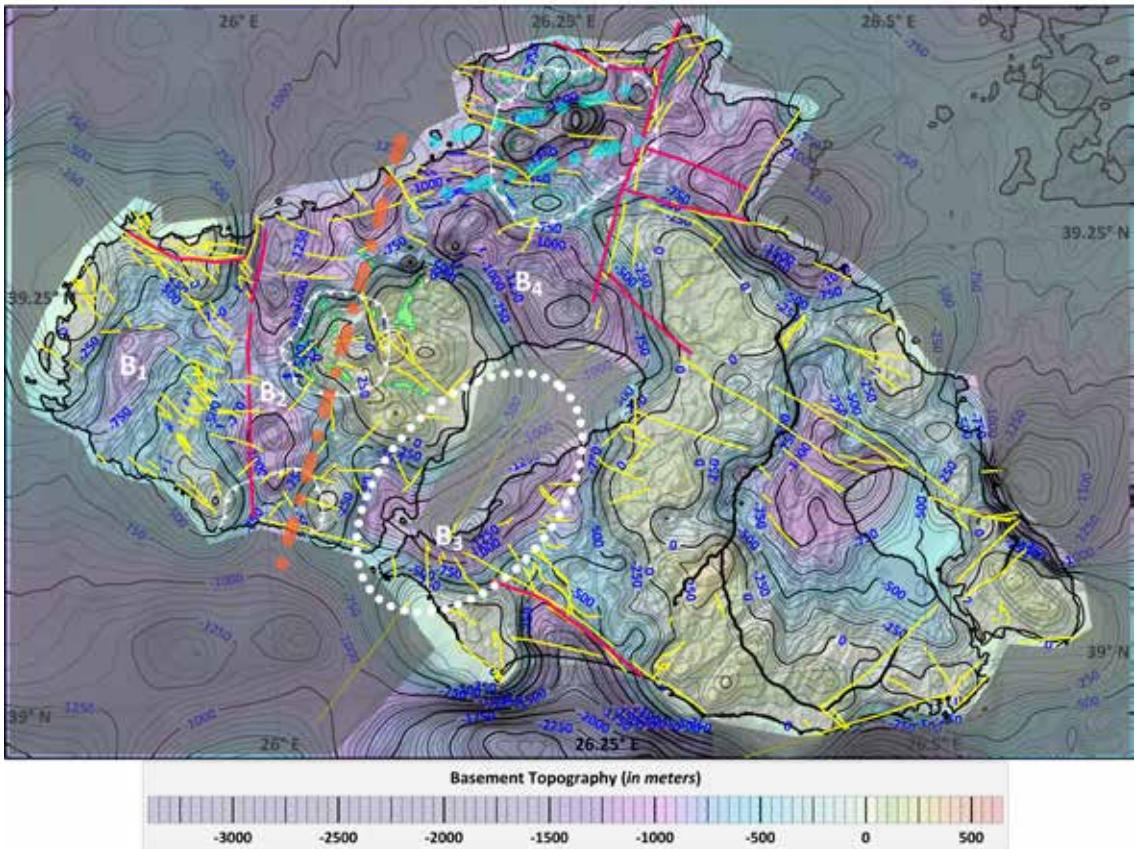

Figure 5. Model of the relief of the pre-volcanic basement

In the caldera of Lepetymnos, a significant NE-SW depression can be observed in the basement, which may be the result of density reduction through chemical alteration by hydrothermal activity facilitated by (past?) active faulting. Finally, in southern Lesvos, the model indicates a structural connection between the Vrissa – Vatera area and the submarine Lesvos basin, with the former feature appearing to fuse smoothly into the latter.

References

Bott, M.H.P., 1960. The use of rapid computing methods for direct interpretation of sedimentary basins, Geophys. J. Royal Astr. Soc., 3, (1), 63-67.

Hecht, J. (1972–1976). Geological map of Greece, Scale 1:50,000: Sheets of Plomari-Mytilene, Hagia Paraskevi, Mithymna, Polychnitos and Eresos. Institute of Geological and Mining Research (IGME), Athens, Greece.

Lagios E., Chailas, S. and Hipkin R., 2007. Gravity and topographic data banks of Greece. Geophysical Journal International. 126,

Pe-Piper, G., 1980. The Cenozoic volcanic sequence of Lesbos, Greece. Zeitschrift Der Deutschen Geologischen Gesellschaft, 131, 889–901.

Pe-Piper, G., & Piper, D. J. W., 1993. Revised stratigraphy of the Miocene volcanic rocks of Lesbos, Greece. Neues Jahrbuch Fur Geologie Und Palaeontologie Monatshefte, 2, 97–110.

Pe-Piper G., Piper D.J.W., Zouros N. and Anastasakis G., 2019. Age, stratigraphy, sedimentology and tectonic setting of the Sigri Pyroclastic Formation and its fossil forests, Early Miocene, Lesbos, Greece, Basin Res., **31,** 1178–1197, doi: 10.1111/bre.12365.

Radhakrishna Murthy, I.V., Rama Rao, P. and Ramakrishna, P., 1989. Gravity Anomalies of Three-dimensional Bodies with Variable Density Contrast., PAGEOPH, 130(4), 711-719.

Radhakrishna Murthy, I.V., Rama Rao, P. and Jagannardha Rao, S., 1990. The density difference and generalized programs for two and three-dimensional gravity modeling., Computers & Geosciences, 16(3), 277-287.

17th INTERNATIONAL CONGRESS of the Geological Society of Greece

BULLETIN OF THE GEOLOGICAL SOCIETY OF GREECE, SP. PUBL.

EXTENDED ABSTRACT 044

Sediment dynamics in the Sperchios river basin and their influence on stevia cultivation

Chantzi P.[1], Doani, S.[1], Albanakis K.[1]
(1) Department of Physical and Environmental Geography, Aristotle University of Thessaloniki, Thessaloniki, Greece, pchantzi@geo.auth.gr

Introduction / Background

The purpose of this study was to conduct sedimentological analyses at selected stations within the Spercheios River basin, corresponding to specific sampling locations in stevia cultivation fields found in the area. The sediments, formed through rock weathering and erosion, transported downstream and deposited within the Spercheios basin, 2) the tectonic structures that determine the available space for sediment deposition, 3) the type of the Spercheios River, which defines the types and forms of deposited sediments, and 4) the lithological differentiation which influence the geochemical characteristics of the sediments, collectively define the cultivation environment. The simultaneous action of these mechanisms creates a unique geological identity for the sedimentary basin of the Spercheios River, framing the cultivation background. Consequently, this geological identity is reflected in the products grown in these specific fields. The focus of the study was to understand the variations between different agricultural areas in terms of their sedimentological identity and to explore the mechanisms driving any observed differences.

Methods

A sedimentological analysis was undertaken in the Laboratory of Sedimentology, Department of Physical and Environmental Geography A.U.Th. More specifically, grain size analysis was conducted on 12 samples from the first sampling period in 2023 (Figure 1). Particles larger than 2 mm were analyzed using the mechanical sieve method and a set of sieves at half-phi (ϕ) intervals. Following the removal of organic matter with a 10% H_2O_2 solution (Trautmann et al., 2000a, b), the finer fractions were analyzed through laser diffraction with a Malvern Master Sizer Hydro 3000.
The grain size statistical parameters were computed using Gradistat software (Blott & Pye, 2001), applying the Folk and Ward (1957) method. The granulometric indices, Mean grain diameter (M_z), Skewness (Sk_I), Sorting (σ_I), and Kurtosis ($K_{.I}$.), were also calculated, and the grain size distributions were visualized through cumulative and frequency curves.

Figure 1: First sampling period in 2023 in the cultivated areas in the Sperchios River basin

Results

The sedimentological analysis of 12 samples from the Spercheios River basin highlighted a variety of grain sizes, textural groups, and granulometric characteristics that reflect diverse sedimentary conditions within the stevia cultivation fields. The mean grain size ranged from coarse-grained material (e.g., gravel) to finer materials (e.g., mud). The samples were categorized into different textural groups, including “Muddy Gravel,” “Muddy Sandy Gravel,” “Gravelly Mud,” and “Sandy Mud,” indicating diverse depositional environments ranging from fluvial to mixed settings. Figures 2 and 3 show the varying percentages of gravel, sand, and mud in the samples. Samples such as Stev1, Stev2, Stev3, and Stev10 exhibit higher gravel percentages (above 40%), indicating coarse-grained sediment deposits. The highest gravel content is observed in Stev10, suggesting proximity to higher-energy conditions, such as active river channels or areas affected by strong fluvial transport. Conversely, Stev7 and Stev8 have significantly lower gravel percentages, indicating deposition in relatively lower-energy environments. Sand content varies moderately across the samples, generally falling within 10% to 30% in most cases. Samples like Stev5 and Stev6 show balanced amounts of sand, suggesting areas where medium-energy conditions persist during sediment deposition. Stev7 shows relatively higher sand content compared to others, but the dominance of mud remains significant in this sample. Stev7 and Stev8 are dominated by high mud content (~60% to 80%), indicating deposition of fine particles. Most other samples, particularly Stev1, Stev2, and Stev10, have lower mud percentages.

Table 1. Results of the grain size statistical parameters: Mean grain size, Sorting, Skewness, Kurtosis; in phi scale, Folk and Ward method (φ).

Sample	Mean (M)	Sorting (σ)	Skewness (Sk)	Kurtosis (Ku)	Textural Group
Stev1	1.515	3.847	-0.103	0.659	Muddy Gravel
Stev2	1.595	3.749	-0.143	0.675	Muddy Gravel
Stev3	1.265	3.880	0.179	0.697	Muddy Gravel
Stev4	0.507	3.130	0.894	0.471	Muddy Sandy Gravel
Stev5	1.858	3.370	0.158	0.718	Muddy Sandy Gravel
Stev6	1.610	3.683	-0.031	0.684	Muddy Sandy Gravel
Stev7	5.148	1.923	0.100	0.933	Sandy Mud
Stev8	2.579	4.141	-0.381	0.614	Muddy Gravel
Stev9	2.555	3.431	-0.255	1.004	Gravelly Mud
Stev10	2.880	3.603	-0.235	0.656	Gravelly Mud
Stev11	0.204	3.484	0.512	0.698	Muddy Sandy Gravel
Stev12	2.101	3.864	-0.273	0.655	Muddy Gravel

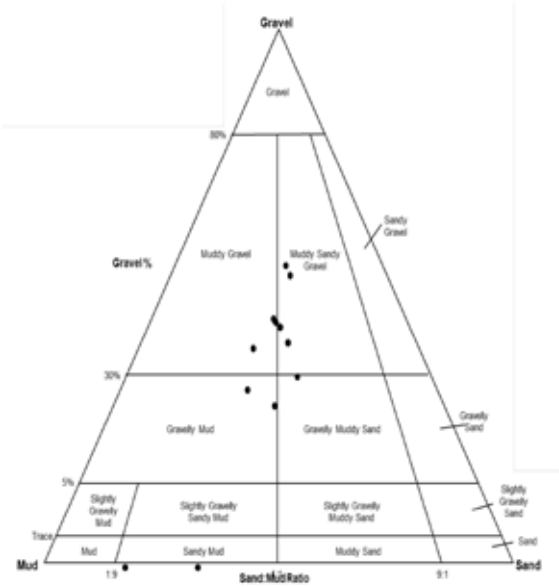

Figure 2. Gravel Sand Mud Diagram for all samples.

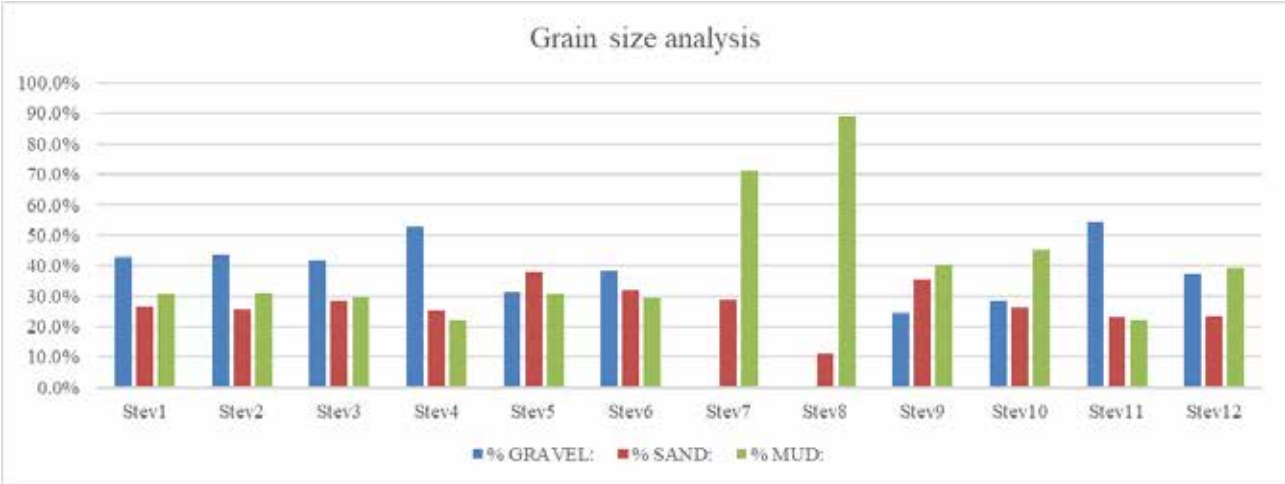

Figure 3. Gravel (%)"; the percentage of gravel fraction, "Sand (%)"; percentage of sand fraction, "Mud (%)"; percentage of silt and clay fraction, for all samples.

Conclusions

The Spercheios River basin exhibits considerable spatial variability in sedimentological characteristics, highlighting the complexity of sediment transport, deposition, and weathering processes within the region. The differences between samples can be attributed to local lithological variations and fluvial dynamics shaping sediment deposition patterns. Fields dominated by finer sediments (e.g., "Sandy Mud") offer higher water retention, potentially benefiting stevia growth, while coarser sediments (e.g., "Muddy Gravel") could enhance drainage but limit moisture availability. Poorly sorted and negatively skewed samples reflect dynamic depositional conditions, likely influenced by periodic floods or sediment influx from upstream erosion. These characteristics may lead to variable nutrient availability and soil fertility across the cultivation areas.

Acknowledgements

The work is funded by"Measure 16 'Cooperation" in the framework of National Rural Development Programme and it is co-financed by the European fund for rural development (EAFRD) and national budgets (GIstevSp: Project code M16SYN2-00237).

References

Blott, S.J., Pye, K., 2001. GRADISTAT: a grain size distribution and statistics package for the analysis of unconsolidated sediments. Earth Surf. Process. Landforms 26 (11), 1237–1248.

Folk, R., Ward, W., 1957. Brazos river bar: a study in the significance of grain size parameters. J. Sediment. Petrol. 27, 2–26.

Trautmann, T., Krbetschek, M.R., Dietrich, A., Stolz, W., 2000a. The basic principle of radioluminescence dating and a localized transition model. Radiat. Meas. vol. 32, 487–492.

Trautmann, T., Krbetschek, M.R., Stolz, W., 2000b. A systematic study of radioluminescence properties of single feldspar grains. Radiat. Meas. vol.32, 685–690.

17th INTERNATIONAL CONGRESS of the Geological Society of Greece

BULLETIN OF THE GEOLOGICAL SOCIETY OF GREECE, SP. PUBL.

EXTENDED ABSTRACT 045

Sustainable Practices for Resilient Hydrosystems at a Municipal Level: Insights from the Greek Island of Chios

Angelos Chasiotis[1], Elissavet Feloni[2], Panagiotis Nastos[1]

(1) Laboratory of Climatology and Atmospheric Environment, Department of Geology and Geoenvironment, National and Kapodistrian University of Athens, University Campus 15784, Athens, Greece; a.chasiotis@geol.uoa.gr

(2) Department of Surveying and Geoinformatics Engineering, University of West Attica, 28 Ag. Spiridonos, 12243 Egaleo, Athens, Greece

Abstract

Ensuring sustainable water resources management is crucial for the long-term resilience of municipal hydrosystems, particularly in Mediterranean island communities where water scarcity, aging infrastructure, and climate variability pose significant challenges. The island of Chios, located in NE Aegean, as many other areas in Greece faces high non-revenue water (NRW) losses, seasonal demand fluctuations, and over-reliance on groundwater abstraction, making it essential to implement innovative and sustainable interventions. This study explores smart water monitoring technologies, nature-based solutions (NBS), and modernized wastewater management to enhance the system's water efficiency, quality, and security. By integrating IoT-enabled leak detection, digital twin modeling, and automated pressure regulation, the island can reduce NRW losses by up to 40%, improving network performance and cost efficiency. Additionally, infrastructure modernization, including pipeline replacements and wastewater treatment upgrades, will enhance water reuse potential and minimize environmental impacts. Finally, studies have demonstrated that digital twin models can optimize network efficiency and reduce NRW losses significantly. The proposed interventions align with EU water management directives and climate adaptation strategies, ensuring resilience to future water challenges. With technological innovation, policy support, and community engagement, Chios has the potential to become a leading example of sustainable island water management, ensuring secure and equitable access to water resources for future generations. These findings align with broader EU climate adaptation policies, reinforcing Chios' commitment to a sustainable water management strategy that remains resilient and adaptable to future challenges.

Keyword: Sustainable water management; Mediterranean islands; Non-revenue water (NRW) losses; Smart water monitoring; Digital twin modeling; IoT-enabled leak detection; Climate adaptation strategies

Introduction

Water scarcity, exacerbated by climate change and increasing population pressures, presents a significant challenge for Mediterranean islands. The Greek island of Chios, like many coastal and insular regions, experiences high non-revenue water (NRW) losses, seasonal demand fluctuations, and heavy reliance on groundwater abstraction, raising concerns over long-term sustainability. Effective water resource management in these environments requires a combination of technological innovation, policy interventions, and nature-based solutions (NBS) to ensure resilience against hydrological variability and climate-induced risks.

Recent studies highlight the effectiveness of GIS-based water management strategies and hydrological modeling techniques in mitigating water resource vulnerabilities in Mediterranean regions. Additionally, nature-based solutions, such as rainwater harvesting, aquifer recharge, and wetland restoration, have been identified as promising approaches to enhance water sustainability while reducing reliance on energy-intensive desalination systems (Monokrousou et al., 2024). However, limited infrastructure investments and governance challenges continue to hinder the adoption of such measures.

Chios offers a unique case study for implementing smart water technologies and decentralized management strategies. By integrating IoT-enabled leak detection, digital twin modeling, and automated water distribution systems, municipalities can significantly reduce NRW, enhance operational efficiency, and ensure equitable access to water resources. Moreover, coastal aquifer conservation and groundwater quality monitoring are critical for protecting the island's freshwater supply from saline intrusion, a growing threat due to over-extraction and rising sea levels.

This study aims to explore sustainable water management interventions tailored to Mediterranean island hydrosystems, with a focus on Chios. The proposed framework leverages smart water governance, digital water technologies, and community-driven conservation strategies to enhance efficiency, resilience, and long-term sustainability. The findings will contribute to EU climate adaptation policies and regional water management frameworks, supporting efforts to

build climate-resilient hydrosystems for future generations.

Proposed Interventions for Sustainable and Resilient Hydrosystems

Water sustainability in municipal hydrosystems requires a multifaceted approach that integrates smart water technologies, nature-based solutions (NBS), and data-driven governance models. This section outlines a series of proposed interventions aimed at enhancing water efficiency, mitigating non-revenue water (NRW), and strengthening climate resilience in the municipal water infrastructure of Chios, a Greek island facing significant water challenges. Recent studies highlight the crucial role of digital water management and decentralized hydrological governance in addressing water scarcity and quality issues (Wendling et al., 2019). By adopting these innovations, Chios can transition toward a more resilient and sustainable water management framework.

One of the primary challenges for municipal hydrosystems is the high level of NRW, which results from leakage, inaccurate metering, and unauthorized water consumption. Implementing IoT-based smart leak detection systems and digital twin models can significantly enhance real-time monitoring and predictive maintenance (Kumar et al., 2023). The deployment of IoT sensors throughout the distribution network enables the identification of leaks and anomalies in real time, potentially reducing water losses by up to 40% (Mounirou et al., 2025). Additionally, digital twin models, such as those employed in EPANET simulations, facilitate scenario testing and infrastructure optimization, allowing municipalities to predict system failures and improve water distribution efficiency (Breil et al., 2022). Alongside these technologies, smart water metering solutions, including Advanced Metering Infrastructure (AMI), play a crucial role in improving monitoring accuracy. These systems allow for real-time tracking of household and commercial water usage, providing behavior-driven insights that help consumers reduce waste. Furthermore, automated billing and demand-based pricing strategies encourage conservation efforts by promoting more responsible water consumption practices (Rodríguez et al., 2021). By integrating these advanced monitoring and metering technologies, Chios can enhance the efficiency and sustainability of its water management system, while ensuring long-term resilience to climate variability and growing water demand.

Expected Outcomes: Reduction in NRW and Cost Savings

The implementation of smart water management technologies is expected to lead to significant reductions in non-revenue water (NRW) and generate substantial cost savings for Greek municipalities. By integrating decentralized water management and nature-based solutions, municipalities can reduce their reliance on traditional water sources while enhancing sustainability (Table 1).

Table 1: Expected Outcomes from Smart Water Management Technologies

Technology	Expected Water Savings (%)	Energy Savings (%)	Reduction in Operational Costs (%)	Estimated Reduction in Maintenance Costs (%)
IoT-Based Leak Detection	30	10	20	25
Smart Water Meters	25	8	15	20
Automated Pressure Management	20	12	18	22
Decision Support Systems (DSS)	15	5	12	18
Nature-Based Solutions (NBS)	10	4	8	10

One promising approach is rainwater harvesting combined with managed aquifer recharge, which offers a low-energy alternative to desalination for securing freshwater supplies (Monokrousou et al., 2024). Key interventions in this area include the installation of green rooftops and permeable pavements that help reduce stormwater runoff and replenish groundwater reserves (Wantzen et al., 2022). Additionally, wetland restoration can naturally filter pollutants while promoting biodiversity (Lewandowski et al., 2019), further supporting water quality and ecosystem health. Urban green infrastructure, such as bioswales and retention basins, also plays a crucial role in enhancing water management. These features reduce urban flood risks by absorbing and storing excess rainfall, improve water purification by filtering runoff before it enters water reservoirs (Meerkhan et al., 2021), and help mitigate the urban heat island effect, which is a growing concern under climate change (Hachem-Vermette, 2024). These solutions not only contribute to water conservation but also enhance urban resilience and adaptability.

Furthermore, the integration of digital water governance through Decision Support Systems (DSS) offers municipalities

tools for optimizing water distribution, energy use, and emergency responses (Jakovljević et al., 2021). Machine learning algorithms can be employed to forecast water demand based on climatic conditions (Chang et al., 2021), while geospatial mapping can help track and prevent groundwater depletion (Zounemat-Kermani et al., 2020). Finally, community-based water conservation programs play a vital role in driving long-term behavioral change. Public engagement through educational campaigns, digital water consumption dashboards, and municipal reward programs can encourage citizens to adopt water-saving practices and reduce domestic water consumption (Majumder and Kale, 2021).

The combined impact of these smart water management interventions is expected to significantly reduce NRW, lower operational costs, and foster more sustainable and resilient water systems, as demonstrated by similar successful practices in other municipalities across Greece (Table 2).

Table 2: Reduction of NRW Losses in Greek Municipalities with Smart Water Management

Municipality	Baseline NRW Losses (%)	Expected NRW Reduction (%)	Estimated Water Savings (m^3/year)	Estimated Cost Savings (€/year)	Number of Beneficiaries
Aigio	48	35	600,000	21,000	20,422
Argos	54	40	1,200,000	42,000	22,209
Paramythia	72	50	600,000	20,000	3,032

(Data from: Chasiotis et al. 2023a; 2023b)

Case Study: Insights from the Island of Chios

Chios, a Greek island in the Aegean Sea, faces significant water management challenges due to seasonal variability, climate change, and high non-revenue water (NRW) losses. As a semi-arid island, Chios experiences long, dry summers and short, intense rainfall periods, which result in frequent water shortages and inefficient groundwater recharge. The municipal water system primarily relies on groundwater abstraction from local aquifers, limited rainwater harvesting, and seawater desalination to meet growing urban and tourism-related demand. However, these sources are increasingly vulnerable to climate variability, saline intrusion, and over-extraction, posing a threat to the island's long-term water security. The Municipal Water and Sewerage Company of Chios oversees the island's water supply and wastewater infrastructure (Table 3), drawing water from over 100 groundwater wells and boreholes, 160 natural springs, and 15 reservoirs, such as the Psaropetra Dam, which stores water during wet seasons. Additionally, four seawater desalination plants supplement supply, particularly during peak demand periods. Despite this diverse water network, Chios struggles with high NRW losses, reaching up to 50% in some areas due to aging pipelines, leaks, and unauthorized consumption. Outdated infrastructure, including asbestos cement and PVC pipes, requires urgent replacement, while the island's limited surface water storage capacity heightens its dependence on groundwater, leading to aquifer depletion and saline intrusion.

Table 3: Major settlements in Chios and their water supply characteristics

Municipal District	Main Water Sources	Challenges
Chios City	Groundwater, desalination, Psaropetra Dam	High seasonal demand, aging infrastructure
Kambos	Wells, springs	Overextraction, groundwater depletion
Mastichochoria	Reservoirs, springs	Insufficient supply during summer months
Volissos & Northern Chios	Springs, boreholes	High NRW losses, insufficient infrastructure
Oinousses Island	Desalination plant	Energy-intensive water production

(Data provided by the Municipal Enterprise for Water and Wastewater of Chios)

The water supply system serves both urban and rural settlements, each facing distinct challenges. Recent efforts to modernize infrastructure, such as replacing outdated asbestos cement pipes with high-density polyethylene (HDPE) alternatives, aim to improve water quality and reduce system inefficiencies. However, three primary challenges continue to impact Chios' water management. First, NRW levels remain high, with system inefficiencies caused by

aging pipelines, leaks, and inaccurate metering contributing to financial and operational losses. Second, climate change and rainfall variability have led to a 20% decline in annual precipitation over the past 30 years (Monokrousou et al., 2024), while rising temperatures and prolonged droughts increase reliance on groundwater, exacerbating the risk of saline intrusion in coastal aquifers. Third, tourism-driven demand surges place additional stress on the system, with water consumption increasing fivefold during peak summer months (Wendling et al., 2019).

The adoption of sustainable water management strategies offers significant environmental, social, and economic benefits for Chios. Environmentally, reducing groundwater over-extraction can help prevent saline intrusion, while minimizing water losses ensures efficient resource utilization. Improved wastewater treatment will further protect marine ecosystems by reducing coastal pollution. Social benefits include securing a continuous and safe water supply, enhancing climate resilience, and promoting water conservation awareness within the community. Economically, modernizing infrastructure and reducing NRW can lower operational costs, while improved water services and environmental sustainability can boost the island's attractiveness as a tourist destination. Additionally, investments in smart water technologies and infrastructure development can create new local employment opportunities.

By implementing smart leak detection systems, automated pressure regulation, expanded wastewater treatment capacity, and increased desalination and rainwater harvesting, Chios can enhance its water security and sustainability. The European Environment Agency in 2021 emphasized that digital water governance frameworks can significantly improve municipal decision-making, further supporting these interventions. Collectively, these measures could lead to a 30–40% reduction in NRW losses, strengthening the island's long-term water resilience. The success of these strategies depends on strong municipal governance, stakeholder collaboration, and sustained investment in digital water solutions, ensuring that Chios becomes a model for sustainable island water management.

Table 4: Expected Impact of Sustainable Water Interventions in Chios

Intervention	Expected Water Savings (%)	Energy Savings (%)	Cost Reduction (%)
Pipe replacement (HDPE)	20	10	25
Smart leak detection	30	8	20
Wastewater treatment upgrades	15	12	18
Rainwater harvesting	10	5	10
Desalination efficiency improvements	25	15	30

Conclusions

Ensuring a sustainable and resilient water management system in Chios requires a holistic approach that integrates technological innovations, nature-based solutions (NBS), and participatory governance. The combination of smart water technologies, such as IoT-enabled leak detection and digital twin modeling, with green infrastructure and adaptive governance frameworks presents a comprehensive strategy to mitigate non-revenue water (NRW) losses, enhance climate resilience, and secure long-term water availability for both residents and seasonal visitors.

The adoption of IoT-based monitoring systems and advanced metering infrastructure (AMI) has already demonstrated its potential in reducing water losses and improving operational efficiency. Simultaneously, investments in rainwater harvesting, managed aquifer recharge, and wetland restoration contribute to natural water retention and purification, reducing dependency on costly and energy-intensive solutions like desalination. These integrated solutions not only optimize water use but also promote ecological sustainability by restoring natural hydrological cycles.

However, for these interventions to achieve their full potential, a strong governance framework is essential. Aligning local policies with EU water management directives, promoting community engagement in conservation efforts, and fostering regional cooperation among Aegean islands will be crucial in ensuring long-term water sustainability. Effective governance will also support the scalability of these solutions and facilitate access to financial and technical resources.

Looking ahead, future research should focus on expanding smart water infrastructure, particularly through the development of digital twins and AI-driven demand forecasting, to optimize resource allocation and emergency response. Additionally, scaling up nature-based interventions can further enhance groundwater recharge and flood mitigation while reducing reliance on non-renewable water sources. Exploring funding opportunities through EU sustainability programs will also be key to supporting large-scale implementation and ensuring the financial viability of these initiatives.

By embracing an integrated and forward-thinking water management approach, Chios can serve as a model for other Mediterranean islands facing similar climatic and hydrological challenges. Sustainable water governance, combined with technological innovation and nature-based solutions, will not only safeguard the island's water security but also enhance its resilience to climate change and environmental pressures, ensuring a sustainable future for generations to come.

Acknowledgements
Authors would like to thank the Municipal Enterprise for Water and Wastewater of Chios for the provision of available data regarding the local water resources and water distribution network.

References

Breil, P., Pons, M.N., Armani, G., Amer, R., Pienaar, H., Oberholster, P. and Namour, P., 2022. Natural□Based Solutions for Bioremediation in Water Environment. Sustainable solutions for environmental pollution: Air, water and soil reclamation, pp.1-93.

Chasiotis, A., Feloni, E., & Nastos, P. 2023a. Strategies towards water leakage monitoring as a good practice under climate change adaptation in Argos City, Greece.

Chasiotis, A., Tsitsifli, S., Panytsidis, K., Nilsen, V., Mantas, N., Theodorou, D., Kyriakidis, T., Chasiotis, S., Bousdeki, M., Feloni, E. and Ratnaweera, H. 2023b. Building a smart green system to control water leakage and monitor drinking water quality in Paramythia city, Greece: the case of SMASH project. EGU General Assembly 2023.

Chang, N.B., Hossain, U., Valencia, A., Qiu, J., Zheng, Q.P., Gu, L., Chen, M., Lu, J.W., Pires, A., Kaandorp, C. and Abraham, E., 2021. Integrative technology hubs for urban food-energy-water nexuses and cost-benefit-risk tradeoffs (II): Design strategies for urban sustainability. Critical Reviews in Environmental Science and Technology, 51(14), pp.1533-1583.

Hachem-Vermette, C., 2024. Enhancing Urban Climate Resistance Through the Application of Selected Strategies and Technologies. Discover Cities, 1(1), p.17.

Jakovljević, D., Pešić, A.M. and Joksimović, D.M., 2021. Protection from harmful effects of water—examples from Serbia. In Water Engineering Modeling and Mathematic Tools (pp. 157-175). Elsevier.

Kumar, A., Button, C., Gupta, S. and Amezaga, J., 2023. Water Sensitive Planning for the Cities in the Global South. Water 2023, 15, 235 [online]

Lewandowski, J., Arnon, S., Banks, E., Batelaan, O., Betterle, A., Broecker, T., Coll, C., Drummond, J.D., Gaona Garcia, J., Galloway, J. and Gomez-Velez, J., 2019. Is the hyporheic zone relevant beyond the scientific community?. Water, 11(11), p.2230.

Majumder, M. and Kale, G.D. eds., 2021. Water and Energy Management in India: Artificial Neural Networks and Multi-Criteria Decision Making Approaches. Springer Nature.

Meerkhan, H., Freitas, L., Teixeira, J., Rocha, F., Pereira, A.J., Afonso, M.J. and Chaminé, H.I., 2021. DISCO-Urban: an updated GIS-based vulnerability mapping method for delineating groundwater protection zones in historic urban areas. Mediterranean Geoscience Reviews, 3, pp.361-377.

Monokrousou, K., Makropoulos, C., Eleftheriou, A., Vasilakos, I., Styllas, M., Dimitriadis, K., Kouris, N., Nyktari, E. and Malamis, S., 2024. From rain to resilience: rainwater harvesting coupled with subsurface storage and recovery as a nature-based solution for arid communities: the case of Mykonos. Urban Water Journal, pp.1-13.

Mounirou, L. A., Yonaba, R., & Faye, M. D. (2025). *Retention basins for urban flood mitigation: Insights from Ouagadougou in Burkina Faso.* ResearchGate.

Rodríguez, D.J., Paltán, H.A., García, L.E., Ray, P. and St. George Freeman, S., 2021. Water-related infrastructure investments in a changing environment: a perspective from the World Bank. Water Policy, 23(S1), pp.31-53.

Wantzen, K.M., Piednoir, T., Cao, Y., Vazhayil, A.M., Tan, C., Kari, F.G., Lagerström, M., Gerner, N.V. and Sommerhäuser, M.M., 2022. Back to the surface–Daylighting urban streams in a Global North–South comparison. Frontiers in Ecology and Evolution, 10, p.838794.

Wendling, L., Rinta-Hiiro, V., Jermakka, J., Fatima, Z., zu Castell Rüdenhausen, M., Ascenso, A., Miranda, A.I., Roebeling, P., Martins, R. and Mendonça, R., 2019. Performance and impact monitoring of nature-based solutions. UNaLab Project, EU H, 2020.

Mounirou, L.A., Yonaba, R., Faye, M.D., Biaou, A.C., Fowé, T., Coulibaly, G., Kafando, M.B. and Karambiri, H., 2025. Retention basins for Urban flood mitigation: Insights from Ouagadougou in Burkina Faso. World Journal of Advanced Research and Reviews, 25(1), pp.1497-1512.

Zounemat-Kermani, M., Matta, E., Cominola, A., Xia, X., Zhang, Q., Liang, Q. and Hinkelmann, R., 2020. Neurocomputing in surface water hydrology and hydraulics: A review of two decades retrospective, current status and future prospects. Journal of Hydrology, 588, p.125085.

17th INTERNATIONAL CONGRESS of the Geological Society of Greece

BULLETIN OF THE GEOLOGICAL SOCIETY OF GREECE, SP. PUBL.

EXTENDED ABSTRACT 046

Kentavros pluton (Thrace, Greece): Geochemistry and Petrogenesis

Chatzakou T.[1], Tsiri A.[1], Koroneos A.[1], Gerontidou I.[1], Drakoulis A.[1]

(1) Department of Mineralogy-Petrology-Economic Geology, Aristotle University of Thessaloniki, Thessaloniki, Greece, theodxat@gmail.com , atsirib@geo.auth.gr , koroneos@geo.auth.gr , ioangero@geo.auth.gr , alexdr@geo.auth.gr

Introduction

Rhodope massif is characterized by the extensive magmatism of Eocene - Miocene age. There are many plutonic rocks intruding the two units (Sidironero and Pangaion) of the Rhodope massif (e.g. Xanthi pluton, Kavala pluton, Vrondou pluton etc.) and most of them have been thoroughly studied (Christofides *et al*., 1998 and references therein). There is one pluton though, the pluton of Kentavros, which has not been petrologically and geochemically studied up to now. The pluton of Kentavros is located 26 km NNE of Xanthi city near the village of Kentavros. The pluton intrudes gneisses and gneiss-schists, marbles and occasionally amphibolites of the Sidironero unit, causing locally contact metamorphic phenomena (Fig.1) (IGME 1973). Liati (1986) using K-Ar method on hornblende gave a Late Eocene - Early Oligocene age (38±1 Ma) for the Kentavros pluton, similar to the age of Xanthi pluton which is 34±0.5 Ma (Christofides *et al*., 2012). The aim of this study is to present for the first time petrological, mineralogical and geochemical characteristics of the Kentavros pluton, to provide evidence on the origin of it as well as to compare it with the nearby Xanthi pluton of similar age.

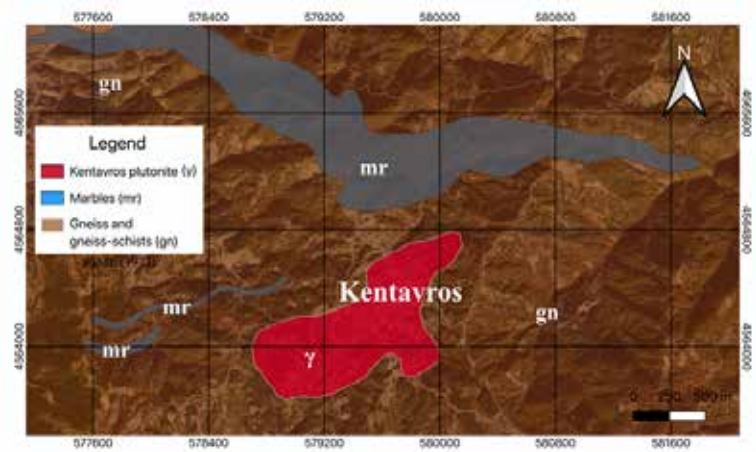

Figure 1: Geologic map of Kentavros area. (IGME, 1973 with modifications using QGIS.3.34, QGIS.org, 2023).

Geological Setting

The Rhodope massif is a thick (10-20 km) continental crust. It extends from southern Bulgaria to Thrace, Thassos, and eastern Macedonia. It is believed to originate either from the Eurasian plate or to be an ancient continental fragment of Gondwana, which was detached and incorporated into Eurasia (Mountrakis, 2021). Its western boundary is the Strymon fault, where it is separated from the Serbomacedonian massif, while to the east it is in contact with the Circum Rhodope zone. The Rhodope massif is divided into two units by Papanikolaou & Panagopoulos (1981): the Upper Tectonic Unit (Sidironero Unit) and the Lower Tectonic Unit (Pangaion Unit). The units were separated by the NE-SW trending and southwest-vergent Nestos thrust, from Xanthi to the Bulgarian border (Christofides *et al*., 2001). The Rhodope massif is intruded by igneous rocks, both plutonic and volcanic, with composition ranging from granitic to gabbroic (Christofides *et al*., 1998). The magmatism ranges from Eocene to Miocene in age and is related to an active continental margin (Mountrakis *et al*., 2006). According to Krohe & Mposkos (2002), Kentavros pluton is an intrusion into the upper Unit Sidironero Complex, which has been exhumed before 50-30 Ma. It is also associated with the Xanthi detachment system. Around the Kentavros pluton there is limited plastic elongation and rotation recrystallization of quartz. The pluton appears highly sheared and it is a syn-detachment intrusion into the Upper Sidironero Complex.

Analytical Methods

The laboratory research includes the determination of the mineralogical and chemical composition of the rocks. Regarding mineralogy, 11 thin sections were prepared and examined under a polarizing microscope. For the chemical analyses, 11 pressed pellets were prepared. The samples were ground to fine powder and mixed with a commercial cellulose based

binder (CEREOX®) at a ratio of 4 parts sample to 1 part binder. The final mixtures were then subjected to a pressure of 15 tons using a hydraulic press, in order to form pellets compatible with the wavelength-dispersive X-ray fluorescence (WDXRF) spectrometry system. The analyses were performed on a RIGAKU Supermini200 tabletop XRF instrument, which operates at 50kV and 4mA with 200W power.

Petrography and Mineralogy

The Kentavros pluton consists of different rock types, from basic to acid, differing to a certain extent in the mafic mineral contents and texture. Based on the TAS classification diagram of Cox *et al*. (1979) (Fig. 2), their texture and modal composition they are classified as: cumulates with pyroxene (Cum Px), cumulates with hornblende (Cum Hb) gabbros (Gb), diorites with hornblende (Hb-Dr) and diorites containing pyroxene and hornblende (Px, Hb-Dr), Qz monzodiorites (Qz-MzDr), tonalites (Ton) and pegmatite veins (Pgm).

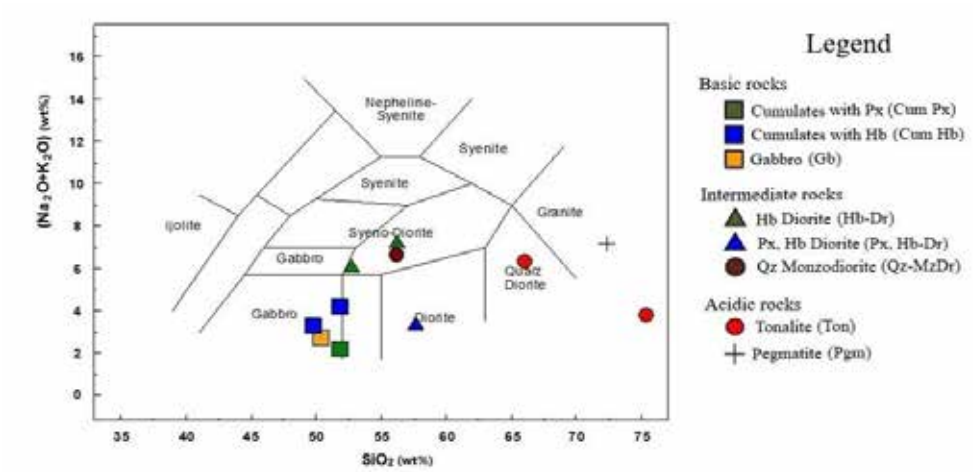

Figure 2: Chemical classification of the Kentavros pluton rock types (TAS after Cox *et al*., 1979).

All the rock types are medium grained apart from the Cum Hb rocks, which contain significantly large hornblende crystals (Fig. 3a). The cumulate rocks consist of hornblende, pyroxene, plagioclase (Fig. 3b), biotite (Fig. 3c) and contain minor amounts of orthoclase and quartz. The accessory minerals are titanite in remarkably large crystals (Fig. 3d), chlorite and apatite. The gabbros consist of plagioclase, hornblende and pyroxene. The diorites and quartz monzodiorites consist of plagioclase, orthoclase, hornblende, biotite, pyroxene and occasionally quartz. The accessory minerals are titanite, allanite, apatite, zircon and opaques. The tonalites consist of quartz, orthoclase, plagioclase, biotite, hornblende and occasionally pyroxene. The accessory minerals are chlorite, allanite and zircon. The pegmatite veins consist of quartz, microcline and plagioclase. The accessory minerals are epidote, clinozoisite and allanite.

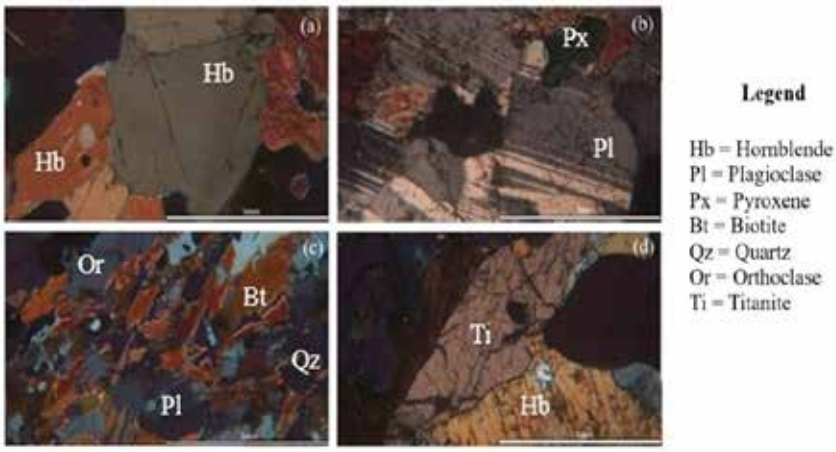

Figure 3: Representative minerals of the Kentavros pluton in N+. (a) Hb crystals, (b) Pl with Px, (c) Bt with Qz, Or and Pl, (d) Ti with Hb.

Geochemistry

The SiO_2 content of the basic rock samples (Cum and Gb) ranges from 49.08 to 51.35%. In the intermediate samples (Dr, Qz-MzDr) it ranges from 50.95 to 57.11%. In the acid samples (Ton, Pgm) it ranges from 65.60 to 71.92% (Table 1). TiO_2, FeO_{tot} (total Fe expressed as Fe^{2+}), MnO, MgO, CaO and P_2O_5 decrease with increasing SiO_2 (Fig. 4 and Table 1), while Al_2O_3, K_2O and Na_2O increase (Fig. 4 and Table 1). Regarding the trace elements, Sr, Ba, Cr, Ni, Zr, Y, Nb, V and Co decrease with increasing SiO_2 (Fig. 5 and Table 1), while Rb and Sc (Fig. 5 and Table 1) increase. According to the SiO_2 - K_2O diagram (Peccerillo & Taylor, 1976) the composition of the pluton varies mostly from calk-alkaline to high-K calc-alkaline (Fig. 4). Also, all the samples are metaluminous and characterized as I-type (Fig. 5).

Table 1: Whole-rock major (wt%) and trace (ppm) element analyses of representative samples from the Kentavros pluton.

Sample name	KE-12	KE-13	KE-03	KE-05	KE-08	KE-07	KE-10	KE-14	KE-11	KE-04	KE-06
Rock type	Cum	Cum	Cum	Gb	Dr	Dr	Dr	Qz-MzDr	Ton	Ton	Pgm
Major elements (wt%)											
SiO_2	49.08	51.29	51.35	49.27	50.95	55.01	57.11	55.80	65.60	74.77	71.92
TiO_2	1.43	1.10	1.01	0.33	0.86	0.42	0.81	1.13	0.18	0.14	0.06
Al_2O_3	8.68	11.45	4.34	18.77	13.97	18.33	7.59	16.09	17.46	11.41	16.14
FeO_{tot}	10.70	9.75	11.26	6.22	7.16	4.94	7.87	7.13	1.88	2.53	0.51
MnO	0.17	0.18	0.28	0.10	0.06	0.07	0.14	0.10	0.02	0.01	0.00
MgO	13.55	10.13	16.35	7.84	4.24	3.18	11.00	5.57	1.25	0.88	0.20
CaO	11.27	10.43	12.03	12.60	12.46	8.19	10.93	6.07	6.38	5.67	3.41
K_2O	0.99	1.07	0.80	0.53	2.18	0.98	0.99	2.54	1.17	0.79	1.23
Na_2O	2.21	3.04	1.36	2.13	3.73	6.12	2.32	4.02	5.04	2.94	5.86
P_2O_5	0.39	0.65	0.19	0.01	0.96	0.61	0.26	0.68	0.26	0.00	0.02
LOI	1.30	0.80	0.87	2.09	3.10	1.95	0.79	0.60	0.60	0.74	0.53
Total	99.77	99.89	99.84	99.89	99.67	99.80	99.81	99.73	99.84	99.88	99.88
Trace elements (ppm)											
Rb	7	4	5	11	50	0	7	47	3	13	5
Sr	646	751	169	210	1318	1308	570	1139	1162	358	836
Ba	234	141	29	18	868	375	124	83	154	18	241
Cr	582	306	576	297	40	38	569	48	27	36	32
Ni	165	103	228	99	18	8	176	30	11	15	10
Zr	128	93	80	36	411	101	102	213	78	464	57
Y	28	26	48	10	28	25	28	20	12	98	3
Nb	19	21	20	0	30	6	13	12	3	5	0
V	242	240	164	163	104	81	187	131	27	8	0
Co	44	38	48	24	25	16	32	25	2	4	0
Sc	21	27	34	39	30	20	30	17	23	27	9

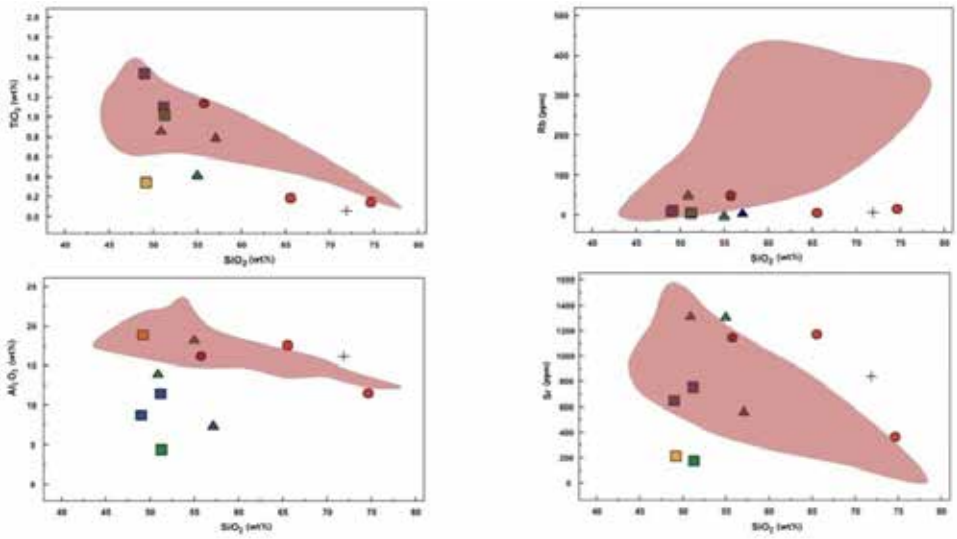

Figure 4: Harker diagrams of representative major and trace elements of the Kentavros pluton (red area: Xanthi pluton). Legend as in Fig. 2.

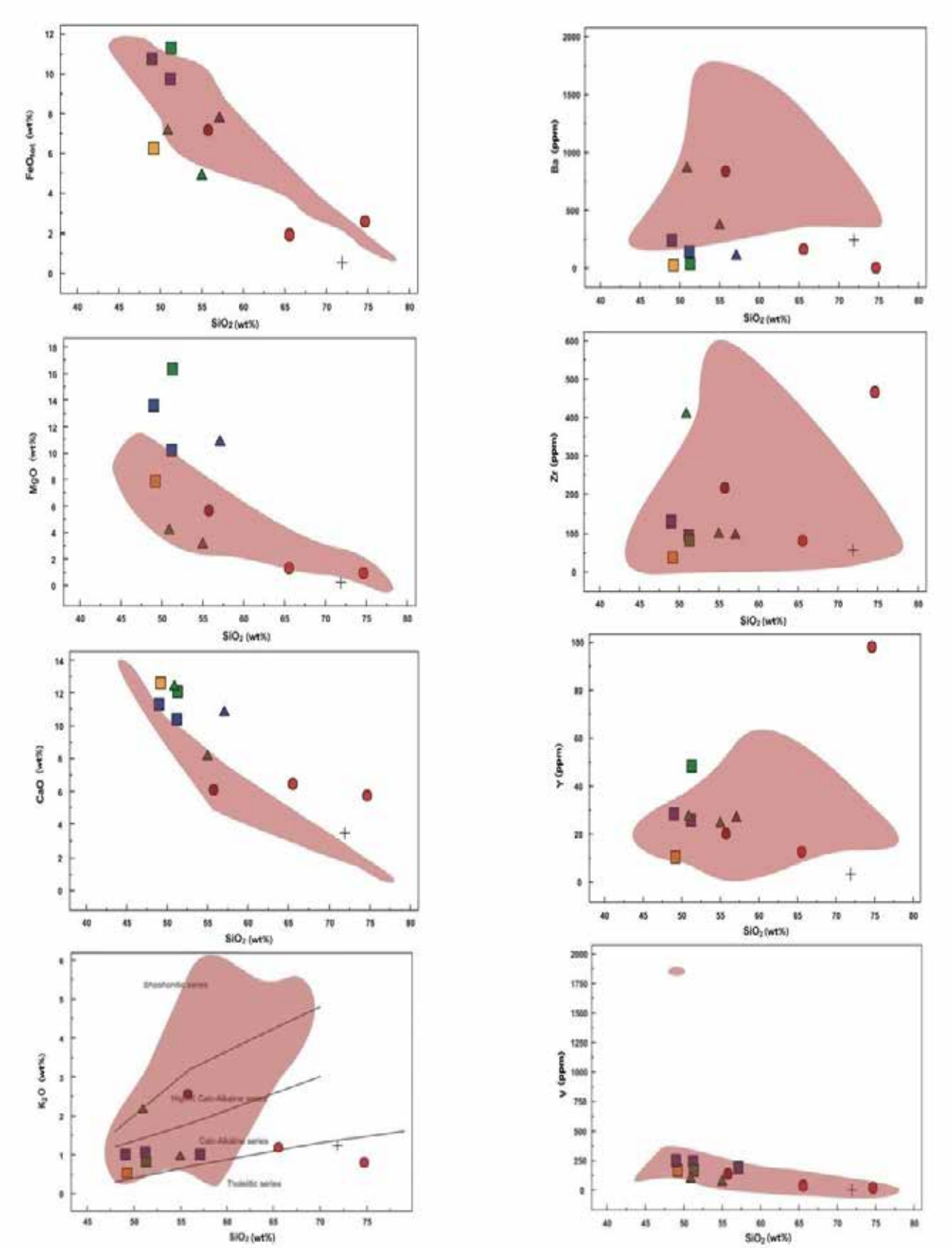

Figure 4 Cont.

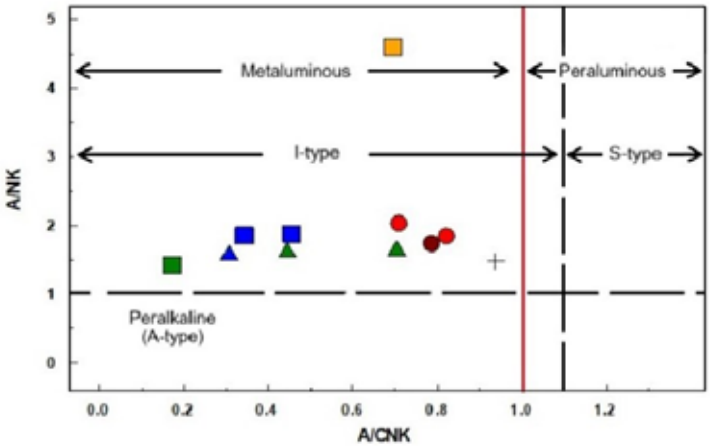

Figure 5: A/CNK - A/NK diagram. Legend as in Fig. 2.

Petrogenesis

According to the tectonic classification diagrams of Pearce *et al*. (1984) (Figs. 6 a and b) the analyzed samples plot mostly in the volcanic arc granitoids (VAG) field. This means that the magmatism of Kentavros is related to a subduction mechanism, which is typical for the Rhodope magmatic rocks of Eocene to Miocene age (Pipera *et al*., 2013).

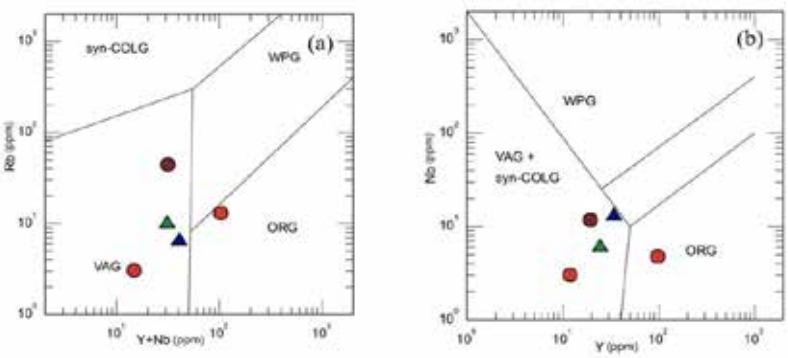

Figure 6: Tectonic classification diagrams (Pearce *et al*., 1984). Legend as in Fig. 2.

Kentavros gabbro represents a mantle-peridotite original melt (Fig. 7, brown area) and diorites are probably the results of evolution of the gabbroic magma although they might represent a high-Mg andesitic magma (Fig. 7, grey area). The tonalitic samples plot in the "Metagreywacke Sources" field (Fig. 7, pink area), indicating association with such sources. It is to note that, alternatively, the intermediate rocks can be probably a result of the metagreywacke's melt interaction with peridotite melt during a mixing procedure.

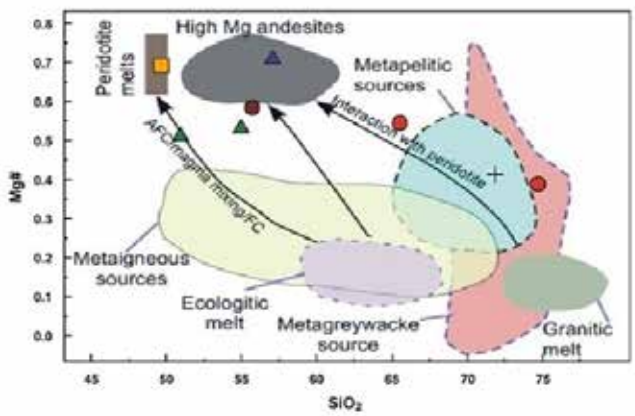

Figure 7: Mg# - SiO_2 diagram showing the melts' origin (Sami *et al*., 2023 and references therein). Legend as in Fig. 2.

Comparison with Xanthi pluton

The fact that the Kentavros and Xanthi plutons are located close to each other (8.8 km apart) combined with their similar ages (Liati, 1986; Christofides *et al*., 2012), lead to the decision of comparing the two plutons, although the geochemical data are limited. Regarding the petrographic types they both contain Qz-MzDr, Dr and Gb, but they differ in the acid rock types. Xanthi pluton contains granodiorites (Gdr) and monzogranites (MzGr), while the Kentavros pluton contains Ton. It must be noted though that Gdr in Xanthi represents ~75% of the pluton. On the contrary, the amount of Ton in Kentavros pluton is limited. Major elements having similar behavior in both plutons are TiO_2, Al_2O_3, FeO_{tot}, MnO, MgO and P_2O_5 (Fig. 4). K_2O has lower values in Kentavros than Xanthi and Na_2O either lower and or higher values than Xanthi. Trace elements showing similar behavior in both plutons are Sr, Cr, Ni, Zr, Y, Co and V (Fig. 4). Rb and Ba have lower values in Kentavros than Xanthi, while Sc has higher values. Moreover, both plutons have calc-alkaline to high-K calc-alkaline affinity, even though Xanthi intermediate (monzonitic) rocks have higher K content (Fig. 4). Both plutons are associated to the same geotectonic environment (VAG) and to the Xanthi detachment system. It should be noted though, that Kentavros pluton is a syn-detachment intrusion while Xanthi pluton is characterized as late or post detachment intrusion (Krohe & Mposkos, 2002).

References

Christofides, G., Soldatos, T., Eleftheriadis, G., Koroneos, A., 1998. Chemical and isotopic evidence for source contamination and crustal assimilation in the Hellenic Rhodope plutonic rocks. Acta Vulcanologica, 10, 305-318.

Christofides, G., Koroneos, A., Soldatos, T., Eleftheriadis, G., Kilias, A., 2001. Eocene magmatism (Sithonia and Elatia plutons) in the Internal Hellenides and implications for Eocene-Miocene geological evolution of the Rhodope massif (Northern Greece). In: Downes, H., Orlando, V. (Eds.), Tertiary Magmatism in the Dinarides Acta Vulcanologica, 13, 73-89.

Christofides, G., Pipera, K., Koroneos, A., Papadopoulos, A., 2012. New geochronological data from the Xanthi pluton: Constraints on the Nestos thrust dating, The School of Prof. Zhivko Ivanov. In International Conference: Exhumation of High-grade Metamorphic Rocks (MCC), Magmatic Arc Systems and Strike-slip Zones (pp. 49-52).

Cox, K. G., Bell, J. D., Pankhurst, R. J., 1979. Compositional variation in magmas. In The interpretation of igneous rocks (pp. 12-41). Dordrecht: Springer Netherlands.

IGME, 1973. Geological map of Greece, Xanthi sheet. Institute of Geology and Mining Research, Athens.

Krohe, A., & Mposkos, E., (2002). Multiple generations of extensional detachments in the Rhodope Mountains (northern Greece): evidence of episodic exhumation of high-pressure rocks.

Liati, A., 1986. Regional metamorphism and overprinting contact metamorphism of the Rhodope Zone, near Xanthi (N. Greece) (Doctoral dissertation, PhD dissertation, Univ. Carolo-Wilhelmina, Braunschweig, Germany).

Mountrakis, D., Tranos, M., Papazachos, C., Thomaidou, E., Karagianni, E., Vamvakaris, D., 2006. Neotectonic and seismological data concerning major active faults, and the stress regimes of Northern Greece. Geological Society, London, Special Publications, 260(1), 649-670.

Mountrakis, D., 2021. Geology and Geotectonic Evolution of Greece. Thessaloniki: University Studio Press, 33-43.

Papanikolaou, D., Panagopoulos, A., 1981. On the structural style of Southern Rhodope, Greece.

Pipera, K., Koroneos, A., Soldatos, T., Poli, G., & Christofides, G., 2013. Origin of the High-K Tertiary magmatism in Northern Greece: Implications for mantle geochemistry and geotectonic setting. Bulletin of the Geological Society of Greece, 47(1), 416–426.

Pearce, J. A., Harris, N. B., Tindle, A. G., 1984. Trace element discrimination diagrams for the tectonic interpretation of granitic rocks. Journal of petrology, 25(4), 956-983.

Peccerillo, A., Taylor, S. R., 1976. Geochemistry of Eocene calc-alkaline volcanic rocks from the Kastamonu area, northern Turkey. Contributions to mineralogy and petrology, 58, 63-81.

Sami, M., Adam, M. M., Lv, X., Lasheen, E. S. R., Ene, A., Zakaly, H. M., Ali, S., 2023. Petrogenesis and tectonic implications of the cryogenian I-type granodiorites from Gabgaba Terrane (NE Sudan). Minerals, 13(3), 331.

17th INTERNATIONAL CONGRESS of the Geological Society of Greece

BULLETIN OF THE GEOLOGICAL SOCIETY OF GREECE, SP. PUBL.

EXTENDED ABSTRACT 047

The Impact of Urban Sprawl on Areas of Natural and Cultural Heritage and Geoheritage. Evidence of Lemnos Island, Greece

Chatzi Efstratia[1] , Derdemezi Evangelia - Theodora[1] , Tsilimigkas Georgios [1]
(1) University of the Aegean, Department of Geography, Mytilene, Greece
Email: efi.chatzi@geo.aegean.gr, ederde@geo.aegean.gr , gtsil@aegean.gr

Research Highlights

Quantitative rendering of the impact of urban sprawl on Natura 2000 areas, Wild Life Refuges, Small Islands Wetlands, Archeological areas and Monuments and the Petrified Forest in Lemnos island. Interpretation of results based on spatial planning system in Greece.

Introduction

Cultural and natural heritage and geoheritage sites are vital for preserving the identity and history of regions, but they are increasingly threatened by urban sprawl, particularly in areas with high development pressures (AbdelMaksoud 2020, Lagarias and Stratigea 2023). Islands are highly vulnerable to such pressures due to their small size and growing tourism (Baldacchino 2004, Spilanis 2012). The urban sprawl on islands is often expanded into critical heritage zones, which are already under pressure from both natural and human factors (Salvati 2013, Tsilimigkas et al.2022). Islands are characterized by spatial fragmentation, which on the one hand makes them fragile socio-spatial systems and on the other hand enhances endemism, creating ecosystems of particular value. This is recognized at the European level, and thus a large part of the island areas is included in the Natura 2000 network (EEC 1992, EC2009). The importance of the natural environment and the need for management and protection is also recognized at the national level with legislation under which, among other things, National Parks (OGG 1986, OGG 2020), Small Island Wetlands (MD 2010, OGG 2011) and Wild Life Refuges (OGG 1998, OGG 2011) are delineated. The cultural heritage of the islands is characterized by an extensive network of traditional settlements and archaeological areas and monuments. The need for cultural heritage protection and management is recognized at European and national level (Council of Europe 1995, OGG 2002, OGG 2021). An important part of the identity of the islands, and a valuable tourist resource is their geoheritage, which consists of physico-geographical elements of geological interest and at the same time, over the years, these areas acquire a cultural significance that makes them landscapes of special value (Sotiriou and Nunes 2024). At the international level, the importance of geoheritage has been recognized mainly through the UNESCO'S Global Geoparks Networks. At the national level, legislation concerning geoparks and geosites is fragmented and falls both within institutional arrangements for the protection of environment and habitats (OGG 2011, OGG 2020) and for the protection of the cultural environment and landscape (OGG 2010).

The study area for this paper is Lemnos Island of the Region of the North Aegean. Covering an area of 478,97 km² and the permanent population is 16409 people. Lemnos has notable natural and cultural heritage, including 3 areas integrated into the Natura 2000 network, 9 wildlife refuges areas, 3 sections of the Petrified Forest, 59 wetlands, 18 traditional settlements and 20 designated archaeological sites. One of the island's most unique features is the Petrified Forest of Lemnos, which contains subtropical vegetation remains dating back at least 20 million years (Dasarxeio, 2020). Designated as a "Preserved Natural Monument" (Decision No. 75247/4865/10-12-2013 by the Secretary General of the Decentralized Administration of the Aegean), this site is protected across three delineated areas and several individual fossil-bearing locations.

Objectives

The aim of this research is the quantitative rendering of urban sprawl in areas of natural and cultural value on the island of Lemnos and its interpretation within the framework of spatial planning. Specifically, the research questions are: (1) What percentage of built-up area is located within and outside settlements' boundaries? (2) What percentage of built-up area outside settlements' boundaries is located within (a) Natura 2000, (b) archaeological areas and (c) petrified forest? The results are interpreted based on spatial planning and applicable legislation.

Methods

To answer the research questions, acquiring the appropriate geospatial data was essential:

- Impervious Built-up (IBU) 2018, provided by the European Environment Agency (EEA) through Copernicus, was used to represent built-up areas. This raster layer contains binary information, with buildings classified as 1 and non-buildings as

0 (EEA 2018). The spatial resolution of IBU is 10m.

- For distinguishing built-up areas inside and outside settlements, the boundaries of official settlements were sourced from the open platform e-poleodomia (MEE 2025). In Lemnos there are 40 settlements of which 18 designated traditional settlements, three traditional settlements were found to lack official boundaries. To avoid considering these built-up areas as exurban, we digitized their boundaries aaccording to the compact residential fabric with reference map the Google Earth. Additionally, the settlement boundaries for Myrina, the capital of the island, were missing. These boundaries were digitized using the General Urban Plan (GUP), with topographical charts georeferenced using the Greek Geodetic Reference System 1987 (GGRS87) at a scale of 1:5.000. This ensures accurate and consistent mapping across all settlements.
- The Natura 2000 areas were retrieved from the EEA (EEA 2022). The Wildlife Refuges were sourced from the Forest Service and forest maps, while the Wetlands were obtained from the Greek Ministry of Environment and Energy. The delineation of archaeological areas came from the Archaeological Cadaster.
- The delineation of the Petrified Forest of Lemnos was based on the map included in the decision declaring it a “Preserved Natural Monument” (Official Decision 2013). To ensure spatial precision, we digitized the forest boundaries from the forest map provided by the Forest Service, georeferencing the map using GGRS87 at a scale of 1:5.000.

The methodology employed was based on raster analysis. Vector-format data were rasterized to align with the raster layers. The identification of exurban built-up areas was achieved by overlaying the layers of IBU and official settlement delineations. This analysis produced quantitative data, which was further examined to assess spatial relationships with the Natura 2000 areas, wildlife refuges areas, wetlands archaeological areas and the Petrified Forest of Lemnos. The resulting insights were interpreted within the framework of spatial planning to evaluate the impact of urban sprawl on these protected areas.

Results

In Lemnos, the total built-up area occupies 4.74 km², which corresponds to 0.99% of the island’s total area. Of this built-up area, 3.41 km² (or 0.71%) lies within the boundaries of settlements, while the remaining 1.33 km² (or 0.28%) is located outside settlement boundaries. Comparatively, the percentage of construction on Lemnos is significantly smaller than on other islands, such as Santorini, where construction occupies 4.04% of the total island area, with 2.08% in extra-urban areas (Tsilimigkas and Derdemezi 2020).

The distribution of built-up areas outside official and traditional settlements in Lemnos highlights their significant impact on zones of natural and cultural significance, as shown in Table 1.Urban sprawl has impacted 8 of the wildlife areas, 6 of the wetlands, 2 of the Natura 2000 sites and 11 of the archaeological sites. Archaeological areas, which cover an impressive 89.44% of the island, are among the most affected by this type of development, hosting a substantial portion of the built-up area outside settlements. This overlap underscores the need for careful management, as interventions within archaeological site boundaries must comply with strict regulations to prevent unplanned and unregulated development.

Table 1. Impact of Built-Up Areas Outside Settlements on Natural and Cultural Zones in Lemnos

Island of Lemnos	Percentage %
Petrified Forest Area B1	2,42
Petrified Forest Area B2	7,67
Wildlife Refuges Areas	32,57
Wetlands	0,61
Natura 2000	14,4
Archaeological	89,44

Other areas of natural significance also show varying degrees of impact from built-up areas outside settlements: Petrified Forest: Area B1 is affected by 2.42%, while Area B2 is affected by 7.67%. Wildlife Refuges Areas: These zones experience significant impact, with 32.57% affected by built-up areas outside settlements. Wetlands: Though wetlands occupy only 0.61% of the island, their exposure to built-up areas outside settlements highlights the need for protection from encroaching development. Natura 2000 Sites: These protected areas are also impacted with 14.4% affected by built-up areas outside settlements, further emphasizing the urgency of integrated spatial planning.

To better visualize the spatial distribution of built-up areas in relation to the zones of natural and cultural significance, Figure 1 provides an overview of Lemnos, while Figure 2 zooms in on two key areas of the island. The labels B1, B2, and B3 in Figure 2 correspond to areas of the Petrified Forest, which are among the zones impacted by built-up areas outside settlements.

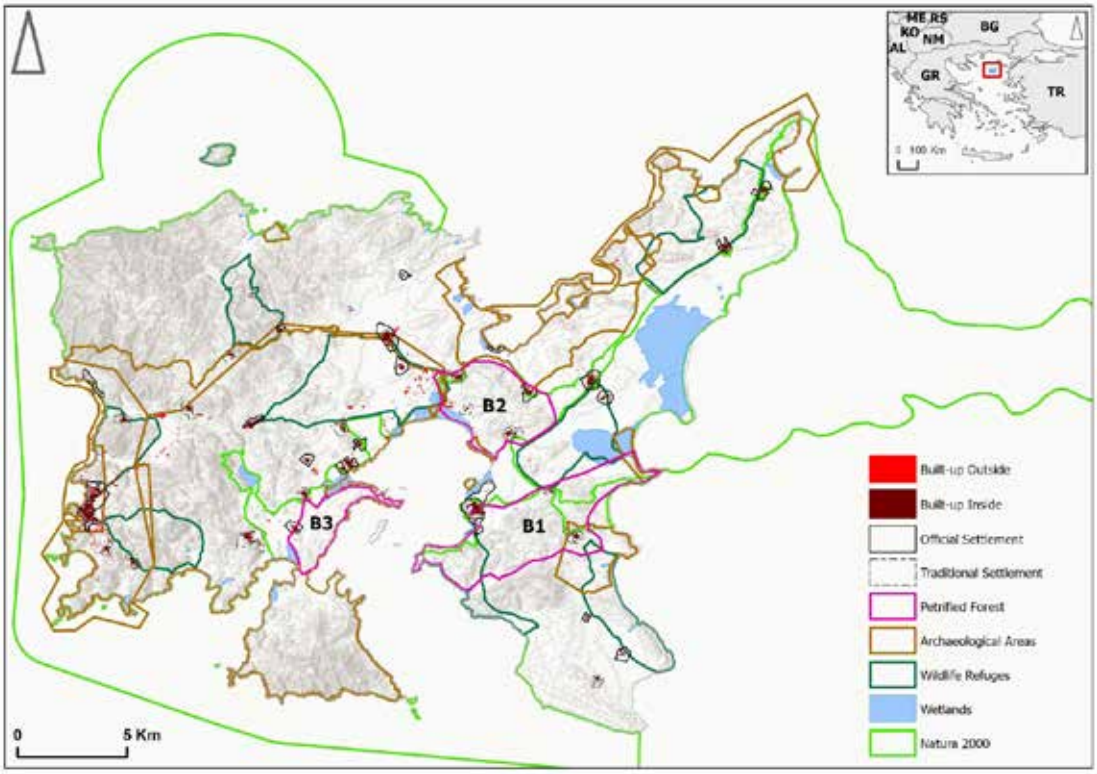

Figure 1: Overview of the Island of Lemnos, showing the spatial distribution of built-up areas, settlements, and protected zones.

Figure 1 provides a comprehensive view of the spatial distribution of built-up areas across Lemnos. The map highlights both built-up areas within settlements (dark red) and outside settlements (bright red). It also delineates key zones of natural and cultural significance, such as archaeological areas, wildlife refuges, wetlands, and Natura 2000 sites. This island-wide perspective allows for a clear visualization of how built-up areas intersect with these protected zones, underscoring the need for spatial planning to mitigate unregulated construction in sensitive areas. The map serves as a foundation for understanding the broader spatial dynamics of built-up development on Lemnos.

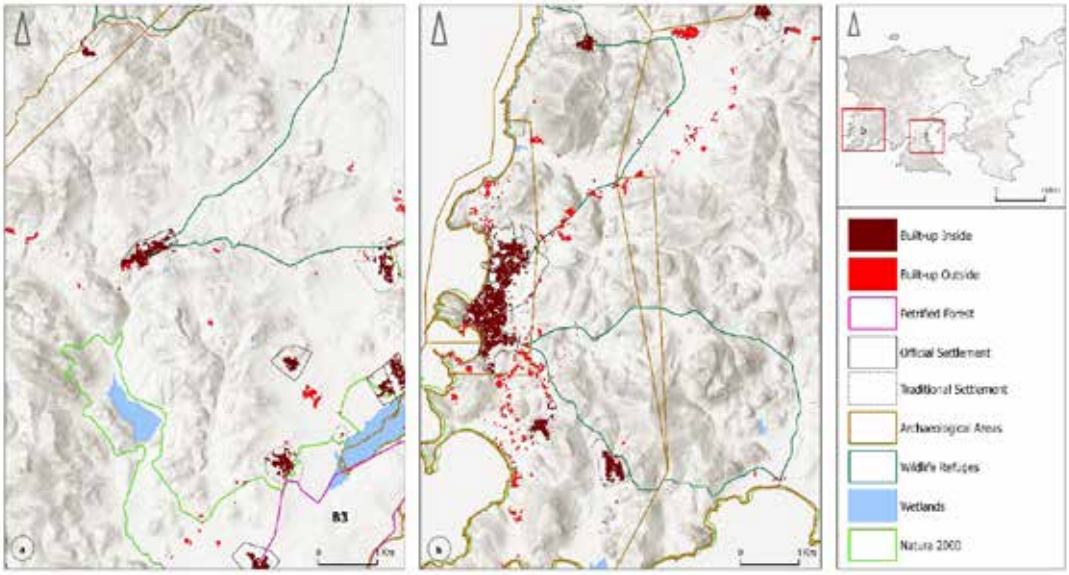

Figure 2: Zoomed-in views of two key areas in Lemnos, highlighting the overlap between built-up areas and protected zones. B1, B2, and B3 represent regions of the Petrified Forest.

Figure 2 zooms in on two critical regions of Lemnos, offering a closer examination of the overlap between built-up areas and zones of natural and cultural importance. The highlighted areas, B1, B2, and B3, represent sections of the Petrified Forest, a unique geological heritage site. The map illustrates the proximity of built-up areas to these sensitive zones, emphasizing the potential risks posed by unregulated construction. The focused view also shows how built-up areas extend beyond settlement boundaries into wildlife refuges, wetlands, and archaeological zones, providing a detailed context for the discussion on sustainable development and spatial planning.

In conclusion, these findings underscore the opportunity to implement a comprehensive and integrated spatial planning framework at the local level, aimed at regulating construction outside settlement boundaries. Such a framework is essential to align development with Lemnos' natural and cultural heritage and geoheritage, prevent the fragmentation of protected zones and balance growth with the preservation of archaeological sites and other critical areas.

Conclusions

This research underscores the critical need for an integrated and cohesive framework for the natural and cultural heritage and geoheritage While legal references and regulations exist, their fragmented nature, coupled with inconsistencies in spatial and temporal application, creates implementation challenges, fosters conflicts and leaves room for unregulated development in sensitive and significant areas (Tzeferis 2018; Tsilimigkas and Derdemezi 2020). A positive step was the inclusion of a section on landscape in the Regional Frameworks on Spatial Planning and Sustainable Development' (RFSPSD) according to European Landscape Convention principles. Although improvements are needed and especially for the island of Lemnos, geoheritage could be included more consistently in landscape zones. The directions of RFSPSD could form the basis to support downstream planning level regulations. The management and promotion of natural and cultural heritage, along with geoheritage, present significant opportunities for strengthening Lemnos' economy. Alternative forms of tourism, such as geotourism, can draw inspiration from neighboring Lesvos, where the Petrified Forest is part of the European Geoparks Network (Zouros 2004). Revised directions in the Special Spatial Framework for Tourism should focus on fostering such sustainable tourism development, emphasizing alternative and eco-friendly tourism models. At the same time, the RFSPSD should be revised to align with the upstream directions and plan a sustainable way of management and development. Finally,a significant challenge remains at the local spatial planning level, which is currently fragmented and incomplete, allowing unregulated built-up area expansion in exurban areas. The upcoming local plans are intented to restrain urban sprawl. . As highlighted in this study, such measures are imperative to prevent the pressures that urban expansion places on natural and cultural heritage and geoheritage.

References

AbdelMaksoud, K.M., El Metwaly, W. Maadi. (2020). Petrified Forest in Cairo, Egypt, as a Geologic Heritage Under Urbanization Pressure. Geoheritage. 12 (44). DOI: 10.1007/s12371-020-00465-4

Baldacchino, G. (2004). The coming of age of island studies. Tijdschrift voor Economische en Sociale Geografie, 95(3), 272–283. DOI:10.1111/j.1467-9663.2004.00307.x

Council of Europe (1995). The European Convention for the Protection of the Archaeological Heritage. Council of Europe Treaty Series no. 143

Dasarxeio. (2020). Giant eight-meter fossilized trunk discovered on Lemnos. Retrieved from https://dasarxeio.com/2013/12/11/10173/. Last Access 20/01/2025

EEA (European Environment Agency). (2022). Natura 2000. Spatial Data. Retrieved from: https://www.eea.europa.eu/data-and-maps/data/natura-14/natura-2000-spatial-data. Last Access 17/01/2025

EEA (European Environment Agency). (2018). Impervious Built - up 2018. Copernicus Land Monitoring Service

European Commission (EC). (2009). Directive 2009/147/EC of the European Parliament and of the Council of 30 November 2009 on the conservation of wild birds

European Economic Community (EEC). (1992). Council Directive 92/43/EEC of 21 May 1992 on the conservation of natural habitats and of wild fauna and flora

Lagarias, A., Stratigea, A. (2023). Coastalization patterns in the Mediterranean: a spatiotemporal analysis of coastal urban sprawl in tourism destination areas. GeoJournal . 88 (2529–2552). DOI:10.1007/s10708-022-10756-8

MD (Ministerial Decision). (2010). Approval of a list of small island wetlands, definition of conditions and restrictions for their protection. 518/2010. OGG B181/2010

Official Decision. (2013). No. 75247/4865/10-12-2013 Decision Declaring the Petrified Forest of Lemnos as a "Preserved

Natural Monument"
OGG (Official Government Gazette). (2021).Ratification of a Code of Legislation for the protection of antiquities and cultural heritage in general. Official Government Gazette 220/A/2021. Law 4858/2021
OGG (Official Government Gazette). (2020). Modernization of environmental legislation, incorporation into Greek legislation of Directives 2018/844 and 2019/692 of the European Parliament and of the Council and other provisions. Official Government Gazette 92/A/2020 Law 4685/2020
OGG (Official Government Gazette). (2011). Conservation of biodiversity and other provisions. Official Government Gazette 60/A/2011. Law 3937/2011
OGG (Official Government Gazette). (2010). 'Ratification of the European Landscape Convention'. Official Government Gazette. 30-A/25.02.2010. Law 3827/2010.
OGG (Official Government Gazette). (2002). 'Protection of Cultural Heritage'. Official Government Gazette 153-A/28.06.2002. Law 3028/2002.
OGG (Official Government Gazette). (1998). Establishment of the Account Certification Agency, the Payments and Control Agency for Community Aids, Guidance and Guarantees, the Certification and Supervision Agency for Agricultural Products, General Directorates and staff positions in the Ministry of Agriculture and "Agricultural Land Development Company" S.A. and other provisions. Official Government Gazette 200/A/1998. Law 2637/1998
OGG (Official Government Gazette). (1986). 'Environmental protection'. Official Government Gazette 160-A/16-10-86. Law 1650/1986.
MEE (Ministry of Environment and Energy). 2025. Geoporta e-poleodomia. Available at: http://gis.epoleodomia.gov.gr/v11/#/10.9313/39.8760/5
Salvati, L. (2013). 'Rural' sprawl, Mykonian style: A scaling paradox. International Journal of Sustainable Development & World Ecology, 20(2), 109–115. DOI:10.1080/13504509.2013.765522
Sotiriou, P. Nunes, P. (2024). The Geoheritage of Madeira: Implications for Natural Heritage and Geotourism. Geoheritage. 16 (74). DOI: 10.1007/s12371-024-00982-6
Spilanis, I. (2012). The islands development: what strategy and what policies to achieve territorial convergence. Gutenberg
Tsilimigkas, G. Gourgiotis, A. Derdemezi, E-T. (2022). Spatial planning incompetence to discourage urban sprawl on Greek Islands. Evidence from Paros, Greece. Journal of Coastal Conservation. 26 (2). DOI: 10.1007/s11852-022-00859-2
Tsilimigkas, G. Derdemezi, E-T. (2020). Unregulated built-up area expansion on Santorini island, Greece. European planning studies. 28 (9). pp. 1790 - 1811. DOI: 0.1080/09654313.2019.1687656
Tzeferis, P. (2018). Institutional framework for the protection of geological sites. Greek Mineral Wealth. Retrieved from: https://www.oryktosploutos.net/2018/04/blog-post_3-5/
Zouros, N. (2004). The European Geoparks Network - Geological heritage protection and local development. IUGS Episodes Journal of International Geoscience. 27(3). DOI: 10.18814/epiiugs/2004/v27i3/002

17th INTERNATIONAL CONGRESS of the Geological Society of Greece

BULLETIN OF THE GEOLOGICAL SOCIETY OF GREECE, SP. PUBL.

EXTENDED ABSTRACT 048

Slope failures of friable sandstone in coastal areas. A Case study from Western Greece.

Chatziangelis E.[1*], Boumpoulis V.[1], Depountis N.[1]
*(1) Department of Geology, University of Patras, 26504 Patras, Greece, *up1089644@upatras.gr*

Research Highlights: **Investigation of the failure mechanism of steep sandstone slopes in coastal areas**

Introduction

Coastal slope failures are major geological phenomena that often lead to environmental degradation, land loss and destruction of property and infrastructure. These failures occur predominantly in regions with weak geological formations, steep slopes and dynamic coastal processes. The Kalamaki coastal zone in Western Achaia, Greece, is a representative example, featuring a stratigraphy of friable sandstone formations overlaying clayey marls, which are inherently prone to weathering, erosion, and slope instability. The susceptibility of these geological formations to failure is exacerbated by structural discontinuities in the sandstone layers, allowing water infiltration and subsequent slope destabilization (Zhang *et al.,* 2020).

Since 2014, progressive slope instability in Kalamaki has been observed through satellite imagery (Figure 1), aerial surveys, and field investigations. The main causes of this instability include natural processes such as wave action and erosion, combined with anthropogenic activities such as irrigation and excavation for road and building construction. In addition, water infiltration along vertical cracks in the sandstone, combined with the penetration of vegetation roots, widens these cracks over time, causing translational slides, rockfalls, and earth flows. These processes deposit significant sediment loads along the coastline, altering beach dynamics (Delgado *et al.,* 2018; Poulos *et al.,* 2019).

Figure 1. Satellite image of Kalamaki in Western Achaia, Greece (Google Earth 05/2015) with the white line representing the failure area as determined in 9/5/2022.

Localized high-wave events and marine undercutting further destabilize the base of the coastal slopes, creating overhangs and weakening the upper geological layers. This underscores the necessity for targeted mitigation measures addressing both geological and marine influences. While prior studies suggest relative stability in some parts of the Kalamaki coastline, high-energy events have repeatedly triggered localized failures, highlighting the importance of assessing these vulnerabilities. For a better understanding of the failures on the coastal slopes of Kalamaki, this paper uses the results of the Coastal Vulnerability Index (CVI) estimation for specific areas (Boumpoulis, 2024; Boumpoulis *et al.,* 2025) in combination with the classical slope stability analysis. Using Hoek et al. (1981) two-dimensional slope stability analysis for weak rocks and general CVI considerations (Gornitz, 1991; Depountis *et al.,* 2023), , this study identifies slope destabilization hotspots in a coastal area, identifying the failure mechanism and providing critical information on areas requiring immediate protection.

Methodology and geological regime

The methodological framework for investigating the sandstone slope failures in the Kalamaki coastal area focuses on the identification of the geological characteristics and the mechanisms of driving slope instability. Fieldwork was conducted to document the state of the slope and identify signs of instability. Observations were made regarding the slope and coast morphology, the distribution of discontinuities in the sandstone mass and the vegetation cover. The field surveys conducted, using UAV and GPS equipment, helped in the production of high resolution orthoimages and mapping of the affected area (Figure 2).

Figure 2. Aerial photograph of the sandstone slope failure occurred in Kalamaki, Western Achaia (UAV campaign, 9/5/2022).

The geological framework of the affected area consists of Plio-Pleistocene sediments, mainly friable sandstones overlying clayey marls (Figure 3) – από το διδακτορικό του Βασίλη και τη δημοσίευση του 2025. Both formations are very susceptible to weathering and have the characteristics of soft rocks; hence, low Uniaxial Compressive Strength (UCS). Moreover, the sandstones exhibit high porosity and permeability, making them susceptible to water infiltration, and are intersected by vertical and sub-vertical cracks, which act as pathways for root penetration and water ingress; thus, further weakening the slope's integrity along the coastline.

Figure 3. Geological map of the study area.

The geological and field surveys carried out allowed the precise delineation of the landslide boundary and its characteristics (Figure 4).

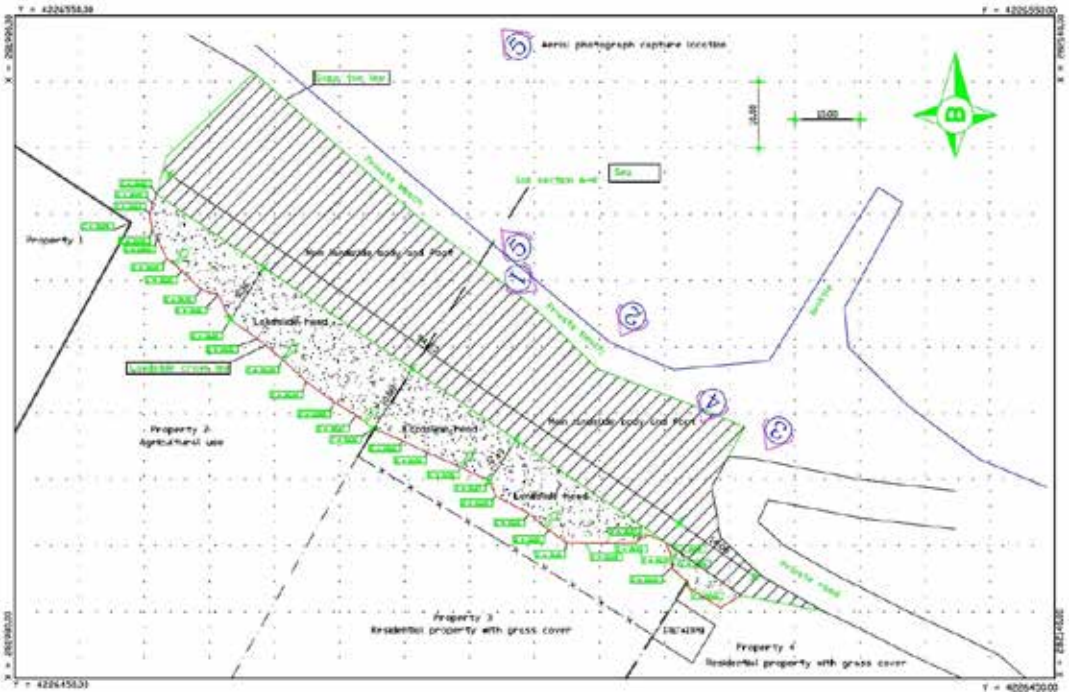

Figure 4. Plan view of the study area with the landslide delineation.

Measurements conducted during field surveys indicated that the landslide's total affected area was approximately 2,750 m², with the crown at an elevation of 18.5–22.5 meters above sea level. The landslide crown extended 120 meters in length, with a scarp of 3 meters and a head of 10.8 meters in width.

Analysis and Results

The failure mechanism was investigated based on the observed field data and geological regime, so a detailed two-dimensional geological cross-section was designed for further analysis (Figure 5).

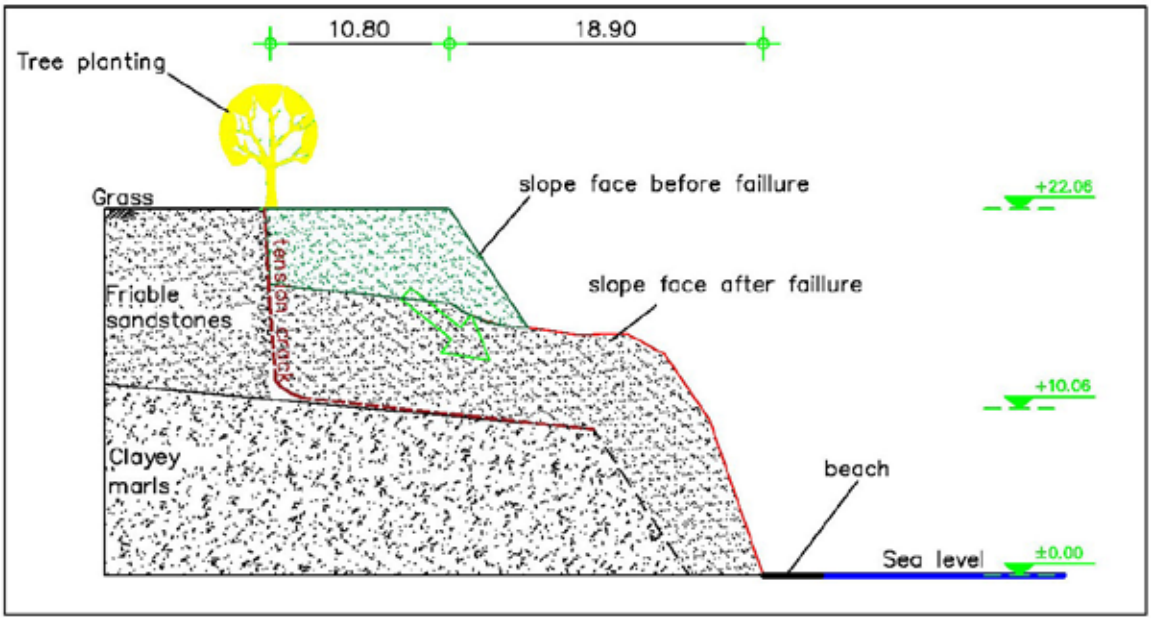

Figure 5. Geological cross-section presenting the landslide characteristics and the failure mechanism

The primary failure mode identified was translational sliding, where sandstone blocks detach along pre-existing discontinuities or tension cracks and slide over the underlying clay marls, even with low stratigraphic gradient between sandstones and clays. These discontinuities acted as tensile cracks, further widened by root penetration and water infiltration and facilitated block detachment and movement downslope. Earlier failure processes were also observed, such as sparse rock falls and earth flow, in places where marine undercutting had reduced the basic support of the slope.
Further destabilization of the slope occurred due to anthropogenic interventions, such as irrigation of vegetation and trees near the slope crest. These activities have contributed to the accumulation of water within the sandstone mass and its discontinuities, exacerbating the instability of the slope.
The failure analysis was based on the principle of a translational slide with tensile crack, as proposed by Hoek et al. (1981), as the most representative for the study area (Figure 6).

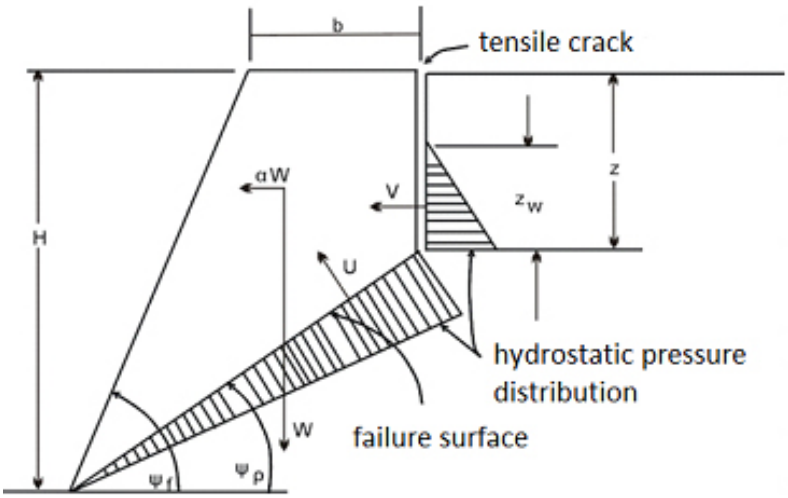

F	Factor of safety
H	Height of the sliding slope
W	Weight of the sliding block
U	Uplifting hydrostatic force
V	Hydrostatic tensile crack force
z	Depth of tensile crack
b	Width of the sliding block
z_w	Water level in tensile crack
ψ_p	Inclination angle of failure surface
ψ_f	Inclination angle of sliding slope
α	Seismic ground acceleration
γ	Unit weight of sliding block

Figure 6. Failure analysis of a rock mass in the form of translational slide with tensile crack (Hoek *et al.,* 1981)

The equations used for the calculation of the Factor of safety for this type of slide are (Hoek *et al.,* 1981):

$$F = \frac{cA + [W\ (\cos\psi_p - \alpha\sin\psi_p) - U - V\sin\psi_p]\ \tan\varphi}{W(\sin\psi_p + \alpha\cos\psi_p) + V\cos\psi_p}$$

$$Z = H(1 - \sqrt{\cot\psi_f\ \tan\psi_p})$$

$$A = (H - Z)cosec(\psi_p)$$

$$W = {}^1/_2\ \gamma\ H^2[(1 - (Z/H)^2)\cot\psi_p - \cot\psi_f]$$

$$U = {}^1/_2\ \gamma_w\ Z_w A$$

$$V = {}^1/_2\ \gamma_w\ Z_w^2$$

The data imported in the above equations are:
H = 12 m, z = 9,5 m, $\psi_\rho = 10^0$, $\psi_f = 80^0$, α = 0.12, γ = 23 kN/m^3, φ = 20^0, c = 10 kPa.
The geometrical data of slope derived by in-situ measurements and the geotechnical data (c and φ) of the sandstone material along the sliding surface considered to be similar to the residual state of a clayey sand with a minimum cohesion. The final calculation of the safety factor of the sandstone slope for three different scenarios is illustrated in Table 1, which shows that the main sliding force is hydrostatic uplift and lateral pressure. When the water level rises

within the discontinuities near the ground surface (0.5 m below the surface), failure occurs. This matches the actual conditions found in the research area and the moisture content of the samples that 1m from the ground surface was in a state of saturation.

Table 1. Factor of safety of the coastal sandstone slopes in the Kalamaki area

Scenario A (dry conditions)		Scenario B (hydrostatic fluctuation)		Scenario C (earthquake)	
Z_w	F	Z_w	F	Z_w	F
0	2.32	3	1.99	0	1.36
		5	1.64		
		7	1.3		
		9	**1**		
		10	0.88		

To exclude the hypothesis that this type of landslide was triggered by coastal erosion, the vulnerability status of the area was also analyzed, along with the calculation of the historical shoreline erosion changes in the coastline. The data was retrieved from two studies carried out in the Gulf of Patras by Boumpoulis (2024) and Boumpoulis *et al.* (2025).

In particular, the results of the Coastal Vulnerability Index (CVI) estimated by the previous studies indicate that the coastal zone of Kalamaki is characterized by very low vulnerability, represented by a green line in Figure 7 (Boumpoulis, 2024; Boumpoulis *et al.*, 2025). The green line in Figure 7 represents a stable coast, with an erosion rate ranging from -0.10 to -0.20 m/year, which suggests a low probability that the landslide event of 2022 was caused by coastal erosion. However, the sandy material of the beach has been created by past landslides, either due to undercutting of part of the slope by wave erosion or similar translational failures.

Figure 7. Coastal Vulnerability Index (CVI) along the Kalamaki coastline as adopted from a previous study conducted by Boumpoulis (2024). The image is a worldview 2018 aerial image and the red line indicates the landslide crown identified in 09/05/2022.

Conclusion/Discussion

This research bridges the perspectives of geology and coastal engineering by investigating the interaction between terrestrial and coastal processes in coastal slope failures. The research focused on finding the failure mechanism of a friable sandstone slope in the coastal area of Kalamaki and revealed that a combination of geological, hydraulic and anthropogenic factors contributed to the slope instability. The friable nature of the sandstone formations, combined with the increased hydrostatic pressure in the discontinuities of the sandstone mass, contributed to the instability of the slope. The vertical discontinuities within the sandstone mass serve as critical pathway for water infiltration, and hydrostatic pressure increases, while marine undercutting weakens the base of the slope; hence creating a complex geological environment for several types of instabilities that have occurred in the past, such as sparse rock falls and earth flows.

A key conclusion of this study is the role of anthropogenic activities in exacerbating slope instability. Practices such as irrigation of vegetation and trees near the top of the slope without any drainage, lead to water accumulation, further destabilizing the slope. These activities, combined with natural processes, highlight the progressive nature of slope failure in the area.

The results of this study underline the importance of an integrated approach to slope stabilization in coastal areas. Mitigation measures should prioritize the reduction of water infiltration in similar geological regimes by implementing appropriate drainage measures and preventing anthropogenic activities such as irrigation and excavation for road and building construction on the crest of coastal sandstone slopes.

References

Boumpoulis, V., 2024. Development of a coastal vulnerability assessment model: application in the pilot area of the Gulf of Patras, Greece. Ph.D. Thesis, University of Patras, 188 p.

Boumpoulis, V., Depountis, N., Dimas, A., Papatheodorou G., 2025. Presentation and analysis of the Geotechnical Coastal Vulnerability Index and validation of its application to coastal erosion problems. Sci Rep 15, 1424.

Delgado, G., Gómez, C., & Fernández, L., 2018. Coastal erosion processes and slope stability in sandy formations. Journal of Coastal Engineering, 42(3), 185-198.

Depountis N., Apostolopoulos D., Boumpoulis V., Christodoulou D., Dimas A., Fakiris E., Leftheriotis G., Menegatos A., Nikolakopoulos K., Pappatheodorou G., Sabatakakis N., 2023. Coastal Erosion Identification and Monitoring in the Patras Gulf (Greece) Using Multi-Discipline Approaches. J Mar Sci Eng 11:654.

Gornitz, V. 1991. Global coastal hazards from future sea level rise. Palaeogeogr Palaeoclimatol Palaeoecol 89:379–398.

Hoek, E., Bray, J., 1981. Rock Slope Engineering, 3rd ed., Inst. Mining and Metallurgy, London, UK, 372p.

Poulos, S.E., Collins, M.B., & Tsimplis, M.N., 2019. Sediment dynamics and slope failures in Mediterranean coastal zones. Coastal Sediments, 101-115.

Zhang, X., Li, Z., Chen, Y., 2020. Geological and geotechnical perspectives on slope failures in coastal regions. Geotechnical Journal, 38(4), 345-362.

17th INTERNATIONAL CONGRESS of the Geological Society of Greece

BULLETIN OF THE GEOLOGICAL SOCIETY OF GREECE, SP. PUBL.

EXTENDED ABSTRACT 049

Settlements in residual soils

Nikolaos Chatzigogos[1] , Agisilaos Poulios[2], Thomas Makedon[3],
(1) Geology, Aristotle University of Thessaloniki, Thessaloniki, Greece (e-mail: chatzi12@gmail.com)
(2) Geology, Aristotle University of Thessaloniki, Thessaloniki, Greece (e-mail: pouliosa@geo.auth.gr)
(3) Geology, Aristotle University of Thessaloniki, Thessaloniki, Greece (e-mail: thomas@geo.auth.gr)

Introduction

The conservation and restoration of cultural heritage structures requires a complete and detailed analysis of the geological and geotechnical hazards that affect them. Thus, it is possible to clarify the failure mechanisms that act upon them or might be activated due to technical interventions and to carry out detailed planning of measures to mitigate their effect at a time scale longer than conventional construction works. In the present paper, geological and geotechnical data from site investigation are presented and evaluated relating to the failure mechanisms affecting the foundation of the Holy Monastery of Chilandari mainly the western wing of the Monastery. The Monastery was founded on artificial backfill material followed by weathered soil formations - most probably residual soils of weathered granodiorite – that lay on top of granodiorite and marble rocks. Specifically, the paper presents the results of the geotechnical investigation carried out via sample drilling in situ and laboratory tests and the formulation of the geotechnical model of the foundation area of Monastery. Based on the model, the nature and mechanical behavior of the foundation soil is investigated against mass movements, deformations and settlement. Finally, the main failure mechanism of the subsoil foundation of the Monastery is established and mitigating measures are proposed.

Methodology

For the purposes of this investigation, a methodology of in situ along with laboratory investigation was followed to examine the physical and mechanical properties of the foundation subsoil of the buildings, aiming to assess its origin and mechanical behavior and identify the failure mechanism responsible for the deformations observed in the western wall of the Monastery. The main steps of this methodology are as follows:

1. Determination of the nature and origin of subsoil formations.
2. Evaluation of in-situ test results and design of a conventional Soil Mechanics testing program.
3. Comparison of in-situ test results with the results of laboratory tests. Tests conducted included the determination of physical properties, soil classification tests, and calculations of mechanical properties.

Based on the above, the following steps were taken:

1. Evaluation of shear strength so as to clarify the mechanical behavior of the foundation subsoil and produce design parameters.
2. Bearing capacity and settlement analysis using specialized software, including the calculation of the safety factor against shear failure and the estimation of expected settlements.
3. Interpretation of computational analyses and assessment of the main geotechnical hazards on site.

Geotechnical Model - Calculations

Based on the results of the geotechnical investigation the geotechnical model is derived via the respective steps and calculations:

- Description of the geological-geotechnical formations.
- Compilation of geotechnical sections of the foundation subsoil based on strength and compressibility parameters, the effect of groundwater levels (maximum annual and 50-year period), foundation levels of the main and neighboring constructions, etc.
- Indication of the main/critical conditions to be observed.

- Calculation of bearing capacity (short-term and long-term). Control of settlement due to consolidation and or hydroconsolidation, estimation of differential settlement etc.
- Full dimensioning of all required retaining and soil improvement works with references to the calculation assumptions and the way of analysis.
- Detailed description of the proposal for the type, level and dimensions of the foundation and a description of the sequence of construction works.
- Investigation and description of suitable alternative construction solutions for the foundation and improvement of

the subsoil, among which the best technically and economically optimal solution will be described.

Discussion

The subsoil formations are residual soils of weathered granodiorite, and the failures recorded to the structures of the western part of the compound of the Monastery are due to differential settlements.

- The differential settlements are due to the subsoils' volumetric change behavior under constant loading as well as changes in the moisture content.
- The changes in moisture content are caused by the seasonal fluctuations of the water table that were measured during the dry and wet periods of the year.
- The stratigraphy is dipping to the west which creates a thicker soil cover of the bedrock to that direction, thus producing differential settlement and failures.
- The drying of the foundation soils causes significant settlements because of swelling under wetting and shrinkage under drying. Overall, it is estimated that wetting affects the surficial deposits (S1, S2 and possibly R1) and drying affects the deeper deposits (layers S3 and C1), resulting in a total amount of settlements throughout a wetting-drying circle over a period of one year.
- No data that indicates possible creep - sliding phenomena or any short of horizontal deformations were observed.

Based on the above, it is suggested that remedial measures against the buildings' failures should adopt an approach to limit vertical deformations. Since it is very difficult to fully control the groundwater regime and the seasonal fluctuations, it is suggested that every structure's foundation separately should be connected to the solid bedrock, so that any further volume changes of the overlain soil layer could not affect them. It must be noted that at a certain point of investigation (location of borehole G3) the compressible layer has a small thickness and therefore the total final settlements in time will not be of great magnitude.

Mitigation Measures

Based on the above and to ensure the safety of the significant and historical structures of the Monastery against further settlements it is proposed that mitigation measures should be implemented along with a monitoring program that can assist possible future interventions. Due to the significance of the structure the suggested measures should have minimal disturbance or effect on the character of the construction and that of the broader area of the Monastery. The solution of micro-piles has several advantages relating to the above considerations:

- They are underground and thus hidden interventions that can be constructed on the perimeter and/or sides of the constructions and anchored to the existing foundations where possible, for further support.
- They can be linked with a capping beam to increase bearing capacity and prevent further differential settlements.

The monitoring should include crack gauges for potential deformations and piezometers for groundwater table measurements. These should be intercorrelated so as to verify the failure mechanism by correlating the rate of deformation with the groundwater levels and its seasonal variations.

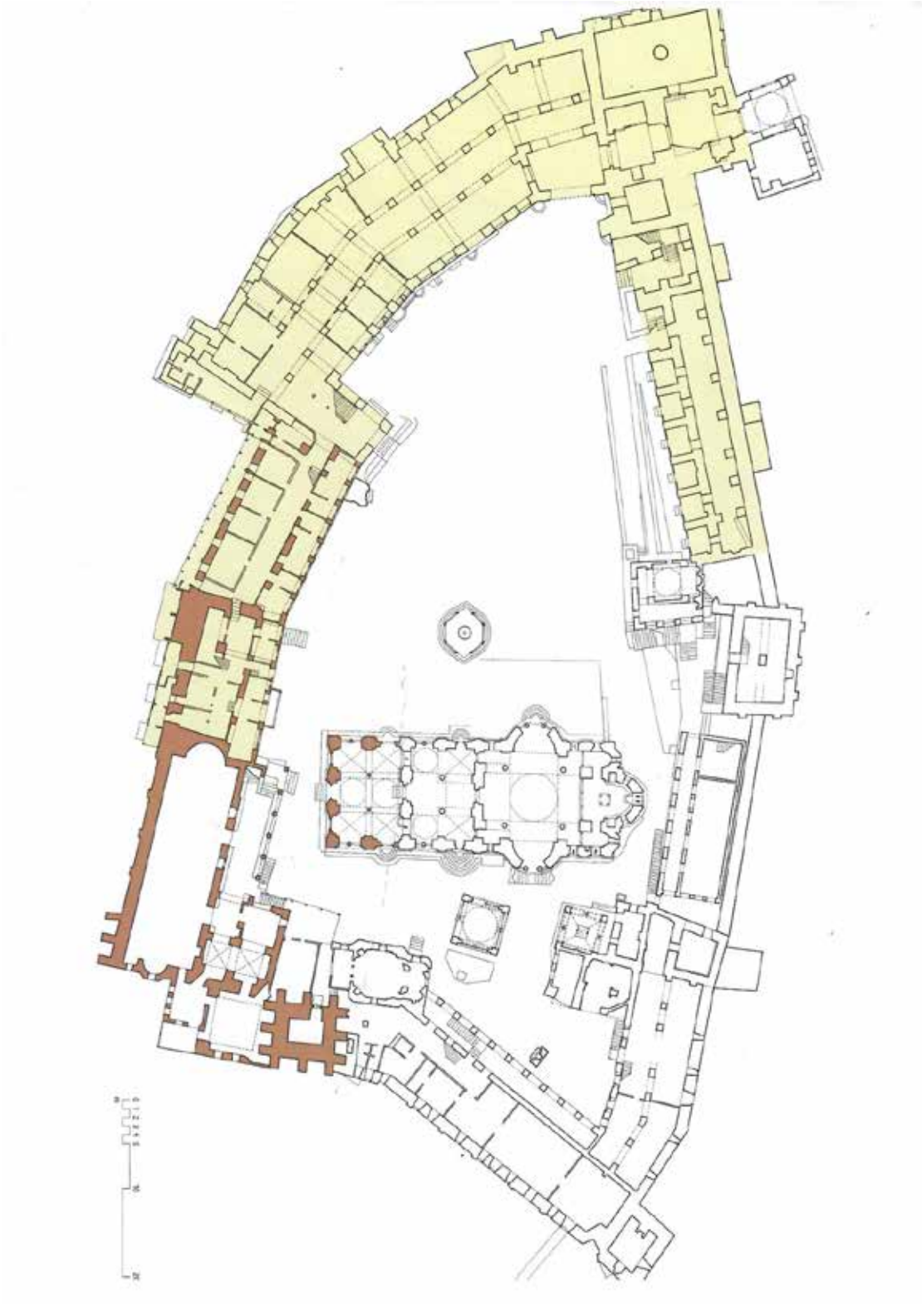

Figure 1: Location of mentioned failures

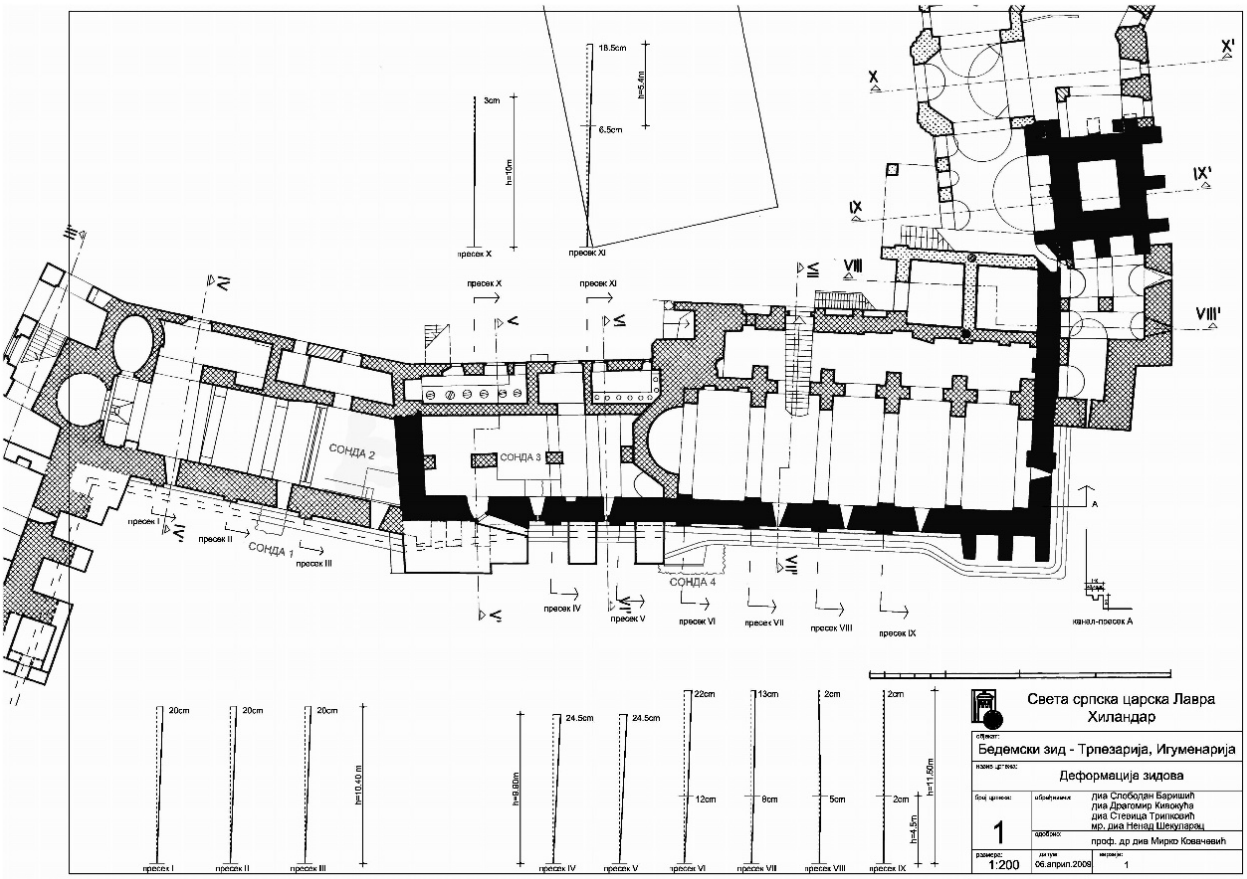

Figure 2: Locations and extent of deviation of structures

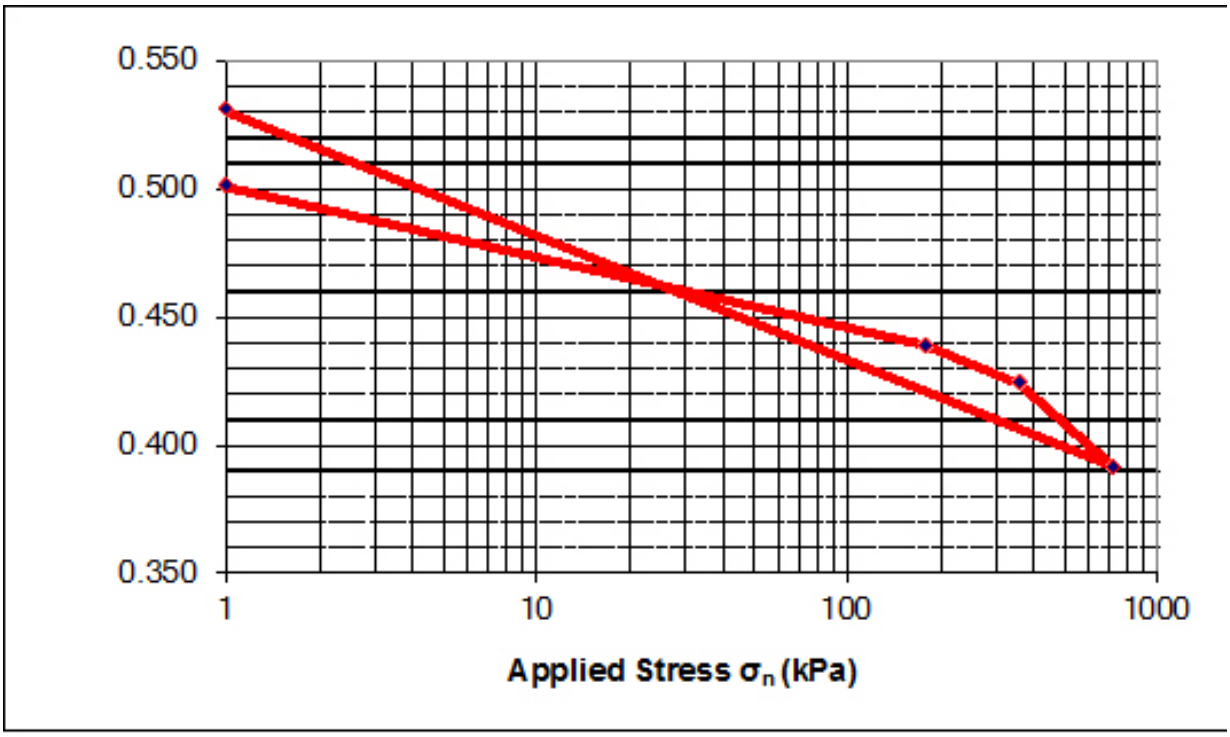

Figure 3:Swelling behavior of layer C1

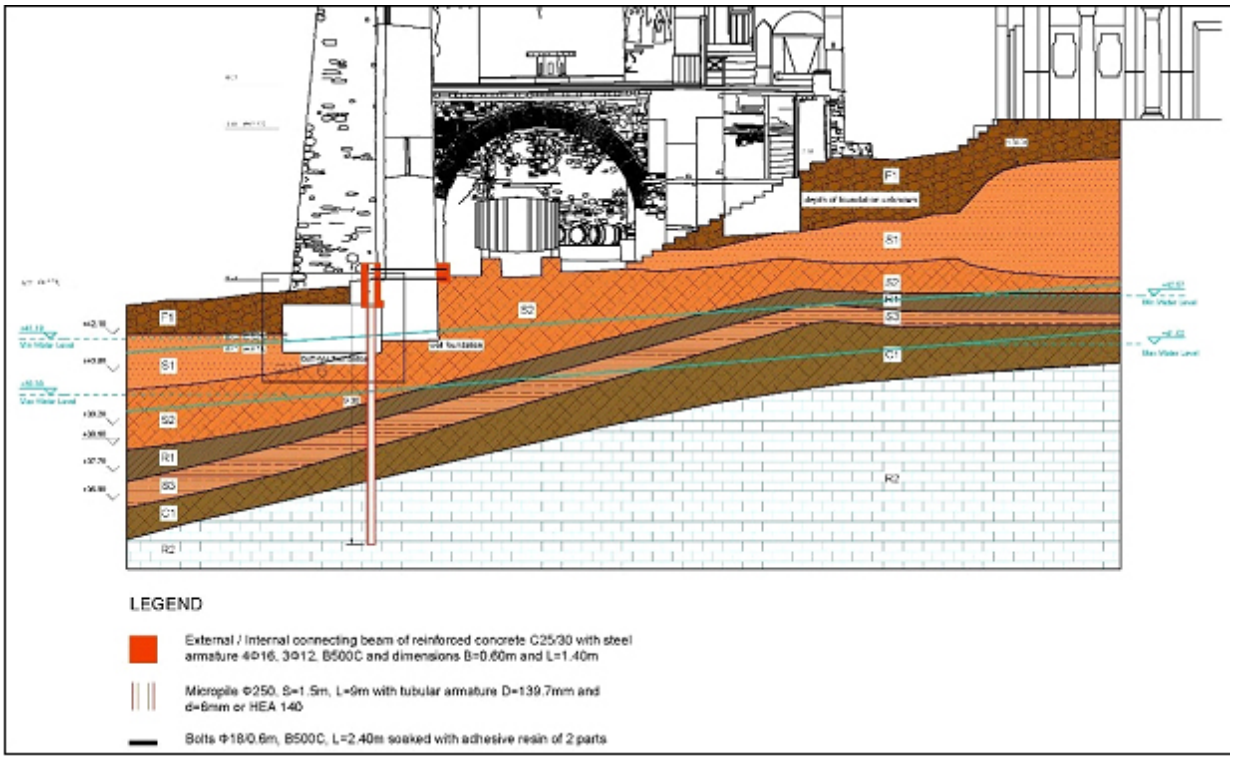

Figure 4:Geotechnical cross section 1-1' with proposed remedial measures

References

Blight, G. E. (1965). A study of effective stresses for volume change. Στο Moisture Equilibria and Moisture Changes in Soils. Beneath Covered Areas (σσ. 259-269). Butterworth, Australia.

Blight, G. E. (1987). Lowering the groundwatertable by deep-rooted vegetation-The geotechnical effects of groundwater recovery. Proc. 9th European Conf. On Soil Mech. and Found. Eng., 1, σσ. 285-288. Dublin.

Blight, G. E. (1997). Mechanics of Residual Soils. Rotterdam, Netherlands: Balkema. Bowles, J. (1957). Foundation Analysis and Design., (σ. 308). New York.

Budhu, M. (2000). Soil Mechanics and Foundations. New York: Wiley.

Craig, R. F. (1992). Soil Mechanics (5 εκδ.). London: Chapman & Hall.

Jennings, J. E., & Knight, K. (1975). A guide to construction on or with materials exhibiting additional settlement due to collapse of grain structure. Proc. 6th Reg. Conf. For Africa on Soil Mech and Found. Eng., 1, σσ. 99-105. Durban.

Knight, K. (1961). The collapse of structure of sandy sub-soils on wetting. PHD Thesis, University of the Witwatersrand, Johannesburg.

Pillissier, J. P. (1991). Piles in deep residual soils. Proc. 10th Conf. For Africa on Soil Mech. and Found. Eng., 1, σσ. 31-40. Maseru, Lesotho.

Tromp, B. E. (1985). Design of stiffened raft foundations for houses on collapsing sands. Johannesburg: Schwarz, Tromp and Associates.

Wesley, L. D. (2010). Geotechnical Engineering in Residual Soils. Hoboken, New Jersey: John Wiley & Sons Inc.

Williams, A. A. (1991). The extraordinary phenomenon of chemical heaving and its effect on buildings and roads. Proc. 10th Reg. Conf. for Africa on Soil Mech. and Found. Eng., 1, σσ. 91-98. Maseru, Lesotho.

17th INTERNATIONAL CONGRESS of the Geological Society of Greece

BULLETIN OF THE GEOLOGICAL SOCIETY OF GREECE, SP. PUBL.

EXTENDED ABSTRACT 050

Geotopes of Thessaly (central Greece) and their educational approach

Chatzipetros A.[1], Samantzi V.[2]

(1) Department of Structural, Historical and Applied Geology, School of Geology, Aristotle University of Thessaloniki, 54124, Greece, ac@geo.auth.gr (2) Department of Geography, University of Aegean, Mytilene, Greece

Introduction / Background

Geotopes play an important role in deducing the geological history and evolution of an area and can contribute to the understanding of geological processes that take place daily. Geotopes can be used for educational purposes, since they can function as natural laboratories in which citizens can come into contact with Geology and understand how the Earth works, thus contributing to the protection of natural monuments. At the same time, economic benefits can also potentially stem from the promotion of a geotope.

Thessaly is an area located in central Greece and is abundant with important geotopes. Tectonic structures, such as faults and folds, rocks, gorges, quarries, caves, monasteries, traditional settlements and more, are some of the impressive locations of Thessaly. Every year there are thousands of visitors in the broader region of Thessaly, who come to admire the treasures of nature and, at the same time, have the potential to come into contact with Geology and its principles.

For this project, six geosites of Thessaly were selected, which are related to different areas of Geology. Each selected geotope is related to a geological phenomenon, which can be presented and analyzed to secondary school students in the context of the course of “Geology – Geography”.

Objectives

This paper aims to help teachers who intend to organize educational trips to the region of Thessaly and for this reason these characteristic landforms have been selected, which have the potential to impress students and attract their interest.

At the same time, the Worksheets and Evaluation Sheets, which correspond to each geotope, include activities and tasks that can be done independently of the educational trip, but can be part of the teaching of the course of “Geology – Geography” of the first and second grade of High School, in order to understand geological concepts, such as weathering and erosion, deposition, faults and earthquakes, volcanos, fossilization, etc. that are phenomena that take place daily in areas of the planet and affect people’s lives.

It is important to mention that by completing the tasks during teaching of the selected geotopes and activities, students will have practiced writing and speaking, team collaboration, and will have developed their self-confidence.

Methods

Geotopes

Geotopes can be used as a source for collecting information about the geological history and paleoenvironment of an area, aiding science, research and education. At the same time, they are of archaeological, historical and folklore importance, while in many cases they host local ecosystems and contribute to the development of tourism in the area. Greece presents great geodiversity with complex geological structures due to geomorphological processes that have taken place and have shaped the image of the country on the surface and the interior of the Earth, thus creating a large number of geotopes throughout the country.

Geosites can contribute to the education of students through activities that lead to an understanding of Geology. Student visits to geological structures can make geotopes a means of understanding geological processes that have taken place in the past (Theodosiou et al., 2006). Educational (geo)tourism can support geoeducation, as geosites are open to the public and are “living museums”. The combination of a geotope with local history and mythology, with archaeology, religion, folk tradition and geological history, can attract the interest of young and old visitors.

Education

Today, courses of environmental interest are taught in Primary and Secondary Education, which bring students into contact with nature and the problems it faces and will face in the future, with the ultimate goal of raising students’ awareness about the protection of natural and geological heritage (Fermeli, 2023).

For the better consolidation of geological concepts, the teacher, in addition to the theoretical approach of the subject, is required to use other assignments or outdoor exercises, in order for the new knowledge to become the property of

the students. Although Greece has a rich geological and geomorphological heritage, few schools form environmental groups to implement environmental programs during the school year that will help students get in touch with the natural environment and love it. Educational activities in the context of Geoeducation, Environmental Education and Education on Natural Disasters is essential for students. Phenomena, such as earthquakes and volcanoes, can affect people's daily lives and even cause human losses.
The proper teaching of a lesson requires proper planning by the teacher, taking into account the general objectives of the course based on the Curriculum. When teaching a lesson, the teacher uses the Lesson Plan and the Worksheets and Evaluation Sheets, which complete the textbooks, for a better understanding and consolidation of the lesson. Initially, the teacher must start with the preexisting knowledge, then continue with the presentation of the lesson, follow the Worksheets for the application of the new knowledge, continue with the evaluation of the lesson through the Evaluation Sheets and finally, after summing up, connect the lesson with the next (Tzovla, 2021).

Geotopes of Thessaly
Thessaly is located in central Greece. It presents a simple geomorphological picture, with the mountainous parts bordering the lowlands in the central areas. Strong earthquakes have occurred in the region from time to time, causing problems, such as the great earthquakes of 1892, 1901, 1941 and the most recent ones of 2021, while the recent floods of 2023 have still left fresh memories, having created serious problems.
Thessaly is an area that combines geological, historical, archaeological and cultural elements. It has many characteristic geological sites, which attract the interest of visitors and scientists. Some geotopes of Thessaly are world famous.
For this paper, six (6) representative geosites of the geological history of Thessaly were selected, in order to develop the interest of students of the first two grades of High School in Geology in general and its individual fields, such as Structural Geology, Physical Geography, Seismology, Volcanology and Palaeobotany. Eventually, students develop into responsible and aware citizens. Initially, general data are given for each geotope, then the necessary geological knowledge is determined, required for the understanding of each geotope by the students, followed by an indicative Lesson Plan for the organization of the teaching of the geological phenomenon and, finally, the Worksheets and Evaluation with activities and homework for the best possible consolidation of the topic.

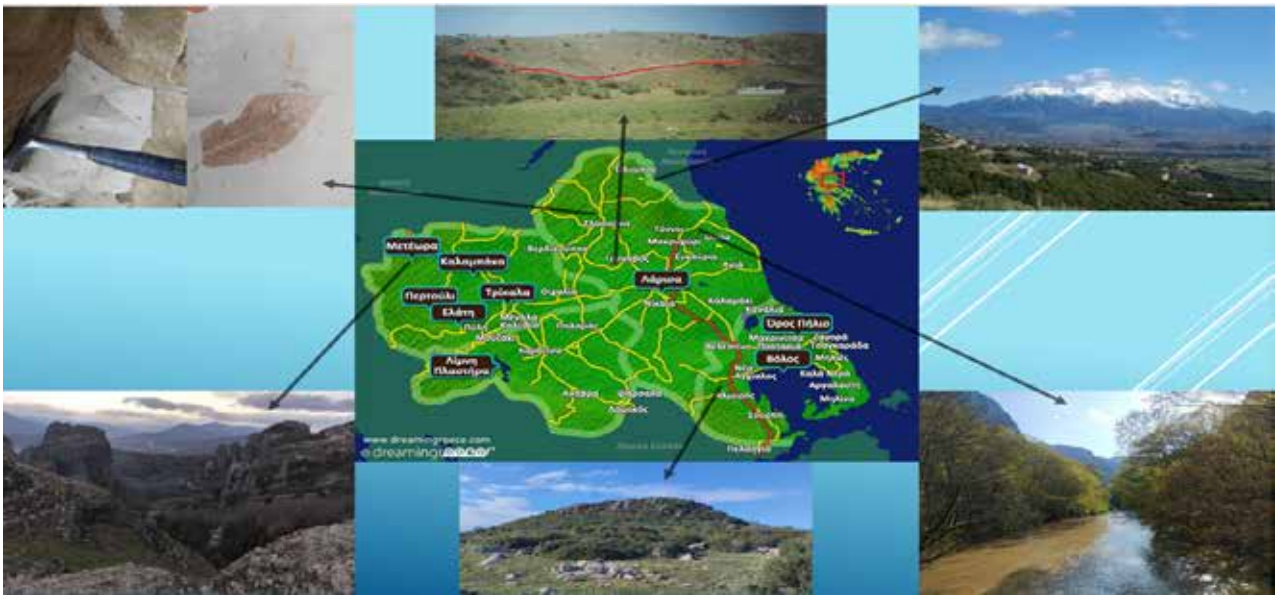

Fig. 1: The six selected geotopes of Thessaly.

The six (6) geotopes are the following (fig. 1, clockwise from top right):
- The **tectonic window of Mount Olympus**, a characteristic geological and tectonic form of Greece,
- The **valley of Tempi**, a characteristic geomorphological form of unique beauty, associated with the mythology of the whole wider area of Olympus and the river Pinios, which flows through it,
- The **volcano of Mikrothives**, as volcanism affected the region of Thessaly in the geological past,
- **Meteora**, a unique global natural monument, with the characteristic huge boulders of conglomerates, which are

a source of awe and admiration,

- The **Neogene basin of Elassona** with numerous flora fossils and
- The **Tyrnavos fault**, which is associated with the seismicity of the wider area, having being the source of a significant number of seismic events in the past.

As part of the work, field work was carried out on Olympus and Ossa mountains, from where one can admire the valley of Tempi, Meteora for the observation of the imposing volumes in western Thessaly, in the area of Tyrnavos – Damasi – Vlachogianni after the earthquakes of March 2021, in the area of Elassona (Sarantaporo, Lykoudi), in order to locate the plant fossils of the Neogene Basin of Elassona, as well as in the interesting, unexploited - but with growth prospects - area of the volcano of Mikrothives.

OLYMPUS

Mount Olympus is an important symbol and monument of Greece, as it is the highest mountain in Greece, known worldwide from Greek mythology, since on its top lived the Twelve "Olympian" Gods, according to the religion of the ancient Greeks. In 1938 it was declared as the first National Park in Greece, for the protection of the area, while later the Ministry of Culture declared Mount Olympus as an archaeological and historical site due to the number of its monuments. It is a compact, relatively small in size, multi-peaked and rocky mountain with an almost circular shape. It hosts about 1,700 plant species, i.e. about 25% of the Greek flora, as well as a multitude of vertebrates.

The "Olympus tectonic window" is of great geological value to scientists and was formed due to the intense pressures and temperatures, but also the intense tectonism, that the region of Greece undergoes. The area is mainly covered by limestone and dolomites of the autochthonous Olympus Unit, but also marble, shale, gneiss and amphibolite of the Pelagonian Zone, intruded by later magnetic products (granitic bodies).

Students of Greek schools come into contact with mythology and the Olympian gods already from the third grade of Primary School. Mount Olympus has a number of characteristic sites that show its geotectonic evolution. However, the concept of "tectonic window" and geological time in Geology is a difficult concept, even for students of Geological Departments. High School students, within the framework of the course of "Geology – Geography", taught in the first and second grades, can come into contact with simpler concepts of Structural Geology, such as faults and folds, which can be found in nature and make a reference to the tectonic window.

For the educational approach of the Geotope of Mount Olympus, the necessary knowledge is provided, which students should know and is mainly related to faults. Geological concepts related to tectonics, endogenous and exogenous factors that shape the relief of the Earth, lithospheric plates, earthquakes and seismicity, are interesting subjects for the students. The teacher can follow the respective lesson plan, which will be called *"Faulting in Greece"*, will be addressed to students of the first grade and will use Worksheets and Evaluation Sheets on faults.

TEMPI VALLEY

The well-known valley of Tempi is in the eastern part of Thessaly plain and located between the mountains of Olympus to the north and Ossa or Kissavos to the south. Along the valley, which has a NE-SW direction, Pinios River flows, which drains the waters of Thessaly into the Aegean Sea with intense meanderings through the plain and flows into the Aegean Sea forming its Delta near Stomio, creating a rich ecosystem. The valley of Tempi consists of mainly limestone, dolomites and marbles, while caves have been created in places, some of which have impressive decoration with stalactites.

The valley of Tempi is inextricably linked to Mount Olympus and mythology. Today the geotope of the Tempi Valley continues to attract visitors, but fewer than in the past, since it is easily accessible to everyone. The picturesque church of Agia Paraskevi, a landmark of the area, continues to attract visitors, who can come into contact with history, mythology, culture, religion and nature. The combination of the above with certain concepts of Geology can attract the interest of students during a visit to the area.

The educational approach of the Tempi Valley Geotope requires knowledge related to concepts of Physical Geography and Geomorphology. The Lesson Plan is related to concepts such as erosion, transport, deposition, weathering, drainage systems, estuary and river delta, but also floods, which in recent years have caused great disasters and human losses in the area. The relevant Lesson Plan with the corresponding Worksheets and Evaluation Sheets can be called *"How water affects the terrain of the Earth"* and addresses students of the second grade of High School.

THE MIKROTHIVES VOLCANO

In the prefecture of Magnesia near Nea Anchialos and Mikrothives is the hill "Kastro", visible and easily accessible from the Volos – Athens National Road, covered by volcanic rocks of the Pleistocene from the volcanic action of the now inactive Mikrothives volcano. The area is of great geological and historical interest, as the lavas of the volcano

cover a large area, while excavations have brought to light parts of an ancient theater, where the sites are made of volcanic rocks, as well as parts of ancient walls of the "Fthiotides Thebes" of the Hellenistic period (Clapsopoulos, 1991, Vavaliou, 2014, Samantzi, 2024).
It is a small low volcano of typical Maar form, where the volcanic cone is absent (Bournovas, 1999). To the SE there is a dome up to 50 meters thick, which is the main crater, from where lava is believed to have flowed and is called "Magoula". Fragments of volcanic rocks are scattered throughout the area of the "Castle" (basalt, andesite) (Clapsopoulos, 1991). The ancient basalt quarries of Phthiotides Thebes operated in the past in the area, probably during the Hellenistic and Roman times, as there are several sites where it seems that healthy rock has been processed and removed. The original rock was solid and hard and could be processed by workers and, in addition, very close was the Pagasetic Gulf and the ancient port of Pyrasos for the transportation of boulders (Vavaliou, 2014). During field work in the area, large basaltic blocks were observed with obvious marks from the tools used by the workers to carve and cut them off the natural rock, which have been altered mainly by wind erosion. The hill "Kastro" perfectly combines Geology with History and Culture, since the ancient inhabitants of the area utilized the "materials" offered by nature for the economic development of the area and come from the volcano.
The educational approach of the Geotope of the volcano of Mikrothebes requires students to possess knowledge of Volcanology, related to the interior of the Earth, lithospheric plates, volcanoes, as well as the volcanism of Greece. The Lesson Plan can be entitled: *"Volcanic activity in Europe and Greece"* and addressed to students of the second grade of High School with the corresponding Worksheets and Evaluation.

METEORA

Meteora is one of the most important geotopes in Greece, being a UNESCO World Heritage Site. It is a geological monument of exceptional value in terms of aesthetics and science, which is the object of study, promotion and protection. More than 50 vertical, steep and cut off dark rocks are located north of the city of Kalambaka and west of the village of Kastraki in the prefecture of Trikala, at the exact point where Pinios enters the plain of Thessaly. At the top of the rocks are the famous Monasteries of Meteora, which attract thousands of visitors every year. Nimas (1987) likens the area of Meteora to a unique in the world *"stone forest",* which during the post-Byzantine era was transformed into *"Lithopolis",* as hundreds of monks settled in the area.
The conglomerates of Meteora (Miocene) are marine sediments of great thickness, in which many marine fossils have been found. Rounded pebbles are of varying consistency, size and origin. The matrix is a fine-grained clay material rich in carbonates. Holes of various sizes are observed in places, created due to the corrosive action of water and wind and in some cases have formed caves (Rassios et al., 2020).
The flora and fauna in the area of Meteora are important. In addition, the Museum of Geological Formations of Meteora operates in Kastraki since 2018, which contributes to Environmental Education. Since 2024, the Meteora-Pyli Geopark has joined the UNESCO Global Geoparks network, where visitors can take part in various activities that will bring them into contact with the natural environment of the area.
For the educational approach of the Geotope of Meteora, concepts of Sedimentology, Physical Geography and Geomorphology are required. Concepts such as Sedimentary Rocks and Sedimentation, exogenous factors that affect the Earth's relief, such as weathering and erosion, lithification and diagenesis, can help students understand how to create forms, like Meteora. The relevant Lesson Plan can be called *"How weathering and erosion affect the relief of the Earth"* and addressed to students of the first grade of High School, while the Worksheets and Evaluation are about weathering and erosion.

NEOGENE BASIN OF ELASSONA

The basin of Elassona hosts a particularly rare and rich fossilized flora assemblage. This is a rare subtropical flora, having forest plants and swamp plants. The Neogene basin of Elassona is the southern part of a NW-SE trending elongated graben consisting also of the Florina, Ptolemaida – Amyntaio and Kozani – Servia ones. Neogene deposits in the region include Miocene, Pliocene and Quaternary sediments. Fossils of leaves, fruits, pollen and seeds have been found in the area and it is one of the most remarkable sites in Europe. However, the area has not yet been exploited (Samantzi, 2024).
'Sequoia', 'Cryptomeria', 'Cathaya', 'Egeria' fossils have been found (Velitzelos and Gregor, 1990; Velitzelos et al., 2014; Bouchal et al., 2020). In the basin of Elassona, plant fossils are enclosed in diatomites of white to yellowish – whitish color and occur in various places, such as Lykoudi, Drymos and Sarantaporos. Diatomite resembles chalk and forms an extremely fine-grained, soft and usually light-colored and friable sedimentary rock, which consists of fossilized diatomaceous remains (Aivaliotis, 2011, Stefanou, 2016). In the basin of Elassona, clay diatomites were deposited in a lagoon environment and their plant fossils correspond to a humid and warm climate in a clean water

lake environment, displaying a brownish yellow to brown color on the surface, while in depth they have a gray color (Stamatakis and Koukouzas, 2001).
For the educational approach of the Geotope of the Neogene Basin of Elassona, students must possess certain knowledge related to Palaeobotany, such as plant fossils, ways of fossilization, petrified forests in Greece. The Lesson Plan can be called *"Plant fossils in Greece"* and addressed to students of the first grade of High School, while the Worksheets and Evaluation Sheets will be related to fossilization and plant fossils.

TYRNAVOS FAULT

The region of Northern Thessaly is of particular interest to scientists, as it consists of several active normal fault zones. In 2021 two large earthquakes of magnitude 6.3 and 5.9 respectively took place in the region between the cities of Tyrnavos and Elassona and were felt in most of mainland Greece, causing significant damage in the epicentral area. Tyrnavos fault, although not directly related to the earthquakes of 2021, is an active normal ENE striking fault, activated during the Middle Pleistocene (Caputo et al., 1993, Kotsis, 1995, Caputo et al., 2004). The trace of the fault is clearly visible and has been mapped for more than 12 km (Koukouvelas et al., 2021), while it is characterized by seismicity of low to moderate magnitude. The maximum expected earthquake is of the order of 6.5R, while it is thought that the fault caused an earthquake of magnitude 6.0 in 1731 (Belesis, 2012).
The School of Geology, Aristotle University of Thessaloniki, the University of Ferrara and the Municipality of Tyrnavos collaborated for the construction of the Palaeoseismological Museum of Tyrnavos, a model research and educational center of Geology and Seismology at the 7th km of Tyrnavos – Damasi road within the valley of the Titarisios River in the middle of the Tyrnavos fault. Paleoseismic trenches in the site show successive reactivations of the fault, aswhile research instruments (seismograph and GNSS) have also been installed (Belesis, 2012). It is the only open museum park in Europe for the geology of earthquakes. Unfortunately, it is still not open to visitors, while today it shows signs of abandonment.
Tyrnavos fault is an important geotope for the region of Thessaly, but also for the whole country due to its seismic potential. The preparation of citizens of all ages is necessary so that their reaction before, during and after the earthquake is optimum and human losses are avoided. Secondary school students can visit the geotope of the Tyrnavos fault, as it is easily accessible, and be informed about the earthquakes of the past.
For the educational approach of the Tyrnavos Fault Geotope, students are required to know about seismology, earthquakes and their characteristics, seismic waves, seismographs, as well as about the surface manifestations of an earthquake (ground ruptures, rockfalls, landslides, subsidence, soil liquefaction). The lesson plan may be entitled: *"The earthquake in everyday life"* and addressed to students of the first grade of High School, while the Worksheets and Evaluation refer to earthquakes.

Results and Conclusions

Several, if not all, geosites can be classified as educational and, in the context of field trips, used by teachers to transfer geological concepts to students. The subject of "Geology – Geography", taught in the first and the second grades of the Greek High Schools, is linked to the natural environment, natural disasters and landforms and can instill a sense of responsibility in students towards the geoenvironment. Students can understand the value of geotopes, get in touch with the place where they live and how they were created.
In addition, the teaching of the subject of "Geology – Geography" needs to change to attract the interest of students. The school must be in accordance with the needs of the time and the students to become efficient and able to prepare them for the new challenges of the future. At the same time, teachers should teach their students topics that interest them and will activate them for the protection of natural and geological heritage, instead of providing them with sterile knowledge. For the above reasons, proper preparation and organization of the lesson by the teacher is required (Iliopoulou, 2006).
In conclusion, it should be mentioned that of the geotopes chosen, Mount Olympus and Meteora are places world famous with thousands of visitors every year. The other four geotopes (Valley of Tempi, Tyrnavos fault, Neogene basin of Elassona, Volcano of Mikrothives) are places that need support, empowerment and promotion in order to attract visitors of all ages while developing Geotourism and economic benefits.

Acknowledgements

This paper is part of the second author's MSc Thesis at the University of the Aegean, completed under the Inter – Institutional "Natural Hazards and Disaster Mitigation" Master Course programme. The authors would like to thank Professor Emeritus Spyros Pavlides, Dr. Charalambos Fassoulas and Professor Nickolas Zouros for their contribution towards the completion of the Postgraduate Program and the MSc Thesis.

References

Aivalioti M. (2011). Remediation of water contaminated by BTEX and MTBE using natural and modified diatomite – Comparison and combination with other natural adsorbents. Doctoral Thesis. Department of Environmental Engineering. Technical University of Crete. Chania.

Belesis A. (2012). Revision and modification of the General Urban Plan (GSP) of the Municipality of Tyrnavos (Stage A – Preliminary Geological Suitability Study.

Bouchal JM, Güner TH, Velitzelos D, Velitzelos E and Denk T. (2020). Messinian vegetation and climate of the intermontane Florina–Ptolemais–Servia Basin, NW Greece inferred from palaeobotanical data: how well do plant fossils reflect past environments? R. Soc. Open Sci. 7: 192067, http://dx.doi.org/10.1098/rsos.192067.

Bournovas, I. (1999). The natural monuments of Greece. Publications: KACTOS.

Caputo, R. and Pavlides, S. (1993). Late Cainozoic geodynamic evolution of Thessaly and surroundings (central-northern Greece). Tectonophysics 223. 339–362, https://doi.org/10.1016/0040-1951(93)90144-9.

Caputo R., Helly B., Pavlides S. and Papadopoulos G. (2004). Palaeoseismological investigation of the Tyrnavos Fault (Thessaly, Central Greece). Tectonophysics 394. 1 –20.

Clapsopoulos I. (1991). Petrology, Geochemistry and origin of Pliocene – Pleistocene potassium – rich volcanic rocks from Greece. Ph.D. Thesis, Department of Geology. Faculty of Science. University of Manchester.

Fermeli, G. (2023). The teaching of geosciences in Greece, through school textbooks: A historical review (1830-2021).

Iliopoulou If. (2006). Storyline: An interdisciplinary approach to the development of environmental issues. 2nd Conference of School Programs of Environmental Education. 15-17/12/2006. Athens.

Kotsis, H. (1998). Neotectonics and paleoseismology in the area of Tyrnavos and Rodia (Thessaly)- Seismic risk assessment for the city of Larissa with geological data. Master's Thesis. Department of Geology. Aristotle University of Thessaloniki.

Koukouvelas I., Nikolakopoulos K., Kyriou A., Caputo R., Belesis A. Zygouri V., Verroios S., Apostolopoulos D. and Tsentzos I. (2021). Damasi Earthquake Sequence, Central Greece. Reactivation Evidence across the Westward Propagating Tyrnavos Graben. Geosciences, 11, 328, https://doi.org/10.3390/geosciences11080328.

Lampaki O., Zouros N. (2007). Geoconservation: Promotion and management of natural monuments – geotopes. The case of the Petrified Forest Geopark of Lesvos. Proceedings of the 8th Panhellenic Geographical Conference of the Hellenic Geographical Society. Athens.

Nimas, T. (1987). Trikala – Kalampaka – Meteora – Pindos – Chasia (Geography – History – Monuments – Tourism). Kyriakides Bros Publications. Thessaloniki.

Rassios Ewing A., Ghikas D., Dilek Y., Vamvaka A., Batsi A. and Koutsovitis P. (2020). Meteora: a Billion Years of Geological History in Greece to Create a World Heritage Site. Geoheritage.

Stamatakis M.G. and Koukouzas N.K. (2001). The occurrence of phosphate minerals in lacustrine clayey diatomite deposits, Thessaly, Central Greece. Sedimentary Geology 139. 33-47.

Stefanou C. E. (2016). The diatomites of Lemnos and their environmental applications. Postgraduate Thesis. Department of Geology. Aristotle University of Thessaloniki. Thessaloniki.

Theodosiou E., Fermeli G. and Koutsouveli A. (2006). Our geological heritage. Publications: Kaleidoscope.

Tzovla E. (2021-22). Teaching Methodology: Lesson Plan – Worksheets. Department of Molecular Biology & Genetics, School of Health Sciences. Democritus University of Thrace.

Vavaliou, M. (2014). Archaeological, mineralogical and geochemical study of the ancient basalt quarries in Mikrothives, Magnesia. Analysis of archaeological basalt material in the wider area. Diploma thesis. Interdepartmental Postgraduate Program "Protection, conservation, restoration of cultural monuments". Aristotle University of Thessaloniki Thessaloniki.

Velitzelos E. and Gregor H.J. (1990). Some aspects of the Neogene floral history in Greece. Review of Palaeobotany and Palynology. 62: 291-307.

Velitzelos D., Bouchal M. J. and Denk T. (2014). Review of the Cenozoic floras and vegetation of Greece. Review of Palaeobotany and Palynology 204. 56–117, http://dx.doi.org/10.1016/j.revpalbo.2014.02.006.

17th INTERNATIONAL CONGRESS of the Geological Society of Greece

BULLETIN OF THE GEOLOGICAL SOCIETY OF GREECE, SP. PUBL.

EXTENDED ABSTRACT 051

Flood risk of a touristic island beach under Climate Change: Komi beach Chios

Chatzistratis D[1]., Monioudi I.N.[1], Chalazas T.[1], Andreadis O.P.[1], Moschopoulos K.[1], Chatzipavlis A.E.[1,2], Psarros F.[1], Velegrakis A.F.[1]
(1) Department of Marine Sciences, University of the Aegean, University Hill, 81100 Mytilene, Greece, mard20007@aegean.gr (2) Department of Physics and Earth Sciences, University of Ferrara, Via Saragat 1, 44122 Ferrara, Italy

Research Highlights

Assessment of beach flood risk using open source geospatial data and models.

Introduction

Coastal floods from extreme marine events have had increasing impacts on the coastal natural and human ecosystems, causing coastline changes, biodiversity losses, human mortality, increased health risks and poverty and induced coastal infrastructure/asset damages (IPCC, 2023). Under climate change, the frequency of extreme events is projected to increase and expose annually a large part of the global coastline to the current 1 in 100 years Extreme Sea Level by 2100 (Vousdoukas *et al*., 2018). 'Sandy' shorelines (i.e., the low-lying coasts built on sediments—beaches), which comprise a large segment of the global coastline (Luijendijk *et al*., 2021) will be particularly vulnerable. In addition to their own importance as ecosystems, beaches form natural buffers that protect backshore ecosystems, infrastructure, and assets from coastal flooding (Toimil *et al*., 2023); they also have high hedonic/recreational value, contributing very significantly to the tourism sector due to the current dominance of the 'Sun, Sea, and Sand—3S' model (UNWTO, 2024). Beaches in touristic islands face increased vulnerability to coastal flooding, due to their generally limited width, scarce sediment supply and the high potential exposure to coastal flooding of their backshore infrastructure and services (Brett, 2021). However, the flood assessment of beaches, presents certain challenges due to the need for accurate geospatial information, as well as the accuracy/costs of the used models (Almar *et al*., 2021).

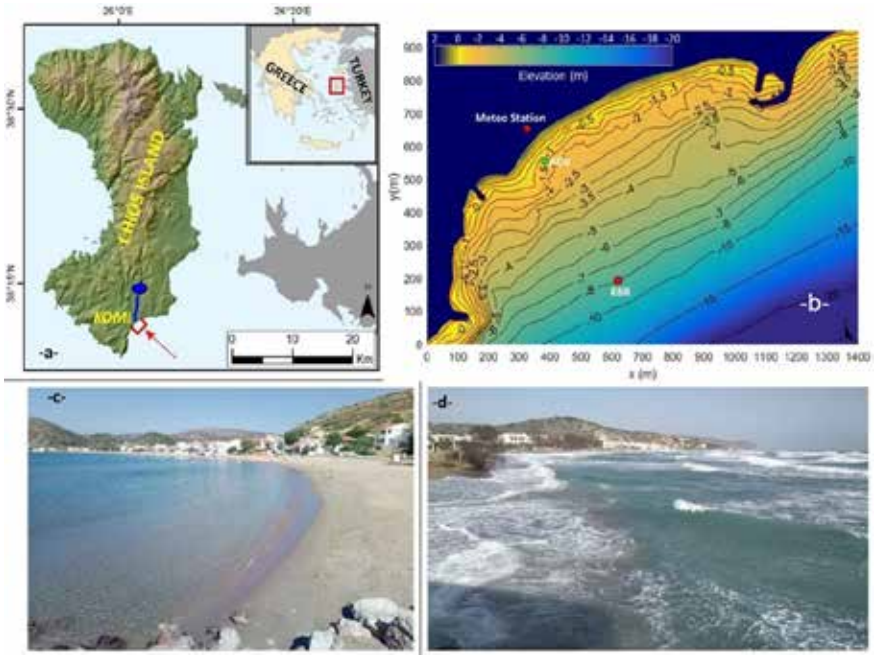

Figure 1. (a) Chios island and Komi beach, showing Katraris river and dam (blue line and circle). (b) Beach nearshore topography/bathymetry. Photos of Komi beach, (c) from the ENE under calm conditions and (d) from WSW during a storm.

Therefore, the objective of this short contribution has been to assess the flood risk of an island beach (Komi, Chios; Fig. 1), using readily available geo-spatial information and an open - source numerical model. Komi is a 1.2 km long barrier beach with a maximum dry width of 38 m. Its backshore hosts a coastal road and many residential and touristic assets, sometimes at a distance of <10 m from the coastline. The beach is characterized by low slopes with elevations that in many areas do not exceed 1.5 m (slopes of approximately 3%). In addition, the backshore elevations are in many areas <1 m. A stream is present at the western segment of the beach, whereas at its eastern end there is a small fishing port. The stream is the outlet of the Katraris river, the land sediment supply of which has been diminished due to the construction of the Kalamoti-Katraris Dam (Andreadis *et al*., 2021).

Methods

In addition to the simple static inundation 'bathtub' model, a simplified two-dimensional finite difference hydrodynamic model LISFLOOD-FP (Bates and de Roo, 2000) was also used. This simulates flood dynamics in a pre-designed grid using a Digital Elevation Model (DEM). Specifically, LISFLOOD-FP applies fluid continuity to calculate the depth at each grid cell while the water flow is channeled along the ground using a simple storage algorithm based on the difference in hydraulic head between adjacent cells (Bates *et al*, 2005). In each cell, the calculated height of the water surface above the topographic elevation as well as the Manning soil friction coefficient are used to calculate the flow rate. The water flow is described by the momentum conservation and mass continuity equations:

$$h_{(i,j)}^{(t+\Delta t)} = h_{(i,j)}^{t} + \frac{\Delta t * Q_{(xi,j-1)}^{t} - Q_{(xi,j-1)}^{t} - Q_{(yi,j-1)}^{t} - Q_{(yi,j)}^{t}}{\Delta x^2} \quad [1]$$

$$Q^{t} = \frac{q_t - \frac{g h_{flow}^{t} * \Delta t * \Delta(h^{t} + z)}{\Delta x}}{1 + g h_{flow}^{t} * \Delta t n^2 * |q^{(t-\Delta t)}| \left(h_{flow}^{t}\right)^{(10/3)}} \Delta x \quad [2]$$

where, (Q^t) is the flow at time (t) between cells, calculated using a centered difference scheme resolved in the (x) or (y) direction; (h_{ij}) is the water depth at the center of cell (i, j); (h_{flow}) is the depth between cells where flow is possible; (z) is the topographic height in the cell; (n) is the ground friction coefficient; (g) is the acceleration of gravity; (q) is the flow from the previous time step; and (Δt, Δx) is the width of the cell.

The flood flows are discretized into a grid of square cells, thus allowing the model to represent two-dimensional flows on the ground surface. LISFLOOD-FP results (ascii files) can be easily imported into a GIS environment for further analysis. The model had been originally designed to simulate river floods, but, in recent years, has been also successfully used to simulate coastal floods (e.g., Monioudi *et al*., 2018; Le Gal *et al*., 2023).

The DEM of Komi beach used the 'Digital Terrain Model of the LSO25 project' (LSO - Large Scale Orthophotos) of the Hellenic Cadastre, which was constructed using high-resolution aerial photographs (2014-2016). The Cadastre DEM has a resolution of 2 m, which allows capture of both the slopes of the coastal topography and adjacent coastal works with much greater accuracy than the EU-DEM (resolution of 25 m, spacedata.copernicus.eu/documents/20123/121239/GEO1988-CopernicusDEM-RP-001Validation_Report_I3.0.pdf). Application of the model at a local level allows the use of this specific spatial resolution with a very reasonable computational cost. The DEM were processed in QGIS software. The Manning friction coefficient was calculated on the basis of the land uses recorded in the Coastal Zone Land Use/Land Cover (LU/LC) geospatial file of the European Copernicus service (https://land.copernicus.eu/en/products/coastal-zones). Manual corrections were applied, which mainly concerned the more accurate design of the beach boundaries (and coastal works and port facilities). As an additional check, the corrections were also taken into account in the DEM of the area to ensure that there were no significant discrepancies between the land uses and the topography, e.g. the polygon corresponding to the sea was checked to overlap pixels with zero elevation. Then, a value for the Manning coefficient was entered for each land use, using the calculations of Papaioannou *et al*. (2018).

The model was driven by the projected Extreme Sea Levels (ESLs) for Chios under the RCP8.5 climatic scenario for 2050 and 2100 extracted from the EU-JRC (Joint Research Centre) database https://webcritech.jrc.ec.europa.eu/SeaLevelsDb detailed in Vousdoukas *et al*. (2018). ESLs were projected using the numerical hydrodynamic model Delft3D-Flow driven by the wind and atmospheric pressure fields corresponding to the climate conditions

of the RCP4.5 and RCP8.5 scenarios calculated by an ensemble of 8 climate models; model performance was assessed for the period 1980 – 2014 (baseline) driven by wind/atmospheric pressure fields extracted from the ERA – Interim database. The ESLs form the sum of the future long-term relative mean sea level rise (RSLR), the astronomical tide (n_t) and the episodic sea level rise (n_{ce}) due to meteorological tides (storm surge) and the storm wave set-up; the latter, which can be quite significant during an energetic event, is set using a generic approximation of 0.2 Hs, i.e., of the offshore significant wave height projected for the same scenarios.

Results

The ESLSs with return period of 100 years (ESL_{100}) projected for the area were 1.12 m and 1.77 m for 2050 and 2100, respectively. The bathtub model results showed inundation of 70,850 and 128,300 m^2 for 2050 and 2100, respectively, with maximum flood extent more than 220 m and 260 m.

The projections show that a large part of the area will be flooded (Fig. 2), with maximum flood extents of 118 m and 190 m for 2050 and 2100 respectively, The beach itself is projected to be completely inundated, presenting a flood risk to all assets at its immediate backshore. Already from 2050 the flood appears to significantly penetrate inshore at the western beach, affecting assets along and to the west of the stream. By 2100, the flood is projected to reach >100 m to the east and west of the stream affecting considerable infrastructure/assets, while the small fishing port will be completely flooded. Overall, it is clear that due to the low relief and many backshore infrastructures/assets there is a high food risk that can cause serious damages/losses, especially if combined floods (i.e., from land and the sea) are considered, which is a likely occurrence during extreme storms.

Figure 2. Flood extent at Komi beach in 2050 (left) and 2100 (right) under theRCP8.5 scenario. The different colors correspond to the estimated beach width that will be flooded.

Discussion and Conclusions

The results show considerable inundation for Komi beach which is projected to be worse by the 'bathtub' approach. However, the static method is considered to overpredict the flood extent, mainly because it ignores bed friction effects on the flood flow as well as its flood inundation predictions for cells are not hydraulically connected with the rest of the flooded area. Similar discrepancies between the two approaches have been found also in other island beaches (Chatzistratis *et al*., 2024). In general, flood simulations with numerical models appear more appropriate for local scales while on regional assessment the bathtub approach may be used as fine grids for numerical modelling increase substantially the computation cost (Seenath *et al*., 2016). Moreover, LISFLOOD-FP provides outputs of flood characteristics at user defined timesteps, providing significant information for flood risk preparedness.

It should be noted that the coastal flood risk in Komi is likely to be exacerbated by the beach erosion/retreat due to the relative sea level rise (RSLR). Andreadis *et al*. (2021) have estimated that Komi beach retreat due to the RSLR will be 3-9 m and 6-9 m by 2050 and 2100, respectively, even under the moderate RCP4.5 climatic scenario. It is noted that these beach erosion/retreat projections are even more conservative, as they

do not take into account the (cumulative) effects of storm events (which, both observations and modeling suggest, could be significant at Komi beach), or the effects of the diminished land-sourced sediment supply due to the construction of the Kalamoti-Katraris Dam. Therefore, in order to assess the flood risk more accurately, coupled beach erosion/flood models will be required. Although such models present large challenges, particularly due to uncertainties at the land/sea boundary condition, future efforts should be focused on it as a response to the major flood disaster risks under climate change.

Acknowledgements

This work was supported by the Project 'Coastal Environment Observatory and Risk Management in island Regions AEGIS+' (MIS 5047038), implemented within the Operational Programme 'Competitiveness, Entrepreneurship and Innovation' (NSRF 2014-2020), co-financed by the Hellenic Government (Ministry of Development and Investments) and the European Union (European Regional Development Fund).

References

Almar, R., Ranasinghe, R., Bergsma, E.W.J. *et al*., 2021. A global analysis of extreme coastal water levels with implications for potential coastal overtopping. Nat. Commun. 12, 3775. https://doi.org/10.1038/s41467-021-24008-9

Andreadis, O., Chatzipavlis, A., Hasiotis, T., Monioudi, I., *et al*., 2021. Assessment of and Adaptation to Beach Erosion in Islands: An Integrated Approach.. J. Mar. Sci. Eng. 9(8), 859. https://doi.org/10.3390/jmse9080859

Bates, Paul D., De Roo, A.P.J., 2000. A simple raster-based model for flood inundation simulation. J. Hydrology 236, 54-77 https://doi.org/10.1016/S0022-1694(00)00278-X

Bates, P., Dawson, R., Hall, J., *et al*., 2005. Simplified two-dimensional numerical modelling of coastal flooding and example applications. Coast. Eng. 52 (9), 793-810. https://doi.org/10.1016/j.coastaleng.2005.06.001

Brett, R., 2021. How Important Is Coastal Tourism for Island Nations? An Assessment of African and Indian Ocean Islands. J. Coast. Res. 37, 568–575. https://doi.org/10.2112/JCOASTRES-D-20-00011.1

Chatzistratis, D., Monioudi, I., Velegrakis, A.F., Chalazas, Th., Tragou, E., 2024. Exposure to coastal erosion and flooding in the Northeastern Aegean islands, Greece, in Briand F. (Ed.), CIESM Monograph 52, Marine hazards, coastal vulnerability, risk (mis)perceptions – a Mediterranean perspective, CIESM Publisher, Paris, Monaco, 115- 130.

IPCC, 2023. Climate Change 2023: Synthesis Report. Contribution of Working Groups I, II and III to the Sixth Assessment Report of the Intergovernmental Panel on Climate Change, Core Writing Team, Lee, H., Romero, J. (Eds.), IPCC: Geneva, Switzerland.

Le Gal, M., Fernández-Montblanc, T., Duo, E., Montes Perez, J., Cabrita, P., Souto Ceccon, P., Gastal, V., Ciavola, P., Armaroli, C., 2023. A new European coastal flood database for low–medium intensity events. Natural Hazards and Earth System Sciences 23, 3585–3602. https://doi.org/10.5194/nhess-23-3585-2023

Luijendijk, A., Hagenaars, G., Ranasinghe, R. *et al*., 2018. The State of the World's Beaches. Sci. Rep. 8, 6641. https://doi.org/10.1038/s41598-018-24630-6

Monioudi, I.N., Asariotis, R., Becker, A., *et al*., 2018. Climate change impacts on critical international transportation assets of Caribbean Small Island Developing States (SIDS): the case of Jamaica and Saint Lucia. Regional Environmental Change 18, 2211-2225. https://doi.org/10.1007/s10113-018-1360-4

Papaioannou, G., Efstratiadis A., Vasiliades, L., Loukas, A., Papalexiou, S.M., Koukouvinos, A., Tsoukalas, I., Kossieris, P., 2018. An operational method for flood directive implementation in ungauged urban areas. Hydrology 5, 24. https://doi.org/10.3390/hydrology5020024

Seenath, A., Wilson, M., Miller, K., 2016. Hydrodyanmic versus GIS modelling for coastal flood vulnerability assessment: Which is better for guiding coastal management? Ocean & Coastal Management 120, 99-109. https://doi.org/10.1016/j.ocecoaman.2015.11.019

Toimil, A., Losada, I.J., Álvarez-Cuesta, M., Le Cozannet, G., 2023. Demonstrating the Value of Beaches for Adaptation to Future Coastal Flood Risk. Nat. Commun. 14, 3474. https://doi.org/10.1038/s41467-023-39168-z

UNWTO, 2024. International Tourism Highlights. World Tourism Organization: Madrid, Spain, ISBN 978-92-844-2579-2.

Vousdoukas, M.I., Mentaschi, L., Voukouvalas, E., *et al*., 2018. Global probabilistic projections of extreme sea levels show intensification of coastal flood hazard. Nat Commun 9, 2360. https://doi.org/10.1038/s41467-018-04692-w

17th INTERNATIONAL CONGRESS of the Geological Society of Greece

BULLETIN OF THE GEOLOGICAL SOCIETY OF GREECE, SP. PUBL.

EXTENDED ABSTRACT 052

Three Years of Progress in Digital Applications and Monitoring Utilizing 3D Reality Capture Technologies for Landslide Hazard Mitigation, the Case in Evritania, Central Greece

Chatzitheodosiou T.[1], Farmakis I.[2], Papouli D.[1], Stoumpos G.[1], Prountzopoulos G.[3], Marinos V.[1]

(1) National Technical University of Athens, Athens, Greece, chatzitheodosiou@mail.ntua.gr

(2) Sapienza University of Rome, Italy

(3) Independent Geotechnical Engineering Consultant, Greece

Introduction / Background

Rockfall and landslide hazards pose significant challenges for mountainous road networks in Central Greece, particularly in the region of Evritania, which is recognized as one of the most susceptible areas to landslides in Greece (Marinos et al., 2015). In cooperation with the Region of Central Greece, the NTUA Engineering Geology & Geohazards Research Group initiated a targeted research program focusing on several key sites in the region. These areas were selected due to their geological complexity, different mechanisms of failure, challenging terrain, and history of documented landslides. Detailed investigations have been conducted to assess slope stability and analyze the mechanisms contributing to slope instability.

Building on these investigations, this study highlights advancements achieved through the research program over the past three years, focusing on the application of innovative technologies and the development of methodologies for geotechnical analysis and hazard monitoring. By leveraging advanced 3D reality capture technologies, the research integrated high-resolution aerial and terrestrial data to produce precise digital replicas of the investigated areas. These replicas enabled the extraction of critical engineering geological information and supported the development of advanced digital tools for terrain analysis and hazard assessment.

Furthermore, the digital replicas formed the foundation of a comprehensive monitoring program designed and implemented by the research team. When combined with ground-based instrument monitoring (e.g., inclinometers), this program provided a continuous stream of data, enabling regular updates to datasets and significantly improving the accuracy and reliability of detailed 2D geotechnical simulations. These analyses, along with 3D numerical simulations, offered valuable insights into slope behavior, advancing landslide hazard assessment and informing the development of site-specific mitigation measures.

Finally, the study evaluates key limitations encountered during data acquisition, processing, and analysis. These insights are examined in the context of each site, demonstrating how challenges were addressed or remain to be resolved to further enhance hazard assessment and optimize mitigation strategies.

Methodology

The methodological framework for this study builds on the integration of advanced digital tools with systematic monitoring programs, aiming to continuously refine geotechnical analyses and optimize solutions to address landslide and rockfall hazards in mountainous terrains. The workflow, illustrated in **Figure 1** begins with detailed engineering geological investigations, including field and laboratory assessments. These investigations enabled the classification of engineering geological units (EGUs) and the development of preliminary hazard maps, geotechnical models and stability analyses that delineated zones of instability and proposed conceptual mitigation designs.

To enhance the accuracy of the preliminary analyses, high-resolution topographic and geospatial data were acquired through UAV-based photogrammetry (Westoby et al., 2012) and terrestrial laser scanning (TLS). UAV surveys using DJI Phantom 4 Pro RTK and Mavic 3 Enterprise drones generated point clouds, digital surface models (DSMs), and orthomosaics with sub-centimeter accuracy, while TLS LiDAR scanning with the Leica ScanStation P40 provided millimeter-level precision for capturing detailed discontinuity characteristics, such as orientation, spacing, and persistence. These datasets facilitated advanced discontinuity mapping using techniques like Principal Component Analysis (PCA) and DBSCAN clustering (Riquelme et al., 2015; Farmakis et al., 2020), as well as the creation of Slope Relief Models (Chatzitheodosiou et al., 2024) to identify overhangs and undercuts. Semantic segmentation tools further refined the analysis by distinguishing vegetation, bedrock, and infrastructure, optimizing the detection of unstable zones and supporting rockfall trajectory analyses (Chatzitheodosiou et al., 2023).

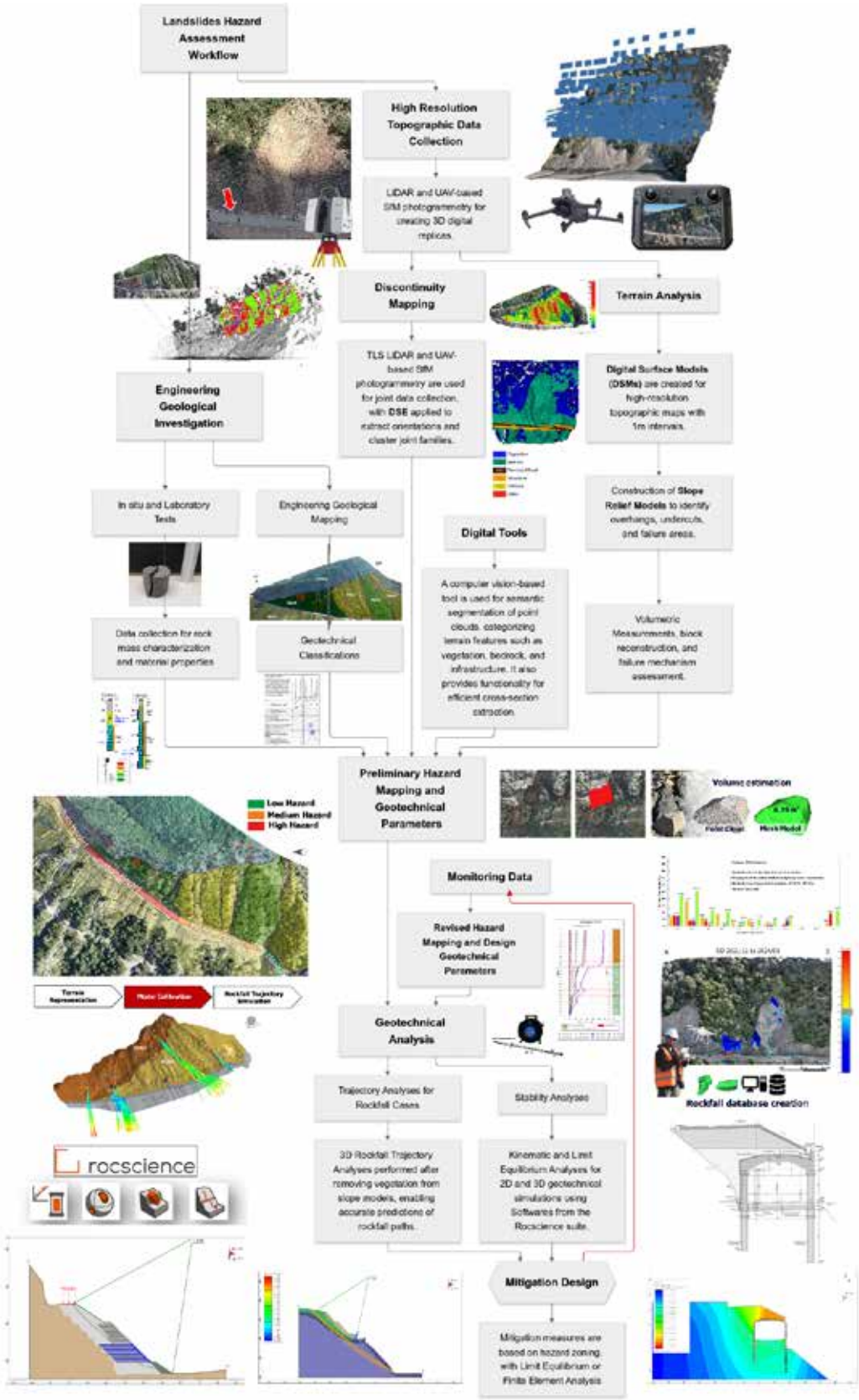

Figure 1. Integrated workflow for Landslide Hazard Assessment.

Monitoring, as illustrated in **Figure 2,** formed a crucial part of the methodology, implemented through a hybrid approach combining UAV surveys (Chatzitheodosiou, 2023) and ground-based instruments. Sequential UAV campaigns produced multi-temporal datasets that were analyzed using the Multiscale Model-to-Model Cloud Comparison (M3C2) algorithm (Lague et al., 2013) to detect and quantify surface deformations and rockfall volumes. Spatial changes were clustered using the Density-Based Spatial Clustering of Applications with Noise (DBSCAN) algorithm (Ester et al., 1996), enabling the identification of discrete events. To enhance volume reconstructions of rockfall events, 3D mesh models were generated using the Iterative Alpha Shape algorithms (Edelsbrunner and Mücke, 1994). Additionally, the VoxFall non-parametric volumetric change detection method (Farmakis et al., 2024) provided an unbiased approach for volumetric rockfall measurements directly between mesh models, cataloging key metrics such as size and location with high accuracy.
Ground-based instruments, such as inclinometers, offered complementary data on subsurface movements, particularly in rotational landslides, where a comparative analysis revealed the attenuation of subsurface displacements near the surface due to material properties and failure plane stratification. The integration of these datasets refined kinematic models and enhanced hazard assessments. Over a three-year period, this dynamic monitoring workflow informed iterative updates to hazard maps and geotechnical models, incorporating stability analyses with kinematic, limit equilibrium, and numerical methods from the Rocscience suite. These analyses, combined with real-time data on rockfall trajectories, guided the design of effective, targeted mitigation measures tailored to the evolving conditions of the study areas.

Results and Conclusions

High-resolution datasets generated through UAV-based photogrammetry and TLS LiDAR enabled the precise identification of critical geohazards, including overhanging rock masses, undercuts, and structurally controlled failure zones in the mountainous terrains of Central Greece. These results underscore the value of combining advanced digital tools with traditional geotechnical methods, providing a robust foundation for hazard mapping, geotechnical modeling, and the classification of engineering geological units (EGUs) with millimeter-level precision. The multitemporal monitoring program provided valuable insights into the dynamic behavior of slopes. The M3C2 change detection algorithm successfully quantified surface deformations and detected rockfall volumes over time. The use of VoxFall for volumetric change detection ensured accurate modeling of these events, minimizing user bias and enhancing the overall reliability of the analysis. The database enabled the team to characterize the frequency, magnitude, and spatial distribution of rockfall events, offering a detailed understanding of hazard zones. For rotational landslides, the comparison between inclinometric data and UAV-based change detection revealed how movement attenuates as it approaches the surface. This attenuation pattern was linked to the geotechnical properties of the subsurface materials and provided critical data for refining stability models and estimating the depth of the failure plane.
Geotechnical analyses, informed by these datasets, identified the predominant failure mechanisms in the study areas. For instance, in structurally controlled limestone slopes, wedge sliding and toppling failures emerged as the dominant modes of instability. Physically based trajectory modeling, calibrated with real-time data, accurately predicted the impact zones of these rockfalls, thereby supporting the design of targeted mitigation measures. Similarly, rotational landslides in weak flysch formations were classified using a modified Geological Strength Index (GSI) tailored for heterogeneous rock masses like flysch (Marinos, 2019) and analyzed in detail, with stability simulations indicating the zones most susceptible to failure and highlighting the effectiveness of potential stabilization interventions. To address the specific challenges at each site, various mitigation measures were proposed to enhance slope stability and safeguard infrastructure. These measures included the installation of rockfall nets and anchored rock bolts to stabilize critical rock masses. Where space constraints limited conventional approaches, reinforced embankments or lane covers were recommended. In areas requiring additional structural support, deep reinforced piles were proposed to provide both lateral and vertical stability by anchoring into stable substrata. Hazard zoning, informed by refined analyses, facilitated proactive planning, while real-time monitoring ensured timely evaluations of the effectiveness of each intervention and allowed for iterative improvements.
Finally, the study addressed several challenges encountered during data collection and processing, such as suboptimal lighting conditions, vegetation interference, and noise in point cloud data. These obstacles were mitigated through adaptive methodologies, including optimized flight paths, advanced clustering algorithms, and rigorous manual validation procedures. Overall, the integration of digital tools with traditional engineering geological and geotechnical approaches has produced significant advances in landslide and rockfall hazard assessment, emphasizing the importance of continuous monitoring, dynamic hazard mapping, and data-driven design proposals for managing geohazards in complex mountainous regions.

Acknowledgements

The authors sincerely thank the Region of Central Greece and the Regional Unit of Evritania for their invaluable support in this research. Their collaboration with the National Technical University of Athens highlights the important role local governments play in advancing scientific efforts to improve infrastructure safety and address geohazards. We are especially grateful for their assistance in facilitating access to key sites, providing logistical support, and contributing to the successful completion of this research.

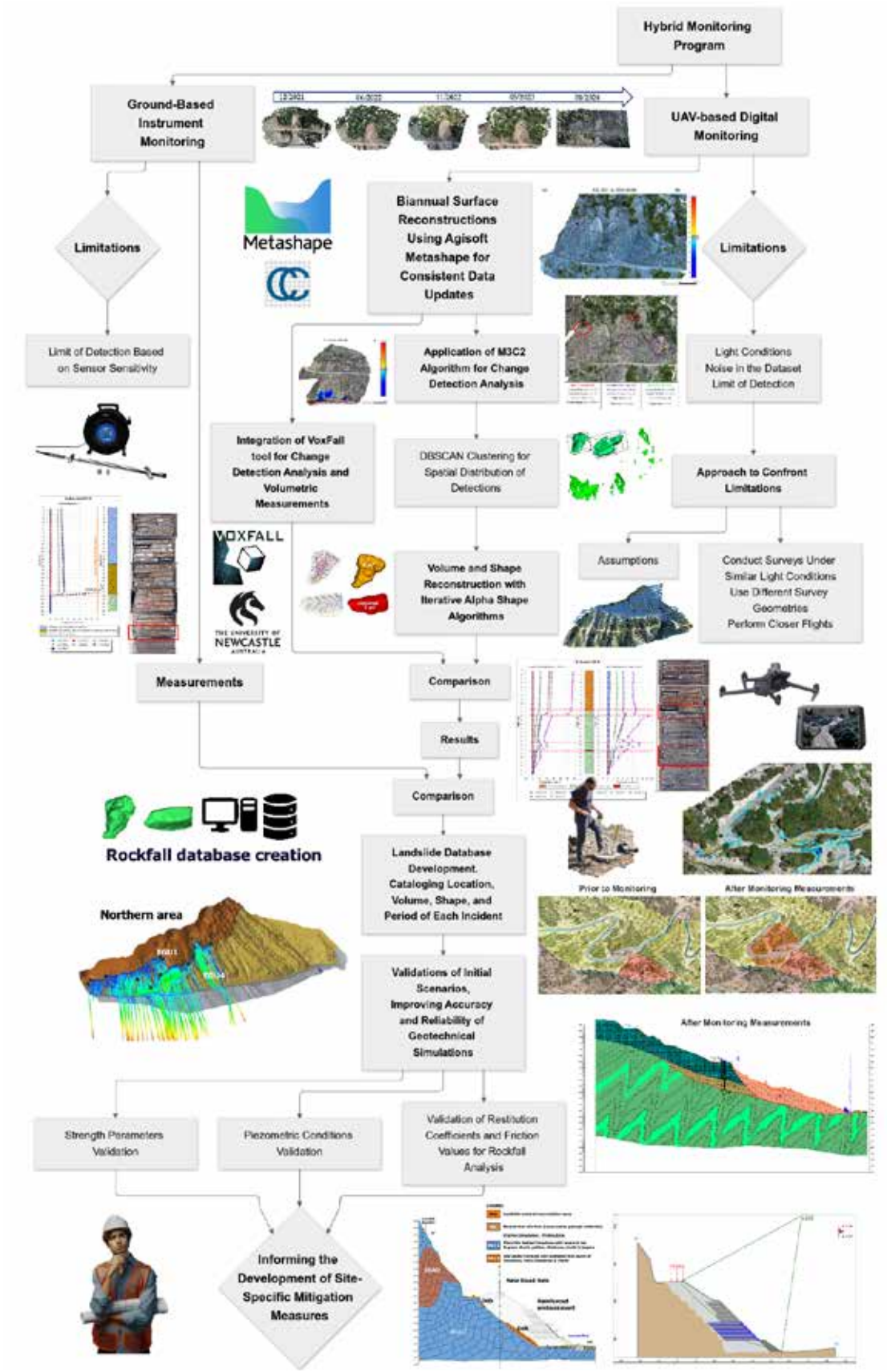

Figure 2. Hybrid monitoring program refining Landslide Hazard Assessment.

References

Chatzitheodosiou, T., Farmakis, I., Prountzopoulos, G., I., Papouli, D., Stoumpos, G., Thomaidis, T., & Marinos, V. (2023). Addressing rockfall challenges in flysch environments – A case study from Greece. In Proceedings of the 6th Regional Symposium on Landslides in the Adriatic-Balkan Region.

Chatzitheodosiou, T. (2023). "One rock at a time" 3D Geology Mini-Series. Available at: https://sketchfab.com/themisto123 [Website]

Chatzitheodosiou, T., Farmakis, I., Papouli, D., Stoumpos, G., & Marinos, V. (2024). SfM photogrammetry for rockfall monitoring and hazard assessment along the Agia Varvara-Agrafa road in Central Greece. 4th European Regional Conference of IAEG – EUROENGEO 2024.

Edelsbrunner, H., & Mücke, E. P., 1994. Three-dimensional alpha shapes. ACM Transactions on Graphics (TOG), 13(1), 43–72.

Ester, M., Kriegel, H. P., Sander, J., & Xu, X., 1996. A density-based algorithm for discovering clusters in large spatial databases with noise. In Proceedings of the 2nd International Conference on Knowledge Discovery and Data Mining (KDD-96), Portland, Oregon, 226–231.

Farmakis, I., Marinos, V., Papathanassiou, G., et al., 2020. Automated 3D jointed rock mass structural analysis and characterization using LiDAR terrestrial laser scanner for rockfall susceptibility assessment. Geotechnical and Geological Engineering, 38(3), 3007–3024.

Farmakis, I., Guccione, D. E., Thoeni, K., & Giacomini, A., 2024. VoxFall: Non-parametric volumetric change detection for rockfalls. Preprint submitted to Elsevier.

Lague, D., Brodu, N., & Leroux, J., 2013. Accurate 3D comparison of complex topography with terrestrial laser scanner: Application to the Rangitikei Canyon (New Zealand). ISPRS Journal of Photogrammetry and Remote Sensing, 82, 10–26. **[Journal Article]**

Marinos, V.; Papathanassiou, G.; Vougiouka, E.; Karantanellis, E., 2015. Towards the Evaluation of Landslide Hazard in the Mountainous Area of Evritania, Central Greece. In: Engineering Geology for Society and Territory, Lollino et al. (eds.), Published by Springer – Volume 2, pp. 989–993.

Marinos, V., 2019. A revised, geotechnical classification GSI system for tectonically disturbed heterogeneous rock masses, such as flysch. Bulletin of Engineering Geology and the Environment, 78(2), 899–912.

Riquelme, A., Abellán, A., & Tomás, R. (2015). Discontinuity spacing analysis in rock masses using 3D point clouds. Engineering Geology, 195, 10.1016/j.enggeo.2015.06.009.

Westoby, M. J., Brasington, J., Glasser, N. F., Hambrey, M. J., & Reynolds, J. M., 2012. Structure-from-Motion photogrammetry: A low-cost, effective tool for geoscience applications. Geomorphology, 179, 300–314.

17th INTERNATIONAL CONGRESS of the Geological Society of Greece

BULLETIN OF THE GEOLOGICAL SOCIETY OF GREECE, SP. PUBL.

EXTENDED ABSTRACT 053

Mapping and Categorization of damage on the built and natural environment caused by the 2023 Daniel and Elias storms in MountPelion, Greece

Eleftheria Christodoulopoulou[1], Olga-Joan Ktenidou[2], Grigorios Tsinidis[3]
1 University of the Aegean, Mytilene, Greece, christodoulopoulouleftheria@gmail.com
2 Institute of Geodynamics, National Observatory of Athens, Athens, Greece
3 University of Thessaly, Volos, Greece

Introduction and motivation

Storms Daniel and Elias occurred in September 2023 with only a 20-day gap between them and left a severe impact on the affected areas, since their aftermath is still clearly visible to date, 16 months later. The meteorological station in Zagora at Mount Pelion recorded the highest daily rainfall value in the country (around 760 mm) during Daniel storm, breaking the previous record of Paliki, Kefalonia (645 mm) recorded during the mediterranean cyclone Ianos in 2020 (Ντάφης κ.ά., 2023; Βουγιούκας κ.ά., 2023). Figure 1 shows the total amount of rainfall (in mm) for September over a period of ten years, as recorded by three different meteorological stations in the vicinity, namely Volos, Zagora and Makrinitsa (see Figure 4 for station locations). Studies exist already analysing the effects of these storms on various aspects of the community and ecosystem; e.g., Dimoudi *et al*. (2024) performed analyses to examine the effect on water quality, He *et al*. (2024) used SAR technologies to map effects on crops and livestock, while Mavroulis *et al*. (2024) highlighted all the risk factors that favor the occurrence of infectious diseases. Here, we consider effects on the built environment and infrastructures through in-situ visits.

In this study we focus on the types of damage that these storms caused in the Pelion region. Through photographic documentation the damage was categorized into six key categories referring to: loss of life, damage to the road network, damage to bridges and other structural elements, soil erosion, debris accumulation, and property loss. These findings provide valuable insights into the diverse and severe impacts of storms and their effects on communities and the environment. We aim to showcase the extent of this destruction caused to the villages and communities of Pelion and provide a comparison between Pelion's three municipalities and the types of damage each one suffered. We also point to the degree to which reparation actions have progressed at the time of writing this abstract, which is 16 months after the incident.

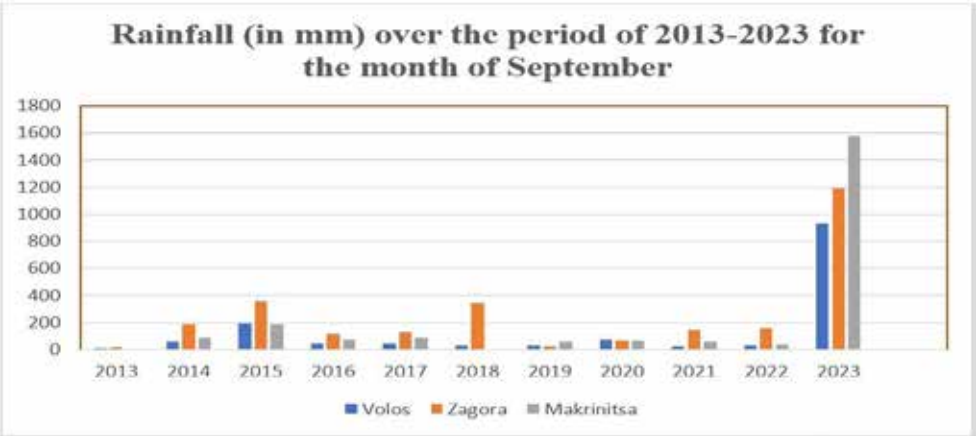

Figure 1. Rainfall of the study area over a ten-year period for the month of September (data from: https://meteo.gr/climatic.cfm)

Method and data collection

In total, seven routes were arranged based on news reports of extensive damage in the region. Data was collected on site through geotagged photographs. A total of 554 photographs were taken, of which 137 were included in the study's detailed analysis. ArcGIS Pro software was used in order to create a map that visualizes the relation between the seven survey routes and the location of damages recorded during field visits. Then, damages were sorted and categorised depending on their content alone, i.e., disregarding their coordinates. Lastly, another map was created to feature the relation between the spatial distribution of damage depending on their type and municipality.

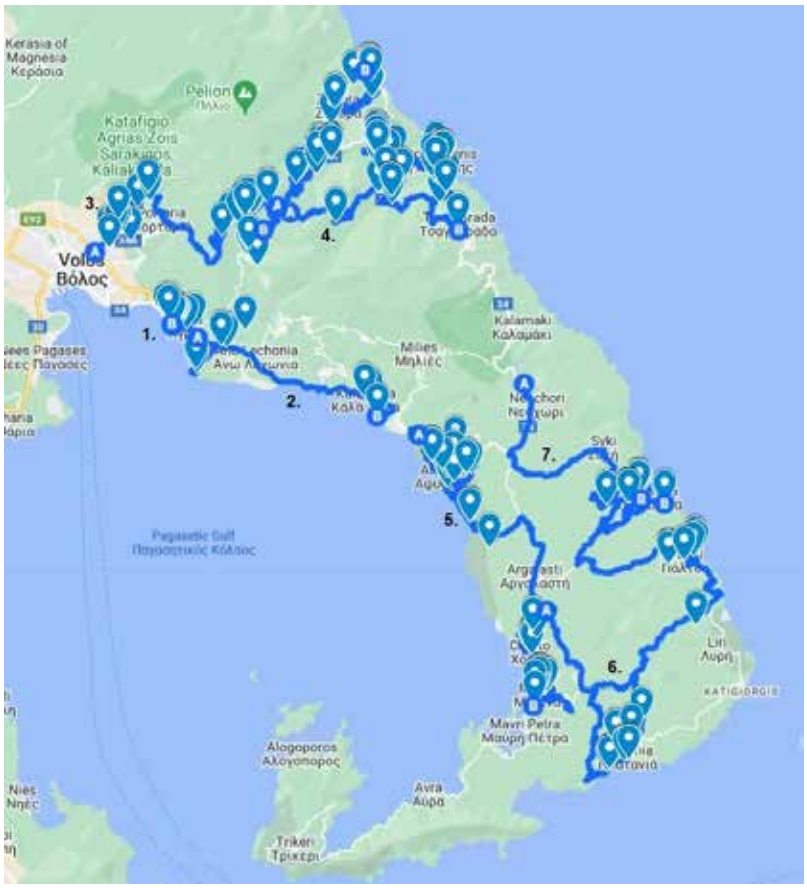

Figure 2. The seven routes that were followed in relation to all damages recorded

Results

Every photograph had georeference through its coordinates, as is standard practice for all post-disaster reconnaissance activities in order for photographs taken in the field to be acceptable for use in the desk analysis. This rendered it possible to visualise all damages and map locations where they were concentrated (Figure 2). After studying the available data, these were categorized into six groups according to the type of damage they were depicting. The groups were formed as shown below:

- Loss of Life: Four fatalities were recorded in the Pelion region alone during Storm Daniel.
- Road Networks: Significant damage was observed, especially near streams and water bodies. Roads were washed away or severely eroded due to the discharge and the high speed of water flow.
- Bridges and Infrastructure: Bridges collapsed or were rendered unsafe, as their structural foundations were compromised. Key access routes were severed. The damage was mainly attributed to scouring phenomena at the approaching embankments of the bridges.
- Property Loss: Houses, vehicles and businesses suffered extensive damage, particularly in areas close to riverbeds.
- Soil Erosion: Landslides and mudflows led to large volumes of soil being moved, exacerbating the damage.
- Debris Deposition: Tree trunks, stones, and other debris clogged waterways, damaged vehicles, and destroyed public spaces.

Figure 3 shows some of the damages recorded, namely: road network destruction in Kala Nera, structural damage of a bridge in Horto, debris deposition on a playground in Agios Onoufrios, extensive damages to a house in Platanias and lastly a large volume of soil that was moved due to a landslide in between Chania and Drakia village. Finally, it was deemed necessary for this study, to create a map where all groups of damages were shown in relation to municipalities (Figure 4), since each one differs from the other regarding environmental conditions (vegetation, gradient).

Figure 3. Different types of damages recorded on site during field visits

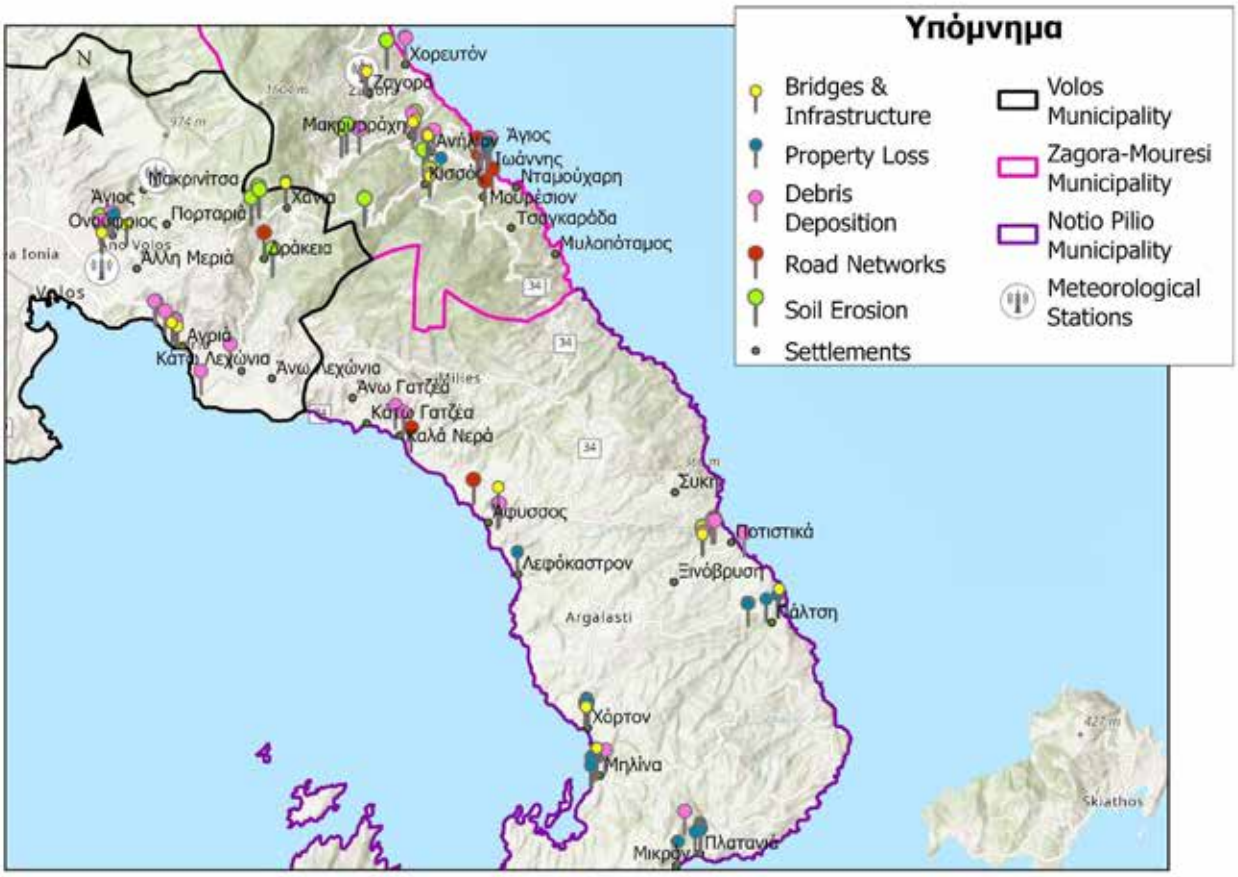

Figure 4. Distribution of types of damages in relation to each municipality of the study area

Conclusions

Proximity of infrastructure and settlements to water bodies played a crucial role in the severity and extensiveness of the damages recorded. Four people lost their lives in Pelion region alone, due to the violent water flow of the torrents. Huge amounts of soil were removed, especially from locations with great inclination (mostly in municipality of Zagora – Mouresi, followed by Volos municipality), and were carried away violently by the water, finally redepositing within riverbeds, private houses, public spaces and the sea. Bridges were washed away or severely damaged, roads were eroded and some settlements were cut off for a few days because of it. These findings highlight the need for improved urban planning and infrastructure resilience in flood-prone areas, but also updated, well-known to all residents evacuation plans. Recovery efforts, one year after these events, indicate slow progress in rebuilding and rehabilitation. In most cases temporary rehabilitation measures have been applied. This study underscores the importance of better disaster management practices, followed by everyone involved, in order to mitigate future risks.

References

Dimoudi, A., Voulgaris, K., Varkoulis, A., Georgiou, K., (2024). The impacts of "DANIEL" and "ELIAS" storms on water quality of Pagasitikos Gulf – a first record. Available at: https://www.researchgate.net/publication/382220692

He, K., Yang Q., Shen, X., Dimitriou, E., Mentzafou, A., Papadaki, C., Stoumboudi, M., Anagnostou, E.N., (2023). 'Brief communication: Storm Daniel Flood Impact in Greece 2023: Mapping Crop and Livestock Exposure from SAR'. Available at: https://doi.org/10.5194/nhess-2023-173.

Mavroulis, S., Mavrouli, M., Lekkas, E., Tsakris, A. Impact of the September 2023 Storm Daniel and Subsequent Flooding in Thessaly (Greece) on the Natural and Built Environment and on Infectious Disease Emergence. Environments 2024, 11, 163. https://doi.org/10.3390/environments11080163

Hewson, T., Ashoor, A., Boussetta, S., Emanuel, K., Lagouvardos, K., Lavers, D., Magnusson, L., Pillosu, F., Zsoter, E., (2024). Medicane Daniel: an extraordinary cyclone with devastating impacts. Available at: https://www.ecmwf.int/en/newsletter/179/earth-system-science/medicane-daniel-extraordinary-cyclone-devastating-impacts

Βουγιούκας, Στρ., Κωλέτσης, Ι., Λαγουβάρδος, Κ., (2023). Αποτίμηση της κακοκαιρίας DANIEL, μέρος 1ο: Ξεπέρασε κατά πολύ τα ύψη βροχόπτωσης του Μεσογειακού Κυκλώνα ΙΑΝΟΥ του 2020. https://meteo.gr/article_view.cfm?entryID=2923

Ντάφης, Σ., Κύρος, Γ., Λαγουβάρδος, Κ. (2023). Κακοκαιρία Daniel: Καταρρίφθηκε το ρεκόρ ημερήσιου ύψους βροχής στη χώρα μας. https://www.meteo.gr/article_view.cfm?entryID=2913

17th INTERNATIONAL CONGRESS of the Geological Society of Greece

BULLETIN OF THE GEOLOGICAL SOCIETY OF GREECE, SP. PUBL.

EXTENDED ABSTRACT 054

ERBE SYMPOSIUM 2027– LAVRION GREECE: Honouring the Values of Geo-Mining Heritage

Demetrios C. Constantinides, RNDr.
Exploration Geologist, Nicosia, Cyprus, email: dimkon46@gmail.com

Introduction

The word Symposium is very understandable to the Greeks, since their ancestors had started organising these events already in the 7th century BC. At such gatherings, the more experienced members of the community were expected to impart practical guidance to younger generations. This mentorship helped maintain the steadiness of certain cultural traditions. A symposium usually took place in a men's dining room of a nobleman. The room was called "andron" and was specially designed for such meetings, with couches placed around the perimeter for guests to lie down, while they while they were eating and drinking (Fig. 1).

Fig. 1: Relief depicting a scene from a symposium in ancient Greece[1]

The ERBE Symposium

An ERBE Symposium has a strong element in common with the ancient Greek symposia: it aims to bring out the cultural heritage of those "who crawl like worms in the earth, denying the sun and the air", as the Cypriot poet Costas Montis describes the miners in one of his poems.

ERBE is a German word that means heritage. The International "ERBE" Symposium, exploring the cultural heritage of geology, mining and metallurgy, has a tradition that goes back more than three decades, since the first one was organised in Freiberg of Germany in 1993. Since then, the Symposium has been organised 15 more times to return to Freiberg in 2023. So far, it has been held in the following cities and countries:

Freiberg/Saxony – Germany (1993)
Leoben – Austria (1995)
St. Petersburg – Russia (1997)
Banská Štiavnica – Slovakia (1999)
Golden/Colorado – USA (2000)
Idrija – Slovenia (2002)
Leiden – The Netherlands (2003)
Schwaz – Austria (2005)
Quebec-City – Canada (2007)
Freiberg/Saxony – Germany (2009)
Real del Monte – Mexiko (2011)
Bozen/Bolzano – Italy (2013)
Banská Štiavnica – Slovakia (2015)
Ravne na Koroskem – Slovenia (2018)
Eggenburg – Austria (2021)
Freiberg/Saxony – Germany (2023)

The next city to host the Symposium will be again Ravne na Koroskem on 22nd – 27th September 2025. Here are some scenes from previous symposia (Fig. 2-6). The source of figures 2 to 6 is https://photos.erbe-symposium.org/index.php?/categories.

Fig. 2: Participants of the last ERBE Symposium in Freiberg during a city sightseeing tour.

Fig. 3: The building of the Old Castle in Banská Štiavnica, the venue of the 13th ERBE Symposium.

Fig. 4-5: Children's performance and miner's choir at the 13th ERBE Symposium.

Fig.6: An old mining locomotive that was exhibited at the ERBE Symposium in Quebec (2007).

For those interested in enjoying thousands of images from all the sixteen symposia, a visit to the website of the ERBE Association is recommended[2].

The Main Goals of an ERBE Symposium

The main objective of an ERBE Symposium is to exhibit the cultural heritage in Geosciences, Mining and Metallurgy. However, each symposium tried to highlight more specific cultural characteristics relating to the local mining tradition. For example, the last Symposium held in Freiberg, focused on libraries, archives and museums associated with historic mining industry. The Principles of the Cultural Heritage of Geosciences, Mining, Metallurgy and Archaeology have been established some time ago[3].

The aim of both international and national commissions of the Symposia is to make available the entire human cultural heritage relating to the earth's crust, including geo-memorials. The committees are made up of personalities who promote and develop the values and the heritage of mining culture.

We could go on presenting the objectives of the Symposia held to date. However, this is not the subject of this paper. What really needs to be highlighted here is the decision of a small group of people to take over the 2027 Symposium that we would like to organise in Lavrion.

Our Initiative

The author of this paper has joined the 13th ERBE Symposium in Banská Štiavnica, where he lived for about 10 years. It is a town of 16,000 inhabitants whose economy is heavily dependent on the tourism generated by its mining heritage.

The idea of applying for one of the next ERBE Symposia, which could be organised by the Lavreotiki Geopark and

the Committee of Geological-Geomorphological Heritage of the Greek Geological Society, was strengthened in our minds after the inclusion of the Lavrion area in the UNESCO Geoparks Group. Nevertheless, the maintenance of a Geopark on this List and its potential inscription on the UNESCO World Heritage Register, will require a great deal of effort. That is why we believe that, apart from the fact that we will be able to present the history, incredible monuments and natural beauty of Lavrion so broadly, the organisation of such a symposium would help us to gain international supporters for the inclusion of the area in the UNESCO World Heritage List.

Why Lavrion?

The beginning of mining and metallurgy in Lavreotiki is placed in the 5th millennium BC. In particular, the inhabitants of Velatouri hill are thought to have been there since the Middle Neolithic, around 4500 BC. At the foot of the hill was the oldest theatre in ancient Greece, that of Thorikos (Fig. 7).

Fig. 7: Thorikon theatre and an ore washing plant.

Next to the amphitheatre is the entrance to the adit where the Ag-Pb ores were mined (Fig. 8). Photo @Richard Kaňa

Fig. 8: The entrance of a mining adit. Photo @Richard Kaňa

The most important technological achievement of this period was mining and metallurgical processing. The archaeological remains of these activities can be found and visited in Souriza (Fig. 9).

Fig. 9: Ruins of the water management system at Souriza. Photo @Richard Kaňa

Not to be missed

Apart from being famous for the exploitation of silver and funding the famous projects of the "Golden Age of Pericles", as well as the fleet of the Naval Battle of Salamis, this mining area contains more minerals than any other region of the Earth, making it also a unique site of mineral heritage.

According to the Mindat Organisation 805 mineral species and varietal names are listed in the abandoned mines of Lavreotiki district[4], whilst it is the type-locality for 23 of them.

Fig. 10: Minerals from Hercules Katsaros collection. Photo @H. Katsaros

Circulars, Sessions and Tours

As soon as our proposal to hold the ERBE Symposium in Greece is officially accepted, the Organising and Scientific Committee of the Symposium will be set up so that the sessions of the Symposium can be decided and the first Circular Letter can be sent out. Of course, the Symposium will include excursions to geological and mining monuments of Lavrion and the surrounding archaeological sites (Sounion and the Temple of Poseidon, the ancient marble quarry at Agrileza and others).

Obviously, the programme will include a full-day trip to Athens including a visit to Acropolis and its modern museum, as well as a lunch in Plaka. Perhaps some delegates who have the time could be offered more distant excursions, e.g., to Serifos and/or Milos.

The Venue

The proposed venue is an important part of the cultural heritage of Lavrion. The buildings are located within the Lavrion Technological and Cultural Park, which was established in 1992 on the site of the former French Mining Company of Lavrion, on the initiative of the National Technical University of Athens. The premises are of high aesthetic and architectural value (Figs. 11), although most of them were built between 1875 and 1940. They include the processing facilities, as well as administrative and other buildings. The site was the location of the company's operations until 1988.

Fig. 11: Historical buildings of the French Mining Company of Lavrion. Photos: @H. Katsaros

The proposed emblem for ERBE Lavrion Symposium

The concept of the ERBE Symposia banner was established at the Freiberg Conference in 1993. With three exceptions, the rest of the countries respected the original emblem by adding only the city and date of the event. It is for this reason that we are proposing the following emblem for the ERBE Symposium to be held in Lavrion in September 2027 (Fig. 12). The exact dates will be added to the logo once they have been finalised in consultation with the International Committee.

Fig. 12: The proposed emblem for the 2027 ERBE Symposium in Lavrion.

What are we looking forward to?

What are we looking forward to?

As the promoters of this initiative, we expect the following:

- The acceptance by the international geological and mining ERBE community of our proposal to hold the 2027 Symposium in Lavrion.
- Effective cooperation between the organising bodies of the Symposium to ensure its success. And above all, to properly promote the cultural heritage of the geological and mining Lavreotiki.
- The General Directorate of Mineral Resources of the Greek Ministry of Environment and Energy to support the efforts of the organisers in an un-bureaucratic way.
- The Greek Geological Society, the Union of Greek Geologists, the Technical Chamber of Greece, the Association of Mining Enterprises, the Eastern Attica Region, the National Technical University of Athens and other relevant bodies to support this initiative.

If all goes well, we believe that Lavrion and its Geopark will not only establish its reputation as one of the world's most Historical Mining Centres and become better known around the world, but also raise the bar for a place on the UNESCO World Heritage List.

(Endnotes)

1 National Geographic.
2 https://photos.erbe-symposium.org/index.php?/categories
3 https://www.erbe-symposium.org/executive-board-committee/cultural-heritage-principles/
4 https://www.mindat.org/search.php?search=Lavrion

17th INTERNATIONAL CONGRESS of the Geological Society of Greece

BULLETIN OF THE GEOLOGICAL SOCIETY OF GREECE, SP. PUBL.

EXTENDED ABSTRACT 055

The Geoheritage of the "Atlantic Geopark" Project (Central Portugal) at a Glance

Custódio, S.C.[1], Henriques, M.H.[2], Sá, A.A.[3]

(1) Geosciences Center, Department of Earth Sciences, University of Coimbra, Rua Sílvio Lima s/n, 3030-070 Coimbra, Portugal; scmcustodio@student.uc.pt

(2) Geosciences Center, Department of Earth Sciences, University of Coimbra, Rua Sílvio Lima s/n, 3030-070 Coimbra, Portugal

(3) Department of Geology and Pole of the Geosciences Center, University of Trás-os-Montes e Alto Douro, Quinta de Prados, 5000-801 Vila Real, Portugal

Introduction

The history of the Proto-Atlantic and the opening up of the Atlantic are particularly well expressed on the Western Iberian Margin (WIM) and are of interest to many geosciences' experts and curiosity to many citizens. The expressiveness of the last 600 million years of the WIM's geological history is particularly eloquent in a territory that covers an east-west strip of the Beira Litoral (Central Portugal), comprising the municipalities of Figueira da Foz, Mira, Cantanhede, Mealhada, Montemor-o-Velho and Penacova (Fig. 1).

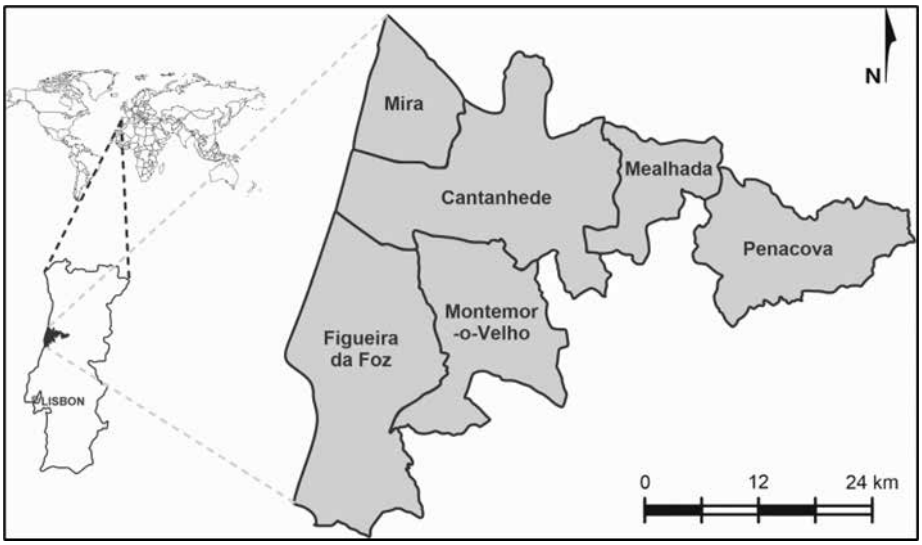

Figure 1: Location map of the "Atlantic Geopark" territory.

The "Atlantic Geopark" Project consists of inventorying and evaluating the geological heritage of those six municipalities, with a view to its conservation, valuation and monitoring for a future application to the Global Geoparks Network (GGN). The results obtained will provide technical support for the application dossier, that has to also include a sustainable management plan for the territory aiming at fostering socio-economic development, conserving the geological heritage and inspirating its replication in similar transatlantic territories.

Conceptual framework

This research assumes that the Earth's natural heritage includes two components - abiotic and biotic - which must be preserved namely through local, regional and national actions/organizations, as well as supranational ones, of which the current UNESCO programs are an example (e.g., Man and the Biosphere Program (since 1971); Convention for the Protection of the World Cultural and Natural Heritage (since 1972) and the International Geosciences and Geoparks Program (since 2015)).

The abiotic component of nature is reflected in its geodiversity, which can be defined as the variety of geological characteristics/features that can be identified in a given territory and taking into account their frequency and distribution, as well as their expressiveness as a reflection of the geological evolution of that territory. When they have scientific, educational and tourist value, such geological sites and elements take on heritage value and are part of the Earth's geological heritage (Carcavilla *et al.*, 2007; Brilha, 2016).

Geoconservation is a geological science that, based on the geodiversity of any territory and/or geological element

(e.g., fossils, rocks and minerals), seeks to safeguard the Earth's geological heritage through specific methods and techniques of inventorying, evaluating, conserving, valuation and monitoring (Henriques *et al*., 2011). From this need emerged the concept of geopark, whose historical foundations date back to the Digne Convention (1991), where an international declaration to protect the geological heritage as a legacy for future generations was approved (IDRME, 1995).

UNESCO defines a geopark as a single, unified area, where sites and landscapes of international geological importance are managed in a holistic concept of protection, education and sustainable development (UNESCO, 2024). UNESCO's link with geoparks officially began in 2004. However, numerous previous initiatives, such as the creation of the European Geoparks Network in 2000, contributed to UNESCO's commitment to the dynamics of geoparks. In 2015, UNESCO enshrined the UNESCO Global Geopark concept within the framework of the new International Geosciences and Geoparks Programme (Henriques & Brilha, 2017).

In 2024, Portugal has six UNESCO Global Geoparks - Azores, Arouca, Estrela, Naturtejo, Terras de Cavaleiros and Oeste (CNU, 2024) – and two Aspirants - Litoral de Viana do Castelo and Algarvensis. The "Atlantic Geopark", which is still in the design phase, emerged from the willingness of six municipalities located in Central Portugal (Cantanhede, Mealhada, Mira, Montemor-o-Velho, Figueira da Foz and Penacova) to apply for their territory to become a UNESCO Global Geopark. To this end, it is necessary to inventory, assess, conserve, valuate and monitor the geological heritage of its territory with a view to incorporating it into the application file for the GGN. This is the main goal of this project which have already produced some relevant results.

First results

The geodiversity of this area, which comprises a strip that crosses Portugal in an approximately east-west direction, allows us to recognize the main episodes in the geological history of the WIM over the last 600 million years (Fig. 2). This is supported by a set of sites of geological interest that illustrate the main episodes related to the opening and closing of the Rheic Ocean, the fragmentation of Pangea, the opening of the North Atlantic Ocean and the Quaternary geodynamics of the North Atlantic Ocean (Custódio *et al.,* 2024; Table 1).

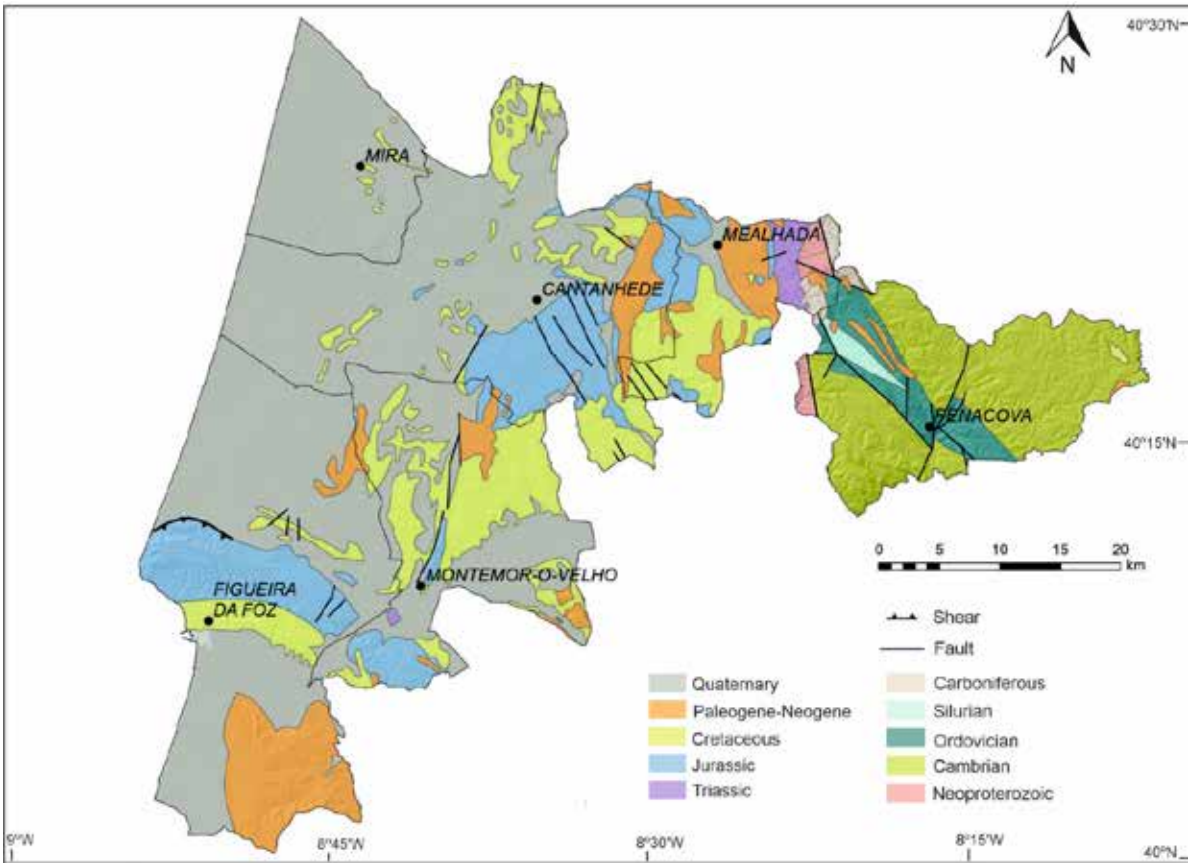

Figure 2: Geological map of the study area. It covers materials from the Neoproterozoic (600 Ma) to the Cenozoic (Vaz *et al*., 2023).

The first geological framework in the study area is the Beiras Supergroup (635 Ma), that represents the oldest record in the study area, outcropping in Penacova Municipality (Fig. 3A). This record is associated with the evolution of a volcanic arc (Cadamian Orogeny; 650-550 Ma) on the margin of the Gondwana continent. It was later inverted by the beginning of the Variscan Cycle (Cambrian—Ordovician; 495–485 Ma), and another deformation episode which is related to the closing of the Rheic Ocean and the Pangea assembly.
The geological record of the Buçaco Synclinal (Lower Ordovician - Silurian; 485-423 Ma) was deposited in a passive margin context of the Rhein Ocean, and it outcrops in Penacova and Mealhada Municipalities (Fig. 3B). In Mealhada Municipality it also crops out the east sector of the Buçaco Carboniferous Basin (Early Ghzelian - 303 Ma), whose units were deposited in a continental basin context located between the Variscan mountains (Fig. 3C).
The next geological framework is represented by the Silves Group (Upper Triassic; Mealhada Municipality a siliciclastic unit that can attest to the central position that Iberia occupied in Pangea just before the opening of the North Atlantic Ocean, marking the break-up of that supercontinent (Fig. 3D).
The Jurassic Carbonate platform of the Proto-Atlantic is well represented in Cantanhede and in Figueira da Foz Municipalities (Figs. 3E and 3F). The reference section of Cabo Mondego (Figueira da Foz) includes the GSSP for Bajocian (170 Ma) and the ASSP for the Bathonian (168 Ma), which represents geoheritage of global relevance. The same section provides a continuous record from the Middle Jurassic fossiliferous marly limestones interpreted as a sag episode of the first rift to the syn-rift episode of the Late Jurassic second rift.
The transition to a passive margin is represented by the next geological framework of the “Atlantic Geopark”, the Carbonate Platform of the Atlantic (Cenomanian—Turonian, 100–93 Ma), which is also well recorded in Figueira da Foz, and in Montemor-o-Velho Municipalities (Fig. 3H).
The Quaternary geodynamics of the Atlantic Margin is well represented throughout the territory, with extensive superficial deposits that cover most of the littoral, dated from the Pleistocene to the Holocene (Fig. 3I).

Table 1. The geological frameworks of the “Atlantic Geopark” and its representative geological site.

Geological framework	Episode	Geological site	Relevance	Municipality
Beiras Supergroup (Neoproterozoic)	Opening of the Rheic Ocean	Aguieira Dam (40°20’24.5”N 8°11’54.6”W)	Regional	Penacova
Buçaco Synclinal (Ordovician - Silurian)	Evolution of the Passive Margin	Livraria do Mondego (40°17’00.9”N 8°15’58.0”W)	Nacional	Penacova
Buçaco Carboniferous Basin (Carboniferous)	Closing of the Rheic Ocean	Santa Cristina Fountain (40°20’55.2”N 8°23’02.8”W)	Regional	Mealhada
Silves Group (Triassic)	Fragmentation of Pangea	Vacariça (40°20’53.6”N 8°23’23.0”W)	Local	Mealhada
Carbonate platform of the Proto-Atlantic (Jurassic)	Opening of the North Atlantic Ocean	Cabo Mondego (40°10’48.4”N 8°54’20.7”W); Ançã limestone (40°17’17.6”N 8°32’22.5”W)	Global	Figueira da Foz; Cantanhede
Carbonate Platform of the Atlantic (Cretaceous)	Marine transgression of the North Atlantic Ocean	Nossa Sra. dos Olivais Chapel (40°14’12.4”N 8°35’20.3”W)	Regional	Montemor-o-Velho
Quaternary Dunes	Quaternary geodynamics of the Atlantic Margin	Barrinha de Mira (Ria de Aveiro; 40°27’05.5”N 8°47’53.3”W)	Local	Mira

Figure 3: The representative geological site of each geological framework recorded at the "Atlantic Geopark". A) Aguieira Dam (Penacova); B) Livraria do Mondego (Penacova); C) Santa Cristina Fountain (Mealhada); D) Vacariça (Mealhada); E) Ançã (Cantanhede); F) Cabo Mondego (Figueira da Foz); G) Nossa Sra. dos Olivais Chapel (Montemor-o-Velho); H) Barrinha de Mira (Mira).

These preliminary results have been reported in several scientific forums, and as geoeducative and geoturistic products (Fig. 4). A promotional video was produced in 2021 by AD ELO, the organization in charge of implementing the future application to GGN (https://youtu.be/NFVJGIL4PX8?si=vPztmIP6BM6vRuMT). The most emblematic geological sites for each municipality were described in detail by Custódio *et al*. (2024). They feature the Oceans Route, a set of outcrops that make it possible to reconstruct the geological history of two oceans—Rheic and Atlantic. Other geo-itineraries (the water route, the stone route and the beach route) were created and are available online (AD ELO, 2024) and as a book in the region's tourist offices (Vaz *et al*., 2024). Other initiatives promoted by municipal authorities regarding the conservation and valuation of local geoheritage resources include the recent designation of the Ançã Limestone as Global Heritage Stone (David Lista *et al*., 2024) and the classification of Livraria do Mondego (in the Buçaco Syncline) as Local Natural Monument included in the National Network of Protected Areas of Portugal (Henriques *et al*., this volume).

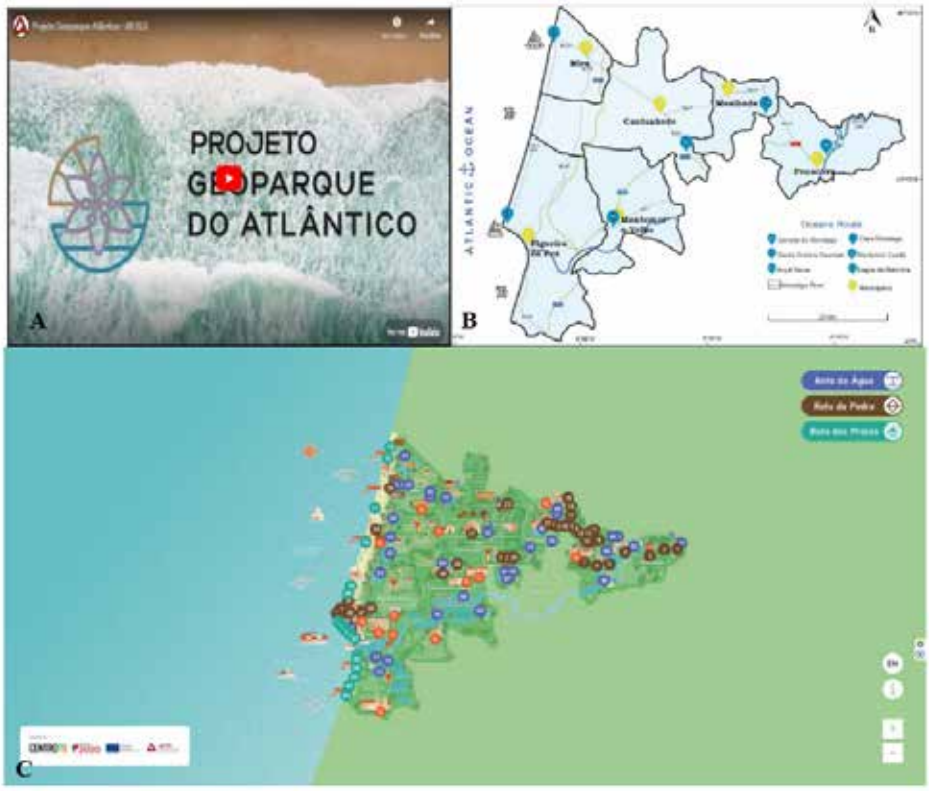

Figure 4: Different types of products resulted from the ongoing "Atlantic Geopark" Project. A: the promotional video (AD ELO, 2021); B: the geo-itinerary with selected geological sites (Custódio *et al*., 2024); C: the geo-itinerary of the heritage routes comprising the water route, the stone route and the beach route (Vaz *et al*., 2024).

Next steps

The results obtained so far allow us to conclude that the territory related to the "Atlantic Geopark" project has geological heritage of international importance, as required by the GGN guidelines (UNESCO, 2022). The geological sites that have been identified so far make it possible to create geotourism routes that tell the story of the various episodes of the geological history of the WIM. But a successful application seeking recognition as a UNESCO Global Geopark requires go through other steps, namely the design and implementation of a comprehensive management plan, covering governance, development, communication, protection, infrastructure, finance, and partnership issues (UNESCO, 2024). This task falls to AD ELO, which has been developing a number of initiatives aimed at publicizing the project through promotional products like a detailed map of the area that connects the area's geological sites and other local resources. Communities' involvement on geoconservation of the "Atlantic Geopark" territory is a challenging goal, and this implies the implementation of a territorial-based program that brings residents closer to the geopark concept.

Acknowledgements
This study was supported by Portuguese funds by FCT - Fundação para a Ciência e a Tecnologia, I.P. (Portugal) in the frame of UIDB/00073/2020 (https://doi.org/10.54499/UIDB/00073/2020) and the UIDP/00073/2020 (https://doi.org/10.54499/UIDP/00073/2020) projects of the I & D unit Geosciences Center (CGeo). S.C.S. benefits from an FCT grant with reference 2024.03829.BD.

References

ADELO, 2021. Projeto Geoparque Atlântico-ADELO. https://www.youtube.com/watch?v=NFVJGIL4PX8&t=1s&ab_channel=ADELOADLBM

AD ELO, 2024. Heritage Routes. https://rotasdopatrimonio.adelo.pt/en/ (retrieved in 17.02.2024)

Carcavilla, L., López-Martínez, J. & Durán, J.J., 2007. Patrimonio geológico y geodiversidad: investigación, conservación, gestión y relación com los espacios naturales protegidos. Instituto Geológico y Minero de España, Serie Cuadernos del Museo Geominero 7, 1-360.

CNU (2024). Geoparques Mundiais da UNESCO. https://unescoportugal.mne.gov.pt/pt/redes-unesco/geoparques-mundiais-da-unesco (retrieved in 17.02.2024).

Custódio, S.C., Henriques, M.H., Rosado-González, E.M., Vaz, N.M. & Sá, A.A., 2024. Selected Geoheritage Resources of “Atlantic Geopark” Project (Central Portugal). Geosciences, 14(3), 81.

Henriques, M.H. & Brilha, J, (2017. UNESCO Global Geoparks: a strategy towards global understanding and sustainability, Episodes 40(4), 349-355.

Henriques, M. H., Pena Dos Reis, R., Brilha, J. & Mota, T.S., 2011. Geoconservation as an emerging geoscience, Geoheritage 3(2), 117-128.

IDRME, (1991). International Declaration of the Rights of the Memory of the Earth. https://www.visitgeoparks.org/geopark-history (retrieved in 17.02.2024).

Freire-Lista, D., Figueiredo, F. & Henriques, M.H., 2024. Ançã Limestone. The stone that carved Portugal, in: Ehling, A., Kaur, G., Jackson, P. N. W., Cassar, J., Lama, E. A. & Heldal, T. (Eds.), The First 55 IUGS Heritage Stones, IUGS Subcommission on Heritage Stones, 22-23. https://iugs-geoheritage.org/publications-dl/IUGS-FIRST-55-STONES-WEB-BOOK.pdf (retrieved in 17.02.2024).

UNESCO, 2022. Application dossier for UNESCO Global Geoparks. https://unesdoc.unesco.org/ark:/48223/pf0000383890 (retrieved in 17.02.2024).

UNESCO, 2024. UNESCO Global Geoparks. https://www.unesco.org/en/iggp/geoparks/about (retrieved in 17.02.2024).

Vaz, N., Rosado-González, E., Lourenço, J.M., Custódio, S., Henriques, M.H., Fidalgo, M., Santos, A. & Sá, A.A., 2024. Rotas do Património - Heritage Routes, Bairrada, Mondego e Atlântico. AD ELO – Associação de Desenvolvimento Local da Bairrada e Mondego.

Vaz, N., Rosado-González, E., Lourenco, J., Correia, P., Custódio, S., Henriques, M.H. & Sá, A.A., 2023. Projeto Geoparque Atlântico–um compêndio com mais de 600 milhões de anos de geodiversidade, in: Font, E., Dinis, P.A., Lopes, F.C. (Eds.), Livro de Roteiros das Excursões do XI Congresso Nacional de Geologia “Geociências e Desafios Globais”, Universidade de Coimbra Coimbra, 114–131.

17th INTERNATIONAL CONGRESS of the Geological Society of Greece

BULLETIN OF THE GEOLOGICAL SOCIETY OF GREECE, SP. PUBL.

EXTENDED ABSTRACT 056

The transitional deposits from carbonates to clastic in the Pindos foreland basin: an example from the Mazia village, Ioannina region, Greece

Dalgkitsi P.[1], Uchman A.[2], Botziolis Ch.[1], Zelilidis P.[3], Bourli N.[1], Zelilidis A.[1]

1 University of Patras, Department of Geology, Laboratory of Sedimentology, 26504, Patras, Greece. giotad19@gmail.com

2 Faculty of Geography and Geology, Institute of Geological Sciences, Jagiellonian University, Gronostajowa 3a, 30-387 Kraków, Poland.

3 University of Patras, Department of Geology, Laboratory of Paleontology and Stratigraphy 26504, Patras, Greece

In the NW part of the Ionian Basin (Ioannina region, Western Greece), Triassic evaporites and Jurassic to upper Eocene carbonates (interbedded with minor cherts and shales) are overlain by Eocene to Miocene siliciclastics. These deposits reflect the depositional environments that prevailed during the pre-orogenic, extensional stage and the following syn-orogenic, contractional stage, respectively. During the Middle Eocene, a transition from extension to compression and growing of the Pindos Orogen took place. This caused a change of sedimentation from slope carbonate to siliciclastic submarine fan deposits. Clastic deposits accumulated in a pre-foreland basin at the margin of the Apulian microcontinent from the Late Eocene to the early Miocene because of the uplift of Pindos Orogen and the activity of Pindos Thrust. This change is relatively rapid, so the total thickness of the transitional beds is up to 12.67 m in the Mazia village. In the lower 5 m, there are only thinly bedded mudstones, whereas in the upper 7.5 m within the thinly bedded mudstones there are sandstones and marly limestones. The mudstone is thin- to medium-bedded (0.01–0.02 m) and is either structureless or parallel-laminated. The sandstone beds display sharp bases and include sedimentary structures, such as parallel and ripple cross-laminations. Individual carbonate beds may be either structureless, parallel, or ripple-cross laminated calcarenites. Some of them show an upward transition from structureless (base of the beds), through parallel-lamination to ripple-cross-lamination (top of the bed). This facies association is interpreted as deep-water abyssal plain deposits, according to the dominant lithology and sedimentary structures. Within the marly limestone beds, the trace fossils *Chondrites intricatus, C. targionii, Planolites isp., Nereites isp.,* and *Avetoichnus* are recognized. In the underlying deposits, *Zoophycos* is present. The overlying clastic deposits in the area contain diverse trace fossils typical of the *Nereites* ichnofacies. The sedimentological and ichnological features point to the transition from the *Zoophycos* to the *Nereites* ichnofacies and slope to abyssal plain deposition.

Key words: slope facies, carbonates, Eocene, Greece.

17th INTERNATIONAL CONGRESS of the Geological Society of Greece

BULLETIN OF THE GEOLOGICAL SOCIETY OF GREECE, SP. PUBL.

EXTENDED ABSTRACT 057

Statistics on seismic moment tensors for the Aegean Sea and surrounding area: preliminary results

Dasoula M. G.[1*], Roumelioti Z.[1], Sokos E.[1], Kokkalas, S.[1]
*(1) Department of Geology, University of Patras, Patras, Greece, *up1074036@ac.upatras.gr*

Abstract

Moment tensors (MTs) are an essential tool for understanding earthquake source processes, improving seismic hazard assessment at various scales, and mitigating earthquake disaster risk. The Aegean Sea and its environs have the highest seismic activity in Europe and the Eastern Mediterranean, providing a wealth of earthquake data that can be used for moment tensor computations. In this work, we summarize moment tensor solutions published by the Global Centroid Moment Tensor Group (GCMT) and compare a subset of them with corresponding moment tensors from the Institute of Geodynamics of the National Observatory of Athens (NOA). We statistically examine the two datasets, primarily from the point of view of the style of faulting implied by the moment tensors in the study area and the associated Mw reporting. We also analyze the metrics of this comparison with respect to various factors, such as the location and magnitude of the associated earthquakes, their hypocentral depth, etc. Overall, we find a good agreement between the moment tensors of GCMT and NOA for 85% of the cases studied. Poor comparisons are mostly restricted to moderate magnitude events along the Hellenic Arc.

Moment tensors of the Global Centroid Moment Tensor Group

There are many institutions and universities around the world that study seismic data and publish MTs. The reliability of each is an issue that often concerns researchers. When conducting seismic research on a particular area, the GCMT project MTs are often used as a reference, as they are the most widely accepted by the seismological community.

For more than 40 years, the GCMT project has provided MTs for strong to moderate earthquakes around the globe using methods that involve inversion of long-period seismic waveforms based on normal mode summation and a 1D Earth model with path corrections (Dziewonski et al., 1981). In 2004, GCMT methods and processing underwent significant changes towards the incorporation of intermediate-period surface waves (Ekström et al., 2014). This led to improvements in shallow earthquake source parameters and a significant reduction in the smallest earthquake size for which GCMT publishes solutions.

In this first part of our work, we review all published GCMT solutions for the wider Aegean region (the exact study area is shown in Figure 1a), with statistics focusing on the implied style of faulting and moment magnitude, Mw, reporting. In total, we review 746 solutions, whose epicenters are shown in Figure 1a. The distribution of solutions unsurprisingly follows the distribution of seismicity in the area, with most MTs corresponding to earthquakes along the Hellenic arc, in the transition area of the Ionian islands, the Gulf of Corinth, and a zone subparallel to the western coast of Turkey. The well-known North Aegean trough zone collects a fair number of solutions, but is not as pronounced as in the seismicity maps. Figure 1b shows the distribution of solutions with Mw or Mw_GCMT to distinguish from another subset in the following. Nearly 80% of the dataset consists of solutions for earthquakes with Mw<5.5. Figure 1c shows how the Mw in GCMT MTs is distributed over time and clearly reflects the methodological change of GCMT in 2004, which resulted in a sudden appearance of much smaller earthquakes in the catalog.

The MTs were classified according to the implied fault style following the projection technique of Kaverina et al. (1996) and the classification scheme of Álvarez-Gómez (2014, 2019) implemented in the FMC software. The scheme is based on the plunges of the three eigenvectors of the moment tensors (P, B, T axes) and their relations and includes seven types of faulting: normal (N), normal with strike-slip component (N-SS), strike-slip with normal component (SS-N), strike-slip (SS), strike-slip with reverse component (SS-R), reverse with strike-slip component (R-SS) and reverse (R). The projection of the classification diagram is shown in the inset of Figure 2a. Figure 2a shows the projections of all 746 MTs, with the dimensions of the circle symbols analogous to the size of the earthquakes and their color reflecting the hypocentral depth. About 43% of the MTs are classified as N or N-SS, 23% as R or R-SS, and 34% as SS, SS-N, or SS-R. Overall, almost half of the GCMT MTs for the study area are normal or have some normal faulting component. However, Figure 2b, which shows the cumulative seismic moment release per faulting class, clearly indicates that reverse faulting is the predominant type. This is also reflected in the concentration of larger earthquakes (larger circles in the lower right part of the plot in Figure 2a). Considering that more than 82% of the total seismic moment released by the 746 earthquakes in our dataset comes from the 55 Mw_GCMT ³ 6.0 events, i.e., above the magnitude of completeness of the GCMT catalog for the Aegean area, at least since 1985 (González,

2024), the statistics in Figure 2b can be considered representative of the total seismic activity in the Aegean region for the examined time period.

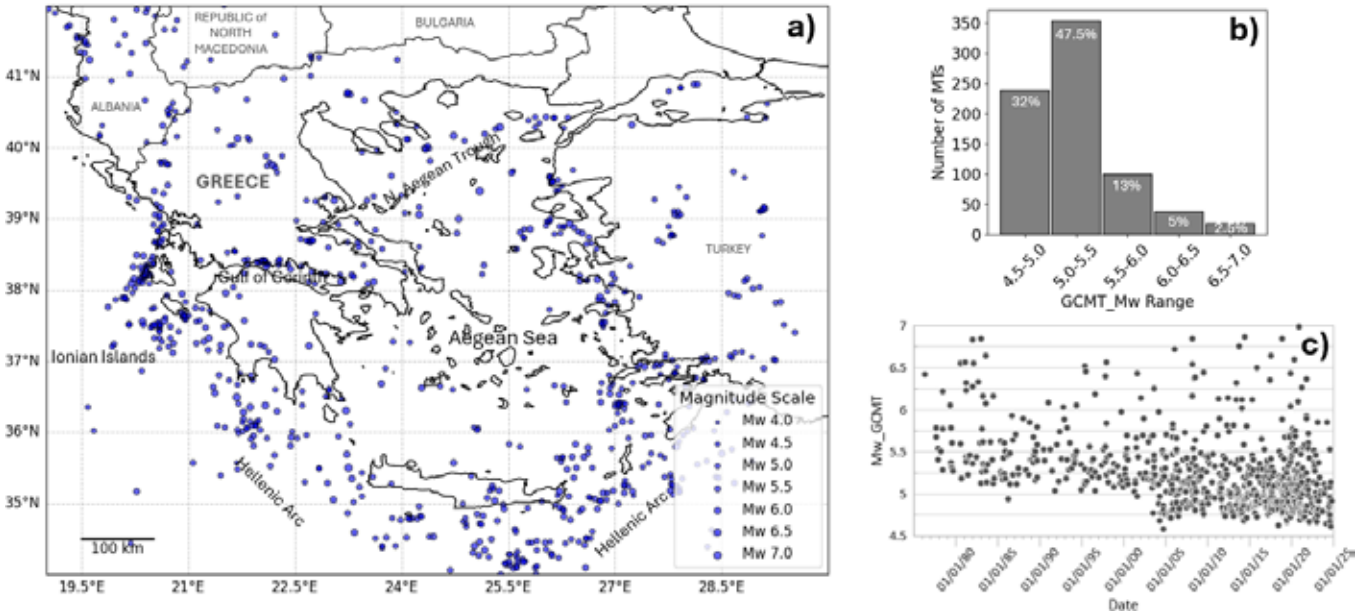

Figure 1. a) Map of the study region showing the epicenters of earthquakes with reported moment tensors in the GCMT catalog and the distributions of b) solutions in M_w bins and c) M_w with time.

Another interesting observation in Figure 2a is the concentration of most intermediate depth earthquake MTs near the center and more generally in the mixed faulting parts of the diagram. This may reflect the increased complexity of the stress field and source processes at greater depths within the subducting system of the Aegean region, the uncertainty of data processing in such depths that result in mixed mode fault-type, the complexity of data from fault branching with decollement surfaces or any combination of these.

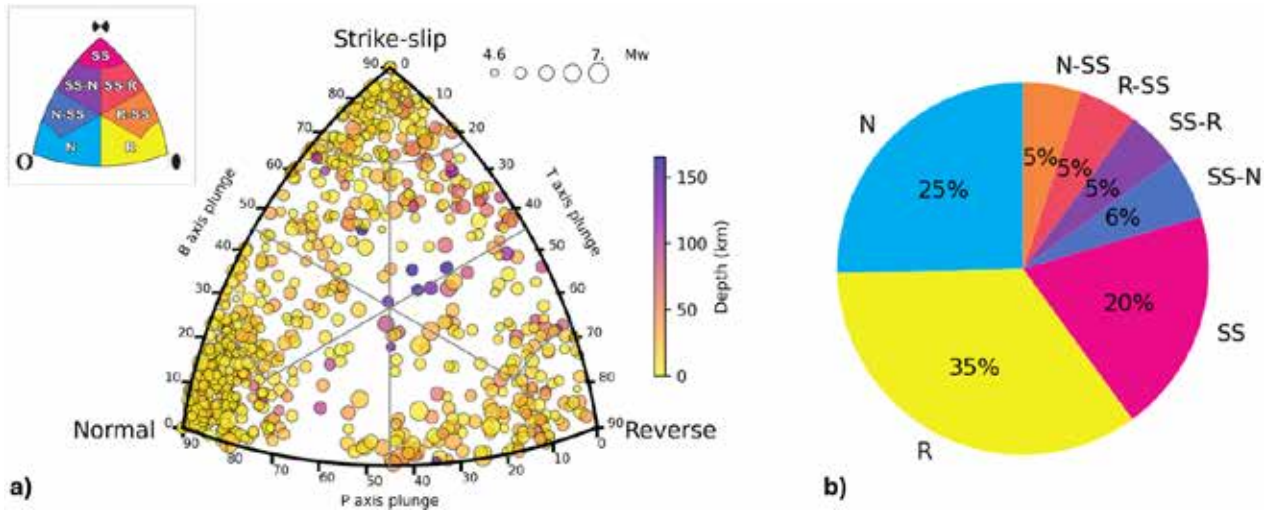

Figure 2. a) Faulting type classification diagram with seven types: N (normal), N-SS (normal with strike-slip component), SS-N (strike-slip with normal component), SS (strike-slip), SS-R (strike-slip with reverse component), R-SS (reverse with strike-slip component), R (reverse). Circle symbols are colored according to the hypocentral depth, and their dimensions are analogous to the magnitude of the earthquakes. The inset (after Álvarez-Gómez, 2014, 2019) shows the sectors of the diagram and corresponding classes b) pie chart with moment release by each class as a percentage of the total moment release from all earthquakes in the examined dataset.

Comparison of GCMT and National Observatory of Athens moment tensors: Faulting Style

The Institute of Geodynamics of the National Observatory of Athens (NOA) provides moment tensors for strong, moderate and even relatively weak earthquakes (down to ~Mw=3.5) as part of its routine services. The MTs published so far by NOA, either automatically derived or manually processed, are based on full waveform inversion of regional broadband waveforms and can be divided into two parts. The first part includes the solutions for the period 2001-2011, when NOA used the method of Hermann and Ammon (2002) (e.g., Konstantinou et al., 2010; Konstantinou, 2015). The second part includes the MTs since 2012, derived by the method of Sokos and Zahradnik (2008), more recently extended by Zahradnik and Sokos (2018) and implemented in the software packages ISOLA and GISOLA (Triantafyllis et al., 2021). This is currently the method routinely used at NOA, and relevant results from its implementation are available on the institute's website (https://bbnet.gein.noa.gr/HL/seismicity/mts).

In order to quantify how well these regional MTs compare to those of the GCMT, we collected the seismic events that occurred in the Aegean and the wider area from 2001 to 2023, for which solutions are available from both sources (i.e., GCMT and NOA). We identified 450 events and as a result we created a database of 450 pairs of MTs. The locations of these events are shown on the map in Figure 3a.

We first examined the pairs of MTs for their similarity in implied fault geometry. To quantify similarity, we adopted an angular measure of the relative orientations of the two MTs in each pair, specifically the smallest angle required to rotate the principal axes of one MT into the principal axes of its paired MT. This angle has been studied extensively by Kagan (e.g., 1991, 2007) and is therefore often referred to as the "Kagan angle". A detailed description of the Kagan angle can be found in the aforementioned publications by Kagan himself and, for example, in Tape and Tape (2012) and references therein.

To define the Kagan angles for our dataset, we used the homonymous MATLAB function (Kolar, 2025). The results are incorporated into the map in Figure 3a by coloring the epicenters based on three classes of Kagan angles: 0˚ - 30˚, indicating that the two focal mechanisms are very similar, 30˚ - 50˚ for acceptable resemblance that allows the focal mechanisms to be identified as similar, and >50˚, where the two focal mechanisms in a pair are very different. Figure 3b shows examples of MT pairs from our dataset for different levels of Kagan angle. The distribution of computed Kagan angles in Figure 3a suggests that there is good agreement between GCMT and NOA solutions, i.e. most epicenters (85%) are colored blue (63%) or yellow (22%), implying Kagan angles <50˚. Red colored epicenters represent only 15% of the cases examined and are almost exclusively located in the outer parts of the study area, where earthquake epicenters are poorly covered in azimuth by the Hellenic Unified Seismological Network, the backbone data source for NOA MT inversions. The largest concentrations of high Kagan angles occur along the southeastern part of the Hellenic Arc and the Ionian Islands.

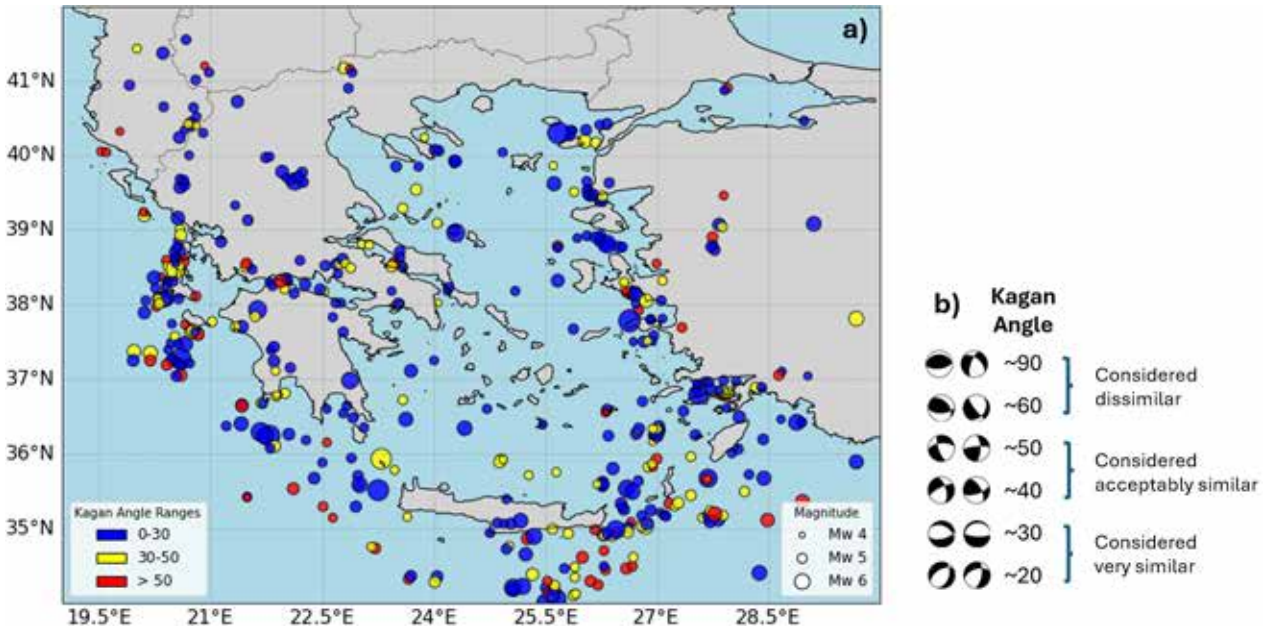

Figure 3. a) Map of the study region with epicenters of earthquakes for which both the GCMT and NOA have published MTs. Circle symbols are colored by Kagan angle ranges. b) Example pairs of MTs from the studied dataset for various levels of the Kagan angle.

Kagan angles were also examined as a function of earthquake magnitude (Mw), hypocenter depth, and time, as shown in Figure 4. Figure 4a shows the distribution of angles with the Mw_GCMT, where it is noticeable that high magnitude events (>6) have low Kagan angles. All angles >50˚ appear at lower magnitudes and especially at Mw<5.5. Combining this observation with the distribution in Figure 3a leads to the expected result that MTs of events with Mw<5.5 in the periphery of our study area are not always accurately resolved.
Figure 4b shows how the Kagan angles vary with the hypocentral depth of the events in our dataset. Most of the high Kagan angle values are concentrated at shallow depths, following the distribution of seismicity. However, several high angles appear to be distributed throughout the sampled depth interval, and the paucity of data at great depths does not allow us to draw any firm conclusions about a possible relationship between changes in the similarity of MT pairs and depth.
Finally, Figure 4c shows the Kagan angles with respect to the date of the events/MTs and gives the impression that the number of events associated with high angles has remained relatively stable over the years (2001-2023), despite the significant methodological changes by both GCMT and NOA. Moreover, since 2012, NOA has adopted GISOLA and has also allowed the release of automatic MT solutions, which has increased the number of events with MT pairs. The high Kagan angles have not followed this increase, indicating that the MT solutions provided by GCMT and NOA have become more similar in recent years.

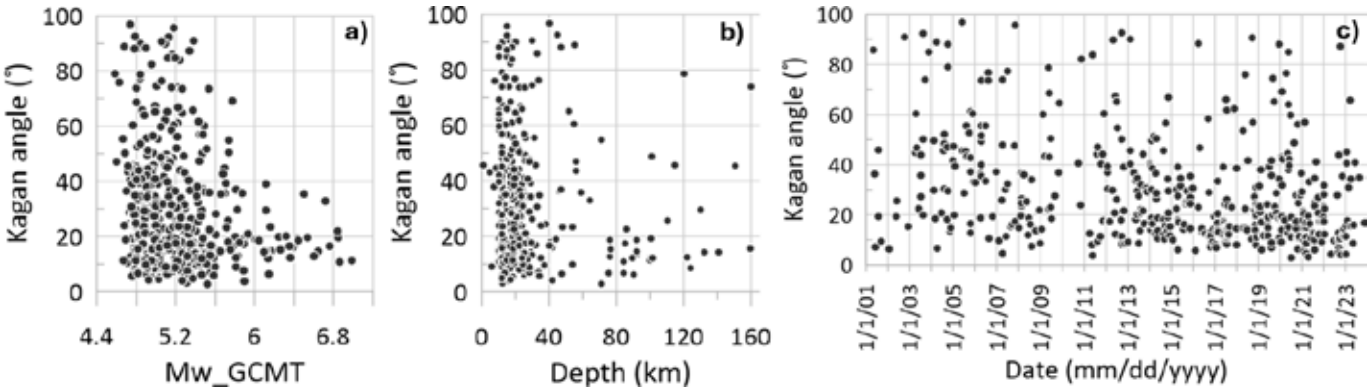

Figure 4. Distribution of computed Kagan angles with respect to a) Mw_GCMT, b) the hypocentral depth of the earthquakes in the examined dataset and c) the date of occurrence of the earthquakes considered to coincide with the date of MT solutions release.

Comparison of GCMT and National Observatory of Athens moment tensors: Mw

The moment tensor is derived by modeling the full waveform and amplitude of the seismic waves, providing the most accurate measure of earthquake energy to date. The radiated seismic energy, in turn, is directly related to the seismic moment and, through it, to the Mw. Thus, the routine computation of MTs has provided a rich dataset of Mw values that should be consistent around the globe. However, it has been shown that different Mw catalogs can show systematic discrepancies. This is, for example, the case of Mw reported by GCMT and Mw reported by NOA based on their respective MT solutions as highlighted by Konstantinou (2015). Konstantinou (2015) collected MTs from GCMT and NOA concerning the same earthquakes and the period May 2001 to October 2014, formed a dataset of 185 paired MTs and examined the differences in their respective Mw values. He concluded that NOA Mw values are smaller than GCMT Mw values by 0.15-0.25 magnitude units and attributed this rather systematic difference to the limited bandwidth in NOA inversions methods with respect to GCMT.
In this final part of our work, we use our paired GCMT-NOA MTs to perform a similar comparison to that performed by Konstantinou (2014). It should be noted that in addition to the differences that may arise from the different methods, data, and metadata of the two MT solution sources, there are also minor differences that may result from the post-processing of the moment tensor metrics. These arise, for example, from the use of a slightly different relation to calculate Mw from the seismic moment, M_0 (Kanamori, 1977; Hanks and Kanamori, 1979), the form of these relations (i.e., to be used with M_0 in N×m or in dyn×cm and rounding tactics of the relations constants), and from different rounding tactics of the reported Mw. To constrain the latter, we have recalculated the Mw of both GCMT and NOA directly from the reported values of M_0 using Kanamori's (1979) relation. The comparison of the derived sets of Mw values is shown in Figure 5a and the result of the standard regression is expressed by the blue thick line described by:

$$Mw_NOA=1.032(\pm0.014)Mw_GCMT-0.367(\pm0.074) \quad (1)$$

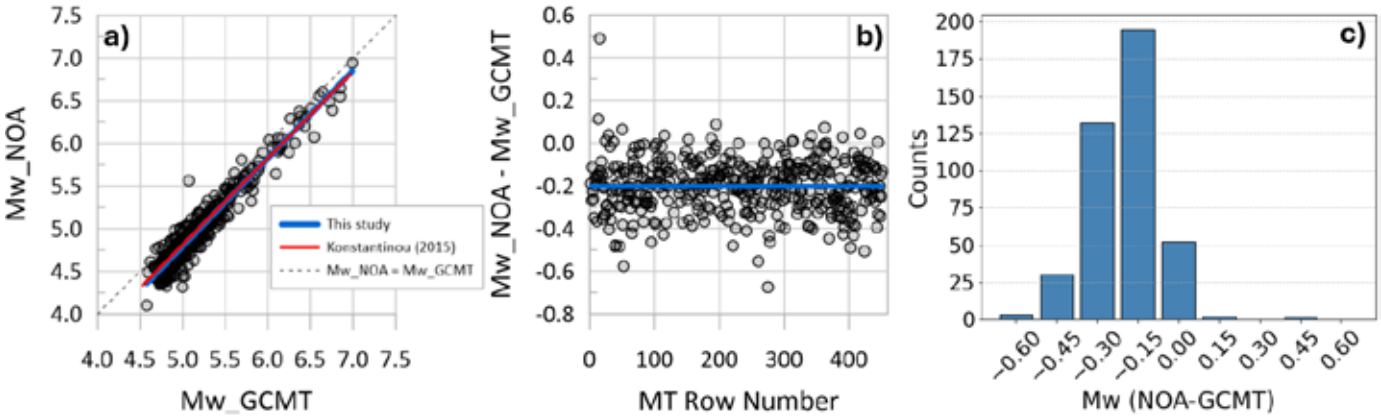

Figure 5. a) Moment magnitude of NOA (Mw_NOA) versus moment magnitude of GCMT (Mw_GCMT) from the corresponding moment tensors. The thick blue line indicates the standard regression result of this study, the red line the orthogonal regression results of Konstantinou (2015) and the dashed gray line the 1:1 relation. b) Differences of the two examined Mw sets with the blue line marking the average difference of 0.2 magnitude units. c) Distribution of Mw differences in 0.15 difference bins.

Equation (1) shows a coefficient of determination R^2=0.93, which is slightly improved (by 0.01) compared to that of the relationship of Konstantinou (2015), despite the fact that our dataset is more than twice as large. Our result is also compared graphically with that of Konstantinou (2015) in Figure 5a, where it is evident that the two lines are practically identical in the upper half and differ only slightly towards lower magnitudes. In fact, our result seems to deviate more from the 1:1 line (gray dashed line) as the magnitude decreases.
Figures 5b,c show the distribution of the differences between the two magnitudes in our dataset, and the blue line shows the practically constant mean of -0.20. Almost all differences are below zero, confirming that Mw_NOA is systematically lower than Mw_GCMT.

Conclusions/Discussion

We present preliminary results of an extensive statistical investigation and comparison of moment tensors (MTs) of earthquakes in the Aegean Sea and surrounding area, using data from the Global Centroid Moment Tensor (GCMT) project and the Institute of Geodynamics of the National Observatory of Athens (NOA). We investigate the MTs with respect to the implied faulting type during strong to moderate magnitude earthquakes in the area, the moment magnitudes (Mw), and the consistency between the two datasets.
Statistical analysis of the GCMT's 40-year archive of 746 MTs for the area showed that approximately 80% of this dataset consists of solutions for earthquakes with Mw<5.5. It also showed that although normal faulting is more frequent, reverse faulting accounts for the largest share of seismic moment release in the form of larger earthquakes. This is consistent with the mechanics involved, which are not facilitated by gravity as in normal faulting, with compressional forces often "locking" large areas and preventing movement for extended periods. This allows for the long build-up of stress that is eventually released in larger magnitude earthquakes.
We also examined the comparison of 450 pairs of MTs from GCMT and NOA for earthquakes from 2001 to 2023. To quantify the similarity/difference in the proposed fault geometry, we used the Kagan angle and concluded that the two compared sets of MTs show good agreement in 85% of the cases studied. Poor comparison of MTs provided by GCMT and NOA for the same events was found for only 15% of the pairs studied and was mostly associated with moderate magnitude events (Mw<5.5) along the Hellenic arc. Over time, despite methodological changes in both GCMT and NOA, the number of events with high Kagan angles has remained stable and the similarity between MT solutions may have increased over time, as suggested by the larger number of good comparisons in recent years.
A comparison of Mw values from GCMT and NOA MTs confirmed previous studies (e.g., Konstantinou, 2015) that NOA Mw values are systematically lower than GCMT Mw values by an average of 0.20 magnitude units. Regression analysis of Mw values showed that this difference is consistent across the magnitude range, with a slightly larger deviation from the 1:1 Mw_NOA - MwGCMT relationship as magnitude decreases.

Acknowledgements

We acknowledge the Global Centroid Moment Tensor project and the National Observatory of Athens for the invaluable moment tensor data provided for decades. The study was carried out in the framework of the research project "UNMASK", supported by the

Hellenic Foundation for Research and Innovation (H.F.R.I.) under the “2nd Call for H.F.R.I. Research Projects to support Faculty Members & Researchers” (Project Number: 2724).

References

Álvarez-Gómez, J. A., 2019. FMC—Earthquake focal mechanisms data management, cluster and classification. SoftwareX, 9, 299-307.

Álvarez-Gómez, J. A., 2014. FMC: a one-liner Python program to manage, classify and plot focal mechanisms. Geophysical Research Abstracts, Vol. 16, EGU2014-10887

Dziewonski, A. M., T.-A. Chou, J. H. Woodhouse, 1981. Determination of earthquake source parameters from waveform data for studies of global and regional seismicity. J. Geophys. Res., 86, 2825-2852, doi:10.1029/JB086iB04p02825

Ekström, G., M. Nettles, A.M. Dziewonski, 2012. The global CMT project 2004-2010: Centroid-moment tensors for 13,017 earthquakes, Phys. Earth Planet. Inter., 200-201, 1-9, doi:10.1016/j.pepi.2012.04.002

González, Á., 2024. Improvements and heterogeneities of the Global Centroid Moment Tensor catalog. Seism. Res. Lett. 95(6), 3566-3578.

Hanks, T.C., H. Kanamori, 1979. A moment magnitude scale, J. Geophys. Res. 84(B5), 2348-2350.

Herrmann, R.B., C.J. Ammon, 2002. Computer programs in seismology source inversions: User’s manual, version 3.30, report, St. Louis University, St. Louis, Missouri.

Kagan, Y. Y., 1991. 3-D rotation of double-coupleearthquake sources, Geophys. J. Int., 106(3), 709-716.

Kagan, Y.Y., 2007. Simplified algorithms for calculating double-couple rotation. Geophys. J. Int. 171, 411–418.

Kanamori, H., 1977. The energy release in great earthquakes. J. Geophys. Res. 82(20), 2981-2987.

Kaverina, A.N., A.V. Lander, A.G. Prozorov, 1996. Global creepex distribution and its relation to earthquake-source geometry and tectonic origin. Geophysical Journal International 125, 249–265.

Kolar, P., 2025. Kagan angle (https://www.mathworks.com/matlabcentral/fileexchange/70040-kagan-angle), MATLAB Central File Exchange. Retrieved January 24, 2025.

Konstantinou, K.I., 2015. Moment Magnitude Estimates for Earthquakes in the Greek Region: A Comprehensive Comparison. Bulletin of the Seismological Society of America 105(5), 2555–2562, doi: https://doi.org/10.1785/0120150088

Konstantinou, K.I., N.S. Melis, K. Boukouras, 2010. Routine Regional Moment Tensor Inversion for Earthquakes in the Greek Region: The National Observatory of Athens (NOA) Database (2001–2006). Seismological Research Letters 81(5), 750–760, doi: https://doi.org/10.1785/gssrl.81.5.750

Sokos, E. N., J. Zahradník, 2008. ISOLA a Fortran code and a Matlab GUI to perform multiple-point source inversion of seismic data. Computers and Geosciences, 34, 967-977.

Tape, W., C. Tape, 2012. Angle between principal axis triples. Geophys. J. Int., 191, 813-831.

Triantafyllis, N., I.E. Venetis, I. Fountoulakis, E.-V. Pikoulis, E. Sokos, Ch.P. Evangelidis, 2021. Gisola: A High-Performance Computing Application for Real-Time Moment Tensor Inversion. Seismological Research Letters, 93(2A), 957–966, doi: https://doi.org/10.1785/0220210153

Zahradník, J., E. Sokos, 2018. ISOLA code for multiple-point source modeling, in: S. D’Amico (ed.), Moment Tensor Solutions, Springer Natural Hazards, https://doi.org/10.1007/978-3-319-77359-9_1

17th INTERNATIONAL CONGRESS of the Geological Society of Greece

BULLETIN OF THE GEOLOGICAL SOCIETY OF GREECE, SP. PUBL.

EXTENDED ABSTRACT 058

Environmental Seismic Intensity Scale (ESI 2007)

Deligianni Stamatia
(1) University of Aegean, Mytilene, Greece, stamatia.deligianni@gmail.com

Introduction / Background

The Environmental Seismic Intensity Scale (ESI 2007), introduced by the International Union for Quaternary Research (INQUA), is an innovative tool for quantitatively assessing macroseismic intensities. The scale comprises 12 levels, based exclusively on the environmental impacts of earthquakes, such as surface ruptures, tectonic uplifts, landslides, liquefaction, and hydrological changes. Unlike traditional macroseismic intensity scales, which focus on damage to anthropogenic structures, ESI 2007 relies on physical observations, eliminating uncertainties associated with socioeconomic and cultural factors (Michetti et al., 2007).

The ESI 2007 scale offers several advantages over traditional macroseismic intensity scales. First, it relies on natural data, providing an independent assessment of earthquake intensity while reducing the influence of anthropogenic factors (Serva, 1994). Second, it enables the comparison of earthquakes from different time periods, geographical locations, and tectonic settings (Porfido et al., 2007). Third, the scale captures local variations in intensity, making it particularly useful in microzonation studies (Ota et al., 2010). Additionally, it is suitable for assessing seismic intensity in areas without anthropogenic infrastructure or population coverage (Tatevossian, 2007). Finally, the integration of paleoseismological data enhances the understanding of seismic hazards and contributes to the development of long-term risk management strategies (Serva et al., 2016).

Despite its advantages, the ESI 2007 scale has certain limitations. Its application requires specialized knowledge of geological phenomena and access to high-quality data. Moreover, it does not replace traditional macroseismic intensity scales but functions complementarily, enhancing the environmental perspective (Papathanasiou et al., 2011).

The ESI 2007 is a crucial tool for site selection in seismic hazard studies. Through the analysis of environmental parameters and the mapping of geological features, the scale identifies areas of increased seismic vulnerability. These include regions with a high probability of liquefaction, active faults, and geomorphological changes. Furthermore, the use of historical and paleoseismological data strengthens predictive capabilities and the effectiveness of risk management strategies. In remote or sparsely populated areas, ESI 2007 provides critical data that cannot be derived from traditional approaches.

In conclusion, ESI 2007 is an exceptional tool for the quantitative and objective assessment of seismic intensity. It expands our understanding of the environmental impacts of earthquakes and enhances the management of natural hazards on a global scale.

Methodology

This study employs a systematic approach involving data collection, the creation of a GIS database, and the generation of maps to analyze earthquakes in western Turkey. The analyzed events include the Gediz, Simav-Kütahya, Samos-Izmir, Marmaris, and Izmit earthquakes. Data were collected from geological observations, historical records, and seismological databases. These data were integrated into a GIS system, enabling the visualization of tectonic structures and affected areas.

The map generation process involved processing geospatial data to highlight active faults, liquefaction zones, and high seismic risk areas. The analysis utilized high-resolution data, enhancing the accuracy of the mapping.

Results

The study focused on the investigation of the environmental, geomorphological, and socioeconomic impacts of five major seismic events that affected the Eastern Mediterranean and Western Turkey. The regions analyzed were Marmaris (1957), Gediz (1970), Izmit (1999), Simav-Kütahya (2011), and Samos-Izmir (2020). The collected and analyzed data provide a comprehensive view of the severity of geodynamic phenomena and their effects on both the natural and anthropogenic environment, contributing to the understanding of the mechanisms governing these phenomena.

In Marmaris, the 1957 earthquake, with an ESI intensity of 8, caused extensive surface ruptures with vertical and horizontal ground displacements of up to 2 meters. Secondary phenomena
such as liquefaction, landslides, and local tsunamis caused severe damage to agricultural lands, infrastructure, and buildings.

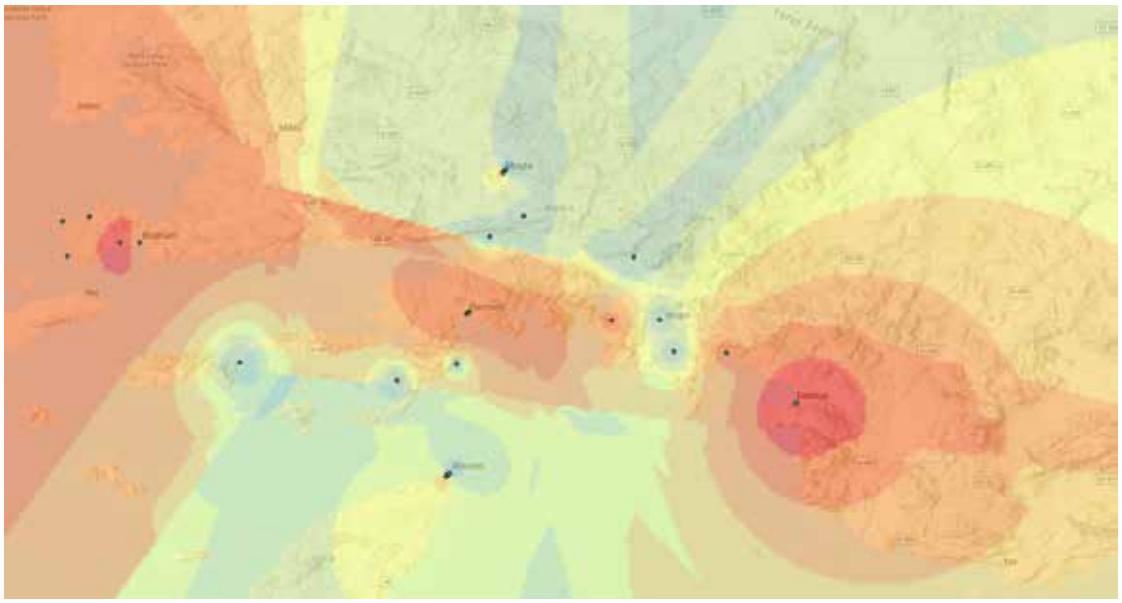

Figure 1. Map of Seismic Intensity Curves for the 1957 Marmaris Earthquake.

The Gediz earthquake of 1970, with an ESI intensity of 7, resulted in intense geomorphological phenomena such as subsidence and landslides. The impacts were catastrophic for the local economy and population, leading to building collapses and disruptions to critical infrastructure, necessitating extensive restoration efforts.

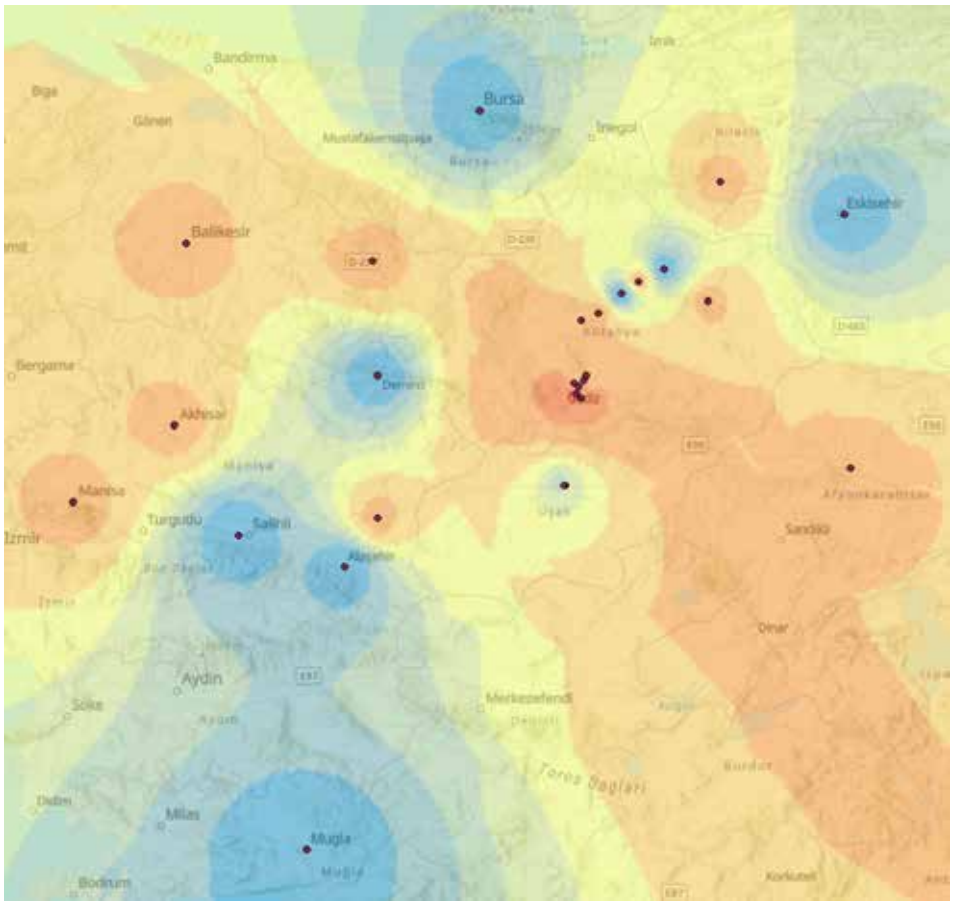

Figure 2. Map of Seismic Intensity Curves for the 1970 Gediz Earthquake

The 1999 Izmit earthquake, with an ESI intensity of 8, was one of the most destructive events, with extensive ruptures exceeding 150 kilometers in length and ground displacements surpassing 5 meters. The geomorphological and anthropogenic impacts were dramatic, as industrial zones and residential areas were destroyed, resulting in numerous fatalities and injuries.

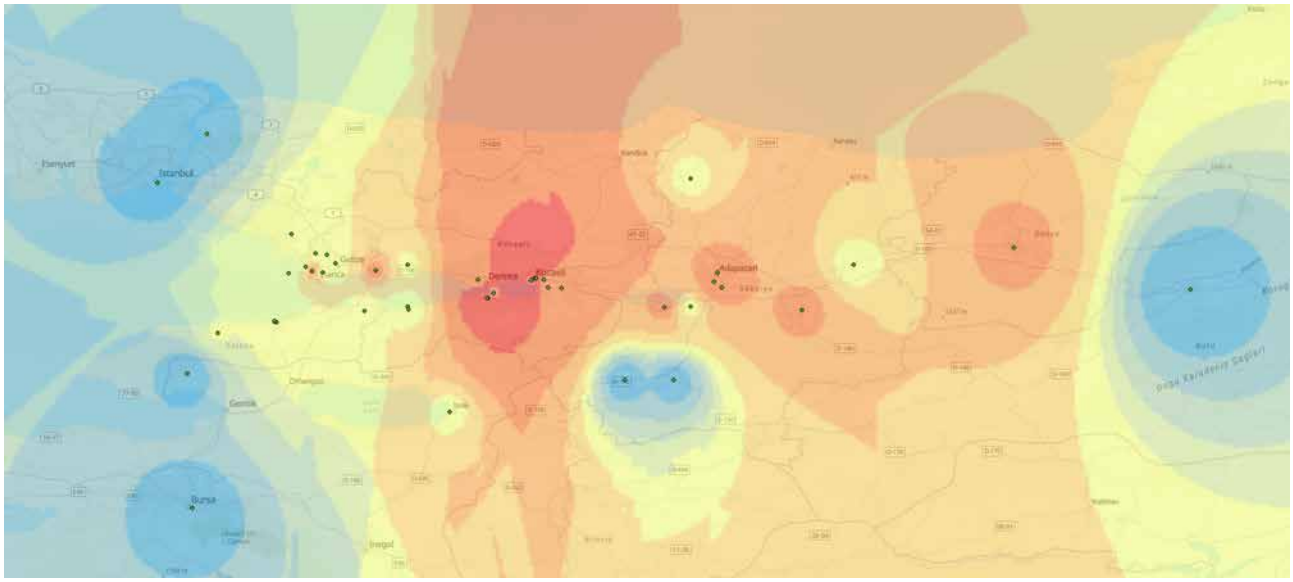

Figure 3. Map of Seismic Intensity Curves for the 1999 Izmit Earthquake.

The 2011 Simav-Kütahya earthquake, with a lower intensity (ESI 6), caused significant geomorphological changes, including widespread subsidence and new landslides. These alterations affected local ecosystems, infrastructure, and the daily lives of residents, requiring substantial restoration efforts.

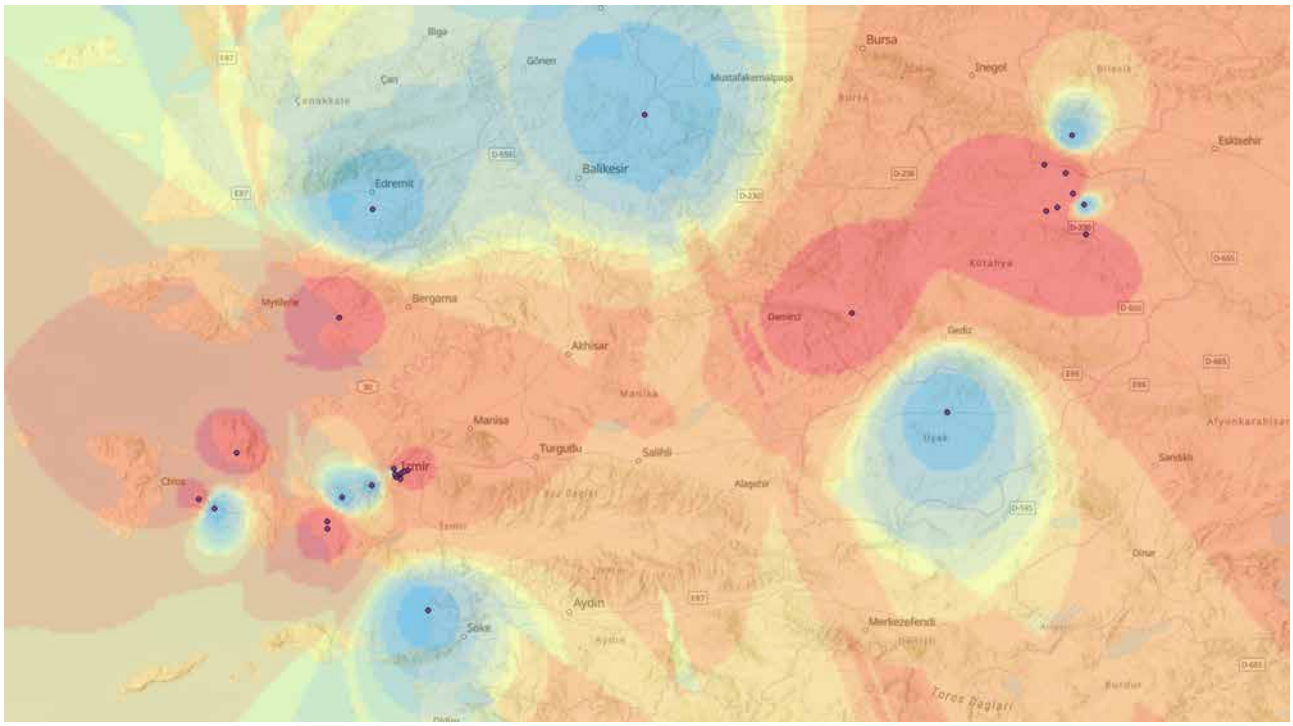

Figure 4. Map of Seismic Intensity Curves for the 2011 Simav - Kutahya Earthquake.

Finally, the 2020 Samos-Izmir earthquake, with an ESI intensity of 8, caused a combination of geodynamic phenomena. Extensive ruptures with displacements of up to 5 meters, as well as secondary impacts such as

liquefaction, landslides, and tsunamis, had devastating consequences for coastal zones and urban centers, with severe socioeconomic impacts.

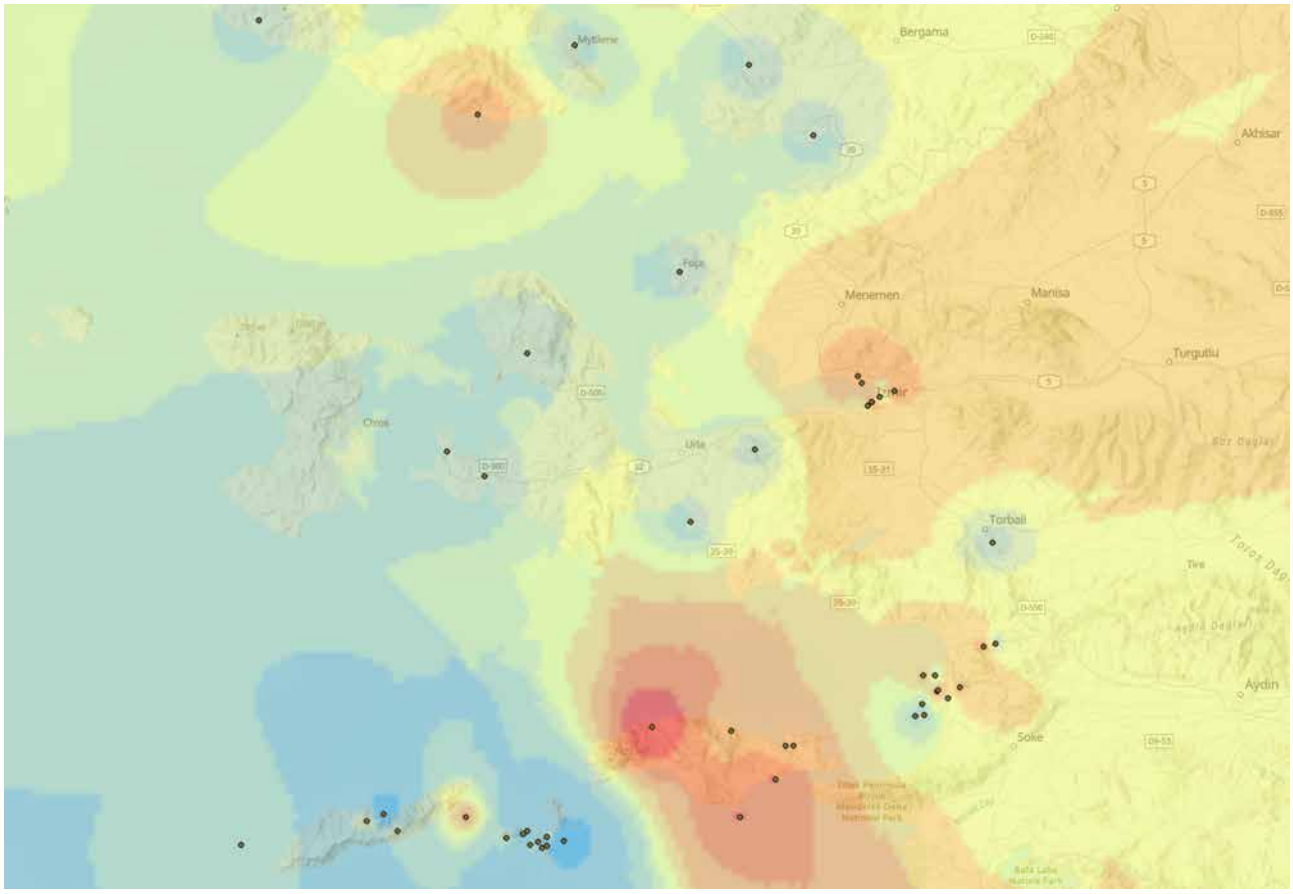

Figure 5. Map of Seismic Intensity Curves for the 2020 Samos - Izmir Earthquake.

Comparison with the Mercalli Scale

This study emphasizes the comparison of earthquakes in five significant regions of the Eastern Mediterranean using the Mercalli and ESI 2007 scales to assess their impacts. The earthquakes of Gediz (1970), Izmit (1999), Simav-Kütahya (2011), Marmaris (1957), and Samos-Izmir (2020) are evaluated based on their primary and secondary consequences on the anthropogenic and natural environments. The Mercalli scale focuses on damage to infrastructure, human casualties, and perceived impacts by human populations, while the ESI 2007 scale records geological and environmental changes, such as ruptures, ground liquefaction, landslides, and morphological alterations.

Specifically, the Izmit and Samos-Izmir earthquakes exhibited intense ruptures and extensive geomorphological changes, demonstrating the utility of the ESI 2007 scale for understanding impacts at a natural level. On the other hand, the Gediz and Simav-Kütahya earthquakes showed more pronounced social impacts, such as residential destruction, effectively captured by the Mercalli scale. The Marmaris earthquake, with its significant effects on both the anthropogenic and natural environment, underscores the need for a combined use of both scales for a more comprehensive understanding of impacts.

The comparison of these scales reveals that their integration provides valuable complementary data for better understanding and managing seismic risks and their impacts. The findings highlight the importance of a multidimensional approach to seismic analysis for improved preparedness and recovery.

Discussion

To visualize the above results, contour maps were created in GIS, capturing the deformation of the Earth's surface. The geometry of the contour lines was examined to determine whether the ellipsoidal shape formed by the contours aligns with the orientation and geometry of the fault responsible for each earthquake. The findings revealed that, in most cases, the shape of the contour lines matches the location and mechanism of the main fault, highlighting the

dynamics of the geodynamic phenomena.
For instance, in the case of the Gediz earthquake (1970), the contour maps depicted deformation aligned with the fault in the area, with the intensity of deformation being stronger near the fault and gradually diminishing with distance. In the case of the Samos-Izmir earthquake (2020), the contour maps captured the deformation caused by the offshore fault between Samos and Izmir in great detail. The ellipsoidal shape of the contours was consistent with the orientation of the fault, highlighting zones of intense deformation concentrated in the coastal areas and urban centers of the region. The contour lines revealed higher deformation values close to the fault, gradually decreasing towards the interior of Izmir and Samos. Moreover, significant secondary impacts such as landslides and liquefaction were recorded in areas of greater deformation. This analysis provided a clear depiction of the dynamics of the seismic event and its geomorphological impacts.
While the comparison between the Mercalli and ESI 2007 scales, presented in the Results section, highlights their complementary nature in evaluating seismic impacts, the Discussion focuses on the limitations and broader implications of these tools. The Mercalli scale, despite its widespread use in capturing human-centric impacts, is limited in its ability to detail geomorphological and environmental changes. Conversely, the ESI 2007 scale excels in documenting geological alterations but may face challenges in highly urbanized regions or in areas where secondary phenomena like tsunamis obscure field evidence.
One critical finding of this study is the role of ESI 2007 in enhancing the spatial and environmental understanding of seismic phenomena. By focusing on physical deformation, such as ruptures and landform changes, ESI 2007 provides insights that are often overlooked by traditional scales like Mercalli. However, its reliance on field observations introduces practical limitations in remote or inaccessible terrains. To address these challenges, future research could incorporate remote sensing technologies, such as LiDAR, InSAR, and satellite imagery, to supplement and expand ESI 2007 analyses.
The integration of both scales offers a multidimensional approach to seismic risk assessment. While the Mercalli scale effectively captures social and structural impacts, ESI 2007 adds a layer of detail about environmental consequences. This dual perspective is particularly valuable for regions like Samos and Izmir, where both anthropogenic and natural environments were significantly affected by the 2020 earthquake.
Furthermore, previous studies, such as Michetti et al. (2007), emphasize the utility of ESI 2007 in regions with significant environmental changes. Our findings build on this by demonstrating how integrating ESI 2007 with Mercalli can provide a more comprehensive framework for seismic preparedness and recovery strategies. This approach could be further refined by applying machine learning algorithms to analyze patterns of seismic impact across multiple datasets, enhancing predictive models for future events.
In conclusion, this study underscores the necessity of a multidimensional framework for analyzing seismic phenomena. The integration of the Mercalli and ESI 2007 scales not only broadens the understanding of seismic impacts but also contributes to more effective disaster risk reduction strategies, emphasizing the value of combining geological, environmental, and social perspectives.

Acknowledgments

I would like to express my heartfelt gratitude to Professors Alexandros Chatzipetros, Spyridon Pavlidis, and Georgios Drakatos for their invaluable guidance and unwavering support during the completion of this dissertation. Their expertise and insightful scientific observations significantly contributed to the shaping of this study and the enhancement of my scientific approach.
Their contribution was pivotal, and I extend my sincere appreciation for their continuous support throughout my academic journey.

References

Ambraseys, N.N., 1988. Engineering seismology. Earthquake Engineering & Structural Dynamics 17, 1-30.]
Caputo, R., Pavlides, S., Chatzipetros, A., 2000. Earthquake surface faulting: Earthquake fault mechanics and implications for seismic hazard assessment. Annals of Geophysics 43, 831-847.
Chatzipetros, A., Pavlides, S., 2003. Active faults in the Aegean region. Tectonophysics 367, 123-136.
Chatzipetros, A., Pavlides, S., 2005. Geological and paleoseismological investigations of active faults in northern Greece. Geological Society of Greece Bulletin 37, 230-245.
Jackson, J., McKenzie, D., 1988. The relationship between plate motions and seismic moment tensors, and the rates of active deformation in the Mediterranean and Middle East. Geophysical Journal International 93, 45-73.
Jenkins, D.G., 1988. Recent developments in seismic hazard assessment in Greece. Tectonophysics 159, 323-339.
McKenzie, D., 1972. Active tectonics of the Mediterranean region. Geophysical Journal International 30, 109-185.
Papazachos, B., Papazachou, C., 2003. The earthquakes of Greece. Ziti Editions.

Papazachos, C., Papazachou, K., Pavlides, S., 1997. Seismicity and neotectonics of the Hellenic arc. Geophysical Journal International 131, 687-699.

Papanikolaou, D., Vassilakis, E., 2008. The neotectonic structure of the Aegean volcanic arc. Journal of the Geological Society 165, 501-512.

Pavlides, S., 1993. Paleoseismicity in the Eastern Mediterranean region. Annals of Geophysics 36, 221-228. [Journal Article]

Pavlides, S.B., Caputo, R., 2004. Magnitude versus faults' surface parameters: quantitative relationships for earthquake geodynamics. Bulletin of the Seismological Society of America 94, 2082-2099.

Scholz, C.H., 2002. The mechanics of earthquakes and faulting. Cambridge University Press.

Stiros, S.C., Pirazzoli, P.A., 1995. Paleoseismicity in the Aegean region. Tectonophysics 249, 195-209.

Taymaz, T., Yolsal-Çevikbilen, S., Ulutaş, E., 2007. Earthquake mechanisms in the Eastern Mediterranean. Bulletin of the Seismological Society of America 97, 273-290.

17th INTERNATIONAL CONGRESS of the Geological Society of Greece

BULLETIN OF THE GEOLOGICAL SOCIETY OF GREECE, SP. PUBL.

EXTENDED ABSTRACT 059

The Triassic post-collisional high-K alkali-calcic granites in the Vertiskos Unit, Serbo-Macedonian Massif: insights from Miriofito granite, Kerkini complex, Greece

Dimitri K.[1], Stouraiti C.[1], Amanatidou D.[1], Soukis K.[1]
(1) Faculty of Geology and Geoenvironment, National and Kapodistrian University of Athens, Athens, Greece;
sge1900022@uoa.gr

Introduction

This paper presents new geochemical and mineral chemistry data of the Early Triassic granitic rocks of Miriofito intrusion, which comprises part of the Kerkini Granite Complex (KGC), in northern Greece (Poli *et al*., 2009). We revisit the issue of petrogenesis of Miriofito granite (MIR) which, according to available literature data, illustrates, together with the main Kerkini intrusion, variable behaviour combining A- and I-type characteristics (Christofides *et al*., 1999; 2007; Poli *et al*., 2009; Himmerkus *et al*., 2009). The main objective of the study is to examine the geochemical characteristics of MIR, as well as to contribute to the existing knowledge regarding the granite's tectonic setting.

Regional Geology

The Serbo-Macedonian massif (SMM) is a NW–SE-trending crystalline complex consisting of amphibolite- to granulite-facies gneisses and schists, and together with the Rhodope massif to the east, constitutes the crystalline core of the internal Hellenides. The SMM comprises two major basement units, the Vertiskos and Kerdilion (Kockel *et al*., 1978; Kilias *et al*., 1999; Himmerkus *et al*., 2007). The Vertiskos unit occupies the central part of the SMM and is mainly composed of felsic augen and mica gneisses which attained amphibolite-facies conditions. U-P zircon dating on the crystalline rocks of this unit revealed three major magmatic episodes: i) 458.8 ± 11 M and 460 Ma (Himmerkus *et al*., 2007; Papapavlou, 2021), ii) 300 ± 1 Ma from the central part of the Arnea Pluton (Abbo *et al*., 2020), and iii) 243.6 ± 1.5 Ma for the Arnea A-type granitoid and 247 Ma for Kerkini granite complex (Poli *et al*., 2009).
The Kerkini granite complex (KGC) comprises a large intrusion, the Muries granite (MUR), and two smaller bodies, the Miriofito granite (MIR) and the Kastanousa granodiorite (KAS) (Christofides *et al*., 1999).

Methods

Seven (7) granite samples were collected from two areas, five (5) from Miriofito and two (2) from Kerkini (Fig. 1). The mineralogical composition of the samples was determined using optical microscopy, Scanning Electron Microscopy accompanied by Energy Dispersive System (SEM/EDS) and X-ray Diffraction analysis (XRD). Geochemical analyses included X-ray Fluorescence Spectroscopy (XRF) and Inductively Coupled Plasma Mass Spectrometry (ICP-MS).

Results and Discussion

The typical MIR rock type is a biotite-bearing (±muscovite) granite which ranges to (±muscovite) leucogranite (Fig.1). It consists of a high content of quartz, K-feldspar, albite and Fe-biotite (annite). The characteristic micrographic texture of quartz in K-feldspar, the perthitic K-feldspar and the occurrence of anorthoclase in the studied rocks indicate that this granite represents the last stage of crystallisation, at shallow intrusion depth and high PH2O (subsolvus granite). Mineral relationships show that biotite is a late magmatic phase after feldspar crystallisation. The mineral chemistry of biotite reveals that the primary ferroan magmatic biotite has been re-equilibrated by a hydrothermal fluid. Muscovite is entirely phengitic in composition and represents a secondary phase forming at the expense of the primary magmatic minerals. In the profoundly altered parts (veins, cracks) minerals such as grossular, fluorite, epidote, monazite, Fe-Ti oxides and sulfides occur.
Geochemically it is a high-K to ultrapotassic granite, variably peraluminous i.e. low- to high-peraluminousity as indicated by the ASI (= mol. Al_2O_3/CaO + Na_2O + K_2O) values i.e. 1 to 1.25. The trace element systematics indicate the dominant role of K-feldspar and minor plagioclase fractionation in the differentiation of Miriofito

intrusion. Advanced fractional crystallisation is supported by large depletions of Sr-Ba-Eu, P and Ti associated with feldspars, apatite/monazite and Fe-Ti-oxides (rutile, ilmenite) respectively.
In the discrimination diagrams for I-S- and A-type granites the Miriofito and Kerkini granite both straddle the field of A-type (Whalen et al. 1987). Our new geochemical data illustrates a strong enrichment of K, Cs, Rb, Th and U relative to the average continental crust, for the Miriofito granite and even more so for Kerkini granite. This enrichment is considered a source characteristic for the high-K calc-alkaline (HKCA), either juvenile crust or K- enriched lithospheric mantle. Further use of tectonic discrimination diagrams for granites (Pearce *et al*., 1984) delineates a trans-discriminant affinity for the MIR samples, between volcanic arc and within-plate environments, while other discrimination diagrams show explicitly a volcanic arc setting, or active continental margin settings. In general, rocks belonging to the high-K calc-alkaline magmatism occurs in a post-collisional setting, commonly after 30 to 50 Ma after the cessation of subduction (Bonin et al. 1990; Liégeois *et al*., 1998).

Figure 1. Field occurrence of Miriofito (left) and Kerkini (right) granites.

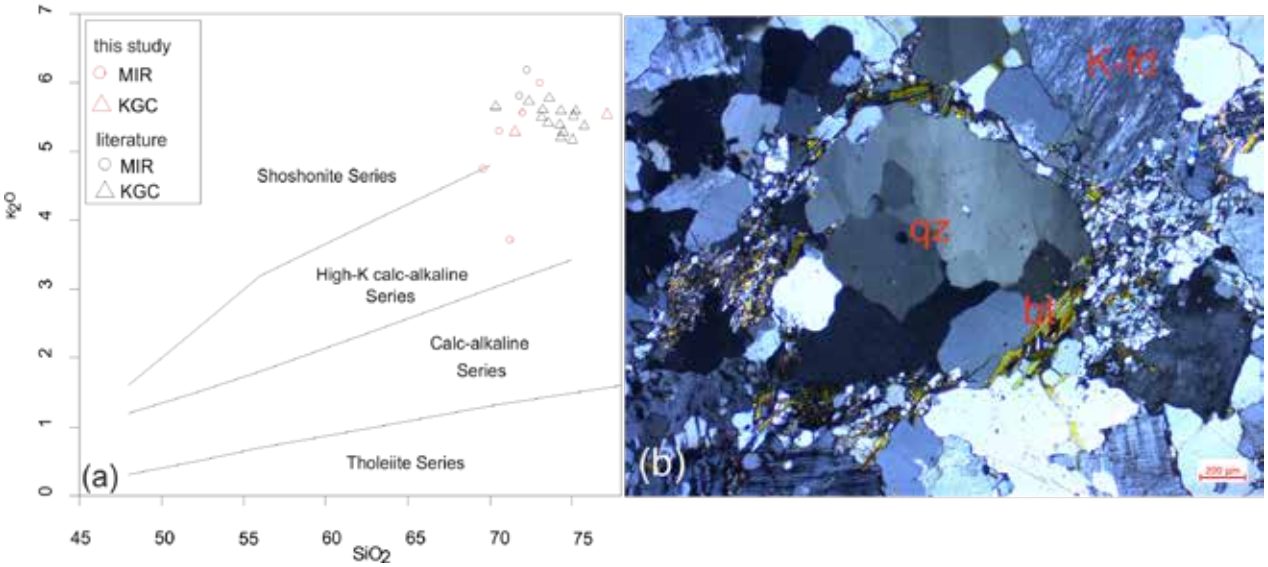

Figure 2(a) Miriofito and Kerkini samples (red symbols) plotted on the SiO_2 *vs.* K_2O classification diagram of Peccerillo and Taylor (1976). Literature data after Christofides *et al*. (1999). (b) Photomicrograph of Miriofito biotite granite (crossed pollars).

Conclusions

- Our new geochemical data agrees with published data for a common origin of Miriofito and Kerkini granite. The Miriofito granite has high SiO_2 (69.5–72.3 wt.%), K_2O (3.7–6.7 wt.%) and Na_2O (3–4 wt.%) and low MgO (0.02–0.4 wt.%) and is ferroan alkali-calcic in composition. It belongs to the high-K magma series and is a highly fractionated and peraluminous A-type granite.
- Petrographic evidence indicates that the granite rose to shallow crustal levels and underwent advanced fractional crystallisation of K-feldspar, minor plagioclase, apatite, and Ti-bearing phases (rutile, ilmenite, titanite).
- Tectonic discrimination diagrams indicate that the whole complex Kerkini-Miriofito-Kastanousa intrusion was likely formed in a post-collisional setting, linked to a transition in the geodynamic setting from an arc-related to a post-collisional extensional setting in the Vertiskos realm.
- The main point is that the generation of the HKCA magma needs the former existence of an important subduction phase to generate this type of source. The K-enrichment event is considered to reflect a subcontinental mantle enrichment /or K-rich mafic crust from the preceding subduction period.

Acknowledgements

The authors are grateful to the Hellenic Survey of Geology and Mineral Exploration (H.S.G.M.E.) for preparing the thin section and providing access to the Scanning Electron Microscope facility.

References

Abbo, A., Avigad, D., Gerdes, A., 2020. Crustal evolution of peri-Gondwana crust into present day Europe: the Serbo-Macedonian and Rhodope massifs as a case study. Lithos 356–357, 105295. http://doi.org/10.1016/j.lithos.2019.105295

Bonin, B., 1990. From orogenic to anorogenic settings: evolution of granitoid suites after a major orogenesis. Geological Journal 25, 261–270. http://doi.org/10.1002/gj.3350250309

Christofides G., Koroneos A., Pe-Piper G., Katirtzoglou K., Chatzikirkou A., 1999. Pre-Tertiary A-Type magmatism in the Serbomacedonian massif (N. Greece): Kerkini granitic complex. Bull. Geol. Soc. Greece, xxxiii, 131-148.

Christofides G., Koroneos A., Liati A., Kral J., 2007. The A-Type Kerkini granitic complex in North Greece: geochronology and geodynamic implications. Bull. Geol. Soc. Greece, xl, 700-711.

Himmerkus, F., Anders, B., Reischmann, T., Kostopoulos, D., 2007. Gondwana-derived terranes in the northern Hellenides. In 4-D Framework of Continental Crust (eds RD Hatcher, MP Carlson, JH McBride and JR Martinez Catalán), pp. 379–90. Geological Society of America, Memoirs no. 200.

Himmerkus, F., Reischmann, T., Kostopoulos, D., 2009. Serbo-Macedonian revisited: a Silurian basement terrane from northern Gondwana in the Internal Hellenides, Greece. Tectonophysics 473, 20–35. doi: 10.1016/j.tecto.2008.10.016.

Kilias, A., Falalakis, G., Mountrakis, D., 1999. Cretaceous–Tertiary structures and kinematics of the Serbomacedonian metamorphic rocks and their relation to the exhumation of the Hellenic hinterland (Macedonia, Greece). International Journal of Earth Sciences 88, 513–31. doi: 10.1007/ s005310050282.

Kockel, F., Mollat, H., Walther, H. W., 1977. *Erlauterungen zur geologicschen karte der Chalkidiki und angrenzender Gebiete 1/100.000 (Nord Griechenland)*. Hanover: Bundesanstalt für Geowissenschaften und Rohstoffe, 119 pp.

Liégeois, J-P., Navez, J., Hertogen, J., Black, R., 1998. Contrasting origin of post-collisional high-K calc-alkaline and shoshonitic versus alkaline and peralkaline granitoids. The use of sliding normalization. Lithos, 45, 1-28.

Papapavlou, K., 2021. Zircon U– Pb–Hf snapshots on the crustal evolution of the Serbo-Macedonian massif: new insights from Ammouliani island (Northern Greece). Geological Magazine 158: 2079–2086. https:// doi.org/10.1017/S0016756821000698.

Pearce, J.A., Harris, N.B.W., Tindle, A.G., 1984. Trace element discrimination diagrams for the tectonic interpretation of granitic rocks. J. Petrol. 25, 956–983.

Peccerillo, A., Taylor, S. R., 1976. Geochemistry of Eocene calc-alkaline volcanic rocks from the Kastamonu area, Northern Turkey. Mineralogy and Petrology, 58, 63–81.

Poli, G., Christofides, G., Koroneos, A., Soldatos, T., Perugini, D., Langone, A., 2009. An Early Triassic granitic magmatism—Arnea Kerkini granitic complexes—In the Vertiskos unit (Serbo-macedonian massif, north-

eastern Greece) and its significance in the geodynamic evolution of the area. *Acta Vulcanologica*, *21*, 47–70.
Whalen, J. B., Currie, K. L., Chappell, B. W., 1987. A-type granites: geochemical characteristics, discrimination and petrogenesis. Contributions to Mineralogy and Petrology, 95, 407-419.

17th INTERNATIONAL CONGRESS of the Geological Society of Greece

BULLETIN OF THE GEOLOGICAL SOCIETY OF GREECE, SP. PUBL.

EXTENDED ABSTRACT 060

Biogenicity of Arsenic Sulfide Biomorphous Structures in Deep-Sea Hydrothermal Vents, Kolumbo Arc Volcano: Morphological, Mineralogical and Geochemical Evidence

Dimou E.[1], Papoutsa A.[1], Pletsas V[1], Zegkinoglou N.[1], Kilias S.[1], Nomikou P.[1], Polymenakou P.[2]
(1) National and Kapodistrian University of Athens, Athens, Greece, evidim25@gmail.com
(2) Hellenic Centre for Marine Research, Heraklion Crete, Greece

Research Highlights

In this study we argue about the biogenicity of biomorphous structures related with As-mineralization from the Kolumbo diffuser chimneys based on their syngenicity and indigenousness, geological context, morphology and composition.

Introduction

Modern seafloor hydrothermal vents present a hostile environment for life which consists of high acidity, discharge of high-temperature magmatic gases and potentially toxic metal(loids) such as As, Sb, Pb, Tl. Arsenic is widely recognized as a major pollutant for marine ecosystems and a potentially toxic element harmful to most living organisms (Hu *et al*., 2020). It is established that hydrothermal vent fields are a vast microbial habitat, hosting a significant population of microorganisms (Runge *et al*., 2023, Kilias *et al*., 2013) Furthermore, this kind of environment is regarded as analogue for the emergence of primordial life while As-enriched oceans are considered a potential cradle for the origin of life (Russel *et al*., 2005, Hu *et al*., 2020). To endure direct exposure to such extreme environments, various microbial species have evolved resistance mechanisms involving detoxification, biotransformation and even generating energy by oxidizing arsenite. (Hu *et al*., 2020). It is well known that microorganisms in the hydrothermal vents can contribute significantly to the formation of mineral deposits rich in metal(loid)s (Southam and Saunders, 2005, Kilias *et al*., 2013). However, little is known about the microbial processes associated with the precipitation of arsenic sulfides. (Hu *et al*., 2020). Here we present morphological, mineralogical and geochemical evidence for the biogenicity of arsenic sulfides on the active hydrothermal diffusers at Kolumbo arc volcano.

Geological Background

The submarine volcano of Kolumbo located in the Anhydros Basin, Aegean Sea as part of the Christiana-Santorini-Kolumbo volcanic field that lies in the center of the Hellenic Volcanic Arc (HVA). Kolumbo crater has a basal diameter of 3 km with NE-SW orientation. (Hector *et al*., 2024). On top of the crater lies an active hydrothermal vent field with diffuser chimneys emitting shimmering water to ~265°C pure gaseous CO2 fluid forming, a polymetallic Au-rich Seafloor Massive Sulfides (SMS) deposit. The studied samples present four distinct mineralogical zones. The thick porous Inner Sulfide-Sulfate Core (ISSC) is composed of barite, pyrite, marcasite, sphalerite, galena, Pb-Sb sulfosalts, minor anglesite, and minor chalcopyrite. Surrounding the ISSC is the Outer Arsenic Layer (OAsL), which contains barite, pyrite, sphalerite, Pb-Sb sulfosalts, stibnite, As-Pb-Sb sulfosalts, and amorphous arsenic-rich sulfides resembling realgar and orpiment. Encasing the OAsL is a gelatinous orange to brown Surface of Fe-rich Microbial Crust (SFeMC), primarily composed of amorphous Fe-(hydrated)-oxyhydroxides. In this study we focus on the OAsL where the As-related biomorphous structures are observed on that layer (Kilias *et al*., 2013).

Materials and methods

Sampling

The samples studied were collected during two oceanographic expeditions collected from the northern part of the Kolumbo crater floor using the Remotely Operated Vehicles (ROV) Hercules and Max Rover.

Optical microscopy and Scanning electron microscopy

All samples were petrographically examined via transmitted and reflected light microscopy at the Department of Geology and Geoenvironment, National and Kapodistrian University of Athens (NKUA). The biomorphous structures were further observed under a Scanning Electron Microscope (SEM) in order to a) examine the morphologies and textural relationships under high magnification, b) obtain semi-quantitative X-ray elemental maps. For that purpose, a Nova NanoSEM Field Emission-SEM (FE-SEM) was utilized, equipped with, a BacksSattered Electron (BSE) detector, a Secondary Electron (SE) detector, and a Bruker X Flash EDS detector. Samples were carbon-coated with an average thickness of 15 nm, to achieve surface conductivity, and the instrument was operated at a 30-kV accelerating voltage, while electron beam stability was calibrated using a copper standard.

Raman spectroscopy

Raman spectroscopy analyses were performed using a Renishaw inVia Raman confocal microscope, equipped with two lasers, emitting at 532 (green) and 785 nm (red). The green and red lasers are coupled with gratings of 1800 and 1200 groves per mm^2, respectively. Spectra were obtained using the 785 nm laser with a power range between 0.5 and 0.05 mW, due to the varying stability and fluorescence of the analysis spots. Samples were exposed to the laser through a long-focal distance, 50X objective lens with 0.55 numerical aperture, and with the measured spectral range extended from 100 to 3200 cm^{-1}. The obtained spectra were then processed by the WiRE software for Windows. Background noise was reduced by the subtraction of a polynomial baseline, and cosmic ray removal corrections were performed for all spectra.

Results

Optical Microscopy

To provide a detailed description, the biomorphous structures are classified in three types based on morphology as well as differences in chemistry. Type 1 structures are identified as diatoms species. Type 2 are filamentous biomorphs. Type 3 are globular biomorphs. Diatom morphology is very evident in Fig. 1. After thorough observation and due to morphology and spectroscopic data (see below) we conclude that it belongs to Chaetoseros sp., one of the most diverse planktonic diatom species (De Luca *et al*., 2019). The main characteristic of the family is the existence of setae that appear to come out from the valve of the cells. Setae help diatoms create chains of cells that a expand for tens of micrometers. To prevent the chains from extending too far, terminal setae are produced from several cells. Each cell exhibits an outer layer known as frustule. It is crucial to mention that diatoms in this study demonstrate different levels of As-mineralization. Diatoms are mostly observed in open spaces and in close association with barite.

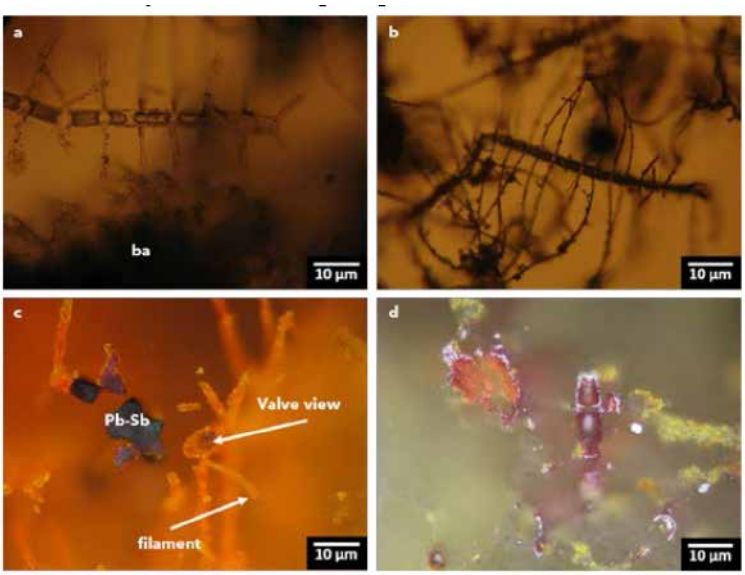

Figure 1. a) Two non-As-mineralized diatom chains with visible intercalary and terminal setae, also the frustule and aperure are very clear b) Partially mineralized diatom with longer setae c) Valve view of a diatom, partially mineralized frustule and setae, also a filamentous type 2 biomorph can be observed d) Fully mineralized diatom, only the cells remain

The type 2 biomorphous structures are filamentous and extend up to several tens of micrometers. Depending on their width, a stibnite core is visible which appears black or gray depending on parallel or crossed polaroids under reflected light, while arsenic is mostly in the form of orpiment. The filaments exhibit a plethora of different characteristics. (Fig. 2). Some of them appear more lineal and demonstrate terminal swelling while others exhibit twisting and branching or even septated structures (Qu *et al*., 2023). Sometimes those can co-exist. The thinner filaments tend to form net-like structures and exhibit pinching (Hu *et al*., 2020). Furthermore, in some cases filaments appear to grow on diatoms (Fig 2. c). It is important to note that even the thinner filaments exhibit a stibnite core, but it is not always visible due to scale. The filaments are usually found as intergrowths with stibnite and Pb-Sb sulphosalts on a barite substrate as they also develop in open space. Type 3 biomorphous orpiment like structures are quite different in morphology

(Fig. 3). They appear as globules either observed on diatoms (mostly on setae) or forming grape-like structures in open spaces. Their diameter is not bigger than 3 micrometers. They can be found in association with filaments as well. (Fig. 4). It is interesting that when a lineal substrate appears (like a diatom seta or a needle-like stibnite) these globular biomorphs can display a string of beads (Qu *et al*., 2023).

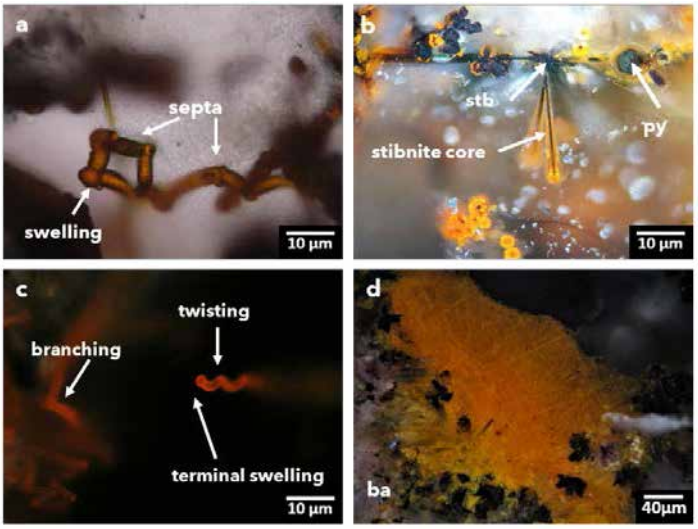

Figure 2. a) Thick filament with swelling and septated structures b) Linear filament with visible stibnite core c) Filaments that exhibit branching as well as twisting and terminal swelling on the same time d) Thinner filaments with net-like structures on a barite substrate.

Mineral Chemistry-SEM EDS

Further detailed geochemical analyses on biomorphous structures were performed by SEM-EDS to evaluate their chemical composition. The results showed the presence of As-sulfide in all the examined biomorphs. Regarding type 1 biomorphs, SEM-EDS confirmed the presence of silica which further proves they are diatoms. As it has been established, diatoms are known to form silica cell walls (Hildebrand, 2008). It is evident (Fig. 5) that silica is distributed on the frustule as well as on setae. When it comes to filamentous biomorphs, SEM-EDS confirms the stibnite core as well as the As-sulfide shell and absence of silica. As for the globular biomorphs, arsenic, antimony and sulfur seem to be equally dispersed.

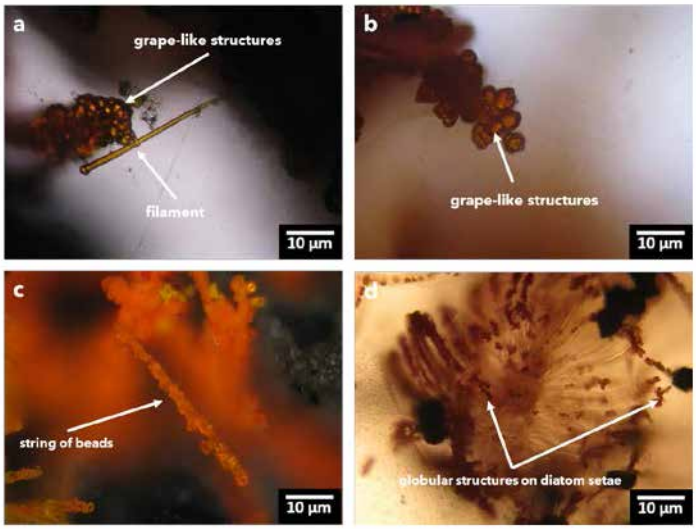

Figure 3. a) Globular structures in asociation with filaments b) Grape-like structures in open space c) Globular biomorphs forming a string of beads d) Globules on diatom setae

Spectral characterization of biomorphous structures

The contribution of Raman spectroscopy for this study was crucial. Point analyses revealed the presence of carbonaceous matter (CM) in all the biomorphs under investigation. Raman mapping was used to better understand the pattern of mineral phases on the studied biomorphs. Spectroscopic data showed the presence of amorphous hydrated silica and orpiment (As_2S_3) and realgar (As_4S_4) mineralization on biomorphous structures (Papoutsa *et al*., 2024). The occurrence of CM as a structural component was verified by the occurrence of first order (1000-1650cm^{-1}) and second-order (2500-3200 cm^{-1}) bands (Papoutsa *et al*., 2024). The notable features consist of a prominent G-band at 1583 cm^{-1}, distinct from the D2 band at approximately 1608 cm^{-1}, along with clearly defined D1 and D4 peaks at 1347 cm^{-1} and 1245 cm^{-1}, respectively. G/D2 band ratio was used to better interpret the distribution of CM. For the type 1 biomorphs, Raman peaks at ~490, 602, 812, 980 and 1000 cm^{-1} are indicative of Si-OH (hydrated silica) that compose the diatomaceous cell wall (Papoutsa *et al*.,2024). The hydrated silica seems to be concentrated mainly on the frustule. Regarding the filamentous biomoprhs, Raman spectroscopy confirmed the presence of stibnite core and orpiment-realgar shell. CM was also identified within the structure.

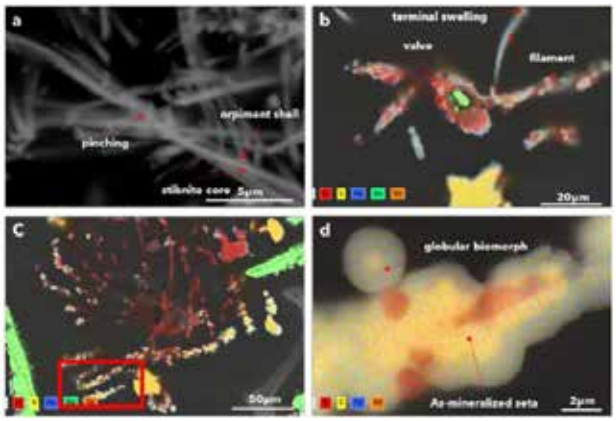

Figure 4:FE-SEM microphotographs and elemental maps of biomorphs. a) Open space filamentous cluster exhibiting pinching features. Note the differentiation in brightness, indicating the presence of a denser stibnite core. b) Microphotograph of As-filament and valve view of a diatom. Note the characteristic presence of Si on the diatom frustule and the absence of Si in the filament. c) Partially mineralized diatom. d) Zoomed area of C (red box) showing the replacement of Si by As and Sb sulfides. Globular biomorphs can be observed growing on the surface of mineralized diatoms. Also displaying a distinct Sb-rich core and an As-rich shell.

As for the globular structures, CM and orpiment were identified as well. However, it is important to note that their small diameter approaches the limit of spatial resolution of Raman mapping with the available objective lens. Regardless that, Raman maps of CM distribution in the type 3 structures, were successfully constructed.

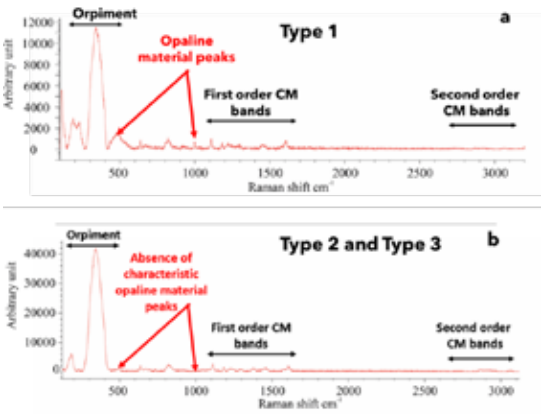

Figure 5. a) Point analysis of a diatom frustule with visible CM peaks, orpiment peaks and opaline material peaks b) Point analysis of filamentous and globular structures with CM and orpiment peaks, also absence of opaline material peaks as it is characteristic for diatoms.

Criteria for biogenicity

To examine the biogenic origin of the aforementioned biomorphs, 4 criteria were tested. (Ivarsson *et al*., 2015)

Geological context

Modern hydrothermal vent fields associated with Seafloor Massive Sulfides (SMS) deposition are widely regarded as significant microbial habitats (Hu *et al*., 2020). They sustain extraordinary biological communities, featuring rare and endemic species uniquely adapted to the conditions of hydrothermal vents (Georgieva *et al*., 2021). SMS being the closest modern analogue of ancient Volcanogenic Massive Sulfides (VMS) deposits, which are proven to be one the earliest known habitats for microbial life (Hu *et al*., 2020). Therefore, these types of environments are closely associated with the history of life and its origination (Hu *et al*., 2020, Georgieva *et al*., 2021). The fossil record of hydrothermal vents possibly represents the earliest direct evidence of life on Earth, highlighting their significance as biological habitats throughout Earth's history. Hydrothermal vent microbial communities consist of relatively high concentrations of a few species that rely on chemosynthesis for survival such as Proteobacteria and Campylobacterota (Georgieva *et al*., 2021).

Syngenicity and indigenousness

All the observed biomorphs, and especially the filaments and the globules, originate from the surface of the minerals present (As-Pyrite, Pb-Sb-sulfosalts, orpiment) at the chimneys and/or the surface of diatoms. The transition from the mineral surface to the filaments are smooth and undisturbed (Fig. 6) indicating that the filaments grow out of the surface of minerals. In cases, the open pore space has been colonized from a biofilm which filamentous net-like and globular grape-like structures grow (Fig. 3). The existence of the biomorphs on the outer layer of the chimneys and their close association with the primary sulfide minerals indicates that microbial activity was synchronous with the arsenic mineralization. These observations coupled with high counts of genes associated with arsenic oxidation (Papoutsa *et al*., 2024) suggest that the filamentous and globular biomorphs are indigenous of the chimneys and syngenetic with the As-sulfide deposition. Diatoms are not usually inhabiting hydrothermal vents, rather they accidentally sink from the upper levels of the water column onto the diffuser chimneys.

Morphology

The occurrence of filaments and globules as whole clusters resemble the culture media precipitates of As-respiring bacterial strain (Hu *et al*., 2020). The growth of clusters over diatoms, orpiment and other As-rich phases, achieved by penetrating and dissolving the mineral surface, mirrors microbial strategies for colonizing mineral surfaces to extract nutrients.

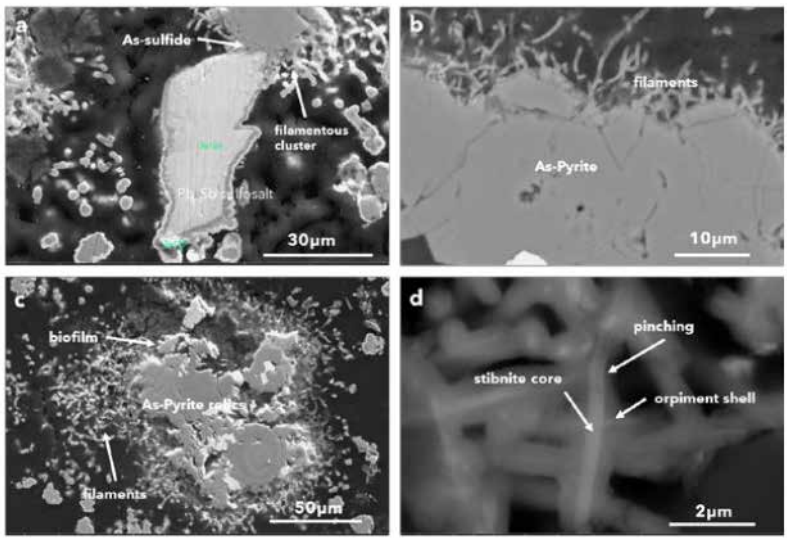

Figure 6. FEG-SEM photomicrographs of filamentous structures. a) Filaments growing on primary As-sulfides showcasing a smooth and undisturbed transition. b) Filaments growing on the surface of As-pyrite. c) Filaments colonization initiated by a biofilm formation around dissolved pyrite crystals. d) Microphotograph of thin filaments exhibiting pinching with a distinct stibnite (brighter color) core and an orpiment shell.

Composition

Despite the filamentous and globular biomorphs being embedded in epoxy resin, Raman spectroscopy revealed distinct CM within their structures. Comparisons with the spectra of the epoxy rule out contamination and confirm

that the carbonaceous matter is indigenous to the structures. Raman mapping (Fig. 7) revealed that CM is localized in specific areas such as the As-rich shell of the filaments rather than the stibnite core (Fig. 8). This suggests that indigenous CM is preserved in the late stages of the mineral paragenesis. The presence of CM in the shell of the structures agrees with other studies arguing about biogenic origin of As-sulfides (Hu *et al*., 2020) and it suggests that microbial activity was synchronous to As-sulfide deposition. Synchrotron X-ray absorption near edge structure analysis has shown that the As-

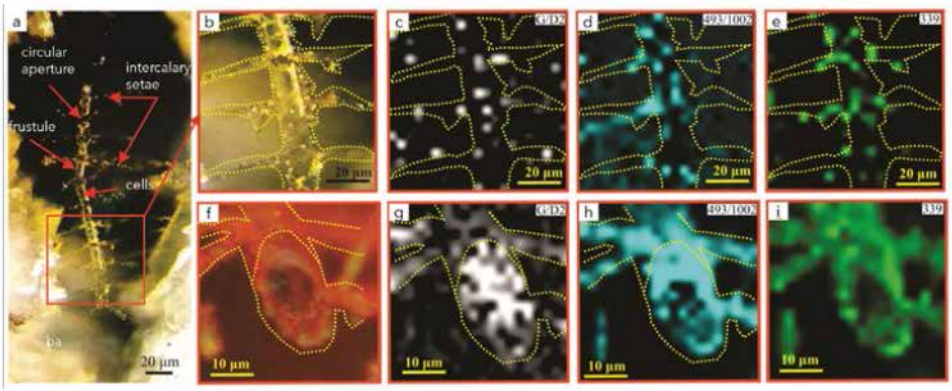

Figure 7. a) site of study b) zoomed area of Raman mapping c) distribution of CM on diatom frustule d) distribution of silica on diatom frustule e) As-Sulfide mineralization f) valve view of a diatom, another site of Raman mapping g) distribution of CM h) distribution of silica on diatom frustule i) As-Sulfide mineralization on diatom frustule and setae, it is also visible that the site in f) is more mineralized than diatom in a) (Papoutsa *et al*., 2024)

sulfides in the diffusers contain a mixture of As (II) and As (III). These heterogeneities in the valence of As can be credited to microbial activity. Metagenomic libraries constructed from the Kolumbo vents, which revealed high counts of functional genes involved in microbial oxidation of As (II) to As (III) (Papoutsa *et al*., 2024) further prove this point.

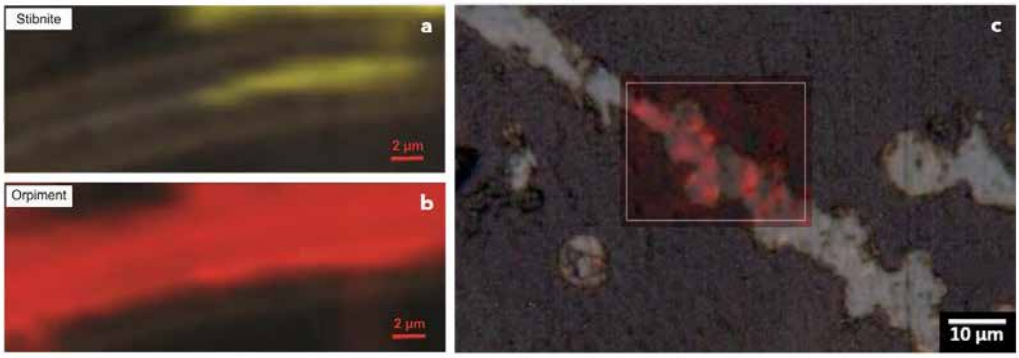

Figure 8. a) Raman map showing the distribution of stibnite in the visible core of a filament b) distribution of orpiment in the outer shell of filament (Papoutsa *et al*., 2024) c) distribution of CM on a string of beads.

Conclusions

In this study we report observations of different biomorphous structures associated with As-sulfides mineralization. Three types of biomorphs have been identified; Type 1) Diatoms, Type 2) Filaments and Type 3) Globules. The morphological features of the studied biomorphs, combined with their distinct spectroscopic characteristics and their geochemical composition along with the metagenomic data suggest that As mineralization was contemporaneous with microbial activity. The lack of diatom related gene counts in the metagenomic libraries shows that diatoms are not directly involved in the mineralization of As, rather they exist as the substrate for microorganisms to develop, providing CM and nutrient from the shallow waters to the deep sea. This theory is further supported by the fact that filamentous and globular structures seem to grow over the diatoms resembling microbial strategies for colonizing mineral surfaces.

Acknowledgments

We are thankful to NKUA for granting us access to Raman Spectroscopy at Core Facility of the School of Science. We are grateful to the Electron Microscopy Facility of the Materials Treatment Centre in VITO (Mol, Belgium) for the use of FE-SEM and the citizen

science Horizon funded project nexus-monARC for fully supporting the analyses that took place in VITO. Also, to Maria-Despoina Chrysafeni for her FE-SEM images.

References

De Luca, D., Sarno, D., Piredda, R., and Kooistra, W.H.C.F., 2019. A multigene phylogeny to infer the evolutionary history of Chaetocerotaceae (Bacillariophyta). Molecular Phylogenetics and Evolution 140, 106575.

Georgieva, M.N., Little C.T., Maslennikov, V.V., Glover, A.G., Ayupova, N.R., & Herrington, R.J. (2021). The history of life at hydrothermal vents. Earth-Science Reviews 217, 103602.

Hector, S., Patten, C.G.C., Beranoaguirre, A., Lanari, P., Kilias, S., Nomikou, P., Peillod, A., Eiche, E., and Kolb, J., 2024. Magmatic evolution of the Kolumbo submarine volcano and its implication to seafloor massive sulfide formation. Mineralium Deposita 59, 1229–1248.

Hildebrand, M., 2008. Diatoms, biomineralization processes, and genomics. Chemical Reviews 108, 4855–4874.

Hu, S.Y., Barnes, S.J., Pagès, A., Parr, J., Binns, R., Verrall, M., Quadir, Z., Rickard, W.D.A., Liu, W., Fougerouse, D., Grice, K., Schoneveld, L., Ryan, C., and Paterson, D., 2020. Life on the edge: Microbial biomineralization in an arsenic- and lead-rich deep-sea hydrothermal vent. Chemical Geology 533, 119438.

Ivarsson, M., Peckmann, J., Tehler, A., Broman, C., Bach, W., Behrens, K., Reitner, J., Böttcher, M.E., and Ivarsson, L.N., 2015. Zygomycetes in vesicular basanites from vesteris seamount, Greenland Basin - A new type of cryptoendolithic fungi. PLoS ONE 10, e0133368.

Kilias, S.P., Nomikou, P., Papanikolaou, D., Polymenakou, P.N., Godelitsas, A., Argyraki, A., Carey, S., Gamaletsos, P., Mertzimekis, T.J., Stathopoulou, E., Goettlicher, J., Steininger, R., Betzelou, K., Livanos, I., Christakis, C., Bell, K.C., Skoullos, M., 2013. New insights into hydrothermal vent processes in the unique shallow-submarine arc-volcano, Kolumbo (Santorini), Greece. Scientific Reports 3, 2421.

Papoutsa, A., Pletsas, V., Kilias, S., Dimou, E., Polymenakou, P., Nomikou, P., Papadimitriou, V., Maak, J., Ivarsson, M., Kyrpides, N.C., 2024. Raman spectroscopy evidence for arsenic-sulfide mineralized diatom-like structures in deep-sea hydrothermal vents at Kolumbo: contribution to arsenic biomineralization. 16th International GeoRAMAN Conference, Rhodes, Greece, p.49-50.

Qu, Y., Yin, Z., Kustatscher, E., Nützel, A., Peckmann, J., Vajda, V., and Ivarsson, M., 2023. Traces of Ancient Life in Oceanic Basalt Preserved as Iron-Mineralized Ultrastructures: Implications for Detecting Extraterrestrial Biosignatures. Astrobiology 23, 769–785.

Runge, E.A., Mansor, M., Kappler, A., and Duda, J.P., 2023. Microbial biosignatures in ancient deep-sea hydrothermal sulfides. Geobiology 21, 355–377.

Russell, M.J., Hall, A.J., Boyce A.J., Fallick A.E., 2005. On hydrothermal convection systems and the emergence of life. 100th anniversary special paper, Economic Geology 100, 259–270.

Southam, G., and Saunders, J.A., 2005. The Geomicrobiology of Ore Deposits. Economic Geology 100, 1067–1084.

17th INTERNATIONAL CONGRESS of the Geological Society of Greece

BULLETIN OF THE GEOLOGICAL SOCIETY OF GREECE, SP. PUBL.

EXTENDED ABSTRACT 061

Microfacies and species richness analyses of middle-late Eocene western Thrace Basin (Neotethys Ocean, Greece): Paleoenvironmental evolution and species-richness hotspot revealed

Dimou V.-G.[1], Koukousioura O.[1,2], Less G.[3], Triantaphyllou M.[4], Dimiza M.[4], Syrides G.[1], Langer M.R.[5]

(1) Aristotle University of Thessaloniki, Thessaloniki, Greece, dimouvaso@geo.auth.gr (2) University of Cologne, Cologne, Germany (3) University of Miskolc, Miskolc-Egyetemváros, Hungary (4) National and Kapodistrian University of Athens, Athens, Greece (5) Rheinische Friedrich-Wilhelms-Universität Bonn, Bonn, Germany

The Thrace region is a large Paleogene-Neogene molassic basin in the northern Aegean (Greece, NW Turkey, Bulgaria). Basin architecture is linked to middle-late Eocene NE-SW extension events, that led to the formation of a supra-detachment basin divided into three sub-basins (Alexandroupolis, Orestias and Petrota) that are characterized by a complex stratigraphy (Kopp, 1965; Papanikolaou and Triantaphyllou, 2010; Kilias *et al.*, 2013). The paleoenvironmental evolution and reconstruction of the Thrace basin (Neotethys Ocean, Greece), were carried out with the help of sedimentological, thin section and microfacies analyses (based on e.g., Flügel, 1982) and, above all, the analysis of larger benthic foraminifera (LBF) as proxies for the middle to upper Eocene carbonate deposits and their species richness.

The studied material derived from a total of 7 new sites (sub-basins of Alexandroupolis and Orestias), covering localities on the mainland [Maronia (MAR-1.2), Palagia (S1-3.2), Avantas (AVT1-15.1), Pylaea (PYL1-10) and Didymoticho (DDM1-5)] and the northeastern Aegean islands of Samothraki (SAM1-2.1) and Lemnos (LM1-2.1) (Fig. 1). In addition, results from the Kirki and Fanari sites were included in the present study (Dimou *et al.*, 2021, 2023).

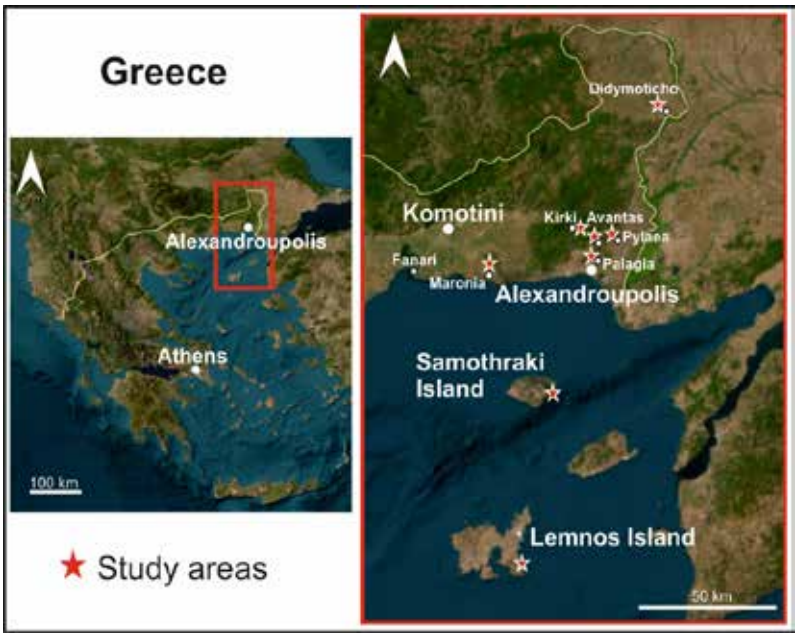

Figure 1. Overview map of Greece with the location of sampled sites marked by red stars (modified from Google Earth, Dimou *et al.*, 2024).

In total, nearly 100 species have been identified. The observed foraminiferal taxa are characterized mainly by benthic foraminifera, while a few planktonic ones were obtained. The assemblage is strongly dominated by calcareous-perforate forms throughout the sequence and less porcelaneous and agglutinated. The calcareous forms are represented by the perforate orders of Rotaliida (>45 species), Vaginulinida (7 species), Polymorphinida (4 species) and Nodosariida (11 species), while porcelaneous forms are represented by *Quinqueloculina* spp. and miliolid casts, that probably belong to more than three genera. Finally, the agglutinated (10 species) forms are represented by the orders of Astrorhizida (4 species), Spirillinida (1 species), Lituolida (2 species) and Textulariida (3 species).

Among them the LBF were very diverse (43 species), with the most abundant *Nummulites fabianii*, *N. incrassatus*, *Heterostegina reticulata*, *Spiroclypeus carpaticus*, *Pellatispira madaraszi*, orthophragmines and *Asterigerina* spp.
The combination of sedimentological features and biogenic components led to the distinction of 5 microfacies types (Table 1). These can be attributed to a sequence of inner to outer shelf environments and support a model of a rimmed carbonate shelf with isolated platforms. Water circulation patterns on and between the platforms were both open and restricted. In particular, the inner shelf is characterized as a restricted environment with vegetation cover and limited water circulation (back-reef settings, MF1 and MF2). The middle shelf refers to the reef-core and platform margins with high energy conditions (MF3a-d), that passes to a lower-energy regime at a fore-reef setting (MF4). Finally, the outer platform refers to its proximal part with maximum depth of 60 m (MF5).
The Thrace Basin region represents a shallow carbonate platform during the middle-late Eocene and comprises two stages of development. Based on the remains of a late Lutetian/early Bartonian assemblage (samples from Kirki; Dimou *et al*., 2021), the existence of an older platform has been suggested, which is either demolished due to the tectonics or underlies a new transgression. The second stage refers to the onset of a late Bartonian to Priabonian platform. The Bartonian is assigned to middle / outer shelf settings and is reported only from Lemnos Island. Unlikely, Priabonian is widespread into the mainland and comprises all three main environments.
During this time interval, the dynamic syn-rifting led to the development of topographic highs, that represent favoring regions on which productive and species-rich reef structures could flourish. Based on an extensive compilation of LBF species richness from the Western Tethys (e.g., Pignatti, 1995; Less *et al*., 2011; Ferràndez-Cañadel *et al.,* 2023), we document in the carbonate deposits of western Thrace basin, well preserved and hyperdiverse, late Eocene assemblages of larger symbiont-bearing foraminifera, characterizing the study area, with 60 species, as a hotspot of LBF diversity in the Neotethys ocean.

Table 1. Summary of distinguished facies and their interpretation.

Major Microfacies (MF) Type	**Texture**	**Main components**	**Minor components**	**Age**	**Paleoenvironmental interpretation**
MF1: encrusting and other rotaliids-miliolids grainstone (PYL10, S3.1.1-S3.1.3)	Sparitic matrix	Encrusting and other rotaliids, coralline red algae, textulariids, miliolids	*Nummulites*	Priabonian (SBZ20)?	Protected environment, lagoon
MF2: Heterosteginid-orthophragminid packstone (AVT5-13.1)	Micritic matrix	Heterosteginids, orthophragminids, coralline red algae	Other nummulitids, small rotaliids, miliolids, agglutinants, bryozoans, corals, molluscs, worm tubes	Priabonian (SBZ20)?	Back reef, close to the reef or as a reef flat
MF3a: coral, coralline red algae, gastropods, aragonite/ magnesian calcite cemented wackestone/ packstone (AVT3-4/14-15, SAM2)	Micritic matrix	Corals, coralline red algae, gastropods, radial fibrous cement	LBF, miliolids, small rotaliids, bryozoans, bivalves, echinoids, ostracods	Priabonian (SBZ20)	Reef core, platform margins
MF3b: Corraline algae, nummulitic, bivalve wackestone/ packstone (MAR1.1, DDM1-5)	Micritic matrix	Coral patches, coralline red algae, nummulitids	Other LBF, small rotaliids, miliolids, planktonic foraminifera, bryozoans, echinoids	Priabonian (SBZ20)	Platform margins, shoal reef areas, patch reef

MF3c: Nummulitic grainstone (MAR, S2F)/ *Assilina alpina*-coral packstone (SAM1)	Sparitic matrix	*Nummulites fabianii, Assilina alpina*	*Operculina* ex. *gr gomezi, Discocyclina* sp., small rotaliids, coralline red algae, molluscs / other nummulitids, *Discocyclina* sp., small rotaliids, *Silvestriella tetraedra*, corals, echinoids, bryozoans	Priabonian (SBZ19)?/ Priabonian (SBZ19B-20)	Platform margins
MF3d: Coralline-LBF wackestone (PYL5-8)	Micritic matrix	Coralline red algae, corals, *Silvestriella tetraedra*	Other LBF, small rotaliids, miliolids, planktonic foraminifera, molluscs	Priabonian (SBZ19-20)	Distal outer platform
MF4: FAN1-16	Micritic matrix	*Nummulites*, small rotaliids	Other LBF, miliolids, planktonic foraminifera, corals, coralline red algae, echinoids, bryozoans, molluscs	Priabonian (SBZ19-20)	Fore-reef
MF5: LBF packstone (PYL1-4,9, LM1-2, AVT1-2, FAN17-21)	Micritic matrix	Orphophragminids, nummulitids	Other LBF, small rotaliids, miliolids, planktonic foraminifera, coralline red algae, echinoids, bryozoans, molluscs, worm tubes	Priabonian (SBZ19-20)	Outer platform

Acknowledgements
The research by V.-G. Dimou was co-financed by Greece and the European Union (European Social Fund-ESF) through the Operational Programme "Human Resources Development, Education and Lifelong Learning" in the context of the Act "Enhancing Human Resources Research Potential by undertaking a Doctoral Research" Sub-action 2, implemented by the Scholarship Programme (IKY) for PhD candidates at Greek Universities.

References
Dimou, V.G., Koukousioura, O., Dimiza, D.M., Triantaphyllou, V.M., Less, G., Pomoni- Papaioannou, F., Syrides, G., 2021. A preliminary investigation of Eocene larger benthic foraminifera assemblages from Alpine and molasse-type deposits of the Hellenic peninsula (Greece). Rev. Micropaleontol., 70, 100468.
Dimou, V.G., Koukousioura, O., Less, G., Triantaphyllou, D.M., Dimiza, V.M., Syrides, G., 2023. Systematic paleontology and biostratigraphy of the upper Eocene Large Benthic Foraminifera of Fanari (Thrace Basin, Greece). Micropaleontology, 69 (4-5), 457-486.
Dimou, V.G., Koukousioura, O., Less, G., Triantaphyllou, D.M., Dimiza, V.M., Syrides, G., 2024. Microfacies and species richness analysis of upper Bartonian and Priabonian carbonate shelf deposits from the Thrace Basin (Tethyan Ocean, Greece): Paleoenvironmental evolution and species-richness hotspot revealed. Marine and Petroleum Geology, 170 (2024) 107126.
Ferràndez-Cañadell, C., Baumgartner-Mora, C., Baumgartner, P.O., Epard, J.-L., 2023. Priabonian (upper Eocene) larger foraminifera from the Helvetic Nappes of the Alps (Western Switzerland): new markers for shallow benthic zones 19-20. Micropaleontology, 69 (4-5), 407-455.
Flügel, E., 1982. Microfacies analysis of limestones. Springer, Berlin Heidelberg New York, 633 pp.
Kilias, A., Falalakis, G., Sfeikos, A., Papadimitriou, E., Vamvaka, A., Gkarlaouni, C., 2013. The Thrace basin in the Rhodope province of NE Greece - a tertiary supradetachment basin and its geodynamic implications. Tectonophysics, 595-596, 90-105.
Kopp, K.O., 1965. Geologie Thrakiens. III: Das Tertiär zwischen Rhodope und Evros. Ann. Géol. Pays Hellén., 16, 315-362.
Less, Gy., Özcan, E., Okay, I.-A., 2011. Stratigraphy and Larger Foraminifera of the Middle Eocene to lower Oligocene shallow-marine units in the northern and eastern parts of the Thrace Basin, NW Turkey. Turkish J. Earth Sci., 20, 793-845.
Papanikolaou, D., Triantaphyllou, M., 2010. Tectonostratigraphic observations in the western Thrace Basin in Greece and correlations with the eastern part in Turkey. Geol. Balcanica, 39 (1-2), 293-294.
Pignatti, J.S., 1995. Biostratigrafia die macroforaminiferi del Paleogene della Maiella nel quadro delle piattaforme periadriatiche. Studi Geol. Camerti sp (1994), 359-405.

17th INTERNATIONAL CONGRESS of the Geological Society of Greece

BULLETIN OF THE GEOLOGICAL SOCIETY OF GREECE, SP. PUBL.

EXTENDED ABSTRACT 062

Using alternative methods to promote geoheritage: the Koziakas Mt., central Greece, case study.

Dittopoulos Panagiotis Sotirios[1], Chatzipetros Alexandros. [1]
Bsc Geologist
(1) School of Geology, Department of Structural, Historical and Applied Geology, Aristotle University of Thessaloniki, 54124, Greece, geo.dittopoulos@gmail.com

***Research Highlights*:** This study demonstrates how GIS software, specifically QGIS, can effectively communicate geological research results to both the scientific community and the general public, enhancing data accessibility and interpretation while promoting geoheritage.

Introduction

Greece is renowned for its rich geological history, characterized by complex tectonic processes, diverse rock formations, and a plethora of geosites that possess scientific, educational, and cultural value. Among these, Koziakas Mt. in central Greece is an example of impressive geological formations, offering significant opportunities for both scientific research and the promotion of geoheritage. Its mountain range forms the edge of Pindos in the western part of Thessaly and rises imposingly from North to South. It covers a total area of about 400 km², making it an important landmark of the area. Geologically, the area is located at the eastern boundary of the Pindus zone and at the western boundary of the Sub-Pelagonian zone, including the important ophiolitic formations of Koziakas. The Koziakas unit, belonging to the Sub-Pelagonian, is the transitional stage from the Pindus to the Pelagonian zone.

The advent of GIS software suites has revolutionized the way geological data is collected, analyzed, and visualized. Open-source GIS programs, provide cost-effective, efficient and user-friendly platforms to create models and visualizations. These tools are instrumental in overcoming challenges associated with communicating geological information. Nonetheless, the effective communication of such data frequently encounters obstacles, such as the complexity of geological concepts, the limitations of impractical and intricate visual editing software, and the absence of user-friendly scientific data presentation platforms. The latter is of particular importance for the effective promotion of geoheritage. QGIS is the most renowned open-source GIS suite, supported by the largest community of users. This community has developed various methods, including the use of plugins, to address a range of challenges. However, the absence of geological modeling features in existing tools, hinders its adoption for geological 3D applications and visualisations. This paper explores how open-source tools, plugins and innovative visualisation techniques can address these challenges, using Koziakas Mt as a case study.

Methodology

The initial input to the area analysis is the geological maps and field data. For selected study areas, field data are collected, consisting of rock samples, images, linear, planar and point data such as rock formation dip planes, faults and locations of fossil finds. In addition, the input includes satellite orthophotos and Digital Elevation Models from the Hellenic Cadastre (Digital Elevation Model -DEM from the LSO25 project 25 m and LSO25 25 cm orthophotos, Hellenic Cadastre), the paths of the area from hellaspath.gr and OpenStreetMap for accessibility purposes (OpenStreetMap contributors, 2015).

The above, combined with the pre-existing geological knowledge for the area, results in the geological output data consisting of the West to East geological cross sections across the mountain, smaller scale flysch cross sections along the western valley, and fault raster and vector layers. Processing the data in QGIS results in the creation of background layers such as hillshade, slope aspect, contours and multispectral satellite layers, as well as vector layers such as the hydrology network.

For the visual results, the input data consists mainly of the above geological and geomorphological outputs. This is followed by processing through QGIS to create well presentable information layers, and later through the qgis2threejs plugin to structure the data using the three.js JavaScript framework and WebGL technology into a locally running 3D web view model. The layers containing the model's data were selected via the plugin's menu, utilising also the data from the National Cadastre. Furthermore, a custom plane was incorporated to facilitate altitude experiments, concurrently serving as a water level surface to simulate local flooding scenarios. To enhance comprehension of the broader area's orientation, geological planes, and azimuth measurements, the north arrow option was enabled. The map's boundaries were defined using a polygon layer, and the model's background was set to resemble the sky. To enable the user to have multiple layers open simultaneously, one focused on the specific study area and

another providing a broader context, the background raster images were separated into two layers: surroundings and background.

The visual outputs are divided into two categories: static and dynamic. The static output comprises 2.5D perspective images, which interpret the geological setting and geomorphology. These images can be used to accompany a digital or printed file. The dynamic output consists of a 3D interactive web model, which showcases all the study's data in multiple layers. This model can be accessed either locally or on the web (as outlined below). The 3D web model can be uploaded for online access, facilitating optimal practicality, via export to an HTML file. Uploading to OneDrive or a similar online drive service platform is then required. The model can be published via Drive2web's free serverless hosting website and viewed through a link on any web browser. The use of a link shortening website can achieve a better optical result. The workflow involved in the publication process can be seen in Figure 1.

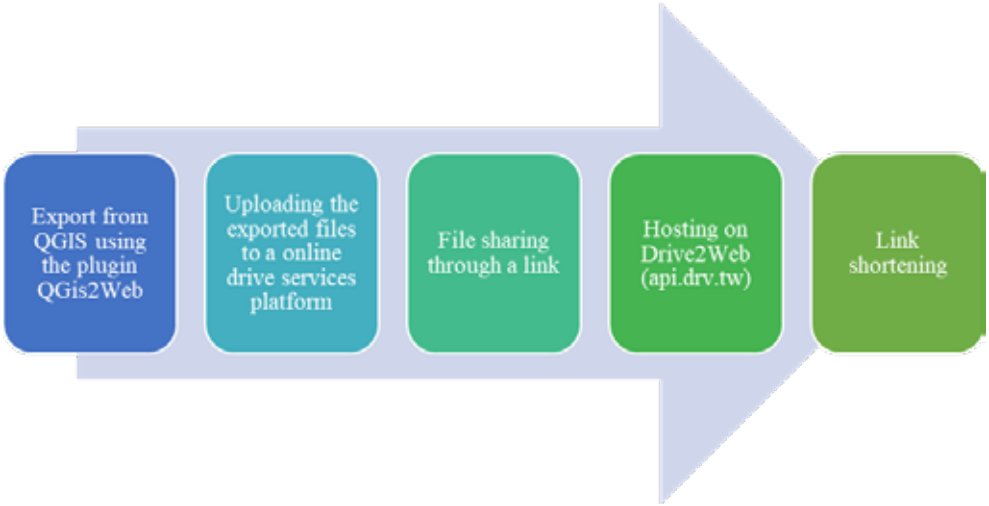

Figure 1. Illustration of the process that was followed from exporting using Qgis2threejs, to the hosting of the model.

Results and conclusions

The geological outcomes of the implemented methodology, which are directly associated with the geological aspect of the study, consist of the 2.5D static images, incorporating the geological cross-sections, as seen in Figure 2. As demonstrated in Figure 3, the integration of the two 2.5D static images in a single illustration serves to emphasize their position in relation to the Koziakas mountain range. The visual results include the most significant element of this study, the 3D web model (Figure 4). The link for the model is the following: https://koziakas-3d-model-qgis2threejs.on.drv.tw/Koziakas%20Website/KoziakasComplete7.html.

Accessible via any web browser, the interactive 3D model provides a detailed visual representation of scientific data while highlighting the geological features of the Koziakas study area. The final model integrates various layers, including geological maps, cross sections, hydrology data, field observations (e.g. fault strike and dip, fossils, faults, and folds), contours, slope aspect maps, hillshade maps, satellite imagery, and nearby hiking trails. The user can create numerous combinations by utilizing all the layers and background data to extract the required information. Background layers, by lacking 3D morphology, place more emphasis on the study region. Hillshade and slope-aspect maps, products from DEM processing from the National Cadastre (Digital Elevation Model -DEM from the LSO25 project (25 m), Hellenic Cadastre), geological maps of IGME (Savoyat and Lalechos, 1972; Karfakis, 1993) and contour topographical map are some of the additional raster layers. Figure 4 displays the model with all information layers activated and Figure 5 demonstrates a different layer combination, showcasing the diverse range of potential applications.

Although not of great significance, the limitations of the plugin have led to the adoption of an alternative visualisation strategy for certain information layers. To address the constraints of the selected plugin and ensure that crucial data remains visible, line elements such as hydrology, faults, and paths have been slightly elevated. Additionally, some product types, like the hillshade-fault map, have been separated into raster and vector layers. This approach mitigates the lower resolution projection caused by the plugin, resulting in improved visualisation. Moreover, the satellite image is observed to exhibit a markedly higher level of clarity when viewed in 3D view within QGIS, in comparison to the final output produced by the Qgis2threejs plugin. Furthermore, it has been demonstrated that the model is efficacious in capturing screenshots, which were subsequently utilized to generate the 2.5D static images.

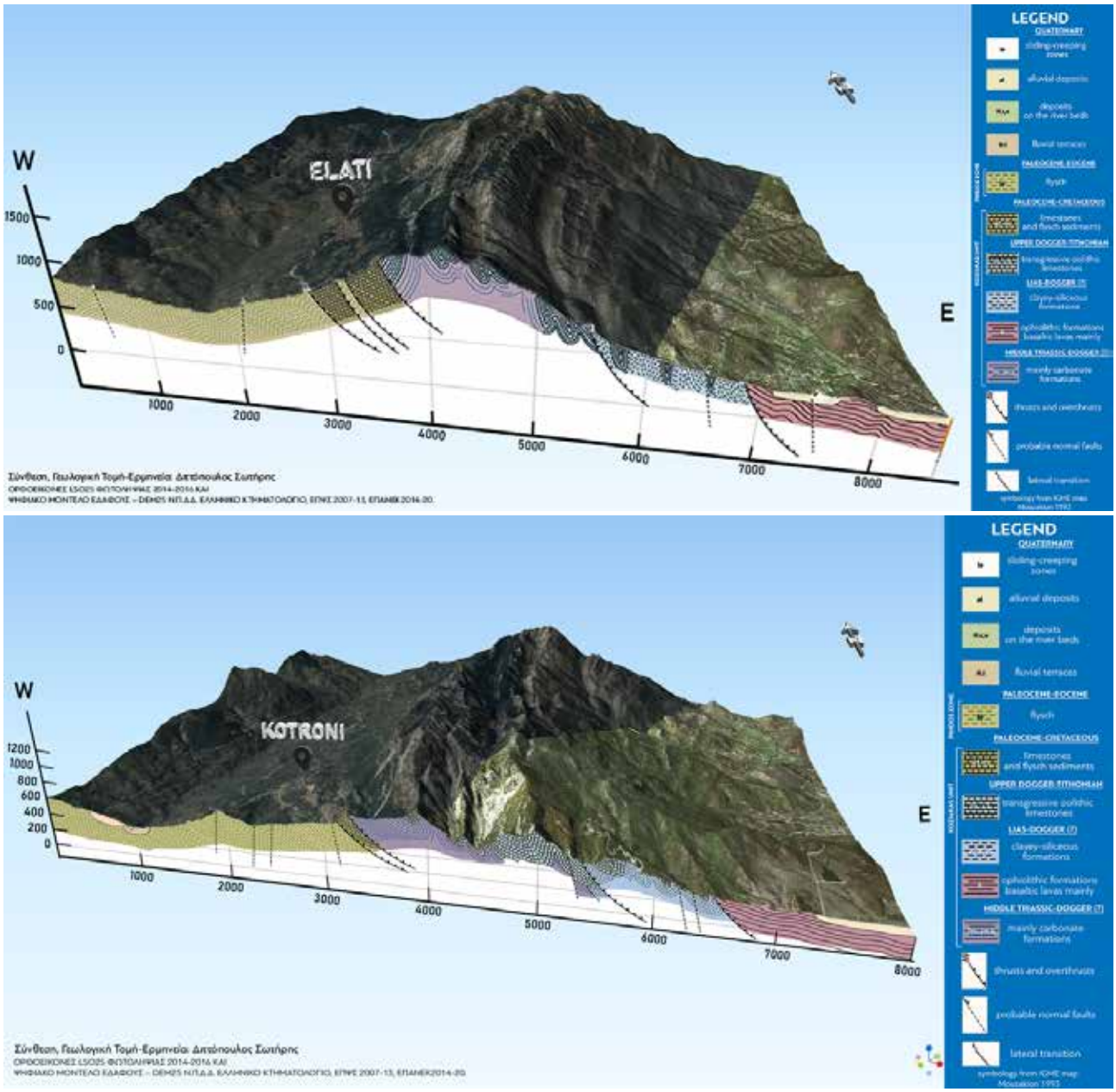

Figure 2. Illustration of the two 2.5D models featuring the geological cross-sections and their respective geological legends. Top: the northernmost geological cross section, located near the settlement of Elati. Bottom: the southernmost geological cross section, located near the settlement of Kotroni. The Qgis2threejs plugin model was utilized to capture the screenshots (Digital Elevation Model -DEM from the LSO25 project (25 m) and LSO25 (25 cm) orthophotos, Hellenic Cadastre).

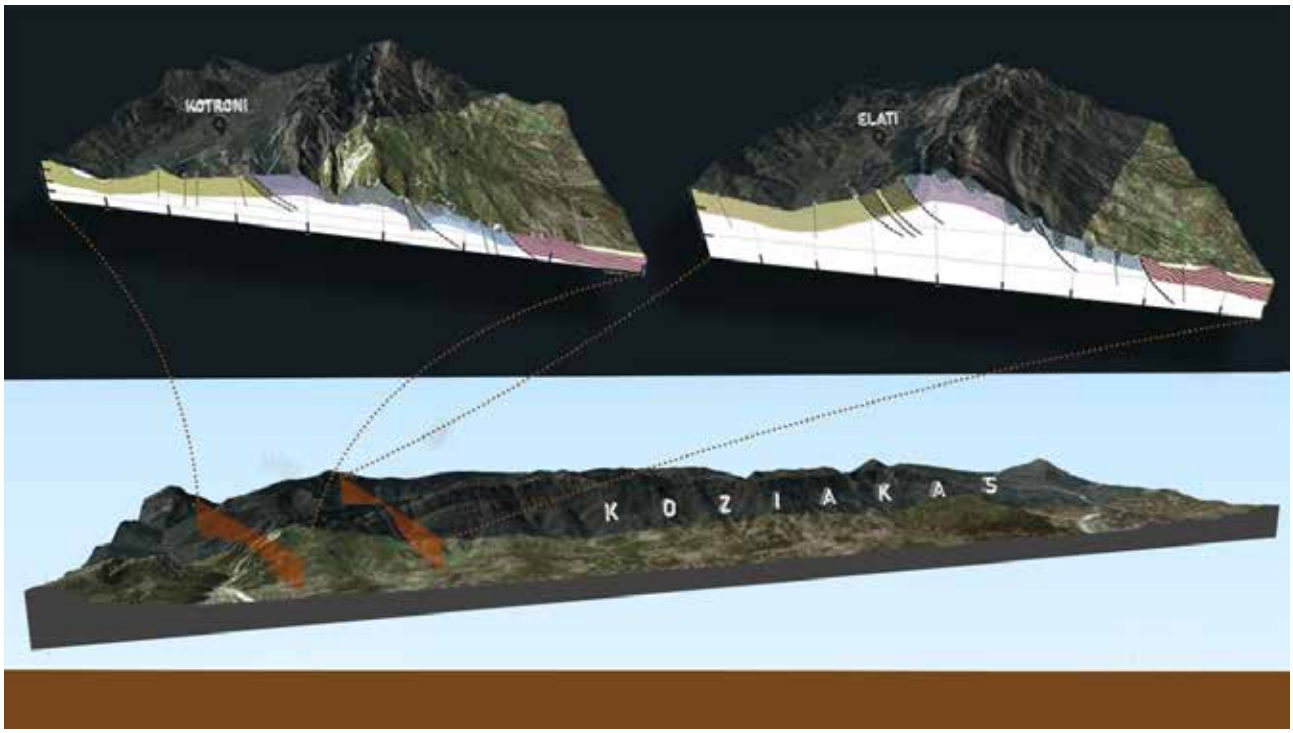

Figure 3. Illustration of the two 2.5D models featuring the geological cross-sections and their position in relation with the Koziakas mountain range. The Qgis2threejs plugin model was utilized to capture the screenshots (Digital Elevation Model -DEM from the LSO25 project (25 m) and LSO25 (25 cm) orthophotos, Hellenic Cadastre).

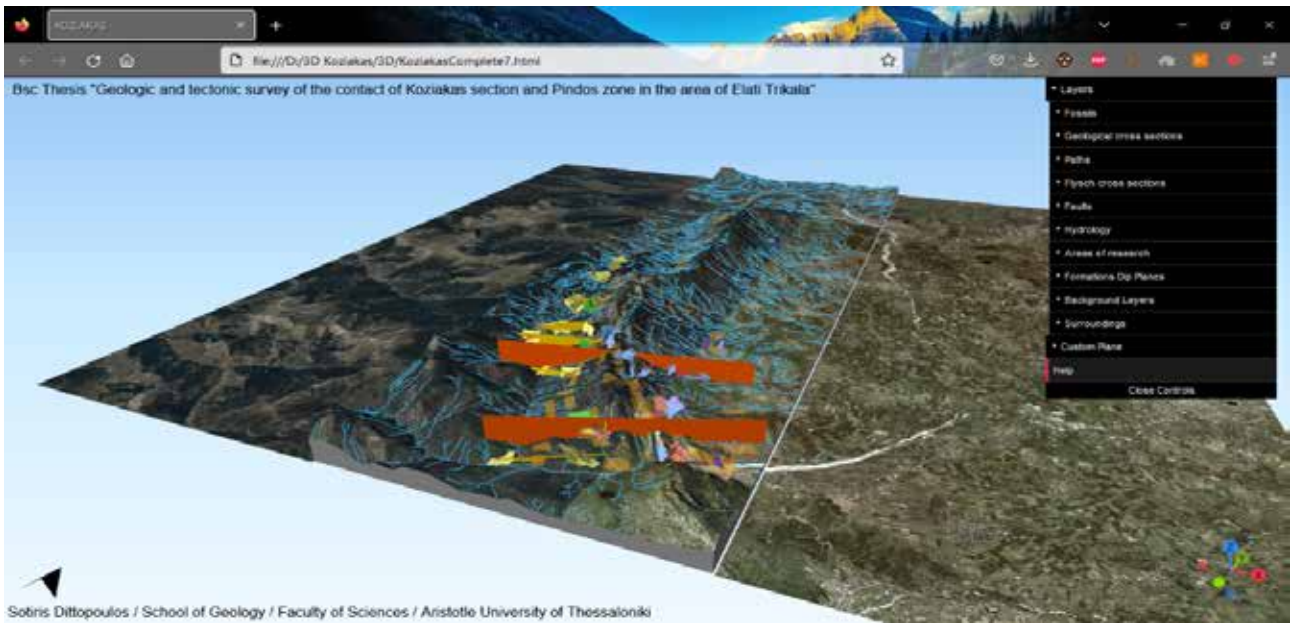

Figure 4. Screenshot of the model, illustrating the information of three layers: locations of geological cross sections (orange), locations of flysch cross sections (yellow), background layers: high resolution satellite image from the Hellenic Cadastre (Digital Elevation Model -DEM from the LSO25 project (25 m) and LSO25 (25 cm) orthophotos, Hellenic Cadastre).

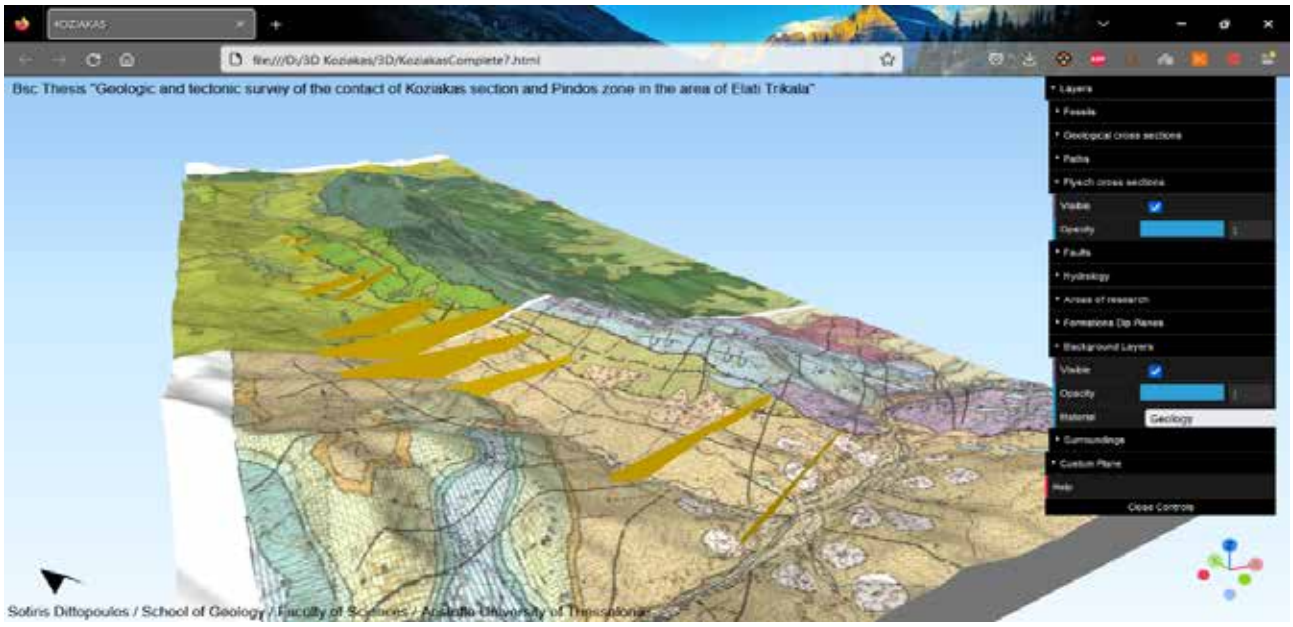

Figure 5. Screenshot of the model, illustrating the information of two layers: locations of flysch cross sections and background layer: geological map of IGME (Mouzakion and Kalambaka sheets, Savoyat and Lalechos, 1972; Karfakis, 1993).

Discussion

The process of transforming complex spatial data into clear, visually engaging outputs is often challenging, particularly when using specialized tools such as the Qgis2threejs plugin. Despite its versatility, the plugin requires experimentation to achieve the intended visualizations, as its performance can be heavily influenced by the underlying hardware. Exporting data, especially in high-resolution formats, can take several hours on systems with outdated or insufficient processing power. To enhance the workflow and optimize efficiency, it is essential to ensure that the hardware capabilities are in alignment with the demands of QGIS and its extensions.

Regarding the enhancements that could be made to improve the end result, one of the primary concerns is the potential to incorporate a geological cross-section illustration within the interactive model. Furthermore, the hydrographic network could be segmented into branches (for example, according to Strahler's classification), integrated into the river basins and accompanied by river name labels. Another significant enhancement would be the capability to include images of the features, visible upon selection. To optimise the presentation for educational purposes, a camera flight plan could be devised to guide the viewer upon entering the model. Faults could be accompanied by arrows, indicating the movement direction, and paths could be equipped with additional information such as distance and estimated walking time. The incorporation of videos and descriptions could further augment the model, resulting in a comprehensive interactive webpage that offers a detailed exposition of the study area.

The Qgis2threejs plugin offers a significant advantage in its ability to export 3D models in the glTF format. This format is a widely recognized standard for 3D computer graphics (3DCG) and 3D printing. This capability opens opportunities for users to move beyond traditional GIS applications, enabling the creation of interactive 3D visualizations or detailed physical models. The potential of these models is significant for the effective promotion and preservation of geoheritage through digital innovation. The visualizations created with this tool facilitate a deeper engagement with geological and cultural heritage sites, providing users with virtual access to areas that may be difficult to visit physically due to geographic or environmental constraints. Moreover, this creates a dynamic way to educate the public about their geological history. Studies have shown that dynamic visualization has a greater positive impact on educational outcomes compared to static visualization. This effect is particularly evident in the learning results and intrinsic motivation of science students, especially in subjects like Biology, Chemistry, and Geology. As highlighted by e.g. Berney & Bétrancourt (2016) and Teplá et al. (2022), dynamic visualization can enhance attention and more effectively demonstrate abstract procedures (Ayres et al. 2009; Schwan & Riempp 2004; Teplá et al. 2022) and processes that change over space and time (Ainsworth & VanLabeke 2004; Rieber 1990; Schnotz & Lowe 2003; Teplá et al. 2022). Furthermore, the 3D printing allows the physical replicas of geoheritage, and features such as

rock formations, fossil sites, faults and folds, to be produced and displayed in educational institutions, museums, or cultural centres. The potential for these models to foster appreciation and awareness is significant, and their capacity to aid in conservation efforts is equally noteworthy.

Acknowledgements

We would like to express our gratitude to the local community of Elati, for their collaboration and the valuable information provided regarding the accessibility of the area. Additionally, we would like to thank the Legal Entity of Public Law Hellenic Cadastre for providing the Digital Elevation Model and Orthophotos used in our analysis.

References

Berney, S., & Bétrancourt, M. (2016). Does animation enhance learning? A meta-analysis. Computers & Education, 101, 150-167.

Karfakis I. (1993). Geological map of Greece, 1:50,000 scale – Mouzakion sheet. Institute of Geological and Mineral Exploration, Athens, Greece.

Savoyat E. and Lalechos N. (1972). Geological map of Greece, 1:50,000 scale – Kalambaka sheet. Institute of Geological and Mineral Exploration, Athens, Greece.

Teplá, M., Teplý, P. & Šmejkal, P. Influence of 3D models and animations on students in natural subjects. IJ STEM Ed 9, 65 (2022). https://doi.org/10.1186/s40594-022-00382-8

Tools

Drive2Web: https://api.drv.tw/

[Github user] Minorua. (2024). Qgis2threejs plugin for QGIS 3.4.0. Originally written by Minoru Akagi. Version 2.7.3. Retrieved from https://github.com/minorua/Qgis2threejs [Accessed: March 30, 2024]

Digital data

Digital Elevation Model -DEM from the LSO25 project (25m), Hellenic Cadastre. Available online: https://www.ktimanet.gr/geoportal/catalog/search/resource/details.page?uuid=%7B2945C504-A861-4CB9-B086-B6244E0D08EF%7D [Accessed: March 30, 2024]

LSO25 (25cm) orthophotos, Hellenic Cadastre. Available online: https://www.ktimanet.gr/geoportal/catalog/search/resource/details.page?uuid=%7B6803818C-284B-442F-8185-707FDB654A22%7D [Accessed: March 30, 2024]

HellasPath: http://www.hellaspath.gr/

One Drive Microsoft: https://onedrive.live.com

OpenStreetMap contributors. (n.d.). OpenStreetMap. Retrieved [Accessed: March 30, 2024], from https://www.openstreetmap.org

17th INTERNATIONAL CONGRESS of the Geological Society of Greece

BULLETIN OF THE GEOLOGICAL SOCIETY OF GREECE, SP. PUBL.

EXTENDED ABSTRACT 063

Assessment of fault hazard in the broader area of Sitia, Eastern Crete

Dretaki A.[1], Chatzipetros A.[1]

(1) School of Geology, Aristotle University of Thessaloniki, , Greece, antoniadret@hotmail.com

Research Highlights: Potential earthquake magnitudes for fault zones in Eastern Crete were determined using empirical relationships, highlighting significant seismic hazards. The Ierapetra, Mesa Mouliana, Sitia, and Xerocampos-Goudouras Fault Zones are identified as the most active and hazardous in the area, indicating the need for further research.

The area of Crete is one of the most tectonically active in Greece and its study has been at the centre of interest of many researchers. Eastern Crete is considered to be the area where 80% of the future normal fault earthquakes will occur (Nicol *et al.,* 2020), so seismic hazard assessment is a necessity. The Ierapetra fault zone is considered the most dangerous and important, as two major earthquakes have occurred in the past, destroying completely the city of Ierapetra. Therefore, the mapping and analysis of the area's major fault zones can provide substantial insight into the seismic hazard of the region.

The study area is located in the eastern part of Lasithi and includes the municipality of Sitia and part of the municipality of Ierapetra. It is characterised by a relatively mountainous landscape with numerous gorges formed in the limestone bedrock. The geological structure of the area, from the lowest to the highest units, consists of the following units: Plattenkalk unit, Tripali unit, Phyllite-Quartzite unit *s. str.,* the pre-alpine basement, the Tyros Unit, the Tripoli Unit, the Pindos Unit and then, above all, the younger post-alpine sedimentary series (Fassoulas, 1995, ten Veen and Postma, 1999, Seidel, 1968; Krahl *et al.*, 1983; Zulauf *et al.,* 2008, Klein *et al.,* 2008, Mountrakis, 2010, Krahl *et al.,* 1986; Zulauf *et al.,* 2013, Robertson, 2006; Robertson, 2008; Robertson, 2022).

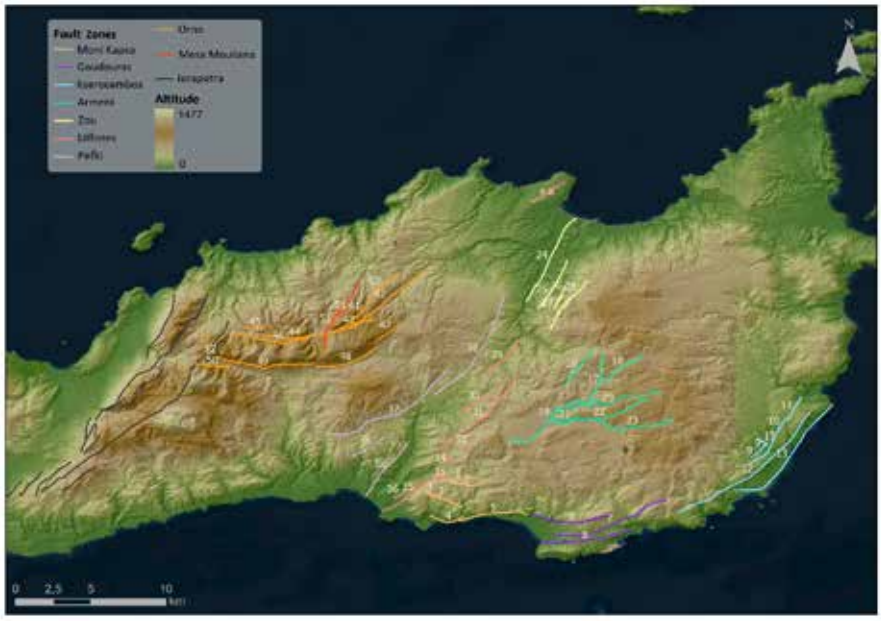

Figure 1. Neotectonic map of fault zones and numbered segments referred on Tables 1 to 3 (Dretaki, 2024). For source of the DEM see text for details.

Active faults in the area are normal or normal-oblique ones. They are numerous and can be grouped into two main trends: the NNE-SSW trending fault group and the E-W to ESE-WNW trending fault group. The Ierapetra Fault Zone, as mentioned above, has been mapped and analysed in detail. Other fault zones mentioned in previous research include the Sitia Fault Zone and other minor offshore and onshore structures, such as the Goudouras Fault, the Mouliana Fault and the Orno Fault (ten Veen and Postma, 1999, Caputo *et al.,* 2010, Caputo and Pavlides, 2013, Mason *et al.,* 2016, Pavlides *et al.,* 2018, Veliz *et al.,* 2018, Mechernich et *al.,* 2023). On 12 October 2021, an M 6.3 earthquake occurred on an offshore NNE-SSW fault, its focal mechanism (data from the National Observatory of Greece, Dretaki *et al.,* 2022), showed that the active stress field is compatible with several onshore fault zones and indicating the need for further research into the tectonic activity of the area.

To estimate the seismic hazard, empirical relationships are used that relate the surface rupture (L) to the energy released by the earthquake (magnitude Ms) (Pavlides, 2016). Many researchers have already calculated the possible magnitudes of some faults

in the area and the results are shown in Table 1.
During the field mapping, measurements of faults and structures were taken where possible. Then, using ArcGIS Pro software, they were analysed and correlated with the satellite imagery and DEM in order to better map them in the field. From the above analysis, the structures were divided into five fault zones, Xerocampos - Goudouras, Sitia, Orno, Mesa Mouliana and Ierapetra (Figure 1). Each was divided into individual fault subzones based on their segmentation and correlated with the satellite data, Digital Elevation Model (Data Source: Legal Entity of Public Law Hellenic Cadastre, Operational Programme Competitiveness, Entrepreneurship and Innovation 2014-2020 (EPAnEK)) and digitized geological map (IGME 1959). The hydrographic network was also used, since the way it develops can be strongly influenced by the tectonic regime of a region.
All of the above, combined with the analysis of morphotectonic indices and data published in the literature, led to the assessment of the activity of each zone. Then, the seismic hazard was calculated, using empirical relationships, for each segment of sufficient length, combinations of segments, the entire fault zone, combinations of fault zones and the entire deformation zone. For the calculation of the Ms magnitude of the faults the empirical relationships of Wells & Coppersmith (1994), Papazachos *et al.* (2004) and Pavlides & Caputo (2004) were used
First, the surface length L or SRL (Surface Rupture Length) of each section was calculated separately in km using the ArcGIS Pro application for the mapped sections. Then the values of the potential magnitudes and the Maximum Vertical Displacement (MVD) were calculated. The values were calculated for each individual segment, combinations of segments and the whole zone and the results are shown in Tables 1, 2 and 3.
Previous work in the area (Dretaki, 2024) confirmed that both groups are active, with the NNE-SSW faults being more active than the E-W ones. The above analysis, in addition with previous studies, shows that the Ierapetra, Mesa Mouliana, Sitia and Xerocampos - Goudoura Fault Zones are the most active in the region. In the Ierapetra Fault Zone there are historical records of its activation. Segment 52 (Figure 1), which was recently mapped during fieldwork (Dretaki, 2024), shows evidence of activity as it deforms recent deposits and has the potential for a magnitude Ms 5.7 event (Pavlides and Caputo, 2004). Further investigation of this fault segment is considered important. The Mesa Mouliana Fault Zone is considered to be as active as the Ierapetra one, with potential similar to that of Lastros fault (Mechernich et al. 2023), with calculated Ms 5.7 (Pavlides and Caputo, 2004). It intersects the Orno Fault Zone, which is also considered to be active, creating strong relief and slope debris have been deposited in the hanging wall. Orno fault has a potential magnitude of Ms 6.8 (Pavlides and Caputo, 2004). Sitia Fault Zone is an active zone with signs of activity migration towards the centre of the basin. The younger parts of it intersect the Neogene deposits, but more importantly they intersect the beachrocks of Sitia beach, indicating that it was active during the Holocene. The activation of the entire fault zone could cause an earthquake of Ms 7.1 (Pavlides and Caputo, 2004), similar to Ierapetra and Xerocambos-Goudouras Fault Zones. Xerocampos Fault Zone, as well as the large expected earthquake magnitude derived from empirical relationships, appears to be part of the same system as the 12 October 2021 earthquake.
Based on the above, as well as the results from Tables 1 to 3, we can conclude that further research on each area is mandatory. This research could include the monitoring of micro-movements by installing instruments in the most active sections, geophysical surveys and paleoseismological trenching. Although the study area is the least developed in terms of tourism compared to the rest of Crete, it receives many visitors each year. Combined with the permanent population, especially in the settlements close to the fault zones, the seismic risk of the area is greatly increased due to the age of most of the settlements, the short distance from the seismic sources and the permanent human presence.

Table 1. Xerocambos – Goudouras Fault Zone

Fault zone	Segment	Length	Wells & Coppersmith (1994)	Papazachos et al. (2004)		Pavlides & Caputo (2004)			
		km	Ms	M	MD (m)	+	Ms	-	MVD (m)
Moni Kapsa	1+2+3	7.0	6.0	5.4		6.4	6.2	5.6	0.20
	4+5	5.8	5.9	5.2		6.4	6.2	5.4	0.16
	1+2+3+4+5	12.8	6.3	5.9		6.7	6.5	5.9	0.37
Goudouras	6	4.4	5.7	5.0		6.2	6.1	5.3	0.12
	7	6.9	6.0	5.4		6.4	6.2	5.5	0.19
	8	5.0	5.8	5.1		6.3	6.1	5.4	0.14
	6+7	11.3	6.3	5.8		6.7	6.4	5.9	0.32
	6+8	9.4	6.1	5.7		6.6	6.4	5.7	0.27
	7+8	11.8	6.3	5.9		6.7	6.4	5.9	0.34
	6+7+8	16.3	6.5	6.1	0.40	6.8	6.6	6.1	0.47

Fault zone	Segment	Length	Wells & Coppersmith (1994)	Papazachos et al. (2004)		Pavlides & Caputo (2004)			
Xerocampos	9	1.5	5.1	4.1		5.8	5.6	4.6	0.04
	12	10.1	6.2	5.7		6.6	6.4	5.8	0.29
	13	8.3	6.1	5.6		6.5	6.3	5.7	0.24
	14+15	0.9	4.8	3.6		5.6	5.4	4.3	
	10+11	5.6	5.8	5.2		6.3	6.2	5.4	0.16
	9+10+11	7.1	6.0	5.4		6.5	6.2	5.6	0.20
	12+13	18.4	6.5	6.2	0.48	6.9	6.6	6.2	0.53
	9+10+11+12+13	25.5	6.7	6.5	0.77	7.0	6.7	6.4	0.74
	9+10+11+12+ 13+14+15	26.4	6.7	6.6	0.80	7.0	6.8	6.4	0.77
Moni Kapsa + Goudoura	5+6	8.2	6.1	5.5		6.5	6.3	5.7	0.23
	4+5+6	10.2	6.2	5.7		6.6	6.4	5.8	0.29
	All segments	29.1	6.8	6.6	0.93	7.1	6.8	6.4	0.85
Goudouras + Xerocambos	8+12	15.1	6.4	6.1	0.36	6.8	6.5	6.0	0.43
	7+12	17.0	6.5	6.2	0.43	6.8	6.6	6.1	0.49
	7+13	15.1	6.4	6.1	0.36	6.8	6.5	6.0	0.43
	8+13	13.3	6.3	6.0	0.30	6.7	6.5	6.0	0.38
	7+8+12+13	30.2	6.8	6.7	0.98	7.1	6.8	6.5	0.88
	All segments	42.7	7.0	7.0	1.61	7.2	6.9	6.7	1.26
Moni Kapsa + Goudouras + Xerocambos	All segments	55.5	7.2	7.2	2.35	7.3	7.1	6.8	1.65

Table 2. Sitia Fault Zone

Fault zone	Segment	Length	Wells & Coppersmith (1994)	Papazachos et al. (2004)		Pavlides & Caputo (2004)			
		km	Ms	M	MD (m)	+	Ms	-	MVD (m)
Armeni	20	6.1	5.9	5.3		6.4	6.2	5.5	0.17
	22	5.7	5.9	5.2		6.4	6.2	5.4	0.16
	23	4.6	5.7	5.0		6.3	6.1	5.3	0.13
	16+19	8.8	6.1	5.6		6.5	6.3	5.7	0.25
	17+18	6.0	5.9	5.3		6.4	6.2	5.5	0.17
	16+17+18+19	14.8	6.4	6.1		6.8	6.5	6.0	0.43
	19+20	12.3	6.3	5.9		6.7	6.5	5.9	0.35
	21+22+23	11.9	6.3	5.9		6.7	6.4	5.9	0.34
	16 to 23	32.9	6.9	6.8	1.10	7.1	6.8	6.5	0.96
Zou	24	6.2	5.9	5.3		6.4	6.2	5.5	0.17
	25	3.6	5.6	4.8		6.2	6.0	5.2	0.10
	28	3.8	5.6	4.9		6.2	6.0	5.2	0.10
	26+27+28	6.2	5.9	5.3		6.4	6.2	5.5	0.17
	24+25	9.8	6.2	5.7		6.6	6.4	5.8	0.28
	24+25+26+27	12.2	6.3	5.9		6.7	6.5	5.9	0.35
	24 to 28	16	6.4	6.1	0.39	6.8	6.6	6.1	0.46

Fault zone	Segment	Length	Wells & Coppersmith (1994)	Papazachos et al. (2004)		Pavlides & Caputo (2004)			
Lithines	29	3.4	5.6	4.8		6.1	6.0	5.1	0.09
	30	1.9	5.2	4.3		5.9	5.7	4.8	0.05
	31	6.7	6.0	5.4		6.4	6.2	5.5	0.19
	35	4.9	5.8	5.1		6.3	6.1	5.3	0.14
	29+30	5.3	5.8	5.2		6.3	6.1	5.4	0.15
	35+36	6.1	5.9	5.3		6.4	6.2	5.5	0.17
	29+30+31	12	6.3	5.9		6.7	6.5	5.9	0.34
	32+33+34+35	6.9	6.0	5.4		6.4	6.2	5.5	0.19
	32+33+34+35+36	8.7	6.1	5.6		6.5	6.3	5.7	0.25
	30+31+32+33+34	10.63	6.2	5.8		6.6	6.4	5.8	0.30
	30+31+32+33+34+35+36	16.73	6.5	6.2	0.42	6.8	6.6	6.1	0.48
	29 to 36	20.1	6.6	6.3	0.54	6.9	6.7	6.2	0.58
Pefki	37	7.9	6.0	5.5		6.5	6.3	5.6	0.22
	38	8.5	6.1	5.6		6.5	6.3	5.7	0.24
	39	2.2	5.3	4.4		5.9	5.8	4.9	0.06
	40	4.2	5.7	5.0		6.2	6.0	5.2	0.12
	37+38	16.4	6.5	6.1	0.41	6.8	6.6	6.1	0.47
	38+39	10.7	6.2	5.8	0.01	6.6	6.4	5.8	0.30
	38+39+40	14.9	6.4	6.1	0.35	6.8	6.5	6.0	0.43
	37+38+39+40	22.8	6.7	6.4	0.65	7.0	6.7	6.3	0.66
Zou + Lithines	All segments	36.1	6.9	6.8	1.26	7.2	6.9	6.6	1.06
Zou + Pefki	All segments	38.8	7.0	6.9	1.40	7.2	6.9	6.6	1.14
Pefki + Lithines	All segments	42.9	7.0	7.0	1.62	7.2	6.9	6.7	1.26
Armeni + Lithines	All segments	53.0	7.1	7.2	2.19	7.3	7.0	6.8	1.57
Zou + Lithines + Pefki	All segments	58.9	7.2	7.3	2.55	7.4	7.1	6.9	1.75
Zou + Lithines + Pefki + Armeni	All segments	91.7	7.5	7.6	4.84	7.6	7.2	7.1	2.76

Table 3. Orno, Mesa Mouliana and Ierapetra Fault Zone

Fault zone	Segment	Length	Wells & Coppersmith (1994)	Papazachos et al. (2004)		Pavlides & Caputo (2004)			
		km	Ms	M	MD (m)	+	Ms	-	MVD (m)

Fault zone	Segment	Length	Wells & Coppersmith (1994)	Papazachos et al. (2004)		Pavlides & Caputo (2004)			
Orno	43	6.7	5.9	5.4		6.4	6.2	5.5	0.19
	44	2.8	5.5	4.6		6.0	5.9	5.0	0.08
	45	2.7	5.4	4.6		6.0	5.9	5.0	0.07
	46	1.4	5.0	4.0		5.7	5.6	4.6	0.04
	47	5.4	5.8	5.2		6.3	6.1	5.4	0.15
	48	1.9	5.2	4.3		5.9	5.7	4.7	0.05
	49	3.8	5.6	4.9		6.2	6.0	5.2	0.10
	50	5.7	5.9	5.2		6.4	6.2	5.4	0.16
	51	1.8	5.2	4.2		5.9	5.7	4.7	0.05
	41+42	4.0	5.7	4.9		6.2	6.0	5.2	0.11
	43+44	9.5	6.1	5.7		6.6	6.4	5.7	0.27
	41+42+43+44	9.5	6.1	5.7		6.6	6.4	5.7	0.27
	43+44+45	12.2	6.3	5.9		6.7	6.5	5.9	0.35
	45+46	4.1	5.7	4.9		6.2	6.0	5.2	0.11
	43+44+45+47	17.6	6.5	6.2	0.45	6.8	6.6	6.1	0.51
	43 to 47	18.9	6.5	6.3	0.50	6.9	6.6	6.2	0.55
	41+42+43+44+45+46+48	20.8	6.6	6.4	0.57	6.9	6.7	6.2	0.60
	48+49	5.6	5.9	5.2		6.4	6.2	5.4	0.16
	48+49+50	11.3	6.3	5.8		6.7	6.4	5.9	0.32
	49+50	9.4	6.1	5.7		6.6	6.4	5.7	0.27
	50+51	7.5	6.0	5.5		6.5	6.3	5.6	0.21
	49+50+51	11.3	6.2	5.8		6.7	6.4	5.9	0.32
	48+49+50+51	13.1	6.3	6.0	0.29	6.7	6.5	5.9	0.38
	41 to 51	32.0	6.8	6.7	1.06	7.1	6.8	6.5	0.94
Mesa Mouliana	51	5.2	5.8	5.2		6.3	6.1	5.4	0.15
Ierapetra	52	1.6	5.1	4.1		5.8	5.7	4.6	0.04

Acknowledgements

The authors would like to acknowledge the invaluable support and contributions that made this research possible. The first author is grateful to Sotiris Dittopoulos, BSc geologist, for his collaboration and assistance. The authors would also like to thank the *Geositia project* for Sitia UNESCO Global Geopark, during which many field data were collected and presented as part of the project deliverables. The administration of the Geopark, as well as the Municipality of Sitia through MADES S.A. provided financial support for part of the research, and their contribution is greatly appreciated. The Digital Elevation Model used in the analysis was kindly provided by the Legal Entity of Public Law Hellenic Cadastre. This paper summarizes part of the first author's MSc Thesis at the University of the Aegean, completed under the Inter-Institutional «Natural Hazards and Disaster Mitigation» Master Course programme. The contributions of Professor Emeritus Spyros Pavlides (Aristotle University of Thessaloniki) and Dr Charalambos Fassoulas (Natural History Museum of Crete of the University of Crete) were crucial, pivotal and greatly improved the Thesis text; the authors would like to express their sincere gratitude towards them.

References

Caputo, R., Pavlides, S., 2013. The Greek Database of Seismogenic Sources (GreDaSS), version 2.0.0: A compilation of potential seismogenic sources (Mw > 5.5) in the Aegean Region. doi:10.15160/unife/gredass/0200

Caputo, R., Catalano, S., Monaco, C., Romagnoli, G., Tortorici, G., Tortorici, L., 2010. Active faulting on the island of Crete (Greece). Geophysical Journal International, 183(3), 111-126. doi:10.1111/j.1365-246x.2010.04749.x

Dretaki, A., Chatzipetros, A., Psomadakis, S., 2022. Site effects and surface deformation associated with the M 6.3 Sitia (eastern Crete). 16th International Congress of the Geological Society of Greece, Bulletin of the Geological Society of Greece, Sp. Publ. 10, p. 418-419. Patra.

Dretaki, A., 2024. Neotectonic study of Sitia area, eastern Crete, and assessment of the faults' seismic potential. Master Thesis, School of Geography, University of the Aegean, Inter-Institutional Postgraduate Studies Program "Natural Hazards and Disaster Mitigation", 236 pp.

Fassoulas, Ch., 1995. Kinematics and deformation of the nappe pile of Central Crete: Aristotle University of Thessaloniki, Phd

thesis (in greek).
IGME., 1959. Geological map of Greece, scale 1:50.000 - sheet ZIROS. Athens: IGME.
IGME., 1959. Geological map of Greece, scale 1:50,000 - sheet IERAPETRA. Athens: IGME.
IGME., 1959. Geological map of Greece, scale 1:50,000 - sheet SITEIA. Athens: IGME.
Klein, T., Reichhardt, H., Klinger, L., Grigull, S., Wostal, G., Kowalczyk, G., Zulauf, G., 2008. Reverse slip along the contact Phyllite-Quartzite Unit/Tripolitsa Unit in eastern Crete: implications for the geodynamic evolution of the External Hellenides. Zeitschrift der deutschen Gesellschaft für Geowissenschaften, 159(3), 375-398. doi:https://doi.org/10.1127/1860-1804/2008/0159-0375
Mason, J., Schneiderwind, S., Pallikarakis, A., Wiatr, T., Mechernich, S., Papanikolaou, I., Reicherter, K., 2016. Fault structure and deformation rates at the Lastros-Sfaka Graben, Crete. Tectonophysics, 638, 216-232. doi:https://doi.org/10.1016/j.tecto.2016.06.036
Mechernich, S., Reicherter, K., Deligiannakis, G., Papanikolaou, I., 2023. Tectonic geomorphology of active faults in Eastern Crete (Greece) with slip rates and earthquake history from cosmogenic 36Cl dating of the Lastros and Orno faults. Quaternary International, 651, 77-91. doi:https://doi.org/10.1016/j.quaint.2022.04.007
Mountrakis, D., 2010. Geology And Geotectonic Evolution Of Greece (1st ed.). Thessaloniki: University Studio Press.
Nicol, A., Mouslopoulou, V., Begg, J., Oncken, O., 2020. Displacement accumulation and sampling of paleoearthquakes on active normal faults of Crete in the eastern Mediterranean. Geochemistry, Geophysics, Geosystems. doi:10.1029/2020gc009265
Papazachos, B., Skordilis, E., Panagiotopoulos, D., Papazachos, C., Karakaisis, G., 2004. Global relations between seismic fault parameters and moment magnitude of earthquakes. Bulletin of the Geological Society of Greece, 36(3), 1482-1489.
Pavlides, S., Caputo, R., 2004. Magnitude versus faults' surface parameters: quantitative relationships from the Aegean Region. Tectonophysics, 380(3-4), 159-188. doi:10.1016/j.tecto.2003.09.019
Pavlides, S., 2016. Geology of earthquakes (2nd ed.). Thessaloniki: University Studio Press.
Pavlides, S., Chatzipetros, A., Sboras, S., 2018. Active faults as seismogenic sources in the Aegean region. 9th International INQUA Meeting on Paleoseismology, Active Tectonics and Archeoseismology. Possidi
Robertson, A., 2006. Sedimentary evidence from the south Mediterranean region (Sicily, Crete, Peloponnese, Evia) used to test alternative models for the regional tectonic setting of Tethys during Late Palaeozoic-Early Mesozoic time. Geological Society, London, Special Publications, 260(1), 91-154.
Robertson, A., 2022. Palaeozoic-Early Mesozoic transition from Palaeotethys to Neotethys: Synthesis of data and interpretations from the northern periphery of Gondwana (central and western Anatolia, Aegean, Balkans and Sicily). Earth-Science Reviews, 230.
Ten Veen, J., Postma., 1999. Neogene tectonics and basin fill patterns in the Hellenic outer-arc (Crete, Greece). . Basin Research, 11(3), 223–241. doi:10.1046/j.1365-2117.1999.00097.x
Veliz, V., Mouslopoulou, V., Nicol, A., Fassoulas, C., Begg, J., Oncken, O., 2018. Millennial to million year normal-fault interactions in the forearc of a subduction margin, Crete, Greece. Journal of Structural Geology, 113, 225-241. doi:10.1016/j.jsg.2018.05.019
Wells, D., Coppersmith, K., 1994. New empirical relationships among magnitude, rupture length, rupture width, rupture area, and surface displacement. Bulletin of the seismological Society of America, 84(4), 974-1002.
Zulauf, G., Blau, J., Dorr, W., Klein, T., Krahl, J., Kustatscher, E., Petschick, R., Van De Schootbrugge, B., 2013. New U-Pb zircon and biostratigraphic data of the Tyros Unit, eastern Crete: Constraints on Triassic palaeogeography and depositional environment of the eastern Mediterranean. Zeitschrift Der Deutschen Gesellschaft Fur Geowissenschaften, 164(2). doi:https://doi.org/10.1127/1860-1804/2013/0009
Zulauf, G., Kowalczyk, G., Krahl, J., Romano, S., 2008. The Mirsini syncline of eastern Crete, Greece: a key area for understanding. At P. Xypolias, G. Zulauf, New results and Concepts on the Regional. Z. dt. Ges. Geowiss.

17th INTERNATIONAL CONGRESS of the Geological Society of Greece

BULLETIN OF THE GEOLOGICAL SOCIETY OF GREECE, SP. PUBL.

EXTENDED ABSTRACT 064

Formation of Sitia's Geopark (Crete Island, Greece) caves in correlation with the structural setting of the area

Dretaki Antonia.[1], Dittopoulos Panagiotis Sotirios[1], Chatzipetros Alexandros[1], Papavasiliou Vasilios[2], Papavasiliou Vasilios[3], Paspaliaris Nikolaos[2], Tsirakakis Georgios[2], Perakis Evangelos[4]

(1) Department of Structural, Historical and Applied Geology, School of Geology Aristotle University of Thessaloniki, 54124, Greece, antoniadret@hotmail.com (2) FORSS, Sitia, Greece (3) Mountaineering Club of Hania, Chania, Greece (4) Sitia UNESCO Global Geopark

Research Highlights: The Sitia Geopark caves, including Pelekita, Kato Peristeras, Ano Peristeras, Chonos, and Vreiko, demonstrate significant tectonic influences on their formation. The tectonic setting, marked by E-W and NNE-SSW faults, shapes the orientation and development of these caves.

Introduction and background

The region of Sitia, distinguished by its topography marked by rugged mountains, intense tectonic activity, and a rich karst landscape, hosts several caves that are of significant historical importance in Greece. Consequently, the area has become a focal point for speleological studies, with numerous teams dedicating their efforts to mapping and exploring the region's cave systems. The caves of the Sitia Geopark include five caves in the Lassithi region, which were studied during a project targeted towards documenting the Geopark's geotopes (Geositia project): Pelekita, Kato Peristeras, Ano Peristeras, Chonos and Vreiko. The formation of these subterranean karst formations is attributed to the combined effects of erosion and chemical dissolution, resulting from the movement of groundwater through fissures in the rock formations. The structural characteristics and three-dimensional patterns of these caves are influenced by the rock type in which they were formed. The hydrochemical factors that influence them depend on petrological, tectonic, climatic, and other conditions. Whether cave forms are composed of active, under-formation or residual features, there is a possibility that they will diversify in the future under completely different conditions (Ford and Williams 2007).

The caves of eastern Crete were primarily formed within limestones and dolomites belonging to the Tripoli and Pindos Units, and along their contact with the Phyllite-Quartzite Unit s.l. (IGME, 1959). This process occurred under the influence of intense tectonic uplift conditions prevailing on the island, caused by the northward subduction of the African plate beneath the Eurasian one (Fassoulas, 2017).

The tectonic history of Crete is marked by significant extensional and compressional episodes. Since the Neogene, the island has experienced three major faulting events that have dissected the island in several blocks. The earliest fault group, formed during the Early Messinian (7-6 Myr), is characterised by E-W trending faults resulting from the southward roll-back of the subduction zone. This was followed by the Late Messinian to Early Pliocene (5 Myr) stage, characterised by N-S trending faults due to the extrusion of the Anatolian plate and regional stress field perturbations. The most recent fault group, dating from the Middle Pliocene to the present (4 Myr), comprises NE-SW and NW-SE trending faults driven by ongoing geodynamic processes (Fassoulas, 2017). More specifically, the active normal faults in the area are numerous and can be grouped into two main trends: the NNE-SSW trending fault group and the E-W to ESE-WNW trending fault group. They can be divided into the following Fault Zones: Ierapetra, Sitia, Orno, Mesa Mouliana and Xerocambos-Goudouras (Dretaki, 2024).

The above tectonic setting can influence the development of the topography of the area, and more precisely, the orientation of the drainage network, which includes the underground network of rivers and caves. The cave structures tend to develop inside fragmented limestone, along pre-existing fractures and faults. The present study is focused on investigating the influence that these intense tectonic settings had on the formation of the caves within Sitia Geopark. Furthermore, the study explores how caves contribute to the unravelling of tectonic structures that remain hidden beneath the surface, leading to a better mapping and understanding of the tectonic setting.

Methodology

Cave mapping is a fundamental aspect of speleology, providing a detailed and accurate representation of the underground environment. These maps are essential tools for understanding the spatial layout, geological features and environmental conditions of caves. The mapping process combines traditional surveying techniques with modern technology to capture the intricate details of cave systems. Cave mapping is carried out by dividing the cave into small imaginary rectilinear sections. In each section, the length, direction relative to magnetic north and inclination relative to the horizontal plane are measured. At the end of each section, the distances from the cave walls are measured to record the dimensions of the

cave. These measurements are processed by a computer program, producing a map in Cartesian coordinates.
The hardware used for mapping included the BRIC5 and DistoX1, an analogue compass, an analogue inclinometer, a tape measure and a laser rangefinder. In terms of software, the BRIC5 measurements were accompanied by the Topodroid app for Android and the processing was done using Visual Topo for Windows.
During the fieldwork of the GeoSitia project and the thesis of Dretaki (2024), fault measurements were obtained using a geological compass and the Android program FieldMove. Further processing and analysis of the data was carried out using QGIS and ArcGIS Pro. The rose diagrams were created using the QGIS plugin “Line direction histogram”. Furthermore, for the creation of the drainage network as well as the hillshade of the study area, the Digital Elevation Model of the Legal Entity of Public Law Hellenic Cadastre was used [Operational Programme Competitiveness, Entrepreneurship and Innovation 2014-2020 (EPAnEK)]. To achieve a more comprehensive interpretation of the landscape, the Digital Elevation Model (DEM) was used in combination with Google Earth Software.

Field data

The cave of Ano Peristeras is located west of the settlement of Karydi and is among the most significant and largest caves in Greece (Figure 1). It is situated within the limestones of Tripoli Unit (IGME, 1959). The cave’s entrance, shaped as a semi-circular doline with a radius measuring approximately 24 m, is situated at an altitude of 600 m. The broader area of the doline exhibits the contact between the Tripoli Unit and the Phyllites-Quartzites Unit. The first chamber is notable for its substantial dimensions, measuring 30 m in width and 90 m in height. This is followed by a second chamber that is comparatively smaller in size, with dimensions of 35 m in width and 13 m in height. Its total length is 8,250 m, making it the third longest cave in Greece. Through hydrologic data and pressure gauges, it is assumed that the Ano Peristeras Cave discharges to the Flega spring (Chailloux, 2015). The entrance of the cave is developed in a SSW-NNE direction, and another branch follows the same direction upstream, to the west of the entrance. The main branch develops in a W-E direction until the central part, where it turns NW-SE. These directions are due to the tectonics of the area and the NNE-SSW fault zone trending (as shown in yellow, Figure 1), as well as the older E-W faults (as shown in orange, Figure 1), which is confirmed by the correlation of the fault trend and cave branches rose diagrams (Figure 5). The dashed yellow lines indicate possible faults along which several branches of the cave were developed, parallel to the younger active Sitia Fault Zone (as shown in yellow, Figure 1). The tectonic stress of the limestone accelerates its disintegration and thus the formation of the cave along the fault zone. In addition, a large part of the cave is situated at the tectonic contact (thrust) of the limestones of the Tripoli Unit, which overlie the phyllites of the Phyllite-Quartzite Unit. A smooth limestone surface appears on the roof of the cave, in the part of the cave that develops within the red phyllites.

Figure 1. Map showing Ano Peristeras (lower, longer red line) and Chonos (upper, shorter red line) cave systems and their correlation with faults in the area. DEM Source: Legal Entity of Public Law Hellenic Cadastre, Operational Programme Competitiveness, Entrepreneurship and Innovation 2014-2020 (EPAnEK).

The cave of Chonos is located south of the homonymous settlement, a term employed in the Cretan dialect to denote a sinkhole (Figure 1). It has been determined that the cave develops at the point of contact between the upper layers of the Toplou beds of the Tyros Unit and the limestones of the Tripoli Unit (IGME, 1959, Klein *et al.*, 2008, Zulauf *et al.,* 2018). The cave's entrance, measuring 120 by 130 m and 25 m in depth, is a doline that appears to have been influenced by probable NE-SW trending faults. The cave development extends for approximately 700 m and reaches a depth of 90 m The first section of the cave is vertical, and then it transitions parallel to the contact between the Tyros Unit and the limestones of the Tripoli Unit. It is plausible that the cave discharges in the same underground drainage system as Ano Peristeras, and the presence of water is seasonal. The presence of speleothems, formed through the accumulation of mineral deposits, indicates that the cave is periodically filled with water, which then escapes through fissures at the cave's end. Mapping of the cave reveals the presence of two branches, which later connect. The main branch of the cave exhibits a WNW-ESE direction (as shown in orange, Figure 1), aligning parallel to the fault zone that brings the Tyros Unit into contact with the limestones of the Tripoli Unit (Klein *et al.,* 2008). The disintegration of limestone is accelerated by tectonic stress, leading to the formation of caves along the fault zone. The second branch, located a short distance west of the entrance and originating at the contact of the two Units, exhibits an NNE-SSW orientation and appears to develop within the same zone as certain branches of the Ano Peristeras (as shown in dashed yellow, Figure 1). The main branch exhibits a bend with a NNE-SSW orientation in its western segment, indicative of its influence by NNE-SSW trending faults (as shown in yellow, Figure 1). The above is confirmed with the correlation between the fault trend and the cave branches' rose diagrams (Figure 5 and 6).

Figure 2. Map showing Kato Peristeras and its correlation with possible faults in the area. Legend as in Figure 1. Basemap: Google Satellite.

The cave of Kato Peristeras is located 1.5 km from the settlement of Karidi, on the road to the settlement of Adravasti (Figure 2). It is located north of the road and can be reached by following a path for 350 m. The cave is developed in limestones of the Pindos Unit (IGME, 1959, Klein *et al.,* 2008). It is a horizontal cave with its entrance at an altitude of 615 m, in the area of Kato Platyvolo. Its entrance is a doline measuring 45 by 25 m and 20-25 m deep, which collapsed to reveal the cave. According to the primary mapping of the E.S.E. (Hellenic Speleological Society) it has a length of 100 m, a maximum ceiling height of 12 m, a depth of 63 m and a total area of 2800 m² (Petrochilou, 1970). The main chamber of the cave measures 75 by 35 m and is 3-10 m high. It is quite steep, with several limestone blocks sloping down towards the interior. At the end of this chamber, water escapes through fractures and discontinuities in the rock. To the left of the main chamber, there is a much smaller one, 19 by 11 m and 1.5-6 m high, with stalagmite speleothems, which joins the main chamber at two points. The cave develops primarily towards the W, in the direction of the NW-SE shear zone (as shown in dashed yellow, Figure 2). Inside the cave, especially in the left part of the chamber, several fault surfaces of a second NW-SE fault zone can be found during the descent. As shown in the rose diagrams (Figures 5 and 6), some smaller branches of the cave follow the NNE-SSW and the E-W trending faults. The tectonic stress on the limestone creates the conditions for faster dissolution and formation of the cave along this zone.

The geotope of the cave of Pelekita is located 3 km away from the settlement of Kato Zakros, following the E4 path to Karoumes beach (Figure 3). The cave is developed in limestones and dolomites of Tripoli Unit (IGME, 1959). The

cave of Pelekita, named after the nearby ancient quarry, is located at an altitude of 100 m in the foothills of Traostalos. According to the primary mapping conducted by the Hellenic Speleological Society (E.S.E.) in 1970, the cave's length is 310 m (Ioannou, 1970). However, more recent mapping by FORS Sitia has revealed a length of 370 m and a depth of 95 m The cave's entrance, measuring 15 m in diameter and 8 m in height, is oriented towards the east (Bruins *et al.,* 2019). The first chamber measures 20 m in length, 20 m in width, and 7.5 m in height. It is a horizontal cave that is developed sub-parallelly to the coastline, oriented NW-SE. The total number of chambers in this cave is four, including the entrance. The second chamber is considered the largest cave chamber in Crete and one of the largest in Greece, with a volume of about 300 m². It is characterized by a rich variety of speleothems, with an abundance of stalactites and stalagmites. At the base of the third and fourth rooms, there are small brackish water ponds, which are at the same altitude as the sea level. Between the last two chambers, there is a pile of limestone fragments, coming from the roof, due to the angle of the limestone bedding, which favours their collapse. In the eastern part of the cave, a relatively smooth surface is found, exhibiting characteristics of a fault surface, which extends to the south and is likely associated with an older possible NW-SE trending fault (as shown in dashed yellow, Figure 3). Based on the rose diagram (Figures 5 and 7), the mean trending direction is similar to Vreiko's cave, while smaller branches follow the NNE-SSW to N-S direction.

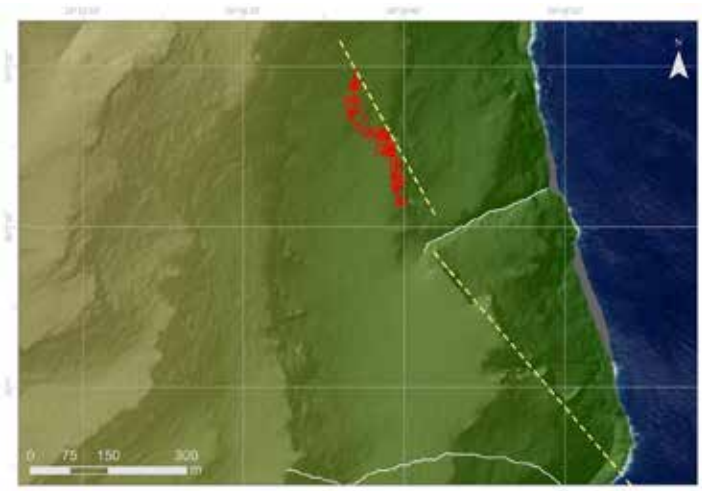

Figure 3. Map showing Pelekita and its correlation with possible faults in the area. Legend as in Figure 1. DEM Source: Legal Entity of Public Law Hellenic Cadastre, Operational Programme Competitiveness, Entrepreneurship and Innovation 2014-2020 (EPAnEK).

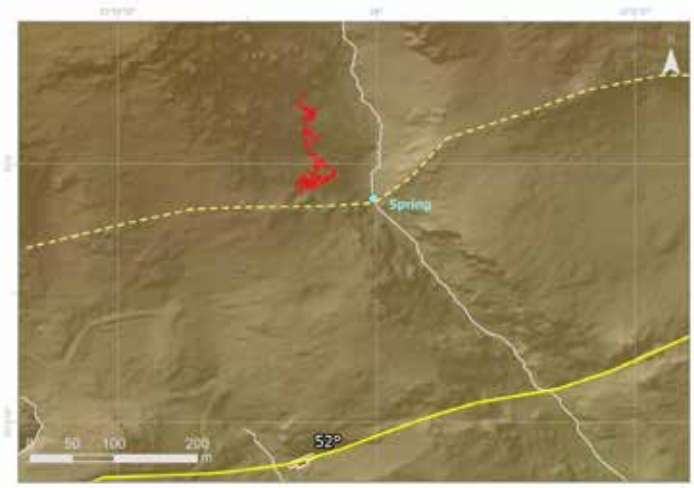

Figure 4. Map showing Vreiko and its correlation with faults in the area. Legend as in Figure 1. DEM Source: Legal Entity of Public Law Hellenic Cadastre, Operational Programme Competitiveness, Entrepreneurship and Innovation 2014-2020 (EPAnEK).

Vreiko Cave is located about 2 km north-east of the village of Pefki, following the road first to Makri Gyalos and then further north to the church of Estavromenos near the peak of Sarakinika (Figure 4). A 300 m path leads to the entrance of the cave. The cave develops within the limestones of the Tripoli Unit (IGME, 1959). The cave entrance is located at an altitude of 565 m and is a 7 m deep depression (Georgiakakis *et al.,* 2006) created by the collapse of the cave ceiling. It has a total length of 277 m and a maximum decline of 47 m. There is one entrance to the NW and two entrances to the south. In the northern part of the cave there are two chambers, the first measuring 60 by 5-22 m with a maximum height of 11.5 m (Georgiakakis *et al.,* 2006). The two chambers are separated by a pile of talus and surface sediments, above which there is an opening at a height of 9.5 m (Georgiakakis *et al.,* 2006), which is the second entrance to the cave. Continuing north, there is a second room leading to an outer porch and the third entrance to the cave . In the southern part of the cave there is a wide opening that leads to the deepest part of the cave, which is 34 m lower. The chamber measures 50 by 22.5-27.5 m and is 3-5.5 m high, with a shallow lake 3-5 m in diameter at its deepest point (Georgiakakis *et al.,* 2006). It has more impressive cave landforms than the northern room, with large stalactite columns and speleothems on the walls. To the left is another room measuring 31 by 7.5 m and 7.5 m high, at the end of which, in a small chamber, Byzantine pottery has been found consolidated with calcite material (Georgiakakis *et al.,* 2006). Just below the entrance to the cave, a spring flows near the vegetated area, which is in line with the southernmost point of the cave. There is a possible ENE-WSW trending fault that contributes to the surface discharge of water, inside the limestone bedrock (as shown in dashed yellow and blue dot as the spring, Figure 4). The fault is indicated by the topography, but also by the parallel development of a synthetic fault structure further south (Dretaki, 2024). The end and lowest part of the cave follows the direction of the above possible fault (Figure 4), which is also evident from the rose diagram (Figure 5 and 7).

Results and conclusions

In most cases, the development of the caves has been directly influenced by the local tectonic setting, including both older and newer faults and lithology. This phenomenon was clear through the correlation of fault zones and cave branch trends, the change in direction of the local drainage network, and in some cases, the existence of springs indicative of fault activity. The major E-W trending development of the caves corresponds with the same trending faults in the area as well as the NNE-SSW trending faults, but to a lesser extent. This finding suggests that the former were active for a longer period than the latter, indicating that the latter are more recent. The data gathered through field measurements offers further evidence to support this interpretation. However, additional field research is necessary to ensure more accurate conclusions. Such research could involve creating a more extensive network of measurements, which would allow for the confirmation or rejection of potential faults and thus correlations. To achieve this, a more in-depth caving mission would be required, with a skilled team that possesses a multidisciplinary understanding of speleology and geology. Regarding the deeper data interpretation, an analysis of 3D models through the software of Visual Topo could also lead to more detailed examination of underground tectonic formations, while experimenting with area proportional and no weighted-on length options in Line Direction Histogram could lead to a safer multivariate rose diagram data analysis.

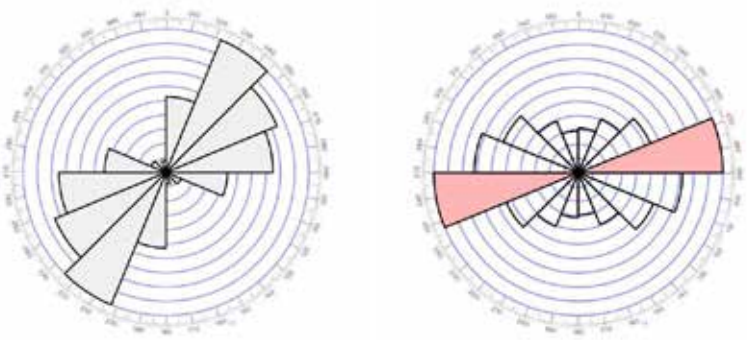

Figure 5. Left: Rose diagram showing the trend of faults in the study area (no weight on length). Right: Rose diagram showing the trend of the cave development of Ano Peristeras (weight on length, red= direction trend).

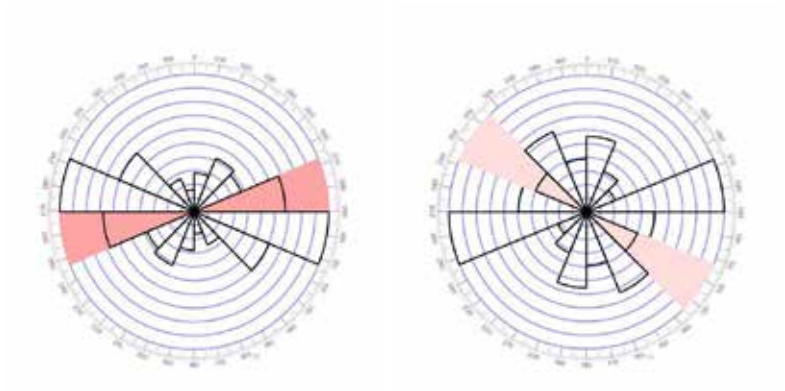

Figure 6. Rose diagram showing the trend of the cave development branches (weight on length, red= direction trend). Left: Chonos, Right: Kato Peristeras.

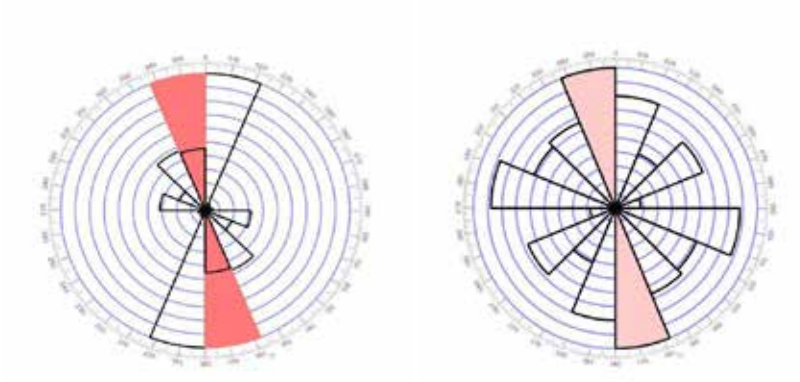

Figure 7. Rose diagram showing the trend of the cave development branches (weight on length, red= direction trend). Left: Pelekita, Right: Vreiko

Acknowledgements

This study is part of the GeoSitia project, which concerns the scientific documentation of Sitia Geopark geotopes. As part of this project, there were many contributors who made it possible, and we are thankful for their invaluable collaboration and guidance. We would like to thank the following speleologists, individuals or teams, for sharing their data: Lille Université Club Spéléo, Bruno Lemee, Christophe Emiel, Caroline Menet, Jean Luc Carron, Aurelien Depret, Frank Maciejak, Stanislas Francfort, Olivier Gaspe, Christophe Depin, Julien Tournois, Olivier Dufourneau, Frederic Bonacossa, Grigoris Anastasopoulos, Panagiotis Vavilis and Rigas Manos. Special thanks to Aristotle University of Thessaloniki and Municipality of Sitia, for supporting the project. We would like to thank the Legal Entity of Public Law Hellenic Cadastre for providing the Digital Elevation Model used in our analysis.

References

Bruins, H. J., Keller, J., Klügel, A., Kisch, H. J., Katra, I., & van der Plicht, J. (2019). Tephra in caves: Distal deposits of the Minoan Santorini eruption and the Campanian super-eruption. Quaternary international, 499, 135-147.

Chailloux, D. (2015). La Perte de la Colombe (Ano Peristeras) Karydi – Crête: Positionnement de la topographie de la Perte de la Colombe par radiolocalisation VLF.

Dretaki, A., 2024. Neotectonic study of Sitia area, eastern Crete, and assessment of the faults' seismic potential. Master Thesis, School of Geography, University of the Aegean, Inter-Institutional Postgraduate Studies Program "Natural Hazards and Disaster Mitigation", 236 pp.

Fassoulas, C., 2017. The geological setting of Crete: An overview. Minoan Earthquakes—Breaking the Myth Through Interdisciplinarity; Jusseret, S., Sintubin, M., Eds, pp.135-164.

Ford, D., & Williams, P. D. (2007). Karst hydrogeology and geomorphology. John Wiley & Sons.

Georgiakakis, P., Paragamian, K., Foteinakis, K., Papadaki, M. & Barlas, P. (2006). The caves Latsida Vreikou and Apoloustres in Pefki of Makry Gialos (Lassithi) [in Greek]. Proceedings of the 2nd Cretan Speleological Symposium in Memoriam of Eleutherios Platakis, May 29 2005, Herakleion, Crete, Greece, Hellenic Speleological Society, Department of Crete, Herakleion, pp. 47-51.

IGME., 1959. Geological map of Greece, scale 1:50.000 - sheet ZIROS. Athens: IGME.

IGME., 1959. Geological map of Greece, scale 1:50,000 - sheet IERAPETRA. Athens: IGME.

IGME., 1959. Geological map of Greece, scale 1:50,000 - sheet SITEIA. Athens: IGME.

Ioannou, I., (1970). The Cave of Pelekita in Kato Zakros, Sitia, Crete. Bulletin of the Hellenic Speleological Society, 10.6, pp. 40-46.
[in Greek].

Klein, T., Reichhardt, H., Klinger, L., Grigull, S., Wostal, G., Kowalczyk, G., Zulauf, G., 2008. Reverse slip along the contact Phyllite-Quartzite Unit/Tripolitsa Unit in eastern Crete: implications for the geodynamic evolution of the External Hellenides. Zeitschrift der deutschen Gesellschaft für Geowissenschaften, 159(3), 375-398. doi:https://doi.org/10.1127/1860-1804/2008/0159-0375

Petrochilou, A. (1970). The Cave of Peristeri, Karydi, Sitia, Crete. Bulletin of the Hellenic Speleological Society, 10.6, pp. 50-54. [in Greek].

Zulauf, G., Dörr, W., Marko, L., & Krahl, J. (2018). The late Eo-Cimmerian evolution of the external Hellenides: constraints from microfabrics and U–Pb detrital zircon ages of Upper Triassic (meta) sediments (Crete, Greece). International Journal of Earth Sciences, 107(8), 2859-2894.

Digital data

Digital Elevation Model-DEM from Legal Entity of Public Law Hellenic Cadastre, Operational Programme Competitiveness, Entrepreneurship and Innovation 2014-2020 (EPAnEK).

17th INTERNATIONAL CONGRESS of the Geological Society of Greece

BULLETIN OF THE GEOLOGICAL SOCIETY OF GREECE, SP. PUBL.

EXTENDED ABSTRACT 065

Enhancing Geoheritage through GEOAM: A Case Study of Tinos Island, central Aegean Sea, Greece

H. Drinia[1] G. Zafeiropoulos[1],

(1) Faculty of Geology & Geoenvironment, National and Kapodistrian University of Athens, Panepistimioupolis 15784, Zographou, Greece, cntrinia@geol.uoa.gr

Introduction

Geoheritage encompasses the recognition, conservation, and promotion of geologically significant sites and their cultural, educational, and ecological value. In this context, Tinos Island in the Cyclades stands out as a remarkable locale due to its complex geological history and the coexistence of geological formations with architectural features tied to human activity. This study employs the GEOAM (Geoeducational Assessment Method), an innovative framework proposed by Zafeiropoulos and Drinia (2023) and Zafeiropoulos (2024), to evaluate the geoheritage potential of Tinos Island and explore the interplay between its natural and built environments.

Tinos Island belongs to the Atticocycladic geological mass and is characterized by its complex metamorphic history and structural geology, deeply influenced by tectonic activities in the Aegean region (Figure 1). This geological mass comprises several distinct metamorphic units, including the Upper Unit, the Cycladic Blueschist Unit, and the Basal Unit. The Upper Unit, which has undergone greenschist-facies metamorphism, consists of serpentinites, meta-gabbros, and phyllitic rocks. The Cycladic Blueschist Unit, notable for its high-pressure metamorphism, includes marbles, calcschists, and various metasediments, reflecting the intense subduction processes that have shaped the region. At the lowest stratigraphic level, the Basal Unit contains a diverse array of metamorphic carbonate rocks. These units collectively highlight a dynamic tectonic environment with multiple detachments, showcasing the geological complexity and ongoing metamorphic processes defining Tinos within the Cyclades complex. Further illustrating this complexity, the island's stratigraphy includes additional divisions such as the Akrotiri Unit, predominantly in the southern region, comprising amphibolites, paragneisses, and minor silicate marbles. This unit is separated from the Upper Unit by the low-angle Vari detachment, emphasizing distinct tectonic settings (Bröcker and Franz, 1998). Beneath the Akrotiri Unit, the Upper Unit presents a metamorphic history shaped by diverse rock types and intricate tectonic interactions. Below these lies the Cycladic Blueschist Unit, marked by high-pressure metamorphism at approximately 450–500°C and pressures around 4–7 kbar. At the lowest level, the Basal Unit, mainly found in the northeastern part of the island, reveals a history of geological transformations influenced by regional metamorphism and magmatic intrusions. The presence of multiple detachments, discussed by Brichau et al. (2007) and Jolivet et al. (2010), underscores the dynamic tectonic regime of Tinos, with the North Cycladic Detachment System reactivating older geological structures such as the Vardar oceanic suture zone. Mapping and analyzing these geological units, based on fieldwork and historical data, provide a comprehensive understanding of Tinos Island's geological framework, offering valuable insights into the Cycladic region's tectonic and metamorphic history while aiding in the prediction of future geological developments in this seismically active area.

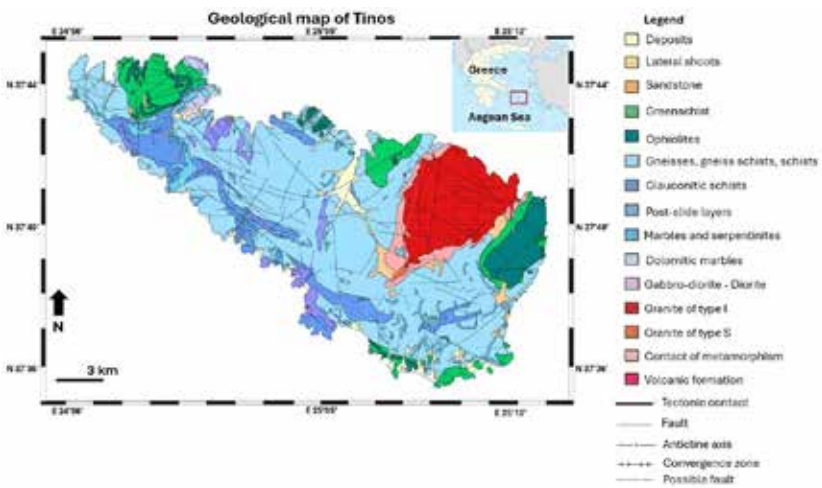

Figure 1. Geological Map of Tinos island after Lamont et al., (2000) and Leonidopoulou (2004), modified

Methodology

To assess and enhance the geoheritage of Tinos, the Geoeducational Assessment Method (GEOAM) was employed. The GEOAM assessment method is a comprehensive framework designed to evaluate the educational value, conservation status, and overall potential of geosites. By applying eight key criteria—Site Management and Visitor Experience (SMVE), Natural Resource Management (NRM), Environmental Education and Interpretation (EEI), Cultural and Historical Significance (CHS), Geoethics (GE), Economic Viability (EV), Community Involvement and Engagement (CIE), and Sustainable Development (SD)—along with their respective subcriteria, GEOAM provides a detailed scoring system that assesses various aspects of a geosite, such as accessibility, biodiversity conservation, interpretive resources, cultural importance, and sustainable practices. Scores are assigned on a scale of 1 to 5 for each subcriterion, weighted according to their importance, and combined to calculate an overall score using a specific formula. The final score categorizes geosites into five levels, from Low Implementation (LI) to Extremely High Implementation (EHI), offering a measurable and adaptable tool for enhancing the geoeducational value and sustainable development of geosites.

The application of GEOAM involved selecting six representative geosites on Tinos, including marble quarries, tafone, alveoles, tors, core stones and the iconic granite outcrop of Exombourgo (Figure 2). Each site was evaluated using a weighted scoring system, highlighting their strengths and areas for improvement. The methodology's focus on education and community involvement ensures that conservation efforts are both inclusive and impactful. This approach is particularly valuable in addressing the dual goals of heritage preservation and tourism promotion according to sustainable principles.

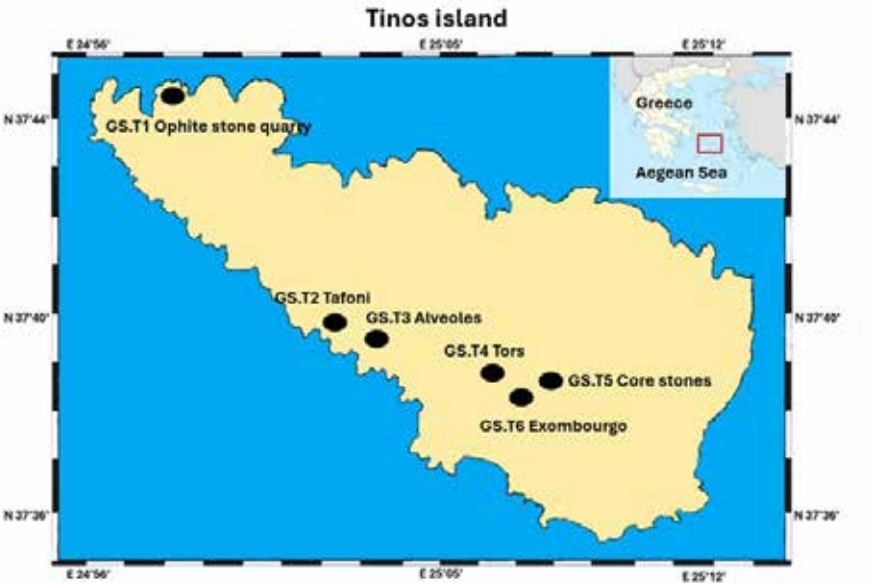

Figure 2. The selected geomorphosites in the island of Tinos

Results

The evaluation of the criteria using the GEOAM intricately revealed the following results (Table 1):

Table 1. Final scores for the geosites of Tinos

Criteria	Weight	GS.T1	GS.T2	GS.T3	GS.T4	GS.T5	GS.T6
SMVE	10%	2.66	2.83	2.5	3.16	2.5	2.66
NRM	10%	2.4	3.2	3	3.4	3	3.4
EEI	30%	2	2.4	2.2	2.4	2	2
CHS	10%	3.25	3	2.5	3.75	2.25	3.5
GE	20%	3.4	3.8	2.6	4	2.4	4
EV	5%	3.6	3.8	2.4	4	2.2	3.8
CIE	5%	3.5	4	2.25	4.5	2.25	4
SD	10%	3	3.33	2.33	3.33	2.66	3
Final Score		2.76	3.10	2.44	3.30	2.34	3.04
Characterization of score		MI	HI	MI	HI	MI	HI

Discussion

According to Table 1, it is evident that all geosites demonstrate significant importance, as none received a low score. Notably, three out of six geosites are classified under High Implementation (HI) in the final score characterization. Specifically, GS.T4 achieves the highest score of 3.30 (Table 10), indicating its strong potential for further development and the initiation of more community-driven strategies for its rational management.

Additionally, GS.T2 and GS.T6 showcase their geoheritage value, offering opportunities to drive collective management efforts. This approach could enable the local community to reap the benefits of their geosites within a sustainable development framework. On the other hand, GS.T1, GS.T3, and GS.T5 record the lowest scores of 2.76, 2.44, and 2.34, respectively. These lower scores highlight a lack of geoenvironmental activities and initiatives to enhance the visibility and value of these geosites. This is further reflected in the fact that the Environmental Education and Interpretation (EEI) criterion consistently receives the lowest scores across all geosites.

To address this issue, collaboration among the local community, stakeholders, and policymakers is essential. Such cooperative efforts would enable a holistic approach to enhancing the geoheritage value of these areas. At the same time, this would safeguard the cultural dynamics of the region, which, according to a European study, face certain threats. Geo-education, through organized geoeducational activities or recreational initiatives, could play a constructive role in benefiting society, delivering economic, social, and environmental advantages.

Furthermore, promoting structured geoeducational activities can foster a geoethical mindset and instill sustainable values in participants. By aligning with the principles of sustainable development, such initiatives would create a society that exists harmoniously with the natural environment..

Conclusions

Tinos Island showcases a remarkable intersection of geology, culture, and geotourism potential. The island's unique geomorphology, shaped by its dynamic tectonic history, offers diverse features such as granitic tors, core stones, and tafoni formations, which contribute to its high geoheritage value. Additionally, Tinos' cultural identity is enriched by its marble craftsmanship, recognized by UNESCO, and its rich tradition of artistic expression.

Evaluating its geosites using the GEOAM method highlighted both strengths and areas for improvement. Geosites like GS.T4 exhibit high implementation potential for geoeducational activities, while others lack necessary infrastructure and environmental education elements. Integrating local communities, stakeholders, and policymakers is critical for sustainable development of the island.

By fostering geoethical awareness and promoting alternative tourism, Tinos can balance cultural preservation with economic and environmental benefits, ensuring its legacy as a dynamic and sustainable destination.

Acknowledgements

The authors extend their heartfelt thanks to the organizing committee of the 17th International Congress of the Geological Society of Greece and the anonymous reviewers for their thorough consideration of this extended abstract.

References

Brichau, S.; Ring, U.; Carter, A.; Monié, P.; Bolhar, R.; Stockli, D.; Brunel, M., 2007. Extensional Faulting on Tinos Island, Aegean Sea, Greece: How Many Detachments? Tectonics , 26, TC4009. https://doi.org/10.1029/2006TC001969.

Bröcker, M.; Franz, L. 1998. Rb–Sr Isotope Studies on Tinos Island (Cyclades, Greece): Additional Time Constraints for Metamorphism, Extent of Infiltration-Controlled Overprinting and Deformational Activity. Geological Magazine, 135, 369–382. https://doi.org/10.1017/S0016756898008681

Jolivet, L.; Lecomte, E.; Huet, B.; Denèle, Y.; Lacombe, O.; Labrousse, L.; Pourhiet, L.; Mehl, C., 2010 The North Cycladic Detachment System. Earth Planet. Sci. Lett., 289, 87–104. https://doi.org/10.1016/j.epsl.2009.10.032 .

Lamont, T.N.; Roberts, N.M.; Searle, M.P.; Gopon, P.; Waters, D.J.; Millar, I., 2020. The Age, Origin, and Emplacement of the Tsiknias Ophiolite, Tinos, Greece. Tectonics, 39, e2019TC005677. https://doi.org/10.1029/2019TC005677

Leonidopoulou, D., 2004. Geological and Geomorphological Factors in the Formation of Intrinsic Vulnerability of Fractured Rocks: Application on the Island of Tinos. Ph.D. Thesis, Department of Physical Geography-Climatology, Department of Geology, National and Kapodistrian University of Athens, Athens, Greece. Available online: http://dx.doi.org/10.12681/eadd/17314 (accessed on 29 June 2024).

Melidonis, N.G.; Triantaphyllis, M., 2003. IGME Geological Map of Greece, Tinos–Yaros Sheet, 1:50000; Institute of Geology and Mineral Exploration: Athens, Greece.

Zafeiropoulos, G. 2024. The Importance of Geoenvironmental Education in Understanding Geological Heritage and Promoting Geoethical Awareness: Development and Implementation of an Innovative Assessment Method, with a Case Study of the Southeast Aegean Islands. Ph.D. Thesis, National and Kapodistrian University of Athens, Faculty of Science, Department of Geology and Geoenvironment, Athens, Greece, 227 p.

Zafeiropoulos, G., Drinia, H., 2023. GEOAM: A Holistic Assessment Tool for Unveiling the Geoeducational Potential of Geosites. Geosciences 2023, 13, 210. https://doi.org/10.3390/geosciences13070210

17th INTERNATIONAL CONGRESS of the Geological Society of Greece

BULLETIN OF THE GEOLOGICAL SOCIETY OF GREECE, SP. PUBL.

EXTENDED ABSTRACT 066

Tinos Island, Aegean Sea, Greece, Geopark: A Pioneering Initiative in Climate Change Resilience and Geoconservation

H. Drinia[1], G. Zafeiropoulos[1]

(1) Faculty of Geology & Geoenvironment, National and Kapodistrian University of Athens, Panepistimioupolis 15784, Zographou, Greece, cntrinia@geol.uoa.gr

Introduction

Tinos Island, part of the Cyclades in Greece, boasts a remarkable granitic landscape with geomorphs of significant geological, cultural, and educational value. These geomorphological features, shaped over millennia, are increasingly vulnerable to the impacts of climate change, which can accelerate erosion, alter landforms, and threaten the preservation of the island's natural heritage. This study explores the feasibility of establishing a Geopark on Tinos Island, with a central mission to protect, promote, and utilize the island's natural and cultural heritage. Special emphasis is placed on addressing climate change and advancing geoconservation practices to mitigate the effects of environmental changes on these unique geomorphs. Unlike existing Geoparks, this project stands out by integrating the unique geological features of Tinos with the island's cultural narratives, offering an innovative approach to linking geoconservation with sustainable development and community engagement.

Geological Setting and Cultural Significance

Tinos Island, part of the Cyclades plateau in the Aegean Sea, boasts a complex geological setting shaped by tectonic processes associated with the Alpine orogeny. It lies within the Attic-Cycladic Metamorphic Complex, a region that showcases the dynamic interplay of subduction, high-pressure metamorphism, and subsequent extensional tectonics during the Tertiary period (Figure 1). These processes have given rise to a diverse range of geological features, making Tinos a natural laboratory for understanding Earth's dynamic systems.

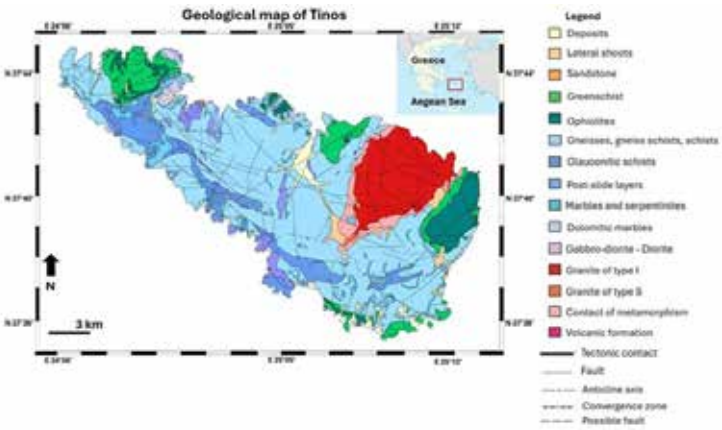

Figure 1. Geological Map of Tinos island after Lamont et al., (2000) and Leonidopoulou (2004), modified

The island's lithology is dominated by metamorphic rocks, including schists, marbles, gneisses, and amphibolites. These rocks were formed under high-pressure, low-temperature conditions during subduction. Tinos is particularly renowned for its high-quality marbles, which have been used extensively in art and architecture since antiquity. Schists and gneisses, characterized by their foliated textures, also contribute to the island's distinct geological character. Adding to this diversity are granitic and granodioritic intrusions from the Miocene period, dated to approximately 18–13 million years ago. These granitoids, formed during post-orogenic extension, are a hallmark of the Cyclades and play a crucial role in shaping Tinos' geomorphology (Stournaras 2006). This granitic landscape, covering 22.6 km², forms a triangular pattern with vertices at Exomvourgo, Livadia Bay, and Kakia Skala. Notable geomorphs, including tors and tafoni, have developed due to spheroidal weathering, creating a visually striking terrain. The area around the village of Falatados, located in the semi-mountainous Pano Meri region between Tinos' highest mountains, Exomvourgo and Tsiknias, contains significant clusters of these geomorphs (Figure 2). These geological features, intertwined with local folklore, architecture, and agricultural traditions, add layers of cultural and social value to the landscape.

Figure 2. Granitic geomorphs around the village of Falatados

Tinos' geology holds significant cultural, scientific, and economic value. Its marbles, known for their exceptional quality, have been used in iconic structures like the Parthenon. The island's geological features attract researchers and geotourists, offering insights into tectonic and metamorphic processes while showcasing the interplay between geological heritage and human history. The unique geomorphic features and the island's potential as a Geopark underscore the importance of integrating geoconservation with sustainable development

Climate Change and Geoconservation Focus

Climate change poses challenges to the preservation of Tinos' granitic landscape. Rising temperatures, shifting precipitation patterns, and increased weathering rates threaten the stability and appearance of the granite geomorphs. The proposed Geopark aims to serve as a hub for studying these impacts while implementing adaptive geoconservation measures. This project is original in its commitment to directly addressing the intersection of climate change, geological heritage, and community well-being, setting a benchmark for future initiatives in similar environments. Key initiatives include a) the establishment of research programs to monitor weathering rates and the effects of climate variability on the granitic formations, b) the development of techniques to stabilize vulnerable geomorphs and preserve traditional stone buildings against climatic impacts, c) the assessment of how climate change influences the surrounding ecosystems and integrating findings into conservation strategies.

To achieve its objectives, the following interventions are proposed:

- Creation of new paths and improvement of existing ones to enhance accessibility while minimizing environmental impact.
- Development of information and visitor service infrastructure, including a central information center.
- Promotion and protection of granite massifs and geomorphs, emphasizing their vulnerability to climate change.
- Restoration, promotion, conservation, and protection of traditional stone buildings as part of the island's cultural heritage.
- Establishment of rest areas and educational zones for visitors.
- Installation of interpretative signs to provide information about the geological, ecological, and cultural significance of the sites.
- Organization of educational and cultural events to raise awareness of climate change and geoconservation

Discussion - Conclusions

The proposed Tinos Island Geopark will serve as a catalyst for addressing climate change and promoting geoconservation while celebrating the island's unique geological and cultural heritage. By combining research, education, and sustainable tourism, the Geopark will enhance the resilience of the local landscape and community, ensuring its preservation for future generations. Its originality lies in its innovative integration of climate change research, community-driven geoconservation, and the sustainable promotion of one of Greece's most distinctive geological landscapes.

Acknowledgements

The authors extend their heartfelt thanks to the organizing committee of the 17th International Congress of the Geological Society of Greece and the anonymous reviewers for their thorough consideration of this extended abstract.

References

Lamont, T.N.; Roberts, N.M.; Searle, M.P.; Gopon, P.; Waters, D.J.; Millar, I., 2020. The Age, Origin, and Emplacement of the Tsiknias Ophiolite, Tinos, Greece. Tectonics, 39, e2019TC005677. https://doi.org/10.1029/2019TC005677

Leonidopoulou, D., 2004. Geological and Geomorphological Factors in the Formation of Intrinsic Vulnerability of Fractured Rocks: Application on the Island of Tinos. Ph.D. Thesis, Department of Physical Geography-Climatology, Department of Geology, National and Kapodistrian University of Athens, Athens, Greece. Available online: http://dx.doi.org/10.12681/eadd/17314 (accessed on 29 June 2024).

Stournaras, G., 2006, “The granite field of Volax (Tinos island, Hellas), Proceedings of the 4th European geoparks meeting, 2-5 October 2003 Anogia Crete, p. 85-91.

17th INTERNATIONAL CONGRESS of the Geological Society of Greece

BULLETIN OF THE GEOLOGICAL SOCIETY OF GREECE, SP. PUBL.

EXTENDED ABSTRACT 067

Hydrogeochemical Characteristics of Alfeios River and the wider hydrographic Network in the Lignite Basin Area of Megalopolis.

Christos Drougas [1] , Efstratios Kelepertzis [1] , Zacharenia Kypritidou [1] , Evangelia Sigala [2], Christos Roumpos [3] , Georgios Louloudis [3] , Eleni Mertiri [3], Evangelos Oikonomopoulos[2]

(1) Department of Geology and Geoenvironment, National and Kapodistrian University of Athens, Panepistimiopolis, Zographou, 15784, Athens, Greece

(2) Laboratory of Environmental Chemistry and Special Materials, Public Power Corporation (PPC) Innovation Hub, Leontariou 9, Leontario 15351, Athens, Greece

(3) Department of Mining Engineering and Closure Planning, Public Power Corporation of Greece,10432 Athens, Greece

Research highlights

- Strong lithological control on dissolved constituents in surface waters, influenced by regional geology.
- Nitrogen species mainly originate from sewage inputs from Megalopolis, with minimal lignite mining impact on Alfeios River water quality.

Abstract

This study aims at the hydrogeochemical evaluation of surface waters and the possible anthropogenic impact affecting the surface water quality in the complex environment of the Megalopolis basin, including over 50 years of lignite mining. The results can guide sustainable restoration strategies and environmental policies in the transition era of mine closure. In March 2024, 24 surface water samples were collected from upstream to downstream locations along the Alfeios River and its tributaries, which flow near the lignite operations. The chemical parameters of NH_4^+ (maximum 3 mg/L), SO_4^{2-} (range from 3 to 1010 mg/L), Mn (range from 1 to 338 μg/L), and Mo (range from 0.2 to 1027 μg/L) were identified as the most of environmental concern, exhibiting significant variability among samples. The presence of SO_4^{2-}, Mn, and Mo in the water samples indicates a geogenic origin, strongly influenced by the regional lithology, including lignite deposits, postAlpine sediments, and geological formations within the Pindos zone. The samples were categorized into three clusters (C1, C2, and C3) according to Hierarchical Cluster Analysis (HCA). Samples in Cluster 3, located near the old mining area, showed the highest concentrations of major and trace elements, exceeding the EU limits for Mn (50 μg/L) and SO_4^{2-} (250 mg/L) and were classified as Ca_2^+-SO_4^{2-} type waters. In contrast, C1 and C2 samples had a Ca^{2+}-HCO_3^- hydrochemical type. The scatter plot of NO_3^-/Cl^- ratios vs Cl^- indicated that the dominant source of NO_3^- was sewage from the town of Megalopolis. The Alfeios River appeared to be minimally affected by lignite activities, with no significant changes in water chemistry observed before and after the mining area, except for slightly elevated Mn and Mo levels, most of which remained below WHO and EU limits.

Keywords: Hydrogeochemistry, Surface Water, Lignite Mining, Post Mining

Introduction / Background

Lignite mining has been a major source of energy, significantly contributing to local and national economies, including that of Greece. Many studies have extensively examined the contamination and geochemistry of surface and groundwater resources near coal mines across various locations and different geological environments (GonzálezMartínez et al., 2019; Yang et al., 2023). However, environmental concerns related to coal mining activities and water resources will remain significant, even after the closure of mines (Liu et al., 2020). The geology of a region is a primary factor influencing the chemical composition of waters and the release of different types of contaminants, including metals and major ions, due to the geochemical conditions and anthropogenic activities (Kelepertzis et al., 2023; Yang et al., 2023). Coal mining can potentially contaminate surface and ground waters with pollutants such as sulfates and metals, resulting from coal processing and the exposure of sulfide minerals in atmospheric conditions (An et al., 2024). Also, various types of wastes affect water quality, including acid mine drainage, waste disposal (e.g. dumping sites), waste rocks, tailing storages, and liquid industrial wastes from power plants (Welch et al., 2021). The post-mining reclamation process has also been shown to affect geochemical conditions in abandoned or closed areas. Studies have shown that exposure of mineral residues and waste from lignite could potentially affect heavy metal and ion concentrations in surface water for many years after mine closure, making monitoring necessary (Liu et al. al., 2020; An et al., 2024). Lastly, differences in the chemical composition of the river are associated with various land uses and activities such as agricultural (fertilizer leaching etc.), domestic sewage, and industrial wastes

(Kypritidou et al., 2024).

Surface water quality of the Alfeios River in Megalopolis has shown elevated concentrations of some ions, e.g. Ca^{2+}, Mg^{2+} and SO_4^{2-} in the river water (Dimitrakopoulos et al., 2007). Louloudis (2017) applied Principal Component Analysis (PCA) to determine the correlation between different types of water in the region, such as surface waters, groundwaters, aquitards, and pit lakes. It was found that karstic waters, surface waters, and aquitard waters are not affected by mine waters in the region. Despite the above studies, there is no comprehensive systematic environmental monitoring of surface water quality in the region. The aim of this study is to cover this gap by sampling all rivers and tributaries flowing through the lignite mining area to define the pollution sources that influence the water hydrochemistry. The findings of this research aim to provide useful information regarding the hydrogeochemical status of surface waters, the geological influence in water geochemistry and imprint the environmental pressures from the human activities in the region. The geochemical stability of the region is one of the main key criteria to consider for the environmental rehabilitation of the Megalopolis Lignite Center (Sokratidou et al., 2018).

This study can establish geochemical baseline conditions before post-mining activities and help for a better understanding of the hydrogeochemical status of the area and support environmental rehabilitation and monitoring plans. The specific objectives are: a) To determine the hydrogeochemistry of all surface waters in the area and their effect on the Alfeios River and, b) to investigate the influence of the regional geological structure and any anthropogenic contamination on major ion and trace element concentration.

Description of the study area

Megalopolis region is located in the center of the Peloponnese peninsula Greece. The basin exhibits an elliptical form, with its major axis oriented in an NNW–SSE direction, stretching over a length of 18 km. The study area could be characterized as small hydrological basin due to the complicated hydromorphology of the region where many small tributaries flow near the Megalopolis town, the lignite mining works and the sites of the external waste dumps. The main river of the area is Alfeios River flowing from the south to Northwest direction, spanning 127 km before discharging into the Gulf of Kyparissia. This study focuses on the Southern part of the basin, where the river traverses the lignite basin of Megalopolis. The biggest tributaries are Elissonas and Xerilas, which flow from East to West and South to North direction and finally flow into Alfeios River.

The geology of the region is shown in Fig. 1. The Pindos unit is the main geological unit in surrounding mountains with limestones, cherts, dolomites, and flysch. In the eastern part of the basin, the Gavrovo-Tripolis Unit appears mainly with limestones, dolomites, Flysch and the Volcano-sedimentary unit (Tyros Beds). Only in small exchanges northeast of the basin does the quartzite-phyllite series show up with marble, schist, and phyllites (IGME, 1997). Lastly, Mesozoic ultramafic rocks also occur in small extensive throughout the basin's marginal rocks. The central part of the basin is covered by different ages of post-alpine sediments from the upper Pliocene with Makryssion formation up to the Holocene Alfeios river terraces with clays, marls, red loam, coarse clastic sediments and lignites.

Figure 1: Geological map of the study area with the sampling locations.

Land use and Mine activity

The main economic sectors are primary (7% of the population) with cultivated land, secondary (36%) by limited industrial and artisanal activity, and tertiary (40%) tourist and economic centres (Energy and Climate Action Plan, 2021). The dominant economic activity was lignite mining by the Public Power Corporation (PPC), starting with the Thoknia mine in 1970. The other lignite fields include: Marathousa (started at 1989) ceased the exploitation in-2015, Kyparissia lignite field (started 1987) finished in 2012 and Choremi lignite field, which was the only active mine site since 1970 until the end of 2024. In the area two (2) Power Plans (PP) exist, with a total of four lignite power units: I and II (19702011), III (1975-2022) (PP A), and IV (1991- end of 2024) (PP B), with a total installed capacity of 850MW. There is also a natural gas Unit V with 811 MW total capacity. In March 2024, only two factories remained operational: a lignitefired power plan (Unit IV), which works when the energy demand is high, and the fully operational natural gas factory (Unit V). By the end of 2024, all lignite power plants were ceased, leaving only the gas unit. New activities like agriculture, renewable energy, and environmental projects will replace lignite operations (Louloudis et al., 2024) considering the master plan for the post mining areas.

Methods

The sampling campaign took place during March 2024 (wet period), collecting 24 surface water samples; ten samples from the Alfeios River (A0-A9) and 12 water samples from tributaries (ZR1, X1, KF1, ZG1, E1, E2, K1, LG1, ZT1, P1, ZM1, T1, SIK1) that discharge directly or indirectly into Alfeios River (Fig. 1). The physicochemical parameters (pH, EC, TDS, Eh, and Dissolved Oxygen) were determined in situ with a pre-calibrated portable multiparameter. The samples were collected in triple-rinsed high-density polyethylene bottles for further analyses. All water samples for analysis of trace elements and major cations were filtered on-site through 0.45 μm membrane filters and acidified down to pH<2 with conc. HNO3 (65%). All water samples were stored at 4 0C or frozen condition until further analysis.

Laboratory analysis and treatment of data

All water samples were analyzed for major cations (Ca^{2+}, K^{+}, Mg^{2+}, Na^{+}) with the ICP-OES (Agilent 5800), trace elements (B, Li, Be, Al, V, Cr, Mn, Fe, Co, Ni, Cu, Zn, As, Se, Sr, Mo, Cd, Sn, Sb, Hg, Ti and Pb) with ICP-MS/MS (Triple Quad 8900), major anions (Cl^{-}, NO_2^{-}, NO_3^{-}, PO_4^{3-}, SO_4^{2-}) with ion chromatography (DIONEX ICS-2000). Ammonium ion (NH4+) was analyzed only in the sampling sites of Alfeios (A0-A9) and Zarzakis (ZR1) with the HACK LANGE DR 3900. All water analyses were carried out in the PPC Innovation hub in the Laboratory of Environmental Chemistry and Special Materials (PPC) and standardized according to ELOT EN ISO/IEC 17025. Bicarbonate (HCO_3^{-}) was measured at the Laboratory of Economic Geology and Geochemistry at the Department of Geology and Geoenvironment (NKUA) by the acid titration method using H2SO4 (1.6 N) until a pH of 4.5. The ionic charge balance error (CBE%) was below 5% for all samples, except for P1 (8.6%) and ZT1 (7.2%). Statistical and graphical analysis of the acquired data was done with the Minitab 7 ® v 17.1 statistical software analysis. Elemental concentrations close to or below the method detection limits were excluded from further data processing. Statistical analysis was restricted to parameters that showed great variability (EC, Ca^{2+}, Mg^{2+}, K^{+}, Na^{+}, Cl, HCO_3^{-}, SO_4^{2-}, NO_3^{-}, Mn, Mo and Sr). The statistical methods that were used are: Hierarchical cluster analysis (HCA) with the Ward method and Boxplot of the parameters.

Results and Discussions

All water samples, except SIK1 (pH 6.5, slightly acidic), were near-neutral to mildly alkaline. Oxidationreduction potential (Eh) in most samples was indicative of oxidizing conditions, except for samples E2 and P1, where Eh values were slightly reduced (-47 and -26 mV, respectively). Electrical conductivity (E.C.) varied widely between 415 μS/cm and 2150 μS/cm, with an average of 788 μS/cm, indicating strong differences in chemical composition. Dissolved oxygen (DO) ranged from 6.6 to 10.3 mg/L. Calcium (Ca^{2+}) levels ranged from 63 mg/L to 421 mg/L, with a median of 115 mg/L; specific samples like P1, T1, SIK1, and ZT1 had elevated levels (>195 mg/L). Bicarbonate (HCO_3^{-}) was stable at 200–300 mg/L, except for SIK1, which exhibited a low value of 98 mg/L. Sodium (Na^{+}), K^{+}, and Mg^{2+} were generally low, except for T1, where Na^{+}, K^{+}, and Mg^{2+} were detected at higher levels 42 mg/L, 22 mg/L, and 44 mg/L, respectively. Sulfate (SO_4^{2-}) ranged from 3 mg/L to 1010 mg/L, with the highest values in SIK1 (553 mg/L) and T1 (1010 mg/L), P1 (274 mg/L) and ZT1 (318 mg/L), exceeded the acceptable drinking water for sulfate ions 250 mg/L(WHO 2022). Chloride (Cl^{-}) was generally below 20 mg/L, except for T1 (61 mg/L) and ZT1 (26 mg/L), both well below the acceptable limit for drinking water of 250 mg/L (WHO 2022).

Nutrient levels were low, with NO_3^{-} ranging from 8 to 16 mg/L in the Alfeios River, and most tributaries below 1 mg/L, except for ZR1 (13 mg/L) and T1 (11 mg/L), all within the WHO-acceptable drinking limit of 50 mg/L. Ammonium (NH_4^{+}) varied from <0.02 mg/L to 3.04 mg/L, with ZR1 showing the highest value above the drinking water

limits of 0.5 mg/L (EU, 2020; WHO, 2022). In the Alfeios River, NH_4^+ values were below 1.45 mg/L and decreased downstream (A8) to 0.34 mg/L. Phosphate (PO_4^{3-}) was generally undetectable, except for ZR1, T1, and ZT1, which had elevated concentrations (0.3 mg/L, 1.8 mg/L, and 0.5 mg/L, respectively). Trace elements such as Pb, Tl, Ag, Sb, Cd, and others were mostly below detection limits, but higher concentrations of Se, Ni, Fe, Mn, and Mo were observed in specific samples. Manganese (Mn) ranged from 1 μg/L to 338 μg/L, with several samples (P1, ZR1, T1) exceeding the WHO, (2022) limit of 80 μg/L. Molybdenum (Mo) had a median value of 3 μg/L, with three samples (E2, T1, ZT1) exceeding the WHO, (2022) limit of 70 μg/L.

Boxplot analysis (Fig. 2) revealed that Cluster 1 shows the lowest concentrations of all chemical parameters, with only a few outliers for Mn (PAN1) and Mo (E2). Cluster 2 exhibits higher concentrations than Cluster 1 across all parameters, especially for NO_3^- (>8 mg/L). Cluster 3 exhibited the highest variability and concentrations for most chemical parameters, except for NO_3^- (<8 mg/L). According to Piper classification diagram (Fig. 3) the water samples of Cluster 1 and Cluster 2 are of Ca^{2+} - HCO_3^- type. The samples from Cluster 3 are of Ca^{2+}-SO_4^{2-} type.

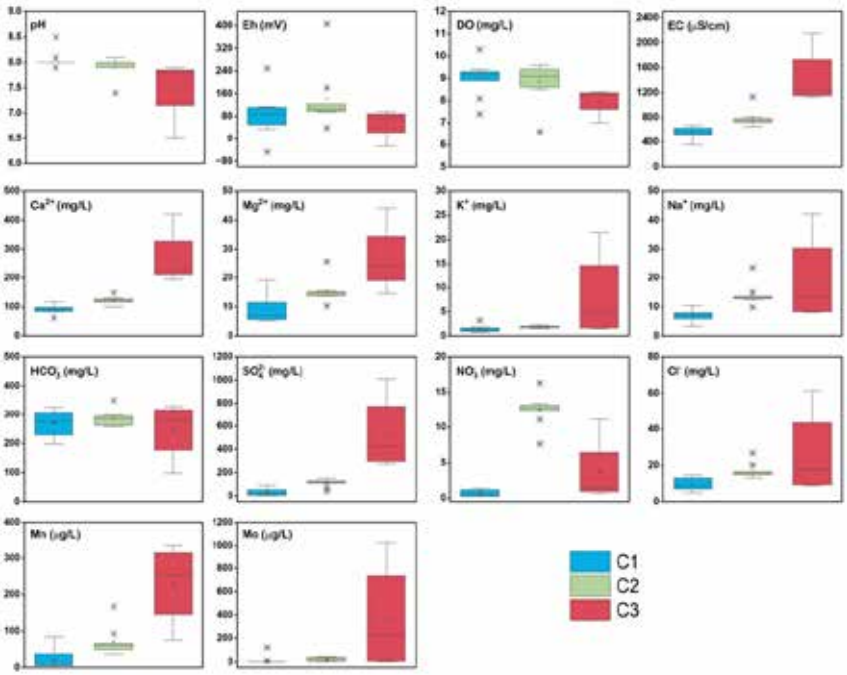

Figure 2: Boxplot of major chemical parameters based on the classification of surface water samples according to HCA.

The presence of Na^+, K^+, and Mg^{2+} in surface waters is associated with the dissolution of the clay minerals existing in the area. Kelepertzis and Kontis (1997) found that these elements have a strong association with clay minerals and plagioclase feldspar. Moreover, the sources of SO_4^{2-} are the geogenic factors of the region, as the composition of lignite is strongly associated with the geological environment of Megalopolis region. The low NO_3^-/Cl^- ratios and high Cl^- concentrations along the Alfeios river indicate sewage contamination from Megalopolis town as the main NO_3^- source (Fig. 4). High Mn content is primarily due to the presence of the Pindos zone in the Peloponnese, which contains high amounts of Mn, with Mn content ranging from 100 ppm to as much as 10,900 ppm, as well as localized small Mn deposits (Pe-Piper & Piper, 1989; Photiades & Perseil, 2002). Secondly Mn originated from the sediments of the area and lastly from the mafic and ultramafic rocks in the area. Mo is generally absent from local waters, except for two notable sources. The first is located downstream in Elissonas river (E2) and the second source of Mo enrichment is associated with the Gavros tributary (T1 sample). As suggested by Dimitrakopoulos et al. (2016), Mo shows high leaching potential because it is mobile and soluble in alkaline environment, and in Megalopolis, the geochemical composition of the lignite ore is particularly enriched in Mo.

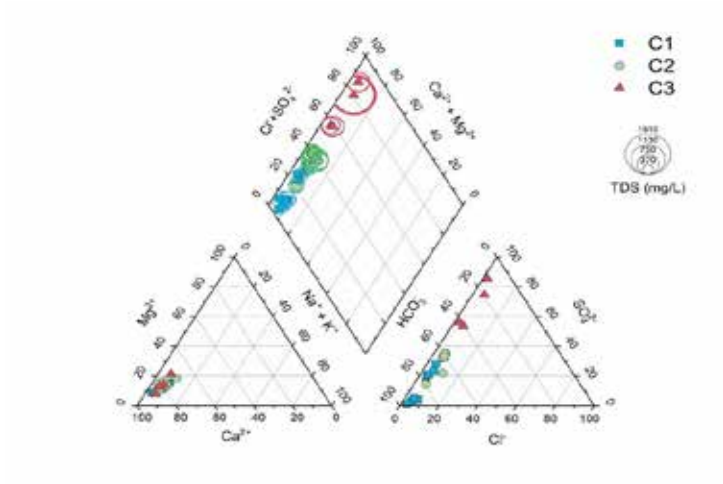

Figure 3: Piper diagram for the surface samples of the study area based on the classification of surface samples according to the results of HCA

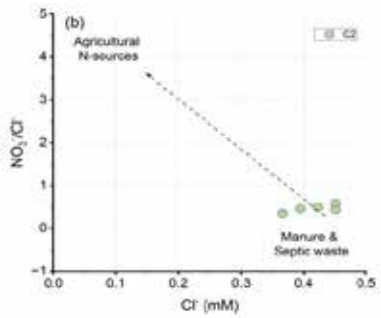

Figure 4: Scatter plot of NO3−/Cl− ratios and Cl−. The limits for agricultural activities and manure/sewage have been taken by Su et al., (2024).

Conclusions

- The Alfeios River appeared to be minimally affected by lignite activities, with no significant changes in water chemistry observed before and after the mining area.
- High Ca^{2+}, Mg^{2+}, Na^{+}, K^{+}, and SO_4^{2-} concentrations are observed in tributaries flowing near the external waste dumps and near Thoknia mine.
- High NH_4^{+}, Cl^{-} concentrations and low NO_3^{-}/Cl^{-} ratios in the Zarzakis stream, point to septic waste from Megalopolis town as the main source of NO_3^{-} contamination that affects the entire length of the Alfeios river.
- Trace elements such as Mn and Mo exhibit distinct sources of enrichment. Manganese appears to originate both from the Chert series (Pindos zone) and post-Alpine sediments in the western basin. In contrast, Mo enrichment is observed in samples after the Elissonas River confluences with the Alfeios River. This enrichment could be attributed to the dissolution of material from the external waste disposal site. The influence of fly ash deposits potentially could be considered as an additional Mo source; however, the external trenches network in the mine perimeter, diverts the surface runoff into external and internal reservoirs, where the concentrated water is pumped and used for the rewetting of desulfurization and fly ash solid waste deposits inside the Thoknia mine area. Therefore, the surface water, that is in contact with the with fly ash deposits, is recycled inside the mine, and leaks in the outside are prevented.

Acknowledgements

This study was partially funded by the Special Account for Research Grants, NKUA project no. 21070 (Educational, research and operational requirements of the Department of Geology & Geoenvironment).

References

An, L., Li, Q., Wu, P., Lu, W., Li, X., Zhang, C., & Zhang, R. (2024). Potential impacts of coal mining activities on nitrate sources and transport in a karst river basin in southwest China. Environmental Science and Pollution Research, 31(10), 15412–15423. https://doi.org/10.1007/s11356-024-32167-7 **[Journal Article]**

Dimitrakopoulos D., Vasileiou E., Stathopoulos N., Dimitrakopoulou S. (2016). Estimation of the qualitative characteristics of post mining lakes in different lignite fields in Greece. **[Journal Article]**

Dimitrakopoulos, D., Vassiliou, E., & Founda, M. (2007). Impacts of mining activities on water resources to Megalopolis lignite district area. In Geophysical Research Abstracts (Vol. 9). **[Journal Article]**

Energy and Climate Action Plan, (2021). The "Sustainable Energy and Climate Action Plan (SECAP) of the Municipality of Megalopolis. (Greek) **[Report]**

EU, 2020. Directive (EU) 2020/2184 of the European Parliament and of the council of 16 December 2020 on the quality of water intended for human consumption. Off. J. Eur. Union 435 (L435), 1–62. **[Report]**

González-Martínez, M. D., Huguet, C., Pearse, J., McIntyre, N., & Camacho, L. A. (2019). Assessment of potential contamination of Paramo soil and downstream water supplies in a coal-mining region of Colombia. Applied Geochemistry, 108. https://doi.org/10.1016/j.apgeochem.2019.104382 **[Journal Article]**

IGME., (1997). Geological Map of Greece, 1:50,000, Megalopolis Sheet. Institute of Geology and Mineral Exploration, Athens, Greece. **[Journal Article]**

Kelepertzis, E., Matiatos, I., Botsou, F., Antonopoulou, C., Lappas, I., Dotsika, E., Chrastný, V., Boeckx, P., Karavoltsos, S., & Komárek, M. (2023). Assessment of natural and anthropogenic contamination sources in a Mediterranean aquifer by combining hydrochemical and stable isotope techniques. Science of the Total Environment, 858. https://doi.org/10.1016/j.scitotenv.2022.159763. **[Journal Article]**

Kelepertsis, A.E., Kontis, E (1997). Geochemical and mineralogical characteristics of Pleistocene lignites and associated sediments of Marathousa coal field, Central Peloponnese, Greece. Chin. J. Geochem. 16, 8–19 (1997). **[Journal Article]**

Kypritidou, Z., Kelepertzis, E., Kritikos, I., Kapaj, E., Skoulika, I., Kostakis, M., Vassilakis, E., Karavoltsos, S., Boeckx, P., & Matiatos, I. (2024). Geochemistry and origin of inorganic contaminants in soil, river sediment and surface water in a heavily urbanized river basin. Science of the Total Environment, 927. https://doi.org/10.1016/j.scitotenv.2024.172250 **[Journal Article]**

Liu, W., Liu, S., Tang, C., Qin, W., Pan, H. & Zhang J. (2020). Evaluation of surface water quality after mine closure in the coalmining region of Guizhou, China. Environ Earth Science 79, 427. **[Journal Article]**

Louloudis G., Kasfikis G., Mertiri E. (2024). Hydrogeological Study for the environmental monitoring and management of the Water potential of Megalopolis mines during the year 2023. Department of Hydrogeological Studies of the Directorate of Mine Exploitation and Completion Studies (DMEPO) of the General Directorate of Production Planning & Development PPC S.A.
(Greek language). **[Report]**

Louloudis G. (2017). The worth of hydrogeochemical data factor analysis (PCA) in interpretation of underground water origin. Megalopolis lignite bearing fields mine water and regional waters relations case study, Proceedings of 15th International Conference on Environmental Science and Technology Rhodes, Greece, 31. **[Journal Article]**

Pe-Piper, G., & Piper, D. J. W. (1989). The geological significance of manganese distribution in Jurassic-Cretaceous rocks of the Pindos Basin, Peloponnese, Greece. In Sedimentary Geology (Vol. 65). https://doi.org/10.1016/0037-0738(89)90010-9 **[Journal Article]**

Photiades, A., Perseil, E.A., 2002. The cu-Ni-Bearing Todorokite from Western Pindos Series (Peloponnese, Greece): Analogous to
Todorokite in Deep-Sea Manganese Nodules, in: Proceedings of XVII. Congress of Carpathian-Balkan Geological Association, Bratislava. [Journal Article]

Sokratidou, A., Roumpos, C., Kaimaki, S., Gkouvatsou, E., Perdiou, A., & Tsagkarakis, G. (2018). Innovative Approaches to Coal Surface Mine Sites Rehabilitation: A Case Study of Megalopolis Lignite Fields. **[Journal Article]**

Su, D., Zhou, Z., Gong, X., Yan, L., Ding, S., Dong, H., Zhang, Y., Wang, X., 2024. Identification of nitrate sources and transformation in karst cave water using hydrochemistry and NO3− isotopes (δ15N/δ18O) combined with a Bayesian mixing model. All Earth 36, 1–17. https://doi.org/10.1080/27669645.2024.2356138 **[Journal Article]**

Welch, C., Barbour, S. L., & Hendry, M. J. (2021). The geochemistry and hydrology of coal waste rock dumps: A systematic global review. In Science of the Total Environment (Vol. 795). Elsevier B.V. https://doi.org/10.1016/j.scitotenv.2021.148798 **[Journal
Article]**

World Health Organization WHO. (2022). Guidelines for drinking-water quality: fourth edition incorporating the first and second addenda. Geneva: World Health Organization; 2022. **[Journal Article]**

Yang, Y., Mei, A., Gao, S., & Zhao, D. (2023). Both natural and anthropogenic factors control surface water and groundwater chemistry and quality in the Ningtiaota coalfield of Ordos Basin, Northwestern China. Environmental Science and Pollution Research, 30(25), 67227–67249. https://doi.org/10.1007/s11356-023-27147-2 **[Journal Article]**

17th INTERNATIONAL CONGRESS of the Geological Society of Greece

BULLETIN OF THE GEOLOGICAL SOCIETY OF GREECE, SP. PUBL.

EXTENDED ABSTRACT 068

Integrating cutting-edge methodological and technological solutions, enabling the development of a next-generation network of Near Fault Observatories across Europe (project TRANSFORM²)

Panagiotis Elias[1], Gaetano Festa[2,3], Lauro Chiaraluce[3], Pascal Bernard[4], George Kaviris[5], Christos Evangelidis[6], Efthimios Sokos[1], John Clinton[7], Alexandru Marmureanu[8], Simona Colombelli[2], Mariano Supino[3], Dimitris Paronis[6], Vassilis Karastathis[6], Men-Andrin Meier[7], Semih Ergintav[9], Alessandro Vuan[10], Tomas Fischer[11], Stanka Sebela[12], Dimitris Paliatsas[1], Anna Serpetsidaki[1] and Andreas Karakonstantis[1]

(1) University of Patras, Patra, Greece
(2) Università di Napoli Federico II, Naples, Italy
(3) Istituto Nazionale di Geofisica e Vulcanologia, Rome, Italy
(4) Institut de Physique du Globe de Paris, Paris, France
(5) Section of Geophysics-Geothermics, Department of Geology and Geoenvironment, National and Kapodistrian University of Athens, 15784 Athens, Greece
(6) National Observatory of Athens, Athens, Greece
(7) ETH Zurich, Switzerland
(8) National Institute for Earth Physics, Bucurest, Romania
(9) Boğaziçi University, Kandilli Observatory and Earthquake Research Institute, Department of Geodesy, Istanbul, (Turkey
(10) National Institute of Oceanography and Applied Geophysics – OGS, Trieste, Italy
(11) Faculty of Natural Sciences, Charles University, Prague, Czechia
(12) Research Centre of the Slovenian Academy of Sciences and Arts – ZRC SAZU, Postojna, Slovenia

Introduction

A Near Fault Observatory (NFO) is a natural laboratory undergoing active, and complex geophysical processes at or in proximity to densely populated urban areas. NFOs bound relatively small areas and provide researchers from various disciplines (e.g. geophysics, geodesy, and geochemistry) the opportunity to access and (re-)use a vast wealth of data and derive scientific products. This allows a better understanding of the multi-scale, physical/chemical processes, responsible for earthquake generation. This can only be achieved by the acquisition of continuous, long-term, high-resolution multidisciplinary data and the application of consistent, reliable state-of-the-art data processing. Six NFOs in Europe have been identified by the European Plate Observing System (EPOS), Figure 1, as long-term Research Infrastructures; three additional NFOs are in observer status. NFOs target the enhanced understanding of the mechanics of earthquakes to unravel the anatomy of complex seismogenic faults.

Figure 1: Map of the Near Fault Observatories (in red) and those being in observer status (in orange) across Europe.

Vision of TRANSFORM²

The TRANSFORM² project has the ambitious goal to improve and transform the existing NFOs, by integrating cutting-edge methodological and technological solutions, paving the way for the next generation of NFOs across Europe. This will be achieved by:

- Conducting tests, horizon scanning and feasibility studies, performing gap-analysis and assessing user needs in order to gain knowledge of the available state-of-the-art sensor equipment, evaluating its appropriateness and applicability for their deployment in the NFOs.
- Accelerating sensor development and testing where possible.
- Creating, developing, and applying workflows that will revolutionize the capacity of NFOs to detect and characterize seismicity and ongoing seismic sequences in real-time, leveraging machine learning as well as the existing and next-generation instrumentation.
- Establishing new paradigms in Earthquake Early Warning (EEW) that are optimized for the dense NFO networks. Assessing the developed workflow's suitability on EEW applications targeting the decision-makers and, consequently, society.
- Transforming the interaction with stakeholders and decision-makers, underpinned by a deeper understanding of their needs and demands and ultimately the benefits that they can gain from the RIs.
- Assessing the capacity and opening of new pathways for the existing NFOs to function as powerful test-beds for the development, calibration, and testing of new measuring equipment and systems.
- Identifying possible funding mechanisms and sources and providing recommendations to national administration authorities and the European Commission on potential calls for the long-term sustainability of the RIs.

Main Pillars

TRANSFORM² is based on the four pillars and on a coherent strategy for communication and liaison activities with researchers, scientists, and stakeholders, securing their active engagement, as well as the assessment and control of the project's outcomes, long-term scientific and socio-economic impact. These are:

Pillar I – New generation of sensors and analytical solutions in basic and applied research related to earthquake processes. These new technologies will contribute to the design of innovative studies and the opening of new perspectives to forecast natural disasters and mitigate associated risks and impact. The scientific and technological advancements of the last decade allowed the scientific community to use a new generation of sensors and analytical solutions in basic and applied research. Near Fault Observatories (NFOs) are the most suitable infrastructures to develop and test advancements in technology because they maintain the facilities and cover a large scientific knowledge to challenge the design, realization, testing, and use of innovative instrumentations. We aim to develop innovative instruments that will go beyond the state-of-the-art, improving NFOs capabilities for interdisciplinary (seismology, acoustics, geodesy, geochemistry) observational and monitoring purposes. We will exploit recent technological advancements (fiber optic-based systems, fully autonomous low-cost seismic devices, ferroelectric acoustic sensors, high-rate multi-constellation GNSS, automated geochemical sensors) to generate a new generation of multidisciplinary data that will allow for the first time to investigate earthquake nucleation processes in more details and from different perspectives.

Pillar II – Novel automatic workflow concept for enhancing detectability and characterization of earthquakes. Development of workflows for improving earthquake detection and source characterization across magnitude ranges. The emergence of Machine Learning (ML) algorithms and Digital Acoustic Sensing (DAS) of fiber optic cables are having a disruptive and transformative effect on seismology today, enabling new and fundamental insights into earthquake processes. The impact of NFOs can be expected to be particularly significant. We aim to exploit these technologies by exploring novel methodologies that will be transformed into operational-quality software, enabling application across the NFOs, with a focus on real-time applications. The first effort focuses on applying machine learning in order to deepen and enrich earthquake catalogues founded on traditional seismic instrumentation. A final effort will be focused on earthquake source characterisation - the elevated event-detectability provides new opportunities for this topic. The characterization of earthquakes might be supplemented by the HR-GNSS instrumentation solutions. Although accelerometers measure the waveform with orders of magnitude higher resolution and at higher frequencies than GNSS, they do not guarantee the representation of the overall event in a unique reference frame and may suffer from the so-called baseline shift (acceleration bias) and data clipping during large events.

Pillar III – New platforms for supporting decision-makers: Earthquake Early Warning concept, combining regional and on-site systems, new communication systems beyond telemetry, and tailored applications to citizens and

stakeholders. In the seconds following earthquake initiation, Earthquake Early Warning Systems (EEWS) can provide prompt notification of the incoming strong ground motion and estimate the potential damage, using real-time, modern information systems, leveraging fast telemetry and data processing from dense instrument arrays deployed in the source region of the event of concern. Despite this scientific and experimental effort, EEWS at the European scale are far from being considered a consolidated and standard technology. The real-time information released by EEWS often suffers from large uncertainties and inaccuracy of the predicted ground shaking amplitude. Additionally, the existing prototype EEWS at European scale are conceived to trigger a generic alert release and are often disconnected from the specific community and environment to be protected. Both factors complicate the effective implementation of EEW methodologies and prevent the use of real-time alerts for automatic decision-making processes during emergencies. Taking advantage of the recent progress in sensors and communication technologies, alongside new theories and observations on the earthquake nucleation process, here we want to set the grounds for the development of the new concept of EEWS, having the next-generation NFOs as backbone infrastructures.

Pillar IV – Next generation of accessibility: Test-bed concept, for testing and development of new cutting-edge measuring sensors. The raised research infrastructure will be exploited as a testbed for the equipment to be developed, workflows, early warning, and decision-making platforms, for demonstration and proof of concept purposes. The main goal is to use and test new measuring sensors and methodologies for studying natural systems at several sites (test-beds). These test-beds might be natural underground cavities, underground basements or even perpendicular escape branches of tunnels. A big challenging task is the in-situ demonstration of new instruments based on innovative optical recordings and processing. These new instruments and technologies, such as the commercial DAS or Brillouin Optical Time-Domain Reflectometer (BOTDR) systems, require long optical cables. For the EEW-ready NFOs, a difficult task will be represented by the improvement of EEW capabilities by extending the EEWS software and exporting the Decision Module, a platform that will be able to issue alerts from multiple locations that act independently. Several prototype applications will be developed to test the end-to-end chain going from data acquisition, and real-time processing of multiple algorithms to output combination and alert release. In several test sites we will involve stakeholders to evaluate the performance of the developed Decision Module.

Communication acivities

TRANSFORM² will focus on the active engagement of the stakeholders through targeted actions.

In the framework of TRANSFORM², industrial partners are given the opportunity to participate by interacting with the scientific and research community through the various planned initiatives. Towards this direction, we propose the development of the SolidEarth Innovation Hub (SEIH), the organization of two dialogue forums and two info-days dedicated to industry.

SolidEarth Innovation Hub is a web-based platform for exposing TRANSFORM²'s activities to stakeholders in a stakeholder-friendly manner and for evolving ideas to innovation and to realized outputs and services

Dialogue forums: Two dialogue forums will be organized by the Region of Western Greece with the participation of invited representatives from local authorities of the countries participating in the NFOs, industrial partners, researchers, scientists, and other target groups. Our aim is to trigger interest and promote the potential opportunities offered to the stakeholders through their active engagement.

Info-days for industry: TRANSFORM² will organize two info-days to engage stakeholders from the commercial world and communicate the projects and NFOs' potential involvement in their domains.

Last but not least, at the project's completion, a comprehensive **'White Book'** will be compiled which will document how associated data, products and services from the next-generation RI can be exploited for the benefit of different target groups among the research community, the stakeholders, and the society and propose ways for a sustainable funding of the RI in the future.

Acknowledgements

TRANSFORM² is funded by the European Union under project number 101188365 within the HORIZON-INFRA-2024-DEV-01-01 call. We would like to acknowledge all the TRANSFORM² colleagues involved in the proposal.

17th INTERNATIONAL CONGRESS of the Geological Society of Greece

BULLETIN OF THE GEOLOGICAL SOCIETY OF GREECE, SP. PUBL.

EXTENDED ABSTRACT 069

The Syros GeoPark Project

Engi M.[1], Gialoglou A.[2], Koutsabasis P.[3], Laurent V.[4], Mavrogonatos C. G.[5]

(1) University of Bern, Switzerland, martin.engi@unibe.ch (2) Syros, Greece agialoglou@mou.gr (3) University of the Aegean, Syros, Greece kgp@aegean.gr (4) Imperial College, London, UK v.laurent@imperial.ac.uk (5) University of Pisa, Italy konstantinos.mavrogonatos@unipi.it

Highlights

Apart from educational and cultural objectives, this project emphasizes the sustainable development of geo-tourism in Syros, with extended seasons, respect for sensitive areas, and supporting ecological preservation efforts.

Background and Motivation

Syros is renowned worldwide among geologists, mainly because its subduction / exhumation history is so well displayed. This realization has attracted countless Earth scientists to Syros since the 1960s, and people on the island have certainly noted these “odd tourists”, equipped with hammers and maps. But hardly any of the locals know what keeps attracting so many field geologists to their island. To this day, a general awareness of the outstanding significance of Syros – and the neighboring Cycladic islands – is lacking. Plenty of scientific research papers on Syros have appeared, but only scientists read these. Sadly, the plate tectonic spectacle evident in Syros remains obscure to most people!

The Syros GeoPark Project aims to change this : The public shall get the opportunity to recognize some of the many geological features visible in Syros and find out how these formed. Interested visitors of the Syros GeoPark shall learn what dramatic history is hidden in the Cyclades. For Syros locals, becoming aware of how their island evolved is part of their cultural identification, their local root system and pride. As a result, ecological sensitivity will spread as well.

Beyond such educational goals, the Syros GeoPark Project aims to form a basis for sustainable economic development by promoting geo-tourism. Opportunities for soft tourism shall be offered in a balanced program combining geological, archaeological, historical and ecological topics. Tourism groups are increasingly keen on discovery programs with an environmental and popular science touch, or on combining physical fitness with family fun. Most hikers prefer moderate weather conditions, they favour spring and fall months over the hot summer. Geo-tourism promises calmer, substantially extended seasons, beyond the brief tourist hype.

Ambitions and Challenges

Over the past 50 years, intense research worldwide has been focusing on subduction-related processes. Studies conducted in the Cyclades have substantially contributed to our current understanding in this field. On Syros in particular, numerous structural, petrological and geochemical investigations have elucidated the evolution in great detail. Hence a vast body of knowledge now exists on the tectonic history of the Aegean-Cycladic archipelago. It is difficult, even for specialists, to integrate so many relevant research results, and bridging the gap to the general public amounts to an enormous challenge.

In view of these considerations, the Syros GeoPark Project has developed two complementary elements : a **GeoCenter** with museum-style displays and activities, and a series of **GeoPaths** offering (self-)guided excursions for hiking-tourists. The goal of both elements is to motivate visitors to enter an enjoyable learning process. The challenge is to stimulate their curiosity, irrespective of prior knowledge and initial interest, so as to guide them to appreciate aspects of Syros beyond sun and fun at the beach…

The ambition of the **GeoPaths** is to provide incentive and information that will motivate locals and tourists to explore *Apano Meria*, the splendid northern part of Syros. An existing network of hiking trails exists, and along these visitors are guided to observe the magnificent landscape, to stop at points of interest (POIs), where they are introduced to specific phenomena, outcrops or (geo)morphological features. A GIS-based app has been specially developed (*Syros GeoPaths App,* Koutsabasis *et al*., 2023) to make necessary information available to visitors, to assist them in planning their hikes and to offer real-time guidance and explanations along each of the GeoPaths. This app will freely be available to download on smartphones or tablets.

The **GeoCenter** will establish the main focus of the Syros GeoPark in a historic building in Ermoupolis. The aim is to immerse visitors in a wide spectrum of geology-related topics relevant to Syros. Fundamental aspects, such as the vast time-scales in Earth science, are introduced, with links from history to archaeology, and from geology to cosmology. The origin of our solar system, its planets and our moon are explained, as are meteorites. From the fundamental structure of planets, displays move on to Earth dynamics, global plate tectonics, and subduction-related processes in particular. The complex history of the Mediterranean is reviewed. Emphasis is placed on showing visitors how researchers combine various disciplines, how progress in Earth science results from working together at many scales. The splendid minerals

and rocks found in Syros are displayed not only for their beauty, but to convey how such samples, metamorphosed at high pressure, provide insight into processes deep inside the Earth, at tectonic plate boundaries. Interactive models, both digital and analog, are used to make many of the concepts understandable, and visitors will also enjoy playing the field assistant to a geologist in a VR game.
Above all, the GeoCenter aims to motivate visitors to explore more of what they learnt by hiking along the GeoPaths. Conversely, observing phenomena in Apano Meria while hiking may well bring up questions that may steer people to visit the GeoCenter.

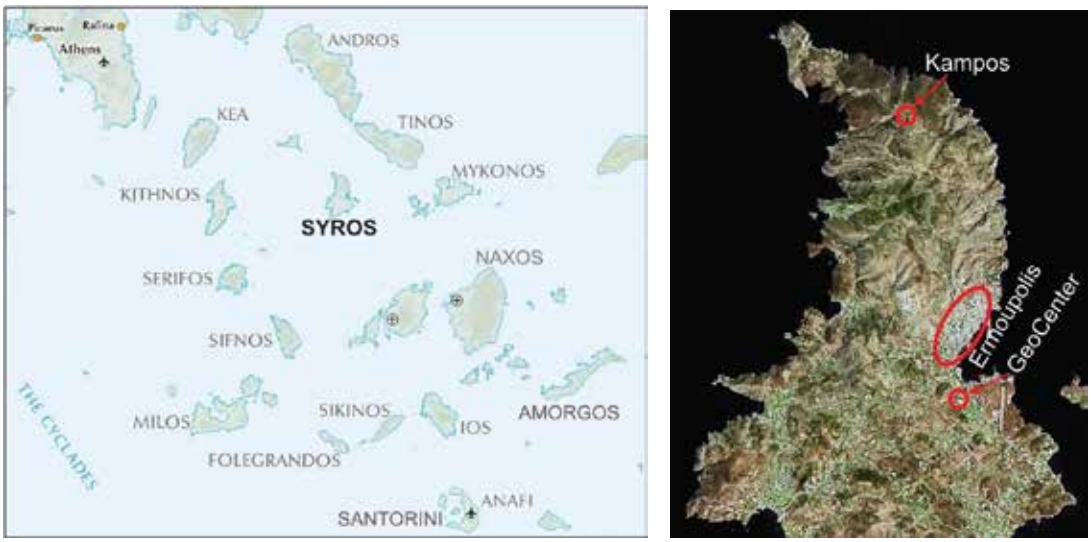

Figure 1. Overview map of the Cyclades (left), with locations relevant for the Syros GeoPark (right).

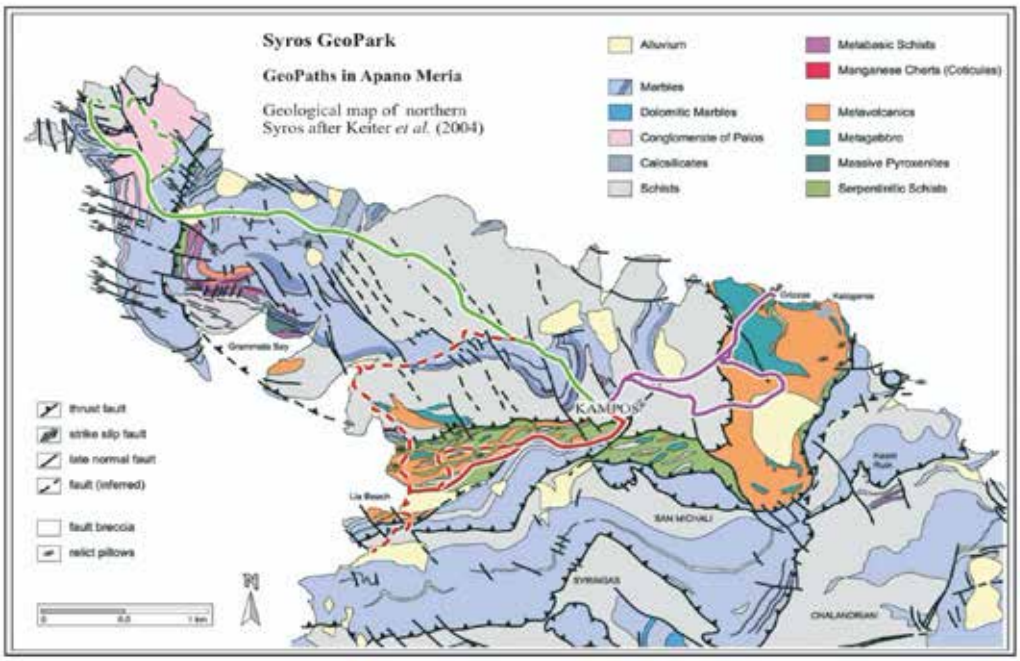

Figure 2. Geological base map of northern Syros (Keiter et al. 2004). GeoPaths from Kampos indicated by colored traces.

The Syros GeoPaths

The network of the GeoPaths is centered at Kampos, a tiny hamlet some 8 km north of Ermoupolis, where the road ends. All hikes start and finish all start at Kampos, they take between 3 and 6 hours round-trip (plus time for swimming etc.). Each GeoPath focuses on one or more geological themes (Table 1), so there is plenty to discover and enjoy.

Table 1. Characteristics of the GeoPaths in the Syros GeoPArk.

Path	Main topics of interest	Distances[1]	POIs, specials
Kampos – Lia	High-pressure shear-zone, tectonic contacts, brittle and ductile deformation, hydration phenomena, metasomatism, eclogite and glaucophane schists, marbles and metavolcanic rocks	H: 3.3 km V: 180 m	10 POIs Pretty beach “Aerolithos”
Kampos – Marmàri – Lia	Marble quarry, lawsonite pseudomorphs, cross section through shear zone, metasomatism, valley formation, mass flow	H: 4.5 km V: 310 m	11 POIs Nice beaches (3!)
Kampos – Diapori – Ryakas	Primary and tectonic contacts, fluid activity, erosional processes and features, soil formation, geomorphology, metaconglomerate, sedimentary *versus* tectonic origin	H: 8.4 km V: 410 m	13 POIs Fabulous views on clear days
Kampos – Grizzas	Intact (primary?) sequence of sedimentary and volcanic origin, metamorphic mineral growth, historic remnants, deformation in metagabbro, magmatic relics, chaotic breccia deposits, erosional morphology	H: 6.2 km V: 420 m	11 POIs Pebble beach “Cyclopic hand”
Kampos - Trochós	Metasediments and metavolcanics, karst formation in marble, eclogite lens, great views to Bronze-age Kastri fortress, historic Trochòs settlement and remnants, magmatic “factory”, veining	H: 2.8 km V: 110 m	5 POI Best view of Kastri

1: Approximate hiking distances. Horizontal (H) in kilometers for round trip. Vertical (V) in meters, necessarily up and down!

Popular destinations include the valley from Kampos to Lia beach, arguably the best researched transect in Syros. It displays an exceptionally well preserved high-pressure shear zone, that is interpreted as an exhumed part of a subduction channel. It presents a tectonic mélange containing massive eclogite fragments, elongate trails of metavolcanics and marble, all immersed in a highly tectonized serpentinite matrix, now composed mainly of talc-chlorite schist. The eclogite lenses display thin metasomatic rims and spectacular glaucophane veins, attesting to hydration of eclogite during exhumation. Most of the giant eclogite lenses are fragmented, but one boulder, known as “Aerolithos”, still stands over to 20 meters high. Its characteristic outline gave the Syros GeoPark its emblem (Fig. 3).

Figure 3. The “Aerolithos”, a giant eclogite fragment overlooking the bay of Lia

The Syros GeoCenter

The GeoCenter utilizes part of a 19th century industrial building, formerly one of the important tanneries in Syros. The impressive architecture of the Kornilaki building (Fig. 4) and its location slightly outside the busiest parts of central Ermoupolis offer a very suitable space for a museum-type installation.

Two floors of very distinct character lend themselves for displays. In preparation, some basic constructions were required to adapt the internal structure, notably to separate the display halls on the top floor from the building’s central

court. In total, the plans (Fig. 5) now encompass an entry and two display spaces at ground level, plus five exhibition halls upstairs.

Figure 4. The Kornilaki building in Ermoupolis, housing the GeoCenter and the library of the University of the Aegean

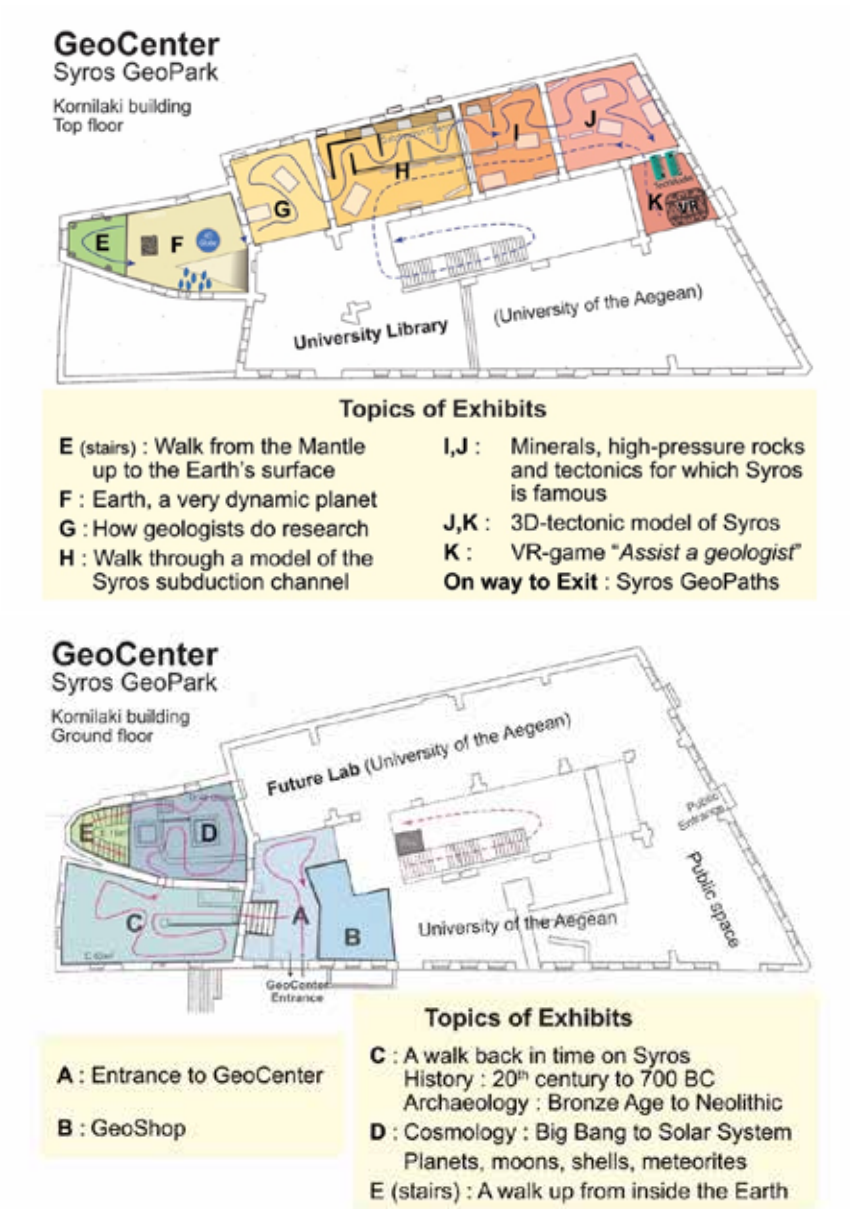

Figure 5. Floor plans at the GeoCenter, space distribution and topics of planned exhibits

Figure 6. Peeking into one of the exhibition halls of the GeoCenter

Project Organisation, Timeline, and Outlook

The Syros GeoPark was conceived as a project in 2017 by M. Engi and A. Gialoglou. In 2018 it received major funding through the SPECIAL PURPOSE DEVELOPMENT PROGRAMME for the SOUTH AEGEAN. In 2023 an extension with additional funds was granted. The project runs under the auspices of the Municipality of Syros, which has provided substantial support as well. A strong partnership with the University of the Aegean was established with P. Koutsabasis in 2018, and several international universities have been actively collaborating.

Regrettably, the initial time plan has been repeatedly disrupted due to the pandemic, an inefficient public administration, and a couple of individuals seeking to harm the project. Serious difficulties still remain due to urgently needed roof repairs on the Kornilaki building, as well as complicated negotiations with some of the land owners. Nevertheless, an optimistic time-plan presently counts on rapid progress over the next months, such that the Syros GeoPark should officially open in October 2025.

All along eight long years of preparation, the prospect of the GeoPark has generated growing enthusiasm in Syros, not only in the tourism sector, but equally among people with ecological, historical and archaeological interests. Strong connections have been established between the GeoCenter and sections of the University of the Aegean, some of which share the Kornilaki building. Beyond Greece, the many partners involved in the project have been spreading news about the project in international geological circles.

The idea of integrating the Syros GeoPark into a larger framework by associating it the with interested neighboring islands, so as to establish a topically broad Cycladic GeoPark has been discussed. No concrete plans exist so far, but at that scale an integration into the global network of UNESCO geoparks would appear both attractive and realistic.

Acknowledgements

Substantial funding for the Syros GeoPark Project by the Greek Public Investment Program is gratefully acknowledged. We thank the Municipality of Syros for all the support provided. Countless friends have collaborated with us – too many to name you all, but we do sincerely thank you, as this project could not be realized without you!

References

Keiter, M., Piepjohn, K., Ballhaus, C., Lagos, M., Bode, M., 2004. Structural development of high-pressure metamorphic rocks on Syros island (Cyclades, Greece). Journal of Structural Geology 26, 1433-1445.

Koutsabasis, P., Nikolarakis, A., Panopoulou, E., Georgiadi, S., Mavrogonatos, C., Engi, M., 2023. Mobile User Experience to Learn About Geology While Hiking: The Syros GeoPaths app. Proceedings of the 2nd International Conference of the ACM Greek SIGCHI, Athens. 1-8.

17th INTERNATIONAL CONGRESS of the Geological Society of Greece

BULLETIN OF THE GEOLOGICAL SOCIETY OF GREECE, SP. PUBL.

EXTENDED ABSTRACT 070

The 2024–2025 Seismic Sequence in the Santorini-Amorgos Region: High-Resolution Seismological Insights into a Volcano-Tectonic Crisis

Evangelidis C.P.[1] and Fountoulakis I. [1]

(1) National Observatory of Athens, Institute of Geodynamics, cevan@noa.gr

Introduction

The Santorini-Amorgos (SA) region lies within one of the most active segments of the South Aegean Volcanic Arc (SAVA), where complex interactions between tectonic structures and volcanic systems are driven by the ongoing subduction of the African plate beneath Eurasia (Fig. 1a). This region is characterized by extensional deformation along NE–SW-trending faults and includes prominent volcanic centers such as Santorini and Kolumbo. In mid-2024, low-level seismicity began beneath Santorini, gradually intensifying and migrating northeastward by early 2025. This development raised significant concern due to its location along known fault systems and in proximity to active volcanic centers. Historically, the area has shown evidence of tectono-magmatic activity, and the emerging sequence prompted the need for detailed monitoring and analysis. The primary objective of this study is to investigate the evolution and underlying processes of the 2024–2025 seismic sequence using high-resolution seismic monitoring. Specifically, we aim to enhance the existing seismic catalog through machine-learning-driven workflows, resolve spatial and temporal patterns of earthquake occurrence, and assess the physical nature of the events—particularly whether they result from tectonic faulting, magmatic intrusion, or a combination of both. A secondary goal is to develop and implement a near-real-time operational framework to support crisis response and long-term scientific research.

Methods

Seismic data were acquired from 23 broadband, short-period, and strong-motion stations, with coverage significantly improved by the installation of station HT.ANYD on Anydros Island in early February 2025. The analysis focused on the period between June 2024 and March 2025. Using continuous waveform data, seismic phases were automatically picked with EQTransformer (Mousavi et al., 2020), a deep-learning tool optimized for volcanic environments, and associated with the PyOcto phase associator (Münchmeyer, 2024). Initial event locations were determined with NonLinLoc and refined using a source-specific station term (SSST) relocation (Lomax et al., 2014; Lomax and Savvaidis, 2022), and the GrowClust algorithm (Trugman and Shearer, 2017) based on waveform cross-correlation. This workflow produced a final catalog of nearly 14,000 high-precision events. For larger earthquakes (ML ≥ 3.5), full moment tensor (MT) solutions were computed using Gisola (Triantafyllis et al., 2021), a high-performance implementation of the ISOLA method. The seismic signals were further analyzed using the Frequency Index (FI) metric, which estimates relative spectral content and provides insight into source complexity and potential magmatic influence.

Results

The relocated seismicity revealed a clear evolution of the sequence, beginning with shallow clusters beneath the Santorini caldera and shifting northeastward to greater depths beneath Kolumbo volcano (~20 km) (Fig.1b, 1a-b). The seismicity then migrated toward Anydros, forming a broad, diffuse seismogenic zone between 10–15 km depth, extending ~20 km in length and aligning with NE–SW-trending tectonic structures. Cross-sections indicate both steeply dipping and antithetic faults, consistent with transtensional deformation (Fig.1a-b, g-h, i-j). Moment tensor solutions display a dominant normal-faulting regime with significant non-double-couple components, especially positive isotropic and CLVD terms, suggesting crack-opening processes linked to magmatic fluid movement. The FI metric further supports this interpretation, revealing spatial variation in frequency content, with higher-FI events concentrated northeast of Anydros, where the activity appears more tectonic in nature, and lower-FI events toward the southwest, potentially indicating stronger magmatic involvement. Seismic migration patterns also exhibit rapid back-and-forth behavior with velocities up to 2.8 km/h.

Conclusions

The 2024–2025 SA sequence presents a compelling case of tectono-magmatic interaction, with seismicity progressing from deep initiation beneath Kolumbo to shallower zones aligned with known tectonic features. The combination of moment tensor inversion and frequency content analysis suggests that the sequence was not purely tectonic but involved magmatic processes such as dike injection or fluid migration. The study demonstrates the effectiveness of machine-learning-based workflows for real-time seismic monitoring during volcanic crises. The resulting high-

resolution catalog provides valuable insights into the geodynamic behavior of the region and is now openly available for future studies. This work establishes an operational framework that may serve as a model for future seismic and volcanic crises in similar geodynamic environments.

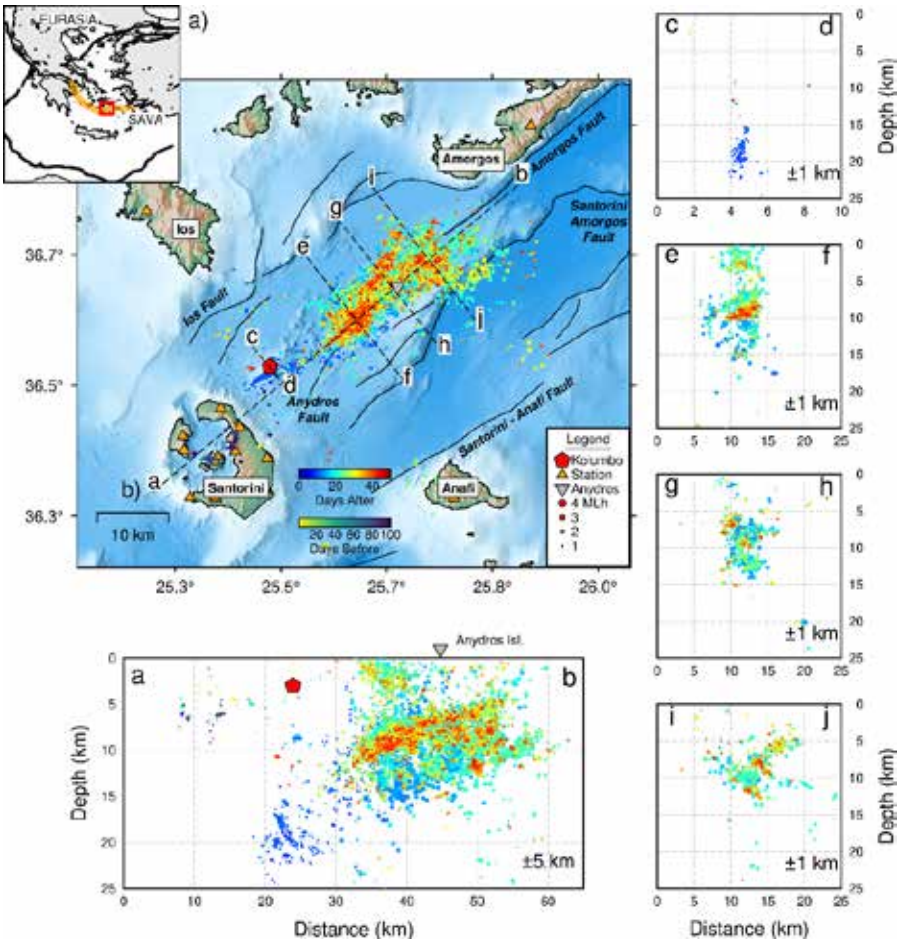

Figure 1. (a) General illustration of the broader Hellenic arc region, showing the main plate boundaries. The SAVA is highlighted in orange, with the study area shown in b) marked by a red rectangle. (b) Relocated seismic events, color-coded based on their occurrence date relative to 20/01/2025 (DD:MM:YYYY) and scaled according to their local magnitude (ML). Black lines represent the main fault traces in the area (Nomikou et al., 2018), while the red polygon defines the Kolumbo volcano chamber (2-4 km depth based on Chrapkiewicz et al. (2022)). The inverted triangle marks the location of Anydros Island, and triangles indicate the seismic stations used in this study. Vertical cross-sections (a-b to i-j) are also shown.

Acknowledgements

Figures and maps were created using the Pythonic interface of the Generic Mapping Tools (PyGMT) software (Tian et al., 2025) and the Matplotlib library (Hunter, 2007). Additionally, parts of the analysis were conducted using ObsPy (Beyreuther et al., 2010). We are thankful to all those scientists and personnel who maintain and operate their networks at the National Observatory of Athens-Institute of Geodynamics, Aristotle University of Thessaloniki-Seismological Station and National Kapodistrian University of Athens-Seismological Laboratory.

References

Beyreuther, M., Barsch, R., Krischer, L., Megies, T., Behr, Y., Wassermann, J., 2010. ObsPy: A Python Toolbox for Seismology. *Seismological Research Letters* 81, 530–533. doi: 10.1785/gssrl.81.3.530.

Chrapkiewicz, K., Paulatto, M., Heath, B.A., Hooft, E.E.E., Nomikou, P., Papazachos, C.B., Schmid, F., Toomey, D.R., Warner, M.R., Morgan, J.V., 2022. Magma Chamber Detected Beneath an Arc Volcano With Full-Waveform Inversion of Active-Source Seismic Data. *Geochemistry, Geophysics, Geosystems* 23(11), e2022GC010475. doi: https://doi.org/10.1029/2022GC010475.

Hunter, J.D., 2007. Matplotlib: A 2D Graphics Environment. *Computing in Science & Engineering* 9(3), 90–95. doi: 10.1109/

MCSE.2007.55.

Lomax, A., Michelini, A., Curtis, A., 2014. Earthquake Location, Direct, Global-Search Methods. In: Lee, W.H.K. (Ed.), *Encyclopedia of Complexity and Systems Science*. Springer New York, pp. 1–33. doi: 10.1007/978-3-642-27737-5150 − 2.

Lomax, A., Savvaidis, A., 2022. High-precision earthquake location using source-specific station terms and inter-event waveform similarity. *Journal of Geophysical Research: Solid Earth* 127(1), e2021JB023190.

Mousavi, S.M., Ellsworth, W.L., Zhu, W., Chuang, L.Y., Beroza, G.C., 2020. Earthquake Transformer—An Attentive Deep-Learning Model for Simultaneous Earthquake Detection and Phase Picking. *Nature Communications* 11, 3952. doi: 10.1038/s41467-020-17591-w.

Münchmeyer, J., 2024. PyOcto: A high-throughput seismic phase associator. *Seismica* 3(1). doi: 10.26443/seismica.v3i1.1130.

Nomikou, P., Hübscher, C., Papanikolaou, D., Farangitakis, G., Ruhnau, M., Lampridou, D., 2018. Expanding extension, subsidence and lateral segmentation within the Santorini - Amorgos basins during Quaternary: Implications for the 1956 Amorgos events, central - south Aegean Sea, Greece. *Tectonophysics* 722, 138–153. doi: https://doi.org/10.1016/j.tecto.2017.10.016.

Tian, D., Uieda, L., Leong, W.J., Fröhlich, Y., Schlitzer, W., Grund, M., Jones, M., Toney, L., Yao, J., Tong, J.-H., et al., 2025. PyGMT: A Python interface for the Generic Mapping Tools. https://doi.org/10.5281/zenodo.14868324.

Triantafyllis, N., Venetis, I.E., Fountoulakis, I., Pikoulis, E., Sokos, E., Evangelidis, C.P., 2021. Gisola: A High-Performance Computing Application for Real-Time Moment Tensor Inversion. *Seismological Research Letters* 93(2A), 957–966. doi: 10.1785/0220210153.

Trugman, D.T., Shearer, P.M., 2017. GrowClust: A Hierarchical Clustering Algorithm for Relative Earthquake Relocation, with Application to the Spanish Springs and Sheldon, Nevada, Earthquake Sequences. *Seismological Research Letters* 88(2A), 379–391. doi: 10.1785/0220160188.

17th INTERNATIONAL CONGRESS of the Geological Society of Greece

BULLETIN OF THE GEOLOGICAL SOCIETY OF GREECE, SP. PUBL.

EXTENDED ABSTRACT 071

Tooth enamel meso- and microstructure of fossilized Hipparionine horses of Pikermi (Attica, Greece)

Fasoli D.[1], Stathopoulou E.[1]

(1) National and Kapodistrian University of Athens, Department of Geology and Geoenvironment, Panepistimiopolis, 15784 Zografou, Greece, dionfasoli@gmail.com , estathop@geol.uoa.gr

Research Highlights

There are no major differences in the microstructure of enamel between the two main subgenera of Pikermi. However, slight distinctions are present, in enamel thickness and Type III enamel presence.

Introduction / Background

Equidae teeth have a highly complex structure, consisting of heavily plicated enamel. Hypsodonty, along with enamel microstructure alterations, helped them adapt to changes in dietary conditions (Pfretzschner, 1993). Due to its unique diversity, enamel often allows for the identification and classification of mammals, shedding light also on their phylogenetic relations. Tooth enamel microstructure is known to be an indicator of dietary adaptations and biomechanical stress due to its unalterable nature (Koenigswald and Pfretzschner, 1991).

The objective of this study was to describe and compare the traits of Hipparionine dental enamel from the famous fossiliferous site of Pikermi (Attica, Greece). Any unique characteristics could offer crucial phylogenetic information and could even be used for the identification of the different species that have been recorded at the site, but till now they were only identified based on macroscopic features. This information was also correlated to the mesoscopic characteristics of tooth enamel, which in the case of these specific animals is extremely complicated, as well as fascinating. Intense plications and variations of the enamel thickness within a single tooth are extraordinary. This is the first attempt to discriminate different hipparionine species at the site based on enamel microstructure.

Materials and Methods

Twenty-four dental samples (upper cheek teeth) from the fossiliferous locality of Pikermi (Attica, Greece) were acquired, to test for distinctions between two subgenera belonging to the Pikermi fauna, in meso- and micro-scale. The physical characteristics and size of Pikermi hipparions allow us to discriminate between at least two species, *Hippotherium brachypus and Cremohipparion meditteraneum* (Böhme *et al.,* 2018) (*H. brachypus* and *H. mediterraneum* in Koufos, 1987, Koufos *et al.,* 2022). These subgenera descended from different lineages and show different cranial and limb bone characters (Koufos, 1987).

The rich terrestrial vertebrate fauna has been extracted from the Pikermi Formation, an up to 30-meter-thick series of mostly reddish silts with subordinate clastic channels of conglomerates and sandstones (Roussiakis *et al.,* 2019), with its deposition starting in the Early Tortonian (Vallesian) (Böhme *et al.,* 2017). The material at the site has been dated back to the Tortonian – Messinian boundary (middle Turolian) (circa. 7,25 Ma B.P.) (Koufos, 2013; Böhme *et al.,* 2017).

The material was grouped based on macroscopic and mesoscopic characters and measurements (height from the root, occlusal length, occlusal width, protocone length, number of enamel plications pointing at the protocone – plis caballins, number of rest of plications, shape of protocone) (Figures. 1,2), according to Eisenmann *et al.,* 1988.

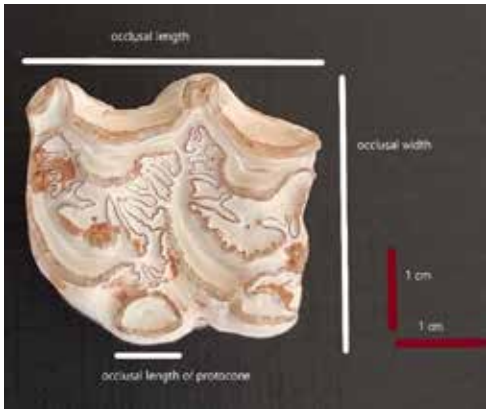

Figure 1. Macroscopic and mesoscopic measurements on the dental occlusal surface of sample Π89/39, according to Eisenmann *et al.,* 1988.

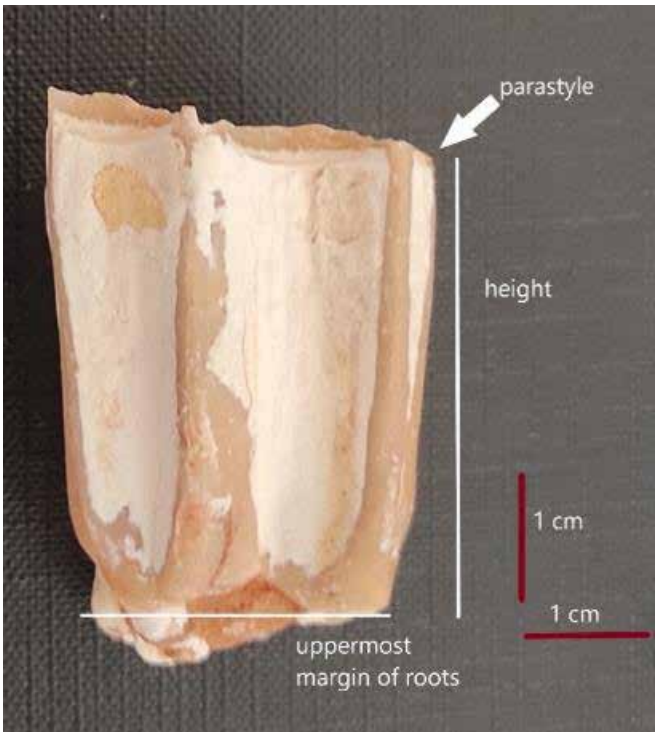

Figure 2. Macroscopic measurements on dental sample Π89/39 (vestibular view), according to Eisenmann et al., 1988.

Samples of each group were examined via stereoscope and Scanning Electron Microscope (SEM), regarding changes in the number of enamel plications while moving closer to the root (cut at 3, 2, and 1 cm from the root), enamel thickness, and enamel types and distribution. To study the enamel microstructure of the selected teeth, they were embedded in resin and cut at 1, 2 and 3 cm above the root of the samples. The embedded samples were prepared according to a specific procedure which includes etching with HCl, to enhance the enamel's characteristic features (Koeningswald and Rose, 2005), and after being coated with Au-Pd they were observed with a Jeol JSM 6390 Scanning Electron Microscope. SEM is considered essential for the observation of specimen histology.

Results – Discussion

No increase/decrease pattern was detected in the number of plications while moving closer to the root, although all samples, at 1 cm from the root, showed a simpler structure. There was the exception of one sample whose plis caballins (8) exceeded the range given by Koufos, 1987 (1-5).

Enamel maximum thickness ranged between 1000 – 1400 μm in peripheral enamel, 800 – 1400 μm in protocones, and 1000 – 1300 in the fossettes. The group with 1 pli caballin showed average maximum thickness of 1,3 mm in peripheral enamel, 1,17 mm in protocone, and 1,21 mm in the fossettes, while the group with >3 plis caballins showed average maximum thickness of 1,16 mm in peripheral enamel, 1,02 mm in protocone, and 1,16 mm in the fossettes.

Three main enamel types are seen in Equidae with hypsodonty. Modified enamel (or Type I enamel) closer to the EDJ (enamel – dentine junction) consisting of radial rows of prisms separated by relatively thick rows of IPM (inter – prismatic matrix), radial enamel (or Type II) closer to the ECJ (enamel – cementum junction) which consists of prisms of various sizes and shapes (horseshoe, keyhole, oval) with noticeably thinner – to – non-existent IPM, and a honeycomb – like structure (or Type III enamel) making small appearances in either the EDJ or the ECJ or both, composed of round- shaped prisms separated by thick IPM (Kilic *et al.,* 1997; Pfretzschner, 1992; Demeshkant *et al.,* 2023).

All samples showed all the aforementioned enamel types (Figures 3 – 5). The samples with 1 pli caballin had more Type III enamel than the ones with >3 plis caballins, in various areas, and even far from the junctions. Most plications showed irregularities regarding the enamel prisms and IPM orientations at the invaginations, with no distinct pattern (irregular enamel type) (Figure 6), while elsewhere the enamel prisms and IPM followed a relatively radial path between the boundaries, and in others HSBs (Hunter – Schreger bands) appeared. The plications of all the samples had triangular - like or rounded shapes and were either deep or shallow.

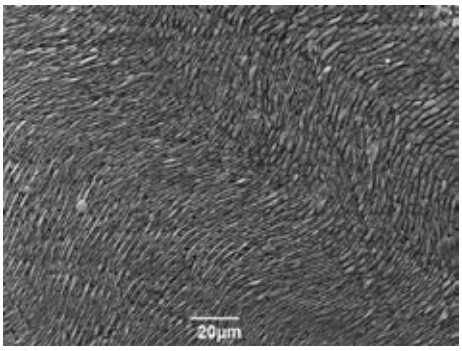

Figure 3. Type I enamel (modified) in sample Π89/9 (2cm distance from the root).

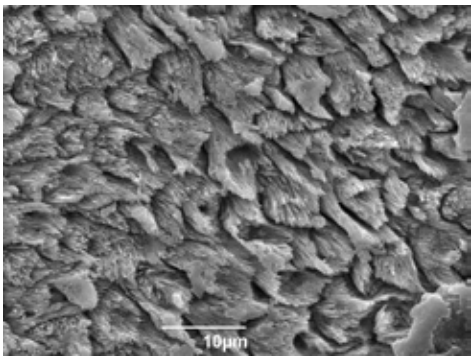

Figure 4. Prisms of Type II enamel (radial) in sample Π89/12 (2cm distance from the root).

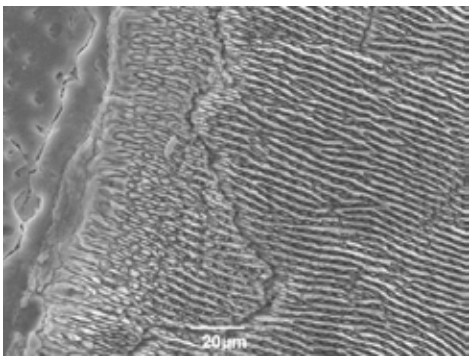

Figure 5. Type III enamel (honeycomb – like) (left) and Type I enamel (modified) (right) in sample Π89/9 (2cm distance from the root).

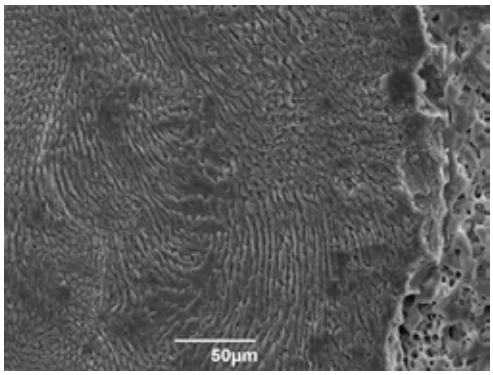

Figure 6. Irregularities appearing in one of the plis caballins of sample Π89/12_2

The presence of modified enamel (Type I) shows the evolutionary track of hipparionine horses, as the diet of Equidae altered from browsing to grazing (Pfretzschner, 1993). As the enamel microstructure in this genus (and in Equidae in general) is very complicated, a clear distinction between the two subgenera was not possible, as all samples exhibited the same features under SEM, similar distribution of enamel types, fragmented protocones, and similar plication forms, with the differences being the number of plications, the enamel thickness, and the more distinct presence of Type III enamel in samples with 1 pli caballin. Ongoing research will allow for further investigation of this hypothesis.

References

Böhme, M., Spassov, N., Ebner, M., Geraads, D., Hristova, L., Kirscher, U., Kötter, S., Linnemann, U., Prieto, J., Roussiakis, S. and Theodorou, G., 2017. Messinian age and savannah environment of the possible hominin Graecopithecus from Europe. PloS one 12(5), e0177347.

Böhme, M., Van Baak, C.G., Prieto, J., Winklhofer, M. and Spassov, N., 2018. Late Miocene stratigraphy, palaeoclimate and evolution of the Sandanski Basin (Bulgaria) and the chronology of the Pikermian faunal changes. Global and planetary change 170, 1-19.

Demeshkant, V., Biegalski, M. and Rekovets, L., 2023. Teeth Enamel Ultrastructural Analysis of Selected Equidae Taxa. Diversity 15(11), 1141.

Eisenmann, V., Alberdi, M.T., De Giuli, C. and Staesche, U., 1988. Studying fossil horses. EJ Brill, Leiden, The Netherlands.

Kilic, S., Dixon, P.M. and Kempson, S.A., 1997. A light microscopic and ultrastructural examination of calcified dental tissues of horses: 2. Ultrastructural enamel findings. Equine Veterinary Journal 29(3), 198-205.

Koenigswald, W. and Pfretzschner, H.U., 1991. Biomechanics in the enamel of mammalian teeth, in: Constructional morphology and evolution. Berlin, Heidelberg: Springer Berlin Heidelberg, 113-125.

Koenigswald, W.V. and Rose, K.D., 2005. The enamel microstructure of the early Eocene pantodont Coryphodon and the nature of the zigzag enamel. Journal of Mammalian Evolution 12, 419-432.

Koufos, G.D., 1987. Study of the Pikermi hipparions. Part I: Generalities and taxonomy. Bulletin du Muséum national d'Histoire naturelle 9, 197-252.

Koufos, G.D., 2013. Chapter 28. Neogene mammal biostratigraphy and chronology of Greece. In Fossil mammals of Asia: Neogene biostratigraphy and chronology. Columbia University Press. pp.595-626

Koufos, G.D., Vlachou, T.D. and Gkeme, A.G., 2022. The fossil record of equids (Mammalia: Perissodactyla: Equidae) in Greece. Fossil vertebrates of Greece Vol. 2: Laurasiatherians, artiodactyles, perissodactyles, carnivorans, and island endemics, 351-401.

Pfretzschner, H.U., 1992. Enamel microstructure and hypsodonty in large mammals. Structure, function and evolution of teeth, 147-162.

Pfretzschner, H.U., 1993. Enamel microstructure in the phylogeny of the Equidae. Journal of vertebrate paleontology 13(3), 342-349.

Roussiakis, S., Filis, P., Sklavounou, S., Giaourtsakis, I., Kargopoulos, N. and Theodorou, G., 2019. Pikermi: a classical European fossil mammal geotope in the spotlight. European Geologist 48, pp.28-32.

17th INTERNATIONAL CONGRESS of the Geological Society of Greece

BULLETIN OF THE GEOLOGICAL SOCIETY OF GREECE, SP. PUBL.

EXTENDED ABSTRACT 072

Local driven protection of a tectonic geosite, in Crete, Greece: The Paligremnos Protected Landscape

Fassoulas C.[1], Staridas S.[2], Nikolakakis E.[3]

(1) Natural History Museum of Crete- University of Crete, Heraklion, Greece, fasoulas@nhmc.uoc.gr (2) Staridas Geography, Heraklion, Greece, (3) University of Crete, Heraklion, Greece

Introduction

Protection of geodiversity is an urgent need of modern societies as it represents the crucial link between abiotic and biotic nature. Although in nowadays protection of biodiversity is one of the highest priorities of our societies, the same does not apply for geodiversity, which is under additional pressures related with row materials and development of big infrastructures that are so necessary for our technology. The oldest efforts for conservation of geoheritage are dated back to the 18th century in several European countries, followed by the establishment of the first National Parks in USA (Grand Canyon, Yellowstone etc.) with core geological features (Gray 2004).

In Greece, the first efforts to protect elements of our geoheritage can be found in the establishment of the two National Parks of Olympus (1938) and Samaria (1962), however without any concern or the direct protection of their geological values (Zouros & Fassoulas 2006). Yet, national legislation is very weak in respect to geoconservation and has changed several times overturing former positive initiatives. The first law with a clear provision for the protection of abiotic nature was the 1650/1986 which was foreseen that some aspects of geodiversity, like caves, gorges, plateau and fossil sites could be preserved as Natural Monuments. Application of this legislation was though incredibly difficult as it was requesting the elaboration of Special Environmental Studies of high cost and time consumption that were approved by the Ministry of Environment. As a consequence, no geological monument was protected under this law. In 1985 Lesvos Petrified Forest was declared by the Ministry of Culture as a Protected Monument of Nature, and in 1988 Meteora were nominated as a World Heritage Site mainly for its cultural value. A big step forward was achieved with the Law 3937/2011 which for the first time defined what a geosite is and foresaw the establishment of geoparks in the form of National or Regional Nature Parks, with much simpler studies checked by Regional Authorities. Implementation of this legislation was relative flexible permitting the protection of two geological monuments as Protected Landscapes, the Almyri Panagia in Lesvos and Limnos Petrified Forest. In 2020 legislation changed again with the Law 4685/2020 which abrogated the Nature Parks and thus geoparks and transferred the decision-making process back to the Ministry of Environment, Energy and Climate Change.

A milestone for the geoconservation in Greece was the establishment in 2015 of the UNESCO Global Geoparks by UNESCO, that recognized five territories in Greece under this program, namely the Lesvos Petrified Forest, Psiloritis, Chelmos-Vouraikos, Vikos-Aoos and Sitia. Still the nine existing UGGps in Greece lack of authorization and recognition by law. Concluding, the geological elements that are under protection in Greece are quit few, despite the extraordinary value of Greek Geological Heritage.

In 2022 an important geosite of Crete, the Paligremnos fault scarp (Fig. 1) was placed under serious threat by the initiation of excavations at the top of its scarp by a private company for the construction of touristic apartments. Being a local landmark, a postcard of Crete since the 1970's, an aesthetic landscape, an international climbing field, a well-studied fault (Angelier 1979) and a mapped geosite for Crete with at least regional value (Fassoulas et al. 2007), Paligremnos received an immense and unexpected support by locals, foreign residents, visitors and the climbing community of Greece. Just a week after the excavations, more than 1500 people gathered at Paligremnos protesting against its destruction and the construction of the apartments, requesting by the regional and local authorities its protection under the moto "We become a rock for the protection of our rock". In July 2022 the Municipality of Agios Vassilios in Rethimno assigned Natural History Museum of Crete the elaboration of a special study for the nomination and protection of Paligremnos as a Protected Landscape, whereas together with the protesting society, undertook legal actions to cancel the building license of the construction. Both actions were successful and finally the Paligremnos was declared in 2023 as a Protected Landscape and Protected Natural Formation due to its geological importance, with the Ministry Decision GGG 535/23-62023. This article presents the main geological features, their assessment and the documentation of the broader area of Paligremnos as a Protected Landscape due to the national value of its geological heritage.

Figure 1. The Paligremnos fault scarp in Plakias bay

Methodology

The Natural History Museum of Crete established a study group including various specialists such as a geologist, geographer, a biologist and an IT specialist with the aim to (1) Identify the area of interest, (2) identify, map, study and document the main geological and biological values of the area (3) Qualitatively and quantitatively assess the geological values of the area (4) identify the potential human and natural risks (5) document the reasons for monument's protection and preparation of a Ministry Decision under the 4685/2020 Law.

In Automn 2022 both geological and biological missions and inventories were contacted at the area, a detailed geological and tectonic mapping at a scale 1:5000 was applied, satellite images were analyzed, an UAV-based photogrammetric survey was conducted and a digital relief model was created for detailed measurements of the scarp, while existing literature was analyzed. Finally, we applied the quantitative geotope assessment method of Fassoulas et al. (2012) to demonstrate the touristic and educational potential of the monument and its vulnerability.

All collected data resulted in the compilation of the Special Geological Study foreseen by the L.3937/2011, which was quite similar to the well-known Special Environmental Studies of the L1650/1986, that was submitted to the regional and national authorities for the characterization of the broader Paligremnos area as Protected Landscape.

Results

The broader area of Paligremnos is characterized by the presence of Jurassic and Eocene limestones of the Tripolitsa nappe and small outcrops of the Eocene flysch, that cover a small peninsula named Psarela, opposite to the well-known tourist destination of Plakias in Rethimnon (Fig. 2). An east-west trending basin exists between the cape Psarela and the Asiderotas mts at the north, covered by late Miocene sediments in which an important amphibian and terrestrial fauna was discovered (Georgalis et al. 2016), while small sand dunes are formed at the southern part of the beach. The monument is located over the north facing steep cliff of the peninsula on which three parallel fault scarps were mapped along the east-west direction (Fig. 2). The first scarp (F1) is the Paligremnos, an almost vertical fault surface with two generations of striations present, as well as large corrugations and kinematic indicators pointing to a normal sense of shear. The second scarp (F2) located uphill is quite long dipping into the sea westwards. This scarp has a moderated dip towards north, and although more weathered it presents also several corrugations, while two coastal caves exist at its surface. A small tunnel was opened during the WWII reaching the caves, to transfer coal excavated inland at the far-most cave where ships could deliver it. The tunnel was supported by fortification establishments too. The higher scarp (F3) has smaller extent, moderate dip with polished surfaces at places, where one set (the oldest) of slickensides can be seen. The analyses of the photogrametric data and the digital relief model (Fig. 3) revealed that the Paligremnos scarp is 132 m long and 42 m high, with a total surface of 5274,1 m^2. Field and other historical data proved that the scarp was naturally exposed. Finally, another older normal fault (F4) oriented northwest-southeast has been mapped on top of the hill forming together the F3 a high escarpment at the Tripolitsa limestone.

Along the coastal cliffs and in several cases on the F2 fault scarp, a sea notch at 1.4m above m.s.l. indicates the tectonic uplift of the whole territory related with the 365 A.D earthquake. Geomorphotectonic mapping and study revealed five distinct marine terraces on the peninsula (Fig.4), the lowest at about 15m height, and the highest at about 120m. showing the gradual rock uplift recorded at the southern coastal zone of Crete during the upper Pleistocene (Ott et al. 2019).

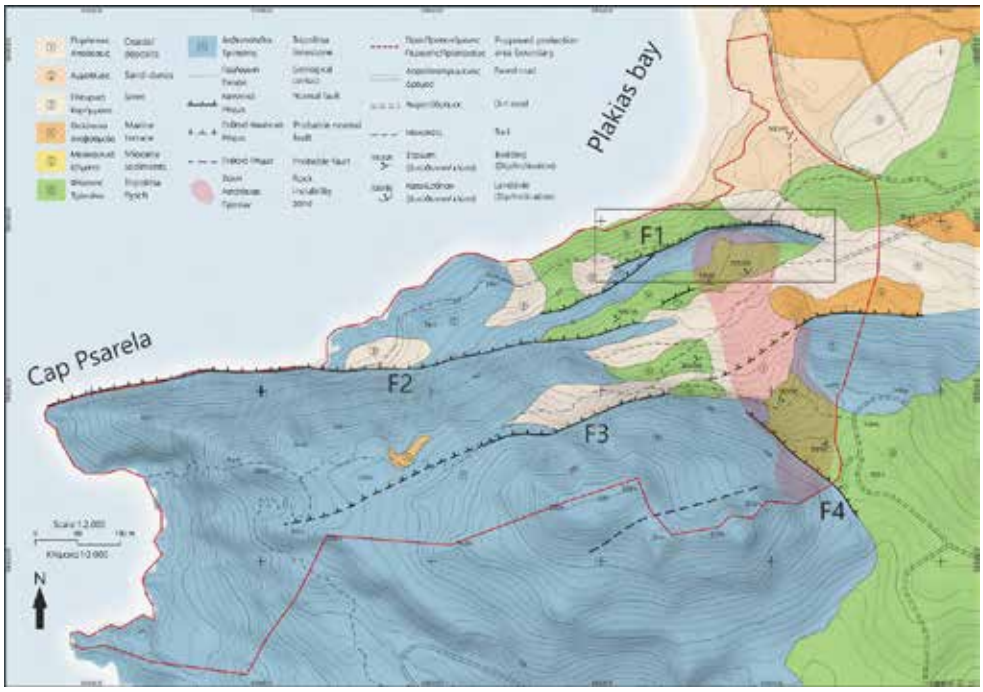

Figure 2. Geological map of study area. F1,..,4 refer to faults in text, square shows Paligremnos scarp

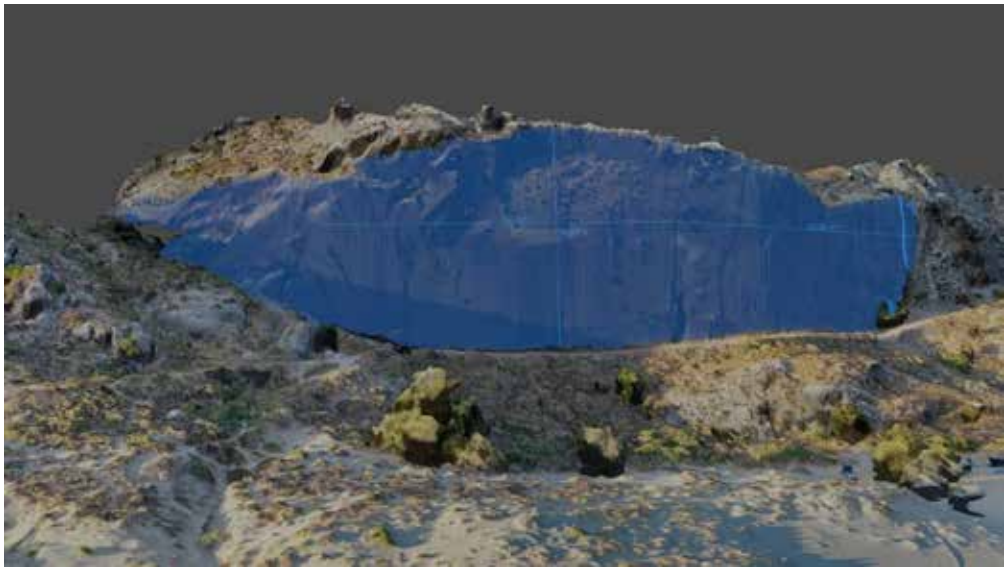

Figure 3. The 3-d relief model of Paligremnos scarp developed for the accurate measurements of its surface

Fault kinematic analyses, using Stereonet software, revealed for the older set of striations a stress field with the maximum extensional axis gently dipping towards the NNW direction and an almost vertical maximum compressional axis, pointing out, together with the kinematic indicators, to a normal sense of shear (Fig 5a). The younger set of lineations indicated a normal sense of shear with considerable lateral component, and the maximum extensional axis almost horizontal dipping towards NNE direction (Fig 5b). This latest stress field is the same with the stress field recognized by Mouslopoulou et al. (2014) for the nearby active Spili fault. In addition, the Paligremnos faults appear to act as antithetic to the main fault zone of Sellia- Assomatos, located north of Plakias basin. Sellia-Assomatos fault zone appears to be the eastwards continuation of the Sfakia fault zone, which is considered as the most important active zone of the southwestern cost of Crete (Nicol et. all, 2020; Ott et al. 2019). The vertical inclination of the Paligremnos scarp was thus interpreted as a rotated surface due to the main activation of the Sellia-Assomatos fault, indicating that the fault zone should be considered as active too.

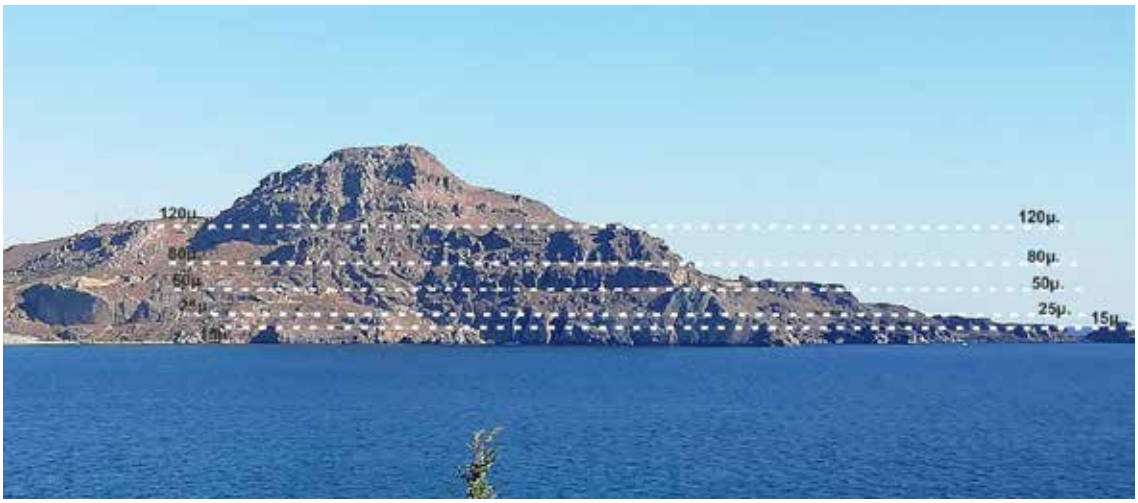

Figure 4. The five marine terraces recognized on the Psarela cape

In respect to other geomorphological features, geological mapping identified a rock instability zone just over the Paligremnos fault scarp initiated at the crosscutting of the F3 and F4 faults on top of the hill. Scattered boulders and large rock blocks seem that have been fallen from the escarpment and then slid on the clay flysch of Tripolitsa reaching finally the edge of the Paligremnos fault scarp. This instability zone covers the area of the touristic constructions imposing a high risk on it.

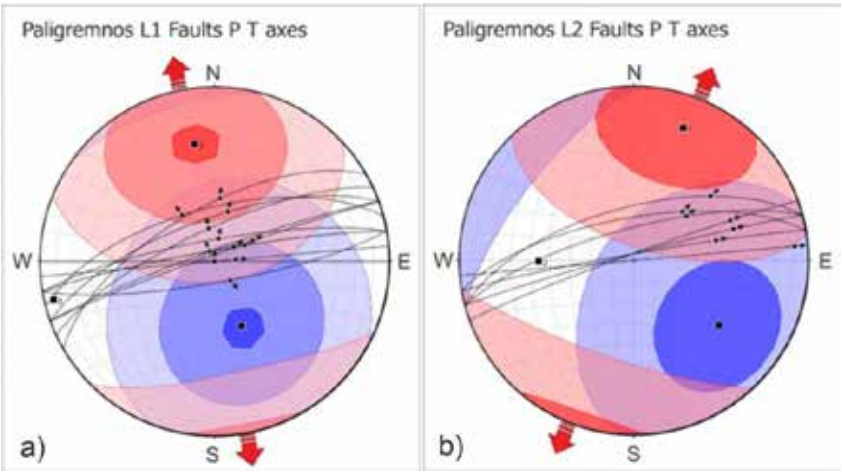

Figure 5. Paleostress analyses of the two striae generations the older a) and newer b)

In what regards the biological value of the area, apart from the sand dunes at the beach that host some very important local flora and are very sensitive ecosystems, the study identified another important area at the western part of the peninsula where, over one of the intermediate marine terraces, a seasonal pond is developed that is crucial for bird fauna. Based on all the above data the suggested area for the protection of the monument was drawn, including all the important geological (fault scarps, notches, marine terraces), biological (part of the dunes and the seasonal pond) and the cultural elements (the tunnel and the remains of the WWII railway and the fortifications) of the monument (Fig. 2).

The qualitative and quantitative assessment that followed documented the value of the area and the reasons to be nominated as a Protected Landscape. The fault scarp is the largest naturally exposed fault scarp in Greece, with the second larger in dimensions but artificially exposed, being the Arkitsa fault (Kokkalas et al. 2007). The Paligremnos fault zone is an active fault zone forming together with the Sellia-Assomatos fault the Plakias graben since the Miocene times. Together with the five marine terraces and the 365 AD notch demonstrate impressively and didactically the Pleistocene rock uplift of the southern coasts of Crete. The Paligremnos fault scarp tucked into the embrace of Plakias bay constitutes a unique and outstanding landscape that forms one of the most attractive landmarks of Crete, listed in geological text books and Atlases (Papanikolaou & Sideris 2013; Mountrakis et al. 2002). Quantitative analyses of the geosite indicated in addition, that the area has of the highest scientific and aesthetic values among the geosites studied with that method in

Greece, and of the highest potential for touristic and educational development. In addition, the vulnerability of the geosite is higher than the normal mean values, mainly due to the thread that touristic constructions may impose.

Conclusions

Based on the processing of bibliographic data, the geological mapping, the analyses of the data collected during the fieldwork and the data provided by residents and visitors of the area, it is demonstrated that the "Paligremnos - Akrotiri Psarela" area of Plakias, Municipality of Agios Vasilios, Rethimno has special and remarkable characteristics of the geological and geomorphological environment, hosts endemic forms of flora and fauna of Crete and gathers some rare and unique for Crete cultural elements related to mining and quarrying activities of the past. It is obvious that the dominant and special characteristics, worthy of protection, are the geomorphological and geological formations that crop out in almost the entire area under consideration, but specifically at the Paligremnos fault scarp that appears to be the largest, naturally exposed fault scarp in Greece. Due to all these values the area finally was declared as a Protected Landscape and Protected Natural Formation under the Greek legislation in 2023, crowning the efforts of local communities to protect their nature.

As an outcome of this study and in order to further promote the values of this area we have developed a virtual tour based on UAV shots and 360° panoramas that virtually guides visitors, step by step, along the main features of the Paligremnos and cape Psarela area. In addition, the tour offers panoramic view of the whole Plakias bay and graben. The tour can be visited thought the following link https://tours.panotours.gr/plakias/.

Acknowledgements

This study is based on the Special Study for the Nomination of the area as Protected Landscape and Protected Natural Formation, assigned to the Natural History Museum of University of Crete by the Municiaplity of Agios Vassilios in Rethimnon. We would like to thank Agios Vassilios Municipality for all the support that has provided during and after the implementation of the Study. We owe special thanks though, to the inhabitants, locals and foreigners, the Climbing and Speleological community of Crete and other specialists who have provided valuable information and data for the development of the Study and the strong motivation and support they offered for the nomination and protection of the area. The final result is dedicated to all of them.

References

Angelier, J., 1979. Neotectonique de l'arc egeen, vol. 3. Society Geologic du Nord Special Publication, pp. 1-418.

Fassoulas C., Paragamian K. & Iliopoulos G. (2007). Identification and assessment of Cretan Geotopes. Bull. Geol. Soc. Greece, vol. XXXVII, 1780 – 1795.

Fassoulas C., Mouriki D., Dimitriou-Nikolakis P. & Iliopoulos G. (2012). Quantitative assessment of geotopes as an effective tool for geoheritage management. GEOHERITAGE, v4, 3, 177-193, DOI 10.1007/s12371-011-0046-9.

Georgalis, G. L., Villa, A., Vlachos, E., & Delfino, M. (2016). Fossil amphibians and reptiles from Plakias, Crete: a glimpse into the earliest late Miocene herpetofaunas of southeastern Europe. Geobios, 49(6), 433-444. https://doi.org/10.1016/j.geobios.2016.09.004

Gray M. (2004). Geodiversity: Valuing and Conserving Abiotic Nature. Wiley-Blackwell eds, 512 p.

Kokkalas S., Jones R. R., McCaffrey K. J. W., and Clegg P. (2007). Quantitative fault Analysis at Arkitsa, central Greece, using terrestrial laser-scanning. Bulletin of the Geological Society of Greece vol. XXXVII, 2007 Proceedings of the 11th International Congress, Athens, May, 2007

Mouslopoulou V., Moraetis D, Benedetti L., Guillou V., Bellier O, & Hristopulos D. 2014. Normal faulting in the forearc of the Hellenic subduction margin: Paleoearthquake history and kinematics of the Spili Fault, Crete, Greece. Journal of Structural Geology 66 (2014) 298-308

Mountrakis, D., Zouros, N. & Soulakelis, N. (2002). Atlas of geological monuments of Aegean, Greece. Ministry of Aegean, Lesvos, pp.352.

Nicol A., Mouslopoulou V., Begg J., Oncken O., (2020). Displacement accumulation and sampling of paleoearthquakes on active normal faults of Crete in the eastern Mediterranean. Geochemistry, Geophysics, Geosystems, https://doi.org/10.1029/2020GC009265

Ott R.F, Gallen S.F., Wegmann K.W., Biswas R.H., Herman F., Willett S.D. (2019). Pleistocene terrace formation, Quaternary rock uplift rates and geodynamics of the Hellenic Subduction Zone revealed from dating of paleoshorelines on Crete, Greece. Earth and Planetary Science Letters, 525(2019, 115757

Papanikolaou D. & Sideris Ch. (2013). Geology the discipline of the earth (in greek). Pattakis eds. Athens, 296 p.

Zouros, N. & Fassoulas, C. (2006). Geodiversity in Greek National Parks. In: 2nd UNESCO Inter. Conf. on Geoparks, Belfast 2006, Abst. Vol., 62.

Tsimi, C., Ganas, A., Ferrier, G., Drakatos, G., Pope, R.J. and C. Fassoulas, (2007). Morphotectonics of the Sfakia normal fault, south-western Crete, Greece. 8th Pan-Hellenic Geographical Conference, volume 1 (186-194), 4 - 7 October 2007, Athens (Greece).

17th INTERNATIONAL CONGRESS of the Geological Society of Greece

BULLETIN OF THE GEOLOGICAL SOCIETY OF GREECE, SP. PUBL.

EXTENDED ABSTRACT 073

Assessing the management of Arkalochori EQ crisis in Crete, Greece under the implementation of RESILIAGE project in order to strengthen community resilience

Fassoulas C.[1], Tamborrino R.[2], Bolca, P.[2], Marra G.[2], Mezzalama G.[2], Tackacs V.[3], Leonhardmair N.[4], Demir M. E.[5]

(1) Natural History Museum, Univ. of Crete, Crete, Greece, fassoulas@nhmc.uoc.gr (2) Politecnico di Torino, Torino, Italy (3) DeepBlue, Rome, Italy (4) Vienna Centre for Social Security, Vienna, Austria (5) Demir Energy, Istanbul, Turkey

Introduction

It is well documented that only preparedness and prevention can support modern communities in respect to the earthquake risk. Being one of the most seismic prone areas in the world, Greece has invested a lot in the prevention of the impacts of future earthquakes and in the increase of preparedness of the structured and non-structured elements of our societies. Prevention is achieved through interventions and actions aiming at the identification of hazard zones, minimizing the exposures on the build environment and developing plans and regulations to manage crises. In most cases preparedness is achieved by strengthening and improving the behavior of material elements and infrastructures, the increase of knowledge regarding the hazard and its impact, as well as the improvement of the self-protection of citizens. In the past years, repeated Earthquake crises revealed that further improvements both on prevention and preparedness are necessary which can be made only if assessment of past crises' management is performed.

The earthquake of Arkalochori in central Crete is of one the most recent and most peculiar crises in Greece. The foreshock sequence started on the beginning of June 2021, just at the end of the COVID 19 crisis, and lasted almost three months having one strong earthquake of 4,8 R on July 24. The long foreshock period enabled the establishment of many seismic instruments in the broader area to monitor the phenomenon. The main shock took place early in the morning on September 21st, 2021 with a magnitude of 6 R scale and focal point 10 kms below the town of Arkalochori (Ganas et al. 2021). The earthquake took place along a well-known active fault in the area, the Kasteli fault (Fassoulas 2001) that has produced a swam of small eq in 1995 too (Delibasis et al. 1999). The town, that is one of the largest of rural Crete with a population of about 4000 inhabitants and many nearby villages were seriously affected with collapses and damages of old and more recent constructions, while even the city of Heraklion experienced moderate intensities with minor impacts. This was the first strong earthquake onshore Crete for more than a century (Papadopoulos 2011), and fortunately, there was only one human victim that was killed by a strong aftershock that happened few hours after the main event.

The most peculiar feature of this crisis was though the very long aftershock period that lasted almost a year with several events between 4 and 5 R scale. It was estimated that more than 4750 earthquakes took place on the broader area over a period of one year (Vallianatos et al. 2022) challenging the structural behavior of the buildings and the mental health of local population. The response of the Civil Protection mechanism was immediate with first responders and civil protection volunteers taking action soon after the main shock installing temporary camps at the Arkalochori and several other villages, and a more organized shelter at the Exhibition Center of Arkalochori few days after. The response of the local population was remarkable with hundreds of them arriving at Arkalochori from the first day to support the victims. This huge offer of volunteers created problems till a mechanism to manage them was set, but their contribution in compensating the burden of the local people and supporting their daily needs was invaluable even months after the earthquake.

The total toll of impacts counts more than 7000 houses heavily damaged by the main shock and its aftershocks with about 3900 of them to be demolished. Within these structures occur many local schools and churches. Apart from the first financial support that state provided soon after the earthquake to those affected by, the recovery process according to the locals failed totally to cover the needs of local societies (p.c. K. Gantatsios, president of "Elpis" the association of the victims of the earthquake 2024). Three years after the earthquake many families still live at preconstructed houses at the temporary shelter, from the 7000 applications for financial aid to repair houses that have been submitted only few tens have been elaborated by the relative services and the broader area presents images of abandonment and depopulation that was obvious at the recent census.

It is important to mention that the psychological burden of the local communities was not only increased by the long-lasting aftershocks but also from rumors and fake news that were circulated at social media but even the national

broadcasting channels. Rumors for stronger earthquakes were appearing after interviews or posts of "earthquake specialists" in national and international media. Fake news about the reasons of the long seismicity were repeatedly circulated connecting the earthquakes with the construction nearby of a new airport, the existence of a dam few kms away from the epicenters, but even the overfilling of a chapel under the runway of the new airport, that further increased the communication chaos.

The Arkalochori earthquake is a case study under RESILIAGE project funded by the Horizon Europe and coordinated by the Polytechnic of Torino, in which the University of Crete is among the 18 partners that aim to build sustainable resilient communities with local heritage drivers (https://resiliage.eu/). In general, recent crises and disasters have affected the European citizens' lives, livelihoods, and environment in unforeseen and unprecedented ways. These disasters are exacerbated by social inequality, lack of adequate information and technology, as well as economic and political crises, that reduce the effective preparedness and response. The main objectives of the project are thus focused on understanding citizen reaction in case of crisis, on cocreating new knowledge encompassing the local heritage drivers that make communities stronger and new tools that provide more accurate information and make it accessible through easy-to-use tools and finally, lightweighting solutions to support first responders and empower citizens in crisis and disaster situations. The project has defined five Systemic Resilience Innovation (SyRI) frameworks focusing on Adaptive Governance, Health and Wellbeing, Active Memory, Social Interaction and Inclusiveness and Socio-economic Resilience that are examined in five European territories facing variable risks. The Region of Crete is one of them addressed to the Active Memory in respect to the earthquake risk.

Hereby we present the results of two workshops that have been developed in Crete under RESILIAGE in order to assess the management of Arkalochori EQ crisis, to identify the cultural factors that may influence local resilience, to build local networks through synergies and collaborative actions, and to identify the gaps in the management crisis operation in order to develop proposals for future improvement.

Figure 1. Implementation of focus groups discussions during the first workshop of RESILIAGE at Cretan CORE Lab on May 2024.

Methodology

The RESILIAGE project has foreseen the organization of five Community Resilience Laboratories (CORE Labs) in five European territories that have suffered in the past from various disasters. These include the City of Trondheim in Norway that faces the risk of landslides (slow clay) and focusses on Health and wellbeing, the Famenne-Ardenne UNESCO Global Geopark in Belgium which has been affected by serious floods several years ago and focuses on Socio-economic resilience, the Region of Crete focusing on the earthquakes and the Active Memory, the Naturtejo UNESCO Global Geopark in Portugal which repeatedly experiences wild fires and focusses on Social Interaction and Inclusiveness and the town of Karsiyaka in Turkey that is facing risks form heatwaves and focusses on the Adaptive Governance.

The relative partners in these counties were obliged to set the CORE Labs by inviting local stakeholders. In Crete the Natural History Museum of Crete invited various stakeholders that are engaged in crisis management, or represent certain local target groups, education and communication organizations and citizens. The CORE Lab was thus formed by representatives of First Responders (National Center of Immediate Aid, Fire Brigade, and Volunteer groups),

Local Municipalities and the Region of Crete, Local Development Companies, The Church of Crete, Local Museums, Educational Centers, Local Cultural Clubs and Associations, Sport Clubs and Citizens.
Two onsite workshops were organized in Crete using the focus group methodology (Wilkinson 1998) associated by structured interviews and web questionnaires. In each workshop we used boards, concept, interaction and territorial maps, discussion recordings and the assistance of facilitators to gather and analyse local data in a qualitative manner. The first WS took place on the 21st and 22nd of May 2024 at the premises of Natural History Museum with 30 participants (Figure 1). The aims of the WS were to understand how the local community define its territory in terms of main environmental, historical, and cultural characterizations, understand how local community interacts with the environment from a cultural and historical perspective, gather local narratives of disaster risk reduction, extract cascade effects related to the historical, cultural and environmental factors that intervene in crisis response, and identify lessons learned related to the historical, cultural and environmental factors that intervene in crisis response, having as case study the Arkalochori EQ crisis. During the WS field visit to Arkalochori and nearby areas was organized to discuss with the local stakeholders and inhabitants there (Figure 2).

Figure 2. Pupils performing local dances during the visit of RESILIAGE partners at the preconstructed classrooms hosting the primary school of Arkalochori on May 2024.

The second workshop took place on the 7th of February 2025 again at the Natural History Museum of Crete with the participation of 19 people (Figure 3). This WS was aiming on mapping certain heritage elements recorded at the collective memory that can be used to strengthen local resilience and improve preparedness planning. Activities were thus focused on the co-mapping of local cultural elements supportive to strengthen citizen's resilience, on the co-creation of synergies and collaborations to safeguard those heritage elements through the establishment of a local agreement to safeguard them, and on proposing actions for the inclusion of local communities and vulnerable groups in the crisis management plans through the improvement of communications, the raise of awareness and sensitization of citizens and improving adaptive governance. In this second workshop more advanced methodologies and means were used like serious game, stickers, card boards, thematic maps etc. (Figure 4).
The data collected through these onsite CORE Lab activities were further elaborated by the research partners to step on and develop soft solutions and digital tools that will be evaluated by CORE Lab in a second phase of the project implementation.

Results
The main priority of Civil Protection is always the proper management of a crisis putting more efforts and means though on the response phase. Preparedness and prevention are less developed, whereas the recovery phase is the one that is less considered. RESILIAGE invests in the improvement of preparedness of local communities using their cultural assets and local heritage as potential drivers for establishing strong community resilience that can contribute in a more effective recovery phase. The inventory of these drivers and the assessment of crisis management is the main tool to identify the local needs, capacities and strengths, on which new tools and actions are being developed. The main results under the scopes of RESILIAGE project from the CORE Lab activities in Crete may be summarized as follows.

Figure 3. Co-mapping of cultural and natural heritage elements during the second workshop of RESILIAGE in February 2025.

Cultural bonds remain very strong in the island of Crete based on traditions and ethics dated back in time. Dances, songs, “mantinades” (local rhymes) and common celebrations under various occasions tightened relationships between communities and helped a lot the citizens to cope with the Arkalochori EQ consequences and long-standing impacts (Figure 2). The oral traditions and transfer of myths and stories between generations appears to be a key channel for the preservation of values and collective memory, connecting generations through shared narratives. The workshops also highlighted issues related to social ethics and values as well as the strong blood bond that highlights the importance of family ties that can influence social interactions and contribute to shaping the resilience of the community. At the same time, the workshops underscore that in each settlement there are dozens of reference points and monuments that connect residents to the place and history and offer relief and a source of encouragement in times of crisis, that must be preserved. The existence of social interaction spaces where people can meet and promote social interactions is an important foundation in the event of crises that must be maintained during the operation of temporary shelters.

In places where social interaction was intense, like in Arkalochori where a local sport club and the community were organizing various annual events, this played a crucial role in managing the crisis and offering immediate support to the victims. Their role was remarkable in providing food, immediate aim, managing and organizing the many volunteers and retaining community alive for long period. The engagement of young people in such social and community activities enforces the local cohesion and reduces the vulnerability of the communities. The local Church is also a very important actor in the post crisis phase because it has the organization and means to support immediately the victims especially at the rural areas, with material and immaterial aid. The existence of local volunteer groups is also a very important factor to manage a crisis as they can offer assistance to CP mechanism, support the victims and palliate the psychological burden.

The need for reliable information and proper communication, before but especially during the crisis, emerged as the top problem in the case of the Arkalochori earthquakes. The absence of reliable and timely information, as well as of corresponding official state communication channels, contributed to the increase in the spreading of fake news and rumors that increased further the stress of those affected. The battle with fake news and incorrect information was lost very early on as there was no way to deal with this on social networks. Throughout the long post-earthquake sequence, residents felt the lack of communication and information from the official authorities, a problem that was much more intense in elder people. In these cases, the Church could play an important role, if proper cooperation has been developed between the Church, the relevant scientific bodies and the State. To enhance disaster preparedness and response, it is crucial to adopt a more proactive and comprehensive approach to communication. This should include regular awareness campaigns before a disaster, accessible guidance for individual groups after a disaster and ensure that all relevant information sources are easily identifiable and accessible.

Figure 4. The concept board for the assessing of Crisis Management plan after the implementation of the second workshop of RESILIAGE in February 2025.

Regarding the crisis management it was obvious that the CP mechanism responded immediately after the main shock establishing shelters and providing support to the affected societies, following a well operational management plan. However, it is apparent that despite the comprehensive national policies and documentation, shortcomings exist in resources evaluation and cooperation mechanisms at the local level, which hinder effective disaster response. The strong building codes and regulations didn't prevent the numerous damages and destructions, mainly because of the weakness of the relative authorities to monitor and ensure their implementation. The case of Arkalochori EQs underpin the fact that in rural areas older infrastructure remains vulnerable, highlighting a need for reinforcement and modernization. In addition, and under the threat of Climate Change it was highlighted that disaster risk management plans are not integrated with climate adaptation strategies, causing missed opportunities to leverage ecosystems in disaster management.

Under this scope it was also stressed that detailed risk assessments are outdated and require revisions. The risk and vulnerability assessments identify key vulnerabilities within the adaptation plan, such as: socio-demographic factors (population distribution and vulnerable groups), impacts on buildings and infrastructure, and cultural heritage considerations. The assessment should thus consider agriculture, forestry, biodiversity, and fisheries, as well as references to vulnerable groups such as the elderly and disabled at the national or regional level.

The crisis management was further exacerbated by the fact that the financial legislation lacks detailed information regarding funding mechanisms available for disaster management. Alternative financing mechanisms for risk reduction are scarce, while state financial resources for risk reduction are insufficient, limiting the implementation of disaster resilience measures. The total failure of the CP mechanism in the recovery phase is indicated by the fact that three years after the crisis from the thousands of applications seeking state support to reconstruct the damaged properties, only few tens have been elaborated so far. This situation is not only socially inappropriate, but ethically and morally too as a large number of the Arkalochori victims were elder.

Acknowledgements

This study is funded under the EU's Horizon Europe, key funding programme for research and innovation, with title: "RESILIAGE – Advancing holistic understanding of community RESILIence and heritAGE drivers through community-based methodologies (GA no. 101121231)".

References

Delibasis, N.D.; Ziazia, M.; Voulgaris, N.; Papadopoulos, T.; Stavrakakis, G.N.; Papanastassiou, D.; Drakatos, G. Microseismic activity and seismotectonics of Heraklion Area (central Crete Island, Greece). Tectonophysics 1999, 308, 237–248.

Fassoulas, C., 2001. The tectonic development of a Neogene basin at the leading edge of the active European margin: the Heraklion basin, Crete, Greece. J. Geodyn. 31, 49–70. https://doi.org/10.1016/S0264-3707(00)00017-X.

Ganas, A., Hamiel, Y., Serpetsidaki, A., Briole, P., Valkaniotis, S., Fassoulas, C., Piatibratova, O., Kranis, H., Tsironi, V.,

Karamitros, I., Elias, P., Vassilakis, E., 2022. The Arkalochori Mw =5.9 earthquake of 27 September 2021 inside the Heraklion basin: a shallow, blind rupture event highlighting the orthogonal extension of central Crete. Geosciences 12, 220. https://doi.org/10.3390/geosciences12060220.

Papadopoulos, G.A. A Seismic History of Crete: Earthquakes and Tsunamis, 2000 B.C.–A.D. 2010, 1st ed.; Ocelotos Publ.: Athens, Greece, 2011; p. 415. ISBN 978-960-9499-68-2.

Vallianatos, F., Karakonstantis, A., Michas, G., Pavlou, K., Kouli, M., Sakkas, V., 2022. On the Patterns and Scaling Properties of the 2021–2022 Arkalochori Earthquake Sequence (Central Crete, Greece) Based on Seismological, Geophysical and Satellite Observations. Appl. Sci. 2022, 12, 7716. https://doi.org/10.3390/app12157716

Wilkinson, S., 1998. Focus group methodology: a review. International Journal of Social Research Methodology, 1(3), 181–203. https://doi.org/10.1080/13645579.1998.10846874

17th INTERNATIONAL CONGRESS of the Geological Society of Greece

BULLETIN OF THE GEOLOGICAL SOCIETY OF GREECE, SP. PUBL.

EXTENDED ABSTRACT 074

Quaternary eustatic cycles and their impact on the Paleoceanography of the Gulf of Corinth (NE Mediterranean Sea)

Fatourou E.[1], Kafetzidou A.[1], Marret F.[2], Panagiotopoulos K.[1,3], Kouli K.[1]

[1]*National and Kapodistrian University of Athens, School of Science, Geology and Geoenvironment, GREECE (efatourou@geol.uoa.gr)*

[2]*School of Environmental Sciences, University of Liverpool, UK*

[3]*Forschungszentrum Jülich, Jülich, GERMANY*

Introduction / Background

The Gulf of Corinth (GoC), which is a semi-isolated marine basin derived from a geologically young active rift (McNeill *et al.,* 2019b), offers a unique opportunity to study changes in environmental conditions during the Quaternary period in a region where long sequences are few. The GoC is linked to the global ocean via the Gulf of Patras in the Ionian Sea. This connection is facilitated by the Rion Strait to the west and the Corinth Isthmus to the east. The Rion Strait forms a narrow and deep marine embayment, resembling a fjord, with fully marine conditions (Poulos *et al.,* 1996). The recent IODP expedition (IODP381) has retrieved three long sequences (M0078A, M0079 and M0080) recovering most of the Quaternary period and providing the first comprehensive insight on the evolution of a young active rift (McNeill *et al.,* 2019b). The sedimentary sequence drilled 610.43 mbsf that were divided into two main Lithostratigraphic Units (LU). Deposition during the upper one, LU1 (0–385.14 mbsf), is primarily controlled by eustatic sea level and dominated by detrital clay- and silt-grade carbonate, this interval has been divided into 16 subunits (LU1.1-1.16) with respect to the alternation of marine and isolated/semi-isolated intervals, while below 385.14 mbsf, LU2 is composed almost entirely of weakly laminated to homogeneous highly bioturbated mud (McNeill *et al.,* 2019a).

Preliminary observations of conventional biological proxies used for determining past palaeoceanographic conditions during the onshore party of IODP 381 expedition (*McNeill et al., 2019b*) have highlighted an unexpected richness in dinoflagellate cyst taxa, notably species that were only known from the Marmara-Black Sea corridor (e.g., Marret *et al.,* 2004; Mudie *et al.,* 2004; 2017). Due to periods of isolation during Quaternary lowstands, the water conditions were not favorable for the occurrence of conventional palaeoceanographical proxies such as planktonic foraminifera. Fatourou *et al.* (2023) presented an initial study of organic-walled dinoflagellate cyst assemblages from site M0078A, covering the upper 384m (~Marine Isotopic Stage 18), highlighting distinct shifts related to fluctuations in sea-surface temperature and salinity in response to global sea-level changes.

Table 1: List of identified dinoflagellate cyst taxa, with micropalaeontological (cyst) name and associated biological name, trophic level (P: Phototrophic; H: Heterotrophic), and environmental conditions (B: brackish; M: marine) of the Gulf of Corinth.

Cyst name	Biological name	Code	Trophic level	Environmental conditions
Achomosphaera sp.	*Gonyaulax* sp.	Achs	P	M
A. choane	*Gonyaulax* sp.	Acho	P	M
B. tepikiense	*Gonyaulax* sp.	Btep	P	M
Brigantedinium sp. (*B. caracoense* and *B. simplex*)	*Protoperidinium* sp. (*Protoperidinium avellanum* and *Protoperidinium conicoides*)	Brisp	H	B to M
C. rugosum	Unknown	Crug	P	B
E. zonneveldii	Unknown	Ezon	H	M
I. caspienense	*Gonyaulax baltica*	Icas	P	B
I. aculeatum	*Gonyaulax sp.*	Iacu	P	M
I. paradoxum	*Gonyaulax sp.*	Ipar	P	M
I. patulum	*Gonyaulax sp.*	Ipat	P	M
I. plicatum	*Gonyaulax sp.*	Ipli	P	M
I. sphaericum	*Gonyaulax sp.*	Isph	P	M
I. strialatum	*Gonyaulax sp.*	Istr	P	M
L. oliva	Unknown	Loli	H	M
L.machaerophorum s.l.	*Lingulodinium polyedrum*	Lmacsl	P	M
L.machaerophorum s.p.	*Lingulodinium polyedrum*	Lmacsp	P	B
N. labyrinthus	*Gonyalax spinifera*	Nlab	P	M

O. centrocarpum sensu Wall and Dale, 1967	*Protoceratium reticulatum*	Ocen	P	M
P. zoharyi	*Pyrodinium bahamense*	Pzoh	P	M
cysts of *P. dalei*	*P. dalei*	Pdal	P	M
P. psilata	Unknown	Ppsi	P	B
Q. concreta	*Protoperidinium leone*	Qcon	H	M
S. nephroides	*Protoperidinium subinerme*	Snep	H	M
S. quanta	*Protoperidinium conicum*	Squa	H	M
S. belerius	*Gonyalax scrippsae*	Sbel	P	M
S. bentorii	*Gonyalax digitale*	Sben	P	B to M
S. bulloideus	*Gonyalax scrippsae*	Sbul	P	M
S. cruciformis	*Gonyalax* sp.	Scru	P	B
S. delicatus	*Gonyalax* sp.	Sdel	P	M
S. hyperacanthus	*Gonyalax* sp.	Shyp	P	M
S. lazus	*Gonyalax* sp.	Slaz	P	M
S. membranaceus	*Gonyalax* sp.	Smem	P	M
S. mirabilis	*Gonyalax spinifera*	Smir	P	M
S. ramosus	*Gonyalax* sp.	Sram	P	M
T. pellitum	*Gonyalax spinifera*	Tpel	P	M
T. vancampoae	*Pyrophacus steinii*	Tvan	P	M
X. xanthum	*Protoperidinium divaricatum*	Xxan	H	M

We present here a continuous record of dinoflagellate cyst assemblages of the last 1.1 Ma aiming to examine the shifts between marine and isolated/semi-isolated depositional environments in response to eustatic sea level changes in the GoC. The dinocyst assemblages encountered within the intervals described below consist of the low salinity indicators *S. cruciformis*, *P. psilata*, *Caspidinium rugosum, Impagidinium caspienense* and *Lingulodinium machaerophorum* s.p.. *Spiniferites cruciformis* and *P. psilata* are the most dominant species during those intervals, however, a distinct variability in those assemblages is recorded. The dinocyst assemblages recovered within the marine intervals of M0078A record are characterised by a high diversity (30 different species) and with mean concentrations of 24,632 cysts/g. In addition, results from other proxies (aquatic palynomorphs, foraminifera and diatoms) offer an integrated perspective on the evolution of the basin and its surroundings. The freshwater and brackish diatoms, as well as the euryhaline foraminifera identified during the onshore phase of the IODP 381 expedition (McNeill *et al.,* 2019) seem to correlate well with the isolated LUs and the brackish dinocyst assemblages. During the Holocene, the presence of several dinoflagellate cysts, alongside with the decreased TOC and TOC/N at the upper part of LU1.1 (Holocene) confirm the occurrence of well-oxygenated bottom waters in the basin.

Figure 1: Shade plot: visual representation of the species encountered in the different LUs (LU1.1 to LU1.16) and Marine Isotope Stages (MIS). Samples were arranged based on core depth. White colour indicates absence, black the highest abundance in the dataset, while all the different colours suggest low (blue colour), medium (green colour) and high presence (orange and red) (Fatourou, 2024).

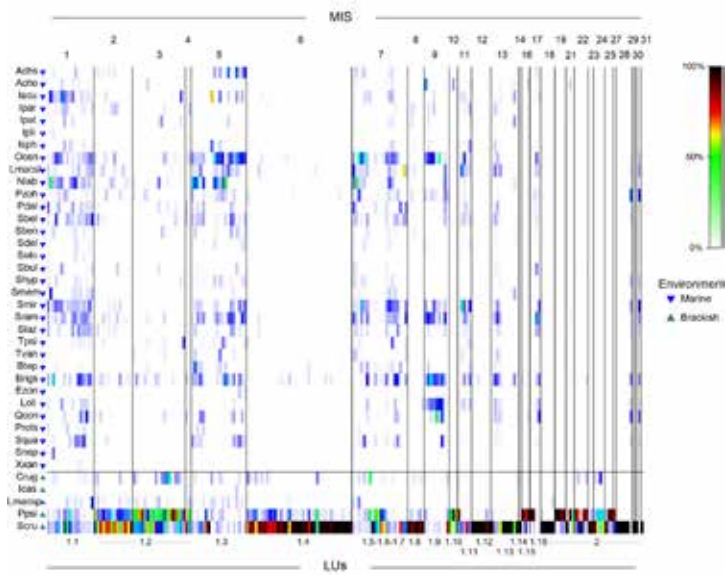

This record aims to fill a gap in palaeoceanographic studies in Eastern Mediterranean region and to provide a better understanding of how shallow-sill connected basins respond to global climate changes. Dinocysts and other palynomorphs (NPPs) suggest that the GoC was repeatedly isolated and reconnected to the Mediterranean Sea during global sea-level lowstands associated with glacials. These proxies combined suggest that marine water flowed into the GoC during the eustatic highstands associated with interglacials. The dinocyst assemblages show a close affinity to modern assemblages from the Black, Caspian, and Marmara Seas (e.g., Marret *et al.,* 2004; Mudie *et al.,* 2004; 2017).

Acknowledgements

The study material was retrieved during the IODP Exp. 381. The research work was supported by the Hellenic Foundation of Research and Innovation (H.F.R.I) under the "First Call for H.F.R.I. Research Projects to support Faculty members and Researchers and the procurement of high-cost research equipment grant" (Project Number: 1026, Quaternary Environmental Changes in the Corinth Rift Area: the IODP 381 palynological record: QECCoRA).

References

Fatourou E., 2024. Depositional environment development and ecosystem response in the Gulf of Corinth during the Quaternary climatic cycles. Ph.D. Thesis, Department of Geology and Geoenvironment, National and Kapodistrian University of Athens, pp. 290.

Fatourou, E., Kafetzidou, A., Marret, F., Panagiotopoulos, K., Kouli, K., 2023. Late Quaternary Ponto-Caspian dinoflagellate cyst assemblages from the Gulf of Corinth, Central Greece (eastern Mediterranean Sea). Mar. Micropaleontol 179. https://doi.org/10.1016/j.marmicro.2023.102211

Marret, F., Leroy, S., Chalié, F., Françoise, F., 2004. New organic-walled dinoflagellate cysts from recent sediments of Central Asian seas. Rev. Palaeobot. Palyno. 129, 1–20. https://doi.org/10.1016/j.revpalbo.2003.10.002

McNeill, L.C., Shillington, D.J., Carter, G., Everest, J.D., Gawthorpe, R.L., Miller, C., Phillips, M.P., Collier, R.E.Ll., Cvetkoska, A., De Gelder, G., Diz, P., Doan M.-L., Ford, M., Geraga, M., Gillespie, J., Hemelsdaël, R., Herrero-Bervera, E., Ismaiel, M., Janikian, L., Kouli, K., Le Ber, E., Li, S., Maffione, M., Mahoney, C., Machlus, M.L., Michas, G., Nixon, C.W., Oflaz, S.A., Omale, A.P., Panagiotopoulos, K., Pechlivanidou, S., Sauer, S., Senguin, J., Sergiou, S., Zakharova, N.V., Green, S., 2019a. High-resolution record reveals climate-driven environmental and sedimentary changes in an active rift. Scientific Reports 9, 1–11.

McNeill, L.C., Shillington, D.J., Carter, G.D.O., Everest, J.D., Le Ber, E., Collier, R.E., Cvetkoska, A., De Gelder, G., Diz P., Doan, M. L., Ford M., Gawthorpe, R. L., Geraga, M., Gillespie, J., Hemelsdaël, R., Herrero-Bervera, E., Ismaiel, M., Janikian, L., Kouli, K., Li, S., Machlus, M.L., Maffione, M., Mahoney, C., Michas, G., Miller, C., Nixon, C. W., Oflaz, S. A., Omale, A.P., Panagiotopoulos, K., Pechlivanidou, S., Phillips, M.P., Sauer S., Seguin, J., Sergiou, S., Zakharova, N.V., 2019b. Corinth active rift development. Proceedings of the International Ocean Discovery Prog, 381. https://doi.org/10.14379/iodp.proc.381.104.2019

Mudie, P.J., Marret, F., Mertens, K.N., Shumilovskikh, L., Leroy, S.A., 2017. Atlas of modern dinoflagellate cyst distributions in the Black Sea Corridor: from Aegean to Aral Seas, including Marmara, Black, Azov and Caspian Seas. Mar. Micropaleontol. 134, 1–152. https://doi.org/10.1016/j.marmicro.2017.05.004

Mudie, P.J., Rochon, A., Aksu, A.E., Gillespie, H., 2004. Late glacial, Holocene, and modern dinoflagellate cyst assemblages in the Aegean–Marmara–Black Sea corridor: statistical analysis and re-interpretation of the early Holocene Noah's Flood hypothesis. Rev. Palaeobot. Palyno. 128, 143–167. 9

Poulos, S.E., Collins, M.B., Pattiaratchi, C., Cramp, A., Gull, W., Tsimplis, M., Papatheodorou, G., 1996. Oceanography and sedimentation in the semi-enclosed, deep-water Gulf of Corinth (Greece). Mar. Geol. 134, 213–235. https://doi.org/10.1016/0025-3227(96)00028-X

17th INTERNATIONAL CONGRESS of the Geological Society of Greece

BULLETIN OF THE GEOLOGICAL SOCIETY OF GREECE, SP. PUBL.

EXTENDED ABSTRACT 075

Underground rivers in Greece

Fellachidou K.[1], Lazaridis G.[1]

(1) Aristotle University of Thessaloniki, School of Geology, Department of Structural, Historical and Applied Geology, Laboratory of Geology and Paleontology, Thessaloniki, Greece, fellachid@gmail.com

Research highlights

This study presents the first national-scale mapping of underground rivers in Greece, documenting a total of 60 systems. It also offers the first systematic classification of the underground rivers, emphasizing their spatial distribution and characteristics in relation to tectonostratigraphic units. Spatial analysis reveals the dominance of the External Hellenides in speleogenesis, as they host 67% of the documented underground rivers. Limestone hosts 21 underground rivers, highlighting its critical role in speleogenesis. High-relief regions (>900m) host the majority of these systems, influenced probably by climatic and hydrological conditions. Conversely, the Internal Hellenides display fewer and more isolated underground rivers due to their complex geological history and diverse lithologies. Overall, the findings enhance the theoretical understanding of underground river systems while providing practical applications for water resource management, environmental protection, and geological risk assessment.

Introduction

Underground rivers represent a unique and significant geological feature, particularly in regions such as Greece, where complex geological formations and hydrological conditions prevail. Their formation is attributed to processes of epigene speleogenesis. These processes occur when meteoric water infiltrates from the surface, utilizing its dissolving capacity derived from surface environmental conditions. Specifically, the water acquires its ability to dissolve carbonate rocks by absorbing carbon dioxide from the atmosphere, particularly within the soil. As the water percolates through limestone or other soluble lithologies, its flow transitions from diffuse pathways to more convergent routes, eventually emerging at discrete springs in adjacent valleys (Audra & Palmer, 2011).

These caves form under specific geological and environmental conditions, influenced by factors such as lithology, tectonics, the type of recharge and base-level changes. In most cases, the passages of epigene caves develop along discontinuities, such as bedding planes, fractures and faults (Gunn, 2004), forming cave patterns that include isolated passages or branchworks, with angular configurations (Audra & Palmer, 2011).

According to Ford (2007), as the frequency of permeable discontinuities increases significantly, resistance to water flow is drastically reduced. This allows water to follow the pathway closest to the water table, which is also the shortest route to spring. This process results in the formation of “ideal” water table caves. As the fluvial base level drops, new phreatic passages form at successively lower levels, while pauses in base-level lowering result in the creation of cave levels that correlate with river terraces (Audra & Palmer, 2011). Vadose shafts and canyons extend downward to the new water table, while older conduits become abandoned, often filled with sediments and intersected by newer passages. This dynamic process leads to the integration of multiple cave levels, preserving a record of successive stages of base-level lowering. A notable example is the Stefanina Cave in northern Greece, where tectonic discontinuities, including joints and bedding planes, have played a key role in guiding water flow and shaping the underground river’s morphology (Lazaridis et al., 2021). Additionally, scallops, small-scale dissolution features typically formed in shallow phreatic environments, found within the cave have enabled the estimation of past flow velocities and discharge rates.

The geotectonic setting of Greece consists of the Hellenides showing an arcuate orogenic belt, subdivided into two distinct tectonostratigraphic domains, the External and Internal Hellenides zones. The Internal Hellenides comprise Paleozoic basement overlain by Mesozoic carbonate platform sediments, obducted by Neo-Tethyan ophiolites during the Mid-Late Jurassic, exhibiting a multiphase tectonic history and significant metamorphism during the Alpine orogeny. During the Eocene-Oligocene, the Internal Hellenides overthrusted the External Hellenides which are primarily composed of Mesozoic and Cenozoic sediments from deep-sea and shallow-water environments, characterized by continuous sedimentation that took place during the Paleocene to Miocene period, forming a complex thrust and fold belt with no significant metamorphism (Kilias, 2024).

Methodological approach

This study employs a systematic approach that combines bibliographic review, data collection, processing and analysis. The methodology follows a structured framework that integrates both primary and secondary data sources, tools and comparative evaluations. The first step involved an extensive bibliographic review to gather relevant scientific

information. Searching was conducted in databases such as Scopus, ScienceDirect, ResearchGate, Google Scholar, Academia and Theophrastos digital library of Aristotle University of Thessaloniki. Additional information was gathered from online resources, archives of speleological associations in Greece and the Bulletin of the Hellenic Speleological Society to address gaps in the existing literature. Each source was critically analyzed for quality and reliability and the literature was categorized based on themes and regions.

Next, the study proceeded with the collection and recording of data, which included both primary and secondary sources. Primary data were derived from spatial analyses, while secondary data were extracted from bibliographic sources and existing studies. Data were systematically stored and classified based on criteria such as geographical region, tectonostratigraphic unit and morphological characteristics of the underground rivers, forming the basis for a detailed catalog of Greece's underground rivers (Fellachidou, 2024 and references therein).

The data processing phase involved both statistical and spatial analyses. Quantitative data were analyzed using tools such as Excel, allowing for the identification of trends and patterns across variables. Spatial analysis was performed using the QGIS tool enabling detailed mapping of underground river distribution and their relationship with geological and tectonic features. Data visualization, including the creation of charts, graphs and maps, further supported the interpretation and presentation of results.

Results and discussion

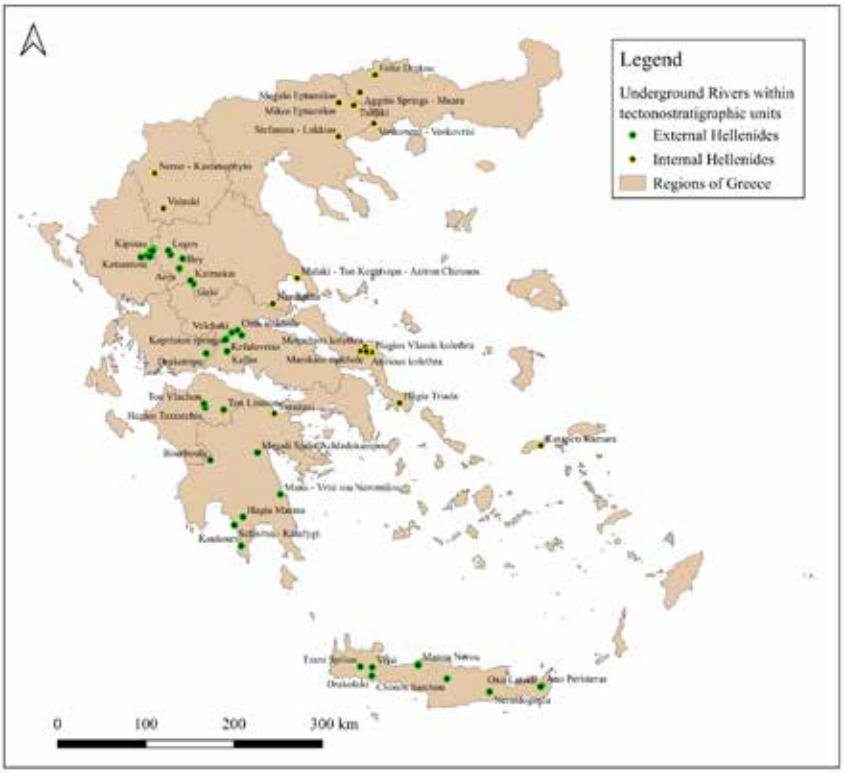

Figure 1. Geographical distribution of underground rivers across 13 Greece's regions, categorized by tectonostratigraphic units. Locations marked green represent underground rivers within the External Hellenides (40 in number), while those in yellow correspond to the Internal Hellenides (20 in number). (Regions of Greece retrieved from https://geodata.gov.gr/en/)

The analysis revealed significant insights into the distribution, geological characteristics and morphology of Greece's underground rivers. The compiled catalog of underground rivers served as the basis for constructing a map depicting their spatial distribution. The map (Fig. 1) presents a detailed spatial representation of underground river systems in Greece, categorized into two primary tectonostratigraphic units: the Internal Hellenides and External Hellenides. It reveals a total of 60 documented underground rivers, with 40 concentrated within the External Hellenides mainly along the Pindos mountain chain. Conversely, only 20 underground rivers are documented within the Internal Hellenides, where they are more sporadically distributed, with notable examples including Karapeti Kamara in the South Aegean and Neron-Kastanophyto in Western Macedonia. Furthermore, Aggitis River, the longest underground

cave of Greece is also located in the Internal Hellenides.
Notable clusters are observed in Epirus region (e.g., Anemotripa, Klifkis, Kipon, Katsantoni, Kipinas, Stafyla, Gouva Mare, Galazio Nero), in Sterea Ellada region (e.g., Koprision springs, Kefalovriso, Velchaki, Oitis sinkhole, Sklithraki) and the Euboea Island (e.g., Metochiou kolethra, Genitsari, Manikion sinkhole, Atsitous kolethra, Hagios Vlassis kolethra). Crete Island also emerges as a significant region, hosting nine underground rivers such as Tzani Spilios, Drakolaki and Chonos Sarochou, Manna Nerou, Ano Peristeras etc.) reflecting its dynamic karstic systems. The geographical distribution highlights regional variability, with certain areas, such as the South Aegean, Ionian Islands and Attica, lacking any recorded underground rivers.
Overall, the External Hellenides account for 67% of the recorded underground rivers in Greece (Fig. 2A), emphasizing their dominant role in karst system development. In contrast, the Internal Hellenides, shaped by a complex geological history involving metamorphic processes, host fewer and more isolated underground rivers.

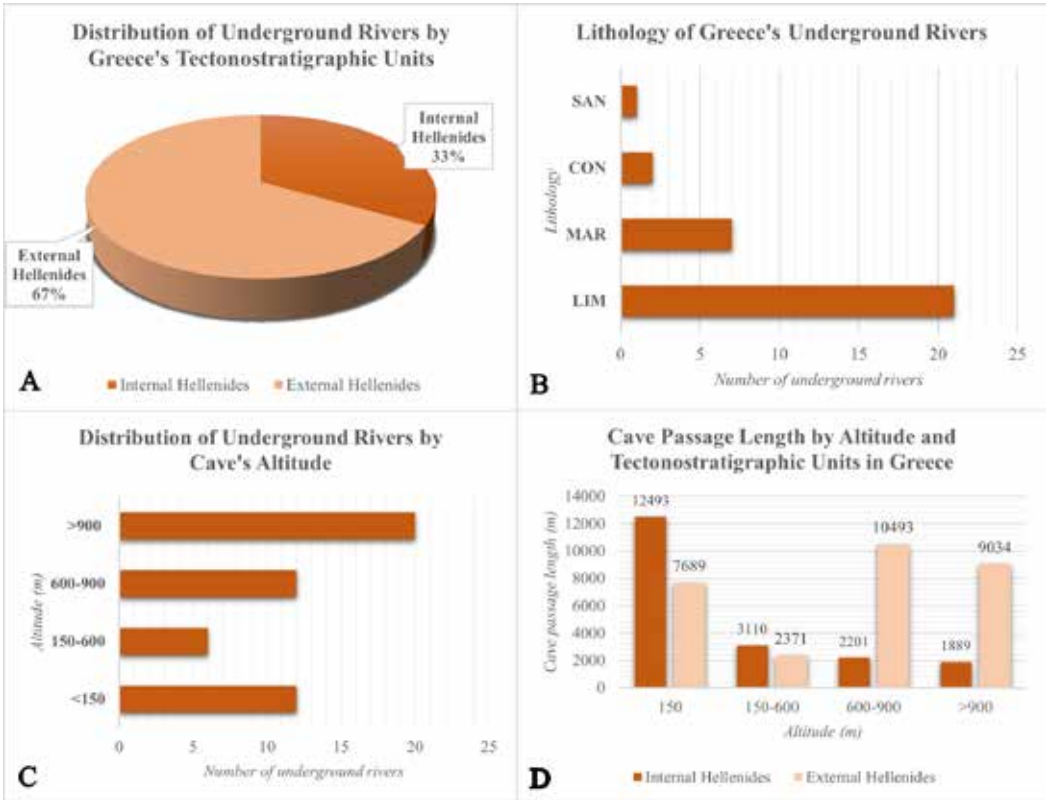

Figure 2. A: Proportion of underground rivers distributed between the two tectonostratigraphic units in Greece, the Internal Hellenides and the External Hellenides. B: Number of underground rivers associated with different lithologies in Greece. SAN: Sandstones, CON: Conglomerates, MAR: Marbles, LIM: Limestones. C: Number of underground rivers found at different elevation ranges in Greece according to Dikau (1989) classification system (>900: mountainous areas, 600-900: semi-mountainous areas, 150-600: hilly areas, <150: lowland areas). D: Total length of underground river cave passages (speleogenesis in meters) within the Internal and External Hellenides across different altitude ranges in Greece.

Figure 2B delves into the influence of lithology on speleogenesis, highlighting the critical role of carbonate rocks. Limestone, due to its high solubility, hosts the majority of underground rivers (21), underscoring its dominance in karst development. Marble, while also capable of supporting karst systems, accommodates fewer rivers (7). Conglomerates and sandstones, which account for just 2 and 1 rivers respectively, further emphasize that lithology is a key determinant in the formation and distribution of underground river systems.
Elevation plays a critical role in the distribution of underground rivers (Fig. 2C). Mountainous areas (>900m) host the highest number of underground rivers (20), followed by semi-mountainous (600-900m) and lowland areas (<150m), each with 12 rivers, while hilly areas (150-600m) contain only 6. This high concentration of underground rivers in high-relief regions can be attributed to the unique climatic and hydrological conditions of these areas. In mountainous regions, colder infiltrating water retains higher levels of carbon dioxide, enhancing its aggressivity and promoting

extended speleogenetic processes. Additionally, seasonal climatic variations, including snow accumulation in winter, rapid snowmelt in spring and intense summer thunderstorms, lead to periods of extreme discharge and flooding, which significantly influence cave development and morphology through the interplay of climatic factors and speleogenesis (White & Culver, 2012).

Finally, the relationship between altitude and tectonostratigraphic units is further elaborated (Fig. 2D). At lower altitudes (<150m), the Internal Hellenides exhibit longer cave passages, reflecting prolonged water flow and underground karst development. In contrast, at higher altitudes (600-900m and >900m), the External Hellenides dominate in terms of cave passage length, highlighting their structural and geological suitability for high-altitude underground river development. These observations reinforce the role of both altitude and tectonostratigraphic context in shaping speleogenetic processes.

Concluding Remarks

In summary, the distribution, lithological dependence, geomorphological and tectonostratigraphic influences collectively reveal the complexity of underground river formation in Greece. Detailed examination of the general geographical distribution to specific geological factors, provides a clear narrative of how various processes interact to shape these unique systems. This multi-layered analysis highlights the intricate interplay between geology, hydrogeology, tectonics and topography in determining the characteristics of underground rivers in Greece.

- This study provides a comprehensive insight into the underground rivers of Greece, representing the first national-scale mapping effort.
- The distribution, lithological dependence, geomorphological and tectonostratigraphic influences collectively reveal the complexity of underground river formation in Greece.
- Significant insights are provided into the spatial and geological dynamics that shape these systems, demonstrating the dominant role of the External Hellenides and carbonate lithologies in underground karst system development.
- Areas within the Internal Hellenides, where geological complexity and mixed lithologies prevail, display fewer and more sporadically distributed underground rivers.
- Low altitude concentration of underground rivers occurs in Internal Hellenides, in contrast to the External Hellenides, where these caves are developed mainly in higher altitudes.
- The results contribute to theoretical knowledge and may have practical implications for water resource management, environmental protection and geological risk assessment.
- Future studies can build upon this foundation to explore more localized patterns and predict potential changes in underground hydrological systems.

References

Audra, P., & Palmer, A.N., 2011. The pattern of caves: controls of epigenic speleogenesis. Structure des réseaux karstiques : Les contrôles de la spéléogenèse épigène. Geomorphologie: Relief, Processus, Environnement, 4, 359–378.

Fellachidou, K.K., 2024. Underground rivers in Greece: Documentation, geology, speleogenesis. Undergraduate Thesis, Department of Geology, Aristotle University of Thessaloniki.

Ford, D., & Williams, P., 2007. Karst Hydrogeology and Geomorphology. John Wiley & Sons.

Gunn, J., 2004. Encyclopedia of caves and karst science. Fitzroy Dearborn, Taylor & Francis Group.

Kilias, A., 2023. The Alpine Geological History of the Hellenides from the Triassic to the Present—Compression vs. Extension, a Dynamic Pair for Orogen Structural Configuration: A Synthesis. Geosciences, 14(1), 10.

Lazaridis, G.T., Fellachidou, K.K., & Georgaki, M.N., 2021. Paleohydrology of the Stefanina Cave (Greece). Bulletin of the Geological Society of Greece, 57(1), p. 52-67.

Dikau, R., 1989. The application of digital relief model to landform analysis in geomorphology. Three Dimensional Application in Geographic Information Systems, 51–77.

White, W.B., & Culver, D.C., 2012. Encyclopedia of caves, 2nd ed. Academic Press.

17th INTERNATIONAL CONGRESS of the Geological Society of Greece

BULLETIN OF THE GEOLOGICAL SOCIETY OF GREECE, SP. PUBL.

EXTENDED ABSTRACT 076

Preliminary estimation of the recession coefficient of the "Kefalari Agios Ioannis" spring, Dimitsana, Peloponnesus, Greece

Filis, C.[1], Skourtsos, E.[1], Korovesai, A.[1], Andreadakis, E.[1], Kapourani, E.[1], Karalemas, N.[1], Alexopoulos, A.[1]

(1) National and Kapodistrian University of Athens, Department of Geology and Geoenvironment, Athens, Greece

chfilis@geol.uoa.gr

Introduction

A hydrograph is the discharge (Q) diagram of a spring or a watercourse as a function of time (t). From the study of hydrographs of karst spring areas, it is possible to (Lundberg & Worsfold, 1993; Ford & Williams, 2007; Zhou & Li, 2010; Ma & Zhang, 2016):

- Find a "transformation coefficient", that is, a relationship that connects the input of the karst system to the output, i.e., the spring.
- Make predictions of the spring discharge and calculate the reserves.
- Provide information about the organization and operation of the karst system.
- Characterize the hydrogeological system that feeds a spring based on the slope of the depletion line between two given discharges (Q_1) and (Q_2). The change in slope from one year to the next indicates either water withdrawals from the aquifer (increase in slope), or recharge of the aquifer during the dry period from irrigation returns (decrease in slope), or changes in the structure of the aquifer, such as due to seismic activity.
- Calculate the water reserves in the system, which are located higher than the outflow point (discharge point) and equal to ($Q_t t_d$) at any given time.

Large values of the depletion coefficient (a) (in the range of 10^{-1} to 10^{-2}) mean that the karst system has conduits and generally large diameter voids with adequate continuity. In contrast, small values of (a) (in the range of 10^{-3}) mean that the water flows through fractures and intra-stratigraphic voids. In the first case, we typically have massive limestones, while in the second case, stratified ones (Soulios, 1985).

The spring "Kefalari Agios Ioannis" is located at an elevation of approximately 871 m, about 1,650 m south-southeast of the picturesque village of Dimitsana (Peloponnesus, Greece) discharging a karst aquifer. Its water is used for drinking water supply and irrigation. The clarification of the hydraulic characteristics of the karst aquifer, through the "Kefalari Agios Ioannis" spring, is of immense importance for the sustainable management of water resources in the broader area of Dimitsana, which is continuously developing in terms of tourism.

Geological Setting

The area of Dimitsana is composed of geological formations belonging to the lower Tripolitza Unit (Blumenthal, 1933; Dercourt, 1964; Lekkas, 1978; Tsaila – Monopolis, 1977; Fleury, 1980; Thiebault, 1982) and the higher Pindos Unit (Aubouin, 1959; Dercourt, 1964; De Wever, 1975; Fleury, 1980). Post-alpine sediments have locally unconformably covered the alpine formations. The post-alpine formations comprise the following (Exindavelonis, 1988):

- Alluvial deposits (H.al) consisting of pebbles, gravels and clayey-sandy materials.
- Scree and talus cones (H.sc,cs) mainly consisting of carbonate fragments of local origin.

The Pindos Unit includes the following formations (Exindavelonis, 1988):

- Platy limestones (Ks-Pc.k) dated Upper Cretaceous to Paleocene of green-gray and locally reddish colour with nodules and thin chert intercalations. The upper parts of the formation correspond to the transitional beds towards the flysch and comprise alternations of thin-platy limestones, sandstones and breccia limestones.
- Red cherts, siltstones and "First Flysch" (Js-Ki.fl) dated Upper Jurassic to Lower Cretaceous consisting of alternations of cherts, siltstones, shales, sandstones and clastic limestones often containing chert angular pebbles.

The Tripolitza Unit comprises the following formations (Exindavelonis, 1988):

- Flysch (Ft) consisting of alternations of grey marls, sandstones with intercalations or lenses of breccia limestones and conglomerates.
- Limestones, dolomites and dolomitic limestones (Ks-Es.k,d) dated Upper Cretaceous to Upper Eocene consisting of grey to black, thick-bedded limestones and dolomitic limestones.

The formations of both the Pindos and Tripolitza Units are juxtaposed through thrust faults and high-angle normal faults. This deformation can be ascribed to a compressional tectonic episode that transpired during the Middle Eocene to the Lower Miocene followed by an extensional one since Middle Miocene.

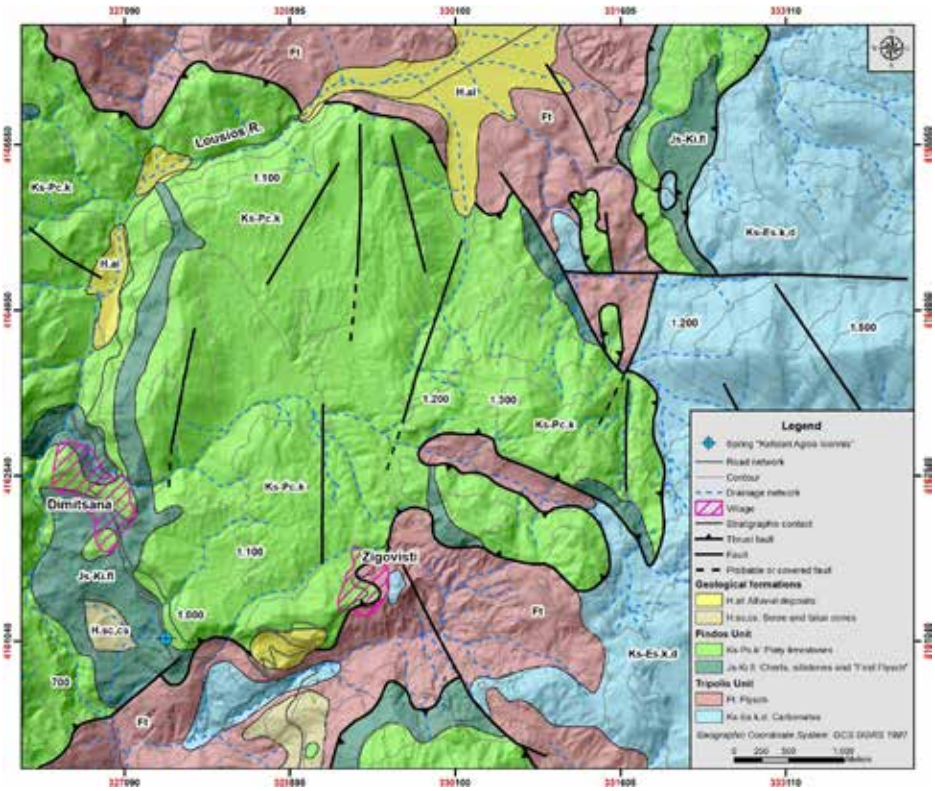

Figure 1. Geological map of the study area (modified from Exindavelonis, 1988).

Hydrogeological Conditions

The geological formations of the study area fall into the following categories, according to the standards of the International Association of Hydrogeologists (Struckmeier & Margat, 1995; Nikas et al., 2010):

- Alluvial deposits (H.al): They develop local and thin aquifers with high yield or extensive aquifers with moderate yield (Subclass 1b).
- Scree and talus cones (H.sc,cs): They develop local and thin aquifers with high yield or extensive aquifers with moderate yield (Subclass 1b).
- Platy limestones (Ks-Pc.k): This formation generates local and thin aquifers with high yield or extensive aquifers with moderate yield (Subclass 2b).
- Red cherts, siltstones and “First Flysch” (Js-Ki.fl): They develop aquifers of minor practical significance or non-aquifer formations (Subclass 3b).
- Flysch (Ft): This formation develops aquifers of minor practical significance or non-aquifer formations (Subclass 3b).
- Carbonates (Ks-Es.k,d): This formation generates extensive aquifers with high yield (Subclass 2a).

The carbonate formations of the Pindos Unit (Ks-Pc.k), characterized by their multifold and fractured structure, give rise to a karst aquifer of moderate capacity situated to the east of Dimitsana. The underlying impermeable substratum is comprised primarily of the flysch (Ft) of the Tripolitza Unit, predominantly located to the north, east, and south, as well as the red cherts and siltstones and “First Flysch” (Js-Ki.fl) of the Pindos Unit, mainly to the west.

Conversely, the carbonate formations of the Tripolitza Unit (Ks-Es.k,d) exhibit considerable fragmentation and fissuring, revealing two or more primary joint systems, accompanied by additional secondary systems that display distinctive karstification. These formations give rise to a deep karst aquifer of substantial capacity.

It is noteworthy that in certain regions, the carbonate formations of the Pindos Unit directly overly those of the Tripolitza Unit, facilitating the transfer of groundwater to greater depths through lateral hydraulic connectivity.

Recession coefficient of the “Kefalari Agios Ioannis” spring

The contact spring “Kefalari Agios Ioannis” (Figure 2) discharges the karst aquifer that develops in the platy limestones (Ks-Pc.k) of the Pindos Unit at their contact with the underlying and impermeable red cherts, siltstones and “First Flysch” (Js-Ki.fl) of the Pindos Unit, as shown in Figure 1.

Figure 2. View of the "Kefalari Agios Ioannis" spring on 26-11-2023. The turbidity of the water is due to the heavy rainfall of the previous days.

For the evaluation of the quantitative status of the "Kefalari Agios Ioannis" spring, flow measurements were conducted using an appropriate flow gauge within the rectangular cross-section of the concrete channel to which the water flows, leading to the Open-Air Water Power Museum of the Piraeus Cultural Foundation (Table 1, Figure 3 & Figure 4).

Table 1. The dates of the flow measurements, along with the quantitative data (discharge) and qualitative data (water temperature, pH, and electrical conductivity) of the "Kefalari Agios Ioannis" spring.

Seq. No.	Date	Discharge (m^3/h)	T °C Water	pH	Electric Conductivity (μS/cm)
1.	18-04-2024	711.1	12.9	7.7	320.0
2.	04-05-2024	468.9	12.7	7.6	320.0
3.	16-05-2024	312.3	12.6	7.7	300.0
4.	30-05-2024	245.2	12.9	7.6	300.0
5.	14-07-2024	101.7	14.4	7.4	310.0
6.	07-08-2024	98.2	13.5	7.4	280.0
7.	07-09-2024	84.7	13.7	7.6	290.0
8.	29-09-2024	70.3	13.7	7.6	260.0
9.	27-10-2024	69.4	13.8	7.6	270.0

Figure 3. Flow measurements taken with an appropriate flow gauge at the "Kefalari Agios Ioannis" spring on 04-05-2024.

Figure 4. Flow measurements taken with an appropriate flow gauge at the "Kefalari Agios Ioannis" spring on 30-05-2024 (up) and on 14-07-2024 (down).

Quantitative analysis of the “Kefalari Agios Ioannis” spring hydrograph is based on the equation proposed by Maillet (1905), who suggested that the discharge of a spring is a function of the volume of water held in storage and is described by an exponential equation.
The “Kefalari Agios Ioannis” spring hydrograph based on the flow measurements, which were conducted from 18-04-2024 to 27-10-2024 (Table 1) is presented in Figure 5. For the calculation of the recession coefficient of the “Kefalari Agios Ioannis” spring, flow measurements which were conducted from 14-07-2024 to 27-10-2024 were used (Table 1 & Figure 5) and if they get plotted to semi-logarithmic graph paper, the curve of Figure 5 is represented as a straight line (Figure 6).

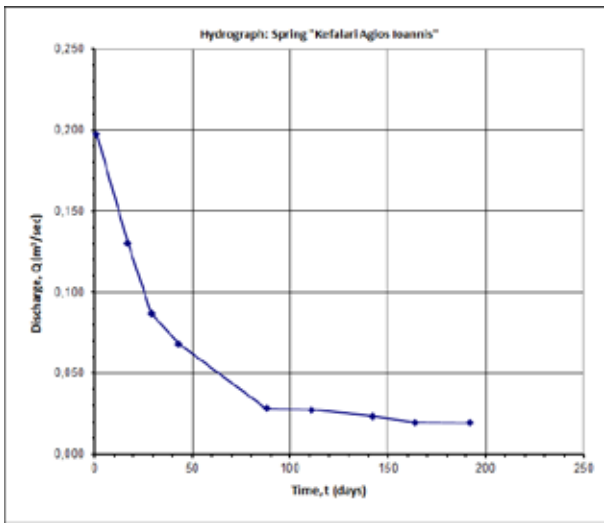

Figure 5. Hydrograph of the “Kefalari Agios Ioannis” spring based on the flow measurements, which were conducted from 18-04-2024 to 27-10-2024.

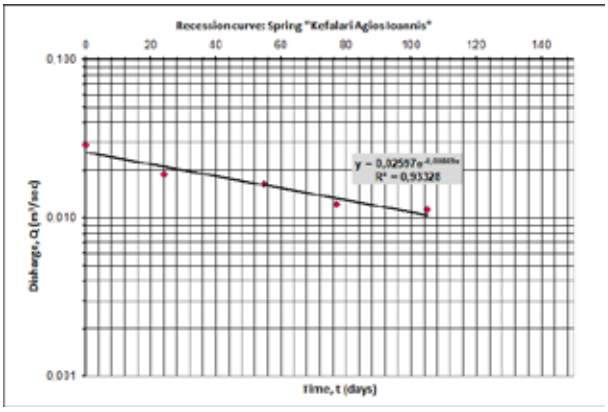

Figure 6. Semi-logarithmic graph paper of the “Kefalari Agios Ioannis” spring flow measurements, which were conducted from 14-07-2024 to 27-10-2024, used for the calculation of its recession coefficient.

The value of the recession coefficient derives from the hydrogeological characteristics of the aquifer, especially effective porosity and transmissivity (T). The recession coefficient of the “Kefalari Agios Ioannis” spring calculated from the flow measurements, which were conducted from 14-07-2024 to 27-10-2024 is 8.69×10^{-3} days^{-1} (Figure 6), which means that the water flows through the fractures and the intra-stratigraphic voids of the platy limestones (Ks-Pc.k) of the Pindos Unit (Soulios, 1985).

Discussion - Conclusions

The contact spring “Kefalari Agios Ioannis” discharges the karst aquifer that develops in the platy limestones (Ks-Pc.k) of the Pindos Unit at their contact with the underlying and impermeable red cherts, siltstones and “First Flysch” (Js-Ki.

fl) of the Pindos Unit.

The clarification of the hydraulic characteristics of the karst aquifer, through the "Kefalari Agios Ioannis" spring, is of immense importance for the sustainable management of water resources in the broader area of Dimitsana, which is continuously developing in terms of tourism. Additionally, the operation of the Open-Air Water Power Museum of the Piraeus Cultural Foundation, which is located immediately downstream of the spring, is inextricably linked to the functioning of the "Kefalari Agios Ioannis" spring.

The recession coefficient of the "Kefalari Agios Ioannis" spring calculated from the flow measurements which were conducted from 14-07-2024 to 27-10-2024 is 8.69×10^{-3} days^{-1}, which means that the water flows through the fractures and the intra-stratigraphic voids of the platy limestones (Ks-Pc.k) of the Pindos Unit. The aforementioned calculated value is consistent with the literature data for the recession coefficient of karst aquifers developed in the Pindos Unit and in equivalent units, which is on the order of 10^{-3} days^{-1} (Soulios, 1985; Giannatos, 1999; Karalemas, 2010).

It is noted that the hydrological year 2023-2024 was particularly dry, and the calculation of the «Kefalari Agios Ioannis" spring's recession coefficient should be considered with special caution, as it has been derived from flow measurements, which are the result of prolonged drought and water scarcity. This might has caused different conditions of groundwater circulation, which are not uniform across the entire hydrogeological basin and becomes apparent under extreme hydrological conditions, either surplus (wet hydrological years) or deficiency (dry hydrological years), during which different sections and levels of the recharge area are activated or operate differently. It is noteworthy that the recession period lasted at least 105 days, from 14-07-2024 to 27-10-2024.

Therefore, the recalculation of the spring's recession coefficient is considered necessary for the hydrological year 2024-2025 as well, which so far appears to be more representative compared to the previous one.

Acknowledgements

The research team extends its most heartfelt gratitude to the director and the staff of the Open-Air Water Power Museum of the Piraeus Cultural Foundation, for the time they dedicated and their invaluable assistance during the fieldwork. Additionally, we express our appreciation to Mayor of Gortynia Mr. Efstathios Koulis for his collaboration.

References

Aubouin, J., 1959. Contribution a l' etude geologique de la Grece septentionale, les confins de l' Epire et de la Thessalie. Ann. Geol. Pays Hell. 10, 526.

Blumenthal, M., 1933. Zur Kennthnis des Querprofils des zentralen und nordlichen Peloponnes. N. Jb. f. Miner. 70, 449-514.

De WeveR, P., 1975. Etude geologique de series apparaisant en fenetre sous l'allocthone pindique (serie de Tripolitza, serie epimetamorphique de Zarouchla), Peloponnese septentrional, Grece. These 3eme cycle.

Dercourt, J., 1964. Contribution a l'etude geologique d'un secteur du Peloponnese septentrional. Ann. Geol. Pays Hell. 15, 418.

Exindavelonis, P., 1988. Geological Map of Greece in scale 1:50,000, sheet "DIMITSANA" published by IGME, Athens.

Fleury, J., 1980. Les zones de Gavrovo-Tripolitza et du Pinde-Olonos (Grece continentale et Peloponnese du Nord). Evolution d'une plateforme et d'un bassin dans leur cadre alpin. In: Memoire de la Soc. Geol. Nord, 651.

Ford, D., Williams, P., 2007. Karst Hydrogeology and Geomorphology. Wiley-Blackwell.

Giannatos, G., 1999. Spring's hydrodynamic analysis from rocks in which the fissure type permeability prevails. The wider area of the Ano Bouraikos catchment in the Pindos geotectonic rock unit. PhD, National and Kapodistrian University.

Karalemas, N., 2010. Qualitative and quantitative status of the water bodies of eastern Taygetos and of Mani and prospects for sustainable development. PhD, National and Kapodistrian University.

Lekkas, S., 1978. Contribution to the geological structure of the area southeast of Tripoli (Central Peloponnese). PhD, National and Kapodistrian University.

Lundberg, L., Worsfold, P., 1993. Hydrological characteristics of karst aquifers. Geological Society of America.

Ma, Y., Zhang, L., 2016. Hydrograph Recession Analysis of Karst Springs. Journal of Hydrology, 543, 107-115.

Maillet, E. 1905. Essais d' hydraulique souterraine et. fluviale. Herman, 218, Paris.

Nikas, K, Antonakos, A, Kallergis, G, Kounis, G., 2010. International Hydrogeological Map of Europe: Sheet D6 "Athina". Proceedings of the 12th International Congress, Patras, 2010 Bulletin of the Geological Society of Greece, Volume XLIII No 4, pages 1821-1830.

Soulios, G., 1985. Contribution to the hydrogeological study of karst aquifer systems in Greece. Aristotle University of Thessaloniki.

Struckmeier, W.F., Margat, J., 1995. Hydrogeological maps: a guide and a standard legend (Vol. 17). Hannover: Heise.

Thiebault, F., 1982. Evolution geodynamique des Hellenides externes en Peloponnese meridional (Grece) 6. Societe Geologique du Nord, 393.

Tsaila-Monopolis, S., 1977. Micropaleontological study and stratigraphic structure of the formations of the geotectonic Tripolis (Gavrovo) zone in the Peloponnese. Geological and Geophysical Studies 20(1), 1-136.

Zhou, Y., Li, W., 2010. Study on hydrograph recession of karst springs using the baseflow separation method. Hydrological Processes, 24(12), 1642-1651.

17th INTERNATIONAL CONGRESS of the Geological Society of Greece

BULLETIN OF THE GEOLOGICAL SOCIETY OF GREECE, SP. PUBL.

EXTENDED ABSTRACT 077

Role of Earth Observation in Monitoring Santorini–Anydros Volcano-Tectonic Crisis

Foumelis M.[1], Papageorgiou E.[1], Trasatti E.[2], Tapete D.[3], Bitharis S.[1], Pikridas C.[1], Papazachos C.[1]
(1) Aristotle University of Thessaloniki (AUTh), Thessaloniki, Greece, mfoumelis@geo.auth.gr (2) Istituto Nazionale di Geofisica e Vulcanologia (INGV), Rome, Italy (3) Agenzia Spaziale Italiana (ASI), Rome, Italy

Background

The Santorini volcano is associated with one of the most destructive volcanic eruptions in human history, yet it remains insufficiently monitored. This is partly due to its behavioral pattern, characterized by long periods of rest interrupted by short and rapid episodes of unrest (Hooper, 2012). Indeed, the last well-documented unrest episode in 2011–2012 (Newman *et al.*, 2012; Parks *et al.*, 2012; Papageorgiou *et al.*, 2012), characterized by comprehensive instrumentation and quantitative measurements, occurred after approximately 60 years of quiescence since the 1950 volcano activity.

Despite the significance of the 2011–2012 unrest, post-crisis monitoring efforts were limited, sustained mainly by the Institute for the Study and Monitoring of Santorini Volcano (ISMOSAV; www.ismosav.gr), and without any coordinated activity at a national level. ISMOSAV is a non-profit organization established in the summer of 1995, with the primary objective of operating volcano monitoring networks and providing informed assessments regarding the state of the volcano. The monitoring efforts over the past 12 years were substantial enough to enable early detection and timely notification to relevant authorities, contributing to the governmental response when a new unrest phase began in mid-summer 2024.

The role of Earth Observation (EO) and geodetic imaging, specifically Interferometric Synthetic Aperture Radar (InSAR), is crucial for the systematic long-term monitoring of Santorini. Several studies utilized archive SAR missions from the European Space Agency (ESA), namely ERS and ENVISAT satellites, to characterize displacement fields from 1992 to 2010 (Papageorgiou *et al.*, 2012; Parks *et al.*, 2015), as well as during the 2011–2012 unrest phase (Foumelis *et al.*, 2013). Since October 2014, Copernicus Sentinel-1 mission has enabled actual continuous monitoring. While the ERS and ENVISAT era allowed accurate annual displacement measurements, the limited temporal sampling (i.e., long satellite repeat-cycles) prevented the detection of short-term behavioral changes of the volcano. On the contrary, systematic acquisitions from Sentinel-1 have proven adequate for capturing early indicators of deviations from background behavior.

EO-based Monitoring

This EO-based monitoring capability was made possible through the deployment of an operational solution using the SNAPPING service of the Geohazards Exploitation Platform (GEP) (Foumelis *et al.*, 2022). SNAPPING is a Persistent Scatterer Interferometry (PSI) chain integrated by AUTh on the GEP platform, facilitating access to Sentinel-1 surface motion measurements for users and EO practitioners. The SNAPPING service generates average Line-of-Sight (LoS) motion rate maps and displacement time series at both reduced spatial (at approx. 100 m) and full sensor resolutions (SNAPPING, 2022). A well-defined set of processing parameters optimized to the specific environment are defined and a dedicated application on GEP is designed to execute SNAPPING in a monitoring framework based on user defined temporal step.

During unrest events, near-real time PSI solutions were generated whenever a new Sentinel-1 acquisition was available, based on both online hosted SNAPPING service, as well as in-house GAMMA Multi-Temporal InSAR (MT-InSAR) processing. This dual-processing methodology serves as a verification mechanism for the detected displacement signals.

Surface Motion Measurements

In the period following the 2011–2012 unrest, the Santorini volcano experienced deflation centered on Nea

Kameni (Figure 1), extending as far as Thera Island, including Cape Skaros and the northern caldera walls. The observed motion rates of approximately -7.8 mm/yr remained elevated compared to pre-unrest levels of around -5 mm/yr, though slightly lower than the -9 mm/yr reported seven years after the 2011 event (Papageorgiou *et al.*, 2019). These observations suggest that the volcano was undergoing a prolonged deflation phase, gradually returning to its pre-unrest state before the onset of a new unrest in July 2024.
Although the initial 2024 inflation signals were detected by InSAR and the local GNSS network of ISMOSAV, the confirmation of a new unrest phase was underlined by the onset of seismicity a few months later (AUTh Seismological Station, 2024). Since summer 2024, inflation of Santorini, the second episode of significant magnitude within the last 15 years, has continued through the end of the year. This local inflation was consistent in both displacement pattern and magma source location with the 2011–2012 unrest. However, it was also soon superimposed by a more significant event that occurred in the early part of February 2025 and originated from the broader Kolumbo–Anydros area. The Anydros event was shorter in duration but associated with deformation nearly two orders of magnitude greater than the prior Santorini caldera inflation. While the inner caldera magma source was deforming the volcanic complex at a rate of 10–12 cm per year over a six-month period, the Kolumbo–Anydros activity exhibited meter-level displacement rates within just two weeks, highlighting their distinct dynamics and potential implications. These differences are further reflected in the number and magnitude of the accompanying seismic events.

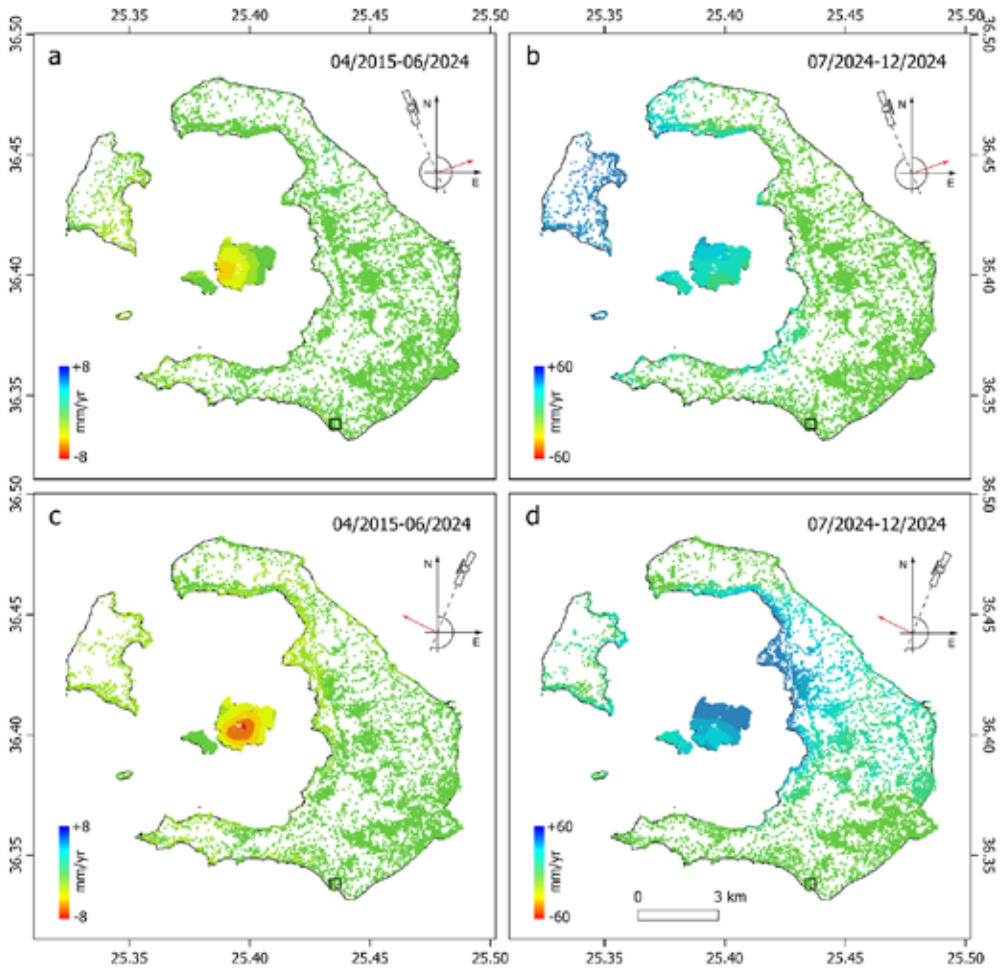

Figure 1. Sentinel-1 MT-InSAR LoS motion rates prior (a,c) and during (b,d) the 2024 unrest for the ascending 029 (a,b) and descending 109 (c,d) satellite tracks. Local reference point for InSAR processing is located in the southern part of the island (black square).

Discussion and Conclusions

The Earth Observation and Geospatial Applications Laboratory (EO.Lab) of AUTh has systematically monitored Santorini through InSAR, as part of the operational framework of ISMOSAV, using automatic solutions such as GEP SNAPPING, internal processing chains based on Copernicus SAR data, and collaborations with space agencies for complementary SAR monitoring. In this work, we present the evolution of surface displacements as measured by satellite InSAR techniques for the broader Santorini–Anydros region. We discuss the role of geodetic imaging techniques in volcano monitoring, their advantages, and complementarities with other geodetic and in-situ networks and finally, we emphasize the need to establish a local volcano observatory, involving scientists across multiple domains, integrating diverse techniques and equipment for real-time monitoring of this volcanic region and its surrounding areas.

Acknowledgements

The authors would like to thank the GEP platform providers for allocating resources to support the execution of services related to the monitoring of the Santorini volcano.

References

AUTh Seismological Station, 2024. Permanent Regional Seismological Network operated by the Aristotle University of Thessaloniki. Available online: http://geophysics.geo.auth.gr/ss/station_index_en.html.

Foumelis, M.; Trasatti, E.; Papageorgiou, E.; Stramondo, S.; Parcharidis, I., 2013. Monitoring Santorini volcano (Greece) breathing from space. Geophys. J. Int., 193, 161–170.

Foumelis, M.; J.M. Delgado Blasco, J.M.;F. Brito, F.; F. Pacini, F.; E. Papageorgiou, E.; P. Pishehvar, P., &and P. Bally, P., 2022. SNAPPING Services on the Geohazards Exploitation Platform for Copernicus Sentinel-1 Surface Motion Mapping, Remote Sensing, 14(23), 6075, https://doi.org/10.3390/rs14236075.

Hooper, A., 2012. A volcano's sharp intake of breath. Nat. Geosci., 5, 686–687.

Newman, A.V., Stiros, S., Feng, L., Psimoulis, P., Moschas, F., Saltogianni, V., Jiang, Y., Papazachos, C., Panagiotopoulos, D., Karagianni, E., & Vamvakaris, D., 2012. Recent geodetic unrest at Santorini Caldera, Greece. Geophys. Res. Lett., 39, L06309.

Papageorgiou, E.; Foumelis, M.; Parcharidis, I., 2012. Long- and Short-Term Deformation Monitoring of Santorini Volcano: Unrest Evidence by DInSAR Analysis. IEEE JSTARS, 5, 1531–1537.

Papageorgiou, E.; Foumelis, M.; Trasatti, E.; Ventura, G.; Raucoules, D.; Mouratidis, A., 2019. Multi-Sensor SAR Geodetic Imaging and Modelling of Santorini Volcano Post-Unrest Response. Remote Sens., 11, 259, https://doi.org/10.3390/rs11030259.

Parks, M., Biggs, J., England, P. et al., 2012. Evolution of Santorini Volcano dominated by episodic and rapid fluxes of melt from depth. Nature Geosci 5, 749–754, https://doi.org/10.1038/ngeo1562.

Parks, M.M., et al., 2015. From quiescence to unrest: 20 years of satellite geodetic measurements at Santorini volcano, Greece, J. Geophys. Res. Solid Earth, 120(2), 1309–1328, doi:10.1002/2014JB011540.

Surface motioN mAPPING (SNAPPING) Service on Geohazards Exploitation Platform. 2022. GEP SNAPPING Tutorial. Available online: https://docs.terradue.com/geohazards-tep/tutorials/Snapping.html.

17th INTERNATIONAL CONGRESS of the Geological Society of Greece

BULLETIN OF THE GEOLOGICAL SOCIETY OF GREECE, SP. PUBL.

EXTENDED ABSTRACT 078

Seismotectonic Features of the 2023 Strong Earthquake Sequence in Southeast Türkiye.

K.E. Fragkouli[1,2], G. Drakatos[2], S. Pavlides[3], S. Sboras[2].

(1) University of the Aegean, Mytilene, Greece, keafrag@gmail.com

(2) Geodynamics Institute, National Observatory of Athens, Athens, Greece

(3) Aristotle University of Thessaloniki, Thessaloniki, Greece.

Introduction / Background

Türkiye is one of the most seismically active countries in the world, and the East Anatolian fault is one of the largest and most active faults in the Eastern Mediterranean, as proven by the recent, destruvtive earthquake sequence in 2023. On February 6th, 2023, three earthquakes with magnitudes Mw > 6.5 struck within 11 hours, followed by another earthquake of Mw > 6 two weeks later. The aftermath of these events were thousands of casualties and an unprecedented infrastructure damage in Türkiye and Syria. Landslide phenomena and widespread liquefactions were a direct consequence of the earthquakes, further worsening the already immense destruction (Chadha, 2023). This study aims to better understand the sequence's behavior through an analysis of Coulomb static stress changes. More specifically, the four strongest earthquakes in the February 2023 sequence were attributed to four respective faults which have been modelled in order to be imported to the Coulomb 3.3 software (Toda et al., 2011). The Coulomb 3.3 software calculates the loading or unloading of stress on the modelled faults and in the surrounding area.

The Coulomb Failure Criterion determines the critical value of maximum shear stress without specifying the point where a rupture starts or how it will evolve. It is expressed by the relation $\Delta\sigma f = \Delta\tau_s + \mu' \Delta\sigma_n$, where $\Delta\sigma f$ is the difference in Coulomb stress failure. When $\Delta\sigma f > 0$, there is stress loading in the surrounding area, suggesting a higher likelihood of fault reactivation (triggering effect). On the contrary, when $\Delta\sigma f < 0$, there is stress release and a reactivation is potentially delayed. The fault or faults that are being triggered are referred to as source-faults, while the fault that receives the transferred stresses is referred as the receiver-fault. The stress change is strongly dependent by the receiver fault's geometric and kinematic attributes (Harris, 1998; Steacy et al., 2005; Toda et al., 2011).

Seismotectonics in East Türkiye

In East Türkiye the major tectonic structures are Caucasus Fault Zone which is a right-lateral strike-slip faults in the NW, Dead Sea Fault Zone (DSFZ) which is a 1000 km zone of left-lateral horizontal slip, Cyprus Arc which is a convergence boundary of the African and Anatolian plates, causing high seismicity begins from Cyprus to the Kahramanmaraş Triple Point, East of Karlıova Triple Junction where there is a compressional tectonic area of N-S and strike-slip faults (right-lateral & left-lateral) and the interconnected strike-slip zones of North Anatolian Fault Zone (NAFZ right-lateral) & East Anatolian Fault Zone (EAFZ left-lateral) (Taymaz et al., 2021; KOKUM & OZCELIK, 2020).

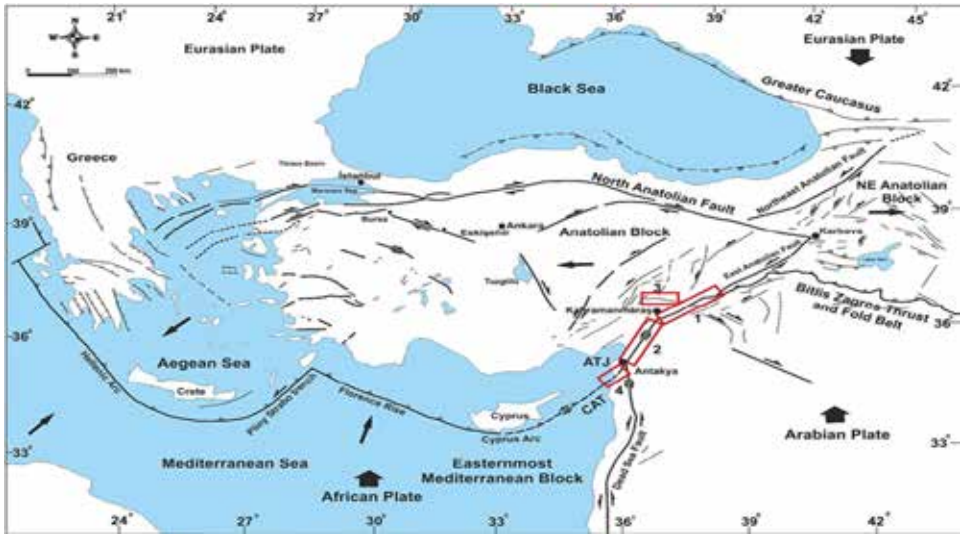

Figure 1: Tectonic map of East Mediterranean region (modified from Barka, 1992; Över et al., 2010).

More specifically, EAFZ facilitates the westward extrusion of the Anatolian plate, has a total length of 700 km. It consists of two branches: i) the Southern one, from Karlıova to Antakya, towards the DSFZ and the Cyprus Arc, and ii) the Northern one, from Celikhan to the Iskenderun Gulf, with a length of ~ 350 km. EAFZ constists of strike-slip faults with a normal component (h < 20 km) and is a zone of high seismic activity with magnitudes M > 6 during the past 300 years (Taymaz et al., 2021; KOKUM & OZCELIK, 2020).

The 2023 earthquake sequence

The study focuses on the four strongest earthquakes of the sequence, with M_w >6, all of which had shallow hypocentral depths. Their focal mechanisms indicate left-lateral strike-slip motion, a characteristic feature of the East Anatolian Fault Zone. The four strongest earthquakes appeal to a really rare phenomenon of multiplet earthquakes where magnitudes differ no more than ±0.4M_w and all shocks are considered to be mainshocks (Goldberg et al., 2023).

- February 6, 2023 (Mw 7.7): known as the earthquake of Nurdağı - Pazarcık - Kahramanmaras Earthquake, at 01:17 (local time) and a total duration of 80 seconds. The ground acceleration reached 1.5 g, with a rupture velocity of 3.2 km/s. It is a shallow earthquake of 8.6 km hypocentral depth with NE-SW stress orientation. Its epicentre is located at the Türkiye-Syria border, in the Kahramanmaraş (KMTJ) – Gaziantep region (32 km NNW). The rupture is considered to be dual, as it initiated on the Narli fault (20 km from the EAF), lasting for 20 seconds and then extended 50 km NE-SW (Karabulut et al., 2023; Wang et al., 2023; Melgar et al., 2023).
- February 6, 2023 (Mw 6.8): this earthquake is reffered as Nurdağı Earthquake and it struck just 11 minutes after the first shock (01:28 UTC), with epicentral depth 6.2 km. Its epicentre is located at the southern end of the EAFZ and its stresses oriented in a NE-SW direction (Karabulut et al., 2023; Wan et al., 2024).
- February 6, 2023 (Mw 7.5): this earthquake is known as Elbistan – Ekinözü Earthquake, it occurred just 9 hours after the first one, at 10:24 (UTC) with a total duration of 50sec. Its epicentral depth is 8.6 km, the maximum slip reached 7m and the length of the rupture was approximately 160 km (SOFTA et al., 2024; Chen et al., 2023; Over et al., 2023).
- February 20, 2023 (Mw 6.3): the earthquake of Uzunba – Antakya took place two weeks after the initial event. M_w 6.3, its epicentre was in the area where the EAF and Cyprus Arc meet, its hypocentral depth was deeper than the first three earthquakes, estimated approximately at 22 km. Despite its smaller magnitude, it caused significant damage, particularly in areas affected by the previous earthquakes. The fault responsible was blind and unmapped, its focal mechanism was a left-lateral strike-slip with a small horizontal component and the length of its rupture is estimated at 25 km (Barbot et al., 2023; Over et al., 2023; Karabulut et al., 2023; Gürboğa et al., 2023).

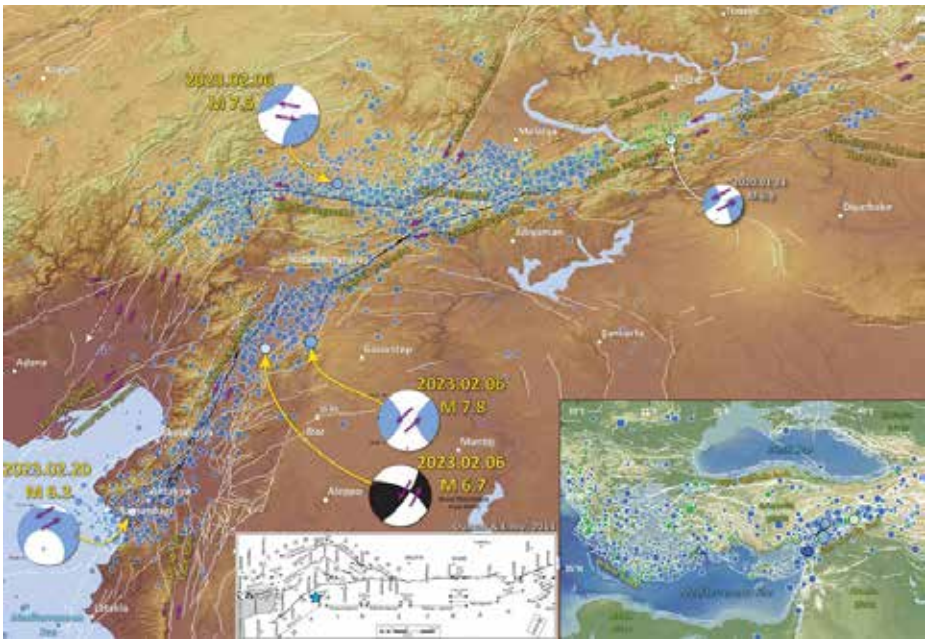

Figure 2: Epicentral map of the 2023 sequence (blue dots) with the four strongest earthquakes highlighted (USGS, 2023) (Duman & Emre, 2013).

Seismic Fault Modelling and static stress changes calculation

Firstly, we selected the nodal plane of the focal mechanisms that best fits: i) the fault direction and ii) the aftershock spatial distributions. The modelling was performed in the Coulomb 3.3 application in which we set the geometric and kinematic parameters (length and width are automatically calculated by the integrated scalar relationships of Wells & Coppersmith, 1994). After modelling the seismic sources, we applied the Coulomb Failure Criterion within the same application under the following scenario: we set in each fault rupture the ruptured fault(s) as the seismic source(s) and the faults that didn't yet rupture as receiver faults. Coulomb 3.3 software is based on the Coulomb Failure Criterion. Thus, we examined all the intermediate change of stress between the successive major ruptures of the earthquake sequence ('in-sequence' investigation).

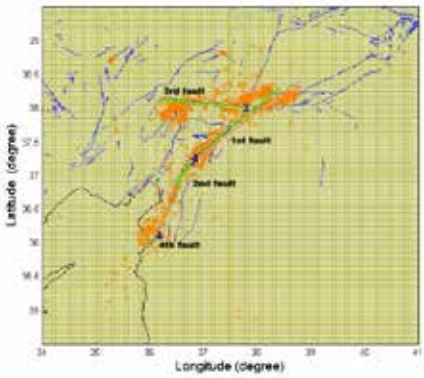

Figure 3: This figure shows the four modelled faults (1, 2, 3, 4) in Coulomb 3.3, along with the overlays of coastline (in black), regional faults (in blue) and seismic sequence of 2023 (in orange circles).

Results and conclusions

During the seismic sequence of the four strongest earthquakes of February 2023 in SE Türkiye, we investigated the Coulomb static stress changes which were caused after the fault rupture of the four strongest events. The results are shown in Figure 4 at depths close to hypocentral depth of the next earthquake. In more detail:

- The investigation of the first earthquake (06.02.2023, 01:17 UTC, 7.7 Mw) and its effect on the second event (06.02.2023, 01:28 UTC, 6.8 Mw) was conducted at the depth of 6.2km, which is close to the hypocentral depth of the latter. The results in Figure 4a indicate that the first earthquake triggered the second one, as the first fault loaded stress on the second fault.
- The investigation of both first and second earthquake suggests that they played a major role in accelerating the occurrence of the third event (06.02.2023, 10:24 UTC, 7.5 Mw). The results in Figure 4b, calculated at depth of 8.6 km which is the hypocentral depth of the third fault, indicate that the third fault was loaded with stress after the first two shocks.
- On the contrary, in the last case, we investigated the total stress change from the three earthquakes and its impact on the fourth event, two weeks later (20.02.2023. 17:04 UTC, 6.3 Mw), at the depth of 22 km, which is close to the hypocentral depth of the fourth fault. The results depicted on Figure 4c indicate that the fourth fault was not affected (white area) from the stress change produced by the first three earthquakes.

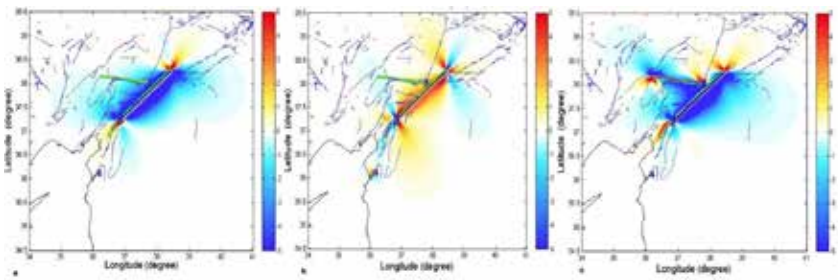

Figure 4: This figure shows the four modelled faults (1, 2, 3, 4) in Coulomb 3.3, along with the overlays of coastline (in black), regional faults (in blue) and the stress bar. The stress bar is coloured: in red tones for Δσf > 0 (loaded stress), in white for Δσf=0 (no stress change) and in blue tones for Δσf < 0 (unloaded stress). Specifically: a. depicts the 1st fault as source-fault (with slip) and the 2nd as receiver fault, being loaded with stess, b. depicts 1st & 2nd faults as source faults and the 3rd fault as the receiver fault, being loaded with stress, c. depicts the cumulative effect of the first three faults as source faults and the 4th fault as receiver fault, which stands in an uncharged area.

Summarizing, the correlation between static stress changes and the local structural pattern played a critical role in determining the stress transfer within the faults. The stress patterns in the region were redistributed after each of the four shocks, with particularly interesting results. At least three of the four strongest earthquakes were related, each one charging stresses for the appearance of the next one. The fourth fault did not receive significant stress increase from the prior events, likely due to its deeper hypocenter and less optimal orientation within the broader stress field. The regional faults that had generated earthquakes in the recent past (Elazig 2020 & Palu 2010) appear to be recharged with stresses, confirmed by the 6 M_W earthquake in Akusagi-Kale, Elazığ, Türkiye, on 16 October 2024. This highlights the importance of integrating structural data when interpreting stress transfer and seismic hazard in complex fault systems.

Acknowledgements
I would like to express my sincere gratitude to all colleagues at NOA and especially Dr. O.J.Ktenidou and A.Papageorgiou for their support and guidance.

References

Barka, A.A., 1992. The North Anatolian Fault zone, Annales Tectonicae 6, 164 -195.
Barbot, S., Luo, H., Wang, T., Hamiel, Y., Piatibratova, O., Javed, M., Braitenberg, C. Gurbuz, G., 2023. Slip distribution of the February 6, 2023 Mw 7.8 and Mw 7.6, Kahramanmaraş, Turkey earthquake sequence in the East Anatolian Fault Zone, Seismica, 2, 1-17.
Chadha, R. K., 2023. An Mw 7.8 Earthquake on 6 February 2023 on the East Anatolian Fault, Turkey, Journal of the Geological Society of India, 99, 449–453.
Chen, W., Rao, G., Kang, D., Wan, Z., & Wang, D., 2023. Early Report of the Source Characteristics, Ground Motions, and Casualty Estimates of the 2023 Mw 7.8 and 7.5 Turkey Earthquakes. Journal of Earth Science, 20, 1-7.
Duman, T., & Emre, Ö., 2013. The East Anatolian Fault: geometry, segmentation and jog characteristics. Geological Society, 372, 495-529.
Goldberg, D., Taymaz, T., Reitman, N., Hatem, A., Yolsal-Çevikbilen, S., Barnhart, W., Serkan Irmak, T., Hatem, D., Ocalan, T., Yeck, W., Ozkan, B. Thompson Jobe, J.A., Shelly, D., Thompson, E., Duross, C., Earle, P., Briggs, R., Benz, H., Erman, C., Dogan, A.H., Altunas, C., 2023. Rapid Characterization of the February 2023 Kahramanmaraş, Türkiye, Earthquake Sequence. The Seismic Record, 3, 156–167.
Gürboğa, S., Kayadibia, O., Akıllıa, H., Arıkana, S., Tana, S., 2023. Preliminary Results of the Great Kahramanmaraş 06 February 2023 Earthquakes (Mw7.7 and 7.6) and 20 Feburary 2023 Antakya Earthquake (Mw 6.4), Eastern Türkiye. Turkish journal of Earth Science, 33, 22-32.
Harris, R., 1998. Introduction to special section: Stress triggers, stress shadows, and implications for seismic hazard. Journal of Geophysical Research B: Solid Earth, 103, 24347-24358.
Karabulut, H., Güvercin, S.E., Hollingsworth, J., Konca, A.O, 2023. Long silence on the East Anatolian Fault Zone (Southern Turkey) ends with devastating double earthquakes (6 February 2023) over a seismic gap: implications for the seismic potential in the Eastern Mediterranean region. Journal of the Geological Society, 180.
Kokum, M., Özcelik, F., 2020. An example study on re-evaluation of historical earthquakes: 1789 Palu (Elazığ) earthquake, Eastern Anatolia, Turkey. Bulletin of the Mineral, 161, 157-170.
Melgar, D., Taymaz, T., A. Ganas, A., Crowell, B., Öcalan, T., Kahraman, M., Tsironi, V., Yoslal-Cevikvil, S., Valkaniotis, S., Irmak, T.S., Eken, T., Erman, C., Ozkan, B., Dogan, A.H., Altuntaş, C., 2023. Sub- and super-shear ruptures during the 2023 Mw 7.8 and Mw 7.6 earthquake doublet in SE Türkiye. SEISMICA, 2.
Över, S., Özden, S., Pınar, A., Yılmaz, H., Ünlügenç, U. C., Kamacı, Z., 2010. Late Cenozoic Stress Field in the Çameli Basin, SW Turkey. Tectonophysics, 492, 60-72.
Över, S., Demirci,A., Ozden, S., 2023. Tectonic implications of the February 2023 Earthquakes (Mw7.7, 7.6 and 6.3) in south-eastern Türkiye, Tectonophysics, 866.
Softa, M., Kocbulut, F., Akgun, E., Aksoy, E., Sozbilir, H., Tatar, O., Karabacak, V., Ozkaymak, C., Utku, M., Ozdag, O.C., Cakir, R., Demir, A., Arslan, G., 2024. Surface rupture during the 6th of February 2023 Mw 7.6 Elbistan-Ekinözü (Kahramanmaraş) earthquake: implications for fault Fault Zone, Turkish Journal of Earth Science, 33, 1-21.
Steacy, S., Gomberg, J., Cocco, M., 2005. Introduction to special section: Stress transfer, earthquake triggering, and time-dependent seismic hazard, Journal of Geophysican Research, 110, 1-12.
Taymaz, T., Ganas, A., Yolsal-Çevikbilen, S., Vera, F., Eken, T., 2021. Source Mechanism and Rupture Process of the 24 January 2020 Mw 6.7 Do˘ganyol–Sivrice Earthquake obtained from Seismological Waveform Analysis and Space Geodetic Observations on the East Anatolian Fault Zone (Turkey), Tectonophysics, 804.
Toda, S., Stein, R., Sevilgen, V., Lin, J., 2011. Coulomb 3.3 Graphic-Rich Deformation and Stress-Change Software for Earthquake, Tectonic, and Volcano Research and Teaching-User Guide, Virginia, USA: U.S. Geological Survey Open-File Report 2011-1060.
Wan, Z., Dong, R., Wang, D., Xu, S., Wang, Z., Wang, Q., 2024. Along-Strike Variation of Rupture Characteristics and Aftershock Patterns of the 2023 Mw 7.8 Türkiye Earthquake Controlled by Fault Structure, Seismological Research Letters, 95, 2071-2080.
Wang, Z., Zhang, W., Taymaz, T., He, Z., Xu, T., Zhang, Z., 2023. Dynamic Rupture Process of the 2023 Mw 7.8 Kahramanmaraş Earthquake (SE Türkiye): Variable Rupture Speed and Implications for Seismic Hazard, Geophysical Research, 50, 1-11.
Wells, D., Coppersmith, J., 1994. New Empirical Relationships among Magnitude, Rupture Length, Rupture Width, Rupture Area, and Surface Displacement, Bulletin of the Seismological Society of America, 84, 974-1002.

17th INTERNATIONAL CONGRESS of the Geological Society of Greece

BULLETIN OF THE GEOLOGICAL SOCIETY OF GREECE, SP. PUBL.

EXTENDED ABSTRACT 079

The Hellenic DataBase of Active Faults (HeDBAF): a new national geodatabase

Dimitrios Galanakis[1], Dimitris Sakellariou[2], Sotiris Sboras[3], Spyros Pavlides[4], Kyriaki Iordanidou[1], Charalambos Georgiou[1], Athanasios Ganas[2], Yiannis Koukouvelas[5], Charalampos Kranis[6], Spiros Lalexos[7] Theodora Rondoyanni[8], Efthymios Lekkas[9] and the EPPO Seismotectonics Committee.

(1) Hellenic Survey of Geology & Mineral Exploration, dgalanakis@eagme.gr (2) Hellenic Centre for Marine Research, (3) Geodynamics Institute National Observatory of Athens, (4) Geology Department, Aristotle University, Thessaloniki, (5) Geology Department, University of Patras, (6) Department Geology and Geoenvironment, National Kapodistrian University of Athens, (7) Earthquake Planning & Protection Organization (EPPO) (8) Head of Seismotectonics Committee of the Earthquake Planning & Protection Organization (EPPO), (9) President of the Earthquake Planning & Protection Organization (EPPO)

Abstract

The Hellenic DataBase of Active Faults (HeDBAF) is a national product of collaboration between scientists of all related to this subject academic and research institutes of Greece under the the auspices of the Earthquake Planning and Protection Organization (EPPO) and the supervision of its Seismotectonics Committee (Fig. 1). The main purpose of the geodatabase is to provide essential information to the scientific community and to whoever wants to have a synoptic or in detail information about the active faults of Greece, as well as to serve as a platform for geologists, engineers and the central and local administration, to in-depth studies. The HeDBAF geospatial database started to realize since 2021, including parametric and descriptive information about the active faults in the broader Hellenic region. The responsibility of implementation, management and hosting is held by the Hellenic Survey of Geology and Mineral Exploration (HSGME).

The HeDBAF adopts conceptual approaches and characteristics from other time-proven national databases of the world (e.g. INGV's DISS, IGME's QAFI, etc.). It is a multi-layered tool that hosts all available literature data (e.g. scientific articles, technical/project reports, thematic maps, etc.), targeting various groups of end-users: the primary target group is the scientific community which often needs medium- to small-scale information for geodynamic interpretations, large-scale data for local seismotectonic analyses, and appropriate parametric information for numerical modelling. The next target group is the engineers who need large-scale detailed surveying of the fault traces and ground ruptures, and fault models for the prediction of ground motion in the context of Seismic Hazard Assessment. Administration, government, security bodies and local authorities can benefit from this geodatabase as a decision-making tool for safety and rescue planning. Last, but not least, a broad range of citizens will be able to access principal theoretical and parametric information about active faults in areas they are interested in.

More important dataset includes faults with geomorphic marks, such as free faces, coseismic ruptures, fault scarps, triangular facets (flat-irons), or sometimes inferred faults based on geomorphological evidence, such as river deflections, linear mountain-fronts, *etc.* It should be mentioned that the geomorphological evidence is a complementary element for the more accurate geographical positioning of the fault trace and not for the existence of the fault. In the case of earthquake-related faults (seismic faults), the traces can correspond to primary ground ruptures. Among the purposes of this dataset is to provide also information necessary for *Surface Faulting Hazard* (SHA). This type of hazard assessment is crucial for building and infrastructure design, considering that a possible fault displacement could damage the foundations of any technical construction. Moreover, the detailed mapping of fault traces can contribute to fault linkage/segmentation scenarios. Such scenarios are also important, since they can inform us whether a possible rupture can be constrained or pass through neighbouring faults, increasing, thus, the magnitude potential.

The core of the geodatabase, i.e. the tectonic information, will be separated into two distinct, but interrelated, datasets: i) the Fault Traces (FT), and ii) the Fault Zones (FZ). The purpose of each dataset is to provide a different level of information covering different needs (Fig. 2). The former focuses on the mapping accuracy of faults, targeting on large- to medium-scale data (> 1:50,000). Faults originating from smaller scale maps are reassessed (if possible) using hi-resolution topographic data. Primary co-seismic ground ruptures are distinguished from geologically detected fault traces to better understand the surficial rupturing process for fault rupture hazard purposes. The Fault Zones dataset involves fault segmentation and earthquake rupture scenarios which are crucial for Seismic Hazard Assessment (SHA).

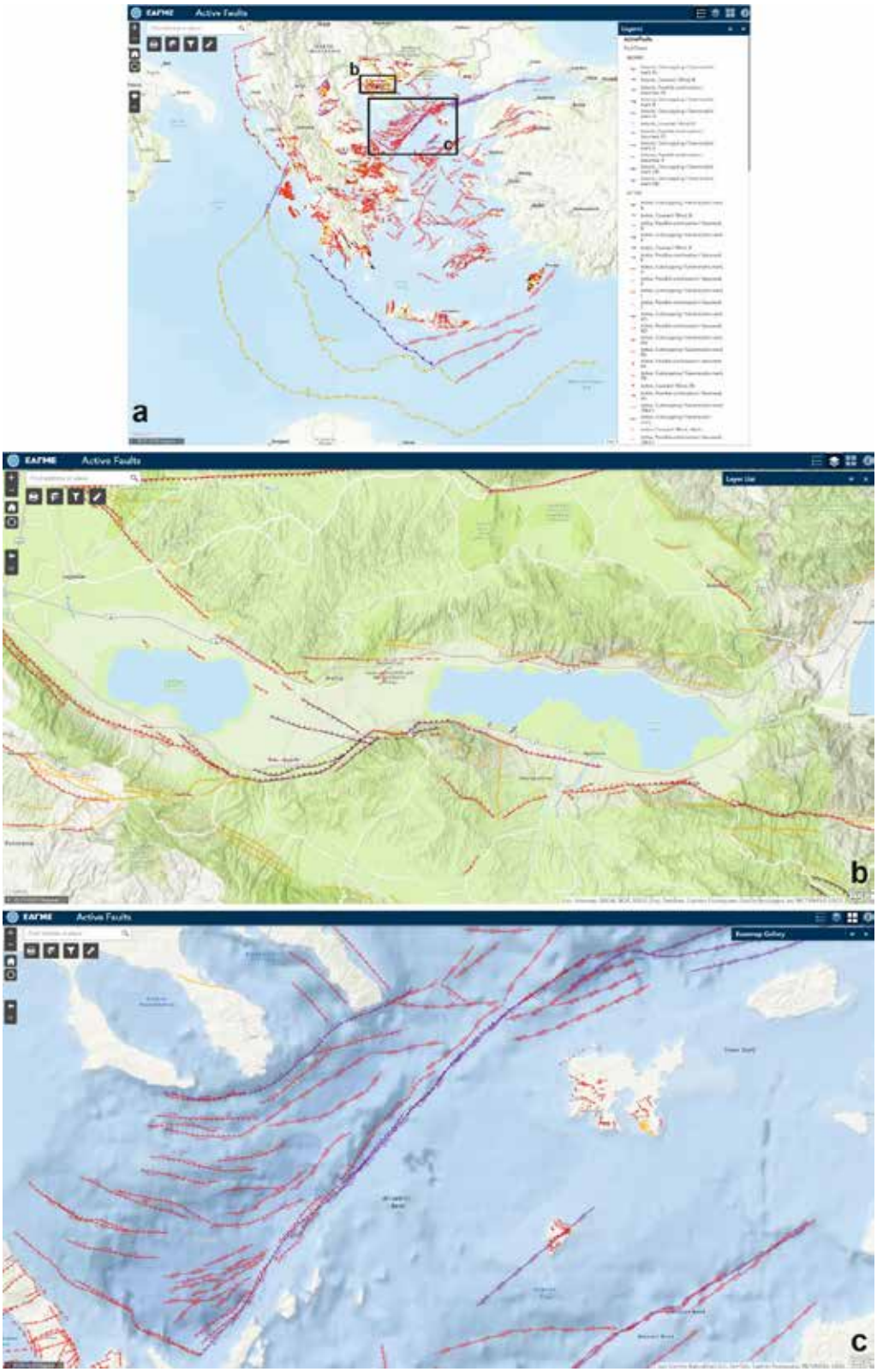

Figure 1. Snapshots of the Hellenic DataBase of Active Faults (HeDBAF) in its current status as seen in the dedicated website (https://activefaults.eagme.gr/en/) for various topographic backgrounds: (a) The broader area of Greece showing the locations of inset maps (b) and (c). (b) Focus on the Mygdonia Basin. (c) Focus on the North Aegean Basin, Lemnos and Aghios Efstratios islands.

Thus, the fault zones are represented by medium- to small-scale lineaments which also facilitate the visualization of large tectonic structures in small-scale maps. The HeDBAF, geodatabase is continuously updateable and upgradeable showing frequent improvements and enrichments.
Following the steps of the Database of DISS (DISS Working Group, 2021) and the Quaternary active faults database of Iberia QAFI (García-Mayordomo et al., 2012), the HeDBAF not only is the source of information, for most of the parametric information, clearly given (whether it is literature data, original data, empirical relationship, or expert judgement, all abbreviated as source-keys), but the methodology followed to extract this information is stated. This means that the end-user has at his/her disposal the origin of the parametric information and the distinction between real data or any other kind of estimation. In this way, the scientific and highly specialized working group of the geodatabase ensures that most of the parametric information will be filled in, leaving as few blank fields as possible.

The classification of the faults used in the Database is based on the definitions decided by the Seismotectonics Committee, as follows:

Seismic fault is defined as an active fault if its activation has been confirmed by a strong earthquake during the instrumental or historical period, by an observed surface seismic rupture or by a palaeoseismological investigation. It should be mentioned that the above definition does not exclude the existence of seismic faults identified by seismological, geophysical, geodetic or other instrumental observations.

A fault is characterized as Active when it documents displacement at least once during the Upper Pleistocene (in the last 126,000 years or so) and can therefore be the source of a future earthquake.
A fault is characterized as active when:

- it has produced a surface rupture associated with a historical or modern earthquake
- it has yielded soil ruptures dated during the Upper Pleistocene-Holocene period, as has been determined by excavating palaeoseismological trenches perpendicular to its trace
- it displaces or affects (e.g. folds) Upper Pleistocene-Holocene geological formations
- free faces with sclickenlines observed along the fault's length have not been eroded at places
- characteristic escarpments and tectonic scarps can be recognized along its length
- debris or talus cones develop at the base of the fault scarp
- morphotectonic structures (e.g. triangular facets, etc.) are shown along its length
- it cuts or displaces river or stream beds in a systematic way
- it demonstrates aseismic slip (proven by geodetic measurements or other indications)
- it is associated with seismic epicentres of the instrumental period or with the alignment of microearthquakes
- it has a structural relationship with another known active fault (it is subparallel, it branches, it has en echelon geometry, etc.)
- it is associated with active volcanism or hot springs
- the stress field of its last activation is roughly the same as the one given by the focal mechanisms in the same area.

A fault is characterized as Potentially Active when it documents displacement at least once during the Quaternary (in the last 2.600.000 years).
The Potentially Active faults:

- displace or affect (e.g. folds) quaternary geological formations but they have not been reactivated during the last 126.000 years
- there is no available geological data indicating their direct relation to strong earthquakes
- they show a small degree of correlation with the distribution of major earthquake epicenters of the instrumental period.
- geomorphological features (eg fault surfaces) along the fault traces are significantly eroded
- they have been identified on the basis of geophysical surveys in areas covered by recent deposits
- their direction is compatible with the active tectonic stresses prevailing in the area.

Non active faults (Inactive or Faults of Undetermined activity) are those for which there are no geological or other (seismological, historical, paleoseismological, geophysical) indications for their activation at least during the Quaternary period (last 2.600.000 years).

References

DISS Working Group (2021). Database of Individual Seismogenic Sources (DISS), Version 3.3.0: A compilation of potential sources for earthquakes larger than M 5.5 in Italy and surrounding areas. Istituto Nazionale di Geofisica e Vulcanologia (INGV). https://doi.org/10.13127/diss3.3.0

García-Mayordomo, J., Insua-Arévalo, J. M., Martínez-Díaz, J. J., Jiménez-Díaz, A., Martín-Banda, R., Martín-Alfageme, S., Álvarez-Gómez, J.A., Rodríguez-Peces, M., Pérez-López, R., Rodríguez-Pascua, M.A., Masana, E.& the QAFI Compilers Working Group (2012). The Quaternary active faults database of Iberia (QAFI v. 2.0). Journal of Iberian Geology, 38(1), 285-302.

EPPO Seismotectonics Committee: Vassiliki Avramea, Constantinos Athanassas, Nikolaos Zouros, Nikolaos Theodoulidis, George Kaviris, Ioannis Kalogeras, Vassiliki Kouskouna, Anastasia Kiratzi, Stylianos Lozios, Constantinos Makropoulos, Maria Manoussaki, Vasileios Margaris, Spyridon Mauroulis, Vassiliki Mouslopoulou, Panayiotis Papadimitriou, Gerasimos Papadopoulos, Constantinos Papazachos, Christos Papaioannou, Efthymios Sokos, Charalambos Fasoulas.

17th INTERNATIONAL CONGRESS of the Geological Society of Greece

BULLETIN OF THE GEOLOGICAL SOCIETY OF GREECE, SP. PUBL.

EXTENDED ABSTRACT 080

An investigation of the use of deep-neural-network-based seismic arrival time picking methods for the automatization of earthquake sequence monitoring: The case of the November 3, 2024 MW 5.3 Kassandra earthquake

Galanis O. [1], Panou A. [1]

(1) Aristotle University of Thessaloniki, Thessaloniki, Greece, ogalanis@geo.auth.gr

We use a pretrained deep neural network to pick seismic arrivals on continuous seismic records. With these picks we locate the events of an earthquake sequence.

Introduction

During the last decade, a number of machine learning techniques have been developed for seismology, and equally importantly, became available as open software. This, combined with the wide availability of open seismological data and open tools for their manipulation, sets the stage for significant improvements in both routine earthquake monitoring and seismological research. In the present work we investigate the use of deep-neural-network-based seismic arrival time picking methods for the automatization of earthquake sequence monitoring and we use the sequence of the November 3, 2024 M_W 5.3 Kassandra earthquake as a case study.

Data

On November 3, 2024, an earthquake of magnitude 5.3 (M_W) occurred off the coast of the Kassandra peninsula of Chalkidiki, Northern Greece, in an area of moderate seismicity. The subsequent aftershock sequence consisted of hundreds of events (indicatively, 430 earthquakes of magnitude 1.5M_L or larger were detected by the automatic location system of the Seismological Station of the Aristotle University of Thessaloniki, within the two months following the mainshock). A selected subset of these events was manually located and included in the bulletin of the Seismological Station of the A.U.Th. These events are shown in Figure 1.

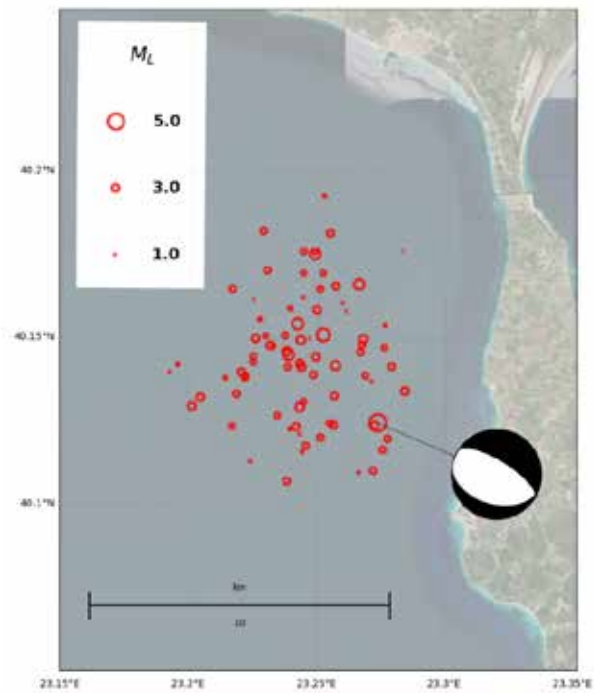

Figure 1. The epicenters of events with a manual solution included in the bulletin of the Seismological Station of the A.U.Th. The beachball plot corresponds to the focal mechanism of the mainshock (Mw=5.3, A.U.Th.).

The input data used in the present study, is the continuous recordings of broadband and strong motion stations in operation in the area around the sequence. These stations are selected from the around 350 stations available to the Seismological Station of A.U.Th., of which 50 are maintained by the A.U.Th. itself while the rest are provided by the other members of the Hellenic Unified

Seismological Network and other partners. The routine procedure is to first automatically calculate hypocenters and magnitudes in real time with the SeisComP seismological software package, which are then refined by designated human analysts. Analysts are instructed to at a minimum perform a manual analysis of every event for which the automatic magnitude (M_L) is 2.5 or greater. This results in two datasets, one of relatively higher quality but limited in size by the available humanpower of the Seismological Station and one of relatively lower quality but more extensive.

In the present study, we use deep-neural-network-based seismic arrival picks to locate the sequence, in order to obtain a dataset of sufficient quality and sufficient size to describe the spatial and temporal distribution of the events.

Implementation

We used the SeisBench toolbox (Woolam et al. 2022) which provides, among other tools, deep neural network models trained with a range of training datasets. Comparing models and training sets is out of the scope of the present work, so we used the EQTransformer model (Mousavi et al., 2020), trained with the Instance dataset which is a good starting point for most cases (Münchmeyer et al., 2022). A sample of the results is shown in figure 2. For associating the picks produced by EQTransformer, we used the GaMMA associator (Zhu et al. 2022). After association, each pick is associated with a specific event. In the final step the events are located using the NonLinLoc software (Lomax et al. 2014), which is also the software used for the routine manual location of earthquakes. For the routine manual location, we use a 1-D velocity model, and we did not change this for the present work. The end product of the process is a catalog of the events of the earthquake sequence. It also has to be mentioned that in addition to all the above software, we had to develop tools for the downloading of the data, as well as manipulation, bookkeeping and reformatting. This also included tools to rapidly visually inspect phase picks and phase associations.

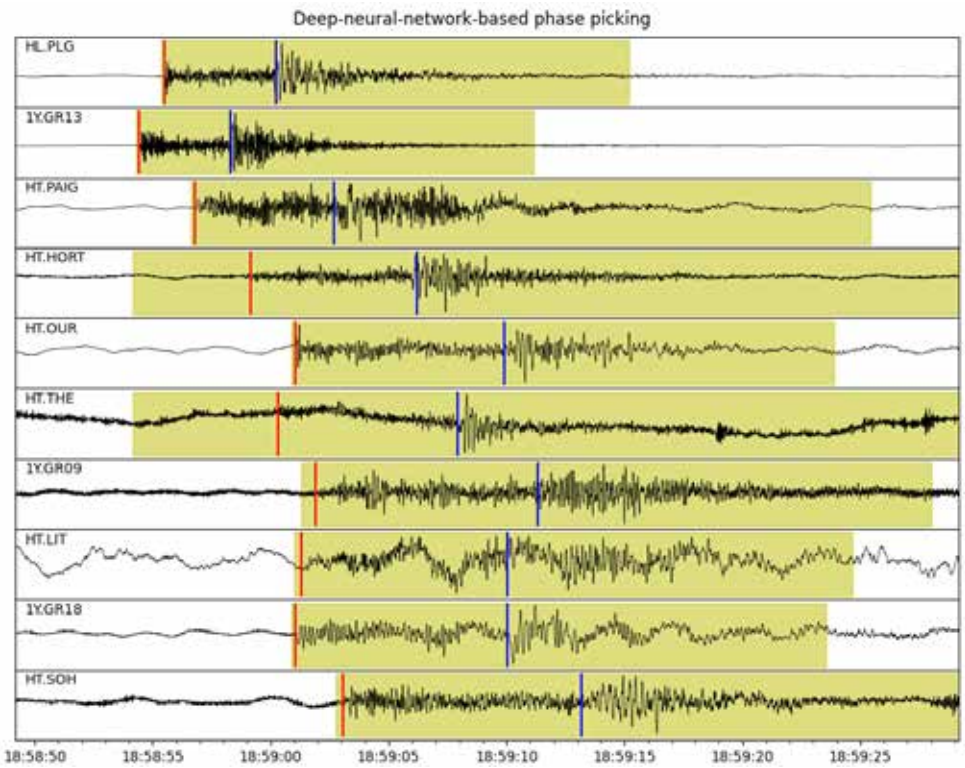

Figure 2. Example of the results of deep-neural-network-based picking. The yellow shadowed area corresponds to the time window characterized as the detection of an earthquake by the model. The red lines correspond to the P arrivals (technically the times where the probability of a P arrival is maximized) and the blue lines correspond to the S arrivals. The event shown has a magnitude of 1.7 (M_L) as determined by the automatic earthquake location system.

Results

The picking – association – location procedure resulted in the events shown in Figure 3. 1085 events were located in total. 11 foreshocks were detected, the first one occurring in October 31st. Although we scanned for P and S wave arrivals for the period starting in October 1st, not a single event was detected in the area of interest until the last hour of the month. This gives an indication of the system's resilience to false detections. The aftershocks persisted for the months following the mainshock with an average of more than one event per day during February 2025.

The focal depths of these events are < 20 km but they are not well constrained. This does not seem to be a problem of the location procedure as it was also observed in the far more rigorous manual locations. The error in the epicenter appears to be at least as small as that of the manual epicenter judging by their spatial distribution, especially taking into account that the deep-neural-network-based sample of earthquakes is about an order of magnitude larger than the manual sample. To confirm this, we also performed a double-difference relocation (hypoDD, Waldhauser and Ellsworth, 2000, Waldhauser, 2001) of all the events. The results of this relocation are shown in Figure 4.

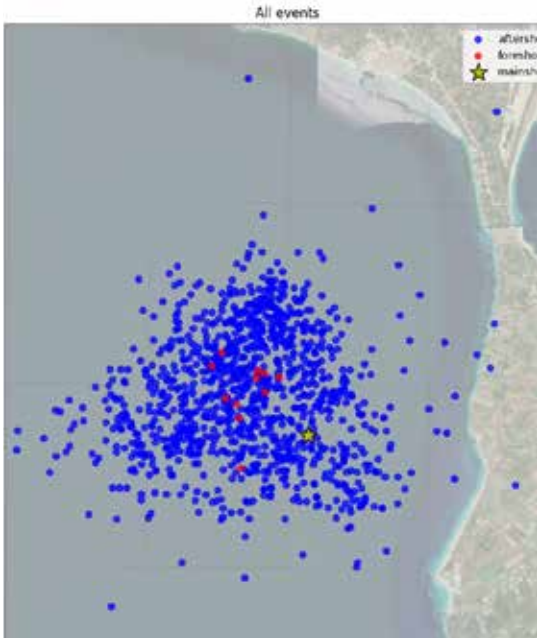

Figure 3. All the events located. The mainshock is marked with a star, while foreshocks and aftershocks are marked by red and blue points respectively.

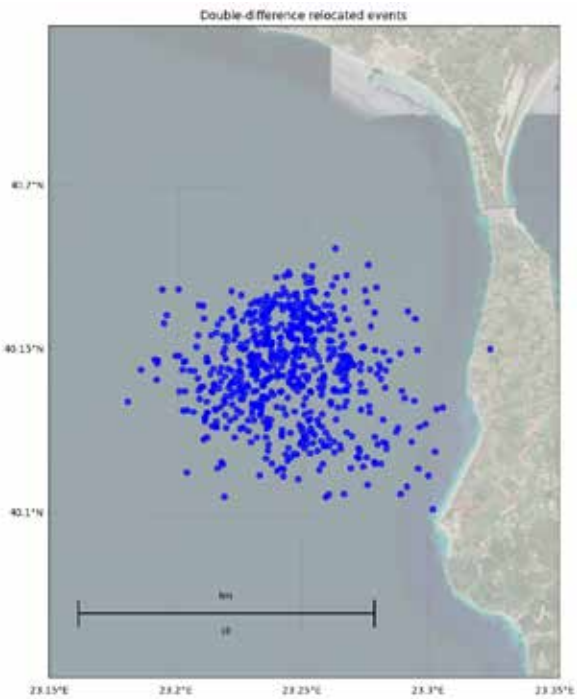

Figure 4. All the events relocated by the double-difference algorithm

The geometry of the fault is not apparent by the epicenter distribution, but taking into account the published focal mechanism it appears that the fault length is at most 10km which is compatible with an event of this magnitude or a slightly larger one. In a real-world application this sort of information would be helpful in the evaluation of the earthquake sequence the hours following the mainshock. For this reason, we mapped the events that occurred in the 12h following the mainshock. The results are shown in figure 5. We conclude that during this particular earthquake sequence there was no significant temporal change in the spatial distribution of the epicenters.

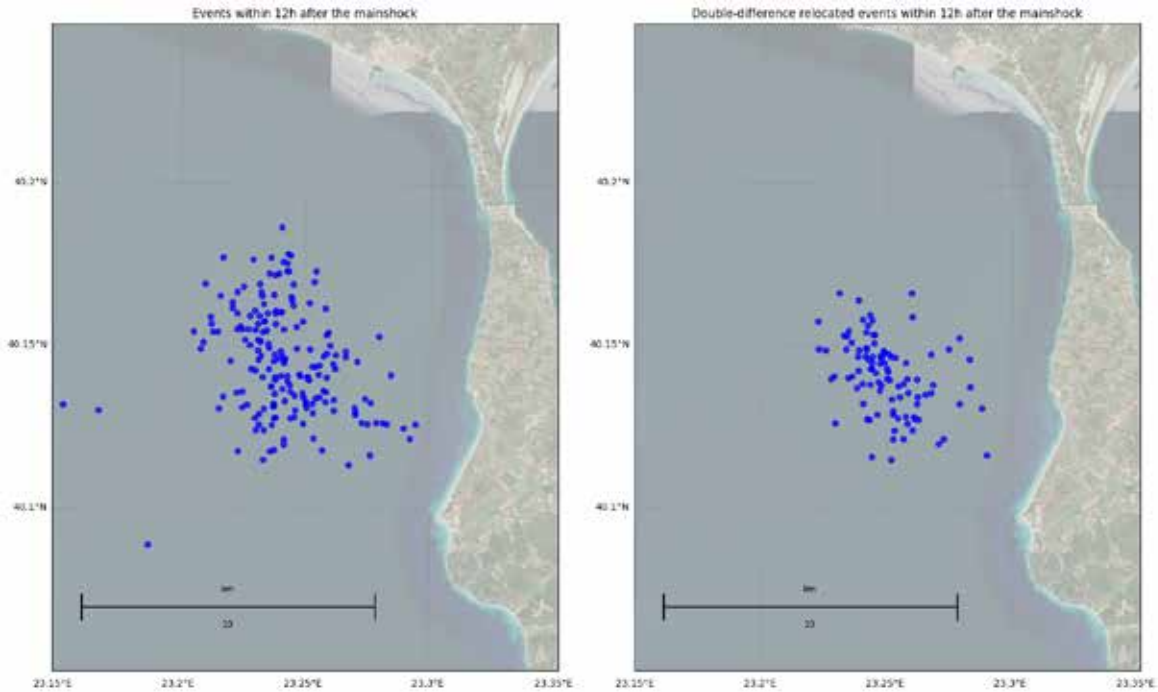

Figure 5. The events that occurred the 12 hours following the mainshock as located by NonLinLoc (left) and the subset that was successfully relocated by hypoDD

Finally, we calculated the rate of occurrence of the aftershocks, as the number of detected events within a 24h moving window. The results are shown in Figures 6, 7 and 8. We conclude that the aftershock sequence is very typical in this respect, as the rate of occurrence of aftershocks follows Omori's law in the short term (days) as well as in the long term (months).

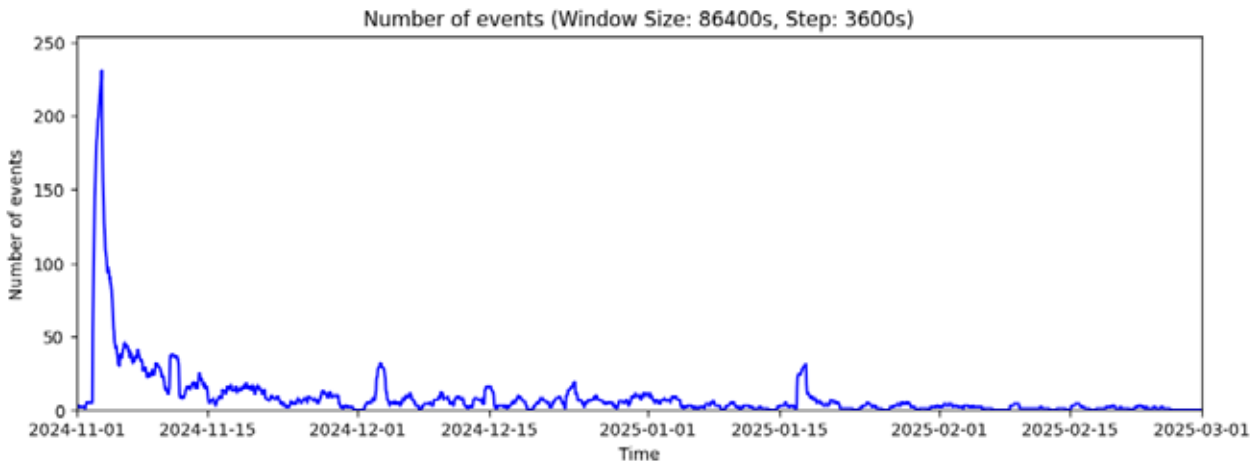

Figure 6. The rate of occurrence of earthquakes given as the number of detected events within a 24h moving window for the period covered by the present study.

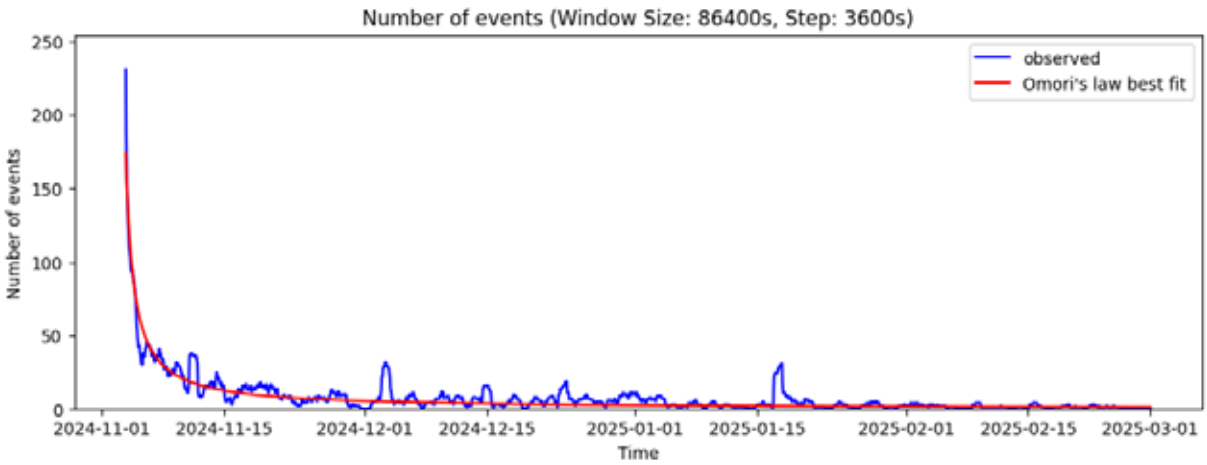

Figure 7. The rate of occurrence of aftershocks given as the number of detected events within a 24h moving window starting at the origin time of the mainshock. The rate of occurrence is shown with a blue line, and the least squares best fit for Omori's law is shown with a red line.

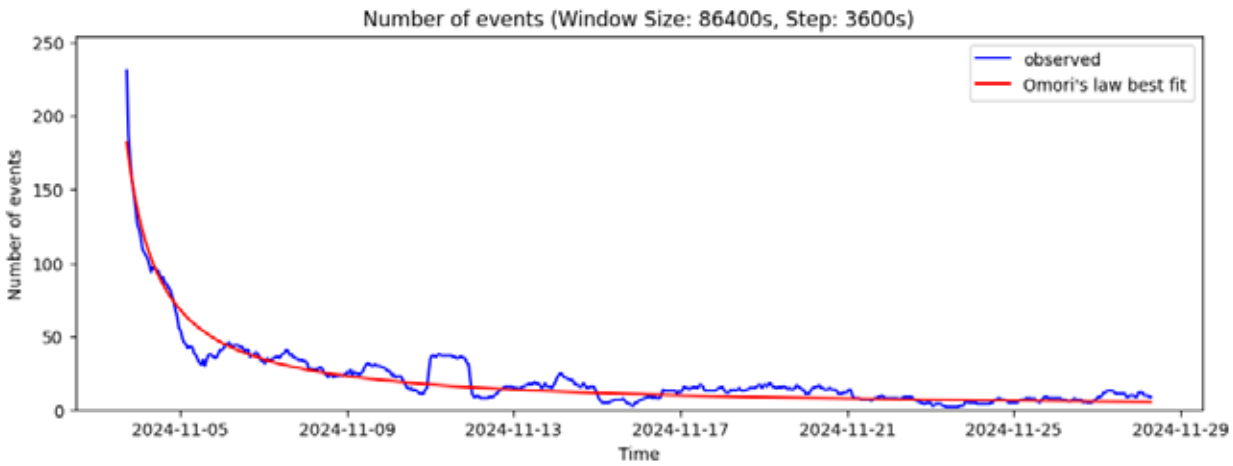

Figure 8. The rate of occurrence of aftershocks given as the number of detected events within a 24h moving window for a few weeks following the mainshock. The rate of occurrence is shown with a blue line, and the least squares best fit for Omori's law is shown with a red line.

Conclusions

Deep-neural-network-based seismic arrival time picking methods, can be used in combination with other tools and methods and using relatively modest computational resources, for the monitoring of earthquake sequences. This sort of automatization is a satisfactory compromise between the higher quality manual locations and larger quantity of "traditional" automatic pickers. We applied them retrospectively to a moderate size earthquake sequence, and we plan to use them in real time in the future.

Data sources

All graphs and maps were created with the Matplotlib library (https://matplotlib.org/). When not stated otherwise, managing and processing seismological data was performed with ObsPy (https://www.obspy.org/). The backgrounds of the maps were developed by ESRI (https://www.esri.com/). We used data from the FDSN networks: 1Y, BS, EG, HA, HI, HL, HP, HT, KO and MK (https://www.fdsn.org/networks/)

References

Beyreuther, M., Barsch, R., Krischer, L., Megies, T., Behr, Y., and Wassermann, J., 2010. ObsPy: A Python Toolbox for Seismology, Seismological Research Letters, 81 (3), 530-533.

Helmholtz-Centre Potsdam - GFZ German Research Centre for Geosciences and gempa GmbH, 2008. The SeisComP

seismological software package. GFZ Data Services. doi: 10.5880/GFZ.2.4.2020.003.

Lomax A., Michelini A., Curtis A., 2014. Earthquake Location, Direct, Global-Search Methods, in: Meyers R. (Eds), Encyclopedia of Complexity and Systems Science. Springer, New York, NY.

Mousavi, S.M., Ellsworth, W.L., Zhu, W., Chuang, L.Y., Beroza, G.C., 2020. Earthquake Transformer: An Attentive Deep-learning Model for Simultaneous Earthquake Detection and Phase Picking. Nature Communications.

Münchmeyer, J., Woollam, J., Rietbrock, A., Tilmann, F., Lange, D., Bornstein, T., et al., 2022. Which picker fits my data? A quantitative evaluation of deep learning based seismic pickers. Journal of Geophysical Research: Solid Earth, 127, e2021JB023499.

Waldhauser, F., Ellsworth W.L., 2000. A Double-Difference Earthquake Location Algorithm: Method and Application to the Northern Hayward Fault, California, Bull. Seism. Soc. Am. 90, 1353-1368.

Waldhauser, F., 2001. hypoDD - A Program to Compute Double Difference Hypocenter Locations, U.S. Geological Survey Open-File Report 01-113, 25p.

Woollam, J., Münchmeyer, J., Tilmann, F., Rietbrock, A., Lange, D., Bornstein, T., Diehl, T., Giunchi, C., Haslinger, F., Jozinović, D., Michelini, A., Saul, J., Soto, H., 2022. SeisBench—A Toolbox for Machine Learning in Seismology. Seismological Research Letters 93 (3): 1695–1709.

Zhu, W., McBrearty, I. W., Mousavi, S. M., Ellsworth, W. L., Beroza, G. C., 2022. Earthquake phase association using a Bayesian Gaussian Mixture Model. Journal of Geophysical Research: Solid Earth, 127, e2021JB023249

17th INTERNATIONAL CONGRESS of the Geological Society of Greece

BULLETIN OF THE GEOLOGICAL SOCIETY OF GREECE, SP. PUBL.

EXTENDED ABSTRACT 081

Evolution of map-making from prehistoric times to the Middle Ages

Galazoudi E.[1], Bathrellos G.D.[2], Skilodimou H.D.[2], Koukouvelas I.K.[2], Nikolakopoulos K.[2]

(1) National & Kapodistrian University of Athens, Athens, Greece, egalaz@uoa.gr, (2) University of Patras, Patras, Greece

Introduction

The history of cartography—the art and science of map-making—is rich and fascinating, spanning millennia of human history. The relationship between humans and the environment dates back to ancient times. Most ancient cultures considered nature sacred (Manolas, 2010).

This connection between man and the environment is reflected, for example, in literary works, art, and maps. Maps have always been among the most important tools for comprehending the world and humanity's place in it, dating back long before the invention of writing.

Prehistoric humans used maps to depict their environment and to transmit their knowledge to future generations (Livieratos, 2007). Ancient Greeks considered themselves part of the natural environment, a perspective that influenced their daily lives, philosophy and religion. In antiquity, maps were created to help people understand and navigate the world.

Objectives

This paper describes the evolution of cartography or map-making from Prehistory to the Middle Ages. It explores the purposes of map-making, highlights the first examples of maps, discusses the contributions of ancient civilizations to map-making, of technology to the evolution of maps, and the role of geopolitical conditions in the formation of maps.

It also describes the significance of maps in understanding our world and the evolution of related theories. It examines the findings and observations concerning their thematic content and materials used in map-making during this period. It also presents the evolution of theories regarding the shape of Earth, its position in the Universe, and maps orientation.

Methods

The methodology for this paper initially included the search and collection of relevant bibliographic references. This bibliography includes Greek and international references about:

- the objectives and purposes of map creation
- the earliest examples of maps
- the contribution of ancient civilizations to the development of map creation
- the influence of geopolitical conditions on the formation and evolution of maps

The bibliography was searched and collected through Greek libraries, bibliographic databases, repositories of Greek - foreign Academic Institutions and online resources.

Subsequently, all the data collected was classified and processed. The maps were analysed in detail based on:

- their thematic content,
- the material used in their construction,
- the evolution of the Earth's outline and shape,
- the evolution of orientation over time.

The findings and observations derived from the data analysis were synthesized to draw conclusions, which are described in the concluding section.

Results

The first maps date back to the Paleolithic era (40,000 to 10,000 BC) and were created before the development of writing. Their purpose was educational and contained simple representations of the environment of primitive man. The material for recording primitive maps is rocks, known as petroglyphs (Brotton, 2015).

Babylonians introduced the fundamental principles of cartography, namely orientation and scale. They created the first map in 2500 BC, using clay tablets - the material - to make maps. They represented properties, city plans, as well as the world. The Babylonian view of the Earth was flat, circular and surrounded by the ocean (Snow et al., 2018).

By the end of the pre-Christian era, the ancient Greeks had laid the foundations of scientific cartography through three significant advances. First, Alexander the Great's expedition extended the then-known world to the Indus River, expanding geographical knowledge and reinforcing the need for cartographic mapping (Hunt, 2000). Second, Eratosthenes proved the sphericity of the Earth and calculated its circumference with remarkable accuracy. Third, Hipparchus invented a system of meridians and parallels, highlighting the need to develop map projections (Hunt, 2000).

Generally, the ancient Greeks contributed decisively to the evolution of cartography, introducing scientific and mathematical principles that formed the basis for its later development. They recognized the spherical shape of the Earth, leading to a more

accurate geographical depiction (Livieratos, 2007). They used geometric methods and developed instruments for measuring geographical quantities. They focused on scientific observation through measurements to understand the universe. They invented projections and, through them, the mathematical organization of the Earth's surface while connecting measurements with precise calculations, such as Eratosthenes' measurement of the Earth's diameter, a pioneering transition from empirical to scientific observation (Livieratos, 2007).

Cartography during the Middle Ages remained stagnant. Maps or mappae mundi showed significant differences from ancient and modern times (Harley & Woodward, 1987). Their purpose was educational as well as to represent the time's geographical, religious and mythological concepts. T and O-type maps were religious and represented the world with Jerusalem in the center and the East at the top of the map (Woodward, 1987). One type of map showed the world as a circle divided into seven geographical zones - the "climates" of Eratosthenes - or the five zones of the Roman writer Macrobius (Hunt, 2000). Portolans are maps that appeared in the 13th century and depicted the coasts, intending to help sailors in their travels (Tolias, 1999).

Table 1. Evolution of the beliefs about Earth's place in the Universe: From Antiquity to Renaissance

Period	Earth's place in the Universe	Important Philosophers/Scientists
Antiquity	Geocentric model	Aristotle (384-322 BC),
	Heliocentric model	Aristarchus of Samos (310 BC - 230 BC)
	Geocentric model	Claudius Ptolemy (85-165 AD)
Middle Ages 5th to 15th century AD	Geocentric model	Official position of the Roman Catholic Church
16th century	Heliocentric model	Nicolaus Copernicus

The place of the Earth in the Universe has been an issue that has concerned humans throughout time. Table 1 shows the evolution of the perception.

In Antiquity, the dominant belief was the geocentric system, in which the Earth was the center of the world. The Sun, the planets and the Stars revolve around the Earth (Livieratos, 2007). However, Aristarchus of Samos (310 BC - 230 BC) introduced the theory of a heliocentric system (Crowe, 1990), in which the Sun is the center of the Universe and the Earth orbits around it, which was not adopted.

The geocentric system was maintained in the Middle Ages, with the official position of the church being that the Earth is stationary and the planets revolve around it. Copernicus refuted this view in the 16th century.

Table 2. Evolution of the theories about Earth's shape. From Antiquity to Middle Ages.

Period	Map	Person	Earth's shape	Orientation
8th century BC	Shield of Achilles	Homer	Flat circular	
600 BC	Babylonian world map	Babylonians	Circular disk	N
550 BC	Anaximander map	Anaximander	Circular disk	
510 BC	Anaximander map	Hecataeus	Circular disk	
580-500 BC		Pythagoras	Spherical and rotation around an axis	
340 BC		Aristotle	Spherical	
250 BC		Eratosthenes *	Spherical	N
270-180 BC		Crates **	Spherical	
180-120 BC		Hipparchus***	Spherica	
85 BC		Poseidonius ****	Spherical	
1st century BC	Geographical	Strabo	Spherical	
2nd century AD	Geographia	Claudius Ptolemy	Spherical	N
536 AD		Cosmas	flat and elongated	S
Middle Ages 5th – 14th century AD		Mappae mundi	One - dimensional or flat, with circular or rectangular shapes that did not reflect the real geomorphology of the earth	E

*First measurement of the Earth, **Created the first Globe, *** Invented a system of meridians and parallels, ****Second measurement of the Earth

The beliefs about the shape of the Earth.

The shape of the Earth has been another topic that has preoccupied people since ancient times. Table 2 displays the transition from simple initial beliefs to more complex scientific theories about the shape of the Earth.

In antiquity, there were differing beliefs about the shape of the Earth:

1. Flat Circular Disk: This idea was held by the Babylonians, Homer, Anaximander, Hecataeus, and the Ionians, who believed the Earth was a flat disk.
2. Spherical Shape: In contrast, philosophers such as Pythagoras, Aristotle, Eratosthenes, Crates, Hipparchus, Posidonius, Strabo, and Ptolemy supported the theory that the Earth is spherical. They based their conclusions on observations of stars and various natural phenomena over time. Eratosthenes played a key role in confirming the Earth's spherical shape by calculating its circumference.

In the Middle Ages, maps depicted the world as one-dimensional or flat, with circular or rectangular shapes that did not reflect the Earth's actual geomorphology. These maps often illustrated the world as a flat disk surrounded by water.

The shape of the Earth played a crucial role in the significant geographical discoveries of the late Middle Ages. An example was the discovery of America in the late 15th century. It prompted the exploration of new sea routes and the establishment of trade relations, while scientific contributions from Arab geographers and European scholars improved the knowledge and confidence of seafarers. This new concept played a significant role in reviving geographical knowledge and initiating the era of great discoveries.

In addition, the above table also illustrates how map orientation has evolved over time.

In Babylonian maps, the orientation was initially towards the North. However, the earliest maps created by the ancient Greeks did not have a precise orientation. It was not until the introduction of geographical coordinates that they began to orient their maps towards the North, as seen in Ptolemy's map. This description resulted from the astronomical, geometric, and physical observations made by the ancient Greeks.

During the Middle Ages, most mappae mundi were oriented toward the East for religious reasons. An exception to the above is the map of Cosmas the Indicator, which was oriented towards the South. The Arab maps were oriented towards the South to align with Mecca. The evolution of map orientation underscores the profound cultural significance of mapmaking.

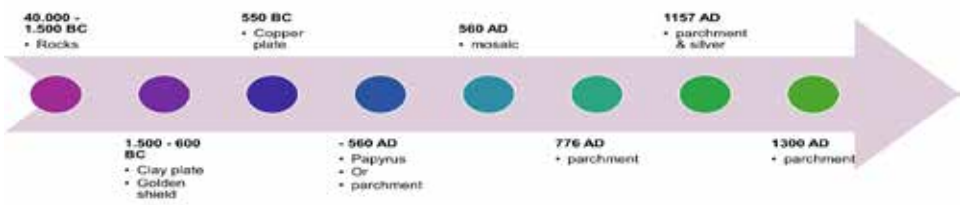

Figure 1. Evolution of the material used to make maps through time.

The above figure presents the evolution of the material used to make maps. Specifically, the depiction of maps began in the Paleolithic era, when prehistoric people drew their environment on rocks. Then, in Antiquity, it progressed from the clay tablets of Babylon to Homer and the golden shield of Achilles to the bronze tablet of Anaximander. During the Middle Ages, the most significant number of maps (or tablets) were either made of papyrus or parchment. Then, in Antiquity, from the clay tablets of Babylon to Homer and the golden shield of Achilles, we move on to the bronze tablet of Anaximander. In Antiquity, most maps (or tablets) were made of papyrus or parchment.

The transition from papyrus to parchment resulted from a combination of factors such as durability compared to papyrus, which was vulnerable to moisture and brittle. This durability allowed the preservation of texts for a more extended period, which was crucial to conserving religious texts and scriptures (di Curci, 2003). In addition, ease of use, availability, and the need for religious writing made parchment an essential material in the history of writing and cartography (di Curci, 2003). This transition began in the fourth, and by the end of the eighth century, most maps used parchment as constructed material.

In the Middle Ages, most maps were made of parchment. Exceptions are the Madaba mosaic map (560 AD) and the

Tabula Rogeriana map (1157 AD), which is made of parchment and silver. Towards the end of the Middle Ages, maps of animal skin (vellum), such as the Carte Pisane (1300 AD), were also made of parchment (Brotton, 2015).

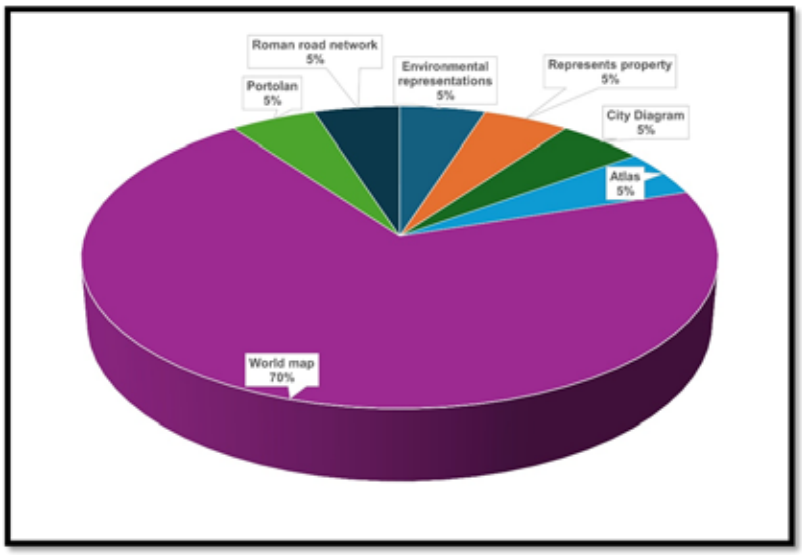

Figure 2. Distribution of types of maps, from Prehistory to the Middle Ages

Figure 2 presents the distribution of types of maps, from Prehistory to the Middle Ages, highlighting the diversity across numerous types.

World maps account for the most significant percentage of concerns, which indicates man's interest in understanding the World on a global scale.

These maps were not only geographical but often incorporated both philosophical and religious concepts of the World.

The remaining types of maps are in the same percentages: Portolans, environmental representations, representations of property, city diagrams, geographical atlases, as well as maps of the Roman road network.

Conclusions

The high percentage of World maps demonstrates humanity's inclination to understand the Earth, which was not only geographical but often incorporated both philosophical and religious concepts of the world.

The materials used for making maps have changed over time. In the past, people used rocks and clay tablets. Later, they made maps from metal, papyrus, and parchment. This progression illustrates technological advancements and emphasizes how these innovations have improved our comprehension of the world.

In Antiquity, the geocentric model of the Universe was dominant until Aristarchus of Samos proposed a heliocentric view, which was largely ignored. During the Middle Ages, the geocentric perspective continued to be upheld and supported by Church doctrine, demonstrating the enduring influence of ancient ideas.

Early thinkers like the Babylonians and Homer viewed the Earth as a flat disk. In contrast, philosophers such as Pythagoras and Aristotle later argued for a spherical Earth. During the Middle Ages, maps often depicted a flat world, ignoring true geomorphology.

Babylonian maps oriented northward, while early Greek maps lacked clear orientation. As the Greeks began to use geographical coordinates, they started orienting their maps to the north. In contrast, medieval mappae mundi were often oriented eastward for religious reasons, and Arab maps pointed south.

References

Brotton, J., 2015. Great maps. Dorling Kindersley Limited.

Crowe, M. J., 1990. Theories of the world from antiquity to the Copernican revolution. New York: Dover Publications.

di Curci, M. 2003. The History and Technology of Parchment Making. Lochac College of Scribes: Parchment Making

Harley, J. B., & Woodward, D. (Eds.)., 1987. The History of Cartography, Vol. 1: Cartography in Prehistoric, Ancient and Medieval Europe and the Mediterranean. (Vol. 1). THE UNIVERSITY OF CHICAGO PRESS.

Hunt, A., 2000. 2000 Years of Map Making. Geography, 85(1), 3–14.

Livieratos, E., 2007. 25 Centuries from Iones to Ptolemy and Rigas: A tour into Cartography and Maps. Ziti (in Greek)

Manolas, E. I. (Ed.). (2010). The Natural Environment in Ancient Greece. Department of Forestry and Environmental and Natural Resources Management, Democritus University of Thrace. (in Greek)

Snow, P., Houston, R., Mumford, S., Merritt, E., Darlison, M., & Stirling, H. (Eds.)., 2018. History of the world map by map. Dorling Kindersley Limited.

Tolias, G., 1999. The Greek nautical charts Portolans, 15th-17th centuries: A contribution to the Mediterranean cartography of recent times (1st ed.). Olkos (in Greek).

Woodward, D., 1987. Medieval Mappaemundi. In Cartography in Prehistoric, Ancient, and Medieval Europe and the Mediterranean Vol. 1, pp. 286–370.

17th INTERNATIONAL CONGRESS of the Geological Society of Greece

BULLETIN OF THE GEOLOGICAL SOCIETY OF GREECE, SP. PUBL.

EXTENDED ABSTRACT 082

Ground motion monitoring with low-cost multi-GNSS installations in Achaia, western Greece

Ganas A.[1], Anastasiou D.[2], Mavropoulos, G.[3], Karamitros, I.[1], Nikolakopoulos, K.[4], Tsironi, V.[1]
(1) National Observatory of Athens, Institute of Geodynamics, Athens, Greece aganas@noa.gr
(2) Dionysos Satellite Observatory, National Technical University of Athens, Heroon Politecniou 9, 157 80, Zografos
(3) ES Systems-Pressure & Flow Sensor Solutions, 62 Ioannou Metaxa Str, Koropi - Athens 19441, Greece
(4) University of Patras, Department of Geology, 26504 University Campus, Rio Patras, Greece

Abstract
In this contribution, we demonstrate the operational status of a new GNSS infrastructure in the western Gulf of Corinth (Greece) that is based on the collaboration of a multidisciplinary research team and on low-cost equipment. Our low-cost instrumentation includes a multi-GNSS dual-frequency chip (Ublox ZED F9P module) mounted on a Raspberry-Pi 4 compute module IO board together with an industry-standard MEMS accelerometer. It provides signal tracking for multi-GNSS systems (GPS, GLONASS, Galileo and BeiDou). The GNSS data are collected 24 hours 7 day 365 days per year, quality-checked and processed by use of the PRIDE-AR open-source software. The E, N, Up velocities for two sites (GEDP & KRHN) were estimated on the IGS20 reference frame. We tested our results against the velocities of neighbouring permanent GNSS stations with overall good agreement.

Introduction
There is a continuous need for integrating multi-parameter instrumental observations and measurements with Satellite Earth observation data towards continuous monitoring of the environment and infrastructures. This task attains more importance within the tectonic and seismically active area of the Greek "Supersite" (Fig. 1; Achaia, western Corinth Gulf). The significant level of geohazards in this region have made necessary the implementation of new technological approaches that could offer reliable augmentation to permanent networks (both geodetic and seismological; Nikolakopoulos et al. 2023). In this contribution, we demonstrate the design, construction and installation of a new GNSS infrastructure that is based on the collaboration of a multidisciplinary research team (funded by the PROION project) and on low-cost equipment.
The aim of the PROION project (https://proion-hellas.eu) was the development of a platform for the continuous monitoring of high importance infrastructures such as public buildings and dams. The methodology combines instrumental and remote sensing measurements along with fuzzy logic networks methods and machine learning algorithms (Nikolakopoulos et al. 2023). Specifically, measurements obtained by three-axis accelerometers, low cost GNSS receivers and Persistent Scatterer Interferometry (PS-InSAR) are fused and validated with high-precision 3D reference data derived from TLS surveys and UAV campaigns. The processing is based on soft computing algorithms while very accurate deformation maps are utilized for making decisions about the current and the future state of each infrastructure.
Our low-cost instrumentation includes a multi-GNSS dual-frequency chip (Ublox ZED F9P module) mounted on a Raspberry-Pi 4 compute module IO board together with an industry-standard MEMS accelerometer. It provides signal tracking for most global-coverage GNSS systems (GPS, GLONASS, Galileo and BeiDou). The GNSS data are collected 24/7/365, quality-checked and processed by use of open-source software. The combined-synergistic use of these new sensors is compatible with ground motion data provided by GNSS reference stations and accelerometers used by seismic agencies. Current work includes collection, reformatting, processing and archiving daily data from three test sites using 4G telemetry. The GNSS data support the on-going, pre-operational monitoring of three test sites (Fig. 1; Asteri dam, Department of Geology U. Patras, Krini landslide; Ganas et al. 2022) together with InSAR Copernicus data (Tsironi et al. 2022). For the first time, the displacement velocities of the NOA low-cost GNSS stations have been estimated to provide additional geodynamic information in an area with high rates of deformation. In this contribution we will present results for two sites GEDP (Patras; Fig. 1) and KRHN (Krini village; Fig. 1), respectively.

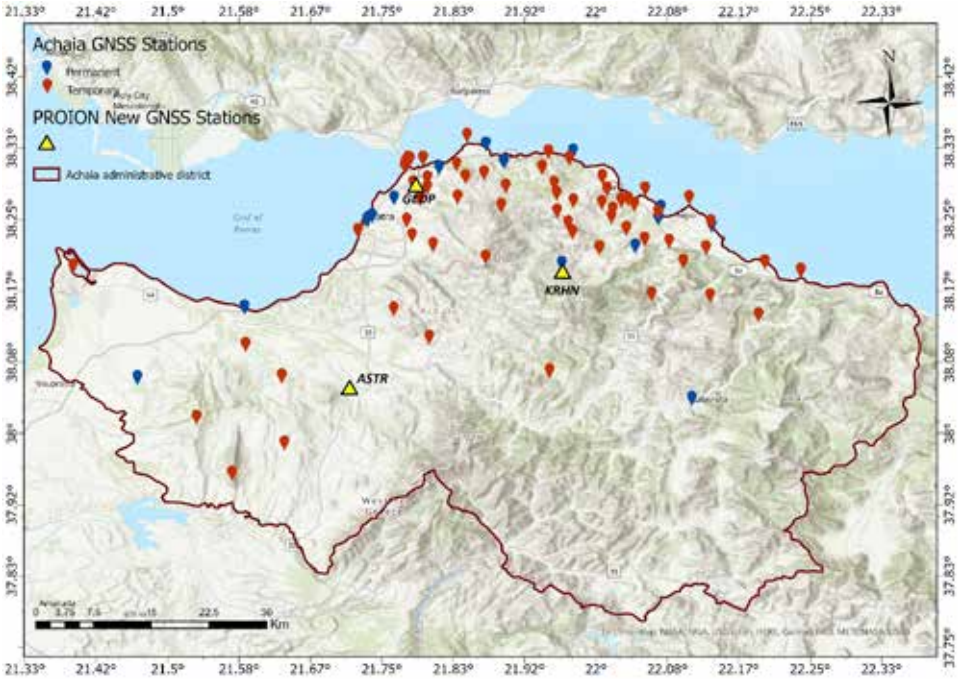

Figure 1. Relief map showing GNSS low-cost installations (yellow triangles; KRHN, GEDP, ASTR) in Achaia (part of the western Gulf of Corinth). Blue and red pins show other GNSS stations in the area.

Data and Methods

In actively deforming areas such as rift systems, it is essential to sample the deformation field thoroughly in both time and space to a) map the pattern of ground changes as well as the speed and direction of movement and b) constrain active fault source models. Surface displacements, tilts, and dilatation are easily measurable with modern geodetic techniques, such as the Global Navigation Satellite System (GNSS; Partheniou et al. 2019; Ganas et al. 2013, 2020; Briole et al. 2021).

In 2021 NOA established a local network of three (3) GNSS stations around the south coast of the Gulf of Corinth (Fig. 1; code names KRHN, GEDP and ASTR; Ganas et al. 2022). All stations were selected on horizon-free buildings, either on bedrock or on syn-rift sedimentary rocks, so that we make sure our data products record either tectonic or local motions. The benchmarks were drilled inside the roof tops and metallic bolts were placed (Fig. 2). GEDP and KRHN are new installations; KRHN occupied the same benchmark as the CRL station KRIN (https://nfo.crlab.eu/KRIN). Continuous measurements have been conducted on this network on a yearly basis since then by use of dual-frequency geodetic receivers (Ganas et al. 2024). With a combination of repeated GNSS measurements and continuous monitoring by 1-D InSAR (i.e., Tsironi et al. 2022), it is now possible to measure ground deformation over broad areas around the three GNSS sites and with satisfactory temporal and spatial resolution.

The data sampling interval was 1 s, and the data were collected on a 24 h basis. The RINEX files that were processed contain 8 observables of GPS satellites: C1C L1C D1C S1C C2W L2W D2W S2W. All station records were complete. Each station has been analyzed independently using the Precise Point Positioning (PPP) method which computes coordinates of each station separately. The low-cost data set was processed to obtain 24-h position solutions using the PRIDE-AR software (V3.0; Geng et al., 2019). Final products from the Wuhan IGS Analysis Center were employed for satellite orbits, clocks, attitude, and bias corrections. Daily files containing Earth Rotation Parameters (ERP) were also included in the processing. The latest ANTEX file published by IGS, including extensions for the station antenna, was also used. Zenith Total Delay (ZTD) was estimated using a stochastic walk model with a process noise of 0.0004 m/√s. The Vienna Mapping Function 3 (VMF3) was used as the troposphere delay model. Tidal

corrections, including solid Earth tides, ocean tides, and pole tides, were applied with the FES2004 model as reference. Daily position files are converted into an annual series of positions, in which we obtain the displacements that have occurred since the beginning of our time series. The linear trend of the position time series was estimated using the Hector software (Bos et al. 2013). The N, E, Up position time series for station GEDP are shown in Fig. 3 (left panel) and for station KRHN in Fig. 3 (right panel), respectively.

Figure 2. Field photographs (2023) showing the GNSS low-cost installations a) top panel: at the Department of Geology University of Patras (code name GEDP). View to the west b) bottom panel: at the building in village Krini (code name KRHN). View to the east).

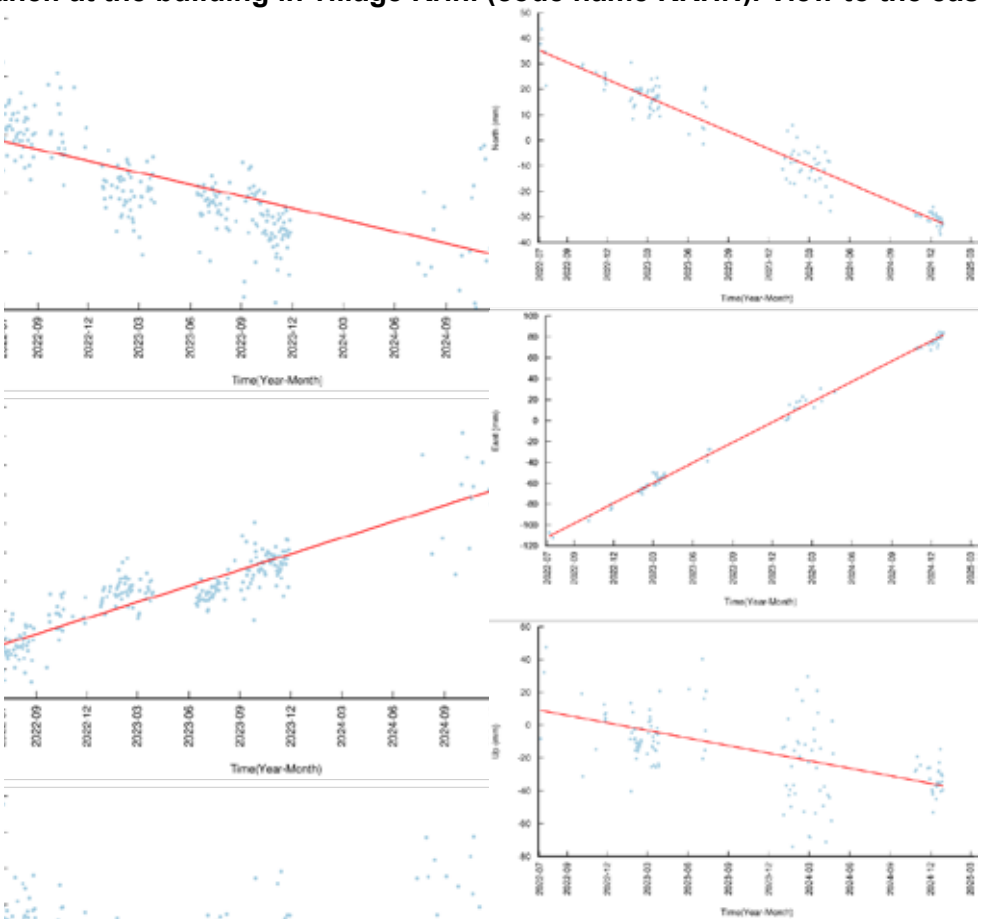

Figure 3. left) displacement vs time diagram of GNSS station GEDP (measurements 2022 – 2024), right) displacement vs time diagram of GNSS station KRHN (measurements 2022 – 2024). Three panels are shown from top to bottom (North, East, Up components). Missing data is due to telemetry gaps.

Results and Conclusions

The low-cost geodetic data were sampled at 1-s intervals, however, for data processing the RINEX files were resampled at 30-s. This is normal when daily coordinates are computed because the default PRIDE-AR configuration is to process 30-s RINEX files. The velocities for two sites (GEDP & KRHN; Fig. 3) were estimated on the IGS20 reference frame (Table 1). For comparison we provide the velocities of the permanent GNSS station PAT0 as reported by a) the Nevada geodetic laboratory (Blewitt et al. 2018; http://geodesy.unr.edu/NGLStationPages/stations/PAT0.sta) and b) by Briole et al (2021). PAT0 is located a few hundred metres to the SW of station GEDP, inside the U. Patras campus. The overall velocity trends between the two stations are in good agreement. We attribute the small differences in all three (3) velocity components to the short duration of the data for station GEDP (2 years) vs PAT0 (14 years) and to the different reference frames used (IGS20 for the low-cost data vs. ITRF14 for the permanent station data). The geology of the Patras University Campus (Palyvos et al. 2007) consists of Quaternary deposits, Plio-Pleistocene sedimentary rocks and unconsolidated soils. Characteristic lithologies include coastal sands, fluvial sands and gravels, Holocene deposits, weathering mantle of Plio-Pleistocene sediments, as well as alluvial and colluvial deposits.

A good agreement is also observed between the velocities of KRHN and KRIN (Table 1; see North and Up components). This station is located inside a slow-moving landslide on the eastern slope of mountain Panachaikon (Fig. 1), which is also monitored by InSAR (Tsironi et al. 2022). The Krini landslide is included in the landslide inventory of north Peloponnese (Koukis et al. 2009) and its formation/activation is attributed to a combination of lithology (Flysch), rainfall and proximity to the large active faults of the Gulf of Corinth. We note that station KRHN is co-located with a NOA meteorological station https://penteli.meteo.gr/stations/krini/ so that the GNSS displacement pattern may correlated with rainfall intensity and duration, especially during winter months. Such a correlation was already found for station KRIN (Tsironi et al. 2022).

Table 1. GNSS station velocities (East, North, Up) and their uncertainties. Values are in mm/yr. Station KRIN and PAT0[1] velocities are after Briole et al. (2021), PAT0 are after the Nevada Geodetic Laboratory (Blewitt et al. 2018).

Point	vEast	vE-unc	vNorth	vN-unc	vUp	vU-unc
KRHN	77.63	0.77	-27.17	0.58	-18.44	4.15
KRIN	111.60	1.30	-31.30	0.60	-19.70	1.30
GEDP	11.03	0.84	-4.03	0.74	-2.22	1.72
PAT0	8.14	0.21	-6.21	0.21	-0.46	0.72
PAT0[1]	8.10	0.30	-5.80	0.30	-0.30	0.60

Acknowledgements

This research has been co financed by the European Union and Greek national funds through the Operational Program Competitiveness, Entrepreneurship and Innovation, under the call RESEARCH – CREATE – INNOVATE (project code: T2EΔK-02396 *Multiparametric monitoring platform with micro-sensors of eNceladus hellenIc supersite*). We thank Vassiliki Charalampopoulou, Theodoros Athanassopoulos, Aggeliki Kyriou, Konstantinos Exarchos, George Bozionelos, Stratos Liadopoulos, Pierre Briole and Panagiotis Elias for their help with network setup and discussions. The low-cost GNSS rinex data are distributed open-access and are available at http://194.177.194.200/GPS/GEDP/ and http://194.177.194.200/GPS/KRHN/.

References

Blewitt, G., W.C. Hammond, C. Kreemer, 2018, Harnessing the GPS Data Explosion for Interdisciplinary Science, Eos, 99, https://doi.org/10.1029/2018EO104623

Bos, M.S., Fernandes, R.M.S., Williams, S.D.P., Bastos, L. 2013. Fast error analysis of continuous GNSS

observations with missing data. J. Geodesy 2013, 87, 351–360.

Briole, P., A. Ganas, P. Elias, D. Dimitrov, 2021. The GPS velocity field of the Aegean. New observations, contribution of the earthquakes, crustal blocks model, Geophysical Journal International, Volume 226, Issue 1, Pages 468–492, https://doi.org/10.1093/gji/ggab089

Ganas, A., Marinou A, Anastasiou D., Paradissis D., Papazissi K., Tzavaras P., Drakatos G. 2013. GPS-derived estimates of crustal deformation in the central and north Ionian Sea, Greece: 3-yr results from NOANET continuous network data. Journal of Geodynamics, 67, 62– 71. http://dx.doi.org/10.1016/j.jog.2012.05.010

Ganas, A., Elias, P., Briole, P., Cannavo, F., Valkaniotis, S., Tsironi, V., Partheniou, E.I. 2020. Ground Deformation and Seismic Fault Model of the M6.4 Durres (Albania) Nov. 26, 2019 Earthquake, Based on GNSS/INSAR Observations. Geosciences, 10 (6), 210 https://doi.org/10.3390/geosciences10060210

Ganas, A., I. Karamitros, G. Mavropoulos, D. Anastasiou, T. Athanassopoulos, K. Nikolakopoulos, A. Kyriou, C. Kontopoulos, V. Charalampopoulou, V. Tsironi, 2022. A New Low-Cost GNSS and Strong Motion Instrument for Monitoring of Slopes and Critical Infrastructures Within the Greek “Supersite”. SafeThessaloniki 2022 – 9th International Conference on Civil Protection & New Technologies, 29 September-1 October, pp. 117-120, SafeThessaloniki 2022 Proceedings, ISSN 2654-1823

Ganas, A., Mavropoulos, G., Karamitros, I., Nikolakopoulos, K., Charalampopoulou, V., Anastasiou, D., Athanassopoulos, T., Kyriou, A., and Tsironi, V. 2024 A new low-cost GNSS instrument for monitoring of ground motions and critical infrastructures within the Greek “Supersite”, EGU General Assembly 2024, Vienna, Austria, 14–19 Apr 2024, EGU24-10188, https://doi.org/10.5194/egusphere-egu24-10188

Geng J, Chen X, Pan Y, Mao S, Li C, Zhou J, Zhang K, 2019. PRIDE PPP-AR: an open-source software for GPS PPP ambiguity resolution. GPS Solutions, 23(91):1-10. doi:10.1007/s10291-019-0888-1

Koukis, G., Sabatakakis, N., Ferentinou, M. et al. 2009. Landslide phenomena related to major fault tectonics: rift zone of Corinth Gulf, Greece. Bull Eng Geol Environ 68, 215–229. https://doi.org/10.1007/s10064-008-0184-8

Nikolakopoulos, K., V. Mpelogianni, P. Groumpos, A. Kyriou, A. Ganas, V. Charalampopoulou, and T. Athanasopoulos, 2023. Soft computing algorithms for infrastructure monitoring: preliminary results of PROION project. Proc. SPIE 12786, Ninth International Conference on Remote Sensing and Geoinformation of the Environment (RSCy2023), 127861S (21 September 2023); https://doi.org/10.1117/12.2680702

Palyvos, N., Pantosti, D., Stamatopoulos, L., & De Martini, P. M. 2007. Geomorphological reconnaissance of the Psathopyrgos and Rion-Patras Fault zones (Achaia, NW Peloponnesus). Bulletin of the Geological Society of Greece, 40(4), 1586–1598. https://doi.org/10.12681/bgsg.17063

Partheniou, E., A. Ganas and Sakkas V., 2019. Ground deformation from GNSS data following strong Ionian Sea earthquakes in 2014 and 2015: co-seismic offsets and station baseline changes. Bull. Geological Society of Greece, Special Publication 7, pp. 253-254.

Tsironi, V., Ganas, A., Karamitros, I., Efstathiou, E., Koukouvelas, I., Sokos, E. 2022. Kinematics of Active Landslides in Achaia (Peloponnese, Greece) through InSAR Time Series Analysis and Relation to Rainfall Patterns. Remote Sens., 14(4), 844. https://doi.org/10.3390/rs14040844

17th INTERNATIONAL CONGRESS of the Geological Society of Greece

BULLETIN OF THE GEOLOGICAL SOCIETY OF GREECE, SP. PUBL.

EXTENDED ABSTRACT 083

Geodetic monitoring of the 2024-2025 Santorini volcanic unrest using GNSS and InSAR data: preliminary results

Ganas A.[1], Briole P.[2], Tsironi, V.[1], Goutsos, G.[1], Madonis N.[1], Liadopoulos E.[1], Mintourakis, I.[1]
(1) National Observatory of Athens, Institute of Geodynamics, Athens, Greece aganas@noa.gr
(2) UMR 8538 CNRS - École Normale Supérieure - PSL, France

Abstract

Santorini is an active stratovolcano emplaced within a region of extensional faulting in South Cyclades, Greece. A two-month-long seismic crisis reaching Amorgos (NE of Santorini), together with GNSS measurements made before and during the crisis, provide insights into the relations between the volcano dynamics and its surroundings. The GNSS data show that Santorini inflated since the summer of 2024. We model this inflation with a magma source of ~ 8 × 10^6 m^3 located ~3.5 km under the north-central floor of the caldera, near the inflation centre of 2011-2012. The inflation phase ceased around 20 January 2025. Contemporaneously, the seismic activity, shifted to the north-east of Santorini near the islet Anydros. This phase lasted about ten days, before leading into a most intense phase that produced ground deformation measurable at large distances over the South Cyclades.

Introduction - Data and Methods

The Santorini volcanic Centre (Fig. 1; Thera, Thirasia, Kammeni etc.) is located within the Aegean micro-plate, which overrides the subducting Tethys lithosphere in a SSW direction. The subduction of Africa over the Cenozoic resulted in calc-alkaline volcanism which is presently distributed along the South Aegean Volcanic Arc, comprising volcanic islands of Quaternary age. The Santorini volcano has been activated during the historical era, producing important explosive eruptions (e.g., Parks et al. 2012). The seismicity of the broader area is related to the Quaternary NW-SE extensional regime, as well as to the volcanic processes (Bohnhoff et al., 2006; Dimitriadis et al., 2009; Briole et al. 2021). In 2011 - 2012, ground deformation was detected by use of GPS and Envisat satellite data confirmed that Santorini have risen as much as 14 cm between January 2011 and March 2012 (Papoutsis et al., 2013).

Since the summer of 2024 the Santorini volcanic Centre entered a new phase of unrest as GNSS data indicate the start of deformation onshore Thera, followed by an increase of the seismicity rates since January 2025. The seismic events were detected first inside the caldera, then spreading with intense activity towards the northeast until the islet Anydros, spanning an overall distance of 30 km, displaying a NE-SW orientation (Figure 1). The seismicity pattern indicates swarm characteristics with larger events not exceeding M_L = 5.3 according to the catalogue of the National Observatory of Athens (NOA, https://www.gein.noa.gr/services/cat.html). This intense phase generated significant activity in the Greek and international scientific community, which worked together to provide rapid scientific assessments of the phenomenon for the purposes of crisis management by the authorities. Figure 1 shows a map of the seismicity and the active faults (ticks on the downthrown block) from the NOAFAULTs database (Ganas, 2024).

In this extended abstract, we analyse the geodetic observations from eleven GNSS stations (Fig. 1): four located on Santorini, including two operating in 2011-2012 and used in previous works (e.g. Lagios et al., 2013), six located on the neighbouring islands, and one installed on 12 February on the islet of Anydros near the centre of the crisis. Figure 2 shows the time series of coordinates (East, North, Up) of GNSS station SANT calculated using the SCRS-PPP software. We also used InSAR time series analysis (ESA Copernicus satellite imagery) to monitor the ground deformation (Figure 3). A sequence of deformation phases appears in the time series of coordinates. There is initially a slow inflation starting during summer 2024, then a second phase that starts around January 20 and lasts until around February 3, followed by the most intense phase that ends on February 16. A fourth phase is underway at the time of writing this extended abstract. The second phase correlates in time with the seismicity shift to the north-east of Santorini. We model this inflation using the software WebObs (Beauducel et al. 2020; Briole et al. 2017) with a magma source of ~ 8 × 10^6 m^3 located ~3.5 km under the north-central floor of the caldera, near the inflation centre of 2011-2012. The inflation phase ceased around 20 January 2025.

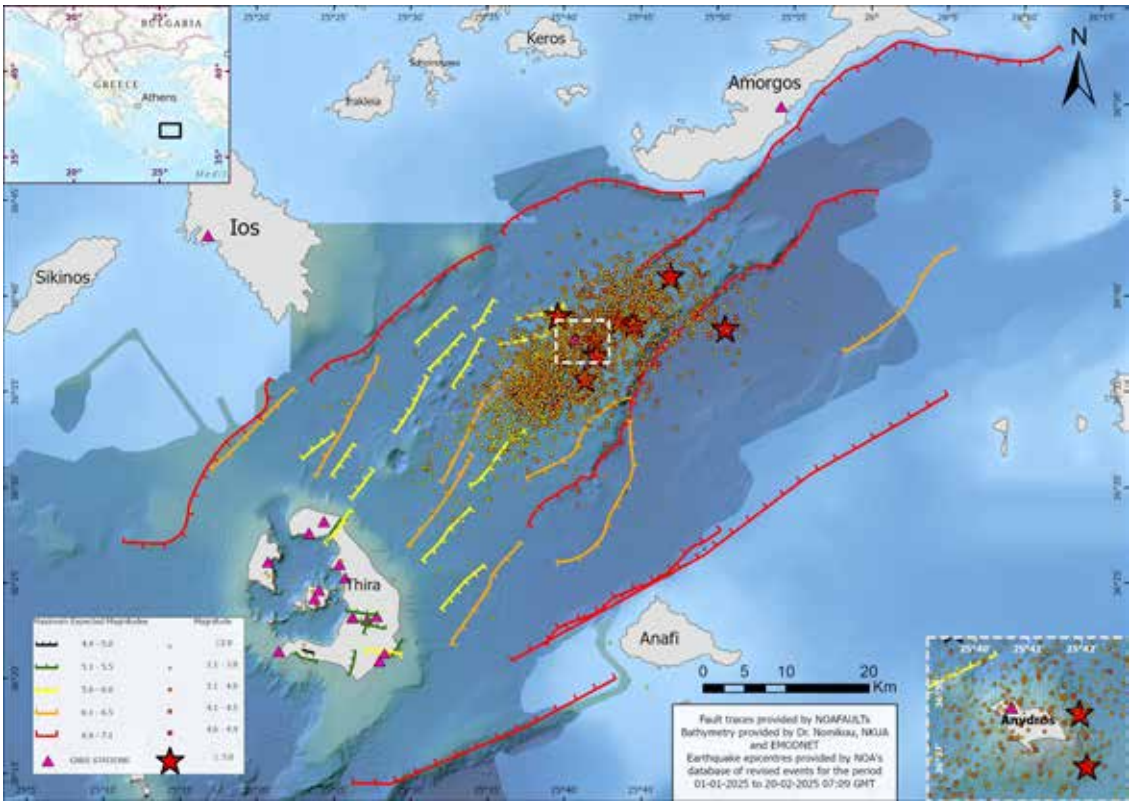

Figure 1. Location map showing GNSS stations (solid triangles) in South Cyclades and earthquake epicentres from the NOA seismicity catalog. Inset map shows location of study area within Greece.

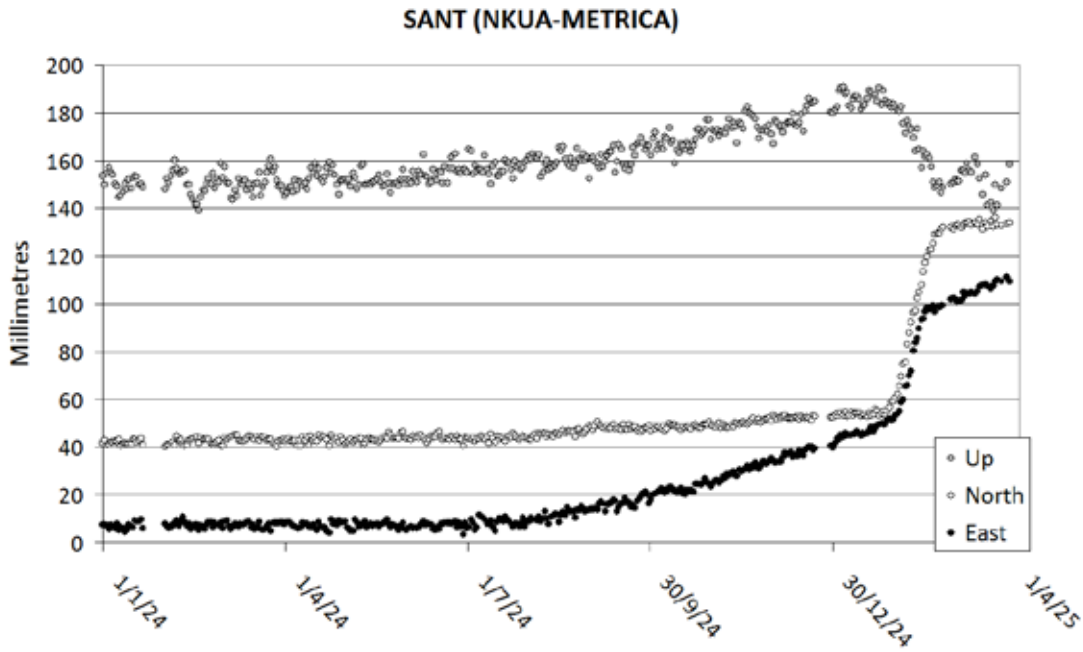

Figure 2. Graph showing time series of coordinates (East, North, Up) of GNSS station SANT (period 1/1/2024-25/3/2025).

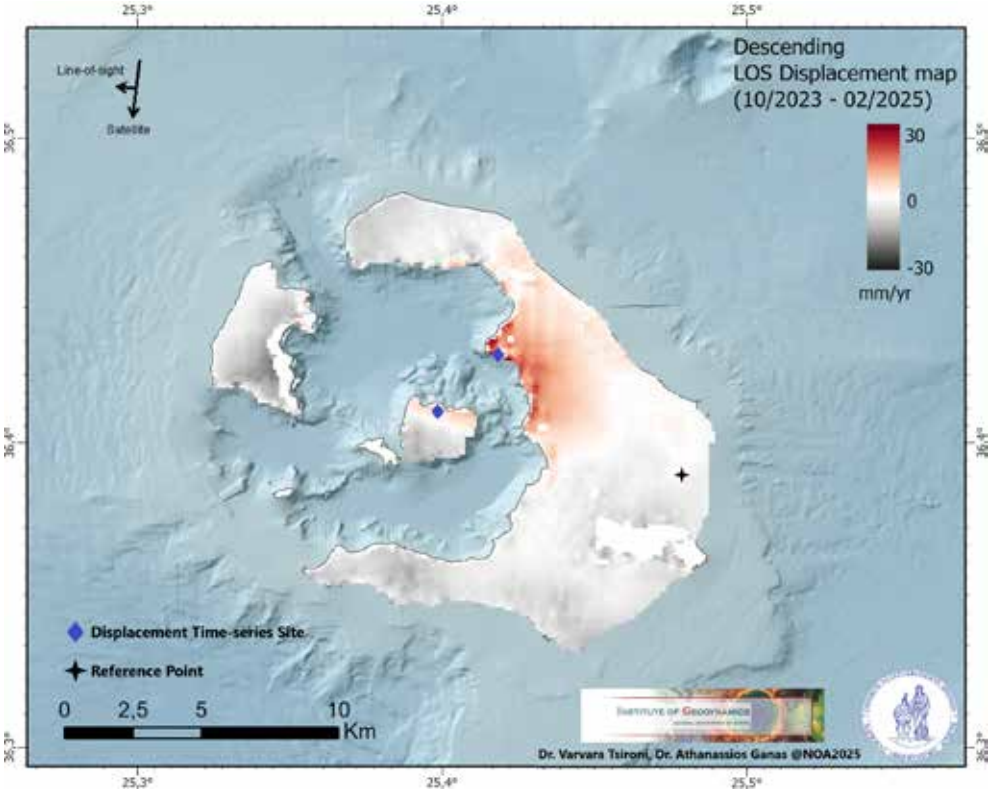

Figure 3. Map of Santorini showing InSAR displacement time series (descending orbit).

Acknowledgements

We acknowledge funding of this research by the project "*SAT4GAIA"*. We thank Betty Charalampopoulou for administrative support. We are indebted to Francois Beauducel, Costas Synolakis, Paraskevi Nomikou, Dimitris Anastasiou and Vassilis Sakkas for discussions. The GNSS data used in this letter are made available by public and private GNSS networks of Greece under the coordination of the Greek Earthquake Planning & Protection Organisation (EPPO, https://oasp.gr/en). The following networks are gratefully acknowledged: HEPOS, NOANET, AUTH-ISMOSAV, NKUA, NTUA, HxGn-METRICA, URANUS & JGC. The geodetic equipment for the Anydros station was provided by the University of Patras (Panagiotis Elias). The GNSS campaigns and station installations were supported by the Hellenic Ministry of the Civil Protection, the Municipalities of Thera, Anafi, Amorgos, Iraklia and Sikinos. The faults mapped in Figure 1 are the "NOAfaults" available at http://doi.org/10.5281/zenodo.4304613

References

Briole, P., A. Ganas, P. Elias, D. Dimitrov, 2021. The GPS velocity field of the Aegean. New observations, contribution of the earthquakes, crustal blocks model, Geophysical Journal International, Volume 226, Issue 1, Pages 468–492, https://doi.org/10.1093/gji/ggab089

Beauducel, F., Lafon, D., Béguin, X., Saurel, J.M., Bosson, A., Mallarino, D., Boissier, P., Brunet, C., Lemarchand, A., Anténor-Habazac, C., Nercessian, A. & Fahmi, A.A., 2020. WebObs: The volcano observatories missing link between research and real-time monitoring, Frontiers in Earth Sciences, 8, https://doi.org/10.3389/feart.2020.00048

Bohnhoff, M., Rische, M., Meier, T., Becker, D., Stavrakakis, G. & Harjes, H.-P., 2006. Microseismic activity in the Hellenic Volcanic Arc, Greece, with emphasis on the seismotectonic setting of the Santorini–Amorgos zone, Tectonophysics, 423(1–4), 17–33, https://doi.org/10.1016/j.tecto.2006.03.024

Briole, P., 2017. Modelling of earthquake slip by inversion of GNSS and InSAR data assuming homogeneous elastic medium, Zenodo, http://doi.org/10.5281/zenodo.1098399

Briole, P., Ganas, A., Elias, P. & Dimitrov, D., 2021. The GPS velocity field of the Aegean. New observations, contribution of the earthquakes, crustal blocks model, Geophysical Journal International, 226(1), 468-492, https://doi.org/10.1093/gji/ggab089

Dimitriadis, I., Karagianni, E., Panagiotopoulos, D.G., Papazachos, C., Hatzidimitriou, P., Bohnhoff, M., Rische, M. & Meier, T., 2009. Seismicity and active tectonics at Coloumbo Reef (Aegean Sea, Greece): monitoring an active volcano at Santorini Volcanic Center using a temporary seismic network, Tectonophysics, 465, 136–149, https://doi.org/10.1016/j.tecto.2008.11.005

Ganas, A., 2024. NOAFAULTS KMZ layer Version 6.0 (version 6.0) [Data set]. Zenodo. https://doi.org/10.5281/zenodo.13168947

Lagios, E., Sakkas, V., Novali, F., Bellotti, F., Ferretti, A., Vlachou, K. & Dietrich, V., 2013. SqueeSAR™ and GPS ground deformation monitoring of Santorini Volcano (1992-2012): Tectonic implications, Tectonophysics, 594, 38-59, https://doi.org/10.1016/j.tecto.2013.03.012

Newman, A. V., S. Stiros, L. Feng, P. Psimoulis, F. Moschas, V. Saltogianni, Y. Jiang, C. Papazachos, D. Panagiotopoulos, E. Karagianni, and D. Vamvakaris (2012), Recent geodetic unrest at Santorini Caldera, Greece, Geophys. Res. Lett., 39, L06,309.

Papoutsis, I., Papanikolaou, M., Floyd, K., Ji, H., Kontoes, C., Paradissis, D. & Zacharis, V., 2013. Mapping inflation at Santorini volcano, Greece, using GPS and InSAR, Geophysical Research Letters, 40, 267-272, https://doi.org/10.1029/2012GL054137

Parks, M.M., Biggs, J., England, P., Mather, T.A., Nomikou, P., Palamartchouk, K., Papanikolaou, X., Paradissis, D., Parsons, B., Pyle, D.M., Raptakis, C. & Zacharis,V., 2012. Evolution of Santorini Volcano dominated by episodic and rapid fluxes of melt from depth, Nature Geosciences, 5, 749-754, https://doi.org/10.1038/ngeo1562

17th INTERNATIONAL CONGRESS of the Geological Society of Greece

BULLETIN OF THE GEOLOGICAL SOCIETY OF GREECE, SP. PUBL.

EXTENDED ABSTRACT 084

Geodetic monitoring of the Methana volcano (central Greece) using campaign GNSS data: preliminary results

Ganas A.[1], Carnemolla F.[2], Karamitros, I.[1], Madonis N.[1], Georgakopoulos V.[1]
(1) National Observatory of Athens, Institute of Geodynamics, Athens, Greece aganas@noa.gr
(2) University of Catania, Department of Biological, Geological and Environmental Sciences, Catania, Italy

Abstract

This work presents the results from six (6) years of GNSS campaign observations on the Methana volcano, central Greece. The observations were collected by occupying five (5) benchmarks using dual frequency geodetic receivers during the period 2018 – 2024. The Methana data set was processed to obtain 24-h position solutions using the GIPSY-X software. For the first time, the displacement velocities of the NOA campaign GNSS stations have been estimated to provide additional geodynamic information in an active volcano area with two permanent stations.

Introduction

Methana peninsula is an active volcano, approximately 50 kilometres southwest of Athens (Central Greece, Fig. 1). The last onshore eruption took place in 230 BC in the Kameni Chora lava dome while the last offshore took place in 1700 AD north of Kameni Chora at a submarine volcano. Methana consists of mostly andesitic and dacitic rocks comprising lava flows and domes (Suesskoch et al. 1984). Volcanic domes are the most characteristic features of Methana, and are primarily andesitic to dacitic composition, are widely distributed across Methana and concentrated in the northern and central areas. They are marked by steep topographies and rugged terrains. Their widespread distribution points to multiple centers of volcanic activity over an extended geologic timeframe. A major increase in volcanic products has been determined at about 0.29–0.34 Ma (Pe-Piper and Piper, 2013), mostly on E–W faults, that was followed by minor andesite flows in the NW of the peninsula. In addition, the available magnetotelluric data (Tzanis et al. 2020) detected what appears to be a geothermal reservoir located underneath the central domes at a depth of approximately 1 km below sea level.

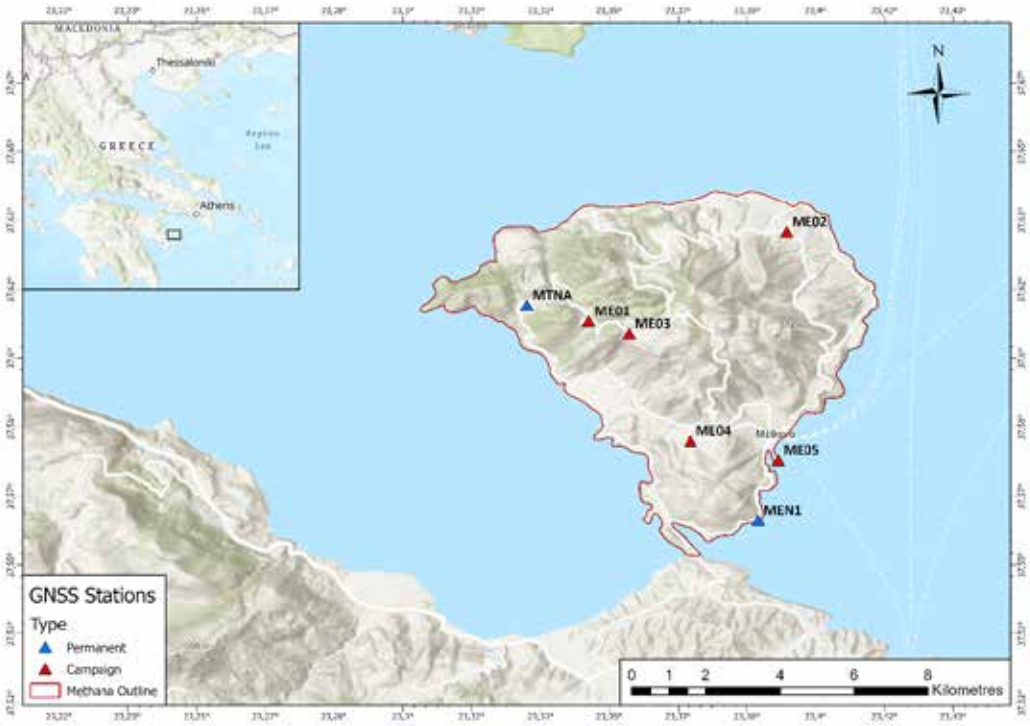

Figure 1. Relief map showing GNSS stations (solid triangles) in Methana peninsula. Inset map shows Methana location.

Data and Methods

In active volcanoes it is essential to sample the deformation field thoroughly in both time and space to adequately a) map the pattern of ground changes as well as the speed and direction of movement and b) constrain volcanic source models. Surface displacements, tilts, and dilatation are easily measurable with modern geodetic techniques, such as the Global Navigation Satellite System (GNSS; Ganas et al. 2016; Briole et al. 2021).

In 2018 NOA established a local network of five (5) geodetic benchmarks around Methana volcano (Table 1, Fig. 1). The local network was established on 20 and 21st October 2018 by Dr Athanassios Ganas and Mr. Ioannis Karamitros, MSc geologist. All points were selected on bedrock areas, either volcanic or limestone, so that we make sure our data products record either tectonic or volcanic motions. The benchmarks were drilled inside the bedrock and metallic bolts were placed (Fig. 2). Episodic measurements have been conducted on this network on a yearly basis since then by use of dual-frequency geodetic receivers. With a combination of repeated GNSS 3-D surveys and continuous monitoring by 1-D InSAR (i.e., Gatsios et al. 2020), it is now possible to measure ground deformation over broad areas in all sides of the volcano and with satisfactory temporal and spatial resolution.

Measurements have been conducted on the local network in 2018, 2019, 2020, 2023 and 2024 with dual-frequency GNSS receivers (LEICA GS08+). The data sampling interval was 10-s & 15 s, and the data were collected on an 8 h basis (2018 and 2019) and on 24-48 hrs (2020 onwards). The RINEX files contain 8 observables of GPS satellites: C1C L1C D1C S1C C2W L2W D2W S2W. All station records were complete. Each station has been analyzed independently using the Precise Point Positioning (PPP) method which computes coordinates of each station separately. The Methana data set was processed to obtain 24-h position solutions using the GIPSY-X software (version 2.2; Bertiger et al., 2020). The processing was performed using the final fiducial-free GPS orbits computed by the Jet Propulsion Laboratory. Ocean tidal loading was modeled using the FES2004 ocean tidal model (Lyard et al., 2006) and the wet zenith troposphere was modeled by the Global mapping Function (Boehm et al., 2006). Moreover, we used the antenna calibration file provided by the IGS and the second order ionospheric correction.

Table 1. List of the NOA local GNSS network locations around the Methana Volcano.

Point	Location	LONG	LAT	Occupation
ME01	Agia Sotira	23.345	37.609	2018, 2019, 2020, 2023, 2024a, 2024b
ME02	Agios Georgios	23.392	37.630	2018, 2019, 2020, 2023, 2024a
ME03	Lava dome Melissa	23.354	37.606	2018, 2019, 2020, 2023, 2024a
ME04	Dritsaiika	23.369	37.580	2018, 2019, 2020, 2023, 2024a, 2024b
ME05	Light House	23.390	37.575	2018, 2019, 2020, 2023, 2024b

Figure 2. Field photographs of GNSS measurements in Methana (2018 – 2019 campaigns).

Results and Conclusions

The Methana volcano geodetic data were sampled at 10-s & 15-s intervals, however, for data processing the RINEX files were resampled at 30-s. This is normal when daily coordinates are computed because the default GIPSY-X configuration is to process 30-s RINEX files. In addition, the station velocities were computed directly by GIPSY-X. The software has a set of scripts (*NetSplit.py*, *staFit.py, staSeries.py* etc.) able to compute time series, to detect outliers and to fit seasonal terms and finally to calculate the East, North & Vertical (Up) velocities based on the position time series. The velocities were estimated on the IGS20 reference frame (Table 2).

Geodetic monitoring using campaign observations could present significant drawbacks compared to continuous GNSS stations, mainly in the lack of data continuity, lower precision, and inability to monitor short-term phenomena (transients) or provide real-time data. Nevertheless, the recorded data quality of the Methana campaigns is high (Fig. 3; results from the Anubis software, open-source version). The GNSS velocity vectors of all volcano stations with available data are plotted in Fig. 4 (red are campaign, blue are permanent). There is notable agreement in the North component of the velocity between the neighbouring stations ME05 – MEN1 and MTNA – ME01 but there is a deviation on the East component which is under investigation.

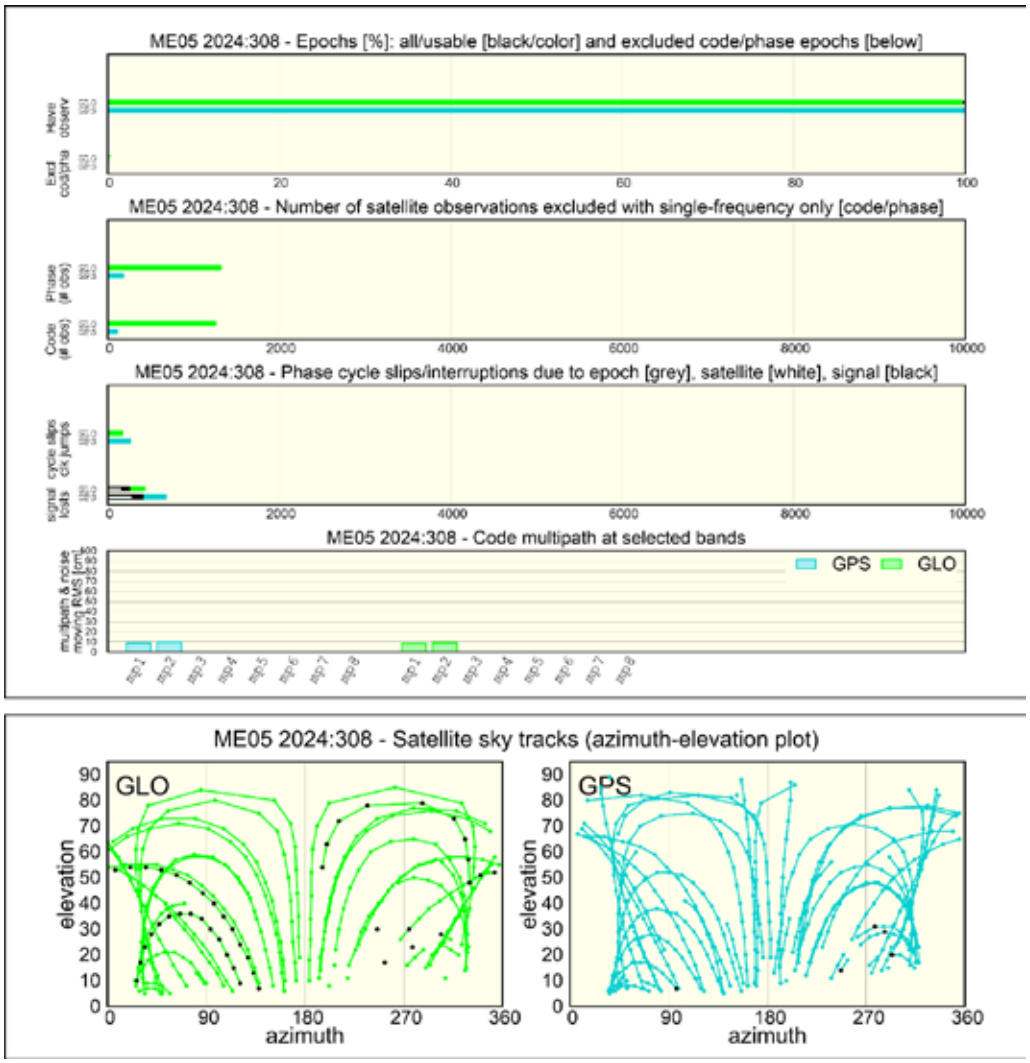

Figure 3. Data quality plot (GPS and GLONASS satellites) for station MEO5 (year 2024 DOY 308): upper panel) quality metrics for satellite observations, bottom panel) sky satellite tracks plot.

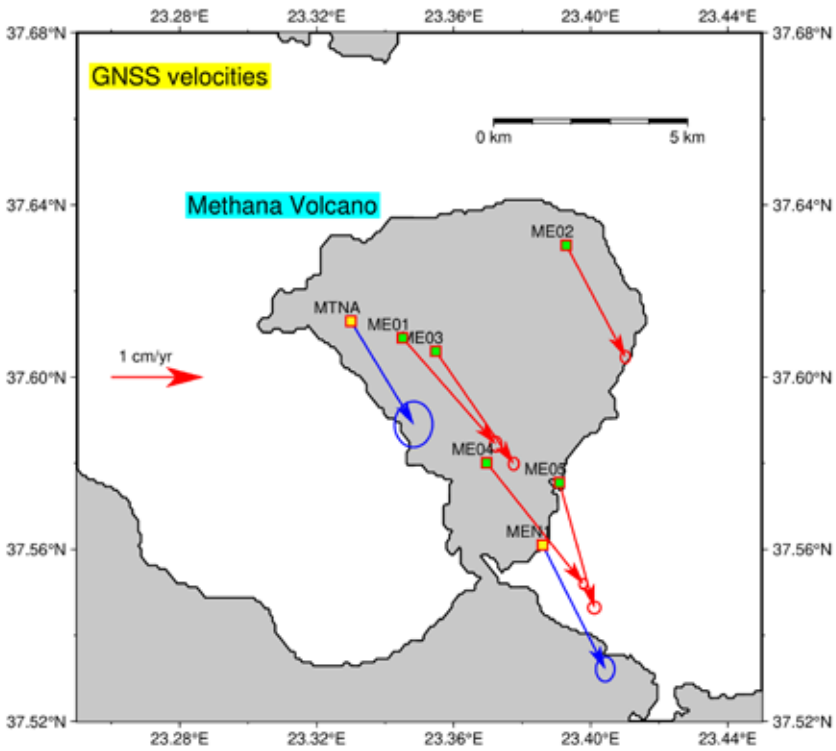

Figure 4. Map showing GNSS velocity vectors on the Methana volcano (campaign period 2018-2024). Blue vectors show permanent stations processed by NGL.

Table 2. GNSS station velocities (East, North, Up) and their uncertainties. The reference frame is IGS20 for the campaign stations and ITRF2014 for the permanent ones, respectively. Station MTHA velocities are provided by the EPOS Analysis Centre SGO-EPND and NTUA (Anastasiou and Papanikolaou pers. Commun.). NGL is the Nevada Geodetic Laboratory solution (Blewitt et al. 2018). Values are in mm/yr. Station MTHA, MENA and MEN1 are the same site with different code names. MTNA is an EPOS GNSS stations (EPOS, 2025).

Point	vEast	vE-unc	vNorth	vN-unc	vUp	vU-unc	Solution
ME01	10.11	0.26	-11.51	0.33	2.17	1.82	This study
ME02	6.41	0.21	-12.12	0.27	-1.23	1.02	This study
ME03	8.44	0.23	-12.20	0.28	0.73	1.05	This study
ME04	10.47	0.18	-13.13	0.23	-4.80	0.81	This study
ME05	3.79	0.28	-13.54	0.27	-2.39	1.43	This study
MTHA	7.12	0.14	-12.68	0.17	-0.55	0.18	SGO-EPND
MTHA	6.79	0.08	-13.08	0.26	-0.84	0.71	NTUA
MENA	7.20	0.30	-13.10	0.40	0.20	1.20	Briole et al. 2021
MEN1	6.78	0.41	-13.45	0.55	0.29	1.63	NGL
MTNA	6.79	0.84	-11.18	1.01	-1.66	3.57	NGL

Acknowledgements
We acknowledge support of this research by the project "*GEORISK – Developing Infrastructure and Provision of Services through Actions of Excellence to Reduce the Impact of Geodynamic Hazards*"

(MIS 5002541) which is implemented under the “Action for the Strategic Development of Research and Technology Organizations”, funded by the Operational Programme “Competitiveness, Entrepreneurship and Innovation” (NSRF 2014-2020) and co-financed by Greece and the European Union (European Regional Development Fund). We thank the four reviewers for constructive comments and our NOA colleagues Dr. G. Drakatos and Dr. Ch. Evangelidis for their administrative support. We are indebted to Ass. Prof. Dimitris Anastasiou and Dr V. Tsironi for discussions.

References

Bertiger, W., Bar-Sever, Dorsey, Y. A., Haines, B., Harvey, N., Hemberger, D., et al. 2020. GipsyX/RTGx, a new tool set for space geodetic operations and research. Advances in Space Research, 66(3), 469–489. https://doi.org/10.1016/j.asr.2020.04.015

Boehm, J., A. Niell, P. Tregoning, and H. Schuh, 2006. Global Mapping Function (GMF): A new empirical mapping function based on numerical weather model data, Geophys. Res. Lett., 33, L07304. https://doi.org/10.1029/2005GL025546.

Blewitt, G., Hammond, W. C., and Kreemer, C. 2018. Harnessing the GPS data explosion for interdisciplinary science, Eos, 99, https://doi.org/10.1029/2018EO104623.

Briole, P., A. Ganas, P. Elias, D. Dimitrov, 2021. The GPS velocity field of the Aegean. New observations, contribution of the earthquakes, crustal blocks model, Geophysical Journal International, 226, 1, 468–492, https://doi.org/10.1093/gji/ggab089

EPOS, 2025 (web site accessed 15 January 2025): https://gnss-metadata.eu/MOID/station.5e67e28bc074fb07db56feb2

Ganas, A., Chousianitis, K., Argyrakis, P., Tsimi, C., Papanikolaou, M., Papathanassiou, G., & Exarchos, K. 2016. Monitoring of surface displacements in the Kalochori area (Thessaloniki, Greece) using a local GNSS network. Bulletin of the Geological Society of Greece, 50(3), 1553-1562. http://dx.doi.org/10.12681/bgsg.11869

Gatsios, T., Cigna, F., Tapete, D., Sakkas, V., Pavlou, K., & Parcharidis, I. 2020. Copernicus Sentinel-1 MT-InSAR, GNSS and Seismic Monitoring of Deformation Patterns and Trends at the Methana Volcano, Greece. Applied Sciences, 10(18), 6445. https://doi.org/10.3390/app10186445

Lyard, F., Lefevre, F., Letellier, T. et al. 2006. Modelling the global ocean tides: modern insights from FES2004. Ocean Dynamics 56, 394–415. https://doi.org/10.1007/s10236-006-0086-x

Pe-Piper, G., Piper, D.J.W., 2013. The effect of changing regional tectonics on an arc volcano: Methana, Greece. J Volc. Geotherm. Research, 260, 146–163. https://doi.org/10.1016/j.jvolgeores.2013.05.011 .

Suesskoch, H., Bannert, D., Kalkreuth, W., Walliner, P., Strauss, M., Fytikas, M., Mazzuoli, R., 1984. Methana sheet, 1:50000 Geological Map of Greece. IGME, Athens.

Tzanis, A., A. Efstathiou, S. Chailas, E. Lagios, M. Stamatakis, 2020. The Methana Volcano – Geothermal Resource, Greece, and its relationship to regional tectonics. J Volc. Geotherm. Research, 404, 107035, https://doi.org/10.1016/j.jvolgeores.2020.107035

17th INTERNATIONAL CONGRESS of the Geological Society of Greece

BULLETIN OF THE GEOLOGICAL SOCIETY OF GREECE, SP. PUBL.

EXTENDED ABSTRACT 085

Integrated monitoring of the Milos geothermal site (Cyclades, Greece) using InSAR, GNSS and local seismic network data

Ganas A.[1], Kapetanidis, V.[2], Tsironi, V.[1], Karakonstantis, A.[2], Karamitros, I.[1]
(1) National Observatory of Athens, Institute of Geodynamics, Athens, Greece aganas@noa.gr
(2) National and Kapodistrian University of Athens, Department of Geology and Geoenvironment, Athens, Greece

Abstract

In this short paper, we update on the findings of a joint geodetic and seismological investigation of Milos (western Cyclades islands, Greece) since 2022 when we published out first short report in BGSG. The integrated monitoring includes the use of geodetic data (InSAR and GNSS) and the continuous recordings of a 24/7/365 local seismic network established by NOA in 2021 and upgraded in 2023. Our objective was to investigate the ground deformation and seismicity patterns and detect activity along fault zones of the island. We present evidence for on-going activity at 5-9 km depths along a NW-SE fault crossing Milos.

Introduction

The South Aegean Volcanic Arc (Kassaras et al. 2020), and in particular the Milos Island in western Cyclades offers a high potential for deep geothermal energy due to the well-known geothermal anomaly (Fytikas, 1977). Milos is a dormant stratovolcano with the most recent volcanic activity recorded about 380 ka-90 ka ago (Fytikas et al., 1986). The oldest K-Ar date on the lowest volcanic outcrops in the SW coast of Milos, gave an age of 3.5 Ma. Basement rocks occur in the SW, S and SE parts of the island. The seismicity around Milos is both shallow (4-15 km; Ganas et al. 2022) and intermediate depth (70-90 km), however, until 2021no clear patterns had emerged due to the lack of sufficient seismic stations. Several swarms have been reported in the literature, linking seismicity and ascent of magmatic fluids but without strong evidence (Sachpazi and Hirn, 1991; Baltatzis et al., 2001).

Figure 1. Relief map showing seismic stations (blue marks) and GNSS stations (red marks) in Milos Island. Inset map shows location of Milos in the south Aegean Sea.

Based on detailed chemical and isotopic analyses Wu et al. (2011) identified three types of hydrothermal vent fluids at Milos: cave vents, submarine brine vents and seawater-like vents. Using this distinction of measured samples, they are suggesting a conceptual geological model that consists of a shallow reservoir (<248°C) which is separated from a deep reservoir (>313°C) where subcritical phase separation happens. This work presents the monitoring strategy and

the preliminary results. We installed a network of campaign & continuous GNSS (see Fig. 1) and INSAR Copernicus data are available in continuous processing (yearly rounds). Our aim is to monitor local surface displacements before and finally during the production states of the geothermal plants. GNSS and INSAR are two spatial geodetic methods with millimeter accuracy. GNSS provides information about the absolute 3D displacement at some point location while InSAR gives high spatial information (100-m pixel size) of relative displacement.

Data and Methods

During May 2021 and May 2023 NOA installed a local seismic network of seven (7) stations in the SE and East Milos (Fig. 1; blue dots). The sensors are GEOBIT C100 and were placed inside shallow (2-m) boreholes. Data telemetry is real-time (at 100 sps) using a commercial GSM network. The seismic network of Milos had a fair response to the main demands such as the increase in detectability of the local microearthquakes, as well as the characterization of seismic properties of the area such as the origin of the recorded noise (natural, anthropogenic). The earthquake magnitudes range from 0.4 to 3.4 on the local magnitude (M_L) scale. The recorded activity is mainly concentrated inside the Gulf of Adamas and in Southern Milos, along the NW-SE striking fault (Ganas et al. 2022), which might be associated with the March 1992 earthquake sequence (Delibasis and Drakopoulos, 1993; Papanikolaou et al. 1993). In 2021 NOA established a local network of three (3) geodetic benchmarks at SE Milos (Fig. 1). The local network was established on 25th September 2021 by Dr Athanassios Ganas and Mr. Ioannis Karamitros, MSc geologist. All sites were selected in bedrock areas, to ensure that our receivers record either tectonic or volcanic motions. The benchmarks were drilled inside the bedrock and metallic bolts were placed. Episodic measurements have been conducted on this network on a yearly basis since then by use of dual-frequency geodetic receivers. In May 2023 NOA installed a low-cost GNSS station in western Milos (Fig. 1; code MILN) following the procedures established by the project PROION (Ganas et al. 2024). This station started recording 1-s GNSS observations on 12 November 2024. With a combination of repeated GNSS 3-D surveys and continuous monitoring by 1-D InSAR (i.e., Tsironi et al. 2024), it will be possible to measure ground deformation over broad areas in all sides of the geothermal site of Milos, and with satisfactory temporal and spatial resolution.

In terms of SAR geodetic data (1-D displacement time series) we used archived SAR Copernicus imagery (C-band) (Fig. 2). For the InSAR time series analysis we applied the SBAS algorithm that is part of LiCSBAS, an open-source package (Morishita et al., 2020). The available interferograms from the LiCSAR platform include 828 (ascending orbit) and 771 (descending orbit, respectively. During the phase unwrapping, decorrelated areas in the interferograms are masked where the phase noise coherence is < 0.2. Wrapped and unwrapped interferograms were geocoded with a pixel spacing of 0.001 degree (~100 m) and converted to the GeoTIFF format. The accuracy of this technique is about 2-3 mm/yr (Morishita et al. 2020; Tsironi et al. 2024).

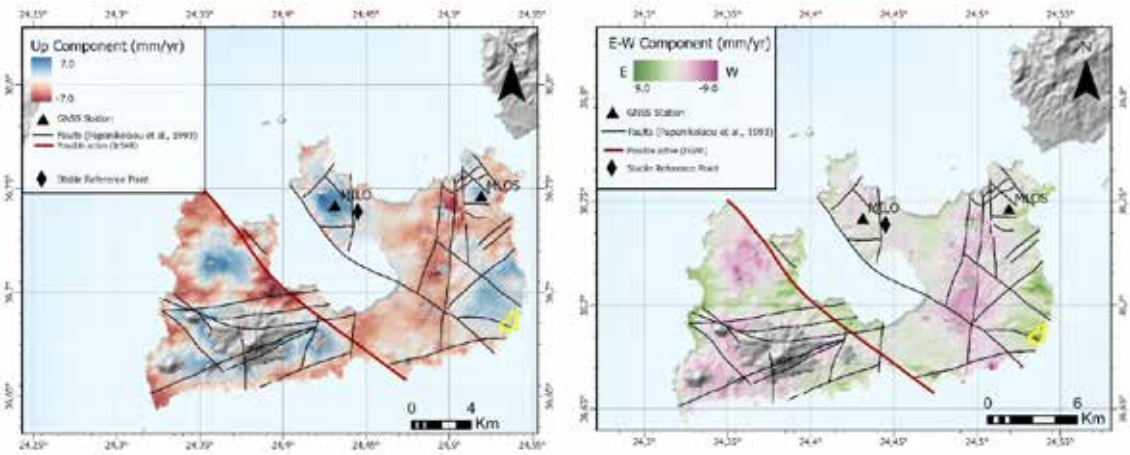

Figure 2. left panel) Up-Down ground motion map in units mm/yr, right panel) East-West velocity map based on InSAR data. Black lines indicate faults after Papanikolaou et al. (1993). The red line is an active fault based on InSAR. Diamond symbol indicates the reference point used in InSAR processing. MILO & MLOS are GNSS stations on the island. Grey areas indicate no data.

The InSAR data processing (period 2016-2024) resulted in the production of Up-Down and E-W velocity maps (Fig. 2; left is vertical and right is E-W motion) which indicates that there is divergent ground motion (opening) across the NW-SE fault onshore Milos (see red line in Fig. 2). The velocity difference across the fault reaches 1 cm/yr, that is well above the error. Moreover, the InSAR data provide evidence that this fault is active, and its surface trace can match an east-dipping fault plane where microseismicity is present (Fig. 3). A second area of interest is the mapped subsidence along the Zafeiria depression in east Milos (reaching 7 mm/yr.; Fig. 2 left) which abuts a N-S normal fault (west-dipping; Papanikolaou et al. 1993). The newly-installed GNSS station MILN will provide additional constraints to the InSAR results when its secular velocity is estimated with confidence (Fig. 3; after a period of 3-4 years; Briole et al. 2021). In western Milos there is no other geodetic point of reference while due to the rugged relief the atmospheric contribution to the InSAR signal may be considerable.

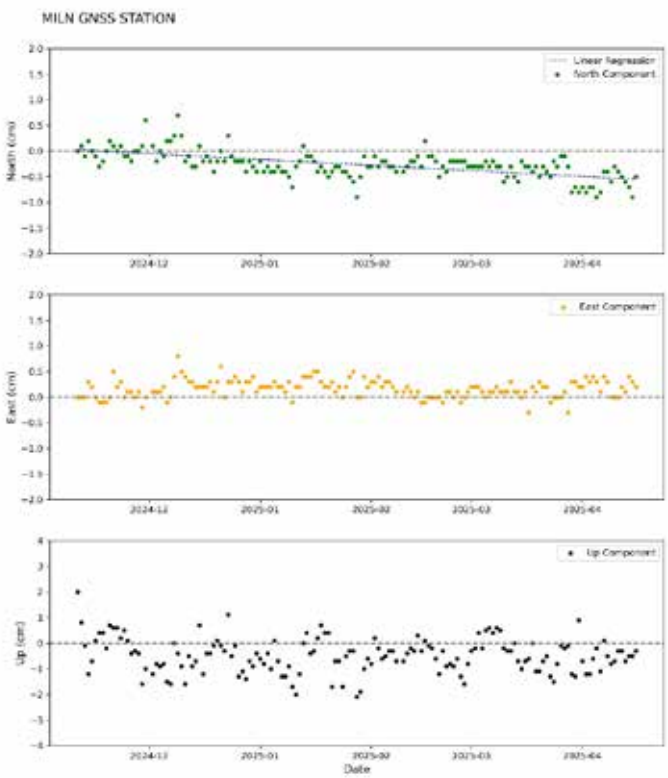

Figure 3. Graphs showing position time series of the low-cost GNSS station MILN (Agia Marina, western Milos). The daily positions were estimated with the on-line CSRS-PPP processing tool from the 30-s observations (code and phase) collected by the u-blox dual-frequency receiver and geodetic antenna. The panels show time series in North, East, Up components, respectively. Units in cm.

Results and Conclusions

During 2021-2024 the local seismic network recorded hundreds of microearthquakes in the broader Milos area, the majority of which occurred at shallow depths (< 10 km; Fig. 4). In order to improve the locations of hypocenters of the initial catalogue, which consists of 109 manually analyzed events and 589 additional detections made with the template matching technique (Chamberlain et al., 2018), we applied double-difference relocation with the HypoDD code (Waldhauser, 2001). Many small earthquakes are concentrated in the middle of the island (Gulf of Adamas) in tight spatial clusters, due to their strong waveform correlation. The clusters are aligned in a NW-SE orientation, following the strike of the main fault line that crosses Milos Island to the west of the epicenters (Papanikolaou et al. 1993). The overall length of

the seismicity belt is 8 km and it is located on the eastern side of the Gulf of Adamas and in the airport area. Fig. 4 shows a seismicity map, where different colours / sizes represent different depths / magnitudes. The map indicates that the clustered seismicity beneath the Gulf of Adamas is located at focal depths of 6±1 km. Assuming a dip of 60° towards NE for the main fault that bounds the western shores of the Gulf (Fig. 2), its plane would roughly cross the hypocenters. It should be noted, however, that for a more precise determination of the absolute hypocentral depths, a local velocity model is required. This could become possible with the accumulation of more data from the local network in the future.

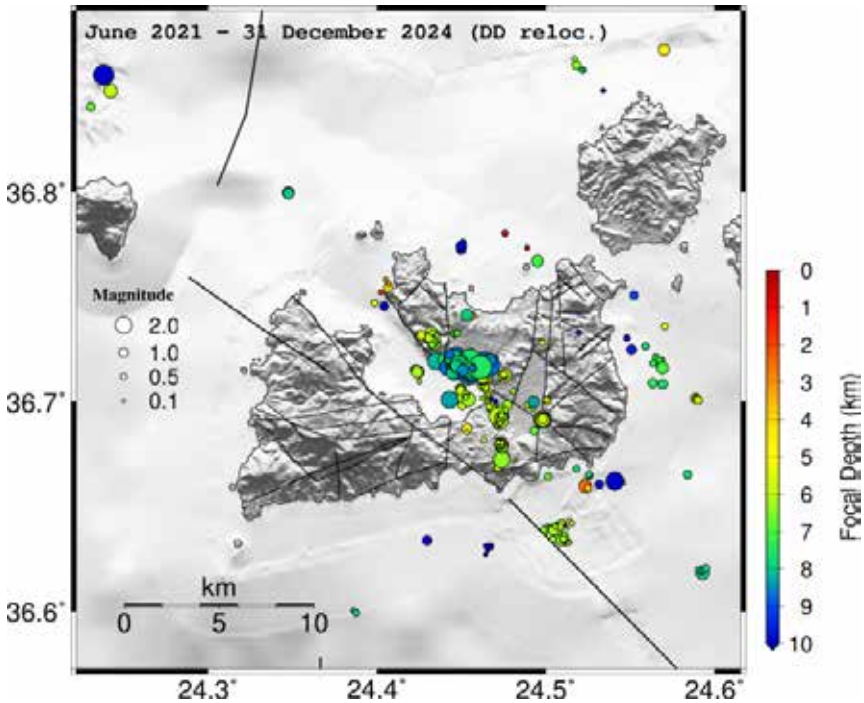

Figure 4. Seismicity map of Milos Island (period June 2021-2024) after relocation using the double-difference method (HypoDD).

Acknowledgements

We acknowledge support of this research by the project "*Seismological Monitoring of Milos Island"* funded by the Public Power Corporation Renewables SA (PPCR). The GNSS data from station MILN are freely available at http://194.177.194.200/GPS/MILN/ We thank Evangelos Spyridonos, Nikos Germenis, Konstantinos Exarchos, Nikolaos Madonis, Giorgos Goutsos and Stratos Liadopoulos for their help with network installations and data collection. We are indebted to our late colleague Ioannis Kassaras for discussions. We thank three reviewers for constructive comments. The views and opinions expressed in this paper are those of the contributors and do not necessarily reflect the views or positions of PPCR.

References

Briole, P., A. Ganas, P. Elias, D. Dimitrov, 2021. The GPS velocity field of the Aegean. New observations, contribution of the earthquakes, crustal blocks model, Geophysical Journal International, 226, 1, 468–492, https://doi.org/10.1093/gji/ggab089

Chamberlain, C.J., Hopp, C.J., Boese, C.M., Warren-Smith, E., Chambers, D., Chu, S.X., Michailos, K., Townend, J., 2018. EQcorrscan: Repeating and Near-Repeating Earthquake Detection and Analysis in Python. Seismol. Res. Lett. 89, 173–181. https://doi.org/10.1785/022017015

Delibasis, N., Drakopoulos, J., 1993: The Milos island earthquake of March 20, 1992 and its tectonic significance. Pageoph, Vol. 141, No 1, p. 43-58.

Fytikas, M. 1977. Geological and geothermal study of Milos island. Geol. & Geoph. Research, (1).

Fytikas, M., Innocenti, F., Kolios, N., Manetti, P., Mazzuoli, R., Poli, G., Rita, F., Villari, L., 1986. Volcanology and petrology of volcanic products from the island of Milos and neighbouring islets. J. Volcanol. Geotherm. Res., 28: 297-317.

Ganas A., A. Karakonstantis, V. Kapetanidis, V. Tsironi, I. Karamitros, E. Efstathiou, I. Karasante, and I. Kassaras, 2022. Ground deformation and microseismicity patterns onshore Milos, Cyclades, Greece. 16th International Congress of the Geological Society of Greece, 17-19 October 2022, Patras, Greece. Bulletin of the Geological Society of Greece, Sp. Publ. 10, pp. 663-664, ISBN: 978-960-98709-8-6.

Ganas, A., Mavropoulos, G., Karamitros, I., Nikolakopoulos, K., Charalampopoulou, V., Anastasiou, D., Athanassopoulos, T., Kyriou, A., and Tsironi, V. 2024. A new low-cost GNSS instrument for monitoring of ground motions and critical infrastructures within the Greek “Supersite”, EGU General Assembly 2024, Vienna, Austria, 14–19 Apr 2024, EGU24-10188, https://doi.org/10.5194/egusphere-egu24-10188

Kassaras, I., Kapetanidis, V., Ganas, A., Tzanis, A., Kosma, C., Karakonstantis, A., Valkaniotis, S., Chailas, S., Kouskouna, V., Papadimitriou, P. 2020. The New Seismotectonic Atlas of Greece (v1.0) and Its Implementation. Geosciences, 10, 447 https://www.mdpi.com/2076-3263/10/11/447

Morishita, Y., Lazecky, M., Wright, T. J., Weiss, J. R., Elliott, J. R., & Hooper, A. 2020. LiCSBAS: An open-source InSAR time series analysis package integrated with the LiCSAR automated Sentinel-1 InSAR processor. Remote Sensing, 12(3), 424

Papanikolaou, D., Lekkas, E., Syskakis, D., Adamopoulou, E., 1993. Correlation of neotectonic structures with the geodynamic activity in Milos during the earthquakes of March 1992. Bull. Geol. Soc. Greece, Vol. XXVIII/3, p. 413-428.

Sachpazi, M., Hirn, A., 1991. Shear-wave anisotropy across the geothermal field of Milos, Aegean Volcanic arc. Geophys. J. Int., Vol. 107, p. 763-785.

Tsironi, V., Ganas, A., Valkaniotis, S., Kouskouna, V., Sokos, E., Koukouvelas, I., 2024. Active shortening and aseismic slip along the Cephalonia Plate Boundary (Paliki Peninsula, Greece): Evidence from InSAR and GNSS data. Tectonophysics, v. 884, 230400, https://doi.org/10.1016/j.tecto.2024.230400

Waldhauser, F., 2001. hypoDD-A Program to Compute Double-Difference Hypocenter Locations, U.S. Geol. Surv. Open File Rep. 01-113, 25 p.

Wu, S.F., You, C.F., Wang, B.S., Valsami-Jones, E., Baltatzis, E., 2011. Two-cells phase separation in shallow submarine hydrothermal system at Milos Island, Greece: Boron isotopic evidence. Geophys. Res. Lett. 38, p. 3–7.

Μπαλτατζής Ε., Δελήμπασης Ν., Valsami-Jones, E., Πυρλή Μ., & Baier, B. 2001. Relationship between hydrothermal fluids and microseismic activity on the south-east coast of Milos Island. Bulletin of the Geological Society of Greece, 34(4), 1441–1447. https://doi.org/10.12681/bgsg.17239 (In Greek, with English abstract).

17th INTERNATIONAL CONGRESS of the Geological Society of Greece

BULLETIN OF THE GEOLOGICAL SOCIETY OF GREECE, SP. PUBL.

EXTENDED ABSTRACT 086

NOAFAULTs: 12-yrs of studies and investigations towards building a geospatial database for active faults in Greece and surrounding areas

Ganas A.[1], Tsironi, V.[1], Goutsos, G.[1,2], Efstathiou E.[1], Tsimi, Chr.[1], Madonis, N.[1], and Georgakopoulos, V.[1],

(1) National Observatory of Athens, Institute of Geodynamics, Athens, Greece aganas@noa.gr

(2) National and Kapodistrian University of Athens, Department of Geology

Abstract

In this short paper, we update on the development of the NOAFAULTs geodatabase since 2013. Our objective was to create a nation-scale database of active faults in Greece and its adjacent regions, supporting the seismicity monitoring at the National Observatory of Athens (NOA) in tandem with an associated web-based query system. In the latest version V6.0 we added new data and fault traces, corrected for missing data, reviewed overlapping fault traces, added new thematic layers, and studied the kinematic and geometrical relations from the parametric data. NOAFAULTs can be used to investigate the ground deformation and seismicity patterns in Greece and surrounding areas and to detect new activity along fault zones. The Greek government, research institutions, and companies have widely used the active faults data from the previous versions of the database.

Introduction – Data and Methods

The NOAFAULTs geospatial database of active faults of Greece was first published in 2013 at BGSG (versions 1.0 & 1.1; Ganas et al. 2013; http://dx.doi.org/10.12681/bgsg.11079). Version 2.1 was published in 2018; Ganas et al. 2018); Version 3.0 was published in 2020 http://doi.org/10.5281/zenodo.4304613; Version 4.0 was published in 2022 https://zenodo.org/record/6326260; Version 5.0 in 2023 (Ganas et al. 2023; https://doi.org/10.5281/zenodo.8075517) followed by Version 6.0 in 2024 (https://doi.org/10.5281/zenodo.13168947).

The NOAFAULTs dataset was created towards compiling a digital database of fault traces, geometry and additional attributes (kinematics, slip rate, associated earthquakes etc.) following the Adria faults community effort in 2007 (Piccardi et al 2007). It has been constructed from published fault maps (that are contained in individual scientific papers) in peer-reviewed journals since 1972. The number of papers that have contributed with fault data in version 6.0 is 145. The authors have modified the fault trace in cases where the original map scale was too coarse, and the topography data (DEM) indicated a large distance between the digitized fault and the trace of the mountain front (in case of normal faults). No unpublished data are included in the database apart from the PhD theses of Caputo (1990), Ganas (1997), Valkaniotis (2009), Zervopoulou (2010) and the Kineta normal fault (fault code GR 3261) that was recently mapped by AG and it is part of a larger study under preparation. Selected fault data were also digitized from the neotectonic fault map series of Greece (Lekkas, 1995, 1996; Mountrakis et al. 1996). Data from neighbouring countries (Albania, North Macedonia, Turkey; e.g., Emre et al. 2018) were also incorporated as active fault systems in the Aegean crosscut national boundaries. The standard commercial software ARCGIS has been used to design and populate the database. The fault layer was produced at NOA by on-screen digitization of fault traces at the original map-scale (as drawn by the reference paper it was taken from) and is available through our web portal application https://arcg.is/04Haer supported by ESRI. The web-content of the database incorporates 27 thematic layers such historical seismicity, seismic and geodetic networks, isodepths of the subducted African slab, geodetic velocities (Briole et al. 2021) and many others. The capability to overlay geospatial data with near real-time earthquake epicentres, achieves an optimal monitoring of areas of high interest.

In version 6.0 (see Fig. 1), the number of 3088 active faults are included. 92% of the active faults are normal faults, 4% are strike-slip faults and only 3% represent the reverse faults. Also, reliable data on slip rates is available for 160 faults. Limited data on instrumental and historical seismicity are linked to 175 and 130 active faults, respectively. Data on fault lengths, slip per event etc. when available may be used to extract kinematic relations such as those pioneered by Wells and Coppersmith (1994).

In addition, a) surface-rupturing geological data and b) data on the proximity of epicentres of strong seismic events to the traces of active faults allows the identification of 173 rupturing faults (seismic faults; both exposed and blind) that are included in version 6.0. The NOAFAULTs database shows that nearly 52% of its active faults imply high seismic risk level in the broader area of Greece. These active faults can generate surface faulting or strong ground motions that can cause serious damage to buildings and infrastructures and therefore represent a significant hazard, particularly in the densely populated and industrialized areas of Greece. Since 2022 NOAFAULTs has contributed to the EFSM20 database (https://www.seismofaults.eu/efsm20; Basili et al. 2022).

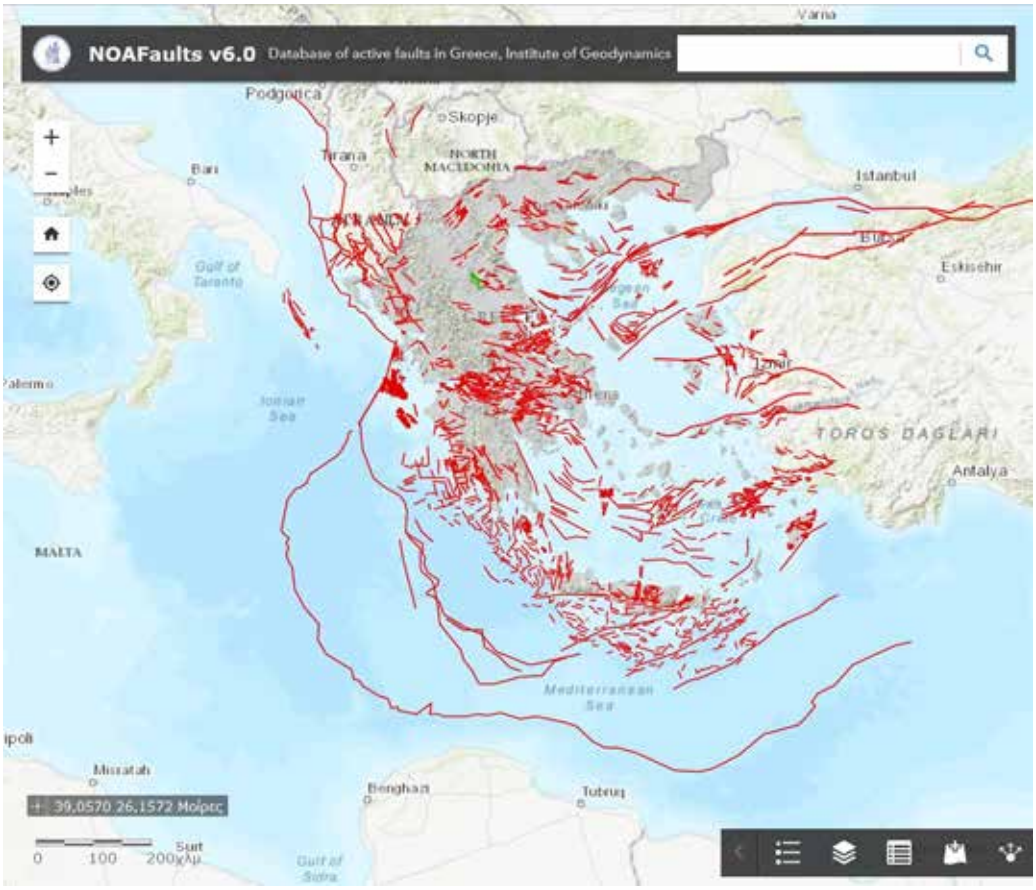

Figure 1. Relef map showing the NOAFAULTs V6.0 fault traces (red lines) in the broader Aegean area.

Results and Conclusions

Active faults serve as sources of strong and destructive earthquakes. Studies and investigations of active faults are necessary for anti-seismic protection and planning and for disaster prevention (Piccardi et al 2007; Emre et al. 2018; Maldonaldo et al. 2021). This study presents the updated nation-scale database of active faults in Greece and its adjacent regions, in tandem with an associated web-based query system. This database includes the active faults data included in 145 peer-reviewed scientific publications during the period 1972-2024. The data integration originates from regional-scale studies and surveys conducted at reference scales from 1:5.000 to 1:500.000. The information collected from these studies and surveys encompasses field mapping, geophysical profiles, measurements of offset horizons and landforms, C^{14} and cosmogenic isotope dating, as well as geometric and kinematic parameters of both exposed and blind faults, earthquake sequences and their characteristics. These data have been acquired and analyzed utilizing a uniform technical standard framework and reviewed by NOA experts. Our system hosts this database accessible through a Web Geographic Information System (GIS) application, enabling browsing, querying, and downloading functionalities via a web browser. Users can incorporate map layers and obtain fault data in OGC-compliant GIS software for further analysis through these services. The Greek government, research institutions, and companies have widely used the active faults data from the previous versions of the database.

Future Objectives

Our aim for the next version of the database (V7.0) is to review the existing data so that the fault traces are digitized in such a way that every user can correctly represent the kinematics of the faults, as well as to correct existing ambiguities. Another important step into the development of the NOAFAULTs is the application of a semi-automatic procedure towards filling out the attribute fields for each new digitized fault trace that will be considered for inclusion into the database.

Acknowledgements

We acknowledge support of this research by the project "*HELPOS - Hellenic Plate Observing System - MIS 5002697)* the GSRT-funded project KRIPIS-ASPIDA "*Infrastructure Upgrade for Seismic Protection of the Country and Strengthen Service Excellence through Action*", the National industry-academia project '*Platform of multidimensional monitoring with micro sensors of Enceladus of Hellenic Supersite-PROION*' with grant number: MIS-5070928 and the HORIZON Geo-Inquire project (EU- project number 101058518). We are indebted to Emmanouela Konstantakopoulou, Nikoletta Andritsou, George Evangelou, Elisavet Kollia, Michael Delagas, Athanassia Oikonomou, Fotini Kounavi, Panagiotis Savvaidis, Anna Fokaefs, and Vasiliki Kanavou for their contribution with earlier versions of the database. We thank many Greek and foreign colleagues from the active tectonics community for their feedback and continuous support.

References

Basili R., Danciu L., Beauval C., Sesetyan K., Vilanova S., Adamia S., Arroucau P., Atanackov J., Baize S., Canora C., Caputo R., Carafa M., Cushing M., Custódio S., Demircioglu Tumsa M., Duarte J., Ganas A., García-Mayordomo J., Gómez de la Peña L., Gràcia E., Jamšek Rupnik P., Jomard H., Kastelic V., Maesano F., Martín-Banda R., Martínez-Loriente S., Neres M., Perea H., Sket-Motnikar B., Tiberti M., Tsereteli N., Tsironi V., Vallone R., Vanneste K., Zupančič P. 2022. European Fault-Source Model 2020 (EFSM20): online data on fault geometry and activity parameters. Istituto Nazionale di Geofisica e Vulcanologia (INGV). https://doi.org/10.13127/efsm20

Briole, P., A. Ganas, P. Elias, D. Dimitrov, 2021. The GPS velocity field of the Aegean. New observations, contribution of the earthquakes, crustal blocks model, Geophysical Journal International, Volume 226, Issue 1, Pages 468–492, https://doi.org/10.1093/gji/ggab089

Caputo, R. (1990). Geological and structural study of the recent and active brittle deformation of the Neogene-Quaternary basins of Thessaly (Central Greece). Ph.D Thesis, Aristotle University of Thessaloniki

Emre, Ö., Duman, T. Y., Özalp, S., Şaroğlu, F., Olgun, Ş., Elmacı, H., and Çan, T. 2018. Active fault database of Turkey, B. Earthq. Eng., 16, 3229–3275, https://doi.org/10.1007/s10518-016-0041-2

Ganas, A., 1997. Fault Segmentation and Seismic Hazard Assessment in the Gulf of Evia Rift, central Greece. Unpublished PhD thesis, University of Reading, November 1997.

Ganas A., Oikonomou I.A. and Tsimi Ch., 2013. NOAfaults: a digital database for active faults in Greece. Bulletin of the Geological Society of Greece, vol. 47 (2), 518-530, http://dx.doi.org/10.12681/bgsg.11079

Ganas, A., Tsironi, V., Kollia, E., Delagas, M., Tsimi, Ch., Oikonomou, Ath. 2018. Recent upgrades of the NOA database of active faults in Greece (NOAFAULTs). 19th General Assembly of WEGENER, September 2018, Grenoble, sciencesconf.org:wegener2018:219400

Ganas, A., V. Tsironi, E. Efstathiou, E. Konstantakopoulou, N. Andritsou, V. Georgakopoulos, Ch. Tsimi, A. Fokaefs and N. Madonis, 2023. The National Observatory of Athens active faults of Greece database (NOAFAULTs) version 2023. In: Book of Abstracts of the 8th International Colloquium on Historical Earthquakes, Palaeo- Macroseismology and Seismotectonics, Bulletin of the Geological Society Special Publication No. 11, pp. 36-38, ISBN: 978-618-86841-1-9.

Ganas, A., 2024. NOAFAULTS KMZ layer Version 6.0 (version 6.0) [Data set]. Zenodo. https://doi.org/10.5281/zenodo.13168947

Lekkas et al., 1995. Neotectonic Map of Zakynthos.

Lekkas et al., 1996. Neotectonic map of Cephalonia.

Maldonado, V., Contreras, M., and Melnick, D. 2021. A comprehensive database of active and potentially-active continental faults in Chile at 1:25 000 scale, Figshare [data set], https://doi.org/10.6084/m9.figshare.13268993

Mountrakis, D., Kilias, A., Pavlides, S., Sotiriadis, L., Psilovikos, A., Astaras Th, V. E., ... & Skordilis, M. 1996. Neotectonic map of Greece, Langadhas sheet. Earthquake planning and protection organisation and European centre on prevention and forecasting of earthquakes. scale, 1:100,000).

Piccardi, L., L, Toth, E. Vittori, S. Aliaj, G. Cello, WD. Cunningham, G. Drakatos, A. Gosar, D. Herak, M. Herak, S. Sebela, E. Sulstarova, G. Windhoffer, B. Glavatovic, A. Kiratzi, A. Ganas, M. Omerbashich, S. Pavlides, L. Petro, G. Sijaric, B. Tomljenovic, & E. Tondi, 2007. A first attempt at compiling a map of active faults of the Adria region. Geophysical Research Abstracts, Vol. 9, 09228, Sref-ID: 1607-7962/gra/EGU2007-A-09228. © European Geosciences Union 2007.

Valkaniotis, S. 2009. Correlation between Neotectonic structures and Seismicity in the broader area of Gulf of Corinth (Central Greece). Unpublished PhD Thesis, Aristotle University

Wells, D.L. and Coppersmith, K. 1994. New empirical relationships among magnitude, rupture length, rupture width, rupture area, and surface displacement. Bull. Seismol. Soc. Am., 84, pp. 974-1002.

Zervopoulou, A. 2010. Neotectonic Faults of the Wide Area of Thessaloniki in association with foundation Soils (Doctoral dissertation, Ph. D. Thesis, University of Thessaloniki.

17th INTERNATIONAL CONGRESS of the Geological Society of Greece

BULLETIN OF THE GEOLOGICAL SOCIETY OF GREECE, SP. PUBL.

EXTENDED ABSTRACT 087

Climatological analysis and Trend Assessment of Climate Indices in two forest areas of Greece experienced extreme fire events in 2023.

Gasteratou Amalia[1], Kostopoulou E.[1]

(1) University of the Aegean / Department of Geography, Mytilene, Greece, geoha22003@aegean.gr

Introduction / Background

Forests cover 39% of the EU's land area. In recent years, large forest fires have repeatedly affected Europe, in particular the Mediterranean countries (EEA, 2024). Particularly, the year 2023 has recorded the highest temperatures in the history of humanity. The year 2023 was a tipping point for the wildfires in Greece (first in EU countries with 42% of the total burnt area), which suffered the largest wildfire ever recorded in Europe. Following the destructive wildfires on the island of Rhodes in July, dozens of new wildfire ignitions in August across the country have been recorded. The most severe one was located in its northeast region, including the Dadia-Lefkimi-Soufli Forest National Park. European Forest Fire Information System (EFFIS) estimates that over 94,000 hectares of natural land were burnt in this single wildfire. Over 45,000 hectares of forests went into flames in Greece, and 65% of areas burnt were within the country's biodiversity reservoir of Natura 2000 (ESOTC, 2023). Fire danger is influenced by weather in the short term, and by climate when considering longer time intervals. In this work, the emphasis is on observed changes of weather and climate patterns on regional scale, as well as trend assessment in climate indices. The extremes considered include temperature extremes and precipitation, as well as compound events. Climate strongly influences fire activity, and the sequence of multiple weather and climate extremes, such as co-occurrence of hot and dry events, leads to more severe fires. Positive temperature, negative humidity and zonal wind anomalies correlate with large fires (Smith et al., 2020). According to the recent report of the United Nations Economic Commission for Europe's International Cooperative Program on Assessment and Monitoring of the Effects of Atmospheric Pollution on Forests (ICP Forests, 2023), it was identified that the outbreaks of forest mortality and their occurrence is partly explained by the simultaneous occurrence of extreme heat and drought events. Weather and climate play an important role in fire occurrence. Therefore, this study aims to provide local-scale understandings of the climatological characteristics of temperature and total precipitation in two Protected Areas in Greece, the National Park of Dadia ("Dadia") and the nature reserve Vounokalathos in Southern Rhodes ("Rhodes"). Therefore, the object of this study is the detailed climatological analysis of these two forest areas in Greece that are among the Protected Areas, which were most affected by the major fires of 2023. The analysis in this study is divided into three parts. The first is the climatological analysis based on key meteorological indicators of Climate Change. Using observed data in the regions of interest from 1981 to 2023, this study characterizes changes observed over the last 43 years for two key climatic parameters (e.g. mean, maximum and minimum air temperature at 2m and precipitation), at the annual and seasonal scales. Second, the analysis of meteorological observations in each site of interest was carried out through calculations of the deviations (commonly called anomalies) of average min/max/mean temperature and total precipitation from the average/total represented by the 30-year normals (1991-2020) according to the standards and requirements of the World Meteorological Organization (WMO). Third, assessment of the co-existence of positive temperature anomalies and negative precipitation anomalies (warm/dry) during the same fire season for the observed period (1981-2023) at each site were conducted. The detection of Dry-Warm each year's fire season is based on the pre-calculated temperature/precipitation anomalies from the 1991-2020 average. We showed that, in "Dadia" the fire season of 2023, with the greatest ecological disaster ever recorded in the region, is described as Dry-Warm, while for "Rhodes" Dry-Warm detected in 2020 and 2021 fire seasons. The results suggest a general trend towards higher temperatures. The statistically significant climatic indices that, according to scientific literature have been linked to both the risk of severe forest fires, stress and tree mortality in forest ecosystems (Carnicer et al. 2022; Guion, et al. 2022; Jones et al. 2022), are defined and examined in this study. Trends in extreme temperature indices were statistically more significant than trends in extreme precipitation indices in both sites of interest.

Objectives

The primary objective of this study is to analyze the trends and variability of extreme weather indices in the Dadia-Lefkimi-Soufli Forest National Park ("Dadia") and the nature reserve Vounokalathos in Southern Rhodes ("Rhodes") study sites of Greece. A secondary objective is to determine whether climate change has caused temporal changes in meteorological elements in the regions of interest. Detecting changes in the temporal patterns of temperature and precipitation is a prerequisite for developing effective adaptation options and strategies for the future. By examining patterns and changes in the local climate system, the study provides new insights into the climate-induced impacts on wildfire activity, as they put into perspective the underlying combinations of weather and climate conditions that are conducive to wildfires based on daily climate data for the period 1981–2023.

Methods

To understand and evaluate the meteorological dynamics, precipitation patterns, and other fundamental climatic elements shaping the environmental landscapes of the study sites, this study employs trend and statistical analysis methods. The methodology consists of three main parts: the selection of the geographical sites in which the indices would be assessed; the collection of daily meteorological data to calculate averages for each parameter at monthly, seasonal and annual timescales, as well as long term averages for the climatological reference period of 1991-2020 (climatological analysis). Additionally, 27 climate indices are calculated on an annual timescale for the observed period (1981-2023) at each site, and finally the performance (existence, magnitude, and statistical significance at 95% level of confidence of potential trends) of the indices is analyzed using Kendall's Tau correlation coefficient and Theil-Sen slope estimator methods (trend analysis). Figure 1 presents a time series graph that shows the annual values of all 27 indices for the observation period and linear regression tests of climate indices. Linear decadal trends are represented by solid red lines, while dashed lines (blue color) represent 10-year smoothed moving average. The study sites are located in two forest areas in Greece that were among the Protected Areas, which were most affected by the major fires of 2023, namely the National Park of Dadia ("Dadia") and the nature reserve Vounokalathos in Southern Rhodes ("Rhodes"). These two sites were selected due to their significant biodiversity that is threatened by the negative impacts associated with the increased, uncontrolled large-scale forest fires over the past decade (Spanos et al., 2021). The climatological analysis is based on long-term observational datasets of meteorological parameters, including temperature, precipitation, wind speed, wind direction and relative air humidity. Meteorological data used in this analysis were obtained from the National Aeronautics and Space Administration Prediction of Worldwide Energy Resources (NASA POWER) satellite-based weather system as a single-point dataset. The analysis also used fire point records from EFFIS. The extreme indices were calculated by using the 'ClimInd' package (Reig-Gracia et al., 2019). Climate indices integrate changes in the frequency, intensity and duration of key extreme climate indicators, as defined by the Expert Team on Climate Change Detection and Indices (ETCCDI). For the calculation of indices, daily values of mean temperature (TM), maximum temperature (TX), minimum temperature (TN), and daily precipitation (RR) are required. Specifically, a total of 27 climate extreme indices were estimated for each location, 15 temperature and 8 precipitation indices. Table 1 provides a description of climate indices. In the second part of the detailed climate analysis, we consider seasonal statistics to analyze "hot and dry" compound extremes focus on precipitation deficits and high temperatures over a common period, in this case fire seasons per year for the observed period (1981-2023) at each site. The condition for characterizing a fire season of a given year as "Dry-Warm" is when the deviation of total precipitation is <10% and the deviation of maximum temperature >0.5 °C. We calculated the anomalies of precipitation and maximum temperature in order to produce the Figure 2 with "Dry-Warm" anomalies located in quadrant I (top-right) and those with wet-cold in quadrant III (bottom-left). It should be noted that for easier interpretation, in the case of the fire season's total precipitation parameter the deviations are expressed as a percentage, with the mean set at 0% instead of 100% (Royé, 2020).

Table 1. Definitions and units of climate air temperature and precipitation indices used in this study.

Indices	Definitions	Units
TXx / TNx	Annual maximum value of daily TX / TN (the hottest days / warmest night of the year)	°C
TX10p / TN10p	Percentage of days when TX < 10th / TN < 10th percentile (cold days / nights) of the year	% days
TN90p	Percentage of days when TN > 90th percentile (warm nights) of the year	% days
XTG / BIO10	Annual max of TM / Mean Temperature of Warmest Quarter of the year	°C
DD17	Difference days above/below Tx17 (days TX > 17 °C)-(days TX < 17 °C)	days
TR	Annual count of Tropical Nights of the year (days TN > 20 °C)	days
WSDI	Annual count of days with at least 6 consecutive days when TX > 90th percentile	days
GD4	Growing degree days. Sum of degree days of TG over 4 °C	degree days
HD17	Heating degree days. Accumulated degree when TG is below 17 °C	degree days
HI	Heat Index. Combines TM and relative humidity to determine equivalent temperature	degree days
STX32	Sums TX32. Sum of degree days when TX ≥ 32 °C on the interval June-August.	degree days
TA_O / TM_S	Growing season (April to October / May to September) mean TM of the hear	degree days
WKI	Winkler index Sum of degree days > 10 °C of TG (April 1 - October 31)	degree days
BIO18	Precipitation of Warmest Quarter of the year	mm
GSR	Growing season (April to October) total precipitation	mm
RTI / PRCPTOT	Annual total precipitation / Annual total precipitation on wet days (rainfall ≥ 1 mm)	mm
R95tot	Annual rainfall that exceeded the 95th percentile in the period from 1981 to 2023	mm
D95p	Very wet days of the year. Days with precipitation > 95th percentile.	days
DR1mm / DR3mm	Wet days 1 / 3mm. Total number of wet days ≥ 1 / ≥ 3mm of the year	days
R10mm	Annual count of days with rainfall ≥ 10 mm	days
SDII	Simple Daily Intensity Index. Mean precipitation on wet days, with rainfall ≥ 1 mm for one year	mm/day

Results

The results of the climatological analysis indicated that 2023 is ranked as the warmest for both sites of interest, according to historical mean temperature data for the period 1981-2023. On the other hand, annual precipitation shows a mixed signal. According to the analysis of the precipitation anomalies (deviations from the long-term mean 1991-2020), it shows that 2008 marked the driest year for “Dadia” and 1990 for “Rhodes” in more than 40 years. Specifically, the calculated annual precipitation deviations for both sites for the period of 1981-2023 showed -44.9% of the mean annual precipitation (569.6 mm) for “Dadia” and -47.8% of the mean annual precipitation (626.2 mm) for “Rhodes” according to the 1991–2020 climatology. The deviations of 2023 average annual mean temperature from the 1991-2020 mean, were 1.9ºC for “Dadia” and 1.0ºC for “Rhodes” above reference mean. Analysis of the climate indices revealed a general warming trend in both sites, which is consistent with global warming (Carnicer et al., 2022). Table 2 presents the decadal trends for the two Greek sites during the period 1981–2023, with bold numbers indicating statistically significant slopes, $p < 0.05$). Increases in the TNx index (see Table 2 and associated plots) indicate a rising potential for Tropical Nights, consistent with global trends for this index (Dunn et al., 2020). Table 2 indicates that computed index related to Tropical Nights (TN > 20 °C) has positive decadal trends for both sites. Decadal increasing trend in Tropical Nights (TR) is more prominent in “Dadia”, statistically significant decadal trend amounting to 10.3 days per decade respectively; TR has a statistically significant positive trend at “Rhodes”, amounting to 5.6 days per decade (Table 2). The increasing intensity of Tropical Nights is clearly evident in “Dadia”, where the value of tropical nights recorded in 1993 increased almost six times, from 10 in 1993 to 56 in 2023, the highest value observed during the 1981–2023 period (Figure 1). In contrast, “Rhodes” increased at a rate of about half of (5.6 tropical nights per decade) the northern “Dadia” (Figure 1). The TXX index observed at “Dadia” has been around 40°C for 12 out of the 43 years (1981-2023), reaching 43.3°C in 2007 (maximum) and 41.4°C in 2023. In “Rhodes”, the maximum and minimum value of TXX is 36.6°C (2021) and 36.4°C (1989) respectively. The northern site (latitude > 40 ◦N) have statistically significant linear increasing decadal trends than the site in the southern Greece (latitude < 40 ◦N) in the annual maximum values of TX (TXx), as displayed in Figure 1. The TXx has statistically significant positive trend of 0.6◦C at “Dadia”, when there was no statistically significant trend at “Rhodes” (Table 2). Dry conditions are also observed by precipitation indicators, where in 2023 the duration of precipitation during the germination period of the plant (GSR) decreased by 17% compared to 2022, while extreme precipitation indicators increased, for example the DR95tot, which increased by 26% in one year, and the D95p, which increased by 5 days in total since 2022. Trends in GSR of statistically significant increasing values are indicative, with a value of +24.2 per decade at “Dadia” (Table 2). For the warm season duration index (WSDI), both sites showed significantly increasing trends. Strong decreasing trends in cold days (TX10p) and cold nights (TN10p) indices were found at both sites. In general, a weak trend towards drier conditions is observed in “Rhodes”, which is in good agreement with previous studies on climate trends in the Mediterranean region and Greece over the recent decades (Kostopoulou et al., 2005; Giannakopoulos et al.,2011; Kostopoulou et al., 2012; Lelieveld et al., 2014; Kostopoulou et al., 2023). A statistically significant upward trend was identified for the extreme climate index STX32 throughout the study period only at “Dadia”. Additionally, the annual mean temperature index for the April-October growing season (TA_O) showed a positive trend of 0.3°C/decade in “Rhodes” and 0.4°C/decade in “Dadia”. Likewise, the annual mean temperature index for the May-September season (TM_S) showed a significant positive trend of 0.5°C/decade in “Dadia”, followed by “Rhodes” with a trend of 0.3°C/decade (Table 2). Figure 1 reveals that the magnitude of heat extremes increased significantly, while cold extremes decreased at a faster rate. Precipitation changes varied between the sites (Figure 1). Results showed a significant increase in temperature and a decrease in precipitation only in “Rhodes” site, indicating a warming and drying trend due to climate change. High rate of change in both regions was observed in the DD17, with a statistically significant positive trend of 12 (20.4) days per decade at “Dadia” (“Rhodes”), as displayed in Table 2.

Table 2. Decadal trends in annual climate indices for 2 Greek sites during the period 1981–2023 (numbers in bold indicate statistically significant slopes, $p < 0.05$).

Indices	«Dadia»	«Rhodes»	Indices	«Dadia»	«Rhodes»
TXx	**+0.6**	+0.3	STX32	**+33.5**	+0.5
TNx	**+0.5**	**+0.3**	TA_O	**+0.4**	**+0.3**
TX10p	**-1.5**	**-1.8**	TM_S	**+0.5**	**+0.3**
TN10p	**-1.6**	**-1.7**	WKI	**+92.1**	**+72.4**
TN90p	**+3.2**	**+3.8**	BIO18	+2.9	-13.7
XTG	**+ 0.5**	**+0.3**	GSR	**+24.2**	+7
BIO10	**+0.7**	**+0.5**	PRCPTOT	**+ 35.8**	-33
DD17	**+12**	**+20.4**	R95tot	+ 1.9	-2.9
TR	**+10.3**	**+5.6**	RTI	**+ 34.7**	-31.5
WSDI	**+8.7**	**+6.5**	D95p	**+ 1.4**	-1.4
GD4	**+175.5**	**+125.3**	DR1mm	**+ 3.6**	0
HD17	**-127.8**	**-44.4**	DR3mm	+2.4	-1.3
HI	**+0.6**	**+0.4**	R10mm	+ 1.2	**-1.8**

A temperature of 18ºC is generally used as the baseline for calculating the scores, as reported in the study by Karagiannidis et al. (2024). Therefore, the findings highlighting a warming trend of the regions under study are particularly concerning. Evergreen oaks can recover better after dry periods than deciduous oaks, as they continue their growth after the summer drought. Low soil water availability in spring is more detrimental to deciduous oak growth (Valeriano et al., 2021). According to the results, a decreasing trend in the HD17 index was found in both study areas. In “Dadia” forest, degree days <17°C are decreasing at a rate of about 128 per decade, while in the “Rhodes” forest, the decrease is quite slower, at about 44 degree days per decade (Table 2). In parallel, the same findings of decreasing trend, were found by Doshi et al. (2023), for the European continent. Conversely, all other degree day indices showed an opposite trend, with the largest increase in the rate of change found in growing degree days (GD4) index (sum of degree days of TM over 4 °C), which increased by 175.5 (125.3) degree days per decade at “Dadia” (“Rhodes”), as shown in Table 2. These findings again agree with those of Doshi et al. (2023), where the GD4 index showed the highest upward trend across all months in Europe. The trend patterns of some extreme precipitation climate indices show geographic variation, large and expected variability, in contrast to the remarkable consistency of extreme temperature climate indices across both study locations. All precipitation indices exhibited increasing trends in the “Dadia” region in the northern parts of the country, while some decreasing trends were observed at “Rhodes” in the southernmost part of the country (Figure 1). Moreover, at the southernmost site of “Rhodes”, the rate of decrease in the total annual precipitation (RTI) reaches 31.5mm/decade (Figures 1). These results for the locations of interest are in general agreement with global findings (IPCC, 2007, 2023; Boegelsack et al., 2018).

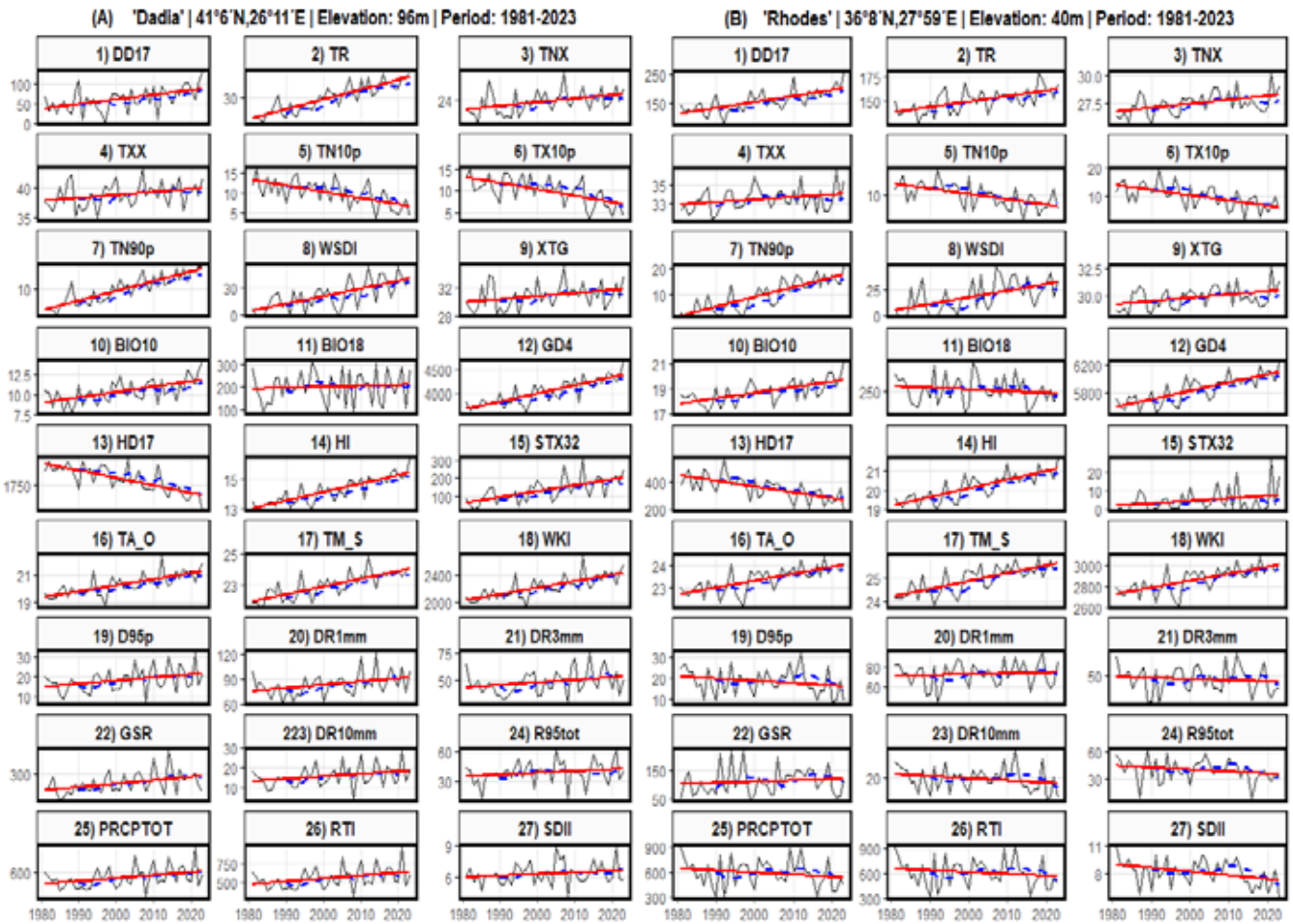

Figure 1: The annual trend magnitudes of all climate indices in (A) “Dadia” and (B) in “Rhodes” (1981-2023).

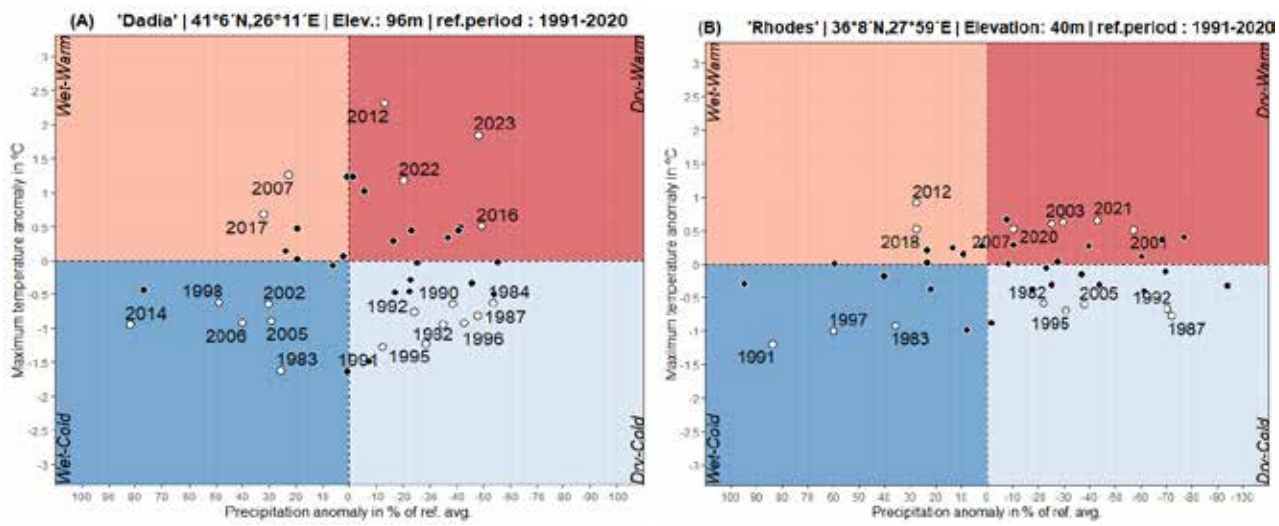

Figure 2: Temperature (maximum) and Precipitation Anomalies in Fire Season (May to October) from 1981 to 2023 (A) in "Dadia" and (B) in "Rhodes" site. Each chart shows each year's characterization as Wet-Warm (top left), Wet-Cold (bottom left), Dry-Warm (top right) and Dry-Cold (bottom right) in quadrants.

The most catastrophic fire season of all, 2023 in "Dadia", is classified as Dry and Warm (Figure 2). Maximum temperature anomalies were 1.8°C above the 1991–2020 average (28.2°C), and a decrease in precipitation amount of 48.4% (mean 214.1 mm). The maximum temperature increased by 0.7 °C compared to 2022. The 2013 fire season's maximum temperature deviation increased from 0.5°C above the 1991–2020 average to 1.8°C over 10 years (2013-2023) and precipitation anomaly values recorded from -40.8% deviation into -48.4% of reference period in the same decade. Respectively in "Rhodes", in 2023 fire season the estimated maximum temperature anomalies were 0.6°C above the 1991–2020 average (26.7°C), and a decrease in precipitation amount of 7.4% (mean 89.8 mm) (not shown in Figure 2). In the same decade from 2013 to 2023 fire season's estimated anomalies of temperatures increased from 0.03°C in 2013 to 0.6°C in 2023 and precipitation anomalies of 2013 increased from -27.6% to -7.5%. Although the 2023 fire season wasn't characterized as Dry and Warm (thus it is not shown in Figure 2), 2022 had remarkable deviations. Maximum temperature anomalies in fire season estimated 0.3°C above the 1991–2020 average, slightly smaller deviation than 2023. Precipitation anomalies in the 2022 fire season estimated negative at 39.6%, a huge difference from 2023 with the enormous damages in the natural reserve of Vounokalathos. According to the literature, the assessment of extreme drought events at both annual and three seasonal scales, i.e., previous winter (December-February), current spring (March-May) and current summer (June-August) best captures absolute water availability (Adams et al. 2017, Senf et al. 2020, Bose et al. 2024). So, these estimations from the year before the disastrous 2023 may be explained the fire severity. Also, 2020 and 2021 fire seasons were estimated as Dry and Warm in "Rhodes" (Figure 2). Thus, three consecutive fire seasons were characterized by favorable fire-weather conditions. Overall, the magnitude of the "Rhodes" 2023 fire season's Dry and Warm event was smaller (in terms of amplitude) compared to the "Dadia" event.

Conclusions

We analyzed the observed climate-driven changes in summer wildfires in two typical Mediterranean forest regions in Greece. The analysis indicates that the northernmost site is most impacted by hot extremes and compound hot-dry extremes, with changes being sensitive to temperature index used, while the southernmost site is most impacted by dry extremes and compound hot-dry extremes, with changes not being sensitive to the precipitation index used. In addition, we propose that climate change affects temperature and precipitation patterns, creating drier and extremely warm conditions that are more likely to lead to forest fires. This strengthens the evidence that climate change increases the frequency and/or severity of fire weather, with a high fire risk due to a combination of high temperatures, low humidity, low rainfall, and often high winds at the sites of interest. However, establishing a direct causal link between a single case and climate change remains challenging as some events would still occur even without climate change. It is therefore important to understand the changes in frequency and intensity at which these events occur. Moreover, it is concluded that to be effective, the management of forest ecosystems and forest fires must be accompanied by long-term knowledge of all the parameters associated with forest fires (climate, vegetation, soil, topography, etc.), which vary locally. More research is, of course, necessary to fully understand the effects of heat stress, which should be supported by real-time data collection and analysis in the field.

References

Adams, H.D.; Zeppel, M.J.B.; Anderegg, W.R.L.; Hartmann, H.; Landhäusser, S.M.; Tissue, D.T.; Huxman, T.E.; Hudson, P.J.; Franz, T.E.; Allen, C.D.; et al. 2017. A Multi-Species Synthesis of Physiological Mechanisms in Drought-Induced Tree Mortality. Nat. Ecol. Evol., 1, 1285–1291

Boegelsack, N., Withey, J., O'Sullivan, G. and McMartin, D. 2018. A Critical Examination of the Relationship between Wildfires and Climate Change with Consideration of the Human Impact. Journal of Environmental Protection, 9, 461-467. DOI 10.4236/jep.2018.95028.

Bose AK, Doležal J, Scherrer D, Altman J, Ziche D, Martínez-Sancho E, Bigler C, Bolte A, Colangelo M, Dorado-Liñán I, et al. 2024. Revealing legacy effects of extreme droughts on tree growth of oaks across the Northern Hemisphere. Sci Total Environ.926:172049. DOI: 10.1016/j.scitotenv.2024.172049. Epub 2024 Mar 27. PMID: 38552974.

Carnicer, J., Alegria, A., Giannakopoulos, C. et al. 2022. Global warming is shifting the relationships between fire weather and realized fire-induced CO2 emissions in Europe. Sci Rep 12, 10365. DOI: https://doi.org/10.1038/s41598-022-14480-8

Copernicus Climate Change Service 2024. European State of the Climate (ESOTC) report of 2023. Press releases Copernicus Climate Change Service (C3S). DOI 10.24381/bs9v-8c66

Doshi S. C., Lohmann G., Rimbu N., Ionita M.(2023. Spatiotemporal trend analysis of climate indices for the European continent. Journal of Water and Climate Change, 14 (9): 3112–3130. DOI 10.2166/wcc.2023.183

Dunn, C. J., O'Connor C. D., Abrams J., Thompson M. P., Calkin D. E., Johnston J. D., Stratton R., and Gilbertson-Day J. 2020. Wildfire risk science facilitates adaptation of fire-prone social-ecological systems to the new fire reality. Environmental Research Letters 15(2):025001. DOI 10.1088/1748-9326/ab6498

European Environment Agency - EEA (2024). Forests and forestry. EU-European Union. Modified 04 Dec 2024. Available from: https://www.eea.europa.eu/en/topics/in-depth/forests-and-forestry [Accessed: on 16 January 2025]

European Forest Fire Information System - EFFIS (2023). Data and services (europa.eu). Data and services. European Centre for Medium-Range Weather Forecasts (ECMWF). EC - European Commission. Available from: https://effis.jrc.ec.europa.eu/applications/data-and-services [Accessed: on 10 June 2024]

Expert Team on Climate Change Detection and Indices, ETCCDI: i) Karl et al., 1999; ii) Peterson, 2005; iii) Klein Tank et al., 2009).

Giannakopoulos C., Kostopoulou E., Varotsos K.V., Tziotziou K., Plitharas A. 2011. An integrated assessment of climate change impacts for Greece in the near future. Reg. Environ. Chang., 11, 829–843.

Intergovernmental Panel on Climate Change-IPCC 2007. Climate Change 2007. The Physical Science Basis Contribution of Working Group I to the Fourth Assessment Report of the IPCC (ISBN 978 0521 88009-1 Hardback; 978 0521 70596-7 Paperback)

Intergovernmental Panel on Climate Change-IPCC 2023. Summary for Policymakers. In: Climate Change 2023: Synthesis Report. Contribution of Working Groups I, II and III to the Sixth Assessment Report of the Intergovernmental Panel on Climate Change [Core Writing Team, Lee H., and Romero J. (eds.)]. IPCC, Geneva, Switzerland, pp. 1-34, DOI 10.59327/IPCC/AR6-9789291691647.001

Karagiannidis, A.; Lagouvardos, K.; Kotroni, V.; Galanaki, E. 2024. Expected Changes in Heating and Cooling Degree Days over Greece in the near Future Based on Climate Scenarios Projections. Atmosphere, 15, 393. https:// doi.org/10.3390/atmos15040393

Kostopoulou, E., Jones, P. 2005. Assessment of climate extremes in the Eastern Mediterranean. Meteorol. Atmos. Phys. 89, 69–85 DOI 10.1007/s00703-005-0122-2

Kostopoulou, E., Giannakopoulos C., Hatzaki M., and Tziotziou K. 2012. Climate extremes in the NE Mediterranean: Assessing the E-OBS dataset and regional climate simulations. Climate Research 54, no. 3: 249 - 270.

Kostopoulou, E.; Giannakopoulos, C. 2023. Projected Changes in Extreme Wet and Dry Conditions in Greece. Climate, 11, 49. DOI 10.3390/cli11030049

Matzarakis, A., Nastos, P. 2024. Greece 2023: Crazy Summer or New Normal—Lessons Not Learned. Atmosphere 15, no. 10: 1241. DOI 10.3390/atmos15101241

Michel A, Kirchner T, Prescher A-K, Schwärzel K, editors (2023) Forest Condition in Europe: The 2023 Assessment. ICP Forests Technical Report under the UNECE Convention on Long-range Transboundary Air Pollution (Air Convention). Online supplementary material, 48 p. Eberswalde: Thünen Institute. Available at http://icp-forests.net/page/icp-forests-technical-report

Paparrizos, S., Matzarakis, A., 2016. Present and future assessment of Growing Degree Days over selected Greek areas with different climate conditions. Meteorology and Atmospheric Physics, DOI 10.1007/s00703-016-0475-8

Reig-Gracia Fergus 2019. ClimInd: Climate Indices. R package version 0.1-3, https://cran.r-project.org/web/packages/ClimInd. Accessed 11 Jan. 2023. DOI 10.32614/CRAN.package.ClimInd.

Royé Dominic. 2020. «Visualize climate anomalies». R-bloggers. www.r-bloggers.com. Accessed 11 Jan. 2023.

Smith, A.J.P., Jones, M.W., Abatzoglou, J.T., Canadell, J.G. & Betts, R.A. 2020. ScienceBrief Review: Climate change increases the risk of wildfires Critical Issues in Climate Change Science, edited by: C. Le Quéré, P. Liss, P. Forster. DOI 10.5281/zenodo.4570195. This ScienceBrief Review was supported by the European Commission via projects CRESCENDO, 4C, and VERIFY (grants no. 641816, 821003, 776810).

Senf, C., Buras, A., Zang, C. S., Rammig, A., & Seidl, R. 2020. Excess forest mortality is consistently linked to drought across Europe. Nature Communications, 11(1), Article 6200. DOI:10.1038/s41467-020-19924-1

Spanos, K.; Skouteri, A.; Gaitanis, D.; Petrakis, P.; Meliadis, I.; Michopoulos, P.; Solomou, A.; Koulelis, P.; Avramidou, E. 2021. Forests of Greece, their multiple functions and uses, sustainable management and biodiversity conservation in the face of climate change. Open J. Ecol., 11, 374–406.

Valeriano, C., Gazol, A., Colangelo, M., Gonzalez de Andres, E., Camarero, J.J., 2021. Modeling climate impacts on tree growth to assess tree vulnerability to drought during forest dieback. Front. Plant Sci. 12, 672855

17th INTERNATIONAL CONGRESS of the Geological Society of Greece

BULLETIN OF THE GEOLOGICAL SOCIETY OF GREECE, SP. PUBL.

EXTENDED ABSTRACT 088

A flood hazard assessment tool using satellite based high resolution land cover dataset within Google Earth Engine

Gemitzi A.[1], Kopsidas O.[1], Stefani F.[2], Polymeros A.[3], Bellos V.[1], Falalakis G.[4]

(1) Department of Environmental Engineering, Democritus University of Thrace, Xanthi, Greece, agkemitz@env.duth.gr (2) National School of Public Administration and Local Government, Athens, Greece (3) Ministry of Rural Development and Food, Athens, Greece (4) Ministry of Education and Religion, Directorate of Secondary Education Rhodope, Greece

Introduction / Background

Floods are one of the natural disasters that pose a real threat for communities all over the world, especially in areas of low altitude with mild slopes and in coastal zones, impacting thus significantly human life. Floods may result in loss of human life, property damage, infrastructure damage and subsequent economic losses (Guha-Sapir *et al.,* 2014; Pabi *et al.,* 2021; Venkataramanan *et al.,* 2019). Another serious flood implication is the displacement of people, which can be temporary or long-term, depending on the severity of the flood and the availability of resources to support those who have been displaced (International Federation of Red Cross and Red Crescent Societies, 2021).

Thus, there is need for proactive flood disaster risk management (Pabi *et al.,* 2021), for any flood type like flash floods, river floods and flooding in urban areas, which can be greatly facilitated nowadays by remotely sensed information (Ajmar *et al.,* 2017)]. The EU Directive 2007/60 requires EU member states to take a number of measures to reduce the negative impacts of floods on human health, the environment, and economic activities, including the identification of areas at risk of flooding, the development of flood risk maps and management plans, and the implementation of flood risk reduction measures. As climate change is expected to bring more frequent extreme precipitation events, floods are expected to pose a serious threat for human society and environment and within this context flood hazard mapping is of major importance for urban and spatial planning and land use management (Hosseini *et al.,* 2020; Ran *et al.,* 2019).

There are several methods to identify flood prone areas, but the main tool is numerical modeling. The conventional way is to identify the catchment which runoffs to the vulnerable area and implement a hydrological rainfall-runoff model which derives a flood hydrograph at the catchment outlet. Except for the previous framework, there are several approaches such as multi-criteria decision-making tools, statistical methods, and Machine Learning techniques [Hosseini *et al.,* 2020; Rafiei-Sardooi *et al.,* 2021), which can be incorporated in the general methodology.

As previously mentioned, the EU Directive 2007/60 is the main tool for the European Union to define the strategy and to derive the policies for flood management. However, this framework has some drawbacks: a) the inundated areas are produced using numerical modeling, which in general suffer from uncertainties. Moreover, the low quality or even the lack of historical data from flood events makes the calibration of the required parameters no feasible and hence uncertainty is increased; b) Flood Hazard Maps are one snapshot in a specific time moment and they cannot incorporate all the changes which affect the flooded area, such as the land use modifications, the urbanization, the construction of several manmade structures, the rainfall variability over time, etc.

Therefore, there is a gap between this static tool of EU Flood Hazard Maps and the real world which changes every day. During the last years, Remote Sensing (RS) techniques to identify the inundated areas after a flood event are rising and indicate a potential. For example, researchers used Sentinel-1 images in order to assess the performance of hydraulic modeling in a historical flood event (Zotou *et al.,* 2020)] Other researchers developed the FLOMPY toolbox to identify flooded areas in the past using Sentinel-1 images (Karamvasis *et al.,* 2021) and they used Synthetic Aperture Radar approaches to support flood modeling (Zotou *et al.,* 2022). There are also works utilized the Google Earth Engine (GEE) based on Sentinel-1 images, in which they identified the flood susceptibility of an area, namely which areas are more vulnerable to be flooded based on historical and topographic data (Mehravar *et al.,* 2023) or they focused on the built-up area effect on flooding.

To the best of our knowledge, flood hazard mapping is based on hydrological modeling while there is no approach that uses remote-sensed and constantly updated images of flood data which can be used to assess the output of the EU Flood Hazard Maps. Besides, this is the first time a constantly updated flood hazard assessment tool is available for use by every interested stakeholder. In this work, a methodology for the assessment of flood hazard and the associated socioeconomic implications is presented based on the land cover dataset produced by Artificial Intelligence (AI) namely Dynamic World (Brown *et al.,* 2022), which is updated constantly following the revisit time of Sentinel 2, i.e., two to five days, and provides information on flooded areas at a 10 m spatial resolution. The

assessment is built within GEE platform, and evaluates the flooding probability at the pixel level, computing the number of times each pixel is categorized as flooded in the Dynamic World dataset for a given time period.
The methodology is applied in the River Basin District (RBD) of Thrace in NE Greece and it was compared against the latest Flood Hazard Maps developed for the study area according to the requirements of the EU Directive 2007/60 (EU Parliament, 2007). Our work highlights the advantages of using near-real time updated information on floods, complementary to the EU Flood Hazard Maps which are derived for a specific time moment. Its simplicity makes it an ideal instrument to overcome barriers encountered between scientific advances and policy adjustments, since it is implemented within a simple GEE code, and hence it is also readily available for use in other areas around the world. Apart from that, we also applied the tool in the region of Thessaly, Greece, in order to identify the flood impact after the recent catastrophe due to the Storm Daniel which hit the Mediterranean basin in early September of 2023.

Methods / Results

The flood hazard assessment approach presented herein builds on the global near-real time land use/land cover (LULC) product Dynamic World (Brown *et al.,* 2022), which is the result of the joint effort of Google and the World Resources Institute. It is available through the GEE platform and can be viewed in the GEE public data catalog. Aim of this initiative was to release a global LULC dataset, updated in near-real time that could capture the dynamic nature of Earth's surface. A detailed description of the methodology and training material can be found in the Dynamic World web page (Google and World Resources Institute Dynamic World App., 2024). Dynamic World is produced applying Artificial Intelligence (AI) principles using GEE and AI Platform. It is based on the European Space Agency's Sentinel-2 Top of Atmosphere (TOA) images, which are classified into 9 land use / land cover classes, using deep learning techniques. It has the spatial resolution of the original Sentinel-2 TOA product, i.e., 10 m, and it is updated globally every 2-5 days depending on the location, following the revisit time of Sentinel-2. The classification technique assigns per-pixel probabilities across nine land cover classes: Water, Trees, Grass, Crops, Shrub and Scrub, Flooded Vegetation, Built-up Area, Bare Ground, Snow and Ice. The Dynamic World classification has been applied to all historic Sentinel-2 TOA images, i.e., from June 2015 and it is constantly updated as soon as new images become available.
Concerning the flood hazard assessment presented in this work, the class of Flooded Vegetation is of particular interest, as it describes vegetated conditions related to flood. In the Dynamic World, each land cover class is represented by a different band. In this work, each pixel in every Dynamic World image of the study area, demonstrating the highest probability in the Flooded Vegetation class, is considered to be flooded area and it is assigned a value of 1, whereas in all other cases the pixel is assigned a zero value. Summing the values of each pixel across the whole time series, i.e., from June 2015 until today, corresponds to the number of times the specific pixel is viewed in flood conditions. All computations were performed within the GEE Platform with a Java Script code freely available using the link provided in the data availability section. The whole process is schematically depicted in Figure 1.

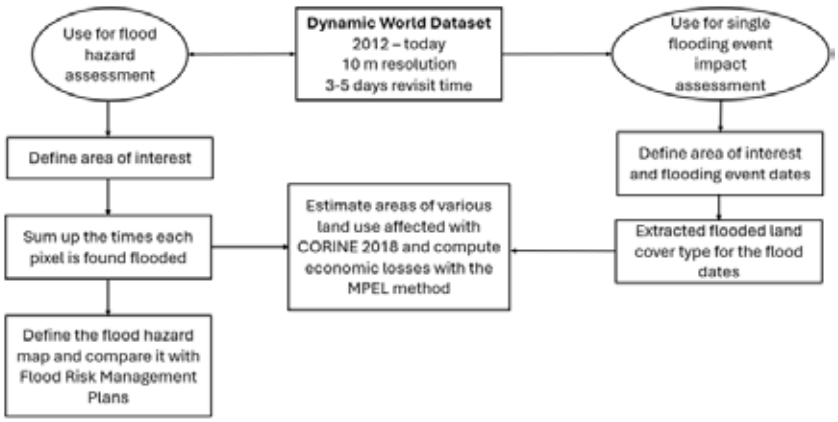

Figure 1. Flow chart of the flood hazard mapping approach

The results obtained with DW dataset in the Thrace RBD are shown in Figure 2a, whereas Figure 2b shows the frequency of flooding of various flooding areas. Comparison of the two independent datasets in Thrace Water District, which occupies an area of 11,250 km^2, revealed certain areas where Dynamic World did not detect flood conditions whereas the Flood Hazard Map indicates them as inundated area which corresponds to the rainfall with return period

of 100 years. This is expected since the two datasets correspond to different repeat periods and does not mean that DW underestimates or the Flood Hazard Map overestimates flood hazard conditions. Those areas correspond to 444,3 km^2 (Figure 3). The areas that both datasets assign as flood cover 122.7 km^2. However, the most interesting outcome is that there is an area of 194.6 km^2 which has been observed as a flooded area at least once since 2015 in DW. This is a certain miss of the 100-year return flood data set. Those areas are observed along the eastern and northeastern areas of Thrace WD, within the basin of River Evros.

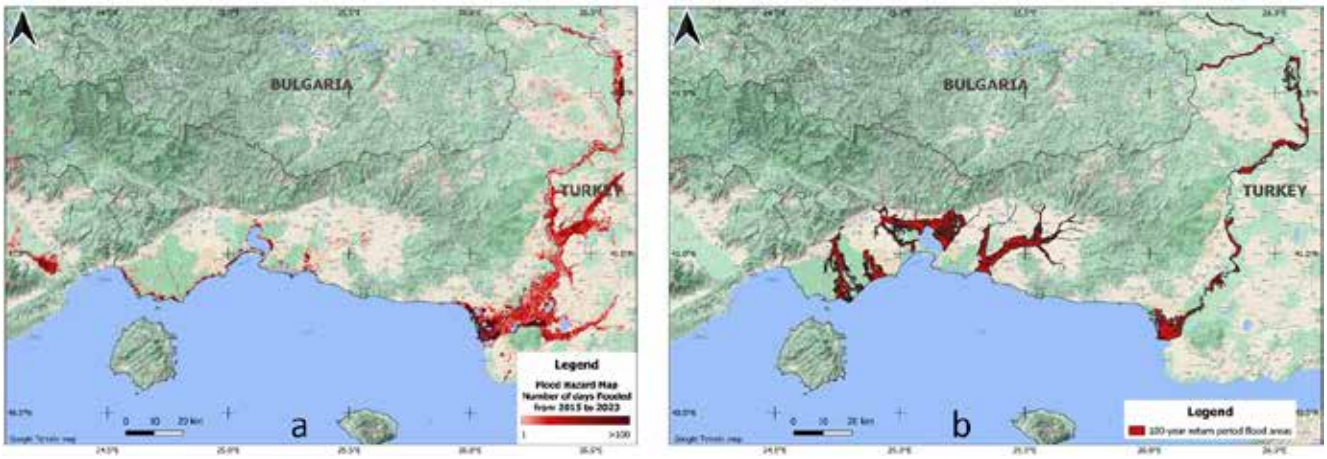

Figure 2. a) Flood Hazard Map of the broader Thrace RBD based on the methodology presented herein, covering the 2015 – 2023 period**, b)** 100-year return period Flood Hazard Map as defined for Thrace RBD, Greece

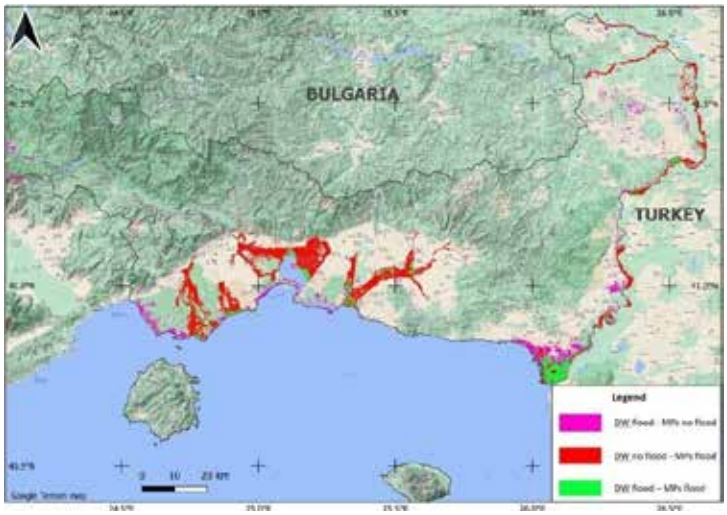

Figure 3. Comparison of the Flood Hazard Map of the Thrace RBD based on the methodology presented herein against the 100-year Flood Hazard Map based on the Flood Management Plan

Except for the application of DW in Thrace, we defined the flooding area prior and after the recent Medicane Daniel. Specifically, a tremendous flood event occurred in early September 2024 as a result of Storm Daniel, which caused dramatic impacts mainly on the region of Thessaly, in Central Greece (Figure 4). More than 750 mm of rainfall were recorded at the meteorological station of Zagora village near Mount Pelion, which approximates twice the annual rain of Athens (Nasa Earth Observatory, A Deluge in Greece). In Figure 5 the flooded area is plotted against how many times it is flooded, demonstrating that the flood impact of Daniel changed dramatically the distribution of flooded areas, with more than 50 km^2 observed as flooded for the first time.

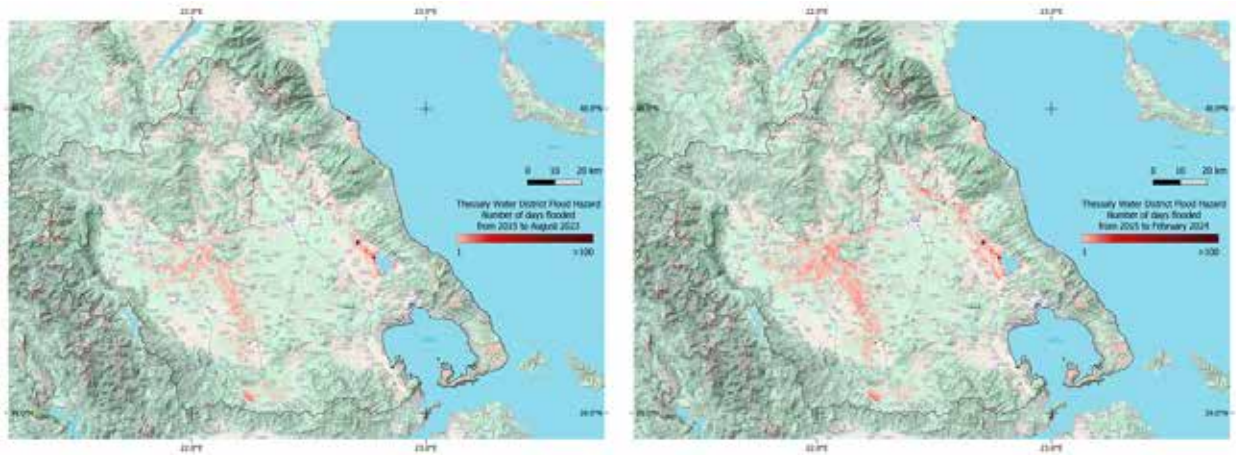

Figure 4. Flooded area prior to storm Daniel (left) and after storm Daniel (right)

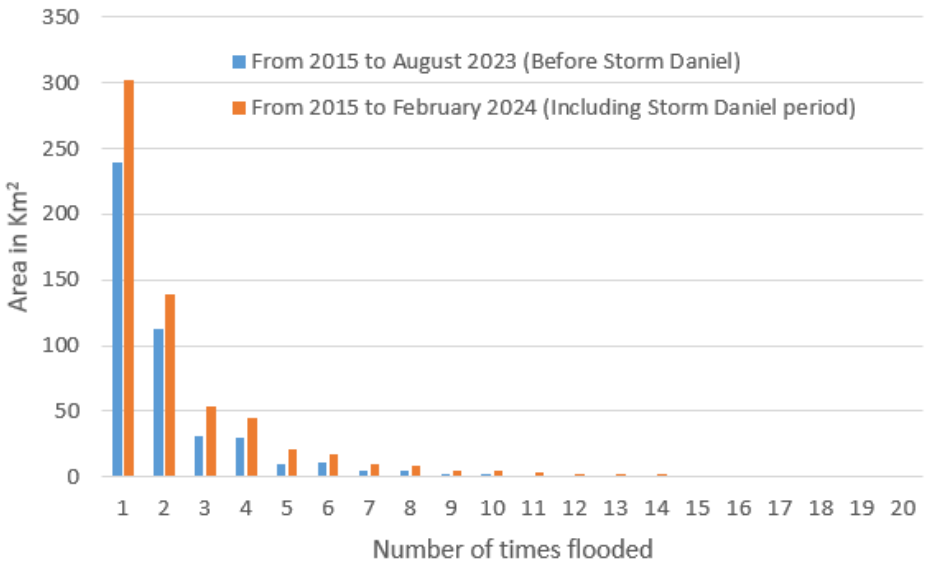

Figure 5. Flooded area against how many times is flooded before and after storm Daniel

Conclusions

In this work, we developed an open tool based on remote sensed images obtained by the Google Earth Engine, and specifically on Sentinel 2 images, for identifying the time series of flooded areas with a continuous update. This tool is implemented in the Thrace water district (Greece) and the outcome of the proposed tool is compared with the corresponding Flood Hazard Maps of the EU Directive 2007/60. It is found that there are discrepancies between the model product (i.e. the Flood Hazard Maps) and the real-world picture. We applied DW tool for identifying the flooded area after the recent Storm Daniel, which hit Greece in September of 2023 and specifically the region of Thessaly. Our major findings are presented in the following paragraphs.

First, we shall keep in mind that the conventional Flood Hazard Maps within the Flood Management Plans, are created on a probability basis using modeling tools and should be regarded as future potential flooding areas. Besides, these maps are derived assuming that there are no changes at the configuration of the vulnerable area. Our results indicated that there is space for improvement in those Flood Hazard Maps combining information from satellite-based observations. The DW dataset approach, presented in this work, offers a means of verification of the modeling results, especially by enhancing them in flooded areas which are not depicted in the Flood Hazard Maps. Regarding the reliability of this dataset, it should be noted that it has been rigorously examined and tested with a large Expert Consensus dataset and the results indicated top qualitative performance in each comparison category among the examined land cover datasets. Hence, the presented methodology, taking advantage of emerging techniques and datasets, helps policy makers acquire better and timely information on flood hazard, so as to improve the planning of protective measures.

Second, Sentinel 2 mission has a global coverage and covers all Earth's continents, large islands, along with inland and coastal

water bodies, with a revisit frequency of 5 days. However, cloud cover may restrict acquisition of useful images, resulting in lower data availability in flooded areas with increased cloud cover and therefore the results obtained with DW dataset should be regarded as the minimum number of days the specific area is observed as flooded. It is very likely that some flood events are not detected by satellite observations due to cloud cover and are not included in the DW dataset. As the methodology is based on AI classification, there is always a slight possibility of misclassification, i.e., a dry pixel may appear falsely flooded and vice versa. Nevertheless, DW is an extensively evaluated dataset of high accuracy. Since it is a constantly updated dataset, its quality is expected to improve in the future versions. The probability for a specific area to have no RS history data is very low and thus the methodology works at the global scale. Moreover, since the Sentinel 2 mission operates from 2015, the data history covers a relatively short time period, which however can be extended back to early '80s combining data from Landsat missions. This can be a very challenging future extension of the present work.

Finally, the growing production of freely available datasets related to environmental monitoring based on remote sensing and AI technologies can be used to tackle the tremendous impacts on natural and human ecosystems due to flooding. The innovation of our approach consists of:

- The development of an algorithm using the Google Earth Engine platform in order to utilize the high-spatial resolution of the Dynamic World data.
- The deployment of a user-friendly tool which can be used for the effective communication of scientific findings to government and policy makers but also to all community actors and will encourage social acceptability of improved flood anticipation policies.
- The evidence of the usefulness of the tool, demonstrating the inadequacy of the River Flood Management Plans against the outcome of the tool in the Thrace Water District.

References

Ajmar, A., Boccardo, P., Broglia, M., Kucera, J., Giulio-Tonolo, F., Wania, A., 2017. Response to Flood Events. In Flood Damage Survey and Assessment, Geophysical Monograph Series, pp. 211–228 ISBN 9781119217930.

Brown, C.F., Brumby, S.P., Guzder-Williams, B., Birch, T., Hyde, S.B., Mazzariello, J., Czerwinski, W., Pasquarella, V.J., Haertel, R., Ilyushchenko, S., 2022. Dynamic World, Near Real-Time Global 10 m Land Use Land Cover Mapping. Sci Data, 9, 251, doi:10.1038/s41597-022-01307-4.

EU Parliament,2007. Floods Directive, Directive 2007/60/EC.

Google and World Resources Institute Dynamic World App, 2024. Available online: https://dynamicworld.app/ (accessed on 25 March 2024).

Guha-Sapir, D., Hoyois, P., Below, R., 2014. Annual Disaster Statistical Review 2014 The Numbers and Trends Centre for Research on the Epidemiology of Disasters (CRED).

Hosseini, F.S., Choubin, B., Mosavi, A., Nabipour, N., Shamshirband, S., Darabi, H., Haghighi, A.T., 2020. Flash-Flood Hazard Assessment Using Ensembles and Bayesian-Based Machine Learning Models: Application of the Simulated Annealing Feature Selection Method. Science of the Total Environment 711, 135161, doi:10.1016/j.scitotenv.2019.135161.

International Federation of Red Cross and Red Crescent Societies, 2021. DISPLACEMENT IN A CHANGING CLIMATE Localized Humanitarian Action at the Forefront of the Climate Crisis, Geneva.

Karamvasis, K., Karathanassi, V., 2021. FLOMPY: An Open-Source Toolbox for Floodwater Mapping Using Sentinel-1 Intensity Time Series. Water (Basel), 13, 2943, doi:10.3390/w13212943.

Mehravar, S., Razavi-Termeh, S.V., Moghimi, A., Ranjgar, B., Foroughnia, F., Amani, M., 2023. Flood Susceptibility Mapping Using Multi-Temporal SAR Imagery and Novel Integration of Nature-Inspired Algorithms into Support Vector Regression. J Hydrol (Amst), 617, 129100, doi:10.1016/j.jhydrol.2023.129100.

Nasa Earth Observatory A Deluge in Greece.

Pabi, O., Egyir, S., Attua, E.M., 2021. Flood Hazard Response to Scenarios of Rainfall Dynamics and Land Use and Land Cover Change in an Urbanized River Basin in Accra, Ghana. City and Environment Interactions 12, doi:10.1016/j.cacint.2021.100075.

Rafiei-Sardooi, E., Azareh, A., Choubin, B., Mosavi, A.H., Clague, J.J., 2021. Evaluating Urban Flood Risk Using Hybrid Method of TOPSIS and Machine Learning. International Journal of Disaster Risk Reduction, 66, doi:10.1016/j.ijdrr.2021.102614.

Ran, J., Nedovic-Budic, Z., 2019. Designing an Information Infrastructure for Policy Integration of Spatial Planning and Flood Risk Management. In Environmental Information Systems, IGI Global, pp. 520–554.

Venkataramanan, V., Packman, A.I., Peters, D.R., Lopez, D., McCuskey, D.J., McDonald, R.I., Miller, W.M., Young, S.L. A , 2019. Systematic Review of the Human Health and Social Well-Being Outcomes of Green Infrastructure for Stormwater and Flood Management. J Environ Manage 246, 868–880, doi:10.1016/j.jenvman.2019.05.028.

Zotou, I., Bellos, V., Gkouma, A., Karathanassi, V., Tsihrintzis, V.A., 2020. Using Sentinel-1 Imagery to Assess Predictive Performance of a Hydraulic Model. Water Resources Management, 34, 4415–4430, doi:10.1007/s11269-020-02592-7.

Zotou, I., Karamvasis, K., Karathanassi, V., Tsihrintzis, V.A., 2022. Potential of Two SAR-Based Flood Mapping Approaches in Supporting an Integrated 1D/2D HEC-RAS Model. Water (Basel), 14, 4020, doi:10.3390/w14244020.

17th INTERNATIONAL CONGRESS of the Geological Society of Greece

BULLETIN OF THE GEOLOGICAL SOCIETY OF GREECE, SP. PUBL.

EXTENDED ABSTRACT 089

How medial tephra records contribute to proximal tephrochronology: Case study of Nisyros Volcano

G. Gençalioğlu Kuşcu [1], G. Uslular [2]
(1) Department of Geological Engineering, Muğla Sıtkı Koçman University, Muğla, Türkiye, gkuscu@mu.edu.tr
(2) Polar Research Institute, TÜBİTAK Marmara Research Center, Kocaeli, Türkiye

Introduction

Santorini and Nisyros are considered the most important caldera-type volcanoes in terms of volcanic risk in the South Aegean Active Volcanic Arc, Figure 1A). The recent earthquake swarms in the Christiana-Santorini-Kolumbo volcanic system between Santorini and Amorgos Islands have been causing concern not only in Santorini and neighboring islands, but also in Türkiye since the end of January 2025. The possibility of a volcanic eruption in this volcanic field reminded us of widespread tephra units in the geological past such as the Santorini Minoan tephra, spread to western Anatolia. Therefore, the other active volcanic field of the SAAVA, Kos-Nisyros-Yali, closer to Turkish mainland becomes more important. Terrestrial medial/distal tephra sequences are especially valuable in the case of island arc volcanoes where most of the tephra deposited within the sea and not readily accessible. The purpose of this study is to document the medial Nisyros tephra on Datça peninsula (Muğla, SW Türkiye) and discuss how they contribute to the understanding of tephrochronological issues in the proximal region.

Kos-Nisyros-Yali Volcanic Field and Nisyros Medial Tephra

Kos-Nisyros-Yali, is the site for one of the most powerful eruptions in the Quaternary (i.e. Kos Plateau Tuff, Keller et al., 1990) (Figure 1B). Despite the well constrained geology, distribution and chronology of tephra units of Santorini, there are some uncertainties in tephra distribution and eruption frequency for Nisyros volcano. The $^{40}Ar/^{39}Ar$ age of Kos Plateau Tuff (KPT) eruption is 161.3 ± 1.1 ka (Smith et al., 1996), and Nisyros-Yali are considered post-KPT volcanic centers. The geochronology of the Nisyros tephra units has been constrained just recently. The K-Ar method was the most widely used for the pre-caldera Nisyros tephra units, but did not provide accurate ages (e.g. Keller et al., 1990). Absence or rarity of K-bearing phases or excess Ar in some crystals were problems related to K/Ar dating, resulting in older ages. Other methods (^{14}C, O isotopes, fission track) were employed for the caldera-forming tephra, and use of distal marine tephra for stratigraphy and correlation also produced conflicting and wide range of ages.
Regarding the Nisyros tephra dispersal, only caldera forming rhyodacitic/rhyolitic Lower and Upper Pumice units (63.1 ± 4.7 ka and 58.4 ± 2.7 ka, respectively; Popa et al., 2020) were considered significant in the literature. Even if deposited on neighboring islands or Turkish coast, pre-caldera tephra was thought to be eroded later on (Longchamp et al., 2011). However, pre-caldera Kyra unit (previously estimated as 24-38 ka) was reported in one locality on Datça (0.9 m) and Tilos (1.2 m) (Keller et al., 1990; Sterba et al., 2011).

Results

In order to contribute to the tephrochronology of Nisyros volcano, we conducted field studies and tephra hunting on Datça peninsula, that revealed 6 new outcrops and confirmed the occurrence of Nisyros Kyra reported earlier (Gençalioğlu-Kuşcu and Uslular, 2018). We collected andesitic and dacitic pumice lapilli deposited on KPT with an unconformity in between (Figure 2). Zircon, monazite, and apatite crystals were separated from Datça pumice fall tephra for U-Th/He geochronology, and abundant apatite crystals proved to be useful. Plagioclase and hornblende crystals were also separated for $^{40}Ar/^{39}Ar$ geochronology from another Kyra tephra location. The weighted mean of combined $^{40}Ar/^{39}Ar$ and (U–Th)/He ages was calculated as 133.5 ± 3.4 ka (Gençalioğlu Kuşcu et al., 2020).

Conclusions

Identification of new medial Nisyros tephra on Datça Peninsula, together with their detailed characterization

contributes to the proximal tephrochronology of Nisyros volcano. The weighted mean age of 133.5 ± 3.4 ka for Kyra tephra conforms with the recent ages of younger explosive and effusive units, revealing a more precise tephrostratigraphy. As a caldera volcano accumulating silicic magma, Nisyros possesses volcanic risk to surrounding islands and Turkish mainland. Therefore, medial tephra distribution and identification, correlation and geochronology of these tephra units are vital to get the full picture of this relatively less known, but potentially dangerous volcanic system. Further volcanological and geochronological work is needed to determine the distribution of medial tephra and determine the eruption frequency for the Nisyros volcano.

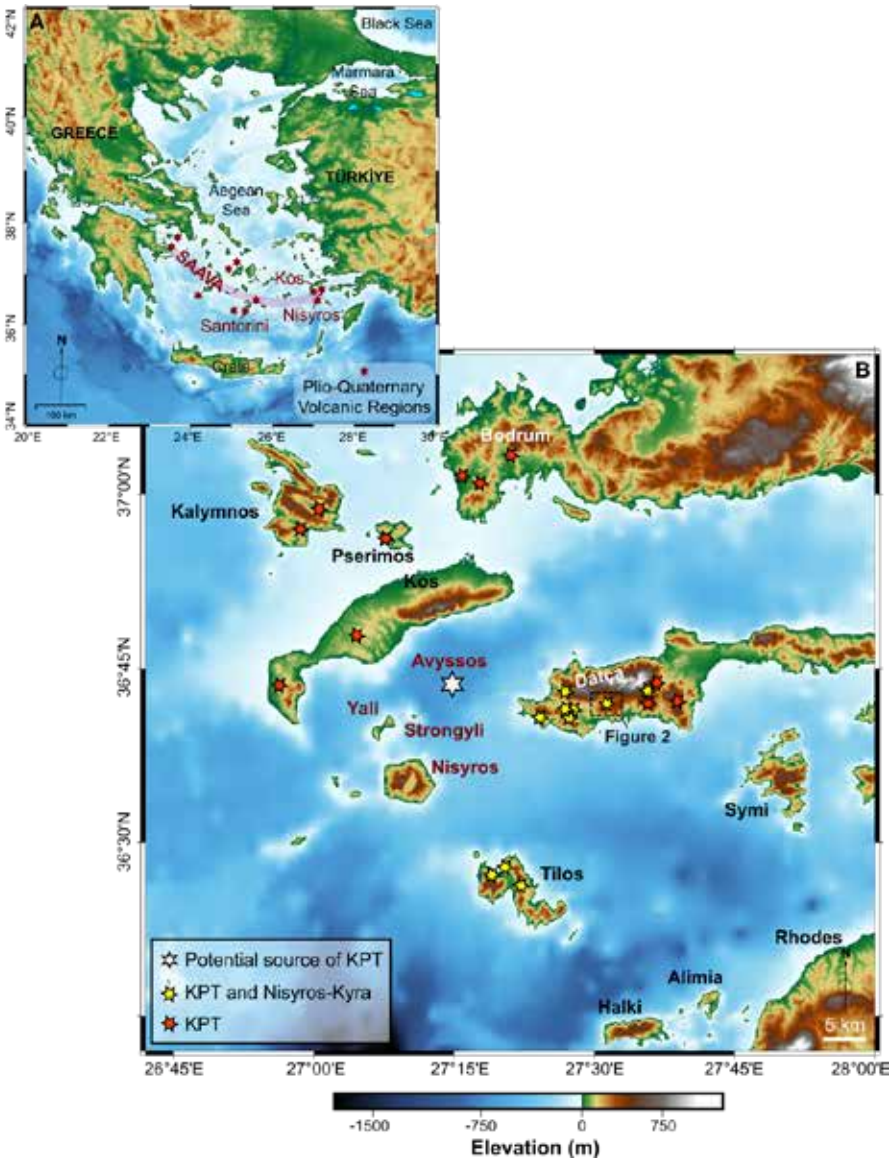

Figure 1A. Map showing the volcanic centers of the South Aegean Active Volcanic Arc (SAAVA); B. DEM image (30-m resolution SRTM) showing the Kos-Nisyros-Yali volcanic system. Occurrences of KPT on Datça-Bodrum Peninsulas and neighboring islands are modified from Ercan et al. (1984), Allen et al. (1999), Pe-Piper et al. (2005), and Gençalioğlu Kuşcu (2012). Nisyros Kyra tephra on Datça peninsula and Tilos island are from Gençalioğlu Kuşcu and Uslular (2018) and Sterba et al. (2011), respectively. The rectangle on the Datça peninsula shows the Sındı location of Figure 2, where Nisyros Kyra overlies the KPT and fluvial deposits.

Figure 2. General view of the andesitic Kyra fallout overlying the KPT and fluvial deposits on Datça peninsula.

Acknowledgements

The research was funded by Scientific Research Project Office of Muğla Sıtkı Koçman University, Türkiye (through BAP Projects 10/47; 15/070 and 15/077), and TÜBİTAK Scientific and Technical Research Council of Türkiye (grant number 113Y328).

References

Allen, S.R., Stadlbauer, E., Keller, J., 1999. Stratigraphy of the Kos Plateau Tuff: product of a major Quaternary explosive rhyolitic eruption in the eastern Aegean, Greece. Int.J. Earth Sci. 88, 132–156.

Ercan, T., Günay, E., Baş, H., Can, B., 1984. Datça Yarımadasındaki Kuvaterner yaşlı volkanik kayaçların petrolojisi ve kökensel yorumu (Petrology and genetical interpretation of the Quaternary volcanic rocks on Datça Peninsula) MTA Dergisi, 97/98. pp. 45–56 (in Turkish).

Gençalioğlu-Kuşcu, G. 2012. Bodrum ve Datça Yarımadası Piroklastik İstiflerinin Jeolojik ve Petrografik İncelenmesi, 10/47 no'lu Muğla Üniversitesi BAP Proje Raporu, (in Turkish).

Gençalioğlu-Kuşcu, G. and Uslular, G., 2018. Geochemical characterization of mid-distal Nisyros tephra on Datça peninsula (southwestern Anatolia). Journal of Volcanology and Geothermal Research, 354, 13-28.

Gençalioğlu-Kuşcu, G., Uslular, G., Danišík, M., Koppers, A., Miggins, D.P., Friedrichs, B. and Schmitt, A.K., 2020. U–Th disequilibrium, (U–Th)/He and 40Ar/39Ar geochronology of distal Nisyros Kyra tephra deposits on Datça peninsula (SW Anatolia). Quaternary Geochronology, 55, 101033.

Keller, J., Rehren, T.H., Stadlbauer, E., 1990. Explosive volcanism in the Hellenic arc. In: Hardy, D.A., Keller, J., Galanopoulos, V.P., Fleming, N.C., Druitt, T.H. (Eds.), Thera and the Aegean World, III, Proceedings of the Third International Congress, Santorini, Greece, 3–9 September 1989. vol. 487. The Thera Foundation, p. 13–26.

Longchamp, C., Bonadonna, C., Bachmann, O., Skopelitis, A., 2011. Characterization of tephra deposits with limited exposure: the example of the two largest explosive eruptions at Nisyros volcano (Greece). Bull. Volcanol. 73, 1337–1352.

Pe-Piper, G., Piper, D.J.W., Perissoratis, C., 2005. Neotectonics and the Kos Plateau Tuff eruption of 161 ka, South Aegean arc. J. Volcanol. Geotherm. Res. 139, 315–338.

Popa, R. G., Guillong, M., Bachmann, O., Szymanowski, D., & Ellis, B. (2020). U-Th zircon dating reveals a correlation between eruptive styles and repose periods at the Nisyros-Yali volcanic area, Greece. Chemical Geology, 555, 119830.

Smith, P.E., York, D., Chen, Y., Evansen, N.M., 1996. Single crystal 40Ar–39Ar dating of Late Quaternary paroxysm on Kos, Greece: concordance of terrestrial and marine ages. Geophys. Res. Lett. 23, 3047–3050.

Sterba, J.H., Steinhauser, G., Bichler, M., 2011. On the geochemistry of the Kyra eruption sequence of Nisyros volcano on Nisyros and Tilos, Greece. Appl. Radiat. Isot. 69, 1605–1612.

17th INTERNATIONAL CONGRESS of the Geological Society of Greece

BULLETIN OF THE GEOLOGICAL SOCIETY OF GREECE, SP. PUBL.

EXTENDED ABSTRACT 090

Evaluation of PAHs sorption behavior in coals and cokes

Georgaki M. [1], Karapanagioti H.K.[2], Wojtaszek-Kalaitzidi M.[3], Kalaitzidis S.[1*]
(1) Department of Geology, University of Patras, Rio-Patras, GR 265 04, Greece, skalait@upatras.gr (2) Department of Chemistry, University of Patras, Rio-Patras, GR 265 04, Greece (3) Institute of Energy and Fuel Processing Technology, 1 Zamkowa Street, Zabrze, Poland

Research Highlights

This study investigates the sorption behavior of phenanthrene in coals and cokes, highlighting the influence of coal rank and maceral composition on phenanthrene sorption capacity.

Introduction / Background

Organic petrography has become an important tool in environmental research, particularly in studying the sorption capacities of polycyclic aromatic hydrocarbons (PAHs) in various types of coal (e.g., Ligouis *et al*., 2005; Kalaitzidis *et al*., 2006; Yan *et al*., 2011). This is important as it provides insights into the interactions between PAHs and organic matter, which are critical for predicting the behavior and environmental fate of these pollutants in natural systems. PAHs refer to a broader category of harmful and toxic organic pollutants widely distributed in nature (Van der Oost *et al*., 2003; White *et al*., 2016; Patel *et al*., 2020). Some of these compounds can be mutagenic or carcinogenic in living organisms, leading to their classification as priority pollutants (ATSDR, 1995).

Phenanthrene ($C_{14}H_{10}$) belongs to PAHs and is a hydrophobic organic pollutant, due to its potential toxicity to humans and other living organisms, as well as its prevalence and persistence in the environment (Hussar *et al*., 2012). It is commonly used in sorption studies as a model organic chemical and is also used in this study. Previous studies showed that the sorption of phenanthrene in low-rank coals is controlled, among others, through the inertinite content (e.g. Kalaitzidis *et al*., 2006).

Objectives

In the current study, the sorption behavior of phenanthrene in a series of various rank coals such as lignite, bituminous coals, semi-anthracite and anthracite, as well as naturally coked coals and industrial cokes, is examined (Figure 1). The rank series represents a wide range of coal basins and coal-forming periods, ranging from Gondwana coals from Australia and South Africa, Laurasian coals from China and Poland, and Neogene lignite from the Czech Republic, thus demonstrating variable physical and chemical characteristics and most importantly, maceral contents (Table 1). The main purpose of this study is to evaluate the impact of coal rank upon sorption attributes, but also to test the hypothesis that sorption will increase proportionally to carbonized material (e.g. inertinite content) in higher-rank coals, as it was observed for low-rank coals (Kalaitzidis *et al*., 2006).

Methods

In total twenty-two samples were analyzed, comprising lignite (ERT_3,_4), bituminous coal (ERT_5,_6,_7,_10,_11, _12,_13,_14,_15,_16), anthracite (ERT_1,_2,_8,_9), naturally coked coals (ERT_18,_19) and industrial cokes (ERT_17,_20,_21,_22). On the representative samples proximate, ultimate and petrographical analyses were conducted. Proximate analysis was performed according to ASTM (D3174; D3175; D3302, 2004). Ultimate analysis was carried out using a Carlo Erba EAGER 200 Automatic Analyzer according to ASTM D5373, 2004. Maceral analysis was performed according to ISO 7404-3 (2009) using a Leica DMRX coal-petrography microscope (ICCP, 1998, 2001; Sýkorová *et al*., 2005; ASTM D5061, 2007; Pickel *et al*., 2017). Vitrinite reflectance (Ro%) and bireflectance (Rbi%) were measured according to ISO 7404-5 (2009) using Leica MPV/SP spectral photometer and AxioImager M1m/Zeiss+MSP 400 Spectrophotometer.

Additionally, all samples were tested for their sorption capacity in batch triplicate reactors at the same initial phenanthrene concentration (Co) of 250 μg/L. Based on the sorption and petrographical analysis results, nine samples were selected for further sorption experiments of phenanthrene at concentrations (Co), ranging from 20 to 200 μg/L (Kleineidam *et al*., 1999; Karapanagioti and Sabatini, 2000; Karapanagioti *et al*., 2001), as well as for BET analysis.

The surface area, pore volume and pore size distribution of selected samples were determined by nitrogen gas (N_2) adsorption-desorption with the Tristar 3000 Analyzer (Micrometrics® GA, USA) using the Brunauer, Emmett, and Teller (BET) equation, at the Laboratory of Heterogeneous Catalysis, Department of Chemistry of the University of Patras.

Results and Discussion

Proximate analysis determines that the moisture varies from 0.7 to 10.0 wt% (on an as-received basis). The ash yield shows a high variability with values ranging from 2.5 to 64.8 wt% (db). The volatile matter yields vary from 2.9 to 58.8

wt% (daf). The carbon content of the samples ranges from 59 to 95 wt% (daf). Hydrogen and nitrogen fluctuate from 0.3 to 6.2 wt% and 1.1 to 2.3 wt% (daf), respectively. Sulfur content varies from 0.1 to 3.9 wt% (daf).

Table 1. Samples characteristic, rank, results of proximate and ultimate analyses, vitrinite reflectance and bireflectance.

Sample	Location	Ash (wt.%, db)	VM (wt.%, daf)	Ro%	Rank
ERT_1	South Africa	14.2	11.3	2.31	Anthracite C
ERT_2	China	12.8	10.6	3.37	Anthracite B
ERT_3	Germany	2.5	58.8	0.32	Lignite B
ERT_4	Czech	2.6	54.4	0.30	Lignite B
ERT_5	Australia	22.2	31.5	0.73	Bituminous C
ERT_6	Australia	11.6	21.7	1.28	Bituminous B
ERT_7	Australia	16.6	20.5	1.52	Bituminous A
ERT_8	Australia	10.1	8.6	4.38	Anthracite A
ERT_9	Australia	12.1	10.9	4.63	Anthracite A
ERT_10	Australia	5.3	24.0	1.20	Bituminous B
ERT_11	Australia	7.0	18.2	1.61	Bituminous A
ERT_12	Australia	47.4	17.4	1.90	Bituminous A
ERT_13	Australia	5.4	19.8	1.20	Bituminous B
ERT_14	Poland	9.6	29.4	1.11	Bituminous B
ERT_15	Poland	6.0	36.8	0.87	Bituminous C
ERT_16	Poland	7.8	25.5	1.25	Bituminous B
				Rbi%	
ERT_17	Australia	12.0	6.3	5.52	Coke
ERT_18	Australia	64.8	18.6	4.75	Coked coal
ERT_19	Australia	64.6	15.8	3.70	Coked coal
ERT_20	Poland	11.0	2.9	4.72	Coke
ERT_21	Poland	13.0	4.1	1.43	Coke
ERT_22	Poland	12.1	3.0	4.89	Coke

VM: volatile matter; Ro%: vitrinite reflectance; Rbi%: bireflectance; ar: as-received basis; db: dry basis; daf: dry, ash-free basis.

The petrographical analysis indicates that huminite is the dominant maceral group in the lignite samples ranging from 85.6 to 92.6 vol%, on an organic matter basis. Vitrinite is the dominant maceral in the bituminous coal and anthracite samples, ranging from 56.9 to 100 vol%, where two of them (ERT_8,9) were anthracite A with 100 vol% vitrinite. Inertinite content in lignite samples is generally low (<9 vol%), while in bituminous coal and anthracite, it ranges from 3.3 to 40.7 vol%. Liptinite content is up to 10.6 in lignite and bituminous coal samples. Naturally coked and coke samples were dominated by binder phase (69.6-95.0 vol%) and less filler phase (5.0-30.0 vol%).

The phenanthrene sorption distribution coefficient (Kd, $Kd = qe \times Ce^{-1}$) at the same initial phenanthrene concentration (Co) of 250 μg/L ranges from 1,024 to 37,329 L/Kg, with samples ERT_14 and ERT_1 displaying the lowest and the highest values, respectively. Of the 9 samples selected for further sorption experiments, samples ERT_3, ERT_18, and ERT_19 show the highest sorption capacity at both high (Co=180 μg/L) and low concentrations (Co=15 μg/L). Anthracite (ERT_1) exhibited nonlinear sorption behavior (Freundlich exponent N > 1), while bituminous coals (ERT_6, _11, _14 _15, _16), showed a correlation between inertinite content and sorption nonlinearity (N < 1). Coke samples (ERT_18, _19) displayed the highest organic carbon-normalized sorption capacity (Koc, $Koc = Kd \times foc^{-1}$) at low phenanthrene concentrations.

The BET analysis reveals that the surface areas vary from 1.0 to 41.2 m^2/g. Pore volume ranges from 0.0056 to 0.062 cm^3/g. Samples ERT_18 and ERT_19 with high surface area also exhibit high pore volume. The pore size ranges from 62 to 303 Å.

Considering the above, the sorption behavior seems to be affected by the coal rank, except for the lignite (ERT_3) sample. However, if the organic carbon content is considered, it follows the same pattern observed in a previous study (Kalaitzidis *et al*., 2006), which found a positive correlation between inertinite content and Koc, indicating that as inertinite content increases, sorption capacity also increases.

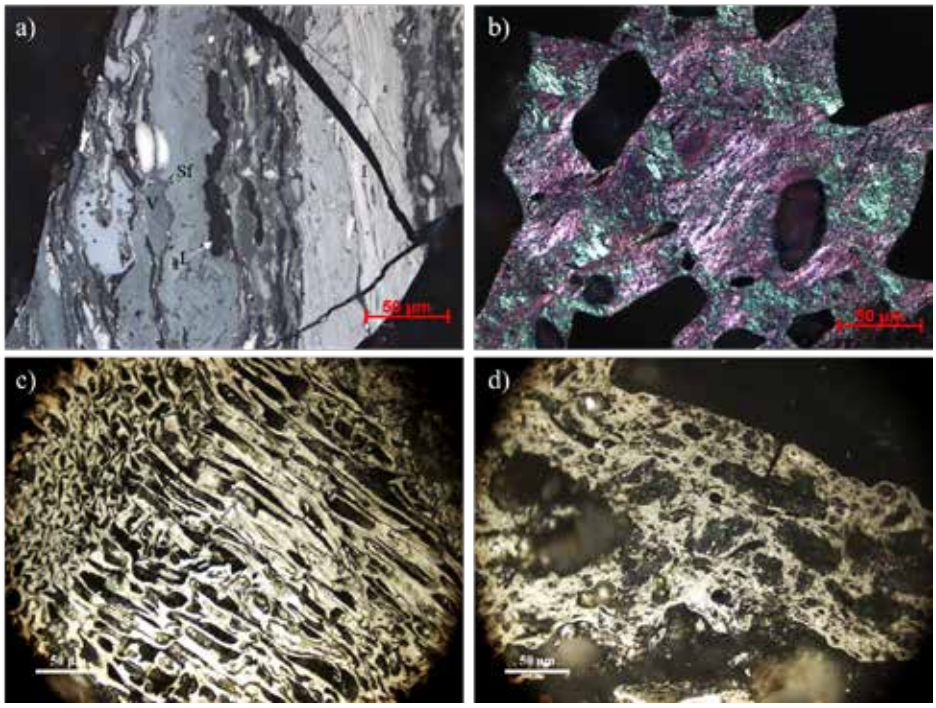

Figure 1. Photomicrographs of selected samples; a) ERT_14 bituminous B coal, V: vitrinite, Sf: semifusinite, L: liptinite, I: inertinite; b) optical texture of coke sample ERT_20; c) view of inertinite in naturally coked coal ERT_19; d) view of naturally coked coal sample ERT_18.

Conclusions

The anthracite (ERT_1) exhibited the highest sorption capacity (Kd) from all samples, but also its behavior was totally different from the rest samples. Anthracite had a nonlinear Freundlich exponent (N) higher than 1, which suggests that the more the sorbed phenanthrene the higher the affinity of the sorbent for phenanthrene. Bituminous coals (ERT_6, _11, _14 _15, _16) sorption behavior seemed to be affected by the inertinite content in terms of their nonlinearity (N<1); nonlinearity increases (N decreases) with increasing inertinite amount. The two coke samples (ERT_18, _19) demonstrated the highest sorption affinity (Koc); which is the sorption capacity normalized for the fraction of organic carbon content for phenanthrene at low concentrations.

Acknowledgments

The authors would like to thank Ms. Vasiliki Kostopoulou and Mr. Dimitrios Bampagenes for conducting laboratory experiments. Dr. Dimitrios Vachliotis, Laboratory of Instrumental Analysis, Faculty of Sciences, University of Patras, is also acknowledged for performing the Carlo Erba analysis.

References

Agency for Toxic Substances and Disease Registry (ATSDR), 1995. Toxicological profile for Polycyclic Aromatic Hydrocarbons (PAHs). Atlanta, GA: U.S. Department of Health and Human Services, Public Health Service.

American Society for Testing and Materials (ASTM) D3174, 2004. Standard Method for Ash in the Analysis Sample of Coal and Coke from Coal. 2004 Annual Book of ASTM Standards, Gaseous Fuels; Coal and Coke, vol. 05. ASTM, Philadelphia, PA, pp. 322–326 06.

American Society for Testing and Materials (ASTM) D3175, 2004. Standard Method for Volatile Matter in the Analysis Sample of Coal and Coke. 2004 Annual Book of ASTM Standards, Gaseous Fuels; Coal and Coke, vol. 05. ASTM, Philadelphia, PA, pp. 327–330 06.

American Society for Testing and Materials (ASTM) D3302, 2004. Standard Method for Total Moisture in Coal. 2004 Annual

Book of ASTM Standards, Gaseous Fuels; Coal and Coke, vol. 05. ASTM, Philadelphia, PA, pp. 352–358 06.

American Society for Testing and Materials (ASTM) D5061, 2019. Standard Test Method for Microscopical Determination of the Textural Components of Metallurgical Coke. 2019 Annual Book of ASTM Standards, Gaseous Fuels; Coal and Coke, vol. 05. ASTM, West Conshohocken, PA, pp. 278–283.Kalaitzidis, S., Karapanagioti, H., Christanis, K., Bouzinos, A. and Iliopoulou, E., 2006. Evaluation of peat and lignite phenanthrene sorption properties in relation to coal petrography: the impact of inertinite. Int. J. Coal Geol., 68: 30-38.

American Society for Testing and Materials (ASTM) D5373, 2004. Standard Test Methods for Instrumental Determination of Carbon, Hydrogen and Nitrogen in Laboratory Samples of Coal and Coke. 2004 Annual Book of ASTM Standards, Gaseous Fuels; Coal and Coke, vol. 05. ASTM, Philadelphia, PA, pp. 504–507 06.

Hussar, E., Richards, S., Lin, Z. Q., Dixon, R. P., & Johnson, K. A., 2012. Human health risk assessment of 16 priority polycyclic aromatic hydrocarbons in soils of Chattanooga, Tennessee, USA. Water, Air, & Soil Pollution, 223, 5535-5548.

International Committee for Coal Petrology (ICCP), 1998. The new vitrinite classification (ICCP System 1994). Fuel 77 (5), 349–358.

International Committee for Coal Petrology (ICCP), 2001. The new inertinite classification (ICCP System 1994). Fuel 80, 459–471.

International Standard Organisation (ISO) 7404-2, 2009: Methods for the Petrographic Analysis of Coals—Part 2: Method of Determining Microscopically the Reflectance of Vitrinite. International Organization for Standardization, Geneva, Switzerland, 7 p.

International Standard Organisation (ISO) 7404-3., 2009. Methods for the Petrographic Analysis of Coals—Part 3: Method of Determining Maceral Group Composition., International Organization for Standardization, Geneva, Switzerland, 7 p.

International Standard Organisation (ISO) 7404-5, 2009. Methods for the Petrographic Analysis of Coals—Part 5: Method of Determining Microscopically the Reflectance of Vitrinite. International Organization for Standardization, Geneva, Switzerland, 12 p.

Kalaitzidis, S., Karapanagioti, H., Christanis, K., Bouzinos, A. and Iliopoulou, E., 2006. Evaluation of peat and lignite phenanthrene sorption properties in relation to coal petrography: the impact of inertinite. Int. J. Coal Geol., 68: 30-38.

Karapanagioti, H.K., Kleineidam, S., Sabatini, D.A., Grathwohl, P. and Ligouis, B., 2000. Impactsof Heterogeneous Organic Matter on Phenanthrene Sorption: Equilibrium and Kinetic Studieswith Aquifer Material, Environ. Sci. Technol., 34, 406-414.

Karapanagioti, H.K., Sabatini, D.A., 2000. Impacts of heterogeneous organic matter on phenanthrene sorption: different aquifer depths. Environ. Sci. Technol. 34, 2453–2460.

Kleineidam, S., Rügner, H., Ligouis, B., & Grathwohl, P., 1999. Organic matter facies and equilibrium sorption of phenanthrene. Environmental Science & Technology, 33(10), 1637-1644.

Ligouis, B., Kleineidam, S., Karapanagioti, H.K., Kiem, R., Grathwohl, P., and Niemz, C., 2005. Organic petrology: a new tool to study contaminants in soils and sediments. In: E. Lichtfouse, J. Schwarzbauer, D. Robert (Eds.), Environmental chemistry, Green Chemistry and Pollutants in Ecosystems. Springer-Verlag, Berlin, p. 89-98.

Patel, A. B., Shaikh, S., Jain, K. R., Desai, C., & Madamwar, D., 2020. Polycyclic aromatic hydrocarbons: sources, toxicity, and remediation approaches. Frontiers in Microbiology, 11, 562813.

Pickel, W., Kus, J., Flores, D., Kalaitzidis, S., Christanis, K., Cardott, B.J., Misz-Kennan, M., Rodrigues, S., Hentschel, A., Hamor-Vido, M., Crosdale, P., Wagner, N., ICCP, 2017. Classification of liptinite–ICCP System 1994. International Journal of Coal Geology, 169, 40-61.

Sýkorová, I., Havelcová, M., Trejtnarová, H., Matysová, P., Vašíček, M., Kříbek, B., Suchý, V., Kotlík, B., 2009. Characterization of organic matter in dusts and fluvial sediments from exposed areas of downtown Prague, Czech Republic. International Journal of Coal Geology, 80(2), 69-86.

Van der Oost, R., Beyer, J., & Vermeulen, N. P., 2003. Fish bioaccumulation and biomarkers in environmental risk assessment: a review. Environmental toxicology and pharmacology, 13(2), 57-149.

White, A.J., Bradshaw, P.T., Herring, A.H., Teitelbaum, S.L., Beyea, J., Stellman, S.D., Steck, S.E., Mordukhovich, I., Eng, S.M., Engel, L.S., Conway, K., Hatch, M., Neugut, A.I., Santella, R.M., Gammon, M.D., 2016. Exposure to multiple sources of polycyclic aromatic hydrocarbons and breast cancer incidence. Environ. Int. 89-90, 185–192.

Yan, C., Yang, Y., Liu, M., Nie, M., & Zhou, J. L., 2011. Phenanthrene sorption to Chinese coal: Importance of coal's geochemical properties. Journal of hazardous materials, 192(1), 86-92.

17th INTERNATIONAL CONGRESS of the Geological Society of Greece

BULLETIN OF THE GEOLOGICAL SOCIETY OF GREECE, SP. PUBL.

EXTENDED ABSTRACT 091

Groundwater Quality Evaluation of Thessaly and Peloponnese: Data Analysis of 2019 year and Evidence of Degradation

Georgaki Maria-Nefeli[1], Georgakis Athanasios[2], Sarigiannis Dimosthenis[1], Kazakis Nerantzis[3]

[1]*Environmental Engineering Laboratory, Department of Chemical Engineering, Aristotle University of Thessaloniki, 54124, Thessaloniki, Greece, nefgeor@gmail.com*

[2]*Democritus Thrace University, Department of Civil Engineering, Section of Transportation, Kimmeria Campus, 67100 Xanthi, Greece*

[3]*Laboratory of Hydrogeology, Department of Geology, University of Patras, Rion, 26500, Patras, Greece*

Introduction / Background

Globally, groundwater is a primary source of water supply and irrigation, often with a balanced distribution (Wada et al., 2012). However, in Greece, water distribution is uneven, both temporally and regionally, with a significant portion of its main water resources being used for agricultural purposes. The chemical status of groundwater in mainland Greece is characterized as particularly degraded (Karavitis et al., 2024). The main sources of groundwater degradation are industrial and mining zones - heavy metal pollution, which is harmful even at low concentrations – the seawater intrusion, and the use of fertilizers and pesticides in areas of agricultural intensification (Dokou et al., 2015).

Objectives

Systematic groundwater monitoring ensures good water quality for water supply and agricultural irrigation in Greece, especially in Thessaly and Peloponnese, regions characterized by intense agricultural activity. The purpose of the study is to determine the distribution of groundwater parameters in the studied regions, the overall groundwater quality of these, and the identification of possible factors that influence groundwater system.

Methods

Based on the "National Water Monitoring System" (Ministry of Environment and Energy), this study aims to include all recently available data of 2019 on the hydrochemical characteristics of groundwater in Greece. This data includes measurements of physicochemical parameters, such as pH, temperature, electrical conductivity (EC), sulfate (SO_4), nitrate (NO_3), total chromium (Cr_{total}) and total phosphates (PO_4), from monitoring stations in the regions of East and West Peloponnese and Thessaly. The available groundwater variables were analyzed using statistical tools in SPSS software version 16.0 and RStudio Desktop (Dammi et al., 2021). Multivariate statistical methods (MSMs) were applied to identify trends and differences in groundwater quality in studied regions of Greece with increasing agricultural activity (Praus 2005; Belkhiri et. al. 2010). Varimax rotation approach and Kaiser normalization, combined with principal component analysis (PCA), which is included in factor analysis (R-mode FA) , were applied as an exploratory tool to identify potential sources of groundwater pollution (Ma et al., 2014).

The limits of detection (LOD) and quantification (LOQ) are the most crucial data that researchers evaluate when assessing approach validity. The parameters LOD and LOQ define analyzed concentrations that may be accurately quantified. The LOQ indicates the lowest concentration that can be quantitatively determined with sufficient accuracy, whereas the LOD indicates the lowest detectable concentration (Taleuzzaman 2018). At chemical concentrations below the limit of quantification, half the value was assigned. References state that censored data are either removed or replaced with specified data, usually half of the LOQ (Cantoni et al., 2020).

Results

The chemical composition of groundwater samples, both from Peloponnese and Thessaly varies significantly (Table 1). Both a descriptive analysis and a test for normality to the data distribution were carried out. The pH, an important parameter for assessing water quality, ranges from slightly acidic to slightly alkaline in the studied regions, mainly within World Health Organization (WHO) limits. WHO recommends a pH of 6.5 to 8.5 (WHO 2008). Although pH does not directly affect human health, it is closely associated with the physicochemical properties of water. Electrical conductivity (EC) is frequently differentiated in water quality data in both the Peloponnese and the Thessaly, indicating moderate to high dissolved salt content. Water hardness is influenced by anions such as chloride and sulfate, as well as calcium and magnesium cations. The Peloponnese and Thessaly regions frequently have significant concentrations of both calcium and magnesium ions. Groundwater's chloride concentrations varied, with some samples having higher concentrations than the permissible limit of 250 mg/L (8062 mg/L). Significant concentrations of chloride in water are frequently used as an indicator of groundwater pollution (Panno et al., 2006). Nevertheless, geological factors, including seawater intrusion in coastal aquifers, or deep saline groundwater upwelling, may also cause naturally high

chloride concentrations in some areas. This could be related to high salt levels, marine pollution, and other activities (such as the use of chemicals in industry or agriculture. In both studied areas, some samples observed high nitrate (534 and 526 mg/L) and sulfate concentrations (2534 and 2423,4 mg/L), possibly due to the use of fertilizers in agriculture, indicating serious water pollution. In Thessaly, high concentrations of nitrite, ammonium and chromium total are observed in some samples, exceeding internationally accepted drinking water limits. In the Peloponnese, the values of these elements, although lower compared to Thessaly, exceed the permitted limits in some cases, especially for total chromium and ammonium samples.
The spatial distribution of trace element concentrations in the groundwater varied significantly. Despite a few exceptions, it was observed that most samples for trace elements (Cr total, Cr^{6+}, Pb, As, Cd, Ni) are either equal to or below the limit of quantification (LOQ or LOD); as a result, trace elements were not used in the factor analysis. This method provides a more accurate representation of the data and enables more accurate statistical analysis.

Table 1. Descriptive Statistics of Groundwater Quality Parameters in studied regions

	Peloponnese (n=235)				Thessaly (n=307)			
Parameter	**Minimum**	**Maximum**	**Mean**	**Std. Deviation**	**Minimum**	**Maximum**	**Mean**	**Std. Deviation**
pH	6,19	8,43	**7,45**	0,27	6,19	9,84	7,59	0,43
Temperature (°C)	9,5	31,6	18,3	2,59	9,5	31,6	18,06	2,55
Electrical Conductivity (EC, μS/cm)	230,5	**24900**	1223,65	2047,97	114	**24900**	1135,74	1815,65
Dissolved Oxygen (DO)	1	7,8	4,42	1,32	1	9,3	4,71	1,56
Calcium (Ca^{2+})	24,7	681,63	127,06	83,84	4,61	674,51	108,84	81,47
Magnesium (Mg^{2+})	0,66	290,81	27,22	38,56	0,66	290,81	30,08	36,61
Sodium (Na^{+})	1,7	5163,2	96,95	401,07	0,9	5163,2	89,67	355,15
Potassium (K^{+})	0,23	187,86	5,08	18,51	0,232	186,66	4,89	16,2
Bicarbonate (HCO_3^{-})	47,28	486,93	301,25	70,88	23,19	851,84	306,46	101,92
Chloride (Cl^{-})	3,51	**8062**	**205,58**	685,30	1,38	**8062**	**171,18**	602,55
Sulphate (SO_4^{2-})	2,57	**2534,5**	84,26	194,13	2,57	**2423,4**	79,06	176,47
Nitrate (NO_3^{-})	0,06	**534**	33,38	61,47	0	**526**	32,29	57,22
Nitrite (NO_2^{-})	0	0,26	0,02	0,03	0	**1,87**	0,05	0,17
Total Phosphates (PO_4^{3-})	0	0,46	0,01	0,04	0	0,364	0,02	0,04
Ammonium (NH_4^{+})	0	**1,73**	0,02	0,12	0	**4,16**	0,04	0,27
Chromium dissolved (Cr)	0	**50,28**	2,91	4,94	0	**50,16**	3,13	4,96

According to Table 2, in the two studied regions, the porous aquifer is the most prevalent aquifer, with a percentage of 48.1% in the Peloponnese and 53.1% in Thessaly. For the supply and storage of groundwater, porous aquifers are frequently important, especially in urban or agricultural settings (Daskalaki & Voudouris, 2008). Porous aquifer's materials are characterized by high permeability, which facilitates the rapid movement of water within the aquifer. This fact creates ideal conditions for storing and pumping groundwater. Increased permeability also makes them more susceptible to contamination by industrial activities or fertilizers, as it makes them accessible quickly to water (Burri et al., 2019).

Table 2. Type of aquifer

	Peloponnese		Thessaly	
	Frequency	**Percent (%)**	**Frequency**	**Percent (%)**
Karst	98	41,7	106	34,5
Porous	**113**	48,1	**163**	53,1
Excavated rocks	24	10,2	38	12,4
Total	**235**	100	**307**	100

In total, there are 307 monitoring stations in Thessaly and 235 in Peloponnese. However, the sample size used in the Kaiser-Meyer-Olkin (KMO) test and Bartlett's Test of Sphericity is smaller due to a lack of measurements for certain groundwater quality parameters at specific monitoring stations. Degrees of freedom (df=120 and df=105, respectively) in Bartlett's test resulted from the factor analysis's inclusion of 16 variables for Peloponnese and 15 for Thessaly. Table 3 shows the KMO statistics values for each case that was studied. KMO statistics values for each region are 0,51 and 0,67, respectively, indicating marginal to moderate suitability for the method (Shrestha, 2021). At p < 0,001, Bartlett's test of sphericity is highly significant, indicating that at least some of the variables of the correlation matrix have significant correlations with one another. In this case, the test values are 4819,16 and 4699,34, and the corresponding significance level is less than 0,001 (Silva et al., 2014).

Table 3. Kaiser-Meyer-Olkin (KMO) and Bartlett's Test of Sphericity

		Peloponnese	Thessaly
	KMO	**0,51**	**0,67**
Bartlett's Test of Sphericity	**Approx. Chi-Square**	4819,16	4699,34
	df	120	105
	Sig.	<0,001	<0,001

This study used principal component analysis (PCA) as the factor extraction method. PCA is often used to identify significant factors which influence groundwater quality, and it may minimize the number of variables without losing information (Bodrud-Doza et al., 2016). According to Table 3, the first four components explain 72,46% of the total variation in Peloponnese, while the other five frequent components account for 77,44% in Thessaly. These elements constitute the essential information of the initial data. The additional variables have an insignificant portion.

Table 3. Total Variance Explained in two regions

Component	Peloponnese						Thessaly					
	IE			RSSL			IE			RSSL		
	Total	%V	C%	Total	%V	C%	Total	%V	C%	Total	%V	C%
1	6,80	42,50	42,50	6,60	**41,23**	41,23	6,01	40,04	40,04	5,62	**37,47**	37,47
2	2,06	12,85	55,34	2,04	**12,77**	53,99	1,79	11,93	51,96	1,68	**11,22**	48,68
3	1,73	10,84	66,18	1,94	**12,13**	66,12	1,55	10,32	62,28	1,66	**11,06**	59,75
4	1,00	6,28	**72,46**	1,01	**6,34**	72,46	1,24	8,29	70,57	1,53	**10,20**	69,95
5							1,03	6,87	**77,44**	1,12	**7,49**	77,44

Extraction Method: Principal Component Analysis; IE:Initial Eigenvalues; %V: % of Variance; C%: Cumulative %;RSSL:Rotation Sums of Squared Loadings

Table 4 highlight the factor loadings after the rotation in each case. In Peloponnese, the first factor is responsible for 41.2% of the total dataset's variation. EC, sodium, chloride, sulfate, potassium, magnesium, and ammonia are the variables in this component with the highest loading coefficients. This factor reflects areas with elevated levels of inorganic salts and metals, which is strongly correlated with salinity. The salinity is primarily attributed to seawater intrusion into the aquifer, leading to an increased concentration of dissolved ions in the water (Han et al., 2015). While ammonia is present in this component with the intrusion ions, it is not a direct indicator of seawater intrusion. Instead, ammonia concentrations are monitored by processes such as organic matter decomposition, which is commonly increased in aquifers with a lack of oxygen (Moore & Joye, 2021). The second factor accounts for 12.8% of the total variation in the data, with high loadings on the nitrate and nitrite variables. This factor indicates agricultural contamination (agricultural runoff) since it contains nitrates, which are commonly found in fertilizers and organic sources, while nitrites are often associated with biogeochemical processes (Rivett et al., 2008; Khan et al., 2018). Their association usually reveals specific nitrogen cycle processes as well as the system's redox state. In oxygenated conditions, nitrite, an unstable intermediate, is frequently transformed to nitrate, indicating that nitrate dominance may be the last stage of oxidation (Nowka et al., 2015). A strong positive loading on the bicarbonate variables, which indicates their relationship to the geochemistry of carbonate rocks and the natural processes of CO_2 dissolution in the soil, characterizes the third component, which accounts for 12.1% of the total variation in the data. At the same time, it has a moderate negative loading on dissolved oxygen and pH, indicating the potential for inadequate oxygenation,

which can be linked with reductive environments or increased biological activity (Koch et al., 1985). The fourth factor expresses 6.3% of the total variation in the data and presents a high loading on the total phosphate's variable, indicating the use of phosphate fertilizers, and therefore potential pollution from fertilizer use and crops (Cheraghi e al., 2012).

Respectively in Thessaly, the first factor expresses 37.5% of the total variation in the data. Respectively in the Peloponnese, the first factor is characterized as a salinity factor, with high loadings on the variables EC, sodium, chloride, sulfate, potassium, and magnesium, describing the salinity and ionic concentration of the water. The second factor represents 11.2% of the total variation in the data and is characterized by a high positive moderate loading on the nitrate variable and a moderate positive loading on the calcium variable. Nitrates are related to the use of fertilizers in crops and to runoff from agricultural activities (Whang & Li, 2019). The existence of moderate calcium loading indicates that agricultural activities may occur in areas with a high geological presence of calcium or that calcium in rocks is dissolved from soils because of water inputs. The third factor is related to low oxygen or organic pollution environments, having a high positive loading on the variable's nitrite and ammonia. The simultaneous presence of both ions implies that reductive processes increase in low-dissolved oxygen environments, probably due to organic matter decomposition. The fourth factor is mainly related to physicochemical characteristics such as dissolved oxygen, temperature, and pH, reflecting the oxygenation processes in the aquatic environment. (Babatunde 2024). A high loading of dissolved oxygen (DO), a moderate negative loading for Temperature, and a moderate positive loading with pH are observed. The fifth factor expresses 7.5% of the total variation of the data and shows a high loading on the variable phosphate salts in water, which is related to agricultural (use of phosphate fertilizers) and biological sources. Phosphates are frequently indicators of eutrophication, or excessive nutrient enrichment of water, which can result in algae development and the degradation of quality of water (Cheraghi e al., 2012; Kundu et al., 2015).

Table 4. Rotated Component Matrix[a] in two regions

	Peloponnese				Thessaly				
	Component								
Parameter	1	2	3	4	1	2	3	4	5
pH	-0,13	-0,29	**-0,69**	-0,03	-0,04	-0,55	0,05	**0,54**	0,31
Water Temperature (°C)	0,39	-0,03	0,57	-0,07	0,34	0,14	-0,01	**-0,64**	0,23
Electrical Conductivity (EC)	**0,99**	0,09	0,07	-0,02	**0,98**	0,11	0,05	-0,10	-0,02
Dissolved Oxygen (DO)	-0,15	0,29	**-0,64**	-0,11	-0,11	0,10	0,01	**0,84**	-0,01
Calcium (Ca^{2+})	0,64	0,47	0,33	-0,04	0,57	**0,62**	0,00	-0,24	-0,21
Magnesium (Mg^{2+})	**0,80**	0,29	0,13	-0,05	**0,76**	0,30	0,18	-0,01	0,17
Sodium (Na^{+})	**0,99**	-0,05	0,00	0,00	**0,98**	-0,06	0,04	-0,07	-0,01
Potassium (K^{+})	**0,90**	-0,06	-0,03	-0,01	**0,92**	-0,07	0,02	-0,01	0,01
Bicarbonate (HCO_3^{-})	-0,15	0,04	**0,74**	-0,09					
Chloride (Cl^{-})	**0,99**	0,04	0,02	-0,02	**0,98**	0,06	0,01	-0,07	-0,05
Sulphate (SO_4^{2-})	**0,93**	0,07	0,11	0,01	**0,89**	0,09	0,11	-0,13	0,02
Nitrate (NO_3^{-})	0,02	**0,89**	0,10	-0,01	0,01	**0,87**	0,07	0,11	0,05
Nitrite (NO_2^{-})	0,05	**0,82**	-0,12	0,03	-0,04	0,08	**0,91**	0,08	0,15
Total Phosphates (PO_4^{3-})	-0,03	0,01	-0,01	**0,96**	-0,01	-0,04	0,06	-0,03	**0,92**
Ammonium (NH_4^{+})	**0,85**	-0,14	0,00	0,03	0,27	-0,04	**0,86**	-0,07	-0,08
Chromium dissolved (Cr)	-0,02	0,24	-0,02	-0,23	0,00	0,29	-0,19	0,09	0,10

Extraction Method: Principal Component Analysis.; Rotation Method: Varimax without Kaiser Normalization.; a. Rotation converged in 5 iterations (Peloponnese); Rotation converged in 6 iterations (Thessaly)

Conclusion

The degradation of groundwater quality makes agricultural production and public health difficult, as drinking water can be enriched with toxic metals. The analysis of hydro chemical data confirms the need for systematic monitoring of the region's stations and management of groundwater quality, especially in areas with high agricultural activity. This study identified significant relationship between anthropogenic variables and water quality parameter concentrations in groundwater wells. Overall, the type of aquifer has an important role in the creation of hydrogeological conditions and the vulnerability of areas to various environmental and anthropogenic stresses (Ashraf et al., 2017). The dominance of porous aquifers in the studied areas indicates increased water storage and transport capacity but at the same time

increased sensitivity to pollution from agricultural activities or other anthropogenic sources of pollution (Machiwal et al., 2018). The presence of sulfate (SO_4), nitrate (NO3), and chloride (Cl) indicates possible contamination due to anthropogenic activities affecting the quality of groundwater. The high concentration of nitrates and sulfates results from chemical pollution from agricultural (e.g. pesticides and fertilizers) and industrial activities, while the increased concentration of chlorides (Cl) is usually associated with excessive amounts of water in coastal areas (Akhtar et al., 2021).

Multivariate approaches like factor analysis can use and correlate numerous parameters. Factor analysis was performed to interpret the statistical methods according to the available data, proving to be a helpful tool for monitoring the groundwater quality. According to the results, this method provides the distribution and origin of water parameters. However, this study shows that additional data are required for the analysis of elements, including trace elements, with sufficient quantified values, so that the factor analysis does not overestimate or underestimate the influence of anthropogenic factors (e.g. industrial or agricultural activity). The estimation of the distribution and the improvement of the measurement methods of trace elements are necessary for the accurate analysis of hydrogeological processes and anthropogenic influences, as well as for enhancing the accuracy of statistical models, facilitating the identification of pollution sources. Furthermore, it is easier and more dependable to evaluate the results when they are presented utilizing Geographic Information Systems techniques (Mathenge et al., 2023; Xu & Zhan 2023). More extensive research can assist in developing a long-term groundwater management strategy for different objectives. Above all, it seems helpful to analyze geographical zones to identify high-pollution areas, the causes of pollution, particularly for heavy metals, and the agricultural applications that have an impact on nitrate levels.

Acknowledgements

The authors gratefully acknowledge the support of the National Monitoring Water Network and HSGME for providing open data that significantly contributed to the completion of this research. This study was conducted as part of the PhD dissertation, funded by the Athens Water Supply and Sewerage Company (E.Y.D.A.P.) within the framework of the IKY-EYDAP Scholarship Program for the academic year 2024-25.

References

Wada, Y., van Beek, L. P., & Bierkens, M. F. (2012). Non sustainable groundwater sustaining irrigation: A global assessment. *Water Resources Research*, *48*(6).

Karavitis, C. A., & Oikonomou, P. D. (2024). Water Resources Management and Policy in Greece: Challenges and Options. In *The Geography of Greece: Managing Crises and Building Resilience* (pp. 113-128). Cham: Springer International Publishing.

Dokou, Z., Kourgialas, N. N., & Karatzas, G. P. (2015). Assessing groundwater quality in Greece based on spatial and temporal analysis. *Environmental monitoring and assessment*, 187, 1-18.

Ministry of Environment and Energy. Retrieved from: http://nmwn.ypeka.gr/

Belkiri L and Mouni L (2012) “Hydrochemical analysis and evaluation of groundwater quality in El Eulma area, Algeria”, Appl. Water Sci.: 2:127-133.

World Health Organization (WHO) (2011) Guidelines for drinking water quality, Geneva, World Health Organization. 515.

Mitchell, E. J., & Frisbie, S. H. (2023). A comprehensive survey and analysis of international drinking water regulations for inorganic chemicals with comparisons to the World Health Organization’s drinking-water guidelines. *Plos one*, 18(11).

Praus, P. (2005). Water quality assessment using SVD-based principal component analysis of hydrological data. Water Sa, 31(4), 417-422.

Dammi Djimi, E. G., Abia, A. L. K., Belibi Belibi, P. D., Takam Soh, P., Che, R. N., Ghogomu, J. N., & Ketcha, J. M. (2021). Multivariate statistical and hydrochemical analysis of drinking water resources in Northern Cameroon watersheds. Water, 13(21), 3055.

Ma, R., Shi, J., Liu, J., & Gui, C. (2014). Combined use of multivariate statistical analysis and hydrochemical analysis for groundwater quality evolution: A case study in north chain plain. *Journal of Earth Science*, *25*, 587-597.

World Health Organization (WHO) (2008). *Guidelines for drinking-water quality: second addendum. Vol. 1, Recommendations*. World Health Organization.

Panno, S. V., Hackley, K. C., Hwang, H. H., Greenberg, S. E., Krapac, I. G., Landsberger, S., & O’kelly, D. J. (2006). Characterization and identification of Na-Cl sources in ground water. *Groundwater*, 44(2), 176-187.

Shrestha, N. (2021). Factor analysis as a tool for survey analysis. *American journal of Applied Mathematics and*

statistics, *9*(1), 4-11.

Silva, D. L., Sabino, L. D., Lanuza, D. M., Adina, E. M., Villaverde, B. S., & Pena, E. G. (2014, October). Silva's management competency theory: a factor-item analytic approach utilizing oblique rotation direct oblimin method under Kaiser-Bartlett's test of sphericity. In *Proceedings of the World Congress on Engineering and Computer Science* (Vol. 1).

Bodrud-Doza, M. D., Islam, A. T., Ahmed, F., Das, S., Saha, N., & Rahman, M. S. (2016). Characterization of groundwater quality using water evaluation indices, multivariate statistics and geostatistics in central Bangladesh. *Water science*, *30*(1), 19-40.

Babatunde, S. (2024). *Evaluating the Impact of Continuous Cover Cropping and Kernza on Nitrate and Orthophosphate Retention in Corn-Soybean Rotations: Implications for Drain Water Quality and Environmental Sustainability* (Doctoral dissertation, Western Illinois University).

Akhtar, N., Syakir Ishak, M. I., Bhawani, S. A., & Umar, K. (2021). Various natural and anthropogenic factors responsible for water quality degradation: A review. *Water*, *13*(19), 2660.

Xu, H., & Zhang, C. (2023). Development and applications of GIS-based spatial analysis in environmental geochemistry in the big data era. *Environmental Geochemistry and Health*, *45*(4), 1079-1090.

Mathenge, M., Sonneveld, B. G., & Broerse, J. E. (2022). Application of GIS in agriculture in promoting evidence-informed decision making for improving agriculture sustainability: a systematic review. *Sustainability*, *14*(16), 9974.

Taleuzzaman, M. (2018). Limit of blank (LOB), limit of detection (LOD), and limit of quantification (LOQ). *Org. Med. Chem. Int. J*, *7*(5).

Nowka, B., Daims, H., & Spieck, E. (2015). Comparison of oxidation kinetics of nitrite-oxidizing bacteria: nitrite availability as a key factor in niche differentiation. *Applied and environmental microbiology*, *81*(2), 745-753.

Daskalaki, P., & Voudouris, K. (2008). Groundwater quality of porous aquifers in Greece: a synoptic review. *Environmental Geology*, *54*, 505-513.

Burri, N. M., Weatherl, R., Moeck, C., & Schirmer, M. (2019). A review of threats to groundwater quality in the anthropocene. *Science of the Total Environment*, *684*, 136-154.

Han, D., Post, V. E., & Song, X. (2015). Groundwater salinization processes and reversibility of seawater intrusion in coastal carbonate aquifers. *Journal of Hydrology*, *531*, 1067-1080.

Moore, W. S., & Joye, S. B. (2021). Saltwater intrusion and submarine groundwater discharge: acceleration of biogeochemical reactions in changing coastal aquifers. *Frontiers in Earth Science*, *9*, 600710.

Khan, M. N., Mobin, M., Abbas, Z. K., & Alamri, S. A. (2018). Fertilizers and their contaminants in soils, surface and groundwater. *Encyclopedia of the Anthropocene*, *5*, 225-240.

Rivett, M. O., Buss, S. R., Morgan, P., Smith, J. W., & Bemment, C. D. (2008). Nitrate attenuation in groundwater: a review of biogeochemical controlling processes. *Water research*, *42*(16), 4215-4232.

Koch, F. A., & Oldham, W. K. (1985). Oxidation-reduction potential–a tool for monitoring, control and optimization of biological nutrient removal systems. *Water science and technology*, *17*(11-12), 259-281.

Cheraghi, M., Lorestani, B., & Merrikhpour, H. (2012). Investigation of the effects of phosphate fertilizer application on the heavy metal content in agricultural soils with different cultivation patterns. *Biological trace element research*, *145*, 87-92.

Wang, Z. H., & Li, S. X. (2019). Nitrate N loss by leaching and surface runoff in agricultural land: A global issue (a review). *Advances in agronomy*, *156*, 159-217.

Kundu, S., Coumar, M. V., Rajendiran, S., Rao, A., & Rao, A. S. (2015). Phosphates from detergents and eutrophication of surface water ecosystem in India. *Current science*, 1320-1325.

Machiwal, D., Jha, M. K., Singh, V. P., & Mohan, C. (2018). Assessment and mapping of groundwater vulnerability to pollution: Current status and challenges. *Earth-Science Reviews*, *185*, 901-927.

Ashraf, B., AghaKouchak, A., Alizadeh, A., Mousavi Baygi, M., R. Moftakhari, H., Mirchi, A., & Madani, K. (2017). Quantifying anthropogenic stress on groundwater resources. *Scientific reports*, *7*(1), 12910.

17th INTERNATIONAL CONGRESS of the Geological Society of Greece

BULLETIN OF THE GEOLOGICAL SOCIETY OF GREECE, SP. PUBL.

EXTENDED ABSTRACT 092

Automatic Detection and Extraction of Geological Lineaments on Amorgos Island Using Satellite Data and Open-Source Software

Georgios P. Georgalas[1], Polychronis Kolokoussis[1], Sofia Laskari[2], Konstantinos Soukis[2]

(1) National Technical University of Athens (NTUA), School of Rural, Surveying & Geoinformatics Engineering, Laboratory of Remote Sensing, Athens, Greece, gp.georgalas@gmail.com

(2) National and Kapodistrian University of Athens, Department of Geology and Geoenvironment, Dynamic, Tectonic and Applied Geology, Athens, Greece

Abstract

This study presents a methodology automatically detecting and extracting geological lineaments on Amorgos Island using satellite data and open-source software. The approach utilizes Landsat 8 satellite images and employs a newly developed Python-based algorithm, GeoLine, for automated lineament detection. The results demonstrate a dominant NE-SW orientation of lineaments, which aligns with previous geological studies of the region. The extracted lineaments show a 53% correlation with existing geological maps, confirming the reliability of the proposed approach.

Introduction

Geological lineaments represent structural discontinuities such as faults and fractures and play a crucial role in geoscientific studies. The ability to extract and analyze these features using remote sensing has been a growing research area. Various remote sensing techniques, including manual, semi-automated, and automated methods, have been employed for lineament detection (Tsilavo et al., 2006). The choice of techniques depends on the research objectives and available datasets, such as optical and radar imagery (Yathunanthan et al., 2014).

This study focuses on the automated extraction of geological lineaments using open-source software. By leveraging satellite data and computational techniques, it aims to develop an efficient and reproducible methodology for detecting geological structures, contributing to advancements in structural geological analysis.

Geological setting

Amorgos Island is located in the southeastern part of the Attic-Cycladic Crystalline Complex of Greece. This region formed as a result of the northward subduction of Gondwanan fragments beneath the Eurasian plate (Pe-Piper and Piper 2002; Papanikolaou 2021). The island's geology includes metamorphosed clastic sequences, carbonates, and flysch deposits, which are divided into three regions: northeastern, central, and southwestern (Figure 1, Laskari et al., 2022). The rocks of Amorgos have undergone multiple deformation events, particularly in the later stages, including alpine and neotectonic faults. The latter are associated with the 1956 offshore earthquakes (Papadopoulos and Pavlides 1992). Therefore, Amorgos provides an ideal setting for applying the automatic detection and extraction method of geological lineaments.

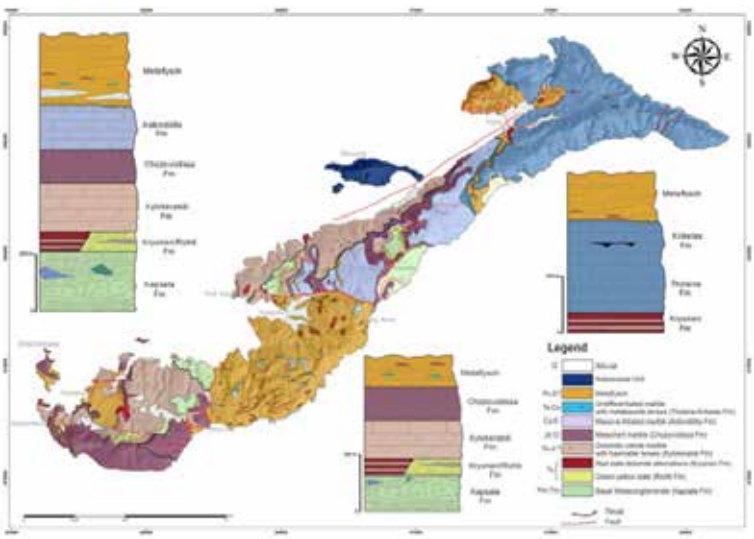

Figure 1. Geological map of Amorgos Island and lithostratigraphic columns of southwestern, central, and northeastern Amorgos (adapted from Laskari et al., 2022)

Data

For the objectives outlined, satellite imagery from the NASA Landsat 8/9 satellites was selected as the primary dataset source, based on accessibility, spatial resolution, spectral range, and enhancement capabilities even though Sentinel-2 imagery could have been used as well.

For this study, one Landsat 8 image acquired on May 27, 2022(Level 2 data product: "LC08_L2SP_181034_202 20527_20220603_02_T1"), has been used. This image included layers such as surface reflectance (SR), surface temperature (ST), intermediate ST bands, angle coefficient files, and quality assessment (QA) bands.

Method

Satellite data pre-processing was conducted in QGIS 3.22.1 using the Semi-Automatic Classification Plugin (SCP). Pansharpening was applied through the GDAL toolbox with Nearest Neighbor (NN) resampling. Dimensional reduction was performed using Principal Component Analysis (PCA) with PC1 selected for analysis. The final processed image had dimensions of 2067×1253 pixels, and a 15×15-meter pixel size. The image was segmented into 400×400-pixel tiles.

For automated tectonic lineament extraction, a Python-based algorithm called GeoLine was developed. Image import and georeferencing were handled using the GDAL library. Edge detection was performed with Canny algorithm. Vectorization was achieved through the Probabilistic Hough Transform (PHT), extracting edges as vector lines while refining parameters such as minimum length and angular tolerance (Fig. 2). The generating shapefiles were merged in QGIS, and a rose diagram was created using the Line Direction Histogram plugin.

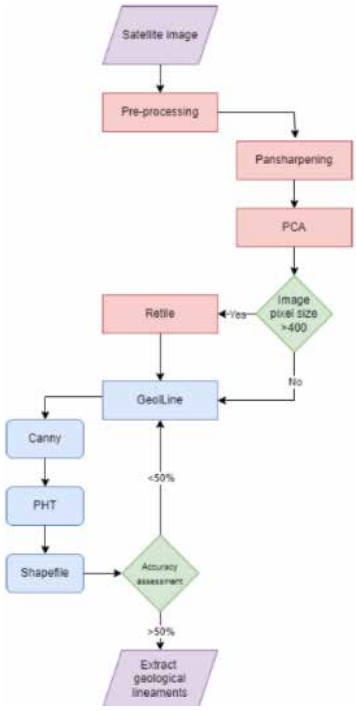

Figure 2. Methodology's Flowchart.

Results And Discussion

This study evaluated the accuracy and relevance of the extracted geological lineaments by comparing them with published geological datasets. Five image sets were generated using different parameter configurations for the Canny and PHT algorithms.

Validation was conducted by comparing the extracted lineaments with datasets from Laskari et al. (2022) and the Hellenic Society of Geology and Mineral Exploration (H.S.G.M.E.) (Fig 3.). Additionally, the results were assessed against PCI Geomatica 9.1 software (Salui, 2018), where seven image sets were generated using different parameter configurations.

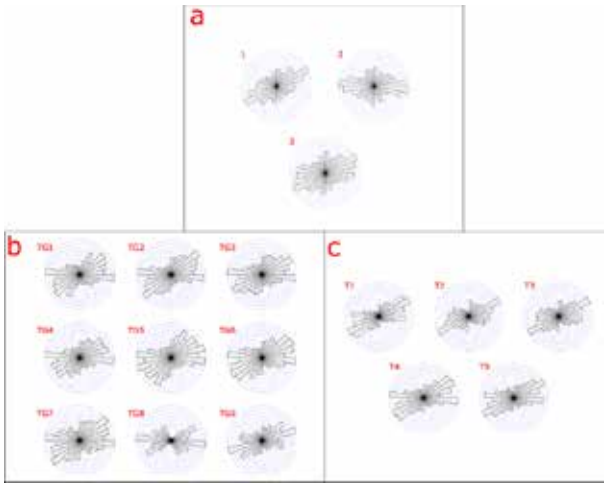

Figure 3. Rose diagrams of lineaments: (a) Ground truth data (1: Laskari et al., 2022; 2: H.S.G.M.E.; 3: combination of 1 & 2), (b) Geomatica Line algorithm, seven datasets with different parameters, (c) GeoLine algorithm, five datasets with different parameters.

Correlation analysis using the LineComparison plugin revealed an overall low correlation due to the limited distribution of control data. However, focused comparisons in specific regions around the control data consistently exceeded 33%. Notably, both Geomatica and GeoLine achieved correlation rates of up to 53%, with the T4 and TG7 datasets displaying the highest correlation percentages (Fig. 4).

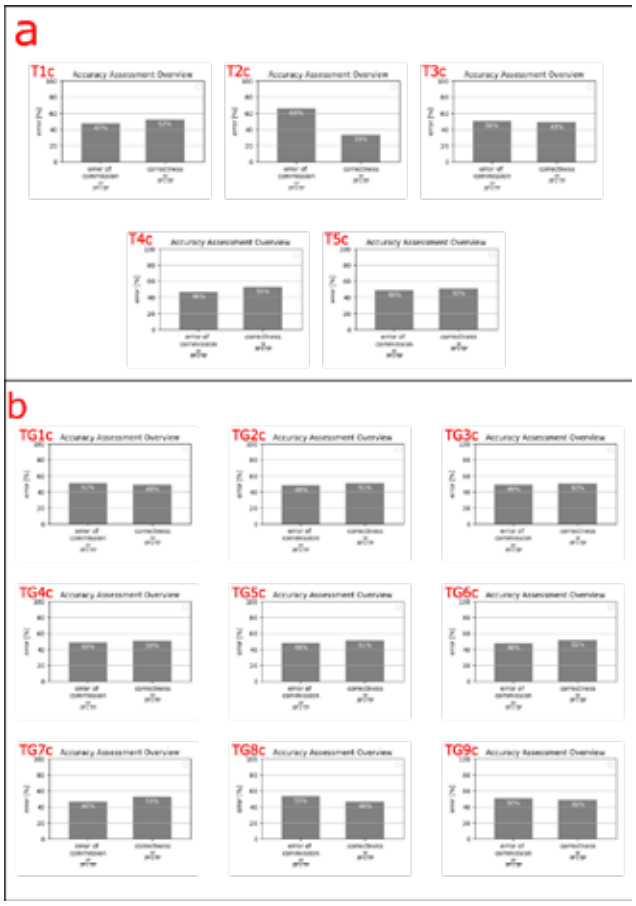

Figure 4. Accuracy assessment in demarcated zone with a) GeoLine dataset, and b) Geomatica dataset.

Although the results are promising, there is still room for improvement in terms of precision, accuracy, and usability. Future efforts will focus on two key areas.

First, enhancing result efficiency by refining GeoLine to improve post-lineament extraction capabilities. This includes achieving better correlation between detected lineaments and generating more accurate polygonal chains. Expanding the methodology to incorporate a wider range of satellite data sources, such as SAR images for terrain relief and high-resolution multispectral imagery like WorldView-3, would further improve accuracy and applicability.

Second, improving usability by automating procedural steps and integrating them into a user-friendly QGIS plugin. This would make the methodology more accessible to researchers with limited programming skills. Developing an open-source plugin would simplify data input and lineament extraction, streamlining workflows and broadening access for geoscientists.

These advancements would greatly enhance both the effectiveness and accessibility of the GeoLine algorithm, establishing it as a more valuable tool for geological research.

Conclusions

This study demonstrates the efficiency and accuracy of the developed methodology in extracting geological lineaments from satellite imagery, by showing a significant correlation with existing geological data. GeoLine shows strong potential for large-scale geological surveys, further refinement is needed to minimize noise and enhance accuracy in complex geological settings. By offering a reproducible and efficient methodology, this research contributes to the growing body of knowledge in the field of automated geological mapping.

References

Tsilavo Raharimahefa, Timothy M. Kusky, Structural and remote sensing studies of the southern Betsimisaraka Suture, Madagascar, Gondwana Research, Volume 10, Issues 1–2, 2006, Pages 186-197, ISSN 1342-937X, https://doi.org/10.1016/j.gr.2005.11.022.

Yathunanthan Vasuki, Eun-Jung Holden, Peter Kovesi, Steven Micklethwaite, Semi-automatic mapping of geological Structures using UAV-based photogrammetric data: An image analysis approach, Computers & Geosciences, Volume 69, 2014, Pages 22-32, ISSN 0098-3004, https://doi.org/10.1016/j.cageo.2014.04.012.

Ahmadi, H.; Pekkan, E. Fault-Based Geological Lineaments Extraction Using Remote Sensing and GIS—A Review. Geosciences 2021, 11, 183. https://doi.org/10.3390/geosciences11050183.

Sichugova L.V., Jamolov A.T., & Movlanov J.J. (2021). Statistical Analysis Of Lineaments Using Landsat 8 Data: A Case Study Of The Fergana Valley (East Uzbekistan). The American Journal of Applied Sciences, 3(3), 83–92. https://doi.org/10.37547/tajas/Volume03Issue03-14. .

Marzouki, A., Dridri, A. Lithological discrimination and structural lineaments extraction using Landsat 8 and ASTER data: a case study of Tiwit (Anti-Atlas, Morocco). Environ Earth Sci 82, 125 (2023). https://doi.org/10.1007/s12665-023-10831-4. El-Qassas, R.A.Y., Ahmed, S.B., Abd-Elsalam, H.F. and Abu-Donia, A.M. (2021) Integrating of Remote Sensing and Airborne Magnetic Data to Outline the Geologic Structural Lineaments That Controlled Mineralization Deposits for the Area around Gabal El-Niteishat, Central Eastern Desert, Egypt. Geomaterials, 11, 1-21. https://doi.org/10.4236/gm.2021.111001.

Papadopoulos, G., Pavlides, B.S., 1992. The large 1956 earthquake in the South Aegean: Macroseismic field configuration, faulting, and neotectonics of Amorgos Island. Earth Planet. Sci. Lett. 113 (3), 383–396. https://doi.org/10.1016/0012-821X(92)90140-Q.

Papanikolaou, D.I., 2021. Regional Geology Reviews The geology of Greece. Springer Nature pp. 345. https://doi.org/10.1007/978-3-030-60731-9.

Pe-Piper, G. and Piper, D.J.W., 2002. The igneous rocks of Greece. The anatomy of an orogen. –Gebrüder Borntraeger, Berlin, Stuttgart. G. Catsadorakis: Determinants of raptor abundance, 573.

Dürr, S., 1985. Geological Map of Greece, 1:50.000, Amorgos-Donousa Sheet.Institute of Geological and Mining Research, Athens.

Sofia Laskari, Konstantinos Soukis, Daniel F. Stockli, Stylianos Lozios, Alexandra Zambetakis-Lekkas, Reconstructing the southern Pelagonian domain in the Aegean Sea: Insights from U-Pb detrital zircon analysis, lithostratigraphic and structural study, and zircon (U-Th)/He thermochronology on Amorgos Island (SE Cyclades, Greece), Gondwana Research, Volume 106, 2022, Pages 329-350, ISSN 1342-937X, https://doi.org/10.1016/j.gr.2022.02.007.

Salui, C.L. Methodological Validation for Automated Lineament Extraction by LINE Method in PCI Geomatica and MATLAB based Hough Transformation. *J Geol Soc India* **92**, 321–328 (2018). https://doi.org/10.1007/s12594-018-1015-6

17th INTERNATIONAL CONGRESS of the Geological Society of Greece

BULLETIN OF THE GEOLOGICAL SOCIETY OF GREECE, SP. PUBL.

EXTENDED ABSTRACT 093

Major and trace element analysis on geological samples using WD-XRF on pressed pellets

I. Gerontidou[1], A. Koroneos [1]

(1) Department of Mineralogy-Petrology-Economic Geology, Faculty of Geology, Aristotle University of Thessaloniki, Thessaloniki, Greece, ioangero@geo.auth.gr.

The sample preparation protocol and the analytical method of elemental analysis using WD-XRF Supermini200 from Rigaku Holdings Corporation, are presented. The use of pressed pellets, traditionally employed for trace element analysis, is examined and proposed for major element analysis as well.

Introduction

Wavelength Dispersive X-ray Fluorescence (WD-XRF) spectrometry has been the cornerstone of elemental analysis for geological samples. It is a non-destructive analytical technique that provides high accuracy and precision, when measuring the composition of both light and heavy elements (Beckhoff et al., 2007; Rainer, 2016). Measuring major elements is quite a challenge because light elements emit weaker fluorescent energies. This problem was approached with the use of fused beads because they offer optimal homogeneity within the sample and a smooth surface for the primary X-ray to hit, minimizing energy scattering and absorption effects (Beckhoff et al., 2007). That's why major element XRF analysis has been, almost exclusively, done on fused glass beads. However, sample fusion is costly, requiring the purchase and maintenance of a fusion machine and Pt-Au ware. Moreover, it is time-intensive due to multiple stages of preheating, prefusion, fusion and air cooling.

In this study, the use of pressed pellets for major element analysis is examined, by creating and calibrating an empirical hybrid quantitative method using certified reference materials. The use of pressed pellets is the most cost effective and time saving sample preparation method. The core of this research is the comparison of certified reference material values with their obtained results using the proposed method. Along with the major elements, the commonly used trace elements in geological research are calibrated into the method, broadening its utility.

Sample preparation

The most important part of calibrating a new analytical method is to maintain a consistent sample preparation protocol (Marguí & Queralt, 2024). The reliability of the results is always dependent on proper sample handling. For this reason, thorough care is taken to keep the lab-ware clean and to work in a laboratory environment with limited dust, ensuring minimal contamination from the surroundings.

Geological samples, due to their inhomogeneity, cannot be analyzed directly as a solid. Instead, the rocks are first crushed using a steel jaw breaker, downsizing them to an approximately 2cm fracture size. The next and most crucial step is pulverizing the rocks to a fine powder. To evaluate the use of pressed pellets over fused beads, it is vital to achieve sample homogeneity. Pulverization is also the most prone step to contamination, which is the reason many researchers have investigated its effects (Thompson & Bankston, 1970; Hickson, 1986; Roser et al., 2003; Mojtahed et al., 2006; Saikia et al., 2009; Takamasa & Nakai, 2009; Morikawa, 2014; Yamasaki, 2018).

Among the available options, using tungsten carbide (WC) pulverizing mill bowl is the most time-efficient choice, and essential for quartz-bearing siliceous rocks. However, it can affect the elemental composition of the sample. Morikawa (2014) presents the contamination of a SiO_2 sample, with W, Cu, Co, Ni and Fe, Yamasaki (2018) and Saikia et al. (2009) confirm the Co and W contamination of volcanic rocks and a quartz sample respectively and Mojtahed et al. (2006) suggests the added impurity of W, Co, C, Ti, Ni, Ta. Those studies point out the drastic effects of the pulverization duration. Morikawa (2014) displays the impurities present at 3, 5 and 10 minutes, Saikia et al. (2009) at 5 minutes, whereas Yamasaki (2018) indicates Co (~10 ppm) and W (up to 100 ppm) contamination at 40 sec and lastly, Roser et al. (2003) confirm the Co and W contamination at 30sec pulverizing time using tungsten carbide mill.

To avoid any contamination mentioned above, the proposed protocol follows strictly the under 10 second duration time in WC pulverizer, preferably at 5 seconds. Another measure taken to ensure the purity of the sample is following the technique of prewash, where a small portion of the sample is grinded and discarded, before continuing with the rest of the sample. For the last step of pulverization, to ensure the fine grain size (smaller than 50μm), the sample is grinded on a manual agate mortar. The agate mortar has been proven to add limited contamination (Takamasa & Nakai, 2009).

The typical procedure for pelletizing geological samples is followed. The sample must be mixed with a reagent to behave

as a binder, guaranteeing the cohesion of the pressed solid disc. These reagents improve uniformity, durability, and increase the density of the pellet, creating a consistent surface to analyze. This study's protocol uses CEROX from FLUXANA GmbH & Co. KG, as a binder, which is known as Hoechst wax ($C_{38}H_{76}N_2O_2$). It is very low on impurities and resistant to X-rays. It is mixed with the sample on a 1:4 ratio (Rainer, 2016), more specifically 2 grams of the binder are mixed with 8 grams of the sample. In the case that the sample has very high relative density, the portions are increased accordingly to achieve infinite thickness (Marguí & Queralt, 2024) of the pressed pellet. X-rays can penetrate the sample up to a few millimeters that's why the pellet must be thick enough (>0.5 cm) for the penetration to not go further to the back of the pellet. The mixture of sample-binder is then inserted into the automatic Retsch 200 mixer mill for homogenization. After testing, the most optimal mixing is achieved at 15 minutes by fluctuating the speed of the mixer, turning it from low to high. This lets the particles mix more efficiently than letting the mixer work on high for the whole period. In the end, the palletization is completed with the Specac 15-ton Hydraulic press with the 40 mm pressing dies. XRF machines are sensitive to dust, so to make sure the pellet won't break inside the instrument, the durability of the pellets is tested with the drop test. The drop test involves the free fall of the pellet from 15 cm distance from a flat surface. The pellets that pass the fall test, show a homogeneous surface without colored spots that would indicate the differentiation within the solid, and have a smooth flat surface, are ready for analysis. The maintenance of the pressing dies is important to achieve the desired smooth flat surface.

Part of the sample preparation is also the calculation of loss on ignition (LOI). Geological samples contain volatiles like CO_2 (e.g. in calcite) and crystalline water (bound H_2O^+ found in OH-bearing minerals like amphiboles or micas). These elements cannot be analyzed with XRF. Modern XRF analytical methods can estimate the LOI without the need of pre-calculation. However, for better accuracy it is recommended to calculate LOI beforehand, by exposing the samples in high temperatures and measuring mass loss (Brouwer, 2003). Approximately 2 grams of the fully dried sample is inserted into a fully dried heat-resistant ceramic capsule and then placed in a high temperature furnace. This protocol suggests first heating the samples at 150°C for 15 minutes and then at 1050°C for 120 minutes, so that the temperature is gradually going up. At 1000°C there is complete removal of volatiles (Lechler & Desilets, 1987). After cooling down, the capsules are weighed to calculate the mass loss. The final goal of this procedure is to calculate the volatile content of the sample so that the LOI % value can be in the sample's final composition to be normalized to 100%. It is highlighted that the samples and crucibles are fully dried before the heating, so that moisture water (H_2O^-) is not confused with bound water (H_2O^+) at the LOI value.

Instrument specifications

The Superimini200 is a benchtop Wavelength Dispersive X-ray Fluorescence (WD-XRF) spectrometer from Rigaku. It is equipped with a Pd anode X-ray tube, operating at 200W power. The X-ray beam is filtered using a Zr filter. The system utilizes two primary crystals: LiF(200) and PET, coupled with two detectors: a flow proportional counter and a scintillation counter. It has a broad elemental detection range from O to U. For analysis on solids, the system operates under vacuum. The instrument requires a P10 gas mixture (10% Ar - 90% CH_4) as its primary consumable. To ensure optimal performance and consistent analytical results, the laboratory environment temperature must be kept below 28°C. The fluctuation in laboratory temperature has been observed to affect drastically the quality of the results, so the importance of maintaining a constant temperature of 20-25°C is highlighted.

Analytical method

The Supermini200 operates using the ZSX Guidance software, which is user-friendly and provides extensive control over the calibration and data analysis. For this study, the analytical method was developed using nineteen certified reference materials (CRMs) from FLUXANA. These standards were carefully selected to cover a wide compositional range, ensuring that the calculated results for unknown samples fall within the calibration range. Specifically, the analytical method achieves optimal precision when the unknown sample's composition lies between the highest standard composition (Point A) and the lowest standard composition (Point B) for each element. Since this analytical method was meant for geological samples, silica content is a useful indicator, so it was essential to cover a large range. The standards that were picked cover the silica range from 35.69% to 73.42%.

The method quantifies major elements in their oxide forms, including SiO_2, Al_2O_3, K_2O, Na_2O, MgO, CaO, TiO_2, MnO, Fe_2O_3, P_2O_5, and SO_3 in percent (%), as well as the trace elements Rb, Sr, Ba, Zr, V, Cr, Co, Ni, Cu, Zn, Pb, Sc, Y, Ga, and Nb in ppm.

The analytical method is classified as a standardized method, more specifically as an empirical analytical method. Its basis is the calibration curve, which is represented graphically from the relationship between the standards' certified analytical values (x axis) and their X-ray fluorescent intensities (y axis). This correlation then is used to obtain the content of the unknown sample by projecting the unknown sample's X-ray intensity on the graph (Brouwer, 2003).

The method includes the «optimizing measuring conditions» (OMC), which determines the measurement conditions for each element. This step is prior to the measurement of the standards and hence the calibration. It is critical because it affects all the next steps, and it would be very time-consuming to go back to adjusting this step after completing the method. For the OMC, standards are first measured with the highest and the lowest content for each element to take scans. The OMC is divided into four parts, determining the peak position, selecting background points position, setting counting time and adjusting the pulse height analyzer (PHA) window. The peak position (2-theta degrees) is unique for each element, there is a theoretical value, but this can vary depending on the laboratory conditions. Background noise from scattered X-rays was negligible for major elements, therefore background points weren't needed. Background points were selected for all the trace elements, with most requiring two points to form linear background (BG) coefficients, except from Co and Sc where three points were selected, forming quadratic BG coefficients. Effective management of measuring time is crucial so that accurate results are achieved without unnecessary delays. Insufficient measuring time can lead to poor precision, while excessive measurement can reduce the efficiency of the method. The measuring times allocated for each element were: 40 seconds (sec) for the peaks of major elements and 40-140 sec for the trace elements, depending on their complexity. For example, 139 sec were chosen for Ba, a challenging element to measure because of its overlap with Ti, whereas 40 sec were sufficient for Ni. Each background point is measured for 10 to 33 sec. The total analysis time is calculated to be 34 minutes per sample. PHA window was widened for all elements to include their entire signal.

Another important part of the analytical method creation is drift correction. Over time, instrument aging, temperature fluctuations and changes in environmental conditions affect the X-ray intensities. To overtake these variations and maintain result stability, drift correction materials are measured on the day the method is created, and the results are stored in the software for the instrument to use during subsequent measurements and adjust accordingly. It works as a monitor to bring the method back to its calibrated state. In this study, the Alpha-Beta drift correction method was applied, using high and low concentration standards for as many elements as possible. Specifically, BR SQ1N and BR SQ3N glass discs from Bruker Corporation were used for Si, Al, K, Na, Mg, Ca, Ti, Mn, Sr, Ba, Zr, Zn and Pb. It is essential to update the drift correction library, before and after any maintenance service of the instrument.

Three corrections were made. First, a mixing ratio correction (0.25) was applied for the binder, using a 1:4 binder-to-sample ratio to account for the dilution effect of the binder on the sample's X-ray fluorescent intensity. Lastly, overlap and matrix corrections were chosen for elements whose peaks overlap or show absorption/enhancement respectively. The analytical element lines with their correction lines are displayed on Table 1.

Table 1. Element lines with their correction line(s)

Element line	Si-KA	Al-KA	K -KA	Ca-KA	Mn-KA	Fe-KA	P -KA	S -KA
Correcting line(s)	Al-KA	Ca-KA Si-KA	Fe-KA	K -KA	Cr-KA	Mn-KA Co-KA Si-KA	Zr-KA Ca-KA	Ti-KA Pb-LA
Element line	Rb-KA	Sr-KA	Ba-LA	Zr-KA	V -KA	Cr-KA	Co-KA	Ni-KA
Correcting line(s)	Sr-KA Al-KA	Ca-KA Rb-KA	Sc-KA Cu-KA Ti-KA	Sr-KA Y -KA	Ti-KA Ba-LA Cr-KA	V -KA	Fe-KA Ni-KA	Y -KA Rb-KA
Element line	Cu-KA	Pb-LA	Sc-KA	Y -KA	Ga-KA	Nb-KA		
Correcting line(s)	Sr-KA	Si-KA Zr-KA	Ca-KA Ti-KA	Rb-KA	Al-KA	Zr-KA V -KA		

The empirical method was converted to Fundamental Parameters (FP) method to achieve greater accuracy (Rousseau, 2013). The empirical method, while effective for calibration, relies heavily on the standards and appears problematic when a sample shows heterogeneity in the matrix. This means that for samples that don't contain a high variety of elements, the empirical method is sufficient to quantify them, with the best accuracy. In the case of rocks where a lot of elements are present and there is a heterogeneous matrix (complex mineral assemblance) there is a misfit (Beckhoff et al., 2007). For a purely empirical method to work well for rocks, an extremely large number of standards would be needed, which is not possible to use. With the conversion of the empirical method to FP, theoretical equations are introduced to correct matrix effects (Rousseau, 2006; Kawai et al., 2019), rather than relying solely on empirical data, but still using them. This way, analysis of samples outside of the exact compositional range of the calibration standards is possible. This hybrid method proved to be more accurate than the purely empirical methods that were developed.

To ensure the ongoing validity of the analytical method, the software provides the ability to input a check sample. This

check sample is used as a consistent reference analyzed every time before a batch of unknown samples is analyzed. It has known composition and standard deviation values, which are predefined within the software. This way, the system automatically flags results that deviate beyond acceptable limits (high and low). It's best to also test the sample preparation process by making new pressed pellets occasionally of the same check sample's powder.

Validation – Accuracy and precision

The validation of an analytical method is a significant step after the calibration, this method was validated in-house (Boqué et al., 2002). For this study, six certified reference materials were used for the validation of the method to cover a wide range of silica content, from 42.38% to 73.42% (CRM values). This is so the validation covers a wide range of concentrations (Boqué et al., 2002) for geological samples. These samples are listed in Table 2 with their basic information.

Table 2. Certified reference materials used for the validation of the method.

No.	FX part number	Manufacturer	Manufacturer's code	Application
1	FI000042	GSJ	JP-1	peridotite
2	FI007834	GSJ	JB-2a	basalt
3	FI000048	GSJ	JSy-1	syenite
4	FI007152	GSJ	JA-1	andesite
5	FI000097	GSJ	DC71302	trachyte
6	FI007981	GSJ	GM	granite

Accuracy and precision are two key properties that determine the quality of the analytical method. Accuracy reflects how close the calculated result is to the true or correct value, while precision indicates the reproducibility of the results (Ragland, 1989).

To assess precision, Ragland (1989) proposes duplicate analyses on five samples, for each major element to calculate the percent deviation or coefficient of variation (V) from equation 1 (Tab. 3). V is perceived as a measure of error or precision. For this study triplicate analyses were carried out on six samples (Tab. 2). Before calculating V, the results per element must be standardized to be comparable. To do that, the average $\bar{x}$ (for each sample) and the grand mean $\bar{x}_G$ (average from all samples) are calculated to find the factor f from equation 2 (Tab. 3). Then, to standardize the results, each calculated value is multiplied with f, equation 3 (Tab. 3). Standard deviation (s) is calculated from the standardized results; hence V is calculated from the standardized results (equation 1 from Tab. 3).

Table 3. Equations used for precision and accuracy measures. Modified from Ragland (1989).

$V = 100s/\bar{x}_G$	equation 1
$f = \bar{x}_G / \bar{x}$	equation 2
f * element %	equation 3
$x^2 = \Sigma[(O-R)^2/R]$	equation 4

For the main major elements Al_2O_3, TiO_2, Fe_2O_3, MgO, CaO, Na_2O, K_2O, Ragland (1989) indicates that V should be < 3-4 % per oxide, whereas for SiO_2 V should be < 2 %. For this study, Al_2O_3, TiO_2, Fe_2O_3, MnO, MgO, CaO, Na_2O, K_2O have V ranging from 0.9 % to 3.9 % and SiO_2 has V = 0.068 %. For P_2O_5 and S_2O_3 V is 4.3 % and 4.9 % respectively, these elements are not approached by Ragland (1989), this V value is accepted because of the small content of P and S in these rocks and the difficulty of quantifying them.

To evaluate accuracy, Ragland (1989) describes the procedure of comparing the certified reference material value and the obtained concentrations for elements in one or more standards. He highlights the importance of these samples not being part of the regression calculations for the calibration curve. As an estimate of accuracy, he uses Chi-Squared (x^2) from equation 4 (Tab. 3), where "O" is the obtained value and "R" is the reference material value. The x^2 is calculated for each single comparison standard for the sum "Σ" of the major elements. This study's major elements had x^2 values ranging from 0.006 to 0.13. Ragland (1989) considers acceptable values for major elements with x^2 < 0.10-0.15.

For better presentation of the results, major and trace elements are projected with their obtained (y-axis) and certified reference material (x-axis) values in figures 1 and 2 respectively. On figures 1 and 2, the equations of the linear regression lines in the form of y = bx + a and the coefficient of determination R squared (R^2) are displayed. The quantity R^2 represents the variation of the data, a value near 1 indicates a good fit, whereas a value near 0 indicates a poor fit (Ross, 2010).

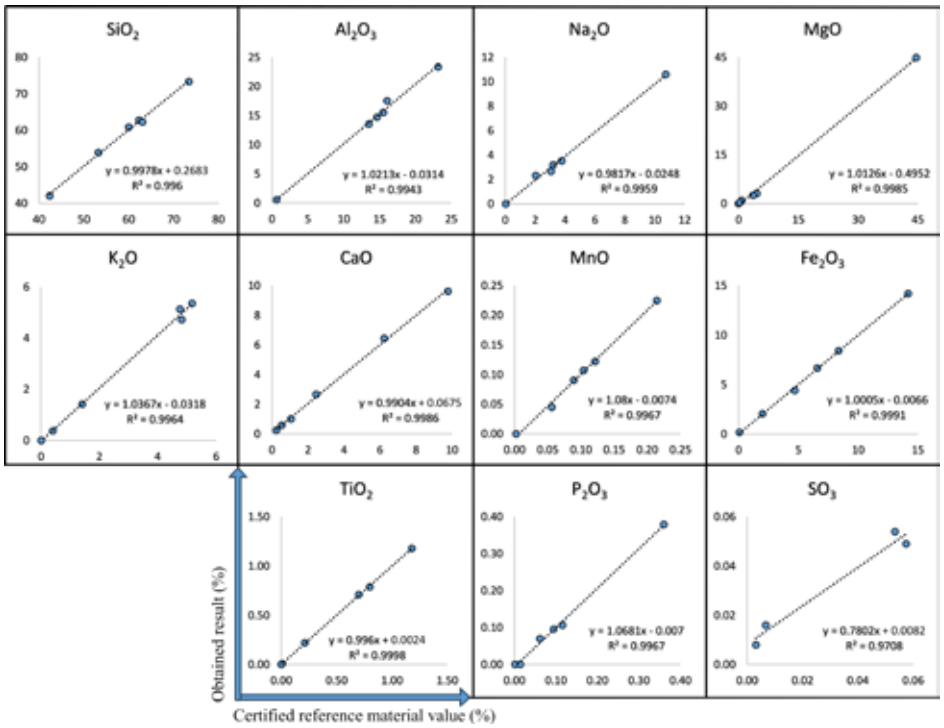

Figure 1. Certified reference material vs obtained result values for the major elements

The results for the major elements showed a coefficient of determination (R^2) higher than 0.99 for the major elements (Fig. 1), except for SO_3 yielding an R^2=0.97, which is considered a challenging element with very low content in the rocks studied. These results show excellent fit ($R^2 > 0.95$). This reflects a strong linear relationship between the obtained and the certified reference values.

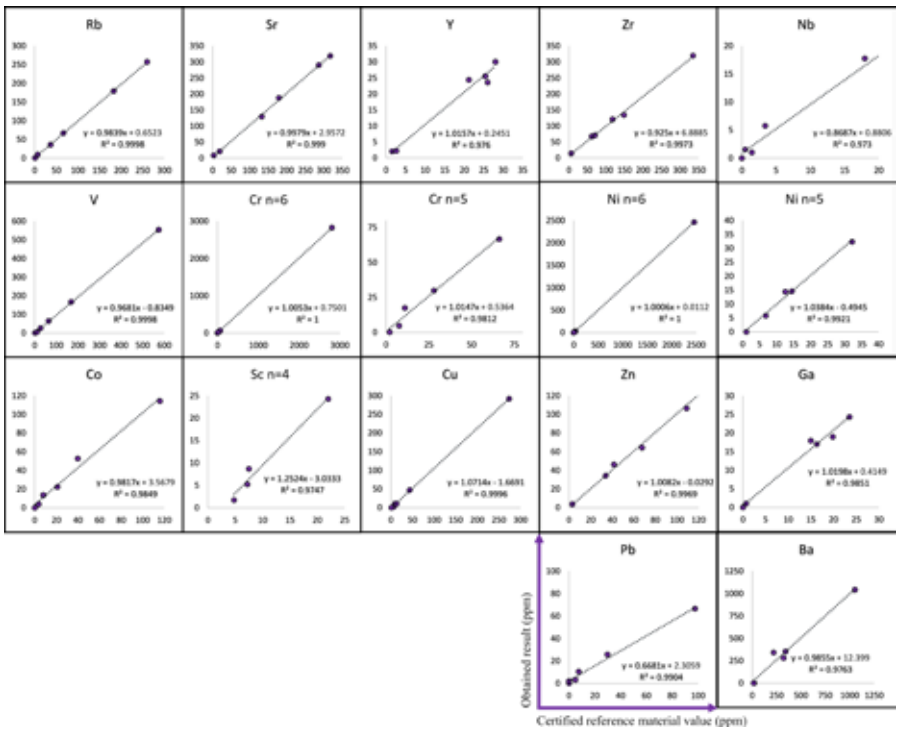

Figure 2. Certified reference material vs obtained result values for the trace elements.

The results for trace elements (Fig. 2) showed a correlation factor R^2 >0.99 for Rb, Sr, Zr, V, Ni, Cu, Zn, Pb and R^2>0.97 for Y, Nb, Cr, Co, Sc, Ga, Ba. For Cr and Ni, two diagrams are presented for 6 of the samples (n=6) and 5 samples (n=5), respectively, as one sample had an extremely high content that skewed the. To accurately test correlation between the samples, they must have comparable contents without extreme outliers. For Sc, 4 samples are plotted on the diagram (n=4) because the other two standards lacked certified values.

Limit of detection and limit of quantification for major elements.

Another important aspect of the analytical method set up is the determination of the limit of detection (LOD) and limit of quantification (LOQ). These values ensure the method's capability to reliably detect and quantify elements across the user's preferred concentration range (Shrivastava & Gupta, 2011). The LOD describes the lowest concentration of an element that can be detected but not necessarily quantified. The LOQ is the minimum concentration that can be quantified with acceptable precision and accuracy. For major elements the LOD and LOQ are calculated using equation i and equation ii respectively, with "s" as the standard deviation and "b" as the slope of the calibration curve (Tab. 4).

Table 4. Equations for LOD and LOQ calculation from Shrivastava & Gupta (2011)

LOD = 3s/b	equation i
LOQ = 10s/b	equation ii

For this study, the standard deviation (s) for each major element was calculated based on the average of the obtained results for the sample with the lowest concentration and its certified value (CRM). The slope (b) was derived from the equation y=bx+a, as determined from the regression lines presented in Fig. 1 and Fig. 2. The LOD and LOQ calculations, along with the obtained and CRM values, as well as the s and b for each oxide, are presented in Table 5.

The low LOD and LOQ values for major elements confirm the sensitivity of the method.

Table 5. LOD and LOQ values for major elements

Oxide	obtained value %	CRM value %	s	b	LOD %	LOQ %
SiO_2	42.30	42.38	0.0566	0.9978	0.170	0.567
Al_2O_3	0.59	0.66	0.0481	1.0213	0.141	0.471
K_2O	0.37	0.41	0.0276	1.0367	0.080	0.266
Na_2O	0.01	0.02	0.0078	0.9817	0.024	0.079
MgO	0.34	0.37	0.0240	1.0126	0.071	0.237
CaO	0.26	0.25	0.0057	0.9904	0.017	0.057
TiO_2	0.01	0.01	0.0007	0.9960	0.002	0.007
MnO	0.05	0.06	0.0078	1.0800	0.022	0.072
Fe_2O_3	0.10	0.08	0.0113	1.0005	0.034	0.113
P_2O_5	0.10	0.10	0.0007	1.0681	0.002	0.007
SO_3	0.02	0.01	0.0066	0.7802	0.025	0.084

Conclusions

Major element analysis has traditionally been done on fused glass beads, however in this study, major element analysis, in addition to trace elements, has been calibrated on pressed pellets. The accuracy and precision of the method were verified through multiple analyses on certified materials to ensure the reproducibility and results close to their true values. Major element analysis on pressed pellets has also been examined by Yamasaki et al., (2023) with a purely standardized method, who reported correlation results ranging from 0.9525 to 0.9989, thus proposing it for semi-quantitative analysis. The correlation results of the examined method range from 0.9943 to 0.9998 for the same ten main major elements (SiO_2, Al_2O_3, K_2O, Na_2O, MgO, CaO, TiO_2, MnO, Fe_2O_3, P_2O_5). The conversion of a purely empirical standardized method to a fundamental parameters method, could be the cause of the increased accuracy of this study's results. This quantitative analytical method was developed through the process of «trial and error», where adjustments were made based on observed errors until the desired accuracy was achieved. Important factors in creating such a method are sample preparation and corrections application. It is worth noting that this analytical method has been employed for two years at Aristotle University of Thessaloniki, in both undergraduate and postgraduate research. To ensure reliability, drift correction is conducted weekly, and the check sample is analyzed daily ensuring that any variations in instrument performance are corrected, and the results remain consistent and accurate over time.

References

Beckhoff, B., Kanngießer, B., Langhoff, N., Wedell, R., Wolff, H., 2007. Handbook of Practical X-Ray Fluorescence Analysis. Springer Berlin Heidelberg.

Boqué, R., Maroto, A., Riu, J., Xavier Rius, F., 2002. Validation of analytical methods. Grasas y Aceites, 53, 128–143.

Brouwer, P., 2003. Theory of XRF: getting acquainted with the principles. PANalytical BV.

Hickson, C., 1986. Sample contamination by grinding. The Canadian mineralogist, 24, 585–589.

Kawai, J., Yamasaki, K., Tanaka, R., 2019. Fundamental Parameter Method in X Ray Fluorescence Analysis, in: Meyers, R.A. (Ed.), Encyclopedia of Analytical Chemistry. Wiley, 1–14.

Lechler, P.J., Desilets, M.O., 1987. A review of the use of loss on ignition as a measurement of total volatiles in whole-rock analysis. Chemical Geology, 63, 341–344.

Marguí, E., Queralt, I., 2024. Sample Preparation for X-Ray Fluorescence Analysis. In Encyclopedia of Analytical Chemistry, R.A. Meyers (Ed.), 1-29.

Mojtahed, S., Kohsary, A., Komuro, K., 2006. Investigation of contaminations resulted by tungsten carbide pulverizer and their spectra interference in xrf analysis method. Iranian journal of crystallography and mineralogy, 13, 177-188.

Morikawa, A., 2014. Sample preparation for X-ray fluorescence analysis II. Pulverizing methods of powder samples. Rigaku Journal, 30, 23-27.

Ragland, P.C., 1989. Basic Analytical Petrology. Oxford University Press.

Rainer, S., 2016. Use of X-ray Fluorescence Analysis for the Determination of Rare Earth Elements. Physical Sciences Reviews 1-17.

Roser, B., Kimura, J.-I., Sifeta, K., 2003. Tantalum and niobium contamination from tungsten carbide ring mills: much ado about nothing. Geoscience Report of Shimane University, 22, 107–110.

Ross, S.M., 2010. Linear Regression, in: Introductory Statistics. Academic Press, 537-604.

Rousseau, R.M., 2006. Corrections for matrix effects in X-ray fluorescence analysis—A tutorial. Spectrochimica Acta Part B: Atomic Spectroscopy, 61, 759–777.

Rousseau, R., 2013. How to Apply the Fundamental Parameters Method to the Quantitative X-ray Fluorescence Analysis of Geological Materials. Journal of Geosciences and Geomatics, 1, 1–7.

Saikia, G. C., Sinha, T. K., Kharshiing, F., 2009. Tungsten–cobalt contamination from pulverizing cup. Current Science, 1, 29–30.

Shrivastava, A., Gupta, V., 2011. Methods for the determination of limit of detection and limit of quantitation of the analytical methods. Chronicles of Young Scientists, 2, 21-25.

Takamasa, A., Nakai, S., 2009. Contamination introduced during rock sample powdering: Effects from different mill materials on trace element contamination. Geochemical Journal, 43, 389–394.

Thompson, G., Bankston, D.C., 1970. Sample Contamination from Grinding and Sieving Determined by Emission Spectrometry. Applied Spectroscopy, 24, 210–219.

Yamasaki, S.-I., Yamagishi, H., Tsuchiya, N., 2023. Major element analysis of geological samples with wavelength Dispersive X-ray Fluorescence (WDXRF) spectrometry using glass disks and pressed powder pellets. Sustainable Environment, 9, 1, 1-10.

Yamasaki, T., 2018. Contamination from mortars and mills during laboratory crushing and pulverizing. Bulletin of the Geological Survey of Japan, 69, 201–210.

17th INTERNATIONAL CONGRESS of the Geological Society of Greece

BULLETIN OF THE GEOLOGICAL SOCIETY OF GREECE, SP. PUBL.

EXTENDED ABSTRACT 094

The Art of Stone in Grevena-Kozani UGGp: Community-led Conservation Efforts

Ghikas D.[1], Batsi A.[1]
(1) Grevena-Kozani UGGp, Kozani, Greece, geowonders@gmail.com

Introduction / Background

Grevena-Kozani UNESCO Global Geopark

Grevena-Kozani UGGp is located in West Macedonia and covers an area of 2.486km2. The territory joined the UNESCO Global Geoparks Network in 2021 and was the 6th geopark in Greece. UNESCO Global Geoparks (UGGp) are single, unified geographical areas where sites and landscapes of international geological significance are managed with a holistic concept of protection, education and sustainable development. A UNESCO Global Geopark uses its geological heritage, in connection with all other aspects of the area's natural and cultural heritage, to enhance awareness and understanding of key issues facing society, such as using our earth's resources sustainably, mitigating the effects of climate change and reducing natural hazard-related risks. At present, there are 213 UNESCO Global Geoparks in 48 countries (unesco.org).

Geologic Background

The territory boasts exceptional geodiversity, spanning the boundary between the internal and external structural zones of the Hellenides (Ferriere *et al.,* 2013). The geopark includes a large swathe of the Mesohellenic Basin (MHB), a Late-Eocene to Late-Miocene intermontane basin (Doutsos *et al*., 1994) filled with mostly siliciclastic turbidite sequences and shelf originally deposited in the Tethys Ocean, until thrusting of the Hellenide orogeny and post-orogenic extensional tectonics completed the structural evolution of this piggyback basin (Vamvaka, 2009 and references therein).

The MHB is a source of high-quality stone for construction, particularly within the Pentalophos and Eptahori formations which contain many sandstone and siltstone units which are well lithified, fine grained, minimally deformed and have low permeability (Tyrologou *et al.,* 2023). Communities living on or adjacent to outcrops of these rocks took advantage of this resource and developed an industry and culture based on stonework.

The Stone Masters of West Macedonia

Communities which were historical centers of stonework and building are collectively known as Mastorohoria (Master Villages). The craftsmen or masters would build structures out of locally available, high-quality stone and other natural materials. A building gang, or *boulouki,* composed of highly skilled masters, variously specialized technicians and artisans, and low-level workers, would depart from their village to a job site and remain there for many months, until the completion of the project (Poravos, 2023). Many mastorohoria are located within Grevena-Kozani UGGp, principally in the townships of Voio and Grevena, and many more communities and areas of the geopark feature stone architecture including homes, churches and bridges built by these masters.

The 20th century saw a precipitous decline of the Mastorohoria, as industrial building materials flooded the market and economic centers shifted elsewhere. Young males migrated away from the area, and remaining craftsmen did not document their knowledge. Today hardly any skilled workers exist, and many of the historic structures of this territory are in a state of decay, and their future is uncertain as their proper restoration depends on increasingly scarce qualifications. Improper or anachronistic renovations risk exacerbating the collapse of already fragile structures (Lianos, 2012) as well as obscuring their historic and aesthetic value.

In recent years, there has been a renewed interest in reviving the craft of stone building, as the region of West Macedonia has begun to invest in tourism and sustainability. For these efforts to be successful, the technical know-how of the original masters is of vital importance, and every means must be taken to preserve what knowledge remains. Additionally, the recognition of geoheritage, or the linking of geologic science with human society (Rassios and Grieco, 2021), is necessary for the region to be able to sustainably realize the touristic potential of its tangible and intangible cultural heritage.

Recent Community-led Conservation Efforts

In 2024, there were several developments in the revitilization of traditional stone architecture. Grevena-Kozani UGGp was able to contribute to these events and we are confident of long-term partnerships with the people and organizations who are working in this direction.

Announcement: School of Traditional Stoneworking, Pentalophos Voio

In May 2024, an assembly was held in the village of Pentalophos, Voio Township, at which the Minister of Culture, Ms. Lina Mendoni, together with professors from the National Metsovio Polytechnic University of Athens and Utah Valley University, announced the upcoming establishment of a School of Stone and Traditional Building Forms, to be based in the village of Pentalophos. From 21-27 October, these two schools held a field study course in Pentalophos, although the geopark was not able to participate in that event.

1st Traditional Stone Workshop, Kyparissi Grevenon

In August 2024, the 1st Workshop in Traditional Building, Art and Customs of the Craftsman Villages took place in the village of Kyparissi, the first workshop of its kind in the Township of Grevena. The 4-day event was a collaboration between the Community Association of Kyparissi, the Aristotelian University of Thessaloniki (AUTh), and a qualified stone master, Mr. Athanasios Poravos. Registered participants numbered about 30, coming from around the country, and had various backgrounds relating to architecture, engineering and history. Mr. Poravos guided the group through techniques for building a dry-stone wall, in the courtyard of the old stone schoolhouse of the village (now a museum). Participants received hands-on training in cutting, shaping and laying stones from Mr. Poravos, one of the few remaining First Masters in mainland Greece. In addition to the practical sessions, participants had lessons on various aspects of the stoneworking traditions of the region, including the history of vernacular architecture, as well as construction considerations including siting, framing, mortaring and repairing traditional stone structures. In the evenings, the group toured the villages of Kyparissi and Kalloni to examine their traditional building practices and current structural problems, and to learn the history of the area. Dr. Constantinos Katakalos (Dept. of Civil Engineering, AUTh) instructed participants on methods and materials for diagnosing, retrofitting and renovating traditional structures. Geopark staff guided the group through the geologic foundations of the Mastorohoria, with a tour of nearby outcrops and a classroom lesson and discussion on the geologic history of the territory.

Cultural practices related to stone working were also on display throughout the workshop, as local cultural societies, musicians, amateur artists and theater groups reenacted the emotional departure of workers from their communities and their arrival at seasonal building sites. Participants also learned words from *Koudaritika* (Stone Talk), the argo or secret language of the craftsmen, who wished not to be understood by their Ottoman rulers (Poravos, 2023). Events for the public included staged reenactments of some of the customs which marked both the annual departure of the workers from their villages, and the completion of a project. In the village of Sydendro, a village which was largely built by the craftsmen of the Mastorohoria, workshop participants and local authorities reenacted the tradition of *Bahcisia* (Tipping) whereby workers would climb onto the roof of a house which was nearly finished, erect a scaffolding and wooden cross, and pay hyperbolic (and somewhat ironic) compliments to the owner of the building and his family, in exchange for gifts. This custom has been submitted to UNESCO for recognition as Intangible Cultural Heritage.

Figure 1. Left: historical photograph of a *boulouki*. Right: reenactment of the *Bachcisia*.

8th Workshop on Traditional Building, Pentalophos Voio

In September 2024, Dr. Constantinos Katakalos (Dept. of Civil Engineering, AUTh) led the 8th Workshop on Traditional Building in the village of Pentalophos. Geopark staff were invited speakers and field experts to give the participants, who numbered about 25, geologic and geoheritage context for their studies. They had the opportunity, for most participants their first, to examine outcrops of Pentalophos sandstone and learn about its formation, age, properties

and what criteria should be used in assessing the quality of the stone as building material. They also learned how the landscape and climate influenced the local environment and culture, and received general information about the geopark and its activities. Local stone craftsmen (masters) were also present as honored guests, and at the conclusion of the workshop, participants received certificates of completion in a ceremony, officiated by the Pentalophos stone masters.

Conclusions

The distinctive vernacular architecture of the Mastorohoria, shaped by the local geologic history, is part of the unique character of the region. As West Macedonia strives to diversify its economy and stanch emigration, there is renewed and growing interest in reviving the craftsman traditions. This imperative will only grow as the stone structures of the territory will face continual need for maintenance. Grevena-Kozani UGGp is dedicated to the preservation of its historic stone structures, the continuance of its intangible cultural heritage, and the spread of knowledge about geoheritage—the indivisible bonds between geology and humanity.

Acknowledgements

The authors wish to thank A. Poravos, K. Katakolos, M. Stephanidou, and Z. Karanikou for sharing your knowledge. The communities of Pentalophos, Kyparissi, Kalloni and Sydendro for hosting these events. The municipal and regional authorities of Grevena and Kozani for welcoming the participants and supporting the geopark in its ongoing efforts for West Macedonia.

References

Doutsos, T., Koukouvelas, I., Zelilidis, A., Kontopoulos, N., 1994. Introcontinental wedging and post-orogenic collapse in the Mesohellenic Trough. Geologische Rundschau 83, 257-275.

Ferrière, J., Chanier, F., Reynaud, J., Pavlopoulos, A., Ditbanjong, P. and Coutand, I. 2013. Evolution of the Mesohellenic Basin (Greece): a synthesis. In: (Ed.) Emmanuel Skourtsos, The Geology of Greece - Part II, Journal of the Virtual Explorer, Electronic Edition, ISSN 1441-8142, volume 45, paper 1.

Lianos, N. A., 2012. The Assumption of Mary Church at Dilofo of Kozani: a brief review of missed goals, documentation of the current condition and a restoration study. Πράκτικα 3ου Πανελλήνιου Συνεδρίου Αναστυλώσεων, Εταιρία Έρευνας και Προώθησης της Επιστημονικής Αναστύλωσης των Μνημείων (ΕΤΕΠΑΜ).

Poravos, A., 2023. Δεύτερο Ταξίδι στην Αιωνιότητα. Ατρειδών Κύκλος.

Rassios, A.E., and Grieco, G., 2021, Is geoheritage a “cutting-edge” science? Promotion of an extension to the definition of geoheritage with emphasis as a significant discipline in geosciences with cultural and societal relevance, in Wakabayashi, J., and Dilek, Y., eds., Plate Tectonics, Ophiolites, and Societal Significance of Geology: A Celebration of the Career of Eldridge Moores: Geological Society of America Special Paper 552, p. 37–53, https://doi.org/10.1130/2021.2552(03).

Tyrologou P., Vamvaka A., Koukouzas N. et al., 2023. Progress for carbon dioxide geological storage in West Macedonia: a field and laboratory-based survey. Open Res Europe, 3:85. DOI: 10.12688/openreseurope.15847.2

Vamvaka, A., 2009. Geometry of deformation and kinematic analysis in Mesohellenic Trough. PhD Thesis, Dept. of Geology, Aristotle University of Thessaloniki, 220p.

www.unesco.org/en/iggp/geoparks/about

17th INTERNATIONAL CONGRESS of the Geological Society of Greece

BULLETIN OF THE GEOLOGICAL SOCIETY OF GREECE, SP. PUBL.

EXTENDED ABSTRACT 095

Paleoecological imprints of pteropod assemblages and their response to sapropel S1 conditions in the eastern Mediterranean Sea

Giamali C.[1], Kontakiotis G.[2], Antonarakou A.[2]

(1) The Goulandris Natural History Museum, Kifissia, Greece, ch.giamali@gnhm.gr, (2) National and Kapodistrian University of Athens, Faculty of Geology and Geoenvironment, Department of Historical Geology and Paleontology, Panepistimiopolis, Zografou, 15784, Athens, Greece

Research Highlights

Environmental factors during the sapropel S1 interval, affect pteropod assemblages in a way that the development of a precise eco-biostratigraphic scheme for the eastern Mediterranean Sea, seems feasible to accomplish.

Introduction

Pteropods are widespread and abundant in the global ocean and entirely adapted to a pelagic life cycle. They are considered valuable tool in paleoceanographic and paleoclimatic reconstructions due to their sensitivity in the environmental changes (Wall-Palmer *et al.*, 2014). Within the Mediterranean Sea, the preservation of pteropod shells is excellent because of the relatively shallow water, high bottom water temperatures, and the limited number of mud feeders (Herman, 1971). A considerable number of studies present the late Quaternary pteropod assemblages and their distribution pattern in the western and/or central Mediterranean basin (Buccheri *et al.*, 2002; Herman, 1971; Wall-Palmer *et al.*, 2014). In the eastern sector and particularly the Aegean Sea the only available data are that extracted from the gravity cores AEX-15, AEX-23, KIM-2A (Giamali *et al.*, 2019; 2020). These three cores constitute the only high-resolution records that depict their pattern during the deposition of the most recent sapropel S1. In the current work, we focus on understanding the response of the pteropod fauna in environmental changes during the sapropel S1 deposition. To do so, correlations with the distributional patterns of planktic foraminifera were also made. This preliminary attempt may lead to a future establishment of eco-biostratigraphic zonation based on pteropod assemblages.

Material & Methods

For the needs of our study, we used the data published by Giamali *et al.*, (2019; 2021), from two gravity cores, one in the north Aegean Sea, AEX-15, and one in the south Aegean Sea, KIM-2A (Fig. 1). In these cores, a total of 13 species of Euthecosomata (*Heliconoides inflatus, Limacina trochiformis, Limacina bulimoides, Limacina retroversa, Creseis acicula, Creseis sp., Boasia chierchiae, Hyalocyclis striata, Styliola subula, Clio pyramidata* s.l., *Clio cuspidata, Diacria trispinosa, Cavolinia* spp.) were identified. Here, we focus on the species that present a notable distributional pattern and were encountered in both cores in the interval from 10.0 ka to 5.0 ka. These are *H. inflatus, L. trochiformis, C. acicula, C. pyramidata,* and *D. trispinosa.* Furthermore, a correlation was made with planktonic foraminifera species that are common within the sapropel S1 (Cassford *et al.*, 2002; Kontakiotis, 2016). Sapropel layers in AEX-15 spans from 9.6 ka to 6.1 ka (with the interval between 7.0 ka and 6.1 ka being the oxidized part) and in KIM-2A from 9.4 ka to 6.4 ka with the sapropel interruption (S1i) placed at 7.8 ka to 6.8 ka. Comparison of these two cores is challenging and demanding as it includes two regions with different hydrographic characteristics and climate contrasts between more humid conditions in the north and semiarid conditions in the south and (Lykousis *et al.*, 2002). Moreover, data availability differs between the cores, due to higher resolution sampling of AEX-15 core. However, the downcore variation of the fauna enables an initial recognition of the imprints left by environmental changes on the pteropod distribution.

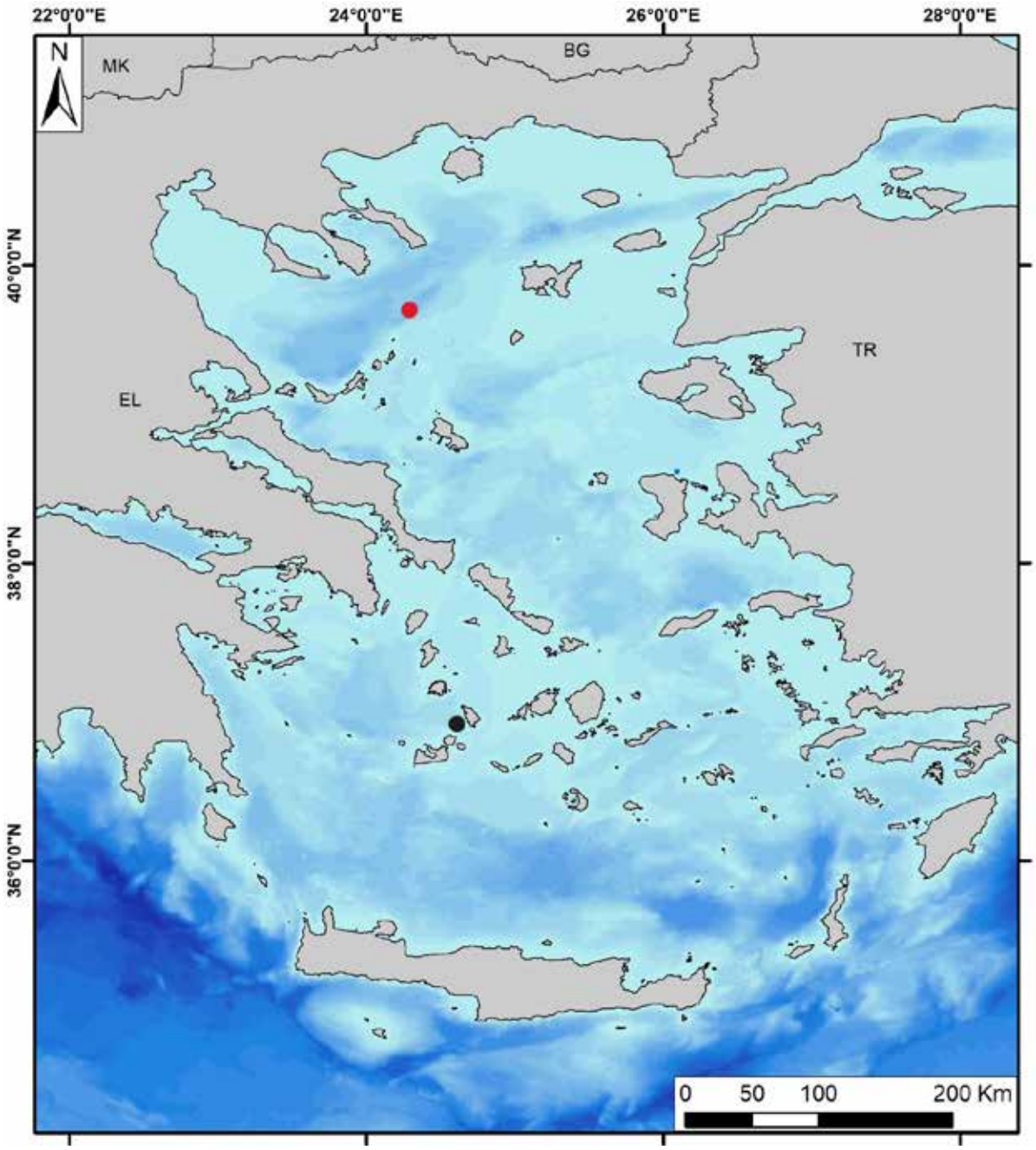

Figure 1. The Aegean Sea and the location of the two gravity cores; AEX-15 with red dot (39°39.900′N, 24°15.369′E; 1242 m water depth, length 178 cm) and KIM-2A with black dot (36°95.4640′N, 24°06.3540′E; 640 m water depth, length 200 cm). Map available via GIS, bathymetry is after (Ioc, 2003) country names are given by © EuroGeographics for the administrative boundaries (Eurostat).

Results & Discussion

As the distributional pattern of the plankton fauna is presented exhaustively in Giamali *et al*., (2019, 2020), herein we focus on the paleoecological aspects that are reflected in the downcore variation of specific pteropod species (Fig. 2). During the sapropel S1 deposition, an increase in temperature and humidity has been documented in all marine records in the eastern Mediterranean region (Giamali *et al*., 2019; Kontakiotis, 2016). This paleoclimate change coincides with the Holocene summer precession-related insolation maximum in the Northern Hemisphere (Laskar *et al*., 2004), and the monsoon intensification that resulted in a widespread increase in humidity over the entire Mediterranean region as well as the concomitant increase of freshwater inputs mainly to the eastern Mediterranean (Rohling, 1994; Rossignol-Strick, 1983).

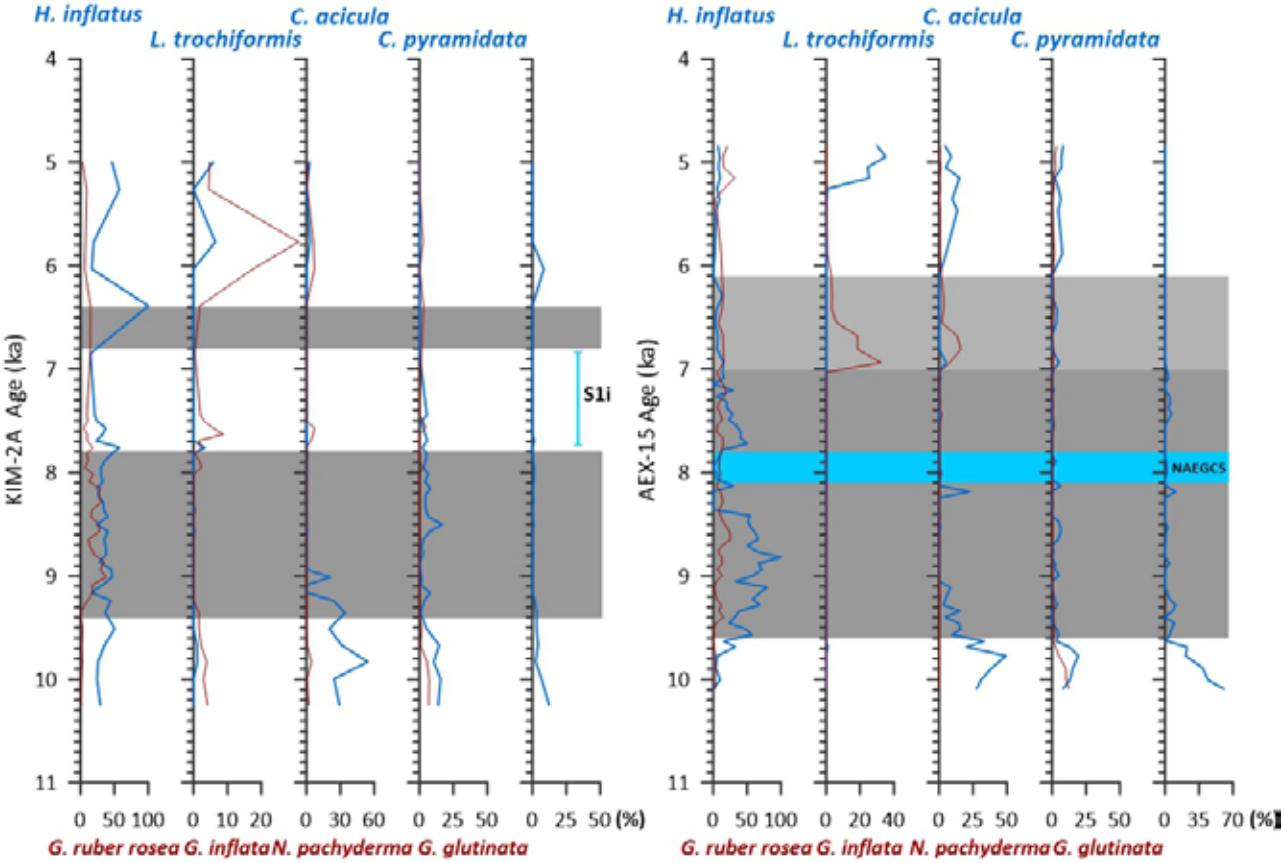

Figure 2. Downcore variations of selected pteropod and planktonic foraminifera species. Blue line corresponds to pteropods, dark red line to planktonic foraminifera. Gray bands correspond to the sapropel S1a and S1b in the core KIM-2A. Gray and light gray bands correspond to the sapropel S1 and its oxidized part in the core AEX-15. S1i interval is depicted in core KIM-2A, and the cooling event NAEGC5 in core AEX-15.

The warm-water mesopelagic *H. inflatus,* presents high percentages during the S1 deposition followed by a notable reduction during the S1i interval in core KIM-2A, and during the cooling event NAEGC5 (Giamali *et al*., 2019). The distribution pattern of this species can be correlated well with that of the warm indicator *Globigerinoides ruber rosea*. Both species can provide a complete overview of the water column as the former lives at a depth ranging from 200-1000 m, whereas the latter is considered as indicative of warm surface waters (Pujol and Vergnaud-Grazzini, 1995). Though *H. inflatus*, seems to reflect better the temperature fluctuations. The epipelagic *L. trochiformis,* is associated with the mixed layer in the upper water column thriving in upwelling conditions (Bé and Gilmer, 1977). Such ecological preferences explain its absence from the S1 interval (Fig. 2). It can be correlated to *Globoconella inflata* which reflects deep seasonal mixing conditions (Hemleben *et al.*, 1989), such as those dominated during the S1i interval characterized by the breakdown of the stratification (Kontakiotis, 2016; Geraga *et al.,* 2010). It is notable that *L. trochiformis* bounds the S1a layer in the core KIM-2A and the termination of S1 layer in core AEX-15 (at 7.0 ka), suggesting the prevalence of homogenization/overturn conditions in the upper water column.
Creseis acicula is a warm-water, euryhaline species that has the shallowest depth habitat amongst all epipelagic pteropods (Liu *et al*., 2022). This specific habitat most probably led to its outbreak as high percentages during the last 0.7 – 1.5 ka before the onset, and the first 0.3 ka of the sapropel S1 are observed (Fig. 2). This pattern may mark both the rising temperature and the increase of freshwater input in the Mediterranean Sea that may increase the ingestion and assimilation rates of the species for algal food (Liu *et al.,* 2022). Its reduction afterwards may mark the change in environmental conditions or an increase in competitors and/or predators (Dai *et al*., 2020).
The mesopelagic species *C. pyramidata* and *D. trispinosa* on the contrary are less tolerant in high temperatures and in salinity fluctuations, and prefer a well-ventilated water column (Buccheri *et al.,* 2002; Giamali *et al*., 2020), which explains their low percentages during the S1 interval. Their abrupt decline is correlated with the onset of S1 deposition in both cores. A similar downcore record can be seen through the distributional pattern of the planktonic foraminifera *Globigerinita glutinata*.

Conclusions

Based on the faunal distribution of two gravity cores of north and south Aegean Sea, the biotic response of specific pteropod species in environmental changes during the sapropel S1 deposition was made. In particular, temperature, salinity, stratification and food availability are the factors that affect the distribution of the examined species. The observed data if enhanced by new records within and beyond the Aegean basin, can give more insights for the establishment of a precise regional eco-biostratigraphic scheme.

Acknowledgements

The gravity cores examined in this work, were collected during the "YPOTHER" project realized at the Hellenic Survey of Geology and Mineral Exploration in collaboration with the Institute of Oceanography of the Hellenic Centre for Marine Research (HCMR).

References

Bé, A.W.H., Gilmer, R.W., 1977. A zoogeographic and taxonomic review of euthecosomatous Pteropoda. Oceanic Micropaleontology 1, 733-808.

Buccheri, G., Capretto, G., Di Donato, V., Esposito, P., Ferruzza, G., Pescatore, T., Russo Ermolli, E., Senatore, M.R., Sprovieri, M., Bertoldo, M., Carella, D., Madonia, G., 2002. A high resolution record of the last deglaciation in the southern Tyrrhenian Sea: environmental and climatic evolution. Marine Geology 186, 3, 447-470.

Casford, J.S.L., Rohling, E.J., Abu-Zied, R., Cooke, S., Fontanier, C., Leng, M., Lykousis, V., 2002. Circulation changes and nutrient concentrations in the late Quaternary Aegean Sea: A nonsteady state concept for sapropel formation. Paleoceanography 17, 2, 14-11-14-11.

Geraga, M., Ioakim, Chr., Lykousis, V., Tsaila Monopolis, St, Mylona, G., 2010. The high resolution palaeoclimatic and palaeoceanographic history of the last 24,000 years in the central Aegean Sea, Greece. Palaeogeography Palaeoclimatology Palaeoecology 287, 101e115.

Giamali, C., Kontakiotis, G., Koskeridou, E., Ioakim, C., Antonarakou, A., 2020. Key Environmental Factors Controlling Planktonic Foraminiferal and Pteropod Community's Response to Late Quaternary Hydroclimate Changes in the South Aegean Sea (Eastern Mediterranean). Journal of Marine Science and Engineering, 8, 9.

Giamali, C., Koskeridou, E., Antonarakou, A., Ioakim, C., Kontakiotis, G., Karageorgis, A. P., Roussakis, G., Karakitsios, V., 2019. Multiproxy ecosystem response of abrupt Holocene climatic changes in the northeastern Mediterranean sedimentary archive and hydrologic regime. Quaternary Research, 92, 3, 665-685.

Kontakiotis, G., 2016. Late Quaternary paleoenvironmental reconstruction and paleoclimatic implications of the Aegean Sea (eastern Mediterranean) based on paleoceanographic indexes and stable isotopes. Quaternary International 401, 28-42.

Laskar, J., Robutel, P., Joutel, F., Gastineau, M., Correia, A.C.M., Levrard, B., 2004. A long-term numerical solution for the insolation quantities of the Earth. A&A, 428, 1, 261-285.

Liu, O., Zhou, L., Zhang, W., Zhang, L., Tan, Y., Han, T., Dai, M., Liao, X., Huang, H., 2022. Rising temperature contributed to the outbreak of a macrozooplankton Creseis acicula by enhancing its feeding and assimilation for algal food nearby the coastal Daya Bay Nuclear Power Plant. Ecotoxicology and Environmental Safety 238, 113606.

Lykousis, V., Chronis, G., Tselepides, A., Price, N.B., Theocharis, A., Siokou-Fragou, I., van Wambeke, F., Danovaro, R., Stavrakakis, S., Duineveld, G., Georgopoulos, D., Ignatiades, L., Souvermezoglou, A., Voutsinou-Taliadouri, F., 2002. Major outputs of the recent multidisciplinary biogeochemical researches undertaken in the Aegean Sea. Journal of Marine Systems 33e34, 313e334.

Dai, M., Qi, Z., Zeng, L., Zhang, S., Wang, L., Qin, X., Liao, X., Yan, J., Huang, H., Shang, S., 2020. An unprecedented outbreak of pelagic molluscs Creseis acicula in Daya Bay, South China Sea. Authorea Prepr.

Hemleben, C., Spindler, M., Anderson, O.R., 1989. Modern planktonic Foraminifera. Springer.

Herman, Y., 1971. Vertical and horizontal distribution of pteropods in Quaternary sequences, in: Funnell, B. M., Reidel, W. R., (Eds.), The Micropalaeontology of Oceans, 463–486.

Pujol, C., Vergnaud-Grazzini, C., 1995. Distribution patterns of live planktic foraminifers as related to regional hydrology and productive systems of the Mediterranean Sea. Marine Micropaleontology 25, 187-217.

Rohling, E.J., 1994. Glacial conditions in the Red Sea. Paleoceanography, 9, 5, 653-660.

Rossignol-Strick, M., 1983. African monsoons, an immediate climate response to orbital insolation. Nature 304, 5921, 46-49.

Wall-Palmer, D., Smart, C. W., Hart, M. B., Leng, M. J., Borghini, M., Manini, E., Aliani, S., Conversi, A., 2014. Late Pleistocene pteropods, heteropods and planktonic foraminifera from the Caribbean Sea, Mediterranean Sea and Indian Ocean. Micropaleontology 60, 6, 557-578.

17th INTERNATIONAL CONGRESS of the Geological Society of Greece

BULLETIN OF THE GEOLOGICAL SOCIETY OF GREECE, SP. PUBL.

EXTENDED ABSTRACT 096

Correlation study of overland and marine aggregates capable to be used in various construction applications

Giannakopoulou, P.P.[1], Rogkala, A.[1], Lampropoulou, P.[1], Koutsovitis, P.[1], Kalpogiannaki M.[2], Giamas V.[1], Seikatis, O.[1], Islam I.[3], Petrounias, P.[1]

(1) Department of Geology, University of Patras, Patras, Greece, peny_giannakopoulou88@outlook.com (2) Section of Mineralogy and Petrology, Department of Geology and Geoenvironment, National and Kapodistrian University of Athens, Panepistimioupolis Zografou, 157 84 Athens, Greece (3) Department of Geology, Shaheed Benazir Bhutto University Sheringal, Dir Upper, 18030, Pakistan

Introduction

Ophiolitic rocks are used extensively as engineering materials in applications such as road construction, concrete and railway ballast (Rigopoulos *et al.*, 2010, Rigopoulos *et al.*, 2015, Petrounias *et al.*, 2016, Petrounias *et al.*, 2018, Giannakopoulou *et al.*, 2018). The suitability of aggregates for their applications is determined by evaluating their physical, physicochemical and mechanical properties, which are collectively known as engineering properties.

Nowadays, natural aggregate sources are depleting, and their mining impacts the environment adversely. In this direction, during the last decades, marine aggregates exploitation increases due to the high demand for material supply regarding construction industry (Velegrakis *et al.*, 2010). Also, marine aggregates play a crucial role in meeting the demand for construction materials, coastal protection, and beach replenishment. On average, in Europe, almost 60 million tonnes of marine aggregates are extracted from the sea used for construction and as a strategic material in supplying large scale coast defense and beach replenishment projects. The contribution of marine dredged sand and gravel resources as part of the wider portfolio of construction aggregate supply is growing in importance. Where local primary aggregates are constrained, either because resources are not geologically present or because existing resources have become depleted, alternative sources of supply have to be found. Economies of scale allow marine aggregate supplies to play an important role using a fleet of highly specialized dredgers to load sand and gravel from licensed areas located around the coast of England and Wales.

"The main use of marine aggregates is in the manufacture of concrete. Nearly 80% of the marine aggregates landed for construction purposes are used as concrete aggregate, increasing to nearly 90% in London and the south-east of England. By contrast 60% of land-won sand and gravel production and 16% of crushed rock is sold as concrete aggregate," says the organization. Indeed, while the largest use of marine aggregates is in construction, they are also widely used for the production of asphalt and coated products; masonry and paving blocks; drainage and fill materials; leisure facilities; sports pitches; golf courses; equestrian facilities; horticulture products; steel manufacture and beach replenishment. So, it is not surprising that worldwide production is on the increase. Therefore, it is necessary to optimize the river sand consumption while, at the same time, increasing the use of alternate sources to replace them. There is a wide use of marine sand as fine aggregate material in cement mortar and concrete (Limeira *et al.*, 2012, Xiao *et al.*, 2017, Ganesan *et al.*, 2022).

Marine aggregate extraction is closely regulated to protect the environment. Expert studies are undertaken to help inform license decisions and permission will be refused if there is any concern about impacts on the coastline or any other environmental or economic interests.

The aim of this study is, on the one hand, to evaluate the engineering properties of the tested aggregates, whether overland or marine, and on the other hand, to conduct a comparative study between them in order to identify whether the properties of aggregates change from the area where it is currently possible to locate them.

Materials and Methods Geological Setting of aggregate samples

Ten block samples of ultramafic rocks (five overland and five marine blocks) from Gerania ophiolite complex were collected according to the EN 932-1 standard to evaluate their suitability as aggregates for construction applications (Figure 1).

Figure 1. (a,b) overland ultramafic aggregate rock samples from Gerania ophiolite complex, (c,d) marine ultramafic aggregate rock samples from Gerania ophiolite complex.

The Gerania Ophiolite Complex belongs to the Pelagonian geotectonic zone of the internal Hellenides. They comprise a Permian sedimentary and volcanic succession overlain by a series of carbonate rocks and lesser radiolarites (Clément, B.,1971, Bornovas, J,. 1981, Vacondios, I., 1997, Giannakopoulou *et al.*, 2018). This succession is tectonically overlain by an ophiolite sequence. The ophiolite is a NE-trending rhomb-shaped outcrop, with approximately 10 km in length and 5 km in width, representing an incomplete and dismembered ophiolite sequence. It is dominated by variably serpentinized and tectonized lherzolite, locally crosscut by thin pyroxenite dykes with subordinate harzburgite and dunite (Figure 2). These serpentinized peridotites are interrupted by gabbro dykes, some of which have been transformed into rodingites. An ophiolite mélange includes fragments of lavas, serpentinized peridotites, gabbros, oceanic sediments previously described as schist-chert formation, as well as an amphibolite metamorphic sole tectonically underlie the ophiolite.

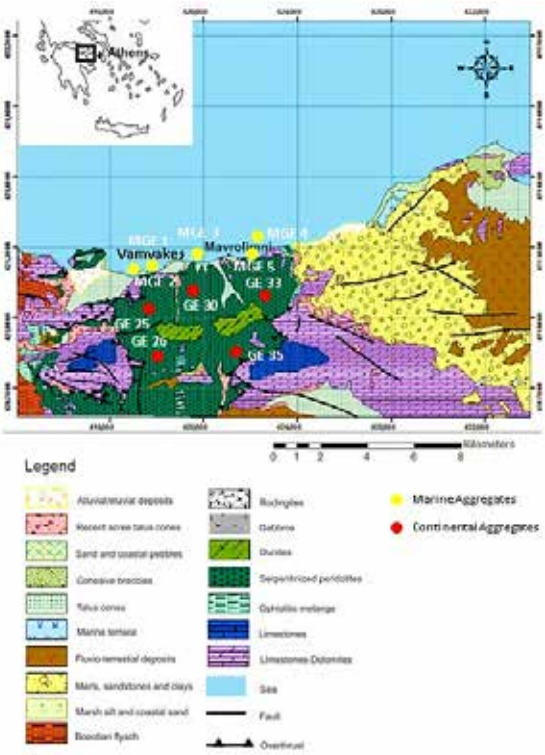

Figure 2. Geological map of the Gerania region (Giannakopoulou *et al.,* 2018), the rectangle in the inset shows the study area.

Analytical methods

All aggregate rock samples have petrographically been observed by variety of petrographic methods. The mineralogical and textural characteristics of the samples were studied in polished-thin sections using a polarizing optical microscope (Leitz Ortholux II POL-BK Ltd., Midland, ON, Canada), according to the EN-932-3 standard for the petrographic description of aggregates. The engineering properties of the tested aggregates were determined in the Research Laboratory of Minerals and Rocks, Department of Geology, University of Patras, Patra, Greece. Moisture content (w) was measured in accordance to the AASHTO T-255 standard, the Los Angeles (LA) test was carried out in accordance to the ASTM C-131 standard using the "B" gradation. The Uniaxial Compressive Strength (UCS) was determined from the average value of six cylindrical rock specimens for each sample with diameters ranging from 51 to 54 mm and their height/diameter ratios between two and three for each sample (ASTM D-2938). As for the geometrical properties of the tested aggregates, the flakiness index (I_F) and the elongation index (I_E) were performed according to the BS 812 Part 105.1 and 105.2 correspondingly.

Results and Discussion

Petrographic features

Peridotites from the Gerania ophiolite complex include lherzolite and harzburgite with low to moderate degrees of serpentinization and deformation even they are overland or marine. Lherzolite shows protogranular, porphyroclastic and locally cataclastic textures. Their primary minerals are olivine, orthopyroxene and clinopyroxene. Opaque minerals (mainly Al-spinel in light brown color) are present in small amounts. Porphyroclastic texture is characterized by large orthopyroxene, clinopyroxene and olivine clasts in a finegrained matrix made up of recrystallized olivine neoblasts. Serpentine is the main secondary mineral, which shows mostly mesh and locally ribbon textures. The effect of serpentinization also leads to the replacement of orthopyroxene from bastite. The secondary assemblage is completed by chlorite and actinolite. Also, a dense network of microcracks is observed. The harzburgite presents mainly porphyroclastic and locally cataclastic textures. Its primary assemblage includes olivine, orthopyroxene and rare clinopyroxene. Olivine appears as porphyroclasts, which present strong deformation, as well as small-sized unstrained neoblasts. Frequent replacement of orthopyroxene from olivine neoblasts is also observed. Al-spinel in light brown color and Cr-spinel characterized in red-brown color are present in small amounts, some of which display embayed margins and rims altered to secondary magnetite. A dense network of microcracks also occurs in the harzburgite. The serpentine comprises the most common secondary phase presenting ribbon texture; minor chlorite occurs as well. Regarding the tested aggregate samples (overland and marine), the only remarkable variation that appears is the degree of oxidation of the metallic minerals, which is likely due to the entry of seawater into the intercrystalline cracks, where it creates conditions for their extensive oxidation. The remaining secondary minerals do not appear to show any change in any environment they have been exposed to.

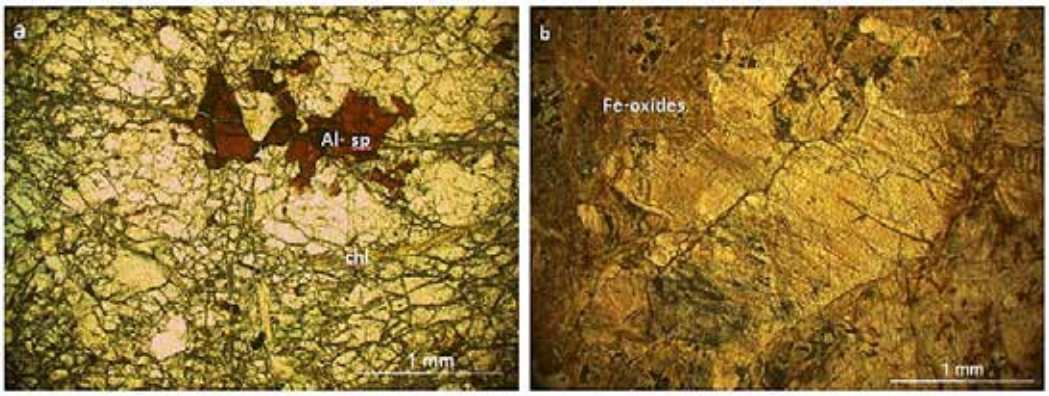

Figure 3. Photomicrographs of (a) overland lherzolite where chlorite is occurred and Al-spinel, (b) marine lherzolite which present high oxidation.

Engineering properties

The values of the engineering properties are summarized below in Table 1. In general, the results show that the overland and marine aggregates present similar physicomechanical characteristics. A small decrease in the mechanical strength of the marine lherzolites is observed compared to the overland ones. More specifically, it seems that the physical properties present a similar variation which may be attributed to the different degree of alteration.

This fact regarding the physical properties is also confirmed by the petrographic study which did not reveal significant differences. The same conclusion has also been conducted by the results of the geometric properties, where the more serpentinized are the aggregates the more elongated grains present. There is no significant difference among them depending on their origin (overland or marine).

Table 1. Engineering properties of the tested aggregate rocks (*GE: overland aggregates, MGE: marine aggregates, w: moisture content, I_F: Flakiness Index, I_E: Elongation Index, LA: Los Angeles, UCS: Uniaxial Compressive Strength).

Samples	Engineering Properties				
	W (%)	I_F (%)	I_E (%)	LA (%)	UCS (MPa)
GE25	0.78	22.54	34.17	15.90	79.0
GE26	0.91	33.90	32.33	19.6	66.0
GE30	0.92	26.84	34.16	16.60	75.0
GE33	0.08	16.25	30.16	20.90	69.1
GE35	0.69	25.15	24.51	23.90	76.0
MGE1	2.60	28.53	27.67	25.60	42.0
MGE2	2.30	29.56	31.25	24.35	49.0
MGE3	2.10	27.84	32.89	26.48	48.0
MGE4	0.90	29.95	34.52	27.00	54.0
MGE5	2.80	31.00	36.01	26.68	39.0

Regarding the mechanical properties UCS and L.A, a small reduction of the properties is shown in marine aggregates, which is probably due to the extensive oxidation of the secondary minerals where they can result in extensive intercrystalline microcracks that can act as surfaces of weakness and cause fractures. Several scientists have conducted similar conclusions when investigated the mechanical behavior of mafic rocks (Petrounias *et al.,* 2018). Giannakopoulou et al. 2018 considered that the increase of alteration such as serpentinization in ultramafic rocks strong influences the physical and mechanical properties of rocks. This happens because the soft and platy nature of serpentine constitutes a critical factor for the development of extensive porous areas, which are weak. The above result, although presented in all the examined samples, it should not be generalized because the mentioned variation may be result of the degree of serpentinization. However, the results of the present study are particularly encouraging as marine aggregates appear to be a quite valuable alternative way to replace overland aggregates.

Conclusions

The engineering characteristics of the tested marine peridotites are generally identical to the tested overland peridotites used as aggregates and hence these results are particularly encouraging for the replacement of the overland aggregates with the corresponding marine. However, it should be mentioned that a study like this in order to conduct a safer conclusion must combine the research results of many scientific fields such as engineering geology, applied petrography and marine geology.

Acknowledgements

We kindly thank Dr. K. Hatzipanagiotou and Dr. B. Tsikoura for their assistance in the fieldwork, in the interpretation of the results and for their whole contribution of this study.

References

AASHTO T255 (American Association of State Highway and Transportation Officials). Standard Method of Test for Total Evaporable Moisture Content of Aggregate by Drying; AASHTO: Washington, DC, USA, 2000.

ASTM C-131. Resistance to Abrasion of Small-Size Coarse Aggregate by Use of the Los Angeles Machine; American Society for Testing and Materials: Philadelphia, PA, USA, 1989.

ASTM D-2938. Standard Test Method of Unconfined Compressive Strength of Intact Rock Core Specimens; Annual Book of Standards, 4.08; American Society for Testing and Materials: Philadelphia, PA, USA, 1986.

Bornovas, J. 1981. Geological map of Greece, Kapareli Sheet, 1:50.000; IGME: Athens, Greece.

BS 812, Testing Aggregates, Part 105: Methods for Determination of Particle Shape. Section: 105.1: Flakiness Index; British Standards Institution: London, UK, 1989.

BS 812, Testing Aggregates, Part 105: Methods for determination of particle Shape. Section: 105.2: Elongation Index; British Standards Institution: London, UK, 1990.

Clément, B. 1971. Découverte d'un flysch éocrétacé en Béotie (Grèce overlande). C. R. Acad. Sci., 272, 791–792.

EN 932. Part 3: Procedure and Terminology for Simplified Petrographic Description; European Standard: Pilsen, Czech Republic, 1996.

EN 932-1. Part 1: Composition, Specifications and Conformity Criteria for Common Cements; European standard: Pilsen, Czech Republic, 2011.

Giannakopoulou, P. P., Petrounias, P., Rogkala, A., Tsikouras, B., Stamatis, P. M., Pomonis, P., Hatzipanagiotou, K. 2018. "The Influence of the Mineralogical Composition of Ultramafic Rocks on Their Engineering Performance: A Case Study from the Veria-Naousa and Gerania Ophiolite Complexes (Greece)" Geosciences 8, no. 7: 251. https://doi.org/10.3390/geosciences8070251

Limeira, J., Agulló, L., Etxeberria, M. 2012. Dredged marine sand as construction material European Journal of Environmental and Civil Engineering 16 906–18.

Petrounias, P., Giannakopoulou, P.P., Rogkala, A., Stamatis, P.M., Tsikouras, B., Papoulis, D., Lampropoulou, P., Hatzipanagiotou, K. 2018. The Influence of Alteration of Aggregates on the Quality of the Concrete: A Case Study from Serpentinites and Andesites from Central Macedonia (North Greece). Geosciences, 8, 115.

Petrounias, P., Rogkala, A., Kalpogiannaki, M., Tsikouras, B., Hatzipanagiotou, K. 2016. Comparative study of physico-mechanical properties of ultrabasic rocks (Veria-Naousa ophiolite) and andesites from central Macedonia (Greece). Bull. Geol. Soc. Gr. 50, 1989–1998.

Petrounias, Petros, Panagiota P. Giannakopoulou, Aikaterini Rogkala, Panagiotis M. Stamatis, Paraskevi Lampropoulou, Basilios Tsikouras, and Konstantin Hatzipanagiotou. 2018. "The Effect of Petrographic Characteristics and Physico-Mechanical Properties of Aggregates on the Quality of Concrete" *Minerals 8*, no. 12: 577. https://doi.org/10.3390/min8120577.

Rigopoulos, I., Tsikouras, B., Pomonis, P., Hatzipanagiotou, K. 2010. The influence of alteration on the engineering properties of dolerites: The example from the Pindos and Vourinos ophiolites (northern Greece). Int. J. Rock Mech. Min. Sci. 47, 69–80.

Rigopoulos, I., Tsikouras, B., Pomonis, P., Hatzipanagiotou, K. 2015. Assessment of the engineering behavior of ultramafic and mafic rocks using chemical indices. Eng. Geol. 196, 222–237.

Vacondios, I. 1997. Etude Metallogenique des Chromites Liees aux Ophiolites de Type Mediterranee Occdentale ou orientale: Le chromites de Tinos et des Gerannees. Ph.D. Thesis, University of Patras, Patras, Greece, Volume 98.

Velegrakis, A., Ballay, A., Poulos, S., Radzevicius, R., Bellec, V., Manso, F. 2010. European marine aggregate resources: Origins, usage, prospecting and dredging techniques. Journal of Coastal Research, S151.

Xiao, J., Qiang, C., Nanni, A., Zhang, K. 2017. Use of sea-sand and seawater in concrete construction: current status and future opportunities Constr. Build. Mater. 155 1101–11.

17th INTERNATIONAL CONGRESS of the Geological Society of Greece

BULLETIN OF THE GEOLOGICAL SOCIETY OF GREECE, SP. PUBL.

EXTENDED ABSTRACT 097

Estimation of an empirical relationship for calculating quantities of demolished materials through three-dimensional visualization of buildings affected by the earthquake of June 12, 2017, in Vrisa, Lesvos.

Giannakou A., Soulakellis N., Zouros N., Kavroudakis D.
Affiliation : University of the Aegean, Department of Geography

Intoduction

Natural disasters, particularly earthquakes, can cause severe social, economic, and environmental disruptions. These include fatalities, injuries, infrastructure failures, and challenges related to waste management. Post-disaster debris management is critical due to its implications for public health, environmental preservation, and the efficiency of relief operations. Accurate estimation of the volume and composition of building debris is essential for effective waste management planning.

Objectives

This study aims to develop a rapid methodology for estimating construction and demolition waste C&DW quantities generated after natural disasters using geospatial data. Initially, an attempt will be made to estimate C&DW production rates based on footprint measurements for different building categories. These estimates can be used both for calculating the quantities of various waste streams according to the European Waste Catalogue classification system and for determining total waste quantities at both the building and area levels. Subsequently, using empirical data from demolished buildings, an effort will be made to construct a mathematical formula that calculates the quantities of construction waste in volume and weight units, utilizing independent variables (building characteristics).

Methods

Specifically, the study will investigate the impact of the number of floors and footprint area of buildings on the estimation of waste quantities resulting from collapses or demolitions of buildings severely affected by a natural disaster. These variables are chosen because empirical data for them can be easily and quickly collected with high accuracy through the use of geoinformatics systems, either before or after the occurrence of the disaster. The estimation of the mathematical model will be performed using the method of multiple linear regression, a widely used and powerful statistical tool for estimation based on empirical data. In this analysis, for the first time, detailed data are available at the building level for 182 structures following a catastrophic event, specifically the Vrisa earthquake of June 12, 2017 (6.3 Mw) analyzed at three different scales: area scale, street scale and building scale.

Map 1: Map of Area B1, Vrisa Settlement

Using 140 point clouds and 240 3D models obtained from terrestrial laser scanners and terrestrial photogrammetry, along with two orthophotos, two digital terrain models and a digital surface model generated by UAVs, a wealth of empirical data has been gathered at both area and building levels. This data facilitates the development of a model to calculate C&DW quantities following a disaster.

Figure 1. A section of the 3D model from July 25, 2017, generated from high-resolution images taken by unmanned aerialvehicles (UAVs), N. Soulakellis, S. Chatzistamatis, C. Vasilakos, G. Tataris, A. Papakonstantinou, D. Kavroudakis, K. Topouzelis, O. Roussou, Ch. Kalloniatis, E. E. Papadopoulou, K. Chaidas, P. Kalaitzis, (2018)

Results

As part of this study, an initial attempt was made to estimate the rates of demolition waste production in volume and weight per square meter of floor plan for various categories of buildings. In the study area, the most prevalent use of buildings consists of residences and warehouses, which is logical for a small traditional village on an island, such as Vrisa. Thus, it was deemed necessary to create a separate categorization of the buildings in these two uses based on the number of floors, the type of exterior masonry, and the method of roofing. These data can easily be derived using GIS, as well as through on-site visits to an affected area after a natural disaster. Four tables of weight and volume values of waste per square meter of floor area were compiled in total for different types and codes of construction waste, in accordance with the European Waste Catalogue, as well as overall for each building category. These values can be used for a quick calculation of potential quantities of waste from collapses and demolitions of buildings that may be damaged after a catastrophic event, as well as the total quantities of waste in an affected area. To summarize, buildings with storage use have an average of 2,470 kg/m² and 1.47 m³/m² of generated construction waste, while buildings with residential use have an average of 4,170 kg/m² and 2.40 m³/m² of generated construction waste.

In addition, using the processed data for 182 buildings in the B1 sector of Vrisa, four mathematical formulas were calculated for estimating construction waste and are presented below in a table format.

Table 1: Consolidated table of the four mathematical formulas with their variables and weights.

Equation of the form $Y = \beta_0 + \beta_1 * x_1 + \beta_2 * x_2$						
	Y	**β_0**	**β_1**	**x_1**	**β_2**	**x_2**
1.	Weight (kg)	-130242.6	48903.4	Building Height (m)	1332.6	Building floor area (m^2)
2.	Volume (m^3)	-58.85607	22.78869	Building Height (m)	0.74388	Building floor area (m^2)
3.	Weight (kg)	-147134.0	154491.7	Number of floors	1734.2	Building floor area (m^2)
4.	Volume (m^3)	-64.66171	70.11125	Number of floors	0.94282	Building floor area (m^2)

To examine the relationship between the variables, four multiple linear regression analyses were conducted, where the dependent variables were waste weight (kg) and waste volume (m³), while the independent variables included building height (m), floor area (m²), and the number of floors.

The results indicated that the fitted models were statistically significant, explaining a substantial proportion of the variance in the dependent variables.

1. Waste weight (kg) as the dependent variable with building height and floor area as independent variables
   - $F(2,179) = 320.30$, $R^2 = 0.782$, $p < 0.001$
   - Building height: $\beta = 48{,}903.4$, $t = 18.092$, $p < 0.001$
   - Floor area: $\beta = 1{,}332.6$, $t = 7.809$, $p < 0.001$
2. Waste volume (m^3) as the dependent variable with building height and floor area as independent variables
   - $F(2,179) = 528.5$, $R^2 = 0.8552$, $p < 0.001$
   - Building height: $\beta = 22.79$, $t = 22.16$, $p < 0.001$
   - Floor area: $\beta = 0.74$, $t = 11.46$, $p < 0.001$
3. Waste weight (kg) as the dependent variable with the number of floors and floor area as independent variables
   - $F(2,179) = 262.40$, $R^2 = 0.7457$, $p < 0.001$
   - Number of floors: $\beta = 154{,}491.7$, $t = 15.992$, $p < 0.001$
   - Floor area: $\beta = 1{,}734.2$, $t = 9.866$, $p < 0.001$
4. Waste volume (m^3) as the dependent variable with the number of floors and floor area as independent variables
   - $F(2,179) = 359.70$, $R^2 = 0.8008$, $p < 0.001$
   - Number of floors: $\beta = 70.11$, $t = 17.55$, $p < 0.001$
   - Floor area: $\beta = 0.94$, $t = 12.97$, $p < 0.001$.
   -

These findings confirm that building height, floor area, and the number of floors are strong predictive factors of waste volume and weight, with all β coefficients being statistically significant.
Subsequently, we created the necessary diagnostic plots to check the assumptions of the linear model regarding the residuals. From the first plot, we observe that the red line partially follows the horizontal dashed line, indicating that there do not appear to be issues with linearity. In the second plot, since the points follow the dashed line, the assumption of normality of the residuals is satisfied. In the third plot, the red line is almost flat, thus fulfilling the assumption of homoscedasticity. In the fourth plot, the solid red line remains close to the grey horizontal dashed line, and none of the points exhibit a Cook's distance greater than 0.5, indicating that there are no influential observations."

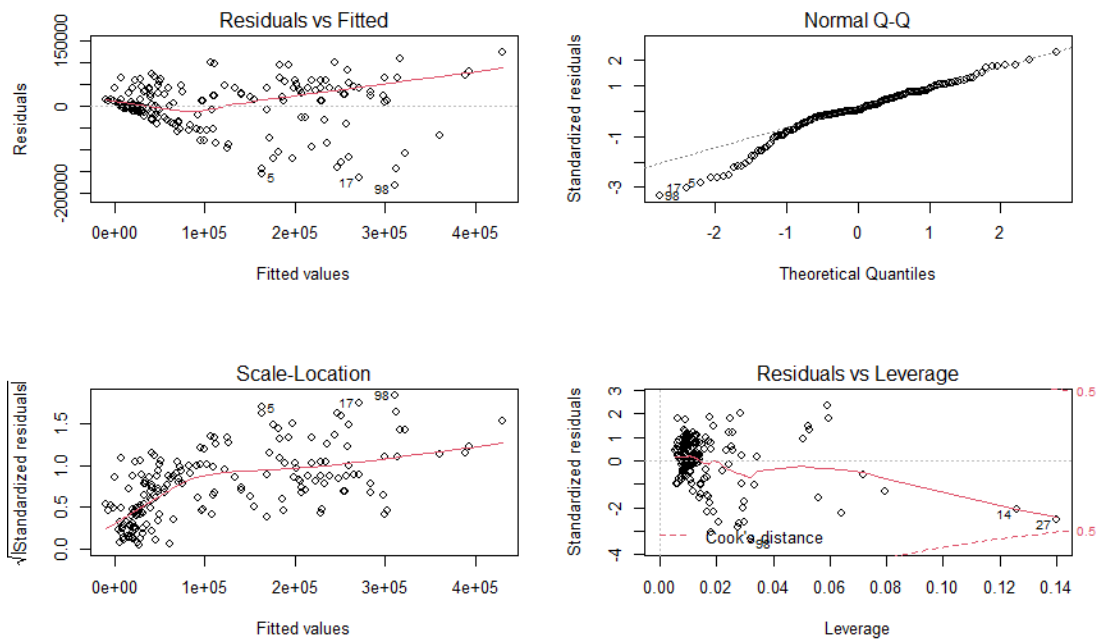

Figure 2. Linear model diagnostic plots

Additionally, an effort was made to study the impact of the number of floors of the buildings in sector B1 of the settlement of Vrisa for three different categories of floor area. Specifically, the study examines how the quantities of

waste in kg, m³, as well as in kg/m² and m³/m², vary on average in the cases of single-story buildings with a floor area ≤ 50 m², two-story buildings with a floor area ≤ 50 m², and three-story buildings with a floor area ≤ 50 m². A similar process is applied for floor areas E > 50 m² and E ≤ 100 m², as well as for E > 100 m². The results are based both on the initial data derived from geographic information systems [Chrysafis, 2018] and on the application of the empirical relationships developed within the framework of this thesis analysis.

Table 2: Comparison of results with the application of empirical relationships

	SINGLE-STORY ≤ 50 m²	**TWO-STORY ≤ 50 m² T**	**THREE-STORY ≤ 50 m²**
KG	41289,16	181945,4	0
KG/M2	2741,83	15651,09	0
M3	23,36	88,5	0
M3/M2	1,56	7,6	0
	SINGLE-STORY > 50 AND ≤ 100 m²	**TWO-STORY > 50 AND ≤ 100 m²**	**THREE-STORY > 50 AND ≤ 100 m²**
KG	143774,5	226939,3	0
KG/M2	2287,66	5371,12	0
M3	76,79	112,78	0
M3/M2	1,22	2,67	0
	SINGLE-STORY > 100 m²	**TWO-STORY > 100 m²**	**THREE-STORY > 100 m²**
KG	214902,8	259520,4	390750,2
KG/M2	1790,6	4277,62	6442,24
M3	116,9	130,29	191,38
M3/M2	0,97	2,15	3,16

Finally, comparison of the results was conducted between the use of the formula developed by the NTUA Chemical Engineering School which has been widely used since 2005 for the preparation of all Regional Solid Waste Management Plans in Greece and the empirical relationships of this thesis. Specifically, the estimation of waste weight using the NTUA formula shows a deviation of approximately 50% upwards compared to empirical relationships and the estimation of waste volume shows a deviation of approximately 60% upwards. This confirms the need for a model to calculate demolition waste quantities that take into account the unique morphological characteristics of an area (e.g., traditional settlements, stone-built structures, etc.) rather than relying solely on statistical data from the Hellenic Statistical Authority (ELSTAT) regarding the number of demolitions.

Conclusions

In conclusion, the availability and collection of empirical data is the most important and necessary step in establishing standardized methods for estimating construction waste, both at the local level and at the building level. The collection of data can precede a disaster and, therefore, facilitate political leadership in organizing immediate and effective recovery plans for areas threatened by various types of natural phenomena. According to the EU Protocol for the management of construction and demolition waste [European Commission, 2016], an inspection must be conducted prior to demolition projects for any material to be reused or recycled, as well as for any hazardous waste. The methodology developed in this study for determining waste generation rates per EWC category can significantly contribute to this inspection and aid in the systematic utilization of materials from debris for subsequent building reconstruction processes. The proposed models from our study can be used for future estimates of waste that may result from a potential natural disaster in various other areas that morphologically resemble the area of our study. Specifically, they can be applied to traditional settlements whose basic morphological characteristics include stone-built walls, wooden internal and external openings, internal partition walls made of bagdati (a type of traditional construction technique), wooden floors, etc. It is understood that they can also be used for predictions and estimates of other traditional settlements on the island of Lesbos, as well as settlements in the Aegean island complex with similar architecture. Our analysis was based on estimates from the available building stock rather than field measurements taken after the disaster occurred. Estimating quantities based on available building stock almost always provides a consistent amount of waste, whereas methods relying on field measurement data after an event can yield significantly fluctuating values.

The need to find a standardized empirical relationship for calculating construction waste with broad application in traditional settlements of Greece, with vulnerable building stock and unauthorized structural interventions, necessitates further research using more empirical data. One attempt is to use existing data for the entire area of Vrisa, so that our mathematical models can be reassessed and adjusted. Additionally, data could be obtained for other areas of the island of Lesbos using GIS methods, so that by knowing the available building stock, we can automatically estimate potential disaster waste quantities, as various natural hazards (earthquakes, floods, fires, etc.) threaten the existence of the island. Furthermore, measurements of construction waste quantities should be made after necessary demolitions by the waste management authorities (AEKK) within their environmental responsibility framework, so that a comparison and verification of the results from the application of the empirical relationships can be made. Finally, other or different variables could be used in the mathematical model so that, using the method of multiple linear regression, it can be determined whether they contribute and to what extent to the correct estimation of quantities, as well as to identify their interdependencies. Such variables could, for example, include the building coefficient, or even categorical variables, such as floor type, roof type etc.

Acknowledgements
I would like to express my gratitude to my supervising professor, Nikolaos Soulakellis, for the guidance he provided throughout the duration of this thesis. I would also like to extend my thanks to the other two members of the committee for their contribution to this thesis.

References

Chrysafis N., 2018. Investigation of geoinformatics methods in the management modeling of C&DW (Construction and Demolition Waste) after a destructive earthquake: The case of Vrisa, Lesvos. Master's thesis, Department of Geography, University of the Aegean.

N. Soulakellis, et al., 2018. Synergistic exploitation of geoinformation methods for post-earthquake 3D mapping of Vrisa traditional settlement, Lesvos island, Greece. Int. Arch. Photogramm. Remote Sens. Spatial Inf. Sci., XLII-3/W4, 491–498.

D. Fatta, et al., 2003. Generation and management of construction and demolition waste in Greece- an existing challenge. Resources Conservation and Recycling 40(1):81-91.

Samy García-Torres et al., 2017. Methodology to characterize and quantify debris generation in residential buildings after seismic events. Resources, Conservation and Recycling, Volume 117, Part B, Pages 151-159.

Askarizadeh A. et al., 2015. Management of post-earthquake construction debris in Tehran Metropolitan. International Journal of Environmental Science and Technology volume 13, pages 639–648.

Koutsoudaki E., 2016. Linear and Non-Linear Regression with Applications in R. Master's thesis, Department of Engineering and Informatics, University of Patras.

17th INTERNATIONAL CONGRESS of the Geological Society of Greece

BULLETIN OF THE GEOLOGICAL SOCIETY OF GREECE, SP. PUBL.

EXTENDED ABSTRACT 098

Preliminary results on the toxic elemental accumulation in the Fe-oxides of the stream sediments from Palea Kavala, Northern Greece

Giouri K.[1], Stergiou C.L.[1,2], Melfos V.[1], Papadopoulou L.[1], Kantiranis N.[1], Peytcheva I.[3], Stefanova E.[3]

(1) School of Geology, Aristotle University of Thessaloniki (AUTH), 54124, Thessaloniki, Greece (2) Chemical Process & Energy Resources Institute (CPERI), Centre for Research and Technology Hellas (CERTH), 50200, Ptolemaida, Greece (3) Geological Institute, Bulgarian Academy of Sciences, 241113, Sofia, Bulgaria

Introduction

The origin of metals in the environment can be both attributed to natural or to anthropogenic sources. The occurrence of mineralization in an area can affect the metals concentration in the geological background. Wastes from past or current mining and metallurgical activities can contribute to these concentrations through natural processes or through the disposal of the wastes encountered during these activities (Kabata-Pendias, 2011; Alloway, 2013). The research area of Palea Kavala in Northern Greece, is distinguished by the presence of diverse mineralizations rich in Pb, Zn, Fe, Mn, As, Cu, Au, and Ag. Mining and metallurgical activities have been conducted in the region in the antiquity and in the beginning of the 20th century, resulting in the disposal of large quantities of mining waste. The presence of Fe-oxides has been identified in the geological background of the Palea Kavala area. Although they can accumulate inorganic pollutants, no detailed study has been carried out concerning the composition of these oxides in the broader district. The main analytical technique applied for the detailed determination of elements accumulated in the oxides was the application of LA-ICP-MS. The advantage of this method in relation with other analytical techniques, is that it does not require the dissolution of the material to be analyzed and is fast. Additionally, its detection limits are very low and no loss of elements concentration could result, since it does not include many steps, which could cause contamination of the samples (Günther et al. 2000, Huelin et al. 2006). This ongoing study is considered as environmentally significant, since it will reveal locations with high concentrations of chemical elements that are often characterized as harmful for the local community.

Geological Setting

The study area belongs to the Pangeon unit, part of the Southern Rhodope Core Complex. The latter represents a large metamorphic core complex, which was exhumed along the Strymon detachment fault between upper Oligocene and middle Miocene. The lithology of the Pangeon unit includes Paleozoic-Mesozoic gneisses overlain by marbles with schist intercalations (Krohe and Mposkos, 2002; Brun and Sokoutis, 2007). These rocks were intruded by the Kavala (or Symvolon) pluton of Miocene age (22-21 Ma) (Kydonakis *et al.*, 2014). This pluton is an I-type intrusion and mainly consists of amphibole-biotite granodiorite with subordinate amounts of tonalite, diorite, monzogranite, and monzodiorite. Alluvial sediments of a Quaternary age consisting of clays, sands and gravels overlie the crystalline rocks in the western part of the studied area and form the Philippi basin (Figure 1).

Approximately 150 major and minor base- and precious metal occurrences, mostly weathered and oxidized, are spread in an area of about 100 km^2. These metal occurrences have a magmatic-hydrothermal origin and are found within the Kavala pluton, as well as in the surrounding metamorphic rocks. Five different metal assemblages, including Fe-Mn-(Pb-Zn-Ag), Fe-Mn-Au, Fe-As-Au, Fe-Cu-Au and Bi-Te-(Pb-Sb-Au), exhibit a zonal distribution around the magmatic intrusion and contain complicated primary and secondary metallic mineral paragenesis. Primary minerals consist of pyrite, arsenopyrite, chalcopyrite, galena, sphalerite, tetrahedrite-tennantite, with subordinate pyrrhotite, bismuthinite, petzite, lillianite, proustite, pyrargyrite, argentite, cosalite, tetradymite, jalpaite, stephanite and native gold and silver. The secondary minerals comprise mainly goethite, lepidocrocite, hematite, covellite, chalcocite, malachite, smithsonite, cerussite, mimetite, siderite, arseniosiderite, scorodite, jarosite, pyrolusite, manganite, manganosite, cryptomelane, todorocite, nsutite (Vavelidis *et al.*, 1997; Fornadel *et al.*, 2011).

Considerable underground and surface mining activities took place during Classical to Roman periods for gold or lead–silver, and during the 20th century (1904-1914) for iron, manganese, zinc and lead. In the vicinity of the mines, large piles of mining wastes, mainly from the recent activities, are spread along the rivers and the streams. The wastes are eroded and significant quantities of the metals are diffused in the aquatic environment of the river drainage systems and are transported downhill, in the Phlippi basin (Giouri et al. 2013, 2016a,b, 2018; Giouri, 2020).

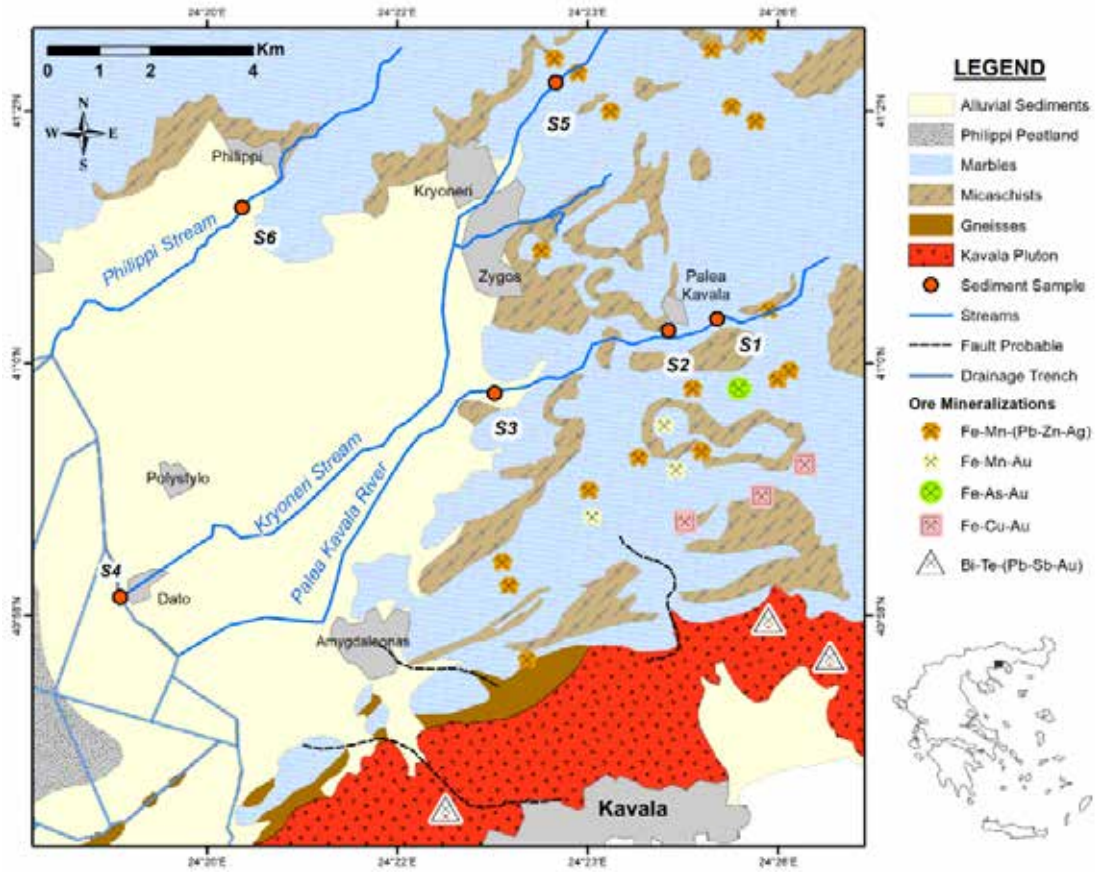

Figure 1. Geological map of the Kavala-Philippi area (modified after Kronberg, 1970 & Kronberg, Melidonis 1970), including the Palea Kavala river and the Kryoneri and Philippi streams. The sampling sites of the stream sediments are also shown.

Methods

Samples collection

Six sampling sites were strategically chosen for sediment collection, distributed across three branches of the main drainage system that traverse areas of ore mineralization and historic mining waste deposits. The site selection considered the expectation that closely situated locations would not exhibit significant variations in geochemical background. Despite the presence of numerous metal occurrences in the study area, their exact dimensions are undefined, and they lack a discernible geometric distribution. Consequently, metal dispersion throughout the region is irregular. Sediments were collected from the following locations: samples S1, S2, and S3 were obtained downstream of the Palea Kavala River, samples S4 and S5 from the Kryoneri Stream, and sample S6 from the Philippi Stream (Figure 1). The collection process involved using an acid-washed plastic shovel to minimize contamination, after which the samples were transferred into clean polyethylene bags. These bags were sealed immediately to preserve sample integrity and transported to the laboratory for further processing and analysis.

Samples preparation

The collected samples were dried at 60 ˚C in an oven, at the Department of Mineralogy-Petrology-Economic Geology of the School of Geology, Aristotle University of Thessaloniki (AUTH), in order to remove the adsorbed moisture. Then they were gently ground in an agate mortar, in order to be disaggregated. The dried and disaggregated samples were sieved through a 0.5 mm and a 0.18 mm sieve in order to obtain the in-between fraction of each sample for the polished sections. Samples were also sieved through a 0.063 mm sieve in order to obtain the fine grained fractions for further chemical analyses.

Samples analysis

In the present study, the fine grained fraction (<0.063 mm) was used for the determination of the mineralogical composition of sediments by the application of X-ray diffraction (XRD), at the Department of Mineralogy-Petrology-Economic Geology, AUTH, using a PHILIPS PW1820/00 X-ray diffractometer, which carry a PW1710 microprocessor. The operating conditions were 35 kV and 25 mA using Ni-filtered CuK radiation. The 2θ scanning range was between 3 and 63 degrees and the scanning speed was 1.2 deg/min. The sediments fraction between 0.5 and 0.18 mm of each sample has been studied under a stereoscopic

microscope in order to separate the Fe-oxide fraction. Subsequently, polished-thin sections were prepared and an initial identification of minerals was carried out by the use of a reflected-transmitted light polarizing microscope. The determination of both composition and morphology of the Fe-oxides, was conducted by the use of scanning electron microscopy (SEM) at the Faculty of Sciences, Aristotle University of Thessaloniki, by the use of a JEOL JSM-840A SEM equipped with an ISIS 300 OXFORD energy-dispersive spectrometer (EDS). The LA-ICP-MS was applied for the determination of the Fe-oxides chemical composition in ultra-trace level. The analyses were conducted at the Geological Institute of the Bulgarian Academy of Sciences in Sofia. Trace elements were measured using a PerkinElmer ELAN DRC-e ICP mass spectrometer coupled with a New Wave UP193-FX excimer laser ablation system, with ablation conducted in a helium medium. The system was optimized daily to ensure sensitivity, using a 35 μm spot size and an energy density of 5.0–5.2 J/cm². The analysis included a 100-second cycle (40 seconds for background, 60 seconds laser-on). Predefined areas in the sections avoided mineral inclusions, and repeated external standardization was performed with NIST SRM 610, USGS GSD-1G, and USGS Mass 1 standards. Data reduction utilized SILLS software (Guillong *et. al,* 2008), with Fe and contents determined by SEM-EDS as internal standards. Fluctuations in isotope intensity were evaluated to exclude contamination by other minerals.

Results

The mineralogical composition of the samples consists mostly of quartz, plagioclase, K-feldspar, mica, calcite, with minor amphiboles. Clay minerals such as chlorite, smectite and kaolinite were also determined (Figure 2a). By the use of a stereoscopic microscope, grains of ore minerals were separated out of the sediments, and randomly oriented samples were analyzed with XRD. These enriched samples consisted of hematite and goethite, along with mica, K-feldspar, quartz and clay minerals (Figure 2b).

The application of optical and scanning electron microscopy on the studied samples revealed that the sediments of the research area comprise ore minerals which are mainly Fe-oxides (Figures 3a,b, 4a,b, 5a,b). According to the results of the scanning electron microscopy (SEM-EDS) these Fe-oxides are mainly hematite and magnetite which are rich in As, Pb and/or Zn. Other identified minerals were goethite, pyrite, galena and titanite. This comes in agreement with the results revealed by Giouri *et al.* (2013, 2016a,b, 2018) and Giouri (2020) according to which most of the sediments in the studied area are enriched in metal(loids), which among others include As, Pb and Zn. More specifically, by the comparison of the mean elements concentrations in the sediments with the corresponding mean concentrations in the rocks of the studied area, it is demonstrated that the sediments are enriched 1.3 times in Fe, 8.7 times in As, 34.9 times in Pb and 4.4 times in Zn (Giouri, 2020). Hence, as concluded by both the bulk sediments geochemistry and the statistical analysis of the results, the enrichment of sediments in As, Pb and Zn is mainly attributed to the neighboring ore deposits.

The LA-ICP-MS further proved As, Pb and Zn accumulation and revealed specific groups of trace elements participating in the studied Fe-oxides (Figures 3c, 4c, 5c). The Fe-oxide from sample S6 contains the highest accumulation of trace elements, while sample S3 is the most depleted one. Based on the chemical composition of the analyzed oxides main accumulations of elements included As (<16,971.57 μg/g in S5), Cd (<10.90 μg/g in S5), Cr (<7,932.26 μg/g in S5), Co (<69.83 μg/g in S6), Cu (<342.02 μg/g in S5), Ni (<716.41 μg/g in S5), Pb (<4,314.55 μg/g in S5) and Zn (<4,180.71 μg/g in S5), as well as the critical and rare metals Ag (<197.30 μg/g in S5), Ce (<211.42 μg/g in S6), La (<440.91 μg/g in S5), Lu (<3.36 μg/g in S6), Th (<16.92 μg/g in S5), and U (<3.29 μg/g in S5, Figures 3c, 4c, 5c).

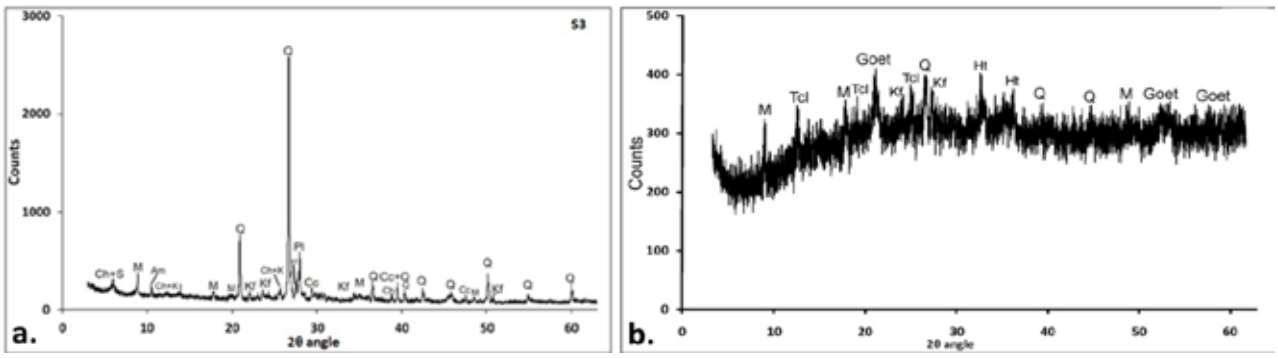

Figure 2. a. XRD pattern of the representative sample S3 (fraction < 0.063 mm). b. XRD pattern of the sample that was enriched in ore minerals. Abbreviations: amphibole (Am), calcite (Cc), chlorite (Ch), goethite-limonite (Goet), hematite (Ht), kaolinite (K), K-feldspars (Kf), micas (M), plagioclase (Pl), smectite (S), quartz (Q), and total clays (Tcl).

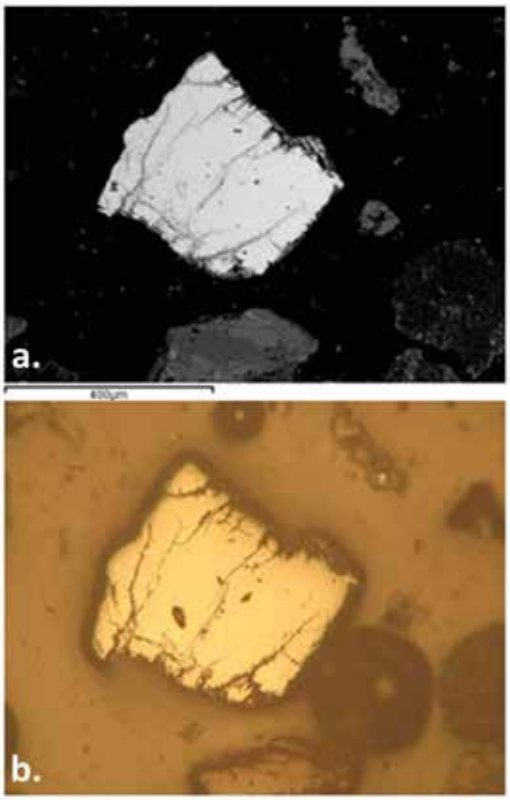

c.

SiO2	wt.%	<0.67235	<0.69319
TiO2	wt.%	0,04	0,11
Al2O3	wt.%	0,20	0,17
FeO	wt.%	99,48	99,20
MnO	wt.%	0,24	0,29
MgO	wt.%	0,02	0,02
CaO	wt.%	<1.1199	<1.1207
Na2O	wt.%	<0.0040615	<0.0039912
K2O	wt.%	<0.0064129	<0.0066573
P2O5	wt.%	<0.035802	<0.034843
V51	µg/g	2472,11	2266,61
Cr52	µg/g	178,13	173,74
Co59	µg/g	45,72	43,29
Ni60	µg/g	43,27	48,45
Cu63	µg/g	33,37	<4.3222
Zn66	µg/g	187,36	231,48
Ga71	µg/g	57,29	45,35
As75	µg/g	<16.8988	<14.725
Zr90	µg/g	<0.67578	<0.63428
Mo95	µg/g	5,13	<14.792
Ag107	µg/g	<6.3156	<4.706
Cd111	µg/g	<14.1094	<7.7669
Sb121	µg/g	1,71	<0.8697
Ba137	µg/g	2,47	<6.9413
Ce140	µg/g	0,41	<0.26137
Ta181	µg/g	<1.1465	<0.88967
W182	µg/g	<4.4624	<4.377
Pt195	µg/g	<1.9608	<1.8222
Au197	µg/g	<0.77605	<0.73012
Tl205	µg/g	<0.73071	<0.63545
Pb208	µg/g	21,55	2,34
Bi209	µg/g	<1.4279	<1.1063
Th232	µg/g	<0.26473	<0.82706

Figure 3. a. SEM back-scattered electron image of a Fe-oxide grain from sample S3. b. The same grain as seen under reflected light. c. Representative chemical analyses by means of LA-ICP-MS.

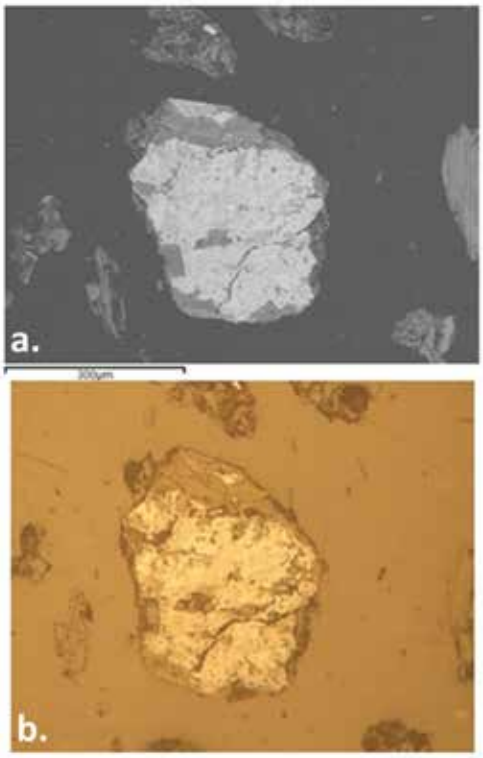

c.

SiO2	wt.%	8,60	7,96	7,67	6,52
TiO2	wt.%	<0.0084243	0,00	<0.0045515	<0.0022378
Al2O3	wt.%	3,56	1,14	0,53	1,94
FeO	wt.%	81,78	85,13	86,90	86,65
MnO	wt.%	0,08	0,06	0,02	0,06
MgO	wt.%	0,34	0,17	0,16	0,21
CaO	wt.%	1,48	2,18	1,59	1,37
Na2O	wt.%	0,02	0,02	0,02	0,01
K2O	wt.%	0,92	0,22	0,14	0,42
P2O5	wt.%	0,14	0,22	0,21	0,13
Sc45	µg/g	32,36	14,17	10,91	32,04
V51	µg/g	1049,52	860,58	653,20	963,91
Cr52	µg/g	2040,26	7932,26	2741,53	4993,08
Co59	µg/g	61,11	8,32	3,53	16,82
Ni60	µg/g	716,41	315,55	102,63	251,96
Cu63	µg/g	342,02	197,49	143,08	240,26
Zn66	µg/g	4180,71	1747,81	1224,61	2926,41
Ga71	µg/g	20,08	3,75	<5.5946	8,17
As75	µg/g	16971,57	12475,98	15160,50	10276,00
Sr88	µg/g	22,82	45,06	49,35	30,76
Y89	µg/g	136,12	220,31	228,67	152,73
Zr90	µg/g	8,53	12,33	23,19	2,28
Ag107	µg/g	2,78	62,00	197,30	<5.7179
Cd111	µg/g	10,90	<11.2481	<14.6181	<13.4059
In113	µg/g	16,24	<14.2782	<12.9922	7,13
Sb121	µg/g	991,40	916,93	279,61	471,73
Ba137	µg/g	126,12	221,70	250,08	151,14
La139	µg/g	243,86	440,91	408,78	305,26
Ce140	µg/g	7,19	7,47	1,03	4,75
Lu175	µg/g	1,54	3,49	2,95	3,32
W182	µg/g	206,52	166,04	156,66	213,01
Tl205	µg/g	1,18	2,87	<1.1754	0,66
Pb208	µg/g	2667,18	3996,59	4314,55	2448,43
Th232	µg/g	16,92	8,38	<0.75173	3,75
U238	µg/g	2,88	3,29	2,39	2,82

Figure 4. a. SEM back-scattered electron image of a Fe-oxide grain from sample S5. b. The same grain as seen under reflected light. c. Representative chemical analyses by means of LA-ICP-MS.

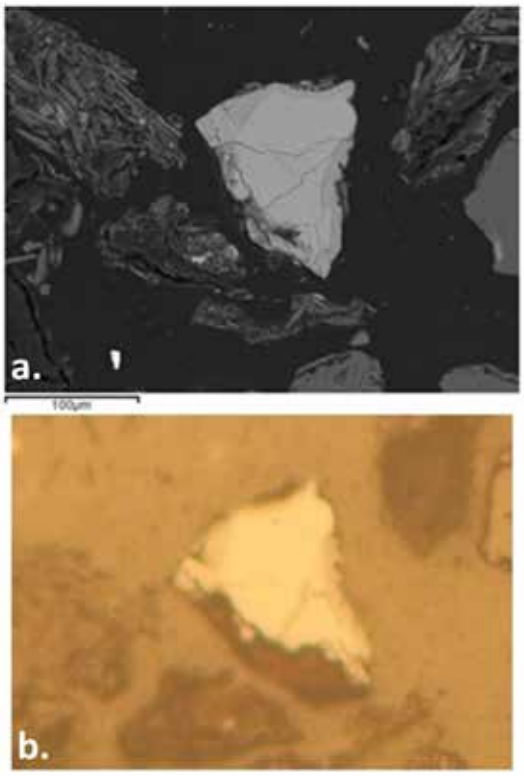

c.

SiO2	wt.%	7,19	6,83
TiO2	wt.%	0,02	<0.0029148
Al2O3	wt.%	3,19	0,55
FeO	wt.%	84,62	91,50
MnO	wt.%	0,11	0,08
MgO	wt.%	0,18	0,11
CaO	wt.%	1,40	<0.81371
Na2O	wt.%	0,10	0,03
K2O	wt.%	0,48	0,09
P2O5	wt.%	2,71	0,54
Sc45	µg/g	24,98	<5.0964
V51	µg/g	327,82	<4.5428
Cr52	µg/g	5380,98	2472,47
Co59	µg/g	25,52	69,83
Ni60	µg/g	209,13	345,97
Cu63	µg/g	258,71	81,97
Zn66	µg/g	993,61	1556,00
Ga71	µg/g	4,62	<5.7906
As75	µg/g	2556,67	162,78
Sr88	µg/g	37,84	6,86
Y89	µg/g	111,89	248,44
Zr90	µg/g	1,87	<1.334
Ag107	µg/g	<2.2784	2,66
Cd111	µg/g	<30.872	<26.9108
In113	µg/g	<16.3518	7,86
Sb121	µg/g	20,32	<4.4107
Ba137	µg/g	210,83	38,97
La139	µg/g	71,48	79,78
Ce140	µg/g	38,72	211,42
Lu175	µg/g	1,79	3,36
Hf177	µg/g	<4.5762	<5.3671
Ta181	µg/g	<1.0394	<0.54105
Au197	µg/g	<1.2756	<2.5155
Pb208	µg/g	879,70	10,24

Figure 5. a. SEM back-scattered electron image of a Fe-oxide grain from sample S6. b. The same grain as seen under reflected light. c. Representative chemical analyses by means of LA-ICP-MS.

Although the mineralogical composition of the studied samples mainly consists of silicate minerals, the presence of chlorite, smectite, and kaolinite among the clay minerals indicates a complex sedimentary matrix (Figure 2a). In addition, the co-occurrence of pyrite and galena with Fe-oxides as indicated by SEM-EDS analysis suggests secondary oxidation processes, leading to the incorporation of trace elements such as As, Pb, and Zn within the oxide matrix.

The trace element contents revealed by LA-ICP-MS, especially for the elements As, Pb, Zn, Cr, and Cd, exceed common environmental thresholds, highlighting potential geochemical hazards (Kabata-Pendias, 2011). The ongoing research includes the co-evaluation of the semi-quantitative mineralogical compositions by XRD and the statistical analysis of LA-ICP-MS results in an effort to estimate the spatial distribution of potentially hazardous concentrations. For example, a 10% Fe-oxide content in contaminated sediment suggests a significant geochemical reservoir of toxic elements, that could be related to a maximum of ~1.7 g in As per kg of sediment (as of <16,971.57 µg/g in S5, Table 4). These advanced mineralogical and geochemical approach, if coupled with leaching studies may help determine whether these elements remain immobilized or may constitute an environmental risk, under natural or disturbed conditions.

Conclusions

The study highlights the significant influence of ore deposits on the geochemical background of the Palea Kavala area, emphasizing the role of Fe-oxides in stream sediments as environmental monitors due to their capacity to accumulate inorganic pollutants. Mineralogical analysis revealed the presence of major components like quartz, K-feldspar, mica, calcite, and clay minerals, with minor presence of amphibole, hematite, and goethite. Analytical techniques such as SEM-EDS, LA-ICP-MS, and XRD identified Fe-oxides as primary carriers of toxic metals, including As, Cd, Cr, Mn, Ni, Pb, Zn, and U. The geochemical variability among samples suggests that local redox conditions, mineralogical composition, and post-depositional alterations have played key roles in element mobility and retention. The strong association of As, Pb, and Zn with Fe-oxides raises concerns about their potential release into the environment under varying physicochemical conditions, emphasizing the need for further geochemical and environmental assessments. The findings underscore the environmental significance of Fe-oxides in tracing pollutant

pathways and their role in geochemical cycling. This comprehensive approach demonstrates how integrating multiple analytical methods provides robust insights into sediment composition and metal distribution. Future research could focus on the mobility and bioavailability of these metals to better assess their environmental impact.

Acknowledgements
Authors would like to thank Aristeidis G. Stamatiadis for the preparation of the polished sections, as well as the Geological Institute of the Bulgarian Academy of Sciences for facilitating the LA-ICP-MS analysis.

References

Alloway B.J., 2013. Bioavailability of Elements in Soil. In: Selinus O. (eds) Essentials of Medical Geology. Springer, Dordrecht.
Brun, J.P., Sokoutis, D. 2007. Kinematics of the Southern Rhodope Core Complex (North Greece). International Journal of Earth Sciences 96, 1079-1099.
Fornadel, A.P., Spry, P.G., Melfos, V., Vavelidis, M.,Voudouris, P., 2011. Is the Palea Kavala Bi–Te–Pb–Sb±Au district, northeastern Greece, an intrusion-related system? Ore Geology Reviews 39, 119–133.
Giouri K., Melfos V., Papadopoulou L., Vavelidis M., Alifragkis D. (2016a). Correlation of selected metals and their binding behavior with sediment fractions in Philippoi area, NE Macedonia, northern Greece. Scientific Annals of the Faculty of Geology, University of Thessaloniki (Honorary Publication in Memory of Professor A. Kasoli-Fournaraki), 105, 1-7.
Giouri A., Melfos V., Papadopoulou L., Vavelidis M., Alifragkis D. (2018). Selected Metal Content and Binding Behaviour in Riverbed Sediments of the Kavala-Philippi Area (Northern Greece). Geosciences, 8, 187, 1-17.
Giouri A., Vavelidis M., Melfos V. (2013). Occurrence of Arsenic in waters and sediments of the Palea Kavala river, NE Macedonia, Northern Greece. Bull Geol Soc Greece, XLVII, 8 p.
Giouri K., Vavelidis M., Melfos V., Papadopoulou L. (2016b). Assessment of selected metals enrichment in sediments from Palea Kavala river, NE Macedonia, Northern Greece. Bull Geol Soc Greece, L, 2137-2144.
Giouri K. (2020). Mineralogical and geochemical environmental research in the wider area of Philippoi, Kavala Prefec. Ph.D. Thesis, School of Geology, Aristotle University of Thessaloniki, Annex Number of Scientific Annals of the School of Geology No 209, 206 pp.
Guillong, M.; Meier, D.L.; Allan, M.M.; Heinrich, C.A.; Yardley, B.W.D. Appendix A6: SILLS: A MATLAB-based program for the reduction of laser ablation ICP-MS data of homogeneous materials and inclusions. In Laser Ablation ICP-MS in the Earth Sciences: Current Practices and Outstanding Issues; Sylvester, P., Ed.; Mineralogical Association of Canada Short Course 40: Vancouver, BC, Canada, 2008; pp. 328-333.
Günther, D., Horn, I., Hattendorf, B., 2000. Recent trends and developments in laser ablation-ICP-mass spectrometry. Journal of Analytical Chemistry, 678, 4–14.
Huelin, S., Longerich, H., Wilton, D., Fryer, B. 2006. The determination of trace elements in Fe–oxide coatings on pebbles using LA-ICP-MS. Journal of Geochemical Exploration, 91, 110–124.
Kabata-Pendias, A., 2011. Trace elements in soils and plants, 4th ed., CRC Press, 548 p.
Krohe, A., Mposkos, E., 2002. Multiple generations of extensional detachments in the Rhodope Mountains (northern Greece): evidence of episodic exhumation of high-pressure rocks, in: Blundell, D.J., Neubauer, F., von Quadt, A. (Eds), The timing and location of major ore deposits in an evolving orogen, Geological Society, London, UK, (204), 151–178.
Kronberg, P. Kavala Sheet, 1970. In Geological map of Greece, Scale 1:50.000. Institute of Geology and Mineral Exploration (IGME), Athens, Greece.
Kronberg, P.; Melidonis, 1970, N. Krinidhes Sheet. In Geological map of Greece, Scale 1:50.000. Institute of Geology and Mineral Exploration (IGME), Athens, Greece.
Kydonakis, K., Gallagher, K., Brun, J.P., Jolivet, M., Gueydan, F., Kostopoulos, D. 2014. Upper Cretaceous exhumation of the western Rhodope Metamorphic Province (Chalkidiki Peninsula, northern Greece). Tectonics 33, 1113–1132.
Melfos, V., Voudouris, P., Vavelidis, M., Spry, P.G., 2008. Microthermometric results and formation conditions of a new intrusion-related Bi–Te–Pb–Sb±Au mineralization in the Kavala Pluton, Greece. Proceedings of the 13th All-Russian Conference on Thermobarogeochemistry in conjuction with the 4th Asian and Pacific International Fluid Inclusion Society Symposium, Moscow, Russia, volume 2, 165-168.
Vavelidis, M., Melfos, V., Eleftheriadis, G., 1997. Mineralogy and microthermometric investigations in the Au-bearing sulphide mineralization of Palea Kavala (Macedonia, Greece), in: Papunen, H. (Eds.), Mineral Deposits: Research and Exploration — Where do They Meet?, Balkema, Rotterdam, NL, 343–346.

17th INTERNATIONAL CONGRESS of the Geological Society of Greece

BULLETIN OF THE GEOLOGICAL SOCIETY OF GREECE, SP. PUBL.

EXTENDED ABSTRACT 099

Investigating the interseismic coupling degree of the northern Apennines external Arc in Emilia Romagna region, (northern Italy).

S. Giuffrida[1-6], L. Anderlini[2], S. Graham[3], F. Carnemolla[1-6], F. Brighenti[4-6], G. de Guidi[1-6], F. Cannavò[5], R. Caputo[4-6]
(1) Department of Biological, Geological and Environmental Sciences (University of Catania, Italy) (2) National Institute of geophysics and Volcanology (INGV, Bologna, Italy) (3) Physics Department (The College of New Jersey-TCNJ, NJ) (4) Department of Physic and Earth Sciences (University of Ferrara, Italy) (5) National Institute of Geophysics and Volcanology-Etnean Observatory (INGV-OE, Italy) (6) CRUST - Interuniversity Center for 3D Seismotectonics with territorial applications, Italy

The Emilia Romagna region, hosts part of the outermost sector of the northern Apennines. This domain is affected by a contractional stress dynamic results from the westward subduction of the Adriatic lithosphere and its flexural retreat. This process leads the formation of a thrusts and fold belt system, migrating toward east and north-east (Malinverno and Ryan, 1986; Fig. 1 a - b). The above-mentioned regional dynamics, determine a shortening deformation pattern, in the interseismic period, probably accommodated by various faults hidden below the Po-Plain, which represents the nowadays foredeep of the northern Apennines. In this work, we apply a kinematic Block Modeling approach (McCaffrey, 2002), to investigate which faults, striking across the Po Plain, is actively accommodating the recognized geodetic velocity field. We use several GNSS data available in these areas (Serpelloni et al., 2022), and exploit all the available fault parameters (e.g., position, strike, dip angle and locking depth) from previous studies and database, to verify the role of major fault segments in accommodating the given velocity field. Our solution shows that the outermost sector of the Northern Apennines, which includes the Mirandola fault and Ferrara Thrusts System, is characterized by contractional slip rates, at most equal to 1.5 mm/yr (dip-slip component), that reproduce the observed velocity field in the long-term (Fig. 2 a). These two above mentioned faults have been widely studied during the last years because of their capability of generating high magnitude earthquakes. An example is the 2012 seismic sequence, characterized by two mainshocks occurred on 20 May (Mw ~ 6) and 29 May (Mw ~ 5.8), (Lavecchia et al., 2012; Fig. 1 b).
Due to the complex seismotectonic history of the studied domain, we discretise the northern Apennines external Arc by means of a Triangular Dislocation Elements (TDEs) mesh to resolve the variability of the slip-deficit rate pattern on fault planes. (Fig. 2 a) According to Meade and Loveless (2009), we calculate the interseismic coupling degree as the ratio of the slip deficit and the long term slip derived from the relative motion of the bounding blocks (Fig 2 b). We therefore investigate each fraction of coupling increment to discern portions of fault planes characterized by a complex behaviour (e.g., aseismic creep vs elastic responses). Finaly, we detect at least three locked asperities, with which we propose a set of possible rupture scenarios and calculate the amount of seismic moment rate that the Emilia Romagna region is accumulating. The obtained seismic moment accumulation rate (3.21 x 1016 Nm/yr) is higher than the rate of the released seismic moment (2.2 x 1016 Nm/yr) in the last ~35 years. Assuming that all this energy (1.01 x 1016 Nm/yr) is released elastically, it would be the equivalent of an earthquake of Mw ~ 4.4, each year..

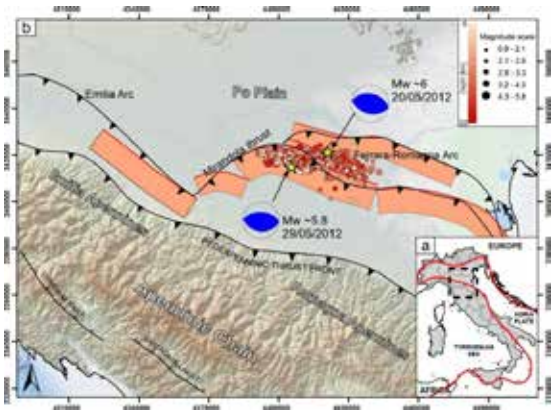

Figure 1. – a) Europe-Africa relative convergence in the context of the Central mediterranean area, (red line represent the front of the collisional domain. – b) Simplified seimotectonic map of the Emilia region (modified after: Toscani et al., 2009; Martelli et al., 2017). Seismogenic sources in orange are from DISS (Database of individual Seismogenic Sources). The microseismicity associated to the 2012 seismic event is from La Torre et al., 2023 (CLASS Database). Focal mechanisms of the May 2012 mainshocks are from INGV (https://terremoti.ingv.it/en). Digital Elevation Model from emodnet (https://emodnet.ec.europa.eu/).

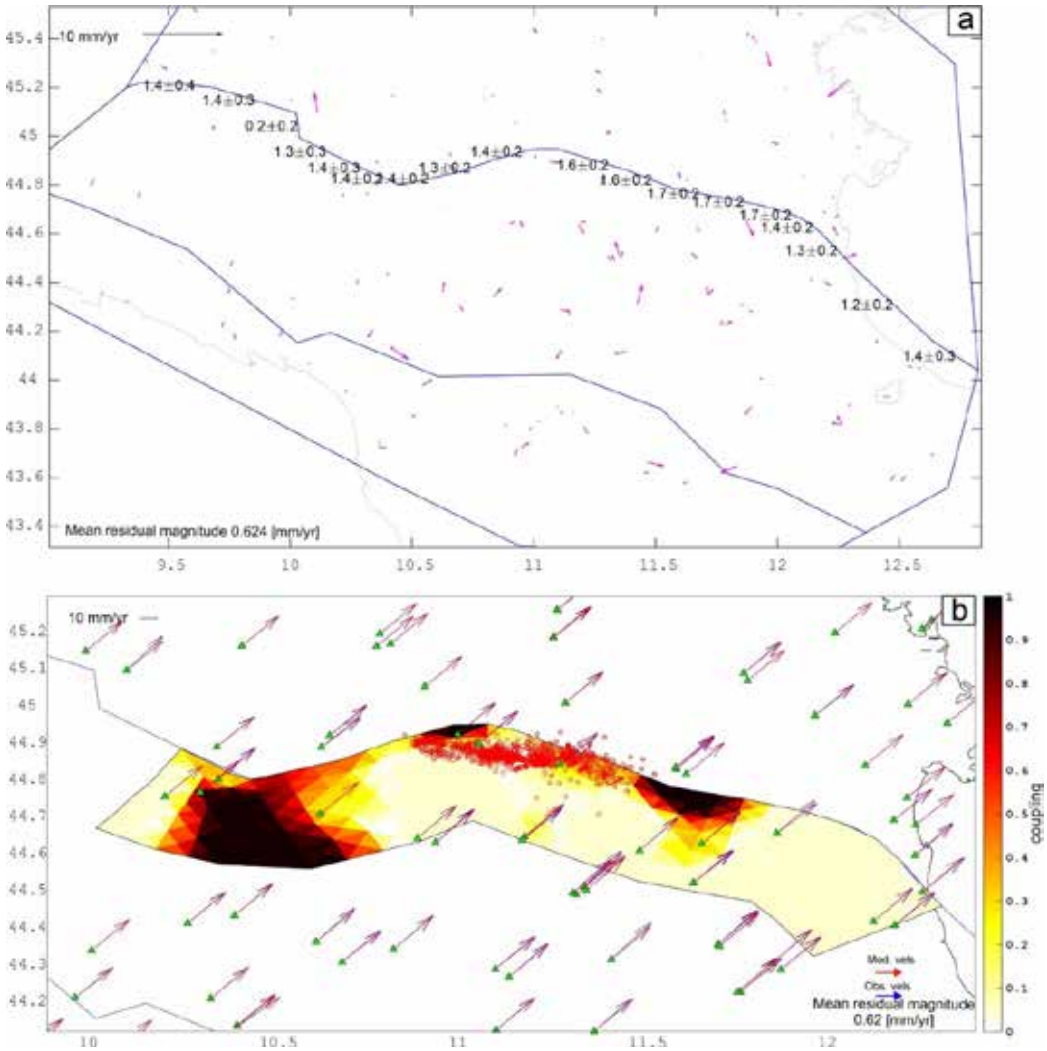

Figure 1. – a) long-term slip rate values (dip slip components) of the northern Apennines external Arc. – b) view of the triangular patches mesh coloured as function of the interseismic coupling distribution, red circles indicate the instrumental seismicity from CLASS database (La Torre et al., 2023), blue and red arrows indicate the observed and the modelled velocity field respectively, green triangles are the permanent GNSS stations of Serpelloni et al., 2022 (in ITRF 2014 reference frame).

References

DISS Working Group (2023). Database of Individual Seismogenic Sources (DISS), Version 3.3.0: A compilation of potential sources for earthquakes larger than M 5.5 in Italy and surrounding areas. Istituto Nazionale di Geofisica e Vulcanologia (INGV). https://doi.org/10.13127/diss3.3.0

Latorre, D. et al. (2023) 'An updated view of the Italian seismicity from probabilistic location in 3D velocity models: The 1981–2018 Italian catalog of absolute earthquake locations (CLASS)', Tectonophysics, 846. Available at: https://doi.org/10.1016/j.tecto.2022.229664.

Lavecchia, G. et al. (2012) 'The May-June 2012 Ferrara Arc earthquakes (northern Italy): Structural control of the spatial evolution of the seismic sequence and of the surface pattern of coseismic fractures', Annals of Geophysics, 55(4), pp. 533–540. Available at: https://doi.org/10.4401/ag-6173.

Malinverno A, Ryan W (1986) Extension in the Tyrrhenian Sea and shortening in the Apennines as result of arc migration driven by sinking of the lithosphere. Tectonics 3:227–245

Martelli, L. et al. (2017) 'Seismic hazard of the Northern Apennines based on 3D seismic sources', Journal of Seismology, 21(5), pp. 1251–1275. Available at: https://doi.org/10.1007/s10950-017-9665-1.

Meade, B.J. and Loveless, J.P. (2009) 'Block modeling with connected fault-network geometries and a linear

elastic coupling estimator in spherical coordinates', Bulletin of the Seismological Society of America, 99(6), pp. 3124–3139. Available at: https://doi.org/10.1785/0120090088.

Mccaffrey, R. (2002) 'Crustal Block Rotations and Plate Coupling', AGU Monograph, pp. 1–40.

Serpelloni, E. et al. (2022) 'Surface Velocities and Strain-Rates in the Euro-Mediterranean Region From Massive GPS Data Processing', Frontiers in Earth Science, 10. Available at: https://doi.org/10.3389/feart.2022.907897.

Toscani, G. et al. (2009) 'Plio-Quaternary tectonic evolution of the Northern Apennines thrust fronts (Bologna-Ferrara section, Italy): Seismotectonic implications', Bollettino della Societa Geologica Italiana, 128(2), pp. 605–613. Available at: https://doi.org/10.3301/IJG.2009.128.2.605.

17th INTERNATIONAL CONGRESS of the Geological Society of Greece

BULLETIN OF THE GEOLOGICAL SOCIETY OF GREECE, SP. PUBL.

EXTENDED ABSTRACT 100

Geochemical and Mineralogical Study of the Antimony (Sb)-mineralization at the north Pelion region, Magnesia, Greece.

Gjika A.[1], Stouraiti C.[1], Voudouris P.[1], Laskaridis K.[2], Anastasatou M.[2], Mavrogonatos C.[3], Strauss H.[4]
(1) Faculty of Geology and Geoenvironment, National and Kapodistrian University of Athens, Athens, Greece, antonelag@geol.uoa.gr; chstouraiti@geol.uoa.gr; voudouris@geol.uoa.gr; (2) Hellenic Survey of Geology and Mineral Exploration (HSGME), Athens, Greece, klaskaridis@eagme.gr; manastasatou@eagme.gr; (3) Department of Earth Sciences, University of Pisa, Pisa, Italy, konstantinos.mavrogonatos@unipi.it; (4) Institut für Geologie und Paläontologie, Westfälische Wilhelms-Universität Münster, Münster, Germany, hstrauss@uni-muenster.de.

Introduction

Antimony (Sb) is consistently included in the European Union's (EU) list of Critical Raw Materials (CRM) since its establishment in 2011, due to its economic importance and the EU's supply reliance on imports from third countries (European Commission, 2023). Greece is one of the EU member states that host a significant number of antimony mineralization (both occurrences and deposits that were exploited in the past), located in central-eastern Macedonia, western Thrace, the eastern Aegean Sea, and the Pelion peninsula (Stergiou *et al.*, 2022,2023; Kanellopoulos *et al.*, 2024). Antimony mineralization at Pelion has never been the subject of systematic research, especially compared to other Greek antimony mineralization. The aim of this study is to determine the mineralogical and geochemical characteristics of the antimony mineralization at the Mantemia and Moni Panagias sites, North Pelion, in an attempt to determine the conditions of ore deposition.

Regional Geology

The Pelion peninsula consists of a HP-LT metasedimentary sequence (e.g., mica schists) of Permian-Cretaceous age, which can be subdivided into two units (i.e. the North Pelion unit and the South Pelion unit) based on dissimilarities regarding their lithology, stratigraphy and provenance (Hinshaw *et al.*, 2024). The metamorphic rocks of North Pelion overlie the Permo-Carboniferous and Neoproterozoic Pelagonian basement and exhibit similar provenance history to the Cycladic Blueschist Unit (CBU) (Hinshaw *et al.*, 2024). Magmatic intrusions of Tertiary age and porphyritic texture occur throughout the North Pelion unit, crosscutting the metamorphic rocks (IGME, 1987). Antimony mineralization occurs in the "Alikopetra" area of N. Pelion, in proximity to the contact of the HP-LT metamorphic rocks of the North Pelion unit and the marbles of the Pelagonian basement.

Methods

Sixteen (16) samples were collected from two Sb-mineralization sites, namely the "Mantemia" and "Moni Panagias", in the broad "Alikopetra" area. The mineralogical content of the samples was determined using optical microscopy, X-ray Diffraction analysis (XRD), and Scanning Electron Microscopy combined with Energy-dispersive X-ray Spectroscopy (SEM-EDS). Geochemical analyses included X-ray Fluorescence Spectroscopy (XRF) and Inductively Coupled Plasma Mass Spectrometry (ICP-MS). The analyses were conducted at the laboratories of the Hellenic Survey of Geology and Mineral Exploration (HSGME).

Results and Discussion

The antimony mineralization at the "Mantemia" site occurs in the form of stibnite lenses within the marble, ranging in size between 2-15 cm (Fig. 2A). The ore assemblage consists of stibnite, pyrite, sphalerite and Sb-Pb sulfosalts, accompanied by the secondary Sb minerals valentinite, a mineral of the roméite group, stibiconite and senarmontite (Fig. 2B, C). Five different species of Sb-Pb sulfosalts were identified, namely zinkenite, fülöppite, plagionite, robinsonite and boulangerite (Fig. 3). Sphalerite exhibits low Fe concentrations (up to 1.65 wt.%). Pyrite has a high As content, reaching up to 10 wt% and being mostly incorporated in the rims of the crystals. Geochemical analysis yielded concentrations up to 29 wt.% Sb, 6.13 wt.% Fe, 6100 ppm Zn, 3550 ppm As, 2400 ppm Pb, 300 ppm Cu, 40 ppm Sn, 167 ppm Ga, 67 ppm Ta, 3 ppm Te and 2 ppm Ag in the ore. The hydrothermal alteration of the host-rock consists of quartz, carbonate minerals (calcite, dolomite), and muscovite.

The antimony ore at "Moni Panagias" occurs in thin and discontinuous quartz veins (Fig. 2D). The ore assemblage at this site appears more diverse, consisting of stibnite, pyrite, sphalerite, arsenopyrite, cinnabar, Bi-Pb-Cu±Ag sulfosalts, (Bi-tennantite, coloradoite and tetradymite, accompanied by the same secondary Sb minerals as in "Mantemia" (Fig. 2E, F). Iron content in sphalerite reaches 2.32 wt.%, while As content in arsenic pyrite reaches 4.98 wt.%. The geochemical composition of the "Moni Panagias" ore consists of 9.10 wt.% Sb, 2.41 wt.% Fe, 7200 ppm Zn, 2240 ppm As, 160 ppm Cu, 2 ppm Ag and 2 ppm Te. The "Moni Panagias" mineralization exhibits a depletion in Pb (up to 210 ppm), Sn (up to 10

ppm), Ga (up to 7 ppm) and Ta (up to 6 ppm), and an enrichment in Bi (up to 30 ppm) compared to the "Mantemia ore". The mineral composition of the hydrothermal alteration remains similar to "Mantemia"; however, the quartz participation is significantly higher in this location.

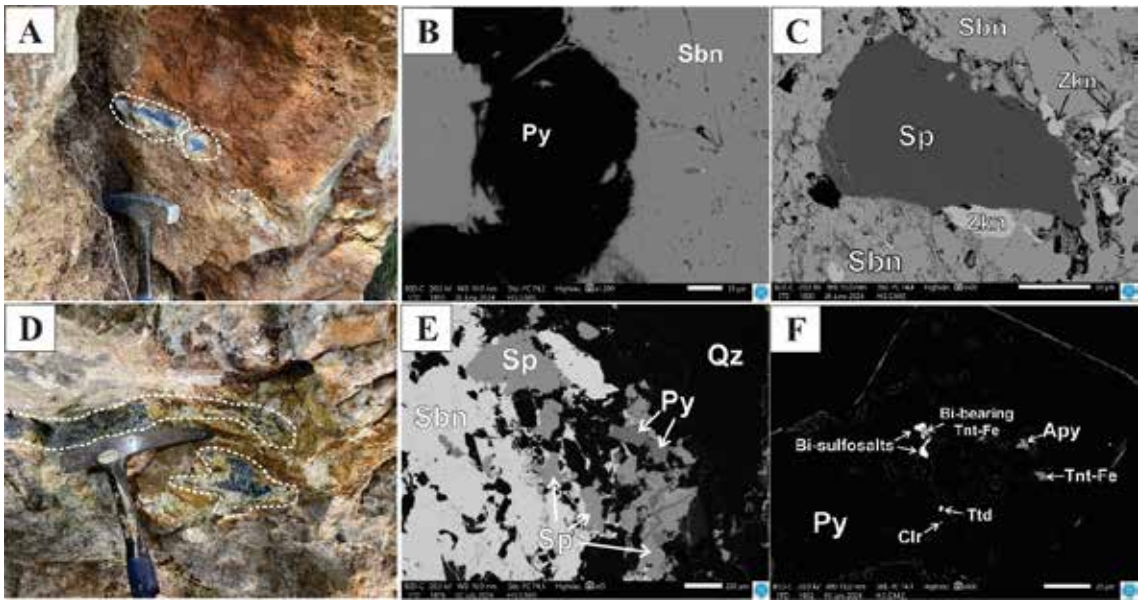

Fig. 2. (A) In-situ antimony mineralization at the "Mantemia" site, (B) Backscattered electron image (BSE) of pyrite and stibnite crystals from the "Mantemia" ore, (C) BSE of sphalerite, zinkenite and stibnite crystals from the "Mantemia" ore, (D) In-situ antimony mineralization at the "Moni Panagias" site, (E) BSE of stibnite, sphalerite, pyrite and quartz from the "Moni Panagias" ore (F) BSE of mineral inclusions inside a pyrite crystal, consisting of Bi-Pb-Cu±Ag sulfosalts, (Bi-)tennantite, arsenopyrite, coloradoite and tetradymite. Abbreviations (according to IMA–CNMNC 2021): Py=pyrite, Sbn=stibnite, Sp=sphalerite, Zkn=zinkenite, Qz=quartz, Tnt=tennantite, Apy=arsenopyrite, Clr=coloradoite, Ttd=tetradymite.

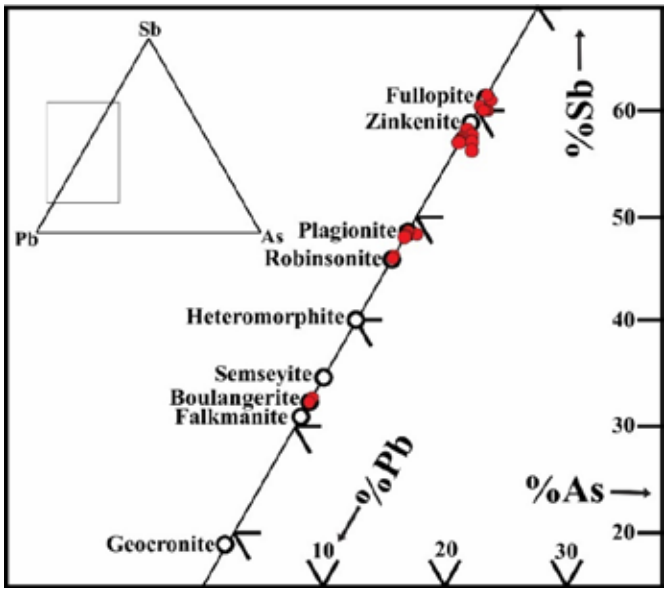

Fig. 3. Composition of Sb-Pb sulfosalts from "Mantemia" plotted on a Sb-Pb-As ternary diagram.

Conclusions

The antimony mineralization in Pelion exhibits characteristics of an epithermal mineralization, formed due to hydrothermal activity, under relatively low temperatures and intermediate to low-sulfidation fluid states. The differences

identified between the two mineralization sites can be attributed to variations of physicochemical conditions during the precipitation of the ore, such as lower fluid sulfidation states and temperatures during the precipitation of the "Moni Panagias" ore (probably due to increased neutralization and/or sulfur consumption), compared to those at "Mantemia" ores.

Acknowledgements
Part of this work was funded by the European Union under the Horizon Europe grant No. 101091374 of MultiMiner project - Multi-source and Multi-scale Earth observation and Novel Machine Learning Methods for Mineral Exploration and Mine Site Monitoring.

References

European Commission, Study on the Critical Raw Materials for the EU 2023 – Final Report. https://data.europa.eu/doi/10.2873/725585

Hinshaw, E.R., Stockli, D.F., and Soukis, K., 2024. Coherent underplating of HP-LT blueschist packages and basement during the Hellenic subduction recorded by zircon U-Pb data, Pelion, Greece. Journal of the Geological Society, vol. 181 (2).

IGME, 1987. *Geological Map of Greece, Scale 1.50,000, "Zagora-Syki" Sheet*. Institute of Geology and Mineral Exploration in Athens.

Kanellopoulos, C., Sboras, S., Voudouris, P., Soukis, K., Moritz, R., 2024. Antimony's significance as a Critical Metal: The global perspective and the Greek Deposits. Minerals, 14, 121, https://doi.org/10.3390/min14020121

Stergiou, C.L., Melfos, V., Voudouris, P., Papadopoulou, L., Spry, P.G., Peytcheva, I., Dimitrova, D., Stefanova, E. 2022. A Fluid Inclusion and Critical/Rare Metal Study of epithermal Quartz-Stibnite Veins associated with the Gerakario Porphyry Deposit, northern Greece. Applied Sciences 12, 909, https://doi.org/10.3390/app12020909

Stergiou, C.L., Sakellaris, G-A., Melfos, V., Voudouris, P., Papadopoulou, L., Kantiranis, N., Skoupras, E., 2023. Mineralogy, Geochemistry and Fluid Inclusion Study of the Stibnite Vein-Type Mineralization at Rizana, Northern Greece. Geosciences, 13, 61. https://doi.org/10.3390/geosciences13020061

17th INTERNATIONAL CONGRESS of the Geological Society of Greece

BULLETIN OF THE GEOLOGICAL SOCIETY OF GREECE, SP. PUBL.

EXTENDED ABSTRACT 101

SantoArray: Densifying station coverage in Santorini amidst the Amorgos-Anydros earthquake swarm crisis

Gkogkas K.[1], Papazachos C.[2], Chatzis N.[2], Vamvakaris D.[2], Karagianni E.[2], Ventouzi C.[2], Vellis A.[2], Anterriotis-Kalpakidis N.[2], Madelis D.[2], Paradisopoulou P.[2], Aidona E.[2], Pikridas Ch.[2]

(1) Institute of Geophysics, Polish Academy of Sciences, Warsaw, Poland, konstantinos.gkogkas@igf.edu.pl

(2) Aristotle University of Thessaloniki, Thessaloniki, Greece, kpapaza@geo.auth.gr

Introduction

During February-March 2025, a seismic swarm occurred near the Santorini-Anydros-Amorgos area, with thousands of earthquakes being recorded with a maximum magnitude of **M**5.2. Hundreds of earthquakes with magnitudes larger than 3 were recorded and felt by inhabitants of Santorini and neighboring islands, to a tentative self-evacuation of Santorini and the declaration of emergency state by the Hellenic government. In light of these events, we rapidly responded to the ongoing crisis by designing and deploying a new seismic array in Santorini (SantoArray). The collaboration between the Aristotle University of Thessaloniki (Greece) and the Institute of Geophysics, Polish Academy of Sciences (Poland) facilitated the preparation, shipment, deployment, maintenance, and data analysis of 7 SmartSolo units and 117 DATA-CUBE instruments. The network operated continuously for approximately 3 weeks (28 February – 23 March 2025) without instrumentation losses, resulting in a plethora of data recorded by the deployed large-N network. We present detailed information on this newly deployed temporary seismic network along with a preliminary example of data analysis.

Over the last decades, the proliferation of equipment for large-N seismic experiments has provided unique opportunities for extensive investigations aiming at resolving the Earth's finer structure and towards a better understanding of seismicity. In the case of Santorini, numerous nodal experiments (e.g., PROTEUS; Hooft et al., 2019; Chatzis et al., 2022) have provided local and fine-scale tomographic images of the crust and uppermost mantle (e.g., Dimitriadis et al., 2010, Hooft et al., 2019; Heath et al., 2019; McVey et al., 2022; Autumn et al., 2025; Huftstetler et al., 2025) with the aim of improving our understanding of the deeper structure of the volcanic plumbing system, as well as the geophysical and geological characteristics of the near-surface structure. The presented SantoArray experiment expands over Santorini, Kammeni and Thirasia islands, providing a unique opportunity to better resolve the islands' shallow structure using land stations.

SantoArray

The SantoArray comprises of continuous records from all permanent (broadband and wide-band; red squares in Figure 1) stations in Santorini operating under the Hellenic Unified Seismic Network (H.U.S.N., Evangelidis et al., 2021), augmented with temporarily deployed nodal stations (117 DATA-CUBE 3-C & 7 SmartSolo 3-C instruments) in two deployment phases (I and II), with distinct instrument configurations and geometries. Phase I (28 February – 11 March, Figure 1a) involved the installation of 7 SmartSolo 5Hz IGU-16HR-3C sensors (blue triangles in Figure 1a) and 117 DATA-CUBE digitizers equipped with 4.5Hz 3-component sensors, set in two different instrument gain configurations (minimum-"low" and maximum-"high" possible) deployed as follows: 50 co-located low- and high-gain sensor sites (grey triangles in Figure 1a), 10 high-gain sensors (white triangles in Figure 1a) and 7 low-gain sensors (black triangles in Figure 1a), with a ~1.3 km average inter-station spacing. Phase II (11-23 March; Figure 1b) was initiated due to instrument battery replacing needs and comprises of the same total instrument number. However, during Phase II we have set all sensors configuration to the maximum possible gain (white triangles in Figure 1b), while sensors co-located at "double" (low- and high-gain) sites and near permanent station locations (grey and several black triangles of Figure 1a) were relocated and distributed throughout Santorini to improve the inter-station spacing to about ~600m. We successfully retrieved all stations and downloaded above 95% of the expected continuous time series for future analyses.

Data examples

Figure 2 presents a preliminary analysis of two local earthquakes that occurred in the vicinity of Anydros (08/03/2025 **M**3.7, Figure 2a) and Kyparissia (09/03/2025 **M**4.7, Figure 2b) recorded during first phase of the SantoArray experiment operation (Phase I). For both events, P- and S-wave phases were manually picked, and P-wave arrival times were calculated relative to the origin time of each event. Then, a simple topographic correction was applied to account for the rapidly changing topography in Santorini, incorporating the mean P and S velocities presented by

Chatzis et al. (2022). A smooth 2D kriging interpolation was applied to the observations to enhance the visualization of spatial wave propagation. The preliminary observations verify the adequate data quality for earthquakes occurring in both near (Anydros sequence example), and large distances (Kiparissia earthquake) from Santorini, and highlight areas of loose formations (sparse time contours in Figure 2b) and near the bedrock (dense time contours in Figure 2b).

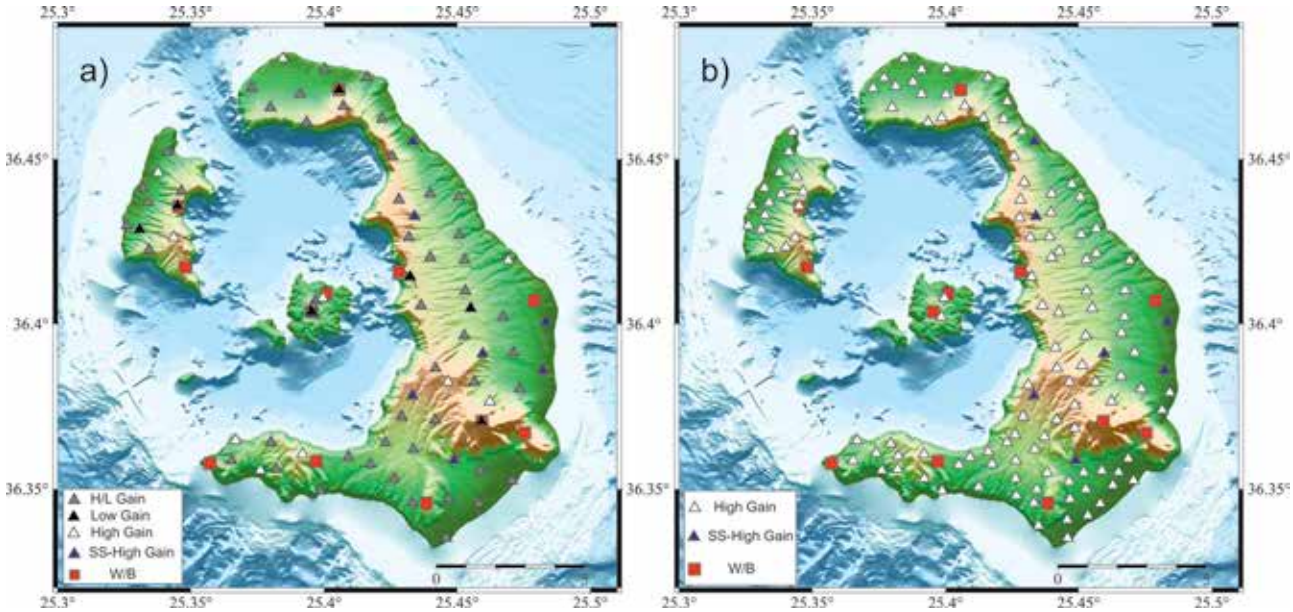

Figure 1. Sensor distribution of the newly deployed SantoArray temporary network. Red squares show permanent Wide-band and Broadband stations from the Hellenic Unified Seismic Network. Blue triangles show deployment locations of the 7 SmartSolo sensors and otherwise colored triangles show the 117 DATA-CUBE sensors. a) SantoArray Phase I, b) SantoArray Phase II.

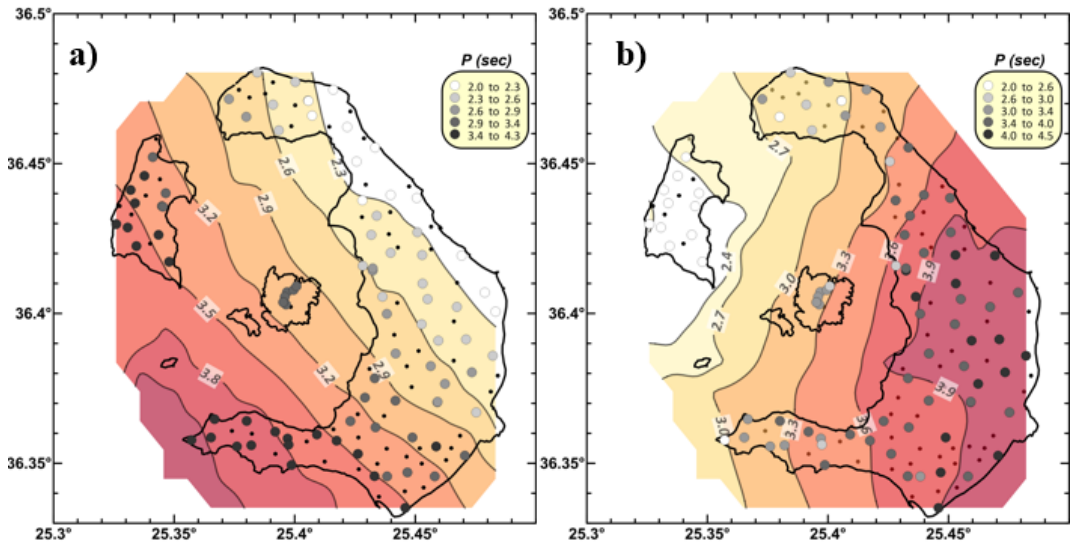

Figure 2. Example of P-wave arrivals from two local earthquakes recorded by SantoArray. Travel-times (colored circles) were calculated for the vertical component measured from the earthquake origin time and corrected for topography. Black dots show locations of SantoArray Phase II stations that were asynchronously deployed and did not record the earthquakes presented here. Smoothed 2-D kriging traveltime contours are plotted in the background. a) the 08/03/2025 M3.7 Anydros earthquake the 08/03/2025 M4.7 Kiparissia earthquake. Traveltimes presented are relative to arbitrary times [00:13:55 for (a) and 20:56:00 for (b)].

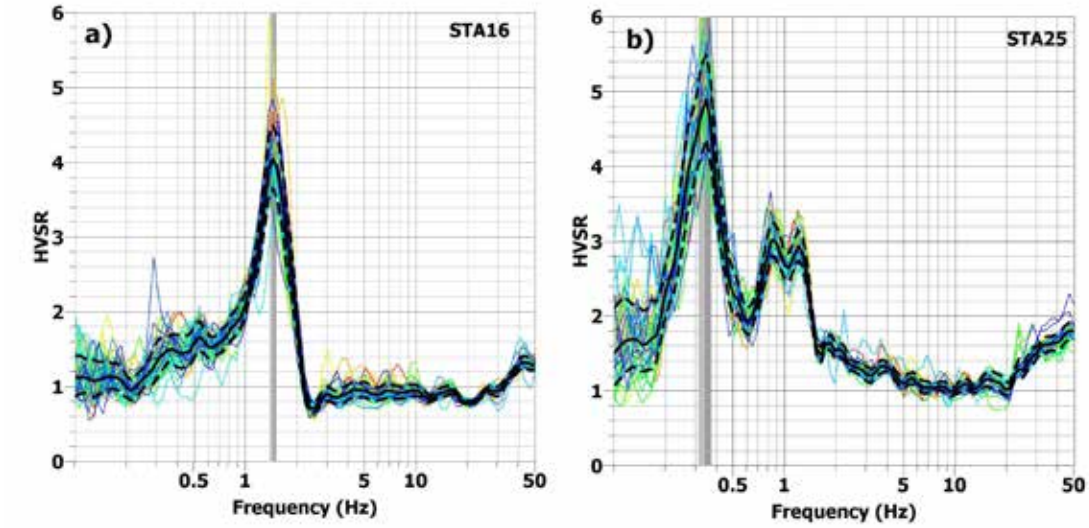

Figure 3. Typical examples of HVSR curves. a) HVSR curve from a site close to the outcrop basement, where a prominent peak is observed at the f_0=1.5 Hz due to impedance contrast between pyroclastic deposits and the underlying metamorphic basement. b) HVSR curve from a site with a very low frequency peak at f_0=0.35 Hz, indicating very deep volcanics above the basement, as well as a secondary frequency peak at f_1~1 Hz, due to shallower impedance contrast within the volcanic layers. The frequency peak is presented in vertical grey line.

In Figure 3, we present two examples of HVSR (Nakamura 1989) curves obtained from single-station 3-component ambient noise measurement at two sites located closer (Fig.3a) and farther (Fig.3b) from the basement outcrop. A sharp fundamental frequency peak is observed in both plot, in agreement with earlier findings (e.g. Chatzis et al., 2022). Moreover, the fundamental frequency, f_0, shifts from ~1.5Hz to 0.35Hz as we move further away from the basement, verifying that the HVSR dataset can be employed to identify the presence of shallow and deep volcanic layers above the metamorphic basement, based on existing and future calibrations of the bedrock depth against the fundamental frequency.

Conclusions

The deployment and operation of SantoArray was completed successfully. The rapid emergency response to the earthquake swarm crisis and the instrument and data retrieval rates underscores the ability of future large-N seismic experiments of similar nature in Greece. The recorded earthquakes presented here provide high quality data encouraging future analysis for several purposes, e.g. earthquake relocation, body-wave tomography, sire-response analysis, etc. Moreover, the hybrid geometry of the network will also allow us to use the recorded ambient noise records for several purposes, such as HVSR and noise autocorrelation, or to compute and use thousands of inter-station pairs for ambient noise cross-correlation tomography, yielding tomographic images of Santorini with unprecedented resolution. Additional inter-disciplinary and collaborative approaches are planned to be realized with the SantoArray data, towards a better understanding of Santorini's seismic structure, the earthquake swarm and the volcano structure and behavior.

Acknowledgement

We are thankful to the people from both institutes who have worked these last few months towards making this experiment happen. We would also like to thank the technicians of the IRIS local technical company who participated in the field work, Manolis Pitsikalis, Ioanna Vamvakouri and other anonymous volunteers for providing local support, as well as the Institute for the Study and Monitoring of Santorini Volcano (ISMOSAV) for covering part of the installation costs.

References

Aristotle University of Thessaloniki. Aristotle University of Thessaloniki Seismological Network, 1981. doi: 10.7914/SN/HT.

Autumn, K. R., Hooft, E. E., & Toomey, D. R. (2025). Exploring Mid-to-Lower Crustal Magma Plumbing of Santorini and Kolumbo Volcanoes using PmP Tomography. Authorea Preprints.

Chatzis, N., Papazachos, C., Theodoulidis, N., Hatzidimitriou, P., Vougioukalakis, G., Paulatto, M., ... & Ventouzi,

C. (2022). Metamorphic bedrock geometry of Santorini using HVSR information and geophysical modeling of ambient noise and active-source surface-wave data. Journal of Volcanology and Geothermal Research, 432, 107692.

Dimitriadis, I., Papazachos, C., Panagiotopoulos, D., Hatzidimitriou, P., Bohnhoff, M., Rische, M., & Meier, T. (2010). P and S velocity structures of the Santorini–Coloumbo volcanic system (Aegean Sea, Greece) obtained by non-linear inversion of travel times and its tectonic implications. Journal of Volcanology and Geothermal Research, 195(1), 13-30.

Evangelidis, C. P., Triantafyllis, N., Samios, M., Boukouras, K., Kontakos, K., Ktenidou, O. J., ... & Tselentis, G. A. (2021). Seismic waveform data from Greece and Cyprus: Integration, archival, and open access. Seismological Society of America, 92(3), 1672-1684.

Heath, B. A., Hooft, E. E. E., Toomey, D. R., Papazachos, C. B., Nomikou, P., Paulatto, M., ... & Warner, M. R. (2019). Tectonism and its relation to magmatism around Santorini Volcano from upper crustal P wave velocity. Journal of Geophysical Research: Solid Earth, 124(10), 10610-10629.

Hooft, E. E. E., Heath, B. A., Toomey, D. R., Paulatto, M., Papazachos, C. B., Nomikou, P., ... & Warner, M. R. (2019). Seismic imaging of Santorini: Subsurface constraints on caldera collapse and present-day magma recharge. Earth and Planetary Science Letters, 514, 48-61.

Hufstetler, R. S., Hooft, E. E., Toomey, D. R., VanderBeek, B. P., Papazachos, C., & Chatzis, N. (2025). Seismic Structure of the Mid to Upper Crust at the Santorini-Kolumbo Magma System from Joint Earthquake and Active Source Vp-Vs Tomography. Authorea Preprints.

Nakamura, Y. (1989). A method for dynamic characteristics estimation of subsurface using microtremor on the ground surface. *Railway Technical Research Institute, Quarterly Reports*, *30*(1).

McVey, B. G., Hooft, E. E. E., Heath, B. A., Toomey, D. R., Paulatto, M., Morgan, J. V., ... & Papazachos, C. B. (2020). Magma accumulation beneath Santorini volcano, Greece, from P-wave tomography. Geology, 48(3), 231-235.

National Observatory of Athens, Institute of Geodynamics, Athens. National Observatory of Athens Seismic Network, 1975. doi: 10.7914/SN/HL.

University of Athens. Hellenic Seismological Network, University of Athens, Seismological Laboratory, 2008. doi: 10.7914/SN/HA.

17th INTERNATIONAL CONGRESS of the Geological Society of Greece

BULLETIN OF THE GEOLOGICAL SOCIETY OF GREECE, SP. PUBL.

EXTENDED ABSTRACT 102

Assessment of assembly point suitability in tsunami-prone South Aegean coasts after the 2025 Santorini-Amorgos earthquake swarm and related risk reduction measures

Gogou M.[1], Spyrou N.I.[1], Mavroulis S.[1], Evelpidou N.[2], Mavrouli, M.[3], Lekkas E.[1,4], Antonarakou A.[5]

(1) Department of Dynamic Tectonic and Applied Geology, Faculty of Geology and Geoenvironment, School of Sciences, National and Kapodistrian University of Athens, Athens, Greece, mgogou@geol.uoa.gr
(2) Department of Geography and Climatology, Faculty of Geology and Geoenvironment, School of Sciences, National and Kapodistrian University of Athens, Athens, Greece
(3) Department of Microbiology, Medical School, National and Kapodistrian University of Athens, Athens, Greece
(4) Earthquake Planning and Protection Organization, Athens, Greece
(5) Department of Historical Geology and Palaeontology, Faculty of Geology and Geoenvironment, School of Sciences, National and Kapodistrian University of Athens, Athens, Greece

Introduction

The early 2025 earthquake swarm between Santorini and Amorgos, in the southern part of the Aegean Sea, triggered an immediate mobilization of the authorities and operational structures of the Civil Protection system in Greece, with a primary focus on increased preparedness actions for an imminent strong earthquake. Among other significant actions, a specially developed web platform was made available for all users (mysafetyplan.gov.gr), for locating designated assembly points in case of an earthquake. These locations were selected by the Independent Department of Civil Protection of the Municipalities, though the methodology used for their selection and the factors considered in the decision-making process were not explicitly defined.

The Aegean Sea, like the broader Eastern Mediterranean region, is characterized by high tsunami hazard (Shaw *et al.* 2008; Sørensen *et al.*, 2012; Papadopoulos and Fokaefs, 2005; Karkani *et al.*, 2022; Gogou *et al.*, 2023). In addition to historical records, three seismic events in the past 70 years have triggered tsunamis with considerable impact on the coastal areas, including those triggered by the 1956 Amorgos earthquake (Galanopoulos, 1956; Ambraseys, 1960; Papadopoulos and Pavlides, 1992; Okal *et al.*, 2009; Leclerc F. *et al.*, 2024), the 2017 Kos earthquake (Lekkas *et al.*, 2018) and the 2020 Samos earthquake (Triantafyllou *et al.*, 2021; Dogan *et al.*, 2021). Furthermore, the study area belongs to the tsunamigenic zone of Cyclades, which is characterized by moderate tsunamigenic potential (Papadopoulos and Fokaefs, 2005; Gogou *et al.*, 2023).

The high tsunami exposure in the region is related to the increasing urbanization on the islands over the past few decades and, most notably, to the continuous expansion of tourism in coastal zones. Moreover, the ongoing climate crisis, which has led to steadily rising temperatures throughout the year (Copernicus Climate Change Service, 2025), has enabled the tourism development in coastal areas even during winter season (Bank of Greece, 2025). This fact has resulted in the extension of the tourist season in Greece, consequently increasing exposure and vulnerability to several natural hazards, including tsunami.

The present study assesses the suitability of designated assembly points in case of an event triggers a tsunami in the southern part of the Aegean Sea. The research methodology was applied to the coastal areas of islands within the Cyclades complex, located close to the activated area surrounding Anydros Islet.

Methodology

Mapping and quantifying tsunami hazard remains a significant challenge, as predicting the occurrence, magnitude, and extent of damage from a tsunami is inherently complex and difficult to model. The wide array of potential causes, combined with the numerous possible source areas, renders it nearly impossible to provide a fully accurate and deterministic risk assessment.

Even in regions with rich tsunami inventory, the potential for a larger, more impactful event persists, despite the exclusion of certain combinations of source and magnitude through prior analysis. This is especially true for areas that are susceptible to tsunamis triggered by any of the primary tsunami-triggering mechanisms (earthquakes, volcanic eruptions, and coastal and offshore landslides) or by their combination, as applicable to the study area.

Based on the literature on tsunami impacts in coastal areas, both within the study area and globally, along with the unique morphological features of the southern part of the Aegean Sea and the exposure and vulnerability of the coasts to potential tsunamis, the delineation of tsunami risk zones of the studied coastal areas was implemented.

When the run-up increases, the tsunami risk usually increases as well, since the inundation covers a larger area. However, there are certain factors that can reduce the risk, even when the run-up is high. These factors include urban and morphological characteristics of the affected area, including natural barriers (such as coastlines with steep slopes, sandy beaches, or wetlands), as well as constructions and infrastructure that avoid contact with sea level.
The used run-up values were obtained from a combination of data from past events (Gogou *et al.*, 2018) and contributed to the effective tsunami risk zoning, which comprises the following six zones characterized by different run-up values (Table 1):

- **Zone 1 with run-up up to 3 m**: These run-up values have been reported during tsunami generation in the southern part of the Aegean Sea, based on the available historical data. They represent the minimum recorded values in the area. However, they are characterized by high occurrence probability. Furthermore, this zone is the most vulnerable and exposed to tsunami impact as it lies along the coastal front. Considering that this zone is where most of the constructions, infrastructure, and the most intense human activity are developed, the Zone 1 is defined as the direct-high risk zone, presented with red colour in Table 1 and Figure 1.
- **Zone 2 with run-up ranging from 3 to 5 m**: This zone is located farther inland compared to the previous zone, making it more distant from the coastal front. It includes run-up values recorded and reported from the majority of the islands of the central and southern part of the Aegean Sea, which were affected by the 1956 Amorgos tsunami. This area is also considered highly vulnerable to tsunami inundation and impact. The Zone 2 is defined as the high risk zone, presented with orange colour in Table 1 and Figure 1.
- **Zone 3 with run-up ranging from 5 to 10 m**: This zone also includes run-up values from the 1956 tsunami. At least five areas in Amorgos, Folegandros and Astypalaea Islands experienced such inundation or larger based on Okal *et al*. (2009). The Zone 3 is defined as the moderate risk zone, presented with yellow colour in Table 1 and Figure 1.
- **Zone 4 with run-up ranging from 10 to 20 m**: In the 1956 tsunami, the highest recorded run-up reached 20 m along the southern coastline of Amorgos Island (Okal et al., 2009). The Zone 4 is defined as the low risk zone presented with light green colour in Table 1 and Figure 1.
- **Zone 5 with run-up ranging from 20 to 30 m**: . This zone includes run-up values that exceed the maximum identified and published run-up in the southern Aegean islands from the 1956 tsunami, which is 20 meters in the southern part of Amorgos. The Zone 5 is defined as the very low risk zone presented with dark green colour in Table 1 and Figure 1.
- Zone **6 with run-up larger than 30 m**: This zone is considered to have a low probability of tsunami impact due to volcanic eruptions along the South Aegean Volcanic Arc based on historical evidence. However, extreme events cannot be entirely ruled out. Similar tsunami events caused by volcanic activity, such as the 1883 Krakatau eruption, have produced run-ups of up to 42 meters (Charles W. et al., 1994). This zone can be considered safe under most scenarios due to the rarity of the phenomenon. This zone is located farther inland compared to the previous zone and has no colour indication in Table 1 and Figure 1.

The proposed zoning for the coastal areas of the southern Aegean islands is presented in Table 1.

Table 1. The Tsunami Risk Zones for the Central Aegean area.

Zone	Max Run-Up (m)	Past events	Tsunami Risk
1	< 3 m	Common events (tsunamis with lowest run-up)	Direct-high
2	3-5	Recorded values from 1956 Amorgos tsunami	High
3	5-10	Recorded values from 1956 Amorgos tsunami	Moderate
4	10-20	Maximum run-up from 1956 Amorgos tsunami	Low
5	20-30	Seabed deformation or largest landslide	Very low
6	> 30	Rare extreme events (volcanic eruptions)	Considered safe under most scenarios

Using a Geographic Information System (GIS), the delineation of tsunami risk zones was conducted based on the local contours of selected islands in the south Aegean and subsequently overlaid with recent satellite imagery. Then,

the thematic layer of the assembly points for earthquake-related emergencies were also added and evaluated based on the tsunami risk zones. This methodological approach enabled the identification of (i) the specific tsunami risk zones in which the designated assembly points are located, and (ii) the corresponding level of tsunami hazard exposure associated with each site.

The aforementioned methodology was applied along the entire coastline of Ios, Folegandros, Naxos, Irakleia, Schoinousa, Ano Koufonisi, Kato Koufonisi, Amorgos, Santorini, and Anafi Islands. These islands were selected due to their short distance from the seismically activated area in early 2025 and the increased probability of being affected by a potential tsunami, which could be triggered in the case of a larger seismic event either by sea-bed displacement or by coastal and submarine landslides.

Results

This section comprises the results of the applied methodology to four locations within the study area: Perissa area in Santorini, Katapola settlement in Amorgos, Chora town in Naxos, and the Ios port (Figure 1). These sites were selected because they are characterized by significant population densities, comprising both residents and visitors, as well as the presence of critical infrastructure essential during emergencies triggered by natural hazards, particularly earthquakes and related geohazards.

In Santorini, the designated assembly points are situated at considerable distances from the coastline. For example, the southeastern assembly point is located approximately 3,100 meters from the coastal settlement of Perivolos and 3,200 meters from Perissa. While such locations may be suitable for seismic safety, they are impractical as immediate, pedestrian-accessible assembly points in the event of a tsunami. In Naxos, many of the designated assembly points fall within the direct-high risk zone (red zone). In Ios, the sole designated assembly point for the port area is located within the inundation zone, even under 0–3 m run-up. This renders the location unsuitable for tsunami evacuation.

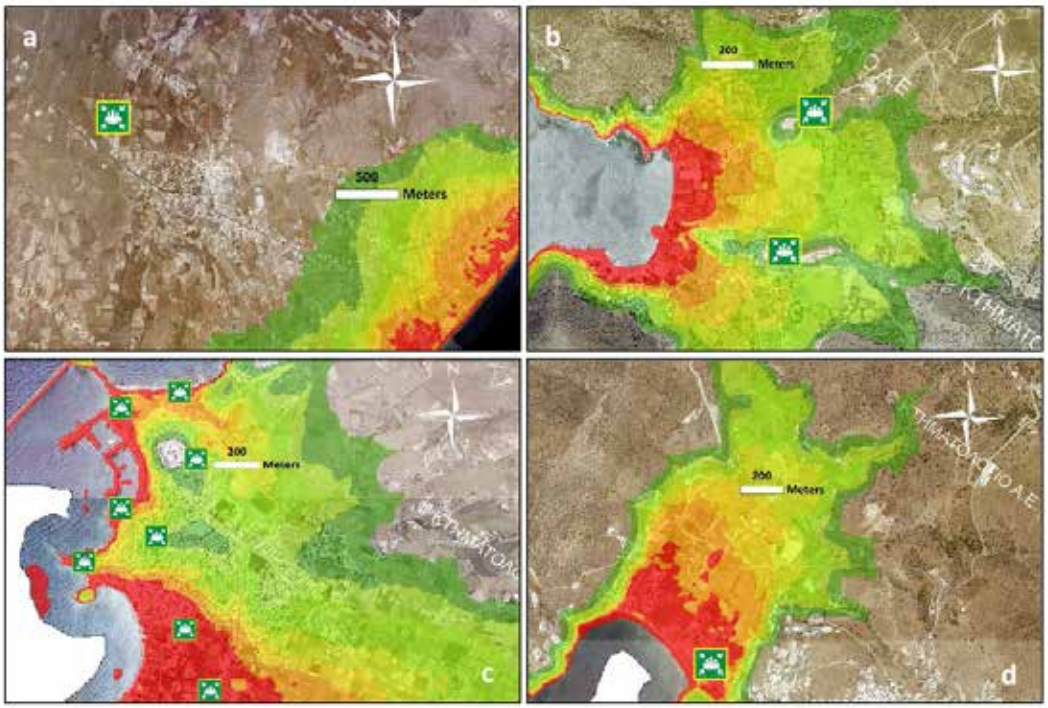

Figure 1. Maps illustrating the results of the applied methodology in selected coastal areas of the Cyclades island complex: (a) Perivolos – Perissa in Santorini. This assembly point is located at a considerable distance from the coastal zone, making it safe from the adverse effects of a potential tsunami, but unsuitable for immediate sheltering of the affected people, who will have to cover many kilometers to reach the site. (b) Katapola in Amorgos. The assembly points have been correctly selected, as they are located both in the safe zone and close to the residential area. (c) Chora town in Naxos. Most of the selected assembly points are considered unsuitable, as the majority is located either along the coastal front or within the direct-high and high risk zones. (d) Ios Port. The designated assembly point is considered unsuitable due to its location within the direct-high risk zone.

This approach enables the integration of additional thematic layers, such as key urban planning characteristics, including land use, road network, and public spaces, into the assessment process. Such integration supports the development of targeted actions aimed at enhancing safety and accessibility, including the updating and optimization of assembly points and the delineation of safe evacuation routes.

A representative application of the aforementioned methodology was conducted within the present study in the area of the port of Ios. The assembly point proposed in the frame of this study (indicated by the blue symbol in Figure 2), is situated on a hillside between the port facilities and Gialos beach and selected to serve the eastern shoreline of the port bay. The site is positioned approximately 15 m above sea level and lies just 130 m from the coastline. Based on the aforementioned zoning, it is classified within a low tsunami risk zone. As such, it may be considered a safe location in the event of tsunami scenarios of equal or lesser intensity than the 1956 Amorgos tsunami, compared to the rejected assembly point located within the port area and in the direct-high risk zone (Figure 2).

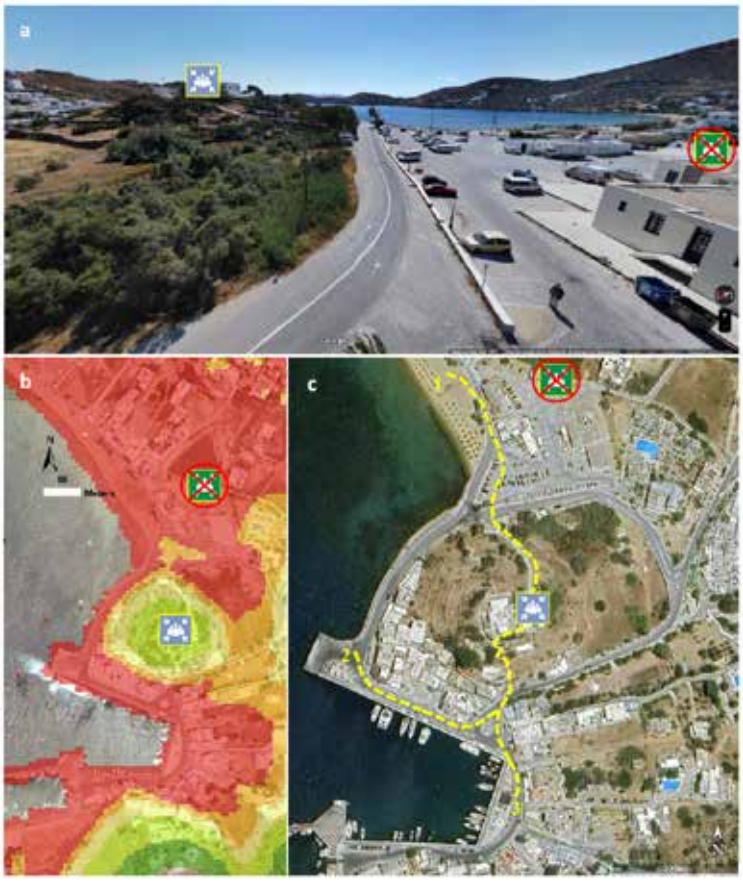

Figure 2. (a) View of the area showing both the rejected assembly point included in the web platform and the new assembly point proposed in the frame of the present study. (b) The old point is located within the direct-high risk zone, while the new point lies within the low risk zone. (c) Delineation of evacuation routes from three important locations to the proposed assembly point in case of an emergency.

The primary accessibility characteristics of the newly designated assembly point in Ios Port (indicated by the blue symbol in Figure 2) are summarized as follows:

- From a representative location within the coastal settlement (Coordinates: 36.726458, 25.274483): approximately 400 meters, with an estimated average arrival time of 6 minutes.
- From Gialos Beach (point 1 in Figure 2): approximately 240 meters, with an estimated average arrival time of 4 minutes.
- From the main port pier (point 2 in Figure 2), the location used for large passenger vessel docking and embarkation/disembarkation: approximately 250 meters, with an average arrival time of 3 minutes.
- From the central area of the marina pier (point 3 in Figure 2): approximately 200 meters, with an estimated average arrival time of 2 minutes.

These distances and times reflect the site's high accessibility from key coastal activity zones, supporting its suitability as an emergency evacuation point.

Conclusions

With the exception of a few cases (e.g., Amorgos), where designated assembly points have been appropriately selected and offer sufficient protection in the event of a tsunami, the majority of sites proposed by local municipalities and currently listed on the aforementioned web platform of assembly points are assessed as inadequate for tsunami response and require urgent reassessment.

In Santorini, additional strategically positioned assembly points should be designated specifically for vulnerable coastal zones. In Naxos, due to the high density of the urban fabric in Chora town, it is essential to reassess current assembly points and develop accessible, well-defined evacuation routes that can be safely followed during emergencies.

With particular focus to the area of the bay where the port of the Ios island is located, , the present study proposes a more appropriate emergency assembly point. Based on calculated distances and estimated pedestrian travel times, the newly proposed site demonstrates an adequate level of protection from tsunami inundation. However, for these evacuation routes to function effectively, targeted urban planning interventions are necessary, such as creating direct, unobstructed paths to safe zones, avoiding bottlenecks, low-lying flood zones, and congested areas, as well as selecting designated multi-modal paths, walkable for pedestrians, accessible for vehicles and people with disabilities, among other actions. Additionally, at least two more assembly points should be established: one for the western section of the bay and another for the southeastern zone.

To mitigate tsunami risk in the study area, several key actions are recommended. These include the systematic reassessment and, where necessary, revision of designated evacuation and assembly points, as well as the clear delineation of tsunami evacuation zones. It is essential to design and mark evacuation routes that are both accessible and efficient, ensuring they can be safely used by all individuals, including individuals with disabilities. Regular operational exercises should be conducted with the active participation of residents and authorities at the central, regional, and local levels, to ensure preparedness and coordination in the event of a tsunami. Furthermore, continuous scientific monitoring of regional seismic and volcanic activity is necessary, as well as the submarine mapping, alongside enhancements to the tsunami early warning system and the supporting sensor network. Finally, public awareness and education initiatives should be implemented, targeting local populations, visitors, and vulnerable groups, in order to foster a culture of preparedness and resilience.

Acknowledgements

The main author would like to express sincere gratitude to the pioneering scientists whose invaluable data and, most importantly, their passion, served as an inspiration to continue working towards making this world safer. Prof. E. Lekkas and Dr. G.A. Papadopoulos are acknowledged for their continuous guidance and encouragement.

References

Ambraseys, N.N., 1960. The seismic sea wave of July 9th 1956, in the Greek Archipelago, Journal of Geophysical Research, 65, 4, 1257-1265, https://doi.org/10.1029/JZ065i004p01257

Mandeville, C.W., Carey, S., Sigurdsson, H, King, J., 1994. Paleomagnetic evidence for high-temperature emplacement of the 1883 subaqueous pyroclastic flows from Krakatau Volcano, Indonesia. Journal of Geophysical Research, 99 (B5), 9487-9504. https://doi.org/10.1029/94JB00239

Copernicus Climate Change Service. Surface Air Temperature Maps. Available online: https://climate.copernicus.eu/surface-air-temperature-maps (accessed on 5 April 2025).

Dogan, G.G., Yalciner, A.C., Yuksel, Y., Ulutaş, E., Polat, O., Güler, I., Şahin, C., Tarih, A., Kânoğlu, U., 2021. The 30 October 2020 Aegean Sea Tsunami: Post-Event Field Survey along Turkish Coast. Pure and Applied Geophysics, 178, 785-812. https://doi.org/10.1007/s00024-021-02693-3

Galanopoulos, A.G., 1956. The seismic sea-wave of July 9, 1956. Proceedings of the Academy of Athens, 82, 90-101.

Gogou, M., Andreadakis, E., Nomikou, P., Lekkas, E., 2018. Previewing (and prioritization) tsunami risk in coastal zone of southern Aegean Sea, 9th International INQUA Meeting on Paleoseismology, Active Tectonics and Archeoseismology (PATA).

Gogou, M., Mavroulis, S., Evelpidou, N., Lekkas, E., 2023. Earthquakes and Tsunamis: Natural Hazards over the Aegean Archipelago. In: The Handbook of Environmental Chemistry. Springer, Berlin, Heidelberg. https://doi.org/10.1007/698_2022_941

Gogou, M., Mavroulis, S., Evelpidou, N., Stagonas, D., Lekkas, E., 2024. Effective estimation of Tsunami Coastal Impacts based on Tsunami Inventories, Satellite Imagery and Inundation Zoning, 18th Plinius Conference on Mediterranean Risks, Chania, Greece, 30 Sep–3 Oct 2024, Plinius18-102, https://doi.org/10.5194/egusphere-plinius18-102

Gogou, M., Triantafyllou, I., Mavroulis, S., Lekkas, E., A. Papadopoulos, G., 2021. The October 30, 2020 tsunami in the eastern Aegean Sea: Intensity mapping on Samos Island based on the Integrated Tsunami Intensity Scale (ITIS 2012). EGU General Assembly 2021, 19–30 Apr 2021, EGU21-5006, https://doi.org/10.5194/egusphere-egu21-5006

Karkani, A.; Evelpidou, N.;Tzouxanioti, M.; Petropoulos, A.; Gogou, M.; Mloukie, E., 2022. Tsunamis in the Greek Region: An Overview of Geological and Geomorphological Evidence. Geosciences, 12, 4. https://doi.org/10.3390/geosciences12010004

Leclerc, F., Palagonia, S., Feuillet, N., Nomikou, P., Lampridou, D., Barrière, P., Dano, A., Ochoa, E., Gracias, N., Escartin, J., 2024. Large seafloor rupture caused by the 1956 Amorgos tsunamigenic earthquake, Greece. Communications Earth & Environment, 5, 663. https://doi.org/10.1038/s43247-024-01839-0

Lekkas, E., Carydis, P., Mavroulis, S., Gogou, M., Andreadakis, Emm., Katsetsiadou, K.-N., Skourtsos, Emm., Minos-Minopoulos, D., Bardouli, P., Voulgaris, N., Papadimitriou, P., Kaviris, G., Tselentis, G.-A., Karakonstantis, A., Parcharidis, I., Papastergios, A., Tsironi, V., Lalechos, S., Avramea, Kleanthi, M., Papaioannou, C., Salonikios, T., Adam, N., Sakellariou, D., 2017. The Mw 6.6, July 21, 2017 Kos Earthquake, Scientific Report (Version 2.0). Newsletter of Environmental, Disaster, and Crises Management Strategies, 1, ISSN 2653-9454.

Okal, E.A., Synolakis, C.E., Uslu, B., Kalligeris, N., Voukouvalas, E., 2009. The 1956 earthquake and tsunami in Amorgos, Greece. Geophysical Journal International, 178: 1533-1554. https://doi.org/10.1111/j.1365-246X.2009.04237.x

Papadopoulos, G.A., Fokaefs, A., 2005. Strong tsunamis in the Mediterranean Sea: a reevaluation. ISET Journal of Earthquake Technology, 42, 159-170.

Papadopoulos, G.A., Pavlides, S.B., 1992. The large 1956 earthquake in the South Aegean: Macroseismic field configuration, faulting, and neotectonics of Amorgos Island, Earth and Planetary Science Letters, 113, 3, 1992, 383-396, https://doi.org/10.1016/0012-821X(92)90140-Q

Shaw, B., Ambraseys, N.N., England, P.C., Floyd, M.A., Gorman, G.J., Higham, T.F.G., Jackson, J.A., Nocquet, J.-M., Pain, C.C., Piggott, M.D., 2008. Eastern Mediterranean tectonics and tsunami hazard inferred from the AD 365 earthquake. Nature Geoscience, 1, 268-276, https://doi.org/10.1038/ngeo151

Sørensen M.B., Spada M., Babeyko A., Wiemer S., Grünthal G., 2012. Probabilistic tsunami hazard in the Mediterranean Sea. Journal of Geophysical Research, 117, B01305, http://dx.doi.org/10.1029/2010JB008169

Triantafyllou, I., Gogou, M., Mavroulis, S., Lekkas, E. Papadopoulos, G.A.; Thravalos, M., 2021. The Tsunami Caused by the30 October 2020 Samos (Aegean Sea) Mw 7.0 Earthquake: Hydrodynamic Features, Source Properties and Impact Assessment from Post-Event Field Survey and Video Records. Journal of Marine Science and Engineering, 9, 68. https://doi.org/10.3390/jmse9010068

17th INTERNATIONAL CONGRESS of the Geological Society of Greece

BULLETIN OF THE GEOLOGICAL SOCIETY OF GREECE, SP. PUBL.

EXTENDED ABSTRACT 103

Palaeoenvironmental Interpretation and Soft Sediment Deformation of the Ionian Basin Lower Jurassic Formations in Astakos (Western Greece)

Golfinopoulos V.[1], Piper J.W.D.[2], Zelilidis A.[1], Pe-Piper G.[3], Papadopoulou P.[1], Bourli N.[1], Iliopoulos G.[1]

(1) University of Patras, Department of Geology, Patras, Greece, gkolfinopoulosv@ac.upatras.gr (2) Dalhousie University, Department of Oceanography Halifax, Canada (3) Saint Mary's University, Department of Geology, Halifax, Canada

Introduction

The Ammonitico Rosso (AR) Formation (Fm) is one of the best-known lithofacies of the Tethys Ocean's history due to its peculiar lithological features (Cecca et al. 1992). During the Early Jurassic, the opening of the Tethys Ocean begun, influenced by intense faulting which led to the development of both shallow marine platforms and deep-sea basins (Bernoulli and Renz, 1970). Extensional stress led to the development of the Ionian Basin (Bernoulli and Renz, 1970; Zelilidis et al., 2015). Intrabasinal differentiations resulted in submarine highs with minimal sediment deposition and continuous deposition in local depressions (Bernoulli and Renz, 1970).

Benthic foraminifera and ostracods are valuable tools for palaeoenvironmental reconstructions (Ansari et al., 2022 and reference therein;). Especially for the Jurassic, they could be useful for the age determinations of the studied formations as well. Thus, a variety of studies on Lower – Middle Jurassic ostracods and benthic foraminifera have been conducted in the Neo-Tethys region. Despite extensive research on Jurassic foraminifera and ostracods in the Tethys Ocean, there is a notable absence of such studies in Greece, except for a few studies on Jurassic benthic foraminifera using thin sections. Nevertheless, the systematic study of ostracods through the study of thin sections is not possible.

Landslides that produce mass-transport deposits occur in loosely consolidated soft sediments in both subaerial and submarine environments (Ferrill et al. 2023). Synsedimentary deformation structures (synsedimentary faults, folds, slide planes, dewatering structures, etc.) are widely distributed in the syn-rift formations of the Ionian Basin of Greece (Golfinopoulos et al. 2025 and reference therein).

The study area is located in the region of Western Greece, in the regional district of Aitoloakarnania, approximately 8 km northwest of Astakos town and 10 km southeast of Mytikas village. In this area, Jurassic and Cretaceous formations of the External Ionian Basin are exposed in coastal sections, road cuts, and sparsely vegetated mountain slopes.

Objectives

The main objectives of this study are: i) to document the first stereoscopic record of Jurassic benthic foraminifera and ostracods in Greece, ii) to reconstruct the palaeoenvironment and determine the age of the AR and Posidonia beds Fms in the Ionian Basin, iii) to unravel the internal structure of AR Fm, which includes several horizons of synsedimentary deformation and iv) to present the revised geological map of the studied area as part of this project.

Methods

In the field, detailed bed-by-bed logs were measured, and then the corresponding lithostratigraphic columns were produced. Fieldwork also included measurements, descriptions, and reconstruction of the studied stratigraphy, bearing in mind the local tectonic activity. A total of 52 rock samples and 8 sediment samples were collected from eight sequences. Thirty of the most characteristic rock samples were thin sectioned for microfacies analysis. Microfacies analysis was conducted using Folk's (Folk, 1959) and Dunham's (Dunham, 1962) classifications. Additionally, the revised Wilson model (Wilson, 1975), which defines 26 standard microfacies (SMF) types that are associated with 10 standard facies zones (FZ), was employed. For all sediments samples, micropalaeontological analysis was carried out. The strongly deformed horizons were recorded in detail, including their thickness, deformation axis, their relation to the underlying and overlying horizons, and the bedding planes' dip and direction. Additionally, the characteristics and kinematics of the faults were recorded and analyzed in relation to the depositional processes.

Results

The Jurassic to Cretaceous formations of the External Ionian sub-basin were studied, focusing on the AR Fm, as it appears fully developed in the study area. Specifically, in this area, the following formations are exposed (from the

base to the top): Pantokrator limestones, Sinies limestones, Lower Posidonia beds, AR, limestones with filaments, and Vigla limestones Fms. The base of the succession consists of massive- to thick-bedded white limestones (Pantokrator Fm, Sequence 1). These are overlain by thin- to medium-bedded siliceous limestones (Sinies Fm) which locally contain ichnofossils, stylolites, and occasional chert nodules (Sequences 2-5). Conformably, on the latter, alternations of laminated green-brown pelites with laminated marly limestones were recognized (possible Posidonia beds, Sequence 6, the beginning of Sequence 7). Above them, alternations of red pelites and calcilutites with grey and red nodular limestones were observed (AR Fm, Sequence 7). In the red pelites, grey nodular limestones, and red nodular limestones, ammonites and ichnofossils were observed. The upper stratigraphic part of this formation consists of pink-beige limestones (Limestones with filaments Fm, the beginning of Sequence 8). These strata are laminated to medium-bedded. In the upper part of the studied section, thin- to thick-bedded beige siliceous limestones with chert nodules and chert bands (Vigla limestone Fm, Sequence 8) are present. Notably, within this upper formation, brown shales containing very small polymetallic nodules were recorded (Golfinopoulos et al. 2025, Figure 1).

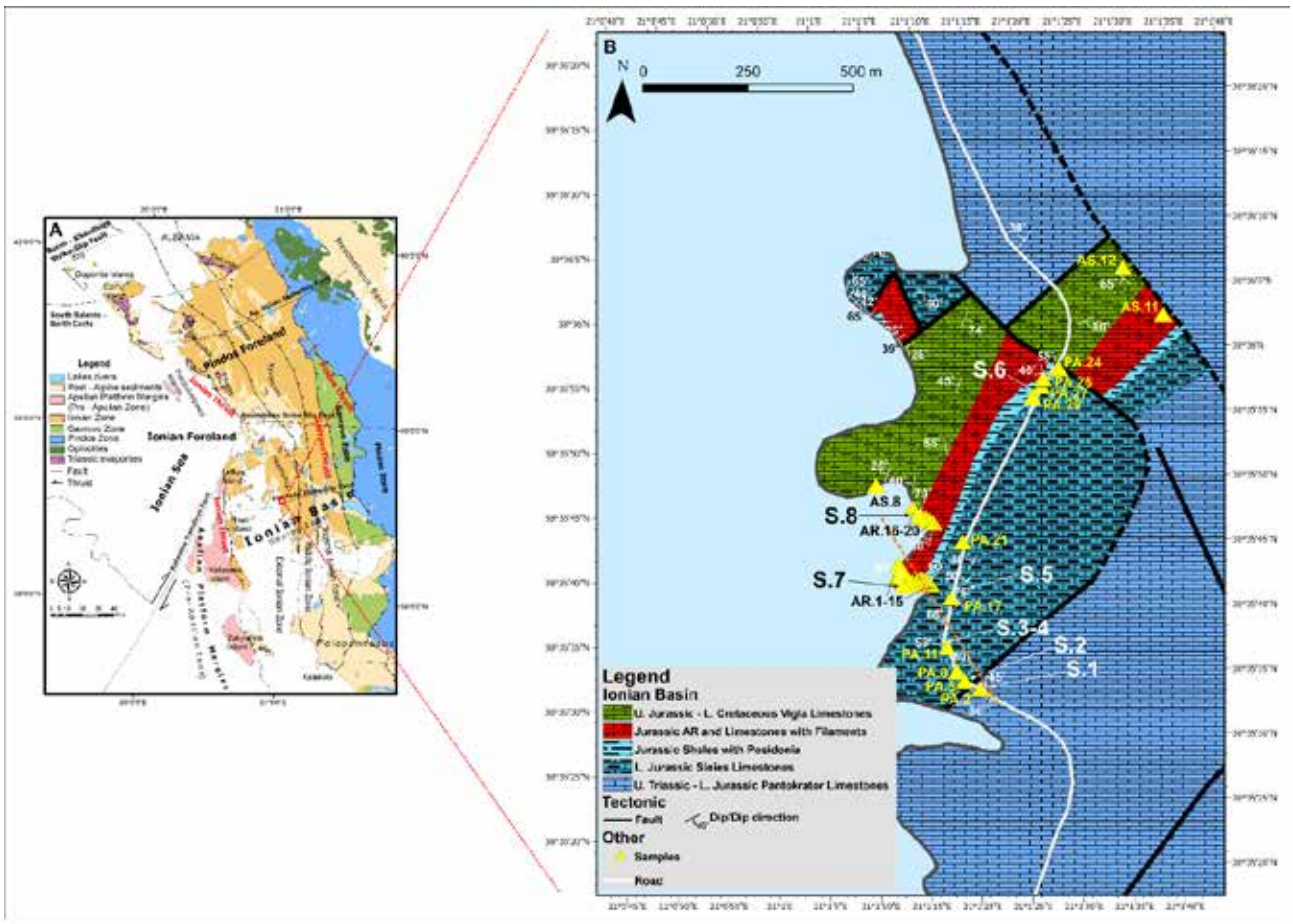

Figure 1: A) Simplified geological map of the External Hellenides in NW Greece, modified from (Zelilidis et al. 2015), where the red box indicates the study area. B) Geological map of the study area. Codes with letter "S" represent the locations of the sequences referred to in the text (modified from Golfinopoulos et al. 2025).

The microfacies analysis of 30 studied thin sections from Sequences 1 - 8 showed two different depositional environments, toe of slope (FZ 3) and platform-margin reefs (FZ 5), corresponding to two different standard microfacies types. Each MF corresponds to a different SMF type. Specifically, MF 1 is classified as biosparite/ boundstone (SMF 7), while MF 2 includes micrites, fossiliferous micrites, and both sparse and packed biomicrites/ wackestones and packstones (SMF 3, SMF 3-RAD, SMF 3-CALP, SMF 3-FIL). The biofacies analysis revealed among others (radiolaria, filaments, benthic and planktonic foraminifera), the existence of planktonic foraminifera of the genus *Globuligerina* in Sequences 5, 6, 7 and 8. The samples of Sequence 5 belong to the upper part of Sinies limestone Fm, based on their lithological features and their relationship to the overlying formations, they appear to have been deposited during the Late Pliensbachian. If verified, this claim would shift the first appearance of

planktonic foraminifera from the Toarcian to the Pliensbachian (Golfinopoulos et al. 2025).
In total 8 sediment samples from Sequences 6-7 were micropalaeontologically studied as well. Two of the samples were barren, while all the other samples contained sufficient numbers of benthic foraminifera tests and ostracod valves. A few fish teeth and sea urchin spines were recorded as well. In total, 15 benthic foraminifera species belonging to 7 families, namely Ichthyolariidae, Vaginulinidae, Lagenidae, Nodosariidae, Polymorphinidae, Spirillinidae and Saccamminidae, were determined. Regarding the ostracod assemblages, at least 10 species belonging to 3 families (Polycopidae, Healdiidae and Bairdiidae), were determined as well. Most of the studied material is moderately to very badly preserved, thus making some of the determinations difficult. Ostracod molds of oval to ellipsoidal shape have been retrieved. Their shape points to a suborder other than Metacopina and Podocopina, whose shape is more sub-triangular. A significant number of the determined in this study benthic foraminifera (Ichthyolariidae, Vaginulinidae, Polymorphinidae and Saccamminidae) and ostracods (Polycopidae and Healdiidae) are characteristic for the Lower Jurassic (Pliensbachian – Toarcian) assemblages of the Tethys Ocean.
In Sequence 7 synsedimentary deformation structures have been developed. The succession of this Sequence begins with greenish-grey shales, quite distinct from the overlying red and white limestones and shales of the AR Fm. The base of the unit is not exposed, whereas at beach level, the top is marked by a few centimetres of greenish deformed fissile shale, conformably overlain by AR-type limestone. Along the strike, in the cliff face, the contact appears rather irregular. As the internal details of this unit are not well exposed, it is simply termed the Lower Unit. It is probably either a complex slide or a debris-flow deposit with rafted blocks of bedded limestone, but the possibility that the unit is in situ and suffered some internal deformation from the overlying slide cannot be excluded. The base of the AR Fm shows considerable synsedimentary deformation. The lowest shale unit has a recumbent fold closure. It is overlain by discontinuous decimeter-scale boudins of micritic limestone enclosed in rubbly AR limestones and shale, with a ghost stratigraphy about 1 m thick. This is overlain by 30 cm of apparently undeformed reddish marl and several meters of alternating nodular limestones and reddish shales with discontinuities between packets of limestone beds, thus creating a series of oblique, bedding-parallel slabs of alternating limestone and shale. In places, limestone beds terminate or are boudinaged, and shales are deformed. The proportion of limestone increases upward. This limestone is overlain by a 2 m thick, polymictic limestone, matrix-supported conglomerate interpreted as a debris-flow deposit, termed debrite 1. Debrite 1 is overlain by about 1 m of reddish shales with discontinuous thin limestone beds. Overlying bedded limestones show brittle deformation into metre-scale tilted blocks, apparently as part of the slide mass. Interbedded with the AR limestones is at least one graded calcirudite to calcarenite turbidite. Debrite 2 overlies the tilted blocks and is about 1 m thick. It is redder in colour than debrites 1 and 3 and is also matrix-supported. Debrite 3 is poorly sorted, with large subangular blocks, supported by a matrix of sand-sized limestone clasts and red mud. The top of debrite 3 is overlain by 30 cm of seemingly undeformed red shale and then an AR limestone section that in its upper part is deformed into a large open fold (Figure 2). The fold is unconformably overlain by about 1 m of bedded limestones with rapid lateral thinning, suggesting that it is also a block within the overall slide. These bedded limestones are overlain by an 1 m bed of sorted conglomerate with an erosional contact with the underlying limestones. The conglomerate consists of rounded limestone pebbles, with the upper part of the bed comprising fine pebbles and granules. Above this conglomerate is a succession of red-grey bedded calcarenites (Golfinopoulos et al. 2025).

Figure 2: Representative view of sequence 7, where the three debrites (1-3) are developing.

Conclusions

During this study, 8 sedimentary sequences in the Astakos area have been studied. Detailed sedimentological, tectonic, and biostratigraphic analyses of both carbonate and clastic sediments have been conducted. Therefore, the following findings have been reported:

- This work presents the first stereoscopic record of Jurassic ostracods and benthic foraminifera in Greece.
- There are indications that some *Globuligerina* tests occurred earlier than previously known; their first appearance probably occurred during the Pliensbachian.
- Lower Posidonia Beds and Ammonitico Rosso Formations were deposited in the shelf and transported in deeper environments during the Pliensbachian to Toarcian.
- The studied sedimentary sequence, though, comprises an allochthonous submarine slide deposit, consisting of four imbricate slices capped by debrites (except the upper one) rather than four discrete slides. Upwards, a conglomerate with reworked limestone clasts has been deposited as a result of a single turbidite. The sequence closes with sediments of the limestone with filaments and Lower Posidonia bed Fms.
- The autochthonous AR Fm depositional setting fits well with a carbonate ramp, on which turbidity currents with a transport distance of several kilometres would have developed from a watery debris flow formed by headwall collapse
- The discovery of the AR Fm slide has a profound effect on the reported sedimentation rates for the area, which until now have not taken under consideration the duplication of the layers, and which thus must be significantly lower.
-

Acknowledgements

This work was supported by the “Andreas Mentzelopoulos Scholarships for the University of Patras” [grant number: 33720000], awarded to Vasilis Golfinopoulos, a PhD student. Special thanks go to the members of the Palaeontology and Stratigraphy Laboratory at the University of Patras, including Marianthi Tzortzi, Irena Pappa, and Maria Groumpou, for their essential support during the fieldwork.

References

Ansari, A.H., Talib, A., Kumar, A., 2022. Tracing ecological fluctuations during the Middle to Late Jurassic of Jhura, Kutch, India, using foraminifera. Marine Micropaleontology, 177, 102183.

Bernoulli, D., Renz, O., 1970. Jurassic Carbonate Facies and New Ammonite Faunas from Western Greece. Eclogae Geologicae Helvetiae, 63, 573–607.

Cecca, F., Fourcade, E., Azéma, J., 1992. The Disappearance of the “Ammonitico Rosso”. Palaeogeography Palaeoclimatology Palaeoecology, 99, 55–70.

Danelian, T., De Wever, P., Azéma, J., 1997. Palaeoceanographic Significance of New and Revised Palaeontological Datings for the Onset of Vigla Limestone Sedimentation in the Ionian Zone of Greece. Geological Magazine, 134, 869–872.

Dunham, R.J., 1962. Spectral Subdivision of Limestone Type. In Classification of Carbonate Rocks. American Association of Petroleum Geologists: Tulsa, OK, USA, Volume 1, pp. 62–84.

Ferrill, D.A., Smart, K.J., Lehrmann, D.J., Morris, A.P., McGinnis, R.N., 2023. Synsedimentary Slump Folding: Examples and Consequences of an under-Recognized Process in Epicratonic Basins. Marine and Petroleum Geology, 152, 106274.

Folk, R.L., 1959. Practical Petrographic Classification of Limestones. American Association of Petroleum Geologists Bulletin, 43, 1–38.

Golfinopoulos, V., Piper, D.J.W., Zelilidis, A., Pe-Piper, G., Papadopoulou, P., Bourli, N., Iliopoulos, G., 2025. Depositional Environments and Soft Sediment Deformation in the Early Jurassic Ammonitico Rosso Formation of Western Greece. Geosciences, 15, 10.

Wilson, J.L., 1975. Carbonate Facies in Geologic History. Springer: New York, NY, USA, 1-471.

Zelilidis, A., Maravelis, A.G., Tserolas, P., Konstantopoulos, P.A., 2015. An Overview of the Petroleum Systems in the Ionian Zone, Onshore NW Greece and Albania. Journal of Petroleum Geology, 38, 331–348.

17th INTERNATIONAL CONGRESS of the Geological Society of Greece

BULLETIN OF THE GEOLOGICAL SOCIETY OF GREECE, SP. PUBL.

EXTENDED ABSTRACT 104

A decade of data: Updating the Hellenic Macroseismic Database for historical earthquakes

Goutsos, G.[1], Sakkas, G.[1,2], Sakellariou, N.[3], Kouskouna, V.[1]

[1]National and Kapodistrian University of Athens, Athens, Greece, goutsos2002@yahoo.com, [2]Center for Security Studies, Athens, Greece, [3]Museo Nacional de Ciencias Naturales, Madrid, Spain

Introduction

The Hellenic Macroseismic Database for historical earthquakes (HMDB.UoA, Kouskouna and Sakkas 2013) was developed at the Laboratory of Seismology of the University of Athens in 2013 within the framework of NERIES and SHARE projects, as a contributor to the Archive of Historical Earthquake Data inventory of Europe. Since then, new studies presenting additional macroseismic intensities from historical earthquakes have been published. Our aim is to update this database with the new Macroseismic Data Points (MDPs) and present its latest version. In addition, amendments regarding the parameters PlaceID, PlaceName and coordinates were introduced in order to better constrain the identity of localities and their multiple names within the centuries. Thus, a separate column containing the latest name of the locality is added, as well as one for comments related to the amendments. We anticipate enhancing the database with earthquakes from the early 20th century in the near future.

Before the update

The first version of HMDB.UoA consists of four tables (Kouskouna and Sakkas, 2013):

The *Earthquake Catalogue table* containing the core information on the available earthquakes such as origin time and date, focal depth, epicentral area, geographical coordinates of the epicentre, maximum observed intensity and epicentral intensity, equivalent moment magnitude, number of available macroseismic data points as well as additional data on methods for estimating magnitude, preferred epicentre and magnitude and errors (Table 1).

Table 1. Example of the Earthquake catalogue table in Excel sheet format.

id_UoA	Date	Year	Mo	Da	Ho	Mi	Se	Comments	Ax	StudyCode	Study	NMDP	Ix	IxNum	EpLat	EpLon	Io	IoNum	Ms	Mw	Mark
1	1040 02 02	1040	02	02					Izmir (TURKEY)	TAXE003	Taxeidis, 2003	1	9	9	38.417	27.150			6.7		IN AHEAD
2	1296 07 17 21	1296	07	17	21				Bergama (TURKEY)	TAXE003	Taxeidis, 2003	3	10	10	39.117	27.183			7.2		IN AHEAD
3	1383 08 06	1383	08	06				Dawn	Mytilene (LESVOS)	TAXE003	Taxeidis, 2003	1	10	10	39.100	26.550			7.2		IN AHEAD
4	1389 03 20 14 30	1389	03	20	14	30		Ho: 14-15	Chios (CHIOS)	KOUS2013	ouna & Sakkas,	4	10	10	38.255	26.573			7.2		IN AHEAD
5	1396 00	1396							Chios (CHIOS)	TAXE003	Taxeidis, 2003	1	7	7	38.367	26.133			5.6		IN AHEAD
6	1471 00	1471						Year: before 1472	Lemnos (LEMNOS)	KOUS2013	ouna & Sakkas,	2	8	8	39.950	25.300			6.2		IN AHEAD
7	1528 00	1528						Year: before 1528	Mytilene (LESVOS)	KOUS2013	ouna & Sakkas,	1	10	10	39.100	26.550			7.2		IN AHEAD
8	1546 00	1546							Mastichochoria (CHIOS)	KOUS2013	ouna & Sakkas,	1	7	7	38.230	26.030			5.6		IN AHEAD
9	1565 00	1565							Chios (CHIOS)	TAXE003	Taxeidis, 2003	1	6-7	6.5	38.367	26.133			5.4		IN AHEAD
10	1577 09 21	1577	09	21				Day: before 21	Balikesir (TURKEY)	KOUS2013	ouna & Sakkas,	1	8	8	39.650	27.883			6.2		IN AHEAD
11	1580 00	1580							Mynia (PHOKIS)	KOUS2013	ouna & Sakkas,	10	8	8							IN AHEAD
12	1595 09 22	1595	09	22					Manisa (TURKEY)	KOUS2013	ouna & Sakkas,	12	7	7	38.657	27.643	6-7	6.5	5.6	6.1	IN AHEAD
13	1611 00	1611						1611-1612	Manisa (TURKEY)	KOUS2013	ouna & Sakkas,	1	6-7	6.5	38.614	27.426			5.4		IN AHEAD
14	1636 02 27 22	1636	02	27	22				Kalloni (LESVOS)	TAXE003	Taxeidis, 2003	1	6-7	6.5	39.233	26.207			5.4		IN AHEAD
15	1646 00	1646							Nazilli (TURKEY)	TAXE003	Taxeidis, 2003	4	8-9	8.5	37.913	28.322			6.4		IN AHEAD
16	1648 10 18	1648	10	18				Night	Chios (CHIOS)	TAXE003	Taxeidis, 2003	1	3-4	3.5	38.367	26.133					NOT IN AHEA
17	1653 02 22	1653	02	22					Aydin (TURKEY)	TAXE003	Taxeidis, 2003	9	9-10	9.5	37.927	28.033	9	9	7.0		IN AHEAD
18	1654 05 20	1654	05	20					Izmir (TURKEY)	TAXE003	Taxeidis, 2003	1	7-8	7.5	38.417	27.150			5.9		IN AHEAD
19	1664 06 02	1664	06	02				night	Izmir (TURKEY)	TAXE003	Taxeidis, 2003	1	6-7	6.5	38.417	27.150			5.4		IN AHEAD
20	1667 11	1667	11						Izmir (TURKEY)	TAXE003	Taxeidis, 2003	1	5	5	38.417	27.150			4.8		IN AHEAD

The *Macroseismic Intensity Data Points* table (Kouskouna and Sakkas, 2013, Tables 2, 4) is the catalogue of available macroseismic data per earthquake. It contains available information on macroseismic data points (MDPs) such as the various available names of the localities, place identifier for seismic history (Locati and Cassera, 2010), locality geographical coordinates, assigned macroseismic intensities, reliability of data, source of data and is directly connected to the earthquake catalogue as well as the sources table (*Studies* table).

The *Reference Places table* (Table 3) containing reference places used as basic input for the online map. It is an independent table, not related to the other tables. Information of this table include the name of locality and the geographical coordinates, country, geographical area that the reference location belongs, availability of the reference location to shown on the map depending on the zoom level.

The *Studies* table (Table 4) contains the necessary information of the sources (original macroseismic studies) of the database. This information includes name of authors, editors, title of the study, original language of the study and links to the studies.

Table 2. Example of the *Macroseismic Intensity Data Points* table in Excel sheet format

id_UoA	EqDate	MDPidUoA	PlaceID	PlaceNameGreek	PlaceNameText	PlaceNameWeb	PlaceNameEng	PlaceNameEngGr	PlaceSc	PlaceLat	PlaceLon	PlaceLatTE	PlaceLonTE	Int	IntNum	MdpCount	Mark	Country
1	1040 02 02	1	TR-00052	Σμύρνη	Izmir	Σμύρνη (Izmir)	Izmir	Izmir Σμύρνη		38.417	27.150			9	9	1	IN AHEAD	TR
2	1296 07 17 21	2	TR-00051	Κωνσταντινούπολη	Istanbul	Κωνσταντινούπολη (Istanbul)	Istanbul	Istanbul Κωνσταντινούπολη		41.008	28.980			6	6	3	IN AHEAD	TR
2	1296 07 17 21	3	TR-00016	Πέργαμος	Bergama	Πέργαμος (Bergama)	Bergama	Bergama Πέργαμος		39.117	27.183			10	10	3	IN AHEAD	TR
2	1296 07 17 21	4	TR-00057	Χλιαρά	Kirkagac	Kirkagac	Kirkagac	Kirkagac Χλιαρά		39.060	27.680			10	10	3	IN AHEAD	TR
3	1383 08 06	5	GR-00132	Μυτιλήνη	Mytilini	Μυτιλήνη (Mytilini)	Mytilini	Mytilini Μυτιλήνη		39.100	26.550			10	10	1	IN AHEAD	GR
4	1389 03 20 14 30	6	GR-00232	Άγιος Κήρυκος Ικαρί	Agios Kirykos, Ikaria	Άγιος Κήρυκος Ικαρίας (Ayios Kirykos, Ikaria)	Agios Kirykos Ikaria	Agios Kirykos Ikaria Άγιος Κήρυκος Ικαρίας	MS	37.583	26.233			9	9	4	IN AHEAD	GR
4	1389 03 20 14 30	7	TR-00124	Νέα Φώκαια	New Foça/YeniFoça	Νέα Φώκαια (New Foça/YeniFoça)	New Foça/YeniFoça	New Foça/YeniFoça Νέα Φώκαια	SS	38.740	26.840			9	9	4	IN AHEAD	TR
4	1389 03 20 14 30	8	TR-00052	Σμύρνη	Izmir	Σμύρνη (Izmir)	Izmir	Izmir Σμύρνη		38.417	27.150			7-8	7.5	4	IN AHEAD	TR
4	1389 03 20 14 30	9	GR-00041	Χίος	Chios	Χίος (Chios)	Chios	Chios Χίος		38.367	26.133			10	10	4	IN AHEAD	GR
5	1396 00	10	GR-00041	Χίος	Chios	Χίος (Chios)	Chios	Chios Χίος		38.367	26.133			7	7	1	IN AHEAD	GR
6	1471 00	11	GR-00095	Κάστρο Κότζινο	Kotzinos castle	Κάστρο Κότζινο (Kotzinos castle)	Kotzinos castle	Kotzinos castle Κάστρο Κότζινο	SS	39.941	25.284			8	8	2	IN AHEAD	GR
6	1471 00	12	GR-00125	Παλαιόκαστρο/Μύρ	Palaiokastro/Mirina	Παλαιόκαστρο/Μύρινα (Palaiokastro/Mirina)	Palaiokastro/Mirina	Palaiokastro/Mirina Παλαιόκαστρο/Μύρινα	SS	39.867	25.067			7	7	2	IN AHEAD	GR
7	1528 00	13	GR-00132	Μυτιλήνη	Mytilini	Μυτιλήνη (Mytilini)	Mytilini	Mytilini Μυτιλήνη		39.100	26.550			10	10	1	IN AHEAD	GR
8	1546 00	14	GR-00116	Μαστιχοχώρια	Mastichochoria	Μαστιχοχώρια (Mastichochoria)	Mastichochoria	Mastichochoria Μαστιχοχώρια	MS	38.230	26.030			7	7	1	IN AHEAD	GR
9	1565 00	15	GR-00041	Χίος	Chios	Χίος (Chios)	Chios	Chios Χίος		38.367	26.133			6-7	6.5	1	IN AHEAD	GR
10	1577 09 21	16	TR-00011	Μπαλικεσίρ	Balikesir	Balikesir	Balikesir	Balikesir Μπαλικεσίρ		39.650	27.883			8	8	1	IN AHEAD	TR
11	1580 00	17	GR-00003	Αγία Ευθυμία	Ayia Efthymia/Mynia	Αγία Ευθυμία/Μυνιά (Ayia Efthymia/Mynia)	Ayia Efthymia/Mynia	Ayia Efthymia/Mynia Αγία Ευθυμία		38.483	22.367			8	8	10	IN AHEAD	GR
11	1580 00	18	GR-00016	Άμφισα	Amfisa	Άμφισα (Amfisa)	Amfisa	Amfisa Άμφισα		38.533	22.383			7	7	10	IN AHEAD	GR
11	1580 00	19	GR-00219	Βουνιχώρα	Vounikhora	Βουνιχώρα (Vounikhora)	Vounikhora	Vounikhora Βουνιχώρα		38.450	22.300			6	6	10	IN AHEAD	GR
11	1580 00	20	GR-00057	Γαλαξείδι	Galaxidi	Γαλαξείδι (Galaxidi)	Galaxidi	Galaxidi Γαλαξείδι		38.377	22.384			7	7	10	IN AHEAD	GR
11	1580 00	21	GR-00225	Ζάκυνθος	Zakinthos	Ζάκυνθος (Zakynthos)	Zakinthos	Zakinthos Ζάκυνθος		37.782	20.896			F	3.9	10	IN AHEAD	GR
11	1580 00	22	GR-00103	Λιδωρίκι	Lidhorikion	Λιδωρίκι (Lidhorikion)	Lidhorikion	Lidhorikion Λιδωρίκι		38.533	22.200			7	7	10	IN AHEAD	GR
11	1580 00	23	GR-00129	Μονή Σωτήρος	Moni Sotiros	Μονή Σωτήρος (Moni Sotiros)	Moni Sotiros	Moni Sotiros Μονή Σωτήρος	IB	38.483	22.367			8	8	10	IN AHEAD	GR
11	1580 00	24	GR-00052	Ναύπακτος	Naupaktos	Ναύπακτος (Nafpaktos)	Naupaktos	Naupaktos Ναύπακτος		38.395	21.833			7	7	10	IN AHEAD	GR
11	1580 00	25	GR-00153	Πεντεόρια	Pendeoria	Πεντεόρια (Pendeoria)	Pendeoria	Pendeoria Πεντεόρια		38.417	22.317			6	6	10	IN AHEAD	GR
11	1580 00	26	GR-00067	Τριταία/Καλοπετινίτ	Tritaia/Kalopetinitsa	Τριταία/Καλοπετινίτσα (Tritaia/Kalopetinitsa)	Tritaia/Kalopetinitsa	Tritaia/Kalopetinitsa Τριταία/Καλοπετινίτσα		38.450	22.367			6	6	10	IN AHEAD	GR

Table 3. Example of the ref_places (reference areas) table in Excel sheet format

RecordID	PlaceNameGreek	PlaceNameText	PlaceNameWeb	PlaceLat	PlaceLon	Country	ZoomLevel	GeographicalArea
GR-00001	Οθωνοί	Othonoi	Οθωνοί (Othonoi)	39.844	19.403	GR	detail	aegean
GR-00002	Ερεικούσσα	Erikoussa	Ερεικούσσα (Erikoussa)	39.883	19.583	GR	detail	aegean
GR-00003	Κέρκυρα	Corfu	Κέρκυρα (Kerkyra)	39.624	19.920	GR	medium	aegean
GR-00004	Παξοί	Paxoi	Παξοί (Paxoi)	39.198	20.170	GR	medium	aegean
GR-00005	Αντίπαξοι	Antipaxoi	Αντίπαξοι (Antipaxoi)	39.152	20.226	GR	medium	aegean
GR-00006	Λευκάδα	Leukada	Λευκάδα (Leukada)	38.836	20.707	GR	medium	aegean
GR-00007	Μεγανήσι	Meganisi	Μεγανήσι (Meganisi)	38.656	20.775	GR	medium	aegean
GR-00008	Αργοστόλι	Argostoli	Αργοστόλι (Argostoli)	38.179	20.487	GR	medium	aegean
GR-00009	Ιθάκη	Ithaki	Ιθάκη (Ithaki)	38.363	20.718	GR	medium	aegean
GR-00010	Ζάκυνθος	Zante (Zakinthos)	Ζάκυνθος (Zakinthos)	37.783	20.900	GR	medium	aegean
GR-00011	Αγρίνιο	Agrinion	Αγρίνιο (Agrinion)	38.633	21.417	GR	large	aegean
GR-00012	Βόνιτσα	Vonitsa	Βόνιτσα (Vonitsa)	38.917	20.833	GR	detail	aegean
GR-00013	Αμφιλοχία	Amfilokhia	Αμφιλοχία (Amfilochia)	38.862	21.166	GR	medium	aegean
GR-00014	Θέρμο	Thermon	Θέρμο (Thermon)	38.583	21.667	GR	detail	aegean
GR-00015	Μεσολόγγι	Messolongi	Μεσολόγγι (Messolongi)	38.367	21.433	GR	medium	aegean
GR-00016	Αστακός	Astakos	Αστακός (Astakos)	38.535	21.081	GR	detail	aegean
GR-00017	Ναύπακτος	Naupaktos	Ναύπακτος (Nafpaktos)	38.395	21.833	GR	medium	aegean
GR-00018	Αίγιο	Aiyion	Αίγιο (Aiyion)	38.250	22.083	GR	medium	aegean

Table 4. Example of the *Studies* table

StudyCode	Study	Authors	Editors	TitleOriginal	CitationOriginal	TitleEnglish	CitationEnglish	PublicationYear	ExtLink	ExtPdfLink	Language
KOUAL998	Kouskouna et al., 1998	Kouskouna V.; Karnassopoulou A.; Makropoulos K.; Taxeidis K.; Tzanis A.		Investigation of earthquakes (1400-1899) in Greece.	Kouskouna V., Karnassopoulou A., Makropoulos K., Taxeidis K. and Tzanis A., 1998. Investigation of earthquakes (1400-1899) in Greece. Internal report for the BEECD project, Department of Geophysics, University of Athens, Athina, 112 pp.	Investigation of earthquakes (1400-1899) in Greece.	Kouskouna V., Karnassopoulou A., Makropoulos K., Taxeidis K. and Tzanis A., 1998. Investigation of earthquakes (1400-1899) in Greece. Internal report for the BEECD project, Department of Geophysics, University of Athens, Athina, 112 pp.	1998		http://macroseismology.geol.uoa.gr/studies/KOUAL998.pdf	English
KOUS001	Kouskouna, 2001	Kouskouna V.	Ελληνική Γεωλογική Εταιρεία	Ο σεισμός της (28ης Δεκεμβρίου 1891) 9ης Ιανουαρίου 1892 στη Λάρισα.	Κουσκουνά Β., 2001. Ο σεισμός της (28ης Δεκεμβρίου 1891) 9ης Ιανουαρίου 1892 στη Λάρισα. Δελτίο της Ελληνικής Γεωλογικής Εταιρείας, τομ. XXXIV/4, 1425-1432, 2001. Πρακτικά 9ου Διεθνούς Συνεδρίου, Αθήνα, Σεπτέμβριος, 2001.	The (December 28th, 1891) January 9th, 1892 Larisa (Central Greece) earthquake.	Kouskouna V., 2001. The (December 28th, 1891) January 9th, 1892 Larisa (Central Greece) earthquake. Bulletin of the Geological Society of Greece, Vol. XXXIV/4, 1425-1432. Proceedings of the 9th International Congress, Athens, September 2001 (in Greek).	2001		http://macroseismology.geol.uoa.gr/studies/KOUS001.pdf	Greek
MAKKO994a	Makrop. & Kous., 1994a	Makropoulos K.C.; Kouskouna V.	Albini P.; Moroni A.	The Ionian Islands earthquakes of 1767 and 1769: seismological aspects. Contribution of historical information to a realistic seismicity and hazard assessment of an area.	Makropoulos K.C. and Kouskouna V., 1994a. The Ionian Islands earthquakes of 1767 and 1769: seismological aspects. Contribution of historical information to a realistic seismicity and hazard assessment of an area. In: P. Albini and A. Moroni (eds.), Materials of the EC Project "Review of Historical Seismicity in Europe", vol. 2, 27-36.	The Ionian Islands earthquakes of 1767 and 1769: seismological aspects. Contribution of historical information to a realistic seismicity and hazard assessment of an area.	Makropoulos K.C. and Kouskouna V., 1994a. The Ionian Islands earthquakes of 1767 and 1769: seismological aspects. Contribution of historical information to a realistic seismicity and hazard assessment of an area. In: P. Albini and A. Moroni (eds.), Materials of the EC Project "Review of Historical Seismicity in Europe", vol. 2, 27-36.	1994		http://macroseismology.geol.uoa.gr/studies/MAKKO994a.pdf	English

Inspections to detect problems

Checks were made to investigate whether the existing MDPs in the respective table needed to be improved. This was achieved by introducing appropriate functions (if, ifand), which identify any points which need amendment, such as:

- localities with the same name (PlaceName) but different identification key (PlaceID)
- localities with the same PlaceID for different PlaceSc (Place Special case: isolated building, multiple settlement…)
- localities with the different name (PlaceName) but same geographical coordinates
- localities with the same identification key (PlaceID) for different localities
- localities with the same identification key (PlaceID) for different coordinates

These points were marked with different colors (Figure 5). It was observed that certain cells present more than one color. All appropriate corrections were made to these cells

Steps followed

Five new columns were added to the mdp_cat table

- OldPlaceNamesEn (containing the old names in English)
- OldPlaceNamesGr (containing the old names in Greek)
- LatestPlaceNameGr (containing the latest names in Greek)
- LatestPlaceNameEn (containing the latest names in English)
- Comments (containing the comments for any changes made to this mdp)

The format of StudyCode column was changed from 5 letters and 3 digits to 4 letters and 4 digits.

Finally, all coordinates were checked on all coordinates and adjustments were made, where necessary (Tables 5, 6 and Figure 1).

Table 5. Examples of points to be amended

PlaceID	PlaceNameGreek	PlaceNameText	PlaceNameEng	PlaceLat	PlaceLon
TR-00076	Ρεϊσντερέ	Reis-dere (Reisdere)	Reis-dere (Reisdere)	38.317	26.417
TR-00076	Τσεσμέκιοϊ	Tcheshmekioi (Reisdere)	Tcheshmekioi (Reisdere)	38.317	26.417
PlaceID	**PlaceNameGreek**	**PlaceNameText**	**PlaceSc**	**PlaceLat**	**PlaceLon**
GR-00003	Αγία Ευθυμία	Ayia Efthymia/Mynia		38.483	22.367
GR-00129	Μονή Σωτήρος	Moni Sotiros	IB	38.483	22.367
PlaceID	**PlaceNameGreek**	**PlaceNameEng**	**PlaceSc**	**PlaceLat**	**PlaceLon**
TR-00088	Τροία	Truva		*39.956*	*26.240*
TR-00088	Τροία	Truva	MS	39.956	26.240
PlaceID	**PlaceNameGreek**	**PlaceNameText**	**PlaceNameWeb**	**PlaceLat**	**PlaceLon**
TR-00053	Καραμπουρούν	Karaburun	Karaburun	38.617	26.517
TR-00107	Καραμπουρούν	Karaburun	Karaburun	38.617	26.517

Color	Meaning
	Same PlaceID for dif. region
	DIF PlaceNameText same COORDIN.
	DIF PlaceNameText same COORDIN2
	Same PlaceID Dif. COORDIN
	Dif. PlaceSc same COORDIN
	same coord dif place id
	Dif. PlaceID, same PlaceName
	Dif. PlaceID, same PlaceName
	Dif. PlaceID, same PlaceName
	Dif. PlaceID, same PlaceName
	Dif. PlaceID, same PlaceName
	Dif. PlaceID, same PlaceName
	Dif. PlaceID, same PlaceName
	Same PlaceID Dif PlaceSc

Corrections and inserting new data can be performed manually, or by using functions such as *vlookup* and *countif*. These functions automatically fill in the necessary parameters.

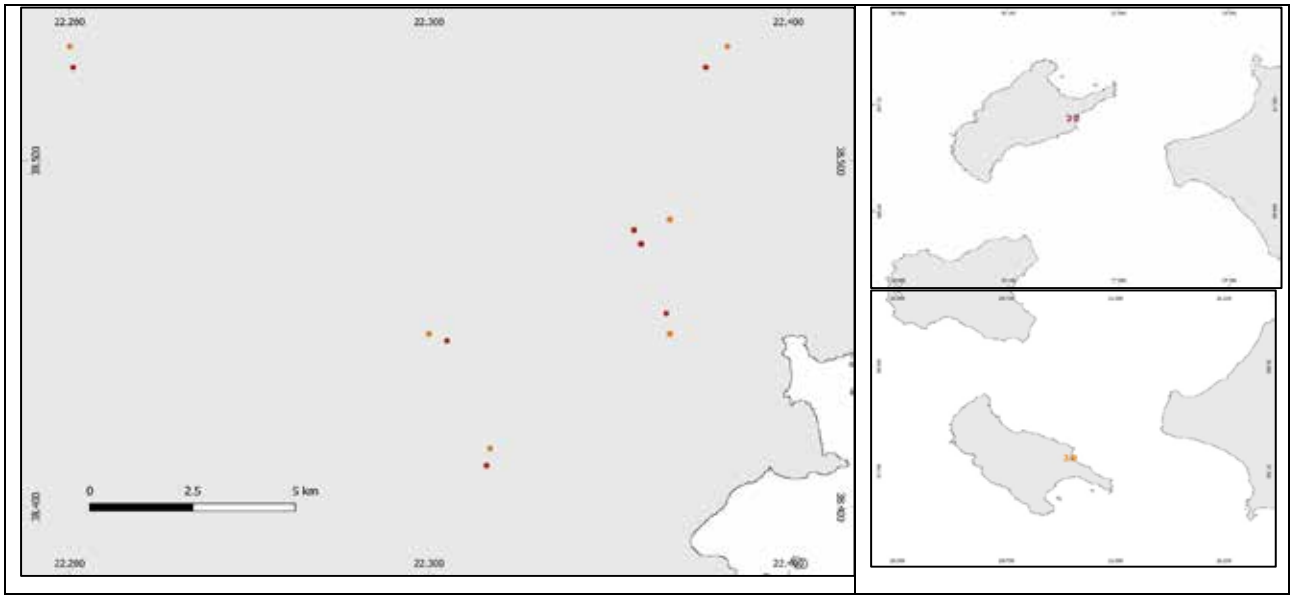

Figure 1. Two examples before (orange) and after (red) adjustments for the 1580 Mynia (PHOKIS) earthquake. Coordinates have been relocated and one intensity value was corrected from 3.9 to 3.5.

Table 6. Two examples before and after adjustments

	PlaceID	PlaceNameGreek	PlaceNameText	PlaceNameWeb	PlaceNameEng	PlaceNameEngGr	PlaceLat	PlaceLon
EXAMPLE 1 BEFORE	GR-00206	Τσουκαλοχώρι	Tsoukalokhorion	Τσουκαλοχώρι (Tsoukalokhorion)	Tsoukalokhorion	Tsoukalokhorion Τσουκαλοχώρι	39.267	26.067
	GR-00185	Σκαλοχώρι	Skalokhorion	Σκαλοχώρι (Skalokhorion)	Skalokhorion	Skalokhorion Σκαλοχώρι	39.267	26.067
EXAMPLE 2 BEFORE	GR-00358	Μηλίτσα (εδώθε)	Militsa (Edhothe)	Μηλίτσα (εδώθε) (Militsa)	Militsa	Militsa Μηλίτσα (εδώθε)	36.867	21.833
	GR-00359	Μηλίτσα (πέρα)	Militsa (Pera)	Μηλίτσα (πέρα) (Militsa)	Militsa	Militsa Μηλίτσα (πέρα)	36.867	21.833
EXAMPLE 1 AFTER	PlaceID	Comments	OldPlaceNamesEn	OlderPlaceNamesGr	LatestPlaceNameGr	LatestPlaceNameEn	PlaceLat	PlaceLon
	GR-00206	PlaceNames and coordinates have been corrected	Tsoukalokhorion	Τσουκαλοχώρι	Σκαλοχώρι	Skalokhorion	39.260	26.075
EXAMPLE 2 AFTER	PlaceID	Comments	OldPlaceNamesEn	OlderPlaceNamesGr	LatestPlaceNameGr	LatestPlaceNameEn	PlaceLat	PlaceLon
	GR-00358	I, PlaceNames and coordinates have been corrected			Μηλίτσα (εδώθε)	Militsa (Edhothe)	36.875	21.839
	GR-00359	I, PlaceNames and coordinates have been corrected			Μηλίτσα (πέρα)	Militsa (Pera)	36.870	21.846

Updating / adding "new" earthquakes

After the automation procedure, the existing database may be considered enriched and corrected. Moreover, we started to enrich this database with new data, either adding MDPs from recent studies in existing earthquakes, or introducing new earthquakes (Tables 7,8 and Figure 2). Thanks to the automation, this process was achieved without difficulty.

Table 7. The re-assessed Intensities and additional MDPs

Place	Date	NMDPs	Studies used for the update
Filiatra	1886 08 27	344	Sakellariou, N., Kouskouna, V. (2014)

Atalanti	1894 04 27	96	Albini, P., Pantosti D. (2004) / Sakellariou, N., Kouskouna, V. (2014)
Atalanti	1894 04 20	65	Albini, P., Pantosti D. (2004) / Sakellariou, N., Kouskouna, V. (2014)
Messini	1885 03 28	40	Sakellariou, N., Kouskouna, V. (2014)
Kyparissia	1899 01 22	109	Sakellariou, N., Kouskouna, V. (2014)

Table 8. "New" earthquakes and their MDPs from recent studies added in the database

Place	Date	NMDPs	Study
Lefkada	1704 11 22	12	Kouskouna et al. 2020
Negreponte	1708 04	3	Kouskouna et al. 2020
Lamia	1740 10 05	6	Kouskouna et al. 2020
Kefallinia	1741 06 23	6	Kouskouna et al. 2020
Corinthia	1742 02 21	11	Kouskouna et al. 2020
Aigio	1748 05 25	5	Kouskouna et al. 2020
Thiva	1853 08 18	41	Kaviris et al. 2022
Thiva	1853 09 29	14	Kaviris et al. 2022
Thiva	1893 05 23	13	Kaviris et al. 2022
Thiva	1893 05 22	3	Kaviris et al. 2022
Thiva	1872 09 26	1	Kaviris et al. 2022
Thiva	1833 12 13	1	Kaviris et al. 2022

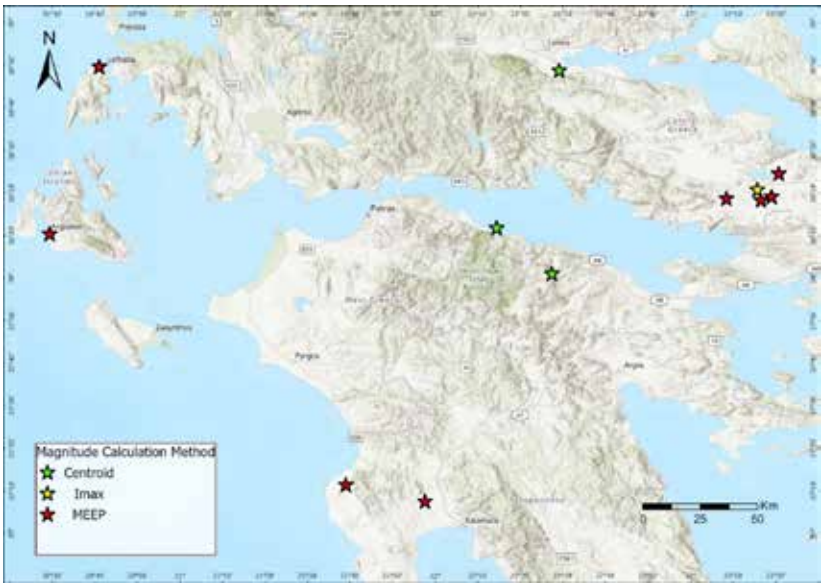

Figure 2. The epicentral areas of the "new" earthquakes (from Table 8)

Future objectives

New data inserted in the database, need previous thorough checks in terms of compatibility with the database format. More importantly, for each earthquake a macroseismic review is necessary to identify the most accurate and reliable source, as well as to double-check the available information from multiple sources in both terms of localities naming, geographical coordinates and avoid duplications that may lead to false data and, consequently, to unreliable results. On the other hand, newer earthquakes may include more data and be easier to calculate reliable equivalent moment magnitudes and epicentral

areas.
We aim to upload the updated database file at the webpage http://macroseismology.geol.uoa.gr/, as described by (Kouskouna and Sakkas 2013) using MIDOP (Locati and Cassera 2010) and also to incorporate early 20th century earthquakes and their MDPs, as it is common knowledge that the parameters determination of earthquakes continued to be based on macroseismic data for a few decades after the turn of the century. However, instrumental data begin to be more and more available and offer an opportunity to apply calibration methods using both macroseismic and instrumental data for improved parameters determination.

Acknowledgements
This research is partially funded by the "TowaRds AdvaNced multidiSciplinary Fault ObseRvatory systeMs²" (TRANSFORM²) project, which is funded by the European Union under project number101188365 within the HORIZON-INFRA-2024-DEV-01-01 call (Special Account for Research Grants of NKUA, project code: 21465).

Bibliography

Albini, P. & Pantosti. D., 2004. The 20 and 27 April 1894 (Locris, Central Greece) Earthquake Sources through Coeval Records on Macroseismic Effects Bulletin of the Seismological Society of America, Vol. 94, No. 4, pp. 1305–1326

Kaviris, G., Kapetanidis, V., Spingos, I., Sakellariou, N., Karakonstantis, A., Kouskouna, V., Elias, P., Karavias, A., Sakkas, V., Gatsios, T., Kassaras, I., Alexopoulos, D.J., Papadimitriou, P., Voulgaris, N., Parcharidis, I., 2022. Investigation of the Thiva 2020–2021 Earthquake Sequence Using Seismological Data and Space Techniques. Appl. Sci. 2022, 12, 2630. https://doi.org/10.3390/app12052630

Kouskouna, V. & Sakkas, G., 2013. The University of Athens Hellenic Macroseismic Database (HMDB.UoA): historical earthquakes DOI 10.1007/s10950-013-9390-3

Kouskouna, V., 2001. The (December 28th, 1891) January 9th, 1892 Larisa (Central Greece) earthquake. Bulletin of the Geological Society of Greece, Vol. XXXIV/4, 1425-1432. Proceedings of the 9th International Congress, Athens, September 2001 (in Greek).

Kouskouna, V., Kaperdas, V., Sakellariou, N., 2020. Comparing calibration coefficients constrained from early to recent macroseismic and instrumental earthquake data in Greece and applied to eighteenth century earthquakes Volume 24, pages 293–317,

Kouskouna, V., Karnassopoulou A., Makropoulos K., Taxeidis K. & Tzanis A., 1998., Investigation of earthquakes (1400-1899) in Greece. Internal report for the BEECD project, Department of Geophysics, University of Athens, Athina, 112 pp.

Kouskouna, V., Makropoulos, K.C. & Tsiknakis, T., 1992. Contribution of historical information to a realistic seismicity and hazard assessment of an area. The Ionian Islands earthquakes of 1767 and 1769: historical investigation. In: P. Albini and A. Moroni (eds.), Materials of the EC Project "Review of Historical Seismicity in Europe", vol. 1, 195-206.

Kouskouna, V., Makropoulos, K.C. & Tsiknakis, K., 1992. Contribution of historical information to a realistic seismicity and hazard assessment of an area. The Ionian Islands earthquakes of 1767 and 1769: historical investigation. In: P. Albini and A. Moroni (eds.), Materials of the EC Project "Review of Historical Seismicity in Europe", vol. 1, 195-206.

Makropoulos, K.C. & Kouskouna, V., 1994a. The Ionian Islands earthquakes of 1767 and 1769: seismological aspects. Contribution of historical information to a realistic seismicity and hazard assessment of an area. In: P. Albini and A. Moroni (eds.), Materials of the EC Project "Review of Historical Seismicity in Europe", vol. 2, 27-36.

Makropoulos, K.C. & Kouskouna, V., 1994b. The 1894 April 20 and 27 Atalanti earthquakes: 100 years after - lessons learnt. Proc. XXIV ESC Gen. Ass., Athens, 19-24 Sept. 1994, vol. 1, 61-71.

Locati, M. & Cassera, A., 2010. MIDOP: Macroseismic Intensity Data Online Publisher. Rapporti Tecnici INGV, 123, 92 pp.

Sakellariou, N., Kouskouna, V. & Makropoulos, K.C., 2010. Macroseismic Intensities in Central-Southern Peloponnese during the 19th century. Laboratory of Seismology, Internal Report, 2010.

Sakelariou, N., & Kouskouna, V., 2014. Assigning Macroseismic Intensities of Historical Earthquakes from late 19th century in SW Peloponnese (Greece). Second European Conference on Earthquake Engineering and Seismology, Istanbul, Aug. 25-29.

Stucchi, M., A. Rovida, A., Gomez Capera, A.A, Alexandre, P., Camelbeeck, T., Demircioglu, M.B., Gasperini, P., Kouskouna, V., Musson, R.M.W., Radulian, M., Sesetyan, K., Vilanova, S., Baumont, D., Bungum, H., Fäh D., Lenhardt, W., Makropoulos, K., Martinez Solares, J.M., Scotti, O., Živčić, M., Albini, P., Batllo J., Papaioannou, C., Tatevossian, R., Locati, M., Meletti C., Viganò, D., Giardini, D., 2013. The SHARE European Earthquake Catalogue (SHEEC) 1000–1899. DOI 10.1007/s10950-012-9335-2.

Taxeidis K., 2003. Study of Historical Seismicity of the Eastern Aegean Islands. PhD thesis, N&K University of Athens, Greece, 301 pp.

17th INTERNATIONAL CONGRESS of the Geological Society of Greece

BULLETIN OF THE GEOLOGICAL SOCIETY OF GREECE, SP. PUBL.

EXTENDED ABSTRACT 105

Seeking for dependencies of the high frequency "kappa" parameter of earthquake spectrum on weather/climate conditions

Grendas I.[1], Roumelioti Z.[1]

(1) Department of Geology, University of Patras, Patras, Greece, grendasioannis@gmail.com

Abstract

We investigate the seasonal variability of the κ_0 parameter, which describes the near-surface high-frequency attenuation of seismic waves. We analyze data from the ARGONET vertical array of accelerometers in Cephalonia, Greece, focusing on comparisons of high-frequency spectral decay between the surface station CK0 and the borehole bedrock station CK83. The study uses the ARGONET database records from July 2015 to October 2022. Results using two different approaches agree on a significant variation of κ_0 at CK0, with lower values in summer (dry period for Cephalonia) and higher values in winter (rainy period). This suggests that weather/climate related factors, such as soil moisture and temperature, influence near-surface attenuation, at least as expressed through the value of κ_0. This result challenges the assumption of a static value for κ_0 often made in site characterization for seismic hazard assessment.

Background

Kappa, κ, is used to quantify the attenuation of high-frequency seismic waves as they travel through the Earth's crust and near-surface materials. First introduced by Anderson and Hough (1984), it is determined from the slope of the high-frequency decay in the Fourier Amplitude Spectrum (FAS) of acceleration, typically using earthquake ground motion records. It is often analyzed in one component that reflects the attenuation occurring along the seismic ray path due to anelastic and scattering processes in the crust and one that quantifies the near-surface attenuation due to the shallow geological conditions, particularly in sedimentary layers.

The component of κ related to site-specific near-surface attenuation, widely called the kappa-zero, κ_0, is a crucial parameter in engineering seismology (e.g., Boore and Joyner, 1997; Ktenidou et al., 2014; Douglas et al., 2020). It enhances the accuracy of ground motion models in predicting high-frequency spectral amplitudes and is directly utilized in developing design spectra and ground motion simulations. By incorporating κ_0, engineers can better estimate seismic demands on structures, especially those sensitive to high-frequency vibrations. That is why it has been considered vital for critical facilities, such as nuclear power plants, where accurate characterization of high-frequency ground motion components is essential.

While κ has been widely adopted by both the seismological and civil engineering communities, several challenges and criticisms have emerged regarding its application. Estimating κ involves subjective decisions, such as selecting the frequency range for analysis and assuming linearity in the spectral decay. This can lead to variability and inconsistencies, which are further amplified by a lack of standardized methodologies in the parameter's computation and data with insufficient high-frequency content (e.g., Ktenidou et al., 2014). Furthermore, κ reflects a combination of attenuation processes, including scattering, anelastic absorption, site amplification effects and even soil-structure interaction and similar effects emerging from sensor installation practices (e.g., Parolai and Bindi, 2004; Hollender et al., 2020). Disentangling these contributions can be difficult and complicates the interpretation of the parameter under discussion. Another recently proposed process that may affect the spectral region where κ is measured is soil-atmosphere interaction, which suggests a seasonal variation in κ (e.g., Roumelioti et al., 2020; Grendas et al., 2025).

Objectives

This study aims to investigate the seasonal variability of κ_0 using data from the ARGONET vertical array, a special infrastructure for site effect studies on Cephalonia Island, Greece. The objective is to use this well-studied site to extract valuable insights about the possible contribution of weather/climate into the complex nature of near-surface, high-frequency attenuation.

Data and Initial Processing

The ARGONET infrastructure includes, among other components, a vertical array of accelerometers located in the sedimentary valley of Koutavos, south-southeast of Argostoli, the capital of the island of Cephalonia in western Greece. Details of the infrastructure can be found in Theodoulidis et al. (2018). In this study, we only use data from the surface and deepest sensor of the vertical array, code-named CK0 and CK83, respectively. CK0 is installed inside a light wooden construction on a relatively soft site. Average shear-wave velocity, V_S, for the upper 30 m depth (VS_{30}) according to the V_S values from different methods (cross-hole, down-hole, seismic interferometry) reported in Cushing et al., (2020), is in the range 201-262 m/s. CK83, on the other hand, installed at a depth of 83 m, is reported to be in the limestone bedrock (Theodoulidis et al., 2018). For the purposes of this study, this station is used as a "reference" station, both in the classical sense of engineering seismology (i.e., absence of

significant site effects), but also in the sense that it is very unlikely to be significantly affected by short-term ground-atmosphere interactions (Roumelioti et al., 2020; Grendas et al., 2025).

Since its launch in 2015, ARGONET has been in continuous recording mode. Earthquake records that include CK83 acceleration time histories with a Peak Ground Acceleration (PGA) ³2mg are processed and organized in the ARGONET database, which is openly available online (https://argonet-kefalonia.org/data/argonet_data/). In this work, we process the horizontal records at CK0 and CK83 stations of 964 earthquakes epicentered in the wider area of Western Greece and occurring from July 2015 to October 2022.

The horizontal acceleration waveforms were first processed for standard corrections and S-wave window selection. The various steps of this processing are not presented here for reasons of space, but are described in detail in Grendas et al. (2021). Briefly, we selected S-wave windows of variable duration, depending on the earthquake-receiver distance and the earthquake magnitude. These S-wave windows were Fast Fourier Transformed (FFT) and smoothed following Konno and Ohmachi (1998) (with the parameter b of the method set to 50). Spectra were first generated for each horizontal component separately, and then combined (square root of the sum of squares) to compute a single horizontal spectrum per station and earthquake.

Computation of κ and κ_0

Kappa values were computed for each horizontal FAS, A(f), based on a linear fit of its amplitudes in the high-frequency spectral region in between user-defined frequencies f_e and f_{end}, following the original work of Anderson and Hough (1984) and the equation:

$$A(f)=A_0 \exp^{(-\pi \cdot \kappa \cdot f)} \qquad (f>f_e) \qquad [1]$$

in which A_0 corresponds to the plateau of spectral amplitudes at $f<f_e$. Figure 1 shows the computation of κ schematically. In addition to the examined earthquake spectrum (in blue), the corresponding Fourier spectrum of a noise window preceding the earthquake signal is shown (in red). The part of the earthquake spectrum used in the analysis is required to be above a certain multiple of the noise spectrum. Figure 1 shows an example of a multiple of 3. In this work, we set a stricter minimum signal-to-noise level of 5.

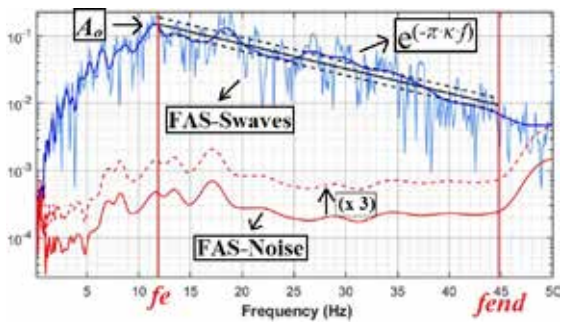

Figure 1. The Fourier Amplitude Spectra (FAS) of the S-wave earthquake motion (light blue line), its smoothed version (bold blue line), and the corresponding smoothed FAS of the noise before the arrival of the P-wave (bold red line). The red dashed line marks the 3-fold noise FAS level as an example of the minimum threshold for the earthquake signal to be considered reliable (Signal-to-Noise Ratio, SNR³3). Black lines show the least-squares regression of log(FAS) values in the frequency range from f_e to f_{end}, ±1 standard deviation (STD) of the mean.

We computed κ values for four different fixed frequency ranges, i.e., 6-25 Hz, 6-35 Hz, 10-25 Hz, and 10-35 Hz. The results for each of the two stations and each frequency range studied are plotted against epicentral distance in Figure 2. By linear regression of the distributions in Figure 2, it is possible to separate the "path" and the epicentral distance independent ("site" or/and "source" considered) terms of kappa. The mean values for the second term of kappa or κ_0, i.e., the values of κ corresponding to zero epicentral distance are reported in Figure 2 and Table 1. We restricted the linear regressions to data corresponding to epicentral distances £60 km, partly because data points were sparse at larger distances and partly because around 60 km there is an obvious change in the regional attenuation that could not be fit by a single line. We also kept the slope of the linear fit, based on the regression of the entire set of ARGONET data (i.e., all stations of the vertical array, not shown in this paper), fixed so as to reasonably assume exactly the same path attenuation factor for the two stations studied, since they are both located at the same epicentral distance.

Results in both Figure 2 and Table 1 show a larger variability of κ values at CK0 compared to CK83. They also highlight that mean κ_0 values are, as expected, larger at the "soft" CK0 stations and much smaller in the "soft rock" CK83 station. Another rather expected result is the dependence of κ and consequently of the κ_0 values on the frequency range used in the analysis, further highlighting the problem in understanding κ in the absence of standardized analysis practices.

Computation of $\Delta\kappa_0$

The exclusive site-specific character of κ_0 has been a subject of debate (e.g., Ktenidou et al., 2014 and references therein). Most studies support it (e.g., Cotton et al., 2006; Drouet et al., 2010; Ktenidou et al., 2013; Ktenidou et al., 2015). However, others also argue for a dependence on the seismic source (e.g., Tsai and Chen, 2000; Purvance and Anderson, 2003; Kilb et al., 2012), a component that would be difficult to isolate based on classical linear regression analysis on the κ measurements of a single site. To overcome this difficulty and secure that we have effectively removed any possible source effects, instead of using κ or κ_0 we used one site as target and one as reference and we computed their κ differences, Δκ. Δκ is equivalent to $\Delta\kappa_0$ under the realistic assumption that the wavefield at both examined stations experiences the same along-path attenuation.

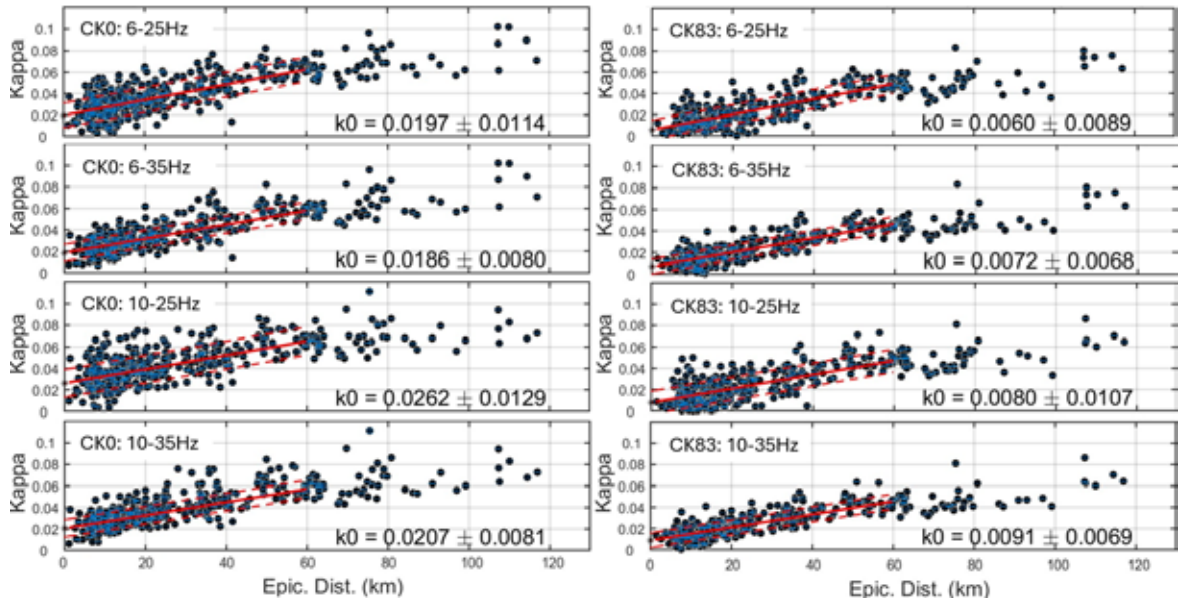

Figure 2. κ values computed from the earthquake records at stations CK0 (left) and CK83(right) considering four different frequency ranges (noted on top left of each subplot). The slope of the linear regression has been kept constant considering all ARGONET data. Mean κ_0 values (κ at zero distance) and the ± 1 STD are also noted in each subplot.

Table 1. Computed κ_0 and $\Delta\kappa_0$ mean values and their standard deviations (σ) for four examined frequency ranges. $\Delta\kappa_0$ results are shown for both applied methods described in the text. Columns named "SV model range" list the quantity "maximum seasonal model amplitude - minimum seasonal model amplitude" for each examined case.

	CK0		CK83		$\Delta\kappa_0$ Method1			$\Delta\kappa_0$ Method2		
f_e-f_{end} (Hz)	κ_0 (ms)	$\sigma\kappa_0$ κ_0 (ms)	κ_0 (ms)	$\sigma\kappa_0$ κ_0 (ms)	$\Delta\kappa_0$ (ms)	$\sigma\Delta\kappa_0$ $\Delta\kappa_0$ (ms)	SV model range	$\Delta\kappa_0$ (ms)	$\sigma\Delta\kappa_0$ $\Delta\kappa_0$ (ms)	Sv model range
6-25	19.7	11.4	6.0	8.9	18	6	7	17.4	0.8	6.5
6-35	18.6	8.0	7.2	6.8	14	6	5	14.4	0.5	4.3
10-25	26.2	12.9	8.0	10.7	20	10	10	20.6	1.1	9.6
10-35	20.7	8.1	9.1	6.9	15	10	6	14.4	0.7	4.5

In our case, CK0 is the target site and we examine its high-frequency shaking characteristics with respect to the borehole station CK83 using two different methods: In "Method 1", we used pairs of κ values from CK0 and CK83 stations to estimate $\Delta\kappa=\kappa_{(CK0)}-\kappa_{(CK83)}$ and equivalently $\Delta\kappa_0$. In "Method 2", we measured $\Delta\kappa_0$ directly on Standard Spectral Ratios (SSRs) of CK0 with respect to CK83. The two approaches will be presented in more detail in the following.

The computation of $\Delta\kappa_0$ from the κ values of CK0 and CK83 is straightforward and resulting values are plotted in Figures 3a and 4. For examining possible variations of $\Delta\kappa_0$ with seasons (Seasonal Variation, SV), we considered a "pseudo-waveform" $\Delta\kappa_0$(day), where "day" is derived from date considering as starting point the 1st of January of each year. We analyzed this pseudo-waveform for its frequency content via FFT. We computed FAS only for periods T_{SV}^{h}, corresponding to 365/h for h=1 and h=2, seeking for possible variations with a return period of the order of a year or half a year and aiming to a smooth model of the phenomenon, if proven significant. The seasonal variation of $\Delta\kappa_0$ ($\Delta\kappa_h(SV)$), was finally modeled as the sum of the 2,

discrete period (T_{SV}^{h}) cosine wavelets, based on the corresponding scaled FAS Amplitude, $\Upsilon(T_{SV}^{h})$, and adopted phase, $\varphi(T_{SV}^{h})$ (in degrees),as in:

$$\Delta\kappa_h(SV) = \Upsilon(T_{SV}^{h}) \cdot \cos\left\{\left(2 \cdot \pi / T_{SV}^{h}\right) \cdot [\mathrm{Date} - \varphi(T_{SV}^{h})]\right\} \quad [2]$$

Figure 3a shows as an example the starting data and resulting model (red dots and cyan lines in Figure 3a) for the frequency range 6-25Hz and the corresponding result of the FFT analysis (Figure 3b). The starting data and final models for the seasonal variation of $\Delta\kappa_0$ for all four tested frequency ranges are presented in Figure 4. If there is a time pattern in $\Delta\kappa_0$, a clear peak is expected to be observed in plots like the example plot in Figure 3b. In the specific example of Figure 3b, a prominent peak is seen at the examined period of 1 year, suggesting a yearly repeating change in $\Delta\kappa_0$.

In general, Figure 3 shows a clear time variation of $\Delta\kappa_0$ measurements, with lower $\Delta\kappa_0$ during summer and highest during winter. The proposed model for this variation also predicts the lowest $\Delta\kappa_0$ values during the first third of July and the highest values during the first third of January of each year. These results were consistent for all four examined frequency ranges and any differences were restricted to the order of a few days.

The modelled seasonal variation of the high-frequency ground motion amplitudes at CK0 with respect to those in CK83 can be characterized as significant, since its range (maximum seasonal model amplitude - minimum seasonal model amplitude) is of the order of 1 standard deviation of the mean $\Delta\kappa_0$ from data (Table 1, $\sigma\Delta\kappa_0\Delta\kappa_0$, Columns 7, 8). This means that the proposed model, if used to "correct" the observed data examined in this study, could lower the variability in κ_0 or $\Delta\kappa_0$ measurements and lead to more robust computations of the mean κ_0. The performance of the seasonal variation model of $\Delta\kappa_0$ shows some dependence on the frequency interval adopted in the analysis, but in all cases explains much of the variability of the examined parameter (Table 1).

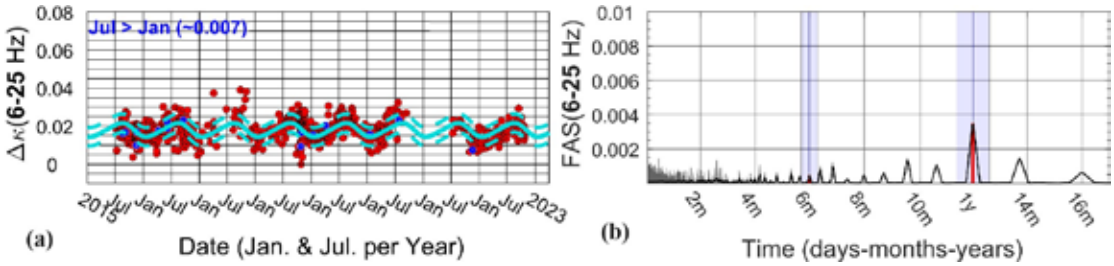

Figure 3. Variation of $\Delta\kappa_0$ with date a) data points of individual $\Delta\kappa_0$ measurements for the frequency range 6-25Hz and superimposed model of the seasonal variation of $\Delta\kappa_0 \pm 1$ standard deviation (STD) of the mean model (cyan curves), b) Fourier Amplitude Spectrum (FAS) of the pseudo-waveform $\Delta\kappa_0$(day) considered. Shaded areas mark the areas of the investigated return periods of the phenomenon (i.e, at 1 year and 6 months). The difference between the lower and higher $\Delta\kappa_0$ values predicted by the proposed model are noted in the top left of a).

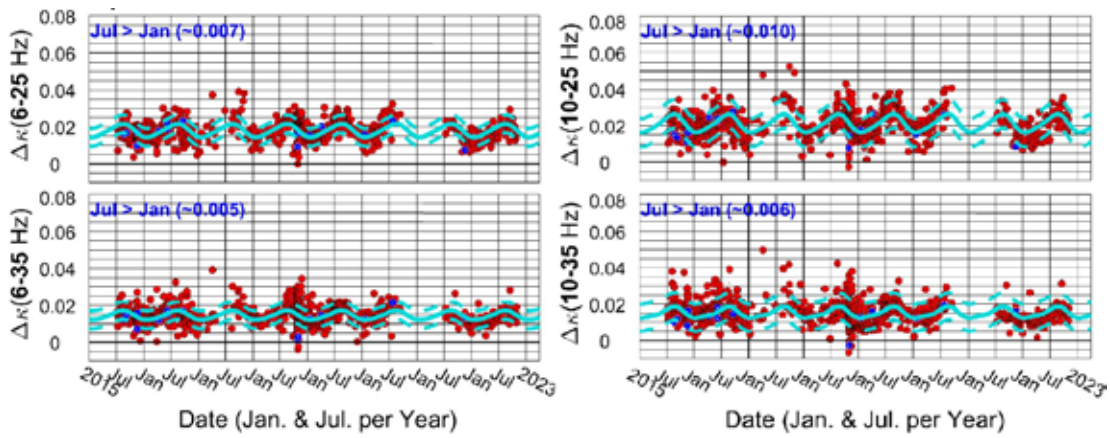

Figure 4. $\Delta\kappa_0$ values based on the κ_0 measurements at CK0 and CK83 stations ($\kappa_{(CK0)}$-$\kappa_{(CK83)}$) for the 4 examined frequency ranges. The modeled seasonal variation of $\Delta\kappa_0$ and its Standard Deviation (STD), are shown in cyan solid and dashed lines, respectively. The highest value of the seasonal $\Delta\kappa_0$ model is predicted to occur in July and the lowest in January of each year. The difference between the lowest and highest predicted $\Delta\kappa_0$, is written in the top left of each subplot.

The alternative approach to compute $\Delta\kappa_0$ (our "Method 2") is to measure it directly on Standard Spectral Ratios (SSRs) of CK0 with respect to CK83. By dividing the FAS of CK0 to those of CK83 and considering that the interstation distance is much smaller compared to any epicentral distance in the examined dataset, we assume that source and path effects are effectively removed (Borcherdt, 1970), including the path-dependent component of κ. In the high-frequency part of the SSR, the spectral division mainly includes the division of the factors $\exp(-\pi\kappa_{(CK0)}f)/\exp(-\pi\kappa_{(CK83)}f)$. The path-dependent component of κ is considered the same for both the surface and borehole station and is eliminated and what remains is the difference $\kappa_{0(CK0)}-\kappa_{0(CK83)}$, i.e., the quantity under study.
SSRs for the horizontal component of the ARGONET dataset have already been computed by Grendas et al. (2025). Herein, we use these published seasonal varying ratios to perform linear regression on their high-frequency parts and more specifically within the same four frequency ranges examined earlier ("Method 2"). The resulting $\Delta\kappa_0$ values are depicted in Figure 5, along with SSRs colored according to the date of their occurrence. Warm colors correspond to dry, summer months and cold colors to winter months and it is evident that the differences in the high-frequency signal of CK0 with respect to CK83 increases during winter and diminishes during the summer.
Linear regressions to compute the mean $\Delta\kappa_0$ and its values during the identified "extreme" seasonal variation periods (i.e., July-August and January-February) have been performed directly on the SSRs of Figure 5. Pertinent results are shown in each subplot, considering the four examined frequency ranges. The linear fits for the two extreme seasonal variation periods are also shown. $\Delta\kappa_0$ values and their STDs are also listed in Table 1, under "Method 2".
By comparing the linear fits in Figure 5, it becomes evident how the seasonal variation can largely affect the computation of $\Delta\kappa_0$ (and directly of κ and κ_0), at least at the specific site examined in this study. Datasets with a biased concentration of summer recordings would provide much larger values of κ_0 compared to non-biased or inversely biased datasets. The effect seems to be more significant when the examined frequency range terminates at frequencies largely affected by seasonal variations. In Figure 5, for example, the left subplots including analysis up to 25Hz present much larger discrepancies between the two "extremes" with respect to subplots to the right where the analysis is extended well beyond the frequency range mostly affected by seasonal variation. All these observations raise another "red flag" when the engineering and seismological communities face the necessity to harmonize κ measurements for comparisons.
Overall, the results of the two methods for computing $\Delta\kappa_0$ are similar and this is demonstrated by the comparison of values reported in Table 1.

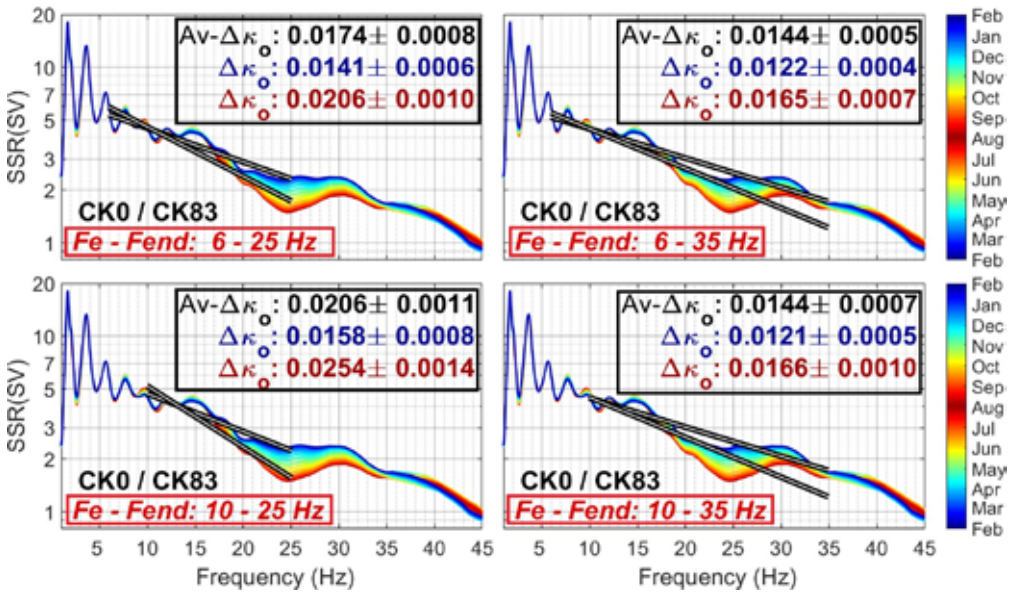

Figure 5. Mean Standard Spectral Ratios (SSRs) (for the 1st day of each month) between CK0 and CK83 stations colored according to the date of occurrence of. Subplots differentiate in the frequency range used for the linear regression. Double lines mark the regression results for the two extreme $\Delta\kappa_0$ cases (summer vs winter). On the top right of each subplot, the mean $\Delta\kappa_0$ and $\Delta\kappa_0$ values corresponding to the two extremes of the modelled seasonal variation are noted.

Conclusions/Discussion

Despite its limitations, kappa remains a valuable parameter for understanding high-frequency attenuation and

conducting site-specific hazard analyses. Its practical utility has made it a significant parameter of engineering seismology, but ongoing research aims to refine its estimation techniques and improve its integration into seismic hazard models. By addressing its limitations and standardizing methodologies, the role of kappa in seismic hazard analysis can be further enhanced.

In this work we addressed an additional process that may add to the lumped character of this single-number descriptor of high-frequency attenuation, i.e., the soil-atmosphere interaction. We specifically examined if the high-frequency part of the earthquake spectrum, i.e., the part commonly used for the computation of kappa, changes with a seasonal periodicity. To do so, we comparatively examined kappa values at one surface and one borehole, bedrock station.

Our results demonstrate that the difference in κ_0 values of the two examined stations exhibit considerable variability due to seasonal weather conditions, the frequency range used in the computation of the parameter, and potentially source processes. The pronounced seasonal variation observed at the surface soft soil site CK0 highlights the influence of rainfall-induced changes in ground humidity on near-surface attenuation. This finding challenges the common assumption of a static, site-specific κ_0 value and requests further research on the possible need to consider seasonal variability of high-frequency ground motion in seismic hazard assessments.

The frequency-dependent behavior of κ_0, evident in the variations observed across different tested frequency ranges, suggests that attenuation slopes might not be uniform across the entire high-frequency spectrum at a given site. This observation warrants further investigation to understand the underlying mechanisms driving these frequency-specific variations. It also adds to previous discussions in the published literature about the need to standardize the methods for computing kappa to be able to compare kappa values from different regions and studies and limit its broader applicability in seismic hazard models (e.g., Ktenidou et al., 2014).

This study also confirms the effectiveness of using SSR(f) for more robust κ_0 estimation, providing lower standard deviations compared to traditional methods based on individual kappa factor differences.

Overall, this research provides additional insights into the complex nature of κ_0 and its potential variability. Further research is needed to investigate seasonal variations of kappa at a statistically significant number of sites, quantify dependencies and develop improved predictive models that incorporate these sources of variability for enhanced accuracy and reliability.

Acknowledgements

The study was carried out in the framework of the research project “UNMASK”, supported by the Hellenic Foundation for Research and Innovation (H.F.R.I.) under the “2nd Call for H.F.R.I. Research Projects to support Faculty Members & Researchers” (Project Number: 2724).

References

Anderson, J.G., Hough, S.E., 1984. A model for the shape of the Fourier Amplitude Spectrum of acceleration at high frequencies. Bull. Seismol. Soc. Am. 74, 1969–1993.

Boore, D. M., Joyner, W. B., 1997. Site amplifications for generic rock sites. Bull. Seism. Soc. Am., 87(2), 327-341.

Borcherdt, R., 1970. Effects of Local Geology on Ground Motion Near San Francisco Rbay. Bull. Seismol. Soc. Am. 60, 29–61.

Cotton, F., Scherbaum, F., Bommer, J.J., Bungum, H., 2006. Criteria for selecting and adjusting ground-motion models for specific target regions: Application to central Europe and rock sites. J. Seismol. 10, 137–156.

Cushing, E.M., Hollender, F., Moiriat, D., Guyonnet-Benaize, C., Theodoulidis, N., Pons-Branchu, E., Sépulcre, S., Bard, P.Y., Cornou, C., Dechamp, A., Mariscal, A., Roumelioti, Z., 2020. Building a three dimensional model of the active Plio-Quaternary basin of Argostoli (Cephalonia Island, Greece): An integrated geophysical and geological approach. Eng. Geol. 265, 105441.

Douglas, J., Edwards, B., Convertito, V., Sharma, N., Tramelli, A., Kotha, S. R., Bora, S. S., 2020. Predicting site-specific kappa (κ) to improve ground-motion models for seismic hazard assessment. Earth-Science Reviews, 203, 103142.

Drouet, S., Cotton, F., Guéguen, P., 2010. VS_{30}, κ, regional attenuation and M_w from accelerograms: Application to magnitude 3-5 French earthquakes. Geophys. J. Int. 182, 880–898.

Grendas, I., Theodoulidis, N., Hollender, F., Hatzidimitriou, P., 2021. Effects of the S-wave time-window selection on Standard Spectral Ratio (SSR): Application to the ARGONET vertical array, Greece. 6th Int. Conf. Earthq. Eng. Seismol., Gebze Turkey.

Grendas, I., Roumelioti, Z., Theodoulidis, N., Hollender, F., 2025. Ground motion dependency on seasonal variations: Observations at the ARGONET array (Cephalonia, Greece). Bull. Seism. Soc. Am., (accepted).

Hollender, F., Roumelioti, Z., Maufroy, E., Traversa, P., Mariscal, A., 2020. Can we trust high-frequency content

in strong-motion database signals? Impact of housing, coupling, and installation depth of seismic sensors. Seismol. Res. Lett. 91, 2192–2205.

Kilb, D., Biasi, G., Anderson, J., Brune, J., Peng, Z., Vernon, F.L., 2012. A comparison of spectral parameter kappa from small and moderate earthquakes using southern california ANZA seismic network data. Bull. Seismol. Soc. Am. 102, 284–300.

Konno, K., Ohmachi, T., 1998. Ground-motion characteristics estimated from spectral ratio between horizontal and vertical components of microtremor. Bull. Seismol. Soc. Am. 88, 228–241.

Ktenidou, O.J., Gélis, C., Bonilla, L.F., 2013. A study on the variability of Kappa (κ) in a Borehole: Implications of the computation process. Bull. Seismol. Soc. Am. 103, 1048–1068.

Ktenidou, O.-J., Abrahamson, N. A., Drouet, S., Cotton, F., 2014. Understanding the physics of kappa (κ): Insights from a global dataset of high-quality ground motion recordings. Bull. Seism. Soc. Am., 104(5), 2313-2332.

Ktenidou, O.J., Abrahamson, N.A., Drouet, S., Cotton, F., 2015. Understanding the physics of kappa (κ): Insights from a downhole array. Geophys. J. Int. 203, 678–691.

Parolai, S., Bindi, D., 2004. Influence of Soil-Layer Properties on k Evaluation. Bull. Seism. Soc. Am., 94(1), 349–356.

Purvance, M.D., Anderson, J.G., 2003. A comprehensive study of the observed spectral decay in strong-motion accelerations recorded in Guerrero, Mexico. Bull. Seism. Soc. Am. 93, 600–611.

Roumelioti, Z., Hollender, F., Guéguen, P., 2020. Rainfall-induced variation of seismic waves velocity in soil and implications for soil response: What the ARGONET (Cephalonia, Greece) vertical array data reveal. Bull. Seism. Soc. Am. 110, 441–451.

Theodoulidis, N., Hollender, F., Mariscal, A., Moiriat, D., Bard, P.Y., Konidaris, A., Cushing, M., Konstantinidou, K., Roumelioti, Z., 2018. The ARGONET (Greece) seismic observatory: An accelerometric vertical array and its data. Seismol. Res. Lett. 89, 1555–156.

Tsai, C.-C.P., Chen, K.-C., 2000. A model for the high-cut process of strong motion accelerations in terms of distance, magnitude, and site condition: an example from the SMART 1 array, Lotung, Taiwan. Bull. Seism. Soc. Am 90, 1535–1542.

17th INTERNATIONAL CONGRESS of the Geological Society of Greece

BULLETIN OF THE GEOLOGICAL SOCIETY OF GREECE, SP. PUBL.

EXTENDED ABSTRACT 106

Digital model of Hydrological components, Mean annual Temperature, Precipitation and Evapotranspiration in Macedonia, Greece

Grimpylakos, Georgios[1]
(1) Department of Geography, University of the Aegean, Mytilene, Greece

Introduction / Background

River hydrology and morphology provide a relationship between flowing water and the physical environment of rivers. The hydromorphological regime (C11) is one of the hydromorphological quality elements of the WFD and is defined by the water flow's characteristics regarding quantity and dynamics hence to each connection to ground waters (Rinaldi et al. 2013b, Belletti et al. 2015, and Kilinc & Kay 2018). In recent years, 2009-2025, the classification of a river's hydromorphology is directly correlated with the classification and characterization of a river's morphology and hydrology which are recognized as fundamental intergrading components for studying, analysing and understanding it's behavior in order to adapt and suggest appropriate river management applications (e.g., Sear et al. 1995, Gilvear 1999, Kondolf et al. 2003, Downs and Gregory 2004, Brierley and Fryirs 2005, Brierley and Fryirs 2008; Meitzen et al. 2013, Tadaki et al. 2014, Belletti et al. 2015). The increased concern of quality, regarding river water and its habitats, combined with their correlation with the river's degradation have become important elements of hydromorphological assessment (Kilinc & Kay 2018). Furthermore, floods are common in certain areas of the world, and there have been more than 400 major floods during 2000-2024 with more than 70 billion Euros (EM-DAT, 2024).

Objectives

This study aims to create digital maps of hydrological components, such as Mean Annual Temperature, Precipitation and Evapotranspiration, which are recognized as essential components for the study and modeling of hydrological cycle, river management and hydrological natural hazards and point out the need for high spatial resolution.

Study area

Macedonia is a district of North Greece as shown at Figure 1. Studying area is a polygon that includes all the watersheds of Macedonia's torrents and rivers, resulting in a polygon the boundaries of which differ from the boundaries of Macedonia's political district and define it as an area of North Greece. The boundaries of each watershed were determined by the Ministry of Rural Development and Food in collaboration with the Institute of Geology and Mineral Exploration and always according to the WFD guidelines for water bodies. The study area is 36.290 km^2, has a perimeter of 2.163 km and includes 77 different torrents in which main rivers are divided according to WFD, and their watersheds area is of 2,9-4.775 km^2.

Data and Methodology

To study the climatic parameters for a given area, a 30-year period with good spatial and temporal distribution is needed.

For our study area, 85 meteorological – climatological stations (mentioned as MCS) from the Ministry of Rural Development and Food (82) and Hellas Gold (3) provided data which correspond to different time periods during an eighty-year period (1930-2010) and include daily, monthly and annual measurements of precipitation, while 43 of them included also daily monthly and annual measurements of temperature. After sorting the data from all 85 MCS the best period corresponded to 1974-2004, as the number of stations with daily and continuous data was higher (Grimpylakos 2020).

Specifically, to estimate the mean annual precipitation, 163.254 measurements belonging respectively to 40 MCS were used (Figure 1,3) and a subset of 20 MCS (figure 2,4). The second map of Precipitation was created using a subset of 20 MCS which also had adequate Temperature data for the creation of the Temperature and Evaporation map.

To estimate the mean annual temperature, approximately 800.000 measurements of daily minimum and maximum temperature, obtained from 43 MCS, during 1930-2010 were examined. The same thirty-year period 1974-2004 with

consistent daily data of 255.326 measurements were used, belonging respectively to the same 20 stations of the second map of precipitation (Figure 2,4).

The average initial MCS spatial distribution was 1/38,7km^2. After sorting and evaluating data, the overall spatial distribution of MCS for the precipitation map at figure 3 is 1/82.25km^2 and for temperature (figure 5), precipitation (figure 4) and corresponding evapotranspiration map (figure 6) is 1/164.5km^2. However, there are areas with lower density of approximately 1/300km^2 for maps at figures 4,5,6 and of 1/180km^2 at figure 3.

A very basic problem in spatial analysis is interpolating a spatially continuous variable from point samples. There are many different spatial interpolation techniques. Some of the most used interpolation methods to model spatially distribution from point data are: Inverse Distance Weighting (IDW), spline and ordinary kriging. Overall, anomalies of local scale can be adjusted without affecting the values derived from interpolation at other points on the surface (Burrough and McDonnell 1998).

Inverse distance weighted (IDW) is a method of interpolation that estimates cell values by averaging the values of nearby measured data points. This technique weighs the points closer to the prediction location greater than those farther away, hence the name inverse distance weighted (Watson and Philip 1985). However, the main problem with this technique is that it assumes that maximum and minimum values are measured at the sampled points and all other points have values between those values.

Spline is an interpolation method in which cell values are estimated using a mathematical function that minimizes overall surface curvature, resulting in a smooth surface that passes exactly through the input points. It is a deterministic, locally stochastic interpolation technique, which represents two-dimensional curves on three-dimensional surfaces (Eckstein 1989; Hutchinson and Gessler 1994).

These methods are known as deterministic interpolation methods because they are directly based on the surrounding measured values and use specified mathematical formulas that determine the smoothness of the resulting surface. On the other hand, kriging uses statistical models that include autocorrelation among measured points, to predict the values at unknown points. The most applied form uses “semivariogram” among pairs of sampled points. The Kriging interpolation method was developed by Matheron (1970).

All data were divided into 2 groups. The first group was named “training” and content 90% of sample points while the second group was named “test” and content 10% of the sample points. Training group’s measurements were used for predicting the values of the examined variable at whole Macedonia by using the aforementioned interpolation methods. Test’s group was used to validate the results of each method as shown at table 1.

The correlation between elevation and mean annual temperature, precipitation and evapotranspiration was checked with SPSS program and the results are shown at table 2.

Table 1. Root mean square error of each applied technique was calculated and IDW shows significant higher accuracy.

Interpolation techniques	IDW	Kriging	Spline	Polynomial
Root Mean Square Error	0,091	0,133	0,159	0,134

Figure 1. Map projecting the spatial distribution of the 20 meteorological – climatological stations with continuous temperature data during period 1974-2004, at North Greece.

Results and Discussion

Mean monthly precipitation was estimated for each month at all 20 (that have also good spatial-temporal distribution of temperature data) and 40 (with no adequate distribution of temperature data) MCS and then the mean annual precipitation was calculated for all of them. The highest possible correlation between Precipitation and elevation was not significant R^2<0,29 (Table 2) and so an equation for the estimation of the mean annual precipitation for each cell of Macedonia could not be used. Four different interpolation techniques were examined, and the root mean square error was estimated for each technique (Table 1). The IDW method was found to be the most accurate one and two thematic maps were created showing the mean annual precipitation in Macedonia North Greece. The spatial distribution of the mean annual precipitation that derived from the 40 MCS during 1974-2004 is projected at Figure 3. The spatial distribution of the mean annual precipitation that derived from the data of 20 MCS, a subset of 40, during 1974-2004 is projected at Figure 4.

The thematic map that derived from the 20 stations at Figure 4 did not include 20 stations of Figure 3, so it was missing mean annual precipitation values between 417,0 – 417,3 and 853,8 – 999,8 as these data did not exist at the 20 stations. The data distribution of the 20 stations at West, Central and South Macedonia is very sparse, resulting in much less precipitation zones. The map of 40 stations has much better spatial distribution and is more accurate than that of 20 stations and is suggested for analysis purposes). Precipitation increases with elevation, but as there is lack of MCS at elevation above 1250m, there are also no values above 1000mm at the produced map for precipitation (figure 6), Koumaria has the highest mean annual precipitation of 1020,4mm at 700m elevation.

Figure 2. Map projecting the spatial distribution of the 40 meteorological – climatological stations with continuous precipitation data during period 1974-2004, at North Greece.

Figure 3. Thematic map projecting the spatial distribution of mean annual precipitation (mm) at Macedonia of North Greece. The data derived from 40 meteorological – climatological stations during period 1974-2004 and the cell size is 750m.

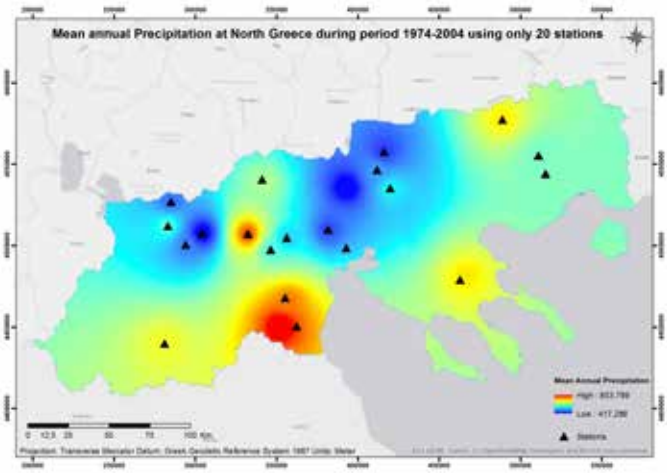

Figure 4. Spatial distribution of mean annual precipitation at Macedonia Greece derived from 20 meteorological stations during period 1974-2004

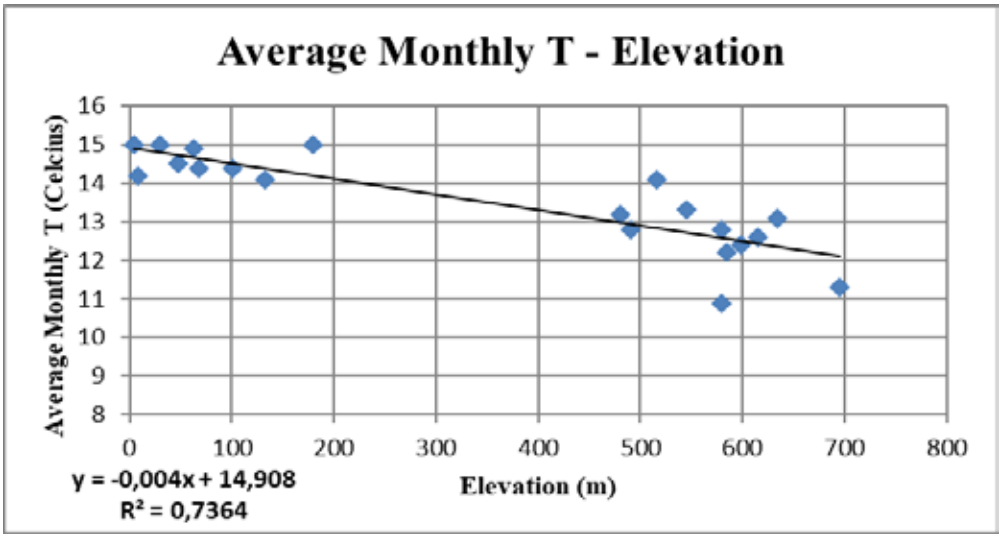

Chart 1. Correlation of mean annual temperature with elevation using linear equation.

The mean monthly temperature for each of the 20 MCS was calculated and then, the mean of these values gave the mean annual temperature for each station. There is a significant correlation between Mean annual Temperature and elevation as shown at (Chart 1), with R^2 = 0,7364, and the corresponding equation shows that the temperature declines as the elevation rises. This equation was applied using the raster calculator of ArcMap 10.3 and high-resolution Digital elevation model (DEM) with 28.3mx28.3m cell size, which was constructed from the Advanced Space borne Thermal Emission and Reflection Radiometer (ASTER) of NASA Terra satellite. The corresponding map was created (Figure 5).

Table 2. Correlation of Variables Temperature, Precipitation and evapotranspiration of each method of Thornthwaite, Turc and Coutagne with Elevation.

Elevation	Examined Variable				
	T (°C)	P(mm)	Thornthwaite	Turc	Coutagne
Pearson	-0,851	0,306	0,156	-0,072	0,108
R-square	0,723	0,094	0,024	0,005	0,012

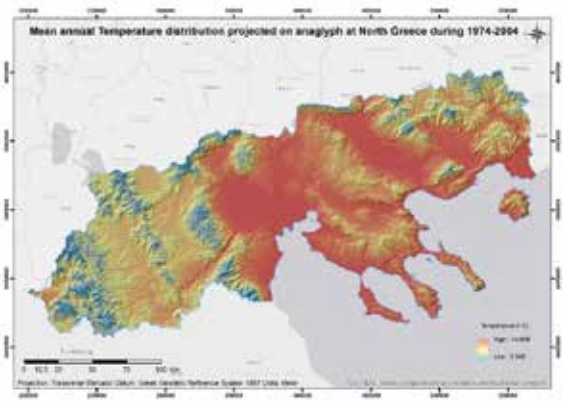

Figure 5. Mean annual temperature distribution at North Greece derived from 20 meteorological – climatological stations during period 1974-2004, projected on anaglyph.

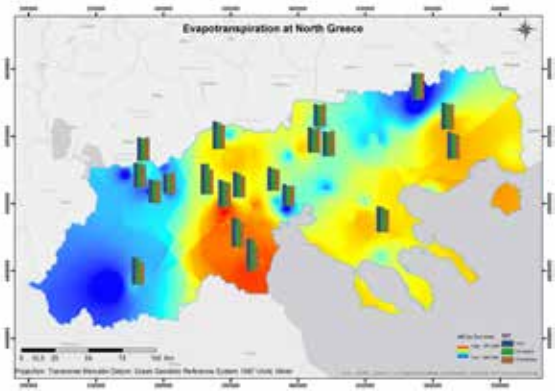

Figure 6. Thematic map of AET by all methods and with IDW by Turc nethod, cell size of 750m.

Actual evapotranspiration was calculated with Turc, Coutagne and Thornthwaite methods for each month at each one of the 20 MCS (Figure 2). AET by Turc method is higher than Thornthwaite method at all stations and in 19 of 20 stations it is higher than Coutagne method, while Coutagne is higher than Thornthwaite method at 15 of 20 stations. On the other hand, Turc method is the most easily applied method of all, as Coutagne method is not always applicable and Thornthwaite's method uses parameters that differ according to elevation and the spatial distribution of each examined place, which makes it very difficult to apply this method at all stations. No significant correlation between elevation and evapotranspiration was found (Table 2). Lastly, the Thornthwaite method is underestimating evapotranspiration in comparison with the other two methods. All AET are projected at each station, while Turc method with the highest AET is projected using IDW spatial interpolation (Figure 6). As Turc method is the easiest applied method, other researchers can use this method and compare their results with figure 6.

Conclusions

A significant correlation, with R^2 = 0,7364 (chart 1), between Mean annual Temperature and elevation was found and the corresponding equation is **T = - 0,004 * E + 14,908** (T is mean annual temperature and E is elevation). The thematic map projecting the distribution of Mean annual Temperature and the elevation is shown at Figure 5. However, there is a significant gap in the MCS regarding elevation 200-450 m, which was necessary for data consistency. The temperature values were estimated through extrapolation, therefore there is also a limitation for areas with elevation above 700m. A better elevation distribution in MCS is suggested for future work.

The mean annual precipitation at each MCS was estimated, but there was no significant correlation between elevation and Precipitation at Macedonia to create an equation. For future work, better elevation distribution of the MCS is suggested. For the creation of the Precipitation maps, 4 different spatial interpolation techniques were examined (Table 2) and IDW method was applied as it had the lowest Root Mean Square Error (Figures 3 and 4). Highest

spatial distribution of stations at figure 3, with 40 MCS, clearly shows the need of good spatial distribution of MCS, as figure 4 with 20 MCS misses values between 417,0 – 417,3 and 853,8 – 999,8.

The mean annual actual evapotranspiration at each one of the 20 MCS was estimated using Turc, Coutagne and Thornthwaite methods and their values are displayed at figure 6. The thematic map (Figure 6) projecting the evapotranspiration distribution by Turc method at Macedonia was created using the IDW spatial interpolation method. The AET used only the Precipitation at the same 20 stations that Temperature data were available and not from the 40 MCS where the precipitation has higher values 853,8 – 999,8. This means that AET at the rest area of the map could be underestimated.

Lastly the need for high spatial-temporal distribution of MCS is clearly shown, but also a good elevation distribution of MCS is also needed and suggested for better results in the future.

Acknowledgments

Special thanks to all geologists that worked during 2011-2012 at the Department of Geology and Hydrology of Ministry of Rural Development and Food and to Emeritus Professor Karakostas Theodoros for scientific advice in the field of methodological approach, selection and evaluation of data station and time series, the interpretation of data and the validation procedure.

References

Belletti, B., Rinaldi, M., Buijse, A.D., Gurnell, A.M. and Mosselman, E (2015) A review of assessment methods for river hydromorphology. Environmental Earth Sciences 73: 2079-2100.

Brierley, G.J.and Fryirs, K.A., 2005. Geomorphology and River management: applications of the River Styles Framework, Blackwell.

Brierley, G.J. and Fryirs, K.A., 2008. River futures: an integrative scientific approach to river repair. Society for Ecological Restoration International, Island Press, Washington, DC 304 pp

Burrough, P.A and McDonnell, R.A., 1998. Principles of geographical information systems. Oxford University Press, New York.

Downs, P.W. and Gregory, K.J., 2004. River channel management. Towards sustainable catchment hydrosystems. Arnold, London, pp 395

Eckstein, B.A., 1989. Evaluation of spline and weighted average interpolation algorithms. Comput Geosci, Vol. 15, p. 79–94.

Grimpylakos I.G. 2020. Contribution of the Hydromorphological - Geological and Climatological parameters to the watershed typology, application in basins of Northern Greece. Ph.D. Thesis, School of Geology, Aristotle University of Thessaloniki, Annex Number of Scientific Annals of the School of Geology No 202, 580 pp

Gilvear, D.J., 1999. Fluvial geomorphology and river engineering: future roles utilizing a fluvial hydrosystems framework. Geomorphology 31:229–245

Hutchinson, M.F. and Gessler, P.E., 1994. Splines-more than just a smooth interpolator. Geoderma, Vol. 62, p. 45–67.

EM-DAT, 2024. The International Disaster Database. Center for Research on Epidemiology of Disasters. Available online: https://www.emdat.be/ (accessed on 02 December 2024).

Kilinc, S.F. and Kay, P., 2018. Determination of the Most Suitable Assessment Methods of River Hydromorphology for Turkey. DOI: 10.31807/tjwsm.322489.

Kondolf, G.M., Montgomery, D.R., Piegay, H. and Schmitt, L., 2003. Geomorphic classification of rivers and streams. In: Kondolf GM, Piegay H, (eds) Tools in fluvial geomorphology. Wiley, Chichester, pp 171–204

Matheron, G., 1970. The theory of regionalized variables and its applications, École Nationale Supérieure des Mine, Les Cahiers du Centre de Morphologie Mathématique de Fontainebleau, Paris, Vol. 5, p. 212.

Meitzen, K.M., Doyle, M.W., Thoms, M.C. and Burns, C.E., 2013. Geomorphology within the interdisciplinary science of environmental flows. Geomorphology 200:143–154

Rinaldi, M., Belletti, B., Van de Bund, W., Bertoldi, W., Gurnell, A., Buijse, T. and Mosselman, E., 2013b. Review on eco-hydromorphological methods. Deliverable 1.1, REFORM (REstoring rivers FOR effective catchment Management), Project funded by the European Commission within the 7th Framework Programme (2007 – 2013), Topic ENV.2011.2.1.2-1 Hydromorphology and ecological objectives of WFD, Grant Agreement 282656.

Sear, D.A., Newson, M.D. and Brookes, A., 1995. Sediment related river maintenance: the role of fluvial geomorphology. Earth Surf Proc Land 20:629–647

Tadaki, M., Brierley, G. and Cullum, C., 2014. River classification: theory, practice, politics. WIREs Water 1:349–367

Water Framework Directive (2000/60/EC). Directive 2000/60/EC of the European Parliament and of the Council of 23 October 2000 establishing a framework for Community action in the field of water policy. Official Journal L 327 , 22/12/2000 P. 0001 – 0073.

Watson, D.F. and Philip, G.M., 1985. A refinement of inverse distance weighted interpolation. Geo-Processing, Vol. 2, p. 315–327.

17th INTERNATIONAL CONGRESS of the Geological Society of Greece

BULLETIN OF THE GEOLOGICAL SOCIETY OF GREECE, SP. PUBL.

EXTENDED ABSTRACT 107

The Pheneos palaeolake in N. Peloponnese, Greece

Groumpou M.[1], Koukouvelas I.[1], Nikolakopoulos K.[1], Sanjuan J.[2], Papadopoulou P.[1], Iliopoulos G.[1].

(1) Geology Department, Patras, Greece, mgroumpos@gmail.com

(2) Department of Earth and Ocean Dynamics, Barcelona, Spain

Introduction

Pheneos polje, located in northern Peloponnese (Greece) is strongly linked to the homonymous mythical lake. Throughout the past millennia, flooding events in the southern part of this polje have given rise to a lake. The myths associated with the lake revolve mostly around its drainage periods, with local populations suggesting that Hercules himself excavated openings to the ground with his bare hands to rescue the villagers from flooding (Jones, 1988). In reality, the water drains through sinkholes that are part of the region's karstic system (Tsoflias, 1973). In the southernmost part of the polje, distinct step-like scarps on the landscape serve as indicators of past lake levels (Figure 1). These scarps, representing notable geomorphological features, have been documented by Pausanias and other historical travelers (Groumpou, 2024). The primary objective of this study was to verify these features as relict shorelines of the ancient Pheneos lake.

Figure 1. Scarps on the landscape in the southern part of Pheneos polje indicating past lake levels.

Methods

Two distinct datasets, consisting of orthophoto maps and digital surface models (DSMs) were used to identify and map the step-like landforms across the landscape. The first dataset consists of a 50 cm spatial resolution orthophoto map and a 5 m pixel size DSM, whereas the second dataset consists of an orthophoto and a DSM of 4 cm spatial resolution. ArcMap 10.8 was used to display and analyze the two datasets. Subsequently, fieldwork was conducted to examine the characteristic features of the stepped landforms, and 35 surface sediment samples were collected from the different step-like scarps across the southern margins of the polje and processed for micropalaeontological analysis.

Results

The results reveal that the step-like scarps in the landscape consist of alternating coarse-grained gravel material and fine-grained material rich in gravel containing lacustrine taxa, which were deposited in a nearshore environment (Groumpou et al., 2023). A pattern of at least four such alternating sediment deposits has been mapped from the orthophoto maps, corresponding to distinct palaeoshorelines (Figure 2). These deposits contain a micropalaeontological assemblage comprising charophyte remains (gyrogonites and oospores), ostracods and gastropods. The most representative taxa of the identified micropalaeontological assemblage are *Nitellopsis obtusa* (Desvaux) Groves, 1919, *Sphaerochara prolifera* (Ziz. Ex. A. Braun) emend. Soulié-Märsche, 1989, *Chara vulgaris* Linnaeus, 1753, *Ilyocypris bradyi* Sars, 1890, *Ilyocypris inermis* Kaufmann, 1900, and *Candona neglecta* Sars, 1887 (Figure 3). Based on the ecological preferences of these taxa and their geographical distribution along the southern margins of the polje, three distinct lacustrine palaeoenvironments are identified: i) ephemeral lake (possibly annual) dominated by *S. prolifera* which is present up to an altitude of 710 m ii) cold and oligotrophic lake environment characterized by

the presence of *N. obtusa* and *I. inermis*, observed up to an altitude of 729 m and iii) warmer and mesotrophic lake, extending to altitudes of up to 744 m.

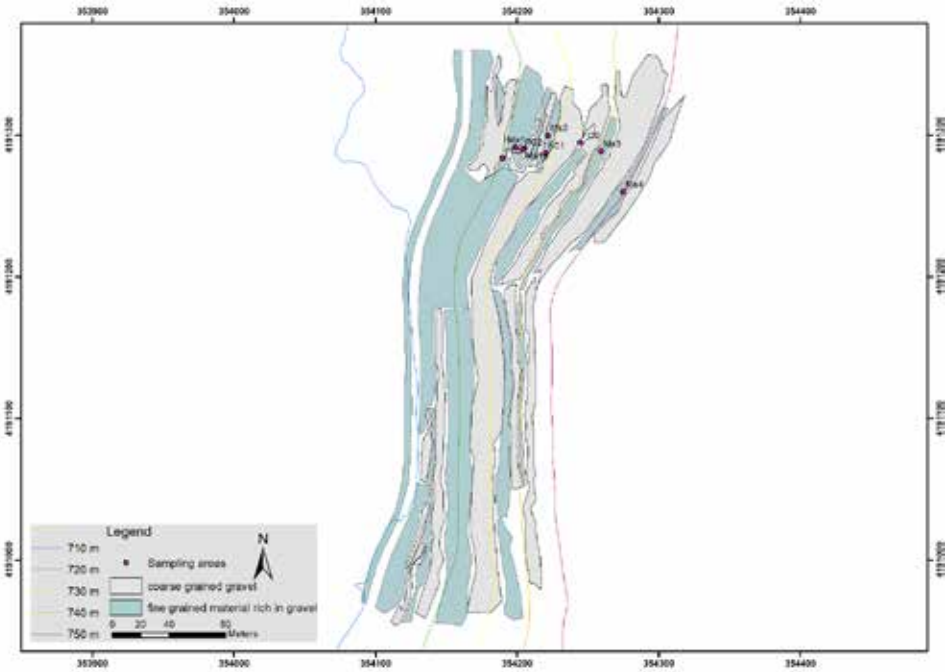

Figure 2. The mapped alternations of the studied sediment material, highlighting distinct palaeoshorelines on the southeastern part of Pheneos polje.

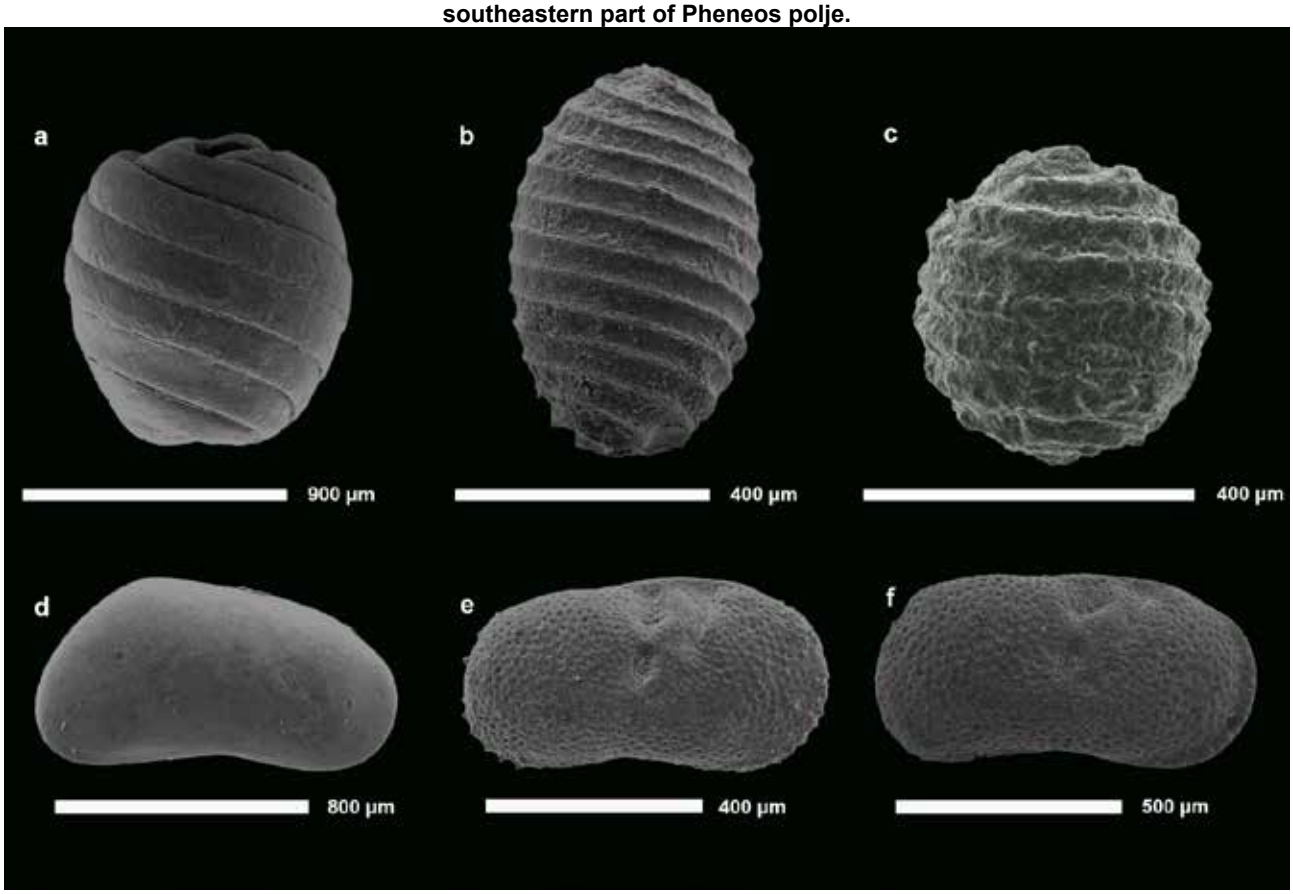

Figure 3. The most representative taxa of the identified micropalaeontological assemblage: a) *Nitellopsis obtusa*, b) *Chara vulgaris*, c) *Sphaerochara prolifera*, d) *Candona neglecta* e) *Ilyocypris bradyi* and f) *Ilyocypris inermis*.

Conclusions

The analysis of the stepped landscape in the southern margins of Pheneos polje revealed a sequence of at least four alternating sedimentary deposits, enriched with lacustrine taxa and which are indicative of near-shore depositional environments. The possible boundaries of Pheneos palaeolake are mapped and three distinct lacustrine palaeoenvironments were recognized based on the ecological preferences of the respective taxa (Groumpou et al., 2023). These findings provide insights into the Holocene dynamics and depositional history of the Pheneos polje.

Acknowledgements

The authors would like to thank: Dr. Carles Martín-Closas who kindly helped us to study the material in the Department of Earth and Ocean Dynamics (Faculty of Earth Sciences, Universitat de Barcelona), Dr. Alejandro Gallardo (technician of the Palaeontology laboratory, Department of Earth and Ocean Dynamics, Faculty of Earth Sciences, Universitat de Barcelona) for sharing his knowledge on how to process the samples and Dr.Vayia Xanthopoulou (technician of the Laboratory of Electron Microscopy and Microanalysis, University of Patras, Greece) for her help during the SEM sessions. We would also like to thank the following projects: Multimeter monitoring platform with micro-sensors of enceladus hellenic supersite, code: (ΦΚ/MIS) 81383/5070928; the European IBERINSULA, code: PID2020-113912GB-100/AEI/10.13039/ 501100011033 of the Spanish Research Agency (AEI) and the European Regional Development Fund (ERDF); and “Geologia Sedimentaria” (2022 SGR 00349) of the AGAUR (Catalan Autonomous Government).

References

Jones, W. H.S., 1988. Pausanias, Description of Greece, Books VIII.22-X (translated by W. H.S. Jones). Harvard University Press, Cambridge MA.

Tsoflias, P., 1973. Geology and Geomorphology of mount Helmos and in the area of Loussi of Kalavrita county (Northern Peloponissos). (in Greek) Digital Library “Theofrastos”, Aristoteleion University of Thessaloniki, Department of Geology. 23-25 p.

Groumpou, M., 2024. Tectonic geomorphology and palaeoenvironments of north Peloponnese, Greece: the Pheneos polje case study. Ph.D. Thesis, University of Patras, Patras, 171 p.

Groumpou, M., Sanjuan, J., Koukouvelas, I., Nikolakopoulos, K., Iliopoulos, G., 2023. Review of Palaeobotany and Palynology 318, 104973.

17th INTERNATIONAL CONGRESS of the Geological Society of Greece

BULLETIN OF THE GEOLOGICAL SOCIETY OF GREECE, SP. PUBL.

EXTENDED ABSTRACT 108

Estimation of soil vulnerability index in the metropolitan area of Thessaloniki (Greece)

Grylionaki M.[1], Theodoulidis N.[2], Panou A.[1], Chatzidimitriou P.[1]

(1) Department of Geophysics, Department of Geology, Aristotle University Thessaloniki, Thessaloniki, Greece

mariagrilionaki@gmail.com

(2) Institute of Engineering Seismology and Earthquake Engineering (ITSAK), Thessaloniki, Greece

This paper presents an effort to assess the liquefaction potential across the Thessaloniki metropolitan area by calculating the Soil Vulnerability Index (SVI or Kg) for the surface geological formations and comparing the results with those of previous research. The SVI is associated with shear strain (γ) imposed on surface geological layers and has been effectively correlated with building damage and soil failures, such as liquefaction. To determine the dynamic properties of surface formations, including fundamental frequency (fo) and corresponding amplitude (Ao), the Horizontal-to-Vertical Spectral Ratio (HVSR) method of microtremor measurements was used. A total of 190 microtremor measurements were analyzed, revealing a good correlation between the SVI and liquefaction potential based on previous studies. High SVI values, indicative of increased liquefaction potential, are linked to low fundamental frequencies, high amplitudes, and are predominantly found in areas near the coast, where thick coastal soft deposits and riverbeds are prevalent. Additionally, strain (γ) values, which are related to SVI, were calculated for various peak ground acceleration scenarios and seismic basement velocities (Vb) specific to Thessaloniki. The results, represented in spatially interpolated maps generated via Geographic Information System (QGIS), align quite well with previous liquefaction potential studies conducted throughout the city using different estimation methods. This agreement encourages the use of microtremor measurements, directly linking them to liquefaction potential by employing the methodology utilized in the current study, in other regions as well.

17th INTERNATIONAL CONGRESS of the Geological Society of Greece

BULLETIN OF THE GEOLOGICAL SOCIETY OF GREECE, SP. PUBL.

EXTENDED ABSTRACT 109

Seismotectonics of the NE Aegean region: The Lesvos Island and the Gulf of Edremit

Levent Gülen
Sakarya University, Serdivan, Sakarya, Türkiye, lgulen@sakarya.edu.tr

Introduction:

Active tectonics of the Aegean is mainly influenced by the interactions of the North Anatolian Fault (NAF) branches, that extend into the Aegean Sea, the counter clockwise rotation and westward extrusion of the Anatolian block, the Hellenic Trench retreat, and the left-lateral strike-slip Pliny-Strabo Shear Zone (PSSZ), that extends towards the Isparta Angle (IA), (Dewey & Şengör, 1979; Taymaz et.al., 1991; Yılmaz & Gürer, 2013). The right-lateral strike-slip NAF gradually gains an additional normal component to the west of 31° E and its branches form the North Aegean Trough (NAT) and Skyros-Edremit Trough (SET) in the North Aegean Sea (Figure-1).

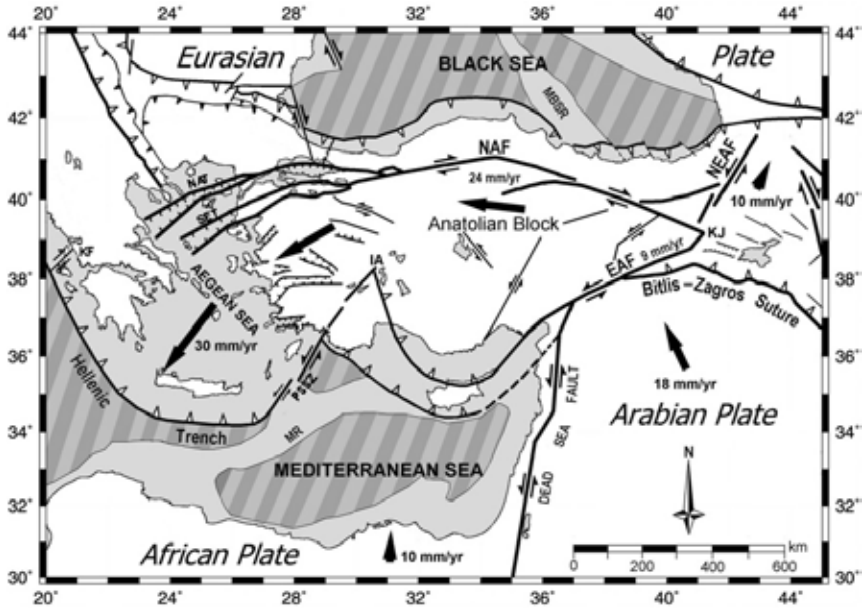

Figure 1. Simplified tectonic map of Turkey and surrounding regions (modified after Gülen et al, 2002).

The Aegean region is one of the rapidly deforming and seismically most active regions of the world as evidenced by historical and instrumental period earthquakes. More than 16 earthquakes with M > 6.5 have occurred since the mid-19th century in the North Aegean Region (Papadopoulos et al., 2002; Ganas et al., 2014). More than 32 major historical earthquakes have occurred just in the Lesvos Island and the Gulf of Edremit area and 22 of them occurred in 1800's (Ambraseys & Jackson, 2000; Ambraseys, 2002; Ambraseys, 2009). The historical earthquakes define an elongate zone extending in NW-SE direction that is parallel to the NE coastline of the Lesvos Island, which may indicate the presence of an unmapped major fault that is orthogonal to the Aghia Paraskevi Fault that traverses the island in NE-SW direction (Figures-2 & 3). The magnitudes of historical Lesvos earthquakes of 1739, 1809, and 1867 were determined as 6.8, 6.6, and 7.0, respectively (Karakaisis et al., 2010). The 1867 Lesvos earthquake was the most destructive among the historical earthquakes. The Oct. 26, 1889 earthquake was also a major earthquake that occurred in the western part of the Gulf of Edremit. This earthquake did not only totally ruin many towns in Lesvos, but also felt strongly as far as Çanakkale in the north and the Rhodes Island in the south (Ambraseys, 2009).
The instrumental period, 6 October, 1944 Gulf of Edremit Earthquake with M_w=6.7 occurred on the Edremit Fault Zone with a normal fault mechanism solution. This earthquake created a minor tsunami with a maximum inundation distance of 170 m. in the town of Ayvalık, on the Turkish coast (Altınok et al., 2012-a; Altınok et al., 2012-b; Sözbilir et al., 2016; Figure-2). Recently the 8 January, 2013 Lemnos Earthquake with M_w=5.7 (Kiratzi & Svigkas, 2013; Kürçer

et. al., 2013; Ganas et al., 2014); the 6 February-20 March, 2017 Gülpınar Earthquake Sequence (Gülen & Yalçın, 2017; Poyraz et al., 2017, Utkucu et al., 2017; Özden et al., 2017; Sözbilir et al., 2018; Ganas et al., 2018; Bekler et al., 2019; Koçyiğit & Gürboğa, 2021), and the 12 June, 2017 Lesvos - Karaburun Earthquake with M_w=6.3 (Kiratzi, 2018; Papadimitriou et al., 2018; Chousianitis & Konca, 2018; Utkucu et al., 2021) occurred in this region (Figure-3). The centroid moment tensor solutions indicate that 2017 Gülpınar, and 2017 Lesvos Earthquakes were caused by normal faulting, whereas the 2013 Lemnos Earthquake was caused by strike-slip faulting (Figure-3). More recently another earthquake sequence had started on 7 January, 2023 with an earthquake of M_w = 5.0 and continued with an earthquake of M_w=5 on 10 January, 2023, both located next to each other on the north coast of the Lesvos Island (Figures-3 and 6).

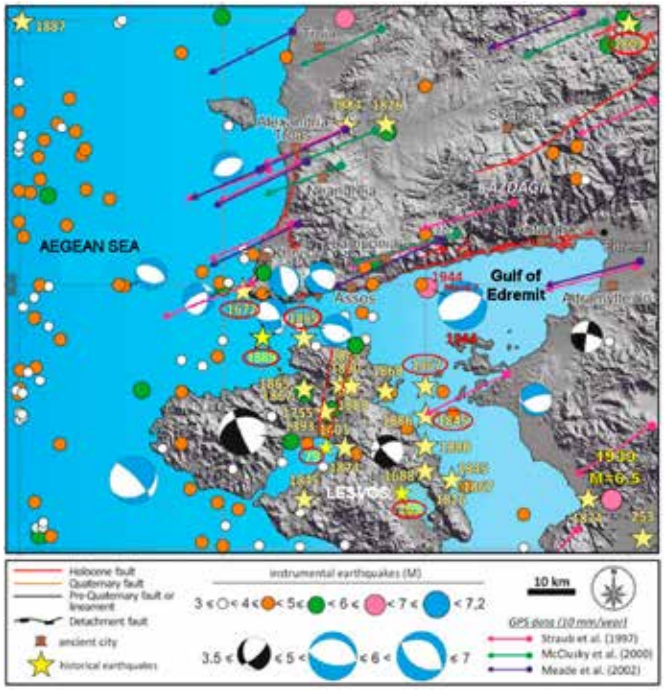

Figure 2. Seismicity map of the Lesvos Island and vicinity until 2017 (modified after Sözbilir et al., 2016).

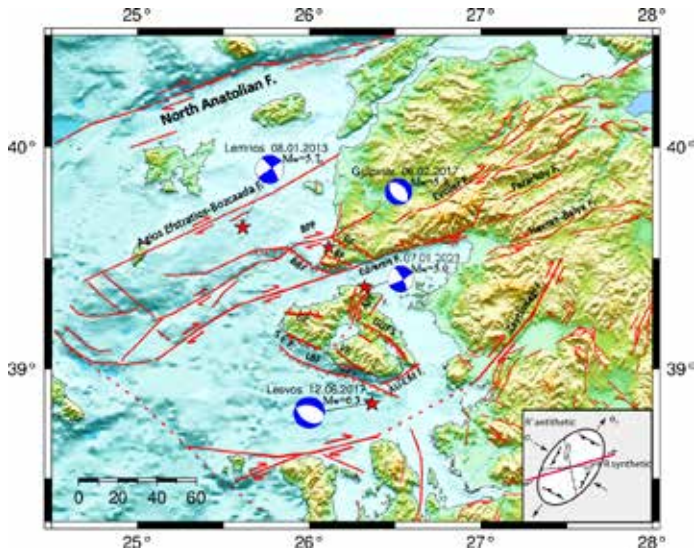

Figure-3. Map of recent earthquakes with $M_w \geq 5.0$ that occurred in the Lesvos Island and the Gulf of Edremit region.

The 6 February-24 March 2017 Gülpınar (Ayvacık, Çanakkale) Earthquake Sequence

An earthquake with moderate magnitude M_w=5.3 occurred on 6 Feb., 2017, at 03:51 (UTC) in the Gülpınar (Ayvacık, Çanakkale) region at a depth of 6 km (Poyraz et al., 2017). A second event with M_w=5.1 on the same day at 10:58; a third event with M_w=5.3 on 7 Feb., 2017, at 2:24; and a fourth event with Mw=5.2 on Feb., 12, 2017 at 13:48 were occurred. 26 aftershocks with M_w=4-5, and more than 2000 aftershocks with M≥2.0 occurred in this region between February 6 – March 24, 2017. These earthquakes occurred where there is a normal fault system (Gülpınar-Tuzla, Balabanlı, and Babakale Faults), which have been mapped by field studies (Yılmaz and Karacık, 2001; Sözbilir et al., 2018; Koçyiğit & Gürboğa, 2021). A panoramic photo taken looking in the NW direction shows the textbook example of stair steps like normal fault system in the Gülpınar-Tuzla area (Figure-4). Epicenters of these earthquakes plot in an elongate zone that strikes in the NW-SE direction (Figure-5). The moment tensor solutions of the main shock and a great majority of the aftershocks indicate normal faulting mechanism with NW-SE fault strike (Poyraz et al, 2017; Gülen & Yalçın, 2017; Bekler et al, 2019). The hypocenter depths of the aftershocks are in the range of 5-20 km and the distribution of aftershock hypocenters define normal faulting with a listric fault geometry that dips to SW (Figure-6).

Figure-4. A panoramic photo showing the normal faults in the Gülpınar-Tuzla area (looking towards the NW direction).

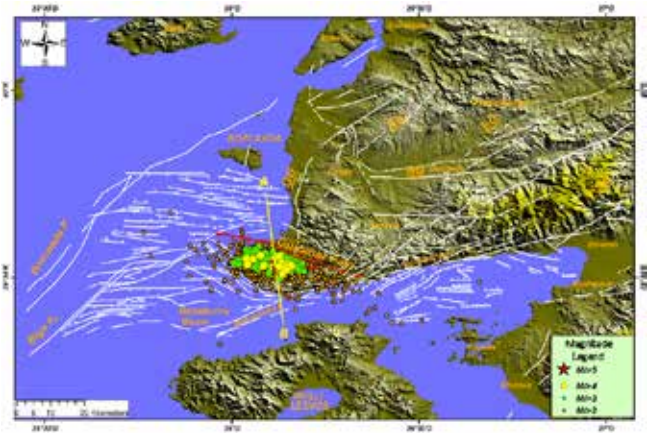

Figure-5.Seismic activity map of the the 6.02-24.3, 2017 Gülpınar Earthquake sequence (modified after Yaltırak et al., 2012).

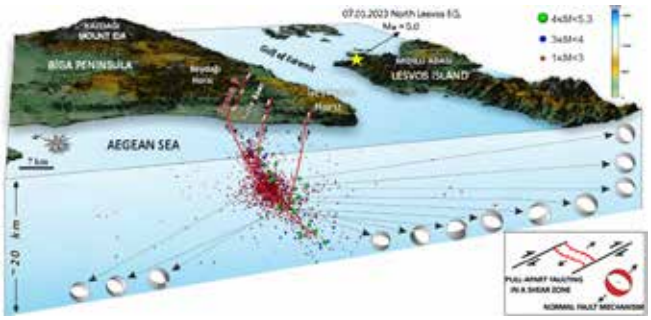

Figure-6. Block diagram of the 6 February- 2017 Gülpınar Earthquake sequence activity (modified after Sözbilir et al, 2018).

The January 7-10, 2023 North Lesvos Earthquake Sequence

An earthquake of moderate magnitude M_w=5.0 occurred on January 7, 2023, at 01:52:57 (GMT) at a depth of 6 km. along the northern coast of the Lesvos Island (Kartal and Kadirioğlu, 2023). The location of this earthquake is shown with a yellow star in Figure-6. On the same day an aftershock of M_w=4.7 occurred at 06:39:30. As of January 7, 2023, nearly one thousand earthquakes with magnitudes; varying between 0.8-5.0 have been recorded by the Disaster and Emergency Management Presidency of Türkiye. On January 10, 2023 another M_w=5 earthquake occurred in the same area. The aftershocks occurred at a depth range of 5-20 km with almost vertical geometry. The epicentral distribution of the aftershocks define an elongate zone extending in the NE-SW direction. Thus, centroid moment tensor solutions of 7 events with $M_w \geq 4.0$ indicate that these earthquakes were caused by a right-lateral strike-slip fault with an average strike of N60°E. The right-lateral strike-slip Aghia Paraskevi Fault is the most prominent tectonic feature on the Lesvos Island and it cuts the central part of the island coast to coast and it was the source fault of the historical 1867 destructive earthquake (Chatzipetros, et al., 2013).. The Aghia Paraskevi Fault has 5 fault segments and the southern 4 of these segments have NNE-SSW strikes (Chatzipetros, et al., 2013). Only the northernmost Sykamia segment has NE-SW strike and the January 7-10, 2023 earthquakes may be associated with the Sykamia segment of the Aghia Paraskevi Fault (Kartal and Kadirioğlu, 2023).

Conclusions

The active tectonics of the NE Aegean region can be explained by the mega-horse-tail geometry of the right-lateral strike-slip North Anatolian Fault's branches and other faults that extend with NE-SW strikes from the mainland Türkiye into the Aegean Sea. The historical and instrumental period seismicity, bathymetry, seismic reflection profiles, field studies, GPS measurements clearly corroborate this conclusion. The insets given in Figures 3 and 6 provide the simplest explanation for the active tectonics of the northern Aegean, which exhibits a NE-SW extensional tectonic regime. In the inset of Figure-3 the strain ellipsoid for a right-lateral strike-slip fault is shown with the positions of σ_1 and σ_3 principle stress axis', as well as the R and R' orientations. Similarly, the inset of Figure-5 also shows how extension takes place in a right-lateral strike-slip shear zone. The fault map given in Figure-5 shows the development of NW-SE trending normal faulting within a NE-SW trending right-lateral strike-slip shear zone that is perfectly consistent with the simple strain ellipsoid and pull-apart faulting explanations.

The fundamental cause of the overall Aegean extensional tectonic regime needs an explanation as well. The subduction transform edge propagator faults (STEP faults or simply tear faults) of the Kefalonia and the Pliny-Strabo Shear zones on both sides of the Hellenic Trench (Özbakır et al., 2023; 2020), as well as the North Anatolian Fault facilitates the Aegean continental lithosphere thrust over the subducting slab (remnant of the Neo-Tethys) causing trench retreat. The trench retreat and the associated mantle flow in that direction causes stretching of the ductile lower crust, which in turn creates an extensional tectonic regime in the brittle upper crust, thus thinning and expanding the surface area of the Aegean continental crust (Gülen, 1990). Supporting evidences for these conclusions were obtained by mantle seismic anisotrophy and seismic tomography studies recently (Jolivet, et al., 2009; Rappisi et al, 2024). In summary, the fundamental cause of the Aegean extension is the drag forces exerted by mantle flow to the Aegean continental lithosphere (Gülen, 1989; 1990).

Acknowledgements

I thank Prof. Athanassios Ganas, Director of the Geological Society of Greece for inviting me to attend the 17th International Congress of the Geological Society of Greece. I thank Yavuz Güneş of Kandilli Observatory and Earthquake Research Institute for generating the base map of Figure-3.

References

Altınok, Y., Alpar, B., Yaltırak, C., and Özer, N., 2012-a. Macroseismic evaluation of the Gulf of Edremit-Ayvacık earthquake, 6 October 1944, İstanbul Yerbilimleri Dergisi, 25, 41-53. **[Journal Article]**

Altınok, Y., Alpar, B., Yaltırak, C., Pınar, A., and Özer, N., 2012-b. The earthquakes and related tsunamis of October 6, 1944 and March 7, 1867; NE Aegean Sea, Nat. Hazards, 60, 3–25. https://doi.org/10.1007/s11069-011-9949-7 **[Journal Article]**

Ambraseys, N., 2002. The seismic activity of the Marmara Sea Region over the last 2000 years. Bull. Seism. Soc. Am., 92,

1-18. **[Journal Article]**

Ambraseys, N., 2009. Earthquakes in the Mediterranean and Middle East: A multidisciplinary study of seismicity up to 1900. Cambridge Univ. Press, 947p. **[Book]**

Ambraseys, N., & Jackson, J., 1998. Faulting associated with historical and recent earthquakes in the Eastern Mediterranean region, Geophys, J. Int. 133, 390–406. **[Journal Article]**

Bekler, T., Demirci, A., and Özden, S., 2019. Biga yarımadası güncel depremleri ve faylanma karakterleri ve sismotektonik değerlendirmesi, 5th International Conference on Earthquake Engineering & Seismology, 8-11 October, 2019, METU, Ankara, Türkiye. **[Conference Proceedings]**

Chatzipetros, A., Kiratzi, A., Sboras, S., Zouros, N., Pavlides, S., 2013. Active faulting in the north-eastern Aegean Sea Islands. Tectonophysics. Vol. 597-598, P.106-122. http://dx.doi.org/10.1016/j.tecto.2012.11.026 **[Journal Article]**

Chousianitis, A. and Konca, A.Ö., 2018. Coseismic slip distribution of the 12 June 2017 Mw = 6.3 Lesvos earthquake and imparted static stress changes to the neighboring crust. Journal of Geophysical Research: Solid Earth, 123, 8926–8936. https://doi.org/10.1029/2018JB015950 **[Journal Article]**

Dewey, J.F.and Sengör, A.M.C., 1979. Aegean and surrounding regions: complex multiple and continuum tectonics in a convergent zone, Geol. Soc. Am. Bull., 90**,** 84–92. **[Journal Article]**

Emre, Ö., Duman, T. Y., Özalp, S., Elmacı, H., Olgun, Ş., & Şaroğlu, F., 2013. Active fault map of Turkey with explanatory text. Ankara: General Directorate of Mineral Research and Exploration, Special Publication Series-30. **[Book]**

Ganas A., Oikonomou,I.A., and Tsimi, C., 2013. NOAFAULTS: A Digital database for active faults in Greece, Bulletin of the Geological Society of Greece, vol. XLVII, Proceedings of the 13th International Congress, Chania, Sept.2013. **[Conference Proceedings]**

Ganas, A., Roumelioti, Z., Karastathis, V., Chousianitis, K., Moshou, A., and Mouzakiotis, E., 2014. The Lemnos 8 January 2013 (Mw=5.7) earthquake: fault slip, aftershock properties and static stress transfer modeling in the north Aegean Sea, J. Seismol., https://doi.org/10.1007/s10950-014-9418-3 **[Journal Article]**

Ganas, A., Kourkouli, P., Briole, P., Moshou, A., Elias, P., and Parcharidis, I., 2018. Coseismic Displacements from Moderate-Size Earthquakes Mapped by Sentinel-1 Differential Interferometry: The Case of February 2017 Gulpinar Earthquake Sequence (Biga Peninsula, Turkey), Remote Sens., 10, 1089, https://doi.org/10.3390/rs10071089 **[Journal Article]**

Gülen, L., 1989. From plate tectonics to global domain tectonics, in Crust/Mantle Recycling at Convergence Zones, S. R. Hart and L. Gülen (Editors), NATO ASI Series, C258, Kluwer Academic Publishers, Boston, 173–179. **[Book]**

Gülen, L., 1990. Isotopic characterization of Aegean magmatism and geodynamic evolution of the Aegean subduction, in Proc. Int. Earth Sci. Cong. on Aegean Regions, M.Y. Savaşcın & A.H. Eronat (Editors), Vol. 2, 143–166. **[Conference Proceedings]**

Gülen, L., Pınar, A., Kalafat, D., Özel, N., Horasan, G., Yılmazer, M., & Işıkara, A.M., 2002. Surface fault breaks, aftershock distribution, and rupture process of the 17 August 1999 İzmit, Turkey earthquake, Bull. Seism. Soc. Am. 92**,** 230–244. **[Journal Article]**

Gülen, L., and Yalçın, H., 2017. February 2017 Ayvacık, Çanakkale Earthquake Swarm:Seismotectonic and morphotectonic constraints, 4. Uluslararası Deprem Mühendisliği ve Sismoloji Konferansı, 11-13 Ekim 2017, Anadolu Üniversitesi, Eskişehir, Türkiye. **[Conference Proceedings]**

Jolivet, L., Faccenna, C., and Piromallo, C., 2009. From mantle to crust: Stretching the Mediterranean, Earth & Planet. Sci. Lett., 285, 198–209. https://doi.org/10.1016/j.epsl.2009.06.017 **[Journal Article]**

Karakaisis, G.F., Papazachos, C.B. and Scordilis, E.M., 2010. Seismic sources and main seismic faults in the Aegean and surrounding area, Proceedings of the 12th International Congress, Patras, May, 2010, Bull. Seism. Soc. Greece. **[Conference Proceedings]**

Kartal, R.F. and Kadirioğlu, F.T., 2023. January 2023 Mytilene Island (North Aegean Sea) Earthquake Activity and Its Relationship with the Tectonics of the region, Proceedings of the 75th Geological Congress of Turkey, April 10-14, 2023, Ankara, Turkey. **[Conference Proceedings]**

Kiratzi, A., 2018. The 12 June 2017 Mw 6.3 Lesvos Island (Aegean Sea) earthquake: Slip model and directivity estimated with finite-fault inversion, Tectonophysics 724–725, 1–10, https://doi.org/10.1016/j.tecto.2018.01.003 **[Journal Article]**

Kiratzi, A. and Svigkas, N., 2013. A study of the 8 January 2013 Mw5.8 earthquake sequence (Lemnos Island, East Aegean Sea), Tectonophysics 608, 452–460. http://dx.doi.org/10.1016/j.tecto.2013.09.002 **[Journal Article]**

Koçyiğit, A. and Gürboğa, Ş., 2021. Active tectonics of Gülpınar-Tuzla area (Biga Peninsula, NW Turkey): the source of 6 February-24 March 2017 earthquake cluster, Bull. Min. Res. Exp. (2021) 166: 85-112. **[Journal Article]**

Kürçer, A., Yalçın, H., Gülen, L., Kalafat, D., 2014. 8 January 2013 Mw = 5.7 North Aegean Sea earthquake and its seismotectonic significance, Geodinamica Acta, https://doi.org/10.1080/09853111.2014.957503 **[Journal Article]**

McClusky, S., et al., 2000. Global Positioning System constraints on plate kinematics and dynamics in the eastern Mediterranean and Caucasus, J. Geophys. Res., 105, 5695– 5719. **[Journal Article]**

Meade B.J., Hager B.H., McClusky, C., Reilinger R.E., et al., 2002. Estimates of seismic potential in the Marmara region from block models of secular deformation constrained by GPS measurements, Bull. Seismol. Soc. Am., 92, 208–215. **[Journal Article]**

Özbakır, A.D., Şengör, A.M.C., Wortel, M.J.R., and Govers, R., 2013. The Pliny–Strabo trench region: A large shear zone resulting from slab tearing, Earth & Planet. Sci. Lett. 375, 188–195. http://dx.doi.org/10.1016/j.epsl.2013.05.025 **[Journal Article]**

Özbakır, A.D., Govers, R., and Fichtner, A., 2020. The Kefalonia Transform Fault: A STEP fault in the making, Tectonophysics, 787, 228471. http://creativecommons.org/licenses/BY/4.0/ **[Journal Article]**

Özden, S., Över, S., Poyraz, S.A., Yavuz Güneş, Y., Pınar, A., 2017. Tectonic implications of the 2017 Ayvacık (Çanakkale) earthquakes, Biga Peninsula, NW Turkey, J. Asian Earth Sci., https://doi.org/10.1016/j.jseaes.2017.12.021 **[Journal Article]**

Papadimitriou, P., Kassaras, I., Kaviris, G., Tselentis, A., Voulgaris, N., Lekkas, E., et al., 2018. The 12th June 2017 Mw=6.3 Lesvos earthquake from detailed seismological observations, Journal of Geodynamics, https://doi.org/10.1016/j.jog.2018.01.009 **[Journal Article]**

Papadopoulos G, Ganas A, Plessa A (2002) The Skyros earthquake (Mw6.5) of 26 July 2001 and precursory seismicity patterns in the North Aegean Sea. Bull Seismol Soc Am 92(30):1141–1145. **[Journal Article]**

Poyraz, S.A., Pınar, A., Kekovalı, K., Güneş, Y., Kalafat, D., et al., 2017. 2017 yılı Ayvacık, Çanakkale deprem aktivitesinin sismotektonik özellikleri, 4. Uluslararası Deprem Mühendisliği ve Sismoloji Konferansı, 11-13 Ekim 2017, Anadolu Üniversitesi, Eskişehir, Türkiye. **[Conference Proceedings]**

Rappisi, F., Bue, R.L., VanderBeek, Confal, J.M., Erman, C., et al., 2024. 3-D Mantle Flow and Structure of the Mediterranean from Combined P-wave and Splitting Intensity Anisotropic Tomography,
https://essopenarchive.org/doi/full/10.22541/essoar.173499076.65970186/v1 **[Journal Article]**

Sözbilir, H., Uzel, B., Sümer, Ö., Eski, S., Softa, M., Tepe, Ç., Özkaymak, Ç., Baba, A., 2018. Çanakkale-Ayvacık deprem fırtınasının (14 Ocak – 20 Mart 2017) sismik kaynakları, Anadolu Üniversitesi Bilim ve Teknoloji Dergisi – B Teorik Bilimler, **6**:1-17. **[Journal Article]**

Sözbilir, H., Sümer, Ö., Özkaymak, Ç., Uzel, B., Güler, T., and Eski, S., 2016. Kinematic analysis and palaeoseismology of the Edremit Fault Zone: evidence for past earthquakes in the southern branch of the North Anatolian Fault Zone, Biga Peninsula, NW Turkey, Geodinamica Acta, 28:4, 273-294, https://doi.org/10.1080/09853111.2016.1175294 **[Journal Article]**

Straub, C., Kahle, H.G., and Schindler, C., 1997. GPS and geologic estimates of the tectonic activity in the Marmara Sea region, J. Geophys. Res., 102, 27587-27601. **[Journal Article]**

Taymaz T., Jackson J. and McKenzie D. 1991. Active tectonics of the north and central Aegean Sea, Geophys. J. Int., 106, 433-490. **[Journal Article]**

Utkucu, M., Budakoğlu, E., Kızılboğa, S., and Yalçın, H., 2017. Şubat 2017 Ayvacık deprem silsilesi geri plan depremsellik analizi, 4. Uluslararası Deprem Mühendisliği ve Sismoloji Konferansı, 11-13 Ekim 2017, Anadolu Üniversitesi, Eskişehir, Türkiye. **[Conference Proceedings]**

Utkucu, M., Nalbant, S.S., Pınar, A., McCloskey, J., Nicbhloscaidh, M., et al., 2021. The June 12, 2017 M6.3 Karaburun-Lesvos earthquake of the Northern Aegean Sea: Aftershock forecasting and stress transfer, Tectonophysics, https://doi.org/10.1016/j.tecto.2021.228945 **[Journal Article]**

Yaltırak, C., İşler, E.B., Aksu, A.E., and Hiscott, R.N., 2012. Evolution of the Bababurnu Basin and shelf of the Biga Peninsula: Western extension of the middle strand of the North Anatolian Fault Zone, Northeast Aegean Sea, Turkey, Journal of Asian Earth Sciences, 57, 103–119. http://dx.doi.org/10.1016/j.jseaes.2012.06.016 **[Journal Article]**

Yılmaz, Y. and Gürer, Ö.F., 2023. Tectonic development of western Anatolian extensional province, International Geology Review, https://doi.org/10.1080/00206814.2023.2209865 **[Journal Article]**

Yılmaz, Y. and Karacık, Z., 2001. Geology of the northern side of the Gulf of Edremit and its tectonic significance for the development of the Aegean grabens, Geodinamica Acta 14, 31- 43. **[Journal Article]**

17th INTERNATIONAL CONGRESS of the Geological Society of Greece

BULLETIN OF THE GEOLOGICAL SOCIETY OF GREECE, SP. PUBL.

EXTENDED ABSTRACT 110

The rocks connect us: Volcanic geoheritage of Lesvos Geopark (Greece) and Ida Madra Geopark (Türkiye)

Erdal Gumus[1], Nikolas Zouros[2]
(1) Balikesir University, Balikesir, Türkiye, erdalgumus08@gmail.com, (2) Aegean University, Mytilene, Greece

Introduction

Both Lesvos UNESCO Global Geopark, (Greece) and Ida Madra Geopark (Türkiye) include a variety of geological heritage sites of international significance and are characterized by rich geodiversity. The majority of the geological heritage sites present in the respective territories are related to volcanism, with the 72% of the geosites in Lesvos Geopark and 62% of the geosites in Ida Madra Geopark found on igneous rocks. Highlighting the shared and complementary geohistorical context of neighboring geoparks can enhance the interpretation, conservation, and promotion of geoheritage in a holistic manner and cooperation between territories.

The Aegean region is among the most tectonically active regions on Earth due to the subduction of the African plate beneath the Eurasian plate and the westward extension of the Anatolian microplate. Consequently, the region saw extensive extrusive and intrusive volcanism during the Miocene period (Bozkurt et al. 2005, Innocenti et al. 2009). The vigorous volcanic activity created complex volcanic formations. The geosites of Lesvos Geopark (Greece) and Ida Madra Geopark (Türkiye) are closely associated with Miocene volcanism and tectonics.

A Geopark might be likened to a chapter in a novel; it may be coherent independently but remains incomplete without the additional chapters that contribute to the overarching narrative. In this regard, the coinciding and complementary geosites of the Lesvos Geopark and Ida Madra Geopark may offer a more comprehensive perspective for both. Both Geoparks belong geologically to the Sakarya - Pelagonia massif (Figure 1).

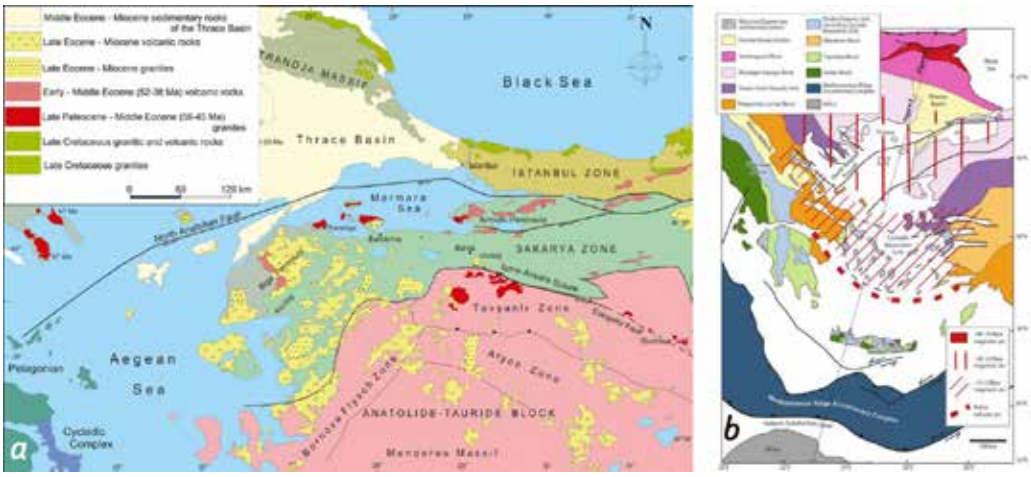

Figure 1. Simplified tectonic map of the North Aegean (a) (Okay et al., 2022) Aegean region (b), (Vouduris, 2018)

The Lesvos Geopark was founded in 2000 as one of the four primary partners of the European Geoparks Network. It is founding member of the Global Geoparks Network since 2004 and recognized as a UNESCO Global Geoparks in 2015. The Lesvos Geopark is distinguished by its exceptional abundance of fossilized trees and volcanic terrains. (Zouros *et al.*, 2003, 2004, 2009, 2010)

The Ida Madra Geopark was established in 2019 and designated as a UNESCO candidate in 2022 (Gumus et al., 2021). The Ida Madra Geopark features the prominent Mt. Ida, composed of metamorphic rocks, alongside Mt. Madra, recognized for its Kozak granitoid (Gumus, 2022).

The two nearby geoparks are close enough to share a common geotectonic setting (Figure 2).

Figure 2. Location map of the Lesvos Geopark (Greece and the Ida Madra Geopark (Türkiye)

Objectives

This study intends to demonstrate how rocks and their geohistorical background can play an important role in bringing together neighboring and geologically interconnected territories. Their geological background can be the basis for the development of common research, educational and geo-touristic activities and provide a stable bridge for collaboration, common activities and cultural exchange.

This study is based on the classification, comparison, and interpretation of the volcanic geosites of the neighboring Lesvos Geopark and Ida Madra Geopark in a comprehensive manner.

Findings

Both Lesvos and the Ida Madra Geopark are significantly influenced by volcanism and associated landscapes, with 72% of geosites in Lesvos Geopark and 62% in Ida Madra Geopark located on igneous lithology (Figure 3).

The geosites of volcanic origin exhibit unique features, including diverse volcanic landscapes, intrusions, domes, columnar lava formations, lava flows, pyroclastics, hot springs, waterfalls, fossils, caves, and canyons.

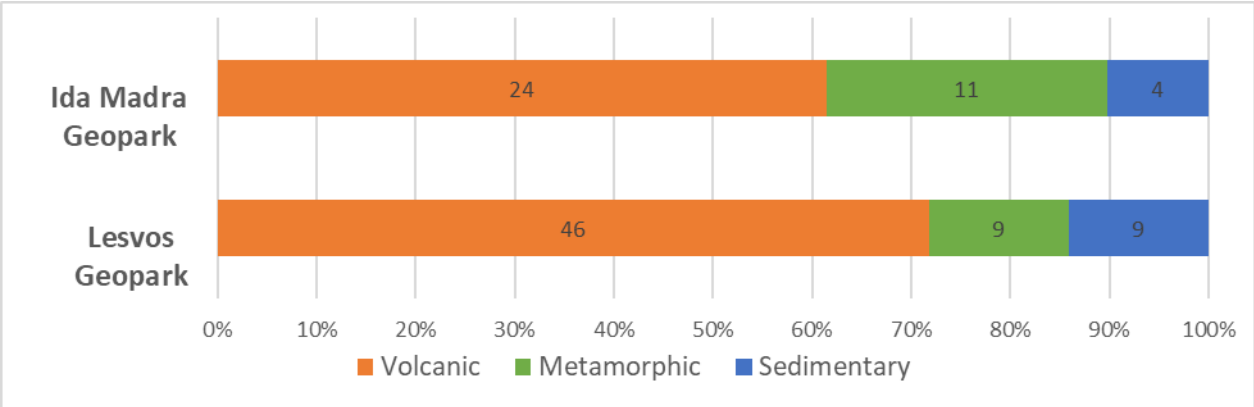

Figure 3. Geosite lithology comparison of Lesvos Geopark and Ida Madra Geopark

The variety of volcanic geosites of both Geopark facilitate a more thorough spatiotemporal interpretation of volcanism in the region. In certain instances, analogous geological processes resulted in comparable

formations, whereas in other cases, they produced distinctly unique appearances. For instance, both geoparks feature characteristic spheroidal exfoliation forms that are nearly identical in size and shape (Figure 4).

Figure 4. Spheroidal exfoliation geosites: Tatlısu geosite /Ida Madra Geopark (a), Vatousa geosite /Lesvos Geopark (b)

The westward extension of the Anatolian microplate dominates the active tectonics that governs both Geoparks. As a result, Miocene volcanics have been affected by major active faults creating impressive fault scarps during Quaternary (Figure 5).
Furthermore, the scientific importance of these geosites is highlighted by their extensive use in geo-education and in enhancing public awareness regarding natural disasters.

Figure 5. Aghia Paraskevi fault scarp geosite/ Lesvos Geopark (a), Pelitköy fault scarp geosite, / Ida Madra Geopark (b)

Conversely, analogous lithologies give rise to entirely distinct geosites and landscapes. For example, the differential weathering of thick ignimbrite deposits along vertical fractures resulted in finger-like columns in Lesvos Geopark, whereas the same lithology, when subjected to a spheroidal fracture pattern, revealed a turtle back-like landscape in Ida Madra Geopark (Figure 6).

Figure 6. Aslanalan geosite/Ida Madra Geopark (a), Candles geosite/Lesvos Geopark (b)

Intrusive volcanics significantly contribute to the geological features of both geoparks. The western section of the Lesvos Geopark features prominent volcanic formations, including the Ipsilou dome, Eressos dome, Mesotopos dome, and Mythimna dome. In contrast, the Ida Madra Geopark is distinguished by its granitic intrusions, exemplified by Mt. Çataldağ and Mt. Madra (Figure 7).

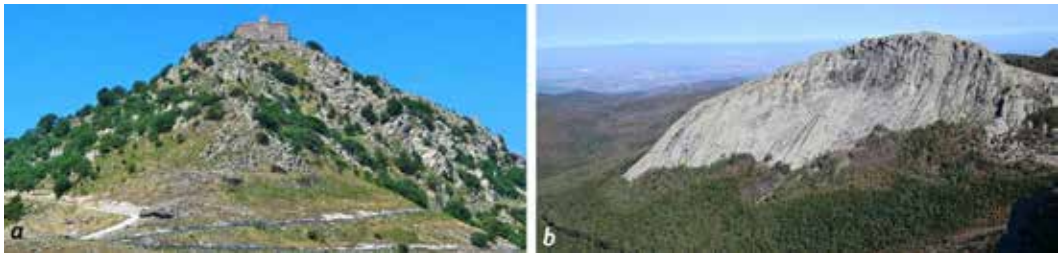

Figure 7. Ipsilou volcanic dome geosite/ Lesvos Geopark (a), Çataldağ granite slab geosite /Ida Madra Geopark (b)

Results and Conclusion

The Miocene volcanism which has significantly shaped both Lesvos Island and the Ida Madra Geopark area, may serve as a geological reference framework frame for cooperation in conservation, education, and research.

This geological continuum hosts inherently related yet fully distinct geosites within both Geoparks. Tracking the geological links between Lesvos Island and Ida Madra Geopark could help to provide a more thorough understanding and interpretation of the region's and Earth's overall geological evolution.

In the last decade, there has been a growing trend in reciprocal visits between Lesvos Island and Balikesir Metropolitan Area, evidenced by the traditional connections between Mytilene and Ayvalik as well as the establishment of new ferry routes and destinations connecting the two territories.

This fact presents significant potential for development of collaborative educational initiatives, including field excursions and Erasmus Exchange programs, as well as geotourism activities like offering inter-geopark tour packages.

References

E. Bozkurt and S. K. Mittwede (2005). Introduction: Evolution of Continental Extensional Tectonics of Western Turkey. Geodinamica Acta 18/3-4: 153–165.

Gumus, E, Soykan, A, Helvacı C, Ulusoy ,İ., (2021) Aspiring Ida Madra Geopark-2021 UNESCO Geoparks Candidate of Turkey. Proceedings of the Digital 9th International Conference on UNESCO Global Geoparks. Juju, South Korea

Gumus, E (2022). Aspiring Ida Madra Geopark. UNESCO Application Dossier

Voudouris, Panagiotis. "A Field Guide on the Geology and Mineralogy of Lavrion, Attica, Greece." (2018).

Innocenti, F., Agostini, S., Tokcaer, M., and Savaşcın, M.E. (2009). Volcanic Rocks from Foça-Karaburun and Ayvalık-Lesvos Grabens (Western Anatolia) and Their Petrogenic-Geodynamic Significance. Turkish Journal of Earth Sciences (Turkish J. Earth Sci.), Vol, 19.

Okay, A. I., Topuz, G., Kylander-Clark, A. R., Sherlock, S., & Zattin, M. (2022). Late Paleocene–Middle Eocene magmatic flare-up in western Anatolia. Lithos, 428, 106816.

Zouros, N., Martini, G., (2003) Introduction to the European Geoparks network. In NHM of Petrified Forest. Proceedings of 2nd International Symposium of Natural Monuments and Geological Heritage, Lesvos (pp. 17-21)

Zouros, N., Fassoulas, Ch., Velitzelos, E., Mountrakis, D., Soulakellis, N., (2005) Monuments geotopes in the aegean islands – Contribution to the protection and promotion of Geological heritage in Greece. 50 Proceedings of the 4th European Geopark's Meeting, 2-5 October

Zouros, N., (2004) European Geoparks Network: geoconservation, promotion, education and local development. Proceedings of the 5th International Symposium on Eastern Mediterranean Geology. Thessaloniki 14-19 April 2004 p. 441-444

Zouros, N., (2009) The petrified forest of Lesvos – a unique natural monument. In: N. Evelpidou, T. De Figueiredo, F. Mauro, V. Tecim, A. Vasilopoulos, (ed.) Natural Heritage monuments – Europe from West to East. Springer Verlag Berlin Heidelberg 2010 p. 15-26

Zouros, N., (2010) Lesvos Petrified Forest Geopark, Greece: geoconservation, geotourism, and local development. In The George Wright Forum Journal (Vol. 27, No. 1, pp. 19-28)

17th INTERNATIONAL CONGRESS of the Geological Society of Greece

BULLETIN OF THE GEOLOGICAL SOCIETY OF GREECE, SP. PUBL.

EXTENDED ABSTRACT 111

Assessing Climate Change Impacts on Troodos Mountain (Troodos UNESCO Global Geopark area) Through Methodological Approaches and Community Engagement in the ClimEmpower Project

Petros Hadjicostas [1], Evi Kazamia [1], Georgios Xekalakis [2], Christos Anastasiou [2], Petros Christou [2, 3]

[1] *Troodos Development Company LTD, Troodos, Cyprus*
[2] *Department of Civil Engineering, School of Engineering, Frederick University, 1036 Nicosia, Cyprus*
[3] *Faculty of Civil Engineering and Architecture, Kaunas University of Technology, 44249 Kaunas, Lithuania*
**Correspondence: info@anetroodos.com*

Abstract

The Troodos Mountain region, including the Troodos UNESCO Global Geopark, is increasingly vulnerable to the impacts of climate change, facing both environmental degradation and socio-political challenges. Within the ClimEmpower project, we apply an integrated methodological framework combining climate modeling, geospatial analysis, and community engagement to assess these effects. Climate projections are based on downscaled outputs from the EURO-CORDEX initiative (RCMs under RCP4.5 and RCP8.5 scenarios), while trends in temperature and precipitation are quantified using 25 years of daily data from local meteorological stations. Geospatial analysis utilizes shapefiles of the study area and climate-related indicators to produce climate risk maps. These maps integrate environmental datasets with socio-economic vulnerability information gathered through Community of Practice (CoP) meetings. The CoP sessions also offer critical insights into local experiences, resource management challenges, and governance gaps faced by residents. Preliminary results indicate rising temperatures and declining precipitation patterns, correlating with increased drought stress, wildfire risks, and biodiversity shifts within the region. This participatory, data-driven approach underscores the need for adaptive and inclusive governance strategies tailored to the specific vulnerabilities of mountain communities. Our findings contribute to evidence-based policymaking aimed at enhancing regional resilience to climate change.

Acknowledgements

The ClimEmpower project has received funding from the EU under Grant Agreement ID: 101112728.

References

Georgios Xekalakis, Lopez, P.M., Ruiz, M.A., Tötzer, T., Kaleta, P., Konstantinos Karystinakis, Moumtzidou, A., Forjan, R., Christou, P., Anastasiou, C., Pavone, V., Gigliola D'Angelo, Cobos, F.S., Bügelmayer-Blaschek, M., Socrates Boutsis, Marija Vurnek, Murano, I., Prete, P.D., Kutschera, P. and Dimitrios Leonidis (2024). User-Driven Climate Resilience Across Southern European Regions. Climate, [online] 13(1), pp.2–2. doi: https://doi.org/10.3390/cli13010002.

Xekalakis, G., Anastasiou, C., Bügelmayer-Blaschek, M., Molina López, P., Gamallo-Paz, I., Tötzer, T., Pavone, V., Kazamia, E., Christou, P., & Havlik, D. (2025). BUILDING CLIMATE RESILIENCE IN MOUNTAIN REGIONS. Eleventh International Conference on Remote Sensing and Geoinformation of Environment (RSCy25), Paphos, Cyprus. Eleventh International Conference on Remote Sensing and Geoinformation of Environment. https://doi.org/10.5281/zenodo.15058105

Climempower.eu. ABOUT—ClimEMPOWER. 2023. Available online: https://climempower.eu/about/ (accessed on 9 January 2025).

Tötzer, T., Bügelmayer-Blaschek, M., Hochebner, A., Kozlowska, A., Schneider, M., Chatzichristaki, C., Molina Lopez, P., Murano, I., Xekalakis, G., and Havlik, D.: Climate change resilience in South-European regions: data, services, indicators and gaps, EGU General Assembly 2025, Vienna, Austria, 27 Apr–2 May 2025, EGU25-9170, https://doi.org/10.5194/egusphere-egu25-9170, 2025.

17th INTERNATIONAL CONGRESS of the Geological Society of Greece

BULLETIN OF THE GEOLOGICAL SOCIETY OF GREECE, SP. PUBL.

EXTENDED ABSTRACT 112

Geoconservation in Portugal: an overview

Henriques M.H.[1], Custódio S.[1], Carvalho I.S.[1,2]

(1) Geosciences Centre, Department of Earth Sciences, Faculty of Sciences and Technology, University of Coimbra (Polo II), Rua Sílvio Lima 3030-790, Coimbra, Portugal, hhenriq@dct.uc.pt (2) Department of Geology, Federal University of Rio de Janeiro, Cidade Universitária - Ilha do Fundão, CCMN/IGEO 21.949-900, Rio de Janeiro, Brazil

Introduction

Geoheritage and geotourism help to promote inclusive and sustainable economic growth, full and productive employment and decent work for all, in line with the Sustainable Development Goals of the 2030 Agenda (Gill, 2017). This is a particularly important issue for peri-Mediterranean countries, whose economy is heavily dependent on tourism, mostly seasonal and concentrated on beaches. Tourism in Portugal reached historic highs last year and contributed to around half of the real growth in Gross Domestic Product (GDP), generating a direct and indirect contribution of 33.8 billion euros to GDP in 2023, which corresponds to 12.7% (INE, 2023). Diversifying the tourism offer and creating products in low-density territories represents a challenge for consolidating the country's tourism industry and making it compatible with sustainable development goals.

Protecting and valuing the geological heritage of Portugal is an important asset in promoting sustainable, non-seasonal tourism which is reflected in the well-being of the residents. It is up to the political authorities to implement public policies that guarantee the effective geoconservation of these territories, and for other sectors of society to become more involved in safeguarding their geoheritage.

There is no specific legislation on geoconservation in Portugal. The national law to protect natural areas (Decree-Law nº19/93 of 23rd July) defines several different categories created mainly for biological purposes with only one category remaining to include sites of geological interest that deserve to have their physical integrity safeguarded (Henriques, 2004). As so, the geological heritage of Portugal is protected at national level through Natural Monuments, which are part of the National Network of Protected Areas (Table 1). These are defined as natural occurrences containing one or more aspects which, due to their uniqueness, rarity or representativeness in ecological, aesthetic, scientific and cultural terms, require their conservation and the maintenance of their integrity (ICNF, 2025).

Table 1. Natural Monuments of Portugal that are part of the National Network of Protected Areas.

Name	Characterization	Classification date	Level
Pegadas de Dinossáurios de Ourém/Torres Novas	The largest Middle Jurassic (Bajocian-Bathonian) sauropod trackside (147 meters long) known in the world.	1996	National
Carenque	One of the largest and earliest (Lower Cretaceous) known continuous dinosaur tracks (127 meters long) produced by two herbivorous quadrupeds and possibly bipedal carnivores.	1997	National
Lagosteiros	High quality Upper Jurassic dinosaur tracks.	1997	National
Pedra da Mua	Trails of Tithonian age that record the first evidence of gregarious behavior among sauropods recognized in Europe.	1997	National
Pedreira do Avelino	The prints of the smallest sauropod known in Europe of Kimmeridgian age.	1997	National
Cabo Mondego	Jurassic record including the Bajocian GSSP and the Bathonian ASSP.	2007	National
Portas do Ródão	An imposing gorge carved out by the River Tagus in the quartzite ridges of the Perdigão mountain range, with a 45 meters wide bottleneck.	2009	National
Canhão Cársico de Ota	One of the most interesting "canyon" valleys in the Portuguese karst regions, with almost vertical escarpments carved into the Upper Jurassic limestones.	2019	Local
Livraria do Mondego	Sequence of subverticalized Armorican quartzites, in thick layers with well-defined stratification surfaces, which resemble the arrangement of a set of books on a shelf, and which refers to the name given to the site.	2024	Local

The first classified geological sites in Portugal date back to 1996 and 1997 and refer exclusively to dinosaur tracks, which reflects how dinosaurs captivate humans and are a charismatic component of our contemporary human existence (Yates and Peacock, 2023). The following decade saw the classification of the last two national Natural Monuments, which no longer refer to geological heritage of the paleontological type like the previous ones but can be included in the stratigraphic type (Habibi *et al*., 2018). Among them is the Cabo Mondego Natural Monument, located on the west coast of the country, with a particularly significant record of the Middle and Upper Jurassic (Fig. 1), and which is part of the territory related to the ongoing "Atlantic Geopark Project", aimed at a future application to the Global Geoparks Network (Custódio et al., 2024, 2025 this volume).

Figure 1. The extraordinary Middle Jurassic stratigraphic record of Cabo Mondego Natural Monument, where the Bajocian GSSP (A and B) and the Bathonian ASSP (C) were defined. The Upper Jurassic record includes dinosaur footprints on the surface bedding plane (D and E), as well as convoluting bedding and soft sediment injection structures (E) interpreted as dinoturbation structures (Carvalho *et al*., 2022).

Natural Monuments of national rank are managed by a national, centralized entity, the Institute for Nature Conservation and Forests (ICNF), which belongs to the Ministry of Environment and Energy. The same Ministry runs a database of geological sites located in national territory intended for scientific, technical, and educational purposes, to support nature conservation and land use policies, with free access and constant updates with the collaboration of the geological community (Fig. 2). It includes nearly four hundred geological sites distributed by 26 thematic categories following a methodology adapted to national-level inventories originally defined by ProGEO (the European Association for the Conservation of Geological Heritage) and IUGS (the International Union of Geological Sciences) (Brilha et al., 2005; LNEG, 2025). But the first national inventory of geological heritage, which brings together the main sites in Portugal where elements of geodiversity (minerals, fossils, rocks, geoforms) with high scientific value occur, was the result of a research project that took place between 2007 and 2010 at University of Minho and is available through the ICNF website (Fig. 3; Geossítios, 2025). The two inventories are currently being merged in a strategy to promote geoconservation in Portugal more effectively (Aires et al., 2023).

Despite being classified and formally protected, the Natural Monuments of national rank have not been the subject of valuation and monitoring interventions, procedures that are required in effective geoconservation practices (Henriques *et al.*, 2011). The classification of a natural monument aims to protect natural values, namely notable

occurrences of geological heritage, in the integrity of their characteristics and in the immediate surrounding areas, and the adoption of measures compatible with the objectives of their classification (ICNF, 2025), i.e., the promotion of scientific research, geoeducation and geotourism. The current conditions of the Portuguese Natural Monuments of national rank are a long way from such goals and the communities that occupy the territories are completely oblivious to the geological heritage that surrounds them.

Figure 2. The official website of the National Inventory of Geological Heritage at the Laboratório Nacional de Energia e Geologia (LNEG, 2025).

Figure 3. The official website of the National Inventory of Geological Heritage at the Instituto da Conservação da Natureza e das Florestas (Geossítios, 2025).

This top-down nature conservation strategy has proved to be totally inappropriate and has not contributed to harmonious integration between communities and nature. In parallel with the Portuguese state's disinvestment in the conservation of the country's geodiversity, a number of local initiatives have sprung up for this purpose. Among them are projects aimed at integrating territories into the UNESCO World Geoparks Network.

The bottom-up approach

The first Portuguese Geopark to join the UNESCO World Geoparks Network was Naturtejo in 2006, followed by Arouca, the Azores, Terras de Cavaleiros, Estrela and Oeste (CNU, 2025; Fig. 4; Table 2). Rather than emerging from

a nationwide political decision, UNESCO Global Geoparks (UGGp) are established through a bottom-up process involving all relevant local and regional stakeholders and authorities in the area, deeply committed to the exploration, development and celebration of the links between the geological heritage and all other aspects of the area's natural, cultural and intangible heritage (UNESCO, 2025).

Figure 4. UNESCO Global and Aspiring Geoparks in Portugal (modified after AG, 2025).

UGGp proved to be a sustainable strategy for protecting the geological heritage of Portugal. This may have inspired the Portuguese political authorities to change the legislation on the protection of geological heritage, allowing the creation of Local Natural Monuments. Proposals for their creation come from the local authority, as well as their management, once the classification has been approved by the national authority. The last two Natural Monuments to be classified by the Portuguese State have this status (Table 1).

Table 2. UNESCO Global Geoparks in Portugal.

Name	Official Website	Designation date
Naturtejo	https://www.naturtejo.com/	2006
Arouca	https://aroucageopark.pt/	2009
Azores	https://www.azoresgeopark.com/	2013
Terras de Cavaleiros	https://geoparkterrasdecavaleiros.pt/p/en/	2014
Estrela	https://www.geoparkestrela.pt/	2020
Oeste	https://www.geoparqueoeste.com/	2024

The relevance of community involvement in geoconservation

Nature conservation in Portugal was initially governed by top-down approaches, based on centralized classification initiatives that resulted in difficulties in the management of protected areas. The geological heritage classified as Natural Monuments covers around 1500 ha, of which around 1000 ha correspond to the Portas do Ródão Natural

Monument (ICNF, 2025), a territory included in the Naturtejo Geopark and therefore subject to the geoconservation requirements of UNESCO's Global Geoparks Network (GGN, 2025). But the rest of the area, although classified, has not been valued and, in some cases, is at risk of destruction due to lack of monitoring. The potential for using these sites of recognized scientific and educational interest is practically nil, since they lack the infrastructure to support visitors and the information to understand how the site record contributes to understanding the history of the Earth. The Natural Monuments are briefly described on the official ICNF website, which is the only information available to anyone wishing to visit them.

The creation of geoparks, which emerge from local initiatives, with extensive community involvement in all stages of geoconservation, has proved to be the most effective way of guaranteeing the integrity of geological objects with heritage value, as well as their enjoyment by society. They demonstrated to be a viable approach to the development of areas with remarkable geological heritage which can be adapted to various social and economic contexts as well as cultural ones (Henriques and Brilha, 2017).

Portuguese authorities recognized the relevance of community involvement, and the last two Natural Monuments to be classified in Portugal are already local in scope, and their geoconservation is expected to be more effective. Moreover, the organization of nature protection at state level was altered to integrate the National Network of Protected Areas (a government initiative and responsibility) with classified areas with alternative management systems like those integrated into the Natura 2000 Network and other areas classified under international commitments assumed by the Portuguese State, such as RAMSAR Sites, Geoparks and Biosphere Reserves (SNAC, 2025). However, the maintenance of national natural monuments without improvements that allow them to be used for educational and/or geotourism purposes is a waste of an economic, social and environmental asset.

Conclusions

With regard to geoconservation in Portugal, there is a state entity that aggregates information on the inventory of the country's geological heritage, in close collaboration with the academic community – the Laboratório Nacional de Energia e Geologia, which is a state laboratory of the Ministry of the Environment and Energy (LNEG, 2025). Within the same Ministry, the ICNF oversees the National Network of Protected Areas, which aims to ensure the protection of the geological heritage and the integrity of its characteristics, in the territorial context in which they are located (ICNF, 2025). In this sense, it is possible to say that the country's geological heritage is reasonably well known and inventoried. But geoconservation refers to more than the inventory of a territory's geological heritage. In Portugal, all the other steps that make it possible to guarantee the physical integrity of geological sites (classification, monitoring), as well as their enjoyment for educational and geotourism purposes (valuation) has been assumed fundamentally by local and/or private initiative. It is essential to provide the ICNF with the necessary means to ensure the monitoring and valuation of the protected areas for which it is responsible, i.e., the National Natural Monuments.

Acknowledgements

The authors acknowledge the support from the Portuguese funds of Fundação para a Ciência e a Tecnologia in the frame of UIDB/00073/2025 (https://doi.org/10.54499/UIDB/00073/2020) and the UIDP/00073/2025 (https://doi.org/10.54499/UIDP/00073/2020) projects, the Conselho Nacional de Desenvolvimento Científico e Tecnológico (303596/2016-3) and Fundação Carlos Chagas Filho de Amparo à Pesquisa do Estado do Rio de Janeiro (E-26/200.998/2024) from Brazil.

References

AG, 2025. Algarvensis Geoparque. https://geoparquealgarvensis.pt/unesco/rede-portuguesa-dos-geoparques-mundiais (retrieved 26.2.2025).

Aires R., Machado, S., Pereira, P., Matos, J.X. & Brilha, J., 2023. A unificação dos inventários de geossítios como estratégia para a geoconservação em Portugal. Resumos do XI CNG 2023, Coimbra, 621-622.

Brilha, J., Andrade, C., Azerêdo, A., Barriga, F.J.A.S., Cachão, M., Couto, H., Cunha, P.P., Crispim, J.A., Dantas, P., Duarte, L.V., Freitas, M.C., Granja, M.H., Henriques, M.H., Henriques, P., Lopes, L., Madeira, J., Matos, J.M.X., Noronha, F., Pais, J., Piçarra, J., Ramalho, M.M., Relvas, J.M.R.S., Ribeiro, A., Santos, A., Santos, V. & Terrinha, P., 2005. Definition of the Portuguese frameworks with international relevance as an input for the European geological heritage characterization. Episodes, 28(3), 177-186. https://doi.org/10.18814/epiiugs/2005/v28i3/004

Carvalho, I.S., Cunha, P.P., Figueiredo, S. D., 2022. Dinoturbation in Upper Jurassic siliciclastic levels at Cabo Mondego (Lusitanian Basin, Portugal): evidences in a fluvial-dominated deltaic succession. Palaeoworld 31(3), 455-477. https://doi.org/10.1016/j.palwor.2021.09.001

CNU, 2025. Geoparques Mundiais da UNESCO. Comissão Nacional da UNESCO. https://unescoportugal.mne.gov.pt/pt/redes-unesco/geoparques-mundiais-da-unesco (retrieved 26.2.2025).

Custódio, S.C., Henriques, M.H., Rosado-González, E.M., Vaz, N.M. & Sá, A.A., 2024. Selected Geoheritage Resources of

"Atlantic Geopark" Project (Central Portugal). Geosciences, 14(3), 81. https://doi.org/10.3390/geosciences14030081

Geossítios, 2025. Inventário Nacional do Património Geológico. https://geossitios.progeo.pt/index.php/about (retrieved 26.2.2025).

GGN, 2025. Global Geoparks Network. https://www.globalgeoparksnetwork.org/ (retrieved 26.2.2025).

Gill, J.C., 2017. Geology and the Sustainable Development Goals. Episodes 40(1), 70-76. http://dx.doi.org/10.18814/epiiugs/2017/v40i1/017010

Habibi, T., A. Ponedelnik, A.A., Yashalova, N.N., Ruban, D.A., 2018. Urban geoheritage complexity: Evidence of a unique natural resource from Shiraz city in Iran. Resources Policy 59:85–94. https://doi.org/10.1016/j.resourpol.2018.06.002

Henriques, M.H., 2004. Jurassic heritage of Portugal: state of the art and open problems. Rivista Italiana di Paleontologia e Stratigrafia 110(1), 389-392. DOI: https://doi.org/10.13130/2039-4942/6317

Henriques, M.H., Brilha, J., 2017. UNESCO Global Geoparks: a strategy towards global understanding and sustainability. Episodes 40(4), 349-355. DOI: 10.18814/epiiugs/2017/v40i4/017036

Henriques, M.H., Pena dos Reis, R., Brilha, J., Mota, T., 2011. Geoconservation as an Emerging Geoscience. Geoheritage 3:117–128. DOI: 10.1007/s12371-011-0039-8

ICNF, 2025. Instituto da Conservação da Natureza e das Florestas. https://www.icnf.pt/conservacao/ordenamentoegestao/snac (retrieved 11.2.2025).

INE, 2023. Estatísticas do Turismo – 2023. Instituto Nacional de Estatística. file:///C:/Users/M%C2%AA.%20Helena%20Henriques/Downloads/ETurismo_2023.pdf (retrieved 13.12.2024).

LNEG (2025). Geoportal Energia e Geologia. National Inventory of Geological Heritage. https://geoportal.lneg.pt/en/databases/geosites/#!/ (retrieved 26.2.2025)

SNAC, 2025. Sistema Nacional de Áreas Classificadas. https://www.icnf.pt/conservacao/ordenamentoegestao/snac (retrieved 11.2.2025)

UNESCO, 2025. UNESCO Global Geoparks. https://www.unesco.org/en/iggp/geoparks/about (retrieved 27.2.2025).

Yates, D., Peacock, E., 2023. T. rex is Fierce, T. rex is Charismatic, T. rex is Litigious: Disruptive Objects in Affective Desirescapes. International Journal of Cultural Property 30(4):396-418. DOI:10.1017/S0940739124000055

17th INTERNATIONAL CONGRESS of the Geological Society of Greece

BULLETIN OF THE GEOLOGICAL SOCIETY OF GREECE, SP. PUBL.

EXTENDED ABSTRACT 113

Beach retreat due to sea level rise induced by climate change: The case of the Korasida, Heromylos and Limnionas beaches in southeastern Evia facing the Aegean Sea

Iatrou[1] A., Karakostas[1] D., Markozanes[1] F., Karditsa[2] A., Poulos[1] S.

(1) Laboratory of Physical Geography, Section of Geography and Climatology, Department of Geology and Geoenvironment, Panepistimioupolis-Zografou 15784, Attiki, Greece.

(2) Department of Port Management and Shipping, National and Kapodistrian University of Athens, Psahcna, Evia, Greece

Introduction

The processes that govern the formation and evolution of beach zones include marine and terrestrial processes; the former, in the case of an essentially tideless environment, refer to the incoming waves, their transformation and breaking conditions that induce nearshore currents and sediment transport, while the latter to the delivery of terrestrial sediment (i.e. cliff erosion, river inputs). These processes acting in different times (from seconds to decades) and spatial (for a few meters to km) scales, are subjected also to the various human (direct or indirect) interventions. Such an indirect anthropogenic intervention is climate change which among other impacts causes the rise of sea level; the latter has a significant impact on beach zone evolution with undesirable consequences to coastal ecosystem services with coastal tourism being among them.

The purpose of the present study is to provide an estimate of shoreline retreat associated with the sea level rise (SLR) for the year 2100, according to the latest IPCC 2021 report (Masson-Delmotte et al., 2021), in the case of three beaches in Evia facing the Aegean Sea (Figure 1). The three beaches are (from north to south) Korasida, Heromylos and Limnionas, selected based on their size in both width and length, together with their direct exposure to incoming waves from the NE, E and SE directions (open Aegean Sea), making them highly relevant for assessing the impact of sea-level rise on coastal retreat. The first two beaches have been formed in front of schist formations while the third one in front of marbles, with both formations belonging to the Styra Nappe of the Cycladic Blueschist Unit (Xypolias et al., 2003).

Figure 1. The location of the beaches under investigation.

Methods

Shore-normal profiles were measured with the use of a Leica Distance Meter (subaerial part) and a Portable Handy Depth Sounder Hondex PS-7 (subaqueous part). For the geographical position of profile, a Topcon GPS was used. Reanalysis of hourly wave data, regarding the neighbouring area of Kimi (shown in Figure 1), were obtained from the Copernicus platform, covering a period of 20 years (1/1/2002 - 31/12/2021).

For the purpose of the present study the highest (1%) of the wave characteristics (height (H) and period (T)) have been identified for each of the three predominant directions. For the estimation of shoreline retreat the most common method, the Bruun's rule (Bruun, 1962), has been used (Figure 2), which is based on the change of the beach's morphometric characteristics due to the rise of the sea level, assuming a shoreline retreat retaining unchanged beach profile, with the eroded sediment deposited on the shoreface, retaining depth unchanged. Therefore, the calculated estimates could be considered as indicative.

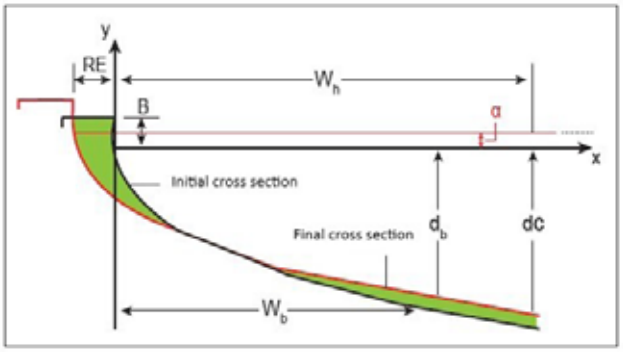

Figure 2: Illustration of Bruun's rule (from Poulos and Karditsa, 2020).

The retreat (RE: retreat) of the beach boundary is given by Brunn's (1962) relationship (equation 1):

$$wE = \frac{W_C \ a}{d_c + B} \qquad (1)$$

Where, (α): the sea level rise; (dc): the maximum depth of bottom sediment mobilization given by Hallermeier (1981) (equation 2); (W_C): the horizontal distance of dc from the shoreline; and (B): is the berm height.

$$dc = 2.28\ H_e - 68.5\ (H_e^2 / gT_e^2) \qquad (2)$$

where, (e: extreme) values (with a yearly exceedance of 0.137%) of wave height (H) and Period (T) and (g) earth's gravity.

The retreat of all beaches was calculated for the various Shared Socio-economic Pathways (SSP) scenarios provided by IPCC (Masson-Delmotte et al., 2021), which are: SLR = 0.28 m (SSP1a-1); SLR = 0.60 m (SSP2-4.5); SLR = 1.01 m (SSP4-8.5).

Results

The basic morphometric and wave characteristics of the three beaches are presented in Table 1. The wave characteristics refer to the wave height (H_e), period (T_e) , direction, closure depth (d_c) and its distance from the shore (W_c) for the extreme values of H and T. Limnionas beach is the widest beach (39 m), followed by Heromylos (28 m) and Korasida (22 m). All three locations have similar beach heights (< 3 m), while Korasida has the steepest subaerial slope. Heromylos and Korasida have higher significant wave heights compared to Limnionas. Finally, Heromylos has the greatest depth of closure, followed by Korasida and Limnionas.

Table 1. The basic morphometric and hydrodynamic characteristics of the 3 beaches.

	Morphometric characteristics			Hydrodynamic characteristics				
	Beach Width (W) (m)	Beach Height (B) (m)	Shoreface slope (β_f)	Wave Direction	H_e (m)	T_e (s)	d_c (m)	W_c (m)
Heromylos	28	2.8	0.045	NE	5.1	8.3	11.3	250.5
Korasida	22	2.6	0.090	SE	5.2	8.9	11.7	129.7
Limnionas	39	2.7	0.060	E	3.7	8.9	7.6	128.2

The estimated retreat for the three SSP sea level rise scenarios is shown in Table 2. For all sites, both the absolute retreat (Re in meters) and the retreat relative to the beach width (Re in %) increase significantly with increasing expected sea level rise (0.28 m from SSP1 to 1.01 m SSP4).

Heromylos is the most vulnerable of the three sites, even under moderate sea level rise (SSP2-4.5), and shows the highest retreat values (Re=18.8 m (67.1%) under the worse scenario SSP4-8.5. Korasida shows moderate retreat values, while under the SSP4-8.5 scenario Re is 9.6 m (43.5%). Limnionas is the least affected but still shows significant impacts. For example, under SSP4-8.5 the overtopping reaches 12.2 m (31.3%), which is the lowest of the three sites.

Table 2. The estimated retreat (RE) for the three beaches with respect to the sea level rise ("α" in equation 1) related to the weak (SSP1a), moderate (SSP2-4.5) and worse (SSP4-8.5) case scenarios due to climate change.

Sea Level Rise Scenarios		**Heromylos**	**Korasida**	**Limnionas**
SSP1a–1: 0.28 m	Re (m)	5.2	2.7	3.4
	Re (%)	18.6	12.1	8.7
SSP2-4.5: 0.60 m	Re (m)	11.2	5.7	7.2
	Re (%)	39.8	25.9	18.6
SSP4-8.5: 1.01 m	Re (m)	18.8	9.6	12.2
	Re (%)	67.1	43.5	31.3

Discussion and Conclusions

The three beaches exposed to the open Aegean Sea are expected to retreat by 2.7-5.2 m for the SSP1a-1 scenario, by 5.7-11.2 m for the moderate SSP2-4.5 scenario and by 9.6-18.8 m for the worse SSP4-8.5 scenario by 2100. The differences between the retreat values are due to their different morphodynamic and hydrodynamic characteristics, as shown in Table 1. Heromylos experiences the highest retreat under all scenarios, reaching 18.8 m (67.1%) under SSP5-8.5. Korasida and Limnionas show lower but still significant retreat values, with Korasida reaching 9.6 m (43.5%) and Limnionas 12.2 m (31.3%). The vulnerability of Heromylos and Korasida beaches is also related to the fact that they are exposed to the highest wave heights (5.1-5.2 m). On the other hand, they show the most dramatic retreat. Limnionas beach is exposed to the lowest wave heights (3.7 m). The relatively lower retreat values under all climate scenarios may also be related to the higher beach elevation or better natural resilience to sea level rise.

Given the economic, ecological, and social importance of these beaches, proactive measures need to be considered to mitigate the effects of rising sea levels and associated coastal hazards. Implementing a combination of continuous monitoring to predict beach response and adaptive strategies (eg. nature based solutions and interventions) will support preserving the value and function of these coastal areas in the face of climate change.

References

Bruun, P., 1962. "Sea-level rise as a cause of shore erosion." Journal of the Waterways and Harbors division 88(1), 117-130.

Hallermeier, R. J., 1981. "A profile Zonation for Seasonal Sand Beaches from Wave Climate". Coastal Engineering, 4, 253 - 277.

Masson-Delmotte, V. P., Zhai, P., Pirani, S. L., Connors, C., Péan, S., Berger, N., ... & Scheel Monteiro, P. M., 2021. IPCC, 2021: Summary for policymakers. *In:* Climate change 2021: The Physical Science Basis. Contribution of Working Group I to the Sixth Assessment Report of the Intergovernmental Panel on Climate Change.

Poulos, S., and, Karditsa, A., 2020. Applied and Environmental Oceanography -An Introduction to coastal zone management, DISIGMA publisher, Thessaloniki

Xypolias, P., Kokkalas, S., & Skourlis, K., 2003. Upward extrusion and subsequent transpression as a possible mechanism for the exhumation of HP/LT rocks in Evia Island (Aegean Sea, Greece). Journal of Geodynamics, 35(3), 303-332.

17th INTERNATIONAL CONGRESS of the Geological Society of Greece

BULLETIN OF THE GEOLOGICAL SOCIETY OF GREECE, SP. PUBL.

EXTENDED ABSTRACT 114

Contribution to the stratigraphic study of the pyroclastic Formations of the Lesvos Petrified Forest, Lesvos Island, Greece.

Iliopoulos, G.[1], Papadopoulou P.[1], Valiakos, I.,[2], Zouros, N.[2,3]

(1) Department of Geology, University of Patras, Patras, Greece, iliopoulosg@upatras.gr (2) Natural History Museum of the Lesvos Petrified Forest, Sigri, Greece (3) Department of Geography, University of the Aegean, Mytilene, Greece

Introduction / Background

Lesvos Petrified Forest represents one of the most important monuments for the geological heritage of Greece. It is located on the western peninsula of Lesvos Island and has been recognized as a Natural Monument since 1985, covering an area of 15.000 hectares. Silicified tree trunks, both lying and in upright position, as well as fossil leaves of lower Miocene age are found enclosed in pyroclastic and volcaniclastic material deriving from a nearby stratovolcano chain (Zouros et al., 2015). The protected area of the Lesvos Petrified Forest became one of the 4 first European Geoparks in 2000 and global geopark in 2004. In 2015 Lesvos Island became a UNESCO Global Geopark with the petrified forest as the main geological heritage area of international significance. Recognized as one of the first 100 IUGS geological heritage sites, the Petrified Forest is a locus for research, education, and sustainable tourism.

Recently, the construction of the new Kalloni-Sigri road brought to light new fossiliferous localities (Zouros at al., 2015, 2022). Construction works with extensive new roadcuts, exposed several artificial sections along the road, which on the one hand brought to light numerous fossilized trees and leaves, and on the other hand enabled the stratigraphic research of the volcanoclastic rocks at Akroheiras Hill (within the protected area of the Lesvos petrified forest) which contain them (Fig. 1A), and allowed the detailed stratigraphic analysis of the Sigri Pyroclastic Formation (Pe-Piper et al. 2019b).

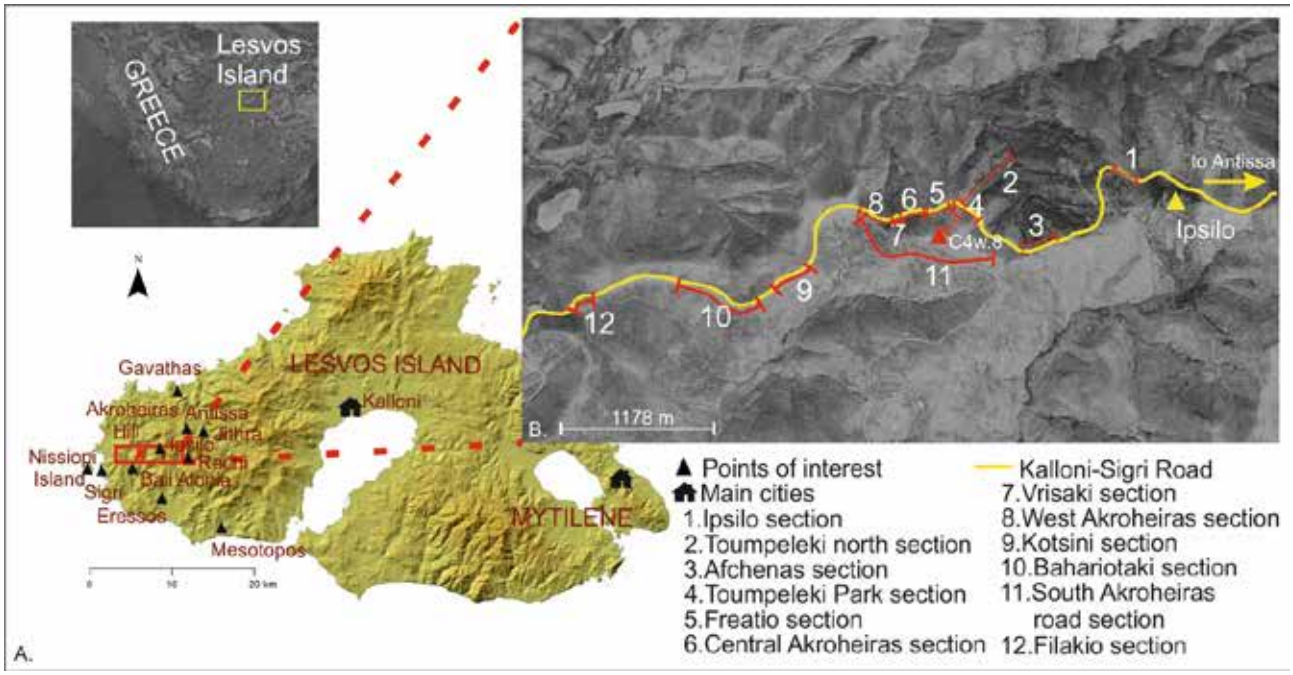

Fig. 1: A. DEM image of Lesvos Island. Main cities, villages and main points of interest are noted. The study area is noted with the red rectangle. B. Satellite image of the study area, where the 12 studied sections (red lines) are highlighted.

Twelve different sections located along the new road that cuts across Akroheiras Hill (Fig. 1B), were stratigraphically recorded and are presented herein, while a new stratigraphic scheme for the pyroclastic deposits of Lesvos is proposed.

Geological setting

During the last fifty years the volcanic rocks of Lesvos have been extensively studied and mapped (Hecht, 1974a, b, c; Pe-Piper, 1978; 1980; Pe-Piper et al., 2019b), and the overall stratigraphic structure of the volcanic formations of the Island has been provided (Pe-Piper & Piper, 1993; Pe-Piper et al., 2019a, b). Pyroclastic and volcaniclastic rocks of several

hundred meters extend at the western part of the Island and are known until now as the Sigri Pyroclastic Formation (Pe-Piper 1980; Pe-Piper et al., 2019b), lying above Permian schists and marbles (Katsikatsos et al., 1982). Sigri pyroclastics are mostly tuffs containing exceptionally preserved silicified trunks and fossilized leaves (Velitzelos & Zouros, 1997; Zouros et al., 2007; Zouros, 2021; Liapi et al., 2022; Tsitsou et al., 2022; Liapi et al., 2024). The age of Sigri pyroclastics has been estimated between 21.5 and 18.0 Ma (Pe-Piper et al., 2019b). The stratovolcano chain follows the dominating NNE-SSW dextral strike-slip tectonic regime of the Aegean-Anatolian microplate (Yilmaz et al., 2000). In Lesvos Island three successive neotectonic stages have been reported since the Miocene: a) the earliest one is of Upper Miocene age, based on its relation to synchronous volcanism and associated rocks, and formed strike–slip faults of E–W to ENE–WSW strike b) the second one took place in the Pliocene and formed normal faults of NW–SE strike, as well as strike–slip faults of NNE–SSW strike c) finally, the active stage since the Pleistocene forms E–W trending normal faults (Chatzipetros et al., 2013)

Material and Methods

Detailed stratigraphic logging was conducted in twelve sections along the new road cuttings from Moni Ipsilou Hill to Fylakio (Fig. 1A). Stratigraphic logging was performed in many places of each site as the lateral continuity of the layers was interrupted by faults, and lateral changes of the pyroclastic material occurred. The lithological characterisation of the pyroclastic rocks follows Fisher & Schmincke (1984) and Francis & Oppenheimer (2003). The presence of the most prominent fallen or standing tree trunks was noted, as well as the respective fossil leaf horizons. Basic sedimentary structures were also recorded. Rough stratigraphic cross sections containing the most important features of each section (characteristic horizons, major faults etc) were recorded and photos of each section were taken. Identification of the stratigraphic discontinuities took place (particularly erosional unconformities which mostly correspond to palaeosoil horizons). These discontinuities as well as some fine tuff layers, which present obvious and recordable lateral continuity, were used for the correlation of the different stratigraphic columns in each section, and subsequently for the correlation of the different sections.

The different formations were distinguished using criteria of the International Commission on Stratigraphy (Murphy and Salvador, 1999), as well as using physical characteristics of the rocks. Subdivision of formations in members took place when possible, taking into account erosional unconformities or/and palaeosoil development. In addition, palaeosoil horizons were also used to distinguish the different eruption phases.

Results

The prevailing lithology of pyroclastic rocks from the study area are tuff layers (fine to lapilli tuffs), with thicknesses ranging from a few millimeters to several meters characterized by sharp contacts. Grading is common (normal, reverse or normal to reverse), and pumice and lithic lapilli are often present. Pyroclastic rocks are often intercalated with volcaniclastic layers namely channeled or layered tuffaceous conglomerates and sandstones. The recorded palaeosoil horizons present thicknesses from a few millimeters to around ten centimeters or more and are easily traced by their black, green or/and red color. Neither their color nor their thickness appears stable laterally. They often evolve to thin horizons of fine tuff or even they disappear leaving only a discontinuity, many times difficult to observe. Their coloring is attributed to alteration due to the circulation of hydrothermal fluids (Pe-Piper et al., 2019a). The layers are dipping with a general NE-SW orientation and low angles (3-16˚). Some differentiations were noticed as NE-SW (sections 4, 12) and NW-SE (sections 10, 12) orientations also occur, which are attributed to the described above tectonic regime.

Several high angled (60-90˚) faults, deforming the studied sections have been observed. Most of them are sinistral strike slip faults with NE-SW or NNE-SSW directions (sections 1, 3, 4, 5, 7, 8, 9, 10, 11, 12). N-S directed faults were also noticed (sections 1, 4, 5, 10, 11). Additionally, E-W or WSW-ENE directed sinistral strike slip faults (sections 3, 6, 7, 10, 11) and a few NW-SE normal faults (sections 1, 10) were also recorded. The lateral continuity of the sections is interrupted by Quaternary channels. Their position is controlled by faults as it has been also implied for the older channels (Lamera et al., 2004), which are uplifting the western blocks.

Twelve sections were lithostratigraphically recorded in detail namely Ipsilo section, Toumpeleki north section, Afchenas section, Toumpeleki section (east and west part), Freatio section, Central Akrocheiras section, Vrisaki section, West Akrocheiras section, Kotsini/Bachariotaki sections, South Akroheiras road cut section and Filakio section (Fig.1B).

Ipsilo section stretches for 250 m at the foot of Ipsilo Hill (Fig.1B, Section 1) and has a recorded thickness ranging between 4 and 20m. It presents pyroclastic tuffs with high pumice content at its base, while at higher levels locally developed palaeosoil horizons were recorded. The stratigraphy of **Toumpeleki north section** was recorded along a narrow natural section across a stream valley north of the road (Fig.1B, Section 2). A total of 65 m of pyroclastic material was recorded. Brown volcanic material was recorded at the base of this section. Upwards the sequence is composed of both coarse and lapilli tuffs with a characteristically high percentage of pumice at the lower part. Further upwards lapilli tuff layers exist for at least 55 m. **Afchenas section (**Fig.1B, Section 3) consists of thick (around 60m) reddish chaotic (poorly sorted) polymictic,

mostly clast supported volcaniclastic deposits with substandard stratification and angular clasts. Wedged laterally secondary fine grained layers with high pumice content can be seen. **Toumpeleki Park section (east part)** (Fig.1B, section 4, Fig. 2) consists mostly of coarse and lapilli tuffs and some volcaniclastic layers, often containing transported trunks and branches (with thickness 16m). Seven palaeosoil horizons were recorded from bottom to top. Standing fossil trunks implying the presence of a respective forest were recorded on six of the palaeosoil horizons. Fossil leaves were recorded on at least three stratigraphic horizons. **Toumpeleki Park section (west part)** presents 90m of pyroclastic rocks. The lower 37 m consist mostly of both coarse and lapilli tuffs with intercalations of palaeosoil horizons and volcaniclastic layers, often containing transported trunks and branches. In total, eight palaeosoil horizons and two disconformities were recorded from bottom to top. Standing fossil trunks were recorded in four palaeosoil horizons and fossil leaves were recorded just in one case. At the upper stratigraphic levels (from 37 to 90 m column height) of this section a concise stratigraphic recording was conducted (due to vegetation cover) revealing a more coarse grained stratigraphic sequence. **Freatio section** (Fig.1B, Section 5) is a very unique and important site because of the exceptionally high number of transported fossilized trunks that have been excavated and are preserved on site. The section has a length of more than 100m and is delimited in both sides and on top of the west end by Quaternary channels. It consists mostly of fine and coarse tuff layers and volcaniclastic sediments with a total thickness of around 14m. Four palaeosoil horizons were recorded. Standing trunks were recorded on three horizons. At its lower part a thick (4.60 m) lahar which turns into a mud flow deposit at the top exists. A large number of transported trunks were excavated lying in different orientations. This accumulation is interpreted as a log jam. **Central Akroheiras section** (Fig. 1B, Section 6) is lying west from Freatio section. It stretches for more than 290m and the thickness of the pyroclastic sequence is more than 40m. It consists mostly of coarse and lapilli tuffs and some very characteristic volcaniclastic sediments that have been deposited in small rivers. The upper stratigraphic levels present an overall more coarse-grained lithology and thicker layers. Nine palaeosoil horizons and a disconformity were recorded. Standing fossil trunks were recorded on three palaeosoil horizons. Fossil leaves were recorded at several stratigraphic levels. **Vrisaki section** (Fig. 1B, section 7) is a small section consisting mostly of tuffs (coarse /lapilli tuffs and tuff breccia) and volcaniclastic sediments with a total thickness of 20m. Seven paleosoil horizons were recorded between the volcaniclastic layers. This section presents lateral continuity with **West Akroheiras section** which lies immediately westwards. It consists of coarse tuffs, lapilli tuffs and less of tuff breccia layers. Volcaniclastic layers also exist. The total thickness of the pyroclastic layers of this section is 22m. Seven palaeosoil horizons were recorded in this section. Standing fossil trunks were recorded in three palaosoil horizons. Fossil leaves were recorded in great numbers in many locations throughout this section. The upper stratigraphic levels show an overall different lithology. Most of the layers are thick and coarse grained and bear a lighter color. **Kotsini-Bachariotaki sections** (Fig. 1B, sections 9 & 10 respectively), stretch for more than 870 m along the road. The total thickness of the pyroclastic layers that were recorded is 21m. A characteristic palaeosoil horizon with multiple standing trunks can be noticed in both sections. Fossilized leaf litter was noticed in the lower part. Its upper part appears thicker and coarser grained with transported volcanic bombs. **South Akroheiras road section** (Fig.1B, section 11) stretches for 1424 m along the road that leads to Bali Alonia Petrified Forest Park. A variety of layers from volcaniclastic layers to tuff breccia with varying thicknesses (from 2 cm to approx. 30 m) were recorded. Palaeosoil horizons, fossil trunks and fossil leaves were also recorded in some places. The stratigraphic sequence is disrupted by faults and thus the correlation with the other sections was difficult. However, the existence of common very thick (1-30m) tuff breccia layers and the decreased frequency of palaeosoil horizons must be noted.

Fig. 2: Panoramic view of east Toubeleki park section (section 4). Toubeleki park section (east) consists a characteristic section where seven palaeosoil horizons (PS4e.1-7) can be seen (red lines). The red arrows indicate the position of standing fossil trunks.

Filakio section (Fig.1B, section 12) stretches for 140 m along the new Kalloni-Sigri road towards Sigri. It is the western of the studied sections, but it is one of the most important since a large number of both standing and fallen trunks were excavated. It is composed of relatively thick lapilli tuffs, tuff breccia, discontinuous thin palaeosoil horizons and conglomerate lenses at its lower part (road level) and thinner tuffs and volcaniclastic layers with intercalations of palaeosoil horizons upwards (Filakio Park level). The total thickness of this sequence is 12.5 m. Five palaeosoil horizons were recorded and standing fossil trunks were recorded in three of them. The lower part of the section shows volcaniclastic characteristics with thin intermittent palaeosoil horizons.

Discussion

The studied sections provide a detailed stratigraphic record of the broader Akroheiras Hill pyroclastics. The lateral continuity of the layers is often interrupted by post deposition Quaternary erosional surfaces, the road construction works and the severe faulting. The recorded faults have vertical displacements from a few centimeters up to 10m (i.e. Freatio section). Thus, the different characteristic horizons (palaeosoils and disconformities) from each section were correlated. The correlation of the different sections revealed that many palaeosoil horizons bear trunks in upright position recorded in at least one of the studied sections (Fig.3).

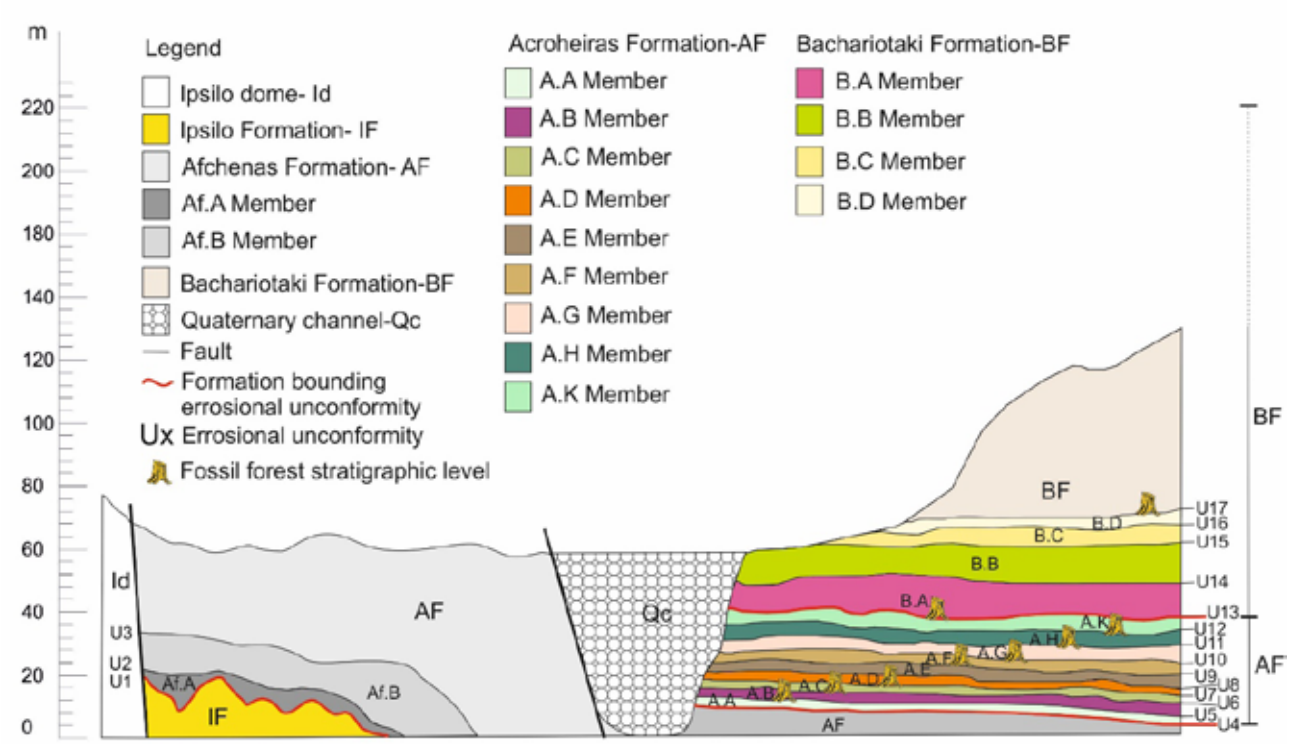

Fig. 3: Simplified synthetic section of Akroheiras Hill presenting the relative position of the described in the text Formations, Members and disconformities/palaeosoils (Us).

Moreover, four new Formations have been established namely Ipsilo Fm, Afchenas Fm, Akroheiras Fm, and Bachariotaki Fm (Fig. 3), replacing Sigri Pyroclastics Fm, which from now on will be considered as the Sigri Pyroclastics Group.

Ipsilo Formation: The pyroclastic rocks of this formation consist coarse and lapilli tuffs with characteristically high percentage of pumice (vitric tuffs) (up to around 50%). Secondary channels also exist. Fossilized wood is scarce in this formation and no trunks in upright position exist. Its lower limit was detected in Toumpeleki North section, where it comes in contact with brown ignimbrite (0-3m). The nature of their contact could not be evaluated due to limited exposure. Its upper limit is a distinct disconformity which can be seen in several sites along the road (U1). In places a weak palaeosoil horizon can be noticed. The total visible thickness of Ipsilo Formation pyroclastic rocks is five m but increases eastwards and may reach up to 20m.

Afchenas Formation: Thick (around 60m) reddish chaotic (poorly sorted) polymictic, mostly clast supported volcaniclastic material with substandard stratification and angular clasts can be seen along the road. Secondary channels can also be noticed. Its upper stratigraphic levels can be seen in the lower part of Freatio section and the lower part of Filakio section. In this part thin intermittent palaeosoil horizons and conglomerate lenses are detected. No or limited fossilized wood can be found in this

formation except its upper limit, where also trunks in upright position were noticed. The material is probably of fluvial origin and may represent hyperconcentrated or gravelly debris flows (Pe-Piper et al., 2019b) carrying mostly andesitic blocks and has been deposited close to the source. This formation outcrops also at Rachi area as mentioned in Pe-Piper et al. (2019b). The total thickness of this Formation is at least 58m. The lower part of this Formation can be divided in two Members, Af.A and Af.B.

Akroheiras Formation: the pyroclastic rocks of this formation are made of relatively thin (0.5 cm to 7m) fine grained secondary pyroclastic layers (predominantly lithic, fine or/and coarse tuffs and minor lapilli tuffs) intercalated by repeated palaeosoil horizons. Standing and fallen fossilized trunks as well as fossilized leaves are found in great numbers in this formation. The different layers are the result of pyroclastic avalanches (lahars, debris and mud flows) as well as river flows with limited lateral continuity. This formation comes in contact with the underlying Afchenas Formation through the disconformity/palaeosoil horizon U5 (Fig.3), while its upper limit is set to the disconformity signified by palaeosoil horizon U14 (Fig.3). Its total thickness is approximately 30m. Parts of the pyroclastics of this formation are exposed in several of the studied sections (Toumpeleki east, Toumpeleki west, Freatio, Central Akroheiras, Vrisaki, West Akroheiras and Filakio). Nine members are distinguished (Members A.A-A.K) separated by 9 palaeosoil horizons respectively (palaeosoils U6-U14, Fig. 3).

Bachariotaki Formation: The pyroclastic layers of this formation appear thicker (up to 30 m in Bali Alonia Section) and overall, more coarse grained than the other formations. They consist mostly of lapilli tuffs and tuff breccia with transported blocks and volcanic bombs. Volcaniclastic layers are also present. The stratigraphy of this part of the sequence appears complicated due to the multiple thick lobes that can be noticed and intense tectonism. Moreover, there are no adequate sections to record the stratigraphy in detail due to the high vegetation cover of the Akroheiras Hill slopes. Based on the total thickness of the recorded layers in the upper part of Akroheiras Fm and in South Akroheiras road section, the total thickness of this formation is estimated as 200m up to the hilltop of Akroheiras Hill. Both transported and standing trunks exist in this formation too although their frequency is reduced. Its upper limit is unknown due to erosion and vegetation cover (on top of Akroheiras Hill). In the lower Bachariotaki Fm, which is exposed in Toumpeleki Park west, Central Akroheiras, Vrisaki and West Akroheiras, four Members have been established (Members B.A, B.B, B.C, BD) bounded by the relative erosional unconformities/palaeosoils (U15-U19). Pyroclastic layers of this formation are also exposed in Kotsini/Bachariotaki sections as also in South Akroheiras road sections, but the existence of multiple faults does not allow the correlation of these layers and thus no other members are established for this formation for the time being.

The high pumice content of Ipsilo Formation may imply pyroclastic deposits deriving from ignimbrite or deposited during the same ignimbrite-forming eruption (Fisher and Heiken, 1982). As implied by Piper et al. (2019b) the location of the main source of Sigri pyroclastics was most likely in the wider Mesotopos area. It is possible that Ipsilo Formation was coeval with an ignimbrite forming eruption happening in Mesotopos prior to Eressos dome intrusion/extrusion as this could account for the high percentage of pumice and the low lithic content of this formation. The presence of the ignimbrite in Toumpeleki north section may contribute to this. On the contrary, due to the high lithic content of Afchenas Formation it may have derived from an Eressos Fm dome that had already been extruded during the formation of this sequence. In both formations a low time gap between the volcanic phases is implied by the reduced number of palaeosoil horizons that were formed or/and preserved. Ipsilo and Afchenas Formations bear little or no fossilized wood, nevertheless, they serve as the base of the fossiliferous Sigri pyroclastics.

Akroheiras Fm shows a high number of palaeosoil horizons and units. Each unit was formed when pyroclastic material deriving from neighboring volcanoes lying eastwards (Kouli and Seymour, 2006) was remobilized, enriched with water and flowed down the pre-existing alluvial system. These secondary pyroclastic flows reached the plain area lying further to the west carrying also fallen trunks and leaves. Each palaeosoil horizon is marking the cessation of the volcanic activity for a certain period of time. Therefore, the recorded palaeosoil horizons can serve as markers for distinguishing between different eruptions as has also been mentioned by Piper et al., (2019b) for the recorded palaeosoil horizons of Central Akroheiras area. At least 9 eruptive phases are evidenced in this part of the sequence corresponding to the establishment of the respective members.

When there was enough time between the previous and the next eruption, forests were developing on the formed soils. Thus, in Akroheiras Fm, nine (9) successive forest forming periods were recorded. The forests were buried later on under water saturated with cold pyroclastic material. Because the flows were not hot enough to burn the trees and because there was water in them the tree trunks and the leaves that were buried under anoxic conditions (otherwise the wood would have been decomposed) were preserved and then had the opportunity to get fossilised.

Within the lower part of Bachariotaki Fm at least four more eruptive phases are assured with one more forest developing period. In total, in Akroheiras and the lower part of Bachariotaki Fms 13 eruptive phases which correspond to the 13 defined members of the formations are mentioned herein. Moreover, at least 10 successive forest forming periods are witnessed by the different stratigraphic levels of the standing trunks.

Conclusions

- A new stratigraphic model is hereby proposed based on the lithology of the layers and the major stratigraphic hiatuses for the previously called Sigri Pyroclastic Formation (Pe-Piper, 1980; Pe-Piper & Piper, 1993; Pe-Piper et al., 2019b), and

which herein is revised as the Sigri Pyroclastic Group.

- Four pyroclastic formations are introduced for the Sigri pyroclastic rocks, Ipsilo Fm, Afchenas Fm, Akroheiras Fm and Bachariotaki Fm, bounded by erosional unconformities.
- Akroheiras Fm is further divided in Members A.A to A.K., as is also the case for the lower part of Afchenas Fm (Members Af.A and Af.B) and the lower part of Bachariotaki Fm (Members B.A to BD). The different Members are also bounded by palaeosoils and respective disconformities that correspond to different volcanic eruptions.
- Thus, at least 13 eruptive phases are identified. The cessation of each eruption was followed by the formation of a palaeosoil and the subsequent development of a forest on it.
- At least 10 successive forest developing periods have been recorded until now in the Akroheiras Hill pyroclastic sequences. It is certain that more forest forming events are hidden below the dense vegetation in the wider area of the Sigri pyroclastics.

References

Chatzipetros, A., Kiratzi, A., Sboras, S., Zouros, N., & Pavlides, S., 2013. Active faulting in the north-eastern Aegean Sea Islands. Tectonophysics, 597–598, 106–122. https://doi.org/10.1016/j.tecto.2012.11.026

Fisher, R.V. and Heiken, G., 1982. Mt. Pelee, Martinique: May 8 and 20, pyroclastic flows and surges. J. Volcanol. Geotherm. Res., 13:339-371

Fisher, R., Schmincke, H.U., 1984. Pyroclastic Rocks, Springer-Verlag Berlin Heidelberg.

Francis, P., Oppenheimer, C., 2003. Volcanoes. Oxford University Press.

Hecht, J., 1974a: Geological map Mithimna sheet. 1:50000. IGME, Athens

Hecht, J., 1974b: Geological map Polychnitos sheet. 1:50000. IGME, Athens.

Hecht, J., 1974c: Geological map Eresos sheet. 1:50000. IGME, Athens.

Katsikatsos, G., Mataragas, D., Migiros, G., Triandafillou, E., 1982. Geological study of Lesbos Island, Special Report, IGME, Athens.

Kouli, M., Seymour, K., 2006. Contribution of remote sensing techniques to the identification and characterization of Miocene calderas, Lesvos Island, Aegean Sea, Hellas. Geomorphology 77, 1-16.

Lamera, S., Kouli, M., Vamvoukakis, C., Seymour, K. St., 2004. Volcanic Stratigraphy, Sources and Mesothermal Au-Ag Deposit in Polychnitos Ignimbrite, Lesvos. Abstract in proceedings 10th International Congress. Bulletin of the Geological Society of Greece. April 2004, Thessaloniki.

Liapi, E., Zidianakis, G., Tsitsou, E., Iliopoulos, G., Zouros, N., 2022. New floristic data of the Early Miocene Lesvos Petrified Forest − Part A: Non-vascular plants, ferns and monocots from the West Akrocheiras outcrop. Bulletin of Geological Society of Greece Sp. Publ. 10, pp. 395–396.

Liapi, E., Iliopoulos, G., Zouros, N., 2024. Documenting the leaf flora of a new fossiliferous locality from the Lesvos Petrified Forest. Folia Musei rerum naturalium Bohemiae occidentalis - Geologica et Paleobiologica 58 (1), pp. 29–33.

Murphy, M., Salvador, A., 1999. International Subcommission on Stratigraphic Classification of IUGS, International Commission on Stratigraphy, International Stratigraphic Guide— An abridged version. Episodes 22 (4).

Pe-Piper, G., 1978. The Cenozoic volcanic rocks of Lesbos (Greece), unpublished readership thesis, University of Patras.

Pe-Piper, G., 1980. The Cenozoic Volcanic Sequence of Lesvos, Greece. Z. dt. geol. Ges., 131, 889- 901.

Pe-Piper, G., Piper, D.J.W., 1993. Revised stratigraphy of the Miocene volcanic rocks of Lesbos, Greece. Neues Jahrbuch für Geologie und Palaeontologie Monatshefte, 1993 (2),97–110.

Pe-Piper, G., Imperial, A.M., Piper, D.J.W., Zouros, N.C., Anastasakis, G., 2019a. Nature of the hydrothermal alteration of the Miocene Sigri Petrified Forest and host pyroclastic rocks, western Lesbos, Greece. Journal of Volcanology and Geothermal Research, 369,172–187.

Pe-Piper, G., Piper, J.W.D., Zouros, N., Anastasakis, G., 2019b. Age, stratigraphy, sedimentology and tectonic setting of the Sigri Pyroclastic Formation and its fossil forests, Early Miocene, Lesbos, Greece. Basin Research 2019, DOI: 10.1111/bre.12365.

Tsitsou, E., Zidianakis, G., Liapi, E., Iliopoulos, G., Zouros, N., 2022. New floristic data of the Early Miocene Lesvos Petrified Forest − Part B: Dicotyledon taxa from the West Akrocheiras outcrop Bulletin of Geological Society of Greece Sp. Publ. 10, pp. 398–399.

Velitzelos, E., Zouros, N., 1997. The petrified forest of Lesvos–Protected natural monument. Proc. Internat. Sympos. On Engineering Geology and the Environment, Athens, 3037-304.

Yılmaz, Y., Genç, Ş. C., Gürer, F., Bozcu, M., Yılmaz, K., Karacik, Z., … Elmas, A., 2000. When did the western Anatolian grabens begin to develop? Geological Society, London, Special Publication, 173, 353–384.

Zouros, N., Velitzelos, E., Valiakos, I., & Labaki, O., 2007. The Plaka Petrified forest park in Western Lesvos -Greece. Bulletin of the Geological Society of Greece, 40, 1880–1891.

Zouros, N.,Valiakos, I., Gribilakos, G., Plougarlis, A., Mpentana, K., Rozakis, V., Agiasoti, M., Tsalkitzi, O., 2015. New fossil findings in the Petrified Forest of Lesvos along the new Kaloni-Sigri road. The forest under the road a new traveling exhibition of the Lesvos Geopark. 13th European Geoparks Conference, Rokua, Finland.

Zouros, N.C., 2021. The Miocene petrified forest of Lesvos, Greece: Research and geoconservation activities. Geoconservation Research. 4(2), 635–649.

Zouros, N., Soulakellis, N.,Valiakos, I., Bentana, K., Theodorou, E., Zgournios, E., Antonakis, E. and Lamprakopoulos, A. 2022. Enhancement and promotion of the new fossiliferous sites along the new Kalloni Sigri road.-An example of good practice in geoconservation in Lesvos Isl. UNESCO Global Geopark Greece. Bulletin of Geological Society of Greece Sp. Publ. 10, pp. 849-850.

17th INTERNATIONAL CONGRESS of the Geological Society of Greece

BULLETIN OF THE GEOLOGICAL SOCIETY OF GREECE, SP. PUBL.

EXTENDED ABSTRACT 115

Geological study of the basement structure in the wider area of Filiro (Circum-Rhodope Belt, Central Macedonia, Greece)

D. Ioannidis, E. Katrivanos, A. Chatzipetros

School of Geology, Department of Structural, Historical and Applied Geology, Aristotle University of Thessaloniki, Greece, dioannif@geo.auth.gr

Abstract

The western border of the Serbo-Macedonian massif with Circum-Rhodope belt has been a subject of discussion in the past. Several questions have been raised about the geological structure of the study area (NE part of Thessaloniki, Pefka, Filiro, Asvestochori), based on variations in structural and lithological characteristics. Field – structural and lithological data were initially collected and then the geological structure and the tectonostratigraphy of the study area were visualised. In the area of interest there are characteristic rocks of both continental and oceanic crust in contact, as a result of past tectonic events (D1-D6 deformation events). Older tectonic events of compressive ductile stress regime (D1-D2) are correlated with the tectonic emplacement of ophiolites and the general terrane accretion, whine newer ones of brittle stress regime (D4-D5) are related with the thrusting and the creation of tectonic slices, as well as the inversion of the whole series. The lithological units of the area have been inverted by these tectonic events (D4-D5). As a result, the older rocks are placed tectonically on top of the younger ones. Compression forces have created a fold-and-thrust belt with a sense of movement to-the-SW. A lithological unit belonging to the Serbo-Macedonian massif is tectonically intercalated between the lithological units of Circum-Rhodope belt. The pre-alpine basement in the study area is of Serbo-Macedonian origin and the tectonic movement of the tectonic slices was accomplished on this basement.

Geological setting

The study area is geologically located mainly within the Circum-Rhodope Belt, which is part of the Internal Hellenides. The Circum-Rhodope Belt is traditionally divided into three units (from north-east to south-west):Deve Coran - Dubya, Melissochori - Cholomontas, Aspri Vrisi - Chortiati (Mountrakis 2010).

The Circum-Rhodope Belt was characterised palaeogeographically as the continental slope of the Greek hinterland during Jurassic. The presence of the oceanic crust of the Axios Zone at its eastern boundary, the turbiditic character of its rocks and the origin of its sediments from the Serbo-Macedonian Massif as described in Meinhold and Kostopoulos (2013) are indications consistent with this model. Structural and lithological features of Circum-Rhodope Belt show many variations. Thus, several questions have been raised about the geological structure of the study area.

The Serbo-Macedonian Massif starts from the Greek-Bulgarian border and extends in a northwest-southeast direction to the coast of Sithonia and Mount Athos peninsulas. Its western boundary is the contact with the Circum-Rhodope Belt , while its eastern boundary is in the basin of the Strimonas river, where it meets the Rhodope Massif. The similarities that appear in the rocks of the Serbo-Macedonian are many, however the massif has been divided into two units, namely Kerdyllia and Vertiskos.

Palaeogeographically, the Serbo-Macedonian Massif, together with the Rhodope Massif, expresses the Greek hinterland. Its rocks represent a continental crust with evidence of orogenies older than the Alpine (Papanikolaou 2015). There are views that consider the Serbo-Macedonian Massif to be part of the Eurasian plate and views that place it within the Cimmerian blocks that were attached to Eurasia. What is important, however, is that the Serbo-Macedonian Massif was not part of Gondwana at the start of the Alpine cycle, but was already in Eurasia undergoing the effects of the Ercynian orogeny (Papanikolaou 2015).

In this paper we present new field and structural data from the study area to investigate the shallow structural configuration and the geological structure of the basement, as well as the deformation phases and geotectonic evolution in general.

Methodology

The identification and differentiation of the cartographic units was the first step in a traditional field-work way (Figure 1). Then, based on field-structural data we decipher the deformation events (Table 1) that affected the units and we construct the tectonostratigraphic column (Figure 2). The final stage is to produce the geological cross-sections (Figure 3). All the field structural data were measured and verified using a geological compass. The points chosen for measurement were the contacts between two cartographic units, the foliation of the rocks, the folds (limbs and b-axis) and the mirror surfaces of the faults. Many structural features (foliation, lineation, folds, faults, kinematic markers, slip lines) were identified, measured and helped to distinguish the tectonic events (Table1), providing information on the stress field of the epoch in which they acted and on the kinematics of deformation. The analysis of the tectonic structures (folds, faults, tectonic contacts and lineation) was carried out in order to distinguish the tectonic events find the temporal succession of the deformation events with the final result being the understanding of the geological history of the area. The tectonic structures studied belong to the macroscopic scale.

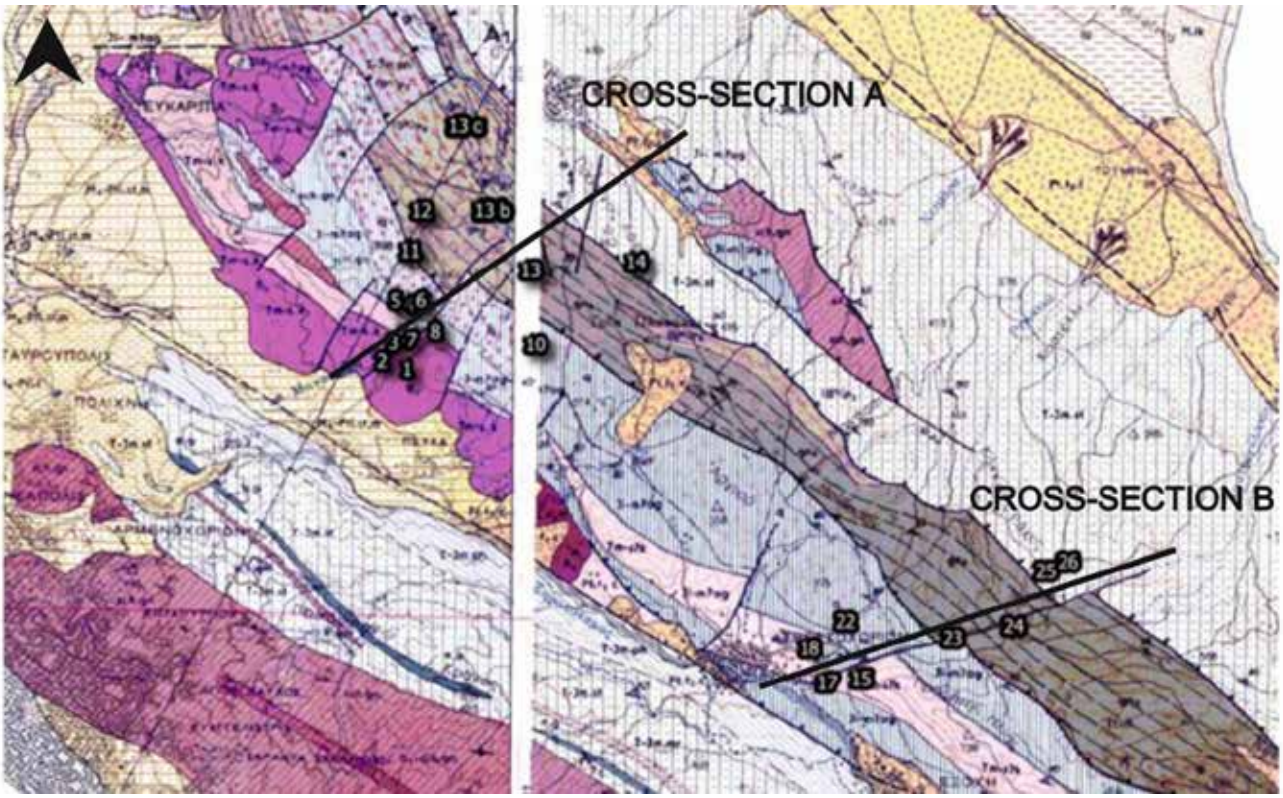

Figure 1.Geological map of the study area with field measurement points and location of geological sections. According to the geological mapping (Kockel et al.1970a Thermi sheet, Kockel et al.1970b Thessaloniki sheet).

Results

The data analysed showed that the geological structure that exists today was not created by a single tectonic episode, but is the result of a series of deformation events. The newer events overprinted the older ones, making it more difficult to identify them. The distinction macroof the deformation events was based on the geometric characteristics of the tectonic structures (orientation, position, shape) and their kinematic analysis. The tectonic structures formed by compressive forces are due to the convergence of the African plate with Eurasia, the destruction of the Tethys Ocean and the increase in the thickness of the continental crust. Extensional structures followed the compressive ones, first with the collapse of the compressive structure and later with back arc extension.

We distinguished six main deformation events (D1-D6) in the study area (Table 1) which is coherent to similar studies in the broader area (Kilias et al. 2010, Katrivanos et al. 2013, 2016, Kilias 2024), revealing that the Internal Hellenides underwent complex deformation and metamorphism during the Alpine orogeny. The rocks appear to be inverted, with the older rocks tectonically superimposed on the newer ones. The degree of metamorphism increases to the northeast, i.e. towards the upper tectonostratigraphic horizons. The tectonic contacts between the formations are due to the action of reverse faults. Parts of the Serbo-Macedonian Massif were trapped between the units of the Circum-Rhodope Belt (Aspris Vrysi - Chortiati, Melissochori - Cholomonta). In this way, continental crustal rocks came into contact with rocks characteristic of the oceanic crust and deep-sea sediments. The sense of movement was from north-east to south-west. The geological structure of the tectonostratigraphic column (Figure 2) and of the two geological sections(Figure 3) prove that they belong to the same geotectonic zone (Circum-Rhodope Belt), have been affected by common deformation events and consist of the same formations.

However, there are some differences between the two areas: In the Asvestochori area, no occurrences of microgneiss and augen gneiss have been found. Thus, the Serbo-Macedonian Massif in the area consists only of greenschist. The degree of metamorphism of the greenschist is obviously greater than that of the surrounding rocks, but it does not reach the degree of metamorphism of the gneiss rocks of the Pefka-Filiro area. In the area of Asvestochori, the formation of clay shales contains interbeds of graphitic shales. In the Pefka area, graphitic shales are absent or could not be found. Finally, the orientation of the formations in the two areas shows a slight deviation from NW-SE in the Pefka-Filiro area to WNW-ESE in the Asvestochori area.

Table 1. Deformation events based on our field- structural observations and on other similar studies (Kilias et al. 1999,2010,Tranos et al. 1999, Katrivanos et al. 2013,2016, Kilias 2024)

DEFORMATION EVENTS (D)	AGE	STRESS REGIME & DEFORMATION CONDITIONS	STRUCTURES	KINEMATICS	GEODYNAMIC RESULTS
D1	MID-LATE JURASSIC	COMPRESSION DUCTILE	NOT FOUND		Ophiolite obduction and thrusting
D2	LATE JURASSIC-EARLY CRETACEOUS	COMPRESSION DUCTILE	CLOSED FOLDS & SCHISTOSITY CREATION		Thrusting and terrain accretion (photo 1,2)
D3	LATE CRETACEOUS	EXTENSION	NOT FOUND		Basin formation
D4	PALEOCENE-EOCENE	COMPRESSION SEMI-BRITTLE	REVERSE FAULTS – OPEN KNICK FOLDS	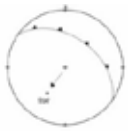	Intense imbrication of all units (photo 3,4,5)
D5	OLIGOCENE-MIOCENE	TRANSPRESSION BRITTLE	STRIKE – SLIP to NORMAL FAULTS - REVERSE FAULTS		Boundary effect between ductile extension in Pangaion unit to the east and brittle extension in Paikon unit to the west. Localized event in CRB as a boundary effect
D6a	MIOCENE-PLIOCENE	EXTENSION BRITTLE	HIGH – ANGLE NORMAL FAULTS		General faulting and basin Formation (Mygdonia)
D6b	PLIOCENE-PLEISTOCENE	EXTENSION BRITTLE	HIGH – ANGLE NORMAL FAULTS	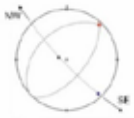	General faulting (photo 6)

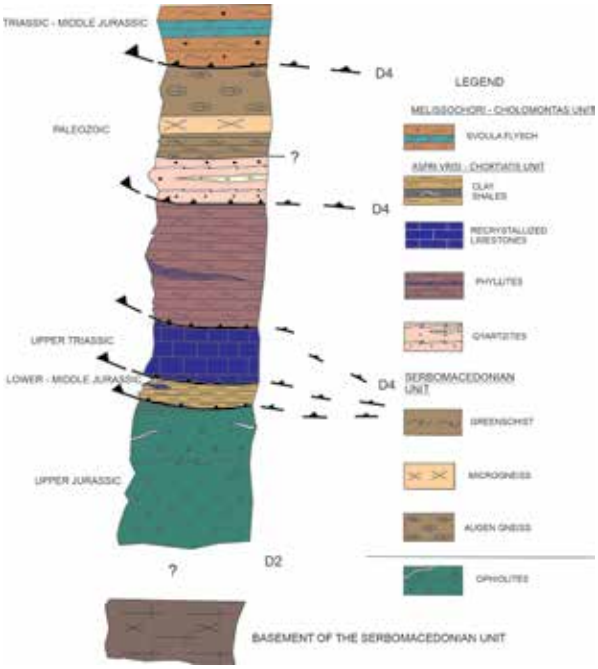

Figure 2. Tectonostratigraphic column of the study area.

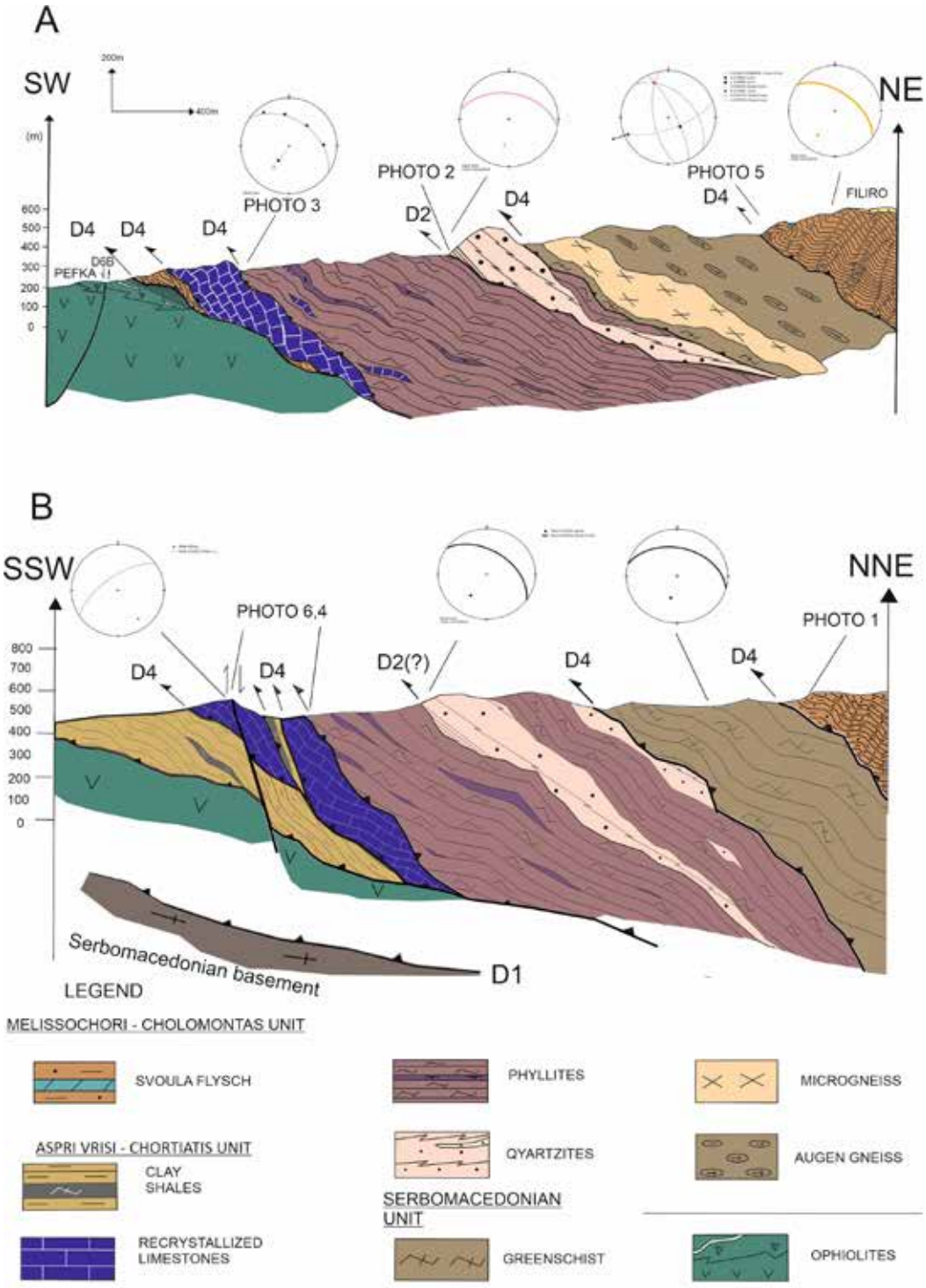

Figure 3.Geological cross - sections in the Pefka - Filiro (A) and Asvestochori (B) study areas (see Figure 1 for location).

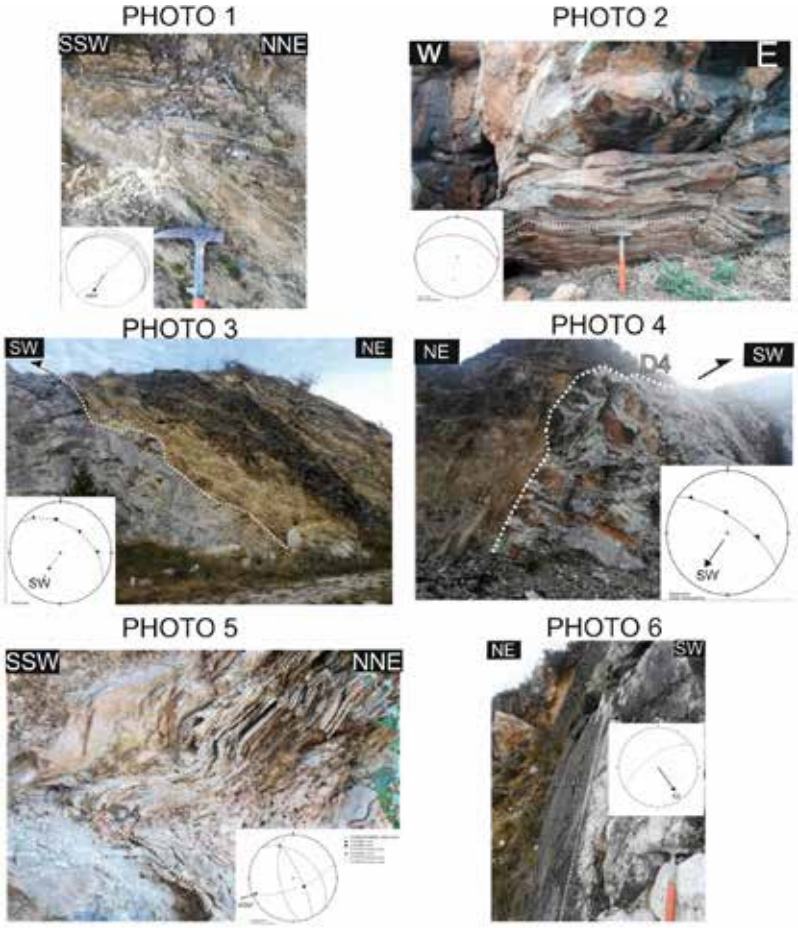

Figure 4. (see Figure 3 for reference).
Photo 1 : D2 event , closed to sub-isoclinal fold , submerged and inverted with a direction to SW (Svoula flysch)
Photo 2: D2 event, schistosity (quartzites-phyllites contact)
Photo 3: D4 event, reverse fault, flat – ramp – flat structure (limestones – phyllites contact , Filiro area)
Photo 4: D4 event, reverse fault, flat – ramp – flat structure (limestones – phyllites contact, Asvestochori area)
Photo 5: D4 event ,open fold with a direction to WSW (Svoula flysch)
Photo 6: D6b event, normal fault

Conclusions

- The whole area was affected by a polyphase deformation (D1-D6 events), that started in ductile conditions (D1-D3) and continued with brittle conditions (D4-D6).
- Older tectonic events of compressive ductile stress regime (D1-D2) are associated with the tectonic emplacement of ophiolites and the general terrane accretion, whine newer ones of brittle stress regime (D4-D5) are related to the thrusting and the creation of tectonic slices, as well as the inversion of the whole series.
- During the D4 deformation event, parts of the Serbo-Macedonian Massif were tectonically intercalated within the Circum-Rhodope Belt formations.
- In Oligocene – Miocene, the localized conditions of the stress regime fall into the category of transpression, while in the same age ductile extension prevails to the east (Pangaion unit) and brittle extension prevails to the west (Paiko unit).
- We consider that the pre-alpine basement in the study area is of Serbo-Macedonian origin and the tectonic movement of tectonic slices was accomplished on this basement.

References

Katrivanos E., Kilias A. and Mountrakis D., 2013. Kinematics of deformation and structural evolution of the Paikon Massif (Central Macedonia, Greece): A Pelagonian tectonic window? Neues jahrbuch fuer Mineralogische Abhandlunger, 269, 149-171.

Katrivanos E., Kilias A. and Mountrakis D., 2016. Deformation history and correlation of Paikon and Tzena terranes (Axios zone, Central Macedonia, Greece) E.G.E. 12

Kilias, A. 2024.The Alpine Geological History of the Hellenides from the Triassic to the Present—Compression vs. Extension, a Dynamic Pair for Orogen Structural Configuration: A Synthesis. 72.

Kilias A. 2021. The Hellenides: A multiphase deformed orogenic belt, its structural architecture, kinematics and geotectonic setting during the Alpine orogeny: Comression vs Extension the dynamic peer for the orogen making. A synthesis. Journal of Geology and Geoscience.1-56.

Kilias A., Frisch W., Avgerinas A., Dunkl I., Falalakis G. and Gawlick H.-J. 2010. Alpine architecture and kinematic of deformation of the northern Pelagonian nappe pile in the Hellenides. Austrian Journal of Earth Sciences.

Kilias A., Falalakis G. and Mountrakis D. 1999.Cretaceous±Tertiary structures and kinematics of the Serbomacedonian metamorphic rocks and their relation to the exhumation of the Hellenic hinterland (Macedonia, Greece).

Kockel, Mollat, Antoniadis P. 1970a Geological map of Greece 1:50.000, Thermi sheet, Institute of Geological and Mineral Exploration, Athens

Kockel, Antoniadis P., Ioannidis K.1970b Geological map of Greece 1:50.000, Thessaloniki sheet, Institute of Geological and Mineral Exploration, Athens

Meinhold G., Kostopoulos D. K. 2013. The Circum-Rhodope Belt, northern Greece: Age, provenance, and tectonic setting.

Mountrakis D. 2010. Geology and geotectonic evolution of Greece. Thessaloniki. :University studio press. 321 p.

Papanikolaou D. 2015. Geology of Greece. Athens: Pataki publication.433 p.

Tranos M., Kilias A. and Mountrakis D., 1999. Geometry and kinematics of the Tertiary post metamorphic Circum- Rhodope Belt Thrust System (CRBTS), Northern Greece.

17th INTERNATIONAL CONGRESS of the Geological Society of Greece

BULLETIN OF THE GEOLOGICAL SOCIETY OF GREECE, SP. PUBL.

EXTENDED ABSTRACT 116

Integrating Geotechnical Data and Site Response Analyses in the Municipality of Chalandri, Athens, Greece

Ioannidou Despoina Civil Engineer T.E. MSc, d.ioannidou12@gmail.com, CLPW, Athens, Greece & University of the Aegean, Greece

Ktenidou Olga – Joan Civil Engineer, PhD, Researcher National Observatory of Athens, Greece

ABSTRACT: I

n this work, the properties and the dynamic response of the soil formations in the area of Chalandri are investigated. Its main points are the collection and synthesis of all available data from 92 sampling boreholes, the estimation of shear velocity (Vs) through empirical correlations, the 1-D dynamic analysis of soil profiles modelled from 42 borehole locations, the zonation of the area according to site response and the production of maps showing the spatial distribution of the main characteristics of ground motions (fundamental period and amplification factor). Finally, these results were correlated with the building damage caused by the 1981 earthquake in Alkyonides.

INTRODUCTION

Local soil conditions are one of the most important factors determining the strong ground motion and consequently the seismic hazard at a specific location. Site effects have been known to modify the duration, amplitude and frequency content of ground shaking. The most commonly considered case is that of increased amplitude at specific frequencies related to the material properties (e.g. shear-wave velocity) and geometry (e.g. layer thickness), which is referred to as site amplification. Simpler cases refer to simple soil layers over bedrock while more complex ones include basin edges, topographic features, and other cases of lateral discontinuities (Bard, 1999, (Kausel & Roesset, 1984), (Pitilakis et al, 1999a) (Chavez-Garcia et al, 2000), (Raptakis et al, 2005).

The present work, which is the result of postgraduate work within the framework of the inter-institutional postgraduate program "Natural Hazards and Disaster Management" (co-organized by the University of the Aegean, the Aristotle University of Thessaloniki and the National Observatory of Athens), aims to utilize as much as possible the available information for an initial assessment of the seismic response at a large number of points in the Municipality of Chalandri, taking into account the influence of local soil conditions and their change within the area. The Municipality of Chalandri was chosen as a study area due to its size and population, but also due to the availability of a large number of data that remained unexploited for decades.

COLLECTION AND PROCESSING OF GEOTECHNICAL AND GEOPHYSICAL DATA

An extensive effort to collect data and technical information from boreholes and geotechnical surveys carried out in past decades for the Municipality of Chalandri in the Prefecture of Attica. This search, resulted in the discovery of 10 geotechnical surveys consisting of 92 sampling boreholes, which occupy most of the Municipality (as it was defined in earlier days, before its extension north), and one cross-hole test site (figure 1).

All boreholes and geotechnical surveys were drawn from the project archive of the "Geotechnical Engineering and Geology" department of the Central Laboratory of Public Works (TGMT/KEDE/YPOME).

The geological background of the Municipality of Chalandri is structured by alpine formations ('Allochthonous Unit of Attica" which includes the 'Athenian Schists" and the 'Upper Cretaceous Limestones") which are covered by significantly thick Post-alpine formations, (Lekkas et al., 1999). The Post-alpine formations are represented by Neogene and Quaternary sediments. The Neogene sediments found in Chalandri are continental formations of Upper Miocene age. (Mariolakos & Fountoulis, 2002). The Quaternary deposits that overlie all of the previous formations are loose deposits from river alluvium, of mixed phase.

From the processing and evaluation of the data from the boreholes, it became possible to distinguish the soils into three soil units I, II, III. These units represent the geological formations of the subsoil of Chalandri and are categorized into geotechnical units Ia, Ib, Ic for the Quaternary deposits and IIa, IIb for the Neogene sediments (Upper Tertiary deposits). This distinction was the result of the evaluation of the physical and geotechnical properties of the soil materials, with the aim of grouping them into specific units, characterized by a certain framework of homogeneity in terms of their mechanical behavior. The geotechnical units (Ia, Ib, Ic) consist of alternations of sandy clay with clayey silty sand and gravels of clayey composition. Unit IIb consists of lean and fat clay and unit IIa consists of marls which overlie unit IIb. Finally, unit III represents the rocky bedrock of the municipality, which consists mainly of clayey shale and cohesive shale (Table 1).

After the thorough recording and detailed statistical processing of 793 samples and 2734 tests, which included data from tests of physical properties (grain size distribution analysis, Atteberg limits, etc.), mechanical properties (unconfined compressive strength, etc.), the SPT standard penetration test, the Chalandri area is characterized by a general geotechnical section, which

consists of recent deposits (manmade fill, sandy clays, sandy silts, sandy gravels), of Upper Tertiary deposits consisting mostly of reddish-brown sandy clay and interspersed in places with layers of clayey marl and loose conglomerates and bedrock, which consists of Athenian Schist, limestone and cohesive conglomerates.

The difference seen in the processing of geological and geotechnical data is the progressive increase in the thickness of the Upper Tertiary deposits and correspondingly the increase in the depth of the rocky bedrock (Figure 2).

Therefore, according to this important detail, the area was divided, depending on the depth of the rocky bedrock, into six (6) zones, which are: Zone A: 0 – 5m., Zone B: 5 – 10m., Zone C: 10 – 20m., Zone D: 20 – 30m., Zone E: 30 – 40m. and Zone ST: >40m. (Figure 3). There is a clear NNW-SSE trending boundary in the zonation map which represents the Chalandri fault (Christoulas, et al 1983), and marks an abrupt change in sediment thickness either side.

It is worth noting that no rocky bedrock was found in zone ST, although the deepest drillings exceeded the drilling depth of 70m. Also, zone ST was deemed appropriate to be divided into two subzones (subzone ST and ST_1), which present a differentiation in terms of stratigraphy. Specifically, subzone ST_1 consists of layers of conglomerates and marls before the reddish-brown sandy clay which is the main material of the Upper Tertiary deposits.

Figure 1: Locations of 92 sampling boreholes

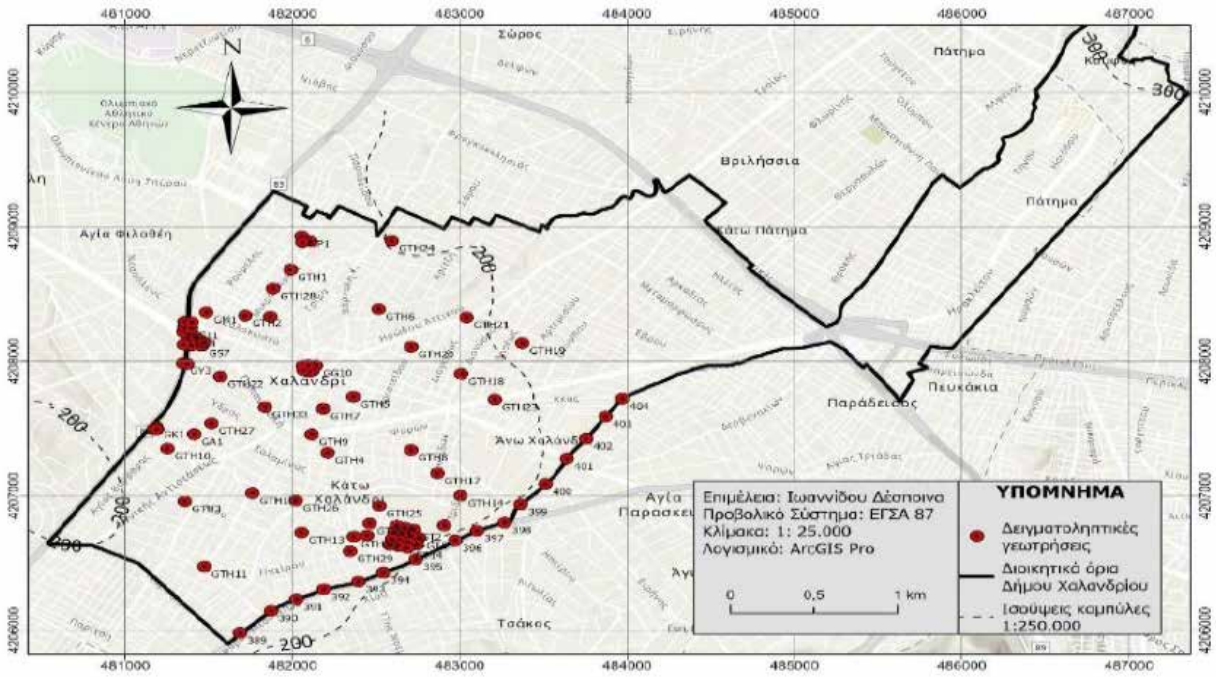

Table 1: Definition of geological – geotechnical units

GEOLOGICAL UNIT	GEOTECHNICAL UNIT	DESCRIPTION OF GEOTECHNICAL UNIT
Quaternary deposits I	A	Manmade fill
	Ia	Brown, reddish brown, yellow brown, white brown, brownish brown silty clay SAND
	Ib	Brown, reddish brown, yellow brown, ash brown sandy CLAY
	Ic	Brown, reddish brown, brownish-ash silty clayey GRAVEL
Upper Tertiary deposits II	IIa	Brown, brownish-yellow clay MARL
	IIb	Reddish brown CLAY with sand
Bedrock III		Red, brownish-ash, ash yellow CONGLOMERATES Brownish-ash, ash yellow, ash green, ash, brownish-brown CLAY SHALE and reddish, whitish-brown LIMESTONE

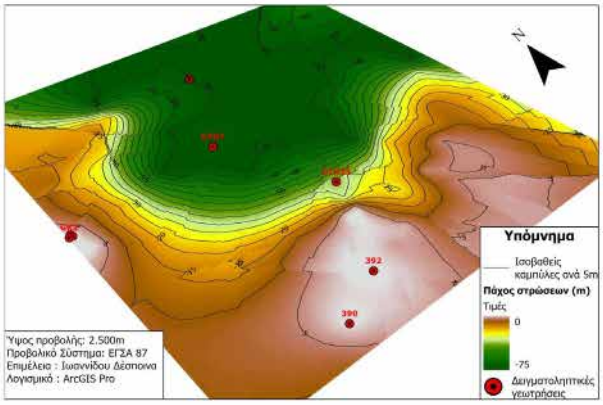

Figure 2: Spatial distribution map of layer thickness

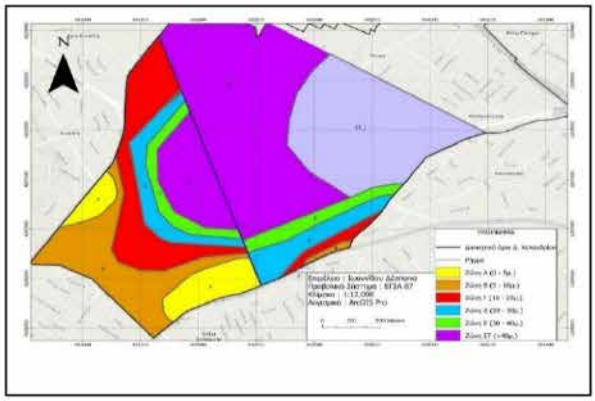

Figure 3: Division of study area into zones according to depth of bedrock

STUDY OF SEISMIC RESPONSE OF SOIL FORMATIONS

The shear wave propagation velocity Vs, in soil formations, due to the lack of a sufficient number of geophysical tests, was estimated approximately through the very extensive data of the standard penetration test Nspt (621 tests). After reviewing the literature and comparing a large number of relationships, the following empirical relationships were selected, from studies in Greek soils.

(Raptakis, et al 1994)

Vs (m/sec) = 99.95 $(N_{60})^{0.237}$ (Medium – Dense sands, Nspt>10) (1)

Vs (m/sec) = 192.41 $(N_{60})^{0.131}$ (Gravel soils) (2)

Vs (m/sec) = 10.78 (N_{60})-299.3 (Marls) (3)

(Athanasopoulos, 1995)

Vs (m/sec) = 85.3 $(Nspt)^{0.42}$ (Gravel soils) (4)

(Tsiabaos & Sabatakakis, 2011)

Vs (m/sec) = 112.2 $(N_{60})^{0.324}$ (Clay soils and marls) (5)

Vs (m/sec) = 79.7 $(N_{60})^{0.365}$ (Sandy soils) (6)

For soils consisting of clays, Vs was estimated approximately by the empirical correlation of the results of the single cross-hole test with the average of the Nspt blows for the corresponding depths of the cross-hole test values, of all the projects under study through the following relationship:

Vs (m/sec) = 7.39 $(Nspt)^{0.95}$ (7)

The data and the trend line for relationship (7) are shown in figure 4.

Figure 4: Correlation between Nspt and Vs values for clays (Nspt>8) (left) and normalized consistency ratio $C_{(d)}$ (right).

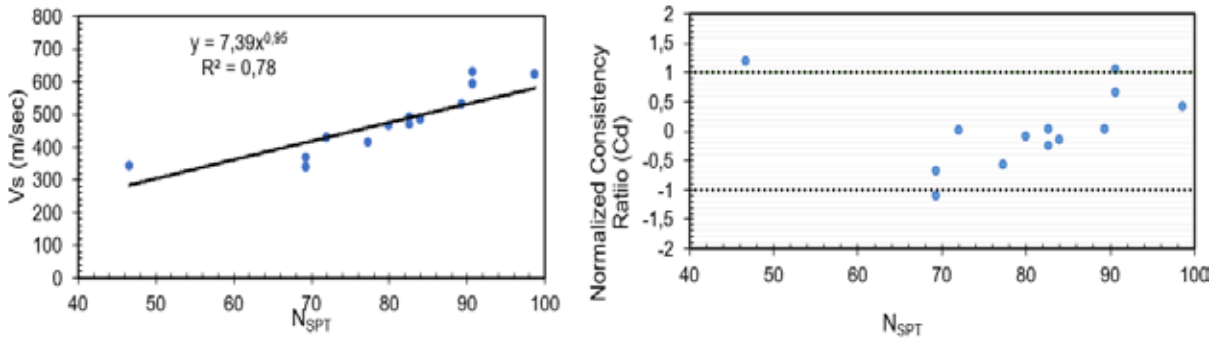

The normalized coherence ratio C(d) is given by equation 8:

C(d) = (Vsm – Vsc) / Nspt (8)

where Vsm are the measured values from the cross-hole test, Vsc are the calculated values from equation (7), and Nspt are the uncorrected values of the SPT blows. Figure 4 (right) shows the comparison between the Vsm and Vsc values. The C(d) values appear close to 0, which means that the proposed equation performs well in predicting Vsc (Table 2).

The Vs adopted for the bedrock of Chalandri is 1600 m/sec for the clayey shale of Athens (Koukis & Sabatakakis, 2000). For the seismic bedrock of zones ST and ST_1 the shear velocities adopted are 750 m/sec and 850 m/sec respectively, values representative of very hard soils and sandy clays (Chen & Ong, 2012), (Jia, 2018).
In every location of the soil profiles analyzed, the average mass density of the rocky bedrock was assumed to be equal

Table 2: Average SPT blow counts and shear wave velocities Vs for the geotechnical units of the Municipality of Chalandri

GEOTECHNICAL UNIT	Nspt	N_{60}	Raptakis et. al (1994)	Tsiambaos G. et. al (2010)	Average	Average	Raptakis et. al (1994)	Athanasopoulos G.A. (1995)	Average	Raptakis et. al (1994)	Tsiambaos G. et. al (2010)	Average	Resulting empirical relationship N_{spt}	Resulting empirical relationship N_{60}	Average
			Medium to dense sands	Sandy soil			Gravelly soil	Gravelly soil		Marls	Marls		Clayey soil	Clayey soil	
			$Vs=99.95N_{60}^{0.237}$	$Vs=79.7N_{60}^{0.365}$			$Vs=192.41N_{60}^{0.131}$	$Vs=85.3N_{spt}^{0.42}$		$Vs=10.78N_{60}-299.3$	$Vs=112.2N_{60}^{0.324}$		$Vs=7.39N_{spt}^{0.95}$	$Vs=9.71N_{60}^{0.95}$	
A	51	38	237	301	**269**										
						271*									
Ia	53	40	240	306	**273**										
Ib	57	43											344	346	**345**
Ic	60	45					317	476	**396**						
IIa	87	65								401	434	**418**			
IIb	101	76											593	594	**593**

*Because geotechnical units A and Ia have similar geotechnical properties and the average velocities Vs estimated are practically the same, for reasons of simplification of the seismic analysis, the two units were merged.

to 23 kN/m3 (Koukis & Sabatakakis, 2000) while the seismic bedrock (zone ST and ST_1) was assumed to be 22 kN/m^3 since no harder formation has been found in this zone and the average density value for the Upper Tertiary deposits was calculated to be 22 kN/m^3. The hysteretic damping ratio was assumed to be equal to 2% for the rocky-seismic bedrock and 3% for the soil layers overlying the bedrock.
The seismic excitation used for the analysis of the seismic ground response is the Athens earthquake of September 7, 1999, with a magnitude of Mw 5.9. The accelerogram chosen as the input motion was recorded at the DMK station (EKEFE Demokritos) of the National Earthquake Research Center in the area of Agia Paraskevi (NOA, 1975) and had an epicentral distance from the rupture of 25 km (esm-db.eu, Luzi et al., 2020) (figure 5). This station was chosen because it is the only one in the vicinity that lies on rock conditions. Figure 6 shows the acceleration time series at DMK station, as well as the acceleration response spectrum in the 3 components of the recording.
After merging similar soil profiles, 42 soil profiles were solved in the Chalandri area using 1D equivalent linear analysis method with the DEEPSOIL software (Hashash et al., 2020). According to this method, for any seismic excitation, the differential equations are solved using Fourier analysis in the frequency domain. Using this model and the corresponding geotechnical and dynamic properties and layer thicknesses for each zone, the corresponding transfer functions were calculated for each soil profile (Figure 7, where the groups of transfer functions for zones A, C, ST and the corresponding response spectra for damping ratio of ξ=5%, i.e. for a reinforced concrete structure, are shown).

Figure 5: Location of the DMK accelerometer (red cicle)

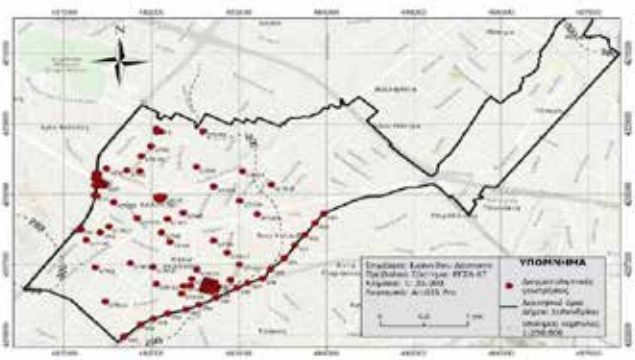

Figure 6: Acceleration time series and response spectra at DMK station

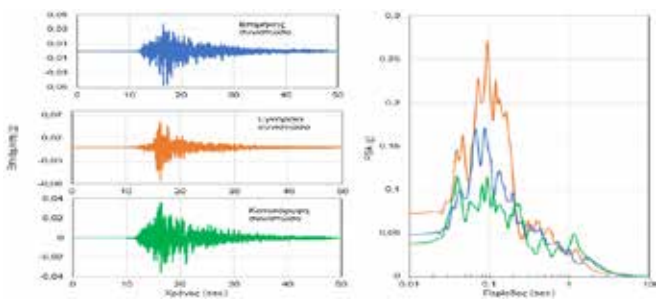

Figures 8 and 9 show the spatial distribution of the fundamental period T0 and the amplification factor in this period A0. Among the calculated values, the other values were estimated using the spatial interpolation method “Krigging”. The maps, in addition to the spatial distribution of the above parameters, also show the locations of the buildings that suffered significant damage from the 1981 Alkyonides earthquake (Christoulas et al., 1983). Also shown are the EC8 soil categories for each soil profile as calculated from the relation for shallow seismic profiles (>30m):

Log Vs 30 = (a + b) log (Vs (d)) (Boore, 2004) (9)

where Vs (d), the average velocity value for a soil profile depth of less than 30 m, a and b, coefficients for each 1m. from 10m. to 29m.

Figure 7: Transfer functions (left) and response spectra (right) computed from the 1D analyses at each borehole location within each zone (zones A,C,ST)

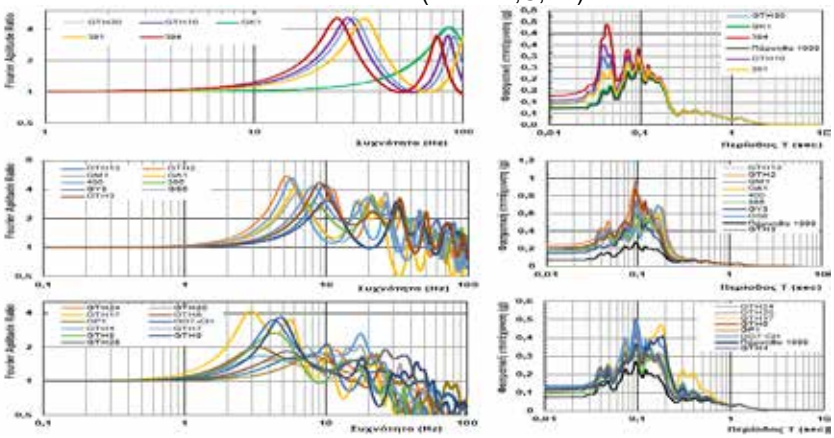

Figure 8: Spatial distribution map of fundamental period T0

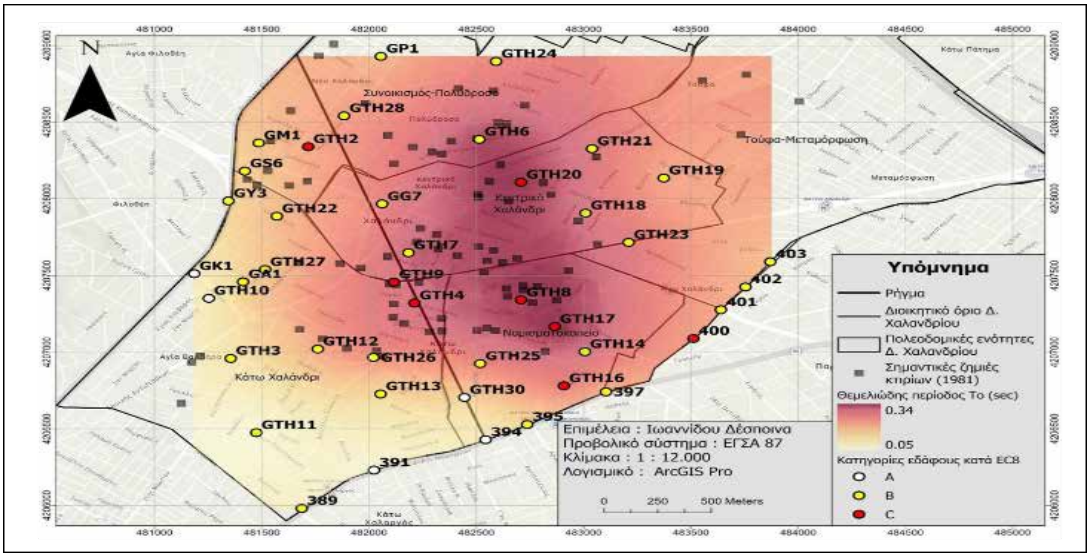

Figure 9: Spatial distribution map of amplification factor A0

Studying the maps of figures 8 and 9, and comparing the most significant building damages caused by the Alkyonides earthquake in 1981, most of the damages are observed in the northeastern and eastern part of Chalandri and mainly in central Chalandri, where the thickness of the soil deposits exceeds 20m. (zones D, E, ST), giving periods from 0.15 to 0.34 sec, values that affect single-storey to four-storey buildings. In the SW part of Chalandri, the damages appear at soil deposit depths of up to 10m. and are clearly less than in the previous case.

Evaluating all the above results and observations and according to the spatial distribution maps that were constructed, we reach the following conclusions:

• In the area of eastern Chalandri (central Chalandri, Synoikismos – Polydroso) the deepest soil deposits prevail without the rocky subsoil being known, resulting in the longest fundamental periods found of the order of 0.12sec – 0.34sec. These conclusions are restricted by the lack of basement rock in the boreholes in zone ST.

• In the area of the Nomismatokopeio, in addition to the deep deposits that prevail, the soils are looser (small number of Nspt blows, category C according to EC8), resulting in large amplification factor of the order of 4 due to the stronger impedance with the considered subsoil.
• Finally, in Kato Chalandri it seems that two areas with different depths of soil deposits prevail. To the west and around the administrative boundaries of the Municipality, shallow soil deposits prevail with cohesive soils with fundamental period of the order of 0.06sec, while further east, the deposits become deeper with looser soils giving amplification factor of the order of 4 and fundamental period of the order of 0.20sec. This is probably why the damage in the Kato Chalandri area is concentrated in its eastern part.

In this study, despite the large amount of geotechnical data collected and analyzed, unfortunately it was not possible to find geophysical data, with the exception of a cross-hole test. Thus, the estimation of Vs was based on empirical formulas in correlation with the Nspt blows and the results of a single cross-hole test. This lack of data constitutes one of the main limitations of the present study, combined with the fact that the depth of most boreholes does not reach 30 meters and often does not reach the bedrock (this latter limitation leads to the lack of content of the seismic analyses at shorter periods that would be associated with the deeper soil layers). On the other hand, the relatively small difference between the Vs of the soil layers leads to relatively low levels of amplification, which for higher impedance values would potentially lead to higher ground motion around the resonance frequencies. In the future, and towards a more theoretical investigation of uncertainties, a new analysis could be carried out including variations in the Vs values, following statistical processing and randomization of the profiles. Furthermore, given that maximum ground accelerations greater than 0.20 g were estimated at the surface of some soil profiles, it would be advisable to carry out a non-linear analysis of the soil formations. This could lead (due to the reduction of the stiffness and the velocity Vs in the shallower layers) to somewhat lower amplifications and natural frequencies.

BIBLIOGRAPHY

Αθανασόπουλος, Γ. (1995). Εμπειρικές συσχετίσεις Vs - Nspt και Go - Nspt από αποτελέσματα δοκιμών σε Ελληνικά εδάφη. Τεχνικά Χρονικά, 7-28.

Λέκκας, Ε., Σούκης, Κ., Λόζιος, Σ., & Αντωνίου, Β. (1999). Χρήση των ΓΠΣ (GIS) στον Αντισεισμικό Σχεδιασμό και την οργάνωση του Δήμου Χαλανδρίου. Πρακτικά 5ου Πανελλήνιου Γεωγραφικού Συνεδρίου. Αθήνα: ΕΓΕ

Χριστούλας, Σ., Τσιαμπάος, Γ., & Σαμπατακάκης, Ν. (1983). Γεωτεχνική Έρευνα: Έδαφος Θεμελιώσεως περιοχής Χαλανδρίου και σεισμοί του 1981. ΚΕΔΕ ΕΚ1α. Αθήνα: Μη δημοσιευμένη έκθεση.

Bard, P. Y., 1999. Local effects on strong ground motion: Physical basis and estimation methods in view of microzoning studies, in Proceedings, Advanced Study Course on Seismotectonic and Microzonation Techniques in Earthquake Engineering 4, Kefallinia, Greece, pp. 127–218

Boore, D. (2004). Estimating Vs(30) (or NEHRP Site Classes) from Shallow Velocity Models (Depths < 30 m). Bulletin of the Seismological Society of America, pp. 591– 597.

Chavez-Garcia, J., Raptakis, G., Makra, A., & Pitilakis, K. (2000). Site Effects at EUROSEIST - II: Results from 2D Numerical Modelling and Comparison with Observations. Soil Dynamics and Earthquake Engineering (1), pp. 23-39.

Chen, S., & Ong, C. (2012). Spectral Analysis of Surface Wave for Empirical Elastic Design of Anchored Foundations. Advances in Civil Engineering. doi:10.1155/2012/635257

Hashash, Y., Musgrove, M., Harmon, J., Ilhan, O., Xing, G., Numanoglu, O., Park, D. (2020). DEEPSOIL 7.0. User Manual. Urbana, Illinois, USA.

Jia, J. (2018). Soil Dynamics and Foundation Modeling (Τόμ. Chapter 2). Springer International Publishing AG.

Kausel, E., & Roesset, J. (1984). Soil amplification: some refinements. International Journal of Soil Dynamics and Earthquake Engineering, pp. 116-123.

Koukis, G., & Sabatakakis, N. (2000). Engineering geological environment of Athens, Greece. Bulletin of Engineering Geology and the Environment, pp. 127-135. doi:10.1007/s100640000058

Mariolakos, I., & Fountoulis, I. (2002). The Athens Earthquake September 7, 1999 Neotectonic Regime and Geodynamic Phenomena. NATO Science Series, pp. 113- 126.

Luzi L., et al. (2020). Engineering Strong Motion Database (ESM) V2.0. INGV. https://doi.org/10.13127/ESM.2

National Observatory of Athens, Institute of Geodynamics, Athens. (1975). https://doi.org/10.7914/SN/HL

Pitilakis, K., Raptakis, G., & Makra, A. (1999a). Site Effects: Recent Consideration and Design Provisions. Proceedings of the 2nd International Conference on Earthquake Geotechnical Engineering. Lisbon.

Raptakis, D., Anastasiadis, A., Pitilakis, K., & Lontzetidis, K. (1994). Shear wave velocities and damping of Greek natural soils. 11th European Conference on Earthquake Engineenng, (pp. 477-482). Vienna.

Raptakis, G., Manakou, M., Chavez-Garcia, J., Makra, A., & Pitilakis, K. (2005). 3D Configuration of Mygdonian Basin and Preliminary Estimate of its Site Responce. Soil Dynamics and Earthquake Engineering (11), pp. 871-887.

Tsiabaos, G., & Sabatakakis, N. (2011). Empirical estimation of shear wave velocity from in situ tests. Bull. Eng. Geol. Environ., pp. 291-297. doi:10.1007/s10064-010-0324- 9

17th INTERNATIONAL CONGRESS of the Geological Society of Greece

BULLETIN OF THE GEOLOGICAL SOCIETY OF GREECE, SP. PUBL.

EXTENDED ABSTRACT 117

Seismic vulnerability of cultural heritage. The case of the archaeological museum of Rhodes: building performance, safety of the public and exhibits

Irakleidis A.-K.[1] Ktenidou O.-J.[2]

(1) Civil Engineer, graduate of the Inter-Institutional Master Course «Natural Hazards and Disaster Mitigation»

(2) Senior Researcher at National Observatory of Athens, Greece

Introduction / Background

Natural disasters and especially earthquakes in seismically active areas such as Greece, constitute the most significant risk that threatens tangible cultural heritage: buildings and other structures (bridges, aqueducts, etc.), archaeological and historical sites but also artifacts of everyday life, funerary objects, works of art, etc. that are kept in warehouses or exhibited in museums.

The vulnerability of buildings belonging to cultural heritage is high: constructed of load-bearing masonry – a brittle material – they do not possess the structural characteristics that allow them to absorb the energy released by an earthquake, without being subject to damage and ultimately collapse. Respectively, objects placed on pedestals, shelves, in display cases or suspended from ceilings and walls, etc., under a strong earthquake run a high risk of suffering damage that is often irreversible, even when the museums themselves remain intact.

In recent major earthquakes in Greece, as well as in other seismically active countries, monuments and museum exhbits were the ones that were most affected.

The aim of this paper is to demonstrate the relationship between the requirement for the protection of human life, while simultaneously protecting the monumental values carried by buildings and objects that belong to cultural heritage.

A case study of a building located in an area with a rich seismic history was examined, for which it was possible to collect data in order to highlight the objectives of the work. The Archaeological Museum of Rhodes was chosen, that is a building built from the island's Hospitaller Knights of St. John (1310-1522) as their New Hospital. The building was completed in 1489 and is located within the Medieval City of Rhodes, an area where data on the dynamic behavior of its soil formations is available from previous studies, while the bibliography is rich in data for the structural types and the mechanical properties of the materials of the buildings of this World Heritage Site.

The seismic vulnerability of the building was studied with modern computational methods, following the provisions of the Code for interventions in buildings made of load-bearing masonry (KADET), while the stability of exhibits on pedestals was calculated with procedures proposed in the American regulation FEMA P-58 and other sources. The results of the preliminary analyzes are interesting. On the one hand, as expected, the iconic medieval building turns out to fall short of modern requirements for the seismic vulnerability of museum buildings. On the other hand, museum exhibits that are placed on the museum floors with conventional support methods (usually on pedestals that are not anchored to the floor) prove to be particularly vulnerable to earthquakes – indeed considerably smaller than those expected to cause damage to the building itself. The above results are consistent with what has been observed in recent and past earthquakes. For this reason, extensive research on this field is undergoing internationally in order to mitigate seismic risk for monuments and museum exhibits.

Seismic vulnerability of the archaeological museum of Rhodes

From an architectural point of view, the building under study is a Gothic building with Renaissance elements. In plan, it covers an area of approximately 3600 m^2 with a maximum dimension in the N-S direction of 65 m and in the E-W direction of 60 m. It has two floors and its main morphological characteristic is the large atrium in the center that covers an area of approximately 500 m^2, which is surrounded by the rooms. The first floor is dominated by the large "patients' hall", an elongated hall on the facade of the building (eastern side) measuring 54.0 m x 14.0 m, with a central arcade consisting of 7 intermediate octagonal columns. The height of the large hall is greater than the rest of the floor by approximately 3.0 m and dominates the facade of the building.

The buildings' load bearing walls are made of three-leaf masonries. The main building material is the local yellowish sandstone, which is the material of all the buildings of the medieval city and its fortresses. The mechanical characteristics of the walls were assumed to be the same as those used in a recent research work for the nearby Arsenal de Milly (Cattari et al, 2015). The ground floor ceiling is made of masonry vaults, while the first floor is covered with reinforced concrete slabs that are the result of the most recent large scale intervention on the building, dated back in the 1920's when Rhodes came under the Italian colonial rule.

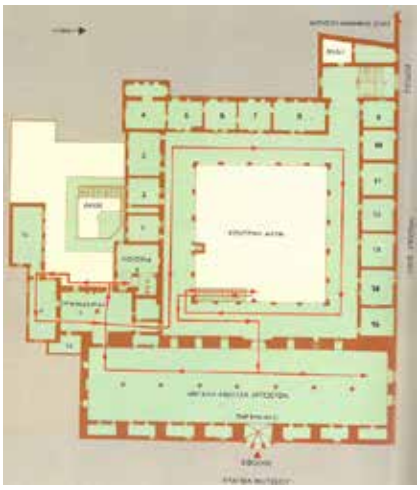

Figure 1: Plan of the 1st floor of the museum (source: I. Kollias, 1991, The Knights of Rhodes)

The underground conditions of the Medieval City of Rhodes were studied in the past by the Aristotle Polytechnic School (1997) and results for the dynamic response at the ground surface were taken into account in the analyses. In the next figure the division of the medieval city of Rhodes in distinct zones is presented.

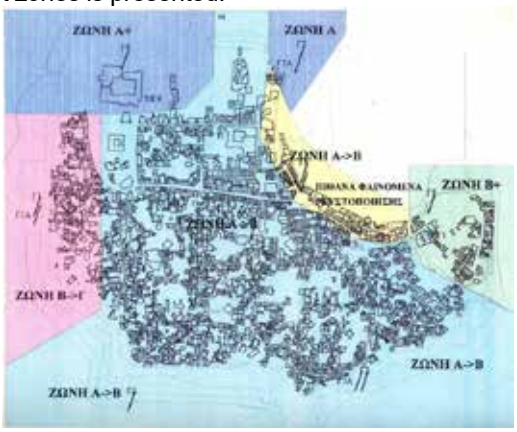

Figure 2: Division of the Medieval City into distinct zones according to their seismic response

The building was simulated with the equivalent frame model method, using the specialized commercial software package 3MURI. This method reduces the plane walls into three types of elements: piers (vertical elements), lintels (horizontal elements) and rigid nodes.

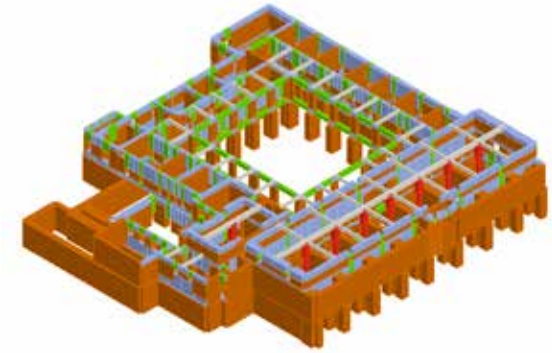

Figure 3: Three-dimensional model of equivalent frames (3MURI software)

Two types of analysis were performed on the geometric model of the building:
a) Modal analysis, which determines the vibration modes of the building and their degree of participation in the overall response of the structure, and

b) equivalent static nonlinear analysis (pushover).
The modal analysis of the model provides all possible eigenmodes of the building's oscillation and contributes to a better understanding of its dynamic behavior in the frequency domain.
From the analysis performed, it was found that the significant eigenmodes that oscillate at least 75% of the seismic mass of the building per direction are more than one and they are ranging between 0,13s and 0,23s – it is a very stiff building indeed. This fact is not surprising. Despite the existence of rigid concrete slabs on the roof of the first floor, diaphragmatic behavior is not ensured. The slabs lack of continuity over the entire surface of the building's floor plan, as they are interrupted by the large atrium in the center the different level of the building's two largest rooms at the first floor.
On the other hand, the pushover analysis helps to identify the weaknesses of the structural system and assess its seismic adequacy for a selected performance level and level of the seismic hazard. A variety of performance levels may be introduced and checked depending on the significance and the level of exposure of the examined building. In the case study, these levels were determined by the current Greek regulation (KADET) for museum buildings, which are significantly higher than those for typical residential buildings.
Despite certain limitations of the application of pushover method to this building, it provides some useful insight to its response. The building shows significant damage for most of the examined scenarios at its upper floor, while the ground floor remains intact. This means that if a desired level of safety, as determined by the current seismic regulations should be reached, measures to strengthen the building's upper floor should be studied and implemented.

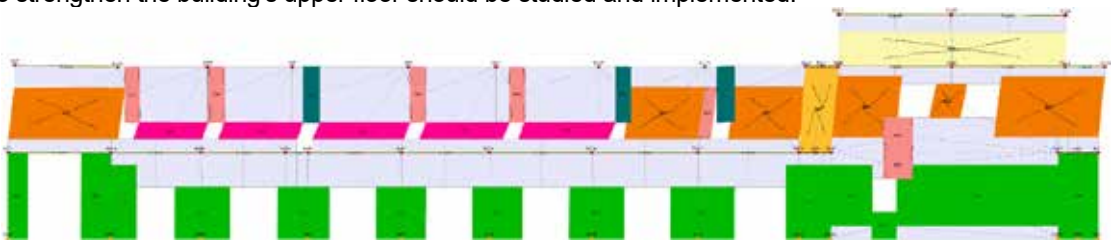

Figure 4: Illustration of the plane model of a characteristic wall of the building at the last step of the pushover analysis (3MURI software). With different colors are shown the different modes and levels of failure of the elements.

Seismic vulnerability of museum artifacts
The stability of museum artifacts depends on many factors, such as the characteristics of the incoming earthquake, the response at each point of the building, the location, the materials involved and the method of support of the exhibits etc. In the present study, a simplified method of analysis of the stability of museum exhibits that are mounted on pedestals that rest freely on the museum floor was used. The procedure is provided in the American code FEMA P-58 and its application field includes the seismic stability of building equipment items, such as libraries, devices freely placed on the floor, etc.
In the method, two limit states are examined: the limit state against overturning and the limit state against sliding, whichever appears first. Its philosophy is based on the assumption that objects are allowed to slide or rock, up to a maximum limit, which is determined by a median maximum floor velocity. This limit is determined in such a way that if the object slides, the distance traveled does not endanger its integrity due to a fall or collision, while if the object rocks, it does not risk overturning after a few rocking cycles. In the present work, although median maximum floor velocity is calculated, a more conservative approach is adopted due to the great importance of the exhibits: it is the onset of rocking or sliding which signals failure. And as the sliding coefficient is a more controllable parameter, the critical acceleration $S_{a0}S_{a0}$ for the onset of rocking was considered as a criterion of failure.

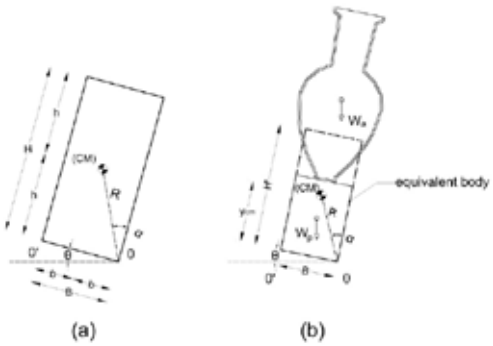

Figure 5: Geometric definitions of the method by Spyrakos et al (2017)

Using the formulas of the aforementioned method, the stability of a large number of objects from the museum's sculpture exhibition was examined, taking into account in a simplified manner their actual geometric characteristics. From the calculations performed, it was found that failure of exhibits is expected even for small earthquakes. The percentage of failure is increased when artifacts are exhibited on a higher floor, where seismic acceleration is amplified compared to the ground acceleration.
It is indicated that for an earthquake for which the museum building should not develop damage (performance level A2 according to the Greek intervention code), at least 7% of the exhibits are expected to begin to rock. This percentage is increasing significantly if these exhibits are placed on a floor.
It is concluded that even if the results of the simplified calculations presented in this chapter are conservative and based on assumptions that have large margins of error, they confirm what is already known from recent international and local experience: museum artifacts are not earthquake-proof and the main risk they run does not come so much from the failure of the building as from the loss of their stability due to strong ground motion.
From this point of view, such simple calculation methods are extremely useful for quickly assessing the risk of overturning or sliding of exhibits, but they certainly do not replace more detailed and accurate methodologies which, however, require reliable data in order to be useful and practically usable.

Discussion

Seismic safety of museums and artifacts is a subject of great scientific and technological interest, on which research is being developed internationally. The building under study, the archaeological museum of Rhodes has a monumental character and at the same time it hosts an important archaeological exhibition. Thus, both the integrity of the building and the safety of the exhibits are of great importance.
The methodology used and analyses performed under the present work meet certain limitations and further work is needed. More specifically, regarding the study of the building, a more detailed knowledge of its structural system and the materials it consists of is required. More sophisticated analyses would give a better insight to its seismic response at every location, which would be particularly useful for a reliable analysis of the seismic performance of the building and for the stability analysis of the exhibits as well. Furthermore, more complex models for the calculation of the rocking characteristics of artifacts, based on detailed geometric mapping would provide a better understanding of their safety margins under earthquake loading and in the selection and development of new appropriate methods of supporting and displaying museum artifacts.

Acknowledgements

Among the people who helped in one way or another in the preparation of this work, we feel the need to acknowledge the contribution of Dr. Dimitrios Vamvatsikos, associate professor at NTUA, whose initial ideas and directions formed the basis for the present work.

References

Αριστοτέλειο Πανεπιστήμιο Θεσσαλονίκης, Τμήμα Πολιτικών Μηχανικών, Τομέας Γεωτεχνικής Μηχανικής. ΤΔΠΕΑΕ Επιτροπή Παρακολούθησης Μνημείων Μεσαιωνικής Πόλης Ρόδου. Ερευνητικό Πρόγραμμα 9233 – Στερεωτικά Προβλήματα Οχυρώσεων της Μεσαιωνικής Πόλης της Ρόδου, Μάρτιος 2000.

Βαδαλούκας Γ., Βιντζηλαίου Ε., Γκανάς Α., Γιαρλέλης Χ.,Ζιωτοπούλου Κ., Θεοδουλίδης Ν., Καρασαντέ Η.,Μάργαρης Β., Μυλωνάκης Γ., Παπαχρηστίδης Α., Ρεπαπής Κ., Ψαρρόπουλος Π., Σέξτος Α. (2020). Σεισμός Σάμου, 30 Οκτωβρίου 2020-Προκαταρκτική Έκθεση της ΕΤΑΜ, 65 σελ.

Βλάχος Ν., Διαμαντόπουλος Σ., Φραγκιαδάκης Μ. Σεισμική συμπεριφορά έργων τέχνης που εδράζονται σε άκαμπτη λικνιζόμενη βάση. 4ο Πανελλήνιο Συνέδριο Αντισεισμικής Μηχανικής και Τεχνικής Σεισμολογίας., Αθήνα, 5-7 Σεπτεμβρίου 2019

Λέκκας, Ε., Σταυρακάκης Γ., Σακελλαρίου Δ., Λόζιος, Σ. (1995). Εφαρμοσμένο ερευνητικό πρόγραμμα: Αντισεισμικός Σχεδιασμός και Οργάνωση Δήμου Ρόδου. Εθνικό και Καποδιστριακό Πανεπιστήμιο Αθηνών. Σχολή Θετικών Επιστημών – Τμήμα Γεωλογίας. Τομέας Δυναμικής Τεκτονικής και Εφαρμοσμένης Γεωλογίας. Έκδοση: ΤΕΕ – ΤΜΗΜΑ ΔΩΔΕΚΑΝΗΣΟΥ, Δεκέμβριος 1995.

Λέκκας, Ε., Λόζιος, Σ., Σκούρτσος, Ε., Βασιλάκης, Ε., Δανάμος, Γ. (2008). Πιλοτικό Πρόγραμμα Πολιτικής Προστασίας για την αντιμετώπιση των Φυσικών Κινδύνων στη Ν.Α. Δωδεκανήσου. Μέρος Β. Ανάλυση Φυσικών Κινδύνων. Τεύχος Β-10. Νήσος Ρόδος. Εθνικό και Καποδιστριακό Πανεπιστήμιο Αθηνών, Τμήμα Γεωλογίας και Γεωπεριβάλλοντος, 56 σελ.

Λέκκας, Ε., Παπανικολάου, Δ., Σακελλαρίου, Δ. (1998). Νεοτεκτονικός Χάρτης της Ελλάδας, Φύλλο Ρόδος, κλίμακα 1:100.000. Ευρωπαϊκό Κέντρο Πρόληψης και Πρόγνωσης Σεισμών, Οργανισμός Αντισεισμικού Σχεδιασμού και Προστασίας, Επιτροπή Τεκτονικής της Ελληνικής Γεωλογικής Εταιρίας.

Μαυρούλης Σπυρίδων. Σύνταξη οδηγιών για τη διεξαγωγή Άσκησης Εκκένωσης της Μεσαιωνικής Πόλης της Ρόδου. Ο.Α.Σ.Π. Δράση του ΕΚΠΠΣ – Preseismic assessment of the traditional dwellings, vulnerability assessment and evacuation of the old town of Rhodes. Νοέμβριος 2021.

Παπαδόπουλος Α. Γεράσιμος (2014), Ρόδος - Οι Σεισμοί και τα Τσουνάμι από την Αρχαιότητα μέχρι Σήμερα. Εκδόσεις Οσελότος

Σπυράκος Κωνσταντίνος. Κατασκευές από τοιχοποιία. Αποτίμηση και επεμβάσεις για σεισμικά φορτία (2019). Α΄ έκδοση ISBN: 9786180012569 Εκδόσεις ΕΡΓΟΝΟΜΟΣ

Υπουργείο Πολιτισμού, Γενική Διεύθυνση Αρχαιοτήτων, Διεύθυνση Συντήρησης Αρχαιοτήτων. Σεισμοί και Αρχαιότητες. Προληπτικά και Πρώτα Σωστικά Μέτρα. Σ.Γκιώση, Μ.Κρίνη, Θ.Μαραγκού, Π.Πρόκος. Αθήνα, 2002 ISBN: 960-214-686-9

Ψυχάρης Ι., Ταφλαμπάς Ι. Προκαταρκτική εκτίμηση της εδαφικής κίνησης στην πόλη της Κω στο σεισμό της 21.07.2017, Νοέμβριος 2017, https://psycharis.weebly.com/uploads/1/6/2/5/16258088/kos.pdf

Ψυχάρης Ι. και συνεργάτες. Καταρρεύσεις αρχαίων μνημείων και καινοτόμες μέθοδοι βελτίωσης της σεισμικής τους συμπεριφοράς. Η περίπτωση του σεισμού της Κω 2017. https://5psamts.eltam.org/katarrefseis-archaion-mnimeion-kai-kainotomes-methodoi-veltiosis-tis-seismikis-tous-syberiforas-i-periptosi-tou-seismou-tis-ko-2017/

Χρήστου Α. (2020). Προσομοιώσεις της ισχυρής σεισμικής κίνησης στο κοντινό πεδίο του σεισμού της Κω-Αλικαρνασσού 2017. Μεταπτυχιακή διπλωματική εργασία. Τμήμα Γεωλογίας, Τομέας Γεωφυσικής ΑΠΘ. Τριμελής Εξεταστική Επιτροπή: Κυρατζή Α., Θεοδουλίδης Ν., Ρουμελιώτη Ζ.

Ambraseys, N.N., Adams, R.D. The Rhodes earthquake of 26 June 1926. *Journal of Seismology* **2**, 267–292 (1998). https://doi.org/10.1023/A:1009706415417

Baggio S., Berto L., Rocca I., Saetta A. Vulnerability assessment and seismic mitigation intervention for artistic assets: from theory to practice, Engineering Structures, Volume 167, 2018, Pages 272-286, ISSN 0141-0296, https://doi.org/10.1016/j.engstruct.2018.03.093.

Bommer, J. J., & Alarcon, J. E. (2006). THE PREDICTION AND USE OF PEAK GROUND VELOCITY. Journal of Earthquake Engineering, 10(1), 1–31. https://doi.org/10.1080/13632460609350586

Booth, E. (2007). The Estimation of Peak Ground-motion Parameters from Spectral Ordinates. Journal of Earthquake Engineering, 11(1), 13–32. https://doi.org/10.1080/13632460601123156

Cattari, S., Karatzetzou, A., Degli Abbati, S., Pitilakis, D., Negulescu, C., Gkoktsi, K. (2015). Seismic Performance Based Assessment of the Arsenal de Milly of the Medieval City of Rhodes. In: Psycharis, I., Pantazopoulou, S., Papadrakakis, M. (eds) Seismic Assessment, Behavior and Retrofit of Heritage Buildings and Monuments. Computational Methods in Applied Sciences, vol 37. Springer, Cham. https://doi.org/10.1007/978-3-319-16130-3_15

Diamantopoulos, Spyridon & Fragiadakis, Michalis & Sextos, Anastasios. (2019). Dynamic response of museum artefacts standing on a pedestal.

EPPO//LCR-NTUA Chronopoulos M., Psycharis I., Trezos K. (2016): Draft proposal for Aseismic Design of Non-Structural Components.

FEMA P-58-1, December 2018. Seismic Performance Assessment of Buildings. Volume 1 – Methodology Second Edition

Fragiadakis, Michalis & DiSarno, L. & Saetta, A. & Castellano, Maria Gabriella & Irene, Rocca & Diamantopoulos, Spyridon & Crozet, Vincent & Politopoulos, Ioannis & Chaudat, Thierry & Vasic, S. & Bal, İhsan & Smyrou, Eleni & Psycharis, I. & Hutchinson, Tara & Berto, L.. (2020). Experimental seismic assessment and protection of museum artefacts. 3381-3396. 10.47964/1120.9277.20698.

Ishiyama Yuji Motions of rigid bodies and criteria for overturning by earthquake excitations. Earthquake engineering and Structural Dynamics, Vol.10, 635-650 (1982)

Karaferi E., Melissianos V., Vamvatsikos D. (2022) A preliminary urban seismic risk model for the City of Rhodes Greece. 3rd European conference on earthquake engineering & seismology Bucharest, Romania, 2022

Karatzetzou, A., Pitilakis, D., Kržan, M. et al. Soil–foundation–structure interaction and vulnerability assessment of the Neoclassical School in Rhodes, Greece. Bull Earthquake Eng 13, 411–428 (2015). https://doi.org/10.1007/s10518-014-9637-6

Karatzetzou, A., Negulescu, C., Manakou, M. et al. Ambient vibration measurements on monuments in the Medieval City of Rhodes, Greece. Bull Earthquake Eng 13, 331–345 (2015). https://doi.org/10.1007/s10518-014-9649-2

Kassaras, I., Kapetanidis, V., Ganas, A., Tzanis, A., Kosma, C., Karakonstantis, A., Valkaniotis, S.,Chailas, S., Kouskouna, V., Papadimitriou, P. (2020). The New Seismotectonic Atlas of Greece (v1.0) and Its Implementation. Geosciences, 10 (11), 447. https://doi.org/10.3390/geosciences10110447

Koumousis Vlasis (2008) Seismic Isolation System for the Statue of Hermes at the Archaeological Museum of Olympia. Advances in Protection of Museum Collections from Earthquake Damage. Pages 125-134. Publisher J. Paul Getty Museum. Symposium held at the J.Paul Getty Museum at the villa on May 3-4, 2006.

Lagomarsino, S. Seismic assessment of rocking masonry structures. Bull Earthquake Eng 13, 97–128 (2015). https://doi.org/10.1007/s10518-014-9609-x

Lekkas, E., Lozios, S., Sakellariou, D. (1997a). Neotectonic and Engineering Geological Mapping of the area of Rhodos Municipality, Greece, as a tool for Earthquake Planning and Organization. Proceedings of the International Symposium on Enginnering Geology and the Environment, organized by the Greek National Group of IAEG / Athens / Greece, 23-27 June 1997, Enginnering Geology and the Environment, Marinos, P.G., Koukis, G.C., Tsiambaos, G.C., Stournaras, G.C. (eds), p. 1335-1340.

Lekkas, E ., Lozios, S ., Sakellariou, D . (1997b). Rhodes Island. In: The Islands of the Aegean World, Lekkas, E., Kaplanides, A., Lozios, S. and Sakellariou, D. (eds), International Symposium Engineering Geology and the Environment, Post Symposium Tour 3 - “The Islands of the Aegean World”.

Lekkas, E., Papanikolaou, D., Sakellariou, D. (1998b). Neotectonic Map of Greece, Rhodes Sheet, scale 1: 100,000. European

Center for Earthquake Prevention and Forecasting, Organization for Earthquake Planning and Protection, Tectonic Committee of the Hellenic Geological Society.

Lekkas, E., Sakellariou, D., Bertakis, G., Lozios, S. (1998a). Location of geohazards at Rhodes island, SE Greece. Proceedings of the Eighth International Association for Engineering Geology and the Environment, 21-25 September 1998, Vancouver, Canada, Moore, D., Hungr, O. (eds), p. 953-958.

Lekkas, E., Sakellariou, D., Lozios, S. (1998c). A Proposal for Earthquake Emergency Planning of Rhodes Municipality (Greece). WIT Press, vol. 31, 10 p., doi: 10.2495/RISK980161

Papayanni I, Stefanidou M,Konopisi S, Anastasiou E, PachtaV (2004) Stability issues of the fortification of the Medieval City of Rhodes, Technical report (in Greek). Laboratory of BuildingMaterials, Civil Engineering Department, Aristotle University of Thessaloniki

Pitilakis, D., Karatzetzou, A. Dynamic stiffness of monumental flexible masonry foundations. Bull Earthquake Eng 13, 67–82 (2015). https://doi.org/10.1007/s10518-014-9611-3

Pitilakis, K., Riga, E., Apostolaki, S. et al. Seismic hazard zonation map and definition of seismic actions for Greece in the context of the ongoing revision of EC8. Bull Earthquake Eng (2024). https://doi.org/10.1007/s10518-024-01919-8

J. Podany, Advances in the Protection of Museum Collections from Earthquake Damage, Los Angeles, USA, J. Paul Getty Museum, 2008.

Prota A., Zito M., D'Angela D., Toscano G., Ceraldi C., Fiorillo A. & Magliulo G. (2022) Preliminary Results of Shake Table Tests of a Typical Museum Display Case Containing an Art Object. Advances in Civil Engineering https://doi.org/10.1155/2022/3975958

Prota A., Zito M., D'Angela D., Toscano G., Ceraldi C., Fiorillo A. & Magliulo G. (2023). Dynamic Properties and Seismic Response of a Museum Display Case with an Art Object. In: Cimellaro, G.P. (eds) Seismic Isolation, Energy Dissipation and Active Vibration Control of Structures. WCSI 2022. Lecture Notes in Civil Engineering, vol 309. Springer, Cham. https://doi.org/10.1007/978-3-031-21187-4_72

Spyrakos, Constantine & Maniatakis, Charilaos & Taflampas, Ioannis. (2008). Assessment of seismic risk for museum artifacts. The 14th World Conference on Earthquake Engineering October 12-17, 2008, Beijing, China

Spyrakos, Constantine & Maniatakis, Charilaos & Taflampas, Ioannis. (2017). Application of predictive models to assess failure of museum artifacts under seismic loads. Journal of Cultural Heritage. 23. 11-21. 10.1016/j.culher.2016.10.001.

Jie Qin, Botao Ma, Maomao Song, Mansheng Zhang, Zhizhong Guan, Ling Zhang and Jiaqi Ge. Preventive Seismic Protection Technologies to Museum Collections: Quanzhou Museum of China Case Study. Journal of Physics: Conference Series, Volume 1624, Advanced Algorithms, Analysis Model, Optimization Design and Its Application DOI 10.1088/1742-6596/1624/4/042073

Weiguo Yang, Xiaoguang Zou, Meng Wang, Pei Liu, Rapid seismic risk assessment method for museum exhibition halls based on seismic safety of artifacts, Engineering Failure Analysis, Volume 153, 2023, 107552, ISSN 1350-6307, https://doi.org/10.1016/j.engfailanal.2023.107552.

http://odysseus.culture.gr/h/4/gh41.jsp?obj_id=3665

https://oasp.gr/eleghos-mi-domikis-trototitas

https://www.archaiologia.gr/blog/2014/01/29/kefalonia-mouseio/

http://www.gein.noa.gr/Documents/pdf/ekthesi_G_I_26-2-2014_v2.pdf

https://www.gein.noa.gr/Documents/pdf/Kefalonia2014_ekthesi_G_I.pdf

https://kefalonianmantata.gr/διεθνής-ημέρα-μουσείων-μια-απογοητευ/

https://www.itsak.gr/uploads/news/earthquake_reports/EQ_COS_20170721_M6.6.pdf

https://www.eltam.org/images/nltr/newsletters/20201125/etam_report_samos2020earthquake.pdf

https://www.protothema.gr/culture/article/1060445/o-seismos-traumatise-mouseia-kai-arhaiologikous-horous-se-samo-kai-hio/

https://www.rodiaki.gr/article/362325/oi-filoi-poybombardizan-alyphta-th-mesaiwnikh-polh

https://culturalheritagestudies.ceu.edu/concept-and-history-cultural-heritage

17th INTERNATIONAL CONGRESS of the Geological Society of Greece

BULLETIN OF THE GEOLOGICAL SOCIETY OF GREECE, SP. PUBL.

EXTENDED ABSTRACT 118

Rock slope stability analysis on the road axis of Kleisoura – Kastoria, Greece

Irakliotis A. W.[1] Papathanassiou G.[1]

(1) School of Geology, Aristotle University of Thessaloniki, Greece, airak@geo.auth.gr

Background

Transport corridors, like other infrastructure such as fuel lines, telecommunication, water, sewage and energy corridors, are highly vulnerable to landslide phenomena. Landslides pose a threat to both infrastructure and human lives, with their impacts ranging from minor disruptions to economic catastrophes (Crozier et al., 2005). A variety of transport infrastructure projects require the excavation of rock cuts. The design process of rock cuts is usually concerned with details of the structural geology, meaning the orientation and characteristics of the discontinuities. In cases where the rock strength is much higher than the stresses in the rock, where there is little concern of fracturing, the design of slopes is primarily concerned with the stability of rock blocks formed by the discontinuities (Wyllie et al., 2017). The process of studying the discontinuities that characterize a certain rock mass should always involve a field investigation where geotechnical data is collected. This typically involves the collection of the discontinuities' orientation measurements using a geological compass, their characteristics, such as spacing, length and roughness, using a line measure and a profilometer, the compressive strength of their surfaces using a Schmidt hammer and more. In recent years remote sensing technologies such as the use of Terrestrial Laser Scanners or Airborne Laser Scanners have been extensively used to help assess hazards in rock slopes, particularly in regard to the mapping of discontinuities. A similar approach can be achieved using an Unmanned Aerial Vehicle (UAV) combined with the application of the photogrammetry method (Papathanassiou, 2022). Useful data, such as discontinuity orientation and certain characteristics, can then be extracted and used in rock slope stability analysis, in combination with the field obtained data.

Objectives

The present study focuses on the stability analysis of a rock slope along the Kleisoura – Kastoria road axis. One of its objectives is to highlight the usage of modern remote sensing techniques, particularly the use of Unmanned Aerial Vehicles, in the mapping of rock slopes and the evaluation of their stability. For the purposes of stability analysis both traditional and modern data collection methods have been utilized. The main objective is the assessment of the rock mass behavior, in order to predict future failures and suggest remedial measures to protect the infrastructure.

Methods

The methodology applied in this study can be divided into three parts.

The first part consists of the site reconnaissance where all available data concerning the study area was collected. This includes geographical, geological and hydrogeological data, as well as information concerning the tectonics and seismicity of the study area.

The second part includes the engineering geological field survey, where all necessary measurements, such as discontinuity orientations and characteristics, Schmidt hammer measurements, photographs and samples were collected. This phase also included the acquisition of all the necessary photographs for the creation of a 3D point cloud, using the methodology of UAV-based photogrammetry, described by Vasuki et al. (2014).

The third part of this study involves processing data acquired through field investigation and the analysis of the 3D point cloud. This includes generating stereographic plots to display discontinuity orientations and conducting relevant kinematic analyses. Noise removal from the 3D point cloud was performed to exclude elements not representing the anisotropic rock mass, such as vegetation, fallen rock blocks, and highly weathered material. The edited point cloud was then used for semi-automatic extraction of the main discontinuity set orientations using the open-source Discontinuity Set Extractor (DSE) software (Riquelme et al., 2014). Discontinuity spacing was then calculated through both manual analysis and automatic methods using DSE as a complementary approach (Riquelme et al., 2015). The volume of formed rock blocks was determined using two approaches: analyzing failed rock blocks present in the point cloud and applying Palmstrom's formula (Palmstrom, 2005) in combination with the previously quantified discontinuity spacings. Finally, areas of the slope most prone to rockfalls were identified, and rockfall trajectory simulations were performed. Based on these results, remedial measures were proposed and quantified for the studied slope.

Results

The studied slope consists of crystalline rock, specifically gneiss, belonging to the bedrock of the Pelagonic geotectonic

zone. It is characterized by three main discontinuity sets, while a fourth set is only observed locally. The rock exhibits varying degrees of weathering; in some areas, it is slightly weathered, while in others it is completely weathered, with some areas locally forming residual soil. The discontinuities vary in roughness, with JRC values ranging between 7 and 12. Clay infill material was observed in some of the discontinuities, and dripping water was also locally present. The minimum representative friction angle used in the kinematic analyses was calculated to be 43°. According to the kinematic analyses, the most common type of potential failure identified was wedge failure, followed by a small number of flexural toppling and planar failures. The blocks formed in the rock mass are characterized as small to medium in volume. The suggested remedial measure to protect the slope from potential rockfalls is the installation of a draped mesh, as there is insufficient space to construct a ditch capable of catching rockfalls on its own.

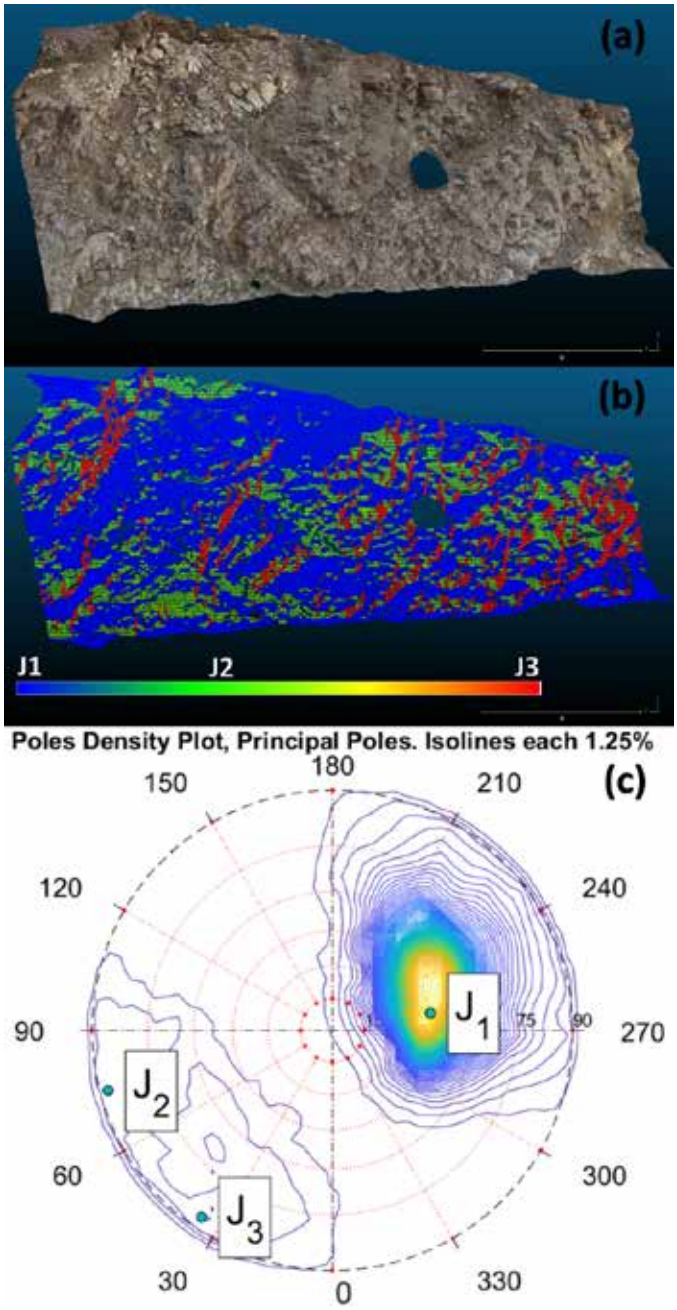

Figure 1. (a) Isometric front view of part of the slope, (b) the visual interpretation of the three main discontinuity sets extracted from the DSE analysis on the 3D point cloud and (c) the stereographic projection of the DSE derived discontinuity sets from the same part of the slope.

Acknowledgements

Part of the transportation costs to the study area were covered by the Research Committee of Aristotle University of Thessaloniki, as part of the corresponding author's master's thesis. Part of the analyses were performed using software provided by RocScience Inc. (Toronto, ON, Canada) under an academic license granted by the Department of Geology, Aristotle University of Thessaloniki.

References

Crozier, M. J., & Glade, T., 2005. Landslide Hazard and Risk: Issues, Concepts and Approach. in: Glade, T., Anderson, M., Crozier, M. J. (Eds.), Landslide Hazard and Risk, 1-40

Palmstrom, A., 2005. Measurements of and correlations between block size and rock quality designation (RQD). Tunnelling and Underground Space Technology, 20(4), 362–377.

Papathanassiou, G., 2022. Engineering Geology and Geohazards, Kallipos Open Academic Editions.

Riquelme, A. J., Abellán, A., Tomás, R., & Jaboyedoff, M., 2014. A new approach for semi-automatic rock mass joints recognition from 3D point clouds. Computers & Geosciences, 68, 38–52.

Riquelme, A. J., Abellán, A., & Tomás, R., 2015. Discontinuity spacing analysis in rock masses using 3D point clouds. Engineering Geology, 195, 185–195.

Vasuki, Y., Holden, E.-J., Kovesi, P., & Micklethwaite, S., 2014. Semi-automatic mapping of geological Structures using UAV-based photogrammetric data: An image analysis approach. Computers & Geosciences, 69, 22–32.

Wyllie, D. C., & Mah, C. (2017). Rock Slope Engineering, 3rd ed. CRC Press.

17th INTERNATIONAL CONGRESS of the Geological Society of Greece

BULLETIN OF THE GEOLOGICAL SOCIETY OF GREECE, SP. PUBL.

EXTENDED ABSTRACT 119

Relict Taxa and Refugial Dynamics in the Corinth Gulf: Insights from the Pollen Record

Kafetzidou A.[1], Fatourou E.[1], Panagiotopoulos K.[2], Marret F.[3], Koukousioura O.[4,5] and Kouli K.[1]
(1) University of Athens, Greece, akafetzidou@geol.uoa.gr (2) Forschungszentrum Jülich, Germany (3) University of Liverpool, UK (4) University of Cologne, Germany (5) Aristotle University of Thessaloniki, Greece

Introduction / Background

Long pollen sequences covering the Quaternary period have enabled us to gain insight into the long-term variability and migration of the vegetation in the Mediterranean Basin in relation to climatic cycles (e.g., Magri *et al.,* 2017). Climatic fluctuations and ecological competition led to the gradual disappearance of several tree taxa, including Taxodioideae*,* Sequoioideae*, Sciadopitys, Tsuga, Castanea, Engelhardia*, and *Diospyros* (Suc *et al.,* 1995; Svenning, 2003; Farjon, 2005; Bertini, 2010; Popescu *et al.*, 2010). Deteriorated climatic conditions during glacial intervals forced the most demanding taxa into refugial areas, such as the Pindus Mountain Range, or southern regions of Italy and Greece (Suc et *al.,* 1995; Svenning, 2003; Bertini, 2010; Popescu *et al.*, 2010). Existing high-resolution pollen records from the southern Balkan show that the amplitude and timing of millennial-scale oscillations in temperate tree abundances depend on the latitude and altitude of the study area as well as its proximity to temperate tree refugia. Long pollen records located in mid-altitudes (between 400 and 850 m above sea level) across the Pindus Mountain Range, such as the Ioannina, Prespa and Ohrid Lakes sites suggest the survival of temperate tree populations during successive glacial-interglacial cycles (Tzedakis *et al.,* 2002, 2004; Panagiotopoulos *et al.,* 2014; Sadori *et al.,* 2016). Opposingly, in the Tenaghi Philippon pollen record from the north-eastern Greece, temperate trees often disappear and only occur during interglacial intervals. The vegetation at Tenaghi Philippon seems to have reacted in a more sensitive way to the climatic cycles, possibly due to the reduction in temperature and moisture (e.g., Tzedakis *et al*., 2006; Pross *et al.,* 2015; Koutsodendris *et al.,* 2023). The Quaternary climate-driven shifts significantly affected ecosystems, particularly at mid-latitudes (Lisiecki and Raymo, 2005; Joannin *et al.,* 2011). In Mediterranean Europe, the shift from the 41,000-year to the 100,000-year climatic oscillations resulted in an increase of in aridity, further impoverishing vegetation communities due to long-term cooling trends (Joannin *et al.,* 2011). This resulted in the gradual extinction of several tree taxa such as *Cedrus, Carya, Pterocarya, Juglans*, and *Zelkova* (Suc *et al.,* 1995; Svenning, 2003; Bertini, 2010). However, the sporadic and scattered nature of records only provides a partial chronostratigraphical overview of their distributions and extinctions, necessitating macroregional-scale adaptations. Despite the existence of some long continuous pollen records from the Balkan Peninsula, most of them are either far from tree refugial areas (e.g. the Tenaghi Philippon record that includes the MPT) or do not include the MPT interval (e.g., Ioannina, Prespa and Kopais). The evolution of north-south and west-east environmental gradients over long time scales, notably the sustained west-east precipitation gradient, has profoundly shaped the plant ecosystems in the southern Balkan Peninsula. This is evidenced by the contrasting vegetational responses observed between Tenaghi Philippon (e.g., Tzedakis *et al.,* 2006; Koutsodendris *et al.,* 2023) in the east and other western Balkan sites such as Lake Ohrid (Sadori et al., 2016; Donders *et al.,* 2021), Ioannina (e.g., Tzedakis *et al.,* 2002, 2003, 2004) and Prespa (Panagiotopoulos *et al.,* 2013, 2014). These findings highlight the need for further analysis of long-term pollen archives from the Balkan Peninsula to better understand the evolution of regional flora and the timing of relict species extinctions in the eastern Mediterranean.

The Gulf of Corinth pollen record provides significant insights into the persistence of relict taxa such as *Liquidambar*, *Carya*, *Pterocarya*, and *Cedrus* throughout the Pleistocene. These taxa, key components of temperate and riparian forests, persisted through multiple glacial-interglacial cycles, indicating the Gulf of Corinth region as a refugium in southeastern Europe. The region's unique climatic, topographic, and hydrological conditions enabled the survival of these taxa despite broader climatic fluctuations. *Liquidambar* displayed remarkable resilience, with a near-continuous presence from MIS 8 (300 ka) to ~13 ka BP, thriving during glacial phases in humid conditions. *Carya* persisted from MIS 24 (~923 ka) to MIS 8, with low percentages correlating with localized humid microclimates influenced by marine humidity. *Pterocarya* was present from MIS 13 (~500 ka) to MIS 3 (~36 ka), reaching higher abundances during glacial periods, indicating stable hydrological conditions in wet environments such as floodplains. Similarly, *Cedrus*, which gradually disappeared from the central and northern Balkans by the end of the Pleistocene, remained present in Gulf of Corinth sediments, suggesting local persistence rather than long-distance transport. These findings underscore the Gulf of Corinth's biogeographical significance as a biodiversity hotspot, providing exceptional conditions that allowed the persistence of relict taxa during the glacial maxima and interglacial periods of Quaternary.

The study highlights the region's role as a corridor for species persistence and migration in the Mediterranean. Understanding the resilience of these taxa offers valuable insights into reconstructing past vegetation dynamics, identifying refugia, and

predicting ecosystem responses to future climate change. The preservation and further study of this paleoenvironmental archive are important for advancing our knowledge of plant resilience, refugial dynamics, and climatic stability in the Mediterranean region.

Acknowledgements

The study material was retrieved during the IODP Exp. 381. The research work was supported by the Hellenic Foundation of Research and Innovation (H.F.R.I) under the "First Call for H.F.R.I. Research Projects to support Faculty members and Researchers and the procurement of high-cost research equipment grant" (Project Number: 1026, Quaternary Environmental Changes in the Corinth Rift Area: the IODP 381 palynological record: QECCoRA).

References

Bertini, A., 2010. Pliocene to Pleistocene palynoflora and vegetation in Italy: State of the art. Quaternary International 225, 5-24.

Combourieu-Nebout, N., Bertini, A., Russo-Ermolli, E., Peyron, O., Klotz, S., Montade, V., Fauquette, S., Allen, J., Fusco, F., Goring, S., Huntley, B., Joannin, S., Lebreton, V., Magri, D., Martinetto, E., Orain, R., Sadori, L., 2015. Climate changes in the central Mediterranean and Italian vegetation dynamics since the Pliocene. Review of Palaeobotany and Palynology 218, 127-147.

Donders, T., Panagiotopoulos, K., Koutsodendris, A., Bertini, A., Mercuri, A. M., Masi, A., Combourieu-Nebout, N., Joannin, S., Kouli, K., Kousis, I., Peyron, O., Torri, P., Florenzano, A., Francke, A., Wagner, B., Sadori, L., 2021. 1.36 million years of Mediterranean forest refugium dynamics in response to glacial–interglacial cycle strength. Proceedings of the National Academy of Sciences 118.

Farjon, A., 2005. A Monograph of Cupressaceae and Sciadopitys. Royal Botanic Garden, Kew.

Joannin, S., Bassinot, F., Nebout, N.C., Peyron, O., Beaudouin, C., 2011. Vegetation response to obliquity and precession forcing during the Mid-Pleistocene Transition in Western Mediterranean region (ODP site 976). Quaternary Science Reviews 30, 280e297

Koutsodendris, A., Dakos, V., Fletcher, W. J., Knipping, M., Kotthoff, U., Milner, A. M., Müller, U.C., Kaboth-Bahr, S., Kern, O.A., Kolb, L., Vakhrameeva, P., Wulf, S., Christanis, K., Schmiedl, G., Pross, J., 2023. Atmospheric CO2 forcing on Mediterranean biomes during the past 500 kyrs. Nature Communications 14, 1664.

Lisiecki L.E., Raymo M.E., 2005. A Pliocene-Pleistocene stack of 57 globally distributed benthic δ18O records. Paleoceanography 20.

Magri, D., Di Rita, F., Aranbarri, J., Fletcher, W., González-Sampériz, P., 2017. Quaternary disappearance of tree taxa from Southern Europe: Timing and trends. Quaternary Science Reviews 163, 23-55.

Magri, D., Palombo, M.R., 2013. Early to Middle Pleistocene dynamics of plant and mammal communities in SouthWest Europe. Quaternary International 288, 63-72.

Panagiotopoulos, K., Aufgebauer, A., Schäbitz, F., Wagner, B., 2013. Vegetation and climate history of the Lake Prespa region since the Lateglacial. Quaternary International 293, 157-169.

Panagiotopoulos, K., Böhm, A., Leng, M. J., Wagner, B., Schäbitz, F., 2014. Climate variability over the last 92 ka in SW Balkans from analysis of sediments from Lake Prespa. Climate of the Past 10, 643-660.

Popescu, S.-M., Biltekin, D., Winter, H., Suc, J.-P., Melinte-Dobrinescu, M.C., Klotz, S., Rabineau, M., Combourieu-Nebout, N., Clauzon, G., Deaconu, F., 2010. Pliocene and Lower Pleistocene vegetation and climate changes at the European scale: long pollen records and climatostratigraphy. Quaternary International 219, 152-167.

Postigo-Mijarra, J.M., Morla, C., Barrón, E., Morales-Molino, C., García, S., 2010. Patterns of extinction and persistence of Arctotertiary flora in Iberia during the Quaternary. Review of Palaeobotany and Palynology 162, 416-426.

Sadori, L., Koutsodendris, A., Panagiotopoulos, K., Masi, A., Bertini, A., Combourieu-Nebout, N., Francke, A., Kouli, K., Joannin, S., Mercuri, A-M., Peyron, O., Torri, P., Wagner, B., Zanchetta, G., Sinopoli, G., Donders, T.H., 2016. Pollen-based paleoenvironmental and paleoclimatic change at Lake Ohrid (south-eastern Europe) during the past 500 ka. Biogeosciences 13, 1423-1437.

Suc, J.P., Bertini, A., Combourieu-Nebout, N., Diniz, F., Leroy, S., Russo-Ermolli, E., Zheng, Z., Bessais, E., Ferrier, J., 1995. Structure of West Mediterranean vegetation and climate since 5.3 ma. Acta Zoologica Cracoviensia 38, 3-16.

Svenning, J., 2003. Deterministic Plio□Pleistocene extinctions in the European cool□temperate tree flora. Ecology Letters 6, 646-653.

Tzedakis, P.C., Frogley, M.R., Heaton, T.H.E., 2003. Last interglacial conditions in southern Europe: evidence from Ioannina, northwest Greece. Global and Planetary Change 36, 157-170.

Tzedakis, P.C., Frogley, M.R., Lawson, I.T., Preece, R.C., Cacho, I., de Abreu, L., 2004. Ecological Thresholds and Patterns of MillennialScale Climate Variability: The Response of Vegetation in Greece during the Last Glacial Period. Geology 32, 109-112.

Tzedakis, P. C., Hooghiemstra, H., Pälike, H., 2006. The last 1.35 million years at Tenaghi Philippon: revised chronostratigraphy and long-term vegetation trends. Quaternary Science Reviews 25, 3416-3430.

Tzedakis, P. C., Lawson, I. T., Frogley, M. R., Hewitt, G. M., Preece, R. C., 2002. Buffered tree population changes in a Quaternary refugium: evolutionary implications. Science 297, 2044-2047.

17th INTERNATIONAL CONGRESS of the Geological Society of Greece

BULLETIN OF THE GEOLOGICAL SOCIETY OF GREECE, SP. PUBL.

EXTENDED ABSTRACT 120

Rare Insights in the Oligocene flora of Thrace (Greece): Preliminary results from the Rhodopi Petrified Forest

Kafetzidou A.[1], Koukousioura O.[2], Zotiadis V.[3], Kouli K.[1]

(1) National and Kapodistrian University of Athens, akafetzidou@geol.uoa.gr (2) Aristotle University of Thessaloniki, Greece (3) Edafomichaniki S.A., Athens, Greece

New fossil discoveries in the area of Thrace offer remarkable insights into the Oligocene vegetation and paleoenvironmental conditions of southeastern Europe. The plant fossil sites, representing some of the oldest Petrified Forests in Greece, preserve a diverse assemblage of both permineralized wood remains as well as leaf imprints of angiosperm trees. The fossil-bearing deposits comprise of successive pyroclastic series mainly consisting of tuffs intercalated with layers of sandstones, clays and marls. The pyroclastic sequence is linked to the volcanic activity in the Rhodope region during the Late Eocene to Oligocene (Georgiev and Marchev, 2005; Voudouris *et al.*, 2007).

Numerous permineralized well preserved wood specimens were identified, exhibiting the dominance of Fagaceae, mainly *Quercoxylon* sp., and the presence of thermophilic Lauraceae. The occurrence of several leaf litter horizons is recorded within the marl layers of the sequence. Among leaf imprints, the key taxa identified include Fagaceae (*Eotrigonobalanus* sp., *Quercus* spp.), *Myrica* spp., *Ziziphus* sp., *Laurophyllum* spp, *Dicotylophyllum* sp. and representatives of the Leguminosae (Figure 1).

Figure 1. a, b) Logging of the petrified trunks; c) branched petrified trunk; d) leaf imprints (scale: 10 cm).

Our findings show great similarities to those from the neighboring Bulgarian fossiliferous sites, as well as the petrified forest of Evros (Iamandei *et al.,* 2014, 2016, 2024; Velitzelos *et al.*, 2014; Velitzelos *et al.*, 1999, 2002). In the Bulgarian sites, petrified trunks within tuffs had provided a radiometric age ($^{40}Ar/^{39}Ar$) of approximately 31 million years (e.g., Iamandei *et al.*, 2014, 2016), confirming the Early Oligocene age of the fossils (Georgiev and Marchev,

2005). The volcanic activity, attributed to centers in Kotyli and Kalotycho (Caracciolo *et al.*, 2011), played a key role in the rapid burial and exceptional preservation of plant material. The studied fossil-bearing area in combination with the petrified forest of Evros (Velitzelos *et al.,* 2014; Velitzelos *et al.,* 1999, 2002) represent some of the oldest occurrences of paleovegetation in Greece.

References

Caracciolo, L., Critelli, S., Innocenti, F., Kolios, N., Manetti P., 2011. Unravelling the provenance from Eocene-Oligocene sandstones of the Thrace Basin, North-East Greece. Sedimentology 58, 1988-2011.

Georgiev, S., Marchev, P., 2005. Oligocene pyroclastic rocks and a petrified forest in the Nanovitsa depression. Bulgarian Academy of Sciences, Geochemistry, Mineralogy and Petrology 42, 47-65.

Iamandei S., Iamandei, E., Bozukov, V., Tsenov, B., 2014. Oligocene fossil woods from Rhodopes, Bulgaria. Acta Palaeontologica Romaniae 9, 15-25.

Iamandei S., Iamandei, E., Bozukov, V., Tsenov, B., 2016. New Oligocene fossil woods from Rhodopes, Bulgaria. Acta Palaeontologica Romaniae 12, 47-65.

Iamandei S., Iamandei E., Velitzelos D., Velitzelos E., 2024. Palaeoxylotomical studies in the Cenozoic petrified forests of Greece. Part three – dicots. Acta Palaeontologica Romaniae 20, 61-96

Velitzelos D., Bouchal J.M., Denk T., 2014. Review of the Cenozoic floras and vegetation of Greece. Review of Palaeobotany and Palynology 204, 56-117

Velitzelos, E., Kvaček, Z., Velitzelos, D., 2002. New Oligocene leaf floras from the volcanic complex of the Evros Mountains. 6th European Paleobotany-Palynology Conference Athens, Greece 2002, Book of Abstracts, 185-186.

Velitzelos, E., Kvaček, Z., Walther, H., 1999. Erster Nachweis von *Eotrigonobalanus furcinervis* (Rossm.) Walther & Kvaček (Fagaceae) in Griechenland. Feddes Repertorium 110, 349-358.

Voudouris, P., Velitzelos, D., Velitzelos, E., Thewald, U., 2007. Petrified wood occurrences in western Thrace and Limnos Island: Mineralogy, geochemistry and depositional environment. Proceedings of the 11th International Congress, Bulletin of the Geological Society of Greece XXXX/1, 238-250.

17th INTERNATIONAL CONGRESS of the Geological Society of Greece

BULLETIN OF THE GEOLOGICAL SOCIETY OF GREECE, SP. PUBL.

EXTENDED ABSTRACT 121

Mapping the Geological Landscape of NW Bay of Navarino Through Time

Kaimakami M.[1]

(1) University of Peloponnese, Kalamata, Greece, mariakaim04@gmail.com

Abstract

This study explores the geological landscape of the northwest bay of Navarino and its influence on human settlement patterns. Using field surveys, GIS mapping, and optical microscopy, the research identifies key geological formations and their relationship with archaeological remains. The findings suggest that elevated limestone areas, such as the hills of Prophitis Ilias and Koukouras, were preferred for habitation, while fewer artifacts were found in the surrounding lagoon and cultivated areas. The study highlights the need for further research to confirm these observations and deepen our understanding of the region's historical development.

Introduction

The northwest bay of Navarino, located between modern Pylos and Romanos, is a significant cultural and environmental area, forming part of the Natura 2000 network. This study focuses on the region's geological and archaeological features, including the Gialova lagoon, Voidokoilia beach, Coryphasium peninsula, and surrounding hills and fields. Major archaeological discoveries include the Mycenaean tholos tomb of Thrasymedes, the Frankish Palaiokastro, and Nestor's Cave with Neolithic occupation traces. Since 2021, the Pylos Geoarchaeological Program (GEAPP) has been conducting research to investigate the area's natural and cultural environment. This study aims to analyze the geological landscape in relation to archaeological findings.

Geomorphology

The study area is part of the Gavrovo-Tripoli geotectonic zone, characterized by carbonate sedimentation from the Upper Triassic to the Upper Eocene. The western region, particularly the Coryphasium peninsula and nearby hills, consists mainly of Paleocene to Eocene limestone, while the Gialova lagoon lies on Holocene alluvial and fluvial deposits. Coastal sand dunes of Holocene-age, reaching up to 10 meters in height, dominate the shoreline. Tectonic movements and erosional processes have shaped the area, with evidence of past marine submersion and gradual land emergence over the past 9,000 years.

Historical Background

The Bay of Navarino has a long history of human presence, with research beginning with the University of Minnesota Messenia Expedition (UMME, 1953-1975) and continuing with the Pylos Regional Archaeological Project (PRAP, 1991-1999). Evidence of habitation dates back to the Paleolithic period, including tools and settlement in Nestor's Cave. During the Bronze Age, important settlements and burial monuments, such as the tholos tomb of Thrasymedes, indicate significant activity. In the Classical period, the region witnessed military conflicts, including the Battle of Sphacteria (425 BC). During the Roman and Byzantine eras, it remained an important center, while in the Frankish and Ottoman periods, fortifications were strengthened. The Battle of Navarino (1827) marked a turning point in Greece's independence.

Methodology

A field survey was conducted to record geological and archaeological features. Samples were collected for analysis using optical microscopy, and the data was digitized in ArcGIS 10.4.1. The mapping process included thematic layers for geological formations and archaeological discoveries. The coordinate system used was the Greek Grid Reference System (EGSA '87), and aerial photographs from 1945 were incorporated to enhance accuracy.

Key Sites of Geological and Archaeological Interest

- Voidokoilia Beach: Known for its circular shape, the beach comprises limestone, travertine, and dunes. Archaeological findings include ceramics and limestone walls, suggesting a Mycenaean harbor.
- Gialova Lagoon: A vital wetland with Holocene alluvial deposits with rich biodiversity. Drainage works in the 1960s uncovered a Classical and Roman cemetery.
- Divari Beach &Coryphasium Peninsula: The beach consists of alluvium and dunes, while the limestone-rich peninsula hosts ceramics, bones, and architectural remains.
- Prophitis Ilias Hill: Features prehistoric cemetery remains, limestone blocks with pillar holes, and ceramic depos-

its.

- Koukouras Hill: A primarily limestone hill with architectural structures and large limestone blocks indicating past settlements.
- Almyrolakka, Agios Nikolaos, and Kolopanas Beaches: Characterized by sandstone and brecciated limestone, with prehistoric ceramics and wall remnants.
- Agricultural Fields: Consisting of fertile alluvial soils, these areas exhibit limited archaeological finds due to extensive plowing.
-

Mapping and Rock Identification

The study area consists mainly of limestone, sandstone, breccia and flint. The Coryphasium Peninsula, as well as the hills of Prophitis Ilias and Koukouras, are primarily composed of limestone, while sandstones andfossilized aeolian sand appear on beaches such as Almyrolakka, Agios Nikolaos, and Kolopanas. Breccia was identified on the Coryphasium Peninsula, and flint was also present in various locations. A field survey was conducted to collect rock samples, some of which were analyzed using an optical microscope for better identification. The geological mapping revealed a more diverse rock distribution than previously indicated, enhancing our understanding of the region's geological composition.

Archaeological Findings and Settlement Patterns

Archaeological findings in the study area are mainly concentrated on the Coryphasium Peninsula and the hills of Prophitis Ilias and Koukouras, where limestone dominates. Few remains were found around the Gialova Lagoon, likely due to agricultural activities that have disturbed the soil over time. The region has been continuously inhabited since prehistoric times, with settlements, tombs, and artifacts indicating human presence. Changes in vegetation and land use over millennia have influenced the preservation and visibility of archaeological sites. Drainage works in the 20th century also exposed significant findings, highlighting the need for further research to understand human activity in relation to the landscape.

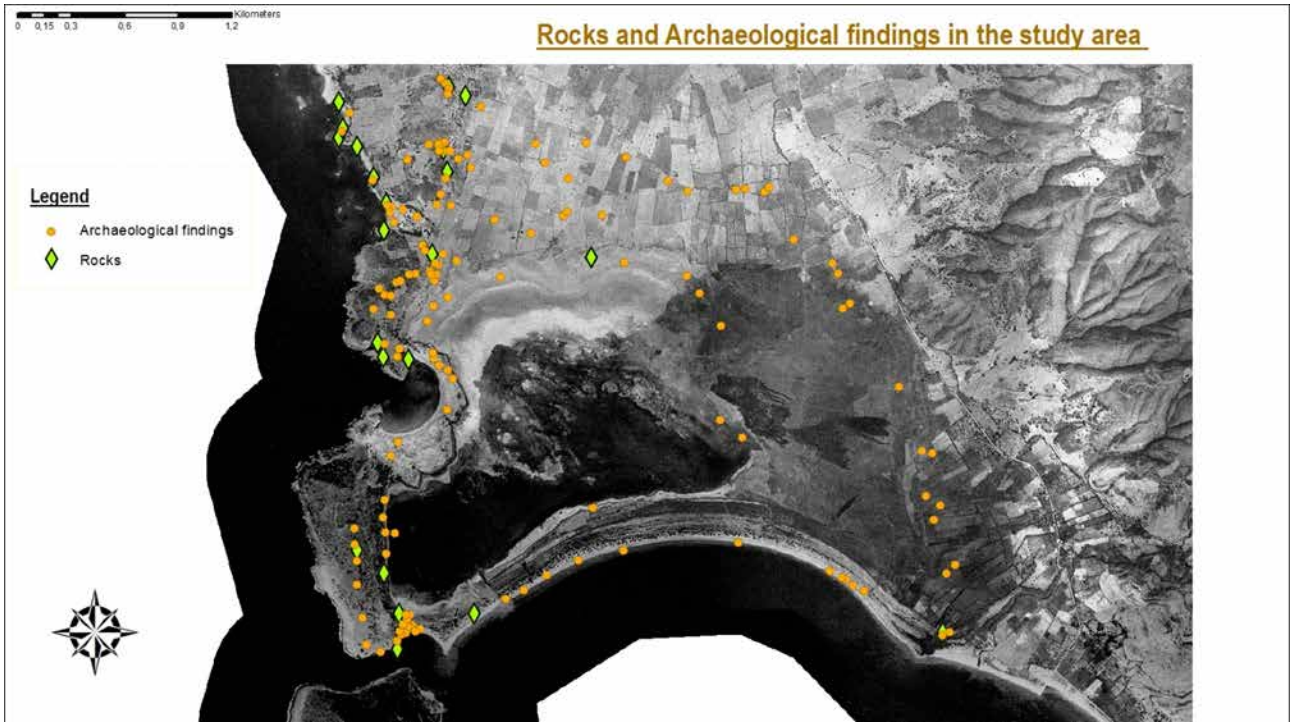

Figure 1. The map of the rocks and the archaeological findings in the study area © Maria Kaimakami.

Discussion

Most archaeological remains are located in elevated limestone areas, suggesting that strategic positioning and material availability influenced settlement choices. The scarcity of finds in the lagoon and cultivated areas may result from erosion, land disturbance, and accessibility issues. Geological mapping identified a wider variety

of rock formations than previously recorded, indicating the need for further research. A deeper understanding of archaeological distribution requires investigating environmental, geological, and socio-political factors that shaped human habitation in the area over time.

Conclusions

This research provides an initial understanding of the interaction between geology and human settlement in the northwest bay of Navarino. The concentration of archaeological remains in elevated limestone areas supports the hypothesis that geology influenced habitation choices. However, further research is needed to confirm these patterns, particularly in areas affected by erosion and modern land use. Increased survey efforts are essential to preserve and document archaeological evidence before it is lost. Understanding the geological factors that influenced human settlement in this region can contribute to broader studies of environmental and cultural history in coastal Mediterranean landscapes.

Acknowledgements

ReI thank Dr. G. Malaperdas, Environmentalist Cartographer – Land Surveyor – GIS & R.S. Analyst – Geoinformatics and Earth Studies, for his invaluable assistance with GIS mapping. I also thank E. Zymi, Associate Professor of Classical Archaeology at the Department of History, Archaeology and Cultural Resources Management at the University of Peloponnese, for her invaluable support with the archaeological part of my research and Dr. K. Theodorakopoulou, specializing in geoarchaeology and the use of archaeometric techniques, for her crucial help with the geological part. The first to assist me, N. Zacharias, Professor of Archaeometry, Environmental and Cultural Technology, sadly passed away before the completion of my research.He will be remembered as a distinguished scientist and professor. I am honored to conduct and present this research, as he greatly supported me throughout this endeavor.

References

Agapiou, A., Lysandrou, V., Alexakis, D.D., Themistocleous, K., Cuca, B., Argyriou, A., Sarris, A. and Hadjimitsis, D.G., 2015. Cultural heritage management and monitoring using remote sensing data and GIS: The case study of Paphos area, Cyprus. Computers, Environment and Urban Systems 54, 230–239.

Alcock, S.E, Berlin, A.M., Harrison, A.B., Heath, S., Spencer, J. and Stone, D.L., 2005. The Pylos Regional Archaeological Project, Part VII: Historic Messenia, Geometric through Late Roman. Hesperia 74 (2), 147-209.

Athanassas, C. and Fountoulis, I., 2013. Quaternary Neotectonic Configuration of the Southwestern Peloponnese, Greece, Based on Luminescence Ages of Marine Terraces, Journal of Earth Science 24 (3), 410–427.

Avramidis, P., Iliopoulos, G., Kontopoulos, N., Panagiotaras, D., Barouchas, P., Nikolaou, K. and Papadopoulou, P., 2015. Deposotional environments, sediment characteristics, palaeoecological analysis and environmental assessment of an internationally protected shallow Mediterranean lagoon, Gialova lagoon – Navarino Bay, Greece. Earth and Environmental Science Transactions of the Royal Society of Endinburgh 105, 189-206.

Darvill, T., 2008. The Concise Oxford Dictionary of Archaeology. Second Edition. Oxford University Press, Oxford.

Doula, M.K. and Sarris, A., 2016. Soil environment. Environment and development. Elsevier.

Emmanouilidis, A., 2017. Mid to Holocene Paleoenvironmental study of Gialova lagoon, SW Peloponnese, Greece. Patra.

Hardar, S.K. and Tisljar J., 2014. Introduction to minerology and petrology. Elsevier.

Katsianis, M., Kalayci, T. and Sarris, A., 2022. Bridging Digital Approaches and Legacy in Archaeology. Digital 2 (4), 538-545.

Kennedy, W., 2021. Terra Petraea. The Archaeological Landscape of the Petraean Hinterland from the Hellenistic to the Byzantine Period. Logos Verlag, Berlin.

Kipfer, B.A., 2021. Encyclopedic Dictionary of Archaeology. Second Edition. Springer Nature, Switzerland.

Konstantopoulos, P., 2009. Περιβάλλοντα ιζηματογένεσης και στρωματογραφική διάρθρωση του φλύσχη της Πελοποννήσου - πιθανή γένεση υδρογονανθράκων. Patra.

Kraft, J.C., Rapp Jr., G.R., Aschenbrenner, S.E., 1980. Late Holocene palaeogeomorphic reconstructions in the area of the Bay of Navarino: Sandy Pylos. Journal of Archaeological Science 7, 187-210.

Loy, M., Stocker, S.R. and Davis, J.L., 2021. From Archive to GIS: Recovering Spatial Information for Tholos IV at the Palace of Nestor from the Notebooks of Lord William Taylour. InternetArchaeol 56 (5).

Μαλαπέρδας, Γ., 2023. Χαρτογραφία, Γεωγραφικά Συστήματα Πληροφοριών και Τηλεπισκόπιση, in: Zacharias, N. (Eds), Πολιτιστική Κληρονομιά και Νέες Τεχνολογίες, Papaizisi, Athens, 11-110.

Malaperdas, G. and Zacharias, N., 2018. A Geospatial Analysis of Mycenaean Habitation Sites Using a Geocumulative versus Habitation Approach. Journal of Geoscience and Environment Protection 6, 111-131.

Malaperdas, G., & Panagopoulos, N., 2021. Mapping shoreline changes over the years: The case study of Navarino bay, Pylos, Messenia, Greece. World Journal of Geomatics and Geosciences 1 (1).

Malaperdas, G. &Barberopoulou, A., 2023. Mapping art: 3D geovisualization and virtual worlds in cultural heritage. International Journal of Visual and Performing Arts 5(2).

Malaperdas, G., Grethe, R. and Zacharias, N., 2023. Depicting the past: The significance of old maps and topographic diagrams in Cultural Heritage via GIS in Cultural Heritage. Journal of Archaeological Science: Reports 52 (104276).

Malaperdas, G., Maggidis, C., Karantzali, E., and Zacharias, N., 2023. Field Surveying, Geostatistical and GIS Methods in Archaeology. The Mycenaean Spercheios-Valley Project (MY. SPE. AR. Project 2018-2022). Journal of Archaeology and Anthropology.

Miller, B.A. and Juilleret, J., 2020. The colluvium and alluvium problem: Historical review and current state of definitions. Earth-Science Reviews 209 (103316).

Raith, M.M., Raase, P. and Reinhardt, J., 2011. Guide to Thin Section Microscopy. Second Edition.

Sarris, A., Chliaoutakis, A., Déderix, S. and Donati, J.C., 2013. Reconstructing archaeo-landscapes: myth versus reality as Exploration / Production Analogues. The 6th Symposium of the Hellenic Society for Archaeometry: Craft-based Cultural Influences in the Mediterranean, Athens.

Secchi, M., Zanatta, M., Borovin, E., Bortolotti, M., Kumar, A., Giarola, M., Sanson, A., Orberger, B., Daldosso, N., Gialanella, S., Mariotto, G., Montagna, M. and Lutterotti, L., 2018. Mineralogical investigations using XRD, XRF, and Raman spectroscopy in a combined approach. Journal Raman Spectroscopy, 1–8.

Simpson, R.H., 2014. Mycenaean Messenia and the Kingdom of Pylos. Academic Press Philadelphia, Pennsylvania.

Stamatopoulou, E., Sotiropoulou, M., Karoglou, M. and Bakolas, A., 2021. Characterization of contemporary artworks made on photosensitized canvas by means of optical microscopy and micro-Raman spectroscopy techniques. Microchemical Journal 165 (106110).

Theodorakopoulou, K., 2020. Ανθρωποϊστορίαγραμμένηστηνπέτρα: εποχή του Λίθου και γεωπεριβάλλον. Kardamitsa.

Tsiafakis, D., Evagelidis, V., 2006. GIS as an Interpretative Tool in Greek Archaeological Research. Nottingham.

Valsamaki, I.A., 2012. Πύλος. Μελέτη Διαχείρισης και Ανάπτυξης του Πολιτισμικού τοπίου του όρμου του Ναυαρίνου. Athens.

Willershäuser, T., Vött, A., Hadler, H., Ntageretzis, K., Emde, K., and Brückner, H., 2015. Holocene palaeotsunami imprints in the stratigraphical record and the coastal geomorphology of the Gialova Lagoon near Pylos (southwestern Peloponnese, Greece). Zeitschrift Für Geomorphologie, Supplementary Issues 59(4), 215–252.

Zacharias, N. and Palamara, E., 2016. Glass Corrosion: Issues and Approaches for Archaeological Science, in: Gan, F., Li, Q., Henderson, J. (Eds), Recent Advances in the Scientific Research on Ancient Glass and Glaze, World Century Publishing Corp. and World Scientific Publishing Co., 233-247.

Zacharias, N., Militsi, E., Kylafi, M., Valantou, V., Kazolias, A., Kompoti, A. and Panagiotidis V.V., 2023. Sand & stones: The Pylos Geoarchaeological Program. Journal of Archaeological Science: Reports 51 (104210).

Zangger, E., Timpson, M.E., Yazvenko, S.B., Kuhnke, F., and Knauss., J., 1997. The Pylos Regional Archaeological Project, Part II: Landscape Evolution and Site Preservation. Hesperia 68 (4), 548-641.

17th INTERNATIONAL CONGRESS of the Geological Society of Greece

BULLETIN OF THE GEOLOGICAL SOCIETY OF GREECE, SP. PUBL.

EXTENDED ABSTRACT 122

The influence of DSMs spatial resolution on rockfall simulation.

Kakavas M.[1], Kyriou A.[1], Nikolakopoulos K.[1], Koukouvelas I. [1]

(1) University of Patras, Department of Geology, Patra, Greece, kakava.maria@upatras.gr

Abstract

Rockfalls are dynamic geological events characterized by the sudden detachment and descent of rock fragments from steep slopes. These events vary greatly in scale, velocity, and trajectory, influenced by factors such as slope geology, topography, and environmental conditions. This study examines rockfall hazards in Platiana, Greece, using simulation tools— RocFall 4.0, QProto, and HY-STONE. By applying Digital Surface Models (DSMs) with spatial resolutions ranging from centimeters to meters, the study demonstrates that higher-resolution DSMs more accurately simulate rockfall trajectories, velocities, and energy distributions. Coarse-resolution DSMs, however, tend to overestimate rockfall runout and simplify topography. The findings highlight the importance of selecting high-resolution DSMs for reliable hazard assessments.

Introduction

Rockfalls are natural phenomena where rock fragments abruptly detach and freefall from steep slopes, posing significant natural hazards in mountainous and hilly areas (Dorren, 2003; Wu et al., 2025). These phenomena exhibit considerable scale variability, velocity, and trajectory, influenced by factors such as the slope's geological composition, topography, and other environmental conditions (Hungr et al., 1999; Guzzetti et al., 2002; Borella et al., 2019). The unpredictable nature of rockfalls makes their risk assessment and mitigation a challenging task, especially in regions with steep and unstable terrains (Fell et al., 2008). To predict and manage rockfall hazards effectively, researchers employ advanced modelling techniques that integrate terrain analysis and remote sensing data, helping to estimate potential impact zones and identify areas at risk of rockfall events (Jaboyedoff et al., 2005). Digital Elevation Models (DEMs) are essential tools in rockfall hazard assessment, as they provide topographical data critical for simulating rockfall behaviour. DEMs allow the extraction of slope parameters that influence rockfall dynamics, including slope angle, roughness, and vegetation cover. The resolution of these models plays a pivotal role in the accuracy of rockfall simulations. Lower-resolution DEMs tend to oversimplify the terrain's features, leading to inaccurate predictions of rockfall trajectories and energy distribution (Keijsers et al., 2011). Alternatively, higher-resolution DEMs capture fine terrain details, improving the precision of simulations and offering more reliable hazard assessments (Pradhan et al., 2017; Kakavas et al., 2021; Kakavas et al., 2024). Consequently, rockfall simulation software incorporates DEMs of varying spatial resolutions to meet different analytical needs with finer-resolution models, typically producing more detailed and accurate results (Acosta et al., 2002; Baillifard et al., 2003; Kakavas et al., 2023). The scope of this study is to examine the influence of DEM resolution on rockfall simulations in Platiana, Greece, via RocFall 4.0, QProto, and HY-STONE software. The aim is to highlight the importance of DEM resolution in improving hazard predictions.

Study Area

Platiana is a village located in the Ilia prefecture of Peloponnese, Greece (Figure 1). The surrounding area is primarily composed of Upper Cretaceous limestones, as indicated by the engineering geological map of Greece, and is part of the Pindos geotectonic unit according to the Hellenic Survey of Geology & Mineral Exploration (HSGME) (Figure 2). This region is a segment of the broader Pindos Unit that has been thrust westward. Near the settlement, there are significant outcrops of limestone with varying thicknesses from thin to medium layers. According to Vagenas (2020), these limestone layers are locally intercalated with chert layers. Platiana experienced the devastating wildfires of 2007 and has been declared reforesting land over the past years. Following the natural reforestation, the vegetation levels have been fully recovered. However, from 2008 to 2018, the mountain slopes adjacent to Platiana were completely barren (Figure 1). Similar to other cases, the lack of vegetation exposed the slopes to corrosion factors that compromised their structural integrity and triggered the release of internal stresses. As a result, rocks of various sizes became detached from the main rock body and sliding, toppling or falling and proceeding downslope. Notably, on December 4, 2018, after heavy rainfall, a massive boulder approximately 10m³ in volume slid down the slope. Fortunately, it came to a stop in a churchyard, causing no casualties. During its down-ward course, the boulder penetrated two gabion retaining wall that served to protect the Platiana village (Figure 1). It is important to mention that, the rockfall simulations using pre-2018 DEMs (ALOS AW3D30, ASTER GDEM, SRTM30, SRTM90, and TanDEM_X), which capture the barren mountain slopes, demonstrated higher kinetic velocities, whereas those based on post-2018 DSMs (UAV, Greek Cadastral, and Ministry of Agriculture), reflecting restored vegetation, yielded lower kinetic energies.

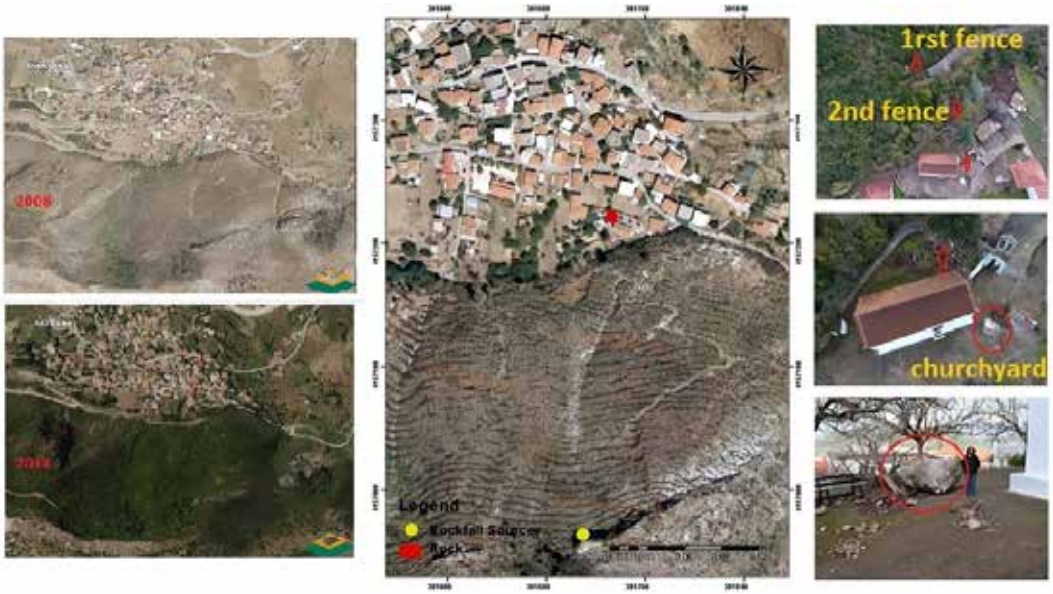

Figure 1. The images on the left (from Greek Cadastral, 2008) and below (2018) illustrate the natural reforestation of the slope adjacent to the Platiana village. The central map indicates both the rockfall source (yellow circle) and the boulder's final point (red circle). On the right, photographs show the aftermath of the rockfall event, including fence damage and the boulder in the churchyard.

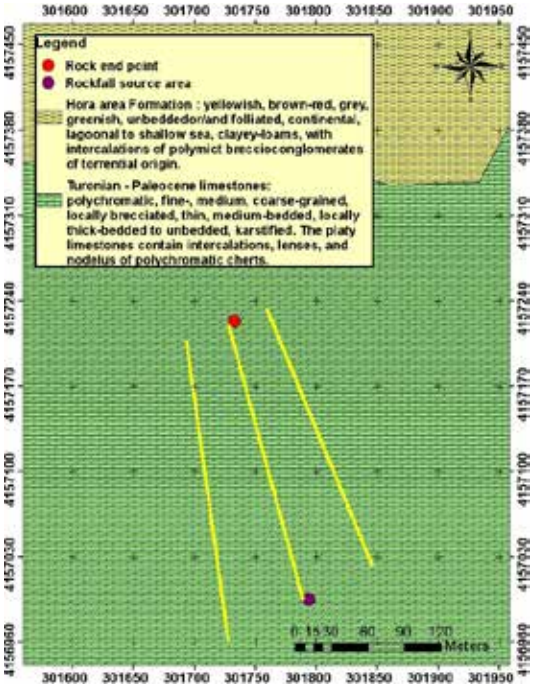

Figure 2. Geological map of the study area according to the Hellenic Survey of Geology & Mineral Exploration (HSGME)

Processing Tools

For this study, three rockfall simulation software were used. The first is RocFall 4.0 from Rocscience, which is a two-dimensional rockfall modeling tool for steep slopes. The detection of rockfall susceptibility is achieved through a lumped mass statistical analysis. This software comprises the collision theory and Newton's laws of motion, so as to simulate the path of the rolling rock mass/boulder (Rocscience, 2002). RocFall software calculates four parameters for the entire slope, including the final position of the rock, bounce height and velocity, as well as energies. The second software is QProto, which is an open-source geographic software and consists a plugin in the QGIS environment

(Castelli et al., 2021). GRASS GIS 7 is the base of this plugin as it optimizes for performance and large geospatial data analysis by offering powerful raster, vector, and geospatial processing engines in a single integrated software suite. It comes with a temporal framework for advanced time series processing and a Python API for rapid geospatial programming (Toma et al., 2021). The third software is HY-STONE which is a software developed for 3D numerical modeling of rockfall processes, including the simulation of the motion of non-interacting blocks, utilizing a high-resolution 3D description of slope geometry for accurate multiscale stochastic modeling (Crosta et al., 2004; Frattini et al., 2008; Agliardi et al., 2009). It is capable of modeling free fall, impact, and rolling of blocks, with energy loss simulations at impacts or by rolling based on a hybrid (cinematic and dynamic) approach.

Rockfall Simulation

For examining Platiana's rockfall phenomenon, slope profiles were selected and extracted from eight different resolution DSMs (Figure 3), aiming at simulations via RocFall, Qproto and HY-STONE software: one 5 cm spatial resolution DSM created by UAV data, one 5 m DSM from the Greek Cadastral, one 20 m DSM from the Ministry of Agriculture, three 30 m resolution DEMs (ALOS AW3D30 DEM, ASTER GDEM and SRTM30 DEM) and two 90 m cell size DEMs (SRTM90 DEM and TanDEM_X). The two barriers, drystone fences, were taken into account in software settings, as well as geological and material characteristics of the slope profiles. In situ surveys and literature data were accomplished (Figure 1) (Depountis et al., 2010; Sabatakakis et al., 2015; Vagenas, 2020).

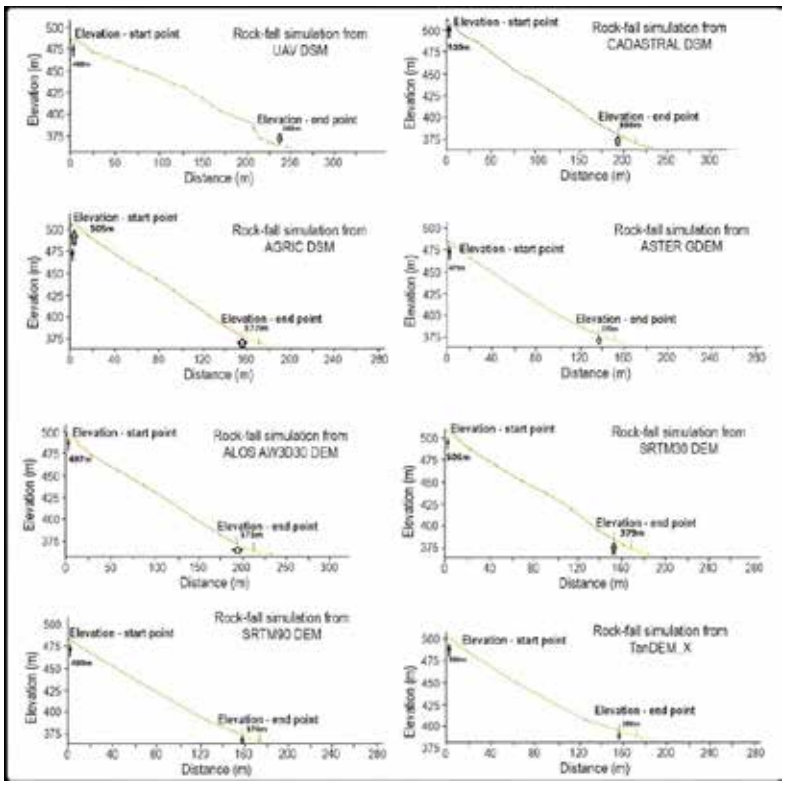

Figure 3. Two-dimensional rockfall simulations via RocFall software for the 2nd slope profile.

According to the figures above, only the UAV DSM created a detailed slope profile, with steep slopes and smooth areas. The other DSMs tended to flatten the topography. The rock in the UAV DSM slope profile jumped the first barrier/fence and broke the second barrier/fence. This result, in comparison with the field observations, is reliable, as the rock stopped a few meters before the end of the slope, in the churchyard (Figure 1). In the DSM from the Greek Cadastral, DSM from the Ministry of Agriculture, ALOS AW3D30 DEM, ASTER GDEM, SRTM30 DEM, SRTM90 DEM and TanDEM_X slope profiles, the rock rolled and stopped in the first barrier/fence. This is in contrast to the real trajectory. Therefore, only the UAV DSM simulated a trajectory close to the real.

- **<u>RocFall results</u>**

The total kinetic energy distribution was computed via RocFall software in the middle of the slope profile, at x = 117.3 m, and is presented below (Figure 4). The geological and material characterizes of the rockfall were taken into

account. More specifically, the coefficient of normal restitution (Rt) has a mean value of 0.39 and a standard deviation of 0.04, while the coefficient of tangential restitution (Rn) has a mean of 0.80 with the same standard deviation. The friction angle (Phi) averages 15° (standard deviation 2°), and the mean horizontal velocity reaches 11 m/s (standard deviation 1.1 m/s).

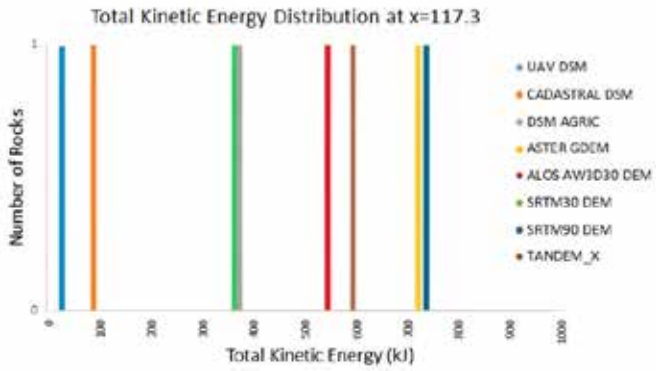

Figure 4. Total kinetic energy distribution at x = 117.3 m for the slope profile via RocFall

Figure 4 illustrates how total kinetic energy—measured at x = 117.3 m along the slope—varies for a single rockfall simulation when using different elevation models in RocFall. Each colored bar corresponds to a specific DSM/DEM, with higher bars positioned farther along the x-axis indicating larger kinetic energies. The UAV DSM and Greek Cadastral DSM (blue and orange bars), which have finer spatial resolutions, yield the lowest kinetic energies (roughly 20–90 kJ). By contrast, the Ministry of Agriculture DSM and SRTM30 DEM (green and grey bars) display moderate energy levels (about 360–380 kJ). The coarsest models, ALOS AW3D30 DEM, ASTER GDEM, SRTM90 DEM, and TanDEM_X (red, yellow, dark-blue, and brown bars) produce the highest energy values (560–730 kJ), since smoothing out the terrain in lower-resolution data allows the rock to accelerate more. Overall, the DSMs with coarser spatial resolution (more than 30 m) flattened the relief; consequently, the rock recorded higher speed than in the other DSMs with high spatial resolution (less than 30 m), which created unsmooth surfaces

- **<u>QProto results</u>**

For examining Platiana rockfall phenomenon and extract maps, in terms of the total weighted kinetic energy (J), QPROTO analysis were accomplished in this section (Figure 5a-5d). The slope and material characteristics which derived from in situ surveys and literature data were defined (Depountis et al., 2010; Sabatakakis et al., 2015; Vagenas, 2020). The energy angle φp is 30°, the forest coverage is dense vegetation in limestones and the propensity index is 1.

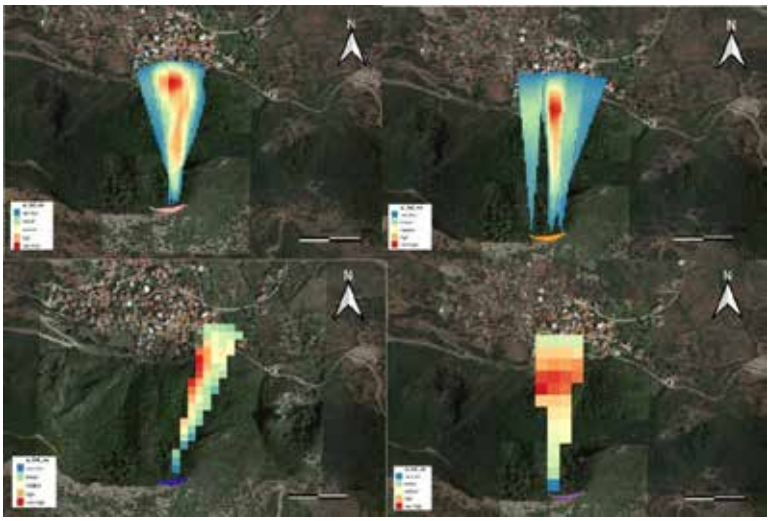

Figure 5. QPROTO results, in terms of total weighted kinetic energy (J), for the site of Platiana. a) UAV DSM, b) Greek Cadastral DEM, c) DSM from the Ministry of Agriculture d) ALOS AW3D30 DEM.

In Figure 5a, the UAV DSM (0.1 m resolution) generated 93,155 source points (pink polygon), necessitating resampling to 5×5 m for faster processing. The QPROTO map shows high to very high total weighted kinetic energies in the slope's center, tapering to very low at the edges, with the northern sector exhibiting the highest values. In Figure 5b, the Greek Cadastral DSM (5 m resolution) yielded just 36 source points (orange polygon), capturing very low to medium energies over two-thirds of the area and higher levels near the slope's end, especially in the north—consistent with in situ observations that place the rock's stopping point in the churchyard, where energies peaked. Although the Greek Cadastral DSM aligns with the UAV DSM, it positions the cone a few meters farther and reveals an exposed block area on the cone's left side. The Ministry of Agriculture DSM (20 m resolution, Figure 5c) produced only two source points (blue region). This analysis shows very low energies in the south, low to medium in the east-north, and high to very high in the west, yet contradicts field data by displaying high values prematurely. Finally, Figure 5d presents the ALOS AW3D30 DEM (30 m resolution) with three source points, indicating low to medium energies over most of the cone, very high in its middle, and an endpoint that stops short of the actual stopping point, rendering this analysis more conservative.

- **HY-STONE results**

For the rockfall analysis, six DEMs were used, covering a resolution range from 5 m to 90 m. The coefficients of restitution E_N and E_T, and the rolling friction coefficient A_T, were back-calibrated on the higher-resolution DEM based on the rockfall event (Table 1). The masonry stone walls were simulated with low values of E_N and E_T and high values of A_T, similarly to buildings. Given that HY-STONE operates on a stochastic model, simulations were performed with 1000 rocks to provide a more accurate representation of rockfall dynamics. The following data presents the maximum translational kinetic energies for the Platiana rockfall, expressed in kJ (Figure 6).

Table 1. Coefficients of restitution and rolling friction in Platiana rockfall, calibrated on the Greek Cadastral DEM

Description	E_N	E_T	A_T
Houses	0.20	0.20	1.00
Road- asphalt	0.55	0.70	0.25
Debris well vegetated	0.35	0.60	0.42
Debris without vegetation	0.40	0.65	0.35
Stone wall	0.20	0.20	1.00

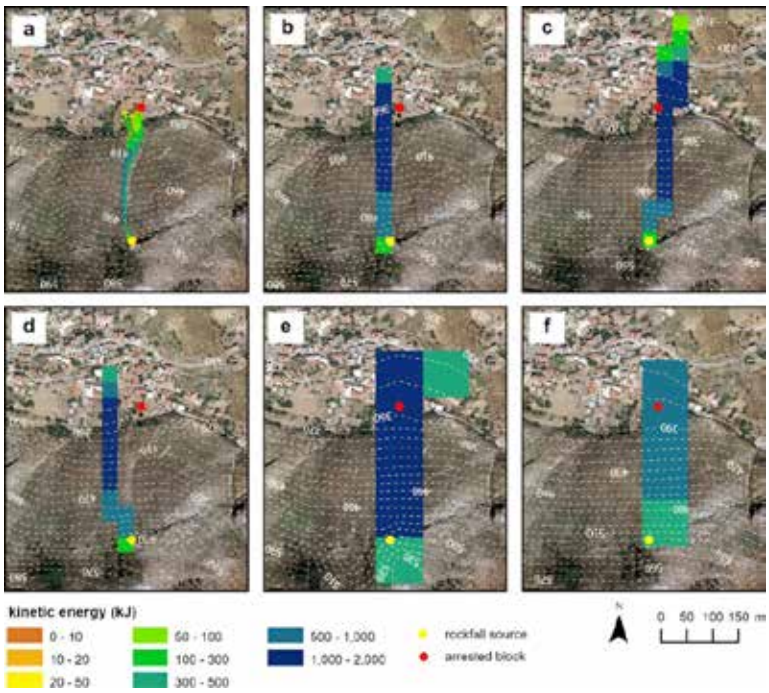

Figure 6. HY-STONE results, in terms of in terms of the maximum translation kinetic energy for the site of Platiana. a) Greek Cadastral DEM, b) ALOS AW3D30 DEM, c) ASTER GDEM, d) SRTM30 DEM, e) SRTM90 DEM and f)TanDEM_X.

In Figure 6, the Greek Cadastral DEM (a) shows high to very high kinetic energies (0–1,500 kJ) near the rockfall source and centrally, then decreasing to very low at the slope's end; the ALOS AW3D30 DEM (b) starts with low energies near the source, rises to high in mid-path, and declines with medium energies at the end; the ASTER GDEM and SRTM30 DEMs (c, d) depict multiple paths with low energies (0–1 kJ) at the source, high energies (100–1,500 kJ) in the middle, and medium levels (0.1–100 kJ) in residential areas—extending beyond the actual endpoint; the SRTM90 DEM (e) generates two paths showing very high energies (500–1,500 kJ) at the endpoint and low energies (0.2–1 kJ) near the source; and TanDEM_X (f) presents a single trajectory transitioning from medium to high, then very high, and finally back to medium and low energies, likewise extending past the real endpoint.

Conclusions

The findings of this study highlight the importance of DSM resolution in rockfall simulations. The area of interest has been extensively observed since the occurrence of the rockfall events. Therefore, a plethora of in situ measurements and observations have been recorded and many geo-data sets have been collected. These data significantly contribute towards the extraction of a reliable 2D rockfall simulation, with relatively small discrepancies from the observations of the real event.

1. DSMs from UAV data with sub-decimeter spatial resolution proved to be the most accurate for a rockfall simulation.
2. The UAV offers a significantly different pathway among different rock paths, whereas the other DSMs have a simplified path of the fallen blocks.
3. The DSMs can be classified into three categories according to their accuracy in rock-fall simulation. In particular:

(i) High accuracy, which corresponds to DSMs with spatial resolution less than 5 m, such as UAV DSM and DSM from the Greek Cadastral. The processing of these DSMs in RocFall software extracted results similar to in situ observations.

(ii) Medium accuracy which corresponds to DSMs with spatial resolutions ranging from 20 m to 30 m, such as DSM derived from the Ministry of Agriculture, ALOS AW3D30 DEM, ASTER GDEM and SRTM30 DEM. Against all these DSMs, only DSM of the Ministry of Agriculture and ALOS AW3D30 DEM offered rockfall illustration relatively close to the real event.

(iii) Low accuracy, which corresponds to DSMs with spatial resolution of 90 m, such as SRTM90 DEM and TanDEM_X, and led to rockfall conclusions that abstain from the reality.

4. The existence of vegetation plays an important role in the simulation of the rockfalls and a recent and very accurate DSM from UAV can represent the real height of the vegetation in contrast to the free available DSMs, such as SRTM 30DEM or ASTER DEM that were created few years ago.
5. The coarse resolution of SRTM 90DEM and TanDEM_X may lead to the inaccurate slope profiles and to the erroneous calculations of the rock kinetic energy. Previous rockfall simulation studies based on SRTM90 or TanDEM_X DSMs should be re-evaluated.

Acknowledgements

The authors would like to thank Prof. Paolo Frattini from the University of Bicocca, Milan, for providing access to the HY-STONE software and for his valuable contributions.

References

Acosta, E., Agliardi, F., Crosta, G.B., Rıos Aragues, S., 2002. Regional Rockfall Hazard Assessment in the Benasque Valley (Central Pyrenees) Using a 3D Numerical Approach. In Proceedings of the 4th EGS Plinius Conference—Mediterranean Storms, Mallorca, Spain, p. 555–563.

Agliardi, F., Crosta, G.B., Frattini, P., 2009. Integrating rockfall risk assessment and countermeasure design by 3D modelling techniques. Nat. Hazards Earth Syst. Sci. 9, 1059–1073.

Baillifard, F., Jaboyedoff, M., Sartori, M., 2003. Rockfall hazard mapping along a mountainous road in Switzerland using a GIS-based parameter rating approach. Nat. Hazards Earth Syst. Sci. 3, 435–442.

Borella, J., Quigley, M., Krauss, Z., Lincoln, K., Attanayake, J., Stamp, L., .. Gravley, D., 2019. Geologic and geomorphic controls on rockfall hazard: how well do past rockfalls predict future distributions?. Natural Hazards and Earth System Sciences, 19(10), 2249-2280.

Castelli, M., Torsello, G., Vallero, G., 2021. Preliminary Modeling of Rockfall Runout: Definition of the Input Parameters for the QGIS Plugin QPROTO, Geosciences 11, 88.

Crosta, G.B., Agliardi, F., 2004. Parametric evaluation of 3D dispersion of rockfall trajectories. Nat. Hazards Earth Syst. Sci. 4, 583–598.

Depountis, N., Lainas, S., Pyrgakis, D., Sabatakakis, N., Koukis, G., 2010. Engineering geological and geotechnical investigation of landslide events in wildfire affected areas of Ilia Prefecture,Western Greece. Bull. Geol. Soc. 43, 1138–1148.

Dorren, L., 2003. A review of rockfall mechanics and modelling approaches. Progress in Physical Geography 27(1), 69–87.
Fell, R., Corominas, J., Bonnard, C., Cascini, L., Leroi, E., Savage, W.Z.; 2008.Guidelines for landslide susceptibility, hazard and risk zoning for land use planning. Eng. Geol. 102, 85–98.
Frattini, P., Crosta, G., Carrara, A., Agliardi, F., 2008. Assessment of rockfall susceptibility by integrating statistical and physically-based approaches. Geomorphology 94, 419–437.
Guzzetti, F., Crosta, G., Detti, R., Agliardi, F., 2002. STONE: A computer program for the three-dimensional simulation of rock-falls. Comput. Geosci. 28, 1079–1093.
https://grass.osgeo.org/grass78/manuals/r.viewshed.html (accessed on 14 January 2021).
Hungr, O., Evans, S.G., Hazzard, J., 1999. Magnitude and frequency of rockfalls and rock slides along the main transportation corridors of southwestern British Columbia. Canadian Geotechnical Journal 36(2), 224-238.
Jaboyedoff, M., Derron, M.-H., Blikra, L.H., 2005. Preliminary assessment of rockslide and rockfall hazards using a DEM (Oppstadhornet, Norway). Natural Hazards and Earth System Sciences 5, 285-292.
Kakavas, M., Frattini, P., Previati, A., Nikolakopoulos, K., 2024. Evaluating the Impact of DEM Spatial Resolution on 3D Rockfall Simulation in GIS Environment. Geosciences, 14(8), 200.
Kakavas, M., Nikolakopoulos, K., 2021. Digital Elevation Models of Rockfalls and Landslides: A Review and Meta-Analysis. Geosciences 11, 256.
Kakavas, M., Nikolakopoulos, K., Kyriou, A., Koukouvelas, I., 2023. The Influence of the DEM Spatial Resolution in Rockfall Simulation and Validation with In Situ Data. Geosciences 13, 57.
Keijsers, J.G.S., Schoorl, J.M., Chang, K.-T., Chiang, S.-H., Claessens, L., Veldkamp, A., 2011. Calibration and resolution effects on model performance for predicting shallow landslide locations in Taiwan. Geomorphology 133, 168–177.
Pradhan, B., Sameen, M.I., 2017. Effects of the Spatial Resolution of Digital Elevation Models and Their Products on Landslide Susceptibility Mapping. In Laser Scanning Applications in Landslide Assessment; Springer: Berlin/Heidelberg, Germany, p. 133–150.
Rocscience., 2002 RocFall software—For risk analysis of falling rocks on steep slopes. In Rocscience User's Guide; Rocscience: Toronto, ON, Canada.
Sabatakakis, N., Depountis, N., Vagenas, N., 2015. Evaluation of Rockfall Restitution Coefficients. Eng. Geol. Soc. Territ. 2, 2023–2026.
Toma, L, Zhuang, Y., Richard, W., Metz, M. GRASS GIS Manual. Available online
Vagenas, N., 2020. Rockfall Simulation by Analytical Methods. Correlation of Rockfall Energy Dissipation Parameters and Rock Mass Characteristics. Ph.D. Thesis, University of Patras, Greece, Department of Geology, Patras, Greece.
Wu, M., Luo, G., Hu, X., Bi, Y., Wang, Y., Ma, N., 2025. Dynamic fragmentation analysis of potential rockfall hazards at Zixia hydropower dam, Qinghai-Tibet plateau. Journal of Rock Mechanics and Geotechnical Engineering.

17th INTERNATIONAL CONGRESS of the Geological Society of Greece

BULLETIN OF THE GEOLOGICAL SOCIETY OF GREECE, SP. PUBL.

EXTENDED ABSTRACT 123

The late Ruscinian leporid *Trischizolagus* (Leporidae, Lagomorpha) from Megalo Emvolon (Thessaloniki, Greece)

Christina N. Kalaitzi[1], Dimitris S. Kostopoulos[1]

(1) Laboratory of Geology and Palaeontology, School of Geology, Aristotle University of Thessaloniki, 54124 Thessaloniki, Greece

Introduction – Fossiliferous site

Since 2017, ongoing field campaigns at Megalo Emvolon have led to the discovery of a new fossil site, Megalo Emvolon-4 (MVL), which has yielded, inter alia, an abundance of lagomorph fossils. This paper introduces the newly discovered leporid collection (Leporidae, Mammalia) at MVL, featuring exceptionally well-preserved cranial, postcranial, and dental fossil remains. All specimens are attributed to *Trischizolagus dumitrescuae*, the most prevalent and widespread species of the genus during the Early Pliocene (Ruscinian) in Europe. Originally discovered in Romania, *Trischizolagus dumitrescuae* has since been identified at more than fifteen fossil sites across Eurasia (Averianov and Tesakov, 1997; Čermák and Wagner, 2013; Čermák *et al.,* 2021; and others).

The sediments in the Megalo Emvolon area are part of the Gonia Formation (Fm) and are indicative of a fluvio-lacustrine depositional environment with frequent river discharges and shallow lakes (Syrides, 1990). Alternating lenses and intercalated beds of clays, silts, marls, sands, sandstones, massive marly limestones, and gravels constitute the sedimentary sequence in the Megalo Emvolon area. Small pockets or spots, ranging from 0.5 to 3 meters in length, typically concentrate fossils at the site, scattered across various stratigraphic levels. Koufos *et al.* (1991) identified three fossil horizons within the Megalo-Emvolon section, with MVL either correlated with the basal or middle fossiliferous level (MEV, MEM) or situated in between both levels. The Megalo Emvolon fauna is dated to the Late Ruscinian, MN 15 (Koufos *et al*., 1991; Koufos, 2006) (about 4.2–3.2 Ma, according to http://paleobiodb.org).

The MVL *T. dumitrescuae*

Overall, the leporid material of this study is in excellent condition, with only a few incomplete specimens or fragments. The MVL material comprises 383 specimens, out of which 26 are cranial, 212 are dental (146 upper and 66 lower), and 145 are postcranial (11 bone groups), all in outstanding condition (Fig 1). Significantly, this study presents the first discovery of well-preserved skulls of *T. dumitrescuae* at Megalo Emvolon, providing unprecedented insights into its cranial morphology. The identification of *T. dumitrescuae* is solely based on the morphology of p3 and is strongly supported by comparisons with Romanian samples among other localities, alongside a detailed analysis of several morphometrical traits. The p3 exhibits the typical tetralobed trigonid form, a well-developed mesoflexid and hypoflexid, and a 1:2 size ratio between the length of the trigonid and the talonid. Moreover, the so-called "*Alilepus* pattern" is the predominant morphotype across all MVL material. Regarding the cranial anatomy, *T. dumitrescuae* has a large and acute cranium that is highly fenestrated, especially in the premaxillary, maxillary, and frontal regions, and exhibits a set of supraorbital processes that are not so well developed. Regarding the postcranial material, the forelimb features a scapula with a broad neck and a narrow coracoid process positioned close to the glenoid cavity. The humerus is characterized by a prominent deltoid crest. In the hindlimb, the femur's proximal trochanters are closely spaced, while the pelvis displays a robust ilium and a wide ischial tuberosity. Additionally, the calcaneus has an elongated body.

Conclusions

The material from MVL significantly expands upon earlier records from the site (Koufos and Koliadimou, 1993), providing valuable new insights into the previously unknown cranial morphology of *T. dumitrescuae*, its intraspecific dental variability, and locomotive tendencies, while also refining the genus and species diagnostic characteristics, correcting earlier misconceptions, and establishing intraspecific variation in comparison to other European records. The description of the cranium of *T. dumitrescuae* reveals a unique combination of *Lepus*- and *Oryctolagus*-like features that differentiate it from both the Eurasian *Alilepus* and the African *Serengetilagus*. The dental shape and size of MVL are consistent with those of dental remains from Megalo Emvolon-1 (Koliadimou and Koufos, 1993), as well as those of *T. dumitrescuae* from the type locality in Măluşteni, Romania. Lastly, preliminary ecomorphological analysis based on limb and skull morphology of *T. dumitrescuae* in MVL reflects adaptations for swift movement, high jumping, and capability for digging.

Figure 1. Craniodental and postcranial material of *T. dumitrescuae* in MVL.

Acknowledgements

The authors express their sincere gratitude to Dr. Lars von den Hoek Ostende and Pepijn Kamminga, MSc, of the Naturalis Biodiversity Center, for providing recent leporid specimens essential to the comparative study. Special thanks are also extended to Dr. Georgios Konidaris and Stylianos Koutalis, MSc, from the Department of Geosciences, Palaeoanthropology section, at Eberhard Karls Universität Tübingen, for their assistance with 3D scanning. Finally, we deeply appreciate Dr. Stanislav Čermák for generously sharing raw data on the *Trischizolagus* p3.

References

Averianov, A.O., Tesakov, A.S., 1997. Evolutionary trends in Mio-Pliocene Leporinae, based on *Trischizolagus* (Mammalia, Lagomorpha). Paläontologische Zeitschrift 71, 145-153.

Čermák, S., Wagner, J., 2013. The Pliocene record of *Trischizolagus* and *Pliopentalagus* (Leporidae, Lagomorpha, Mammalia) in Central Europe, with comments on taxonomy and evolutionary history of Leporinae. Neues Jahrbuch für Geologie und Paläontologie 268, 97-111.

Čermák, S., Angelone, C., Moncunill-Solé, B., 2021. *Prolagus* Pomel, 1853 (Lagomorpha, Mammalia) in the framework of the Pliocene faunal rearrangements in central Europe. Comptes Rendus Palevol 28, 597-617.

Koufos, G.D., 2006. The Neogene mammal localities of Greece: faunas, chronology and biostratigraphy. Hellenic Journal of Geosciences 41, 183-214.

Koufos, G.D., Syrides, G., Koliadimou, K., 1991. A Pliocene primate from Macedonia. Journal of Human Evolution 21, 283-294.

Koufos, G.D., Koliadimou, K., 1993. Two lagomorphs from the Pliocene of Macedonia (Greece). Bulletin of the Geological Society of Greece 28, 117-129.

Syrides, G., 1990. Lithostratigraphic, biostratigraphic and palaeogeographic study of the Neogene – Quaternary sedimentary deposits of Chalkidiki Peninsula, Macedonia, Greece. Ph.D. Thesis, Aristotle University of Thessaloniki, Thessaloniki, 243 p.

17th INTERNATIONAL CONGRESS of the Geological Society of Greece

BULLETIN OF THE GEOLOGICAL SOCIETY OF GREECE, SP. PUBL.

EXTENDED ABSTRACT 124

Multiscale Geo-visualization Dashboard of Persistent Scatterer Interferometry SAR Data, Lesvos Island, Greece

Panagiotis Kalaitzis[1], Michael Foumelis[2], Antonios Mouratidis[2] and Nikolaos Soulakellis[1]
(1) Department of Geography, University of the Aegean, Mytilene, Greece, p.kalaitzis@geo.aegean.gr
(2) Department of Physical and Environmental Geography, Aristotle University of Thessaloniki, Thessaloniki, Greece

Research Highlights

This study emphasizes the importance of effective visualization for Persistent Scatterer Interferometry (PSI) data, particularly in capturing the dynamic and spatiotemporal aspects of ground displacement. A novel multiscale generalization algorithm was developed to optimize PSI dataset visualization across eight predefined cartographic scales, ensuring suitability in each cartographic scale. An interactive dashboard was designed to properly visualize PSI data of different geographic, cartographic, spatial, and temporal scales, combined with auxiliary geospatial data, addressing the need for intuitive cartographic tools. The results highlight the importance of visualizing and studying PSI data through interactive dashboards, applying the classic principles of cartography. This approach underscores their role as innovative tools for understanding and monitoring the dynamic behavior of surface motion.

Introduction / Background

The rapid increase in the availability of earth observation (EO) data has introduced a critical demand for precise, user-friendly, and interactive dashboards that facilitate the thorough analysis of these vast and complex datasets (Gehlot & Hanssen, 2008). Despite significant advancements, the interpretation of EO data remains a challenging endeavor due to their spatial and temporal intricacies. Advances in geospatial data visualization have provided efficient, low-cost methodologies for analyzing and interpreting geospatial information (Kraak & Ormeling, 2020). Among these, Persistent Scatterer Interferometry (PSI) has emerged as a highly effective technique for monitoring ground deformation and instability phenomena. Utilizing spaceborne synthetic-aperture radar (SAR) imagery, PSI achieves millimeter-level precision in detecting surface motion over extensive spatial domains, serving as a key tool in geosciences, urban planning, and environmental disciplines (Crosetto *et al*., 2016).

PSI data provide valuable insights into a broad spectrum of dynamic processes, including land subsidence, landslides, volcanic activity, and infrastructure stability. However, the technique is inherently dependent on persistent scatterers (PS), which exhibit consistent radar reflectivity over time. The spatial density of PS can be limited in non-urban environments where suitable targets are sparse. To overcome this limitation, distributed scatterers (DS)—targets with consistent scattering behavior within radar resolution cells—are integrated with PS measurements, significantly enhancing spatial coverage. The combined PS/DS solution enables more detailed analyses by increasing point density, particularly in densely vegetated or sparsely built-up areas (Foumelis *et al*., 2022).

Recently, algorithms for performing multi-temporal interferometric analysis have been seamlessly integrated into cloud platforms, providing users with operational and automated services. This integration significantly reduces the need for extensive data storage, computational resources, and specialized expertise in executing complex processing chains. An example of such a service is the surface motion mapping (SNAPPING) service integrated on the Geohazards Exploitation Platform (GEP). SNAPPING is a PSI chain designed specifically for the Copernicus Sentinel-1 mission, capable of generating average motion and corresponding displacement time-series at various spatial resolutions.

However, effective visualization of PSI data remains a challenge, particularly at multiple scales and resolutions. The spatial and temporal complexity of PSI data necessitates the development of innovative visualization methods to support comprehensive analysis. Generalization techniques, such as point aggregation and elimination, are employed to adapt datasets to predefined cartographic scales while mitigating challenges posed by overlapping points in high-density areas (Kalaitzis *et al*., 2023; Poncoş *et al*., 2022).

Existing platforms, such as the European Ground Motion Service and national services in Germany, Norway and the Netherlands, demonstrate the utility of PSI web applications in monitoring ground motion. The dashboard employs a cohesive, interactive design centered around a web map that serves as a primary visualization element. Complementing this, key performance indicators (KPIs) provide high-level insights, while dynamic graphs depict trends and relationships in the data. Accompanying these are structured **lists** that offer detailed tabular information.

All components are interconnected: any selection or interaction within one-such as clicking on a map region, a data point in a graph, or a list item-immediately updates the other components, ensuring a synchronized and contextualized user experience. This architecture enables seamless data exploration and decision-making (Bach *et al*., 2022).
Interactive dashboards offer dynamic tools for visualizing and exploring PSI datasets. Providing tools such as data filtering, time-series graphs creation and comparison with auxiliary geospatial data, dashboards enable both expert and novice users to interact with and interpret ground deformation data effectively. By combining original and generalized datasets in areas with varying densities, dashboards help manage cartographic challenges and offer insights into intricate geospatial information.
This study introduces a novel approach to address the challenges of visualizing and exploring PSI datasets of different spatial resolutions, in predefined cartographic scales. This approach is based on the development of a standalone dashboard, providing interactive cartographic tools designed to optimize the visualization and exploration of PSI datasets. The dashboard represents a low-cost solution that can be tailored with any generic PSI dataset, in order to offer users invaluable insights into such intricate geospatial information.

Methods

The methodology of this study is represented by the flowchart in Figure 1, consisting of three main steps.

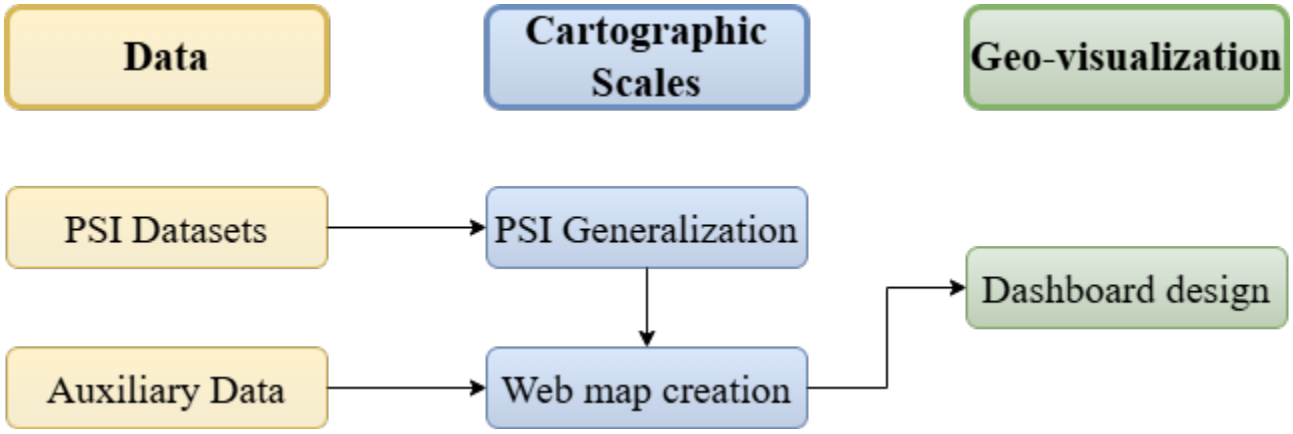

Figure 1: Overall workflow chart of the methodology followed for the integration of the research

1. Data: Describing all the PSI datasets generated and the auxiliary data used for the needs of the current study, as well as for visualization.

   PSI Data

   The processing of Sentinel-1 SAR data is performed using the SNAPPING service on GEP, where PSI services are available at different spatial resolutions. For this study, two resolution datasets (PSI Med and PSI Full) were utilized. SNAPPING offers three distinct services: the SNAPPING IFG service, which generates interferometric stacks, and the SNAPPING PSI Med (i) and SNAPPING PSI Full (ii) services, which conduct PSI analyses at medium and full resolutions, respectively. Additionally, SNAPPING provides a PSI time-series analysis service for both resolutions (Foumelis et al., 2022).
   PSI processing focused on PS/DS (iii) scatterers was carried out using the infrastructure of Aristotle University of Thessaloniki (AUTh), utilizing the SNAPPING IFG outputs, including differential interferograms and auxiliary data, previously generated on GEP. To ensure measurement consistency, common processing parameters were applied to all solutions, with adjustments made for deviations caused by different references.
   According to specific criteria, the detected Persistent Scatterer (PS) targets from the SNAPPING PSI Med dataset were initially merged within a 100-meter search radius, reducing the number of targets in areas with high point density. For SNAPPING PSI Full, no merging of neighbouring PS targets was performed, preserving the original sensor resolution. Compared to PS-InSAR, DS-InSAR results significantly enhance the spatial distribution density of point targets, particularly in regions with lower coherence (Foumelis *et al*., 2022).
   PSI Med and Full resolution datasets consist of 45,749 and 283,419 PSs respectively, geolocated in the broader area of Lesvos Island, for the period between 2015–2020. PS/DS dataset consists of 11,169 points for the period between 2019-2021 and located in the broader area of Bali Alonia Park.

   Auxiliary data

PSI data are integrated with auxiliary datasets to meet visualization requirements and enable enhanced utilization. The auxiliary datasets include: A geology layer, digitized from the freely available geological map of Greece (1:500,000), provided by the Hellenic Geological and Mining Research Authority (E.A.G.M.E) and ESA Land Cover 2020 dataset, with a spatial resolution of 10 meters.

2. Cartographic scales: Based on previous studies (Kalaitzis *et al*., 2023; Poncoş *et al*., 2022), the necessity for PSI interpretation aligned with pre-specified scales becomes evident. By combining the coverage area of each PSI dataset with various geographic scales (e.g., regional scale, local scale), eight predefined cartographic scales are derived:

- 1:1,000,000
- 1:500,000
- 1:200,000
- 1:100,000
- 1:50,000
- 1:20,000
- 1:10,000
- 1:5,000

An algorithm for generalizing PSI datasets was developed, in order to avoid point overlapping especially on smaller cartographic scales (Kalaitzis *et al*., 2024). More extensively, based on the visual acuity of the human eye in each predefined cartographic scale, eight grids with corresponding cell sizes were created, as presented in Table 1.

Table1: Predefined cartographic scales used for visualization, followed by the PSI dataset visualized in each case. For generalization needs, a grid was created for each cartographic scale, with the corresponding cell size. For each cartographic scale, a dataset (either generalized or not) is generated with the corresponding number of points and point density.

Cartographic Scale	Cell Size (m)	PSI Dataset	No. of Points	Point Density (points/km^2)
1:1,000,000	250	PSI Med	14,348	15
1:500,000	125	PSI Med	31,189	66
1:200,000	50	PSI Med	45,749	99
1:100,000	25	PSI Full	158,030	376
1:50,000	12,5	PSI Full	231,166	507
1:20,000	5	PSI Full	283,419	580
1:10,000	2,5	PS/DS	11,169	9422
1:5,000	1,25	PS/DS	11,169	9422

After applying a generalization algorithm to all available PSI datasets, it is derived that each original PSI dataset is best visualized at a specific cartographic scale, determined by the point density of the dataset. In every other cartographic scale, generalized datasets are used for visualization.

After this procedure, all PSI datasets were joined with auxiliary data and uploaded on a server provided by ArcGIS Enterprise™ platform. Through this platform a web map, consisting of all available data, was created.

3. Geo-visualization: Based on the web map created, an interactive dashboard was created consisting of the basic viewer of the application (web map), combined with several cartographic tools, providing crucial information about each points' attributes (mean v
4. elocity, velocity uncertainty, temporal coherence, cumulative deformation, time-series, geology and land use).

Results

An interactive dashboard developed, contributing in proper visualization and exploration of different resolution PSI datasets in multiple cartographic scales. The main component of this platform, is the web map, providing visualization of mean velocities of PSI datasets and exploration through the study area. Navigation along the study area, is also enhanced by predefined bookmarks, zooming in specific areas of Lesvos Island. A base map list is also available, allowing users to customize it according to their preferences. The map is combined with four different indicators about mean velocity, temporal coherence, velocity uncertainty and cumulative deformation. Time-series graph, presenting ground deformation of points through time, is also available. The time-series graph tool allows users to zoom in on shorter time periods within the graph using a scrollbar. The indicators and the time-series graph display the mean values of the attributes they represent. Lists of geology and land use of points, are also provided as tools. Each one of the tools is linked with the map, so every adjustment by the users (selection, pan, zoom) affects both the map

and the tools. Selection of single or multiple points from the map, also updates indicators, time-series graph and lists. Dashboard is accessible by the link: Multiscale Geo-visualization Dashboard for PSI Measurements, Lesvos A preview of the dashboard is presented in Figure 2.

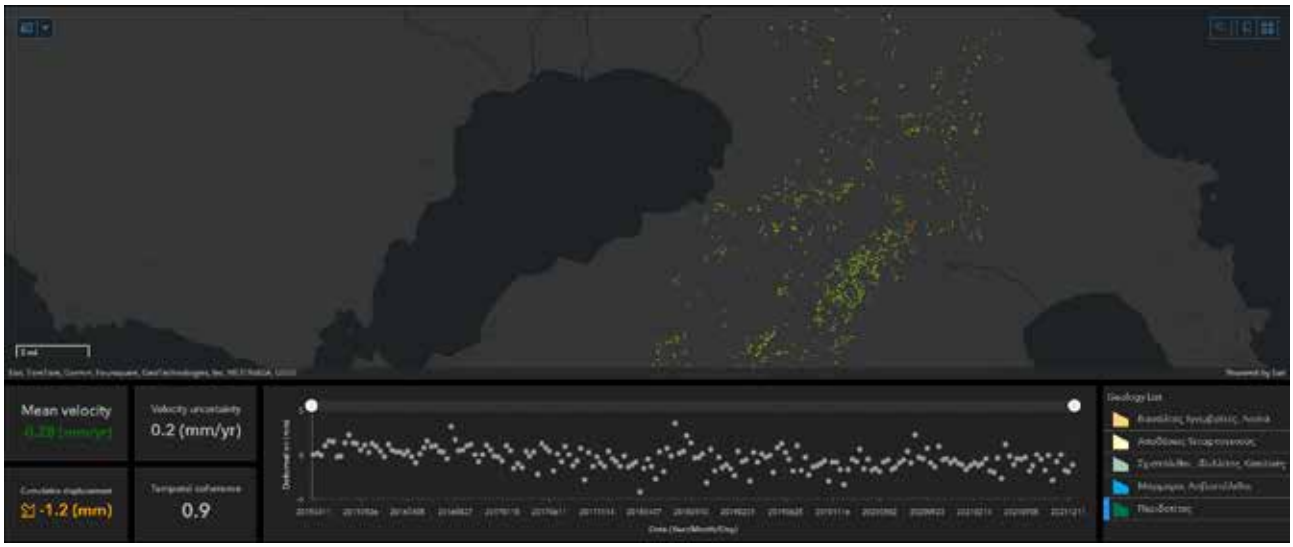

Figure2: A preview of the dashboard, visualizing mean velocities of PSI med resolution dataset, in scale 1:200.000. Only points referring to peridotites are filtered and displayed; cartographic tools are adjusted accordingly. Mean velocity of filtered points is -0.28mm/yr with a velocity uncertainty of 0.2mm/yr, cumulative deformation is -1.2mm and temporal coherence is 0.9.

Limitations mainly refer in the availability of cartographic tools, which may not cover all user needs for advanced data analysis or visualization. Customization options for the tools are restricted, making it challenging to tailor the dashboard to specific workflows or preferences. While functional, the dashboard's tools are constrained by its simplified design, prioritizing ease of use over extensive configurability. Another limitation arises concerning the application of generalization algorithm on PSI datasets. More specifically, during the generalization process, the number of points in each generalized dataset is reduced compared to the original. In the cartographic scales where generalized datasets are used, information regarding individual ground displacement values per date is absent. Consequently, time-series analysis is not feasible at these cartographic scales. To address this limitation, time-series graphs are exclusively generated for the original datasets at their corresponding cartographic scales.

Conclusions

The utilization of the multiscale geo-visualization dashboard facilitates the effective exploration of various PSI datasets, enabling easier extraction of ground motion information and valuable insights into the prevailing conditions. The integration and seamless interaction between the web map and the cartographic components result in an accessible and fully operational tool for interactive data visualization applicable to any generic PSI dataset and individual case studies.

Generalized PSI datasets enable accurate and effective visualization of measurements across multiple cartographic scales, facilitating qualitative data interpretation. Each original PSI dataset is optimally visualized at a specific cartographic scale, dictated by the dataset's point density. Visualizing original datasets at their corresponding optimal cartographic scales not only ensures precise depiction of ground displacement but also enables comprehensive qualitative and quantitative spatiotemporal analyses, such as time-series graphs generation.

By visualizing mean velocities of different resolution PSI datasets, via the multiscale geo-visualization dashboard, reveals that Lesvos Island is not characterized by significant ground deformation. Negative velocity rates between -5 mm/year and -8 mm/year, indicative of land subsidence, are observed in the eastern part of the island near Lampou Mili village. Conversely, positive velocity rates indicating uplift, reaching up to 2 mm/year, are concentrated in the northern region, between Mythimna and Efthalou.

References

Bach, B., Freeman, E., Abdul-Rahman, A., Turkay, C., Khan, S., Fan, Y., & Chen, M., 2022. Dashboard Design Patterns. IEEE

Transactions on Visualization and Computer Graphics 29(1), 1–11. https://doi.org/10.1109/TVCG.2022.3209448

Crosetto, M., Monserrat, O., Cuevas-González, M., Devanthéry, N., & Crippa, B., 2016. Persistent Scatterer Interferometry: A review. ISPRS Journal of Photogrammetry and Remote Sensing 115, 78–89. https://doi.org/10.1016/j.isprsjprs.2015.10.011

Foumelis, M., Delgado Blasco, J. M., Brito, F., Pacini, F., Papageorgiou, E., Pishehvar, P., & Bally, P., 2022. SNAPPING Services on the Geohazards Exploitation Platform for Copernicus Sentinel-1 Surface Motion Mapping. Remote Sensing 14(23), 6075. https://doi.org/10.3390/rs14236075

Gehlot, S., & Hanssen, R. F., 2008. Monitoring and Interpretation of Urban Land Subsidence Using Radar Interferometric Time Series and Multi-Source GIS Database, in: Nayak, S., & Zlatanova, S. (Eds.), Remote Sensing and GIS Technologies for Monitoring and Prediction of Disasters, 137–148. https://doi.org/10.1007/978-3-540-79259-8_8

Kalaitzis, P., Foumelis, M., Mouratidis, A., Kavroudakis, D., & Soulakellis, N., 2024. Multiscale Visualization of Surface Motion Point Measurements Associated with Persistent Scatterer Interferometry. ISPRS International Journal of Geo-Information 13(7). https://doi.org/10.3390/ijgi13070236

Kalaitzis, P., Foumelis, M., Vasilakos, C., Mouratidis, A., & Soulakellis, N., 2023. Interactive Web Mapping Applications for 2D and 3D Geo-Visualization of Persistent Scatterer Interferometry SAR Data. ISPRS International Journal of Geo-Information 12(2), 54. https://doi.org/10.3390/ijgi12020054

Kraak, M.-J., & Ormeling, F., 2020. Cartography: visualization of geospatial data. CRC Press.

Poncoş, V., Stanciu, I., Teleagă, D., Maţenco, L., Bozsó, I., Szakács, A., Birtas, D., Toma, Ş.-A., Stănică, A., & Rădulescu, V., 2022. An Integrated Platform for Ground-Motion Mapping, Local to Regional Scale; Examples from SE Europe. Remote Sensing 14(4), 1046. https://doi.org/10.3390/rs14041046

17th INTERNATIONAL CONGRESS of the Geological Society of Greece

BULLETIN OF THE GEOLOGICAL SOCIETY OF GREECE, SP. PUBL.

EXTENDED ABSTRACT 125

Methodology of cave mapping: comparison of surveys

Kalogeropoulos I.[1], Lazaridis G.[2,*], Tsekoura A.[1]

(1) Hellenic Speleological Society, branch of northern Greece

*(2) Faculty of Sciences, Aristotle University of Thessaloniki (AUTH), 54124 Thessaloniki, Greece, *geolaz@geo.auth.gr*

Research Highlights

The aim of the present article is to investigate the factors that affect the cave mapping. This investigation is based on comparisons of topographical diagrams of a given space made by different surveys of the same stations. A classroom of a known topography has been used for that purpose. The used traverses are the circumference survey, splay shots, zig-zagging survey and radial survey (after Dasher 1994). The comparisons concern the shape, the area and the direction of the cave map as well as the time that is needed for the survey and the affect of errors in certain station to the general topography of a map. The results are summarized and the significance of reference in the used methodology in any cave surveying is concluded. Among the different traverses the radial one and the splay shots are considered as the most accurate.

Introduction to Cave Mapping

Cave mapping is a crucial aspect of speleology. Due to the complex nature of caves, the perception of distances often does not align with reality. A well-drawn map allows speleologists to assess the cave's size, identify hazardous areas, anticipate challenges during exploration, and determine the necessary equipment. Furthermore, the systematic study of caves requires detailed and reliable mapping in a suitable format and scale, addressing various geoscience disciplines such as geology, speleology, and paleontology (Pagounis et al., 2004; Doggouris et al., 1986). Cave mapping is complicated by numerous factors, the two most prominent being the non-ideal conditions explorers face due to the challenging environment (Doggouris et al., 1986), which makes the mapping process arduous, and the cave's inherent complexity. This often requires documenting points located at vastly different elevations, necessitating a comprehensive representation of a three-dimensional space.

The first stage of cave mapping involves collecting data to create the map, which includes measurements taken by a mapping team. Ideally, this team consists of 3-4 members to optimize time, particularly in large caves, though a two-person team often exhibits better coordination (Judson, 1974). The team leader determines the locations of the measurement stations, records data in a logbook, sketches the cave, and typically designs the map, as they are most familiar with the notes. The other team members operate the instruments and relay measurements to the leader (Savvaidis et al., 2007).

The mapping process begins by establishing a station (which may or may not have pre-defined coordinates relative to a reference system). Subsequent stations are positioned to accurately depict the cave's shape. For each new station, the distance from the previous one, the azimuth, and the elevation difference (or slope) are measured and recorded. With these data, the stations can be drawn to scale and oriented on paper. This process is repeated as needed for all required stations.

The measurements collected form a path within the cave, known as a traverse, which can be either open or closed. In a closed traverse, the start and end points coincide, while in an open traverse, they do not. Closed traverses provide greater accuracy in mapping, as they allow the mapper to detect potential errors (Dasher, 1994). There are four types of traverses: central, radial, circular, and zig-zag, each suited to different cave shapes and sizes.

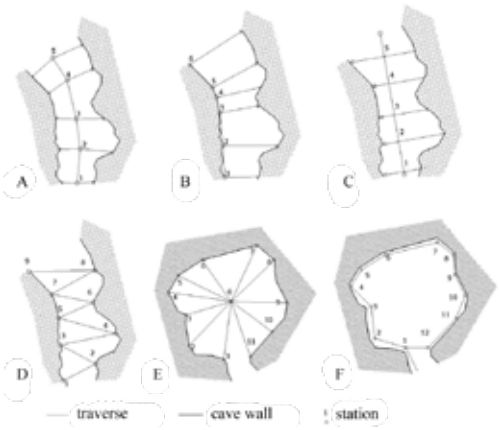

Figure 1. Illustrates various types of traverses: (a) central traverse, (b) central traverse with the main line along the wall, (c) central traverse with vertical measurements from the main line, (d) zig-zag traverse, (e) radial traverse, and (f) circular traverse.

- In a central traverse, a central line of stations is established down the middle of the cave passage, and the distance to the

cave walls is measured from each station on both sides (Judson, 1974). Lateral measurements always include azimuth readings (Fig. 1a). When the cave's morphology permits, the central line can run along one wall, with measurements taken only toward that wall (Dasher, 1994; Fig. 1b). In some cases, a straight central line is used, and wall distances are measured perpendicular to this line without needing azimuth readings (Fig. 1c; Savvaidis et al., 2007).

- In a zig-zag traverse, measurements alternate between the left and right sides of a narrow passage, creating a zig-zag path (Fig. 1d). This method provides more detail about each cave wall. Some explorers believe this technique distorts the cave's length, but it offers more comprehensive information for the final map (Dasher, 1994).
- In a radial traverse, measurements are taken from a central station (usually in a chamber) toward the boundaries of the area being mapped. The subsequent stations are radially arranged around the central station. This method is ideal for chambers that are roughly circular, allowing a clear line of sight from all stations to the center (Fig. 1e).
- In a circular traverse, measurements follow the perimeter of the mapped area. In this case, the traverse's shape matches that of the mapped space (Fig. 1f). This method is commonly used in circular chambers, where completing the traverse by taking measurements from the last station back to the first helps identify potential errors during map creation (Dasher, 1994).

Mapping Instruments

The primary instruments used in cave mapping are tape measures and laser meters for distance measurement, compasses for azimuth readings, and clinometers for slope measurements (Tarsoly, 2006).

Tape measures are the standard tool for direct distance measurement. They are made from various materials (metal, plastic, linen, or plastic) and typically come in lengths of 20, 25, 30, and 50 meters. Their accuracy is approximately 2-3 cm per 100 meters under standard tension (marked on the tape) and at 20°C. Proper care should be taken when rewinding the tape into its case, as mud and dirt in caves can jam the tape, rendering it unusable (Savvaidis et al., 2007).

Laser meters, which use electromagnetic waves to measure distance, are particularly useful in large caves. Many laser meters can also measure slope (Doggouris et al., 1986).

For angle measurements, a magnetic compass is used to measure the azimuth, or the angle between the target and magnetic north, which differs from true north. Compasses can be divided in several ways, with the most common being a 0–360° system providing a clockwise azimuth relative to north. Other systems include quadrant-based systems, military mils (6400 divisions), and grads (400 divisions) (Dasher, 1994). More precise angle measurements can be made using theodolites or total stations, though their size can make them cumbersome in caves. 3D scanners, which capture real-time three-dimensional coordinates to generate a 3D model, are another tool used in cave mapping (Pagounis et al., 2004).

A clinometer measures ground slope to calculate elevation differences. Simple clinometers consist of a protractor and a plumb line and can sometimes be integrated with a compass. Geometrical leveling is another method for measuring elevations, though it is difficult to apply in steep environments (Doggouris et al., 1986).

Error Correction and Map Drawing

After data collection, the next step is to correct for measurement errors (Tarsoly, 2006). Errors during mapping can distort the final result, deviating from reality. These errors fall into several categories:

- **Random errors**, such as deviations from a straight line, horizontal position, or recording inaccuracies (Savvaidis et al., 2007).
- **Systematic errors** caused by instrument imperfections, differences from the standard, or incorrect tension applied to the tape measure. Tape sag due to weight is another common source of error. Calibrating the instruments outside the cave to account for these errors is a recommended procedure (Savvaidis et al., 2007).
- **Blunders**, the most critical type of error, arise from human factors such as inexperience or extreme fatigue, making them unpredictable.

The final stage of mapping is creating the map based on the corrected measurements. It is crucial that the cave map is aligned with the country's triangulation network (or other reference systems) (Tarsoly, 2006).

Different mapping techniques can yield slightly varied results for the same cave. This study examines the case of mapping a specific space while keeping parameters like stations, team composition, and instruments constant but varying the traverse technique.

Mapping of a Room with Different Survey Routes

To compare different mapping techniques, a room and its antechamber from the Department of Geology at Aristotle University of Thessaloniki (AUTH) were selected for mapping. This choice was made because the shape of the space was already known, and a topographic plan existed, allowing for a comparison of each route's results with the topographic model (Fig. 2).

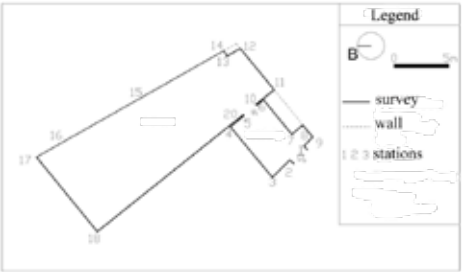

Figure 2. Topographic plan of the chamber mapped in this study, showing the locations and numbering of the stations used.

Instruments Used and Stations

The instruments used included a laser meter, a measuring tape, and a Suunto compass with a clinometer. A total of 21 stations were defined, remaining the same for each survey route to ensure accurate comparison of results, even in specific points. Additionally, on the eastern side, stations 15 and 16 were marked along with stations 14 and 17 to examine the deformation caused by redundant stations.

It was noted that the length of each measurement should be as large as possible to limit the number of stations, as suggested by Judson (1974).

Different Mapping Routes

The mapping was repeated, keeping the same instruments and team composition, but changing the route. The routes used were:

1. Radial route: Measurements were taken from three central stations (0, 21, 19).
2. Circular and zigzag routes: Mapping started from station 1, located at the entrance of the antechamber.
3.Central route: Measurements were taken perpendicularly from two central lines (19-21 and 21-22) toward the walls.

After collecting the data, four different maps of the same area were produced without any error correction (Fig. 3).

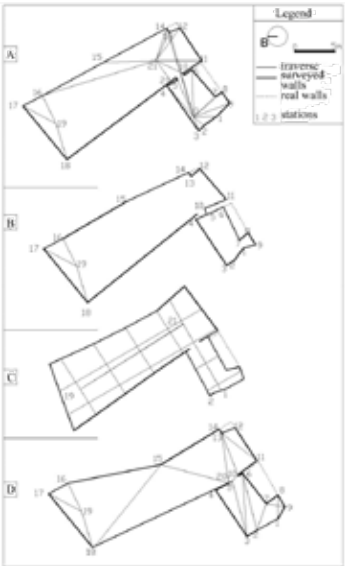

Figure 3. Topographic diagrams in "speleological style" of the chamber with different traverses: a) radial traverse, b) circular traverse, c) central traverse, d) zigzag traverse.

Discussion and conlusions

Radial Route Map (Fig. 3a, Table 1): This map closely aligns with the topographic plan of the room. The measured area matches the actual size (171 m²). Points 15, 16, and 17 are on the same straight line, with only minor deformations in some spots, such as the turn of the antechamber, which do not affect the overall shape of the room.

Circular Route Map (Fig. 3b, Table 1): This map shows deformation compared to the room's topographic plan, affecting the calculated area, which is smaller than the actual size by 7 m². Significant deformations were observed at the corners, which influence the overall shape. However, the advantage of the circular route is that there is a direct relationship between the measurement and the area represented.

Central Route Map (Fig. 3c, Table 1): This map presents minor deformations and a good overall correlation with the topographic plan. The measured area deviates slightly from the actual size (by 3 m²), with stations 15, 16, and 17 aligning correctly. The corners are also accurate. The central route, especially when measurements are taken at right angles, yields very good results but is time-consuming (Savvaidis et al., 2007).
Zigzag Route Map (Fig. 3d, Table 1): This map exhibits significant deformation compared to the actual shape. A notable discrepancy was found in the length of the room, which is a known issue with this route (Dasher, 1994). This also affects the area, which is calculated larger than the actual size by 15 m². Additionally, a slight shift in the map's orientation relative to the north was observed. Although the zigzag route requires less time for measurements compared to other routes, a single error can greatly distort the overall shape of the map and, with it, many important data points such as area and length.

Table 1. Summary description of the results of each traverse and evaluation regarding the main characteristics of cave mapping.

Type of Traverse	**Radial**	**Circular**	**Central**	**Zigzag**	**Type of Traverse**
Deformation	Minimal	Considerable	Minimal	Considerable	Deformation
Area Accuracy	Very good	Shows deviation	Relatively good	Shows significant deviation	Area Accuracy
Retention of Straight Lines	Yes	Yes	Yes	No	Retention of Straight Lines
Effect of an Error on Subsequent Measurements	Small to minimal	Significant	Small to minimal	Very large	Effect of an Error on Subsequent Measurements
Mapping Speed	Fast	Fast	Time-consuming process*	Fast	Mapping Speed
Deviation from Actual Orientation	No	No	No	Slight angle	Deviation from Actual Orientation

Dermitzakis & Dikaioulia (1981) emphasize the importance of a unified methodology in cave mapping. This study highlights the significance of:
a) the chosen survey route (Table 1),
b) the number of stations, and
c) the location of those stations in the mapping process.
As a result, maps produced using different methodologies are not directly comparable. Although references to the specific mapping methodology used are rarely found in the literature, it is deemed essential that each map be accompanied by these details for clarity and accuracy.

Acknowledgements
This paper was originally presented in Greek at the 4th Pancretan Speleological Conference in 2008, held in Zoniana, Crete, Greece. It is resubmitted with the approval of the organizing committee, represented by biologist Kaloust Paragamian, head of the Hellenic Institute of Speleological Research.

References

Dasher, G.R., 1994. ON STATION - A complete handbook for surveying and mapping caves. National Speleological Society, pp. 1-242, USA.
Dermitzakis, M.D., Georgiadou-Dikaioulia, E., 1981. Methods for calculating and measuring cave development parameters. Bulletin of the Hellenic Speleological Society, 18: 391-410.
Doggouris, S.N., Makris, G.N., Balodimos, D.D., 1986. Cave surveys. Proceedings of the Conference on Modern Methods of Surveying and Documenting Monuments and Archaeological Sites, pp. 188-221.
Judson, D., 1974. Cave survey for expeditions, The Geographical Journal, 140(2): 292-300.
Pagounis, V., Kalykakis, S., Biza, P., Papadopoulos, CH., 2004. The use of 3D scanning as a methodology for cave mapping: Application to the St. George Cave in Kilkis. Proceedings of the 10th International Conference, Bulletin of the Hellenic Geological Society, 36: 1244-1251.
Savvaidis, P., Yfantis, I., Lakakis, K., 2007. Topography and thematic cartography. Lecture Notes - Department of Architecture, Aristotle University of Thessaloniki.
Tarsoly, P., 2006. Cave Information System. Shaping the shape. XXIII FIG Congress, GIS Applications - Special Issues, pp. 1-9, Munich.

17th INTERNATIONAL CONGRESS of the Geological Society of Greece

BULLETIN OF THE GEOLOGICAL SOCIETY OF GREECE, SP. PUBL.

EXTENDED ABSTRACT 126

Geoeducational and Geotourism values of geological resources as novel path for Geosciences Education

Kalpogiannaki M.[1], Rogkala A.[2], Giannakopoulou P.P.[2], Koutsovitis P.[2], Lampropoulou, P.[2] Petrounias P.[2], Papoulis D.[2], Koukouzas N.C.[3], Pomonis P.[1]

(1) Section of Mineralogy and Petrology, Department of Geology and Geoenvironment, National and Kapodistrian University of Athens, Panepistimioupolis Zografou, 157 84 Athens, Greece, maria.kalpogiannaki@gmail.com (2) Department of Geology, University of Patras, Patras, Greece, (3) Chemical Process and Energy Resources Institute, Centre for Research and Technology Hellas (CERTH), Greece

Introduction

The modern trends of nowadays force us to adapt more and more to them in order to achieve the European as well as the international goals of smooth and sustainable development. Specifically, the evolution of data in Greece reveals that we are increasingly moving towards a new model of overtourism, where, in addition to the increase of revenue from an economic perspective, we must also identify any other ways to use these visitors from the geosciences viewpoint. This will indirectly help us to create a more conscientious audience capable of receiving any additional information regarding environmental protection in a more fruitful manner.

The only way to balance the strong relationship between human and nature is the sustainable development as it will solve problems between the increasing demands for resources and the environment. Living in a world where the climate change is increasingly apparent, the risk of depletion of mineral resources as well as the environmental pollution is becoming our daily routine, it is imperative as geo-scientists to reconsider our views and our actions in order to promote a more sustainable development model for a more sustainable society. Nowadays, the general public awareness of daily environmental challenges and sustainable development is low. Young people are by nature receptive to learn, while at the same time, they are also the key drivers of change in a society. In order to play a such role, they need to become environmentally aware. In this way, they could devise action programs to solve problems as they considered as active citizens and also exploited their relationship with all social media. Environmental education and geo-education, "which is promoted as the new educational trend that will make learning more comprehensive, more effective, more conscious and based on the research-scientific method of collecting, processing, presenting and utilizing information" will contribute to addressing this necessity. Thus, the purpose of knowledge of the environment is not the domination of man over nature but, in the context of the total environment, the relation of competition and domination are transformed into relations of complicity, cooperation and creation, where man must lead and follow the nature (Zouros *et al.*, 2004). In fact, at the 1977 International Conference in Tbilisi, Georgia, participants agreed that environmental education should be regarded as a separate scientific field of crucial significance. It is worth mentioning that UNESCO never gave up on the concept and initiative of environmental education. Following the above philosophy, UNESCO started to demarcate some areas with important geocultural monuments and designate them as UNESCO geoparks after strict geotope parameter controls (Iliopoulos *et al.*, 2024).

Geoturism has created techniques for geoeducation that enable geo-interpretation and the attainment of cognitive objectives by the audience, i.e., a broad education in geology, in order to promote awareness of geoheritage values, mainly in geoparks and geosites (and in Greece, in legal forms of protection – reserves of geoheritage and documentation sites or monuments of geoheritage).

This study aims to investigate the perception and the cognitive level of Tourists in Kefalonia Island (Greece) as one of the famous Geoparks in Europe. To achieve the main objective of improving the knowledge about geosites, mineral raw materials, and geological heritage, a targeted public outreach took place based in a hotel in Argostoli (Kefalonia) within one of designated UNESCO Geoparks focusing on teaching and rapid learning about the basic principles of geoeducation, when at the same time is giving emphasis in the importance of sustainable environmental practices about the mineral raw materials by increasing geoethical awareness and education. Through this type of study, it is possible to identify immediately and interactively the cognitive gaps for a better and sustainable society.

Geological setting of studied area

Kefalonia Island, one of the biggest Ionian Islands, is mainly separated through alpine formations (Paxoi and Ionian geotectonic units) and Plio–Quaternary sediments (Underhill 1989, Lekkas *et al.*, 2001). The Paxoi unit composed of Triassic–Middle Miocene carbonates and clay-clastic sequence of flysch from the Middle Miocene–Early Pliocene, including alternations of marls, clays and mudstones, while the Ionia unit composed of Triassic evaporitic series and Jurassic–Cretaceous limestones and slates (Lekkas *et al.*, 2001). Pliocene–Calabrian and Middle-Upper Pleistocene–Holocene series make up the Plio–Quaternary sediments, which characterized through the presence of a marine sequence, yellowish marls with siltstones, sandstones, sands

and coarse calcarenites. Pliocene–Calabrian series prevail in the Lixouri area, where the marine sequence is observed as an uplifted coastal zone with 2 to 10 km width range. Such formations have a thickness variation between 200 and 500 m and are developed transgressively over Paxoi unit (Figure 1) (Lekkas *et al.*, 2001).

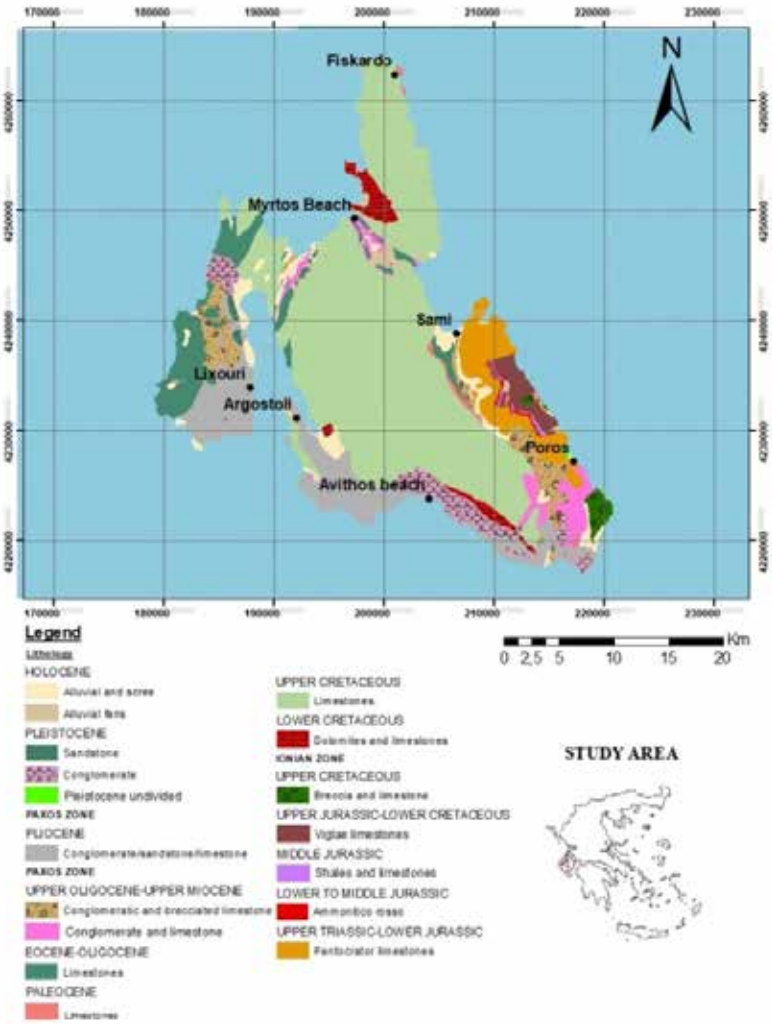

Figure 1. Geological map of Kefalonia (after IGME) (Lampropoulou *et al.*, 2023).

Analytical methods

In order to investigate how informed the European citizens about Geosites, geology, petrology and raw materials issues are, as well as whether they agree with the necessity of geoeducation to the general public, a number of questions accompanied by a geological map were given to a variety of European citizens. For this reason, a random sample of visitors was selected from May 25 to June 25, 2024, which is a peak period, and 300 European citizens coming from various European countries were selected in order to obtain a representative statistical sample. The questions were given in visitors of a hotel located in Kefalonia Island, which constitutes one of the most famous European tourist destinations and now has air connection with almost all European countries. Moreover, this hotel was chosen as it contains a geological stand which has a display case of rocks of various types and provides explanatory information about each one as well as at the reception the employees are geology graduates. The island of Kefalonia was strategically chosen, as in 2021, it was included in the UNESCO Geoparks, as a result of which it attracts many European citizens who visit the island to discover the natural beauty of the geopark. All the answers were statistically analyzed in order to draw important conclusions.

Questionnaire

In order to investigate how informed European citizens are about geoparks and more specifically about the Kefalonia-Ithaca Geopark, a series of questions were given in a preliminary survey stage to 300 European citizens/visitors in

order to obtain a representative statistical sample. The design of the questionnaire was based on determining the elements necessary for the research and then the questions were screened and the most representative ones were selected, following all European standards. The questionnaires were distributed/given to the partner hotel from 25 May to 25 June of 2024 and at this point the questionnaires were purely diagnostic in nature and statistically analyzed in order to draw significant conclusions. In the context of this study, we present a part of the overall questionnaire that was given to the guests of the hotel as well as the wider research that was conducted.

Below, the questions used in the questionnaire are listed:

1. What is your academic backround?
2. Have you visited another Geopark or Geo-invastigation in the current/last year? (yes, no)
3. Do you have any special interests about geosciences as a subject at school?
4. Have you ever encountered the term geotourism? (yes, no)
5. What do you think about the mineral raw materials in our life, are they very important? (yes, no)
6. Do you think geoheritage sites (specific rocks, caves as Melisani Lake) can be an important tourist attraction? (yes, no)
7. Does the school, universities, or public teams, organize field trips or lessons in your country/ region to the geoheritage sites? (yes, no)

At this point, representative Geologist in collaboration with the hotel's reception service informed and educated the tourists about the concept of Geopark and the geology of Kefalonia island, while they also guided them how to navigate in the geopark so they could better understand the geological history of the area. Actually, through this way, we pursued to achieve the reconnection of human society, at all levels, with the planet known as home. However, extremely important was to make them understand and also to accept that our planet and its 4,600 million of years history have shaped every aspect of our lives and our societies. As a result, the aim was to strengthen the feeling of respect of the environment and the preservation of this natural heritage.

The way to achieve what was mentioned above was to organize short trips through the georoutes map of the geopark (Figure 2). Along with the selected and suggested geo-routes for exploration, all the necessary instructions and information relative to what they were going to visit was given to the guests. The aim of this step was the tourists to see in depth the geological history reflected in each geosite and to become a part of the history and geological processes.

Figure 2. Map of the Geopark of Kefalonia Ithaka

Statistical analysis

Statistical interpretation of the results (tourist's answers) was performed with SPSS statistical analysis in order to investigate the interdependence of the questions. The methodological approach of the process of the present study has been directed to the area of the quantitative research approach to collect and analyse the research data. The study focuses on the quantification of collected data and on the interpretation of the results.

Results and Discussion

A total of 300 questionnaires were filled out. The age of those which were filled out the questionnaires was from 18 to 75 years old, while the 55% of the respondents were men. Based on the questionnaire survey conducted in

collaboration with a geo-friendly hotel in Kefalonia, on a representative sample of 300 people in low-stress conditions for respondents and in a beautiful and natural environment, important points that should be considered in any future research or in a pilot work were identified, while at the same time, concerning the issue of geoeducation in general public. More specifically, the following results indicate that even a large amount of the respondents had heard about the geotourism, they have been trained in a substantial and in-depth way on the subject.
While the majority of respondents has finished high school and they have subsequent activities or studies, as shown by the answers of the first question, it does not seem that they have been substantially educated on geoeducation issues and natural resources protection (questions 5 & 7). Particularly important seem to be the results of questions 2, 3 and 4. Even the general public has visited a geopark or a geotope in the past, the 91% may not be able to understand the concept of a geotope as a geological unit of increased and timeless value.
On the other hand, the answers of question 3, 4 and 6 reveal the potential interest that the general public seems to have in geoeducation as long as they are aware of it and have been guided on this knowledge, which makes geosciences education from the young people possible to be a key focus. Finally, the results of questions 5 and 7 clearly indicate that there is a clear gap in the education (answers of question 7) regarding the use and the importance of mineral raw materials due to the absence of a strategic and common public awareness of geoeducation in all countries. Electrical and electronic devices such as mobile phones, computers, TV are made by a large amount of mineral raw materials (i.e. minerals, metals).

Table 1. Statistical results of the respondents.

1 Question	Primary school 15%	Secondary school 65%	Master degree 18%	PhD 2%
2 Question	YES 9%	NO 91%		
3 Question	YES 74%	NO 26%		
4 Question	YES 90%	NO 10%		
5 Question	YES 56%	NO 44%		
6 Question	YES 93%	NO 7%		
7 Question	YES 23%	NO 77%		

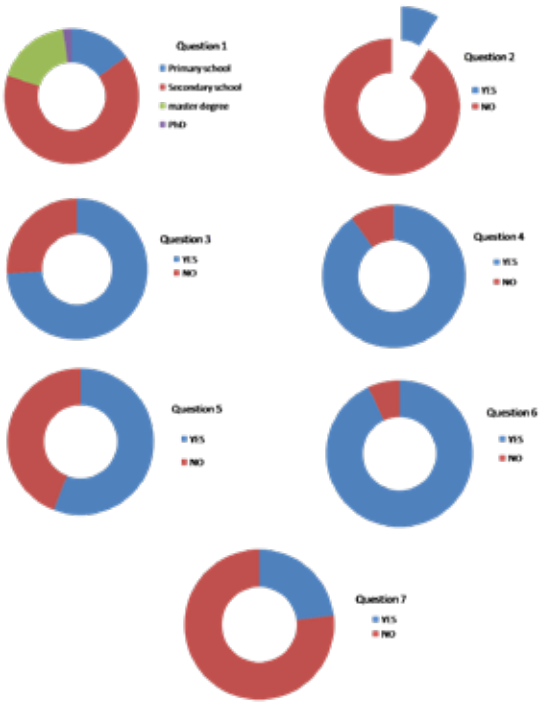

Figure 3. Excel pie charts showing the answers from the questionnaires (answers to questions 1 to 7).

Conclusions

The conclusions of this study seem to be double. The first one is related to the poor knowledge about the mineral raw materials, geo-investigations and Geoparks, while the second is related to the social acceptance of Geoeducation.

The main conclusions of the study are summarized below:

- Geosites play significant role in geoeducation even they have not always been used properly often due to lack of knowledge.
- Schools play a crucial role in the development of geoeducation and geotourism, as cognitive needs are formed.
- The majority of the respondents consider that geotourism constitutes an important tourist activity.
- It should be mentioned that there should be an organized project in all European countries in order to communicate the scientific knowledge to a wider European audience, with having as an ultimate goal the consolidation of sustainable development in Europe.

References

Zouros, N. The European Geoparks Network. Episodes 2004, 27, 165–171.

Underhill, J.R., 1989. Late Cenozoic deformation of the Hellenide foreland, western Greece. GSA Bull. 101, 613–634.

Lekkas, E., Danamos, G., Mavrikas, G., 2001. Geological Structure and Evolution of Kefallonia and Ithaki islands. Bulletin of Geological Society of Greece 34, 11–17.

Iliopoulos, G., Golfinopoulos, V., Kalampalika, A., Karanika, K., Kolendrianou, M., Papadopoulou, P., Tsacos, S., Tzortzi, M., Valavani, D., Zoumpouli, E., Bourli, N., Zelilidis, A., 2024. From the Ground to the Public: Old and New Fossil Discoveries from Kefalonia–Ithaca UNESCO Global Geopark and Their Value in Research, Education, and Local Palaeontological Heritage. Sustainability 16(6), 2521.

Lampropoulou, P., Petrounias, P., Rogkala, A., Giannakopoulou, P.P., Gianni, E., Mantzoukas, S., Lagogiannis, I., Koukouzas, N., Hatziantoniou, S., Papoulis, D., 2023. Microstructural and Microbiological Properties of Peloids and Clay Materials from Lixouri (Kefalonia Island, Greece) Used in Pelotherapy. Applied Sciences 13(9), 5772.

17th INTERNATIONAL CONGRESS of the Geological Society of Greece

BULLETIN OF THE GEOLOGICAL SOCIETY OF GREECE, SP. PUBL.

EXTENDED ABSTRACT 127

The pseudokarst at the Kaki Thalassa Bay reveals unknown ancient mining activities (Lavreotiki UNESCO Global Geopark)

Kampolis I.[1,3], Voudouris P.[2], Moraiti E.[1]

(1) Lavreotiki UNESCO Global Geopark, Lavrion, Greece, kampolisigeo@gmail.com (2) National and Kapodistrian University of Athens, Zografou, Greece (3) National Technical University of Athens, Zografou, Greece

Research Highlights

Pseudokarst features at the small islet of Kaki Thalassa, reveal previously unknown ancient mining activities.

The Lavreotiki UNESCO Global Geopark comprises one of the nine Greek UNESCO Geoparks, promoting the significant geological heritage of Greece. It is the only geopark located close to Athens, the capital city of Greece and bears a long and rich mining history. Lavreotiki Geopark occupies the southeastern part of the Attica Prefecture and its spatial extent coincides with the region of the Lavreotiki Municipality. Although, mining heritage represents the core of the Lavreotiki Geopark, other geological features such as coastal, geomorphological landforms enclose high scientific and educational value, revealing unknown aspects of this deep-in-time heritage.

The Lavrion mining district covers an area of >100 km^2 and has been exploited nearly continuously for silver (Ag) and lead (Pb) from 4000 BC until the late Roman times (Conophagos, 1980; Rosenthal *et al*., 2012). It is also considered that Lavrion was a source of copper (Cu) for a large part of the latter period (Gale *et al*., 2009; Kayafa, 2020). Monumental sites and structures such as the Industrial District, as well as the Thorikos theater at the flanks of the Velatouri hill, reveal the inseparable connection of the ancient local people with their peculiar local geology. This type of geology provided the appropriate resources to the Athenian Democratic Polis to be transformed during the Classical period and fund the trireme fleet, which determined the naval battle at Salamis against the Persians.

Apart from this mining wealth, the Lavreotiki Geopark includes a 73-km long coastline, hosting a rich geodiversity and biodiversity. With the aim of assessing the impact of the future sea level rise on the coastal landforms, which can also be potential future geosites, the geopark's personnel undertook an extended project between 2022-2024 for surveying and mapping the geological/geomorphological sites on the coastline. During these activities at the Kaki Thalassa Bay (Keratea, Lavrion), a small rocky islet was surveyed (Fig. 1). This islet consisting of Pounta marble, is located 128 m from the closest coast and hosts two strange pool-like structures at its eastern side (Fig. 2).

These morphological structures were considered to be the result of natural processes and were often referred as natural pools. On the contrary, detailed geomorphological mapping with the application of drone-assisted technology and S-f-M (Structure-from-Motion) technique in combination to geological observations, resulted in anthropogenic pseudokarst features in the sense of Veress (2022).

The assessment of the origin of these pools was implemented with the use of sophisticated, low-cost, non-destructive photogrammetrical technique, employing two-dimensional (2D) aerial mapping and geological-geomorphological field-based observations. The same technology has been applied in other locations of the geopark (Kampolis *et al*., 2024) as well as in other sites of interest (Kampolis *et al*., 2021) with valuable results.

Figure 1. The small islet close to the northern coast of the Kaki Thalassa Bay.

Figure 2. Aerial photo of the two pool-like structures at the islet. The red dashed line represents the fault crossing the western part of the islet.

The followed methodology was arranged in two separate phases. The first phase included the aerial 2D mapping and the photogrammetry of the small islet and the second one comprised the in-situ geological and geomorphological observations, as well as the extraction of samples for subsequent analysis.

During the first phase of the project, a *DJI Mavic Air 2* drone was employed for the 2D mapping of the islet, after setting up its flight mission within the *Copterus* app, running on an "*iphone 13 mini*" mobile phone. The drone's flight was programmed at an altitude of 30 m with a 75% frontal and lateral overlap, yielding a total (real) flight duration of 13 min. The collected aerial photos were then inserted in *Agisoft Photoscan Pro* software and following the photogrammetrical work-flow without ground control points, the three-dimensional (3D) reconstruction of the small islet was generated (Fig. 3). The Agisoft work-flow includes certain stages of multi-image processing: A) photos alignment, B) point cloud building, C) mesh reconstruction and D) Digital Elevation Model (DEM) generation (Semaan and Salama, 2019). For the in-depth exploitation of the islet's 3D reconstruction, the exported mesh file from Agisoft was input in *CloudCompare* software and converted into a point cloud for further geometric measurements. The latter enables various measurements such as inclinations, azimuths, lengths, areas and geometrical features of plane surfaces (dip and dip direction) on certain features.

The second phase consisted of the mineralogical observations on mineral assemblies found on the perimetry of these pool-like structures. Also, geomorphological observations on the morphology of the pools took place in-situ. The depths of their bottom were measured with a SUUNTO D3 digital depth gauge (accuracy ±0.1 m).

The generated 3D model of the small islet in combination to the field-based geomorphological measurements, provided the ability to assess the formation origin of the pools, present at the eastern side of it. According to the geomorphology of the coastal part of the islet and the bathymetry of the pools' bottom, it is unlikely for the pools to be the result of natural erosional processes. This can be supported by the bathymetry of the connection passage between the open sea and the easter pool (Fig. 4). The depth at this point reaches only 0.3 m and thus prevents the wave activity and its subsequent erosive force to enter the eastern and western pool and form them, as the erosive force is consumed on the shallow coastal part. Additionally, the eastern pool reaches a depth of 2.5 m, which cannot be justified by natural processes (i.e. waves, karstification).

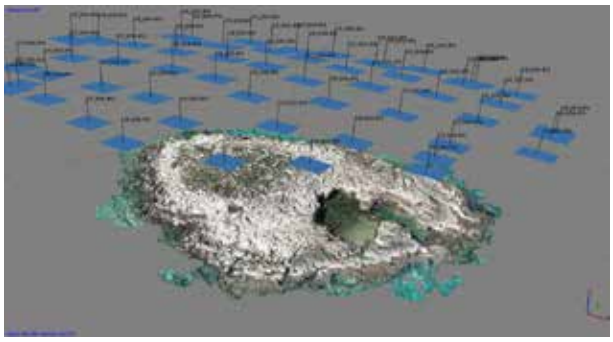

Figure 3. The 3D model of the small islet and the acquired aerial photos during the flight mission of the 2D mapping.

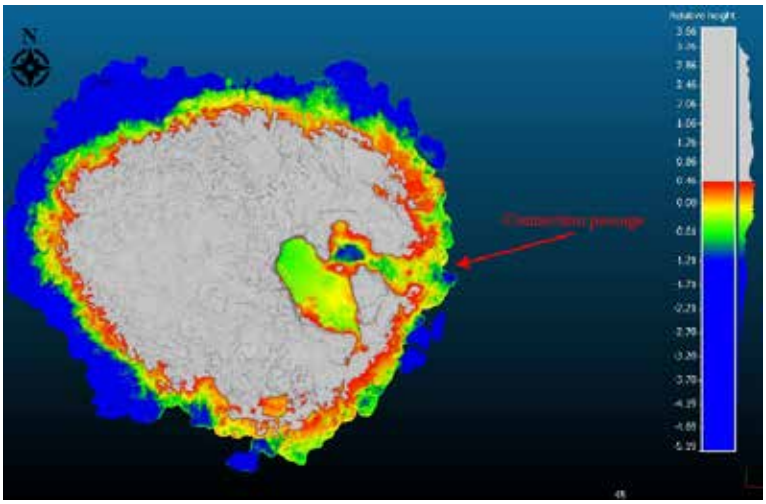

Figure 4. The bathymetry of the coastal part of the islet, generated in the CloudCompare software. The colored scale on the right provides the depth.

Moreover, the presence of a tectonic structure trending NW-SE (15°/204° – Dip/DipDir) and crossing the western part of the islet (Fig. 2) may be an extension structure related to the Miocene low-angle detachment fault developed during the top-to-SSW crustal extension, resulting in the Western Cycladic Detachment System (Loisl *et al.,* 2014), and locally referred as the South Attic Detachment (SAD) (Ross *et al*., 2021). This fault seems to play a role on the presence of sulfide mineralization (now oxidized to iron oxides), recorded on the periphery of the pools and along its surface (Fig. 5). The oxidized mineralization occurs above the SAD, where it replaces, and also cements brecciated fragments of the Punta marble. Ross *et al.* (2021) mentioned that normal faults rooted within the SAD are linked to its movement and have hydrothermally affected the Pounta marble. Consequently, it is possible that this NW-SE fault has designated the oxidized sulfide mineralization on the Pounta marble of the islet, which also attracted the interest of the ancient people. The latter must have started exploiting this mineralization, leaving open depressions that were later inundated by the sea level rise since the antiquity. Ancient miners extracted the mineralized layer, and this is probably the reason for the flat, shallow bottom of the western pool. The pool was excavated for the extraction of the mineralization, whereas natural processes like karstification would have resulted in a more uneven bottom. Therefore, these depressions originated by the anthropogenic activity on the carbonate rock of the islet, can be falsely interpreted as karst landforms and thus, represent the so-called anthropogenic pseudokarst. The nature of the latter revealed these previously unidentified ancient mining works.

Figure 5. The oxidized sulfide mineralization on the eastern side of the eastern pool.

Acknowledgements

Warm thanks are addressed to DANETAL S.A. for the support on the research activities of the Lavreotiki UNESCO Global Geopark.

References

Conophagos, C. E., 1980. Le Laurium antique et la technique grecque de la production de l'argent, Ekdotiki Athinon.

Gale, N. H., Kayafa, M., Stos□Gale, Z. A., 2009. Further evidence for Bronze Age production of copper from ores in the Lavrion ore district, Attica, Greece, in: A. Giumlia□Mair et al. (Eds.), Proceedings of the Second International Conference: Archaeometallurgy in Europe, 158–176.

Kampolis, I., Iossifidis, Th., Moraiti, E., 2024. The 3D reconstruction of an ancient quay at the Thorikos Bay (Lavreotiki UNESCO Global Geopark). International Conference "Widening the Big Blue Horizon" Innovative Technologies & Sustainable Strategies for the Protection and Management of Underwater Cultural Heritage, Volos, Greece, p. 50.

Kampolis, I., Dimakopoulou, A., Vakalas, I., Loukidis, N., Dimitriadis, Kl., 2021. Geotechnical study of the ancient Phyle Fort. Directorate of Restoration of Ancient Monuments, Ministry of Culture.

Kayafa, M., 2020. The metal resources of Laurion during the Early Bronze Age: A synthesis of the archaeological and archaeometric data, in: Papadimitriou, N., Wright, J., Fachard, S., Polychronakou□ Sgouritsa, N., Andrikou E. (Eds.), Athens and Attica in prehistory, 193-201.

Loisl, J., Linder, K., Huet, B., Graseman, B., Rice, N.H.N., Soukis, K., Schneider, D., 2014. The Western Cycladic Detachment System on Makronisos, Greece, EGU General Assembly, Vol. 16, EGU2014-11587.

Rosenthal, P., Morin, D., Herbach, R., Photiades, A., Delpech, S., Jacquemot, D., Fadin, L., 2012. Mining technologies at deep level in antiquity: The Laurion mines (Attica, Greece). Second Mining in European History Conference of the FZ HiMAT, Innsbruck, Austria, pp. 89–95.

Ross, J., Voudouris, P., Melfos, V., Vaxevanopoulos, M., Soukis, K., Merigot, K., 2021. The Lavrion silver district: reassessing its ancient mining history, Geoarchaeology, 36, 4, 617-642.

Semaan, L., Salama, M.S., 2019. Underwater Photogrammetric Recording at the Site of Anfeh, Lebanon, in: McCarthy, J., Benjamin, J., Winton, T., van Duivenvoorde, W. (Eds), 3D Recording and Interpretation for Maritime Archaeology, 67-87.

Veress, M., 2022. The Effect of Mining Activities on the Paleokarstic Features, Recent Karstic Features, and Karst Water of the Bakony Region (Hungary). Mining, 2, 757–768.

17th INTERNATIONAL CONGRESS of the Geological Society of Greece

BULLETIN OF THE GEOLOGICAL SOCIETY OF GREECE, SP. PUBL.

EXTENDED ABSTRACT 128

Preliminary results of black sands in Corfu Island (Ionian Sea, Greece)

Kanellopoulos C.[1*], Aggelatou, V.[1], Papatrechas C.[1]

[1] *Hellenic Survey of Geology and Mineral Exploration (HSGME), 1 Spirou Loui str., Olympic Villa, 13677, Acharnae, Attiki, Greece; ckanellopoulos@gmail.com , vaggelatou@eagme.gr , chpapatrechas@eagme.gr*

The grains of beach sand results from the weathering and transportation of geological formations. From a mineralogical perspective, beach sand typically consists of the durable remnants of weathering, providing insights into the original rock formation, while the transport process may involve a combination of factors such as river, wind, and sea transportation.
Typically, near the coastline, an accumulation of heavy minerals is found in certain limited places, such as the swash zone of wave run-up. These accumulations are typically distinguished by their dark color (black sands). The accumulation sites could change rapidly over time due to varying factors that influence transportation routes, such as changes in wind or sea current patterns.
In some cases, black sands are enriched with economically significant minerals, forming placer deposits in coastal regions through gravitational segregation. Their minerals exhibit weathering resistance and, in numerous cases, are enriched with elements characterized as critical in adequate concentration and quantity that they can be extracted.
The mineral phases commonly found in black sands include quartz and other tectosilicates, phyllosilicates such as micas, chlorite, and serpentine, orthosilicates such as zircon, olivine group, and garnet group minerals, as well as spinels, titanite, rutile, and minerals from the epidote group, such as allanite.
In Greece, in recent years, numerous studies have been conducted on black sands, especially in the Northern Aegean Sea, i.e., Eastern Macedonia coastline, such as the Kavala region (Papadakis, 1975; Perissoratis et al., 1988; Pergamalis et al., 2001a, 2001b; Aggelatou et al., 2018; Papadopoulos et al., 2015, 2016, 2019; Tzifas et al., 2019; Stouraiti et al., 2020; Peristeridou et al., 2022) and in few cases in volcanic islands in Aegean Sea, such as Nisyros (Tzifas et al., 2017). Significant geochemical anomalies specifically in La and Zr, were detected along the Eastern Macedonia coastline, prompting further exploration and study to ascertain the source geological formation.
No occurrences of black sand have been reported in the Ionian Sea until now. For the first time, regions of black sand accumulation have been discovered on Corfu Island (Fig. 1). The deposits were located in the swash zone of wave run-up. Mineralogical (optical microscopy, XRD and SEM-EDS) and geochemical analyses (XRF, ICP-MS) were performed at the laboratories of the Hellenic Survey of Geology and Mineral Exploration (HSGME). Preliminary mineralogical and geochemical analyses revealed that the black sand mostly consists of chromium-rich mineral phases, iron-titanium oxides, and shows elevated concentrations of chromium, iron, and titanium, among other elements. The comprehensive investigation and characterization of areas displaying these characteristics, together with the identification of the parent geological formation, is of significant importance.

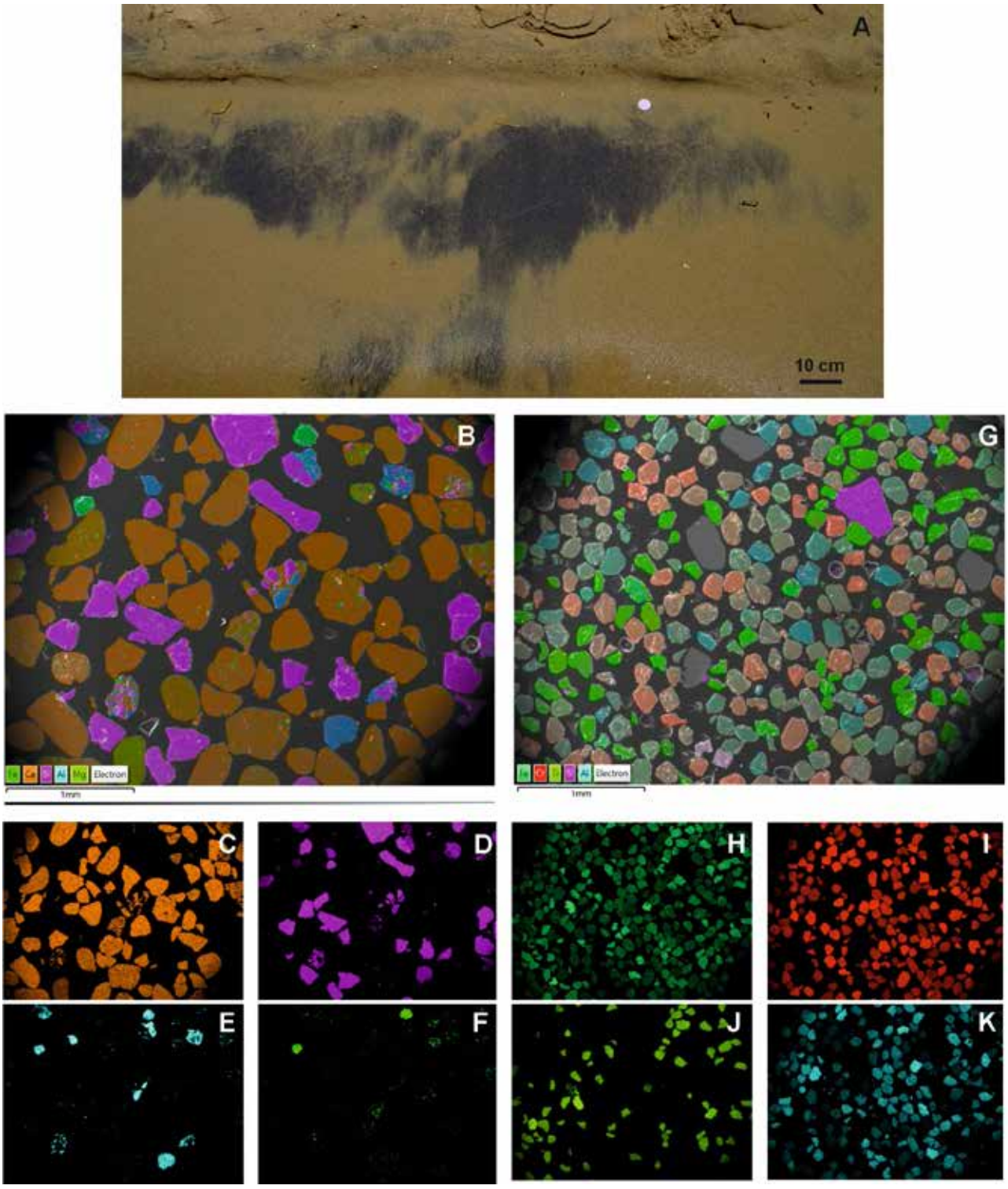

Figure 1. (A) The swash zone of wave run-up with black sand accumulation from Corfu Island. (B) Combined false color back-scattered electron image (BSEI) presenting the mapping of Fe, Ca, Si, Al, and Mg from a typical beach sand sample in the area. (C-F) False color BSEI results of the mapping, displaying only the distribution of Ca, Si, Al, and Fe. (G) Combined false color back-scattered electron image (BSEI) presenting the mapping of Fe, Cr, Ti, Si, and Al from the beneficiated black sand sample. (H-K) False color BSEI results of the mapping display only the distribution of Fe, Cr, Ti, and Al.

References

Aggelatou, V., Papamanoli, S., Stouraiti, C., Papavasileiou, K., 2018. REE distributions in the black sands of Kavala coastal zone, northern Greece: Mineralogical and geochemical characterization of beneficiation products. In Proceedings of the 1st International Electronic Conference on Mineral Science, virtual, 16–31 July 2018, Volume 1.

Papadakis, A. 1975. The black sands of Loutra Eleftheron near Kavala, Greece. Sci. Ann. Fac. Phys. Math. Univ. Thessaloniki, 15, 331–390.

Papadopoulos, A., Koroneos, A., Christofides, G., Papadopoulou, L., 2016. Geochemistry of Beach Sands from Kavala, Northern Greece. Ital. J. Geosci. , 135, 526–539.

Papadopoulos, A., Koroneos, A., Christofides, G., Stoulos, S., 2015. Natural Radioactivity Distribution and Gamma Radiation Exposure of Beach Sands Close to Kavala Pluton, Greece. Open Geosci., 7, 407–422.

Papadopoulos, A., Tzifas, I.T., Tsikos, H., 2019. The Potential for REE and Associated Critical Metals in Coastal Sand (Placer) Deposits of Greece: A Review. Minerals, 9, 469.

Pergamalis, F., Karageorgiou, D.E., Koukoulis, A., 2001a. The location of Ti, REE, Th, U, Au deposits in the seafront zones of Nea Peramos-Loutra Eleftheron area, Kavala (N. Greece) using radiation. Bull. Geol. Soc. Greece, 34, 1023–1029.

Pergamalis, F., Karageorgiou, D.E., Koukoulis, A., Katsikis, I., 2001b. Mineralogical and chemical composition of sand ore deposits in the seashore zone N. Peramos-L. Eleftheron (N. Greece). Bull. Geol. Soc. Greece, 34, 845–850.

Perissoratis, C., Moorby, S.A., Angelopoulos, I., Cronan, D.S., Papavasiliou, C., Konispoliatis, N., Sakellariadou, F., Mitropoulos, D. 1988. Mineral Concentrations in the Recent Sediments Off Eastern Macedonia, Northern Greece: Geological and Geochemical Considerations. In Mineral Deposits within the European Community, Springer: Berlin/Heidelberg, Germany.

Peristeridou, E., Melfos, V., Papadopoulou, L., Kantiranis, N., Voudouris, P., 2022. Mineralogy and Mineral Chemistry of the REE-Rich Black Sands in Beaches of the Kavala District, Northern Greece. Geosciences, 12, 277.

Stouraiti, C., Angelatou, V., Petushok, S., Soukis, K., Eliopoulos, D., 2020. Effect of Mineralogy on the Beneficiation of REE from Heavy Mineral Sands: The Case of Nea Peramos, Kavala, Northern Greece. Minerals, 10, 387.

Tzifas, I.T., Misaelides, P., Godelitsas, A., Gamaletsos, P.N., Nomikou, P., Karydas, A.G., Kantarelou, V., Papadopoulos, A., 2017. Geochemistry of coastal sands of Eastern Mediterranean: The case of Nisyros volcanic materials. Geochemistry, 77(3), 487-501.

Tzifas, I.T., Papadopoulos, A., Misaelides, P., Godelitsas, A., Göttlicher, J., Tsikos, H., Gamaletsos, P.N., Luvizotto, G., Karydas, A.G., Petrelli, M., et al. 2019. New Insights into Mineralogy and Geochemistry of Allanite-Bearing Mediterranean Coastal Sands from Northern Greece. Chem. Der. Erde., 79, 247–267.

17th INTERNATIONAL CONGRESS of the Geological Society of Greece

BULLETIN OF THE GEOLOGICAL SOCIETY OF GREECE, SP. PUBL.

EXTENDED ABSTRACT 129

Preliminary results on Agios Efstratios island (NE Aegean Sea, Greece) geology

Kanellopoulos C.[1*], Galanakis D.[1], Moforis L.[2], Sboras S.[3], Chalkiadaki O.[1], Xirokostas N.[1], Vougioukalakis G.[1]

[1] *Hellenic Survey of Geology and Mineral Exploration (HSGME), 1 Spirou Loui str., Olympic Villa, 13677, Acharnae, Attiki, Greece; ckanellopoulos@gmail.com, dgalanakis@eagme.gr, ochalkiadaki@eagme.gr, nxirokostas@eagme.gr, gvougioukalakis@eagme.gr*

[2] *Faculty of Geology and Geoenvironment, Department of Historical Geology-Paleontology, Panepistimioupolis, Zografou, Athens; leonidasmoforis@gmail.com*

[3] *Institute of Geodynamics, National Observatory of Athens, Lofos Nymphon, Thesio, 11810 Athens, Greece; sboras@noa.gr*

Agios Efstratios Island is a small, isolated island located in the northeastern Aegean Sea. The island is situated approximately 30 km southwest of Limnos Island and approximately 80 km northwest of Lesbos Island. It covers an area of approximately 43,000 km² and is distinguished by its rocky geomorphology. Despite its closeness to the volcanic islands of Lesvos and Limnos, as well as its location near the North Aegean Trough, geological data regarding it is limited (i.e., Fytikas et al., 1980, IGME, 1983, Pavlidis and Tranos, 1991).

In light of these conditions and the limited geological understanding of the region, the Hellenic Survey of Geology and Mineral Exploration (HSGME) organized a field expedition. The objectives of the expedition were to achieve a more thorough comprehension of the geology of Agios Efstratios through the creation of a new geological map (Fig. 1), identifying and mapping new geological formations, and an assessment of the island's volcanic formations.

Seven distinct geological formations were recognized and sampled on Agios Efstratios island. No Alpine basement formation has been identified on the island; However, many volcano-tectonic data and structures have been documented. The two primary formations are volcanoclastic-pyroclastic formations of significant thickness (several tens of meters) of Oligocene to Lower Miocene age, covering most of the island. The volcanoclastic formations consist mostly of epiclastics (debri flows, lahars, hypercocentrated flood flows) and in a less extension of tuffs and tuffites, primarily of intermediate to acid composition. These formations typically have well-defined stratified layers (Fig. 1). Irregular, scattered, and ungraded fragments of volcanic rocks, mostly boulders of lavas, are incorporated into the tuffs, alongside ejecta and bombs predominantly of high-K calc-alkaline tracyandesitic to andesitic-dacitic composition (Fig. 2), based on new geochemical analysis. The southern volcaniclastic-pyroclastic formation developed from nonvisible nowadays volcanic center(s) south of Agios Efstratios, whereas the northern volcanoclastic formation also formed from nonvisible nowadays volcanic center(s) north-east of Agios Efstratios. According to Fytikas et al. (1980), these deposits belong to the late Oligocene-early Miocene (17 Ma, 22 Ma), similar to the age of Lemnos Island volcanic products. Volcanic vents and block and ash flows were detected on the island's southeastern coast. Intense fault-related hydrothermal alteration has been reported on the island, leading to the development of bentonites and zeolites (Pe-Piper and Piper, 2002).

The other five geological formations of the island occur mainly in the northern and northeastern parts; there are small occurrences of the recent Holocene alluvial deposits, coastal deposits, talus cones and scree, Upper Miocene marine limestones, and Oligocene clastic formations (Fig. 1).

The recent Holocene alluvial deposit reaches a thickness of up to 20 m and is predominantly composed of sandy, clay, and pebble materials; in the NE part of the island, there appears to be a fluvial deposit of dunes. The Oligocene sediments consist of clays, mudstones, sandstones, and conglomerates (Fig. 3). The IGME (1983) mentions that lignite intercalations occur in the deeper sections of the Oligocene sediments. The Miocene limestone consists of bedded to massive calcite-marly organogenic limestones from a shallow water environment (Fig. 4), with dip 10-15° to the E-SE, including pieces of lamellibranchs, gastropods, algae, ostracods, and foraminifera (Milliolidae, Rotaliidae). The formation unconformably overlays the pyroclastic formation (IGME, 1983).

The geological formations of the island demonstrate substantial evidence of neotectonic movements from the post-middle Miocene to the present (Pavlidis and Tranos, 1991). Mercier et al. (1989) suggest that the neotectonic regime of the island is extensional and can be categorized into two separate periods. The minimal primary stress ($\sigma 3$) during the Pliocene-early Pleistocene epoch was oriented NE-SW, whereas the $\sigma 3$ axis from the middle Pleistocene to the present phase trends N-S.

The current geodynamic regime activates NE-SW direction strike-slip dextral faults, which displace older neotectonic structures and geological formations. The last activation occurred in 20th February 1968 after a strong 6.8 earthquake when the seismic strike-slip fault cut the island in half with a NE-SW direction (Fig. 1).

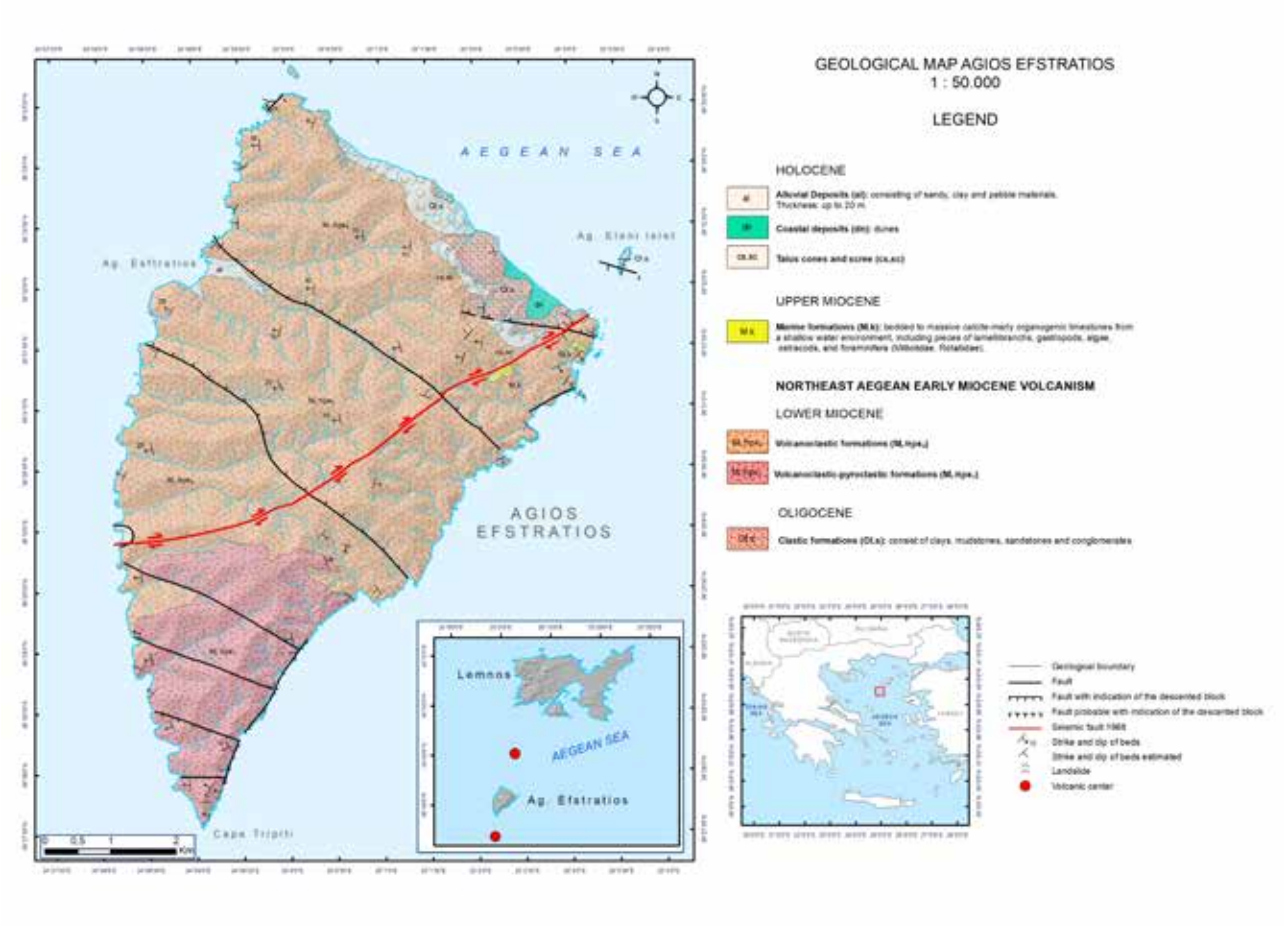

Figure 1. Geological map of Agios Efstratios island.

Figure 1. Well-developed thick stratified layers of pyroclastic formations (several tens of meters).

Figure 2. Characteristic example of a fragment of volcanic rock embedded in the tuffs (see red arrow).

Figure 3. Oligocene sediments.

Figure 4. Miocene limestone formation.

References

Fytikas, M., Giullani, O., Innocenti, F., Manetti, P., Mazzuoli, R., Peccerillo, A. & Villari, L. 1980. Neogene Volcanism of the Northern and Central Aegean Region. Annls g~ol. Pays Hell. 30, 106-129.

IGME, 1983. Geological map of Greece, Agios Efstratios sheet (scale 1: 50,000). IGME, Athnes, by Latsoudas, Ch., Tsaila-Monopolis, St. & Chorianopoulou, P.

Mercier, J. L., Simeakis, K., Sorel, D. & Vergely, P. 1989. Extensional tectonic regimes in the Aegean basins during the Cenozoic. Bas/n Res. 2, 49-71.

Pavlidis S.B., Tranos, M.D., 1991. Structural characteristics of two strong earthquakes in the North Aegean: Ierissos (1932) and Agios Efstratios (1968). Journal of Structural Geology, Vol. 13, No. 2, pp. 205-214

Pe-Piper, G. and Piper, D., 2002. The igneous rocks of Greece, the anatomy of an orogeny. Gebruder Borntraeger, Berlin.

17th INTERNATIONAL CONGRESS of the Geological Society of Greece

BULLETIN OF THE GEOLOGICAL SOCIETY OF GREECE, SP. PUBL.

EXTENDED ABSTRACT 130

Pagasitikos volcanism (Lichades-Kamena Vourla-Achillio-Mikrothives-Porfyrio-Psathoura): Preliminary results on a Quaternary tectonically related volcanism.

Kanellopoulos C.[1], Galanakis D.[1], Sboras S.[2], Iordanidou, K.[2], Moforis L.[1,3], Xirokostas N.[1], Chalkiadaki O.[1], Vougioukalakis G.[1]

[1] *Hellenic Survey of Geology and Mineral Exploration (HSGME), 1 Spirou Loui str., Olympic Villa, 13677, Acharnae, Attiki, Greece; ckanellopoulos@gmail.com , dgalanakis@eagme.gr , kiordanidou@eagme.gr , nxirokostas@eagme.gr , ochalkiadaki@eagme.gr , gvougioukalakis@eagme.gr*
[2] *Institute of Geodynamics, National Observatory of Athens, Lofos Nymphon, Thesio, 11810 Athens, Greece; sboras@noa.gr*
[3] *Faculty of Geology and Geoenvironment, Department of Historical Geology-Paleontology, Panepistimioupolis, Zografou, Athens, Greece; leonidasmoforis@gmail.com*

In the greater Pagasitikos Gulf, Oreoi Strait, northern Euboea Gulfand NW Aegean Sea regions, a series of volcanic centers, namely Lichades, Kamena Vourla, Achillio, Mikrothives, and Porfyrio, occur at the western extremity of the southwestern segment of the North Anatolian Fault, (e.g. Ktenas, 1927; Georgalas, 1938; 1940; Georgiades, 1958; Marinos, 1958; Pe & Panagos, 1976, Innocenti *et al.*, 1979, Clapsopoulos, 1991, Pe-Piper and Piper, 2002, Fig. 1). Despite their early identification and studies (e.g., Ktenas, 1927, Georgalas, 1938, 1940), their proximity to important tectonic structures, and their correlation with other geological features, i.e. presence of hot springs/geothermal fields (Kanellopoulos *et al.*, 2017a, 2017b, 2018), there are no further systematic geological studies conducted for these occurrences.

The Lichades island complex consists of a series of trachyandesite volcanic islands (Georgalas, 1938; Georgiades, 1958), with a characteristic dome on the island of Strongili. The geochronological dating for the lava flows of the Lichades islands indicate an age of 0.5 Ma (K-Ar, Fytikas *et al.*, 1976).

Adjacent to Lichades is the trachyandesitic lava outcrop of Kamena Vourla (formerly known as Agios Ioannis), located on the mainland (Georgalas, 1938; Georgiades, 1958, Kanellopoulos *et al.*, 2019). The geochronological data for Kamena Vourla indicate an age of 1.7 Ma (K-Ar, Bellon *et al.*, 1979).

At Achilleon, occur a trachyandesite dome, located near Tymbanos Hill (Marinos, 1958). The geochronological data at Kamena Vourla indicate an age of 2.68-3.4 Ma (K-Ar, Innocenti *et al.*, 1979; Pe-Piper and Piper, 1979).

At Porphyrion near Volos, a trachyandesite lava flow is present (formerly known as Kadir Agas in earlier literature) (Georgiades, 1958). Geochronological data indicate an age of 1.2-1.6 Ma (K-Ar, Innocenti *et al.*, 1979; Pe-Piper and Piper, 1979).

At Microthibes, a plateau of trachyandesite lavas, with a total volume of around 0.2 km³, is present (Ktenas, 1927). Geochronological data indicates an age of 1.5 Ma (K-Ar, Innocenti *et al.*, 1979).

At Psathoura island in the NW Aegean Sea, basaltic trachyandesite lavas compose the island (Koutsovitis *et al.*, 2015; Ntaflos *et al.*, 2017). Geochronological data indicate an age of 0.7 Ma (K-Ar, Fytikas *et al.*, 1984).

In the past, multiple theories have been proposed regarding these volcanic centers; among which is that are related to the western extension of the South Aegean active volcanic arc (Pe and Panagos, 1976; Pe-Piper and Piper, 1989), and they are associated with a deep source likely linked to the continuation of the North Anatolia fault, and unrelated to the plate subduction context (Fytikas *et al.*, 1985). Innocenti *et al.* (2010) utilized Sr–Nd–Pb isotopic data to associate this volcanic center with the extensive volcanic belt that formed north of the Pelagonian–Attic–Cycladic–Menderes massifs, which spans a considerable region from NW Greece–Macedonia to the Aegean–western Anatolia, covering a duration of 35 Ma.

Kanellopoulos *et al.* (2017a, 2017b, 2018) proposed that the volcanic center of Lichades and its associated magmatic chamber serve as the thermal source and contribute a fraction of deep magmatic fluid to the geothermal fluid of the Euboea-Sperchios system, in conjunction with seawater and minimal meteoric water input. Northern Euboea (or Evia) and the adjacent region of the mainland in eastern Central Greece (Sperchios area) are acknowledged as possessing one of the highest geothermal gradients in Greece, following the active volcanic arc of the southern Aegean (Fytikas and Kolios, 1979).

New data derived from geochemical and mineralogical analyses, tectonic measurements, and field observations confirmed the strong geochemical correlation between these volcanic centres and simultaneously elucidated their connection to the region's dynamic tectonic setting.

Based on geological, seismological, and geodetic data (e.g. Galanakis, 1997; Galanakis *et al.*, 1998; Chousianitis *et al.*, 2024 and references therein), the study area undergoes a roughly N-S oriented extension. As a result, E-W- to ESE-WNW-striking normal faults dominate in the area. However, the shear that prevails in the North Aegean Sea, as the western continuation of the North Anatolian Fault, seems to affect the eastern part of the Pagasitikos Gulf and North Euboea, forming a locally transtensional regime. Neotectonic investigations in central Greece suggest that the current extensional stress field dates back to Middle

Pleistocene, following a NE-SW trending extensional phase which was active from Pliocene to Early Pleistocene (e.g., Caputo & Pavlides, 1993). The faulting due to the current stress field has significantly affected the topographic relief by forming horst-graben systems of various scales.

The volcanic centers are located along neotectonic structures (Fig. 1). The Porphyrio and Microthebes centers are related to the Nea Anchialos fault zone, an active structure responsible for the July 9, 1980, double earthquake (two strong earthquakes of M_W 6.5 and M_W 6.1, 24 mins apart). The Achillio center is located next to the Oreoi Strait, in a small fault system that is affected by the narrow graben that forms this NE-SW trending channel. The Kamena Vourla center outcrops along an area of dense faulting where the western prolongation of the Atalanti and the eastern tip of the Kamena Vourla faults occur. The Lichades center is situated on the western prolongation of the Gialtra – Agios Georgios fault, which shapes the southern coastline of the westmost part of Euboea. It is obvious that all volcanic occurrences coincide and are associated to the active tectonic of this region.

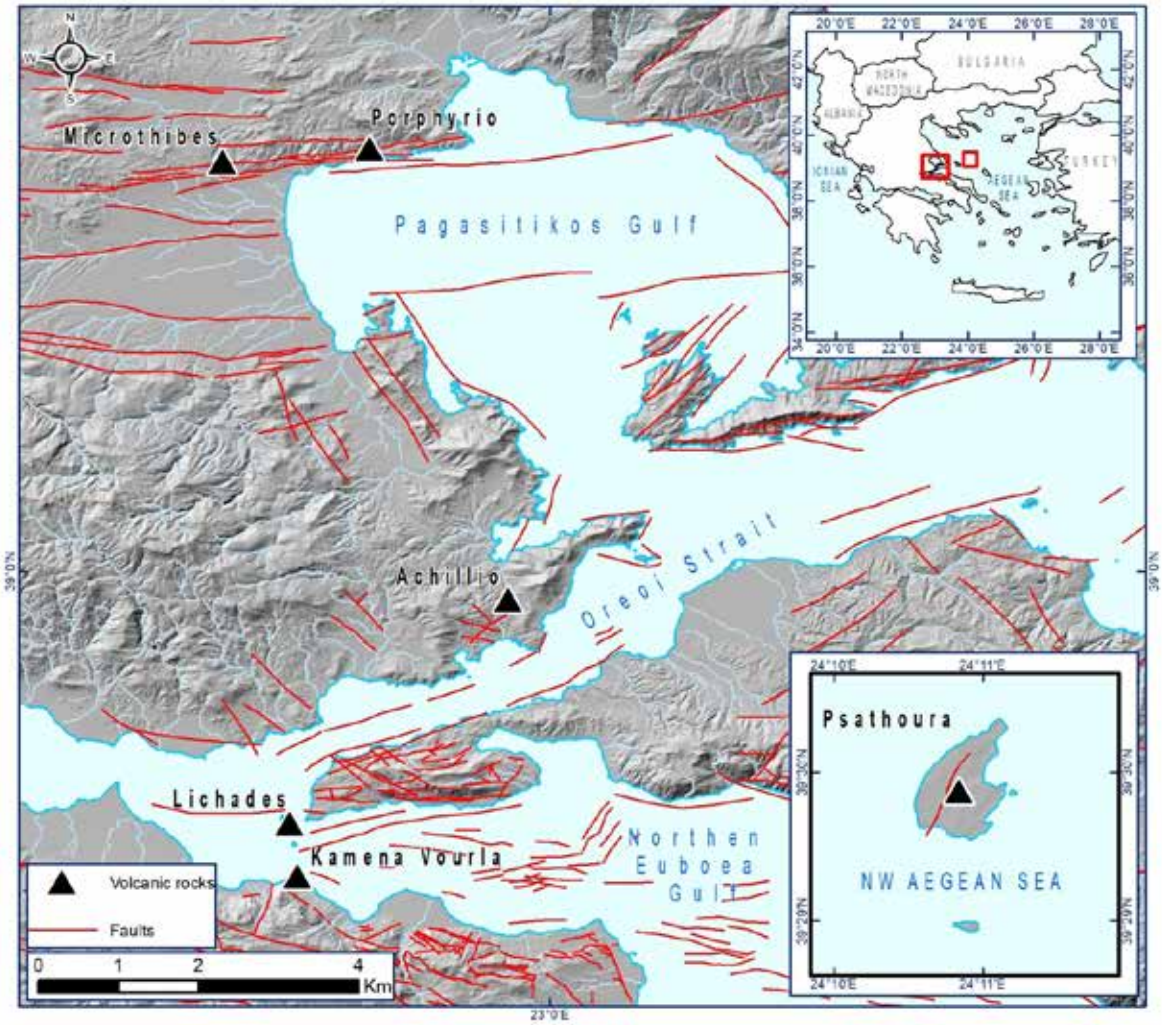

Figure 1. Geological map of the area of interest.

References

Bellon, H., Jarrige, J.J., Sorel, D., 1979. Les activites magmatiques egeennes de l'Oligocene a nos jours et leurs cadres geodynamiques. Donnees nouvelles et synthese. Rev. Géol. Dynam. Géog. Phys. 21, 41–55

Caputo, R., & Pavlides, S. (1993). Late Cainozoic geodynamic evolution of Thessaly and surroundings (central-northern Greece). Tectonophysics, 223(3-4), 339-362.

Clapsopoulos, I., 1991. Petrology, geochemistry and origin of Pliocene - Pleistocene potassium-rich volcanic rocks from Greece. PhD thesis, University of Manchester (UK), 252pp.

Chousianitis, K., Sboras, S., Mouslopoulou, V., Chouliaras, G., & Hristopulos, D. T. (2024). The upper crustal deformation field of Greece inferred from GPS data and its correlation with earthquake occurrence. Journal of Geophysical Research: Solid Earth, 129(4), e2023JB028004.

Ntaflos, T., Wegner, W., Hauzenberger, C., Vatougios, K., Kitipis, C., 2017. Geochemical evolution of the monogenetic volcanic islet Psathoura in the NE Aegean region, Greece. EGU, vol. 19, EGU2017-13601-2.

Fytikas, M., Giuliani, O., Innocenti, F., Marinelli, G., Mazzuoli, R., 1976. Geochronological data on recent magmatism of the Aegean Sea. Tectonophysics, 31, T29-T34.

Fytikas, M. and Kolios, N., 1979. Preliminary heat flow map of Greece. In: Cermak, V., Rybach, L. (Eds.), Terrestrial Heat Flow in Europe. Springer-Verlag, 197-205.

Fytikas, M., Innocenti, F., Manetti, P., Mazzuoli, R., Peccerillo, A., and Villari, L., 1985. Tertiary to Quaternary evolution of volcanism in the Aegean region, The Geological Evolution of the Eastern Mediterranean, Special Publ. Geol. Soc., 17, 687–699.

Galanakis D., 1997. Neotectonic structure and stratigraphy Neogene and Quaternary sediments of Almyros-Pagasitikos basin, Pilio, Oreoi-Trikeri chanel and Maliakos gulf. Ph.D.Thesis.Aristot. Univer.Thessaloniki, Unpub., (in Greek), 260p.

Galanakis D., Pavlides S., Mountrakis D., 1998. Recent Brittle Tectonic in Almyros -Pagasitikos, Maliakos, N. Euboia & Pilio. Bull. Geol. Society of Greece, XXXII/1, 263-273.

Georgalas, G.C., 1938. Le volcan des îles Likhades et de Hagios Ioannis (Kammena Vourla). Praktika Academia Athinion, 13, 86–98.

Georgalas, G.C, 1940. Über den chemismus der laven der vulkane von Lichadonissia, Wromolimni und Hagios Ioannis (Kamena Wourla). Praktika Academia Athinon 1940, 15, 116–131.

Georgiades, A.N., 1958. Sur une nouveau centre volcanique Pleistocène sur la route de Volo à Almyrosen Théssalie. Praktika Academia Athinion 33, 257–269.

Innocenti, F., Manetti, P., Peccerillo, A., Poli, G., 1979. Inner arc volcanism in NW Aegean arc: geochemical and geochronological data. - N.Jb. Miner., Mh. 1979: 145-158.

Innocenti, F., Agostini, S., Doglioni, C., Manetti, P., Tonarini, S., 2010. Geodynamic evolution of the Aegean: constraints from the Plio-Pleistocene volcanism of the Volos–Evia area. J. Geol. Soc., London, 167, 475–489.

Kanellopoulos, C., Mitropoulos, P., Valsami-Jones, E., Voudouris, P., 2017a. A new terrestrial active mineralizing hydrothermal system associated with ore-bearing travertines in Greece (northern Euboea Island and Sperchios area). Journal of Geochemical Exploration 179, 9-24, DOI: https://doi.org/10.1016/j.gexplo.2017.05.003

Kanellopoulos C., Stouraiti C., Xenakis M., Vakalopoulos P., Vougioukalakis G., 2017b. The geothermal system of northwestern Euboea Island and eastern Sperchios areas, Greece: Geological characteristics and suggested direct use applications. 11th International Hydrogeological Congress of Greece, vol. 2, 263-273.

Kanellopoulos, C., Mitropoulos, P., Argyraki, A., 2018. Radiological and hydrochemical study of thermal and fresh groundwater samples of northern Euboea and Sperchios areas, Greece: Insights into groundwater natural radioactivity and geology. Environmental Monitoring and Assessment Journal 190:265, DOI: https://doi.org/10.1007/s10661-018-6643-1.

Kanellopoulos, C., Vougioukalakis, G., Mavrogonatos, C., Megremi, I., & Iliopoulos, I., 2019. Mineralogical, Petrological and Geochemical Study of the Agios Ioannis Volcanic Rocks, Kamena Vourla Area, Greece. Bulletin of the Geological Society of Greece, 55(1), 274-289. doi:http://dx.doi.org/10.12681/bgsg.21128

Koutsovitis, P., Vougioukalakis, G., Economou, G., Xirokostas, N., Tarenidis, D., Ioakim, C., Karageorgis, A., 2015. Petrogenetic implications from Pleistocene volcanic rocks of Psathoura

Island, Greece: Mineral chemistry and geochemical data. EGU, Vol. 17, EGU2015-13365-7.

Ktenas, C.A., 1927. Le volcan de Thebes (Persouphli) en Thessalie [in Greek]. - Praktika Akad.Athinon 2: 35-44.

Kranis, H., 1999. Neotectonic activity of Fault Zones in central-eastern mainland Greece (Lokris). Ph.D. Thesis, University of Athens, Greece (in Greek).

Marinos, G., 1958. The Achilleon volcano in eastern Greece. [in Greek]. Bull. Geol. Soc. Greece 3: 64-72

Pe, G. and Panagos, A., 1976. Comparative geochemistry of the Northern Eubeoecos 26 lavas. Bulletin of the Geological Society of Greece, 9, 95–133 (in Greek).

Pe-Piper, G. & Piper, D.J.W (1979): Plio-Pleistocene age of high-potassium volcanism in the northwestern part of the Hellenic arc. Tschermaks Miner. Petrograph. Mitt. 26: 163-165.

Pe-Piper, G. and Piper, D., 1989. Spatial and temporal variation in Late Cenozoic back-arc volcanic rocks, Aegean Sea region. Tectonophysics, 169 (1–3), 113-134.

Pe-Piper, G. and Piper, D., 2002. The igneous rocks of Greece, the anatomy of an orogeny. Gebruder Borntraeger, Berlin.

17th INTERNATIONAL CONGRESS of the Geological Society of Greece

BULLETIN OF THE GEOLOGICAL SOCIETY OF GREECE, SP. PUBL.

EXTENDED ABSTRACT 131

Investigating crustal deformation of Zakynthos Island using Satellite Interferometry (InSAR): pre- and post- seismic analysis of the October 25, 2018 earthquake.

Kantareli K.[1], Sakkas V.[1].

(1) Geophysics Laboratory, Department of Geology and Geoenvironment, National and Kapodistrian University of Athens, Greece, ntinakanta@gmail.com

Introduction

This study focuses on the analysis of crustal deformation the period before and after the strong M_w6.8, 2018 Zakynthos earthquake, utilizing Interferometric Synthetic Aperture Radar (InSAR) data detecting ground surface changes over a period of six years. The earthquake took place southwest of Zakynthos Island on October 25, 2018, with an estimated magnitude of M_w6.8 (Papadimitriou et al., 2021). The earthquake was one of the most significant events in recent years in the broad region, producing noticeable ground displacement (~40 mm in the southern part of Zakynthos), reflecting the dynamic tectonic processes on the south Ionian Islands. Analysing pre- and post- seismic InSAR datasets, patterns of ground motion were identified and quantified aiming to assess the deformation processes before and after the earthquake based on the estimated velocity changes and its spatial distribution across Zakynthos.

Geology and Seismicity

Zakynthos island, located in the southern Ionian Sea, is part of the External Hellenides, a geotectonic domain shaped by the convergence of the African and European plates (Papanikolaou, 2021). The island's tectonic framework is influenced by its position along the Hellenic Subduction Zone, the active boundary of the subduction of the eastern Mediterranean oceanic lithosphere under the Aegean microplate. The island consists of series of stacked tectonostratigraphic units that were accreted during the alpine orogenic system. A significant part of the island in its western part is mainly structured by the Paxoi Unit and represents the primary tectonostratigraphic feature. In the eastern part, the Paxoi Unit is overthrusted by the Ionian unit, a structural feature that emphasizes the tectonic complexity of the region (Figure 1).

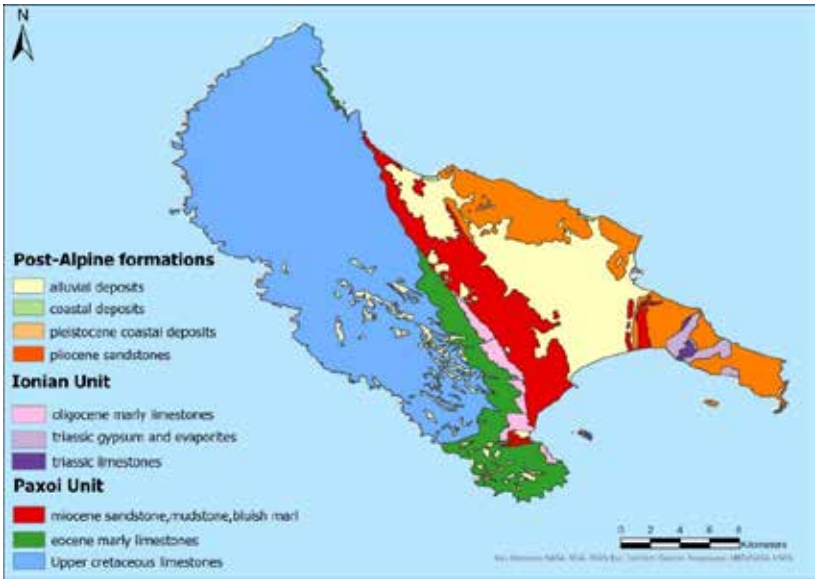

Figure 1:Geological map of Zakynthos Island (IGME, Geological Map of Greece, 1983)

The Paxoi Unit consists of a well-developed carbonate sequence that spans from the Upper Cretaceous to the Oligocene (Papanikolaou, 2021). This sequence is characterized by thick fossiliferous limestones and marly limestones, and above these carbonate rocks lie Miocene deposits, made up of marls, sandstones, and mudstones. This stratigraphic succession captures the evolving depositional setting which was influenced by the tectonic changes over millions of years. The Ionian unit comprises a Triassic sequence of limestones, evaporites and breccias, which

represent different geological episodes, consisting of restricted marine deposition and subsequent tectonic disruption (Papanikolaou 2021). Overlying both units are post-Alpine Quaternary deposits, which consist of alluvial and coastal sediments, deposited during the Pleistocene and Holocene. The presence of the two distinctive geological units, Paxoi and Ionian, that dominate the eastern and western part of the island, respectively, may infer different kinematic behaviour. However, the absence of a clear tectonic feature (i.e. fault) in between these two units is questioning this assumption. Using the InSAR technique the latter will be studied aiming to examine this hypothesis.
The earthquakes that occur in the Ionian Sea are mainly generated along the Cephalonia-Lefkada transform fault zone (CLTFZ), which plays a significant role in the kinematic field of the region (Sakkas et al., 2022). This zone divides the Ionian margin into two areas, the North Ionian islands, which move north-northwestward at rates slower than 5mm/year relative to Eurasia, and the South Ionian islands that move southwestward with velocities of 6-30mm/year (Sakkas et al., 2022). The intense seismicity on the southern Ionian Sea is attributed to the proximity of this area to the CLTFZ and the Hellenic Trench (Figure 2). Zakynthos in particular, experiences intense seismic activity frequently, as it lies at the northwesternmost edge of the Hellenic arc, near the boundary where the eastern Mediterranean lithosphere subducts beneath the Aegean microplate. This complicated geotectonic setting highlights its significance in understanding regional deformation processes.

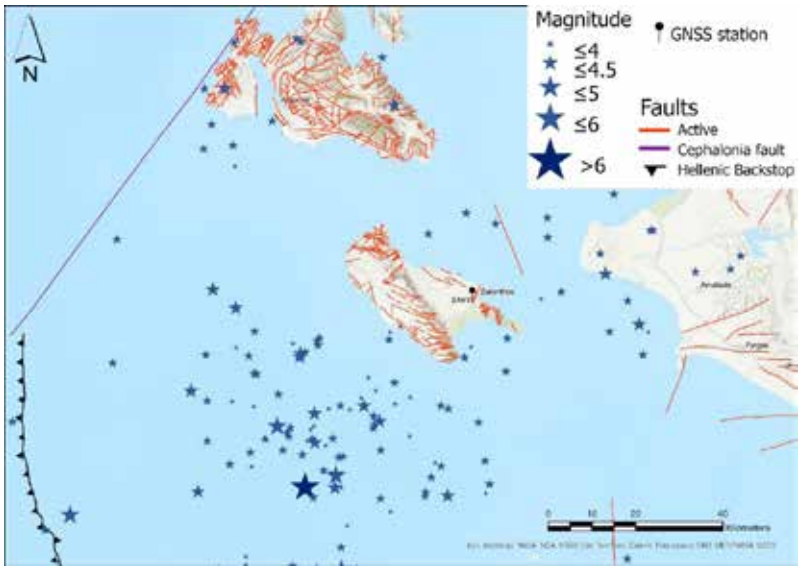

Figure 2: Seismicity of the broad area of Zakynthos Island (2015-2021) with M≥4.0 based on the catalogue of Seismological laboratory of NKUA (Fault lines from Ganas, et al., 2024)

Radar Interferometry

Interferometric Synthetic Aperture Radar (InSAR) is an advanced geodetic technique used for precise measurements of surface deformations and topographic variations on the Earth's surface. Utilizing radar signals transmitted and received by satellites, InSAR exploits the phase differences between radar acquisitions taken at different times or from slightly varied perspectives to derive changes in ground displacement. SAR satellites collect data during ascending (asc; from south to north) and descending (desc; from north to south), with the radar sensor looking to the right of the orbit trajectory. The two viewing geometries result in different line-of-sight (LOS) observations of the ground surface and refer to the displacements along the direction in which the satellite's radar beam travels, which is inclined relative to the vertical and horizontal axes. Since ground deformation occurs in multiple directions, LOS data from both ascending and descending passes are combined, to resolve the ground motion into its vertical (Vup) and horizontal eastward (Veast) components.
The decomposition of the LOS displacements into vertical and horizontal components requires knowledge of both the incidence angle (θ) and the track/azimuth angle (α) of the satellite's orbit geometry, as they define the orientation of the radar signal and the satellite's path relative to the Earth's surface (Figure 3). The incidence angle is the angle between the radar beam and the vertical axis at the point in reference, on the Earth's surface. SAR sensors typically have an incidence angle of 20-45 degrees depending on the satellite's orbit. The track angle is the angle between the satellite's orbital path and the true north. Combining the LOS displacements of ascending and descending orbital geometries (Ulos asc and Ulos desc) the vertical and horizontal components of the displacement vector are extracted

based on the following expression (Fuhrmann, 2019):

$$\begin{pmatrix} U_E \\ U_U \end{pmatrix} = \begin{pmatrix} -sin\theta_{asc}\, cos\alpha_{asc} & cos\theta_{asc} \\ -sin\theta_{desc}\, cos\alpha_{desc} & cos\theta_{desc} \end{pmatrix}^{-1} \begin{pmatrix} U_{asc} \\ U_{desc} \end{pmatrix} \quad (1)$$

Where U_U is vertical component, U_E the east component, Uasc and Udesc are the velocities in LOS direction, and θ and α are the incidence and track angles as descripted above.

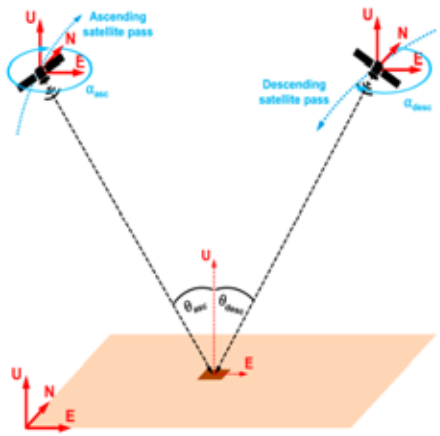

Figure 3:Schematic view of the interferometric aperture radar (InSAR) geometry for line of sight (LOS) measurements on ascending and descending satellite passes (after Fuhrmann T. 2019)

Data processing and analysis

In this study, the data utilized were derived from the European Ground Motion Service (EGMS, https://egms.land.copernicus.eu/). This service provides processed results in LOS direction, called "*Basic Product*". In this study the used results are covering the period 2015-2021 in the Island of Zakynthos. The *Basic Product* provides for each measurement point time series of displacement in the satellite LOS geometry, the estimated LOS velocity and the acceleration value for the whole-time span of the product (in this case 2015-2021). Additionally, the service offers annotated geo-localization and quality measures per measurement point. The dataset is generated from the interferometric analysis of Sentinel-1 radar images and is visualized as a vector map of measurement points color coded, both as *Ascending* and *Descending* data. The ascending measurement points were approximately 600000 and the descending approximately 380000, where each has a mean velocity and acceleration value, estimated on the time-series residuals (measured in mm/yr), and incidence and track angle values (degrees).

To estimate the velocity field before and after the October 25, 2018, a MATLAB code was used to calculate the mean velocity of each data point before and after the main shock occurrence, utilizing the time series of each one. The velocity for each period was realized applying linear least squares fitting process, using the MATLAB curve fitting tool. This toolbox utilizes the least squares method to fit a polynomial to a set of data, through minimizing the sum of the squared residuals between the observed and the predicted values of the line. The final dataset that was used, included approximately 500000 measurement points on ascending and 300000 points in descending orbit.

Data calibration

The raw time series of each measurement point provided from the EGMS dataset were divided to pre- and post-seismic periods, to enable independent analysis of each phase. These categorized data were then absolute calibrated using the velocity vector of a permanent GNSS station on Zakynthos Island (station ZAKY) with well-established ground displacement components for both these periods. Table 1 presents the velocity components of the ZAKY station, for the pre- and post- seismic period. Indicative of the calibration procedure are Figures 4 that present the calibrated velocity maps for the Ascending data set. The GNSS velocity vector was projected on the LOS direction of the two orbital geometries based on the average (due to the relatively small spatial extent of the Island) incidence and track angles for each geometry, using the expression (Hansen 2001).

$$LOS = U_U cos\theta - sin\theta \left[U_N \cos\left(a - \frac{3\pi}{2}\right) + U_E\, sin\left(a - \frac{3\pi}{2}\right) \right] \quad (2)$$

Where U_N is the real north component, rest of the annotations are presented above.

Table 1: Velocity components of ZAKY GNSS site and its LOS projection

	Pre-seismic period (mm/yr)	Post-seismic period (mm/yr)
Vup	-0.33	0.03
Veast	12.81	11.51
Vnorth	-2.50	-1.89
Vlos Ascending	-3.45	-2.62
Vlos Descending	-0.13	-0.09

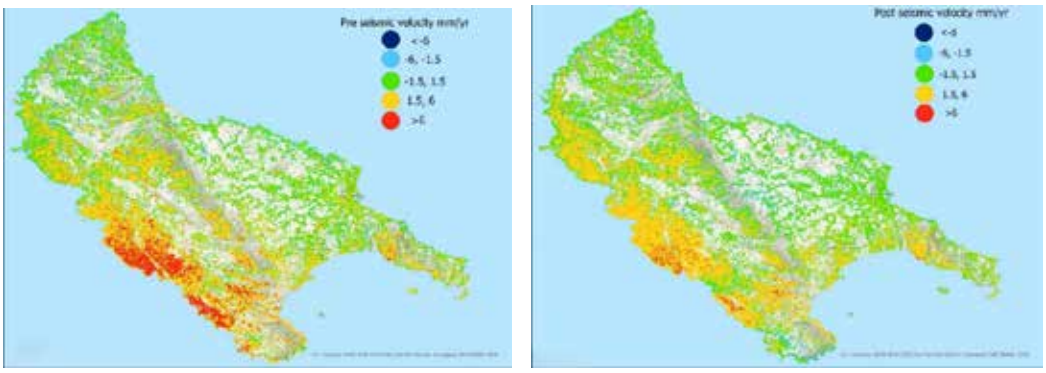

Figures 4: Ascending absolute calibrated pre- seismic (left) and post-seismic (right) velocity maps as calculated in the LOS direction.

The overall image of the crustal velocity field before and after the M_w6.8 event shows a similar pattern but of slightly different amplitudes mainly in the SW part of Zakynthos. The pre-seismic motion on the southwest part of the Island seems more intense compared to the post–seismic one, which shows smaller velocity range. As, as it is revealed by the approximately 70000 more points that have calibrated velocity value above 6mm/yr in the pre-seismic period compared to the post-seismic one.

Ortho map generation

The calibrated LOS velocity vector was then decomposed into its east-west and vertical component using the expression (1). Both incidence and track angles were measured in degrees, but in the velocity calculations were converted into radians. The used angles for both acquisition geometries are summarized in Table 2. Since the two acquisition geometries cannot have common data points, additional processing steps were adopted aiming to combine the ascending and descending data sets. As to generate the ortho maps, first a *kriging* interpolation technique was applied, to estimate values at unsampled locations based on the spatial correlation of measurement points, ensuring that the dataset is spatially continuous. This process resulted in a dataset of approximately 68000 points for the ascending and descending dataset individually. Then a *contour* tool was used, to create contour lines that visualize the variations within the dataset, and a *grid to point* conversion tool, to convert the raster data of points (grid cells) into vector point data and create a grid over the area of Zakynthos. Finally using the *extract by mask* tool, with the shoreline of the Island as a mask, the grid was refined as to include only the island and not the broad area that was automatically calculated during previous steps (Esri. *Anatomy of a Tool Reference Page*. ArcGIS Pro Documentation). With the *extract by mask* tool the dataset was reduced to 60000 points per orbital geometry, equally divided for the pre- and post- periods.

Table 2: Summary of the angles that were used in the estimation of the vertical and east-westward velocities.

Orbital geometry	Incidence angle (degrees)	Track angle (degrees)
Ascending	44.88	-9.22
Descending	38.72	190.18

The final east-west and vertical velocity field for the pre- and post- seismic period are presented in Figures 5 and 6, respectively. For the east-west velocity field, positive values indicate eastward motion, while negative values represent westward motion. Both components show similar pattern of ground motion before and after the earthquake,

but of different amplitudes and spatial coverage. The central part of the Island is the area that shows the more intense discrepancies, while in the SW part of Zakynthos the overall surface motion retains its basic characteristics in between the two periods.

Discussion

The east-west displacement maps (Figure 5) reveal distinct patterns of deformation in between the two-time spans. In the pre-seismic period, the western and mostly the southern regions exhibit westward velocities below -5mm/yr, while the central and northern ones show relatively stable conditions, with velocities ranging between -2 to 1mm/yr. After the 2018 earthquake (post-seismic period), the Island shows a slight shift to the east, with more data points assigning velocities above 2mm/yr, this kinematic behaviour is more evident in the eastern and southeastern part. The more significant changes in velocity are shown near fault zones that may indicating possible co-seismic fault-related movements and ground deformation, as well as, across the main geological boundary (in the central part of the island) in between the Paxoi and Ionian units (Figure 1), since there are significant more data points exhibiting velocities over 2mm/yr.

The vertical displacement maps (Figure 6) have noticeable changes across the two periods. Before the earthquake, the southern-most region shows subsidence with velocities even lower than -10mm/yr, while the central-southern part remains relatively stable, without any clear pattern of subsidence or uplift (the velocities range between -2 to 2mm/yr). However, the northern part of the Island reveals an uplifted character, with areas exhibiting vertical velocities up to 10mm/yr. In the post-seismic period, the southern part of Zakynthos does not alter its motional pattern, except that the velocities of several data points are dropping quite a lot below -10mm/yr (up to -18mm/yr). The most considerable changes are observed in the rest of the Island (northern, central and SE part) where the pre-seismic uplift pattern alters to minor subsiding motion (up to -5mm/yr). In comparison to the east-west displacement maps, the vertical ones, also seem to have fault related deformation, with differential motion across them, but not so noticeable in the geological boundary between the two units.

The overall image of the two displacement components (E-W and Up), indicates major changes primarily on the northern and central-eastern part of Zakynthos. The pre seismic period is characterised by mostly stable conditions, with small westward motion and slight uplift. The post-seismic period shows change on the sign in both components. After the M_w6.8 main shock, the geological boundary seems to play a less significant role in terms of vertical displacement, since there is no clear differentiation between the two geological units. In contrast the east-west component shows a more noticeable differentiation, with the motion gaining an eastward character. The vertical component highlights a more distinctive change in between the northern and southern part of the Island, since the northern part is clearly changing its kinematic behaviour, from uplift before the earthquake to subsidence after it. Conclusively, the comparison between the pre- and post-seismic period highlights a kinematic differentiation between the northern and southern part of the Island, which does not coincide with any geological boundary or tectonic feature. This change takes place in a zone that crosscuts the Island (with east-west direction) along the centre of the island (Figure 6, lower part).

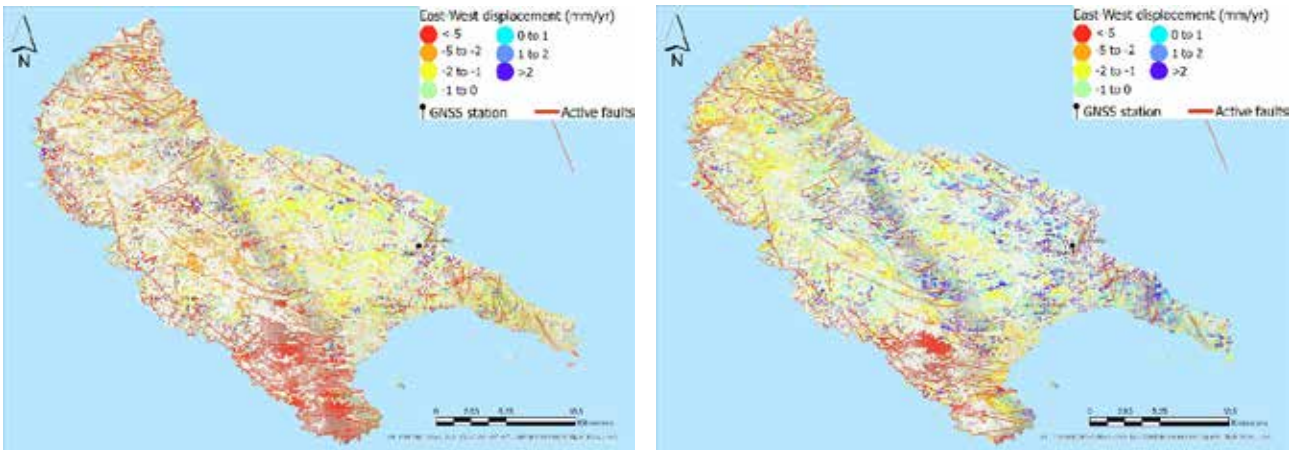

Figures 5: Pre- seismic (left) and post-seismic (right) east-west displacement in the island.

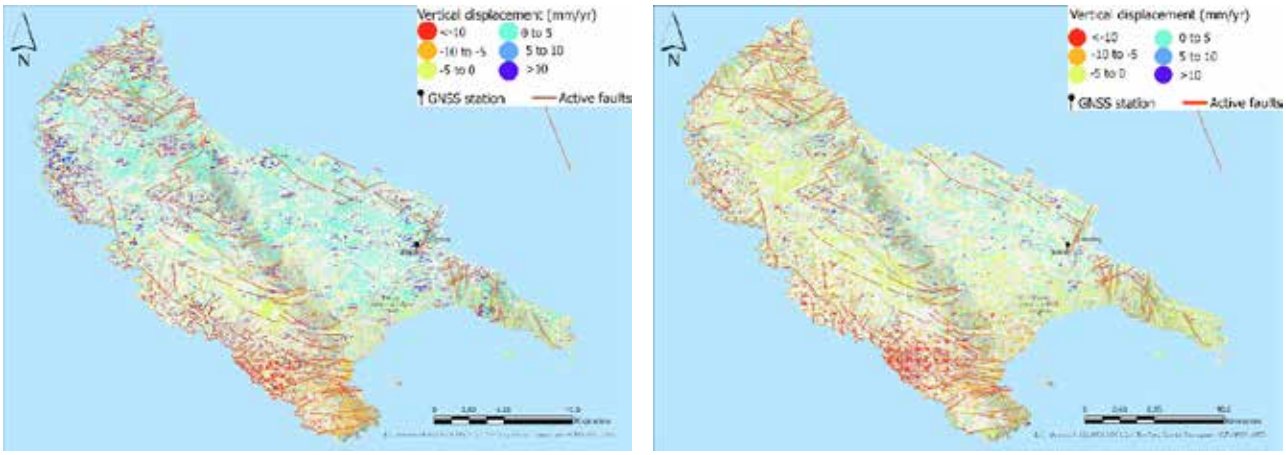

Figure 6: Pre- seismic(left) and post- seismic (right) vertical displacement in the island. The dash line indicates the approximate position of the zone that differentiates the northern and the southern kinematic behavior of Zakynthos.

Acknowledgements

The authors would like to thank Prof. A. Tzanis (Department of Geology and Geoenvironment, NKUA) for his help on the MATLAB codes used in this work. The Seismological data were obtained by the Seismological Laboratory of NKUA.

References

Esri. Anatomy of a Tool Reference Page. ArcGIS Pro Documentation https://pro.arcgis.com/en/pro-app/latest/tool-reference/introduction-anatomy/anatomy-of-a-tool-reference-page.htm

European Ground Motion Service, https://egms.land.copernicus.eu/

Fuhrmann, T., Garthwaite, M.C., 2019. Resolving three-dimensional surface motion with InSAR: Constraints from multi-geometry data fusion. Remote Sensing, 11(10), 1206. https://doi.org/10.3390/rs11101206

Ganas, A. et al. 2024. NOAFaults v6.0: New upgrades of the NOA Geospatial database of Active Faults in the broader Aegean area. https://zenodo.org/records/1316894

Hanssen, R.F., 2001. Radar interferometry: data interpretation and error analysis. Springer, Berlin.

Papadimitriou, P., Kapetanidis, V., Karakonstantis, A., Spingos, I., Pavlou, K., Kaviris, G., Kassaras, I., Sakkas, V., Voulgaris, N. 2021. The 25 October 2018 Zakynthos (Greece) earthquake: Seismic activity at the transition between a transform fault and a subduction zone. *Geophys. J. Int.*, *225*, 15–36. https://doi.org/10.1093/gji/ggaa575

Papanikolaou, D., 2021. The Geology of Greece, 1st ed. Springer International Publishing, pp. 1-345.

Sakkas V., Kapetanidis V., Kaviris G., Spingos I., Mavroulis S., Diakakis M., Alexopoulos J.D., Kazantzidou□Firtinidou D., Kassaras I., Dilalos S., Vassilakis E., Kotsi E., Tselentis G., Lekkas E., Voulgaris N. 2022. Seismological and Ground Deformation Study of the Ionian Islands (W. Greece) during 2014–2018, a Period of Intense Seismic Activity. App. Sciences 12 (5), art. no. 2331. DOI: 10.3390/app12052331.

17th INTERNATIONAL CONGRESS of the Geological Society of Greece

BULLETIN OF THE GEOLOGICAL SOCIETY OF GREECE, SP. PUBL.

EXTENDED ABSTRACT 132

Application of a machine-learning model for the determination of focal mechanisms in the area of the Corinth Rift Laboratory Near-Fault Observatory (CRL NFO), Central Greece

Kapetanidis V.[1], Spingos I.[1], Kaltsas, C.[1], Kaviris G.[1]

(1) National and Kapodistrian University of Athens, Section of Geophysics-Geothermy, Seismological Laboratory, Athens, Greece, vkapetan@geol.uoa.gr

Research Highlights

- First motion polarities determined using an ML model yielded results comparable with manual measurements.
- Discrepancies were mainly observed at stations in larger epicentral distances or equipped with accelerometers.

Introduction

The large quantities of available seismic waveform data have rendered their manual analysis a challenging task. The unification of seismic networks in Greece (e.g., Evangelidis et al., 2021) has improved the completeness of the routine analysis seismic catalogs. However, as the number of earthquakes is multiplied almost tenfold for every lowering of a magnitude unit, manual analysis can only go so far before the workload becomes prohibiting. Conventional automatic seismic P- and S-wave arrival-time picking methods also have downsides, depending upon the objective function used in each case. Despite providing quick solutions, the measurements of these automatic methods are usually less accurate than those performed by human analysts, and they need to be manually revised for their quality to be improved. However, in recent years, the rise of Machine-Learning (ML) models has revolutionized the automatic processing of seismological data. ML models, such as PhaseNet (Zhu & Beroza, 2019) and EQTransformer (Mousavi et al., 2020), are now used for the automatic analysis of huge datasets, greatly augmenting the number of detected events and lowering the completeness magnitude of seismic catalogs. Even more surprisingly, in terms of accuracy, these ML methods provide results that are on par with manually analyzed data (e.g., Mousavi et al., 2020) and can even recognize P- and S-wave arrivals in noisy signals without filter application (e.g., Zhu & Beroza, 2019).

An even more challenging task is the automatic identification of P-wave First Motion Polarities (FMPs). For earthquakes of moderate or higher magnitude (e.g., M³3.6), the focal mechanisms can usually be determined through moment tensor inversion, by fitting synthetic to the observed waveforms. FMPs, on the other hand, are useful for determining focal mechanisms for weak events (M£3.5), particularly when the network density is adequate near the epicentral area. The distribution of FMPs depends on the radiation pattern of seismic energy at the source. In the double-couple model, FMPs are distributed in four quadrants, characterized by the alternating sign of the first motion recorded at the vertical component of the seismic stations. These first pulses can be impulsive or emergent, depending on the angle of emergence of the seismic ray at the focus, relative to the radiation pattern of the faulting, which defines the focal mechanism; i.e., the strike, dip, and rake of the rupture. Rays originating near the P or T principal axes of the moment tensor are expected to produce impulsive negative or positive first motions, respectively. On the other hand, rays originating near the nodal planes or the null axis are likely to produce emergent first motions, which cannot be easily distinguished (small, nearly zero amplitude). Furthermore, the Signal-to-Noise Ratio (SNR) of weak-magnitude events can be too low for even a P-wave arrival to be picked. The application of filters to lower the noise level and improve SNR can distort the first pulse and lead to an erroneous FMP measurement. Even when a P-wave arrival-time can be roughly assessed, the analyst must decide whether to characterize the polarity of the first motion or skip it to avoid an error. Other measurements that can help constraining the focal mechanisms of weak events include the S-to-P amplitude ratio and the S-wave polarization direction (e.g., Kapetanidis et al., 2015).

As the characterization of the FMP is a pattern recognition task, it has also been the subject of studies employing methods based on artificial intelligence. Such ML models can recognize these patterns and classify the first pulse as being positive or negative, assess whether it is impulsive or emergent, or decide to dismiss a measurement if the polarity cannot be safely determined. Examples of such ML models include those presented by Ross et al. (2018) and Zhao et al. (2023). Both models were trained on a large dataset of seismic waveforms from Southern California, and the authors reported a precision of ~95% or more compared to the respective FMP measurements by human analysts.

Background

The Corinth Rift Laboratory is a dense local seismological network that has been established in the Western Gulf of

Corinth (WGoC; Figure 1) since the early 2000s (Chiaraluce et al., 2022). It is one of the Near-Fault Observatories (NFOs) of the European Plate Observing System (EPOS), complemented by stations of the regional Hellenic Unified Seismic Network (HUSN). WGoC is one of the most seismically active areas in Greece, due to a high extension rate, reaching ~16 mm/yr in a ~N-S direction (Avallone et al., 2004), mainly characterized by E-W-striking normal faulting. Between December 2020 and February 2021, an intense seismic swarm occurred in WGoC (Kaviris et al., 2021; Papadimitriou et al., 2022; Serpetsidaki et al., 2023). The swarm mainly evolved in three phases, each triggered by a significant earthquake: an M_w=4.6 event on 23 December 2020 near Marathias; an M_w=5.0 event on 12 January 2021 near Trizonia Island; and an M_w=5.3 event on 17 February 2021 (Zahradník et al., 2022), north of Psathopyrgos. An examination of the aftermath period up to December 2022, showed that the swarm activity diminished after March 2021, and a background seismicity level was established, with only a few spatiotemporal clusters and two significant earthquakes of M_w=4.2 and M_w=4.3, on 30 November 2021 and 29 July 2022, respectively (Kaltsas et al., 2024). In the framework of the studies of Serpetsidaki et al. (2023) and Kaltsas et al. (2024), a total of 117 focal mechanisms were calculated between December 2020 and December 2022, with 20 from the former study being assessed through moment tensor inversion, while the rest were determined using P-wave first motion polarities. Most focal mechanisms indicate normal faulting, with a smaller proportion of strike-slip or oblique-normal events also being detected.

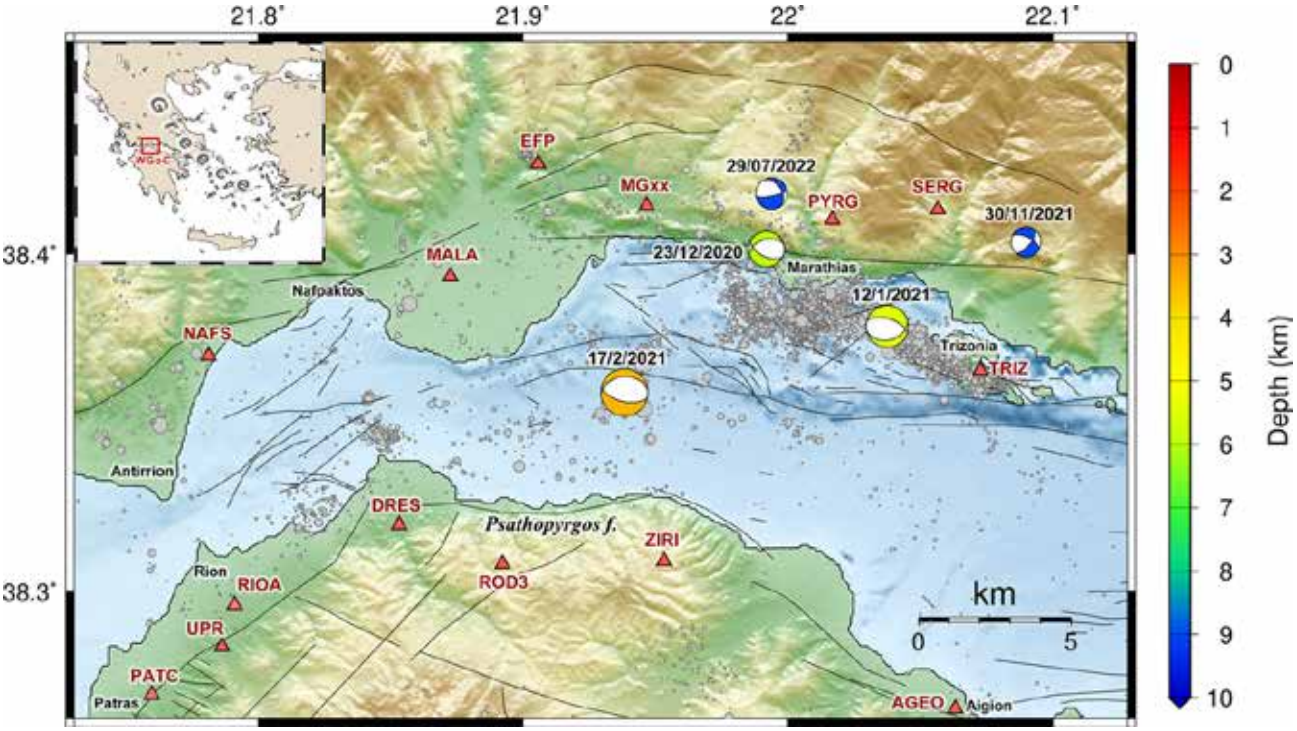

Figure 1. The Western Gulf of Corinth (WGoC) in Central Greece. Seismological and accelerometric stations of the Corinth Rift Laboratory Near-Fault Observatory (CRL-NFO) are depicted as triangles. The focal mechanisms of selected significant (M_w ³ 4.2) earthquakes of the period December 2020 – December 2022 are presented with beachball symbols. The relocated seismicity of the period December 2020 – February 2021 (gray circles) is after Serpetsidaki et al. (2023). The fault lines are from the NOAfaults database (Ganas et al., 2013).

Objectives

In this work, we apply a machine-learning model to identify the FMPs and determine the focal mechanisms of earthquakes that occurred between December 2020 and December 2022 in the western Gulf of Corinth. This will provide a perspective on the efficiency and accuracy of the applied model on the abovementioned dataset, as there are also available manually defined FMPs for a subset of the events that will be processed. The latter will be used to examine the validity of the FMPs, but also to quantify the difference in the resulting focal mechanisms derived from the herein-applied method compared to previous results of manually measured FMPs.

Data and Methods

We use a catalog of ~460 manually analyzed and relocated events from the seismic crisis in WGoC between December 2020 and February 2021 (Serpetsidaki et al., 2023), as well as 82 events from the aftermath period between March

2021 and December 2022 (Kaltsas et al., 2024); the selected events have M³2.0. In both cases, there is a subset of events with available manually measured FMPs and calculated focal mechanisms with a grid-search method, that will be used for comparison. We acquire seismic waveform data from the EIDA nodes of Reseau Sismologique et Geodesique Francais (RESIF; https://seismology.resif.fr/eida/), for stations of the CRL network, and the National Observatory of Athens – Geodynamics Institute (NOA-GI; http://eida.gein.noa.gr/webdc3/), for stations of HUSN.
We employ the DiTing-Motion (DTM) machine-learning model (Zhao et al., 2023) to automatically identify the FMPs at local stations in the area of WGoC. For each station, the waveform recording of the vertical component is detrended, resampled to 100 sps, if necessary (e.g., for accelerometric stations, which are usually at 200 sps), and cropped to a 128-sample window of ±0.64 s around the P-arrival. We follow the workflow established by Zhao et al. (2023), also measuring the S-to-P amplitude ratio (SPR) and employing the HASH code (Hardebeck & Shearer, 2002, 2003) to determine the focal mechanisms using both FMPs and SPR. To assess the influence of the P-wave's arrival-time accuracy on FMP identifications, we also test the procedure after re-picking the P-wave in the vicinity of the previously available arrival-time with Phasenet, pre-trained with data from the INSTANCE dataset (Michelini et al., 2021). We examine DTM results in terms of FMP identification accuracy, compared to manually analyzed events, both automatically and by visually reviewing the automatic FMP characterizations (Figure 2, left). The discrepancies are also examined on a per-station level to identify any systematic issues related to particular stations. For the difference between the newly determined focal mechanisms and the previously available ones from the common subset, we calculate the Kagan angle between the two solutions and also examine the whole image of their beachball projections on the map for visible similarities or differences.

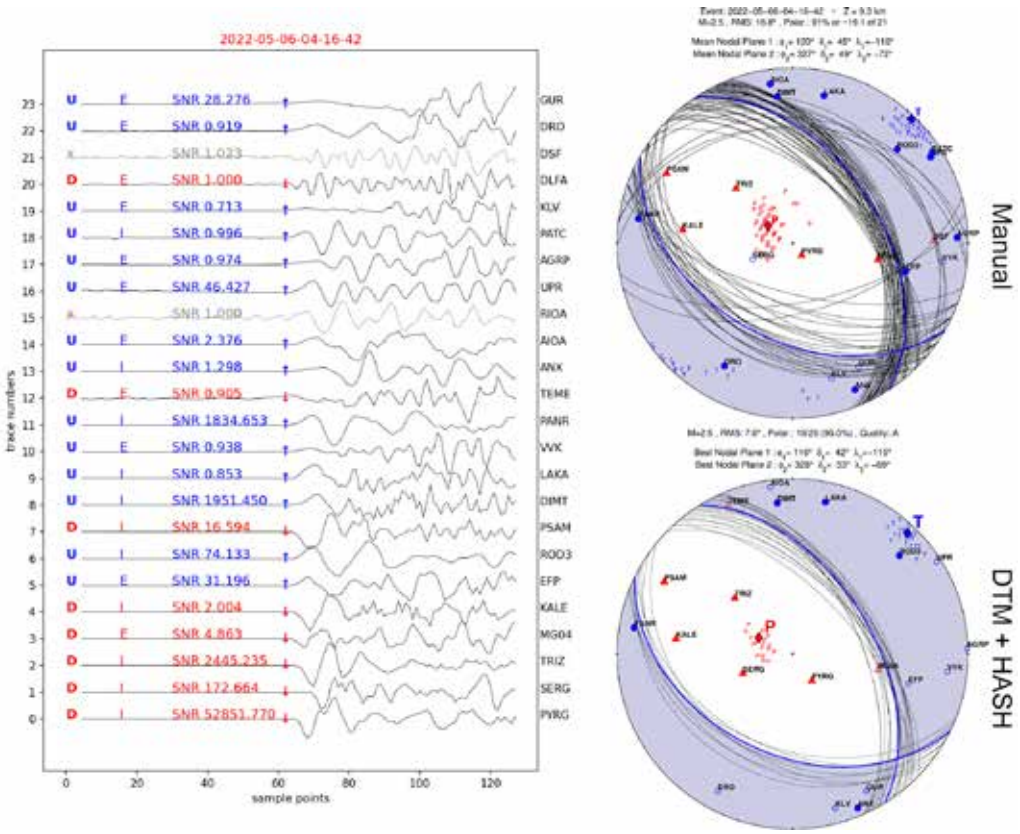

Figure 2. (Left) Example of automatic FMP identifications derived by the DiTing-Motion machine-learning model. The blue letters marked with "U" denote compression whereas the red letters marked with "D" denote dilatation. Gray lines (marked with "x") denote no measurement. "I" and "E" denote impulsive and emergent first motion, respectively. SNR is the Signal-to-Noise Ratio. (Right, Top) focal mechanism derived from manually measured FMPs and a grid-search over fault plane solutions that are consistent with the FMPs. (Right, Bottom) focal mechanism for the same event derived by HASH using the FMPs of the left panel. The RMS value refers to the angular difference between the best solution (bold blue nodal planes) and the valid individual fault planes (thin nodal planes). Blue circles denote compression and red triangles denote dilatation. Small red P and blue T symbols show the distribution of the P- and T-axes projections for valid individual solutions.

Results

The automated workflow yielded 370 focal mechanisms for the 2020-2021 WGoC seismic crisis and 65 for the aftermath period, classified by HASH with a quality grade “A”. Figure 3 (left) shows a confusion matrix comparison between characterized polarities by the applied workflow and FMPs identified for the second period by Kaltsas et al. (2024), for 65 common events. The comparison shows that 82-89% of the FMPs were assessed in a similar manner both automatically and manually. Notably, however, 10-13% of FMPs were discarded by DTM. A closer examination revealed that the cases of “missed” FMPs by DTM mostly belong to either stations with accelerometric instruments, or stations at larger epicentral distances (>30 km). With the more distant stations removed from the comparison, the percentages of consistent FMP measurements rise to 87-91% and “missed” FMPs drop to 7-8% (Figure 3, right). Still, ~1% of compressional and 6% dilatational manual FMPs were characterized as being of the opposite polarity by DTM. A more detailed example is presented in Figure 4 for common events of the crisis period, where FMPs are additionally characterized as impulsive or emergent. This is a more subjective matter from the point of view of a human analyst, as an “emergent” characterization may refer to either a “gentle slope” first motion or a low-amplitude first motion, which can also be due to low SNR. DTM results show a larger percentage of agreement for impulsive FMPs than for emergent ones. A larger percentage of manually characterized “emergent” FMPs also tend to be rejected by DTM, which indicates that the classification of the ML model is generally on the more conservative side. An emergent FMP can probably be misjudged as an impulsive FMP of the same polarity, less probably as an emergent FMP of the opposite polarity, and even more rarely as an impulsive FMP of the opposite polarity.

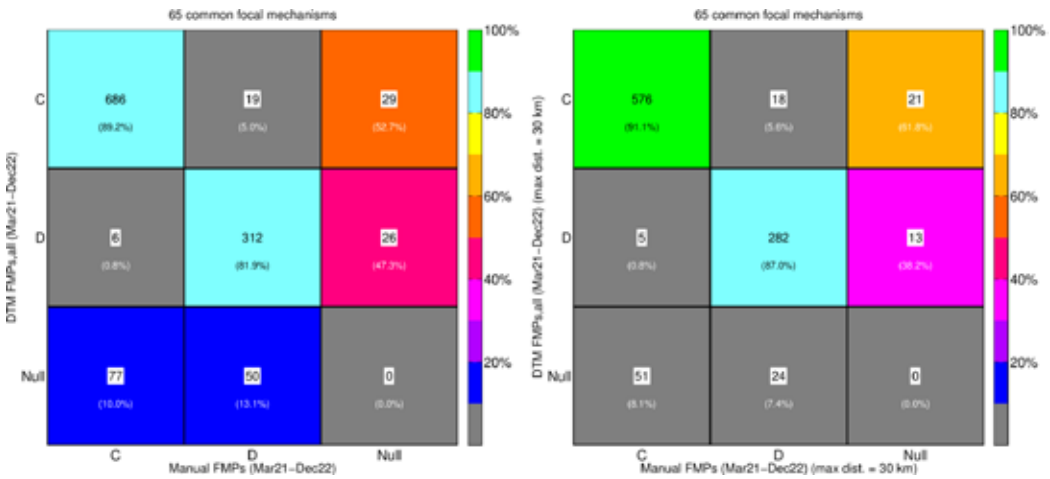

Figure 3. Confusion matrix between FMPs identified with DTM (rows) and manually (columns) for the aftermath period (March 2021 – December 2022). (Left) for all available stations, (Right) only for stations at epicentral distances < 30 km. Letters “C” and “D” denote Compression and Dilatation, respectively. The “Null” row indicates “missed” FMPs, while the “Null” column corresponds to additional automatic FMPs missing from the manual dataset.

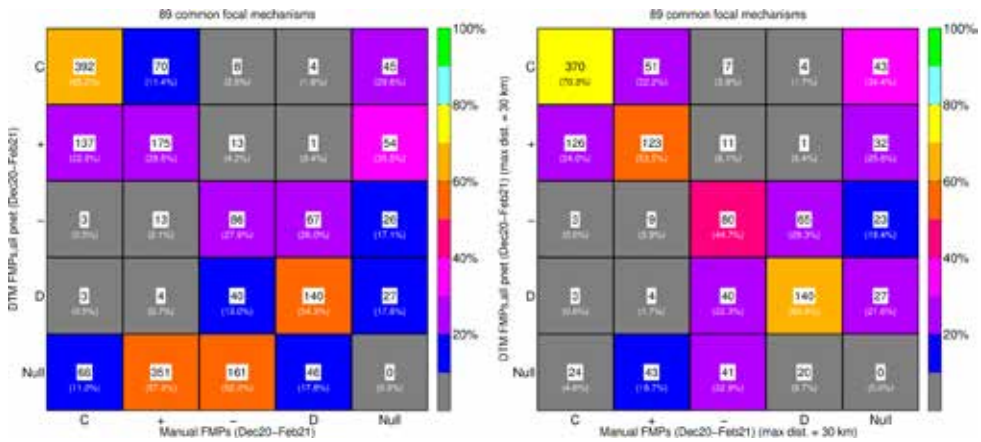

Figure 4. Same as Figure 3, but for the crisis period (December 2020 – February 2021). Symbols “+” and “-” denote emergent, whereas letters “C” and “D” denote impulsive compressional and dilatational FMPs, respectively.

A visual inspection of a subset of identified FMPs alongside the respective P-wave first pulses on the vertical component (e.g., Figure 2, left) confirmed the findings of the confusion matrices, with a generally impressive accuracy of FMP measurement in the majority of instances. There were, however, cases where the polarity of the first motion was seemingly evident to the human eye, but for some reason DTM either dismissed the measurement or misjudged the polarity. As previously noted, null measurements were mostly observed at more distant stations, where the first motion usually has a larger-period pulse than at stations near the epicenter. Erroneous DTM measurements mainly occurred in instances where the P-wave arrival-time pick was not accurate enough, which may be attributed to the applied filter during picking. We tested re-picking on the vertical component with Phasenet, retaining the P-wave pick that was found within ±1 sec of the previously available pick. When the DTM model was re-applied, some results were changed, with new FMPs added, but also with some polarities being reversed and, in some cases, previous FMP measurements being rejected. For the dataset of the 2020-2021 crisis period, the confusion matrix showed an accuracy of 89% and 80% for positive and negative polarities, respectively, taking into account stations at epicentral distances < 30 km and excluding accelerometric stations, after re-picking the P-waves with PhaseNet.

Concerning the focal mechanisms, the similarities between the solutions of the automated workflow with DTM+HASH and those with manually measured FMPs and a grid-search over all fault plane solutions that satisfy a minimum percentage of measured FMPs are quite strong (Figures 5 and 6). HASH was configured to allow for one (1) assumed erroneous FMP for each event. Most of the common solutions with quality grade A, for both the crisis and aftermath periods, exhibit a Kagan angle of less than 30°. Larger deviations can be visibly noticed as a rotation in the focal sphere, mainly affecting the strike-slip component of the focal mechanism. Although the DTM+HASH solutions usually include fewer FMPs than the manual ones, the additional measurement of the S-to-P amplitude ratio likely helps with providing a constrained solution. However, the lack of data from some local stations, particularly for small-magnitude events, can significantly reduce the available FMPs, making the derivation of a quality grade A focal mechanism more difficult. This is especially true during the crisis period (Figure 5), as several local stations experienced technical issues that were later resolved during the aftermath period. Significant differences may also occur as the manual solutions were constrained by the addition of FMP measurements at more distant HUSN stations, where the DTM approach seems to fail to measure the FMP, as also happens sometimes at accelerometric stations due to low SNR. Figure 6 shows a comparison between 57 common solutions of manual and DTM+HASH grade A solutions for the aftermath period, indicating very similar focal mechanisms in both cases, with few notable discrepancies.

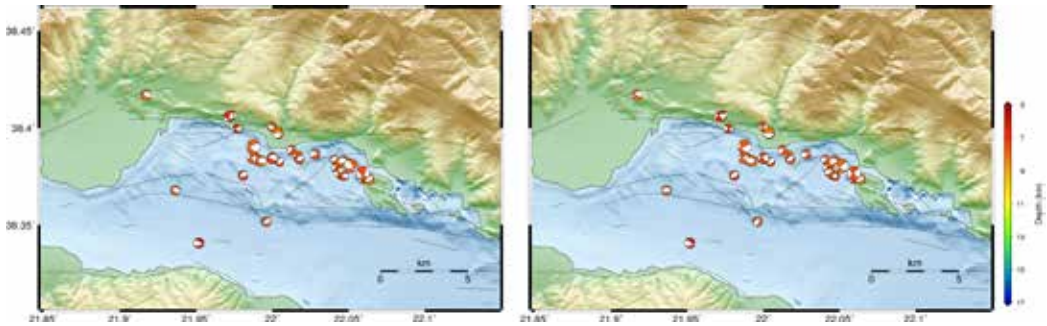

Figure 5. Focal mechanisms of 31 earthquakes during the crisis period, (Left) derived from manually determined FMPs and grid-search over adequate fault plane solutions, (Right) derived with DTM+HASH. The common events presented are those for which the DTM+HASH solutions yielded a quality grade A.

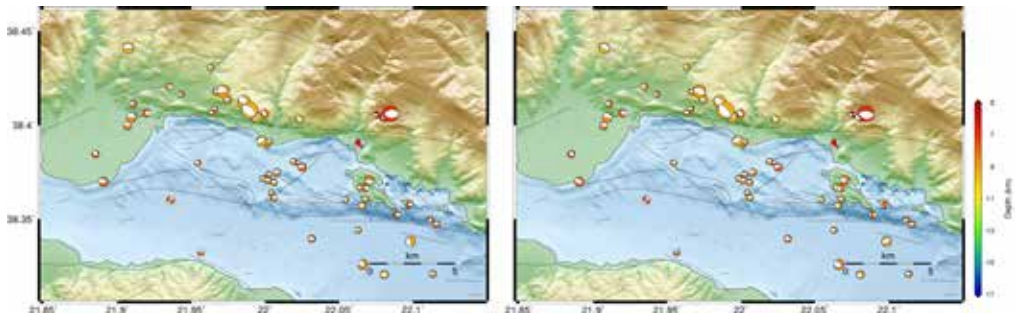

Figure 6. Same as Figure 5, but for the focal mechanisms of 57 common earthquakes during the aftermath period.

Conclusions

In this work, we showcased an application of the DiTing-Motion machine-learning model to fully automate the procedure of first motion polarity measurements in order to determine focal mechanisms of small earthquakes in the Western Gulf of Corinth, Central Greece. As with other methods that employ artificial intelligence, this is a useful tool that can automatically extract a large amount of information that was previously unavailable. We assess the accuracy of the model to identify the polarity of the first motion and examine the cases where it rejects or produces an erroneous measurement. The method requires the availability of accurate P-wave arrival picks at local velocimetric stations for best results. With enough FMP data, even allowing for 1 or 2 erroneous measurements, an accurate focal mechanism can be determined. Despite the abovementioned issues, the results are still remarkable, given that they were produced with a model that was trained with a completely different dataset at a different site. As ML models can be improved by re-training, using site-specific data, this method is promising, regarding the generation of large datasets of focal mechanisms of small earthquakes. The latter could be useful for studies of fault geometries, spatial stress patterns, and even temporal stress changes prior to impending large earthquakes.

Acknowledgements

Waveform data from the following networks were used: CL (Corinth Rift Laboratory Team And RESIF Datacenter, 2013), HA (University of Athens, 2008), HP (University of Patras, 2000), HL (National Observatory of Athens, Institute of Geodynamics, Athens, 1975), and HT (Aristotle University of Thessaloniki, 1981). Maps were drawn using the Generic Mapping Tools (GMT) software (Wessel and Smith, 1998). This research is partially funded by the “TowaRds AdvaNced multidiSciplinary Fault ObseRvatory systeMs²” (TRANSFORM²) project, which is funded by the European Union under project number 101188365 within the HORIZON-INFRA-2024-DEV-01-01 call (Special Account for Research Grants of NKUA, project code: 21465).

References

Aristotle University of Thessaloniki, 1981. Aristotle University of Thessaloniki Seismological Network. International Federation of Digital Seismograph Networks. https://doi.org/10.7914/SN/HT]

Avallone, A., Briole, P., Agatza-Balodimou, A.M., Billiris, H., Charade, O., Mitsakaki, C., Nercessian, A., Papazissi, K., Paradissis, D., Veis, G., 2004. Analysis of eleven years of deformation measured by GPS in the Corinth Rift Laboratory area. Comptes Rendus Geosci. 336, 301–311. https://doi.org/10.1016/j.crte.2003.12.007]

Corinth Rift Laboratory Team And RESIF Datacenter, 2013. CL - Corinth Rift Laboratory Seismological Network (CRLNET). RESIF - Réseau Sismologique et géodésique Français. https://doi.org/10.15778/RESIF.CL

Chiaraluce, L., Festa, G., Bernard, P., Caracausi, A., Carluccio, I., Clinton, J.F., Di Stefano, R., Elia, L., Evangelidis, C.P., Ergintav, S., Jianu, O., Kaviris, G., Marmureanu, A., Šebela, S., Sokos, E., 2022. The Near Fault Observatory community in Europe. Annals of Geophysics 65, 3, DM316. https://doi.org/10.4401/ag-8778

Evangelidis, C.P., Triantafyllis, N., Samios, M., Boukouras, K., Kontakos, K., Ktenidou, O.-J., Fountoulakis, I., Kalogeras, I., Melis, N.S., Galanis, O., Papazachos, C.B., Hatzidimitriou, P., Scordilis, E., Sokos, E., Paraskevopoulos, P., Serpetsidaki, A., Kaviris, G., Kapetanidis, V., Papadimitriou, P., Voulgaris, N., Kassaras, I., Chatzopoulos, G., Makris, I., Vallianatos, F., Kostantinidou, K., et al., 2021. Seismic Waveform Data from Greece and Cyprus: Integration, Archival, and Open Access. Seismol. Res. Lett. 92, 1672–1684. https://doi.org/10.1785/0220200408

Ganas, A., Oikonomou, I.A., Tsimi, C., 2013. NOAfaults: a digital database for active faults in Greece. Bull. Geol. Soc. Greece 47, 518. https://doi.org/10.12681/bgsg.11079

Hardebeck, J.L., 2002. A New Method for Determining First-Motion Focal Mechanisms. Bull. Seismol. Soc. Am. 92, 2264–2276. https://doi.org/10.1785/0120010200

Hardebeck, J.L., Shearer, P.M., 2003. Using S/P amplitude ratios to constrain the focal mechanisms of small earthquakes. Bull. Seismol. Soc. Am. 93, 2434–2444. https://doi.org/10.1785/0120020236

Kaltsas, C., Kaviris, G., Kranis, H., Kapetanidis, V., 2024. The aftermath of the 2020-2021 seismic crisis in the Western Gulf of Corinth (Central Greece). Proceedings of 39th General Assembly of the European Seismological Commission, ESC2024-S44-622, p. 752.

Kapetanidis, V., Deschamps, A., Papadimitriou, P., Matrullo, E., Karakonstantis, A., Bozionelos, G., Kaviris, G., Serpetsidaki, A., Lyon-Caen, H., Voulgaris, N., Bernard, P., Sokos, E., Makropoulos, K., 2015. The 2013 earthquake swarm in Helike, Greece: seismic activity at the root of old normal faults. Geophys. J. Int. 202, 2044–2073. https://doi.org/10.1093/gji/ggv249

Kaviris, G., Elias, P., Kapetanidis, V., Serpetsidaki, A., Karakonstantis, A., Plicka, V., De Barros, L., Sokos, E., Kassaras, I., Sakkas, V., Spingos, I., Lambotte, S., Duverger, C., Lengliné, O., Evangelidis, C.P., Fountoulakis, I., Ktenidou, O.-J., Gallovič, F., Bufféral, S., Klein, E., Aissaoui, E.M., Scotti, O., Lyon-Caen, H., Rigo, A., Papadimitriou, P., Voulgaris, N., Zahradnik, J., et al., 2021. The Western Gulf of Corinth (Greece) 2020–2021 Seismic Crisis and Cascading Events: First Results from the Corinth Rift Laboratory Network. Seism. Rec. 1, 85–95. https://doi.org/10.1785/0320210021

Michelini, A., Cianetti, S., Gaviano, S., Giunchi, C., Jozinović, D., Lauciani, V., 2021. INSTANCE – the Italian seismic dataset for machine learning. Earth Syst. Sci. Data 13, 5509–5544. https://doi.org/10.5194/essd-13-5509-2021

Mousavi, S.M., Ellsworth, W.L., Zhu, W., Chuang, L.Y., Beroza, G.C., 2020. Earthquake transformer—an attentive deep-learning model for simultaneous earthquake detection and phase picking. Nat. Commun. 11, 3952. https://doi.org/10.1038/

s41467-020-17591-w

National Observatory of Athens, Institute of Geodynamics, Athens, 1975. National Observatory of Athens Seismic Network. International Federation of Digital Seismograph Networks. https://doi.org/10.7914/SN/HL

Papadimitriou, E., Bonatis, P., Bountzis, P., Kostoglou, A., Kourouklas, Ch. & Karakostas, V, 2022. The intense 2020–2021 earthquake swarm in Corinth Gulf: Cluster analysis and seismotectonic implications from high resolution microseismicity. *Pure & Applied Geophysics*, 179, 3121–3155. https://doi.org/10.1007/s00024-022-03135-4

Ross, Z.E., Meier, M., Hauksson, E., 2018. P Wave Arrival Picking and First□Motion Polarity Determination With Deep Learning. J. Geophys. Res. Solid Earth 123, 5120–5129. https://doi.org/10.1029/2017JB015251

Serpetsidaki, A., Kapetanidis, V., Elias, P., Rigo, A., Spingos, I., De Barros, L., Lengliné, O., Bufféral, S., Karakonstantis, A., Bernard, P., Briole, P., Zahradník, J., Kaviris, G., Plicka, V., Sokos, E., Voulgaris, N., 2023. The 2020–2021 seismic sequence in the Western Gulf of Corinth: Insights on the triggering mechanisms through high resolution seismological and geodetic data analysis. Tectonophysics 863, 230011. https://doi.org/10.1016/j.tecto.2023.230011

University of Athens, 2008. Hellenic Seismological Network, University of Athens, Seismological Laboratory. International Federation of Digital Seismograph Networks. https://doi.org/10.7914/SN/HA

University of Patras, 2000. University of Patras, Seismological Laboratory. International Federation of Digital Seismograph Networks. https://doi.org/10.7914/SN/HP

Wessel, P., Smith, W.H.F., 1998. New, improved version of generic mapping tools released. Eos, Trans. Am. Geophys. Union. https://doi.org/10.1029/98eo00426

Zahradnik, J., Aissaoui, E.M., Bernard, P., Briole, P., Bufferal, S., De Barros, L., Deschamps, A., Elias, P., Evangelidis, C.P., Fountoulakis, I., Gallovic, F., Kapetanidis, V., Kaviris, G., Ktenidou, O., Lambotte, S., Lengline, O., Lyon-Caen, H., Noble, M., Plicka, V., Rigo, A., Roumelioti, Z., Serpetsidaki, A., Sokos, E., Voulgaris, N., 2022. An atypical shallow Mw 5.3, 2021 earthquake in the Western Corinth Rift (Greece). J. Geophys. Res. Solid Earth 127. https://doi.org/10.1029/2022JB024221

Zhao, M., Xiao, Z., Zhang, M., Yang, Y., Tang, L., Chen, S., 2023. DiTingMotion: A deep-learning first-motion-polarity classifier and its application to focal mechanism inversion. Front. Earth Sci. 11. https://doi.org/10.3389/feart.2023.1103914

Zhu, W., Beroza, G.C., 2019. PhaseNet: A deep-neural-network-based seismic arrival-time picking method. Geophys. J. Int. 216, 261–273. https://doi.org/10.1093/gji/ggy423

17th INTERNATIONAL CONGRESS of the Geological Society of Greece

BULLETIN OF THE GEOLOGICAL SOCIETY OF GREECE, SP. PUBL.

EXTENDED ABSTRACT 133

Preliminary results of physicomechanical properties of lightweight mortars using palygorskite as sand replacement

Karachaliou A.T., Vogiatzis D., Kantiranis N.

Dept. of Mineralogy-Petrology-Economic Geology, School of Geology, Aristotle University, Thessaloniki, Greece, akaracha@geo.auth.gr

Introduction

Cements are any kind of solid or liquid fine-grained material that can be used as a binder for aggregates. After mixing with a liquid, which is mainly water, the cements harden and eventually solidify gradually. During this period of time, i.e. the change from harden to solidification, cement acquires its final form but also it develops specific properties (bonding and mechanical strength). Cements are divided either on the basis of their origin, into natural and artificial cements (Mohammed, 1996), or on the basis of the way of solidification and hardening, into air hardening and hydraulic mortars (Legakis, 1954 & Zacharopoulou, 2004).

Mortars are mixtures consisting of one or more cements, aggregates, any other special materials and mainly water and/or other mixing liquids. The strength of the mortars is mainly dependent on the type of aggregates they contain. Before drying they have good plasticity, but also workability, while after setting and hardening they develop high compressive strength, but also physical and chemical properties that depend on the materials they contain. Lightweight mortars are a subcategory of mortars. These are those with an apparent density of a dry powdered mortar of less than or equal to 1500 kg/m^3 (1.5 g/cm^3) according to ELOT EN 1015-10 (2000). They are characterized by low specific weight and high porosity. Depending on the aggregates used to prepare them, they can be fire-resistance or have sound and heat insulation properties. In general, the category of lightweight mortars is one of the many categories of mortar classification based on specific characteristics such as specific weight, application, type of cement, type of aggregate, etc. (Papagianni, 2000 & Vogiatzis, 2009).

According to the Greek Concrete Technology Regulation (2016), aggregates are defined as all those materials of geological or industrial origin, which are used either together with some kind of cement (in order to create mortars, concretes, etc.), or on their own in all kinds of technical works. This includes natural or artificial materials used either in their original form or after crushing, grinding or grading for the production of concrete and other applications. Included raw materials for the production of lime, cement or metallurgical fluxes.

The natural materials used in mortars include, among others, pumice, zeolites, vermiculite, perlite, diatomite, etc., while the artificial materials include fly ash, blast furnace slag, etc. The use of clays, particularly those rich in palygorskite, has not been studied in this particular application as a substitute for conventional sand for the production of lightweight mortars.

Palygorskite is a hydrated magnesium aluminosilicate mineral with the general chemical formula $(Mg,Al)_2Si_4O_{10}(OH)\cdot 4(H_2O)$. It occurs in the form of elongated (vacuum tube type) crystals and a structure that can be characterized as chain type. When dispersed its crystals remain inert and without any expansion. It retains liquids and gives thickening, thixotropic and other properties. It has a highly porous structure which makes it a very absorbent material but also shows resistance to high temperatures and to environments of high salinity and alkalinity.

The aim of this study is to evaluate the ability of a clay rich in palygkorskite from the Ventzia basin of the region of Grevena, Macedonia, Greece, in the preparation of lightweight mortars when used as a partial substitute of sand. A mixture was prepared, and standard samples were used to evaluate specific physicomechanical properties such as specific weight, porosity, uniaxial compressive strength and mineralogical composition of the standard samples of the prepared mixture.

Materials and methods

The materials used in the present work, for the creation of the mixtures, are palygorskite from the company Geohellas SA, commercial quality sand, which comes from the riverbed of the Axios river and Portland cement type CEM II/B-M 42.5 from the company ISOMAT. For the present study, ten 5 cm cubic specimens were prepared according to ASTM C109/109M, in which 50% of the sand was replaced by palygorskite and the specific weight, porosity, uniaxial compressive strength and mineralogical composition were evaluated for hardening period of 3, 7, 28 and 90 days. For the evaluation of the results, standard specimens were used which were prepared in previous work (Vogiatzis, 2009).

The specific weight was obtained as the result of dividing the volume of each cubic specimen by its weight after weighing on a high precision balance and is expressed in units of g/cm^3. This constitutes the most important property for classifying a mortar as lightweight. The porosity was calculated from the formula of Wyllie *et al.* (1956):

$$\frac{1}{Vp} = \frac{\varphi}{Vpf} + \frac{1-\varphi}{Vpm}$$

where the velocity V_p of primary (P) waves, in a material with porosity φ is given by the above relation in which V_{pf} is the velocity of wave travelling through the material with which the pores of the rock are filled, whether this is air (330 m/sec) or water (1,450 m/sec), and V_{pm} is the velocity of the wave travelling through the studied material without pores. The V_{pm} value used for this work is 5,840 m/sec (Berge *et al.,* 1995). A Pundit Lab type ultrasonic device was used to measure the velocity of the primary (P) waves in the studied specimens.
For the evaluation of the uniaxial compressive strength, a hydraulic press was used directly on the prepared specimens. The strength is calculated as the ratio of the value of the applied crushing force to its applied area, with the result given in MPa.
In order to determine the mineralogical composition of the samples both quantitatively and qualitatively, the X-ray diffraction method was used on a powder sample. A Bruker diffractometer (D8 ADVANCE), Cu tube and Ni filter were used to isolate Cu_{Ka} radiation, at operating conditions of 40 kV & 40 mA, for a scanning range of 3-63° 2θ, step 0.02° and a step time of 0.25 sec. The results were qualitatively evaluated using the DIFFRAC.EVA (v7.1) software with PDF4+ (2004) database, while the quantification of the minerals identified was performed using Bruker's DIFFRAC.TOPAS v6 (2018).
All measurements were conducted in the laboratories of the School of Geology of Aristotle University of Thessaloniki.

Results and discussion

Concerning the raw materials, the sand mainly consists of feldspars, quartz and mica, while minor amounts of amphibole chlorite, serpentine and talc were also measured. As for the clay, the mineralogical analysis showed that it consists mainly of palygorskite (90 wt.%) and in minor amounts of serpentine and chlorite. The mineralogical analysis of the cement showed that it consists of hatrurite (33 wt.%), larnite (24 wt.%), anhydrite (12 wt.%), calcite (12 wt.%), dolomite (10 wt.%), gypsum (5 wt.%), brownmillerite (3 wt.%) and quartz (1 wt.%). In figure 1 the X-ray patterns of the raw materials were shown.

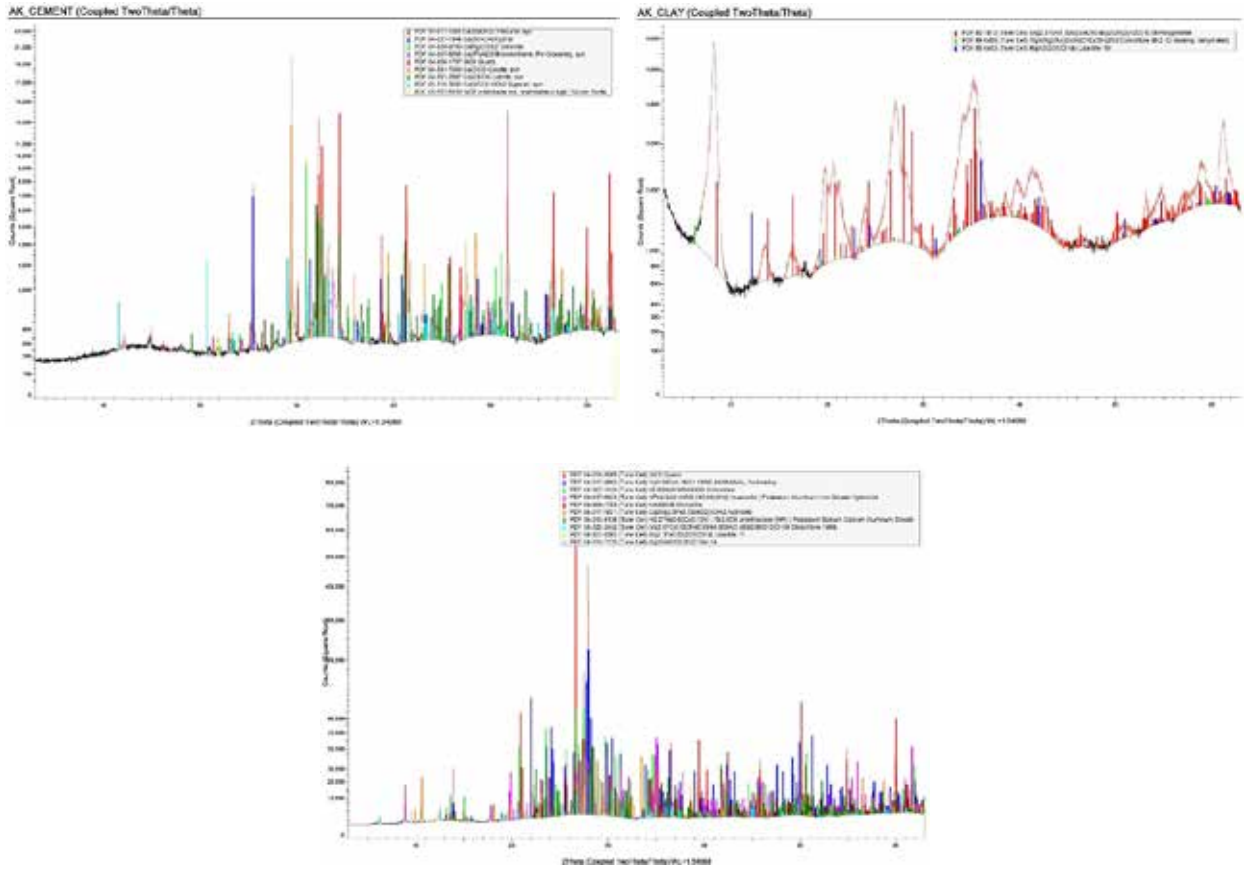

Figure 1. X-ray patterns of the raw materials (cement, clay, sand).

The physical properties of the studied mortar are presented in Table 1. Regarding the specific weight, the studied mortar does not show any change in the first 3 (1.298 g/cm^3) and 7 (1.300 g/cm^3) days, while a significant change in the specific weight occurs on the 28th (1.114 g/cm^3) day, which becomes more obvious on the 90th (0.731 g/cm^3) day. This continuous decrease in specific weight is caused by the porous structure of the palygorskite and the loss of water from

the pores of the specimen throughout its compaction mainly due to hardening reactions and secondly to its contact with the atmosphere. This results in a relatively large and continuous final reduction in the specific weight of the mortar (90 days 0.731 g/cm^3) of 43.7% compared to the initial values (3 days 1.298 g/cm^3).
The velocity of the primary (P) waves (Tab. 1) has a decreasing trend from day 7 to day 90 which is mainly due to the increase in porosity during the same period. At 3 days of hardening the average P-wave velocity was measured 1414 m/sec, which at 90 days was measured at 1068 m/sec, i.e. the P-wave velocity at 90 days decrease to approximately 25% of the 3-day value. Standard cement:sand mortar (conventional mortar) shows at 90 days a P-wave velocity of 3.126 m/sec, while zeolitic mortar (50 wt.% replacement of sand by natural zeolite) specimens showed after 90-day of hardening a P-wave velocity of 2.736 m/sec (Vogiatzis *et al.,* 2008 & Vogiatzis, 2009).
Porosity, which is negatively correlated with P-wave velocity (Wyllie *et al.* 1956), showed an increasing trend throughout the hardening period. In the first week (3 and 7 days) of hardening a relatively similar values of 28.9 and 30.7% v/v, were calculated, while after 28 and 90 days of hardening porosity gradually increases to 35.9 and 38.7% v/v, respectively. This variation in porosity can be attributed to the porous structure of palygorskite, the gradual removal of pore water after day 7 until the end of hardening, but also to the hardening reactions that take place until the 90th day.

Table 1. Measurements of the physical properties of the mortar under testing.

Sample	Consolidation days	Specific weight, S.W. (g/cm^3)	Average value of S.W.	Vpx (m/sec)	Vpz (m/sec)	Vpy (m/sec)	Average Vp (m/sec)	Porosity (% v/v)
K3.1	3	1.390	1.298	1450	1405	1400	1414	30.7
K3.2		1.207		1398	1444	1387		
K7.1	7	1.364	1.300	1526	1522	1509	1525	28.9
K7.2		1.236		1408	1594	1589		
K28.1	28	1.114	1.114	1184	1143	1108	1172	35.9
K28.2		1.086		1126	1169	1154		
K28.3		1.125		1234	1235	1194		
K90.1	90	0.731	0.731	1026	1042	1065	1068	38.7
K90.2		0.686		1141	1188	1225		
K90.3		0.778		1044	958	923		

Uniaxial compression tests showed low strength values, varying from 1.6 MPa at 3 days to 1.0 MPa at 90 days of hardening. The uniaxial compressive strength values show an inversely proportional variation with P-wave velocity and porosity (Fig. 2), a behavior that is attributed to the increase of empty spaces in the specimens from the studied mortar which cause their break by applying a smaller force on the same specimen surface (Kantiranis *et al.,* 2000 & Kantiranis, 2001, Vogiatzis *et al.,* 2008).

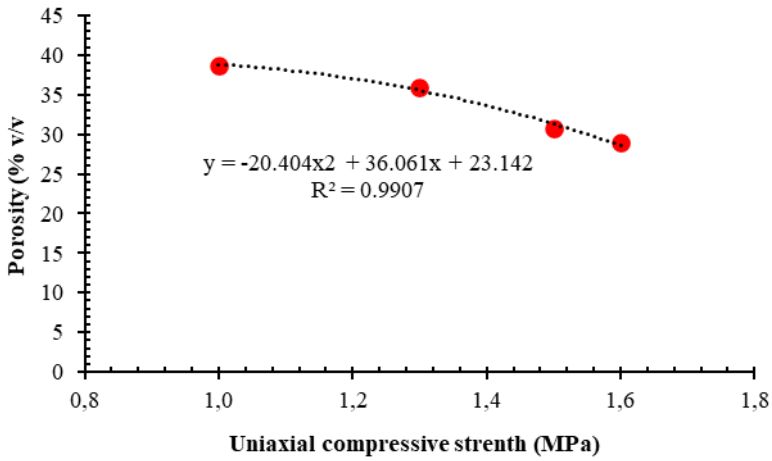

Figure 2. Variation of uniaxial compressive strength (MPa) with porosity (% v/v).

Mineralogical analysis of the studied mortar sample (Fig. 3) showed that the quantities of the mineral constituents (quartz, feldspar, mica, amphibolite, olivine, dolomite, calcite, chlorite, serpentine and palygorskite) of the original materials remain stable compared to the 90 days of compaction, with some variations in the relative variation of these phases on the intermediate days of compaction (3, 7 and 28 days). As for the cement phases, brownmillerite, tobermorite and larnite

show stable values with relatively low percentages, while hatrurite shows an increase of 14% between day 3 and day 28. Finally, portlandite remains stable for the first 28 days, then gradually decreases, reaching a very low rate (0.5% w/w) on day 90. The findings of the present study are similar to previous studies, e.g. Vogiatzis *et al.* (2012).

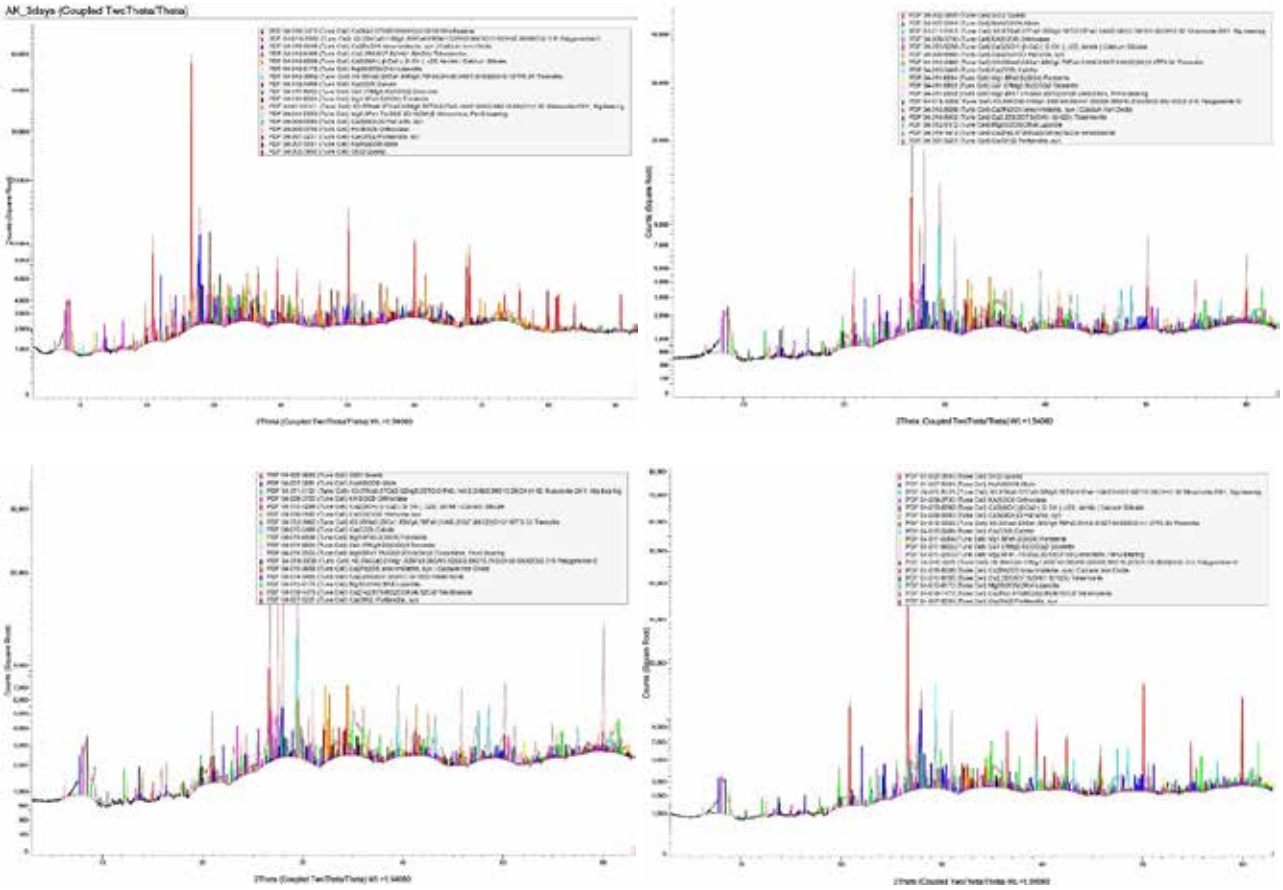

Figure 3. X-ray patterns of the studied mortar at 3, 7, 28 and 90 days of hardening.

It is worth mentioning that the use of clay minerals in mortars, more specifically that of palygorskite, can provide useful properties to the final products, which are the higher porosity and lower specific weight compared to conventional mortars or mortars using natural zeolites. Specifically, Table 2 presents the physical and mechanical properties of three different mortars: the conventional mortar (sand-cement-water) according to ASTM C109-109M (2002), the mortar with 50% wt. replacement of sand by natural zeolite and the mortar with 50% wt. replacement of sand by palygorskite clay. From the evaluation of the data in Tab. 2 it is clear that the use of palygorskite clay produces a much lighter mortar compared to both other mixes. It is observed a decrease in specific weight and an increase in porosity due to the unique microstructure (vacuum tube type) of palygorskite, which decisively affects the development of the final characteristics of the studied mortar. This variation is also observed in the mortar with natural zeolite content, which although not very pronounced, is attributed to the macro, micro & nano pores of zeolitic rock and the contained zeolite (clinoptilolite), respectively. In addition, the cementation and hardening reactions of the mortars play an important role in the change in specific weight and porosity, with zeolitic water having a significant influence on the progression and completion of these reactions (Vogiatzis, 2009).

Table 2. Comparative results of the physical and mechanical properties of mortars with different aggregates.

Samples	Specific weight (g/cm^3)	Porosity (% v/v)	Uniaxial strength (MPa)
Cement:Sand (conventional mortar)	1.869	19.0	14.6
Cement:1/2Sand:1/2 Natural zeolite	1.657	25.0	9.0
Cement:1/2 Sand:1/2 Palygorskite clay	0.731	38.7	1.0

Regarding the uniaxial compressive strength of these three mortars, the use of sand as the only aggregate (conventional mortar) produces the mortar with the highest strength values compared to mortars with natural zeolite rich in clinoptilolite and clay rich in palygorskite, since both these components, with their porous structure, give the mortars a higher porosity and therefore lead to lower uniaxial compressive strength. In comparison between mortars with clinoptilolite and those with palygorskite, the use of natural zeolite leads to higher uniaxial compressive strength values. According to ELOT EN 998-2 (2003), the mortar with palygorskite is classified as M1 (class with minimum compressive strength of 1 MPa), while that with natural zeolite is classified in M5 (class with minimum compressive strength of 5 MPa).
The specific weight was measured at lower values both in the mortar with palygorskite and in the one with natural zeolite, compared to the conventional mortar. Between them the mortars with sand replacement show a relatively large difference in specific weight, with palygorskite clay providing the mortar with values up to 50% lower than those of the mortar with natural zeolite. According to ELOT EN 1015-10 (2009), the specific weight value of palygorskite mortar meets the criteria for lightweight mortars.
Therefore, the addition of palygorskite clay can provide mortars with properties that classify them as lightweight, thus allowing their application in special uses, such as for thermal insulation, sound insulation, etc.

Conclusions

In the present study, the preparation and properties of lightweight mortars were studied through the partial replacement of sand, which is a basic aggregate component of conventional mortars, by palygorskite-rich clay, which is a natural clay material. The materials used include CEM II/B-M 42.5 type cement of the company ISOMAT, commercial sand from the Axios riverbed and palygorskite clay of GEOELLAS S.A. The mixing ratios of cement:aggregates:water were 1:2.75:0.485, with the aggregates consisting equally of sand and palygorskite clay. The aim of this study was to produce a mortar of lower specific weight than conventional mortars, which would be classified as a lightweight mortar, using palygorskite clay as a natural substitute for sand.
The specific weight showed a 43.7% reduction at 90 days, with values varying from 1.298 (3 days) to 0.731 g/cm³ (90 days), with the 90-day value being within the specifications for lightweight mortars. The porosity increased gradually during hardening, mainly due to the removal of pore water from the mixture, but also due to the mirco-structure of the palygorskite. Primary waves (P-waves) velocity showed a 25% decrease from 3 to 90 days of hardening, with mean values decreasing from 1.414 m/sec at 3 days to 1.068 m/sec at 90 days. This decrease is attributed to an increase in porosity, as the velocity of P-waves is inversely proportional to the porosity of a material. Consequently, the uniaxial compressive strength decreased, classifying the studied mortar in class M1 (minimum compressive strength of 1 MPa). Mineralogical analyses of the cement phases showed significant changes. Brownmillerite showed similar values in the first few (3 and 7) days of hardening, with a gradual increase thereafter due to its slow reaction with water. Hatrurite showed a strong increase in the first 28 days of hardening, with a decrease thereafter, as it reacts rapidly with water, contributing to the early increase in the strength of the mortal. Larnite decreased at 90 days of hardening, while tobermorite and portlandite showed constant values or a slight increase at the beginning, followed by a decrease at the end of hardening due to their involvement in hydration reactions. The use of palygorskite clay as a natural aggregate resulted in the production of mortar with low specific weight (0.73 g/cm³) and high porosity (38.7% v/v) at 90 days of hardening, fulfilling the criteria for lightweight mortars. The studied mortar, with 50% substitution of palygorskite clay for sand, was prepared without chemical or other treatment and based on its characteristics it is a lightweight mortar of low specific weight and high porosity.
Finally, further research on mixtures with different percentages of sand replacement by palygorskite-rich clay could lead to a complete evaluation of the specific properties and the identification of the optimal mixture for specific applications, especially in the field of thermal and acoustic insulation, making these mortars a promising material for construction applications.

Bibliography

ASTM C109/C109M, 2002. Standard Test Method for Compressive Strength of Hydraulic Cement Mortars (Using 2-in. or [50-mm] Cube Specimens).
Berge P.A., Bonner B.P., and Berryman J.G., 1995. Ultrasonic velocity□porosity relationships for sandstone analogs made from fused glass beads, Society of exploration geophysicists, Geophysics, Volume 60, Issue 1,January-February 1995.
DIFFRAC.TOPAS V6 (2018). A profile fitting based software for quantitative phase analysis, microstructure analysis and crystal structure analysis. Bruker Corporation, The Netherlands.
ΕΛΟΤ EN 1015-10, 2009. Methods of test for mortar for masonry - Part 10: Determination of dry bulk density of hardened mortar.

ΕΛΟΤ EN 998-2, 2003. Specification for mortar for masonry - Part 2: Masonry mortar.

Kantiranis N., 2001. Calcination study of the crystalline limestone from Agios Panteleimonas, Florina, Greece. PhD Thesis, School of Geology, Aristotle University, Thessaloniki, Greece, 194 p.

Kantiranis N., Christaras B., Filippidis A. and Tsirambides A., 2000. The usage of ultrasonic techniques at calcination studies. *European Commission, Directorate General X, Compatible materials recommendations for the preservation of European cultural heritage, PACT*, 59: 231-237.

Legakis A., 1954. Structural Materials, Library of the Technician, Volume A, Eugenidou Foundation, Athens.

Muhammad M., 1996. Preparation of new mortars with traditional materials for Venetian monuments conservation applications - Study of the compatibility of building stones, their strength and marine corrosion, School of Mineral Resources Engineering, MSc Thesis, Technical University of Crete, Chania.

Papayianni I., Stefanidou M., 2000, Repair mortars for monuments in Byzantine Architecture, 5th International Congress on Restoration of Architectural Heritage, Firenze, 1671-1683.

Regulation on the Technology of Concrete, 2016. Approval of the Concrete Technology Regulation 2016 (CTS-2016). FEK B'1561/2-6-2016, 18057-18171.

Vogiatzis D., 2009. Use of fly ash and natural zeolite in the preparation of lightweight mortars, School of Geology, Ph.D Thesis (in Greek), Aristotle University, Thessaloniki, Greece.

Vogiatzis D., Christaras V., Filippidis A., Kassoli-Fournaraki A., Kantiranis N., Moropoulou A., and Bakolas A., 2008. Evaluation of cement-sand-natural zeolite mortar hardening by ultrasonic techniques. 1st Panhellenic Conference on Structural Materials and Elements, T.C.G., Athens, Greece, Proceedings, B: 1099-1110.

Vogiatzis D., Kantiranis N., Filippidis A., Tzamos E. and Sikalidis C., 2012. Hellenic Natural Zeolite as a replacement of sand in mortar: Mineralogy monitoring and evaluation of its influence on mechanical properties. Geosciences, 2(4), 298-307.

Wyllie M. R. J., Gregory A. R., and Gardner L. W., 1965. Elastic wave velocities in heterogeneous and porous media, Geophysics 21: 41-70.

Zacharopoulou G., 2004. Production of high reactivity building lime suitable for conservation of monuments and historical buildings, School of Civil Engineering, PhD Thesis (in Greek), Aristotle University, Thessaloniki, Greece.

17th INTERNATIONAL CONGRESS of the Geological Society of Greece

BULLETIN OF THE GEOLOGICAL SOCIETY OF GREECE, SP. PUBL.

EXTENDED ABSTRACT 134

Microtremor array explorations and the importance of local site effect in Western Türkiye

Karagöz Ö.[1], Tan O.[2]

(1) Çanakkale Onsekiz Mart University, Faculty of Engineering, Department of Geophysical Engineering, Çanakkale, Türkiye. ozlemkaragoz@comu.edu.tr

(2) İstanbul University-Cerrahpaşa, Faculty of Engineering, Department of Geophysical Engineering, İstanbul, Türkiye.

Introduction

The seismic hazard analysis aims to minimize the damage by determining local site conditions and peak ground acceleration before an earthquake as much as possible. Engineering geophysical methods are one of the fast and economical ways to determine the strength of the soil that will carry engineering structures, the thickness of the layers, water content, behavior under dynamic load, etc. The surface wave analyses allow to S-wave velocity model of the soil layers from the shallow surface to the engineering/seismic bedrock at a site.

In the last 25 years, seismic hazard studies have become important for seismological and earthquake engineering applications in the world. Turkey is one of the countries that have suffered from destructive earthquakes, especially since the 1999 Kocaeli earthquake. The latest 6 February 2023 Kahramanmaraş earthquakes, defined as catastrophe earthquakes, show that we have not made enough progress in reducing earthquake risk since 1999.

Western Türkiye covers rapidly growing areas and encompasses the main financial and industrial centers, especially Istanbul, which is one of the most populated cities in the world, and the other cities in the Marmara Region, such as Tekirdag, Çanakkale, and Balıkesir are the part of the Marmara Supersite that are a high priority to the geohazard community (Figure 1). Additionally, Izmir, the third biggest city, is also located in western Türkiye and affected by earthquakes.

Historical records show that destructive earthquakes frequently visit the region. In the last century, the 9 August 1912 Mürefte (Mw 7.3) earthquake hit the western part while the 17 August 1999 Kocaeli (Mw 7.4) earthquake destroyed the eastern part of the Marmara Region. The Gokceada earthquake (24 May 2014, Mw 6.9) also affected the west of the region. The last destructive earthquake occurred on 30 October 2020, in the north of Samos Island. Even the Bornova Basin, where the city of İzmir is mainly settled, is 70 km away from the earthquake epicenter, significant damage occurred in the city center because of the tick sediment basin. The number of collapsed, heavily damaged and moderately damaged buildings in İzmir is 54, 676 and 789, respectively. A total of 7,683 buildings were labeled as slightly damaged. Totally 117 people died during the mainshock.

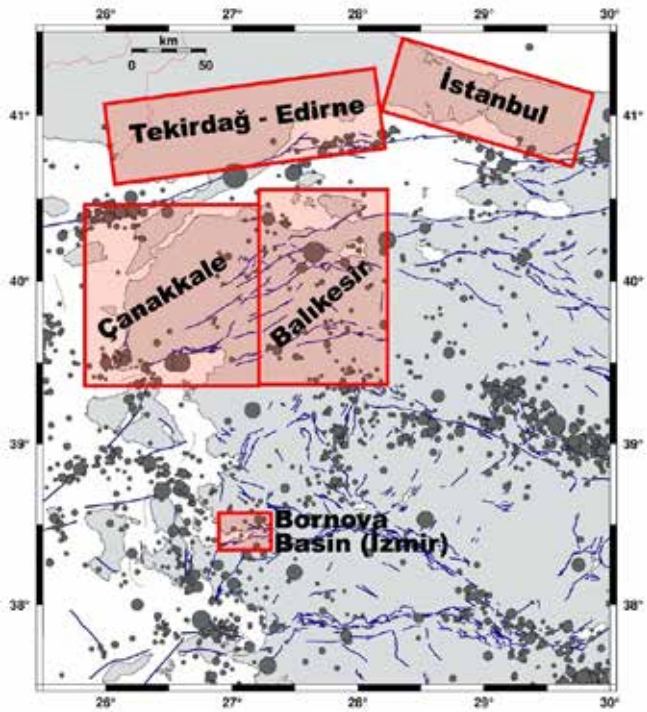

Figure 1. Microtremor study areas in the western Türkiye.

One of the important points for local seismic hazard studies is to define 1D S-wave velocity (Vs) structures from the surface to the seismic or engineering bedrock. This is necessary to know site responses to estimate the ground motion impact on the buildings. The local geology significantly modifies ground motion characteristics and controls the irregular distribution of damage during large earthquakes. Therefore, shallow low-velocity layers are responsible for the variation of earthquake ground motion amplification at a site. Heterogeneity of the soil structures, velocity impedance differences between layers, resonant effects, irregular topography of the layers beneath a basin, the effect of the surface topography, nonlinear soil behavior, fault geometry and lateral variation of Vs causes variation of earthquake ground motion amplifications. It is important to estimate the Vs structure in near-surface layers for estimating strong motion characteristics during an earthquake. Furthermore, investigating the amplification of shallow soil structures is essential as accurately as possible to close the real ones. It is the first step to reduce casualties and collapse buildings before an earthquake for damage assessment. The amplitude, frequency content, and duration of strong ground motions are generally controlled by the local soil structures and have the main role for building damage during an earthquake.

To reduce the earthquake local site effect, a 1D soil profile can be obtained by different geophysical methods, using earthquake data or ambient noise recording to retrieve the vertical soil structure as well as borehole logging. The 1D assumption of the soil structure is widely accepted and easy to implement. Array explorations of microtremors (i.e. SPAC) and MASW methods have been gaining much popularity in the world to obtain 1D Vs profiles. Because they are one of the economic methods and easily applicable for the estimation of Vs structure by a simple circular array with a few seismometers (Figure 2). The Rayleigh waves are considered when vertical sensors are used for microtremor records. Surface wave phase velocity dispersion curves from microtremor records can be utilized to investigate 1D S-wave velocity structures for shallow soil structures.

In this study, the results of array microtremor studies in western Türkiye are presented. The data are collected by the international and national projects from October 2013 to August 2024. The projects were focused on different methods and practices for disaster mitigation for western Türkiye. One of the main research fields of the projects is the determination of the deep and shallow velocity structure for “seismic characterization and damage prediction” that aims to improve the prediction accuracy of estimating the damages induced by strong ground motions.

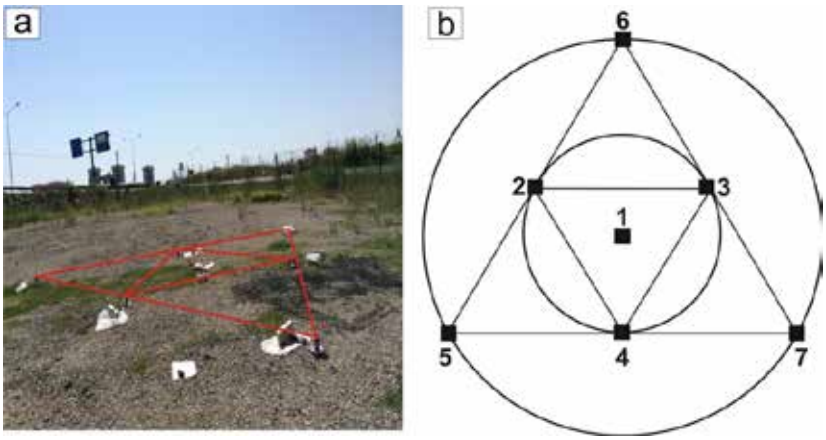

Figure 2. Photo from field measurement in Tekirdag city center (a) and diagram (b) of microtremor array configuration. Numbers show sensor location.

Results and Conclusions

1D Vs structures of shallow sedimentary layers down to the engineering bedrock were explored by applying short-period microtremor Spatial Autocorrelation (SPAC) array measurements (Aki, 1957; Okada, 2003) on the different geological units in Istanbul (Zeytinburnu), Tekirdağ, Edirne, Çanakkale, Balıkesir and İzmir in western Türkiye (Figure 1, 2).

The microtremor array data was gathered with temporarily installed seismic sensors, which were set by using the small and large array circles measurements (Figure 2). Phase velocities of Rayleigh waves were estimated from vertical components of microtremors using the SPAC method proposed by Okada (2003). The SPAC method computes cross-correlations between station pairs in the array with the SPAC coefficients for the calculation of phase velocity at different frequencies. Each vertical-component record was divided into 81.92 s time segments. Then, the transient and artificial noises generated by local conditions, such as pedestrians and cars near the sensors during the measurements, were removed. The Parzen window with a bandwidth of 0.2 Hz was chosen for smoothing in the data processing. We used the 6-14 segments (average 10) for averaging to get the phase velocity at each frequency (Karagoz et al., 2015).

The observed phase velocities were used for the estimation of 1D S-wave velocity structure profiles using the hybrid heuristic

method (Yamanaka 2007) as an inversion method to find an optimal S-wave velocity model. This method searches a 1D soil profile by minimizing the misfit function that is defined as a sum of squared differences between the observed and calculated phase velocities. The method used for theoretical dispersion curves of the fundamental mode of Rayleigh waves is based on Haskell (1953). We assumed a horizontally layered, isotropic and homogenous model. The layer model is characterized by four parameters; thickness (h), density (ρ), P-wave velocity (Vp) and S-wave velocity (Vs) for each layer. Thicknesses and shear-wave velocities are the unknown parameters in the inversion. The density was assumed to increase with increasing S-wave velocity. P-wave velocity is not inverted but derived from S-wave velocity by using the empirical relation by Kitsunezaki et al. (1990), defined as

$$Vp = 1.29+1.11*Vs$$

where the units of Vp and Vs are expressed in km/s (Karagoz et al., 2015).

The observed Rayleigh wave phase velocities from field studies were between ~200 and 1000 m/s, ~90 and 930 m/s, ~120 and 850 m/s, ~200 and 1000 m/s in a frequency range from 2 to 30 Hz, respectively, for Zeytinburnu, Tekirdag, Çanakkale and İzmir, respectively. Most of the sites in Tekirdag had predominant frequencies higher than 2 Hz., 0.5 Hz for Zeytinburnu, 0.8 Hz Çanakale, and 0.5 Hz for Izmir (Figure 3). The high amplifications at low frequencies are related to the thick sedimentary layers beneath the cities. Therefore, the reality of the seismic risk of the cities where close to the potential seismic sources (faults) and are on sedimentary basins must be considered for a sustainable future.

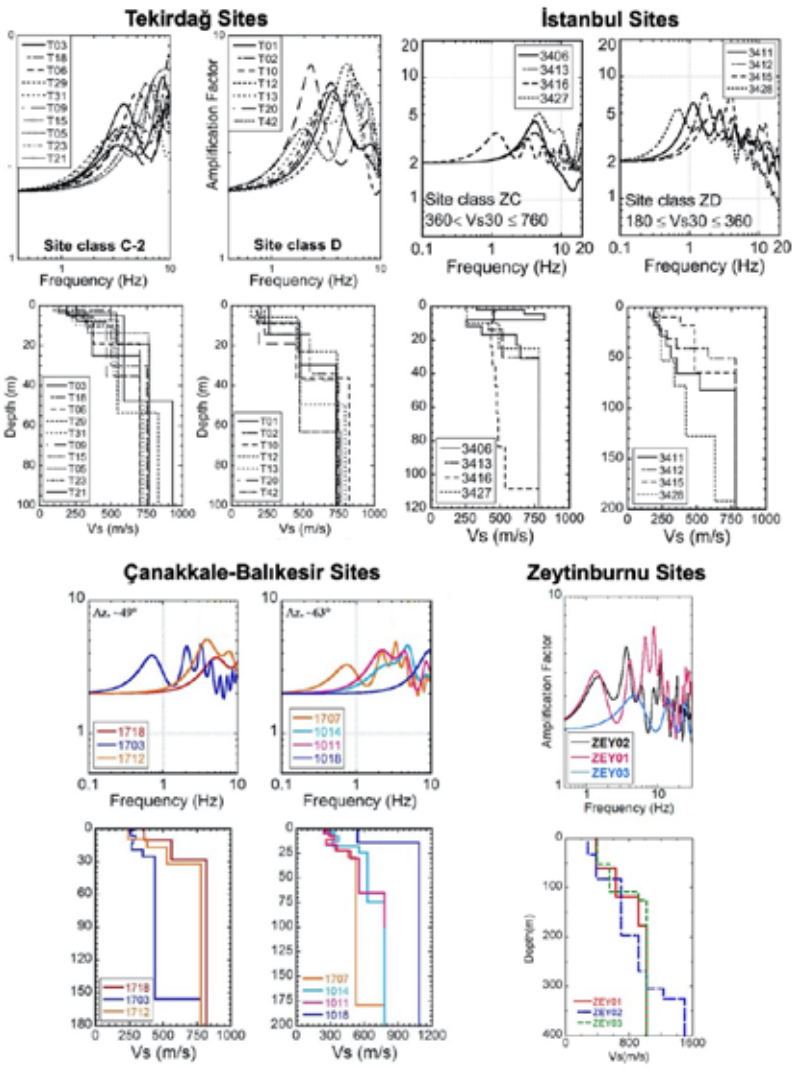

Figure 3. Examples of shallow soil structures and corresponding site amplifications from western Türkiye.

References

Aki, K., 1957. Space and time spectra of stationary stochastic waves, with special reference to microtremors. BERI, 35, 415-456.

Haskell NA (1953) The dispersion of surface waves on multilayered media. Bull Seism Soc Am 43:17–34

Karagoz, O., Chimoto, K., Citak, S., Ozel, O., Yamanaka, H., Hatayama, K., 2015. Estimation of shallow S-wave velocity structure and site response characteristics by microtremor array measurements in Tekirdag region, NW Turkey. Earth, Planets and Space, 67(1), 1-17.

Kitsunezaki C, Goto N, Kobayashi Y, Ikawa T, Horike M, Saito T, Kurota T, Yamabe K, Okuzumi K (1990) Estimation of P- and S-wave velocities in deep soil deposits for evaluating ground vibrations in earthquake. J Japan Soc for Natural Disaster Scie 9:1–17

Okada H., 2003. The microtremor survey method. Geoph. Monog. Series. SEG, 12.

Yamanaka H (2007) Inversion of surface-wave phase velocity using hybrid heuristic search method. Butsuri Tansa 60:265–275. doi:10.3124/segj.60.265 (in Japanese)

17th INTERNATIONAL CONGRESS of the Geological Society of Greece

BULLETIN OF THE GEOLOGICAL SOCIETY OF GREECE, SP. PUBL.

EXTENDED ABSTRACT 135

The 2025 seismicity burst in the Santorini – Amorgos seismovolcanic zone

Karakostas, V.[1], Lomax, A.[2], Anagnostou, V.[1], Papadimitriou, E.[1], Acocella, V.[3], Hicks, S.[4], Henry, P.[5]

(1) Geophysics Department, Aristotle University of Thessaloniki, GR54124, Greece, vkarak@geo.auth.gr (2) ALomax Scientific, Mouans Sartoux, France, (3) Universita Roma Tre, Rome, Italy, (4) University College London, UK, (5) Aix Marseille University, CNRS, IRD, INRAE, College de France, CEREGE, Aix–en–Provence, France

Introduction

In January 2025, an intense earthquake activity started in the Santorini volcano area, southern Aegean, causing great concern among the local population and resulting in actions such as school closures and spontaneous evacuation. Seismic activity and geodetic motion increased inside the Santorini caldera in the last second half of 2024, intensifying in mid–January 2025 and extending offshore to the northeast around the Anydros islet between Santorini and Amorgos islands. This activity was remarkably dense, with turbulent variations over space and time (Figure 1). Up to 13 March 2025 over 4000 earthquakes exceeding *M*1.0 occurred and analyzed.

Santorini is an active stratovolcano in the volcanic arc of the Hellenic subduction zone, with several smaller craters in addition to a main caldera, which collapsed around 1625 BC (known as Minoan eruption). Volcanic centers (volcanoes, fumaroles or solfatara fields), epicenters of strong shallow earthquakes (with focal depths up to 20 km) and epicenters of intermediate depth strong earthquakes (with focal depths between 120 and 160 km) in the southern Aegean volcanic arc can be grouped into five well defined, linear clusters trending about N60°E, corresponding to five extensional zones (Papazachos and Panagiotopoulos, 1993).

Regional seismicity is mostly low-rate crustal activity. However, the largest instrumental earthquake in Greece during the 20th century is an *Mw*7.7 rupture in 1956 (Pacheco and Sykes, 1992), just south of Amorgos Island, caused extensive destruction in the southern Aegean. The earthquake ruptured an ENE–striking normal fault that lies parallel to the southern coastline of Amorgos (Papadimitriou et al., 2005). The area of the 2025 swarm coincides with the rupture area of the *M*6.9 main shock, that occurred 13 minutes after the first 1956 M_w7.7 main shock.

Relocated microseismicity recorded by a temporary network deployed in 2003 to investigate microseismicity of the Santorini volcanic center, revealed two clusters. The main cluster was located at the Columbo Reef, which is the top of a submarine volcano, whereas a smaller cluster was located near the Anydros islet, without seismicity inside Santorini caldera, both clusters were aligned in a NE–SW direction (Dimitriadis et al., 2009). During February 2011 an intense microseismicity was initiated within the caldera and lasted until March 2012. In addition to increased seismicity, the volcano showed significant ground uplift, reaching 14 cm within this period (Foumelis et al., 2013). Manual analysis and relocation provided high-resolution image of the activated fault segments (Papadimitriou et al., 2015). The NE–SW activity inside the caldera, with dextral strike slip motion, was rapidly diminished after the activation of an offshore area to its southwest. Normal faulting activity expanded to the northeast offshore area, near Anydros, where the 2025 swarm is manifested. Since 2012, the activity inside the caldera was low and with relative quiescent periods, whereas near Columbo it has been more frequent and continuous (Karakostas and Papadimitriou, 2025).

High–precision earthquake locations

We used the NLL algorithm (Lomax et al., 2000, 2014) and the multiscale high precision NLL–SSST–coherence procedure (Lomax and Savvaidis, 2022) to relocate a manually picked set of earthquakes with data taken from the bulletins from the Geophysics Department of Aristotle University of Thessaloniki (doi:10.7914/SN/HT) and National Observatory of Athens (doi:10.7914/SN/HL) and a set of picks obtained with machine learning (ML). For the relocation of the manually picked earthquakes the recordings of 31 seismic stations were used. Fourteen of them were in operation on Santorini Island since the beginning of our study (January 2024). Seven stations were installed or started their operation after long interruption in February 2025 [Anydros (Feb. 03), Anafi and Amorgos (Feb. 04), Gavrilos (Feb. 07), Astypalaia (Feb. 10), Ios (Feb. 12), Christiana (Feb. 26)]. For the ML picking we analysed waveform data during 1 January–28 February 2025, from 21 broadband stations located in distances up 120 km from the seismicity centroid (https://eida.gein.noa.gr/). The earthquake detection and phase picking were performed by Phasenet (Zhu and Beroza, 2018), a deep–neural–network–based arrival-time picker. Phase picks are then associated using the REAL software (Zhang et al., 2019). REAL is a grid–search phase association algorithm that performs phase association and an initial location of earthquakes, primarily through counting the number of P

and S picks that appear within a travel–time curve threshold determined by the user and secondarily from travel time residuals (Zhang et al., 2019).

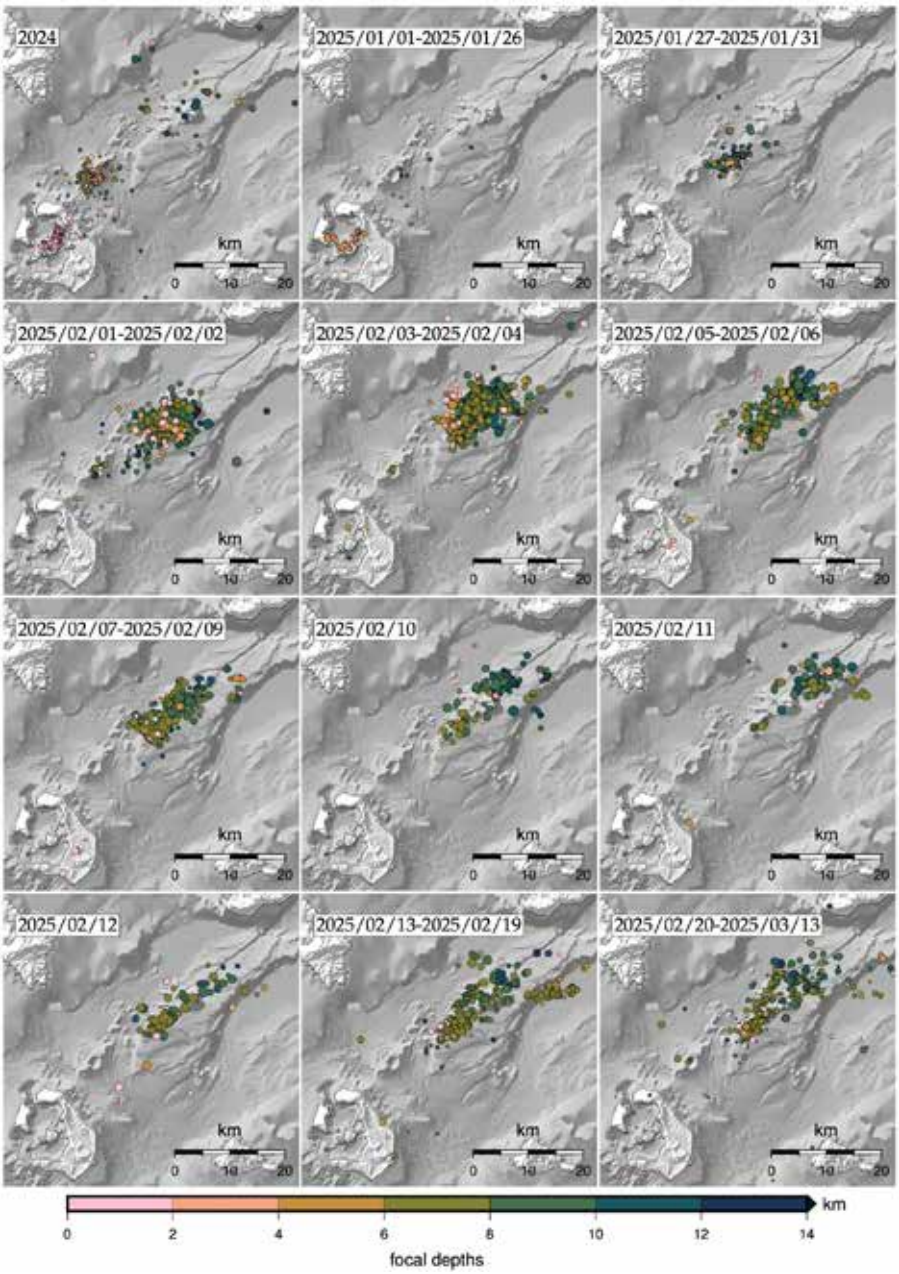

Figure 1. Seismicity evolution in map views for consecutive time windows as indicated inside each snapshot. The size of the symbols is proportional to the earthquake magnitude.

Relocated manually picked seismicity is shown in the maps of Figure 1, covering consecutive time intervals. Background seismicity during 2024 exhibits quite shallow clustering inside Santorini caldera (pink symbols), more dense clustering around the Columbo reef (offshore area NE of Santorini Island) with seismicity up to ~10 km deep, and a third cluster, along with sparse activity, to the northeast and around Anydros islet with focal depths in the brittle crust (5–15 km, inside the seismogenic layer of the back–arc Aegean area, Hatzfeld et al., 1999; among others) with the majority of them getting focal depths between 6–12 km.

With the Machine Learning detection and picking we obtained a catalog with 34442 earthquakes. We relocated the detected seismicity using the same procedure as the manually picked catalogue (Figure 2).

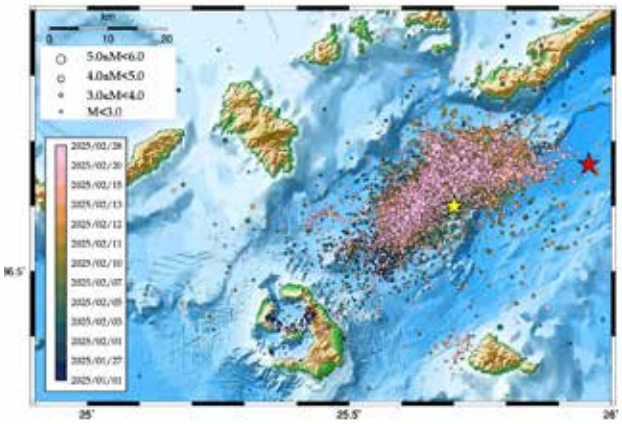

Figure 2. Relocated seismicity during 01/01/2025–28/02/2025 using machine learning detection and NLL–coherence location. The red and yellow stars depict the epicenters of the 1956 M7.7 and M6.9 main shocks, respectively (Bondar et al., 2015; ISC, 2024).

Discussion

Seismic activity intensified during the first weeks of 2025 (1–26 January), including mainly small magnitude seismic activity within the caldera at shallow depths. The main activity abruptly jumped to the northeast offshore area during 27–31 January. Beginning on 1 and up to 4 February, an unusually high number of moderate magnitude earthquakes occurred, the most intense ever reported during the instrumental era anywhere in Greece, with three earthquakes of M≥5.0 and eighty with M≥4.0. The activity formed a ~20 km–long NE–SW trend, in accordance with the strike of the 1956 second main shock (M6.9).

The epicentral area of the 2025 swarm was strictly confined within the Anydros basin, which is bounded on both sides by NE–SW striking normal faults. It appears that further migration of the activity along the Amorgos fault zone almost ceased. The shallower focal depths occupy the southwestern part of the seismicity zone, where NE–SW trending small volcanic cones are also located. Over the next two days (on 5 and 6 February) the main seismicity to the northeast became slightly more compact, with 47 (forty–seven) M4+ earthquakes, and around 10 km depth, whereas activity near Columbo decreased. Between 7 and 9 February, 39 (thirty–nine) M4+ earthquakes were concentrated in an even more localized area, but sparser seismicity extends as far as 40 km NE of Santorini. Two additional M5+ earthquakes struck on 10 and 12 February, with the M4+ occurrence rate appearing to decline. The main concentration of activity from 10–11 February migrated and jumped to over 10 km NE of Anydros Island, before rapidly returning back to the SW of Anydros by 12 February. During these last days, when the M4+ activity was more constrained we could distinguish multiple small structures within the fault network that hosts the seismicity burst.

By 13 February, seismic activity had dramatically decreased, to only a few M4+ earthquakes per day, and the last recorded M5+ earthquake on 17 February. From 13 February and through at least 13 March (Figure 1), small clusters took place to the north and eastern edges of the activated area.

Coulomb seismicity–stress imaging of the swarm

The 3D, scalar ΔCFS field due to finite–fault slip or dike opening can be obtained through integration over the fault or dike of the point–source ΔCFS field of stresses due to a point shear dislocation or tensile opening in an elastic half–space (Haskell 1964; Kikuchi & Kanamori 1982; Okada 1992; King et al. 1994; Materna & Wong 2023). This procedure is a forward calculation, with the resulting ΔCFS field often assessed by how well it agrees with the surrounding distribution of seismicity. The corresponding inverse problem is to infer a distribution of finite–fault slip or dike opening given the 3D distribution of aftershocks or other seismicity and the physics of the Coulomb failure stress criteria. Here we infer the space–time distribution of fault slip or dike opening through an imaging methodology: for specified point source slip or dike opening and receiver fault orientations, we obtain 3D maps of extended slip or dike opening through correlation of point–source ΔCFS kernels across the spatial distribution of seismicity. This seismicity–stress procedure finds a 3D distribution of relative fault slip or dike opening which can explain, in accordance with the physics of the Coulomb failure stress criteria, the surrounding distribution of seismicity.

We performed Coulomb seismicity – stress imaging (Lomax, 2025) of the 2025 Santorini – Amorgos earthquake swarm to determine whether the swarm activity could be driven by ΔCFS either from pure normal faulting source (Figure 3) or a vertical dike source with tensile opening (Figure 4). The results for the normal faulting source (Figure 3) show broad lobes of maximum source potential which are separated from and extend far to the northwest and southeast of the swarm seismicity, and which are

not parallel to the steep, 65°SE dip of the target normal faulting source. Seismicity-stress imaging supports a given source and receiver configuration when the maximum source potential is a) concentrated within the seismicity distribution and in areas of no or low seismicity, and b) flattened and extended parallel to a source fault or fracture plane orientation. Thus, these seismicity-stress imaging results do not support extended normal faulting as a driver of the swarm seismicity.

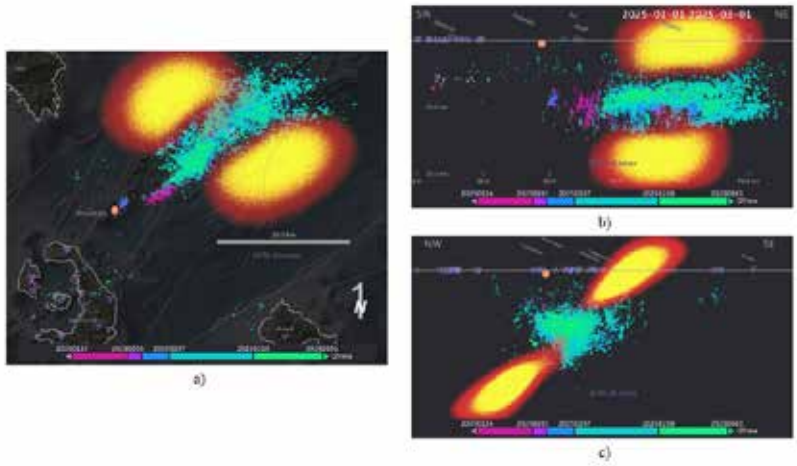

Figure 3. Seismicity-stress imaging of the 2025 Santorini-Amorgos swarm seismicity using a pure normal faulting source specified by a representative mechanism for the M_w7.7, 1956 Amorgos earthquake from Brüstle et al. (2014; strike N36°E, dip 65°SE, rake -102°). 3D density clouds of relative amplitudes of the high-potential portions of the imaged seismicity-stress finite-source fields (yellow and red show normalized correlation ≥ 0.8 and ≥ 0.7, respectively) are shown in a) map view, b) profile view from the SE, and c) profile view from the SW. Dots show NLL-SC-ML relocated swarm seismicity from 2025-01-01 through 2025-02-28, color coded according to occurrence time. Light red lines show mapped surface faults (NOAFaults v6.0); blue inverted pyramids show seismic stations used for ML picking and NLL-SC relocation.

In contrast, the 3D maps of seismicity-stress imaging over the swarm seismicity for a vertical tensile source (Figure 4) show an elongated volume of highest source potential that is mainly below and partly surrounded by the seismicity, abuts high-density limits of the seismicity, is aligned parallel to the trend of the swarm, and is flattened towards a vertical plane. All of these characteristics are compatible with and support a vertical, opening fracture or dyke as a stress source that causes the swarm seismicity.

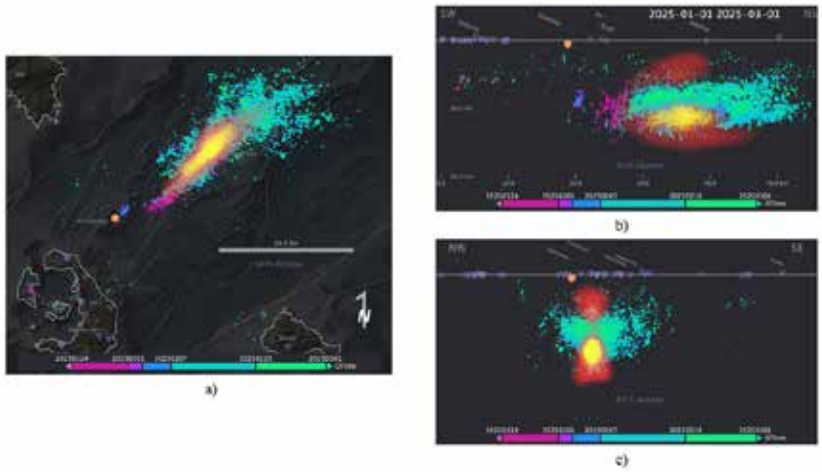

Figure 4. Seismicity-stress imaging of the 2025 Santorini-Amorgos swarm seismicity for a dike source with tensile opening on vertical planes. 3D density clouds of relative amplitudes of the high-potential portions of the imaged seismicity-stress finite-source fields (yellow and red show normalized correlation ≥ 0.8 and ≥ 0.7, respectively) are shown in a) map view, b) profile view from the SE, and c) profile view from the SW. Dots show NLL-SC-ML relocated swarm seismicity from 2025-01-01 through 2025-02-28, color coded according to occurrence time. Light red lines show mapped surface faults (NOAFaults v6.0); blue inverted pyramids show seismic stations used for ML picking and NLL-SC relocation.

Acknowledgements
The authors acknowledge the OSCARS project, which has received funding from the European Commission's Horizon Europe Research and Innovation programme under grant agreement No. 10112975.

References

Bondár, I., Engdahl, E.R., Villaseñor, A., J. Harris, J., Storchak, D. A., 2015. ISC-GEM: Global Instrumental Earthquake Catalogue (1900-2009): II. Location and seismicity patterns. Physics Earth Planetary Interiors 239, 2–13, doi:10.1016/j.pepi.2014.06.002.

Brüstle, A., Friederich, W., Meier, T., & Gross, C., 2014. Focal mechanism and depth of the 1956 Amorgos twin earthquakes from waveform matching of analogue seismograms. Solid Earth, 5(2), 1027–1044. https://doi.org/10.5194/se-5-1027-2014

Dimitriadis, I., Karagianni, E., Panagiotopoulos, D., Papazachos, C., Hatzidimitriou, P., Bohnhoff, M., Rische, M., Meier, T., 2009. Seismicity and active tectonics at Coloumbo Reef (Aegean Sea, Greece): monitoring an active volcano at Santorini volcanic center using a temporary seismic network. Tectonophysics 465, 136–149. http://dx.doi.org/10.1016/j.tecto.2008.11.005

Foumelis, M., Trasatti, E., Papageorgiou, E., Stramondo, S. Parcharidis, I., 2013. Monitoring Santorini volcano (Greece) breathing from space. Geophysical Journal International 193, 161–170 doi:10.1093/gji/ggs135

Haskell, N.A., 1964. Total energy and energy spectral density of elastic wave radiation from propagating faults. Bulletin Seismological Society America 54, 1811–1841 doi:10.1785/BSSA05406A1811

Hatzfeld, D., Ziazia, M., Kementzetzidou, D., Hatzidimitriou, P., Panagiotopoulos, D., Makropoulos, K., Papadimitriou, P. and Deschamps, A., 1999. Microseismicity and focal mechanisms at the western termination of the North Anatolian Fault and their implications for continental tectonics. Geophysical Journal International 137, 891–908.

International Seismological Centre, 2024. ISC-GEM Earthquake Catalogue, https://doi.org/10.31905/d808b825

Karakostas, V., Papadimitriou, E., 2025. A review of the relationship between seismicity and volcanic activity in Santorini volcano. AGU Chapman conference, Caldera – Forming Eruptions at Basaltic Volcanoes, Hilo, Hawaii, February 10–14, 2025.

Kikuchi, M., Kanamori, H., 1982. Inversion of complex body waves. Bulletin Seismological Society America 72, 491–506 doi:10.1785/BSSA0720020491

King, G. C. P., Stein, R. S., Lin, J., 1994. Static stress changes and the triggering of earthquakes. Bulletin Seismological Society America 84, 935–953.

Lomax, A., 2025. Mapping finite fault earthquake slip using spatial correlation between seismicity and point source Coulomb failure stress change. Seismica 4(1), https://doi.org/10.26443/seismica.v4i1.1412

Lomax, A., Savvaidis, A., 2022. High–precision earthquake location using source–specific station terms and inter–event waveform similarity. Journal Geophysical Research: Solid Earth 127(1), e2021JB023190. https://doi.org/10.1029/2021JB023190

Lomax, A., Virieux, J., Volant, P., Berge–Thierry, C., 2000. Probabilistic earthquake location in 3D and layered models. In: C. H. Thurber and N. Rabinowitz (Eds.). Advances in Seismic Event Location (vol. 18, pp. 101 – 134). Dordrecht: Springer Netherlands, https://doi.org/10.1007/978-94-015-9536-0_5

Lomax, A., Michelini, A., Curtis, A., 2014. Earthquake Location, Direct, Global-Search Methods. in Encyclopedia of Complexity and Systems Science, pp. 1–33, ed. Meyers, R.A., Springer New York. doi:10.1007/978-3-642-27737-5_150-2

Materna, K., Wong, J., 2023, May 20. Elastic_stresses_py (version 1.0.0). https://github.com/kmaterna/Elastic_stresses_py, Zenodo. doi:10.5281/zenodo.7951979

Okada, Y., 1992. Internal deformation due to shear and tensile faults in a half–space. Bulletin Seismological Society America 82, 1018–1040.

Pacheco, J. F. and Sykes, L. R. (1992). Seismic moment catalog of large shallow earthquakes, 1900 to 1989. Bulletin Seismological Society America 82, 1306–1349.

Papadimitriou, E. E., Sourlas, G., Karakostas, B. G., 2005. Seismicity variations in the southern Aegean, Greece, before and after the large (Mw7.7) 1956 Amorgos earthquake due to evolving stress. Pure Applied Geophysics 162, 783–804.

Papadimitriou, P., Kapetanidis, V., Karakonstantis, A., Kaviris, G., Voulgaris, N. and Makropoulos, K., 2015. The Santorini Volcanic Complex: a detailed multi – parameter seismological approach with emphasis on the 2011–2012 unrest period. Journal Geodynamics 85, 32–57. http://dx.doi.org/10.1016/j.jog.2014.12.004

Papazachos, B. C., Panagiotopoulos, D. G., 1993. Normal faults associated with volcanic activity and deep rupture zones in the southern Aegean volcanic arc. Tectonophysics 220, 301–308.

Zhang, M., Ellsworth, W. L. and Beroza, G. C., 2019. Rapid Earthquake Association and Location. Seismological Research Letters 90(6), 2276–2284. https://doi.org/10.1785/0220190052

Zhu, W. and Beroza, G. C., 2019. PhaseNet: a deep-neural-network-based seismic arrival-time picking method. Geophysical Journal International 216(1), 261–273. https://doi.org/10.1093/gji/ggy423

17th INTERNATIONAL CONGRESS of the Geological Society of Greece

BULLETIN OF THE GEOLOGICAL SOCIETY OF GREECE, SP. PUBL.

EXTENDED ABSTRACT 136

Climate changes, neglected and emerging diseases.

P. Karanis[1]

(1) Department of Basic and Clinical Sciences, University of Nicosia Medical School, Cyprus, karanis.p@unic.ac.cy

The climate crisis is one of humanity's most pressing challenges and has visible and widespread impacts on public health. The presentation links the climate crisis to disease distribution, research, and control. From rising temperatures and the increasing frequency of extreme weather events to the emergence of climate-related diseases and nutritional inequalities, the climate crisis seriously threatens the health and well-being of the population. Using the interdisciplinary approach, we report on the challenges emerging, reemerging, and neglected diseases arising and being influenced by the climate crisis and how they affect our health and everyday life.

Climate change is expected to significantly impact neglected tropical diseases (NTDs), affecting their transmission patterns and geographic distribution. Vector-borne NTDs are particularly susceptible to environmental changes, as climate influences vector biology and habitat. Rising temperatures and altered rainfall patterns may lead to the emergence and re-emergence of NTDs in previously unaffected regions. Current NTD mitigation strategies, including mass drug administrations, are vulnerable to global events like the COVID-19 pandemic. There is a need for improved surveillance, monitoring, and research to understand better and address the complex interactions between climate change and NTDs. We will highlight the synergistic effects and advocate for a One Health concept by integrating insights from climate science, ecology, geology, water resources and medicine to address the interdisciplinary relation and the gaps to strengthen the resilience of Mediterranean health systems.

Neglected tropical diseases (NTDs) are diverse tropical infections caused by various pathogens, including viruses, bacteria, protozoa, and parasitic worms or helminths. Globalization and increased international trade and travel bring vectors and pathogens together, even where they are limited and prevalent. Climate change is another force driving the expansion of NTDs. A warmer and wetter climate has made the continent more welcoming to vectors of debilitating and sometimes deadly pathogens.

Although the impact of these diseases is not on the same scale in any country compared to tropical countries, cases of vector-borne diseases have become endemic in countries where they were not prevalent before, and they are on the rise. No one country long thought itself safe from NTDs is free. Old certainties that antibiotics and drugs will defend against the risks have evaporated. As Earth warms, the creatures that spread neglected tropical diseases are gaining a foothold in many countries.

Climate, demographic, geological, and geopolitical changes and floods pose new challenges in surface water quality monitoring. They bring forth usual or unusual pathogens, thus requiring new test designs. This demands the development of faster and easier tests to control the quality of drinking or reusing treated wastewater at all points, from plants to end users.

NTDs are also characterized by inequity, which is closely associated with poverty. This inequity has given rise to neglect. Wealthy countries must prepare themselves for more cases. We will discuss and propose options for action and innovative approaches that we can adopt to address these challenges and safeguard public health in an era of climate uncertainty and existing, emerging, reemerging, and neglected diseases related to water supply and vector disease distribution.

One of the most concerning impacts of climate change on human health is the rising prevalence and altered distribution of vector-borne diseases greatly influenced by environmental factors. Tick-borne diseases represent a particularly pressing threat, as climatic shifts influence pathogen transmission dynamics, host-vector interactions, and the geographic spread of key vector species. Ticks are blood-feeding ectoparasites found in mammals, birds, and reptiles worldwide. Unlike nest-dwelling tick species, non-nidicolous ticks are found on vegetation, such as grasses and bushes, onto which they climb and wait to attach themselves to their prey. They feed by sucking blood from their hosts, which can be pets, farm or wild animals, and humans. Ticks are known as carriers for a wide range of pathogens, including viruses, bacteria, protozoa, and helminths, and therefore, numerous tick-borne diseases are transmitted through their bite. Ticks, like mosquitoes, are recognized as the leading global arthropod vectors of human diseases and of primary medical and veterinary importance. Beyond these immediate concerns, ticks are vectors for pathogens that significantly increase morbidity and mortality, amplifying rising public health costs and disease management challenges.

Greece is a popular summer destination for tourists worldwide. Tourists and immigrants represent a melting pot of human activities that brings many people from all over the world together and potentially serves as a source of contamination that can cause endemic infectious diseases on the islands and the whole country. During their

visit, they overconsume diverse water resources by swimming, drinking a lot of water, and eating a lot of fresh produce with minimal preparation, especially salad ingredients and leafy greens. The objective evaluation of the epidemiological status is complex due to the unknown levels of pathogenic contamination in the water supplies, the degree of swimming pool contamination, and the distribution of contaminated food irrigated with contaminated water. Environmental pressure thereby is created and affects both humans and wildlife.

The annual average temperature increases (°C) in four Mediterranean basin countries (Greece, Cyprus, Italy, and Tunisia) from 1960 to the present. Since the 1990s, temperatures in the region have accelerated, with projections suggesting further increases, particularly in the summer months. Under different climate scenarios, the temperature could rise by 2 to 6°C by the end of the century, with a potential summer temperature increase of up to 3°C if global temperatures rise by 2°C. These warming trends are expected to lead to more frequent and intense heat waves, which will pose significant challenges to humans.

Infections have been reported, although outbreaks have been reported in limited numbers. The absence of outbreak documentation indicates the lack of an efficient screening and detection system and that these threats are not on the authorities ‘ alarm agenda until an outbreak occurs. Global warming negatively influences public health, the environment, and wildlife. Responding to these One Health threats promptly is critical. Specific pathogens were the leading etiological agents of waterborne and foodborne outbreaks. The parasites ‘ dormant and transmissive stages can infect a broad host range with multiple transmission routes. Consumption of various vegetables, direct or indirect contact with infected food products and ingesting contaminated water through drinking or swimming can lead to a foodborne and waterborne outbreak. Food and water safety are critical global health concerns, with specific foodborne and waterborne pathogens threatening human and animal health and environmental stability. Addressing the detection and monitoring challenges to water resources, leafy greens, and water supplies will overlap two questions.

Climate change and its influence on emerging disease transmission threaten public health and countries ‘ economies. This perspective emphasizes a critical knowledge gap by exploring how climate-induced environmental changes interact synergistically with disease transmission dynamics to heighten disease risks in Mediterranean countries. Research on the combined effects of climate change and disease transmission will establish bridges and fill the gaps, offering an integrated perspective on the interconnected pathways through which climate change affects public health. By integrating climate science, ecology/ecological modelling, geology and public health aspects, research efforts will advance existing part of knowledge by developing a holistic framework for assessing climate-driven threats. It underscores the necessity of adaptive strategies, including improved disease surveillance, integrated disease management, and climate-informed policy interventions. One Health approach is a cornerstone of the proposed solutions, fostering cross-sectoral collaboration to enhance resilience against climate-driven emerging risks

17th INTERNATIONAL CONGRESS of the Geological Society of Greece

BULLETIN OF THE GEOLOGICAL SOCIETY OF GREECE, SP. PUBL.

EXTENDED ABSTRACT 137

AI-Driven Approaches for Landslide Modeling: Challenges and Opportunities

Karantanellis E.[1], Marinos V.[2], Braun A.[3]

(1) University of Michigan, Ann Arbor, USA, stratis@umich.com

(2) National Technical University of Athens, Athens, Greece

(3) Technische Universität Berlin, Germany

Introduction

Landslides are among the most pervasive and destructive natural hazards, threatening lives, infrastructure, and ecosystems worldwide. Triggered by factors such as intense rainfall, earthquakes, volcanic activity, and human-induced changes, landslides are inherently complex phenomena influenced by dynamic interactions between geological, hydrological, and climatic conditions. Effective prediction and risk mitigation are critical to minimizing their societal and environmental impacts. However, traditional modeling approaches, which often rely on deterministic or statistical frameworks, face significant limitations in capturing the multifaceted and nonlinear processes underlying landslide occurrence. In recent years, artificial intelligence (AI) has emerged as a transformative tool in addressing complex problems across various scientific domains (Catani, Nava, and Bhuyan 2025). In the field of landslide modeling, AI-driven approaches leverage machine learning (ML), deep learning (DL), and advanced data analytics to process large, heterogeneous datasets, uncover hidden patterns, and make predictions with unprecedented accuracy (Sun, Bocchini, and Davison 2020). These technologies offer new opportunities to improve landslide susceptibility mapping, hazard assessment, and early warning systems.

The integration of AI into landslide modeling is particularly timely given the increasing availability of high-resolution remote sensing data, real-time sensor networks, and global climate models. These data sources provide the foundational input for AI algorithms to identify correlations and interactions among diverse variables such as slope angle, soil properties, rainfall intensity, and vegetation cover. Moreover, AI's adaptability allows models to evolve with changing environmental conditions, making them highly suited for long-term hazard management in a rapidly changing world (Dahal and Lombardo 2022). Despite its promise, the application of AI in landslide modeling is not without challenges. Issues such as data quality and availability, model interpretability, and uncertainty quantification remain significant hurdles. Furthermore, the successful implementation of AI requires interdisciplinary collaboration, bridging expertise in geosciences, computer science, and engineering, and transparency for decision-makers. Addressing these challenges is crucial to unlocking the full potential of AI in landslide risk reduction. This study aims to explore the opportunities and challenges associated with AI-driven in landslide modeling. It provides a review of methodologies, evaluates effectiveness, and highlights emerging trends and research directions.

Challenges and Opportunities

In recent years, the integration of AI with geotechnical and environmental sciences has opened new avenues for enhancing landslide modeling accuracy and effectiveness. AI approaches leverage computational algorithms to learn from data, enabling the extraction of hidden insights and the development of robust predictive frameworks (Zhao et al. 2024). Data complexity and availability remain significant barriers in landslide modeling, largely because these models require input from diverse datasets spanning geological attributes, hydrological dynamics, land cover, and climatic variables. The heterogeneity of these data sources often complicates their integration into cohesive models. Geological maps, satellite imagery, rainfall records, and field measurements vary in scale, resolution, and format, necessitating extensive preprocessing pipelines to harmonize inputs. This process can be computationally intensive and prone to errors. Additionally, data scarcity in remote or underdeveloped regions limits the accuracy and scope of modeling efforts. For instance, in areas without detailed geological surveys, proxy variables are often used, introducing uncertainties. Noise and errors in data, such as interference in remote sensing imagery due to cloud cover or inaccuracies in manually collected field data, further exacerbate the challenge. High temporal resolution data, critical for capturing dynamic triggers such as rainfall or seismic events, are frequently unavailable, reducing the model's ability to identify precursors to landslide events.

The temporal and spatial variability of landslide occurrences adds another layer of complexity. Landslides are influenced by short-term events like extreme rainfall, as well as long-term processes such as progressive slope deformation driven by climate change. AI models must therefore be capable of addressing these overlapping timescales. On the spatial front, landslides range from localized slope failures to regional mass movements, and models trained on small-scale events may not generalize well to larger-scale phenomena. Variability in lithology, vegetation, and human

activities such as deforestation and construction introduces nonlinear and region-specific interactions, complicating predictions further. Capturing these dynamics requires multi-scale modeling approaches capable of representing both broad regional trends and localized instabilities (Dahal, Huser, and Lombardo 2024). Uncertainty in AI-driven landslide models is another critical challenge, stemming from both the inherent unpredictability of landslides and limitations in data and algorithms. Quantifying uncertainty is essential for practical applications, as decision-makers must understand the confidence level of predictions. Probabilistic approaches, such as Bayesian neural networks or ensemble methods, can address this need but often demand substantial computational resources. Validation of model outputs against historical landslide inventories is another challenge, as such inventories are frequently incomplete or biased toward more visible events. This bias can reduce the reliability of model predictions. Furthermore, high-dimensional AI models risk overfitting to limited training data, underscoring the importance of rigorous cross-validation and feature selection to ensure generalizability.

Despite these challenges, AI offers transformative opportunities for advancing landslide modeling. One of the most significant benefits is enhanced prediction accuracy. AI algorithms can analyze large, complex datasets to uncover intricate patterns and nonlinear relationships that traditional methods often overlook. For example, deep learning models can extract geomorphological features indicative of slope instability from high-resolution satellite imagery, leading to improved landslide susceptibility mapping. These models also provide insights into the relative importance of input variables, such as rainfall intensity versus slope angle, which can guide future data collection and mitigation strategies. The scalability of AI further enables the development of regional and global models with unprecedented detail. Real-time monitoring and early warning systems represent another area where AI can have a profound impact. By integrating with data sources such as Internet of Things (IoT) sensors (Mendoza-Cano et al. 2021), AI models can continuously update landslide risk assessments in near real-time. Advanced algorithms, including recurrent neural networks and long short-term memory networks, excel at detecting anomalies in time-series data, serving as early indicators of potential slope instability (Zhao et al. 2024). These systems can also facilitate community engagement by delivering timely warnings through mobile applications, empowering at-risk populations to take preventive action and minimizing casualties. AI-driven models are inherently adaptive, evolving with new data inputs and changing environmental conditions. This adaptability is particularly valuable in the context of climate change, where shifting weather patterns and land-use practices continuously alter landslide dynamics (Ajraoui et al. 2024). Continuous retraining ensures that models remain relevant and accurate over time. AI can also simulate hypothetical scenarios, such as the impact of land-use changes or extreme weather events, aiding long-term planning and resilience building. Moreover, by automating data analysis and hazard mapping tasks, AI reduces the cost of landslide risk management, making advanced solutions accessible even to regions with limited resources. Numerous open-source libraries e.g. for R and python, such as the Scikit-learn library, and the implementation of AI algorithms in GIS platforms or Google Earth Engine make AI methods highly accessible. AI is being used in a variety of ways to improve landslide modeling, including data collection and integration, real-time monitoring, predictive modeling and early warning systems.

Figure 1. Conceptual schematic plot of landslide modeling where different conceptual elements are integrated (created in Gemini).

Discussion

This review has examined the burgeoning field of AI-driven approaches for landslide modeling, highlighting their potential to revolutionize our understanding and management of these geohazards. We have observed a growing body of research demonstrating the superior performance of AI algorithms, particularly deep learning models, in capturing complex non-linear relationships within landslide datasets. This has resulted in improved accuracy, enhanced prediction capabilities, and the ability to handle high-dimensional and heterogeneous data. However, several critical challenges persist. Data scarcity and heterogeneity remain significant hurdles, hindering the development and validation of robust AI models. The lack of standardized data collection and sharing protocols exacerbates these issues. Furthermore, the inherent "black-box" nature of many AI models raises concerns regarding interpretability and the potential for unintended biases. This lack of transparency can hinder trust and limit the widespread adoption of AI-based landslide prediction systems. Despite these challenges, the potential benefits of AI are substantial. AI-driven approaches can significantly enhance early warning systems, enabling more accurate and timely predictions of landslide events. This can facilitate proactive evacuation procedures and minimize human casualties. Moving forward, several key research directions are crucial.

- **Data-centric workflows:** Prioritizing the development of robust data acquisition and sharing frameworks, including initiatives to improve data quality, standardize formats, and enhance data accessibility.
- **Cognitive AI:** Developing and implementing techniques to enhance the interpretability of AI models, such as feature importance analysis, visualization methods, and rule extraction algorithms.
- **Hybrid approaches:** Exploring hybrid models that combine the strengths of AI with traditional geotechnical and statistical methods, leveraging the interpretability and domain expertise of traditional approaches while benefiting from the predictive power of AI.
- **Real-world applications:** Focusing on the practical implementation of AI-based landslide models in real-world settings, including their integration into operational systems and decision-making processes.

Ultimately, the successful application of AI in landslide modeling requires a multidisciplinary approach. Collaboration between researchers, practitioners, policymakers, and the public is essential to address the challenges, maximize the benefits, and ensure the responsible and ethical development and deployment of AI-based landslide prediction and mitigation systems.

References

Ajraoui, Abdelrhani, Said Chakiri, Hammou Mansouri, Mohamed Benhaddou, Oussama Laassilia, and Abdelkrim Saouabe. 2024. "Landslide Prediction Methods: A Comparative Overview of Traditional and AI-Based Decision-Making Approaches." In *2024 International Conference on Decision Aid Sciences and Applications (DASA)*, 1–5. Manama, Bahrain: IEEE. https://doi.org/10.1109/DASA63652.2024.10836546.

Catani, Filippo, Lorenzo Nava, and Kushanav Bhuyan. 2025. "Artificial Intelligence Applications for Landslide Mapping and Monitoring on EO Data." In *Earth Observation Applications to Landslide Mapping, Monitoring and Modeling*, 119–45. Elsevier. https://doi.org/10.1016/B978-0-12-823868-4.00007-6.

Dahal, Ashok, Raphaël Huser, and Luigi Lombardo. 2024. "At the Junction Between Deep Learning and Statistics of Extremes: Formalizing the Landslide Hazard Definition." *Journal of Geophysical Research: Machine Learning and Computation* 1 (3): e2024JH000164. https://doi.org/10.1029/2024JH000164.

Dahal, Ashok, and Luigi Lombardo. 2022. "Explainable Artificial Intelligence in Geoscience: A Glimpse into the Future of Landslide Susceptibility Modeling." https://doi.org/10.1002/essoar.10512130.1.

Mendoza-Cano, O., R. Aquino-Santos, J. López-de La Cruz, R. M. Edwards, A. Khouakhi, I. Pattison, V. Rangel-Licea, et al. 2021. "Experiments of an IoT-Based Wireless Sensor Network for Flood Monitoring in Colima, Mexico." *Journal of Hydroinformatics* 23 (3): 385–401. https://doi.org/10.2166/hydro.2021.126.

Sun, Wenjuan, Paolo Bocchini, and Brian D. Davison. 2020. "Applications of Artificial Intelligence for Disaster Management." *Natural Hazards* 103 (3): 2631–89. https://doi.org/10.1007/s11069-020-04124-3.

Zhao, Tianjie, Sheng Wang, Chaojun Ouyang, Min Chen, Chenying Liu, Jin Zhang, Long Yu, et al. 2024. "Artificial Intelligence for Geoscience: Progress, Challenges, and Perspectives." *The Innovation* 5 (5): 100691. https://doi.org/10.1016/j.xinn.2024.100691.

17th INTERNATIONAL CONGRESS of the Geological Society of Greece

BULLETIN OF THE GEOLOGICAL SOCIETY OF GREECE, SP. PUBL.

EXTENDED ABSTRACT 138

Evaluation of Greek clay for pottery applications

Karountzou G.[1], Panagiotaki M.[1], Semitekolos D.[1], Charitidis C[1]

(1) Research Lab of Advanced, Composite, Nano-Materials and Nanotechnology (R-NanoLab), School of Chemical Engineering, National Technical University of Athens, 9 Heroon Polytechniou St., Zographos, Athens 15780, Greece, karountzou@chemeng.ntua.gr

Abstract

The use of clay in the ceramics industry is significant, because the properties influence greatly the final product's quality and performance. Greece has clay deposits that remain underexploited for artisanal and handicraft applications and imported clays are predominantly used. This study aims to evaluate the suitability of specific clayey raw materials for ceramic applications such as pottery, through characterization and mechanical testing. The research involves granulometric analysis, particle size analysis, and determination of Atterberg limits to assess plasticity. Experimental clay specimens are manufactured and subjected to mechanical strength tests, including flexural, tensile and compression testing, at two different firing temperatures. Additionally, mineralogical characterization is performed on both clayey raw materials and sintered specimens to investigate phase transformations. Particle size analysis and other complementary techniques are employed to further understand the material's behavior. Raw material prospection and sampling were undertaken, in accordance with the data provided from Mineral & Aggregate Resources Division of Greek Ministry of Environment, Energy and Climate Change. The clay samples are sourced from active quarries in Greece, specifically from Central Euboea, Central and Western Macedonia, and Central Greece, as potential material sources for pottery applications. The results will provide critical insights into the clay's applicability in ceramic production, highlighting its structural integrity and performance under different conditions. Additionally, these findings will promote the use of Greek clays in pottery applications.

Introduction

Clay-based ceramics have been extensively used in artistic and functional applications due to their durability and versatility. However, the performance of ceramic products depends on the properties of the clay raw materials. This study focuses on evaluating the suitability of selected clay sources for pottery through a comprehensive characterization approach. The main objective is to determine whether the studied Greek clays have the required mechanical and mineralogical properties for industrial use.

Methodology

The methodology consists of several steps. Initially, granulometric analysis is conducted to determine the textural properties and particle size distribution of the clay samples. Atterberg limits are measured to evaluate plasticity, which are critical for workability in artisanal applications. Then, the selected clay materials are processed into standard experimental specimens, which undergo mechanical strength testing. To study the influence of temperature on material properties, the specimens are fired at two different temperatures. Furthermore, mineralogical characterization using X-ray diffraction (XRD) and other techniques are performed to identify phase transformations occurring before and after firing. Additional particle size analysis and complementary characterization methods provide further insights into the structural and functional suitability of the clay for artisanal pottery applications.

Expected Results and Discussion

This study will reveal critical information regarding the development of clay materials during the ceramic production process. The impact of particle size distribution and mineral composition on mechanical strength is expected to be significant. The results will offer insights into how firing temperature influences phase transformations and overall material performance.

Conclusion

This study will contribute valuable data on the potential application of selected clays in pottery industry. Future work may include further refinement of processing parameters and extended mechanical testing to improve ceramic product development.

Acknowledgements

This study is funded by Hellenic Ministry of Culture under the program titled Study of value chains and materials investigation in cottage industry – craftsmanship.

17th INTERNATIONAL CONGRESS of the Geological Society of Greece

BULLETIN OF THE GEOLOGICAL SOCIETY OF GREECE, SP. PUBL.

EXTENDED ABSTRACT 139

The 2025 seismic crisis reveals a coupled magma feeding system at Santorini and Kolumbo

Jens Karstens[1], Paraskevi Nomikou[2], Marius Isken[3], Michelle Maree Parks[4], Vincent Drouin[4], Emilie E.E. Hooft[5], Thomas R. Walter[3,6], Mahmud Haghshenas Haghighi[7], Dimitris Anastasiou[8] and the research team

(1) GEOMAR Helmholtz Centre for Ocean Research Kiel, Kiel, Germany
(2) National and Kapodistrian University of Athens, Laboratory of Geography and Climatology, Department of Geology and Geoenvironment
(3) GFZ Helmholtz Centre for Geosciences, Potsdam, Germany
(4) Icelandic Meteorological Office, Reykjavík, Iceland
(5) Department of Earth Science, University of Oregon, Eugene, OR, USA
(6) Institute of Geosciences, University of Potsdam, Potsdam, Germany
(7) Institute of Photogrammetry and GeoInformation, Leibniz University Hannover, Hannover, Germany
(8) School of Rural, Surveying and Geoinformatics Engineering, National Technical University of Athens, Zographos, Greece

Abstract

The 2025 volcano-tectonic crisis of Santorini and Kolumbo volcanoes in the Greek Aegean Sea has provided unprecedented insights into the complex, interconnected magmatic systems beneath these neighbouring volcanic centres. Through the integrated analysis of seismological data and geodetic measurements, the migration of magma prior to and during this significant event has been reconstructed. The crisis began with a gradual deformation of the ground within the Santorini caldera from July 2024, with an uplift of about 45-50 mm detected by GNSS and satellite data, accompanied by increased H_2 and CO_2 gas emissions. On 27 January 2025, an intense earthquake swarm initiated 10 km northeast of Santorini, near Kolumbo volcano. The seismic activity continued for a period of over 30 days, during which time the intensity fluctuated. The seismic activity can be subdivided into distinct phases, beginning with deep seismicity (12-18 km) accompanied by strong tremors. This was followed by northward migration of increasingly shallow earthquakes towards Anhydros Island at velocities of approximately 1 km/h. The identification of at least 12 seismic surges, characterised by sharp increases in seismicity rate, magnitude intensification, and concurrent tremor activity, followed by lateral migration of seismic fronts, underscores the complexity of the crisis. A thorough analysis of 180 earthquake moment tensors for events with MW>3.6 revealed a consistent NW-SE-oriented tension axis perpendicular to the earthquake migration path, consistent with normal faulting patterns typical of dike intrusions. Our high-resolution earthquake catalogue, which contains over 28,000 events, shows a segmented, laterally ascending complex dike intrusion characterised by incremental, non-uniform and rapid expansion. Furthermore, periods of dike growth coincided with intense seismicity and large-magnitude earthquakes (MW>5) concentrated at the advancing dike tip. Between surges, when the dike boundary was stationary, seismicity was predominantly lower magnitude (MW 1-3), consistent with gradual pressurisation due to continuous magma inflow. Joint inversion of ground deformation data suggests two primary sources: a volume decrease within a mid-crustal reservoir beneath Kolumbo volcano and a uniform opening along a ~13km long dislocation between Kolumbo and Anhydros, representing the emplacement of a dike. The deflation source has been estimated at a depth of ~7.6 km beneath Kolumbo, with an inferred volume decrease of ~0.08 km³. In contrast, the volume increase in the dike has been calculated at ~0.3 km³. Following the initiation of the dike, there was a rapid increase in the magma inflow rate, which peaked between 4-12 February, with average inflow rates exceeding 200 m³/s, before decreasing to almost zero by 24 February, which is likely to mark the end of the intrusion. The sequential timing of these events – shallow magma chamber inflation at Santorini, followed by dike intrusion into the Anhydros Block with concurrent deflation at Kolumbo – points to coupling between reservoirs of both volcanoes. The interaction between the reservoirs likely occured through crustal stress transfer or pressure changes within the fluid plumbing system at depth, while there is no evidence for direct

connection between the shallow magma reservoirs.

Acknowledgements
The authors would like to acknowledge the research team: Eleonora Rivalta, Gareth J. Crutchley, Simone Cesca, Sebastian Hainzl, Joachim Saul, Kostas Raptakis, Nikolai M. Shapiro, Jannes Münchmeyer, Quentin Higueret, Jean Soubestre, Florent Brenguier, Rebeckah S. Hufstetler, Kaisa R. Autumn, Maria Tsakiri, Dietrich Lange, Heidrun Kopp, Morelia Urlaub, María Blanch Jover, Jonas Preine, Christian Hübscher, Mahdi Motagh, Daniel Müller, Torsten Dahm, Christian Berndt for their contribution.

17th INTERNATIONAL CONGRESS of the Geological Society of Greece

BULLETIN OF THE GEOLOGICAL SOCIETY OF GREECE, SP. PUBL.

EXTENDED ABSTRACT 140

The role of painting as historical evidence of relative sea-level change: a review

Karymbali Th.[1]

(1) School of Humanities, Hellenic Open University, Patras, Greece, theodorak2000@gmail.com

Background

Certain artworks can provide important perspectives on historical environmental and climate changes and may be used by scientists as proxies in measuring such changes. The extent to which they can be utilized depends greatly on the nature of the artwork, ranging from abstract and interpretive to strikingly precise, and the specific climate phenomenon being studied (Smithers, 2011). For instance, the variety of animals depicted in prehistoric cave and rock art offers clues about the prevailing climate at the time, though such interpretations must account for critical limitations. Pieter Bruegel's paintings, while inconclusive, have been linked to evidence of the onset of the Little Ice Age (Mann, 2002), while Mid-19th-century depictions of glaciers serve as useful benchmarks for assessing modern glacial retreat. Additionally, analyses of sunsets in various artworks have provided precise data on the atmospheric effects of volcanic eruptions (Zerefos *et al*., 2007).

When studying mean sea-level fluctuations, geomorphological data are valuable for identifying long-term rates of relative sea-level change, while historical data and records can be used to study local sea-level variations over recent centuries. By identifying and locating these indicators and determining their age and elevation relative to present-day sea-level, changes in relative sea-level can be established.

Geomorphological sea-level indicators can have the form of erosional landforms (such as marine notches, sea caves, arches, shore platforms, and marine terraces) or depositional landforms (such as beachrocks, beach ridges, tidal flats, and coral formations) (Vacchi, 2016). When these erosional or depositional features become inactive (fossilized) and appear above or below the current level at which similar landforms are currently forming, they provide evidence of sea-level changes since the time of their formation. In addition, various organisms (corals, algae, various types of shells, worms etc.) or their remnants that, when alive, inhabited known specific tidal levels, can now be found fossilized at different elevations. These biological sea-level indicators reflect changes in sea level that occurred after the organisms' death. The fossils mark the location of the ancient shoreline, representing the time when these organisms lived (Karymbalis, 2010). Sea-level indicators may also include archaeological evidence, such as ancient coastal cities or harbor structures that are now situated above or below the current sea-level (Kolaiti *et al*., 2024). These findings demonstrate that during their period of peak activity, sea-level was at a different position than it is today.

Historical data and records often serve as valuable indicators of more recent sea-level changes. These include written documentary evidence, as well as old tidal gauge measurements, which span over 100 years but are available for only a few regions worldwide (such as northwestern France). Additionally, old high precision paintings that accurately depict coastal landscapes, whether natural or urban, can serve as historic sea-level indicators, providing valuable insights into the sea-level's position at the time they were created.

An example of using paintings to study changes in relative sea-level and the geomorphological evolution of a coastal area is the work by Mattei *et al*. (2020). Among the various geomorphological and historical elements they interpreted to reconstruct the relative sea-level variations and associated morpho-evolutive trends of the Naples coast since the mid-Holocene, they utilized five paintings created between 1790 and 1836 by different artists. However, the most notable example of how paintings can be successfully used to reconstruct recent relative sea-level changes is Venice. For centuries, Venice has long wrestled with the effects of subsidence and the rising sea-level, well before the onset of the industrial era and has abundant evidence of rising sea-level and historical evdence of past high waters. High precision 18th century paintings have been systematically used by Camuffo *et al*., 2017, Camuffo and Sturaro (2003), and Camuffo (2001; 2021)to identify water levels in Venice in the period before instrumental records were kept.

This review paper explores how sea-level evidence on buildings in Venice, as well as architectural features captured in paintings, serve as powerful witnesses to geological and climatic processes. These indicators reveal the recent rise in sea-level driven by both global eustatic sea-level rise and local land subsidence caused by natural and human forces. It primarily focuses on how the height of algae line on palaces, accurately depicted by two painters, has been used as a sea-level proxy over the last three centuries, demonstrating how art and geomorphology can collaborate in reconstructing past sea-level fluctuation.

Methodology

The methodology for this study is based on a comprehensive review of existing literature on the topic. A systematic approach was employed to identify key studies addressing long-term land subsidence and relative sea-lever rise, as well as the use of historical evidence depicted on paintings in Venice. The literature search led to a series of papers and book chapters on the

topic published mostly by Dario Camuffo and his co-authors who have been exhaustively studying these types of historical sea-level indicators in Venice over the past few decades.

Venice

Venice is located in northeastern Italy and is the capital of the Veneto region (Figure 1). It rests atop a network of 127 islands, interconnected by 472 bridges and divided by canals and open waterways. These islands are nestled within the shallow Venice Lagoon, a sheltered bay located between the mouths of the Po and Piave rivers. The lagoon has been a hub of human activity since pre-historic times, with early inhabitants relying on its rich resources for fishing and hunting. By the Neolithic period, the area was already settled, and by the Bronze Age, significant communities, such as Altinum, had emerged. From its very origins, Venice's identity has been inseparable from water. The lagoon offered natural protection against invaders and served as a vital lifeline for its people. Yet, life in this extraordinary setting has always demanded resilience, as Venetians have faced and adapted to the challenges of land subsidence and shifting sea-level.

Carminati *et al*. (2003) assessed a long-term subsidence rate of 0.7–1.0 mm/yr for the greater Venice area, which aligns closely with the slightly lower rate of 0.5 mm/yr estimated by Kent *et al*. (2002) for the past 2.6 million years. The geological-scale subsidence affecting Venice is primarily driven by the subduction of the Adriatic plate beneath the Apennines (Carminati and Di Donato, 1999), as the city lies at the northeastern edge of the Po Plain, which is the foreland basin for two fold-and-thrust belts: the Northern Apennines and the Southern Alps (Cuffaro *et al*., 2010). A natural subsidence rate of 0.45±0.09 mm/yr has also been calculated for the last 124 ka (Rovere *et al.*, 2024), consistent with all the above-mentioned long-term rates. However, it is important to note that subsidence rates in regions as geologically complex as the Venice lagoon and its surrounding coastal plain can vary significantly over space and time. Holocene subsidence rates appear to be greater than those observed over extended geological periods. Tosi *et al*. (2009) offer a possible explanation for this difference, suggesting that sediment compaction could be a contributing factor. They propose that this process significantly impacts Holocene sediments, whereas its effect on older sediments is minimal.

Figure 1. Location of Venice (Source: Google Earth).

Paintings as historical relative sea level change indicator

While geological data are essential for determining long-term rates of relative sea-level change, accounting for eustatic, isostatic, and tectonic components, understanding localized sea-level fluctuations over recent centuries is particularly critical for a city like Venice. This period spans both the pre-industrial and post-industrial eras, the latter marked by accelerated ice melt and rising sea-level driven by human-induced greenhouse gas emissions (Fox-Kemper *et al*. 2021). For the past century, modern tools such as tide gauges and satellite altimetry have provided accurate sea-level measurements. Venice presents a unique case study as its centuries-old architecture, constructed in close proximity to the water's edge, combined with artistic depictions of the city by painters, allows the reconstruction of sea-level changes dating back as far as 1300 CE (Camuffo, 2021). This rich historical and cultural record offers insights unavailable in most other coastal locations.

The contributions of the paintings by two prominent Venetian painters, Antonio Canal (better known as Canaletto, 1697–1768) and Bernardo Bellotto (1722–1780) were of great importance in sea-level change reconstruction (Camuffo, 2001). Born in Venice on October 18, 1697, Canaletto grew up in a family of artists. He initially worked as a theatrical scene painter but eventually embraced a new artistic direction that shaped his legacy: veduta, or "view painting." This genre, which originated in the 17th century, focuses on exceptionally detailed portrayals of cityscapes and urban landmarks (Kowalczyk, 2018). Drawn to this style, Canaletto turned his attention to capturing the essence of daily life in Venice through his meticulously crafted cityscapes and architectural views often referred to as "veduta". In his paintings, Venice is portrayed as a grand theatrical production, with the

Grand Canal serving as the stage, the buildings forming the curtains, and the intricate architecture creating the backdrop of the scenery (Kowalczyk, 2018). Bernardo Bellotto (1721–1780) was a nephew and pupil of Canaletto known also for his stunning "veduta" painting. He even signed some of his works as "Bernardo Canaletto", capitalizing on his uncle's fame. However, Bellotto developed his own distinct style, marked by highly detailed and often large-scale depictions of cities, dramatic lighting, and a cooler palette (Kowalczyk, 2016).

To discuss the role of paintings as indicators of sea-level change, it is essential to understand the concept of the "Comon Mark" ("CM") or "Marine Common Level" in sea-level reconstruction studies, both generally and specifically in the context of Venice. The "CM" refers to reference benchmarks used to measure and monitor sea-level changes. These benchmarks might include tidal markers, which are physical markers set at specific locations that serve as references for mean-sea level, tidal datums, or other standardized elevations for data comparison (Rovere *et al*., 2024). Essentially, common marks agreed-upon reference points or datasets that allow for consistent comparisons across different regions or time periods. The role of the "CM" in sea-level change studies is crucial because it provides consistency across locations. A shared CM or "common level" ensures that measurements are comparable on a global scale. Additionally, using standard baselines allows researchers to track global sea-level rise and its impacts on coastal regions making "CM"s indispensable for understanding long-term trends.

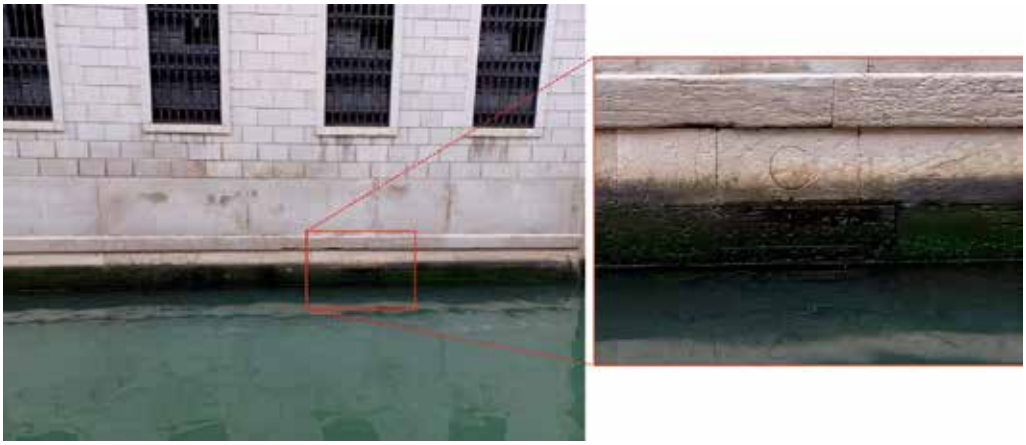

Figure 2. Photo showing the present brown-green microorganisms mark on a building wall facing a canal and the letter "C" (the official sea-level reference engraved when the benchmark was made in 970).

In the case of Venice, the "CM" refers to the distinctive dark green-brown belt formed by photic algae that grows on buildings, walkways, and bridges throughout the city (Rovere *et al*., 2024). This belt's elevation is slightly above the high tide level, influenced by the standing waves generated by boats during calm days in the lagoon. As noted by Camuffo (2023), the ancient Venetians sometimes formalized this marker by engraving it onto walls as "CM" or simply "C", designating it as an official sea-level reference at the time the benchmark was made (Figure 2). The use of the "CM" as a benchmark for water level in Venice has been well-documented in historical sources, including a 16th century book by Cornaro, (1560) and the writings of Temanza (1761).

Canaletto and Bellotto achieved an almost photographic precision in their depictions of urban landscapes, faithfully reproducing buildings down to the smallest details, a realism made possible by their use of the camera obscura (Camuffo and Sturaro, 2003). The camera obscura, an early precursor to the modern camera, functions by allowing a beam of light to pass through a lens or small opening, it is then reflected by a mirror or prism and subsequently projected onto a glass surface (Figure 3a). The painter would position a canvas or sheet of paper over the glass surface to trace the outlines of the projected image, creating a highly detailed, almost "photographic" rendering. Although the overall proportions of the scene might not always be maintained, Cannaleto and Bellotto meticulously reproduced intricate details, including the "CM" on buildings. This technique enabled painters to achieve remarkable detail and realism in their cityscapes. Canaletto's camera obscura, is kept at the Correr Museum in Venice (Figure 3b). The accuracy of detail in Canaletto and Bellotto's works can be tested by scaling and comparing elements across multiple paintings of the same building, all created using a camera obscura. Although these paintings are often regarded as copies of an original, the varied patterns of minor discrepancies suggest that the two artists likely revisited the site at different times to produce fresh sketches of the same structure. The precision in depicting even the smallest details highlights that their paintings are faithful, high-quality representations of the real world rather than imaginative or fictional compositions.

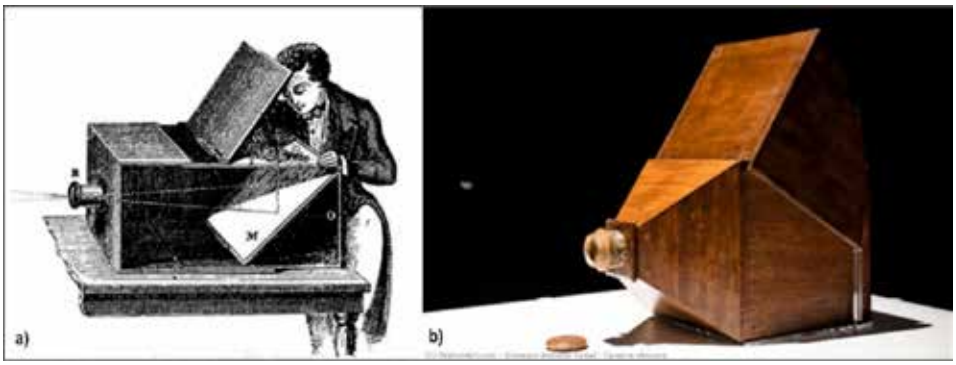

Figure 3. (a) An artist sketching from life using a 19th century camera obscura. The device includes: B (lens), M (mirror), and O (the path of light if unobstructed by the mirror). The artist used thin tracing paper to outline the image, then transferred it onto canvas, board or paper to complete the drawing. (Source: Wikipedia Commons) (b) A camera obscura made, or perhaps simply owned, by Canaletto, as revealed by the inscription.

From the above it is clear that it becomes possible to reconstruct the sea-level at the time the painting was created. Although the exact tidal stage during the painting's execution cannot be determined, both Canaletto and Bellotto incorporated the "CM" into their works, providing a reliable reference point. The process begins by identifying the precise location of the "CM" in the painting, relative to recognizable architectural features. Next, the site is visited, typically by boat, to locate the building, where the "CM" (level reached by algae) from the painting is compared to the current algae line on the structure. The difference between the two levels indicates the rise in relative sea-level from the time the painting was made to the present. Before arriving at a final estimate, several adjustments must be made. Key factors, such as the difference in wave patterns created by motorboats today compared to those caused by the rowing and sailing vessels of the 18th century, as well as the amplification of tidal wave due to dynamic effects, must be carefully taken into consideration (Rovere *et al*., 2024). The analysis of eleven paintings of Canaletto and Bellotto (Figure 4) revealed that the "CM" has risen on average by 69±11 cm since the early 18th century (Camuffo and Sturaro, 2003) as shown in Figure 5a.

Figure 4. Four of the paintings of Canaletto and Bellotto that were used as historical relative sea level change indicator (a) "The Punta della Dogana" by Canaletto (1727); (b) "View of the Grand Canal at San Stae" by B. Bellotto (1740); (c) "The Grand Canal, Venice, Looking East from the Palazzo Flangini to the Palazzo Venramin Calergi" by B. Bellotto (1741); (d) "Grand Canal From the Campo Santa Sofia Towards the Rialto Bridge" by Canaletto (1730-31). (Source: WikiArt, Visual Art Encyclopedia).

Beyond changes in the "CM" elevation shown in paintings, another architectural feature that can act as a proxy for relative sea level is the positioning of steps in front of residential buildings or leading to canal walkways. Camuffo *et al*. (2017) explored this proxy, grounded in the principle that stairs were designed for practical use—allowing people to descend from buildings into boats, and vice versa. To facilitate this, the lowest step was typically aligned with the boat's gunwale (side level), ensuring it was free of algae, meaning it was positioned slightly above the "CM".
By integrating evidence from paintings, staircases, and historical written documents detailing changes in "CM" elevation relative to known architectural features, Camuffo *et al*. (2017) reconstructed trend in relative sea-level from 1300 to around 1800 CE. Camuffo *et al*. (2017) and Camuffo (2021; 2022a) identified an exponential rise in relative sea-level from 1350 to the present. This acceleration in sea-level rise is also exponential, indicating the importance of long-term processes (such as melting continental glacier, isostatic adjustments, and tectonic movements) alongside climate change. While the precise mechanisms driving this exponential trend remain to be fully understood, they likely involve a complex interaction of Glacial Isostatic Adjustment, historical subduction, and post-industrial sea-level rise. Over the entire period from 1350 to 2016 CE, the average local sea-level change is estimated at 1.9±0.1 mm/yr. A key unresolved issue lies in the significant discrepancies between historical records and geological data reported by Vacchi *et al*. (2016). These differences suggest the possibility of substantial pre-industrial sea-level fluctuations that remain unexplained. Bridging the gap between geological and historical relative sea-level data is essential and represents a promising direction for future research in understanding long-term sea-level dynamics.

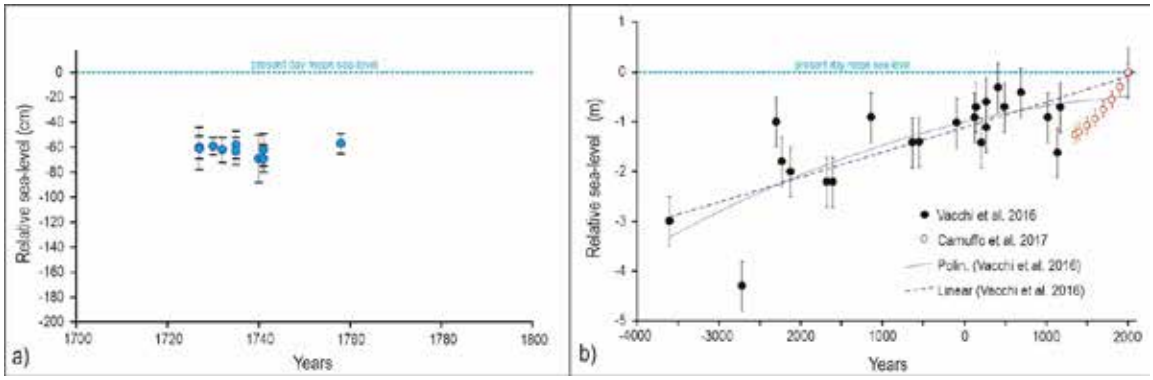

Figure 5. Data on relative sea level (RSL) changes in Venice through multiple sources. (a) The graph illustrates RSL trends based on estimations derived from the paintings of Canaletto and Bellotto (white dots with error bars, covering 1727–1758). The RSL values from the paintings were inferred by comparing the algae belt's position depicted in the artwork to its present-day level; (b) a long-term reconstruction of relative sea-level rise over the past 6000 years. Black dots represent data from natural proxies as compiled in Vacchi *et al*. (2016), while red circles indicate sea-level estimates reconstructed by Camuffo et al. (2017). (Source: Camuffo *et al*. (2022b).

In the context of climate change, the study area is expected to face significant challenges due to both short- and long-term sea-level rise (Tosi et al., 2002; Zanchettin et al., 2021; Lionello et al., 2021).
Taking into account the spatial distribution of vertical land movement (1–3 mm/year of subsidence, with peak values reaching 7 mm/year) and tide gauge data, projections indicate that by 2150, more than 112 km² could be at risk of flooding under the SSP1-2.6 low-emission scenario, with this figure increasing to 139 km² under the SSP5-8.5 high-emission scenario. During extreme high-water events—driven by the combined effects of astronomical tides, seiches, and atmospheric forcing—the relative sea-level rise (RSLR) in 2150 could temporarily reach up to 3.47 m (Andizei et al., 2024, 2025). These findings emphasize the urgent need for local communities to strengthen flood resilience strategies to mitigate the projected impacts of RSLR by 2150, particularly in the UNESCO-listed city of Venice and its ecologically significant lagoon (Alberti et al., 2023; Andizei et al., 2024).

Closing Remarks

Painting and other forms of art have emerged as significant proxies for understanding climate change impacts including sea-level rise. Venice, with its continuous habitation and unique coastal environment characterized by significant interaction between water and buildings, stands out as a one-of-a-kind region globally where painting can play a pivotal role in studying sea-level changes. The distinctive technique and faithful depiction of the city's urban landscape by painters such as Canaletto and Bellotto have significantly contributed to the investigation of relative sea level changes since the early 18th century, making Venice one of the finest examples of the collaboration between

painting and geomorphology, yielding impressive results. While paintings can help reconstruct historical sea-levels from the time they were created, several critical factors that further complicating accurate interpretations must be taken into account. In the case of Venice such issues include significant differences in wave patterns generated by modern motorboats compared to those produced by the rowing and sailing vessels of the 18th century, as well as the amplification of tidal wave due to dynamic effects.

The integration of artistic expression with scientific data allows for a unique communication of climate change, particularly in relation to sea-level rise. Beyond utilizing works of art to study changes in relative sea-level, art can also motivate audiences to consider the implications of climate change more seriously. Artists often depict landscapes threatened by rising waters, creating a visual narrative that underscores the urgency of climate change and the need for a sustainable future.

References

Alberti, T., Anzidei, M., Faranda, D., Vecchio, A., Favaro, M., Papa, A., 2023. Dynamical diagnostic of extreme events in Venice lagoon and their mitigation with the MoSE. Sci. Rep., 13, 10475.

Anzidei, M., Tolomei, C., Trippanera, D., Alberti, T., Bosman, A., Brunori, C.A., Serpelloni, E., Vecchio, A., Falciano, A., Deli, G., 2025. Multi-temporal Relative Sea Level Rise Scenarios up to 2150 for the Venice Lagoon (Italy). Remote Sens., 17, 820.

Anzidei, M., Alberti, T., Vecchio, A., Loizidou, X., Orthodoxou, D., Serpelloni, E., Falciano, A., Ferrari, C., 2024. Sea level rise and extreme events along the Mediterranean coasts: the case of Venice and the awareness of local population, stakeholders and policy makers. Rendiconti Lince Sci. Fis. Nat., 35, 359–370

Camuffo, D., 2023. The Treatise on Waters by Cornaro (1560) and a quantitative assessment of the historical sea surges “Acqua Alta” in Venice. Climatic Change 176, 18.

Camuffo, D., 2022a. A discussion on sea level rise, rate ad acceleration. Venice as a case study. Environmental Earth Sciences, 81, 349.

Camuffo, D., 2022b. Historical Documents as Proxy Data in Venice and Its Marine Environment. Oxford Research Encyclopedia of Climate Science. Retrieved 31 Jan. 2025, Historical Documents as Proxy Data in Venice and Its Marine Environment.

Camuffo, D., 2021. Four centuries of documentary sources concerning the sea level rise in Venice. Climatic Change, 167, 54.

Camuffo, D., 2001. Canaletto’s paintings open a new window on the relative sea level rise in Venice. Journal of Cultural Heritage, 4, 227–281.

Camuffo, D., Sturaro, G., 2003. Sixty-cm submersion of Venice discovered thanks to Canaletto’s paintings. Climatic Change, 58(3), 333-343.

Carminati, E., Doglioni, C., Scrocca, D., 2003. Apennines subduction-related subsidence of Venice (Italy). Geophysical Research Letters, 30(13), 1717.

Carminati, E., Donato, G.D., 1999. Separating natural and anthropogenic vertical movements in fast subsiding areas: The Po plain (N. Italy) case. Geophysical Research Letters, 26(15), 2291-2294.

Cornaro, L., 1560 Trattato di Acque, Perchacino, Padua.

Cuffaro, M., Riguzzi, F., Scrocca, D. Antonioli, F., Carminati, E., Livani, M., Doglioni, C., 2010. On the geodynamics of the northern Adriatic plate. Rendiconti. Fis. Acc. Lincei 21(Suppl 1), 253–279.

Fox-Kemper, B., Hewitt, H.T., Xiao, C., Aðalgeirsdóttir, G., Drijfhout, S.S., Edwards, T.L., Golledge, N.R., Hemer, M., Kopp, R.E., Krinner, G., Mix, A., Notz, D., Nowicki, S., Nurhati, I.S., Ruiz, L., Sallée, J.-B., Slangen, A.B.A., Yu, Y., 2021: Ocean, Cryosphere and Sea Level Change. In: Masson-Delmotte, V., Zhai, P., Pirani, A., Connors, S.L., Péan, C., Berger, S., Caud, N., Chen, Y., Goldfarb, L., Gomis, M.I., Huang, M., Leitzell, K., Lonnoy, E., Matthews, J.B.R., Maycock, T.K., Waterfield, T., Yelekçi, O., Yu, R., Zhou, B. (Eds.), Climate Change 2021: The Physical Science Basis. Contribution of Working Group I to the Sixth Assessment Report of the Intergovernmental Panel on Climate Change. Cambridge University Press, Cambridge, United Kingdom and New York, NY, USA, 1211–1362.

Karymbalis, E., 2010. Coastal Geomorphology, ION Publishing Group, p. 240.

Kent, D.V., Rio, D., Massari, F., Kukla, G., Lanci, L., 2002. Emergence of Venice during the Pleistocene. Quaternary Science Reviews, 21(14-15), 1719-1727.

Kolaiti, E., Simosi, A., Mourtzas, N., 2024. Archaeological sea level indicators in the Argolic Gulf since the 14th century AD: Bourtzi Fortress, Myloi Lernas and Mylos Beach in Agios Andreas. In: M. Xanthopoulou et al. (Eds), Archaeological Work in the Peloponnese 3, Proceedings of the 3rd International Scientific Meeting AWOP3, Kalamata, 2-5 June 2021, University of the Peloponnese, Kalamata, 837-853.

Kowalczyk, B.A., 2018. Canaletto1697-1768. p. 256.

Kowalczyk, B.A., 2016. Bellotto e Canaletto Lo stupore e la luce. p. 304.

Lionello, P., Nicholls, R.J., Umgiesser, G., Zanchettin, D., 2021. Venice Flooding and Sea Level: Past Evolution, Present Issues, and Future Projections (Introduction to the Special Issue). Nat. Hazards Earth Syst. Sci., 21, 2633–2641.

Mann, M.E., 2002. Little Ice Age, in: MacCracken, M.C., Perry, J.S. (Eds.), Encyclopedia of Global Environmental Change, Vol 1: The Earth system: physical and chemical dimensions of global environmental change, 504-509.

Mattei, G., Aucelli, P.P., Caporizzo, C., Rizzo, A., Pappone, G., 2020. New geomorphological and historical elements on morpho-evolutive trends and relative sea-level changes of Naples coast in the last 6000 years. Water, 12(9), 2651.

Rovere, A., Camuffo, D., Cerrone, C., 2024. Living on the water towards 2100. Fieldtric guide. Ca´ Foscari University of Venice. p. 26.

Smithers, S., 2011. Sea-level indicators. in: Hopley, D. (Ed.), Encyclopedia of modern coral reefs. Encyclopedia of earth sciences series. Springer, 978–991.

Temanza, T. 1761. Dissertazione sopra l'antichissimo territorio di Sant'Ilario nella diocesi di Olivolo. Pasquali, Venice.

Tosi, L., Teatini, P., Carbognin, L., Brancolini, G., 2009. Using high resolution data to reveal depth-dependent mechanisms that drive land subsidence: The Venice coast, Italy. Tectonophysics, 474(1-2), 271-284.

Tosi, L., Carbognin, L., Teatini, P., Strozzi, T., Wegmüller, U., 2002. Evidence of the present relative land stability of Venice, Italy, from land, sea, and space observations. Geophys. Res. Lett., 29, 3-1–3-4

Vacchi, M., Marriner, N., Morhange, C., Spada, G., Fontana, A., Rovere, A., 2016. Multiproxy assessment of Holocene relative sea-level changes in the western Mediterranean: Sea-level variability and improvements in the definition of the isostatic signal. Earth-Science Reviews, 155, 172-197.

Zanchettin, D., Bruni, S., Raicich, F., Lionello, P., Adloff, F., Androsov, A., Antonioli, F., Artale, V., Carminati, E., Ferrarin, C., et al., 2021. Sea-level rise in Venice: historic and future trends (review article). Nat. Hazards Earth Syst. Sci., 21, 2643–2678.

Zerefos, C.S., Gerogiannis, V.T., Balis, D., Zerefos, S.C., Kazantzidis, A., 2007. Atmospheric effects of volcanic eruptions as seen by famous artists and depicted in their paintings. Atmospheric Chemistry and Physics, 7, 4027–4042.

17th INTERNATIONAL CONGRESS of the Geological Society of Greece

BULLETIN OF THE GEOLOGICAL SOCIETY OF GREECE, SP. PUBL.

EXTENDED ABSTRACT 141

Challenges and Opportunities in the AI Era: Promoting Earth Science Education for Deaf and Hard of Hearing Students

Katheri M.[1], Koumoutsakou O.[1], Antonarakou A.[1]

(1) Department of Geology and Geoenvironment, Kapodistrian University of Athens, Ilisia, Greece, mar.katheri@hotmail.com

Introduction / Background

The formal education of Deaf and Hard of Hearing (DHH) students has a long and often controversial history, particularly in Earth Sciences. Despite the legal guarantee of equal education for DHH students, its practical implementation often lacks inclusivity. Many students, while physically present in the classroom, are academically and socially excluded due to deficiencies in the education system (Howerton-Fox & Falk, 2019), though these deficiencies may vary by region or institution. Considering inclusion, accessibility, and the greater representation of persons with disabilities in science and engineering fields (NCSES, 2023), including Earth Sciences, the need for redesigning Earth Science teaching at all educational levels becomes evident, especially in the new AI era.

The Challenges of DHH Students in Geosciences

DHH students are often discouraged from participating in Earth Science due to practical constraints and social biases (Connors, 2023). Fieldwork, which is a cornerstone of Geosciences (Whitmeyer & Mogk, 2009), presents significant difficulties. Challenges such as outdoor communication difficulties, insufficient educational materials, and the absence of sign language for specialized terms create significant barriers to equal participation.

At the same time, inclusive pedagogical approaches often omit deafness as a key factor, ignoring the need for tailored solutions. The responsibility for accommodation is often placed on DHH students, burdening them with additional stress and challenges (Carabajal *et al.*, 2017). The challenges faced by DHH students considering intersectionality (e.g., gender, ethnicity, socioeconomic status) may compound these challenges.

Assistive Technologies and Innovations

Today, technology is providing new opportunities to support DHH students. Tools such as Communication Access Real-time Translation (CART) and sign language interpreters improve communication (NAD, 2023). However, these tools often have limitations, such as incomplete coverage of specialized terms in Earth Sciences. Newer technologies like real-time AI-based sign language generation, tactile feedback devices, virtual and augmented reality education platforms, and AI tools and datasets reflect recent innovations (Kouremenos & Ntalianis, 2025; Hossain, 2024; Ulrich et al., 2024).

In addition, initiatives such as the Signing Earth Science Dictionary (SESD) offer access to approximately 750 Earth Science terms for DHH students (Vesel & Hurdich, 2014). Similar efforts are being extended to British Sign Language, with the addition of terms related to biodiversity and ecology. Thus, maintaining and expanding such dictionaries and similar efforts to address evolving terminology remains a challenge.

Innovative Pedagogical Methods

Virtual technologies provide unique teaching opportunities in Earth Sciences. Research projects, such as the use of virtual worlds, have demonstrated that virtual fieldwork can effectively simulate the experience of outdoor teaching (Allison & Miller, 2012) especially for students who might not have access to physical field experiences due to disabilities or other constraints. Moreover, devices such as the deformational sandbox demonstrate that hands-on learning can be effectively adapted for DHH students, enhancing their understanding of complex geological processes (Kahn *et al.,* 2013).

Fieldwork and Inclusive Education

Fieldwork remains a critical area for adaptation to support DHH students. Despite these barriers, educators have developed practices to improve accessibility in field experiences. Virtual field applications, while not a full replacement for the experience, offer significant support and learning opportunities (Guillaume *et al.,* 2023).

The Role of Inclusion in the Earth Sciences

Inclusion in geoscience is not only about DHH students' access to education but also about creating a more diverse and welcoming science environment. Research shows that the presence of minority faculty encourages students to remain in the field, fostering a sense of community (Dutt, 2020). Peer support networks, accessibility policies, and inclusive course design, also play a significant role in retention and fostering community.

Conclusions and Perspectives

Addressing the challenges DHH students face in geosciences requires a multi-dimensional approach. From the development of assistive technologies and customized pedagogies to the creation of inclusive learning environments, progress in this area is essential. An education system emphasizing intellectual abilities over physical limitations can unlock the full potential of DHH individuals and enrich Earth Sciences with diverse perspectives and ideas. In addition, wider social and professional barriers, including funding challenges, recruitment biases, and the need for more mentoring programs need to be taken seriously.

References

Allison, C. and Miller, A. (2012). Open virtual worlds for open learning. Higher Education Academy St. Andrews, UK.

Carabajal, I.G., Marshall, A.M., Atchison, C.L. (2017). A synthesis of instructional strategies in geoscience education literature that address barriers to inclusion for students with disabilities. Journal of Geoscience Education 65(4), 531–541, https://doi.org/10.5408/16-211.1.

Connors, I.C. (2023). Racial diversity in the Geosciences: Engaging community cultural wealth for success. J of Women & Minor. in Sc. and Eng. 29(2), 1-23.

Dutt, K. (2020). Race and racism in the geosciences. Nature Geoscience 13(1), 2–3, https://doi.org/10.1038/s41561-019-0519-z.

Guillaume, L., Laurent, V., Genge, M.J. (2023). Immersive and interactive three-dimensional virtual fieldwork: Assessing the student learning experience and value to improve inclusivity of geosciences degrees. Journal of Geoscience Education 71(4), 462–475, https://doi.org/10.1080/10899995.2023.2200361.

Hossain, S. (2024). Human AI Collaborative Framework to Aid in Computer Science Technical Sign Generation: Towards Enhancing Deaf and Hard Of Hearing Participation in Technical Higher Education. Thesis. Arizona State University.

Kahn, S., Feldman, A., Cooke, M.L. (2013). Signs of Autonomy: Facilitating Independence and Inquiry. Journal of Science Education for Students with Disabilities 17(1), 2.

Kouremenos, D., & Ntalianis, K. (2025). GLaM-Sign: Greek Language Multimodal Lip Reading with Integrated Sign Language Accessibility. https://arxiv.org/pdf/2501.05213 (retrieved 21/01/2025) https://doi.org/10.5281/zenodo.14610495

NAD, 2023. Position Statement on Inclusion. National Association of the Deaf, https://www.nad.org/about-us/positionstatements/position-statement-on-inclusion.

NCSES (2023). Diversity and STEM: Women, Minorities, and Persons with Disabilities. National Center for Science and Engineering Statistics. Special Report NSF 23-315, Alexandria, VA: National Science Foundation, https://ncses.nsf.gov/wmpd.

Ulrich, L., Carmassi, G., Garelli, P., Lo Presti, G., Ramondetti, G., Marullo, G., Innocente, C., Vezzetti, E. (2024). SIGNIFY: Leveraging Machine Learning and Gesture Recognition for Sign Language Teaching Through a Serious Game. *Future Internet* **2024**, *16*, 447. https://doi.org/10.3390/fi16120447

Vesel, J. and Hurdich, J. (2014). Signing Earth Science: Accommodations for Students Who Are Deaf or Hard of Hearing and Whose First Language Is Sign. In: Proceedings of American Geophysical Union, Fall Meeting 2014, abstract id: ED31I-04.

Whitmeyer, S. and Mogk, D. (2009). Geoscience field education: A recent resurgence. Transactions American Geophysical Union, Eos 90(43), 385–386, https://doi.org/10.1029/2009EO430001.

17th INTERNATIONAL CONGRESS of the Geological Society of Greece

BULLETIN OF THE GEOLOGICAL SOCIETY OF GREECE, SP. PUBL.

EXTENDED ABSTRACT 142

Preliminary results of displacements from the recent seismic and volcanic crisis in the Santorini Island complex, Greece

Katsafados I.[1,2], Anastasiou D.[2], Paraskevas M.[1,2], Tsakiri M.[2], Nomikou P.[3], Synolakis C.[4]

(1) Hellenic Military Geographical Service, john.katsafados@gmail.com
(2) National Technical University of Athens
(3) National and Kapodistrian University of Athens
(4)University of Southern California

Research Highlights

GNSS campaign measurements conducted in February 2025 reveal measurable displacements across the Santorini caldera, with patterns consistent with low-level magmatic deflation. Comparison with 2012 benchmark data confirms ongoing deformation and underscores both the value and the limitations of campaign-based observations relative to continuous GNSS monitoring.

Introduction

The Santorini Island complex, located in the southern Aegean Sea, is one of the most active volcanic regions in the Eastern Mediterranean. It forms part of the Hellenic Volcanic Arc and comprises several islands, including Thera (Santorini), Therasia, and Nea Kameni, which collectively outline a partially submerged caldera formed during the catastrophic Minoan eruption around 1600 BCE (Friedrich et al., 2006; Druitt et al., 1999). Volcanic activity in the region is driven by the subduction of the African plate beneath the Eurasian plate, resulting in both tectonic and magmatic processes that have shaped the morphology and evolution of the caldera (Nomikou et al., 2014; Pyle & Elliott, 2006).

In recent years, the Santorini complex has experienced a period of renewed geophysical unrest, marked by increased seismic activity, observed ground displacements, and subtle geochemical anomalies (Parks et al., 2012; Bagnardi et al., 2013). This ongoing activity—reminiscent of the 2011–2012 unrest episode—has raised concerns about the potential reactivation of the volcanic system. Early detection and monitoring of ground deformation are therefore essential for understanding subsurface processes and assessing potential volcanic hazards (Newhall et al., 2000).

This study presents preliminary results of ground displacements associated with the most recent seismic and volcanic activity in the Santorini Island complex. Our analysis is based on a combination of continuous GNSS (cGNSS) data from permanent stations established and maintained by various Institute, Universities and private companies and measurements from GNSS campaign surveys conducted at selected pillars of the National Triangulation Network of Greece, established and maintained by the Hellenic Military Geographical Service, across the island complex. By comparing recent observations with historical GNSS datasets, we detect and quantify ground deformation patterns related to the ongoing unrest. The aim is to identify spatial trends, evaluate the magnitude and direction of surface displacements, and explore possible links to underlying volcanic and tectonic processes. These results contribute to a better understanding of Santorini's geodynamic behavior and provide valuable input for hazard monitoring and risk assessment in the region.

Previous Measurements (2011–2012 Unrest)

During the period of increased volcanic unrest in the Santorini Island complex between 2011 and 2012, an extensive geodetic campaign was conducted to detect and quantify ground deformation. The network consisted of ten permanent GNSS stations established progressively across the islands, with dense spatial coverage especially after mid-2011 in response to the signs of volcanic reactivation. Key stations were operated by several institutions including the Dionysos Satellite Observatory of the NTUA, the University of Patras, the University of Oxford, UNAVCO, and the University of Athens. To enhance spatial resolution, the permanent network was supplemented by 19 non-permanent (campaign) stations, measured during two epochs: the first in September 2011 and the second between January and early October 2012. These campaigns allowed for the detection of short-term displacements by comparing coordinates between the two time periods. GNSS data were processed using the Gamit/Globk software package (10.4), with results validated against independent solutions produced using the Bernese software (Version 5.0) at the Dionysos Satellite Observatory (Dimitriou, 2013).

The analysis revealed measurable displacements across the caldera, particularly evident in the radial outward motion and uplift consistent with magmatic inflation processes. Linear velocities and coordinate time series were derived for both campaign and permanent stations, referenced to the ITRF08/IGS08 Reference Frame (Altamimi et al., 2012), using IGS stations to ensure geodetic consistency.

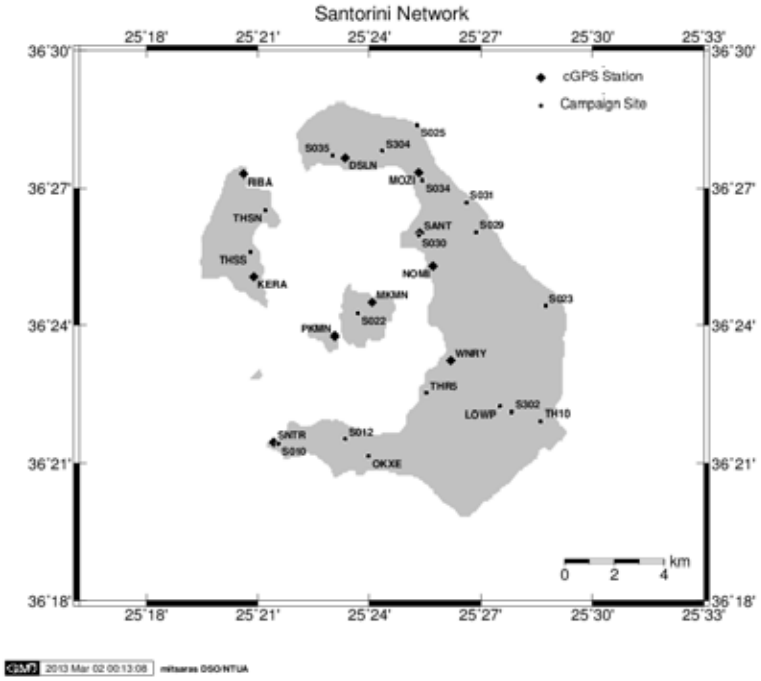

Figure 1. Santorini GNSS Network (Dimitriou, 2013)

3. Recent GNSS Campaign

In the framework of the current study, GNSS measurements were carried out at 16 benchmarks that had originally been observed during the 2012 measurement campaign (Fig. 2). The 2025 observations were conducted using dual-frequency GNSS receivers, with each session lasting at least two hours to ensure high-precision positioning suitable for geodetic applications. The measurement campaign was conducted over the period 6 – 13 February 2025, a period of time during which the seismic phenomenon was in full swing. The raw data were processed using the Bernese GNSS Software (Version 5.2) via the AUSPOS service, which delivers precise coordinate solutions in the ITRF2020 reference frame (Table 1 & 2).

However, the coordinates of the benchmarks measured at 2012 were originally computed in the IGS08 reference frame. To allow a reliable and rigorous comparison between the two epochs, a dedicated transformation and alignment procedure was implemented to bring both datasets into a common reference system and epoch.

Table 1 – GNSS Data processing parameters

Processing – Adjustment strategy	Phase preprocessing is undertaken in a baseline-by-baseline mode using triple-difference and weighted least-squares algorithm.
Reference Stations	11 IGS permanent GNSS stations
Tidal displacements	Solid earth tidal: IERS Conventions 2010 Ocean tide loading: Not applied
Tropospheric Mapping Function	DRY/WET - GMF
Orbits	IGS precise orbits
Data Windowing	7^0 elevation mask
Ambiguity resolution	Ambiguities are resolved using the Code-Based strategy for 200-6000km baselines, the Phase-Based L5/L3 strategy for 20-200km, the Quasi-Ionosphere-Free (QIF) strategy for 20-2000km and the Direct L1/L2 strategy for 0-20km.

Figure 2 - GNSS campaign (February 2025)

Table 2 - Preliminary results of GNSS processing (m)

id	X	Y	Z	σx	σy	σz
S012	4645987.168	2205009.115	3760475.682	0.007	0.008	0.026
S022	4642998.614	2204148.098	3764501.625	0.009	0.007	0.024
S023	4639536.759	2210862.974	3764705.381	0.009	0.007	0.025
S025	4637854.918	2204331.020	3770555.816	0.006	0.005	0.016
S029	4639171.945	2207601.822	3767093.660	0.01	0.008	0.03
S030	4640442.048	2205642.223	3767168.724	0.007	0.007	0.026
S031	4638679.806	2206932.288	3768055.825	0.008	0.007	0.03
S034	4639145.943	2205182.794	3768936.203	0.01	0.006	0.024
S035	4640030.934	2201621.482	3769625.629	0.007	0.007	0.029
S302	4642794.671	2210899.110	3761560.174	0.008	0.007	0.022
S304	4639217.564	2203433.204	3769888.083	0.008	0.006	0.025
TH10	4642339.911	2211981.450	3761145.342	0.008	0.006	0.021
THR5	4643592.806	2207486.308	3761951.473	0.006	0.005	0.021
THSN	4642430.113	2199760.327	3767915.240	0.019	0.008	0.039
THSS	4643652.696	2199681.385	3766578.974	0.006	0.006	0.019
OKXE	4645876.061	2205981.162	3759846.953	0.009	0.008	0.027

3.1 Methods of data analysis

To achieve compatibility between the two datasets, the 2012 coordinates in IGS08 were first transformed into the ITRF2020 reference frame using the official seven-parameter Helmert transformation, including both positional offsets and their associated rates (Altamimi et al., 2023). Additionally, to ensure that the coordinate comparisons reflect only the true displacements between the two measurement epochs, both datasets were referred to a common epoch. This step is critical because the 2012 and 2025 observations are separated by more than a decade, during which secular tectonic motion could contribute significantly to the apparent coordinate differences. For this purpose, the velocity field of Bitharis et al. (2016)—which provides high-resolution horizontal and vertical velocities for the Hellenic region based on long-term GNSS observations—was used to propagate the transformed coordinates forward in time to the epoch of the 2025 campaign. This allowed the separation of long-term tectonic trends from potential volcanic or local ground deformation signals between the two periods (Figure 3).

Once the coordinates of the campaign of 2012 were transformed into the ITRF2020 frame and propagated to the epoch of the 2025 measurements, the coordinate differences between the two epochs were computed for each benchmark. These differences were initially expressed in geocentric Cartesian coordinates (X, Y, Z), but for geophysical interpretation, they were further transformed into topocentric displacements, in the local North, East, Up (NEU) reference frame.

This transformation allows a clearer visualization and analysis of horizontal and vertical displacements relative to each station's location on the Earth's surface. The NEU components were computed using each station's geodetic latitude and longitude, following standard local frame rotation techniques. This step enables the detection of meaningful surface movements such as uplift, subsidence, or horizontal spreading that may be associated with magmatic or tectonic processes in the Santorini volcanic complex.

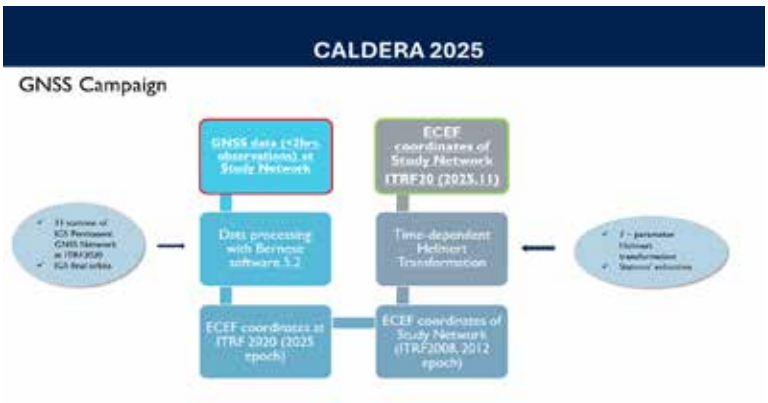

Figure 3 - Schema of the methodology for the data analysis

3.2 Preliminary Results

The comparison between the two GNSS campaign data revealed measurable displacements at the benchmarks across the Santorini Island complex. The displacements are presented both in terms of horizontal (East–North) and vertical (Up) components. The horizontal displacement vectors exhibit a radial pattern centered around the north part of the caldera, with the largest motions observed at stations located near Nea Kameni and the northern part of the island. The magnitude of horizontal displacements generally ranges from 2.5 cm to over 9 cm, suggesting a subtle but coherent deformation field (Figure 4).

Vertical displacements also show spatial variability, with most of the stations inside the caldera experiencing subsidence of up to 15 cm, while peripheral stations remain stable or exhibit minor uplift. These patterns are consistent with low-level deflation of a magmatic source beneath the caldera (Figure 5).

In addition to the comparison between the 2012 and 2025 campaigns, a short-term repeatability test was conducted to assess the internal consistency and reliability of the recent GNSS measurements. Specifically, three benchmarks were successfully re-measured with a time difference of only five days during the February 2025 campaign. These repeat measurements refer to the same reference frame (ITRF2020) and the same epoch, thus eliminating the need for any transformations or epoch propagation. Although limited in number, these observations provide a more detailed snapshot of the ongoing deformation, free from long-term tectonic signals or processing-related uncertainties. The high internal consistency between the repeated measurements enhances confidence in the reliability of the broader displacement patterns observed in the full network.

Figure 4 - Horizontal Displacements (2012-2025)

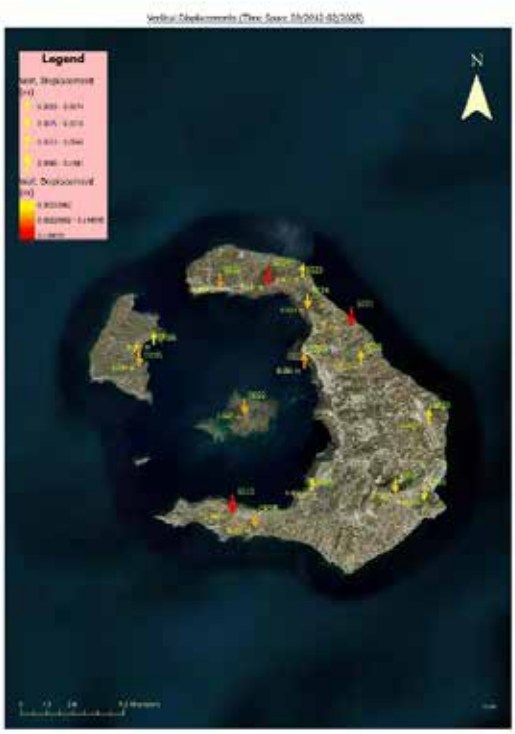

Figure 5 - Vertical Displacements (2012-2025)

The displacements derived from these short-term measurements provide an internally consistent snapshot of ongoing deformation. The horizontal displacements at these three sites range between 2.4 cm and 6.3 cm, indicating significant surface motion over just a few days. In the vertical component, the measurements revealed distinct vertical behavior: no vertical displacement at the caldera center, uplift at the southwestern station, and subsidence at the northeastern station. This spatial variation suggests that deformation is not driven by a simple, symmetric source. Instead, it may reflect a heterogeneous deflation process, possibly involving lateral magma migration or localized hydrothermal activity. The absence of uplift at the caldera center further supports the interpretation of a deflating or stabilizing magmatic system with distributed or compartmentalized subsurface dynamics. Similar patterns of spatially variable deformation were observed during the 2011–2012 unrest and attributed to complex pressurization processes within a multi-level magmatic system (Parks et al., 2012).

Figure 6 - Horizontal Displacements (2025)

Figure 7 - Vertical Displacements (2025)

4 cGNSS station analysis

The data described above were analyzed using the Bernese GNSS Software (v. 5.2) (Dach et al., 2015). Both GPS and
GLONASS observations were used when available. IGS20 was used as the frame of reference, using a set of 19 IGS stations for alignment. CODE final products were incorporated in the analysis, consistent with the frame of choice. The key parameter of interest was station coordinates (Anastasiou et al., 2024).

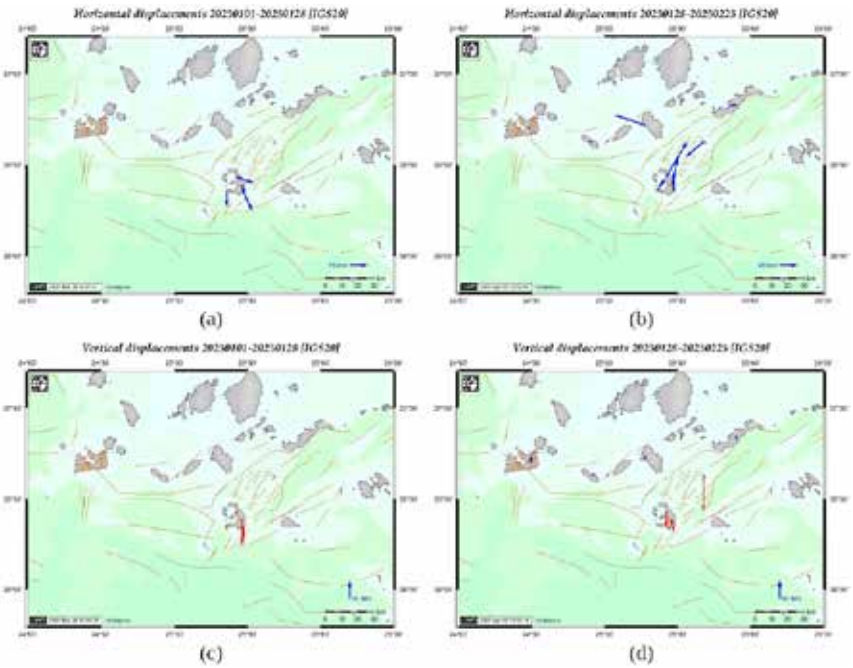

Figure 7 - Horizontal Displacements and vertical displacement of cGNSS stations for two different phases a,c: 01.01.2025-28.01.2025 and b,d: 28.01.2025-25.02.2025

Position time series analysis depicts the different movement of the stations that occurred toward the end of January 2025. Figure 7 illustrates the station displacements in different phases. In Figure 7a, a radial motion of the stations is observed up until the end of January, while in Figure 7b, the stations on Santorini Island are moving in a northeastward direction. A southwestward displacement is observed for the islet of Anydros, and displacements are also estimated on the islands of Amorgos and Ios.

Conclusions

This study presents preliminary results of ground deformation in the Santorini volcanic complex based on a comparison between GNSS campaign measurements from February 2025 and a previous geodetic campaign conducted during the 2011–2012 volcanic unrest. The data analysis, following rigorous transformations and epoch adjustments, revealed coherent displacements in both horizontal and vertical directions, indicating ongoing low-level deflation of a magmatic source beneath the caldera.

While the campaign-based measurements provided valuable spatial coverage and enabled the detection of long-term displacements, the approach has certain inherent limitations when compared to continuous GNSS (cGNSS) monitoring. Continuous GNSS stations offer high temporal resolution, allowing for the detection of short-term deformation transients, long-term trends, and episodic events that may be missed during isolated campaign observations. Moreover, cGNSS data are less affected by field-related errors such as antenna setup inconsistencies, multipath, or variations in session duration—factors that can introduce uncertainty into campaign-based results.

In contrast, the campaign method, while logistically simpler and cost-effective, captures only snapshots in time, making it less suitable for detecting subtle temporal variations or dynamic deformation processes. Nevertheless, it remains a useful tool for benchmarking long-term change, especially when co-located with cGNSS stations for cross-validation.

Future work should aim to integrate campaign results with continuous time series and InSAR data, enabling a more complete and time-resolved picture of the geodynamic processes at Santorini. Expansion of the permanent GNSS network and reoccupation of additional historical benchmarks will further improve spatial resolution and strengthen long-term volcanic monitoring in the region.

Acknowledgements

We thank the GNSS data providers NOA, NKUA, University of Patra, Hellenic Cadastre, Metrica, and JGC. These institutes and private companies provide RINEX data of permanent stations free of charge.

References

Altamimi, Z., Collilieux, X., & Métivier, L. (2011). ITRF2008: An improved solution of the International Terrestrial Reference Frame. Journal of Geodesy, 85(8), 457–473. https://doi.org/10.1007/s00190-011-0444-4

Altamimi, Z., Rebischung, P., Métivier, L., & Collilieux, X. (2023). ITRF2020: An improved realization of the International Terrestrial Reference Frame accounting for non-linear station motions. Journal of Geodesy, 97(2), 23. https://doi.org/10.1007/s00190-023-01739-2

Anastasiou D., Papanikolaou X., Serelis G., Tsakiri M. (2024). Velocity field estimated from HEPOS permanent GNSS network in Greece, preliminary results. EGU General Assembly 2024, https://doi.org/10.5194/egusphere-egu24-17390

Bagnardi, M., Hooper, A., & Wright, T. J. (2013). Revisiting the 2011–2012 unrest at Santorini: New insights from InSAR and GPS observations. Geophysical Research Letters, 40(19), 4954–4958. https://doi.org/10.1002/grl.50952

Bitharis, S., Fotiou, A., Pikridas, C., & Rossikopoulos, D. (2016). Velocity field and crustal deformation of the Hellenic area derived from GPS data (1993–2014). Journal of Geodynamics, 97, 1–16. https://doi.org/10.1016/j.jog.2016.03.003

Dimitriou, D. (2013). Processing of satellite geodetic observations in Santorini [Diploma thesis, National Technical University of Athens]. NTUA Library. (In Greek)

Dach, R., Lutz, P. Walser, P. Fridez (Eds); 2015: Bernese GNSS Software Version 5.2. User manual, Astronomical Institute, University of Bern, Bern Open Publishing.DOI: 10.7892/boris.72297; ISBN: 978-3-906813-05-9.

Druitt, T. H., Edwards, L., Mellors, R. M., Pyle, D. M., Sparks, R. S. J., Lanphere, M., & Collier, L. (1999). Santorini volcano. Geological Society, London, Memoirs, 19(1), 13–18. https://doi.org/10.1144/GSL.MEM.1999.019.01.02

Friedrich, W. L., Kromer, B., Friedrich, M., Heinemeier, J., Pfeiffer, T., & Talamo, S. (2006). Santorini eruption radiocarbon dated to 1627–1600 B.C. Science, 312(5773), 548. https://doi.org/10.1126/science.1125087

Newhall, C. G., & Punongbayan, R. S. (Eds.). (2000). Fire and mud: Eruptions and lahars of Mount Pinatubo, Philippines. University of Washington Press.

Nomikou, P., Papanikolaou, D., Parks, M. M., Pyle, D. M., Mather, T. A., Carey, S., & Livanos, I. (2014). The emergence and growth of a submarine volcano: The Kameni Islands, Santorini (Greece). GeoResJ, 1–2, 8–18. https://doi.org/10.1016/j.grj.2014.02.002

Parks, M. M., Biggs, J., England, P. C., Mather, T. A., Nomikou, P., Palamartchouk, K., ... & Pyle, D. M. (2012). Evolution of Santorini Volcano dominated by episodic and rapid fluxes of melt from depth. Nature Geoscience, 5(10), 749–754. https://doi.org/10.1038/ngeo1562

Pyle, D. M., & Elliott, J. R. (2006). Quantitative morphology, recent evolution, and future activity of the Kameni Islands volcano, Santorini, Greece. Geomorphology, 73(3–4), 242–254. https://doi.org/10.1016/j.geomorph.2005.07.009

17th INTERNATIONAL CONGRESS of the Geological Society of Greece

BULLETIN OF THE GEOLOGICAL SOCIETY OF GREECE, SP. PUBL.

EXTENDED ABSTRACT 143

SANTORY shallow seafloor observatory: First time series data from an active submarine volcano

Katsigera A.[1], Nomikou P.[1], Polymenakou P.[2], Sciré Scappuzzo S.[3], Lazzaro G.[3], Mallios A.[4], Ntouskos V.[5], Spanos S.[5], Antoniou C.[5], Rizzo A.L.[6], Longo M.[3], Escartin J.[7], Karantzalos K.[5], D Alessandro W.[3], Heimburger L.[8], Kilias S[1], Mertzimekis T[1], Grassa F.[3], Lampridou D.[1], Anagnostou E.[1]

(1) National and Kapodistrian University of Athens, Athens, Greece, evinom@geol.uoa.gr (2) Hellenic Centre for Marine Research, Heraklion, Greece (3) Istituto Nazionale di Geofisica e Vulcanologia, Sezione di Palermo, Palermo, Italy (4) Ploa Technology Consultants S.L, Girona, Spain (5) National Technical University of Athens, Athens, Greece (6) University of Milano-Bicocca, Milano, Italy (7) École Normale Supérieure, Paris Sciences Letters (PSL) University, Paris, France (8) Aix-Marseille-University, Marseille, France

Managing volcanic risk encompasses a multifaceted and crucial field, aimed at reducing the hazards posed by volcanic eruptions to human life, infrastructure, and the surrounding environment. This endeavor includes preparedness planning, monitoring, and responsive actions, with continuous monitoring of volcanic activity using state-of-the-art technology and geophysical tools being the first and most essential step (Katsigera et al., 2024).

SANTORY is a state-of-the-art project aiming at submarine volcanic hazard monitoring in the Aegean Sea. Focused on the Kolumbo submarine volcano NE of Santorini Island, this cutting-edge observatory combines advanced imaging, geophysical and geochemical measurements, and real-time monitoring technologies to address one of the region's most important volcanic threats (Nomikou et al., 2022).

For the operation of the observatory, three oceanographic cruises were conducted, during which specialized scientific instruments were deployed inside the crater for several months (Figure 1), later retrieved to collect data, and subsequently re-deployed. These instruments included: the SANTORY underwater observatory, which comprised sensors for collecting acoustic data, temperature (T°C), CO_2, H_2S, O_2, pressure, electrical conductivity (EC), pH, and turbidity; tilt current meters for measuring marine currents within the crater; specialized thermometers for monitoring temperature changes in the polymetallic chimneys of the hydrothermal field; optical cameras positioned in front of active polymetallic chimneys to record hydrothermal fluid flow; and advanced underwater recording stations for measuring physical parameters in water, such as turbidity, temperature, conductivity, pressure, and oxygen levels. Additionally, the ROV was equipped with the following instruments for real-time data collection: a multispectral and stereo camera ("THEIA") for capturing the texture of the seafloor with multispectral data; the gSniffer device for real-time γ-radiation measurements; the γ-radiation imager ("SUGI") for real-time γ-radiation imaging; and a UV camera ("CHERI") for detecting Cherenkov radiation, marking a global first in underwater applications (Figure 2).

Over the past two years, SANTORY has provided unprecedented insights into Kolumbo's geological dynamics and volcanic activity. High-resolution 3D mapping revealed steep slopes, mass-wasting deposits, and hydrothermal vent fields, critical for assessing seafloor instability and potential eruption risks. Novel hyperspectral imaging and autonomous video systems have captured persistent vent activity, bubbling plumes, and environmental changes, thus providing the most complete assessment of hydrothermal processes to date and establishing a baseline for potential tracking of underlying volcanic processes.

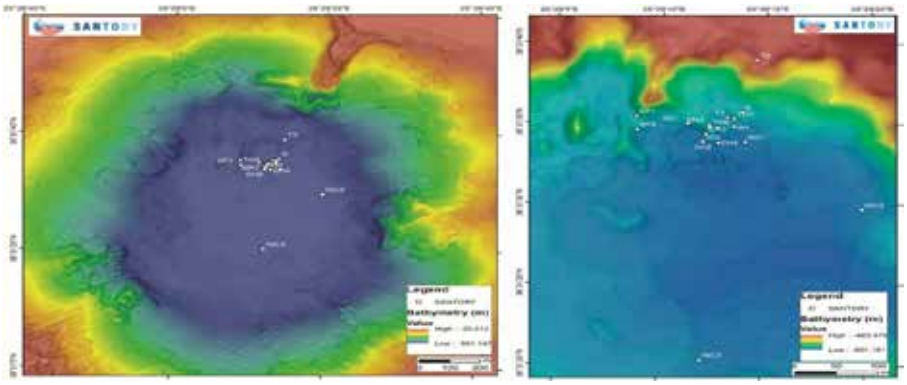

Figure 1. Bathymetry map of Kolumbo crater. Bathymetric data were collected by GEOMAR's autonomous underwater vehicle (AUV) Abyss during mission POS 510 (Hannington et al, 2018). The points indicate the location of the SANTORY observatory and its instruments along the hydrothermal vent field.

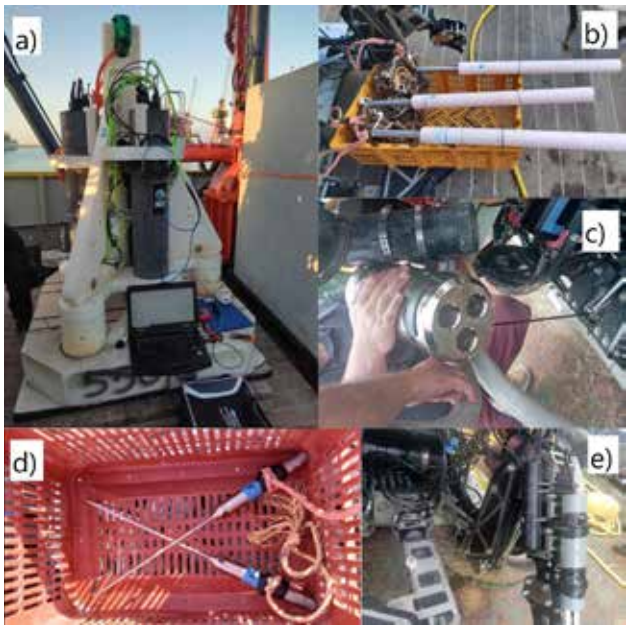

Figure 2. Photographs showing a) the SANTORY observatory, b) The tilt current meters of SANTORY placed in the Kolumbo crater, c) the multispectra and stereo camera "THEIA", d) the sensitive high-temperature thermometers and e) gSniffer for real-time γ-radiation measurements, conducted for the first time on a global scale.

Autonomous sensors deployed on the crater floor have been monitoring hydrothermal outflow temperature, pressure, and chemistry of fluids; these parameters will help quantify chemical fluxes, and reveal periodic variations driven by tides, in addition to magmatic activity. Datasets revealing these hydrothermal fluctuations may thus be critical in detecting precursor signals of volcanic unrest (e.g., changes in subsurface permeability, magmatic degassing). Chemical and isotopic analyses of hydrothermal fluids have revealed the degassing of CO_2-rich fluids characterized by a mantle-like 3He/4He signature. These findings highlight Kolumbo's potential for hazardous eruptions and its classification as a high-risk volcanic system.

Through the program, innovative results emerged, highlighting the uniqueness of the Kolumbo submarine volcano. Acoustic data collected every 30 minutes included one-minute recordings that revealed local hydrothermal events and bubble activity related to CO2 release in the 4000-8000 Hz range (Figure 3). Algorithms were developed to differentiate hydrothermal noise from environmental background noise, identifying bubble radii primarily in the range of 0.20-0.54 mm. Persistent and active bubble activity was observed within the hydrothermal field, with high temperature recordings (232°C) inside hydrothermal chimneys. Local hydrothermal events and fluid dynamics were identified, showing synchronized variations and anomalies in current meters, significant cooling phenomena, and high-velocity currents regulated by tidal forces.

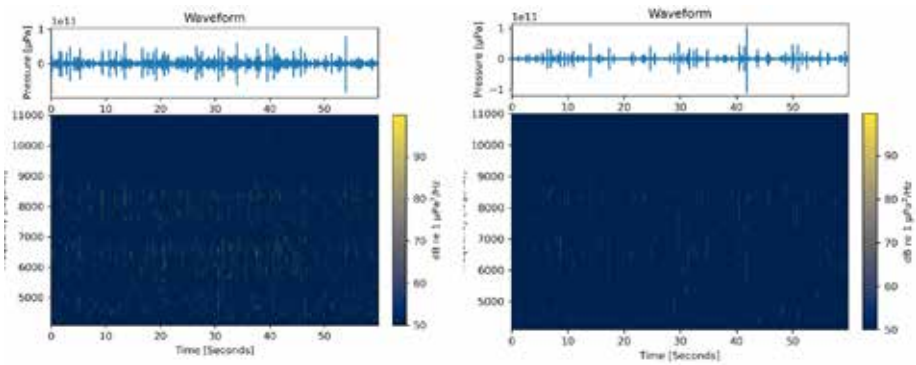

Figure 3. Bubble activity recording from the SANTORY observatory. Bubble activity was detected in the range of 4000-8000 Hz. Due to the presence of ambient noise overlapping the same band, a specialized algorithm was developed to better isolate bubble noise events.

Geochemical analysis confirmed acidic and slightly reducing conditions on the crater floor, helium isotopic composition indicating mixing of atmospheric and magmatic sources, and high concentrations of mercury (Hg) and methylmercury (MeHg) pointing to potential natural pollution. CO2 concentrations were extremely high (96%). Water samples collected at various depths showed anomalies in magmatic/geothermal gases, while trace elements such as Mn, Cs, and Hg exhibited significant deviations. A pH decrease above active chimneys was observed between December 2022 and October 2023, with the lowest value recorded during the last expedition (pH=5.33; 10/2023).
For the first time, natural radioactivity data were recorded within the Kolumbo hydrothermal field. The typical radioactivity measurement rate recorded away from the seafloor and known hydrothermal fields ranges around 1–2 counts per second. In contrast, radioactivity near the hydrothermal chimneys of Kolumbo reaches an impressive level, approximately three orders of magnitude higher, with a maximum of 996 counts per second (Figure 4).

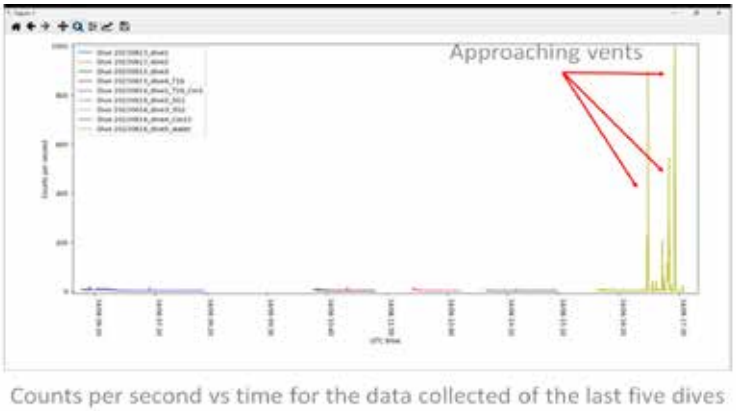

Figure 4. Radioactivity measurements inside the Kolumbo crater. Radioactivity near the hydrothermal chimneys reaches an impressive level, approximately three orders of magnitude higher, with a maximum of 996 counts per second.

Additionally, isolation of microorganisms from Kolumbo's extreme environment was achieved, where these microorganisms are of particular interest for biotechnological applications as they possess unique mechanisms for adapting to extreme conditions. Microbial data also unveiled diverse communities thriving in hydrothermal vent systems, offering insights into their metabolic pathways and resilience mechanisms. Metagenomic analyses uncovered new information about the carbon and methane cycles, which directly impact our planet's climate.
The project results provide valuable information for assessing volcanic hazards, contributing to the protection of the region from natural disasters, safeguarding human lives, and supporting the local economy. SANTORY is more than a research project—it is an initiative for developing a protocol for volcanic hazard mitigation that can be extrapolated to other submarine systems. By integrating cutting-edge technologies and multidisciplinary expertise, the project delivers actionable insights to improve early warning systems and protect vulnerable coastal communities. SANTORY sets a new benchmark in safeguarding against submarine volcanic threats.
All scientific data are accessible through the SANTORY Open Data Hub platform, available to both the residents of the Municipality of Thira and the scientific community. https://santory-open-data-hub-nom.hub.arcgis.com/

Acknowledgements
We are thankful to the International Ocean Discovery Program (IODP), the technical staff of the JOIDES Resolution, and all of the shipboard personnel for a great expedition. We also thank the member organizations of IODP for financial aid, and the Municipality of Thera for help in preparing for the expedition.

References
Katsigera, A., Nomikou, P., & Pavlopoulos, K. (2024). A Preliminary Hazard Assessment of Kolumbo Volcano (Santorini, Greece). GeoHazards, 5(3), 816-832. https://doi.org/10.3390/geohazards5030041
Nomikou P, Polymenakou PN, Rizzo AL, Petersen S, Hannington M, Kilias SP, Papanikolaou D, Escartin J, Karantzalos K, Mertzimekis TJ, Antoniou V, Krokos M, Grammatikopoulos L, Italiano F, Caruso CG, Lazzaro G, Longo M, Scire´ Scappuzzo S, D'Alessandro W, Grassa F, Bejelou K, Lampridou D, Katsigera A and Dura A (2022) SANTORY: SANTORini's Seafloor Volcanic ObservatorY. Front. Mar. Sci. 9:796376. doi: 10.3389/fmars.2022.796376
Hannington, M. D. (2018). RV POSEIDON Fahrtbericht/Cruise Report POS510-ANYDROS: Rifting and Hydrothermal Activity in the Cyclades Back-Arc Basin, Catania (Italy)–Heraklion (Greece) 06.03.-29.03. 2017.

17th INTERNATIONAL CONGRESS of the Geological Society of Greece

BULLETIN OF THE GEOLOGICAL SOCIETY OF GREECE, SP. PUBL.

EXTENDED ABSTRACT 144

Flash drought assessment: insights from Lesvos island, Greece

Katsora, C.[1], Leivadiotis, E.[2], Tzoraki, O. [1], Papadopoulou, N.[1]
(1) University of the Aegean, Mytilini, Lesvos, Greece, geoha23008@geo.aegean.gr, ckatsora@gmail.com
(2) University of Thessaly, Volos, Greece

Traditional drought definitions characterize them as prolonged periods of below-average precipitation, resulting in gradual soil moisture depletion (Wilhite & Glantz, 1985). However, the emergence of flash droughts (Christian et al., 2021), characterized by rapid onset and intensification, challenges this traditional view. While a universally accepted definition remains elusive, key characteristics include rapid soil moisture depletion, often within days or weeks, and significant impacts on agriculture, livestock, and water resources (Oetkin et al., 2018).

Effective flash drought monitoring is crucial for early warning systems and mitigation efforts (Pakkasagi et al., 2023). Monitoring techniques (Lisonbee et al., 2021) encompass satellite remote sensing for soil moisture, vegetation health, and precipitation; ground-based observations from weather stations and soil moisture networks; meteorological models for forecasting; and drought indices such as the Standardized Precipitation Index (SPI) (McKee, 1993), the Evaporative Demand Drought Index (EDDI) (Li et al., 2024), and the Standardized Precipitation Evapotranspiration Index (SPEI) (Spinani et al., 2017).

This study investigates historical flash drought occurrences on Lesvos island (Figure 1a), Greece, an island characterized by a hot-summer Mediterranean climate (Csa), that experiences significant seasonal and spatial rainfall variability, high temperature oscillations, and an average annual temperature of 17.78 °C. The island exhibits diverse vegetation types, reflecting its natural environment and historical agricultural practices (Figure 1b), which can influence vulnerability to flash drought events.

The historical flash drought events have been identified by employing two indices, requiring minimal datasets while yielding reliable results: the Standardized Precipitation Evapotranspiration Index (SPEI) and Soil Moisture (SM).

Figure 2 provides a graphical illustration of the methodology employed for FD identification using the SPEI. This represents a simple climatic water balance (i.e. difference between precipitation and potential evapotranspiration (PET). Meteorological data, comprising precipitation and temperature records from the Agia Paraskevi, Akrasi, and Sigri stations (Figure 1a), were analyzed using R scripts to identify historical flash drought events. This analysis identified forty flash drought events within the past 15 years (Figure 3), with a peak occurrence between March and June (Figure 4a) and an average duration of approximately eight pentads (Figure 4b). The years 2018 and 2012 experienced the most intense (Figure 4c) and severe (Figure 4d) flash drought events within the northeast and north regions, respectively.

Hourly soil moisture data from the ERA5 reanalysis dataset (1950-2024) were used to evaluate the spatial extent, frequency, magnitude, and intensity of flash drought events across Lesvos island. Following the methodology outlined in Figure 5, the results show a higher frequency of flash droughts in the northern part of the island (Figure 6a). The most severe events, characterized by higher magnitude and intensity (graphically presented as percentages), were also observed in the north-northeastern region (Figure 6b,c).

Given the success of this methodology, which integrates meteorological data (precipitation and temperature) with satellite-derived soil moisture, it has the potential for application in other Mediterranean regions with similar climatic characteristics. This approach can be valuable for identifying flash drought occurrences, assessing associated risks, and developing effective mitigation and adaptation plans.

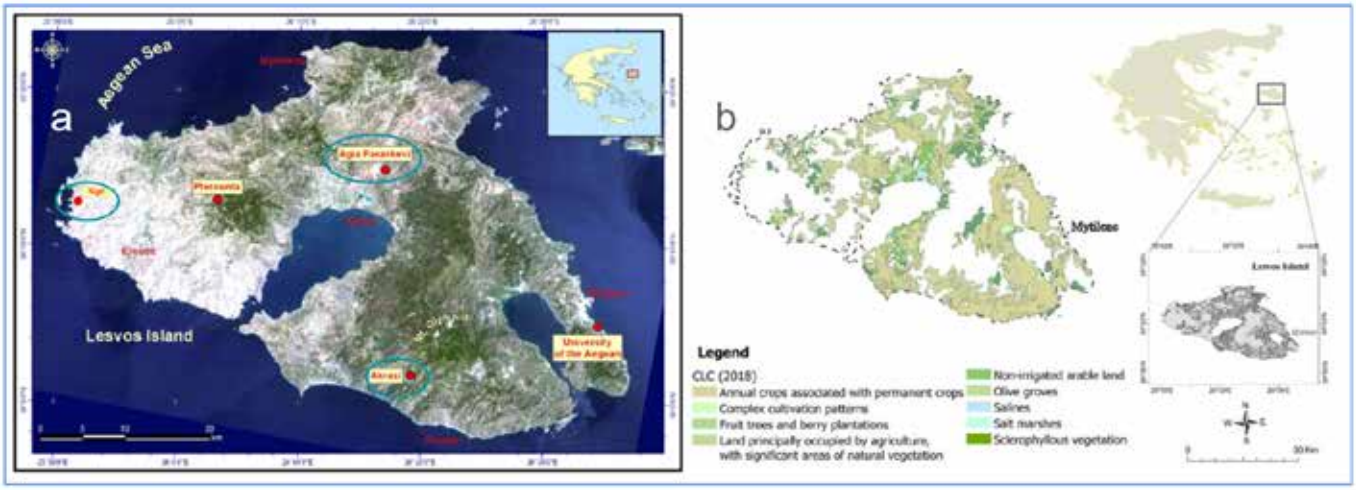

Figure 1: a. Area of interest with available meteorological stations, b. Vegetation types in Lesvos (Palaiologou *et al*., 2012)

Step 1

Prepare data (precipitation, maximum temperature and minimum temperature):

- remove missing values,
- define the analysis period,
- aggregate the daily data into pentads (five-day periods).

Step 2

Calculate SPEI for each pentad:

- calculate potential evapotraspiration (PET), using Thornthwaite method,
- compute the water balance as the difference between precipitation and PET (Precipitation - PET).

Step 3

Identify flash drought events when SM value falls between the 40th and 20th percentile, with event durations up to 8 pentads (40 days):

- exclude events shorter than 4 weeks from further analysis,
- focus on detecting valid endpoints of FD events that meet the defined criteria,
- remove overlapping onset-endpoint pairs to ensure independent event identification.

Step 4

Calculate flash drought characteristics:

- Frequency: Calculate the total frequency of the FD events,
- Duration: calculate the duration of each FD event, as the absolute value between the start and end pentad, divided by 5 (expressed in days),
- Magnitude: calculate the magnitude of each FD events as the absolute difference between the endpoint and the SPEI value at the onset,
- Intensity, calculate the intensity of each FD event by dividing the magnitude by the duration.

Figure 2: Methodology for identifying flash droughts (based on SPEI)

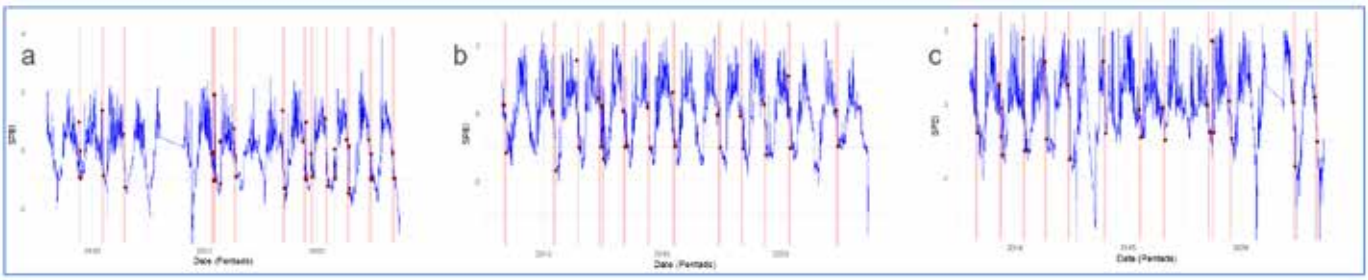

Figure 3: Identification of flash droughts events (based on SPEI), in a. Agia Paraskevi, b. Akrasi and c. Sigri

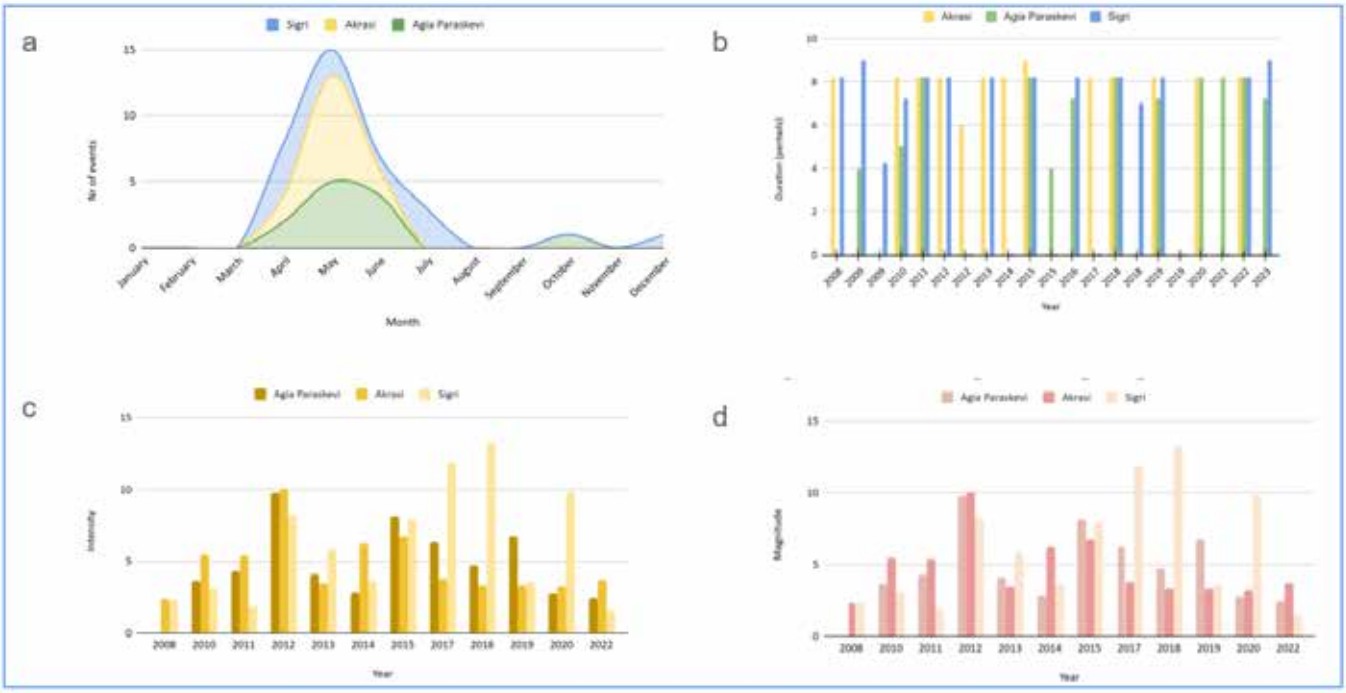

Figure 4: a. Seasonality, b. Duration in pentads, c.Intensity and d. Magnitude of flash droughts (based on SPEI)

Step 1

Prepare Soil Moisture (SM) data (volumetric soil water layer 1, volumetric soil water layer 2, volumetric soil water layer 3, volumetric soil water layer 4):

- remove missing values,
- define the analysis period,
- aggregate the hourly data into daily
- aggregate the daily data into pentads (five-day periods).

Step 2

Calculate percentiles of SM and define the 40th and 20th percentiles

Step 3

Identify flash drought events when SM value falls between the 40th and 20th percentile, with event durations up to 8 pentads (40 days):

- exclude events shorter than 4 weeks from further analysis,
- focus on detecting valid endpoints of FD events that meet the defined criteria,
- remove overlapping onset-endpoint pairs to ensure independent event identification.

Step 4

Calculate for the identified flash drought events the characteristics:

- Duration
- Magnitude
- Intensity
- Frequency

Figure 5: Methodology for identifying flash droughts (based on SM)

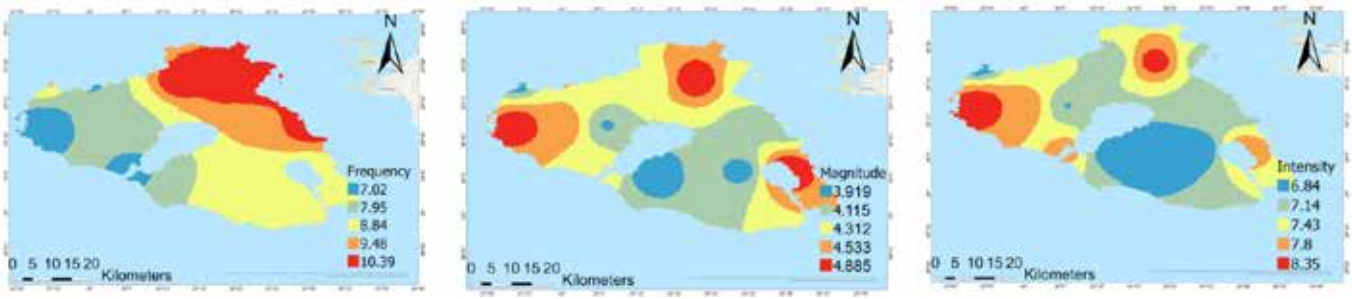

Figure 6: Flash droughts frequency, magnitude and intensity (based on Soil Moisture)

References

Christian, J.I., Basara, J.B., Hunt, E.D., Otkin, J. A., Furtado, J.C., Mishra, V., Xiao, X., & Randall, R.M., 2021. Global distribution, trends, and drivers of flash drought occurrence. Nature Communication 12, 6330. https://doi.org/10.1038/s41467-021-26692-z.

Li, H., Choy, S., Zaminpardaz, S., Wang, X., Liang, H., Zhang, K., 2024. Flash drought monitoring using diurnal-provided evaporative demand drought index, Journal of Hydrology, Volume 633, 130961, ISSN 0022-1694, https://doi.org/10.1016/j.jhydrol.2024.130961.

Lisonbee, J., Woloszyn, M.,Skumanich, M., 2021: Making sense of flash drought: Definitions, indicators, and where we go from here. Journal of Applied and Service Climatology, (1), 1–19, https://doi.org/10.46275/JOASC.2021.02.001.

McKee, T.B., Doesken, N.J., Kleist J., 1993. The relationship of drought frequency and duration to time scales. In: Paper Presented at Eighth Conference on Applied Climatology, American Meteorological Society, Anaheim, CA.

Otkin, J. A., Svoboda, M., Hunt, E. D., Ford, T. W., Anderson, M. C., Hain, C., & Basara, J. B., 2018. Flash droughts: A review and assessment of the challenges imposed by rapid-onset droughts in the United States. *Bulletin of the American Meteorological Society*, *99*(5), 911-919.

Palaiologou, P., Kalabokidis, K., Haralambopoulos, D., Feidas, H., Polatidis, H., 2011. Wind characteristics and mapping for power production in the Island of Lesvos, Greece. Computers & Geosciences 37 (7), 962-972.

Rakkasagi, S., Poonia, V., & Goyal, M. K., 2023. Flash drought as a new climate threat: drought indices, insights from a study in India and implications for future research. Journal of Water and Climate Change, 14(9), 3368-3384.

Spinoni, J., Naumann, G., Vogt, J., 2017. Pan-European seasonal trends and recent changes of drought frequency and severity. Global Planetary Change. 148, 113–130.

Wilhite, D.A., and M.H. Glantz, 1985. Understanding the drought phenomenon: The role of definitions. Water International. 10, 111-120.

Zeng, Z., Wu, W., Peñuelas, J., Li, Y., Jiao, W., Li, Z., Ren, X., Wang, K., Ge, Q., 2023. Increased risk of flash droughts with raised concurrent hot and dry extremes under global warming. Climate and Atmospheric Science 6, 134. https://doi.org/10.1038/s41612-023-00468-2.

17th INTERNATIONAL CONGRESS of the Geological Society of Greece

BULLETIN OF THE GEOLOGICAL SOCIETY OF GREECE, SP. PUBL.

EXTENDED ABSTRACT 145

Rainfall-induced landslides in Corfu island: effectiveness of the regional scale landslide susceptibility map

Kavoura K.[1], Konstantopoulou G.[1], Paschos P.[1]
(1) Hellenic Survey of Geology and Mineral Exploration, Acharnaes, Greece, aikavoura@eagme.gr

Research Highlights

Introduction

A long term investigation on landslide phenomena in Corfu Island, consumes that the majority of them are strongly connected with rainfall events hit Western Greece and Ionian Sea islands, annually. The last years an increasing number of precipitation events occurred in Greece are characterized by meteorologists as extreme events, with a large amount of rain falls in a short time. Depending on the geomorphological and geological conditions of a specific area, this kind of events usually induce soil erosion moreover lead to landslides and floods. For Corfu island, according to the Hellenic National Meteorological Survey the mean annual rainfall is around 1100mm, while high rainfall frequency between October and November is recorded. Additionally, the abundance of recent landslides occur in this period. Based on the landslide database of the Hellenic Survey and Mineral Exploration (H.S.G.M.E.) from 1959 to 2022, 203 landslides in a 592 km^2 area have been officially recorded and mapped into a multi-temporal landslide inventory map.

Analyzing the landslides inventory some interesting results are extracted about landslide features. It is shown that 77% of the landslides are hosted in Neogene sediments followed by Quaternary formations and artificial fills while several rockfalls occur in limestones. Serious instability phenomena are often observed as rotational or translational slides (80%), while in some cases complex landslides occur. Moreover, soil creep often be an important process on extensive areas of the island. Almost 85% of the recorded landslides are located within residential areas and road network, while the rest within forests and cultivated lands (Konstantopoulou *et al*., 2019). In addition, it is stated that rainfall consists the main triggering factor of landslides in this area.

In general, the study area is prone to landslides, but where? Landslide susceptibility assessment is an important tool for identifying areas prone to landsliding. A preliminary landslide susceptibility map of the Corfu Island was presented by Konstantopoulou *et al*., 2022, using the Frequency Ratio (FR) statistical model and four commonly used predisposing factors (lithology, land use, slope, distance from road network). That assessment had a very good ability to classify landslides in susceptibility zones with ROC curves analysis give an AUC=0.895. A newer landslide susceptibility assessment was presented by Kavoura *et al*., 2024 using FR model and six predisposing factors (lithology, land use, slope, road network density, distance from rivers, distance from faults).

An important stage in landslide susceptibility assessment is to evaluate the effectiveness of the produced landslide susceptibility map by transparent validation. The standard evaluation approach is to analyze the agreement between the resulting map and observed data (Corominas *et al*., 2014). This study discusses the quality of the final landslide susceptibility map highlighting the transparency and the acceptance of such maps.

Objectives

Many techniques have improved in order to evaluate the quality of landslide susceptibility models. In this study besides the ordinary validation checks, such as Receiver Operating Characteristics (ROC), the actual predictive performance of future landslide phenomena also be assessed.

The objective of this study was to provide a coordinated approach for quality assessment of landslide susceptibility analysis by focusing not only on the calculation, but also on the evaluation process, even if the landslide susceptibility assessment was prepared under a statistical based method (FR model). More precisely, this approach uses retrospective data from landslides to examine the predictive performance of landslide susceptibility map (Fleuchaus *et al*., 2021). The predictive performance of the susceptibility map was evaluated based on different landslide events triggered by heavy rainfall events between 2022 and 2024.

Methods

For the assessment of susceptibility at regional (1:50,000) scale, six key-role predisposing factors were selected that are often used in such analyses based on literature review and experience in landslide studies. The factors were chosen to reflect the general geological, topographic and environmental settings in the study area:

1. Road network density, represents the impact of road network in occurrence of landslides (Figure 1a)
2. Slope angle, is a fundamental factor in slope stability analysis leading also the landslide mechanism (Figure 1b)

3. Land cover, this factor is associated with human activities. Changes in land uses bring changes to landslide susceptibility (Figure 1c)
4. Geotechnical units, one of the most important factors while failure occurs because the force of gravity becomes greater than either friction or the internal strength of the rock or soil (Figure 1d)
5. Distance from faults, refers to the geotechnical quality of rockmass and soil formations (Figure 1e)
6. Distance from hydrographic network (Figure 1f)

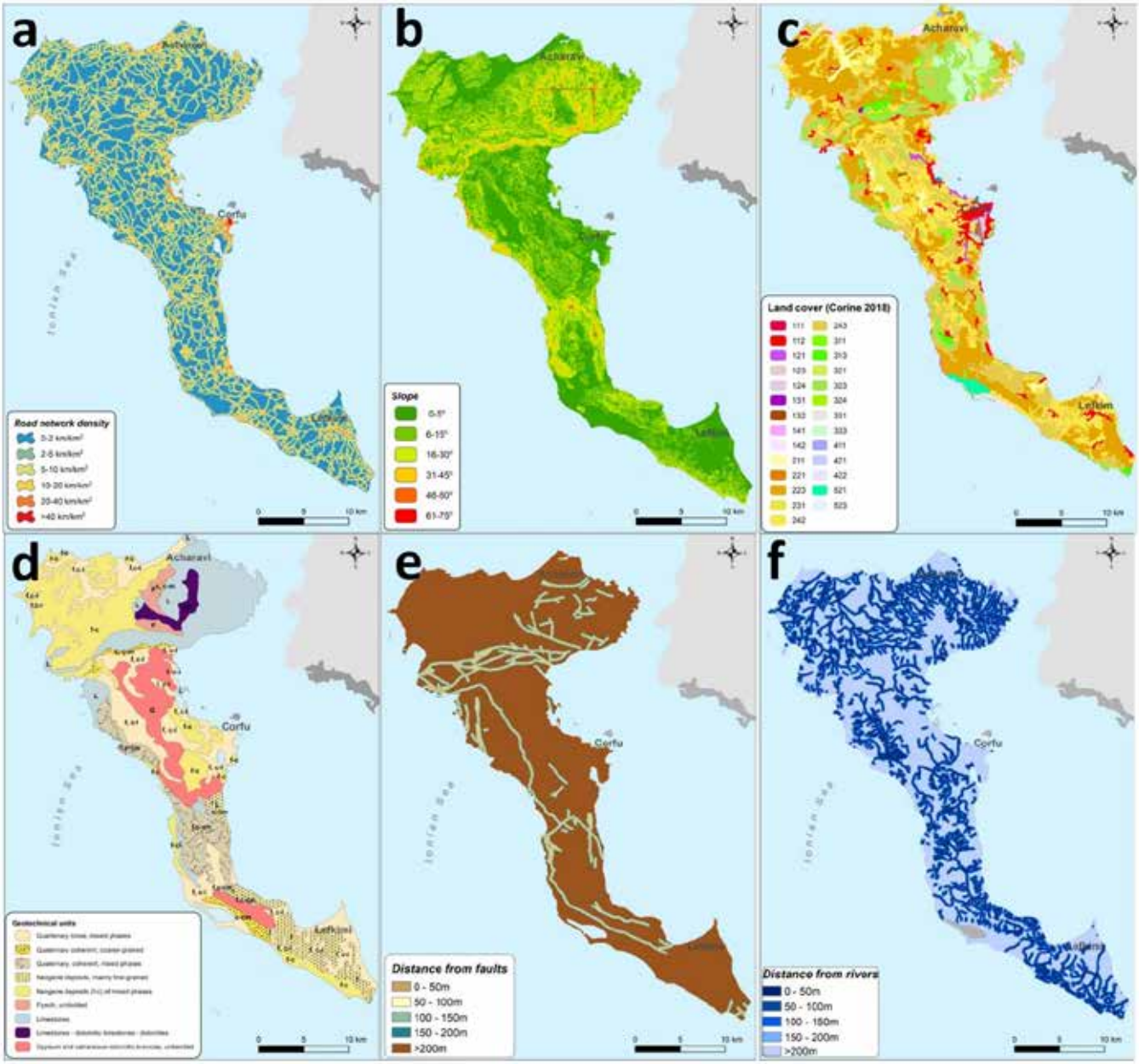

Figure 1. Predisposing factors a) Road network density, b) Slope angle, c) Land cover, d) Geotechnical units, e) Distance from faults and f) Distance from hydrographic network

The Frequency Ration (FR) model was applied to define weights for each factor, using the ratio of the per-centage of landslides in a class of the selected factor to the percentage of the area of this class in the study area. The classification of the susceptibility level is given in a percentage scale of 10%, so that each class differs from the next in terms of the degree of susceptibility, i.e. the probability of a landslide occurring in the area according to the conditions of the area, by 10%. The lower the percentage the lower the susceptibility level (Figure 2).

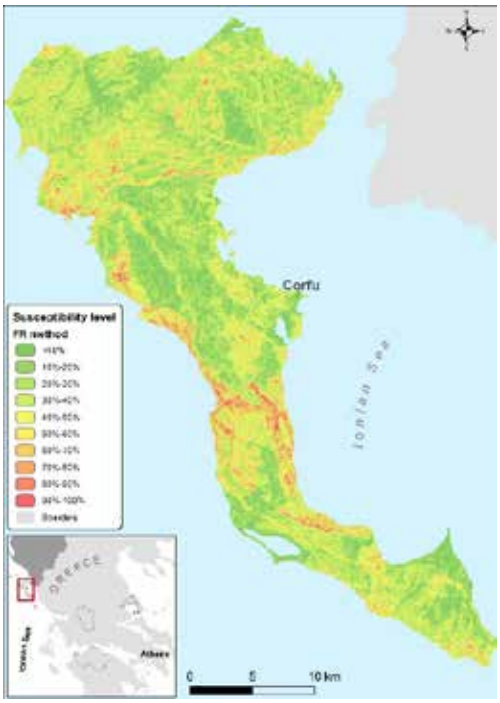

Figure 2. Landslide susceptibility map of Corfu Island

Receiver Operating Characteristic (ROC) curves were used, firstly for checking the reliability of the proposed model (success rate curves) as well as to check the ability of the model to pinpoint landslide-prone areas (prediction rate curves). In the first face, the model was checked using a training set of landslides (landslides were activated before 2020) and an equal number random set of points free of landslides. The process was repeated for the validation set of landslides (landslides were activated after 2020) in order to find if these independent landslide occurrences were correctly adapted in different susceptible areas. It is indicated that in Corfu Island the model can correctly predict the susceptible areas while AUC value is approximately 0.9 ($AUC_{success}$= 0.893 and $AUC_{predict}$=0.906).
Although the study achieves an AUC value higher than 80%, the landslide susceptibility map is subject to the predictive power of landslides activated after 2022, considering the impact of inaccurate input data or the over- and underestimation of causative factors. For this reason, a brief search was made in the local press to find unrecorded landslides in the HSGME database that were activated after 2022. This resulted in the identification of four independent rainfall – induced landslide events in different parts of the island according toTable1.

Table 1. Landslide events after 2022

Landslide event	Rainfall event	Rainfall[1]	Area
1st	8-13/12/2022	57.4 mm	Agios Dimitrios – Chlomos
2nd	19/8/2024	19.4 mm	Ano Garouna
3rd	9-10/9/2024	133 mm	Sinarades – Agios Gordios
4rth	8/1/2025	19.2 mm	Episkepsi (Megas Lakkos)

1: Weather station of Gouvia, Corfu (National Observatory of Athens network).

Results and Conclusions

The posterior validation of the landslide susceptibility map was performed based on the distribution of landslides for individual susceptibility classes (Pareek *et al*., 2024). According to Figure 3a, the majority of landslides are located along slopes in the Chlomos area predicted as being highly susceptible to landslides over 75%. Both landslides of 2024 were activated in Ano Garouna village (Figure 3b) and Sinarades – Agios Gordios (Figure 3c) area were well predicted and plotted into the susceptibility class of 70%-80%. The most recent landslide occurred in January 2025 on a slope of a mountainous road in North Corfu. As illustrated in the Figure 3d the phenomenon is closely linked to a highly susceptible zone along the road.

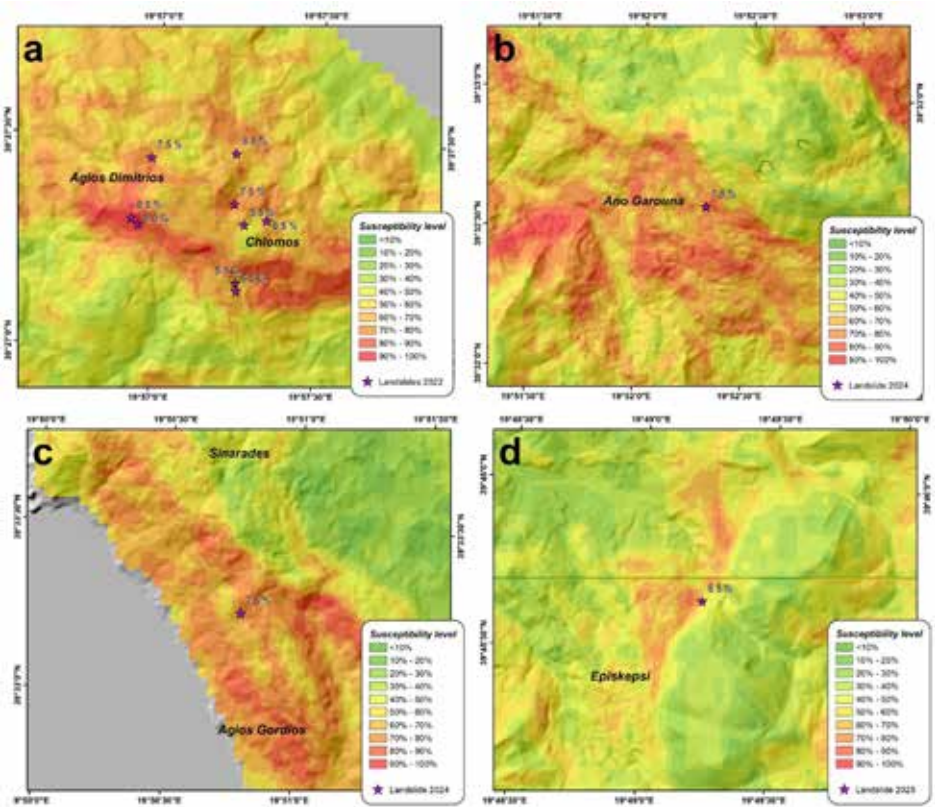

Figure 3. Evaluation of landslide susceptibility map abstracts with overlaid recent landslides at a) Chlomos and Agios Dimitrios villages, b) Ano Garouna village, c) area between Sinarades and Agios Gordios and d) wider area of Episkopi village

The retrospective validation presented in this study revealed significant correlation of the landslide susceptibility map of Corfu Island with respect to recent landslides for the period 2022 – 2025. In particular, the 60 % of the landslides, were activated into the susceptibility class of 70%-80%. This work highlights that the retrospective validation approach could be a promising assessment tool in the field of landslide susceptibility evaluation. While HSGME serves the Nation by providing reliable scientific information and thus minimizing loss of life and property from natural disasters, this research could be a basic tool for managing a sustainable hazard and risk mitigation program in landslide prone areas

References

Corominas, J., Van Westen, C., Frattini, P., Cascini, L., Malet, J.-P., Fotopoulou, S., Catani, F., Van Den Eeckhaut, M., Mavrouli, O., Agliardi, F., Pitilakis, K., Winter, M.G., Pastor, M., Ferlisi, S., Tofani, V., Hervás, J., Smith, J.T., (2014) Recommendations for the quantitative analysis of landslide risk. Bull Eng Geol Environ 73(2):209–263.

Fleuchaus, P., Blum, P., Wilde, M. Terhorst, B., Butscher, C., 2021. Retrospective evaluation of landslide susceptibility maps and review of validation practice. *Environ Earth Sci* **80**, 485. https://doi.org/10.1007/s12665-021-09770-9

Kavoura, K., Spanou, S., Apostolidis, E., Kokkali, P., 2024. Regional Landslide Susceptibility Assessment: Case Studies from Greece. Proceedings of the 6th Regional Symposium on Landslides in the Adriatic-Balkan Region, ReSyLAB2024, ISBN 978-86-7352-402-3. - Vol. 6:193–197. https://doi.org/10.18485/resylab.2024.6.ch27

Konstantopoulou, G., Exintaridi, A., Paschos, P., Nikolaou, N., 2019. Landslide hazard in Corfu Island, Greece. SafeCorfu 2019 6th International Conference on Civil Protection & New Technology

Konstantopoulou, G., Kavoura, K., Exintaridi, A., Paschos, P., 2022. Landslide inventory and preliminary susceptibility mapping of Corfu Island, Greece. 16th International Congress of the Geological Society of Greece, Patras, Greece, Sp. Publ. 10, Ext. Abs. GSG2022-197

Pareek, T., Bhuyan, K., van Westen, C., Rajaneesh, A., Sajinkumar, K. S., Lombardo, L., 2024. Analyzing the posterior predictive capability and usability of landslide susceptibility maps: a case of Kerala, India. Landslides. https://doi.org/10.1007/s10346-024-02389-4

17th INTERNATIONAL CONGRESS of the Geological Society of Greece

BULLETIN OF THE GEOLOGICAL SOCIETY OF GREECE, SP. PUBL.

EXTENDED ABSTRACT 146

Origin of nitrate pollution in groundwater of Mygdonia Plain, Greece

Kazakis Nerantzis[1*], Sideri Ioanna[1], Ntona Maria Margarita[2], Stavropoulou Vasiliki[1], Lampropoulou Dimitra [3], Zagana Eleni[1], Voudouris Konstantinos[2]

(1) Laboratory of Hydrogeology, Department of Geology, University of Patras, Faculty of Natural Sciences, 26504 Rion, Patras, Greece, nkazakis@upatras.gr (2) Laboratory of Engineering Geology & Hydrogeology, Department of Geology, Aristotle University of Thessaloniki, 54124 Thessaloniki, Greece (3) Department of Chemistry, Aristotle University of Thessaloniki, 54124 Thessaloniki, Greece

Research Highlights

- The highest concentration of nitrate is 208 mg/L occurring during the dry period.
- Dual nitrate isotopes in groundwater samples from deep boreholes indicate manure and sewage as primary nitrate sources.

Introduction / Background

Groundwater and surface water nitrate pollution constitute an important environmental issue worldwide. The primary source of nitrate pollution is usually human activities, particularly in regions heavily influenced by agriculture and livestock farming (Kazakis *et al*., 2020). In numerous aquifers across Greece, nitrate concentrations exceed the maximum permissible limit for drinking water (50 mg/L), raising significant concerns due to their potential adverse impacts on human health (Daskalaki and Voudouris, 2008). This research was conducted in a Mediterranean region affected by nitrate pollution where the groundwater originates from porous, karsts and fractured rock aquifers.

This study is focused on the administrative boundaries of DEYA Oraiokastrou due to the elevated concentrations of nitrate in drinking water. The determination of nitrate origin and regime in the porous aquifer is of utmost importance in order to map the polluted aquifer layers and locate zones with nitrate concentration below the permitted drinking limit (50 mg/L).

Study area

The study area is located in Mygdonia Basin, northern Greece. It has a typical Mediterranean climate with a mean annual rainfall of 496 mm for the period of 2015-2022, while the minimum and maximum values observed were 391 mm and 550 mm, respectively. The temperature varies from 11.9 ˚C to 20.6 ˚C with a mean annual temperature of 15.8 ˚C (data from meteo.gr). From a geotectonic perspective, the basin includes two major structural zones: the central and eastern parts are associated with the Serbo-Macedonian Massif, while the western region, where the study area is located, belongs to the Circum Rhodope Belt (Meinhold and Kostopoulos, 2013). The geological substratum comprises Paleozoic two-mica gneisses and amphibolites of the Serbomacedonian Massif, along with Mesozoic phyllites, quartzites, clay-schists, marbles, and granites of the Circum Rhodope Belt (Mountrakis *et al.*, 2006). Neogene deposits, primarily red clays, overlay these bedrock formations, with extensive Quaternary materials, including sandy clays, sands, and gravels, dominating the geological formations of the area (Figure 1). The study site is hydrologically divided into two sub-catchments: Koronia sub-basin and Volvi sub-basin. The study area belongs to the 10th Water District of Greece (GR10) and mainly falls within the Cholomontas – Oraiokastro and Koronia Groundwater Systems. According to the second revision, the qualitative and quantitative status of the Koronia Groundwater System is characterized as poor. The aquifer systems in the basin exhibit considerable heterogeneity, with alluvial deposits hosting both shallow unconfined and deeper confined aquifers, while fractured rock aquifers with variable permeability are found within the metamorphic formations (Mylopoulos *et al*., 2007; Devlioti *et al*., 2023).

This complex geological and hydrogeological setting highlights the importance of the Mygdonia Basin as a critical area for tracing nitrate sources in groundwater. The land use in the study area, based on the data from the Corine land cover, is provided in pie diagrams of Figure 2. Based on these data the landscape is primarily allocated to agriculture, with moderate forest coverage and limited urban and industrial development. Agricultural land is the dominant land use, with non-irrigated arable land constituting the largest portion (62%), followed by complex cultivation patterns (26%). Forested areas are primarily broad-leaved forests (45%) and coniferous forests (42%), with smaller contributions from natural grassland and other vegetation types. Artificial surfaces cover the minimum part of the study area and are mainly composed of discontinuous urban fabric (41%) and industrial or commercial units (27%).

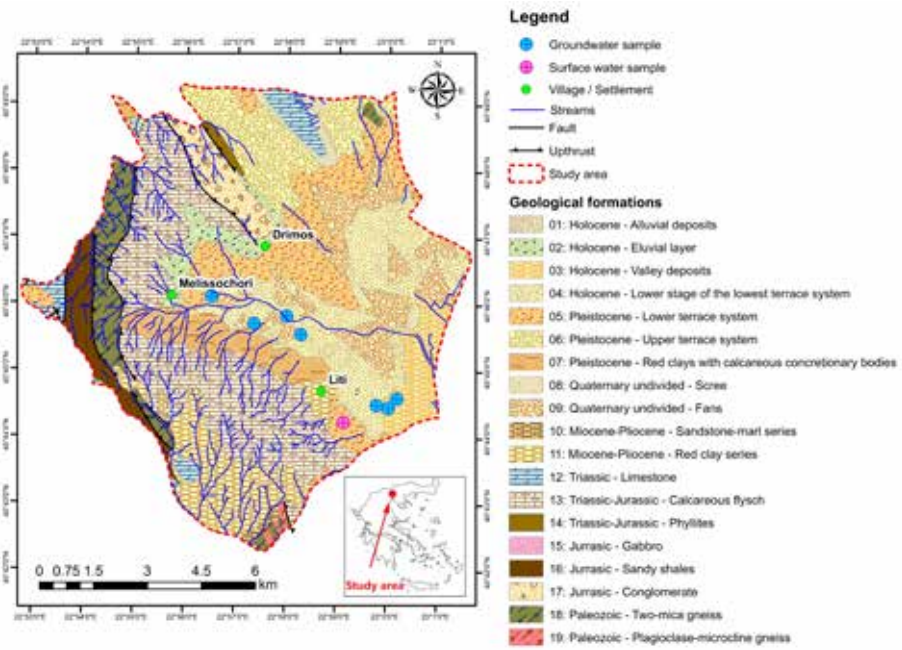

Figure 1. Study area with the groundwater and surface water sampling points.

Methodology

Groundwater and surface water samples were collected from the Mygdonia Basin during two field campaigns conducted in June and September 2023. Sampling locations were strategically selected following a judgmental sampling approach, as described by Ntona *et al.* (2023). The collected samples were analyzed to determine the concentrations of major ions and to perform stable nitrate isotope analyses of $\delta^{15}N\text{-}NO_3^-$ and $\delta^{18}O\text{-}NO_3^-$. Prior to collection, the sampling equipment was thoroughly cleaned with distilled water. Groundwater samples were collected from the well monitoring points and filtered through 0.45 μm filters to remove particulates. The filtered samples were then divided into aliquots, for isotopic analysis. The isotopic data was analyzed to distinguish between different nitrate sources, including synthetic fertilizers, animal manure, and organic matter decomposition. The chemical analyses of water samples were conducted by a private laboratory. The nitrogen isotopes in water ($\delta^{15}N$ and $\delta^{18}O$) were measured in the Isotopic Biotechnology Laboratory of the University of Ghent.

Results and discussion

The results of the chemical and isotope analysis provide important information to understand and investigate the hydrogeological regime of the groundwater in the study area. The water samples have been categorized in various diagrams providing their suitability for human consumption and irrigation purposes. Based on the Durov (Durov, 1948) diagram (Figure 3a), specifically in the square section, in most samples the predominant ions are HCO_3^- and Ca^{2+}, usually indicating rapid water recharge. The rest of the samples plotted higher with primary ions Ca^{2+} and Mg^{2+}, are due to the ion exchange processes. Referring to the Piper diagram (Piper, 1944), in the anion triangle, all samples are concentrated in the HCO_3^- section, while in the cation triangle, all groundwater samples are projected towards Ca^{2+} and the surface water samples have no dominant type (Figure 3b). Most samples are characterized as Ca^{2+}-Mg^{2+}-HCO_3^- water type, while the surface water sample collected in June is separated from the rest samples with higher concentrations of sodium compared to calcium.

The EC values of the same sample vary from 837 to 880 μS/cm, while the pH is 8.1 in the sampling periods. Regarding the suitability of water bodies for irrigation purposes, the Wilcox (Wilcox, 1995) diagram (Figure 4a) was used, which depends on the sodium percentage against electrical conductivity, and indicated that water is of good to permissible quality for irrigation, while only one groundwater sample collected in September showed good to excellent quality. In addition, Richard's plot (Richards, 1954) (Figure 4b) was applied to classify water samples in terms of the degree to which they can cause difficulty in the permeability of soils and the infiltration process, based on their electrical conductivity and the sodium adsorption ratio. Most samples are classified as high salinity hazard and low sodium hazard, indicating that the water

quality is medium and not suitable for semi-tolerant crops (Jafar Ahamed, 2013). Some samples collected in September are categorized as having medium salinity hazard and low sodium hazard, which means they do not require special measures for managing salinity.

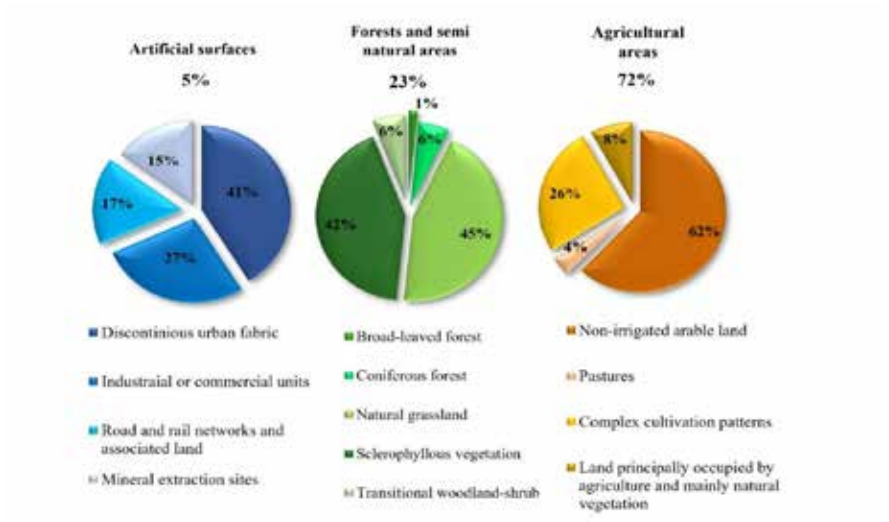

Figure 2. Pie diagrams with the percentages of land use in the study area.

The results of the physicochemical analyses (Table 1 and Table 2) on the samples showed that the pH values in June 2023 ranged from 7.3 to 7.7 and in September 2023 from 7.4 to 7.7 characterizing the groundwater as neutral to alkaline. Electrical conductivity (EC) varies from 831.0 to 1315.0 μS/cm and 734.0 to 1315.0 μS/cm during wet and dry periods, respectively. It is noted that the wider area is characterized by the presence of geothermal fields (Chantzi and Dotsika, 2016).

Nitrate concentrations for the two sampling periods showed a range from 47.8 mg/L to 154.0 mg/L in June and from 49.3 mg/L to 208.0 mg/L in September. The average concentration increased from 100.9 mg/L in June to 128.6 mg/L in September, representing a 27.5% rise.

In addition, almost all samples exceeded the permissible limit of nitrate concentration in drinking water (50 mg/L), with the exception of two samples, one for each period, which are quite close to this limit. With regard to the remaining nitrogen species, NH_4^+ appeared in all the samples with values lower than the detection limit of 0.06 mg/L, while NO_2^- concentration values were below the detection limit of 0.03 mg/L in almost all samples, with maximum values of 0.3 mg/L and 0.1 mg/L for June and September, respectively.

Land use data and field surveys highlight several potential anthropogenic sources of nitrate, including the extensive application of fertilizers, both manure and chemical types, as well as sewage effluent and solid waste disposal practices. To enrich the current results, the dual nitrate isotopes have also been utilized to investigate the contributors of nitrate pollution in the study area (Table 3). The dual nitrate isotope cross-plot diagram (Figure 5) serves as a key analytical tool for identifying the predominant nitrate sources.

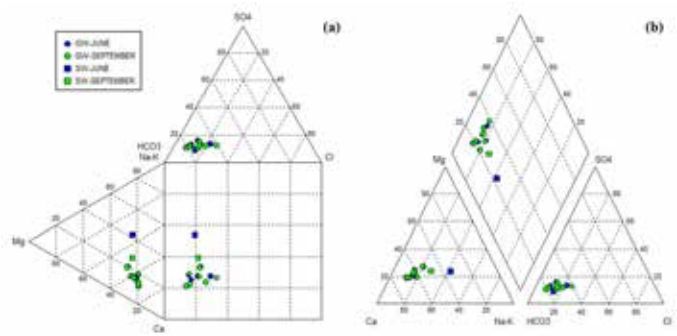

Figure 3. Classification of samples in Durov (a) and Piper (b) diagrams.

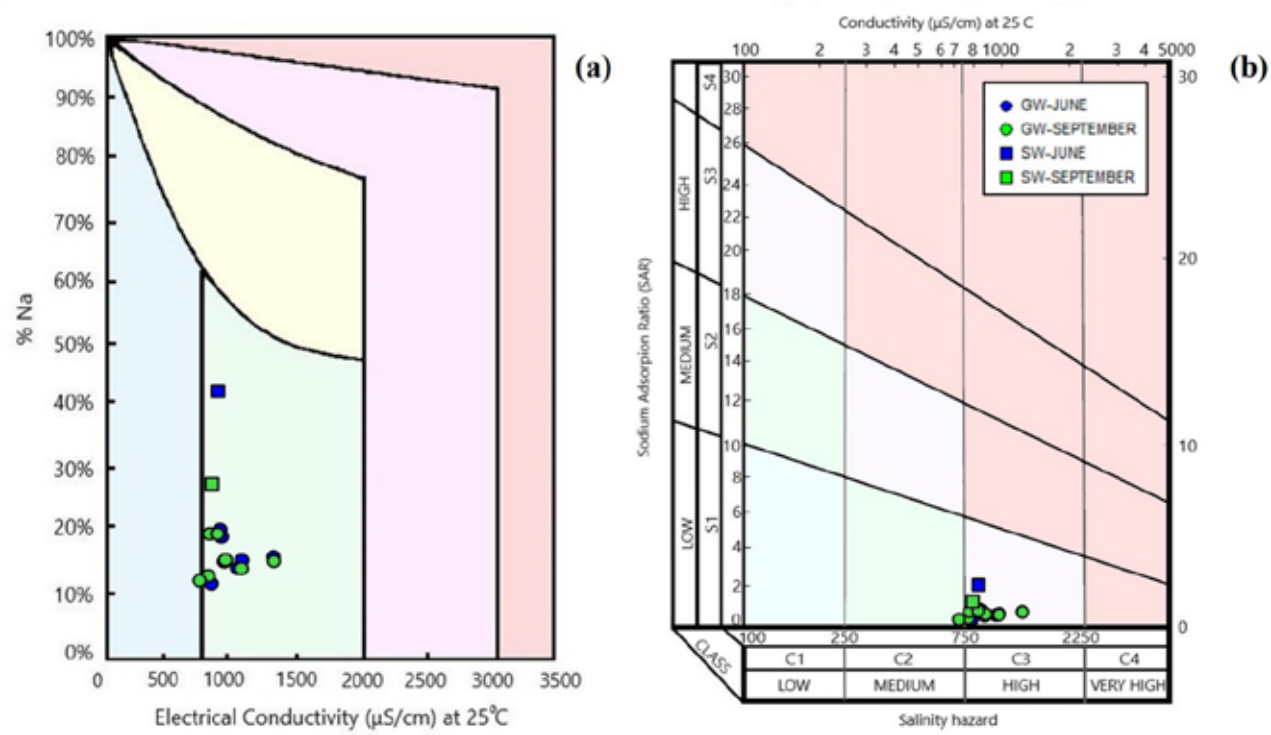

Figure 4. Classification of samples in Wilcox (a) and SAR (b) diagrams.

Table 1. Statistical analysis of the groundwater samples during the wet period of 2023.

Parameter	EC	pH	Ca^{2+}	Mg^{2+}	K^{+}	Na^{+}	NO_3^-	SO_4^{2-}	Cl^-	HCO_3^-
Values	µS/cm		mg/L	mg/L	mg/L	mg/L	mg/L	mg/L	mg/L	mg/L
Minimum	831.0	7.3	104.0	20.1	0.6	23.2	47.8	39.3	21.6	375.0
Average	998.0	7.5	131.1	28.6	0.9	39.3	85.1	58.0	48.6	408.4
Maximum	1315.0	7.7	164.0	39.3	1.5	50.3	154.0	77.7	88.8	437.0
St. Deviation	149.4	0.2	19.66	6.3	0.3	8.4	35.89	12.3	22.7	25.7

Table 2. Statistical analysis of the groundwater samples during the dry period of 2023.

Parameter	EC	pH	Ca^{2+}	Mg^{2+}	K^{+}	Na^{+}	NO_3^-	SO_4^{2-}	Cl^-	HCO_3^-
Values	µS/cm		mg/L	mg/L	mg/L	mg/L	mg/L	mg/L	mg/L	mg/L
Minimum	734.0	7.4	110	19.6	0.5	24.0	49.3	37.7	22.4	375.0
Average	934.0	7.5	136.9	29.0	0.9	39.6	100.7	57.3	53.2	414.3
Maximum	1315.0	7.7	187.0	41.7	1.2	53.7	208.0	74.4	112.0	442.0
St. Deviation	183.9	0.1	26.0	7.4	0.2	9.7	49.4	12.2	29.2	26.6

The results indicate that the majority of the groundwater samples fall within the isotopic range of manure and sewage nitrate sources, as the primary contributors to nitrate pollution in the Mygdonia Plain aquifer. In contrast, chemical fertilizers and soil organic nitrogen were found to play a key role in sample OR1.

The source identification of pollutants such as nitrate constitute the first step for the detection of unaffected aquifer layers. It is obvious that in the study area, chemical fertilizers and manure were excessively used neglecting the protection of groundwater. The upper layers of the aquifer are characterized by extensive nitrate pollution. The next step to secure the water supply for domestic use in the site is the isolation of these layers and pumping from deeper zones. Additionally, the assessment of groundwater vulnerability to nitrate pollution and pollution risk mapping constitutes a further step for water resource management and protection in the wider area of Mygdonia basin.

Table 3. Nitrate concentrations and isotopic composition of groundwater samples.

Sample	$d^{15}N\text{-}NO_3$	$d^{18}O\text{-}NO_3$
	‰	‰
OR1	5.6	3.5
OR2	11.2	4.0
OR3	9.9	3.5
OR4	8.4	4.0
OR5	9.9	3.8
OR6	9.90	3.70
OR7	8.60	4.40

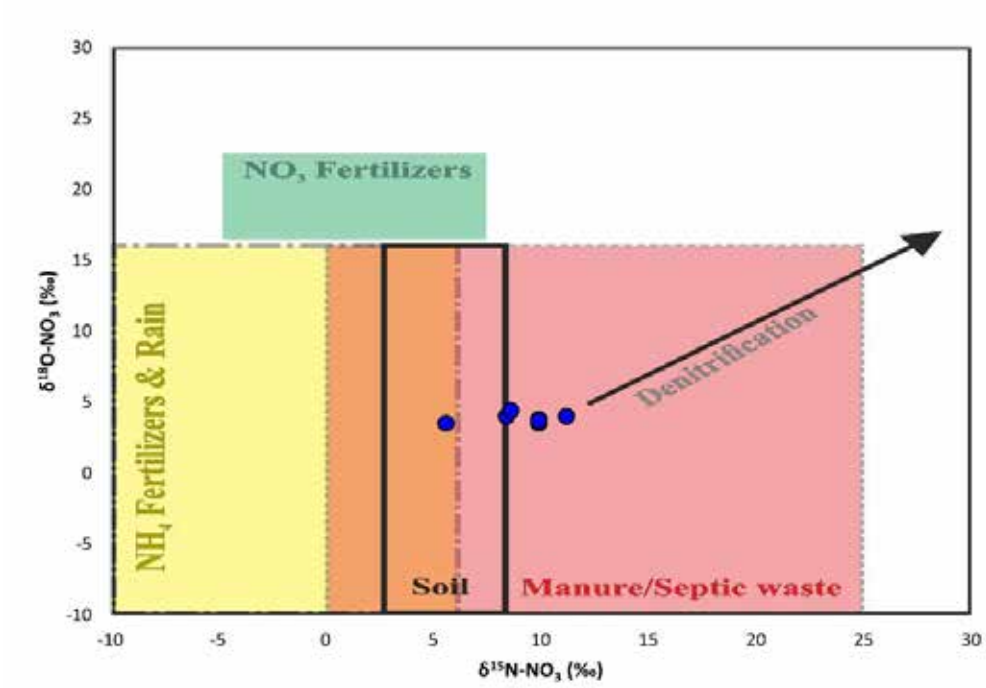

Figure 5. Cross plot of $\delta^{18}O\text{-}NO_3$ and $\delta^{15}N\text{-}NO_3$ of groundwater samples (Kendall, 1998).

Conclusions

This research provides a robust basis for tracing nitrate sources and enhances understanding of groundwater nitrate pollution in the Mediterranean region. The groundwater and surface water samples were collected during June and September 2023, revealing nitrate concentrations that reached up to 154.0 mg/L and 208.0 mg/L, respectively. Using stable nitrate isotopes on groundwater samples plotted on a Kendall diagram, nitrate sources were identified. The main nitrate pollution sources in the Mygdonia Plain aquifer are due to manure and sewage. The hydrochemical analysis of groundwater samples and the plot of water samples on the Piper diagram reveals the Ca^{2+}-Mg^{2+}-HCO_3^- water type of samples.

Further investigation into the role of the geothermal fields on groundwater quality should be implemented in the wider area. Management strategies to mitigate nitrate pollution from these identified sources and protect groundwater quality in the area are of paramount importance. This requires a systematic and continuous monitoring of groundwater quality in Mygdonia Basin.

Acknowledgments

This research was carried out within the framework of the project entitled “Water resources research and nitrate origin in groundwater of the Municipal Unit of Mygdonia” and was funded by the Water and Sewage Management Company of Oraiokastro (DEYAO).

References

Jafar Ahamed, A., Ananthakrishnan, S., Loganathan, K., Manikandan, K., 2013. Assessment of groundwater quality for irrigation use in Alathur Block, Perambalur District, Tamilnadu, South India. Applied Water Science 3, 763-771.

Chantzi, P., Dotsika, E., 2016. Mygdonia Basin (N. Greece) in the view of Isotope Geochemistry. In Energy, Transportation and Global Warming, Green Energy and Technology (Grammelis, P., Ed.). Springer International Publishing: Cham, Switzerland. https://doi.org/10.1007/978-3-319-30127-3_49.

Daskalaki, P., Voudouris, K., 2008. Groundwater quality of porous aquifers in Greece: a synoptic review. Environmental Geology 54, 505-513.

Devlioti, K., Mattas, C., Kaklis, T., Voudouris, K., 2023. Groundwater quality analysis in Mygdonia basin, Greece. Proc. of the 7th International Electronic Conference on Water Sciences (ECWS-7), MDPI (Ed. Loukas, A.), 2023, 25, 45, 313-319.

Durov, S.A., 1948. Natural Waters and Graphic Representation of Their Composition. Doklady Akademii Nauk SSSR, 59, 87-90.

Kazakis, N., Matiatos, I., Ntona, M.M., Bannenberg, M., Kalaitzidou, K., Kaprara, E., Mitrakas, M., Ioannidou, A., Vargemezis, G., Voudouris, K., 2020. Origin, implications and management strategies for nitrate pollution in surface and ground waters of Anthemountas basin based on a δ15N-NO3− and δ18O-NO3− isotope approach. Science of the Total Environment 724, 138211.

Kendall, C., 1998. Tracing nitrogen sources and cycling in catchments, in: Kendall, C., McDonnell, J.J. (Eds.), Isotope Tracers in Catchment Hydrology, 519–576.

Meinhold, G., Kostopoulos, D., 2013. The Circum-Rhodope Belt, northern Greece: Age, provenance, and tectonic setting. Tectonophysics 595-596, 55-68.

Mountrakis, D., Tranos, M., Papazachos, C., Thomaidou, E., Karagianni, E., Vamvakaris, D., 2006. Neotectonic and seismological data concerning major active faults, and the stress regimes of Northern Greece. Geological Society, London, Special Publications 260, 649-670.

Mylopoulos, N., Mylopoulos, Y., Tolikas, D., Veranis, N., 2007. Groundwater modeling and management in a complex lake-aquifer system. Water Resources Management 21, 469-494.

Ntona, M.M., Chalikakis, K., Busico, G., Mastrocicco, M., Kalaitzidou, K., Kazakis, N., 2023. Application of Judgmental Sampling Approach for the Monitoring of Groundwater Quality and Quantity Evolution in Mediterranean Catchments. Water 15, 4018.

Piper, A.M., 1944. A graphic procedure in the geochemical interpretation of water-analyses. Eos, Transactions American Geophysical Union 25, 914-928.

Raptakis, D.G., Manakou, M.V., Chávez-García, F.J., Makra, K.A., Pitilakis, K.D., 2005. 3D configuration of Mygdonian basin and preliminary estimate of its site response. Soil Dynamics and Earthquake Engineering 25, 871-887.

Richards, L.A., 1954. Diagnosis and Improvement of Saline Alkali Soils, Agriculture, 160, Handbook 60. US Department of Agriculture, Washington DC.

Wilcox, L.V., 1995. Classification and use of irrigation waters. Washington, USA Department of Agriculture, pp. 19.

17th INTERNATIONAL CONGRESS of the Geological Society of Greece

BULLETIN OF THE GEOLOGICAL SOCIETY OF GREECE, SP. PUBL.

EXTENDED ABSTRACT 147

Micropaleontological and paleoenvironmental study of carbonate intercalations within Boeotia (Greece) clastic formations

Khan S.A[1,2], Tsourou Th.[1], Skourtsos E.[1], Soukis K. [1], Michailidis I.[1], Skampa E.[1], Triantaphyllou M.V.[1]

(1) National and Kapodistrian University of Athens, Department of Geology and Geoenvironment, Athens, Greece, mtriant@geol.uoa.gr (2) Department of Earth Sciences, University of Lille 1, Villeneuve d'Ascq, France

This study aims to define the age and the paleoenvironmental depositional conditions of various carbonate facies within the Western Boeotia-Thessaly Unit in the broader area of Boeotia, central Greece, through the integration of calcareous nannofossil biostratigraphy and sedimentary microfacies analysis.

The existence of an Upper Jurassic–Lower Cretaceous "flysch" spread across multiple paleogeographic regions, both neritic and pelagic, is the main distinctive characteristic of the Western Thessaly–Boeotia unit that belongs to the outermost part of the Internal Hellenides (Papanikolaou, 2013; Papanikolaou, 2021).

The study area (Figure 1) is comprised of the outcrops of the Western Thessaly-Boeotia and the Parnassos units in Central Greece. The Western Thessaly–Boeotia, Late Jurassic–Early Cretaceous Boeotian flysch is followed by Late Cretaceous pelagic breccia limestones of the Thymiama facies, in contrast to the other more internal units, which remain below the Late Cretaceous transgression (e.g., Papanikolaou, 2021). The investigated successions are mainly composed of carbonate intercalations within the clastic sequences of the Boeotian flysch and the limestone of Thymiama. A selection of samples has been analyzed for the present research (Historical Geology and BioGeosciences Laboratory; National and Kapodistrian University of Athens), representing the carbonate intercalations and/or carbonate sequences from the various geological units and facies defined in the fieldwork campaign. Emphasis has been attributed to the calcareous nannofossil biostratigraphic assignment of the sampled clastic sequences (Figure 2).

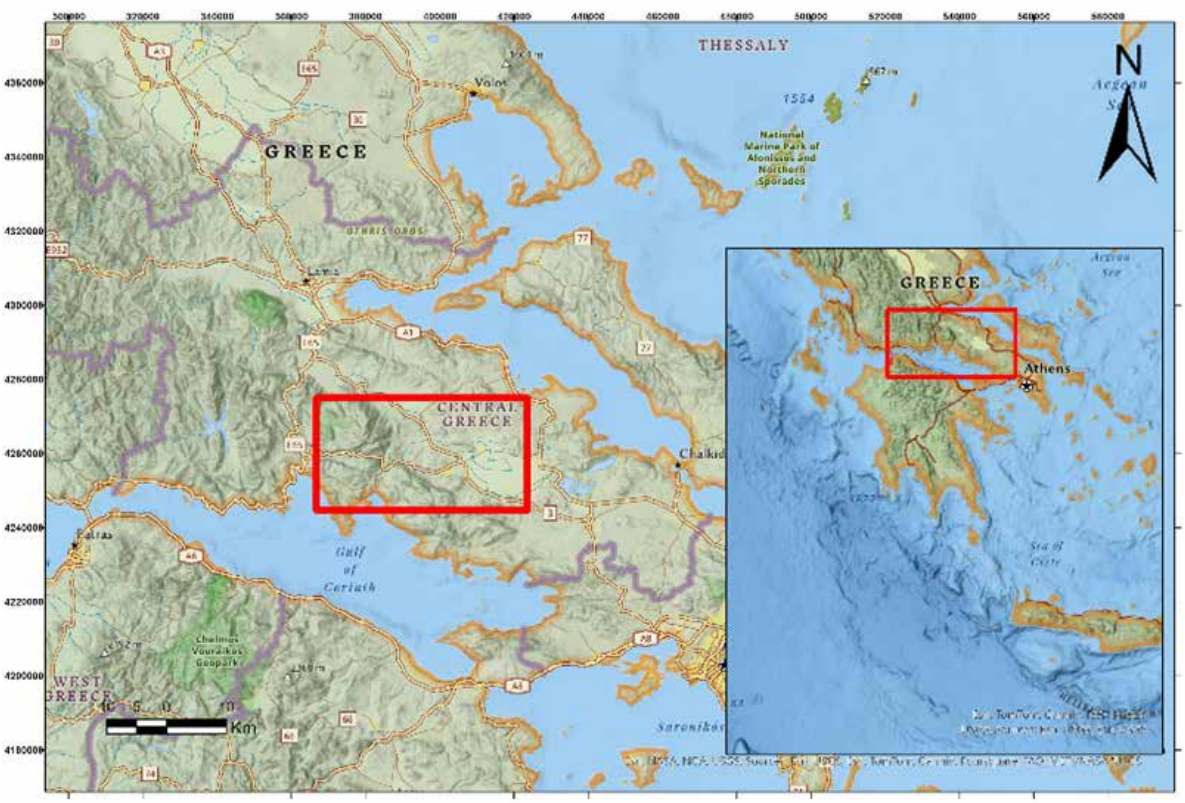

Figure 1. Location map of the study area in Central Greece.

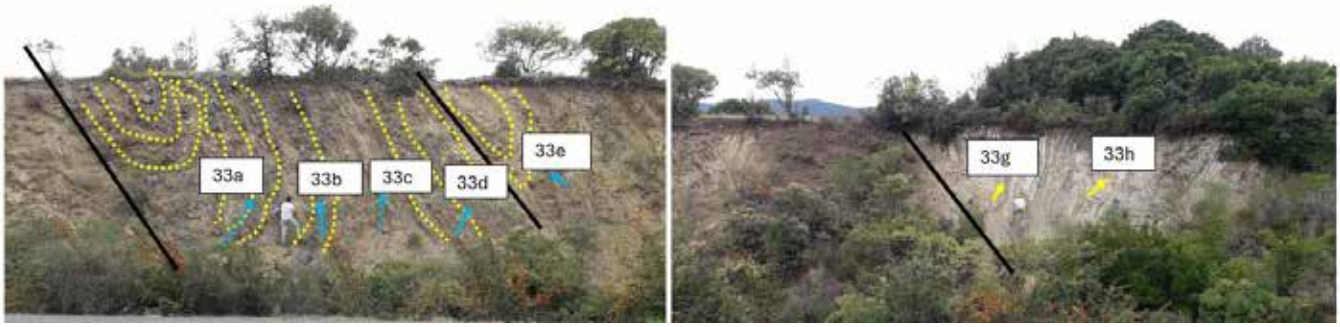

Figure 2. Studied outcrop showing the carbonate intercalations within the clastic sequences of the Boeotian flysch in Karakolithos section.

The nannofossil-based biostratigraphy performed in the clastic sequences being either intercalated or in contact with the studied carbonate samples, suggests that the samples from the Boeotian flysch are of Early Cretaceous age (Berriasian-Valanginian up to Aptian; Nirta et al., 2015; present study). The intercalated carbonate sequences of the Early Cretaceous age Karakolithos section comprise of pelagic biota. Based on the microfacies details, the sediments of the Boeotian flysch have been deposited in toe-of-slope to deep shelf setting in low-energy conditions (FZ-2 and FZ-3). This is evident by the intense presence of radiolarian and planktonic foraminifera within pelagic lime mud.

The Thymiama limestones in Boeotia represent reworked sediments from a reef or platform-derived environments as evidenced by rudist fragments and echinoderms. These have been transported during multiple sedimentary cycles and were redeposited to deeper settings (FZ-4), i.e., a low-energy gradient slope setting, also supported by the occurrence of Orbitolinidae. The nannofossil-based biostratigraphic results from marly intercalations within the Thymiama-type brecciated limestones suggest Turonian age. Also, the Aptian-Cenomanian has been identified in other locations, supporting an overall Aptian-Turonian age for the Thymiama limestones in the Boeotia area.

References

Nirta, G., Moratti, G., Piccardi, L., Montanari, D., Catanzariti, R., Carras, N., Papini, M., 2015. The boeotian flysch revisited: New constraints on ophiolite obduction in central Greece. Ofioliti 40(2), 107–123. https://doi.org/10.4454/ofioliti.v40i2.438

Papanikolaou, D., 2013. Tectonostratigraphic models of the Alpine terranes and subduction history of the Hellenides. Tectonophysics
595–596, 1–24.

Papanikolaou, D. I., 2021. Regional Geology Reviews The Geology of Greece. http://www.springer.com/series/8643.

17th INTERNATIONAL CONGRESS of the Geological Society of Greece

BULLETIN OF THE GEOLOGICAL SOCIETY OF GREECE, SP. PUBL.

EXTENDED ABSTRACT 148

" Vikos-Aoos Geopark: Toponyms as a Link Between Geological Heritage and Culture"

Georgia Kitsaki[1], Christos Stergiou[2], Haritakis Papaioannou[3]

(1) Vikos-Aoos UNESCO Global Geopark - Development Agency of Epirus S.A. (EPIRUS S.A.), Ioannina, Greece, gkitsaki@epirussa.gr (2) Stergiou C.L., Faculty of Geology, Aristotle University of Thessaloniki (AUTH), Thessaloniki, Greece / Vikos-Aoos UNESCO Global Geopark, Ioannina, Greece (3) Vikos-Aoos UNESCO Global Geopark - Development Agency of Epirus S.A. (EPIRUS S.A.), Ioannina, Greece

The Vikos-Aoos Geopark serves as a unique example of the interaction between geological formations, the natural environment, and culture, highlighting the enduring relationship between geological heritage and human activity. The region's geodiversity, characterized by designated geosites and a wide variety of geological formations, provides evidence of long-term geodynamic processes that have significantly shaped local ecosystems and biodiversity. At the same time, these geological features have been utilized by local communities, contributing to the development of a biocultural heritage, where the geoenvironment and human activity have jointly shaped the landscape and cultural identity of the area.

The integration of the geological environment into the daily lives of local communities extends beyond the mere exploitation of natural resources, such as the use of rocks in traditional architecture. Instead, it is deeply embedded in the toponymic tradition, the process by which geographical features are named, allowing communities to attribute distinct characteristics and meaning to the landscape. Toponyms are not merely linguistic data; rather, they function as carriers of valuable information across multiple disciplines, including history, archaeology, geology, and folklore. Geology, by examining the gradual transformations of the Earth's surface, contributes to the understanding of geographic and cultural migrations of populations, as well as the selection of specific sites for human settlement. Meanwhile, folklore studies investigate how toponyms encapsulate religious beliefs, local traditions, and ritual practices, establishing a profound connection between inhabitants and their natural surroundings, transforming the landscape from a natural into a humanized space.

Research Methodology and Objectives

The present research aims to identify and highlight examples that demonstrate the dynamic relationship between geological formations and human activity, illustrating the connection between geological heritage and cultural identity. Additionally, it seeks to enhance the participation of local communities in the management and promotion of the Vikos-Aoos Geopark, recognizing the significance of local knowledge in preserving both natural and cultural heritage. To collect, analyze, and interpret data, a qualitative research methodology was applied, aiming at an in-depth investigation of experiences and social processes related to the region's geological heritage. Data collection techniques included:

- Literature review and content analysis of scientific and historical sources.
- Interviews with local residents of the Geopark to document local perceptions and oral traditions.
- Participant observation through field research in locations of particular geological and cultural interest.

As part of the field research, studies were conducted in the community of Pyrgos in Konitsa, where an on-site visit was carried out with its President, Mr. Christos Papadimitriou, and in the village of Laista in Zagori, where data was collected in collaboration with the President of the Laista Mountaineering Association, Ms. Toula Poala.

Findings and Conclusions

Preliminary research findings indicate that the Vikos-Aoos Geopark hosts numerous locations of significant geological interest and designated geosites that have been incorporated into the collective memory of local communities through toponymic tradition. Notable examples include "Nterti", "Vrachos tou Chodza" ("Hodja's Rock"), "Kokkino Lithari" ("Red Rock"), as well as the well-known Dragon Lakes of Smolikas and Tymfi. These findings suggest that diverse geological formations—ranging from steep cliffs to crystalline springs—have acquired profound significance for local populations, becoming an integral part of their cultural heritage.

This exploration of the interplay between geology and culture underscores that geology is not merely a science that interprets the Earth's past but also a bridge to sustainable development and cultural empowerment. The Vikos-Aoos Geopark serves as a living example of the intricate relationship between the natural environment and human activity, emphasizing the need for holistic approaches in the management and promotion of geological heritage.

Prospects and Management of Geocultural Heritage

The management of the region's geocultural heritage aligns with the principles of UNESCO, fostering the systematic

interpretation of geological and cultural heritage while promoting sustainable development. Strengthening the connection between humans, nature, and culture through the management of the Vikos-Aoos Geopark is a priority, ensuring the preservation of the geological and cultural elements that make the area unique.
Thus, understanding the relationship between geological structures and cultural practices not only contributes to scientific knowledge but also plays a crucial role in reinforcing local identity and ensuring the sustainable development of the region.

References

Toponymy of Zagori, Konstantinos Ev. Oikonomou, Ph.D. Dissertation, University of Ioannina, 1986
Toponymics, N.G. Politis, P.D. Sakellariou Publications, Athens, 1914 and 1916
Our Toponyms: Their Value and Their Problems, Thomopoulos I., Thessaloniki, 1958
Toponyms & Oikonyms of the Mason Villages of Konitsa: Documentation, Interpretation, Etymology, Comments, Ziogas Th., Athens, 2013
A Tree Spreads Its Branches, G. Poala, Laista Zagori Mountaineering Club, Ioannina, 2006
The Echoing Rock of Sellio and Stratiani, Soureli-Galani Eleni, Kaktos Publications, Athens, 2023
Miscellaneous Folklore Studies, Nitsiakos V., Odysseas Publications, 1997
Building Space and Time, Nitsiakos V., Odysseas Publications, 2003
The Kantsiotika", Informational and Cultural Publication of the Drosopigi Brotherhood, Issue No. 22, August 2015
Technical Report on the Geological Formations of the Vikos-Aoos UNESCO Global Geopark, EPIRUS S.A., Ioannina, 2023
Vikos-Aoos Geopark: Nature Narrates Its History, Papaioannou Ch. & Kitsaki G. (eds.), IPIROS S.A., Region of Epirus, 2014

17th INTERNATIONAL CONGRESS of the Geological Society of Greece

BULLETIN OF THE GEOLOGICAL SOCIETY OF GREECE, SP. PUBL.

EXTENDED ABSTRACT 149

A Duration Model for Strong Seismic Motions of Intermediate-Depth Earthquakes in the Southern Aegean and its implication for stochastic simulations

Kkallas Ch.[1], Papazachos C.[2], Margaris B.[3]

(1) Aristotle University of Thessaloniki, Thessaloniki, Greece, chkkalla@geo.auth.gr

(2) Aristotle University of Thessaloniki, Thessaloniki, Greece, kpapaza@geo.auth.gr

(3) Institute of Engineering Seismology & Earthquake Engineering (EPPO-ITSAK), Thessaloniki, Greece, margaris@itsak.gr

Introduction

The southern Aegean subduction zone experiences the highest active deformation rates along the entire Africa-Eurasia collision zone, accounting for over 60% of Europe's seismicity. The Aegean microplate is moving southwestward at an average velocity of ~35 mm/yr relative to Eurasia, while the nearly stalled Mediterranean-Nubian plate system moves slowly toward Europe at ~5 mm/yr (Reilinger et al., 1997; Papazachos et al., 1998; Papazachos, 1999; McClusky et al., 2000; Ganas and Parsons, 2009) (Figure 1). This subduction process of the Eastern Mediterranean lithosphere beneath the Aegean microplate leads to the presence of partial melt in the mantle wedge above the subducting slab. As a result, P and S waves from intermediate-depth earthquakes (depths >45-50 km) are strongly attenuated along the South Aegean volcanic arc, while body waves from in-slab events that propagate toward the outer Hellenic arc experience high-frequency amplification (Skarlatoudis et al., 2013). The attenuation of seismic wave energy observed in the recordings appears to affect the durations of their seismic records. The ground motion duration is usually defined using the segment of the seismogram corresponding to the 0% (or 5%) to 95% energy range, as determined by Husid plots (Husid, 1969). A typical example is presented in Figure 2 which shows the corresponding Husid durations at a back-arc station (KOSI) and along-arc station (KAPA) for the 09 July 2016 **M**4.6 intermediate-depth earthquake. As we can see from both plots, there is a notable difference in the duration between the back-arc and along-arc stations, with the back-arc region exhibiting longer durations compared to the along-arc stations. This variation highlights the influence of the geotectonic setting on seismic wave propagation and attenuation. In this study, we examine the variation of strong ground motion duration as a function of hypocentral distance for intermediate-depth earthquakes. Previous attempts to correlate epicentral distance with quantitative measures of recorded ground motion duration have been performed by several researchers (e.g. Papazachos et al., 1992; Koutrakis et al., 2002; Tselentis and Danciu 2008), using shallow earthquake data (typically h < 50 km) for the broader Aegean area. No such relationships have been proposed for intermediate-depth earthquakes, mainly due to the limited data available.

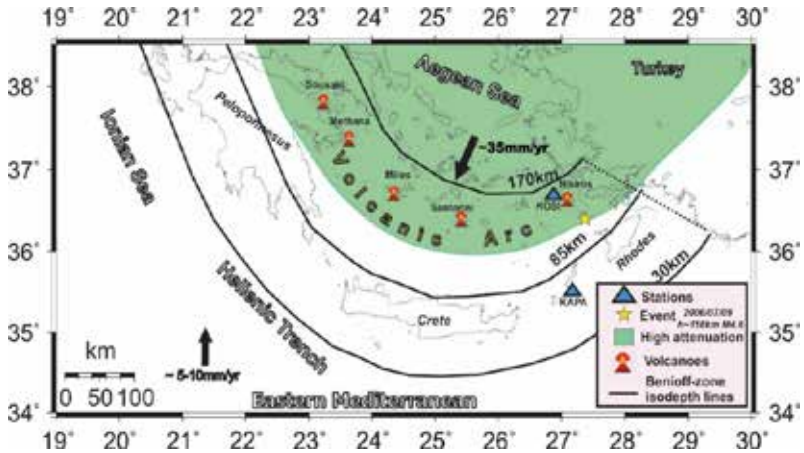

Figure 1. Schematic geotectonic map of the southern Aegean Sea subduction (southern Greece). Plate motions relative to stable Europe are shown with solid vectors. Indicative Benioff-zone isodepths are also indicated. The shaded area identifies the high-attenuation back-arc region (Skarlatoudis et al., 2013). We also present the 09 July 2006 M4.6 intermediate-depth earthquake with a yellow star, while the stations of Fig. 2 (KOSI and KAPA) are depicted with blue triangles.

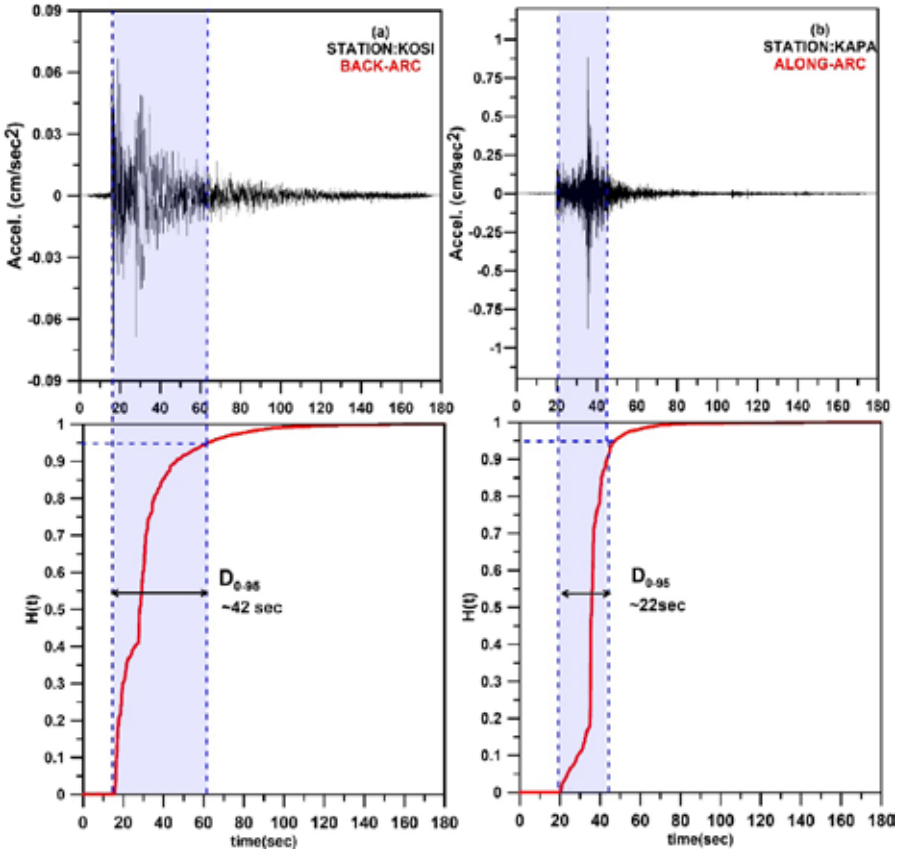

Figure 2. Husid duration for the 0%–95% range of the Arias intensity computed only for S-waves, for a back-arc station (KOSI) and a along-arc station (KAPA) [2006/07/09 M4.6 earthquake, h~118 km]. Although the stations are located at approximately the same epicentral distance, the back-arc station (KOSI) shows a significantly longer duration compared to the along-arc station (KAPA).

Data and method

We estimated the Husid duration for back-arc and along-arc area using a larger number of instrumental recordings based on previous works (Kkallas et al., 2018 and Skarlatoudis et al., 2013). Waveform data were collected and processed for the Southern Aegean subduction, providing the basis for a detailed study of the duration model, using information provided by horizontal components. To calculate the ground motion durations, we used waveform data from both acceleration and broadband-velocity sensor instruments for intermediate-depth earthquakes (depths >45km) with **M**4.5-6.7 that occurred along the southern Aegean Sea Wadati-Benioff zone. We considered the "significant" duration, as this was examined for the energy range 0% –95% of the Arias intensity of both P and S wavetrains. It should be noticed that the selection of 0% rather than the 5% often used refers to our choice to define a duration that starts exactly at the arrival time of the S (or P) waves, indicating the onset of the wave under study. We also excluded data from very large hypocentral distances (R^{hyp} > 450km), as the data for very large distances showed a very large scatter and corresponded to very small levels of ground motions.

Data from intermediate-depth earthquakes were analyzed and grouped into three categories based on their focal depths (≤60 km, 60–100 km, >100 km). This classification enabled us to quantitatively examine a possible correlation between S-wave durations and hypocentral distance. Figure 3a depicts a characteristic example, illustrating the spatial variation of Husid durations observed for the 09 July 2006 **M**4.6 intermediate-depth earthquake. Longer duration values are recorded in the back-arc region, at stations more than 100 km from the epicenter, driven by significant back-arc attenuation for events with depths >100 km. Figure 3b shows the variation of strong seismic motion duration, as defined by Husid diagrams, with respect to hypocentral distance. These differences are clearly due to the presence of the mantle wedge, characterized by a low Qs quality factor (Ventouzi et al., 2018), as well as low Vp and Vs velocities (Papazachos and Nolet, 1997), which primarily accounts for the strong attenuation of S-wave energy.

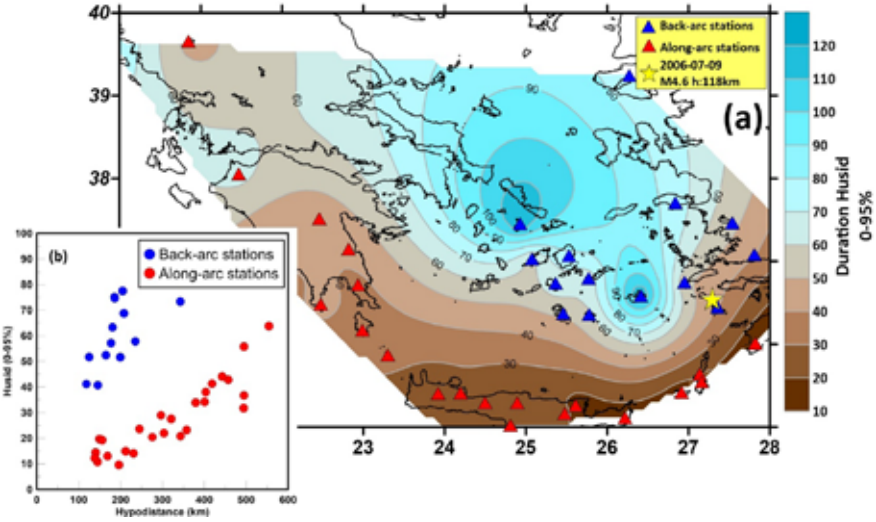

Figure 3. a) Spatial variation of the 0-95% Husid duration for S-waves for the 09 July 2006 M4.6 intermediate-depth earthquake, showing significant spatial variability between the outer Hellenic arc and the back-arc area. b) Variation of the same duration as a function of the hypocentral distance and back-arc/along-arc location of the recording station, showing a ~4 times larger durations for back-arc stations.

Figure 4 shows the variation of the strong motion duration, as defined by Husid diagrams, against the hypocentral distance for the three focal depth intervals (Figures 4a, 4b, 4c). Significant differences in the S-wave duration for earthquakes with focal depths greater than 100 km are identified between stations in the back-arc region and stations along the Hellenic Arc, leading to different linear regressions between duration and hypocentral distance (Figure 4d). This was not the case for shallower intermediate-depth events, where back-arc and along-arc stations exhibit rather similar durations.

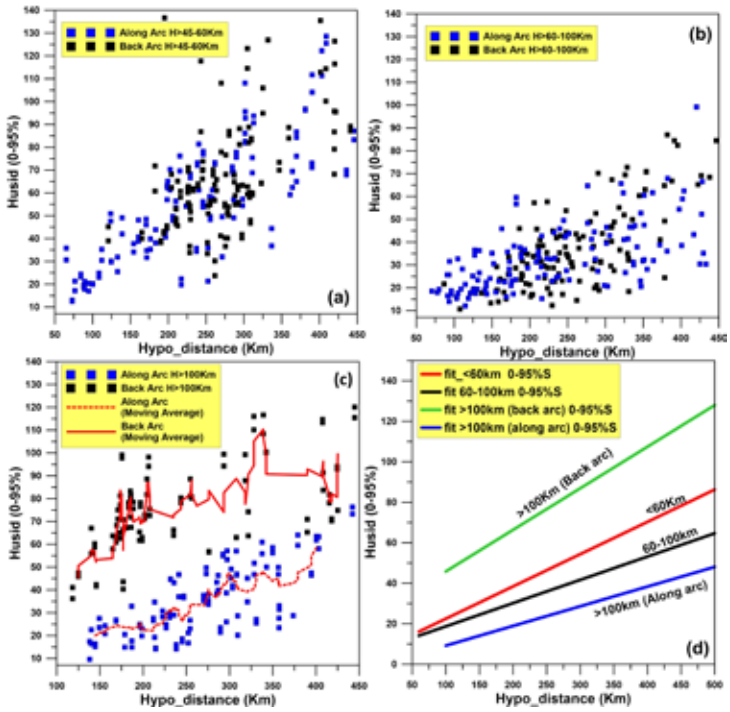

Figure 4. Variation of S-wave significant duration measures (Husid 0%-95%) with hypocentral distance for along-arc and back-arc seismic stations, categorized by depth: a) h≤60 km, b) h:60–100 km, c) h>100 km. d) Linear regression between duration and hypocentral distance for along-arc and back-arc stations, based on the depth classification.

The final relations regarding the duration of strong seismic motion (S-waves) are:

$$S-wave\ durarion(h, R_{hyp}) = \begin{cases} if\ 45km \le h < 60km \\ 0.1594 * (R_{hyp}) + 6.5355 \\ \\ if\ 60km \le h < 100km \\ 0.11493 * (R_{hyp}) + 7.1973 \\ \\ if\ h \ge 100km \\ [Back-arc]\ \ 0.2053 * (R_{hyp}) + 25.293 \\ [Along-arc]\ \ 0.0972 * (R_{hyp}) - 0.53475 \end{cases} \quad (1)$$

It should be noticed that no magnitude term is included in the linear equations (1), which may appear rather strange, considering that the input data span a rather wide moment magnitude range (**M**4.5-6.7). However, attempts to simultaneously solve for both distance and magnitude terms using an appropriate linear formulation rendered a very weak dependance on moment magnitude, which is equivalent to a total difference of ~4 sec for the aforementioned magnitude range. Due to the very poor control on the magnitude effect on durations we decided to use the simple form of eq. (1), until a larger dataset is available for intermediate-depth events of the southern Aegean area. We should consider that eq. (1) corresponds to significant durations, which do not reflect the actual level of seismic motions, but rather the time interval within which the largest part of S-wave energy is released by the mainshock. As a result, it is expected that the event magnitude is less critical and that the duration increases with the coda envelope that critically depends on the hypocentral distance.
The results in eq. 1 can be employed in a stochastic simulation scheme to determine synthetic but realistic waveforms using the stochastic approach of Motazedian and Atkinson (2005), as adapted by Boore (2009), and implemented in the EXSIM algorithm. It is important to emphasize that EXSIM does not determine ground motion duration using peak-based or threshold-based criteria, such as the time interval during which acceleration exceeds a fixed value commonly referred to as “strong-motion duration.” Instead, EXSIM adopts a more physically meaningful approach by utilizing energy-based duration metrics, which are derived from Husid plots. These plots represent the cumulative energy of the ground motion over time, allowing the modeled duration to reflect the overall energy content of the seismic signal, rather than being influenced by isolated acceleration peaks or arbitrary thresholds. We used the method as adapted by Kkallas et al. (2018) for the southern Aegean Benioff zone. Moreover, we used the same approach to generate P-wavetrains, using the travel-time curves for intermediate-depth earthquakes of Ventouzi et al. (2013) to deternine the S-P duration, which we considered as the duration of longitudinal (P) waves. The final seismogram was created as the superposition of both P and S waveforms. A typical example is presented in Figure 5 for the 24 July 2015 **M**5.0 Nisyros earthquake (h=133 km). The waveforms (containing both P and S waves) from the stochastic simulation modeling are quite similar with the actual records for stations from both the along-arc (ARG) and back-arc area (VLY), suggesting that the employed duration model can be considered as realistic.

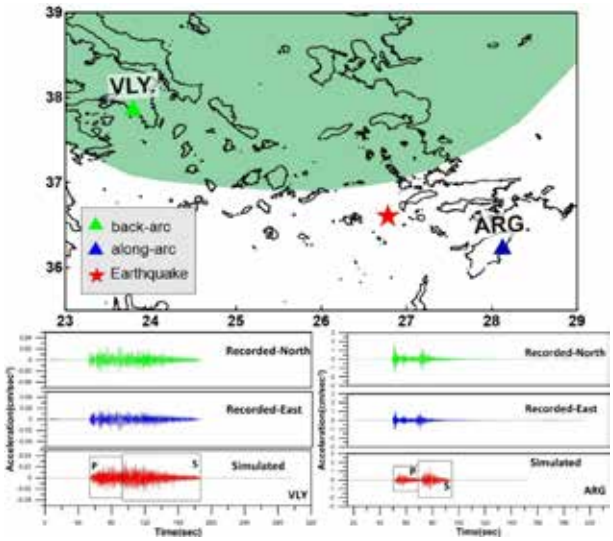

Figure 5. Synthetic acceleration waveforms (P and S waves) for back-arc and along-arc stations for the 24 July 2015 M5.0 Nisyros earthquake from stochastic simulation modeling. Notice the significant differences in the duration of strong ground motion time histories between the back-arc and along-arc stations, with the final composition of the waveforms (P and S waves) being in good agreement with the actual records for both stations (along-arc station ARG and back-arc station VLY).

Conclusions

The study of the strong seismic motion duration for intermediate-depth events of the Southern Aegean Benioff zone revealed that for earthquakes with depths greater than 100 km, the recording stations can be divided into two categories: stations along the external Hellenic Arc (along-arc) and stations in the back-arc region. Stations in the back-arc region exhibit records with longer Husid durations of seismic motion, though with low amplitudes due to the strong attenuation of S-waves caused by the presence of the mantle wedge beneath the volcanic arc. In contrast, records from stations along the Hellenic arc have significantly higher amplitudes and shorter Husid durations. On the contrary, events at shallower depths seem to have comparable significant durations for both back-arc and along-arc stations. It should be noted that this conclusion may seem counterintuitive at first, since it is known that the duration of strong seismic motions for intermediate-depth earthquakes is shorter at stations in the back-arc region compared to those in the along-arc region. However, by "duration", we define the time during which the motion accumulates the total energy of the seismic record, regardless of the level of seismic motion. Consequently, the low-amplitude back-arc records "delay" the accumulation of the total cumulative energy, leading (typically) to a longer strong duration. In contrast, records from stations along the external Hellenic Arc have significantly higher amplitudes (similar to those of shallow earthquakes), resulting in the rapid accumulation of a larger percentage of the energy in the record (shorter strong duration). As we demonstrate in this work, a simple distant-dependent duration model can be adopted and employed in stochastic simulation modeling, allowing the efficient reconstruction of wavetrains for intermediate-depth events in the Southern Aegean subduction zone. The observed weak dependence of duration on moment magnitude is most likely attributed to the limited dataset. Further clarification on the uncertainty quantification in linear regressions could be explored in the future once additional data becomes available, allowing to assess the actual influence of moment magnitude on duration.

References

Boore, D. M. (2009), Comparing Stochastic Point-Source and Finite-Source Ground-Motion Simulations: SMSIM and EXSIM, Bull. *Seism. Soc. Am*., 99(6), 3202-3216, doi:10.1785/0120090056

Ganas, A., Parsons, T., 2009. Three-dimensional model of Hellenic arc deformation and origin of the cretan uplift. Journal of *Geophysical Research: Solid Earth* 114.

Husid, L. R. "Características de Terremotos, Análisis General." Revista del IDIEM 8, Santiago, Chile, 1969: 21–42Kkallas, C., C. B. Papazachos, B. N. Margaris, D. M. Boore, Ch. Ventouzi, and A. Skarlatoudis (2018) Stochastic strong ground motion simulation of the southern Aegean Sea Benioff zone intermediate-depth earthquakes, *Bull Seismol Soc Am*, 108(2), 946-965

Koutrakis, S.I., P.K. Koliopoulos, G.F. Karakaisis, B.N. Margaris and P.M. Hatzidimitriou (2002). Seismic hazard in Greece based on different strong ground motion parameters, *Jour. of Earthquake Engineering*, 6, 75-109.

McClusky, S., Balassanian, S., Barka, A., Demir, C., Ergintav, S., Georgiev, I., Gurkan, O., Hamburger, M., Hurst, K., Kahle, H. and Kastens, K., 2000. Global Positioning System constrains on plate kinematics and dynamics in the eastern Mediterranean and Caucasus. *Journal of Geophysical Research: Solid Earth*, 105(B3), pp.5695-5719.

Motazedian, D., and G. M. Atkinson (2005), Stochastic Finite-Fault Modeling Based on a Dynamic Corner Frequency, *Bulletin of the Seismological Society of America*, 95(3), 995-1010, doi:10.1785/0120030207

Papazachos, B., E. Papadimitriou, A. Kiratzi, C. Papazachos, and E. Louvari, (1998). Fault plane solutions in the Aegean Sea and the surrounding area and their tectonic implications, *Boll. Geof. Teor. Appl*, 39(3), 199-218.

Papazachos, B.C., B.N. Margaris, N.P. Theodulidis and C. A. Papaioannou (1992). Seismic hazard assessment in Greece based on strong motion duration, *Proc. 10th Wor. Conf. Earthq*. Eng., Madrid, July 19-24, I, 425-430.

Papazachos, C. B. (1999). Seismological and GPS evidence for the Aegean□Anatolia Interaction. *Geophysical Research Letters*, 26(17), 2653-2656.

Papazachos, C., and G. Nolet (1997), P and S deep velocity structure of the Hellenic area obtained by robust nonlinear inversion of travel times, Journal of Geophysical Research B: *Solid Earth*, 102(B4), 8349-8367. **[**

Reilinger, R. E., S. C. McClusky, M. B. Qral, R. W. King, M. N. Toksoz, A. A. Barka, I. Kinik, O. Lenk, and I. Sanli (1997), Global positioning system measurements of present-day crustal movements in the Arabia-Africa-Eurasia plate collision zone, Journal of *Geophysical Research B: Solid Earth*, 102(B5), 9983-9999.

Skarlatoudis, A. A., C. B. Papazachos, B. N. Margaris, C. Ventouzi, and I. Kalogeras (2013), Ground-Motion Prediction Equations of Intermediate-Depth Earthquakes in the Hellenic Arc, Southern Aegean Subduction Area, *Bulletin of the Seismological Society of America*, 103(3), 1952-1968, doi:10.1785/0120120265.

Tselentis, G. A., and L. Danciu (2008), Empirical Relationships between Modified Mercalli Intensity and Engineering Ground-Motion Parameters in Greece, *Bulletin of the Seismological Society of America*, 98(4), 1863-1875, doi:10.1785/0120070172.

Ventouzi, C., Papazachos, C., Hatzidimitriou, P., Papaioannou, C., & EGELADOS Working Group. (2018). Anelastic P-and S-upper mantle attenuation tomography of the southern Aegean Sea subduction area (Hellenic Arc) using intermediate-depth earthquake data. *Geophysical Journal International*, 215(1), 635-658.

Ventouzi, C., Papazachos, C., Papaioannou, C. and Hatzidimitriou, P., 2013. Obtaining information on the Q-structure of the southern Aegean subduction area by spectral slopes from temporary and permanent networks. *Bulletin of the Geological Society of Greece*, 47(3), pp.1366-1375.

17th INTERNATIONAL CONGRESS of the Geological Society of Greece

BULLETIN OF THE GEOLOGICAL SOCIETY OF GREECE, SP. PUBL.

EXTENDED ABSTRACT 150

Lunar Pits: Statistical Analysis of Morphometric and Geophysical Properties

Klimis F.[1], Sykioti O.[2], Karymbalis E.[1], Parcharidis I.[1]

(1) Department of Geography, Harokopio University of Athens, Athens, Greece, gs219116@hua.gr (2) Institute of Astronomy, Astrophysics, Space Applications and Remote Sensing, National Observatory of Athens, Athens, Greece

Background and Objectives

Lunar pits are distinct geological features scattered across the Moon's surface that offer significant insights to the subsurface structure of the Moon, potentially indicating the existence of ancient lava tubes formed by volcanic activity. Lava caves or lava tubes are formed when the external part of the a lava flow cools more quickly and makes a hardened crust over the internal lava flow. As the lava flow drains out of the tube, it leaves an empty space. The thin part of the ceiling of lava tube could then collapse to expose the entrance to the lava tube which is called a pit (Haruyama et al., 2009; Robinson et al., 2012; Hong et al., 2014; Wagner & Robinson, 2014). They vary from a few meters to several hundred meters in diameter and display differing depths. Morphologically, these pits can be broadly categorized into two types: those with a direct vertical drop (shaft-like pits) and those that slowly narrow down like a funnel (Figure 1). Lunar pits are mostly identified in near crater impact sites and within maria (large basaltic plains formed by ancient volcanic activity). Much of the original volume of most pits is now filled with debris, but some exhibit significant overhangs and may have present-day cave access (Wagner & Robinson, 2022). As these formations may be linked to subsurface lava tubes, they are not only significant for understanding the geological history of the Moon but also for future lunar exploration, water ice detection and habitat development (Zu et al., 2024; Carrer et al., 2024). According to Horvath et al. (2022), lunar tubes and caves could provide a temperate, stable, and safe thermal environment for long term exploration and habitation. Although, the investigation of pits may be challenging due to steep slopes of loose material at their walls and floors, it could help clarify their formation mechanisms and their implications for the evolution of lunar volcanic and tectonic processes (Nesnas et al., 2023).

This study carries out a statistical morphometric and geophysical analysis of 278 currently observed lunar pits in order to detect and quantify their main attributes. A dataset of morphometric and geophysical measurements was collected in order to perform descriptive statistics and correlation analysis. The analysis is performed on a 2-point axis: (1) descriptive and correlation analysis of morphometric variables, (2) descriptive and correlation analysis of geophysical variables. The main conclusions of the analyses are presented proposing future directions for the continuation of this work.

Data and method

For the purpose of this study, morphometric and geophysical data issued from various satellite and topographic measurements of the lunar surface were collected. The main data source of the morphometric variables was the Lunar Reconnaissance Orbiter Camera Planetary Data System (PDS) archive. A detailed catalogue of 278 lunar pits containing geographical, topographical and morphological data was retrieved and utilized. The Catalogue of Lunar Pits receives updates as more pits are detected manually or by the Pitscan Algorithm developed by Wanger & Robinson (2022). According to Wagner & Robinson (2022), the up-to-date observed pits are 321. However, due to the unavailability of morphometric and geophysical variables of the newly recently detected lunar pits, in this study we used the 2021 pit catalogue that includes 278 pits. The main data source of the geophysical variables was the web platform Lunar QuickMap, implemented by the collaboration between NASA, Arizona State University and Applied Coherent Technology Corporation (https://quickmap.lroc.asu.edu/). Through the QuickMap platform (the platform employs the Wagner & Robinson (2022) pit catalogue), we retrieved the files containing the geophysical variables of 278 pits (example in Figure 2, variables in Table 1).

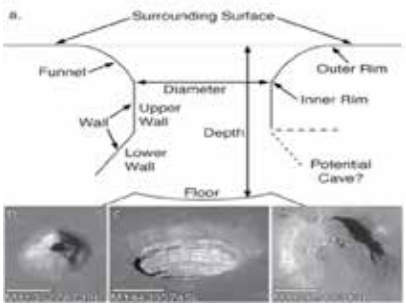

Figure 1. Cross-section of a generic lunar pit (Source: Wagner & Robinson, 2022). Not all pits exhibit all these features, or show these shapes. The inner rim is exaggerated for visibility.

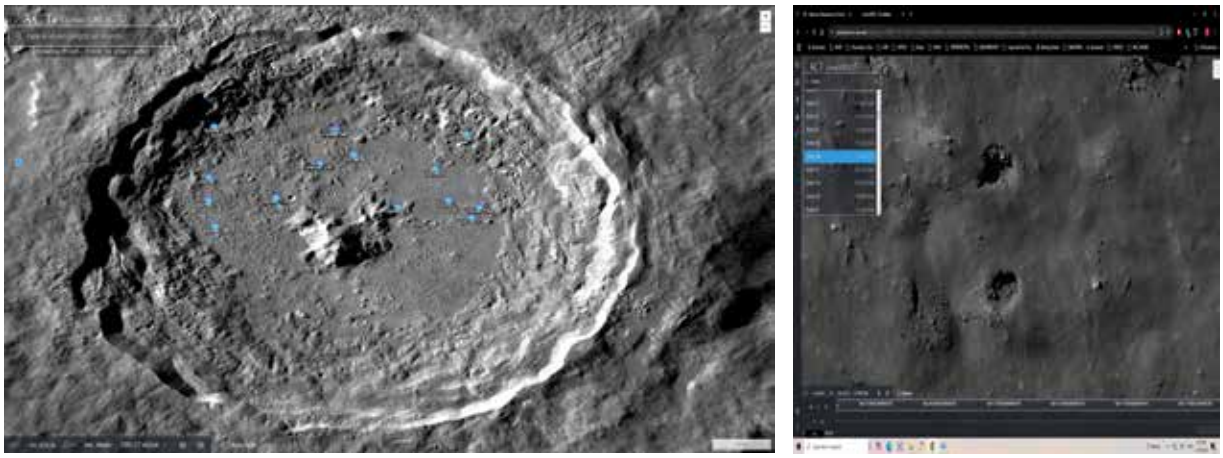

Figure 2. Tycho crater (formed 108 mya, Tycho crater has a diameter of 85km and is one among the thousands of similarly-sized craters on the Moon). Left image: screenshot featuring lunar pit locations within Tycho Crater using the QuickMap Platform (blue dots); Right image: zoom to pits Tycho 17a and Tycho 17b (located within the yellow circle in the left image). The left image scale is shown at the bottom right corner (10km) and the spatial resolution of the image is app. 100m/pixel. The spatial resolution of the right image is app. 0.6m/pixel.

All variables examined in this study are presented in Table 1. For the purpose of the morphometric statistical analysis, the variables were classified into two distinct categories, continuous and nominal variables. Statistical measures were used to provide a comprehensive understanding of the continuous variables, namely mean value, standard deviation, kurtosis and skewness. The Shapiro Wilk Test was also employed to evaluate whether the data follow a distribution. Correlation matrices were employed to determine the strength and correlation type (positive or negative) among pairs of variables such as funnel diameter, depth, slope measurements and terrain characteristics. The Jamovi open-source statistical software was utilized along with plug-ins of the R software in order to perform the correlation analysis. For the nominal variables, histograms were created to explore the distribution of categorical data, such as terrain type, host feature, and other binary indicators like the presence of an entrance ramp, overhangs, etc. Similar to the morphometric analysis, the geophysical analysis involved the use of descriptive statistics, distribution examination and correlation analysis.

Table 1. List of all morphometric and geophysical variables used in this study. The use of "?" shows the boolean character of the variable, meaning the presence or absence of a certain morphometric characteristic.

Morphometric continuous variables	Morphometric categorical variables	Geophysical continuous variables
Funnel max Diameter (m), Funnel min Diameter (m), Inner max Diameter (m), Inner min Diameter (m), Azimuth of the long axis of the inner pit (deg), Depth (m), SLDEM2015 (+LOLA) elevation (m), SLDEMDEM Slope (dynamic) (deg), SLDEM src Azimuth (deg), SLDEM src Slope (deg), Terrain Height (m), Terrain slope (deg)	Terrain type, Host feature, Geometry, Entrance Ramp ?, Overhangs ?, Nearby Pits ?, Nearby Fractures ?, Nearny Depressions ?, In Dome ?, In Depression ?, Colinear Pits ?, Colinear Depressions ?, Colinear Fractures ?, Is Copernical Crater ?, Is Mare ?, Is permanent shadow ?	Clinopyroxene abundance (wt%), FeO abundance (wt%), Olivine abundance (wt%), Orthopyroxene abundance (wt%), Plagioclase abundance (wt%), Thorium abundance (ppm), UVVIS FeO abundance (wt%), Nighttime soil temperature (normalized) (K), Nighttime soil temperature (K), Derived optical maturity (unitless), Diviner H-parameter (m), Rock abundance (unitless)

Results and Conclusions

Statistical analysis of pit morphometric characteristics

With the completion of the morphometric analysis, several key conclusions were drawn regarding the physical characteristics, geophysical context, and local distribution of lunar pits. The statistical results of the descriptive statistical analyses of the continuous variables (Table 1) are presented in Table 2 and examples of the distributions of pit continuous and nominal morphometric characteristics are presented in Figure 3.

Table 2. Results of the main descriptive statistical analysis of the continuous variables.

Variable	Number	Missing	Mean	Median	SD	Skewness	Kurtosis	Shapiro –Wilk
Funnel Max Diam	266	12	48.55	29.00	62.56	3.375	12.885	0.571
Funnel Min Diam	273	5	36.33	21.00	49.66	3.887	17.018	0.518
Inner Max Diam	266	12	31.00	16.00	48.78	4.328	21.931	0.483
Inner Min Diam	261	17	22.82	11.00	40.65	4.631	24.244	0.440
Azimuth	277	1	87.48	70.00	54.08	0.172	-1.364	0.927
Depth	237	41	13.15	9	13.89	3.310	13.072	0.609
SLDEM2015(+LOLA)(m)	278	0	-2008.63	-2293.34	1703.75	1.041	0.351	0.870

The results show significant skewness and kurtosis in both funnel and inner diameters, with the majority of pit dimensions ranging between 22 and 48 meters (Table 2 and Figure 3a). While most lunar pits are relatively shallow, with depths between 10 and 15 meters, there exists a subset of significantly deeper pits, indicating potential variations in formation processes or geological setting (Figure 3b). The azimuth analysis reveals a uniform distribution of pit orientations, suggesting no particular alignment or external directional influence in the formation of these pits (Table 2). Furthermore, the majority of lunar pits are found in impact melt terrains (mostly located within mare regions), and relatively few within mare and highlands (Figure 3c). This suggests a strong association between impact-related processes and pit formation. Many pits tend to cluster near other geological features, especially craters. This clustering suggests that pit formation may be influenced by nearby structural weaknesses, crustal thinning due to impacts or collapse processes related to crater formation. The study identified 28 distinct clusters of pits across various lunar regions. A significant number of pits (228 out of 278) are located near depressions, while very few are located within depressions. This distribution pattern could be related to crustal weakening in the broader area or subsurface voids influencing pit formation. Elevation data show that lunar pits are predominantly located in elevations well below the Moon's reference elevation sphere (Figure 3d).
Regarding the geometric variability, the majority of pits display undefined or elliptical or circular geometries with a variability that could be due to different collapse dynamics or variable composition of the host regolith (Table 3). Examining the overhangs, the presence of overhangs is observed only in a small percentage of lunar pits. Overhangs may be the result of mechanical weathering or collapse of pit walls due to gravitational forces. The majority of pits do not exhibit entrance ramps. Finally, no pits are observed in permanently shadowed regions of the Moon, which could be explained either by lack of data or by poor illumination conditions (e.g. areas of permanent shadow near the lunar poles and inside craters that are not directly illuminated by the sun).

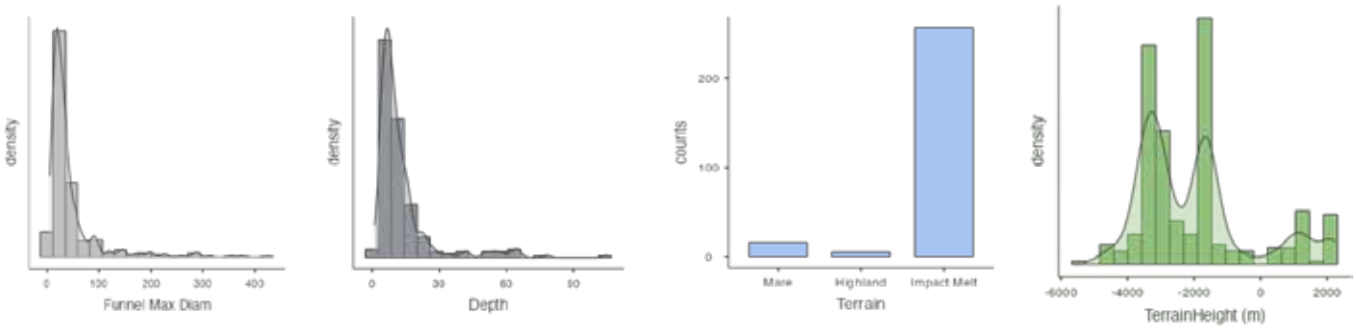

Figure 3. Examples of distributions of pit continuous and nominal morphometric variables: (a) funnel maximum diameter, (b) depth, (c) terrain type and (d) terrain elevation issued from LOLA DEM (elevation values are the distance above or below the reference sphere). Most of the pits show less than 10m funnel maximum diameter, they are rather shallow (10-15m) located in impact melts at altitudes well below the lunar reference elevation sphere.

Table 1. Most frequent pit geometries (shape) (occurrence >5% of total number of pits).

Geometry (shape)	Number of pits	% of total
Elliptical	52	18.7
Rectangular	21	7.6
Irregular	25	9.0
Triangular	19	6.8
Circular	38	13.7
Undefined	57	20.5

Concerning the linear correlation analysis, the first notable observation in the correlation matrix (Figure 4) is the strong relationship between pit dimensions. More specifically, Funnel Max Diameter and Funnel Min Diameter show a very strong positive correlation (Pearson's $r = 0.94$, $p < .001$). Similarly, both Inner Max Diameter and Inner Min Diameter show strong positive correlations with Funnel Max and Min Diameters ($r > 0.9$, $p < .001$), suggesting that the size of the inner pit is closely linked to the size of the outer funnel. Additionally, the strong positive correlation between Funnel Diameter and Inner Diameter ($r > 0.7$, $p < .001$) suggests that deep pits tend to present large diameters.

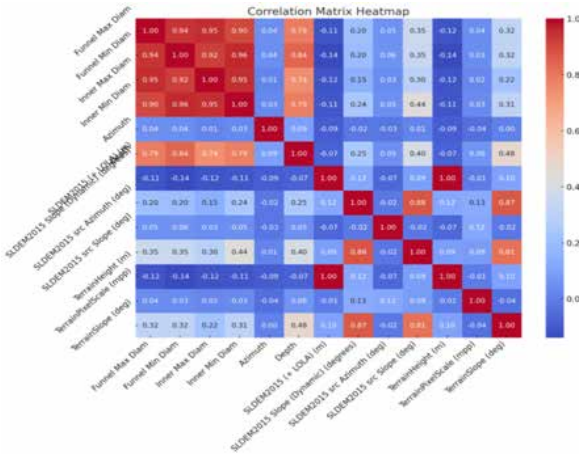

Figure 4. Correlation matrix between morphometric variables. The matrix is symmetric. The highest linear correlations are observed between the funnel diameter (man and min) and the inner diameter (max and min) of the pit.

Statistical analysis of pit geophysical characteristics

The results of the statistical analysis of the geophysical characteristics of the pit areas are in general consistent with the already known geological patterns on the lunar surface. In terms of mineralogy, maria, corresponding to secondary lunar crust formed by basaltic volcanism, exhibit the highest olivine, pyroxene (both clinopyroxene and orthopyroxene) content and the lowest content in plagioclase (32-35 wt%) (Figure 5a). Highlands, corresponding to the primordial lunar crust of anorthositic composition, present medium content in olivines and pyroxenes and a high content in plagioclase (anorthite) (62-65 wt%). Impact melts, corresponding to areas of intense cratering (where most of pits are located), present the lowest content in olivine and pyroxenes and the highest content in plagioclase (70-75 wt%). Correspondingly in terms of chemical composition, iron (Fe) and titanium (Ti) contents are high (15-17wt% and 2.5 – 3.5 wt% correspondingly) within maria pit areas, which are consistent with the maria basaltic compositions (Figure 5b). Highlands present relatively low Ti and Fe-content (7-10 wt%), which is expected due to the predominance of anorthositic rocks. Finally, pit areas within impact melts present the lowest Fe and Ti-content (7-10 wt%), which is consistent with their general low content in mafic minerals (olivines and pyroxenes). Concerning thorium (Th), it seems that maria and highland pit areas show higher Th content (3-3.5 ppm) than impact melts. Finally, impact melts present high rock abundances within regolith, low thermal intertia (0.03m) while they seem to retain higher nighttime soil temperatures (~ -271.15°C) compared to the maria and the highlands, reflecting thus a distinct thermal behavior (Figures 5c and d).

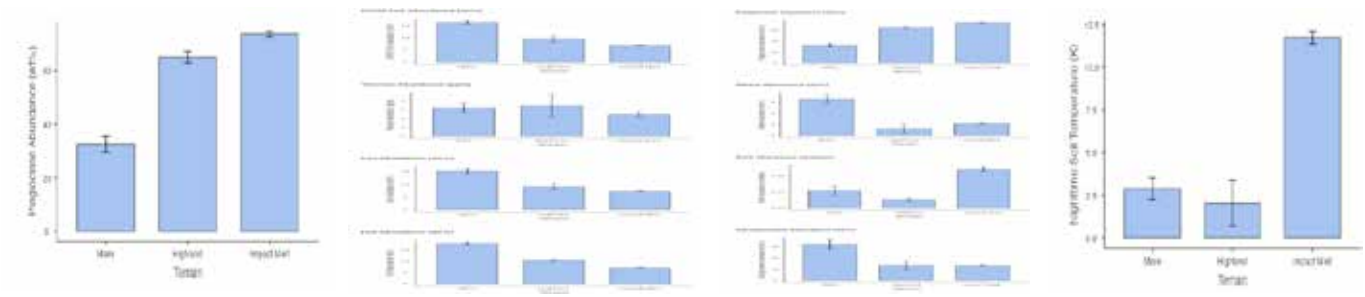

Figure 5. Examples of geophysical variables for the three different lunar terrain types (maria, highlands and impact melts; (a) plagioclase content (%wt), (b) iron content (%wt), (c) rock abundance in regolith (unitless) and (d) nighttime soil temperature (in K). Vertical bars correspond to value variations.

The linear correlation analysis reveals strong relationships between geophysical variables (Figure 6). Notably, Fe-content presents a high positive correlation with nighttime soil temperature (r = 0.92). Additionally, there is a strong positive correlation (r = 0.89) between rock abundances within the regolith and nighttime soil temperatures, which is consistent with Powell *et al.* (2023). In parallel, a significant negative correlation observed between nighttime soil temperatures and thermal inertia (Diviner H-Parameter) (r = -0.97) shows that nighttime temperatures are sensitive to the thermophysical properties of the regolith. High thermal inertia materials, such as large rocks, seem to remain warmer during the lunar night and thus result to anomalously warm nighttime temperatures (Williams *et al.*, 2017).

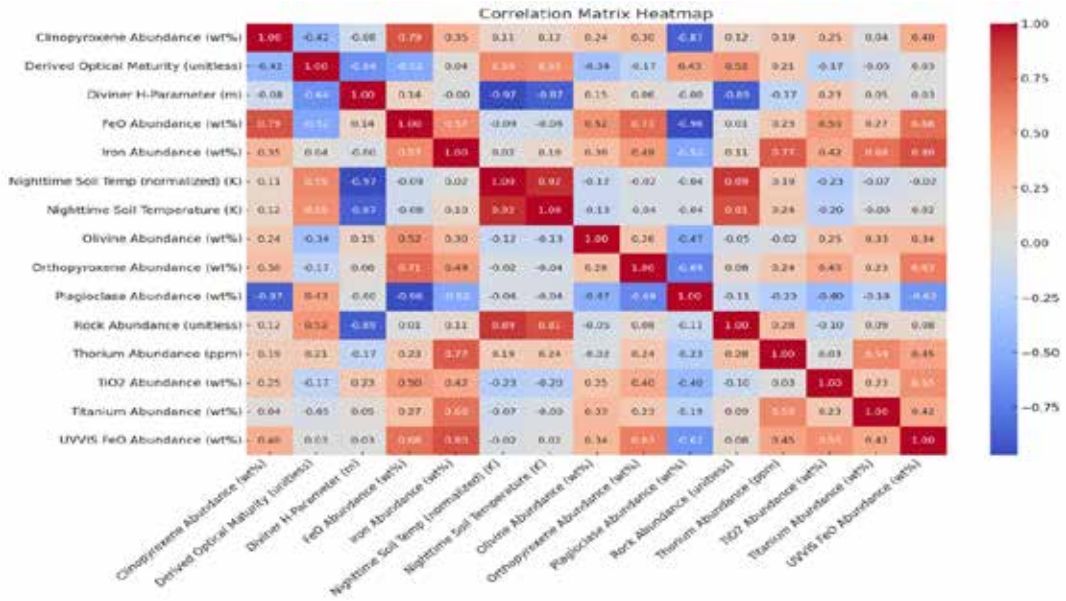

Figure 6. Correlation matrix heatmap of geophysical characteristics. The matrix is symmetric.

In conclusion, the examination of the morphometric and geophysical properties of lunar pits showed that they often have undefined or elliptical shape, varying geometry and are often present in several clusters, near depressions located within crater impact melts. Mineralogy and chemistry are consistent with the geological context of their locations. Although the spatial resolution of the current available data is often a limiting factor, the examination of their properties provides insights to the Moon's geological history, surface processes and stability. Furthermore, lunar pits are potentially linked to subsurface lava tubes or caves which could be promising sites for future human exploration, human habitats and infrastructures. Their unique structure potentially offers natural protection from extreme temperatures, cosmic radiation, and meteorite impacts, making them prime candidates for sustainable lunar bases, landing site selection and long-term lunar sustainability research.

This study is part of Mr. Klimis' BSc thesis. Future continuation of this work includes the study of the each pit cluster, comparison of different pit clusters within different geological contexts, thermal properties (outside and within pits), and the detection of new pits potentially linked to subsurface lava tubes or caves.

References

Carrer, L., Pozzobon, R., Sauro, F., et al., 2024. Radar evidence of an accessible cave conduit on the Moon below the Mare Tranquillitatis pit. Nature Astronomy 8, 1119–1126. (https://doi.org/10.1038/s41550-024-02302-y)

Haruyama J, Hioki K, Shirao M, Morota T, Hiesinger H, Van Der Bogert C, Miyamoto H, Iwasaki A, Yokota Y, Ohtake M, Matsunaga T, Hara S, Nakanotani S, Pieters C.M., 2009. Possible lunar lava tube skylight observed by SELENE cameras. Geophysical Research Letters, 36, L21206.(https://doi.org/10.1029/2009GL040635)

Hong, I-S., Yi, Y., Kim, E., 2014. Lunar Pit Craters Presumed to be the Entrances of Lava Caves by Analogy to the Earth Lava Tube Pits. Journal of Astronomy and Space Sciences 31(2), 131-140. (https://doi.org/10.5140/JASS.2014.31.2.131)

Horvath, T., Hayne, P.O., Paige, D.A., 2022. Thermal and Illumination Environments of Lunar Pits and Caves: Models and Observations from the Diviner Lunar Radiometer Experiment. Geophysical Research Letters 49(14), e2022GL099710. (https://doi.org/10.1029/2022GL099710)

Nesnas, I.A.D., Kerber, L., Sellar, G., Balint, T., Denevi, B., Parness, A.J., Kornfeld, R.P., Smith, M., McGarey, P., Brown, T., Sunada, E., Gonter, K.A., Hockman, B., Hayne, P., et al., 2023. Moon Diver: Exploring a pit's exposed strata to understand

lunar volcanism, Acta Astronautica 211, 163-176, (https://doi.org/10.1016/j.actaastro.2023.05.042)

Powell, T.M., Horvath T., Robles, V.L., Williams, J.-P., Hayne, P.O., Gallinger, B.T., Greenhagen, D.S., McDougall, D.S., Paige, D.A, 2023. High-Resolution Nighttime Temperature and Rock Abundance Mapping of the Moon Using the Diviner Lunar Radiometer Experiment With a Model for Topographic Removal. JGR Planets 128(2), e2022JE007532 (https://doi.org/10.1029/2022JE007532)

Robinson, M.S., et al. 2012. Confirmation of sublunarean voids and thin layering in mare deposits. Planetary and Space Science 69(1), 18-27. (https://doi.org/10.1016/j.pss.2012.05.008)

Wagner, R.V., Robinson, M.S., 2022. Lunar Pit Morphology: Implications for Exploration and Science. Journal of Geophysical Research: Planets 127(8), e2022JE007328. (https://doi.org/10.1029/2022JE007328)

Wagner, R.V., Robinson, M.S., 2014. Distribution, formation mechanisms, and significance of lunar pits. Icarus 237, 52-60. (https://doi.org/10.1016/j.icarus.2014.04.002)

Williams, J.P., Paige, D.A., Greenhagen, B.T., Sefton-Nash, E., 2017. The global surface temperatures of the Moon as measured by the Diviner Lunar Radiometer Experiment, Icarus 283, 300-325. (https://doi.org/10.1016/j.icarus.2016.08.012)

Zhu, K., Yang, M., Yan, XY, Li, WK., Feng, W., Zhong,M., 2024. GRAIL gravity gradients evidence for a potential lava tube at Marius Hills on the moon, Icarus 408,115814, (https://doi.org/10.1016/j.icarus.2023.115814)

17th INTERNATIONAL CONGRESS of the Geological Society of Greece

BULLETIN OF THE GEOLOGICAL SOCIETY OF GREECE, SP. PUBL.

EXTENDED ABSTRACT 151

Utilizing engineering geological database for urban geohazard assessment: a case study from Thessaloniki, Greece

Kokkala A.[1], Marinos V.[2], Papathanassiou G.[1]

(1) School of Geology, Aristotle University of Thessaloniki, Thessaloniki, Greece, kokkalaaliki@gmail.com

(2) School of Civil Engineering, National Technical University of Athens, Athens, Greece

Introduction

This research presents an advanced engineering geological database, designed to comprehensively manage extensive geological and geotechnical data (Kokkala, 2023). Based on the Tunnel Information and Analysis System (TIAS) framework (AGS, 1999; Marinos et al., 2013), the database integrates information from numerous boreholes and geotechnical investigations conducted in Thessaloniki's urban area, northern Greece, focusing on Quaternary and Neogene sediments, as well as fill deposits. Its primary aim is to reduce geological uncertainties and address geotechnical challenges critical for urban safety and planning, by means of numerous database applications (Kokkala and Marinos, 2022). Emphasizing the utility of big data management, the study explores how geological heterogeneity, subsurface variations, and engineering geological conditions can be better understood to mitigate geohazards (e.g. liquefaction as the application example used here) and support early-stage infrastructure design.

Methods

In this study, Standard Penetration Test (SPT) and Cone Penetration Test (CPT) results were analyzed to investigate liquefaction susceptibility and potential in an area located at the vicinity of Thessaloniki airport (Figure 1), as a database application for urban geohazard assessment. Based on the outcome arisen by the geotechnical investigation, it was concluded that the subsoil profile predominantly consists of sandy clays and silts, interspersed with medium-density sand layers. Two distinct sub-areas (A and B), differentiated based on their proximity to the stream located to the south, were analyzed to evaluate in situ conditions and liquefaction susceptibility.

A series of cross-sections, such as the example shown in Figure 2, was developed to illustrate the distribution of the Soil Behavior Type Index-SBTn (Ic) based on the liquefaction susceptibility criterion proposed by Robertson and Wride (1998). Further analysis involved the assessment of the liquefaction potential index (LPI) alongside estimations of vertical and lateral displacements for each sub-area, utilizing the available CPT data. For this purpose, two distinct seismic scenarios were considered: the first one involves the activation of the Anthemoundas fault, resulting in a seismic event with a magnitude of M 6.9 and peak ground acceleration of 0.4 g, while the second scenario refers to the activation of the Gerakarou fault, generating a seismic event with a magnitude of M 7.0 and peak ground acceleration of 0.5 g (Lin and Smerzini, 2022).

Results

The analysis revealed stratigraphic differences between the sub-areas. Sub-area A exhibited a higher concentration of coarse-grained materials in places, whereas sub-area B was dominated by fine-grained deposits, reflecting variations in the depositional environment. In most soil columns, LPI values exceeding 5% were observed throughout the study area under the first seismic scenario, indicating a high to very high liquefaction potential. Additionally, vertical displacements ranged from 16 to 19 cm and lateral displacements reached up to 220 cm were estimated under both seismic scenarios for the two sub-areas.

Conclusions

This study highlights the essential role of integrating primary geological and geotechnical data into a well-structured database for detailed geohazard analysis. The proposed methodology showcases the utility of an engineering geological database in evaluating and mitigating liquefaction, providing critical insights for enhancing urban safety and optimizing infrastructure design.

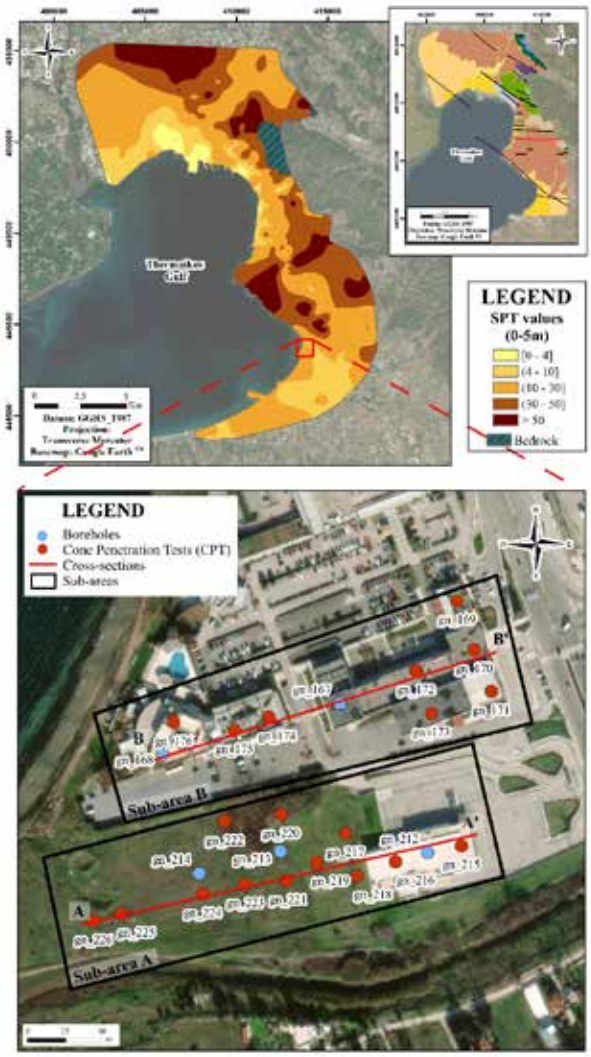

Figure 1. Spatial distribution map of SPT for depth 0-5 m accompained by the updated engineering geological map of Thessaloniki city (for detailed engineering geological map refer to Kokkala and Marinos, 2022, from Rozos *et al.*, 1998), illustrating the studied area used as an engineering geological database application (Kokkala, 2023).

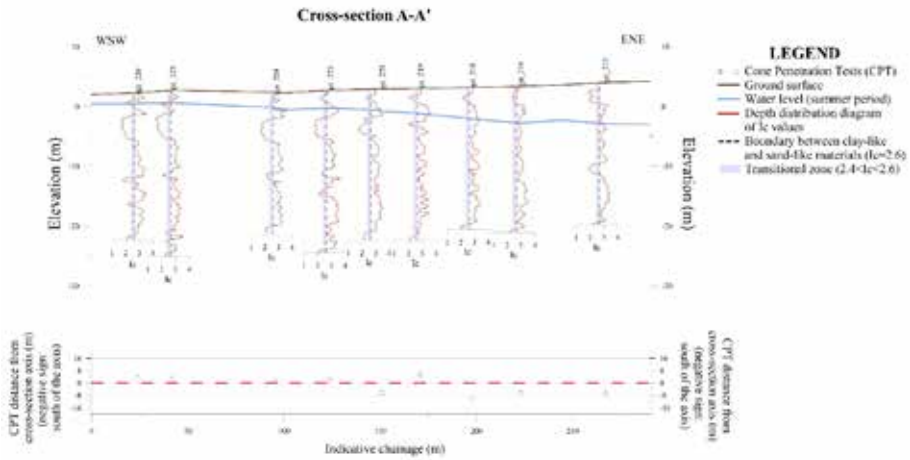

Figure 2. Cross-section A-A' (see Figure 1), presenting the graphical distribution of Ic values (Kokkala, 2023).

Acknowledgements

The research was funded by the Hellenic Foundation for Research and Innovation (HFRI) through the HFRI PhD Fellowship grant (Fellowship Number: 99319). The authors extend their gratitude to the Central Laboratory of Public Works, Geognosi S.A., Attiko Metro S.A., Egnatia Odos S.A., and the National Cadastre and Mapping Agency S.A. for generously providing the data used in this study.

References

Association of Geotechnical and Geoenvironmental Specialists (AGS), 1999. Electronic Transfer of Geotechnical and Geoenvironmental Data, 3rd ed.

Kokkala, A., 2023. Engineering geological assessment and classification of Thessaloniki's urban area formations using a geotechnical database. Research on the technical behavior and applications in the design of engineering projects. Ph.D. Thesis, Aristotle University of Thessaloniki, Thessaloniki, 570 p.

Kokkala, A., Marinos, V., 2022. An engineering geological database for managing, planning and protecting intelligent cities: The case of Thessaloniki city in Northern Greece. Engineering Geology 301, 106617, https://doi.org/10.1016/j.enggeo.2022.106617

Lin, J., Smerzini. C., 2022. Variability of physics-based simulated ground motions in Thessaloniki urban area and its implications for seismic risk assessment. Frontiers in Earth Science, 10: 951781. https://doi.org/10.3389/feart.2022.951781

Marinos, V., Prountzopoulos, G., Fortsakis, P., Koumoutsakos, D., Korkaris, K., Papouli, D., 2013. Tunnel information and analysis system: a geotechnical database for tunnels. Geotechnical and Geological Engineering 31, 891–910, https://doi.org/10.1007/s10706-012-9570-x

Robertson, P.K., Wride, C.E., 1998. Evaluating cyclic liquefaction potential using the cone penetration test. Canadian Geotechnical Journal, 35 (3): 442–459

Rozos, D., Apostolidis, E., Hadzinakos, I., 1998. Engineering-Geological Map of the Wider Thessaloniki Area, 1:25,000 Scale. I.G.M.E, Athens

17th INTERNATIONAL CONGRESS of the Geological Society of Greece

BULLETIN OF THE GEOLOGICAL SOCIETY OF GREECE, SP. PUBL.

EXTENDED ABSTRACT 152

Diapiric structures in evaporites of Western Greece as potential geoenergy storage areas

Kokkalas S.[1], Psarros V.[1], Koutsovitis P.[1]
(1) Department of Geology, University of Patras, Greece, skokalas@upatras.gr

Introduction-Research background

The capture and storage of CO_2 is an important process as it helps to prevent the negative impacts of CO_2 emissions in the atmosphere, such as the greenhouse effect and ocean acidification among others. On the other hand, the storage of H_2 is an environment-friendly process, as it allows for large-scale controlled and flexible energy conversion. Storage of both hydrogen and carbon dioxide in salt caverns has emerged recently as a favorable option due to its numerous benefits, such as the high withdrawal capacity, favorable mechanical properties, and enhanced safety (Tackie-Otoo & Haq, 2024). Despite the increasing demand in geo-energy storage, there is limited relevant literature, mainly on underground geoenergy storage in geological structures in Greece (Arvanitis et al., 2020; Makri et al., 2022). Triassic evaporites diapirism, which involves the buoyant uprise of large evaporite masses through piercing and displacing, are either reaching the surface or halting at a depth, as is evidenced in several seismic profiles. They mainly occur in Western Greece along the Ionian zone, such as in the areas of Aitolo-Akarnania, Hepirus, the Ionian islands, as well as in the Western Peloponnese (Underhill, 1988; Kamberis et al., 2022; Soto et al., 2024). Salt caverns provide significantly higher storage volumes compared to traditional fuel tanks, making them ideal for large-scale energy storage (Fig. 1). The geological suitability for geo-energy storage in salt caverns is determined by certain fundamental geological criteria such as: i) the depth of the storage cavities, ii) the minimum thickness of the salt formation, (iii) the mineralogical composition of the salt formations and (iv) the petrophysical properties of the host rock (i.e., low porosity and permeability, pore structure etc.), in order to ensure that the supercritical gas remains in the cavity and to prevent the potential risk of leakage.

The above criteria for geological suitability for subsurface storage were examined and evaluated in some representative areas in Western Greece, where evaporitic rock samples were collected and analyzed, by applying several laboratory techniques, upon samples from the areas of Katouna (Aitolo-Akarnania), Pagos (Corfu), and various sites in the proximity to Preveza (Kanalaki-Aidonia-Chimadio). Based on the interpretation of these preliminary results, and the percentage of coverage of the required geological criteria for underground energy storage, the prospects of underground storage in artificial cavities in evaporite rock formations are discussed and the adverse factors that require further study in the future research stages are presented.

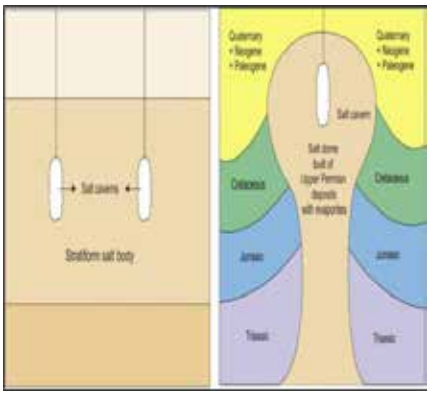

Figure 1. Salt cavern in a salt diapiric structure (Tarkowski and Czapowski 2018).

CO_2 and H_2, as representative gases for underground gas storage, exhibit significant differences in physical properties, particularly in density and viscosity. Storage of CO_2 in salt caverns is a promising solution, since it not only provides permanent storage but can also operate as a renewable and sustainable method for utilizing CO_2 as a valuable industrial resource.

For the underground storage of geoenergy, salt caverns are currently considered to offer the most promising option owing to their low investment cost, high sealing capacity, the inert nature of salt structures, and the low cushion gas requirement (Fig. 1; Caglayan et al., 2020). Rock salt properties such as permeability, porosity, and pore pressure, are crucial parameters to consider for hydrogen storage and to evaluate potential migration (AbuAisha and Billiotte, 2021).

Several sites for hydrogen storage in salt caverns in UK (Teeside), USA (Clemens Dome, Moss Bluff) operate for nearly 50 years, at depths below 1 km, demonstrating that underground storage is a technically-feasible option (Landinger and Crotogino, 2007; Tarkowski, 2019). For the Greek region a total cavern storage potential mainly onshore (within 50 km from the shore) is estimated around 10^2 TWh (Caglayan et al., 2020).

Geological setting

Although the Ionian Zone has been extensively studied, having attracted the interest for hydrocarbon exploration in Greece (Zelilidis et al., 2015), there is still much ambiguity in the deeper structures of the crust of the External Hellenides. Western Greece is considered as a region with mainly thin, or possibly coexistence of thin and thick-skinned deformation of the Mesozoic-Cenozoic succession above the Triassic evaporites and Permian sequences (Kokkalas et al., 2013). The Ionian Zone consists of sedimentary rocks ranging from Triassic evaporites at the base, to Jurassic–upper Eocene carbonates with minor cherts and shales (Karakitsios, 1995; Rigakis et al., 2007; Karakitsios et al., 2015; Bourli et al., 2019; Kamberis et al., 2022). Thick Upper Eocene to Miocene flysch deposits overlie the carbonate sequence (Avramidis et al., 2002; Vakalas et al., 2024). The Ionian Zone boundary towards the west is marked by intrusive evaporites that represent the lowest detachment level of individual overthrust sheets in the External Hellenides.

The Ionian Zone consists of three distinct stratigraphic sequences (Karakitsios, 2013): a) a pre-rift sequence (Triassic – Early Jurassic) represented by a thick evaporitic succession (with an estimated thickness that exceeds 2 km) overlain by shallow marine carbonates. Regarding the depositional environment, the alternating sulphate and carbonate constituents correspond probably to an arid and shallow depositional setting (Karakitsios, 1995). Evaporites are often related to extensive exposures of dissolution breccia of Triassic age (Triassic breccia); b) a syn-rift sequence (Early to Late Jurassic) where the basin was compartmentalized, and a half-graben geometry was favored, as reflected in variations in sediment type (pelagic carbonates and deep water clastics) and thickness (Karakitsios, 2013). During this stage, the evaporites were mobilized forming several types of diapiric structures; c) A post-rift sequence (Early Cretaceous to Eocene) marking by the deposition of pelagic limestones.

However, new insights into the evolutionary structural model of the Ionian fold-and-thrust belt in central-south Albania and Western Greece have been revealed, based on significant information provided from detailed fieldwork and new seismic data, suggesting an alternative model that places the rifting stage earlier in the Triassic and demonstrating the clear influence of salt tectonics since the Early Jurassic (Hernandez et al., 2019; Vakalas et al., 2023; Soto et al., 2024).

Methods

Fieldwork and preliminary sampling were conducted in five areas along western Greece, specifically on Corfu Island (Pagoi), in several sites of Preveza region (Aidonia, Chimadio and Tsouknida) and along a continuous road outcrop near Katouna area (Table 1). The rock samples were carefully selected to avoid areas of high dissolution and internal fracturing, in order to comply with the requirements for each of the following analytical techniques. For the determination of the mineralogical and quantitative composition of the samples, X-Ray Powder Diffraction analyses (XRD) and Fourier-Transform Infrared Spectrometry (FTIR) were conducted. For the characterization of their petrophysical properties, such as porosity, pore size distribution (PSD), permeability and specific surface area, Brunauer-Emmett-Teller (BET) analysis with nitrogen and Mercury Injection Capillary Pressure (MICP) analysis (Table 2), were carried out in parallel, in the facilities of the Department of Material Sciences and FORTH/ICE-HT (Upatras), respectively. Investigation of the sealing capacity and pore-throat-aperture size distribution in samples was conducted via mercury porosimetry using the latest Micromeritics Autopore III porosimeter, which is capable of injecting non-wetting phase (mercury) in user-defined, step-like pressure increments (0.5 to 2 psi) up to 60,000 psi (~413 MPa) into an evacuated, cleaned, and dried rock sample.

Results

The analyzed evaporite samples can generally be distinguished into those being rich in gypsum and those being rich in anhydrite (Table 1). The samples have a dominance of gypsum in the samples Pg2, KAT, KAT1, KAT2, Aid2, whereas anhydrite is the predominant phase in samples Pg1, Pg3, and Chm1b.

Mercury porosimetry showed porosity values that range from 0.17% to 5.06% (Table 2), with a wide distribution of pore diameters D (Fig. 2). The mean pore-throat diameter values in the samples indicate macroporous materials, with samples Pg2, Chm_1b and Aid2 showing the lowest mean values (0.55-0.57 μm), whereas the highest value is shown in sample KAT1 (1.10 μm). Since these samples were collected from surface outcrops, a reference evaporite sample (Mo1#7) from a borehole in southwest Montenegro at a depth of ~ 3 km, (kindly provided by Energean Montenegro Ltd.) was used for comparison; it showed a mean PSD value of 0.19 μm (Table 2). The permeability exhibits relatively low values, ranging from 0.01549 to 0.46367 mD. For comparison the reference sample Mo1#7 showed a permeability of 0.00587 mD.

Table 1. Results of XRD-analysis in the studied samples.

Samples ID	Location	Mineral content (in %)						
		Gypsum	Anhydrite	Halite	Dolomite	Calcite	Celestite	Quartz
KAT	Katouna	30	4	9	10	17	7	20
KAT 1	Katouna	35	4	13	13	21	6	5
KAT 2	Katouna	36	3	11	9	20	8	9
Aid2	Aidonia (Preveza)	98	-	-	<2	-	-	-
Chm	Chimadio (Preveza)	15	-	-	-	85	-	-
Chm_1b	Chimadio (Preveza)	4	30	<3	<3	34	<3	27
Tsk	Tsouknida (Preveza)	10	-	-	-	90	-	-
Pg 1	Pagoi (Corfu)	4	43	<3	<3	44	<3	7
Pg 2	Pagoi (Corfu)	37	<3	8	10	18	7	18
Pg 3	Pagoi (Corfu)	4	30	<3	<3	30	<3	29

In order to additionally investigate the presence and size of the micro-mesopores BET-analysis was performed, which has a different resolution capability than MICP. The BET-analysis confirmed the wide distribution of pore width ranging from micropores (width 1.6-3 nm), mainly mesopores (width 7-10 nm), and also macropores (width 50-100 nm). A mean pore diameter of approximately 3.8 nm is observed, indicating the presence of micro-mesoporosity in the samples, which would be unfeasible to determine by applying only the mercury porosimetry measurement technique. Furthermore, the specific surface area shows values ranging from 19.9 to 22.7 m^2/g.

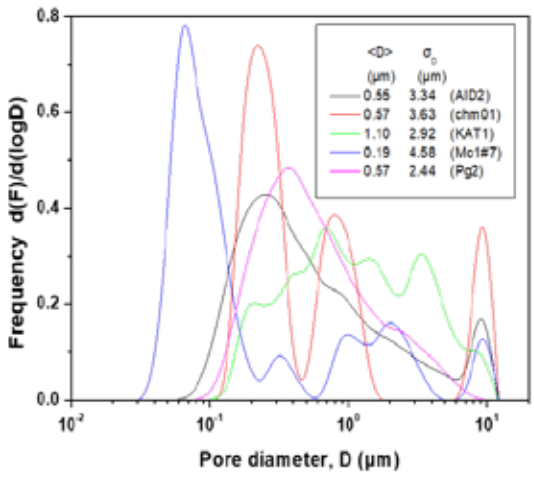

Figure 2. Pore size distribution diagram of the samples from the MICP analysis.

In the BET analyses, it is observed that all samples belong to the type III isotherm adsorption. Type III isothermal adsorption is convex on the P/Po axis throughout the entire adsorption process, and for this reason, there are no inflection points (Fig. 3). From the types of adsorption-desorption isotherm (type III), which are not common, it appears that there is little interaction between the gas and the adsorbing surface. Regarding the type of hysteresis loop, all samples exhibit an H3-type hysteresis loop, which appears only in the mesoporous structure due to capillary condensation, and this is confirmed by the pore size distribution (PSD) assessed through analytical techniques. This indicates that the pores exhibit slit-like shapes and it is considered that materials with such characteristics tend to behave as microporous materials, regardless of the PSD.

Table 2. Results from MICP-analysis in selected samples.

Sample	Pore volume, V_p (cm^3/g)	Specific surface area, S_p (m^2/g)	Porosity (%)	Mean value of PSD (μm)	Standard deviation of PSD (μm)	Tortuosity τ	$k = \varphi < D_p >^2 / (16\tau)$ (mD)
Aid2	0.0220	0.258	4.74	0.55	3.34	2.217	0.40422
Chm1b	0.0007	0.007	0.17	0.57	3.63	2.229	0.01549
KAT1	0.0028	0.018	0.63	1.10	2.92	2.228	0.21384
Pg2	0.0235	0.222	5.06	0.57	2.44	2.216	0.46367
Mo1#7	0.0020	0.079	0.58	0.19	4.58	2.229	0.00587

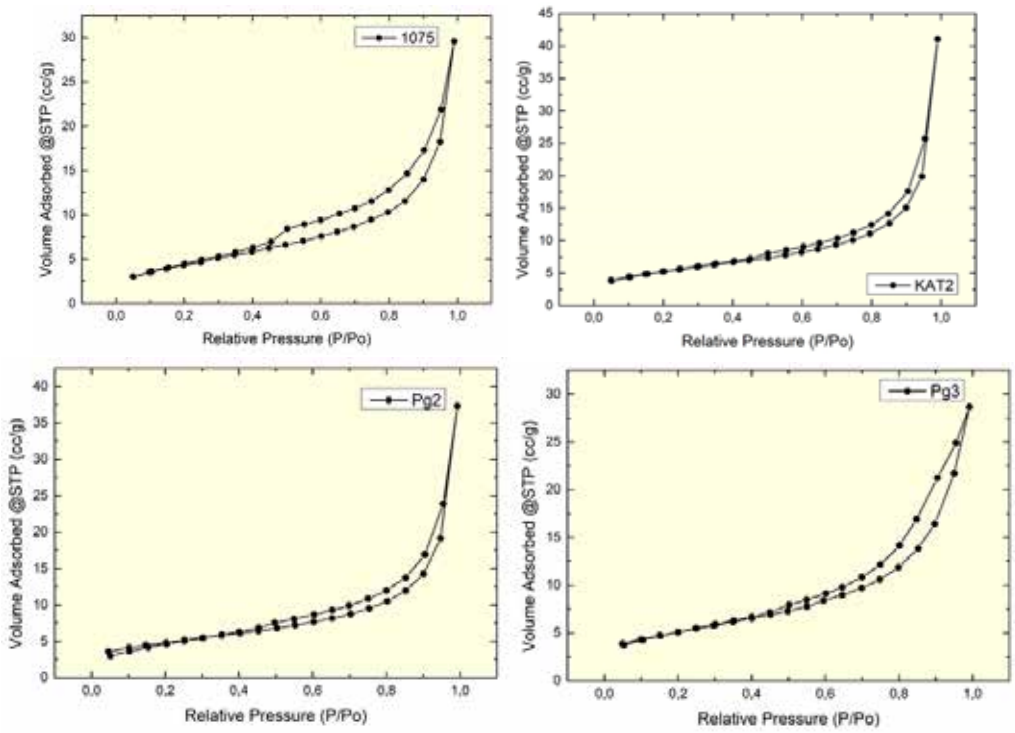

Figure 3. Isotherm absorption curves and hysteresis loops for the examined samples in BET analysis.

Discussion-Conclusions

The porosity of the studied evaporite samples appear to exhibit a complex structure involving micro-, meso-, and macropores, and potentially interconnected pores (microcavities due to dissolution). The range of their pore size (diameter) distribution values was estimated by combining results from both BET and MICP techniques, as there is a different resolution capability between these techniques. In general, the porosity of the samples shows low values ranging from 0.17 to 5% and relatively low permeabilities (0.01-0.46 mD). Since these are preliminary data and the research is still ongoing on this subject, more data will be required from other evaporitic rock sites in western Greece to have a better overview of their petrophysical properties.

The halite (NaCl) at a percentage higher than 95%, the depth of the cavity formation (which ideally should range between a min of 800 m and max of 1300 m for the higher capacity of hydrogen storage), and the ideal thickness of the evaporite formation, in the range of 150-200 m, are some of the most important required factors for the underground geological storage of carbon dioxide and hydrogen in salt cavities to be considered.

Existing data from boreholes and seismic interpretations of salt structures (pillows, plugs and diapirs) in western Greece (Fig. 4, Kamberis et al., 2022; Soto et al., 2024), suggest that in the area of Filiates the presence of thick halite appears at a non-ideal depth of 1700 m and deeper, as anhydrite predominates at shallower depths (from 300-1600 m in Filiates-1 well). In Delvinaki, halite predominates at the desired depth (700-1000 m) with sufficient thickness (approx. 400 m) and minimal presence

of dolomite. In Tryfos, (Aitolo-Akarnania) and Parakalamos, although the formation depth is ideal, the lack of halite and the presence mainly of anhydrite-gypsum and dolostone sequence requires further investigation and analyses, mainly due to the slower dissolution of the formation compared to halite and issues of stability and sealing of the walls of the artificially formed cavity. Despite that, the visco-plastic properties of evaporitic rocks may improve their sealing function, since they have the ability for "self-sealing" the potential microfractures under cyclic stress (Lyu et al., 2023). Thus, detailed studies on the mechanical properties of the evaporitic rocks are crucial when selecting a site for underground storage.

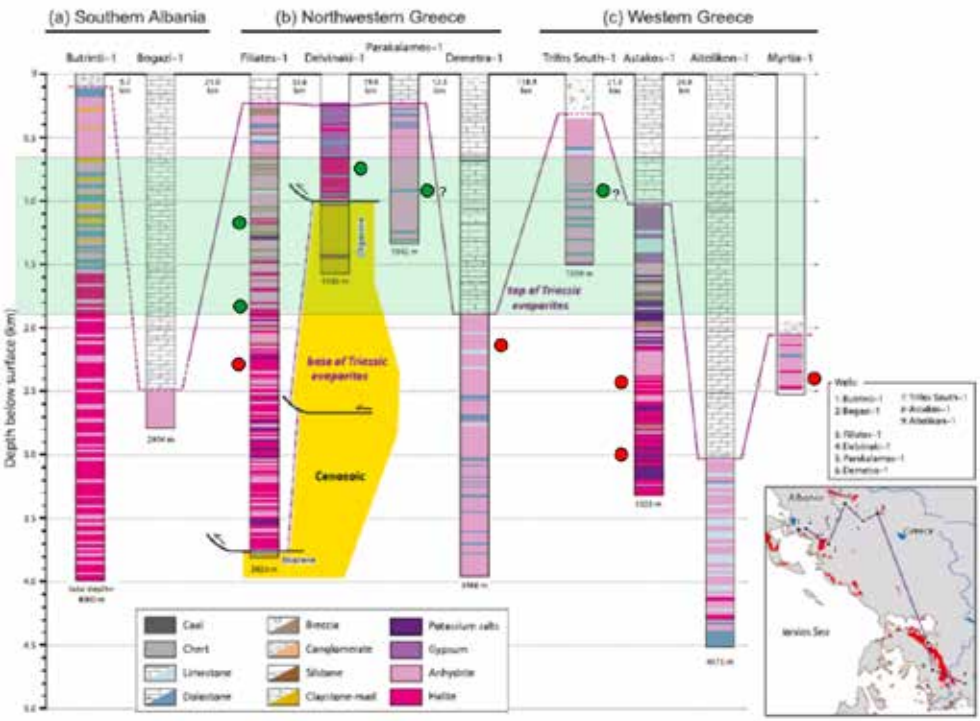

Figure 4. Triassic evaporite sequences with well correlation in north-western and western Greece and inset showing the position of wells and main outcrops of Triassic evaporites in the Ionian zone (from Soto et al., 2024). Original figure is modified showing the ideal depths for subsurface geoenergy storage with green shading, while green/red circles indicate the potential sites with favorable/unfavorable conditions for storage, respectively, based on combined depth/lithology selection criteria.

Although until recently, the construction of artificial cavities in evaporitic formations has been carried out exclusively in areas with a high percentage of halite (>95%), recent studies have shown that salt-rich gypsum rocks can also be characterized as high-quality seals for hydrocarbon reservoirs, due to their strong plasticity, and their excellent petrophysical and mechanical properties (Lyu et al., 2023). However, the effect of cyclic loading on their sealing capacity in a cavity needs further investigation, which limits progress in such storage plans (Lyu et al., 2023). Furthermore, a recent experimental study suggests that the geochemical reactivity of hydrogen with salt cavern minerals (halite-anhydrite-gypsum) is very weak at relatively low temperatures, within short period of time with hydrogen treatment, demonstrating high stability and integrity of salt caverns during short hydrogen storage cycles, with no major alterations in pore structure analysis (Fatah et al., 2024).

Based on these new published data (Fig. 4), and in conjunction with the analytical results of the present study, areas such as Pagoi (Corfu Island) and Katouna (Aitolo-Akarnania region), exhibit promising petrophysical characteristics, which, together with the aforementioned areas of Delvinaki and Filiates (mostly based on the available well data and the seismic profile interpretations; Soto et al., 2024), provide favorable prospects for further research as potential underground storage sites for H_2 and/or CO_2. The areas of Corfu and Trifos (north of Katouna) in Aitolo-Akarnania have been proposed also by Arvanitis et al. (2020), as potential H_2 storage sites, based mainly on their storage capacity (367 km^3), taking as a scenario a capsule-shaped cavern, with dimensions of 300 m height and 60 m in diameter, at a depth of 650 m.

It is also worth to mention that a significant issue in the development of such areas for subsurface storage of hydrogen is the lack of a specific legislation that regulates, based on technical-geological and economic-technical criteria, the entire process related to underground hydrogen storage, from the selection of the site to the injection process, including the monitoring and an action plan after the exploitation of the storage facility.

Acknowledgements
We would like to thank our colleague Ass. Prof. P. Lampropoulou (University of Patras) for her assistance with XRD analysis, Prof. G. Avgouropoulos and Dr. St. Tombros (Department of Material Science, University of Patras) for their help with BET-analysis and Dr. Ch. Tsakiroglou for conducting the MICP-analysis in FORTH/ICE-HT at the University of Patras.

References

AbuAisha, M., Billiotte, J., 2021. A discussion on hydrogen migration in rock salt for tight underground storage with an insight into a laboratory setup. Journal of Energy Storage 38, art. #102589.

Arvanitis, A., Koutsovitis, P., Koukouzas, N., Tyroglou, P., Karapanos, D., Karkalis, C., Pomonis, P., 2020. Potential sites for underground energy and CO_2 storage in Greece: A geological and petrological approach. Energies 13, art. #2707.

Avramidis, P., Zelilidis, A., Vakalas, I., Kontopoulos, N., 2002. Interactions between tectonic activity and eustatic sea-level changes in the Pindos and Mesohellenic Basins, NW Greece: Basin evolution and hydrocarbon potential. Journal of Petroleum Geology 25(1), 53–82.

Bourli, N., Pantopoulos, G., Maravelis, A. G., Zoumpoulis, E., Iliopoulos, G., Pomoni-Papaioannou, F., et al., 2019. Late Cretaceous to early Eocene geological history of the eastern Ionian Basin, southwestern Greece: A sedimentological approach. Cretaceous Research 98, 47–71.

Caglayan, D.G., Weber N., Heinrichs, H., Linßen, J., Robinious, M., Kukla, P.A., Stolten D., 2020. Technical Potential of Salt Caverns for Hydrogen Storage in Europe. International Journal of Hydrogen Energy 45, 6793-6805.

Fatah, A., Al-Yaseri, A., Theravalappil, R., Radwan, O., Amao, A., Al-Qasim, A., 2024. Geochemical reactions and pore structure analysis of anhydrite/gypsum/halite bearing reservoirs relevant to subsurface hydrogen storage in salt caverns. Fuel 371, Part A. art. #131857,

Hernández, P., Pérez Martín, R., Pita, J.P., Ponte, A., Rubio, B., Malmcrona, Y., Chambers, A., Martin, A., Cascone, L., Konstantopoulos, T., et al., 2019. New structural and petroleum system models of the Ionian Zone, North-Western Greece. In 15th International Congress of the Geological Society of Greece, Athens, Greece, p. 527–528.

Kamberis, E., Kokinou, E., Koci, F., Lioni, K., Alves, T.M., Velaj, T., 2022. Triassic evaporites and the structural architecture of the External Hellenides and Albanides (SE Europe): Controls on the petroleum and geoenergy systems of Greece and Albania. International Journal of Earth Sciences 111(3), 789–821.

Karakitsios, V., 1995. The influence of preexisting structure and halokinesis on organic matter preservation and thrust system evolution in the Ionian Basin, Northwest Greece. AAPG Bulletin 79(7), 960–980.

Karakitsios, V., 2013. Western Greece and Ionian Sea petroleum systems. AAPG Bulletin 97(9), 1567–1595.

Kokkalas, S., Kamberis, E., Xypolias, P., Sotiropoulos, S., Koukouvelas, I., 2013. Coexistence of thin- and thick-skinned tectonics in Zakynthos area (western Greece): Insights from seismic sections and regional seismicity. Tectonophysics 597–598, 73–84.

Landinger, H., Crotogino, F., 2007. The role of large-scale hydrogen storage for future renewable energy utilisation. In Second international renewable energy storage conference (IRES II), 19-21.

Lyu, X., Yun, L., Xu, J., Liu, H., Yu, X., Peng, P., Ouyang, M., Luo, Y., 2023. Sealing capacity evolution of gypsum salt caprocks under multi-cycle alternating stress during operations of underground gas storage. Journal of Petroleum Science and Engineering 220, art. #111244.

Makri, V.I., Bellas, S., Gaganis, V., 2021. Assessing Natural Gas Versus CO_2 Potential Underground Storage Sites in Greece: A Pragmatic Approach. Materials Proceedings 5(1), 98.

Rigakis, N., Nikolaou, K., Marnelis, F., Pakos, T., 2007. The utility of oil shows in the hydrocarbon exploration of western Greece. Bulletin of the Geological Society of Greece 40(2), 959–971.

Soto, J. I., Tranos, M. D., Bega, Z., Dooley, T. P., Hernández, P., Hudec, M. R., et al. 2024. Contrasting styles of salt-tectonic processes in the Ionian Zone (Greece and Albania): Integrating surface geology, subsurface data, and experimental models. Tectonics, 43, e2023TC008104, https://doi.org/10.1029/2023TC008104.

Tackie-Otoo, B.N., Haq, M.B., 2024. A comprehensive review on geo-storage of H_2 in salt caverns: Prospect and research advances. Fuel 356, p. 129609.

Tarkowski R. 2019. Underground hydrogen storage: characteristics and prospects. Renew Sustain Energy Rev. 105, 86-94.

Tarkowski, R., Czapowski, G., 2018. Salt domes in Poland-Potential sites for hydrogen storage in caverns. International Journal of Hydrogen Energy, 43, 21414-21427.

Vakalas, I., Kokkalas, S., Konstantopoulos, P., Tzimeas, C., Kampolis, I., Tsiglifi, H., et al., 2023. Implications of salt diapirism in syn-depositional architecture of a carbonate margin-to-edge transition: An example from Plataria syncline, Ionian Zone, NW Greece. Applied Sciences 13(2), 7043.

Zelilidis, A., Maravelis, A.G., Tserolas, P., Konstantopoulos, P.A., 2015. An overview of the petroleum systems in the Ionian Zone, onshore NW Greece and Albania. Journal of Petroleum Geology 38(3), 331–348.

17th INTERNATIONAL CONGRESS of the Geological Society of Greece

BULLETIN OF THE GEOLOGICAL SOCIETY OF GREECE, SP. PUBL.

EXTENDED ABSTRACT 153

The Argo-Beachrock Project: web mapping and geovisualisation of beachrocks using UAS along the coast of the Argolic Gulf, Greece

Kolaiti E. [1], Soulakellis N.[2], Tataris G.[2], Mourtzas N.[3]

(1) Society for the Study of Ancient Coastlines - AKTES NPO; National Hellenic Research Foundation, Institute of Historical Research; University of Nottingham, Department of Classics and Archaeology; Chalandri, Athens, Greece, kolaitieleni@gmail.com (2) University of the Aegean, Department of Geography, Cartography and Geoinformatics Laboratory, Mytilene, Lesvos, Greece (3) Society for the Study of Ancient Coastlines - AKTES NPO; University of Nottingham, Department of Classics and Archaeology; Chalandri, Athens, Greece

Research Highlights

Web mapping and geovisualisation of beachrocks using UAS along the littoral zone of the Argolic Gulf: a methodological approach to surveying the nearshore zone, with advantages and constraints for bathymetric reconstruction.

Introduction - Background

Beachrocks are rocky coastal deposits that form during relatively short periods along the shoreline within the intertidal zone, under complex physicochemical (e.g., Ginsburg, 1953; Taylor and Illing, 1969; Moore, 1973; Hanor, 1978; Meyers, 1987) and biological (e.g., Webb *et al.*, 1999; Neumeier, 1999) cementation processes. They consist of coastal sediments, such as sand, gravels, pebbles, cobbles and other coarse materials of both clastic and biogenic origin, and even of anthropogenic origin (e.g., ancient remains), usually cemented with calcium carbonate, high/low magnesian calcite and aragonite. It is generally accepted that beachrock lithification takes place in the intertidal zone (e.g., Scholle and Ulmer-Scholle, 2003; Vousdoukas *et al.*, 2007; Mauz *et al.*, 2015). In microtidal environments such as this, in the central Aegean where the maximum and mean tidal ranges do not exceed 0.30 m and 0.15 m, respectively (HNHS, 2015), the cementation of coastal sediments exceeds the tidal range and expands into the swash, saturated, zone (Gifford, 1995; Kolaiti *et al.*, 2017; Kolaiti, 2019). Diagenesis is similar in both the intertidal and the swash and backwash zones, and the cementation results are indistinguishable (Bernier and Dalongeville, 1996). Therefore, beachrocks demarcate an ancient coast during their formation, with the base of the seaward end of a beachrock slab, in its well-preserved parts that have not undergone erosion or fragmentation, representing the mean low tide of a former sea level (e.g., Kolaiti and Mourtzas, 2023). Different sea level stands form distinct beachrock slabs at various elevations that correspond to different generations of a fossilized palaeoshoreline (e.g., Vousdoukas *et al.*, 2007; Desruelles *et al.*, 2009; Mauz *et al.*, 2015 and references therein; Mourtzas and Kolaiti, 2020). The loose, unconsolidated, sandy/sandy-gravel sediments laid on the sea bottom between two different beachrock generations represent a period of relative sea level (rsl) change (e.g., Desruelles *et al.*, 2009). Fossils, organic material or archaeological remains embedded in a beachrock are a *terminus post quem* for the beachrock formation, postdating the embedded material (Kolaiti, 2019).

The study of beachrocks provides valuable knowledge about the ancient environmental, geological, sedimentological, and geomorphological conditions that prevailed in the littoral zone during their formation process (Mauz *et al.*, 2015 and references therein). Their development along a sandy coastline contributes to mitigating the effects of marine erosion, i.e., the irreversible retreat of the coastline caused by natural (e.g., storms, waves, ocean currents, sea level rise) and anthropogenic (e.g., residential and touristic development, coastal infrastructure) processes in the coastal zone. This results in a systematic alteration of the coastscape, with the sea covering large sections of the vulnerable sandy beach. The submerged beachrock slabs in the nearshore zone due to relative sea level rise can act as natural barriers against coastal erosion, despite the loss of sediment during their initial cementation, thus changing the seascape and affecting the coastal morphodynamics (Psomiadis *et al.*, 2010). On the other hand, the rsl rise results in exposure of beachrocks along the contemporary coast (typical example from the study area: the Ververonta beachrock), which were previously buried under beach sediments, thus turning a sandy beach into rocky. This may have several social-economic impacts on the touristic exploitation of a beach and requires appropriate coastal management (Vousdoukas et al., 2009), in order to avoid inconsiderate destruction by locals (typical example from the study area: the Plaka-Drepano beachrock). As an alternative protection measure against coastal erosion, of lower

cost and more environmentally friendly than heavy engineering structures, several studies have focused on coastal ground improvement based on bio-stimulation, that is cementation of coastal sediments on the erosion-prone beach following the formation process of beachrocks and using local bacteria and seawater (e.g., Danjo and Kawasaki, 2016; Saitis *et al.*, 2022).
Due to their lateral spread and, often, their significant thickness, beachrocks contribute to the preservation of biodiversity in the nearshore marine ecosystems, effectively acting as a natural reef on the sandy seabed and a safe habitat of several species of marine life (seaweed, algae, organisms, fish, etc.).
Finally, recently initiated experimental researches attempt to link beachrocks with natural CO_2 storage exploring their role in reducing the environmental footprint of a region, as it has been demonstrated for CO_2 sequestration in sandstone reservoirs (e.g., Koukouzas *et al.*, 2018; Gholami and Raza, 2022).

Project area - Objective
The pilot area for the implementation of the Argo-Beachrock Project is the nearshore of the south Argolic Peninsula, from the southern part of the Saronic Gulf, at the eastern edge of the Hydra Strait, to the mouth of the Argolic Gulf, on the western coast of the Myrtoan Sea. The study area stretches across 255 km of coastline and includes 20 locations with beachrock formations, which collectively cover a total length of 20 km (Fig. 1).
This area was chosen partly because numerous submerged beachrock generations have already been recorded at various locations and depths, indicating distinct ancient lithified beaches formed during different periods. Notably, it includes the deepest recorded occurrence of Holocene beachrock observed in Greece to date (i.e., -8.85 m below mean sea level, Tigani coast, Tyros Bay) (Kolaiti, 2019). Additionally, it is a region undergoing systematic tourism development.

Figure 1. Map of the project area. The survey areas are indicated by red bullets.

The objectives of the Argo-Beachrock Project could be outlined as follows:
- UAV mapping and documenting of beachrock formations, including UAV and underwater survey, and depth measuring and validation.
- Analysis and processing of spatial data, production of high-resolution orthophoto maps, digital surface models (DSM), and 3D models.
- Visualisation of 2D information on an open-access web-map platform, creation of thematic maps, photographic material.
- Understanding coastal dynamics, environmental conditions, and natural processes through the comprehension and synthesis of all available data on the formation and evolution of beachrocks.
- Creating a comprehensive database (incl. location, depth per generation, mineralogical composition, if available, and absolute and indirect dating for each survey site), thus enhancing scientific knowledge and providing data available for future research.

- Disseminating the project results in order to raise public awareness of the importance of coastal protection through the study and preservation of beachrock formations, highlighting their role in mitigating erosion and preserving ecosystems. Collaboration with local communities, researchers, and stakeholders.

Methods

The submerged beachrock formations throughout the survey area have been previously mapped, their features (length, width and thickness) recorded, and the depth of the seaward and landward end of the top and base of each beachrock generation in each location were measured during previous snorkel geological surveys using customary methods. The depth measurements were subsequently corrected for tide at the time of the surveys with respect to mean sea level and for the effect of atmospheric pressure on the sea level (Kolaiti, 2019, 2024).

In this study, aerial digital photogrammetry was applied to produce high-resolution digital surface models (DSM) of the seashore and nearshore zone in all the survey areas. The low altitude imagery captured during aerial surveys conducted in two different periods (October 2024 and April 2025), under extremely calm wind conditions (<1 bf), in order to achieve the best shoreline reconstruction and avoid any distortion in the coastline position caused by sea waves and water refraction. High-resolution images have been acquired using an RTK DJI Mavic 3E with global shutter camera (FOV 84°, 24mm lens equivalent, 20MPixel, ¾ sensor size) in aerial surveys. Side overlap was set at 60%, frontal overlap at 80%, and flight speed at 4-7 m/sec. During the two survey periods 30 flights were conducted, of a maximum duration 20 min each, depending on the extent of the survey area. The relative height of the flights was 80 m with terrain follow adjustments, whereas in two sites (Tyros and Plaka-Drepano) a flight height of 60 m and 40 m was applied, in order to compare the images in shallow waters. At the 80 m-flight level, the resulting ground sample distance (GSD) was 2.2 cm/pixel, which produced a high detailed orthomosaic. A total of 4,534 images were collected, while the sum of the 20 survey areas amounts to 454 ha (4.54 km^2).

The image-based 3D modelling process was carried out using Agisoft Metashape Pro software. The GGRS 1987 coordinate system was used, with Geoid Model D applied for vertical adjustments. After the modelling process was completed, the following outputs were produced for each surveyed site: (i) 3D dense point cloud (in LAS/LAZ format) (ii) mesh (in FBX format) (iii) GeoTIFF Digital Surface Model (DSM) with a spatial resolution of 8.5 cm, and (iv) orthomosaic with a spatial resolution of 2.1 cm.

The 3D modelling workflow involved several key steps: (a) *Sparse Point Cloud Generation*: an initial sparse point cloud was created as a preliminary representation of the geometry derived from UAV-acquired imagery using the Structure from Motion (SfM) algorithm, (b) *Dense Point Cloud Generation*: high-resolution dense point clouds were generated from the aligned images using multi-view stereo algorithms, after feature detection with the Scale-Invariant Feature Transform (SIFT) algorithm. The dense point cloud enhanced model precision by capturing detailed surface features necessary for accurate representation, (c) *3D Mesh Creation*: The dense point cloud data was interpolated to construct 3D meshes, providing a continuous surface representation, and (d) *3D mesh Texturing*: the 3D meshes were textured to produce a photorealistic visual output.

This systematic approach ensured the generation of high-precision 3D models suitable for detailed analysis and visualisation (Papadopoulou *et al*., 2021, 2022).

Results - Discussion

The orthomosaics generated from the Argo-Beachrock Project's geospatial survey were used to delineate the boundaries of each beachrock generation, now submerged in the nearshore zone of each surveyed area, to assess its current situation (e.g., erosion, fragmentation), and to identify remains of ancient structures integrated into the beachrock formations.

For each surveyed area, a comprehensive suite of geospatial products has been generated, including detailed 3D models, high-resolution visualisations, orthophoto maps, and associated datasets. These outputs are integral to the project's objectives and will be made publicly available on open-access platforms by the project's conclusion. The data dissemination strategy includes the following components:

- *Web-Map Platform*: an interactive web map will enable users to visually explore all orthomosaics. This platform will allow seamless navigation, zooming, and layer toggling for enhanced spatial analysis and visualisation. The

web map will cater to diverse user needs, from researchers and planners to educators and the general public.

- *YouTube Channel for 3D models*: a dedicated YouTube channel will host a collection of 3D animated maps, providing dynamic visualisations of the generated 3D models. These animations will facilitate an in-depth visual inspection of the models, showcasing intricate surface details and the spatial relationships within each survey area. The channel will serve as an accessible resource for presentations, educational purposes, and broader dissemination to non-specialist audiences.

By leveraging open-access platforms, the project ensures that these datasets are preserved and accessible for future research, education, and practical applications. This approach promotes collaboration, supports transparency, and maximizes the impact of the generated geospatial resources.

Next, we provide an example of the photogrammetric mapping and visualisation data generated for one out of the twenty survey sites (Figs. 2 and 3).

Figure 2. Part of the orthomosaic of the Plaka beach (Drepano, N Argolic Gulf), providing a clear and detailed image of the beachrock formation extending to a depth of -1.20±0.05 m below mean sea level.

Figure 3. Part of the 3D model of the Plaka beach (Drepano, N Argolic Gulf), corresponding to the same coastal zone as Figure 2.

The depths in the nearshore zone, as derived from the Digital Surface Models (DSMs) produced in the context of the Argo-Beachrock Project, were compared with those obtained through mechanical methods during previous snorkel geological surveys. The comparison shows a good match in shallow waters (up to a maximum depth of 2 m), with deviations well below the mean tidal range. However, this comparison is not meaningful for greater depths.

Shallow-water bathymetry is a dynamic and evolving field of research, with modern drone imagery-based methods enabling unprecedented levels of detail and accuracy (Makris *et al.*, 2024 and references therein). Among the methodologies commonly employed in the literature, spectral and geometry-based approaches are predominant. These techniques are often utilized individually or in combination to enhance bathymetric accuracy and resolution.

In the context of the present study, the produced Digital Surface Models (DSMs) were utilized exclusively for geovisualisation purposes rather than as a true bathymetric dataset. This distinction aligns with prior research, where DSMs

derived from drone-based imagery are often leveraged for visual representation but they lack the precision required for accurate depth measurements in bathymetric studies, as it is widely accepted that the accuracy of DSMs decreases with increasing water depth (Sefercik *et al.*, 2024 and references therein).

Conclusions

By combining UAV image-based 3D modelling, field observations, and systematic documentation of coastal natural features and manmade structures, alongside the use of geovisualisation tools, we can better understand the extent of past marine transgression and coastline retreat driven by ongoing relative sea level rise along the entire coast of the Argolic Gulf during the Late Holocene.

Modern methodological approaches to studying the dynamic coastal system have proven invaluable tools for monitoring and managing one of the wealthiest littoral zones of the Peloponnese, which is experiencing steady tourist growth. However, this region, rich in natural geomorphs and cultural heritage, has already been significantly affected by rising sea levels over both prehistoric and historic timescales. It will face even greater challenges as sea levels continues to rise at an accelerating rate, in line with global temperature increases, a dire consequence of climate change.

Beyond the methodological aspects, the results of this fully open-access research project will assist scientists, local communities, and stakeholders to design early response systems for coastal retreat, extreme weather events, and civil protection and adaptation measures, ultimately contributing to a sustainable regional development. More analytically, integration of UAV-based remote sensing and advanced geovisualisation techniques has significantly enhanced the accuracy and efficiency of coastal monitoring and analysis. Geovisualisation platforms further enable interactive exploration and interpretation of 2D and 3D data, fostering a deeper understanding of spatial-temporal trends and facilitating data-driven decision-making for coastal management and climate resilience strategies. Finally, UAV-based mapping can serve as a foundation for the long-term monitoring of the changes in the coastal zone over time.

Acknowledgements

The Argo-Beachrock Project was implemented with the support of the Athanasios C. Laskaridis Charitable Foundation within the framework of "*Points of Support*", a co-funded programme by 10 public benefit foundations. The project was assigned to the Society for the Study of Ancient Coastlines NPO – AKTES on October 1, 2024, and was carried out in close and effective collaboration with the Cartography and Geoinformatics Laboratory, Department of Geography, University of the Aegean. It was completed on May 31, 2025. The final deliverables are displayed on the *ArcGis Enterprise Portal* of the University of the Aegean (https://sdi-portal.aegean.gr/portal/apps/experiencebuilder/experience/?id=602a22c307b34e7cb0211f0f6b58220e), uploaded on the fully open access *sketchfab platform* (https://sketchfab.com/aegean_cartolab/collections/the-argo-beachrock-project), and published on the *AKTES YouTube channel* (https://www.youtube.com/@aktes7509/playlists).

References

Bernier, P., Dalongeville, R., 1996. Mediterranean coastal changes recorded in beachrock cementation. Zeit. Geomorphol. NF, Suppl.-Bd, 102, 185–198.

Danjo, T., Kawasaki, S., 2016. Microbially Induced Sand Cementation Method Using Pararhodobacter sp. Strain SO1, Inspired by Beachrock Formation Mechanism. Materials Transactions, 57(3), 428-437.

Desruelles, S., Fouache, É., Çiner, A., Dalongeville, R., Pavlopoulos, K., Kosun, E., Coquinot, Y., Potdevin, J.-L., 2009. Beachrocks and sea level changes since Middle Holocene: Comparison between the Insular Group of Mykonos-Delos-Rhenia (Cyclades, Greece) and the southern coast of Turkey. Global and Planetary Change, 66(1), 19-33.

Gholami, R., Raza, A., 2022. CO_2 sequestration in sandstone reservoirs: How does reactive flow alter trapping mechanisms? Fuel, 324, part C, 124781.

Gifford, J.A., 1995. The physical geology of the western Messara and Kommos. In: Shaw, J.W., Shaw, M.C. (Eds.), Kommos I: the Kommos Region and Houses of the Minoan Town, 30-90, Princeton University Press, NJ.

Ginsburg, N.R., 1953. Beach rock in south Florida. Journal of Sedimentary Petrology, 23, 85-92.

Hanor, S.J., 1978. Precipitation of beachrock cements: mixing of marine and meteoric waters vs CO2-degassing. Journal of Sedimentary Petrology, 48, 489-501.

HNHS - Hellenic Navy Hydrographic Service, 2015. Statistical data on sea level from Greek ports, 2nd revised edition.

Kolaiti, E., 2019. Changes in the anthropogenic environment along the eastern coast of the Peloponnese on the basis

of archaeological and morphological indicators of the Late Holocene relative sea level changes. Proposing a geoarchaeological method of approach. Ph.D. Thesis, University of the Peloponnese, Kalamata, 674 p. (available at www.didaktorika.gr/eadd.)

Kolaiti, E., 2024. The 'vanished port' of ancient Asine: a geoarchaeological approach, in: Xanthopoulou, M. et al. (Eds), Archaeological Work in the Peloponnese 3 (Proceedings of the 3rd International Scientific Meeting AWOP3 - 2021, University of the Peloponnese Kalamata, Greece), 821-835.

Kolaiti, E., Mourtzas, N., 2023. Late Holocene relative sea-level changes and coastal landscape readings in the island group of Mykonos, Delos, and Rheneia (Cyclades, Greece). Mediterranean Geoscience Reviews, 5(3), 99-128.

Kolaiti, E., Papadopoulos, G., Morhange, C., Vacchi, M., Triantafyllou, I., Mourtzas, N., 2017. Palaeoenvironmental evolution of the ancient harbour of Lechaion (Corinth Gulf, Greece): were changes driven by human impacts and gradual coastal processes or catastrophic tsunamis? Marine Geology, 392, 105-121.

Koukouzas, N., Kypritidou, Z., Purser, G., Rochelle, C.A., Vasilatos, C., Tsoukalas, N., 2018. Assessment of the impact of CO_2 storage in sandstone formations by experimental studies and geochemical modeling: The case of the Mesohellenic Trough, NW Greece. International Journal of Greenhouse Gas Control, 71, 116-132.

Makris, A., Nicodemou, V.C., Alevizos, E., Oikonomidis, I., Alexakis, D.D., Roussos, A., 2024. Refraction-Aware Structure from Motion for Airborne Bathymetry. Remote Sensing, 16(22), 4253.

Mauz, B., Vacchi, M., Green, A., Hoffmann, G., Cooper, A., 2015. Beachrock: a tool for reconstructing relative sea level in the far-field. Marine Geology, 362, 1-16.

Meyers, J.H., 1987. Marine vadose beachrock cementation by cryptocrystalline magnesian calcite, Maui, Hawaii. Journal of Sedimentary Petrology, 57, 558-570.

Moore, C.H., 1973. Intertidal carbonate cementation in Grand Cayman, West Indies. Journal of Sedimentary Petrology, 43, 591-602.

Mourtzas, N., Kolaiti, E., 2020. Palaeogeographic reconstruction of the Messara Gulf and Matala Bay (Crete, Greece): coastal response to sea level changes during prehistoric and historic times. Alpine and Mediterranean Quaternary 33(1), 61-87.

Neumeier, U., 1999. Experimental modeling of beachrock cementation under microbial influence. Sedimentary Geology, 126, 35-46.

Papadopoulou, E.E., Papakonstantinou, A., Zouros, N., Soulakellis, N., 2021. Scale-variant flight planning for the creation of 3d geovisualization and augmented reality maps of geosites: The case of Voulgaris Gorge, Lesvos, Greece. Applied Sciences, 11(22), 11(22), 10733.

Papadopoulou, E.E., Papakonstantinou, A., Vasilakos, C., Zouros, N., Tataris, G., Proestakis, S., Soulakellis, N., 2022. Scale issues for geoheritage 3D mapping: The case of Lesvos Geopark, Greece. International Journal of Geoheritage and Parks, 10(3), 435-446.

Psomiadis, D., Albanakis, K., Tsourlos, P., 2010. Evaluation of sea-level rise impact on cemented and uncemented beach. Case study from Thassos Island, Greece. Scientific Annals, School of Geology, Aristotle University of Thessaloniki (Proceedings of the XIX CBGA Congress, Thessaloniki, Greece), Special Volume 99, 483-48.

Saitis, G., Karkani, A., Koutsopoulou, E., Tsanakas, K., Kawasaki, S., Evelpidou, N., 2022. Beachrock Formation Mechanism Using Multiproxy Experimental Data from Natural and Artificial Beachrocks: Insights for a Potential Soft Engineering Method. Journal Marine Science and Engineering, 10, 87.

Scholle, P.A., Ulmer-Scholle, D.S., 2003. A color guide to the petrography of carbonate rocks: grains, textures, porosity, diagenesis. American Association of Petroleum Geologists, Tulsa, Oklahoma.

Sefercik, U.G., Nazar, M., Aydin, I., Büyüksalih, G., Gazioglu, C., Bayirhan, I., 2024. Comparative analyses for determining shallow water bathymetry potential of multispectral UAVs: case study in Tavsan Island, Sea of Marmara. Frontiers in Marine Science, 11, 1388704.

Taylor, M.C.J., Illing, V.L., 1969. Holocene intertidal calcium carbonate cementation, Qatar, Persian Gulf. Sedimentology, 12, 69-107.

Vousdoukas, M., Velegrakis, A., Plomaritis, T.A., 2007. Beachrock occurrence, characteristics, formation mechanisms and impacts. Earth-Science Reviews, 85, 23-46.

Vousdoukas, M.I., Velegrakis, F., Kontogianni, A., Makrykosta, E.-N., 2009. Implications of the cementation of beach sediments for the recreational use of the beach. Tourism Management, 30(4), 544-552.

Webb, G.E., Jell, J.S., Baker, J.C., 1999. Cryptic intertidal microbialites in beachrock, Heron Island, Great Barrier Reef: implications for the origin of microcrystalline beachrock cement. Sedimentary Geology, 126 (1–4), 317-334.

17th INTERNATIONAL CONGRESS of the Geological Society of Greece

BULLETIN OF THE GEOLOGICAL SOCIETY OF GREECE, SP. PUBL.

EXTENDED ABSTRACT 154

The Corinth Canal (Greece): monumentality and protection

Kolaiti E.[1], Zouros N.[2], Mourtzas N.[3]

(1) Society for the Study of Ancient Coastlines - AKTES NPO; National Hellenic Research Foundation, Institute of Historical Research; University of Nottingham, Department of Classics and Archaeology; Chalandri, Athens, Greece, kolaitieleni@gmail.com (2) University of the Aegean, Department of Geography, Mytilene, Lesvos, Greece; Natural History Museum of the Lesvos Petrified Forest (3) Society for the Study of Ancient Coastlines - AKTES NPO; University of Nottingham, Department of Classics and Archaeology; Chalandri, Athens, Greece

Introduction

The Corinth Canal is an artificial waterway in Greece that connects the Corinth and Saronic Gulfs. It crosses the narrow Isthmus of Corinth, a 79 m high ridge which once linked the Peloponnese peninsula to the Greek mainland, creating a natural barrier between the Ionian and Aegean Seas. The Canal extends in a straight line for 6,343 m. It is 24.60 m wide at the sea surface narrowing to 21.30 m at its bottom, while the water height in it ranges from 7.50 to 8 m (CorinthCanal). In this paper, we present an overview of the technical aspects of this admirable engineering work tracking the historical route of its opening from antiquity until the late 19th century and briefly describe the accompanying infrastructure works and the ongoing interventions, mainly driven by the geotectonic setting of the area. We argue for the monumentality of the Corinth Canal that mandate its future preservation and we propose a framework of actions to protect this prominent heritage.

The diolkos and the history of the canal

The idea of avoiding the dangerous and long circumnavigation of the Peloponnese taking advantage of the strategic position of the Isthmus of Corinth dates back to the late 7th – early 6th century BC, when ancient Corinth flourished, ruled by the tyrant Periander, having two harbours (Lechaion in Corinth Gulf and Kenchreai in Saronic Gulf) and a fleet to control maritime traffic on both seas. It was then that a paved trackway along the isthmus was constructed, the famous *diolkos*, across which goods and small boats, mainly warships, were hauled and transported on a platform (*olkos*). It followed the path of the present-day canal for a length of about 8 km. It was 3.40-6.0 m wide and carried two grooves in the middle, spaced 1.50 m apart. It ended on a paved quay on its western side, where it has been excavated for 255 m and 204 m on the Peloponnese (Kolaiti *et al.*, 2017) and Sterea Hellas sides, respectively, whereas its eastern end facing the Saronic Gulf, located in the area of ancient Schinous (today's Kalamaki) has not been found yet. Several phases of reconstruction followed during the 5th and 4th centuries BC. It remained in use until the AD 9th century (Ministry of Culture and Sports, 2012).

Strabo (1.3.11) reports that Dimitrios Poliorkitis (307 BC) planned to cut a passage through the Isthmus of Corinth, but he was prevented by his engineers, and also Julius Caesar (AD 44) and Caligula (AD 37) had probably the same intention. The most important works were carried out by Nero in AD 67, who, using slaves (at least 6,000 Jewish prisoners), began excavations on both sides of the Isthmus with notable progress, remains of which are either still visible (e.g. Nero's relief) or recorded (e.g. trenches, pits) during the construction of the modern canal (Gerster, 1884). The project was eventually interrupted due to either logistic difficulties or political instability (CorinthCanal). This was certainly the commencement of an ambitious project. The Venetians attempted to resume it in 1687 but were unsuccessful.

In 1830, Ioannis Kapodistrias, the first Governor of the new Greek State, assigned the project to the French engineer Virle d'Uct, who estimated that an enormous amount of 40 million gold francs would be needed for its completion. In 1869, the inauguration of the Suez Canal revived interest in constructing the Corinth Canal, and the government of Thrasyvoulos Zaimis passed a law "on the Isthmus canalization", under the provisions of which in 1870 a contract was signed with French entrepreneurs, but it was not implemented due to lack of funds (Papafotiou, 2010). In 1882, the French company 'Société Internationale du Canal Maritime de Corinthe' was formed with the purpose of completing and operating the Corinth Canal. The 99-year canal's concession, granted by a royal decree in 1881 to Hungarian General, canal architect, and engineer Istvan Türr, was transferred to the French company (Société Internationale). The project commenced on April 23, 1882, based on Nero's plans and the final design by the Hungarian engineer Bella Gerster. In 1890, the company was dissolved and put into liquidation, and the project halted. However, efforts to secure additional funding succeeded, and constructions was resumed by the Greek construction company 'Geniki Etaireia Ergolipsion', founded in 1889 (Pepelasis, 2010). With a generous contribution from Greek benefactor Andreas Syggros, the canal opened with great ceremony on July 25, 1893 (CorinthCanal).

Isthmus Infrastructure: The bridges

The 19th-century railway bridge was blown by the German occupying troops during their withdrawal from Greece in 1944, to be later rebuilt in the late 1940's. Two submersible road bridges operate at both ends of the canal (Posidonia and Istmia), which continuously facilitate the communication between central Greece and the Peloponnese.

In the late 1990s, as part of the construction projects of the new P.A.TH.E. motorway and the high-speed railway line Athens-

Thessaloniki funded by the European Union, the design of the new canal bridges was decided. The initial design was based on the geometric characteristics of the new alignments, while ensuring the stability of the bridges with the least possible excavations in the canal's slopes so that its shape would not be altered. The span of the bridges was determined after the idea of widening the canal was rejected. However, the geotectonic setting of the Isthmus area finally played a decisive role in the final position and foundation of the new bridges. The secondary tectonic activation of the faults crossing the Corinth Isthmus, as it was evidenced by their quantitative and qualitative tectonic analysis, and the thorough study of the stratigraphic, lithological and neotectonic features of the canal's slopes, demonstrated that the abutments and the piers of the new bridges had been positioned in different tectonic blocks on both sides of the canal (Peloponnese and Attica). This led to the redesign of the new bridges and the implementation of specific construction techniques using seismic isolation bearings. The new motorway and railway bridges were opened to traffic in 1997 and 2003, respectively.

The geological and geotectonic context of the Corinth Isthmus

The Corinth Isthmus is crossed by at least 46 large-scale normal faults, traverse to its direction, which have caused successive displacements on the Plio-Pleistocene and Quaternary strata, and on the recent artificial deposits from the Isthmus excavation, affecting the morphology on both sides of the canal. The faults have a NE-SW direction, with the fault mirrors dipping toward S, SE, and WNW at 60°-85°, and strike-slip lineation plunging S and SW. They have been repeatedly activated within a NNE-SNE extensional regime and are still considered to be active (Fig. 1A, 1B). With a total visible displacement of 7.50-21 m during the Quaternary, they have caused the gradual rotation of the tectonic blocks they delimit by about 10° toward the SE. The Corinth Isthmus is affected by two vectors of tectonic displacement: uplift and extensional fault-induced subsidence, which may be accompanied by block rotations. Neogene and Quaternary sediments are cut by numerous, nearly E-W striking, sub-vertical normal faults, which can be observed all along the canal. As these faults belong to two different groups dipping toward N and S, respectively, the isthmus has been interpreted as a horst (Fig. 1C). The oldest sediments are at the base of the central horst block, dominated on the NW by white and grey calcareous silts (Fig. 1B). There is an upwards transition within the central horst block from freshwater or brackish facies to sediments of a marine environment (Papanikolaou *et al.*, 2015; Mourtzas and Kolaiti, 2017 and references therein).

The crossing area of the new bridges consists of three distinct tectonic blocks, each of an average width of 60 m, bounded by four main normal faults striking NW-SE to NNE-NNW and dipping toward SE to SSW at angles 70°-90°, with a visible displacement of 4-5 m (Fig. 1D, 1E). The faults have been activated during various neotectonic deformation phases, causing a gradual displacement toward the SE and a counter-clockwise rotation of about 10°. The main faults and the accompanied parallel small-scale structures were surveyed, not only on both slopes, but also in deep trenches that were excavated parallel to the canal axis, while their geometric and kinematic features were measured (Fig. 1E). The stratigraphy of the Neogene and Quaternary units on both the canal's slopes was mapped and the relative position of the layers within the distinct tectonic blocks was recorded, thus ascertaining their spatial continuity (Fig. 1D, 1E). Moreover, the lithology, physical characteristics, and mechanical properties of the layers were determined by means of drilling of fifteen boreholes and wells (Fig. 1D). The identification of recent fault activations that have resulted in displacements of several centimetres, which are visible even in the debris of the canal's excavations, imposed the positioning of the abutments and piers of the bridges within the same tectonic block with their axes parallel to the direction of the fault lines, in order to avoid failures in case of differential movements (Mourtzas and Kolaiti, 2017 and references therein).

Landslides and Recent interventions

The high (>60 m), steep, marly slopes of the Corinth Canal, prone to landslides, have caused ongoing instability, rock falls, and slide of large volumes of materials since almost the inception of the canal, leading to interruptions in vessel passage and even extended closures. In addition to geological factors (e.g., rock type and structure, steep gradients, active tectonism, seismic activity, lack of vegetation, soil erosion), human-related factors (e.g., excavation, construction, undermining, sabotage) have further increased slope vulnerability to failure. Between 1923 and 1997, it is estimated that approximately 900,000 m³ of material fell into the canal, resulting in a total closure period of eight years (CorinthCanal). The destructive 1981 Alkyonides earthquake sequence (24.2.1981 M=6.7, 25.2.1981 M=6.4, 4.3.1981 M=6.3) at the eastern end of Corinth Gulf, resulted in two major ruptures in the Isthmus horst, fault activation and displacement, and rock failure and serious landslides in the canal's slopes. The ENE-WSW trending Kalamaki-Isthmia normal fault downthrown to SSE, located at the eastern tip of the canal, was passively ruptured by up to 6 cm during the 1981 earthquake sequence (Papanikolaou *et al.*, 2015; Mourtzas and Kolaiti, 2017 and references therein). Between November 2020 and February 2021, frequent landslides occurred, culminating in a major collapse of 15,000-20,000 m³ on February 3, 2021 (CorinthCanal), mainly near the wastewater treatment plant on the Peloponnese side. This serious instability resulted in the closure of the canal and disruption of navigation through it. Although the landslides affected the upper part of the slope over a 100 m-stretch near the wastewater bridge, they did not impact the bridge's stability.

In November 2021, the final design of the slope restoration project was approved by the Ministry of Infrastructure and Transportation

–now responsible for the design and construction of the slope restoration works at the request of the

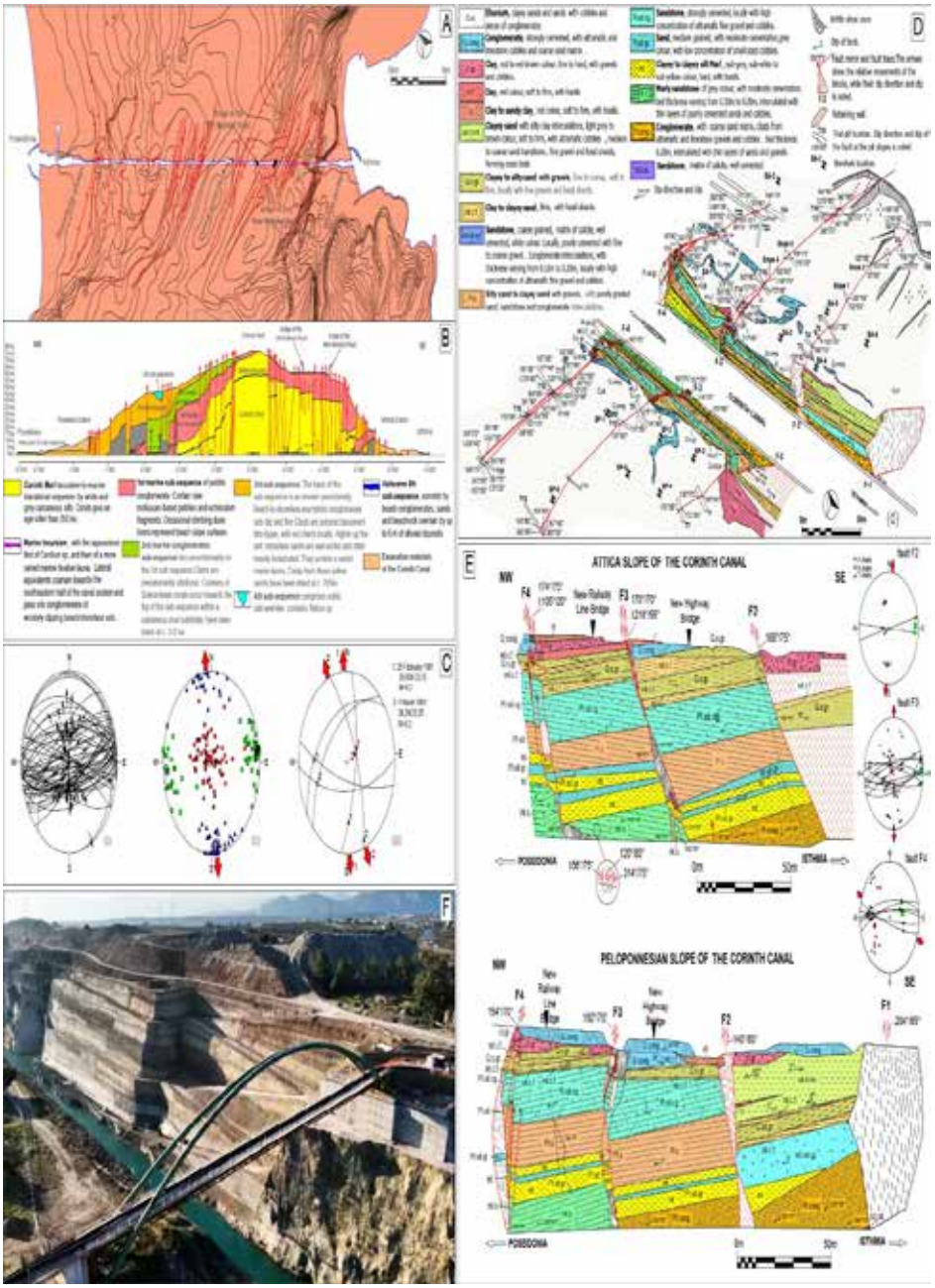

Figure 1. A: Plan view, and B: Longitudinal section of the Isthmus horst, indicating the geological structure and main faults. C: (i) Stereogram, and (ii) calculated stress axes of the Isthmus main faults, and (iii) focal mechanism solutions of the 1981 Alkyonides earthquake sequence. D: Geological plan view, and E: Front views of the two slopes of the Corinth Canal in the area of the new bridges, indicating the main faults that demarcate the tectonic blocks and their palaeostress analysis. F: Aerial view of the slope stabilisation works in 2022 at the area of the wastewater treatment plant on the Peloponnese side, showing the slope excavations and, in the foreground, the wastewater bridge [A, B, C, D, E: after Mourtzas and Kolaiti (2017) and references therein, F: modified from Papamanolakis].

Corinth Canal S.A.– especially characterized as a '*complex and special national-level project*' (Dec. 29307/ Σ6651/3.2.2021). Due to its urgent nature for civil protection ensuring public safety and restoring normal navigation, the project is exempting from environmental approval (Dec. 103435/6635/9.2.2021), with the only obligation for the operating company to submit an Environmental Impact Study for the operation and maintenance of the canal within

two years from the exemption. In December 2021, the project was assigned to the contacting company AKTOR S.A., with a budget of 30.57 million euros and a completion period of 24 months. The restoration engineering works are divided into two distinct phases: Phase A includes slope excavations for a total length of 600 m on both sides of the wastewater bridge, creation of three terraces (10 m-wide with intermediate slopes 6 m/11 m/9 m/8 m high), construction of permanent roads-ramps for heavy vehicles, strengthening with piles of the southern pier of the wastewater bridge, slope stabilisation with anchors and grouting, hydraulic works for surface water drainage management, construction and waterproofing of the western and eastern embankments. Phase B involves the construction of a toe pile wall to prevent coastal erosion and slope undermining.
The first phase of the project has been completed, leaving a significant environmental footprint (Fig. 1F). The second phase has not yet started. Furthermore, the recent approval by the Ministry of Infrastructure and Transportation to replace the seismic isolation bearings of the new motorway bridge, at the request of Olympia Odos S.A. (concessionaire of the Elefsis-Corinth-Patras-Pyrgos Motorway), and the looming plans of widening the canal (Papafotiou, 2022), will further alter this outstanding landmark, without substantial financial benefits for the Corinth Canal S.A. (A.E.DI.K), the company which exercises and exploits the rights associated with the Corinth Canal. Although outside the scope of this paper, the long-term viability of the company remains crucial. Official data (Growthfund) shows that the Corinth Canal handles over 11,000 vessels annually, mainly tourist ships. Published financial statements for the period 2019-2023 (GEMI-Publicity) reveal net profits of 1 million euros in 2019 when the canal's passage was unhindered, but losses of over 3.3 million euros in 2021 and 1.7 million euros in 2022, due to the canal's closure for restoration after the 2020-landslides.

Monumentality of the Corinth Canal or Infrastructure and Monumentality

The term '*monumentality*', introduced by several scientists with different connotations, is hard to define in a few words, although several methodological approaches and tools explore its concept, mainly for ancient civilisations (Buccellati, 2019). Despite the unfruitful attempts to find a unifying definition for the complex notion of monumentality (Levenson, 2019), it has been adopted by architectural and archaeological theory, while it has a broader approval to other disciplines and different types of structures, which reflect the cultural and socio-political context they belong to. Osborne (2014) argues that '*monumentality is something more than the shape, or size, or visibility, or permanence of the monument – though these variables absolutely carry their own significance. Monumentality lies in the meaning created by the relationship that is negotiated between object and person, and between object and the surrounding constellation of values and symbols in a culture*'. Others support that monumentality exceeds physical scale and it is '*a combination of great technical ingenuity, extraordinarily high levels of skill, the devotion of vast amounts of time to build the monument, the type and range of the resources invested and the sheer size of the task*' (Brunke *et al.*, 2016). Monumental structures can be related to four primary attributes: permanence of the structure, the place or the memory (lasting endurance: connection to the past and projection into the future), integration within a specific landscape or urban environment, statement of vision, compelling effect, strength, and social and political relations, and, projection of public values, symbols, and political authority (Brunke *et al.*, 2016; Hageneuer and van der Heyden, 2016; Horn and Proudfoot, 2016). Although there has been much discussion of monumentality, it is mainly focused on monumental architectures, in diverse archaeological and historical contexts. Infrastructures (e.g. dams, bridges, canals, roads, power stations, etc.) are often overlooked in discussions, due to the weakness of perception of their symbolic power or the profound effects they have on society. Nevertheless, large-scale technical works are undeniably significant in terms of constructional energetics and social impact. According to Levenson (2019), they possess a distinct form of monumentality rooted in their capacity to innovate, improve daily life, and create social dependencies, arguably making them even more integral to the survival of societies than palaces, temples, or other public buildings. Infrastructure and monumentality intersect in how large-scale constructions embody both functional utility and symbolic significance. Beyond serving as tools for transportation and labour, they synthesise surrounding landscape, public space, and architecture (MIT Center for Advanced Urbanism, 2016). Large-scale technical projects, while fulfilling essential societal functions, can also be monumental in design and impact, symbolizing power, progress, and cultural significance.
Under these considerations, the Corinth Canal is an infrastructure necessary for navigation, primarily designed for function, efficiency, and sustainability. The canal connected the Saronic with the Corinth Gulfs, thus making navigation faster (time), easier (risk), and more environmentally-friendly (energy). Its geographic and geopolitical position renders it to '*a communication hub between the Aegean and Ionian Seas*' (Dec. 29307/Σ6651/3.2.2021). The opening of the canal, in fact, created a man-made, geographic boundary between the Greek mainland (Sterea Hellas) and the Peloponnese, the latter now shaping the largest island of Greece. From this perspective, the canal is an outstanding landmark. The geology and faulting of the Isthmus horst adds an invaluable value to the Corinth

Canal. Crossed by at least 46 normal and oblique normal faults, all recognised and surveyed (Mourtzas and Kolaiti, 2017), the canal's slopes compose an open geo-archive, providing a great opportunity to visualise them. This unique structure shapes an '*impressive mega-trench*' (Papanikolaou *et al.*, 2015), a precious geoheritage (Velitzelos *et al.*, 2003).

Its monumentality, on the other hand, lies in its symbolic and cultural importance, emphasising permanence, vision, political power, and historical significance. First conceived 2,300 years ago, the initial design plans date back to the 1st century AD. Remains from Nero's works testify to the ambitious idea and efforts to implement the grand project. The canal's construction was organized and completed only after the emergence of the Modern Greek state. The various actors of this grand project, either known or unknown, may have had different motivations, but its completion is the result of the development policy of the Prime Minister Charilaos Trikoupis, who, through major infrastructure projects, aimed to create a modern, economically developed state and provide models for future growth. The project was also deemed necessary by the international trade and shipping conditions of the time. Though the Corinth Canal was a 2,300-year-old dream, it was the technological progress of the 19th-century Industrial Revolution that ultimately drove its realisation. Therefore, large-scale public projects, such as the Corinth Canal, serve to enhance community infrastructure and identity, reflecting the vision of their inspirers, and the cultural values and technological advancements of the society, in most cases tied to political power. It is authoritatively perceived as '*a unique landmark*' and '*a project-symbol, completely identified with the modernization of Greece*' (Hellenic Republic, 2022).

The Corinth Canal is tightly connected to the collective historical memory of the WWII period. Images of the blow up of the railway bridge by the Germans and knocking of locomotives and wagons down into the canal to block it, remain still strong to remind this period of the Greek history. Landscape transformations (e.g. earth movements) and bunkers still preserved there, reveal the strategic importance the isthmus had for the German occupiers, contributing to the historical memory.

The approaching method of '*constructional energetics*' would help to understand the canal monumentality in numbers. Records of the cost of the individual constructional processes (e.g. excavation, debris transportation, labour, etc.), aids in understanding the resources required and calculating the energy expended (Buccelatti, 2019). Beyond the quantitative approach, the study of the workforce (skills, composition, social setting) would be interesting. Therefore, the consequential correlation between cost and final result, given the limitations of data availability, adequacy, and accuracy, provides a better understanding of what the canal meant to those who produced it. Urban changes imposed by the needs of construction in the project's area can also signal its social impact, such as the creation of two settlements, Posidonia (divided in two sections, area: 139,000 m^2 and 72,000 m^2) and Isthmia (area: 144,000 m^2) (Papafotiou, 2010) to house the people occupied in the project and their families.

In addition, the huge quantities (millions of cubic metres) of excavated material from the opening of the canal and recent construction activities, have actually reshaped the landscape of the Isthmus territories (e.g., the artificial slopes on the road leading from Isthmia to Loutraki), offering insights into the design process. Recent approaches to moving grounds from the 'AlpTransit Infrastructure' project (new rail link crossing the Alps and connecting Germany to Italy through Switzerland) highlight how depots, landfills, and wastelands are shaping a collective imagination about the idea of landscape, giving rise to major political, economic, and ecological implications (Pradel, 2020).

From an engineering point of view, the Corinth Canal has no parallel in Greece and Europe. It is numbered among the three existing canals in the world, and is an excellent technological achievement of the time. Its engineering uniqueness has been authoritatively recognised: '*together with the Panama and Suez Canals, (it) constitutes the three technical canals that exist in the world today*' (Dec. 29307/Σ6651/3.2.2021). Furthermore, the implementation of the canal project opened new routes to mobilisation of scarce capital and technical know-how for the construction of public infrastructure through the collective entrepreneurial initiatives of S.A. banks (Pepelasis, 2010). Together with the construction of the 1,548 km-long national railway network, were decisive for the establishment of an integrated national economy and administrative centralization, both required for the building of the newly Greek state (Papayiannakis, 1982; Pepelasis, 2010). In particular, the mobilisation of national technical know-how was seminal to the Greek technical community. A notable example is Greek engineer-entrepreneur Antonios Z. Matsas, co-founder of 'Geniki Etaireia Ergolipsion', who replaced the foreign engineer Istvan Türr after the liquidation of the French company, ultimately leading to the canal's completion.

The long-lasting project of the canal's opening evokes the perception of a connection to a distant past, while its continuous operation for over 130 years reinforces a sense of permanence. Integrated into the unique geotectonic landscape of the Isthmus, the canal stands as a striking and timeless landmark with a dominant form, whose monumentality is constantly experienced. In terms of reception, it commemorates people, events, eras, practices, and techniques—not only from its creation, but also its lasting impact—embedded both in the structure and in collective memory (Belavilas, 2015). Numerous textual and artistic sources depict the canal, in an iconic way, further enhancing

this shared memory.

Thoughts on the future of the Corinth Canal

Nowadays navigation through the canal appears to be limited to mainly tourist vessels, as large ships prefer other easier sea routes in the open sea than a restricted canal to get from the Ionian to the Aegean Sea, thus downgrading its economic importance. The Corinth Canal is mainly a tourist attraction, thus its widening to accommodate ships larger than its current capacity seems to have no effect in conjunction with the exorbitant construction costs and the loss of its monumentality. After all, this proposal was rejected during the design of the new bridges in the 1990s. Although it seems that the Greek state is moving in this direction ['*the Canal should not only be a project that facilitates navigation, but also in itself be a visitable destination in order to highlight the overall tourism product of the region*' (Hellenic Republic, 2022)], at the same time the Ministry of Infrastructure and Transportation approves large-scale interventions for slope stabilisation on the Peloponnese side, without any environmental restrictions under the guise of urgent user safety, sadly causing significant alterations in the physiognomy of this unique monument. Immediate restoration of the canal's slope to its original form by a reinforced earth wall is required, while any future interventions of this scale will invalidate its monumentality.

Unfortunately, political decisions appear to be driven by development policies, yet they lack a clear strategy for ensuring the long-term viability of the canal. However, it seems that only an alternative management of the Corinth Canal, while maintaining its existing function, creates a development perspective. The production and promotion of a new tourism product is suggested, which will offer an immersive experience and tour of the canal through its historic path. Though it be focused on the Corinth Canal highlighting its monumental qualities and geological features, will also include accompanying monuments (e.g. ancient diolkos, bunkers, new bridges, submersible bridges, etc.). This tourism product would be flexible, catering to different types of tourism (both conventional and alternative), visitor demand, and available time, while ensuring accessibility and safety to visitors of all ages.

The Corinth Canal, a prominent engineering project of the time with an outstanding universal value, is a monumental infrastructure, highlighting how certain structures, while fulfilling necessary functions, transcend their utility and become symbols of cultural identity, history, and human achievement. It should have long since been classified as a recent monument of Greek cultural heritage, fully protected and subject to sustainable interventions under the provisions of Law No. 3028/2002, as in force. In addition, coordinated efforts ought to make the competent bodies so that the area of the Corinth Canal could be designated UNESCO World Heritage Site, recognizing its global significance both historically and culturally, as well as for its geological features. Thinking that *'monuments have shaped and are still shaping contemporary views on the past*' (Bußmann, 2019), we marvel at how this monumental, man-made '*mega-trench*' shapes perceptions of the geotectonic processes reflected on its slopes. It is our duty to preserve engineering achievements and historical memory for present and future generations, thereby substantially enhancing our social and cultural identity.

References

Belavilas, N., 2015. On monuments and memory: the material aspects of history, in: Papadimitriou, N., Anagnostopoulos, A. (Eds), The past in the present: Memory, history, and antiquity in modern Greece, 64-82.

Brunke, H., Bukowiecki, E., Cancik-Kirschbaum, E. *et al.*, 2016. Thinking Big. Research in Monumental Constructions in Antiquity. eTopoi - Journal of Ancient Studies, Spec.Vol. 6, 250–305.

Buccellati, F., 2019. Monumentality: Research Approaches and Methodology, in: Buccellati., F, Hageneuer, S., van der Heyden, S., Levenson, F. (Eds), Size Matters – Understanding Monumentality Across Ancient Civilizations, 41-63.

Bußmann, R. 2019. Monumentality in context – a reply from Egyptology, in: Buccellati., F., Hageneuer, S., van der Heyden, S., Levenson, F. (Eds), Size Matters – Understanding Monumentality Across Ancient Civilizations, 99-104.

CorinthCanal, Corinth Canal S.A. (A.E.DI.K.). The Canal - Specifications - The history of the canal - Press release of January 15, 2021, retrieved from: https://corinthcanal.com/the-canal/?lang=en.

Papamanolakis, M., Korinthognosia (YouTube channel). Latest news about the small wagon found in the Corinth Canal, retrieved from: https://www.youtube.com/Papamanolakis.

Dec. 29307/Σ6651/3.2.2021. Ministerial Decision No 29307/Σ6651 3 February 2021, Ministry of Infrastructure and Transportation.

Dec. 103435/6635/9.2.2021. Decision of the G. D. of Env. Policy No 103435/6635 9/12/2021, Ministry of Environment and Energy.

GEMI-Publicity. Financial Reports: A.E.DI.K. S.A., retrieved from: https://publicity.businessportal.gr/.

Gerster, B., 1884. L'Isthme de Corinthe, tentatives de percement dans l'antiquité. BCH, 8, 225-232.

GrowthFund. Corinth Canal S.A. (AEDIK), retrieved from: https://growthfund.gr/corinth-canal-sa/.

Hageneuer, S., van der Heyden, S., 2016. Perceiving monumentality, in: Buccellati., F, Hageneuer, S., van der Heyden, S., Levenson, F. (Eds), Size Matters – Understanding Monumentality Across Ancient Civilizations, 65-89.

Hellenic Republic, 2022. Hellenic Republic, Information note on the visit of Prime Minister Kyriakos Mitsotakis to the Corinth Canal, retrieved from: https://www.primeminister.gr/2022/07/01/29702.

Horn, E.T., Proudfoot, P.R., 2016. Ideas of monumentality in architecture. Quadrant, 60(9), no. 529, 75-80.

Kolaiti, E., Papadopoulos, G.A., Morhange, C., Vacchi, M., Triantafyllou, I., Mourtzas, N.D., 2017. Palaeoenvironmental evolution of the ancient harbor of Lechaion (Corinth Gulf, Greece): Were changes driven by human impacts and gradual coastal processes or catastrophic tsunamis? Marine Geology, 392, 105-121.

Levenson, F., 2019. Monuments and Monumentality – different perspectives, in: Buccellati., F, Hageneuer, S., van der Heyden, S., Levenson, F. (Eds), Size Matters – Understanding Monumentality Across Ancient Civilizations, 17-39.

Ministry of Culture and Sports. Diolkos of Corinthian Isthmus, retrieved from: http://odysseus.culture.gr/.

MIT Center for Advanced Urbanism, 2016. Infrastructural Monument. Princeton Architectural Press.

Mourtzas N., Kolaiti E., 2017. Relative sea level changes on the NE coast of the Peloponnese after the late roman period: the ancient Corinth harbours of Lechaion and Kenchreai, in: D. Katsonopoloulou, D. (ed.), Ancient Helike and Aigialeia: Poseidon God of Earthquakes and Waters Cult and Sanctuaries, 275-308.

Osborne, J.F., 2014. Monuments and Monumentality, in: Osborne, J.F. (ed.), Approaching Monumentality in Archaeology, IEMA Proceedings, 1-19.

Papafotiou, A.E., 2010. The Corinth Canal: a technological miracle of the 19th century, retrieved from: https://www.teepelop.gr/.

Papafotiou, A.E., 2022. The Corinth Canal – a pharaonic intervention with negligible results, retrieved from: https://gnomipoliton.com/2022/.

Papanikolaou, D., Triantaphyllou, M., Pallikarakis, A., Migiros, G., 2015. Active faulting at the Corinth Canal based on surface observations, borehole data and paleoenvironmental interpretations. Passive rupture during the 1981 earthquake sequence? Geomorphology, 237, 65-78.

Papayiannakis, L., 1982. Greek Railways (1882-1910) Geopolitical, economic, and social aspects, MIET.

Pepelasis, I.S., 2010. Entrepreneurial Typologies in a Young Nation State: Evidence from the founding charters of Greek Société Anonymes, 1830-1909. Discussion Paper No 200, Athens Univ. Econ. Business, 1-24, available at: https://www.dept.aueb.gr/sites/.

Pradel, C., 2020. Moving Ground. The Construction of AlpTransit Infrastructure and its Monumental Landscapes, Ardeth, 7, 67-83.

Société Internationale. Numistoria, retrieved from: https://numistoria.com/.

Velitzelos, E., Mountrakis, D., Zouros, N., Soulakellis, N., 2003. Atlas of the Geological Monuments of the Aegean. Ministry of the Aegean, Adam editions.

17th INTERNATIONAL CONGRESS of the Geological Society of Greece

BULLETIN OF THE GEOLOGICAL SOCIETY OF GREECE, SP. PUBL.

EXTENDED ABSTRACT 155

Synergies for geo- education: materials and initiatives from Psiloritis UNESCO Global Geopark and the Center for Environmental Education and Sustainability of Anogia, (Crete) Greece.

Kolendrianou M .[1], Kefalogianni Z.[2], Kalomoiri A. [2], Fassoulas C. [1,3]

(1) Psiloritis UNESCO Global Geopark, Anogia, Greece, info@psiloritisgeopark.gr (2) Center for Environmental Education and Sustainability of Anogia, Anogia, Greece, (3) Natural History Museum of Crete- University of Crete, Heraklion, Greece

Research Highlights

The present work includes a summary of the main materials used and initiatives undertaken by Psiloritis UNESCO Global Geopark and the Center for Environmental Education and Sustainability of Anogia for the education of children and adults on Geology and Geology- related topics in the area of Psiloritis UNESCO Global Geopark, (Crete) Greece.

Introduction / Background

UNESCO Global Geoparks (UGGps) are single, unified geographical areas with exceptional geological features of international significance. They are managed with a holistic approach towards the protection, education and sustainable development of their territories, adopting a bottom-up approach through the active involvement of their local communities in their efforts (UNESCO, 2024). For any UGGp, education at all levels is one of the main focus areas of its operation (UNESCO, 2015). It is essential for a UGGp to develop and perform educational activities to disseminate knowledge and raise awareness on geodiversity and its connections to biodiversity and other traits of the tangible and intangible cultural heritage, with the purpose to educate and inspire on the significance of the territory and to increase local involvement and engage the audiences into more effective conservation.

Many UGGps form synergies with specialized educational institutions, at the national or local level, to achieve better pedagogical and more widespread results in their initiatives for education. One such example is the cooperation between Psiloritis UGGp and the Center for Environmental Education and Sustainability (CEES) of Anogia. CEESs are an institution of multiple different centers throughout Greece, established by the Greek Ministry of Education, Religious Affairs and Sports as a bridge between the school and society. In the CEESs' philosophy of operation, emphasis is put on the need to raise interest in all forms of life towards the development of an environmental ethic and by linking the education for the environment and sustainability with the need to also instill a system of values.

Objectives

Presently, there are 213 UGGps in 48 countries and, even though they produce numerous and innovative educational materials, the amount of published works on UGGp- education still remains limited in comparison to research on other topics concerning UGGps and with an availability of resources not much broader than that of local implementation and dissemination through conference participation (Martínez-Martín *et al.*, 2023). The present work aims to present the materials, programs and digital tools developed and used for education by Psiloritis UGGp and its education partner, the CEES of Anogia, as they are currently being implemented in the area.

Area

Psiloritis Geopark was established in 2001 and since 2015 it has been recognized as a UGGp. It is located in the central part of the island of Crete (Greece) with the mountain of Psiloritis, or ancient Idi (2456m), being the main point of reference for the territory, thus, also providing the name for the Geopark. It has a total area of 1272 km^2, including villages and settlements from 8 different Municipalities and a population of approximately 38.000 residents. The complex topography of the area and the variety of rocks combined with the isolation of the entire island of Crete, make the mountainous mass of the geopark a hotspot for biodiversity and endemism, leading to the inclusion of ~56% of the territory in the European NATURA 2000 Network. The connection of the area with the people has been strong and persistent since the times of antiquity, as can be demonstrated by the numerous findings and monuments spanning from the Minoan era to the Roman times and the many religious and cultural monuments of our days. The intangible cultural heritage of Psiloritis is also worldwide famous with the traditional handicrafts, cuisine, and music being only some of the examples.

Concerning the geodiversity of Psiloritis UGGp, it spans over a period of about 360 million years, with a variety of rocks attributed in 7 different tectonic nappes and ranging from the most common limestones and dolomites to the

more rare stromatolites and ophiolites. The fossils of Psiloritis UGGp also bear witness to its history and evolution of life, including findings such as the rare Fodele fossils (corals, brachiopods and bivalves of about 360-300 million years ago) or the most recent fossils from terrestrial vertebrates (dwarf elephants and deer, giant mice from the Pleistocene) as evidence of a special adaptation mechanism to island life.
The geodiversity of the Geopark bears witness to the geological history of the area that has been (and is still being) dominated by tectonism, uplift of the mountains and karstic erosion. Large- and small-scale folds and faults and all kinds of karstic features (surface and subterranean) appear throughout the area of Psiloritis, providing the opportunity for the visitor to find all the evidence that explain the formation of the high mountains and their continuous transformation through the creation of impressive gorges, mystical caves and fertile plateaus, as well as fascinating landscapes.

Results and Discussion

Psiloritis UGGp and Anogia CEES are both institutions with a long history of operation in the area (Psiloritis Geopark was established in 2001 and Anogia CEES in 2006), offering formal and non- formal educational activities in the wider area of Psiloritis. Both organizations have so far informed and trained thousands of students, teachers and also local professionals, residents and visitors. It is characteristically mentioned that for the year 2024, Psiloritis UGGp and Anogia CEES received a total of approximately 1035 children aged 5-18 (students, scouts), with whom educational activities were implemented either indoors or in the field. Most of the developed materials and tools used within this context, could be broadly categorized in the following general thematic categories: Geodiversity, Biodiversity, Human History/ Traditions and Arts, Sustainable way of life. These are briefly presented in the table below (Table) according to the typology of each material that is currently being implemented, its title and a brief description, the thematic category it falls into, whether it's being implemented by the staff of Psiloritis UGGp, Anogia CEES or by the two in cooperation and finally, the age of the audiences each material is addressed to.

Table. Summary of main materials for education implemented by Psiloritis UGGp and Anogia CEES, at the area of Psiloritis UGGp.

#	Typology of material	Title	Brief description	Thematic Category	Partner that implements the activity	Age of targeted audience
1	Multiple	Visit to the Psiloritis UGGp Information Center.	Includes informative and educational materials and small experimental displays, dioramas (cave, mountain ecosystem and traditional house), an exhibition of local products, while there is also a small collection of rocks and fossils from the geopark area as well as digital educational tools and references to the SDGs.	Geodiversity, Biodiversity, Human History and Traditions, Sustainable way of life	Psiloritis UGGp	NS
2	Educational program, field visit, simple experiments, hands- on activities	Meet Psiloritis UNESCO Global Geopark!	Includes a presentation on what is a UGGp and what are its purposes, Geopark networks, examples of geosites from Psiloritis UGGp, interpretation of the main geological processes (complementarily with simple experiments or displays) characteristic of the geodiversity and geological history of Psiloritis UGGp (and Crete), holistic approach of UGGps and links between geodiversity, biodiversity and human history and traditions. The presentation is usually followed by a field visit and/ or worksheets, hands- on activities.	Geodiversity	Psiloritis UGGp & Anogia CEES	NS

3a	Educational program	Where is the water?	Aims to explore the processes of karst erosion that have formed the relief of Psiloritis and the relationship between underground water and water availability/ management issues in the area. It may be followed by a field visit (#3c) in one of the caves of Psiloritis UGGp that are open for visitors.	Geodiversity	Anogia CEES	Kindergarten - mid-Elementary School students
3b	Educational program	When water hugged the stone…				Mid-Elementary-High School students and adult students
3c	Field visit	Discovering the secret world of caves!	This field visit incudes a visit in one of the three open for visitors caves of Psiloritis UGGp, where the students experience the geology of caves and their unique biodiversity and local legends.	Geodiversity, Biodiversity, Human History and Traditions		Elementary-High School students and adult students
4a	Hands-on activity	What makes the most common rock of Psiloritis UGGp special?	This aims to highlight the diversity of karst formations, including posters of caves, gorges, plateaus and karst springs and complementary smaller cards depicting characteristic plants, animals or human activities linked to them, that the students need to “match”. This activity is used independently (during public outreach events) or follows the implementation of #2 or #5a (when there isn’t an option for a field visit).	Geodiversity, Biodiversity	Psiloritis UGGp	Elementary-High School students and adults (during public outreach events)
4b		Threats for mountain ecosystems!	Includes 12 cards with different threats for mountain ecosystems (soil erosion, pollution, habitat fragmentation etc.) with pictures from the territory and different Greek mountains. This activity is used independently (during public outreach events) or follows the implementation of #2 or #5a. It can also be implemented in the field, where the students try to identify in- situ a bad practice from the cards (if present) and discuss if other threats could apply in the territory.	Geodiversity, Biodiversity, Sustainable way of life		
5a	Educational program, field visit, worksheets, hands- on activities	Biodiversity and Psiloritis UGGp.	Includes a presentation on what is a UGGp and what are its purposes, interpretation of geodiversity and biodiversity and how they are linked, introduction to endemic plants and animals of Psiloritis UGGp- mainly focusing on the species’ history and threats. The presentation is usually followed by a field visit and/ or worksheets, hands- on activities in the Information Center or in the field.	Geodiversity, Biodiversity	Psiloritis UGGp	mid-Elementary -High School students
5b		In the land of Amalthea: earth, scent, life!	Includes a presentation on the typical ecosystems of Psiloritis, examples of local biodiversity and endemism, the concepts of diversity in nature and society and familiarization with the scientific approach of studying the natural world. The presentation is usually followed by a field visit and/ or worksheets, hands- on activities in the Information Center or in the field.	Geodiversity, Biodiversity	Anogia CEES	Elementary-High School students and adult students
6	Educational program, hands- on activities	A tale from Psiloritis UGGp!	Includes a presentation on what is geology and what is a UGGp, what could be a geosite and what could not (with visual examples from the territory), who are the people of the Geopark (who studies rocks? what are the main professions of the people in our geopark?), interactive narration of a local myth and activities exploring the characters/ natural setting of the story.	Geodiversity, Human History/ Traditions and Arts	Psiloritis UGGp	Kindergarten - mid-Elementary School students

7	Educational program, worksheets, activity book	How does the natural environment give birth to civilization?	This is a program that aims to highlight the connections between the natural environment of Psiloritis and the cultural heritage of its people, focusing on the local economy and the traditional arts (especially loom weaving).	Geodiversity, Human History/ Traditions and Arts	Anogia CEES	Kindergarten -High School students and adult students
8	Educational program, field visit	Visiting the shepherd's shelter!	This program aims to present the shepherd's way of life in Psiloritis, highlighting the role of the natural environment, through a field visit in a mountain plateau to experientially explore concepts of ecosystem services and visit a mitato (traditional shepherd's refuge built with the dry- stone walling practice).	Geodiversity, Biodiversity, Human History/ Traditions and Arts	Anogia CEES	Kindergarten -High School students and adult students
9	Educational kit	The underground journey of water.	Explores the relationship between limestone and water, the underground journey of water through the rocks, the formation of karst structures and the ecosystems and biodiversity found in them. The kit includes theoretical background for the teacher, instructions and materials for different activities e.g. crosswords, board games.	Geodiversity, Biodiversity	Psiloritis UGGp	Elementary -High School students
10	Educational kit	Climate Change and Island Geoparks.	Explores themes such as climate change, the "footprint" of the modern lifestyle and the natural phenomena associated with the effects of these factors. The kit includes theoretical background for the teacher, instructions and materials for different activities e.g., card- games, board game.	Sustainable way of life	Psiloritis UGGp	Mid Elementary -High School students
11	Digital tool	e-Geodiscover app (available for two different geo-trails)	This is an app for mobile devices (smartphones, tablets) that aims to provide knowledge about the geology, culture and environment of the geopark, as well as map reading, orientation and navigation skills, in the form of a pop-up "hidden treasure" quiz, which the child follows along an easy and smooth short route in the area of the Stefana plateau (Mygia's geo- trail) and/or in Gonies geo- trail.	Geodiversity, Biodiversity, Human History/ Traditions and Arts	Psiloritis UGGp	NS
12	Network for collaboration on education	National Thematic Network entitled "Feeling the memory of the Earth through geodiversity, Geoparks and anthropogenic activities"	Anogia CEES has established this Thematic Network with the aim to connect teachers and educators all over Greece, interested in topics related to geodiversity and UGGps and keep them engaged through a series of actions and initiatives (trainings, production of textbooks and education material etc.).	Geodiversity, Biodiversity, Human History/ Traditions and Arts	Anogia CEES	Teachers of all levels, Educators
13	Training seminars, field visits	Multiple themes	Both partners design, organize and implement training seminars (many times jointly) addressed to adult professionals of the area (e.g., teacher trainings, seminars for local producers). These seminars usually include a series of theoretical presentations from experts, followed by field visits to experience the examples and good practices, regarding each topic.	Geodiversity, Biodiversity, Human History and Traditions, Sustainable way of life	Psiloritis UGGp & Anogia CEES	Adults

14	Public events	Multiple themes	Both partners design, organize and implement public events (many times jointly), addressed to issues that concern the local communities with the purpose to responsibly inform and sensitize them. These events may concern public talks on Natural heritage & Conservation, Natural Hazards, debates on Clean Energy etc. and on many occasions they are organized within the context of International Days.	Geodiversity, Biodiversity, Human History and Traditions, Sustainable way of life	Psiloritis UGGp & Anogia CEES	NS
15	Partnerships-synergies	Multiple partnerships	Both partners have a close cooperation between each other, but they have also developed numerous synergies with other Educational/ Research Institutions over the years to further support their initiatives concerning education.	Geodiversity, Biodiversity, Human History and Traditions, Sustainable way of life	Psiloritis UGGp & Anogia CEES	NS

NS: Not- Specified (for "Age of targeted audience"), when there is no limit to the age of the targeted audiences to whom the material/ activity is addressed to, but is modified for different ages and situation of implementation (educational activity, public outreach event etc.).

Figure 1. Picture from a school visit in the geosite Petradolakia after an educational program at CEES of Anogia (left) and at the geosite Vossakos Folds during a three-day teacher- training seminar in 2019, within the context of the National Thematic Network of CEES of Anogia "Feeling the memory of the Earth through geodiversity, Geoparks and anthropogenic activities" with the cooperation of Psiloritis UGGp (right).

Based on the quantity and multidisciplinarity of the materials provided for geo- education and geology- related topics in Psiloritis UGGp (Table), it becomes once again evident that these territories are important loci for the interpretation and education on themes and phenomena related to the formation and conservation of the natural world. In Psiloritis UGGp, educational activities are implemented by the staff of the organization as well as by the Anogia CEES, one of the geopark' s partners for education within the territory. Interestingly, even though the educators in the CEES of Anogia are not trained geologists, they have exhibited a consistent passion for geo- education since the early years of their operation, recognizing the importance of the local geodiversity and promoting it through the numerous education programs and initiatives they implement (Table). The excellent cooperation between Anogia CEES and Psiloritis UGGp has provided high- quality (scientifically and pedagogically) education materials and initiatives, educating an overall of approximately 10.000 students and 5.000 teachers on relevant topics (Fig. 1) in the territory so far (data from Anogia CEES).

Both organizations have developed and are implementing activities in the form of complete and structured educational programs or individual materials (activity books, short experiments etc.) for students of different levels, but also adults that may be university students, teachers or professionals of the area, receiving training on Geopark- related subjects in the form of workshops. Other forms of education initiatives may include field trips, textbooks and other activities performed during special occasions (i.e., celebration of International Days, special visits etc.) (Catana & Brilha, 2020; Rossi et al., 2022) also potentially aiming at locals or visitors, within the context of communication/ public outreach- that share some goals and principles with education- on what concerns the interpretation of the natural world of a territory (Crofts et al., 2020).

A wide range of pedagogical techniques is embedded in these educational activities: step-based education, familiarization and empowerment games, field studies, observation and orientation games, experiments that visualize

natural processes, inquiry-based learning and many more, while at the same time they enhance critical thinking, cooperation between students/ student groups, and empirical knowledge. The multidisciplinary approach and the promotion of links between themes is obvious in most materials while the successful communication between the organizations itself can be seen in the complementarity of some of the materials/ initiatives e.g., the CEES of Anogia has a greater experience in organizing training seminars for teachers and educators and Psiloritis UGGp has a larger set of options of digital tools (Tab. #11; Fig.2; Fassoulas *et al.*, 2022). All the above observations (quantitatively, qualitatively) generally agree with findings and conclusions from Catana & Brilha (2020) and Rossi *et al.*, (2022) on the mode of how educational tools and activities are designed and executed in most geopark territories.
Furthermore, with reference to the seventeen United Nations Sustainable Development Goals (SDGs), the potential of the tools presented here can easily be grasped within the context of SDG 4 “Quality Education” and SDG 17 “Partnership for the Goals”. Additional SDGs can also be observed in, for example, materials #4b- 5b (Table) that are clearly linked to SDG 15 “Life on Land” and material #10 (Table) that is linked to SDG 13 “Climate Action”. Furthermore, other stand- alone activities and individual actions from initiatives #13, 14, 15 (Table)- that are not mentioned here in detail for reasons of space availability and overall relevance- are directly related to SDGs focusing on the triplet People- Prosperity- Planet. This further underlines the role of UGGps as areas for the promotion of the natural sciences but, also, sustainability (Catana & Brilha, 2020; da Silva, 2020).

Figure 2. Picture from a school visit where the e-Geodiscover app was used by students following Mygia’s geo-trail.

Conclusions

Geology is all around us through the rocks and minerals that we use, the processes that shape our surroundings and the very substrate we walk on! However, as a scientific field, it unfortunately still remains rather unpopular and non-understandable by most of the public. UGGps as organizations and as territories are, indeed, playing a significant role addressing this issue, since they have the background and experience to “translate” this often-inaccessible knowledge for the local communities (students and adults) in a way that is scientifically and pedagogically appropriate. Thus, educational tools developed and implemented in UGGp territories, especially in cooperation with local educational partners, are numerous, innovative and extremely useful if one considers the overall limited and very much needed interpretive and teaching resources on geology for the more effective protection of this aspect of the natural heritage of our territories. Extending the conversation to other relevant issues of sustainability such as the climate crisis, natural hazards, water availability and many more, we could find ourselves in the position to also inform, sensitize, engage, and prepare members of local communities on matters that are extremely pressing nowadays. The impact of this effort increases significantly if we, as organizations, share all these tools and practices within our networks and more broadly into the scientific community and other conservation organizations and protected areas, with whom we share the same goals.

References

Catana, M. M., Brilha, J. B., 2020. The role of UNESCO global geoparks in promoting geosciences education for sustainability. Geoheritage 12 (1), 1.

Crofts, R., Gordon, J.E., Brilha, J., Gray, M., Gunn, J., Larwood, J., Santucci, V.L., Tormey, D., Worboys, G.L., 2020. Guidelines

for geoconservation in protected and conserved areas. Best Practice Protected Area Guidelines Series No. 31. Gland, Switzerland: IUCN.

da Silva, E. M. R., 2020. The contribution of the European UNESCO Global Geoparks for the 2030 Agenda for Sustainable Development–a study based on several data sources. Ph.D. Thesis, Universidade NOVA de Lisboa, Portugal, 344p.

Fassoulas, C., Nikolakakis, E., Staridas, S., 2022. Digital tools to serve geotourism and sustainable development at Psiloritis UNESCO Global Geopark in COVID times and beyond. Geosciences 12 (2), 78.

Martínez-Martín, J. E., Mariñoso, P. E., Rosado-González, E. M., Sá, A. A., 2023. UNESCO Global Geoparks vs. Education: A 10-Year Bibliometric Analysis. Geoheritage 15(1), 34.

Rossi, G.S., Motta Garcia, M.G., Marie Bourotte, C.L., 2022. Educational Materials on Geosciences: Analysis from UNESCO Global Geoparks and Potential for Application to Protected Areas. Geoconservation Research 5(2): 165-194.

UNESCO, 2015. Operational Guidelines for UNESCO Global Geoparks. https://unesdoc.unesco.org/ark:/48223/pf0000391354. Accessed 21 January 2025.

UNESCO, 2024. UNESCO Global Geoparks (UGGp). https://en.unesco.org/global-geoparks. Accessed 21 January 2025.

17th INTERNATIONAL CONGRESS of the Geological Society of Greece

BULLETIN OF THE GEOLOGICAL SOCIETY OF GREECE, SP. PUBL.

EXTENDED ABSTRACT 156

The Role of Fairy Tales in Fostering Geoscience Understanding in Early Childhood

Kolyva P. [1], Koumoutsakou O.[1], Antonarakou A.[1]
(1) Department of Geology and Geoenvironment, Kapodistrian University, Athens, Greece, pavlinak03@yahoo.com

Introduction

Storytelling through oral traditions has long been a powerful way to pass down cultural values and beliefs while nurturing imagination and creativity in children. Similarly, children's literature plays a pivotal role in education by effectively blending learning with entertainment (Pulimeno et al., 2020). This research is a small case study in which the use of fairy tales and storytelling, in general, is examined to understand geoscience and its subsections, such as earthquakes. Regarding the utilization of fairy tales as instructional resources, an extensive examination of a wide range of fairy tales was undertaken, focusing on their various attributes and potential educational significance. A fairy tale about earthquakes was created and evaluated with primary school children.

The Evolution and Impact of Fairy Tales: From Cultural Narratives to Educational and Scientific Insights

Fairy tales stimulate creativity and emotional development by embodying deep themes, offering comfort and security even when exploring conflict or danger. They nurture emotional intelligence, impart moral lessons, and inspire critical thinking. These stories are vital tools for fostering creativity, moral maturity, and thoughtful engagement with the world. (Bakaraki et al., 2018).

Fairy tales have transitioned from oral traditions to a significant presence in mass media, with geomythology—a field studying myths tied to geological phenomena—revealing how narratives about earthquakes, tsunamis, and volcanic eruptions reflect cultural efforts to explain natural events (Rahman, 2017; Dewi, 2024; Piccardi & Masse, 2007; Vitaliano, 2007). These myths, often holding sacred and cultural significance, provide valuable insights into geological science and resilience-building, especially for children living in areas prone to natural disasters (Dewi, 2024). Local myths have also contributed to addressing geological challenges, with geological terminology itself drawing inspiration from mythological figures (Vitaliano, 2007). Prominent authors like Jules Verne, Arthur Conan Doyle, and H.P. Lovecraft have integrated geological concepts into their adventure and fantasy literature, illustrating how literature can blend science and storytelling (Gargallo, 2023).

Research Methodology:

The research was conducted as a small-scale case study involving a class of 20 second-grade students from a primary school in Vasiliko Evoias, Greece. The prototype fairy tale was introduced during the school's annual earthquake drill. Data collection methods included direct observation, semi-structured interviews with the teachers, and a post-activity reflection task using visual prompts tailored for children. The research aimed to evaluate student engagement, their conceptual understanding of earthquakes, and their emotional response to the narrative.

Developing a Prototype Fairy Tale to Educate Children About Earthquakes

The initial phase of this research involved an exploration of effective strategies for the implementation of fairy tale-based instruction within the context of elementary science classrooms (Kwon & Lee, 2010). To investigate the pedagogical effectiveness of fairy tales in geoscience education, a prototype fairy tale was developed specifically for preschool and elementary school-aged children. This narrative addresses the phenomenon of earthquakes, emphasizing the importance of preparedness and mitigation strategies to minimize potential damage, destruction, and human loss. The protagonist of this tale is a small rock named Rhea, who embarks on a journey to the Earth's surface to convey an urgent message about an impending earthquake.

The prototype fairy tale was introduced to elementary school students during their annual earthquake drill. Teachers observed that the students were highly engaged throughout the process. The classroom was soon filled with exciting questions and discussions about earthquakes, sparked by the captivating story. The fairy tale not only ignited children's imaginations but also stimulated their critical thinking skills, helping them understand the appropriate actions to take during an earthquake. Importantly, these results demonstrate that incorporating fairy tales into children's education can effectively cultivate valuable character traits.

Mitigating the Risk of Misconceptions

To prevent the development of misconceptions, the fairy tale content was co-reviewed by a geoscience expert and an

early childhood education specialist. Scientific elements, such as the causes of earthquakes and safety measures, were presented clearly and accurately within the fictional framework. Educators facilitated follow-up discussions to reinforce key concepts and clarify any confusion that might arise between fiction and scientific fact.

Discussion of Results

Teachers reported increased attentiveness and participation from students, indicating the effectiveness of the narrative-driven approach. Many students could accurately recall appropriate earthquake safety measures, such as "Drop, Cover, and Hold On," and showed greater confidence in discussing natural disasters. Some students even shared how they planned to inform family members about what they had learned. These findings suggest that the integration of storytelling not only supported cognitive learning but also fostered emotional readiness and resilience. The use of relatable characters like Rhea helped students better internalize abstract scientific ideas, which is consistent with previous research emphasizing the benefits of narrative pedagogy (Dewi, 2024; Fleer, 2013).

Enhancing Scientific Learning and Motivation Through Fairy Tale-Based Pedagogy

This research revealed that students effectively connected fairy tales to their personal experiences and actively engaged in classroom activities incorporating them. Many expressed increased interest in science classes, attributing this to the engaging nature of the fairy tale-based approach. This method not only motivated students to study diligently but also facilitated a deeper understanding of scientific concepts in context.

The study concluded that instruction using fairy tales is an effective pedagogical approach that enhances learning motivation, fosters scientific inquiry, provides opportunities to apply scientific concepts, and cultivates a positive attitude toward science.

Conclusion

Recognizing the crucial role of imagination in early childhood science education is vital (Fleer, 2013). Children's literature and storytelling could help promote "*students' global development and well-being when included in school curricular activities*" (Pulimeno, et al., 2020). This study offers promising evidence that integrating scientifically accurate storytelling into early education can not only reduce fear and confusion about natural disasters but also lay the groundwork for informed and resilient future citizens. Further research with larger samples and longitudinal follow-ups is recommended to explore the long-term impact of this approach.

Acknowledgments

I would like to express my sincere gratitude to the teachers and elementary school children who have given their time to be respondents in this research, to my professor for her invaluable guidance, and to my sister for her significant contributions throughout the project.

References

Bakaraki, M.P., Dourbois, T., Kosiva, A. (2024). Therapeutic and developmental benefits of fairy tales in early childhood: A mini-review. Brazilian Journal of Science, 3(8), 19-23. https://doi.org/10.14295/bjs.v3i8.600

Dewi, D.J.K. 2024 Storytelling to develop resilience in early childhood in facing earthquake disasters. Proceedings of the International Conference on Current Issues in Education (ICCIE 2023), Atlantis Press, pp. 410-420. Doi: 10.2991/978-2-38476-245-3_43

Fleer, M. (2013). Affective Imagination in Science Education: Determining the Emotional Nature of Scientific and Technological Learning of Young Children. Research in Science Education, 43, 2085-2106. https://doi.org/10.1007/S11165-012-9344-8

Gargallo, J. (2023). Geology and literary fiction. BOLETÍN GEOLÓGICO Y MINERO. https://doi.org/10.21701/bolgeomin/134.1/004

Kwon, N., & Lee, K. (2010). The Development and Application of Strategies using Fairy Tales in Elementary School Science Instruction. Journal of the Korean Association for Research in Science Education, 30, 1-12. https://doi.org/10.14697/JKASE.2010.30.1.001

Piccardi, L., & Masse, W. (2007). Myth and geology. Geological Society, London, Special Publications, 273, 366-368. https://doi.org/10.1144/GSL.SP.2007.273

Pulimeno, M., Piscitelli, P., Colazzo, S. (2019). Children's literature to promote students' global development and well-being. Health Promotion Perspectives, 2020, 10(1), 13-23. https://hpp.tbzmed.ac.ir/Article/hpp-31914

Rahman, F. (2017). The Revival of Local Fairy Tales for Children Education. Theory and Practice in Language Studies, Vol. 7, No. 5, pp. 336-344. http://dx.doi.org/10.17507/tpls.0705.02

Sherbaeva, Z. (2021). Fairy Tales World Specifics in the Perception of a Child. Bulletin of Science and Practice. https://doi.org/10.33619/2414-2948/69/36

Vitaliano, D. (2007). Geomythology: geological origins of myths and legends. Geological Society, London, Special Publications, 273, 1 - 7. https://doi.org/10.1144/GSL.SP.2007.273.01.01

17th INTERNATIONAL CONGRESS of the Geological Society of Greece

BULLETIN OF THE GEOLOGICAL SOCIETY OF GREECE, SP. PUBL.

EXTENDED ABSTRACT 157

Application of the educational proposal for geoscience: geology in secondary education through educational geopaths in the urban environment

Kontokostas G.E.[1], Antonarakou A.[1]

(1) National and Kapodistrian University of Athens, Faculty of Geology and Geoenvironment, Panepistimiopolis, Zografos, Greece, geokon@geol.uoa.gr

Introduction / Background

The research project, entitled: An educational walk in the historical centre of Athens, is an innovative educational proposal that approaches different scientific fields in an interdisciplinary way. Conducted as part of the research work (project) by 14 school girls and 13 school boys of secondary education of the high school, during the second semester of the 2019-2020 school year. In addition to the historical, social and literary approach to the selected sites, this educational process uses the area around the square in Monastiraki in the light of urban geology and can increase children's knowledge and improve their attitude towards geosciences.

1. Background and Objectives

A route guide was prepared by the students, in which each site, along with its historical and cultural characteristics, describes the geological and hydrological potential of the area.

In the course of the educational process, using techniques entailed in the scientific/educational methodology by inquiry, suggesting educational walking paths through the historical center of Athens, (Dermott, L.,1996), Selected places of the walk trail served our educational aims: Ag, Asomaton-Monastiraki-Eridanos-Stoa of Attalos-Roman Agora –Hadrian's Library-Kapnikarea.

The locations chosen for the route served our educational purposes. I am referring, for example, to the optimal understanding of the formation of rocks, the recognition of the type of rocks, information on the geological and hydrographic potential, in pupils of the Secondary Education of Attica.

2. Research Methodology

The research sample consist of 14 school girls and 13 school boys of secondary education of the high school. In this research the educational aims for the students were: a) to recognize rocks b) to be informed about geological and hydrological potential, and finally, c) to understand the geological notions in time and in space, that means to recognize the geological time and to comprehend the rock cycle (Kaliet al.,2003). The educational goals of our proposal were: a) to inform students about the urban environment of Attica, b) to show that geology is an attractive and important science, c) to study geological phenomena with an interdependence procedure with geosciences and d) to view physical phenomena with a holistic approach, improving students' ecological consciousness.

In this work, we attempted to follow research steps, (Kalkanis, 2010) set forth by inquiry-based learning (Dermott, 1996) : a) trigger for interest, b) reminder of basic knowledge/formulation of hypotheses, c) experimentation/trials, d)formulation of conclusions, e) applications/generalization according to learning.

Trigger of interest (step 1) : Initially, the students visited the exterior and interior of the Temple of Kapnikarea, where they noted with interest the diversification of the rocks and the geological relief of the area.

Reminder of basic knowledge/formulation of hypotheses: Then the necessary knowledge was presented in the way presented by the relevant school lesson of the analytical program (orogenesis, types of rocks) and by the most widely used international reference books (Kali, 2003, Tillery, 1996), - ways of rock formation and the cycle of rocks, so that the pupils could formulate hypotheses. Then, the male and female students completed an appropriately coded questionnaire (pre-test), (Bakopoulou, 2016). The pre-test examined if the students are informed of the geological and hydrological potential of the area , if they could recognize rocks (marbles, granites, limestone and fossils) and if they know the rock cycle.

Experimentation/trials: After studying the relevant literature (Bouras, 2017), the students researched the area and the sites through the internet, collecting historical, cultural and geological information, and visited the places around the area of the square in Monastiraki. They revisited the sites, observed and studied the stones with the aid of a magnifying glass in different buildings. Then they selected sites of hydrological interest (rivers, wells) and of geological interest, combining building materials (limestone, marble and granite).

Formulation of conclusions: Then, we asked the students to summarize their conclusions and to write down

observations and comments. Finally, they designed a suitable route with the selected locations and entered it in a mobile application with all the relevant information.
Applications/generalization according to learning: The successful completion of the students' survey prompted them to suggest additional routes in the surrounding area. Finally, we asked them (increasing the difficulty further) to generalize their conclusions by interpreting the creation of other sedimentary, siliceous and metamorphic rocks. They also completed a post-test questionnaire.

3. Results

The control group was also the experimental group. After the questionnaires were deleted (pre-tests are different from post-tests), the answers and observations were compared, and the following was recorded as regards the main research questions and objectives: In general, the pre-tests showed difficulties in identifying the different rocks, in understanding the geological processes and the cyclicity of the rocks. On the contrary, their responses to the post-test after the completion of the project and following the methodological steps, showed that all the students had understood the geological processes and the cycle of rocks in geological time, had the ability to recognize rocks and learned about the geological and hydrological potential of the area (Figure 1).

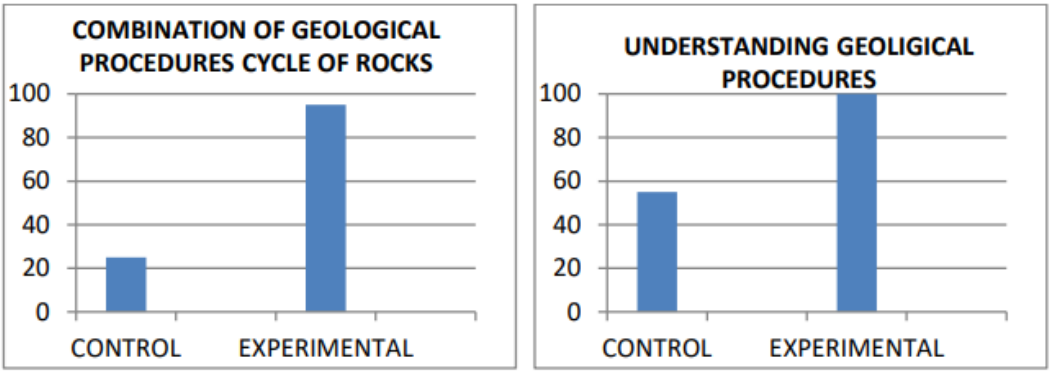

Figure 1 a. We observed an improvement in a) the understanding of geological processes by the pupils (%) and (b) the combination of geological processes in the rock cyclicity by the pupils (%), before and after the teaching intervention, respectively.

4. Conclusions

The results of the post-test show that all the pupils in the class understood the geological processes (Figure 1a) and the rock cycle (Figure 1b). The children's own design of the georoutes proved to be functional and highly useful in terms of understanding and interpreting the phenomena involved. After the educational intervention the pupils improved their geological knowledge, developed their critical thinking, their creativity and found the science of geology interesting.

Figure 2 A mobile app that acts as a compass for our route.

References

Καλκάνης, Γ.Θ., 2010. ΕκΠαιδευτικό ΕΡΓΑΣΤΗΡΙΟ και ΕκΠαιδευτικές ΤΕΧΝΟΛΟΓΙΕΣ, Ι. το Εργαστήριο, ΙΙ. οι Τεχνολογίες, Αθήνα (in Greek).

Bakopoulou, A., Antonarakou, A., Loizos, S., Zambetakis –Lekkas, 2016. Development and precodification of a lithosphere questionnaire as a tool in educational research (Geosciences). Bulletin of the Geological Society of Greece, 50(1), 201-208 https://doi.org/10.12681/bgsg.11720

Bloom, B.S. (Ed.), 1984. Taxonomy of educational objectives. 1: Cognitive domain. White Plains, Longman, NY.

Bouras, Ch., 2017, Byzantine Athens. 10th-12th centuries, Routledge – Benaki Museum, Athens.

Dermott, L.,1996. Physics by Inquiry: Physics Education Group University of Washington, Washington.

Kali, Y., Orion, N. & Eylon, B-S, 2003. The effect of knowledge integration activities on students' perceptions of the Earth's crust as a cyclic system. Journal of Research in Science Teaching, 40(6), 545–565.

Manion, L, Cohen, L., and Morrison, K., 2000. Methodologia ekpaideftikis erevnas, publ. Metaixmio, 737 pp. (in Greek), Athens.

Zervopoulou, A., Pavlides, S., 2016. Geological mapping in urban areas. a case study from the inner city of Thessaloniki, Greece. Bulletin of the Geological Society of Greece, 50 (2), 1027-1023 https://doi.org/10.12681/bgsg.11807.

17th INTERNATIONAL CONGRESS of the Geological Society of Greece

BULLETIN OF THE GEOLOGICAL SOCIETY OF GREECE, SP. PUBL.

EXTENDED ABSTRACT 158

Interpretation of CPTu data for mining slope stability assessment in reclamation projects: The case of pit Lake Most, Czech Republic

Kontopidis O.N.[1], Theocharis A.I.[2], Koukouzas N.C.[3], Burda J.[4,5], Zevgolis I.E.[1]

(1) School of Mining and Metallurgical Engineering, National Technical University of Athens, Greece izevgolis@metal.ntua.gr (2) Department of Civil Engineering, University of Patras, Greece (3) Chemical Process & Energy Resources Institute, Centre for Research & Technology Hellas, Athens, Greece (4) Brown Coal Research Institute (VUHU), Most, Czech Republic (5) Faculty of Mining and Geology, VSB Technical University Ostrava, 17 Listopadu 2172-15,70800 Ostrava, Czech Republic

Spoil heterogeneity poses geotechnical challenges during mine reclamation. CPTu data-driven slope stability analyses are crucial for safe and effective restoration.

Introduction

During the last decades, coal (also in the form of lignite) has been the main raw material for electricity production. The leading European producing countries include Germany, Czech Republic, Poland and Greece (BGR, 2014, Euracoal, 2017, EY, 2014). Due to the climate crisis, lignite mines have now entered a final phase in Europe and worldwide, heading towards decarbonization. As the transition to the post-lignite era is underway, the choice of land use after mine closure is a crucial decision, and must obviously be in line with the expectations of local communities and with the principles of sustainable development (Pavloudakis *et al*., 2009).

One of the most common practices of restoring a mine is the formation of a lake within its excavation. The creation of lakes can be done either artificially or naturally through hydrological processes, such as rainfall or groundwater infiltration. Lakes offer local communities social, recreational, ecological and economic benefits by landscaping and revegetation, creating aquatic life and maintaining water quality. However, the creation of lakes in lignite mines may cause instabilities and landslide phenomena, with social and economic consequences (Zevgolis *et al*., 2019). The elevation of the aquifer during flooding affects the stability of the slopes by increasing the water pressures of the submerged soil pores. However, increasing the water body within open excavation also acts as a supporting force, and lake creation has been reported to improve slope stability as lake height increases (Kontopidis *et al*., 2022).

The surface exploitation of lignite requires the extraction, transport and deposition of the overlying intermediate soil layers called spoil materials (spoils). According to estimates, spoil heaps reach 1.45 Gt annually worldwide (Bian *et al*., 2012). The disposal spoil takes place mainly in areas where the mining phase has been completed, so that there is the possibility of restoring the paid areas with the aim of minimal environmental impact during the transition to the post-lignite era. The variability of their characteristics and the absence of good deposition practices result in geotechnical problems, including slope stability issues, which need to be investigated both during the deposition phase and during the restoration phase of the area.

This work deals with the assessment of stability issues in the area of the artificial lake Most in the Czech Republic, which was formed in a former surface lignite mine with an average excavation depth of 100 m. At the current boundaries of the lake, spoil materials were deposited during the operation of the mine, forming artificial slopes. Due to the uncertainty about the properties of spoil, 24 cone penetration tests were performed around the lake by measuring pore pressure (CPTu) at depths up to 50 m, mainly within spoils. Raw test data were used to evaluate them and estimate undrained shear strength (c_u) based on empirical correlations. The stability analysis was performed using the commercial software Slide2 applying the limit equilibrium method.

CPTu raw data interpretation

In 2020, 5 years after the final elevation of the lake Most, 24 CPTu were performed with measurement of pore pressures, at depths up to 50 m. The purpose of the tests was to investigate and identify adverse soil conditions in terms of lake's banks stability. Figure 1 shows a sketch of Lake Most (floor plan) with the relative locations of the CPTu tests. A star symbol indicates test P20 whose primary results are shown in Figure 2. CPTu raw data consist of cone tip resistance (q_c), sleeve friction (f_s), friction ratio (R_F) and pore water pressure (u_2). Cone tip resistance (q_c) is observed to increase with depth smoothly from 2 MPa at the surface to 5 MPa at the depth of 40 m and then increase relatively sharply up to 15 MPa. Local peaks, such as those occurring at depths of 22 m, 33 m and 45 m, may be due to the presence of isolated conglomerates which momentarily hinder the advance of the cone. Sleeve friction (f_s) shows a similar increase from 0.1 MPa on the surface to 0.2 MPa at a depth of 40 m and in the last 10 m increases sharply to 0.6 with 0.8 MPa. The friction ratio (R_F) varies from 2% to 6%, while two peaks of 10% are observed at 15 m and 25 m. In the first 20 m the average R_F value is about 3.5%, while from 20 m to 45 m the average value increases to 5%. Pore water pressure (u_2) shows a small rate of increase up to 120 kPa at a depth of 40 m with no local peaks.

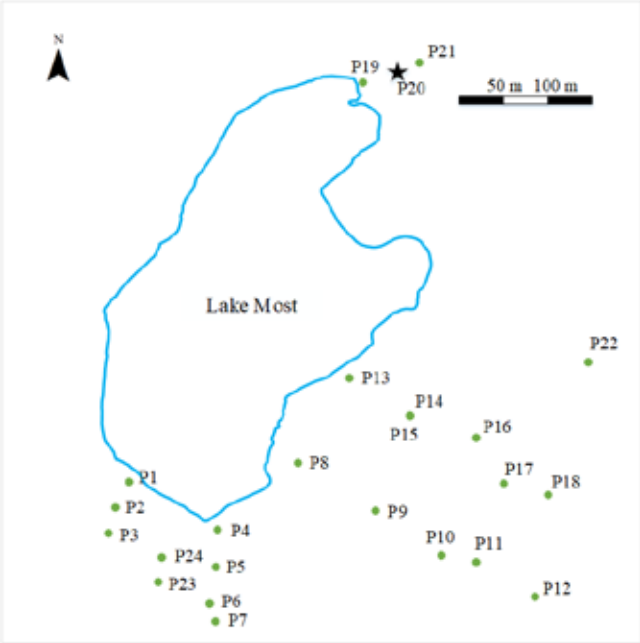

Figure 1. Overview of the lake Most with the locations of the CPTu tests.

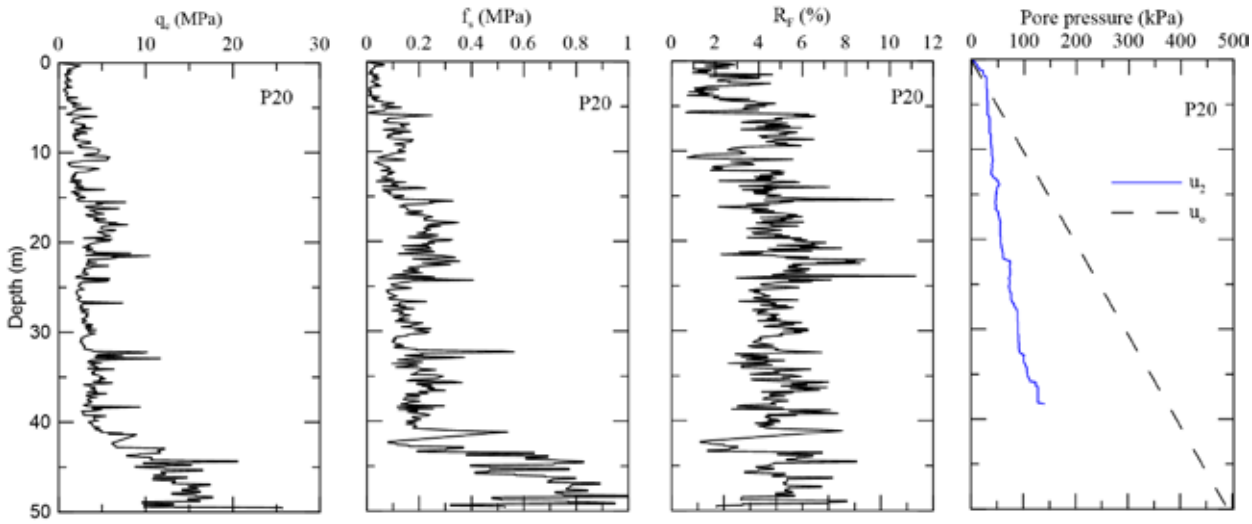

Figure 2. Measurements of q_c, f_s, R_F, and u_2 with depth for test P20.

The measurement of pore pressure allows for improved interpretation of soil conditions. In particular, several diagrams have been proposed for the determination of soil types by CPTu using the combined overburden stress (σ_v)-corrected total tip resistance (Q_t), overburden stress-corrected sleeve friction (F_r), and pore pressure, u_2. In this paper the following I_c index is used (Robertson, 2009, Mayne, 2014):

$$I_c = ((3.47 - \log Q_t)^2 + (\log F_r + 1.22)^2)^{0.5} I_c = ((3.47 - \log Q_t)^2 + (\log F_r + 1.22)^2)^{0.5} \quad (1)$$

Figure 3 presents the soil classification as a function of depth for the P20 test according to the I_c index. The values on the horizontal axis correspond to specific values of I_c associated with specific soil types. Up to 5 m sandy silty and silty sand are the main soil type and then up to 10 m sandy silt/silty sand. At a depth of 10 m to 42 m, clay prevails with sporadic silty layers. In the last 8 m, until the end of the test, silty clay is returned. Generally based on the 24 CPTu, the soil type mainly in fine-grained soils, i.e. silt, silty clays and clays.

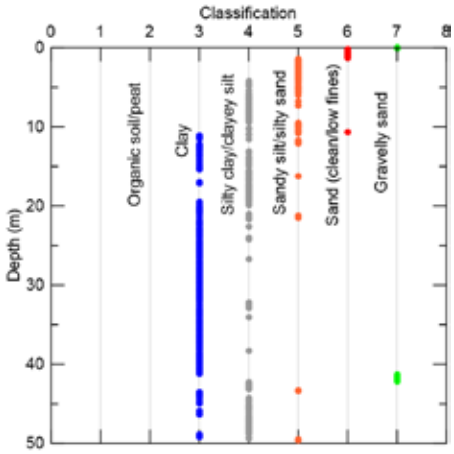

Figure 3. Soil classification using I_c index for test P20.

The undrained shear strength (c_u) is calculated based on the values of pore-pressure-corrected cone resistance (q_t):

$$c_u = \frac{q_t - \sigma_{vo}}{N_{kt}} c_u = \frac{q_t - \sigma_{vo}}{N_{kt}} \quad (2)$$

where N_{kt} is a factor taking values 10 to 18. In the context of this analysis, the mean value N_{kt}=14 was used (Robertson, 2009). Initially, a regression analysis of the q_t population was performed where a trendline equation was derived:

$$q_t = 0.12D + 1.27 \text{ (MPa)} q_t = 0.12D + 1.27 \text{ (MPa)} \quad (3)$$

where D is the depth.
The equation (2) was used for the function of undrained shear strength (c_u). For the calculation of total stress σ_{vo} a constant value of unit weight γ=18.2 kN/m^3 was considered as the population mean. Figure 4 illustrates the change of c_u with depth. Therefore, the mean function (c_u) is obtained:

$$c_u = 7.27D + 90.7 c_u = 7.27D + 90.7 \text{ (} c_u \text{ in kPa, D in m)} \quad (4)$$

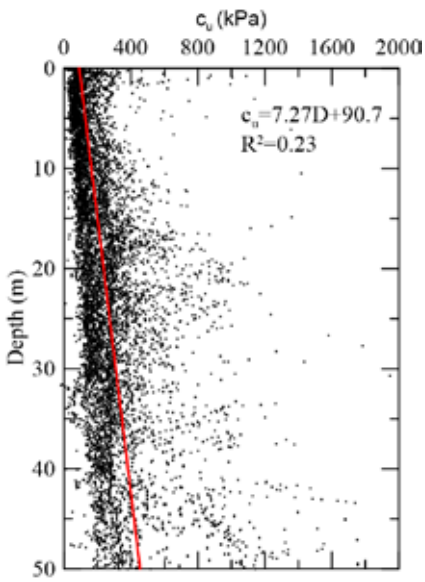

Figure 4. Variation of c_u as a function of depth.

Slope stability analysis

Slope stability analyses were performed with Slide2 software (Rocscience, 2019). The strength of spoils is determined by the function c_u=7.27D+90.7 (Eq. 4). Figure 5 illustrates a typical slope model considered for stability analysis. Specifically, the analyses are performed on two-layer slopes of (H) 100 m and inclination (β) 11°, where a clayey layer with φ´=9.5° and c´=57 kPa underling spoils. An unfavorable condition in lignite mines, usually, is the presence of weak zones at the marl-lignite or between the layers of lignite. In this work, an inclined (β_z=3°) weak zone is located at the base of spoils with low strength (φ´= 6°, c´= 6 kPa) is considered (Mikroutsikos *et al*., 2021). This weak zone was simulated with a weak layer interface condition (proposed in limit equilibrium analysis to simulate narrow layers or interfaces with low strength) through software tools (Rocscience, 2023). Table 1 shows the strength values for the layers considered in the slope model.

Table 1. Input strength values.

Layer	Strength
Spoils	c_u=7.27D+90.7
Weak zone	φ´= 6°, c´= 6 kPa
Clay	φ´= 9.5°, c´= 57 kPa

The analyses used the advanced method "cuckoo" search for non-circular surfaces, which does not require the surface to be determined from the outset, but determines it through linear sections and optimization of solutions. To calculate the safety factor, the Spencer method was used, which satisfies the equations of equilibrium of both forces and moments. The Mohr-Coulomb failure criterion was used to determine the shear strength of the clayey layer and the weak zone. The lake was considered to have been filled by about 1/3 (so the ratio of the level of the lake (H_w) to the height of the slope is H_w/H = 0.3) as the most critical condition for the stability where the safety factor (FS) becomes minimal (Zevgolis *et al*., 2021). Finally, steady-state flow conditions were considered with the water table defined by H'_w = 0.1H at the left limit of the slope and the height of the lake on the right.
Figure 6 illustrates the non-circular/bi-linear failure surface which travels along the weak zone and daylights at the toe of slope. The safety factor (FS) is equal to 1.19, which is deemed tolerable for temporary mining slopes. However, this value is insufficient for civil engineering slopes, especially when considered in the context of reclamation projects, where a minimum FS of 1.4 is required. This higher standard is crucial to ensure the stability and safety of the slopes in the long term, as reclamation projects often involve the restoration of disturbed land and the safeguarding of the surrounding environment.

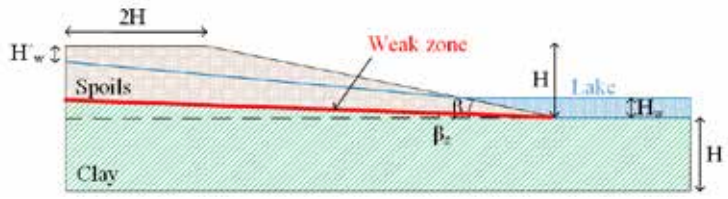

Figure 5. Two-layered slope model with inclined weak zone.

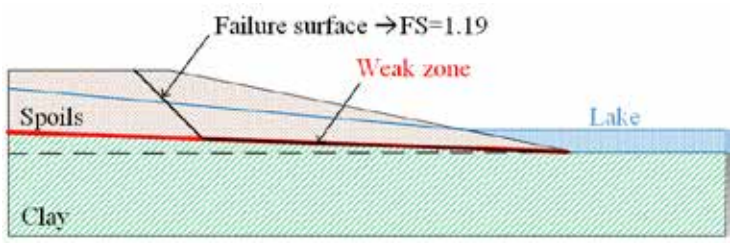

Figure 6. Bi-linear failure surface with FS=1.19.

Conclusions

This paper deals with slope stability in the area of the artificial lake Most in the Czech Republic, which was formed in a former surface lignite mine with an average excavation depth of 100 m. A key element of the slopes and their stability is the existence of spoi materials from the excavations of lignite mines. To investigate the characteristics of spoil materials around the lake, 24 cone penetration tests were performed by measuring pore pressure (CPTu) at

depths up to 50 m. Each test produced different deep primary results, confirming uncertainty and spatial variability as the main characteristics of the nature of spoil materials. Through the empirical soil index I_c spoils are mainly characterized as fine-grained materials, silts, silty clays and clays. Due to the presence of several types of soils in random spatial arrangement, it was not possible to locate a distinct stratigraphy. Consequently, a single soil material with significant heterogeneity was assumed. Evaluation of CPTu results showed that undrained shear strength c_u increases as a function of depth. The strength c_u was calculated through empirical correlations from the total cone peak resistance (q_t). A regression analysis of q_t resulted in the change function with the depth D q_t=0.12D+1.27 (in MPa). The change function of q_t derived the function of change of c_u=7.27D+90.7 (in kPa).
The use of CPTu data, although displaying some data dispersion, proved valuable for characterizing the soil properties and informing the stability analysis. The stability analysis revealed a safety factor (FS) of 1.19, deemed acceptable for temporary mining slopes but inadequate for long-term stability in civil engineering applications, especially reclamation projects. A minimum FS of 1.4 is recommended for such projects to ensure stability and safety. The analysis employed a two-layer slope model incorporating an inclined weak zone, a common feature in lignite mines, further emphasizing the need for a higher FS. The lower FS obtained highlights the potential for slope instability and underlines the risks associated with insufficient consideration of long-term stability requirements during reclamation.

Acknowledgements
This research has received funding from the European Union's Research Fund for Coal and Steel (RFCS) under the project "MidSafe" grant agreement No. 101157379 and the Hellenic Foundation for Research under the 5th Call for HFRI PhD Fellowships (Fellowship Number: 61518400).

References

BGR 2014. Energy study 2014: reserves, resources and availability of energy resources,Hanover. Federal Institute for Geosciences and Natural Resources (BGR).
Bian, Z., Miao, X., Lei, S., Chen, S.-E., Wang, W. & Struthers, S. 2012. The challenges of reusing mining and mineral-processing wastes. Science, 337, 702-703.
Euracoal 2017. Annual Report. European Association for Coal and Lignite,Brussels, Belgium.
EY 2014. European lignite mines benchmarking—sanitized report.
Kontopidis, O.N, Theocharis, A.I., Koukouzas, N.C. & Zevgolis, I.E. 2022. Stability of open pit lignite excavations during flooding. Comparison of a simplified analytical tool with limit equilibrium computational analysis. Górnictwo Odkrywkowe, 63.
Kontopidis, O., Theocharis. A.I., Zevgolis, I.E., Koukouzas. N.C. (2022). Stability of open pit lignite excavations during flooding: comparison of a simplified analytical tool with limit equilibrium computational analysis, Górnictwo Odkrywkowe – Surface Mining (ISSN 0043-2075), Poltegor-Instytut, Vol. LXIII, Nr. 3, p. 4-9
Mayne, P. Interpretation of geotechnical parameters from seismic piezocone tests. Proceedings, 3rd international symposium on cone penetration testing, 2014. 47-73.
Mikroutsikos, A., Theocharis, A.I., Koukouzas, N.C. & Zevgolis, I.E. 2021. Slope stability of deep surface coal mines in the presence of a weak zone. Geomechanics and Geophysics for Geo-energy and Geo-resources, 7, 1-17.
Pavloudakis, F., Galetakis, M. & Roumpos, C. 2009. A spatial decision support system for the optimal environmental reclamation of open-pit coal mines in Greece. International Journal of Mining, Reclamation and Environment, 291-303.
Robertson, P. K. 2009. Interpretation of cone penetration tests—a unified approach. Canadian geotechnical journal, 46, 1337-1355.
Rocscience 2019. Slide2 Version 7.0 - 2D Limit Equilibrium Slope Stability Analysis. https://www.rocscience.com/, Toronto, Ontario, Canada.
Rocscience 2023. Slide2 User Guide. Documentation/Slide model/Boundaries/Weak Layer Overview. https://www.rocscience.com/help/slide2/documentation/slide-model/boundaries/weak-layer/weak-layer-overview. Accessed on 10-1-2025. Toronto, Ontario, Canada.
Zevgolis, I.E, Mikroutsikos, A., Theocharis A.I. & Koukouzas, N.C. 2021. The effect of water filling on slope stability of open pits: A numerical investigation. The Evolution of Geotech-25 Years of Innovation. CRC Press.
Zevgolis, I.E., Deliveris, A.V. & Koukouzas, N. C. 2019. Slope failure incidents and other stability concerns in surface lignite mines in Greece. Journal of Sustainable Mining, 18, 182-19

17th INTERNATIONAL CONGRESS of the Geological Society of Greece

BULLETIN OF THE GEOLOGICAL SOCIETY OF GREECE, SP. PUBL.

EXTENDED ABSTRACT 159

A semi-quantitative multi-hazard approach for Tailings Storage Facilities

Kontopidis O.N.[1], Theocharis A.I.[2], Zevgolis I.E.[1]
(1) School of Mining and Metallurgical Engineering, National Technical University of Athens, Greece izevgolis@metal.ntua.gr (2) Department of Civil Engineering, University of Patras, Greece

A semi-quantitative approach presents a new way to assess multiple natural hazards' interactions affecting the stability of tailings storage facilities, leading to a semi-quantitative hazard index.

Introduction

The extraction and exploitation of raw materials are necessary activities for the sustainable development of society and the evolution of technology. The mining sector consists of successive stages initiating from the extraction of raw material to the storage and management of waste. Mine wastes include overlying soils that are removed to reveal the mineral, spoil materials with a content of raw material below the cut of grade and tailings. Tailings are defined as the waste of ore processing during the removal of economically important components (Vick, 1990). These can be in solid or liquid form (slurry) depending on the drying and deposition techniques chosen by the enrichment plants. The tailings, in the form of slurry, are transported by pipelines from the enrichment plant to the Tailings Storage Facilities (TSFs). TSFs are high-risk infrastructures as tailings contain a high pollutant load mainly due to the chemicals used to extract minerals. Also, the volume of tailings stored is in the order of millions of cubic meters. In general, tailings storage is often recognized as the most important source of environmental impact for many mining activities (Vick, 1990). A large number of TSFs are located in countries with a severe mining sector such as the USA, Canada, Brazil, Chile, South Africa and Australia (Piciullo *et al*., 2022).

TSFs, like any infrastructure, interact with and are affected by the environmental conditions of the surrounding area. These conditions are related to the particular geological, hydrogeological, geotechnical, climatic and topographical characteristics of the area, which potentially constitute sources of natural hazards. Infrastructures with components that perform various functions (storage, transportation, drainage), such as TSFs, tend to show vulnerability to multiple natural hazards. Indicative components are pipelines, dams, geomembranes, spillways and impoundments. In the recent past, attempts are made to review significant failures over the last 100 years by statistically recording the natural hazards and more generally the conditions under which TSFs have failed (Azam & Li, 2010; Piciullo *et al*., 2022; Rico *et al*., 2008). In this direction, on line bases are also moving, indicatively mentioning the CSP2-Tailings Dam Failures. The difference between single and multi-hazard is important, as. In a multi-hazard framework, the consequences of interrelated hazards in the components are often more significant than those deriving from individual hazard summation. These failure mechanisms, most frequently mentioned as "failure modes", are defines as the ways, or modes, in which something (in this case the various components of the TSF) might fail.

This paper presents a new way to assess the interaction of natural hazards among them, and natural hazards with failure modes of TSFs. A semi-quantitative multi-hazard method developed by Liu *et al*., 2021, hereinafter Liu's method, is adapted for TSFs. This method evaluates each hazard individually, builds triggering interactions between hazards and failure modes using adjusted factors, and aims to quantify the multi-hazard intensity of different scenarios, which trigger specific failure modes. This method has been applied once in the wider mining sector and specifically in post-mining lignite regions (Nalmpant-Sarikaki *et al*., 2023).

Methodology

Three categories of methodologies are typically encountered to explore the interaction of hazards and calculate the multi-hazard intensity: qualitative and semi-quantitative quantitative. Focusing on semi-quantitative methods, they either use correlation coefficients or calibrate hazard occurrence characteristics to capture the interaction of hazards. The current work is based on a semi-quantitative method, which is described in four main steps. The initial step involves the identification of the main hazards in the study area as typically conducted in risk assessment. In the case of TSFs, the hazard categories are related to the specific conditions of the surrounding area as described above (geological, hydrogeological, geotechnical, climatic and topographical characteristics of the area). Anthropogenic (technological hazards) also affect TSFs and are often combined with natural ones to trigger a failure mode. However, in this work, only natural hazards are employed and the scenarios that will be developed consider only natural hazards. It focuses on the methodological framework and does not extend to a large number of natural hazards that could potentially threaten the area. Thus, four natural hazards are considered for this analysis, specifically earthquake, rainfall, flooding and landslide. Individual hazards are characterized based on their predisposing factors

and associated triggering factors. For example, a landslide is influenced by its predisposing factors, such as the topography of the ground and the soil conditions, and can be triggered by climate conditions, e.g., heavy rainfall (Zevgolis, Deliveris *et al*., 2019). Moreover, in a multi-hazard scenario, a landslide can be triggered by other hazards, such as flooding and earthquakes.

The second step deals with typical failure modes identification. The most critical components of TSFs are the tailings dam as they are earthen confining structures whose failure results in the release of tailings. As geotechnical works similar to earthen water dams and levees, they mainly present geotechnical failure modes. The failure modes that will be considered in this work are the overtopping, the slope instability, the liquefaction, the foundation failure, the internal erosion and the external erosion (Clarkson & Williams, 2021).

- Overtopping can occur from excessive inflows (flooding), malfunctioning spillway or outlet structures, insufficient spillway capacity, dam settlement, external landslide into reservoir, or by waves driven by wind running up and overtopping the dam (Clarkson & Williams, 2021).
- Slope instability refers to the failure of the upstream and downstream slopes of the dam either due to static or dynamic loading.
- Liquefaction is the instant loss of saturated soil's strength in response to strong ground shaking. A particular type, which the upstream constructed dams face, is the static liquefaction, namely the brittle loss of strength in loose, saturated, nonplastic or low plasticity soil under monotonic loading (i.e., static rather than dynamic).
- Foundation failure has three components, the overcoming of the bearing capacity, the development of excessive settlements and its permeability, which will result in the seepage of water and tailings under the dam body.
- Internal erosion (called "piping" by dam engineers) of a tailings dam takes place when water that seeps through the dam carries soil particles away from the embankment, filters, drains, foundation or abutments of the dam. If the seepage that discharges at the downstream side of the dam carries particles of soil, an elongated cavity or "pipe" may be eroded backward (working upstream) toward the reservoir through the embankment, foundation or abutment. When a backward-eroding pipe reaches the reservoir, a catastrophic breaching of the dam can occur (ASDSO).
- Surface erosion is a physical process that occurs when tailings flow removes soil particles from the surface of the dam so that its cross section to thin.
- An additional failure mode is the structural failure, which refers to any non-earth-related parts, such as corrosion of pumps and fractures in reinforced concrete. However, this failure mode is ignored in this study.

The third step deals with interactions between natural hazards and failure modes determining multi-hazard scenarios. Although the type of interactions between hazards and failure modes can be of diverse types such as trigger and coincidence (when they occur simultaneously and independently), hazards that act as triggering factors for other hazards are associated to failure modes to define multi-hazard scenarios. Scenarios in the form of "chains" will therefore be built, with cause-and-effect relationships.

The final (fourth) step focuses on identifying the level of interactions among hazards and failure modes. This assessment is based on the intensity of individual hazards and the level interaction of a hazard that causes a failure mode. The multi-hazard analysis demonstrates that interacting hazards can be more destructive as the principles of Liu's method demonstrate. Thus, it is challenging to consider multiple hazards and not only assess single ones because the overall risk is underestimated in the latter case.

Application

The application of Liu's method requires the selection of a study area to assign intensity values to natural hazards according to characteristics such as seismicity, precipitation and topography as well as the history of hazard occurrence in the area surrounding the TSF. It does not require knowledge of the technical specifications of a specific TSF. The identification of failure modes and their interaction with hazards is generally applicable, regardless of the specific study area. The indicative area employed in this work refers to the area of Halkidiki in the central Macedonia in northern Greece. In Halkidiki, due to intense mining operations, various TSFs with dry tailings have been constructed. Table 1 presents the identified natural hazards that potentially affect the study area and their initial intensities considering its location, topography and the historical data. There are six intensity classes ranging from 0 to 5; the higher the number, the greater the hazard intensity, and zero means that the hazard has no impact.

The earthquake's initial intensity is related to the classification of Greek seismic hazard. According to the latest Greek seismic code, the country was divided into three seismic hazard zones. Regarding the horizontal peak ground acceleration, the study area falls into zone II. In addition, according to National Observatory of Athens two strong earthquakes have occurred in the past in the wider area, 1932 Ierissos earthquake and 1978 Thessaloniki earthquake with M=7 and 6 respectively. Therefore, the initial intensity was selected as three. Precipitation data reserved from the Hellenic National

Meteorological Service. The annual precipitation of the Halkidiki area has a moderate value, 400-450 mm, with a low to moderate duration regarding the recordings; thus, the initial intensity was selected as two. Flooding is expected, locally, on both sides of the riverbeds and streams and considering the value given to rainfall the initial intensity selected equally as 2. Finally, initial intensity for landslides is selected as 4 due to mine wastes heaps prone to instabilities. Regarding bedrock formations, there are amphibolites – amphibolitic gneisses and biotic gneisses. These rock types exhibit high strength, whenever their rock mass characteristics indicate gravitational-movement type landslides governed by their discontinuities.

Table 1. Initial intensities of hazards (scale 0-5).

Natural hazards	Initial intensity
Earthquake (EQ)	3
Rainfall (RF)	2
Flooding (FL)	2
Landslide (LA)	4

The triggering relationships among hazards and between hazards and failure modes are summarized by hazard matrices, as shown in Figure 1 and Figure 2, respectively. The interactions among them are categorized into two levels: dark blue indicates high probability of interaction; light blue indicates low probability of interaction. In Figure 1 the diagonal cells are filled with dashes and represent the interaction of each hazard with itself, which is meaningful because the current study is focused on interactions between different hazards. Indicatively, earthquake has a high probability of triggering landslide, the flood has a low probability to trigger landslide, and the earthquake is unlikely to trigger rain and vice versa. Regarding the interaction between hazards and failure modes, flooding has a high probability to trigger overtopping, the landslide has a low probability to trigger external erosion and finally the earthquake is not associated with internal and external erosion as these phenomena are inextricably related to the action of water.

		Natural hazards			
		EQ	RF	FL	LA
Natural hazards	EQ	-			
	RF		-		
	FL			-	
	LA				-

Figure 1. Interaction matrix of natural hazards; dark blue cells: high probability of interaction, light blue cells: low probability of interaction, white cells: no interaction.

		Failure modes					
		OT	SI	LIQ	FOUN	IE	EE
Natural hazards	EQ						
	RF						
	FL						
	LA						

Figure 2. Interaction matrix between natural hazards and failure modes. OT= overtopping, SI=slope instabilities, LIQ= liquefaction, FOUN= foundation failure, IE= internal erosion, EE= external erosion.

The above qualitative characterization of the interactions is converted into semi-quantitative by introducing some sub-coefficients of approximation of the initial intensities of hazards. In the context of multi-hazard analysis, the intensities of hazards are greater when they occur in combination compared to the simple hazards analysis approach. Liu's method proposes multiplying the initial intensities by coefficients from 1.1 to 1.5 depending on the initial intensity value and the type of correlation (low or high) among hazards. Coefficient 1.1 is applied when the initial intensity value equals to 1-2 and there is a low interaction while on the other side 1.5 with initial intensity value 5 and high interaction. Liu's method presents a detailed table for coefficients. The same principle applies to this work and in addition the coefficients are similarly applied to the correlation between hazards and failure modes.

The combination of Figure 1 and Figure 2 results in scenarios development. The scenarios consist of 2 hazards and a

failure mode. In particular, a primary hazard causes a second hazard which in turn causes a failure mode. The scenarios are therefore in the form of a chain, for example, rainfall trigger flooding and the latter trigger overtopping. Thus, the building of scenarios involves pairing elements (hazards or failure modes) according to the degree of interaction observed between them. Earthquake and rainfall cannot be triggered by the other hazards (as shown in Figure 1) so, they cannot be placed as second hazards in the multi-hazards scenarios. The final multi-hazard intensity (MH) is calculated by summing up the trigger and the triggered hazard's adjusted intensity.

Table 2 presents all scenarios sorted by failure modes. Each scenario receives an MH, so for each failure mode a total MH summing up the individual MH corresponding to each failure mode is obtained. In addition, It is determined a higher (each hazard has an initial intensity of 5 and high probability to trigger other hazards or failure mode) and a lower (each hazard has an initial intensity of 1 and low probability to trigger other hazards or failure mode) limit. The range is normalized (0-1), and the MH is scaled accordingly through Norm. MH to improve visualization of scenario intensities. Table 2 presents scenarios shorted by failure mode to assess their criticality according to MH. Similarly, we could short them by hazards to find their criticality. Overtopping appears to be the most critical failure mode as 0.438 is the highest norm. MH. This is because FL and LA has high interaction with it as well as LA, which is involved in 4 out of 6 scenarios has an initial intensity of 4. SI, LIQ and FOUN have equal MH as 3 scenarios lead to them and FL acts as triggering hazards for each failure mode. They present low MH as FL and RF receive the lowest initial intensity of 2. IE shows slightly higher MH than SI, LIQ and FOUN because although equally similarly in 3 scenarios, FL has low interaction with IE. In final, EE appears to be the second most critical after OT, as LA has low interaction with EE while LA has high interaction with OT. Therefore, the criticality of FM depends on the number of scenarios involved, on the initial intensities of hazards and on the type of interaction between hazards and between hazards and between hazards and failure modes.

Table 2. Multi-hazards scenarios shorted by failure modes (FM). OT= overtopping, SI=slope instabilities, LIQ= liquefaction, FOUN= foundation failure, IE= internal erosion, EE= external erosion

FM	Scenario	Total MH	Min total MH	Max total MH	Norm. MH
OT	EQ → FL → OT	46.8	13.2	90	0.438
	RF → FL → OT				
	LA → FL → OT				
	EQ → LA → OT				
	RF → LA → OT				
	FL → LA → OT				
SI	EQ → FL → SI	18.4	6.6	45	0.307
	RF → FL → SI				
	LA → FL → SI				
LIQ	EQ → FL → LIQ	18.4	6.6	45	0.307
	RF → FL → LIQ				
	LA → FL → LIQ				
FOUN	EQ → FL → FOUN	18.4	6.6	45	0.307
	RF → FL → FOUN				
	LA → FL → FOUN				
IE	EQ → FL → IE	19.6	6.6	45	0.339
	RF → FL → IE				
	LA → FL → IE				
EE	EQ → FL → EE	44.4	13.2	90	0.406
	RF → FL → EE				
	LA → FL → EE				
	EQ → LA → EE				
	RF → LA → EE				
	FL → LA → EE				

Conclusions

The present work adjusted an existing multi-hazard methodology, originally designed to analyze the interaction of natural and technological hazards, adapting it to fit a framework of interactions between hazards and failure modes in the context of TSFs. Multi-hazard analysis constitutes a critical component of modern risk assessment; this assessment must also include a detailed analysis of the consequences of TSF failures in the downstream region. The initial steps involved identifying the most significant natural hazards and possible failure modes of TSFs. The region of Halkidiki, operating intense mining, was selected as an indicative area. Then, the hazards' initial intensities and levels of interaction determined using appropriate interaction matrixes. The initial intensities were modified and increased, and the resulting values were appropriately summed up to create various multi-hazard scenario intensities (MH). The ultimate objective was to identify the most critical failure by comparing various scenarios via the total multi-hazard (MH) intensities. The study showed that the criticality of failure mode for this methodology is a function of the number of scenarios involved, the initial intensities of hazards and the type of interaction among hazards and between hazards and failure modes. Based on the analysis overtopping is the most critical, with external erosion following. Finally, some limitations of the modified method and the general assumptions considered in this work should be mentioned. The scenarios were built under the premise of developing a cause-and-effect relationship among their components. However, in nature this assumption does not always apply. For example, earthquakes and rainfall, although independent, can occur simultaneously without having a causal relationship. Rainfall and earthquakes are not triggered by other hazards. Subsequently, they were not placed as second components in scenarios, consequently, they were not included as direct triggering factors of failure modes. In future work, these interactions will be better studied, and anthropogenic-technological hazards will be included in the analysis.

Acknowledgements

The research work was supported by the Hellenic Foundation for Research and Innovation (HFRI) under the 5th Call for HFRI PhD Fellowships (Fellowship Number: 61518400).

References

Azam, S., & Li, Q. (2010). Tailings dam failures: a review of the last one hundred years. Geotechnical news, 28(4), 50-54.

Clarkson, L., & Williams, D. (2021). An overview of conventional tailings dam geotechnical failure mechanisms. Mining, Metallurgy & Exploration, 38(3), 1305-1328.

CSP2- Tailings Dam Failures. (2024). Retrieved 11/12/2024 http://www.csp2.org/tsf-failures-from-1915

Liu, B., Han, X., Qin, L., Xu, W., & Fan, J. (2021). Multi-hazard risk mapping for coupling of natural and technological hazards. Geomatics, Natural Hazards and Risk, 12(1), 2544-2560. doi:10.1080/19475705.2021.1969451

Nalmpant-Sarikaki, D. M., Theocharis, A. I., Koukouzas, N. C., Benardos, A. G., & Zevgolis, I. E. (2023). Multi-Risk Assessment in Post-Mining Lignite Areas. Materials Proceedings, 15(1), 65.

Piciullo, L., Storrøsten, E. B., Liu, Z., Nadim, F., & Lacasse, S. (2022). A new look at the statistics of tailings dam failures. Engineering Geology, 303, 106657.

Rico, M., Benito, G., Salgueiro, A., Díez-Herrero, A., & Pereira, H. (2008). Reported tailings dam failures: a review of the European incidents in the worldwide context. Journal of hazardous materials, 152(2), 846-852.

Vick, S. G. (1990). Planning, Design, and Analysis of Tailings Dams. Vick, S. G. (1990). BiTech Publishers Ltd.

Zevgolis, I. E., Deliveris, A. V., & Koukouzas, N. C. (2019). Slope failure incidents and other stability concerns in surface lignite mines in Greece. Journal of Sustainable Mining, 18(4), 182-197.

17th INTERNATIONAL CONGRESS of the Geological Society of Greece

BULLETIN OF THE GEOLOGICAL SOCIETY OF GREECE, SP. PUBL.

EXTENDED ABSTRACT 160

The role of the museums in the geoscience education

Efterpi Koskeridou[1], Christos Psarras[1], Evangelia Rentoumi[1], Ioannis Giaourtsakis[1], Marija Bosniak[2]

(1) Faculty of Geology and Geoenvironment, National and Kapodistrian University of Athens, Greece, ekosker@geol.uoa.gr (2), Croatian Natural History Museum, Zagreb, Croatia

Introduction

Museum curators and museum staff working in the field of education face the challenges of enrolling museums in the geoscience education. The knowledge gained from the scientific work on museums' collections is transferred and communicated to public using various tools. That way public is acquainted with the current and ongoing research in the museums, has the opportunity to be part of it, and it is educated on various topics.

In this paper we show ways of communicating with the audience based on the examples from the Museum of Paleontology and Geology of the National and Kapodistrian University of Athens, Greece and the Croatian Natural History Museum, Zagreb, Croatia.

Objectives

The goal of this work is to highlight the role of museums in Geosciences and education, acting as a mediator between scientific research and public understanding. By combining traditional and digital tools, museums potentially offer learning opportunities to diverse audiences, from the general public to university students and educators. This work demonstrates how museums can communicate the complex concepts of Natural History, containing geological and paleontological terms, by fostering curiosity and providing accessible educational experiences that enamor people to science. By showcasing innovative methodologies and case studies, we underscore the importance of museums as dynamic hubs of learning and science communication.

Methods

Museum education encompass various tools that can be used in the science communication, e.g., exhibitions, catalogues related to the exhibitions and collections, workshops, lectures, conferences, flyers, etc. Examples here presented are based on the incorporation of virtual tools in the museum work, which are in recent time becoming more and more popular and applied.

First example is a new virtual online tour at the Museum of Paleontology and Geology of Athens, titled: Advanced Tour and Education Services in the virtual Paleontology and Geology Museum/v-PalM.

Second example is a virtual exhibition "Oysters of the ancient seas" available on the website of the Croatian Natural History Museum.

Results

Museum of Geology and Paleontology

- The Museum of Geology and Paleontology at the National and Kapodistrian University of Athens has long been a beacon for scientific research and public education in the fields of Paleontology and Earth Sciences in Greece. Founded in the 19th century, the institute's roots go back to the founding of the Hellenic Society of Naturalists in 1835, which began collecting specimens of animals, plants, fossils, rocks and minerals. These early collections laid the foundations for one of the most important paleontological and geological museums in Greece. Throughout its history, the Museum has grown through continuous acquisitions, research and collaborations, so that today it can preserve a rich selection of more than one million specimens documenting more than 550 million years of the Earths' geological history.

A significant enhancement to the Museum's educational output has recently been the "v-PalM" project (fig. 1), which has developed a dynamic virtual experience to increase the museum's reach and educational effectiveness. Through the collaboration with the National Technical University of Athens and the technology company OMEGA, the project has successfully integrated 3D models, multimedia content, games and interactive educational programs, offering a digital extension of the museum's physical exhibits (Konstantakis *et al*., 2023; Thanou *et al*., 2023). In this virtual museum, visitors can explore thematic educational material such as the organisms and evolution of life during the Paleozoic, Mesozoic and Cenozoic Eras, the famous Pikermian Fauna, examples of island dwarfism in Greece and the evolution of marine organisms through time. Each program is carefully coordinated

with the exhibits that are on display in the actual Museum exhibition. For the first time, these educational programs have been specifically designed to engage the public with the Museum's unique collection and enhance the learning experience through the use of detailed illustrations of specimens, 3D models and in-depth information.

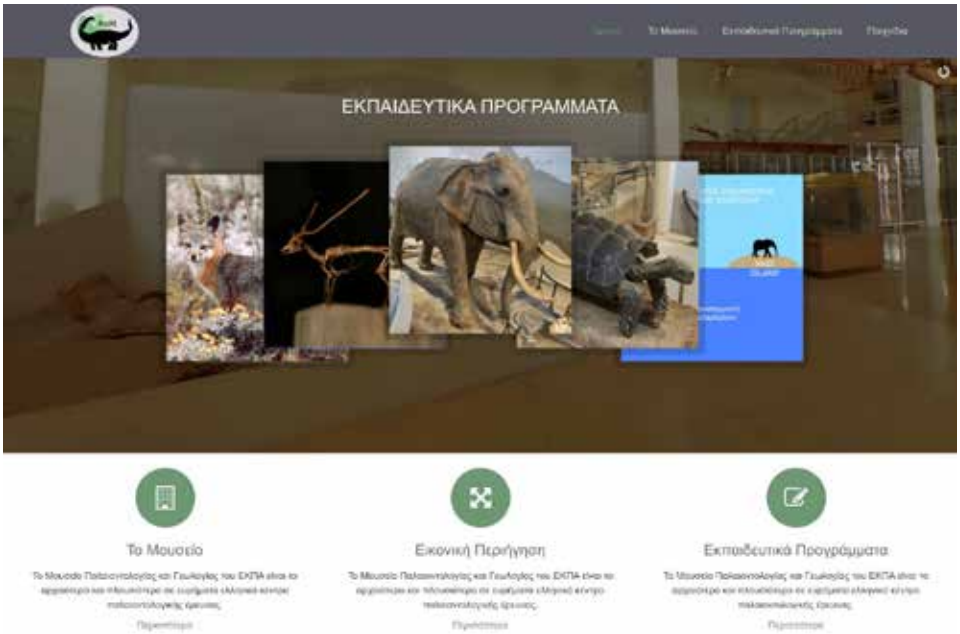

Figure 1. V-Palm Web application.

Furthermore, the Museum's impact on the educational landscape goes beyond its exhibits and digital initiatives. It has long been a center for educating students in fields such as Geology, Paleontology and Museology, providing hands-on learning opportunities through its extensive collections and research programs. The Museum hosts a variety of educational initiatives, including fieldwork, workshops and guided tours, providing opportunities for both school groups, university students and the general public to engage with the sciences of Geology and Paleontology. The Museum, through the expansion of educational offers, particularly through digital platforms such as the "v-PalM" project, makes science learning more accessible, especially for those who cannot visit the Museum in person, and promotes a deeper understanding of the natural world.

The completion of the "v-PalM" project is a milestone in the museum's mission to make science education more accessible and interesting for several target groups. By integrating advanced technology with curated educational content, the Museum has not only enriched its physical exhibitions through illustrations and paleoenvironmental reconstructions but has also made a lasting impact on the way Earth Science education is delivered in Greece. Visitors –whether in person or virtually– can now experience an interactive and enriching learning environment that emphasizes on the importance of scientific knowledge and understanding our planet's past, present and future.

Croatian Natural History Museum

- Due to the earthquake, renovation of the museum building and work on the new permanent exhibition, Croatian Natural History Museum was closed for public from 2020 until 2024. In order to continue presenting the museum collections, virtual exhibition "Oysters of the ancient seas" was prepared. That was the first virtual exhibition of the CNHM completely prepared from the scratch in the virtual environment. For the purposes of the exhibition, virtual exhibits of the Middle Miocene oysters were presented not only as photographs, but also as 3D scanned objects, that could be moved in various directions, as the visitors decided. The exhibition involved a guide in each section, who would briefly describe what can be seen in this part of the exhibition. Storytelling was a great part of the preparation of this exhibition, since the texts for the exhibition' guide were prepared based on the work with a communicator.

  Currently, the exhibition is presented in its classical form in the renovated CNHM museum building. Together with original specimens of the fossil and recent oysters, 3D prints of fossil oysters are available for touching. That way,

visitors having disabilities can feel the morphology of the fossil oysters and imagine how they looked like. Additionally, one original specimen of partial fossil oyster-reef can be studied by the magnifier and visitors can look for various inhabitants preserved as fossils, e.g., oysters, coralline algae, corals, bryozoans, etc. We noticed the positive feedback of visitors on these types of exhibits, enabling them to discover for themselves something that is not so familiar to them on everyday basis, and encouraging them to find out more.

Methods used in geoscience education include also workshops and seminars. As museum curators, we can be involved in the education of the pupils and students, as well as the schoolteachers.

One of the examples of geoscience education is the action called “Meet the Earth - Peek under the microscope” organized by the Croatian Geological Society since 2013 (e.g., Galović & Bošnjak, 2014). Geologists from various institutions are involved in this promotion of geoscience, as well as students. In the agreement with schools, geoscientists show various exhibits of macro samples of minerals, rocks, fossils, and petroleum, and thin sections of different fossils and crystals using the microscopes. Geological maps, posters from conferences, and geological models can also be shown. This type of exhibition can be followed by a presentation. Exhibiting specimens from different geological field, the students and teachers can learn more about geoscience, and specifics of each discipline.

Other example of educating teachers is the Spring seminar, organized by the Education and Teacher Training Agency, Croatia and the Croatian Geological Summer School. Each year, under one topic researchers hold lectures to the teachers of geography, taking in account the curriculum of the geographic class for the current year. Topics include various geoscience themes, e.g., vulcanism, climatic changes, catastrophic events, etc.

Conclusions

Museums are crucial in promoting and educating people about geosciences by serving as accessible platforms that combine science, culture, and education. The two examples presented here in the two museums illustrate how museums are modernized to meet the needs of modern educational practices. By adopting tools like 3D modeling, virtual exhibitions, and interactive workshops, museums are extending their reach to visitors but also enhancing their experience. These initiatives display the importance of museums not just as repositories of knowledge but as active participants in its acquisition and promotion. Finally, continued collaboration between museums, researchers, and educators is necessary for the further enhancement and impact of geoscience education worldwide.

References

Galović, L., Bošnjak, M., 2014: Meet the Earth – Peek under the microscope!’’ – promotion of geology and geoheritage protection. XVI Serbian Geological Congress “ Optimal research and sustainable usage of the geological resources”, Belgrade, Serbia, p. 846-849.

Konstantakis, M., Trichopoulos, G., Aliprantis, J., Michalakis, K., Caridakis, G., Thanou, A., Zafeiropoulos, A., Sklavounou, S., Psarras, C., Papavassiliou, S., Koskeridou, E., 2023. An Enhanced Methodology for Creating Digital Twins within a Paleontological Museum Using Photogrammetry and Laser Scanning Techniques. Heritage 6(9), 5967-5980.

Thanou, A., Stavropoulou, G., Tsitseklis, K., Zafeiropoulos, A., Orfanidou, V., Kotsopoulos, K., Papastamatiou, N., Koskeridou, E., Giaourtsakis, I., Filis, P., Papavassiliou S., 2023. A Dynamic Interactive Virtual Museum for Enhancing Students Engagement. 13th Pan-Hellenic and International Conference “ICT in Education”, Kavala, Greece, p. 235-242.

17th INTERNATIONAL CONGRESS of the Geological Society of Greece

BULLETIN OF THE GEOLOGICAL SOCIETY OF GREECE, SP. PUBL.

EXTENDED ABSTRACT 161

Ultrasonic analysis of the structural stones of the Parthenon at the Acropolis of Athens - Investigation of the physical / mechanical properties and integrity control of the grouted Joints

Kosmas P.[1], Loupasakis C.[1], Eleftheriou V.[2], Christodoulopoulou R.[2], Vrouva A.[2]

(1) Laboratory of Engineering Geology and Hydrogeology, School of Mining and Metallurgical Engineering, National Technical University of Athens, Athens, Greece, kosmas.panagiotis9@gmail.com

(2) Acropolis Restoration Service, Ministry of Culture and Sports, Athens, Greece

In this research, a non-destructive ultrasonic method was used to evaluate both the physicomechanical properties of the Parthenon's stones and the integrity of the grouted joints in the restoration works. Over 600 measurements of ultrasound velocity were conducted: 320 measurements for estimating the physicomechanical characteristics and 280 for assessing the integrity of the joints (Fig 1).

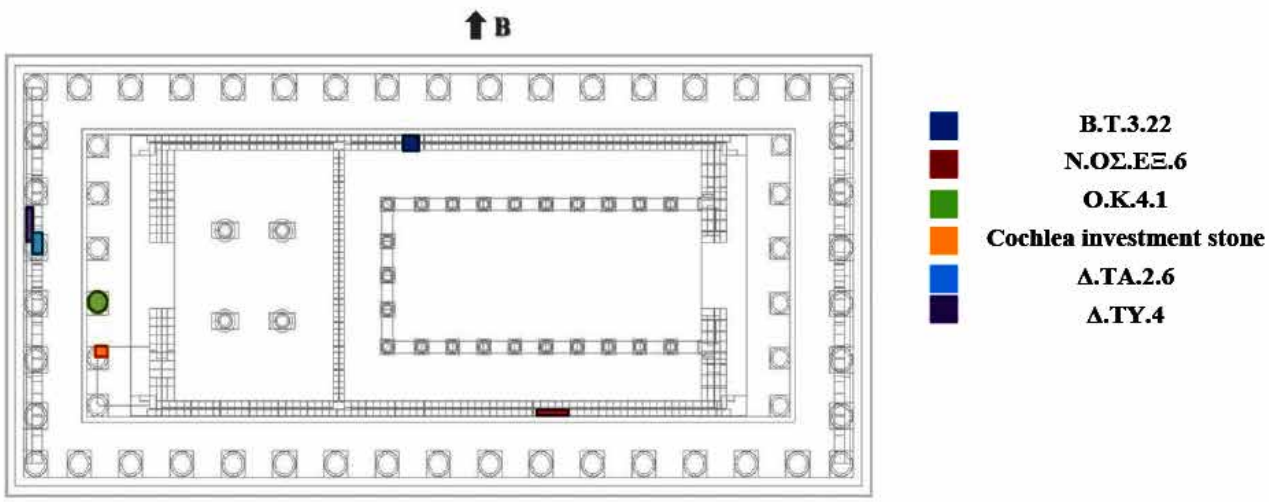

Figure1.Parthenon's layout. The physical location of the measured structural stones.

The measurements were made with the PUNDIT ultrasonic pulse propagation measurement device using P-wave piezoelectric transducers at 54 kHz, 150 kHz, and 250 kHz. After several measurements, it was concluded that, due to the roughness of the surfaces, plasticine was best suited as a contact material. Additionally, the transducers that provided the most consistent readings were those at 54 kHz, especially when used for the evaluation of the integrity of the joints.

The physicomechanical properties of the marbles were determined by taking measurements perpendicular and parallel to the unconformities (bedding or schistosity). The distance between the transducers was 10 cm, and distance between two successive rows 3 cm. A canvas was designed over the surfaces to ensure an accurate distance was maintained between the transducers (Fig 2). Physical pressure was applied to the transducers to ensure proper contact.

The properties of the Dionysos marble, after applying the above-described procedure, are presented in Table 1, and those of the Pentelikon marble are presented in Table 2. It should be noted that, according to Skoulikidis (2000) and Korres & Mpouras (1983) the density of Dionysos and Pentelic marble is 2720 kg/m^3 and 2720 to 2710 kg/m^3, respectively.

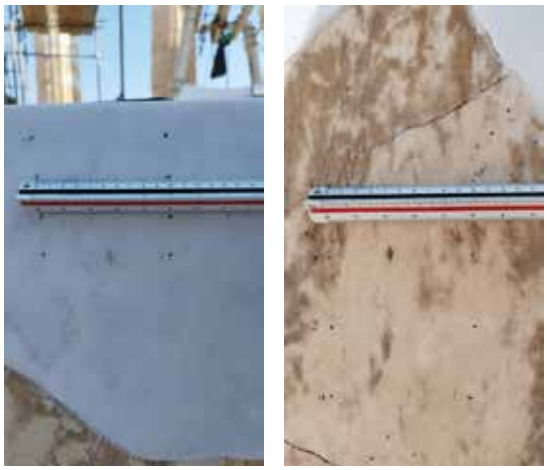

(a) (b)

Figure 2. a) "New" Dionysos and b) "Ancient" Pentelic marble with the canvas designed for measuring the physicomechanical properties.

Table1.The physicomechanical properties estimated for the Dionysos marble (Pd: Density, Eo: modulus of elasticity, v: Poisson's ratio, Go: shear modulus).

Transducers parallel to the unconformities				
Code No.	**Marble**	**Pd (kN /m3)**	**Eo (Gpa)**	**Go (Gpa)**
BT322	Dionysos	27.2	12.68~13.14	5.13~5.31
ΝΟΣΕΞ6	Dionysos	27.2	20.52~23.23	8.30~9.40
Transducers perpendicular to the unconformities				
Code No.	**Marble**	**Pd (kN /m3)**	**Eo (Gpa)**	**Go (Gpa)**
BT322	Dionysos	27.2	11.99~12.84	4.85~5.20
ΝΟΣΕΞ6	Dionysos	27.2	12.74~15.43	5.16~6.24
ΝΟΣΕΞ6	Dionysos	27.2	20.00~21.50	8.09~8.70

Table2. The physicomechanical properties estimated for the Pentelikon marble (Pd: Density, Eo: modulus of elasticity, v: Poisson's ratio, Go: shear modulus).

Transducers perpendicular to the unconformities				
Code No.	**Marble**	**Pd (kN /m^3)**	**Eo (Gpa)**	**Go (Gpa)**
BT322	Pentelikon	27.1-27.2	10.20~15.45	4.13~6.25
ΝΟΣΕΞ6	Pentelikon	27.1-27.2	8.26~ 14.80	3.34~5.99
ΝΟΣΕΞ6	Pentelikon	27.1-27.2	9.78~ 12.67	3.96~ 5.13
O.K.4.1	Pentelikon	27.1-27.2	5.55~15.28	2.25~ 6.18
ΔΤΥ4	Pentelikon	27.1-27.2	7.78~8.32	3.15~3.37
ΔΤΑ2.6 1ο	Pentelikon	27.1-27.2	9.34~11.76	3.77~ 4.76
ΔΤΑ2.6 2ο	Pentelikon	27.1-27.2	7.47~13.47	3.02 – 5.45
Transducers parallel to the unconformities				
BT322	Pentelikon	27.1-27.2	15.76~19.44	6.38~7.85
ΝΟΣΕΞ6	Pentelikon	27.1-27.2	14.17~26.49	5.74~10.72
ΝΟΣΕΞ6	Pentelikon	27.1-27.2	27.61~29.76	11.17~12.04
ΔΤΑ2.6 1ο	Pentelikon	27.1-27.2	11.43~22.47	4.63~9.10

The measurements conducted for assessing the integrity of the joints are based on a two-step procedure. An initial measurement is taken with the transducers placed 2 cm from both sides of the joint, followed by a second measurement at a distance of 4 cm. After the completion of the measurements, the PUNDIT provides a clear reading of the depth of the open joint. The process is repeated until a sufficient number of readings, indicating a clear value of the depth of the open joint, is provided. Note that an open joint is considered to be the part of the joint not filled with grout, or the part where grout has detached due to shrinkage from the walls of the joint.

(a) (b)

Figure 3. (a) Joint between ancient and ancient marble pieces and (b) joint between ancient and new marble. The canvas designed for measuring the integrity of the joints is clearly illustrated.

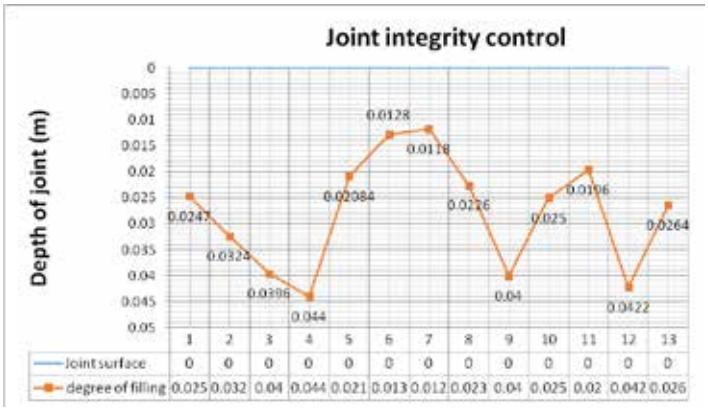

Figure 4. Graph presenting the depth of the open joint; the part of the joint that failed to get properly filed with grout. The graph presents the readings obtained at the joint depicted in Figure3.a.

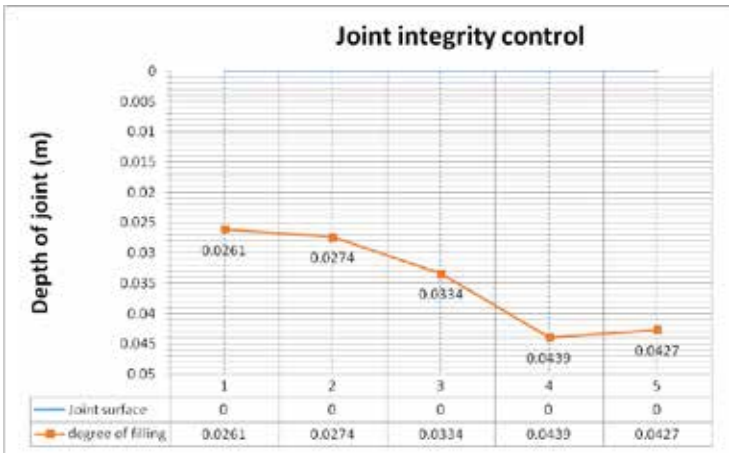

Figure 5. Graph presenting the depth of the open joint; the part of the joint that failed to get properly filed with grout. The graph presents the readings obtained at the joint depicted in Figure3.b.

Measurements of ultrasound velocity was used to examine Dionysos “new” and Pentelic “old” marble, which have been used to construct and reconstruct the Parthenon from antiquity to the present.
According to the ultrasonic measurements, both marbles’ properties appear to be compatible to each other.

Furthermore, higher values of the dynamic characteristics (shear modulus and dynamic modulus of elasticity) are noted in the measurements made parallel to the marbles' unconformities (bedding or schistosity) than those perpendicular.

Additionally, the superficial deterioration—such as cellular corrosion or gypsum formation—ultimately affects only the marbles' surface and not their interior structure and characteristics. This indicates that even though there is significant surface damage, which obviously and irrevocably alters the stone's external relief, it does not damage their mechanical properties.

When evaluating the integrity of the joints, it can be safely stated that the joints are shielded, as the mean depth of the open cracks is less than 2 cm, with only a few identified as reaching the maximum depth of 5 cm. As the ultrasound machine does not allow for the determination of the cracks' width, capillary cracks can only be observed along the joints.

References

Asef M.R., Farrokhrouz M. (2017): A semi-empirical relation between static and dynamic elastic modulus; Journal of Petroleum Science and Engineering 157, pp.359-363.

Christaras, B., (1994): Anisotropy effects on the elastic parameters of rocks; determination using ultrasonic techniques. 7o Intern. Congr. Geol. Soc. Gr.4, pp. 381-387.

Christaras B. (1996): Particularities In Studying The Fpysical And Mechanical Properties Of Stones In Monuments. Examples From The Mediterranean Basin. 8th International Congress on the Deterioration and Conservation of Stone, Berlin, pp. 819-829.

Christaras B. (1997): Estimation Of Damage At The Surface Of Stones Using Non Destructive Techniques. STREMAH V (5th Int. Congr. Structural Studies, Repairs and Maintaince of Historical Buildings). San Sebastian. Advances in Architectural Series of Computetional Mechanics Publications, Southampton, pp. 121-128.

Korres M. and Mpouros Ch. (1983): Study for the restoration of the Parthenon, Athens. Ministry of Culture and Sports - Acropolis Restoration Service (YSMA).

Salvatici T., Centauro I., Segabinazzi E., Intrieri E., Garzonio G.A., (2023): Non destructive methods applied for in situ mechanical diagnosis: Florentine historical buildings in Pietra Serena, Salvatici et al. Heritage Science, pp.1-11.

Skoulikidis Th. (2000): Erosion and conservation of structural monuments, Heraklion, University of Crete Press.

17th INTERNATIONAL CONGRESS of the Geological Society of Greece

BULLETIN OF THE GEOLOGICAL SOCIETY OF GREECE, SP. PUBL.

EXTENDED ABSTRACT 162

The Koziakas Mélange Unit: New perspectives on Its Mesozoic paleogeographic and geotectonic evolution (Central Greece)

Kostaki G.[1], Gawlick H.-J.[2], Kilias A.[1], Missoni S., Ghon G.[2], Katrivanos E.[1]
(1) Aristotle University Thessaloniki, Thessaloniki, Greece, gkostaki@geo.auth.gr (2) Montanuniversität Leoben, Leoben, Austria

The Koziakas ophiolites in central Greece, along with their underlying mélanges, represent a part of the obducted Neo-Tethys ophiolites. During the Middle to early Late Jurassic, west-directed ophiolite obduction led to the formation of various mélanges, incorporating blocks from the Triassic Neo-Tethys Ocean floor (radiolarites) and the outer open-marine shelf (Hallstatt Facies). The Middle to Late Triassic Hallstatt Limestones, in particular, are crucial in defining the migration path of the obducting ophiolites. During Oxfordian, obduction stopped, and a shallow-water carbonate platform devolved on top of the ophiolites, shedding material into the remaining underfilled foreland basin in front of the obducted ophiolites. In the latest Jurassic to early Early Cretaceous, mountain uplift and erosion began, and the erosional products of this evolving continent were transported into this foreland basin. During the Tertiary (Eocene-Oligocene), the Koziakas ophiolite and mélange system thrust westward as a whole, together with Pindos unit, over the Gavrovo carbonate platform.

Background/Objectives

The Koziakas mélange unit, traditionally referred to as the Koziakas massif, is located in central Greece and is geologically characterized by an ophiolite nappe and associated underlying Jurassic mélanges. The unit was thrust southwestward as a whole during the Early Cretaceous over the Early Cretaceous Boeotian 'flysch', and during subsequent Paleocene-Eocene tectonics, it was displaced together with the Boeotian 'flysch' over the Late Cretaceous Thymiama succession or directly onto the Paleocene-Eocene Pindos orogenic sediments (Bortolotti *et al*., 2004, Chiari *et al.,* 2012; Fig. 1a). To the east of the Koziakas mélange unit, a Neogene basin developed, primarily receiving erosional products from the ophiolites to the west. The Koziakas ophiolites crop out between the well-known Pindos and Vourinos ophiolites to the north and the Othrys and Argolis ophiolites to the south, forming part of an ophiolite belt whose derivation remains a subject of ongoing debate. Several geodynamic models have been proposed to interpret the origin of these ophiolites, with the most prevalent divided on whether they originated: a) from a parautochthonous Triassic-Jurassic oceanic basin (Pindos Ocean) or b) represent remnants of a far-traveled ophiolite nappe stack derived from the Triassic-Jurassic Neo-Tethys Ocean floor located east of the Pelagonian units (see Robertson, 2012, for an extended review). To unravel the origin of these ophiolites is essential to understanding the Mesozoic paleogeography and mountain-building processes. A key aspect of this understanding is the study of the sedimentary and facies evolution of the passive continental margin(s) that existed prior to plate convergence and ophiolite obduction. Comprehending their evolution would assist in determining the number of the oceanic realms involved, as a multi-ocean reconstruction requires the presence of multiple passive continental margins. An important contribution to this is the study of mélanges formed in front of the advancing ophiolites, as they contain material that provide critical insights into the route taken by the ophiolites during their emplacement. A typical Triassic-Jurassic passive continental margin adjacent to an oceanic realm, from which the ophiolites originate, is characterized by shallow-water carbonates on the central shelf and open-marine carbonates dominating the outer shelf. During the obduction processes, the arrangement of the passive continental margin is disrupted, leading to the formation of a nappe stack and associated trench-like deep water basins in the lower plate position (Frisch & Gawlick, 2003). These trench-like deep-water basins receive synorogenic sediments derived from formations of the passive margin and the ophiolites, while experiencing thrusting into the foreland following the ophiolite emplacement (Gawlick & Missoni, 2019). As a result, the synorogenic sediments within these basins can undergo deformation, with most of their primary sedimentological characteristics being destructed by subsequent tectonics. However, in some cases, distinctive primary sedimentary features can still be observed in such sedimentary mélanges (in sense of Festa *et al*., 2016**)**. During the overthrust of the higher nappe (i.e., obducting ophiolites), material from the lower plate (former passive continental margin sedimentary rocks) can also be scraped off and incorporated into such mélanges (Schmid *et al*., 2008). These mélanges are characterized by a fine-grain matrix incorporating diverse exotic blocks and mass-transport deposits (Gawlick & Missoni, 2019). In this paper, we present new stratigraphic and paleontological data from the Koziakas mélange unit, integrated with structural observations to provide new insights toward a comprehensive understanding. Our analysis focuses on the carbonate exotic blocks incorporated within the mélange associated with the obduction of Koziakas ophiolites. These exotic blocks serve as a valuable tool for reconstructing the original configuration of the overridden passive continental margin. Moreover, we conducted microfacies analyses on a sedimentary sequence composed of carbonate resediments intercalated in radiolarites. This sedimentary sequence, which overlies the Koziakas mélange with the incorporated exotic carbonate and radiolarite

blocks, offers new insights into the subsequent events after the ophiolite emplacement. By combining our diverse data, we aim to contribute to the ongoing discussion surrounding the provenance of the ophiolites and the geotectonic evolution of the Hellenides during the Middle Jurassic to Early Cretaceous. Specifically, we address whether a Triassic-Jurassic Pindos Ocean or Pindos Basin existed and investigate the timing and direction of ophiolite obduction on the Pelagonian margin(s), providing new geodynamic implications and perspectives on the Mesozoic paleogeography of the region.

Methods

In the laboratory, approximately 100 thin sections, each measuring 5 cm x 5 cm, were prepared for detailed examination. Microfacies analyses were conducted to identify microfossils and paleontological characteristics, aiming to determine the paleogeographical environment and the age of the original deposition of the various components and blocks within the studied successions. For conodont age dating, carbonate samples were subjected to 10% diluted acetic acid digestion to dissolve the rock matrix, with the resulting residues examined under a binocular microscope.

Results

Microfacies analysis and conodont age dating were conducted on samples from various outcrops of the Koziakas mélange unit, situated on the eastern slopes of the Koziakas massif, west of the Koziakas ophiolites. This mélange comprises a lower section dominated by an argillaceous-radiolaritic matrix of Middle to early Late Jurassic age, containing, beside Triassic radiolarite pebbles, exotic open-marine Late Triassic carbonate blocks and slides of varying sizes and colors, resembling typical Hallstatt Limestones. Overlying this mélange follow basin-fill sediments consisting of thick, multicolored Late Jurassic radiolarites intercalated by carbonate turbidites and oolitic limestones, transitioning at higher stratigraphic levels into Late Jurassic to earliest Cretaceous shallow-water carbonate-clastic resediments (Fig. 1b, c).

- *Conodont age dating and microfacies analysis on open-marine carbonate blocks*: Samples from exotic blocks and mass-transport deposits within the Jurassic matrix of the Koziakas mélange were collected along the local road connecting Gorgogyri to Kori, as well in the vicinity of the Monastery of Vytoumas (Fig. 1d, e). Sample GR (62), obtained from a polymictic breccia, yielded conodont taxa such as *Gladigondolella*-ME, *Gladigondolella* cf. *malayensis*, *Paragondolella foliata*, and *Paragondolella* cf. *inclinata*, indicating a latest Longobardian to earliest Carnian age. Sample GR (69), collected from a filament limestone block beneath radiolarites with turbidites containing shallow-water debris, revealed taxa *Gladigondolella*-ME, *Paragondolella foliata*, *Paragondolella* cf. *inclinata*, and *Paragondolella polygnathiformis*, suggesting a lowermost Carnian (Cordevolian) age. Sample GR (70), collected from a grey micritic limestone block with red chert nodules, included taxa *Epigondolella rigoi* and *Norigondolella hallstattensis*, indicating an Early Norian age. Sample GR (71), derived from a polymictic breccia, contained the conodont *Paragondolella polygnathiformis*, corresponding to a Carnian age. Sample GR (235), obtained from mass-transport deposits with grey and red limestones, included *Metapolygnathus* cf. *commusti*, suggesting the Carnian/Norian boundary; *Epigondolella slovakensis*, indicative of Alaunian 2-3; and *Epigondolella bidentata*, corresponding to the Sevatian. Sample GR (236), collected from a reddish limestone block, yielded conodont taxa *Paragondolella polygnathiformis* and *Paragondolella nodosa*, indicating Tuvalian 3/1, as well as *Metapolygnathus* sp., suggesting the Carnian/Norian boundary. Sample GR (237), derived from a reddish limestone block, included several species of the latest Carnian (Orchard). Sample GR (238), also collected from a reddish limestone block, yielded *Paragondolella polygnathiformis* and *Paragondolella carpathica*, which are indicative of Tuvalian 2. Sample GR (240), obtained from a grey limestone block, included *Epigondolella rigoi*, indicating Lacian 2 age. Finally, sample GR (43) was collected from a medium-bedded grey siliceous limestone block and thin section analysis revealed a dark reddish-grey pelagic non-laminated wackestone with radiolarians, filaments, and a biofabric characterized by loose packing, medium sorting, and size variation of bioclasts. These facies suggest open-marine deposition on an outer shelf, with most radiolarians recrystallized into quartz.
- *Microfacies analysis of shallow-water carbonate-clastic resediments*: Shallow-water carbonate-clastic resediments are observed near Kori village, occurring at the higher stratigraphic levels of the Late Jurassic radiolarite sequence (Fig. 1f, g). Based on the examination of thin sections, the microfacies of the collected samples are identified as bioclastic packstones and grainstones, with shallow-water bioclasts being the most frequent components. In these thin sections, the bioclasts consist of bryozoans, foraminifera, crinoids, and debris from reef-building organisms. The presence of encrusting organisms is characteristic, such as the microencruster *Crescentiella morronensis* (Crescenti). Additionally, other bioclasts, such as calcareous algae *Thaumatoporella*, foraminifera *Litualinida*, and *Aptychus*, have been identified. These taxa indicate reefal facies from the Tithonian age. In specific thin sections, reworked shallow-water bioclasts are observed to be mixed with older Late Triassic clasts containing the benthic foraminifera *Aulotortus sinuosus*. The identification of radiolarian wackestone containing poorly preserved calpionellids, such as *Crassicollaria brevis* or *Calpionella elliptica*, mixed in the resediments suggests that the oldest age of redeposition can be estimated as Berriasian (Ghon *et al.*, 2018).

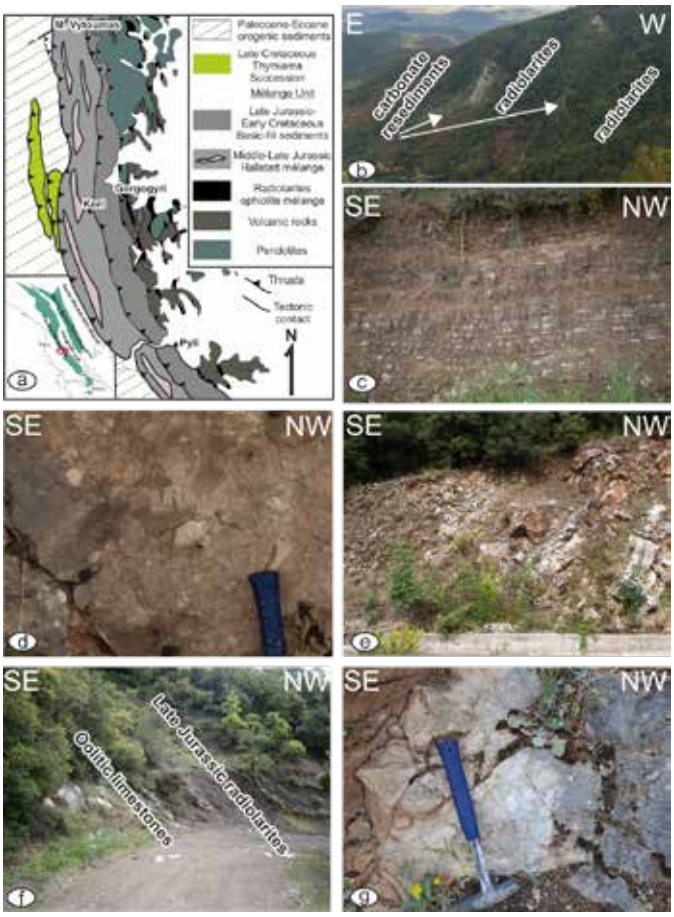

Figure 1. a) Simplified geological map of Koziakas massif (modified after Chiari et al., 2012). b) Panoramic view of the Late Jurassic-Early Cretaceous carbonate resediments intercalated in radiolarites. c) Radiolarite sequence. d) Polymictic breccia with Hallstatt components. e) Hallstatt Limestone block within Middle to early Late Jurassic argillaceous-radiolaritic matrix. f) Late Jurassic radiolarites intercalated by oolitic limestones. g) Late Jurassic to earliest Cretaceous shallow-water carbonate-clastic resediments.

Discussion/Conclusions

Carbonate rocks originating from formations of the outer passive continental margin (Hallstatt Facies) are often found as exotic blocks incorporated within mélanges, a phenomenon widely observed in collisional belts (Gawlick & Missoni, 2019). These exotic blocks serve as valuable tools for reconstructing the original configuration of passive continental margins, as demonstrated in studies of the Dinarides, Albanides, and more recently, the Hellenides (Kostaki *et al.*, 2024, and references therein). Similarly, the exotic open-marine carbonate blocks within the Koziakas mélange provide critical insights into the disrupted architecture of the former passive margin preceding ophiolite obduction. Our analysis reveals that these blocks, spanning ages from the latest Ladinian–earliest Carnian, Late Carnian, and the entire Norian, correspond to a dismembered Triassic Hallstatt Limestone succession characterized by distinctive lithology, microfacies, and stratigraphy. The Hallstatt Facies were originally deposited on the outer shelf during the Middle Anisian to Rhaetian, along with the continental slope Meliata Facies, shaping the eastern Adriatic passive continental margin that faced Neo-Tethys Ocean to the east (e.g., Sudar *et al.*, 2013; Fig. 2a). However, in most instances, the Hallstatt Facies have been disrupted during Middle-Late Jurassic ophiolite obduction and preserved as components or complete successions within massive blocks and slides found in Middle to Late Jurassic far-traveled mélanges along the Alpine-Carpathian-Dinaridic collisional belt (e.g., Gawlick & Frisch, 2003). The Hallstatt Facies can be subdivided into (Gawlick *et al.*, 2018): the reef-proximal facies, characterized by light grey hemipelagic limestones intercalated with shallow-water turbidites, and the distal outer shelf facies, which consists of variously colored limestones. Within the distal outer shelf facies, two types are recognized (Krystyn, 2008): a) the famous fossil-rich facies featuring red bioclastic condensed limestone layers with local enrichment in cephalopods, and b) the facies poor in megafauna, characterized by red to whitish to grey bedded limestones with local enrichment in filaments, radiolarians and echinoderms. The biostratigraphy of the latter facies primarily relies on conodonts. In the Hellenides, the reef-proximal facies are well-

represented by Middle Triassic to Early Jurassic cherty limestones intercalated with turbidites with shallow-water material, notably observed in the Argolis Peninsula, Orthis, and Hydra (Baumgartner, 1985, Ferrière *et al.*, 2016). These limestones are interpreted as west-directed, far-traveled nappes associated with a Jurassic obduction of ophiolites originating from an oceanic realm east of the Pelagonian units (for an alternative view, see Clift & Robertson, 1990). Representing the central shelf dominated by shallow-water carbonates, the Pelagonian units served as a source for sedimentary input into the adjacent reef-proximal outer shelf environment during the Middle Triassic to Early Jurassic. A west-directed ophiolite obduction over the Pelagonian units during the late Middle to early Late Jurassic aligns with our structural observations and other published works (e.g., Kilias *et al.*, 2010, Bortollotti *et al*. 2012, and references therein). In the Avdella mélange, an equivavent mélange to the Koziakas mélange, NW-SE trending asymmetric tight to sub-isoclinal folds with a predominant top-to-the-SW sense of movement are well-preserved and associated with the emplacement of the Pindos ophiolites (Kostaki *et al.*, 2024). Additionally, ductile to semi-ductile shear zones, characterized by well-developed cinematic indicators (e.g. σ-clasts, shear bands, S-C-C` structures), clearly show a west to southwestward sense of shear, although, in some places, they are affected by the younger Tertiary brittle deformation, which typically characterizes the post-obduction phase. Furthermore, similar to the Koziakas mélange, the Avdella mélange contains open-marine Triassic blocks, from which a dismembered Hallstatt succession has been reconstructed (Kostaki *et al.*, 2024). Both mélanges, exhibiting identical characteristics, developed during the Middle to early Late Jurassic as a result of westward ophiolite obduction. Ahead of the advancing ophiolites, trench-like deep-water basins formed, receiving material from the progressing nappe stack, including Hallstatt Facies and ophiolites (Fig. 2b). These basins were subsequently sheared and incorporated into the nappe stack, resulting in the characteristic features of mélanges. Notably, the reconstructed Hallstatt succession from exotic blocks within the Avdella and Koziakas mélanges closely resemble the complete open-marine Middle Triassic to Early Jurassic succession preserved in the Western Pindos, indicating that the Western Pindos succession is the paleogeographic source of the open-marine exotic blocks (complete correlation in Kostaki *et al.*, 2024, Kostaki, 2024). This succession, attributed to the Hallstatt Facies due to its identical lithological and stratigraphic characteristics, represents the distal outer shelf facies. The original deposition of the Western Pindos succession is identified as taking place on the outer shelf from the Middle Triassic until the Early Jurassic east of the Pelagonian units, constituting the easternmost segment of the Adriatic plate (Kostaki *et al.*, 2024). During the late Middle to early Late Jurassic, the west-directed obduction of the Neo-Tethys ophiolites led to the formation of a nappe stack (Fig. 2b**)**. As a result, the Western Pindos succession also became part of this nappe stack and was subsequently bulldozed westward, providing material to trench-like deep-water basins that later evolved into mélanges. This Jurassic westward movement, reflected in both the mélanges and the ophiolites (Kilias, 2024), ultimately transported the Western Pindos succession onto the foreland, reaching the inner parts of the Pelagonian units. Consequently, in its new position during the early Late Jurassic, the Western Pindos succession underwent new sedimentation, resulting in its coverage by a subsequent Late Jurassic to Paleogene sequence. This sequence contributed to a misconception regarding its original deposition, which was perceived as parautochthonous and referred to as Pindos basin. Our biostratigraphic analysis of the exotic blocks found in the Koziakas mélange indicates that the lowermost Carnian blocks are characterized by the influence of shallow-water material, suggesting their original deposition in proximity to the central shelf. This interpretation aligns with the development of the Wetterstein Carbonate Platform, which evolved during the Late Ladinian and lasted until the Early Carnian, shedding debris into the outer shelf region.

Furthermore, our study of the Koziakas mélange unit provides additional insights into nappe stacking processes, the timing of events, and the Middle Jurassic to Early Cretaceous paleogeography. Based on our structural observations, the Koziakas mélange unit can be divided into three tectono-sedimentary sub-units: a) an ophiolitic mélange at the base, consisting exclusively of components derived from the ophiolites and their radiolarite cover, predominantly Triassic radiolarite components (see also Chiari *et al.*, 2012); b) a mélange upsection, dominated by Triassic Hallstatt limestone blocks within an argillaceous-radiolaritic matrix; c) an overlying sequence of radiolarites intercalated by carbonate turbidites and oolitic limestones, transitioning at higher stratigraphic levels into shallow-water carbonate-clastic resediments. The formation of ophiolitic mélanges occurred at the base of the advancing ophiolites, following the onset of intra-oceanic subduction and the development of metamorphic soles. Radiometric dating and geochemical analysis indicate a Middle Jurassic age (174 ± 3 Ma and 161 ± 1 Ma) for the formation of Koziakas ophiolites' metamorphic sole within a MORB-type lithosphere influenced by IAT characteristics (Pomonis *et al.*, 2002). This setting initiated a west-directed ophiolite obduction onto the passive continental margin during the Bajocian-Bathonian, imbricating the lower plate and leading to the formation of trench-like deep-water basins (Fig. 2b). These basins received material from the advancing nappe stack, which later evolved into the mélange with the Hallstatt blocks (Fig. 2c). The timing of ophiolite obduction and the formation of trench-like deep-water basins as Middle to early Late Jurassic is supported by biostratigraphic data obtained from equivalent mélanges across the Albanides and Dinarides (Gawlick *et al.*, 2017), aligning with radiolarian age dating from the Koziakas mélange, which indicate a latest Bajocian to Early Callovian age (Chiari *et al.*, 2012). This is further supported by the evolution of Kimmeridgian–Tithonian shallow-water platforms atop the obducted ophiolites, suggesting that ophiolite emplacement over the Pelagonian units predates the formation of these platforms (Kostaki *et al.*, 2013, 2024). By that time, the nappe stack had advanced into the foreland, and the progressing

basin system developed into a trench-like foreland basin in front of the obducted Koziakas ophiolites, where the radiolarite sequence of the Koziakas was deposited above the mélange with the Hallstatt blocks (Fig. 2c, d). Extending for several meters, this radiolarite sequence reflects a period of relative tectonic silence during the Oxfordian to the Kimmeridgian, as indicated by radiolarian age dating (Kostaki, 2024). The influence of a shallow-water environment from the Kimmeridgian-Tithonian platform atop of the ophiolites during the late Oxfordian to Tithonian became evident through the deposition of radiolarites intercalated with carbonate turbidites and oolitic limestones. Subsequently, from the latest Tithonian onwards, erosional products of this platform were redeposited in this remaining underfilled foreland basin, forming carbonate-clastic resediments. Microfacies analysis of these resediments reveals Kimmeridgian Saccocoma-bearing limestones and Tithonian shallow-water clasts mixed with Late Triassic carbonate clasts. This phase of erosion is attributed to the tectonic uplift of the accreted former Pelagonian margin from the Tithonian onwards, initially affecting the Late Jurassic shallow-water platform, then the ophiolites and their radiolarite cover, and later extending to the Triassic to Early Jurassic shallow-water Pelagonian carbonates. The ongoing uplift and unroofing led to further westward transport of the ophiolites and the overlying shallow-water platform, bringing them closer to the under-filled foreland basin (Fig 2d). In this setting, erosional products, including reworked Late Jurassic shallow-water platform clasts and Triassic carbonate clasts, were redeposited, forming carbonate-clastic resediments. The basin remained under-filled, allowing sedimentation to continue until the earliest Cretaceous (Ghon *et al.*, 2018). In contrast to the Koziakas setting, which partially escaped complete overthrusting by the ophiolites and allowed for prolonged sedimentation with minimal deformation of the basin fill sediments, the Avdella mélange was totally overthrust by the ophiolites, exhibiting the typical characteristics of a mélange.

Our perspective aligns with paleogeographic reconstructions of other regions within the Alpine-Carpathian-Dinaridic belt, characterized by a well-organized passive continental margin consisting of a central shelf (the Pelagonian unit) and an outer shelf dominated by Hallstatt Facies. In the Hellenides, these facies are represented by the Triassic–Early Jurassic Western Pindos succession, which we interpret as a west-directed, far-traveled nappe during Middle to early Late Jurassic. Our findings support the existence of a single Neo-Tethys Ocean located east of the broader Adria, with the Pelagonian unit forming its easternmost continuation without any interruption of an autonomous Pindos Ocean or a Triassic-Jurassic deep-water Pindos Basin.

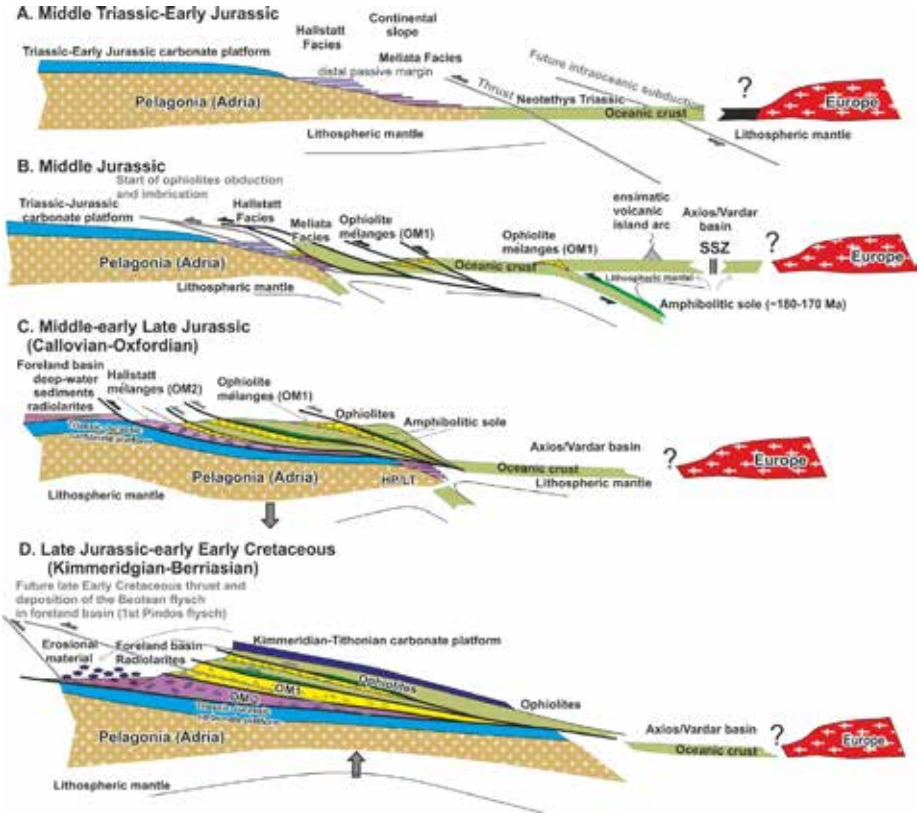

Figure 2. Reconstruction of the Middle Triassic to Early Cretaceous paleogeographic and geotectonic evolution.

Acknowledgements

We acknowledge the late Sigrid Missoni, whose contributions to this research were invaluable. The assistance of Dr. Agni

Vamvaka and Dr. Aristides Sfeikos during fieldwork is greatly appreciated. We also thank the editors for their support throughout the publication process.

References

Baumgartner, P.O., 1985. Jurassic sedimentary evolution and nappe emplacement in the Argolis Peninsula (Peloponnesus; Greece). Mémoires de la Société Helvétique des Sciences Naturelles 99, 111 p.

Bortolotti, V., Chiari, M., Marcucci, M., Marroni, M., Pandolfi, L., Principi, G., Saccani, E., 2004. Comparison among the Albanian and Greek ophiolites: In search of constraints for the evolution of the Mesozoic Tethys Ocean. Ofioliti 29(1), 19-35.

Bortolotti, V., Chiari, M., Marroni, M., Pandolfi, L., Principi, G., Saccani, E., 2012. Geodynamic evolution of ophiolites from Albania and Greece (Dinaric-Hellenic –belt): one, two or more oceanic basins? International Journal of Earth Sciences 102, 783-811.

Chiari, M., Bortolotti, V., Marcucci, M.C. and Saccani, E., 2012. Radiolarian Biostratigraphy and Geochemistry of the Koziakas Massif Ophiolites (Greece). Bulletin de la Societe Geologique de France 183, 287-306.

Clift, P.D. and Robertson, A.H.F., 1990. Deep-water basins within the Mesozoic carbonate platform of Argolis, Greece. Journal of the Geological Society London 147, 825-836.

Ferrière, J., Baumgarthner, P.O., Chanier, F., 2016. The Maliac Ocean: the origin of the Tethyan Hellenic ophiolites. International Journal Earth Sciences 105, 1941-1963.

Festa, A., Ogata, K., Pini, G.A., Dilek, Y., Alonso, J.L., 2016. Origin and significance of the olistostromes in the evolution of the orogenic belts: a global syntheisis. Gondwana Research 39, 180-203.

Frisch, W., Gawlick, H.J., 2003. The nappe structure of the central Nothern Calcareous Alps and its disintegration during Miocene tectonic extrusion-A contribution to understanding the orogenic evolution of the Eastern Alps. International Journal of Earth Science 92, 712-727.

Gawlick, H.-J., Frisch, W., 2003. The Middle to Late Jurassic carbonate clastic radiolaritic flysch sediments in the Northern Calcareous Alps: sedimentology, basin evolution and tectonics - an overview. Neues Jahrbuch für Geologie und Paläontologie, Abh. 230, 163–213

Gawlick, H.-J., Sudar, M.N., Missoni, S., Suzuki, H., Lein, R., Jovanovic, D., 2017. Triassic- Jurassic geodynamic evolution of the Dinaridic Ophiolite Belt (Inner Dinarides, SW Serbia). Journal of Alpine Geology 55, 1–167.

Gawlick, H.-J., Missoni, S., Sudar, M.N., Suzuki, H., Meres, S., Lein, R., Jovanovic, D., 2018. The Jurassic Hallstatt Mélange of the Inner Dinarides (SW Serbia): implications for Triassic-Jurassic geodynamic and palaeogeographic reconstructions of the Western Tethyan realm. Neues Jahrbuch Geologie Paläontologie, Abh. 288, 1–47.

Gawlick, H.-J., Missoni, S., 2019. Middle-Late Jurassic sedimentary melange formation related to ophiolite obduction in the Alpine-Carpathian-Dinaridic Mountain Range. Godwana Research 74, 144-172.

Ghon, G., Gawlick, H.-J., Missoni, S., Djeric, N., Kilias, A., Gorican, S., 2018. Age and microfacies of a carbonate-clastic radiolaritic basin fill above the Koziakas Mélange (Hellenides, Greece). XXI International Congress of CBGA, Salzburg, Austria.

Kilias, A., Frisch, W., Avgerinas, A., Dunkl, I., Falalakis, G., Gawlick, H.-J., 2010. Alpine architecture and kinematics of deformation of the northern Pelagonian nappe pile in the Hellenides. Austrian Journal of Earth Sciences 103/1, 4-28.

Kilias, A., (2024). The Alpine Geological History of the Hellenides from the Triassic to the Present—Compression vs. Extension, a Dynamic Pair for Orogen Structural Configuration: A Synthesis. Geosciences 14, 10.

Kostaki, G., Kilias, A., Gawlick, H-J., Schlagintweit, F., 2013. Kimmeridgian- Tithonian shallow-water platform clasts from mass flows on top of the Vardar/Axios ophiolites. Bulletin of the Geological Society of Greece 47, 184–193.

Kostaki, G., Gawlick, H.-J., Missoni, S., Kilias, A., Katrivanos, E., 2024. New stratigraphic and paleontological data from carbonates related to the Vourinos-Pindos ophiolite emplacement: Implications for the provenance of the ophiolites (Hellenides). Journal of Geological Society of London 181.

Kostaki, G., 2024. Late Jurassic-Early Cretaceous shallow water sediments on the top of the Tethyan ophiolites of the Hellenides (Northern Greece). Ph.D. Thesis, Aristotle University of Thessaloniki, Thessaloniki, 200 p.

Krystyn, L., 2008. The Hallstatt pelagics- Norian and Rhaetian Fossillagerstaetten of Hallstatt. Berichte der Geologischen Bundesanstalt Wien 76, 81-98.

Pomonis, P., Tsikouras, B., Hatzipanagiotou, K., 2002. Origin, evolution and radiometric dating of the sub-ophiolitic metamorphic rocks from the Koziakas ophiolite (W. Thessaly, Greece). Neues Jahrbuch für Mineral, Abh. 177, 255-276.

Robertson, A.H.F., 2012. Late Paleozoic-Cenozoic tectonic development of Greece and Albania in context of alternative reconstructions of Tethys in the Eastern Mediterranean region. International Geology Review 54, 373-454.

Schmid, S.M., Bernoulli, D., Fugenschuh, B., Matenco, L., Scheffer, S., Schuster, R., Tischler, M., Ustaszewski, K., 2008. The Alpine-Carpathian-Dinaric orogenic system: correlation and evolution of tectonic units. Swiss Journal of Geosciences 101, 139-183.

Sudar, M.N., Gawlick, H.-J., Lein, R., Missoni, S., Kovacs, S., Jovanovic, D., 2013. Depositional environment, age and facies of the Middle Triassic Bulog and Rid formation in the Inner Dinarides (Zlatidor Mountain, SW Serbia): evidence for the Anisian break-up of the Neotethys Ocean. Neues Jahrbuch fur Geologie und Palaontologie, Abh. 269, 291-320.

17th INTERNATIONAL CONGRESS of the Geological Society of Greece

BULLETIN OF THE GEOLOGICAL SOCIETY OF GREECE, SP. PUBL.

EXTENDED ABSTRACT 163

Assessing Climate Extremes as Drivers of Geohazards in Greece

Kostopoulou E.[1], Giannakopoulos C.[2], Nefros C.[3], Loupasakis C.[3]

(1) Department of Geography, University of the Aegean, Greece, ekostopoulou@aegean.gr (2) Institute for Environmental Research and Sustainable Development, National Observatory of Athens, Greece, (3) School of Mining and Metallurgical Engineering, National Technical University of Athens, Athens 15780, Greece

Climate extremes have become more frequent and intense in recent years due to global climate change, leading to an increased risk of geohazard occurrences. Extreme events, such as heavy precipitation, can contribute directly to the occurrence of geohazards, including floods and landslides. Additionally, prolonged heatwaves can directly lead to increased soil erosion and indirectly to more frequent and intense wildfires, which, in turn, can increase landslide hazard, by reducing vegetation cover and destabilizing the soil. This study examines historical climate data and future projections, to identify potential climatic changes, which may induce geohazards in Greece.

Introduction

The Mediterranean, a climate change hotspot, is warming 20% faster than the global average (Lionello and Scarascia, 2018; MedECC, 2020; IPCC, 2021), with Greece, as part of the region, following a similar trend. The impact of climate change becomes evident with the increasing variability in temperature, precipitation, and wind patterns leading to more frequent and severe climatic extremes (Giannakopoulos et al., 2011; Lelieveld et al., 2012; Zittis et al., 2016; 2014, Politi et al., 2022, Kostopoulou and Giannakopoulos, 2023 Kostopoulou et al., 2024). Rising temperatures and shifting rainfall patterns exacerbate soil erosion, increase the frequency of floods, and destabilize slopes. This study focuses on the assessment of climate extreme indices in Greece and their direct and indirect impacts on potential future geohazards. Using climate data from the Copernicus Climate Change Service/Climate Data Store (https://cds.climate.copernicus.eu/) we analyze climate variables, indices, based on historical data and projections of future climate scenarios. The ERA5-Land is a global land-surface climate reanalysis produced by the European Centre for Medium-Range Weather Forecasts (ECMWF), providing data at various temporal resolutions from 1950 onward (Muñoz-Sabater et al., 2021). The high-resolution regional climate model data were extracted from the EURO-CORDEX database (Jacob et al., 2014). The climate projections cover the period 1971–2100 and have been used to examine future changes. The projections were estimated for two future emissions scenarios, the moderate RCP4.5 and the more extreme RCP8.5 (Moss et al., 2010). Furthermore, we study maps from the European Climate Risk Typology (https://european-crt.org/) projecting changes in representative climate indices, under the high-emissions 'RCP8.5' global warming scenario, which are related to specific hazards in Greece at regional scale. In the following sections, historical and model-projected time series of temperature and precipitation are analyzed. Subsequently, changes in climate indices and hazard indicators across Greece are presented.

Time Series Analysis of Climate Data and Projections

Reanalysis data from the ERA5-Land dataset are used to describe present climate conditions in Greece. Over the historical period 1950–2022, the mean annual temperature (TM) averaged 13.9°C. In the first half of the period, the annual TM was 13.6°C, while in the second half, it increased to 14.2°C. Anomalies from the 1991–2020 mean range from -1.5°C to 0.8°C, with nine of the ten warmest years occurring after 2010.

Increasing trends are particularly observed in daily mean, minimum, and maximum temperatures (hereafter TM, TN, and TX) on both annual and seasonal scales. Figure 1 illustrates the variations in TN and TX during winter (December to February – DJF) and summer (June to August – JJA) over the historical period. Both seasons show increasing trends, with summer temperatures exhibiting a steeper rise. Focusing on the positive anomalies, we observed deviations of 2.1°C and 1.5°C for TN, and 2.4°C and 2.3°C for TX in winter and summer, respectively, compared to the 30-year average for the period 1991–2020. However, when comparing to the average of the earlier 30-year period (1951–1980), the positive deviations reach up to 2.3°C for TN in both winter and summer, 2.9°C for winter TX, and 3.1°C for summer TX. Hence, both seasonal TN and TX are increasing in Greece, with TX exhibiting a faster rate of warming. The increasing temperatures can contribute to more frequent and severe wildfires, which, in turn, increase the risk of soil erosion (Depountis et al., 2020) and landslides (Nefros and Loupasakis, 2023), especially in mountainous areas. The rise in temperatures may also lead to increased droughts, further stressing water resources and enhancing the risk of desertification in certain regions.

Warming is projected to continue in the future, with both seasonal TN and TX expected to rise further in Greece. Figure 2 shows future projections for the near term (2021–2040), medium term (2041–2060), and long term (2081–

2100). As revealed under both RCP4.5 and RCP8.5 scenarios, not only TX and TN are projected to increase, but the number of heatwave days (TX exceeding 35° C) is expected to rise, while the number of frost days (TN below 0° C) is anticipated to decline. Moreover, according to the CORDEX-EUR-11 climate model, TX and TN are anticipated to increase, with changes ranging from 2°C to over 4°C by the end of the 21st century under the RCP4.5 and RCP8.5 scenarios, respectively.

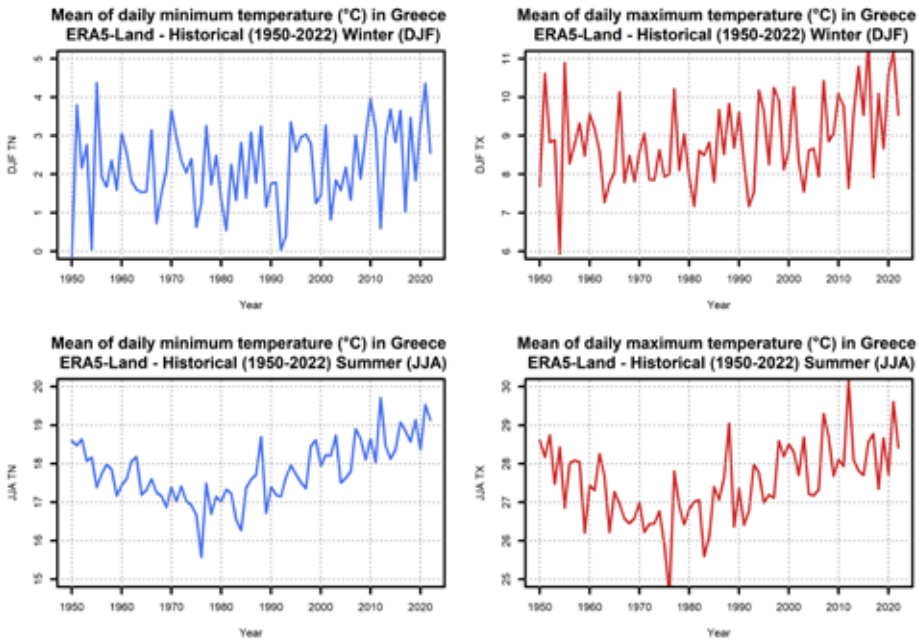

Figure 1. Variations in TN -mean daily minimum (blue) and TX -maximum (red) temperatures over the historical period 1950–2022 during winter (top) and summer (bottom) in Greece.

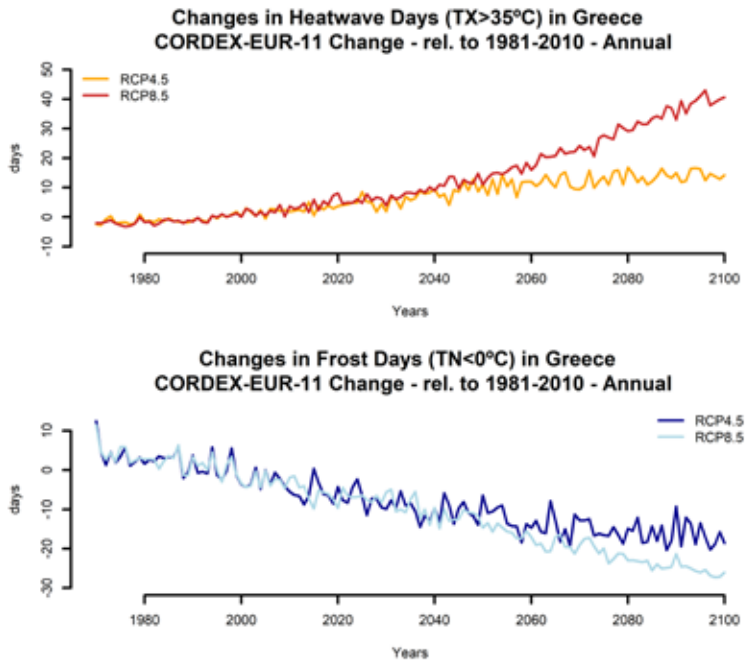

Figure 2. Simulated changes in the number of days with TX above 35°C (top) and TN below 0°C (bottom) in Greece, relative to the 30-year historical period 1981–2010.

Concerning precipitation, the mean daily accumulated precipitation fluctuates around its average over the historical period 1950-2022 (Figure 3, left column panels), with both wetter and drier years evident. An increasing trend has been observed in the annual maximum 1-day precipitation over the past decade, although this is not a long-term pattern and the trend remains uncertain. However, a more distinct trend is evident in the annual mean daily evaporation, likely driven by the rising temperatures. Regarding future changes (Figure 3, right column panels), the mean daily accumulated precipitation is projected to slightly decrease in the medium term (2041–2060) under both RCP4.5 and RCP8.5 scenarios, with a more pronounced decline under RCP8.5 in the long term (2081–2100). The annual maximum 1-day precipitation is expected to increase under both scenarios, particularly under RCP8.5, with an approximate increase of 5 mm per day. The combined effect of these changes suggests that while daily precipitation may decrease, precipitation on wet days could become more intense. The scenarios do not show a clear trend in the annual mean daily evaporation. The Standardized Precipitation Index (SPI; McKee et al., 1993) is of particular relevance, as it shows changes in precipitation relative to the average of a reference period and defines precipitation anomalies over time (i.e., dry and wet spells). The two maps shown in Figure 3, located at the far right of the figure, present the annual index values calculated over a 6-month period (SPI-6) for the medium and long term under RCP8.5. This index is typically used to identify short-term trends in precipitation. In both cases, negative values of the index are observed over Greece, indicating that the region is expected to experience drier-than-normal conditions. More specifically, the SPI-6 suggests moderate drought conditions in the medium term, which could become more severe towards the long-term period.

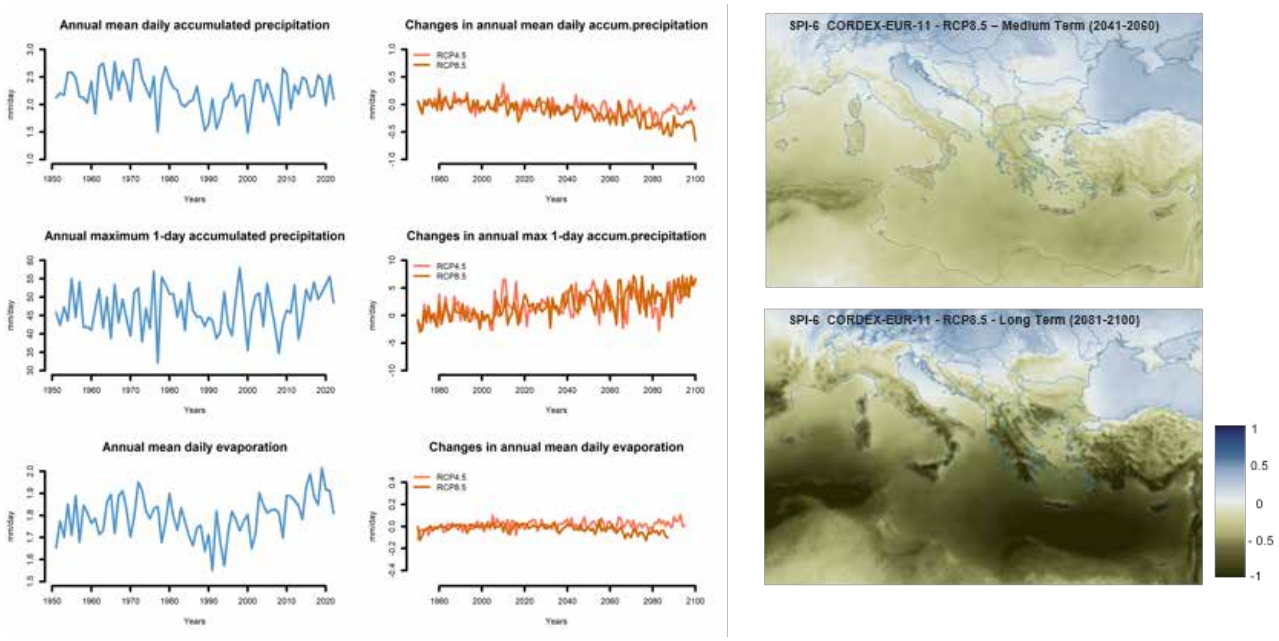

Figure 3. The diagrams show the observed values (left) and simulated changes (right) in mean daily precipitation (top), maximum 1-day precipitation (middle), and daily evaporation (bottom) in Greece. The maps, located at the far right of the figure, depict the annual SPI-6 under RCP8.5 for the medium term (2041–2060, top) and the long term (2081–2100, bottom).

Spatial Representation of Changes in Climate Indices and Hazard Indicators

Subsequently, data from the European Climate Risk Typology (European CRT, Carter et al., 2018) are utilized to examine the spatial distribution of projected climate index changes in Greece at regional unit scale (NUTS3 scale). The European CRT provides a systematic framework for assessing and classifying climate risks across Europe, facilitating a comprehensive understanding of their spatial distribution and intensity. This approach supports researchers and policymakers in developing targeted, region-specific climate adaptation strategies.

Extreme climate indices potentially related to the occurrence of specific hazards are shown and discussed. For example, the combined effect of increased temperatures and consecutive dry days creates favorable conditions for the development of drought hazards. Similarly, projections of changes in the number of consecutive wet days and extreme precipitation events provide insights into the potential for flood hazards. These maps present changes for the medium term (in this case the period 2036-2065, with respect to the reference period 1981-2010) under the RCP8.5 scenario.

The projected changes in heatwave days (TX > 35°C) are shown in Figure 4a. The Greek region is expected to experience positive changes across the entire area. Most regions are projected to see an additional 6–15 heatwave days by the mid-21st century. Notably, increases are observed in the islands of the eastern Aegean Sea. The most impacted areas, highlighted in red, are located in the central continental parts of the country. Increases are also observed in consecutive dry days (Figure 4b), with the eastern and southern parts of the country projected to experience the greatest impact. The number of consecutive dry days (precipitation < 1mm) may increase by 8 days in eastern Peloponnese and by 11 days in eastern Crete. In line with this finding, the next index refers to changes in wet spells, using the number of consecutive wet days (precipitation > 1mm). Here, we observe minimal changes, indicating a future trend toward increasing dryness in the region. The fourth index, presented in Figure 4d, shows the projected changes in heavy precipitation days. All Greek sub-regions show negative trends in heavy precipitation events. However, it is important to note that smaller-scale extreme events, such as localized heavy rainfall, may not be accurately captured by the model's long-term projections, particularly in areas with complex topography (e.g., mountains or coastal regions). As a result, extreme precipitation events may still occur despite the overall negative trend.

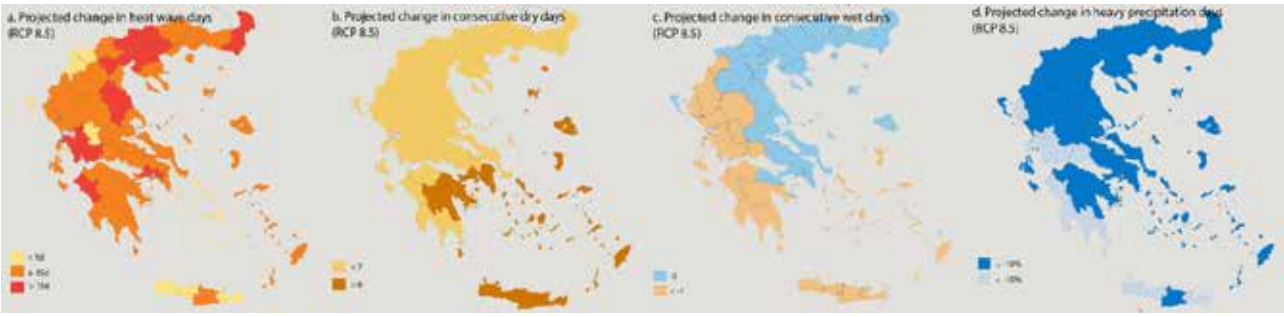

Figure 4. Projected changes under RCP8.5 in (a) heatwave days, (b) consecutive dry days, (c) consecutive wet days, and (d) heavy precipitation days (data source: european-crt.org).

Finally, maps showing several hazards over Greece were reproduced from the European CRT datasets. Figure 5 presents four types of hazards related to climate conditions. The indicator that defines 'Drought hazard' utilizes the Standardized Precipitation-Evapotranspiration Index (SPEI; Vicente-Serrano et al., 2010) at nine month timescales to provide a measure of meteorological drought. Negative values of SPEI reflect regions where precipitation over a nine-month period is reduced. Although most of the Greek region shows values below the European average, the light colors in northeastern Greece, the small islands of the Aegean, and eastern Crete indicates regions more susceptible to drought. This is of particular importance, especially for eastern Crete and the Cyclades islands in the Aegean, which are among the driest areas of the country and at high risk of desertification. The "Fluvial flooding" indicator highlights areas susceptible to flooding in the event of a 1-in-100-year fluvial flood. Parts of northeastern Greece, as well as the regions of Larissa, Voiotia, Ileia, Thesprotia, and especially Evros, are identified as areas prone to fluvial flooding. The "Landslide hazard" indicator highlights areas with moderate or higher susceptibility to landslides, considering both predisposing and triggering factors. While steep slopes are a key factor influencing landslide susceptibility, landslide hazard is determined by combining susceptibility with triggering factors, such as intense precipitation (Nadim et al., 2006). Landslides in Greece are usually triggered by heavy rainfall, seismic activity, and human activity such as deforestation, and constructions on geologically unstable or steep terrain. Changes in soil erosion can also impact landslide susceptibility (Huang et al., 2020), significantly also heighten the landslides hazard in various regions. Moreover, high temperatures and prolonged dry spells may exacerbate soil erosion, which can further increase landslides susceptibility. This indicator identifies several Greek sub-regions with values above the European average, indicating a higher susceptibility to landslides. The "Wildfire hazard" indicator uses data on past wildfire occurrences, vegetation types, climate variables, and the Canadian Forest Fire Weather Index (FWI; Van Wagner, 1987) to identify regions at risk. Most of Greece shows values above the European average, which can be attributed to the combination of rising temperatures and extended dry periods, particularly in subregions located in the eastern and southern parts of the country. Similarly, the increased wildfire hazard is expected to indirectly affect the occurrence of geohazards, such as soil erosion and landslides.

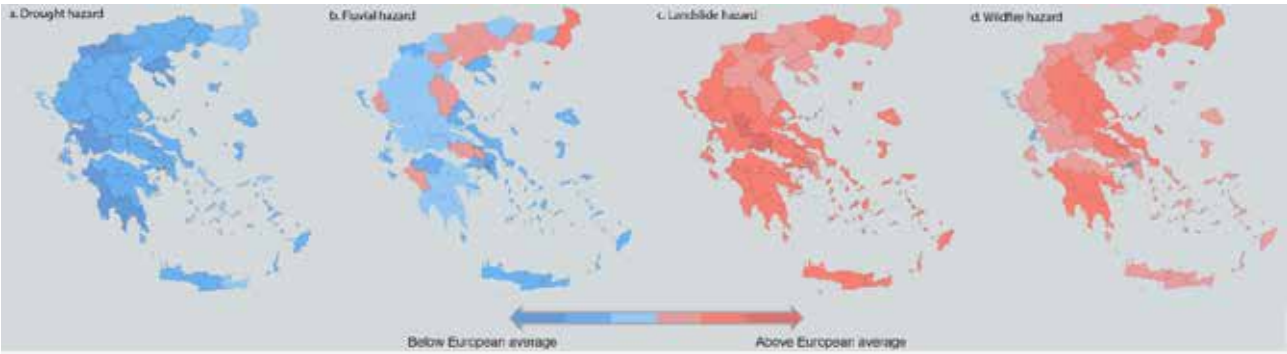

Figure 5. Estimated hazards under RCP8.5 for (a) drought, (b) fluvial flooding, (c) landslides, and (d) wildfires (data source: european-crt.org).

Conclusions

Analysis of climate data reveals a clear warming trend across Greece, with annual and seasonal temperatures rising, especially during summer. Projections suggest further warming of 2°C to beyond 4°C, by the century's end, depending on emission scenarios. Combined with prolonged dry spells, this will lead to more frequent and intense heatwaves, droughts, and wildfire risks, and in turn, to an increased occurrence of geohazards. While precipitation trends remain variable, heavy rainfall events do not show a clear increase, though models have difficulty capturing localized extremes. Future projections indicate a decline in mean daily accumulated precipitation, but an increase in the individual daily rainfall amounts, raising the risk of both droughts and floods, which can, in turn, impact accordingly soil erosion and landslides. The SPI-6 indicates drier conditions, especially under high-emission scenarios. Eastern and southern Greece is most vulnerable to drought, while coastal and mountainous areas face increased flooding, landslides, and soil erosion. Wildfire risks will also rise, especially in the east and south. These findings highlight the need for targeted adaptation strategies to mitigate extreme climate impacts on geohazards, particularly in high-risk regions.

Acknowledgements

We acknowledge the use of data from the Copernicus Climate Change Service (C3S) and the Climate Data Store (CDS), specifically the ERA5-Land dataset and the CORDEX-EUR-11 climate model data. We also thank the European Climate Risk Typology for contributing essential data on climate risk indicators.

References

Carter, J.G, Hincks, S, Vlastaras, V, Connelly, A., Handley, J., 2018. European Climate Risk Typology. [ONLINE] Available at: http://european-crt.org/index.html

Depountis, N., Michalopoulou, M., Kavoura, K., Nikolakopoulos, K., Sabatakakis, N., 2020. Estimating Soil Erosion Rate Changes in Areas Affected by Wildfires. ISPRS International Journal of Geo-Information 9, 562.

Giannakopoulos, C., Kostopoulou, E., Varotsos, K.V., Tziotziou, K., Plitharas, A., 2011. An integrated assessment of climate change impacts for Greece in the near future. Reg Environ Change 11, 829–843.

Huang, F., Jiawu C., Zhen D., Chi Y., Jinsong H., Qinghui J., Zhilu C., Shu L., 2020. Landslide Susceptibility Prediction Considering Regional Soil Erosion Based on Machine-Learning Models. ISPRS International Journal of Geo-Information 9, no. 6, 377.

IPCC, 2021. Climate Change 2021: The Physical Science Basis. Contribution of Working Group I to the Sixth Assessment Report of the Intergovernmental Panel on Climate Change[Masson-Delmotte, V., P. Zhai, A. Pirani, S.L. Connors, C. Péan, S. Berger, N. Caud, Y. Chen, L. Goldfarb, M.I. Gomis, M. Huang, K. Leitzell, E. Lonnoy, J.B.R. Matthews, T.K. Maycock, T. Waterfield, O. Yelekçi, R. Yu, and B. Zhou (eds.)]. Cambridge University Press, Cambridge, United Kingdom and New York, NY, USA.

Jacob, D., Petersen, J., Eggert, B., Alias, A., Christensen, O.B., Bouwer, L.M., Braun, A., Colette, A., Déqué, M.; Georgievski, G., et al., 2014. EURO-CORDEX: New high-resolution climate change projections for European impact research. Reg Environ. Change 14, 563–578.

Kostopoulou, E., Giannakopoulos, C., 2023. Projected Changes in Extreme Wet and Dry Conditions in Greece. Climate 11(3), 49.

Kostopoulou, E., Giannakopoulos, C., Mirasgedis, S., 2024. Aspects of Climate Change in Greece. In: Darques, R., Sidiropoulos, G., Kalabokidis, K. (eds) The Geography of Greece. World Regional Geography Book Series. Springer.

Lelieveld, J., Hadjinicolaou, P., Kostopoulou, E., Chenoweth, J., El Maayar, M., Giannakopoulos, C., Hannides, C., Lange,

M.A., Tanarhte, M., Tyrlis, E., Xoplaki, E., 2012. Climate change and impacts in the Eastern Mediterranean and the Middle East. Climatic Change 114, 667–687.

Lelieveld J, Hadjinicolaou P, Kostopoulou E, Giannakopoulos C, Pozzer A, Tanarhte M, Tyrlis E., 2014. Model projected heat extremes and air pollution in the eastern Mediterranean and Middle East in the twenty-first century. Regional Environmental Change 14, 1937-1949.

McKee, T.B., Doesken, N.J., Kleist, J., 1993. The relationship of drought frequency and duration to time scale. In: Proceedings of the Eighth Conference on Applied Climatology, Anaheim, California, 17–22 January 1993. Boston, AMS, 179–184.

MedECC, 2020. Climate and Environmental Change in the Mediterranean Basin – Current Situation and Risks for the Future. First Mediterranean Assessment Report [Cramer, W., Guiot, J., Marini, K. (eds.)] Union for the Mediterranean, Plan Bleu, UNEP/MAP, Marseille, France, 632pp.

Moss, R.H., Edmonds, J.A., Hibbard, K.A., Manning, M.R., Rose, S.K., Van Vuuren, D.P., Carter, T.R., Emori, S., Kainuma, M., Kram, T., 2010. The next generation of scenarios for climate change research and assessment. Nature 463, 747–756.

Muñoz-Sabater, J., Dutra, E., Agustí-Panareda, A., Albergel, C., Arduini, G., Balsamo, G., Boussetta, S., Choulga, M., Harrigan, S., Hersbach, H., Martens, B., Miralles, D. G., Piles, M., Rodríguez-Fernández, N. J., Zsoter, E., Buontempo, C., and Thépaut, J.-N., 2021. ERA5-Land: A state-of-the-art global reanalysis dataset for land applications, Earth Syst. Sci. Data 13, 4349–4383.

Nadim, F., Jaedicke, C., Smebye, H., Kalsnes, B., 2006. Assessment of global landslide hazard hotspots. International Centre for Geohazards (ICG) / Norwegian Geotechnical Institute (NGI), Oslo, Norway. IPL Project C102

Nefros, C., Loupasakis, C., 2023. Landslide Risk Management in Areas Affected by Wildfires or Floods: A Comprehensive Framework Integrating GIS, Remote Sensing Techniques, and Regional Climate Models. Bull. Geol. Soc. Greece 60 (1), 27–68.

Politi, N., Vlachogiannis, D., Sfetsos, A., Nastos, P.T., 2023. High resolution projections for extreme temperatures and precipitation over Greece. Clim Dyn 61, 633–667.

Vicente-Serrano, S.M., Berguería, S., López-Moreno, J.I., 2010. A multi-scalar drought index sensitive to global warming: the standardized precipitation evapotranspiration index - SPEI. Journal of Climate 23 (7), 1696-1718.

Van Wagner, C.E. 1987. Development and structure of the Canadian forest fire weather index system. Forestry Technical Report 35. Canadian Forestry Service.

Zittis, G., Hadjinicolaou, P., Fnais, M., Lelieveld, J., 2016. Projected changes in heat wave characteristics in the eastern Mediterranean and the Middle East. Reg Environ Change 16, 1863–1876.

17th INTERNATIONAL CONGRESS of the Geological Society of Greece

BULLETIN OF THE GEOLOGICAL SOCIETY OF GREECE, SP. PUBL.

EXTENDED ABSTRACT 164

Submarine geomorphological structures in the Ionian Sea, Greece

Kothri S.[1], Nomikou P.[1], Loreto M.F.[2], Ranero R.C.[3,4], Lampridou D.[1], Nikoli E.[1], Merino I.[5], Ferrante V.[2], Poulos S.[1], Ganas A.[6]

(1) National and Kapodistrian University of Athens, Athens, Greece, skothri@geol.uoa.gr, (2) CNR – ISMAR, Istituto di Scienze Marine, Bologna, Italy, (3) Institució Catalana de Recerca i Estudis Avançats, ICREA, Barcelona, Spain, (4) Barcelona Center for Subsurface Imaging, ICM, CSIC, Barcelona, Spain, (5) Faculty of Geosciences, University of Bremen, Bremen, Germany, (6) Institute of Geodynamics – National Observatory of Athens, Greece

Introduction

The underwater geomorphology of tectonically active regions is essential for understanding seismic hazards, particularly in areas with a history of destructive earthquakes. The Ionian Sea, situated at the convergence of major tectonic domains in the Mediterranean, represents a region of significant scientific interest (Fig.1). It likely features an upper crustal fault system overlying the megathrust fault system of the Hellenic Subduction Zone, trending NW-SE to NNW-SSE, which contributes to its high seismic hazard potential (Ranero et al., 2023).

Figure 1. The location of the study area in relation to continental Greece (the bathymetry is from EMODnet, while in red are shown simplified fault lines of on- and offshore Greece)

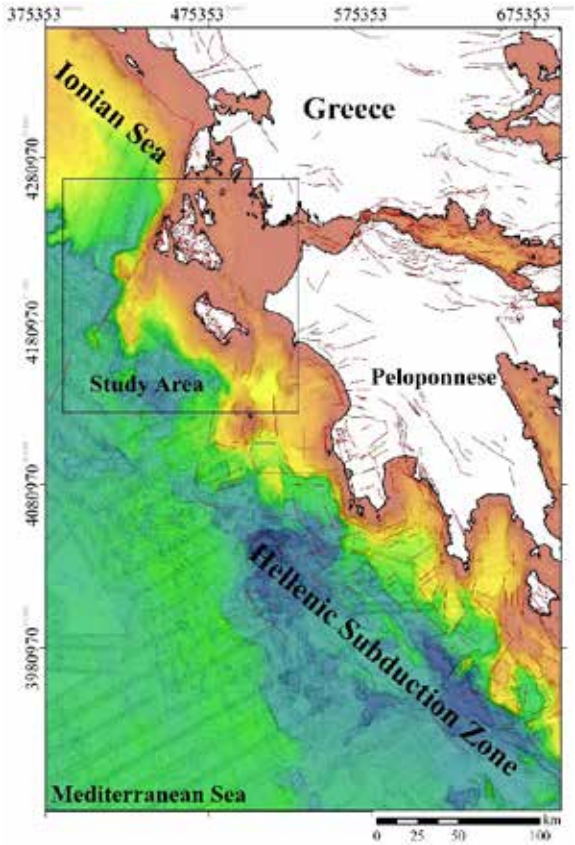

The POSEIDON Eurofleet+ cruise (10–22 June 2023) aboard Research Vessel (R/V) *Laura Bassi* focused on mapping the tectonic structure of the Ionian Sea, particularly near the western Peloponnese and Ionian Islands, including Lefkada, Cephalonia, and Zakynthos (Fig.1). This region is characterized by a complex fault network and exhibits the highest instrumentally recorded seismic activity in the Mediterranean, often associated with tsunamigenic potential, as exemplified by the 1953 Cephalonia Mw ~6.8 earthquake (Stiros et al., 1994).

Methods

During the cruise, approximately 1,940 km of high-resolution swath bathymetry data were collected using the keel-mounted EM304 (Kongsberg Maritime) system. To enhance data accuracy, adjustments were made to optimize swath

width, and sound velocity profiles (SVP) were acquired in shallow and deep waters to correct refraction errors. Data acquisition was performed using SIS and Quincy software, while processing—including sound speed corrections, line cleaning, and CUBE surface creation—was completed using Qimera software. The processed data was gridded at a 50 m resolution.

The high-resolution bathymetric data were then integrated with medium-resolution data from the EMODnet database, along with single- and multibeam datasets provided by the Hellenic Navy Hydrographic Service (HNHS) (Fig.2). These combined datasets were visualized and analyzed using the ESRI GIS software suite, producing a comprehensive morpho-bathymetric map of the region.

The bathymetric data reveal a rugged seafloor with significant variability, especially in the northern sections. Offshore Lefkada Island, a well-defined continental slope extends from 150 m to 680 m water depth, marked by amphitheater-shaped canyon heads at the continental shelf's edge. This area can be divided into two distinct zones: a relatively flat section up to 600 m depth, hosting sediment waves in the northern part, and deeper regions characterized by NE-SW trending canyons. These canyons exhibit flanks indicating multiple, coalescent and nested landslides, with their mouths reaching depths of nearly 2800 m (Fig.2).

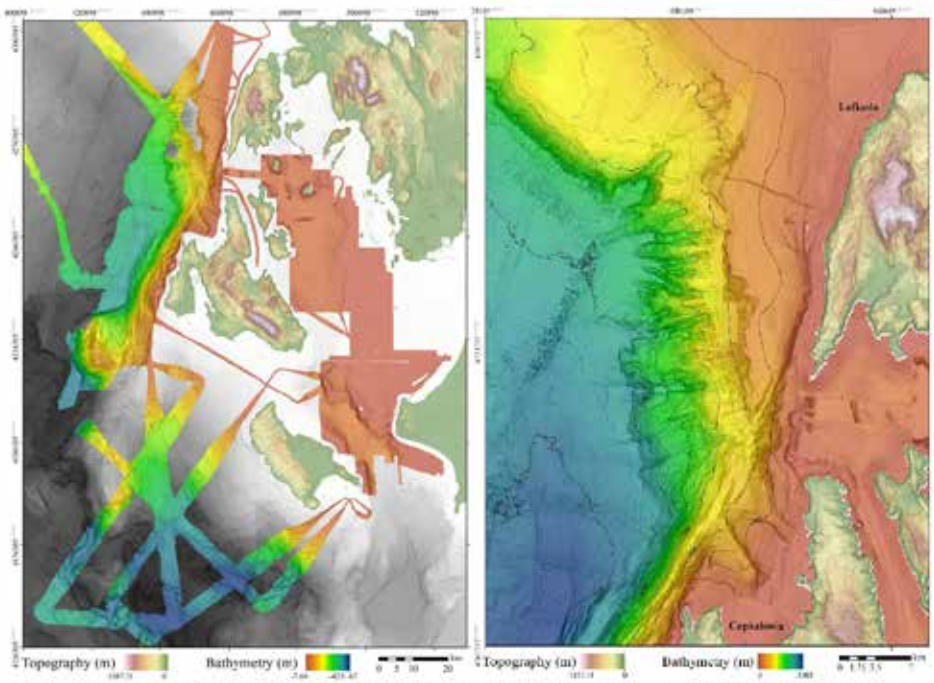

Figure 2. Integrated bathymetric data from the Poseidon Cruise and the HNHS (left) and offshore Lefkada region (right)

Results

The bathymetry of Cephalonia and Zakynthos shows stark contrasts. Northwest of Cephalonia, a steep (>40°) slope connects the abyssal plain to a narrow continental shelf or directly to the coastline. Southward, the slope becomes gentler (~21°) with NE-SW trending steps along the Cephalonia Transform Fault (CTF) system, forming a corrugated seabed (Fig. 4). The CTF trends in a NE-SW direction and extends morphologically to the northern edge of Cephalonia. To the west, the CTF system connects to the Lixouri Seamount, which transitions from a N-S to an E-W orientation. Another Unnamed Seamount further south features steep (36°), triangular, E-dipping faces (Fig.3).

The SW-facing slopes of Cephalonia and Zakynthos are even steeper, with angles up to 40° (Fig. 4), lacking features like canyons or gullies, but are marked by crescent-shaped landslide scars and large-scale landslides, such as a 51 km-long and 2 km-wide feature south of the Paliki Peninsula (Cephalonia) and Zakynthos. These areas display morphological steps indicative of landslides, with E to ENE-dipping detachment planes. The Argostoli Ridge runs NNE-SSW and is bounded by the CTF system and several crescent-shaped landslide scars. Further south, this ridge fragments and collapses. The southernmost area features two elongated abyssal basins reaching depths of 4230 m and 4220 m (Fig.3).

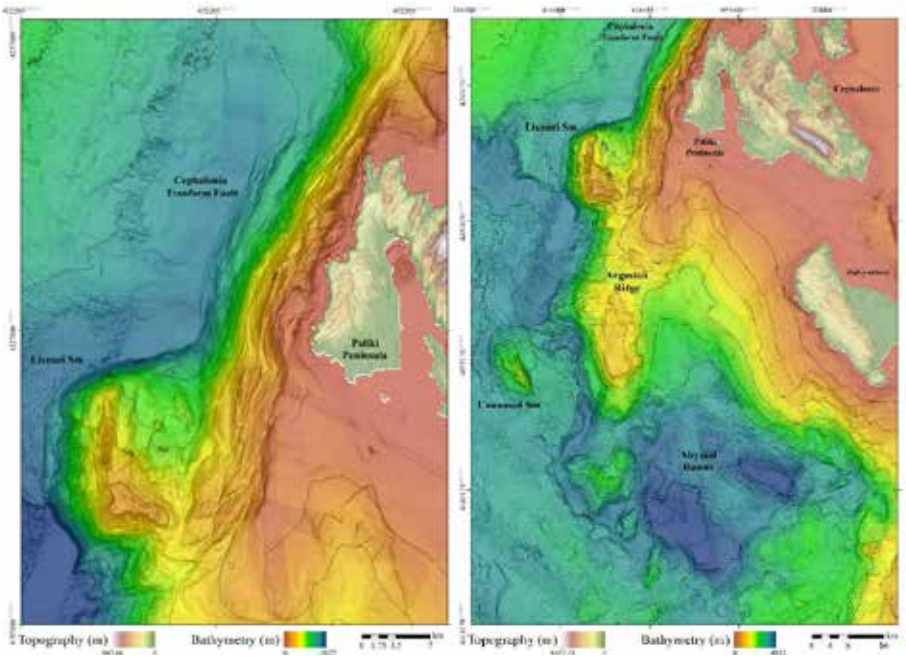

Figure 3. The Cephalonia Transform Fault and the Lixouri Seamount (left) and the SW Cephalonia and Zakynthos area (right)

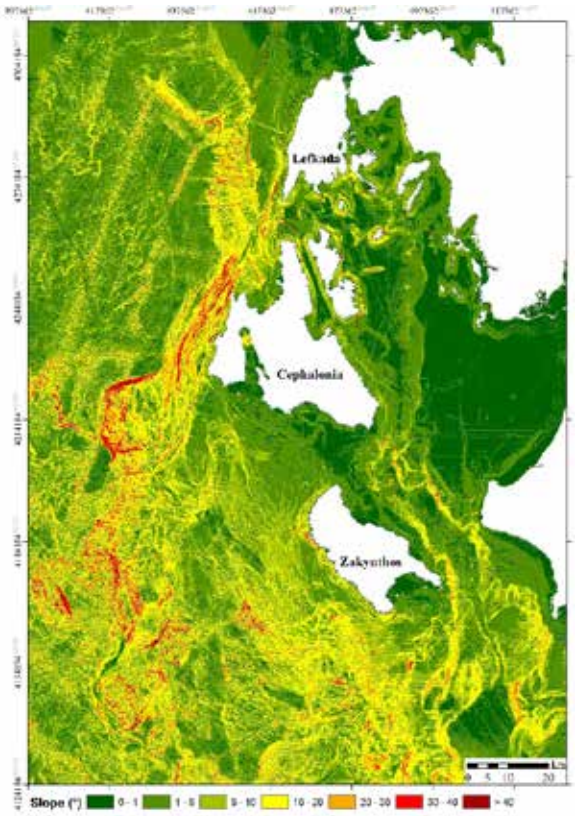

Figure 4. Morphological slope map of the Ionian Sea

Acknowledgements

We acknowledge the professional and dedicated work of the master, officers and crew of the R/V Laura Bassi as well as the technical parties that made this acquisition possible.

References

Ranero C. R., Nomikou P., Loreto M.F., Merino I., Ferrante V., Lampridou D., Nikoli E., Poulos S., 2023. POSEIDON: New data on offshore structures in the west Peloponnese - Ionian Islands Domain and implications for seismic hazards. Bulletin of the Geological Society of Greece, Sp. Publ. 11, 28-31.

Stiros, S.C., et al.,1994. The 1953 earthquake in Cephalonia (western Hellenic arc): coastal uplift and halotectonic faulting. Geophys. J. Int.

17th INTERNATIONAL CONGRESS of the Geological Society of Greece

BULLETIN OF THE GEOLOGICAL SOCIETY OF GREECE, SP. PUBL.

EXTENDED ABSTRACT 165

Heavy metal concentrations in indoor house dusts from the city of Thessaloniki, N. Greece: a small-scale study

Kotsakostoudi Ch.[1], Bourliva A.[2], Mytiglaki Ch.[1], Papadopoulou L.[1], Kantiranis N.[1]

(1) Department of Mineralogy-Petrology-Economic Geology, School of Geology, Aristotle University of Thessaloniki, 54124 Thessaloniki, Greece, kchristina91@gmail.com

(2) Soil Science Laboratory, School of Agriculture, Faculty of Agriculture, Forestry and Natural Environment, Aristotle University of Thessaloniki, 541 24Thessaloniki, Greece

Introduction

Heavy metals in indoor environments have raised growing concern due to their potential adverse health effects, especially in residential settings where individuals, including vulnerable populations such as children and the elderly, spend a significant amount of time (Cheng et al., 2018). Among various indoor substrates, house dust serves as a significant reservoir for heavy metal contamination, often reflecting the combined influence of outdoor pollution, household activities, and the use of materials containing toxic metals. These metals, including lead (Pb), cadmium (Cd), arsenic (As), and chromium (Cr), can be introduced into indoor spaces through numerous pathways, such as outdoor air deposition, contaminated building materials, household products, and the wear and tear of everyday items (Isley et al., 2021).

The presence of these toxic elements in house dust poses serious health risks, with evidence linking exposure to neurological, respiratory, and developmental disorders, particularly in children. Furthermore, long-term exposure to even low concentrations of heavy metals can contribute to chronic health conditions, including cancer, kidney damage, and cardiovascular diseases (Thomas et al., 2009). The variability in the distribution and concentration of heavy metals across different homes highlights the complex interplay between environmental factors, socio-economic status, and lifestyle choices, making the study of house dust as a vector for heavy metal exposure a crucial area of research.

This study aims to explore the concentration of heavy metals in house dust from diverse residential settings in the city of Thessaloniki, with an emphasis on understanding the indoor environmental quality and promoting healthier living spaces.

Materials and Methods

A total of 10 house dust samples were collected from residences within the city of Thessaloniki (Fig1). An effort was made to ensure that the selected residences are uniformly distributed within the city. Sampling was performed during June 2024. House dust was collected by vacuuming repeatedly hard floor surfaces of all living spaces in the house. Vacuum bags were sealed, labeled and stored. Dust samples were sieved to 150 μm using a stainless-steel sieve and analyzed for seven (7) trace metals: arsenic (As), chromium (Cr), copper (Cu), manganese (Mn), nickel (Ni), lead (Pb) and zinc (Zn) as they are known to occur in potentially toxic concentrations in residential environments and to allow comparison with other international dust studies (Isley et al., 2021). Trace metal concentrations were determined via pXRF. A Bruker S1 Titan 600 with a 4 W Rh X-ray tube, 5 mm spot size, a silicon drift detector (resolution < 145 eV), and the inbuilt Geoexploration mode, a factory calibration method for soils, was applied for pXRF analysis. The analysis was conducted in three energy ranges (15, 30 and 50 kV) for 30 s each (a total of 90 s). The elemental contents calculated with the Geoexploration mode were calibrated using certified reference materials (CRMs); calibration curves with R^2 values higher than 0.9 were obtained.

Results and Discussion

The summary statistics of heavy metals in house dusts are given in Table 1 and graphically shown in Figure 2. Heavy metals in house dusts exhibited ranges as: 4 to 11 mg kg^{-1} for As, 106 to 279 mg kg^{-1} for Cr, 62 to 614 mg kg^{-1} for Cu, 263 to 544 mg kg^{-1} for Mn, 23 to 160 mg kg^{-1} for Ni, 22 to 77 mg kg^{-1} for Pb and 339 to 885 mg kg^{-1} for Zn. The median concentration values are following a descending order as: Zn > Mn > Cr > Cu > Ni > Pb > As in line with previous studies (Kelepertzis et al., 2020). In particular, sampled house dusts exhibited higher contents in Zn (650 mg kg^{-1}) followed by Mn (384 mg kg^{-1}), Cr (179 mg kg^{-1}) and Cu (166 mg kg^{-1}), while As presented the lowest concentrations (9 mg kg^{-1}).

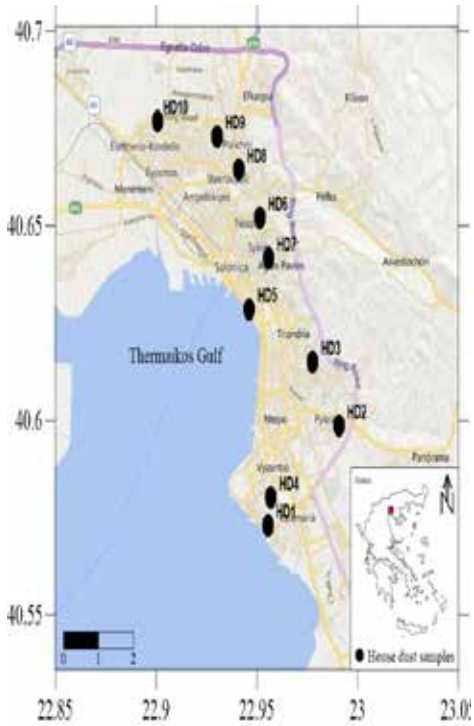

Figure 1. Map of house dust sampling sites in the city of Thessaloniki, N. Greece.

Compared to global crustal values (Isley et al., 2021), most of the elements (except Mn and Ni) are presented moderately to significantly enriched in house dust samples (Fig. 2). Specifically, enrichment ranges of 1-2.6 for As, 1.5-4.0 for Cr, 1.6-15.7 for Cu, 0.7-1.5 for Mn, 0.4-2.9 fon Ni, 1.3-4.5 for Pb and 5.1-13.2 for Zn, were estimated. On the contrary, heavy metal levels (except Cr and Mn) are relatively lower (Fig. 2) than those reported for a dataset of 2265 vacuum dust samples from 35 countries (Isley et al., 2021).

Table 1. Summary statistics of heavy metal contents (mg kg^{-1}) in house dust samples. Background crustal values and international vacuum dust values are also given.

Element	Indoor house dusts (n=10)					Upper Continental Crust [2]	Global Crustal Values[3]	International Vacuum Dust Values[4]
	Mean	SD[1]	Median	Minimum	Maximum			
As	8	3	9	4	11	4.8	4.2	25
Cr	185	49	179	106	279	92	69	128
Cu	204	158	166	62	614	28	39	264
Mn	392	92	384	263	544	1000	363	333
Ni	66	43	50	23	160	47	55	78
Pb	51	21	52	22	77	17	17	224
Zn	623	197	650	339	885	67	67	1470

1: standard deviation, 2: Rudnick & Gao, 2004, 3: Isley et al., 2021, 4: average values from 35 countries (Isley et al., 2021)

Although a direct comparison of heavy metal contents is difficult due to the different sampling protocols, analytical procedures and examined dust fractions, the obtained elemental contents were compared with reported values worldwide (Table 2). As shown, heavy metal contents were relatively higher than those reported for residences from Turkey, Croatia or Ghana; however the sampled house dusts are relatively enriched in Cr and Mn compared to other Greek cities such as Athens (Kelepertzis et al., 2019). Moreover, sampled residential environments display elevated Cr, Mn and Ni contents compared to data from an international vacuum dust analysis program including values from 35 countries worldwide (Isley et al., 2021). Specifically, median Cr levels of 179 mg kg^{-1} were recorded, in contrast to 86 mg kg^{-1} exported from a dataset of 2265 samples from 35 countries. Though Cr sources mainly reflect natural inputs from ultramafic rocks and soils, anthropogenic or industrial inputs cannot be excluded.

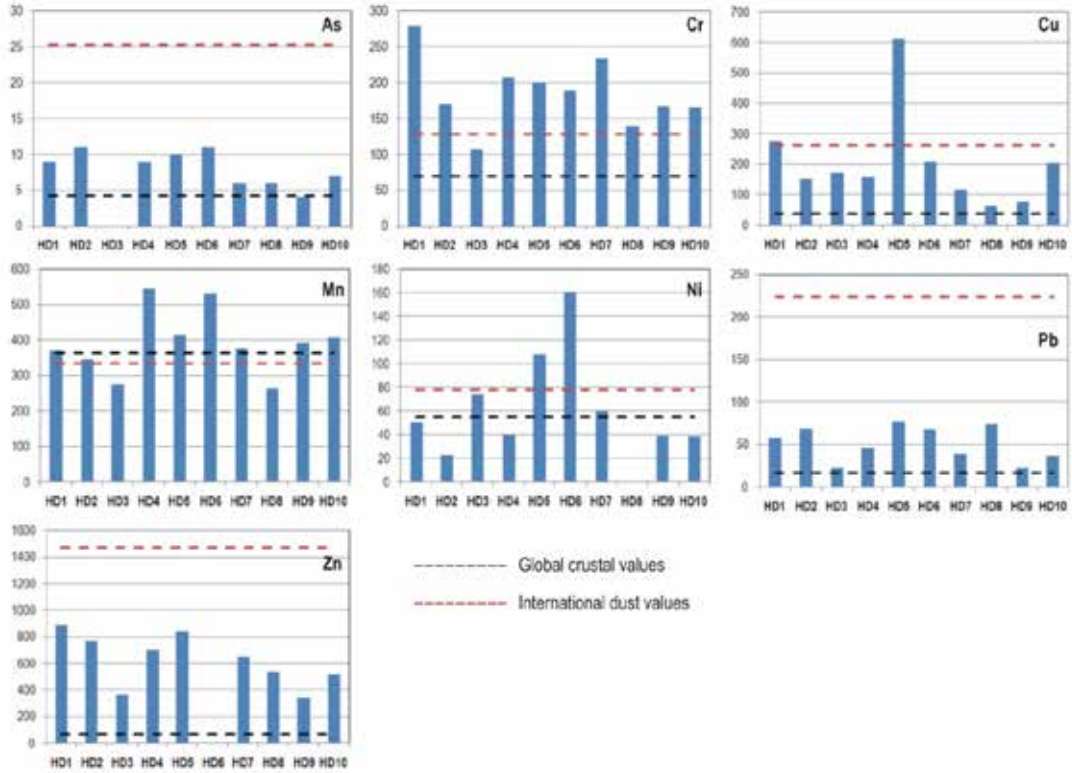

Figure 2. Heavy metal contents (mg kg^{-1}) in house dust samples. Global crustal elemental concentrations (black dashed line, data in Table 1) and international dust values (red dashed line, data in Table 1).

Table 2. Bibliographic data of median heavy metal contents in indoor dust from previous studies.

Study areas	n	Concentrations (mg kg^{-1})							References
		As	Cr	Cu	Mn	Ni	Pb	Zn	
Thessaloniki, Greece	10	9.0	179	166	384	50	52	650	This study
Volos, Greece	24	31.7	163.0	167	274	81	63.2	785	Kelepertzis et al., 2020
Athens, Greece	43		82.9	217	132	89.5	92.2	786	Kelepertzis et al., 2019
Greece	35	6.9	97.9	158	230	52.3	57.0	664	Isley et al., 2021
Australia	1310	19	86	186	246	36	126	1260	Doyi et al., 2019
UK	32			301	524	53.1	150	622	Turner & Simmonds, 2006
Turkey	85	4.41	23.8	65.7	65.9	32.3	27.5	263	Gul et al., 2023
Croatia	34	4.5	88.5	133	225	32.5	59	669	Isley et al., 2021
Ghana	54	1.75	51	55.5	161.5	17	60.5	114	Isley et al., 2021
International vacuum dust values (mean of 35 countries)	2265	13.3	86	176	257	39	94	1110	Isley et al., 2021

To decipher the influence of anthropogenic activities on indoor dust concentrations, Enrichment Factors (EFs) were calculated for As, Cr, Cu, Ni, Pb, and Zn by normalizing vacuum dust trace metal ratios to ratios from global crustal values selected from relevant crustal assessments in the literature and the results are illustrated in Figure 3. The EF was calculated using the following equation:

$$EF = \left(\frac{C_n}{C_{ref}}\right)_{sample} / \left(\frac{B_n}{B_{ref}}\right)_{background}$$

where $(C_n/C_{ref})_{sample}$ and $(B_n/B_{ref})_{background}$ refer to the concentration ratios of a target metal and the reference metal in the house dust samples and the background material, respectively (Yuen et al. 2012). In this study, aluminum (Al)

was taken as a normalization factor and concentrations of elements in the upper crust (Rudnick and Gao, 2004) were taken as background values.

An enrichment factor (EF) less than 2 indicates natural conditions, while EFs larger than 2 suggest anthropogenic influence (Isley et al., 2021). Overall, enrichment of Zn was the greatest, followed by Cu > Pb > Cr > As. Zinc and copper returned values EF > 2 in all sampled house dusts, while EFs for As, Cr and Pb were above 2 in more than 80% of the sampled residences. Specifically, the median EF values of Zn (13.7), Cu (8.8), Pb (4.3), Cr (3.1) and As (2.4) were higher than 2, implying that these heavy metals in house dusts are related to anthropogenic activities (Kelepertzis et al., 2020). For instance, pigments of the wall paints are an important source of heavy metals in household dust (Chattopadhyay et al., 2003). On the contrary, the median EFs for Ni (1.5) and Mn (0.6) indicate a minimal enrichment, which therefore, is linked to the lithogenic component of the house dust mainly inherited from the outdoor soil. However, Ni moderate enrichment in 40% of the sampled residences (maximum values of 4) cannot exclude an anthropogenic input. Moreover, EF values did not exhibit great variability among sampled house dusts suggesting the absence of local anthropogenic activities adjacent to the sampled residential environments. However, residences close to city center presented significantly higher EF values reflecting possible outdoor input from adjacent roadside environments as enhanced heavy metal contents in road dusts have already been reported (Bourliva et al., 2018).

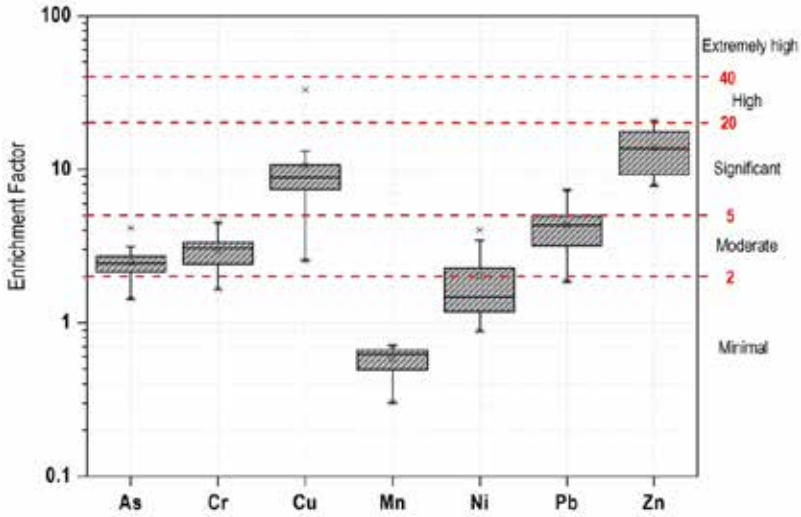

Figure 3. Box plots of enrichment factor (EF) calculations for the assessed trace metals in house dusts, normalized against the reference element Al. Red dashed lines indicate the level of enrichment.

Conclusions

People spend increasing amount of time at home, yet household environments remain understudied. The present study investigated the heavy metal contents in house dust samples from 10 residences within the city of Thessaloniki. Concentration values exhibited a descending order as: Zn > Mn > Cr > Cu > Ni > Pb > As, while concentration levels of these elements were high when compared with those from countries such as Turkey and Croatia. Moreover, the concentrations of As, Cu, Pb and Zn are lower than that of a global vacuum dust dataset. However, Cr levels were relatively higher than those reported from other countries or areas. Values of EFs larger than 2 suggested anthropogenic inputs (except of Ni and Mn), while higher EF values in residences close to city center suggest vehicular traffic as a factor contributing to the rise of heavy metal levels in household environments. Thus, distance to city center could be suggested as an important consideration for the choice of housing.

References

Bourliva, A., Kantiranis, N., Papadopoulou, L., Aidona, E., Christophoridis, C., Kollias, P., Evgenakis, M., Fytianos, K., 2018. Seasonal and spatial variations of magnetic susceptibility and potentially toxic elements (PTEs) in road dusts of Thessaloniki city, Greece: A one-year monitoring period. Science of the Total Environment 639, 417-427.

Chattopadhyay, G., Lin, C.P., Feitz, A.J., 2003. Household dust metal levels in the Sydney metropolitan area. Environmental Research 93, 301-307.

Cheng, Z., Chen, L.-J., Li, H.-H., Lin, J.-Q., Yang, Z.-B., Yang, Y.-X., Xu, X.-X., Xian, J.-R., Shao, J.-R., Zhu, X.-M., 2018. Characteristics and health risk assessment of heavy metals exposure via household dust from urban area in Chengdu,

China. Science of the Total Environment 619-620, 621-629.

Doyi, I.N.Y., Isley, C.F., Soltani, N.S., Taylor, M.P., 2019. Human exposure and risk associated with trace element concentrations in indoor dust from Australian homes. Environment International 133, 105-125

Gul, H.K., Gullu, G., Babaei, P., Nikravan, A., Kurt-Karakus, P.B., Salihoglu, G., 2023. Assessment of house dust trace elements and human exposure in Ankara, Turkey. Environmental Science and Pollution Research 30, 7718–7735.

Isley, C.F., Fry, K.L., Liu, X., Filippelli, G.M., Entwistle, J.A., Martin, A.P., Kah, M., Meza-Figueroa, D., et al., 2021. International Analysis of Sources and Human Health Risk Associated with Trace Metal Contaminants in Residential Indoor Dust. Environmental Science and Technology 56, 1053-1068.

Kelepertzis, E., Argyraki, A., Botsou, F., Aidona, E., Szabó, Á., Szabó, C., 2019. Tracking the occurrence of anthropogenic magnetic particles and potentially toxic elements (PTEs) in house dust using magnetic and geochemical analyses. Environmental Pollution 245, 909-920.

Kelepertzis, E., Argyraki, A., Chrastný, V., Botsou, F., Skordas, K., Komárek, M., Fouskas, A., 2020. Metal(loid) and isotopic tracing of Pb in soils, road and house dusts from the industrial area of Volos (central Greece). Science of the Total Environment 725, 138300.

Rudnick, R.L., Gao, S., 2004. Composition of the continental crust, in: Rudnick, R.L. (Ed.), The Crust, 1–64.

Thomas, L.D., Hodgson, S., Nieuwenhuijsen, M., Jarup, L., 2009. Early kidney damage in population exposed to cadmium and other heavy metals. Environmental Health Perspectives 117, 181-184.

Turner, A., Simmonds, L., 2006. Elemental concentrations and metal bioaccessibility in UK household dust. Science of the Total Environment 371, 74-81.

Yuen, J.Q., Olin, P.H., Lim, H.S., Benner, S.G., Sutherland, R.A., Ziegler, A.D., 2012. Accumulation of potentially toxic elements in road deposited sediments in residential and light industrial neighborhoods of Singapore. Journal of Environmental Management 101, 151–163.

17th INTERNATIONAL CONGRESS of the Geological Society of Greece

BULLETIN OF THE GEOLOGICAL SOCIETY OF GREECE, SP. PUBL.

EXTENDED ABSTRACT 166

New *Clypeaster* fossils from South Crete (Rodakino, Rethymno)

Kotsomitopoulou A.[1], Tsaparas N.[1], Galazoudi E.[1]

(1) National and Kapodistrian University of Athens, Athens, Greece, artemiskots@gmail.com

Introduction

The study area is located near the village of Rodakino in the southwestern part of the Rethymno prefecture (Crete). In this region, the marine Neogene deposits overly the Phyllite-Quartzite unit, which structure the wider area.

The Neogene deposits of Crete are extensive covering a large part of the island. Many researchers have described them throughout the years, classifying them into four lithostratigraphic units ranging from Upper Tortonian to Lower Pleistocene. From oldest to youngest these units are: Tefeli Group (conglomerates and coarse-grained sands to claystone and siltstone with turbidites), Vrysses Group (white marls, calcarenites and bio-calcarenites of Tortonian-Messinian age), Foinikia Group (marls and marly silts of lower Pleistocene age) and Agia Galini Group (conglomerates and coarse-grained sands of lower-middle Pleistocene age) (van Hinsbergen & Meulenkamp, 2006; Tortorici et al., 2010).

The fossiliferous section is 20 meters thick and consists of fine marly sandstones alternating with blue marls. In detail, from the bottom of the section and for 5 meters, thick layers of marly sandstones (~ 70cm) alternate with very thin layers (~5cm), while towards the top, the marly layers are thicker (~ 20 cm). The studied sea urchins were found in the marly sandstones from the first 5m of the outcrop.

Objectives

The purpose of this paper is to present findings from a new fossiliferous site in Crete with echinoids of the genus *Clypeaster*, a taxon now extinct from the Mediterranean. Additionally, data about the age of the studied site were based on calcareous nannoplankton.

Materials and methods

Samples and data collected during the area's mapping were used to create the stratigraphical section. The *Clypeaster* species were identified according to Marcopoulou-Diakantoni (1985), by measuring length (l), width (L), height (h), ratio width-length (L/l) and ratio height-width (h/L).

The material was transported to the Laboratory of Historical Geology and Biogeosciences (Department of Geology and Geoenvironment, National and Kapodistrian University of Athens), where it was cleaned and, when necessary, reconstructed to restore its original shape in cases of fracturing.

A preliminary investigation was conducted on the age of the section based on calcareous nannofossils, but it needs further and more detailed analysis. The sample preparation for the study of calcareous nannoplankton followed standard smear slide techniques. The slides were analyzed using a polarising light microscope LEICA DMLP at 1,250×..

Results

Five different *Clypeaster* species were determined: *Clypeaster altus, C. calabrus, C. campalanatus f. portentosus, C. tauriqus, and C. altostratus*. Several of the specimens could not identified in species level as they were not well preserved. The descriptions of the species presented herein were created according to Markopoulou-Diakantoni (1985), Kroh (2005) and Tsaparas (2005).

Classification

Phylum: Echinodermata KLEIN 1734
Subphylum: Echinozoa HECKEL in ZITTEL, 1895
Class: Echinoidea LESKE, 1778
Subclass: Euechinoidea BRONN, 1860
Superorder: Gnathostomata ZITTEL, 1879
Order: Clypeasteroida A. AGASSIZ, 1873
Suborder: Clypeasterina A. AGASSIZ, 1872
Family: Clypeasteridae L. AGASSIZ, 1835
Genus: Clypeaster LAMARCK, 1801

***Clypeaster campanulatus f. portentosus* MICHELIN, 1861**

(Figure 1.a, b)

Large size species with long pentagonal shape. It has slightly curved edges and very distinct surface ridging and it's characterized by a very elevated petal area, which gives the animal the shape of a bell. The sides are very inclined and not well developed, while the petals are curved and slightly open. Its underside is particularly flat.

***Clypeaster altus* KLEIN, 1734**
(Figure 1.c)
Pentagonal symmetry, elongated, angular on the front and almost straight on the back. Its upper side is erect, the upper surface is relatively high, erect, hypoconical and thick on the sides. Sides very poorly developed and oblique like petals, with their edges rounded and thick. The lower surface is smooth and has prominent peripatetic grooves. The upper side sports a madreporite with ten pores. Ambulacral zones are protruding and petal shaped, with their sides open.

***Clypeaster calabrus* SEGUENZA, 1880**
(Figure 1.d)
Medium to large sized, elongated with pentagonal shape. Its front side is blunt and pointed and its back side is transversely truncated, with well-defined recess and a margin that gets thinner from the front to the back side. The margin of the test is rounded off.

***Clypeaster tauricus* DESOR, 1859**
(Figure 1.e)
Medium height, with its test size pentagonal, elongated and angular, with the 5 points rounded off. The ambulacral zones are petal like in shape, long, protruding, wide open and form a bulge when they come to the side. The lower surface is smooth, the peristome is not well developed while the peripectorium is small and circular.

***Clypeaster alticostatus* MICHELIN 1861**
(Figure 1.f)
Large sized species, with its upper surface very elevated and conical and the madreporite plate submerged. Its sides are underdeveloped, thick and curved, and less extended. The periphery is slightly elongated and the ambulacral zones are petal and almost lance like. The test margin is thin and slightly angular.

Table 1. Measurements of the *Clypeaster* species

Species	Length (l)	Width (L)	Height (h)	L/l	h/l
C. campanulatus f. portentonsus	228	181	96	0.79	0.42
C. altus	152	135	64	0.88	0.42
C. calabrus	158	134	72	0.86	0.45
C. tauricus	189	151	70	0.80	0.37
C. alticostatus	165	142	68	0.86	0.41

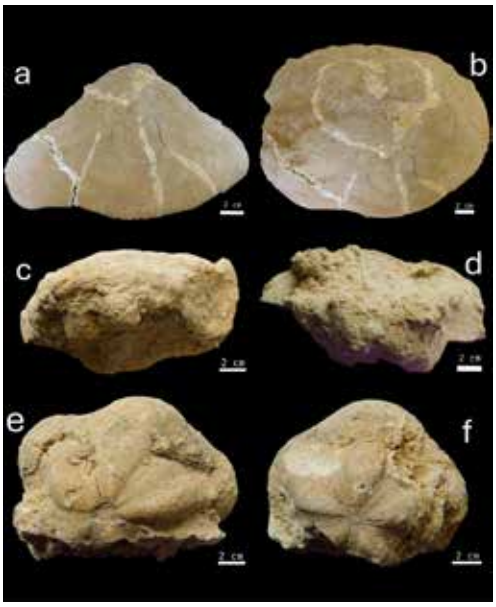

Figure 1. ***a, b. Clypeaster campanulatus* f. *portentosus*. C: *Clypeaster altus* d. *Clypeaster calabrus*. E. *Clypeaster tauricus*. F. *Clypeaster alticostatus***

Several specimens of the large benthic foraminifera *Heterostegina* were found on the echinoids (Figure 2) and in the sediment that was collected after cleaning the specimens. This large benthic calcareous foraminifer is a circum-tropical nummulitid foraminifer with photosymbionts, which prefers forereef environments (Boudagher-Fadel, 2008; Benedetti *et al*., 2017).

The micropaleontological analysis for calcareous nannoplankton (Young *et al*., 2022) of the sediment from the interior of a sea urchin determined two species of the genus *Discoaster* : *Discoaster variabilis* MARTINI AND BRAMLETTE, 1963 and *Discoaster exilis* MARTINI AND BRAMLETTE, 1963 (Figure 3).

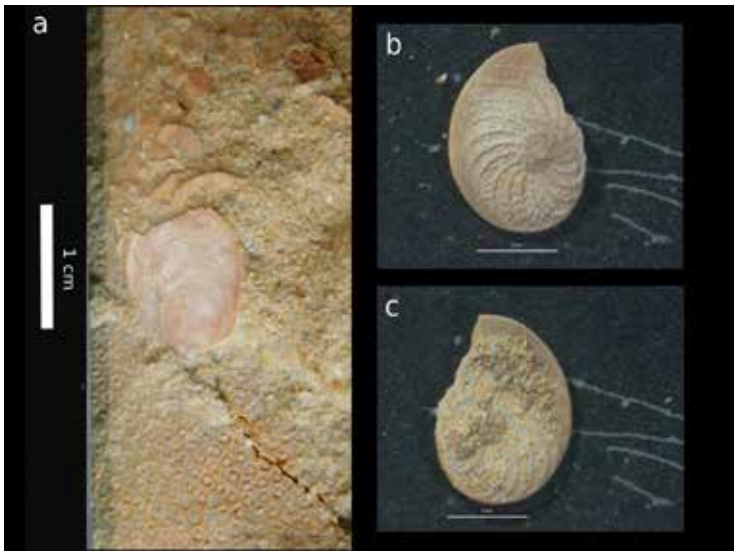

Figure 2. *Heterostegina* members found on the echinoids

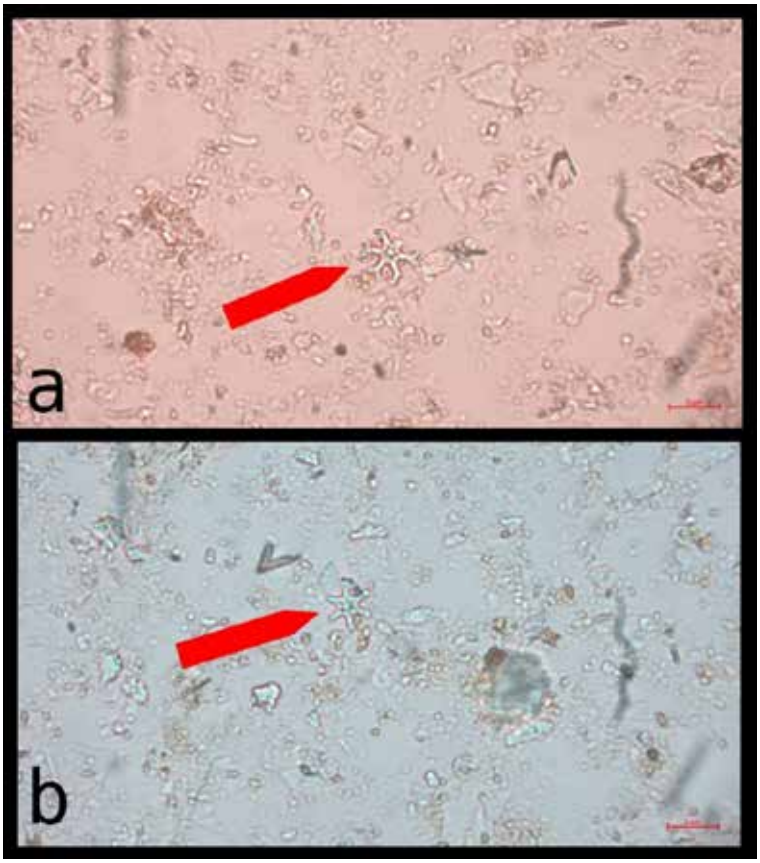

Figure 3. a. *Discoaster variabilis.* b. *Discoaster exilis*

Conclusions

After measurements were made, the following *Clypeaster* species were determined*: C. altus, C. calabrus, C. campalanatus f. portentonsus, C. tauriqus, C. alticostatus*. Based on the presence of *Discoaster variabilis* and *Discoaster exilis* individuals that were found in the sediment, their age was identified as Middle Tortonian (NN9-NN10). Further study on calcareous nannoplankton will determine the age. The environmental conditions inferred from the presence of *Heterostegina*, which coexisted with the sea urchins, suggest a shallow, warm marine environment, similar to that of Gavdos, where comparable findings had been reported.

Acknowledgements

We would like to thank Mr. Nils Sappok for his kind gesture to provide us with the large, complete specimen of *Clypeaster* for our study and for indicating the location where he found it. This enabled us to conduct extensive sampling, the results of which are presented in this paper.

References

Aubry, M.P, 1984. Handbook of Cenozoic Nannoplankton Book 1: Ortholithae (Discoasters), Micropaleontology Press, The American Museum of Natural History.

Benedetti, A., Less G., Parente M., Pignatti J., Cahuzac B., Torres-Silva A.I. & Dieter Buhl D., 2017. Heterostegina matteuccii sp. nov. (Foraminiferida: Nummulitidae) from the lower Oligocene of Sicily and Aquitaine: a possible transatlantic immigrant. Journal of Systematic Palaeontology, 16(2), 87–110.

BouDagher-Fadel, M. K. (2008). Evolution and Geological Significance of Larger Benthic Foraminifera (Vol. 21). Elsevier. https://doi.org/10.1016/S0920-5446(08)00012-5

Kroh, A., 2005. Catalogus Fossilium Austriae. Band 2. Echinoidea neogenica. Österreichische Akademie der Wissenschaften.

Markopoulou-Diakantoni, A., 1985. Morphology and Evolution of the Genus Clypeaster (Clypeasteroida). Aristotle University of Thessaloniki. (in Greek)

Tortorici L., Caputo R., Monaco C., 2010. Late Neogene to Quaternary contractional structures in Crete (Greece), Tectonophysics, 483 (3–4), 203-213.

Tsaparas, N., 2005. Contribution to the history of sedimentation of the upper Cenozoic marine formations in Gavdos island. Faculty of Geology and Geoenvironment. Ph.D. Thesis, National and Kapodistrian University of Athens, 325 p. (in Greek).

van Hinsbergen, D.J.J., Meulenkamp, J.E., 2006. Neogene supradetachment basin development on Crete (Greece) during exhumation of the South Aegean core complex. Basin Research, 18(1), 103–124.

Young, J.R., Bown P.R., Lees J.A., 2022. Nannotax3 website. International Nannoplankton Association.

17th INTERNATIONAL CONGRESS of the Geological Society of Greece

BULLETIN OF THE GEOLOGICAL SOCIETY OF GREECE, SP. PUBL.

EXTENDED ABSTRACT 167

Measurements of soil gas emissions (radon and thoron) in the municipality of occidental Lesbos, Stypsis – Petras, and correlation with tectonic structures (rift zone) of the subsidence coast of Petra

Koukoulis A.[1], Xenakis M.[1]
(1) H.S.G.M.E., Athens, Greece, akoukoulis@eagme.gr

Panoramic view of the measurement area.

Summary

In this work, a radiological, geological and tectonic approach is carried out, for the evaluation of radon-thorium soil, in two predetermined areas of Petra, which have been designed by PPC RENEWABLES S.M.S.A. for the needs of geothermal research conducted in the region. The objective of the HSGME service project was to identify the optimal pathways for radon increase in the soil and their possible connection to the mapped tectonic structures and the corresponding optimal geothermal fluid pathways in the research area.

The most important results of the work are that radon and thoron concentrations in the soil, which reach high levels of up to 57.448 and 10.357 Bq/cm3 respectively, are independent of the activity of local geological formations and are fed by deeper bottom horizons via fault zones. The spatial distribution of radon shows high concentrations with growths of about 200 to 400m on the ground, correlated with the corresponding tectonic structures.

From the shape and the particular characteristics of the distribution of soil gases (radon and thoron), the data so far change, and from the lines of the mapped tectonic structures, we have the identification of rift zones, with optimal circulation of soil gases and possibly also of geothermal fluids.

Methodology-Measures

In situ measurements (N=435) were performed at predetermined positions of a 400m orthocanonical cell grid, with some thickening in the center of the squares and at the 200m edge vertices, which cover the entire area of the research field with a total of 87 situations (Fig. 1).

For each location, underground air is pumped to a depth of about 50cm, and radon and thoron are measured on site using an automatic semi conductor detector (RTM-1688-2, Sarad), for an average time of about 45 minutes. At the same time, with the help of special detectors (Camberra smart probes), the variation of activity on the ground surface, three radiological parameters is recorded (Fig. 2) :

(a) total contamination of α-β-γ radiation, by the Radiagem 2000 instrument and the SABG 15 probe

b) the equivalent dose rate when detecting a gamma photon flux by the Radiagem 2000 instrument and the external 2΄X2΄ SG-2R gamma probe

c) total γ radiation, by scintillation meter SPP2 (Saphymo-Stel).

The measurements of these quantities (Table 1) give a satisfactory consistency of the arguments in favour of the activity of the radiation emitted by the ground in the field of research, and above all make it possible to assess the origin of the high concentrations of radon in the soil, since it is known that among the factors that influence it are geology, geotectonic, radiology, geothermal field, etc., with which an investigation is attempted.

Discussion of the results

In the study area, radon-thoron increases are independent of the type of volcano and the primary or secondary stages of volcanism (Fig. 3, 4), which have a high radiological background, several times higher than that of other regions of the country (Table 1, Fig. 5, 6). However, there is no direct relationship between radon-thoron and volcanism, which is essentially identical (Fig. 2, Fig. 9. 10, 11) to the upper unit of lavas of Hehct 1974, or to that of the subalkaline potassic series (shoshonites) as identified by G. Piper 1992, and which is more uranium-rich and potassic, with accessory minerals responsible for uranium concentrations, selective aggregation of thorite-titanite-allanite-zirconium-apatite (Koukoulis A. et al., IGME, 2001).

A few kilometers from the Stypsi geothermal field, there are high concentrations of radon and thoron in the ground, with small isolated developments (about 200-400m on the ground), which are located both in the research field and its extension, which requires further research (Fig. 7, 8).

On the descending side of the Avlaki and Petra faults, maximum radon values were recorded in the upper unit of lavas (53.522Bq/cm3) and in the alluvial deposits (48.015Bq/cm3), which structure individual soil extenctions (about 200-400m), at the boundaries of the research field, suggesting a possible expansion beyond these.

On these margins and approximately above the Petra ring road, private and municipal water supply and irrigation wells have been recorded, with high temperatures (25-45°C), at depths of a few tens of meters, which is considered particularly encouraging for further research.

In the field of research, the individual high concentrations of radon, with a growth of more than about 600m, have a NE-SW direction, which is affected by deep long-range faults, which form the important sunkens of the island.

This development of high radon concentrations seems to have been dismembered towards the SW, under the influence of the more frequent and later NW-SE faults. In the fragment descending echelon to SW of the NW-SE faults, the highest radon concentrations in the research field were recorded (45.175 and 55.578 Bq/cm3), with NW direction and a development greater than 400m in the upper unit of lavas.

Further research is also needed in the north-western extension of the search area, in which the high concentrations of thoron appear (maximum value 10.357 Bq/m3), with a NW-SE direction of about 200m on the ground.

References

Hecht, J. (1974): Geological mapping of at a scale of 1:50.000, I.G.M.E.

Koukoulis, A., 1982. The granitoids of the Vrondou massif, Serres, Greece, Magmatic typology and evolution, Mineralogy and geochemistry of uranium and thorium, 3rd cycle thesis (Mineral and Energy Raw Materials), I.N.P.L. (E.N.S.G.), Nancy, France, 179 pp.

Koukoulis, A., Karageorgiou, E.D., Pergamalis, F., (2001). Uranium detection research on the island of Lesvos, IGME Report, Athens p.173.

Koukoulis A., 2016a. Primary radiological investigation (radon-thoron, etc.) of the urban and suburban area of Volos (under geological control), IGME Report, Athens, p. 61.

Koukoulis A., 2016b. Primary radiological investigation (radon-thhoron, etc.) of the urban and suburban area of Igoumenitsa (under geological control), IGME Report, Athens, p. 67.

Koukoulis A, 2024. Primary radiological investigation (radon-thoron, etc.) of the urban and suburban area of Lamia (under geological control), EAGME Report, Athens, p. 57.

Pe-Piper, G. and Piper, D.J.W. (1992): Geochemical variation with time in high-K Cenozoic volcanic rocks of shoshonite petrogenesis. Journal of Volcanology and Geothermal Research, 53 pp. 371-387.

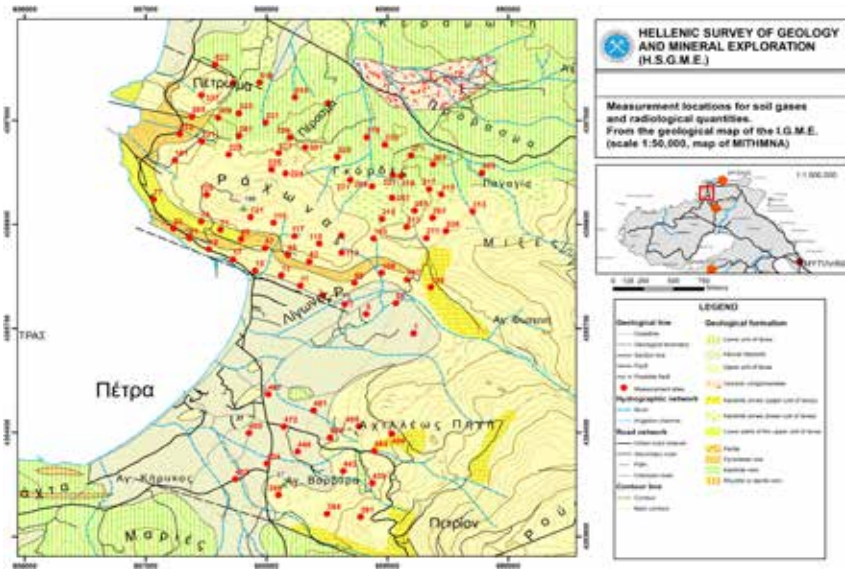

Figure 1: Soil measurement locations in the predefined research area, on a geological map of the I.G.M.E. (excerpt from sheet MITHMNA, scale 1:50,000).

Radon-thoron analyzer RTM-1688-2 (Sarad)

Radiagem 2000 (Camberra)

Alpha beta gamma probe SABG 15

Gamma external 2´X2´ probe SG-2R

Scintillation meter SPP2 (Saphymo–Stel)

Figure 2 : Radio Measuring Instruments

Table 1: Statistical descriptive data of the soil measurements in the area between Stypsi and Petra (Lesvos). In parentheses, corresponding data from the urban and suburban areas of Lamia, Volos and Igoumenitsa (Koukoulis A., 2016 a-b and Koukoulis A.2024).

Measurements	On the ground surface			At a depth of 50cm (approximately)	
Radiation measurement	α-β-γ	γ		γ	
Radiological Size	Total Radiation contamination α-β-γ	Dose rate	Total Radiation γ	Thoron	Radon
Measuring instrument	SABG 15 & RADIAGEM 2000	SG-2R & RADIAGEM 2000	SPP2	RTM 1688-2	
Unit of measurement	Bq/cm2	nSv/h	c/s (SPP2)	Bq/m3	Bq/m3
Number of measurements	87 (258_211_160)	87 (258_215_160)	87 (258_163_160)	87 (258_133_160)	87 (258_214_160)
Minimum measurement value	0,61 (0,05_0,22_0,21)	3170 (248_242_371)	50 (5_5_10)	25 (40_84_47)	290 (46_78_72)
Maximum measurement value	1,99 (0,76_1,51_0,88)	10900 (4080_3000_2960)	180 (75_40_75)	10357 (4206_16324_28223)	57448 (33290_36522_153781)
Average measurements	1,21 (0,45_0,44_0,42)	6258 (1196_1083_1240)	99 (22_21_22)	1297 (707_1144_2069)	16622 (4016_5920_12582)
Standard deviation of measurements (σ)	0,32 (0,12_0,12_0,10)	1972 (514_462_450)	32 (8,49_5,98_7,90)	1698 (771_1559_2959)	13010 (5422_6195_14323)
coefficient of dispersion of measurements (σ/γ)	0,26 (0,28_0,27_0,23)	0,32 (0,43_0,43_0,35)	0,32 (0,39_0,29_0,35)	1,31 (1,09_1,36_1,43)	0,78 (1,35_1,05_1,14)

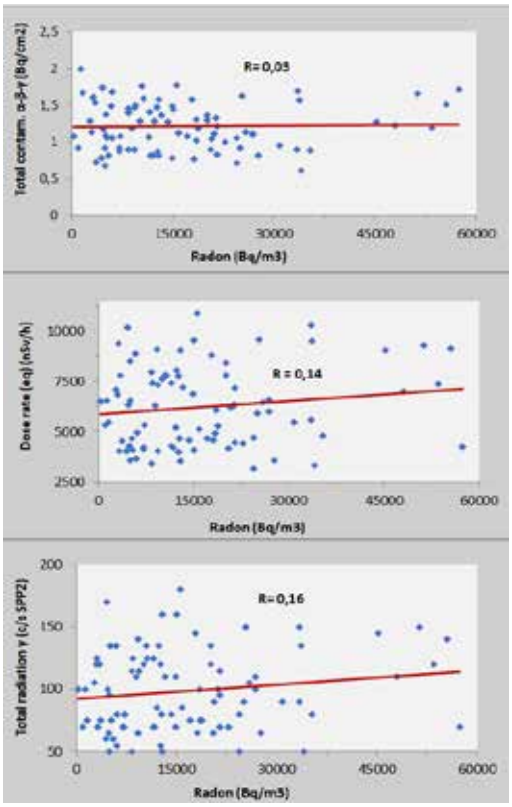

Figure 3: Independent increase in radon from surface soil activity, expressed as:: (i) the total contamination α-β-γ radiations, (ii) the equivalent dose rate, and (iii) the total γ radiation (correlation coefficients almost zero, R=0.03-0.16).

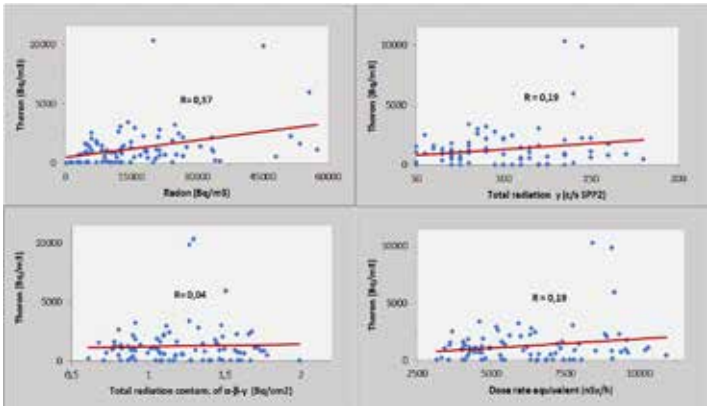

Figure 4 : Relatively independent increase between thoron and radon (r=0.37) and greater independence of thoron from soil activity (r=0.04-0.19) expressed as: i) surfacic contamination of α-β-γ radiation, ii) equivalent dose rate and iii) total γ radiation.

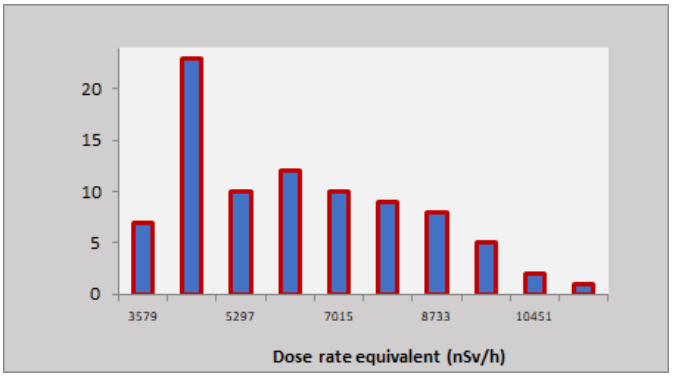

Figure 5 : High values of soil activity in the research area with the equivalent dose rate being above normal levels (1μSv/h) and slightly increased (3.17μSv/h-10.9 μSv/h).

Geological formation		Symbols	0-2,5 KBq/m3	2,5-5 KBq/m3	5-10 KBq/m3	10-15 KBq/m3	15-20 KBq/m3	20-25 KBq/m3	25-30 KBq/m3	30-40 KBq/m3	40-50 KBq/m3	50-60 KBq/m3	Total
Upper unit of lavas		Ng-ul	1	5	4	7	6	4	5	2	0	2	36
	Lower parts	Ng-ul1	1	1	1								3
	Kaolinite zone	kl Ng-ul			1								1
	Limits	Ng-ul/Ng-pc		1		1				1	1	1	5
Pyroclastic row		Ng-pc	1		1								2
Lover unit of lavas		Ng-ll		2	5	2	1	3	1	3			17
	Kaolinite zone	kl Ng-ll	1	1	3	3	0	2				1	11
Alluvial deposits		Q.al			3	4	2	2			1		12
		Total	4	10	18	17	9	11	6	6	2	4	87

Table 2: Relationship of soil radon with geological formations of the field of investigation (number of measurements in some classes from 0-60KBq/m3)

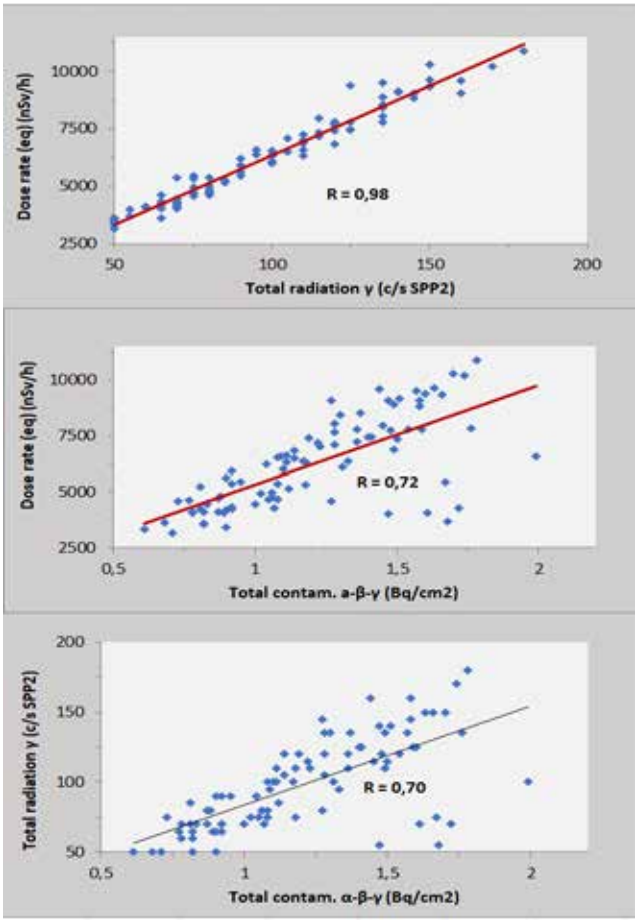

Figure 6 : Strong correlations between radiological values measured at the soil surface, with very strong correlation coefficients (R≥0.70 and up to 0.98).

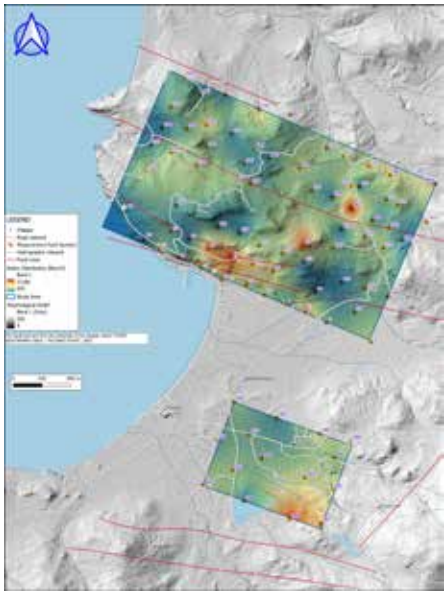

Figure 7: Spatial distribution of radon

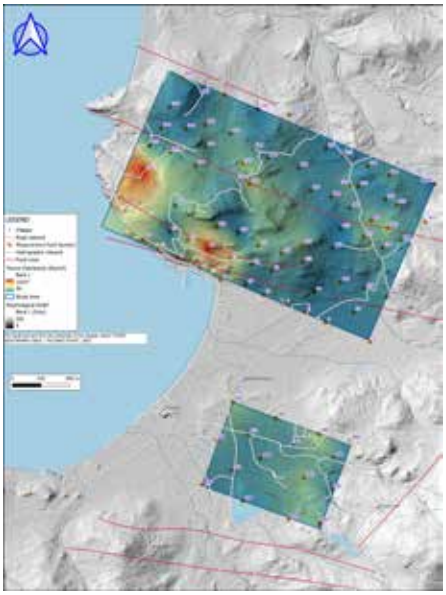

Figure 8 : Spatial distribution of thoron

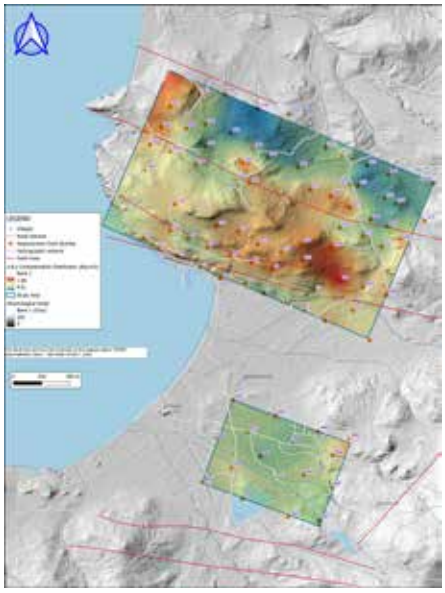

Figure 9 : Spatial distribution of total contamination of radiations α-β-γ

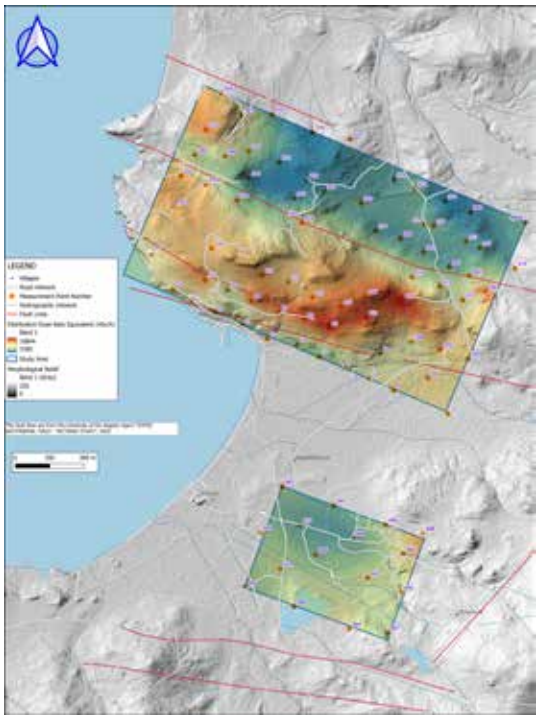

Figure 10 : Spatial distribution of dose rate equivalent

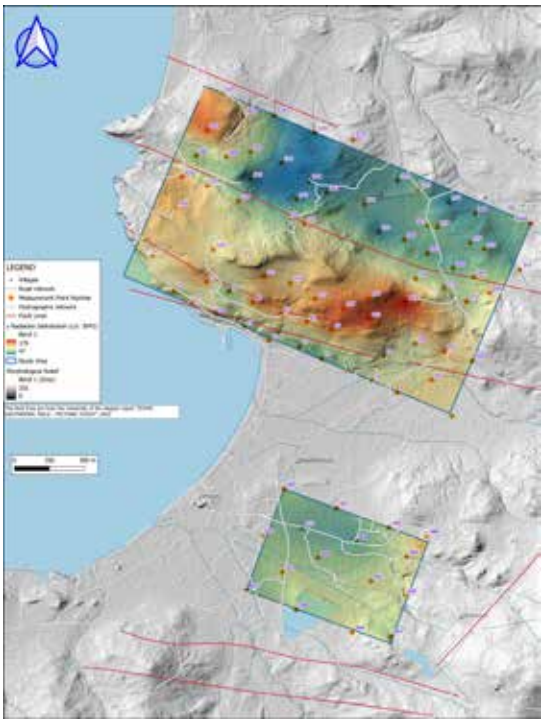

Figure 11 : Spatial distribution of total radiation γ

17th INTERNATIONAL CONGRESS of the Geological Society of Greece

BULLETIN OF THE GEOLOGICAL SOCIETY OF GREECE, SP. PUBL.

EXTENDED ABSTRACT 168

Foraminiferal response to a giant shallow-marine pyroclastic-flow-eruption from ancestral Santorini discovered by IODP Expedition 398 - Objectives, challenges and results of deep drilling into Christiana-Santorini-Kolumbo volcanic field

Koukousioura O.[1,2], Nomikou P.[3], Woodhouse A.[4], Chiyonobu S.[5], Polymenakou P.[6], Druitt T.[7], Kutterolf S.[8], Ronge T.[9], Beethe S.[10], Bernard A.[11], Berthod C.[12], Chen H.[13], Clark A.[14], DeBari S.[15], Della Sala S.[16], Fernandez-Perez T.I.[17], Gertisser R.[18], Hübscher C.[19], Johnston R.M.[20], Jones C.[21], Joshi K.B.[22], Katsigera A.[3], Kilias S.[3], Kletetschka G.[23], Li X.[24], Manga M.[25], McCanta M.[26], McIntosh I.[27], Metcalfe A.[7], Morris A.[28], Pank K.[8], Papadimitriou V.[3,6], Peccia A.[29], Preine J.[19], Tominaga M.[30], Yamamoto Y.[31], Yoshimoto T.[31], Papanikolaou D.[3]

(1) Aristotle University of Thessaloniki, Thessaloniki, Greece, okoukous@geo.auth.gr (2) University of Cologne, Cologne, Germany (3) National and Kapodistrian University of Athens, Athens, Greece (4) Cardiff University, Cardiff, UK (5) Akita University, Akita, Japan (6) Hellenic Centre for Marine Research, Heraklion, Greece (7) University Clermont-Auvergne, CNRS, IRD, OPGC, Clermont-Ferrand, France (8) GEOMAR Helmholtz Centre for Ocean Research Kiel, Kiel, Germany (9) International Ocean Discovery Program, Texas A&M University, Texas, US (10) Oregon State University, Corvallis, US (11) Université de Pau et des Pays de l'Adour, Pau, France (12) Centre National de la Recherche Scientifique (CNRS), Paris, France (13) China University of Geosciences, Beijing, China (14) University of Tasmania, Hobart, Australia (15) Western Washington University, Bellingham, US (16) University of Oxford, Oxford, UK (17) Kent State University, Kent, USA (18) Keele University, Keele, UK (19) University of Hamburg, Hamburg, Germany (20) University of South Florida, Tampa, US (21) University of California, Riverside, US (22) National Centre for Earth Science Studies, Thiruvananthapuram, India (23) University of Alaska Fairbanks, Fairbanks, US (24) Ocean University of China, Qingdao, China (25) University of California, Berkeley, US (26) University of Tennessee, Knoxville, US (27) Japan Agency for Marine-Earth Science and Technology, Yokosuka, Japan (28) Plymouth University, Plymouth, UK (29) Columbia University, New York, US (30) Woods Hole Oceanographic Institution, Woods Hole, US (31) Kobe University, Kobe, Japan

International Ocean Discovery Program Expedition 398 'Hellenic-Arc-Volcanic-Field' took place in the Christiana-Santorini-Kolumbo Volcanic-Field (CSKVF) in the central Hellenic Volcanic Arc. The CSKVF is one of the most hazardous volcano-tectonic regions in the world, as the volcano has produced many and highly explosive eruptions in the past and could be of a threat for at least eastern Mediterranean (Druitt *et al.*, 1999; Nomikou *et al.*, 2013, 2019). This volcanic field produced the notorious Late Bronze age Minoan eruption that is considered to have contributed to the fall of an entire civilization (Bruins et al., 2008). The overall objectives of the expedition were to investigate the links and feedbacks between volcanism/magmatism, crustal tectonics and sea level, to groundtruth the seismic stratigraphy of the Santorini caldera, to reconstruct the subsidence history of the southern Aegean Sea and to search for deep life inside and outside of Santorini caldera (Druitt *et al.*, 2022).

IODP Expedition 398 was conducted with the R/V JOIDES Resolution, from 11 December 2022 to 10 February 2023. During the expedition despite the very challenging drilling conditions, twelve sites were drilled, for a total of 7345 meter in 28 holes, retrieving 780 cores with a total recovery of 3356 meters (Druitt *et al.*, 2024b; Figure 1). Outside of Santorini caldera, drilling penetrated the thick basin fills of the crustal rift system hosting the CSKVF, and identified more than 1000 tephra layers, some known from onland and others formerly unknown. The seismic stratigraphy was groundtruthed (Preine *et al.*, 2024), detailed age-depth constraints were provided mainly by biostratigraphy. Drilling penetrated the Alpine basement and ancient life DNA was recovered, proving that most of the volcano-tectonic history of the CSK field, as the volcano-sedimentary sequences, lies under the sea.

One of the first results, constrained by a multidisciplinary approach and highlighting the hazards of submarine explosive eruptions, includes the discovery of a giant rhyolitic pumice, the Archaeos Tuff, as the result of a shallow marine eruption of ancestral Santorini Volcano (Druitt *et al.*, 2024a). The Archaeos Tuff was emplaced during the Middle Pleistocene at water depths of 200 to 1000 m, as suggested by foraminiferal and calcareous nannoplankton biostratigraphic markers and benthic foraminiferal paleodepth indicators. It formed a 90 km^3 volcaniclastic megaturbidite up to 150m thick in the marine basins (Druitt *et al.*, 2024a), six times bigger than the pyroclastic current deposit from the Minoan eruption (~15 km^3; Karstens *et al.*, 2023).

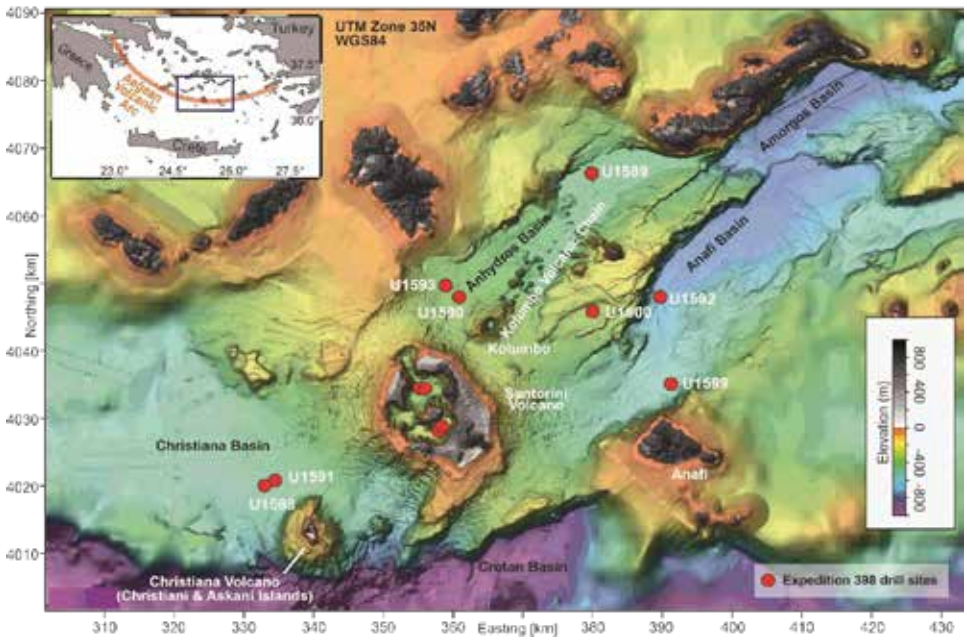

Figure 1. The IODP Expedition 398 drill sites (modified by Druitt *et al.*, 2024a).

These kind of large explosive volcanic eruptions from island arcs pour pyroclastic currents into marine basins, causing high plumes of ash, earthquakes and associated tsunamis and severely affecting coastal communities and infrastructures. Marine ecosystems are particularly vulnerable to eruptions and their consequences (ocean acidification, fertilization, debris flows, increased temperatures, ash falls) leading to diversity changes and even biodiversity loss (e.g., Finger and Lipps, 1981; Hart *et al.*, 2022). The effects in foraminiferal microfauna of such extreme events, as volcanic eruptions, were investigated in the sediments deposited prior and after the emplacement of Archaeos Tuff.

The exact intervals before, during and after this pyroclastic flow (for interval details on the Archaeos Tuff see Druitt *et al.*, 2024a) were studied in six cores along the different basins, and here we present our preliminary results on its impacts on foraminiferal community structure. During deposition of the submarine pumice, benthic foraminifera species were severely affected both in terms of density and diversity, with survivor infaunal species, shelf species and damaged specimens likely representing downslope reworking. Some samples were barren even from accompanying ostracods, molluscs and pteropods, while planktonic foraminifera were also rarely present. Following deposition of the pumice, the foraminiferal repopulation took place, with high numbers and diversity values, suggesting the recovery of the stressed environment and the restoration of the oligotrophic and well-oxygenated conditions.

Our findings highlight the foraminiferal fauna ability to tolerate major catastrophic events in their environment and to recover and recolonize, which is both admirable and extremely useful as a tool to interpret biostratigraphic correlations and paleoenvironmental conditions.

Acknowledgements

We are thankful to the International Ocean Discovery Program (IODP), the technical staff of the JOIDES Resolution, and all of the shipboard personnel for a great expedition. We also thank the member organizations of IODP for financial aid, and the Municipality of Thera for help in preparing for the expedition.

References

Bruins, H.J., MacGillivray, J.A., Synolakis, C.E., Benjamini, C., Keller, J., Kisch, H.J., Klügel, A., van der Plicht, J., 2008. Geoarchaeological tsunami deposits at Palaikastro (Crete) and the late Minoan IA eruption of Santorini. Journal of Archaeological Science 35(1), 191-212.

Druitt, T.H., Edwards, L., Mellors, R.M., Pyle, D.M., Sparks, R.S.J., Lanphere, M., Davies, M., Barreirio, B., 1999. Santorini Volcano. Memoir - Geological Society of London 19, 165pp.

Druitt, T., Kutterolf, S., Höfig, T.W., 2022. Expedition 398 Scientific Prospectus: Hellenic Arc Volcanic Field. International Ocean Discovery Program. https://doi.org/10.14379/iodp.sp.398.2022

Druitt, T., Kutterolf, S., Ronge, T.A., Hübscher, C., Nomikou, P., Preine, J., Gertisser, R., Karstens, J., Keller, J., Koukousioura,

O., Manga, M., Metcalfe, A., McCanta, M., McIntosh, I., Pank, K., Woodhouse, A., Beethe, S., Berthod, C., Chiyonobu, S., Chen, H., Clark, A., DeBari, S., Johnston, R., Peccia, A., Yamamoto, Y., Bernard, A., Fernandez Perez, T., Jones, C., Joshi, K.B., Kletetschka, G., Li, X., Morris, A., Polymenakou, P., Tominaga, M., Papanikolaou, D., Wang, K.-L., Lee, H.-Y., 2024a. Giant offshore pumice deposit records a shallow submarine explosive eruption of ancestral Santorini. Communications Earth and Environment 5, 24.

Druitt, T.H., Kutterolf, S., Ronge, T.A., Beethe, S., Bernard, A., Berthod, C., Chen, H., Chiyonobu, S., Clark, A., DeBari, S., Fernandez Perez, T.I., Gertisser, R., Hübscher, C., Johnston, R.M., Jones, C., Joshi, K.B., Kletetschka, G., Koukousioura, O., Li, X., Manga, M., McCanta, M., McIntosh, I., Morris, A., Nomikou, P., Pank, K., Peccia, A., Polymenakou, P.N., Preine, J., Tominaga, M., Woodhouse, A., and Yamamoto, Y., 2024b. Expedition 398 summary, in: Druitt, T.H., Kutterolf, S., Ronge, T.A., and the Expedition 398 Scientists, Hellenic Arc Volcanic Field. Proceedings of the International Ocean Discovery Program, 398: College Station, TX (International Ocean Discovery Program). https://doi.org/10.14379/iodp.proc.398.101.2024

Finger, K.L., Lipps, J.H., 1981. Foraminiferal decimation and repopulation in an active volcanic caldera, Deception Island, Antarctica. Micropaleontology 27, 111-139.

Hart, M.B., Fisher, J.K., Smart, C.W., Speers, R., Wall-Palmer, D., 2022. Re-colonization of hostile environments by benthic foraminifera: an example from Montserrat, Lesser Antilles Volcanic Arc. Micropaleontology 68(1), 1-27.

Karstens, J., Preine, J., Crutchley, G.J., Kutterolf, S., van der Bilt, W.G.M., Hooft, E.E.E., Druitt, T.H., Schmid, F., Cederstrøm, J.M., Hübscher, C., Nomikou, P., Carey, S., Kühn, M., Elger, J., Berndt, C., 2023. Revised Minoan eruption volume as benchmark for large volcanic eruptions. Nature Communications 14, 2497.

Nomikou, P., Papanikolaou, D., Alexandri, M., Sakellariou, D., Rousakis, G., 2013. Submarine volcanoes along the Aegean volcanic arc. Tectonophysics 597-598, 123-146.

Nomikou, P., Hübscher, C., Carey, S., 2019. The Christiana-Santorini-Kolumbo Volcanic Field. Elements 15(3), 171-176.

Preine, J., Karstens, J., Hübscher, C., Druitt, T., Kutterolf, S., Nomikou, P., Manga, M., Gertisser, R., Pank, K., Beethe, S., Berthod, C., Crutchley, G., McIntosh, I., Ronge, T., Tominaga, M., Clark, A., DeBari, S., Johnston, R., Mateo, Z., Peccia, A., Jones, C., Kletetschka, G., Metcalfe, A., Bernard, A., Chen, H., Chiyonobu, S., Fernandez-Perez, T., Joshi, K.B., Koukousioura, O., McCanta, M., Morris, A., Polymenakou, P., Woodhouse, A., Yamamoto, Y., Wang, K.-L., Lee, H.-Y., Li, X., Papanikolaou, D., 2024. Hazardous explosive eruptions of a recharging multi-cyclic island arc caldera. Nature Geoscience 17, 323-331.

17th INTERNATIONAL CONGRESS of the Geological Society of Greece

BULLETIN OF THE GEOLOGICAL SOCIETY OF GREECE, SP. PUBL.

EXTENDED ABSTRACT 169

Late Quaternary dynamics of paleoenvironments and ecosystems in the Gulf of Corinth (eastern Mediterranean): IODP Expedition 381

Koukousioura O.[1,2], Panagiotopoulos K.,[1,3], Fatourou E.[4], Kafetzidou A.[4], Diz P.[5], Kouli K.[4], Grunert P.[1]

(1) University of Cologne, Cologne, Germany (2) Aristotle University of Thessaloniki, Thessaloniki, Greece, okoukous@geo.auth.gr (3) Forschungszentrum Jülich, Jülich, Germany (4) National and Kapodistrian University of Athens, Athens, Greece (5) Universidade de Vigo, Vigo, Spain

Abundance and assemblage composition of benthic foraminifera, dinoflagellate cysts and pollen grains were analysed together with sedimentological (grain size) and geochemical (organic and inorganic carbon content, XRF, benthic foraminifera oxygen and carbon isotopes) proxies to investigate paleoenvironmental changes recorded in the Gulf of Corinth during MIS 1-5, from IODP Expedition 381 core M0080. The Gulf of Corinth is a relatively young (<5 Ma) and active continental rift zone in the eastern Mediterranean Sea, with a length of about 120 km (McNeil *et al.*, 2019a and references therein; Gawthrope et al., 2022). The Gulf is currently connected to the Ionian Sea through a shallow sill (Rion sill; 60 m-deep) and to the Aegean Sea via the Corinth Canal (Isthmus; 6 km-wide). The eastern part is divided by the Perachora Peninsula into the Lecheon Gulf in the south, and the Alkyonides Gulf in the north, a shallow semi-enclosed sub-basin within the northeastern part of the Gulf of Corinth, where core M0080 is located (Fig. 1; McNeil et al., 2019b). The closed drainage system and the high sedimentation rates (approx. 0.5-3 mm/yr; McNeil et al., 2019a) make the study area a natural laboratory for the investigation of the complex interaction between sedimentary input, tectonics and climate through the basin's evolution.

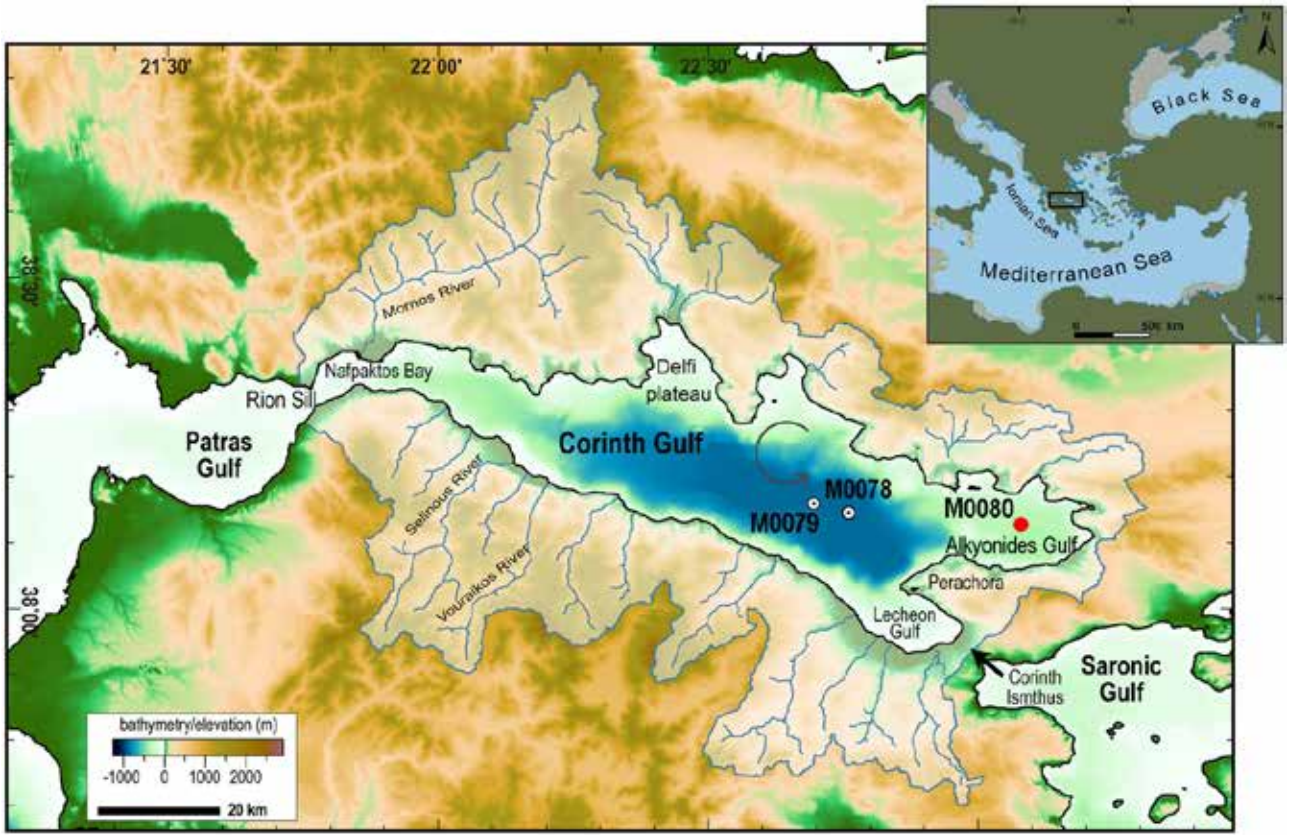

Figure 1. The IODP Expedition 381 drill sites with the location of M0080 indicated by the red dot (modified from Fatourou *et al.*, 2023 and Kafetzidou *et al.*, 2023).

The benthic foraminiferal, dinocyst and pollen records are highly variable during both the Last Interglacial complex and the Holocene. Infaunal foraminiferal species characterize these assemblages with high abundances of *Bolivina* spp.,

Melonis affinis, *Bulimina* spp. and *Cassidulina carinata*, indicating mesotrophic to eutrophic marine conditions, with marine dinocysts (*Nemaosphaeropsis labyrinthus*, *Spinifireties ramosus*) and montane trees likely to have occurred during high sea-levels. During glacial and interstadial intervals, benthic foraminifers are very low in numbers or even absent, whereas abundant brackish dinocysts (*Pyxidinopsis psilata*) suggest a sea-level drop below sill level and the subsequent (semi-)isolation of the basin. Inorganic carbon content and elemental counts varied following the inferred sea-level fluctuations, while the benthic foraminifera oxygen isotope record is discontinuous and conditioned to the presence of well-preserved benthic foraminifera. The beginning of the Holocene is marked by the re-establishment of marine conditions as the sea-level rose above the sill and the basin re-connected to the Mediterranean Sea.
Ongoing high-resolution studies and a refinement of the age model will improve our understanding of paleoenvironmental changes in the Gulf of Corinth during glacial and interglacial stages and allow us to define the factors driving changes in this unique active rift of the eastern Mediterranean.

Acknowledgements
This study is funded through projects GR 5285/3-1 "*Late Quaternary dynamics of marine paleoenvironments and ecosystems in the Gulf of Corinth (eastern Mediterranean)*" and PA 2664/8-1 "*Linking marine and terrestrial ecosystem responses to climate variability since the Last interglacial in the Eastern Mediterranean*" of the Deutsche Forschungsgemeinschaft (DFG).

References

Fatourou, E., Kafetzidou, A., Marret, F., Panagiotopoulos, K., Kouli, K., 2023. Late Quaternary Ponto-Caspian dinoflagellate cyst assemblages from the Gulf of Corinth, Central Greece (eastern Mediterranean Sea). Marine Micropaleontology 179, 102211.

Gawthrope, R.L., Fabregas, N., Pechlivanidou, S., Ford, M., Collier, R.E.L., Carter, G.D.O., McNeil, L.C., Shillington, D.J., 2022. Late Quaternary mud-dominated, basin-floor sedimentation of the Gulf of Corinth, Greece: Implications for deep-water depositional processes and controls on syn-rift sedimentation. Basin Research 34, 1567-1600.

Kafetzidou, A., Fatourou, E., Panagiotopoulos, K., Marret, F., Kouli, K., 2023. Vegetation Composition in a Typical Mediterranean Setting (Gulf of Corinth, Greece) during Successive Quaternary Climatic Cycles. Quaternary 6(2), 30.

McNeil, L.C., Shillington, D.J., Carter, G.D.O., Everest, J.D., Gawthorpe, R.L., Miller, C., Phillips, M.P., Collier, R.E.Ll., Cvetkoska, A., De Gelder, G., Diz, P., Doan, M.-L., Ford, M., Geraga, M., Gillespie, J., Hemelsdaël, R., Herrero-Bervera, E., Ismaiel, M., Janikian, L., Kouli, K., Le Ber, E., Li, S., Maffione, M., Mahoney, C., Machlus, M.L., Michas, G., Nixon, C.W., Oflaz, S.A., Omale, A.P., Panagiotopoulos, K., Pechlivanidou, S., Sauer, S., Seguin, J., Sergiou, S., Zakharova, N.V., Green, S., 2019a. High-resolution record reveals climate-driven environmental and sedimentary changes in an active rift. Scientific Reports 9, 3116.

McNeill, L.C., Shillington, D.J., Carter, G.D.O., Everest J.D., Le Ber E., Collier R.E., Cvetkoska A., De Gelder G., Diz P., Doan M.L., Ford M., Gawthorpe R.L., Geraga M., Gillespie J., Hemelsdaël R., Herrero-Bervera E., Ismaiel M., Janikian L., Kouli K., Li S., Machlus M.L., Maffione M., Mahoney C., Michas G., Miller C., Nixon C.W., Oflaz S.A., Omale A.P., Panagiotopoulos K., Pechlivanidou S., Phillips M.P., Sauer S., Seguin J., Sergiou S., Zakharova N.V., 2019b. Site M0078, in Program, I.O.D.P. (Ed.), McNeill, L.C., Shillington, D.J., Carter, G.D.O., and the Expedition 381 Participants, Corinth Active Rift Development. Proceedings of the International Ocean Discovery Program. International Ocean Discovery Program, College Station, Texas.

17th INTERNATIONAL CONGRESS of the Geological Society of Greece

BULLETIN OF THE GEOLOGICAL SOCIETY OF GREECE, SP. PUBL.

EXTENDED ABSTRACT 170

Characterization of Sandstone Formations in the Mesohellenic Trough for CO_2 Storage: Insights from the Integration of Optical Mineralogy, Geochemistry, and Automated Imaging Techniques

Koukouzas N.[1], Tyrologou P.[1], Stergiou C.L.[2,3], Carneiro J.[4], Fernández-Canteli P.[5], Karatrantou C.[1], Asimakopoulou S.[1],

(1) Chemical Process & Energy Resources Institute (CPERI), Centre for Research and Technology Hellas (CERTH), 15125 Athens, Greece, koukouzas@certh.gr (2) Chemical Process & Energy Resources Institute (CPERI), Centre for Research and Technology Hellas (CERTH), 50200 Ptolemaida, Greece (3) School of Geology, Aristotle University of Thessaloniki (AUTH), 54124 Thessaloniki, Greece (4) ICT/IIFA, Geosciences Department, Universidade de Évora, 7000-671 Évora, Portugal (5) Instituto Geológico y Minero de España (IGME-CSIC), 28003 Madrid, Spain

Introduction

Carbon Capture, Utilization, and Storage (CCUS) is critical for reducing CO_2 emissions from industry and energy generation, aligning with net-zero goals under the Paris Agreement (Koukouzas *et al.,* 2021). CCUS captures CO_2 for reuse or secure storage in geological formations, including saline aquifers and depleted fields, offering flexibility through enhanced recovery and mineralization (Koukouzas *et al.,* 2018, 2021, Tyrologou *et al.,* 2023). While cost remains a challenge, technological advancements and successful projects (e.g. Sleipner, Norway) highlight its potential for supporting the low-carbon transition (Tyrologou *et al.,* 2023).

The Horizon 2020-funded PilotSTRATEGY project advances CO_2 storage research in Southern and Eastern Europe, focusing on deep saline aquifers in five basins, including the Mesohellenic Trough (M.T.) in northern Greece (e.g. Ayala *et al.,* 2023, Berrezueta *et al.,* 2023, Tyrologou *et al.,* 2023, Ordóñez *et al.,* 2024). Geological modeling in the M.T. identified the Pentalofos and Eptachori Formations (Fms) as prime storage sites, with capacities of 1 Gt and 0.85 Gt, respectively (Koukouzas *et al.,* 2021). Petrophysical studies confirm low porosity and water permeability in specific sedimentary strata, designating sedimentary layers in the Eptachori, Pentalofos, and Tsotyli Fms as effective cap rocks for secure CO_2 storage (Tyrologou *et al.,* 2023). This publication presents preliminary findings on the geological characterization of sandstone formations in the M.T. using a multidisciplinary approach. Methods include thin section analysis under optical and SEM microscopy for grain and texture evaluation, XRD and XRF for mineralogical and chemical characterization, and automated image analysis for macro-porosity assessment.

Geological Setting

The Mesohellenic Trough (M.T.) is a Tertiary sedimentary basin along the suture zone between the Apulian platform and the Pelagonian nappe, marking the Hellenide orogenic belt boundary (Vamvaka *et al.,* 2006, Fig. 1a). Extending over 200 km in length and 40 km in width, it features five siliciclastic formations – Krania, Eptachori, Pentalofos, Tsotyli, and Ondria – deposited from the Late Eocene to the Middle Miocene in environments varying from fan-deltas to turbiditic sandstones, and deltaic sediments, reflecting a transition from marine to terrestrial settings (Vamvaka *et al.,* 2006). The asymmetrical syncline, with up to 4.5 km thick sediments near Grevena, reflects orogenic and extensional tectonics. Its evolution involves Eocene-Oligocene and Miocene faults and N-S extension linked to recent seismicity, shaping fault zones and river alignments (Tyrologou *et al.,* 2023).

Methods

Three sedimentary rock samples were selected for study, originating from the Tsotyli (sample Tsot-1; marly sandstone; Burdigalian; Lower Miocene), Eptachori (sample Ept-2; fine sandstone; Rupelian; Upper Oligocene), and Pentalofos (sample Pent-3; sandstone; Chattian-Aquitanian; Upper Oligocene-Lower Miocene) Fms of the M.T. (Figs 1b-g). Three thin-polished sections were prepared at the School of Geology, AUTH, and analyzed using a ZEISS Axioskop 40 polarizing microscope to examine mineral composition. SEM-EDS analysis was conducted with a JEOL JSM-IT500 equipped with an OXFORD INCA X-ACT system at Analytical Services Unit, CPERI, CERTH, under 20 kV accelerating voltage, 0.4 mA probe current, 20 s analysis time, and ~1 μm beam diameter in BSE mode. Elemental mapping revealed mineralogical variations, and pore characteristics were evaluated with representative photomicrographs. Automated image analysis (×200 magnification, BSE mode) was performed using ImageJ software (Schneider *et al.*, 2012).

X-ray diffractometry (XRD) was performed using a Bruker D8 Advance diffractometer with a CuKα anode (λ = 0.1542 nm) operating at 40 kV and 30 mA at the School of Geology, AUTH. The counting statistics of the XRD study were, step size: 0.019° 2θ, start angle: 3.000°, end angle: 93.009° and scan speed: 0.19° 2θ/s. Rietveld refinement

were implemented by using the Profex5 (v.5.2.7, Doebelin and Kleeberg, 2015) software acquiring semi-quantitative estimates on the abundance of the mineral phases and on the chemical composition of the analyzed samples.
X-ray fluorescence (XRF) analysis was conducted using a Bruker S4-PIONEER WDXRF system at the School of Geology, AUTH, to determine the geochemical composition of the samples. Equipped with a Rh lamp, five crystals, and dual detectors, the system operated at 50–60 kV, analyzing Ka and La lines for elements. Corrections for spectral overlaps and matrix effects ensured accuracy.

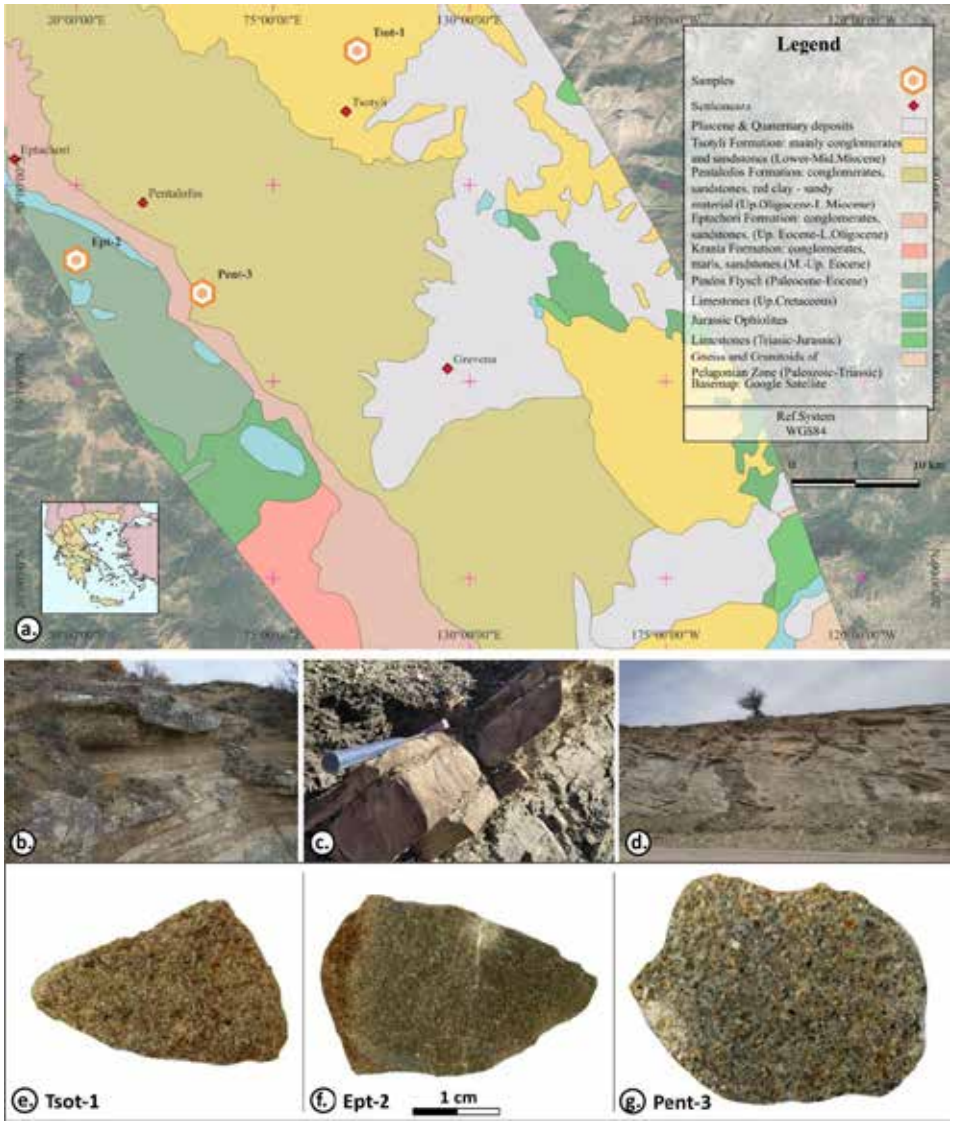

Figure 1. a. Geological map of the Mesohellenic Trough at Grevena region, showing the sampling locations of Tsot-1, Ept-2 and Pent-3 samples (modified after Savoyat & Monopolis, 1972, Bornovas & Rondogianni-Tsiambaou, 1983). b-d. Field photographs of the sampled outcrops (b: Tsot-1, c: Ept-2, Pent-3: d). d-f. Macro-photographs of the analyzed samples.

Results & Discussion

Field survey and macroscopic observations revealed that Tsot-1, Ept-2, and Pent-3 outcrops share similarities, including their light-colored sandstones, medium bedding (200 to 600 mm in thickness), and slightly weathered (Grade 1) tabular rock masses, and very strong material strength (100-250 MPa, Fig. 1b-d). However, they differ in texture, features, and bedding orientation: Tsot-1 lacks fossils, has a homogeneous marly texture, and bedding striking 322°/12°, Ept-2 exhibits burrows, plant fragments, Liesegang discoloration, and bedding striking 122°/33°, while Pent-3 shows alternating clast-rich and mudstone units with diverse compositions and bedding striking 128°/33°.

Optical microscopy and SEM-EDS analysis and petrographic examination of bulk samples and thin-polished sections from Tsot-1, Ept-2, and Pent-3 highlighted distinct mineralogical and compositional characteristics. In Tsot-1, the identified minerals include calcite (30 wt.%), quartz (29 wt.%), and albite (21 wt.%), minor muscovite, chlorite, dolomite and aragonite, as well as microcline, zircon and jacobsite in traces (Table 1, Figs 2a, 3a). The sample consists of well-cemented grains dominated in average by Si (52 wt.%) and Ca (24 wt.%), with additional Al (11 wt.%), K (11 wt.%), Fe (7.0 wt.%), Mg (4.0 wt.%), and Na (3.0 wt.%, Table 3). Macro-pores are rounded to irregular, averaging 45 μm in width, and the siliceous cement is locally crystalline, containing up to 9.9 wt.% Fe (Tables 2, 3). Sample Ept-2 includes quartz (37 wt.%), calcite (29 wt.%), albite (13 wt.%) and muscovite (13 wt.%), minor dolomite and chamosite, while as traces are found biotite, titanite, pyrite, crichtonite, actinolite and zircon (Table 1, Figs 2b, 3b). It is well-cemented, with a bulk composition dominated by Ca (<53 wt.%) and Si (≤26 wt.%), alongside Mg (<8.8 wt.%), Fe (<8.3 wt.%), and Al (3.7 wt.%, Table 3). The calcareous microcrystalline cement contains up to 41 wt.% Si and 18 wt.% Fe, with macro-pores averaging 66 μm and smaller pores at 11 μm (Tables 2, 3). In Pent-3, calcite (41 wt.%), dolomite (18 wt.%), quartz (15 wt.%), and albite (12 wt.%) are found, while minor minerals include microcline, muscovite and aragonite, with trace amounts of chlorite, titanite, chromite, pyrite, Fe-chromite, actinolite, apatite, andradite and enstatite (Table 1, Figs 2c, 3c). The sample displays the largest grains among the analyzed material, with grains occasionally exceeding 500 μm, with a dominantly calcareous composition (61 wt.%) and cement enriched in Mg and Si (Fig. 3c). Rare elongated macro-pores average 65 μm, while smaller pores within the cement average 6.0 μm.

Table 1. Sample identification numbers, localities (coordinates), main, minor and trace mineralogy. Abundances (%) of the main and minor mineral phases are given after the Rietveld refinement.

Sample	Coordinates WGS84 (Latitude/Longitude)	Main minerals	Minor minerals	Trace mineralogy	Qtz/ Fsp ratio
Tsot-1	N 40.3075°/ E 21.3354°	Cal: 30%, Qz: 29%, Ab: 21%	Ms: 7.2%, Chl: 7.1%, Dol: 4.5%, Arg: 1.4%,	Mc, Zrn, Jcb	1.4
Ept-2	N 40.1535°/ E 21.0824°	Qz: 37%, Cal: 29%, Ab: 13%, Ms: 13%,	Dol: 4.6%, Chm: 3.1%	Bt, Ttn, Py, Cic, Act, Zrn	2.9
Pent-3	N 40.1332°/ E 21.1997°	Cal: 41% , Dol: 18%, Qz: 15%, Ab: 12%	Mc: 8.0%, Ms: 4.3%, Arg: 2.6%	Chl, Ttn, Chr, Py, Fe-Chr, Act, Ap, Adr, En	0.8

Abbreviations: Ab = Albite, Act = actinolite, Adr = andradite, Ap = apatite, Arg = aragonite, Bt = biotite, Cal = calcite, Chl = chlorite, Chm = chamosite, Cic = crichtonite, Chr = chromite, Dol = dolomite, Fe-Chr = Iron-chromite, Fsp = feldspar, Mc = microcline, Ms = muscovite, Py = pyrite, Ttn = titanite, Qz = quartz, Zrn = zircon.

Relative abundances of quartz and feldspars (albite, microcline) were obtained by XRD analysis and plotted in the QFR (Quartz-Feldspar-Rock fragments) triangular classification diagram (McBride, 1963). The analyzed samples fall within the “Feldspathic litharenite” field, with Tsot-1 and Ept-2 clustering closely, while Pent-3 exhibits relative enrichment in lithic fragments (Fig. 2d). In addition, the mineralogical analysis conducted via XRD and Rietveld refinement, revealed that for sample Tsot-1 the quartz/feldspar (albite) ratio is 1.38 (Table 1), while Ca/Si ratio of 0.6 complements SEM-EDS results (Ca/Si = 0.5), indicating a consistent siliceous matrix (Table 3). Sample Ept-2 has a quartz/feldspar (albite) ratio of 2.9 (Table 1). Although SEM-EDS geochemistry highlights a Ca-enriched matrix (Ca ≤53 wt.%), the Rietveld refinement analysis revealed a siliceous chemical composition (25 wt.% Si) with a Ca/Si ratio of 0.5, underscoring the complex interplay between primary mineral inputs and diagenetic processes (Table 3). The quartz/feldspar (albite, microcline) ratio of 0.8 for sample Pent-3, reflects feldspathic contributions, while the Rietveld-derived Ca/Si ratio of 1.5 aligns with SEM-EDS findings (Ca/Si = 1.5), indicating a calcite-dominated cement matrix (Tables 1 & 3).

Bulk geochemical analysis applying XRF spectrometry reveals the compositional variability among samples Tsot-1, Ept-2, and Pent-3, with calcium and silica identified as the most enriched elements (Table 3). Sample Tsot-1 (25 wt.% SiO_2) is slightly siliceous, Ept-2 (36 wt.% SiO_2) is dominantly siliceous, and Pent-3 (42 wt.% CaO) is dominantly calcareous (Table 3). These findings align closely with the semi-quantitative mineralogical data derived from XRD and SEM-EDS analyses. In sample Tsot-1, the XRF results support the mineralogical profile established by XRD, where calcite (30 wt.%) and siliceous components, quartz (29 wt.%) and albite (19 wt.%), collectively constitute 50 wt.%, confirming its slightly siliceous composition. For Ept-2, XRF results indicating a dominantly siliceous composition (36 wt.% SiO_2) are consistent with the XRD data, which identified quartz (37 wt.%) as the primary phase, followed by calcite (29 wt.%). Similarly, the calcareous dominance of Pent-3 (42 wt.% CaO by XRF) corroborates XRD findings, which showed calcite as the most abundant phase (41 wt.%). The XRF data also reveal insights into trace element distributions, particularly for Ept-2, which

exhibits the highest enrichment in minor elements, including Cr (1680 ppm) and V (990 ppm), alongside Co, Cu, Ni, and Zn (Table 3). These variations in trace element content are associated to minor mineral phases, such as chromite and pyrite, which were detected through the SEM-EDS analysis of the thin-polished sections (Table 1, Fig. 3c), and suggest a significant contribution of detrital material, likely derived from the erosion of ophiolitic basement rocks surrounding the Mesohellenic Trough.

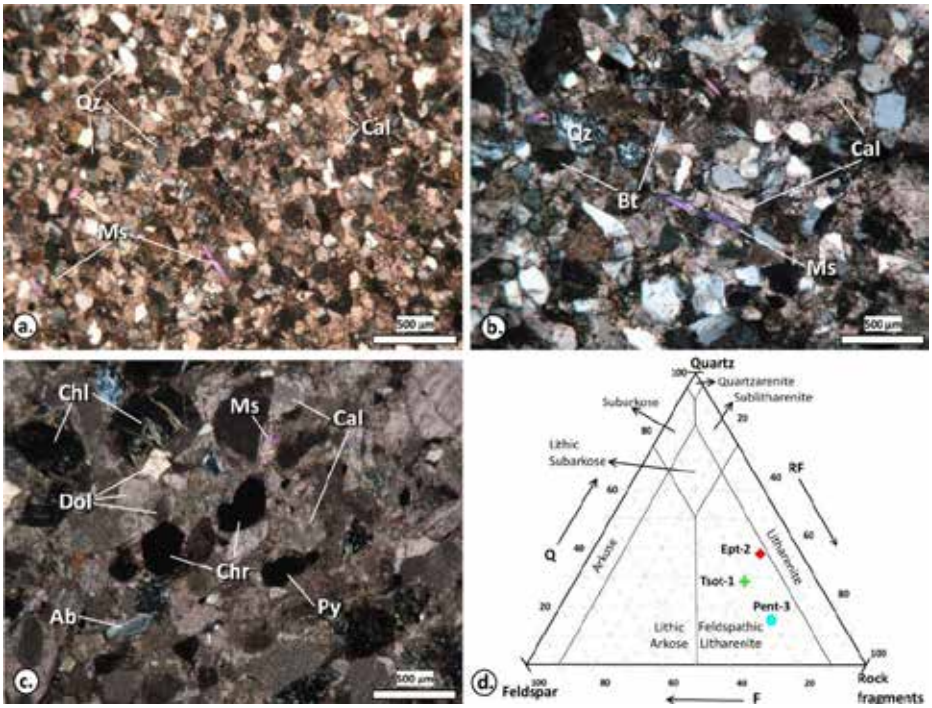

Figure 2. Photomicrographs of the studied samples: a. Well-cemented quartz (Qz), calcite (Cal) and muscovite (Ms) in sample Tsot-1. b Quartz (Qz), biotite (Bt), calcite (Cal) and muscovite (Ms) in sample Ept-2. c. Calcite (Cal) and dolomite (Dol) with chlorite (Chl) and minor albite (Ab), chromite (Chr) and pyrite (Py) in sample Pent-3. Dolomite was identified by SEM-EDS analysis. d. QFR (Quartz-Feldspar-Rock fragments) triangular plot diagram for classification of the studied samples after McBride (1963).

Table 2. Average morphometric characteristics by SEM-EDS analysis of the pores width between grains and in cement for samples Tsot-1, Ept-2, and Pent-3, along with macro-porosity data obtained through automated image analysis.

	Average morphometric characteristics				**Macro-porosity data**				
Sample	**Pores between grains**	**Pore shape**	**Pores in cement**	**Pore shape**	**Sample**	**MIN**	**MAX**	**STDEV**	**AVG**
Tsot-1	45 µm (n = 12)	Irregular, rounded, elongated	-	-	**Tsot-1** (n = 5)	1.4	1.9	0.2	1.7
Ept-2	66 µm (n = 8)		11 µm (n = 5)	Rounded	**Ept-2** (n = 9)	1.7	1.9	0.1	1.8
Pent-3	65 µm (n = 4)	Irregular, elongated	6.0 µm (n = 3)	Rounded	**Pent-3** (n = 12)	1.0	4.0	1.4	2.0

Abbreviation: average = AVG, maximum = MAX, minimum = MIN, standard deviation = STDEV.

The maximum porosity (4%) measured after automated image analysis is related to sample Pent-3 (Table 2). The results are in accordance with these previously published where porosity was measured at 6.0%, 7.4% and, 4.9 to 10.8% for the samples Tsot-1, Ept-2 and Pent-3, respectively (Tyrologou *et al.,* 2023). The lower porosity values from ImageJ analysis compared to petrophysical testing reflect differences in methodology, as ImageJ focuses on 2D observable pores, potentially overlooking micro-porosity (Figs 3d-f). Petrophysical testing, measuring bulk porosity provides a more comprehensive view of the porosity of the samples. Despite this, ImageJ remains a valuable and cost-effective tool for identifying porosity trends and comparing samples, particularly for macro- and meso-pores.

Table 3. Bulk geochemical composition, determined through elemental mapping via SEM-EDS, XRD and Rietveld refinement, and XRF analysis of major elements in samples Tsot-1, Ept-2, and Pent-3. Values are in weight percent (wt.%), except for the trace elements where they are reported in parts per million (ppm).

Element by SEM-EDS	**Si**	**Al**	**Fe**	**Ca**	**Mg**	**Na**	**K**	**Mn**	**Ti**	**P**	**Ca/Si**	
Tsot-1 in average (n = 6)	52	11	7.0	24	4.0	3.0	11	n.a.	n.a.	n.a.	0.5	
Ept-2 in average (n = 6)	26	3.7	8.3	53	8.8	n.a.	n.a.	n.a.	n.a.	n.a.	2.0	
Pent-3 in average (n = 6)	21	3.3	3.6	48	7.9	1.8	1.4	n.a.	n.a.	n.a.	2.3	
Element by XRD	**Si**	**Al**	**Fe**	**Ca**	**Mg**	**Na**	**K**	**Mn**	**Ti**	**P**	**Ca:Si**	
Tsot-1	23	4.3	0.8	14	1.8	1.8	0.7	n.a.	n.a.	n.a.	0.6	
Ept-2	25	4.0	1.1	13	0.8	1.1	0.8	n.a.	n.a.	n.a.	0.5	
Pent-3	14	2.8	0.1	21	2.3	1.0	1.4	n.a.	n.a.	n.a.	1.5	
Element by XRF	**SiO_2**	**Al_2O_3**	**Fe_2O_3**	**CaO**	**MgO**	**Na_2O**	**K_2O**	**MnO**	**TiO_2**	**P_2O_5**	**LOI**	**Total**
Tsot-1	35	7.0	2.7	31	4.2	1.0	2.2	0.1	0.3	0.08	17	100
Ept-2	36	6.6	3.3	26	7.2	0.7	1.4	0.1	0.4	0.1	18	100
Pent-3	16	2.9	1.2	42	6.0	0.4	0.9	0.03	0.1	0.06	30	100
Trace element by XRF	**Ba**	**Co**	**Cr**	**Cu**	**Ni**	**Rb**	**Sc**	**Sr**	**V**	**Zn**	**Zr**	**Total**
Tsot-1	189	7.0	749	14	112	192	bdl	298	650	31	100	
Ept-2	149	13	1680	23	221	95	bdl	342	990	38	113	
Pent-3	66	4.0	512	7.0	78	82	bdl	242	306	15	54	

Abbreviations: LOI = Loss of ignition, n.a. = not available.

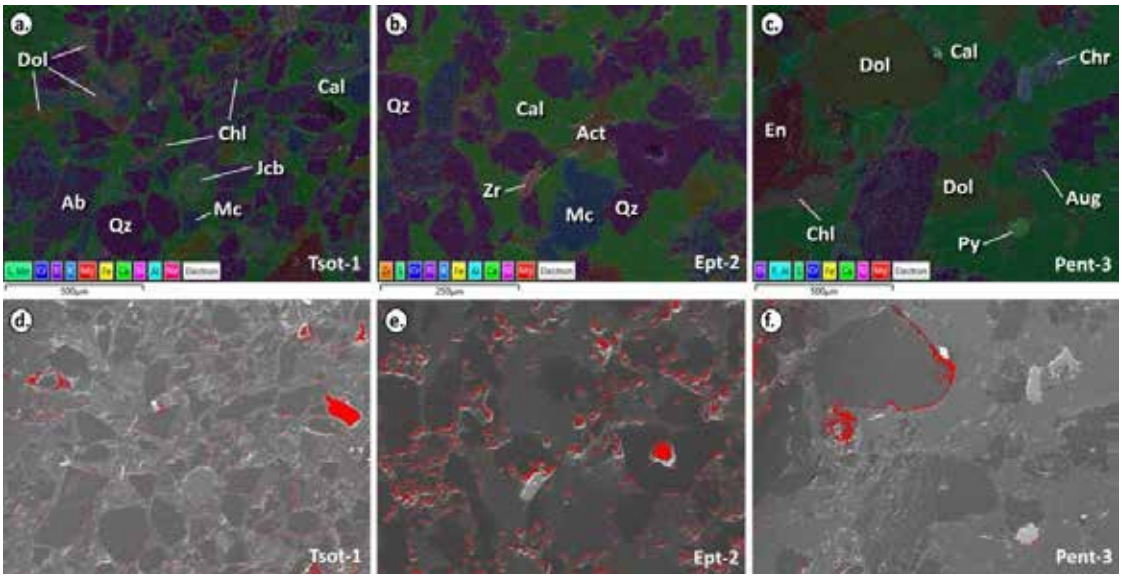

Figure 3. Representative photomicrographs illustrate elemental mapping (a–b) and porosity assessment (d–f) via automated image analysis for samples Tsot-1, Ept-2, and Pent-3. The calculated porosity values are 1.8% for Tsot-1 (d), 1.9% for Ept-2 (e), and 1.1% for Pent-3 (f).

Conclusions and Ongoing Research

The combined mineralogical, geochemical, and textural analysis of samples Tsot-1, Ept-2, and Pent-3 reveals significant variability in depositional environments and diagenetic processes. In addition, SEM-EDS analysis and automated image analysis enables fast, cost-effective macro-porosity characterization. Sample Tsot-1, with its siliceous dominance, moderate macro-porosity, and traces of microcline and zircon, suggests deposition in a high-energy environment with significant siliciclastic input, consistent with its well-bedded sandstone structure. Sample Ept-2, characterized by its carbonate-rich composition and microcrystalline cement, indicates deposition in a marine-influenced or lacustrine setting, supported by bedding features and burrow evidence. In contrast, the complex mineralogy of sample Pent-3, including high calcite content and inclusions like titanite and chromite, reflects a mixed depositional environment influenced by the erosion of the ophiolitic rocks surrounding the Mesohellenic Trough.

These findings highlight the interplay between provenance, depositional energy, and diagenetic processes in shaping the regional sedimentary formations, offering insights into the tectonic and sedimentological evolution of the basin.

Acknowledgements
This research was funded by the EU Horizon 2020 program under grant No. 101022664 (PilotSTRATEGY). The funders had no role in study design, data collection, analysis, publication decisions, or manuscript preparation. Special thanks to Agnes Vamvaka, Dina Ghikas, and Anna Mpatsi for their assistance in field sample collection. XRF analyses were conducted under a service agreement between CERTH and the Laboratory of Mineralogy and Petrology, Faculty of Geology, AUTH.

References

Ayala, C., Benjumea, B., Mediato, J.F., García-Crespo, J., Clariana, P., Soto, R., Rubio, F., Rey-Moral, C., Pueyo, E.L., Martín-León, J., García, A.G., Fernández-Canteli, P. Martinez Orio, R., 2023. Developing a new innovative methodology to integrate geophysical techniques into characterization of potential CO_2 storage sites: Lopín structure (Southern Ebro basin, Spain), in: Miocic, J.M., Heinemann, N., Edlmann, K., Alcalde, J., Schultz, R.A. (Eds.), Enabling Secure Subsurface Storage in Future Energy Systems, The Geological Society of London, Lyell Collections, 528, 227–243.

Berrezueta, E., Kovacs, T., Herrera-Franco, G., Mora-Frank, C., Caicedo-Potosí, J., Carrion-Mero, P., Carneiro, J., 2023. Laboratory studies on CO_2-brine-rock interaction: an analysis of research trends and current knowledge. International Journal of Greenhouse Gas Control 123, 103842.

Bornovas, J., Rondogianni-Tsiambaou, Th., 1983. Geological Map of Greece, 1:500.000. 2nd edition, Institute of Geology and Mineral Exlporation, Athens.

Doebelin, N., Kleeberg, R., 2015. Profex: a graphical user interface for the Rietveld refinement program BGMN. Journal of Applied Crystallography 48(5), 1573-1580.

Koukouzas N., Kypritidou Z., Purser G., Rochelle, C.A., Vasilatos, Ch., Tsoukalas, N., 2018. Assessment of the impact of CO_2 storage in sandstone formations by experimental studies and geochemical modeling: The case of the Mesohellenic Trough, NW Greece. International Journal of Greenhouse Gas Control 71, 116–132.

Koukouzas, N., Tyrologou, P., Karapanos, D., Carneiro, J., Pereira, P., de Mesquita Lobo Veloso, F., Koutsovitis, P., Karkalis, C., Manoukian, E., Karametou, R., 2021. Carbon Capture, Utilisation and Storage as a Defense Tool against Climate Change: Current Developments in West Macedonia (Greece). Energies 14, 3321.

McBride, E.F., 1963. A classification of common sandstones. Journal of Sedimentary Petrology 33, 664–669.

Ordóñez, B., Mediato, J., Kovacs, T., Martínez-Martínez, J., Fernández-Canteli, P., González-Menéndez, L., del Moral, B., Berrezueta, E., 2024. Experimental geochemical assessment of a seal-reservoir system exposed to supercritical CO_2: A case study from the Ebro Basin, Spain. International Journal of Greenhouse Gas Control 137, 104233.

Savoyat, E., Monopolis, D., 1972. Geological map sheet Grevena, 1:50.000. Institute of Geology and Mineral Exlporation, Athens.

Schneider, C.A., Rasband, W.S., Eliceiri, K.W., 2012. NIH Image to ImageJ: 25 years of image analysis. Nature Methods 9(7), 671–675.

Tyrologou, P., Vamvaka, A., Koukouzas, N., Pedro, J., Fleury, M., Carneiro, J., Ribeiro, C., Ghikas, D., Mpatsi, A., Barradas, J.P., Faria, P., de Mesquita Lobo Veloso, F., 2023. Progress for carbon dioxide geological storage in West Macedonia: A field and laboratory-based survey. Open Research Europe 3, 85.

Vamvaka, A., Kilias, A., Mountrakis, D., Papaoikonomou, J., 2006. Geometry and structural evolution of the Mesohellenic Trough (Greece): a new approach, in: Robertson, A.H.F., Mountrakis, D. (Eds.), Tectonic Development of the Eastern Mediterranean Region, Geological Society, London, Special Publications 260(1), 521-538.

17th INTERNATIONAL CONGRESS of the Geological Society of Greece

BULLETIN OF THE GEOLOGICAL SOCIETY OF GREECE, SP. PUBL.

EXTENDED ABSTRACT 171

Unveiling the Potential of AI in Geoscience Education: A Student-Centered Perspective

Koumoutsakou O.[1], Antonarakou A.[1]
(1) Department of Geology and Geoenvironment, University of Athens, Ilisia, Greece, okoumout@geol.uoa.gr

Introduction / Background

According to a recent survey by the Digital Education Council, 86% of students globally incorporate artificial intelligence into their studies, with 24% using it every day and 54% using it at least once a week (Digital Education Council, 2024). This highlights the growing integration of AI into students' academic routines. Integrating Artificial Intelligence (AI) into geoscience education is rapidly transforming the learning landscape, presenting unprecedented opportunities and significant ethical challenges (Patra et al., 2024). This research explores the multifaceted impact of AI on geoscience students, focusing on their perspectives regarding the future of their field in this era of technological advancement. It draws upon a range of studies that examine the practical applications, ethical dilemmas, and prospects of AI in Earth sciences.

AI's Role in Geoscience Education

AI is becoming increasingly prevalent in geoscience, from data collection and processing to complex modeling and interpretation (Sun et al., 2024; Zhao et al., 2024). Artificial intelligence techniques, such as machine learning (ML) and deep learning (DL), allow for the analysis of large datasets, improving our insights into Earth's systems (Sun et al., 2024). "AI can help students analyze satellite imagery to detect land-use changes, monitor environmental degradation, and study natural disasters. In mineral exploration, AI algorithms can identify mineral deposits based on geophysical data patterns" (Sun et al., 2024). AI can also improve the analysis of seismic data, enhance our understanding of the Earth's interior, and aid in the prediction of earthquakes. Furthermore, AI techniques can optimize climate modeling, making the process more accurate and efficient despite its complexity and time demands (Sun et al., 2024).

Furthermore, AI tools such as ChatGPT, Gemini, etc., can help with tasks such as scientific writing, data interpretation, and hypothesis generation (Baucon et al., 2024). GeologyOracle, a specialized artificial intelligence system created by Baucon and his colleagues, can handle complex geoscientific tasks, interpret geological sites, and provide support in educational environments (Baucon et al., 2024). Such tools can accelerate scientific discovery, automate research tasks, and support educators, students, and geotourists (Baucon et al., 2024). However, this technological integration also presents considerable challenges.

Ethical Considerations and Student Perspectives

Ethical concerns are central to discussions of AI in education. Plagiarism and academic integrity present significant challenges, as students might rely on AI to produce written content, potentially hindering the development of their skills (Assapari et al., 2025; Patra et al., 2024; Weijemars et al., 2023). There is a concern that some students may use AI to complete assignments, bypassing plagiarism detectors, and there are concerns regarding the authenticity of written work. Additionally, the potential for AI to generate biased or inaccurate information raises questions about the reliability of these tools in an academic setting (Ghotbi & Ho, 2021).

Student perceptions of AI in education are varied

While many recognize the potential benefits of AI, particularly for improving learning and research activities, there are also concerns about over-reliance on technology, its impact on critical thinking, and the need for human oversight (Patra et al., 2024; Sarwari & Adnan, 2024; Kumar & Ramanm, 2022; Crawford et al., 2024). Many students find AI tools like ChatGPT valuable for everyday learning activities, as they provide access to information anytime and anywhere without limitations. "However, they also prefer traditional teaching methods and consider human teachers indispensable" (Patra et al., 2024; Sarwari & Andnan, 2024).

Research conducted among 94 geoscience students in Mumbai (Patra et al., 2024) revealed that most students disapprove of AI-generated texts bypassing plagiarism detection, emphasizing their concern for academic integrity. There is also concern that using AI may diminish critical thinking and problem-solving skills. Furthermore, some students believe AI should be excluded from specific academic processes, like admissions, exams, and placements, due to concerns about accuracy and fairness (Kumar & Raman, 2022).

The Future of Geoscience in the AI Era

Although challenges exist, AI is anticipated to become increasingly important in shaping the future of geoscience (Zhao et al., 2024, Sun et al., 2024). Many scientists envision a hybrid environment where AI and numerical models coexist, working collaboratively to solve complex environmental issues (Sun et al., 2024). Advancing explainable and physics-based AI models is crucial for improving accuracy and building trust (Sun et al., 2024). It is also important to address the ethical implications of AI in geoscience, including algorithmic bias and data privacy (Ghotbi & Ho, 2021; Sun et al., 2024; Zhao et al., 2024).

AI is also anticipated to aid in creating personalized learning experiences that are customized to meet the specific needs of each student and support educators in providing effective interventions (Burner et al., 2025; Miller, 2025). AI-powered tools can provide tailored feedback, assist with language barriers, and offer adaptive testing, which is particularly beneficial for international students (Wang et al., 2023). However, some scholars highlight gaps in understanding the long-term psychosocial effects of AI usage in education (Crawford et al., 2024).

According to Sun et al. (2024), the success of AI in geoscience will rely on collaboration between computer scientists, mathematicians, and geoscientists to develop tailored tools and training. It is critical to foster a culture of innovation and ethical AI use, educating students on the importance of critical thinking and responsible application of AI technologies (Sun et al., 2024; Baucon et al., 2024; Patra et al., 2024; Ghotbi & Ho, 2021).

Preliminary research results

The preliminary results of our survey of students and graduates of Earth Science in Greece reveal important findings about students' understanding, use, and opinions about Artificial Intelligence (AI). Although AI is embedded in their daily lives, a small percentage of students remain unaware of its presence. The majority use AI tools mainly for information access, data analysis, and task automation, with a particular focus on geoscientific data. Familiarity with these tools ranges from moderate to high, with voice assistants and recommendation systems emerging as more popular applications. However, the use of more specialized tools, such as for music production, video, navigation or translation tools, and bibliographic analysis, remains in high demand, much more frequently than the use of chatbots. Students appear divided on the reliability of AI responses, with several expressing concerns about privacy and human autonomy, while very few feel adequately informed about the ethical issues arising from its use.

Conclusion

The integration of AI in geoscience education is a complex, evolving process that requires a balanced approach. AI is expected to assist in developing tailored learning experiences that address the unique needs of each student (AI-powered personalized learning systems, adoption of artificial intelligence). (Sun et al., 2024; Zhao et al., 2024; Sarwari & Andnan, 2024; Wang et al., 2023). Students have expressed concern regarding potential over-reliance on AI, and their role as future geoscientists in a rapidly changing world (Patra et al., 2024; Kumar & Raman, 2022; Crawford et al., 2024; Ghotbi & Ho, 2021). Therefore, the future of geoscience in the AI era will depend on our capacity to integrate these technologies responsibly and ethically while prioritizing human expertise, critical thinking, and environmental responsibility.

Acknowledgments

Thank you to all the students who participated in my research questionnaire. Your valuable insights were greatly appreciated and contributed significantly to this study.

References

Assapari, M.M., Hidayati, R., Mukti, S.R.W. (2025). Unlocking the Future: EFL Students' Insights on Artificial Intelligences for Academic Writing. Indonesian Journal of Artificial Intelligence and Data Mining (IJAIDM) Vol. 8, No. 1, March 2025, pp. 120 – 129. doi: http://dx.doi.org/10.24014/ijaidm.v8i1.30307

Baucon, A., de Carvalho, C.N. (2024). Can AI Get a Degree in Geoscience? Performance Analysis of a GPT-Based Artificial Intelligence System Trained for Earth Science (GeologyOracle). Geoheritage 16, 121 (2024). https://doi.org/10.1007/s12371-024-01011-2

Burner, T.; Lindvig, Y.; Wærness, J.I. "We Should Not Be Like a Dinosaur"—Using AI Technologies to Provide Formative Feedback to Students. Educ. Sci. 2025, 15, 58. https://doi.org/10.3390/educsci15010058

Crawford, J., Allen, K. A., Pani, B., & Cowling, M. (2024). When artificial intelligence substitutes humans in higher education: the cost of loneliness, student success, and retention. Studies in Higher Education, 49(5), 883–897. https://doi.org/10.1080/03075079.2024.2326956

Digital Education Council (2024). Digital Education Council Global AI Student Survey 2024. https://www.digitaleducationcouncil.

com/post/digital-education-council-global-ai-student-survey-2024 (retrieved 9/1/2025)

Ghotbi N., Ho M.T. (2021). Moral Awareness of College Students Regarding Artificial Intelligence. Asian Bioeth Rev. 2021 Sep 3;13(4):421-433. doi: 10.1007/s41649-021-00182-2. PMID: 34616496; PMCID: PMC8486910

Kumar, V.V. R and Raman, R. (2022). Student Perceptions on Artificial Intelligence (AI) in higher education, 2022 IEEE Integrated STEM Education Conference (ISEC), Princeton, NJ, USA, 2022, pp. 450-454, doi: 10.1109/ISEC54952.2022.10025165.

Miller, M.D. (2025). Generative AI as a challenge to faculty development: ugly advice at the dawn of generative AI. (ch. 13, pp. 179-191). In: Generative AI in Higher Education, (Eds.: Kätlin Pulk & Riina Koris), https://doi.org/10.4337/9781035326020

Patra, S., Singha, T. S., Kanvinde, M., Mazumder, A., and Kanjilal, S. (2024). Harnessing AI for Geosciences Education: A Deep Dive into ChatGPT's Impact,/ChatGPT in Geoscience Education: Revolutionizing Learning or Ethical Minefield? ((b), EGU General Assembly 2024, Vienna, Austria, 14–19 Apr 2024, EGU24-16918, https://doi.org/10.5194/gc-2023-7, 2024., https://doi.org/10.5194/egusphere-egu24-16918, (b) 2024.

Sarwari, A. Q., & Mohd Adnan, H. (2024). The effectiveness of artificial intelligence (AI) on daily educational activities of undergraduates in a modern and diversified university environment. Advances in Mobile Learning Educational Research, 4(1), 927-930. https://doi.org/10.25082/AMLER.2024.01.004

Sun, Z., ten Brink, T., Carande, W., Koren, G., Cristea, N., Jorgenson, C., Janga, B., Asamani, G. P., Achan, S., Mahoney, M., Huang, Q., Mehrabian, A. Munasinghe, T., Liu, Z., Margolis, A., Webley, P., Gong, B., Rao, Y., Burgess, A., Huang, A., Sandoval, L., Pagán, B. R. and Duzgun, S. (2024) Towards practical artificial intelligence in Earth sciences. Comput Geosci 28, 1305–1329 (2024). https://doi.org/10.1007/s10596-024-10317-7

Zhao, T., Wang, S., Ouyang, C., Chen, M., Liu, Ch., Zhang, J., Yu, L., Wang, F., Xie, Y., Li, J., Wang, F., Grunwald, S., Wong, B., Zhang, F., Qian, Z., Xu, Y. J., Yu, C., Han, W., Sun, T., Wang, L. (2024). Artificial intelligence for geoscience: Progress, challenges, and perspectives. The Innovation. Vol. 5 100691. 10.1016/j.xinn.2024.100691.

Wang, T., Lund, B. D., Marengo, A. Pagano, A., Mannuru, N. R., Teel, Z. A., & Pange, J. (2023). Exploring the Potential Impact of Artificial Intelligence (AI) on International Students in Higher Education: Generative AI, Chatbots, Analytics, and International Student Success. Applied Sciences 13(11):6716, doi: 10.3390/app13116716

Weijermars, R., Waheed, U. B., Suleymanli, K. (2023). Will ChatGPT and Related AI Tools Alter the Future of Geosciences and Petroleum Engineering? First Break 41(6):53-61 doi: 10.3997/1365-2397.fb2023043

17th INTERNATIONAL CONGRESS of the Geological Society of Greece

BULLETIN OF THE GEOLOGICAL SOCIETY OF GREECE, SP. PUBL.

EXTENDED ABSTRACT 172

An insight to grain size composition of the beach sediment along the north coast of the Messiniakos Gulf (Greek Mainland).

Koumpou[1] V., Poulos[1] S.E., Karditsa[2] A., Petrakis[3] S., Kapsimalis[3] V.

(1) Laboratory of Physical Geography, Section of Geography and Climatology, Department of Geology and Geoenvironment, Panepistimioupolis-Zografou 15794, Attiki, Greece.

(2) Department of Post Managerment and Shipping, National and Kapodistrian University of Athens, Psahcna, Evia, Greece

(3) Instiute of Oceanography, National Centre for Marine Research, 46,7 km Athens Sounio ave., P.C. 19013, Anavyssos, Attiki, Greece

Introduction

Among the processes that govern the formation and evolution of beach zones is the grain-size of beach material; the latter together with slope have recognized as key geomorphological elements for characterizing the beaches as they appear interrelated with each other and with the oceanographic conditions (Carter, 1988; Wright and Short, 1984).

The scope of the present study is to provide an insight to the grain size distribution of the sediments consisting of both subaerial and submarine sectors of beach zone that extends along the north coastline of the Messiniakos Gulf from Messini to Kalamata with a West – East trending shoreline, a length of 21 km and an average width of 20 m. It is exposed to southerly wind-generated waves, with average significant wave height of 1.2 m and period of 7.6 s (Koumpou et al., 2018). The subaerial beach zone gentles smoothly, having rhythmic morphological features (e.g. beach cusps, berms) at its central and western part and crescentic / longshore bars at its subaqueous part. In addition, low dunes, river mouths (central and western sector) and artificial coastal structures (eastern sector) are also present.

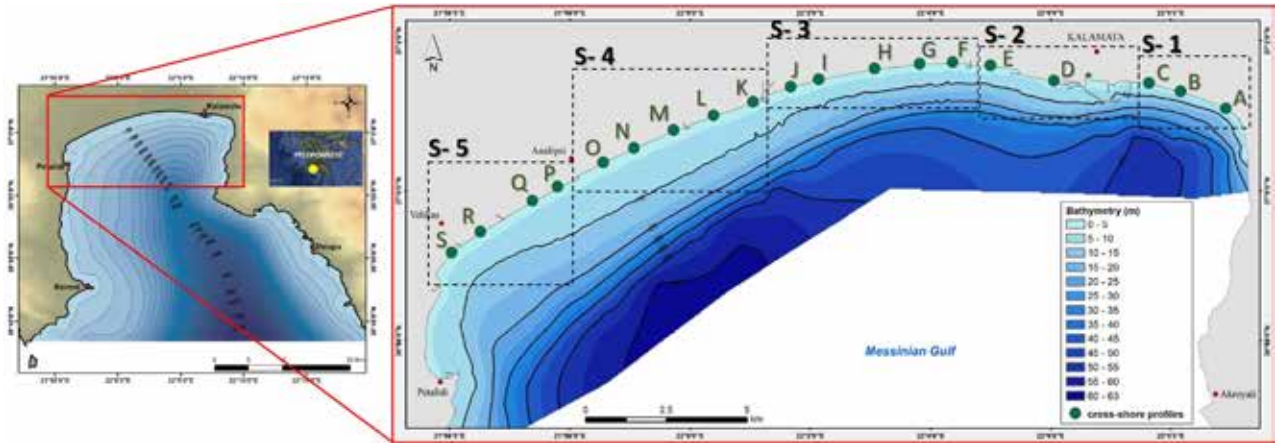

Figure 1. The study area with the positions of the shore-normal profiles (A-S) and the five beach sectors (1-5).

Methods

Nineteen (19) shore-normal profiles (A to S, from east to west) (Fig.1) were measured with the use of a Leica Distance Meter (subaerial part) and a Portable Handy Depth Sounder Hondex PS-7 (subaqueous part). For the geographical position of the profiles a Topcon GPS was used. 118 ssurficial (upper 2 cm) sediment samples were selected along these profiles, i.e., 60 subaerial, 19 from the beach face (shoreline) and 39 subaqueous samples (see Table A).

Subsequently sediment samples >625μm were subjected to dry sieving according to the Folk (1974) procedure, whilst sediment samples (<625 μm) were analyzed with a Sedigraph-Micrometrics using X-rays (type III PLUS). The statistical elaboration of the grain size identification included the determination of the graphical mean grain size (Mz; equation 1), the graphical standard deviation (σI; equation 2) and the mean diameter (D50), while the samples were classified according to their content in gravels, sand and mud following the Folk' (1974).

Results

The subaerial, beach-face and subaqueous slopes of the 19 normal to shoreline profiles (A-S) are presented in Table 1, while the types of sediment samples, according to their grain size composition, is presented in Table 2.

Table 1. Average slopes of subaerial, subaqueous and beacface of the 5 beach sectors (T1-T5)

Sectors	**1A**	**T1B**	**T-2a**	**T2b**	**T3a**	**T3b**	**T4**	**T5a**	**T5b**
Profiles	**A**	**B, C**	**D**	**E**	**F, G**	**H, I, J**	**K, L, M, N, O**	**P, Q, R**	**S**
Backshore (%)	0.07	0.115 (±0.045)	0.21	0.11	0.065 (±0.005)	0.145 (±0.055)	0.03 (±0.01)	0.105 (±0.015)	0.13
Beach face (%)	0.15	0.13 (±0.01)	0.16	0.19	0.16 (±0.02)	0.175 ±(0.025)	0.105 (±0.015)	0.10	0.11
Foreshore (%)	0.04	0.03 (±0.01)	0.01	0.01	0.035 (±0.025)	0.03 ±0.02	0.015 (±0.005)	0.01	0.01

Table 2. Types of sediment according to their size at the 5 beach sectors (T1-T5)

Sectors	**T1A**	**T1B**	**T2a**	**T2b**	**T3a**	**T3b**	**T4**	**T5a**	**T5b**
Profiles	**A**	**B, C**	**D**	**E**	**F, G**	**H, I, J**	**K, L, M, N, O**	**P, Q, R**	**S**
2,0-2,5							g(S)-gS		
1,5-2,0	G					sG-gS-(g)S	g(S)-gS	(g)S	
1,0-1,5	G	(g)S			sG	gS	(g)S - gS -sG	(g)S -S	
0,5-1	G	G-sG		(g)S	G	(g)S	gS -sG	G	(g)S
0-0,5	G	G	G	G	G	G-sG	(g)S - gS -sG	sG -G	G
0	G	gS -sG	sG	gS	gS	sG-gS	S -sG	sG-gS	gS
1,5-2,5	S	sG	G	(g)S	S-gS	(g)S-sG	(g)S -sG	sG	S
4-5	S	(g)S-S	mS	S	S	S-mS	S-mS	mS -S	sM
5-7,5	S	S		S	S	S-mS	mS	mS	sM
7,5-10	mS	mS		S	S	S-mS	mS	sM	sM
10-15	mS	mS		S	S	S-mS	mS	M	M
15-20	mS	mS			sM	sM	mS - sM		

Key. G: Gravel; S: Sand; M: Mud; sG: sandy Gravel; (g)S: slightly sandy Gravel; gS: gravelly Sand; sG: sandy Gravel; mS: muddy Sand; sM: sandy Mud

Discussion and Conclusions

The beach zone along the northern coast of the Messiniakos Gulf consists predominantly of mixed sediments, with sand-sized material being the primary component. As expected, the subaerial sediments are coarser, with gravel-sized particles being as significant as the sand-sized ones. In contrast, the subaqueous sediments are dominated by sand, particularly in water depths greater than 2 meters. Beyond 5 meters of depth, the proportion of mud increases, becoming the dominant sediment type at depths exceeding 15 meters. Along the beach face (±0.5 m), the sediment consists of a mixture of sand and gravel in varying ratios. Additionally, the results of the grain size analysis align with the classification of the 19 profiles into five main sectors, based on shoreline orientation and beach slope (Table 1).

There is a notable similarity between the eastern Sector 1 and the central Sector 3, particularly in the slopes of their beach face and shoreface. Both end sectors are characterized by relatively coarser material and exhibit similar slopes. This similarity is likely influenced by the original terrestrial material and the presence of coastal structures, such as port breakwaters, in the eastern Sector. The observed differences between the sectors may be attributed to variations in sediment input from rivers discharging along the shore, combined with the effects of longshore sediment transport in the nearshore zone and wave runup on the subaerial beach.

References

Carter, R.W.G., 1988. *Coastal Environments: An Introduction to the Physical, Ecological, and Cultural Systems of Coastlines*; Academic Press: London, UK.

Folk, R. L. (1980). *Petrology of sedimentary rocks*. Hemphill publishing company.

Koumpou V., Petrakis S., Karditsa A., Kapsimalis V. and Poulos S., 2018. Morphological changes induced by storm event, along the Messini- Kalamata beach zone. 12th Panhellenic Symposium of Oceanography & Fisheries, Corfu, 30 May – 3 June 2018, p.93.

Wright, L.;and Short, A., 1984. Morphodynamic variability of surf zones and beaches: A synthesis. *Mar. Geol*, *56*, 93–118.

17th INTERNATIONAL CONGRESS of the Geological Society of Greece

BULLETIN OF THE GEOLOGICAL SOCIETY OF GREECE, SP. PUBL.

EXTENDED ABSTRACT 173

A systematic review of grey literature in Greek universities repositories to uncover Greek UNESCO Global Geoparks

Alexandros Aristotelis Koupatsiaris[1], Hara Drinia[1]

(1) Department of Geology and Geoenvironment, National and Kapodistrian University of Athens, 15784 Athens, Greece, alkoup@geol.uoa.gr

Research Highlights

A systematic review of grey literature from Greek university repositories reveals a growing interest in UNESCO Global Geoparks, primarily focusing on geotourism, geology, management, and education, but also identifies gaps in social sciences and community engagement. Future research should adopt a holistic approach, integrating socio-economic, cultural, and environmental aspects, while enhancing geoenvironmental education and stakeholder involvement to support the United Nations' seventeen Sustainable Development Goals.

Introduction / Background

Our world is experiencing rapid urbanization, interconnectivity, and environmental changes. The global population is projected to reach 9.7 billion by 2030 and 10.4 billion by 2050. Currently, 55% of the population lives in urban areas, a figure expected to rise to 68% by 2050. This trend impacts land use, biodiversity, and ecosystems, with significant urban land development anticipated by 2030 (Fragkias, 2013). Environmental challenges, such as pollution, erosion, desertification, deforestation, fires, intensified agriculture, overgrazing, invasive species, overfishing (Scoullos, 2008), climate change, greenhouse effects, droughts, floods, habitat loss, chemical pollution (Krasny, 2020), environmental emergencies, and anthropogenic impacts on economic systems, global warming, natural disasters, declining biodiversity, land degradation, water pollution, mineral resource exploitation, coastal vulnerability, and geodiversity alterations (Peppoloni et al., 2022) threaten our planet's natural capital (Gray, 2018). These issues necessitate proactive measures and community involvement to protect our environment for future generations.

UNESCO Global Geoparks (UGGps) play a crucial role in sustainable development by managing areas with significant geological heritage. Established in 2000 and supported by UNESCO since 2001, these UGGps promote awareness of societal issues through geoconservation, geotourism, and geoeducation, enhancing community well-being and sustainability (Zouros, 2016). There are currently 213 UGGps in 48 countries. In Greece, nine areas are designated as UGGps (Lesvos Island UGGp, Psiloritis UGGp, Chelmos-Vouraikos UGGp, Vikos-Aoos UGGp, Sitia UGGp, Grevena-Kozani UGGp, Kefalonia-Ithaca UGGp, Lavreotiki UGGp, Meteora-Pyli UGGp), with one more in the nomination process (Nisyros aspiring UGGp).

Greece's geotectonic position offers a rich geological landscape, making its UGGps invaluable. These sites serve as "natural geological laboratories," chronicling Earth's history from the Proterozoic Eon to today and providing insights into tectonics, sedimentation, volcanic activity, and landscape evolution. The geoconservation and sustainable development of these UGGps are crucial. Scientific research helps formulate effective conservation strategies. Greek UGGps also serve as effective platforms for teaching about the environment, enhancing public awareness of the connections between geology, ecology, culture, and sustainability (Koupatsiaris et al., 2023). They promote social, economic, and cultural growth through educational programs, geotourism, and geoethics (Zafeiropoulos et al., 2021). The study of UGGps supports interdisciplinary research in geosciences and geoconservation, informing global efforts in sustainability and environmental stewardship.

Objectives

The systematic review aims to evaluate the repositories of Greek universities to identify and catalog research topics related to Greek UGGps. It seeks to provide a comprehensive overview of the research landscape, highlight underexplored areas, and suggest directions for future research, offering insights to the academic community, policymakers, and stakeholders.

The research questions addressed are:

- What research topics and themes are covered in Greek university grey literature about Greek UGGps?
- What research gaps exist in this literature?
- What are the potential future research directions for Greek UGGps?
-

Methods

This study gathers research evidence on Greek UGGps to guide future research studies. Using a systematic review

approach, specific steps were followed to ensure replicability and reliability. The criteria included publications from Greek university repositories published between 2000 and 2022, using the keyword "Geopark." The search focused on publications primarily discussing Geoparks as holistic entities, rather than specific geological or other features within Geopark boundaries. A total of 138 items were accessed, with 28 theses deemed relevant after applying selection criteria. The process followed PRISMA guidelines for a thorough review (Figure 1).

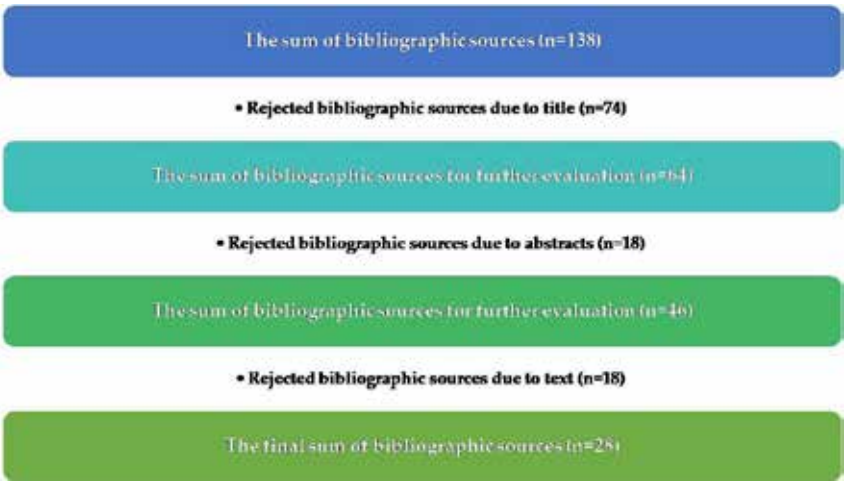

Figure 1. Flow chart for the grey literature review in Greek university repositories.

Limitations included reliance on a single keyword and variations in search capabilities across institutions, which may have resulted in omissions. External literature from global databases related to Greek UGGps was not examined.

Results

The review identified 28 theses on UGGPs: 23 master's, 3 graduate, and 2 doctoral theses. This indicates a growing academic interest, although there was a notable dip in publications during 2021 due to the SARS-CoV-2 pandemic (Figure 2).

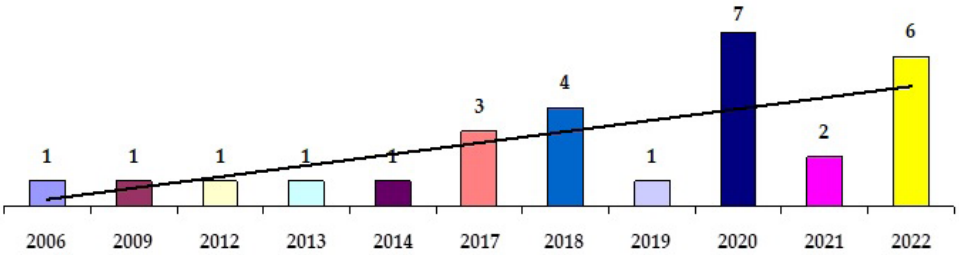

Figure 2. Distribution of the theses by the year of publication in Greek university repositories.

Most theses were found at the University of the Aegean (n=9), likely due to its collaboration with the Lesvos Island UGGp, followed by the Hellenic Open University (n=6) and the National Kapodistrian University of Athens (n=4) (Figure 3).

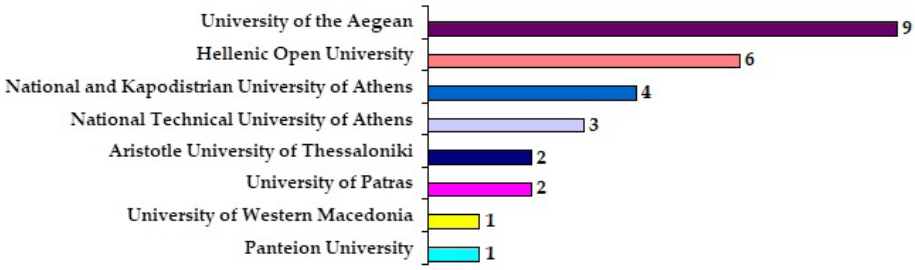

Figure 3. Distribution of the theses by Greek university repositories.

The Department of Geography had the most theses (n=7), followed by the Department of Geology and Geoenvironment at the National and Kapodistrian University of Athens (n=4) and the Tourism Business Administration at the Hellenic Open University (n=4) (Figure 4).

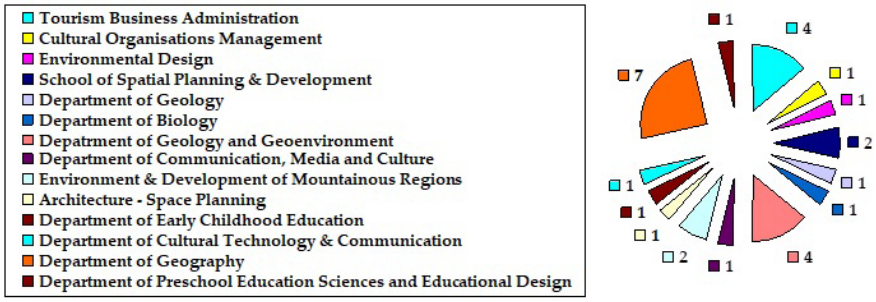

Figure 4. Distribution of the theses by Greek university department.

The 28 university theses focused on Lesvos Island (n=11) and Sitia UGGps (n=6), with newer UGGps like Grevena-Kozani, Kefalonia-Ithaca, and Lavreotiki having fewer studies due to their recent establishment (Figure 5).

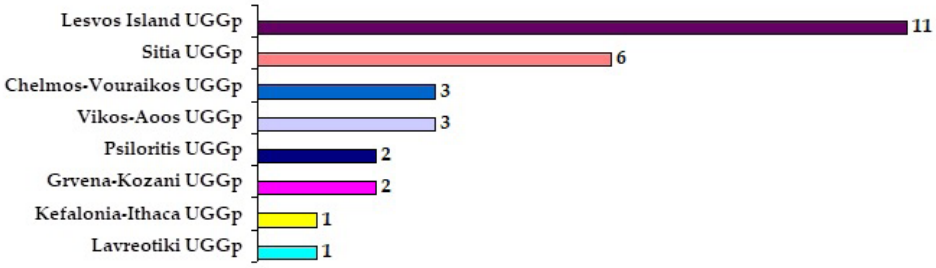

Figure 5. Distribution of the theses according to their Greek UNESCO Global Geopark focus.

Research topics included geotourism (n=7), geodiversity and geology (n=6), sustainable management (n=4), and geoeducation (n=4). Other areas were geoinformatics, biodiversity, cartography, cultural development, spatial planning, and georoute promotion, highlighting the multidisciplinary nature of UGGps studies (Figure 6).

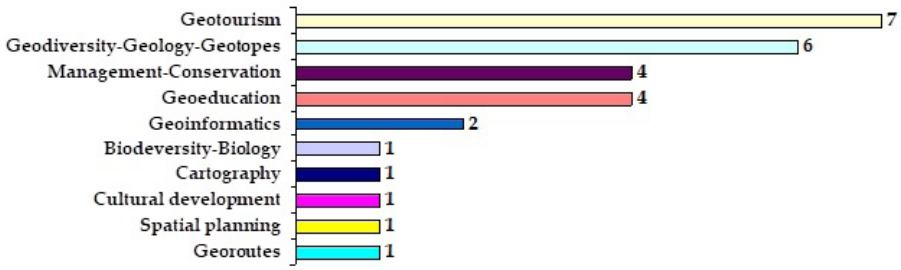

Figure 6. Content classification of the grey literature in Greek university repositories.

Conclusions

This review underscores the importance of Greek UGGps as globally recognized assets supporting scientific research and societal contributions. It addresses key global issues such as urbanization, environmental challenges, and the alienation from nature, emphasizing the need for new sustainability and resilience policies. Greece, renowned for its geological richness, hosts nine UGGps, offering opportunities for geoconservation, geodiversity and biodiversity, and cultural appreciation. The review focused on grey literature from Greek universities to identify research gaps and align domestic efforts with international trends. There is strong academic interest in Greek UGGps, particularly in geology, biology, tourism, and culture.

Recent proposals, such as Martini et al. (2022), suggest a roadmap for UGGps focusing on climate change, water

resources, sustainable tourism, and community engagement. International research emphasizes interdisciplinary studies and community involvement. Stoffelen's (2020) review focused on geomorphological aspects, while Herrera-Franco et al. (2021) noted this area's dominance in research, particularly in Asia and Europe. Ferreira et al. (2023) highlighted the need to explore UGGps' role in sustainable development and their benefits to local populations. Evaluations of the International Geoscience and Geoparks Programme showed UGGps' contributions to the United Nation's Sustainable Development Goals, including quality education (UNESCO, 2019). However, educational topics remain underrepresented in research.

Greek research aligns with international trends but often focuses on geotourism, geology, and management, with limited attention to social and humanitarian aspects. To fully harness the potential of UGGps, Greek studies should expand to include social development and stakeholder engagement, drawing from successful international models aligning with the United Nations' Sustainable Development Goals and fostering a sense of belonging and responsibility among future generations in Greece and beyond (Koupatsiaris et al., 2023). Addressing these research gaps can enhance the role of UGGps in environmental awareness, sustainability, and education, providing a roadmap for future academic research.

Future research within UGGps, highlighted in the grey literature of Greek university repositories, should focus on:

- Socio-economic and cultural aspects: Explore the socio-cultural dimensions of UGGps, integrating historical and cultural narratives with geological significance. This holistic approach can transform UGGps into cultural and economic hubs, enhancing their role in local identity and advancement.
- Collaborative management and governance: Investigate stakeholder participation in UGGps management, involving local communities, students, and special interest groups. Innovative governance structures can improve UGGps' visibility and recognition, reflecting their significance in local culture.
- Climate change and environmental challenges: UGGps can educate the public on climate change and resilience. They serve as living laboratories for studying environmental impacts and engaging communities in climate action through science initiatives, contributing to public health and well-being.
- Geoenvironmental education: Emphasize education with a focus on integrating UGGps into educational curricula to raise awareness about geoconservation, sustainability, and environmental challenges. This can enhance public understanding and foster a sense of responsibility towards preserving geological heritage.

By addressing these areas, future research can strengthen the role of Greek UGGps in promoting sustainability.

Acknowledgements

The authors extend their heartfelt thanks to the organizing committee of the 17th International Congress of the Geological Society of Greece and the anonymous reviewers for their thorough consideration of this extended abstract.

References

Ferreira, D.R., Valdati, J., 2023. Geoparks and Sustainable Development: Systematic Review. Geoheritage 15, 6. https://doi.org/10.1007/s12371-022-00775-9

Fragkias, M., Güneralp, B., Seto, K.C., Goodness, J., 2013. A synthesis of global urbanization projections, in: Elmqvist, T., Fragkias, M., Goodness, J., Günerlap, B., Marcotullio, P.J., McDonald, R.I., Parnell, S., Schewenius, M., Sendstad, M., Seto, K.C., et al. (Eds.), Urbanization, Biodiversity and Ecosystem Services: Challenges and Opportunities, 409-435.

Gray, M., 2018. The Confused Position of the Geosciences within the "Natural Capital" and "Ecosystem Services" Approaches. Ecosystem Services 34, 106-112. https://doi.org/10.1016/j.ecoser.2018.10.000

Herrera-Franco, G., Montalván-Burbano, N., Carrión-Mero, P., Jaya-Montalvo, M., Gurumendi-Noriega, M. 2021. Worldwide Research on Geoparks through Bibliometric Analysis. Sustainability 13, 1175. https://doi.org/10.3390/su13031175

Koupatsiaris, A.A., Drinia, H., 2023. Exploring Greek UNESCO Global Geoparks: A Systematic Review of Grey Literature on Greek Universities and Future Research Avenues for Sustainable Development. *Geosciences 13*(10), 296. https://doi.org/10.3390/geosciences13100296

Krasny, M.E., 2020. Advancing environmental education practice, Cornell University Press.

Martini, G., Zouros, N., Zhang, J., Jin, X., Komoo, I., Border, M., Watanabe, M., Frey, M.L., Rangnes, K., et al., 2022. UNESCO Global Geoparks in the "World After": A Multiple Goals Roadmap Proposal for Future Discussion. Episodes 45, 29-35. https://doi.org/10.18814/epiiugs/2021/021002

Peppoloni, S., Di Capua, G., 2022. Geoethics: Manifesto for an Ethics of Responsibility towards the Earth, Springer International Publishing.

Scoullos, M., Alambei, B., Kouroutos, B., Malotidi, M., Mantzara, M., Psallidas, B. (Eds.) Environmental Education and Education for Sustainable Development in Protected Areas: Educational Material, MIO-ECSDE. (In Greek).

Stoffelen, A., 2020. Where is the Community in Geoparks? A Systematic Literature Review and Call for Attention to the Societal Embedding of Geoparks. Area 52, 97-104. https://doi.org/10.1111/area.12549

UNESCO, 2019. International Geoscience and Geoparks Programme, in: Evaluation of the International Geosciences and

Geoparks Programme, Zhechkov, R., Hinohosa, C., Knee, P., Pinzon, L., Buchs, D., Chernet, T. (Eds.), IOS/EVS/PI/182.
Zafeiropoulos, G., Drinia, H., Antonarakou, A., Zouros, N., 2021. From Geoheritage to Geoeducation, Geoethics and Geotourism: A Critical Evaluation of the Greek Region. *Geosciences 11*(9), 381. https://doi.org/10.3390/geosciences11090381
Zouros, N., 2016. Global Geoparks Network and the new UNESCO Global Geoparks Programme. Bulletin of the Geological Society of Greece 50, 284-292. https://doi.org/10.12681/bgsg.11729

17th INTERNATIONAL CONGRESS of the Geological Society of Greece

BULLETIN OF THE GEOLOGICAL SOCIETY OF GREECE, SP. PUBL.

EXTENDED ABSTRACT 174

Assessing Educators' Sense of Place and Geoethical Awareness at the 4th Summer School of Sitia UNESCO Global Geopark

Alexandros Aristotelis Koupatsiaris[1], Hara Drinia[1]

(1) Department of Geology and Geoenvironment, National and Kapodistrian University of Athens, 15784 Athens, Greece, alkoup@geol.uoa.gr

Introduction / Background

The environment is shaped by a complex interplay of natural and human influences affecting ecological balance, quality of life, public health, cultural traditions, and aesthetic values. Current environmental challenges, intensified by urbanization, threaten natural resources and cultural and geological heritage. The United Nations' Sustainable Development Goals provide a strategic framework to address these issues. In the Anthropocene Era, it is crucial to adopt modern geoenvironmental strategies grounded in geoethics (Koupatsiaris et al., 2024). Pro-environmental behavior, aimed at enhancing environmental quality and sustainability, is essential for confronting these challenges.

UNESCO Global Geoparks (UGGps) play a vital role in conserving and promoting areas with notable geodiversity, biodiversity, and geotourism, while also advancing education, public understanding, sustainability, and resilience. These UGGps inspire a sense of belonging and responsibility, encouraging local communities to re-evaluate their heritage through tourism and eco-friendly activities (Fassoulas et al., 2010). At present, there are 213 UGGps across 48 countries, with Greece hosting nine, including the Sitia UGGp, established in 2015. It is located on the eastern edge of Crete, encompassing an area of 713.5 km² with internationally significant geology.

For over six decades, environmental education has aimed to develop environmentally conscious citizens capable of addressing complex environmental problems (Krasny, 2020). Geoeducation integrates natural and cultural features with geology to raise awareness and foster participation in geoconservation efforts (Gordon, 2019). Place-based education (Sobel, 2004) emphasizes the importance of local geoenvironments in a globalized world, countering the alienation from nature. The sense of place (Kudryavtsev et al., 2012), a key concept in environmental education, involves the connections people have with locations, influenced by physical, psychological, and emotional factors (Semken et al., 2009). It intersects with geoethics (Peppoloni et al., 2022), which explores the ethical dimensions of human interactions with the natural environment, promoting sustainability, environmental responsibility, and social justice.

Objectives

In response to the increasing global interest in geoenvironmental education, geoheritage, geoconservation, and geoethics, this study presents a novel approach to exploring the interrelations between sense of place and geoethical awareness within the context of UGGps. The research addresses the following questions:

- What changes occur in participants' sense of place (including place attachment and place meaning) and geoethical awareness before and after attending the summer school?
- Is there a relationship between place attachment, place meaning, and geoethical awareness among the summer school participants?
-

Methods

The study was conducted during the 4th Summer School of Environmental Education on Geotopes and Sustainability at the Sitia UNESCO Global Geopark from June 29 to July 4, 2024, involving 50 educators from Greece. A quasi-experimental design with a single experimental group and a pre-post technique was employed. Convenience sampling resulted in 41 questionnaires at the start and 36 at the end, with 33 matched pre-post questionnaires analyzed. The comprehensive survey included four sections: Section A (place attachment)—12 items, Section B (place meaning)—28 items, Section C (geoethical awareness)—32 items, and Section D (demographics)—15 items. The place attachment scale was adapted from Williams and Vaske (2003), and the place meaning scale was a modified version of Young's (1999) scale. A new geoethical awareness scale was developed based on geoethics literature. All items used a Likert scale from 1 to 5. Ethical standards were strictly followed. Data analysis was conducted using IBM SPSS Statistics version 29. Normality tests (Kolmogorov–Smirnov and Shapiro–Wilk) indicated a non-normal distribution ($p > 0.05$), so non-parametric tests (Spearman's rho, and Wilcoxon signed-rank) were used for correlation analyses and multiple linear regression.

Results

The questionnaire's internal consistency was assessed using Cronbach's Alpha. Section A had $\alpha = 0.942$ (pre) and $\alpha = 0.929$ (post) with 12 items. Section B had $\alpha = 0.917$ (pre) and $\alpha = 0.914$ (post) with 28 items. Section C had $\alpha = 0.945$ (pre) and $\alpha =$

0.955 (post) with 32 items. For all 72 items, both pre- and post-summer school consistency was α = 0.967.
Among participants, 36.4% were male and 63.6% female. Age distribution: 9.1% were 25–34, 27.3% were 35–44, 33.3% were 45–54, and 30.3% were 55 and above. Educational qualifications included 66.7% with a postgraduate degree, 24.2% with an undergraduate degree, and 9.1% with a Ph.D. Employment varied: 6.1% in kindergarten, 30.3% in primary school, 33.3% in middle school, 21.2% in high school, and 6.1% in other institutions.
In analyzing the ''Place Attachment'' section of the questionnaire, notable changes in participants' responses were observed before and after attending the summer school (Table 2).

Table 2. Distribution of mean value, standard deviation, and total score for place attachment.

Items		PRE M.V.	PRE S.D.	POST M.V.	POST S.D.	SUM PRE	SUM POST
A1	I feel Sitia Geopark is part of me.	3.58	0.204	4.06	0.168	118	134
A3	Sitia Geopark is very special for me.	3.79	0.178	4.33	0.142	125	143
A5	I identify strongly with Sitia Geopark.	3.39	0.162	3.88	0.161	112	128
A7	I am very attached to Sitia Geopark.	3.36	0.203	4.12	0.167	111	136
A9	Visiting Sitia Geopark says a lot about who I am.	3.52	0.145	4.12	0.149	116	136
A11	Sitia Geopark means a lot to me.	3.48	0.185	4.18	0.154	115	138
Total (place identity)		3.52	0.157	4.12	0.137	697	815
A2	Sitia Geopark is the best place for what I like to do.	3.39	0.157	3.79	0.167	112	125
A4	No other place can compare to Sitia Geopark.	2.58	0.123	3.24	0.163	85	107
A6	I get more satisfaction out of visiting Sitia Geopark than any other.	3.12	0.167	3.61	0.157	103	119
A8	Doing what I do at Sitia Geopark is more important to me than doing it in any other place.	3.24	0.174	3.61	0.130	107	119
A10	I wouldn't substitute any other area for doing the types of things I do at Sitia Geopark.	2.82	0.154	3.24	0.180	93	107
A12	The things I do at Sitia Geopark I would enjoy doing just as much at a similar site.	3.30	0.119	3.39	0.137	89	86
Total (place dependence)		3.08	0.115	3.48	0.113	589	663
Total (place attachment)		3.30	0.130	3.80	0.118	1286	1478

Note: Odd-numbered items measure place identity, and even-numbered items measure place dependence. The final item is reverse-scored. Responses are based on a Likert scale where 1 corresponds to ''Strongly disagree,'' 2 to ''Disagree,'' 3 to ''Neither disagree nor agree,'' 4 to ''Agree,'' a nd 5 to ''Strongly agree.''

Overall, the measure of place attachment, which includes both place identity and place dependence, showed a notable increase. The average score for place attachment rose from 3.30 (S.D. = 0.130) before the summer school to 3.80 (S.D. = 0.118) after the event. The total score for place attachment also increased from 1286 to 1478 units. Participation in the summer school positively influenced participants' place attachment, enhancing their emotional connections and deepening their bonds with Sitia UGGp in the context of geoenvironmental education.
The analysis of the ''Place Meaning'' section revealed significant shifts in participants' perceptions of Sitia UGGp both before and after their attendance at the summer school (Table 3).

Table 3. Distribution of mean value, standard deviation, and total score for place meaning.

Sitia Geopark is for me:		PRE M.V.	PRE S.D.	POST M.V.	POST S.D.	SUM PRE	SUM POST
B1	Ancient place	3.52	0.200	4.03	0.177	116	133
B2	Pristine place	3.61	0.213	4.21	0.167	119	139
B3	Scenic place	3.70	0.215	4.36	0.156	122	144
B4	Beautiful place	4.30	0.141	4.58	0.115	142	151
B5	Remote place	4.03	0.197	4.18	0.182	133	138
B6	Unique place	4.15	0.152	4.64	0.105	137	153
B7	Important place to preserve	4.55	0.116	4.73	0.090	150	156
B8	Authentic place	4.55	0.107	4.70	0.111	150	155
B9	Privilege to visit	3.73	0.191	4.42	0.131	123	146
B10	Relaxing place	4.21	0.136	4.70	0.081	139	155
B11	Important place for local culture	4.12	0.143	4.64	0.105	136	153
B12	Overdeveloped place	1.64	0.143	1.73	0.152	144	141
B13	Unusual place	3.94	0.174	4.42	0.138	130	146

B14	Scientific valuable place	4.09	0.165	4.33	0.155	135	143
B15	Ecologically important place	4.42	0.151	4.58	0.123	146	151
B16	Place for fun	2.85	0.209	3.15	0.243	94	104
B17	Threatened place	3.76	0.151	4.09	0.171	74	63
B18	Crowded place	1.70	0.141	1.82	0.177	142	138
B19	Dangerous place	1.58	0.151	1.94	0.184	140	134
B20	Interesting place	4.3	0.111	4.48	0.131	142	148
B21	Educational place	4.18	0.127	4.48	0.098	138	148
B22	Tranquil place	4.52	0.088	4.64	0.085	149	153
B23	Spiritually valuable place	2.79	0.188	3.15	0.247	92	104
B24	Fragile place	4.00	0.144	4.39	0.123	132	145
B25	Wilderness place	3.85	0.169	4.15	0.200	127	137
B26	Historical place	4.06	0.130	4.24	0.180	134	140
B27	Place for adventure	4.15	0.116	4.61	0.144	137	152
B28	Tourism place	3.52	0.200	3.94	0.204	116	130
Total (place meaning)		3.71	0.089	4.05	0.085	3639	3900

Note: Items 12, 17, 18, and 19 are reverse-scored. This instrument uses a Likert scale where 1 corresponds to ‘‘Does not fit at all,’’, 2 to ‘‘Fits to some extent,’’ 3 to ‘‘Neither fits nor does not fit,’’ 4 to ‘‘Fits sufficiently well,’’ and 5 to ‘‘Fits perfectly.’’

Overall, the comprehensive measure of place meaning increased from a mean of 3.71 (S.D. = 0.089) to 4.05 (S.D. = 0.085). This reflects a stronger alignment with the idea that Sitia UGGp ‘‘fits perfectly’’ with the positive attributes assessed. The total score for place meaning rose from 3639 to 3900 units. Participation in the summer school significantly enhanced participants’ perceptions of the symbolic meanings of Sitia UGGp, reinforcing its cultural, ecological, and aesthetic value.
The analysis of the ‘‘Geoethical Awareness’’ section revealed significant shifts in participants’ perceptions regarding geoethical issues before and after attending the summer school (Table 4).

Table 4. Distribution of mean value, standard deviation, and total score for geoethical awareness.

Items		PRE M.V.	PRE S.D.	POST M.V.	POST S.D.	SUM PRE	SUM POST
C1	The preservation of geoheritage is essential for maintaining cultural and scientific values in Sitia Geopark.	4.33	0.112	4.70	0.081	143	155
C2	Public awareness programs about geoheritage in Sitia Geopark significantly enhance community appreciation and protection efforts.	4.42	0.098	4.70	0.081	146	155
C3	Effective geoconservation strategies in Sitia Geopark are crucial for protecting geological features from degradation.	4.39	0.106	4.64	0.085	145	153
C4	Geoconservation in Sitia Geopark should be integrated into local development plans to ensure the sustainable use of geological resources.	4.42	0.107	4.58	0.098	146	151
C5	Geotourism activities within Sitia Geopark should prioritize sustainability.	4.45	0.098	4.58	0.107	147	151
C6	The promotion of geotourism in Sitia Geopark can help boost local economies without compromising geological integrity.	4.30	0.141	4.52	0.098	142	149
C7	It is important to recognize and protect the geodiversity of Sitia Geopark as it contributes to ecological balance.	4.48	0.098	4.58	0.098	148	151
C8	Educational programs about geodiversity in Sitia Geopark can foster a deeper understanding of geological processes among visitors.	4.33	0.120	4.55	0.098	143	150
C9	The protection of biodiversity within Sitia Geopark is as important as preserving geological features.	4.18	0.187	4.73	0.079	138	156
C10	Biodiversity and geodiversity conservation in Sitia Geopark should be managed in a complementary manner.	3.88	0.167	4.15	0.175	128	137
C11	Responsible use of georesources within Sitia Geopark can support local communities without harming the environment.	4.09	0.159	4.42	0.098	135	146
C12	Regulations on the extraction of geosources in Sitia Geopark are necessary to prevent environmental degradation.	4.12	0.183	4.58	0.107	136	151
C13	Sustainable water management practices are essential to maintain the ecological balance within Sitia Geopark.	4.30	0.119	4.58	0.087	142	151
C14	Community involvement in water management decisions within Sitia Geopark can lead to more effective conservation outcomes.	4.18	0.119	4.55	0.098	138	150
C15	Sitia Geopark should implement strategies to mitigate the impacts of the climate crisis on its geological and biological resources.	4.33	0.128	4.48	0.116	143	148

C16	Raising awareness about the climate crisis in Sitia Geopark can motivate visitors and locals to adopt more sustainable practices.	4.27	0.117	4.45	0.116	141	147
C17	Risk prevention measures are necessary to protect both geological and human resources within Sitia Geopark.	4.39	0.115	4.42	0.098	145	146
C18	Adequate infrastructure and planning can significantly reduce the risks of natural disasters within Sitia Geopark.	4.18	0.134	4.45	0.107	138	147
C19	Sitia Geopark must develop adaptive strategies to cope with environmental changes and their impacts.	4.06	0.130	4.36	0.114	134	144
C20	Continuous research and monitoring are vital for effective adaptation to changing conditions within Sitia Geopark.	4.33	0.104	4.58	0.098	143	151
C21	All activities within Sitia Geopark should be guided by principles of sustainability to ensure long-term conservation.	4.55	0.107	4.70	0.081	150	155
C22	Sustainable development within Sitia Geopark can serve as a model for other protected areas.	4.36	0.114	4.48	0.088	144	148
C23	Enhancing the resilience of Sitia Geopark's ecosystems is crucial for coping with environmental pressures.	4.00	0.179	4.39	0.123	132	145
C24	Community resilience in Sitia Geopark can be bolstered through education and involvement in conservation efforts.	4.15	0.158	4.55	0.098	137	150
C25	Active community engagement is crucial for the success of conservation initiatives in Sitia Geopark.	4.33	0.104	4.48	0.116	143	148
C26	Local communities should have a significant role in decision-making processes related to Sitia Geopark.	4.18	0.134	4.45	0.116	138	147
C27	Strong environmental advocacy initiatives are essential for raising awareness about conservation issues within Sitia Geopark.	4.42	0.098	4.67	0.083	146	154
C28	Collaborating with environmental advocacy groups can amplify the impact of conservation efforts within Sitia Geopark.	4.42	0.087	4.45	0.163	146	147
C29	Programs that connect visitors emotionally to Sitia Geopark can lead to stronger conservation efforts.	4.30	0.111	4.52	0.098	142	149
C30	Ecological experiences within Sitia Geopark should be designed to foster a sense of responsibility towards nature.	4.45	0.116	4.70	0.092	147	155
C31	Geoenvironmental education programs are essential for raising awareness about the importance of geological conservation in Sitia Geopark.	4.27	0.109	4.39	0.162	141	145
C32	Schools and educational institutions should be actively involved in geoenvironmental education initiatives within Sitia Geopark.	4.52	0.098	4.61	0.097	149	152
Total (geoethical awareness)		4.30	0.770	4.53	0.069	4536	4784

Note: Items 1–2 evaluate the geoheritage value; items 3–4 focus on the geoconservation; items 5–6 examine geotourism; items 7–8 address the geodiversity; items 9–10 pertain to the biodiversity; items 11–12 consider georesources; items 13–14 discuss water management; items 15–16 relate to climate crisis issues; items 17–18 involve risk prevention; items 19–20 explore adaptation to changes; items 21–22 assess sustainability; items 23–24 reflect on resilience; items 25–26 cover community engagement; items 27–28 focus on environmental advocacy; items 29–30 evaluate the value of concrete ecological feelings; and items 31–32 consider the geoenvironmental education potential. The instrument uses a Likert scale as follows: 1 corresponds to ''Strongly disagree,'' 2 to ''Disagree,'' 3 to ''Neither disagree nor agree,'' 4 to ''Agree,'' and 5 to ''Strongly agree.''

Overall, the average rating for geoethical awareness increased from 4.30 (S.D. = 0.770) to 4.53 (S.D. = 0.069), with total scores rising from 4536 to 4784, highlighting the program's positive impact on participants' understanding and attitudes towards geoethical issues. These findings demonstrate a marked enhancement in geoethical awareness, with increased agreement on management, sustainability, preservation, community involvement, and advocacy. The summer school enhanced participants' commitment to geoethical principles, supporting geoconservation efforts in Sitia UGGp.

To explore the relationships between key scales of the questionnaire —place attachment (Scale A), place meaning (Scale B), and geoethical awareness (Scale C)—Spearman's rho correlation coefficients were calculated. The strongest correlation was observed between place attachment and place meaning ($\rho = 0.734$, $p < 0.001$, $N = 33$), indicating a strong link between emotional connection and perceived significance. Place meaning and geoethical awareness also showed a significant correlation ($\rho = 0.699$, $p < 0.001$), as did place attachment and geoethical awareness ($\rho = 0.664$, $p < 0.001$). All correlations were positive and significant, indicating interconnectedness of the scales and suggesting that the summer school enhanced participants' understanding of geoethical issues at Sitia UGGp.

A Wilcoxon signed-rank test was used to evaluate the impact of the summer school program on participants' connection to Sitia UGGp by comparing median place attachment levels before (APRE) and after (APOST) the program. This test is suitable for related samples. Notably, 30 of 33 participants reported a stronger connection post-program, while only 2 reported a decrease, and 1 remained unchanged. The test showed a statistically significant difference ($Z = -4.785$, $p < 0.001$), confirming the changes were not due to chance. The median place attachment score increased from 41.00 to 45.00, indicating a stronger connection to Sitia UGGp. The total scores for place attachment for each participant illustrate a clear trend toward stronger connections with

Sitia UGGp (Figure 1).

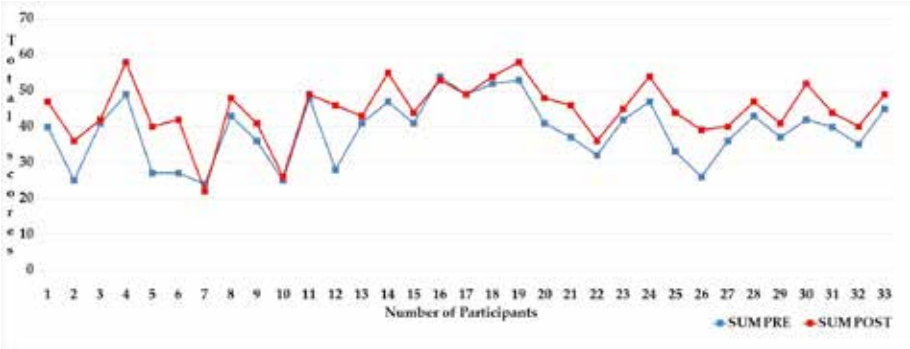

Figure 1. Distribution of total place attachment scores among summer school participants.

The results from the Wilcoxon signed-rank test and descriptive statistics demonstrate that the summer school significantly enhanced participants' attachment to Sitia UGGp. The increased median scores and the large number of participants reporting stronger connections highlight the program's success in deepening emotional and cognitive bonds with Sitia UGGp. This underscores the effectiveness of the summer school in fostering greater appreciation and attachment among participants.

To assess the summer school's impact on participants' perceptions of the Sitia UGGp's significance, a Wilcoxon signed-rank test compared median place meaning scores before (BPRE) and after (BPOST) the program. Of the 33 participants, 28 reported an enhanced perception of the site's importance, while only 2 noted a decrease, and 3 remained unchanged. The test showed a statistically significant difference ($Z = -4.282$, $p < 0.001$), indicating the changes were not due to chance. The median score for place meaning increased from 110.00 to 121.00 after the program. The upward shift in total scores for place meaning reflects a notable enhancement in participants' valuation of the Sitia UGGp, attributable to the summer school experience (Figure 2).

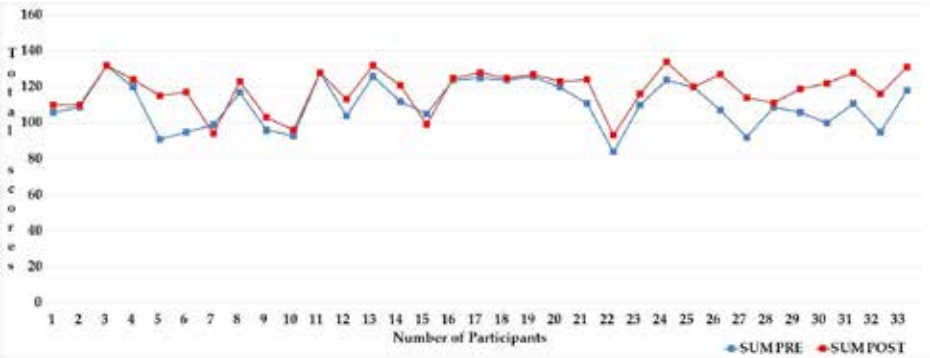

Figure 2. Distribution of total place meaning scores among summer school participants.

The results show that the summer school positively influenced participants' perceptions of the importance of the Sitia UGGp. The significant increase in median place meaning scores underscores the program's effectiveness in enhancing appreciation and recognition of the site's cultural and natural value. This highlights the role of educational initiatives in elevating the significance of heritage sites.

A Wilcoxon signed-rank test was also used to evaluate the impact of the summer school on participants' geoethical awareness, comparing median scores before (CPRE) and after (CPOST) the program. Among 33 participants, 26 reported increased geoethical awareness, 4 experienced a decrease, and 3 showed no change. The test revealed a statistically significant difference ($Z = -4.085$, $p < 0.001$), indicating the changes were not due to chance. The median geoethical awareness score rose from 139.00 to 152.00, demonstrating a significant improvement following the summer school. The notable increase in total scores for geoethical awareness indicates a positive shift in participants' geoethical perceptions of the Sitia UGGp, reflecting the summer school's effectiveness in enhancing their awareness (Figure 3).

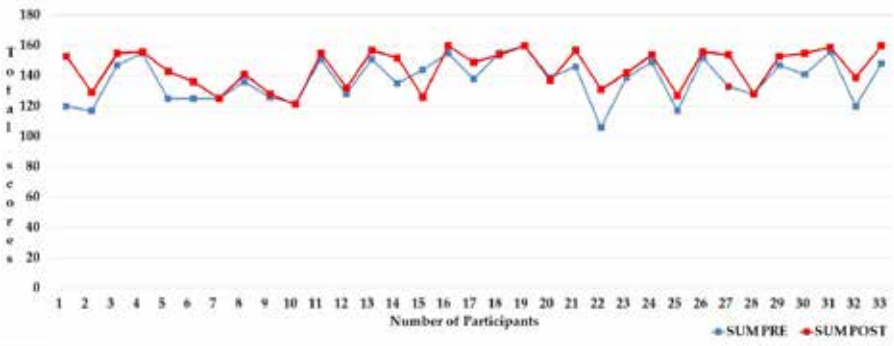

Figure 3. Distribution of total geoethical awareness scores among summer school participants.

The results show that the summer school significantly enhanced participants' geoethical awareness regarding the Sitia UGGp. The increase in median scores underscores the program's success in deepening understanding of ethical considerations. These findings affirm the summer school's effectiveness in enhancing geoethical perspectives and achieving its educational goals.

To explore the potential for predicting geoethical awareness (CPRE), a multiple linear regression analysis was conducted. The goal was to identify variables that reliably predict geoethical awareness before the summer school. Independent variables included place attachment (APRE), place meaning (BPRE), gender, years of teaching experience, and other factors related to environmental involvement. The stepwise procedure revealed that place attachment (APRE) and place meaning (BPRE) significantly contributed to the model, with an adjusted R^2 of 0.583, explaining 58.3% of the variance in geoethical awareness. ANOVA confirmed statistically significant differences for place attachment [$F(1,29) = 34.330$, $p < 0.001$] and place meaning [$F(2,28) = 21.990$, $p < 0.001$]. The regression equation is: Geoethical Awareness = 2.128 + 0.281 × Place Attachment + 0.332 × Place Meaning. A one-unit increase in place attachment predicts a 0.281 unit increase in geoethical awareness, while a one-unit increase in place meaning predicts a 0.332 unit increase. Place attachment showed a stronger effect, with a standardized coefficient B = 0.458. Multicollinearity checks showed no significant issues (max VIF < 5, Tolerance > 0.2), and the Durbin–Watson value (1.928) indicated independent residuals. Residuals met normal distribution assumptions, with Spearman's rho showing no significant correlation ($\rho = -0.128$, $p = 0.477$).

In summary, place attachment and place meaning are significant predictors of geoethical awareness, with place attachment being a stronger predictor. The model's reliability is confirmed by meeting statistical assumptions, highlighting the importance of emotional and cognitive connections in fostering geoethical awareness.

Conclusions

In the realm of geosciences, safeguarding biotic, abiotic, and cultural elements is crucial for sustainability and resilience. Geoconservation emphasizes geodiversity and biodiversity, highlighting biological, geological, and cultural heritage. Developing a strong sense of place can foster a responsible and cooperative world, enhancing emotional connections and promoting protective behaviors. Geoethics provides a framework for viewing Earth as a system of complex relationships, advocating sustainable practices.

This study on sense of place and geoethics at the Sitia UGGp found high reliability in scales measuring place attachment, place meaning, and geoethical awareness, both before and after summer school. Significant increases in these scales indicated enhanced emotional connections and understanding. Positive correlations among the scales highlighted their interrelation, with regression analysis confirming place attachment and place meaning as predictors of geoethical awareness.

Future research could explore changes in geoethical awareness over time, use interdisciplinary approaches for holistic understanding, and conduct comparative studies across UGGps. Investigating how awareness translates into behaviors and evaluating geoenvironmental education programs could enhance effectiveness. Validating the geoethical awareness scale in diverse contexts is also important.

This research has limitations, including a small sample size, lack of a control group, and potential biases. The focus on Sitia UGGp may limit applicability to other regions.

Acknowledgements

The authors want to express gratitude to the 4th Summer School of Environmental Education on Geotopes and Sustainability organizing committee at Sitia UNESCO Global Geopark and all the participants involved in our study. They also extend their heartfelt thanks to the organizing committee of the 17th International Congress of the Geological Society of Greece and the anonymous reviewers for their thorough consideration of this extended abstract.

References

Fassoulas, C., Staridas, S., Perakis, V., Mavrokosta, C., 2013. Revealing the Geoheritage of Eastern Crete through the Development of Sitia Geopark, Crete, Greece. Bulletin of the Geological Society of Greece 47, 1004-1016. https://doi.org/10.12681/bgsg.11143

Gordon, J.E., 2019. Geoconservation Principles and Protected Area Management. International Journal of Geoheritage and Parks 7, 199-210. https://doi.org/10.1016/j.ijgeop.2019.12.005

Koupatsiaris, A.A., Drinia, H., 2024. Expanding Geoethics: Interrelations with Geoenvironmental Education and Sense of Place. Sustainability 16, 1819. https://doi.org/10.3390/su16051819

Krasny, M.E., 2020. Advancing environmental education practice, Cornell University Press.

Kudryavtsev, A., Stedman, R., Krasny, M., 2012. Sense of Place in Environmental Education. Environmental Education Research 18, 229-250. https://doi.org/10.1080/13504622.2011.609615

Peppoloni, S., Di Capua, G., 2022. Geoethics: Manifesto for an Ethics of Responsibility towards the Earth, Springer International Publishing.

Semken, S., Freeman, C.B., Watts, N.B., Neakrase, J.J., Dial, R.E., Baker, D.R., 2009. Factors that Influence Sense of Place as a Learning Outcome and Assessment Measure of Place-Based Geoscience Teaching. The Electronic Journal for Research in Science and Mathematics Education 13, 136–159.

Sobel, D., 2004. Place-based education: Connecting classrooms and communities, 2nd ed. The Orion Society.

Williams, D., Vaske, J., 2003. The Measurement of Place Attachment: Validity and Generalizability of a Psychometric Approach. Forest Science 49, 830-840. https://doi.org/10.1093/forestscience/49.6.830

Young, M., 1999. The Social Construction of Tourist Places. Australian Geographer 30, 373-389. https://doi.org/10.1080/00049189993648

17th INTERNATIONAL CONGRESS of the Geological Society of Greece

BULLETIN OF THE GEOLOGICAL SOCIETY OF GREECE, SP. PUBL.

EXTENDED ABSTRACT 175

Fault–based recurrence models and occurrence probabilities of large earthquakes (M≥6.0) in the Corinth Rift, Greece

Kourouklas C. [1], Bonatis P.[1], Papadimitriou E.[1], Karakostas V.[1]

(1) Geophysics Department, School of Geology, Aristotle University of Thessaloniki, Thessaloniki, Greece, ckouroukl@geo.auth.gr.

Research Highlights

- The $M^3$6.0 earthquakes recurrence times, T_r, exhibit high variability from 40 to 1500 years, with the southern Corinth Rift fault segments reaching values up to 350 years and their antithetic ones ranging from 400 to 1500 years.
- The fault segments in the Corinth Rift can be devided into three groups, according to their recurrence behaviour, with some of them exhibiting significantly lower renewal model probabilities than the Poisson model, others showing nearly equal probabilities, and one segment where the renewal model probabilities are much higher than the Poisson one.
-

Introduction

The main objectives of the current study include the determination of the mean recurrence time, T_r, of large ($M^3$6.0) earthquakes associated with the major fault segments of the Corinth Rift, Greece, and the estimation of the conditional occurrence probabilities of an impending $M^3$6.0 earthquake on each major fault segment.

The recurrence behavior of large earthquakes (e.g. $M^3$6.0) on specific fault segments is one of the primary input parameters for developing long–term Earthquake Rupture Forecast (ERF) models. These models integrate a series of parameters (maximum observed magnitude, fault dimensions, long–term slip rates, available recurrence times) to estimate the occurrence likelihood of nearly characteristic magnitude earthquakes in a specific time span. The primary output of such models is the mean recurrence time, which can later be used for the application of statistical models, which, in turn, return the likelihood of the occurrence of near characteristic magnitude earthquakes over specific time intervals and can be based on either a time–independent or an elastic rebound motivated renewal assumption.

A precise and robust estimation of T_r requires the inclusion of as many large earthquakes associated with individual fault segments as possible, including both historical and instrumental data along with the selection of the appropriate statistical model. However, large earthquakes associated with specific fault segments are often limited, with only a few cases having about 3 to 10 observations due to the long duration required for stress accumulation and the short time span of available large earthquake records.

To address these challenges and limitations, an alternative approach is the estimation of T_r through the application of the seismic moment rate conservation method (Field *et al.*, 1999). This method defines the mean recurrence time as the ratio of the maximum expected seismic moment corresponding to a large earthquake with the maximum observed magnitude (M_{max}) occurring on a given fault segment, to the seismic moment that might be released by the respective fault segment due to the tectonic loading, assuming a nearly characteristic earthquake model. This approach can provide more precise T_r estimates because the overall rate and size distribution of earthquakes should reflect the tectonic loading in the brittle part of the crust, and this function is typically constrained by the principle of seismic moment rate conservation.

Seismotectonic Setting of Corinth Rift

The Corinth Rift, a prominent E–W oriented elongated graben stretching over 100 km in length, separates the Peloponnese from mainland Greece. It exhibits a remarkable extension rate that varies spatially, with the western section extending at approximately 10 mm/yr and the eastern section at around 5.5 mm/yr (Briole *et al.*, 2021). As a result, the Corinth Rift is one of the most seismically active regions, frequently experiencing large ($M^3$6.0) earthquakes during both the instrumental and historical seismicity periods (Papazachos & Papazachou, 2003), with the most recent one being the 1995 M_w=6.5 Aigion earthquake (Bernard *et al.*, 1997). The intense seismic activity along the Corinth Rift has made it one of the most well studied areas, resulting in the detailed determination of its main fault segments. Information on the M≥6.0 earthquakes are derived from the catalogue provided by Papazachos & Papazachou (2003) and regional parametric earthquake catalog of the Geophysics Department of the Aristotle University of Thessaloniki, consisting of 35 large earthquakes since 373 BC. Studies by Console *et al.* (2013, 2015), after concluding that the large earthquakes catalog could be considered as complete after 1700 AD (since 1714 AD) as well as Kourouklas (2022), suggest that they are not regularly distributed but they are clustered in time. This latter dataset includes 22 M≥6.0 earthquakes (Figure 1).

The southern margin of the Corinth Rift is bounded by eight (8) normal faults, listed from west to east as Psathopyrgos (FS 01), Aigion (FS 02), Eliki (FS 03), Akrata (FS 04), Xylokastro (FS 05), Perachora (FS 06), Skinos (FS 07) and Alepochori

(FS 08) fault segments (Figure 1). Their strike values are almost the same 260° – 280° and their dip angles vary between 30° and 45°. The northeastern boundary of study area is demarcated by the Kapareli fault segment (FS 09), also a normal fault with a strike of 50° and a dip angle of 50°. The fault segment lengths range from 8 km (Akrata Fault Segment) to 22 km (Eliki Fault Segment). All their geometrical and kinematic were summarized by Console *et al.* (2013, and references therein). To the north the Delfoi (FS 10), Makrygialos (FS 11), Sykia (FS 12) and Marathias (FS 13) fault segments are defined from east to west (Figure 1; Ganas 2024, and references therein). Their lengths range from 10 km (Makrygialos and Sykia fault segments) to 18 km (Delfoi fault segment).

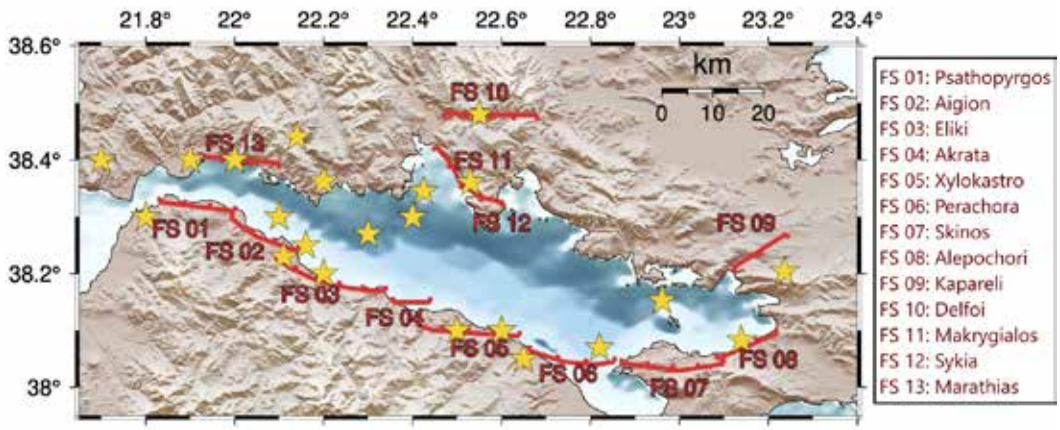

Figure 1. Geomorphological map of Corinth Rift, where the major normal fault segments are represented by red solid lines. Yellow stars depict the *M*≥6.0 earthquakes occurred in the study area since 1714.

Although the number of large earthquakes (both historical and instrumental) is adequate for regional statistical studies, the number of recurrence intervals become limited when subdivided into subsets associated with specific fault segments. For this reason, Kourouklas (2022, and references therein) attempted to associate the 22 *M*≥6.0 earthquakes since 1714 with their respective causative fault segments. The analysis suggested that 2 out of 8 fault segments of the western Corinth Rift were associated with two (2) *M*≥6.0 earthquakes each (Psathopyrgos and Eliki). The Aigion fault segment was linked to four (4) events, whereas the Xylokastro and Perachora segments were each associated with three (3). The Alepochori and Skinos fault segments were associated with one (1) *M*≥6.0 earthquake each. It is noteworthy that the Akrata fault segment, the shortest in length, has not been associated with any *M*≥6.0 earthquake since 1714. Similarly, the Kapareli fault segment was also associated with only one (1) *M*≥6.0 earthquake. In the northern part, the Delfoi, Makrygialos and Sykia segments were associated with one (1) *M*≥6.0 historical earthquake each, whereas the Marathias fault was linked to two (2) such events. Thus, although the study area is among the most seismically active areas where several large earthquakes rather frequently take place, the insufficient number of *M*≥6.0 earthquake events per segment restricts the ability to determine T_r by using their observational recurrence intervals as input.

Method

We estimated the mean recurrence time, T_r, by applying the seismic moment rate conservation technique (Field *et al.*, 1999) in the absence of a sufficient number of recurrence intervals for each of the 13 normal faults in the Corinth Rift. This technique assumes that a large earthquake of nearly characteristic magnitude can release the total accumulated seismic moment on a fault. It takes into account the maximum observed magnitude (M_{max_obs}) and its corresponding uncertainty (ΔM) and the maximum seismic moment corresponding to the accumulated strain on the specific fault segment due to tectonic loading. The mean recurrence time is then calculated as the ratio of the seismic moment rate that can be released by the maximum magnitude earthquake to the seismic moment due to strain accumulation on the fault:

$$T_r = \frac{M_{o\,max}}{\mu L w V} \quad (1)$$

where $M_{o,\,max}$ is the maximum possible seismic moment released by a large earthquake with a magnitude within the range $M_{max_obs} \pm \Delta M$. μ is the shear modulus, whose typical value for faults in the Earth's crust is equal to 3.3×10^5 bar ($\mu = 3.3\times10^5$ bar), L and w *are* the length and width of the fault segment (in km), respectively, and V the long–term slip rate.

The maximum expected seismic moment is computed via the definition of seismic moment. The variability of T_r is also computed via the method of formal error propagation technique proposed by Peruzza *et al.* (2010), considering the uncertainties related

to the maximum magnitude and slip rate values. Knowing the variability of mean recurrence time, the standard deviation, σ, can then be easily calculated. The advantage of this approach is that, once T_r and σ are estimated, the corresponding aperiodicity values, α, can be calculated as the coefficient of variation, C_v, of T_r, which is the second appropriate parameter of renewal model applications (Pace *et al.*, 2016).
Using the estimated T_r and σ as the primary inputs, we model the M≥6.0 earthquakes recurrence times by applying both the time–independent Poisson model and the Brownian Passage Time (BPT; Matthews *et al.*, 2002) renewal model, aiming at the estimation of the occurrence probabilities of the next M≥6.0 earthquake to be occurred on each fault segment for the next 10, 20 and 30 years, starting from 1 January 2025.
The Poisson process can be expressed by the exponential distribution with probability density function (pdf) given by:

$$f(t|T_r) = \frac{1}{T_r}\exp\{-\frac{t}{T_r}\} \quad (2)$$

where T_r is the mean recurrence time of large earthquakes associated with a specific fault segment. To model the occurrence of large earthquakes as a renewal process, the BPT distribution is applied. The PDF of the BPT model is given by:

$$f(t|T_r, \alpha) = \left(\frac{T_r}{2\pi\alpha^2 t^3}\right)^{1/2} \exp\{-\frac{(t-T_r)^2}{2T_r\alpha t}\} \quad (3)$$

where T_r is also the mean recurrence time and α is the aperiodicity, which can be considered as analogous to the coefficient of variation, C_v, of the normal distribution.
The occurrence probabilities of a next large earthquake on certain fault in a specific time span can be computed by applying the simple Poisson probability model given by:

$$P(t \le T \le t + \delta t) = 1 - e^{-\delta t/T_r} \quad (4)$$

where $\delta t \delta t$ is the forecast duration and the conditional probability corresponding to the BPT renewal given by:

$$P(t \le T \le t + \delta t) = \frac{\int_t^{t+\delta t} f(t)dt}{\int_t^{\infty} f(t)dt} \quad (5)$$

where t is relative to the date of last earthquake, conditioned by the fact that it has been $t + \delta t t + \delta t$ years since the last one.
Alternatively, the occurrence probabilities of the next large earthquake can be evaluated by the estimation of the hazard function, $H(t)$, of both Exponential and BPT models. This analysis is particularly useful for predicting future rupture scenarios as the values of the hazard function or, in other words, the hazard rate is equivalent to the conditional probability estimate within a specific time span. The hazard function of a given distribution can be easily defined using its corresponding probability density, $f(t)$, and cumulative density, $F(t)$, functions as follows:

$$H(t) = \frac{f(t)}{S(t)} = \frac{f(t)}{1-F(t)} \quad (6)$$

where $S(t)$ is the survival function of the distribution.

Application & Results

The mean recurrence times, T_r, of M≥6.0 earthquakes are estimated through Equation (1) after defining all the appropriate parameters for the application of the seismic moment rate conservation method. These parameters include the fault dimensions (L, w), the maximum observed magnitude, M_{max_obs}, their long-term slip rates (V) and the corresponding uncertainties (ΔM and σV, respectively) which are summarized in Kourouklas (2022). It should be noted that for the definition of the long-term slip rates assigned to each fault segment, 60% of the geodetic slip rates proposed by Briole *et al.* (2021) are used. As previously mentioned, the Akrata fault segment was not associated with any M≥6.0 earthquake and the estimation of the mean recurrence time and the maximum expected magnitude, were calculated using scaling relations, The absence of any M≥6.0 earthquake associated with this fault segment prevents the estimation of any elapsed time, which is necessary for renewal recurrence modeling. For this reason, the Akrata fault segment is excluded from the next steps of the statistical analysis.
The estimated T_r values (Figure 2a) range from a few years (Akrata fault segment; T_r=35 years) to about 1500 years (Makrygialos fault segment; T_r=1511.5 years). These variations are clearly related to the dimensions and slip rates of each segment, which results in different stressing rate values and maximum observed magnitudes. Starting from the southern Corinth Rift fault zone (excluding the Akrata fault segment), mean recurrence times vary from almost 120 years (Psathopyrgos fault segment; T_r=119.4 years) to 359 years (Skinos fault segment; T_r=359.3 years) (Figure 2a). The T_r of M≥6.0 earthquakes increase from the western

part to the eastern one (Figure 2a), due to the gradual decrease of deformation rates from the western to eastern part of our study area. Regarding the respective *Cv* values, it is reported that they exhibit minimal variations, ranging from 0.6 to 0.7 in 6 out of 7 cases (Psathopyrgos, Aigion, Xylokastro, Perachora, Skinos, Alepochori). This suggests that the recurrence behavior of $M \geq 6.0$ earthquakes associated with these fault segments can be characterized as slightly aperiodic. On the other hand, results of our analysis for $M \geq 6.0$ earthquakes associated with the Eliki fault segment indicates that its recurrence behavior can be characterized as highly aperiodic (almost random), given that its *Cv* value is equal to 0.9 (*Cv*=0.9).
Moving to the mean recurrence time results for the northern part, higher values are reported, ranging from 426 years to 1511 years. Specifically, the T_r of $M \geq 6.0$ earthquakes associated with the Kapareli fault segment is found equal to 426 years, with a *Cv* value of 0.6. The mean recurrence time for the Delfoi fault segment is equal to T_r=933.1 years, whereas the T_r of $M \geq 6.0$ earthquakes associated with Makrygialos and Sykia fault segments are even larger, with T_r=1511.5 years and T_r=1070.1 years, respectively. The mean recurrence time of $M \geq 6.0$ earthquakes associated with the Marathias fault segment is T_r=546.1 years. The coefficient of variation for all four these cases (Delfoi, Makrygialos, Sykia, Marathias) is estimated equal to *Cv*=0.7.

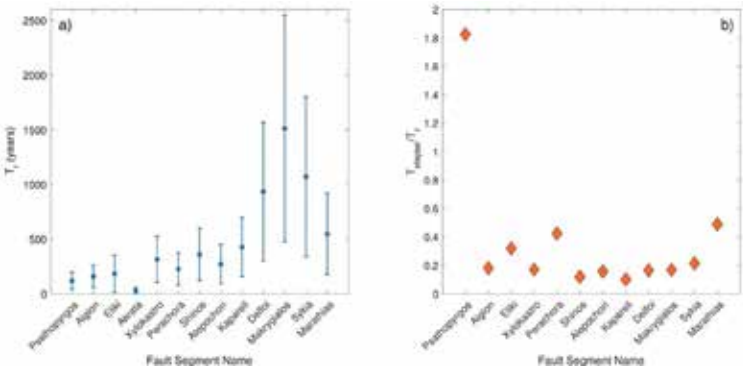

Figure 2. (a) Mean recurrence time, T_r, estimates of $M \geq 6.0$ earthquakes (blue circles), along with their ±1σ (vertical blue solid line) for the 13 normal fault segments of the Corinth Rift. (b) The ratio of elapsed time, T_e, of the last $M \geq 6.0$ earthquake that occurred in each fault segment (except from Akrata fault segment) and the mean recurrence time, T_r, estimates.

One more important factor for the statistical modeling of T_r, especially for time–dependent approaches, is the elapsed time, T_e, since the last earthquake. Specifically, the ratio of T_e over T_r can serve as an initial indicator of the stage of the earthquake cycle for a given fault. Values of this ratio approaching zero indicate the early stage of a new earthquake cycle, while more increased values indicate that the fault is closer to the next rupture. Figure 2b shows the ratio of the elapsed time to the mean recurrence time for the seven fault segments. The smallest value is reported for the Aigion fault segment, which is the most recently ruptured (T_e = 28.57 years). For 10 out of the other 11 fault segments, the ratio ranges between 0.17 and 0.55, also showing that the elapsed time is considerably shorter than the mean recurrence time. This suggests that these faults are likely in the early stages of their seismic cycle. The only case in which the ratio is larger than 1.0 is the Psathopyrgos fault segment (Figure 2b), meaning that the elapsed time since the last $M \geq 6.0$ is much larger than the estimated T_r.
Next, we applied the exponential and BPT distributions, representing the Poisson and renewal models, using the mean recurrence time, T_r, and *Cv* values obtained from the seismic moment rate conservation approach. The ultimate goal is to model the recurrence behavior of the $M \geq 6.0$ earthquakes associated with the normal faults of the study area. We focused primarily on the hazard functions of both statistical models, as their (hazard) rates can be considered equivalent to the conditional probability estimates over a specific time span. Figure 3 shows the hazard functions of the exponential and BPT distributions for the seven (7) fault segments of the southern part (Psathopyrgos, Aigion, Eliki, Xylokastro, Perachora, Skinos and Alepochori), in which their significant differences in modeling T_r are highlighted.
Starting from the Psathopyrgos fault segment (Figure 3a) the constant hazard rate of the Poisson model (blue solid line) is considerably lower than the hazard rate of the BPT model (red solid line), which exhibits a decreasing trend, at the time corresponding to T_e (until 31-12-2024). On the other hand, in the case of the Aigion fault segment (Figure 3b), the most recently ruptured segment in the study area, the hazard function values of the Poisson model (blue solid line) are considerably larger than the values obtained from the application of the BPT, at the time corresponding to T_e. The BPT model application on the Eliki fault segment (Figure 3c) reports hazard rates slightly higher than those of the Poisson model around the time corresponding to the elapsed time (black dashed line in Figure 3c). More specifically, the BPT hazard function values exhibit an increasing trend for the next 10, 20 and 30 years after 31-12-2024. Similarly, for the Aigion fault segment, the hazard function values of the Poisson model (blue solid line) are considerably larger than the values of the BPT model for the recurrence behavior of the $M \geq 6.0$ earthquakes associated with the Xylokastro fault segment (Figure 3d), indicating that the fault segment is at an early stage of a

new earthquake cycle at time *t* corresponding to the elapsed time. For the Perachora fault segment both models report almost equal hazard rates (Figure 3e) and lastly, for the Skinos and Alepochori fault segments (Figures 3f and 3g, respectively) the hazard function values of the BPT model are significantly lower than the ones of the Poisson model at time *t* corresponding to the elapsed time, highlighting that both segments are at an early stage of a new earthquake cycle according to the renewal model.

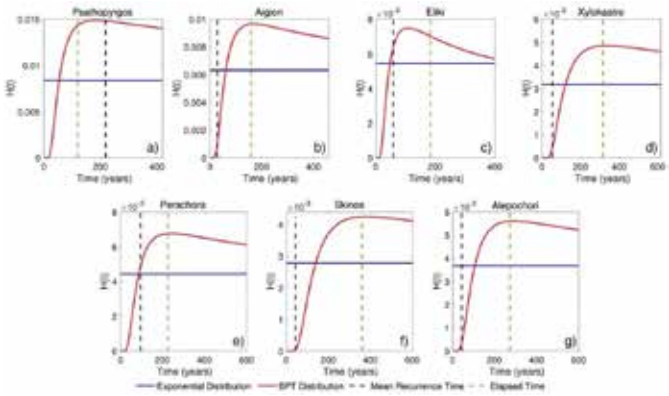

Figure 3. Hazard functions, *H(t)*, for the Psathopyrgos (a), Aigion (b), Eliki (c), Xylokastro (d), Perachora (e), Skinos (f) and Alepochori (g) fault segments according to the Exponential (blue solid lines) and the BPT (solid red lines) distributions. Vertical dashed lines denote the elapsed time since the last *M*≥6.0 earthquake (*t* = 0) occurred on each fault segment, whereas the vertical dashed black lines denote the mean recurrence time of *M*≥6.0 earthquake for each fault segment.

Focusing on the recurrence modeling results for the five (5) fault segments of the northern Corinth Rift fault zone, in 4 out of 5 cases the hazard rate values of the renewal model are significantly lower than those of the Poisson model. Specifically, the statistical modeling of *M*≥6.0 earthquakes associated with the Kapareli (Figure 4a), Delfoi (Figure 4b), Makrygialos (Figure 4c) and Sykia (Figure 4d) fault segments show that the hazard rate estimates of the time–independent Poisson model are considerably higher (blue solid lines in Figures 4a, 4b, 4c and 4d) than the ones of the BPT model (solid red lines). More specifically, for the Kapareli fault segment, the BPT model hazard function values are almost zero at the time corresponding to the elapsed time, whereas the constant hazard rate of the Poisson mode is equal to 2.4×10^{-3}. Statistical modeling for Delfoi, Makrygialos and Sykia fault segments indicates slightly different results for the renewal model, with its hazard function values exhibiting an increasing trend for the next 10, 20 and 30 years after elapsed time (vertical dashed black lines in Figures 4b, 4c and 4d) in all cases. On the contrary, the recurrence modeling of *M*≥6.0 earthquakes associated with the Marathias fault segment (Figure 4e) reports hazard rates slightly higher than the ones of the Poisson model around the time corresponding to the elapsed time.

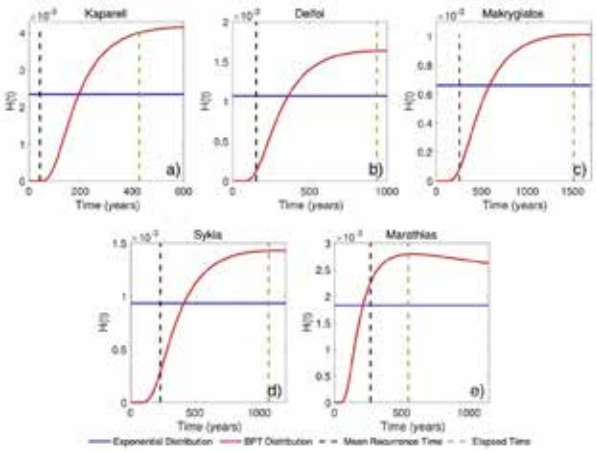

Figure 4. Hazard functions, *H(t)*, for the Kapareli (a), Delfoi (b), Makrygialos (c), Sykia (d) and Marathias (e) fault segments according to the Exponential (blue solid lines) and the BPT (solid red lines) distributions. The vertical dashed lines denote the elapsed time since the last *M*≥6.0 earthquake (*t* = 0) occurred on each fault segment, whereas the vertical dashed black lines denote the mean recurrence time of *M*≥6.0 earthquake for each fault segment.

Conclusions

In this study, we present both time–dependent and time–independent recurrence models to investigate the mean recurrence time of $M \geq 6.0$ earthquakes associated with the main normal faults of the Corinth Rift. We used the most detailed available input data (fault network model, long–term slip rates) for the estimation of the mean recurrence time, T_r, by applying the physics–based seismic moment rate conservation method. The results show that T_r ranges from about 40 years to almost 1500 years, depending on the combination of the input parameters. The statistical analysis of T_r via the Exponential and BPT distributions (representing the Poisson and a renewal model, respectively) reveals that the recurrence behavior of the Corinth Rift fault segments can be divided into three distinct groups. The first group includes fault segments where the elapsed time since the last earthquake is considerable smaller than the T_r. This group includes the Aigion, Xylokastro, Skinos, Alepochori, Kapareli, Delfoi, Makrygialos and Sykia fault segments. For all these cases the renewal model's hazard function values and the corresponding conditional occurrence probabilities for the next 10, 20 and 30 years show significant differences among the two applied models, with the BPT model yielding much lower values than the Poisson model. These findings indicate that the aforementioned fault segments are at an early stage of a new earthquake cycle according to the renewal model. The second group includes the Eliki, Perachora and Marathias fault segments for which the hazard rates of both models are almost equal, resulting in similar occurrence probabilities for the next 10, 20 and 30 years. The last group includes only the Psathopyrgos fault segment for which the BPT model reports significantly larger hazard rate values than the Poisson model. The Psathopyrgos fault segment is the only case where the elapsed time since the last $M \geq 6.0$ earthquake exceeds the mean recurrence time, indicating that from a statistical point of view, it is at a later stage of a new earthquake cycle. Consequently, the occurrence probabilities for the next $M \geq 6.0$ earthquake to occur in the next 10, 20 and 30 years are the highest within the study area. The results of our analysis could serve as the basis for fault–based large earthquake occurrence models. By considering time–dependent occurrence models in probabilistic seismic hazard analysis (PSHA) one can account for epistemic uncertainties, quantify the range of seismic hazard for a given exceedance probability and illustrate which model assumptions lead to the most significant variations in the estimated seismic hazard (Akinci *et al.*, 2017). By utilizing these models, stakeholders can better determine when and where protective measures are most urgently needed, particularly in regions with higher short-term earthquake probabilities, leading to more effective seismic risk management.

Acknowledgements

Funded by the European Union

This research is financially supported by the artEmis Project funded by the European Union, under Grant Agreement nr 101061712. Views and opinions expressed are however those of the author(s) only and do not necessarily reflect those of the European Union or European Commission – Euratom. Neither the European Union nor the granting authority can be held responsible for them.

References

Akinci, A., Vannoli, P., Falcone, G., Taroni, M., Tiberti, M.M., Murru, M., Burrato, P., Mariucci, M.T., 2017. When time and faults matters: Towards a time-dependent probabilistic SHA in Calabria, Italy. Bulletin of Earthquake Engineering 15, 2497-2524.

Bernard, P., Briole, P., Meyer, B., Lyon-Caen, H., Gomez, J.-M., Tiberi, C., Berge, C., Cattin, R., Hatzfeld, D., Lachet, C., Lebrun, B., Deschamps, A., Courboulex, F., Larroque, C., Rigo, A., Massonet, D., Papadimitriou, P., Kassaras, I., Diagourtas, D., Makropoulos, K., Veis, G., Papazisi, E., Mitsakaki, C., Karakostas, V., Papadimitriou, E., Papanastassiou, D., Chouliaras, G., Stavrakakis, G., 1997. The Ms = 6.2, June 15, 1995 Aigion earthquake (Greece): Evidence for low angle normal faulting in the Corinth rift. Journal of Seismology 1, 131–150. Doi:https://doi.org/10.1023/A:1009795618839.

Briole, P., Ganas, A., Elias, P., Dimitrov, D., 2021. The GPS velocity field of Aegean. New observations, contribution of the earthquakes, crustal blocks model, Geophysical Journal International 226, 468-492.

Console, R., Falcone, G., Karakostas, V., Murru, M., Papadimitriou, E., Rhoades, D., 2013. Renewal models and coseismic stress transfer in the Corinth Gulf, Greece, fault system/ Journal of Geophysical Research, Solid Earth 118, 3655–3673. Doi:https://doi.org/10.1002/jgrb.50277.

Console, R., Carluccio, R., Papadimitriou, E., Karakostas, V., 2015. Synthetic earthquake catalogs simulating seismic activity in the Corinth Gulf, Greece, fault system. Journal of Geophysical Research 120, 326–343. Doi:https://doi.org.10.1002/2014JB011765.

Field, E.H., Jackson, D.D., Dolan, J.F., 1999. A mutually consistent seismic hazard source model for Southern California. Bulletin of Seismological Society of America 89, 559–578.

Ganas, A., 2024. NOAFAULTS KMZ layer Version 6.0 (version 6.0) [Data set]. Zenodo. Doi: https://doi.org/10.5281/zenodo.13168947

Kourouklas, C., 2022. Determination and simulation of strong earthquakes' recurrence times in Greece via the application of stochastic models: contribution on seismic hazard assessment. Ph.D. Thesis, Aristotle University of Thessaloniki,

Thessaloniki, 329 p. Doi: http://dx.doi.org/10.12681/eadd/53270
Matthews, M.V., Ellsworth, W.L., Reasenberg, P.A., 2002. A Brownian model for recurrent earthquakes, Bulletin of Seismological Society of America 92, 2233–2250.
Pace, B., Visini, F., Peruzza, L., (2016). FiSH: MATLAB Tools to Turn Fault Data into Seismic-Hazard Models, Seismological Research Letters, 87, 375-386.
Papazachos, B.C., Papazachou, C.C., 2003. The earthquakes of Greece, Ziti Publications.
Peruzza, L., Pace, B., Cavallini, F., 2010. Error propagation in time- dependent probability of occurrence for characteristic earthquakes in Italy, Journal of Seismology, 14, 119–141.

17th INTERNATIONAL CONGRESS of the Geological Society of Greece

BULLETIN OF THE GEOLOGICAL SOCIETY OF GREECE, SP. PUBL.

EXTENDED ABSTRACT 176

A preliminary petrographic approach to the pyroclastic rocks (tuffs) of Tilos island

Petros Koutsovitis[1], Gerasimina Pahaki[1], Vasileios Giamas[1], and Lemonia Kalantzi[1]

(1) University of Patras, Greece, pkoutsovitis@upatras.gr

Introduction

Volcanism in the Aegean results after the subduction of the African plate beneath the European. The present-day active volcanic arc consists of five major volcanic centers (Sousaki, Methana-Aegina, Milos-Antimilos, Santorini-Kolumbo, and Nisyros-Kos). In the eastern Aegean, several large-scale volcanic eruptions took place during Late Pleistocene, which produced large quantities and relatively thick layers of pumice and vitric ash. These were distributed throughout various regions, but they are more evident in proximity to the volcanic centers. Their origin is mainly associated with the phreatomagmatic volcanic eruption of Nisyros volcano at eastern flank, which corresponds to the Kyra sequence at 161 ka (Sterba, 2007; Sterba *et al.,* 2011). Pyroclastic deposits in the form of pumice from this eruption have been recorded not only to the southeast at Tilos island but also to the north at Kalymnos Island, and to the east at Datça peninsula in Turkey, expanding over an area of approximately 3000 km^2. KPT pyroclastic deposits have been investigated by Smith *et al.* (1996) and Steinhauser *et al*. (2007) in order to refine the chemical fingerprint of the KPT eruption

Explosive rhyolitic eruptions form one of the most hazardous catastrophic events that can occur on earth (Allen 1999). The eruption of the Kos Plateau Tuff (KPT) produced massive rhyolitic fallout, high-density pyroclastic flows, and massive ignimbrites (Allen, 2001). The inflow of seawater to the magmatic chamber at the early stages of the eruption can be considered as the mechanism that led to a phreatomagmatic type of eruption. The fact that the lithic breccia is followed by the deposition of ignimbrites forms an important volcanological feature which implies the collapse of the caldera and links with its initial stages. This feature has also been noticed in the Minoan eruption of Santorini (Heiken and McCoy,1984). During caldera collapse, the pressure and the mass flux increase simultaneously (Wilson *et al.,* 1980; Carey and Sparks, 1986; Carey and Sigurdsson, 1989). Pyroclastic deposits withhold information about the eruption and/or mass flux nevertheless the precise classification of internal stratigraphy and lithofacies combined with petrographical and geochemical results can pose fundamental objectives regarding the dynamics of the eruption.

Geological Setting

The non-volcanic island of Tilos lies to the southeast of the volcanic islands of Kos and Nisyros. Stratigraphically, Tilos consists of biosparudites limestones and dolomites, locally representing the 'Hallstatt' phase. These rocks date from Triassic to the Lower Jurassic. Furthermore, it consists of Upper Jurassic thin-bedded pelagic plate micritic limestones, Upper Cretaceous pelagic biomicritic limestones as well as pyroclastic deposits from the KPT eruption (Stadlbauer, 1988; Johannes and Sterba, 2007). The pyroclastic rocks are mostly represented by tuffs and pumices, which in most cases correspond to acid compositions (e.g., rhyolite), and date to the Quaternary. According to Allen and Cas (1998), Tilos pyroclastic rocks are subdivided into i) ash-rich facies (~1 meter), ii) pumice-rich facies (~50 centimeters) and iii) pumiceous ignimbrites. The pumiceous ignimbrites, which are correlated with the E stromatographic unit of Nisyros (Allen and Cas, 1998), contain basaltic lithic fragments (Figure 1a) and are rather restricted in only a few outcrops in the field. Based on field observations, pumice-rich facies underlain the ash-rich facies. The ash-rich facies are coarse-grained and exhibit internal wavy and irregular bedforms (Figure 1b), whilst pumice-rich facies display fine lithic lapilli. The lithic clasts of this layer are rather small in size (< 40 centimeters) and the matrix material is fine-grained compared to the overlying pumiceous ignimbrite.

Figure 1. (a) Field photograph from the lower pyroclastic unit, comprising of lithic fragments, many of which are basaltic, (b) Field photograph from pumice succession of pyroclastic tuffs.

Materials and Methods

Twenty rock samples were collected from Tilos Island. These were macroscopically classified into two major groups i) pumices and ii) basaltic lithic fragments taking into account field observations as well. All samples were subsequently crushed and pulverized for conducting bulk mineralogy investigation through X-ray Diffractometry (XRD) as well as polished thin sections were prepared for conducting petrographic examination through transmitted light optical microscopy. Bulk mineralogy of the studied samples was determined using a Bruker D8 Advance Diffractometer with Ni-filtered CuKα radiation at the Research Laboratory of Rocks and Minerals of the University of Patras. The scanning angle (2θ) interval was 2–70° with an angular step size of 0.015° and a time step of 0.1 s. Subsequently, mineral phases were determined using the DIFFRACplus EVA 12® software (Bruker-AXS GmbH, Karlsruhe, Germany) and the ICDD Powder Diffraction File of PDF-2 2006. Petrographic examination was performed using a polarizing petrographic microscope (Leitz Ortholux II POL-BK Ltd., Midland, ON, Canada) at the Research Laboratory of Rocks and Minerals of the University of Patras.

Results-Discussion

In the present study, three main types of pyroclastic rocks were observed based on field observations. Most of the thin layers are ash-rich layers and pumice-rich layers that collapsed and flattened as they were re-heated, whereas in some cases the pumice clasts have relatively high vescularity, revealing high intensity phases. The matrix material is quite friable and finely crystalline, with yellow ash dominating the most outcrops. Lithic fragments show a diversity (e.g., basaltic, pumice) and in restricted outcrops has also established obsidian. Basaltic lithic fragments are mainly found within the lower pyroclastic unit (Figure 1a) are well preserved and have been subjected to only minor alterations. Pumice samples show an excellent color contrast between the various clasts (red, orange, brown, etc.) and the compressed ash (white). The pinkish to brownish hue characteristic for some samples is mainly due to oxidation but could also related to the presence of xenoliths (i.e., basaltic blocks; Figure 2b).

Pyroclastic rocks present vitrophyritic texture and contain plagioclase (mainly albite-oligoclase), clinopyroxenes (augite) and alkali feldspars. They also contain tubular fragments of pumice as well as bonded clay margins on glassy and crystalline surfaces, which record the initial stage of diagenesis in this semi-molten pumice breccia. These clay margins in many cases enclose crystalline and glassy fragments. In some cases, microfossils were also established within the matrix. The pyroclastic texture of most tuffs is not so evidently identified. Basaltic lithic fragments contain plagioclase, clinopyroxene, and alkali feldspars (Figure 3). Despite the glassy and fine-grained nature of the studied rocks, they display trachytic texture and, in some cases, glomeroporphyritic textures (Figure 3).

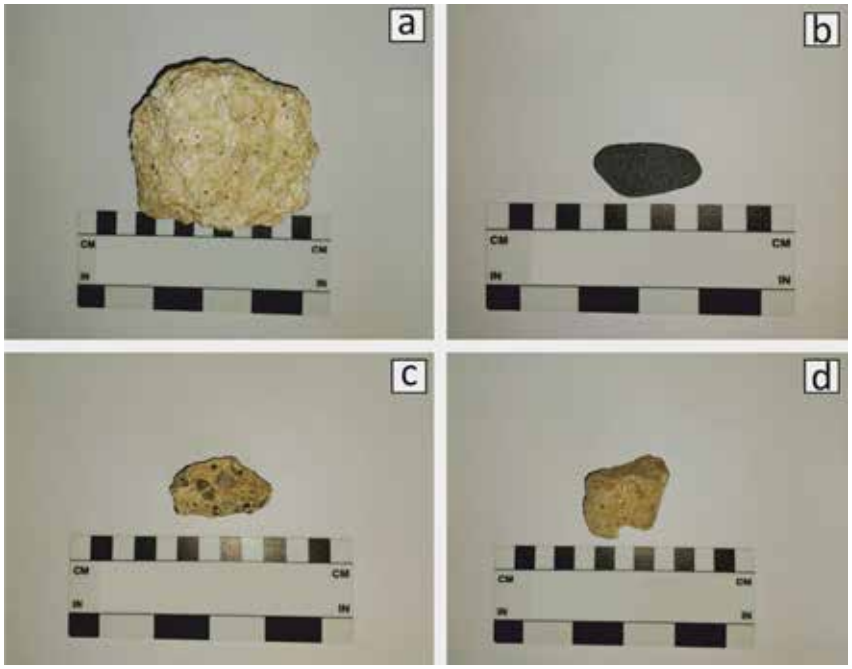

Figure 2: Representative samples from Tilos Island, a) Vesicular pumice, b) Basaltic lithic fragment, c) Pumice with individual clasts, and d) Pumice with low porosity.

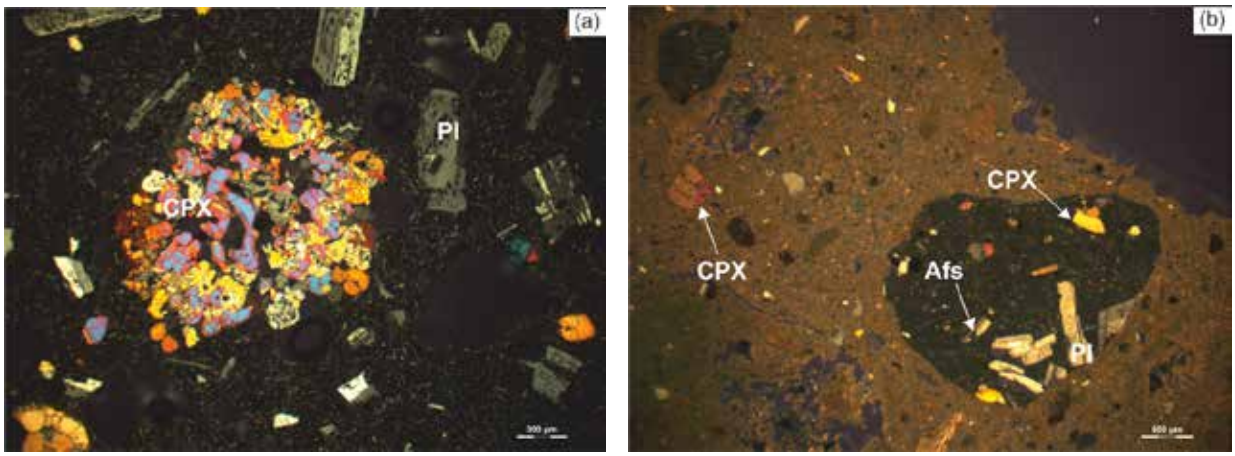

Figure 3. Photomicrographs of: (a) hornblende basaltic lithic fragment with quenched glomerophyric clinopyroxenes (CPX) and plagioclase (Pl) and b) pyroclastic lapilli tuff with devitrified glass with clinopyroxene (CPX) phenocryst and basaltic lithic fragment with clinopyroxene phenocrysts (CPX), plagioclase (Pl) and alkali feldspar (AFS).

Conclusion

The internal stratigraphy and the deposition of the lithofacies reflect a dynamic high-intensity eruption. In particular, the deposition of these basaltic lithic fragments seems to be vent-derived, resulting from the deposition of voluminous ignimbrites. For the case of Tilos, the conduit type of lithic fragments can be an eruptive indicator. Also, the textural changes in the vesicularity of the pumice show possibly two stages of depressurization and the influence of the volatiles during the phreatomagmatic eruption. These patterns have a strong impact, and their understanding would be critical for potential hazard assessment. Through a more comprehensive volcanological view, further investigation combining field observations and detailed mineral chemistry analyses of the fluid inclusion on the lithic fragments and the pumice will highlight the importance of volatiles in post-caldera forming reactions.

References

Allen, S. R. (2001). Reconstruction of a major caldera-forming eruption from pyroclastic deposit characteristics: Kos Plateau Tuff, eastern Aegean Sea. Journal of Volcanology and Geothermal Research, 105, 141–162.

Carey, S., & Sigurdsson, H. (1989). The intensity of plinian eruptions. Bulleting of Volcanology, 51, 28–40.

Carey, S., & Sparks,. (1986). Quantitative models of the fallout and dispersal of tephra from volcanic eruption columns. *Bulleting of Volcanology*, 48, 109–125.

Caliro, S., Chiodini, G., Galluzzo, D., Granieri, D., La Rocca, M., Saccorotti, G., Ventura, G., 2005. Recent activity of Nisyros volcano (Greece) inferred from structural, geochemical and seismological data. Bulletin of Volcanology 67, 358–369.

Johannes, D.I., Sterba., J.H, 2007, Anwendung der Neutronen Aktivierungsanalyse zum Aufbau der Chemostratigraphie einer vulkanischen Eruptionssequenz auf Tilos und Nisyros, Griechenland., pages 7-120.

Heiken, G., & Jr, M. (1984). Caldera development during the Minoan eruption, Thira, Cyclades, Greece. *J. Geophys. Res.*, *89*(B10), 8441–8462.

Nomikou, P., Krassakis, P., Kazana, S., Papanikolaou, D., Koukouzas, N. 2021. The Volcanic Relief within the Kos-Nisyros-Tilos Tectonic Graben at the Eastern Edge of the Aegean Volcanic Arc, Greece and Geohazard Implications, Geosciences 11, 231.

R, A. S., & Cas,. (2001). Transport of pyroclastic flows across the sea during the explosive, rhyolitic eruption of the Kos Plateau Tuff, Greece. *Bulletin of Volcanology*, *62*(6), 441–456.

R, A. S., Stadlbauer, E., & Keller, J. (1999). Stratigraphy of the Kos Plateau Tuff: product of a major Quaternary explosive rhyolitic eruption in the eastern Aegean, Greece. *International Journal of Earth Sciences*, *88*(1), 132–156.

Smith, P.E., York, D., Chen, Y., Evensen, N.M., 1996. Single crystal 40Ar–39Ar dating of a Late Quaternary paroxysm on Kos, Greece: concordance of terrestrial and marine ages. Geophys. Res. Lett. 23, 3047–3050.

Stadlbauer, E., 1988. Vulkanologisch-geochemische Analyse eines jungen Ignimbrites: Der Kos-Plateau-Tuff (Südost-Ägäis). PhD thesis, Freiburg.

Steinhauser, G., Sterba, J.H., Bichler, M., 2007. Chemical fingerprints of pumice from Cappadocia (Turkey) and Kos (Greece) for archaeological applications. Appl. Radiat. Isot. 65, 488–503

Sterba, J.H., 2007. Anwendung der Neutronen-Aktivierungsanalyse zum Aufbau der Chemostratigraphie einer vulkanischen Eruptionssequenz auf Tilos und Nisyros, Griechenland. Ph.D. Thesis, Vienna University of Technology

Sterba, J.H., Steinhauser, G., Bichler, M., 2011. On the geochemistry of the Kyra eruption sequence of Nisyros volcano on

Nisyros and Tilos, Greece. Applied Radiation and Isotopes 69, 1605–1612.
Vougioukalakis, G., 1993. Volcanic stratigraphy and evolution of Nisyros island (Abstracts). Bull. Geol. Soc. Greece 1993, 28, 239–258
.Wilson, L., Stephen, & George, W. (1980). Explosive volcanic eruptions — IV. The control of magma properties and conduit geometry on eruption column behaviour. Geophysical Journal of the Royal Astronomical Society, 63, 117-148

17th INTERNATIONAL CONGRESS of the Geological Society of Greece

BULLETIN OF THE GEOLOGICAL SOCIETY OF GREECE, SP. PUBL.

EXTENDED ABSTRACT 177

A preliminary petrographic approach of the altered Triassic volcanic lavas in Argolis, Greece

Petros Koutsovitis[1], Aikaterini Papaioannou[1]
(1) University of Patras, Department of Geology, GR-26504 Patras, Greece
E-mail address: pkoutsovitis@upatras.

Introduction

In the northeastern Peloponnese lies the region of Argolis, an area of significant geological interest, as its geotectonic position belongs to the Sub-Pelagonian zone, characterized by intense and extensive tectonism, involving the presence of five distinct tectonic units. These comprise of: i) Trapezona Unit (M. Triassic - L. Jurassic: limestones, radiolarites, lavas), ii) Demaina Ophiolite Unit (L. – L. Cretaceous: ophiolites, basalts, pillow lavas, limestones, radiolarites, dolerites), iii) Adheres Melange Unit (Palaeocene – Eocene: silt, sandstone, marl and Triassic: limestones, radiolarites and Jurassic: metagranodiorites, andesites, basalts, mineralized sediments, dolomites), iv) Iliokastron Melange Unit (ophiolite melange), v) Faniskos Unit (L. Cretaceous: above the "Trapezona" and "Demaina Ophiolite Unit" units). The region primarily consists of Triassic and Jurassic-aged rocks (Bortolotti et al., 2003; Celet & Ferriere, 1978; Jacobshagen et al., 1978; Gioni, 2021). The study was mostly focused on the Middle Unit, occurring in Central and Northern Argolis (Bortolotti et al., 2001, 2002; Baumgartner, 1985). This investigation integrates field observations with detailed microscopic analyses of the most representative rock samples. Emphasis was given to interpret alteration effects that are a key characteristic of these rocks. The Triassic basaltic rocks of the Middle Unit are classified as trachybasalts (Saccani et al., 2015), mostly in the form of pillow lavas, with OIB and E-MORB geochemical signatures (Baumgartner, 1985; Dostal et al., 1991). The vast majority of these exposed rocks in the field exhibit evidence of low-grade metamorphism and metasomatic processes. The research focuses on characterizing the secondary processes that influenced the Triassic volcanic lavas of the area, with an emphasis on their petrographic and mineralogical classification.

Results - Discussion

The most representative samples were selected for the preparation of thin sections. Through pulverization, the samples were prepared for analyses via X-ray diffractometry (XRD). In addition, the Petrographic study was carried out using an optical microscope for observation of the rocks' mineralogical characteristics.

Residual phases of primary minerals were recorded, due to the significant degree of alteration. These mainly include clinopyroxene (Cpx) and plagioclase (Pl), with the presence of plagioclases being more Ca-rich in their center (An) and more Na-rich at the periphery (Ab), exhibiting the albitization phenomenon. The microcrystals of clinopyroxene appear altered and with intense colors throughout the fundamental mass of the samples. It is observed that the entire glass has been transformed into secondary chlorite, actinolite, and montmorillonite. Additionally, we have the presence of accessory mineral of ilmenite (Ilm), as well as secondary alteration of primary mineralogical components with concurrent formation of chlorite (Chl), epidote (Ep), prehnite (Prh), calcite (Cc) with characteristic zoning and the form of spherical mineral amygdales, while in small-length veinlets analcime (Anl), as well as other zeolites (Zeo), are present.

Additionally, in certain samples, actinolite (Act) and tremolite (Tr) were observed replacing clinopyroxene (Cpx), while there are also microlites of alkaline feldspars (K-feld) and paragonite (Pg). The phenocrysts of quartz (Qz) represent a secondary phase, complementary to chlorite, and they are intensely deformed. The modal composition of secondary zeolites found in some of the samples is estimated to be ~10 vol.%. The type of zeolite observed in most of the samples from the area is Mordenite, as well as Analcime. Specifically, the zeolites appearing in the form of small-sized crystals were observed filling voids and microfractures, indicating hydrothermal processes and a low degree of metamorphism.

The petrographic study of the Triassic lavas of Argolis reveals the significant secondary processes that occurred after the intense volcanic activity during the Triassic period. These processes are generally common for the various Triassic lavas of the Hellenic region (Castorina et al. 2020 - Koutsovitis et al. 2012 - Magganas et al. 1997 - Magganas and Kyriakopoulos 2005 - Pe-Piper and Piper 2002). However, in the study area, the significant involvement of zeolites in the secondary phases stands out, as they locally constitute the dominant metasomatic phase, fully replacing the primary phases. A more precise characterization of the zeolitic phases requires further investigation through mineral chemical analyses methods, while it is also deemed necessary to conduct geochemical analyses to detect trace

element variations during the secondary processes.

References

Bortolotti, B., D'Souza, J., Fantini, M., & Megginson, W. L. (2002). Privatization and the sources of performance improvement in the global telecommunications industry. Telecommunications Policy, 26(5-6), 243-268.

Bortolotti, V., Carras, N., Chiari, M., Fazzuoli, M., Marcucci, M., Photiades, A., & Principi, G. (2003). The Argolis Peninsula in the palaeogeographic and geodynamic frame of the Hellenides. Ofioliti, 28(2), 79-94.

Castorina, F., Magganas, A., Masi, U., & Kyriakopoulos, K. (2020). Geochemical and Sr-Nd isotopic evidence for petrogenesis and geodynamic setting of Lower-Middle Triassic volcanogenic rocks from central Greece: Implications for the Neotethyan Pindos ocean. Mineralogy and Petrology, 114, 39-56.

Koutsovitis, P., Magganas, A., Ntaflos, T., Koukouzas, N., Rassios, A.E., Soukis, K., 2020. Petrogenetic constraints on the origin and formation of the Hellenic Triassic rift-related lavas. Lithos 368-369, 105604.

Saccani, E. (2015). A new method of discriminating different types of post-Archean ophiolitic basalts and their tectonic significance using Th-Nb and Ce-Dy-Yb systematics. Geoscience Frontiers, 6(4), 481-501.

17th INTERNATIONAL CONGRESS of the Geological Society of Greece

BULLETIN OF THE GEOLOGICAL SOCIETY OF GREECE, SP. PUBL.

EXTENDED ABSTRACT 178

Petrographic evidence for the metamorphic conditions in ultramafic rocks at Makrymalli - Evia Island

Petros Koutsovitis[1], Konstantinos Tetisis[1], Georgia Kolovadi[1]
(1) University of Patras, Department of Geology, GR-26504 Patras, Greece
E-mail address: pkoutsovitis@upatras.gr

Introduction

The aim of this announcement is to highlight the greenschist facies as the main metamorphic facies that affected the ultramafic rocks of the Makrymalli area, based on petrographic data. Makrymalli is a region in central Evia (Central Greece). In geotectonic terms, the region belongs to the Pelagonian zone and is mainly comprised of mafic and ultramafic volcanic and sedimentary rocks (Danelian and Robertson, 2001). The extensive ophiolitic complex that represents the ultramafic rocks of the area consists mainly of harzburgites (Danelian and Robertson, 2001), variably serpentinized, including both serpentinites and serpentinized harzburgites, although serpentinized lherzolites were also identified. Their metamorphic grade is classified as greenschist facies, though some evidence suggests that, on local scale, metamorphic conditions may have been more intense (Simantov et al., 1990). These ophiolites are related to the subduction of the oceanic crust of the Tethys Ocean and the subsequent closure of the Pindos and Vardar Oceanic basins; the Pelagonian platform host ophiolitic thrust sheets from both basins.

Results- Discussion

The samples analyzed in this study comprise of serpentinized harzburgites, lherzolites and also serpentinites. They are clearly serpentinized, with lizardite and antigorite occurring in rather balanced amounts. Serpentinization occurs at rates of 75% to 85% on average in microscopic sections. Uralitization is also observed in certain lherzolites, at the expense of relict clinopyroxene. Mesh textures are frequently observed especially in the highly serpentinized varieties. The presence of lizardite and antigorite in the ultramafic rocks of Makrymalli in rather balanced amounts, suggests that metamorphism did not exceed greenschist facies (~320°C - 340°C, P ≈ 6-7 kbar; Guillot et al., 2015). This is further supported by the fact that spinel rims were not altered to Cr-magnetites but also because orthopyroxene bastites were pseudomorphically retained their former crystal appearance. These metamorphic conditions are evidently lower than those that were established for the adjacent East Thessaly serpentinites, where the predominance of antigorite corresponds to blueschist facies metamorphism (~ 360–400 °C, P ≈ 11–12 kbar) (Koutsovitis, 2017). Furthermore, thin crosscutting chrysotile veinlets, as well as the presence of talc and minor chlorite, point to retrograde low-metamorphic conditions during exhumation. Serpentinization subsequently led to the formation of Fe-oxides such as magnetite in the serpentinite matrix. In some of the serpentinized lherzolites, distinct deformation and undulose extinction was observed in clinopyroxene crystals, suggesting local deformation phenomena. Serpentinites in few cases were locally subjected to local mylotinization and even brecciation, being characterized by their mylonitic fabric and by the higher modal amount of antigorite.

References

Danelian, T., Robertson, A.H.F., 2001. Neotethyan evolution of eastern Greece (Pagondas Mélange, Evia island) inferred from radiolarian biostratigraphy and the geochemistry of associated extrusive rocks. Geological Magazine (3) 138, 345–363.

Guillot, S., Schwartz, S., Reynard, B., Agard, P., Prigent, C., 2015. Tectonic significance of serpentinites. Tectonophysics 646, 1–19.

Koutsovitis, P., 2017. High-pressure subduction-related serpentinites and metarodingites from East Thessaly (Greece): Implications for their metamorphic, geochemical and geodynamic evolution in the Hellenic–Dinaric ophiolite context, Lithos 276, 122-145.

Simantov, J., Economou, C., Bertrand, J., 1990. Metamorphic rocks associated with the central Euboea ophiolite (southern Greece). Some new occurrences. In Ophiolites and Oceanic Crust (eds J. Malpas, E. M. Moores and C. Xenophontos), pp. 285–94. Ophiolites and Oceanic Crustal Analogues. Proceedings of the International Symposium “Troodos 1987”. Geological Survey Department Cyprus, Nicosia.

17th INTERNATIONAL CONGRESS of the Geological Society of Greece

BULLETIN OF THE GEOLOGICAL SOCIETY OF GREECE, SP. PUBL.

EXTENDED ABSTRACT 179

An outline on some of the recently reported granitoids from St. Martin Island

Petros Koutsovitis[1,*], Michiel J. van der Meulen[2], Tirza van Daalen[2], Pavlos Tyrologou[3], Nikolaos Koukouzas[3], Alkiviadis Sideridis[1], Christos Karkalis[3], Michel Grégoire[2], Petros Petrounias[1], Theodoros Ntaflos[5], Konstantinos Lentas[6]

(1) University of Patras, Department of Geology, GR-26504 Patras, Greece
(2) TNO, Geological Survey of the Netherlands, P.O. Box 80015, 2508 TA, Utrecht, the Netherlands
(3) Centre for Research and Technology, Hellas (CERTH), Egialias 52, Marousi 15125, Attica, Greece
(4) Géosciences Environnement Toulouse (GET), CNRS, UPS, IRD, CNES, Université de Toulouse, Observatoire Midi Pyrénées (OMP), 14 Av. E. Belin, 31400 Toulouse, France
(5) University of Vienna, Department of Lithospheric Research, Althanstr. 14, Vienna, Austria
(6) National Observatory of Athens, Institute of Geodynamics, Lofos Nymfon, Athens 11810, Greece
** Corresponding author: Tel.: +30 2610997737; E-mail address: pkoutsovitis@upatras.gr.*

Introduction

St. Martin is located at the northern parts of the Lesser Antilles (Caribbean). Oligocene magmatic rocks include plutonic intrusions and volcanics (Davidson et al., 1993). Their age has been determined between 26 to 31 Ma relying upon K-Ar data (Davidson et al., 1993). The plutonic granitoids mostly comprise of tonalites, quartz-monzodiorites and granodiorites (Davidson et al., 1993, Noury et al. 2021, Koutsovitis et al. 2025). Granitoid plutonism is assigned to subduction and subsequent convergence of the Farallon, South American and North American plates (Lidiak and Jolly, 1996).

For the purposes of the present announcement, we briefly outline some of the findings, recently outlined in detail by Koutsovitis et al. (2025), concerning some of the St. martin granitoids that encompass relatively high modal amounts of mafic minerals.

Results

The recently reported St. Martin melatonalites (Koutsovitis et al. 2025), clearly correspond to granitoids, with their total modal composition of quartz, plagioclase and alkali feldspars exceeding 50 vol.%. Most participating mineral phases are medium grained, suggesting plutonic crystallization condition. Their modal composition was determined through point counting and CIPW calculations. Accessory minerals were determined through microprobe facility. Classification relied upon normative Q, A, P percentages. Their M' colour index, based on the mafic minerals, suggests that these are in fact melatonalites with elevated M' values. They are also characterized by the following features: i) relatively restricted modal amount of quartz, ii) higher normative anorthite than albite, iii) participation of cordierite, orthopyroxene and phlogopite. iv) low LOI contents, in accordance with the presence of phlogopite and complete absence of any alteration effects. Accessory minerals comprise of ilmenite, Ti-magnetite and apatite.

Plagioclase of the St. Martin melatonalites are characterized by their relatively high An components, displaying normal compositional zoning (Koutsovitis et al. 2025); K-feldspars are absent. Orthopyroxenes are enstatites with moderate Mg#, low Al, Cr and Ni contents (Koutsovitis et al. 2025). Clinopyroxenes and amphiboles are absent, in contrast to the other granodiorites present in St. Martin. Phlogopites display rather enhanced Ti and Ba contents, whereas cordierites exhibit rather high Mg values. Geochemical results show that the melatonalites are characterized by their enhanced Ti, Fe and Mg contents (Koutsovitis et al. 2025). Based upon various geochemical classification plots, these rocks correspond to low-K, calcic and magnesian granitoids, with a transitional character between calc-alkaline to tholeiitic (Koutsovitis et al. 2025).

Discussion-Conclusions

Apparently, the presence of cordierite within the melatonalites signifies that these may correspond to S-type granitoids. This is further supported by their peraluminous character (Koutsovitis et al. 2025). However, this is not consistent with their very low-K, as well as their behavior in Harker binary plots, pointing to an I-type character. Furthermore, additional major and trace element ratios comply with restricted involvement of sediments in the source and were more affected by hydrous and slab-derived fluids (Koutsovitis et al. 2025). Geothermometry applications reveal relatively high temperatures for the melatonalites compared to the other granitoids. Pressure calculations show that these were crystallized at the relatively deep parts of the arc (Koutsovitis et al. 2025). It seems that these rocks

formed at the early stages of subduction and may likely represent one of the few traces of CLIP influence, associated with early hybridization of the mantle wedge (Koutsovitis et al. 2025).

References

Davidson, J., Boghossian, N.D., Wilson, M., 1993. The Geochemistry of the Igneous Rock Suite of St Martin, Northern Lesser Antilles. Journal of Petrology, 34 (5), pp. 839-866. https://doi.org/10.1093/petrology/34.5.839

Lidiak, E.G., Jolly, W.T., 1996. Circum-Caribbean granitoids: Characteristics and Origin. Int. Geol. Rev. 38, 1098 – 1133. https://doi.org/10.1080/00206819709465385.

Noury, M., Philippon, M., Cornee, J.-J., Bernet, M., Bruguier, O., Montheil, L., Legendre, L., Dugamin, E., Bonno, M., Münch, P., 2021. Evolution of a shallow volcanic arc pluton during arc migration: a tectono-thermal integrated study of the St. Martin granodiorites (Northern Lesser Antilles). Geochem. Geophys. Geosyst. 22, e2020GC009627. https://doi.org/10.1029/2020GC009627.

Koutsovitis, P., van der Meulen, M.J., van Daalen, T., Tyrologou, P., Koukouzas, N., Sideridis, A., Karkalis, C., Grégoire, M., Petrounias, P., Ntaflos, T., Lentas, K., 2025. Granitoids from St. Martin/Maarten Island, Caribbean: Insights on the role of mantle processes in the Lesser Antilles arc. Lithos 494–495, 107926. https://doi.org/10.1016/j.lithos.2024.107926

17th INTERNATIONAL CONGRESS of the Geological Society of Greece

BULLETIN OF THE GEOLOGICAL SOCIETY OF GREECE, SP. PUBL.

EXTENDED ABSTRACT 180

Mineral mapping using satellite multispectral and hyperspectral data for a pyrite mine in the frame of the m4mining project

Evlampia Kouzeli[1], Olga Sykioti,[2] Konstantinos Nikolakopoulos[1], Saeid Asadzadeh[3], Friederike Koerting[4], Daniel Schläpfer[5]

[1] GIS and Remote Sensing Lab, Department of Geology, University of Patras, Patras 26504, Greece; e.kouzeli@upatras.gr (E.K.); knikolakop@upatras.gr (K.N.)

[2] National Observatory of Athens, Institute for Astronomy, Astrophysics, Space Applications and Remote Sensing, Athens Greece; sykioti@noa.gr (O.S.)

[3] Helmholtz Centre Potsdam, GFZ German Research Centre for Geosciences,14473, Potsdam, Germany; saeid@gfz-potsdam.de (S.A.);

[4] Norsk Elektro Optikk AS—HySpex Division, Østensjøvei 34, 0667 Oslo, Norway; friederike@neo.no (F.K.);

[5] ReSe Applications LLC Langeggweg 3 9500 Wil Switzerland daniel@rese-apps.com (D.S.)

Introduction and objectives

Mafic sulfide deposits in Cyprus were studied by Hannington et al. (1998) and Adamides et al. (2010). They are composed mostly of pyrite (Parvaz, 2014). The acid mine drainage (AMD) is the result of sulfide minerals and waste oxidation due to exposure to water and oxygen conditions affecting large areas. The case study is the Memi inactive pyrite mine in Nicosia, Cyprus. Herein, we applied Remote Sensing (RS) techniques for the monitoring of the mine area. To this purpose, the Visible Near Infrared and Shortwave Infrared (VNIR-SWIR) spectral bands of multispectral (MSI) and hyperspectral satellite imagery (HSI) were used. More specifically, a combination of Sentinel-2, WorldView-3 (WV3), both VNIR and SWIR, and Environmental Mapping and Analysis Program (EnMap) data were employed. Two different spectral libraries, namely the United States Geological Survey (USGS) and Jet Propulsion Laboratory (JPL) spectral libraries, and three spectral processing methods were selected to analyze the data in the frame of the m4mining project.

The m4mining project aims to provide an integrated remote sensing approach for mapping and monitoring active and inactive mining sites. MSI and HSI imaging are combined with in situ measurements and are utilized for material identification from the detailed mine face to the site scale using unmanned aerial vehicles (UAVs) and satellite sensors. Central to the proposed work is a synergistic combination of UAV and satellite-based processing algorithms, workflows, and decision-making tools at timescales required to impact active operations and environmental and risk management of tailings and waste sites.

This study aims to investigate the suitability of EnMap, Sentinel-2, and WV3 data for the detection and mapping of minerals related to pyrite -AMD.

Data and methodology

The Memi mine is located in Nicosia district, Cyprus (35° 2’30.11”N, 33° 2’19.61”E). Six minerals (Table 1, Figure 1) namely hematite, goethite, ferrihydrite, jarosite, schwertmannite, and copiapite (hereafter endmembers) were selected for AMD identification within the inactive pyrite mine study area. USGS and JPL spectral libraries were used to retrieve the spectral signatures of hematite, goethite, and jarosite which were convolved to EnMap, Sentinel-2, and WV3 spectral bands while spectral signatures of ferrihydrite, schwertmannite, and copiapite were not available in the JPL library.

The endmember selection criteria were the grain size and the spectral purity of the sample. A spectral signature with fine to medium grain size approximated the grain size of the minerals in the study area while the spectral purity defined the presence and/or the absence of contaminants. We selected spectral signatures with the least possible contaminants and a fine to medium grain size.

Table 1. Description of endmembers used in this study. For each mineral in the second column, the first row corresponds to the spectral signature name in the USGS spectral library, and the second row corresponds to the spectral signature name in the JPL spectral library. The spectrum title and information were retrieved from the corresponding ancillary file of each mineral from each spectral library.

Mineral	Spectrum title	Reference
Hematite	Hematite_FE2602_BECKb Hematite alpha Fe 2O 3 [oxide-none-fine-o01a]	Meerdink et al, 2019 Kokaly et al., 2017 Baldridge et al., 2009
Goethite	Goethite_HS36.3_BECKb Goethite alpha Fe^3+O(OH) [hydroxide-none-fine-oh02a]	
Ferrihydrite	Ferrihydrite_GDS75_Syn_F6_BECKb	
Jarosite	Jarosite_JR2501_(K)_BECKb Jarosite KFe 3^3+(SO 4) 2(OH) 6 [sulfate-none-fine-so07a]	
Schwertmannite	Schwertmannite_BZ93-1_BECKb	
Copiapite	Copiapite_GDS21_BECKb	

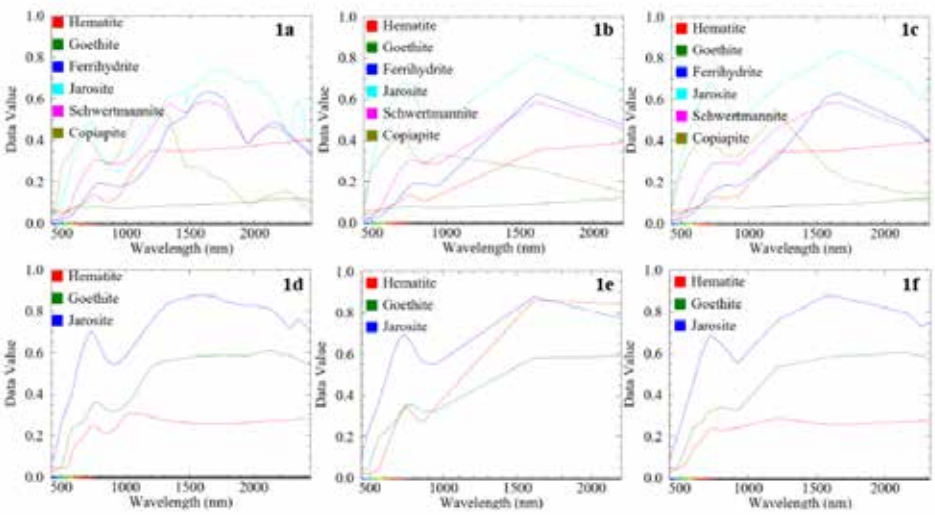

Figure 1. Mineral spectral signatures used in this study, (a) retrieved from the USGS spectral library convolved to the EnMap spectral bands; (b) retrieved from the USGS spectral library convolved to the Sentinel-2 spectral bands; (c) retrieved from the USGS spectral library convolved to the WV3 VNIR and SWIR spectral bands; (d) retrieved from the JPL spectral library convolved to the EnMap spectral bands; (e) retrieved from the JPL spectral library convolved to the Sentinel-2 spectral bands; (f) retrieved from the JPL spectral library convolved to WV3 VNIR and SWIR spectral bands.

For the purpose of this study, a Sentinel-2 Level 2A VNIR-SWIR image (12 spectral bands) was used, acquired on 2024/07/26. The archived WV3-VNIR and SWIR datasets (16 spectral bands) were also used (acquired on 2018/04/03-VNIR and 2020/09/12-SWIR). The WV3 data were atmospherically corrected by ReSe Applications. Although the WV3 data were acquired on two different dates, namely 2020 and 2018, after atmospheric corrections they were handled as one dataset (a total of 16 spectral bands). The atmospherically corrected EnMap data (acquired 2024/07/14) VNIR-SWIR (224 spectral bands) were conceded by the Helmholtz Centre Potsdam - GFZ German Research Centre for Geosciences (GFZ). The EnMap spectral bands 131-135 (1342.82-1390.48nm) were set as bad bands and excluded from the analysis. The spatial resolutions of EnMap, Sentinel-2, and WV3 data used in this study are 30m, 10m, and 3.7m respectively. The EnMap, Sentinel-2, and WV3 datasets were analyzed as layer-stacked (VNIR-SWIR) data: one layer stack for each sensor (EnMap, Sentinel-2, and WV3). To discriminate the spectral bands between the different types of sensors, we hereafter named the EnMap spectral bands Ebx (e.g. Eb1), the Sentinel-2 ones Sbx (e.g. Sb1), and WV3 ones Wbx (e.g. Wb1). The reflectance values were between 0 and 1 and each scene was cropped to the mine area extent. The mineral reflectance values issued from the spectral libraries vary between 0 and 1 as well. An NDVI threshold of 0.25 was applied to mask vegetation.

Three different processing methods were employed: spectral indices (SI), band depth (BD) analysis using continuum removal, and spectral angle mapping (SAM). The selected spectral indices used in this study are given in Table 2 and some of the results are presented in Figure 2. For BD and SAM calculations, six USGS endmembers and three JPL endmembers were used to detect the wavelength/band of the minerals' diagnostic absorption features (Sykioti et al, 2023) and compare the spectral angle between the spectral vectors of image pixels and reference spectra, respectively. Moreover, in BD, pixels with absorption <0.01 were masked while the threshold angle for SAM was set to 0.35 for EnMap (USGS endmember), 0.30 for EnMap (JPL endmember), 0.40 for Sentinel-2 (USGS & JPL endmembers), and 0.25 for WV3 (USGS and JPL endmembers).

Table 2. Overview of used spectral indices applied to this study. The SIs for EnMap and Sentinel-2 were retrieved from van der Meer et al. (2014), Ge et al. (2020), and the Index DataBase (https://www.indexdatabase.de/, accessed 02/11/2025). The SIs for WV3 were retrieved from Hildebrand (2022).

Spectral Index	EnMap	Sentinel-2	WV3
Ferrous Iron	(Eb216/Eb60) + (Eb22/Eb37)	(Sb12/Sb8a) + (Sb3/Sb4)	(Wb13/Wb7) + (Wb3/Wb5)
Ferric Iron	(Eb37/Eb22)	(Sb4/Sb2)	Wb5/Wb3
Ferric Oxides	(Eb164/Eb60)	(Sb11/Sb8a)	Wb11/Wb7

Results and Conclusions

SI maps: Using the SIs, we mapped ferric iron, ferrous iron, and ferric oxides in different spectral and spatial resolutions (Figure 2). As seen in Figure 2, generally, the SI ferrous iron values obtained were higher than the SI ferric iron ones. Furthermore, the EnMap and Sentinel-2 ferric iron maps were presented a similar spatial pattern and generally the same SI values. On the other hand, the SI ferrous iron showed higher values in EnMap data than in Sentinel-2 data. As for WV3, we observed locally high values (mostly on the roads) but generally, the SI values were lower than the corresponding ones in the EnMap and Sentinel-2 data.

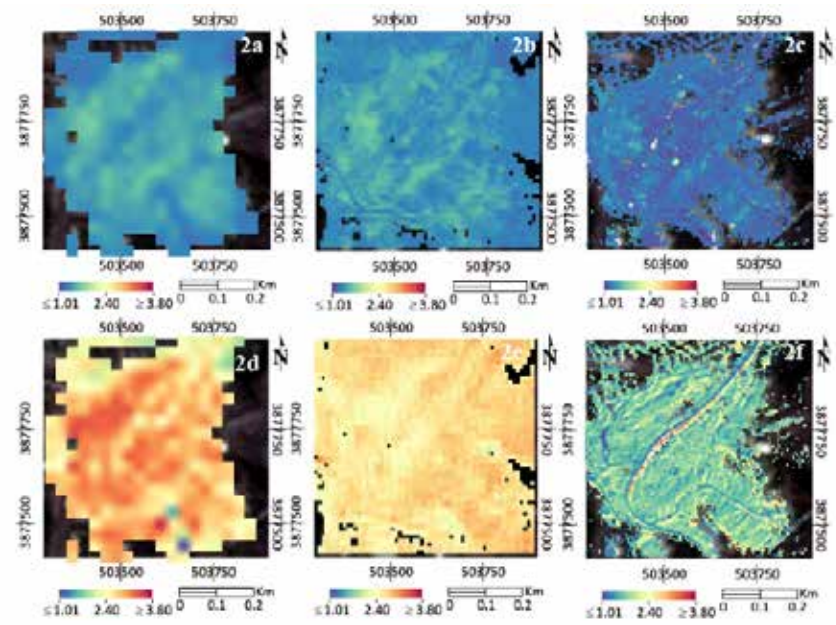

Figure 2. SI maps of ferric iron index applied on (a) EnMap (2024/07/14); (b) Sentinel-2 (2024/07/26); and (c) WV3 (2020/2018) and ferrous iron index applied on (d) EnMap (2024/07/14); (e) Sentinel-2 (2024/07/26); and (f) WV3 (2020/2018). For comparison purposes, all images have a common color scale (1.01-3.80). The background image is the TCI of Sentinel-2 (2024/07/26). SI values <1.01, indicating the absence of the material, are masked.

Absorption maps: the absorption feature maps (BD method) were also created from each one of the EnMap, Sentinel-2, and WV3 datasets. Based on the maximum absorption features observed within each endmember spectrum (issued from both the USGS and JPL spectral libraries and for each endmember), we located the unique diagnostic feature

which was not observed in the other mineral spectral signatures and thus, it spectrally differentiates the specific mineral from the others. The spectral bands/wavelengths corresponding to these absorption features were presented in Table 3 and Figure 3. In Figure 3, we presented indicative the hematite, goethite, and jarosite absorption maps. In particular for the EnMap dataset, we identified more than one characteristic absorption features for each endmember. However in Table 3, for EnMap, we presented the spectral band with the highest absorption of all other bands.

Table 3. Wavelength position (and corresponding band) and corresponding band depths (in the continuum removed (CR) spectra) of the characteristic diagnostic absorption feature of each one of the six minerals, namely hematite, goethite, ferrihydrite, schwertmannite, copiapite, and jarosite in (a) EnMap, (b) Sentinel-2 and (c) WV3 spectral bands retrieved from both USGS and JPL spectral libraries. Not available: mineral's spectral signature was not available in the specific spectral library, and -: no spectral feature was detected that differentiates this mineral from the others.

	EnMap		**Sentinel-2**	**WV3**	
Endmember	USGS	JPL	JPL	USGS	JPL
Hematite	871.7nm (Eb76) CR value 0.45	540.4nm (Eb26) CR value 0.40	864.7nm (Sb9) CR value 0.63	660.3nm (Wb5) CR value 0.64	546.6nm (Wb3) CR value 0.53
Goethite	501.2nm (Eb18) CR value 0.77	482.4nm (Eb14) CR value 0.38	664.6nm (Sb4) CR value 0.94	-	660.3nm (Wb5) CR value 0.95
Ferrihydrite	515.6nm (Eb21) CR value 0.34	Not available	Not available	-	Not available
Jarosite	2265.7nm (Eb196) CR value 0.61	439.7nm (Eb5) CR value 0.75	-	-	2259.8nm (Wb15) CR value 0.95
Schwertmannite	482.4 (Eb196) CR value 0.34	Not available	Not available	-	Not available
Copiapite	879.6nm (Eb77) CR value 0.59	Not available	Not available	-	Not available

Concerning the USGS endmembers, for hematite the characteristic absorption features were possible to define with EnMap and WV3 data. For goethite, ferrihydrite, jarosite, schwertmannite, and copiapite, this was possible only with the EnMap dataset. For Sentinel-2 data, no characteristic absorption feature was identified for these minerals. As for the JPL endmembers, hematite and goethite were differentiated with EnMap, Sentinel-2, and WV3 data while jarosite only with EnMap and WV3. The corresponding absorption maps (1-CR values) are presented in Figure 3.

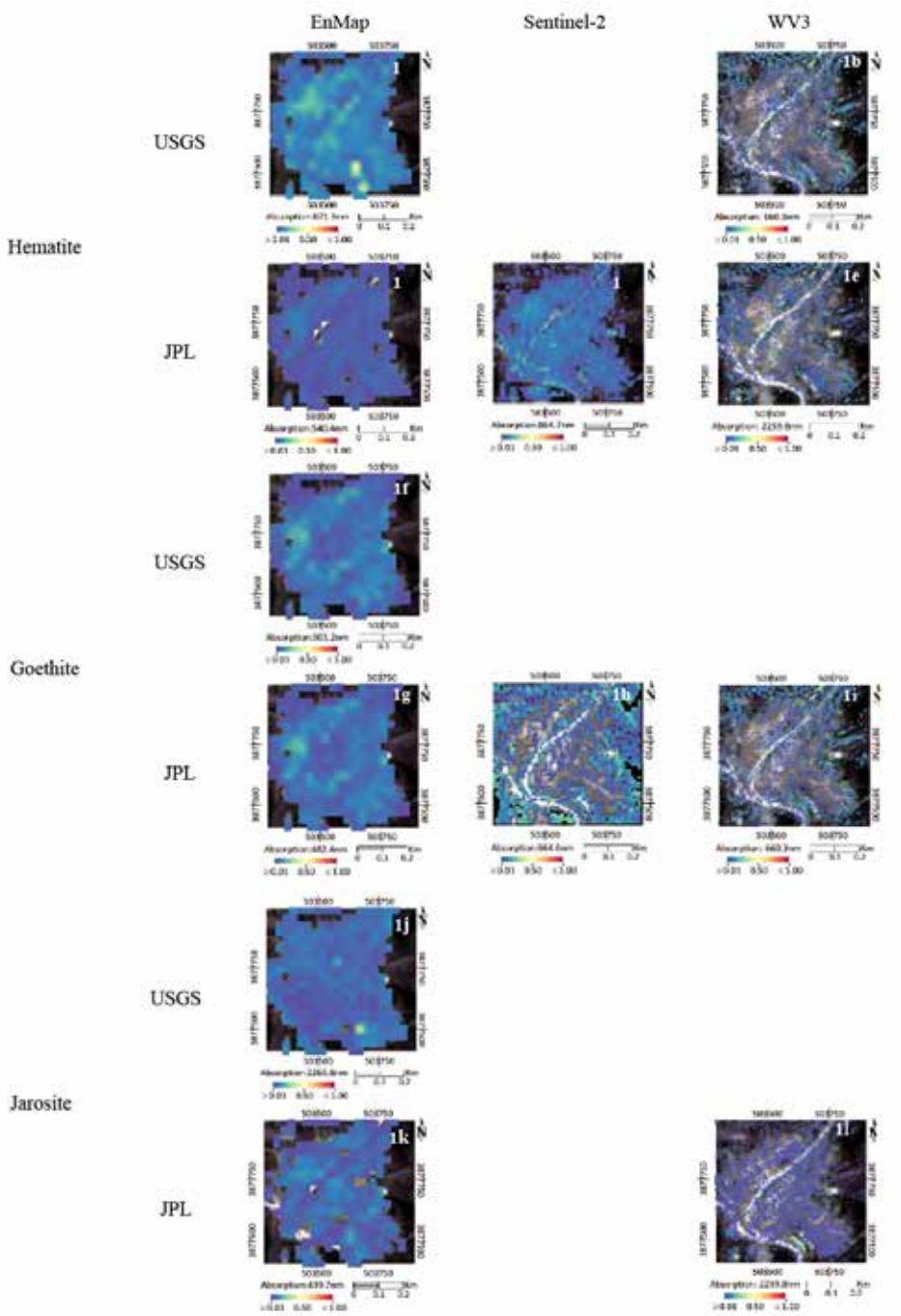

Figure 3. Absorption (1- CR) maps: Hematite-USGS (a) EnMap (2024/07/14) centred at 871.7nm; (b) WV3 (2020/2018) centred at 660.3nm. Hematite- JPL (c) EnMap (2024/07/26) centred at 540.4nm; (d) Sentinel-2 (2024/07/26) at 864.7nm; (e) WV3 (2020/2018) at 546.6nm. Goethite – USGS (f) EnMap (2024/07/14) centred at 501.2nm. Goethite -JPL (g) EnMap (2024/07/14) centred at 482.4nm; (h) Sentinel-2 (2024/07/26) centred at 664.6nm (i) WV3 (2020/2018) centred at 660.3nm. Jarosite-USGS (j) EnMap (2024/07/14) centred at 2265.7nm. Jarosite-JPL (k) EnMap (2024/07/14) centred at 439.7nm; and (l) WV3 (2020/2018) at 2259.8nm. The values range from 0.01 to 1 with 0.01 corresponding to minimum absorption and 1.0. to maximum absorption. The background image is the TCI of Sentinel-2 (2024/07/26)

SAM classification maps: Concerning SAM using the USGS endmembers (Figure 4), we mapped goethite, jarosite, copiapite, and schwertmannite with EnMap data with a threshold angle of 0.35, we mapped jarosite and copiapite with Sentinel-2 data using a threshold angle of 0.40, and all minerals with WV3 with a threshold angle of 0.25, except

from hematite. Concerning SAM using the JPL endmembers, we mapped hematite, goethite, and jarosite with EnMap data using a threshold angle of 0.30, we mapped hematite and jarosite with Sentinel-2 data using a threshold angle of 0.40, and we mapped hematite, goethite, and jarosite with WV3 data using a threshold angle of 0.25. Hematite and jarosite were mapped with all three datasets.

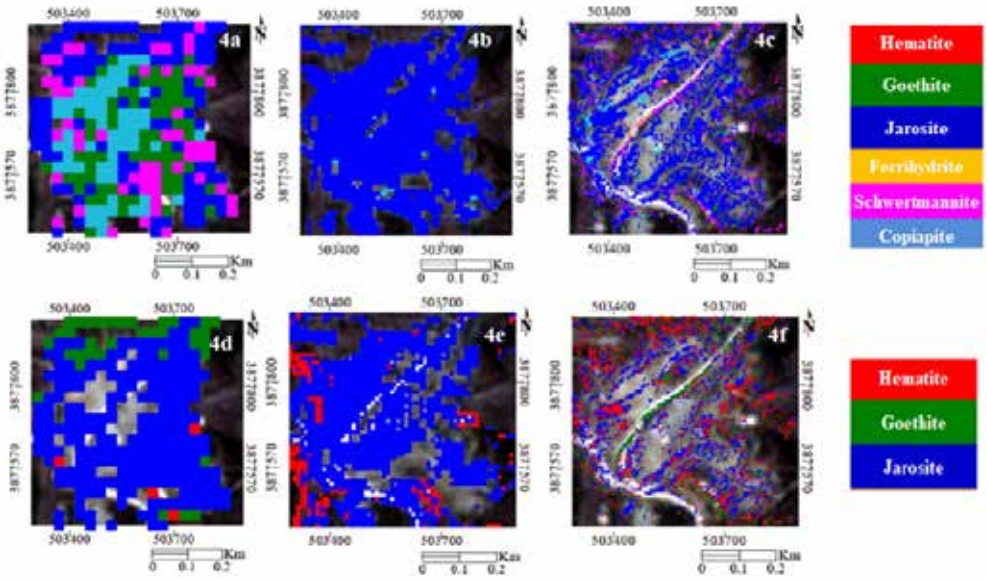

Figure 4. SAM classification maps. In the top row, SAM classification maps using the USGS endmembers for (a) EnMap (2024/07/14); (b) Sentinel-2 (2024/07/26); and (c) WV3 (2020/2018). In the bottom row, the SAM classification maps using JPL endmembers for (d) EnMap (2024/07/26); (e) Sentinel-2 (2024/07/26); and (f) WV3 (2020/2018). The background image is the TCI of Sentinel-2 (2024/07/26).

Overall, ferric iron, ferric oxides, and ferrous iron were mapped with EnMap, Sentinel-2, and WV3 data (SI method) (Figure 2). The presence of ferric iron could be considered as an indicator for the presence of several iron oxide/ hydroxides minerals such as hematite, goethite, and ferrihydrite while the ferrous index for copiapite. In this case study, ferric and ferrous iron seem to be present within the entire study area but the highest SI values were observed in pixels corresponding to the weathered slope areas of the tailings. As expected, the SI maps issued from WV3 data provide more details due to the high spatial resolution of the dataset (3.7m). The observed higher ferrous iron values compared with the ferric iron ones could be attributed to the copiapite presence. It must be noted here, that the higher the value, the higher the probability of the mineral's presence within the pixel.

Based on the analysis of the characteristic absorption features (BD analysis), concerning the USGS endmembers, in EnMap data the higheest absorptions (1-CR) were observed for hematite (0.41), jarosite (0.39), and copiapite (0.40), and the lowest ones for goethite (0.23) and schwertmannite (0.23). In WV3, the corresponding hematite absorption is 0.50. As for the JPL endmembers, we identified hematite (0.11), goethite (0.23), and jarosite (0.15) with EnMap, hematite (0.23) and goethite (0.33) with Sentinel-2, and hematite (0.53), goethite (0.60), and jarosite (0.35) with WV3. The highest absorption values were obtained for hematite, goethite, and jarosite using WV3 data but for a relatively small number of pixels within the image located mainly at the weathered slope areas and in certain flat areas (the same locations observed in the SI maps). Among the JPL-endmembers, hematite and goethite were detected in all three types of datasets and among the USGS-endmembers, only hematite and jarosite were identified using EnMap and WV3.

In the case of SAM using USGS endmembers, we note that jarosite and copiapite were mapped using EnMap, Sentinel-2, and WV3. Goethite and schwertmannite were also mapped using EnMap and WV3 but by applying a different threshold angle. Jarosite seems to be the spatially dominant mineral in the Sentinel-2 image. In the case of SAM using the JPL endmembers, jarosite also seems to be present within most image pixels followed by hematite and goethite.

The multispectral and hyperspectral images were acquired under optimal conditions: between late spring and early autumn with high sun elevation and no precipitation weather conditions. The temporal pattern of the data does not affect the results while there were no terrain modifications (e.g., human interventions) in the area during the study

period. Results were not affected by possible vegetation changes while a) bare soil dominates the study area, b) a 0.25 NDVI threshold was applied to mask the sparse vegetation, or c) remained unchanged which cross-validated with historical Google Earth imagery. Finally, the viewing angle of each satellite is practically vertical and combined with the smooth terrain slopes in the study area, resulting in no shadow effects on one or more images.

Concluding, the detection of the specific minerals (using USGS or JPL endmembers) at different wavelengths using EnMap, Sentinel-2, and WV3 data seems to be influenced by each sensors' specifications (e.g. band wavelength position, spectral range, spectral band, spatial resolution, acquisition date etc.) and the inherent physical properties of the samples the spectral signatures of which are retrieved from the spectral library and used as endmembers (e.g. particle size, specific chemistry, environmental context). The SI, BD, and SAM indicate the presence of AMD-related minerals in the study area revealing higher values within the mine area. This is an ongoing work. The verification of the obtained results using in-situ samplings, chemical and mineral laboratory analyses, and in-situ spectral measurements is currently under study.

Acknowledgements

Funded by the European Union

"m4mining" project is funded by the European Union's Horizon Europe programme under Grant Agreement ID 101091462.

References

Adamides, N.G., 2010. Mafic-dominated volcanogenic sulphide deposits in the Troodos ophiolite, Cyprus Part 2-A review of genetic models and guides for exploration. Applied Earth Science 119, 193–204.

Baldridge, A.M., Hook, S.J., Grove, C.I., Rivera, G., 2009. The ASTER Spectral Library Version 2.0. Remote Sensing of Environment, 113, 711-715.

Ge, W., Cheng, Q., Jing, L., Fei, W., Zhao, M., & Ding, H. (2020). Assessment of the capability of Sentinel-2 imagery for iron-bearing minerals mapping: A Case Study in the Cuprite area, Nevada. Remote Sensing, 12(18), 3028.

Hannington, M.D., Galley, A.G., Herzig, P.M., Petersen, S., 1998. Comparison of the tag mound and stockwork with Cyprus-type massive sulfide deposits. Proceedings of the ocean drilling program, scientific results, 158

Hildebrand, J.C., 2022. Acid Mine Drainage and Tailing Monitoring using Satellite Imagery for VMS-type deposits in the Republic of Cyprus MSc. Thesis, (Scientific Technical Report STR; 22/08), Potsdam: GFZ German Research Centre for Geosciences, 16p.

Meerdink, S.K., Hook, S.J., Roberts, D.A.,Abbott, E.A., 2019. The ecostress spectral library version 1.0. Remote sensing of environment, 230(111196), 1–8.

Kokaly, R.F., Clark, R.N., Swayze, G.A., Livo, K.R, Hoefen, T.M., Pearson, N.C., Wise, R.A., Benzel, W.M., Lowers, H.A., Driscoll, R.L., Klein, A.J., 2017. USGS Spectral Library Version 7, Data series 1035

Parvaz, D.B., 2014. Oxidation Zones of Volcanogenic Massive Sulphide Deposits in the Troodos Ophiolite, Cyprus: Targeting Secondary Copper Deposits. Ph.D. Thesis, University of Exeter, Exeter, 58 p.

Sykioti, O., Ganas, A., Vasilatos, C., Kypritidou, Z., 2023. Investigating the capability of Sentinel-2 and Worldview-3 VNIR satellite data to detect mineralized zones at an igneous intrusion in the Koutala islet (Lavreotiki, Greece) using laboratory mineralogical analysis, reflectance spectroscopy and spectral indices. Bulletin of the Geological Society of Greece, 59, 175–213.

van der Meer, F.D., van der Werff, H.M.A., van Ruitenbeek, F.J.A., 2014. Potential of ESA's Sentinel-2 for geological applications. Remote Sensing of Environment 148, 124–133.

17th INTERNATIONAL CONGRESS of the Geological Society of Greece

BULLETIN OF THE GEOLOGICAL SOCIETY OF GREECE, SP. PUBL.

EXTENDED ABSTRACT 181

A Novel Approach to Flood and Drought Management in Arid Regions using Multi-Agent Systems

Kravari K.[1], Emmanouloudis D.[1]

(1) UNESCO Chair for the Conservation and Ecotourism of Riparian and Deltaic Ecosystems, Democritus University of Thrace, Greece, kkravari@affil.duth.gr; kkravari@csd.auth.gr

Research Highlights

Multi-Agent Systems offer a promising decentralized approach for integrated flood and drought management in arid Greek regions, enabling more effective responses to extreme weather events. A conceptual case study demonstrates the potential of this framework to improve real-time decision-making and promote sustainable water resource management in the face of climate change.

Introduction

In Greece, like worldwide, arid and semi-arid regions face the alternating challenge of water scarcity and erratic rainfall patterns (Kourgialas, 2021; Nabinejad et al., 2023; El-Hamid et al., 2024). Hence, they are highly vulnerable to both droughts and floods. Unfortunately, the frequency and intensity of such extreme weather events are increasing, making traditional management methods obsolete. As a result, both the scientific community and society are now looking for more dynamic and adaptive approaches. This paper studies a novel approach to integrated flood and drought management using Multi-Agent Systems (MAS), an Artificial Intelligence technology. The proposed MAS framework consists of a network of intelligent agents, each responsible for a specific aspect of water resource management, including real-time data collection, flood prediction, drought monitoring, water allocation, and infrastructure control. This distributed and adaptive approach enables autonomous agents to have common goals, allowing them to interact and cooperate to achieve them. As a result, they will contribute to effective responses in case of extreme weather events, promoting sustainable water resource management. More specifically, Intelligent Agents in the context of a water resource management system, can integrate diverse data sources, support real-time decision-making, and enable responses to floods and droughts. The rest paper presents the architecture of the proposed MAS, including the types of agents, their interactions, and the data they utilize. A case study for a representative arid region presents the added value of the proposed approach.

The Challenge of Flood and Drought Management

It is known that arid regions have a low rainfall average and limited water resources. Yet, something is changing revealing serious challenges. The frequency and intensity of droughts are constantly increasing but at the same time, extreme precipitation events are more frequent nowadays. This is quite confusing for the traditional approaches that are often based on historical data and centralized control. On one side, droughts create a shortage of water for agriculture and industry besides domestic use, on the other side, flooding destroys infrastructure and causes loss of life, while even water sources can be polluted. The aim, therefore, of this paper is to deal with such challenges, proposing an integrated MAS approach that will be able to deal with both flood and drought management at the same time. To this end, a complex architecture with various intelligent agents is needed. Agents like Sensor Agents, Prediction Agents, Decision-Making Agents, and Infrastructure Control Agents should be represented in the framework. Each of these agents types should have specific responsibilities and well-designed knowledge-based interaction strategies.

Multi-Agent Systems for Flood and Drought Management

Although Artificial Intelligence (AI) is not new, over the last few years it reached a broader audience since it seems to be everywhere. However, despite the available technology in so many fields, there is still a lack of scientific approaches that could be used effectively in environmental real-life problems. Typically, AI approaches tend to enable machines to perform tasks that typically require human intelligence. But what we really need is approaches that can think, act and decide like humans when there are complex phenomena, unusual pattern and urgent situations (Chen, 2022; Sarker, 2022). In this context, an AI technology that is promising is the intelligent agents (Anshuka, 2022). An intelligent agent is an autonomous entity that can monitor its environment through sensors and act upon that to achieve its goals. The simplest type of agents is the reactive agents but here we need the complex cognitive agents those that are equipped with knowledge base and inference capabilities. These agents are able to know facts about their environment, when needed they can use this knowledge for reasoning and decision-making. In atypical form, a knowledge base includes facts, rules, and other forms of structured information. This allow agents to deal with complex cases, learn from their experience, and even explain their actions. Hence, this type of agents is appropriate for

the needs of a water resource management systems, since they are capable of understanding complex hydrological processes and take critical decisions under uncertainty, and as such they are adopted in the current proposed approach.

The Architecture of the Multi-Agent System Approach

As already discussed, multi-agent systems are a promising solution for flood and drought management. The proposed MAS approach consists of a diverse network of intelligent agents, representing different roles and assigned with different responsibilities. The architecture of the system consists of five agent types (Figure 1); namely Sensor Agents, Prediction Agents, Decision-Making Agents, Infrastructure Control Agents, and Communication Agents.

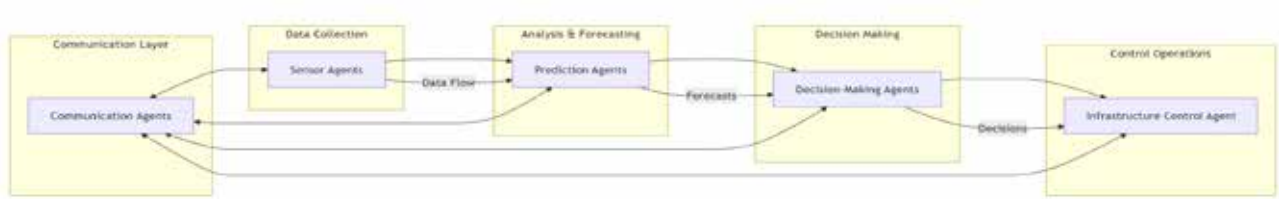

Figure 1. Agent types in the Multi-Agent System approach.

Sensor Agents are able to collect real-time data from various sources. These may include weather stations, river gauges, soil moisture sensors, and reservoir levels. Prediction Agents then receive the data and feed hydrological models or machine learning algorithms to forecast, for instance, flood risks and drought severity. Later, the Decision-Making Agents based on these predictions and some pre-defined rules could make decisions depending on the case. The decision could be related to water allocation, reservoir operation, or flood control measures. Of course, these decisions should somehow be implemented, hence, the Infrastructure Control Agents will follow by implementing the decisions made by the decision-making agents. They could for instance control pumps, gates, and other infrastructure components. Finally, the Communication Agents are responsible for keeping the team informed and functioning by sharing the necessary information between agents. It is worth mentioning here that there are approaches where agents communicate and negotiate with each other without the need for communication agents, however, in this approach we adopted their use to ensure smooth information sharing, making the already complex architecture of the system more light. In this context, consider the following example; during a heavy rainfall event, sensor agents collect data on rainfall intensity and river levels. Prediction agents use this data to forecast flood risk. Decision-making agents then determine the appropriate flood control measures, such as opening floodgates or diverting water to retention basins. Infrastructure control agents execute these decisions.

The mathematical background of the proposed approach is quite complex since the Multi-Agent System (MAS) should deal with different cases of flood and drought. The agents should be able to provide specific functionalities complying with different upcoming events to remain flexible and efficient. Figure 2 presents the mathematical components for each agent type but it should be clear that in a specific use case or scenario, only some of these components are triggered based on the agents' strategies and some pre-defined rules that depict the potential case. More specifically, Sensor Agents primarily deal with data. Hence, their case is quite straightforward. For calibration purposes, they use linear or non-linear functions to convert raw sensor readings into meaningful units, such as voltage to water level. For purposes of filtering, they use some statistical methods like Kalman and Savitzky-Golay filters to reduce noise in the data. Finally, they can use common statistical measures like mean, median, and standard deviation for aggregation since they have to summarize data from multiple sensors or time steps. On the other hand, Prediction Agents are responsible for hydrological modeling and, in some cases, machine learning. Hence, they are the most mathematically intensive agents in the system. As far as it concerns the hydrological models, the approach is based on sound physical laws, like conservation of mass, momentum, and energy, and some empirical relationships which is more difficult to incorporate in the system. Some of the examples that are studied are the rainfall-runoff models, in an attempt to use equations for describing how rainfall translates into streamflow. The unit hydrograph theory is the core theory here but the Horton's infiltration equation will follow. Of course, these models are not enough, hence, hydraulic models are also studied in an attempt to describe water flow in rivers and channels. Manning's and Saint-Venant's equations are some of the studied approaches. In the cases in which machine learning is needed, namely, cases where we have plenty of datasets, linear, polynomial, and support vector regression are the core cases. These models learn patterns from data and can be used to predict water level or flow. Sometimes, we need to classify cases and predict the type of an event. In such cases, the decision trees, random forests, and neural networks are mainly used to predict flood risk in terms of low, medium, or high. It should be mentioned that optimization is not part of this approach yet but gradient descent, genetic algorithms, or particle swarm optimization seem promising for the aforementioned hydrological and machine learning models.

The following simplified example explains better the approach; a prediction agent that uses historical data to estimate the values

of a and b using the least squares regression method. The agent has to predict river flow (Q) based on rainfall (R). A simple linear regression model used by this agent is $Q = a + bR + \varepsilon$, where Q is the predicted river flow, R is the rainfall, a is the intercept, and b is the slope which represents the relationship between rainfall and flow, and ε is the error term. Now consider a more complex event like heavy rainfall. During the event, Sensor Agents collect data on rainfall intensity, river levels, and soil moisture. Prediction Agents have to use this data to forecast river flow and flood risk. Later the Decision-Making Agents will determine appropriate flood control measures, such as opening floodgates. For this example, the rainfall intensity r(t) will be constant at 20 mm/hr for 3 hours. So, r(t) = 20 mm/hr for $0 \leq t \leq 3$ hours, and r(t) = 0 otherwise. We also assume that the river water level h(t) is initially h(0) = 1.5 m while the initial soil moisture is s(0) = 60%. For demonstration purposes, we assume that it remains relatively constant during the short period of the rainfall event. Firstly, we use a simplified unit hydrograph with a peak of 10 $m^3/s/hr$ at t = 2 hours and a base width of 4 hours. For simplicity, we assume also that all the rainfall becomes excess rainfall r_e(t). So, r_e(t) = r(t) = 20 mm/hr for $0 \leq t \leq 3$ hours. We need to convert this to consistent units with the unit hydrograph (m^3/s), assuming a catchment area of 1 km^2 (10^6 m^2). So, r_e(t) = (20 mm/hr) * (1 m/1000 mm) * (10^6 m^2) * (1 hr/3600 s) = 5.56 m^3/s for $0 \leq t \leq 3$ hours. Based on the aforementioned simplified assumptions, the direct runoff will rise linearly to a peak and then fall linearly. Peak flow q_peak = r_e * (area under unit hydrograph) = 5.56 m^3/s * (0.5 * 4 hr * 10 $m^3/s/hr$) = 111.2 m^3/s and time to peak 2 hours. Hence, the direct runoff q(t) will be a triangle, rising linearly from 0 to 111.2 m^3/s in 2 hours, then falling linearly back to 0 over the next 2 hours. Now, the machine learning model, an LSTM Network, will follow. Here we assume that the network is trained, so given the rainfall initial river level and soil moisture, predicts a peak flow of 120 m^3/s at t = 2.5 hours. The agent trusts the LSTM slightly more in this heavy rainfall scenario and uses weights $w_1 = 0.4$ for the unit hydrograph model, and $w_2 = 0.6$ for the LSTM. Hence, at the LSTM peak time, t = 2.5 hours, the fused prediction is q_fused(2.5) = (0.4 * 111.2 m^3/s) + (0.6 * 120 m^3/s) = 44.48 m^3/s + 72 m^3/s = 116.48 m^3/s. Finally, the agent proceeds with the flood risk assessment which is simplified for the example since in real cases many factors beyond just river flow should be taken into account. Yet, in the context of the example. We set a flood warning threshold of 100 m^3/s. so, since q_fused(2.5) > 100 m^3/s, the agent outputs a fused river flow forecast with a peak of approximately 116.5 m^3/s around 2.5 hours and gives a flood warning, like "High Flood Risk" or similar.

Following the work conducted from the prediction agents, Decision-Making Agents are responsible for decision making, proposing specific actions. These agents have to use the predictions provided by the aforementioned agents along with some pre-defined rules. Although, there various technologies that can be used, in this approach the agents are rule-based. This means that they are based mainly on if-then-else rules and thresholds. For instance, a simple example is "If water level > X, then open floodgate Y". Hence, these agents are actually based on logic, pretty much like humans, making the decision-making process transparent and explainable. More specifically, the core of these agents is their knowledge base, which consists of a set of rules. Each rule has a set of conditions and an action. Typically, the conditions are comparisons between predicted values, like water level and flow rate, and predefined thresholds. The actions are specific guidelines like opening floodgates or adjusting pump rates. A typical rule is in the form of *IF (Condition 1) AND (Condition 2) AND ... AND (Condition N) THEN (Action)*. Below are presented some examples for purposes of better understanding. R1 and R2 are related to flood control, R3 and R4 are related to drought management while are related to water allocation.

R1: IF (Predicted Water Level > Flood Warning Threshold) AND (Rainfall Intensity > Heavy Rainfall Threshold) THEN (Open Floodgate Y to Level Z)

R2: F (Predicted River Flow > Critical Flow Rate) THEN (Activate Emergency Flood Protocol)

R3: IF (Soil Moisture < Drought Threshold) AND (Reservoir Level < Low Reservoir Threshold) THEN (Implement Water Restrictions – Level 1)

R4: IF (Groundwater Level < Critical Groundwater Level) THEN (Issue Drought Warning to Farmers)

R5: IF (Reservoir Level > Optimal Level) AND (Downstream Flow Requirements Met) THEN (Increase Water Release for Irrigation)

R6: IF (Water Demand Forecast > Available Water) THEN (Implement Water Conservation Measures)

It is clear from these examples that thresholds are crucial, since they define the boundaries that trigger specific actions. These thresholds can be pre-defined and fixed or dynamic, adjusted on real-time conditions or historical data. For example, the "Flood Warning Threshold" might be a fixed water level, or it could be dynamically adjusted based on the current river flow and downstream conditions. Sometimes Decision-Making Agents have to also use logical operators like AND, OR, and NOT to create complex rules with multiple conditions, like in the following example.

R7: IF (Predicted Water Level > Flood Warning Threshold) AND (Rainfall Intensity > Heavy Rainfall Threshold) AND (Downstream Reservoirs Not Full) THEN (Open Floodgate Y to Level Z)

Of course, all these rules would be useless without the proper inference engine. The inference engine checks the conditions of each rule and if they are met, the rule is "fired," and the corresponding conclusion is extracted. Hence, this agent type is equipped with proper inference engines. Currently, explainability is not included in the system but it is still quite easy to understand why a particular action was taken because the rules are clearly defined. It is also worth mentioning that rules can be easily added, modified, or removed, making the system adaptable to changing conditions or new knowledge. This approach is actually mainly

based on rules because rule-based systems provide a good balance between complexity and performance which is convenient for many water resource management problems.
Next, Infrastructure Control Agents will take the conclusions and turn them into actions. For this purpose, depending on the available infrastructure, equations describing the behavior of pumps, gates, and other infrastructure components are used when there is an automation possibility. In cases where this is not possible, the information provided by the prediction agents can be used by humans to manually take the necessary actions. Finally, the Communication Agents will handle the information exchange throughout the whole procedure. Typically, they use graphs to create a communication network between agents allowing them to reach each other more easily.

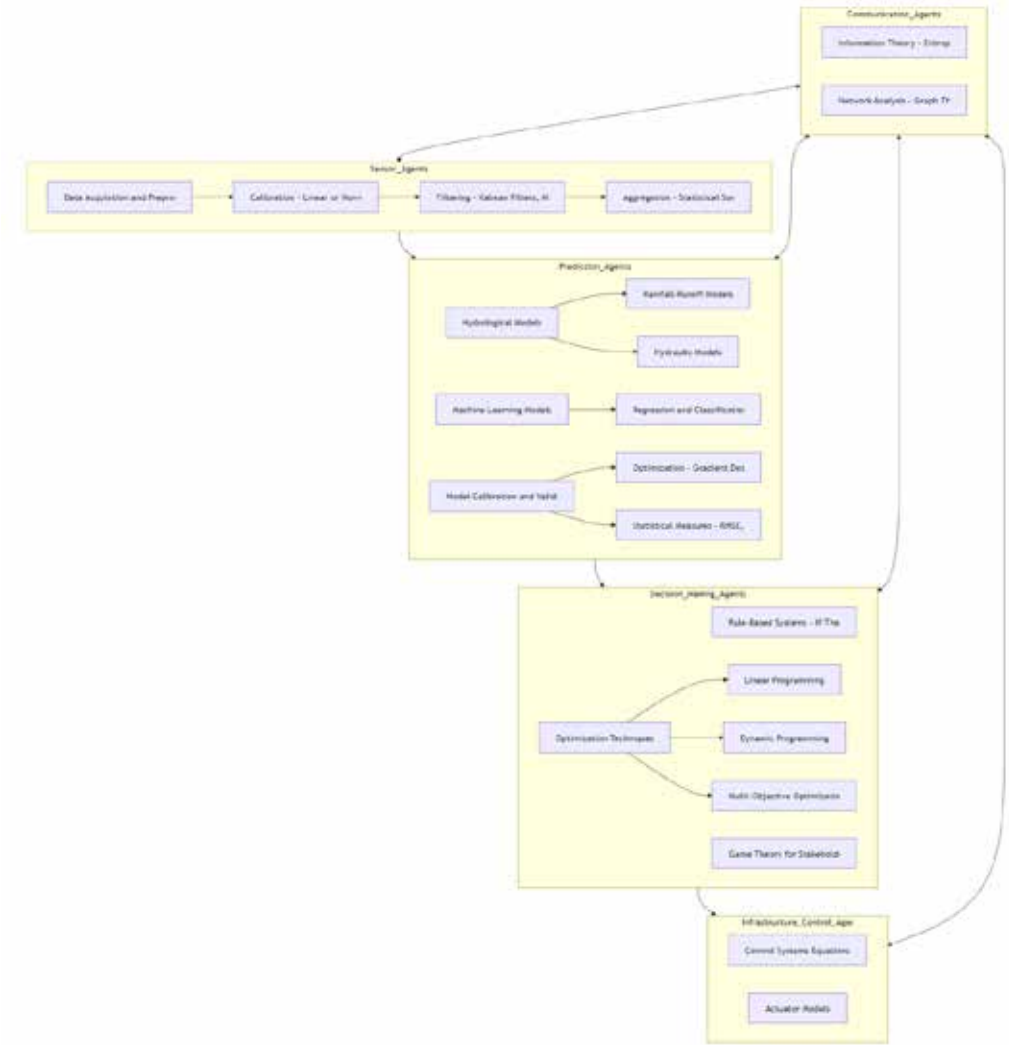

Figure 1. Background of the agent types.

The Technical Implementation of the Multi-Agent System

This section discuss core concepts of the technical implementation of the proposed Multi-Agent System. The chosen implementation language is Python which provided flexibility with several libraries for data handling, numerical computation, allowing integration with hydrological and machine learning models. The system implements the five aforementioned agent types as follows.
Each SensorAgent is initialized with a sensor_type, like “rainfall” or “river_level”, and a location identifier. For simulation purposes, the collect_data() method simulates the data acquisition process, generating a random value within a realistic range for the specified sensor type but in case of real datasets the method will process sensor data. Additionally, this method adds a timestamp to each data point, enabling temporal analysis which important when we have to adapt to pattern changes.
Each PredictionAgent is initialized with model_weights, allowing for flexible configuration of the weighting between different prediction models. The predict_flood_risk() method combines the outputs of a simplified unit hydrograph calculation and a

placeholder machine learning prediction. The unit hydrograph calculation is simplified for research purposes but it could be replaced with a proper SWAT model integration using a library like pyswat in a real application. Libraries like TensorFlow or PyTorch (Ansel et al., 2024) are used here. The outputs from the simplified unit hydrograph and the placeholder are combined using a weighted average, controlled by the model_weights.

Each DecisionMakingAgent is initialized with a set of rules. The make_decision() method iterates through the rules, evaluating the conditions using Python's eval() function. This allows for flexible definition of conditions using comparison operators and logical connectives. However, using eval() can pose security risks if the rules are defined by untrusted sources. Hence, in the future a safer rule evaluation method will be implemented. The agent returns the action associated with the first rule whose conditions are met. The rules as discussed are designed to trigger actions based on predicted flood risk, soil moisture levels, and river levels.

Each InfrastructureControlAgent uses the execute_action() method to receive the action as input and prints a simulated execution message or in cases that there is an APIs or hardware control interface this method can interface with the physical infrastructure like floodgates or pumps.

Each CommunicationAgents uses the broadcast_message() method to allow agents to communicate with each other. The log_data() method is also crucial for recording the simulation results. It uses the json library to store the data in a structured JSON format, making it easy to parse and analyze the results later.

The interactions between the agents follow a defined sequence where Sensor Agents collect data, which is then used by Prediction Agents to forecast flood risk. Decision-Making Agents use these forecasts and their rule base to determine appropriate actions. Finally, Infrastructure Control Agents execute these actions. The Communication Agent logs all relevant data at each time step.

Mention that sensor data is stored as a list of dictionaries within each SensorAgent. Each dictionary contains the timestamp, value, and location of the sensor reading while the CommunicationAgent uses the json library to log the data from all agents in a structured JSON format.

The current implementation uses placeholder values for the hydrological and machine learning models. Later, when the system will be used in real-world scenario some integrations will be needed such as the integration with SWAT by using a Python library like pyswat to interact with the SWAT model or the integration with a pre-trained LSTM network by loading the trained model, i.e. from a saved file, into the PredictionAgent. Libraries like TensorFlow or PyTorch are already used and could support this. For the current research phase, the simulation loop consists of a predefined number of time steps. At each time step, sensor data is collected, predictions are made, decisions are taken, actions are executed, and all relevant data is logged. This loop structure allows for simulating the system's behavior over time and analyzing its response to different events.

Conceptual Case Study: Thessaly, Greece

A conceptual case study for the Thessaly region in Greece demonstrates the added value of the proposed Multi-Agent System (MAS) approach. Thessaly is a representative arid region which is characterized by limited water resources, rainfall patterns, and a high vulnerability to both drought and flood events. This conceptual case study discusses how the MAS approach can address the challenges in the area by integrating real-time data, employing intelligent prediction, and facilitating coordinated decision-making. More specifically, thessaly is an agricultural region, heavily reliant on irrigation. Its water resources are under significant pressure due to increasing demand and decreasing rainfall. The region experiences frequent droughts, leading to water shortages and economic losses. Yet, the last years intense rainfall events triggered flash floods, causing life losses, damage to infrastructure and agricultural lands. This makes Thessaly a really complex hydrological case (Xafoulis, 2023).

The proposed MAS can integrate data from existing meteorological and hydrological networks in Thessaly since there are ready installed stations there. This includes mainly rainfall data from weather stations, but also some river level data from gauging stations, soil moisture data from dedicated sensors, and reservoir level data. Of course, additional sensor deployments in strategic locations would be needed to cover the area. For the purposes of this case study, the agents within the MAS are trained using historical data from these sources. This historical data are used to calibrate the hydrological models and train the machine learning modelsemployed by the Prediction Agents. In real-life, real-time data streams would continuously update the models and inform the decision-making process. For now, a simulated heavy rainfall event, similar in magnitude to historical flood events in Thessaly, is introduced into the model. The Sensor Agents collect "real-time" rainfall data, which are transmitted to the Prediction Agents. The Prediction Agents, utilizing the calibrated hydrological and machine learning models, forecast the river flow and potential flood inundation areas. The Decision-Making Agents, based on pre-defined rules and the flood forecast, then optimize reservoir operations, determining the appropriate release rates to minimize downstream impacts. Simultaneously, the MAS generate timely warnings to local communities through communication channels like, SMS alerts. The Infrastructure Control Agents execute the reservoir operation decisions, adjusting gate openings and water releases.

This simulation takes into account three locations, Larissa, Trikala, and Volos, where the Sensor Agents record the rainfall intensities during a simulated heavy rainfall event as depicted in Table 1.

Table 1. Simulation values for the heavy rainfall event.

Time (hours)	Larissa (mm/hr)	Trikala (mm/hr)	Volos (mm/hr)
0	5	7	3
1	15	20	10
2	25	30	18
3	20	25	15
4	10	12	8

Based on this rainfall data and other relevant inputs, the Prediction Agent predicts a peak river flow of 280 m^3/s at 4 hours. Part of the Decision-Making Agent knowledge base is presented below.

Rule1: IF (Predicted River Flow > 250 m^3/s) AND (Reservoir Level < 90%) THEN (Open Floodgate A to 70% and Floodgate B to 50%)

Rule2: IF (Predicted River Flow > 200 m^3/s) AND (Reservoir Level < 80%) THEN (Open Floodgate A to 50%)

Rule3: IF (Predicted River Flow > 150 m^3/s) THEN (Issue Flood Warning to Larissa and Trikala)

Hence, since the predicted river flow exceeds 250 m^3/s, and assuming that the reservoir level is at 85%, Rule1 is triggered. The Decision-Making Agent instructs the Infrastructure Control Agent to open Floodgate A to 70% and Floodgate B to 50%. A flood warning is also issued to Larissa and Trikala (Rule3). As a result, the floodgates are opened, reducing the peak flow downstream to 220 m^3/s.

Conclusion and Future Work

This paper proposed an integrated approach towards flood and drought management within an arid area using a MAS. The MAS framework consists of Sensor, Prediction, Decision-Making, Infrastructure Control, and Communication Agents presents a novel, decentralized solution for mitigating the challenges imposed by extreme weather events. The Python implementation of the MAS was developed in a flexible language with extensive libraries, detailing both the functionalities of each agent type and how they interact. A conceptual case study for the Thessaly region in Greece showcased the potential benefits from the MAS in managing a flood scenario. The obtained results were promising, although there are a number of limitations regarding the present research. The existing implementation is using simplified models and placeholder values. A subsequent step would be to embed real-world hydrological models, such as SWAT, along with the trained machine learning models, like LSTMs, into the Prediction Agents. This will involve access and processing of real-world datasets from the Thessaly region or elsewhere, including historical rainfall, river flow, soil moisture, and other relevant variables. Furhermore, the rule-based decision-making could be further enriched with fuzzy logic or defeasible logic, to handle uncertainties and increase the accuracy of decision-making. Interaction between agents may be explored further either by implementing negotiation protocols or other collaborative mechanisms. The Infrastructure Control Agents need to be connected with the real physical infrastructure through APIs or hardware interfaces, enabling automated control of floodgates, pumps, and other devices.

References

Kourgialas, N.N., 2021. A critical review of water resources in Greece: The key role of agricultural adaptation to climate-water effects. Science of The Total Environment. 775, 145857.

El-Hamid, H.F., Zeleňáková, M., Soľáková, T., Saleh, O.K., El-Dakak, A.M., 2024. Monitoring flood and drought risks in arid and semi-arid regions using remote sensing data and standardized precipitation index: A case study of Syria. Journal of Flood Risk Management 17(1), e12961. https://doi.org/10.1111/jfr3.12961

Nabinejad, S., Schüttrumpf, H., 2023. Flood Risk Management in Arid and Semi-Arid Areas: A Comprehensive Review of Challenges, Needs, and Opportunities. Water, 15(17), 3113. https://doi.org/10.3390/w15173113

Xafoulis, N., Kontos, Y., Farsirotou, E., Kotsopoulos, S., Perifanos, K., Alamanis, N., Dedousis, D., Katsifarakis, K., 2023. Evaluation of Various Resolution DEMs in Flood Risk Assessment and Practical Rules for Flood Mapping in Data-Scarce Geospatial Areas: A Case Study in Thessaly, Greece. Hydrology, 10(4), 91. https://doi.org/10.3390/hydrology10040091

Sarker, I.H. , 2022. AI-Based Modeling: Techniques, Applications and Research Issues Towards Automation, Intelligent and Smart Systems. SN COMPUT. SCI. 3, 158. https://doi.org/10.1007/s42979-022-01043-x

Chen, J., Sun, J., & Wang, G., 2022. From Unmanned Systems to Autonomous Intelligent Systems. Engineering, 12, 16–19. https://doi.org/10.1016/j.eng.2021.10.007

Ansel, J., Yang, E., He, H., Gimelshein, N., Jain, A., Voznesensky, M., ... & Chintala, S., 2024. PyTorch 2: Faster Machine Learning Through Dynamic Python Bytecode Transformation and Graph Compilation. In Proceedings of the 29th ACM International Conference on Architectural Support for Programming Languages and Operating Systems, 2, 929–947. Association for Computing Machinery. https://doi.org/10.1145/3620665.3640366

Anshuka, A., van Ogtrop, F.F., Sanderson, D.,Leao Z. S., 2022. A systematic review of agent-based model for flood risk management and assessment using the ODD protocol. Nat Hazards 112, 2739–2771. https://doi.org/10.1007/s11069-022-05286-y

17th INTERNATIONAL CONGRESS of the Geological Society of Greece

BULLETIN OF THE GEOLOGICAL SOCIETY OF GREECE, SP. PUBL.

EXTENDED ABSTRACT 182

Contemporary distributed block deformation in the South Aegean Sea (Greece), deduced by the analysis of continuous GNSS measurements

Kravvariti Ph.[1], Tzanis, A.[1], Sakkas, V.[1], Kranis H.[2]

(1) Section of Geophysics and Geothermy, Department of Geology and the Geo-environment, National and Kapodistrian University of Athens; atzanis@geol.uoa.gr.

(2) Section of Dynamic, Tectonic and Applied Geology, Department of Geology and the Geo-environment, National and Kapodistrian University of Athens

Introduction / Background

The south Aegean Sea and its adjacent areas are a highly segmented tectonically active domain, characterised by high-rate extension and severe crustal thinning. The different segments (blocks) that make up the south Aegean crust are bounded by significant fault zones and/or dislocation surfaces whose relative motion varies in size and direction. Over the past several decades, the recorded seismicity of the S. Aegean was sparse, scarce, and of generally low intensity. Thus, it cannot assist in adequately resolving regional tectonics.

Hitherto knowledge of tectonic regime was mainly based on the sparse earthquake record, a significant number of shallow marine seismic surveys, minimal use of geophysical potential field data, bathymetry and Differential GPS measurements. All these efforts achieved remarkable results for the methods employed and some resulted in block tectonic models. One of the first approaches by McClusky et al. (2000) identified a South Aegean microplate and determined its motion. Later, Nyst and Thatcher (2004), observed NW-SE trending extension on the Dodecanese Islands, proposing as well that the Peloponnese and the Central and South Aegean belong to a block with internal deformation zones. Reilinger et *al*. (2006) suggested that the kinematics of the south Aegean could be explained by a three-microplate model. Floyd et *al*. (2010) introduced a 15-block model and Briole et *al*. (2021) a 5-block model consistent with known regional-scale structures of the area, but is also rather coarse and with awkwardly shaped blocks (e.g. that of the Central Aegean. Finally, by interpreting a combination of GPS and palaeomagnetic data Lazos et *al*. (2022) propose the existence of an NNE-SSW 'boundary' extending from the west coast of Chios Island and through Paros Island terminating offshore to the south of western Crete; this is referred to as the Mid-Cycladic Lineament and is suggested to delimit areas rotating clockwise to its west counterclockwise to it east.

Herein, we use Differential GNSS measurements augmented with Seismotectonic information and geophysical data to outline the regional tectonic structure and kinematics of the South Aegean Region. Most hitherto work based on GNSS data has studied the deformation of the S. Aegean area by *referring* the velocity or displacement vectors to *remote* locations, usually in Eurasia (e.g. Potsdam, Germany), or the ITRF system as in Fig. 2). While this approach is informative and very useful in studying the *large-scale (whole-plate)* deformation of the Aegean, *it fails* to *resolve* the kinematics/pattern of relative block motions at local- and regional-scales and, therefore, assist in understanding the regional tectonics regime(s). The present study *departs* from this norm by attempting to inquire about *relative block motions* using *local reference points*, thus assisting in understanding the regional pattern(s) of tectonic deformation. Along this vein, if the regional tectonic structure comprises a mosaic of moving rigid blocks separated by active major faulting, it is straightforward to study the motion of any given block *relative* to others by letting some fixed observation point on the immobile block define the origin of a *local reference frame* and subtracting the velocity vectors of *all* other observations points from the velocity vector of the origin. Effectively, the present work expands on that of Sakkas et al. (2020) but incorporates additional cGNSS measurements, strain field computations and seismotectonic information. The resulting tectonic model has significant similarities to that of Sakkas et *al*. (2020), albeit with differences in the configuration and boundaries of the crustal blocks.

Data and Methods

We use data from 54 permanent, continuously recording GNSS stations (cGNSS), all of which are onshore and distributed over the Cyclades, Dodecanese, Crete, Eastern Peloponnese, Attica and Euboea as shown in Fig. 1. They belong to several networks operated by different institutions and agencies. Specifically, two belong to the network of the National and Kapodistrian University of Athens; www.remsenslab.geol.uoa.gr), one to the COMET network (Centre for the Observation and Modelling of Earthquakes, Volcanoes and Tectonics; comet.nerc.ac.uk/), eight to the NCAD (National Cadastre and Mapping Agency S.A. (www.hepos.gr), nine to the NOANET (Geodynamic Institute of National Observatory of Athens; Ganas *et al.*, 2008; Chousianitis *et al.*, 2021) and 32 to the private sector METRICA S.A. network (www.metrica.gr/diktyo-hxgn-smartnet). All data sets span a mean period of five (5) years, but

their majority exceeds three years with many spanning almost one decade. The primary data were processed with the Bernese v5.2 software (Dach et *al*., 2015) to generate high-precision time series of daily coordinates. We also considered (processed) displacement time series from two stations of the Geodetic Laboratory of Nevada (MAGNET + Global GPS Network Map (unr.edu). The annual velocity of each station was obtained from the slope of the least-squares line best fitting the coordinate time series.
The observed velocity field in the ITRF 2008 reference frame was subjected to strain analysis using the *grid*_strain package by Pesci and Teza (2007), a grid with a cell dimension of 30km and no interpolation. The results are shown in Fig. 6. The recovered strain values correspond to high and mid-significance, so that only points sufficiently close to the cGNSS stations would be included in the calculations. This prevented the introduction of potentially misleading information in areas with sparse or no station coverage. Even so, in cases where the distribution of GNNS stations is one-sided, the calculated strain values should be interpreted with caution.
Finally, to further constrain the relative motion between blocks and the resulting tectonic model, we included seismo-tectonic information in the form of 1147 focal mechanisms of *crustal* (less than 30km deep) earthquakes with $M_w \geq 4$, spanning the period 1904–2022. This dataset is a combination of the data bank used by Kassaras *et al.* (2016), which covers the period 1904-2016, as augmented by the first Author to the year 2022 using the same criteria to ensure homogeneity. The focal mechanisms are also illustrated in Fig. 6.

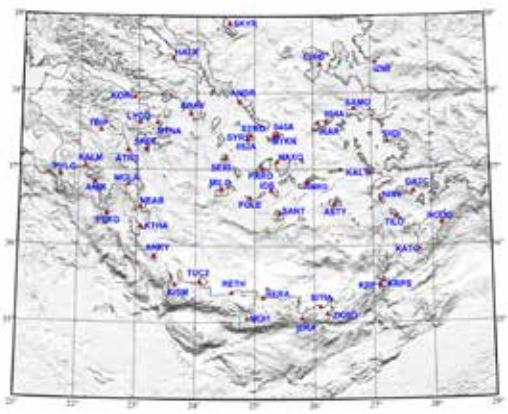

Figure 1. The continuously recording permanent GNSS network used in the analysis. See text for details.

Results

Motion Relative to the ITRF 2008 Reference Frame: The horizontal velocity vectors relative to the ITRF 2008 reference frame are shown in Figure 2. Error ellipses are drawn at the tips of the velocity vectors at the 95% confidence level (used throughout). In this frame, the motion of the entire South Aegean area appears quasi-uniform in a south-westerly direction and at rates of the order of 20mm/year. Minor local differentiations are evident in the rate and/or direction of the velocity vectors, but their interpretation in terms of local to regional kinematics is not easy, if at all possible. The same difficulty arises when the velocity is referred to a remote point on the surface, located in Eurasia or Africa. The local differentiations in crustal deformation can be resolved by using local reference points: herein we use the stations ASTY (Astypalaea Island in the Dodecanese), NAXO (Naxos Island in the Cyclades), ANAV (Anavyssos, Attica).
Motion Relative to ASTY (25.38°E, 37.10°N) on Astypalaea Island (Figure 3): Significant changes in the sense of motion can be observed (a) Relative to a NE-SW line joining the islands of Kos, Astypalaea (ASTY) and Anafi (ANF), and b) relative to a line between Anafi (ANF) and Kasos islands, extending in a NW-SE direction between Crete and Karpathos (KRP). In addition, the stations located in the north and west sectors of the study area *diverge* from those in the south and east sectors. Moreover, and importantly, the SE Dodecanese (Nisyros, Tilos, Rhodes etc.) appears to comprise a block moving to the east-northeast relative to the KOS-ASTY-ANF and ANF-Kasos lines in a sense *sinistral* with respect to the KOS-ASTY-ANF line. Accordingly, the KOS-ASTY-ANF and ANF–KASOS lines appear to be parts of significant tectonic boundaries.
Motion Relative to NAXO (25.38°E, 37.10°N) on Naxos Island (Figure 4): Here we observe a *very* significant change in the sense of motion relative to a NE-SW line joining Kalymnos (KALY), Amorgos (AMRG) and Santorini (SANT). The southeastern part of this line coincides with the southern boundary of the Anhydros Basin, forming between Amorgos and Santorini. All stations located in the Cyclades Archipelago generally drift with very low relative velocities associated

with significant error ellipses that hinder their interpretation, while they exhibit significantly non-uniform orientations. These may be attributed partly to their proximity to the local reference point (small displacement/ large error) and partly to small-scale distributed internal deformation in the "Cyclades Block" (non-uniform orientations). Exceptions to this pattern appear to be the islands Santorini (SANT) and Folegandros (FOLE), which diverge from the rest of the Cyclades relative to an NW-SE line extending between the islands Anafi (ANF) and Ios (IOS). In addition, there is evidence of convergence between east Crete (TUC2) - Anthikethyra (ANKY)and Kythera (KTHA) on one hand, and Santorini (SANT) – Folegandros (FOLE) on the other. Finally, the SE Dodecanese, to the south of the KOS-ASTY-ANF and east of the ANF-KASOS lines respectively, *diverges* from the areas to the north and west of these boundaries at *very high rates*.

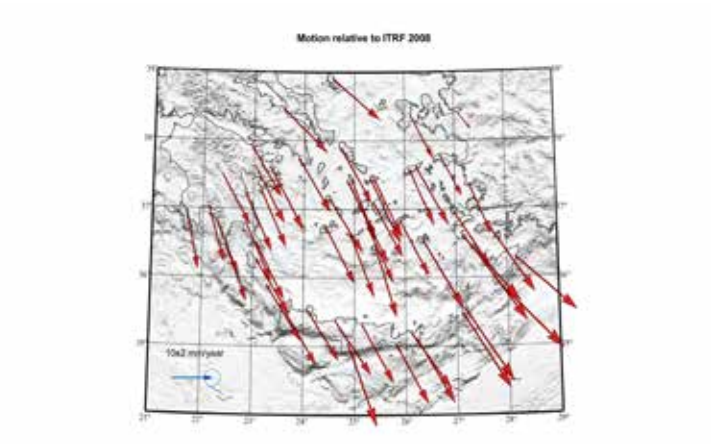

Figure 2. Horizontal velocities of the GNSS stations data in the ITRF2008 reference frame.

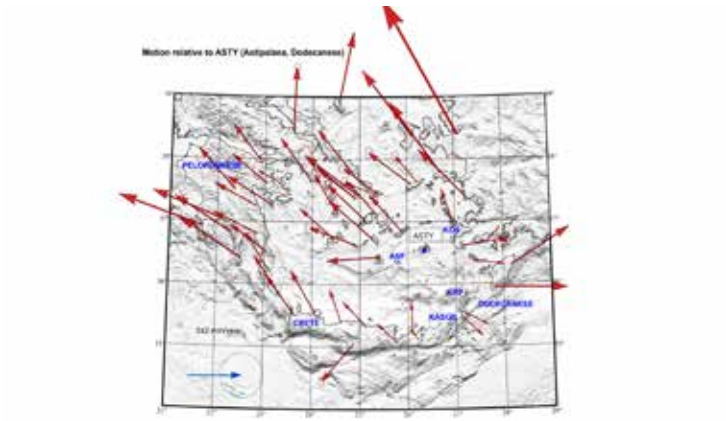

Figure 3. Horizontal velocities of the GNSS relative to the ASTY station.

Motion Relative to ANAV (23.91°E, 37.74°N) at Anavyssos, Attica (Figure 5): It is evident that in this local reference frame, the line Ikaria (IKAR) – Naxos (NAXO) – Paros (PARO) – Milos (MILO) defines a boundary so that: a) Stations to the north of the line and the west of longitude W of 24°E describe mainly NE-SW trajectories, approximately parallel to the south branches of the westward extension of the North Anatolian Fault into the Aegean; b) stations to the north of the line diverge northwards and, c) stations in the vicinity of this line describe NE-SW to E-W trajectories. Significantly, all stations south of the KOS-ASTY-ANF line and east of the ANF-KASOS lines, i.e. the Dodecanese, *diverge* rapidly in a South-Easterly direction. Because all stations located to the south of the Peloponnese and on western Crete are relatively stationary relative to ANAV, the trajectories of MILO, FOLE and SANT, as well as of all stations in eastern Crete indicate that the area within MILO, FOLE, SANT, western Crete, KASOS and ANF may undergo *counterclockwise rotation* which can only be effected by sinistral NW-SE and dextral NE-SW faulting along the KASOS-ANF line. Accordingly, it appears that the horizontal sense of NW-SE faulting changes from *dextral* north of the KALY-AMRG-SANT line to *sinistral* south of the KOS-ASTY-ANF line.

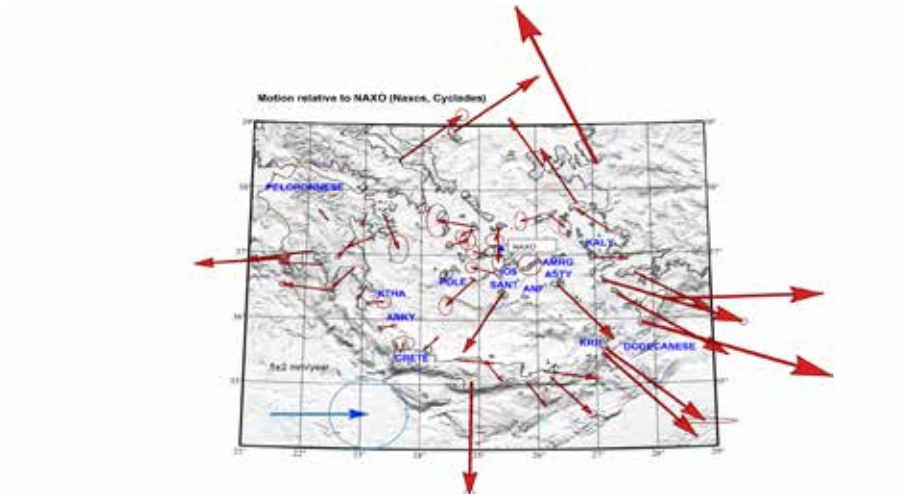

Figure 4. Horizontal velocities of the GNSS relative to the ASTY station.

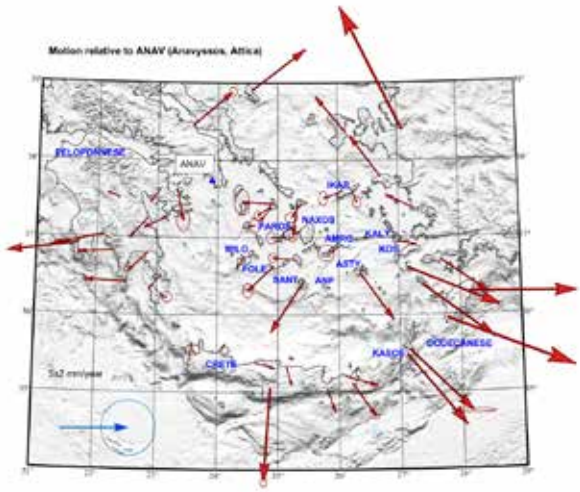

Figure 5. Horizontal velocities of the GNSS relative to the ANAV station.

Strain analysis and focal mechanisms: The calculated two-dimensional strain rate tensor is presented in Fig. 6. Extension (positive eigenvalues) is indicated with blue vectors and compression (negative eigenvalues) with red. The Cyclades Islands and the western coasts of Anatolia are characterized by an almost N-S extensional field, which rotates to NNW-SSE south of IKAR (Ikaria) – NAXO (Naxos) – Paros (PARO) – MILO (Milos) line discussed earlier. This counterclockwise rotation of the extensional field continues to the south and southeast, with the transition apparently associated with KOS (Kos) – ASTY (Astypalaea) – ANF (Anafi) line also discussed above. The Dodecanese Islands experience NW-SE to NNW-ESE extension. This changes to NE-SW compression in Crete. The transition appears to be almost abrupt and occurs just west of an (obvious in the focal mechanism distribution) NNE-SSW oriented extensional feature between the Kasos (KASOS)/ Karpathos (KPR) and Nisyros/Kos (KOS) islands, which we tentatively dub "the *Karpathos – Nisyros detachment*", as well as west of the Kasos – Anafi line which is hereby confirmed. Minor differentiations in the strain field are also evident near Santorini and Folegandros Islands, confirming their separation from the rest of the Cyclades bounded by a line through Santorini (SANT) and Ios/Folegandros (FOLE). Finally, Euboea and the eastern part of central Greece are characterized by NNE-SSW extension, while the south Peloponnese is dominated by E-W extension. Similar findings concerning the Peloponnese, the eastern part of the central Aegean and Euboea were also reported by Chousianitis *et al.* (2015). The results of our strain analysis agree remarkably well with the crustal stress field derived from the inversion of earthquake focal mechanisms, e.g. as reported by Kassaras *et al.* (2020).

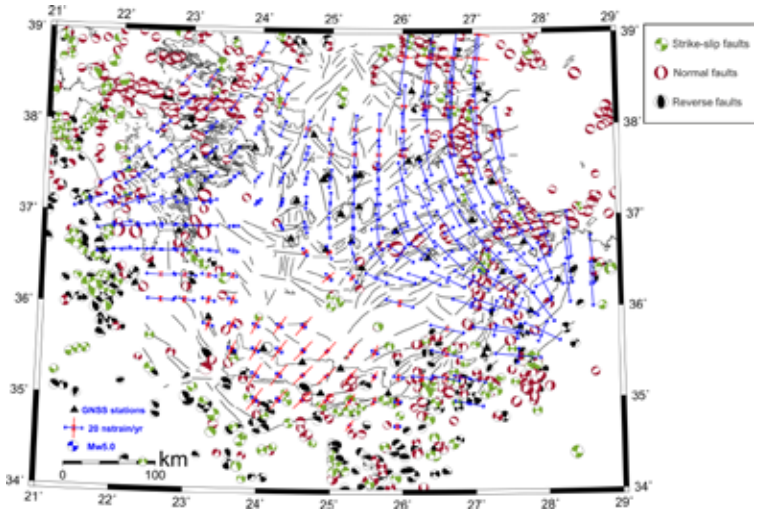

Figure 6. The strain field derived by inversion of the regional velocity field and focal mechanisms of crustal earthquakes with M≥4 over the period 1904-2022. The locations of the cGNSS stations are also indicated with black triangles.

Conclusions

The joint evaluation of all the above information confirms the distributed block deformation of the South Aegean and allows for the tentative identification of 7 major crustal blocks, of which block 1 is further partitioned into three sub-blocks. These are illustrated in Fig. 7 and are numbered from 1 to 7, with the sense of *horizontal* relative motion at their interfaces being as follows:

Block 1a: This includes the area to the north of the Ikaria – Paros/Naxos – Milos line and to the east of longitude 24°E. It is separated from Block 1b by a tentative, N-S oriented, apparently right-lateral discontinuity approximately extending along a line passing east of the Milos and Serifos islands and between the Euboea – Andros strait. It is also separated from Block 2 by a right-lateral and apparently aseismic discontinuity.

Block 1b: The Myrtoan Sea, separated from Block 1a by the Milos – Serifos – Andros line. The western boundary of this block exhibits null horizontal displacement as it comprises the NNW-SSE normal faults bounding the east coast of the Peloponnese. Moreover, the nature of its interface with Block 5 (Cretan Sea) remains undetermined.

Block 2: This comprises the southern Cyclades except for the island east of the Santorini – Ios line, Ikaria, Samos and others. It is separated from Block 1b by the Ikaria – Paros/Naxos – Milos line to the north, from Block 3 by the Kalymnos – Amorgos – Santorini line and from Block 4 by the Santorini – Ios line. The first interface has tentatively been identified as right lateral, the second appears to be normal with a left-lateral horizontal component and the third is tentatively identified as right lateral.

Block 3: The northern part of the Dodecanese. It is separated from Block 2 by the Kalymnos – Amorgos – Santorini line, to the east by the Kasos/Karpathos – Nisyros/Kos line and to the west by the Kasos Anafi line. The sense of horizontal motion here changes abruptly from left-lateral to practically null at the normal faults of the Kasos/Karpathos – Nisyros/Kos line (*Karpathos–Nisyros detachment*). The interface with Block 5 appears to be right lateral.

Block 4: Located at the southeast end of the Cyclades, it includes the islands Santorini, Sikinos, Folegandros. It is separated from Block 2 by the NNE-SSW right-lateral Santorini – Ios line, from Block 1a by the NW-SE right-lateral Paros/Naxos – Milos line and from Block 5 by the continental slope of the Cretan Sea, which is assumed to comprise normal faults with some right-lateral horizontal component. If this configuration is correct, Block appears to experience south-westward translation with simultaneous counterclockwise rotation.

Block 5 is the Cretan Sea. As indicated above, the eastern half of this block may undergo counterclockwise rotation effected by NW-SE left-lateral displacement and NE-SW right-lateral faulting.

Block 6 includes the southeast Dodecanese, Karpathos and Kasos. It is bounded to the southeast by the left lateral faulting of the Aegean – African plates interface and to the west by the normal faults of the Karpathos – Nisyros detachment.

Block 7 is the Karpathos – Nisyros detachment.

In a final comment, it is noted that this configuration and relative motion of crustal block amply explains the geographical configuration of the Cycladic islands.

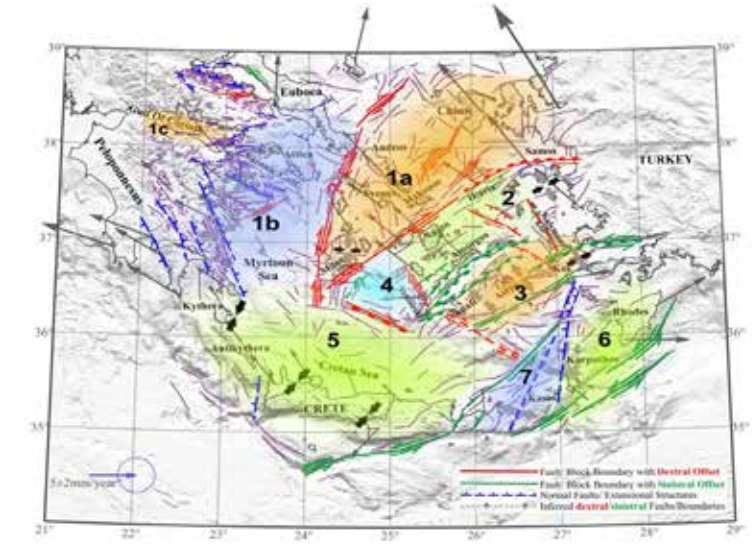

Figure 7. A model of contemporary distributed block deformation in the South Aegean.

Acknowledgements

This research was supported by the Hellenic Foundation for Research and Innovation (HFRI) under the HFRI PhD Fellowship grant (Fellowship Number: 841).

References

Briole, P., Ganas, A., Elias, P. and Dimitrov, D., 2021. The GPS velocity field of the Aegean: new observations, contribution of the Earthquakes, crustal blocks model, *Geophys. J. Int.*, 226, 468–492, doi:10.1093/gji/ggab089.

Chousianitis, K., Ganas, A. and Evangelidis, C.P., 2015. Strain and rotation rate patterns of mainland Greece from continuous GPS data and comparison between seismic and geodetic moment release, *J. Geophys. Res.*, Solid Earth, 120, 3909–3931, doi:10.1002/2014jb011762.

Chousianitis, K., Papanikolaou, X., Drakatos, G. and Tselentis, G-A, 2021. NOANET: A continuously operating GNSS network for solid-earth sciences in Greece, *Seismol. Res. Lett.*, 92, 2050–2064, doi:10.1785/0220200340.

Floyd, M.A. et *al.*, 2010. A new velocity field for Greece: Implications for the kinematics and dynamics of the Aegean, *J. Geophys. Res.: Solid Earth*, 115, doi:10.1029/2009jb007040.

Ganas, A. et *al.*, 2008. NOANET: The new permanent GPS network for Geodynamics in Greece: *Geophys. Res. Abs.*, 10, EGU2008-A-04380, SRef-ID: 1607-7962/gra/EGU2008-A-04380.

Kassaras, I., Kapetanidis, V. and Karakonstantis, A., 2016. On the spatial distribution of seismicity and the 3D Tectonic stress field in Western Greece, *Phys. Chem. Earth.*, *Parts A/B/C*, 95, 50–72, doi:10.1016/j.pce.2016.03.012.

Kassaras, I. et *al.*, 2020. The New Seismotectonic Atlas of Greece (v1.0) and its implementation, *Geosci. J.*, 10, 447, doi:10.3390/geosciences10110447.

Lazos, I. et *al.*, 2022. Temporal evolution of crustal rotation in the Aegean region based on primary geodetically-derived results and palaeomagnetism, *Acta Geod. Geophys.* , 57, 317–334, doi:10.1007/s40328-022-00379-3.

McClusky, S. et *al.*, 2000. Global Positioning System constraints on plate kinematics and dynamics in the eastern Mediterranean and Caucasus, *J. Geophys. Res.*, 105, 5695–5719, doi:10.1029/1996jb900351.

Nyst, M. and Thatcher, W., 2004. New constraints on the active tectonic deformation of the Aegean, *J. Geophys. Res.: Solid Earth*, 109, doi:10.1029/2003jb002830.

Pesci, A. and Teza, G., 2007. Strain rate analysis over the central Apennines from GPS velocities: the development of a new free software, *Bollettino di Geodesia e Scienze Affini*, 56, 69–88.

Reilinger, R. et *al.*, 2006. GPS constraints on continental deformation in the Africa□Arabia□Eurasia continental collision zone and implications for the dynamics of plate interactions, *J. Geophys. Res.: Solid Earth*, 111, doi:10.1029/2005jb004051.

Sakkas, V. et *al.*, 2020. Contemporary kinematics of the South Aegean area (Greece) detected with continuous GNSS measurements: *Proc., 2020 EGU General Assembly*, No EGU2020-7656, doi:10.5194/egusphere-egu2020-7656.

17th INTERNATIONAL CONGRESS of the Geological Society of Greece

BULLETIN OF THE GEOLOGICAL SOCIETY OF GREECE, SP. PUBL.

EXTENDED ABSTRACT 183

Geophysical investigation of landslide phenomena in the Perivoli area, Grevena, using the electrical resistivity tomography method.

Krotka K.[1], Fikos I.[1], Papathanasiou G.[2]

(1) Laboratory of Applied Geophysics Aristotle University of Thessaloniki, Thessaloniki, Greece, konstantinakrkt2000@gmail.com , ifikos@geo.auth.gr

(2) Laboratory of Engineering Geology & Hydrogeology, School of Geology, Aristotle University of Thessaloniki, Greece,

gpapath@geo.auth.gr

Introduction

This study focuses on the identification of the boundaries of a landslide in a remote but inhabited area, laterally and in depth, as well as analyzing the characteristics of it using geoelectrical surveying methods. The landslade is located on the provincial road of Grevena - Vovousa (Fig. 1), limiting access to the country's main road network from remote areas. This study emphasizes on the importance of further investigetion, since the landslade often reactivates, damaging the road and posing a threat to the people of the area. The results showcase the geometry of the landslide's subsurface and the thickness of the layers comprising it.

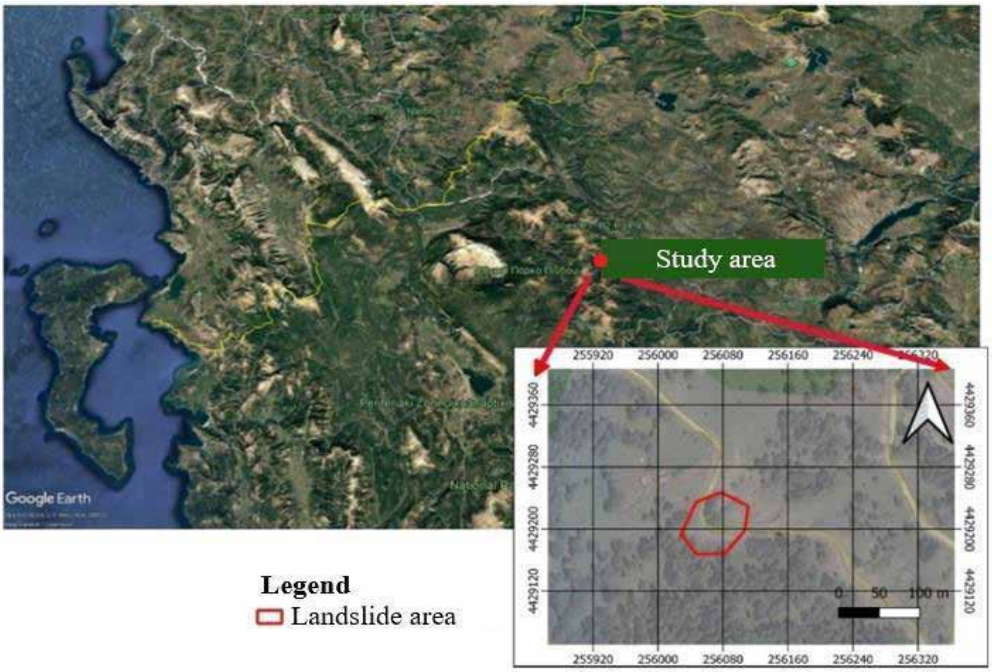

Figure 1: Location of the landslide (Google earth with modifications).

Geological Setting

The investigated area is part of the External Hellenides and more specifically it is located in the tectonostratigraphic zone of Pindos. The dominant formations of this zone are flysch, limestones and platy limestones. The Pindos flysch is divided into two layers, the 1st and 2nd flysch, both consisting of clastic sediments. The 1st is characterized by alterations of pebbles, sandstones and marls and was deposited during the Lower Cretaceous, while the 2nd has a calcareous-marl composition and was formed between the Danian and the Upper Eocene (Mountrakis, 2020). In the geologic map of Pentalofos (IGME, 1977) it can be seen that the landslide is entirely located in the area's flysch (Fig. 2), which overlies the limestone. The flysch in the area occurs with a chaotic structure, sandy and clayey composition and the limestones in the area are white (Mountrakis, 2020). The geological map also shows that the main formations include the undivided Pindos flysch (Danian-Eocene), which coexists with sandstone masses, marls and clay slates. In addition, Mesozoic limestones are found, either as platy/well-stratified ashy or reddish limestones, or as white limestone masses. Peridotites, serpentinites, dolerites and microlithic rocks also occur in the area, either individually or in combinations.

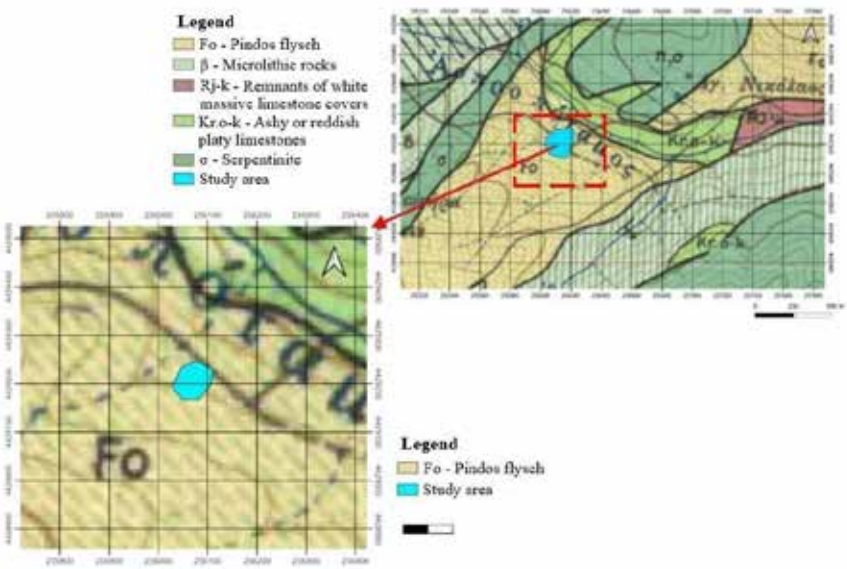

Figure 2: Geologic map of the area (IGME 1977, with modifications).

During the field research a stream was found acting as a natural boundary between the superficial geological formations (flysch and limestone). Flysch appears SE of the stream, while limestone predominates the NW side of it (fig. 3). This holds great importance, as it offers a clear view of the layers comprising the landslide. The subsurface consists of remnants of white limestone covers (Rj-k, Fig. 2), followed by a metabase layer. The upper layer/weathering mantle, which is the moving part of the landslide, consists of Pindos flysch. (Mountrakis D., 2020)

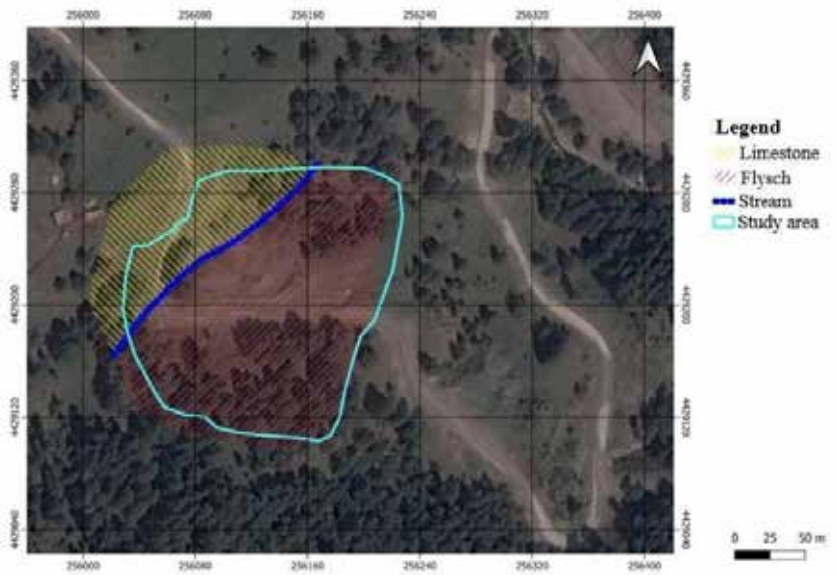

Figure 3: Stream as a natural boundary between the formations (Google earth with modifications).

Geotechnical characteristics

The flysch in the Perivoli area was geotechnically classified as category XI, characterized as strongly sheared siltstone or clayey shale with chaotic structure and clay pockets. It includes thin layers of sandstone that have been transformed into small fragments, making it particularly unstable and associated with landslide phenomena in areas of Western Greece. Its mechanical behaviour is characterised by great anisotropy, due to the degree of weathering, the orientation of discontinuities, high slope gradients and the presence of water. Furthermore, category XI flysch has increased clay content which creates impermeable and semi-permeable barriers, causing slope stability problems (Marinos *et al*., 2013). Limestone on the other hand, has high strength values due to its natural state. It is particularly

vulnerable to erosion due to the presence of water, which can lead to karstification and decrease its durability. The geotechnical characteristics of it depend on the degree of weathering, secondary relaxation and the presence of water. The weathering mantle occuring in the composition of the landslide, has a loose structure and the grain size of the material varies. Its mechanical strength values are lower than those of the original rock, while its limestone composition makes it permeable to groundwater, contributing to the occurrence of failures in the area.

Applied methodology

The geophysical method used in this study is electrical resistivity tomography (ERT). This offers a detailed depiction of the geological formations underground and provides insight on changes or possible movements in the landslide, helping to comprehend the phenomenon better. The arrangements used were the dipole-dipole, for the definition of the lateral boundaries, and the multi-gradient, for the definition of the landslide's depth. This combination provided a more complete depiction of the subsurface structure (Tsourlos P., 2021). A differential GPS (Trimble GNSS System) was used for the precise placement of the electrodes and the measurements were taken with the Syscal Pro instrument (IRIS Instruments). The first tomography (ERT1) was carried out along the movement axis of the landslide (Fig. 4). Its purpose was to determine the depth of the slip surface and the upper limit of the landslide. A limestone outcrop was observed in the southern part, which posed the question of whether it was the crown or just an eyebrow of the landslide. The tomography was 115 meters long and 23 electrodes were used (due to the road network) with 5 meters spacing in between. No increase in resistance was observed at a depth of 20 meters in ERT1, which affected the decisions regarding the length of the next two tomographies ERT2 & ERT3. The second tomography (ERT2) was carried out across the movement axis of the landslide (east to west) and a few meters north of the limestone outcrop mentioned earlier (Fig. 4). After a quick view of the preliminary results of ERT2, signs of clear increase in the resistivity were not identified, therefore this tomography was also 115 meters long in order to provide insight as deep as possible. As in the case of ERT1, 24 electrodes were used with 5 meters spacing in between. The third tomography (ERT3) was almost parallel with ERT2 at the landslide's foot area (Fig. 4). The tomography was 92 meters long and 24 electrodes were used with 4 meters spacing in between, providing slightly better resolution at expense of the maximum depth of investigation.

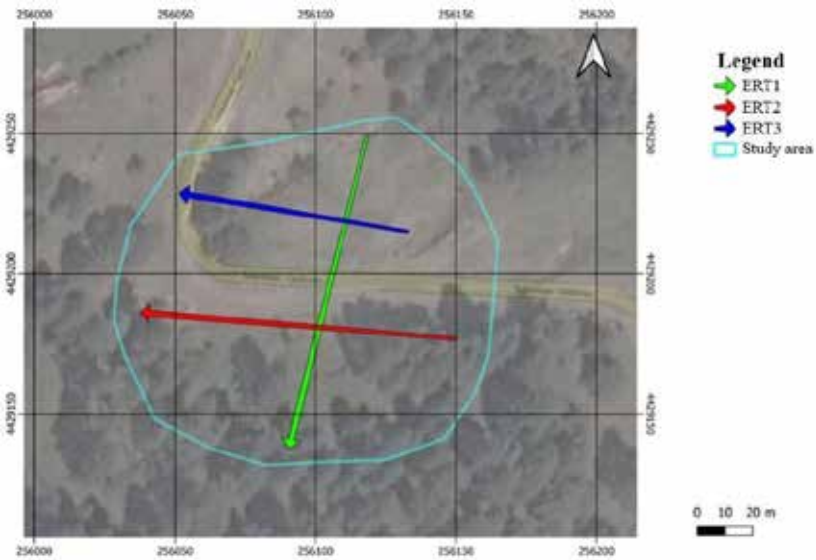

Figure 4: Orientation of the tomographies (Google earth with modifications).

Afterwards the results were subjected to mathematical inversion in the ResIPy open source software. Specifically, this software processed, filtered and finally modeled the geoelectrical data from the tomographies. The results of this process were easy to interpret images, depicting the layers' resistivity in representative colours.

Results

The inversion program ResIPy created two-dimensional models depicting the specific electrical resistivities of the subsurface (Fig. 5, 6, 7). The scale in the models ranges from dark blue for low resistivity values, to dark red for the highest resistivity values. In ERT1 (Fig. 5) 642 values were used by merging both the dipole-dipole and multi-gradient

arrangements and the final error (RMS) was 2.36%. The analysis of the results shows that the subsurface can be divided into three main layers. The first layer (Fig.5, blue area) had the lowest resistivity (20-45 Ohmm) and was about 10 meters thick throughout the entire tomography, except for the area between the 11th and 13th electrodes, where there was a lack of data due to the road network. The second layer (Fig. 5, green and yellow area) had a resistivity of 45-75 Ohm*m and was also 10 meters thick, which remained the same through the entire tomography, with the same anomaly on the road area.

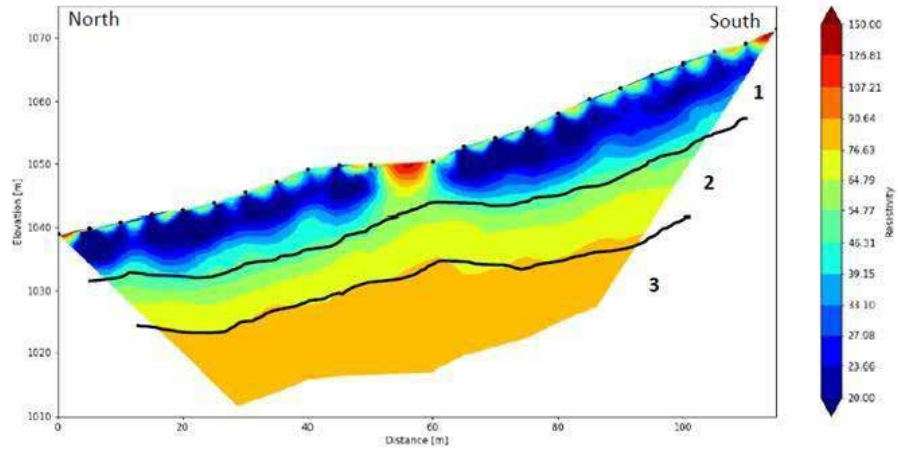

Figure 5: ERT1 resistivity distribution model.

In ERT2 (Fig. 6), 792 values were used by merging the dipole-dipole and multi-gradient arrangements and the final error (RMS) was 2.42%. The subsurface was divided into three main layers with different specific electrical resistivity. The first layer (Fig. 6, blue area), had the lower resistivity values (20-45 Ohmm) and was about 10 m thick. There were no obstacles, and all 24 electrodes were used this time. In this area, increased electrical resistivity values were observed at two points: eastern, between the 1st and 3rd electrode (90 – 105 Ohm*m) and between the 3rd and 4th electrode (45-75 Ohm*m) and western, between the 21st and 24th electrode (45-105 Ohm*m). In the central part of the section, between the 4th and 21st electrodes, the first layer dominates, which probably corresponds to the moving mass of the landslide. The second layer (Fig. 6, green and yellow area) had intermediate resistivity values (45-75 Ohm*m) and was also about 10 meters thick. In areas of increased resistivity, the second layer is locally thicker. Finally, at a depth of about 20 meters, a third layer appeared, which had higher resistivity values (75 to 90 Ohm*m) and was observed uniformly along the entire length of the tomography.

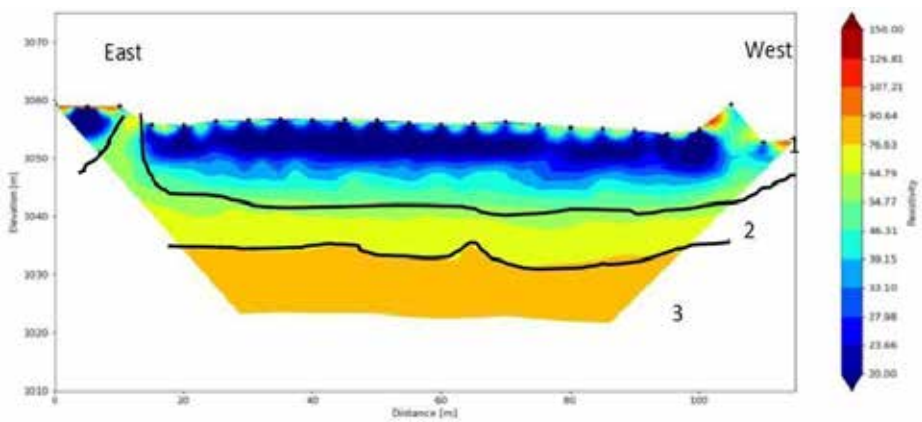

Figure 6: ERT2 resistivity distribution model.

In ERT3 (Fig. 7) 693 values were used by merging the dipole-dipole and multi-gradient arrangements and the final inversion error (RMS) was 2.92%. In this tomography only 23 electrodes were recording, due to the presence of the road network. As previously, three main layers are identified based on the specific electrical resistivities. The first layer is characterized by low resistivity values (20-45 Ohm*m), uniformly observed over most of the section, with the thickness being around 10

m. However, in the western part of the tomography, local variations are recorded, with increased resistivity values reaching 125 Ohmm between the 17th and 18th electrodes, and 45-90 Ohmm values in other areas. In the western part, where the tomography crosses the provincial road network, even higher resistance values were observed, reaching 150 Ohmm. The second layer, located at a depth of 10 meters, has intermediate resistivity values (45-75 Ohm*m), while its thickness reached 15 m locally, mainly in the area between the 6th and 10th electrode. Finally, the third layer appears at a depth of about 20 meters where higher resistivity values (75-90 Ohmm) are observed throughout the entire length of the tomography.

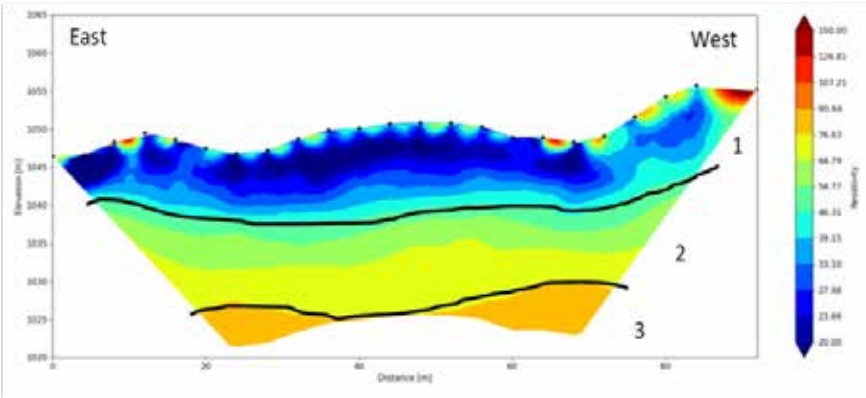

Figure 7: ERT3 resistivity distribution model.

The study of the area through three electrical tomographies (ERT1, ERT2, ERT3), revealed three main geoelectric layers corresponding to geological layers: the flysch (low resistivity values), the weathering mantle (intermediate resistivity values) and the limestone (high resistivity values). These geoelectric characteristics are directly related to the geotechnical properties of the formations, such as their strength, with limestone having the highest strength and flysch having the lowest. The analysis of ERT1 revealed ground subsidence, but it has not appeared as the main crown of the landslide. Instead, it is attributed to the heterogeneity of the flysch. Sections ERT1, ERT2 and ERT3 are cross each other at points used to confirm the validity of the results and to better understand the subsurface of the area. As the ERT1 was vertical to the other electrical tomographies (ERT2 & ERT3), there are two intersection points. The first one (Fig. 7), between ERT1 and ERT2, is located at the absolute altitude of 1.055 meters. On ERT1 this one is found between the 14th and 15th electrode and on the ERT2 it is found between the 9th and 10th electrode. For this common area were found both similar geoelectrical characteristics of the formations and thicknesses of them all, flysch was found 13 meters thick and weathering mantle 10 meters. The limestone basement is found at 23 meters depth.

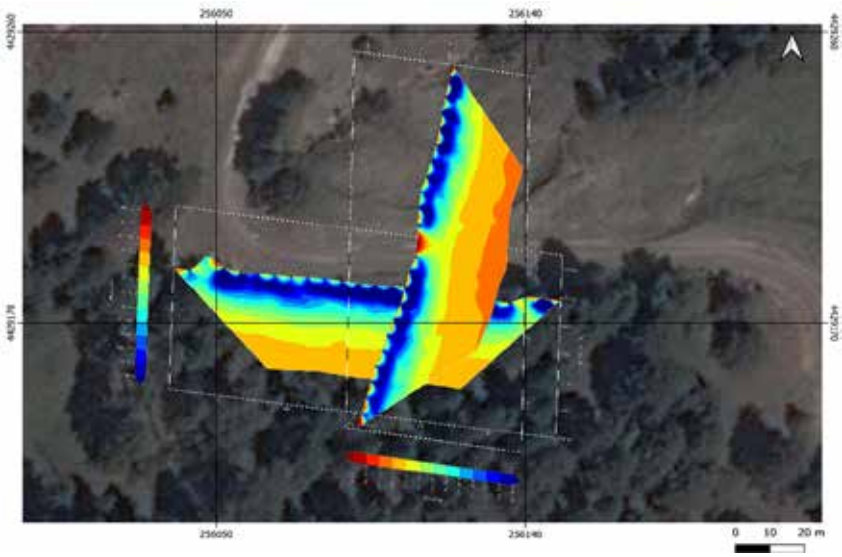

Figure7: Intersection point between ERT1 and ERT2

The second intersection point (Fig. 8), between ERT1 and ERT3, is located at the absolute altitude of 1.046 meters. This point is found between the 7th and 8th electrode on both first and third electrical tomography. At this intersection point the flysch appears with only 10 meters thickness and the weathering layer with 11 meters. The limestone basement is found at 21 meters depth.

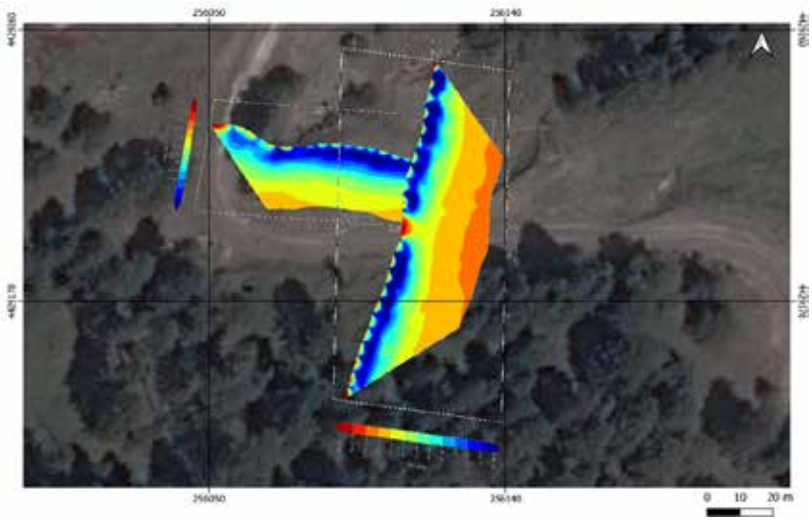

Figure 8: Intersection point between ERT1 and ERT3

Tomographies ERT2 & ERT3 were almost parallel and therefore provide data about the three formations on different elevations of the landslide. On ERT2 the subsurface flysch is found at 1046 meters altitude and on ERT3 at 1037 meters while the weathering layer is located at 1046 meters and 1037 meters and the base layer of limestone is located at 1035 meters altitude on ERT2 and at 1025 meters on ERT3. It becomes clear that the thickness of all the formations remain the same in the examined area even though the altitude decreases constantly, the distance between the two parallels is 37.5 meters.. According to these data, the altitude difference and the distance between the parallels, it follows the total slope of the landslide which is calculated as 13,5 degrees.

References

Brunn, J., 1977. Geological Map of Greece 1:50.000, Sheet Pentalofos. I.G.M.E., Athens.

Marinos, V., Kilias A., Makedon Th. & Thomaidou E., 2013. Guide to Field Trip West Macedonia - Epirus - Central Greece, Technical Geology, Aristotle University of Thessaloniki, Thessaloniki, Greece.

Mountrakis, D., 2020. Geology and Geotectonic Evolution of Greece, 2nd Edition, Part 1, Chapter A', 25-28, Thessaloniki, Greece.

Mountrakis, D., 2020. Geology and Geotectonic Evolution of Greece, 2nd Edition, Part 1, Chapter D', 153, Thessaloniki, Greece.

Tsourlos, P., 2021. Electromagnetic Methods of Geophysical Surveys, Notes, Aristotle University of Thessaloniki, Greece

17th INTERNATIONAL CONGRESS of the Geological Society of Greece

BULLETIN OF THE GEOLOGICAL SOCIETY OF GREECE, SP. PUBL.

EXTENDED ABSTRACT 184

A holistic proposition for assessing reference station conditions

Olga-Joan Ktenidou[1], Antonia Papageorgiou[12], Fevronia Gkika[1], Erion-Vasilis Pikoulis[1], Kalliopi Fragouli[1], Fanis Chalaris[1], Spyros Liakopoulos[1], Ziya Cekinmez[13], Panagiotis Savvaidis[14], Christos Evangelidis[1]

[1] *National Observatory of Athens, Greece*

[1] *University of Patras, Greece*

[1] *National Technical University of Athens, Greece*

[1] *Aristotle University of Thessaloniki, Greece*

Introduction and background

The assumption of reference station conditions is an important one, yet is often taken for granted, especially at seismological stations or those presumably lying on rock. Stations are not always installed on true bedrock or in ideal free-field conditions, and –what is more– rock formations do not always exhibit negligible amplification, as assumed. In Greece, few site effects studies or field surveys have been conducted to characterise seismic networks in their entirety. Here, we first investigate broadband and accelerometric stations from the HL network, run by the National Observatory of Athens (NOA) throughout mainland and island Greece. We propose a solution that does not need significant nationwide resources (time and funding at a massive scale) such as would be required for in-situ geophysical campaigns. Instead of waiting for a time when funding and personmonths will be available at a massive scale to characterise all stations with measurements on site, we propose efficient desk studies that capitalize on the existing recordings collected so far, supplemented by additional desk work and existing knowledge that network operators have acquired from their site visits already. There are 60 such stations with publicly available data streams in the period 2012-2024 which are thought to lie on rock. We address the reference station question compiling a wide variety of parameters: waveform-derived (site-specific amplification characteristics), operator-derived (on-site observations from station visits and walk-overs), and external sources (geological maps and literature). We co-evaluate all these factors to propose a transparent scheme for assessing reference stations for the HL network. Finally, we propose the extension of this pilot study to include other networks, in the region of Macedonia and Thrace, as they can be of use in studying seismicity and seismic hazard in the Kavala-Prinos area, in the framework of EU project COREu.

Methodology

We follow the methodology set forth in detail in Ktenidou et al. (2024). We compile all types of information to create a comprehensive, systematic and holistic set of station metadata as follows.

1. We first compile all publicly available information from external sources. These include notes on geology and topography from the literature (e.g. the ESM ORFEUS website, (https://esm-db.eu/; Lanzano et al., 2021 & Luzi et al., 2016; the NOA/GEIN website, https://accelnet.gein.noa.gr/; Margaris et al., 2021 – M2021). We then collect and analyse geological maps to provide a consistent description of geological unit and geological age. We mostly use geological maps (1:50,000 scale) published by the Hellenic Survey of Geology and Mineral Exploration (HSGME). We then combine this with observations by the operators regarding the geology, topography, and the installation and housing conditions on site, which are attributed high accuracy and reliability owing to the site visits. These parameters are shown in Tables 1, 2 and 3. We acknowledge the limitations of using this kind of geological map, where the scale is more appropriate for nationwide studies than site-specific ones, where inconsistencies are likely between map sheets due to them having been compiles by different persons and even with several decades' time difference, and where simplifications are likely made in the presence of complexities. But there is no other readily available resource for deriving geological information homogeneously across the country, and in this sense the geological information we compile suffers from issues of granularity for the sake of some –relative- consistency and homogeneity.
2. The second and most demanding stage of this study is to create a strong-motion database to study amplification. We collect waveforms available from the past decade from events with M4 and above, and we perform a detailed analysis to estimate the local site response per station. To do this, the dataset first goes through quality control by visually inspecting and meticulously processing the data on a waveform-specific basis, both in the time and frequency domain. Single-station amplification functions are then estimated from the dataset using the horizontal-to-vertical spectral ratio (HVSR) technique of Lermo and Chavez-Garcia (1993). A good reference station should have low and flat amplification, as e.g. some of the Northern Greece stations shown in Figure 1. Moreover, it should exhibit no significant azimuthal variation, and to assess this we not only assess the features of the mean HVSR per station but also its directional sensitivity as per Ktenidou et al. (2016), which serves as a means to identify departure from the 1D assumption (Figure 2 shows the low sensitivity for two of those stations). We propose that three values of standard deviation at different frequency ranges (0.3-30 Hz, 1-10 Hz, and fo) can be used as approximate indicators of the azimuthal stability of site response. These parameters are shown in Table 4.

We evaluate each criterion independently and assess whether each station can be considered a reference station from the point of view of geology, topographic relief, installation conditions, Vs30, and the characteristics of the HVSR in terms of mean amplification level and shape as well as in terms of directional stability. These assessments are shown in the following tables for the three stations in Northern Greece, which ranked very high among the 60 Greek stations studied.
It is well known that the amplification (A_0, A_1 in table 4) is usually underestimated by HVSR, since the vertical component is of course amplified to an unknown degree yet assumed unaffected. We also attempt some preliminary corrections to the amplitude based on the methodology of Ito et al. (2020), which however was calibrated on regional data from Japan, and so may not reflect vertical amplification levels in Greece. Hence we show these results only in an indicative capacity. Figure 3 shows examples of the Ito correction of the mean HVSR shown in Figure 1, and Table 4 also includes characteristics of resonance (e.g. A0_corr) based on these corrections. Clustering was also performed based on corrected HVSRs and similar clusters were found (more details in Ktenidou et al., 2024).

Table 1. Parameters describing housing/installation conditions and Vs30 for 3 example stations.

Station code	Building type (GEIN)	Installation con-dition	Potential reference (Inst/on)?	EC8 (ESM)	Vs30 (ESM)	Vs30 geology (M2021)	Vs30 terrain (M2021)	Preferred Vs30 (M2021)	Potential reference site (Vs30)?
KVLA	2-floor RC	Not free field	**no**	B	782	528	475	501	**yes (ESM)**
NVR	1-floor RC	free field	**yes**	A	955	556	475	514	**yes - ESM**
PLG	1floor RC	Vault in building	**yes**	B	608	492	519	506	**no**

Table 2. Parameters describing topography and slope for 3 example stations.

Station code	Station elevation (m)	Topographic code (ESM)	Slope angle (ESM)	Slope angle (M2021)	Slope (M2021)	Assessment from site visit	Potential reference site (Topography)?
KVLA	122	T1	9	7	0.122	Flat/shallow (<15) within 200 m	**yes**
NVR	627	T1	15	0.259	15	Flat/shallow (<15) within 200 m	**yes**
PLG	566	T1	5	4	0.073	Flat/shallow (<15) within 200 m	**yes**

Table 3. Parameters describing geological conditions for 3 example stations.

Station code	Geologic description (GEIN)	Description (M2021)	Geologic Age (M2021)	Geologic unit - this study	Geologic age - this study	Reference map used (HSGME)	Potential reference site?
KVLA	limestone	Alluvial deposits	Oligocene	Kavala granite	Quartenary	Kavala Sheet	**yes**
NVR	sandstone	Scree and Talus Cones	Pleistocene		Metamorphic rocks/upper series (schists, schist-gneisses, gneisses, amphibolites and marbles)	Oligocene - Miocene	**yes**
PLG	gneiss	Basal Conglome-rate Series	Upper Miocene -Lower Pliocene	Quartzites and quartzitic sandstones of Svoula group	Triassic - middle Jurassic	Polygyros Sheet	**yes**

Table 4. Waveform-derived parameters for 3 example stations.

Station code	f0 inspected >2.7 (Hz)	A0	Peaky / flat?	f1 (Hz)	A1	f0_corr if not seen in HVSR (Hz)	A0_corr (/ A1_corr)	Potential reference site (HV mean)?
KVLA	-	-	f	-	-		-	**yes**

NVR	-	-	**p**	-	-	5.0	4	**ok**
PLG	-	-	f	-	-		-	**yes**
Station code	**SD (1-10 Hz)**	**SD (0.3-30 Hz)**	**Directional variability < 10 Hz**	**Directional variability - HF**	**Cluster no. from mean HV**	**Cluster no. from HV_corr**	**Response description (mean HV)**	**Potential reference site (HV directionality)?**
KVLA	1.04	1.07	Low		6	5	Reference station	**yes**
NVR	1.05	1.09	Low		5	5	Flat, near-reference	**yes**
PLG	1.05	1.09	Low		6	5	Reference station	**yes**

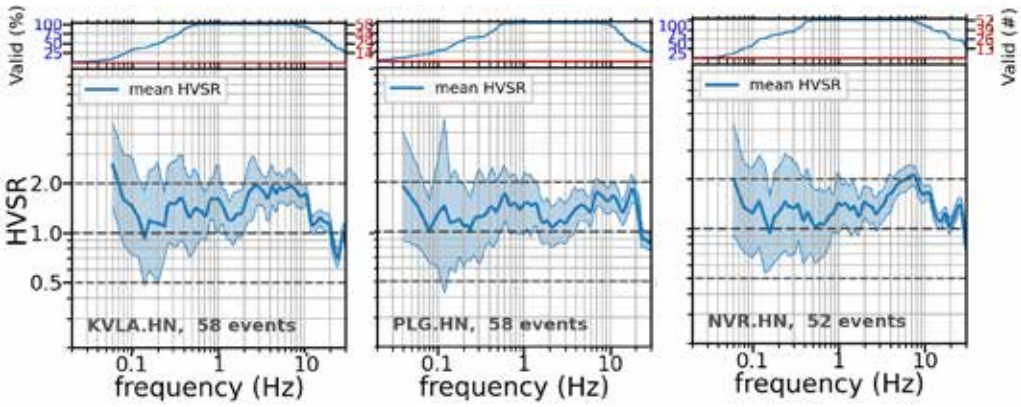

Figure 1. Mean HVSR ± 1 standard deviation for 2 stations in Northern Greece (left to right: HL.KVLA, HL.PLG and HL.NVR); inset on top indicates the number of available recordings per frequency.

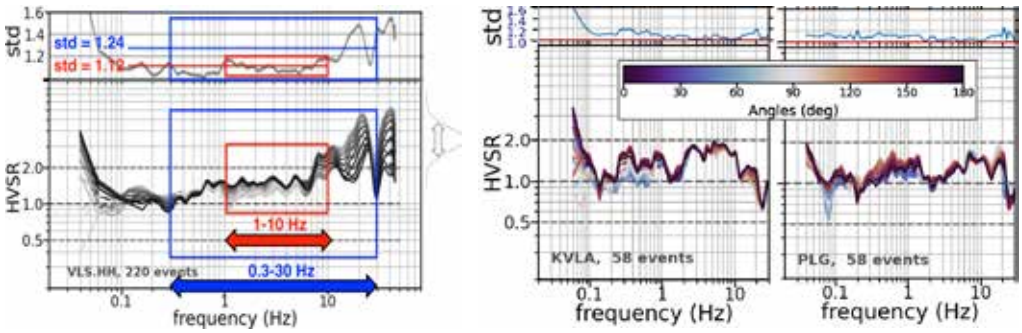

Figure 2. HVSR per component for 2 stations (left to right: HL.KVLA, HL.PLG), as those are rotated by 10º intervals from North to East; inset on top indicates the standard deviation (hence, directional sensitivity or variability) per frequency.

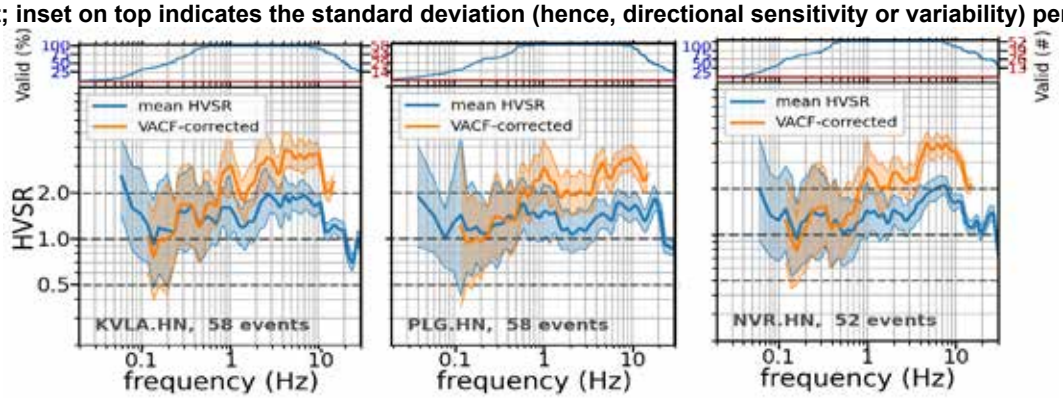

Figure 3. Mean HVSR±1 standard deviation (in blue) for 3 stations in Northern Greece (left to right: HL.KVLA, HL.PLG and HL.NVR) and corrected HVSR using Ito et al. (2020) correction function for the vertical component (in orange). The latter is only computed within the method's range of applicable frequencies and is offered in an indicative quality; inset on top indicates the number of available recordings per frequency.

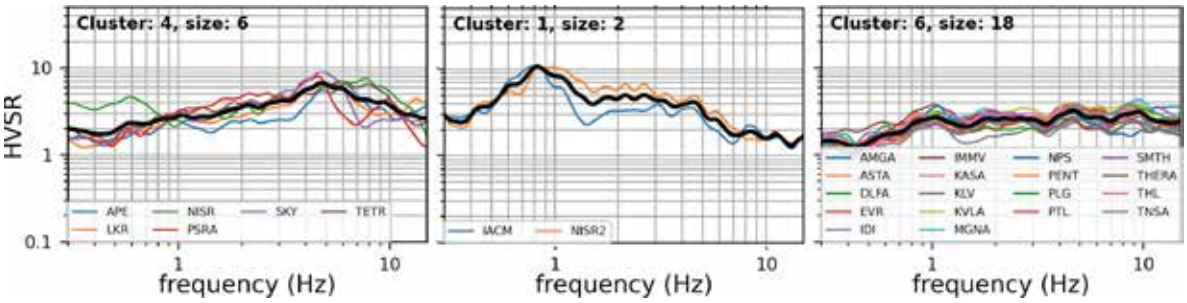

Figure 4. Example station clusters with different style of HVSR response.

Finally, we use clustering techniques to group stations with different response characteristics (Figure 4) and finally combine this data-derived characterization with the previously compiled metadata to evaluate the stations' overall capacity as reference sites.

Results and discussion

In this study, we compiled several descriptors from literature, geological maps and direct network operator observations from site visits and we also derived site-specific amplification characteristics from strong-motion data analysis. We brought everything together to co-evaluate the overall potential of our stations as reference stations. We proposed a solution that does not need significant nationwide resources (time and funding at a massive scale) such as would be required for in-situ geophysical campaigns. Instead of waiting for a time when funding and personmonths will be available at a massive scale to characterise all stations with measurements on site, we propose efficient desk studies that capitalize on the existing recordings collected so far, supplemented by additional desk work and existing knowledge that network operators have acquired from their site visits already. We acknowledge the limitations of HVSR, namely the underestimation of amplification level, and hence propose that our amplification results be regarded as potential lower-bounds. However we do stress that even with a full-blown budget for geophysical campaigns, the resulting Vs profiles would still suffer from that method's own drawbacks – they would be non-unique and any forward site response modeling using them would also heavily rely on the 1D assumption: this, HVSR does not – it actually reveals at least some of nature's departure from it.

This work has been completed for all HL network stations that lie on rock and is currently underway for stations from other networks in the regions of Macedonia and Thrace. The special focus on this region intends to add value and help decrease epistemic uncertainties for future applications that will take place within the European project COREU (https://coreu.eu/), which will involve seismic monitoring and hazard assessment in the Kavala-Prinos area in the framework of a CCS pilot study.

Acknowledgements

All waveforms and station metadata are freely accessible at https://eida.gein.noa.gr/, the regional node of EIDA hosted by the Institute of Geodynamics of the National Observatory of Athens (NOA). Event parameters come from the seismic catalogue of NOA, freely accessible here: https://eida.gein.noa.gr/fdsnws/availability/1. We gratefully acknowledge partial financial support from EU project COREU.

References

Ito, E., Nakano, K., Nagashima, F. and Kawase H. (2020): A Method to Directly Estimate S-Wave Site Amplification Factor from Horizontal-to-Vertical Spectral Ratio of Earthquakes (eHVSRs), Bull. Seismol. Soc. Am., 110, 2892–2911, doi: 10.1785/0120190315.

Ktenidou, O.-J., Pikoulis, E.-V., Papageorgiou, A., Gkika, F., Liakopoulos, S., Cekinmez, Z., Savvaidis, P., Fragouli, K., and Evangelidis, C. P. (2024): The quest for reference stations at the National Observatory of Athens, Greece, Nat. Hazards Earth Syst. Sci. Discuss. doi:10.5194/nhess-2023-233

Ktenidou, O.-J., Chávez-García, F.J., Raptakis, D. and Pitilakis, K.D. (2016): Directional dependence of site effects observed near a basin edge at Aegion, Greece, Bull. Earth. Eng., 14(3), 623-645, doi:10.1007/s10518-015-9843-x.

Lanzano, G., Luzi, L., Cauzzi, C., Bienkowski, J., Bindi, D., Clinton, J., Cocco, M., D'Amico, M., Douglas, J., Faenza, L., Felicetta, C., Gallovic, F., Giardini, D., Ktenidou, O-J. and 12 others: Accessing European Strong-Motion Data: An Update on ORFEUS Coordinated Services, Seismol. Res. Letts, 92, 1642–1658

Lermo, J., and Chávez-García, F.G. (1993): Site effect evaluation using spectral ratios with only one station, Bull. Seismol. Soc. Am., 83,1574–1594.

Luzi, L., Puglia, R., Russo, E., D'Amico, M., Felicetta, C., Pacor, F., Lanzano, G., Çeken, U., Clinton, J., Costa, G., Duni, L., Farzanegan, E., Gueguen, P., Ionescu, C., Kalogeras, I., Özener, H., Pesaresi, D., Sleeman, R., Strollo, A. and Zare, M.: The engineering strong motion database: A platform to access pan□European accelerometric data, Seismol. Res. Letters, 87, 987–99

Margaris, B.E., Scordilis, M., Stewart, J.P., Boore, D.M., Theodulidis, N., Kalogeras, I., Melis, N., Skarlatoudis, A., Klimis, N. and Seyhan, E. (2021). Hellenic strong-motion database with uniformly assigned source and site metadata for period of 1972-2015, Seismol. Res. Letts, 92, 2065-2080.

National Observatory of Athens, Institute of Geodynamics, Athens – NOA-GI (1975). National Observatory of Athens Seismic Network [Data set]. International Federation of Digital Seismograph Networks. https://doi.org/10.7914/SN/HL

17th INTERNATIONAL CONGRESS of the Geological Society of Greece

BULLETIN OF THE GEOLOGICAL SOCIETY OF GREECE, SP. PUBL.

EXTENDED ABSTRACT 185

The Xerias Window near Argos (Peloponnesus)

Dipl.-Geol. Dr. Erwin Kunz, retired geologist, Bad Oeynhausen, Germany

Introduction and methodology

The area considered in this paper comprises a section of the mountains that separate the regions of Argolis and Arcadia. This mountain range is part of the Hellenides, and it is built up by the rock sequences of Tripolitza and Pindos Zone. Its tectonic architecture is deeply exposed in the Xerias Window (Jacobshagen 1986) (fig. 1). Key structures (Schwan 1964) are worked out for every lithological unit, for clarifying the large-scale architecture of the mountains.

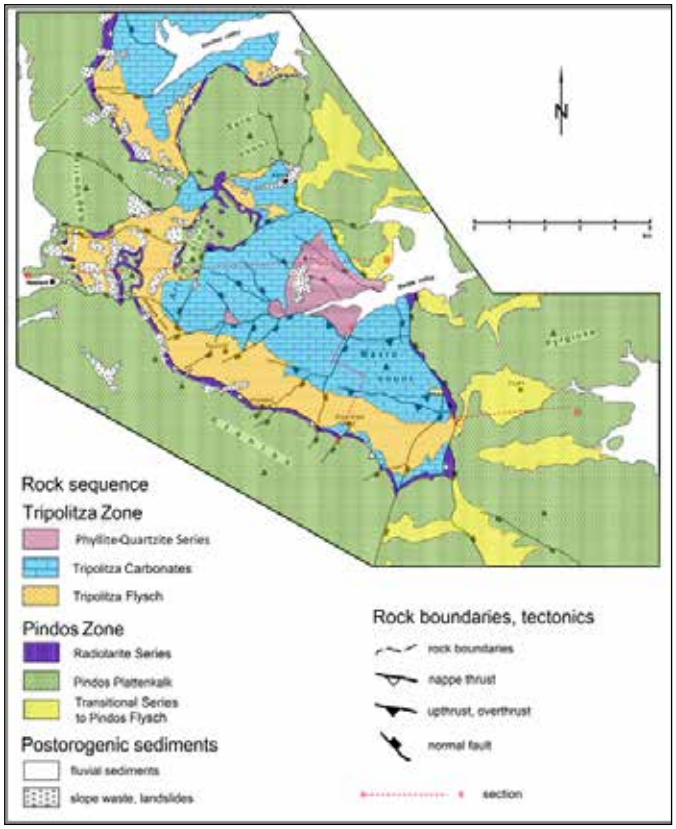

Fig. 1: Generalised geological map of the Xerias Window and its frame

Varying geodynamic stress fields

The nappe-shaped position of the Pindos Zone is obvious in the frame of the Xerias Window. The vergence of the key structures of the latter varies everywhere between W and SW, which proves a relative transport of the Pindos Zone as a whole in that direction.

In contrast, the Tripolitza Zone does not show evidence for such a transport. The folds and overthrusts within Tripolitza Carbonates and Flysch around Krya Vrysi trend resp. strike from WNW to ESE with their vergence to the NNE, which can be explained only by a compressional stress in this direction. Also, at the contact between Phyllite-Quartzite Series and Tripolitza Carbonates south of the Xerias valley, corresponding tectonic structures can be found.

Round about since Upper Miocene, the compressive stress was followed by young extensional tectonics, which continues until today. Its influence on the development of the Xerias Window and on the forming of its frame is described. The important faults created in this time (Xerias faults) show clear parallels to the Corinthian and the Argolic Gulf.

References

Dercourt, J., Wever, P. de, Fleury, J.-J., 1976. Données sur le style tectonique de la nappe de Tripolitza en Péloponnèse septentrional (Grèce). *Bull. Soc. Géol. France,* 7e s., t. XVIII, no. 2, p. 317 – 326.

Doert, U., Richter, D., Mariolakos, I., 1977. Ein tektonisches Querprofil durch die Olonos-Pindos-Zone im Gebiet südwestlich Argos und seine Bedeutung für den Gebirgsbau des Peloponnes (Griechenland). *Ann. Géol. Pays Hellén.,* 28, p. 368 – 386.

Eckl, H., 1979. Beitrag zum Gebirgsbau des NE-Peloponnes im Grenzbereich Olonos-Pindos-Zone/Gavrovo-Tripolitza-Zone. *Z. dt. geol. Ges.,* 130, p. 347 – 351.

Fleury, J.-J., 1980. Les zones de Gavrovo-Tripolitza et du Pinde-Olonos (Grèce continentale et Péloponnèse du Nord). Evolution d'une plate-forme et d'un bassin dans leur cadre alpin. 2 vol. *Soc. Géol. du Nord,* publ. no. **4**: 651 pp.

Jacobshagen, V., 1986. Geologie von Griechenland. – *Beitr. reg. Geol. d. Erde*, vol. 19, 363 pp., Borntraeger, Berlin, Stuttgart.

Papanikolaou, D. I. 2021. The Geology of Greece. – 345 pp., 293 fig., Springer, Cham/Schweiz.

Schwan, W. 1964. Begriff und Bedeutung der Leitstrukturen. Ein Beitrag zur tektonischen Forschungsmethodik. *Geotekt. Forsch.,* 19, p. 1 – 47, 7 pl., 6 fig.

Xypolias, P., Doutsos, T. 2000. Kinematics of rock flow in a crustal-scale shear zone: Implication for the orogenic evolution of the southwestern Hellenides. *Geol. Mag.,* 137 (1), p. 81 – 96.

17th INTERNATIONAL CONGRESS of the Geological Society of Greece

BULLETIN OF THE GEOLOGICAL SOCIETY OF GREECE, SP. PUBL.

EXTENDED ABSTRACT 186

Mineralogy and Geochemistry of the Non-Sulfide Zinc-Lead Deposits, Thasos Island, North Aegean, Greece

Kyriakos A.[1], Sakellaris G.A.[1], Melfos V.[1], Stergiou C.L.[1,2], Papadopoulou L.[1], Kantiranis N.[1]
(1) School of Geology, Aristotle University of Thessaloniki, Greece, axkyriak@geo.auth.gr (2) Chemical Process & Energy Resources Institute (CPERI), Centre for Research and Technology Hellas (CERTH), 50200 Ptolemaida, Greece

Introduction

Thasos Island has long been recognized as an important mining center with its prehistoric ochre mines in the area of Tzines representing some of the earliest mining activities in Europe, dating back to 20,000 BCE (Koukouli *et al.,* 1988). The island was also renowned for its gold, silver, copper and lead production, referenced by Herodotus and Strabo. Due to its abundant Zn occurrences, and particularly calamine ore (smithsonite), Thasos witnessed significant mining activity in the early 20th century. On that time, calamine, a non-sulfide type of zinc ore, was the primary source of Zn worldwide. In 1902, the German company "Minengesellschaft Fr. Speidel" established a mining complex in the Limenaria town to exploit zinc and argentiferous lead ores. However, operations ceased in 1913 due to declining ore grades. In 1925, a subsidiary of the Belgian company "Société des Mines et Fonderies de Zinc de la Vieille Montagne" undertook the restoration and the expansion of the mining facilities. Despite these efforts, the global economic crisis of the 1930s along with the development of flotation and smelting processes for zinc sulfide ores (sphalerite), resulted in cease of the lead-zinc mining activity on the island (Epitropou, 2005). Further exploration on the island during the 1970s and 1980s failed to locate new significant resource of either non-sulfide or sulfide zinc mineralization.

Non-sulfide zinc deposits in Europe were used since Roman times for the production of brass (zinc-copper ± tin alloy). These ores are mostly secondary and form through supergene oxidation of primary sulfide deposits (Boni and Large, 2003). According to Large (2001), the non-sulfide zinc deposits are classified into three main groups based on their geologic characteristics: a) calamine-dominated deposits formed through supergene oxidation of primary sulfides in carbonate environments, often preserved as karst cavity infillings, with main minerals smithsonite ($ZnCO_3$), hydrozincite, and hemimorphite; b) willemite-dominated (Zn_2SiO_4) deposits of primary hydrothermal origin, associated with fault zones and brecciation, and; c) supergene zinc deposits formed by residual surface oxidation, hydromorphic dispersion, and precipitation in carbonate environments, with a complex mineralogy including smithsonite, sauconite, and hydrozincite.

This research work investigates the most important non-sulfide zinc-lead-silver deposits, as well as, the iron-manganese deposits of Thasos. Despite the extensive studies on the metamorphic lithologies and core complex structures of Thasos, these deposits have remained understudied, and no comprehensive data regarding the processes of formation and the characteristics of primary mineralization exist. The aim of this work is to classify the mineralization in respect to mineralogy, the metal concentrations, and the correlations between major and trace elements, contributing to a better understanding of their genesis and economic potential.

Geological Context

Thasos Island located in the northern Aegean Sea, Greece, is geologically part of the Rhodope Metamorphic Core Complex. This complex comprises Paleozoic to Mesozoic high-grade metamorphic rocks that were exhumed during the Late Oligocene to Miocene extension (Wawrzenitz & Krohe, 1998). The metamorphic complex of Thasos is divided into three units (Brun & Sokoutis, 2007): a) a lower unit of marbles (Profitis Ilias), and dolomitic marbles with intercalations of paragneisses and mica schists (Potamia series), which covers the eastern part of the island; b) an intermediate slab of orthogneisses with paragneisses, mica schists (Maries series), and marbles (Kastro), which dominates the western and central part and; c) an upper unit of Tertiary conglomerates and non-mylonitic metamorphic rocks, migmatites and pegmatoids, with minor amphibolites and marbles in southwestern Thasos (Figure 1). These tectonic units are separated by two major southwest-dipping, low-angle extensional fault systems. These low-angle faults were originally thrust faults that transported the migmatites and the overlying intermediate unit over the lower unit. However, during the Miocene, these faults were reactivated as detachment faults. Most of the zinc deposits are located in the western part of the island, within the intermediate marble-gneissic unit along the major detachment faults and can be characterized as stratabound.

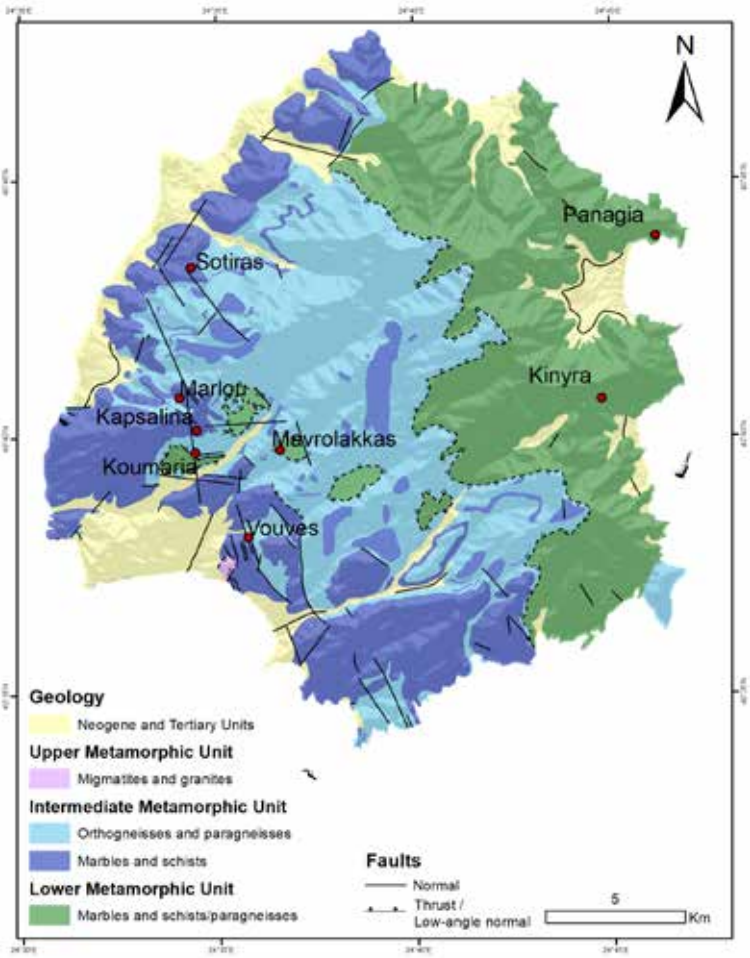

Figure 1. Geological map of Thasos illustrating the locations of the most significant zinc-lead and iron-manganese mines visited and sampled on the island, modified after Brun & Sokoutis (2007).

Samples and Methods

Representative hand specimens were collected from outcrops at the former (ancient and modern) mining sites of Sotiras, Koumaria, Kapsalina, Maries, and Vouves zinc-lead-silver deposits, as well as Mavrolakkas iron-manganese deposit during a two-day field work. Polished thin sections were prepared for microscopic examination using a Zeiss Axioscope 40 Pol, and by backscattered electron imaging (BSE) with a JEOL JSM- 6390LV scanning electron microscope (SEM) equipped with an OXFORD INCA 300 energy-dispersive X-ray spectroscopy (EDS). Powdered samples were proceeded for chemical analysis of major and trace elements, utilizing a wavelength-dispersive X-ray fluorescence (WD-XRF) spectrometry system. The instrument employs a Rhodium (Rh) X-ray tube with a Zirconium (Zr) filter, a three-crystal system (LiF(200), PET, RX25), and two detectors. The X-ray beam operated at high energy, with settings of 50 kV and 4 mA. The oxides measured include: Na_2O, MgO, Al_2O_3, SiO_2, P_2O_5, SO_3, K_2O, CaO, TiO_2, MnO, Fe_2O_3, and trace elements: Cl, Cu, Zn, Sr, Ag, Ba, and Pb (Table 1). All sample preparation and analytical procedures were carried out in the laboratory facilities of the Department of Mineralogy-Petrology-Economic Geology at the School of of Geology, Aristotle University of Thessaloniki.

Results

1. Structural setting

All visited zinc-lead-silver deposits are localized within certain layers of the marble units (Kastro) along major low-dipping detachment faults that bring the gneiss in contact to the marble (Figure 1). The geometry of deposits is highly dependent on the structural setting, with common morphologies including stratabound, stratiform, karst-hosted, lenticular, breccia-hosted, and tabular forms. The stratiform bodies are typically 1 to 3 meters thick extending for several 100s of meters to kilometers within the detachment zones (Figure 2).

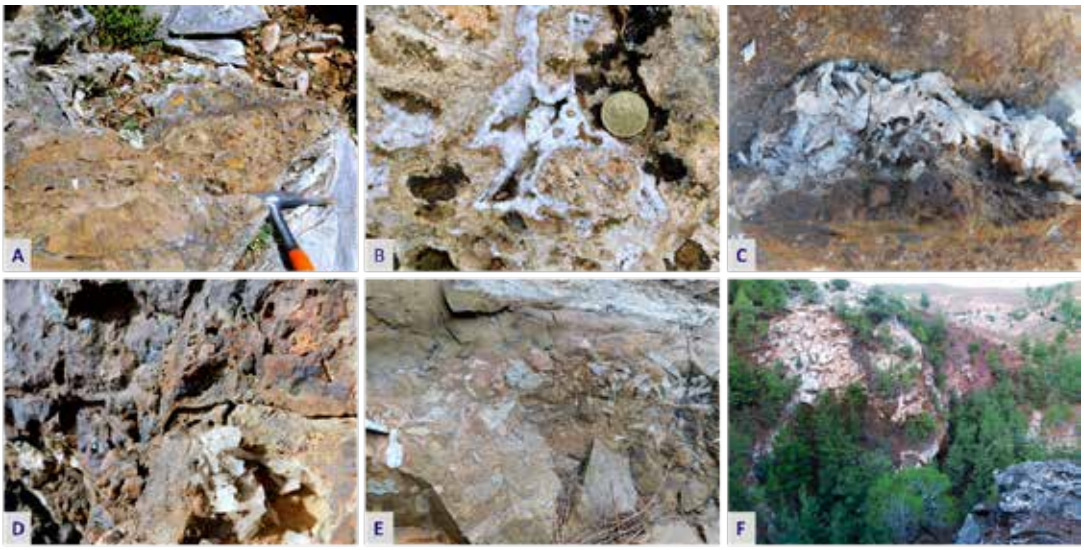

Figure 2. (A) Brecciated Zn-Pb mineralization within a low-angle detachment fault in marble at the contact with gneiss (Sotiras mine). (B) Zinc-rich aragonite filling fractures at the Sotiras mine. (C) Tabular barite crystal aggregates within Zn-Pb mineralization (Koumaria mine). (D) Well-formed barite crystals associated with massive stratiform Zn-Pb mineralization (Kapsalina outcrop). (E) Angular marble fragments within iron oxides-Zn-Pb breccia (Vouves mine). (F) Karst-hosted Fe-Mn (±Cu) mineralization within marbles (Mavrolakkas mine).

2. Mineralogy

The paragenesis of zinc-lead (±copper) minerals in all studied deposits consists predominately of the secondary carbonate minerals smithsonite ($ZnCO_3$) and cerussite ($PbCO_3$), and lesser lead-rich aragonite ($CaPbCO_3$), malachite ($Cu_2CO_3(OH)_2$), and azurite ($Cu_2(CO_3)_2(OH)_2$) (Figure 3). Notably, except Koumaria, where traces of sphalerite (ZnS) and galena were recognized, in none of the samples, primary sulfides were identified. Barite is a major gangue mineral constituent in most ore zones. More detailed:

Sotiras Zn-Pb mine:

The most abundant mineral phases in the ore samples are iron oxides enriched in Zn, smithsonite, and cerussite. Pure smithsonite or smithsonite with elevated Ca contents (up to 20%), is found as dispersed crystals in calcite-aragonite that replace dolomitic marble within breccia (Fig.2a,b and 3a,b).

Vouves Zn-Pb mine:

Mineralogical zoning within the ore breccia zones (Figure 2e) includes: a) a core zone with large euhedral crystals of barite, b) a botryoidal zone with Pb-rich calcite-aragonite, iron oxides enriched in lead, zinc, and occasionally in As and Si, as well as, calcite, c) an outer zone characterized by zinc-rich aragonite. Tiny flakes (less than 5 μm) of jarosite ($KFe_3(SO_4)_2(OH)_6$) and calcium-jarosite (jarosite with calcium impurities) are locally abundant within calcite, occurring between barite crystals. Additionally, concentric zoning in dolomite features iron-rich, Zn-rich and Pb-rich zones. An interesting mineral which occurs in botryoidal form is cesarolite, a rare secondary Pb-Mn oxide phase with the formula $PbMn_4O_6(OH)_2$ (Figure 3c, d).

Koumaria Zn-Pb mine:

Mineralization appears in breccia, consisting of cerussite, iron oxides, and Fe- and Zn-rich cesarolite, with frequent occurrences of barite veins (Figure 2c). The iron oxides are enriched in Pb, Zn, Si, and Mn, and, together with cesarolite, form euhedral structures related with the dissolution of primary mineral phases. Cesarolite appears as irregularly shaped and dispersed grains, suggesting its formation either as a secondary oxidation product or a replacement phase derived from earlier Pb-Mn-bearing minerals (Figure 3e,f). The iron oxides exhibit zoning and irregular morphologies, potentially indicating the oxidation of primary Fe-rich minerals. Their strong enrichment in Pb, Zn, Si, and Mn suggests remobilization and incorporation of these elements during post-depositional processes.

Mavrolakkas Fe-Mn mine:

The karst-filling mineralogy of this deposit within marble follows a distinct zoned pattern with an inner zone dominated by Mn-rich and Si-rich iron oxides, prismatic barite crystals, and quartz; and an outer zone composed of barren calcite/dolomite with minimal Fe and Mn enrichment (Figure 2f). The Fe oxides exhibit distinctive structures at the boundaries of what are likely primary crystals that have undergone oxidation. Additionally, apatite ($Ca_5(PO_4)_3(OH,F,Cl)$) crystals are occasionally observed among the Fe oxides.

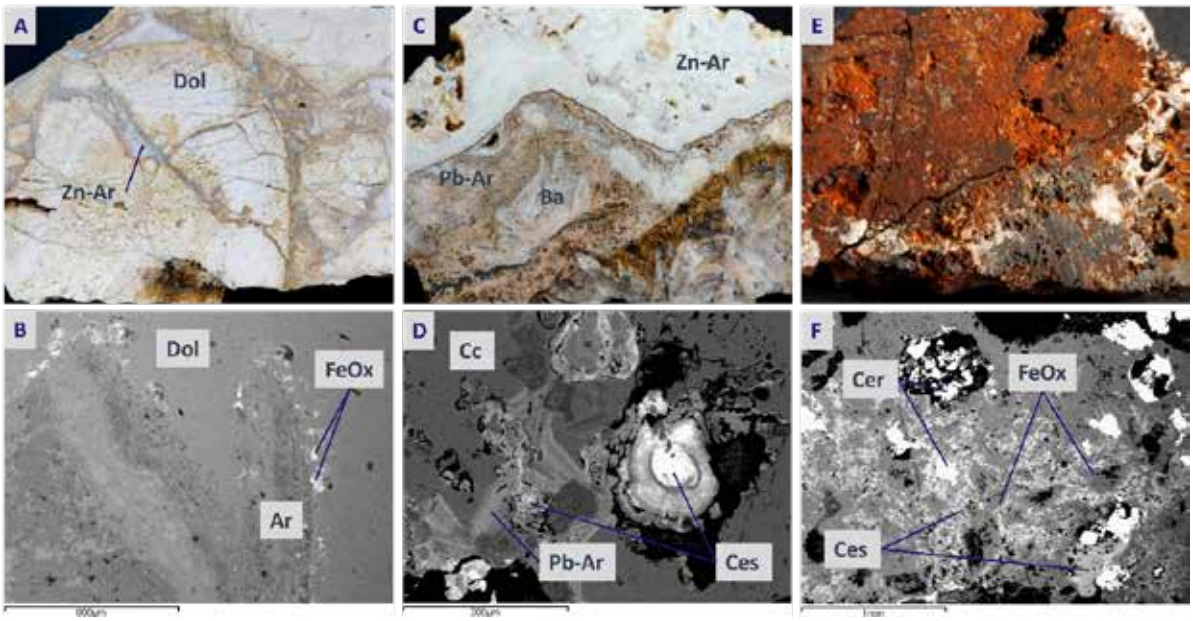

Figure 3. (A) Specimen from Sotiras showing Zn-rich aragonite veins within dolomite breccia. (B) BSE image from Sotiras depicting an aragonite vein within dolomite, with iron oxides forming along the contact zone. (C) Sample from Vouves displaying distinct mineralogical zonation. (D) Botryoidal cesarolite associated with Pb-rich aragonite. (E) Brecciated formation from Koumaria featuring a barite vein. (F) Typical Koumaria mineralization, characterized by cerussite, iron oxides, and cesarolite forming euhedral structures related to primary mineral phases. Mineral abbreviations: Cer: Cerussite, Ces: Cesarolite, Cc: Calcite, Ar: Aragonite, Pb-Ar: Pb-rich aragonite, Zn-Ar: Zn-rich aragonite, FeOx: Iron oxides, Dol: Dolomite.

3. Geochemistry

All samples from the Zn-Pb-Ag deposits exhibit several notable similarities, including consistently low bulk concentrations of Na, K, Al, Si, and Ti, while being enriched in Ca. This suggests a limited contribution from silicate phases and reinforces the strong association of the mineralization with carbonate-dominated host rocks.Sotiras Zn-Pb mine:

Elevated Mg and Ca concentrations are attributed to the presence of carbonates. Copper, Pb, and S exhibit the lowest amounts among all samples, with 0.002 wt.% Cu, 0.05 wt.% Pb, and 0.1 wt.% SO_3. Zinc is present at 0.48 wt.% Zn. Unlike all other samples, Ba was not detected, as its levels were below the detection limit. Iron and manganese concentrations are 1.37 wt.% Fe_2O_3 and 0.084 wt.% MnO, respectively.

Koumaria Zn-Pb mine:

The Koumaria samples are notable for the exceptionally high lead concentration, reaching 43 wt.% Pb, and the highest quantities of zinc (up to2.12 wt.% Zn) and manganese (up to 2.65 wt.% MnO), along with significant amounts of iron (up to 29 wt.% Fe_2O_3). Additionally, it contains notable silver (Ag) values up to 0,137 wt.% and the highest recorded copper (Cu) concentration of 0,104 wt.% among all analyzed samples. In contrast, calcium is the lowest among all samples at 1.05 wt.% Ca. Silicon and sulfur are present at similar levels, with 1.76 wt.% SiO_2 and 0.93 wt.% SO_2, respectively.

Vouves Zn-Pb mine:

The Vouves samples, similar to those from Sotiras, display high Ca and Mg concentrations (due to calcite-aragonite and dolomitic marble) along with notable amounts of zinc and lead. Zinc content ranges from 0.6 to 1.6 wt.%, while Pb varies from 0.25 to 0.64 wt.%. These samples also exhibit the highest recorded levels of barium and sulfur, reaching up to 16 wt.% Ba and 8 wt.% SO_3. Copper concentrations reach up to 0.049 wt.% Cu, while Fe and Mn are present in significant amounts, with values up to 4.12 wt.% Fe_2O_3 and 0.445 wt.% MnO.

Mavrolakkas Fe-Mn mine:

This site exhibits the highest iron and silicon quantities, exceeding 32.5 wt.% Fe_2O_3 and 11.1 wt.% SiO_2, respectively. Additionally, significant amounts of barium 10.5 wt.% Ba, sulfur 5.6 wt.% SO3 are observed, Manganese was measured at 1.8 wt.% MnO. In contrast, copper and zinc concentrations are relatively low at 0.007 wt.% Cu and 0.047 wt.% Zn, while lead is present at 0.36 wt.% Pb.

Table 1. Representative concentrations of major oxides and trace elements (wt.%), using X-ray fluorescence (WD-XRF).

Wt.%	Sot1	Vouv1	Vouv2	Vouv3	Koum1	Mavr1
Na2O	0.07	0.09	0.21	bdl	bdl	0.15
MgO	6.1	0.85	1.13	5.29	0.09	0.78
Al2O3	0.06	0.09	0.08	0.09	0.11	0.85
SiO2	0.24	0.32	0.25	0.36	1.76	11.1
P2O5	0.04	0.06	0.06	0.04	0.05	0.02
SO3	0.10	0.23	8.0	3.43	0.93	5.6
Cl	0.02	0.02	0.03	0.01	bdl	0.01
K2O	0.03	0.06	0.09	0.06	0.16	0.31
CaO	47.3	52.86	38.0	39.47	1.05	19.50
TiO2	0.003*	0.01	0.06	0.04	0.01	0.06
MnO	0.08	0.02	0.02	0.45	2.65	1.8
Fe2O3	1.37	0.23	3.90	4.12	29.0	32.5
Cu	0.002*	0.03	0.049*	0.002*	0.10	0.007*
Zn	0.48	0.60	1.17	1.67	2.12	0.047*
Sr	0.005*	0.03	0.26	0.13	bdl	0.13
Ag	bdl	bdl	bdl	bdl	0.137*	bdl
Ba	bdl	0.65	16.0	7.34	2.30	10.5
Pb	0.05	0.25	0.64	0.57	43.0	0.36
LOI	43.95	43.33	28.94	35.54	14.68	14.94

* For the above samples, rounding was maintained to the third decimal place.

Discussion and conclusions

Most non-sulfide Zn-Pb deposits in Europe are classified as “calamine” ores, defined as concentrations of oxidized Zn and Pb minerals formed through deep weathering of carbonate-hosted primary sulfide ores (Large, 2001). These calamine-type ores are predominantly composed of smithsonite and hydrozincite, which result from the interaction of low-pH, Zn-rich groundwater with carbonate host rocks. Lead-bearing minerals, such as anglesite and cerussite, may also be present if the primary sulfide paragenesis contains galena (Hitzman et al., 2003).

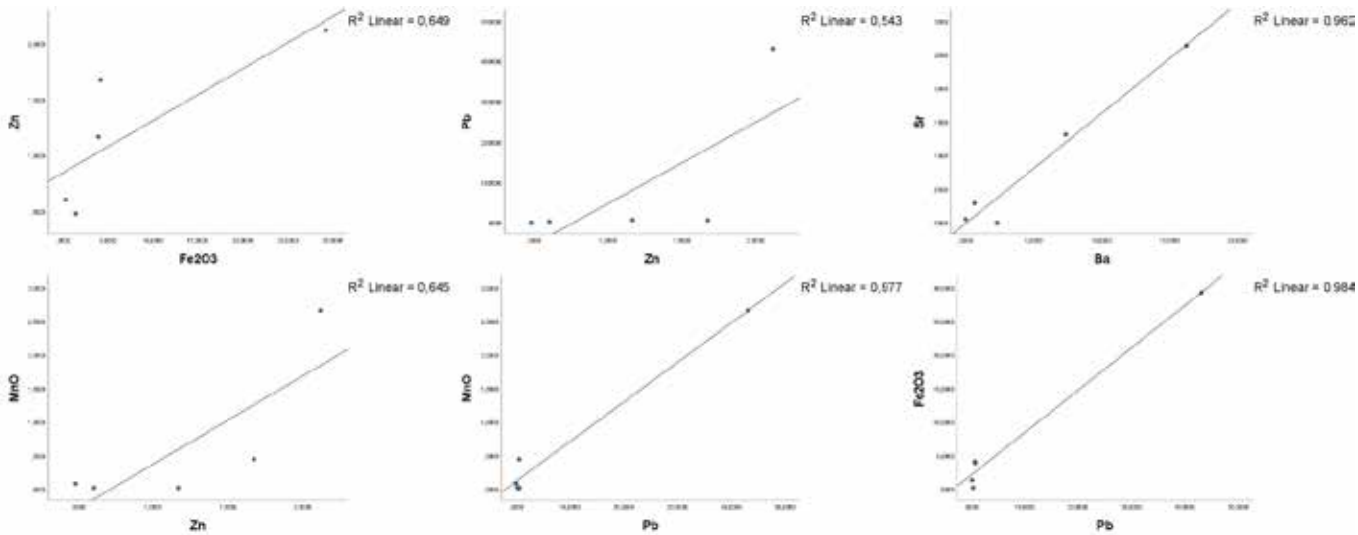

Figure 4. Positive correlation diagrams between major oxides and trace elements of the samples from Sotiras, Vouves and Koumaria.

The smithsonite and cerussite mineralization on Thasos Island is primarily hosted within breccia along large scale low-dipping (0–20°) detachment faults, which are likely of Middle Eocene to Early Miocene age, according to the studies of Brun and Sokoutis (2018) on the Kerdilion detachment fault. The ores are predominantly found within marbles at the contact zones with gneisses of the intermediate unit. The related Fe-oxides are enriched in Mn, Pb, and Zn, as well as As, Si. Other minerals include cesarolite, Pb-bearing aragonite-calcite, jarosite, and barite.
Chemical analyses reveal significant bulk concentrations of zinc and lead across the studied deposits, with Koumaria showing in addition to very high Zn and Pb content, notable enrichment in silver and copper (malachite, azurite). The correlation diagrams in Figure 4 provide insights into the geochemical relationships between different elements in the analyzed non-sulfide Zn-Pb deposits. The strong correlations of Pb with Fe and Mn oxides (Fe_2O_3 and MnO) suggest that lead was significantly remobilized (from oxidation of galena) and precipitated in oxidation zones either as cesarolite ($PbMn_4O_6(OH)_2$) and cerussite or was adsorbed onto Fe oxides/hydroxides. Moderate correlation of Zn with Fe and Mn oxides indicates that zinc liberated through oxidation from sphalerite and was partly incorporated into smithsonite and partly within the iron oxides (Fe-Zn-Si-As oxides). The moderate correlation between Pb and Zn indicates that these metals may have been liberated, transported and deposited together, although their geochemical behavior differs during formation of e.g., smithsonite vs. cerussite. The near-perfect correlation between Sr and Ba indicates the barite ($BaSO_4$) mineralization, with Sr substituting for Ba in the crystal lattice. In conclusion, the geochemistry supports a supergene enrichment model in which primary sulfides (galena, sphalerite) have undergone oxidation, leading to the formation of secondary carbonates (smithsonite, cerussite) and Pb-Mn oxides (cesarolite).
According to Hitzman *et al.* (2003), three main genetic models are considered as potential proto-ore types: Mississippi Valley Type (MVT), SEDEX, and Carbonate Replacement. Thasos deposits share almost all the typical characteristics of MVT Zn–Pb deposits. These include: a) carbonate sedimentary (dolomite) host rock, b) lead (Pb) and zinc (Zn) mineralization, with copper (Cu), silver (Ag), c) the presence of barite, d) stratiform morphology, and f) spatial relation with shale platform that contains hydrocarbon reservoir (Prinos oil district).
The development of the supergene mineralization may be attributed to the oxidation of the primary sphalerite-galena deposits which likely occurred through the infiltration of meteoric waters along post-Messinian normal faults. According to Boulvais *et al.* (2007) two distinct fluid flow events are associated with the normal faulting of Thasos: a) an early-stage, high-temperature fluid, likely of hydrothermal origin, and a later-stage, low-temperature fluid, possibly meteoric in nature, which appears to have driven the oxidative mineralization.

References

Boni, M., & Large, D. 2003. Non-sulfide zinc deposits: A new classification scheme based on geological and metallogenic criteria, Economic Geology 98(4), pp. 685–714.
Boulvais, P., Tistarelli, D., Laignel, B., and Lévêque, F., 2007. Fluid flow and supergene alteration in the Thasos Zn-Pb deposits, Greece: Evidence from fluid inclusions and stable isotope data. Geofluids 7(2), pp. 122-141.
Brun, J.P. & Sokoutis, D. 2007. Kinematics of the southern Rhodope core complex (North Greece), International Journal of Earth Sciences 96(6), pp. 1079–1099.
Brun, J. P., & Sokoutis, D. (2018). Core complex segmentation in North Aegean, a dynamic view. *Tectonics*, *37*(6), 1797-1830.
Epitropou, P. 2005. Historical overview of mining activity in Thasos.
Hitzman, M.W., Large, R.R., and Ludden, J.N., 2003. The Mississippi Valley-type deposits: A summary of their genesis and significance. Economic Geology 98(4), pp. 639-668.
Koukouli, E., Liritzis, I. & Zacharias, N. 1988. The prehistoric ochre mines of Tzines, Thasos, Greece: A mineralogical and geochemical approach, Archaeometry 30(2), pp. 231–243.
Large, R.R., 2001. The genesis of calamine deposits and their role as an indicator of supergene enrichment. Mineralium Deposita 36(5), pp. 392-409.
Wawrzenitz, N., & Krohe, A. 1998. Exhumation and doming of the Thasos metamorphic core complex (S Rhodope, Greece): structural and geochronological constraints. Tectonophysics 285(3-4), 301-332.

17th INTERNATIONAL CONGRESS of the Geological Society of Greece

BULLETIN OF THE GEOLOGICAL SOCIETY OF GREECE, SP. PUBL.

EXTENDED ABSTRACT 187

Study of the geochemical distribution of uranium and thorium in the soils of the Sarigiol Basin, Ptolemais, and their environmental significance.

Ladas, A.[1], Melfos, V.[2], Papadopoulou, L.[3], Kantiranis, N.[4]

(1) Aristotle University of Thessaloniki, Thessaloniki, Greece, anastladas@geo.auth.gr, (2) Aristotle University of Thessaloniki, Thessaloniki, Greece, melfosv@geo.auth.gr, (3) Aristotle University of Thessaloniki, Thessaloniki, Greece, lambrini@geo.auth.gr, (4) Aristotle University of Thessaloniki, Thessaloniki, Greece, kantira@geo.auth.gr

Introduction

The region of Kozani-Ptolemaida-Amynteo Basin hosts the largest lignite deposits in Greece. For decades, lignite has been extracted, stockpiled, and subsequently burned in the thermal power plants (TPPs) of the area. During combustion, many potentially trace elements, with some of them being harmful, are enriched in the fly ash dispersed into the broader region (Kassoli-Fournaraki et al., 1993; Sahanidis et al., 2001). Although previous research indicates that few elements from the region's fly ash exhibit a high degree of leaching, environmental concerns may arise due to the large volume of the fly ash produced (Georgakopoulos et al., 2002b).

The aim of this study was to investigate the geochemical distribution of uranium (U) and thorium (Th) in the soils of the Sarigkiol Basin, SE of Ptolemais town, as well as to evaluate their potential environmental impact. Additionally, an important environmental question addressed in this study is whether the origin of these two trace elements is lithogenic or anthropogenic.

Materials and Methods

For the purposes of this study, 24 soil samples were collected from the Sarigkiol Basin, Ptolemais. Eleven (11) of these samples were provided by Kantiranis et al. (2016) as part of research on assessing the origin of Cr(VI) in the groundwater supplying the municipal districts of Akrini, Agios Dimitrios, and Ryaki in the Municipality of Kozani. The data for these samples derived from the same study. The remaining thirteen (13) samples were collected in October 2023 for the purposes of this study. The sampling locations for each sample can be found in Table 1.

Table 1. Sampling locations for each sample (WGS 84, in decimal degrees).

Sample Name	Longitude	Latitude	Sample name	Longitude	Latitude
2A	329990.19	4471289.72	**15A**	323098.45	4474913.69
4A	326645.56	4471952.36	**52A**	313162.93	4473818.06
5A	326071.14	4471191.24	**54A**	315574.01	4473258.98
8A	323297.78	4475566.17	**55A**	315932.25	4471924.25
11A	322602.77	4477489.33	**56A**	314824.76	4470738.92
12A	321720.56	4476578.47	**57A**	317918.63	4470747.89
Sample name	**Longitude**	**Latitude**	**Sample name**	**Longitude**	**Latitude**
59A	318922.41	4473486.02	**36A**	320025.63	4472172.87
45A	315863.21	4469271.60	**30A**	322677.43	4473964.08
43A	317280.18	4468718.66	**38A**	322902.25	4471394.86
41A	319251.14	4470284.69	**39A**	323945.05	4470281.23
13A	321552.29	4475650.68	**19A**	325023.98	4473946.03
35A	321139.5	4473371.16	**23A**	324758.48	4472070.20

The sampling area and the sample locations are presented in Figure 1. Sampling was conducted using an "Edelman" auger from the top, 10-cm-thick soil horizon. The samples were subsequently dried in an oven at 110°C for 24 hours, then grinded with a mechanical grinder, quartered with a mechanical splitter, and final grinded using an agate mortar.

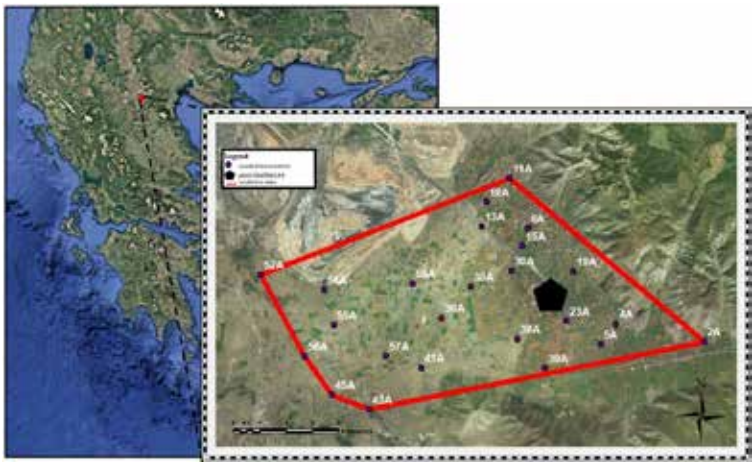

Figure 1. The sampling area and sampling sites (map taken from Google Earth).

The mineralogical analysis was performed using the X-ray diffraction (XRD) on randomly oriented powder preparations. A D8 ADVANCE diffractometer by BRUKER, housed in the Department of Mineralogy–Petrology–Economic Geology at the School of Geology, Aristotle University of Thessaloniki (AUTH), was used for this purpose. For the chemical analysis, the X-ray fluorescence (XRF) spectrometry was employed, using an S1 Titan 600 fluorometer by BRUKER, also located in the Department of Mineralogy–Petrology–Economic Geology at AUTH. The concentrations of the major oxides SiO_2, TiO_2, Al_2O_3, Fe_2O_3, MnO, MgO, CaO, K_2O, P_2O_5, SO_3, as well as the trace elements Cr, Ni, Cu, Zn, As, Rb, Sr, Y, Zr, Ba, Pb, Th and U were determined. Loss on ignition was determined as the percentage weight loss after heating 1 g of each sample at 1050/2h. The concentrations of the chemical elements were calculated using the Geoexploration reference curves integrated into the fluorosimeter. The accuracy of the values was ensured through the measurement of standard samples and the creation of calibration curves, with R^2 exceeding 0.9 in all cases.

The pre-existing measurements were conducted by the internationally certified and reliable Canadian Activation Laboratories LTD, located at 1336 Sandhill Drive, Ancaster, Ontario, Canada L9G 4V5 (http://www.actlabs.com). The following methods were applied: Inductively Coupled Plasma Optical Emission Spectrometry (ICP-OES) on fused pellets prepared with lithium metaborate ($LiBO_2$) and lithium tetraborate ($Li_2B_4O_7$) fusion; Inductively Coupled Plasma Mass Spectrometry (ICP-MS) on fused pellets prepared similarly; Instrumental Neutron Activation Analysis (INAA); and ICP after total digestion in a solution of $HClO_4$, HNO_3, HCl, and HF at 200°C (Kantiranis et al., 2016).

Due to the small number of samples, simple statistical processing was applied, and correlations of U and Th were performed with mineral phases, major oxides, and trace elements. Correlation diagrams were created, and the correlation coefficient R^2 was calculated. Finally, geochemical distribution maps were created in the ArcGIS 10.8.1 environment using the geostatistical Natural Neighbor (NN) method. Additionally, prediction models were generated using the deterministic Inverse Distance Weighted (IDW) method.

Results and Discussion

The mineralogical analysis of the soil samples identified the major mineral phases as calcite, quartz, dolomite, and feldspars. Chlorite, muscovite, amphiboles, serpentine, talc, pyroxenes, and clay minerals were also contained in the soils of the basin in minor amounts. A summary of their statistical distribution is provided in Table 2. The presence of these minerals is largely attributed to the lithology of the area, originating from the carbonate and ophiolitic rocks surrounding the mountainous regions of the basin (Kazakis et al., 2017, 2018), which enrich the detrital material in the study area, a region being now a drained mire (Pavlidis, 1985; Kazakis et al., 2018). Part of the calcite, quartz, feldspars, as well as pyroxenes and dolomite, is also attributed to lignite combustion (Filippidis and Georgakopoulos, 1992; Filippidis et al., 1996; Kolovos et al., 2002; Kostakis, 2009).

Table 2. Descriptive statistics of the mineralogical analysis (%w/w).

	Qz	Cc	Do	F	Ch	M	Am	Serp	Ta	Px	Cl
Mean	30.3	33.3	9.1	10.7	4.8	6.0	1.2	1.9	1.4	0.2	1.0
Median	22.0	25.3	2.3	9.6	3.7	3.1	0.8	0.6	1.2	-	-
STDev	17.6	23.4	12.7	6.6	3.6	7.5	1.4	2.3	1.5	0.8	2.2
Max	76	78.9	47.7	29.1	12.1	27.6	4.2	8	4.7	3.4	10.3
Min	51	-	-	-	-	-	-	-	-	-	-

1: STDev: standard deviation; Max: Maximum Value; Min: Minimum Value; Qz; quartz, Cc: calcite; Do: dolomite; F: feldspar (plagioclase + K-feldspar); Ch: chlorite and kaolinite; M: mica; Am: amphiboles; Serp: serpentine; Ta: talc; Px: pyroxenes; Cl: clay minerals.

Tables 3 and 4 present the summary statistics of the chemical analyses of major oxides and trace elements, respectively. Additionally, the following trace elements were analyzed: Cr, Ni, Cu, Zn, As, Rb, Sr, Zr, Ba, and Pb. The presence of major oxides is attributed to the mineralogical composition of the soil. Nickel (Ni) exhibits a lithogenic origin, while arsenic (As), the third most enriched element, has a mixed origin (Nanos et al., 2015; Kantiranis et al. 2016). All other trace elements, including Cr, Cu, Zn, Rb, Sr, Y, Zr, Ba, Pb, Th, and U, have been identified in previous studies as being present in the region's lignites, as well as in the fly ash and bottom ash produced by the area's thermal power stations (Georgakopoulos et al., 1996; 2002a,b;c). For each major oxide and trace element, the pollution coefficient was calculated by comparing the results to the global average soil values (Hansford and Boerngen, 1984; Kabata-Pendias, 2011).

Table 3. Descriptive statistics of the major oxides (%w/w) of the samples studied.

	SiO_2	TiO_2	Al_2O_3	MnO	MgO	CaO	K_2O	P_2O_5	SO_3	LOI
Mean	41.68	0.62	10.73	5.89	0.12	5.79	15.32	1.63	0.23	0.17
Median	39.75	0.63	10.86	5.49	0.12	4.19	16.55	1.43	0.22	0.14
STDev	10.58	0.18	2.65	1.39	0.03	3.39	8.22	0.62	0.08	0.16
Max	65.31	1.06	15.37	8.71	0.21	13.55	33.25	2.93	0.38	0.75
Min	23.87	0.34	6.40	3.73	0.06	1.25	1.28	0.78	0.08	0.00

1: STDev: standard deviation

Table 4. Descriptive statistics of the trace elements contents (in mg/kg) of the samples studied.

	Cr	Ni	Cu	Zn	As	Rb	Sr	Y	Zr	Ba	Pb	Th	U
Mean	593.3	287.1	33.1	68.7	9.8	80.7	103.7	24.8	183.1	246.5	16.6	7.9	3.3
Median	395.0	248.5	32.0	67.5	9.0	65.5	103.0	24.0	175.0	196.0	17.0	8.3	2.2
STDev	516.4	163.8	9.5	17.4	5.3	54.5	26.8	8.2	82.8	137.7	6.3	2.4	3.4
Max	2230.0	803.0	52.0	105.0	26.0	220.0	167.0	48.0	438.0	803.0	32.0	12.1	12.0
Min	33.0	80.0	16.0	41.0	2.0	15.0	14.0	13.0	72.0	107.0	3.0	4.0	0.5

1: STDev: standard deviation

The pollution coefficients calculated for U and Th (Table 5) showed relatively low values. In the case of Th, most samples had pollution coefficient values below 1, classifying them as non-polluted. Additionally, six samples had values between 1 and 3, characterizing them as moderately polluted. Similarly, U exhibited pollution coefficient values <1 for the majority of the samples, classifying them as non-polluted. Two samples showed values between 1 and 3, indicating moderate pollution, while four samples had pollution coefficient values between 3 and 6, classifying them as significantly polluted for U.

The correlation of U and Th concentrations with mineral phases, major oxides, and trace elements revealed environmentally significant trends. Initially, U correlated with Th, yielding an R^2 value of 0.42, indicating a mild correlation and suggesting a partially common origin. Both radioactive elements showed positive correlations with quartz and feldspars but negative correlations with calcite and dolomite, with no correlation observed with other mineral phases.

For quartz, U had an R^2 value of 0.48 and Th an R^2 of 0.46 (mild correlations), while for feldspars, U showed R^2 = 0.46 and Th R^2 = 0.43 (mild correlations). Consequently, due to their positive correlations with quartz and feldspars, both elements also exhibited positive correlations with the major oxides SiO_2, Al_2O_3, and K_2O. For U, the R^2 values for these oxides were 0.50, 0.41, and 0.46 (mild correlations), respectively, while for Th, the R^2 values were 0.59, 0.60, and 0.63 (strong correlations), respectively. Positive correlations were also observed for Fe_2O_3 and TiO_2, although with lower correlation values. The other major oxides exhibited negative or negligible correlations with U and Th.

Regarding trace elements, U had the strongest correlation with Zr, Y, and Zn, with R^2 values of 0.75, 0.56, and 0.41, respectively (strong to mild correlations). Other trace elements showed weaker positive or negligible correlations. Th exhibited its highest correlation with Zn, Ba, Y, and Pb, with R^2 values of 0.72, 0.50, 0.48, and 0.44, respectively (strong to mild correlations). Figure 2 presents correlation diagrams for U and Th with various minerals, major oxides, and trace elements.

Table 5. Pollution coefficient for U and Th of the samples studied.

Sample	**2A**	**4A**	**5A**	**8A**	**11A**	**12A**	**15A**	**52A**	**54A**	**55A**	**56A**	**57A**
C.U (ppm)	12	1	0.5	2.2	0.5	0.5	11	2.2	1.6	2	10	9
P.C.	4	0.33	0.17	0.17	0.73	0.17	3.67	0.73	0.53	0.67	3.33	3
C.Th (ppm)	9	8	8	4	5	4	11	9	6	10	9	9
P.C	0.98	0.87	0.87	0.43	0.54	0.43	1.2	0.98	0.65	1.09	0.98	0.98
Sample	**59A**	**45A**	**43A**	**41A**	**13A**	**35A**	**36A**	**30A**	**38A**	**39A**	**19A**	**23A**
C.U (ppm)	1.2	2.6	0.5	2.5	4.9	1.2	1.5	3.9	2.6	2.5	1.3	2.1
P.C.	0.4	0.87	0.17	0.83	1.63	0.4	0.5	1.3	0.87	0.83	0.43	0.70
C.Th (ppm)	4	11.4	6.8	9.3	6.8	4.7	6.8	9	11.4	12.1	6.1	8.6
P.C.	0.43	1.24	0.74	1.01	0.74	0.51	0.74	0.98	1.24	1.32	0.66	0.93

C.U: uranium concentration in ppm; C.Th: thorium concentration in ppm; P.C.; pollution coefficient

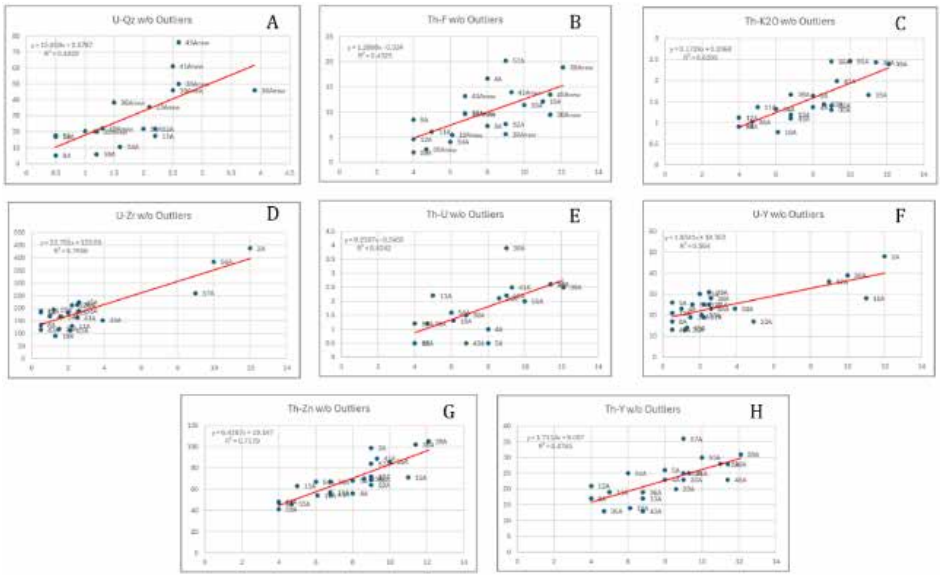

Figure 2. Correlation of U and Th. A) U with quartz, B) Th with feldspar, C) Th with K_2O, D) U with Zr, E) Th with U, F) U with Y, G) Th with Zn και H) Th with Y.

Finally, geochemical distribution maps were created for U, Th, and all other determined major oxides and trace elements. Alongside these distribution maps, predictive models were constructed for all chemical elements analyzed in the soils of the studied area.

The distribution maps for U and Th are presented in Figures 3 and 4, respectively. Additionally, the predictive model for K_2O is presented in Figure 5, which demonstrates very low errors (ME = -0.002 and RMSE = 0.6) based on the method applied.

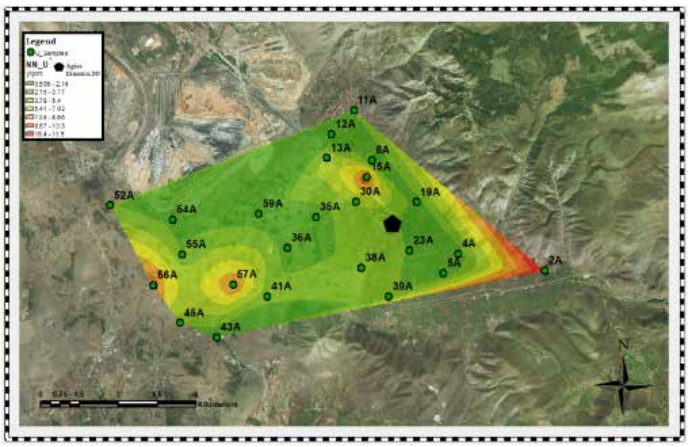

Figure 3. Geochemical distribution map of U using the NN method.

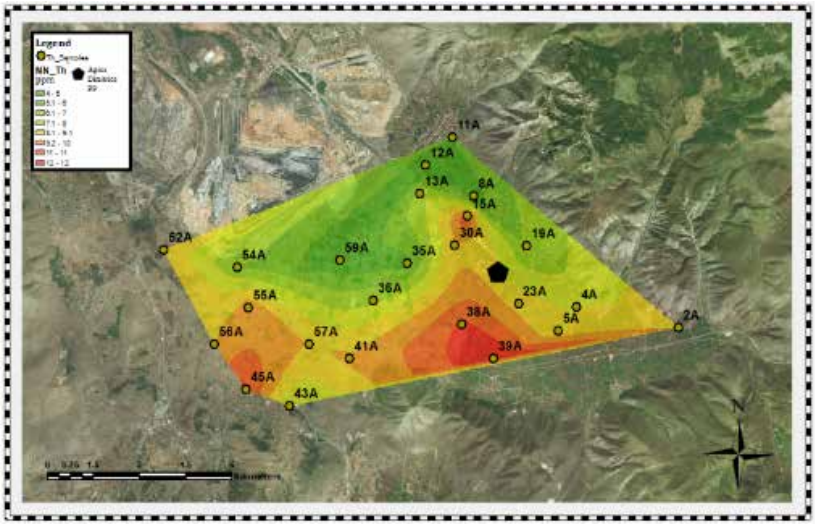

Figure 4. Geochemical distribution map of Th using the NN method.

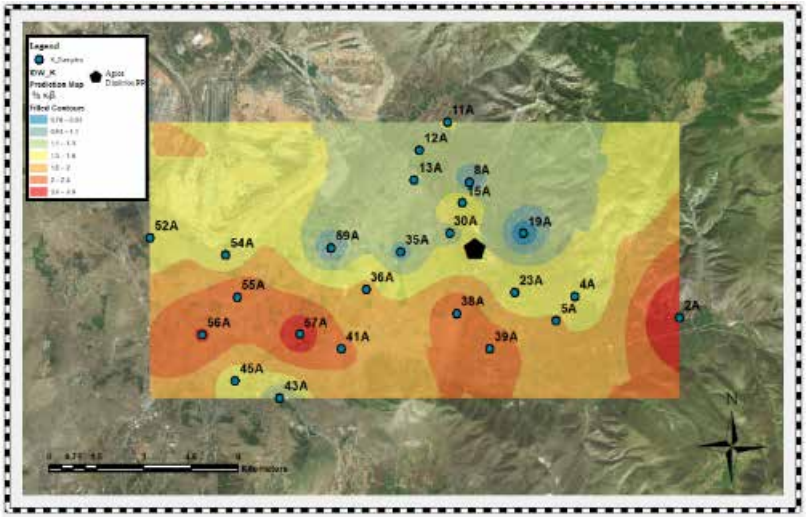

Figure 5. Geochemical distribution map of K_2O using the IDW method.

Conclusions

The results of this study present the geochemical distribution of U and Th in the soils of the Sarigiol Basin in the Ptolemais region, as well as their environmental significance. The main conclusions are as follows:

- Both radioactive elements, U and Th, are present in the basin's soils and show strong correlations with minerals such as quartz and feldspars, as well as with the oxides SiO_2, Al_2O_3, and K_2O.
- A strong correlation was observed between U and Th with the trace elements yttrium (Y), zirconium (Zr), zinc (Zn), and lead (Pb). These four trace elements exhibited a similar distribution pattern in the basin to this of U and Th and are primarily of anthropogenic origin, as they have been linked to industrial activities by previous studies, especially coal burning for energy production as they present high enrichment factors in fly ash.
- The high correlation values of these minerals, major oxides, and trace elements with U and Th, along with their geochemical distribution—showing higher concentrations near industrial activities—indicate anthropogenic activity, likely including lignite combustion and the dispersion of fly ash.
- According to the predictive models, K_2O could serve as a guiding element for identifying elevated concentrations of both radioactive elements.
- The concentrations of U and Th were considered relatively low based on the pollution index for each sample. However, their levels are not negligible, as both elements are radioactive and toxic at high concentrations, necessitating ongoing monitoring of their levels.

References

Filippidis, A., Georgakopoulos, A., 1992. Mineralogical and chemical investigation of fly ash from the Main and Northern lignite fields in Ptolemais, Greece. Fuel 71(4), 373-376.

Filippidis, A., Georgakopoulos, A., Kassoli-Fournaraki, A., 1996. Mineralogical components of some thermally decomposed lignite and lignite ash from the Ptolemais basin, Greece. International Journal of Coal Geology 30, 309-311.

Georgakopoulos, A., Fillipidis A., Kassoli-Fournaraki A., Fernandez-Turiel J.L., Llorens J.F., 1996. The content of some trace elements in surface soils and fly ash of Ptolemais lignite basin, Macedonia, Greece. 3rd International Conference on Environmental Pollution, 16-20/09/1996, Thessaloniki, 114-118.

Georgakopoulos, A., Filippidis, A., Kassoli-Fournaraki, A., Iordanidis, A., Fernandez-Turiel, J.L., Llorens, J.F., Gimeno, D., 2002a. Environmentally Important Elements in Fly Ashes and Their Leachates of the Power Stations of Greece. Energy Sources 24, 83-91.

Georgakopoulos, A., Filippidis, A., Kassoli-Fournaraki, A., Fernandez-Turiel, J.L., Llorens, J.F., Mousty, F., 2002b. Leachability of Major and Trace Elements of Fly Ash from Ptolemais Power Station, Northern Greece, Energy Sources 24(2), 103-113.

Georgakopoulos, A., Filippidis, A., Fernandez-Turiel, J.L., Kasoli-Fournaraki, A., Iordanidis, A., 2002c. Lithogenic and anthropogenic origin of trace elements in surface soils of the lignite-bearing basin of Amyntaio-Ptolemaida-Kozani. 6th Panhellenic Geographic Conference, Proceedings, 03-06/10/2002, Thessaloniki, pp. 335-344.

Hansford, T.S., Boerngen, G.J., 1984. Element Concentrations in Soils and Other Surficial Materials of the Conterminous United States. U.S. Geological Survey, Professional paper 1270, 105p.

Kabata-Pendias, A., 2011. Trace Elements in Soils and Plants. 4th ed., Taylor and Francis Group, LLC, U.S.A, p. 37-45, 50, 82-83, 158-164, 505.

Kantiranis, N., Mitrakas, M., Filippidis, A., Vargemezis, G., Zoumboulis, A., Tsourlos, P., Fikos, H., Vamvakaris, D., Karagianni, E., Paradeisopoulou, P., Kazakis, N., Vogiatzis, D., Kaprara, E., Kalaitzidou, K., Drakoulis, A., Ioannidis, M., Kollias, P., Georgiou, I., 2016. Assessment of the origin of Cr(VI) in the groundwater supplying the Municipal Districts of Akrini - Agios Dimitrios - Ryaki in the Municipality of Kozani. Final report, Aristotle University of Thessaloniki, Department of Chemical Engineering, Department of Geology, and Department of Chemistry, pp. 7-32, 85-105, 135-243.

Kassoli-Fournaraki, A., Georgakopoulos, A., Michailidis, A., Filippidis, A., 1993. Morphology, mineralogy and chemistry of the respirable-size (<5μm) fly ash fraction from the Main and Northern lignite fields in Ptolemais, Macedonia, Greece. In: Current Research in Geology Applied to Ore Deposits (P. Fenoll Hach-Ali, J. Torres-Ruiz, F. Gervilla, eds), La Guioconda. Second Biennial SGA Meeting, Granada, Spain, 727-730.

Kazakis, N., Kantiranis, N., Kalaitzidou, K., Kaprara, E., Mitrakas, M., Frei, R., Vargemezis, G., Tsourlos, P., Zouboulis, A., Filippidis, A., 2017. Origin of hexavalent chromium in groundwater: The example of Sarigkiol Basin, Northern Greece. Science of the Total Environment 593-594, 552-566.

Kazakis, N., Kantiranis, N., Kalaitzidou, K., Kaprara, E., Mitrakas, M., Frei, R., Vargemezis, G., Vogiatzis, D., Zouboulis, A., Filippidis, A., 2018. Environmentally available hexavalent chromium in soils and sediments impacted by dispersed fly ash in Sarigkiol basin (Northern Greece). Environmental Pollution 235, 635-637.

Kolovos, N., Georgakopoulos, A., Filippidis, A., Kavouridis, C., 2002. Environmental Effects of Lignite and Intermediate Steriles Coexcavation in the Southern Lignite Field Mine of Ptolemais, Northern Greece. Energy Sources 24(6), 561-573.

Kostakis, G., 2009. Characterization of the fly ashes from the lignite burning power plants of northern Greece based on their quantitative mineralogical composition. Journal of Hazardous Materials 166(2–3), 972-977.

Nanos, N., Grigoratos, T., Rodríguez Martín, J.A., Samara, C., 2015. Scale-dependent correlations between soil heavy metals and As around four coal-fired power plants of northern Greece. Stoch Environ Res Risk Assess 29, 1531–1543.

Pavlides, S., 1985. Neotectonic evolution of the Florina–Vegoritis–Ptolemaida basin (Western Macedonia). PhD Thesis, Department of Geology, Aristotle University of Thessaloniki, pp. 38-45 [Παυλίδης, Σ., 1985. Νεοτεκτονική εξέλιξη της λεκάνης Φλώρινας – Βεγορίτιδας – Πτολεμαΐδας (Δ. Μακεδονία), Διδακτορική Διατριβή, Τμήμα Γεωλογίας ΑΠΘ, σελ 38-45.].

Sahanidis, Ch., Georgakopoulos, A., Filippidis, A., Kasoli-Fournaraki, A., 2001. Trace element content of marl layers in the lignite-bearing basin of Ptolemaida-Amynteon, Western Macedonia. Bulletin of the Geological Society of Greece 34(3), 1115-1122.

17th INTERNATIONAL CONGRESS of the Geological Society of Greece

BULLETIN OF THE GEOLOGICAL SOCIETY OF GREECE, SP. PUBL.

EXTENDED ABSTRACT 188

Flood Dredge Spoils Mapping with the Use of UAS and GIS: The Case of 2020 Evia Flood

Lida Lakidi[1], Nafsika Ioanna Spyrou[1], Michalis Diakakis[2], Christos Filis[1], Evelina Kotsi[1], Spyridon Mavroulis[1], Emmanuel Skourtsos[1], Haralambos Kranis[1] and Efthymios Lekkas[1]

(1) Department of Dynamic, Tectonic, Applied Geology, Faculty of Geology and Geoenvironment, School of Sciences, National and Kapodistrian University of Athens, 15784 Athens, Greece

(2) Department of Geography and Climatology, Faculty of Geology and Geoenvironment, School of Sciences, National and Kapodistrian University of Athens, 15784 Athens, Greece

Introduction / Background

Natural disasters increasingly threaten human health, the environment, and the economy over time. The rise in frequency is attributed to two key factors: climate change and escalating human activity. Climate change intensifies natural phenomena, while human activity disrupts landscapes, leading to environmental imbalances. In 2023 alone, over 400 natural disasters were recorded globally, resulting in the deaths of 93 million people and damages amounting to
$498 billion USD. As shown in the accompanying image, from 1970 to 2024, the number of disasters has increased, with an average of 266.26 events per year (Burgueño Salas, 2024).

Dredge Spoils refers to the collection of solid and organic materials transported through water, which either flow in the watercourse and on the land surface or accumulate at the bottom of it. The accumulation of materials in aquatic environments is caused by factors such as urban development, agriculture, natural disasters, tidal effects, etc.

Flash floods carry a lot of dredged spoils due to the passage of water through vast areas, which then accumulate in floodplains, causing significant damage. They can roll boulders, cut trees, destroy buildings, and carry fabrics and metals. The resulting materials are transported to water channels and eventually to floodplains, leading to the contamination of the natural environment and acting as waste (Rao, 2017). Dredge materials are divided into two categories: Debris and Solid waste.

The flow of debris is one of the most destructive processes and can be defined as a rapid movement of mass composed of granular solids, water, and air (Varnes, 1978). The usual conditions for debris flow activity include steep slopes, loose materials, and wet conditions (Varnes, 1978). Debris flows can travel long distances and carry large amounts of debris along the way (Zimmermann & Haeberli, 1992). Moreover, in coastal environments, large volumes of debris are created and deposited after natural disasters such as tropical storms, floods, volcanic activity, earthquakes, fires, or explosions (Zimmermann & Haeberli, 1992).

Debris can sometimes be caused by human intervention due to uncontrolled land occupation and deforestation. For example, in Japan, most debris flows are created because of deforestation for building homes and temples. Acid rain could also be a factor, as seen in the Cubatáo area (Zimmermann & Haeberli, 1992).

The main types of debris are (Luther, 2006) (TCEQ Regulatory Guidance, 2017):

(a) Trees, shrubs, and other plant materials
(b) Building or demolition debris, such as construction materials, drywall, timber, treated wood, plastics, etc.
(c) Furniture and appliances such as carpets, furniture, mattresses, plumbing fixtures.
(d) Household hazardous waste such as cleaners, vehicle products, paints, oils, pesticides, solvents, etc.
(e) White goods like refrigerators, freezers, washing machines, dryers, stoves, water heaters, air conditioners
(f) Electronic waste such as computers, televisions, printers, stereos, DVD players, phones.

Other debris may include urban solid waste, including animal carcasses and trash that can cause unpleasant odors as they decompose.

Solid waste refers to any discarded material that is neither in a gaseous nor liquid phase. They can be defined as all discarded household, non-hazardous, industrial, and commercial waste. Additionally, construction waste, street garbage, agricultural waste, and all other non-hazardous, non-toxic waste are included. However, it does not include human excrement. They are produced by activities related to households, healthcare, agriculture, industry, commerce, and mineral extraction, and are piled on municipal streets and other public spaces (Goel, 2017).

Solid waste can generally be categorized as follows (Goel, 2017):

(a) Industrial and mining waste: Metal extraction and related industries represent significant factors for the economic development of many countries, and thus, mining waste represents most of the mining waste.
(b) Urban solid waste: City centers and commercial, institutional, residential, and municipal activities create this waste. This category is the most visible part, although it represents comparatively a small portion of the total solid waste produced.
(c) Hazardous waste: Refers to any waste considered toxic, reactive, radioactive, corrosive, flammable, or infectious. This category of waste also includes biomedical waste, plastics, and electronic waste. Hazardous waste is produced in relatively

small quantities compared to other categories of waste. This category has significant impacts on public health and the environment and is thus considered the most dangerous type of waste.

(d) Ash from thermal power plants: Thermal power plants that use coal are the primary source of electricity worldwide, although renewable energy sources are continuously increasing. Large amounts of ash are produced from coal combustion in thermal power plants. Thus, a significant solid waste management issue today is the management and disposal of this ash.

(e) Agricultural and related industries: Large amounts of agricultural waste are produced by these economic activities during harvesting and in food processing industries.

Other waste streams include oil waste, packaging waste, medical waste, scrap metal, and waste from tires and batteries. Cleaner manufacturing machinery can be developed to minimize waste at the point of production. Additionally, the environmental impact of solid waste can be reduced by sorting and processing waste before final disposal of the various components (Goel, 2017).

Disasters can generate enormous volumes of dredge spoils. During a debris flow, a liquefied mass of rocks, gravel, sand, soil, and other materials travel rapidly over long distances, causing severe destruction and intense erosion along its path. In most cases, the environmental consequences are significant. In terms of natural ecosystems, debris flows can devastate land and vegetation. Additionally, local populations may suffer fatalities, injuries, and displacement due to property loss (Kanji, 2001).

After a disaster, the removal of dredge spoils presents numerous challenges. The process often takes a long time, sometimes years—to complete. The most difficult aspect is finding effective management solutions. The dredge spoils management process should first address existing conditions and then gradually improve as follows ((ILO-OSH), 2001):

- Reduction of industrial, commercial, and household waste
- Increase in waste reuse and recycling
- Promotion of waste collection, processing, and disposal

Case Study

Between August 5 and 9, 2020, the storm “Thalia” struck Greece. This storm was caused by a cut-off low-pressure system in the mid and upper troposphere, located over the southern Adriatic and Ionian Seas. On August 8, the storm’s center was over the Ionian Sea before moving southeast toward the central Aegean on August 9.

By 19:00 UTC on August 8, thunderstorm clouds formed over Evia and organized into a severe storm within two hours. By 05:00 UTC, the storm began to weaken and soon dissipated. The main flooding event in Evia occurred on Sunday, August 9, with the Steni meteorological station recording 75 mm of rain from 23:20 to 02:40, 24 mm from 02:40 to 03:30, 200 mm from 03:30 to 07:30 and a total rainfall of 299 mm (Lekkas E., 2020).

The August 2020 flash floods primarily affected two riverbeds in the Politika area and the floodplain/coastal plains of the Lilandas and Messapios rivers. This study focuses on regions along the Lilandas River (Golubovic - Deligianni M., 2019), (Lekkas E., 2020).

According to the National Observatory of Athens, the storm resulted from a nearly stationary cut-off low-pressure system over the southern Adriatic and Ionian Seas. Early on August 8, 2020, the storm’s center was over the Ionian Sea, later moving southeast across mainland Greece. By the morning of August 9, 2020, the system’s center was detected over the central Aegean Sea (Lekkas E., 2020).

Methodology

The mapping of dredge spoils was based on field data collected by the research team from the Department of Dynamic, Tectonic, and Applied Geology at the University of Athens (NKUA). Immediately after the flood events, the team assessed the disaster’s impact. Data collection took place on August 9-10, 2020, using aerial imagery, videos, and ground-based photographs.

For aerial documentation, a Mavic 2 drone was deployed, flying at an altitude of 20-40 meters, depending on research needs, under sunny conditions.

The data collected was analyzed to identify and categorize dredge spoils in the study area. The categories observed included:

- Trees, shrubs, and other vegetation
- Construction and demolition debris
- Vehicles
- Mud, gravel, and boulders
- Waste
- Furniture and appliances

These categories slightly differ from those referenced in existing literature.

Google Earth was used to compare the aerial data with existing maps and determine the exact locations of the dredge spoils. Each identified deposit was outlined with a polygon to represent its occurrence. These polygons were then exported as Keyhole Markup Language (KML) files for use in Geographic Information Systems (GIS).

For final mapping and visualization, ArcGIS Pro was utilized. The KML file was imported into GIS and converted into a Feature Class, where descriptive data was processed, and each dredge spoil was classified based on its type and size.
Two separate layers were created, one illustrating sediment categories and another representing sediment sizes
To enhance visualization, the base map included Google Maps and a Digital Elevation Model (DEM), which provided elevation data for realistic terrain representation.

Results

The results present the mapping of dredge spoils through a series of maps, which illustrate the subregions within the study area to enhance the visualization of dredge spoils. These subregions, shown in figure 1, include Lilantas Delta, Lefkanti, Bourtzi, Vasiliko, Fylla, Afrati, Afrati/Pissonas, Pissonas, Pissonas/Pournos, and Pournos. For each subregion, two maps have been created, one categorizing the dredge spoils (a) and another representing their sizes (b).

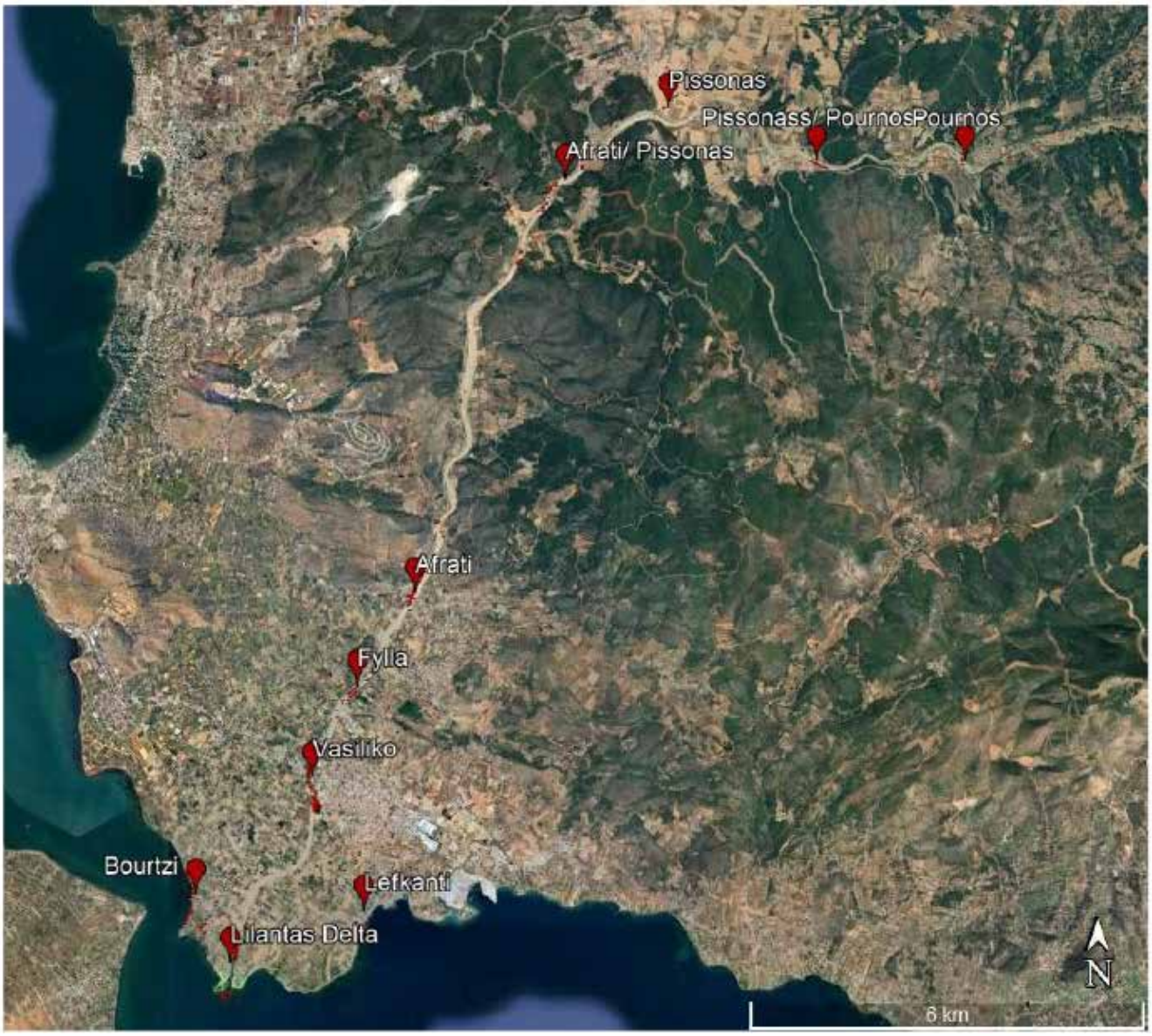

Figure 1. Map of subregions

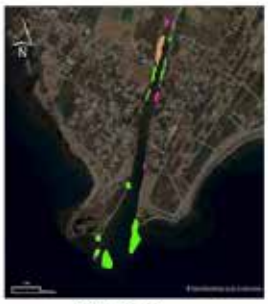
Figure 2a.

Figure 2b.

Figure 3a.

Figure 3b.

Figure 4a.

Figure 4b.

Figure 5a.

Figure 5b.

Figure 6a.

Figure 6b.

Figure 7a.

Figure 7b.

Figure 8a.

Figure 8b.

Figure 9a.

Figure 9b.

Figure 10a.

Figure 10b.

Figure 11a.

Figure 11b.

Categories

Plant materials
Construction debris
Mud, gravel, boulders
Waste
Vehicles
Furniture, appliances

Sizes

Small
Medium
Large

Table 1: Captions of figures 2-11.

Figures	Captions
Figure 2a	Map of dredge spoils by category in the area “Lilantas Delta”.
Figure 2b	Map of dredge spoils by size in the area “Lilantas Delta”.
Figure 3a	Map of dredge spoils by category in the area “Lefkanti”.
Figure 3b	Map of dredge spoils by size in the area “Lefkanti”.
Figure 4a	Map of dredge spoils by category in the area “Bourtzi”.
Figure 4b	Map of dredge spoils by size in the area “Bourtzi”.
Figure 5a	Map of dredge spoils by category in the area “Vasiliko”.
Figure 5b	Map of dredge spoils by size in the area “Vasiliko”.
Figure 6a	Map of dredge spoils by category in the area “Fylla”.
Figure 6b	Map of dredge spoils by size in the area “Fylla”.
Figure 7a	Map of dredge spoils by category in the area “Afrati”.
Figure 7b	Map of dredge spoils by size in the area “Afrati”.
Figure 8a	Map of dredge spoils by category in the area “Afrati/Pissonas”.
Figure 8b	Map of dredge spoils by size in the area “Afrati/Pissonas”.
Figure 9a	Map of dredge spoils by category in the area “Pissonas”.
Figure 9b	Map of dredge spoils by size in the area “Pissonas”.
Figure 10a	Map of dredge spoils by category in the area “Pissonas/Pournos”.
Figure 10b	Map of dredge spoils by size in the area “Pissonas/Pournos”.
Figure 11a	Map of dredge spoils by category in the area “Pournos”.
Figure 11b	Map of dredge spoils by size in the area “Pournos”.

From this study, the following conclusions can be drawn dredge spoils of various sizes are observed across different locations. In Lilandas Delta, small materials at the river delta increase in size upstream. The spoils are predominantly “Trees, Shrubs, and Other Vegetation”, along with “Construction or Demolition Debris”, “Mud, Gravel, and Boulders”, and “Vehicles”. In Lefkanti, small to medium-sized dredge spoils are mainly “Construction or Demolition Debris” and “Furniture and Appliances”, with some “Waste” and “Trees, Shrubs, and Other Vegetation”. In Bourtsi, dredge spoils of all sizes are mostly “Construction or Demolition Debris”, plus “Trees, Shrubs, and Other Vegetation”, “Mud, Gravel, and Boulders”, “Waste”, and “Vehicles”. In Vasiliko, dredge spoils of various sizes are mainly “Construction or Demolition Debris” and “Trees, Shrubs, and Other Vegetation”, with some “Mud, Gravel, and Boulders” and “Waste”. In Fylla, all sizes of dredge spoils are present, primarily “Construction or Demolition Debris” and “Trees, Shrubs, and Other Vegetation”, plus some “Mud, Gravel, and Boulders”. In Afrati, large-sized dredge spoils predominate, mainly “Construction or Demolition Debris” and “Trees, Shrubs, and Other Vegetation”, with some “Mud, Gravel, and Boulders”. In the Afrati/Pissonas area, medium and large dredge spoils are mostly “Mud, Gravel, and Boulders”, followed by “Construction or Demolition Debris” and “Trees, Shrubs, and Other Vegetation”. In Pissonas, medium and large spoils are mainly “Trees, Shrubs, and Other Vegetation” and “Mud, Gravel, and Boulders”. In the Pissonas/Pournos area, large amounts of medium and large “Construction or Demolition Debris” are observed. In Pournos, medium and large spoils are mainly “Mud, Gravel, and Boulders”, with “Trees, Shrubs, and Other Vegetation” and “Construction or Demolition Debris”.

Conclusions / Discussion

Dredge spoils of various sizes are observed across different locations, with materials ranging from small debris in river deltas to larger deposits upstream. The most observed categories include “Trees, Shrubs, and Other Vegetation,” “Construction or Demolition Debris,” and “Mud, Gravel, and Boulders.” In some areas, “Vehicles,” “Furniture and Appliances,” and “Waste” are also present. Larger spoils dominate locations like Afrati and Pissonas, while smaller to medium-sized materials are prevalent in places like Lefkanti and Vasiliko. Effective management and strategic land use planning are essential to mitigate risks associated with dredge spoil accumulation.

The state and relevant authorities must be aware of the extent of the destruction to reduce the likelihood of a similar future event. Identifying high-risk areas is crucial for implementing appropriate measures. Land use should be modified where necessary, such as prohibiting construction near riverbeds to prevent erosion risks. A rapid response is essential, including the removal of debris and financial recovery for affected environments. Protecting human life, health, safety, and the environment must be a priority. Public health risks should be minimized to ensure a swift return to normal activities. Additionally, securing basic needs and creating immediate short-term employment

opportunities will support recovery efforts. Enhancing governmental preparedness and establishing sustainable debris management systems are key to long-term resilience and disaster prevention.

Acknowledgements

I would like to express my sincere gratitude to all those who contributed to the completion of this research. First and foremost, I am deeply thankful to Professor Dr. Efthymios Lekkas and Nafsica-Ioanna Spyrou, for their invaluable guidance, support, and expertise throughout the course of this project. Their insights and encouragement have been instrumental in shaping the direction and quality of my work. A special thanks to the members of the scientific team, who gathered the primary data, as without their efforts none of this could have been possible.

References

(ILO-OSH), I. L. (2001). Guidelines on Occupational Safety and Health Management.

Burgueño Salas, E. (2024). *Statista*. Retrieved from https://www.statista.com/statistics/510959/number-of-natural-disasters-events- globally/

Goel, S. (2017). Advances in Solid and Hazardous Waste Management. *Springer*.

Golubovic - Deligianni M., P. S. (2019). *Investigation of the causes of the flooding in the karst areas.* Govotsis Publishing Co.

Kanji, M. A. (2001). Environmental effects of debris flows and their protection measures. *In: The International Conference On Soil Mechanics and Geotechnical Engineering, AA Balkema Publishers*, pp. 1913-1916.

Lekkas E., S. N.-I.-E.-N. (2020). The August 9, 2020 Evia (Central Greece) Flood. *Newsletter of Environmental, Disaster, and Crises Management Strategies*.

Lewin, J., & Warburto, J. (1994). Debris flows in an alpine environment. *Geography*(79), pp. 98-107.

Luther, L. (2006). Disaster Debris Removal After Hurricane Katrina: Status and Associated Issues. *Congressional Research Service, The Library of Congress, USA*.

Rao, S. (2017). Ground water managment in river flood plains. *In: Sustainable Holistic Water Resources in a Changing Climate*, pp.
401-415.

Research Planning, I. (2014). Best Management Practices for Removal of Debris From Wetlands and Other. *Columbia SC, USA*, p.
29201.

TCEQ Regulatory Guidance. (2017). Managing Debris from Declared Disasters. *TCEQ publication RG-518*.

Urio, A., & Brent, A. (2006). Solid waste management strategy in Botswana : The reduction of construction waste. *Journal of the South African Institution of Civil Engineering, 48*, pp. 18-22.

Varnes, D. (1978). Slope Movement Types and Processes. *Special Report No. 176, National Academy of Sciences, Washington, DC, USA*, pp. 11-33.

Zimmermann, M., & Haeberli, W. (1992). Climatic change and debris flow activity in high-mountain areas. *Catena Supplement*(22),
pp. 59-72.

17th INTERNATIONAL CONGRESS of the Geological Society of Greece

BULLETIN OF THE GEOLOGICAL SOCIETY OF GREECE, SP. PUBL.

EXTENDED ABSTRACT 189

Contribution to the neotectonic study of West Lesvos.

Lamprakopoulos Aggelos[1], Zouros Nikolaos[1,2]
(1) Department of Geography, University of the Aegean, Lesvos, Greece, geod20007@geo.aegean.gr
(2) Natural History Museum of the Lesvos Petrified Forest, Lesvos, Greece

Introduction / Background

Lesvos island, located on the Northeast Aegean region, Greece, is characterized by active tectonics associated with the evolution and deformation of the broader Northeast Aegean Sea.

The Northeast Aegean region is characterized by complex tectonics controlled by interplay of moving tectonic plates in the broader area. The area is affected by the dextral strike-slip movement of the North Anatolian fault, which ends in the Aegean basin and creates significant tectonic structures such as the North Aegean trough and the Skyros trough. The area is also affected by E-W trending normal faults.

Several studies show that the region of the Northeast Aegean region is characterized by complex transtensional stress pattern due to the influence of the NAF, which in combination with the N-S extension stress field of the Aegean micro-plate, creates several secondary faults. (Pavlides & Caputo, 1994; Bellier et al., 1997; Kiratzi, 2002; Flerit et al., 2004; McNeill et al., 2004; Chatzipetros et al., 2013; Konstantinou, 2017; Sakellariou et al., 2017). Except from the well-developed NE-SW faults, the reflection profiles also show the existence of E-W and NW-SE oriented faults which were interpreted as Riedel fractures resulting from the transtensional character of the stress field (Pavlides & Tranos, 1991; Chatzipetros et al., 2013; Konstantinou, 2017).

The tectonic structure of Lesvos Island, both offshore and onshore, is similar to the overall regional deformation of the North Aegean area, where the two main strands of the western prolongation of the North Anatolian Fault form the North Aegean and the Skyros basins. In the Northeast Aegean region there are several E-W trending normal faults due to the active N-S extension stress field, but also there are several other strike-slip faults which are compatible that created in combination of the North Anatolian Fault that pass very close to Lesvos Island. These strike-slip faults have primarily NE-SW orientation and secondarily a NW-SE orientation (Chatzipetros et al., 2013; Kiratzi, 2018; Nomikou et al., 2021).

Figure 1: Seismic and active faults map of the Lesvos Island (Zouros et al., 2008).

The neotectonic studies in Lesvos Island have identified and mapped the major active tectonic structures of the island which are both normal and strike-slip strike (Zouros et al., 2008, 2011; Chatzipetros et al., 2013, Mourouzidou, 2021). In Lesvos Island are represented three neotectonic stages from since the Miocene. A) The recent active stage since

the Pleistocene forms E-W trending normal faults (fig. 2&3), B) the second one took place in the Pliocene and formed normal faults of NW–SE strike, as well as strike–slip faults of NNE–SSW strike and finally, C) the earliest one of Upper Miocene age, based on its relation to synchronous volcanism and associated rocks, and formed strike–slip faults of E–W to ENE–WSW (fig. 4) strike (Chatzipetros et al., 2013).
In the area of west Lesvos there is a gap in tectonic data, due to the lithology which make difficult to identify fault traces. Since the relief is directly affected by erosional processes, among other factors, its intensity is associated with the age of faulting: younger activity generally produces steeper relief. Therefore, geomorphic structures associated with faulting are indicative of relatively recent age (Chatzipetros et al., 2013).
Intense volcanic activity appeared on Lesvos Island during Lower Miocene (23.5 to 16 million years ago) and the volcanic rocks are covering the 2/3 of the island's surface. Several volcanic rock units have been identified (Pe-Piper and Piper, 1993).
West Lesvos is covered mainly by pyroclastic material of the Sigri pyroclastic formation (Pe-Piper et al, 2019). Pyroclastic formations are easily eroded and thus the geomorphological indicators related with the recent tectonic activity are not well-preserved in the relief.

N°	Fault-slip data			Input row data (User format)										
	Definition			Fracture plane		Slip Line		Slip	Conf.	Weigh	Activ.	Striae	Subset	Comments
	Id	Format	Type	Dip-Dir	Dip	Pitch/Tr		Sense	Level	Factor	Type	Intens	Input	
1	1	23	1	181	45	74N		N	C	2.0	2	2	1.0	
2	2	23	1	179	46	80N		N	C	2.0	2	2	1.0	
3	3	23	1	178	52	61N		N	C	2.0	2	2	1.0	
4	4	23	1	204	50	70N		N	C	2.0	2	2	1.0	
5	5	23	1	196	47	76N		N	C	2.0	2	2	1.0	
6	6	23	1	203	46	85N		N	C	2.0	2	2	1.0	
7	7	23	1	200	49	70N		N	C	2.0	2	2	1.0	
8	8	23	1	202	51	63N		N	C	2.0	2	2	1.0	
9	9	23	1	185	47	63N		N	C	2.0	2	2	1.0	
10	10	23	1	183	54	74N		N	C	2.0	2	2	1.0	
11	11	23	1	204	47	83N		N	C	2.0	2	2	1.0	
12	12	23	1	188	46	74N		N	C	2.0	2	2	1.0	
13	13	23	1	189	47	87N		N	C	2.0	2	2	1.0	
14	14	23	1	200	51	74N		N	C	2.0	2	2	1.0	
15	15	23	1	200	49	84N		N	C	2.0	2	2	1.0	
16	16	23	1	205	50	88N		N	C	2.0	2	2	1.0	
17	17	23	1	204	47	81N		N	C	2.0	2	2	1.0	
18	18	23	1	212	71	86N		N	C	2.0	2	2	1.0	
19	19	23	1	215	72	085		N	C	2.0	2	2	1.0	
20	20	23	1	213	70	86N		N	C	2.0	2	2	1.0	

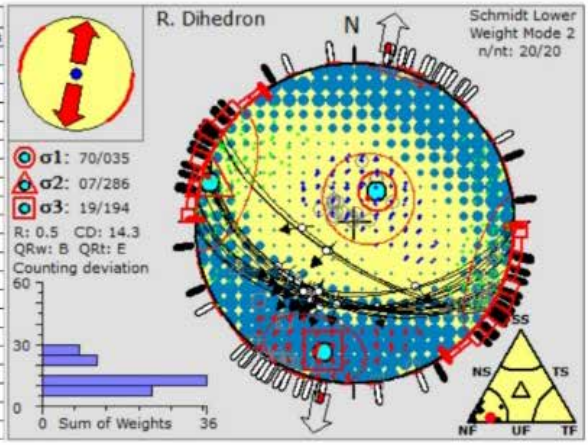

Figure 2: W – E to WNW – ESE trending normal faults affecting the Miocene lavas along the Voulgaris gorge.

Extensive field work was carried out for the study of tectonic structures in order to identify the tectonic deformation in the broader area, according to the new data.
Our study was based on the observations of the fresh road cuts created due to public works for the reconstruction of the new Kalloni – Sigri road. Lots of new tectonic data in the area of West Lesvos, were revealed. The fault planes affecting the volcanic formations consist significant indicators for the tectonic deformation in the area.

Objectives and Methodology

The extensive field work and study on several new faults in the western peninsula of Lesvos Island gave us the opportunity to identify active tectonic structures in a broad area. The faults in the study area are variable in strike and character. Their activity level is determined based on their geological, geometrical and geomorphological characteristics.

The faults of West Lesvos affecting the volcanic rocks present various orientations and types of striking with very clear striations on their fault surfaces.

The tectonic analysis of field data was conducted using Win Tensor 5.9.0 software (Delvaux & Sperner, 2003) to determine the kinematic axes of the main stress pattern in the area. Developed by Damien Delvaux, this software defines stress fields based on geological data, including faults, fractures, and striations, as well as earthquake focal mechanisms.

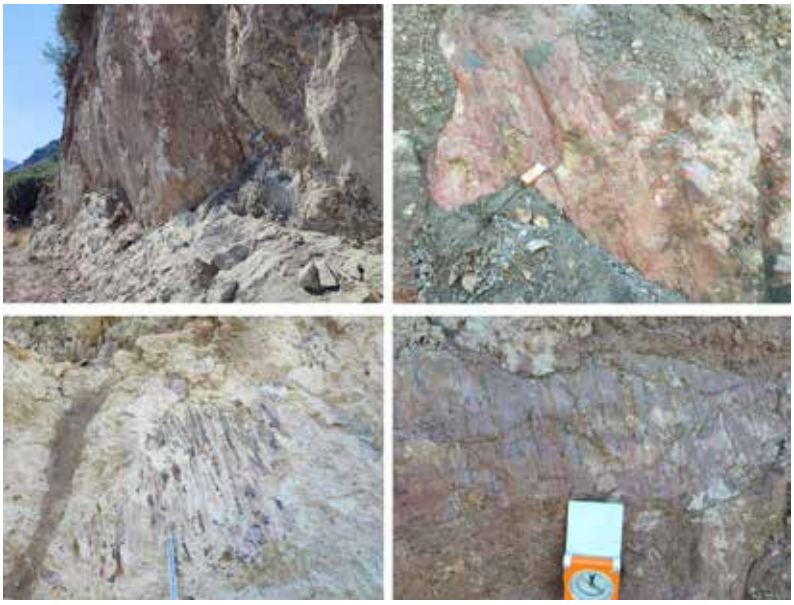

N°	Fault-slip data			Input row data (User format)										
	Definition			Fracture plane		Slip Line		Slip	Conf.	Weigh	Activ	Striae	Subset	Comments
	Id	Format	Type	Dip-Dir	Dip	Pitch/Tr		Sense	Level	Factor	Type	Intens	Input	
1	1	23	1	050	79	62N		N	C	2.0	2	2	1.0	
2	2	23	1	045	76	88N		N	C	2.0	2	2	1.0	
3	3	23	1	024	53	76N		N	C	2.0	2	2	1.0	
4	4	23	1	044	72	60N		N	C	2.0	2	2	1.0	
5	5	23	1	037	71	65N		N	C	2.0	2	2	1.0	
6	6	23	1	070	83	54N		N	C	2.0	2	2	1.0	
7	7	23	1	039	72	70N		N	C	2.0	2	2	1.0	
8	8	23	1	008	62	65N		N	C	2.0	2	2	1.0	
9	9	23	1	019	60	76N		N	C	2.0	2	2	1.0	
10	10	23	1	021	73	68N		N	C	2.0	2	2	1.0	
11	11	23	1	032	72	50N		N	C	2.0	2	2	1.0	
12	12	23	1	063	63	69N		N	C	2.0	2	2	1.0	
13	13	23	1	040	58	76N		N	C	2.0	2	2	1.0	
14	14	23	1	042	69	83N		N	C	2.0	2	2	1.0	
15	15	23	1	069	62	84N		N	C	2.0	2	2	1.0	
16	16	23	1	232	62	70N		N	C	2.0	2	2	1.0	
17	17	23	1	215	76	55N		N	C	2.0	2	2	1.0	
18	18	23	1	057	82	60N		N	C	2.0	2	2	1.0	
19	19	23	1	032	60	70N		N	C	2.0	2	2	1.0	
20	20	23	1	033	58	74N		N	C	2.0	2	2	1.0	
21	21	23	1	030	65	76N		N	C	2.0	2	2	1.0	
22	22	23	1	034	54	80N		N	C	2.0	2	2	1.0	
23	23	23	1	051	75	62N		N	C	2.0	2	2	1.0	

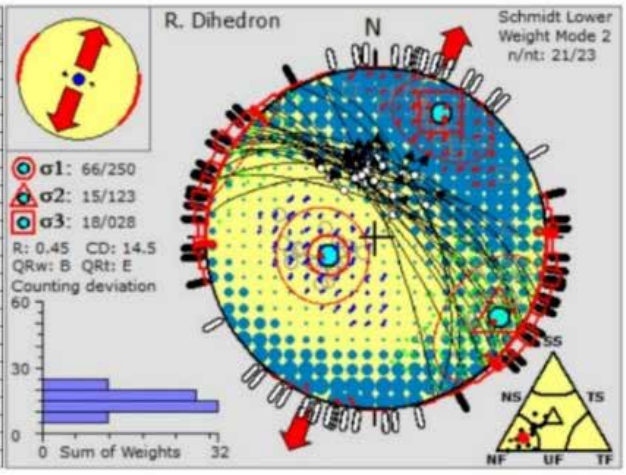

Figure 3: WNW – ESE to NW – SE trending normal faults affecting the Miocene lavas along the Voulgaris gorge.

Initially, tectonic data are entered into a worksheet, specifying the dip direction, dip angle, pitch angle and orientation. The fault type (normal, reverse, or strike-slip), certainty factor, and striation intensity are also assigned.

In the processing stage, the software generates rose diagrams, statistical summaries of fault surfaces, and applies the Right Dihedron method for stress analysis.

Also, Dextral Strike-Slip faults were also identified and measured with NE – SW orientation and less Sinistral Strike-Slip faults with NW – SE orientation (fig. 4 & 5).

N°	Fault-slip data			Input row data (User format)										
	Definition			Fracture plane		Slip Line		Slip	Conf.	Weigh	Activ.	Striae	Subset	Comments
	Id	Format	Type	Dip-Dir	Dip	Pitch/Tr		Sense	Level	Factor	Type	Intens	Input	
1	1	23	1	155	59	15E		D	C	2.0	2	2	1.0	
2	2	23	1	154	61	20E		D	C	2.0	2	2	1.0	
3	3	23	1	170	71	12E		D	C	2.0	2	2	1.0	
4	4	23	1	332	82	11E		D	C	2.0	2	2	1.0	
5	5	23	1	337	79	15E		D	C	2.0	2	2	1.0	
6	6	23	1	342	84	10E		D	C	2.0	2	2	1.0	
7	7	23	1	334	86	15E		D	C	2.0	2	2	1.0	
8	8	23	1	352	85	08E		D	C	2.0	2	2	1.0	

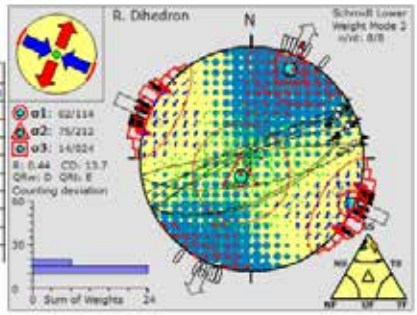

Figure 4: NE – SW trending strike-slip faults with dextral component faults.

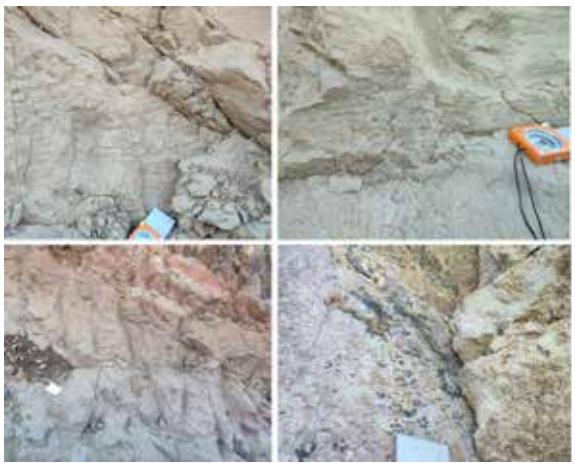

N°	Fault-slip data			Input row data (User format)										
	Definition			Fracture plane		Slip Line		Slip	Conf.	Weigh	Activ.	Striae	Subset	Comments
	Id	Format	Type	Dip-Dir	Dip	Pitch/Tr		Sense	Level	Factor	Type	Intens	Input	
1	1	23	1	204	89	06W		S	C	2.0	2	2	1.0	
2	2	23	1	196	82	02W		S	C	2.0	2	2	1.0	
3	3	23	1	019	87	02W		S	C	2.0	2	2	1.0	
4	4	23	1	014	86	03W		S	C	2.0	2	2	1.0	

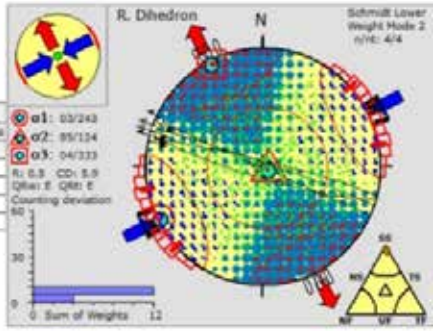

Figure 5: NW-SE trending strike-slip faults with sinistral component.

Results and Conclusions

The neotectonic evolution of Lesvos Island reflects the complex interplay of regional tectonic forces in the NE Aegean. The North Anatolian Fault (NAF), a major dextral strike-slip fault, exerts significant influence, generating numerous secondary strike-slip faults. Simultaneously, the general N-S extension of the Aegean microplate has led to the formation of large W-E trending normal faults (Chatzipetros et al., 2013). This interaction results in a transtensional stress field, producing a diverse array of tectonic structures.

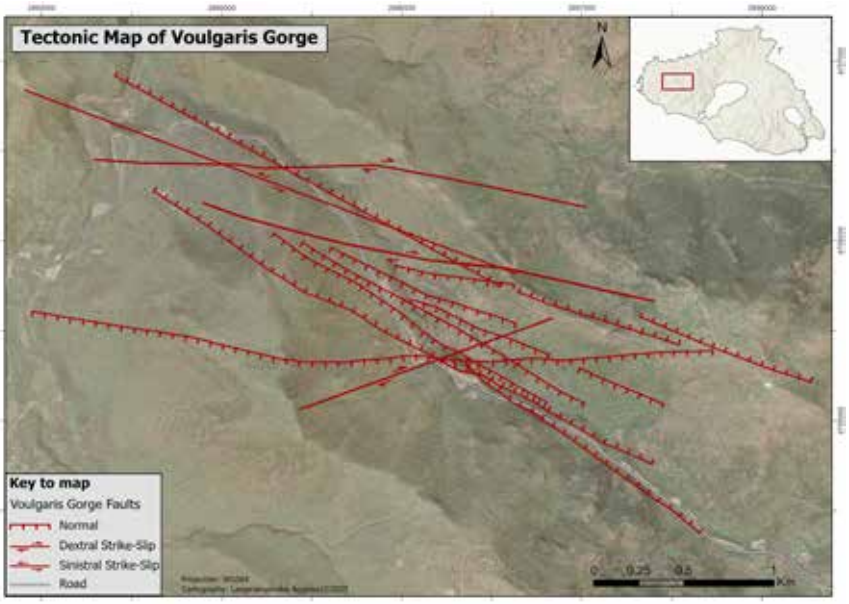

Figure 6: Tectonic map of Voulgaris Gorge area, where 3 different types of faults are presented. Can be observed E-W and NW-SE Normal faults, E-W and NE-SW Dextral Strike-Slip Faults, as well as NW-SE Sinistral Strike-Slip Fauts.

The transtensional field of NE Aegean region is formed by the dextral strike-slip fault of NAF and its stress pattern creates a variety of secondary tectonic structures (Fig. 6), such as secondary NW – SE strike-slip faults which are compatible with the active tectonics of the NE Aegean.

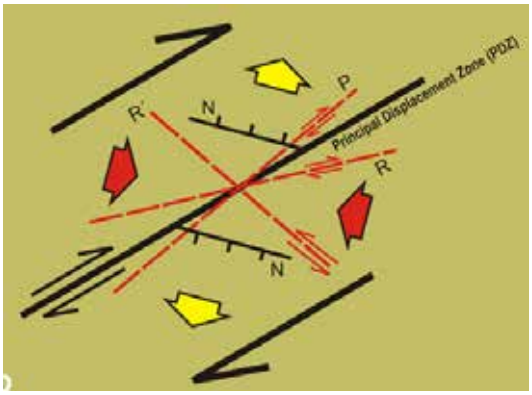

Figure 7: Schematic diagram showing the angular relationships between Riedel shears and the Principal Displacement Zone (PDZ) in a dextral strike–slip deformation zone R, R and P shears are strike slip faults, while N are normal faults perpendicular to the maximum extensional stress. This is a typical arrangement of faulting pattern in the close area of major strike–slip faults; not all types of faults however are always formed in such a setting (Chatzipetros et al., 2013).

In addition to W-E normal faults and NE-SW dextral strike-slip faults, a secondary set of sinistral strike-slip faults has been identified. These faults, which were previously underestimated, can now be considered potentially active structures within the broader stress regime. Their presence suggests a more intricate fault network than previously recognized, influencing seismic hazard assessments and regional tectonic models.

Findings from this study further indicate that the island's extensive tectonic activity has played a crucial role in shaping significant geological formations, such as Voulgaris Gorge. The gorge, along with similar landforms, is likely the result of long-term fault activation and progressive deformation under the prevailing transtensional stress field. These observations highlight the dynamic nature of Lesvos' neotectonic landscape and its ongoing structural evolution.

References

Bellier, O., Over, S., Poisson, A., Andrieux, J. (1997). Recent temporal change in the stress state and Modern Stress Field along the North Anatolian Fault Zone (Turkey). Geophysical Journal International, 131(1), pp. 61–86. doi:10.1111/j.1365-246x.1997.tb00595.x.

Chatzipetros, A., Kiratzi, A., Sboras, S., Zouros, N., & Pavlides, S. (2013). Active faulting in the north-eastern Aegean Sea Islands. Tectonophysics, 597–598, 106–122. https://doi.org/10.1016/j.tecto.2012.11.026.

Delvaux, D. and Sperner, B. (2003). Stress tensor inversion from fault kinematic indicators and focal mechanism data: the TENSOR program. In: New Insights into Structural Interpretation and Modelling (D. Nieuwland Ed.). Geological Society, London, Special Publications, 212, 75-100.

Flerit, F., Armijo, R., King, G., Meyer, B. (2004). The mechanical interaction between the propagating North Anatolian Fault and the back-arc extension of the Aegean. Earth and Planetary Science Letters, 224, 347–362.

Kiratzi, A. A. (2002). Stress tensor inversions along the westernmost North Anatolian Fault Zone and its continuation into the North Aegean Sea. Geophysical Journal International, 151(2), 360–376. https://doi.org/10.1046/j.1365-246X.2002.01753.x.

Kiratzi, A. (2018). The 12 June 2017 Mw 6.3 Lesvos Island (Aegean Sea) earthquake: Slip model and directivity estimated with finite-fault inversion. Tectonophysics 724–725 (2018) 1–10.

Kiratzi, A., Louvari, E. (2003). Focal mechanisms of shallow earthquakes in the Aegean Sea and the surrounding lands determined by waveform modelling: a new database. Journal of Geodynamics 36, 251–274.

Konstantinou, K.I. (2017). Accurate relocation of seismicity along the North Aegean Trough and its relation to active tectonics. Tectonophysics, 717, pp. 372–382. doi:10.1016/j.tecto.2017.08.021.

McNeill, L.C., Mille, A., Minshull, T. A., Bull, J. M., Kenyon, N. H. (2004). Extension of the North Anatolian Fault into the North Aegean Trough: Evidence for transtension, strain partitioning, and analogues for sea of marmara basin models. Tectonics, 23(2). doi:10.1029/2002tc001490.

Mourouzidou, O. (2021). Neotectonics of NE Aegean (Lesvos- Edremit Fault), Faculty of Sciences, Geology. Ph.D. Thesis, Aristotle University of Thessaloniki, Thessaloniki, 284 p.

Nomikou, P., Papanikolaou, D., Lampridou, D., Blum, M., & Hübscher, C. (2021). The active tectonic structures along the southern margin of Lesvos Island, related to the seismic activity of July 2017, Aegean Sea, Greece. Geo-Marine Letters, 41(4). https://doi.org/10.1007/s00367-021-00723-6.

Pavlides, S. B., & Tranos, M. D. (1991). Structural characteristics of two strong earthquakes in the North Aegean: Ierissos (1932) and Agios Efstratios (1968). Journal of Structural Geology, 13(2), 205–214. doi:10.1016/0191-8141(91)90067-s.

Pavlides, S. and Caputo, R. (1994). The north aegean region: A tectonic paradox?. Terra Nova, 6(1), pp. 37–44. doi:10.1111/j.1365-3121.1994.tb00631.x.

Pavlides, S., Mountrakis, D., Kilias, A., Tranos, M. (1990). The role of strike-slip movements in the extensional area of Northern Aegean (Greece). A case of transtensional tectonics. Annales Tectonicae.

Pavlides S, Tsapanos Th, Zouros N, Sboras S, Koravos G, Chatzipetros A. (2009) Using active fault data for assessing seismic hazard: a case study from NE Aegean sea, Greece. Earthquake Geotechnical Engineering Satellite Conference XVIIth International Conference on Soil Mechanics & Geotechnical Engineering 2–3. 10. 2009, Alexandria, Egypt.

Pe-Piper, G., & Piper, D. J. W. (1993). Revised stratigraphy of the Miocene volcanic rocks of Lesbos, Greece. Neues Jahrbuch für Geologie und Paläontologie - Monatshefte, 1993(2), 97–110. https://doi.org/10.1127/njgpm/1993/1993/97.

Pe-Piper, G., Piper, D., Zouros, N., Anastasakis, G. (2019). Age, stratigraphy, sedimentology and tectonic setting of the Sigri Pyroclastic Formation and its fossil forests, Early Miocene, Lesbos, Greece. Basin Research, 31(6), pp. 1178–1197. doi:10.1111/bre.12365.

Sakellariou, D., Mascle, J., Lykousis, V. (2017). Strike slip tectonics and transtensional deformation in the Aegean region and the Hellenic Arc: Preliminary results. Bulletin of the Geological Society of Greece, 47(2), p. 647. doi:10.12681/bgsg.11098.

Soulakellis, N., Novak, I., Zouros, N., Lowman, P., Yates, J. (2006). Fusing Landsat-5/TM imagery and shaded relief maps in tectonic and geomorphic mapping: Lesvos Island, Greece. Photogrammetric Engineering & Remote Sensing 6, 693–700.

Zouros, N., Pavlides, S., Kiratzi, A., Kakakaisis, G., Drakatos G., Soulakellis, N., Vaitis, M., Tsapanos, Th., Chatzipetros, A., Ganas, A., Sboras, S., Koravos, G., Koukourouvli, N., Lampaki, O., Valiakos, I., 2008. Active fault and seismicity maps of the North Aegean region (6 maps, 1:200.000, 1:100.000). Research project: use of modern research tools in geosciences for seismic hazard management in NE Aegean islands, Natural History Museum of the Lesvos Petrified Forest, Mytilene, Lesvos, Greece.

Zouros, N., Pavlides, S., Soulakellis, N., Chatzipetros, A., Vasileiadou, K., Valiakos, I., & Mpentana, K. (2011). Using active fault studies for raising public awareness and sensitisation on seismic hazard: A case study from Lesvos petrified forest Geopark, NE Aegean sea, Greece. Geoheritage, 3(4), 317–327. https://doi.org/10.1007/s12371-011-0044-y.

17th INTERNATIONAL CONGRESS of the Geological Society of Greece

BULLETIN OF THE GEOLOGICAL SOCIETY OF GREECE, SP. PUBL.

EXTENDED ABSTRACT 190

Field-Work Methods in Speleology: A Multidisciplinary Training Approach

Lazaridis G.[1,*], Onac B. P[2], De Waele J.[3], Vouvalidis K.[1], Gkelis S.[1], Gerovasileiou V.[4], Trimmis P. K.[5], Papadimitriou K.[6], Georgiakakis P.[7], Paragamian K.[8], Dora D.[1], Paragkamian S.[8], Digenis M.[4], Sdraka F.[1], Alexandropoulou C.[9], Alikakou T.[9], Arvaniti C.[9], Chatzinikolaou N.[9], Chavanidis K.[9], Georgopoulou X.[9], Giannopoulou A.[9], Koumparelou D.[9], Lytra C.[9], Simoglou I.[9]

*(1) Faculty of Sciences, Aristotle University of Thessaloniki (AUTH), 54124 Thessaloniki, Greece, *geolaz@geo.auth.gr*
(2) School of Geosciences, University of South Florida, 4202 Tampa, FL, 33620, USA
(3) Department of Biological, Geological and Environmental Sciences, Bologna University, 40126 Bologna, Italy
(4) Department of Environment, Faculty of Environment, Ionian University, 29100 Zakynthos, Greece
(5) School of Forestry and Natural Environment, Aristotle University of Thessaloniki, 54124 Thessaloniki, Greece
(6) School of Rural and Surveying Engineering, Aristotle University of Thessaloniki, Thessaloniki, 54124, Greece
(7) Natural History Museum of Crete, University of Crete, 71409 Heraklion, Greece
(8) Hellenic Institute of Speleological Research, 71306 Heraklion, Greece
(9) (participant) Center for Education and Lifelong Learning, AUTH, 54124 Thessaloniki, Greece

Research Highlights

This paper introduces a newly developed 55-hour educational program designed for higher education graduates to bridge knowledge gaps in speleology. The multidisciplinary course covered geosciences, biology, and archaeology, combining theoretical learning with practical fieldwork and advanced technologies. Emphasizing safety, data collection, and interdisciplinary methodologies, the program prepared participants for comprehensive cave research. Offering 4 ECTS credits and a specialized certificate, it significantly advanced speleological education while promoting sustainable research practices.

Introduction

Speleology, the scientific study of caves, requires a multidisciplinary approach to address the unique challenges of cave environments. This paper outlines a newly implemented educational program designed to bridge knowledge gaps and provide participants with practical and theoretical expertise. Based on the absence of dedicated training programs for cave studies highlights the need for such initiatives. This led to the development of a comprehensive curriculum that integrates various disciplines and ensures sustainability and safety in speleological research. Under the title “Field-Work Methods in Speleology”, a 55 instructional hours program, including synchronous and asynchronous components was created. The target audience consisted of graduates from higher education institutions who were interested in acquiring specialized skills in cave research.

Educational Framework

The program was structured around three key thematic units:

1. Geosciences: Covering cave morphology, stratigraphy, sampling and dating methods, paleoenvironmental reconstructions, and safety protocols along with topographic and geomorphological knowledge.
2. Biology: Focusing on terrestrial and aquatic cave ecosystems and organisms, sampling techniques, and data management.
3. Archaeology and Paleontology: Addressing excavation methodologies, anthropological artifact handling, and technological tools for research; cave clastic sediments and paleontological finds with emphasis on processes and taphonomy.

This educational package was developed in accordance with the Regulation of Studies of the Center of Education and Lifelong Learning of the Aristotle University of Thessaloniki (Greece). It underwent a peer-review evaluation process, which was approved to officially invite participants. The final program of the course provided 4 ECTS (European Credit Transfer System) and awarded a certificate of specialized training.

Methodology and outcomes

The program employed a blended learning approach that combined interactive lectures by leading experts with hands-on exercises in real-world cave settings. Participants actively engaged with advanced technologies to enhance their learning experience. By completing the program, they gained a comprehensive understanding of cave environments

and processes while developing practical skills in data collection, analysis, and, most importantly, interpretation. This preparation equipped the participants to confidently and expertly address complex research questions in speleology.

Field-work guide – the scientific approach

As a measure of the course's success, we developed an evaluation scheme designed to produce a field protocol for working in caves, based on the participants' understanding. By integrating the correct answers and addressing specific aspects, we created a comprehensive general guide outlined below.

1. Basic steps for preparing cave field research: Cave fieldwork preparation involves several steps to ensure safety and thorough data collection. Initially, the research objectives and the team involved should be determined. This includes gathering relevant background data from cave maps, previous studies and local knowledge (non-scientific). Equipment preparation is crucial, ensuring that suitable tools are available. Additionally, safety should be prioritized, including evaluating the cave's morphology, checking atmospheric conditions, and having proper first aid kits. Lastly, obtaining permits and considering logistical factors, like weather forecasts and cave access, should be addressed.
2. Determining cave mapping routes: Mapping cave routes accurately is essential for understanding the cave's internal structure. As caves often feature intricate branches and complex passageways, it is crucial to track changes in direction and elevation with precision. By using a laser meter and clinometer, surveyors can obtain accurate measurements of distances and angles. In addition, photogrammetry has revolutionized cave surveying, providing high-accuracy three-dimensional (3D) models of cave systems. Softwares like Polycam, allow precise spatial data collection. These 3D models are not only useful for research but also provide an interactive way for others to explore the cave virtually. This technology can save considerable time and effort while ensuring that the resulting data is accurate and comprehensive.
3. The role of geological research in cave exploration: Geological mapping in caves provides crucial data for understanding the processes that shape cave formation. By documenting sediment layers, mineral deposits, and other geological features, researchers gain insights into past environmental conditions and the processes that have shaped the cave's structure. They identify areas of particular interest for further study, such as areas with rare deposits or specific speleothems. The information gathered during geological research can also aid in conservation efforts. After data are collected, the next step is their analysis. This involves synthesizing measurements, observations, and geological data to create a comprehensive report. The report should include maps, diagrams, and photographs that illustrate the cave's features and structure. This report is an essential document for both scientific research and future cave evaluation from a conservation perspective, as it ensures that the cave's layout and characteristics are intact. For geological recording, several tools are necessary, such as measuring tools (e.g., clinometers, distance meters, compass), recording tools (e.g., gas detectors, data loggers), documentation tools (e.g., camera, notebook) and as technology progresses, apps such as FieldMove Clino assist in collecting and recording data, while LiDAR-based apps help in creating 3D models.
4. Assessing safety: Safety during cave exploration requires assessing weather conditions, especially in cases where rising water levels could be a risk. It is vital to monitor cave stability to avoid collapses, which could result in injury or entrapment. Atmospheric conditions should be regularly monitored using gas detectors for oxygen, carbon dioxide, hydrogen sulfide etc. In certain caves, radon meters may also be used. Descending and climbing in caves demands special training and equipment.
5. Importance of documenting the location and characteristics of deposits: Deposits in caves, including chemical, clastic, and biogenic, offer significant insights into the cave's geological and environmental history. Recording their location, size, shape, color etc. is vital for understanding various processes. For example, clastic deposits provide information about their origin and the conditions under which they accumulated. Speleothems, on the other hand, provide evidence about airflow, microbial activity, precipitation, paleoenvironment etc.
6. Data to record geomorphological features in caves: For geomorphological cave features, data should be collected on the size, shape, color, and location of features like dissolution forms, notches, and sediment deposits. The relationship of these features to other geological elements such as fault lines or water supply sources must be recorded. Information about mesomorphological features, such as passage shapes and their relationship to water levels, is also essential. When recording these data, it is crucial to take detailed measurements, considering the three-dimensional distribution.
7. Following a sampling protocol for geological studies: clear guidelines for selecting, collecting, and storing samples, with the aim of representing the geological diversity of the cave. Sampling should follow strict rules to avoid contamination or alteration. Data regarding the exact location, date, and conditions at the time of sampling must be recorded. Furthermore, documentation of the sampling site on cave maps and in photos with scales is needed.

8. Sampling protocol for excavation research: careful documentation of sample locations, with special attention to the sites of archaeological/paleontological finds. In particular, the stratigraphy of findings is essential for understanding historical periods and their chronological framework. Aadditionally, documentation of the type of findings (e.g., ceramics, tools, bones) and the method of storage, preservation, and analysis are important.
9. Use of maps and topographic measurements in cave studies: These are essential tools for understanding the structure of a cave. The use of topographic maps allows for precise representation of cave formations and the creation of 3D models that facilitate study.
10. Ensuring accuracy in cave observations requires precise measurement of geometric characteristics and the appropriate use of specialized instruments. Measuring instruments must be calibrated and regularly checked to avoid errors during research. Additionally, the use of GIS software for storing and analyzing data aids in recording and verifying observations based on geometric parameters and geological models.
11. Key data in cave studies and their management: In cave studies, the data typically recorded include geological parameters (such as rock types and formations), geometric characteristics (width, height, depth), and ecological data (abiotic factors and cave biological communities). Managing this data requires the use of digital tools and databases for categorizing, storing, and extracting it for analysis, as well as fostering collaboration among scientists.
12. Key features and requirements of biological research in caves: Biological research in caves requires documentation of species inhabiting the caves, the assessment of ecological conditions, and evaluating the conservation needs. Key features include the utilization of specialized instruments and techniques for abiotic data acquisition, biological sampling, sample preservation, and subsequent laboratory procedures for species identification and analysis.

Interdisciplinary relationships – a synthesis

Multiple questions were tested during and at the end of course; a summary of which is given in the following section by providing a relevance scale of scientific fields to cave research (Table 1) along with a key table about the utilization of research fields in multidisciplinary studies (Table 2).

The relevance scale was created to assess and compare the significance of various scientific fields in the study of cave environments. It is based on seven key criteria, each designed to evaluate the contribution of each field to understanding different aspects of caves. These criteria are: 1) Contribution to understanding the processes that created and influenced the evolution of the cave; 2) Contribution to describing the structures and forms found within the cave; 3) Contribution to reconstructing the paleoenvironment and broader geophysical environment that influenced the cave; 4) Understanding the conditions (e.g., pH, temperature, nutrient levels) prevailing in the cave; 5) Contribution to developing a protection plan for caves as natural and cultural landscapes; 6) Understanding the impact of humans on the evolution of caves; and 7) Provision of technologies, methods, and data that facilitate cave study. For each field of study (Geology, Geomorphology, Mineralogy-Geochemistry, Paleontology, Biology, Topography, and Archaeology), scores were assigned based on how well the field meets these criteria. The scale provides a clear, comparative analysis of the relevance of each discipline in cave research. It serves as a guide for prioritizing which aspects of cave studies are most central to specific research objectives (such as geological, geomorphological, or biological studies), but it should not be interpreted as suggesting that fields with lower scores are unimportant. Each field plays an integral role in providing a comprehensive understanding of caves and their significance, both scientifically and culturally.

In this relevance scale, the “total” represents the average score for each scientific field in relation to the criteria established. Higher values indicate a strong relevance of a field to the corresponding criteria, while lower values indicate weaker relevance.

Table 1. Relevance scale for scientific fields to speleology.

Scientific fields	Criterion 1	Criterion 2	Criterion 3	Criterion 4	Criterion 5	Criterion 6	Criterion 7	Total
Geology	5	5	4	4	5	4	5	4.6
Geomorphology	5	5	4	5	5	3	5	4.6
Mineralogy-Geochemistry	4	5	5	5	3	5	5	4.6
Paleontology	3	4	5	5	3	4	4	4.1
Biology	4	4	4	4	5	3	4	4.0
Topography	3	5	3	2	4	1	5	3.3
Archaeology	2	3	4	2	5	5	1	3.1

Cave studies are a prime example of interdisciplinary research, where various scientific fields converge to offer a more

comprehensive understanding of cave environments, their formation, evolution, and their preservation. Research from different disciplines contribute their unique methods, knowledge, and insights, allowing for the exploration of caves from multiple perspectives. Table 2 demonstrates the interaction among scientific disciplines and their contributions to cave research, showcasing how one field's tools or methods can yield valuable outcomes for another. Fields such as geology, biology, archaeology, and paleontology, play crucial roles in addressing different scientific questions and broader environmental, historical, and ecological contexts.

Table 2. Interdisciplinary connections between scientific fields and their contribution to cave research, highlighting how tools and insights from one discipline enhance the understanding and study of caves.

Utilization of	Applied on	Result
Geology	Geomorphology	Understanding the structural, petrographic and hydrologic conditions that led to the formation of specific landforms.
Geology	Archaeology	Use of stratigraphy for the relative dating of cultural artifacts; understanding processes; interpreting formation of spaces and deposition of sediments.
Geomorphology	Biology	Correlation of geomorphological structures and microhabitats with the distribution of various species inside the cave.
Mineralogy – Geochemistry	Archaeology	Determining the origin of raw materials used in artifacts and their processing techniques. This study provides information about human activities (e.g., presence of organic remains); identifying human use of fire, spaces, materials etc.
Archaeology	Geology	Study of the impact of human activity on cave formation and dating of classic sediments through archaeological findings.
Topography	Geology	Cave mapping to understand the creation and evolution of the cave; cave morphometrics; marking sample site.
Topography	Geomorphology	3D representation and survey of caves, landforms and dissolution and depositional features.
Paleontology	Archaeology	Study of fossils can provide information about the relationship between humans, animals and the environment (e.g., hunters, gatherers, domestication of animals) and their dietary habits.
Paleontology	Biology	Comparative study of anatomical structures and ancient DNA (aDNA) to draw conclusions about the evolution and adaptations of organisms in the cave environment and through time.
Biology	Archaeology	Study of the corrosive effect of microorganisms on archaeological finds.
Biology	Geomorphology	Influence of various biological factors on the formation of geological cave structures (e.g., guano-related minerals; biologically mediated deposits, dissolution structures).

Conclusive remarks

This program marks a significant advancement in speleological education, equipping participants with the essential tools and knowledge to thrive in this specialized field. Future iterations will focus on enhancing international collaborations and incorporating emerging technologies.

The program's multidisciplinary approach ensures participants to be prepared for diverse applications, from scientific research to heritage conservation. It also emphasizes sustainable practices to protect fragile cave ecosystems.

The relevance scale serves as a practical tool to prioritize efforts in cave-related research, with the importance of each scientific discipline varying based on the context and specific research goals.

The interdisciplinary nature of cave studies is clearly demonstrated, with various scientific fields working together to provide valuable insights that enrich and support one another. This highlights how methods and tools from one discipline can yield crucial outcomes for other areas, fostering a more integrated understanding of cave environments.

Acknowledgements

This educational program is offered by the Center for Education and Lifelong Learning at Aristotle University of Thessaloniki. We would like to thank the reviewers and staff for their approval and support of the course.

17th INTERNATIONAL CONGRESS of the Geological Society of Greece

BULLETIN OF THE GEOLOGICAL SOCIETY OF GREECE, SP. PUBL.

EXTENDED ABSTRACT 191

Evaluation of karst geosites in Grevena-Kozani UNESCO Global Geopark

Lazaridis G.[1,*], Sdraka F.[1], Georgiadou M. E.[1], Batsi A.[2], Ghikas D.[2], Dora D.[1], Trimmis K. P.[3]

*(1) Faculty of Sciences, Aristotle University of Thessaloniki (AUTH), 54124 Thessaloniki, Greece, *geolaz@geo.auth.gr*

(2) Grevena-Kozani UNESCO Global Geopark, Grevena 51100, Greece

(3) School of Forestry and Natural Environment, Aristotle University of Thessaloniki, 54124 Thessaloniki, Greece

Research Highlights

This study undertakes a comprehensive assessment of karst landforms within the Grevena-Kozani UNESCO Global Geopark, focusing on scoring and analyzing the area's speleological features. By applying six evaluation criteria—scientific, ecological, cultural, aesthetic, economic, and potential utilization—previously used in Crete's Psiloritis and Lasithi Mountains (Fasoulas et al., 2011), the study employs a multidisciplinary methodology to explore management prospects for these unique landforms. It also aims to promote sustainable use and geoconservation of the geopark's caves, aligning with principles advocated by the European Geoparks and the International Union for Conservation of Nature (IUCN).

Introduction

There is a growing global interest in sustainable and alternative tourism that leverages natural and cultural resources. This trend has emerged as a reaction to the challenges of urban lifestyle. The term "Geotourism" refers to a type of alternative tourism that highlights the geological heritage of a location, offering visitors educational and nature-focused experiences. It addresses to individuals interested in geology and the geological processes that created landforms such as caves, gorges valleys, fossil sites and more. Importantly, the study of geosites extends beyond geological interest, contributing to a broader understanding of the environmental conditions in these areas. These conditions have significantly influenced historical human events as well as the evolution of other species and habitats (Rassios & Grieco, 2021).

Caves hold substantial importance within the tourism industry and have historically been the primary geological features of interest to tourists and they continue to be among the most popular geological sites. Cave tourism gained significant popularity in Europe during the 18th century, and today, caves worldwide attract hundreds of thousands of visitors annually (Theodosiadis, 2020). Greece is rich in carbonate rocks, the majority of which have undergone karstification, leading to the formation of thousands of caves across the country. Landforms of karst are of interest not only for natural and geological sciences, but also in other multidisciplinary fields. From a geological perspective caves provide invaluable insights into the conditions that led to their formation, their impressive internal features and their unique microclimate (Mammola et al., 2019). Biologists study caves as habitats, focusing on biodiversity and the ecosystems they sustain (Culver & Pipan, 2019). Fundamental is also the relationship of caves with anthropocentric sciences such as archaeology since caves are considered the earliest human habitation, while from a religious standpoint, caves remain significant as sites of worship and spiritual reverence (Trimmis, 2015).

UNESCO Global Geopark Grevena-Kozani geological settings

The Grevena-Kozani Geopark has been assigned as the UNESCO Global Geopark since 2021. Spanning an area of 2,486 km2 across five regional units in the geographic region of Western Macedonia,the geopark is renowned for its significant geological phenomena related to the formation processes of the Hellenic Orogeny. The area features Greece's oldest rocks, dated at 1 billion years, located in the Deskati region. These formations reveal the geological history and rifting processes that marked the formation of the Tethyan Ocean and the emergence of Europe as a distinct continental landmass. Oceanic crust rocks of the Tethys Ocean are found in Mount Vourinos, alongside sedimentary rocks of the Mesohellenic Trough.

The study area consists of rocks of the Pelagonian and Sub-Pelagonian geological zones (Mountrakis, 1985). The Pelagonian zone comprises Alpine and pre-Alpine rocks, originating from the Paleozoic, Mesozoic and Tertiary periods, which form the bedrock of the region. Overlying these bedrock formations are post-alpine formations, including the molassic sediments of the Mesohellenic Trough and the Plio-Pleistocene terrestrial deposits found in the Kozani-Servia and Grevena basins. These formations are the most recent deposits, consisting primarily of alluvial fans and younger river sediments.

The carbonate rocks of the area were formed during the main sedimentation that took place during the Triassic-Jurassic period. In the Vourinos area, these rocks are represented by crystalline, thickly layered, and tectonized limestones with interbedded layers of dolomites and dolomitic limestones. They form the carbonate cover on which the ophiolites were deposited. Upper Jurassic limestones which were formed in relatively shallow environments, are not distinctly separated from the overlying Cretaceous limestones and are typically mapped as a single unit. These massive carbonate formations are found in contact with the underlying ophiolithic rocks and the overlying Cretaceous limestones (Batsi, 2011).

Data and Methods

The methodological approach employed in this study combined fieldwork, bibliographic research and the application of the evaluation criteria proposed by Fassoulas et al. (2011). Karstic landforms in the area were studied in situ and documented. In specific cases, such as the Crystal Cave, which exhibits vertical development, specialized rope equipment was required for descent and documentation. A detailed catalog of all caves in the area was created, providing an extensive overview of the locations and landforms within Geopark. Precise cave mapping was performed using a Light Detection and Ranging (LiDAR) sensor Numerous 3D models of previously scanned caves, are available on the project website "Virtual speleological field trip in Greece" (Fig. 1).

According to Fassoulas et al. (2011), a systematic methodology for evaluating and assessing geotopes was developed to standardize scoring and minimize subjectivity in geological heritage management. This method categorizes evaluation criteria into six primary groups: scientific, ecological, cultural, aesthetic, economic, and potential for use. Each group is further subdivided into specific criteria that assess attributes such as geological history, ecological impact, cultural significance, landscape visibility, visitor appeal and future use potential. Scores are assigned on a scale from 1 to 10, incorporating qualitative and quantitative factors to account for intangible heritage elements.

This scoring system (Table 1) identifies geotopes of national and international significance, aligning with previous assessments (Grandgirard 1995; Rivas et al. 1997; Pralong, 2005; Zouros, 2007; Reynard et al., 2007). Based on the scores from different groups of criteria, three value indices were developed (Fassoulas et al, 2011): touristic value (Vtour), educational value (Vedu), and protection-need value (Vprot). Each index uses weighted coefficients to reflect the importance of different criteria. For example, Vedu prioritizes scientific value, while Vtour emphasizes aesthetic appeal, reflecting their respective focuses in education and tourism. The Vprot index incorporates scientific scores, integrity, and ecological risk factor, balancing ecological impact with protection status to assess conservation priorities.

- V_{tour}=0.4 Aesthetic + 0.2 Cultural + 0.2 Potential of Use + 0.2 Economic
- V_{edu}=0.4 Scientific + 0.2 Cultural + 0.2 Aesthetic + 0.2 Ecological
- V_{prot}= {Scientific + F_{ecol} + (11-Integrity)}/3

This methodology advances geotope evaluation by incorporating weighting coefficients, enabling a nuanced understanding of geotopes' multifaceted values. It supports sustainable tourism, education, and geoconservation, offering a replicable framework for assessing geological heritage in diverse contexts.

An inventory of caves in the area was compiled based on an unpublished archive of public documents provided by the late speleologist Konstantinos Ataktidis to Georgios Lazaridis. A total of 53 caves were reported, 10 of which are located within the municipality of Siatista, with the majority being potholes. The predominant rock in the broader region where the caves are located is limestone from the Pelagonian zone. The caves exhibit a variety of characteristics, including vertical and horizontal formations, as well as a range of sizes from small to large caves, with some featuring notable speleothems. However, many of these caves remain unexplored or insufficiently studied. This study focuses on analyzing four of these caves: Keli Kalogrias, Kalogria Cave, Orliakas Cave, and Vainaki Cave in the vicinity of the Geopark. These caves were selected for their unique and significant features, as well as the fact that they have been more thoroughly studied compared to others in the region.

Keli Kalogrias

Keli Kalogrias is a rock shelter formed in the limestone of the western banks of the Venetikos River, situated within the Portitsa Canyon. The shelter is located in close proximity to the historic village of "Spilaio" and derives its name, "Keli Kalogrias" (Nun's Cell), from a local legend suggesting that a nun once lived there. This characteristic enhances the cultural value of the landform. The cave is adorned with various speleothems, adding to its scientific and aesthetic significance.

Kalogrias Cave

This cave is located in the slopes of Orliakas Mt. It is small, a few meters long with an ascending branch that exits to a small opening. It is mainly fracture guided and displays a few common speleothems. It is also a cave of significant cultural and religious importance, deeply rooted in the local traditions of the area.

Table 1. Explanation of criteria and scoring system used in the evaluation framework for geosites as proposed in Fassoulas et al (2011).

Criteria	Explanation	Score 1	Score 10
1.1 Geologic history	Diversity of geological history represented at the site.	Simple type history	Tells the whole local story
1.2 Representativeness	How well the site exemplifies typical geological processes or features.	No representativeness	Very high representativeness
1.3 Geodiversity	Proportion of geological elements present.	<5%	>75%

1.4 Rarity	Frequency of similar features in the region or globally.	>7 (least rare)	Unique (most rare)
1.5 Integrity	Preservation state of the geosite	Almost destroyed	Intact
2.1 Ecological impact	Ecological significance of the geosite	No impact	Very high impact
2.2 Protection status	Level of ecological protection measures in place.	No protection	Complete protection
3.1 Ethics	Ethical value of the site.	No ethical significance	Very high significance
3.2 History	Historical importance of the site.	No historical relevance	Very high relevance
3.3 Religious	Spiritual or religious significance of the site.	No religious significance	Very high significance
3.4 Art and culture	Artistic and cultural relevance of the site.	No significance	Very high relevance
4.1 Viewpoints	Number of viewpoints the site offers.	None	>4
4.2 Landscape difference	Degree of visual contrast in the landscape.	No difference	Very high diversity
5.1 Visitors	Annual visitor number	<5,000	>75,000
5.2 Attraction	Site's appeal to visitors	No attraction	International recognition
5.3 Official protection	Level of official protection	International protection	No official protection
6.1 Intensity of use	Extent of site usage and potential overuse.	Very intense	No use
6.2 Impacts	Degree of human-induced impacts.	Very high impact	No impact
6.3 Fragility	Susceptibility to damage	No fragility	Very high fragility
6.4 Accessibility	Proximity to infrastructure	Close to hiking trail	Close to highway or town
6.5 Acceptable changes	Tolerance of the site to change.	No acceptable change	Very high tolerance

Orliakas Cave

The Orliakas Pothole (Fig.1), also known as the Cave of Crystals, is located to the west of the col of Mount Orliakas and reaches a depth of about 15 meters. Its entrance comprises two openings at nearly the same elevation, both of similar size and elliptical in shape. Transparent scalenohedral calcite crystals are adorn the walls and the ceiling of the cave. These crystals are remarkable in size, exceeding 30 cm in length. The cave is formed within Upper Cretaceous reef limestones, which unconformably overlain by sediments from the Mesohellenic Trough (Lazaridis, 2024).

Vainaki

Vainaki cave (Fig.1) comprises a phreatic passage now located several tens of meters above the current water table of the region. It is partially eroded and features two entrances, one at each end. The side walls retain well-defined scallops (Fig.1), offering valuable insights into the paleoflow and specifically the velocity and the flow direction that led the formation of the scallops within the passage.

Figure 1. 3D models of caves: Left – Orliakas Cave, Right – Vainaki Cave, Below – Close-up view of the Vainaki Cave 3D model showcasing well-defined scallop formations. (Source: https://speleology8.wordpress.com).

Results

Results According to the methodology outlined by Fasoulas et al. (2011), the corresponding scoring values for these geosites are presented in Table 2. As shown, the highest educational values are attributed to Orliakas Cave, due to its rarity and uniqueness in the area, its distinct morphology and its high integrity. Remarkably high ecological impact of Orliakas Cave reflects the geotope's role in supporting the development of specific ecotopes or the presence of endemic species in the region. Orliakas cave also receives the highest score for protection-need value because of its significant ecological impact, and its low actual protection status and preservation. The greatest potential for tourism development is attributed to Kalogrias Cave, which is known as a religious site. Its connection with local traditions and historical events in the region is of considerable importance.

Table 2. Evaluation results of geosites in the Grevena-Kozani UNESCO Global Geopark using the Fassoulas et al. (2011) method.

Cave Name	Keli Kalogrias	Kalogrias Cave	Orliakas Cave	Vainaki
1. Scientific score	2.9	2.9	7	5.5
1.1 Geological history	2.5	2.5	7.5	5
1.2 Representativeness	2.5	2.5	5	5
1.3 Geodiversity	1	1	5	2.5
1.4 Rarity	1	1	10	7.5
1.5 Intergrity	7.5	7.5	7.5	7.5
2. Ecological score	4.25	4.25	5.5	4.25
2.1 Ecological impact	7.5	7.5	10	7.5
2.2 Protection status	1	1	1	1
3. Cultural score	7.5	7.5	1.75	4.63
3.1 Ethics	10	10	2.5	10
3.2 History	7.5	7.5	2.5	5
3.3 Religious	10	10	1	1
3.4 Art and culture	2.5	2.5	1	2.5
4. Aesthetic score	5.5	5.5	5.5	6.25
4.1 Viewpoints	1	1	1	2.5
4.2 Landscape difference	10	10	10	10
5. Economic score	2	2	2	2
5.1 Visitors	1	1	1	1
5.2 Attraction	2.5	2.5	2.5	2.5
5.3 Official protection	2.5	2.5	2.5	2.5
6. Potential use score	5.7	6.5	4.7	6.5
6.1 Intensity of use	7.5	7.5	7.5	7.5
6.2 Impacts	7.5	7.5	2.5	7.5
6.3 Fragility	10	10	10	10
6.4 Accessibility	1	5	1	5
6.5 Acceptable changes	2.5	2.5	2.5	2.5
Fecol[1]	7.5	7.5	10	7.5
Vedu[2]	4.61	4.61	5.35	5.23
Vprot[3]	4.63	4.63	6.83	5.5
Vtour[4]	5.24	5.4	3.89	5.13

[1]Fecol: ecological factor, [2]Vedu: educational value, [3]Vprot: protection-need value, [4]Vtour: touristic value

Discussion

The evaluation was conducted on 8% of the caves within the geopark territory. Observing the analysis results, it appears that the economic, aesthetic, and ecological scores exhibit the greatest uniformity in their values. Specifically, the low ecological score is attributed to the limited tourist visitation, as these caves are considered local destinations, are not widely known, and some of them are difficult to access. Regarding the aesthetic score, there are small variations in values, with the average score across all caves exceeding 5. This indicates moderate landscape contrast, which evaluates differences in shape, color, or morphology between the geotope and its surroundings. Additionally, limited viewpoints are considered, focusing on visibility from roads or trails a few meters apart. The ecological score generally displays moderate to low values due to the high ecological impact and low protection status, as these caves are categorized as having no protection.

The most significant variations are observed in the cultural score. The Kalogrias Cave and Keli Kalogrias are religious sites of historical importance, and together with the Vainaki cave, they highlight the traditions and customs of the region. In contrast, no sufficient evidence has been found for Orliakas Cave to provide information supporting such an evaluation.

Previous work by Fasoulas et al. (2011) has provided information and analysis from caves in the Cretan region, allowing us to compare our results and form a more comprehensive picture. Especially at Psiloritis Geopark, the main tourist attractions in the area and the most suitable geotopes for educational activities are Idaion Andro and Sfentoni caves. These sites are already used for various educational programs and initiatives organized by the Geopark and

local educational centers. It is important to note that the low tourist value score attributed to the aforementioned geotopes, is either due to restrictions on visitor numbers, or due to the site's fragility (Sfentoni cave) or ongoing excavations (Idaion Andro Cave). Compared to the touristic score values of Grevena-Kozani Geopark, similarly low value scores are observed, as they are limited to the local level.

At Lassithi Mountain most of the studied geosites lack proper protection or are inadequately managed due to the absence of centralized oversight. As a result, they face significant risks and threats. Many of these geotopes are deeply tied to the history and culture of Crete, such as the renowned Diktaion Andro, mythologically known as the birthplace of Zeus, and hold importance for both educational and tourism purposes. Notably, Dikation Andro, the area's most popular attraction with approximately 70.000 visitors annually, receives a tourism value score of only 4.8. This low score is primarily due to severe discoloration of stalagmites and stalactites caused by decades of improper lighting.

Conclusions

The application of evaluation frameworks is an invaluable tool for geopark management authorities, facilitating informed decision-making, sustainable exploitation, and the effective protection of natural resources and landforms. While criteria such as Scientific, Cultural, and Aesthetic scores largely depend on the natural characteristics of the geosite and its surroundings, Ecological, Economic, and Potential of Use criteria are significantly influenced by management practices and the applicable regional legislation. This distinction emphasizes dual dependency on both natural features and human interventions in the evaluation process.

The uniqueness of the Scientific criterion lies in its potential for enhancement, as it is directly tied to the extent and quality of interdisciplinary research conducted on the geosite. For example, incorporating advanced studies in geology, biology, and cultural heritage can elevate its scientific value. Similarly, the viewpoints of a geosite have a profound impact on its Aesthetic score. Although this factor is an inherent part of the landscape, it can be significantly improved through targeted management initiatives, such as the development of well-planned trails and the installation of strategically positioned viewpoints. These efforts not only enhance the visual appeal but also improve Accessibility scores, ultimately contributing to the geosite's Potential of Use.

The karstic geosites within the Grevena-Kozani UNESCO Global Geopark demonstrate strong performance in Cultural, Aesthetic, and Potential of Use categories. These promising results provide a solid foundation for more detailed investigations into the geosites, aimed at further promoting and showcasing their unique features. A comparative analysis of parameter values between the Grevena-Kozani Geopark and other geoparks reveals that these caves possess significant potential to be recognized as key geotopes within the geopark. Their inclusion would undoubtedly contribute to the geopark's enrichment and global significance.

Upon closer analysis of the applied criteria, it becomes clear that more specialized metrics are necessary for the comprehensive evaluation of karstic landforms, particularly karstic caves. Essential criteria include the accessible length of the cave, the level of technical expertise required for entry, and the suitability of its atmosphere for safe exploration. These parameters are critical for determining the potential for sustainable utilization while ensuring the protection of these fragile environments.

In conclusion, the evaluation frameworks not only serve as a cornerstone for effective geosite management but also underscore the necessity of refining assessment tools to address the specific needs of karstic caves. This step-by-step approach will enable more accurate evaluations, fostering both conservation and sustainable tourism development, and ultimately contributing to the long-term success of geoparks.

Acknowledgements

The authors would like to express their sincere gratitude to Iraklis Kalogeropoulos and Antonis Kleisiaris for their valuable contributions to the fieldwork. 3D cave scans conducted as part of the 'Virtual Speleological Field Trip in Greece' project, formally supported by the International Union of Speleology (UIS).

References

Batsi A., 2011. Tectonic evolution of the area of Rodiani, West Macedonia. MSc Thesis, Aristotle University of Thessaloniki, Thessaloniki.

Culver, D. C., Pipan, T., 2019. The biology of caves and other subterranean habitats. 2nd ed. Oxford University Press. Oxford.

Fassoulas, C., Mouriki, D., Dimitriou, P. D., Iliopoulos, G., 2011. Quantitative assessment of geotopes as an effective tool for geoheritage Management. Geoheritage, 4(3), 177–193.

Grandgirard, V., 1995. Méthode pour la réalisation d'un inventaire de geotopes géomorphologiques. UKPIK Cahiers de l'Institut de Géographie de l'Université de Fribourg 10:121–137.

Lazaridis, G. T., 2024. Formation conditions of hypogene caves in the Hellenic orogen: mineralogy, geochemistry, stable

isotopes (C, O, S), fluid inclusions. .Ph.D Thesis, Aristotle University of Thessaloniki, Thessaloniki.
Mammola, S., Piano, E., Cardoso, P., Vernon, P., Domínguez-Villar, D., Culver, D. C., Pipan, T., Isaia, M., 2019. Climate change going deep: The effects of global climatic alterations on cave ecosystems. The Anthropocene Review, 6(1–2), 98–116.116.
Mountrakis, D., 1985. Geology of Greece, University Studio Press, Thessaloniki.
Pralong, J. P., 2005. A method for assessing the touristic potential and use of geomorphological sites. Geomorphologie: Relief, Processus, Environment 3:189–196.
Rassios, A. E., Grieco, G., 2021. Is geoheritage a “cutting-edge” science? Promotion of an extension to the definition of geoheritage with emphasis as a significant discipline in geosciences with cultural and societal relevance. In Geological Society of America eBooks, pp. 37–53.
Reynard, E., Fontana, G. D., Kozlik, L., Scapozza, C., 2007. A method for assessing “scientific” and “additional values” of geomorphosites. Geographica Helvetica, 62(3), 148–158. https://doi.org/10.5194/gh-62-148-2007
Rivas, V., Rix, K., Frances, E., Cendrero, A., Brunsden, D., 1997. Geomorphological indicators for environmental impact assessment: consumable and non-consumable geomorphological resources. Geomorphology 18:169–182.
Theodosiadis, T., 2020. Cave Tourism. International Developments and Greek Reality, with Emphasis on the Maara Cave in Drama, Alistratis Cave in Serres, and Vlychada Cave in Diros, Laconia MSc Thesis, Hellenic Open University, Greece.
Trimmis, K. P., 2015. Hidden Treasures in Forgotten Archives: Exploring the Archaeology of Greek Caves into the archives and the bulletin of the Hellenic Speleological Society. Chronika, 5, 32-41.
Zouros, N., 2007. Geomorphosite assessment and management in protected areas of Greece. Case study of the Lesvos Island-coastal geomorphosites. Geographica Helvetica 62(3):69–180.

17th INTERNATIONAL CONGRESS of the Geological Society of Greece

BULLETIN OF THE GEOLOGICAL SOCIETY OF GREECE, SP. PUBL.

EXTENDED ABSTRACT 192

Utilizing Information and Communication Technology for geosite development: The case of sulfuric acid caves in the Vikos-Aoos UNESCO Global Geopark

Lazaridis G.[1,*], Stergiou C. L.[1,2], Chatzipetros A.[1], Stamoulis K.[3], Dora D.[1], Georgopoulou X.[4], Vouvalidis K.[1], Nikolaou E[5], Paschos P.[5], Kitsaki G.[6], Papaioannou H.[6]

*(1) Faculty of Geology, Aristotle University of Thessaloniki (AUTH), 54124 Thessaloniki, Greece, *geolaz@geo.auth.gr*

(2) Chemical Process & Energy Resources Institute (CPERI), Centre for Research and Technology Hellas (CERTH), 50200 Ptolemaida, Greece

(3) Archaeometry Center, University of Ioannina, 45110 Ioannina, Greece

(4) Department of Theatre Studies, National and Kapodistrian University of Athens, 15784 Ilissia, Greece

(5) Hellenic Survey of Geology and Mineral Exploration, Region of Epirus, Eleonas, 48100 Preveza, Greece

(6) Vikos-Aoos UNESCO Global Geopark - Development Agency of Epirus S.A. (EPIRUS S.A.), Ioannina, Greece

Research Highlights

Recent research within the Vikos-Aoos UNESCO Global Geopark and neighboring Albania has highlighted the significance of sulfuric acid speleogenesis (SAS) caves, drawing the attention of explorers and researchers alike. Collaborative efforts by the Geopark and the School of Geology at Aristotle University of Thessaloniki focus on mapping these caves and investigating their unique processes. Their presence in a Greek Geopark underscores their scientific importance and potential for fostering awareness and sustainable tourism. However, the challenges posed by toxic atmospheres and fragile ecosystems necessitate strict protection measures, advocating for innovative approaches such as Information and Communication Technologies (ICT) to ensure responsible geosite development.

The Geopark

The Vikos-Aoos Geopark, located in Epirus, Greece, spans 1,200 sq. km across the municipalities of Zagori and Konitsa and includes 62 villages whose residents primarily engage in tourism, agriculture, livestock farming, forestry, and small-scale manufacturing. Dominated by the Vikos and Aoos Gorges, the towering mountains of Northern Pindos, and rivers like Aoos, Voidomatis, and Sarantaporos, the geopark showcases a geologically diverse history starting 200 million years ago. Comprising sedimentary, metamorphic, and igneous rocks, including ophiolitic formations from the Tethys Ocean, the area reflects tectonic processes of the Alpine Orogeny and extensive faulting during the Quaternary, which shaped its rugged karstic landscape (Telbisz et al., 2019). Recognized as a UNESCO Global Geopark since 2010, it supports conservation, education, and sustainable development while protecting unique ecosystems and fostering public engagement through its exceptional geological and natural heritage.

The diverse geological processes in the Vikos-Aoos Geopark are reflected in its landforms and geomorphology, offering unique insights into the geological evolution of Greece. The park features 51 geosites classified into seven categories: springs, tectonic structures (faults and folds), river terraces, rock shelters, panoramic viewpoints, karstic formations, and glacial landforms. These sites showcase significant geological interest, rarity, and beauty.

Classic caves, such as the vertical shafts of “Vulture’s Hole” (Geosite 39, -584m depth, 650m length), and “Chasm of Epos” (Geosite 40, -455m depth), and Gailotrypa (Geosite 44, -155 m deep), exemplify the dissolution of limestone along fractures and faults. Additionally, smaller rock shelters like Boila (Geosite 25), Kleidi (Geosite 24), and Megalakkos served as Paleolithic refuges for hunter-gatherers

While classic caves are well-recognized geosites within the park, SAS caves do not form a distinct category, emphasizing the broad diversity and representation of geological phenomena in the Geopark, and suggesting future actions on geoheritage recognition and preservation.

The SAS geosites of the Geopark

Landforms associated with sulfuric acid dissolution within the geopark include notable caves and springs (Fig.1 & Fig.2). Among them is the Skordyli Cave, situated on the northern bank of the Sarantaporos River, close to the Albanian border and approximately 2.5 km west-southwest of the Kavasila thermal springs. The cave entrance serves as the outlet for an underground sulfuric river that traverses a series of large chambers connected by smaller passages. Extending about half a kilometer from the underground spring to the outlet, the cave’s sidewalls are coated with gypsum and native sulfur. Its ecosystem is remarkable for the presence of chemoautotrophic microorganisms and a high level of endemism (Sarbu et al., 2024).

Pixaria Cave, located east-northeast of the Kavasila thermal springs in a limestone outcrop, is similarly influenced by sulfur springs near its entrance, which lies close to the Sarantaporos River. The cave features fracture-guided passages forming

a maze-like pattern, with a slightly inclined floor and median feeders. The walls of the passages are covered with gypsum, reflecting its speleogenetic processes.

Neles Cave is found near the Neles spring in Kleidonia Village, at the escarpment of the Konitsa Fault that borders Papigo Mountain to the west. The cave entrance is aligned along a fault plane, leading to a vertically developed passage. At its deepest point, 13 meters below the entrance, a horizontally oriented passage carries a stream of sulfuric water. The atmosphere is rich in hydrogen sulfide, and gypsum coats the walls and boulders. Although the cave and the spring appear interconnected, a direct link has yet to be confirmed.

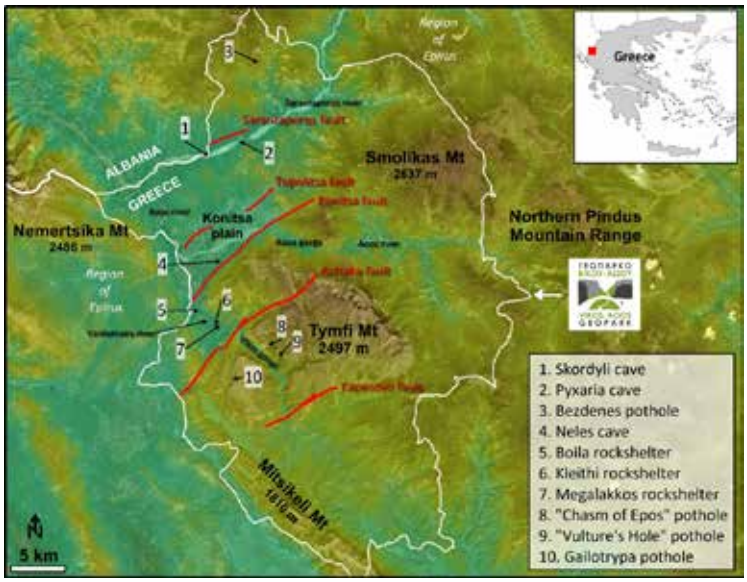

Figure 1. A map of the Vikos-Aoos Geopark showing the locations of the major caves, faults, mountains and rivers of the region (modified after Chatzipetros et al., 2024).

Lastly, Bezdenes Pothole, near the Amarantos thermal springs, is preliminarily included due to gypsum-like deposits found in its deeper sections. This impressive vertical void has a reported depth of 268 meters. Ongoing research aims to confirm its sulfuric acid dissolution origin and further clarify its speleogenetic context.

Figure 2. Entrances of Sulfuric Acid Speleogenesis caves in the Vikos-Aoos UNESCO Global Geopark: A. Skordyli sulfur Cave; B. Pixaria Cave; C., Neles Cave; D., Neles Spring; E. Bezdenes Pothole.

Application of Information and Communication Technologies

Information and Communication Technologies (ICT) have been utilized to support the study and promotion of sulfuric acid speleogenesis (SAS) geosites. Tools such as multimedia, data management systems, and virtual reality (VR) facilitate map creation, data analysis, and immersive public experiences. Their application varies across SAS geosites, addressing site-specific challenges while prioritizing safety.

In the field, a flexible suite of tools—primarily mobile-based applications—has been utilized. These tools facilitate the capture of georeferenced photographs of cave entrances, springs, and related features, as well as 3D scans of the caves. These scans form the foundation for VR or augmented reality (AR) experiences. Notable applications include FieldMove Clino by Midland Valley (specialized in petroleum engineering and structural geology software) for structural data collection and Polycam for 3D scanning. Polycam utilizes LiDAR (Light Detection and Ranging) technology, which works by emitting laser pulses and calculating the time taken for the light to bounce back, generating a precise 3D map of the cave. Advanced machine learning algorithms refine the scans, while AI plays a crucial role in enhancing 3D models by cleaning them, optimizing textures, and filling in missing data. The combined use of these applications, already validated in scientific cave research (Lazaridis et al., 2024), produces cave maps that meet the highest standards as defined by mapping grades (Häuselmann, 2011).

In the Vikos-Aoos Geopark, various 3D models have been developed to document the key features of SAS geosites. At the Neles location, two models were created to capture the spring and the cave, offering ground plans and depth measurements of the vertically developed cave. Similarly, at Pixaria Cave m (Fig.3), three models were produced: one documenting the entrance area with distinct dissolution forms, another capturing a passage characterized by a median sulfuric feeder, and a partial scan of the cave's initial section, highlighting its maze-like pattern of passages with consistent size and morphology.

Some of these scans are featured on the webpage "Virtual Speleological Field Trip in Greece" (https://speleology8.wordpress.com/pixaria-cave/) and are linked to related publications (e.g., Lazaridis et al., 2024). This makes these significant landforms accessible to a broad audience, including researchers, cavers, and the general public.

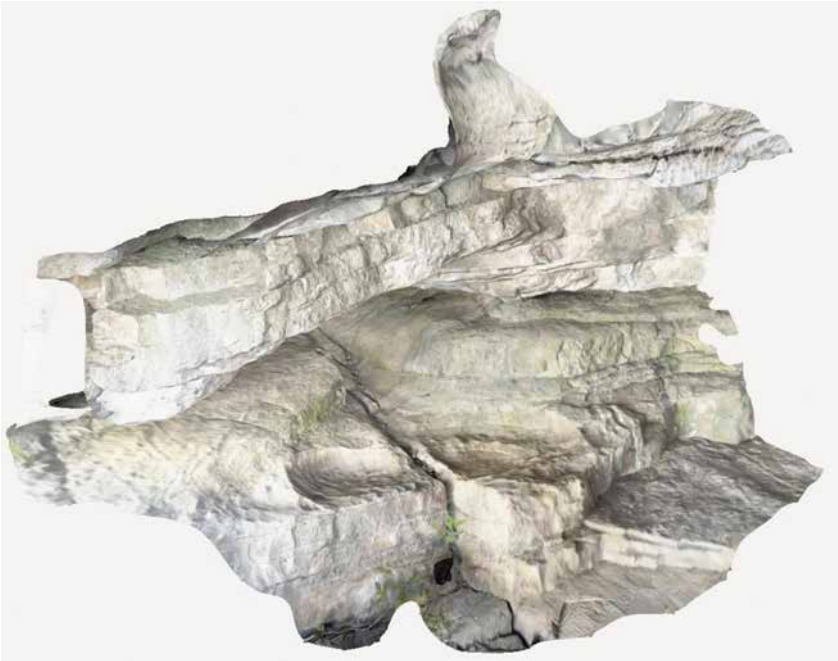

Figure 3. Example of a 3D-model from the entrance area of Pixaria Cave in Kavasila thermal springs of the Vikos-Aoos UNESCO Global Geopark.

Discussion

During the initial phase of this project, several challenges were encountered in applying ICT for geosite development. The primary concerns were identifying a time-efficient, safe, and cost-effective method capable of providing accurate data. To address these concerns, well-trained field participants were involved, equipped with real-time gas detectors and data loggers for monitoring radon levels. The use of smartphone-based tools proved to be an effective solution,

helping minimize factors such as equipment costs and the time required for data acquisition. While this approach sometimes results in lower resolution or precision—such as in the point cloud data from 3D scans—it is a necessary trade-off, as safely entering these caves with highly specialized instruments is virtually impossible.

The fieldwork techniques employed in this study enabled the efficient collection of data and the development of a solid methodology that can be adapted for use in other karst geosites. The combination of ICT tools allowed the team to gather data quickly, facilitating the creation of comprehensive datasets while maintaining a rigorous approach to scientific research.

The implementation of ICT offers several advantages for overcoming speleological challenges and addressing preservation needs, while simultaneously promoting public engagement. In particular, the toxicity of hydrogen sulfide in the cave atmosphere and the elevated radon levels present significant obstacles for fieldwork, increasing the need for safety equipment and monitoring, especially for non-trained visitors. Furthermore, caves with vertical extents, such as Bezdenes Pothole and Neles Cave, pose accessibility challenges for both researchers and the public.

ICTs provide a way for the authorities of the Vikos-Aoos Geopark to offer virtual access to these geosites, enabling the public to explore them remotely while ensuring their protection. Moreover, these technologies support the creation of a management plan that safeguards both the caves and the sensitive ecosystems they contain, which are home to unique species with high levels of endemism. In addition to enhancing visitor safety, the geopark fulfills its role in the conservation and protection of these valuable geological sites.

The integration of ICT in geosite development not only advances scientific research but also provides a sustainable method for preserving these delicate ecosystems. By offering virtual access to otherwise inaccessible caves, such as Bezdenes Pothole and Neles Cave, the Vikos-Aoos Geopark can engage a wider public without compromising safety or the integrity of the sites (e.g. Evelpidou et al., 2021). This virtual experience, coupled with 3D scanning and augmented reality tools, allows visitors to explore these caves remotely, fostering greater awareness and interest in their preservation. The successful application of ICT in this context could serve as a model for other geosites, demonstrating the potential for technological advancements to enhance both public engagement and conservation efforts. Looking ahead, the continued use and advancement of these technologies will help ensure the long-term protection of these valuable natural resources, while also supporting local communities through increased tourism and educational opportunities (see for example Lazaridis et al., 2023).

The sulfuric acid caves in the Vikos-Aoos Geopark are the only known examples of this type of speleogenesis in Greece that are located in the area of an UNESCO Global Geopark, adding critical value to the promotion of these landforms. Their unique morphology also makes them ideal for educational purposes.

Finally, this work aligns with UNESCO's policies by fostering sustainable development, education, and cultural heritage preservation. By utilizing ICT to provide virtual access to inaccessible geosites, we promote inclusivity, enabling broader public engagement while protecting fragile ecosystems. The project supports education through innovative tools like 3D scanning and augmented reality, which enhance understanding of unique geological features. Additionally, our efforts contribute to local communities by encouraging geotourism and raising awareness about the importance of conserving these natural and cultural assets, reflecting UNESCO's goals of balancing accessibility, education, and preservation.

Conclusions

The use of ICT in the Vikos-Aoos Geopark has proven effective in overcoming challenges like toxic cave environments and limited accessibility. Smartphone-based tools and virtual technologies allowed for efficient data collection while keeping costs and time in check. These technologies not only helped gather accurate data but also enabled virtual access to caves, ensuring public safety while promoting awareness of these unique geological sites.

By offering virtual experiences, the Geopark can engage the public without compromising preservation efforts. This approach, using 3D scanning and augmented reality, sets a good example for other geosites looking to balance access and protection. Continued use of ICT will help safeguard these fragile ecosystems, support local tourism, and provide educational opportunities. The sulfuric acid caves in the geopark are particularly valuable for educational purposes and conservation, offering a unique opportunity for both research and public engagement.

This work supports UNESCO's policies by promoting sustainable geosite management, enhancing public engagement through virtual access, and fostering education and conservation of unique geological and cultural heritage.

Acknowledgements

Cave visits for this work have been approved by the Greek Ministry of Culture – Ephorate of Paleoanthropology and Speleology. Special thanks to the cavers who participated in the various expeditions for research in the area. 3D cave scans conducted as part of the 'Virtual Speleological Field Trip in Greece' project, formally supported by the International Union of Speleology (UIS).

References

Audy, M., Bouda, R., Bruthans, J., Rÿžiÿka, V., 2022. Albanian hypogene caves in the area of Vromoner thermal springs on the Sarandaporo River. Speleoforum, 41, 42–49.

Audy, M., Bruthans, J., Mareš, J., Sarbu, S., Galdenzi, S., Bouda, R., 2024. Sulfur 2023, hypogenni jeskyne Albanie a Recka Kavasila, Vromoner, Langarica. Speleoforum, 43, 104–111.

Benassi, A., 2024. Lengarices 2023: inseguendo il Soffi o del Drago (Albania). Speleologia, 89: 4-6.

Chatzipetros, A., Stergiou, C.L., Papaioannou, H., 2024. Seismic hazard in an actively uplifting area: the case of Vikos-Aoos UNESCO Global Geopark, NW Greece. In: Pellicer, M.X., Aytac, A., Amorfini, A., Delaby, S., (Eds.), Geohazards in European Geoparks, Akademisyen Yayınevi Kitabevi, Ankara, Turkey, pp. 150-153.

De Waele, J., D'Angeli, I. M., Audra, P., Plan, L., Palmer, A. N., 2024. Sulfuric acid caves of the world: A review. Earth-Science Reviews, 104693.

Evelpidou, N., Karkani, A., Saitis, G., Spyrou, E., 2021. Virtual field trips as a tool for indirect geomorphological experience: A case study from the southeast part of the Gulf of Corinth, Greece. Geoscience Communication Discussions, 2021, 1-16.

Kovařík, F., Audy, M., Sarbu, S.M., Fet, V., 2023. Euscorpius sulfur sp. n. (Scorpiones: Euscoriidae), a new cave scorpion from Albania and northwestern Greece. Euscorpius, 376:1-14.

Lazaridis, G., Dora, D., Sdraka, F. and Vouvalidis, K., 2023. Virtual speleological field trip in Greece – project report. UIS Bulettin, 61-1: 46-48.

Lazaridis, G., Melfos, V., Papadopoulou, L., 2011. The first cave occurrence of orpiment (As□S□) from the sulfuric acid caves of Aghia Paraskevi (Kassandra Peninsula, N. Greece). International Journal of Speleology, 40(2), 6.

Lazaridis, G., Melfos, V., Papadopoulou, L., Onac, B., Stergiou, Ch., Maravelis, A., Voudouris, P., Dora, D., Fitros, M., Papaioannou, H., Vouvalidis, K., 2024. Sulfuric acid speleogenesis in Greece. Acta Carsologica, 53/2-3, 127-144.

Lazaridis, G., Trimmis, K.P., Drnić, I., Brkić Drnić, K., 2024. Deciphering rock surface origins in a karst cave: insights from the Rača Cave, Lastovo, Croatia. Geologia Croatica, 77(3), pp.235-242.

Polymenakou, P., Mandalakis, M., Dailianis, T., Dimitriadis, C., Medvecky, M., Magoulas, A., Gerovasileiou, V., 2018. Preliminary assessment of methanogenic microbial communities in marine caves of Zakynthos Island (Ionian Sea, Greece). Mediterranean Marine Science, 19(2), 284-289.

Sarbu, S.M., Brad, T., Băncilă, R.I., Stefan, A., 2024. Exploring Biodiversity and Food Webs in Sulfur Cave in the Vromoner Canyon on the Greek–Albanian Border. Diversity 16, 477.

Telbisz, T., Stergiou, C.L., Mindszenty, A., Chatzipetros, A., 2019. Karst features and related social processes in the region of the Vikos gorge and Tymphi mountain (Northern Pindos National Park, Greece). Acta Carsologica 48(1), 29-42.

17th INTERNATIONAL CONGRESS of the Geological Society of Greece

BULLETIN OF THE GEOLOGICAL SOCIETY OF GREECE, SP. PUBL.

EXTENDED ABSTRACT 193

Management of solid wastes from offshore oil drilling, based on their geochemical properties: A case study from the Prinos facilities in the Northern Aegean Sea.

Lianou Vasiliki[1], Tsakiridis Petros[2]
(1) National and Kapodistrian University of Athens, Athens, Greece, vlianou@geol.uoa.gr (2) National Technical University of Athens, Athens, Greece

Introduction

The increasing growth of the oil and gas industry has resulted in the generation of huge amounts of waste, most of which is produced during the drilling of wells for the exploration, extraction and production of hydrocarbons. The solid phase of drilling waste, also known as drill cuttings or DCs, is a major concern for oil companies, mainly due to the organic and inorganic contaminants it contains (Onwukwe & Nwakaudu, 2012). Increasing regulations and environmental concerns require the proper treatment and disposal of this waste (EU, 2013). However, the complexity, slow pace, and high cost of traditional debris remediation methods have, in recent years, shifted research focus toward its use as a raw material for manufacturing various products. The reuse of drilling waste in various applications, particularly in the construction sector, aligns with the principles of the circular economy and serves as a key solution for sustainable development (Asim *et al*., 2021). Research has already presented various proposals for the use of DCs, but choosing the appropriate solution is not an easy task. Each case is unique and demands a thorough understanding of the waste material's physical and chemical properties.

In Greece, the management of drill cuttings from hydrocarbon extraction has not been thoroughly studied. A significant challenge in exploring alternative management solutions is the lack of data on the composition and microstructure of this debris. Addressing this gap, this paper takes an initial step in analyzing and characterizing the geochemical properties of solid drilling cuttings from the country's sole hydrocarbon production facility.

Materials and Methods

A series of laboratory tests were carried out on a sample of DCs from Prinos facilities (fig. 1), using advanced X-ray (XRF and XRD) and scanning electron microscope (SEM) analysis methods to investigate its physical/mechanical properties, measure its hydrocarbon content (as these are its major contaminants) and determine its geochemical composition.

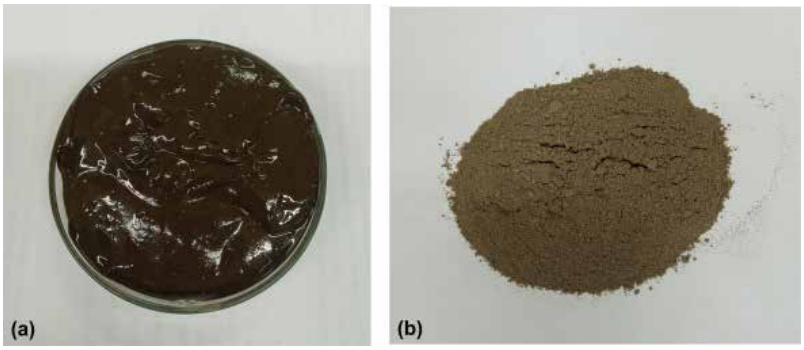

Figure 1. Sample of the study material: (a) coated with drilling mud, and (b) after drying at 110 °C for 24 hours.

Results

The results showed that the physical properties as well as the chemical and mineralogical composition of the DCs from Prinos depend on the rocks of the mining area, mainly on the calcium sources and the residual drilling mud. The debris material was characterized as silt, with the main oxides in its composition being BaO (21.98%), CaO (16.1%), SiO2 (14.21%) and SO3 (8.54%). The sample had a high loss on ignition (LOI ≈25.83% w/w) and contained organic material at 10.04% w/w and total petroleum hydrocarbons (TPH with C>12) at 7.34% w/w (fig. 3). It was also contaminated with polyaromatic hydrocarbons (PAHs: ≈180 mg/kg) (fig. 2). In terms of mineralogical composition, it contained: quartz (SiO2), calcite (CaCO3), dolomite [CaMg(CO3)2], anhydrite (CaSO4), barite (BaSO4) and alite (NaCl), with the dominant phase being quartz (excluding barite).

Molecular weight (gr/mol)	Polycyclic aromatic hydrocarbon (PAH)	Quantity (mg/kg)	Group of rings	Composition (%)
128	Naphtalene	122	2-rings	67,9
166	Accenaphthalene	2,33	3-rings	6,2
	Acenaphtene	6,18		
	Fluorene	0,095		
178	Phenanthrene	0,86		
	Anthracene	1,67		
202	Fluoranthene	3,04	4-rings	2,2
	Pyrene	0,65		
228	Benzo (a) anthracene	0,044		
	Chrysene	0,152		
252	Benzo (b) fluoranthene	0,122	5-rings	0,4
	Benzo (k) fluoranthene	0,089		
	Benzo (a) pyrene	0,033		
278	Dibenzoanthracene	0,522		
276	Benzo (g,h,i) perylene	26,2	6-rings	23,28
	Indeno (1,2,3-c,d) pyrene	15,6		
	Total	179,59		100

Figure 2. PAHs concentrations and percentage distribution of their fractions based on their ring group, in the sample.

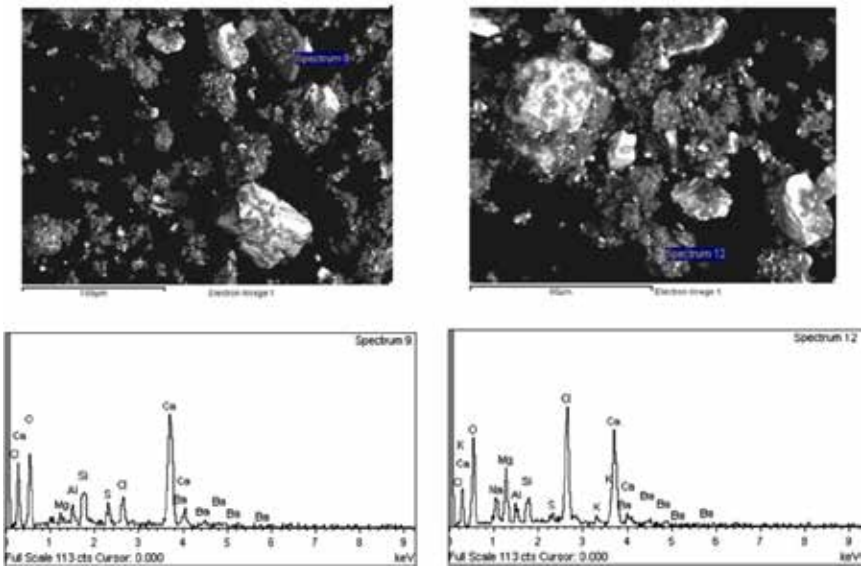

Figure 3. Characteristic mineral phases of the DCs sample from Prinos.

Conclusions

The main conclusions from the study of the results are summarized as follows: (a) the inorganic phases identified indicate that the material under consideration is of evaporite origin, (b) the very high percentage of Ba indicates the presence of drilling mud residues in the sample, (c) the contents of the remaining elements can be attributed mainly to the rocks of the mining area, and (d) the concentrations of trace elements in the DCs are probably controlled by the composition of the individual grains, with the exception of strontium, which is probably associated with the barite in the drilling mud.

Finally, to support the reuse and recycling of DCS, this study also explored three potential scenarios for utilizing Prinos drill cuttings. While the analysis was theoretical, the findings indicate promising opportunities for incorporating this type of solid waste into various products, demonstrating viable alternatives for its management.

Acknowledgements

I extend my gratitude to ENERGEAN OIL & GAS – ENERGIAKI AEGEAN S.A., with special thanks to Mr. V. Tsetoglou and Mr. P. Kokkini for supplying the material necessary for this study.

References

Asim, N., Badiei, M., Torkashvand, M., Mohammad, M., Alghoul, M.A., Gasaymeh, S.S., Sopian, K., 2021. Wastes from the petroleum industries as sustainable resource materials in construction sectors: Opportunities, limitations, and directions. Journal of Cleaner Production, 284, 125459.

EU, 2013. The Council Decision of 17 December 2012 on the accession of the European Union to the Protocol for the Protection of the Mediterranean Sea against pollution resulting from exploration and exploitation of the continental shelf and the seabed and its subsoil https://eur-lex.europa.eu/legal-content/EN/TXT/?uri=CELEX%3A32013D0005.

Onwukwe, S.I., Nwakaudu, M.S., 2012. Drilling wastes generation and management approach. Int J Environ Sci Dev 3(3), 252–257.

17th INTERNATIONAL CONGRESS of the Geological Society of Greece

BULLETIN OF THE GEOLOGICAL SOCIETY OF GREECE, SP. PUBL.

EXTENDED ABSTRACT 194

Palaeobotanical study of the Vrisaki flora from the Lesvos Petrified Forest

Eleni M. Liapi[1,2], George Iliopoulos[3], Nikolaos Zouros[1,2]

(1) Natural History Museum of the Lesvos Petrified Forest, Sigri/Lesvos, Greece, geod22002@aegean.gr (2) Department of Geography, University of the Aegean, Mytilene/Lesvos, Greece (3) Department of Geology, University of Patras, Rio/Patras, Greece

Research highlights

New insights into the plant palaeoassemblages from the Petrified Forest of Lesvos Island are revealed through the documentation and taxonomic determination of the leaf macro-remains from Vrisaki fossiliferous locality.

Background

The Petrified Forest, located at the western peninsula of the Lesvos Island, Greece, and recognized as a UNESCO Global Geopark, plays a pivotal role in preserving and showcasing the natural heritage of the Lesvos Island through efforts in scientific research, geo-conservation, geo-education and geo-tourism.

The recent construction of the new Kalloni-Sigri road, crossing the protected area of the Lesvos Petrified Forest in Western Lesvos, has exposed a remarkable wealth of plant fossil sites (Fig. 1). Especially, twelve fossiliferous localities were identified and excavated along the road, carefully protected, and studied to ensure their preservation and to advance knowledge. The findings include a wide variety of fallen and in situ fossilized tree trunks along with mass occurrences of leaf macro-remains revealing the great palaeobotanical richness of the region (Zouros, 2021).

The unearthed fossil material surpasses all prior expectations establishing the Lesvos Petrified Forest as one of the most significant areas for scientific investigations worldwide. Recent studies on both wood anatomy and leaf macro-morphology have provided new insights into the preserved volcanic flora of the broader protected area of the Petrified Forest (Velitzelos et al., 2019; Iamandei et al., 2022, 2024; Kafetzidou et al., 2022; Tsitsou et al., 2022; Liapi et al., 2022, 2023, 2024; Zhu et al. 2024).

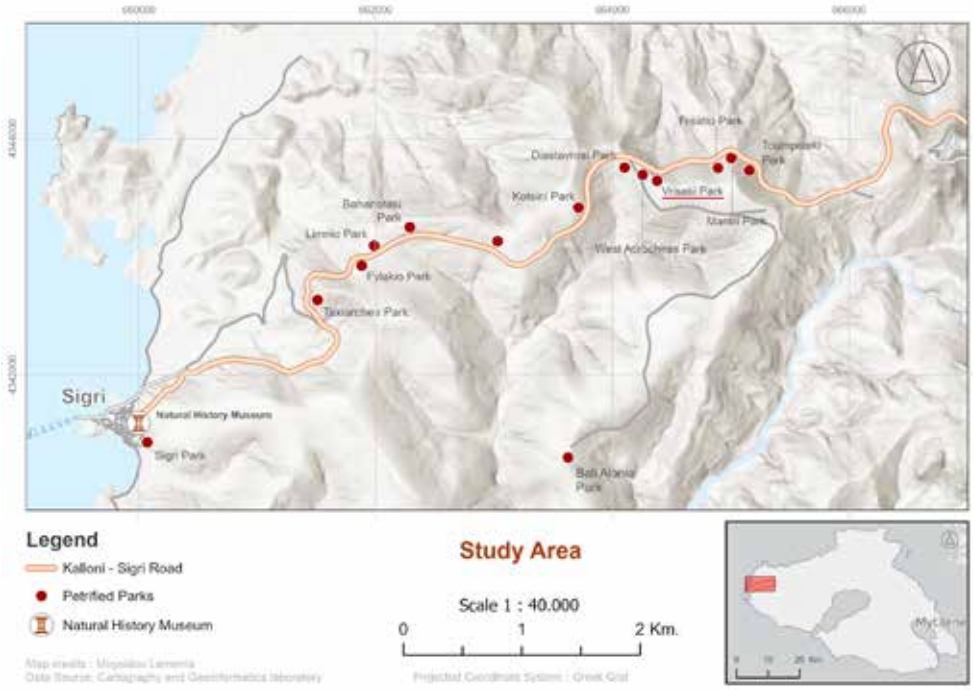

Figure 1. Location map of Western Lesvos where several new fossiliferous localities have been unearthed in the broader area of the Akroheiras hill range along Kalloni-Sigri road. The studied fossil material originates from Vrisaki Park (underlined on the map).

Objectives

The primary objective of this work is to enhance the study of the palaeobotanical record of the Petrified Forest through the documentation and taxonomic determination of leaf macro-remains from the new fossil sites along the Kalloni-Sigri road which traverses the Akrocheiras hill range (Fig. 1). In this context, several leaf macro-remains from Vrisaki

fossiliferous locality have been examined, described and determined. Additionally, the palaeoecological signals of the plant taxa have been assessed to reconstruct the environmental conditions that prevailed during the Early Miocene.

Material and Methods

The studied material consists 500 fossiliferous slabs comprising over 6930 leaves and a small number of reproductive organs. These remains have been preserved within different fine- to coarse-grained tuff layers, occurring both as leaf litter accumulated in the fine tuff layers, and as scattered leaves intermixed with pyroclastic material. The slabs were collected, conserved and cataloged by the research and technical team of the Natural History Museum of the Lesvos Petrified Forest (Zouros et al., 2022). The fossils were evaluated, with the majority of the material examined under an OPTIKA SLX-5 stereomicroscope. The taxonomic determination was conducted following the manual of leaf architecture with a focus on the key macro-morphological features of the fossils, including margin type, apex and base shapes, as well as venation architecture (Ellis et al., 2009).

Preliminary Results

To date, the palaeoflora of Vrisaki consists of at least one bryophyte, three ferns and more than 50 different angiosperm taxa, 21 of which are determined at a high taxonomic rank (family, genus and/or species). The determined taxa based on foliage include Bryophyta gen. et sp. indet., Thelypteridaceae gen. et sp. indet., aff. *Rumohra recentior* (Unger) Barthel, *Daphnogene polymorpha* (A. Braun) Ettingshausen, *Laurophyllum* sp. 1, *Laurophyllum* sp. 2, *Smilax weberi* P.Wessel, *Phoenicites* sp., *Calamus* sp., Zingiberaceae gen. et sp. indet., aff. Zingiberales, Fagaceae gen. et sp. indet. 1, Fagaceae gen. et sp. indet. 2, Juglandaceae gen. et sp. indet., *Alnus* vel *Rubus*, *Rubus* sp., aff. *Celtis japeti* Unger, *Populus* sp., *Nerium* sp., *Myrtophyllum* sp., and *Pungiphyllum cruciatum* (A. Braun) Frankenhäuser & V. Wilde. Additionally, the leaf material has been grouped into several distinct morphotypes, each requiring further investigation for a more detailed classification (Fig. 4, 4.4–4.7). Based on reproductive organs, the flora includes a solely infructescence of *Alnus* ?*kefersteinii* (Göppert) Unger, winged fruits of *Acer* sp. and cf. *Acer* sp., and a few buds probably of lauraceous affinity. Different representative plant taxa of the studied area are illustrated in Figures 2–4, underscoring the floral diversity of Vrisaki.

Discussion

The enormous quantities of leaf macro-remains and the numerous petrified tree trunks preserved in various fossiliferous localities within the pyroclastic rocks of the Lesvos Petrified Forest provides a great opportunity to decipher the Early Miocene subtropical history of the island. This ongoing research focuses on the documentation and systematic taxonomy of the abundant leaf material from the fossiliferous locality of Vrisaki. So far, more than 54 plant taxa have been documented and analyzed based on their macro-morphological characteristics. The palaeoflora of the Vrisaki fossiliferous locality represents a diverse array of vegetation types, ranging from riparian habitats to lowland and upland mesophytic forest regions. The determined taxa are linked to one or more vegetation units, reflecting the ecological diversity and complexity of the palaeoenvironment. Evidence of a riparian plant association is suggested by taxa such as aff. *Rumohra recentior*, *Daphnogene polymorpha*, *Phoenicites* sp., *Alnus* ?*kefersteinii*, *Alnus* vel *Rubus*, *Populus* sp. and possibly *Pungiphyllum cruciatum*. The occurrence of members of the Lauraceae and Fagaceae families, Juglandaceae gen. et sp. indet., aff. *Celtis japeti* and *Nerium* sp. is indicative of well-drained forests. Herbaceous monocots, including members of Zingiberales, were likely adapted to the shaded understory beneath the forest canopy of the riparian or well-drained forests. In addition, lianas such as *Smilax weberi* and *Calamus* sp. may have been part of riparian or well-drained forests, suggesting a forest structure with multiple layers. The preliminary results from the systematic taxonomy of the Vrisaki fossiliferous locality reveal sufficient floristic similarities with the West Akrocheiras fossiliferous locality from the Akrocheiras hill (Kafetzidou et al., 2022; Tsitsou et al., 2022; Liapi et al., 2022, 2023). Both palaeofloras share plant taxa such as Thelypteridaceae gen. et sp. indet., *Daphnogene polymorpha*, *Laurophyllum* sp. 1, *Smilax weberi, Phoenicites* sp., *Calamus* sp., Zingiberaceae gen. et sp. indet., Fagaceae gen. et sp. indet. 1, *Rubus* sp., aff. *Celtis japeti*, *Populus* sp., *Acer* sp., *Nerium* sp., *Myrtophyllum* sp., and *Pungiphyllum cruciatum*. Notably, the Vrisaki palaeoflora appears to exhibit a greater diversity based on fruit remains, including *Alnus* ?*kefersteinii*, *Acer* sp. and cf. *Acer*.

Despite the progress that has been made in recent years, further investigation is required as several morphotypes still remain under study. The systematic taxonomy of the plant macro-remains from Akrocheiras hill poses challenges due to the extensive abundance of collected specimens and the overlapping morphological features exhibited by certain leaf types. Completing the systematic classification in the future will provide a more comprehensive floristic knowledge and offer valuable insights into the palaeoenvironmental history of the Early Miocene of Lesvos.

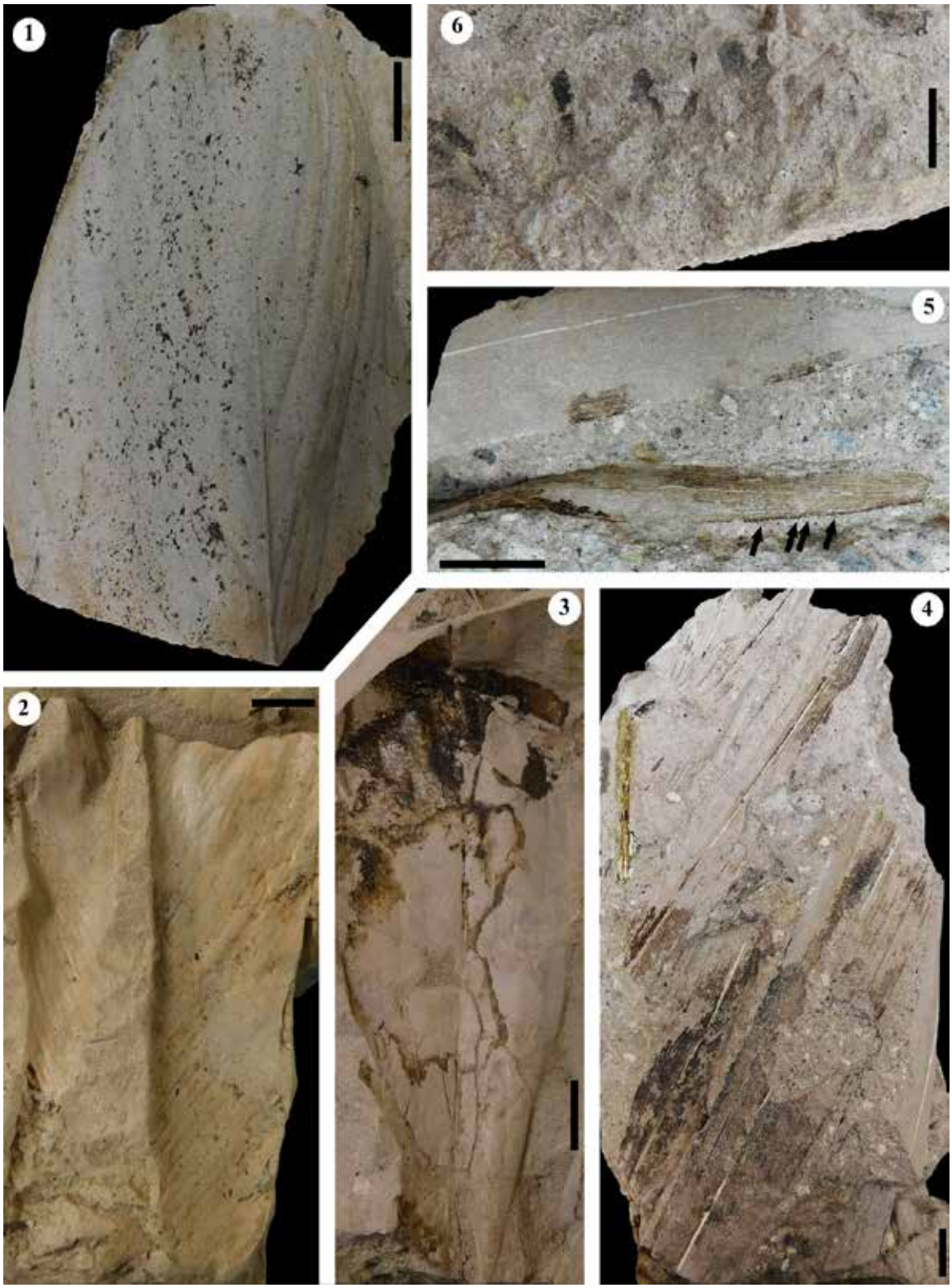

Figure 2. Characteristic plant taxa from the Vrisaki fossiliferous locality of the Lesvos Petrified Forest: 1. aff. Zingiberaceae gen. et sp. indet., leaf, ВРФ1805; 2. aff. Zingiberaceae gen. et sp. indet., leaf, ВРФ2371; 3. Monocotyledoneae fam. gen. et sp. indet. (aff. Zingiberales) leaf, ВРФ467; 4–5. *Calamus* sp., leaf, ВРФ1814, 4. Two leaflets attached to a rachis at the top of the figure, 5. Close up of the leaflets where the black arrows show the distinctive spines in the margin; 6. Bryophyta gen. et sp. indet., thallus, ВРФ2130. Scale bars equal 2 cm (1, 3, 4–5) and 1 cm (2, 6).

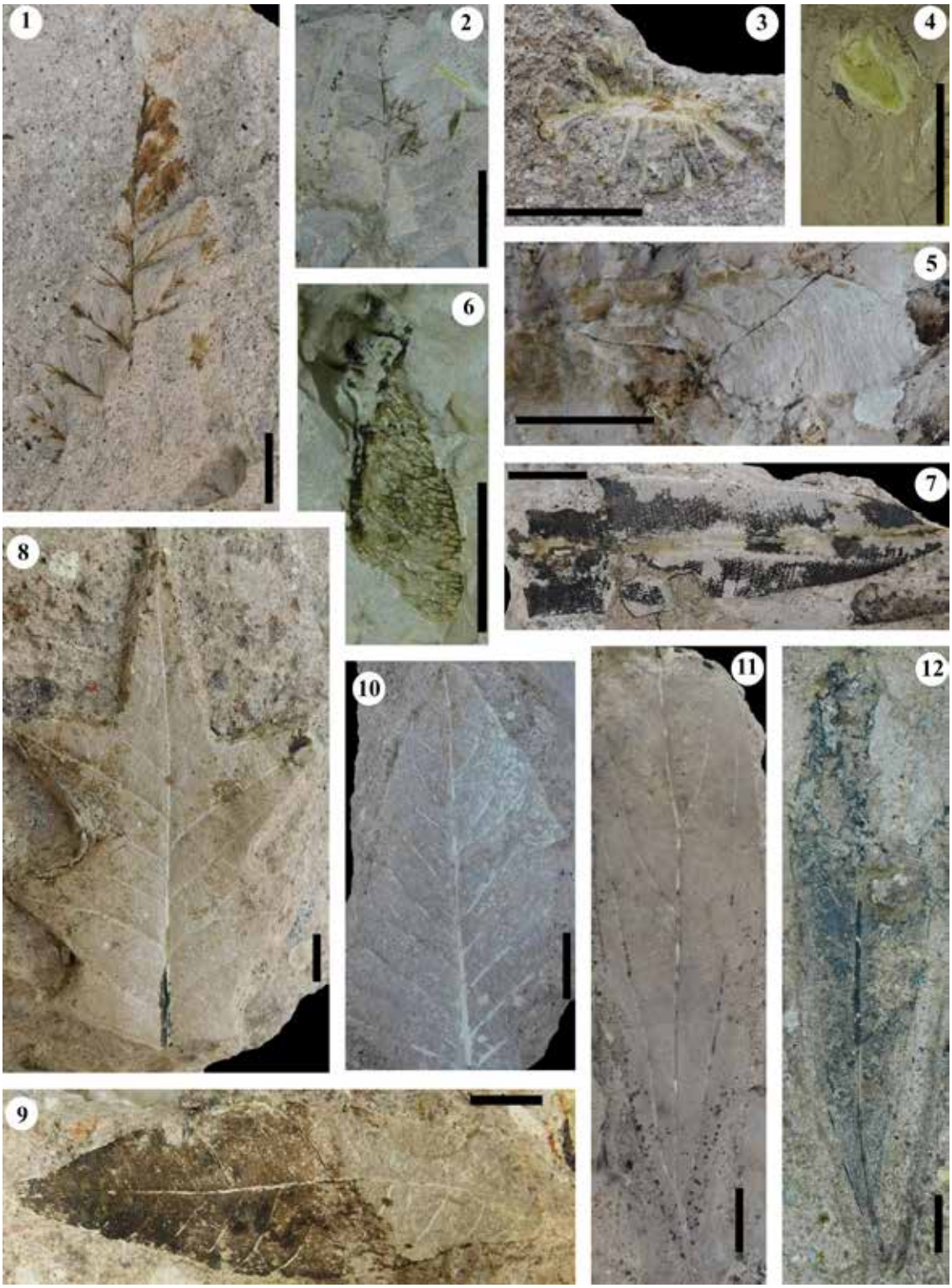

Figure 3. Characteristic plant taxa from the Vrisaki fossiliferous locality of the Lesvos Petrified Forest: 1. aff. *Rumohra recentior*, frond, ΒΡΦ880; 2. Thelypteridaceae gen. et sp. indet., frond, ΒΡΦ317; 3. *Alnus ?kefersteinii*, infructescense, ΒΡΦ1805; 4–5. *Acer* sp., winged fruits, ΒΡΦ1739, 4. Preserved nutlet, 5. Samara; 6. cf. *Acer* sp., winged fruit, ΒΡΦ763; 7. *Nerium* sp., leaf, ΒΡΦ823; 8. *Pungiphyllum cruciatum*, leaf, ΒΡΦ2461A; 9. Fagaceae gen. et sp. indet. 1, leaf, ΒΡΦ2099; 10. Fagaceae gen. et sp. indet. 2, leaf, ΒΡΦ1070; 11. *Daphnogene polymorpha*, leaf, ΒΡΦ2394; 12. *Laurophyllum* sp. 1, leaf, ΒΡΦ349.
Scale bars equal 1 cm.

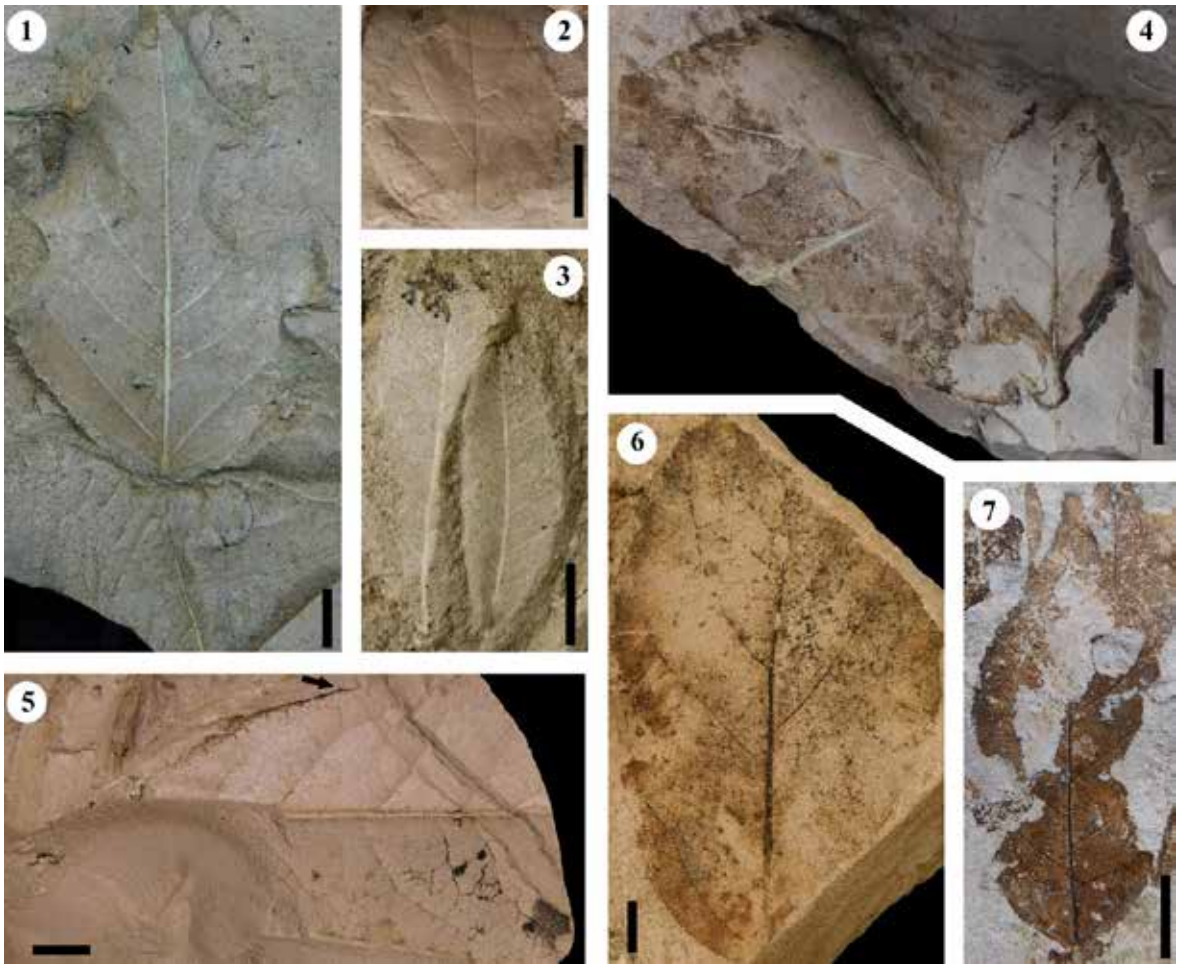

Figure 4. Diverse plant taxa from the Vrisaki fossiliferous locality of the Lesvos Petrified Forest: 1. *Populus* sp., leaf, ΒΡΦ915; 2. *Rubus* sp., leaf, ΒΡΦ2371; 3. *Myrtophyllum* sp., leaf, ΒΡΦ469; 4–7. Dicotyledonous angiosperms of unknown systematic affinity, 4. Leaves, ΒΡΦ1915; 5. Leaf (black arrow indicates the small glandular teeth), ΒΡΦ758; 6. Leaf, ΒΡΦ2199; 7. Leaf, ΒΡΦ1890.
Scale bars equal 1 cm.

Acknowledgments
The authors would like to express appreciation to the research and technical team of the Natural History Museum of the Lesvos Petrified Forest for their contribution and support to the current palaeobotanical research.

References

Ellis, B., Daly, D.C., Hickey, L.J., Johnson, K.R., Mitchell, J.D., Wilf, P., Wing, S.L., 2009. Manual of Leaf Architecture. Cornell University Press, New York.

Iamandei, S., Iamandei, E., Velitzelos, D., Velitzelos, E., 2022. Palaeoxylotomical studies in the Cenozoic petrified forests of Greece. Part two – conifers. Acta Palaeontologica Romaniae 18 (1), 65–111.

Iamandei, S., Iamandei, E., Velitzelos, D., Velitzelos, E., 2024. Palaeoxylotomical studies in the Cenozoic petrified forests of Greece. Part three – dicots. Acta Palaeontologica Romaniae 20 (2), 61–96.

Kafetzidou, A., Kouli, K., Zidianakis, G., Kostopoulos, D., Zouros, N., 2022. The early Miocene angiosperm flora of Akrocheiras in Lesvos Petrified Forest (North Aegean, Greece) – Preliminary results. Review of Palaeobotany and Palynology 296, 104559.

Liapi, E., Zidianakis, G., Tsitsou, E., Iliopoulos, G., Zouros, N., 2022. New floristic data of the Early Miocene Lesvos Petrified Forest − Part A: Non-vascular plants, ferns and monocots from the West Akrocheiras outcrop. Bulletin of Geological Society of Greece Sp. Publ. 10, 64–65.

Liapi, E., Tsitsou, E., Iliopoulos, G., Zouros, N., 2023. Taxonomic investigations of the West Akrocheiras plant assemblage of the Lesvos Petrified Forest. 8th Agora Paleobotanica Meeting, abstracts volume, Belver de Cerdanya, pp. 39–40.

Liapi, E., Iliopoulos, G., Zouros, N., 2024. Documenting the leaf flora of a new fossiliferous locality from the Lesvos Petrified

Forest. Folia Musei Rerum Naturalium Bohemiae Occidentalis - Geologica et Paleobiologica 58 (1), 29–33.

Tsitsou, E., Zidianakis, G., Liapi, E., Iliopoulos, G., Zouros, N., 2022. New floristic data of the Early Miocene Lesvos Petrified Forest − Part B: Dicotyledon taxa from the West Akrocheiras outcrop. Bulletin of Geological Society of Greece Sp. Publ. 10, 66–67.

Velitzelos, D., Iamandei, S., Iamandei, E., Velitzelos, E., 2019. Palaeoxylotomical studies in the Cenozoic petrified forests of Greece. Part one – palms. Acta Palaeobotanica 59 (2), 289–350.

Zhu, Y.B., Li, Y., Zhang, J.P., Wang, Y.D., Zouros, N., 2024. A new species of *Pseudotsuga* (Pinaceae) from the lower Miocene of Lesvos, Greece, and its palaeogeographical and palaeoclimatic implications, Palaeoworld 34, 100852.

Zouros, N.C., 2021. The Miocene petrified forest of Lesvos, Greece: Research and geoconservation activities. Geoconservation Research. 4 (2), 635–649.

Zouros, N., Soulakellis, N., Valiakos, I., Bentana, K., Theodorou, E., Zgournios, E., Antonakis, E., Lamprakopoulos, A., 2022. Enhancement and promotion of the new fossiliferous sites along the new Kalloni Sigri road–An example of good practice of geoconservation in Lesvos Island UNESCO Global Geopark Greece. Bulletin of Geological Society of Greece Sp. Publ. 10, 849–850.

17th INTERNATIONAL CONGRESS of the Geological Society of Greece

BULLETIN OF THE GEOLOGICAL SOCIETY OF GREECE, SP. PUBL.

EXTENDED ABSTRACT 195

Preliminary results of the fluid geochemistry surveillance campaigns on Santorini island (Greece) after the 2025 Anydros seismic sequence

Liuzzo M.[1], Federico C.[1], Grassa F.[1], Kanellopoulos Ch.[2], Kyriakopoulos K.[1,3], Lalechos S.[4], Manousaki M.[4], Nisi B.[5], Tamburello G.[6], Tassi F.[5,7], Vaselli O.[5,7], Vougioukalakis G.[2], Paonita A.[1], Bianco F.[8], D'Alessandro W.[1]

(1) Istituto Nazionale di Geofisica e Vulcanologia, Palermo, Italy, marco.liuzzo@ingv.it; walter.dalessandro@ingv.it (2) Hellenic Survey of Geology and Mineral Exploration, Acharnae, Greece (3) National and Kapodistrian University of Athens, Athens, Greece (4) Earthquake Planning & Protection Organization of Greece, Athens, Greece (5) Consiglio Nazionale delle Ricerche (IGG), Italy (6) Istituto Nazionale di Geofisica e Vulcanologia, Bologna, Italy (7) University of Florence, Florence, Italy (8) Istituto Nazionale di Geofisica e Vulcanologia, Naples, Italy

Recent seismic activity in the Santorini region has attracted global attention and raised concerns about ongoing volcanic hazards. Santorini, a large volcanic caldera featuring the central islets of Nea Kameni and Palea Kameni, has a complex eruptive history spanning approximately 650,000 years, including the catastrophic eruption (~1560 B.C.) linked to the decline of the Minoan civilization. Since 27 January 2025, the region has experienced a major seismic crisis, with over 2,000 earthquakes recorded, including 14 events with magnitudes ≥5.0 and a maximum magnitude of 5.3. Seismicity has been concentrated approximately 25 km northeast of Santorini and 25 km southwest of Amorgos.

We present the results of two geochemical surveys conducted between March and April 2025, involving water sampling from 10 wells, measurements of soil CO□ fluxes and d^{13}C-CO□ values in Santorini and Nea Kameni, as well as sampling of fumarolic gases at Nea Kameni and bubbling gases at Palea Kameni. These data provide a preliminary assessment of the current degassing dynamics of the area. Comparison and integration with existing literature indicate that the post-seismic volcanic phase following the January–February 2025 seismic crisis is marked by an increased degassing rate in the Nea Kameni region. However, the chemical and isotopic compositions of the gases (^{3}He/^{4}He and d^{13}C values) exhibit only minor variations relative to pre-crisis measurements reported in previous studies.

Although preliminary, these findings underscore the critical need for continuous monitoring of the Santorini volcanic system, in order to deliver timely and reliable information to the local community and to support effective volcanic risk mitigation strategies.

17th INTERNATIONAL CONGRESS of the Geological Society of Greece

BULLETIN OF THE GEOLOGICAL SOCIETY OF GREECE, SP. PUBL.

EXTENDED ABSTRACT 196

Automated Seismic signals' identification: A statistical criterion for decreasing the false alarm rate; Implementation on synthetic data.

Lois A.[1], Giannopoulos D.[1], Sokos E.[1]
(1) University of Patras, Department of Geology, Patras, Greece, lois@upatras.gr

Abstract
Algorithms dealing with the problem of the identification of micro-earthquakes constitute a topic of ongoing research. The development of methodologies dealing with the specific problem has gained considerable attention during the last decades in the context of research, appearing at the same time to be the central issue in various application areas. The extraction and efficient analysis of the useful information from continuous recordings are of great importance, since it is a prerequisite for reliable interpretations. Nevertheless, such processes usually suffer from a number of false alarms, which tends to be significantly increased in extremely noisy environments. In this paper, we propose a "decision-making" scenario to be applied on the extracted intervals, for the purpose of decreasing the probability of false alarms. The specific statistical criterion can be implemented regardless of the detection algorithm that has been applied for the identification of the seismic events and its efficiency is confirmed by its application on a series of experiments on synthetic data.

Introduction
The most widely used algorithms, mainly due to their simplicity and the low computational resources that they demand, are the energy-based algorithms, which are also referred to in the literature as STA/LTA detectors. In its simplest form, the STA/LTA algorithm processes the initial recordings, or some characteristic function derived from raw data, using two moving windows and compares their absolute values' ratio to a user-defined threshold value, to declare a seismic event. This idea was firstly adopted by Allen (1978), who applied energy criteria on the characteristic function that resulted from the signal's positive envelope. Baer & Kradolfer (1987) proposed a modified and improved version of Allen's method, aiming in overcoming specific drawbacks that characterize the latter, which are mainly associated to the user-defined parameters of the technique, such as the selection of the appropriate characteristic function, as well as the threshold value, in order to increase the detection rate. Another class of techniques that are commonly used for the solution of the seismic event detection problem, as well as the picking of phase arrivals are the methodologies which utilize autoregressive modeling along with the Akaike Information Criterion (AIC) (Leonard & Kennett 1999). The basic assumption constituting the base of these algorithms is that the seismic recordings can be segmented into locally stationary parts, which can be described by autoregressive models of different orders. This property can be used as a diagnostic tool to discriminate useful information from the background noise. Moreover, several methodologies based on classical statistical concepts, such as the maximum likelihood, hypothesis testing scenarios, higher order statistics etc., were introduced as possible solutions for the signal identification problem. Since the statistical properties of seismic noise are not easily predictable, as it is widely reported (Arrowsmith et al. 2008) Lois et al. (2013, 2019) proposed the solution of the problem under examination, using a thresholding type technique, which is applied under a non–strict hypothesis testing framework. Higher order statistics (HOS) also constitute an important tool that has been exploited by geoscientists, during the last two decades, for the purpose of solving the event detection problem, as well as the accurate estimation of the phase arrival times (Saragiotis et al. 2002). Apart from the above-mentioned techniques, which mainly rely on classical seismic signal analysis applied on either 1C or 3C data, there are also more sophisticated approaches that are referred to in the literature, using artificial neural networks (Mousavi et al. 2018), machine learning (Chen 2018), fuzzy logic theory (Chu & Mendel 1994), etc. Nevertheless, it is obvious that the above-listed methodologies are affected by several factors, such as the source type, the instrument response, the noise level of the study area, the epicentral distance of the recorded events etc. Thus, the development of robust algorithms that provide stable results for general situations is of vital importance. In this study we propose a statistical criterion serving as an "outcome control" process, adopted to refine the initial outcome acquired by any detection algorithm.

Methodology
Once the extraction of the segments of the seismic record is achieved (using any of the well-known detection algorithms), the main effort of the proposed methodology is focused in performing the implementation of a mechanism capable to control the results by retaining the useful, for our analysis, information and eliminating the intervals corresponding to false alarms. In that scope, pure seismic noise is initially isolated, using energy criteria, and, thereafter, we introduce

a "decision-making" criterion, based on the comparison among autoregressive models estimated on the isolated seismic noise, as well as the detected segments resulting from the application of the detection algorithm.

Let us consider that $\mathfrak{B}$ is a set containing *I* blocks $\boldsymbol{b}_i$of length *L* that have been drawn independently and with replacement from the initial stationary record $\mathbf{z}_n$, corresponding to the vertical component, that is:

$$\mathfrak{B} = \{\boldsymbol{b}_1, \boldsymbol{b}_2, \dots, \boldsymbol{b}_I\},\ \boldsymbol{b}_i = [z_i, z_{i+1}, \dots, z_{i+L-1}], i \in [1, N-L+1]. \quad (1)$$

It is clear that the *i*–th element $\boldsymbol{b}_i$of the set $\mathfrak{B}$ is a block of length *L* consisting of consecutive samples, with its starting index *i* being a uniformly distributed discrete random variable ensuring equiprobable selection of each *L*-length block from the available $N-L+1$ that are contained in the initial record $\mathbf{z}_n$ (Lois et al 2013). Apparently, $\mathfrak{B}$ can also be formulated as a $I \times L$ matrix, having in its *i*–th row the block $\boldsymbol{b}_i$.

Having formed the set $\mathfrak{B}$ by applying the previously mentioned sampling procedure, the goal now is to identify blocks consisting solely of noise samples. This constitutes a clustering problem that can be addressed using various approaches. For instance, Lois et al. (2013) proposed the application of a modified "k-median" algorithm that exploits as input autoregressive models estimated on blocks $\boldsymbol{b}_i$, instead of the blocks themselves, in order to reduce the dimensionality of the problem. Following the specific approach, a robust separation among "noise" and "signal" models is achieved, but in general high computational resources are demanded, due to the modeling procedures that have to be applied on each block that is selected during the sampling process. In this work, a simple energy-based procedure is applied in order to establish the desirable isolation of the noise blocks. In general, given a stationary recording, samples forming a noise block are expected to be characterized by insignificant fluctuations in amplitude, thus resulting in low values of the block's variation. On the other hand, the presence of a seismic signal or part of it in a block causes an increase in the block's variation, due to high fluctuations among the samples within the block. Therefore, the selection of the desirable intervals is based on the comparison of their standard deviations to a predefined value.

More particularly, assuming that $\boldsymbol{S}$ is a set including the standard deviations of the blocks $\boldsymbol{b}_i\boldsymbol{b}_i$:

$$\boldsymbol{S} = \{\sigma(\boldsymbol{b}_i)\}_{i\in[1,I]} = [\sigma(\boldsymbol{b}_1), \sigma(\boldsymbol{b}_2), \dots, \sigma(\boldsymbol{b}_I)], \quad (2)$$

the desirable set $\mathfrak{B}_{noise} \subseteq \mathfrak{B}$, containing the noise blocks is selected using the following relation:

$$\mathfrak{B}_{noise} = \{\boldsymbol{b}_i \in \mathfrak{B}; \sigma(\boldsymbol{b}_i) \le median(\boldsymbol{S})\} \quad (3)$$

It is apparent that since the median value of the set $\boldsymbol{S}$ constitutes the "middle observation" of its sorted values, the latter can equally be formulated as an $\frac{I}{2} \times L$ or $\left(\frac{I}{2}+1\right) \times L$ matrix, depending on whether *L* is an odd or an even number. What we need now is to calculate a time series, representative of the noise characteristics of the given recording, in order to use it as a "reference vector" for the next step of our analysis. In that scope, we calculate and denote as $\bar{\boldsymbol{b}}_n\bar{\boldsymbol{b}}_n$ the average of the noise blocks, calculated column-wise, such as:

$$\bar{\boldsymbol{b}}_n = \left[\frac{1}{r}\sum_{j=1}^{r}\mathfrak{B}_{noise}^{j}(1), \frac{1}{r}\sum_{j=1}^{r}\mathfrak{B}_{noise}^{j}(2), \dots, \frac{1}{r}\sum_{j=1}^{r}\mathfrak{B}_{noise}^{j}(L)\right] \quad (3)$$

where the first element of the reference vector is the average of the first column of matrix $\mathfrak{B}_{noise}$, the second element is the average of the second one etc. and *r* equals to $\frac{I}{2} \times L$ or $\left(\frac{I}{2}+1\right) \times L$, depending on whether *L* is an odd or an even number, as it has already been mentioned. Index jj refers to each selected noise block that fulfils eq. (2).

Since the "average" noise block has been isolated using the above-mentioned energy-based procedure, our goal is to estimate the stochastic models that best describe both the noise and the "candidate" seismic signals. These models will be the tools that will permit the elimination of any "false" information that may have been included in the initial results. To this end, we apply autoregressive (AR) modeling procedures to the specific time series, selecting the optimal model orders by using the corrected Akaike Information Criterion (*AICc*). In general, the *AICc* for finite sample sizes and for a model order *P* is defined as follows:

$$AICc = 2P - 2\ln\{l(\theta^*)\} + \frac{2P(P+1)}{L-P-1} \quad (4)$$

where $l(\theta^*)l(\theta^*)$ is the achieved maximum of the likelihood function $l(\theta)$ and θ^* is the maximum likelihood parameter estimator of length *P*, resulting from the solution of the following optimization problem:

$$\theta^* = arg\max_{\theta}\{l(\theta)\} \quad (5)$$

Moreover, it is known that *AIC* (so *AICc*) provides a means of model selection by estimating the amount of information that is lost by a given model. Hence, the less information a model loses, the higher the quality of that model is. Therefore, given a set of models, the optimum model is the one corresponding to the minimum value of the *AICc*, so if $P_i, P_i \in \mathbb{P} \subseteq \mathbb{N}$ are the candidate AR model orders, then the optimum order *P* is estimated by:

$$P = arg \min_{P_i \in \mathbb{P}} \{AICc(P_i)\} \quad (6)$$

Now, we can formulate the average PP-order noise model $\bar{m}_n \bar{m}_n$ which is described as follows:

$$\bar{x}_t = c + \sum_{j=1}^{P} \varphi_j \bar{x}_{t-j} + \varepsilon_t, \quad \varepsilon_t \sim N(0, \sigma_\varepsilon^2) \quad (7)$$

where c is a constant value, φ_j are the parameters of the model and ε_t is white noise with zero mean value and variation equal to σ_ε^2.

Furthermore, assuming that the algorithm has detected *k* segments in the initial recording, we derive in the same way *k* AR(Q_i) models, where the *i*-th model m_i of order Q_i is given by:

$$x_t^i = c^i + \sum_{j=1}^{Q_i} \theta_j^i x_{t-j}^i + \varepsilon_t^i, \quad \varepsilon_t^i \sim N\left(0, \sigma_{\varepsilon^i}^2\right) \quad (8)$$

where c^i is a constant value, θ_j^i are the parameters of each model m_i and ε_t^i is again a process of white noise with zero mean and variation equal to $\sigma_{\varepsilon^i}^2$. Apparently, the model orders Q_i are also computed using the *AICc*. The remaining step, in order to complete the presentation of the proposed algorithm, is a "Decision-Making" criterion which will allow controlling the outcome of detection algorithm, thus ensuring the best possible final result. The general idea lies on the fact that, given the AR models describing the average noise block, as well as the detected intervals from the initial record, we can conclude on the "nature" of each candidate segment by examining whether it converges to the estimated noise model or not. Here, the concept of convergence implies the notion of the distance among these models. In other words, in an ideal case, a model describing a detected segment, which is close to the estimated noise model, is more likely to correspond to a false detection, than to a seismic signal. Alternatively, a model that deviates sufficiently from the noise model probably corresponds to a microseismic event or to any other signal with dynamical characteristics that differ from the characteristics of the background noise. The main question arising from the proposed approach concerns the measure of similarity or the appropriate criterion that must be adopted in order to conclude to secure results. For example, Picolo (2010) proposed the autoregressive metric for comparing time series models, by introducing the Euclidean distance between the coefficients of their AR formulations. Even though the specific distance is a well-defined measure of structural dissimilarity between two stochastic models, its implementation to models associated with passive seismic data leads to unstable conclusions, especially in extremely noisy environments.

Taking into consideration the fact that changes in both the order and the values of the AR coefficients are diagnostic of the differences between noise and signal (Leonard & Kennett 1999), we propose the following scenario in order to decide about the "nature" of the detected intervals under investigation:

$$(P \leq Q_i) \cap \left(\sigma(|\boldsymbol{\varphi}|) < \sigma\left(\left|\boldsymbol{\theta}^i\right|\right)\right), \forall\, i \epsilon [1, k], k \epsilon \mathbb{Z} \quad (9)$$

where $\sigma(.)$ refers to the standard deviation of the quantities $\boldsymbol{\varphi} = [\varphi_1, \varphi_2, \dots, \varphi_P]$, which is the vector containing the coefficients of the noise model, and $\boldsymbol{\theta}^i = [\theta_1^i, \theta_2^i, \dots, \theta_{Q_i}^i]$ is the respective vector corresponding to the *i*–th detected interval.

Experimental Results

The simulations with synthetic data were performed using two different noise process scenarios. To this end, two first-order AR processes were utilized (denoted by AR1 and AR2 respectively) with poles of different magnitude, in order to simulate, as realistically as possible, a "normal" case (pole magnitude = 0.73), as well as an extreme case (pole magnitude = 0.9), where the assumption of stationarity almost fails. For each of the two noise process scenarios, 500 records of synthetic seismic data were constructed (each having a duration of 10 min and a sampling rate of 100 Hz), containing a total number of 2500 events. More specifically, to construct each data record, we initially created the noise process, using the above-mentioned AR processes, and then 5 synthetic seismic events, with the desired SNR in the range [-5, 5] dB, were superimposed. The SNR was estimated using a window of 100 samples (1s) in the vicinity of the first arrival of each seismic event. Moreover, the seismic events were created according to Lois et al. (2013). Initially, a window of white Gaussian noise was low-pass filtered and the resulting sequence was multiplied by a half-Gaussian window of the same length, for the purpose of simulating the exponential decay (attenuation) of the signal's amplitude. Then, the vector representing the seismic signal was multiplied by a constant gain, in order to control the SNR in the desirable range. The detected segments were acquired using an improved 3C version of the well-known STA/LTA algorithm (STA/LTA_{3C}). According to the classical approach (STA/LTA), the ratio between a short-term average (STA) and a long-term average (LTA) window is usually calculated using data from the vertical component. In our experiments (STA/LTA_{3C}), in order to increase the SNR of the ratio function and, consequently, its capability to detect small-magnitude events, we exploit information from all three components of the recorded signal, using their L_2–norm, that is:

$$f_i^{sl} = \sum_{i=1}^{N}\left(\sqrt{z_i^2 + x_i^2 + y_i^2}\right) \quad (10)$$

where z_i corresponds to the vertical component, while x_i and y_i to the East-West and North-South horizontal components, respectively. The results regarding the false alarm rate prior and after the application of the proposed statistical criterion is presented in table 1.

Table 1. False alarm rate prior and after the application of the proposed statistical criterion on synthetic data

False Alarm Rate	AR[1]		AR[2]	
SNR (dB)	Prior (%)	After (%)	Prior (%)	After (%)
-5	33.87	14.47	66	37.33
-2	15.13	8.07	52.63	28.97
0	7.92	1.96	25.15	16.79
2	4.03	0.86	13.35	7.38
5	0.39	0	6.74	2.03

1: Results from the application of the proposed "Decision Making" criterion on the two different noise process scenarios.

By inspecting the results presented in table 1, associated with both noise scenarios it becomes evident that the implementation of the proposed criterion significantly reduces the false alarm rate of the initial outcome derived by (any) detection algorithm. Regarding the first noise scenario and for noise levels down to 2 dB the results are acceptable even without the application of the "decision – making" scenario. But for extreme noise levels, corresponding to negative values of SNR the proposed technique provides a reduction of almost 50% to false detections. Moreover, for the second noise scenario where the useful information is buried to strongly correlated synthetic seismic noise, the attempt is focused on testing the performance of the method in cases where basic assumptions, such as the stationarity, almost fail. Nevertheless, and by considering the extremely noisy environment (-2 and -5 dB), the rate of false signal identifications reduced significantly, approaching again a reduction of 50%.

Conclusions

In this study, we introduce a statistical criterion which can be applied on the initial outcome obtained by the implementation of each well-known detection algorithm on seismic data. This "Decision-Making" scheme relies on stochastic modeling applied on both the detected intervals and a signal representative to the recorded seismic noise. Comparisons among the calculated models provide us an indication about the nature of the "candidate" seismic signals. The advantages of the proposed approach were confirmed through a series of experiments, using synthetic seismic data, providing a significant reduction of the false alarm rate even in extremely noise environments.

References

Allen, R. V., 1978. Automatic earthquake recognition and timing from single traces, Bull. seismol. Soc. Am.68, 1521–1532.

Arrowsmith, S. J., Whitaker, R., Taylor, S. R., Burlacu, R., Stump, B., Hedlin, M., Randall, G., Hayward, C. & ReVelle, D., 2008. Regional monitoring of infrasound events using multiple arrays: Application to Utah and Washington State, Geophys. J. Int., vol. 175(1), pp. 291–300, https://doi.org/10.1111/j.1365-246X.2008.03912.x.

Baer, M. & Kradolfer, U., 1987. An automatic phase picker for local and teleseismic events, Bull. seismol. Soc. Am., 77, 1437–1445.

Chen, Y., Hill, J. C., Lei, W., Lefebvre, M., Bozdag, E., Komatitsch, D. & Tromp, J., 2017. Automated time-window selection based on machine learning for full-waveform inversion, 87th Annual International Meeting, SEG, Expanded Abstracts, 1604-1609.

Chu, C. K., & Mendel, J., 1994. First break refraction event picking using fuzzy logic systems, IEEE T FUZZY SYST., 2, 255–266,doi: 10.1109/91.324805.

Lois, A. E., Psarakis, E. Z. & Pikoulis, E., 2013. A new thresholding type technique for the detection of seismic events, 21st European Signal Processing Conference (EUSIPCO 2013), Marrakech, 1-5.

Lois, A., Sokos, E., Martakis, N, Paraskevopoulos, P. & Tselentis, G.-A., 2013. A new automatic S-onset detection technique: Application in local earthquake data, Geophysics, 78, KS1–KS11.

Leonard, M. & Kennet, B. L. N., 1999. Multi-component autoregressive techniques for the analysis of seismograms, PHYS EARTH PLANET IN, 113, 247–263, doi: 10.1016/S0031-9201(99)00054-0.

Mousavi, S. M., Zhu, W., Sheng, Y., & Beroza, G. C., 2019. CRED: A Deep Residual Network of Convolutional and Recurrent Units for Earthquake Signal Detection, Sci. Rep., 9(1), doi:10.1038/s41598-019-45748-1.

Piccolo, D., 2010. The Autoregressive metric for comparing time series models, Statistica, Department of Statistics, University of Bologna, 70(4), 459-480.

Saragiotis, C., Hadjileontiadis, L. & Panas, S., 2002. Pai-S/K: A robust automatic seismic p phase arrival identification scheme, IEEE T GEOSCI REMOTE, 40(6), 1395–1404.

17th INTERNATIONAL CONGRESS of the Geological Society of Greece

BULLETIN OF THE GEOLOGICAL SOCIETY OF GREECE, SP. PUBL.

EXTENDED ABSTRACT 197

Mapping the active Faults affecting Ionians Islands, Western Hellenic Arc

Loreto M.F.[1], Ferrante V. [1], Ligi M.[1], Muccini F.[2,3], Palmiotto C.[1], Petracchini L.[3], Romano S.[1], Ganas A.[4], Argnani A.[1], Conti A.[3], Cuffaro M.[3], Pensa A.[5], Kothri S.[6], Lampridou D.[6], Merino I.[7], Ranero R.C.[8,9] and Nomikou P.[6]

(1) CNR, Istituto di Scienze Marine (ISMAR), Bologna, Italy, mariafilomena.loreto@cnr.it
(2) Istituto Nazionale di Geofisica e Vulcanologia (INGV), Roma, Italy
(3) CNR, Istituto di Geologia Ambientale e Geoingegneria (IGAG), Roma, Italy
(4) Institute of Geodynamics - National Observatory of Athens (NOA), Greece
(5) Italian Institute for Environmental Protection and Research, Rome, Italy
(6) Department of Geography and Climatology - National and Kapodistrian University of Athens (NKUA), Greece
(7) Faculty of Geosciences, University of Bremen, Bremen, Germany
(8) Institució Catalana de Recerca i Estudis Avançats (ICREA), Barcelona, Spain
(9) Barcelona Center for Subsurface Imaging, ICM, CSIC, Barcelona, Spain

Introduction / Background

The area offshore the central Ionian Islands (Cephalonia, Lefkada, Zakynthos, and Ithaca), western Greece (Fig. 1A; 1B), is within the Mediterranean regions one with the highest seismic activity and tsunamigenic potential (Fig. 1C). Here, the Hellenic frontal thrust system stops against the right-lateral Cephalonia Transform Fault, a fault more than 100 km-long (Louvari et al. 1999), to step back towards Corfu (Sachpazi et al., 2000). In recent decades, this area experienced several destructive events, such as the 1953 Cephalonia earthquakes (three M6+ events) and the more recent the Mw 6.8 Zakynthos event occurred the 28 October 2018 (Ganas et al., 2020) and the swarm of moderate size events ranging from 5.3 to 5.7 occurred in 2006 (Papadimitriou et al. 2012). Although this area has a high exposure to geological risk, offshore remains little explored. In order to improve the knowledge on shallow deformation, fault geometry and on the hazard potential of tsunamigenic faults, we carried out two oceanographic cruises, in May 2022 (aboard of the R/V G. Dallaporta supported by the Italian National Research Council - CNR) and in June 2023 (aboard of the R/V L. Bassi from the National Institute of Oceanography and Applied Geophysics - OGS in the frame of the POSEIDON project supported by the Eurofleet+ Program). During these two cruises we collected a multidisciplinary and multiscale dataset composed of geophysical (e.g., bathymetry, multichannel seismic data, magnetometry) and geological data (gravity cores).

Results

The newly collected high-resolution multichannel seismic data (Fig. 1B), integrated with high-resolution swath bathymetry, allowed us to define the sediment deformation patterns at the intersection between the Cephalonia Fault and the thrust fronts of the Hellenic Arc. To south of Cephalonia, the high-resolution multichannel seismic profile highlights a series of small bulges with internal discontinuities close to small drops of the seafloor (Fig. 2) interpreted as reverse faults bounding positive flower structures dipping toward southeast. Amongst two well-imaged flower structures, a shallow layer of sediments is dislocated by E-verging thrusts forming reverse structures. More eastward, the Argostoli Ridge is bounded on its west side by a strike-slip fault with inverse component, interpreted as a west-verging transpressive fault. The ridge internally is affected by a series of minor compressive faults, as revealed by the dislocations of sedimentary layers L1 and L2, and by a series of minor normal faults related to gas escape that have generated a Giant Pockmark. Further south, the Cephalonia Fault still shows this transpressive character and the Argostoli Ridge looks bounded even on its east side by a strike-slip fault with inverse component (Fig. 3).

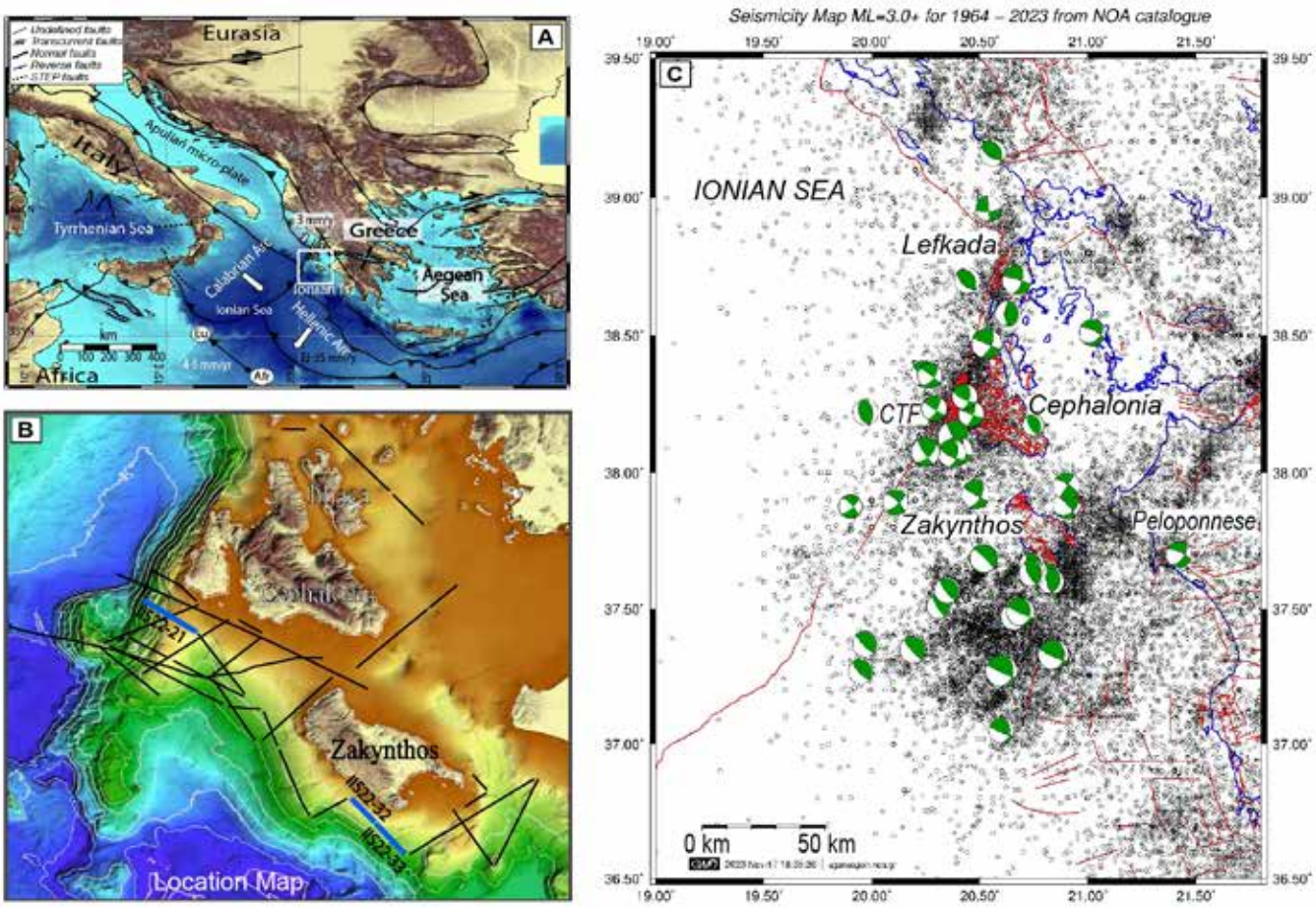

Figure 1. A) Tectonic map of the central Mediterranean showing location of the study area (white box). Mediterranean structural sketch modified after an online Tectonic Map (Woudloper - Own work, CC BY-SA 1.0) and by Loreto et al., (2021). B) Relief map of the study area. It shows the dataset collected during the IONIANS2022 survey. The multichannel seismic profiles shown in this abstract are pointed out with thick blue lines. Bathymetry data were downloaded from EMODnet portal (https://emodnet.ec.europa.eu/en/bathymetry#bathymetry-approach) and gridded using GMT software (Wessel et al., 2019). Inset (upper right): GPS velocity vectors map from https://www.unavco.org/. C) Map showing the distribution of the instrumental seismicity (black dots) with focal mechanisms (beachballs; events with 5.5 ≤ M ≤ 6.8; period 1959 - 2022). Green beachballs are focal mechanisms downloaded from the Global Centroid Moment Tensor database (www.globalcmt.org). Seismicity data collected from 1964 to 2023 by the NOA Institute of Geodynamics (only events with local magnitude M≥3 are shown; https://www.gein.noa.gr/en/services-products/earthquake-catalogs/). Faults are after Ganas et al. (2013, 2018). Map projection is geographic, Datum WGS84.

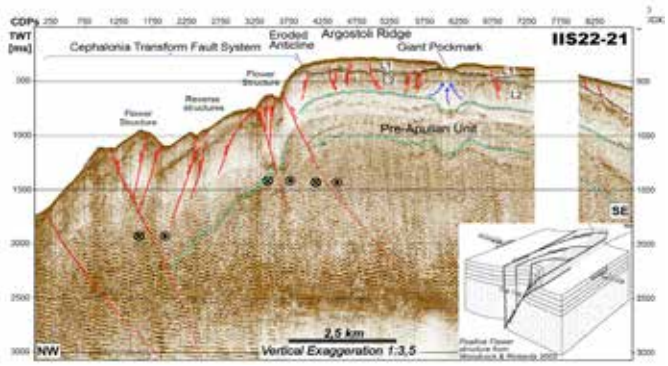

Figure 2. High-resolution multichannel seismic profiles crossing IIS22-21 the Cephalonia Transform Fault system. Faults are marked with red lines, while the kinematics (normal, reverse) are inferred by arrows direction. Blue lines mark the multiple signals. Black lines bound two sedimentary units. A sketch of a strike-slip fault with compressive component modified by Woodcock & Rickards (2003) has been included.

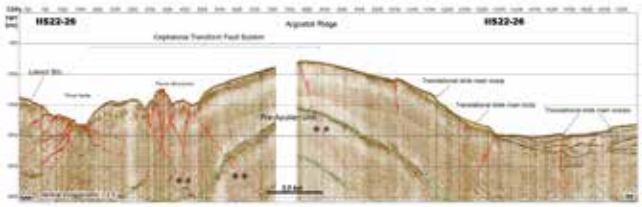

Figure 3. High-resolution multichannel seismic profiles crossing IIS22-26 the Cephalonia Transform Fault system further south of Cephalonia Isl. Faults are marked with red lines, while the kinematics is inferred by arrows direction. Light blue lines mark multiple signals.

South of Zakynthos, the deformation setting changes with respect to the CTF system zone. Here a well-stratified shallow unit, likely of Plio-Quaternary age, overlies a unit internally low reflective facies; we interpreted belonging to the Pre-Apulian unit (Fig. 4). The sedimentary unit is cut by widespread SE and NW dipping faults with extensional kinematics. Some of these faults affect the stratified unit and part of the underlaying Pre-Apulian Unit. These faults frequently reach the seafloor forming small steps. A series of sedimentary unconformities and a deep graben filled by sediments have been mapped in the surroundings of this gentle anticline. This complex setting suggests that there is a strong interplay between tectonics and sedimentary processes.

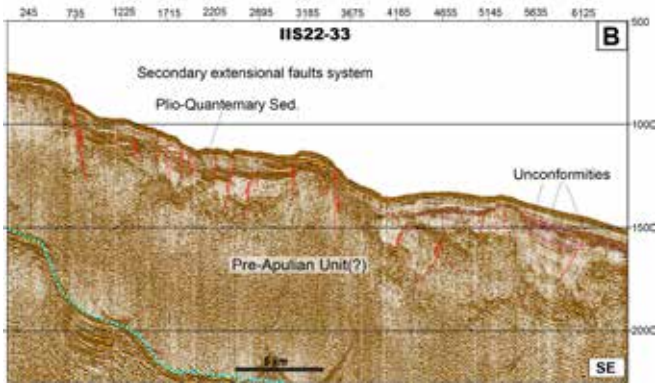

Figure 4. High-resolution multichannel seismic profiles IIS22-33 crossing the slope offshore Zakynthos. Faults are marked with red lines, while the kinematics is inferred by arrows direction. Light blue lines mark the multiple signals.

Discussion

The morphotectonic setting of the CTF fault system results show more complexity than previously mapped (Fig. 2, 3 4). Shallow sediment deformation in the central sector of the CTF system is controlled by a series of strike-slip faults with a compressive component, locally expressed by positive flower structures, generally E-dipping. The Cephalonia fault system splays into several branches, similar to a compressive strike-slip duplex (Woodcock and Fischer, 1986), and changes size passing from ~6 km (Fig. 1B), to west of Cephalonia Is., to 25 km-wide in the southern part. Our new findings completely change the previous published interpretation of the geometry of CTF system, inferred only from seismological data and modelling (Louvari et al., 1999; Papadimitriou et al., 2021). Given that the single fault "widens" into a fault system, the overall slip rate (~17 mm/yr; Tsironi et al. 2024) is partitioned, which might decrease the earthquake magnitude over several active faults and increases the distribution of events over a large area, as inferred from recorded seismicity (Fig. 2 and Fig. 4 in Kassaras et al., 2016). This new fault anatomy, with a multi-segment geometry, should have an effect over the seismological models proposed in the future for the CTF system. Southwest of Zakynthos, a series of normal faults dissecting the shallow marine sediments SE-ward (Fig. 4) indicate that this area is dominated by extensional stress. However, this area has been struck during last decades by several earthquakes, most of which with thrust mechanisms (Figs. 1c and 2a; Kassaras et al., 2016). Combining MCS data (Fig. 4) with swath bathymetry (fig. 1B) and seismological data (Fig. 1C) and considering the orientation of faults with respect to the morphologic features of the area (Fig. 4), we interpret these extensional structures as a secondary system that is able also to trigger earthquakes. This idea is also supported by some focal mechanisms with extensional kinematics recorded on-land (see Figs. 4 and 7 in Kassaras et al., 2016). This extensional secondary system may accommodate deformation induced by a deep compressive fault system, whose orientation remains still to be determined, or may result by a local extensional stress field controlled by gravitational instability, suggested by the large slump and morphological steps along the slope (Figs. 1B, 3 and 4).

Conclusions

The new geophysical data, including high-resolution and high-penetration multichannel seismic data and high-resolution swath bathymetry, allowed us to map the anatomy of the Cephalonia Transform Fault system in its southern sector and deformation affecting the slope to south of Zakynthos. We studied the sediment deformation patterns at the intersection between the Cephalonia strike-slip fault and the thrust fronts of the Hellenic System revealing a larger system and more complex structure than anticipated from previous works. The main outcome of the present work is a new morpho-structural map of Cephalonia and Zakynthos offshore. South of Cephalonia Island, the CTF "widens" to a 25 km-wide system of splays composed of elongated sigmoidal, positive-flower structures, possibly merging at depth into a single strike-slip fault. To west of Cephalonia Island, CTF narrows into a 6 km-wide strike-slip structure. Our data supports a dominant strike-slip kinematics with compressive component of the CTF. South of Zakynthos, the tectonic regime in the shallow sediments is dominated by extension, possibly representing a secondary tectonic system controlled by a local extensional stress field associated with a gravitational instability.

Acknowledgements

Seismic data interpretation was carried out using the Kingdom Suite software (S&P Global), freely available under the S&P Global University Grant Program. Geophysical data were collected during the IONIANS cruise supported by internal CNR funding (https://www.ismar.cnr.it/web-content/rapporto-tecnico-n-11/) and aboard of the R/V L. Bassi – INOGS during POSEIDON cruise supported by the Eurofleet+ program (http://eurofleet.maris2.nl/cds-report/25). The open source for seismological data is https://www.gein.noa.gr/en/services-products/earthquake-catalogs/

References

Ganas, A., Briole, P., Bozionelos, G., Barberopoulou, A., Elias, P., Tsironi, V., Valkaniotis S., Moshou A., Mintourakis, I., 2020. The 25 October 2018 Mw= 6.7 Zakynthos earthquake (Ionian Sea, Greece): A low-angle fault model based on GNSS data, relocated seismicity, small tsunami and implications for the seismic hazard in the west Hellenic Arc. Journal of Geodynamics, 137, 101731. https://doi.org/10.1016/j.jog.2020.101731

Ganas, A., Oikonomou, I.A., Tsimi, C. 2013. NOAfaults: a digital database for active faults in Greece, *Bull. Geological Society of Greece 47* (2), 518–530. https://doi.org/10.12681/bgsg.11079 .

Ganas, A., Tsironi, V., Kollia, E., Delagas, M., Tsimi, C., Oikonomou, A. 2018. Recent upgrades of the NOA database of active faults in Greece (NOAFAULTs), In: Proceedings of the 19th *General Assembly of WEGENER*, pp. 10–13. Grenoble, France.

Kassaras, I., Kapetanidis, V., Karakonstantis, A. 2016. On the spatial distribution of seismicity and the 3D tectonic stress field in western Greece, *Physics and Chemistry of the Earth, 95*, 50–72. https://doi.org/10.1016/j.pce.2016.03.012 .

Loreto, M. F., Zitellini, N., Ranero, C. R., Palmiotto, C., & Prada, M. 2021. Extensional tectonics during the Tyrrhenian back□arc basin formation and a new morpho□tectonic map. *Basin Research*, *33*(1), 138-158.

Louvari, E., Kiratzi, A. A., & Papazachos, B. C. 1999. The Cephalonia transform fault and its extension to western Lefkada Island (Greece). Tectonophysics, 308(1-2), 223-236.

Papadimitriou, P., Chousianitis, K., Agalos, A., Moshou, A., Lagios, E., & Makropoulos, K. 2012. The spatially extended 2006 April Zakynthos (Ionian Islands, Greece) seismic sequence and evidence for stress transfer. *Geophysical Journal International*, *190*(2), 1025-1040.

Papadimitriou, P., Kapetanidis, V., Karakonstantis, A., Spingos, I., Pavlou, K., Kaviris, G., ... & Voulgaris, N. 2021. The 25 October 2018 Zakynthos (Greece) earthquake: seismic activity at the transition between a transform fault and a subduction zone. *Geophysical Journal International*, *225*(1), 15-36.

Sachpazi, M., Hirn, A., Clément, C., Haslinger, F., Laigle, M., Kissling, E., ... & Ansorge, J. 2000. Western Hellenic subduction and Cephalonia Transform: local earthquakes and plate transport and strain. Tectonophysics, 319(4), 301-319.

Tsironi, V., Ganas, A., Valkaniotis, S., Kouskouna, V., Sokos, E., Koukouvelas, I. 2024. Active shortening and aseismic slip along the Cephalonia Plate Boundary (Paliki Peninsula, Greece): Evidence from InSAR and GNSS data, *Tectonophysics, 884*, 230400. https://doi.org/10.1016/j.tecto.2024.230400

Wessel, P., Luis, J. F., Uieda, L., Scharroo, R., Wobbe, F., Smith, W. H. F., & Tian, D. 2019. The Generic Mapping Tools Version 6, *Geochemistry, Geophysics, Geosystems*, 20(11), 5556–5564. https://doi.org/10.1029/2019GC008515.

Woodcock, N. H., & Fischer, M. 1986. Strike-slip duplexes. *Journal of structural geology*, *8*(7), 725-735.

Woodcock, N. H., & Rickards, B. 2003. Transpressive duplex and flower structure: Dent fault system, NW England. *Journal of Structural Geology*, *25*(12), 1981-1992.

17th INTERNATIONAL CONGRESS of the Geological Society of Greece

BULLETIN OF THE GEOLOGICAL SOCIETY OF GREECE, SP. PUBL.

EXTENDED ABSTRACT 198

The Early Pleistocene vertebrate fauna of Vatera, Lesbos, Greece

George Lyras[1], Athanassios Athanassiou[2], Alexandra van der Geer[3], George Kontakiotis[1], Evangelia Besiou[1], Asimina Antonarakou[1]

(1) Department of Historical Geology-Paleontology, Faculty of Geology and Geoenvironment, School of Earth Sciences, National and Kapodistrian University of Athens, Panepistimiopolis, Zografou, 15784 Athens, Greece, glyras@geol.uoa.gr (2) Hellenic Ministry of Culture, Superintendence of Palaeoanthropology–Speleology, Athens, Greece (3) Naturalis Biodiversity Center, Leiden, the Netherlands.

Background and objectives

Fossil-rich areas are found around the area of Vatera near Vrissa, about 6 km south of the town Polichnitos in the southern region of Lesbos Island. Systematic excavations were conducted here between 1996 and 2007 (Lyras & van der Geer, 2007). Fossil remains from these excavations were deposited in a local museum, alongside fish fossils (Drinia *et al*., 2007) and plant remains (Mantzouka *et al*., 2013) collected from the broader Polichnitos area. This year, renewed interest in Vatera's fossil record has brought the University of Athens back to the region. This contribution aims to provide a context and rationale for the new project in the light of the current knowledge on the terrestrial vertebrate fossils discovered thus far at Vatera.

The Vatera sites and fauna

The terrestrial vertebrate fossils at Vatera were discovered within the fluvial deposits of the Vatera Formation. This formation comprises alternating layers of breccia-conglomerates, sandy clays, sandy conglomerates, and silt. A total of 630 vertebrate fossils have been recovered from seven sites (Figure 1), coded with E, F, DS, H, T, U, and V for the different sites. The mammalian fauna includes the papionine monkey *Paradolichopithecus arvernesis* (van der Geer & Sondaar, 2002), the raccoon dog *Nyctereutes megamastoides*, the badger *Meles thorali*, the scimitar-toothed cat cf. *Homotherium latidens*, the rhinoceros *Stephanorhinus* cf. *etruscus*, the gomphothere *Anancus arvernensis*, the southern mammoth *Mammuthus meridionalis*, the giraffid *Palaeotragus* cf. *inexspectatus*, the small Tegelen deer cf. *Metacervocerus rhenanus*, the antelope *Gazellospira torticornis*, and the large bovine *Leptobos* sp. (de Vos *et al*., 1997). Additional finds include two horse morphotypes: *Equus stenonis* and *Equus* sp. (Eisenmann, 2002), three species of gazelle (*Gazella aegaea*, *G.* cf. *bouvrainae*, and *G.* aff. *borbonica*) (Athanassiou, 2002), and birds. Furthermore, remains of the spur-thighed tortoise (*Testudo graeca*), and a giant tortoise (*Titanochelon* sp.) (de Lapparent de Broin, 2002) were also described.

The monkey of Vatera

Paradolichopithecus arvernensis is a large Old-World monkey. In morphology, it resembles macaques cranially but baboons postcranially (Szalay & Delson, 1979). Among the material thus far excavated at Vatera is a juvenile male mandible (van der Geer & Dermitzakis, 2008), an adult female mandible, an upper canine and, notably, several postcranial elements (van der Geer & Sondaar, 2002). This species is known from several European localities, including three in Greece (van der Geer & Sondaar, 2002; Kostopoulos *et al*., 2018; Sianis *et al*., 2023). However, significant insights into its postcranial morphology are provided by only two sites: Vatera and Valea Grăunceanului (Romania). The postcranial elements suggest that *Paradolichopithecus* was a highly terrestrial monkey, exhibiting a notable frequency of bipedalism in its daily locomotor behavior (Sondaar & van der Geer, 2002; Sondaar et al., 2006).

The giant tortoise of Vatera

A rare and exceptional find in the fauna of F-site is a sample of limb bones and osteoderms, which may belong to a single individual of a giant tortoise. The recovered skeletal elements represent a very large form with an estimated carapace length of approximately 186 cm, one of the largest individuals known in the fossil record (de Lapparent de Broin, 2002). Taxonomically, the giant tortoise from Vatera was originally referred to the species cf. *Cheirogaster* aff. *schafferi*. A recent revision of the fossil Testudines from Greek localities reclassified it to the genus *Titanochelon*, refraining from a species-level attribution (Vlachos, 2022). Given the current biochronological placement of F-site (see below), the Vatera form represents the last giant tortoise of Europe.

Palaeoenvironment and age

The presence of horses, a palaeotragine giraffe, and four bovid species indicates a relatively dry and open landscape. Additionally, the terrestrial characteristics observed in the postcranial elements of *Paradolichopithecus* further support

the idea of an open savanna /bushland environment. Based on the faunal composition the sites have been attributed to the biozone MN 17, or the Saint-Vallier Faunal Unit, or the Dafnero Faunal Unit (middle Villafranchian, earliest Pleistocene) (de Vos *et al*., 2002; Konidaris & Kostopoulos, 2024). However, the presence of two horse species is puzzling and may suggest that more than one faunal assemblage is represented at Vatera (Eisenmann, 2002).

Figure 1. Location of the fossil sites of the Vatera Formation

Conclusion and future work

Vatera is a key locality, because here the remains of two rare and puzzling creatures have been found together: the highly terrestrial macaque *Paradolichopithecus arvenensis* and the giant tortoise *Titanochelon sp.*, one of the largest tortoises in the world. Our future work will focus on reconstructing in detail (a) the stratigraphy of the Vatera sites, (b) the relation between the individual sites, and (c) the palaeoenvironment(s) of Vatera, in order to build a robust local biochronological–biostratigraphic scheme that can be integrated in the broader Eurasian context.

Acknowledgements

We are thankful to Michael Dermitzakis, Konstandinos Taxidis, John de Vos, Jan van der Made and the late Paul Sondaar for making the excavations and the research in Vatera possible.

References

Athanassiou, A., 2002. A new gazelle species (Artiodactyla, Bovidae) from the Late Pliocene of Greece. Annales Géologiques des Pays Helléniques 39, 299-310.

Drinia, H., Dermitzakis M.D., Kouli, K., Tsourou, T., 2002. Sedimentary facies analysis and paleoenvironmental interpretation of Vatera Formation, Lesvos Island, Greece. Annales Géologiques des Pays Helléniques 39, 15-35.

De Lapparent de Broin, F., 2002. A giant tortoise from the late Pliocene of Lesvos Island (Greece) and its possible relationships. Annales Géologiques des Pays Helléniques 39, 99-130.

De Vos, J., van der Made, J., Athanassiou, A., Lyras, G., Sondaar, P., Dermitzakis, M.D., 2002. Preliminary note on the Late Pliocene fauna from Vatera (Lesvos, Greece). Annales Géologiques des Pays Helléniques 39, 37-70.

Eisenmann, V., 2002. The primitive horses of the Vatera formation (Lesvos). Annales Géologiques des Pays Helléniques 39, 131-153.

Konidaris, G.E., Kostopoulos, D.S., 2024. The Late Pliocene–Middle Pleistocene Large Mammal Faunal Units of Greece, Quaternary, 7(2), 27.

Kostopoulos, D.S., Guy, F., Kynigopoulou, Z., Koufos, G.D., Valentin, X., Merceron, G., 2018. A 2Ma old baboon-like monkey from Northern Greece and new evidence to support the *Paradolichopithecus* – *Procynocephalus* synonymy (Primates: Cercopithecidae). Journal of Human Evolution 121, 178-192.

Lyras, G.A., van der Geer, A.A.E., 2007. The Late Pliocene vertebrate fauna of Vatera (Lesvos Island, Greece). Cranium 24 (2), 11-24.

Mantzouka, D., Sakala, J., Kvaček, Z., Karakitsios, V., 2013. Palaeobotanical study of Polichnitos region, southern part of Lesbos island, Greece (preliminary results on angiosperm wood). Proceedings of the 13th International Congress of the Geological Society of Greece, Chania, Sept. 2013, Bulletin of the Geological Society of Greece, 47 (1), 204-015.

Sianis, P.D., Athanassiou A., Kostopoulos D.D., Roussiakis, S., Kargopoulos, N., Iliopoulos, G., 2023. The remains of a large

cercopithecid from the Lower Pleistocene locality of Karnezeika (southern Greece). Earth and Environmental Science Transactions of the Royal Society of Edinburgh 114 (sp. issue 1-2), 177-182.

Sondaar, P.Y., van der Geer, A.A.E., 2002. Arboreal and terrestrial traits as revealed by the primate ankle joint. Annales Géologiques des Pays Helléniques 39, 87-98.

Sondaar P.Y., van der Geer, A.A.E., Dermitzakis, M., 2006. The unique postcranial of the Old World monkey *Paradolichopithecus*: more similar to *Australopithecus* than to baboons. Hellenic Journal of Geosciences 41 (1), 19-28.

Szalay, F.S., Delson, E., 1979. Evolutionary history of the Primates. Academic Press.

Van der Geer, A.A.E., Dermitzakis, D.M., 2008. Dental eruption sequence in the Pliocene Papionini *Paradolichopithecus arvernensis* (Mammalia: Primates) from Greece. Journal of Vertebrate Paleontology 28 (4), 1238-1244.

Van der Geer, A.A.E., Sondaar, P.Y., 2002. The postcranial elements of *Paradolichopithecus arvernensis* (Primates, Cercopithecidae, Papionini) from Lesvos, Greece. Annales Géologiques des Pays Helléniques 39, 71-86.

Vlachos, E., 2022. The fossil record of turtles and tortoises (Reptilia: Testudines) in Greece, in Vlachos, E. (Ed.), Fossil Vertebrates of Greece, vol. 1: Basal Vertebrates, Amphibians, Reptiles, Afrotherians, Glires, and Primates, 245-281.

17th INTERNATIONAL CONGRESS of the Geological Society of Greece

BULLETIN OF THE GEOLOGICAL SOCIETY OF GREECE, SP. PUBL.

EXTENDED ABSTRACT 199

Assessing the impact of climate change on olive cultivation in the Peloponnese, Greece: A long-term analysis using climate indices

P. Machaira[1,2], E. Kostopoulou[2], M. Gratsea[1], G. Kitsara[1], C. Giannakopoulos[1]

(1) Institute for Environmental Research and Sustainable Development, National Observatory of Athens, Greece, p.machaira@noa.gr (2) Department of Geography, University of Aegean, Greece

Introduction

Climate change is expected to significantly impact olive cultivation in the Peloponnese, through rising temperatures and decreasing rainfall. Additionally, geological processes, such as soil erosion and changes in hydrological conditions, may intensify the effects of climate change on olive trees. This study aims to evaluate the long-term impacts of climate change on olive cultivation in the region, utilizing climate indices related to temperature and rainfall patterns.

The Peloponnese, a key olive-producing area, is particularly vulnerable to the combination of future climatic changes and geological processes, which could disrupt olive cultivation. Rising temperatures and shifts in rainfall patterns are anticipated to affect flowering dates, irrigation needs, and overall production. Changes in hydrological conditions and soil erosion may negatively affect soil quality and water absorption, further stressing cultivation. The reduction in winter rainfall is expected to negatively impact on olive yields, while an increase in hot days may influence the phenology of olive trees, leading to higher irrigation requirements.

Moreover, climate change, along with increased CO_2 concentrations, is expected to have extensive impacts on olive cultivation. These changes will affect water availability and distribution, pest and disease occurrences, and overall socio-economic development. Key variables likely to be most affected include the duration of phenological stages, crop evapotranspiration, irrigation demands, and biomass growth and yield. These projected changes underscore the importance of adapting agricultural practices to the new climatological and geological conditions to ensure the sustainability of olive oil production in the region.

Material and Methods

Study Area

The Mediterranean has been identified as a climate change "hot-spot" and the impacts are expected to be particularly intense (IPCC, 2021). This specific area is warming 20% faster than the global average (MedECC, 2020). The olive tree (Olea europaea L.) is one of the most significant crops in the Mediterranean basin, which accounts for almost 95% of the global olive oil production. It also holds considerable importance in the Peloponnese region, representing approximately 40% of Greece's olive production. The Peloponnese features a predominantly Mediterranean climate, characterized by mild, wet winters and hot, dry summers. However, significant climatic variation occurs with altitude. Coastal areas experience milder conditions, while mountainous regions, such as Arcadia, have lower temperatures and higher rainfall. These altitudinal gradient influences local agricultural practices, including olive cultivation.

Climate data

For this study, a three-member GCM-RCM sub-ensemble from the Euro-Cordex database (Jacob *et al*., 2014), with a horizontal resolution of 0.11° was used for the study area (Table 1). Daily climate data, including precipitation and temperature, were obtained for three climate periods: historical (1971-2000), near future (2031-2060), and distant future (2071-2100). These data were evaluated under two future emission scenarios: RCP4.5 (a medium mitigation scenario) an RCP8.5 (a high emissions scenario without climate mitigation policies) (Moss *et al*., 2010). The model data were validated against observational data from local meteorological stations, confirming its suitability for this study

Table 1. Three-member GCM-RCM sub-ensemble from the Euro-Cordex database.

Institute	Institute Code	Regional Climate Model (RCM)	Global Climate Model (GCM)	GCM, RCM Pair as Used
Swedish Meteorological and Hydrological Institute	SMHI	RCA4	MPI-ESM-LR	1.MPI-ESM-LR_r1i1pi_RCA4 rca4-mpi-lr
Swedish Meteorological and Hydrological Institute	SMHI	RCA4	HadGEM2-ES	2.HadGEM2-ES_r1i1pi_RCA4 rca4-mohc
Royal Netherlands Meteorological Institute, De Bilt, The Netherlands	KNMI	RACMO22E	HadGEM2-ES	2.HadGEM2-ES_r1i1pi_RACMO22E racmo22e-mohc

Climate indices

For the assessment of the impacts of climate change on olive cultivation, climatic indices based on temperature and precipitation were used. These indices were identified by agricultural sector scientists as appropriate for the olive sector within the framework of the MedGold project. The selection of these indices is in accordance with previous studies on the impact of climate change on olive cultivation in Mediterranean agricultural environments, such as research conducted in Andalusia (Gratsea *et al*., 2022). Specifically, the climatic indices used to assess the impacts of climate change on olive cultivation include the SPRTX index, which is related to the average maximum temperature during the spring months (April-May) and is considered the best indicator for the flowering period of olive trees, aiding in decisions regarding irrigation and management of the olive fruit fly (Perez-Lopez *et al.,* 2008). The SPR32 index, calculated as the number of days with Tmax >32° C in May and June, is linked to early flowering and increased pest and disease risk, providing crucial information for plant management and yield prediction (Ribeiro *et al.,* 2009). The SU38 and SU40 indices, representing the number of days with Tmax >38°C and Tmax >40°C, respectively, are associated with early olive ripening , influencing decisions on harvesting, pest control, and additional irrigation. Additionally, SU40 negatively affects the photosynthesis rate of olive trees (Garcia-Inza *et al.,* 2014). Finally, the WINRR index, which calculates total precipitation from October to May, is crucial for water availability and crop yield. Water deficits during winter and early spring have been shown to reduce yield, while also influencing soil management and long-term crop variety selection (Aissaoui *et al.,* 2016).

Results

Climate indices are essential for characterizing climate variability and investigating the impacts of climate change on olive crops. The effects of climate change on olive cultivation were assessed by analyzing the relationships between primary production, temperature, precipitation, and water availability. Water availability is critical before flowering, while temperature affects fruit development. High summer temperatures can damage fruit surfaces, accelerate ripening and affect overall yield. Climatic indices were calculated annually for three climate periods (historical period, near and distant future) under two emission scenarios (RCP4.5, RCP8.5), focusing on spatial distributions and mean differences. These simulations allow comparison of emission scenario impacts on olive crops and support future agricultural decisions.

Regarding the SPRTX index, it represents the average maximum temperature during spring (April–May), calculated as the mean of daily maximum temperatures between April 1 and May 31. It is a key indicator for olive tree flowering, linked to evapotranspiration and pest development. Warmer climates may accelerate flowering, potentially requiring new varieties or relocation to cooler areas. Higher temperatures will increase evapotranspiration, necessitating more irrigation. While pests and diseases may rise, the olive fly is expected to decrease. In the Peloponnese, the average increase for the near future is about 2°C for RCP4.5 and 3°C for RCP8.5, and for the distant future, 3°C and 5°C, respectively (Figure 1). Similar results were observed by Fraga et al. (2019) for the average temperature of the growing season in the Peloponnese.

Concerning the SPR32 index, it refers to the number of spring days (May and June) with Tmax >32° C. It is linked to early flowering, increasing the risk of pests and diseases (Ribeiro *et al.,* 2009). Rising temperatures will impact flowering and necessitate adjustments in cultivation practices. At temperatures above 35° C, stomatal closure hinders crop growth and productivity (Mavromatis *et al*., 2022). Adaptations such as improved soil management, pruning and increased irrigation during spring will be essential for olive cultivation. Based on the RCP8.5 scenario, the greatest increase in the number of spring days with Tmax >32° C is projected for the distant future (Figure 2), consistent with Mavromatis *et al*. (2022). Specifically, an additional 10 and 14 days with Tmax >32° C per year are projected for the near future under RCP4.5 and RCP8.5, respectively, and 12 and 24 days for the distant future.

The SU38 and SU40 indices represent the number of summer (June, July, August) days with Tmax >38° C and Tmax >40° C, respectively. They are calculated as the annual number of days exceeding these temperature thresholds. Increases in these indices are linked to earlier olive ripening (Garcia-Inza *et al.,* 2014). Notably, SU40 is associated with reduced photosynthetic capacity due to heat stress. Olive production is negatively affected by summer drought, as this is when fruit formation and growth occur (Mavromatis *et al*., 2022). Mitigation measures include adjusting harvest timing, pest control treatments and additional irrigation to support plant resilience. The number of summer days with maximum temperatures exceeding 38° C is expected to increase. The most significant rise is projected for the distant future under the RCP8.5 scenario (Figure 3). Specifically, for the near future, an additional 10 (RCP4.5) and 13 (RCP8.5) days per year are anticipated, while for the distant future, the increase is projected at approximately 15 (RCP4.5) and 40 (RCP8.5) additional days per year, mainly impacting coastal zones. Extreme heat stress, as indicated by the SU40 index, is projected to increase during summer months. The largest rise is expected under the RCP8.5 scenario in the distant future (Figure 4). Average increases for the near future are about 3 (RCP4.5) and 4 (RCP8.5) additional days per year, while for the distant future, the SU40 index is projected to rise by approximately 5 (RCP4.5) and 22 (RCP8.5) additional days annually. Similar to the SU38 index, these changes will primarily impact coastal areas.

Regarding the WINRR index, it refers to the total rainfall from October to May and is closely related to crop yield, as water availability is a crucial factor for the physiological activity of olive trees (Aissaoui *et al.,* 2016). Negative impacts of reduced winter rainfall include increased irrigation demands, decreased water availability due to prolonged droughts, changes in soil

fertility and higher risks of soil erosion associated with droughts and extreme precipitation variability. Projected reductions during winter and early spring are significant for decision-making related to crop yield, soil management and long-term changes in crop varieties (Gratsea *et al*., 2022). The WINRR index is projected to decline in both the near and distant future. The most significant reductions are expected on the western side of the Peloponnese, with largest decreases projected under the RCP8.5 scenario (Figure 5), consistent with Fraga *et al.* (2019). Specifically, for the near future, average reductions are estimated at 9% (RCP4.5) and 16% (RCP8.5). The greatest declines (>20%) are projected for southern-western Peloponnese (Messenia), while the north-eastern regions (Corinthia) may experience smaller reductions (5-10%).

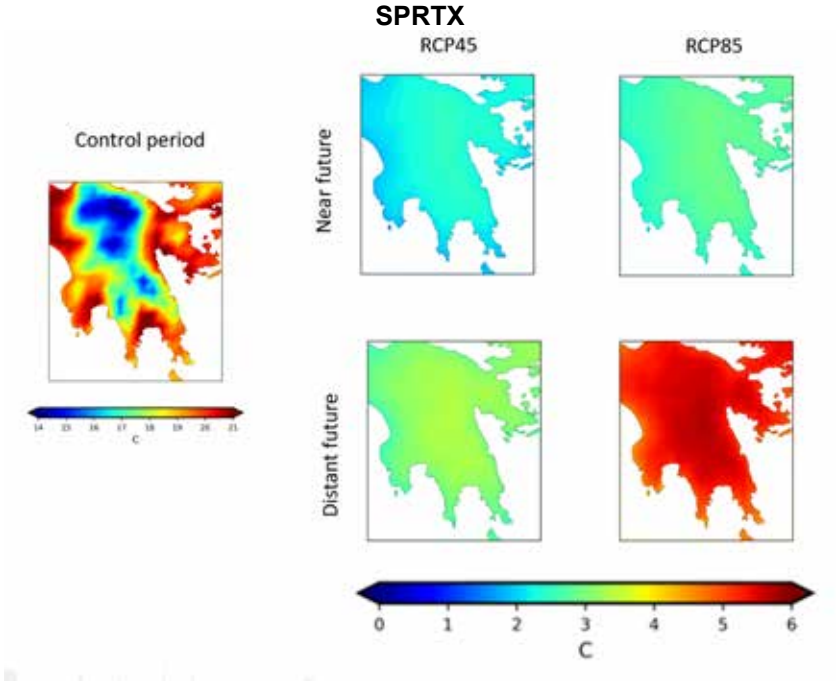

Figure 1. Absolute differences of spring (April-May) maximum temperature, between the reference period and the near or distant for two climate scenarios (RCP4.5, RCP8.5)

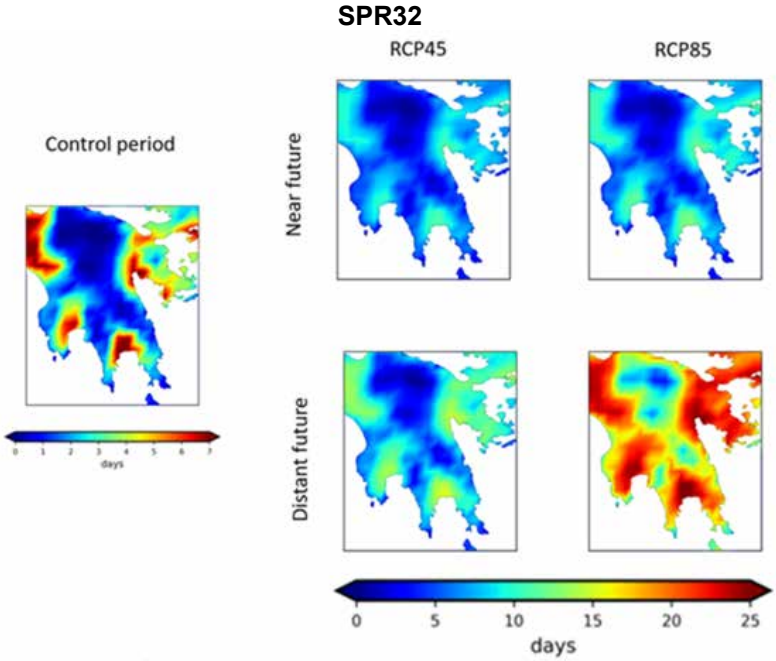

Figure 2. Absolute differences of the number of spring heat days (Tmax>32°C), between the reference period and the near or distant for two climate scenarios (RCP4.5, RCP8.5)

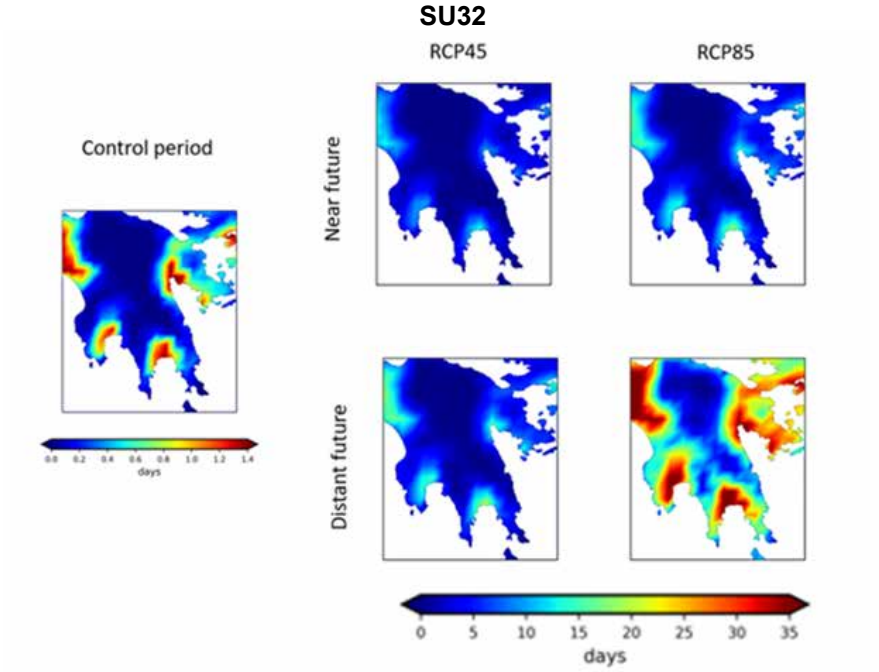

Figure 3. Absolute differences of the number of summer heat days (Tmax>38°C), between the reference period and the near or distant for two climate scenarios (RCP4.5, RCP8.5)

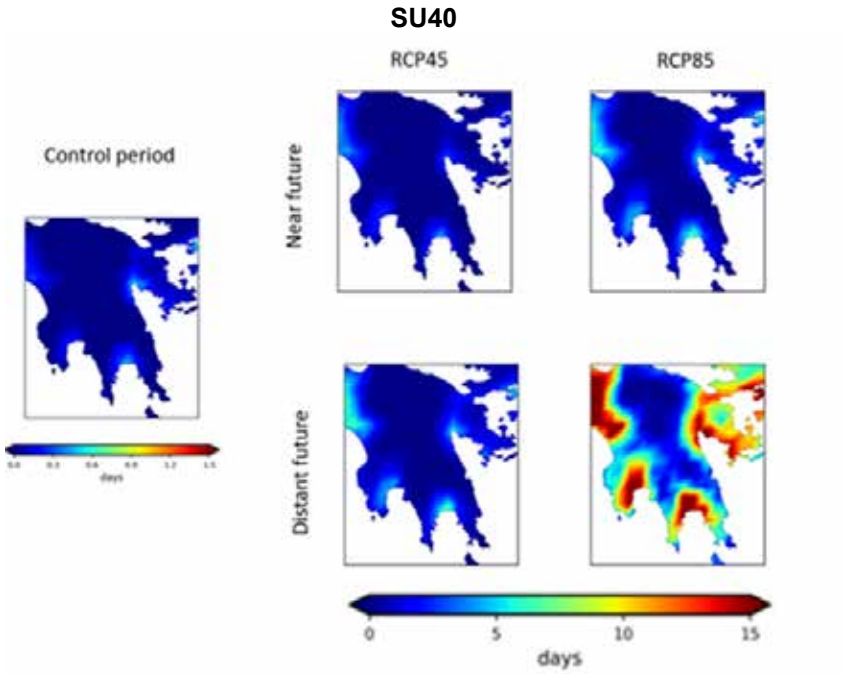

Figure 4. Absolute differences of the number of summer heat days (Tmax>40°C), between the reference period and the near or distant for two climate scenarios (RCP4.5, RCP8.5)

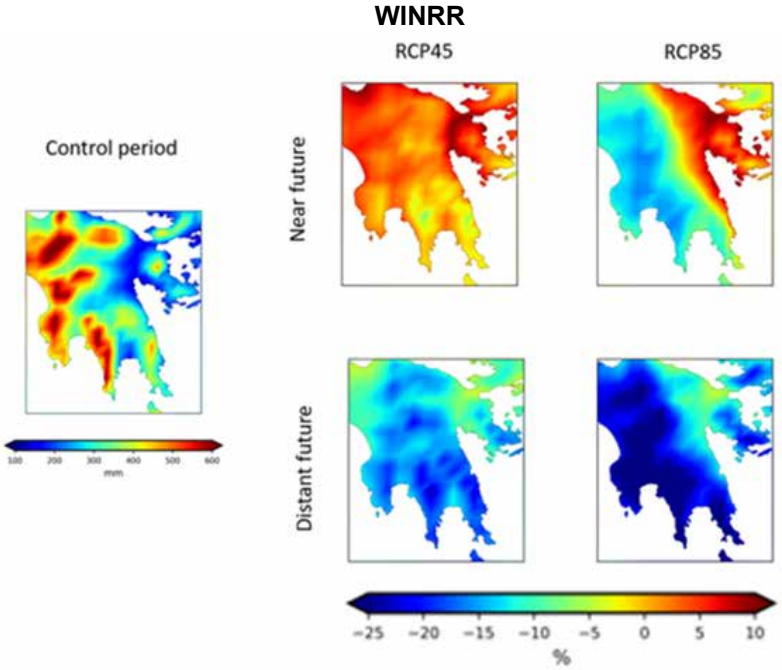

Figure 5. : Relative differences for total winter (Oct-May) precipitation, between the reference period and the near or distant for two climate scenarios (RCP4.5, RCP8.5)

Conclusions

The assessment of climate change impacts on olive cultivation in the Peloponnese, using adapted climate indices highlights significant future challenges. Temperature-related indices, SPRTX and SPR32, show projected increases, indicating accelerated flowering, particularly in coastal areas. Mitigation measures include introducing olive varieties with lower chilling requirements, relocating cultivation to cooler regions, enhancing irrigation and adopting soil conservation practices. Elevated summer temperatures, linked to the SU40 index, are expected to reduce fruit weight (Garcia-Inza *et al.,* 2014), and photosynthetic capacity, particularly in erosion-prone coastal areas, emphasizing the need for additional irrigation and land management strategies. The WINRR index, associated with winter precipitation, is crucial for olive yield. Projected reductions, exceeding 20% in the south-western Peloponnese, highlight the need for integrated water and soil management to sustain cultivation under evolving climatic and geological conditions. Based on these projections, the cultivation requirements of olive trees will change, requiring adaptation to future climate conditions. High temperatures are expected to negatively impact growth and, consequently, productivity. Adaptation strategies will include modifying cultivation practices and land management practices introducing olive varieties with lower chilling requirements or relocating production to cooler areas may become necessary. Water availability is critical during pre-flowering stages (Aissaoui et al., 2016), and reduced annual rainfall is expected to increase water demand. Effective management of soil fertility and optimized irrigation practices will be crucial for sustaining olive cultivation, ensuring both productivity and resilience under changing climatic conditions.

The overall impact of climate change on the expected yields of olive cultivation is expected to be negative, primarily due to rising temperatures and decreasing rainfall. Elevated temperatures are expected to cause heat stress on crops, negatively impacting their growth and development. Heatwaves can damage sensitive crops, reduce yields, and affect the quality of olive products. Additionally, climate change is likely to alter rainfall patterns, potentially leading to droughts and fluctuations in soil moisture levels, which will affect crop growth and irrigation needs. As a result, agricultural production is projected to decline, with an increased risk of diseases and pests. Moreover, the growing frequency and intensity of extreme weather events may cause significant damage to olive trees and their production. Consequently, climate change is expected to affect the dynamics of olive cultivation, with the projected yield losses leading to significant changes in the sector's economy across the Peloponnese, potentially resulting in social impacts.

Short-term adaptation strategies in olive cultivation aim to mitigate the immediate impacts of climate change. Improved water resource management through efficient irrigation systems, the implementation of early warning systems for diseases, and the adoption of sustainable agricultural practices contribute to maintaining productivity.

Additionally, farmers' access to climate information enables the adjustment of cultivation practices to changing conditions, enhancing the sector's sustainability. These strategies provide immediately applicable solutions which, in combination with long-term interventions, can significantly contribute to preserving the productivity and quality of olive production.

Acknowledgements
We acknowledge the use of data from the Copernicus Climate Change Service (C3S) and the Climate Data Store (CDS), specifically the CORDEX-EUR-11 climate model data.

References

Aissaoui, F., Chehab, H., Bader, B., Salem, A. B., M'barki, N., Laamari, S., Chihaoui, B., Mahjoub, Z. and Boujnah, D., 2016. Early water stress detection on olive trees (Olea europaea L. cvs "chemlali" and "Chetoui") using the leaf patch clamp pressure probe. Computers and Electronics in Agriculture, 131, 20–28. doi:10.1016/j.compag.2016.11.007.

Fraga, H., Pinto, J. G., Viola, F. and Santos, J. A., 2019. Climate change projections for olive yields in the Mediterranean Basin. International Journal of Climatology. doi:10.1002/joc.6237.

García-Inza, G. P., Castro, D. N., Hall, A. J., and Rousseaux, M. C., 2014. Responses to temperature of fruit dry weight, oil concentration, and oil fatty acid composition in olive (Olea europaea L. var. "Arauco"). European Journal of Agronomy, 54, 107–115. doi:10.1016/j.eja.2013.12.005.

Gratsea, M., Varotsos, K. V., López-Nevado, J., López-Feria, S. and Giannakopoulos, C., 2022. Assessing the Long-Term Impact of Climate Change on Olive Crops and Olive Fly in Andalusia, Spain, through Climate Indices and Return Period Analysis. Climate Services, vol. 28, no. October, https://doi.org/10.1016/j.cliser.2022.100325.

IPCC, 2021: Climate Change 2021. The Physical Science Basis. Contribution of Working Group I to the Sixth Assessment Report of the Intergovernmental Panel on Climate Change [Masson-Delmotte, V., et al.]. Cambridge University Press, Cambridge, United Kingdom and New York, NY, USA, 2391 pp.

Jacob, D., Petersen, J., Eggert, B., Alias, A., Christensen, O.B., Bouwer, L.M., Braun, A., Colette, A., Déqué, M.; Georgievski, G., et al., 2014. EURO-CORDEX: New high-resolution climate change projections for European impact research. Reg Environ. Change 14, 563–578.

Mavromatis, T., Georgoulias, A. K., Akritidis, D., Melas, D. and Zanis, P., 2022. Spatiotemporal Evolution of Seasonal Crop-Specific Climatic Indices under Climate Change in Greece Based on EURO-CORDEX RCM Simulations. Sustainability, 14, 17048. https://doi.org/10.3390/ su142417048.

MedECC, 2020. Climate and Environmental Change in the Mediterranean Basin – Current Situation and Risks for the Future. First Mediterranean Assessment Report [Cramer, W., Guiot, J., Marini, K. (eds.)]. Union for the Mediterranean, Plan Bleu, UNEP/MAP, Marseille, France, 632 pp., ISBN: 978-2-9577416-0-1.

Moss, R.H., Edmonds, J.A., Hibbard, K.A., Manning, M.R., Rose, S.K., Van Vuuren, D.P., Carter, T.R., Emori, S., Kainuma, M., Kram, T., 2010. The next generation of scenarios for climate change research and assessment. Nature 463, 747–756.

Pérez-López, D., Ribas, F., Moriana, A., Rapoport, H. F., & De Juan, A., 2008. Influence of temperature on the growth and development of olive (Olea europaea L.) trees. The Journal of Horticultural Science and Biotechnology, 83(2), 171–176. https://doi.org/10.1080/14620316.2008.11512366.

Ribeiro, H., Abreu, L. and Cunha, M., 2009. A bioclimatic model for forecasting olive yield. Journal of Agricultural Science 147, 647–656, https://doi.org/10.1017/ s0021859609990256.

17th INTERNATIONAL CONGRESS of the Geological Society of Greece

BULLETIN OF THE GEOLOGICAL SOCIETY OF GREECE, SP. PUBL.

EXTENDED ABSTRACT 200

A WebGIS platform for the multiparametric monitoring of ground deformation and critical infrastructures under the name PROION

Efthymios Magkoufis[1], Athanassios Ganas[2], Konstantinos Nikolakopoulos[3], Betty (Vasiliki) Charalampopoulou[1]

(1) Geosystems Hellas S.A., 11632 Athens, Greece, e.magkoufis@geosystems-hellas.gr

(2) Institute of Geodynamics, National Observatory of Athens, 11810 Athens, Greece, aganas@gein.noa.gr

(3) Department of Geology, University of Patras, 26504 Patra, Greece, knikolakop@upatras.gr

Introduction

Both the modern human-made and natural environment face numerous challenges and risks that have direct and indirect consequences on their sustainability and security. Climate change, combined with the accumulated pressures, ageing infrastructure, and the impact of natural hazards, contributes to the rising frequency of phenomena and events that demand effective and intelligent responses (Kyriou *et al.*, 2023). In this context, the need for a modern, multiparametric framework to monitor and provide up-to-date information on the pressures affecting both the environment and critical infrastructure led to the proposal and successful implementation of the research project, "PROION". The project was based on innovative technologies and methodologies that make use of the latest available infrastructure and development tools. From the perspective of optimal observation of critical infrastructure and the surrounding physical environment, the PROION project aimed to acquire, process, organise and make available measurement data both through the use of in-situ sensors and free satellite products that provide valuable information on the ground deformation, as well as the stability of critical infrastructure. Receiving co-funding from the European Union and the Greek Government, PROION (T2EDK-02396) was invited to implement its vision in the region of Achaia (Fig. 1), part of the Enceladus Hellenic Supersite (EHS).

Methodology

The three main study areas were, i) the building of the Department of Geology at the University of Patras campus, ii) the Asterion dam and iii) an active landslide that includes the boundaries of the mountainous settlement of Krini.

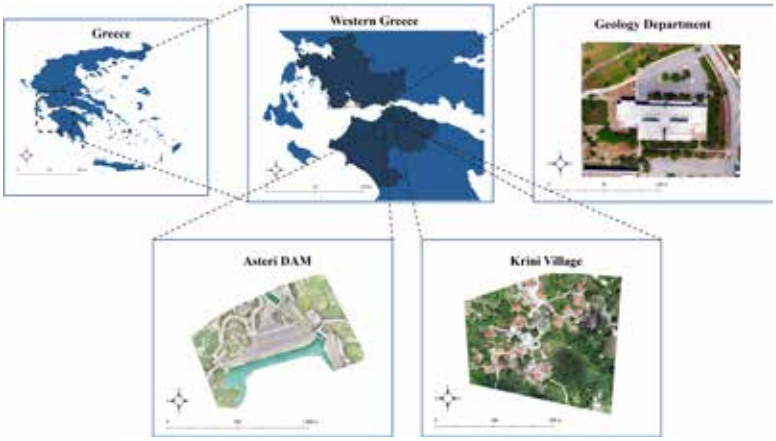

Figure 1. The three sites selected for monitoring in the framework of the PROION project.

In addition, in order to provide the best quality of the final ground displacement products, three SAR triangular aperture reflectors were designed, constructed and installed in the project study areas. For the observation of the study areas, SAR satellite data from the European Sentinel-1 space mission (Tsironi et al. 2022) as well as low-cost GNSS (Ganas *et al.*, 2024) in-situ sensors and accelerometers were used to record local micro-vibrations and seismic events in a timely and accurate manner (Nikolakopoulos *et al.*, 2023). With the acquisition of the multidimensional observations, the InSAR interferometry method was exploited to produce time-series of displacements with 6-12 days repeatability, while GNSS measurements were used to observe the 3-D change in the precise position of the ground and reflectors. In order to accurately render and observe the study areas, regular mapping of these areas was carried out using TLS and UAVs to produce point clouds of high geometric accuracy (Nikolakopoulos *et al.*, 2023). Subsequently, aiming to fully exploit the available information, fuzzy logic algorithms capable of adapting to the temporal behaviour of the observed points and ultimately achieving accurate predictions of their future position were developed. The following graphs (Fig. 2) illustrate the GNSS measurements of the Department of Geology station, acquired and processed for the period of July 2022 to December 2024.

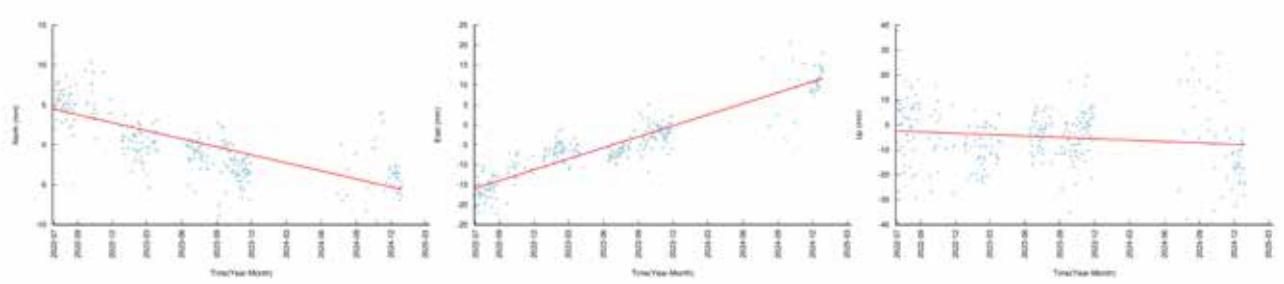

Figure 2. The GNSS measurements of the Department of Geology station from July 2022 to December 2024.

For the success of the overall system, a geospatial database was created both for the organisation and storage of the collected observations and for the subsequent retrieval of these through the compilation of complex spatio-temporal queries. The need for a powerful high-performance relational database led to the use of PostgreSQL with PostGIS software extension to manage spatial information and optimally retrieve it by applying specialised techniques such as spatial indexing (Ďuračiová *et al.*, 2018).

WebGIS platform

Subsequently, to offer an integrated framework for the disposal and visualisation of the generated data, a modern WebGIS platform for multiparametric monitoring was designed and implemented following the most advanced technological standards and specifications. Utilising cutting-edge technologies and modern libraries for the development of web-based geographic information systems, such as Mapbox GL JS, Deck GL, React JS, Chart.js, Flask, etc., a web platform capable of retrieving, managing and visualising spatially and diagrammatically the generated project data in an optimal and user-friendly way was developed. The platform was developed in Software-as-a-Service (SaaS) architectural standard (Capodiferro, *et al.*, 2024), offering easy access and interaction, also achieving easy maintenance and deployment both throughout the project and after its completion. Recognising the advantages of using 3D data visualisation methods for maximum understanding of the projected information, the Mapbox GL JS library was chosen (Zunino *et al.*, 2020), achieving the most complete 3D representation of the observed information through its direct correlation with the topography and morphology of the wider area (Fig. 3).

Figure 3. Illustration of the possibilities for end-user interaction and visualisation with the provided datasets in a cartographic environment. Coloured dots represent Copernicus SAR data (Sentinel-1 time series).

In addition, the platform offers tools for spatio-temporal analysis of longitudinal observations, geospatial data overlay as well as near real-time earthquake epicentres, achieving optimal monitoring of areas of high interest. Finally, in pursuit of a more complete user experience, the Deck GL library was exploited to represent cloud points within the cartographic environment, offering an additional dimension to the observation and understanding of the specific conditions governing each area and infrastructure of interest (Fig. 4), through direct spatial correlation with the ground deformation, geology and seismic phenomena that may occur within or near them.

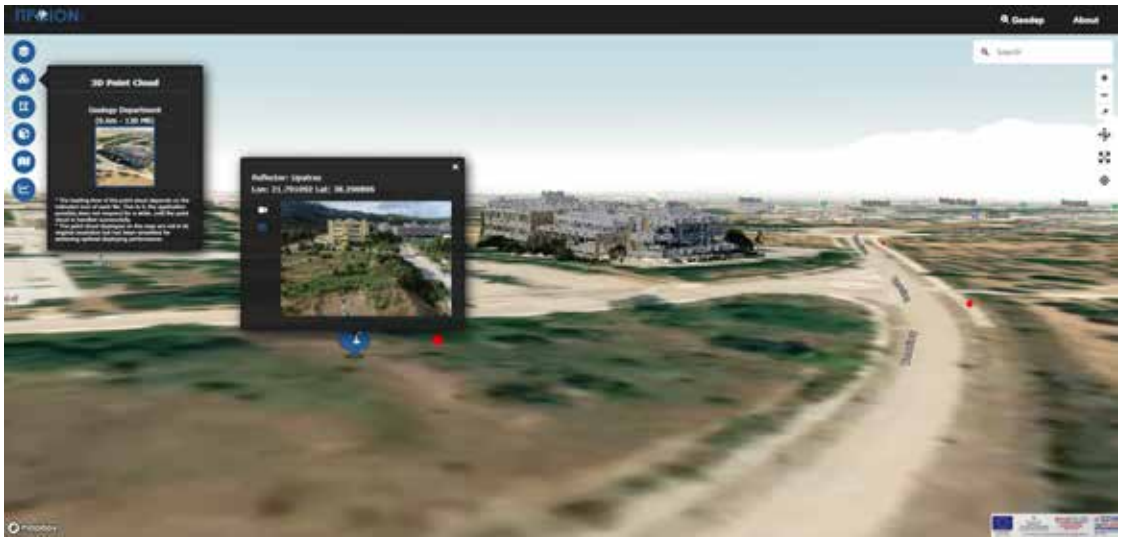

Figure 4. The point cloud of the Department of Geology on the 3D map environment.

Platform Accessibility and Future Prospects

The PROION's WebGIS platform, developed through this project, represents a significant advancement in presenting and analysing ground deformation data to end users. Considering the sensitive insights provided by the platform and the commercialisation of the overall product, the accessibility of the platform remains strict, allowing only authorised users to access the provided data. Therefore, interested parties are able to request access to an online demo of the platform by contacting the authors of the current publication directly via the provided e-mails. Furthermore, the platform shows strong potential for integration into future scientific research or operational monitoring systems, particularly in critical infrastructures and geohazard-prone regions. Its adaptability and scalability could support ongoing efforts in early warning and near-real-time infrastructure monitoring, while further integration of Machine Learning techniques has been explored to expand the current capabilities, aiming to serve as a supporting tool for data-driven decision-making.

Results and Conclusions

The successful implementation of the PROION project and the development of the WebGIS platform have resulted in the provision of a highly relevant system for the monitoring and evaluation of the longitudinal territorial behaviour and mobility of the areas of high interest. In conclusion, the continuous evolution of Remote Sensing and the creation of new and more powerful software technologies extend the possibilities of designing and implementing a sophisticated tool of higher performance and greater added value for the shielding of Greek territory.

Acknowledgements

This research has been co□financed by the European Regional Development Fund of the European Union and Greek national funds through the Operational Program Competitiveness, Entrepreneurship and Innovation, under the call RESEARCH – CREATE – INNOVATE (project code: T2EΔK-02396 Multiparametric monitoring platform with micro-sensors of eNceladus hellenIc supersite).

References

Capodiferro, C., De Maria, M., Mazzei, M., Spreafico, M., Bik, O.V., Palma, A.L., Solovyeva, A.V., 2024. Cultural itineraries generated by smart data on the Web. ISPRS Int. J. Geo-Inf. 13(2), 47.

Ďuračiová, R., Faixová Chalachanová, J., 2018. Fuzzy spatio-temporal querying the PostgreSQL/PostGIS database for multiple criteria decision making. In: Lecture Notes in Geoinformation and Cartography, Springer International Publishing, pp. 81-97.

Ganas, A., Mavropoulos, G., Karamitros, I., Nikolakopoulos, K., Charalampopoulou, V., Anastasiou, D., Athanassopoulos, T., Kyriou, A., Tsironi, V., 2024. A new low-cost GNSS instrument for monitoring of ground motions and critical infrastructures within the Greek "Supersite." EGU General Assembly 2024, Vienna, Austria, 14–19 Apr 2024, EGU24-10188, https://doi.org/10.5194/egusphere-egu24-10188

Kraak, M.-J., Ormeling, F., 2023. Cartography: Visualization of Geospatial Data, Fourth Edition, 4th ed. CRC Press, London, England.

Kyriou, A., Mpelogianni, V., Nikolakopoulos, K., Groumpos, P., 2023. Review of Remote Sensing Approaches and Soft

Computing for Infrastructure Monitoring. Geomatics 3, 367-392.

Nikolakopoulos, K., Kyriou, A., Sokos, E., Bousias, S., Strepelias, E., Groumpos, P., Mpelogianni, V., Roumelioti, Z., Serpetsidaki, A., Paliatsas, D., Ganas, A., Charalampoulou, V. (Betty), Athanasopoulos, T., 2023. Synergy of accelerometer, GNSS, InSAR and TLS measurements in the light of PROION Project.

Nikolakopoulos, K.G., Kyriou, A., 2023. Creation of 3D infrastructure model from UAV and TLS data in the frame of PROION project. In: Themistocleous, K., Michaelides, S., Hadjimitsis, D.G., Papadavid, G. (Eds.), Ninth International Conference on Remote Sensing and Geoinformation of the Environment (RSCy2023). SPIE, p. 10.

Tsironi, V., Ganas, A., Karamitros, I., Efstathiou, E., Koukouvelas, I., Sokos, E. 2022. Kinematics of Active Landslides in Achaia (Peloponnese, Greece) through InSAR Time Series Analysis and Relation to Rainfall Patterns. Remote Sens., 14(4), 844. https://doi.org/10.3390/rs14040844

Zunino, A., Velázquez, G., Celemín, J., Mateos, C., Hirsch, M., Rodriguez, J., 2020. Evaluating the performance of three popular Web mapping libraries: A case study using Argentina's life quality index. ISPRS Int. J. Geo-Inf. 9(10), 563.

17th INTERNATIONAL CONGRESS of the Geological Society of Greece

BULLETIN OF THE GEOLOGICAL SOCIETY OF GREECE, SP. PUBL.

EXTENDED ABSTRACT 201

An example of DsGSDs in Abruzzo Region (Central Italy): the complex case of Civitella del Tronto

Mangifesta M.[1], Scalella G.[2], Sciarra N.[1]

(1) Science Department, University of Chieti-Pescara, 66100 Chieti, Italy, mmangifesta@unich.it

(2) Special Office for the Reconstruction-Earthquake 2016 Extraordinary Commissary, Bureau of the Council of Ministers, 00187 Rome, Italy

Abstract

Deep gravitational slope deformations (DsGSDs) are geological and engineering challenge with important implications for slope stability, reliability of existing infrastructures, land use and, above all, the safety of settlements. This work focuses on the DsGSD (Cappadonia *et. al.,* 2024) phenomenon that affects a large part of the Borrano hamlet, located in the municipality of Civitella del Tronto (Teramo, Abruzzo, Italy). In the area a monoclinal structure of the Laga Formation (Casero *et. al.* 2006) is present, with dips towards the north-east (Artoni, 2013). The terrigenous fill sediments were generated by turbiditic currents, creating characteristic stratified deposits. The deposits consist mainly of marly clays and clayey marls alternating with pelitic-arenaceous intervals with a thickness of about 1500 m. They are characterised by structures elongated in a north-south direction to the east of the main carbonate-covered fronts of the Central Apennine chain. This process is visible within the Teramo Flysch (Artoni, 2003), where two distinct lithostratigraphic units can be observed (figure 1):

- Arenaceous facies: the structural framework shows a trending monocline, with dips ranging from 38° to 60°. The arenaceous component increases the resistance to erosion, allowing these formations to define the geological subsoil.
- Pelitic facies: they are constituted by marly clays, with intercalations of thin layer arenaceous; the structural arrangement follows that of the predominantly arenaceous interval (higher stiffness), with the direction of the layers approximately N-N-E, but with extremely variable dip of the layers.

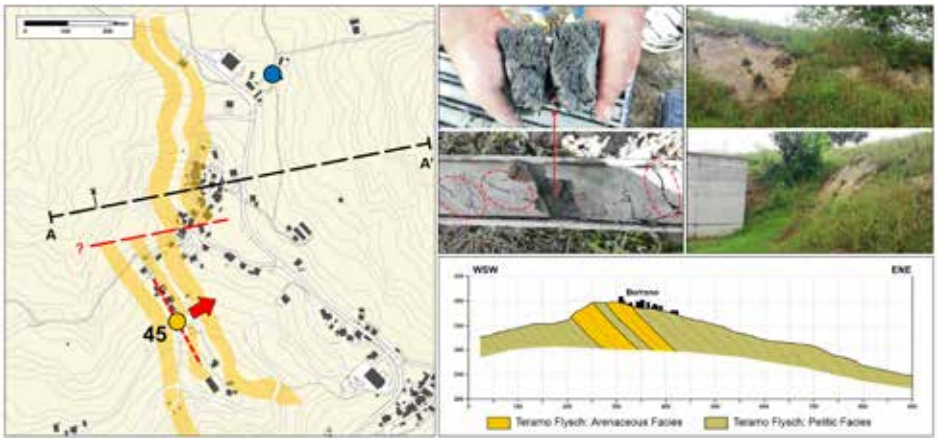

Figure 1. Detail of the Teramo Flysch in predominantly pelitic facies identified in the drill hole at depths of over 30 metres.

In the Borrano area, the identified landslides are of variable extension and mainly consist of slow movements of roto-translative type. The study of the area was carried out using aerial-photographs and Lidar data (Höfle *et al.,* 2011, Gaidzik *e. al.,* 2017) to identify shapes and structural features. The morphology of the terrain, shaped over time by geological processes, reflects the lithological nature of the materials present. The analysis showed that the slopes in the study area are dominated by values between 10° and 30°, with only a few local parts exceeding this range, and the energy of the survey is useful for identifying areas of greater erosion potential and instability. Following the seismic events of 2016/2017, the Borrano area was subjected to a detailed geognostic survey to evaluate slope stability and the vulnerability of existing structures. The damage observed to several local buildings and infrastructure raised significant concerns, indicating the presence of active or potentially reactivatable landslide movements triggered by further seismic or meteorological events. For this, the need arose for a continuous monitoring system capable of detecting any acceleration of the landslide phenomenon in real time and issuing timely warnings to the population to mitigate risk and ensure effective emergency response. A surface monitoring system, shown schematically in figure

2, was installed throughout the area, providing an integrated and technologically advanced system for detecting and analysing the site deformations.

Figure 2. Detail of the installation of the superficial monitoring instruments.

The geognostic survey was realized by boreholes and installed inclinometers and piezometers to a depth of 80 meters. The drilled material shows a complex stratigraphic sequence typical of geological contexts influenced by tectonic and depositional dynamics. The photo-interpretation study has shown a significant evolution of the area. Since the 2000s, it is evident that the entire built-up area was progressively affected by slope movement, indicating a state of activity over time. Significant deformations were identified by deep inclinometers. The image in figure 3 shows the inclinometric analysis (Allasia *et. al.*, 2020) carried out in the area, which provides a complete understanding of the dynamics of the system. It is possible to define a progressive intensification of movements, with significant displacements concentrated at very high depths, suggesting that the deep slip surfaces are active.

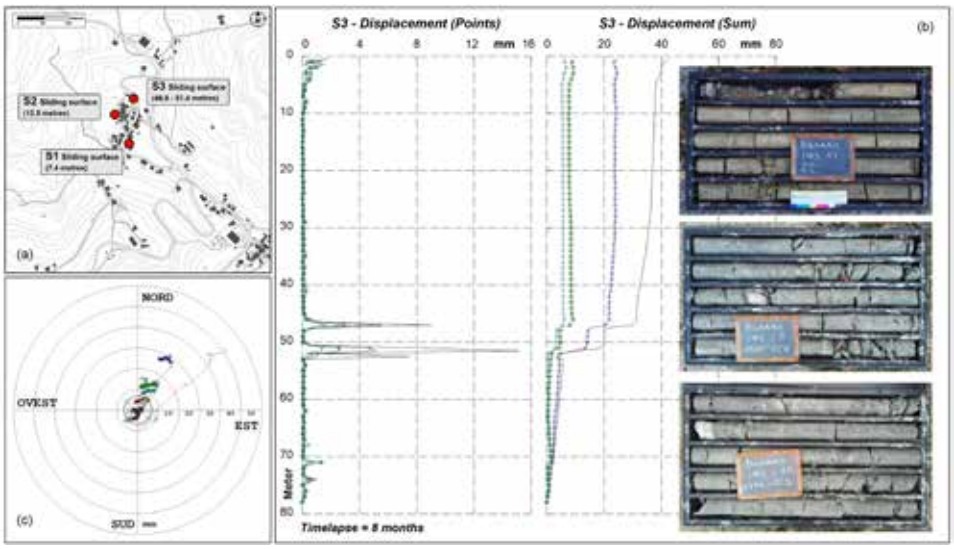

Figure 3. Detail of the inclinometric monitoring.

The successive numerical analyses (Borgatti, 2024) established a good correlation with the monitoring data, revealing in detail the instability of both local and territorial processes. A two-dimensional numerical analysis was carried out in the most critical part of the area to simulate the behaviour of the soil under different loading and saturation conditions. The model parameters (table 1) were calibrated using geognostic data obtained during the investigations, allowing the determination of deformations and stresses at different soil depths.

Table 1. Geotechnical parameters used in numerical analysis.

	Cover Layer	Subsoil	Weakness Planes
Unit weight	19.0 kN/m^3	20.0 kN/m^3	--
Friction angle (j′)	22°	24°	12°
Cohesion (c′)	10.0 kPa	100.0 kPa	0.0 kPa
Elastic modulus	0.01GPa	1.0 GPa	--

The map in figure 3b shows a zone of maximum displacement at the most superficial part, where the alteration cover with less mechanical properties encounters the more compact geological substrate. This transition zone may be affected by alteration, erosion or frictional forces that facilitate movement of the overlying material. At greater depths, secondary failure surfaces develop, which may result from fractures or structural deformation caused by tectonic forces or excessive increase pore pressure. These planes, although less visible on the surface, are critical to the stability of the overall system as they can determine the intensity and direction of deeper and more complex movements of large masses of material. In addition, the graph in figure 3c can be used to identify areas in critical condition where the applied stress exceeds the strength of the material along weakness planes, resulting in creep to failure.

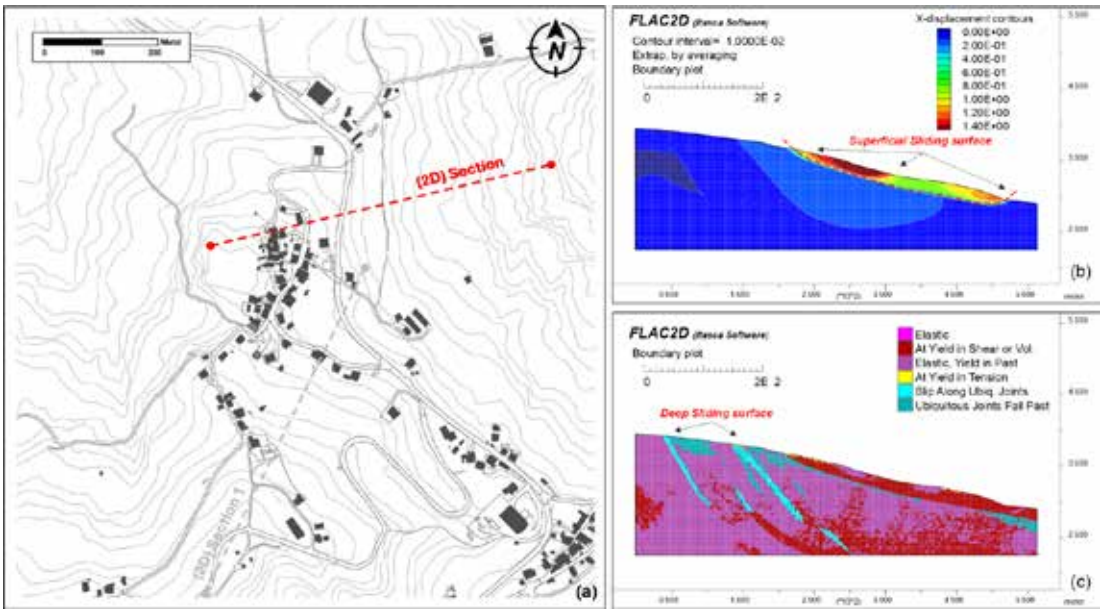

Figure 3. Two-Dimensional Numerical modelling of the section-2.

Because the extent of the potentially unstable area, a three-dimensional numerical model was developed to integrate all the available data and to represent in detail the stress-strain behaviour of the entire analysed area. The model was constructed by incorporating two fundamental components: the surface layers, identified in all the boreholes, and the substrate layer. Particular attention was paid to the modelling of the deep layers, by implementing a constitutive Ubiquitous Joint Plasticity Model (Yang, 1998), capable of describing in three dimensions both the overall mechanical behaviour of the mass (Mohr-Coulomb) and the internal planes of weakness (Zhou *et. al.,* 2018, Azadi *et. al.* 2024). In this specific case, these planes were schematized with a 45° inclination and a preferential north-north-east direction, in accordance with the stratigraphic and structural information obtained from the geological investigations. The mechanical parametrization and the definition of the boundary conditions followed the same criteria as in the two-dimensional model, to ensure consistency and comparability with the real conditions. The three-dimensional approach allowed a detailed analysis of the plastic deformations and their evolution on a local scale, highlighting that a significant part of the inhabited area is affected by widespread plastic deformations, indicating an active instability process. The map of SSI shear rate increments (figure 4) shows red areas of maximum deformation that are large, continuous and characterized by an elongated north-north-east trend. This configuration reflects the geometry of the fracture system and the assumed planes of weakness within the substrate, suggesting significant structural control over the way the ground deforms and slides. These planes of weakness act as stress concentration surfaces, promoting material movement along predefined directions. The results of the three-dimensional model (figure 4) also show good agreement with the real conditions. There is a good comparison with inclinometer measurements (fig. 3), both for deep deformations (inclinometer S3) and surface deformations (inclinometer S1).

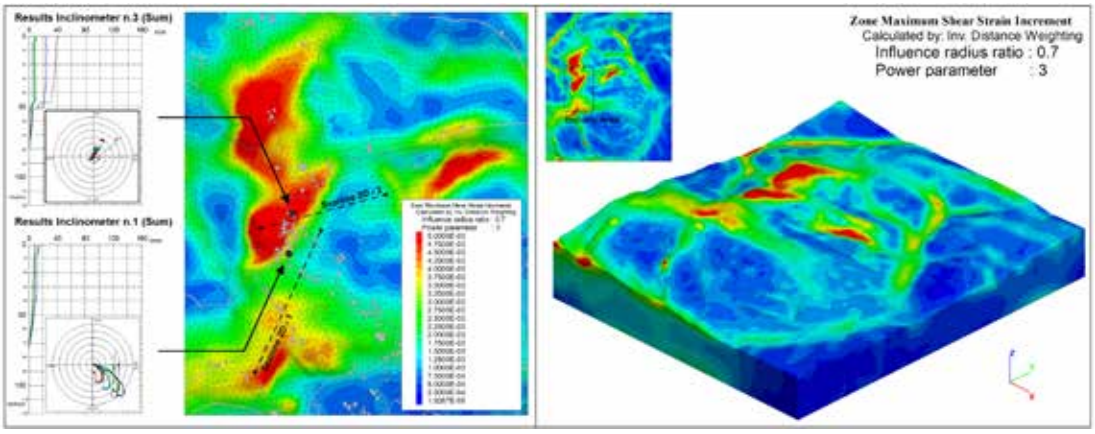

Figure 4. Three-Dimensional Numerical modelling: Shear Strain Increment map.

One crucial aspect is certainly the need to refine the hypotheses on the distribution of water saturation, a parameter that decisively influences the mechanical response of the materials and the local stability conditions. A better understanding of the spatial and temporal variations of saturation could significantly improve the predictive capacity of the models, especially in contexts characterized by intense rainfall or significant seasonal variations. In addition, the detailed study of the local responses of the weakening planes is another fundamental topic of investigation. A more accurate characterization of the geotechnical properties of these surfaces, such as residual shear strength or cohesion under partially saturated conditions, could allow a more realistic representation of the natural processes involved. This would be particularly relevant for improving predictions of surface instabilities, which are often more difficult to model due to their sensitivity to local parameters and variations in environmental conditions. The results of the study provide an essential basis for the development of strategies aimed at planning mitigation and/or relocation measures, which are crucial for the protection of infrastructure and the safety of local communities. The work also highlights the importance of integrated spatial planning, which can combine innovative detection technologies with traditional methods. This approach also makes it possible to optimize land management, making it more effective and sustainable, especially in geologically complex and vulnerable contexts.

Acknowledgements
The Authors thank the Special Office for Reconstruction of the Italian Government's for providing funds for the geognostic surveys.

References
Allasia, P., Godone, D., Giordan, D., Guenzi, D., Lollino, G. 2020. Advances on Measuring Deep-Seated Ground Deformations Using Robotized Inclinometer System. Sensors 2020, 20, 3769. https://doi.org/10.3390/s20133769

Artoni, A. 2003. Messinian events within the tectono-stratigraphic evolution of the Southern Laga Basin (Central Apennines, Italy). Boll. Soc. Geol. Ital.

Artoni A. 2013. The Pliocene-Pleistocene stratigraphic and tectonic evolution of the Central sector of the Western Periadriatic Basin of Italy. Marine and Petroleum Geology: 42, 82-106.

Azadi, A., Momayez, M. 2024. Review on Constitutive Model for Simulation of Weak Rock Mass. Geotechnics 2024, 4, 872-892

Borgatti, L., Donati, D., Hu, L., Landi, G., Zama, F. 2024. A Regularization Method for Landslide Thickness Estimation. J. Imaging 2024, 10, 314.

Cappadonia, C., Confuorto, P., Di Martire, D., Calcaterra, D., Moretti, S., Rotigliano, E., & Guerriero, L. 2024. Geomorphological Insights to Analyze the Kinematics of a DSGSD in Western Sicily (Southern Italy). Remote Sensing, 16(21), 4040. https://doi.org/10.3390/rs16214040.

Casero, P., and Bigi, S., 2006. Deep structure of the Laga Basin. Poster session TS7.2 - XY0591, EGU General Assembly 2006.

Gaidzik, K., Ramírez-Herrera, M. T., Bunn, M., Leshchinsky, B. A., Olsen, M., & Regmi, N. R. 2017. Landslide manual and automated inventories, and susceptibility mapping using LIDAR in the forested mountains of Guerrero, Mexico. Geomatics, Natural Hazards and Risk, 8 (2), 1054–1079.

Höfle, B., & Rutzinger, M. 2011. Topographic airborne LiDAR in geomorphology: A technological perspective. Zeitschrift Fur Geomorphologie , 55 , 1–29.

Yang, Z., Chen, J., Huang, T. 1998. Effect of joint sets on the strength and deformation of rock mass models. Int. J. Rock Mech. Min. Sci. 1998, 35, 75–84.

Zhou, X., Tang, C.A., Li, W. 2018. Modeling the mechanical behavior of jointed rock masses with the synthetic rock mass approach. Eng. Geol. 2018, 110, 136–148.

17th INTERNATIONAL CONGRESS of the Geological Society of Greece

BULLETIN OF THE GEOLOGICAL SOCIETY OF GREECE, SP. PUBL.

EXTENDED ABSTRACT 202

The 'treasure' of aeolianites on the coastal front of Marathopoli Dialiskari, Messinia, Western Coast of the Peloponnese: rhizoliths petrified forest and historical abandoned quarries

Manoutsoglou Emmanouil
Technical University of Crete, School of Mineral Resources Engineering, University Campus, 73500 Akrotiri, Chania, Greece, emanoutsoglou@tuc.gr

Introduction

Aeolianites and rhizoliths are geological structures that occur rarely in spatially limited coastal areas along the coasts of our country (Moraiti & Alexopoulos, 2019; Manoutsoglou, 2022; Μανούτσογλου, 2023). Aeolianites and rhizoliths are associated with the action of natural factors, such as marine activity, wind and vegetation. As fossil dune deposits with carbonate cement mainly of Quaternary age, aeolianites provide key clues for understanding sea-level fluctuations from the Late Quaternary to the Holocene and the dynamic transport of sediments by wind in coastal environments. Since their characteristics are similar to those of recent coastal dunes, such as cross-bedded structures, sand-dominated grain size, and long parallel axes on the shore, these rocks provide records of both past coastal wind-driven dynamics and the complex interactions between aeolian and colluvial river depositional processes in coastal environments. Generally, the morphology of aeolianites reflects the marine dynamics of the region combined with wind direction and changes in climatic conditions during their deposition (Brooke, 2001). Similarly, rhizoliths record the geochemical interaction of soil roots with their environment, indicating the presence of plants and the environmental conditions that prevailed during their formation (Alonso-Zarza, 1999). The description and detailed study of rhizoliths in coastal aeolianites can provide crucial information on the paleoenvironmental conditions of the western coast of the Peloponnese, particularly in the Marathopoli – Dialiskari area (Municipality of Trifylia, Messinia). This study represents one of the first comprehensive attempts to document these features in the region, contributing to a broader understanding of the dynamics of Mediterranean coasts and the interaction between biological and sedimentary processes. While the aeolianites tell a story of natural processes, the historically abandoned quarries in the area, carved into these formations, speak of human ingenuity and resourcefulness. Historically, aeolianite deposits have been exploited as a source of building stone, particularly in coastal areas where other durable rock types are rare. The soft, flexible nature of freshly cut aeolianites makes it an ideal construction material, while its hardening over time ensures the durability of structures built from it. This work aims to highlight the significance of coastal aeolianite rhizoliths forest and abandoned quarries, which represent natural and historically technological 'treasures' for the broader region.

Geological outline

The SW Peloponnese, mainly Messinia, located in the western part of the Aegean arc system, represents one of the most tectonically and seismically active areas of the Africa-Eurasia collision zone. The topographic relief of the SW Peloponnese is characterized by the presence of several mountains and drainage basins with a trend mainly NW-SSE and E-W (Figure 1). The outer part of the western Peloponnese is dominated by extensional tectonics as expressed by the normal faults oriented E-W in its central-western part (Fountoulis *et al*., 2014). According to Αθανασάς (2010), typical marine sedimentation in the submarine areas of Western Messinia seems to start in the Lower Pliocene with a large surface spread. It consists mainly of sandstone formations whose thickness varies. They mainly occupy the plateau between the Pylos-Gargaliannoi-Filiatra heights in the west and the Kyparissia Mountains in the east. They also occur in isolated locations south of Pylos. However, disagreement exists regarding the partial division of the sand-margin formations into Pliocene and Pleistocene. Older stratigraphic studies of the area indicate that this sedimentation began in the Lower Pliocene and became generalized in the Upper Pliocene. Marine deposits consist of calcitic sandstones, marly sandstones, marls and conglomerates of different thicknesses from place to place. Φυτρολάκης (1980) in the geological map (Koroni – Pylos – Skhiza Sheet) considers the calcitic sandstones in the area north of the Romanos to be of Tyrrhenian age, while Αντωνίου και Φυτρολάκης (1988) recognize within the calcareous sandstones of the Petrochori-Romanos coastal front both the aeolian and marine phases and relate them to eustatic events of the Late Pleistocene (Eu- and Neo- Tyrrhenian). Terrestrial deposits consist mainly of conglomerates, red-coloured siliceous sands and sandstones. The multi-coloured sandstones above the marine post-alpine deposits are likely from the Middle and Upper Pleistocene.

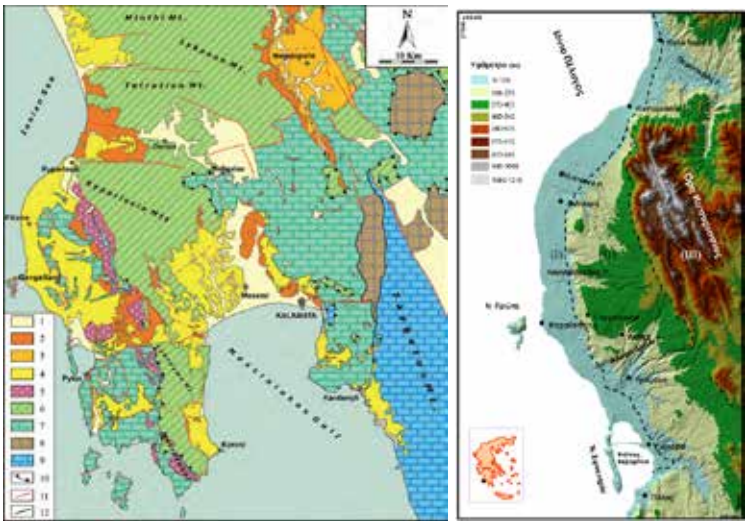

Figure 1. Left, Map depicting the geotectonic units and the post-Alpine deposits of the study area. 1: Holocene deposits; 2: continental deposits; 3: lacustrine deposits; 4: marine deposits; 5: conglomerates of Messinia (molasse); 6: Pindos Unit; 7: Gavrovo-Tripolis Unit; 8: Arna Unit (Phyllites-Quartzites); 9: Mani Unit; 10: thrust; 11: fault zone; 12: detachment fault zone [from Fountoulis et al., 2014]. Right, Three-dimensional visualization of the study area in Western Messinia using ArcGIS. Three basic physical geographical units are distinguished. A smooth surface west of the locations Gialova-Gargalianoi-Filiatra (I), a second, equally smooth but of higher altitudeseast of the previous one (II), which is interrupted by a third even further east that includes the Kyparissia Mountains (III). The altitudes are provided as a graduated color scale every 135 m. The coordinates (top left and bottom right) are given in the EGSA '87 system (from Athanasas, 2010). The study area is in the red boxes.

Sandstones appear in a relatively narrow coastal zone of 50-100 meters that starts north of the Bay of Navarino and extends up to Kyparrissia. Within these sandstones, aeolian deposits were found over a length of approximately two kilometres, spanning from the area north of Marathopolis to the south of Dialiskari. Numerous sites featuring extensive occurrences of rhizoliths were identified within these aeolianites, confirming the presence of a fossilized rhizolith forest in the region. In addition, four abandoned historical quarries were identified nearby, along with the well-known historical salt pan at Dialiskari.

Objectives

According to Brooke (2001), Aeolianite is a type of limestone found in coastal areas, demonstrating the reworking of vast amounts of carbonate sediments of biogenic origin from shallow marine environments into coastal sand dunes. Most aeolianites are calcareous sandstones originating from the biogenic carbonate sediments of shallow marine environments formed through the diagenesis of coastal sand dunes. The cementation of Quaternary-period dunes is the primary source of the aeolianites observed today in numerous island regions of both the northern and southern hemispheres. Most aeolianites consist of multiple generations of older dunes that have undergone diagenesis. When these dunes are cemented (lithified), they preserve the structures imparted by aeolian processes, often retaining their cross-bedded, parabolic, or barchanoid forms. While aeolianites are typical sedimentary deposits of the Quaternary period, instances of Paleozoic and Mesozoic carbonate aeolianites have also been documented (Brooke, 2001). Segments of sand dunes have been identified as distinct due to their association with well-developed paleosols, correlating with sea-level changes driven by glacial cycles. Geochronological records of extensive aeolianite deposits in both hemispheres indicate that eustatic sea-level changes largely controlled the timing of large-scale coastal carbonate dune formations. For an extended period, interpretations of coastal carbonate dunes were limited to their formation during glacial periods, with the majority dating to the Late Tertiary and Quaternary periods. Recent discoveries of aeolianites from interglacial periods challenge the belief that aeolianite formations are exclusive to glacial periods. Instead, these findings highlight the impact of large sea-level fluctuations, which reflect the cyclical growth and melting of continental ice sheets (Frébourg *et al*., 2008).

In the studied region, aeolianites are extensively developed in a relatively narrow coastal zone of 50-100 meters over a length of approximately two kilometres, spanning from the area north of Marathopolis to the south of Dialiskari. These deposits exhibit prominent and distinctive cross-bedding and served historically as a source of quarry material. The study of ancient quarries has evolved from a historical focus in the 19th century to a multidisciplinary field involving archaeologists, geologists, and engineers. Initially perceived as secondary production sites, quarries gained importance with the realization that their technical and economic aspects were crucial to understanding ancient construction. The late 20th century saw systematic excavation methods and geochemical analyses enhancing research. Today, quarry studies integrate archaeological surveys, geological

mapping, and digital tools, providing insights into ancient economies and craftsmanship. Despite challenges, interest persists in medieval quarries, revealing their cultural and economic significance (Lamesa *et al*., 2021). The historical abandoned quarries described for the first time in this work in the area are not registered in the databases and catalogues of historical quarries in Greece (Κουκουβού, 2010; Κοκκορού-Αλευρά κ.α., 2014; Τσιλιγκάκη, 2014). The only historical abandoned quarry in the area has been recorded in the corpus of ancient quarries with number 713. ''location: Pylos, Dialiskari-Marathoupoli". At the same location (Figure 2), a possible salt marsh has been described from the first excavations of the Swedish archaeological mission about a century ago in the area: "..On the rock they have carved half a meter above the sea a 6mx3m. On two sides a groove allows the tank to communicate with the sea. It is probably a salt marsh.." (Valmin, 1930).

Figure 2. Left is the place where the ancient salt lake was built. On the right, you can still see the excavation of the seawater supply channel.

The first quarry that bears traces of recent exploitation (Figure 3) is the largest in dimensions and is located north of Marathopolis, where the coastal aeolianites have the greatest width and width in front of the coast, exceeding one hundred meters. What is left is an abandoned ancient quarry with rugged and uneven terrain filled with large rocks and boulders. The quarry is surrounded by steep, weathered rock walls, which appear eroded over time. There are no exploitation levels, only a front located on the east side, as opposed to the coastal front located on the west side of the site. The quarry's remnants highlight the historical stone extraction, possibly for construction or other purposes, with evidence of human intervention still visible in the surrounding formations.

Figure 3. The first and largest abandoned quarry is located north of Marathopolis.

The second quarry (Figure 4) is located about 500 meters south of the Church of Agios Nikolaos, which was built in the small bay of Dialiskari. The second quarry is an abandoned ancient quarry with visible layers of stone extraction. The quarry's rock face is marked by precisely cut, rectangular sections, indicating past human activity and extraction methods. The ground appears rugged and uneven, strewn with smaller rocks and debris, characteristic of a long-abandoned excavation site. On the right, the image displays visible wedge marks on the rock surface, indicating the stone extraction techniques used in antiquity. These wedge marks appear as small, evenly spaced holes or indentations, likely created by inserting wooden or metal wedges to split the stone. Over time, natural weathering and erosion have partially obscured some of these marks, but their distinct pattern remains visible. The presence of these wedge marks provides valuable insight into the methods employed by ancient quarry workers to extract large stone blocks for construction and other purposes.

Figure 4. Left, the second abandoned quarry is located about 500 meters south of the Church of Agios Nikolaos, which was built in the small bay of Dialiskari; on the right, traces of wasps associated with the method of exploitation.

The third quarry is located next to Barlas beach, 4 km from Marathopoli (Figure 5) and is approximately 10 m above sea level. The colour of the aeolianites without containing layers of paleo-soil is red. However, the colour of the extracted material is uniform throughout the quarry. The surface of the rocky aeolianites shows distinct cutting marks and stepped formations, indicating systematic quarrying techniques. The surrounding area consists of weathered stone with patches of sand and small debris. The layout of the quarry suggests that it was used for the quarrying of large stones, with clear signs of chiselling and splitting methods. Throughout the quarry surface, there are characteristic residual cut marks and grooves indicating wedging techniques, where wooden or metal wedges were inserted into pre-cut grooves to split the stone. These grooves, often arranged in parallel, herringbone, or lattice patterns, suggest a systematic technique in stone quarrying. In addition, the presence of tool marks, such as chisel marks and wedge holes, provides valuable information about the methods used by ancient workers to extract large stones with precision. The creation of stepped steps during quarrying suggests an excavation process preserved to this day, where successive layers of stone were removed. The surrounding environment, with scattered debris and partially worked boulders, reflects the operational phases of the quarry, from initial extraction to preparation for transport. The erosion and weathering of the exposed rock faces suggest that the quarry has been abandoned for a long time. The 1 m wooden stick has been placed on the surface for scale reference.

Figure 5. The third quarry is located by Barlas Beach, 4 kilometres from Marathopoli. On the right, the image shows a close-up view of an abandoned ancient quarry with clear signs of quarrying activity. The rock face exhibits distinct vertical and horizontal tool marks, likely created using chisels and wedges to extract stone blocks. The marks are characterized by parallel grooves and stepped formations, which indicate a systematic quarrying process used to detach large stone blocks from the bedrock.

Comparing the image with documentation and visual records from ancient quarries, the quarrying methods shown here are consistent with those used in classical antiquity. In this era, a combination of hand tools and water-based wedge techniques was employed to split the rock along desired lines. These techniques allowed for the efficient production of stone blocks for construction purposes, such as temples, fortifications, and public buildings.

As well as building material mined in many places, the aeolianite formations along the Marathopoli – Dialiskari coastline exhibit well-preserved examples of fossilized root structures, i.e. rhizoliths, indicative of ancient dune stabilization by vegetation. These features were mapped and analyzed to determine their spatial distribution and morphological characteristics. The fossilized roots appear as vertical to sub-vertical tubular structures, often branching, which are associated with paleo-vegetation that thrives under specific climatic and geomorphic conditions. Rhizoliths, formed by the mineralization of root systems, were observed in association with paleosol layers within the aeolianite sequence, reflecting periods of dune stability and soil development. Klappa (1980) identified five primary types of rhizoliths: (1) root molds, which are tubular cavities left by roots that no longer exist; (2) root casts, formed by the infilling of root molds with sediment and/or cement; (3) root tubules, which are cemented cylindrical structures surrounding root molds; (4) rhizocretions, representing pedo diagenetic mineral accumulations around plant roots; and (5) root petrifactions, involving the mineral impregnation or replacement of organic material, preserving root anatomical features either wholly or partially.

Dozens of rhizoliths were counted in a relatively small area of a few hundred square meters. The first rhizoliths in the area were found within the first quarry north of Marathopolis. The second place is located in Dialiskari (Figure 6). Rhizoliths are visible as irregular, branching grooves and cavities, creating a rugged and porous texture across the terrain. Like many other fossils in the study area, rhizoliths in full development can be observed on aeolianite surfaces formed by marine erosion. The erosion has exposed these rhizoliths, revealing their complex network, which likely developed through the gradual dissolution of sandstone. The excellent preservation of a multitude of roots of various sizes indicates that most rhizoliths in the study area possess greater resistance to marine mechanical erosion compared to the surrounding aeolianites. This observation serves as an initial indication that the majority of the rhizoliths are not mere “root casts” but are very likely mineralized, fossilized roots. If they were simply root casts filled with the surrounding sediment of the aeolianites, they would not have withstood marine mechanical erosion. Detailed mapping has revealed that the distribution of rhizoliths corresponds to distinct stratigraphic horizons, suggesting episodic phases of vegetation growth and sediment stabilization. These intervals are interspersed with layers of reworked aeolian sands, indicative of dune reactivation during climatic aridity or increased wind intensity. The stratigraphic position of the rhizoliths provides a valuable framework for reconstructing the paleoecological and climatic history of the region.

Figure 6. Extensive surface with rhizoliths within the quarry at the Dialiskari location. The settlement and the bay are clearly visible.

Apart from the root system, they were distinguished by positions and remains of fossilized tree trunks (Figure 7). The fossilized tree trunks exhibit significant erosion, with their surfaces marked by deep grooves and cavities resulting from prolonged exposure to marine erosion. Despite the wear, the cylindrical shape and woody texture remain discernible, indicating their origin as tree trunks. The size and orientation of these trunks suggest they were once part of a forested landscape, subsequently buried and preserved through geological processes. Surrounding and connected to the fossilized trunks are rhizoliths.

Figure 7. The provided images depict heavily eroded fossilized tree trunks accompanied by rhizoliths, showcasing the intricate interplay between ancient vegetation and sedimentary processes.

Rhizoliths occur and spread on the flat erosional surfaces of aeolianites (Figure 8 and Figure 9). At the same time, they start from the underlying paleosoil that appears by position. The various rhizoliths differ in size (length, diameter, branching, etc.). Mega-rhizoliths and biokarst dissolution pipes were recognized.

Figure 8. A coastal landscape is characterized by a dense network of rhizoliths and mineralized root structures formed through the diagenetic processes of ancient vegetation. These rhizoliths are visible as elongated, branching, and interconnected features across the eroded limestone surface.

Figure 9. A more detailed look at the rhizolith structures reveals intricate branching patterns with visible root voids and mineralized traces. The rhizoliths exhibit a well-preserved morphology, retaining their cylindrical and tapered shapes

Conclusions

The coexistence of rhizoliths and historical abandoned quarries within aeolianites presents an intriguing juxtaposition: on the one hand, fossilized roots offer a glimpse into ancient ecosystems shaped by natural forces; on the other, quarries stand as monuments to human adaptation and transformation of the landscape. These elements underscore the dynamic relationship between nature and culture, revealing how landscapes evolve under the combined influence of environmental change and human activity. Studying this intersection enhances our understanding of past environments and societies and has contemporary relevance. Understanding how ancient communities adapted to their environments can offer valuable lessons as we face ongoing climate change and increasing pressure on natural resources.

References

\Αθανασάς, Κ., 2010. Νεοτεκτονική εξέλιξη της Μεσσηνίας κατά το ανώτερο τεταρτογενές, βασισμένη σε γεωχρονολογήσεις με τη μέθοδο της φωταύγειας: συμβολή στην αρχαιομετρία. Διδακτορική διατριβή, ΕΚΠΑ, Σχολή Θετικών Επιστημών, Τμήμα Γεωλογίας και Γεωπεριβάλλοντος. Τομέας Δυναμικής, Τεκτονικής και Εφαρμοσμένης Γεωλογίας, σελ.264.

Αντωνίου, Μ., Φυτρολάκης, Ν., 1988. Ιζηματολογικές και νεοτεκτονικές παρατηρήσεις σε νεοπλειστοκαινικούς και ολοκαινικούς σχηματισμούς της Νότιας και Δυτικής Πυλίας (Δυτική Μεσσηνία), Μεταλλειολογικά και Μεταλλευτικά Χρονικά, 85-66.

Κοκκορού-Αλευρά, Γ., Πουπάκη, Ε., Ευσταθόπουλος, Α., Χατζηκωνσταντίνου, Α., 2014. Corpus αρχαίων Λατομείων, ΕΛΚΕ ΕΚΠΑ, Ερευνητικό πρόγραμμα «ΚΑΠΟΔΙΣΤΡΙΑΣ», Αθήνα.

Κουκουβού, Α., 2010. Λατομεία πωρόλιθου στην περιοχή της αρχαίας Βέροιας: μελέτη για την λατομία οικοδομικού λίθου στην αρχαιότητα. Διδακτορική διατριβή, ΑΠΘ, Σχολή Φιλοσοφική, Τμήμα Ιστορίας και Αρχαιολογίας, Τομέας Αρχαιολογίας, σ. 546.

Μανούτσογλου, Ε., 2023. Χαρτογραφώντας το απολιθωμένο δάσος στον Σταυρό Ακρωτηρίου στα Χανιά. Πρακτικά 16ου Εθνικού Συνεδρίου Χαρτογραφίας "Η Χαρτογραφία στον σύγχρονο πολυθεματικό κόσμο" Αιγάλεω, 2/11- 4/11/2023, 819-833.

Τσιλιγκάκη, Ε., 2014. Τα αρχαία λατομεία της Κρήτης, Διδακτορική διατριβή, Παν. Κρήτης, Τμήμα Ιστορίας και Αρχαιολογίας, σ. 937.

Φυτρολάκης, Ν., 1980. Γεωλογικός χάρτης Ελλάδας 1:50,000, Φύλλο Κορώνη-Πύλος-Σχίζα, Ι.Γ.Μ.Ε..

Alonso-Zarza, A.M., 1999. Initial stages of laminar calcrete formation by roots: examples from the Neogene of central Spain. Sedimentary Geology 126, 177-191.

Brooke, B., 2001. The distribution of carbonate eolianite, Earth-Science Reviews, 55, 135-164.

Fountoulis, I., Mariolakos, I., Ladas, I., 2014. Quaternary basin sedimentation and geodynamics in SW Peloponnese (Greece) and late stage uplift of Taygetos Mt., Bollettino di Geofisica: teorica ed applicata, (55), 303-324, 2014, Istituto Nazionale di Oceanografia e di Geofisica Sperimentale, 0006-6729.

Frébourg, G., Hasler, C., Le Guern, P., Davaud, E., 2008. Facies characteristics and diversity in carbonate eolianites, Facies, 54(2), 175-191.

Klappa, C.F., 1980. Rhizoliths in terrestrial carbonates: classification, recognition, genesis, and significance, Sedimentology, 26, 613-629.

Lamesa, A., Bessac, J.-C., Sciuto, C., 2021. The archaeology of quarries and rock-cutsites. In: Claudia Sciuto, Anaïs Lamesa, Katy Whitaker and Ali Yamaç, .Carved in Stone. The Archaeology of rock-cut sites and stones quarries, BAR Publishing, pp. 1-8.

Manoutsoglou, E,. 2022. Rhizoliths within aeolianites at the ancient quarry of Stavros Akrotiri Chania Greece, 16th International Congress of the Geological Society of Greece 17-19 October, 2022 - Patras, Greece, Bulletin of the Geological Society of Greece, Sp. Publ. 10 Ext. Abs., GSG2022-193, 2022.

Moraiti, E., Alexopoulos, A., 2019. Geopark of Aghios Nikolaos–Neapolis, Lakonia, Peloponnese, 15th International Congress of the Geological Society of Greece Athens, 22-24 May, 2019, Harokopio University of Athens, Greece Bulletin of the Geological Society of Greece, Sp. Pub. 7 Ext. Abs. GSG2019-376.

Valmin, N., 1930. Etudes topographiques sur la Messénie ancienne, Lund. 1931. Aten genom tiderna, Stockholm.

17th INTERNATIONAL CONGRESS of the Geological Society of Greece

BULLETIN OF THE GEOLOGICAL SOCIETY OF GREECE, SP. PUBL.

EXTENDED ABSTRACT 203

Monitoring sea water intrusion at Samaria gorge National Park

Manoutsoglou E.[1], Andronikidis N.[1], Lazos I.[1], Kritikakis G.[1], Steiakakis E.[1], Xirouchakis, G.[1] and, Vafidis A.[1]

(1) School of Mineral Resources Engineering of the Technical University of Crete, Chania, Greece, emanoutsoglou@tuc.gr

Introduction

Samaria gorge National Parks is located at the White Mountains mass, at the southwestern part of Crete (Figure 1). It is one of the most significant geomorphological structures in the Mediterranean region globally recognized by numerous international distinctions: 1) UNESCO Man and the Biosphere Reserve, 2) European Diploma of Protected Areas, awarded by the Council of Europe, 3) European Biogenetic Reserve of the Council of Europe, 4) Important Bird Areas by the Birdlife international, 5) NATURA 2000 protected area, under code GR4340014 (Zone of Special Protection: ZSP). The wider area of White Mountains belongs to the Natura 2000 European Network of Protected Areas (under code GR4340008H) and it is certified as a Place of Universal Importance (PUI).

Among geophysical methods, electrical resistivity tomography (ERT) has become a valuable tool for imaging seawater intrusion due to its low cost in combination with the effectiveness and quick interpretation. Automated data collection using multi-electrode resistivity surveying instruments, made the electrical tomography ERT method one of the most widely used geophysical methods for near-surface investigations. Fast acquisition 3D data instruments and inversion algorithms enhance the reliability of the method (Hamdan and Vafidis, 2009).

This study employs the ERT and seismic tomography geophysical methods for sea water intrusion imaging and monitoring at Samaria gorge. The geophysical survey conducted in the National Park of Samaria gorge employed the 3D ERT method which is more efficient due to the 3D nature of this geological structure. Dipole-dipole and gradient arrays were chosen to detect both lateral and vertical resistivity variations.

Geological setting

Crete located just over the active subduction zone of the eastern Mediterranean oceanic plate beneath the Eurasian one, exhibits a gradual uplift and complicated active tectonics (Pavlaki and Perleros, 2015; Manoutsoglou, et al., 2022) The Alpine tectonostratigraphic regime indicates compression tectonics, such as folding. The major tectonic units of Crete (stratigraphically from the lower to the upper one) are:

i) Plattenkalk Group (para-autochthonous),
ii) Phyllite Nappe,
iii) Tripolis Nappe,
iv) Pindos Nappe and
v) Uppermost Nappe.

Various lithological formations, composing these nappes, tectonically overlie different parts of the Plattenkalk Group formations. Plattenkalk Group is predominantly structured by HP/LT affected metamorphic rocks. Furthermore, the Ravdoucha (slate-carbonate) beds tectonically overlie the dynamo-metamorphic sequence in different parts of Western Crete, constituting the lower part of Tripolis Zone, while its upper part includes the carbonate sequence and flysch.

Considering the model relating geological processes and geomorphological features, the following remarks arise for the Samaria gorge area:

1. The entire region is a part of mega structure, consisting of metamorphic unsorted stromatolite limestones (Mt Gigilos). On either side of this mountain, the dip direction of the formations is differentiated, maintaining the same NNE-SSW striking and indicating that Mt Gigilos is a tectonic window.
2. The Trypali Unit occurs at the southwestern part of Samaria gorge according to field observations (Figure 1c).
3. The formations inclination is directly associated with the tectonic processes and the geomorphological evolution of the region.
4. The phyllites and slates (Gigilos formation) are characterized by medium dip angles and smooth relief. On the contrary, the meta-carbonate formations with cherts of Plattenkalk Group are accompanied by high (up to vertical) dip angles. These formations exhibit sharp slopes with height up to 300 m in some locations on both sides of the stream that crosses Samaria gorge.
5. Overall, Samaria gorge constitutes a typical catchment area, in which the surface runoff is favored at the northern part, due to outcropping lithological formations, while the underground one is favored at the southern part.

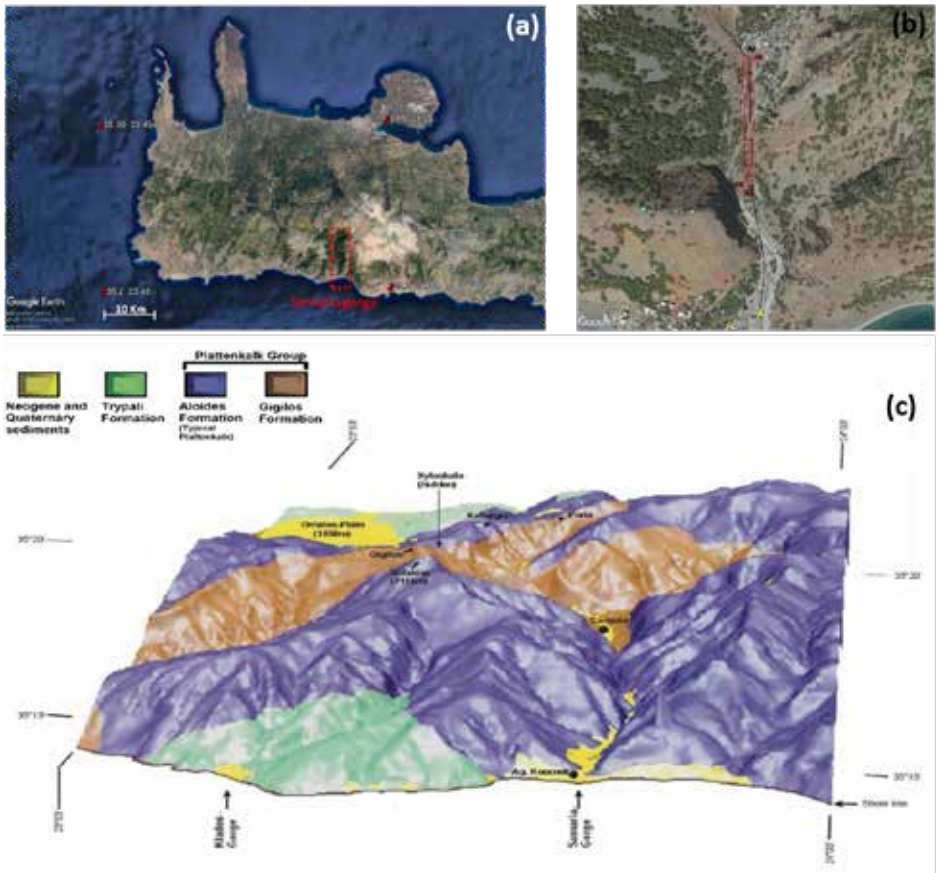

Figure 1. (a) Aerial photograph of Western Crete indicating in red dotted box the Samaria gorge area, (b) South portion of Samaria gorge wherein red are the geophysical lines and (c) the geological model for the wider region of Samaria gorge (modified from Manoutsoglou, et al., 2001).

Electrical tomography survey

The electrical tomography survey scanned the Samaria gorge area during four periods (October 2022, September 2023, June 2024 and October 2024) with 2 ERT lines and a grid (900 m x 30 m) consisting of 4 lines (A0, A1, A2 and A3 from east to west) to inspect seawater intrusion at different time periods. ERT data were acquired using Dipole-Dipole and Gradient arrays and 21 electrodes. The electrode spacing ranges from 10m to 45m. Apparent resistivity data were collected with a 10-channel SYSCAL Pro Switch™, IRIS Instruments system at 19-30 depth levels per line. Resistivity data were processed using the RES2Dinv™ software. Outliers from the original 2D data were removed by trimming data which contributed to high errors. Trimmed data were used for 3D inversion using both the RES3Dinv™ and EarthImager3D™ software packages resulting to a volume of electrical resistivity for the surveyed grid.

The inversion technique gives reasonably accurate images of three-dimensional structures, enabling the 3D imaging of the subsurface using cost–effective 2D electric tomography techniques (Dahlin and Loke, 1997). Since the inversion results deduced from 2 different software packages were similar, the EarthImager3D™ software was utilized for the visualization of 3D data.

The geoelectrical sections (Fig. 2) and the 3D geoelectrical model (Fig. 3) exhibit a lower resistivity zone with resistivity values between 5-40 Ohm.m attributed to sea water intrusion. The geoelectric section along Line A1, acquired during 2022 (Fig. 2a), exhibits lower resistivity values in this zone indicating that the seawater intrusion front extents to more than 650 m from the beginning of the line. Comparing the geoelectrical section Line A1 with the one acquired during 2023, (Fig.2b), the lower resistivity zone is reduced to approximately 600 m from the beginning of the 2023 lines. Finally, the geophysical survey of 2024 (June and October, Fig.2c-d) has shown that the sea water intrusion front is withdrawn to 550m of line A1 on June (Fig.2c), while on October, extents again to more than 650 m from the beginning of the line. The absolute altitude of the sea water intrusion front in the hinterland ranges from -50 to -120 meters.

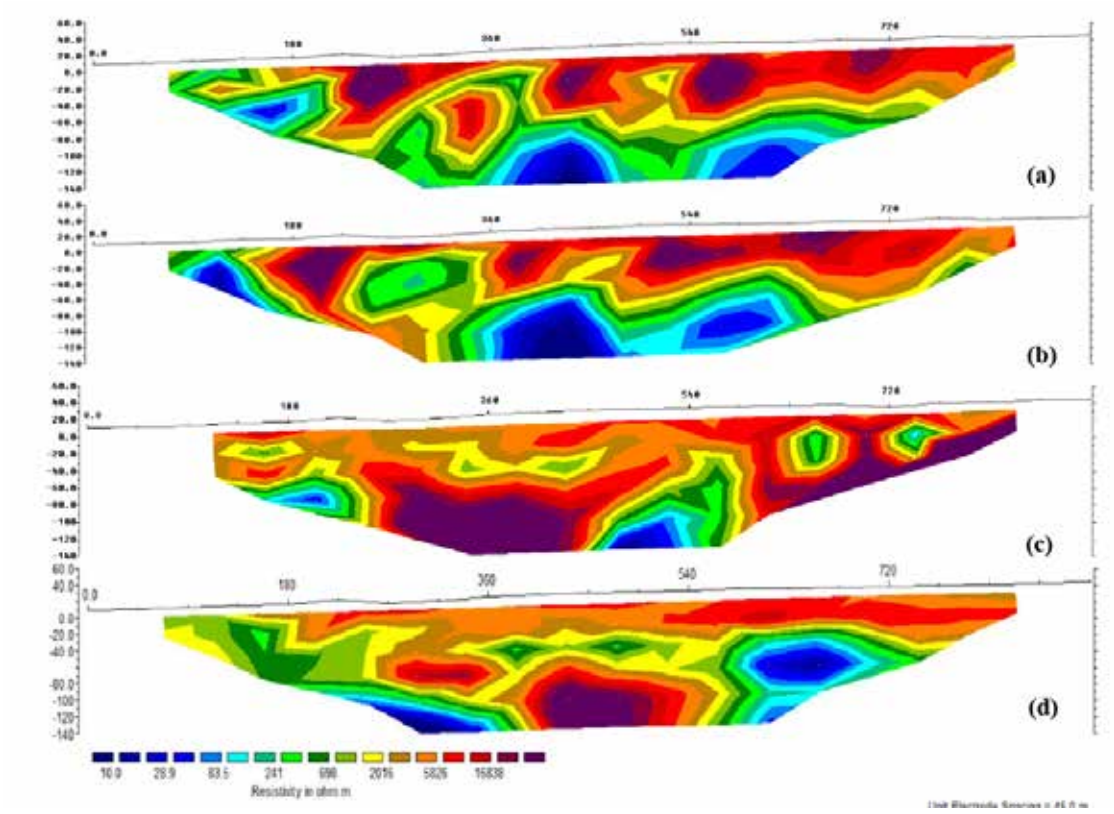

Figure 2. 2D geoelectrical sections along Line A1 surveyed using Gradient electrode array. Data collected during (a) 2022, (b) 2023 and (c-d) 2024 survey (June and October, respectively).

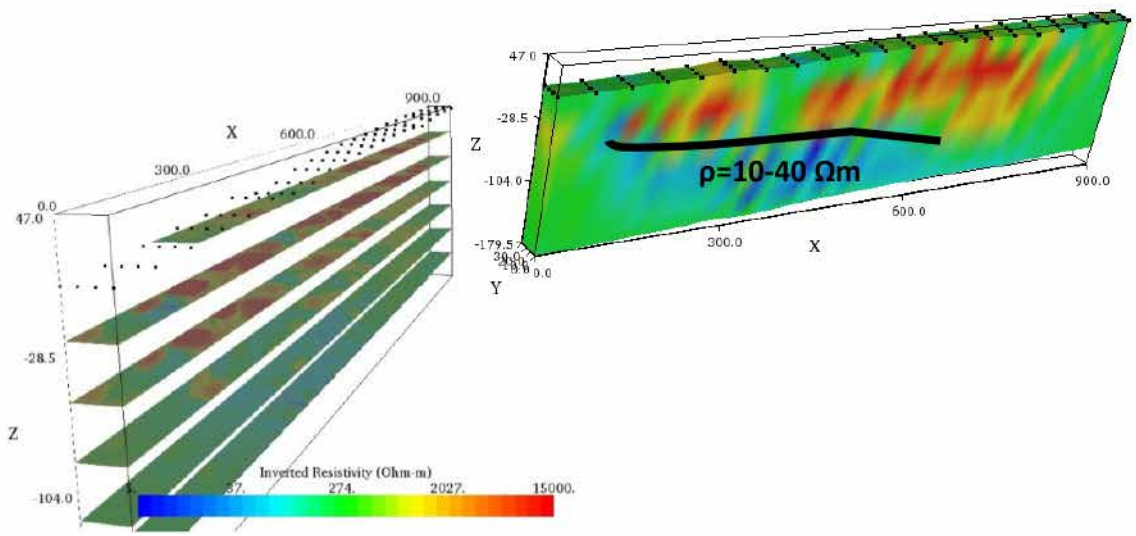

Figure 3. (a) 3D resistivity model (c) Horizontal slices from 3D model for the grid scanned during the 2023 survey.

Seismic tomography survey

The seismic refraction tomography (SRT) survey was conducted at Samaria gorge area during two periods (June and October of 2024) with 2 lines at different positions along ERT line A1. The main target of SRT survey was to delineate the interface between the alluvial deposits and the carbonate bedrock, as well as to estimate the depth to the healthy (unfractured) limestone (with Vp ≥ 3500m/s). SRT data were acquired using 24 geophones in 5m spacing and an 8gk sledgehammer as seismic source. The seismic section acquired on June of 2024 shown that alluvial deposits do not

exceed the thickness of 3-4m, while the fractured limestone appears up to the depth of 20m at the northern part of the section (Fig. 4).

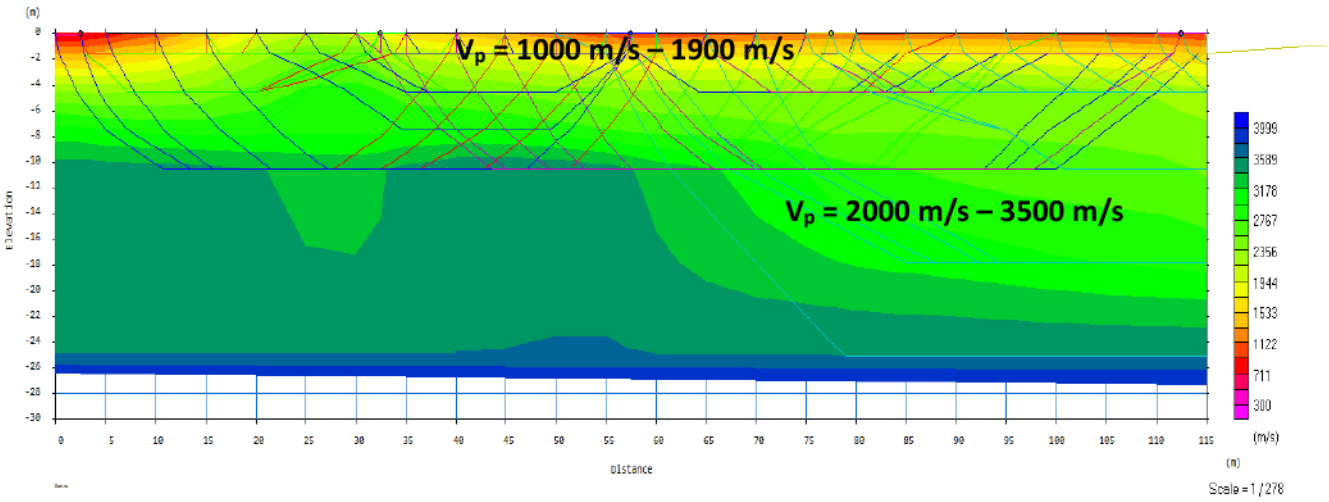

Figure 4. P-wave seismic refraction tomography section acquired during June 2024 survey.

Conclusions

A geophysical survey conducted during two periods namely 2022 and 2023 in the National Park of Samaria gorge employed the ERT method and dipole-dipole and gradient arrays to image the intrusion of sea water whose front appeared at 600 m from the beginning of the scanned lines during the 2023 survey and more than 650 m from the beginning of the scanned lines during the 2022 survey. The geophysical survey of 2024 (June and October) has shown that the sea water intrusion front was withdrawn to 550m of line A1 on June, while on October, extended again to more than 650 m from the beginning of the same line. This rapid change between June and October 2024 can be explained by the fact that infiltration of seawater into the hinterland is performed through the existing faults of the studied area.

Acknowledgements

This research was funded by the Applied Research Project “3D geological structure modeling of Samaria Gorge, aiming at the investigation of hydrogeological conditions and water reservoir levels in the core of Samaria National Park (Lefka Ori), Western Crete” (funding number: 82230), which is financially supported by the Green Fund “Forest Protection and Upgrading 2019” under “Other Nationals. Green Fund”.

References

Dahlin, T. and Loke, M. H., 1997, Quasi-3D resistivity imaging - mapping of three dimensional structures using two dimensional DC resistivity techniques, 3rd EEGS Meeting, Aug 1997, cp-95-00037, DOI: https://doi.org/10.3997/2214-4609.201407298.

Hamdan, H. and Vafidis, A., 2009, Inversion techniques to improve the resistivity images over karstic structures, Proceedings of the «15th European Meeting of Environmental and Engineering Geophysics», 3–5 September, Dublin, Ireland.

Manoutsoglou, E., Lazos, I., Steiakakis, E. And Vafeidis, A., 2022, The Geomorphological and Geological Structure of the Samaria Gorge, Crete, Greece – Geological Models Comprehensive Review and the Link with the Geomorphological Evolution. Applied Sciences, 12(20), 10670.

Manoutsoglou, E.; Spyridonos, E.; Soujon, A.; Jacobshagen, V., 2001, Revision of the Geological Map and 3D Modelling of the Geological Structure of the Samaria Gorge Region, W. Crete. Bulletin of the Geological Society of Greece, 34, 29–36, doi:10.12681/bgsg.16940.

Pavlaki, A., and Perleros, V., 2015. Updated Geological Map of the Lefka Ori National Park with Determination and Mapping of Geotope Locations (in greek). Development Organization of Crete S.A.

17th INTERNATIONAL CONGRESS of the Geological Society of Greece

BULLETIN OF THE GEOLOGICAL SOCIETY OF GREECE, SP. PUBL.

EXTENDED ABSTRACT 204

Preliminary results on sedimentological characteristics of Mass Transport Deposits (MTDs) during the Amorgos tsunami 1956: sediment provenance and geochemical elements.

Manta K.[1,2], Rousakis G.[1], Geraga M.[2], Papatheodorou G.[2], Sakellariou D.[1], Karageorgis A.P[1]

[1] Institute of Oceanography, Hellenic Centre for Marine Research (HCMR), 46.7 km Athens-Sounion, Greece, kmanta@hcmr.gr, [2] Department of Geology, University of Patras, 26504 Rio, Greece

Introduction

On July 9, 1956, two earthquakes struck in the central Aegean Sea (Perissoratis and Papadopoulos, 1999; Okal et al., 2009; Friederich et al., 2014; Brüstle et al., 2014)in Greece and adjacent regions, constitute the most tsunamigenic areas in Europe. The most recent large tsunami was a 20 m high wave that generated on 9 July 1956 in the Amorgos Basin, South Aegean Sea, in association with a M(s. The first earthquake had a magnitude of Ms = 7.4 and was located SE of Amorgos Is. (Fig 1) and occurred at 25 km depth. The second earthquake, M_S= 7.2 occurred just 13 min later close to Anafi Is. at more than 100 km depth. The tsunami that followed reached run-up heights of up to 30 meters along the southern coast of Amorgos marking the highest run-up value in the 20th century in the Mediterranean Basin (Soloviev et al., 2000). Detailed investigation of the run-up values along the Cyclades, Crete, Dodecanese Islands and the Turkish shoreline and propagation modeling by Okal et al. (2009) showed that the tsunami can't be explained by the co-seismic fault-rupture alone. These authors suggested that submarine landslide(s) must have been triggered by the earthquake(s) and contributed to the generation of the tsunami.

The sea floor between Amorgos and Astypalaia Islands is underlain by thick sediments, primarily due to the deposition of slumps debris and mass flows, which mostly consist of fine sand and silt, with occasional coarse sand present (Perissoratis and Papadopoulos, 1999; Tsampouraki-Kraounaki et al., 2021)in Greece and adjacent regions, constitute the most tsunamigenic areas in Europe. The most recent large tsunami was a 20 m high wave that generated on 9 July 1956 in the Amorgos Basin, South Aegean Sea, in association with a M(s. Sakellariou et al. (2021) and Manta et al. (2022) have shown high-resolution seafloor mapping, sub-bottom profiling, and sediment coring descriptions, which provide clear evidence of recent mass transport deposits below the seafloor in the area triggered by the 1956 earthquake(s).

This study provides new sedimentological and geochemical evidence derived from two gravity cores collected south of Amorgos and Anafi Islands, respectively, which confirm the occurrence of submarine landslide deposits linked to the 1956 earthquake(s). The 1956 Mass Transport Deposits (MTDs) vary in thickness from 55 to 100 cm. They are characterized by a gray color, calcite dilution, higher gamma density values, a terrestrial origin, sharp boundaries, and a mixture of cohesive and non-cohesive flows. Additionally, they contain lower amounts of phosphorus (P), calcium (Ca), magnesium (Mg), cobalt (Co), chromium (Cr), iodine (I), manganese (Mn), nickel (Ni), and strontium (Sr). The differences in sedimentological characteristics of the MTDs are attributed to their proximity to the seismic event. The rapid deposition during the seismic shaking preserved the old seafloor, maintaining its physical and chemical characteristics. The predominant fraction of the sediments is clay, followed by sand, while silt is negligible.

Methods

Two sediment cores (Fig. 1) retrieved from water depths between 720 and 1,030 meters. The core from the Amorgos basin (SA-1B: 25°52.974' E, 36°40.304 N) was obtained from a depth of 320 meters and has a length of 144 cm. The second core, SA-4 (26°00.835 E, 36°04.873 N), with a total length of 133 cm and was collected from the South East Aegean Sea. Initially, both cores were scanned using a multi-sensor core logger (Geotek) at 1 cm sample intervals to determine key attributes such as magnetic susceptibility, gamma-ray density, and P-wave velocity. Subsequently, the cores were longitudinally split into two halves. One half was photographed and described macroscopically, and samples were collected for grain size analysis, total organic carbon (TOC), total carbon (C), nitrogen (N), and both major and minor elements. In total, 83 samples were collected from core SA-1B, and 62 samples were obtained from core SA-4. The second half of each sediment core subjected to X-radiography using a Faxitron apparatus (cabinet X-ray). Grain size analysis was performed using a SediGraph device (Micromeritics SediGraph III Plus). Textural sediment classification followed the criteria established by Folk (1974). For carbon and TOC measurements, samples were processed in a CHN Elemental Analyzer (Fisons Elemental Analyzer EA1108) according to standard analytical procedures. The C/N ratios were calculated to estimate terrestrial organic matter inputs, according to Meyers (1994). The chemical composition of major and trace elements was analyzed through fuse beads in an X-ray fluorescence spectrometer (Phillips PW–2400). Terminology that used in this study follows Shanmugam and Wang (2015).

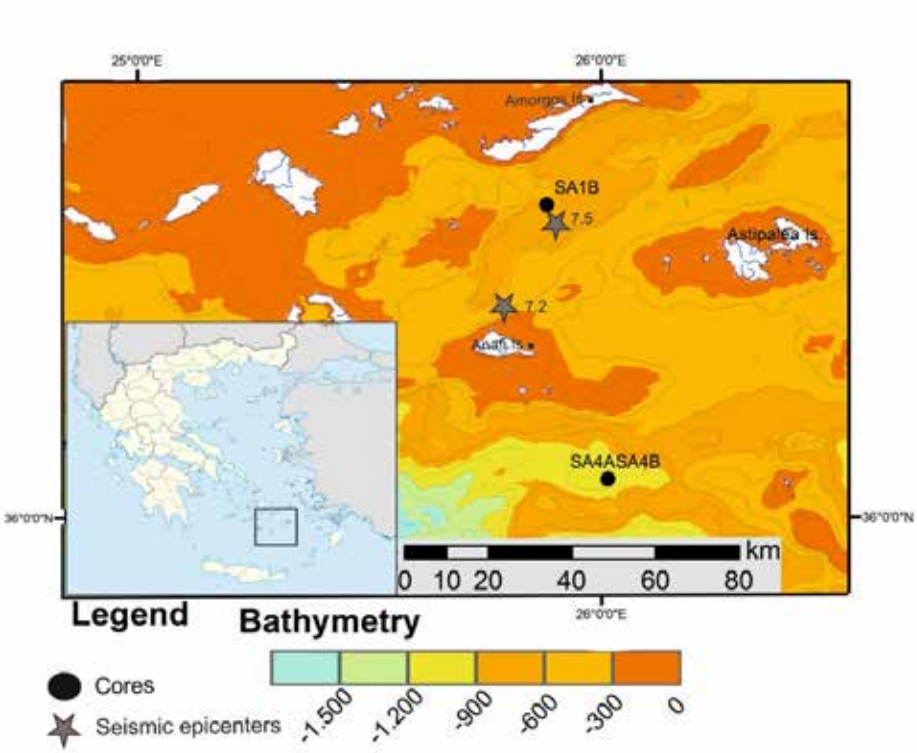

Figure 1. Location and bathymetry (in meters; grid interval of100 m) of the study area. Black circles show the location of the cores. Brown stars show the proposed epicenters for the two seismic events with their magnitude from Perissoratis and Papadopoulos (1999) and Okal et al., 2009.

Results

In core SA-1B, the uppermost 10 cm are characterized by a dull yellow color. Below this layer, the sediment transitions to a light gray hue, extending to a depth of 88 cm. Between 88 cm and 110 cm, the sediment exhibits a gray coloration. From 110 cm to 117 cm, the sediment is light yellow, followed by a dull yellow interval. Finally, the lowermost 19 cm (126–145 cm) of the core are composed of yellowish-gray sediment. The core is mostly composed of clay fractions except for some centimeters wherein sand fractions are dominant. X-radiographic analysis reveals a diagonal erosional surface with pumice at 2–5 cm, and a sandy horizon with pumice at 9 cm. At 79–82 cm, undisturbed sediment is observed at the bottom with an intrusion of sand, while the upper section of this interval is distorted. Hummocky cross-stratification is identified at 85 cm, and horizontal laminations are evident from 95–100 cm. These sediments exhibit high water content. Mud clasts and bioturbation are observed between 33–103 cm, while sand injection and erosional surfaces are present from 105–120 cm. Physical properties, including P-wave velocity and fractional porosity, exhibit similar downcore distributions, with maximum values recorded at 93–94 cm. In contrast, gamma density demonstrates an inverse trend. Total Organic Carbon (TOC) values and calcium carbonate ($CaCO_3$) exhibit parallel downcore trends, while the C/N ratio indicates a mixture of marine and terrestrial input, with the highest value (55) at 10 cm and the lowest (6.2) at 40 cm. Major element profiles reveal abrupt changes at key depths. Elements such as Al, Ba, Si, and K show significant declines at 115 cm, whereas P, Ca, Ti, Fe, Co, Cr, I, Ni, Sr, and V display pronounced increases at the same depth. Maximum values for As, Bi, Br, Sb, and Te occur at 119 cm, while Ce, Ga, and La reach their lowest values at the same depth. Proxies including Fe/Al, Mg/Al, Ca/Al, Br/Al, and Mn/Al show minimum values between 15 and 115 cm, whereas Zr/Sr peaks in this interval (Fig.3).

The uppermost section of the core represents the modern seafloor, consisting of a mixture of hemipelagic sediment and turbidites. Between 10 and 110 cm, mass transport deposits (MTDs) dominate, likely triggered by the 1956 earthquake. Below this, from 110 to 130 cm, the core records ‘old’ seafloor processes. The final section, from 130 to 144 cm, also reflects MTD deposition (Fig. 2).

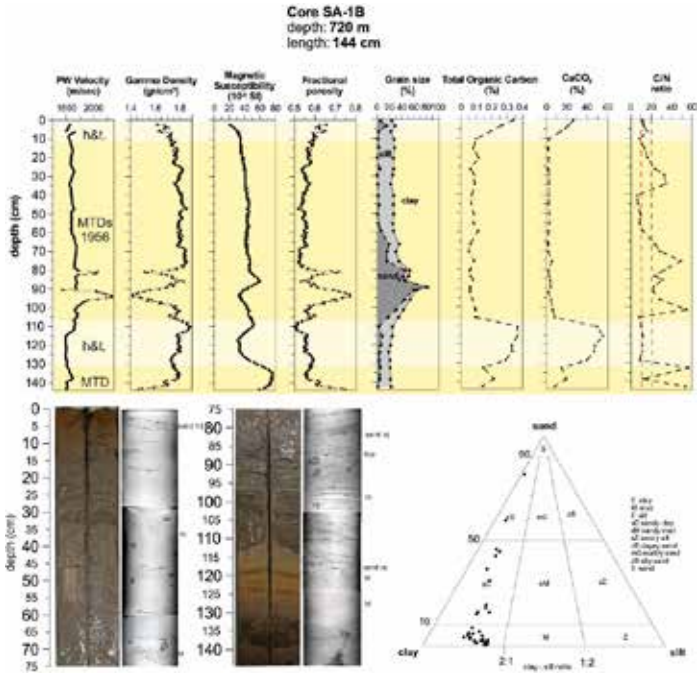

Figure 2. Downcore of plots: P Wave Velocity (m/s), Gamma-ray Density (g/cm³), Magnetic Susceptibility (10^{-5}), Fractional Porosity, Grain size distribution (dw%), Total Organic Carbon (dw%), CaC03 (dw%) and, C/N ratio, with red lines being discriminator between marine or terrigenous origin according to Meyers (1994). Photographs and X-radiographs (negative), as well as the Folk classification of grain assemblages. With light pink the sea floor is noted (h&t) and with pale yellow are marked the MTDs.

In core SA-4, the upper 18 centimeters exhibit a dull yellow-orange coloration (Fig. 4). Between 18 and 28 centimeters, the sediment transitions to a grayish-yellow hue. From 30 to 81 centimeters, the sediment is predominantly gray. The color reverts to dull yellow-orange from 81 to 89 centimeters before darkening further between 89 and 98 centimeters. From 98 to 123 centimeters, the sediment is characterized as grayish yellow, while the final 9 centimeters (123–132 cm) are dark grayish yellow. The core is primarily composed of clay, with the exception of the interval between 30 and 38 centimeters, which consists of sandy clay. Limited occurrences of broken shell fragments are found in the uppermost centimeters and at 95–96 centimeters. Small amounts of sand and pebbles are present at 4–5 centimeters and 90–91 centimeters. Pumice fragments are observed at 20–21 centimeters and 119–120 centimeters, along with volcanic sand identified at 130–131 centimeters. X-radiography of the core reveals a diagonal erosional surface at 3–5 centimeters, accompanied by a few pebbles and mud clasts. Another erosional surface is noted at 18–20 centimeters. Changes in sediment stiffness are observed at depths of 25 and 126 centimeters. P-wave velocity values generally increase downcore, reaching a depth of 77 centimeters, except for an anomaly at 24 centimeters where a value of 1500 m/s is recorded. Gamma density values range between 1.71 and 1.92 g/cm³, showing an overall increase downcore until 80 centimeters, where a local decrease to 1.65 g/cm³ is observed. Magnetic susceptibility values demonstrate an increasing trend, ranging from 23×10^{-5} at 1 centimeter to 143×10^{-5} at 59–60 centimeters. Fractional porosity displays an inverse relationship with gamma density, decreasing with depth. Total Organic Carbon (TOC) and calcium carbonate diagrams exhibit similar trends, with both showing decreasing values until 80 centimeters, followed by a peak and subsequent decline at greater depths. The C/N ratio indicates that sediments in the upper 30 centimeters and between 80 and 120 centimeters are of marine origin, while the rest of the core is composed of terrestrial material. Major element trends reveal an increase in aluminum (Al), silicon (Si), and potassium (K), from 27 to 75 centimeters. In contrast calcium (Ca), phosphorus (P), magnesium (Mg), manganese (Mn), and sulfur (S) show a decline over the same interval, with Ca and Mg reaching their lowest values. Trace elements such as arsenic (As), cobalt (Co), chromium (Cr), copper (Cu), iodine (I), nickel (Ni), antimony (Sb), and strontium (Sr) display reduced concentrations between 25 and 82 centimeters. Elements such as gallium (Ga), molybdenum (Mo), rubidium (Rb), zirconium (Zr), and yttrium (Y) increase until 40 centimeters, followed by a minor decline and subsequent increase at greater depths. Fe/Al, Mg/Al, Ca/Al, Br/Al, Mn/Al, and Zn/Al ratios decrease between 27 and 75 centimeters, while the Zr/Sr ratio exhibits an opposite trend (Fig. 3).
The uppermost centimeters of the core represent the seafloor and consist of a mixture of hemipelagic sediment

and turbidites. Between 25 and 80 centimeters, mass transport deposits (MTDs), triggered by the 1956 earthquake, dominate the stratigraphy. Below 80 centimeters, extending to 102 centimeters, the “old” seafloor processes are evident. The final section from 102 to 134 centimeters is composed of MTDs, reflecting both marine and terrestrial contributions (Fig. 4).

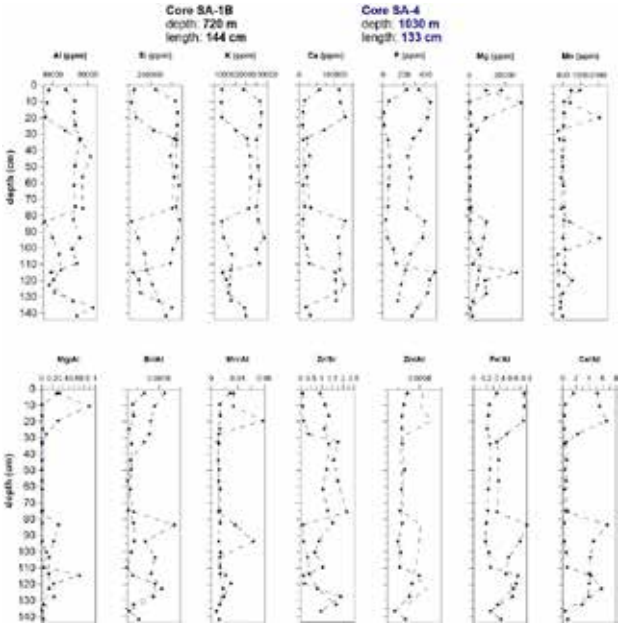

Figure 3. Downcore of plots: Al (ppm), Si (ppm), K (ppm), Ca (ppm), P (ppm), Mg (ppm), Mn (ppm), Mg/Al, Br/Al, Mn/Al, Zr/Sr, Zn/Al, Fe/Al, Ca/Al. Black dashed line are values of core SA-1B and blue dashed line for core SA-4.

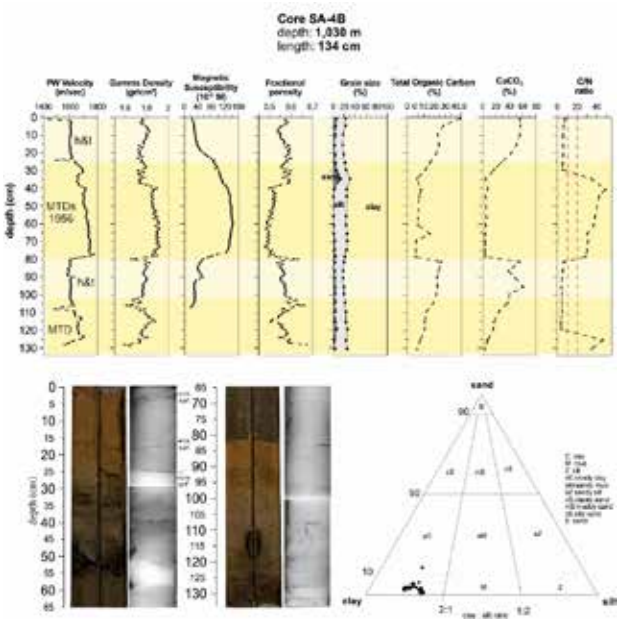

Figure 4. Downcore of plots: P Wave Velocity (m/s), Gamma-ray Density (g/cm^3), Magnetic Susceptibility (10^{-5}), Fractional Porosity, Grain size distribution (dw%), Total Organic Carbon (dw%), CaC03 (dw%) and, C/N ratio, with red lines being discriminator between marine or terrigenous origin according to Meyers (1994). Photographs and X-radiographs (negative), as well as the Folk classification of grain assemblages. With light pink the sea floor is noted (h&t) and with pale yellow are marked the MTDs.

Synthesis

The sediment cores in this study consist of mass transport deposits (MTDs), hemipelagites and turbidites, focusing on MTDs triggered by the 1956 Amorgos earthquakes. The MTDs identified in the cores are classified as debris flows, which can exhibit both cohesive and cohesionless behaviors. In core SA-4, the clayey debris flows are structure-

less, while in core SA-1B from the Amorgos Basin, mud clasts and sedimentary structures are observed. Notably, in core SA-1B, the flow demonstrates a mix of cohesive and non-cohesive behavior, featuring approximately 20 cm of non-cohesive sandy debris flows at depths ranging from 80 to 100 cm. This core also exhibits soft-sediment deformation structures (SSDS), including hummocky cross-stratification, which indicate liquefaction processes potentially triggered by seismic events such as the 1956 earthquake. Both cores share similarities in their sedimentological facies, as illustrated in Figures 2 and 4. The uppermost sections of both cores represent the "present" seafloor, followed by the deposition of large gravity flows (debrites and sandy debrites) during the 1956 earthquake(s). Beneath these layers lies the "old" seafloor, containing older MTDs that predate the 1956 earthquake. These findings align with the work of Perissoratis and Papadopoulos (1999), who reported that sediments between Amorgos and Astypalaia Islands predominantly consist of mass flows, slumps, and debrites.

Core SA-1B, retrieved from the Amorgos Basin, shows a significantly high sand content, reaching up to 80%. This elevated sand fraction is likely attributed to two factors: a) the proximity to Amorgos Island, contributing coarser material to the basin, and b) the location near the epicenter of the 1956 seismic event. The currents generated by the earthquake are believed to have flowed into several channels on the seafloor, resulting in high-energy flows that deposited thick sediment layers. Near the epicenter, MTDs reach up to 1 meter in thickness, while nearly 50 km away measure about 55 cm thick.

The MTDs in both cores consist of a mixture of marine and terrestrial material, as confirmed by various geochemical indicators. The C/N ratio in these sediments shows values up to 60, and a clear decrease in $CaCO_3$ content correlates with the dilution of the sediments by terrigenous material. Additional proxies, such as the calcium-to-aluminum (Ca/Al) ratio (Rothwell and Croudace, 2015), along with elevated levels of silicon (Si), aluminum (Al), potassium (K), and rubidium (Rb), further corroborate this observation. These deposits exhibit high gamma density values and lower fractional porosity, which can serve as diagnostic criteria for classifying similar deposits in the region.

The rapid deposition of MTDs in the study area enabled the underlying sediments to retain their original characteristics. The "old" seafloor layers in both cores are composed of oxidized clay, marked by a distinct color change at the transition to these deposits. Although some differences exist between the two cores, the overall trends remain consistent. Both cores display marine-origin sediments in the present and old seafloor layers, as indicated by the C/N ratio, bromine (Br), and total organic carbon (TOC) values. Furthermore, calcium (Ca) in these deposits is primarily sourced from biogenic $CaCO_3$, as evidenced by the co-variation of calcium (Ca) and strontium (Sr). Manganese (Mn) values tend to be higher in the upper layers than underlying sediments, decreasing downcore. Nevertheless, distinct peaks in Mn concentrations are observed at the same depth intervals where the "old" seafloor is found.

These findings enhance our understanding of the sedimentological and geochemical features of mass transport deposits (MTDs) in the central Aegean Sea, particularly those associated with the 1956 Amorgos earthquakes. The characteristics of these deposits can serve as diagnostic criteria for identifying similar deposits in the surrounding area. By applying the thickness of these facies to a model alongside other numerical calculations, we can gain insights into the volume and direction of the flows generated during these seismic events. Furthermore, numerical modeling of the 1956 tsunamis, combined with the sediment characteristics, is essential for evaluating the impact of tsunamis and providing predictive insights for future seismic events.

Conclusion

- The mass transport deposits resulting from the twin earthquakes exhibit similar characteristics. These deposits consist of both cohesive and cohesionless flows, show a gray color, and vary in thickness from 55 cm to 1 m. They are primarily composed of a very high clay content and possess similar chemical properties. The variation in thickness is attributed to their proximity to the epicenter of the main earthquake.
- The chemical signatures reveal that core SA-4 contains terrestrial materials, while core SA-1B consists of a mixture of terrestrial and marine origins. This suggests that most deposits have traveled from shallower depths and undergone intense remobilization.
- During the seismic shaking and the rapid deposition of these mass transport deposits (MTDs), the old seafloor remains intact, preserving its physical characteristics, color, and geochemical composition. The seafloors before and after the deposition of the MTDs in 1956 show similar characteristics.
- The sedimentological and geochemical signatures of the aforementioned deposits are reliable criteria for distinguishing similar deposits from the 1956 twin earthquakes in the central Aegean Sea.

References

Brüstle, A., Friederich, W., Meier, T., Gross, C., 2014. Focal mechanism and depth of the 1956 Amorgos twin earthquakes from waveform matching of analogue seismograms. Solid Earth 5, 1027–1044. https://doi.org/10.5194/se-5-1027-2014

Friederich, W., Brüstle, A., Küperkoch, L., Meier, T., Lamara, S., 2014. Focal mechanisms in the southern Aegean from

temporary seismic networks – Implications for the regional stress field and ongoing deformation processes. Solid Earth 5, 275–297. https://doi.org/10.5194/se-5-275-2014

Manta, K., Tsampouraki-Kraounaki, K., Sakellariou, D., Rousakis, G., Chiocci, F., Casalbore, D., Migeon, S., Estrada, F., Alonso, B., Gross, F., Morfis, I., Livanos, I., Panagiotopoulos, I., Kalaitzis, M., 2022. Marine geophysical & sedimentological data reveal multiple submarine landslides triggered by the July 1956 Amorgos earthquake in the South Aegean Sea, Greece. Int. Conf. Seafloor Landforms, Processes and Evolution, Valetta, Malta, 4-6 July 2022.

Meyers, P.A., 1994. Preservation of elemental and isotopic source identification of sediemntary organic matter. Chem. Geol. 114, 289–302. https://doi.org/10.1016/0009-2541(94)90059-0

Okal, E.A., Synolakis, C.E., Uslu, B., Kalligeris, N., Voukouvalas, E., 2009. The 1956 earthquake and tsunami in Amorgos, Greece, in: Geophysical Journal International. John Wiley & Sons, Ltd (10.1111), pp. 1533–1554. https://doi.org/10.1111/j.1365-246X.2009.04237.x

Perissoratis, C., Papadopoulos, G., 1999. Sediment instability and slumping in the southern Aegean Sea and the case history of the 1956 tsunami. Mar. Geol. 161, 287–305. https://doi.org/10.1016/S0025-3227(99)00039-0

Rothwell, R.G., Croudace, I. w., 2015. Twenty Years of XRF Core Scanning Marine Sediments: What Do Geochemical Proxies Tell Us? Springer, Dordrecht, pp. 25–102. https://doi.org/10.1007/978-94-017-9849-5_2

Sakellariou, D., Manta, K., Rousakis, G., Tsampouraki-Kraounaki, K, Chiocci, F., Casalbore, D., Migeon, S., Estrada, F., Alonso, B., Gross, F., Morfis, I., Livanos, I., Panagiotopoulos, I., Kalaitzis, M., 2021. Multiple, earthquake-triggered, submarine landslides generated the July 1956 devastating tsunami(s) in the South Aegean Sea, Greece. General Assembly European Seismological Commission, ESC2021, 19-24 Sept. 2021

Shanmugam, G., Wang, Y., 2015. The landslide problem. J Palaeogeogr 4: 109–166. https://doi.org/10.3724/SP.J.1261.2015.00071

Soloviev, S.L., Solovieva, O.N., Go, C.N., Kim, K.S., Shchetnikov, N.A., 2000. Tsunamis in the Mediterranean Sea 2000 B.C.-2000 A.D. https://doi.org/https://doi.org/10.1007/978-94-015-9510-0

Tsampouraki-Kraounaki, K., Sakellariou, D., Rousakis, G., Morfis, I., Panagiotopoulos, I., Livanos, I., Manta, K., Paraschos, F., Papatheodorou, G., 2021. The Santorini-Amorgos Shear Zone: Evidence for Dextral Transtension in the South Aegean Back-Arc Region, Greece. Geosciences 2021, 11, 216, https://doi.org/10.3390/ geosciences11050216

17th INTERNATIONAL CONGRESS of the Geological Society of Greece

BULLETIN OF THE GEOLOGICAL SOCIETY OF GREECE, SP. PUBL.

EXTENDED ABSTRACT 205

Increased preparedness in anticipation of an imminent disaster: actions during the early 2025 Santorini – Amorgos (Aegean Sea, Greece) earthquake crisis and lessons learned

Mavroulis S.[1], Sarantopoulou A.[1], Mavrouli M.[2], Antonarakou A.[3], Lekkas E.[1,4]

(1) Department of Dynamic Tectonic and Applied Geology, Faculty of Geology and Geoenvironment, School of Sciences, National and Kapodistrian University of Athens, Athens, Greece, smavroulis@geol.uoa.gr

(2) Department of Microbiology, Medical School, National and Kapodistrian University of Athens, Athens, Greece

(3) Department of Historical Geology and Palaeontology, Faculty of Geology and Geoenvironment, School of Sciences, National and Kapodistrian University of Athens, Athens, Greece

(4) Earthquake Planning and Protection Organization, Athens, Greece

1. Introduction

Seismic waves from earthquakes propagate quickly, impacting natural and built environments before emergency measures can be implemented, posing challenges for Civil Protection authorities. Earthquake early warning systems (EEWS), which detect primary seismic waves and issue alerts, help mitigate damage and casualties by enabling timely precautionary actions (Cremen and Galasso, 2020). Despite their benefits, EEW systems are not universally applicable due to the complex geodynamic and seismotectonic characteristics of many regions. In such cases, seismic risk reduction depends largely on preparedness actions taken during standard operational phases, as reliable short-term earthquake forecasts remain elusive. Therefore, for most seismic events, the transition from standard preparedness to emergency response is immediate, making the enhanced preparedness phase impractical. In case of experiencing increased seismic activity, Civil Protection authorities may implement increased preparedness actions through public risk communication, structural assessments, and stakeholder engagement, aiming to enhance awareness, influence behavior, and improve community resilience (Musacchio et al., 2023). A notable case occurred during the early 2025 seismic sequence between the Santorini and Amorgos Islands in the southern part of the Aegean Sea (Greece), a rare and unprecedented event globally. This sequence raised significant concerns regarding its evolution, duration, and potential link to magmatic and volcanic activity. It affected mainly the daily activities of the population, affecting services, and economic sectors such as tourism and transportation. This event marked the first instance in Greece where increased preparedness measures were activated in anticipation of a potential major earthquake. This study examines the measures implemented by the Greek Civil Protection authorities and operational agencies in response to the ongoing and escalating seismic sequence. Emphasis is placed on safeguarding both residents and visitors, while proactively reducing the potential risks associated with the occurrence of a more powerful earthquake that could have significant consequences for both the natural and built environments.

2. Disaster Prevention and Management Framework in Greece

Civil Protection in Greece is primarily governed by Law 4662/2020 (Government Gazette of the Hellenic Republic - GGHR, 2020), as amended by Law 5075/2023 (GGHR, 2023), which enhance disaster management and reorganize operational structures. These laws define the roles and coordination mechanisms among key agencies, including the General Secretariat for Civil Protection (GSCP), Fire Service, Hellenic Police, and Armed Forces, across all disaster phases. The GSCP, under the Ministry of Climate Crisis and Civil Protection (MCCCP), coordinates emergency responses for natural and technological hazards at all levels of administration. Strategic disaster management is guided by the national “Xenocrates” Plan, which ensures interagency coordination for disaster risk reduction and response (GGHR, 2003). Earthquake management is outlined in the “Enceladus” Plan, initially issued in 2020 and then updated in the version “Enceladus 2” (GSCP, 2022), while the “Talos 2” Plan focuses on volcanic hazards, particularly for the Santorini volcanic complex (GSCP, 2023). These earthquake plans have been tested through operational exercises (Mavroulis et al., 2025) and real events, including the 2020 Samos (eastern Aegean) earthquake and the 2021 Thessaly (central Greece) and Crete (southern Greece) earthquakes (Mavroulis et al., 2022).

The earthquake contingency plan outlines a four-phase disaster management framework: (i) standard prevention and preparedness measures, (ii) heightened preparedness in anticipation of an imminent earthquake, (iii) emergency response involving immediate mobilization and impact management, and (iv) short-term relief and rehabilitation of affected populations (GSCP, 2022). However, due to the unpredictability of seismic events and the absence of reliable short-term forecasting, the second phase has never been activated. In practice, the standard preparedness before a strong earthquake is followed by emergency response and subsequent relief and recovery after its generation. Notably, the second phase was conceived as an enhancement, not an acceleration, of standard preparedness activities.

2.1. Standard Preparedness Prevention Actions

During the prevention phase of standard preparedness, all involved stakeholders implement measures aimed at enhancing preparedness for earthquake emergencies and the rapid management of their effects. These actions include pre-seismic building inspections, contingency plan revisions, development of action memoranda, and allocation of financial resources. The functionality of emergency communication systems and the efficiency of information exchange are assessed to support coordinated decision-making. Maintenance of emergency equipment, identification of assembly sites and waste disposal areas, and readiness of shelters are also prioritized. Memoranda of understanding with private entities are established to secure additional resources, while public awareness campaigns promote self-protection. Local and regional Coordination Bodies convene to strengthen interagency collaboration, supported by structured training programs and operational exercises for Civil Protection personnel.

2.2. Enhanced Earthquake Preparedness Actions

Given the limitations of short-term earthquake forecasting, early warning systems are not included in Greece's seismic risk management framework. Nonetheless, the Secretary General of Civil Protection may increase operational readiness based on evaluations from the specialized seismic hazard committees of the Earthquake Planning and Protection Organization (EPPO). In response, Municipal and Regional authorities are responsible for implementing or accelerating preventive actions, while local coordination bodies, convened by Mayors or Deputy Mayors, facilitate interagency collaboration. Simultaneously, Civil Protection operational structures review and update emergency plans, enhance capabilities in high-risk zones, and actively participate in coordination efforts at both local and regional levels.

2.3. Emergency response and short-term earthquake impact management

Upon a strong earthquake, the Civil Protection mobilization system is activated under the "Enceladus 2" Plan, coordinating response actions across six areas: (i) search and rescue (SAR) and emergency medical services, (ii) restoration of critical infrastructure and essential services, (iii) protection of affected populations, (iv) operational coordination and administrative measures, (v) public communication and awareness, and (vi) international cooperation (Mavroulis et al., 2022, 2025). The Fire Brigade leads SAR, provides medical aid, and oversees evacuations. Authorities collect real-time data for decision-making, while infrastructure rehabilitation includes inspections, debris clearance, and restoration of utilities. Civil Protection Coordination Bodies manage response efforts locally and regionally, with support from the Armed Forces, volunteers, and public communication initiatives. If needed, evacuations are organized, and international support is requested through the European Civil Protection Mechanism

.

2.4. Immediate relief and rapid rehabilitation actions

In the post-earthquake relief phase, immediate recovery efforts focus on supporting affected populations, conducting damage assessments, and facilitating efficient administrative response. Priority is given to assisting homeless and displaced individuals through municipal welfare services, which provide financial aid for basic needs and essential household replacements. Concurrently, damage to buildings is documented, affected zones are delineated, and housing assistance is granted based on official decisions. Financial support is also extended to impacted businesses, including industrial, commercial, agricultural, and non-profit entities. Restoration of critical infrastructure, such as water, electricity, telecommunications, and road networks, is undertaken by the responsible technical services.

3. The early 2025 Santorini – Amorgos Earthquake Swarm and its Impact

3.1. Seismotectonic Setting of Santorini-Amorgos Area

The central Aegean region, dominated by the Cyclades islands, is geologically defined by the NE-SW trending Anydros, Santorini-Anafi, and Amorgos grabens, within the Santorini-Amorgos Tectonic Zone, an extensional structure 60-70 km long and 20-25 km wide between the Cyclades and Anafi-Astypalaea Plateaus (Tsampouraki-Kraounaki et al., 2021). These grabens, bounded by major faults and separated by horsts, exhibit NW-ward tilt and reach depths of up to 755 m. The area has a history of destructive seismicity, most notably the 9 July 1956 Amorgos earthquake, the strongest in 20th-century Greece. It caused widespread damage across several islands, resulting in 53 fatalities and 100 injuries (Papazachos and Papazachou, 2003). It also triggered the largest tsunami reported in the 20th century over the whole Mediterranean Basin with run-up values up to 30 m in several islands of the southern Aegean Sea (Okal et al., 2009). It was triggered either by offshore landslides (Ambraseys, 1960) or large seafloor rupture (Leclerc et al., 2024).

3.2. Evolution, Seismological Properties and Environmental Effects of the 2025 Earthquake Swarm

After the first significant episode since 2011-2012, seismic activity reemerged between June 2024 and January 2025 within the Santorini caldera, with intensification observed from mid-September. Over 1,200 earthquakes were detected in the Santorini–Kolumbo area using machine-learning-based methods, with the largest event (M=3.8) occurring off Thirassia Island on 25 January

(Interdisciplinary Risk and Crisis Management Committee of the University of Athens, 2025). A new seismic cluster emerged east of Kolumbo on 26 January, with activity peaking on 3 and 4 February at 136 and 140 events, respectively (Seismological Laboratory of the National and Kapodistrian University of Athens – SL-NKUA, 2025) (**Figure 1**). Earthquakes with M ≥ 4.0 were most frequent between 1–12 February, particularly on 4–5 February (19 events per day), and the strongest event (M 5.2) was recorded on 10 February (SL-NKUA, 2025). Seismic activity gradually declined after mid-February, with no M ≥ 4.0 earthquakes after 27 February (SL-NKUA, 2025).

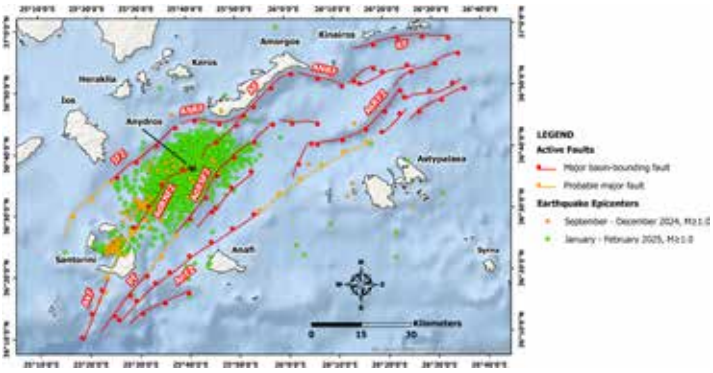

Figure 1. The Santorini – Amorgos area that was mainly affected by the early 2025 earthquake swarm along with the major basin bounding faults and the probable major faults based on Tsampouraki-Kraounaki et al. (2021). The epicenters in the affected area from September 2024 to February 2025 were recorded from the SL-NKUA (2025). AdRNFZ: Anydros Ridge North Fault Zone; AdRSFZ: Anydros Ridge South Fault Zone; AF: Amorgos Fault; AkF: Akrotiri Fault; AnFZ: Anafi Fault Zone; ANRF: Amorgos North Relay Fault; ASRF: Amorgos South Relay Fault; AsRFZ: Astypalaea Ridge Fault Zone; IFZ: Ios Fault Zone; KF: Kinairos Fault; PF: Perissa Fault.

Spatially, initial epicenters were located northeast of Santorini and east of the offshore Kolumbo volcano, later migrating toward and around Anydros islet (SL-NKUA, 2025). Most seismicity occurred southwest of Anydros, though epicenters periodically shifted northeast or appeared simultaneously on both sides of the islet (SL-NKUA, 2025). This pattern highlights a dynamic and evolving seismic sequence concentrated within the Santorini – Amorgos area.
The early 2025 earthquake swarm triggered landslides in three areas: the southern coastal zone (e.g., Red and Vlichada beaches), the central-eastern caldera slopes (e.g., Athinios, Alonaki, Fira, Imerovigli and Skaros), and the northern part of the island along the Fira-Oia road (**Figure 2**).

Figure 2. The spatial distribution of the landslides in Santorini triggered by the 2025 earthquake swarm.

Common geomorphological features at these sites include steep slopes, unstable volcanic formations, and landslide deposits. Impacts varied from debris accumulation at Red beach to sediment mobilization at Vlichada. Minor landslides in the Athinios area posed no threat to infrastructures, while rockfalls near Fira occurred downslope of residential zones without damage. In the north, rockfalls along the Fira-Oia road created hazardous conditions, requiring caution for drivers.

4. Increased preparedness actions for anticipation of an imminent earthquake

4.1. Joint meetings of seismic and volcanic risk assessment committees and public information dissemination

In response to ongoing seismic activity in the Santorini–Anydros–Amorgos region, the EPPO's Permanent Scientific Committees for Seismic Hazard Assessment and Volcanic Arc Monitoring convened to analyze the evolving seismic sequence. Official communications from the MCCCP summarized their findings, noting potential links between seismicity, offshore faults, and magmatic and volcanic processes. Recommended preventive measures included suspending educational activities, avoiding gatherings in unstable structures, restricting port access, removing hazardous building elements, selecting safer routes near landslide-prone areas, and evacuating coastal zones. Key meetings took place in January and February 2025, including a major session on 5 February chaired by the Prime Minister and Minister for Climate Crisis and Civil Protection, followed by a public broadcast featuring experts from the National and Kapodistrian University of Athens and Aristotle University of Thessaloniki, discussing related hazards and risks.

4.2. Awareness raising efforts

The EPPO, Greece's authority on earthquake policy implementation, also plays a vital role in public education and awareness to reduce seismic risk and assess seismic hazard. Its initiatives target diverse groups, including professionals, educators, Civil Protection personnel, tourism workers, and vulnerable populations such as individuals with disabilities. In response to the 2025 seismic sequence, and alongside committee meetings and official announcements on risk reduction, the EPPO conducted awareness and training activities for the affected population. Notably, it organized a webinar titled "Experiencing an Earthquake Period: Earthquake Protection of School Units" in collaboration with the Municipality of Thira, which was attended by local school directors, kindergarten heads, and nursery managers.

4.3. Strengthening security forces in affected islands

In response to the seismic sequence in Santorini and the surrounding islands, multiple Greek authorities coordinated efforts to increase preparedness and public safety. The Hellenic Fire Service deployed specialized disaster management units (EMAK in Greek), rescue dogs, drones, forest operations teams, and a mobile operations center ("Olympos") equipped with advanced technology to monitor and manage disaster response. Additional search and rescue teams were stationed across nearby islands, with aerial rescue teams on standby. Concurrently, the Hellenic Police reinforced local law enforcement with personnel and vehicles from Athens, the capital of Greece, implementing nightly patrols and security checks to prevent criminal activity and safeguard abandoned properties, ensuring public order and a sense of security amid widespread evacuations. The Hellenic Coast Guard implemented strict emergency measures in Santorini's ports, including restricted access, vessel movement controls, and safety protocols for mooring and navigation, backed by enforcement of legal sanctions. The Coast Guard also instructed vessel operators to maintain high alert for both seismic and potential hydrometeorological hazards. Meanwhile, the Hellenic Armed Forces remained on standby, deploying essential logistics infrastructure such as cranes, lighting systems, tents, portable kitchens, and liaison officers to coordinate with Civil Protection authorities. Strategic naval assets, including a tank landing ship and a support vessel, were positioned near Santorini to enable rapid response capabilities across the affected island region.

4.4. Strengthening health services in affected islands

In response to the ongoing seismic activity, all leaves for medical, nursing, and support staff at Santorini Hospital were revoked to ensure full operational readiness. The National Center for Emergency Assistance, under the MCCCP, reinforced its teams on Santorini, Amorgos, and Ios with personnel from the Special Department of Disaster Medicine, including doctors, rescuers, medical equipment, and additional ambulances. The Health Operations Centre and the Unified Coordination Operations Centre maintained high alert for continuous coordination. The 2nd Health Region of Piraeus and Aegean also enhanced readiness by deploying medical teams from "Attikon" General University Hospital and Naxos General Hospital – Health Center, and a psychological support unit from "Dafni" Psychiatric Hospital of Attica. Plans were in place to mobilize all private doctors in the affected islands if needed. Additionally, an evacuation exercise was conducted at Thira General Hospital, supervised by the Deputy Minister of Health and hospital leadership, reflecting the elevated state of preparedness.

4.5. Contribution of public utilities

To mitigate the risk of a widespread blackout during a major earthquake, the Hellenic Electricity Distribution Network Operator deployed generator-equipped trucks to Santorini, while the Municipality enhanced the island's electrical infrastructure by reinforcing networks and installing additional poles and conductors. Simultaneously, the Ministry of Digital Governance, in collaboration with mobile and satellite communication providers, ensured the deployment of mobile units and generators across the affected islands to maintain uninterrupted telecommunications during potential power failures. In response to the increasing number of residents leaving Santorini due to escalating seismic activity, and following a request from the MCCCP, airlines introduced extra flights, offering free tickets to children and teachers, along with a free return ticket valid until 20 August 2025 for those who had evacuated. Ferry companies also initiated emergency services and committed to adjusting schedules as needed to support residents and visitors departing the island.

4.6. Notifying the population via European Emergency Number 112

During the January – February 2025 seismic sequence, Greece's 112 emergency warning system was activated for the first time in response to landslide hazard. On 3 February, a geotargeted alert was issued to Santorini residents warning of landslides due to seismic activity and prohibiting access to Ammoudi and Armeni ports and the old port of Fira, while urging compliance with official instructions. A second message followed, sent to residents of Ios, Amorgos, Santorini, and Anafi, advising heightened alertness and adherence to Civil Protection directives amid ongoing seismic activity.

4.7. Municipal authorities' coordination with Civil Protection agencies

In February 2025, the Municipality of Thira issued the updated Civil Protection plan "Thiras 2" (Municipality of Thira, 2024) emphasizing preventive evacuation of at-risk populations. The plan featured thematic maps identifying emergency shelters, coastal embarkation points, and airdrop zones, selected based on terrain, accessibility, evacuation routes, and minimal tsunami risk. Designated pick-up points for vulnerable groups and students were included, and shelter locations were widely shared through social media and local announcements. To support seismic risk management, the municipality ensured continuous public communication in line with EPPO guidelines. Pre-seismic inspections by the Ministry of Infrastructure confirmed the structural safety of schools. Following landslides in Santorini and, to a lesser extent, in Amorgos, causing limited disruption, authorities enforced access restrictions and installed warning signs near hazardous areas and unstable structures to protect residents.

4.8. Municipality of Thira emergency declaration

On 6 February 2025, the MCCCP declared a State of Emergency in Civil Protection for the Municipality of Thira (MCCCP, 2025a), within the Regional Unit of Thira in the South Aegean Region. This measure was taken to address emergency needs and manage the impact of seismic activity that occurred between January and February in the study area. The declaration was in effect from February 1 to March 1. This action primarily facilitates the bypassing of bureaucratic procedures in public administration to ensure a more efficient response to the seismic crisis.

4.9. Ministerial decisions on earthquake impact mitigation and risk reduction

To mitigate the risks associated with seismic activity and secondary hazards such as landslides, preventive measures were enacted on Thira and Thirassia Islands through a ministerial decision (GGHR, 2025), co-signed by key governmental bodies including the MCCCP. In force from March 14 to May 14, 2025, these temporary restrictions targeted high-risk zones, particularly those with frequent tourist activity or proximity to landslide-prone areas. Measures included limitations on access to ports and adjacent offshore areas without port authority approval, restricted movement on selected roadways and footpaths, controlled access within specific settlement zones, suspension of operations in residential, hospitality, and healthcare facilities, and a ban on vehicular traffic in designated road sections.

4.10. Voluntary team actions for the public and vulnerable groups

During the earthquake swarm in the southern Aegean, the Hellenic Red Cross (HRC) played a crucial role by deploying specialized volunteer teams to Santorini, including Samaritan-Rescuers, psychosocial health professionals, and trained K9 units. These teams provided psychological support to vulnerable populations such as the elderly, chronically ill, and disabled individuals, conducting home visits and counseling for 60 families to address uncertainties regarding emergency contacts and shelter. Additionally, the HRC organized mental health first aid courses, training 198 residents in crisis-response skills, and conducted an evacuation exercise at the Elderly Care Center. On Amorgos, HRC teams collaborated with local Civil Protection agencies to provide community-wide psychosocial support and established a temporary Operations Center in Aegiali area. Volunteers also led awareness campaigns in schools to improve seismic preparedness. These efforts enhanced local capabilities for psychological support, emergency readiness, and resilience.

4.11. Web platform for emergency shelter dissemination

Amid the ongoing seismic activity, the Ministry of Digital Governance, in collaboration with the National Observatory of Athens, launched a web platform to inform and guide citizens on the location of safe assembly points across Greece (MCCCP, 2025b), including seismically affected islands of Santorini, Amorgos, and Ios. The platform ensures user-friendly, real-time access to officially approved assembly points without requiring application installation, and is progressively updated with additional information tailored to various natural hazard scenarios.

5. Discussion

5.1. Adequacy of implemented measures during the early 2025 seismic sequence

During the early 2025 crisis, Civil Protection authorities focused on institutional preparedness through infrastructure assessments, operational readiness, and public announcements. However, community engagement was limited, with minimal participation of

residents and visitors in preparedness actions. Although seismic inspections and safety measures were implemented, the lack of inclusive actions reduced the overall effectiveness of public preparedness efforts. This gap was addressed by the HRC, which deployed trained volunteers to provide psychosocial support, first aid training, and mental health awareness programs, particularly to vulnerable groups such as people with disabilities and the elderly. These interventions played a critical role in enhancing individual psychological preparedness and social resilience, complementing the institutional response and filling crucial gaps in community-level risk reduction. Holistic preparedness also included physical measures like retrofitting and emergency planning for key infrastructure, alongside campaigns promoting risk awareness. The integration of psychological and physical preparedness, as seen in both Civil Protection and HRC efforts, underlines the importance of multi-dimensional strategies for enhancing resilience.

5.2. Further proposed measures to reduce risk

To reduce risks in the Santorini volcanic complex and surrounding areas, early actions are vital, particularly through continuous geophysical, seismological, and geochemical monitoring. Predictive models, combined with real-time data, enable authorities to issue timely warnings and initiate preparatory actions to mitigate human and economic losses. Risk communication, including regular exercises and training for Civil Protection authorities and the public, is crucial for effective disaster preparedness. However, challenges remain, as no full-scale exercises have been conducted since the approval of the “Enceladus” and “Talos” plans in 2020. While awareness efforts are important, they must be more frequent, especially for vulnerable populations. Infrastructure improvements, including safe evacuation routes and emergency ports, are essential, as delays during the 2025 crisis hindered timely responses. Pre-seismic inspections and strengthening critical infrastructure, such as schools and healthcare facilities, are necessary for long-term resilience.

6. Conclusions

The unpredictability of early 2025 Santorini-Amorgos seismic sequence emphasized the need for increased preparedness actions. In response, the authorities and the operational structures of the Civil Protection system in Greece implemented unprecedented preparedness measures, marking the first time in the country that proactive actions were taken in anticipation of an imminent earthquake. These included strengthening security and health services, activating the European Emergency Number 112, enhancing infrastructure resilience, updating emergency plans, and launching public awareness campaigns. Volunteer groups also provided support to vulnerable populations. This comprehensive practice, tailored to the specific geological conditions of the region, can be considered a model approach for managing seismic emergencies and offers valuable lessons for other areas with similar geodynamic risks.

References

Ambraseys, N.N., 1960. The seismic sea wave of July 9th 1956, in the Greek Archipelago. Journal of Geophysical Research 65, 1257–1265. https://doi.org/10.1029/JZ065i004p01257

Cremen, G., Galasso, C., 2020. Earthquake early warning: Recent advances and perspectives. Earth-Science Reviews 205, 103184. https://doi.org/10.1016/j.earscirev.2020.103184

General Secretariat for Civil Protection, 2022. General Plan for Emergency Response and Immediate/Short-Term Management of the Earthquake Impact, Code-Named “Enceladus 2”. Ministry of Climate Crisis and Civil Protection, General Secretariat of Civil Protection, Directorate of Emergency Response Planning.

General Secretariat for Civil Protection, 2023. General Plan for Emergency Response and Immediate/Short-Term Management of the Impact of Volcanic Activity in the Volcanic Complex of Santorini, Code-Named “Talos 2”. Ministry of Climate Crisis and Civil Protection, General Secretariat of Civil Protection, Directorate of Emergency Response Planning.

Government Gazette of the Hellenic Republic, 2003. Ministerial Decision No. 1299/2003. Approval of the 7.4.2003 General Civil Protection Plan with the Keyword “XENOCRATES”. Second Volume, Sheet No. 423.

Government Gazette of the Hellenic Republic, 2020. Law No. 4662/2020. National Mechanism for Crisis and Risks Management and Risk Management, Restructuring of the General Secretariat for Civil Protection, Upgrading of the Civil Protection Volunteer System, Reorganization of the Fire Service and Other Provisions. First Volume, Sheet No. 27.

Government Gazette of the Hellenic Republic, 2023. Law No. 5075/2023. Restructuring of Civil Protection—National Air Rescue and Air Ambulance Mechanism and Other Urgent Provisions on State Aid. First Volume, Sheet No. 206.

Government Gazette of the Hellenic Republic, 2025. Emergency Civil Protection measures in the Island Complex of Santorini. Second Volume, Sheet No. 1267.

Interdisciplinary Risk and Crisis Management Committee of the University of Athens, 2025. Special Announcement, Tuesday 4-2-25 at 9.00 am. Available online: https://hub.uoa.gr/diepistimoniki-epitropi-diacheirisis-kindynon-kai-kriseon-ekpa-ektakto-deltio-typou-triti-4-2-25-kai-ora-9-00/ (accessed on 04/02/2025).

Leclerc, F., Palagonia, S., Feuillet, N., Nomikou, P., Lampridou, D., Barrière, P., Dano, A., Ochoa, E., Gracias, N., Escartin, J., 2024. Large seafloor rupture caused by the 1956 Amorgos tsunamigenic earthquake, Greece. Communications Earth & Environment 5, 663. https://doi.org/10.1038/s43247-024-01839-0

Mavroulis, S., Lekkas, E., Grambas, A., Mavrouli, M., Mokos, V., Kourou, A., Thoma, T., Karagiannis, F., Stamati, E., Kaviris, G., et al., 2025. Enhancing Preparedness and Resilience for Seismic Risk Reduction: The "Minoas 2024" Full-Scale Exercise for Earthquakes and Related Geohazards in Crete (Southern Greece). Geosciences 15, 59. https://doi.org/10.3390/geosciences15020059

Mavroulis, S., Mavrouli, M., Kourou, A., Thoma, T., Lekkas, E., 2022. Multi-Hazard Emergency Response for Geological Hazards Amid the Evolving COVID-19 Pandemic: Good Practices and Lessons Learned from Earthquake Disaster Management in Greece. Sustainability 14, 8486. https://doi.org/10.3390/su14148486

Musacchio, G., Saraò, A., Falsaperla, S., Scolobig, A., 2023. A scoping review of seismic risk communication in Europe. Frontiers in Earth Science 11, 1155576. https://doi.org/10.3389/feart.2023.1155576

Ministry for Climate Crisis and Civil Protection, 2025a. Declaration of State of Emergency for the Municipality of Thira. General Secretariat for Civil Protection, Athens, Greece. Document No. A479.

Ministry for Climate Crisis and Civil Protection, 2025b. Map of safe assembly points – mySafetyPlan. Available online: https://mysafetyplan.gov.gr (accessed on 06/04/2025).

Municipality of Thira, 2024. Second Issue of the Special Civil Protection Plan for the Preventive Organized Evacuation of the Citizens of the Municipality of Thira with the Code Word "THIRAS 2".

Okal, E.A., Synolakis, C.E., Uslu, B., Kalligeris, N., Voukouvalas, E., 2009. The 1956 earthquake and tsunami in Amorgos, Greece. Geophysical Journal International 178, 1533–1554. https://doi.org/10.1111/j.1365-246X.2009.04237.x

Papazachos, B., Papazachou, C., 2003. The earthquakes of Greece. Ziti Publications, Thessaloniki, 286 p.

Seismological Laboratory of the National and Kapodistrian University of Athens. Earthquake Catalogue Search. Available online: http://www.geophysics.geol.uoa.gr/stations/gmapv3_db/index.php (accessed on 10/01/2024).

Tsampouraki-Kraounaki, K., Sakellariou, D., Rousakis, G., Morfis, I., Panagiotopoulos, I., Livanos, I., Manta, K., Paraschos, F., Papatheodorou, G., 2021. The Santorini-Amorgos Shear Zone: Evidence for Dextral Transtension in the South Aegean Back-Arc Region, Greece. Geosciences 11, 216. https://doi.org/10.3390/geosciences11050216

17th INTERNATIONAL CONGRESS of the Geological Society of Greece

BULLETIN OF THE GEOLOGICAL SOCIETY OF GREECE, SP. PUBL.

EXTENDED ABSTRACT 206

Application of GIS-Based Multicriteria Decision Analysis and Analytic Hierarchy Process for Flood-Hazard Mapping in the Messapios River Basin, Central Evia Island, Greece

Mazarakis V.[1], Tsanakas K.[1], Greenbaum N.[2], Batzakis D.-V.[1], Sorrentino A[3], Tsodoulos I.[1], Valkanou K.[1], Karymbalis E.[1]

(1) Department of Geography, Harokopio University, Athens, Greece, karymbalis@hua.gr (2) School of Environmental Sciences, University of Haifa, Israel (3) Department of Science and Technology, Parthenope University of Naples, Italy

Introduction

Floods are among the most frequent and devastating natural hazards worldwide, causing widespread fatalities, significant property damage, and environmental degradation. In recent decades, the occurrence of extreme flood events has risen dramatically, leading to both immediate impacts, such as loss of life, property and infrastructure destruction, and longer-term effects, including health issues caused by pollution and financial difficulties for individuals and communities. Statistics emphasize the scale of the issue, with floods consistently accounting for a large proportion of natural disasters, deaths, and economic losses globally (CRED, 2023). The increasing frequency and intensity of floods highlight the pressing need to understand their underlying causes and implement effective strategies for risk mitigation. Flood-hazard assessment and mapping have become essential tools for prevention and spatial management. A widely used approach involves integrating GIS-based Multi-Criteria Decision Analysis (MCDA) with the Analytic Hierarchy Process (AHP), which allows for a systematic evaluation of multiple factors contributing to flooding and their relative importance (Ouma & Tateishi, 2014; Gigovic *et al*., 2017; Das, 2018; Radwan *et al*., 2019).

This study applies a GIS-based MCDA methodology in combination with AHP to assess and map flood hazard in the Messapios River catchment, a flood-prone area in Central Evia Island, Greece. The analysis incorporates critical factors influencing flooding, including those that affect water flow during extreme runoff events, and assigns weights to these factors based on expert input. This approach aligns with similar studies conducted across Greece, indicating its effectiveness in flood-hazard assessment and providing significant insights for spatial planning and disaster prevention.

Study Area

The Messapios River, an ephemeral stream in central Evia Island, is approximately 34 km long with a catchment area of 216 km² (Figure 1).

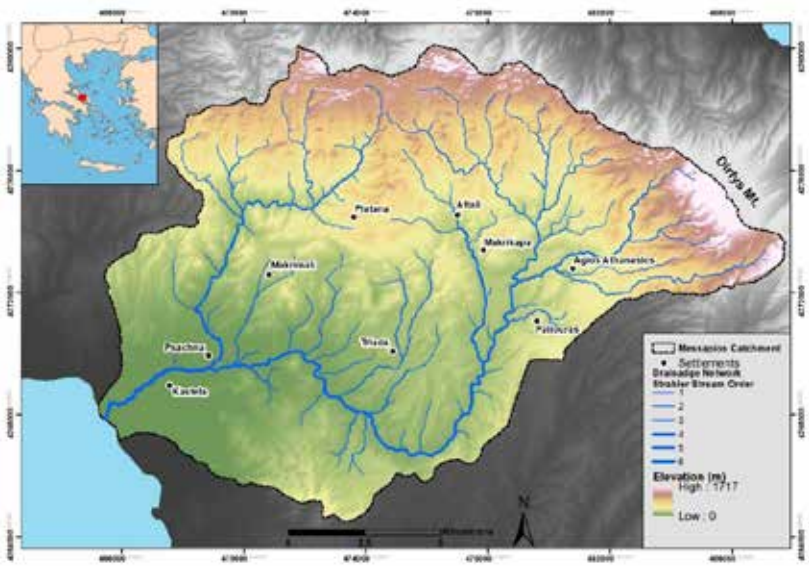

Figure 1. Map of the Messapios River drainage network and catchment.

The drainage network drains a rugged mountainous area, reaching elevations of up to 1,743 m on Mount Dirfys, with steep slopes averaging 24.1% that promote surface runoff. The lowland fan delta near the river's mouth, characterized by gentle slopes, enhances sediment deposition and rainwater infiltration. The catchment consists of geological formations of the Sub-Pelagonian geotectonic zone, including ophiolites, limestones, and flysch, as well as Neogene sedimentary rocks, and Holocene

alluvial deposits.
The climate of the study area is subtropical Mediterranean with hot, dry summers and mild, wet winters, with annual precipitation averaging 450 mm. Hydrologically, the Messapios River catchment falls within the Eastern Sterea Hellas Water District, which recorded 181 flood events between 1939 and 2018. Severe floods in 2006 and 2020 caused significant damage to settlements, infrastructure, and farmland, particularly during the 2020 "Thalia" storm, which resulted in eight fatalities and extensive property destruction.
Administratively, the catchment is part of the Municipality of Dirfys-Messapia, with 15,934 residents, half of whom live in the low-lying plains. Key settlements include Psachna, Kastella, Triada, and Makrykapa. The rural economy relies heavily on agriculture, with 35% of the population engaged in farming, supported by the fertile soils over the plains, and olive cultivation.

Methodology
This study aims to assess and map flood risk within the Messapios River catchment using a model that integrates Multi-Criteria Decision Analysis (MCDA) and the Analytic Hierarchy Process (AHP). This approach enabled the selection, calibration, and integration of five critical factors: slope, elevation, proximity to higher-order stream channels, land cover, and hydro-lithological characteristics of the geological formations. These factors, identified from a review of established methodologies in the literature (Haan *et al*., 1994; Kazakis *et al*., 2015; Bathrellos *et al*., 2016; Patrikaki *et al*., 2018; Skilodimou *et al*., 2021; Feloni *et al*., 2020; Karymbalis *et al*., 2021), influence water flow when drainage systems are overwhelmed by high runoff. A single-level hierarchy was used to maintain a straightforward weighting process for each factor's impact on flood hazard, avoiding potential subjectivity in grouping criteria and following the approach used in similar studies.
Each factor was initially divided into five classes with defined boundaries and then reclassified on a standardized scale from 1 to 5, representing increasing flood hazard levels, as shown in Table 1. A rating of "1" corresponds to a very low flood hazard level, while a rating of "5" represents a very high flood hazard level. The spatial distribution of each factor was visualized through thematic maps, where the values were classified and standardized to ensure consistency in assessing overall flood hazard.
The slope analysis for the study area was conducted using ArcGIS/ArcMap ESRI® software, utilizing a high-resolution 5-meter Digital Elevation Model (DEM) provided by the Hellenic Cadastre (Ktimatologio S.A.). This DEM also served to derive the elevation grid for the area and to extract the drainage network. The stream channels were ranked according to Strahler's stream order system (Strahler, 1957) using ArcGIS/ArcMap. To determine the "proximity to the stream channel" factor, buffer zones were created in ArcMap, generating polygons around both sides of stream channels with a Strahler order greater than 3, at specified distances. A Strahler order greater than 3 was chosen to prioritize larger channels that have a greater potential to contribute to flood hazards due to their size and drainage capacity. Land cover data was obtained from the Copernicus CORINE Land Cover database (Copernicus CORINE Land Cover, 2018) and the Agricultural Blocks dataset (ILOTS 2012) provided by the Ministry of Rural Development and Food. Geological formations in the catchment were sourced from the 1:50,000 scale geological map provided by the Institute of Geology & Mineral Exploration of Greece (IGME, 1981).
The AHP was employed to assign weights to each criterion (Saaty, 1990a; Saaty, 1990b). A pairwise comparison was conducted by the authors based on their expertise in flood hazard assessment from similar studies to assess and rank the criteria based on their relative significance. After determining the weights, the overall flood-hazard score for the Messapios River catchment was calculated by linearly combining the weighted criteria. This process involved overlaying the thematic maps of the factors, each assigned a specific weight, within a vector-based GIS environment. The criteria were integrated using the Weighted Linear Combination (WLC) method, expressed by the formula:

$$H = \sum_{i=1}^{n} w_i X_i$$

where H represents the flood hazard degree, n is the number of criteria, w_i is the weight of criterion i, and X_i is the rating of criterion i.
The result was a final thematic layer depicting the flood hazard across the entire catchment. A sensitivity analysis was also conducted to assess the robustness of the model. This involved applying a slight adjustment to the weight of the most influential criterion while proportionally modifying the weight of the second most influential criterion, ensuring that the changes did not undermine the model's effectiveness.
To validate the flood hazard map, it was compared with the Zoning of Flood-Prone Areas established by the Special Secretariat of Water, Ministry of Environment and Energy, as well as with past flood records in the study area. This comparison helped to assess the consistency of the results. Additionally, to provide an initial estimate of the catchment's vulnerability to flooding, the spatial distribution of settlements and critical infrastructure—such as roads, bridges, schools, industrial facilities, and electricity substations—was analyzed in relation to the mapped flood hazard zones.

Table 1. Classification matrix for flood-hazard criteria, detailing the assigned rating categories and the corresponding area covered by each category for every criterion.

Flood-hazard Criterion	Class	Rating	Area (km^2)	Area (%)
Slope (°)	>40	1	10.03	4.65
	25–40	2	50.42	23.35
	15–25	3	45.01	20.24
	5–15	4	61.06	28.27
	<5	5	49.44	22.89
Elevation (m a.m.s.l.)	901-1717	1	14.97	3.93
	501-900	2	39.29	18.19
	301-500	3	27.92	12.93
	151-300	4	55.58	25.74
	<150	5	78.20	39.21
Proximity to the stream channels (m)	>80 for the 3rd order streams, >100 for 4th order streams, >120 for 5th order streams, and >150 for 6th order stream	1	205.03	94.94
	60-80 for the 3rd order streams, 80-100 for 4th order streams, 100-120 for 5th order streams, and 130-150 for 6th order stream	2	1.88	0.87
	40-60 for the 3rd order streams, 60-80 for 4th order streams, 80-100 for 5th order streams, and 100-130 for 6th order stream	3	2.15	0.99
	20-40 for the 3rd order streams, 30-60 for 4th order streams, 40-80 for 5th order streams, and 50-100 for 6th order stream	4	3.15	1.46
	<20 for the 3rd order streams, <30 for 4th order streams, <40 for 5th order streams, and <50 for 6th order stream	5	3.75	1.74
Land cover	Forests (broad-leaved, coniferous, mixed), Sclerophyllous vegetation, Transitional woodland-shrub	1	129.90	60.13
	Olive groves, natural grasslands, shrub and/or herbaceous vegetation associations	2	16.15	7.47
	Complex cultivation patterns, and principally occupied by agriculture, with significant areas of natural vegetation	3	23.54	10.90
	Non-irrigated arable land, sparsely vegetated areas	4	41.38	19.19
	Discontinuous urban fabric, industrial or commercial units,	5	4.99	2.31
Geological formations	Permeable alluvial deposits	1	49.85	23.08
	Permeable carbonate rocks	2	103.44	47.90
	Semi-permeable alternations of conglomerates, marls, clays, sandstones	3	20.91	9.68
	Semi-permeable igneous and metamorphic rocks	4	27.79	12.87
	Flysch formation	5	13.97	6.47

Results

The thematic maps in Figure 2 illustrate the spatial distribution of the five criteria employed in flood hazard assessment, categorized into five hazard levels according to their respective impact on flooding. The slope in the study area ranges from 0° to 76°, with 51% (~110 km^2) of the catchment categorized as “highly” or “very highly” susceptible to flooding, primarily in the central, southern, and western plains of Psachna and Triada. Steeper slopes with “low” to “very low” flood risk are located in the northern and eastern mountainous regions, including Mount Dirfys (Figure 2a). Regarding the elevation criterion, approximately 65% of the area (~137 km^2), which includes most settlements and all documented flood events, lies below 300 m and falls within the “high” and “very high” flood hazard susceptibility zones (Figure 2b). Based on the classification used for the “proximity to the stream channels” criterion, flood-prone zones are primarily along the 6th order Messapios River main channel, as well as along its major 5th order tributaries, the Mantania and Vailelekas streams (Figure 2c). Regarding the “land cover” criterion, areas covered by forests and semi-natural vegetation, which have “very low” flood susceptibility, account for approximately 60% of the catchment. The highly susceptible areas (~19%) with arable land and sparse vegetation are concentrated in the central and

western parts of the catchment, while less resistant agricultural land and artificial surfaces account for approximately 18% and 3.5% of the catchment area, respectively (Figure 2d). Finally, substantial portions of the catchment are occupied by permeable carbonate rock formations (~48%) and highly permeable alluvial deposits (~23%), which reduce flood susceptibility (Figure 2e).

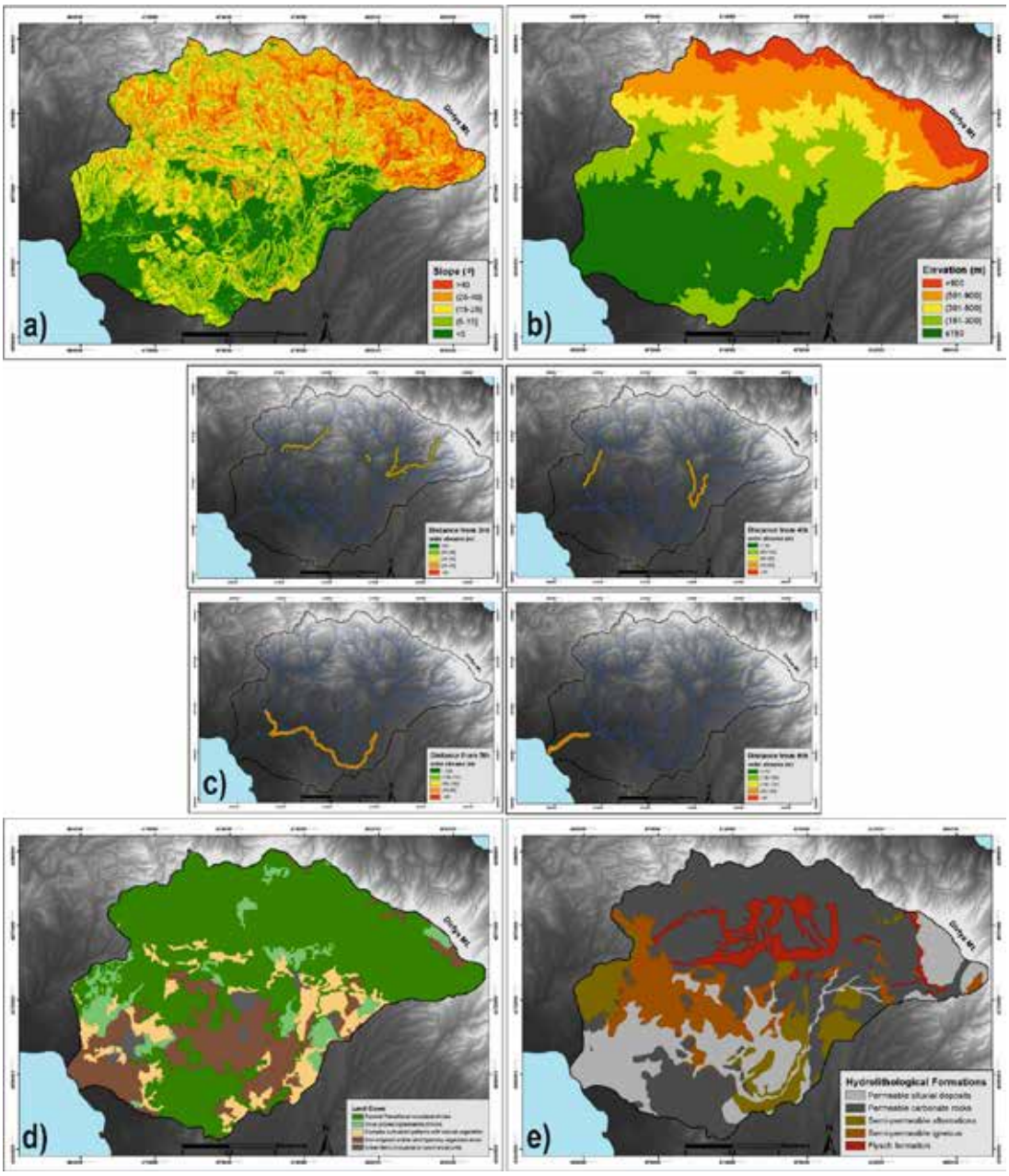

Figure 2. Maps of the Messapios River catchment illustrating the classification of: a) slope values, b) elevation, c) proximity to the stream channel, d) land cover, and e) geological formations into five categories. The rating for each criterion class is presented in Table 1.

The results of the AHP, including the pairwise comparisons matrix and the criteria weights, are given in Table 2. The estimated value of the Consistency Ratio is 0.0296, which is well below the 0.1 threshold, confirming that the hierarchy and pairwise comparisons of the criteria exhibit an acceptable level of consistency.

Two scenarios were considered for the sensitivity analysis: in Scenario 1, the weight of Slope was increased by 0.05, and the weight of Elevation was decreased by 0.05; in Scenario 2, the adjustments were reversed. The updated weights resulted in minimal deviations between the scenarios and the original AHP model, with the largest deviation being -1.57% in Scenario 1 and +1.71% in Scenario 2. These small variations indicate that the model is stable and significantly not affected by minor

changes in the weights.

Table 2. Pairwise comparison values, derived from expert insights grounded in experience with fluvial geomorphology and flood-hazard analysis, reflecting a consensus of their recommendations. W represents the relative weight of the criteria.

	Slope	Elevation	Proximity to the stream channel	Land cover	Geological formations	W
Slope	1.00	2	3	3	4	0.395
Elevation	0.50	1.00	2	2	3	0.239
Proximity to the stream channel	0.33	0.50	1.00	2	3	0.173
Land cover	0.33	0.50	0.50	1.00	2	0.119
Geological Formations	0.25	0.33	0.33	0.50	1.00	0.073
Sum	2.41	4.33	6.83	8.50	13	

To validate the results, the AHP-based flood hazard map, produced using the WLC method, was compared with the Flood Prone Zones from Greece's Special Secretariat of Water and with past flood event locations within the Messapios River catchment (Figure 3). The comparison revealed strong alignment between "high" and "very high' flood hazard areas obtained using the AHP method and the Flood Prone Zones provided by the Special Secretariat of Water of the Ministry of Environment and Energy of Greece. In addition, all past flood events (5 in total) have occurred within the "very high" flood hazard zone. This confirms that the model is reliable for flood risk assessment and management in the Messapios River catchment.

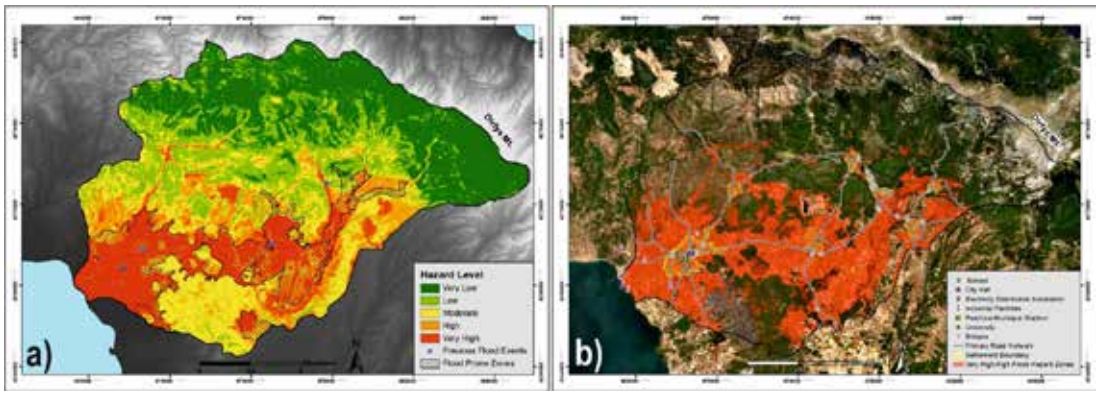

Figure 3. a) Flood hazard map of the Messapios River catchment, which also includes the Flood Prone Zones delineated by the Special Secretariat of Water of the Ministry of Environment and Energy of Greece, as well as the locations of past flood events. b) A comparative map showing the flood hazard zones identified in this study, juxtaposed with the distribution of settlements and critical infrastructure, including the primary road network, bridges, schools, industrial facilities, and electricity distribution substations.

Table 3 summarizes the areas corresponding to each of the five flood susceptibility zones from the flood hazard assessment map of Figure 3a. Approximately one-third of the catchment is classified as "very high" (17.86%) and "high" (18.02%) flood hazard areas. These zones are primarily concentrated in the central, southern, and western parts of the study area, primarily along the channels of the main streams (Messapios, Mantania, Makrimalli, Vailelekas, Makrikapiatiko), in the lower reaches of the catchment, and at the fan delta near the mouth of the river. In contrast, the "very low" and "low" flood-hazard areas are found in the northern and eastern parts, characterized by a rough mountainous relief with steep slopes and dense vegetation.

Table 3. Area (in km² and percentage) of the Messapios River catchment classified by flood-hazard levels, as determined through the Weighted Linear Combination (WLC) method using criteria weights derived from the AHP approach.

Flood Hazard Ranking	Area (km²)	Area (%)
Very low	47.14	21.83
Low	44.85	20.77
Moderate	46.48	21.52
High	38.91	18.02
Very high	38.58	17.86

The spatial comparison of settlements and critical infrastructure—such as roads, bridges, schools, industrial facilities, and power substations—with flood hazard zones highlights the area's significant vulnerability to flooding (Figure 3b). Nearly all settlements, except Platana, are in "high" or "very high" flood-prone areas, exposing approximately 9,000 residents. Psachna and Makrykapa are at greatest risk due to their proximity to major rivers with a history of severe flooding, including recent events like the "Elias" storm on September 27, 2023. Key infrastructure is also at risk: a substantial portion of the road network (~60 km) and all bridges are in "high" and "very high" flood hazard zones, as well as five major industrial facilities in the Messapios River fan delta. The General High School of Psachna, attended by students from across the municipality, and the adjacent municipal stadium are also within this zone, while the Psachna and Triada plains, vital for local agriculture, lie almost entirely in the "very high" flood hazard area, posing severe economic risk. Additionally, the Public Power Corporation substation's location in this zone signifies the potential for widespread disruption during floods.
The flood-hazard assessment map is a crucial tool for regional land-use planning, helping identify areas suitable for development while guiding long-term policies. This is particularly relevant in the study area, where ongoing land cover changes, primarily due to wildfires, have enlarged flood risk.

Concluding Remarks

This study led to the following conclusions:

- The MCDA approach effectively assessed flood hazard in the Messapios River catchment, integrating factors like topography (slope, elevation, and proximity to stream channels), land cover, and hydro-lithological characteristics of the geological formations.
- About one-third of the catchment, primarily its central, southern, and western parts, is classified as "high" or "very high" flood hazard zones, while the mountainous northern and eastern regions are less susceptible.
- Approximately 9,000 residents, key settlements (Psachna, Triada, Kastella, Makrykapa), critical infrastructure (five industrial facilities, one school, one stadium, and the power substation), and vital agricultural plains are situated in highly flood-prone zones.
- The findings emphasize the need for targeted flood mitigation measures and strategic land-use planning to reduce risk and safeguard lives, infrastructure, and economic assets.
- MCDA offers a structured, objective framework to prioritize vulnerable areas, optimize resource allocation, and guide efficient flood management strategies.
-

References

Bathrellos, G., Karymbalis, E., Skilodimou, H., Gaki-Papanastassiou, K., Baltas, E., 2016. Urban flood hazard assessment in the basin of Athens Metropolitan city, Greece. Environmental Earth Science 75, 319.

Centre for Research on the Epidemiology of Disasters (CRED) (2023) 2023 Disasters in Numbers available at: https://files. emdat.be/ reports/2023_EMDAT_report.pdf

Copernicus CORINE Land Cover, 2018. https://land.copernicus.eu/en/products/corine-land-cover

Das, S., 2018. Geographic information system and AHP-based flood hazard zonation of Vaitarna basin, Maharashtra, India. Arabian Journal of Geosciences 11, 1–13.

Feloni, E., Mousadis, I., Baltas, E. 2020. Flood vulnerability assessment using a GIS-based multi-criteria approach–The case of Attica region. Journal of Flood Risk Management 13, e12563.

Gigovic, L., Pamucar, D., Bajic, Z., Drobnjak, S., 2017. Application of GIS-Interval Rough AHP Methodology for Flood Hazard Mapping in Urban Areas. Water 9(6), 360.

Haan, C.T., Barfield, B.J., Hayes, J.C., 1994. Design Hydrology and Sedimentology for Small Catchments; Elsevier: San Diego, CA, USA, p. 608.

Institute of Geology and Mineral Exploration of Greece (IGME), 1981. Geological Map of Greece, in scale 1:50,000, Prachna and Steni Sheets.

Karymbalis, E., Andreou, M., Batzakis, D., Tsanakas, K., & Karalis, S., 2021. Integration of GIS-Based Multicriteria Decision Analysis and Analytic Hierarchy Process for Flood-Hazard Assessment in the Megalo Rema River Catchment (East Attica, Greece). Sustainability 13(18), 10232.

Kazakis, N., Kougias, I., Patsialis, T., 2015. Assessment of flood hazard areas at a regional scale using an index-based approach and Analytical Hierarchy Process: Application in Rhodope-Evros region, Greece. Science of the Total Environment 538, 555–563.

Ouma, Y.O., Tateishi, R., 2014. Urban flood vulnerability and risk mapping using integrated multi-parametric AHP and GIS: Method ological overview and case study assessment. Water 6, 1515–1545.

Patrikaki, O., Kazakis, N., Kougias, I., Patsialis, T., Theodossiou, N., Voudouris, K., 2018. Assessing Flood Hazard at River Basin Scale with an Index-Based Approach: The Case of Mouriki, Greece. Geosciences 8, 50.

Radwan, F., Alazba, A.A., Mossad, A., 2019. Flood risk assessment and mapping using AHP in arid and semiarid regions. Acta

Geophysica 67, 215–229.
Saaty, T.L., 1990a. An exposition of the ahp in reply to the paper remarks on the analytic hierarchy process. Management Science 36, 259–268.
Saaty, T.L., 1990b. How to make a decision: The analytic hierarchy process. European Journal of Operational Research 48, 9–26.
Skilodimou, H.D., Bathrellos, G.D., Alexakis, D.E., 2021. Flood Hazard Assessment Mapping in Burned and Urban Areas. Sustainability 13, 4455.
Special Secretariat of Water, Ministry of Environment and Energy, Greece. Flood Risk Management Plan for the East Sterea Hellas River Basins, Stage I, 1st Phase—Deliverable 1, Analysis of the Areas' Features and Flood Mechanisms; The Hellenic Government: Athens, Greece, 2017. 46.
Strahler, A.N., 1957. Quantitative analysis of watershed geomorphology. Eos, Transactions American Geophysical Union 38, 913–920.

17th INTERNATIONAL CONGRESS of the Geological Society of Greece

BULLETIN OF THE GEOLOGICAL SOCIETY OF GREECE, SP. PUBL.

EXTENDED ABSTRACT 207

Indium and tellurium enrichment in sulfides and sulfosalts at the Pefka high- to intermediate-sulfidation epithermal deposit, Rhodope, Greece

Melfou M.[1], Voudouris P.[2], Klemd R.[3], Keith M.[3], Melfos V.[1], Tarantola A.[4], Papadopoulou L.[1], Kantiranis N.[1]

(1) Faculty of Geology, Aristotle University of Thessaloniki, Greece, melfoumv@geo.auth.gr (2) Faculty of Geology and Geoenvironment, National and Kapodistrian University of Athens, Greece (3) GeoZentrum Nordbayern of Friedrich-Alexander-Universität (FAU) Erlangen-Nürnberg, Germany (4) Université de Lorraine, CNRS, GeoRessources Laboratory, France

Introduction / Background

Indium and tellurium are critical metals for renewable energy and advanced technologies. Tellurium is essential for cadmium telluride (CdTe) solar cells, while indium is vital for indium tin oxide (ITO) coatings used in displays and solar panels (Müller et al. 2025). Both elements are primarily obtained as by-products of base-metal mining (e.g., zinc and copper refining), making their production highly dependent on these industries. Understanding their geological occurrences is crucial for enabling more targeted exploration and efficient extraction, thereby reducing reliance on imports. This is of high significance, as China dominates global production, creating supply chain vulnerabilities (Müller et al. 2025). The Pefka high- to intermediate-sulfidation deposit hosts the highest indium and tellurium grades in Greece (1160 ppm In and >1000 ppm Te), making it an ideal case to study the enrichment processes of these metals in an epithermal environment (Voudouris et al. 2022; Melfou et al. 2023). Studies on the distribution of elements like In and Te in multi-mineral assemblages, where sphalerite is rare, remain scarce, despite their importance (Cook and Ciobanu 2015). The objective of this study is to investigate the capacity of minerals to incorporate indium and tellurium at various stages of mineralization and the processes that control their enrichment. These particularly include roquesite for indium and tellurides/goldfieldite for tellurium, but also in minor proportions galena, luzonite, chalcopyrite, and Cu-rich varieties of tennantite-tetrahedrite. This study also aims to assess the potential of pyrite to provide insights into ore-forming conditions within a deposit characterized by a complex paragenetic sequence with numerous mineral phases.

Geological context

The Rhodope metallogenic province in Greece (Fig. 1a), located within the broader Western Tethyan metallogenic belt, is a highly productive district for epithermal mineralization hosted in Oligocene-Miocene volcanic rocks (Melfos and Voudouris 2017; Voudouris et al. 2019). This region is characterized by metamorphic core complexes exhumed during the Late Cretaceous and Tertiary, as well as supra-detachment sedimentary basins, and mafic to felsic magmatism dating from the Late Eocene to Early Miocene (Marchev et al. 2005; Voudouris et al. 2022). The Pefka-Loutros area, as part of the supra-detachment northern Hellenic Thrace basin, is associated with both sedimentary and calc-alkaline to locally shoshonitic volcanic rocks. These formations are linked to the Tertiary syn- to late-orogenic extensional processes in the Rhodope province (Kilias et al. 2013). The Pefka deposit, located within this area, is one of many high- (HS) and intermediate-sulfidation (IS) epithermal mineralizations hosted in hydrothermally altered volcanic rocks and tuffs, which exhibit intermediate argillic to sericitic-argillic and locally adularia alteration (Fig. 1b). The HS to IS epithermal Pefka deposit is structurally controlled and is characterized by multistage quartz and quartz-carbonate veins and breccias with a complex ore mineralogy. This includes sulfosalts (e.g., enargite, luzonite, tennantite), sulfides (e.g., pyrite, chalcopyrite, galena), and tellurides (e.g., hessite, altaite, coloradoite). The mineralization is enriched in base, rare, and critical metals (e.g., Cu, Fe, Au, Ag, Pb, Zn, Bi, Sn, Ge, Ga, In, Mo, V, As, Hg, Te, and Se), exhibiting an exceptional ore mineralogy that includes a wide variety of sulfides, sulfosalts, tellurides, and native metals (Dimou et al. 1994; Voudouris 2006; Melfos and Voudouris 2012; Repstock et al. 2015; Voudouris et al. 2019, 2022). Bulk ore concentrations in rock chips reach up to 2300 ppm Se, 1160 ppm In, >1000 ppm Te, 390 ppm Ag, 345 ppm Au, and 250 ppm Bi, making the deposit the richest one in Te and In grades in Greece (Melfou et al. 2023). The deposit displays at least three distinct mineralization styles. The early NNW-trending Se-rich galena-quartz vein system crosscuts the altered host rocks. This early stage is followed by an NE-trending HS vein system composed of quartz, enargite/luzonite, goldfieldite, watanabeite (Biagioni et al. 2024), colusite, chalcopyrite, roquesite, tennantite/tetrahedrite-(Cu), tennantite-(In), and native gold (Voudouris 2006; Repstock et al. 2015; Voudouris et al. 2022). Tennantite-(Cu) marks the transition from the HS to the IS stage (Voudouris et al. 2022). The late-stage mineralization is characterized by a NE-trending IS vein system primarily composed of carbonates, tellurides, and tetrahedrite-(Zn), tetrahedrite/tennantite-(Fe) (Voudouris 2006; Repstock et al. 2015; Voudouris et al. 2022). The galena-bearing assemblages are the most In-rich, while the samples with carbonate gangue are the most Te-rich.

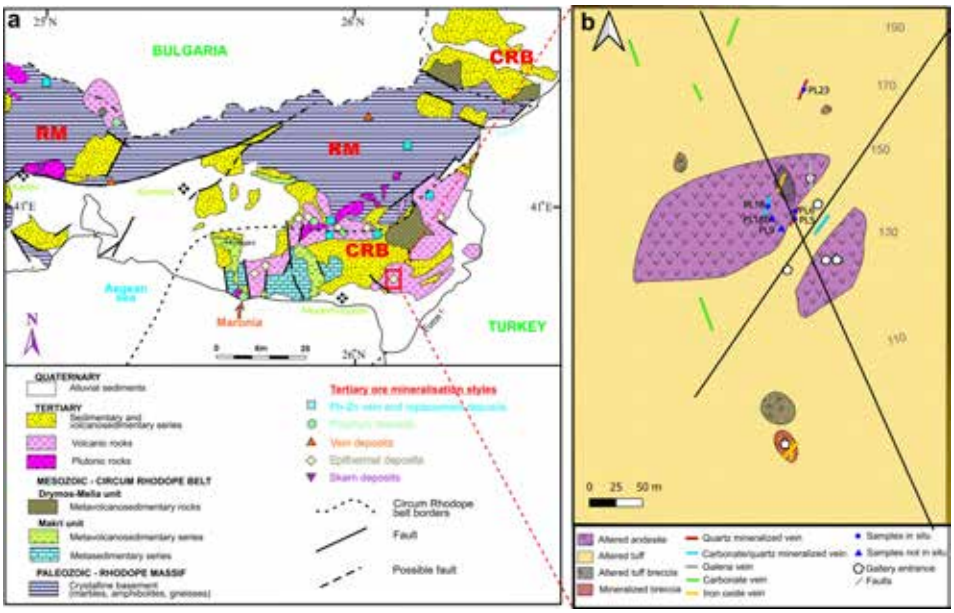

Figure 1. Regional and local simplified geological maps of the study area. (a) Geological map of the Rhodope Metallogenic Province in northern Greece, highlighting the different styles of mineralization (Melfos and Voudouris 2012). (b) Local lithological map of the Pefka HS-IS epithermal deposit, showing the locations of the samples used in this study.

Methods

Ore samples were collected from outcrops of the vein systems in the Pefka deposit and from piles outside abandoned galleries (Fig. 1a, b). Six polished sections and three polished mounts were analyzed using Electron Microprobe Analysis (EMPA) to determine the major and minor element composition of various sulfide and sulfosalt minerals. The analyses were performed with a JEOL JXA-8200 Superprobe equipped with five wavelength-dispersive X-ray spectrometers (WDS) at the GeoZentrum Nordbayern, Germany. The trace element content of sulfide and sulfosalt grains from the Pefka deposit was further analyzed by Laser Ablation Inductively Coupled Plasma Mass Spectrometry (LA-ICP-MS), which was conducted at the GeoZentrum Nordbayern, Germany. An Analyte Excite 193 nm laser (Teledyne Photon Machines) coupled to an Agilent 7500a ICP-MS was used for this purpose, using beam diameters of 20 to 35 μm. Data processing for LA-ICP-MS measurements were performed using GLITTER. Where significant interferences were observed, such as between ^{115}In and ^{115}Sn or between ^{74}Ge and ^{74}Se, mathematical corrections were applied. Due to reduced accuracy in ^{74}Ge measurements on most analytical days, only ^{73}Ge was used.

Results

A modified paragenetic sequence of ore formation at the Pefka deposit, compared to that of Voudouris et al. (2022), is presented in Figure 2a. This study focuses on the most abundant minerals analyzed using LA-ICP-MS to link the petrographic and geochemical observations. The mineralization was divided into three main stages: Pb-Se stage 1, Cu-As-Au-In-V-Sn stage 2a and 2b, and Zn-Te-Sb stage 3 (Fig. 2b-m). Stage 1 is characterized by massive Se-rich galena veins. Stage 2a hosts luzonite and enargite that are typical for high-sulfidation (HS) environments, while Stage 2b (tennantite/tetrahedrite-(Cu) and -(Fe), watanabeite, goldfieldite, colusite) marks the transition from high- (HS) to intermediate-sulfidation (IS) conditions. Stage 3 is characterized by chalcopyrite, tellurides, tetrahedrite-(Zn) that are associated with IS environments. Galena (Fig. 2b, f, g) commonly has enargite and tetrahedrite-(Cd) inclusions in Stage 1, which is accompanied by gangue quartz, forming massive 1–2 cm thick veins. Roquesite forms at the edges of the galena (Fig. 2g), suggesting their close genetic relation (Fig. 2f). The galena is crosscut by Stage 2a-b enargite, bournonite, tennantite-(In), tennantite-(Fe), and tennantite-(Cu) (Fig. 2f). The Stage 2a mineralization predominantly consists of luzonite (Fig. 2c) or enargite, often associated with pyrite. However, the enargite and luzonite of this stage are replaced and usually appear as tennantite-(Cu) of stage 2b (Fig. 2j). Pyrite occurs in two varieties, including py_{1a} that is bright in BSE images and inclusion-rich py_{1b} that is darker in BSE mode. Py_{1a} forms thin semi-massive veins (up to 0.5 cm) (Fig. 2d) and microscopically consists of anhedral grains surrounded by tennantite-(Cu) (Fig. 2i). $Pyrite_{1a}$ usually hosts large luzonite inclusions (Fig. 2h). $Pyrite_{1b}$ is found as disseminations in quartz veins related to sericite or along with barite, sometimes enclosing py_{1a} (Fig. 2i). Chalcopyrite (ccp_1) accompanies enargite in this stage. This stage includes gray quartz containing native gold grains associated with subhedral

py_2, goldfieldite, or tennantite-(Fe) (Fig. 2k). Other sulfosalts, such as colusite and watanabeite, hosting metals like V and Sn, are part of the sulfosalt assemblage in this stage (Fig. 2j). Quartz veins from Stages 2a and 2b are associated with sericite and minor APS (aluminum phosphate-sulfate) minerals, including svanbergite ($SrAl_3(PO_4)(SO_4)(OH)_6$).

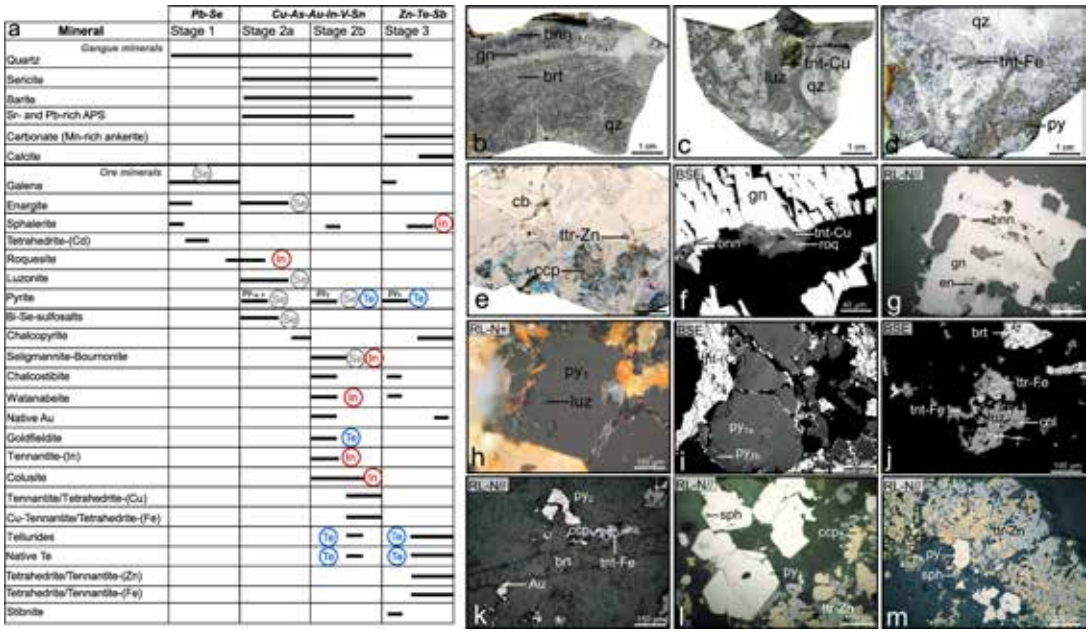

Figure 2. Simplified paragenetic sequence and macroscopic/microscopic photographs of the high-grade ore at the Pefka deposit. (a) Simplified paragenetic sequence of the Pefka deposit, focusing on analyzed sulfides and sulfosalts. (b) Galena (gn)-quartz (qz) vein of stage I, replaced by bournonite (bnn) and crosscut by an Au-rich quartz (qz) vein with barite (brt) grains. (c) Quartz vein with massive luzonite (luz), surrounded by tennantite-(Cu) (tnt-Cu). (d) Quartz vein from HS stage 2a with massive pyrite (py_{1a}) surrounded by tennantite-(Fe) (tnt-Fe) and disseminated pyrite (py_{1b}) within a sericite-rich matrix. (e) Carbonate (cb) vein of the IS stage, containing minor quartz, chalcopyrite (ccp), tetrahedrite-(Zn) (ttr-Zn), tellurides, and pyrite (py_3). (f) Galena replaced by bournonite, tennantite-(In) (tnt-In), and roquesite (roq). Remnants of galena are observed between roquesite and tnt-In. (g) Galena replaced by bournonite and enargite (en). (h) Subhedral py_1 containing luzonite mineral inclusions. (i) Anhedral, bright (in BSE) inclusion-poor py_{1a} and darker, inclusion-rich py_{1b} at the rims, surrounded by tennantite-(Cu). (j) Luzonite crosscut by barite and replaced by tetrahedrite-(Fe) (ttr-Fe) and colusite (col), accompanied by barite veins. (k) Native Au at the rims of a barite grain, accompanied by subhedral py_2 and tennantite-(Fe). (l) Euhedral py_3 hosting sphalerite (sph) and tetrahedrite-(Zn) inclusions in contact with chalcopyrite and tetrahedrite-(Zn) (m) Euhedral py_3 surrounded by chalcopyrite and tennantite-(Zn), which hosts telluride inclusions and minor sphalerite.

Stage 3 represents the IS stage, characterized by quartz and carbonate veins (Fig. 2e) comprising chalcopyrite, tetrahedrite-(Zn) and -(Fe), sphalerite, and tellurides. These are associated with euhedral pyrite (py_3), which contains numerous mineral inclusions (Fig. 2l-m). This stage is also accompanied by sericite and barite.

Variations in the elemental composition of the different pyrite generations, combined with the presence of other elements, offer valuable insights into the physico-chemical conditions of ore formation (Fig. 3a). Selenium and Te concentrations have high median values of 113 ppm and 2 ppm, respectively in py_2, while Ge is higher in py_1, with median at 2 ppm. Silver concentrations are elevated in py_1, with median values at 5 ppm, while Co is elevated in py_2, reaching 150 ppm (Fig. 3a).

Indium and Te concentrations obtained from LA-ICP-MS analyses vary among the sulfide groups, including pyrite (py_1–py_3), chalcopyrite (ccp_1-ccp_2), and galena. In pyrite, In and Te reach up to 0.5 ppm and 22 ppm, respectively, while in galena, they reach up to 30 ppm and 20 ppm, and in chalcopyrite ccp_2, up to 500 ppm and 100 ppm, respectively (Fig. 3b). LA-ICP-MS analyses of sulfosalts include luzonite from Stage 2a and bournonite, colusite and watanabeite from Stage 2b. Luzonite exhibits high Te contents of up to 3000 ppm. Luzonite is In-depleted, while bournonite of stage 2b hosts up to 30 ppm In. Colusite and watanabeite contain up to 550 ppm In and 7000 ppm Te (Fig. 3c). Indium in tennantite and tetrahedrite species reaches up to 2 wt% in the analyzed data, while previous reports noted up to 6 wt% In in the tennantite-(In) (Voudouris et al. 2022). Stage 2b tennantite/tetrahedrite-(Cu) and -(Fe) ranges from In- and Te-poor to In- and Te-rich, with tennantite/tetrahedrite-(Zn) reaching up to 1500 ppm In and 1.3 wt% Te (Fig. 3d). A slight positive correlation between In and Te content ($R^2 = 0.5$) is observed in these minerals.

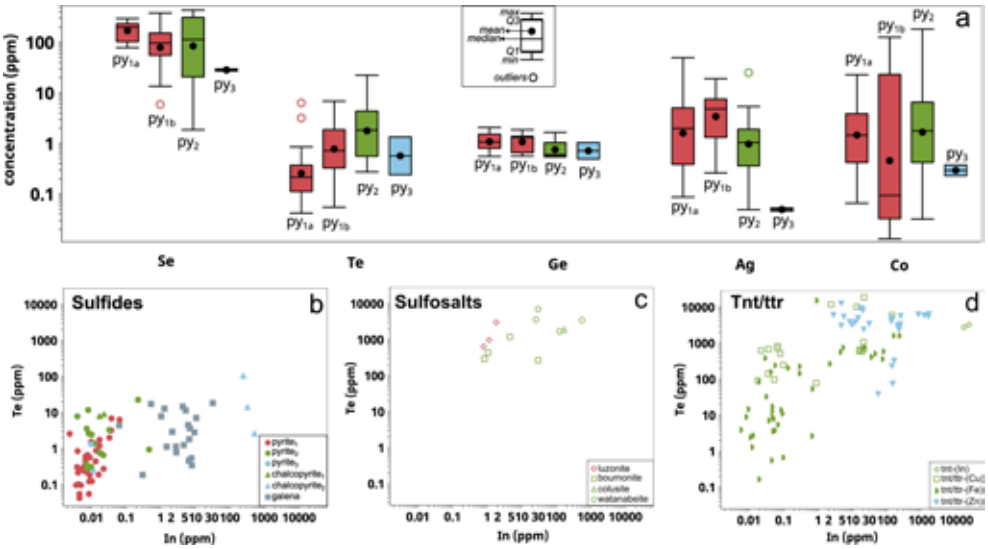

Figure 3. Geochemical variations analyzed with LA-ICP-MS from the Pefka deposit across different stages of pyrite (a), sulfides (b), sulfosalts (c), and varieties of tennantite and tetrahedrite (tnt/ttr) (d). (a) Selenium, Te, ^{73}Ge, Ag, and Co variations in the different pyrite generations. (b) In versus Te contents in different types of pyrite, chalcopyrite, and galena. (c) Indium versus Te contents in stage 2a minerals (luzonite) and stage 2b minerals (bournonite, colusite, watanabeite). (d) In versus Te contents in tennantite/tetrahedrite varieties from stage 2a (tennantite-(In), tennantite/tetrahedrite-(Cu) or -(Fe), and stage 3 (tennantite/tetrahedrite-(Zn)). Colors are indicative of the different stages: Stage 1 is grey, stage 2a is red, stage 2b is green and stage 3 is pale blue.

LA-ICP-MS profiles focusing on In and Te patterns (Fig. 4) in the different minerals suggest either micro-inclusions or the presence of these elements in solid solution. Other elements, such as Cu, Au, Ag, and Pb, were monitored to detect inclusions potentially forming phases with In and Te. Notably, only galena shows evidence of inclusions in the LA-ICP-MS patterns (Fig. 4a). In contrast, sulfosalts display smooth patterns for In and Te, suggesting that In and Te are within the mineral structures (Fig. 4b-h). However, Pb exhibits spiky patterns in tennantite-(In) and tetrahedrite-(Zn) (Fig. 4d, g), likely due to remnants of earlier galena.

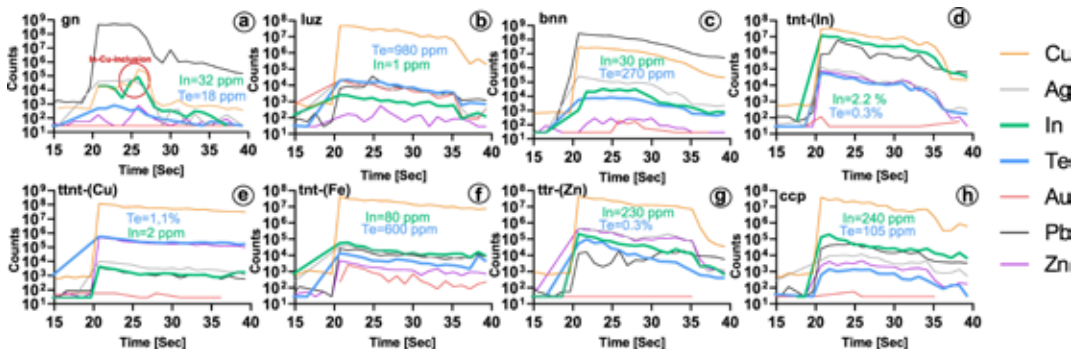

Figure 4. LA-ICP-MS time patterns of (a) galena (gn), (b) luzonite (luz), (c) bournonite (bnn), (d) tennantite-(In) (tnt-In), (e) tennantite-(Cu) (tnt-Cu), (f) Tennantite-(Fe) (tnt-Fe), (g) tetrahedrite-(Zn) (ttr-Zn), and (h) chalcopyrite (ccp). Indium and Te are illustrated with thick green and blue lines, respectively, and their concentrations after data reduction are stated. These patterns are also accompanied by those of Cu, Ag, Au, Pb, and Zn to highlight the presence of mineral inclusions or zonation.

Discussion

The Pefka deposit hosts, to our knowledge the most In and Te rich mineralization in Greece, with the presence of these two metals in a variety of minerals. The main carriers of In are roquesite that hosts 48 wt% In and tennantite-(In) that hosts up to 6 wt% In (Voudouris et al. 2022, 2023). Both minerals belong to stage 2, while roquesite also appears at the end of stage 1. Indium is also present in sphalerite of stage 3 (up to 0.31 wt%; Voudouris et al. 2022). The main carriers of Te are stage 2b goldfieldite that host up to 23 wt% Te and stage 3 tellurides (e.g., hessite, petzite, coloradoite, native Te, etc), in which Te is the main constituent of the minerals. The tellurides also occur in minor amounts in stage 2b in association with goldfieldite. The in-situ LA-ICP-MS analyses revealed the ability of sulfides, including pyrite, galena, and chalcopyrite, as well as sulfosalts like tennantite-tetrahedrite, enargite, colusite, bournonite, and watanabeite to host In and Te in their

structure or in the form of micro-inclusions. Galena shows a moderate enrichment of In, but as revealed by the LA-ICP-MS spectra, this is related to the presence of micro-inclusions, probably of roquesite. Stage 2a minerals like luzonite show no enrichment in In (up to 2 ppm) and a moderate enrichment in Te (up to 3000 ppm) (Fig. 4c and 5b). The sulfosalts of stage 2b, excluding the main carriers (i.e. roquesite), host up to 550 ppm In and 1.9 wt% Te. Stage 3 of the mineralization hosts up to 2500 ppm of In and 2 wt% of Te. Therefore, it is indicated that all stages host In, while Te is mainly hosted in stages 2b and 3. Higher In grades in global epithermal/polymetallic deposits have been detected in Sn-rich systems (Mejías et al. 2023). This fact is also seen at the Pefka deposit with the co-occurrence of In-rich minerals of stage b like tennantite-(In)/bournonite and Sn-rich minerals like colusite that have also high In-contents.

Pyrite, a well-studied and ubiquitous mineral in epithermal deposits, serves as a valuable indicator of ore-forming conditions throughout the different mineralization stages. Different pyrite generations in the Pefka deposit show a progressive evolution in chemistry, particularly in specific elemental ratios, which provide insights into processes like cooling, fluid mixing, and boiling (Keith et al. 2022; Falkenberg et al. 2024). The Se/Te ratio has been used to indicate temperature changes (Keith et al., 2022; Falkenberg et al., 2024). Pyrite data from the Pefka show that py_{1a} formed at higher temperatures, with median Se/Te ratios around 1000, while py_3 exhibits median Se/Te ratios closer to 1, suggesting lower temperatures of formation (Fig. 5a). Other pyrite generations fall progressively between these values: py_{1b} has a median ratio of ~100, while py_2 displays median values around 10. In the Koloula (Solomon Islands) and Maronia (Greece) porphyry-epithermal systems, pyrite formed above 350 °C has median Se/Te ratios >50, while lower-temperature pyrite shows ratios <50 (Keith et al., 2022; Falkenberg et al., 2024). This aligns with mineralogical evidence from Pefka, suggesting its initial HS sulfidation occurred above 300 °C (Voudouris et al., 2022).

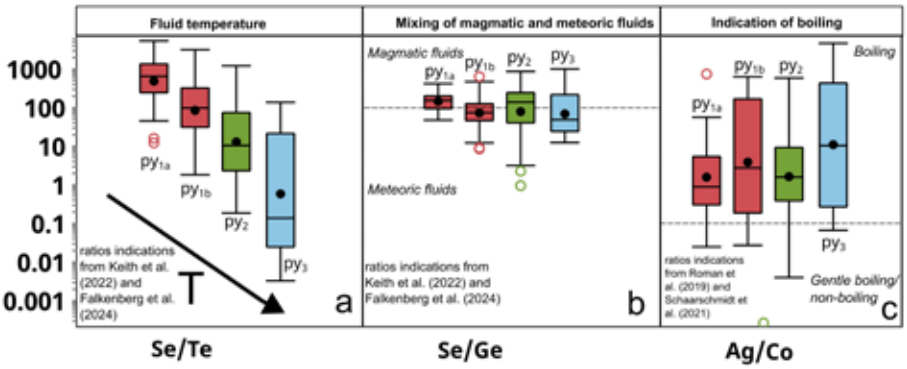

Figure 5. Boxplots from ratios derived from in-situ LA-ICP-MS data in pyrite from the Pefka deposit, used to infer physicochemical parameters of the ore-forming conditions. (a) The Se/Te ratio, which indicates cooling of the fluid temperature (Keith et al., 2022; Falkenberg et al., 2024). (b) The Se/Ge ratio, which reflects the mixing of magmatic and meteoric fluids (Keith et al., 2022; Falkenberg et al., 2024). (c) The Ag/Co ratio, that reflects boiling or non-boiling conditions (Román et al., 2019; Schaarschmidt et al., 2021). Colors are indicative of the different stages: Stage 1 is grey, stage 2a is red, stage 2b is green and stage 3 is pale blue.

The Se/Ge ratio has been applied to indicate fluid mixing, particularly between magmatic and meteoric fluids (Keith et al. 2022; Falkenberg et al. 2024). $Pyrite_{1a}$ and py_2, have median Se/Ge ratios that fall within the magmatic fluid field while the Se/Ge ratio of py_{1b} and py_3 points towards ore fluids with a mixed magmatic and meteoric fluid component (Fig. 5b). It is notable that the high-In stage 2b shows elevated Se/Ge ratios, suggesting important contribution of the magmatic fluids at the In-rich stage. The Ag/Co ratio of pyrite has been used in studies to differentiate boiling from non-boiling environments (Román et al. 2019; Schaarschmidt et al. 2021). At Pefka, all pyrite grains have Ag/Co ratios above 1, indicative of boiling conditions (Fig. 5c). Evidence for boiling at Pefka is also provided by the telluride mineralogy and the presence of adularia alteration in the surrounding rocks, including the andesitic host rock (i.e. Voudouris et al., 2022).

Conclusion

The outcome of this study is the In and Te partitioning in a multi-mineral assemblage where sphalerite is volumetrically rare, providing valuable insights into their distribution in various sulfide and sulfosalt species. Early-stage galena shows moderate enrichment, with In and Te concentrations reaching up to 30 ppm and 20 ppm, respectively, possibly because of the presence of inclusions. In contrast, later-stage tetrahedrite-tennantite varieties exhibit significantly higher concentrations, with up to 6 wt% In and 1.9 wt% Te. Pyrite, analyzed across multiple generations, provides valuable insights into the evolution of the hydrothermal system. A systematic decrease in the Se/Te ratio of pyrite—from magnitudes around 1000 to values close to 1—indicates progressive cooling of the ore-forming fluids. Additionally, Ag/Co ratios in pyrite suggest boiling conditions during both the high-

sulfidation (HS) and intermediate-sulfidation (IS) stages. The LA-ICP-MS analyses reveal that sulfosalts play a critical role in hosting In and Te, from HS, during the transition and final IS stages. Minerals such as tennantite-tetrahedrite, colusite, and watanabeite act as significant carriers, with In and Te present both in solid solution and as inclusions. These findings underscore the importance of sulfides and sulfosalts not only as repositories of critical metals but also as proxies for reconstructing the physicochemical processes that governed ore deposition in the Pefka deposit. Future research will focus on the distribution of other elements in sulfosalts and sulfides, such as Se, Ag, and Au, which are particularly enriched at Pefka. Additionally, pyrite trace element ratios, which provide insights into ore-forming conditions, will be compared with those from similar systems.

Acknowledgements

Dr. H. Brätz is thanked for her assistance during the LA-ICP-MS analyses and data processing. Boliden Mineral AB is gratefully acknowledged for providing financial support to the PhD thesis of M. Melfou entitled “Mineralogy geochemistry and ore genesis of the critical and rare metals enrichment in the high- to intermediate-sulfidation epithermal systems at the Pefka-Loutros area, Rhodope, Greece”.

References

Biagioni, C., Voudouris, P., Moëlo, Y., Sejkora, J., Dolníček, Z., Musetti, S., and Mauro, D., 2024, Crystal structure of Pb-bearing watanabeite from Pefka, Greece: Mineralogical Magazine, v. 88, no. 3, p. 218–227.

Cook, N.J., and Ciobanu, C.L. (2015) Mineral hosts for critical metals in hydrothermal ores. In Mineral Resources in a Sustainable World, Proceedings of the 13th SGA Biennial Meeting, Nancy, France. 24-27

Dimou, E., Michael, C., and Serment, R., 1994, Mineralogical composition of epithermal polymetallic mineralization at Pefka. Rhodope., in Bull. Geol. Soc. Greece. 30, 553–1550.:, p. 553–1550.

Falkenberg, J.J., Keith, M., Melfos, V., Hohl, M., Haase, K.M., Voudouris, P., Höss, A., Wenske, J., Klemd, R., Beier, C., Kutzschbach, M., and Strauss, H., 2024, Insights into fluid evolution and Re enrichment by mineral micro-analysis and fluid inclusion constraints: Evidence from the Maronia Cu-Mo±Re±Au porphyry system in NE Greece: Mineralium Deposita.

Keith, M., Haase, K.M., Chivas, A.R., and Klemd, R., 2022, Phase separation and fluid mixing revealed by trace element signatures in pyrite from porphyry systems: Geochimica et Cosmochimica Acta, v. 329, p. 185–205.

Kilias, A., Falalakis, G., Sfeikos, A., Papadimitriou, E., Vamvaka, A., and Gkarlaouni, C., 2013, The Thrace basin in the Rhodope province of NE Greece — A tertiary supradetachment basin and its geodynamic implications: Tectonophysics, v. 595–596, p. 90–105.

Marchev, P., Kaiser-Rohrmeier, M., Heinrich, C., Ovtcharova, M., von Quadt, A., and Raicheva, R., 2005, 2: Hydrothermal ore deposits related to post-orogenic extensional magmatism and core complex formation: The Rhodope Massif of Bulgaria and Greece: Ore Geology Reviews, v. 27, no. 1, p. 53–89.

Mejías, O., Parbhakar-Fox, A., Jackson, L., Valenta, R., and Townley, B., 2023, Indium in ore deposits and mine waste environments: Geochemistry, mineralogy, and opportunities for recovery: Journal of Geochemical Exploration, p. 107312.

Melfos, V., and Voudouris, P., 2017, Cenozoic metallogeny of Greece and potential for precious, critical and rare metals exploration: Ore Geology Reviews, v. 89, p. 1030–1057.

Melfos, V., and Voudouris, P.Ch., 2012, Geological, Mineralogical and Geochemical Aspects for Critical and Rare Metals in Greece: Minerals, v. 2, no. 4, p. 300–317.

Melfou, M., Voudouris, P., Klemd, R., Keith, M., Melfos, V., and Kantiranis, N., 2023, In-situ trace element analyses of pyrite from the Pefka epithermal Cu-Au-Te-In-Se deposit, Rhodope, Northern Greece, in 17th Biennial SGA Meeting, Minerals in a changing world, Zurich.

Müller D, Groves DI, Santosh M, Yang C-X (2025) Critical metals: Their applications with emphasis on the clean energy transition. Geosystems and Geoenvironment 4:100310.

Repstock, A., Voudouris, P., and Kolitsch, U., 2015, New occurrences of watanabeite, colusite, “arsenosulvanite” and “Cu-excess” tetrahedrite-tennantite at the Pefka high-sulfidation epithermal deposit, northeastern Greece: Neues Jahrbuch für Mineralogie - Abhandlungen, v. 192, no. 2, p. 135–149.

Román, N., Reich, M., Leisen, M., Morata, D., Barra, F., and Deditius, A.P., 2019, Geochemical and micro-textural fingerprints of boiling in pyrite: Geochimica et Cosmochimica Acta, v. 246, p. 60–85.

Schaarschmidt, A., Haase, K.M., Klemd, R., Keith, M., Voudouris, P.C., Alfieris, D., Strauss, H., and Wiedenbeck, M., 2021, Boiling effects on trace element and sulfur isotope compositions of sulfides in shallow-marine hydrothermal systems: Evidence from Milos Island, Greece: Chemical Geology, v. 583, p. 120457.

Voudouris, P., 2006, A comparative mineralogical study of Te-rich magmatic-hydrothermal systems in northeastern Greece: Mineralogy and Petrology, v. 87, nos. 3–4, p. 241–275.

Voudouris, P., Mavrogonatos, C., Spry, P.G., Baker, T., Melfos, V., Klemd, R., Haase, K., Repstock, A., Djiba, A., Bismayer, U., Tarantola, A., Scheffer, C., Moritz, R., Kouzmanov, K., et al., 2019, Porphyry and epithermal deposits in Greece: An overview, new discoveries, and mineralogical constraints on their genesis: Ore Geology Reviews, v. 107, p. 654–691.

Voudouris, P., Repstock, A., Spry, P., Frenzel, M., Mavrogonatos, C., Keith, M., Tarantola, A., Melfos, V., Tombros, S., Zhai, D., Cook, N., Ciobanu, C., Schaarschmidt, A., Rieck, B., et al., 2022, Physicochemical constraints on indium-, tin-, germanium-, gallium-, gold-, and tellurium-bearing mineralizations in the Pefka and St Philippos polymetallic vein- and breccia-type deposits, Greece: Ore Geology Reviews.

Voudouris P., Biagioni C., Sejkora J. and Musetti S. (2023) Tennantite-(In), IMA 2023-011. In: CNMNC Newsletter, 73. European Journal of Mineralogy, 35, 397–402.

17th INTERNATIONAL CONGRESS of the Geological Society of Greece

BULLETIN OF THE GEOLOGICAL SOCIETY OF GREECE, SP. PUBL.

EXTENDED ABSTRACT 208

An Overview of Geological Map Sheets of Crete by HSGME.

I. Michalakis[1], A. Photiades[2], Sp. Staridas[1]

(1) Hellenic Survey of Geology and Mineral Exploration, Regional Branch of Crete, Rethymno, Greece, michalakis@eagme.gr (2) Hellenic Survey of Geology and Mineral Exploration, Department of General and Applied Geology, Acharnes, Greece, afotiadis@eagme.gr

Research Highlights

The geological mapping of Crete, undertaken over several decades, represents a monumental effort to document the island's complex and diverse geology. However, the varying methodologies, technologies, and scientific approaches employed during different survey periods have resulted heterogeneity in the maps produced. This paper highlights advancements in the visualization and integration of geological data within a GIS environment, providing new opportunities for cohesive and comprehensive geological interpretations of Crete.

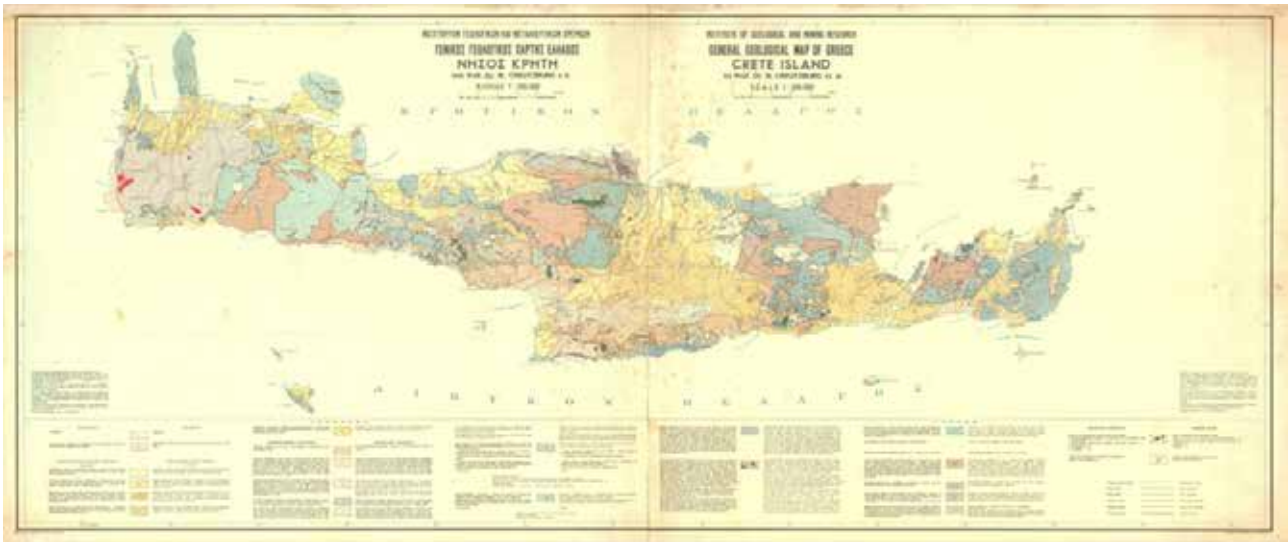

Figure 1. The General Geological Map of Greece / Island of Crete, published by the Institute of Geological and Mining Research (IGMR) in 1977, at a scale of 1:200k (*Commonly known as the Geological Map of Crete by Creutzburg et al.*).

Introduction / History of Publication of Geological Maps of Crete

The geological framework of the island of Crete is extensively documented in the General Geological Map of Greece / Island of Crete, published in 1977 by the Institute of Geological and Mining Research (IGMR), at a scale of 1:200k (Figure 1). This foundational and legacy map represents one of the most significant milestones in capturing the geological complexities of the island. Crete (including Gavdos island) is covered by 24 map sheets (Figure 2) that form part of the Basic Geological Map of Greece (BGMG), produced by the Institute for Geology and Subsurface Research (IGSR)—later renamed the Institute of Geology and Mineral Exploration (IGME), and now known as the Hellenic Survey of Geology and Mineral Exploration (HSGME). These maps, published at a scale of 1:50k between 1956 and 2013, provide a more detailed account of Crete's geological units and structures. The geological mapping of Crete reflects a systematic and iterative process spanning several decades, undertaken by HSGME and its predecessor organizations (IGSR, IGMR, and IGME).

Background / Geological Map Sheets of Crete

The geological mapping of Crete has undergone remarkable advancements over decades of systematic surveys, as summarized in Table 1 and illustrated in Figure 2. The need for a detailed geological map to capture the island's complex geological framework became evident as early as the mid-20th century (Aronis, 1949). In the following years, the IGSR focused on extensive fieldwork, resulting in foundational geological maps at a scale of 1:50k. Notable examples include the Alikianos (Vatolakkos) map sheet in Western Crete (Christodoulou & Tataris, 1969; Figure 4.2) and the Kato Chorio (former Ierapetra) map sheet in Eastern Crete (Papastamatiou et al., 1959; Figure 4.1). These pioneering efforts provided critical insights into the geological structure of the island and paved the way for future

advancements. Figures 4.1 and 4.2 depict the updated versions of these map sheets—soon to be released by the HSGME—showcasing significant progress in geological mapping techniques and visualization. These updates are part of the BGMG series, reflecting the integration of modern methodologies and technologies focused on creating a more cohesive and accurate geological framework for the region.

In 1977, the IGMR published the General Geological Map of Crete at a scale of 1:200k, consolidating decades of geological research (Creutzburg & Papastamatiou, 1966; Creutzburg et al., 1977) and serving as a foundational resource for understanding the island's geology. In the subsequent decades, the IGME (now the HSGME) advanced this work by completing the island's detailed geological framework as part of the BGMG series (Table 1). These endeavors were concentrated on diverse methodologies and advancements in earth science techniques, including petrographic and micropaleontological analyses. The historical evolution of geological mapping in Crete reflects monumental scientific labor, laying the groundwork for modern geological studies while addressing the challenges of heterogeneity in methodologies and outputs over time.

Table 1 (as a reference) provides an overview of the geological map context of Crete (including Gavdos sheet), summarizing critical data such as map sheets, scales, publication bodies, years of publication, and survey periods. This information underscores the extensive involved effort in documenting the island's complex geological framework (Figure 2). The figure effectively organizes these map sheets across the region, optimized by their publication years, showcasing the chronological progression of geological surveys. This dataset highlights the evolution of geological documentation in Crete, beginning with foundational surveys in the mid-20th century and advancing to modern updates that incorporate sophisticated methodologies. However, despite these extensive efforts, several objective difficulties and challenges remain. These include the integration and evaluation of historical and modern bibliographic data, georeferencing older map sheets to contemporary grids, and homogenizing geological data across varied methodologies and periods. Addressing these challenges is critical for achieving a cohesive and accurate geological framework for the region.

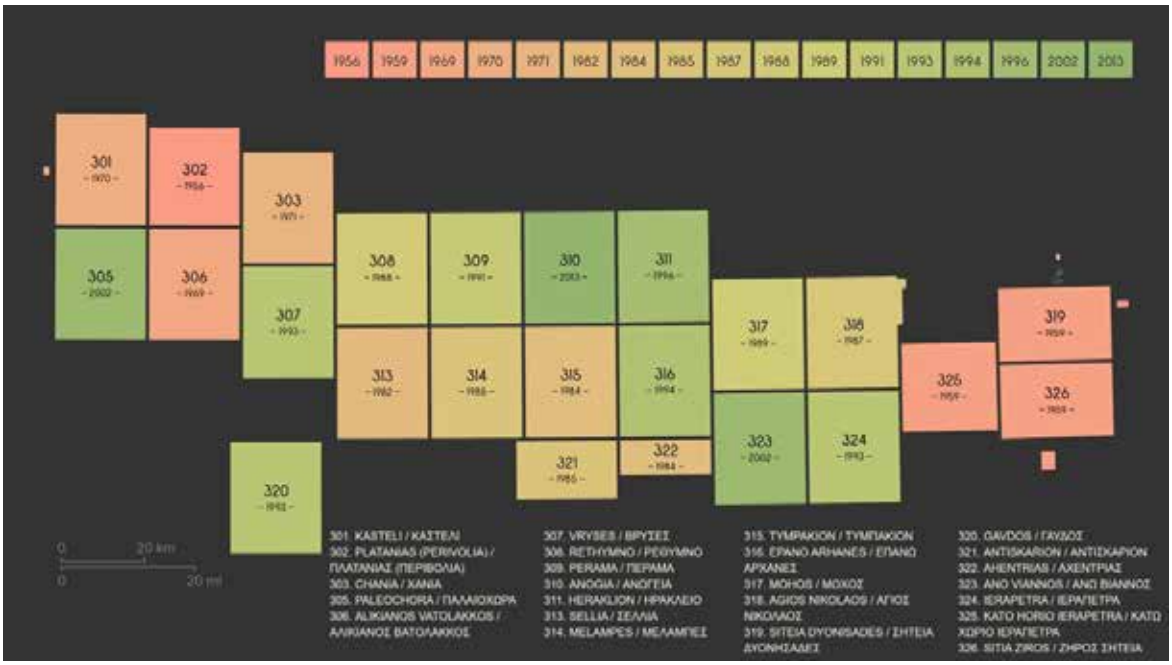

Figure 2. The spatial distribution of the 24 map sheets of the BGMG series, covering the region of the island of Crete (and Gavdos). Optimization based on the publication year.

Objectives

The geological mapping of Crete, conducted over several decades, represents a monumental effort to document the island's intricate and diverse geology. However, the use of varying methodologies, technologies, and scientific approaches during different survey periods has introduced heterogeneity into the resulting maps. This study aims to provide an overview of the Geological Map Sheets of Crete produced by IGME, as well as the ongoing progress by HSGME in advancing this work. A critical focus is on the integration of these maps within a GIS environment, which represents a significant step toward achieving a comprehensive and cohesive geological understanding of Crete.

Table 1. The geological context of the island of Crete is documented in the "General Geological Map of Greece / Island of Crete", published by the IGMR in 1977 at a scale of 1:200k. Additionally, the region of Crete is covered by 24 map sheets from the BGMG series produced by the IGSR (later IGME and now known as HSGME) between 1956 and 2013.

s/n	Code	Scale	Geological Sheet	Geological Sheet (Name after ELOT 743)	by	Year	Period of Survey
1	-	200k	GENERAL GEOLOGICAL MAP OF GREECE / CRETE ISLAND (CREUTZBURG)	CREUTZBURG	IGMR	1977	PRE-NEOGENE 1957-1973, NEOGENE 1961-1974
2	301	50k	KASTELLI	KASTELLI	IGSR	1970	1968
3	305	50k	PALAEOHORA	PALAIOCHORA	IGME	2002	1984, 1994-1995
4	302	50k	PLATANIAS	PLATANIAS	IGSR	1956	1950
5	306	50k	ALIKIANOS VATOLAKKOS	ALIKIANOS VATOLAKKOS	IGSR	1969	1960-1961
6	303	50k	KHANIA	CHANIA	IGSR	1971	1951, 1969
7	307	50k	VRISSES	VRYSES	IGME	1993	1985-1987
8	320	50k	GAVDOS	GAVDOS	IGME	1993	1988
9	308	50k	RETHYMNO	RETHYMNO	IGME	1988	1980-1984
10	313	50k	SELLIA	SELLIA	IGME	1982	1977-1978
11	309	50k	PERAMA	PERAMA	IGME	1991	1982-1987
12	314	50k	MELAMBES	MELAMPES	IGME	1985	1972-1974
13	310	50k	ANOGHIA	ANOGEIA	IGME (IGMEM)	2013	2005-2007
14	315	50k	TIMBAKION	TYMPAKION	IGME	1984	1973-1977
15	321	50k	ANTDISKARION	ANTISKARION	IGME	1985	1970-1972
16	311	50k	HERAKLION	IRAKLEIO	IGME	1996	ALPINE 1983, POST-ALPINE 1973
17	316	50k	EPANO ARCHANAE	EPANO ARCHANAI	IGME	1994	ALPINE 1983, POST-ALPINE 1973-1977
18	322	50k	AKHENDHRIAS	ACHENTRIAS	IGME	1984	1970-1974
19	317	50k	MOCHOS	MOCHOS	IGME	1989	ALPINE 1982-1983, POST-ALPINE 1973-1977
20	323	50k	ANO VIANNOS	ANO VIANNOS	IGME	2002	ALPINE 1975, 1987, POST-ALPINE 1987 (WEST SECTION), 1976 (EAST SECTION)
21	318	50k	AYIOS NIKOLAOS	AGIOS NIKOLAOS	IGME	1987	1976, 1977, 1981
22	324	50k	IERAPETRA	IERAPETRA	IGME	1993	ALPINE 1982, POST-ALPINE 1976
23	325	50k	KATO CHORIO IERAPETRA	KATO CHORIO IERAPETRA	IGSR	1959	1955
24	319	50k	SITIA DIONYSSIADES	SITEIA DYONISADES	IGSR	1959	1953, 1954
25	326	50k	ZIROS SITIA	ZIROS SITEIA	IGSR	1959	1954

Methods and Challenges

The revision of the geological mapping of Crete and its tectono-stratigraphic structure of alpine and post-alpine formations involved a combination of intensive field mapping, field tectonic measurements, sampling, and laboratory analysis. These efforts were further supported by the application of remote sensing techniques and Geographic

Information Systems (GIS) methods (Figures 3.1 & 3.2). The integration of these tools allowed for detailed geological cartographic results, which were subsequently homogenized and correlated with neighboring geological map sheets. This ongoing process (as part of the projects referenced in the Acknowledgements), has contributed to the development of the BGMG at a scale of 1:50,000, accompanied by a detailed explanatory document for each map sheet.

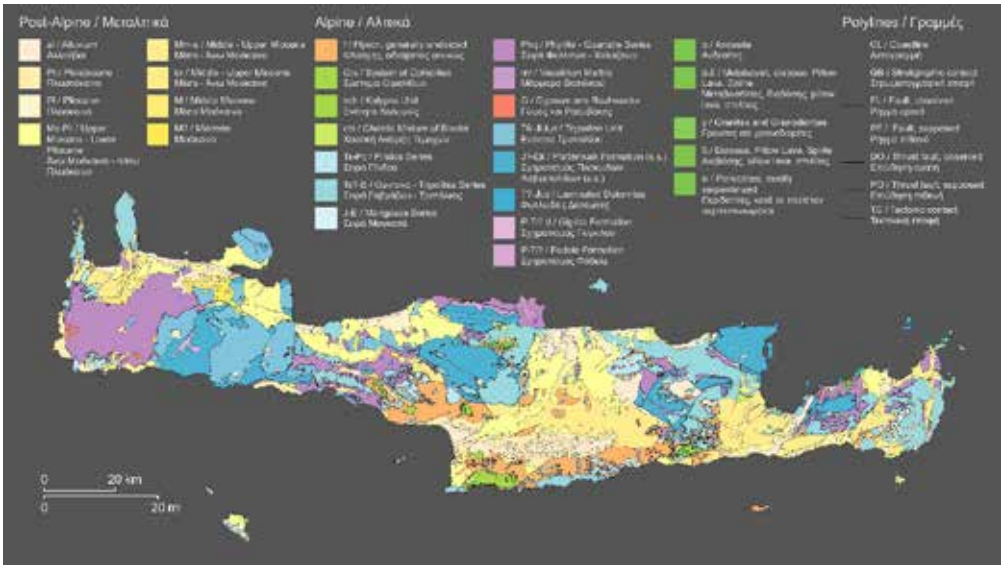

Figure 3.1. The geological setting of the island of Crete, as depicted in the 1:200k Geological Map by Creutzburg et al. (1977), has been further optimized and refined through the application of GIS for enhanced spatial analysis and accuracy.

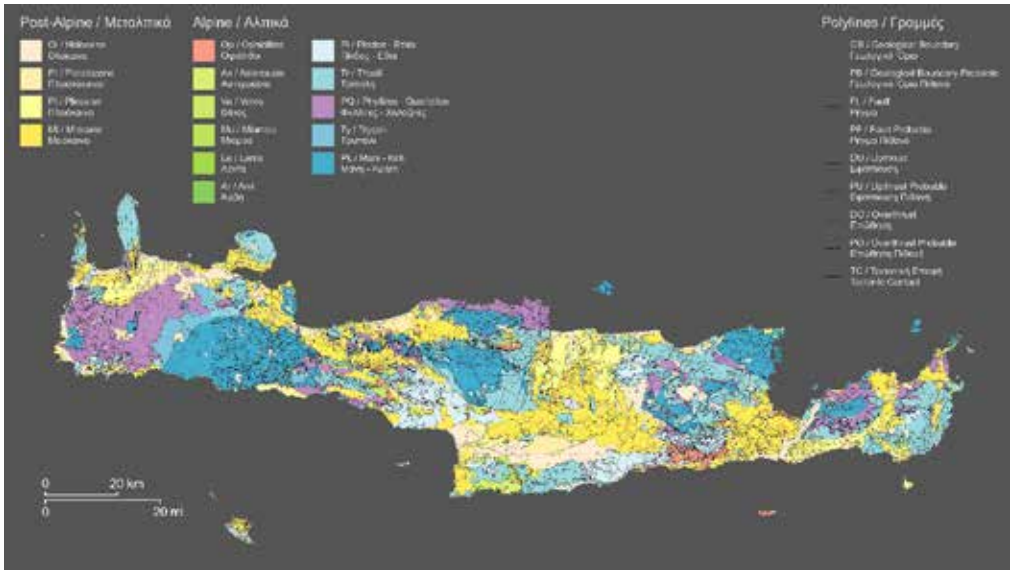

Figure 3.2. The geological setting of the island of Crete, as depicted by the 24 map sheets of the BGMG series, produced by the IGME (1956-2013).

Over the decades, numerous researchers contributed to geological maps of Crete, but these were often based on different methodologies and topographic bases. As a result, discontinuities emerged in the positioning of geological boundaries, in the classification of lithological formations, and in the depiction of tectonic elements, leading to problems, not only in the margins of adjoining map sheets. Various researchers from various schools of thought have carried out geological maps over extended periods, and their results have consequently been projected on different topographic maps. This resulted in the accommodation of geological boundaries in the exact locations and content of the lithological formations with tectonic elements, not coinciding with neighboring sheets.

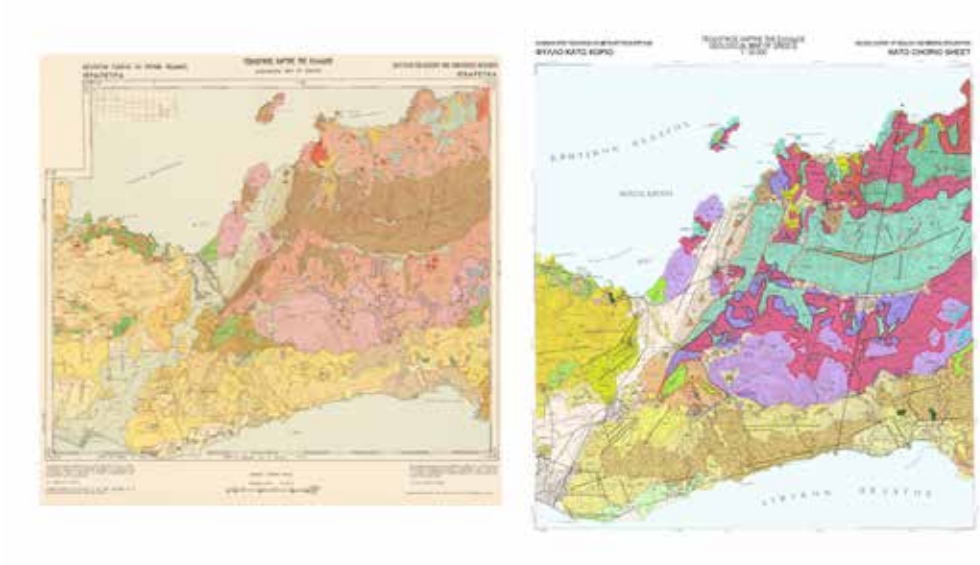

Figure 4.1. The evolution of geological mapping for the Kato Chorio (Ierapetra) map sheet in Eastern Crete. On the left is a segment of the original map, published in 1959 by IGSR, representing one of the foundational efforts in geological documentation. The right panel presents the updated version of the same sheet—soon to be released by HSGME.

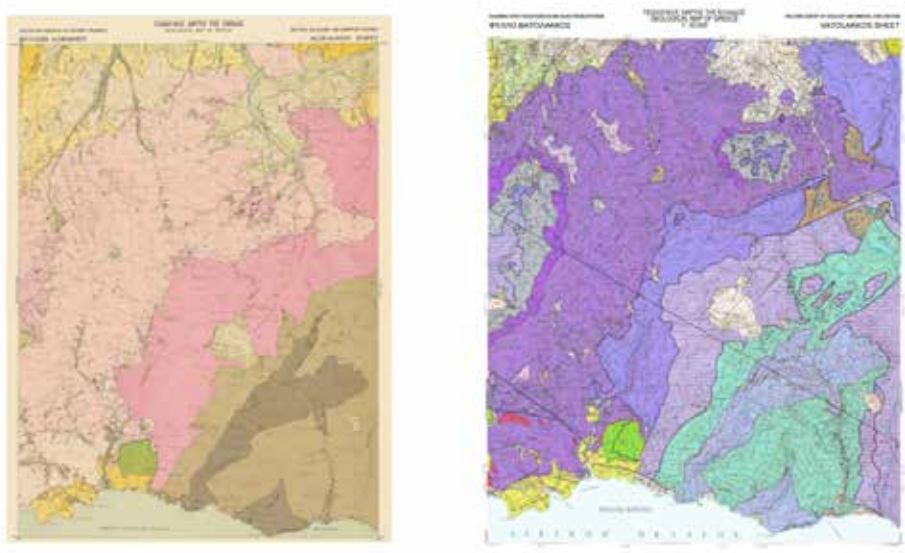

Figure 4.2. The evolution of geological mapping for the Alikianos (Vatolakkos) map sheet in Western Crete. On the left is a segment of the original map, published in 1969 by the IGSR, showcasing one of the foundational efforts in documenting the region's geology. On the right is the updated version of the same sheet—soon to be published by the HSGME.

Addressing these challenges required a multifaceted approach including collection, evaluation, and utilization of bibliography, georeferencing of older maps, grouping and homogenization of geological data, integration of modern geological perspectives, field mapping and data collection, physical and logistical barriers, GIS and cartographic optimization. To meet the objective difficulties and challenges, the fieldwork mapping effort was based on sampling and evaluation of on-site data along with parallel laboratory information and using broadly a modern bibliography. With the georeferencing of older map sheets in Greek Grid (*in Greek EGSA 87'*), in the documentation and appropriate interpretation, grouping-homogenization of geological elements, significant problems were identified within the boundaries of the formations, in the compilation and integration of new data (e.g. geochronological data) and tectonostratigraphic views on the geological structure of Greece. All observations and correlations were focused on the grouping and differentiation of geological formations, primarily categorized into basic lithostratigraphic sequences.

Results

Significant progress has been achieved in revising and homogenizing the 24 geological map sheets of Crete, including Gavdos. Two prominent examples illustrate this advancement: the geological map sheets of Vatolakkos (Western Crete) and Kato Chorio (Eastern Crete). These revised maps (Galanakis et al., 2024; Photiades & Kalogiannis, 2024) incorporate detailed geological cross-sections and tectonostratigraphic unit columns (pre-alpine and post-alpine formations), all compiled using a unified legend. Comparative analyses of these sheets highlight significant differences in both cartographic quality and geological structure (Figures 4.1 and 4.2). For instance, the Vatolakkos sheet in Western Crete extensively represents the full Plattenkalk sequence, ranging from the Upper Triassic to the Eocene, overlain by a meta-flysch formation dated to the Upper Eocene–Lower Oligocene (Figure 4.2). In contrast, the Kato Chorio sheet in Eastern Crete depicts only the uppermost members of the Plattenkalk sequence (Eocene) and the meta-flysch formation (Figure 4.1). Based on these maps, a new comprehensive geological map of Crete has been compiled. This updated map addresses many of the interregional inconsistencies and challenges that arose due to temporal and methodological gaps in the historical geological mapping of Crete (Table 1). The systematic revision and digitization of geological maps provides a valuable foundation for addressing modern challenges. These maps contribute substantially to sustainable development by enabling better planning for large infrastructure projects, optimizing the utilization of natural resources, and improving the management of natural hazards associated with the climate crisis.

Conclusions

The historical progression of geological mapping in Crete represents a monumental scientific endeavor, highlighting decades of systematic surveys that have substantially advanced knowledge of the island's intricate geology. Despite these achievements, challenges such as inconsistencies in methodologies, outdated bibliographic data, and issues in georeferencing older map sheets must be addressed to achieve a unified and accurate representation of Crete's geological context. Moving forward, continued efforts to integrate, update, and modernize the island's geological data are essential. These initiatives will not only build upon the foundational work of past surveys but also ensure that the resulting geological framework supports future research and contributes to the sustainable management of Crete's natural resources.

Acknowledgements

The authors would like to express their sincere gratitude to the personnel of the HSGME who contributed to *the Hydrogeological Mapping at a Scale of 1:100,000: Case Study of the Island of Crete* (part of the National Development Programs for the period 2021–2025, Ministry of Environment & Energy) and to the personnel involved in the revision and homogenization project of the Basic Geological Map of Greece (2019–2023), carried out within the framework of Project GEOINFRA: *Geological Mapping of Greece towards Support of Innovation and Entrepreneurship* (NSRF 2014–2020).

References

Aronis, G. (1949). *General Hydrological Survey of the Island of Crete (Includes Geological Map of Crete, Scale 1:500,000)*. Institute for Geology and Subsurface Research (IGSR), Athens.

Christodoulou, G., & Tataris, A. (1969). *Geological map of VATOLAKKOS sheet (1st ed., scale 1:50,000)*. Institute for Geology and Subsurface Research (IGSR), Athens.

Creutzburg, N., & Papastamatiou, J. (1966). *New Contribution to the Geology of the Island of Crete*. Institute for Geology and Subsurface Research (IGSR), Athens.

Creutzburg, N., Drooger, C. W., Meulenkamp, J. E., Papastamatiou, J., Sannemann, W., Seidel, E., & Tataris, A. (1977). *The General Geological Map of Greece: Island of Crete*. Institute of Geological and Mining Research (IGMR), Athens.

Galanakis, D., Moforis, L., & Carras, N. (2024). *Geological map of VATOLAKKOS sheet (2nd ed., scale 1:50,000)*. Hellenic Survey of Geology and Mineral Exploration (HSGME), Acharnes.

Papastamatiou, J., Vetoulis, D., Tataris, A., Bornovas, J., Christodoulou, G., & Katsikatsos, G. (1959). *Geological map of KATO CHORIO sheet (1st ed., scale 1:50,000)*. Institute for Geology and Subsurface Research (IGSR), Athens.

Photiades, A., & Kalogiannis, N. (2024). *Geological map of KATO CHORIO sheet (2nd ed., scale 1:50,000)*. Hellenic Survey of Geology and Mineral Exploration (HSGME), Acharnes.

17th INTERNATIONAL CONGRESS of the Geological Society of Greece

BULLETIN OF THE GEOLOGICAL SOCIETY OF GREECE, SP. PUBL.

EXTENDED ABSTRACT 209

Water Wells in Crete: Distribution by Municipality, Use, and Ownership—Results of a Systematic Inventory in Greece.

I. Michalakis[1], E. Tsolaki[1]

(1) Hellenic Survey of Geology and Mineral Exploration, Regional Branch of Crete, Rethymno, Greece, michalakis@eagme.gr

Research Highlights

One of the recent projects undertaken by the Department of Hydrogeology at the Hellenic Survey of Geology and Mineral Exploration (HSGME), co-financed under the European Union's Corporate Regional Development Agreement for the 2014-2020 period, involved a systematic inventory of water wells (boreholes) throughout the country of Greece. In Crete and the island of Gavdos, extensive fieldwork conducted by experienced personnel from HSGME spanned from July 2019 to January 2023, lasting a total of 43 months. This comprehensive effort resulted in the identification and documentation of 5,349 water wells (boreholes) across the 24 municipalities of the region (Figure 1).

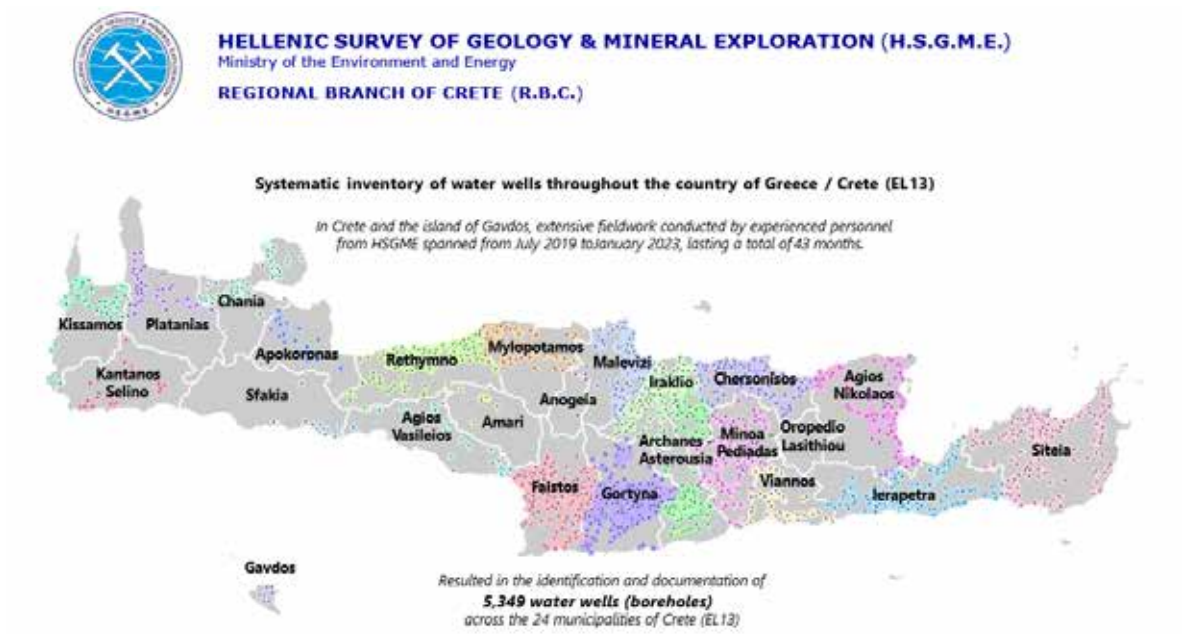

Figure 1. Results of a systematic inventory of water wells (boreholes) conducted across Water District EL13, which identified and documented 5,349 water wells within the 24 municipalities of the region. Different colored dots represent boreholes categorized by their respective municipalities, while white lines delineate municipal boundaries.

Introduction

Since the early 2000s, the European Union has implemented transformative water resource management policies, most notably the Water Framework Directive (Directive 2000/60/EC). Effective from 22 December 2000, this Directive establishes integrated quality, ecological, and quantitative targets for the protection of aquatic ecosystems, aiming to achieve "*good status*" for all water resources through a holistic, basin-scale approach. The Directive expands the definition of a River Basin to include inland surface waters (e.g., rivers, lakes), groundwater, and transitional and coastal ecosystems (e.g., deltas and estuaries). To realize its objectives, the Directive mandates the development and implementation of Management Plans at the River Basin level, as outlined in Article 13 and Annex VII. These plans incorporate Programs of Measures for the Protection and Rehabilitation of Waters, as specified in Article 11 and Annex VI.

In Greece, River Basin Management Plans have been developed in alignment with Directive 2000/60/EC and formalized through Law 3199/2003 and Presidential Decree 51/2007. These plans provide comprehensive details on River Basin Districts, River Basins, and surface and groundwater bodies.

As a complement to the "*Groundwater Monitoring Network of Greece*" (HSGME/RBC, 2019-2023), the Department of Hydrogeology at HSGME initiated the "*Systematic Inventory of Water Wells for All Uses Throughout the Country of*

Greece" (HSGME, 2019-2023). Co-financed under the European Union's Corporate Regional Development Agreement for the 2014–2020 period, this project sought to address critical gaps in groundwater data and understanding. The outcomes of this project directly support the initiatives of the General Directorate of Water within the Ministry of Environment and Energy, strengthening national water policies. These efforts ensure the protection of both the quality and quantity of Greece's water resources, fulfilling obligations under European Union Directives 2000/60/EC, 2006/118/EC, and 91/676/EEC. The project's functionality is integrated with the geospatial database and services system of the National Register of Water Abstraction Points (*in Greek: "EMSY"*). Established in January 2014, EMSY is an electronic register maintained by the General Directorate of Water (formerly the Special Secretariat for Water) in compliance with Greek Law 3882/2010, which was adopted following Directive 2007/2/EC.

Background / Project Overview (EL13)

For Water District EL13, which includes the Island of Crete and the Island of Gavdos, the majority of water needs are met through water wells (boreholes) and the exploitation of groundwater reserves (IGME, 2009). Groundwater management in Crete poses significant challenges, as it requires the collaboration of multiple stakeholders. Various authorities are involved in managing groundwater resources, including municipalities, municipal enterprises for water supply and sewerage, local land reclamation organizations, and the Water Directorate of the Decentralized Administration of Crete, alongside numerous individual stakeholders. This multiplicity of actors complicates coordination efforts and hinders effective management. The widespread prevalence of illegal water wells (boreholes) further exacerbates these challenges, making it increasingly difficult to achieve sustainable groundwater resource management. Despite significant progress made by the Department of Water Management within the Decentralized Administration of Crete in implementing the River Basin Management Plan and its updates, several obstacles persist (General Directorate of Water, 2024).

Between July 2019 and January 2023, extensive fieldwork conducted by experienced HSGME personnel across Crete and the island of Gavdos yielded valuable insights (HSGME/RBC, 2019–2023). This systematic inventory not only documented the distribution and status of water wells (boreholes) but also enhanced understanding of the geological and hydrogeological conditions of the region. These findings establish a robust foundation for future investigations and make a significant contribution to the sustainable management of groundwater resources on the island.

Objectives

This study aims to present aggregate data on the spatial and percentage distribution of water wells by municipality, use, and ownership, derived from a systematic inventory conducted across Water District EL13 (Island of Crete and Island of Gavdos). Site inspections, carried out in collaboration with local authorities—including municipalities, local communities, municipal water and sewerage enterprises, local land reclamation organizations, and the Water Directorate of the Decentralized Administration of Crete—as well as with individual stakeholders. These efforts resulted in the identification and documentation of 5,349 water wells (boreholes) across the 24 municipalities of the region.

Methods

To implement the objectives of the project *"Systematic Inventory of Water Wells for All Uses Throughout the Country of Greece*" (Subproject 1: "*On-site inspections, direct inventory of water wells and completion of inventory forms*") in Crete (Water District EL13), the Regional Branch of Crete, in collaboration with the Hydrogeology Directorate of HSGME, was designated as the responsible department.

The project commenced with organizational meetings at the Water Directorate of the Decentralized Administration of Crete, followed by the coordination efforts of the Regional Branch to conduct on-site visits municipality by municipality. Initial meetings were held with key local stakeholders, including mayors, deputy mayors responsible for water management, presidents and directors of municipal water and sewerage enterprises, presidents of local communities, local water distributors, and presidents and staff of local land reclamation organizations. Following these discussions, field campaigns were organized to carry out the inventory (Figure 5). To guide field inspections, all available datasets from local authorities were collected, compiled into geodatabases, and thoroughly reviewed. These geodatabases served as a critical resource for planning and optimizing fieldwork efforts. For instance, the geodatabase of the Water Directorate of the Decentralized Administration of Crete recorded 3,657 boreholes as of July 2019 and 3,884 boreholes as of October 2021 (Water Directorate of Crete, accessed: July 2019; October 2021; December 2024).

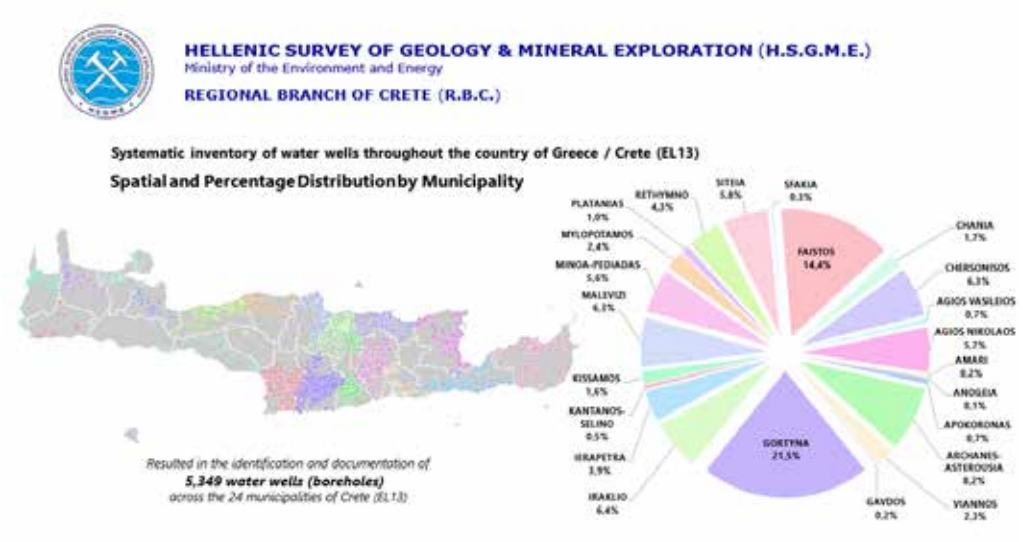

Figure 2. Spatial and Percentage Distribution of Water Wells (Boreholes) in Water District EL13 (Island of Crete and Island of Gavdos). This figure presents the results of a systematic inventory of water wells (boreholes) conducted across Water District EL13, documenting a total of 5,349 wells within the region's 24 municipalities. Colored dots represent boreholes associated with individual municipalities, while white lines delineate municipal boundaries. The accompanying pie chart illustrates the percentage distribution of boreholes by municipality within the district.

Experienced personnel from HSGME were organized into teams of two for field inspections, collaborating with available staff from local authority stakeholders. With their assistance, field inspections were conducted in coordination with individual stakeholders within their respective areas of responsibility.
The on-site inventory of water wells involved completing inventory forms with technical data (e.g., depth, pump specifications), informational details (e.g., ownership, location, coordinates in the Greek Grid), usage information (e.g., irrigation, drinking, period and hours of pumping), and field measurements (e.g., depth of water level, discharge, physicochemical parameters).
All collected data was entered into the project's geodatabase, providing a critical resource for assessing water balances, evaluating the status of the island's groundwater systems, and estimating the pressures exerted on them. This comprehensive data supports the development of appropriate measures aimed at achieving rational and sustainable groundwater management.
As part of the project, Technical Reports on Groundwater Systems within Water District EL13 are being prepared in alignment with the requirements outlined in Greece's River Basin Management Plans.

Results

Aggregate data on the spatial and percentage distribution of water wells (boreholes) by municipality, use, and ownership, derived from a systematic inventory conducted across Water District EL13 (Island of Crete and Island of Gavdos), are presented in Table 1 and Figures 2–4. The inventory resulted in the identification and documentation of **5,349 water wells (boreholes)** across the **24 municipalities** of the region (Table 1; Figures 1 and 2).
The **Municipality of Gortyna** accounts for **21.5%** of all water wells in Crete, followed by the **Municipality of Faistos** with **14.4%** and the **Municipality of Archanes-Asterousia** with **8.2%** (Figure 2). Notably, **52% of all water wells in Crete** are located within the municipalities of Faistos, Gortyna, Archanes-Asterousia, Minoa-Pediadas, and Viannos (Michalakis et al., 2022; HSGME/RBC, 2019–2023). Within the **wider area of the Messara Basin, 46.3%** of all water wells in Crete are concentrated (Michalakis, I., 2024).
Regarding usage, **79.4% of the wells on the Water District EL13 are designated for irrigation**, while **10.5% are used for water supply (drinking water)**. A further **7.6% of the wells are abandoned or no longer in use** (Figure 3).
Ownership data indicate that **68.6% of water wells are privately owned**, followed by **16.4% owned by municipalities**, **9.4% by municipal water and sewerage enterprises**, and **4.6% operated by local land reclamation organizations** (Figure 4).

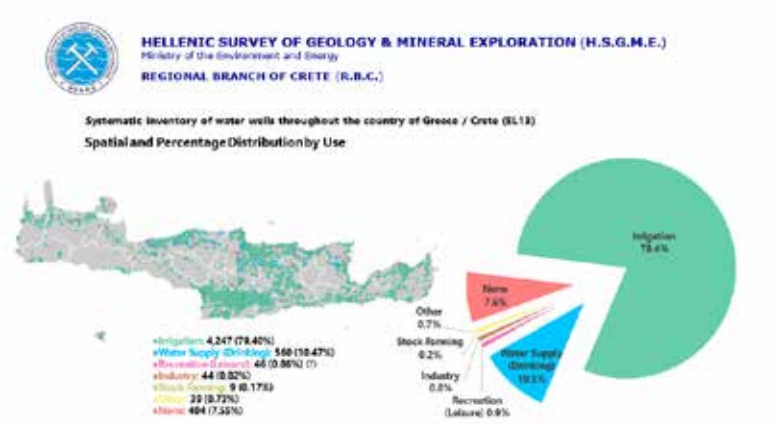

Figure 3. Spatial and Percentage Distribution by Use of Water Wells (Boreholes) in Water District EL13 (Island of Crete and Island of Gavdos) and corresponding pie chart. Different colored dots on the map represent boreholes categorized by specific usage, as detailed in the map legend.

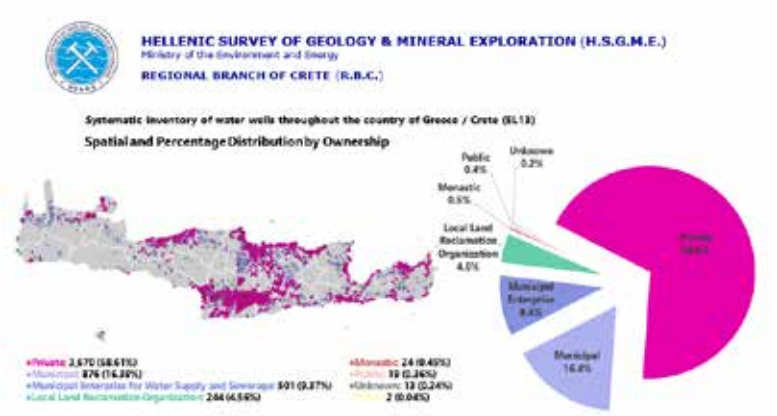

Figure 4. Spatial and Percentage Distribution by Ownership of Water Wells (Boreholes) in Water District EL13 (Island of Crete and Island of Gavdos) and corresponding pie chart. Different colored dots on the map represent boreholes categorized by ownership type, as detailed in the map legend.

Table 1 presents aggregate data by municipality, classified according to the respective main use and ownership of water wells (boreholes). Numeric values indicate the total number of wells, with corresponding percentages (%) shown in parentheses, and are provided for reference.

Table 1. Aggregate data by municipality, main use, and ownership derived from the inventory of water wells (boreholes) conducted across Water District EL13.

		Main Use		Main Ownership			
Municipality	**Total Number of Water Wells (%)**	**Irrigation (%)**	**Water Supply (%)**	**Private (%)**	**Municipal (%)**	**Municipal Enterprises (%)**	**Local Land Reclamation Organization (%)**
Agios Vasileios	35 (0.65)	28 (93.3)	2 (6.7)	16 (45.7)	18 (51.4)	-	1 (2.9)
Agios Nikolaos	306 (5.72)	169 (67.9)	49 (19.7)	200 (65.4)	33 (10.8)	39 (12.7)	27 (8.8)
Amari	10 (0.19)	4 (57.1)	3 (42.9)	-	10 (100.0)	-	-
Anogeia	4 (0.07)	-	4 (100.0)	-	2 (50.0)	2 (50.0)	-
Apokoronas	39 (0.73)	20 (83.3)	3 (12.5)	3 (7.7)	34 (87.2)	2 (5.1)	-
Archanes-Asterousia	440 (8.23)	300 (92.0)	25 (7.7)	341 (77.5)	94 (21.4)	1 (0.2)	-
Viannos	123 (2.30)	106 (88.4)	13 (10.8)	60 (48.8)	54 (43.9)	-	8 (6.5)
Gavdos	9 (0.17)	1 (20.0)	4 (80.0)	1 (11.1)	8 (88.9)	-	-

Gortyna	1,151 (21.52)	800 (95.2)	37 (4.4)	962 (83.6)	157 (13.6)	1 (0.1)	28 (2.4)
Iraklio	341 (6.38)	283 (87.1)	36 (11.1)	256 (75.0)	6 (1.8)	78 (22.9)	-
Ierapetra	209 (3.91)	161 (89.0)	13 (7.2)	144 (68.9)	48 (23.0)	-	15 (7.1)
Kantanos-Selino	26 (0.49)	15 (62.5)	9 (37.5)	9 (34.6)	-	5 (19.2)	4 (15.4)
Kissamos	87 (1.63)	61 (80.3)	15 (19.7)	20 (23.0)	-	4 (4.6)	9 (10.3)
Malevizi	335 (6.26)	169 (70.4)	58 (24.2)	213 (63.6)	22 (6.5)	80 (23.9)	-
Minoa-Pediadas	297 (5.55)	202 (89.9)	21 (9.3)	166 (55.9)	105 (35.4)	24 (8.1)	-
Mylopotamos	127 (2.37)	70 (68.6)	28 (27.5)	56 (44.1)	36 (28.3)	33 (26.0)	1 (0.8)
Oropedio Lasithiou	-	-	-	-	-	-	-
Platanias	55 (1.03)	42 (82.4)	9 (17.6)	8 (14.5)	-	38 (69.1)	9 (16.4)
Rethymno	232 (4.34)	126 (63.0)	47 (23.5)	144 (62.1)	1 (0.4)	86 (37.1)	-
Siteia	309 (5.78)	242 (91.3)	18 (6.8)	183 (59.2)	61 (19.7)	33 (10.7)	24 (7.8)
Sfakia	15 (0.28)	9 (75.0)	3 (25.0)	2 (13.3)	11 (73.4)	-	2 (13.3)
Faistos	770 (14.40)	555 (96.6)	14 (2.4)	585 (76.0)	64 (8.3)	2 (0.3)	115 (14.9)
Chania	92 (1.72)	63 (79.7)	12 (15.2)	69 (75.0)	1 (1.1)	17 (18.5)	1 (1.1)
Chersonisos	337 (6.30)	209 (77.7)	50 (18.5)	232 (68.9)	49 (14.5)	56 (16.6)	-

Conclusions

This study provides a comprehensive overview of the systematic inventory of water wells conducted across Water District EL13. The identification and documentation of **5,349 water wells (boreholes)** across **24 municipalities** represent a significant milestone in understanding the spatial and functional distribution of groundwater abstraction points. The findings reveal key insights into the distribution and use of water wells. The **wider area of the Messara Basin**, a critical agricultural and hydrogeological region in central-southern Crete, accounts for **2,474 wells** (**46.3% of the island's total**), highlighting the region's significant dependency on groundwater for irrigation.

Irrigation dominates water use, representing **79.4% of all wells**, followed by **water supply** (**10.5%**) and a smaller fraction of wells (**7.6%**) that are abandoned or not in use. Ownership patterns indicate a high prevalence of **private wells** (**68.6%**), highlighting the challenges of regulatory oversight and sustainable resource management.

The geodatabases developed as part of this inventory serve as a vital tool for planning and decision-making. They provide a foundation for assessing water balances, evaluating groundwater pressures, and formulating appropriate management strategies. By integrating technical, informational, and usage data, the inventory supports compliance with Greece's River Basin Management Plans and aligns with the European Union's Water Framework Directive and related policies.

The successful implementation of this project demonstrates the importance of collaboration among stakeholders, including local authorities, municipal enterprises, land reclamation organizations, and individual users. Despite challenges such as the prevalence of illegal wells and the complexity of coordinating multiple actors, this initiative contributes significantly to improving the management and sustainability of Crete's groundwater resources.

Future efforts should focus on strengthening the monitoring of groundwater systems, enforcing regulations on illegal wells, and promoting sustainable water use practices. These actions are crucial to safeguarding groundwater resources and addressing the growing pressures of agricultural demand, climate variability, and population growth in the region.

Figure 5. Random photographs from fieldwork conducted during the systematic inventory across Water District EL13.

Acknowledgements
Fieldwork was conducted by the executive staff—Athanasouli Elpida, Davrados Michalis, Lionakis Ioannis, Papanikolaou Kassiani, Pavlidou Saia, Tsolaki Eleni, Zourmpakis Evangelos, and the first author—from the Regional Branch of Crete and the Department of Hydrogeology of HSGME as part of the project "*Systematic Inventory of Water Wells for All Uses Throughout the Country of Greece".* The authors express their gratitude to the personnel of local authorities, including mayors, deputy mayors responsible for water management, presidents and directors of municipal water and sewerage enterprises, presidents of local communities, local water distributors, presidents and staff of local land reclamation organizations, as well as the personnel of the Water Directorate of the Decentralized Administration of Crete. The authors also express their sincere gratitude to all individuals who provided their cooperation, particularly during field activities.

References

Council Directive 91/676/EEC of 12 December 1991 concerning the protection of waters against pollution caused by nitrates from agricultural sources, 1991. [http://data.europa.eu/eli/dir/1991/676/oj].

Directive 2000/60/EC of the European Parliament and of the Council of 23 October 2000 establishing a framework for Community action in the field of water policy, 2000. [http://data.europa.eu/eli/dir/2000/60/oj].

Directive 2006/118/EC of the European Parliament and of the Council of 12 December 2006 on the protection of groundwater against pollution and deterioration, 2006. [http://data.europa.eu/eli/dir/2006/118/oj].

Directive 2007/2/EC of the European Parliament and of the Council of 14 March 2007 establishing an Infrastructure for Spatial Information in the European Community (INSPIRE), 2007. [http://data.europa.eu/eli/dir/2007/2/oj].

General Directorate of Water, 2024. 2nd Revision of the River Basin Management Plan of the Water District of Crete and the corresponding Strategic Environmental Impact Assessment. Ministry of Environment and Energy. [https://wfdver.ypeka.gr/wp-content/uploads/2024/07/EL13_2REV_sdlap.pdf].

General Directorate of Water, 2025. National Register of Water Intake Points (in Greek: *EMSY*). Ministry of Environment and Energy. [http://lmt.ypeka.gr/].

HSGME/RBC, 2019-2023. Systematic inventory of water wells of every use throughout the country of Greece. (Municipalities of Crete. Preliminary Technical Reports, Rethymno, Greece.

HSGME/RBC, 2018-2023. Groundwater Monitoring Network of Greece, Preliminary Reports, Rethymno, Greece.

IGME, 2009. Project: "Recording and Evaluation of the Hydrogeological Characteristics of the Groundwater and Aquifer Systems of Greece. Water District EL13". Rethymno, Greece.

Michalakis, I., Tsolaki, E., Loupasakis, C., Voudouris, K., Kontoes, Ch., 2022. Groundwater level dynamics of the Messara Basin, Crete Island [Bulletin of the Geological Society of Greece, Special Publication 10, Ext. Abs. GSS2022-162, pp 553-554].

Michalakis, I., 2024. Hydrogeological Conditions and Sustainability Challenges in the Messara Basin. Agia Pelagia, Crete. [SIPS 2024. 10th Intl. Symp. on Sustainable Mineral Processing].

Water Directorate of Crete, (2019; 2021; 2024). Decentralized Administration of Crete [Retrieved from https://data.apdkritis.gov.gr/el].

17th INTERNATIONAL CONGRESS of the Geological Society of Greece

BULLETIN OF THE GEOLOGICAL SOCIETY OF GREECE, SP. PUBL.

EXTENDED ABSTRACT 210

Preliminary Results on Land Subsidence Induced by Groundwater Overexploitation Using Copernicus Sentinel Data: Insights from the Messara Basin, Crete

Michalakis I.[1,2], Tsolaki E.[2], Loupasakis C.[1], Voudouris K.[3], Kontoes Ch.[4]

(1) Laboratory of Engineering Geology and Hydrogeology, School of Mining and Metallurgical Engineering, National Technical University of Athens, Athens, Greece, michalakis@eagme.gr, (2) Hellenic Survey of Geology and Mineral Exploration, Regional Branch of Crete, Rethymno, Greece, (3) Aristotle University of Thessaloniki, Dept. of Geology, Thessaloniki, Greece (4) National Observatory of Athens, Institute for Astronomy and Astrophysics, Space Applications and Remote Sensing, BEYOND Center for EO Research and Satellite RS, Athens, Greece.

Research Highlights

Areas of significant groundwater depression have been identified, alongside potential geohazards linked to land subsidence resulting from excessive groundwater withdrawal and significant level decline. Data from the European Ground Motion Service (EGMS) were analyzed to detect land subsidence induced by groundwater exploitation, with findings subsequently validated through site inspections.

Introduction / Background

In cases of overpumping with significant lowering of the piezometric surface across large aquifers subsidence phenomena are often observed (Zhang et al., 2008; Loupasakis et al., 2014; Raspini et al. 2014; Svigkas et al., 2016; Papoutsis et. al., 2020; Kamali et al., 2021). The Messara Basin, a key agricultural and hydrogeological region in central-southern Crete (Figure 2), is characterized by complex geological formations, intensive agricultural activities, and increasing water demand. Geodetic satellite measurements for the period 2007-2009 indicate a subsidence rate of approximately 2 cm per year in the central part of the Messara Plain (Mertikas et al., 2010).

Groundwater demand has approximately doubled the number of recorded boreholes in the area over the past decades. By 2007, the number of boreholes was estimated at 1,400. Recent data from a systematic inventory of water wells (boreholes) in Greece, documented 2,474 boreholes in the Messara Basin (Figure 1), accounting for 46.3% of all water wells in Crete (H.S.G.M.E./ R.B.C., 2023; Michalakis, 2024).

Figure 1. The Spatial Distribution of 2,474 water wells across the broader area of Messara Basin. Results from Project: Systematic inventory of water wells (boreholes) throughout the country of Greece / Crete (EL13). This comprehensive effort resulted in the identification and documentation of 2,474 boreholes across Messara Basin. This represents 46.3% of all water wells in Crete.

Groundwater levels in the Messara Basin exhibit notable seasonal fluctuations (Michalakis, 2024), primarily driven by overexploitation for irrigation, particularly in the aftermath of a prolonged drought. This unsustainable usage raises significant concerns regarding the sustainability of water resources and heightened the basin's vulnerability to climate-induced stresses. Remote sensing technologies, such as the Copernicus Sentinel satellite program, provide valuable tools for monitoring environmental changes and guiding field inspections (Delgado Blasco et al., 2019). This study outlines the integration of Sentinel data with site inspections to address potential geohazards identifying notable displacements and detect induced land subsidence associated with groundwater over-exploitation.

Objectives

This study presents preliminary results from site inspections conducted using Copernicus ground motion data from EGMS. The results highlight the utility of Sentinel data in enhancing field observations and addressing potential geohazards by identifying notable displacements and detecting induced land subsidence associated with groundwater overexploitation.

Methods

Groundwater levels in the basin exhibit significant seasonal variations, largely due to over-exploitation for irrigation, raising critical sustainability concerns. Effective groundwater management requires systematic data collection and precise utilization of primary data. Changes in groundwater head within the Messara Basin were studied from May 2021 to October 2023, leading to the identification of areas with generalized groundwater depressions (Michalakis et al., 2022; Michalakis, 2024). During this period, field observations were conducted, and local authorities and civilians were engaged to assist in identifying notable displacements in their respective areas, with particular emphasis on those linked to groundwater overexploitation. It is worth noting that deformation phenomena occur in several areas; however, as these areas are under cultivation, such phenomena often go unnoticed due to erosion and plowing or are not given adequate consideration.

Following, mean vertical velocities (weekly measurements) from two datasets (80,014 Persistent Scatterers -PSs-) —ORTHO (Level 3) Vertical for 2016–2021 (spanning 5 January 2016 to 22 December 2021) and 2018–2022 (spanning 6 January 2018 to 23 December 2022)—were analyzed using geostatistical methods to identify regions of significant subsidence (Figure 2). Subsequently, an analysis of the ORTHO (Level 3) Vertical dataset for 2019–2023 (spanning 13 January 2019 to 18 December 2023), obtained from the European Ground Motion Service (EGMS) Explorer (accessed on 30 October 2024), led to the selection of 86 PSs for site inspections (EGMS Data Explorer, 2024).

Finally, targeted site inspections at the narrow areas surrounding the 86 selected EGMS PSs were conducted from 11 to 29 November 2024.

Figure 3 presents a plot of vertical displacements and vertical mean velocities for the 86 PSs selected for site inspections in the Messara Basin. In the plot, vertical displacement values range from +48.10 mm (EGMS_08) to -152.40 mm (EGMS_82), while vertical mean velocities range from +9.8 mm/year to -30.80 mm/year, respectively.

Figure 2. The Spatial Distribution of the Mean Vertical Velocities (weekly measurements spanning from 5 January 2016 to 22 December 2021) from dataset: [ORTHO (Level 3) Vertical for 2016–2021 / 80,014 PSs]

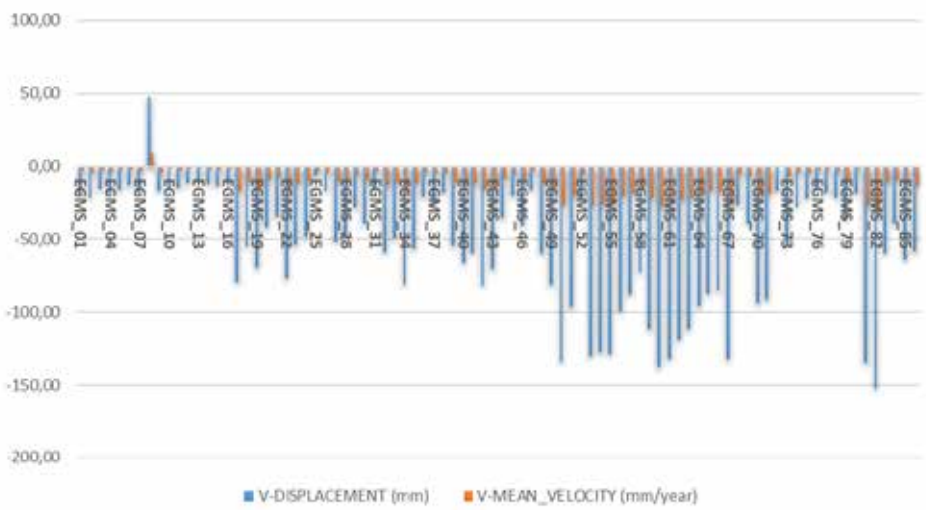

Figure 3. Plot of Vertical Displacements and Vertical Mean Velocities of the 86 PSs selected for site inspections in the Messara Basin.

These values were derived from the ORTHO (Level 3) Vertical dataset for 2019–2023 (spanning 13 January 2019 to 18 December 2023), obtained from the European Ground Motion Service (EGMS) Explorer (accessed on 30 October 2024).

Description and Documentation: An Example

The applied method highlights the utility of Sentinel data in complementing field observations and addressing potential geohazards by identifying displacements and detecting induced land subsidence associated with groundwater overexploitation. Preliminary findings indicate that areas of significant displacement can be identified, while the study of geological and hydrogeological conditions provides a valuable tool for evaluating ongoing geohazards.

An example of the inventory form designed for reporting the findings of the 86 selected sites is presented in figure 3, referring to a Location Southwest of Moires (Kalamiari) (Date of site inspection: 09 December 2024). In Figure 4, embedded Figure 86.1 shows a snapshot from the EGMS Data Explorer, incorporated into the inventory form of EGMS_86.

The reference measurement point (10HQYNAEOU, EGMS_86) is located southwest of Moires, within an olive grove (Figure 4; embedded Figure 86.1). At the reference point and within a radius of ~30m, significant ground ruptures were identified, both within the olive grove and on the paved road to the east. Openings due to pipe-laying phenomena are observed within the olive grove, which are related to underlying deformations (Figure 4; embedded Figure 86.2a). Ground ruptures were observed to the west and at a distance of ~20m, on the eastern margin of the road (Figures 4; embedded Figures 86.2b and 86.2c). Significant deformations and ruptures (Figure 4; embedded Figure 86.2d) are observed over a length of ~70m of the eastern road and are located mainly east and south of the reference point. Two more reference points (EGMS_19 and EGMS_22, shown in figures 5.1 and 5.2) in a short distance gave similar phenomena after site inspections helping to identify an area of high geohazard risk.

Geological Setting. The geological framework of the area is presented in figure 5.2. where **alluvium (al) deposits** comprising unconsolidated sediments such as sands, silts, clays, and gravels deposited by rivers and streams during the Quaternary (thickness up to 20m) overlaying **Pleistocene (Pt) deposits** consisting of marine terraces (typically composed of consolidated beach deposits such as sand, gravel, and occasionally shells) and non-marine clastics including fluviatile beds and fans (consist of coarse-grained materials like sand and gravel).

Hydrolithological Setting.

Alluvium deposits typically form highly permeable and productive aquifer systems where variable yet generally favorable conditions for groundwater storage and movement within these deposits can create a heterogeneous permeability profile. The hydrogeological behavior of alluvial deposits is influenced by the sorting, size distribution, and interbedding of the different sediment types. These factors contribute to a complex and layered aquifer system where hydrological properties can vary significantly over short distances. The hydrogeological properties can vary based on the clast size, sorting, and degree of cementation. This complexity can lead to heterogeneous aquifer properties within short distances, influenced by changes in sediment characteristics and depositional processes (Michalakis et al., 2024).

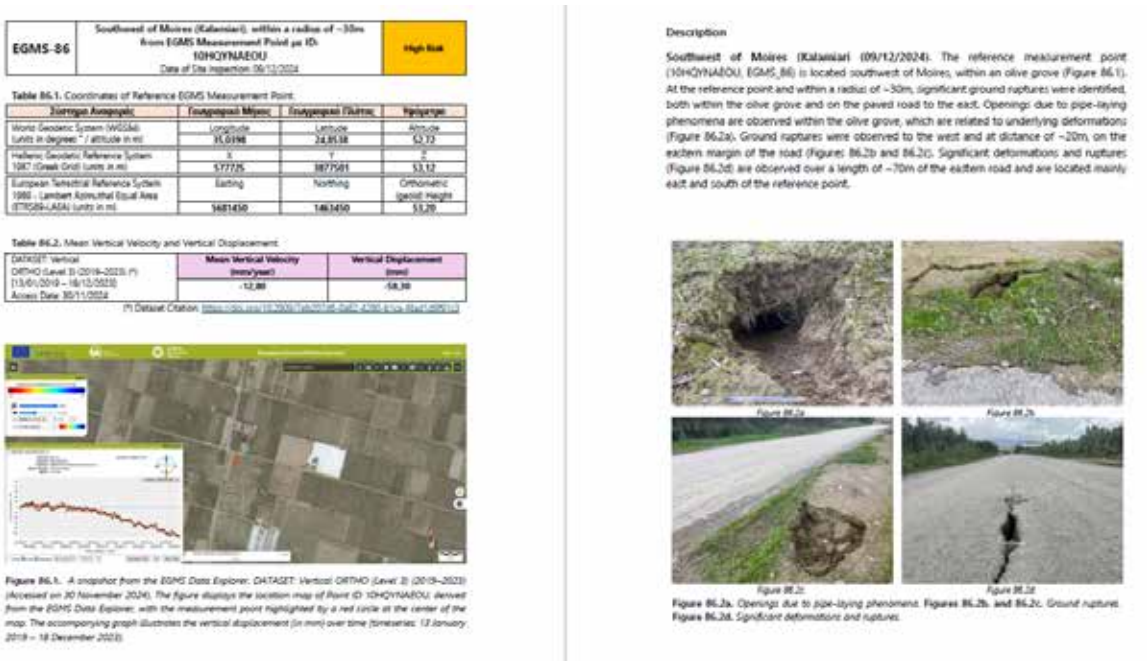

Figure 4. Inventory Form of EGMS Measurement Point: 10HQYNAEOU (EGMS-86).

Pleistocene deposits, presents a stratified aquifer system where the lithological diversity significantly influences hydrogeological properties. Marine terraces, typically composed of consolidated beach deposits such as sand, gravel, and occasionally shells. The degree of cementation varies, but where less consolidated, these terraces often exhibit high porosity and permeability, conducive to effective groundwater storage and flow. The porosity and permeability in marine terraces depend on the degree of lithification. In areas where the terrace deposits are less cemented, they can exhibit high porosity and permeability. Non-marine clastics (fluviatile beds and fans) formed from river and alluvial fan processes, generally consist of coarse-grained materials like sand and gravel. The sorting and layering of these materials can significantly affect their hydrogeological characteristics. Typically, these materials have high porosity due to the loose packing of coarse grains, coupled with high permeability that facilitates effective water infiltration and movement. The hydrogeological properties can vary based on the clast size, sorting, and degree of cementation. The unit exhibits a complex hydrogeological behavior due to the mixture of marine and non-marine depositional environments. This complexity can lead to heterogeneous aquifer properties within short distances, influenced by changes in sediment characteristics and depositional processes. The groundwater flow in these areas is generally robust, especially in regions where the sediments are coarse and well-sorted. The yield from these aquifers can vary depending on local conditions such as sediment depth, degree of consolidation, and the presence of impermeable layers or lenses within the deposits (Michalakis et al., 2024).

Hydrogeological Setting and Deformations

Hydrogeological conditions in the Messara Basin were studied from May 2021 to October 2023, resulting in the identification of areas with generalized groundwater depressions (Michalakis et al., 2022; Michalakis, 2024). Potentiometric data, collected during wet and dry seasons in 2021 and 2023, were derived from an extensive network of 767 measurement points across the basin. These data allowed for the analysis of groundwater head changes, leading to the documentation of significant depressions.

Groundwater overexploitation near the reference measurement point has created a cone of depression, with groundwater levels dropping to negative elevations (below mean sea level). Figure 5.1 illustrates this phenomenon, where the purple-shaded area represents a cone of depression with groundwater head values reaching as low as -31.08 m by the end of the dry season in 2023. Within this zone of excessive groundwater withdrawal (Figures 5.1 and 5.2) lies reference measurement point 10HQYNAEOU (EGMS_86), along with EGMS_19 and EGMS_22, where notable deformations and ruptures were observed.

During the wet season, groundwater levels in alluvial deposits rise to +50 m, influenced by the Geropotamos River located approximately 550 m to the north. However, significant seasonal fluctuations—up to 85 m in vertical water level—are observed in the area, which has an altitude of 53.12 m (EGMS_86). These fluctuations are exacerbated by extensive groundwater overexploitation and occur within highly permeable hydrolithological units that facilitate rapid water infiltration and movement. Embedded Table 86.2 in Figure 3 presents the mean vertical velocity and total vertical displacement of EGMS_86, as derived from the EGMS Data Explorer (accessed on 30 October 2024).

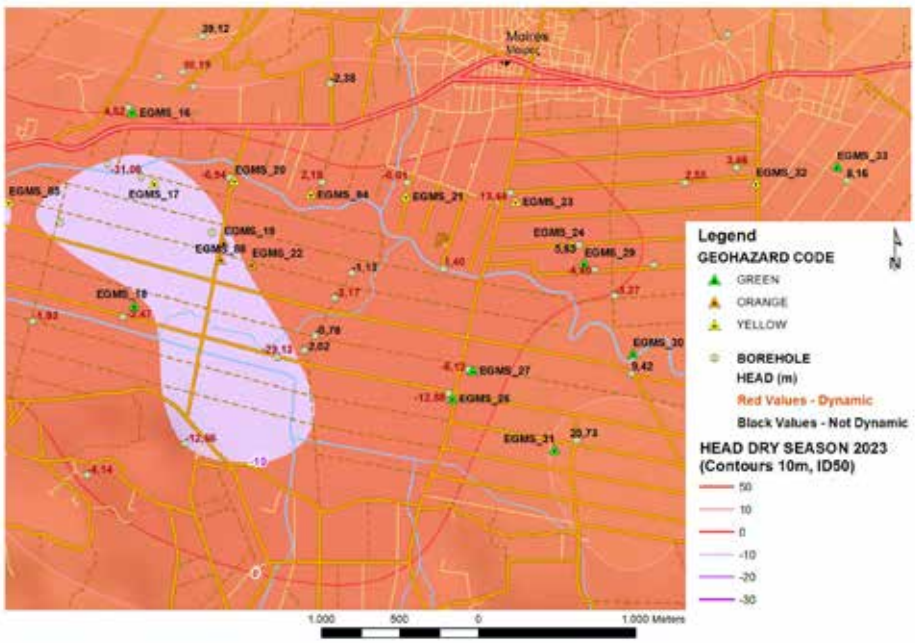

Figure 5.1. Groundwater overexploitation near the reference measurement point has created a cone of depression, with groundwater levels dropping to negative altitude.

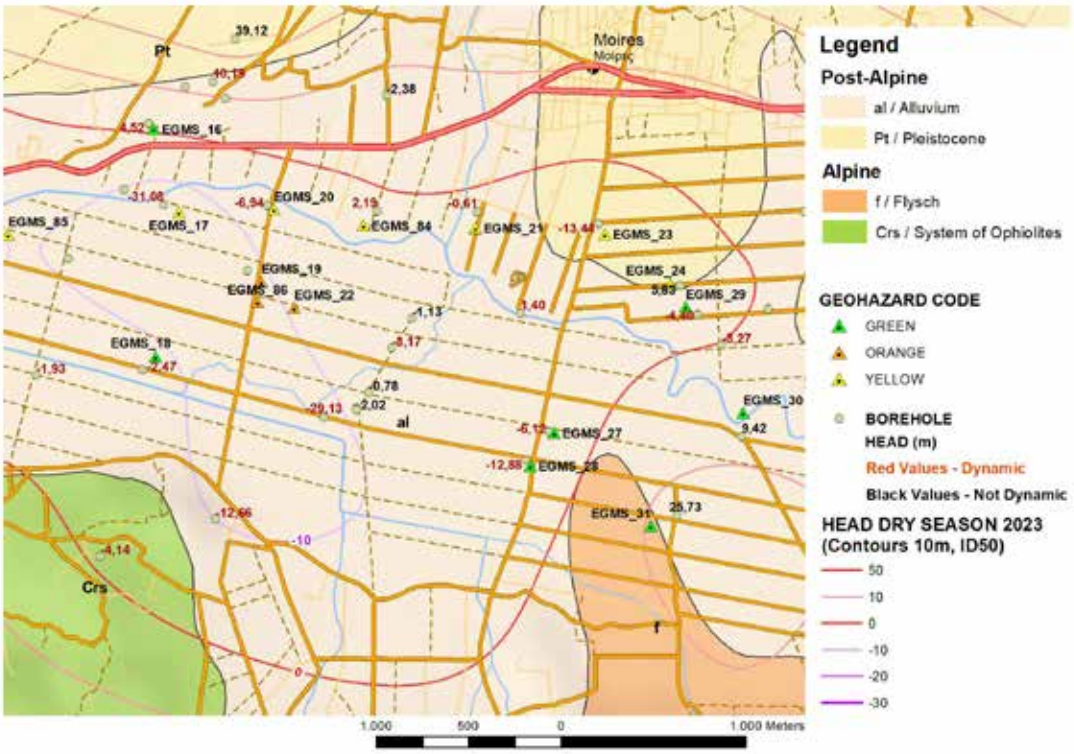

Figure 5.2. The geological framework of the area, illustrating potentiometric contours and head values.

The loose packing of alluvial deposits in the upper layers and the unconsolidated Pleistocene deposits (e.g., sand and gravel) beneath them are particularly affected by these changes. This interaction leads to significant ground ruptures and openings due to pipe-laying phenomena, which are attributed to underlying deformations caused by groundwater-level fluctuations.

It is worth noting that similar phenomena (subsidence - ground movements due to groundwater depletion) occur in other comparable areas; however, because these areas are under cultivation, deformation phenomena often go unnoticed due to erosion and plowing or are not given sufficient consideration. Documenting these areas where such phenomena occur can enhance the understanding of the geological background's response in regions affected by overexploitation and contribute to the assessment of existing or potentially emerging geohazards, ultimately aiding in risk reduction. In addition, it will help in the design of mitigation measures, such as the application of artificial recharge.

Conclusions

Ground movements caused by groundwater decline are an increasingly significant issue worldwide, often due to excessive water extraction and pronounced rainfall seasonality. In agricultural and peri-urban areas, such as the Messara Basin on the island of Crete, these drawdowns are predominantly anthropogenic, with excessive groundwater extraction for agriculture leading to land subsidence. Understanding the geological and hydrogeological conditions of an area, combined with the use of satellite data, offers a critical tool for mitigating risks and minimizing the impacts of potential geohazards. Such integration is particularly valuable for civil engineering applications, including the structural assessment of buildings and infrastructure, detection of differential displacements, evaluation of terrain stability, and other related challenges.

Acknowledgements

Field surveys have been conducted within the framework of the PhD thesis assigned to the first author at the N.T.U.A. We acknowledge the use of data from the European Ground Motion Service (EGMS) Data Explorer in this study. The datasets provided valuable insights for analyzing induced land subsidence and geohazards. We gratefully acknowledge the European Environment Agency (EEA) for maintaining and providing access to the EGMS data, which significantly contributed to the outcomes of this research.

References

Delgado Blasco, J.M., Foumelis, M., Stewart, C., Hooper, A., 2019. Measuring Urban Subsidence in the Rome Metropolitan Area (Italy) with Sentinel-1 SNAP-StaMPS Persistent Scatterer Interferometry. Remote Sensing 11, 129. [https://doi.org/10.3390/rs11020129].

European Ground Motion Service / Land Monitoring / EGMS Explorer. Dataset: ORTHO (Level 3) East/West (2019–2023) & Vertical (2019–2023) [https://doi.org/10.2909/7eb207d6-0a62-4280-b1ca-f4ad1d9f91c3EGMS-01].

H.S.G.M.E./R.B.C., 2023. Project: "Systematic inventory of water wells of every use throughout the country of Greece" of the Municipalities: Phaistos, Gortyna, Archanon Asterousion, Minoa Pediadas, Viannos (Period: 2020-2022). Preliminary Technical Reports, Rethymno, Greece.

Kamali, M., Papoutsis, I., Loupasakis, C., Abuelgasim, A., Omari, K., Kontoes, C., 2021. Monitoring of land surface subsidence using persistent scatterer interferometry techniques and ground truth data in arid and semi-arid regions, the case of Remah, UAE, Science of The Total Environment, Volume 776 [https://doi.org/10.1016/j.scitotenv.2021.145946].

Loupasakis, C., Angelitsa, V., Rozos, D., Spanou, N., 2014. Mining geohazards—land subsidence caused by the dewatering of opencast coal mines: The case study of the Amyntaio coal mine, Florina, Greece. Natural Hazards, vol. 70(1), pages 675-691.

Mertikas, S., Papadaki, E., Paleologos, E., 2010. Radar interferometry technique for monitoring subsidence induced by excessive groundwater pumping in Crete, Greece. ESA Proceedings for the Living Planet Symposium, pp. 6, Bergen, Norway.

Michalakis, I., Tsolaki, E., Loupasakis, C., Voudouris, K., Kontoes, Ch., 2022. Groundwater level dynamics of the Messara Basin, Crete Island. [Bulletin of the Geological Society of Greece, Sp. Publ. 10. Ext. Abs. GSS2022-162. 553-554 p.].

Michalakis, I., Staridas Sp., Tsolaki, E., 2024. Hydrolithological Classification of the Island of Crete: Based on the 1:200,000 Geological Map by Creutzburg et al. (1977) / First Report on the Hydrolithological Properties and Spatial Distribution of Geological Units on the Island of Crete. Rethymno [H.S.G.M.E./R.B.C. Library Code: 377/HG231].

Michalakis, I., Staridas Sp., Tsolaki, E., 2024. Hydrolithological Classification of the Island of Crete: Based on the 1:200,000 Geological Map by Creutzburg et al. (1977) / Second Report on the Hydrolithological Properties and Spatial Distribution of Geological Units on the Island of Crete / Hydrolithological Classification of the Island of Crete. Rethymno [H.S.G.M.E./R.B.C. Library Code: 379/HG233].

Michalakis, I., 2024. Hydrogeological Conditions and Sustainability Challenges in the Messara Basin, Crete. [SIPS 2024. 10th Intl. Symp. on Sustainable Mineral Processing. Paper ID: 493].

Papoutsis, I., Kontoes, C., Alatza, S., Apostolakis, A., Loupasakis, C., 2020. InSAR Greece with Parallelized Persistent Scatterer Interferometry: A National Ground Motion Service for Big Copernicus Sentinel-1 Data. Remote Sensing 12, no. 19: 3207. [https://doi.org/10.3390/rs12193207].

Raspini, F., Loupasakis, C., Rozos, D., Adam, N., Moretti, S., 2014. Ground subsidence phenomena in the Delta municipality region

(Northern Greece): Geotechnical modeling and validation with Persistent Scatterer Interferometry. International Journal of Applied Earth Observation and Geoinformation, Volume 28, Pages 78-89, [https://doi.org/10.1016/j.jag.2013.11.010].

Svigkas, N., Papoutsis I., Loupasakis C., Tsangaratos P., Kiratzi, A., Kontoes C., 2016. Land subsidence rebound detected via multi-temporal InSAR and ground truth data in Kalochori and Sindos regions, Northern Greece. Engineering Geology, Volume 209, Pages 175-186, ISSN 0013-7952, [https://doi.org/10.1016/j.enggeo.2016.05.017].

Zhang, Y., Xue, Y.Q., Wu, J.C., Yu, J., Wei, Z.X., Li, Q.F., 2008. Land subsidence and earth fissures due to groundwater withdrawal in the southern Yangtse Delta, China. Environmental Geology 55, No 4, 751-762.

17th INTERNATIONAL CONGRESS of the Geological Society of Greece

BULLETIN OF THE GEOLOGICAL SOCIETY OF GREECE, SP. PUBL.

EXTENDED ABSTRACT 211

Application of geochemical indices for heavy metal evaluation in the Pinios Dam, Greece

Michalopoulou M.[1], Depountis N.[1], Zagana E.[1], Avramidis P.[1]
(1) Department of Geology, University of Patras, Patra, Greece, maria_michalopoulou@ac.upatras.gr

Research Highlights: Application of geochemical indices for the evaluation of sediment and water samples in the Pinios Dam drainage basin in Western Greece

Introduction

Reservoirs are essential for water supply and flood management; yet numerous reservoirs encounter quality challenges caused by heavy metal concentration. This study investigates the extent of heavy metal concentration in the Pinios Dam drainage basin in the Ilia Regional Unit in Western Greece by analyzing sediment and water samples from the dam reservoir as well as water samples from the river tributaries. The main focus is to evaluate heavy metal concentration levels using established geochemical indices. The indices that were used for this purpose include the Geo-Accumulation Index (Igeo), the Contamination Factor (CF), the Pollution Load Index (PLI), and the Heavy Metal Pollution Index (HPI).

Study area

The Pinios Dam is an earth-filled structure characterized by a heterogeneous design, standing 50 meters high and spanning a length of 2,175 meters, with a final crest elevation of 100 meters. Constructed in 1968, the reservoir associated with the dam covers a total surface area of 19.87 km² and it collects surface runoff from a catchment area of 673.41 km². The water that is collected serves dual purposes, supplying both drinking and irrigation needs (Michalopoulou et al., 2024). Geologically, the catchment area is predominantly underlain by Alpine bedrock, which includes formations from the Ionian, Gavrovo-Tripolis, and Pindos geotectonic zones. These formations primarily consist of flysch and limestone. Additionally, the area features Neogene and Quaternary sediments. To provide a detailed representation of the area's geological framework, a geological map was developed using ArcGIS Pro 3.4.0. This map integrates unified data from four geological sheets produced by the Hellenic Survey of Geological and Mineral Exploration and presents the sampling points of this research (Figure 1).

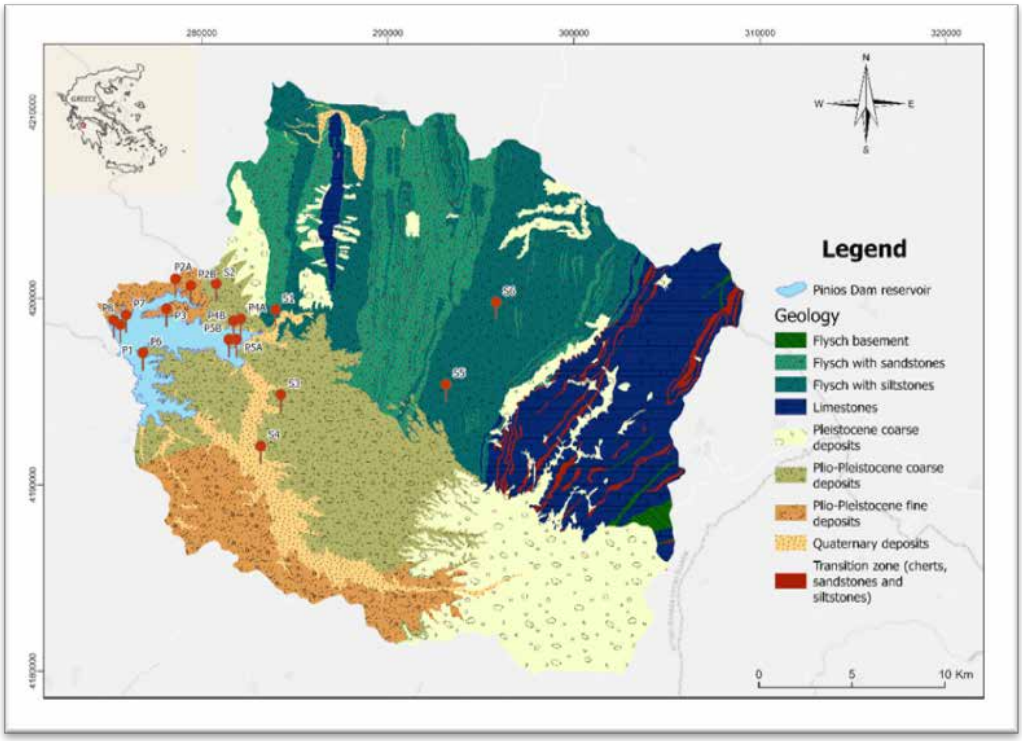

Figure 1. The sampling points and the geological formations of the research area (modified from Michalopoulou et al., 2024).

The surrounding region has experienced high rates of soil erosion and shallow landslide activity in recent decades, largely attributed to the extensive wildfires that have occurred over the past 20 years (Depountis *et al.*, 2020; Lainas *et al.*, 2021; Michalopoulou *et al.*, 2022). These processes have accelerated sediment deposition within the reservoir, significantly influencing the distribution and concentration of heavy metals in the water body and the deposited sediments; thus, altering the geochemical dynamics of the artificial lake.

Methods

Within the research area, monitoring and sampling stations (Figure 1) were established for the analysis of sediments, as well as the incoming and stagnant water. Sediment samples were obtained from the reservoir's bottom using a Van Veen grab sampler at seven stations (P1-P7), covering a collection area of 0.04 m². At locations P3 and P7, in situ measurements were performed during the autumn and winter seasons to record the physicochemical properties of the water column. Both sediment and water samples were transported to the laboratory in a portable refrigerator. Sediment samples were stored at −4 °C to ensure preservation, while water samples were analyzed within 24 hours for nutrient content and acidified for subsequent heavy metal analysis. Regarding the sediment analysis, major elements were analyzed using WD-XRF (Rigaku ZSX PRIMUS II), and the total organic carbon was quantified using the potassium dichromate oxidation method. Fe and Mn in water samples were measured via atomic absorption spectroscopy (Perkin Elmer Pinacle 900). pH, Eh, and other parameters were recorded in situ with a YSI 63 multiparameter probe.

Runoff water sampling was carried out at six sites (S1–S6), representing the tributaries and the main branch of the Pinios River basin. Samples were collected in two polyethylene bottles, one with a capacity of 1 L and the other 100 mL. The 100 mL samples were filtered on-site through a 0.45 μm filter to remove particles, followed by acidification with HNO_3. Following each sampling, water samples were transported to the laboratory for chemical analysis using atomic absorption spectroscopy. The elements analyzed in the sediments are Fe, Mn, Ni, Cr, Pb, Zn, Cu, Co, and Zr. The water samples were analyzed for Fe, Mn and major cations/anions Ca^{2+}, Mg^{2+}, Na^{+}, K^{+}, HCO_3^{-}, SO_4^{2-}, Cl^{-}, NO_3^{-}, NO_2^{-}, PO_4^{3-}, NH_4^{+}.

The Geo-Accumulation Index (Igeo) was used for the assessment of heavy metal enrichment in sediments and soil as suggested by Muller (1969), Sojka *et al.* (2022), Wu *et al.* (2022), and Wang *et al.* (2023) from another similar research. According to Muller (1969), the Igeo index is calculated by the following formula.

$$I_{geo} = \log_2\left(\frac{C_n}{K * B_n}\right), \quad (1)$$

The Cn value represents the measured heavy metal concentrations of the sediment samples (mg/kg), the K coefficient is typically equal to 1.5 and demonstrates the adjustment of the standard variation of heavy-metal concentrations during diagenesis (Wu *et al.*, 2022) and the Bn is the background concentrations of each heavy metal (mg/kg) displaying the composition of the upper continental crust (Taylor *et al.*, 1985; McLennan, 2001). The classes of the Igeo index describing the level of contamination are the following: Igeo ≤ 0: uncontaminated, 0 < Igeo ≤ 1: uncontaminated to moderately contaminated, 1 < Igeo ≤ 2: Moderately contaminated, 2 < Igeo ≤ 3: Moderately to heavily contaminated, 3 < Igeo ≤ 4: Heavily contaminated, 4 < Igeo ≤ 5: Heavily to extremely contaminated and Igeo > 5: Extremely contaminated sediment sample.

The Contamination Factor (CF) is an index proposed by Hakanson (1980) and is widely used for the evaluation of the contamination level of sediments by metals and it is calculated by dividing the measured heavy metal concentration (C_{metal}) with their corresponding background value ($C_{background}$). CF values below 1 show low contamination, values between 1 and 3 show moderate contamination, values between 3 and 6 indicate considerable contamination and values higher than 6 show very high contamination.

$$CF = \frac{C_{metal}}{C_{background}} \quad (2)$$

The Pollution Load Index (PLI) is another index suggested by Tomlinson *et al.* (1980), that intends to evaluate the degree of heavy metal enrichment in sediment samples, and it is calculated by the following formula (Tomlinson *et al.*, 1980).

$$PLI = \sqrt[n]{CF_1 \times CF_2 \times \cdots \times CF_n} \quad (3)$$

The CF component refers to the calculated contamination factor for each element mentioned above. The PLI is

estimated as the n root of the n contamination factors multiplied together. The classifications of the PLI values are the following: no pollution for PLI ≤1, moderate pollution for 1 <PLI ≤2, strong pollution for 2 <PLI ≤3, and extremely strong pollution for PLI ≥3.
The Heavy Metal Pollution Index (HPI) is suggested by Mohan *et al.* (1996) for the assessment of the water quality. In this study, HPI is used for the examination of lake and stream surface water quality concerning Fe and Mn concentrations. The formulas for the estimation of this index are presented below (Mohan *et al.*, 1996; Moldovan *et al.*, 2022; Sur *et al.*, 2022).

$$Q_i = \frac{M_i}{S_i} \times 100 \quad (4)$$

$$W_i = \frac{1}{S_i} \quad (5)$$

$$HPI = \frac{\sum_{i=1}^{n} W_i Q_i}{\sum_{i=1}^{n} W_i} \quad (6)$$

The Q_i refers to the sub index of the *i*th parameter, the W_i is the unit weightage of the *i*th parameter, the n is the number of the examined heavy metals, the Si demonstrates the standard permissible values of the examined heavy metals, and the Mi presents the measured heavy metal concentrations of the water samples. Concerning the Si values for Fe and Mn, the European Directive 2020/2184 on water quality was assessed. When the HPI is less than 100, it indicates low levels of heavy metal concentrations; when it is estimated to be more than 100, it indicates that the water is unsafe for consumption and can have adverse health implications.

Results

The indices that were chosen for the pollution assessment are Igeo, CF, PLI for sediments and HPI for water samples. The values of Igeo for all sampling sites are shown in Figure 2. For most heavy metal elements, the Igeo values are calculated below 1 in every station which means that the samples are practically uncontaminated. Igeo values above unity indicate moderate heavy metal enrichment and were calculated for Ni in all stations (range: 1.02-1.44) except P5 (0.67), and for Cr only in station P2 (1.05). The average Igeo values were ranked as: Ni> Cr> Pb> Zn> Cu> Co> Zr. The Igeo values suggest a heterogeneous distribution of heavy metal enrichment, which is related to natural geological processes as the metal concentrations could be influenced by natural mineral deposits, or even historical land use patterns.

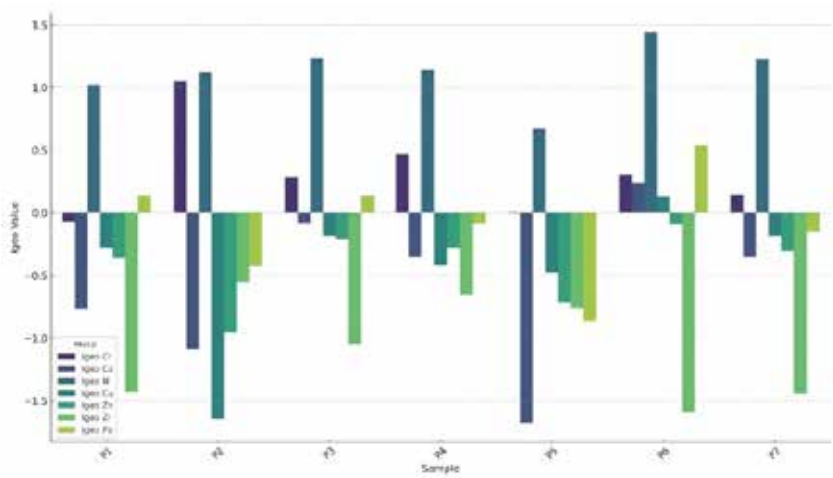

Figure 2. Bar chart of the Igeo values of the examined heavy metals for each station.

The Contamination Factor (CF) values for heavy metals offer insight into the degree of heavy metal enrichment in the examined samples. The ranges of the CF values for Zr, Co, Zn, Cu, Pb, Cr and Ni are 0.50 to 1.02, 0.47 to 1.76, 0.77 to 1.41, 0.48 to 1.64, 0.82 to 2.18, 1.43 to 3.11 and 2.39 to 4.07, respectively. Average CF values for all metals were ordered as presented in the following sequence Ni>Cr>Pb>Cu>Zn>Co>Zr. Low to moderate contamination based

on CF values was calculated for Cu, Zn, Pb, Zr, Co and Cr. The CF values for Ni showed moderate to considerable contamination with a minimum value of 2.39 and a maximum value equal to 4.07. The CF concentrations for all samples indicate varying degrees of heavy metal enrichment, with certain metals like Ni showing consistently higher levels across all samples reflecting mainly natural geological variations (Figure 3).

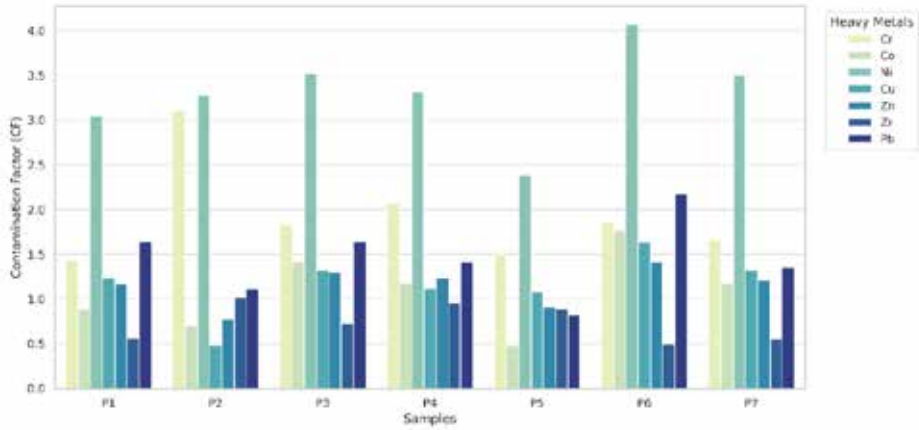

Figure 3. Bar chart of the CF values of the examined heavy metals for each station.

The Pollution Load Index (PLI) for heavy metals offers insight into the degree of contamination in each of the reservoir stations where samples were collected. PLI values below 1 show negligible concentrations while values greater than 1 suggest significant concentrations. The calculated PLI values range between 1.03 to 1.65, indicating moderate degrees of heavy metal enrichment across the stations. The bar graph below visualizes the PLI values across the different stations with the red dashed line representing the PLI threshold (Figure 4).

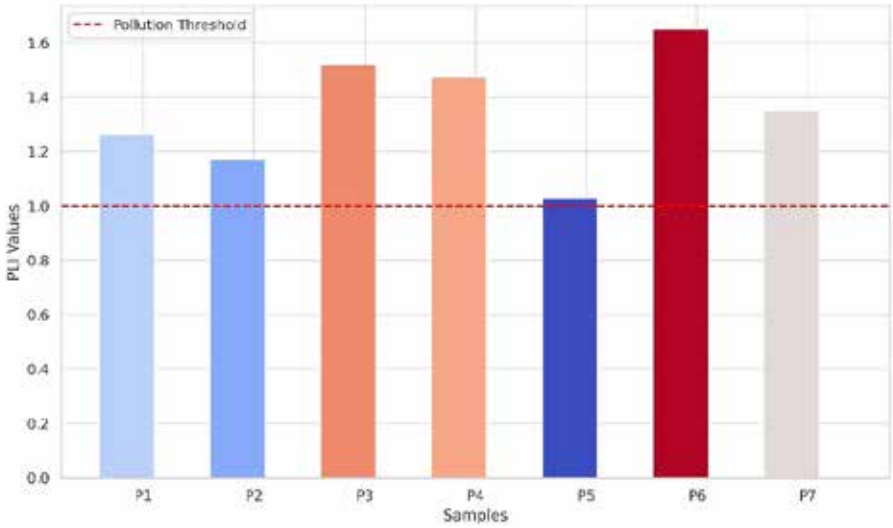

Figure 4. Bar chart of the PLI values of the examined heavy metals for each station.

The Heavy-Metal Pollution Index (HPI) is a vital index for evaluating heavy metal concentrations in water sources as it assesses several heavy metals in the water and their combined effects on water quality in a thorough manner. Each heavy metal is given a weighting factor according to its toxicity and possible health effect in order to calculate the HPI (Badeenezhad *et al.*, 2023). The HPI index was calculated for lake and stream samples for different periods of time. The bar charts for each type of sample are presented in Figure 5. The results showed that the surface lake water samples exceed the threshold of 100 in 22/02/2019 in stations P1, P2, P5, P6, P7 and P8, where in 09/10/2018 the HPI value is considerably high mainly because of the high measured concentration of Mn (226 μg/l). This is likely due to seasonal redox cycling and stratification, which influence metal mobility in the hypolimnion.

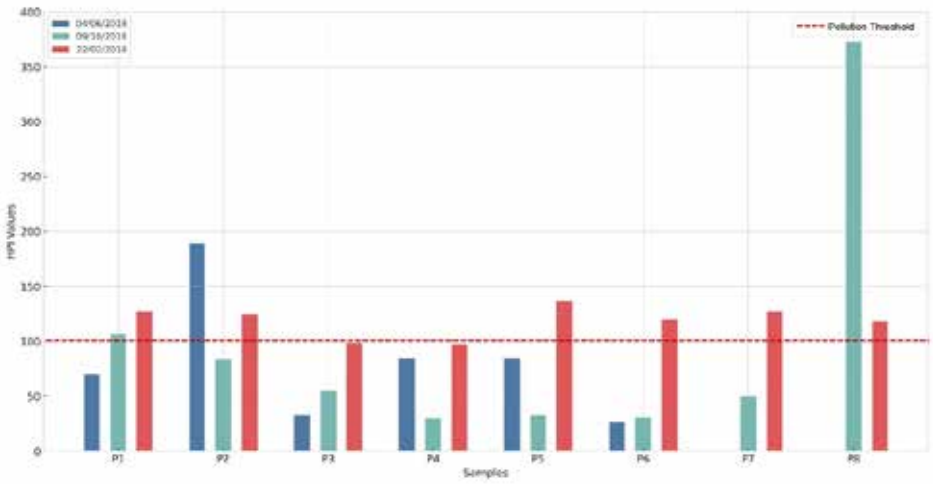

Figure 5. Bar chart of the HPI values of the lake samples for different dates.

Concerning the stream water samples (Figure 6), stations S2, S3, S4 and S6 presented HPI values above the threshold 100. The S2 station is the one with the highest values which exceeded the threshold in almost all samples except for the ones that were taken on 29/11/2018 and at 22/02/2019.

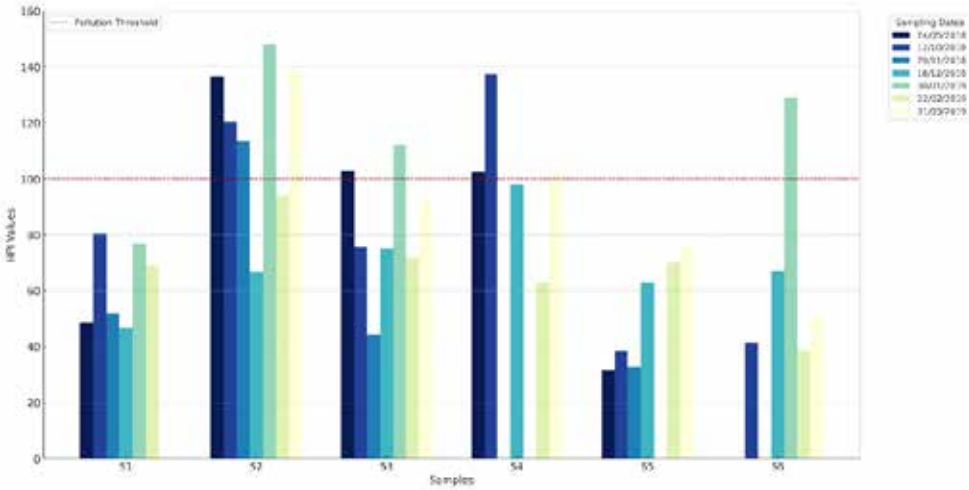

Figure 6. Bar chart of the HPI values of the stream samples for different dates.

Discussion & Conclusions

The application of geochemical indices in the Pinios Dam drainage basin provided valuable insights into the extent and distribution of heavy metal enrichment in sediments and concentrations in water. Regarding the evaluation of sediments, the Igeo values indicate that most heavy metals in the sediment samples are within uncontaminated to moderately contaminated levels, with exceptions observed for Ni and Cr in specific stations. The CF values further suggest low to moderate contamination for most metals, with Ni showing moderate to considerable concentrations, likely due to natural enrichment. The PLI values, ranging from 1.03 to 1.65, point to moderate pollution levels in the sediments across the study area. The examination of the water quality was based on the HPI index which reveals that lake and stream water samples frequently exceed the pollution threshold, primarily due to elevated Fe and Mn concentrations. Temporal variations suggest that certain periods are more prone to higher Fe and Mn concentrations, potentially due to hydrological or seasonal factors. More specifically, in this case, seasonal stratification plays a crucial role in shaping the distribution and mobility of Fe and Mn within the water column of the reservoir, as seasonal fluctuations in their concentrations were evident, with higher levels of these elements observed in the hypolimnion during the autumn/dry season (Michalopoulou *et al.,* 2024).The observed heavy metal indices strongly reflect the strong influence of natural geological processes, such as weathering of metal-rich formations, erosion,

and sediment deposition. These processes dominate the geochemical dynamics of the study area as the observed metal enrichment in the examined sediments originated from natural processes as well as the high concentration of organic carbon and the clayey composition of the fine sediments. So, the geoaccumulation in sediments occurs due to the ability of organic matter and clay minerals to adsorb trace element cations. Anthropogenic activities, such as agriculture, appear to have a secondary role, as suggested by the localized and relatively moderate contamination levels for most metals, and needs further investigation to better quantify their impact. Evaluating pollution levels using multiple indices for the same region can yield varying pollution classifications and lead to different interpretations as these discrepancies arise from the distinct mathematical formulations of each index (Karaouzas et al., 2021). Thus, to ensure effective management, it is essential to prioritize continuous monitoring and utilize modeling techniques to better understand the long-term behavior of metals in the system and to mitigate the potential environmental impacts of metal enrichment.

Acknowledgements

The authors are grateful for the financial and administrative support of the research by the Region of Western Greece and the Municipality of Ilida (project contract 82334).

References

Badeenezhad, A., Soleimani, H., Shahsavani, S., Parseh, I., Mohammadpour, A., Azadbakht, O., ... & Babakrpur Nalosi, K., 2023. Comprehensive health risk analysis of heavy metal pollution using water quality indices and Monte Carlo simulation in R software. Scientific Reports, 13(1), 15817.

Depountis, N., Michalopoulou, M., Kavoura, K., Nikolakopoulos, K., Sabatakakis, N., 2020. Estimating Soil Erosion Rate Changes in Areas Affected by Wildfires. *ISPRS Int. J. Geo-Inf.*, *9*, 562.

Directive (EU) 2020/2184 of the European Parliament and of the Council of 16 December 2020 on the quality of water intended for human consumption. Available online: https://eur-lex.europa.eu/eli/dir/2020/2184/oj. (accessed on 11 November 2024).

Hakanson, L., 1980. An ecological risk index for aquatic pollution control. A sedimentological approach. Water research, 14(8), 975-1001.

Karaouzas, I., Kapetanaki, N., Mentzafou, A., Kanellopoulos, T. D., & Skoulikidis, N., 2021. Heavy metal contamination status in Greek surface waters: A review with application and evaluation of pollution indices. *Chemosphere*, *263*, 128192.

Lainas, S., Depountis, N., Sabatakakis, N., 2021. Preliminary Forecasting of Rainfall-Induced Shallow Landslides in the Wildfire Burned Areas of Western Greece. *Land*, *10*, 877.

McLennan, S. M., 2001. Relationships between the trace element composition of sedimentary rocks and upper continental crust. Geochemistry, Geophysics, Geosystems, 2(4).

Michalopoulou, M., Depountis, N., Nikolakopoulos, K., Boumpoulis, V., 2022. The Significance of Digital Elevation Models in the Calculation of LS Factor and Soil Erosion. *Land*, *11*, 1592.

Michalopoulou, M., Depountis, N., Zagana, E., Avramidis, P., 2024. Investigation of the Origin of Elevated Amounts of Iron and Manganese in a Dam Reservoir. Geosciences, 14, 336.

Mohan, S. V., Nithila, P., & Reddy, S. J., 1996. Estimation of heavy metals in drinking water and development of heavy metal pollution index. Journal of Environmental Science & Health Part A, 31(2), 283-289.

Moldovan, A., Török, A. I., Kovacs, E., Cadar, O., Mirea, I. C., & Micle, V., 2022. Metal contents and pollution indices assessment of surface water, soil, and sediment from the Arieș River Basin Mining Area, Romania. Sustainability, 14(13), 8024.

Muller, G. M. M. G. M. G. M. G. P., 1969. Index of geoaccumulation in sediments of the Rhine River. Geojournal, 2, 108-118.

Sojka, M., Jaskuła, J., Barabach, J., Ptak, M., & Zhu, S., 2022. Heavy metals in lake surface sediments in protected areas in Poland: concentration, pollution, ecological risk, sources and spatial distribution. Scientific Reports, 12(1), 15006.

Sur, I. M., Moldovan, A., Micle, V., & Polyak, E. T., 2022. Assessment of surface water quality in the Baia Mare area, Romania. Water, 14(19), 3118.

Taylor, S. R., & McLennan, S. M., 1985. The continental crust: its composition and evolution. Blackwell, Malden, Mass.

Tomlinson, D. L., Wilson, J. G., Harris, C. R., & Jeffrey, D. W., 1980. Problems in the assessment of heavy-metal levels in estuaries and the formation of a pollution index. Helgoländer meeresuntersuchungen, 33, 566-575.

Wang, M., Wang, M., Yang, L., Yang, T., Li, J., & Chen, Y., 2023. Distribution Characteristics and Genesis of Iron and Manganese Ions in Groundwater of Eastern Sanjiang Plain, China. Water, 15(11), 2068.

Wu, D., Liu, H., Wu, J., & Gao, X., 2022. Spatial distribution, ecological risk assessment and source analysis of heavy metals pollution in urban lake sediments of Huaihe River Basin. International Journal of Environmental Research and Public Health, 19(22), 14653.

17th INTERNATIONAL CONGRESS of the Geological Society of Greece

BULLETIN OF THE GEOLOGICAL SOCIETY OF GREECE, SP. PUBL.

EXTENDED ABSTRACT 212

The impact of aquaculture units on Copper (Cu) concentrations in marine sediments

Michalopoulou S.[1], Faulwetter S.[1], Christodoulopoulos D.[1], Ramfos A.[2], Avramidis P.[1]
(1) Department of Geology, University of Patras, Greece, mich.sofi6@gmail.com (2) Department of Biology, University of Patras, Greece

Introduction / Background

Copper (Cu) is a trace element commonly found in various rocks and minerals, well known for its antimicrobial properties (Wang et al. 2022). Due to these properties, copper is widely used in aquaculture nets to control biofouling (e.g. Nikolaou et al. 2014). More specifically, it is applied in the form of copper sulfate (CuSO□), which dissolves in water and eventually settles on the seabed. However, at elevated concentrations, copper becomes toxic, particularly in marine sediments where the accumulation of heavy metals is significantly elevated and therefore poses a serious threat to aquatic organisms (Emenike et al. 2022). The effects of fish farm operations on copper concentrations have been the focus of several studies worldwide (e.g. Dean et al. 2007) but in Greece, research has focused mainly on individual fish farms (e.g. Farmaki et al. 2014), and overall knowledge on copper concentrations, their spatial distributions and their accumulation processes in the sediment near fish farms in Greece is limited.

Objectives

While the fate and consequences of organic wastes for the benthic ecosystem are relatively well understood worldwide, less attention has been given to metallic wastes from fish farms and to the changes in marine sediments from copper concentrations. Therefore, the main objectives of our study are:

- To determine the impact of copper originating from marine fish farms on marine sediments
- To examine which environmental and farm parameters influence the copper concentration in marine sediments in different regions of Greece.
- To determine the spatial extent of the impact of fish farms of copper concentration in the sediment
-

Methods

We examined the impact of aquaculture activities across four different regions: Aegean Sea, Corinthian Gulf, Euboea and Ionian Sea (Fig. 1). Sediments were collected from 32 fish farms at 50 m distance from the cages, in accordance with the Greek legislation, as well as from reference stations. In addition, we used a dataset assembled between 2020 and 2023 that included samples collected at distances of approximately 0, 25, 50 and 100 m from the cages, as well as reference samples (Fig. 1). Sediment samples were analyzed for total organic carbon (TOC) and total nitrogen (TN) using a Shimadzu TOC-VCSH TOC/TN analyzer. Total phosphorus (TP) was measured with a Hach photometer according to the APHA 2005-4500-P method. Sediment grain size was determined through dry sieving for coarser materials and with a Malvern Mastersizer 2000 Hydro for the finer fractions. Heavy metal content in the sediment was determined (Cu, Mn, Pb, Zn, Fe) using a Bruker Handheld X-ray Fluorescence Analyzer (Titan S1).
For the dataset from 2024, we assembled additional information on the surface area of the farm, the geomorphology of the coastline (farm located within open or closed embayment) and the distance from the coast.
To test the effects of various environmental parameters on the copper concentration in marine sediments two different analyses were performed, using a general linear model (GLM) with a gamma distribution and inverse link function. For the dataset from 2020-2023, the model included the distance from the farm, depth of the seafloor, percentage of sand, sediment type and geographical region as explanatory variables. For the dataset from 2024, the model included the distance from the farm, depth of the seafloor, percentage of mud, sediment type, geographical region, surface area of the farm, distance from the coast, and bay type (open or enclosed) as explanatory variables. The significance level for all tests was set to α=0.05 and all analysis were performed in R (R Core Team 2024).
Two geochemical indices- Contamination Factor (CF), and the Geo-Accumulation Index (Igeo)- were calculated to identify the enrichment or depletion of metal distribution in sediment samples. The calculation of the CF values contacted using the following equation:

$C_F=\bar{c_s}/ C_b$

where the $\bar{c_s}$ represents the mean copper concentration from positions (0, 25, 50, 100m) around the cages and C_b is the background concentration from reference data for each region. The Igeo was calculated using the following equation:

$Igeo=\log_2(Cs/1.5\times Cb)$

where the $\overline{c_s}\overline{c_s}$ represents the mean copper concentration from positions (0, 25, 50, 100m) around the cages, C_b is the background concentration of the same metal in an uncontaminated environment and the factor 1.5 is used as a correction factor to account for natural variability in background levels.

Figure 1. Sampling stations.

Results

The results of the analysis indicated a decrease in copper concentrations with increasing distance from the fish cages (Fig.3a,b). Specifically, the highest concentrations of copper were found directly beneath and around the fish farm cages, but significantly elevated concentration (in comparison to the reference stations) were still found at distances of up to 100 m from the farms (Fig. 2). The dataset from 2024 which included only stations from 50 m distance as well as reference stations showed likewise significantly elevated concentrations at 50 m distance compared to the reference stations.

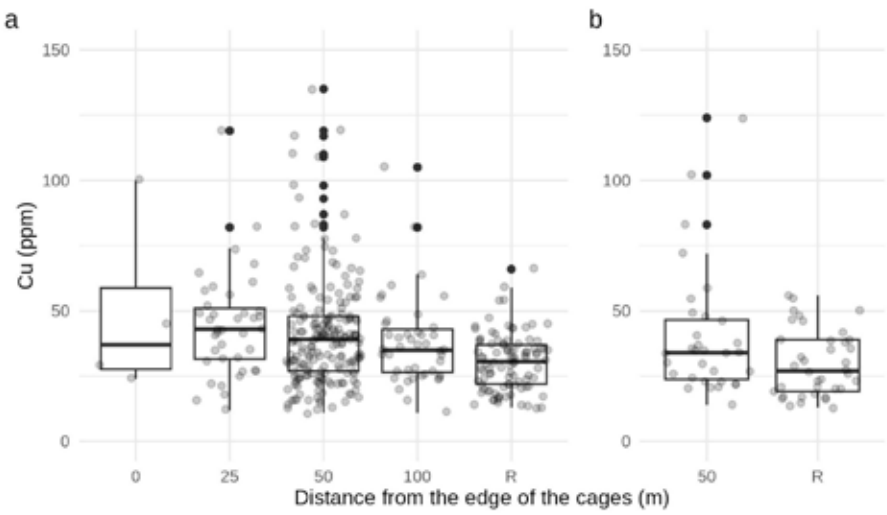

Figure 2. Copper concentration for different distances from the farm distance from the farm. R = Reference station. a) Dataset of 2020-2023, b) Dataset of 2024.

The sediment type was also associated with copper absorption, as finer-grained sediments exhibited a higher capacity for copper absorption in both datasets (Fig. 3). This correlation was weak but statistically significant.

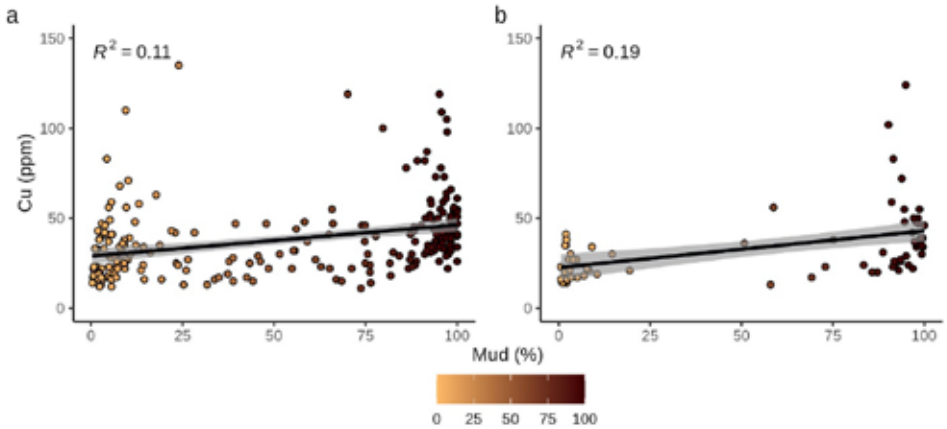

Figure 3. Copper concentration vs percentage of mud in the sediment. a) Dataset of 2020-2023, b) Dataset of 2024.

Additionally, there was an association between copper (Cu) concentration and the geographical region (Fig. 4) Copper concentrations were notably higher in the Ionian region compared to other regions. The Ionian exhibited the highest copper concentrations across all distances from the farm, including reference samples that reflected the natural copper levels of the area. The general pattern of decreasing copper concentrations with increasing distance from the cages was consistent across most regions. However, slight exceptions were observed in regions like Euboea and the Ionian Sea, likely due to a limited number of samples at certain distances.

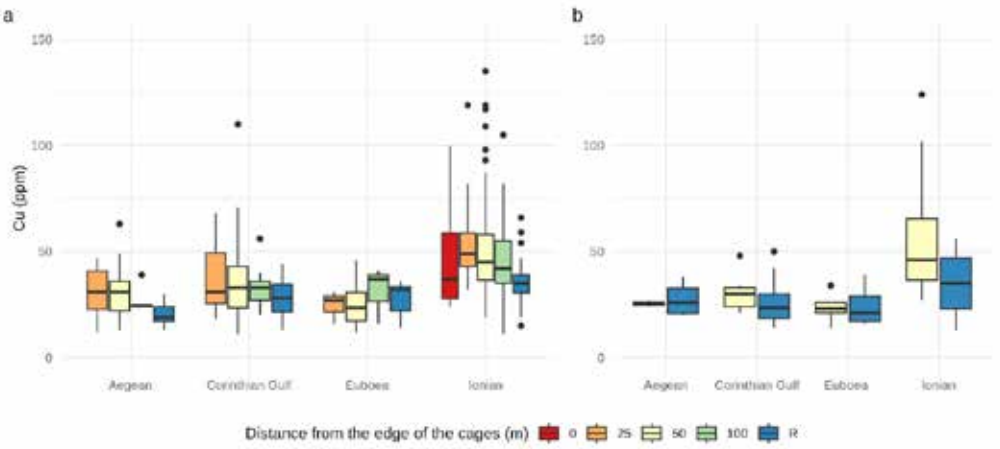

Figure 4. Copper concentration at different distances from the farm, across different regions of Greece. R = Reference station. a) Dataset of 2020-2023, b) Dataset of 2024.

The other variables included in the statistical models (depth of the sea floor, surface area of the farm, the distance from the coast and the bay type (open or enclosed)) did not show any statistically significant effects on copper concentrations.

Overall, the dataset for 2024 confirmed the results of the 2020-2023 dataset. Similar factors were identified to play an important role for copper concentrations in marine sediments.

The contamination factor (CF) provides insight into the extent of pollution in each region. As shown in Table 1, all regions exhibit moderate contamination ($1 \leq CF < 3$), except for Euboea, which falls slightly below this threshold (CF = 0.97), indicating low contamination. Among the regions, the Ionian Sea displays the highest CF value (1.46), suggesting a relatively greater pollutant concentration compared to its natural background levels.

The geoaccumulation index (Igeo) results suggest that all regions are classified as uncontaminated (Igeo<0). The lowest Igeo value was recorded in Euboea (-0,62), significantly lower than the other regions, indicating a natural background concentration very close to or even higher than the sample concentration. The Ionian Sea had the highest Igeo value (-0.04) but still remained within the uncontaminated category.

Table 1. Contamination Factor (CF) and Geoaccumulation Index (Igeo) in Four Study Areas

Region	Sample Concentration (Cs) ppm	Background Concentration (Cb) ppm	CF	Igeo
Aegean	29,4	21,57	1,36	-0,14
Corinthian Gulf	34,81	27,61	1,26	-0,25
Euboea	25,55	26,25	0,97	-0,62
Ionian	51,34	35,13	1,46	-0,04

Conclusions

The present study shows that the determining factors for copper concentration are related to certain individual characteristics of the environment of each farm, such as sediment type and the geographical region. Findings of the present study are of great interest as it highlights that copper concentration is not only determined by the aquaculture activities but also by local environmental conditions.

In both datasets, 2020-2023 and 2024, the results of the analysis indicated that the highest copper concentrations were found directly beneath and around the fish farm cages, within a range of at least 100 m from the cages (no distances further than that were examined). Greek legislation mandates regular environmental monitoring at a distance of 50m from the cages, and while no thresholds or allowed limits for copper concentrations exist in Greece, it is implied that the environmental impact of the farms should overall be limited to this distance. The elevated concentrations found here indicate an effect of the farm on the surrounding marine environment and highlights the impact of feed and faecal inputs as well as the footprint of antifouling products in aquaculture. The spatial extent found in this study is in line with the literature, where effects have been found up to several hundred meters (e.g. Farmaki *et al.* 2014).

The correlation between sediment type and copper concentration in both datasets indicated a weak but significant association, with finer-grained sediments exhibiting a higher capacity for copper absorption. This can be attributed to the solid physio-chemical properties, as smaller particles provide larger surface area per unit mass, facilitating greater adsorption of copper ions.

The spatial differences in copper concentration, particularly in the Ionian region, may be linked to the natural copper concentrations of the area and the geological features, such as inflowing river waters, seasonal variations, hydrodynamic conditions, the rather sheltered conditions of many of the farms and sediment type. In addition, the Ionian region hosts a high number of large fish farms, and cumulative and far-field effects that could even affect the reference stations might likewise play a role and are in need of investigation.

Copper thresholds in marine sediments are crucial for assessing the environmental impacts of aquaculture activities. These thresholds can vary depending on factors such as sediment characteristics, the local species, and environmental conditions. As no copper thresholds have been established by the National or EU Legislation for marine sediments, as well as with SQGs recommended by the Canadian Council of Minister of the Environment (Farmaki et al., 2014), direct comparison of our findings is rather difficult. We found that mean copper concentrations near the cages (42.67 ppm) including extreme values, exceed the Canadian guidelines, set at 18.7 ppm and remain below the Probable Effects Level (PEL=108 ppm). While levels below the PEL suggest that severe biological effects are unlikely, exceeding the ISQGs indicates potential risks to benthic organisms, particularly with prolonged exposure. Additionally, the mean copper concentration in Greece is below 65 ppm, aligning with the threshold set by the Australian & New Zealand Guidelines for Fresh & Marine Water Quality. These findings underscore the need for regular monitoring and targeted mitigation measures.

Other studies in the Mediterranean Sea have found that there is a definite enrichment for copper under the cages, up to 28 ppm in Gulluk Bay in the southeastern Aegean Sea (Dalman et al., 2006). In E. Aegean Sea, Balci Küçüksezgin (1994) found copper concentrations from 8 to 29 ppm and lower copper levels of 15 ppm have been reported in the Bay of Cádiz in Spain, by Mendiguchía et al. (2006) . Outside the Mediterranean, significantly higher copper concentrations were documented in areas with intense industrial activity, such as the mining and smelting region of Rouyn-Noranda, Quebec in Canada (216–2984 ppm) (Borgmann et al., 2004). According to another Canadian study (Brooks and Mahnken, 2003) that compared surface sediment samples from salmon farms that (a) were using copper anti-foulant products, (b) used no copper-based anti-foulant and (c) from reference stations remote from fish farms, concluded that sediment copper levels were higher at farms using copper based anti-foulants.

Overall, this study is an important contribution to the understanding of the impact of fish farms on copper concentrations in the marine sediments and the results should be taken into account for designing environmental monitoring

programs and adopting sustainable farming practices.

Acknowledgements
The authors would like to thank the personnel of all involved fish farms for assistance in field work as well as the personnel of the Research Group for the Environmental Monitoring of Aquaculture of the Department of Geology, University of Patras, for support in sampling and laboratory analyses.

References
Borgmann, U., Nowierski, M., Grapentine, L.C., Dixon, D.G., 2004. Assessing the cause of impacts on benthic organisms near Rouyn-Noranda, Quebec. Environmental Pollution 129, 39–48. https://doi.org/10.1016/j.envpol.2003.09.023

Brooks, K.M., Mahnken, C.V.W., 2003. Interactions of Atlantic salmon in the Pacific Northwest environment. Fisheries Research 62, 295–305. https://doi.org/10.1016/S0165-7836(03)00065-1

Dalman, Ö., Demirak, A., Balcı, A., 2006. Determination of heavy metals (Cd, Pb) and trace elements (Cu, Zn) in sediments and fish of the Southeastern Aegean Sea (Turkey) by atomic absorption spectrometry. Food Chemistry 95, 157–162. https://doi.org/10.1016/j.foodchem.2005.02.009

Dean, R.J., Shimmield, T.M., Black, K.D., 2007. Copper, zinc and cadmium in marine cage fish farm sediments: An extensive survey. Environmental Pollution 145, 84–95. https://doi.org/10.1016/j.envpol.2006.03.050

Emenike, E.C., Iwuozor, K.O., Anidiobi, S.U., 2022. Heavy Metal Pollution in Aquaculture: Sources, Impacts and Mitigation Techniques. Biol Trace Elem Res 200, 4476–4492. https://doi.org/10.1007/s12011-021-03037-x

Farmaki, E.G., Thomaidis, N.S., Pasias, I.N., Baulard, C., Papaharisis, L., Efstathiou, C.E., 2014. Environmental impact of intensive aquaculture: Investigation on the accumulation of metals and nutrients in marine sediments of Greece. Science of The Total Environment 485–486, 554–562. https://doi.org/10.1016/j.scitotenv.2014.03.125

Mendiguchía, C., Moreno, C., Mánuel-Vez, M.P., García-Vargas, M., 2006. Preliminary investigation on the enrichment of heavy metals in marine sediments originated from intensive aquaculture effluents. Aquaculture 254, 317–325. https://doi.org/10.1016/j.aquaculture.2005.10.049

Nikolaou, M., Neofitou, N., Skordas, K., Castritsi-Catharios, I., Tziantziou, L., 2014. Fish farming and anti-fouling paints: a potential source of Cu and Zn in farmed fish. Aquaculture Environment Interactions 5, 163–171. https://doi.org/10.3354/aei00101

R Core Team, 2024. R: A Language and Environment for Statistical Computing_. R Foundation for Statistical Computing, Vienna, Austria. https://www.R-project.org

Wang, Y., Li, H., Yuan, X., Jiang, Y., Xiao, Z., Li, Z., 2022. Review of copper and copper alloys as immune and antibacterial element. Transactions of Nonferrous Metals Society of China 32, 3163–3181. https://doi.org/10.1016/S1003-6326(22)66011-4

17th INTERNATIONAL CONGRESS of the Geological Society of Greece

BULLETIN OF THE GEOLOGICAL SOCIETY OF GREECE, SP. PUBL.

EXTENDED ABSTRACT 213

Spatiotemporal diffusion variability in seismic swarms

Michas G.[1]
(1) Institute of Geodynamics, National Observatory of Athens, Athens, Greece, gmichas@noa.gr

Research Highlights

- The spatiotemporal diffusion properties of seismic swarms can well be reproduced with the Continuous Time Random Walk (CTRW) model and the fractional diffusion equation
- The results show intrinsic variability in earthquake diffusion that may highlight the physical mechanisms at play

Introduction

Seismic swarms are characterized by intense seismic activity strongly clustered in time and space and without the occurrence of a major event that can be considered as the mainshock. Such intense seismic activity is most commonly associated with external aseismic factors, as pore-fluid pressure diffusion, aseismic creep, or magmatic intrusion that can perturb the regional stresses locally triggering the observed seismicity (Vidale & Shearer, 2006). These factors can control the spatiotemporal evolution of seismic swarms, frequently exhibiting spatial expansion and migration of event hypocenters with time (Michas *et al.*, 2021). This phenomenon, termed as earthquake diffusion, can be highly anisotropic and complex, with earthquakes occurring preferentially along fractures and zones of weakness within the heterogeneous crust, presenting anisotropic diffusivities that may locally vary over several orders of magnitude (Michas & Vallianatos, 2018a). The efficient modelling of the complex spatiotemporal evolution of seismic swarms, thus, represents a major challenge.

Herein, we apply a stochastic framework based on the well-established Continuous Time Random Walk (CTRW) model, to map the spatiotemporal evolution of seismic swarms. The CTRW model is a well-established stochastic framework for modelling anomalous diffusion phenomena in complex heterogeneous media (Berkowitz *et al.*, 2006), including fluid flow in fault zones (O'Brien *et al.*, 2003; Brixel *et al.*, 2020) and seismicity (Sotolongo-Costa *et al.*, 2000; Helmstetter & Sornette, 2002; Michas & Vallianatos, 2018a; 2024) among others. The term "anomalous" is used to signify the deviation of the triggered earthquake diffusion from linear diffusion equations and normal (Gaussian) diffusion. Within this context, earthquake occurrence is considered as a point- process in space and time, with jump lengths and waiting times between successive earthquakes drawn from a joint probability density function. The spatiotemporal evolution of seismicity is then described with an appropriate master equation and the time-fractional diffusion equation (TFDE). The applicability of the model is herein demonstrated for the 2014 Long Valley Caldera (California) seismic swarm that has been associated with pore-fluid pressure diffusion at depth (Shelly *et al.*, 2016) and the results are compared with seismic swarms that have occurred in the Corinth Rift (Greece) (Michas & Vallianatos, 2018a; Michas *et al.*, 2021; 2022) and elsewhere, including injection-induced seismicity (Michas & Vallianatos, 2024) and the 2025 seismic crisis in the offshore area between Santorini and Amorgos.

Methods

Within the CTRW context, we consider seismicity as a point-process in time and space, marked by the magnitude of the event. Starting from an origin, seismicity undergoes a random walk in space and time, where the hypocenter of each new event is the new position of the random walk that occurs after waiting some time τ in the previous position. This process can be described with the joint probability density $\psi(x, t)$, which, in the case of seismicity, expresses the probability of an earthquake to occur at some position x after some time t (Michas & Vallianatos, 2018a). By further considering that jump lengths and waiting times between the successive earthquakes are independent random variables, the probability densities of jump lengths $\lambda(x)$ and waiting times $\varphi(t)$ can be deduced from $\psi(x, t)$. In this case, finite or divergent moments of $\lambda(x)$ and $\varphi(t)$ determine the type of the diffusive process. If both are finite, then the random walk corresponds to the well-known Brownian motion (normal diffusion). If, however, $\lambda(x)$ and $\varphi(t)$ present broad distributions with power-law scaling behavior that signifies long-range interactions, then anomalous diffusion arises (e.g., Metzler & Klafter, 2000). In this case, the mean squared distance (MSD) $\langle x^2(t)\rangle$ of seismicity deviates from its linear growth with time t, a function that characterizes normal diffusion. Instead, for various complex systems that present anomalous diffusion, MSD frequently takes the mathematical form:

$$\langle x^2(t)\rangle \propto t^a. \quad (1)$$

The latter equation manifests the power-law growth of the MSD with time, with the diffusion exponent a characterizing

the various domains of anomalous diffusion. Thereby, for $a > 1$ we get superdiffusion, for $0 < a < 1$ subdiffusion, while for $a = 1$ normal (Gaussian) diffusion is recovered.
In the case of seismicity, the diffusion exponent a can provide a proxy for the rate of triggered earthquake diffusion (McKernon & Main, 2005). The MSD is estimated from an origin that is considered to be the mean position of the first ten events in the beginning of each seismic sequence. Then, $x(t)$ is the 3D Euclidean distance between each event and the origin. The MSD is then calculated from the following equation (Michas & Vallianatos, 2018a):

$$\langle x^2(t)\rangle = \frac{1}{N}\sum_{n=1}^{N} x_n^2(t), \tag{2}$$

where N is the total number of events and $x_n(t)$ the distance of the nth event from the origin that have occurred at time t.
In addition, subdiffusion in terms of the probability density function (pdf) $P(x,t)$ to find the variable under observation (e.g., an earthquake) at some position x after some time t, is interchangeable with the time-fractional diffusion equation (TFDE) (Metzler & Klafter, 2000):

$$\frac{\partial}{\partial t}P(x,t) = {}_0D_t^{1-a} K_a \frac{\partial^2}{\partial x^2}P(x,t), \tag{3}$$

where K_a is the generalized diffusion coefficient and ${}_0D_t^{1-a}$ is the Riemann – Liouville fractional operator of order $1 - a$ ($0 < a < 1$) applied to $P(x,t)$. The standard approach to find the position of the propagator $P(x,t)$ is the Fourier-in-space Laplace-in-time transform (Metzler & Klafter, 2000). In terms of $F(x,t)$, i.e. the pdf of the number of earthquake events having just occurred at some position x after some time t, the solution of the TFDE can be found by using the Riemann – Liouville derivation and in terms of the Fox hypergeometric functions, providing the asymptotic behavior of $F(x,t)$ for large x (Helmstetter & Sornette, 2002; Michas & Vallianatos, 2024):

$$F(x,t) \sim \frac{(\tau')^{-a}}{\sqrt{K_a}\, t^{1-(a/2)}} \left(\frac{|x|}{\sqrt{K_a t^a}}\right)^{d(1-a)/(2-a)} \times \exp\left[-\left(1-\frac{a}{2}\right)\left(\frac{a}{2}\right)^{a/(2-a)}\left(\frac{|x|}{\sqrt{K_a t^a}}\right)^{2/(2-a)}\right], \tag{4}$$

where $\tau' = T\left(\Gamma(1-a)\right)^{1/a}$ ($a < 1$) and d the spatial dimensions. The latter equation manifests a power-law increase of the earthquake density for short distances from the origin and an exponential decay of seismicity as distance increases.

Results

First, we consider the probability distribution of waiting times τ between the successive events with magnitude $M \geq -0.4$ for the 2014 Long Valley Caldera seismic swarm (Shelly *et al.*, 2016). The probability density $p(\tau)$ is calculated by counting the number of τ that fall into logarithmically spaced bins and then normalized by the bin width and by the total number of counts (Michas & Vallianatos, 2018b). In Fig. 1b the probability density $p(\tau)$ is shown that presents asymptotic power-law behavior with exponent -1.51. For comparison, the probability density $p(\tau)$ of the waiting times τ ($M \geq 0$) for the 2020 Perachora (Corinth Rift) seismic swarm (Michas *et al.*, 2022) is shown in Fig. 1a, using a seismic catalogue enriched more than thirty-fold with template-matching (Kapetanidis *et al.*, 2023). In this case, $p(\tau)$ shows an almost flat regime for short τ and a rapid decay for larger τ, exhibiting a bimodal behavior. This trend is approximated with the q-generalized gamma function (Michas & Vallianatos, 2018b):

$$f(\tau) = C\left(\frac{\tau}{\tau_0}\right)^{\gamma-1} \exp_q\left(-\frac{\tau}{\tau_0}\right), \tag{5}$$

where C is a normalization constant, τ_0 a positive scaling parameter and γ the scaling exponent. The last term in the right-hand side is the q-exponential function:

$$\exp_q(x) = [1 + (1-q)x]^{1/(1-q)}. \tag{6}$$

For $q > 1$, the q-exponential function exhibits asymptotic power-law behavior, while in the limit of $q \to 1$ it exactly recovers the exponential function and the q-generalized gamma the ordinary gamma function, respectively (Michas & Vallianatos, 2018b).

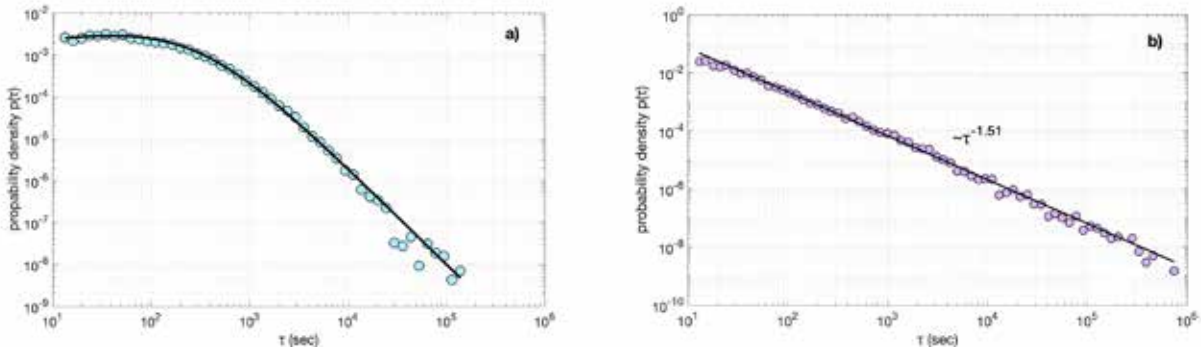

Figure 1. a) Probability density $p(\tau)$ of the waiting times τ (symbols) for the 2020 Perachora swarm according to a template matching catalogue. The solid line represents the q-generalized gamma function fitted to the data, with parameter values C = 0.0012, γ = 1.33, τ_0 = 105.37 and q = 1.38. b) Probability density $p(\tau)$ of the waiting times τ (symbols) for the Long Valley Caldera swarm. The solid line represents a power-law function fitted to the data.

As observed in Fig. 1a, the q-generalized gamma function fits rather well the normalized probability density $p(\tau)$ for the 2020 Perachora swarm, indicating clustering effects in the long-term occurrence of seismicity at breaking asperities that interact with each other. Similar scaling behavior was found for multiplet families during the Perachora swarm (Kapetanidis *et al*., 2023), for the Agios Ioannis seismic swarm that occurred in the western Corinth rift in 2001 (Michas & Vallianatos, 2018a), as well as for injection-induced seismicity in Enhanced Geothermal Systems (Michas & Vallianatos, 2024; Michas, 2025).

Next, the mean squared distance (MSD) $\sqrt{\langle x^2(t)\rangle}$ of seismicity, as estimated from Eq. 2, is analyzed. For the 2014 Long Valley Caldera swarm, the MSD scales according to Eq. 1 (R^2=0.97), for a diffusion exponent a=0.34 ±0.03 (Fig.2b), showing subdiffusion. The 2020 Perachora swarm presents the higher diffusion exponent of a=0.89 ±0.06 (R^2=0.98), still lower than unity, indicating once more subdiffusion of seismicity (Michas *et al*., 2022). Similar behavior and subdiffusion have also been found for other seismic swarms in the western Corinth rift (Michas *et al*., 2021) and for injection-induced seismicity during hydraulic stimulations in EGS (Michas & Vallianatos, 2024; Michas, 2025). However, diffusion exponents higher than unity and superdiffusion have also been found in seismic sequences and injection-induced seismicity, as for the 2006 hydraulic stimulation in Basel (Michas, 2025) and the 2025 seismic sequence in Anydros, in the Santorini-Amorgos tectonic zone, where a rapid diffusive regime with diffusion exponent >3 is encountered during the first days of intense activity. Such diffusion exponents, close to or even greater than unity, are consistent with pore-fluid pressure diffusion phenomena in fractured media and fault zones (Berkowitz *et al*., 2006; O'Brien *et al*., 2003), implying fluid diffusion as the dominant triggering mechanism. In addition, aftershock sequences associated with stress transfer effects show considerably lower diffusion exponents, generally lower than 0.1 (Huc & Main, 2003; Helmstetter *et al*., 2003; Michas *et al*., 2021), suggesting that diffusion variability may be used to infer the main triggering mechanism of seismicity.

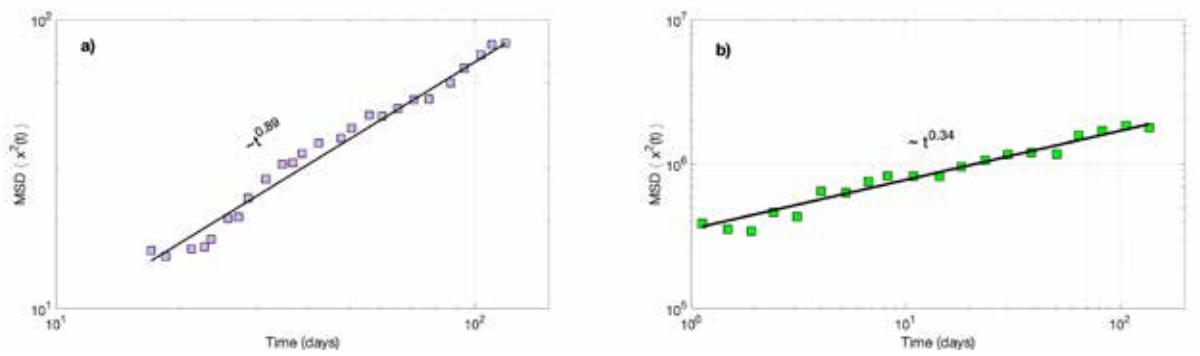

Figure 2. Mean squared distance (MSD) of seismicity with time for a) the Perachora (modified from Michas *et al*., 2022) and b) the Long Valley Caldera seismic swarms (filled squares). Solid lines represent the best-fitting solutions according to Eq. 1 for the diffusion exponents shown in the image.

Furthermore, as discussed previously, the subdiffusive regime of the CTRW model is interchangeable with the time-

fractional diffusion equation (TFDE). Fig. 3 shows the application of its asymptotic solution (Eq. 4) to the observed concentration profiles of seismicity for the Long Valley Caldera swarm for two time periods. In practice, the concentration profile shows the histogram of the absolute 3D distances between each event (for $M \geq M_c$) and the origin. Then, $F(x,t)$ is normalized such that $\int dx F(x,t) = 1$. $F(x,t)$ shows a peak closer to the origin and a tail that stretches towards greater distances. For comparison, the concentration profiles of seismicity for the 2001 Agios Ioannis swarm (Corinth Rift) (Michas & Vallianatos, 2018a) is also shown in Fig. 3 for two time periods. The model successfully captures the main features of earthquake occurrence regarding the peak of concentration close to the origin, the narrowing down and broadening of the peak with time and the stretched relaxation of seismicity with distance.

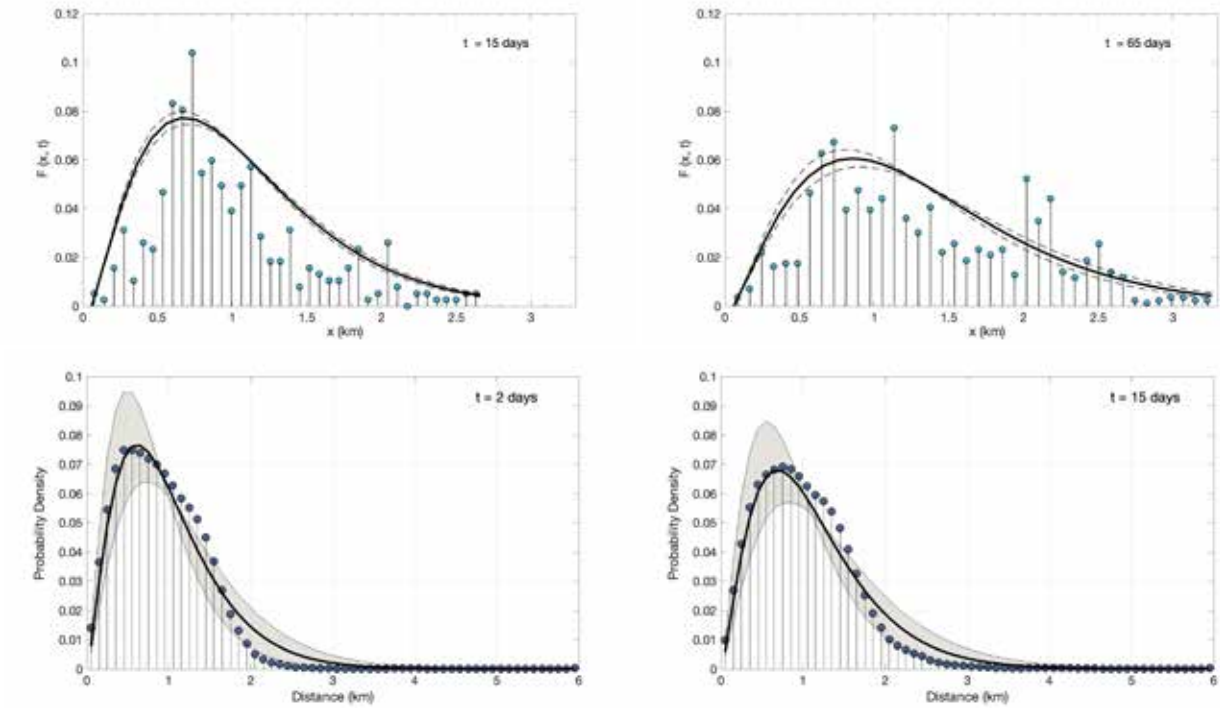

Figure 3. Concertation profiles of seismicity for two time periods, for the 2001 Agios Ioannis seismic swarm (top) (modified from Michas & Vallianatos, 2018a) and the 2014 Long Valley Caldera swarm (bottom). The solid line and the shaded area, or the dashed lines, indicate the asymptotic solution of the TFDE (Eq. 4) and the corresponding confidence intervals, respectively.

Conclusions

Statistical analysis of the studied cases in the light of the CTRW model shows that the mean squared distance of event hypocenters from an origin departs from its linear growth with time, while the temporal occurrence of seismicity exhibits broad waiting times distributions with asymptotic power-law behavior, indicating long-term inter-erathquake interactions. Such properties are intrinsic characteristics of anomalous earthquake diffusion. In such cases, the asymptotic solution of the TFDE can successfully capture the main features of earthquake progression in time and space, showing a peak of event concentration close to the initial source of the stress perturbation and a stretched relaxation of seismicity with distance. Furthermore, the spatiotemporal diffusion variability encountered in various seismic swarms, as well as in injection-induced seismic sequences associated with hydraulic stimulations in EGS, may highlight the main triggering mechanims at play, showing higher diffusion exponents for fluid-related sequences. Overall, the results demonstrate that the CTRW model and the TFDE can efficiently be used to decipher the complex spatiotemporal evolution of seismicity.

References

Berkowitz, B., Cortis, A., Dentz, M., Scher, H., 2006. Modeling non-Fickian transport in geological formations as a continuous time random walk. Reviews of Geophysics, 44, RG2003.

Brixel, B., Klepikova, M., Lei, Q., Roques, C., Jalali, M.R., Krietsch, H., Loew, S., 2020. Tracking fluid flow in shallow crustal fault zones: 2. Insights from cross□hole forced flow experiments in damage zones. J. Geophys. Res. Solid Earth, 125(4), e2019JB019108.

Helmstetter, A., Sornette, D., 2002. Diffusion of epicenters of earthquake aftershocks, Omori's law, and generalized continuous-time random walk models. Physical Review E, 66(6), 061104.

Helmstetter, A., Ouillon, G., Sornette, D., 2003. Are aftershocks of large Californian earthquakes diffusing? J. Geophys. Res. Solid Earth, 108, 2483.

Huc, M., Main, I.G., 2003. Anomalous stress diffusion in earthquake triggering: Correlation length, time dependence, and directionality. J. Geophys. Res. Solid Earth, 108, 2324.

Kapetanidis, V., Michas, G., Spingos, I., Kaviris, G., Vallianatos, F., 2023. Cluster Analysis of Seismicity in the Eastern Gulf of Corinth Based on a Waveform Template Matching Catalog. Sensors, 23, 2923.

McKernon, C., Main, I.G., 2005. Regional variations in the diffusion of triggered seismicity. J. Geophys. Res. Solid Earth, 110, 1–12.

Metzler, R., Klafter, J., 2000. The random walk's guide to anomalous diffusion: A fractional dynamics approach. Physics Reports, 339, 1–77.

Michas, G., 2025. Spatiotemporal Diffusion Variability of Injection-Induced Seismicity in Enhanced Geothermal Systems. Pure and Applied Geophysics, 182, 405–417.

Michas, G., Vallianatos, F., 2018a. Modelling earthquake diffusion as a continuous-time random walk with fractional kinetics: the case of the 2001 Agios Ioannis earthquake swarm (Corinth Rift). Geophysical Journal International, 215(1), 333-345.

Michas, G., Vallianatos, F., 2018b. Stochastic Modeling of Nonstationary Earthquake Time Series with Long-Term Clustering Effects. Physical Review E, 98, 042107.

Michas, G., Vallianatos, F., 2024. Stochastic modeling of injection induced seismicity based on the continuous time random walk model. Scientific Reports, 14(1), 4951.

Michas, G., Kapetanidis, V., Kaviris, G., Vallianatos, F., 2021. Earthquake diffusion variations in the Western Gulf of Corinth (Greece). Pure and Applied Geophysics, 178(8), 2855-2870.

Michas, G., Kapetanidis, V., Spingos, I., Kaviris, G., Vallianatos, F., 2022. The 2020 Perachora peninsula earthquake sequence (East Corinth Rift, Greece): spatiotemporal evolution and implications for the triggering mechanism. Acta Geophysica, 70(6), 2581-2601.

O'Brien, G.S., Bean, C.J., McDermott, F, 2003. A numerical study of passive transport through fault zones. Earth Planet. Sci. Lett., 214, 633–643.

Shelly, D.R., Ellsworth, W.L., Hill, D.P., 2016, Fluid-faulting evolution in high definition: Connecting fault structure and frequency-magnitude variations during the 2014 Long Valley Caldera, California, earthquake swarm. J. Geophys. Res. Solid Earth, 121, 1776–1795.

Sotolongo-Costa, O., Antoranz, J.C., Posadas, A., Vidal, F., Vazquez, A., 2000. Levy flights and earthquakes. Geophysical Research Letters, 27, 1965–1968.

Vidale, J.E., Shearer, P.M., 2006. A survey of 71 earthquake bursts across southern California: Exploring the role of pore fluid pressure fluctuations and aseismic slip as drivers. J. Geophys. Res. Solid Earth, 111(B5), B05312.

17th INTERNATIONAL CONGRESS of the Geological Society of Greece

BULLETIN OF THE GEOLOGICAL SOCIETY OF GREECE, SP. PUBL.

EXTENDED ABSTRACT 214

Hellenic Landslide Platform (He.L.P.): A Geospatial Landslide Inventory for Western Greece.

Misiri Z.[1], Lainas S.[1], Depountis N.[1]
(1) University of Patras, Department of Geology, Patra, Greece, geo07060@ac.upatras.gr

Research Highlights: **Development of a comprehensive landslide inventory for Western Greece**

Introduction

Landslides pose a significant risk to communities, infrastructures, and the natural environment throughout Europe and worldwide. Driven by complex geological settings, increasing urban development, and infrastructure expansion, as well as the occurrence of extreme climatic events, landslides are becoming more frequent and severe. This presents a growing hazard for both human activities and economic assets.

Landslides are widely spatially distributed across Europe, with their occurrence influenced by various topographic and geo-environmental factors, often dictated by each Country's unique geological, geomorphological, and environmental conditions. In Greece, landslides are predominantly associated with mountainous and hilly areas, road network, coastal regions, and riverbanks. Specific site conditions, such as lithology, hydrology, hydrogeology, active tectonics, as well as slope gradient and directionn, are critical in determining landslide susceptibility, hazard and risk status.

The complex geological and tectonic settings in Greece contribute to the complexity and variety of landslide types observed. The classification of landslides in the country generally follows established international standards, including those by Varnes (1978), Cruden *et al.* (1996), and Hungr *et al.* (2014). These classifications are based on the type of movement and the material involved. According to these classifications, the most identified landslide types in Greece include earth slides (rotational and translational), earth flows, debris flows, rockfalls, rockslides, and complex landslides.

While the aforementioned conditions predispose areas to landslides, external triggers serve as the immediate causes of landslide activation. In Greece, the most frequent triggers are related to increasingly extreme weather events, such as intense or prolonged rainfalls, often associated with floods. Other natural triggers include earthquakes, as well as natural erosion along coastlines and riverbanks. Human activities also significantly contribute to landslide initiation, as any interference with a slope influences its equilibrium.

Given for certain that landslides triggered by extreme rainfall events will increase in the future due to climate change, there is an urgent need for landslide recording, enhanced monitoring, risk assessment, and predictive capabilities in affected areas to protect communities, infrastructures, and preserve human activities.

To address this, landslide inventories and susceptibility maps have been developed in many countries worldwide, including at small-scale European and Global levels. A European Landslide Susceptibility Map (ELSUS v2) developed by Günther *et al.* (2014) and Wilde *et al.* (2018) is already available at the European Soil Data Centre (ESDAC) web page. Furthermore, a Global Landslide Catalog (GLC), published in 2019, which includes NASA's landslide datasets and other reports contributed by scientists, is available on-line, but should be updated in the future and with other available landslide datasets.

According to the definition given by Fell *et. al.* (2008) a landslide inventory is an inventory of the location, classification, volume, activity and date of occurrence of landsliding. So far in Greece there is no web application with the of landslide inventory in Greece. However, a national landslide inventory is under construction by the Hellenic Survey of Geology and Mineral Exploration (H.S.G.M.E.), which is the competent authority for the identification, recording, investigation and study of geohazards, as well as for the preparation of susceptibility, hazard and risk maps.

The presented in this work Landslide Inventory Platform named as He.L.P. (Hellenic Landslide Platform) is a first attempt to publish a web-based GIS platform that provides information on landslide phenomena which have been recorded over time in the geographic territory of Western Greece, as defined by the administrative regions of Western Greece, Epirus, and Ionian Islands.

The aim of the platform is to manage geographic information from multiple sources that can be applied to administrative departments and agencies, scientific and general applications, with the management of the volume of information having multiple feed points.

Presentation of the platform

The design and development of HeLP (Hellenic Landslide Platform) (Figure 1) is the achievement of many years of effort by all the members of the Laboratory of Engineering Geology of University of Patras (Professors, PhDs,

Postgraduate students) and was prepared after years of collection, processing and analysis of data from landslide surveys and studies performed by the Laboratory members, satellite images, historical records, as well as studies from Public Authorities, Organizations, Institutes, as well as Technical and Engineering Consulting Companies. Moreover, the possibility for continuous completion and updating with additional records, gives the Platform a "dynamic" character with the prospect of its expansion throughout Greece.

Figure 1: The HeLP (Hellenic Landslide Platform) developed by the EnGeo lab. The red dots represent the landslide events

The Platform draws all its data from geographic databases maintained by the Laboratory of Engineering Geology. In this way, the end user has at his disposal the satellite image of the area with information such as, inventory code, geographical location based on the administrative division of Greece, coordinates in GGRS87, type of landslide and a Landslide Inventory Form (LIF) as a pdf sheet.
In a more advanced process, the platform can display various lists of layers concerning a) the administrative boundaries of a region or a municipality, b) the elevation, c) geological data (engineering-geological units, etc), d) the land use patterns, e) boreholes, f) information on geotechnical monitoring, etc. (Figure 2)

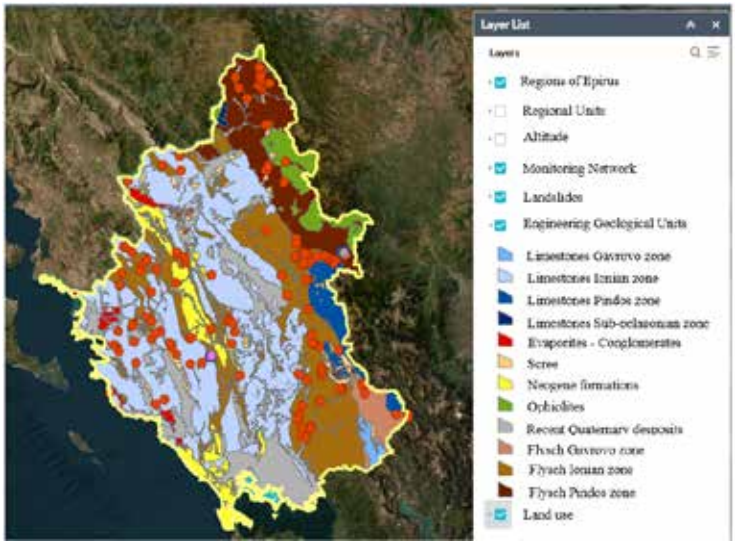

Figure 2. Display of He.L.P. (https://gis.geodory.gr/) for the Region of Epirus. The red dots represent landslide events.

The platform presently includes 1176 landslides. The detailed inventory and the corresponding descriptive data are stored in a database, separately from the graphical part of the inventory map in the form of tables, which allows the visualization of queries and analysing.

The main requirement for predicting future landslides is a well-documented Landslide Inventory Form (LIF). LIF has as its main purpose the recording of all landslides under a common code to achieve an objective in comparison between them and to make it easier to register a new landslide. The design of LIF, used in the He.L.P. platform, was based on the landslide report (WP/WLI, 1990), summary (WP/WLI, 1991), activity (WP/WLI, 1993), landslide causes (WP/WLI, 1994), and rate of movements (WP/WLI, 1995) as well as on corresponding forms of international organizations (United States Geological Survey) and the experience of the Laboratory's staff in the field of landslides. The presented LIF (Figure 3) provides all the necessary information in a condensed form so that it can be easy to rapidly assess the possible risk of each landslide to the natural and man-made environment. It includes seventeen (17) basic fields of information, some of which are subdivided into other categories, as described below.

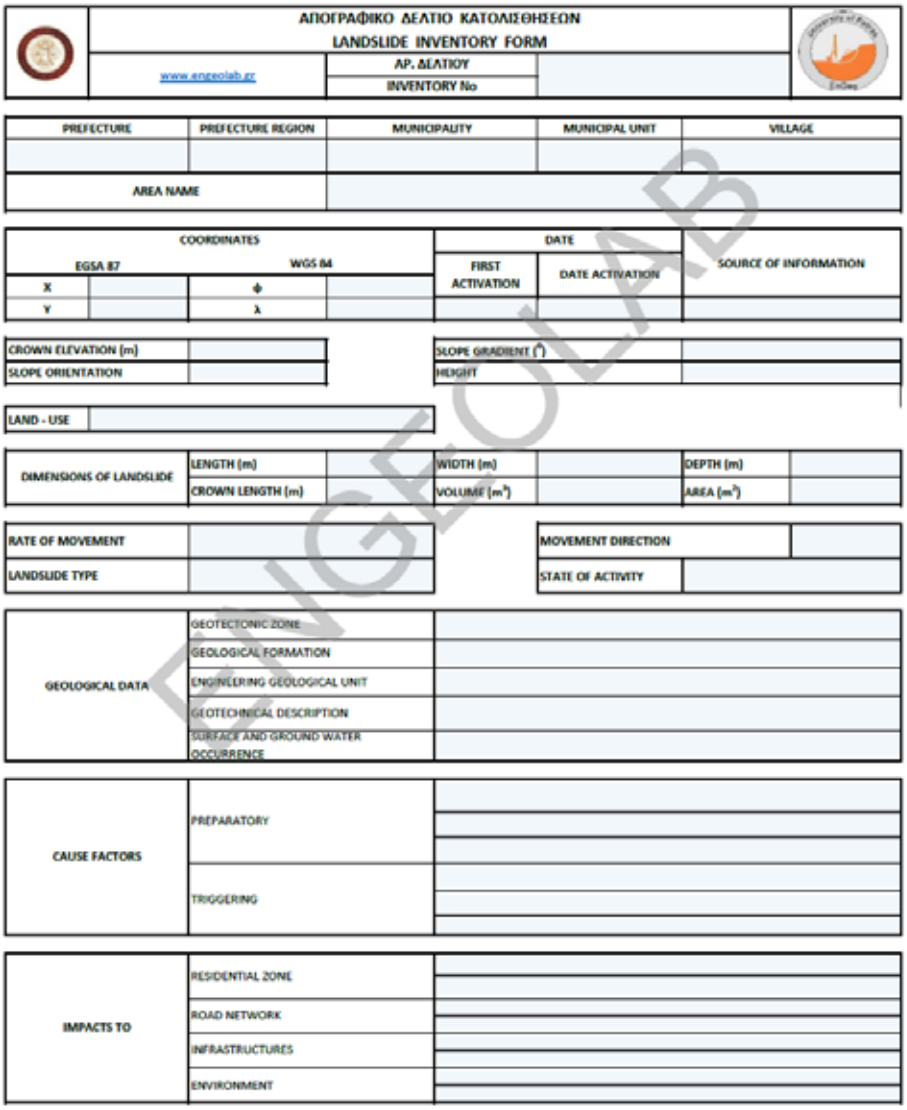
ΑΠΟΓΡΑΦΙΚΟ ΔΕΛΤΙΟ ΚΑΤΟΛΙΣΘΗΣΕΩΝ
LANDSLIDE INVENTORY FORM
www.engeolab.gr
ΑΡ. ΔΕΛΤΙΟΥ
INVENTORY No

PREFECTURE	PREFECTURE REGION	MUNICIPALITY	MUNICIPAL UNIT	VILLAGE
AREA NAME				

COORDINATES				DATE		SOURCE OF INFORMATION
EGSA 87		WGS 84		FIRST ACTIVATION	DATE ACTIVATION	
X		φ				
Y		λ				

CROWN ELEVATION (m)		SLOPE GRADIENT (°)	
SLOPE ORIENTATION		HEIGHT	

LAND - USE	

DIMENSIONS OF LANDSLIDE	LENGTH (m)		WIDTH (m)		DEPTH (m)	
	CROWN LENGTH (m)		VOLUME (m^3)		AREA (m^2)	

RATE OF MOVEMENT		MOVEMENT DIRECTION	
LANDSLIDE TYPE		STATE OF ACTIVITY	

GEOLOGICAL DATA	GEOTECTONIC ZONE	
	GEOLOGICAL FORMATION	
	ENGINEERING GEOLOGICAL UNIT	
	GEOTECHNICAL DESCRIPTION	
	SURFACE AND GROUND WATER OCCURRENCE	
CAUSE FACTORS	PREPARATORY	
	TRIGGERING	
IMPACTS TO	RESIDENTIAL ZONE	
	ROAD NETWORK	
	INFRASTRUCTURES	
	ENVIRONMENT	

ENGEOLAB

Figure 3. The Landslide Inventory Form used in the He.L.P. platform

Land use classification was based on the Corine Land Cover 2018 project, which is part of the Pan-European Land Use Database and includes residential areas, cultivated areas, forest areas, wetlands and fire-affected areas.

Landslide type was indicated according to the classification of Varnes (1978), whose main criteria are the type of movement and the type of material (Figure 4).

TYPE OF MOVEMENT		TYPE OF MATERIAL		
		BEDROCK	ENGINEERING SOILS	
			Predominantly coarse	Predominantly fine
FALLS		Rock fall	Debris fall	Earth fall
TOPPLES		Rock topple	Debris topple	Earth topple
SLIDES	ROTATIONAL	Rock slide	Debris slide	Earth slide
	TRANSLATIONAL			
LATERAL SPREADS		Rock spread	Debris spread	Earth spread
FLOWS		Rock flow (deep creep)	Debris flow (soil creep)	Earth flow
COMPLEX		Combination of two or more principal types of movement		

Figure 4: Classification of landslides according to Varnes (1978)

The geological data are a decisive factor for the likelihood of a landslide occurrence. In the LIF Geotectonic Zone refers to the Geotectonic Zones of Greece, for example Ionian, Sub-pelagonian, Pelagonian, Paxon zone, while the Engineering Geological Unit describes the lithology, and the properties of the materials involved in the movement.
The landslide causal factors are divided into preparatory and triggering factors (Varnes 1978). A preparatory factor can act for years preparing the conditions for the occurrence of a landslide, while a triggering is the factor that under certain conditions can shift the slope from a marginally stable to an actively unstable state. Some of the preparatory factors are surface erosion, annual or seasonal rainfall, slope and tectonics, while triggering factors are earthquakes, volcanic action, and intense or prolonged rainfall.
Landslides have various effects on both the natural and human environment. Effects can be quantitative or qualitative, extensive or not. Table 1 lists examples of the landslide impacts in Residential Zones, Road Network, Infrastructures and the Environment.

Table 1. Impacts of landslides

IMPACTS	RESIDENTIAL ZONE	Damage to buildings
	ROAD NETWORK	Failure of embankments
	INFRASTRUCTURES	Failure of public service networks
	ENVIRONMENT	Loss of arable land

Conclusions

Landslides are a major geohazard, as they are widespread and rank high on the list of natural disasters. In Greece, their occurrence is frequent and controlled mainly by geomorphology, geological structure, seismicity and rainfall. Therefore, their recording is of utmost importance and aims to process their data for scientific and civil protection purposes.
The grouping of the most important parameters describing landslides from a huge number of different information sources created the need for the creation of the presented in this paper Hellenic Landslide Platform names as He.L.P., and the creation of a Landslide Inventory Form (LIF) for each landslide. The design of the Landslide Inventory Form as well as the selection and grouping of its parameters (geological conditions, type of landslides, causative factors, etc.) was made according to the current International Standards and guidelines for landslide recording.
The main objective of this work is the presentation of He.L.P., which is a web-based GIS platform, and by today includes 1176 landslides that have occurred in the regions of Western Greece, Epirus, and Ionian Islands. The simplicity of the platform as well as its accompanying LIF, gives to the Platform a “dynamic” character of continuous completion and updating with additional landslide records, with the prospect of its expansion throughout Greece.

References

Cruden, D.M., Varnes D.J., 1996. Landslides Types and Processes. In: Turner A.K. & Schuster R.L. (Eds.) Landslides: Investigation and Mitigation. Transportation Research Board, Special Report 247, p.36-72, National Academy Press, Washington D.C

Fell, R., Corominas, J., Bonnard, C., Cascini, L., Leroi, E., Savage, W.Z. on behalf of the JTC-1 Joint Technical Committee on Landslides and Engineered Slopes, 2008. *Guidelines for landslide susceptibility, hazard and risk zoning for land use planning*. Engineering Geology, 102: 85-98. doi: 10.1016/j.enggeo.2008.03.022

Günther, A., Van Den Eeckhaut, M., Malet, J.-P., Reichenbach, P., Hervás, J., 2014. *Climate-physiographically differentiated Pan-European landslide susceptibility assessment using spatial multi-criteria evaluation and transnational landslide information*. Geomorphology, 224: 69-85. doi: 10.1016/j.geomorph.2014.07.011

Wilde, M., Günther, A., Reichenbach, P., Malet, J.-P., Hervás, J., 2018. *Pan-European landslide susceptibility mapping: ELSUS Version 2.* Journal of Maps, 14(2): 97-104 and supplemental map. doi: 10.1080/17445647.2018.1432511

Varnes, D.J., 1978. Slope Movement Types and Pro*cesses. In Special Report 176: Landslides: Analysis* and Control (R.L. Schuster and R.J. Krizek, eds.), TRB, National Research Council, Washington, D.C., pp. 11-33.

Hungr, O., Leroueil, S. & Picarelli, L., 2014. The Varnes classification of landslide types, an update. *Landslides 11: 167–194* . https://doi.org/10.1007/s10346-013-0436-y

Varnes, D.J., 1978. Slope movement types and processes. In: Schuster R.L. & Krizek R.J. (Eds.) Landslides: Analysis and control. Transportation Research Board, Special Report 176, p.11–33, National Research Council, Washington D.C.

WP/WLI. 1990. A suggested method for reporting a landslide. International Geotechnical Societies' UNESCO Working Party on World Landslide Inventory (Chairman D Cruden), Bull Eng Geol Env, 41(1), 5–12, doi:10.1007/BF02590201.

WP/WLI. 1991. A suggested method for a landslide summary, International Geotechnical Societies' UNESCO Working Party on World Landslide Inventory (Chairman D Cruden), Bull Eng Geol Env, 43, 101–110, doi:10.1007/BF02590177.

WP/WLI. 1993. Multilingual landslide glossary. International Geotechnical Societies' UNESCO Working Party on World Landslide Inventory (Chairman D Cruden), BiTech, Richmond, p p 59.

WP/WLI. 1994. International Geotechnical Societies' UNESCO Working Party on World Landslides Inventory. Working group on Landslide causes (Chairman: Popescu ME) "A Suggested Method for Reporting Landslide Causes". *Bull IAEG 50:71-74*.

WP/WLI. 1995. A suggested method for describing the rate of movement of a landslide. International Geotechnical Societies' UNESCO Working Party for World Landslide Inventory (Chairman ME Popescu), Bull Eng Geol Env, 52(1), 75–78 doi:10.1007/BF02602683.

17th INTERNATIONAL CONGRESS of the Geological Society of Greece

BULLETIN OF THE GEOLOGICAL SOCIETY OF GREECE, SP. PUBL.

EXTENDED ABSTRACT 215

Biostratigraphy, Sedimentary Microfacies, and Depositional Environment of the Paleocene-Early Eocene Calciturbidites in Gardiki Section (Epirus, Western Greece)

Moforis L.[1], Kontakiotis G.[1], Antonarakou A.[1], Zambetakis-Lekkas A.[1], Ahmad S.[2], Paschos P.[3], Galanakis D.[3], Kanellopoulos C.[3], Sboras S.[4], Janjuhah H.T.[5], Lazos I.[4], Karakitsios V.[1]

(1) National and Kapodistrian University of Athens, Faculty of Geology and Geoenvironment, Department of Historical Geology and Paleontology, Panepistimiopolis, Zografou, 15784, Athens, Greece, leonidasmoforis@gmail.com (2) Department of Geology, University of Peshawar, Peshawar, Pakistan (3) H.S.G.M.E., Hellenic Survey of Geology and Mineral Exploration, Athens, Greece (4) Institute of Geodynamics, National Observatory of Athens, Lofos Nymphon, Thesio, 11810 Athens, Greece (5) INTI International University, Nilai, Negeri Sembilan, 170000, Malaysia

Introduction

The present study examines the depositional processes as well as the sedimentary microfacies types of the Paleocene-early Eocene carbonates of the Gardiki section, situated in Epirus region (western Ionian basin, Paramythia, Greece). This study defines the Paleocene-early Eocene depositional evolution of the area, based mainly on litho-stratigraphic characteristics in the external Ionian domain, which is regarded as a significant hydrocarbon prolific basin in western Greece. This work was accomplished by an extensive sedimentological analysis of the carbonate succession, alongside a synthetic paleoenvironmental reconstruction of the study area. Furthermore, the results provide valuable insights into regional geology and contribute to a deeper understanding of the Ionian basin in western Greece.

Study area

The study area is situated in the Ionian zone, a key element of the fold-and-thrust belt of the External Hellenides orogenic belt in western Greece. The External Hellinides are divided into three tectonostratigraphic zones, namely the pre-Apulian, Ionian, and Gavrovo-Tripoli tectono-stratigraphic zones. At a regional scale, this Alpine belt records the initiation, development, and final destruction of the southeastern margin of the Tethys Ocean and the consequent continent-to-continent collision between the Apulian and the Pelagonian micro-continents to the east. On a local scale, the various sub-basins of the Hellenic Tethys margin have been inverted to produce the main Hellenic thrust sheet folded zones. The Ionian zone, bounded westwards by the Ionian thrust and eastwards by the Gavrovo thrust, extends from Albania to the north most of the Epirus region and parts of the Ionian islands and continues southwards to Central Greece, Crete, and the Dodecanese. According to Auboin (1959) and IGRS-IFP (1966), the Ionian zone is subdivided into the Internal, Middle and External sub-basins (Figure 1a).

Materials and methods

A total of 126 samples were systematically collected from Gardiki area (lat: 39°20´22,08´´ N, long: 20°33´5,63´´ E) (Figure 1b), covering the Paleocene-early Eocene carbonate formations. The fieldwork included detailed logging, measurements and sampling, along with additional observations made on the litho-stratigraphic properties of the limestones, such as colour, lithological and textural variations, bed thickness, syn- and post-depositional features etc. Sampling resolution varied along the section, influenced by outcrop conditions, thickness and the lateral extend of each carbonate unit.

All samples undergone microfacies analysis, focusing mainly on lithofacies and biofacies, to ascertain their age and depositional environment. Thin sections were prepared at the Hellenic Survey of Geology and Mineral Exploration (H.S.G.M.E.) and examined biostratigraphically and sedimentologically using a polarized LEICA DM LP microscope, with photographs captured via an OLYMPUS UC30 microscope digital camera.

The microfacies description and textural characters analysis of the limestones were defined according to Dunham (1962) classification scheme, which was later modified by Embry and Klovan (1971) and Flügel (2004), based on the Standard Microfacies Types (SMF) in the Facies Zone (FZ) of the rimmed carbonate platform model. Depositional paleoenvironments were reconstructed by analyzing sedimentological characteristics observed during the fieldwork and interpreted sedimentary facies analysis. This analysis was supplemented by comparing additional data from existing time-equivalent sections of the same formation known from the literature.

Finally, the basic geological information was provided by the geological map (PARAMYTHIA SHEET 1:50.000) of the Hellenic Survey of Geology and Mineral Exploration (H.S.G.M.E.).

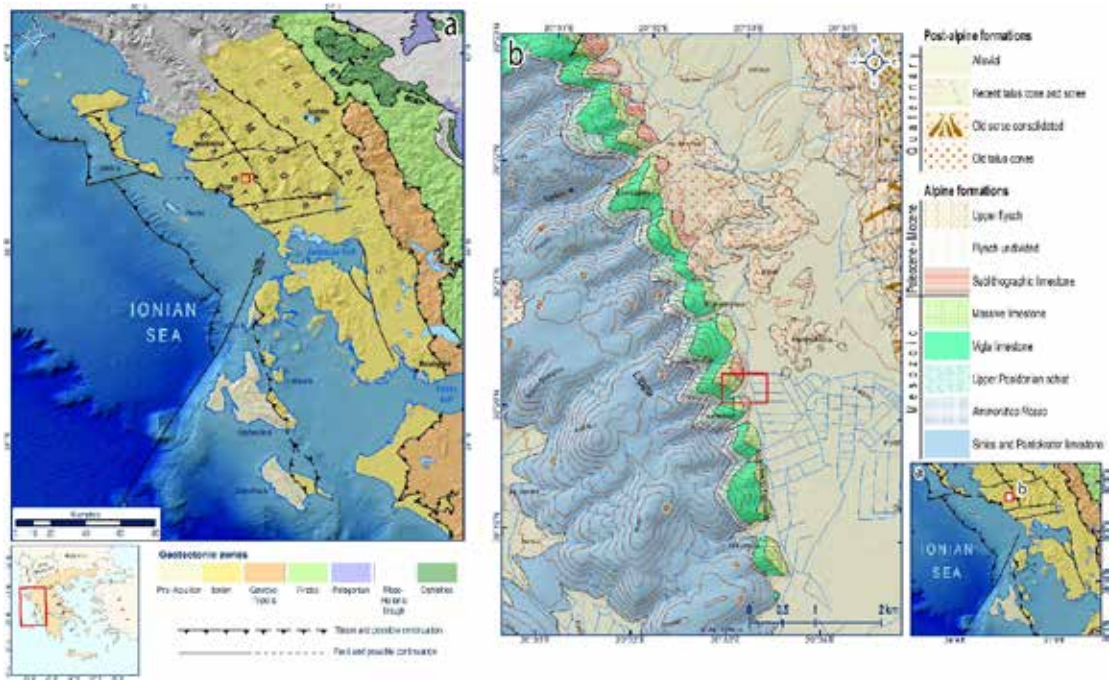

Figure 1(a,b). a) Geological map of the External Hellinides in NW Greece, illustrating the principal tectono-stratigraphic zones: Pre-Apulian, Ionian, Gavrovo, Pindos. b) Geological map of the study area. The red square shows the location of the study area. Legend interpretations are presented in the inset.

Biostratigraphy

The biostratigraphic analysis based on planktonic foraminifera presented in Table 1, revealed that the study part of Gardiki section covers the Paleocene-early Eocene time span based on the existence of *Morozovella* sp., *Operculina* sp., *Miscellanea* sp., *Melobesia* sp., Globorotaliidae and Globigerinidae. In addition, the appearance of radiolarians, rudist fragments, Dasycladacea algae, Siderolites spicules, Globotruncanidae, *Orbitoides* fragments, Miliolidae, *Idalina sp.*, supports their transportation form the underlying Upper Cretaceous Senonian limestones.

The age determination is in partial accordance with the geological map (PARAMYTHIA SHEET 1:50.000) concerning the Ionian rock exposures in Epirus area.

Sedimentary Microfacies Analysis

The key textural and compositional attributes, along with the sedimentary features of the identified microfacies are outlined in Table 1, corresponding to various depositional environments or facies zones. More specifically, within the studied carbonate succession, we observed 4 distinct sedimentary microfacies (Figure 2), which correspond to environments ranging from the upper part of the slope to the deep shelf. They mostly include in-situ wackestone-packstone lithofacies enriched in keeled planktonic foraminifera of Paleocene age, accompanied by faunal fragments indicative of shallower conditions due to their erosion and transportation by turbiditic currents along the slope, e.g., from the nearby platform to the basin. Within these deposits, the presence of bioclasts like the pelagic Globotruncanids in the micritic matrix of the basal samples was interpreted that they have been transferred from the underlying Upper Cretaceous strata. In the Ionian zone, such “clastic limestones” are usually alternated with sub-lithographic pelagic limestones reflected mostly by bioclastic mudstone facies (Kontakiotis *et al.*, 2020; Bourli *et al.*, 2021; Moforis *et al.*, 2022).

More explicitly, the lower part of the succession was characterized by alterations of a pelagic biomicrite mudstone mostly with planktonic foraminifera and more rarely radiolarian (SMF 2-3) with a bioclastic biomicrite wackestone-packstone with abundant planktonic foraminifera (SMF 3-4), reflecting deposition in a low energy, relatively deep environment such as the toe of slope (FZ3) and/or the deep shelf (FZ2). A microbreccia bioclastic rudstone enriched in planktonic foraminifera along with fragments of shallow water fauna (benthic foraminifera, rudists, echinoderms and algae) (SMF 5), represents deep slope depositional conditions (FZ 4). A biomicrite packstone-grainstone (SMF 5) with mixed fauna and reworked lithoclasts was also observed and could be considered as indicative of a medium to high energy environment in the upper part of the slope close enough to the platform.

Samples	Description of Microfacies Analysis	Facies Zone	Lithology	Age
K69-K126	Biomicrite packstone-grainstone (SMF 5) Biomicrite mudstone (SMF 2-3)	Slope (FZ 4) Deep shelf (FZ 2)	Turbiditic limestone	Paleocene-early Eocene
K60-K68	Bioclastic rudstone (SMF 5)	Slope (FZ 4)	Micro-brecciated limestones	Paleocene
K1-K59	Bioclastic biomicrite wackestone-packstone (SMF 3-4) Biomicrite mudstone (SMF 2-3)	Toe of slope (FZ 3) and/or Deep shelf (FZ 2)	Turbiditic limestone	Paleocene

Table 1. Description of microfacies analysis of samples from Gardiki section (Epirus, western Greece).

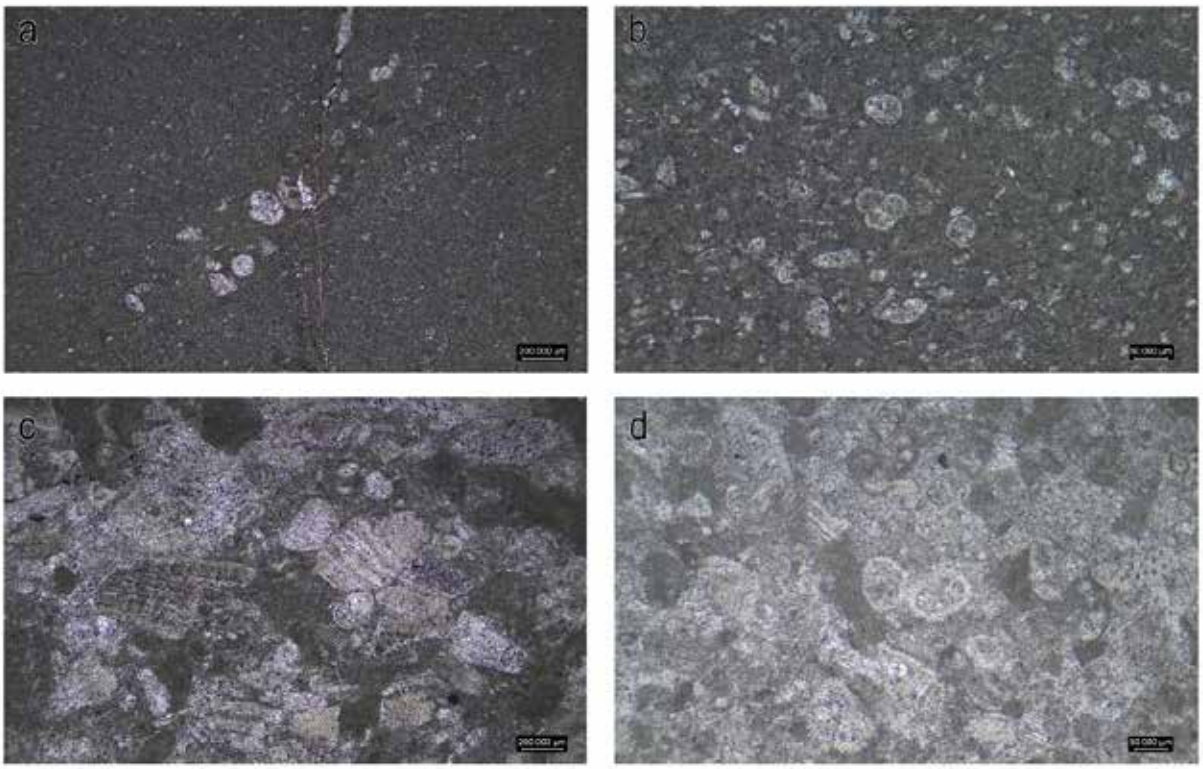

Figure 2. Representative figures of the 4 distinct sedimentary facies. a) Biomicrite mudstone with planktonic foraminifera, b) bioclastic biomicrite wackestone-packstone, c) bioclastic rudstone with planktonic and benthic foraminifera and rudist fragments, d) biomicrite packstone-grainstone with planktonic and benthic foraminifera

References

Aubouin, J.; Le Pichon, X.; Winterer, E.; Bonneau, M. Les Hellénides dans l'optique de la tectonique des plaques, 6th Colloquium on the Geology of the Aegean Region, Athens, 1977; Reprinted from proceedings vol. III; IGME: Athens, Greece, 1979; Volume 3, pp. 1333–1354

Bourli, N., Pantopoulos, G., Maravelis, A.G., Zoumpoulis, E., Iliopoulos, G., Pomoni-Papaioannou, F., Kostopoulou, S., Zelilidis, A., 2018. Late Cretaceous to early Eocene geological history of the eastern Ionian Basin, southwestern Greece: A sedimentological approach. Cretaceous Research 98, 47-71

Bourli, N., Iliopoulos, G., Papadopoulou, P., Zelilidis, A., 2021. Microfacies and Depositional Conditions of Jurassic to Eocene Carbonates: Implication on Ionian Basin Evolution. Geosciences 11 (7), 288]

Dunham, R.J. Classification of Carbonate Rocks According to Depositional Textures; American Association of Petroleum Geologists: Tulsa, OK, USA, 1962

Embry, A.F., Klovan, J.E., 1971 A late Devonian reef tract on northeastern Banks Island, NWT. Bull. Can. Pet. Geol., 19, 730–781

Flügel, E., 2004. Microfacies analysis of carbonate rocks. In Analysis, Interpretation and Application; Springer: Berlin/ Heidelberg, Germany

IGRS-IFP., 1966. Étude Géologique de l'Epire (Grèce Nord—Occidentale); Technip & Ophrys Editions: Paris, France]

IGME., 1966. Geological Map of Greek Series, Paramythia Sheet, Scale 1:50.000; Institute for Geology and Subsurface Research: Athens, Greece,

Karakitsios, V., 1995. The influence of pre-existing structure and halokinesis on organic matter preservation and thrust system evolution in the Ionian basin, northwestern Greece. AAPG Bulletin 79, 960-980

Kontakiotis, G., Moforis, L., Karakitsios, V., Antonarakou, A., 2020. Sedimentary Facies Analysis, Reservoir Characteristics and Paleogeography Significance of the Early Jurassic to Eocene Carbonates in Epirus (Ionian Zone, Western Greece). Journal of Marine Science and Engineering 8 (9), 706

Moforis, L., Kontakiotis, G., Janjuhah, T.H., Zambetakis-Lekkas, A., Galanakis, D., Paschos, P., Kanellopoulos, C., Sboras, S., Besiou, E., Karakitsios, V., Antonarakou, A., 2022. Sedimentary and Diagenetic controls across the Cretaceous-Paleogene Transition: New Paleoenvironmental Insights of the External Ionian Zone from the Pelagic Carbonates of the Gardiki Section (Epirus, Western Greece). Journal of Marine Science and Engineering 10 (12)

17th INTERNATIONAL CONGRESS of the Geological Society of Greece

BULLETIN OF THE GEOLOGICAL SOCIETY OF GREECE, SP. PUBL.

EXTENDED ABSTRACT 216

The geospatial characteristics of island beaches: the case of Kos, Greece

Monioudi I.N.[1], Chatzistratis D.[1], Velegrakis A.F.[1], Rigos A.[1], Chatzipavlis A.E.[1,2], Nikolaou A.[1,3], Andreadis O.P.[1]
(1) Department of Marine Sciences, University of the Aegean, University Hill, 81100 Mytilene, Greece, imonioudi@marine.aegean.gr (2) Department of Physics and Earth Sciences, University of Ferrara, Ferrara, Italy (3) ROGAN ASSOCIATES S.A., Athens, Greece

Research Highlights

Acquisition analysis of widely available geospatial information to assess the state and dynamics of island beaches.

Introduction

Assessing the state and dynamics of sandy shorelines (beaches) is vital for developing efficient management strategies (e.g. Karditsa *et al*., 2024; Chalazas *et al*., 2024), with the approaches used depending on their spatio-temporal scales and the available information and resources. In regional (island) scales, the extensive scope of studies and the high potential costs of adaptation (Narayan *et al*., 2016) may require prioritization of responses and efficient allocation of the (mostly) limited resources. This requires, among others, information of the geospatial characteristics and their interrelationships which may provide much needed information and identify potential controls of beach dynamics. Therefore, the objective of this short contribution is to present an approach that could acquire such information at a regional (island) scale on the basis of widely available geospatial data; the approach is demonstrated for the island of Kos, South Aegean Sea, Greece (Fig.1).

Study area

Kos has an area of about 295 km^2, a coastline length of 112 km and a resident population of about 37,100. Kos is a highly touristic island: in 2023, 1.3 million passengers arrived at the island of Kos. There are > 57,000 hotel beds in Kos, tourism density and intensity being very high (28,917 tourist nights/km^2). Most of this infrastructure and the tourist activities are associated with the island's beaches, as Kos is a global tourist destination for Sea-Sand-Sun - 3S tourism (SETE, 2024). Kos coast is microtidal (0.1 m astronomical tidal range). In the north NNW waves dominate with the largest waves showing heights Hs of 3.8 m and periods Tp of 7.5 s. Energetic waves occasionally impinge on western and southern coasts, with the largest waves having heights of 4–5 m and periods of 9–10 s (Monioudi *et al*., 2025). Kos is a part of the easternmost South Aegean volcanic arc. Its northeastern part is mostly formed on Plio-Quaternary sediments, whereas its southeastern highlands are made mostly of alpine and pre-alpine metamorphics and some Miocene volcanics (Pe-Piper *et al*., 2024). Following a hiatus, volcanism, resumed 3 million years ago (mostly) in the island's west; the large eruption of the Kos Plateau Tuff volcano (161 ka BP) deposited pyroclastics up to 15 m thick that covered most of the western Kos and the adjacent islands (Piper and Pe-Piper, 2020). Most large/wide beaches are found in the low-relief, sedimentary northeastern Kos (Fig. 1), indicating a potential geological control.

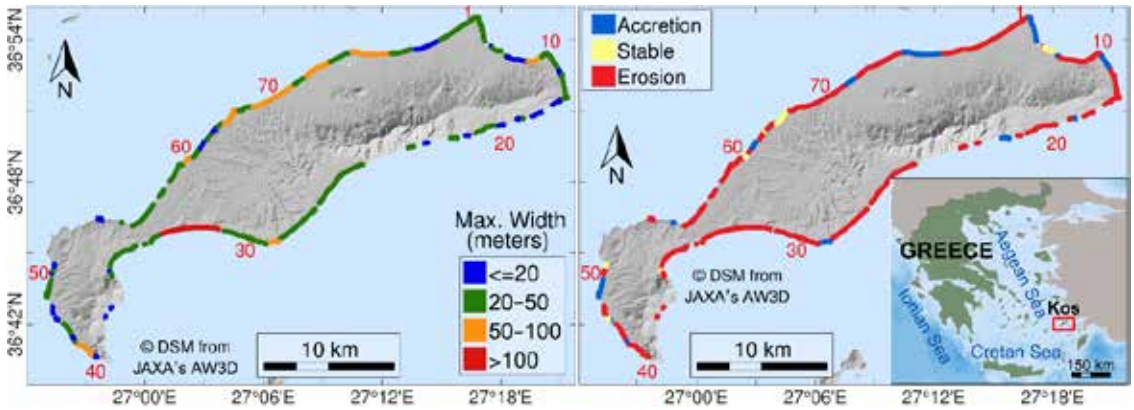

Figure 1. Kos: Beach maximum width (BMW) and long-term beach erosion trends. Numbers refer to the ID of the 78 beaches of Kos (after Monioudi *et al*., 2025).

Methods

The compiled inventory of the Kos beaches provides information on the dimensions, sediment types and the presence of outflowing streams, coastal defenses or artificial and natural features. Using satellite images available in the Google Earth Pro application, subaerial (dry) beaches were digitized as polygons based on clearly visible boundaries: natural features like vegetated dunes or cliffs and permanent artificial structures such as embankments, seawalls, or buildings and the shoreline define the landward and seaward limits, respectively. To ensure consistency, all digitization was conducted by a single analyst adhering to strict delimitation rules. The database was constructed through the digitization of beach polygons from selected images obtained in the period 2003–2021, which allowed an estimation of the recent historical changes. The beach (CNES/Airbus and Maxar) imagery has a spatial resolution about 0.5 m, but its results are constrained by the image accuracy; comparison of satellite images with concurrent RTK-DGPS ground observations showed an RMSE of about 2 m. Moreover, although tidal effects on the shoreline position are very small care was taken to analyze satellite images from the same season and under low hydrodynamic conditions; however as the available images along the islands' coasts have been collected at different times and under different preceding hydrodynamic conditions, recorded beach dimensions may not represent synoptic conditions at the island scale. Such limitations, however, cannot be avoided in the analysis of (historical) satellite imagery at large spatial scales (Monioudi *et al*., 2023). Following these procedures, the characteristics of 78 (Kos) beaches (Fig. 1) were identified, recorded and compared.

Results

The majority of beaches (53%) were found to have maximum widths (BMWs) of 20-50 m, 35% had widths < 20 m and 10 beaches had widths > 50 m (Fig. 1); the average maximum width was found to be 31 m. Despite the higher wave energy of the north- and west-facing beaches, a clear trend was observed in the development of northwest-facing beaches (303.75°- 348.75°). Fewer beaches were found to develop with southeast (16%) and south (12%) orientations, with the remaining beaches exhibiting other orientations (Fig. 2). This supports the hypothesis that the development of the Kos beaches is not controlled by the hydrodynamics, but is mainly subject to geological controls.

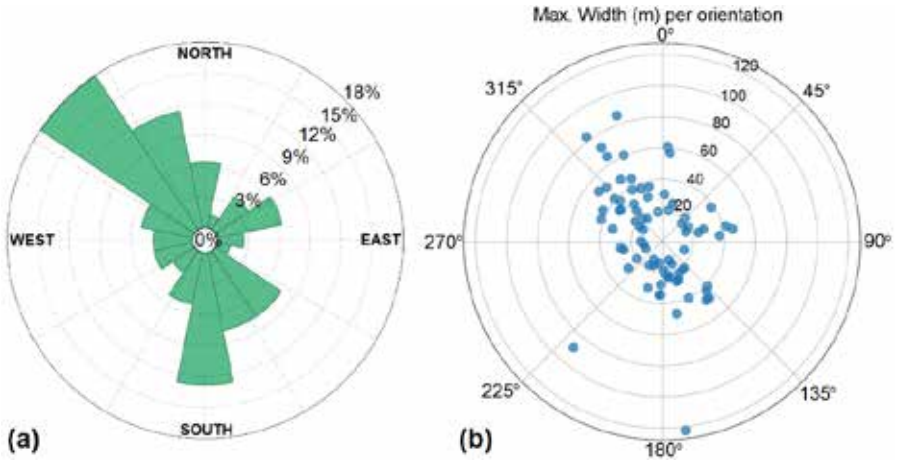

Figure 2. (a) Distribution of the Kos beach orientation. (b) Rose diagram of the beach maximum widths.

The relationship between orientation and the BMWs was further investigated using Angular-Linear correlation (Mardia, 1976; Zar, 2014) was used. This statistical test assesses the null hypothesis H_0 of no correlation between the two variables against the alternative hypothesis H_1 of a significant correlation. The results showed an $R^2 = 0.0327$ and $p = 0.279$, suggesting rejection of the H_0 hypothesis as $p > 0.05$; thus, there is no statistically significant correlation between the two variables.

There are outflowing streams in many Kos beaches (49%), indicating (potential) terrestrial sediment supply. Comparison of the BMWs with the occurrence of streams, shows that stream presence affects the beach size. In 2021, beaches with streams were found to have an average maximum width of 40.4 m which was almost double the

width of beaches without streams (22.8 m). In order to examine the potential correlation between stream presence and BMWs it was checked whether the BMWs follow a normal distribution. Using the Shapiro-Wilk regularity test (Shapino and Wilk, 1965), it was found that the BMWs do not show 'normality' in terms of distribution (the Shapiro-Wilk regularity control gave W = 0.772, p <0.001); thus, the non-parametric Mann-Whitney test was used. Its result showed that these two types of beaches differ (U = 307.5, p <0.001), i.e., there is a correlation between beaches without streams and smaller BMWs with a median width of 22 m (Fig. 3a).

Regarding beach sediments, the majority of Kos beaches (53%) form on sandy sediments, whereas 32 % of the beaches on mixed sediments (gravels/sands) and 15% on pebbles. Comparison of the BMWs with the different sediment types showed good correlations; sandy beaches had an average BMW of 40.8 m (standard deviation 20), i.e. they are significantly wider than mixed sediment beaches and pebble beaches which showed average BMWs of 23.4 m (10.8 standard deviation) and 16 m (7.3 standard deviation), respectively. Even when the mixed sediment and pebble beaches were grouped together, their comparison with the sandy beaches showed a clear difference. Sandy beaches were found to have significantly greater BMWs (40.8 m) compared to the grouped mixed sediment/pebble beaches (21 m). It appears that the coarse sediment beaches attain BMWs 10-25 m, whereas the sand beach BMWs 30-50 m and 50-80 m (Fig. 3b).

In addition, it appears that about 60% of sandy beaches are also associated with outflowing streams, compared with those beaches forming on mixed sediments (45%) and pebbles (17%). To check this hypothesis the non-parametric Kruskal-Wallis test was used (the BMWs do not follow a normal distribution). The test checked the hypotheses: H_0, no correlation between the BMWs and the local sediment; and H_1, correlation between BMWs and the local sediments. The test showed that there is a clear difference between the maximum widths of beaches forming on sand and those forming on mixed/coarse sediments (H_1 = 25.911, p < 0.001). Beaches forming on pebbles have a median BMW of 14.9 m, whereas those formed on mixed sediments and sands 22.6 m and 40.5 m, respectively. A Kruskal-Wallis test (Kruskal and Wallis, 1952) was also applied in the case that beaches divided into two classes: those with sand sediments and those with mixed sediments and pebbles. The test showed a clear difference between these beach classes (H_1 = 25.090, p <0.001).

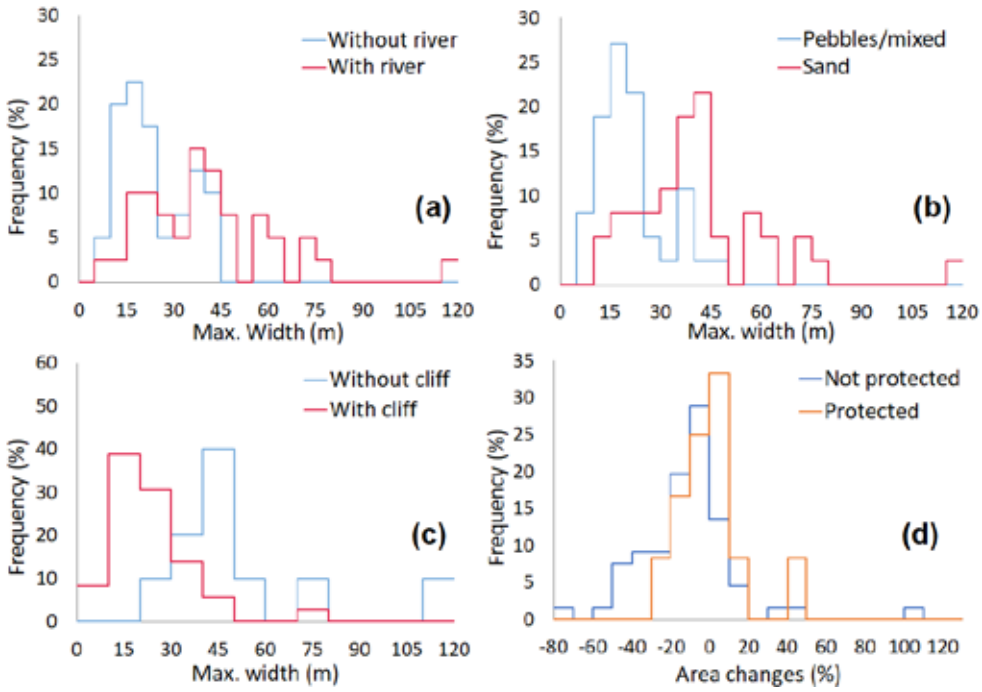

Figure 3. (a) Beach maximum widths (BMW) and the presence of beach streams (5 m steps), (b) BMWs and sediment texture (2 categories), (c) BMWs with the presence of backshore cliffs (10 m steps) excluding beaches with backshore infrastructure, and (d) Histogram of frequencies of areal changes.

A total of 50% of the island's beaches are characterized by the presence of backshore coastal cliffs. An initial investigation of the potential correlation with the BMWs did not reveal a significant relationship. However, as the presence of infrastructure/assets along the immediate backshore might affect the BMWs and other beach dimensions due to e.g., reduction/interruption of the land sediment supply and, thus, the correlation. Excluding beaches where there are backshore infrastructure/assets (about 50% of the total), a significant relationship is apparent (Fig. 3c). Many beaches with cliffs show BMWs of 10-20 m (and up to 30-50 m), whereas the beaches without cliffs attain obviously greater BMWs. The relationship was tested using the Mann-Whitney method excluding beaches with backshore infrastructure/assets. It appears that there is a statistically significant relationship ($U = 34$, $p < 0.001$). Those beaches without a backshore cliff are larger (a median BMW of 46 m) than those with a backshore cliff (median of 22 m). It seems that the coastal topography controls beach formation and size.
To assess the impact and effectiveness of coastal protection schemes, the areal changes between the beach polygons obtained from older imagery (2004-2009) and 2021 were considered which was preferred over more recent ones, as images were taken in spring/summer months (Fig. 3d). The Shapiro-Wilk regularity test for the variable 'beach area change' yielded results $W = 0.889$ and $p < 0.001$ showing that the data do not follow a normal distribution. Thus, the non-parametric Mann-Whitney control was also applied by controlling the following assumptions: H_0, the distribution of the continuous variable "percentage of change of beach area" is similar between beaches with coastal protection works and beaches without protection works; and H_1, the distribution of the continuous variable "percentage of change of beach area" differs between beaches with protection works and beaches without works. The test results show there is a significant areal difference ($U= 260$, $p=0.050$) between beaches with and without coastal works.

Discussion and Conclusions

The analysis of the geo-spatial data using both basic statistical metrics and more complex parametric and non-parametric tests, led to interesting findings regarding the Kos beaches. Comparison of the digitized polygons of the beaches showed erosion trends (Fig. 1) with the average BMW having decreased in 76% of the beaches compared to the period 2004-2009 (average decrease of 3 m). In addition, the area was reduced in 61 beaches out of the 78 beaches of the island, with an average decrease of 15% per beach. As the maximum dry width is considered a relatively conservative indicator of beach erosion (Monioudi and Velegrakis, 2022), the estimation of the areal reduction offers a more comprehensive picture. The analysis also showed that the detection of long-term erosive trends requires availability of time series of data with spatio-temporal resolution better than that currently available in open source imagery. In the near future, when it is expected that the availability of such data will increase significantly (Velegrakis *et al*., 2024), the approach developed/applied in the present study can be used more for the detection (and management) of coastal morphodynamics (erosion). In Kos, the orientation of the beaches does appear to affect the size of the beach, which on the contrary is related to stream presence and sediment texture size. In addition, the presence of backshore cliffs is correlated with small BMWs. Generally, it appears the Kos beach dimensions are primarily controlled by the geology rather the hydrodynamics.

Acknowledgements

This research was supported by the Hellenic Foundation for Research and Innovation (H.F.R.I.) under the '2nd Call for H.F.R.I. Research Projects to Support Post-Doctoral Researchers' (MARICC, Project Number: 211).

References

Chalazas, T., Bove, G., Chatzistratis, D., Monioudi, I.N., Velegrakis, A.F., 2024. A system for the management of sandy shorelines under climate change: United States Virgin Islands (USVI). Ambio 53, 406 - 420. https://doi.org/10.1007/s13280-023-01946-w

Karditsa, A., Niavis, S., Paramana, T., Monioudi, I, *et al*., 2024. Is the insular coastal tourism of western Greece at risk due to climate induced sea level rise? Ocean & Coastal Management 251, 107088. https://doi.org/10.1016/j.

ocecoaman.2024.107088.

Kruskal, W.H., Wallis, W.A., 1952. Use of ranks in one-criterion variance analysis. Journal of the American statistical Association 47(260), 583-621. https://doi.org/10.1080/01621459.1952.10483441

Monioudi I.N., Velegrakis, A.F., 2022. Beach Carrying Capacity at Touristic 3S Destinations: Its Significance, Projected Decreases and Adaptation Options under Climate Change. Journal Of Tourism and Hospitality 11, 500.

Monioudi, I.N., Velegrakis, A.F., Chatzistratis, D. *et al*., 2023. Climate change—induced hazards on touristic island beaches: Cyprus, Eastern Mediterranean. Front. Mar. Sci. 10, 1188896. https://doi.org/10.3389/fmars.2023.1188896

Monioudi, I.N., Chatzistratis, D., Chalazas, T. *et al*. 2025. A prioritization framework for adaptation responses for climate change-induced erosion in island beaches—Cases from the Aegean islands, Greece. J. Mar. Sci. Eng. 13, 491. https://doi.org/10.3390/jmse13030491

Mardia, K., 1976. Linear-Circular Correlation Coefficients and Rhythmometry. Biometrika 63 (2), 403–405, https://doi.org/10.2307/2335637

Narayan, S., Beck, M.W., Reguero, B.G. *et al*., 2016. The effectiveness, costs and coastal protection benefits of natural and nature-based defences. PLoS ONE 2016, 11, e0154735. https://doi.org/10.1371/journal.pone.0154735

Pe-Piper, G., Piper, D.J., Tsoukalas, N., 2024. Mineralogy and Geochemistry of Upper Miocene Igneous Rocks, Kos Island, Greece: Extension during Strike-Slip Faulting and Subduction Rollback. Minerals 14(10), 989. https://doi.org/10.3390/min14100989

Piper, D.J.W., Pe-Piper, G., 2020. A reworked isolated deposit of the Kos Plateau Tuff and its significance for dating raised marine terraces, Kos, Greece. Geol. Mag. 157, 2021–2032. https://doi.org/10.1017/S0016756820000254

SETE, 2024. Annual Report of Competitiveness and Structural Adjustment in the Touristic Sector for 2023: South Aegean. https://insete.gr/wp-content/uploads/2024/12/24-12_South_Aegean-1.pdf (in Greek)

Shapiro, S.S., Wilk, M.B., 1965. An analysis of variance test for normality (complete samples). Biometrika 52(3–4), 591–611. https://doi.org/10.1093/biomet/52.3-4.591

Velegrakis, A.F, Chatzistratis, D., Chalazas, T., *et al*., 2024. Earth observation technologies, policies and legislation for the coastal flood risk assessment and management: a European perspective. Anthropocene Coasts 7, 3. https://doi.org/10.1007/s44218-024-00037-x

Zar, J.H., 2014. Biostatistical Analysis. Pearson Education Limited

17th INTERNATIONAL CONGRESS of the Geological Society of Greece

BULLETIN OF THE GEOLOGICAL SOCIETY OF GREECE, SP. PUBL.

EXTENDED ABSTRACT 217

Innovative educational programs at the Lavreotiki UNESCO Global Geopark: the ERASMUS+ "ARTeMIS" Program Action for Research and Teaching Mineral exploration Inclusive School, Greece

Moraiti E.[1], Voudouris P.[2], Tarantola A. & Barsaki V.

(1) Lavreotiki UNESCO Global Geopark, Lavrion, Greece, eugeniamoraiti@gmail.com (2) National and Kapodistrian University of Athens, Ilissia, Greece

Introduction

UNESCO Global Geoparks (UGGp) are single, unified geographical areas where sites and landscapes of international geological significance are managed with a holistic concept of protection, education and sustainable development. Their bottom-up approach of combining conservation with sustainable development while involving local communities is a fundamental principal and is becoming increasingly popular.

The UNESCO Global Geoparks are ideal destinations that can support local communities and serve the 17 goals of the United Nations' Green Agenda in various ways.

In particular geoparks educate and prepare societies and youths for the new challenges that climate crisis has triggered. Education holds a pivotal role in the operation and management of a geopark. Every member is obliged to implement educational programs based on its geodiversity and biodiversity wealth. Geosites function as experiential laboratories, welcoming students, educators, and visitors to offer them unique experiences and communicate a sustainable way of living.

The ARTeMIS ERASMUS+ program

In the frame of collaboration and the accomplishment of the 17, Lavreotiki UNESCO Global Geopark has joined the ARTeMIS Erasmus + project. This project (funded with 385.000 euros per year and three years duration in total) is led by Alexandre Tarantola, Professor (Associate), head of the first year of the Master's degree in "Earth and Planetary Sciences, Environment", "Earth-Resources System" course of the University of Lorraine, Nancy. Its objective is to develop the methods and tools of geoscience professions through a research-based training approach. It aims to allow students to confront the realities and expectations of the field in geology, to complete their academic career and to broaden their horizons by allowing collaboration with students from other European Universities. This approach brings together various players working on the theme of mineral exploration such as the Friedrich-Alexander-University of Erlangen-Nuremberg, the National and Kapodistrian University of Athens (Scientific Responsible, Professor Panagiotis Voudouris), the Aristotle University of Thessaloniki (Scientific Responsible, Professor Vassilis Melfos) as well as Hellas Gold SA, a subsidiary of the Canadian company Eldorado Gold Corporation, which specializes in the exploration and exploitation of mines worldwide and the Lavreotiki UNESCO Global Geopark with its famous deposits. The Lavrion deposit comprises five different styles of related deposits, a unique geological phenomenon recorded only in Greece and in the Lavreotiki UGG's territory.

Its minerals contain the highest number of different elements (48) of any known mining district and thus more diverse than anywhere else in the world. Lavrion area offers the best opportunity to study the interplay between large-scale tectonic processes which took place during earlier Alpine collision and compression, followed by Miocene extension in the back-arc region of the Hellenic subduction zone; magmatic activity, expressed by emplacement of various igneous rocks in a syn- to post-tectonic regime; hydrothermal activity and fluid circulation within various lithologies, resulting in enormous quantities of ore deposition and related base and precious metal mineralization, later supergene weathering processes, resulting in a unique zone of supergene ore oxidation, which contains, in addition to the primary ores, the most mineral species ever found on a single mining district on earth and the way, geological processes have profoundly influenced ore deposition and the course of human history and technology.

Among many courses and actions, the "ARTeMIS" program includes a 4-days training course in the field (at the geopark's mining galleries) for teachers and students, using spectroscopic analysis tools and the implementation of classroom lessons in mineral resource geochemistry. These actions provide an opportunity to carry out exercises in the use of spectroscopic analysis tools, mapping and reflection on the establishment of metallogenic systems on geological objects that are at the heart of the research carried out by the various partners. The 4-days training course took place in April with great success.

Figure 1. Photography captions during the 4-day training course in the field, at the Lavreotiki UGGp geosites / sites of mining heritage.

Results

The expected results of the "ARTeMIS" ERASMUS+ program are:

- The creation of complementary teaching units for teachers and second-cycle university students engaged in an "exploration and mineral resources" course.
- The use and development of portable field tools suitable for mineral exploration.
- The application of an ergonomic approach to training and research in geology.
- The publication of an educational field guide dedicated to the mineral resources of northeastern Greece.
- The creation of a logistics preparation methodology.

Last but not least, an important aspect of the ARTeMIS project also aims to promote the integration of students with disabilities by making training accessible in order to offer them new opportunities for professional integration. To this end, a collaboration has been initiated with occupational therapists from the Lorraine-Champagne-Ardennes Occupational Therapy Training Institute with a view to identifying avenues for improvement and proposing alternatives. Workshops will be held, bringing together teachers, students, Earth Sciences stakeholders and occupational therapists. In the long term, these solutions will lead to a diversification of jobs and the development of processes that are more in line with the specificities of field geology.

Such substantive partnerships become models of good practices for the adaptation and sustainability of the local communities and the organizations involved in education. These partnerships foster interdisciplinarity and communicate science and universal values, such as collaboration, respect, inclusion, and quality education, to the youth and the next generations. These values are included and promoted by the United Nations Sustainable Development Goals (such as SDG 4, SDG 11, SDG 12, SDG 13, and SDG 17).

Figure 2. SDG 4: Ensure inclusive and equitable quality education and promote lifelong learning opportunities for all, SDG 12: Ensure sustainable consumption and production patterns, SDG 16: Promote peaceful and inclusive societies for sustainable development, provide access to justice for all and build effective, accountable and inclusive institutions at all levels & SDG 17: Strengthen the means of implementation and revitalize the Global Partnership for Sustainable Development.

References

Voudouris, P., et al. 2008. Mineralogical and fluid inclusion study of the Kamariza carbonate-replacement deposit, Lavrion, Greece. **[Mineralogy and Petrology, 94, 85–106.]**

Rieck B. (2024) Lavrion Mining District, Lavreotiki, East Attica, Attica, Greece https://www.mindat.org/loc-1942.html

https://hub.uoa.gr/erasmus-artemis/

https://master-stpe.formation.univ-lorraine.fr/projet-erasmus-artemis-terrain-en-grece-m2-smge/

17th INTERNATIONAL CONGRESS of the Geological Society of Greece

BULLETIN OF THE GEOLOGICAL SOCIETY OF GREECE, SP. PUBL.

EXTENDED ABSTRACT 218

Empowering Future Generations: Incorporating Geo - Environmental Education on Climate Change into Greek Compulsory Education

Moshou H., Drinia H.

Department of Geology and Geoenvironment, National and Kapodistrian University of Athens, Panepistimiopolis, 15784 Athens, moshouhara@geol.uoa.gr

Introduction

The urgent need to address climate change has never been more critical, as its impacts are being felt globally, with severe consequences for ecosystems, economy, and human communities. Adapting to a rapidly changing world is equally essential. Climate change poses one of the greatest challenges of our era, making immediate action imperative. Education, including geoeducation, can serve as a key tool in preparing future generations to mitigate and adapt to these challenges. Geoeducation, enriched with geoconservation principles, emphasizes the importance of protecting geological heritage while fostering an understanding of Earth's processes and their relevance to the climate crisis. Therefore, it provides a unique opportunity to equip students with the knowledge and skills to grasp the complexities of climate change and its impact on our planet.

This paper underscores the significance of education, particularly environmental education and geoeducation, in addressing the climate crisis, while also exploring obstacles and challenges regarding the implementation of climate change education in Greece. Additionally, it proposes general strategic approaches for systematically integrating climate change education into the compulsory education system, with the objective of fostering both mitigation and adaptation in response to the climate crisis. The study employs a mixed-method approach to explore integrating climate change education (CCE) into Greek compulsory education. A systematic review of national and international studies identifies best practices, challenges, and gaps in implementing CCE. SWOT analysis evaluates internal factors like teacher preparedness and resources, while PEST examines external political, economic, social, and technological influences.

The Importance of Geo - Environmental Education in Addressing the Climate Crisis

Recognizing the critical role of education in addressing climate change is essential. Environmental education fosters ecological awareness and equips citizens with the skills and attitudes necessary to adopt sustainable practices and social responsibility (Damoah, 2023; Daskolia, 2023; Nantsopoulos & Mogias, 2020). Geoeducation, with its emphasis on understanding Earth's systems, geological processes, and their interaction with the environment, complements this effort by providing a scientific foundation for grasping the complexities of climate change. Together, environmental education and geoeducation not only raise public awareness but also encourage proactive behavior, leading to significant behavioral shifts. Coupled with effective government policies (see Figure 1), they can mitigate climate impacts and enhance societal resilience to environmental challenges.

Georgousis et al. (2021) emphasize that geoeducation, or geoenvironmental education, plays a pivotal role in connecting students with Earth's dynamic processes, promoting a deeper understanding of the natural environment, and fostering sustainable attitudes. They argue that integrating geoenvironmental education into curricula can bridge the gap between theoretical knowledge and practical applications, empowering learners to critically assess and address environmental issues such as climate change. Geoeducation, coupled with geoconservation, not only deepens students' understanding of Earth's dynamic systems but also emphasizes the preservation of geosites, which serve as critical records of past climatic conditions. This dual approach empowers learners to appreciate the interplay between geological heritage and environmental sustainability. By focusing on interdisciplinary learning, geoeducation highlights the interplay between geology, geography, and environmental science, making it an essential component of climate-focused education.

The urgency for climate-focused education is greater than ever, as new generations face complex challenges from the climate crisis. Integrating climate change into school curricula fosters early environmental and geoscientific awareness, shaping responsible citizens (Nantsopoulos & Mogias, 2020). Early education is vital, as misconceptions formed in childhood can persist into adulthood (Boyes & Stanisstreet, 1993). Geoeducation is particularly valuable in helping students understand how climate change affects Earth's physical processes and ecosystems, fostering a holistic perspective. Preparing students with solid knowledge and its geological dimensions about climate change enhances their willingness to act and fosters active participation in addressing future challenges (Lester et al., 2006)..

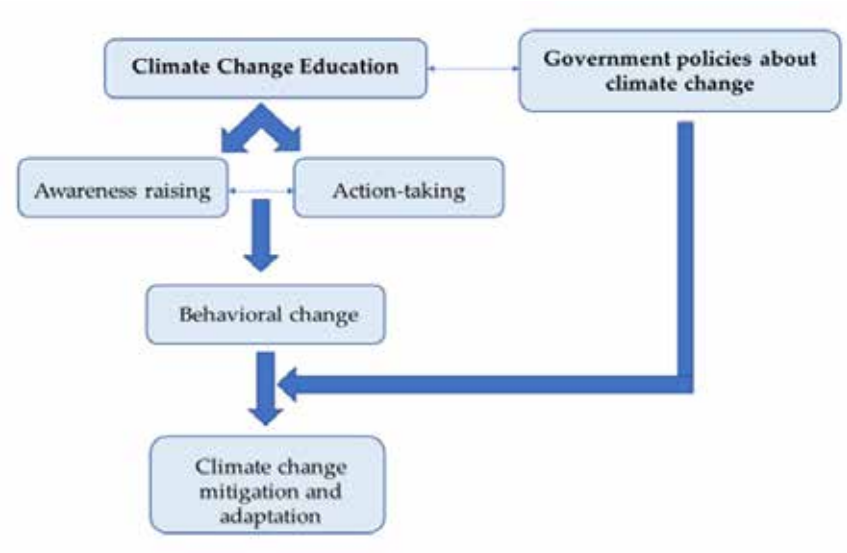

Figure 1. Climate change education as an important part of climate change mitigation and adaptation. (Figure from Moshou & Drinia, 2023)

Challenges and Barriers in Implementing Climate Change Education in Greece

The implementation of climate change education in Greece encounters significant challenges linked to social, political, economic, and educational factors. Although 83% of Greeks recognize climate change as a critical issue of the 21st century (EIB, 2021), integrating environmental education into the national curriculum remains problematic. Since its introduction in 1987, environmental education has been optional and limited to specific programs (Farangitakis & Sbarounis, 2020). Textbooks present environmental topics in a fragmented way, leading to knowledge gaps and misconceptions, such as confusion between the greenhouse effect and ozone layer depletion (Nantsopoulos & Mogias, 2020). Incorporating geoconservation into environmental education could bridge gaps in understanding Earth's history and its relevance to climate change, while fostering a sense of responsibility for preserving unique geological sites as natural laboratories for scientific inquiry. Additionally, inadequate teacher training exacerbates the issue, as many educators lack sufficient preparation in environmental topics (Moshou & Drinia, 2023). These deficiencies are further illustrated in Figure 2, which highlights how early misconceptions formed in childhood persist into adulthood, impacting future educational efforts.

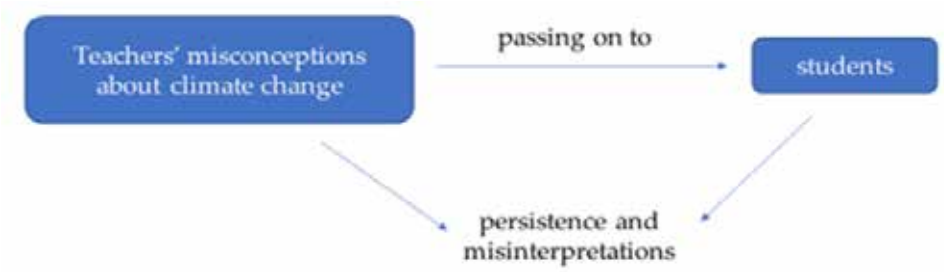

Figure 2. Teachers' misconceptions pass on to students and lead to misconceptions' persistence and misinterpretations (Figure from Moshou & Drinia, 2023)

Further challenges are rooted in Greece's prolonged economic crisis, which limits funding for programs, infrastructure, and teacher training. Environmental Education Centers, critical for raising awareness, face resource shortages, reducing their ability to operate effectively (Farangitakis & Sbarounis, 2020). Psychological distance also plays a role, as many Greeks have yet to experience direct impacts of climate change, diminishing the urgency and public engagement necessary to address the issue. Additionally, unclear legislation and delays in decision-making, coupled with insufficient collaboration among stakeholders, hinder progress. Figure 3 presents a SWOT analysis summarizing these barriers, categorizing them as weaknesses and threats while identifying opportunities for improvement through international best practices and stronger political support.

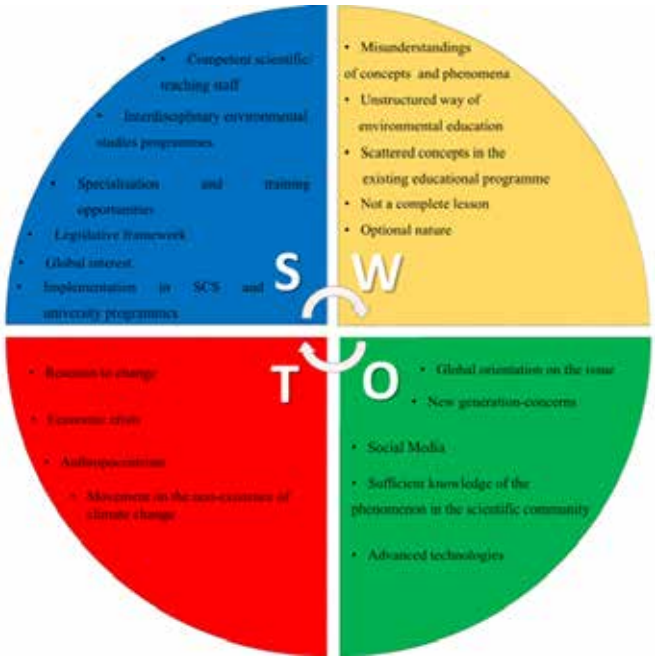

Figure 3. SWOT analysis of environmental education for climate change in Greek Compulsory Education (Figure from Moshou & Drinia, 2025)

Strategic Guidelines for the Effective Integration of Climate Change Education in Greece

The integration of climate change education (CCE) into Greece's educational framework demands a well-structured approach addressing existing challenges. Based on a thorough analysis, including literature reviews, SWOT, and PEST analyses (Moshou & Drinia, 2023; 2025), the following strategic framework is proposed to enhance CCE in Greece:

- Mandatory Environmental Education. CCE must be incorporated as a compulsory subject at all levels of education, ensuring that all students acquire essential knowledge about the environment and climate change. The purpose of this initiative is to provide both theoretical and practical knowledge for reducing environmental risks in the short term and to strengthen students' connection with nature, fostering a lasting environmental consciousness, as well as addressing the main goal of mitigating and adapting to climate crisis.
- Cross-Disciplinary Integration. Given the multidimensional nature of climate change, its integration across various school subjects can promote a holistic understanding of its impact on different aspects of daily life, such as health, the economy, and social equity (Damoah, 2023). While embedding climate change education into existing subjects can be beneficial, it should complement, rather than replace, a distinct compulsory course on environmental education (Moshou & Drinia, 2025). Moreover, it is proposed the inclusion of geoconservation as a key topic within cross-disciplinary education, linking geology, geography, and environmental science to highlight the significance of preserving geosites and their role in understanding climate change.
- Teaching by Specialized Educators. Environmental education, particularly on complex topics like climate change, should be taught by educators with specialized environmental scientists with pedagogical competence. These professionals possess the interdisciplinary knowledge needed to convey accurate information and minimize misconceptions (Moshou & Drinia, 2023).
- Comprehensive Teacher Training. Specialized training programs for teachers are essential to equip them with the necessary knowledge and skills to teach environmental education effectively. Continuous professional development, even for specialized educators, is equally critical to keep pace with the latest scientific developments and pedagogical practices.
- Collaboration with Key Stakeholders. Strengthening collaboration between schools, universities, and local communities is vital for developing innovative educational programs. Partnerships with research institutions can facilitate the design of advanced curricula and educational tools, fostering a culture of environmental responsibility. The collaboration with geologists, conservationists, and UNESCO Global Geoparks to create programs that promote geoconservation and its connection to climate change education aims to foster a deeper

understanding of how geological heritage can play a crucial role in mitigating and adapting to climate change, while also raising awareness about the sustainable management and protection of these invaluable resources for future generations.

- Reducing Psychological Distance. CCE must address the psychological distance that prevents students from relating to climate change. Incorporating local issues and tangible examples into the curriculum can bridge this gap, making the topic relevant and engaging. Emotional and personal connections can motivate students to participate in advocacy and sustainability initiatives actively.
- Utilizing Technology. Technology can play a pivotal role in enhancing environmental education. Digital platforms, interactive applications, and multimedia learning tools can make learning more engaging and effective for students (Nantsopoulos & Mogias, 2020). Moreover, the use of simulations can help reduce psychological distance, allowing learners to better grasp complex environmental issues by visualizing potential outcomes and real-world scenarios.
- Policy Recommendations and Curriculum Policymakers should collaborate with universities and research centers to revise educational frameworks. A clear national framework must outline goals, objectives, and action plans for integrating CCE, alongside timelines and regular program evaluations. The incorporation of geoconservation into national educational policies as a framework to protect geological heritage while enhancing students' understanding of climate and environmental challenges seeks to empower future generations with the knowledge and skills needed to address pressing global issues. By integrating geoconservation into curricula, students can develop a greater appreciation for the role of Earth sciences in tackling climate change and promoting sustainable environmental practices.
- Developing a National Strategy for Climate Change Education. A comprehensive national strategy should be created, taking into account Greece's international obligations and promoting a holistic approach to understanding the climate crisis. This strategy should aim to elevate environmental education as a core component of the educational system, fostering both knowledge acquisition and behavioural change towards sustainability.

Conclusion

Environmental education for climate change is one of the most essential pillars for shaping responsible citizens and fostering a sustainable society. Despite the challenges, integrating environmental education into greek educational system can play a decisive role in developing active and responsible citizens who will be equipped to face and adapt to future environmental challenges.

Developing a cohesive strategy, investing in well-trained educators, and enhancing appropriate teaching methods are key priorities for advancing environmental education. Only through coordinated actions and collaborations can we hope for a sustainable future for the next generations.

Emphasizing sustainable development, cultivating critical thinking, and encouraging active student participation are crucial for achieving this goal. Greece has the potential to become a model country in climate change education if it invests in the appropriate resources and strategies.

Moreover, integrating geoconservation into climate change education not only protects our geological heritage but also provides students with tangible examples of climate change's impact over time, fostering a deeper connection to Earth's history and its future.

Acknowledgements

References

Boyes, E., Stanisstreet, M., 1993. The "greenhouse effect": Children's perceptions of causes, consequences and cures. International Journal of Science Education 15, 531–552.

Damoah, B., 2023. Reimagining climate change education as a panacea to climate emergencies. International Journal of Environmental, Sustainability & Social Science 4, 977–987.

Daskolia, M., 2023. The climate crisis as a "wicked" problem and a learning subject: Theoretical, research, and teaching insights with a focus on education for climate change. Environmental Education for Sustainability 5, 48–65.

EIB (European Investment Bank)

Farangitakis, G., Sbarounis, Th., 2020. SWOT analysis of education for environmental citizenship — Country report: Greece, in: Hadjichambis, A.Ch., Reeis, P., Paraskeva-Hadjichambi, D. (Eds.), European SWOT analysis on education for environmental citizenship. European Network for Environmental Citizenship (ENEC) COST Action Report, 137–148.

Georgousis, E., Savelides, S., Mosios, S., Holokolos, M.-V., & Drinia, H., 2021. The Need for Geoethical Awareness: The Importance of Geoenvironmental Education in Geoheritage Understanding in the Case of Meteora Geomorphes, Greece. Sustainability, 13(12), 6626.

Lester, B.T., Ma, L., Lee, O., Lambert, J., 2006. Social activism in elementary science education: A science, technology, and society approach to teach global warming. International Journal of Science Education 28, 315–339.

Moshou, H., Drinia, H., 2023. Climate Change Education and Preparedness of Future Teachers—A Review: The Case of Greece. Sustainability 15, 1177.

Moshou, H., Drinia, H., 2025. Strategic Insights for Environmental Education in Greece: SWOT & PEST Analyses in the Context of the Climate Change Crisis. Sustainability 17, 2633.

Nantsopoulos, M., Mogias, A., 2020. Climate change and the role of education: The case of environmental study textbooks in primary education. Environmental Education for Sustainability 2, 1–15.

17th INTERNATIONAL CONGRESS of the Geological Society of Greece

BULLETIN OF THE GEOLOGICAL SOCIETY OF GREECE, SP. PUBL.

EXTENDED ABSTRACT 219

Slope stability rehabilitation in the traditional settlement of Chora, Andros Island, Greece

Mourtzas N.[1], Gkiolas A.[2], Papacharalambous G.[2], Tsakonas A[2]., Kolaiti E.[3]

(1) Society for the Study of Ancient Coastlines - AKTES NPO; University of Nottingham, Department of Classics and Archaeology, Kefallinias 18, 15231 Chalandri, Athens, Greece, nikosmourtzas@gmail.com (2) ATENEIA Geotechnical Consultants Private Technical Company (ATENEIA P.C.), Athens, Greece (3) Society for the Study of Ancient Coastlines - AKTES NPO; National Hellenic Research Foundation, Institute of Historical Research; University of Nottingham, Department of Classics and Archaeology, Chalandri, Athens, Greece

Research Highlights

Engineering geological and geotechnical design for slope stability to ensure the long-term protection of the overlying buildings and footpath along a coastal slope in a traditional settlement in the Cyclades, including design implementation, rehabilitation works, and aesthetic interventions.

Introduction - Project area

The failed slope is located in the traditional settlement of Chora on Andros Island, on the northern side of the Chora peninsula, along the southern coast of Nimporio Bay, in the Plakoura area, and approximately 75m southwest of the church of Agia Thalassini. It extends from an elevation of between +2.60m and +3.80m at the slope toe to between +16.80m and +17.40m at the crest, with an average height of 15m. The sickle-shaped slope features a 30m-long arch and a corresponding 25m-long chord, trending NE-SW with a plunge of 85° towards the NW (Fig. 1).

Figure 1. Satellite images of the project area (Google Earth Pro, v. 7.3.4., accessed on 3 October 2021). The yellow outline indicates the location of the failed slope.

Description of the failure

In March 2021, a large volume of rock detached from the central part of the slope, between elevations +9.50m and +14.70m. This event created unsafe conditions for the buildings immediately above the slope's crest and posed a risk of accidents in case of additional rockfalls along the footpath, which runs close to the slope's base. The failed area, measuring approximately 30m^2, is located in the central part of the slope. The failure occurred along a weakness zone in the schist formation, resulting in an 8m-wide, 5m-high and approximately 3m-deep caving (Fig. 2). Moreover, three older, smaller-scale slides, ranging in size from 2m^2 to 4.5m^2, are observed in the central part of the slope at lower elevations, between +4m and +7m (Fig. 2).

Figure 2. General view of the failed slope, the overlying buildings along the slope crest, and the footpath along the slope toe. The location of the failure is indicated by a red outline.

Geology of the landslide area

The slope consists of mica schists (Mehl *et al.*, 2007; Höhn *et al.*, 2022) that are moderately, and in some zones, intensely tectonized. Tectonization of the rock occurred due to four major inverse shear zones (R1, R2, R3, and R4), as well as additional zones parallel to these (R5, R6, and R7), which can be observed on the adjacent property slope (Fig. 3A, 3B). The shear zones extend for several meters, trending NW with plunges ranging from 15° to 25°, and are associated with a compressive tectonic regime, oriented NE-SW. The four major shear zones divide the slope area into five zones, one of which is where the recent slide occurred, while smaller failures have occurred in the other zones in the past.

To investigate the stability conditions, engineering geological characteristics, and properties of the rock mass along the slope, a comprehensive microtectonic analysis was conducted in order to form a complete picture of the tectonism of the rock mass (Fig. 3C). Subsequently, to examine the tectonism of the individual sections of the slope, it was divided into eight sub-sectors: two sectors at the NE end (sectors A and B), one at the SW end (sector H), and five sectors between the faults with a slope direction parallel to that of the slope (sectors C, D, E, F, G, and H). In each sector, a microtectonic analysis was performed (using the software DIPS, v. 5.1, Rocscience) to assess the stability and support of the rock mass (Hoek and Bray, 1981; ISRM Suggested Methods, 1981) (Fig. 3C).

The schistosity is well-developed, showing dips towards the SW in the NE part of the slope, towards the SE to SSW in the central part, and towards the SW to WSW in the SW part, with dips ranging from 15° to 30°. The general dip of the schistosity is oriented towards the SW, with an average dip of 20° (Fig. 3A, 3B). The main joint systems crossing the slope are two: one trending NE-SW with dips towards the NE, and the other trending NNE-SSW with dips towards the ENE. A third, less frequent joint system, with a dip direction parallel to the slope, trends ENE-WSW and dips towards the NNE (Fig. 3A, 3B).

Stability analyses of the slope against wedge and planar failure were conducted (using the software Swedge, v. 5.01 for wedge failures and RocPlane, v. 2.029 for plane failures, Rocscience), based on conservative assumptions (Norrish and Wyllie, 1996; Wyllie and Mah, 2004). Discontinuities were considered planar and of infinite length. The length of the slope was assumed to be L=20m and the rock mass unit weight was taken as γ=26 kN/m^3. Regarding the angle of internal friction, taking into account the characteristics of the schist formation, the condition of discontinuities, and based on literature, a range of values from 25° to 30° was considered (Wyllie and Norrish, 1996). The minimum value of 25° was conservatively selected for the analyses. Regarding cohesion, a value of zero was conservatively assumed, considering the possibility of infilling material being washed out due to groundwater circulation. Analyses were performed for static loading, static loading with hydrostatic pressure on the discontinuities for a 50-year return period (even though a permanent water table was not encountered), assuming partial filling of the discontinuities with water for short periods following intense rainfall, in cases where infiltrating water does not dissipate quickly to lower elevations, and seismic loading.

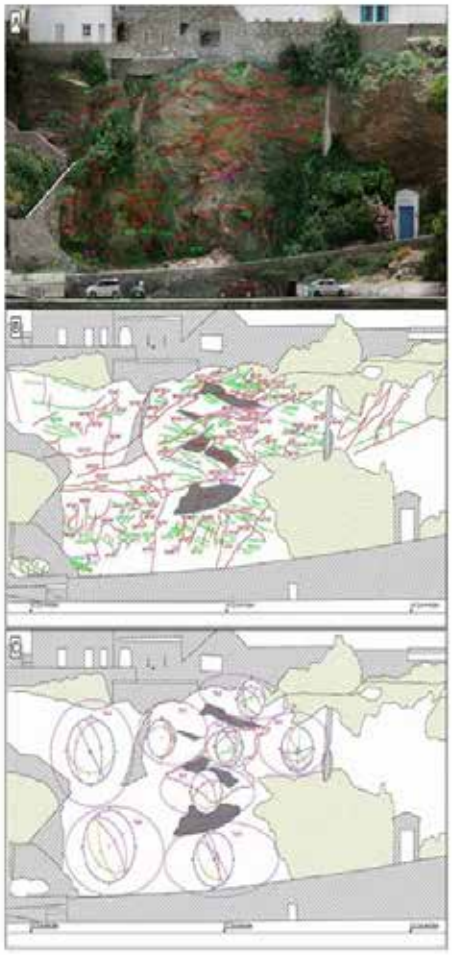

Figure 3. (A, B): View and front view of the failed slope, indicating joints (red lines), schist planes (green lines) and their geometric features. (C): Stereonets of the eight sub-sectors into which the slope was divided. The grey areas in 3B and 3C indicate the locations of recent and older failures.

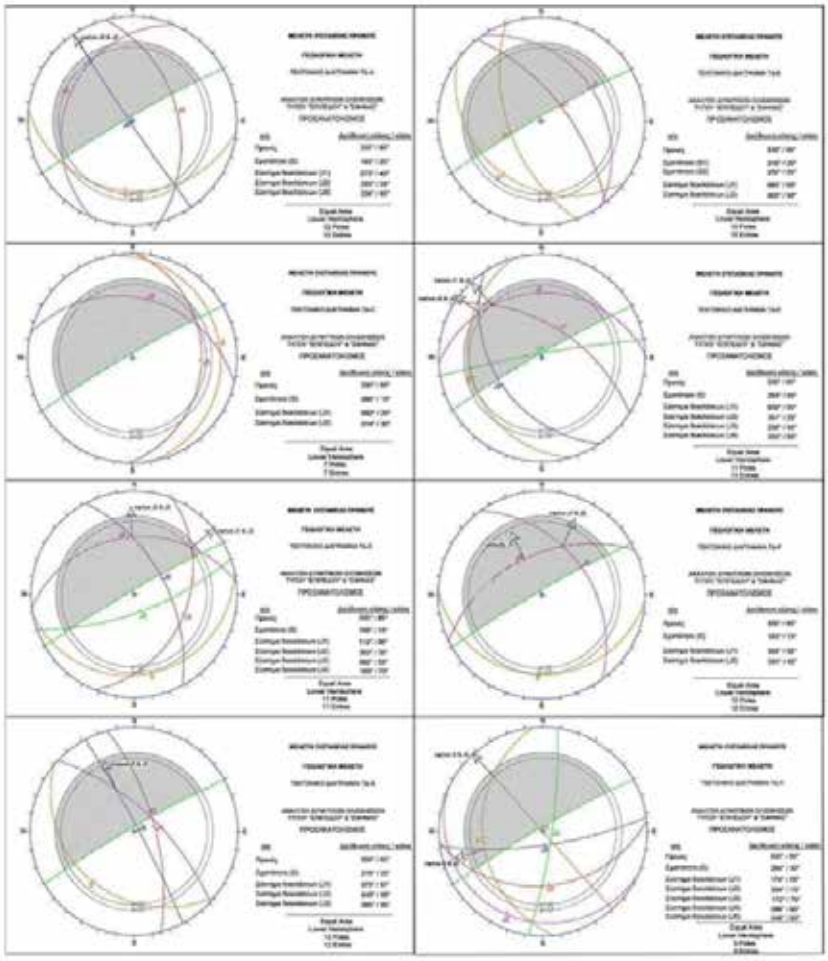

Figure 4. Stereonets of the eight sub-sectors into which the slope was divided. Sliding Kinematic Analysis

Based on the results of the analysis of wedge failure for the overall discontinuity stereonet, as well as for the stereonets of the individual zones of the slope (TΔ-A to TΔ-H, Fig. 3C, Fig. 4), it is inferred that achieving slope stability requires the application of 6m-long rock bolts in a 3m x 3m (v:h) pattern. Furthermore, based on the results of the analysis against planar failure, it is concluded that stabilize the upper six meters of the slope, where planar failures may occur, 6m-long rock bolts in a 2m x 2m (v:h) pattern are needed.

Therefore, from the results of both wedge and planar failures analyses, a rock bolt pattern of 2m x 2m (v:h) was selected for the upper part of the slope, above elevation +9.80m (the higher six meters), and a 2m x 2.50m (v:h) pattern for the lower part of the slope. A rock bolt length of L=6m was chosen for both areas to ensure sufficient anchoring depth (Fig. 5).

Rehabilitation of the slide area

In order to ensure the stability of the slope and provide long-term protection of the rock mass against wedge and planar failure, erosion induced from water runoff, coastal erosion due to the slope's proximity to the sea, and its continuous exposure to wind and waves, as well as to rehabilitate the caving and overall geometry of the slope from both recent and older failures, the most efficient and aesthetically acceptable rehabilitation scheme comprises the combination of rock bolts, shotcrete, and wire mesh across the entire slope surface. The proposed shotcrete coverage aims to provide long-term protection of the rock mass against both surface and in-depth erosion of schist,

while also rehabilitating the slope geometry in areas of failure (recent and older), where cavings and locally negative slope gradients develop. Furthermore, shotcrete in combination with steel wire mesh effectively retain smaller-scale structural failures that may occur between the rock bolts (Fig. 5).

Figure 5. Front view of the slope showing the support and protection measures.

Specifically, the construction of seven rows of rock bolts was proposed for the section of the slope between cross-sections S3 and S12, and six rows for the section beyond cross-section S12 (Fig. 5, 6). In all rows, a horizontal distance of 2m between consecutive bolts is foreseen. The rock bolts are fully grouted steel bars, 24mm or 25mm in diameter, made of S650 steel (for □24mm) or S500 steel (for □ 25mm), with nominal tensile capacity of 200kN, 6m in length, and installed with a downward inclination of 15°. The drillhole diameter for the rock bolts was proposed at least 100mm. Continuous threaded steel bars will be used to ensure good bonding with the grout and also to allow easy screwing of the nut and cutting of any possibly protruding parts of the bars. Additionally, given the proximity of the slope to the sea, all steel bars and relevant materials (e.g. nuts, rock bolt plates) will be hot-dip galvanized to ensure resistance to corrosion.

For the environmental integration of shotcrete, appropriate pigments will be used during mixing, based on relevant in-situ test, to match the natural color of the slope's rock mass. A minimum structural thickness of 10cm of shotcrete was proposed, applied in two layers of 5cm each, with one layer of steel wire mesh placed between them.

In areas of the slope where relatively deep cavings have occurred, consecutive layers of shotcrete will be applied, with additional layers of steel wire mesh installed every 20-30cm of shotcrete thickness. For the first layer of steel wire mesh, to be installed on top of the first five centimeters of shotcrete across the entire slope, T131 wire mesh will be used to provide enough flexibility to conform to the rough slope surface. In areas with extensive and/or deep cavings, the wire mesh layers in between the shotcrete layers will be made of T188 type wire mesh and steel grade B500C. For fixing the additional steel wire mesh layers, bolts consisting of □16mm or □18mm solid steel bars will be used, arranged in an appropriate configuration.

To prevent pore pressure build-up behind the shotcrete facing, drilling of three rows of weep holes (water pressure relief holes), was proposed, each with a diameter of 3'' and ranging from 0.50m to 1.50m in length, depending on the local thickness of the applied shotcrete, and spaced every 2m horizontally. Specifically, the lower row of weep holes was proposed at approximately elevation +7.80m, the second row at +9.80m and the upper row at +13.80m. In addition to the weep holes, two rows of raking drains, transverse to the slope, were proposed, spaced every 2m horizontally. The raking drains will have a diameter of 3'', a length of 6m, and a slight upward inclination of 5° to relieve water pressure in case of a seasonal groundwater table. Inside the raking drains drillholes, □2'' perforated PVC tubes will be installed, coated with separation geotextile to prevent clogging by fines from the surrounding eroding schist rock mass. The lower row of raking drains was proposed at approximately elevation +11.80m (Fig. 6).

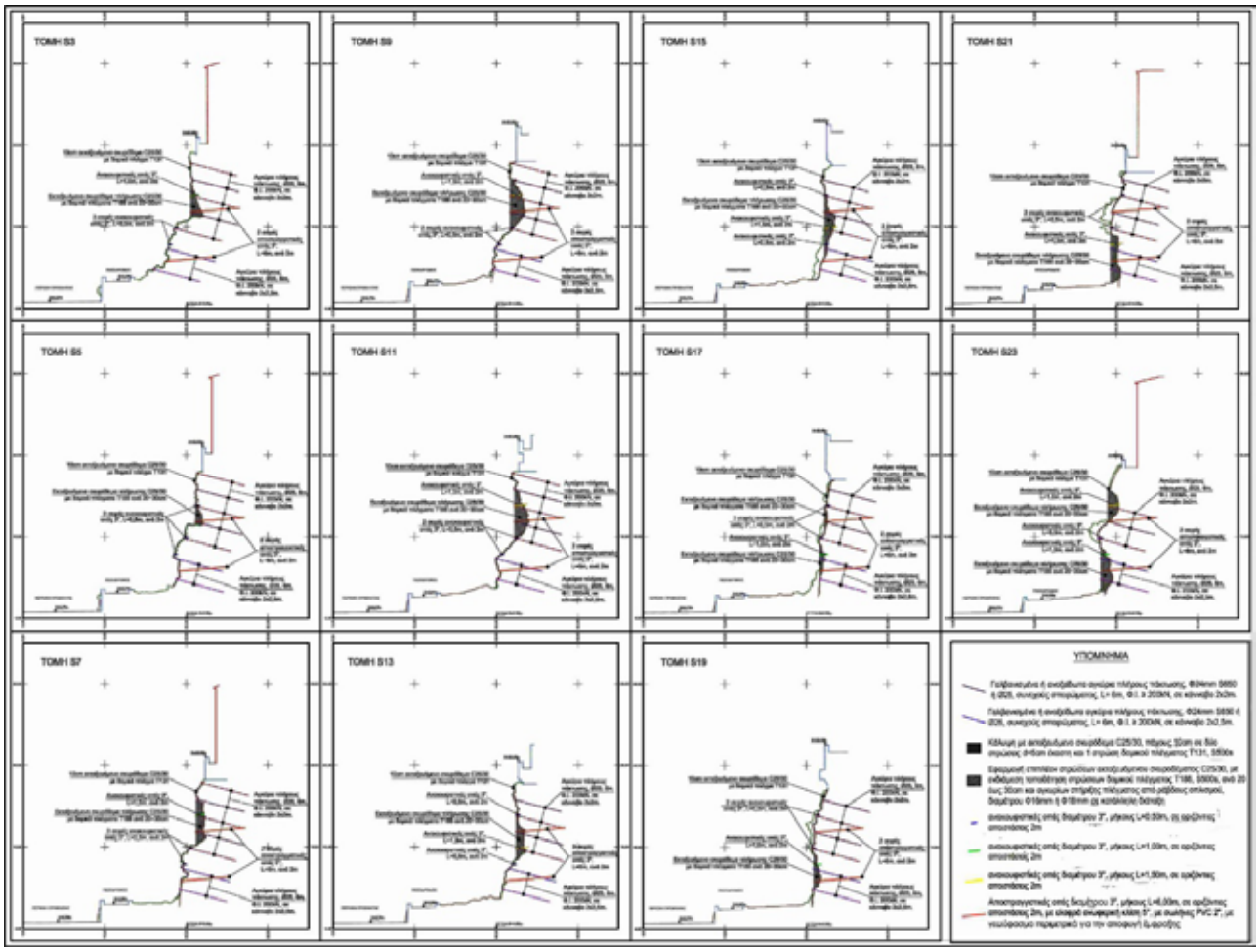

Figure 6. Cross-sections of the failed slope showing the support and protection measures.

Design Implementation

Stabilization and rehabilitation works on the rock slope began in October 2023, following the end of the summer tourist season, to minimize disruption and inconvenience to the visitors of the Agia Thalassini church and those visiting the Andros Chora Castle area, on the northern side of the Chora peninsula (Fig. 7).

Figure 7. Views of the slope after the application of the support and protection measures, before (left) and after (right) the final aesthetic interventions.

Special attention was given to shaping the final slope surface to closely resemble its condition prior to the rehabilitation works, with aesthetic interventions made in consideration of the features of the traditional settlement. Therefore, the shotcrete layers followed the natural slope surface, in accordance with the approved design. Final coloring of the

slope was carried out after the winter of 2024, allowing time for precipitation, sea spray from waves, intense winds, and storms in the area, as well as water seepage (both groundwater and surface water), to naturally balance the color of the shotcrete, which had been already pigmented during shotcreting. An aesthetic intervention followed, involving planting at the slope toe and the reconstruction of the low wall on the footpath side, which was damaged by the slide (Fig. 7).

References

Hoek, E., Bray, J.W., 1981. Rock Slope Engineering, Revised 3rd ed. Institution of Mining and Metallurgy, London.
Höhn, M., Bröcker, M., Berndt, J., 2022. The Jurassic meta-ophiolitic rocks of Cape Steno, Andros, Greece: a high-pressure/low-temperature mélange with Pelagonian affinity in the Cycladic Blueschist Unit? International Journal of Earth Sciences 111, 949-968.
ISRM Suggested Methods, 1981. Rock Characterization Testing & Monitoring, E.T. Brown (ed.), Pergamon Press.
Mehl, C., Jolivet, L., Lacombe, O., Labrousse, L., Rimmele, G., 2007. Structural evolution of Andros (Cyclades, Greece): a key to the behaviour of a (flat) detachment within an extending continental crust, in: Taymaz, T., Yilmaz, Y., Dilek, Y. (Eds), The Geodynamics of the Aegean and Anatolia. Geological Society, London, Special Publications, 291, 41-73.
Norrish, N.I., Wyllie, D.C., 1996. Rock slope stability analysis. in: Turner, A.K., Schuster, R.L. (Eds), Landslides: Investigation and Mitigation, Transportation Research Board, Special Report 247, 391-425.
Wyllie D.C., Norrish N.I., 1996. Rock Strength Properties and their Measurement, in: Turner, A.K., Schuster, R.L. (Eds), Landslides: Investigation and Mitigation, Transportation Research Board, Special Report 247, 372-390.
Wyllie, D.C., Mah, C.W., 2004. Rock Slope Engineering – Civil and Mining, 4th ed. Spon Press.

17th INTERNATIONAL CONGRESS of the Geological Society of Greece

BULLETIN OF THE GEOLOGICAL SOCIETY OF GREECE, SP. PUBL.

EXTENDED ABSTRACT 220

The Horizontal-to-Vertical Spectral Ratio Method for Underground Voids Detection: Testing Over Mycenaean Tombs

Moustakas H. I.[1], Roumelioti Z.[1], Sokos E.[1], Evangelidis Ch.[2]

(1) Department of Geology, University of Patras, Patras, Greece, up1060600@upnet.gr (2) Institute of Geodynamics, National Observatory of Athens, Athens, Greece

Abstract

This study investigates the potential of the Horizontal-to-Vertical (H/V) spectral ratio method, a technique typically used for site characterization, as a complementary tool for detecting underground voids. We leverage ambient noise measurements conducted at the Mycenaean cemetery of Voudeni, Peloponnese, Greece, utilizing the site's numerous underground tombs as test targets. We analyzed the H/V spectral amplitudes above the centers of various sized tombs and the spatial variation of horizontal and vertical spectral amplitudes and of their ratio along trial linear arrays. We verify the suggestion of previous research that over voids the H/V curve shows a characteristic drop below unity at high frequencies (in our test cases, typically >20Hz), which remains below unity for a considerable frequency interval. This phenomenon is attributed to a velocity reversal caused by the void within the surrounding rock. We attempt a first-order comparison of the void size and frequency of initiation of the characteristic drop and conclude that larger subsurface voids tend to affect the H/V curve at lower frequencies compared to smaller voids, exhibiting an exponential relationship. We also observe that the H/V drop over our test voids is primarily driven by the amplification of the vertical component rather than de-amplification of the horizontal component and this suggests that using linear arrays of vertical component geophones alone could be effective for void detection, particularly as a complement to other geophysical methods. We demonstrate this possibility through trial linear arrays of vertical sensors. We conclude that the H/V method and linear arrays of vertical sensors hinder promising advancements as void detection techniques, especially considering their readily deployable and cost-effective character, although theoretical modeling and extensive testing in various geological settings and void characteristics are required to better understand the observed phenomena.

Background and Objective

The Horizontal to Vertical Spectral Ratio (H/V or HVSR) method (Nogoshi and Igarashi, 1971; Nakamura, 1989) involves the analysis of earthquakes or microtremor (ambient noise) records to compute the ratio of the spectral amplitudes of the horizontal components to the vertical component. It was originally proposed as a method to calculate the local amplification and resonance frequency resulting from sedimentary layers overlying the bedrock. For the simplified case of a viscoelastic sedimentary soil layer of thickness h and shear wave velocity Vs, over a viscoelastic bedrock, the resonance frequency f_n is calculated by the formula:

$$f_n = (2n+1)\frac{V_s}{4h}, (n = 0,1,2,\dots)$$

Empirical data have shown that the lowest frequency at which the maximum value of the H/V curve is observed at a site, is identical or very close to the resonance frequency, f_0, of the soil by shear waves SH. In addition to f_0, the method can provide information on the thickness of the soil over bedrock, the presence of high density layers, lateral discontinuities of the subsoil layers from variations of the curves at different locations and velocity reversals (e.g. from natural or artificial hard layer over softer soil) (e.g., Field and Jacob 1993; Lermo and Chávez-García 1994a; Bonilla et al. 1997; Bour et al. 1998; Bard 1998; Fäh et al. 2001; Woolery and Street 2002; Molnar and Cassidy 2006; Haghshenas et al. 2008).

As the popularity of the H/V method increases, several aspects of its practical application are being examined in more detail. One such aspect involves the performance of the method at sites where there is a strong velocity reversal very close to the ground surface. This situation often arises when measurements are collected on top of concrete slabs, asphalt, etc, as discussed in detail in Castellaro and Mulargia (2009). A special case falling under this category is the presence of underground voids close to the surface, either natural or man-made (e.g., cellars, underground parking spaces). Castellaro and Mulargia (2009) present H/V curves for several example cases and discuss that under the absence of shallow velocity reversals, the common plot of the spectra of the horizontal and vertical components presents a characteristic oval shape around f_0, what the authors describe as 'eye shape'. According to the same study, the appearance of this feature suggests that the H/V peak is of stratigraphic origin. Also, when there are no velocity reversals the vertical component remains less than or equal to the horizontal component at all frequencies, hence H/V≥ 1, except for a small range near $2\times f_0$ where it can drop below unity due to the elliptic motion of Rayleigh waves (Fäh et al., 2001). In contrast, if the amplitudes of the H/V curve fall below 1 in regions distant from $2\times f_0$ and remain below 1 for a considerable range of frequencies, this may be evidence for a velocity reversal.

In this work, we further investigate the suggestion of Castellaro and Mulargia (2009) that the H/V curve over voids is expected to show characteristic drops below unity. More generally, we examine the working hypothesis that the method could be useful, at least as a complementary method, in the detection of underground voids. For this purpose, we have chosen as test site the Mycenaean cemetery of Voudeni in the Peloponnese, ~4 km east-northeast of the city of Patras. The archaeological site contains

numerous underground tombs that the Mycenaeans constructed more than 3000 years ago by carving into the soft rock (marl) of the area. Many tombs of different sizes and depths have been excavated and their geometry has been studied in detail by Turner (2020), making them ideal targets for our study.

Our study included three phases of ambient noise data collection and processing, which will be presented sequentially in the following. Data collection was conducted during daylight hours and when the archaeological site was not in operation to minimize nearby anthropogenic noise.

Three-Component Single-Point Ambient Noise Measurements Over Voids of Various Dimensions

In the first phase of our study, we performed single-point H/V measurements over several tombs of different dimensions targeting to 1) identify a characteristic imprint of voids on the shape of the H/V curves, as suggested by previous researchers, and 2) identify a possible correlation between the dimensions of the voids on the characteristics of this imprint. Data were collected using a Geometrics Atom-3C seismic acquisition unit with a 2Hz, three-component (3C) geophone and sampling rate of 4 ms (Nyquist frequency of 125 Hz). The sensor was placed over the centers of several ancient burial chambers, i.e. our target underground cavities, it was oriented to the North and was left to record ambient noise for at least 15 minutes. Since all targets are located at shallow depths (<1m to a maximum of 7-8m), longer recordings were not considered necessary.

Figure 1 shows an example measurement setting. The upper part of the Figure contains the plan view of a measured tomb (a; circled in red) and the side view of its detailed reconstruction (b; wireframe from photogrammetry) by Turner (2020). The lower part of Figure 1 (c-d) contains photographs of the tomb. In general, Mycenaean tombs include an entrance passage or “dromos”, a threshold or “stomion”, and the burial chamber/vault or “thalamos”. The facets of excavated tombs extend from the stomion floor to the ground, and we used them as reference planes to measure the distance to the center of the void chamber, first underground and then on the ground surface.

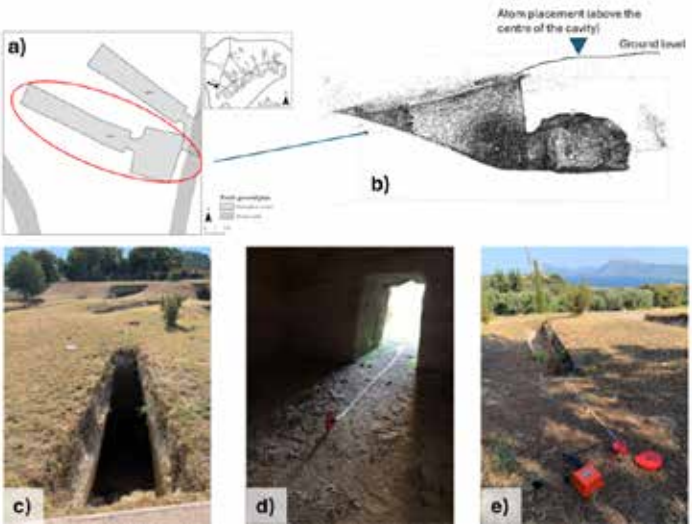

Figure 1. Example measurement setting: a) tomb (circled in red) ground plan and b) side view of its textured photogrammetric model by Turner (2020), c) photograph of the entrance pathway (dromos), d) photograph from the inside of the tomb (thalamos) looking at the stomion and e) photograph of the Atom-3C on the ground surface, over the void chamber.

Although our test site includes 78 excavated burial monuments, we were only able to measure 24, mostly because many chamber tops collapsed over the years or access to their tops was dangerous. Some geometric characteristics of these tombs, as provided by Turner (2020), are summarized in Table 1. The difference between the height of the dromos and the height of the vault is often a good proxy for the depth of the vault top.

The collected data were processed using using SPACPlus module of the SeisImager-sw software from Geometrics Inc. (https://www.geometrics.com/software/seisimager-sw/). Ambient noise time histories were trimmed at the beginning and end of each measurement to remove noise during instrument installation and removal. The common recording for the three components was then divided into segments of 512 samples, i.e. ~ 2 s duration, with an overlap of 50%. Fourier amplitude spectra were computed for each component and each recording segment, and the horizontal component spectra were geometrically averaged. Finally, the H/V ratio was computed for each segment and the results were visually inspected (both in terms of H/V curve shape and directly on the ambient noise records) to remove irregularly noisy segments and spectra. The remaining measurements were used to derive the mean H/V curve for each measured location.

Table 1. Geometric characteristics of the 24 Mycenaean tombs (after Turner, 2020, except those with * vault volume measured in the frame of this study) over which we performed ambient noise measurements.

Tomb Code	Vault Volume (m^3)	Dromos Height (m)	Vault Length (m)	Vault Width (m)	Vault Heigh (m)	Tomb Code	Vault Volume (m^3)	Dromos Height (m)	Vault Length (m)	Vault Width (m)	Vault Heigh (m)
01	20.63	2.33	2.47	2.94	2.05	34	32.9	3.16	3.16	3.09	2.33
02	17.42	2.36	2.2	4.04	1.83	42	18.7	2.11	2.48	2.66	1.71
06	16.98	2.24	2.16	2.51	1.76	43*	13.1	-	2.8	2.6	2.5
07	47.03	3.47	3.21	1.11	1.14	53	65.5	4.34	3.57	3.71	2.79
08	21.9	2.84	2.79	2.73	1.79	54	81.4	5.09	3.15	4.55	2.87
09	27.3	2.71	3.01	2.96	2.4	55	-	3.89	-	-	-
16	11.14	2.37	1.96	2.82	1.36	60	18.9	2.61	2.69	2.62	1.96
22	42.6	4.5	3.37	3.36	2.91	64	40	2.85	3.25	3.27	2.41
23*	20.4	-	2.3	2.3	1.8	71	28.3	3.64	3.18	3.15	2.7
25	126.3	4.29	4.79	3.9	4.09	72	17.11	2.92	2.63	2.71	2.21
28	13.49	2.21	2.39	2.65	1.96	75	257	6.6	5.08	7.6	4.57
29	82.1	3.93	3.66	4.7	3.29	78	106	5.47	3.8	4.58	3.23

Figure 2a shows an example output for the measurement over tomb 78 (Table 1). In the upper part of Figure 2a, the horizontal and vertical component spectra are compared, and it is clearly seen that, for a significantly wide range of frequencies (~22-38Hz), the vertical spectral amplitudes are larger than the horizontal, i.e., opposite to what is usually expected. This results in a drop of the H/V curve in the corresponding frequency range, as shown in the lower part of Figure 2a. The H/V returns to amplitude >1 at frequencies ~>35Hz.

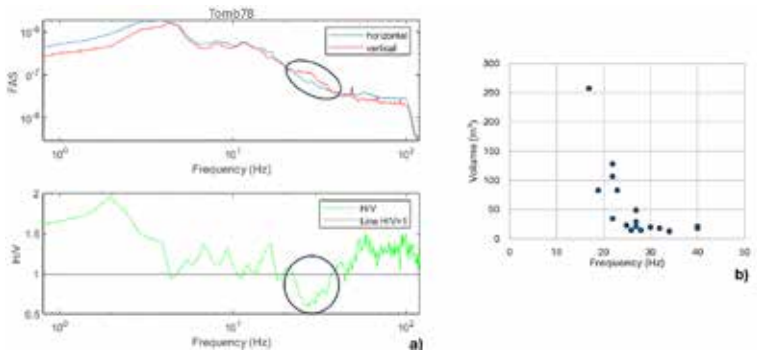

Figure 2. a) Example results of the H/V analysis of data over tomb 78. Upper part: Fourier amplitude spectra (FAS) of the horizontal and vertical components (in blue and red, respectively). The circled area is where the vertical component spectral amplitudes appear larger than the horizontal. Lower part: H/V spectral ratio. The circle marks the characteristic drop of the H/V ratio below unity, at high frequencies and for a significantly wide range. b) Underground void volume (in m^3) with respect to f_{DL} the frequency of initiation of the persistent H/V drop below 1Hz.

We define f_{DL} as the frequency above which we observe a sustained drop in H/V amplitude below 1, and we examined whether this discrete frequency is related to the volume of the underground void. The corresponding plot is shown in Figure 2b and implies an exponential relationship between the compared quantities, i.e. as the void volume increases, the frequency where H/V first drops below 1, in a clear and systematic manner, shifts to lower frequencies. This suggests that larger subsurface voids, at least at the shallow depths investigated here, affect the H/V curve at lower frequencies compared to smaller voids. However, this relationship appears to saturate (flattens) as void volumes become smaller (~<20-30m^3). A similar examination with respect to the depth of the tomb ceilings did not provide evidence for a clear relation, most probably because most ceilings are at very shallow depths of 0.5-1.5m and their geometry varies.

Three-Component Linear Array Ambient Noise Measurements Over a Large Void

One question raised by the previous measurements is how the persistent H/V drop varies spatially, and whether an underground void can be detected even if the ambient noise measurement is not taken directly over its center. Therefore, in the second part of our study, we collected data along a line over one example tomb to investigate, to some extent, the spatial variability of the shape of the H/V curve over a void. The test was conducted on tomb 75, which is the largest of the tombs examined in terms of volume (Table 1). The measurements were made in a linear arrangement across the center of the tomb. The total number of measuring

points was 13, with 2 m between successive measurements. The first was placed 6 m from the north side of the chamber and the last 10 m from the south side (Figure 3a, b).
Examples of results for two of the 13 sites are shown in Figure 3c, d. Specifically, results are shown for location S6, just above the center of the tomb (Figure 3c), and for S12, 5-6 m south of the tomb (Figure 3d). Focusing on the high frequency part of the results, the differences are quite pronounced with a very wide H/V drop below unity at S6 and a flat H/V curve around 1 at S12. Looking at the corresponding results for all 13 sites (not all are shown for reasons of space), the drop of the H/V curve below 1 clearly occurs at sites S4, S5, S6, S7, and S8 (Figure 3b), while at the remaining sites either no drop below 1 or drops within quite short ranges are observed.

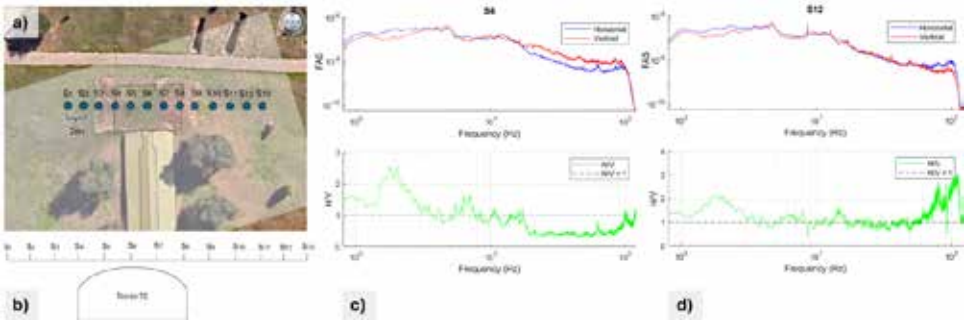

Figure 3. Linear array of 3C measurement points over one of the largest tombs (codenamed 75) in the Mycenaean Park of Voudeni a) in plan view and b) in cross section (depth and volume not to scale); c) Results for the example locations S6 right over the tomb and d) for S12, several meters to the south of the tomb. Top panels in c, d show the Fourier amplitude spectra of the horizontal and the vertical components and bottom panels the H/V curves.

From plots such as those in Figure 3c, d, it is difficult to understand the spatial variability of the results and even more difficult to understand whether the H/V drop is mostly due to de-amplification of the horizontal signal or amplification of the vertical signal. To better demonstrate the spatial variability of our results, we created spectrogram-like plot, but instead of time in the horizontal axis, we plotted the distance of each spectrum or H/V curve from S1. This creates a pseudo-2d spatial variation, which we show in Figure 4 in separate subplots for the amplitudes of the horizontal and vertical Fourier spectra and the H/V curve. The subplots for the horizontal and vertical components (Figure 4a, b) have the same color scale and are directly comparable. Note that since the horizontal axis shows the distance from S1, the measurements directly above the tomb are in the range of 6-14 m. This exact range is clearly colored differently in the H/V subplot (cool colors, mostly <1), starting from frequencies close to 20 Hz and continuing to much higher frequencies. This means that the changes in the wavefield due to the underground void are clearly imprinted on the spatial variability of the H/V amplitudes at high frequencies over the entire structure and not just over its center. In fact, the lateral extent of the structure is well captured in this subplot. By examining the individual component plots, we conclude that the H/V variation is mostly due to a corresponding spatial variation in the vertical component amplitudes (circled areas in Figure 4b). This means that the H/V drop over the studied underground void is mostly due to an increase of the vertical component amplitudes at high frequencies rather than a decrease of the horizontal component spectral amplitudes in the same range.

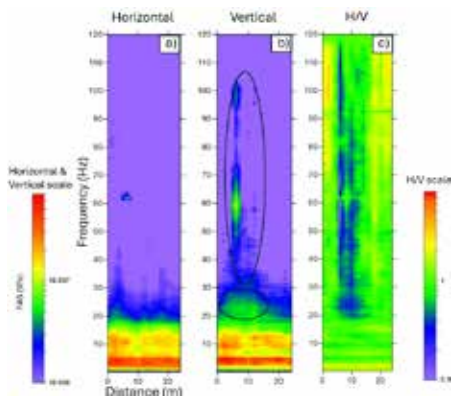

Figure 4. Pseudo-2D plot of results (spectral amplitudes or amplitude ratio vs distance from the starting measurement in the linear array) over tomb 75 for a) the horizontal Fourier amplitude spectra, b) the vertical Fourier amplitude spectra and c) the H/V amplitude. In the central plot for the vertical component, two prominent areas of spectral amplitude amplification are circled.

Vertical Component Linear Array Measurements Over Selected Voids

The preceding results indicated that it is possible to detect the presence of underground voids just by using the vertical component of ambient noise measurements. We further examined this potential by conducting measurements along a second linear array above two adjacent, smaller tombs. In this third phase of our work, we used 6 2Hz, 1-component geophones (Atom-1C, Geometrics), spaced every 1m along a line crossing over the chambers of tombs 28 and 29 (Table 1, Figure 5). The chambers of these two tombs are right next to each other and their separating "wall" was so thin that a small part collapsed, partly joining the two void spaces. It should also be noted that the chamber of tomb 29 is about 6-7 times larger in volume than the chamber of tomb 28 and that their floor depths differ by ~1.5m (Table 1). Fourier amplitude spectra for each recording were computed following the same processing steps as before and plotted against distance. The exact geometry and location of the linear array and the pseudo-2D variation of spectral amplitudes are shown in Figure 5. Distances are measured from geophone A1 (Figure 5a, b). At high frequencies (i.e., >~20Hz) in Figure 5b, we can clearly observe higher spectral amplitudes at distances corresponding to the locations of geophones A1 and A3-A5. A1 was placed exactly over the centre of tomb 28, whereas A3-A5 were over the chamber of tomb 29. A2 and A6 are close to the boundaries of the voids and although they also present elevated amplitudes at high frequencies, these are not as high, either because they are not directly over the voids or because of the lateral deepening of the vaulted tombs ceilings.

Another interesting observation in Figure 5b is that the spatial variation of the elevated spectral amplitudes suggests both the existence of two different voids (lower high frequency amplitudes at the location of A2 compared to those to the left and right of it) and their different dimensions (stronger imprint for tomb 29 and for a larger distance, comparable to the length of its chamber, ~4m). This suggests that denser measurements could provide an even better description of the geometry of the voids as well as their separation.

Figure 5. a) Geophones (A1-A6) placement over the void chambers of tombs codenamed 28 and 29 in the Mycenaean Park of Voudeni. b) Spatial variability of the spectral amplitudes of the vertical component of ambient noise recordings. Black frames mark the interpreted imprints of the two voids in the form of elevated amplitudes at high frequencies.

Conclusions/Discussion

We have tested the H/V method for its ability to contribute to the detection of underground voids as suggested by Castellaro and Mulargia (2009), using as test targets the chambers of Mycenaean tombs of various sizes in the archaeological park of Voudeni in the Peloponnese. We performed single point measurements over the center of the chambers as well as linear arrays over selected chambers using both 3C and 1C geophones. We have shown that the detection and even mapping of the lateral extent of voids by the H/V method is feasible considering the persistent drop of the H/V curve below 1 at high frequencies (in our test cases generally >20Hz). We also showed a correlation between void size and the frequency above which the H/V curve drops below 1. By separately examining the spatial variation of the horizontal and vertical spectral amplitudes over the voids, we concluded that the H/V drop below 1 is mostly due to an amplification of the vertical component rather than a de-amplification of the horizontal. This motivated us to further investigate the potential of detecting subsurface voids based on array measurements with 1C, vertical sensors alone, and we concluded that such an approach is indeed feasible.

Of the 24 single point measurements of ambient noise that we made over voids, 17 of them showed the expected drop in the H/V curve at high frequencies. The reason why the method "failed" in some cases is not yet understood and requires theoretical modelling beyond the scope of this initial feasibility study. It should be noted that although our test site is ideal in terms of the variety of void target sizes, it is also very complicated due to the density and often close proximity of tombs of different sizes, as well as the different shapes of chamber roofs (pyramidal, hipped, vaulted, arched). This was partly demonstrated in the third phase of our measurements, where we measured along a line over two adjacent tombs of different sizes.

Contrary to the preferred interpretation of Castellaro and Mulargia (2009), our results suggest that the drop of the H/V curve below 1 over voids is mainly due to increased spectral amplitudes in the vertical component. This does not mean that the horizontal component is not de-amplified, as would be expected above such an extreme velocity reversal (void within rock), but

that the amplification of the vertical component is more distinct, localized, and easier to detect in terms of its spatial variation. A possible explanation for why the vertical component is amplified above a void was proposed by Kolesnikov and Fedin (2017), who studied an experimental model and proposed the occurrence of standing P waves between the ground surface and the top of the void. This implies a vertical amplification at higher frequencies for shallower voids compared to deeper ones.

In conclusion, our tests support the findings and suggestions of the work of Castellaro and Mulargia (2009) that the H/V curve has special characteristics over voids. This means that the H/V method could be used in the geophysical prospection of underground voids, at least as a complementary method to other more tested and robust methods. Considering that the method is gaining popularity due to its ease of use and cost-effectiveness, it is important for the community to further investigate this possible additional use for void detection, a very common need in geophysical exploration with diverse applications such as archaeological prospection, geological hazard assessment, and infrastructure monitoring.

Our work also suggests that linear array measurements of the vertical component alone may be equally useful. Such measurements are routinely performed by most research groups for site characterization with low-cost equipment, and only require some targeted additional processing to be useful for void detection.

It should be emphasized that, as with all geophysical methods, the interpretation of the results of the proposed methods outside the geological context of a studied site is insecure, and there is always the potential - if not the certainty - that multiple other factors influence the measurements. Several such factors are reviewed and discussed in detail in Castellaro and Mulargia (2009), particularly in relation to the topic discussed here. H/V results can be useful for void detection but should always be corroborated with other geophysical methods for accurate subsurface characterization.

Acknowledgements

The study was carried out in the framework of the research project “UNMASK”, supported by the Hellenic Foundation for Research and Innovation (H.F.R.I.) under the “2nd Call for H.F.R.I. Research Projects to support Faculty Members & Researchers” (Project Number: 2724). We are greatly indebted to the Ephorate of Antiquities of Achaea, and more specifically to its director Dr. A. Koumousi and the archaeologists K. Aktypi and M. Gkazis, for providing the permit and facilitating us in every possible way to perform our measurements in the Mycenaean Park of Voudeni. We also thank them for providing us with supporting archaeological material.

References

Bard, P.-Y. (1998). Microtremor measurements: A tool for site effect estimation? In H. Irikura, K. Kudo, H. Okada, & T. Sasatani (Eds.), The Effects of Surface Geology on Seismic Motion (pp. 1251–1279). A.A. Balkema.

Bonilla, L. F., Steidl, J. H., Lindley, G. T., Tumarkin, A. G., & Archuleta, R. J. (1997). Site amplification in the San Fernando Valley, California: Variability of site effect estimation using the S-wave, coda, and H/V methods. Bulletin of the Seismological Society of America, 87(3), 710–730.

Bour, M., Fouissac, D., Dominique, P., & Martin, C. (1998). On the use of microtremor recordings for site effects studies: Application to the city of Nice (France). Pure and Applied Geophysics, 152(2), 275–288.

Castellaro S., Mulargia, F., 2009. The effect of velocity inversions on H/V. Pure appl. Geophys. 166, 567-592

Chen, Q.-F., Wang, W., & Zhao, J.-X. (2014). Ambient noise as the new source for urban engineering seismology and earthquake engineering: A case study from Beijing metropolitan area. Earthquake Science, 27(1), 89–100. https://doi.org/10.1007/s11589-013-0052-x

Fäh, D., Kind, F., & Giardini, D. (2001). A theoretical investigation of average H/V ratios. Geophysical Journal International, 145(2), 535–549.

Field, E. H., & Jacob, K. H. (1993). The theoretical response of sedimentary layers to ambient seismic noise. Geophysical Research Letters, 20(24), 2925–2928. https://doi.org/10.1029/93GL03168

Haghshenas, E., Bard, P.-Y., & Theodulidis, N. (2008). Empirical evaluation of microtremor H/V spectral ratio. Bulletin of Earthquake Engineering, 6(1), 75–108.

Kolesnikov Yu.I., Fedin K.V., 2017. Detecting underground cavities using microtremor data: physical modelling and field experiment. Geophysical Prospecting, 66, 342–353

Lermo, J., & Chávez-García, F. J. (1994). Are microtremors useful in site response evaluation? Bulletin of the Seismological Society of America, 84(5), 1350–1364.

Molnar, S., & Cassidy, J. F. (2006). A comparison of site response techniques using weak-motion earthquakes and microtremors. Earthquake Spectra, 22(1), 169–188.

Molnar S., Cassidy J. F., Castellaro S., Cornou C., Crow H., Hunter J. A., Matsushima S., Sánchez-Sesma F. J., Yong A., 2018. Application of Microtremor Horizontal-to-Vertical Spectral Ratio (MHVSR) Analysis for Site Characterization: State of the Art. Surv. Geophys. 39 ,613-631.

Nakamura, Y. (1989). A method for dynamic characteristics estimation of subsurface using microtremors on the ground surface. Quarterly Report of Railway Technical Research Institute (RTRI), 30(1), 25–33.

Nogoshi, M., & Igarashi, T. (1971). On the amplitude characteristics of microtremor (Part 2). Journal of Seismological Society of Japan, 24, 26–40.

Turner R. D., 2020. Grave reminders: Comparing Mycenaean tomb building with labour and memory, Sidestone Press.

Woolery, E. W., & Street, R. L. (2002). 3D near-surface soil response from H/V ambient-noise ratios. Soil Dynamics and Earthquake Engineering, 22(9–12), 865–876.

17th INTERNATIONAL CONGRESS of the Geological Society of Greece

BULLETIN OF THE GEOLOGICAL SOCIETY OF GREECE, SP. PUBL.

EXTENDED ABSTRACT 221

Multiscale 3D mapping and Geovisualization of a Petrified Forest Park in Lesvos, Greece, using UAV.

Moysidou L.[1], Papadopoulou E.E.[1], Proestakis S.[1], Zouros N.[1], Soulakellis N.[1]

(1) Cartography and Geoinformation laboratory, Department of Geography, University Of the Aegean, Mytilene, Greece.

Introduction / Background

The Petrified Forest of Lesvos, located in the western region of Lesvos Island, Greece, represents a unique petrified ecosystem that encompasses a significant number of fossilized tree trunks and animal remains. This exceptional natural monument was formed approximately 20 million years ago when volcanic activity covered the area in volcanic material, preserving the organisms in ashes. The volcanic deposits revealed an extensive array of fossils, including standing and recumbent fossilized trunks and petrified branches. (Natural History Museum of the Lesvos Petrified Forest, 2020)

To ensure the protection and systematic study of the Petrified Forest, the Natural History Museum of the Lesvos Petrified Forest was established in Sigri in 1994. The museum manages the petrified forest protected area, which spans an area of 15,000 hectares (Geo-Naturpark Bergstrasse-Odenwald., 2022). The Lesvos Petrified Forest was a founding member of the European Geoparks Network in 2000 and was later designated a Global Geopark in 2004, underscoring its geological and cultural significance (Zouros, 2007). Since 2015 the Lesvos island, is recognized as a UNESCO Global Geopark, including the Lesvos Petrified Forest as the geological heritage area of international significance.

Recent infrastructure projects, including the construction of the Kalloni-Sigri road, led to the discovery of numerous fossiliferous sites, including hundreds of fossilized tree trunks, branches, leaves and cones. The research activities for the excavation, conservation and protection of these findings as well as the presentation, interpretation and promotion of this important site facilitated by the integration of innovative geoinformation technologies, using unmanned aerial vehicles (UAVs), for multiscale and multitemporal 2D and 3D mapping.

This study specifically describes the 3D mapping methodology used for the Ioannis Toumpelekis Park (*Map 1*), a fossil site located in Akrocheiras hill, which comprises 212 fossilized tree trunks and branches (Apostolopoulou, 2024). The fossils within the park are categorized into two distinct stratigraphic sections. The lower section predominantly contains lying fossilized trunks, while the upper section is characterized by standing fossilized trunks belonging primarily to the hardwood tree family. The 3D mapping of the fossiliferous area of I. Toumpelekis park provides critical insights into the paleoenvironmental and geological conditions that contributed to the preservation of the forest.

This research emphasizes the use of advanced geoinformation technologies to study and visualize the fossilized ecosystem comprehensively. A multi-scale 3D geovisualization workflow is employed, encompassing data acquisition, processing, modeling, and visualization. UAV technology plays a central role in data acquisition, delivering high-resolution imagery that forms the foundation for detailed 3D models. By integrating UAV-derived images, photogrammetric 3D models, and panoramic imagery, this study creates an immersive and interactive virtual environment, enhancing the understanding and presentation of this unique paleontological and geological heritage.

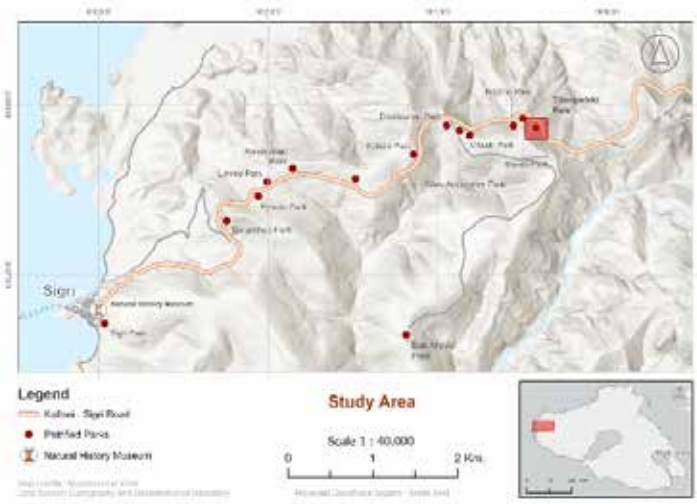

Map 1. Study Area located at the western part of Lesvos island, North Aegean, Greece

Objectives

The primary objective of this research is to explore and implement multi-scale 3D mapping and geovisualization methods for the study area. To achieve this goal, a comprehensive methodology was developed, encompassing both data acquisition and the presentation of findings. This approach involves the following key steps:

1. Data acquisition: High-resolution data were collected at two different ground sampling distances (GSD) using the DJI Mavic 3E, ensuring the accuracy and detail required for subsequent analysis.
2. 2D thematic orthophoto map construction: The collected data were processed to generate detailed thematic orthophoto maps, providing a georeferenced representation of the study area.
3. Development of a multiscale 3D model: A multi-scale 3D model of the study area was created, enabling a detailed representation of both park and fossil-scale features.
4. Creation of 3D animated maps: Animated visualizations were developed to enhance the communication of spatial and temporal data, offering dynamic perspectives of the study area.
5. Construction of an immersive virtual reality (VR) application: A VR application was designed to provide an interactive and immersive experience, allowing users to explore the fossilized park in a virtual environment.

This methodology integrates state-of-the-art geoinformation technologies to advance the study and presentation of complex fossilized ecosystems. The resulting outputs contribute to a deeper understanding of the site and demonstrate the potential of innovative mapping and visualization tools in geoscientific research.

Materials and Methods

In the following workflow, all the stages of the methodology are presented in detail, structured into three (3) main stages: 1. Data Acquisition, 2. Data Processing, and 3. Geovisualizations. (*Figure 1.*):

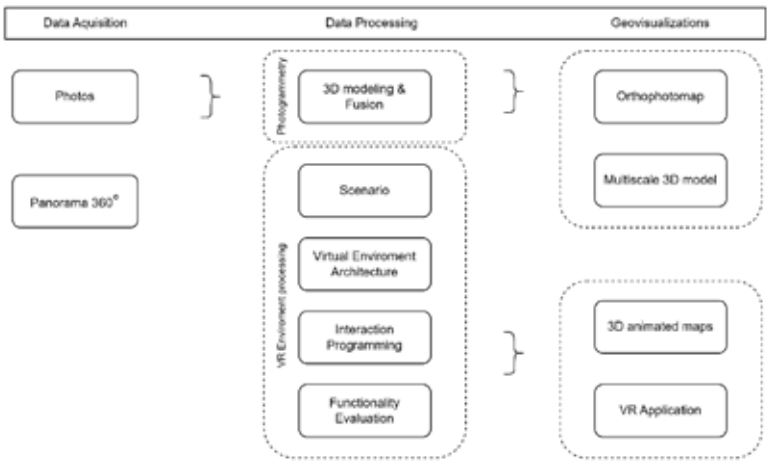

Figure 1. Methodology workflow.

Data Collection

The dataset for the present study was acquired through the deployment of unmanned aerial vehicles (UAVs) for the cartographic documentation of Ioannis Toumpelekis Park and its fossilized tree trunks at two different mapping scales. Specifically, a DJI Mavic 3 Enterprise UAV, featuring a 48 MP camera and a Real-Time Kinematic (RTK) positioning system, was employed to ensure the collection of high-precision spatial data.

Flight operations were carried out in two sessions, on May 1, 2023, and August 31, 2023, at flight altitudes of 70 meters and 2 meters, respectively. These sessions were planned under favorable weather conditions and optimal sunlight to reduce shadow interference and enhance the quality of the captured data. The utilization of the RTK system facilitated positional accuracy, achieving precision of up to 1 cm horizontally and 1.5 cm vertically, thereby obviating the requirement for ground control points. The data acquisition was conducted at two different scales: 1. park-scale (1:150) and 2. petrified tree trunk-scale (1:10). Overlap parameters were set at 80% frontally and horizontally to optimize the creation of image based 3D models and the orthophoto-map. Additionally, 360° panorama was captured at 50m height of flight, providing contextual visuals of the study area for VR geovisualization. (*Table 1.*)

Date	Height of flight	Type of data	Gimbal pitch	Scale	Type of flight
01/05/2023	70m.	Photos	Nadir	Park	Flight plan
	60m.	Photos	Oblique	Park	Manual
	50m.	Panorama	-	Broader Study area	Automatic
	2m.	Photos	Oblique	Fossil 109	Manual
				Fossil 111	
				Fossil 116	
				Fossil 117	
				Fossils F1-F9	
31/08/2023	2m.	Photos	Oblique	Fossil 105	Manual
				Fossil 119	

Table 1. Data acquisition information

Image based 3D Modelling

The 3D models for this study were constructed using a systematic workflow designed to ensure high precision and photorealistic outputs. The process began with the generation of a sparse point cloud, followed by the creation of dense point clouds from UAV imagery utilizing the Structure from Motion (SfM) algorithm (Papadopoulou et al., 2022). The sparse point cloud provided an initial geometric framework, while the dense point cloud added detail, accurately capturing surface features essential for realistic modelling.

.

Subsequently, a total of thirteen (13) 3D models were generated by interpolating the dense point cloud data. Twelve (12) of these 3D models were the fossilized trees within the study area and one (1) 3D model depicting the entirety of the park. Textures were then applied to the meshes, ensuring photorealistic visual fidelity. The fusion approach was employed to refine and fuse the models, maintaining high accuracy across both park-scale and tree trunk-scale. This process involved extracting areas containing fossilized tree trunks from the park-scale model and replacing them with high-detail fossil 3D models derived from data captured at a 2-meter flight altitude. (*Figure 2*). The resulting multiscale 3D model of the park enabled seamless transitions between different scales, providing detailed visualizations of the fossilized tree trunks while retaining the broader contextual information of the park.

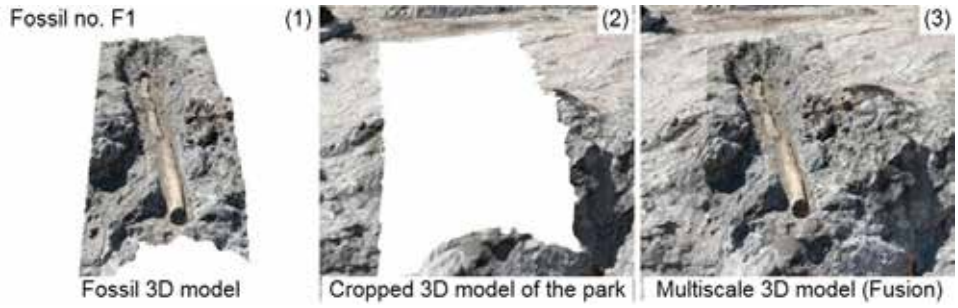

Figure 2. Multi-scale 3D model.

Geovisualization Methods

In the final stage, the 3D models were integrated into a virtual reality (VR) environment utilizing Twinmotion, a real-time 3D visualization software powered by Unreal Engine. This integration facilitated the development of an immersive and interactive experience, enabling users to virtually explore the park. Key features included 3D animated maps, interactive hotspots, and supplementary information highlighting the park's petrified tree trunks.

The development of the VR environment required the establishment of a structured methodology to define the content and features to be presented within the application (Papadopoulou et al., 2022). The process involved the following stages:.

- Scenario Design.
- Virtual Environment Architecture.
- Interaction Programming.
- Functionality Evaluation.

The Virtual Reality (VR) application integrated a 360° panoramic backdrop to enhance spatial awareness and realism within the virtual environment. The incorporation of thematic maps, dynamic animations, and supplementary 3D models—such as fences, staircases, animated human figures, vehicles, and vegetation—further enriched the immersive experience. By adhering to interactive design principles, the application facilitated both free exploration and structured, guided tours, offering users an engaging and intuitive navigation experience.

Results – Discussion

Multiscale 3D Model

The multiscale 3D model was developed through the integration of twelve (12) high level of detail 3D models of fossilized tree trunks with a single (1) overarching model representing the entire Park. This multiscale 3D modeling approach was employed to enhance the overall quality and accuracy of the park's virtual representation by incorporating detailed reconstructions of the petrified tree trunks. The seamless integration of these models enabled a comprehensive visualization of the fossils within their broader natural environment, supporting both interpretative analysis and educational outreach. *(Table 2)*

Fossilized Tree Trunks	Points	Surfaces	Photos	Quality
Fossil no. 105	1,176,473	78,431	53	medium
Fossil no. 109	352,540	47,428	16	medium
Fossil no. 111	552,250	26,381	26	medium
Fossil no. 116	563,681	144,295	35	medium
Fossil no. 117	1,745,749	349,149	57	medium
Fossil no. 119	3,095,251	619,049	76	medium
Fossil no. F1	777,563	200,155	20	medium
Fossil complex no. F2, F3	1,822,312	424,745	23	medium
Fossil complex no. F4, F5	167,888	75,720	38	medium
Fossil no. F6	2,440,954	162,185	103	medium
Fossil complex no. F7, F8	12,488,838	2,102,240	24	High
Fossil F9	1,032,177	203,383	82	medium
Multiscale 3D model	**24,497,102**	**4,835,635**	**594**	**medium**

Table 2. 3D models information

3D Animated Maps

To further enhance the visualization of the park's multiscale 3D model, a series of 3D animated maps were developed. These maps provided detailed visual representations, accurately depicting both standing and lying petrified tree trunks in their natural positions. The implementation of 3D animated maps offers significant potential as an educational tool for students, researchers, and educators, facilitating a deeper understanding of complex geological processes associated with the evolutionary history of the Petrified Forest of Lesvos.

A total of nine (9) 3D animated maps were generated utilizing two specialized software platforms: Agisoft Metashape and Twinmotion. Of these, seven (7) animations focused on individual petrified tree trunks, while two (2) provided comprehensive visualizations of the entire park. To enhance accessibility, these animations have been made available via the YouTube platform and can also be accessed through QR codes embedded within the park's orthophoto map, offering user-friendly experience. (link : https://www.youtube.com/watch?v=GwVFHR6T2EY&t=150s)

Virtual Reality Application

A virtual reality (VR) application was developed to present the multiscale 3D model of the park and to highlight the high level of detail 3D models of petrified trunks in their natural environment. This application also provides users with information A Virtual Reality (VR) application was developed to showcase the multiscale 3D model of the park, emphasizing the high level of detail in the 3D representations of the petrified tree trunks within their natural environment. In addition to immersive visualization, the application provides users with valuable information regarding: (1) the Petrified Forest of Lesvos, (2) the newly established petrified parks along the Kalloni–Sigri road, and (3) the specific study area. This interactive platform enhances user engagement and serves as an educational tool for exploring the geological and cultural significance of the site.

In the Virtual Reality (VR) application, users commence their experience at the entrance of I. Toumpelekis Park, where an introductory series of maps provides insights into the park's geological significance and spatial context. The application incorporates dynamic interactive features, such as the automatic opening of the park gate and the exploration of a detailed 3D animated map—developed in Twinmotion—that illustrates the walking paths and the distribution of petrified tree trunks. A key feature of the experience is the interactive engagement with tree trunk no. 105, which, when approached, activates a 1:1 scale visualization of the fossil's current state. The immersive journey concludes with a 360° panoramic view, offering users a comprehensive spatial perception of the site. (Figures 3-4)

.

Figure 3-4. VR application contents

Conclusions.

.The development of a multiscale 3D model and its integration into a virtual reality (VR) application for the Park, demonstrated both the potential and challenges associated with employing advanced geospatial technologies for the geovisualization of geosites.

Multiscale 3D model:.

1. The multiscale 3D model successfully combined detailed reconstructions of the petrified tree trunks with a broader, lower-level of detail 3D model of the park, enhancing visual fidelity while preserving environmental context. However, challenges were encountered during the management of the multi scale 3D model within platforms such as Twinmotion and Blender. Issues such as the misalignment of models required manual adjustments, including relocating pivot points and realigning coordinates, to ensure seamless integration.
2. **3D animated maps**:.
3. The 3D animated maps provided an innovative way to visualize the multi-scale 3D model, delivering significant educational value. Nevertheless, certain limitations emerged, including incomplete models and texture distortions caused by insufficient image overlap during UAV data acquisition. Furthermore, user interactivity was constrained to predefined perspectives, limiting the ability to explore specific points of interest freely.
4. **VR application**:.
5. The VR application offered an immersive and educational experience, enabling users to explore the park and visualize the detailed petrified tree trunks in their natural environment at a 1:1 scale. Despite its potential, the implementation revealed technical challenges, including scaling 3D models accurately and managing panoramic displays without distortion. Additionally, the requirement for high-performance computational systems imposed financial constraints, potentially limiting accessibility for institutions with restricted resources.

These findings highlight the potential of multiscale 3D modeling and VR applications to revolutionize geovisualization in geosites while emphasizing the need for further advancements in technology to overcome existing limitations.

References

The Forest under the Road, 2020. Natural History Museum of the Lesvos Petrified Forest. https://www.lesvosmuseum.gr/en/exhibitions/forest-under-road [Online Resource]

Lesbos Island UNESCO Global Geopark, 2022. Geo-Naturpark Bergstrasse-Odenwald. https://geo-naturpark.net/en/network/geopark-partnerships/lesbos-island-unesco-global-geopark/ [Online Resource]

Zouros, N., 2007. Geomorphosite assessment and management in protected areas of Greece: Case study of the Lesvos island – coastal

geomorphosites. Geographica Helvetica 62(3), 169–180. https://doi.org/10.5194/gh-62-169-2007 [Journal Article]

Apostolopoulou, N., 2024. Στρωματογραφική αποτύπωση των πυροκλαστικών αποθέσεων του όρους Ακρόχειρας (Λέσβος) με τη χρήση ψηφιακών μέσων. University of Patras, Patras, Greece.

Papadopoulou, E.-E., Papakonstantinou, A., Kapogianni, N.-A., Zouros, N., Soulakellis, N., 2022. VR multiscale geovisualization based on UAS multitemporal data: The case of geological monuments. Remote Sensing 14(17), 4259. https://doi.org/10.3390/rs141742590 [Journal Article]

17th INTERNATIONAL CONGRESS of the Geological Society of Greece

BULLETIN OF THE GEOLOGICAL SOCIETY OF GREECE, SP. PUBL.

EXTENDED ABSTRACT 222

Investigating Drought Dynamics in Greece Using Climate and Meteorological Indicators

Mpakopoulou Ch.[1], Tsesmelis D.[2], Kalogeropoulos K.[3], Vasilakou K.[4], Feloni E.[3,*], Zervas E.[5], Tsatsaris A.[3]

(1) Laboratory of Technology and Policy of Energy and Environment, School of Applied Arts and Sustain-able Design, Hellenic Open University, 26335 Patras, Greece
(2) Department of Agriculture, University of Patras, Messolonghi Campus, 30200 Messolonghi, Greece
(3) Department of Surveying and Geoinformatics Engineering, University of West Attica, 28 Ag. Spiridonos, 12243 Egaleo, Athens, Greece; efeloni@uniwa.gr
(4) Department of Natural Resources Development and Agricultural Engineering, Agricultural University of Athens, 11855 Athens, Greece (5) Laboratory of Technology and Policy of Energy and Environment, School of Applied Arts and Sustainable Design, Hellenic Open University, 26335 Patras, Greece

Background

This study investigates droughts in Greece based on the meteorological relative humidity index (Tsesmelis *et al.*, 2019, 2021, 2022). Droughts, temporary natural conditions tied to water availability, result from low regional rainfall (Karavitis, 1996; Lujala *et al.*, 2015; Feloni *et al.*, 2017). Their frequency, duration, and severity vary, impacting water resources and ecosystem recovery (Fleming-Muñoz *et al.*, 2023; Pizzorni *et al.*, 2024). Relative humidity (RH) measures air moisture relative to its maximum capacity under the same temperature and pressure (Kiem *et al.*, 2016). Using RH data from 42 Hellenic National Meteorological Service (HNMS) stations (1971–2004), the Standardized Relative Humidity Index (SRHI) was calculated at 1, 3, 6, 9, and 12-month intervals. Diagrams illustrated index changes, while drought maps, created via Inverse Distance Weighting, visualized annual SRHI12 and SRHI6 values. Analysis identified 1989–1990 as the most severe drought, followed by 2000–2001. Additionally, this study explores climate variability in Greece through statistical analysis of RH data from the same stations (1975–2004).

RH measures water vapor in relation to air temperature (US Department of Commerce, n.d.). It is the most used humidity index. It is defined as the ratio of the actual amount of water vapor in the air to the maximum amount it can hold under the same temperature and pressure conditions. In other words, it is defined as the ratio of hydrometric parameters to their corresponding values at saturation, as follows:

$$RH = mv/mvs \textit{ or } RH = e/es \textit{ or } RH = r/rs \textit{ or } RH = q/qs$$

Where: RH: relative humidity, m and mvs: mass of water vapor and the corresponding value at saturation, e and es: vapor pressure and the corresponding value at saturation, r and rs: mixing ratio of air and the corresponding value at saturation, q and qs: specific humidity and the corresponding value at saturation.

Relative humidity is expressed as a percentage (%) and always has a value ≤1. In practical terms, its value indicates how far the current state is from the corresponding saturation state, which occurs when there is fog or rain.

Drought is a complex climatic phenomenon that often occurs over large spatial and temporal scales. It is frequently accompanied by severe social impacts resulting from the reduction in the available quantity of water for human consumption, as well as for agricultural and livestock activities. The attempt to find a precise definition has led to the conclusion that it is a temporary natural phenomenon related to water availability, which usually results from low average rainfall values. It has an uncertain frequency, duration, and severity, causing significant impacts on water availability and the ability of the ecosystem to recover to its original state (Stathopoulos *et al.*, 2018).

Objectives

This study aims to investigate the impact of climate change (CC) in Greece by analyzing climate indices using meteorological data. The primary research question focuses on determining whether and to what extent global CC has influenced the climate of Greece. The literature offers a wide range of indices for assessing both qualitative and quantitative changes in climate. Through the processing and statistical analysis of carefully selected and formatted indices, a more in-depth analysis will be conducted compared to previous reports and records (Tsesmelis, 2017; Tsesmelis *et al.*, 2022, 2023). This study can comprehensively define the key elements related to climate, CC and drought phenomena.

Methods

The lack of studies correlating humidity with the occurrence of potential drought phenomena was the impetus for

further study and analysis in this work. In the first stage, humidity measurement data were collected from 42 HNMS stations across the country. These values were processed to produce daily and then monthly data. For each station, a file was created using a spreadsheet program (Excel) in which the minimum, maximum, mean, median, and standard deviation for each month of each year (from 1971 to 2004) were recorded, in order to make an initial estimate of the general trend of humidity measurements. The same process was followed again after the humidity measurements for each station were grouped to obtain the above statistical values for each study year. Subsequently, the monthly humidity values for each station were entered into a suitable programming language where the SRHI (Standardized Relative Humidity Index) was calculated for each station separately. The index was calculated for all time steps: one month (SRHI1), three months (SRHI3), six months (SRHI6), nine months (SRHI9), and twelve months (SRHI12). Using the values obtained from the program, graphs were created to depict the monthly variations of the indices for all years. In this way, an initial qualitative check of the processed data was performed. In order to study, understand, and interpret the results of the above analysis more extensively and ultimately draw conclusions, the creation of maps was initiated in the next stage. Using the spreadsheet program (Excel) again, a workbook was created in which the codes and names of the stations, the coordinates of each station (x and y in EGSA 87), and the results of SRHI6 and SRHI12 were recorded. Subsequently, 3 maps were created for each year based on the values of SRHI6 for the 6th and 12th month and SRHI12 for the 12th month, respectively. The creation of the maps using the geostatistical method of Inverse Distance Weighting, in which both the extreme values and the colors that represent them with blue (wet period) and red (dry period) were defined. The index used for the analysis is the Standardized Relative Humidity Index (SRHI). The SRHI uses a non-parametric standardization approach. First, the empirical probabilities of the relative humidity data are calculated using the empirical plotting position of Gringorten (Farahmand *et al.*, 2015).

$$p(RHi) = (i-0,44)/(n+0,12)$$

where i: the rank of the relative humidity data from the smallest, n: the sample size

The empirical probabilities of the relative humidity data are standardized as follows:

$$SRHI = \Phi\text{-}1(p(RHi))$$

where: Φ-1 is the inverse standard normal distribution function with mean zero and standard deviation one. The standardization is based on the following approximation:

$$SRHI = \begin{cases} \quad 1+d_1t+d_2t^2+d_3t^3 \\ \quad c_0+c_1t+c_2t^2 \end{cases}$$

where: c_0=2,52, c_1=0,80, c_2=0,01, d_1=1,43, d_2=0,19, d_3=0,00

and:

$$t = \begin{cases} \sqrt{\quad} \\ \quad p(RHi)^2 \end{cases}$$

Negative values of the SRHI index indicate relative humidity below the average and are suggested as a measure of dryness according to climatology. The following table (Table 1) presents the scale of the index values.

Table 1. Categorization of SRHI index values.

SRHI values	Category
> 2.00	Extremely Wet
1.50 to 1.99	Very Wet
1.00 to 1.49	Moderate Wet
0.50 to 0.99	Mild Wet
-0.49 to 0.49	Normal Conditions
-0.50 to -0.99	Mild Drought
-1.00 to -1.49	Moderate Drought
-1.50 to -1.99	Severe Drought
<-2.00	Extreme Drought

The HNMS operates 178 surface stations across Greece and three upper-air stations (Elliniko, Heraklion, Macedonia-Mikra). These stations record primary climate data every three hours, 24/7, for analysis and processing. This study utilized humidity data from 42 stations nationwide.

Results and Discussion

Although the index was analyzed at 1-, 3-, and 9-month intervals, SRHI6 was emphasized in diagrams and maps due to Greece's typically high humidity from October to March. Since humidity varies across regions, SRHI12 was also included. Calculating SRHI at these intervals produced 42 diagrams, with two representative examples shown (Figure 1).

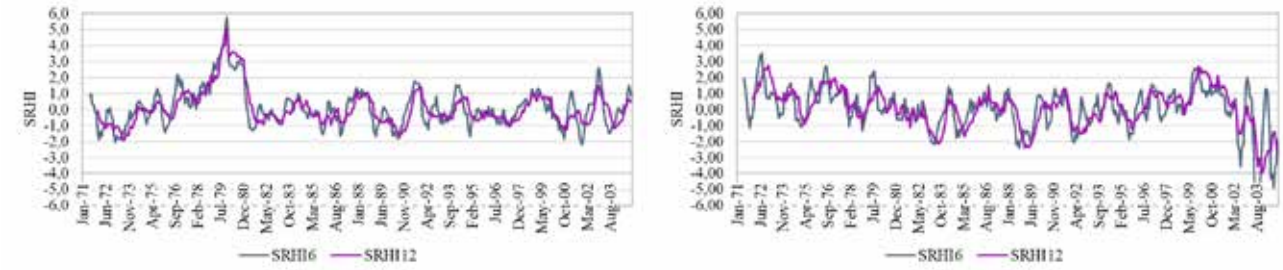

Figure 1. The SRHI index with a time scale of 6 and 12 months for the Lemnos meteorological station where a period of exceptional humidity is observed (left panel) and Methoni where a period of extreme drought is observed (right).

Analysis of the diagrams reveals multiple instances of low index values, indicating past droughts, even before rapid urbanization and increased water consumption. To better visualize drought periods nationwide, 102 maps were generated using Inverse Distance Weighting (IDW) in ArcGIS Pro 3.3—one for SRHI12 and two for SRHI6 annually. Drought patterns varied over the years. Severe droughts affected Arta, southern Peloponnese, Rhodes, and Sitia in 1971–1973, culminating in an extreme nationwide drought in 1974. Another severe drought occurred in 1977, mainly impacting Central Greece and Sitia. From 1979 to 1982, conditions were mostly normal, with localized wet and dry periods. Moderate droughts emerged in southeastern Greece in 1983, followed by a wet phase in 1984, which ended in late 1984 with recurring droughts through 1986, particularly in northern and western Central Greece. A significant shift began in 1988 with moderate drought across western Greece (SRHI12) and nearly the entire country (SRHI6). The most extreme drought occurred in 1989–1990, affecting almost the entire country, with SRHI6 showing more intensity than SRHI12. After milder droughts in 1992–1993, Crete (1995) and Evros (1996) faced localized dry conditions. In 1997, severe drought impacted Epirus, western Macedonia, Thira, and Rhodes. Moderate to severe drought appeared in central Peloponnese (1999), escalating nationwide in 2000–2001, especially in eastern Greece and later across nearly the entire country. In 2002, while Evros faced mild drought, much of Greece experienced unusually wet conditions, particularly Central Greece and Crete. By 2003, extreme drought was again localized in western Peloponnese, Evros, and the Cyclades. This study highlights key drought years: 1974, 1977–1978, 1983–1984, 1985–1986, 1989–1990, 2000–2001, and 2003. In contrast, 2002 was a year of high humidity. Notably, Pyrgella recorded extreme drought values of -6.60 in 1974 and an unprecedented -7.86 in 1975, despite the latter year not being generally dry (Figure 2).

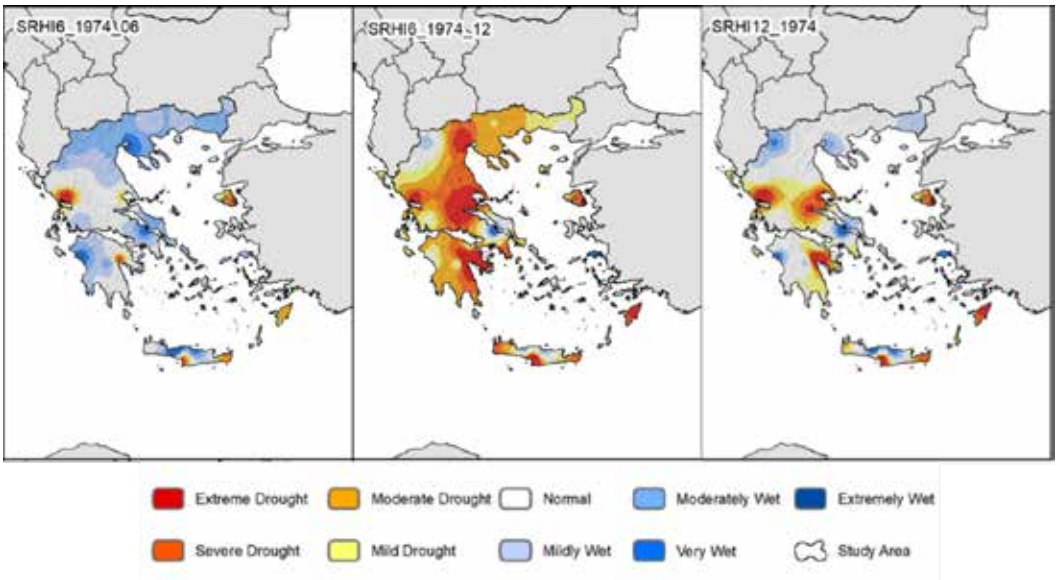

Figure 2. SRHI6 and SRHI12 maps for the year 1974.

The 1977–1978 drought was severe in many regions but not the most extreme recorded. This was followed by 1983–1984, when SRHI6 indicated moderate to high humidity across much of Greece, while SRHI12 showed a milder trend. A similar pattern occurred in 1985–1986, with severe to extreme drought in some areas (SRHI6), but a less intense picture from SRHI12.

In 1988, an extreme drought began, culminating in the devastating 1989–1990 drought—one of Greece's longest and most intense. Nearly the entire country experienced extreme drought, severely impacting agriculture and the economy. June 1990 was the worst month (SRHI6) (Figure 4). To mitigate the crisis, authorities explored solutions, including a proposal by the National Technical University of Athens to transport water by ship, prompting immediate government action (Tsesmelis, 2010).
The next significant drought occurred in 1993, though milder than previous events. It affected much of Northern Greece, Thrace, the Aegean islands, and the Dodecanese. Islands faced heightened drought issues in summer due to increased water consumption from tourism.
In 2000, Greece experienced the most severe drought since 1990, initially impacting Central Greece and northeastern Aegean islands. By year's end, drought spread across the country, with severe crop damage in northern Greece (Figure 5).
In 2001, drought conditions persisted, notably affecting central Peloponnese, Central Greece, and Thrace, but weakened towards the end of the year, returning the country to normal conditions.
Although 2003 had minimal drought issues, localized extremes were observed, such as in Methoni, where SRHI6 recorded the study's most extreme value of -8.11 in August (Figure 6).
Notably, unlike the recorded droughts, 2002 saw exceptionally wet conditions across most of Greece (Figure 7).
Monthly relative humidity analysis revealed two distinct periods: October–March, characterized by high humidity, and April–September, when levels are generally lower. This pattern is evident in station diagrams, though more pronounced in some locations than others.

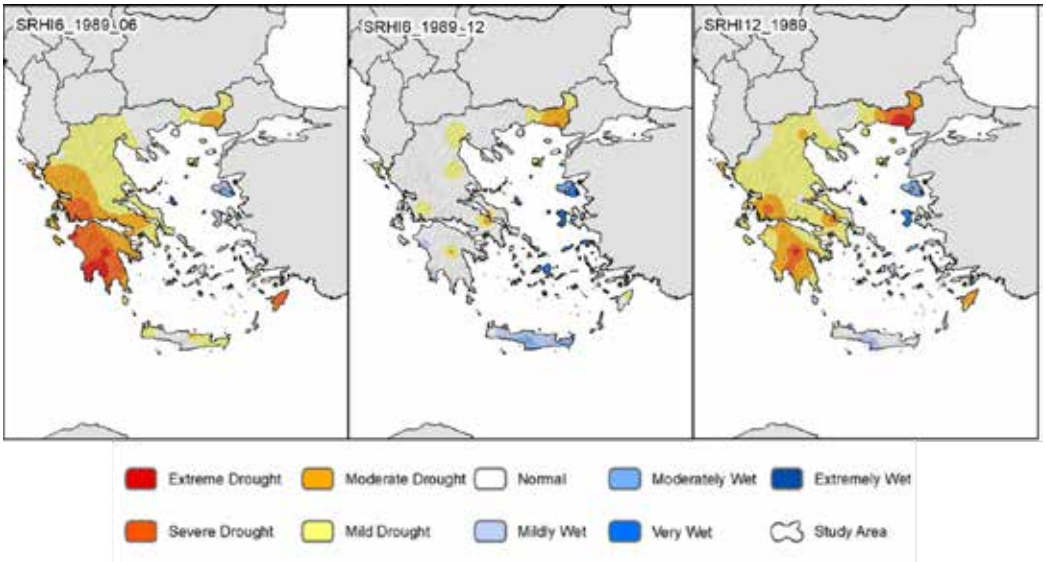

Figure 3. SRHI6 and SRHI12 maps for the year 1989.

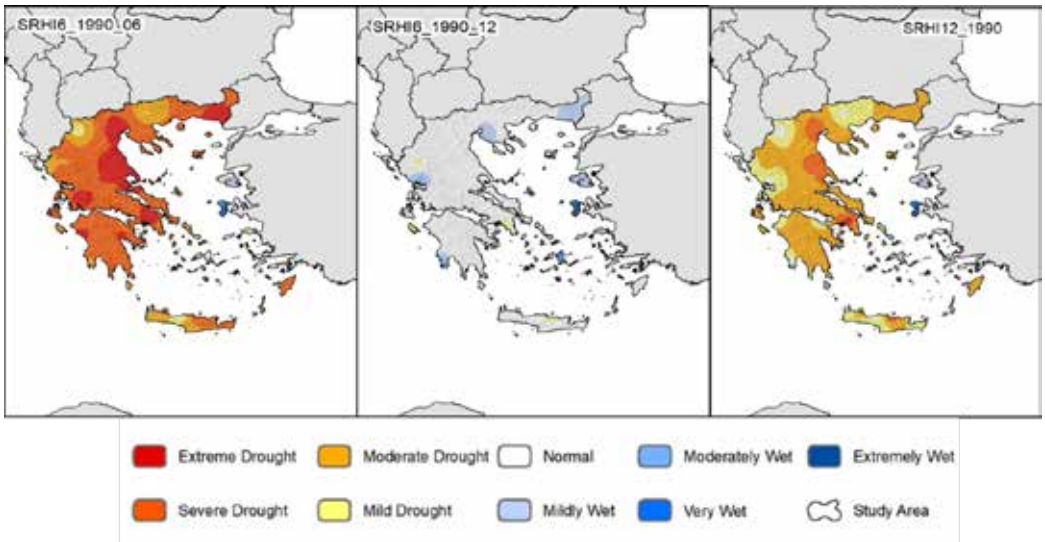

Figure 4. SRHI6 and SRHI12 maps for the year 1990.

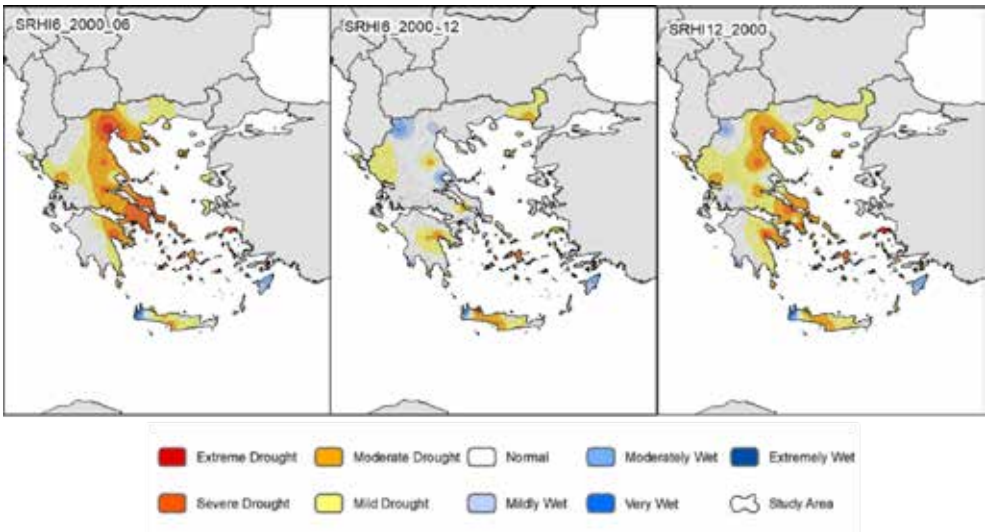

Figure 5. SRHI6 and SRHI12 maps for the year 2000.

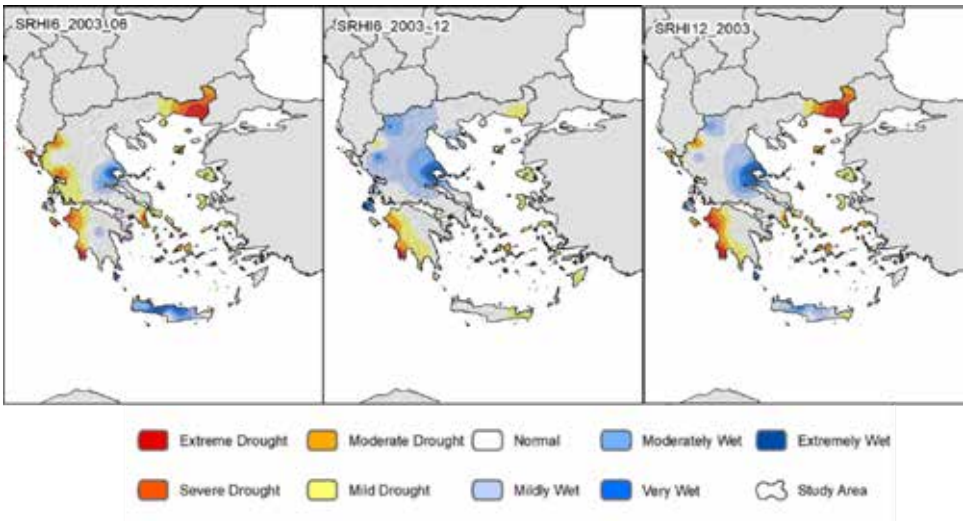

Figure 6. SRHI6 and SRHI12 maps for the year 2003.

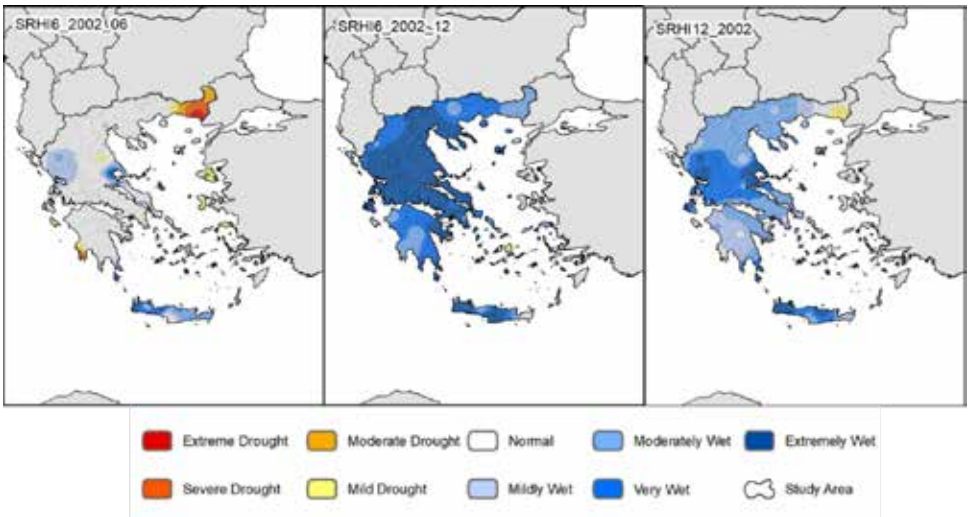

Figure 7. SRHI6 and SRHI12 maps for the year 2002.

Conclusions

This study investigates the drought phenomena in Greece from 1971 to 2004 to assess the long-term variability of climate over the years. Using humidity data from 42 HNMS stations across the country, the Standardized Relative Humidity Index (SRHI) was employed for analysis, with results presented through diagrams and maps. The findings highlight the widespread impact of droughts, particularly in island regions, which face unique challenges due to their geographic and socio-economic characteristics. Island areas, especially during the summer months, are particularly vulnerable to droughts. The increased influx of tourists significantly raises water consumption, exacerbating the already limited water resources available. This effect was observed notably in the Aegean islands and the Dodecanese, where droughts became more severe during peak tourist seasons. The study showed that, while mainland regions experience droughts of varying severity, the islands are often at greater risk due to their dependence on limited freshwater supplies, which are further strained by seasonal population increases.

The severe droughts of 1993, 2000, and 2001 particularly impacted the eastern islands, such as those in the northeastern Aegean. These regions experienced significant agricultural losses, which were compounded by the added strain of water scarcity caused by tourism. The 2000–2001 drought was among the most severe since 1990, with widespread consequences for both agriculture and the local economy, disproportionately affecting northern Greece and the islands. This pattern underlines the critical importance of addressing the unique vulnerabilities of island areas in future drought management strategies.

The overall trend shows that Greece's vulnerability to droughts has intensified, driven by both global CC and the substantial increase in water use. The combination of rising temperatures and heightened water consumption calls for immediate and proactive measures to mitigate drought impacts. The study underscores the urgent need for comprehensive drought prevention and management plans, tailored to both mainland and island regions, to minimize the economic and ecological consequences of future droughts. Given the significant challenges posed by droughts, particularly in island areas, further research is essential to develop more robust strategies for water conservation, sustainable tourism, and regional drought preparedness. With proper planning and management, the impact of droughts can be better mitigated, making their management more effective and less disruptive.

References

Farahmand, A., AghaKouchak, A., & Teixeira, J. (2015). A Vantage from Space Can Detect Earlier Drought Onset: An Approach Using Relative Humidity. *Scientific Reports*, *5*(1), 8553. https://doi.org/10.1038/srep08553

Feloni, E.G., Kotsifakis, K.G., Nastos, P.T. & Baltas, E.A. (2017). SPI analysis over Greece using high resolution precipitation gridded datasets. Eur. Water, 60, pp.319-326.

Fleming Muñoz, D. A., Whitten, S., & Bonnett, G. D. (2023). The economics of drought: A review of impacts and costs. *Australian Journal of Agricultural and Resource Economics*, *67*(4), 501–523. https://doi.org/10.1111/1467-8489.12527

Karavitis, C. A. (1996). Regional Water Transfers and Drought Management Strategies. In J. Ganoulis, L. Duckstein, P. Literathy, & I. Bogardi (Eds.), *Transboundary Water Resources Management* (pp. 451–457). Springer Berlin Heidelberg. https://doi.org/10.1007/978-3-642-61438-5_29

Kiem, A. S., Johnson, F., Westra, S., Van Dijk, A., Evans, J. P., O'Donnell, A., Rouillard, A., Barr, C., Tyler, J., Thyer, M., Jakob, D., Woldemeskel, F., Sivakumar, B., & Mehrotra, R. (2016). Natural hazards in Australia: Droughts. *Climatic Change*, *139*(1), 37–54. https://doi.org/10.1007/s10584-016-1798-7

Lujala, P., Lein, H., & Rød, J. K. (2015). Climate change, natural hazards, and risk perception: The role of proximity and personal experience. *Local Environment*, *20*(4), 489–509. https://doi.org/10.1080/13549839.2014.887666

Pizzorni, M., Innocenti, A., & Tollin, N. (2024). Droughts and floods in a changing climate and implications for multi-hazard urban planning: A review. *City and Environment Interactions*, *24*, 100169. https://doi.org/10.1016/j.cacint.2024.100169

Stathopoulos, N., Skrimizeas, P., Kalogeropoulos, K., Louka, P., & Tragaki, A. (2018, October). *Statistical Analysis and Spatial correlation of rainfall in Greece for a 20-year time period*.

Tsesmelis, D. E. (2017). *Development, implementation and evaluation of drought and desertification risk indicators for the Integrated Management of Water Resources* [Ph.D. Dissertation, Department of Natural Resources Management & Agricultural Engineering, Agricultural University of Athens]. http://hdl.handle.net/10329/6743

Tsesmelis, D. E., Karavitis, C. A., Kalogeropoulos, K., Tsatsaris, A., Zervas, E., Vasilakou, C. G., Stathopoulos, N., Skondras, N. A., Alexandris, S. G., Chalkias, C., & Kosmas, C. (2021). Development and Application of Water and Land Resources Degradation Index (WLDI). *Earth*, *2*(3), 515–531. https://doi.org/10.3390/earth2030030

Tsesmelis, D. E., Karavitis, C. A., Kalogeropoulos, K., Zervas, E., Vasilakou, C. G., Skondras, N. A., Oikonomou, P. D., Stathopoulos, N., Alexandris, S. G., Tsatsaris, A., & Kosmas, C. (2022). Evaluating the Degradation of Natural Resources in the Mediterranean Environment Using the Water and Land Resources Degradation Index, the Case of Crete Island. *Atmosphere*, *13*(1), 135. https://doi.org/10.3390/atmos13010135

Tsesmelis, D. E., Karavitis, C. A., Oikonomou, P. D., Alexandris, S., & Kosmas, C. (2019). Assessment of the Vulnerability to Drought and Desertification Characteristics Using the Standardized Drought Vulnerability Index (SDVI) and the Environmentally Sensitive Areas Index (ESAI). *Resources*, *8*(1), Article 1. https://doi.org/10.3390/resources8010006

Tsesmelis, D. E., Leveidioti, I., Karavitis, C. A., Kalogeropoulos, K., Vasilakou, C. G., Tsatsaris, A., & Zervas, E. (2023). Spatiotemporal Application of the Standardized Precipitation Index (SPI) in the Eastern Mediterranean. *Climate*, *11*(5), 95. https://doi.org/10.3390/cli11050095

17th INTERNATIONAL CONGRESS of the Geological Society of Greece

BULLETIN OF THE GEOLOGICAL SOCIETY OF GREECE, SP. PUBL.

EXTENDED ABSTRACT 223

Density modeling based on gravity survey at faulted area around Aigion, Gulf of Corinth, Greece

Mrlina J.[1]
(1) Institute of Geophysics CAS, Prague, Czechia, jan@ig.cas.cz

Introduction and objectives

This paper is based on the gravity survey data and highlights a quite important difference between former geological models and the new density/gravity model along two NNE-SSW oriented profiles crossing three principal normal faults in the Aigion area of the Gulf of Corinth.

The geological models were presented by Ghisetti *et al.* (2001), Ghisetti and Vezzani (2005), and Moretti *et al*. (2003).The current gravity model actually comprises much less conglomerate formations between the Helike and Pirgaki faults.

For this study, a new gravity map of the area was needed, so a gravity survey was carried out in a few steps, and the data were processed into the Bouguer gravity anomaly values. Then a gravity map and a residual gravity maps were constructed as a base for gravity field evaluation. As well, extensive rock sampling of the principal rock types was performed, as no such data were available from former investigations, as stated by Mrlina (2001). Rock densities and porosity were measured in a laboratory in Czechia.

The principal objective of the gravity surveying was to determine tectonic and structural setting of the area which forms the southern side of the Corinth Rift. The principal tectonic features are the WNW-ESE trending normal faults expressed in the topography of the region (Armijo *et al*., 1996, Rigo *et al.,* 1996). The region is prone to strong earthquakes (Bernard *et al.,* 1997). The target was to perform 2D and 2.5D gravity/density modeling to constrain existing tentative geological profiles. No such gravity models had been published in literature to that date.

The location of the study area is presented in Fig. 1

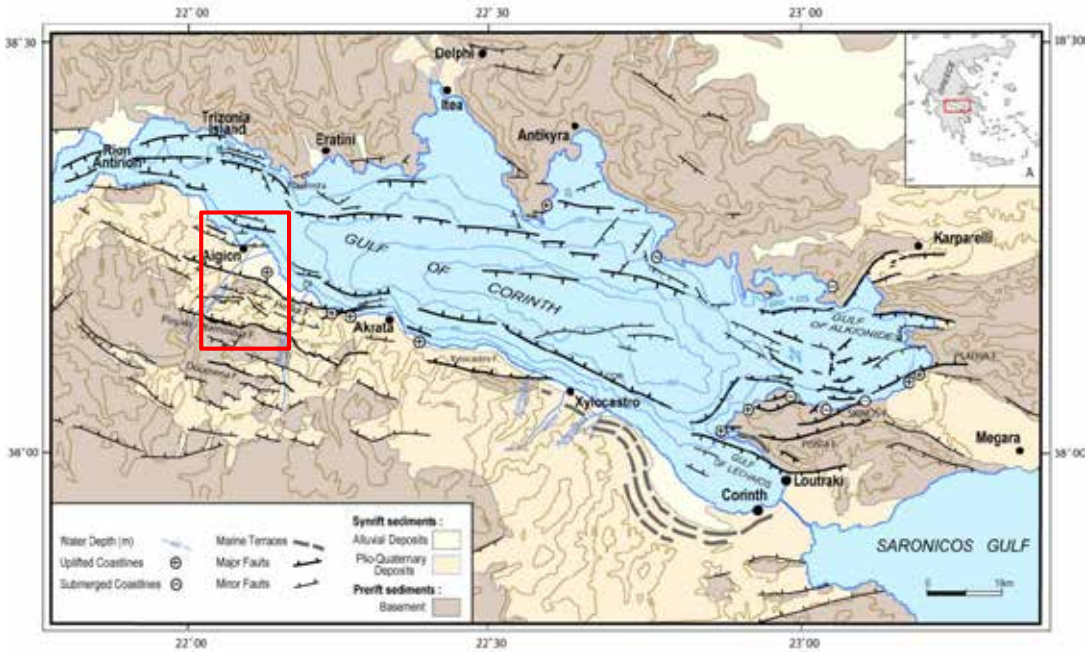

Figure 1. Tectonic map of Gulf of Corinth (after Moretti *et al.,* 2003). The study area around Aigion is marked by a red rectangle. Principal normal WNW-ESE faults are presented in the map.

Methods

The gravity survey was performed using the LaCoste&Romberg D-188 and LCR Graviton-EG gravimeters supported by the Trimble GNSS instrumentation. GNSS survey was connected to a few local Greek geodetic network stations (Lagios *et al.,* 1994), while the gravity measurements were referenced to relative gravity bases. One such base was established in the drill site of the AG10 well (see Fig. 2 for location) that was bored within the EC project Corinth Rift Laboratory.

Daily gravity loops included a few repeated points in order to define an accurate secular drift of a gravimeter. Also, independent control points were observed in order to define the repeatability of the gravity measurements that was evaluated to 0.010 mGal (1 mGal = 10^{-5} m/s^2). The rms of the Complete Bouguer anomaly values was 0.017 mGal. The final range of the gravity field within the gravity map in Fig. 2 was 17 mGal.
The Complete Bouguer anomaly (CBA) was calculated with a traditional formula with normal gravity field correction, elevation correction and Bouguer plate reduction for density of 2.50 g/cm3. Terrain corrections were computed to the distance of 167 km from each point. Terrain model included both onshore and offshore topography. The gravity map is shown in Fig. 2.

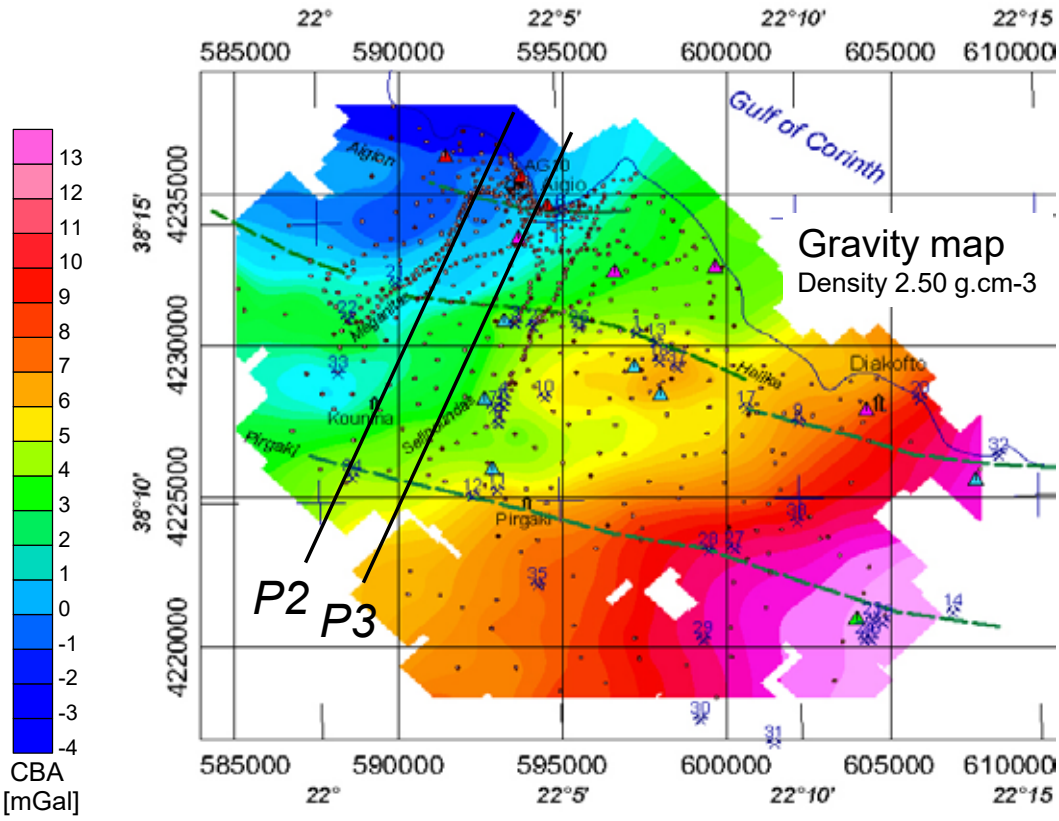

Figure 2. Gravity map of the Aigion area for reduction density 2.50 g/cm3. The total range of the map is 17 mGal. Principal faults are presented as green dashed lines. Two geological profiles P2 and P3 are located in western side of the map. Rock sampling locations are marked by crossed-hammers (mining) symbols. Blue triangles show gravity monitoring stations. Coordinates are WGS84 (degrees) and UTM34N (meters).

Density analysis was performed based on 135 rock samples collected during the field work. Sampling locations are shown in Fig. 2 as 'mining' symbols with numbers; each number represents a few samples from the given location (a,b,c, etc.). Relatively fresh samples were attempted in order to represent respective rock type as well as possible. Still, it is necessary to keep in mind that the samples cannot provide a complete idea on real rock fracturing inside a rock massif. Therefore, they provide approximate values of densities of the given rock types and keep certain freedom for the gravity/density modeling.
In the laboratory, five parameters were determined: bulk (volume), wet (saturated) and grain densities, porosity, and magnetic susceptibility.
The first collection of samples focused on the two principal rock types – limestone and conglomerate. The respective values are presented in Fig. 3, where wet (saturated) density is used, as it represents the most probable status of rocks in the natural conditions inside rock formations. There are 31 samples in the graph showing also average values for limestones and conglomerates, respectively.
As the sampling was further extended, the final collection contained 135 samples. They were separated into 8 groups, while limestone and conglomerate were still the most frequent rock types, see Fig. 4

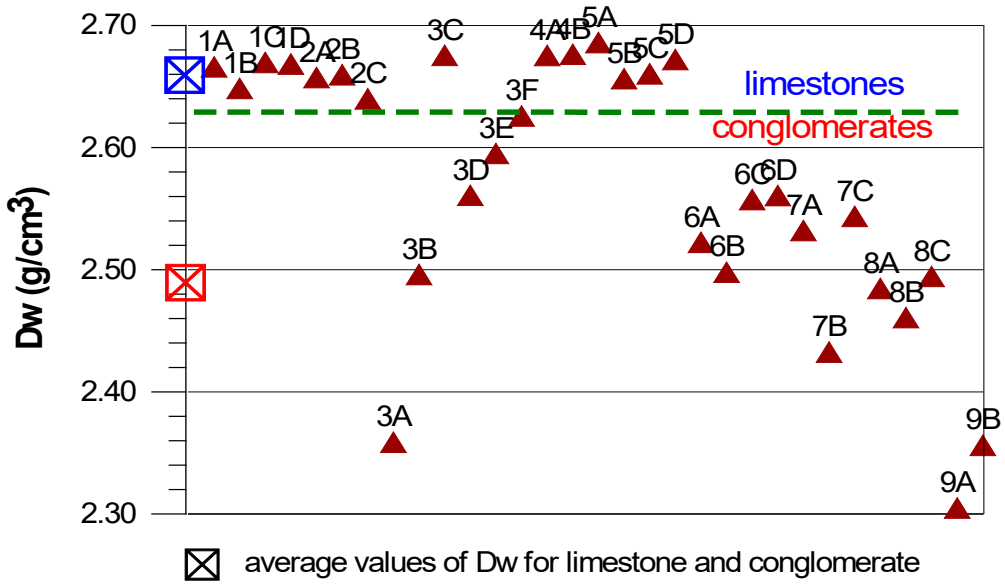

Figure 3. Collection of 31 rock samples (14 samples of limestone, and 17 of conglomerates). Average values of both groups are shown on wet density axis, blue for limestone, red for conglomerate.

rock	n	Db	range	Dw	range	Dg	range	P	range	MS	range
		g.cm-3		g.cm-3		g.cm-3		%		10-6 SI	
L	50	2.66	2.43-2.71	2.67	2.53-2.71	2.70	2.66-2.74	1.6	0.1-10.0	58	5-256
LB	6	2.56	2.45-2.65	2.61	2.55-2.67	2.70	2.65-2.74	5.4	2.0-9.8	71	32-157
R	15	2.58	2.43-2.73	2.61	2.49-2.73	2.66	2.53-2.73	2.9	0.2-10.5	152	30-342
Cst	11	1.82	1.50-2.10	2.14	1.94-2.32	2.70	2.64-2.74	32.7	21.9-43.3	81	18-126
C	39	2.46	2.11-2.66	2.55	2.30-2.68	2.68	2.62-2.76	8.5	5.5-27.2	89	18-353
S	8	2.55	2.42-2.66	2.60	2.51-2.68	2.69	2.67-2.71	5.2	1.9-9.7	244	205-296
GW	3	2.62	2.61-2.63	2.65	2.64-2.66	2.70	2.69-2.70	2.7	2.6-3.0	0	no data
Cal	3	2.66	2.61-2.68	2.67	2.65-2.69	2.70	2.70-2.70	1.7	0.9-3.3	12	7-17

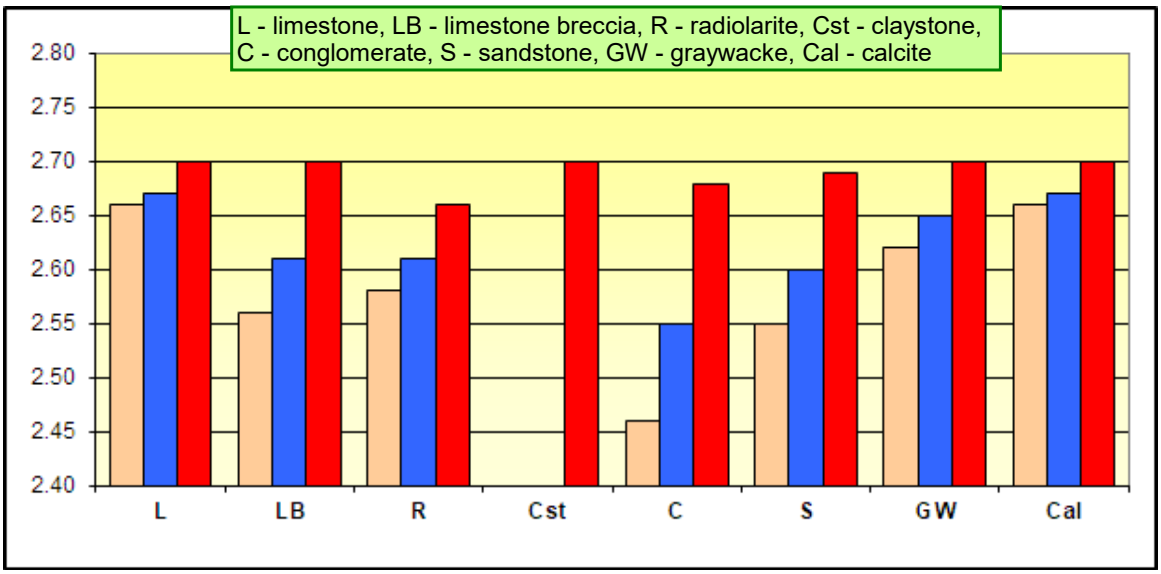

Figure 4. Up: Database of 135 rock samples and respective average values of particular density parameters, as well as porosity and magnetic susceptibility. Each parameter has also respective range of values. Down: Column graph of 3 density parameters for all 8 rock types. It is evident, that grain density Dg has a quite small range (red column), while bulk/volume (Db, orange) and wet/saturated (Dw, blue) densities show much larger differences. Rock type abbreviations are explained in the green window between the two parts of the figure.

Results and discussion

The analysis preceding the gravity modeling focused on the existing geological models. Average density values were attributed to particular formations present in the geological model. The density model was simplified into just two formations – limestone basement, and young rift-related sediments formed mainly by conglomerates (marls, claystones, radiolarites were neglected). Two differential densities were used to calculate these geological models – 0.11 and 0.18 g/cm^3, respectively. The calculated gravity response curves were printed on top of the models.

An example of this procedure is given in Fig. 5. Profile P2 is shown in color where green is limestone formation (basement) and yellow to brown formations are the young sediments. The two calculated gravity curves for both differential densities are presented above the geological model. The general trend is the gravity decrease from south to north due to increase of the thickness of the young sediments. The important features on the calculated curves are the local positive spikes related to fault zones, where the basement is elevated towards the surface – the best example is related to the Helike fault.

However, on top of the figure there are two other lines which show the real observed gravity data on P2 and P3. It is evident that theoretically calculated curves of the model do not fit with the observed data. Therefore, a new density model was developed with certain significant changes with respect to the original geological model, see Fig. 6.

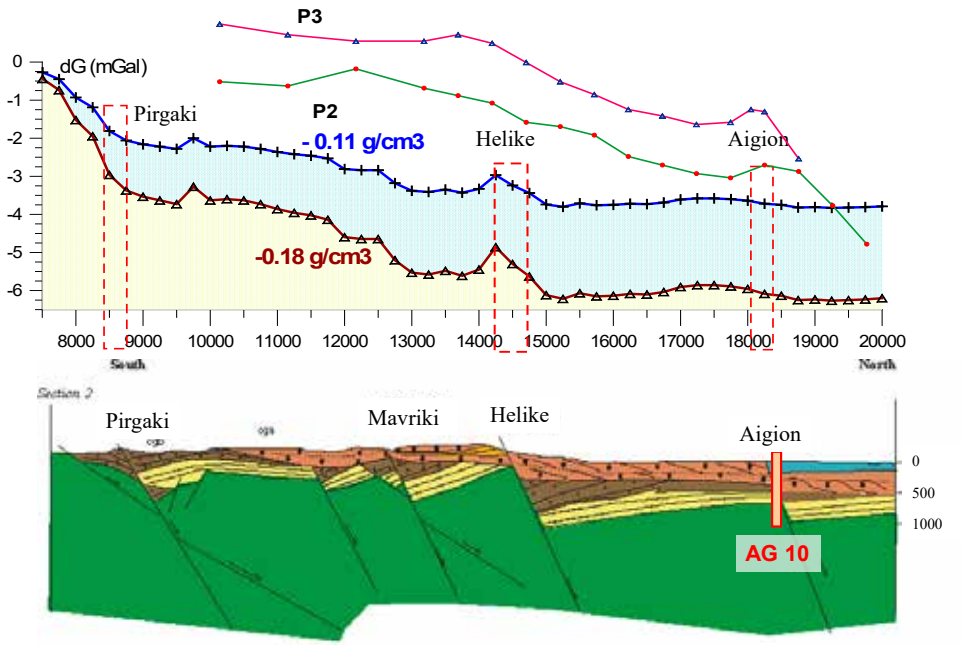

Figure 5. Geological tentative Profile 2 by Ghisetti *et al.* (2001). 2D gravity modeling performed for two differential densities between conglomerates and limestones (0.11 and 0.18 g/cm^3). Residual anomalies based on real observed Bouguer gravity values are different, as shown by two colored lines on top (for both P2 and P3). This justified significant changes in the models, as demonstrated on P3 in Fig. 6.

In the complex Fig. 6 there are actually 4 partial figures. At the bottom (D) the original geological model of Profile P3 (location in Fig 2) is presented. It is evident that all the section between the Pirgaki fault and the Gulf of Corinth is covered by the young sediments of variable thickness which is reaching even more than 1000 m in a few places. The smallest thickness is near the Helike fault where the blocks of the young sediment are strongly tilted to the south.

However, the gravity modelling could not fit the data until in the central part of the profile was completely changed and almost all young sediment removed. Like this the basement has only shallow cover of those young sediments. In part C a simple sketch of the density model is presented so that the descriptions are better visible, contrary to B where the geological formations are presented with raster and colors.

During the modeling process it was necessary to introduce two densities for the limestone formation – 2.70 g/cm^3 at deeper section, and 2.67 g/cm^3 in the upper parts. As well, within young sediments also claystone was incorporated (beside conglomerates) with low density of about 2.35 – 2.40 g/cm^3.

The A part shows observed and calculated gravity curves. In the substantial part of the profile the fit of the two curves is perfect, just in the southern end the data deviated from each other. This may be due to limited extend of the profile,

but also due to too high thickness of conglomerates on the hanging wall side of the Pirgaki fault.
It should be mentioned that the geological and gravity profiles are not completely identical in the field and they differ as for morphology, especially near the Helike fault, where the gravity survey avoided the steep slope of this fault. However, this does not affect the existence of the evaluated difference of the geological and gravity models.

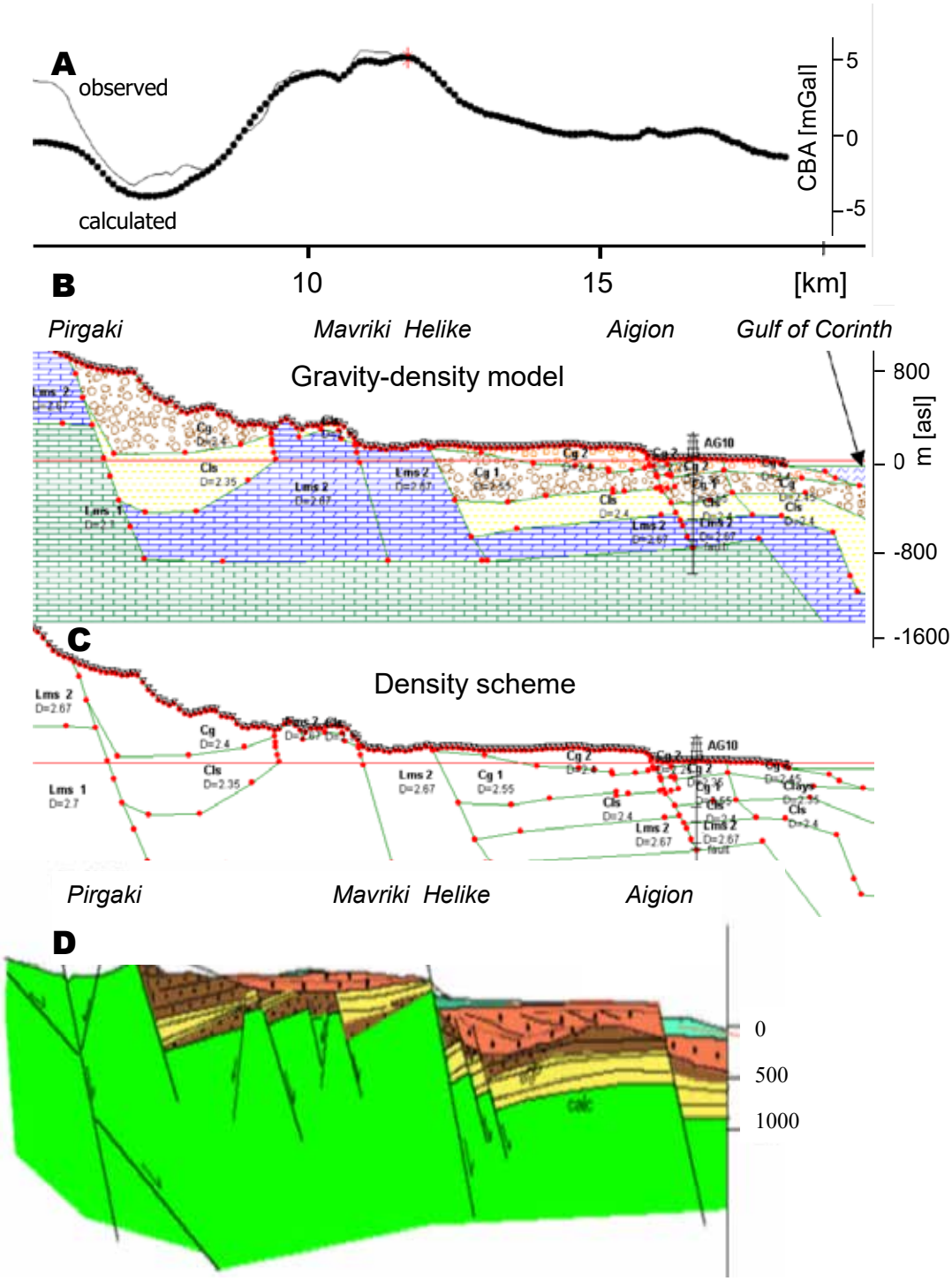

Figure 6. Residual (observed) and calculated gravity (A) for the new model of P3 shown in (B). In (C) simplified density model with rock types (Lms = limestone, Cg = conglomerate) is presented. Gravity/density model (B) is confronted with structural geological model (D) of Ghisetti et al. (2001). The principal difference of the models is exhibited between Helike and Pirgaki faults.

Conclusion

The presented work showed that the geological tentative profiles in complex tectonic and structural setting may suffer from inaccuracies. Therefore, some constraining techniques are recommended to be applied. For geological structures study the gravity method is a suitable geophysical tool.

It is also important to evaluate the rock densities for correct interpretation of the data. In this study we determined the difference between the two principal rock types, limestone and conglomerates, to range from 0.11 to 0.18 g/cm^3. In the Gulf of Corinth rift region it was found (by the gravity surveying and modeling) that the volumes (blocks) of particular formations significantly differ from the geological idea. Along the given NNE-SSW profiles P2 and P3, passing around Aigion city, especially in their central part between the Helike and Pirgaki faults, the volume of young rift-related sediments is much smaller than previously expected. Even if the density difference between basement (limestone) and young sediments cannot be perfectly determined, despite extensive sampling and laboratory work, the density models fit the observed data. In Fig. 6 such a result is presented.

Acknowledgements

The author wishes to appreciate I. Moretti for supporting the idea of a field gravity investigation, F. Ghisetti for sharing geological knowledge of the area, the assistance of M. Seidl with GNSS measurements during the gravity survey, and E. Lagios for providing information on geodetic/gravity networks in Greece. Field operation was supported by the EC project Corinth Rift Laboratory ENK6-CT2000-00056 NAS-3F-CORINTH.

References

Armijo R., Meyer B., King G.C.P., Rigo A., and Papanastassiou D., 1996. Quaternary evolution of the Corinth Rift and its implication for the Late Cenozoic evolution of the Aegean. Geophys. J. Int., 126, 11-53.

Bernard, P. et al., 1997. The Ms=6.2, June 15, 1995 Aigion earthquake (Greece): evidence for low angle normal faulting in the Corinth rift. J. Seism., 1, 131-150.

Ghisetti, F.C. and Vezzani, L., 2005. Inherited structural controls on normal fault architecture in the Gulf of Corinth (Greece). TECTONICS, Vol. 24, TC4016, doi:10.1029/2004TC001696

Ghisetti, F.C., Vezzani, L., Agosta, F., Sibson, R. and Moretti, I., 2001. Tectonic setting and sedimentary evolution of the south-west margin of the Corinth rift (Aigion – Xylokastro area). Report 56 207, IFP Paris, 22 p.

Lagios, E., Chailas, S., Hipkin, R.G. and Drakopoulos, J., 1994: Gravity and topographic data banks of Greece. NKUA, Publ. 4/94, 1-38.

Moretti, I., Sakellariou, D., Lykousis, V. and Micarelli, L., 2003. The Gulf of Corinth: an active half graben? J. Geodynamics, 36, 323-340.

Mrlina, J. (2001): Density measurements and plans for gravity survey and monitoring in the Aigion area. Corinth Rift Laboratory Workshop, Aigion, 2001.

Rigo, A., Lyon-Caen, H., Armijo, R., Deschamps, R., Hatzfeld, D., Makropoulos, K., Papadimitriou, P. and Kassaras, I., 1996. A micro-seismic study in the western part of the Gulf of Corinth (Greece): implication for large-scale normal faulting mechanisms. Geophys. J. Int., 126, 663-688.

17th INTERNATIONAL CONGRESS of the Geological Society of Greece

BULLETIN OF THE GEOLOGICAL SOCIETY OF GREECE, SP. PUBL.

EXTENDED ABSTRACT 224

Gravity monitoring at Santorini volcanic island, Greece

Mrlina J.[1]
(1) Institute of Geophysics CAS, Prague, Czechia, jan@ig.cas.cz

Introduction and objectives

Santorini island in the Aegean Sea is a famous volcanic structure, not only because of its beauty, but mainly for its catastrophic eruption about 3500 years ago. This eruption eliminated the Minoan civilization in Crete, and caused the volcano collapse forming the current day caldera. The volcano is one of the principal volcanoes of the Greek volcanic arc related to the collision of the African and Eurasian plates. The arc comprises also Kos-Nisyros volcanic system, the Milos island, and the Methana peninsula, see Fig. 1.
This volcano is still active, with the last lava flow in the central island of Nea Kameni in 1950. The island hosts numerous population and therefore is a subject of multiparameter control, starting with seismological permanent observations, GNSS (Global Navigation Satellite System) with permanent and campaign-style stations, gas monitoring, etc.
This situation was a motivation of introducing repeated gravity monitoring campaigns in 2013, after the volcano increased activity in 2011-2012. There was no lava eruption, however, the signals from GNSS were showing the inflation of the caldera with the central point in Nea Kamenni. Previously, there was an attempt of such research, but actually only two campaigns could be compared – the one in the 1970s, and the other in 2012-2014 (Paraskevas et al., 2021). Such gravity monitoring was applied e.g. in the Merapi volcano area (Indriana et al., 2023).
IGCAS (Institute of Geophysics, Czech Academy of Sciences) could support and perform this 4D gravity investigation thanks to the EPOS/CzechGeo project, see Acknowledgement. The objective was to indicate possible changes in the gravity field that may be related to mass changes and/or fluids movements inside the caldera.

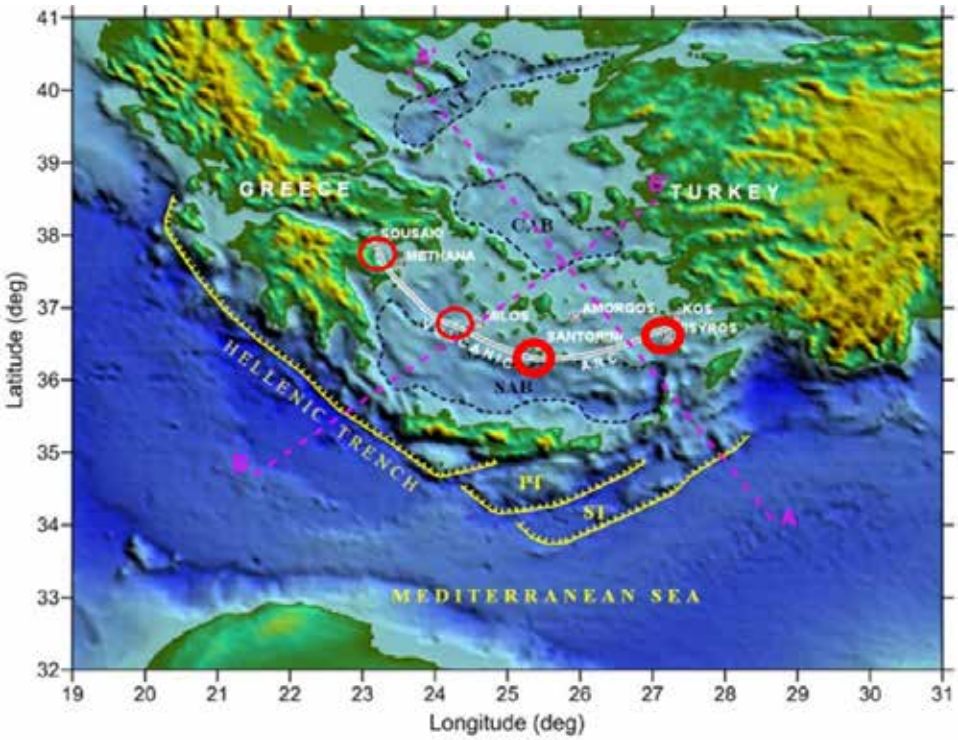

Figure 1. Position of Greek volcanic arc with four principal volcanic edifices – from left to right – Methana, Milos, Santorini, Nisyros.

The island is formed by lava extrusions of dacite, ryodacite, andesit and basalt, but the surface is covered mainly by pyroclastic formations of various composition, see Fig. 2. There are also outcrops of basement formed by carbonates (E, SE), but also metamorphics (slope to the new port) on the western side of Thira (Thera in Fig. 2). Tectonic zones are marked by white lines, as the principal ones of Columbo and Kammeni ones.

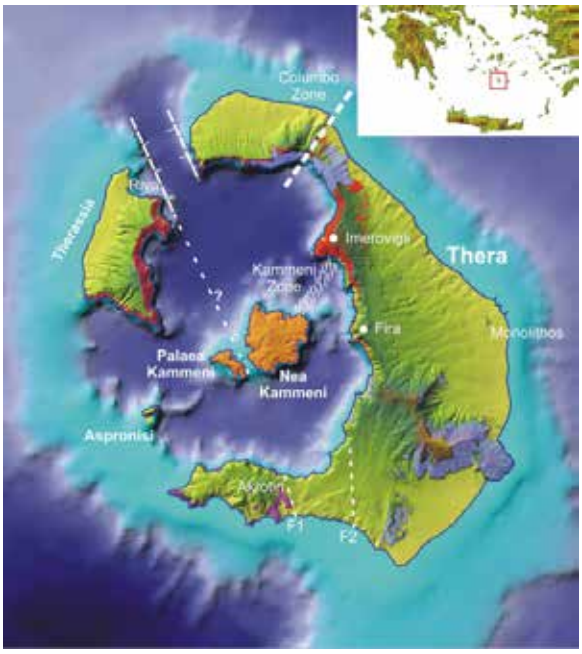

Figure 2. Position of principal tectonic features (Kammeni zone, Columbo zone) in Santorini, and principal lava flows (brown – dacite, ryodacite, andesite; light violet – basalts; medium violet – carbonate basement; green – various pyroclastic formations); after Lagios et al. (2013) and Druitte et al. (1999). Bathymetry after Nomikou et al. (2012).

The primary geophysical method for monitoring volcanoes and active faults is seismology, showing the active regions within the Earth crust. In Santorini two areas of different type of seismicity are located in the center of the caldera, and to the NE of Thira part of Santorini, see Fig. 3. Around Nea Kameni the epicenters are concentrated to a small area of about 5 x 3 km, actually along the Kammeni fault zone (see Figs. 2, 3), while in the NE they are spread on a large area with a diameter of more than 10 km.

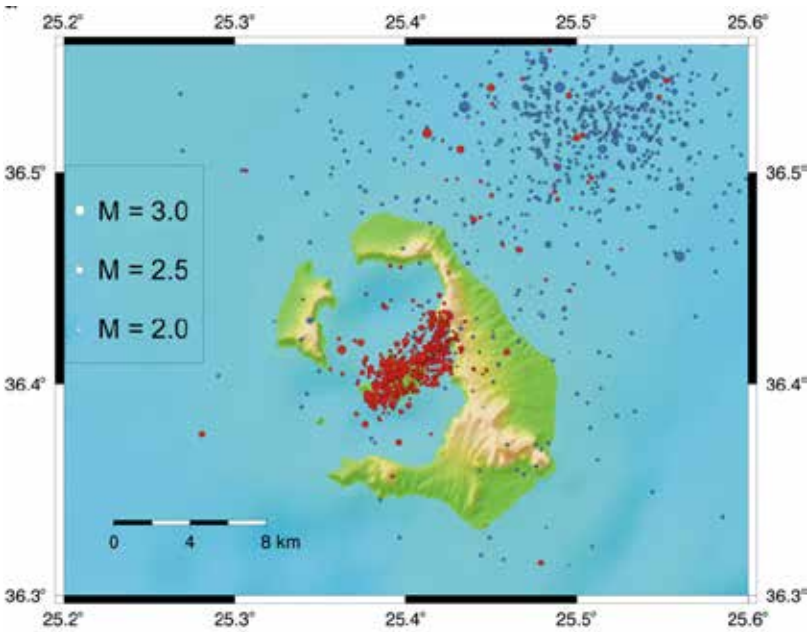

Figure 3. Seismicity around Santorini volcano in 1990-2010 (Lagios et al., 2013). It is evident that many events were recorded inside the caldera where Nea Kameni island is located. Earthquakes epicenters are accumulated within quite small elliptical area with longer axis less than 5 km. On the other side, in the area NE of Santorini seismicity shows much larger spread of epicenters around submarine volcano Kolumbos.

Gravity monitoring

The gravity monitoring is based on repeated measurements of gravity at a fixed network of stations. The observations at each station consist of a set of gravimeter readings, when a homogenous set has to be achieved (outlying readings are cancelled), as presented e.g. by Mrlina (2009, 2024).

Most, or all stations of the daily observation loop are measured three to five times in order to evaluate daily drift of the gravimeter. In this project one LaCoste&Romberg D-188 was used (2013-2021), later the Scintrex CG-6 gravimeter (2019-2024) was used, while in 2019 and 2021 both gravimeters were used simultaneously to provide enough overlap, see Fig. 4.

The network was based on the stations of NKUA (National Kapodistrian University of Athens) with the reference base stations No. 20, see the photos in Fig. 4. This base seems to be a reference point also for other gravity surveys in the Santorini island.

The old stations were continuously supplemented by new stations, as the author wished to cover some areas more densely, or to focus on some areas of higher interest, see Fig. 5. These new stations were selected in stable locations near churches, or similar, to ensure stable gravity observations. However, due to the general noise from the sea and from the volcano itself, exceptionally also of vehicles/people movement, some disturbed readings had to be eliminated. Some stations are increasingly difficult to operate due to difficult access in towns with enormous traffic (Fira, Oia).

The gravity campaigns usually lasted 9-13 days and also included one or two days to connect to Nea Kameni island stations by boat.

Each tie between any two stations was measured normally four times, which required a lot of driving by car (about 4 – 5 thousand km), or, in some cases, walking.

All these measurements, even simultaneous with two gravimeters, were performed as a single-man-job by the same operator (author), with the same gravimeters, and in the same period of a year.

Figure 4. Position of the principal reference base station in Monolithos to NE of the airport. It is a solid pillar with concrete filling at the parking near Monolithos church, built on the limestone basement block (see the hill behind the base). Gravity readings were always stable at this base. Gravimeter Scintrex CG-6 is presented at the bottom photo, LaCoste&Romberg D-188 gravimeter is inside to black box to stay protected from sunshine.

Some ties were repeated in other days in order to evaluate the repeatability. Standard deviation of the measurements was usually better than 4 uGal.
Each campaign was processed and the differences (ties) between stations were calculated. Then these differences were compared between any couple of campaigns. In this way the temporal changes of gravity field were evaluated. Then, the changes for each point were obtained and could be interpolated into a map. Such differential map is presented in Fig. 6 for the years 2013 versus 2021.

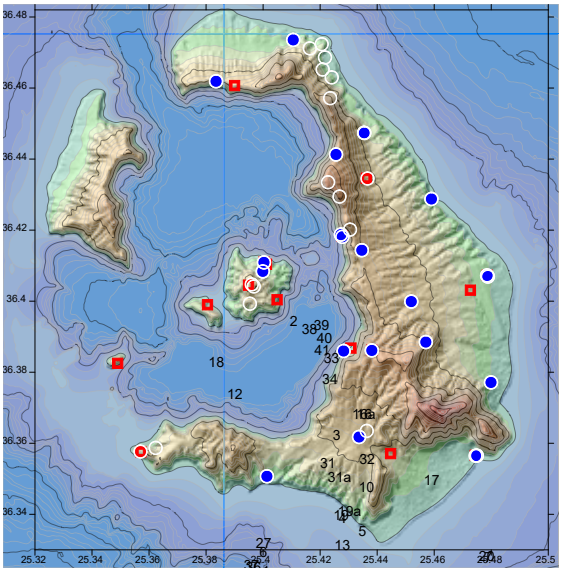

Figure 5. Position of the gravity monitoring network. Red rectangles are the old stations of the 1970s, full blue circles are the stations established by NKUA (Lagios et al., 1988), and white circles are stations used and established by author (IGCAS). Reference base station is No. 20 located in Monolithos to NE of the airport.

Results and discussion

The analysis of the data was focused on the temporal gravity difference between 2013 and 2021 (as in 2021 the campaign was performed with the LaCoste&Romberg D-188 gravimeter for the last time).
As mentioned above, the gravity differences at each station were used to interpolate all the differential values and the differential map was obtained, see Fig. 6.
There are two principal features in the map. The negative gravity changes in the northeastern side of Thira at the stations 3 and 16, and the positive change at the station 26 in the new port.
Most important is the negative change. It can be caused by continuous extension along the Kolumbo fault zone, which may decrease the volume density of the rocks within this zone. At the same time it may be responsible for the development of the Kolumbo submarine volcano with huge amount of fluids emissions through the opening fractures.
In order to exclude the impact of elevation change (that affect gravity values), the vertical component of the permanent GNSS station SANT was checked (courtesy of V.Sakkas). It is clear that within the period under study there was just a slight uplift 2013-2015 of less than 10 mm. Such value cause a gravity change of 2 uGal, which is almost negligible in respect to the amplitude of the negative zone (-50 uGal). Therefore the vertical displacement cannot be responsible of that significant decrease of gravity.
Another potential cause of the gravity decrease could be the emissions of fluids, but this is less probable as the released fluids would be substituted by water or other fluids coming from the deeper subsurface.
On the other hand, the old data 1976-2012 were showing the principal gravity increase in Nea Kameni (evaluated from data of Paraskevas et al., 2021), which was probably related to the magma and fluids rising to surface before the 2011-2012 crisis. During this crisis no lava erupted to surface, but the GNSS data showed inflation of the caldera and active fluid emissions were also encountered. In the NE there was also relative gravity decrease recorded.
This may justify the hypothesis that in the NE side of Santorini there may be an ongoing extension process.
For this reason the Author established another four new gravity monitoring stations 38-41 in the northeastern side of the island, see the white circles 38-41 in Fig. 5 and dark red triangles in Fig. 6. These stations were observed in 2023 and 2024, which is too short period for making any conclusions. The stations will be repeated in each potential future gravity monitoring campaign in the Santorini caldera.

The sharp gravity change between two nearby stations 10 and 26 (Fig. 6) can be affected by very sharp vertical difference, as 10 is located on the top of the cliff, while 26 is down in the new port. Here more investigation is needed to evaluate the impact of enormous change of air pressure during the measuring of this tie.

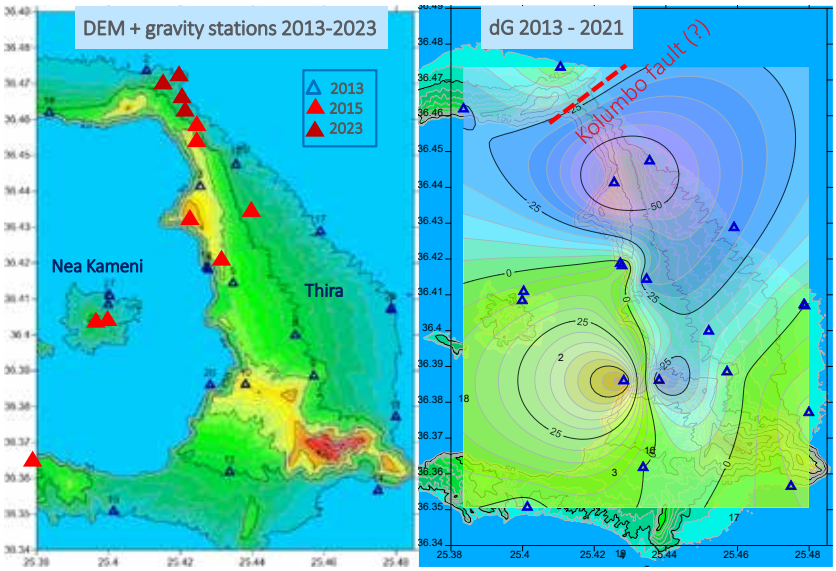

Figure 6. Left: Gravity monitoring stations used by IGCAS in 2013 (blue triangles established by Lagios et al., 1988), and established by IGCAS in later years 2015 and 2023 (red and brown triangles) for 4D gravity measurement campaigns. Right: Gravity difference between 2013 to 2021 in uGal (10^{-8} ms^{-2}) - principal feature is the gravity decrease in NE part of Thira (over -50 uGal) at stations 3 and 16.

Conclusion

This paper documents that the gravity monitoring of the Santorini volcanic island shows temporal gravity changes. As the vertical surface displacements play negligible role in affecting the gravity changes in the study period 2013 – 2021, the changes must be explained by geological/geodynamic processes.

Most significant is the temporal gravity decrease in the northeastern side of Santorini (Thira) where a long-term extension process in the underground may be causing the decrease of the volume density of the rock massif. Such extension within the Kolumbo fault zone also enables the opening for the currently active volcanic process around the Kolumbo underwater volcano with active fluids emissions.

In order to investigate this feature of the gravity field change, dense network of the monitoring stations was established in 2023 around the assumed Kolumbo fault zone.

Additional Comments

- In 2024 the author performed a small gravity survey in the NE part of Thira in order to investigate the Kolumbo fault zone which is related to the Kolumbo underwater volcano. This volcano has been recently very active with a lot of gas emissions. Seventy gravity stations were measured and data processed into the Complete Bouguer anomaly (CBA) with a traditional formula with normal gravity field correction, elevation correction and Bouguer plate reduction for density of 2.50 g/cm3. Terrain corrections were computed to the distance of 167 km from each point. Terrain model included both onshore and offshore topography. The gravity map has to be enlarged during next campaigns so that the tectonic pattern of this part of Thira can be updated.
- Similar gravity monitoring is performed by Author in Kos- Nisyros caldera, to be presented next time.

Acknowledgements

The author appreciates the financial support of the EPOS/CzechGeo project No. LM2015089. As well, Author thanks E.Lagios for introducing the existing stations in 2013 and V.Sakkas for performing random GNSS campaigns in Santorini and providing info on vertical movement trend from the permanent GNSS station SANT.

References

Druitt, T.H., Edwards, L., Mellors, R.A., Pyle, D.M., Sparks, R.S.J., Lanphere, M., Davies, M., Barriero, B., 1999. Santorini Volcano. Geological Society Memoir 19, 165.

Indriana, R. D., Nurwidiyanto, M. I. and Mrlina, J. 2023. Merapi complete Bouguer anomaly changes based on gravity data of Merapi in 2020-2019. AIP Conference Proceedings. Vol. 2738. Melville: American Institute of Physics, 2023 DOI: 10.1063/5.0140956.

Lagios, E., Drakopoulos, J., Hipkin, R.G. and Gizeli, C., 1988. Microgravimetry in Greece: applications to earthquake and volcano-eruption prediction. Tectonophysics, 152, p.197-207.

Lagios, E., Sakkas, V., Novali, F., Bellotti, F., Ferretti, A., Vlachou, K. and Dietrich, V., 2013. SqueeSAR™and GPS ground deformation monitoring of Santorini Volcano (1992–2012): Tectonic implications. Tectonophysics, TECTO-125831, 22p. http://dx.doi.org/10.1016/j.tecto.2013.03.012.

Mrlina, J., 2009. 4D Gravity – fluids monitoring in reservoirs. – Proc. Int. Petroleum Technology Conf., Doha, Qatar, 7-9 Dec., 6 pp., ISBN 978-1-55563-272-4.

Mrlina J., 2024. Application of Gravimetry to Investigation of Volcanism – Examples from West Bohemian Massif and Greece. Int. Journal of Geology and Earth Sciences (IJGES), Vol 10, No. 2, p.38-42. doi: 10.18178/ijges.10.2.38-42.

Nomikou, P., Carey, S., Papanikolaou, D., Croff Bell, K., Sakellariou, D., Alexandri, M., Bejelou, K., 2012. Submarine volcanoes of the Columbo Volcanic Zone NE of Santorini Caldera, Greece. Global and Planetary Change. http://dx.doi.org/10.1016/j.gloplacha.2012.01.001.

Paraskevas, M., Paradissis, D., Raptakis, K., Nomikou, P., Hooft, E. and Bejelou, K., 2021. Gravity observations on Santorini island (Greece): Historical and recent campaigns. Contributions to Geophysics and Geodesy Vol. 51/1, 1–24.

17th INTERNATIONAL CONGRESS of the Geological Society of Greece

BULLETIN OF THE GEOLOGICAL SOCIETY OF GREECE, SP. PUBL.

EXTENDED ABSTRACT 225

Ostracod-based environmental reconstruction of Lake Koronia, (Central Greece) during the Holocene

Navrozidou, V.[1,5], Koukousioura, O.[1,2], Doani, S.[1], Frenzel, P.[3], Triantaphyllou, M.[4], Albanakis, K.[1], Syrides, G.[1]

(1) Aristotle University of Thessaloniki, Thessaloniki, Greece, vnavrozi@geo.auth.gr (2) University of Cologne, Cologne, Germany (3) Institute of Earth Sciences, Friedrich-Schiller-Universität Jena, Jena, Germany (4) National and Kapodistrian University of Athens, Athens, Greece (5) The Goulandris Natural History Museum – Greek Biotope/Wetland Centre Thermi, Greece

Introduction

Lake Koronia is located in the western lowland area of the Mygdonia Basin, northeast of the city of Thessaloniki in northern Greece (40° 41′ N, 23° 09′ E, 75 m a.s.l.). It is the remnant of a once larger lake in the region (Psilovikos, 1977), but is now a shallow, hypertrophic and heavily polluted water body (Moustaka-Gouni *et al.*, 2012). It has experienced substantial degradation over time due to human activities, but has also dried up several times in the past two decades (2002, 2007, 2009 and 2014), resulting in its current state, formerly the fourth largest lake in Greece (Demertzioglou *et al.*, 2022). Despite its current ecological challenges, Lake Koronia is recognized as a protected wetland under international and national legislation, highlighting its importance (Malamataris *et al.*, 2017).

The aim of the present study was to investigate the paleoenvironmental evolution of Lake Koronia and the distribution of ostracod assemblages through time using a combination of core and recent surface sediment samples.

Methods

The KOR core (40°41'45.4" N, 23°11'08.8"E; Fig. 1) was drilled at 71 m b.s.l. and reached a depth of 368 cm. A total of 36 sediment samples were studied in order to reconstruct the paleoenvironmental evolution of the lake. In addition, two sediment samples were collected by boat, using an Ekman grabber from the upper 1 cm of the lake bottom for the analysis of the recent ostracod fauna. For ostracod analysis, 50 ml of each surface bottom sediment sample was wet sieved with tap water through a 125 μm pore size standard sieve. For core samples, 10 g of dried sediment was treated with hydrogen peroxide (H_2O_2) and wet sieved as described above. The residue was oven dried at 60°C and all ostracod valves over the >125 μm fraction were hand-picked under a Zeiss Stemi 305 binocular stereoscope. Species were identified, counted, and stored in microslides. Taxonomic identification of the species was based on the morphological features of the carapace using several published works, ostracod atlases and ostracod databases. In addition, radiocarbon dating was performed using accelerator mass spectrometry (AMS ^{14}C; Beta Analytic USA laboratory). Finally, a Q-mode cluster analysis was performed for the sediment samples of the core.

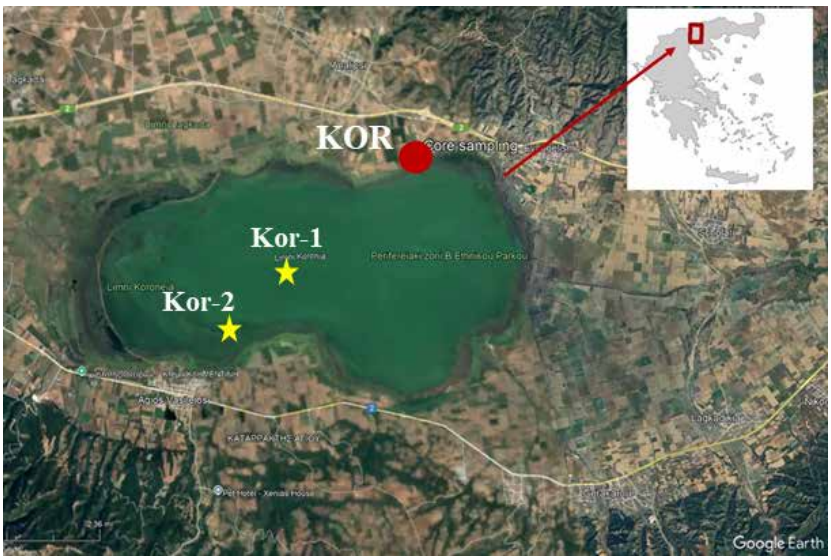

Figure 1. Sampling stations of surface sediments and the location of KOR core in Lake Koronia (modified from Google Earth).

Results and conclusions

The ostracod assemblage of Lake Koronia, both in the surface sediments and in the KOR sedimentary sequence, consisted of five taxa: ex gr. *Candona* juveniles, *Cyprideis torosa*, *Darwinula stevensoni*, *Heterocypris salina* and *Limnocythere inopinata*. In the recent surface sediments, station Kor-1 had a significantly higher abundance compared to station Kor-2. The *Candona* species dominated the assemblage, while *L. inopinata* was the second most abundant species of the total ostracod fauna recorded in the lake, with all other taxa showing relatively low abundances.

The ostracod valves obtained from the core (KOR) were well preserved and relatively abundant, with the number of valves/g reaching high values in some intervals, while the diversity indices showed relatively low values. The species *L. inopinata* dominated the assemblages, reaching even 100% in several intervals, followed by ex gr. *Candona* juveniles and *H. salina*. The species *D. stevensoni* and *C. torosa* accompanied the assemblage with lower but significant values.

The resulting dendrogram of the Q-mode cluster analysis performed on the KOR core sedimentary sequence, pointed out three distinct groups of samples associated with different assemblages and thus different paleoenvironmental conditions. The paleoenvironmental record of Lake Koronia revealed conditions of slightly elevated salinity between 2752-1437 cal. yr BP, occurring in a shallow environment with clear water and the absence of benthic macrophytes. The presence of *Cyprideis torosa*, a true brackish species (Meisch, 2000), further confirmed the elevated salinity during this period. After 1437 cal. yr BP, the fauna diverged significantly, and the environment transitioned to a purely lacustrine system, extremely shallow and with extensive macrophyte vegetation. At the top of the sedimentary sequence, the environment undergoes a further change, characterized by a significant increase in diversity, a deepening of the environment, and the establishment of well-oxygenated water conditions. This interval is comparable with the recent surface sediments in terms of faunal composition and diversity, but not in terms of abundance which was significantly higher at the recent stations.

Lake Koronia is a severely impacted lake that has faced significant degradation over the past few decades. Over the last 20 years, the lake has experienced a dramatic decrease in volume, surface area, and maximum depth (currently almost 2 meters) due to unsustainable water resource management. Further investigation of the benthic conditions and biota, coupled with the paleoenvironmental record of the lake, will be invaluable in this important biotope ecological assessment.

Acknowledgements

Sampling support for the recent sediment samples was provided by the Greek Biotope Wetland Centre.

References

Demertzioglou, M., Genitsaris, S., Mazaris, A.D., Kyparissis, A., Voutsa, D., Kozari, A., Kormas, K.A., Stefanidou, N., Katsiapi, M., Michaloudi, E., Moustaka-Gouni, M., 2022. A catastrophic change in a European protected wetland: From harmful phytoplankton blooms to fish and bird kill. Environmental Pollution 312, 120038.

Malamataris, D., Kolokytha, E., Mylopoulos, I., Loukas, A., 2017. Critical review of adaptation strategies for the restoration of Lake Koronia. European Water 58, 203-208.

Meisch, C., 2000. Freshwater Ostracoda of Western and Central Europe. In Schwoerbel, J. and P. Zwick (eds), Süßwasserfauna von Mitteleuropa 8/3, Spektrum Akademischer Verlag, Heidelberg, Berlin, 522 pp.

Moustaka-Gouni, M., Michaloudi, E., Kormas, K.A., Katsiapi, M., Vardaka, E., Genitsaris, S., 2012. Plankton changes as critical processes for restoration plans of lakes Kastoria and Koronia. European Water 40, 43-51.

Psilovikos, A., 1977. Paleogeographic development of the basin and lake of Mygdonia (Langada-Volvi area) GreecePh.D. Thesis, Aristotle University of Thessaloniki, Thessaloniki, 156 p.

17th INTERNATIONAL CONGRESS of the Geological Society of Greece

BULLETIN OF THE GEOLOGICAL SOCIETY OF GREECE, SP. PUBL.

EXTENDED ABSTRACT 226

Rapid Detection of Landslides Triggered by Mediterranean Cyclones Using Google Earth Engine and Open-Access Data

Nefros C.[1], Kitsara G.[2], Loupasakis C.[1], Giannakopoulos C.

(1) Laboratory of Engineering Geology and Hydrogeology, School of Mining and Metallurgical Engineering, National Technical University of Athens, Athens, Greece, email: kostasnefros@central.ntua.gr

(2) Institute for Environmental Research and Sustainable Development, National Observatory of Athens, Athens, Greece

This research introduces a methodological framework integrating Google Earth Engine and open-access data, to rapidly detect landslides triggered by Mediterranean Cyclones, which nowadays pose an increasing threat for the eastern Mediterranean region. This framework aims to enhance the timely identification and management of these hazards.

Introduction / Background

Medicanes or Mediterranean Cyclones are extreme meteorological phenomena, characterized by intense rainfall and winds speeds approaching hurricane strength (Lagouvardos et al., 1999). Their intensity and duration are expected to increase, along with a spatial shift toward the Ionian Sea and the eastern coasts of southern Italy (González□Alemán et al., 2019). Beyond causing floods and coastal waves, medicanes can trigger a series of landslide events within a short timeframe. These landslides often affect extensive areas and have impacts on various sectors (social, economic, transportation), making their management challenging for local authorities. This study introduces a methodological framework that integrates open access data, including Sentinel-2 and Google Earth imagery, combined with the computational power of Google Earth Engine (GEE), for the rapid identification and mapping of landslides activated by medicanes. The frequent revisit times of Sentinel-2 satellites over Europe and the high processing capabilities of GEE make this framework a valuable tool for the timely mapping of landslides. By enabling authorities to quickly assess the extent of landslide activity, following a medicane, the framework facilitates more effective management. The Ianos medicane, which struck the Cephalonia Island, Greece, in September 2020, was selected as a case study. Using the proposed approach, the activated landslides were identified and mapped. Moreover, the framework proved particularly effective in detecting landslides in remote, mountainous regions, underscoring its potential in difficult to reach areas.

Methods

The proposed framework is illustrated in Figure 1 and it leads to the creation of a comprehensive landslide inventory after a medicane, by using remote sensing techniques and open access data. The data used in the proposed methodology is derived exclusively from open-access or publicly available databases.

Case Study – Ianos Medicane

A medicane named Ianos by the National Observatory of Athens (NOA), struck Greece between 17 to 19 September 2020, severely impacting areas such as Cephalonia Island, Karditsa, and Fthiotida (Lekkas et al., 2020; Zekkos et al., 2020). According to Lagouvardos et al. (2022), the daily accumulated rainfall at the “Antipata” meteorological station in northern Cephalonia reached 644.7mm, which is the highest ever recorded value during a medicane and among the highest ever recorded in Greece. This extreme precipitation significantly exceeded the local precipitation thresholds for landslide activation across the Cephalonia Island, triggering widespread landslides. These landslides caused numerous damages to buildings, bridges, the local road network and other critical infrastructure. The large number of the activated landslides, combined with their extensive distribution, including remote and mountainous areas, posed significant challenges for local authorities in promptly documenting and mapping these events for their effective management. Cephalonia Island, situated in the Ionian Sea, in the west Greece, is characterized by steep terrain, limestone-dominated geology prone to karstification, and a dynamic hydrological network. These features, along with its history of frequent landslide activity, render Cephalonia particularly susceptible to landslides during heavy rainfall events. For these reasons, the island of Cephalonia was selected as a case study to examine the landslides activated by Ianos, highlighting the potential of the proposed framework.

Figure 1. Proposed Framework

Results and Discussion

As illustrated in Figure 2, by using the GEE, the Cephalonia Island was established as the Area of Interest (AoI) along with the time period before and after Ianos medicane. Sentinel-2 images were downloaded for the AoI.

Figure 2. GEE Environment

Cloud cover was mitigated in the Sentinel-2 images using the QA60 band. Specifically, bit 10 (value 1), was used to detect opaque clouds, while bit 11 (value 1) identified cirrus clouds, ensuring clearer imagery for analysis. The Normalized Difference Vegetation Index (NDVI) was then calculated for pre and post Ianos conditions, using the following equation:

$$NDVI = \frac{NIR-R}{NIR+R} \quad (1)$$

where the R factor corresponds to the red band, and NIR the near infrared band of the electromagnetic spectrum. NDVI values range between -1 and 1, reflecting vegetation health and coverage. Slope information was assessed using the Shuttle Radar Topography Mission (SRTM) Digital Elevation Model (DEM) provided by the of the United States Geological Survey (USGS). The SRTM DEM is version GL1, obtained from OpenTopography (portal.opentopography.org). This version provides a 30-meter resolution, ensuring reliable topographic representation. Potential landslide areas were identified based on two criteria: NDVI differences greater than 0.2 between pre and post Ianos, and slope angles exceeding 15°.

Subsequently, CHIRPS (Climate Hazards Group InfraRed Precipitation with Station data) precipitation data provided by the University of California, Santa Barbara (UCSB), were integrated into GEE to estimate the local/regional precipitation values that activated the landslides. CHIRPS were used to generate a raster file representing rainfall distribution over the AOI on the date medicane Ianos impacted Cephalonia. This dataset enables the spatial correlation of each detected landslide with the precipitation values, responsible for its activation. Thus, it facilitates the creation of a comprehensive landslide inventory, which

can be further used during the assessment of the local precipitation Intensity Duration (ID) thresholds.
Figure 3, illustrates the areas identified as potential landslides using the proposed framework, focusing on the Myrtos Beach area in north-western Cephalonia.

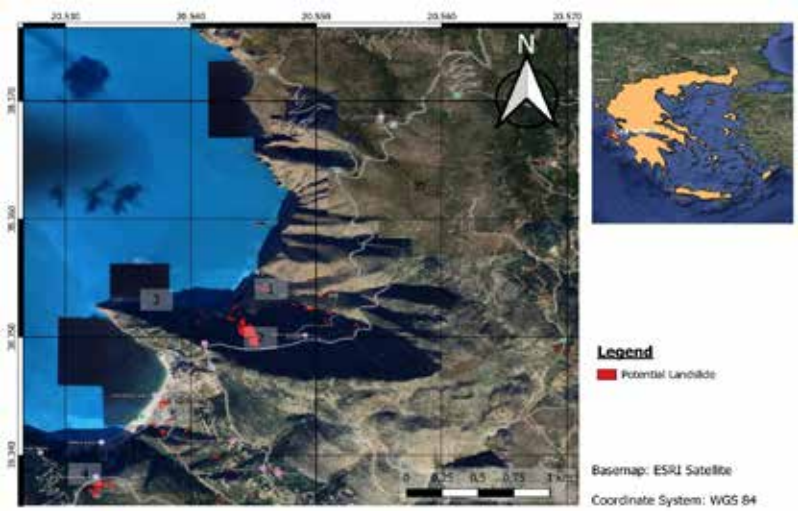

Figure 3. Potential Landslides according to GEE

Verification of these areas was conducted using high-resolution Google Earth imagery, as shown in Figure 4.

(a) (b)

Figure 4. Validation of the landslides using Google Earth Images before Ianos (a) (14-5-20) (Google Earth a) and after Ianos (b) (26-6-2021) (Google Earth b).
Results verification was also achieved using open-access landslide inventories derived from in situ investigations carried out after Medicane Ianos (Lekkas et al., 2020; Zekkos et al., 2020). These independent datasets provide ground-truth validation, supporting the accuracy and reliability of the detected landslides.
As it was revealed, the framework did not provide sufficient results in areas with sparse or absent vegetation, due to its reliance on NDVI changes. To address this issue, the landslide inventory was enriched with additional open access data and advanced remote sensing techniques, such as Persistent Scatterers Interferometry (PSI) processed using SNAP software provided by ESA. Specifically, PSI derived ground displacement velocities were analyzed, and a threshold of -2 mm/year was applied to identify areas exhibiting significant motion, improving landslide detection in non- vegetation regions.
The proposed framework introduces an efficient and rapid methodology for landslide detection by integrating GEE. Nevertheless, it has limitations, particularly in areas with sparse or absent vegetation, as it relies primarily on two criteria: slope angle and NDVI change. In the current study, this limitation was mitigated by incorporating supplementary open -access data and additional remote sensing techniques. However, future studies could address this issue further by enriching the GEE code with additional criteria, improving the framework's performance in diverse landscapes and enhancing its applicability. The final landslide inventory containing more than 600 landslides, is presented in Figure 5

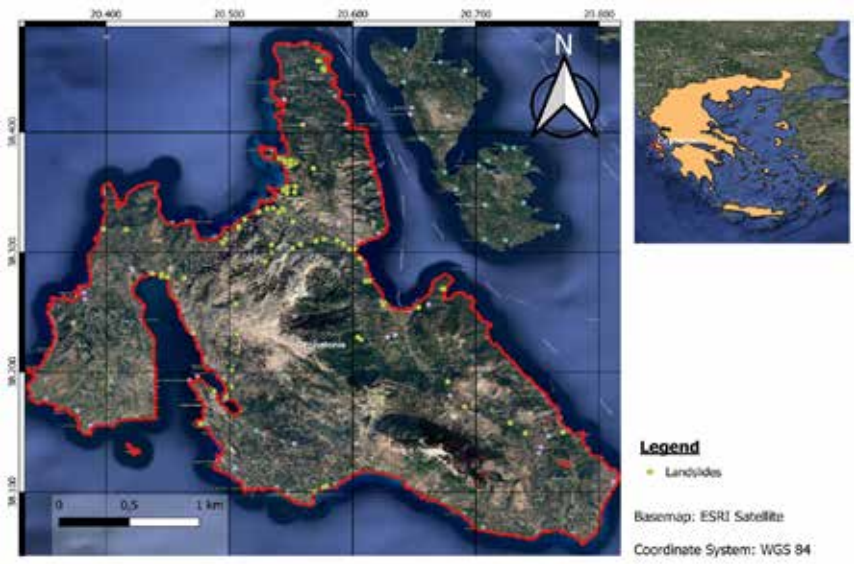

Figure 5. Landslide Inventory Map

These findings confirm the high intensity of the Ianos medicane and provide insight into the exceptionally large number of landslides it triggered. As illustrated in Figure 5, the activated landslides are distributed widely across the island. This widespread impact underscores the challenge of relying solely on in situ investigations for their identification and mapping, which require significant resources, time, and effort, particularly in remote and difficult to access areas.

The proposed framework, integrating open-access data and the computational power of Google Earth Engine (GEE), emerged as an effective, low-cost solution to tackle these challenges. By automating and accelerating the identification and mapping process, this framework minimizes the reliance on extensive field surveys while maintaining accuracy and spatial coverage.

Furthermore, this study highlights the potential of GEE, as a fundamental component of the proposed framework, demonstrating its ability to rapidly process and analyze large volumes of geospatial data. This capability is critical for the prompt identification and mapping of landslides, enabling authorities to respond more effectively. By facilitating timely decision-making and resource allocation, the framework contributes to the broader goal of efficient disaster management and mitigation, even to such extreme events, as the medicanes.

Conclusions

Medicanes are extreme phenomena that, due to climate change, pose nowadays a significant threat to regional or/and local communities in the Mediterranean region. Their destructive impact, including landslides activation, underscores the urgent need for effective disaster management strategies. This study not only highlights the severity of this threat but also introduces a practical solution through the proposed framework.

By leveraging the computational capabilities of GEE and open-access data, the framework offers a cost-effective solution that can assist authorities in promptly identifying regions most vulnerable to landslides. This enables them to implement promptly the necessary mitigation and civil protection measures and apply the necessary recovery measures.

References

Google Earth image (a), received at 14 May 2020. Publicly available at: https://earth.google.com/web/@38.35289638,20.54812259,137.18058809a,4112.50825678d,35y,120.97375048h,61.47762184t,-0r/data=ChYqEAgBEgoyMDIwLTA1LTE0GAFCAggBOgMKATBCAggASg0I_____ARAA (accessed 7 January 2025)

Google Earth image (b), received at 26 June 2021. Publicly available at: https://earth.google.com/web/@38.35289638,20.54812259,137.18058809a,4112.50825678d,35y,120.97375048h,61.47762184t,-0r/data=ChYqEAgBEgoyMDIxLTA2LTI2GAFCAggBOgMKATBCAggASg0I_____ARAA (accessed 7 January 2025)

González□Alemán, J. J. et al., 2019. Potential Increase in Hazard from Mediterranean Hurricane Activity with Global Warming,"

Geophys Res Lett, vol. 46, no. 3, pp.1754–1764, Feb.2019. https://doi.org/10.1029/2018GL081253

Lagouvardos, K., Kotroni, V., Nickovic, S., Jovic, D., Kallos, G. and Tremback, C.J., 1999. Observations and model simulations of a winter sub-synoptic vortex over the central Mediterranean. Met. Apps, 6: 371-383. https://doi.org/10.1017/S1350482799001309

Lagouvardos, K. et al., 2022. “Ianos—A Hurricane in the Mediterranean,” Bull Am Meteorol Soc, vol. 103, no. 6, pp. E1621–E1636, Jun.2022. https://doi.org/10.1175/BAMS-D-20-0274.1

Lekkas, E. et al., 2020. “Impact of medicane IANOS on Cephalonia,” Newsletter of EDCMS, National Kapodistrian University of Athens, Greece. ISSN 2653□9454.

Zekkos D., Zalachoris G., Alvertos, A. E., et al., 2020. “The September 18-20 2020 Medicane Ianos Impact on Greece - Phase I Reconnaissance Report”. Geotechnical Extreme Events Reconnaissance Report, GEER-068, https://doi.org/10.18118/G6MT1T.

17th INTERNATIONAL CONGRESS of the Geological Society of Greece

BULLETIN OF THE GEOLOGICAL SOCIETY OF GREECE, SP. PUBL.

EXTENDED ABSTRACT 227

Integrating Volcanic Geoheritage and Community Engagement: The Case of Nisyros aspiring UNESCO Global Geopark

Nikoli E.[1], Nomikou P.[2], Tasioulas E.[1], Koroneos C.[3], Sakkali K.[1], Koukourakis G.[1], Nastos P.[2], Antoniou V.[2], Emmanouloudis D.[3], Pehlivanides G.[4], Batis A.[5]

(1) Municipal Public Benefit Enterprise of Nisyros (DIKEN) (2) National and Kapodistrian University of Athens, Athens, Greece, evinom@geol.uoa.gr (3) International Hellenic University, Drama, Greece (4) (hands-on studio), Research & Art Direction, Branding, UX/UI Design, Project Management (5) Econtent Systems P.C, Software, Website and Mobile application development, Athens, Greece

Nisyros Geopark, located in the Southeastern Aegean, is a candidate for inclusion in the UNESCO Global Geoparks Network, recognized for its exceptional volcanic heritage and its integration of geological, natural, and cultural elements. Covering 481 km², the geopark is centered on the active Nisyros volcano and nearby islands, forming a dynamic landscape shaped by the South Aegean Volcanic Arc. Among its 24 geosites are active hydrothermal craters, a collapse caldera, volcanic domes, and numerous coastal hot springs, all of which serve as key focal points for educational activities.

Education is a cornerstone of the Geopark's mission, with a range of ongoing programs designed to share its unique geological story with diverse audiences. Workshops, guided tours, summer schools and educational programs are regularly organized to connect participants—ranging from local students to international visitors—with the island's volcanic and cultural history (Fig. 1,2). These activities have yielded significant outcomes, including increased local awareness of geohazards, active participation from hundreds of students annually, and strengthened collaboration with academic institutions. Evaluations indicate that participants develop a deeper understanding of volcanic processes and their environmental implications, contributing to a broader appreciation of geoconservation. These activities aim to foster an understanding of the dynamic processes that shaped the island and their relevance to contemporary environmental issues.

Figure 1. CIVIS Summer School "NATRISKS", May 2024
"Vulnerability of the Eastern Mediterranean: Natural Processes and Climate Risks "

Modern communication tools further enhance the educational experience. The Geopark's official website (www.nisyrosgeopark.gr), along with dedicated mobile applications, provides accessible and engaging resources, enabling visitors to explore the region's geoheritage independently or as part of structured activities. Partnerships with schools, universities, and cultural institutions ensure that educational outreach is deeply integrated into the community, encouraging active participation and fostering a long-term appreciation of the island's natural and cultural heritage.

By combining hands-on experiences, innovative communication techniques, and collaborations with educational organizations, Nisyros Geopark is establishing itself as a hub for learning and discovery. These efforts position the Geopark as a model for integrating education with the preservation and celebration of volcanic heritage, ensuring its significance is understood and valued by future generations.

Figure 2. European Geoscience Day 2023 in Nisyros Geopark

Acknowledgements

We sincerely thank the management body of Nisyros Geopark (DIKEN) and the Mayor of Nisyros, Mr. Koroneos Christofis, for their invaluable contributions and steadfast support. Their dedication has been pivotal in fostering sustainable development, preserving the region's unique geological and cultural heritage, and enriching its educational activities. These efforts have greatly enhanced the geopark's role as a center for learning and exploration, while also advancing its candidacy as a UNESCO Global Geopark.

17th INTERNATIONAL CONGRESS of the Geological Society of Greece

BULLETIN OF THE GEOLOGICAL SOCIETY OF GREECE, SP. PUBL.

EXTENDED ABSTRACT 228

The 2024 March 29, 5.9 M_L Strofades Earthquake (Greece) and its Seismic Sequence: Relocation, Focal Mechanism Solutions and Stress Inversion

Nikolopoulou I.[1], Bocchini G. M.[2], Roth M. P.[2], Essing D.[2], Harrington R. M.[2], Serpetsidaki A.[1], Fountoulakis I.[3], Evangelidis C.[3], Sokos E.[1]

(1) Seismological Laboratory, University of Patras, Patras, Greece, inikolopoulou@ac.upatras.gr

(2) Ruhr University of Bochum, Bochum, Germany

(3) National Observatory of Athens, Athens, Greece

Introduction

On March 29, 2024, a M_L 5.9 earthquake occurred offshore western Peloponesse, near the Strofades Islands in Western Greece. The region lies within the complex tectonic setting of the western segment of the Hellenic Subduction System (HSS), where the African plate is being subducted beneath the Aegean microplate with rates of 30-35 mm/yr (e.g., Chousianitis et al., 2015). The seismotectonic setting is controlled by the active subduction and the Kefalonia Transform Fault, which hosts the lateral transition from subduction to collision between Eurasian and Apulian plates. The mainshock was preceded by a M_L 4.1 foreshock and followed by an aftershock sequence consisting of hundreds of events that continued until June. The sequence occurred at depths ranging from 25 to 35 km, with the mainshock located at 33 km depth within the subducting slab.

The seismic sequence occurred in a region with limited station coverage, particularly offshore, where the azimuthal gap exceeds 180°. Onshore station coverage in western Peloponnese is adequate, but offshore seismic monitoring is significantly constrained. However, the mainshock and its aftershock sequence were well-recorded by the newly installed Pelops network (Harrington et al., 2023), consisting of eight broadband stations deployed by Ruhr University of Bochum in collaboration with the University of Patras and the Institute of Geodynamics of the National Observatory of Athens (NOA).

Using high-resolution seismic data from the Pelops, HUSN and Adria Array networks, we apply machine learning techniques to develop an enhanced catalog. We analyze the sequence through earthquake relocation, focal mechanism solutions, and stress tensor analysis, aiming to provide new insights into the seismic activity and fault dynamics in the western segment of the Hellenic Subduction System.

Data & Methods

To investigate the M_L 5.9 seismic sequence, we analyze the seismicity recorded across the broader region following the deployment of the Pelops network in December 2023. Seismic data include waveforms recorded from December 2023 to September 2024 by the Hellenic Unified Seismological Network (HUSN), Pelops, and Adria Array networks. Using machine learning techniques, we construct a joint catalog, by applying the PhaseNet picker (Zhu and Beroza, 2019) for automatic phase-arrival picking and the PyOcto associator (Münchmeyer, 2024) for correlating phase picks with corresponding events.

We obtain earthquake locations using NLLoc (Lomax et al., 2000) and achieve high-quality hypocentral solutions by applying Source-Specific Station Terms (SSST) travel-time corrections and a coherency analysis of earthquake waveforms (Lomax & Savvaidis, 2022). We use the 1D Vp velocity model of Sachpazi et al. (2020) that we edit by replacing the first two layers with those from the velocity model of Kassaras et al. (2014). We assume a Vp/Vs ratio of 1.81, derived from events in our catalog that have at least 10 reliable Vp/Vs pairs.

We further investigate the sequence by obtaining moment tensors for five events, consisting of the foreshock, mainshock and three larger aftershocks, through full-waveform inversion using the ISOLA code (Sokos & Zahradnik, 2008). We analyze 20 additional aftershocks of lower magnitudes and determine their focal mechanism solutions from first-motion polarity data using the FPFIT program (Reasenberg & Oppenheimer, 1985). Finally, we conduct stress tensor analysis with the StressInverse code (Vavryčuk, 2014) using moment tensor-solutions and well-constrained focal mechanisms.

Results & Discussion

The M 5.9 March 2024 Strofades earthquake ruptured a NE-SW left-lateral strike-slip fault. The distribution of relocated aftershocks aligns with the NE-SW strike inferred from the focal mechanism solution of the mainshock and delineates a structure approximately 10-12 km in length and 6-8 km in width (Figure 1). The foreshock and the mainshock occurred at 30 and 33km depth, respectively, while aftershocks were distributed between 25 to 35 km (Figures 1,3).

The top of the subducting slab in the region is estimated to lie at approximately 20 km depth (Makris & Papoulia 2014, Sachpazi et al. 2016, Bocchini et al. 2018), suggesting that the rupture occurred within the subducting slab.
Focal mechanism solutions derived from moment tensor inversion and first-motion polarities, predominantly indicate strike-slip and normal faulting (Figure 2). The moment tensor solutions of the foreshock, mainshock and largest aftershocks suggest NE-SW strike-slip faulting, with the exception of one event, which exhibits normal faulting with a significant strike-slip component (Figure 2). Focal mechanisms derived from first-motion polarities are compatible with the kinematics of the mainshock (Figure 2, inset).
The geometry of the ruptured area is well-constrained in the two cross-sections, which were constructed parallel and perpendicular to the strike of the aftershock sequence, in SW-NE and NW-SE directions, respectively (Figure 3). The spatial distribution of the sequence is evident in the A-A´ profile, showing the width and length of the ruptured area. The B-B´ cross-section reveals a well-constrained vertical structure, with hypocenters aligned with the dip inferred from the focal mechanisms (Figure 3). Stress tensor analysis indicates a σ_3 axis oriented in an E-W direction, σ_1 oriented horizontally in a N-S direction and a vertically oriented σ_2 (Figure 2). P- and T-axes azimuths are consistent with the inferred stress axes within the subducting plate (Shaw & Jackson, 2010).
The mainshock and its aftershock sequence are not related to any mapped faults at the surface, as their location, geometry and kinematics do not align with the observed spatial distribution of the sequnce (Figure 1). The rupture occurred within the subducting slab, with no evidence of slip along any mapped offshore structures, as further indicated by the cross-sections (Figure 3).
After the mainshock, a sequence consisting of numerous events was recorded onshore in the eastern part of the study area (Figure 1). Future work will assess any potential connection to the Strofades seismic sequence.

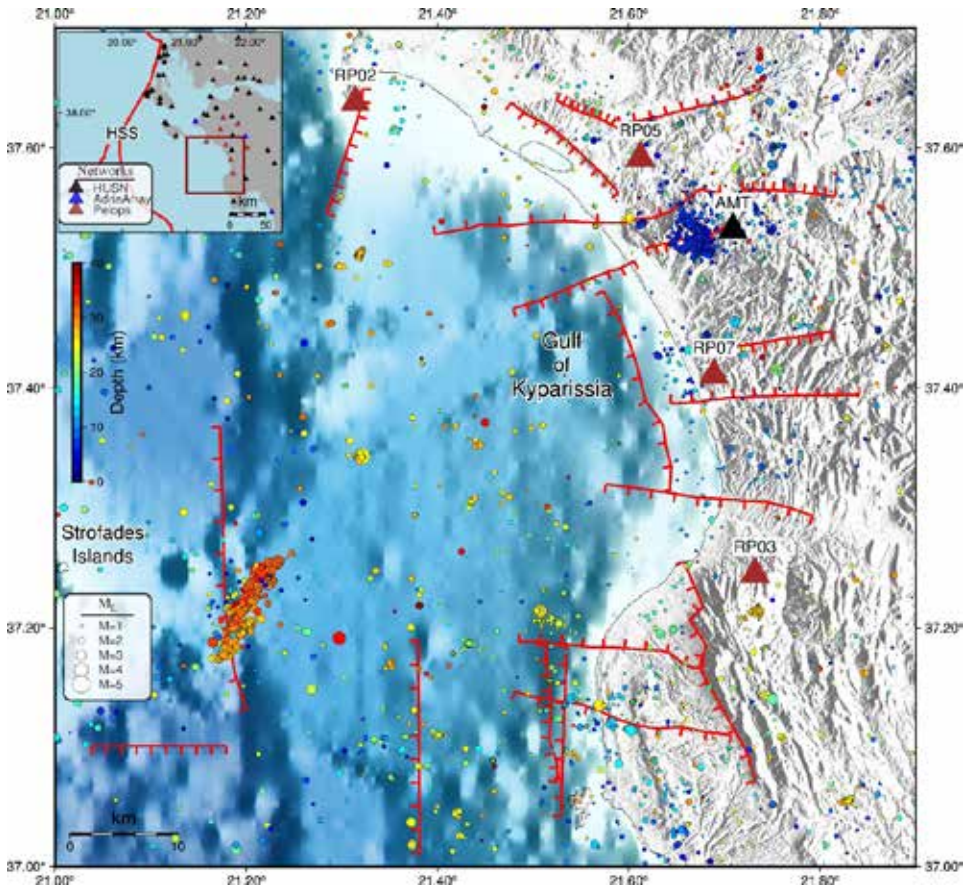

Figure 1. Seismicity map of the broader Gulf of Kyparissia region, showing relocated earthquakes of the M 5.9 earthquake sequence and regional seismicity recorded between December 2023 and September 2024. Earthquakes are depicted as circles, scaled by magnitude and color-coded by depth. Triangles denote the seismic stations operating within the study area. The inset map shows the location of the study area, station coverage across western Greece, and the Hellenic Subduction System (HSS), the main seismotectonic feature of the region. Mapped active faults (in red colour) from Ganas (2024).

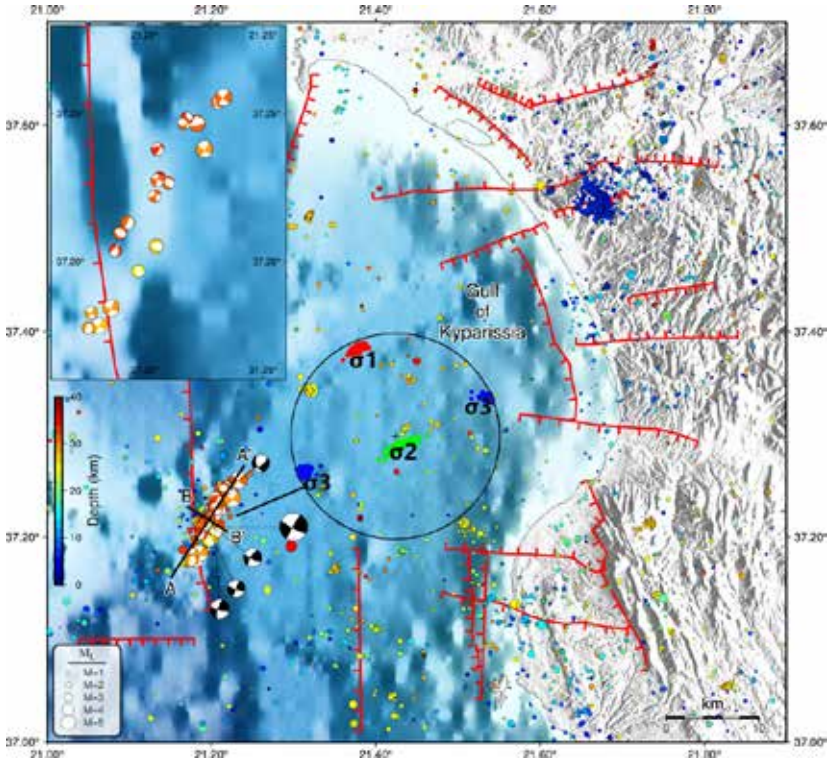

Figure 2. Focal mechanisms of the foreshock, mainshock and 23 major aftershocks of the Strofades sequence, polarity-based solutions are color-coded by depth, centroid moment tensors are the black beachballs, black lines connect the beachball with the centroid location. The location of the A-A´ cross-section and its perpendicular B-B´ cross-section is also shown. A zoomed-in view of the focal mechanisms of the aftershocks in the inset. Principal stress axes (σ1, σ2 and σ3) orientation is shown in the stereographic plot. Mapped active faults (in red colour) from Ganas (2024).

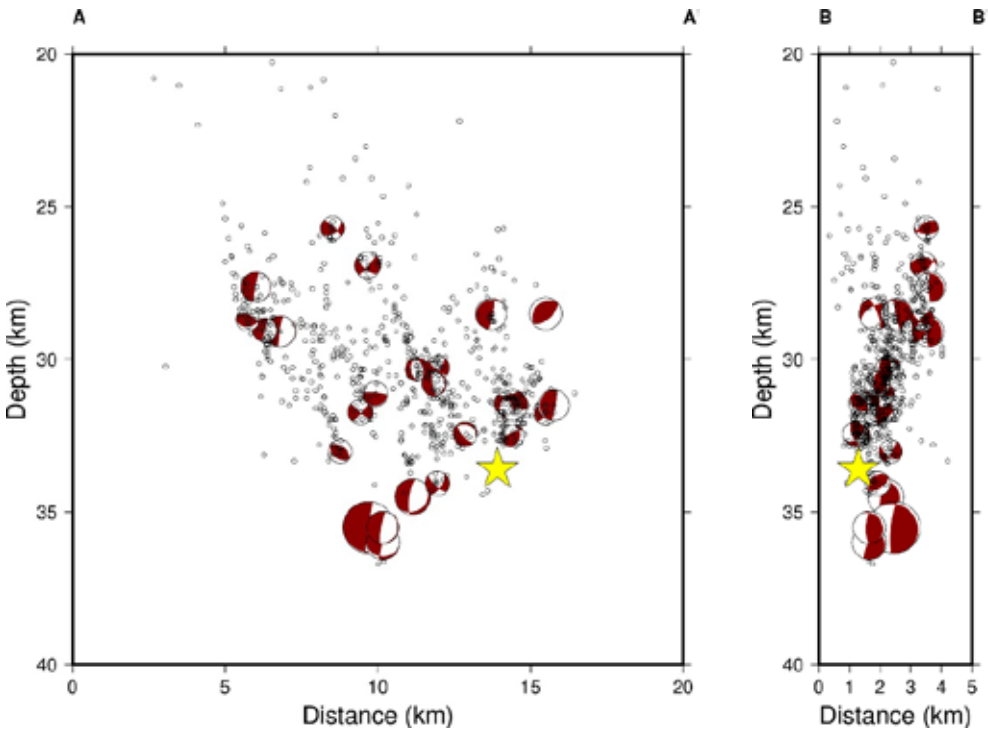

Figure 3. Distribution of the relocated hypocenters in A-A´ (along strike) and B-B´ (along dip) profiles. Beachballs are projected at the centroid location, yellow star denotes mainshock's hypocenter.

Acknowledgements

Waveforn seismic data were retrieved from EIDA@NOA (https://eida.gein.noa.gr/) and the following networks were used. HL (NOA, Hellenic Seismic Network), DOI:10.7914/SN/HL, HT (Aristotle University of Thessaloniki Seismological Network), DOI:10.7914/SN/HT, HP (University of Patras, Seismological Laboratory), DOI:10.7914/SN/HP, HA (National and Kapodistrian University of Athens, Seismological Laboratory), DOI:10.7914/SN/HA, HI (Institute of Engineering Seismology and Earthquake Engineering), DOI:10.7914/SN/HI, HC (TEI of Crete, Seismological Network of Crete), DOI:10.7914/SN/HC, 1Y (2022-2026) (Greece/North Macedonia Contribution to AdriaArray Temporary Network), DOI:10.7914/y0t2-3b67, 5B (2023-2027) (RUB Observational Geophysics Lab Deployment: Northwestern Peloponnese (Pelops), DOI:10.7914/pxkt-x819.

References

Bocchini, G. M., Brüstle, A., Becker, D., Meier, T., van Keken, P.E., Ruscic, M., Papadopoulos, G.A., Rische, M., Friederich, W., 2018. Tearing, segmentation, and backstepping of subduction in the Aegean: New insights from seismicity. Tectonophysics 734-735, 96-118.

Chousianitis, K., Ganas, A., & Evangelidis, C. P. (2015). Strain and rotation rate patterns of mainland Greece from continuous GPS data and comparison between seismic and geodetic moment release. Journal of Geophysical Research: Solid Earth, 120(5), 3909–3931.

Friederich, W., Evangelidis, C., Papazachos, C., Sokos, E., Kaviris, G., & Cernih, D. (2022). AdriaArray Temporary Network: Greece, North Macedonia [Data set]. International Federation of Digital Seismograph Networks.

Ganas, A. (2024). NOAFAULTS KMZ layer Version 6.0 (version 6.0) [Data set]. Zenodo.

Harrington, M., Bocchini, G. M., Roth, M., Sokos, E., & Evangelidis, C. (2023). RUB Observational Geophysics Lab Deployment: Northwestern Peloponnese [Data set]. International Federation of Digital Seismograph Networks.

Kassaras, I., Kapetanidis, V., Karakonstantis, A., Kaviris, G., Papadimitriou, P., Voulgaris, N., Makropoulos, K., Popandopoulos, G., Moschou, A., 2014. Journal of Geodynamics 73, 60-80.

Lomax, A., & Savvaidis, A., 2022. High-Precision Earthquake Location Using Source-Specific Station Terms and Inter-Event Waveform Similarity. Journal of Geophysical Research: Solid Earth 127, e2021JB023190.

Lomax, A., Virieux, J., Volant, P., Berge, C., 2000. Probabilistic earthquake location in 3D and layered models: introduction of a Metropolis-Gibbs method and comparison with linear locations, in: Thurber, C.H., Rabinowitz, N. (Eds.), Advances in Seismic Event Location. Kluwer, Amsterdam, 101–134.

Makris, J., & Papoulia, J., 2014. The backstop between the Mediterranean Ridge and western Peloponnese, Greece: its crust and tectonization. An active seismic experiment with ocean bottom seismographs. Bollettino di Geofisica Teorica ed Applicata 55(2), 249-279.

Münchmeyer J., 2024. PyOcto: A high-throughput seismic phase associator. Seismica 3.

Reasenberg, P. & Oppenheimer, D., (1985). FPFIT, FPPLOT and FPPAGE: Fortran computer programs for calculating and displaying earthquake fault plane solutions, Open-File Report, U.S. Geological Survey, 95-515.

Sachpazi, M., Laigle, M., Charalampakis, M., Diaz, J., Kissling, E., Gesret, A., Becel, A., Flueh, E., Miles, P., Hirn, A., 2016. Segmented Hellenic slab rollback driving Aegean deformation and seismicity. Geophysical Research Letters 43 (2), 651–658.

Sachpazi, M., Kapetanidis, V., Charalampakis, M., Laigle, M., Kissling, E., Fokaefs, A., Daskalaki, E., Flueh, E., Hirn. A., 2020. Methoni Mw 6.8 rupture and aftershocks distribution from a dense array of OBS and land seismometers, offshore SW Hellenic subduction. Tectonophysics (796) 228643.

Shaw B., & Jackson J. (2010). Earthquake mechanisms and active tectonics of the Hellenic subduction zone. Geophysical Journal International, 181(2), 966-984.

Sokos, E. N., & Zahradnik, J. (2008). ISOLA a Fortran code and a Matlab GUI to perform multiple-point source inversion of seismic data. Computers and Geosciences, 34(8), 967–977.

Vavryčuk, V. (2014). Iterative joint inversion for stress and fault orientations from focal mechanisms. Geophysical Journal International, 199(1), 69–77.

Zhu, W., Beroza, G.C., 2019. PhaseNet: a deep-neural-network-based seismic arrival-time picking method. Geophysical Journal International 216(1), 261-273.

17th INTERNATIONAL CONGRESS of the Geological Society of Greece

BULLETIN OF THE GEOLOGICAL SOCIETY OF GREECE, SP. PUBL.

EXTENDED ABSTRACT 229

Sinkholes, roads and exceptional transports, a risk to be assessed

Stefania Nisio[1], Sergio Madonna[2], Giancarlo Ciotoli[3], Francesco Gentili[2], Livio Ruggiero[3]

1 ISPRA – Dipartimento per il Servizio Geologico d'Italia , Via Vitaliano Brancati 48, 00144 Roma

2 Università degli Studi della Tuscia - Via San Camillo de Lellis, 01100 VITERBO (VT).

3 CNR – Consiglio Nazionale delle Ricerche, Italy Piazzale Aldo Moro 7 Roma

Introduction / Background

The Italian territory, characterised by its complex geological and geomorphological features, faces a unique combination of natural hazards, including volcanic activity, landslides, floods, sinkholes and seismic events.

These hazards, which affect nearly the entire country, pose significant challenges to the safety and resilience of transportation networks. Among these geohazards, natural and anthropogenic sinkholes represent a particularly insidious threat due to their sudden and unpredictable nature, often resulting in severe disruptions to road infrastructure.

This danger is further exacerbated by exceptional transports (ETs)—vehicles carrying oversized or heavy loads—which require stable and robust roadways to ensure operational safety.

Italy's urban centres' historical and archaeological richness introduces an additional layer of complexity. Many Italian cities, with their millennia-old history, rest on a network of underground cavities, often remnants of ancient quarries, tunnels, and cisterns. These subterranean voids, many of which remain undocumented, frequently intersect the modern road network, creating hidden vulnerabilities. In historical centres where traffic is already constrained, the passage

A critical dimension of this issue lies in Italy's current nuclear waste management challenges. The absence of a national repository for radioactive waste has necessitated the storage of such materials in numerous temporary facilities scattered across the country, many of which are considered suboptimal in terms of security and stability. Once a national repository is identified, extraordinary transport will play a central role in transferring these hazardous materials to a single site.

The combination of geohazards, infrastructure vulnerabilities, and the logistical demands of nuclear waste transport underscores the critical need for comprehensive risk assessment and mitigation strategies

Comprehending the relationship between sinkhole formation and the transportation of heavy loads is essential, as incidents can increase the risk of human life loss, environmental pollution problems, and significant economic and infrastructure damage.

Objectives

This study aims to raise awareness among public administrations, as well as public and private entities about the significant hazards posed by natural or anthropogenic sinkholes, particularly in the context of exceptional transport planning. The goal is to ensure that this geohazard is systematically accounted for in decision-making processes to mitigate potential safety threats and infrastructure damage.

The issue is especially critical in the historical centers of Italy's art cities, where intricate networks of underground cavities create hidden vulnerabilities that can be exacerbated by exceptional transports or by the placement of heavy temporary structures. The concentrated stress from such activities can trigger or accelerate sinkhole formation, posing a serious threat not only to the stability of the ground but also to the preservation of invaluable cultural and architectural heritage.

Beyond urban areas, this problem is equally relevant in sparsely populated rural and extra-urban regions. Here, the planning of exceptional transports—particularly those involving extremely heavy or high-risk cargo, such as nuclear waste. By highlighting these risks, this study seeks to provide a comprehensive framework for integrating sinkhole hazard assessments into the planning and execution of exceptional transports. This includes developing guidelines for evaluating subsurface stability, strengthening coordination between public and private stakeholders, and implementing preventive measures to enhance the resilience of both urban and rural infrastructures.

By emphasising the importance of continuously updating datasets and integrating diverse geospatial layers, this study seeks to establish a best-practice model for sinkhole risk assessment and mitigation, facilitating safer and more informed decision-making for exceptional transport and infrastructure planning.

Methods

The foundation of this study is the recently updated database of sinkholes and underground cavities developed as part of the PNRR Geosciences IR Project (figure 1A, B). This comprehensive dataset provides a crucial resource for understanding the spatial distribution of sinkholes across Italy and their potential impact on infrastructure. By leveraging Geographic Information System (GIS) technologies, it is now possible to overlay the mapped distribution of currently catalogued sinkholes (point vector layer) with the layout of primary and secondary road networks (line vector layer). The distance from each sinkhole to the nearest road segment can be calculated using GIS tools, such as QGIS's "Distance to Nearest Hub," ArcGIS's "Near" tool,

or GRASS GIS's v. distance. Specific sections of roads can be classified into hazard categories according to their distance from sinkholes. To refine this assessment, additional geospatial layers, including structural elements (e.g., tectonic features), gas emission distributions, geological (e.g., karst terrains, soluble rock types, etc.) or hydrogeological data (e.g., groundwater flow, water table fluctuations, etc.), historical variations of hydrography, land use, etc. can be integrated to identify areas where environmental, geological or anthropogenic conditions may exacerbate sinkhole hazard along specific road segments. Finally, thematic maps are created to visualise risk zones; statistical analyses can identify high-risk clusters, and the results with field data or expert knowledge to ensure accuracy and local relevance. This approach provides a comprehensive framework for evaluating sinkhole hazards near road networks while allowing for site-specific adjustments based on additional data.
Thematic maps, like susceptibility maps, could be created to visualise the likelihood of sinkhole occurrence across large hazard zones. Still, the results must be validated with field data, analysis, and expert knowledge to ensure accuracy and local relevance. Particularly, the development of susceptibility maps for major urban areas offers invaluable tools for planning exceptional transport and positioning temporary heavy loads, such as those used for events or maintenance activities on buildings and infrastructure.

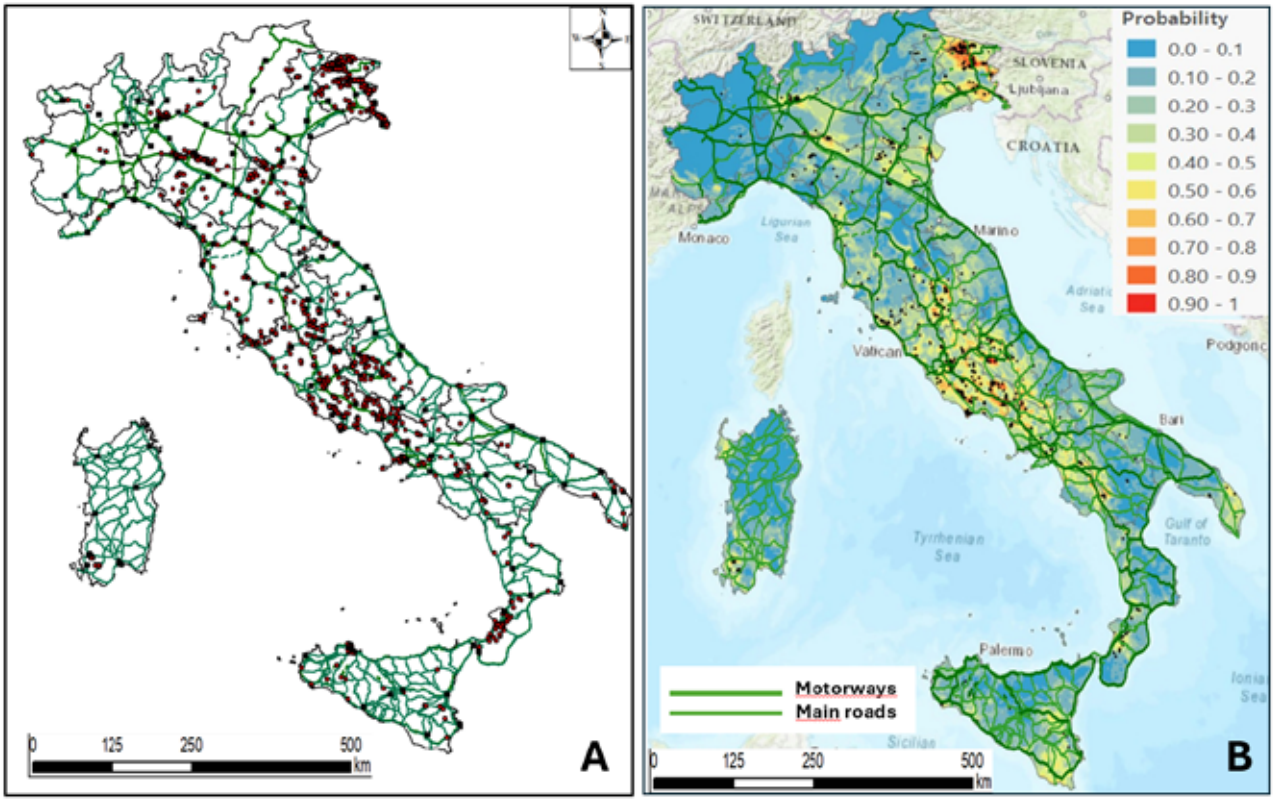

Fig. 1 - Main roads in Italy and: A) Natural sinkhole distribution B) susceptibility maps. From the GIS database PNNR-Geosciences-IR

The first phase of constructing an anthropogenic sinkhole susceptibility map involved constructing a conceptual model identifying potential predisposing factors for anthropogenic sinkholes in urban areas. All selected factors (independent variables), along with the sinkhole database (response variable), were entered into a geodatabase managed in a GIS environment in shapefile format (point, linear, and polygonal geometries) and/or raster format (grid). All grid layers (original and/or produced) were constructed with a resolution appropriate for the purpose of the study. The density analysis of event distribution is a fundamental and straightforward technique to determine the area most prone to a specific geographical phenomenon. The density model is based on the hypothesis that areas with a higher presence of events are more likely to experience additional occurrences. The density analysis was carried out using the "Kernel Density Estimation" (KDE) (Silverman, 1986). The KDE produces a density map representing the number of elements per unit area based on the neighbourhood distance around those elements. The neighbourhood distance is determined by the observed mean distance using the NNI. Density analysis can be calculated for both point and linear elements. Density maps provide preliminary zoning of the territory; a sinkhole density map constitutes an initial evaluation element of an area's susceptibility to this phenomenon.

Random forest regression, a supervised machine learning model that combines decision trees to make accurate predictions, was used to develop a sinkhole susceptibility map (figure.1B). Sinkhole presence, transformed into a binary variable (presence/absence), was used as target variable. Predisposing factors of various types were considered as predictors, organised into a national 10x10 km grid. These included geological variables (GEO, KA), geomorphological factors (DTM, TPI, HAND, Slope), hydrogeochemical indicators (DensGas, DistGasCat, DensSpring, DistSpringCat), seismic features (EQD) and structural parameters (FD). Both continuous and categorical variables were processed to capture detailed local environmental conditions. The supervised method split the data into training and test sets to ensure robust model evaluation and validation. With its ability to handle non-linear relationships and complex variable interactions, the Random Forest model was trained on these data to identify areas with higher susceptibility to sinkhole formation. In addition, the model provided insight into the key drivers of sinkhole susceptibility by providing a Receiver Operating Characteristic (ROC) curve to assess its predictive performance and quantify the importance of each variable.

Results and discussion

Sinkholes are large depressions that suddenly open in the ground catastrophically, with diameters and depths varying from a few to hundred of meters. They are divided into two main categories: natural sinkholes that mostly occur in plain areas and anthropogenic sinkholes affecting basically urban centres, particularly in large metropolitan areas. Natural sinkholes are related to the area's geological, structural, and hydrogeological context, while anthropogenic sinkholes are directly or indirectly related to human activities, particularly the presence of underground cavities.

In recent decades, many sinkholes have opened up in or near important road arteries in extra-urban (figure 2A, B) or urban (figure 2C, D) areas.

Fig. 2 - Examples of sinkholes affecting extra-urban and urban roads: A) provincial road near Ravenna; B) provincial road that crosses the Vepe-Latera caldera (Volsini Volcanic Complex - Latium); C) Viterbo - collapse of the vaults of underground environments under an urban road; D) Rome urban road Via Sestio Mensas.

The recent event that occurred inside the Latera-Vepe caldera (figure.2B) near (about 5m) from Provincial Road 118 leading to Lake Mezzano points out that even volcanic areas are not exempt from these phenomena, which are too often underestimated (Puzzilli et al., 2024). This case also shows that sinkholes are very easily filled with water almost simultaneously with their formation. It is common, after their formation, for groundwater or water rising from deep aquifers to flow into the cavity, turning it into a small lake, and this could lead to further complications in the sinkholes open in communication infrastructure.

The National Database of ISPRA is a fundamental tool for mitigating sinkhole hazards (Caramanna et al. 2008; Nisio et al.

2007; Nisio 2008). Among its various applications, we want to emphasise its usefulness in managing and planning exceptional transport and positioning temporary large loads. ISPRA's National Sinkhole Database was developed using ESRI's ArcGIS software with the WGS84/UTM Zone 33N reference system and has been updated to include further natural sinkhole inventory in the flat areas of Italy, plateau regions, and the transition zones between plains and slopes. The current census is up to date, with more than 6,000 sinkhole phenomena catalogued and classified according to the Italian case typology proposed by Nisio (2008) (Fig. 1A), creating a unique database in Italy.

More than 6000 cases of natural subsidence in plain or slope areas, attributed to natural sinkhole phenomena, have been catalogued and studied by ISPRA through field investigations and archival studies. Many of the catalogued phenomena are hypothesized to relate to the upward migration of aggressive fluids. The areas most susceptible to sinkholes are concentrated in the central Tyrrhenian slope, particularly in the regions of Friuli Venezia Giulia, Lazio, Puglia, Abruzzo, Campania, and Tuscany. Due to its geological-structural setting, the Adriatic side is not affected by these types of sinkholes, nor are the Alpine arc and the Dolomites.

The conditions are different in Northern Italy (where the census is still ongoing). Small diameter depressions with modest depth (known as "occhi pollini") are also widespread in the Po Valley and Lombard plains. The genetic mechanisms of these depressions, probably caused by surface suffusion phenomena, are currently being studied. In the plains and internal basins of Veneto, Friuli-Venezia Giulia (Calligaris 2019 a, b; 2020), Puglia, and Sicily, as well as the Autonomous Province of Bolzano, subsidence phenomena are closely controlled by the dissolution of evaporitic and carbonate lithotypes found beneath relatively thin covers, which are therefore attributable to cover-collapse sinkhole types.

On the other hand, the phenomena reported in Calabria are linked to small cavities, now filled in, whose location is difficult to pinpoint. These originated entirely during seismic events and are associated with liquefaction phenomena in the soils. The geological context appears substantially different in Sicily and Puglia, where subsidence cases are influenced by the presence of evaporitic (gypsum and salt) or calcareous soils and by thinner clayey or sandy covers.

Anthropogenic sinkholes typically occur in large metropolitan cities and are primarily associated with the presence of a complex network of underground cavities (figure 2C), many of which are still unknown. The cities most affected by this phenomenon are Rome, Naples, Cagliari, and Palermo (figure 3A), for which more detailed time series data is available (Ciotoli et al. 2013, 2015 a, b, c; Nisio et al. 2017; Tufano et al. 2022). Similarly, the regions with extensive outcrops of volcanic rocks, such as Lazio and Campania (figure 3B), are the most affected by anthropogenic sinkholes, given the millenary history of occupation and exploitation of its subsoil.

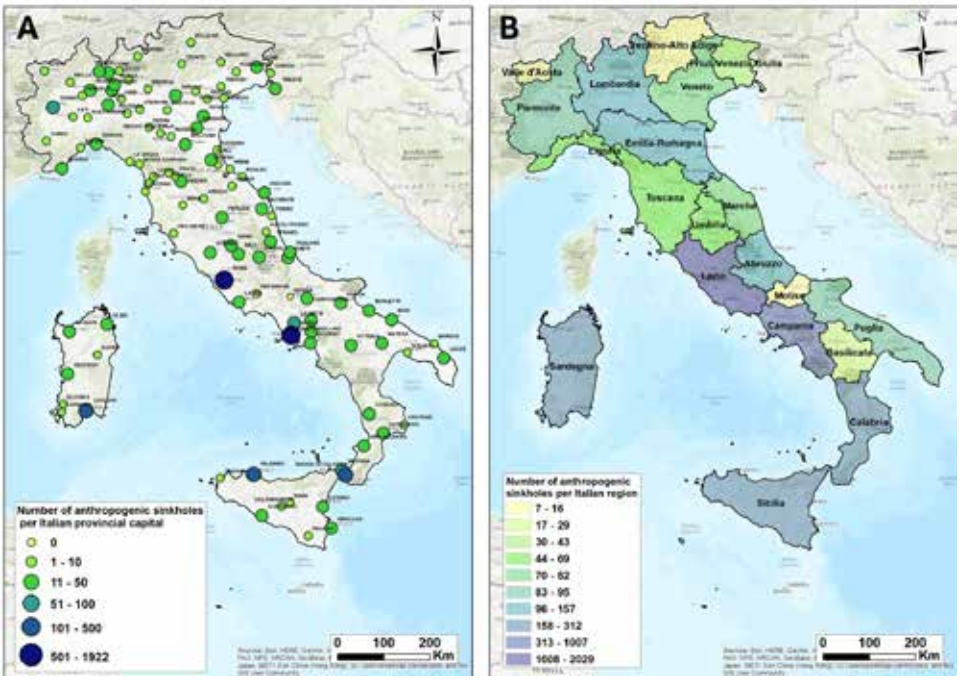

Figure 3-- - Number of anthropogenic sinkholes per Italian provincial capital A) and region B). From the database PNNR-Geosciences-IR.

These cavities have been created by human activity at various times over more than two thousand years. The presence of underground cavities can, under certain conditions, cause the more superficial soil layers to collapse, resulting

in sinkholes (anthropogenic sinkholes). An additional factor that contributes to the formation of such anthropogenic sinkholes is the malfunction, leakage and general dysfunction of the hydraulic network of the underground services. In the last forty years, the frequency of these phenomena has increased due to the denser and more indiscriminate urbanization of the area, and possibly also due to changes in rainfall patterns, which in recent years have led to very intense rainfall events and permanent flooding in certain areas of the city.
The application of the Random Forest Regression model provides a sinkhole susceptibility map, integrating predisposing factors such as geological, geomorphological, hydrogeochemical, and structural variables. The model achieved high predictive performance, as evidenced by the ROC curve with an AUC of 0.96 for the test data, indicating excellent discrimination between sinkhole-prone and non-prone areas. The variable importance analysis revealed that earthquake density (11.5%), gas emission density (11.4%), and karst areas (10%) were the most significant predictors, followed by fault density, mineral spring density, and slope.
The sinkhole susceptibility map (Fig. 1B) highlights areas of high probability, concentrated in karstic and faulted regions, as well as areas with high seismic activity or significant hydrogeochemical anomalies (Di Salvo et al.2024) The map provides valuable insights for land-use planning and risk mitigation, helping prioritise monitoring and intervention efforts in vulnerable areas. The updated sinkhole inventory, combined with this susceptibility analysis, represents a critical resource for understanding and managing sinkhole risks at a national scale.
The processes that create sinkholes are very complex and sometimes difficult to define, not solely attributed to gravity or karst dissolution but to a series of predisposing and triggering causes: liquefaction phenomena, the presence of cavities deep underground, easily erodible cover soils, tectonic features such as faults or fractures, CO_2 and H_2S upwelling, seismic events, heavy rainfall, and human activities like water extraction, mining, excavation, etc.
In urbanised areas, the most significant predisposing factor is generally related to the presence of pre-existing underground cavities, such as catacombs, hypogea, quarries, etc. The collapse or instability of these cavities can propagate to the surface, causing sudden collapses. Another critical element is associated with underground erosion processes caused by infiltration or exfiltration due to the deterioration of the sewer drainage system or underground water supply network. This progressive deterioration of underground cavities can lead to sudden collapses on the surface. Additionally, extreme meteorological events (prolonged or intense rainfall) can act as a triggering factor, especially in urban areas prone to flooding (Di Salvo et al., 2018).
In all these cases, however, the presence of heavy loads and vibrations caused by exceptional transports (ETs) can act as a significant triggering factor for sinkhole formation. These vibrations, combined with the concentrated weight of vehicles, can exacerbate the instability of subsurface voids or weakened geological structures, particularly in karst terrains or areas with soluble rock formations. Repeated mechanical stress from traffic can accelerate the collapse of cavities by dislodging loose sediment, compacting unconsolidated materials, or increasing subsurface pressure, leading to sudden subsidence. This effect is particularly pronounced in areas where groundwater flow or fluctuating water tables have weakened the subsurface, making it more susceptible to external forces. Such dynamics highlight the importance of monitoring high-traffic zones for sinkhole risks, especially in regions with vulnerable geological conditions.

Conclusion

In Italy, natural sinkholes predominantly affect extra-urban areas, while anthropogenic sinkholes are more prevalent in towns and cities. These phenomena pose significant dangers to road infrastructure, threatening public safety and causing substantial economic losses. Among the triggering factors for sinkholes, both natural and anthropogenic, are vibrations and overloads generated by human activities. Specifically, vibrations induced by heavy mechanical equipment used in construction or agriculture, as well as traffic from heavy vehicles, contribute to subsurface instability. Similarly, overloads from exceptional transports (ETs) or the temporary placement of very heavy loads create additional stress concentrations in the soil, further exacerbating pre-existing geological vulnerabilities.
These activities are particularly hazardous in areas prone to sinkhole formation, as they can destabilize subsurface structures and trigger collapses. In urban centres, most sinkholes occur on roadways due to the concentrated impact of traffic and infrastructure stress. In extra-urban areas, sinkholes are frequently found near major road infrastructures and railways, where the cumulative effects of vibrations and heavy loads are most pronounced. The hazard is heightened in regions with karst or pseudokarst formations, where underground cavities or soluble rock layers create a predisposition to collapse. Similarly, areas with unconsolidated soils or shallow water tables are at increased risk, as the additional stress from ETs can lead to soil liquefaction, suffusion, or piping phenomena. The impact of these overloads is not confined to natural sinkholes but extends to urban environments, where anthropogenic sinkholes are linked to underground cavities, failing hydraulic infrastructure or malfunctions of sub-service networks. Most Italian cities are built on a complex network of underground cavities, many of which are still unknown. In the last forty years,

the frequency of these phenomena has increased due to the denser and more indiscriminate urbanisation of the area and possibly also due to changes in rainfall patterns, which in recent years have led to very intense rainfall events and permanent flooding in certain areas of the city. Addressing these risks is essential to safeguard infrastructure, minimise hazards, and mitigate the socio-economic impacts associated with sinkhole formation.

The ISPRA dataset provides a crucial resource for understanding the spatial distribution of sinkholes across Italy and their potential impact on infrastructure. This has practical implications for improving the planning and management of exceptional transport and temporary heavy loads. The sinkhole susceptibility maps can guide decision-makers in prioritising monitoring efforts, implementing preventive measures, and mitigating risks associated with ETs and road infrastructure.

Integrating advanced modelling techniques, such as random forest regression, has proven essential for understanding and predicting natural sinkhole susceptibility. Through the combination of geological, geomorphological, hydrogeochemical and structural factors, the model provides a robust framework for assessing the likelihood of sinkhole formation across Italy. The model's high prediction performance (AUC of 0.96) demonstrates its reliability, while variable importance analysis identifies key drivers, including seismicity, gas emission densities and karst regions. These findings provide a better understanding of the sinkhole phenomenon and demonstrate the potential of machine learning to deal with complex geohazard scenarios.

Future work should focus on refining predictive models by incorporating time-series data, climate change projections, and emerging urbanisation trends. Enhancing these models will improve their reliability and applicability to complex geohazard scenarios. Ultimately, integrating advanced modelling techniques with historical and geospatial data provides a scalable and reproducible methodology for addressing sinkhole hazards.

Acknowledgements

This research was partially funded by PNRR—European Union—NextGenerationEU—Mission 4 "Education and Research"—Component 2 "From Research to Business"—Investment 3.1 "Fund for the realization of an integrated system of research and innovation infrastructures". CUP:I53C22000800006..

References

Calligaris C., Zini L., Nisio S., Piano C. (2019 a) - Sinkholes in the Friuli Venezia Giulia Region: state of the art of the of territorial analyses in the evaporites.Springer Book "Applied Geology: Approaches to Future Resource.

Calligaris C., Zini L., Nisio S., Piano C. (2019 b) - Sinkholes in the Friuli Venezia Giulia Region: state of the art of the of territorial analyses in the evaporites. Springer Book "Applied Geology: Approaches to Future Resource.

Calligaris, C., Zini, L., Nisio, S., & Piano, C. (2020). Sinkholes in the Friuli Venezia Giulia Region focus on the evaporites. Applied Geology: Approaches to Future Resource Management, 73-90.

Caramanna G., Ciotoli G., Nisio S. (2008) - A review of natural sinkhole phenomena in Italian plain areas. Journal of Natural Hazard, 45, 145- 172, DOI 10.1007/s, 11069-007-9165-7.

Ciotoli G. Corazza A., Finoia M.G., Nisio S. Succhiarelli C. (2013) – Gli sprofondamenti antropogenici nell'aria urbana di Roma. Mem. Descr. Carta Geol. D'IT. 93, 143-182.

Ciotoli G., Di Loreto E, Liperi L., Meloni F., Nisio S., Sericola A. (2015a) - Carta dei Sinkhole Naturali del Lazio 2012 e sviluppo futuro del Progetto Sinkholes Regione Lazio. Mem. Descr. Carta Geol. D'It. 99, 189-202.

Ciotoli G., Finoia m.G., Liperi L., Meloni F., Nisio S., Tonelli V., Zizzari P. (2015 b) - Sinkhole susceptibility map of the Lazio Region, central Italy. Journal of Maps 12-2, 287-294, 1/2015.

Ciotoli G., Nisio S., Serafini R. (2015 c) – Analisi della suscettibilità ai sinkholes antropogenici nel centro urbano di Roma: analisi previsionale. (2015) Mem. Descr. Carta Geol. D'IT. 99, 167-188.

Di Salvo, C., Ciotoli, G., Mancini, M., Nisio, S., & Stigliano, F. (2024) - Analysis of Geological Multi-Hazards in an Urban District. Geosciences, 14(2), 27.

Nisio S. (2008) - I fenomeni naturali di sinkhole nelle aree di pianura italiane. Monografia Memorie descrittive della Carta Geologica d'It. Vol. LXXXV; 475pp.

Nisio S., Caramanna G. & Ciotoli G. (2007) Sinkholes in Italy: First results on the inventory and analysis. Geological Society London Special Publications 279(1):23-45. DOI:10.1144/SP279.4

Nisio S., Allevi A., Ciotoli G., Ferri G., Fiore R., Pascucci R., Stranieri I., Succhiarelli C., (2017) Carta delle Cavità sotterranee di Roma. ISPRA

Puzzilli, L. M., Ruscito, V., Madonna, S., Gentili, F., Ruggiero, L., Ciotoli, G., & Nisio, S. (2024). Natural Sinkhole Monitoring and Characterization: The Case of Latera Sinkhole (Latium, Central Italy). Geosciences, 14(1), 18.

Silverman, B. W. (1986). Kernel density estimation technique for statistics and data analysis. *Monographs on statistics and applied probability*, *26*.

Tufano, R., Guerriero, L., Annibali Corona, M., Bausilio, G., Di Martire, D., Nisio, S., & Calcaterra, D. (2022). Anthropogenic sinkholes of the city of Naples, Italy: An update. Natural Hazards, 112(3), 2577-2608.

17th INTERNATIONAL CONGRESS of the Geological Society of Greece

BULLETIN OF THE GEOLOGICAL SOCIETY OF GREECE, SP. PUBL.

EXTENDED ABSTRACT 230

Nisyros Geopark: A Living Laboratory of Volcanic Geoheritage in the South Aegean

Nomikou P.1, Nikoli E.[2], Tasioulas E.[2], Koroneos C.[3], Sakkali K.[2], Koukourakis G.[2], Nastos P.[1], Antoniou V.[1], Emmanouloudis D.[3], Pehlivanides G.[4], Batis A.[5]

(1) National and Kapodistrian University of Athens, Athens, Greece, evinom@geol.uoa.gr (2) Municipal Public Benefit Enterprise of Nisyros (DIKEN) (3) International Hellenic University, Drama, Greece (4) (hands-on studio), Research & Art Direction, Branding, UX/UI Design, Project Management (5) Econtent Systems P.C, Software, Website and Mobile application development, Athens, Greece

Nisyros Geopark, a candidate for nomination as a UNESCO Global Geopark, is distinguished by its remarkable geological, natural, and cultural features. Situated in the Southeastern Aegean, it spans 481 km² and includes the active Nisyros volcano along with nearby islands (Fig. 1). Positioned at the southeastern edge of the South Aegean Volcanic Arc—one of the world's most significant active volcanic systems—the geopark offers a unique terrestrial and submarine landscape shaped by its volcanic origins. The geopark encompasses 24 geosites (Fig. 2), showcasing its rich geological history. Visitors can explore the impressive collapse caldera, hydrothermal craters and lava domes on the western side, stratified layers of lava, ash, and pyroclastics, which chronicle its extensive geological evolution (Parcharidis et al., 2018). Active hydrothermal craters and numerous coastal hot springs highlight ongoing hydrothermal activity, while the submarine aspects of the geopark are key to its formation and development. These features attract international scientific research, positioning Nisyros Geopark as a prominent natural geological laboratory in the Eastern Mediterranean. As part of the South Aegean Volcanic Arc, the geopark features a striking landscape shaped by five eruptive cycles over the past 160,000 years (Dietrich & Lagios, 2018). These cycles have left their mark on both the land and the seabed (Nomikou & Papanikolaou, 2011). The offshore region continues this volcanic landscape beneath the sea, hosting basins, underwater volcanic structures like craters and lava domes, fractures, and even a prehistoric caldera, Avyssos, located northeast of Strongyli islet (Tibaldi et al., 2008; Nomikou et al., 2021).

Figure 1. Nisyros Geopark location map

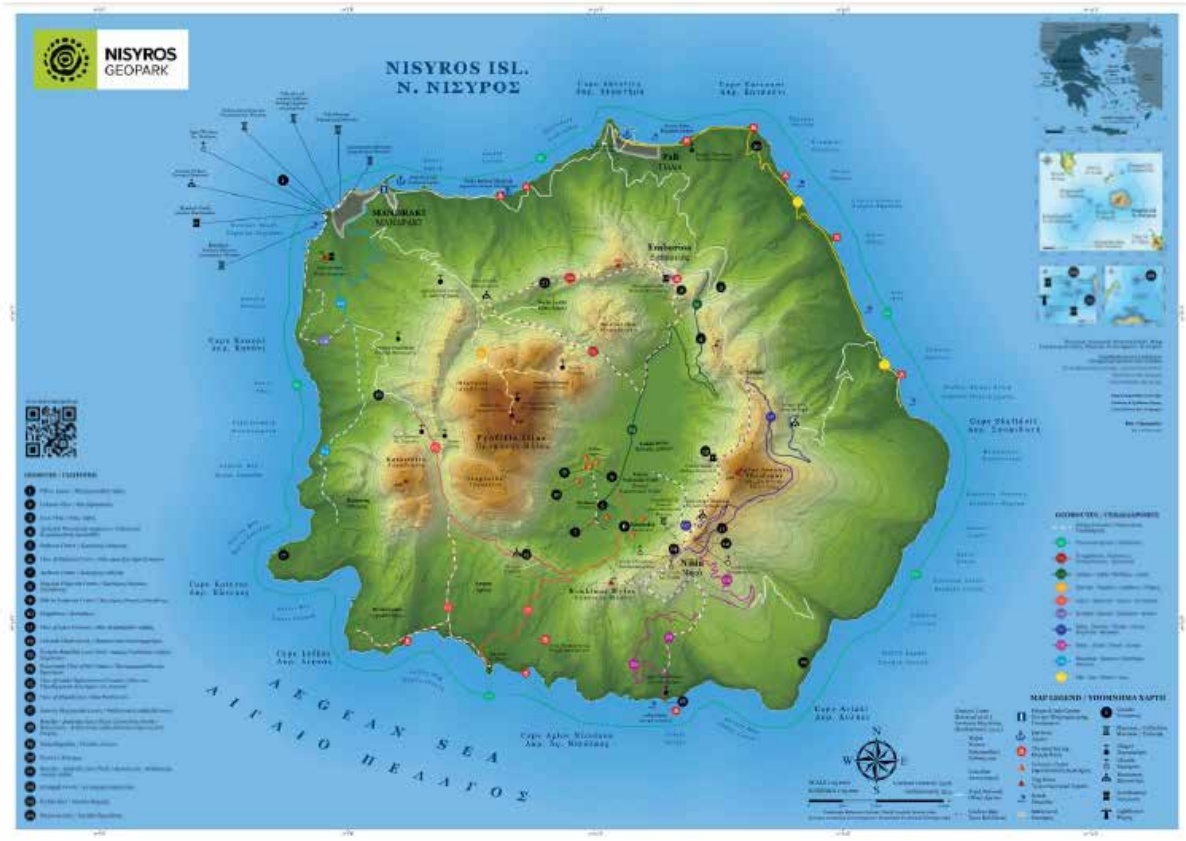

Figure 2. Nisyros Geopark geotouristic map

Beyond its geological wonders, the geopark is steeped in cultural heritage. Despite its modest size, the region has been continuously inhabited for millennia and is linked to the myth of Gigantomachy. The region's cultural heritage has stood steadfast through the ages, showcasing the brilliance of art and civilization through its prehistoric and historic sites and monuments. It is home to remarkable archaeological and cultural landmarks, including fortresses such as Paleokastro and the Mandraki castle, remnants of ancient settlements, numerous Byzantine-era churches and monasteries like the famous Panagia Spliani Monastery (Fig. 3), as well as thermal springs tied to its long-standing tradition of thermal baths. Together, these elements have shaped the region's history, fostering the traditions and preserving the tangible and intangible heritage cherished by its local communities today. Moreover, the Geopark features rich biodiversity protected by the two internationally designated Natura 2000 areas including its entire surface, as well as three wildlife refuge areas recognized at a national level. A great number of species of flora, avifauna and reptiles thrive within the geopark's area (Antoniou et al., 2019).

Figure 3. Panagia Spiliani Monastery (left) and ancient wall of Paleokastro (right)

To enhance visitor engagement and educational opportunities, Nisyros Geopark is upgrading its services. Current initiatives include the development of two free mobile applications, Nisyros Geopark App and Nisyros Volcano App, an informative website (www.nisyrosgeopark.gr) and a variety of educational materials. The geopark actively promotes awareness through talks, workshops, summer schools, and media campaigns, fostering an appreciation of its unique geological and cultural significance among residents and visitors alike.

Acknowledgements
We extend our heartfelt gratitude to the management body of Nisyros Geopark (DIKEN) and the Mayor of Nisyros, Mr. Koroneos Christofis, for their invaluable contribution, unwavering support, and dedication to the vision of the geopark. Their efforts have been instrumental in promoting the sustainable development of the region, preserving its unique geological and cultural heritage, and advancing its candidacy as a UNESCO Global Geopark.

References

Antoniou, V., Nomikou, P., Zafeirakopoulou E., Bardouli P., Ioannou T., 2019. Geo-biodiversity and cultural environment of Nisyros volcano, 15th International Congress of the Geological Society of Greece, Athens, 22-24 May, 2019 | Harokopio University of Athens, Greece. Bulletin of the Geological Society of Greece, Sp. Pub. 7 Ext. Abs. GSG2019-195.

Dietrich, V. and Lagios, E., 2018. Nisyros Volcano, The Kos - Yali - Nisyros Volcanic Field. 1st ed. Springer, Cham.

Nomikou P., Papanikolaou D. (2011). Extension of active fault zones on Nisyros volcano across the Yali-Nisyros Channel based on onshore and offshore data. Marine Geophysical Research 32 (1), pp.181. DOI 10.1007/s11001-011-9119-z.

Nomikou, P., Krassakis, P., Kazana, S., Papanikolaou, D. and Koukouzas, N., 2021. The Volcanic Relief within the Kos-Nisyros-Tilos Tectonic Graben at the Eastern Edge of the Aegean Volcanic Arc, Greece and Geohazard Implications. Geosciences, 11(6), p.231.

Parcharidis, I., Lagios, E. and Sakkas, V., 2018. Differential interferometry as a tool of an early warning system in reducing the volcano risk: the case of Nisyros volcano. Bulletin of the Geological Society of Greece, 36(2), p.913.

Tibaldi A., Pasquarè F.A., Papanikolaou D., Nomikou P. (2008). Tectonics of Nisyros Island, Greece, by field and offshore data, and analogue modeling. Journal of Structural Geology 30 (12), pp.1489.

17th INTERNATIONAL CONGRESS of the Geological Society of Greece

BULLETIN OF THE GEOLOGICAL SOCIETY OF GREECE, SP. PUBL.

EXTENDED ABSTRACT 231

Assessment of groundwater quality and seasonal dynamics in Chortiatis, northern Greece: Insights for sustainable resource management

Ntona Maria Margarita [1], Stavropoulou Vasiliki [2], Lampropoulou Dimitra [3], Zagana Eleni [2], Pouliaris Christos[2], Kazakis Nerantzis [2]

(1) Laboratory of Engineering Geology & Hydrogeology, Department of Geology, Aristotle University of Thessaloniki, 54124 Thessaloniki, Greece, margaritantona@yahoo.com (2) Laboratory of Hydrogeology, Department of Geology, University of Patras, Faculty of Natural Sciences, 26504 Rion, Patras, Greece, nkazakis@upatras.gr (3) Department of Chemistry, Aristotle University of Thessaloniki, 54124 Thessaloniki, Greece

Research Highlights:

- Groundwater samples are characterized by Ca-HCO□ water type.
- Seasonal groundwater level variations reveal various recharge patterns based on precipitation events.

Introduction / Background

Various geological formations and significant seasonal variability in precipitation influence complex hydrogeological environments (Luo *et al.*, 2023). In these cases, effective groundwater management requires a comprehensive understanding of both groundwater levels and quality parameters, especially under the pressures of the climate crisis (Davamani *et al.*, 2024). This study presents the results of field measurements as well as hydrochemical and statistical analysis to assess groundwater quality in the Chrotiatis region, Greece. By combining these methodologies, a comprehensive hydrogeological profile of the region is provided with valuable insights for future resource management. In this aspect, hydrochemical analyses of groundwater samples reveal potential sources of pollution, while groundwater level data provide insights into seasonal fluctuations and recharge patterns of the study area. Additionally, groundwater level measurements reveal temporal trends, including seasonal declines offering key insights into the dynamics of the region's water resources. The findings are expected to benefit water authorities and local stakeholders by offering reliable insights for sustainable groundwater management, protection strategies, and the mitigation of pollution risks.

Study area

The study area is located in northern Greece in the Central Macedonia region (Figure 1). The upper geological units in the area comprise alluvial deposits and red clays, while the Alpine formations, including clay schists, limestones, and igneous rocks, reflect significant tectonic and magmatic activity in the study area. The presence of quartzites and various igneous rocks, such as gabbros and peridotites indicates volcanic processes. These formations contribute to the area's aquifer systems and play a key role in water storage and water movement through the complex lithology. The presence of these diverse geological formations contributes to several types of aquifers in the area, namely alluvial, fractured, and karst aquifers. Based on the Copernicus database, the study area is occupied by transitional forested and shrubland (27.9%), agricultural activities with significant parts of natural vegetation (18.7%), and non-irrigated-arable land (15.7%). Mineral mining sites of limestones and mixed forests are also noted.

Methodology

The combination of qualitative and quantitative data can provide significant information about groundwater dynamics, the influence of local geological formations, and the potential sources of pollution in the aquifers (Kazakis *et al.*, 2015). In this study, monthly groundwater level measurements were obtained across the study area during the period of 2023-2024 to establish a hydrogeological framework using a judgmental sampling approach (Ntona *et al.*, 2023). Additionally, chemical analyses of sixteen (16) groundwater samples from deep boreholes were performed in June 2024 to assess the concentrations of major ions and trace elements, revealing mixing processes and ion exchange reactions in the study area. Piper and Durov diagrams are constructed in AquaChem software, while the maps were designed in ArcMap software. Precipitation data was obtained from the meteorological station Eptapurgio (meteo.gr), located near the study area. Raster file of digital elevation model (DEM) downloaded by NASA open data.

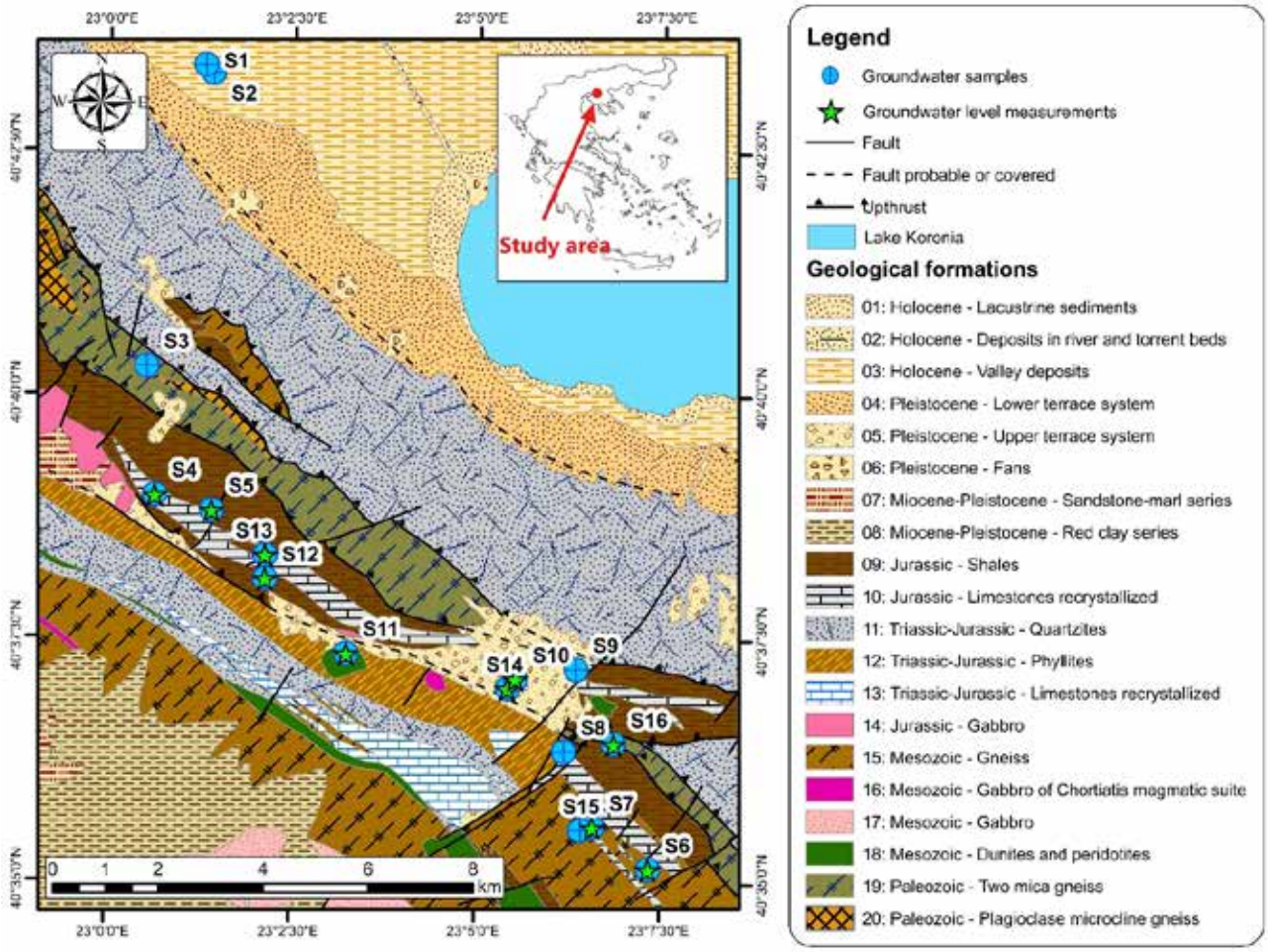

Figure 1. Geological map of the study area (HSGME with modifications, scale 1:50,000, sheets: Thessaloniki and Thermi).

Results and discussion

The chemical composition of all samples is shown in Table 1 and on Piper (Piper, 1944) and Durov (Durov, 1948) diagrams (Figure 2), which demonstrate the proportions between the major water components of the study area. The results of groundwater chemical analyses reflect both natural processes and some potential pollution sources. The pH levels range from 7.4 to 8.5, pointing to slightly alkaline conditions likely influenced by the local carbonate rocks. Electrical conductivity (EC) values vary from 525 to 1640 μS/cm with a mean value of 833 μS/cm (Figure 3a). High concentrations of calcium (Ca) and magnesium (Mg) indicate the presence of calcite and dolomite rocks. Sodium (Na) and chloride (Cl) concentrations vary from 3.7 to 63 mg/L and from 7.5 to 59 mg/L, respectively. These values indicate a mix of natural mineral dissolution and possible pollution from human activities in the area. Nitrate (NO_3^-) concentrations vary between 2.7 and 78.5 mg/L with a mean value of 18.6 mg/L, indicating agricultural or/and urban pollution. According to Piper and Durov diagrams, the most dominant water types are Ca-Mg-HCO_3, while samples S1 and S2 indicate Ca-Na-K-HCO_3 and sample S11 indicate Na-HCO_3 and Mg-Ca-HCO_3 water types, respectively. Samples S1 and S2 are projected at the center of the cations' triangle, indicating the groundwater origin from different sources of ion exchange processes.

The ratios of the major ions are provided in Table 2. The obtained proportions indicate insightful information about the geochemical characteristics of groundwater and potential sources of pollution in the study area. The results noted elevated Na/Cl and Mg/Cl ratios in several samples, suggesting varying degrees of cation exchange and mineral dissolution, possibly linked to carbonate geological formations (Figure 3b). High values of the ration (Ca+Mg)/(K+Na) in groundwater samples indicate a dominant presence of calcium and magnesium, which could be linked to natural mineralization processes from limestone and dolomite rocks. Within the study area the value of (Ca+Mg)/(K+Na) is higher than 1 highlighting the continuous recharge of the aquifer. On the other hand, values <1 of the Cl/SO_4^{2-} ratio observed in ten (10) samples highlight sulphate concentration, possibly from gypsum dissolution or agricultural activities.

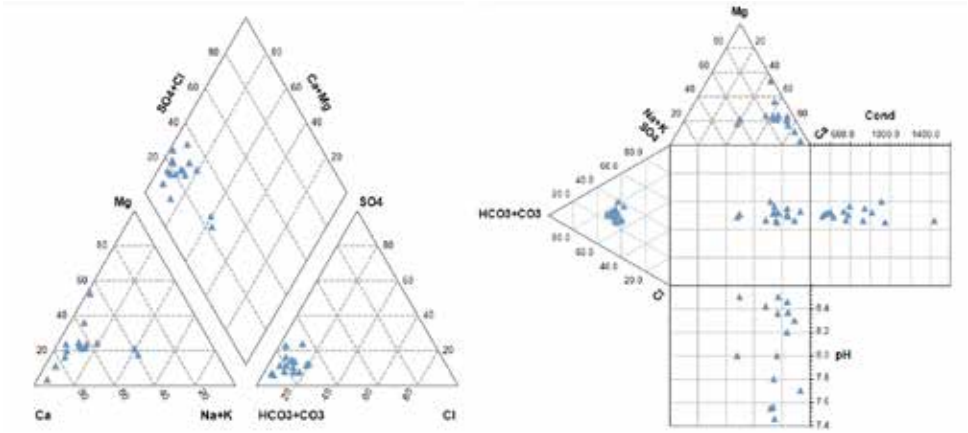

Figure 2. Classification of groundwater samples in Piper and Durov diagrams for the period of June 2024.

Table 1. Descriptive statistics of water quality parameters in the study area for the period of June 2024.

Parameter	Unit	Min value	Max value	Mean value	St.dev.
pH	-	7.4	8.5	8.0	0.4
T	°C	12.0	22.3	17.4	2.8
ORP	mV	-87.0	-20.0	-38.6	16.0
O_2	mg/l	0.0	9.9	4.6	3.3
EC	μS/cm	525.0	1640.0	833.5	295.0
Ca^{2+}	mg/l	50.0	124.0	95.8	25.0
Mg^{2+}	mg/l	2.7	56.8	21.3	13.1
Na^{+}	mg/l	3.7	63.0	21.9	17.2
K^{+}	mg/l	0.3	2.1	1.1	0.5
HCO_3^{-}	mg/l	272.1	451.4	335.7	51.8
SO_4^{2-}	mg/l	16.0	109.0	44.4	26.4
Cl^{-}	mg/l	7.5	59.0	27.8	14.5
NO_3^{-}	mg/l	2.7	78.5	18.6	20.6
NO_2^{-}	mg/l	0.0	0.0	0.0	0.0
NH_4^{+}	mg/l	0.0	0.1	0.1	0.0
PO_4^{2-}	mg/l	0.0	0.2	0.1	0.1

Table 2. Descriptive statistics of components ratios of groundwater samples in the study area.

Ion ratio	Min value	Average value	Max value	St.dev.
Mg^{2+}/Cl^{-}	0.5	3.0	14.4	3.2
Na^{+}/Cl^{-}	0.4	1.3	3.3	1.0
Cl^{-}/SO_4^{2-}	0.1	1.0	2.3	0.6
Mg^{2+}/Ca^{2+}	0.0	0.4	1.2	0.2
Na^{+}/K^{+}	12.7	39.1	148.8	33.5
$(Ca^{2+}+Mg^{2+})/(K^{+}+Na^{+})$	1.3	12.2	51.8	11.7

The trace element analysis of groundwater samples reveals a diverse chemical composition influenced by both the geological regime and possible pollution sources. The concentrations of iron (Fe) in the samples vary from 30.5 to 875.0 μg/L with a mean value of 141.9 μg/l, while the potable limit for Fe is 200 μg/L (EU Council directive 2020/2184). Strontium (Sr) concentrations vary from 52.1 to 581.3 μg/L with a mean value of 374.4 μg/L. High concentrations are also noted by the elements of boron (B) and zinc (Zn). It is worth noting that B element is only presented in the samples at the northern part of the sampling area, with a mean value of 216.7 μg/L and a maximum of 284.0 μg/L, potentially indicating anthropogenic activities such as agricultural fertilizers. Uranium (U) concentrations are below the potable limit of 30 μg/L and range from 0.1 μg/L to 12.7 μg/L.

Table 3. Descriptive statistics of trace element concentrations in groundwater samples of the study area (μg/L).

Trace elements	Min	Max	Mean	St.dev.
Al	ND	13.5	2.5	3.7
As	0.1	3.6	1.0	1.1
B	ND	284.0	216.7	95.2
Ba	8.3	212.5	70.6	56.9
Cr	5.9	42.4	11.0	8.6
Cs	0.0	0.2	0.1	0.1
Cu	1.3	15.8	4.7	4.3
Fe	30.5	875.0	141.9	209.0
Li	0.7	17.1	5.4	4.8
Mn	0.7	199.4	26.8	57.7
Mo	0.2	2.9	0.9	0.9
Ni	3.0	7.4	5.1	1.3
P	16.3	50.1	32.9	10.8
Rb	0.1	1.6	0.7	0.5
Se	ND	3.7	0.7	0.9
Sn	0.2	0.6	0.4	0.1
Sr	52.1	581.3	374.4	119.8
U	0.1	12.7	3.4	3.3
V	ND	4.7	0.8	1.7
Zn	ND	211.6	26.4	50.6

*ND: Not detected

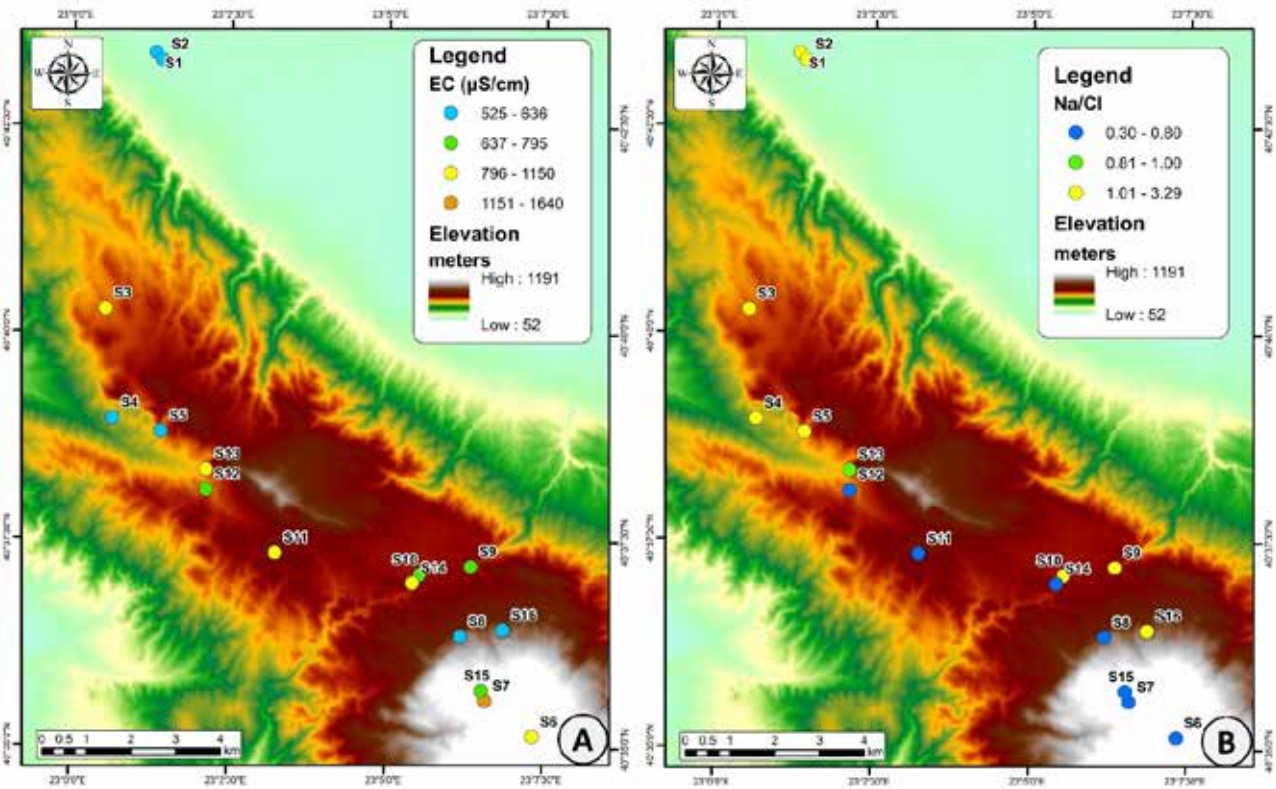

Figure 3. Spatial distribution of the (a) EC (μS/cm) and (b) Na/Cl ion ratio in the study area.

The monthly variation of precipitation and groundwater level for the monitoring wells are also provided in Figure 4, highlighting the groundwater dynamics and spatial heterogeneity of the aquifers. In the diagram of Figure 4a, the groundwater level exhibits a gradual decline over the year, despite a rainfall peak in March 2024. In Figure 4b, a marked rise in groundwater levels is noted following significant rainfall in March and April 2024. No significant variations are mentioned in the diagram of Figure 4c for a long period, on the contrary, low recharge and/or high groundwater exploitation values are noted during the period of June to September 2024. Higher groundwater levels, compared to the other wells, are noted in Figure 4d with a clear seasonal recharge pattern. It should be noted that this particular well has been out of operation for more than a year.

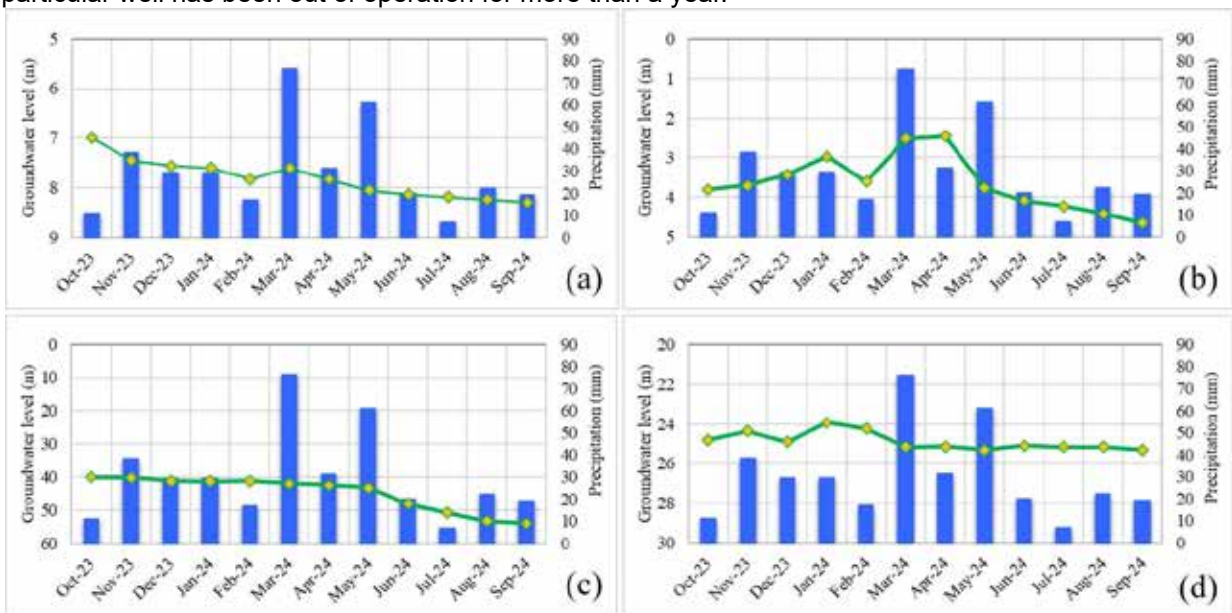

Figure 4. Groundwater level measurements in the hydrological year 2023-2024.

Conclusions

In this study, the hydrochemistry of major ions and trace elements is used to define the hydrochemical characteristics of groundwater in the Chortiatis region. Based on the results, the quality of groundwater is affected by geological regime and human activities. This research indicates that Ca-HCO_3 is the predominant groundwater type, with notable concentrations of sodium-chloride ions. Additionally, elevated concentrations of trace elements such as iron (Fe) and manganese (Mn) highlight the interactions with mineralized rock layers and potential contamination risks that require further monitoring. The results also reveal groundwater level variations across the hydrological year, characterized by seasonal recharge patterns following significant precipitation events and notable declines during dry months. Spatial heterogeneity among the monitoring wells highlights differences in recharge capacity and aquifer exploitation intensity, providing valuable insights for sustainable groundwater management.

Acknowledgment

This research was carried out within the framework of the project entitled “Development of a methodology for investigating the phenomenon of groundwater flooding and defining protection measures and zones for water abstraction projects and infrastructure in the Municipal Unit of Chortiatis.” with Scientific Coordinator Prof. Kazakis Nerantzis and was funded by the Water and Sewage Management Company of Pylaias-Chortiati (DEYA) and the Municipality of Pylaias-Chortiati.

References

Davamani, V., John, J.E., Poornachandhra, C., Gopalakrishnan, B., Arulmani, S., Parameswari, E., Santhosh, A., Srinivasulu, A., Lal, A., Naidu, R., 2024. A Critical Review of Climate Change Impacts on Groundwater Resources: A Focus on the Current Status, Future Possibilities, and Role of Simulation Models. Atmosphere 15(1), 122.

Digital Elevation Model (DEM), raster file downloaded by NASA open data. https://asterweb.jpl.nasa.gov/gdem.asp (accessed on 10 January 2024).

Durov, S.A., 1948. Natural Waters and Graphic Representation of Their Composition. Doklady Akademii Nauk

SSSR, 59, 87-90.
Hellenic Survey of Geology & Mineral Exploration (HSGME), 1978. Geological Map of Greece, Scale 1:50,000, Sheets: Thessaloniki and Thermi.
Kazakis, N., Oikonomidis, D., Voudouris, K., 2015. Groundwater vulnerability and pollution risk assessment with disparate models in karstic, porous and fissured rock aquifers using remote sensing techniques and GIS in Anthemountas basin, Greece. Environmental Earth Science 74(7), 6199-6209.
Luo, Y., Zhou, Q., Peng, D., Yan, W., Zhao, M., 2023. Key influence of hydrogeological, geochemical, and geological structure factors on runoff characteristics in karst catchments. Journal of Hydrology 623, 129852.
Ntona, M.M., Chalikakis, K., Busico, G., Mastrocicco, M., Kalaitzidou, K., Kazakis, N., 2023. Application of Judgmental Sampling Approach for the Monitoring of Groundwater Quality and Quantity Evolution in Mediterranean Catchments. Water, 15, 4018.
Piper, A.M., 1944. A graphic procedure in the geochemical interpretation of water analyses. Eos, Transactions American Geophysical Union 25(6), 914–928.

17th INTERNATIONAL CONGRESS of the Geological Society of Greece

BULLETIN OF THE GEOLOGICAL SOCIETY OF GREECE, SP. PUBL.

EXTENDED ABSTRACT 232

Evaluation of National Groundwater Monitoring Network at the Peloponnese, Greece

Ntontos P.
Freelance Geologist, Naflpio, Greece, ntontosp@gmail.com

Abstract

The Water Framework Directive requires the establishment of monitoring programmes covering groundwater quantitative status, chemical status and the assessment of significant, long-term pollutant trends resulting from human activity. Greece has a significant disadvantage in developing such a monitoring programme because of its geological complexity. This disadvantage is further magnified by the obligatory choice of Greece, due to lack of data, to delineate «Groundwater Systems» and not «Groundwater Bodies» as Guidance Documents describes.

The basic principles that Guidance Documents suggest are not followed by the developed monitoring network in the region of the Peloponnese. There are fewer than the necessary number of monitoring sites, which are badly distributed over the area and, in many cases, not representative of the monitored aquifers. In contrast to the particularly costly and time-consuming solution of developing an adequate and representative ground water monitoring network, the alteration of all existing wells/boreholes to monitoring sites by establishing of institution of "Well Inspector" seems to be the only direct and sustainable solution to the problem.

Background

The WFD 2000/60/ec for groundwater aims to prevent further qualitative degradation, prevent or contain pollutants, restore groundwater quantity, restore groundwater quality by progressively reduce pollutants, and ensure a balance between abstraction and recharge of groundwater.

To achieve these objectives, the member-countries were obliged to describe "Groundwater Bodies" which are defined as "distinct volumes of groundwater within one or more aquifers". According to the specifications the GroundWater Bodies (GWBs) should be defined in all three dimensions. The GWBs are not necessarily homogenous in their natural characteristics or the concentration of pollutants in them. However, the GWBs should be defined in such a way that the definition of their qualitative and quantitative state is possible (Guidance Document No. 2).

For the accurate definition of the quantitative and chemical status of the GWBs, the appropriate selection of the measures necessary for the achievement of the environmental objectives of the directive, the evaluation of the effectiveness of these measures and the detection and reversal of the pollutants of human intervention in the groundwater, the member-countries should develop a monitoring programme. For this programme to be representative, it should be designed according to the theoretical model and the understanding of the general schema of "recharge-pathway-discharge" for each GWB. The determination of the monitoring sites in the design of the monitoring network should be made by taking into consideration the three-dimensional nature of the GWBs, as well as their spatial and temporal variability. The number of the monitoring sites and the frequency of the sampling procedure should be proportionate to the difficulty in evaluating the UWB status, the presence of pollutants, and the probability of wrongful estimations which the restoration measures may be based on. For GWBs which are at risk, a minimum number of 3 monitoring sites is recommended (Guidance Document No. 15).

The monitoring programmes comprise 3 network categories which are of quantitative monitoring, surveillance monitoring, and operational monitoring, The operational monitoring takes place in the GWBs that are at risk of not fulfilling or are already not fulfilling the objectives of the 2000/60 directive (Guidance Document No. 15). To implement this monitoring programme, Greece enforced the National Monitoring Water Network for the first time in 2011, which was amended in 2021. Groundwater is monitored by part of this network.

Delineation of the GWBs and the Groundwater Monitoring Network

In Greece, the implementation of the 2000/60 directive did not lead to the delineation of "GroundWater Bodies", but of "GroundWater Systems" (GWSs). This was according to the hydrolithological classification of the geological formations that accommodate the underground aquifers. The boundaries were determined according to the outcrop at the surface of these formations, without attempting to evaluate their three-dimensional development or the possible differentiation in the hydraulic behaviour of the formations.

The first River Basin Management Plans (RBMPs) of the 14 Water Districts of the country were conducted either through studies assigned to 5 different joint-venture study groups, or by studies of the Special Secretariat for Water itself. The weaknesses and errors that emerged during the process are the disagreement of the philosophy in the

determination of the GWSs according to the study group, the merging of different aquifers in a single GWS and the determination of the GWSs with geological and not hydrogeological criteria (Ntontos, 2022(a)).
In the first RBMPs, 539 GWSs were determined. Later, in their first revision in 2017, the GWSs were redefined, and the number reached 553, while in their second revision in 2024, the total number reached 598.
The complex and complicated structure of the GWSs which have been determined requires the development of a similarly complex and complicated monitoring network, so that it can be representative and adequate. It should be noted that for a GWS to be characterized as in poor quantitative status, the monitoring sites should present an established water level decline for more than a year, at a rate of at least 20% of the monitoring sites. For a GWS to be characterized as in poor chemical status, at least 20% of the monitoring sites should present exceedance (due to human activities) of the highest acceptable value regardless of the parameters measured. Both characterizations are valid on condition that monitoring sites are uniformly distributed in the whole area of the GWS and not locally placed.
The first governmental attempt to develop such a network was in 2011 with JMD 140384/2011, which included 1,392 groundwater monitoring sites. This network, which is in operation today, was enriched and slightly amended in 2021 with JMD 107168/1444/2021 and now includes 1,895 monitoring sites. The development and monitoring of this network was conducted by an informal assignment to H.S.G.M.E.

Adequacy Inspection Methodology of the Groundwater Monitoring Network

A statistical index, the Representative Index, Ru, has been developed (Grath et al., 2001) for the evaluation of the monitoring network with the following form:

$$R_U = \frac{37.7}{dist_{ave}\sqrt{k / Area}} \ [\%]$$

where

- $dist_{ave}$ is the minimum average distance of any site of the GWS from the closest monitoring site
- k the number of monitoring sites
- Area the area of the GWS

However, this index can be used only in hydrogeologically uniform GWSs. When they are heterogenous, the representation should be estimated solely on hydrogeological criteria. For this reason, the methodology for examining the network quantitative adequacy should abide by the following rules:

- The GWSs that are in a good quantitative and qualitative status, the minimum number is established at 3 monitoring sites (Guidance Document No 15).
- The GWSs that are in poor quantitative and/or chemical status and are hydrogeologically uniform, the minimum number is established at 5 monitoring sites so that 20% of these sites is at least 1 site.
- When the GWSs consist of different aquifer systems (karstic, granular, fissured), the minimum number is established at 3 monitoring sites for every type of significant aquifer. For an aquifer system to be considered as significant, we arbitrarily establish as the minimum area the 10% of the total area of the GWS, or it should accommodate at least 10% of the current productive wells/boreholes in the GWS.

For a monitoring network to be qualitatively adequate, the monitoring sites should be well distributed in the area, and, at the same time, they should be representative of the aquifer formations that form the GWSs. Furthermore, they should not be productive wells/boreholes, except if the measurement frequency is at least every hour (Guidance Document No. 15, ANNEX 2).

Groundwater Monitoring Network of the Peloponnese

According to the 2nd revision of the RBMPs, in the Peloponnese there are 90 Groundwater Systems or Subsystems. These systems have been separated into hydrolithological units, the surface area of which has been calculated. According to the quantitative and chemical status of the GWSs, 71 are in good quantitative and chemical status, 8 in poor quantitative and chemical status, 8 only in poor quantitative status, and 3 in only poor chemical status.
The Groundwater Monitoring Network as defined by the J.M.D. 140384/2011 (O.G.G. 2017/B΄/9-9-2011) included 294 monitoring sites in the Peloponnese. Of these sites, 198 were productive boreholes, 36 productive wells and 60 springs. After revising the network according to J.M.D. 107168/1444/2021 (O.G.G. 5384/B΄/19-11-2021) monitoring sites increased approximately 26%, to 371 sites. Of these sites, 270 are productive boreholes, 35 productive wells and 66 springs. In only 3 of the boreholes the measurement frequency is every hour.

Network Evaluation in the Peloponnese

According to the methodology developed, the first rule for the 71 GWSs that were of good quantitative and chemical status, and the second one for the 19 GWBs that were of bad quantitative and/or chemical status were examined. Table 1 presents the number of GWSs per number of monitoring sites. This table shows that 31 GWSs that are of good quantitative and chemical status, and 5 GWSs that are of poor quantitative and/or chemical status, do not have quantitative adequacy of monitoring sites.

Table 1. Number of GWSs with specific number of monitoring sites in them.

	Number of monitoring sites												
	0	**1**	**2**	**3**	**4**	**5**	**6**	**7**	**8**	**9**	**10**	**13**	**14**
GWSs of good quantitative and chemical status	10	7	14	14	10	3	2	5	1		2	2	1
GWSs of poor quantitative and/or chemical status	2	1		1	1	2	2	3	1	3	1	2	

The third rule was examined for the 14 GWSs that are in poor quantitative and/or chemical status (Table 2) and have more than 5 monitoring sites. It was found that GWSs comprised more than one significant hydrolithological systems, 4 of which have less than the minimum required monitoring sites.

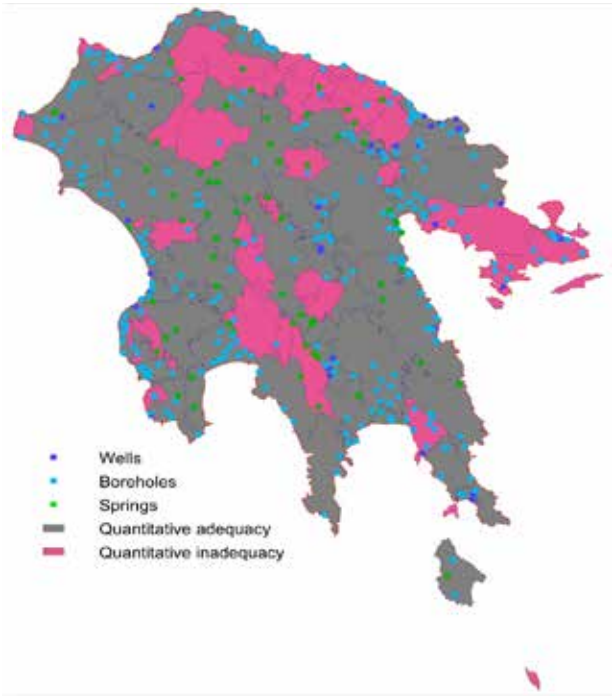

Figure 1. Illustration of the quantitative status of GWSs in the Peloponnese.

Table 2. Area of each significant hydrolithological system (%) of the total GWS area, and number of existing and required monitoring sites.

GWS's code	K1	P1	P2	P3	P4	A1	A2	Number of existing sites	Minimum number required
EL0100100		52,2		45,4				13	6
EL0100170		10,0		87,1				9	6
EL0200091		95,9						7	5
EL0200171		22,3	19,6	48,6				9	9
EL0200173		14,2	11	72,1				6	9
EL0200190		96,3						9	5
EL0300030		98,6						10	5
EL0300040		99,0						13	5
EL0300050	58,4	17,9				8,3*	6,9*	8	12
EL0300060		91,0						6	5
EL0300070	9,4*	9,7*				69,8	7,7*	5	12
EL0300090		71,5			26,2			7	6
EL0300130				95,0				5	5
EL0300150		15,9		43,8			30,2	7	9

K1: Calcareous formations of high to medium permeability. P1: Granular, mainly fluvial deposits of variable permeability. P2: Neogene/Pleistocene deposits of medium to low permeability. P3: Granular, non fluvial deposits of low to very low permeability. P4: Scree of variable permeability. A1:

Fissured formations of low to very low permeability (flysch). A2: Fissured formations of low to very low permeability (phyllites, quartzites, schists).
* Hydrolithological formation accommodating at least 10% of the current wells in the GWS

According to the previous evaluation, the 40 GWSs of good quantitative and chemical status, and the 10 GWSs of poor qualitative and/or chemical status that have quantitative adequacy of monitoring sites were examined for the good spatial distribution of the monitoring sites. Only 23 of them were found to have good spatial distribution of the monitoring sites, with 2 of them not presenting good representation of the aquifer formations. It should be noted that good spatial distribution of monitoring sites means not only to be spread in the area of GWS but mainly near clustered sites of productive wells/boreholes.

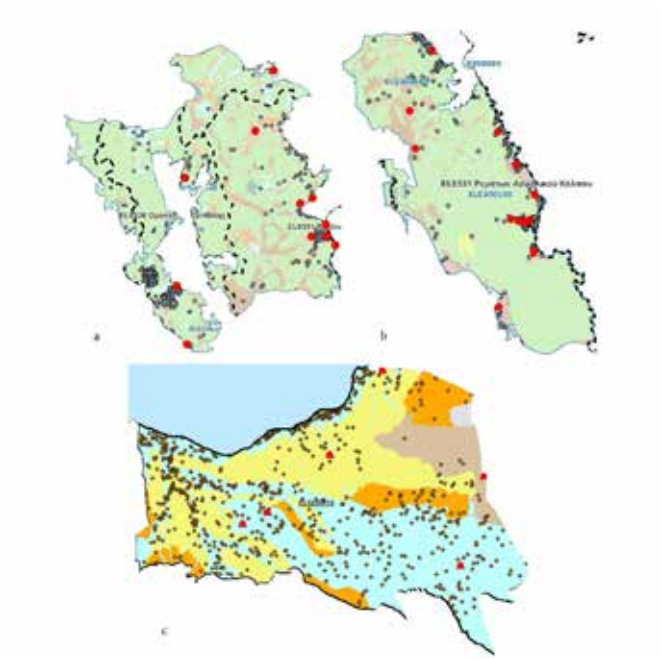

Figure 2. Example of poor (a) and good (b) spatial distribution of monitoring sites (red spots) that need to be not only spread but also near clustered sites of productive wells/boreholes (circles).

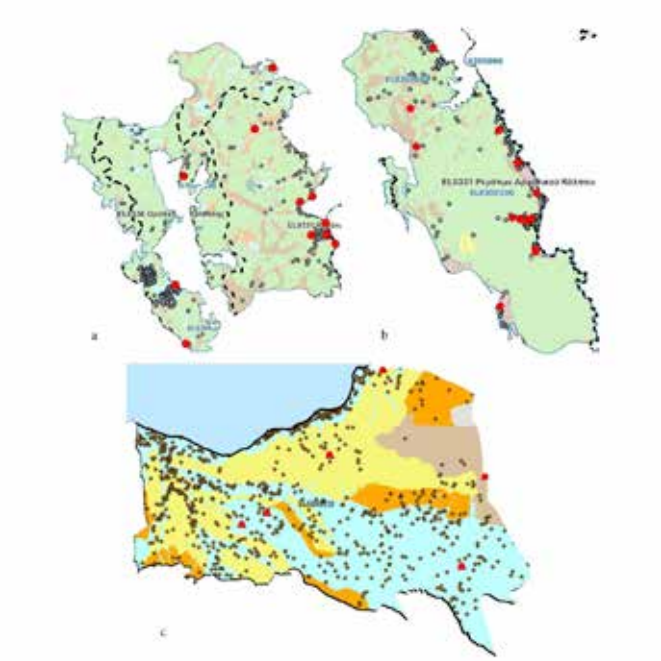

Figure 3. Example of poor representation of aquifer types, as monitoring sites (red spots) need to be not only spread in the area but also within significantly exploited hydrolithological units of the GWS.

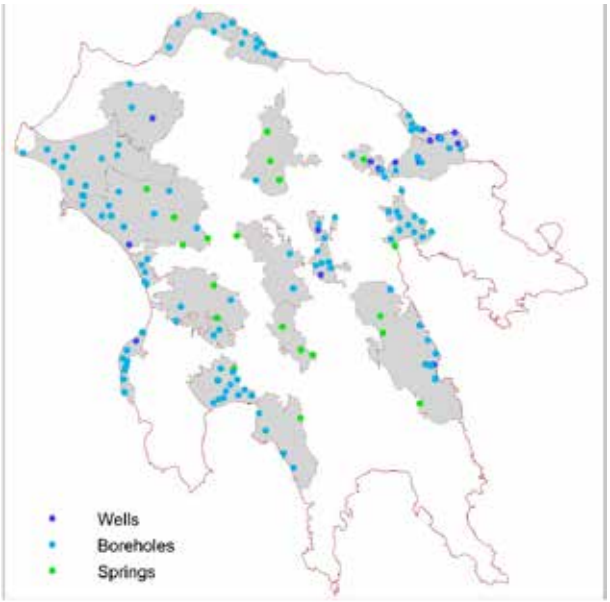

Figure 4. Three types of monitoring sites in 21 GWSs of good spatial and qualitative distribution. Only in 1 borehole measurements were conducted every hour.

Furthermore, 154 sites of the monitoring system were found in the 21 GWSs which were of good spatial and qualitative distribution of monitoring sites. Of those, 134 sites are productive wells/boreholes and only 20 of those sites are springs. However, only in 1 borehole measurements were conducted with the required frequency (eg hourly frequency). In only 4 GWSs the springs comprise the majority of the monitoring sites or are adequate in number (≥3). In the Peloponnese and Western Greece Prefectures, the number of existing productive wells/boreholes is estimated at 83,000 and in Greece at 250,000 respectively (Ntontos, 2017). These wells/boreholes can easily become unofficial monitoring sites for water level and water electric conductivity measurements. These measurements can be conducted twice a year or more frequently by geologists in the private sector who are paid by well/boreholes owners. Such an extended network, with no cost for the state, can contribute to the full understanding of the hydrogeological regime of every aquifer. This in turn can contribute to the appropriate selection of the measures necessary for the achievement of the environmental objectives of the directive.
This procedure is described in the Institution of Well Inspectors (Ntontos, 2022 (b)) and can produce hundreds or even thousands of work positions for geologists. According to the Geotechnical Chamber of Greece data for the year 2023, unemployment rates reach 40%.

Conclusions

According to the recommended methodology, after the examination of the qualitative and quantitative adequacy of the National Monitoring Network of Ground Water, it was found that, from the total of 90 GWSs that are found in the Peloponnese, only 4 of them have quantitatively adequate monitoring sites of good spatial and qualitative distribution. For it to be quantitative adequacy in all GWSs, the monitoring sites must increase in number by at 25%, selectively, and wherever this is imperative. The rearrangement of the monitoring sites is also of significance in many of the GWSs, so that they are distributed well, both spatially and quantitively. Finally, there should be water level loggers installed in all productive wells that are used as monitoring sites, to ensure the frequent monitoring of the water level according to the current European specifications.
It should also be noted that the existence of a minimum number of monitoring sites in each GWS does not, lead to the understanding of the hydrogeological status of the GWS by itself, nor does it contribute to the accurate determination of their quantitative and chemical status. Moreover, the development of a dense underwater monitoring system maintained by the state is extremely costly. Therefore, the implementation of the institution of the well inspector can contribute to the prompt development of an extensive monitoring network, which will consist of all the active wells/boreholes of the country estimated at more than 250,000. In this way, hundreds or even thousands of work positions will be created for geologists, thus the unemployment rates, which reach 40% according to Geotechnical Chamber of Greece data for the year 2023, will be reduced.

References

Ntontos, P., 2022 (a). Well Inspectors: Giving Greek Geologists a Chance. G.S.G. International Congress, Patras, Greece, p. 454 [Bulletin of GSG, Special Publication No. 10]

Ntontos, P., 2022 (b). River Water Management Plans: Weaknesses and Errors. Hellenic Chapter of IAH & CAGME International Hydrogeological Conference, Nicosia, Cyprus, p. 362.

Ntontos, P., 2017. Hydrowells permit issuing: Existing legislation, current situation and future prospects. Hellenic Chapter of IAH & CAGME International Hydrogeological Conference, Athens, Greece, p. 309.

Guidance Document No.15, 2007: Guidance on Groundwater Monitoring. European Communities [Guidance Document of CIS for the WFD 2000/60/EC]

Guidance Document No2, 2003. Identification of water bodies. European Communities. [Guidance Document of CIS for the WFD 2000/60/EC]

Grath, J., Scheidleder, A., Uhlig, S., Weber, K., Kralik, M., Keimel, T., Gruber, D., 2001: “The EU Water Framework Directive: Statistical aspects of the identification of groundwater pollution trends, and aggregation of monitoring results”. Final Report. Austrian Federal Ministry of Agriculture and Forestry, Environment and Water Management (Ref.: 41.046/01-IV1/00 and GZ 16 2500/2-I/6/00), European Commission (Grant Agreement Ref.: Subv 99/130794), in kind contributions by project partners. Vienna. [Technical Report of CIS for the WFD 2000/60/EC]

17th INTERNATIONAL CONGRESS of the Geological Society of Greece

BULLETIN OF THE GEOLOGICAL SOCIETY OF GREECE, SP. PUBL.

EXTENDED ABSTRACT 233

Characteristics of REE mineralization in bauxite strata and in bauxite residue deposited into the Corinth Gulf, Greece

Ntouros E. [1], Sofis N. [1], Damoulianou, M.E. [1], Iatrou M.[2,3], Grammatikopoulos T.[4], Papatheodorou G.[2], Kalaitzidis S.[1*]

(1) Laboratory of Economic Geology, Department of Geology, University of Patras, Rio-Patras Greece, skalait@upatras.gr (2) Laboratory of Oceanography, Department of Geology, University of Patras, Rio-Patras Greece (3) Institute of Oceanography Hellenic Centre for Marine Research (HCMR) (4) SGS Canada Inc.

Research Highlights

Authigenic cerianite mineralization and elevated REE values in b1 and b3 bauxites at the Parnassos-Ghiona Unit and bauxite residues from the Corinth Gulf

Introduction

The Mesozoic carbonate sequence of the Parnassus-Ghiona Unit mainly attracts research and economic interest, particularly around the three karstic-type bauxite strata it hosts, namely b1, b2, b3, which were deposited between Middle Jurassic and Upper Cretaceous times (e.g. Valeton *et al.*, 1987; Kalaitzidis *et al.*, 2010; Laskou & Economou-Eliopoulos, 2013; Economou-Eliopoulos *et al.*, 2016; Gamaletsos *et al.*, 2017). Nowadays mainly b3 horizon is exploited, b2 has been the subject of mining in the past, whereas b1 was never extracted, as it occurs sporadically, with limited quantities and low grade in terms of Al. Diaspore, boehmite and gibbsite are the main Al-minerals of interest, whereas the mineralogical composition frequently includes hematite, goethite, kaolinite, chlorite, anatase and pyrite (Mondillo *et al.*, 2022 and references therein).

Although bauxite mining in Greece takes place for almost a century, nowadays the focus shifts towards the REE, which occur either within the bauxite or the bauxite residues after metallurgical processes and are a key part of the EU Green Deal, in order to transit to a greener and more sustainable future for the EU (European Commission, 2020). REE are characterized by unique electrochemical and magnetic properties, thus making them “critical metals” for technological and industrial development for both developed and developing economies around the world (Borra et al., 2016; Panda et al., 2021). For the reasons above, REE are widely used in green technologies such as electric car batteries, solar panels, special magnets for wind turbines and others (Narayanan, 2019; Deady et al., 2016; Wall, 2014). The REE are traced within the bauxite residue (BR), being enriched in comparison to the bauxite with a factor of about two (Borra *et al.*, 2016; Ujaczki, 2017). In Greece, the bauxite residue is produced during the Bayer method by the alumina and aluminum production plant “Aluminum of Greece SA”(ATE) at Aspra Spitia of Boeotia, and for several decades it was disposed in the gulf of Antikyra in the northern and central part of the Corinthian Gulf. Its discharge began in the 1970s through a submarine pipeline and it ceased in 2012. In total, it is estimated that more than 20 Mt of bauxite residue have been discharged in the Corinthian Gulf, covering up to 12% of its total surface area (Iatrou, 2013). According to Ochsenkiihn-Petropulu et al. (1994) and Borra et al. (2015) the mean value of the ΣREE in the Greek BR is approximately 974 mg/kg. In this study bauxite, from the Parnassus-Ghiona Unit, and bauxite residue samples from the Corinth Gulf were examined in order to record and evaluate their main mineralogical, geochemical and mineral-chemical characteristics, with emphasis on the REE, which has not been systematically studied till now. The aim of this study is to assess the REE mode of occurrence in bauxites and wastes from the metallurgical process of bauxites (BR) and determine their origin.

Methods

Bauxite samples represent a b1 outcrop (EL2, EL3, EL3A and EL4 samples) (in total 17 samples) from Elateia site (near the small town of Elateia, Central Greece) and two b3 outcrops from Kardarrorahi (KR3 samples) (in total 3 samples) and Vargiani (PBF1-2-2 sample) (in total 1 sample) sites (near Delphi area), whereas samples of bauxite residue (RM samples) (in total 12 samples) represent deposition within Corinth Gulf; BR samples were obtained during a drilling campaign in 1994 and 2007 as part of an environmental study.

X-Ray diffraction analysis was performed in all samples, as well as geochemical analyses for major, minor and trace elements. SEM-EDS measurements were also conducted both in bauxite and bauxite residue samples.

Results

The b3 samples mainly consist of Al_2O_3 ranging between 36.81 and 51.55 wt.-%, Fe_2O_3 in a range of 11.26-28.33 wt.-% and SiO_2 fluctuating greatly from 4.23 to 23.97 wt.-%, while the b1 samples consist of Al_2O_3 ranging within

26.39 and 63.9 wt.-%, Fe_2O_3 in a range of 4.80-25.92 wt.-% and SiO_2 fluctuating greatly from 1.85 to 12.9 wt.-%. The bauxite residue samples mainly consisting of Fe_2O_3 (9.85-25.2 wt.-%), CaO (14.85-22.2 wt.-%), SiO_2 (14.2-23.9 wt.-%), and Al_2O_3 (9-11.1 wt.-%).

The ΣREE at the b3 samples vary greatly between 771.67-1961.8 mg/kg, while at the b1 samples varies between 510.23 and 1090.73 mg/kg. Finally, the total REE contents (ΣREE) of the bauxite residue samples vary between 484 and 771 mg/Kg.

The mineralogical examination of the bauxite samples presented similar mineralogical features in the bauxite samples (for both b1 and b3 samples), with small variations among diaspore, boehmite and gibbsite, as well as for the iron oxides and hydroxides. Furthermore, rutile concentration is always low between 1-3%, while Kaolinite seem to be more dominant in the b1 samples.

EDS analysis on individual particles in the bauxite residue samples, was challenging due to the small average size of the crystals. However, several mineral phases were identified with hematite, ilmenite, quartz and calcite being the predominant ones. Various accessory minerals were also rarely detected, including pyrite, and zircon. REE minerals were also found in bauxite and bauxite residues and more specifically individual cerianite crystals.

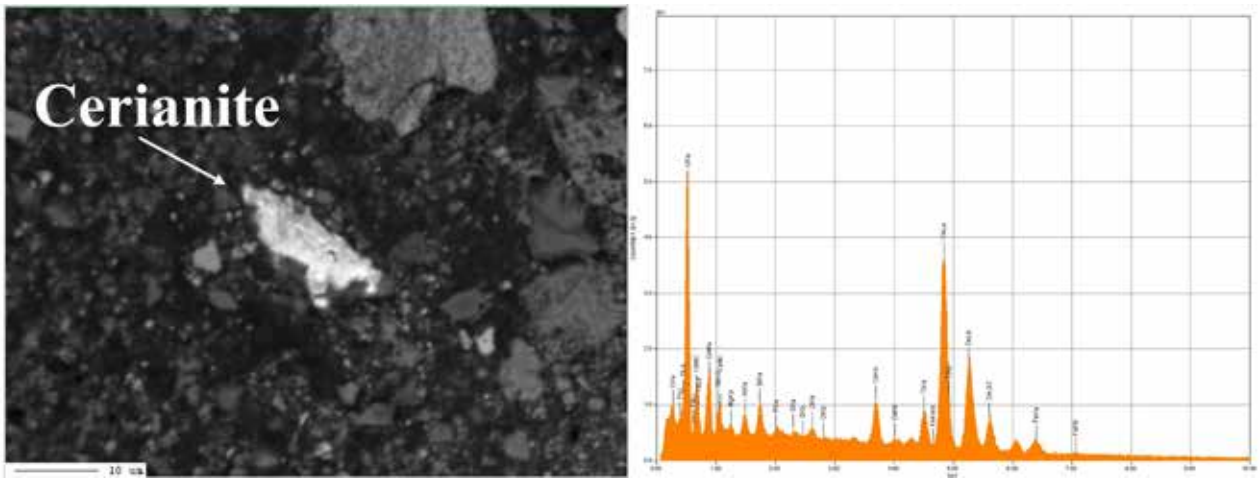

Figure 1. Back-scattered electron image of sample RM13 depicting cerianite in the bauxite residue and relative EDX spectra.

Conclusions

Both bauxite (b1 and b3) and bauxite residue samples seem to be enriched in REE, and show similar ranges in the total content of them. By comparing the ΣREE of the herein studied BR samples with those from previous studies of pure BR from Greece, the former values seem slightly decreased. This divergence is justified due to the mixing of the bauxite residue with the sediments of the Corinth Gulf. Authigenic REE-bearing minerals were identified in all samples and more specifically cerianite.

References

Economou-Eliopoulos, M., Frei, R., & Megremi, I., 2016. Potential leaching of Cr (VI) from laterite mines and residues of metallurgical products (red mud and slag): An integrated approach. Journal of Geochemical Exploration, 162, 40-49.

European Commission, 2020. Report on Critical Raw Materials Resilience: Charting a Path towards greater Security and Sustainability. https://ec.europa.eu/docsroom/documents/ 42849.

Borra, C.R., Blanpain, B., Pontikes, Y., 2016. Recovery of Rare Earths and Other Valuable Metals From Bauxite Residue (Red Mud): A Review. J. Sustain. Metall., 2, 365-386.

Borra C. R., Pontikes Y., Binnemans K., Gerven T. V., 2015. a Leaching of rare earths from bauxite residue (red mud), Minerals Engineering, Volume 76, 20-27

Deady, É, Mouchos, E., Goodenough, K., Williamson, B., & Wall, F., 2016. A review of the potential for rare-earth element resources from European red muds: Examples from Seydişehir, Turkey and Parnassus-Giona, Greece. Mineralogical Magazine, 80(1), 43-61.

Gamaletsos, P. N., Godelitsas, A., Filippidis, A., & Pontikes, Y., 2019. The rare earth elements potential of Greek bauxite active mines in the light of a sustainable REE demand. Journal of Sustainable Metallurgy, 5, 20-47.

Gamaletsos, P.N., Godelitsas, A., Kasama, T., Church, N.S., Douvalis, A.P., Gottlicher, J., Steininger, R., Boubnov, A., Pontikes, Y., Tzamos, E., Bakas, T., Filippidis, A., 2017. Nano-mineralogy and -geochemistry of high-grade diasporic karst-type

bauxite from Parnassos-Ghiona mines. Greece. 84, 228–244.
Iatrou. M., 2013. Oceanographic-Geomorphological surveys in the central Corinthian Gulf in relation to the dispersion of red mud. PhD thesis, University of Patras, Department of Geology.
Kalaitzidis S., Siavalas G., Skarpelis N., Araujo V., Christanis K., 2010. Late Cretaceous coal overlying karstic bauxite deposits in the Parnassus-Ghiona Unit, Central Greece: Coal characteristics and depositional environment. International Journal of Coal Geology, 81(4), 211-226.
Laskou, M. and Economou-Eliopoulos, M. 2013. Biomineralization and potential biogeochemical processes in bauxite deposits: Genetic and ore quality significance. Mineralogy and Petrology, 107, 471-486.
Mondillo, N., Di Nuzzo, M., Kalaitzidis, S., Boni, M., Santoro, L., Balassone, G., 2022. Petrographic and geochemical features of the B3 bauxite horizon (Cenomanian-Turonian) in the Parnassos-Ghiona area: A contribution towards the genesis of the Greek karst bauxites. Ore Geology Reviews, 143, 104759.
Mouchos, E., 2015. A Geological Study of the Potential for Rare Earth Element By-Product Recovery from Greek Bauxite Deposits. University of Exeter (United Kingdom).
Narayanan Remya P., 2019. Recovery of Rare Earth Elements from Bauxite Residue: A Comparative Economic Analysis. International Journal for Multidisciplinary Research, 1(2), 21-40.
Ochsenkühn-Petropulu, M., Lyberopulu, Th., Parissakis, G., 1994. Direct determination of landthanides, yttrium and scandium in bauxites and red mud from alumina production. Anal. Chim. Acta 296 (3), 305-313.
Panda S., Biancalana C. R., Sikandar S. S., Mishra S., Bevilaqua D., Akcil A., 2021. Biotechnological trends and market impact on the recovery of rare earth elements from bauxite residue (red mud) – A review, Resources, Conservation and Recycling, Volume 171, 105645.
Ujaczki, É., Zimmermann, Y.S., Gasser, C.A., Molnár, M., Feigl, V. and Lenz, M. 2017. Red mud as secondary source for critical raw materials – extraction study. J. Chem. Technol. Biotechnol, 92, 2835-2844.
Valeton, I., Biermann, M., Reche, R. and Rosenberg, F., 1987. Genesis of nickel laterites and bauxites in Greece during the Jurassic and Cretaceous, and their relation to ultrabasic parent rocks. Ore Geology Reviews, 2, 359-404.
Wall, F., 2014. Rare earth elements.: Critical Metals Handbook (G. Gunn, editor). First Edition. John Wiley & Sons, Ltd., 312-339.

17th INTERNATIONAL CONGRESS of the Geological Society of Greece

BULLETIN OF THE GEOLOGICAL SOCIETY OF GREECE, SP. PUBL.

EXTENDED ABSTRACT 234

Characterization and timing of charcoal in geoheritage sites preserved by major volcanic destructions – Geoarcheological and paleo-environmental considerations in Ecuador

Grace Tatiana Páez-Barrera[1] Karla Vizuete[1], Alexis Debut[1], Mario Cruz-D´Howitt, Juan José Ortiz-Aguilu, Theofilos Toulkeridis[3,4]

(1) Universidad de las Fuerzas Armadas ESPE, Sangolquí, Ecuador; (2) Universidad Técnica de Manabí, Portoviejo, Ecuador; (3) Aristotle University of Thessaloniki, Thessaloniki, Greece (4) Universidad UDET, Quito Ecuador

Research Highlights

The variety of microfossils identified allowed to reconstruct the original ecosystem of the lake areas of the Pululahua Volcano after its destructive volcanic events. Based on the characterization and timing of charcoal pebbles encountered within a distant but prominent ash-layer, it has been possible to identify how an ancient culture has been destroyed in coastal Ecuador, some 3,5 ka ago.

Introduction / Background

Throughout phanerozoic times, past botanic fossil records are often preserved when ironically huge catastrophic events take place, allowing the reconstruction of past evolutionary processes in the diversity and developments of plant life. These catastrophic events may include flooding of which newly deposited sedimentary material remains above previous existing vegetation, a number of volcanic events or hazards such as lava flows, ash and pyroclastic flows as well as avalanche deposits, ice or glacial deposits and also due to drought and landslides among many others (Ukraintseva *et al.*, 2014; Svoboda *et al.*, 2019; Vallé *et al.*, 2024). Nonetheless, there are a variety of studies where older plants and their corresponding flora and even fauna have been preserved in a variety of forms, due to severe volcanic events such as by even famous eruptive phases of the past (Ayala-Usma *et al.*, 2024).

As it is a challenge to encounter preserved paleoenvironmental areas with corresponding vegetation, it is even more difficult to find paleobotanic remains of wetlands, lagoonal or fluvial environments. Such environments not only preserve the flora and fauna of the given time of its existence, but they are also able to reveal the paleoclimatic and paleoecologic conditions of its time, allowing to reconstruct past events in order to understand the recent and future atmospheric behavior and their fluctuation. Such information may be reconstructed by the content of such wet environments which may include either macro or microfossils. Therefore, paleobotanic research of wet environments may be based on the findings of preserved macrofossil plants within sedimentary layers as impressions or compressions, as casts or molds, and also as petrification. However, many more details are preserved in form of microfossils, when looking with magnifying glasses, binoculars or microscopes of any kind. Such findings may be plants, algae, diatoms, fungi, pollen, spores, bacteria, biomass in general and other kind of microfossils of some animal remains. These discoveries are the basic results for a subsequent declaration of geoheritage sites.

Unfortunately, in Ecuador paleobotanic research is scarce, although there are many reports of charcoals inside of volcanic environments within a high amount of extinct and active volcanoes in the continental part of the country as well as on the Galapagos islands. However, such findings have been mostly used in past for carbon dating without further specification or characterization of the plant or wood fossil content. There are also petrified forests of the Mesozoic period, like the well-known in Puyango in the southern part of Ecuador, but also of limited information concerning paleobotanic findings (Cadena & Román-Carrión, 2018).

Based on the aforementioned context, the current study´s predominant aim has been to identify and characterize microfossil content of charcoal deposits of a fluvial-lagunar environment and a coastal site, being preserved by the volcanic activity of two volcanic complexes in north-central Ecuador. This shall be achieved by a detailed volcanic reconstruction of the catastrophic events of the past, in combination of a microscopic inventory of encountered charcoal horizons within the volcaniclastic deposits. As we deal with two different events in time, the first results may allow to establish the environmental conditions of a so far unknown humid landscape of local to regional importance within the Ecuadorian highlands, shortly after glaciation and almost simultaneously to the first appearance of human settlings, while the second results may allow to reconstruct the almost complete disappearance of a flourishing culture in the coast of Ecuador.

Geological background and study areas

The four Ecuadorian continental volcanic arcs are the result of the subduction of the Nazca oceanic plate below the Caribbean and South American continental plates. The NNE-SSW aligned volcanoes within these arcs correspond to the Western, Inter-Andean, Eastern and Subandean Volcanic Arcs or Cordilleras of Ecuador. In the central part of the Western Volcanic Arc is situated the Pululahua caldera and dome complex as well as the Pichincha Volcanic Complex (PVC), both being located just a few km outside of Ecuador´s capital Quito (Toulkeridis and Zach, 2017).

For the Pululahua volcano, at least 16 predominantly andesitic to dacitic domes have been identified, belonging to four different units (Units I-IV; Andrade *et al.*, 2021). The oldest domes are heavily eroded, porphyritic amphibole-bearing dacitic pelean lava domes of unknown emplacement ages belong to the so-called Unit I. Some further older domes (La Marca among others), belong to the Unit II yielded ages of 18 to 10 ka, while later single or major events took place at 6.75 ka, 2.6 – 2.3 ka and some 2.24 ka ago. Those events resulted into wide and thick successions of pumice-rich, pyroclastic deposits, which include charcoal rich layers, which is evidence of previous vegetation in times of volcanic activity. The most prominent outcrops with charcoal rich layers are situated on the southeastern side of the Pululahua dome complex, along the Monjas river.

A big part of the western mountain flank of the city of Quito, occupies the PVC, which is composed of five successive volcanoes, of which the first four are extinct reaching ages of 1.1 Ma to 4 ka. The El Cinto basal edifice (1.1 to 0.9 Ma) is followed by the Rucu Pichincha stratovolcano (850 to 150 ka), Guagua Pichincha stratocone (60 to 11 ka), Toaza volcanic dome complex (11 to 4 ka) within the collapsed, avalanche amphitheater of Guagua Pichincha and finally the presently active Cristal volcanic dome complex (3,700 years to present day) within the Toaza caldera. The Cristal volcanic dome complex gave rise of repeated growth and collapse of volcanic domes, which occurred in the period of 1998 to 2001 (Monzier *et al.*, 2002; Robin *et al.*, 2010).

Results and discussion

Pyroclastic flows and pyroclastic surges produced by directed, sub-plinian explosions of the outer caldera of Pululahua situated older domes, whose activity represents the second phase of its eruptive period, occurred some 12-10 ka ago. Close-by to the La Marca dome, prominent charcoal deposits of a fluvial-lagoon environment along the Monjas river have been identified and dated, correspond to this time period and event.

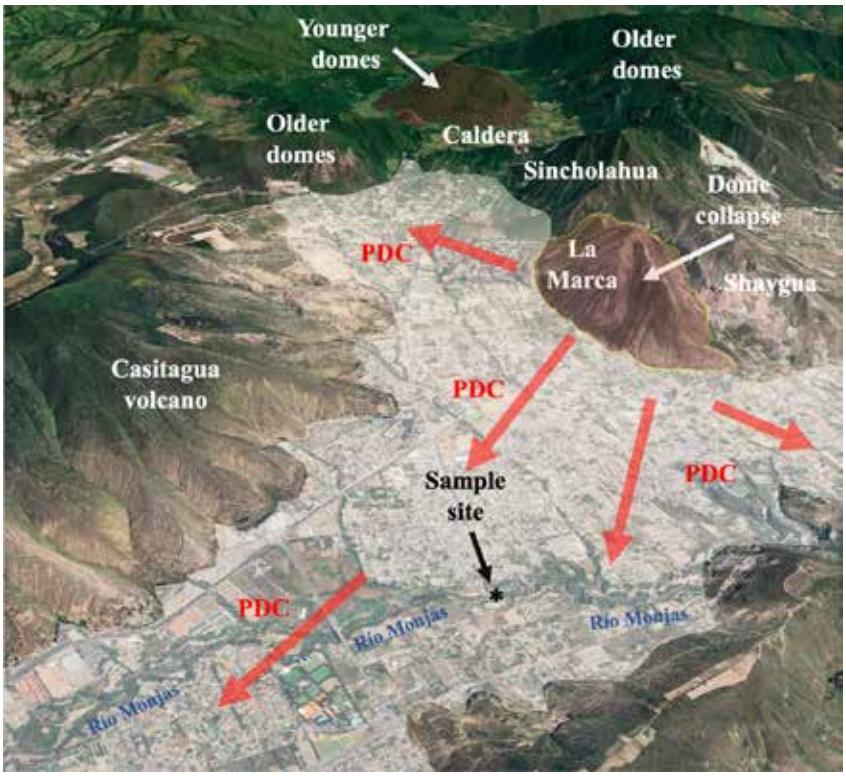

Fig. 1. South (left) to north (right) panoramic, bird-view of the result of the directed blast situation of the older collapsed domes of the Pululahua caldera and dome complex, generating pyroclastic density currents (PDC), which cover a vast area of the Inter-Andean Valley, forming what is now the base of the San Antonio de Pichincha village.

Fig. 2. Charcoal horizons of the Río Monjas type section (A-D). Note that the most prominent charcoal deposit is of about 65 cm thick (A: 45 cm plus 20 cm of the basal part), while others are mixed with pumaceous ash particles (B). Furthermore, there appear charcoal lenses within the pyroclastic deposits (C). Uppermost charcoal layers above an erosional contact (D).

We analyzed and characterized the charcoal deposits and encountered microorganisms such as benthic diatoms, saprophytic fungi and nitrogen-fixing bacteria, as well as herbaceous vascular plants such as horsetails, lycopods, bamboos, ferns, and small shrubs. These identified organisms originated from temperate and cold ecosystems, probably from flooded or seasonally flooded areas. The charcoal fragments perfectly preserved by the favorable conditions suggest that the original ecosystems of the Pululahua paleoflora correspond to areas of humid and lacustrine environments typical of swampy ecosystems, humid mountains and Andean moorlands.

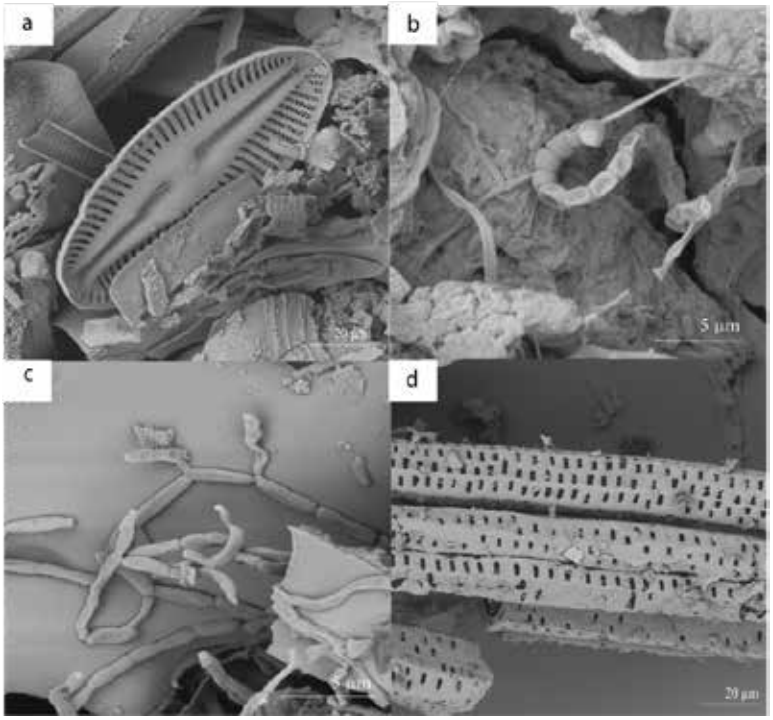

Fig. 3. SEM photomicrographs: a. Diatom Bacillariophyceae, valves oval, elongated, symmetrical, with raphe. Linear, marked transverse striations; b. Streptomyces well-developed filamentous vegetative hyphae; c. Bacillus sp., rods in branched chains; and d. Polypodiophyta, Equisetaceae adjacent nodal metaxylem tracheids.

In the coastal area of Ecuador, close to the city of Portoviejo, at the site called Papayita, an ash layer which includes charcoal pebbles (fossilized wood), with an impressive thickness of 85 centimeters was encountered above an underlying paleosol. A fact that is striking when considering that the closest volcano with sufficient eruptive power to produce such ash volumes, Quilotoa, is around 165 km away in a direct line. Nonetheless, provenance analysis based on geochemistry analysis and mineralogy revealed that the volcano responsible for the high amounts of the expelled material must have been the PVC with a distance of some 225 km in a SW direction. The stratigraphic sequence at Papayita is of significant interest, with a base consisting of geological material layer, succeeded by a paleosol and a cultural layer. The latter contains several discernible activity areas, including a hearth and small midden areas. Two separate features contained human remains associated with the Valdivia ceramics found at the site.

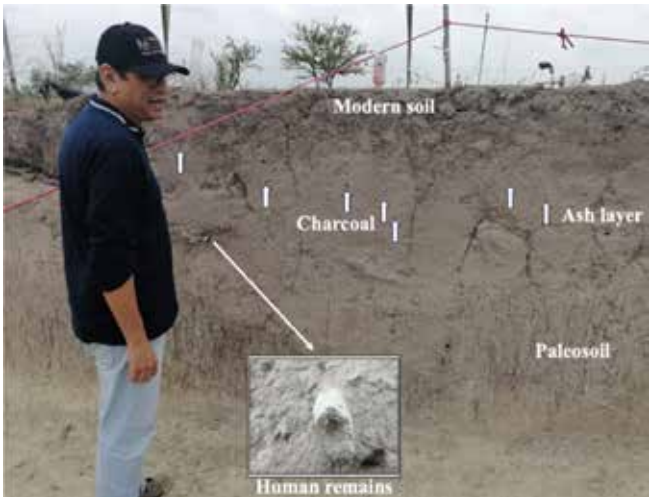

Figure 4. Exposed machine cut due to farmer's construction of a traditional water reservoir. It provided a pro file that indicates the main stratigraphic components of the Papayita site. The most important sections of the profile sequence being (from bottom to top): the paleosol, the ash layer, and the modern soil or plow zone. The position of the human remains and other artifacts, as well as several charcoal fragments, can be discerned in the profile.

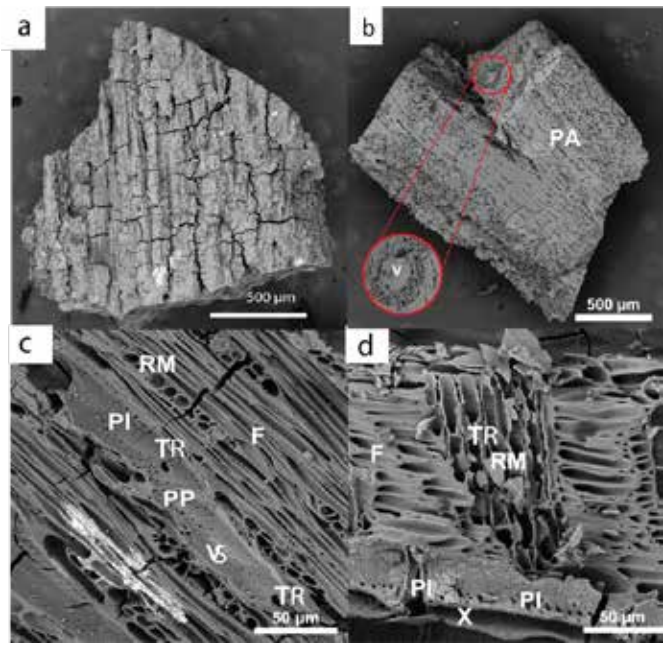

Figure 5. SEM photomicrographs of charred plant material, anatomical features of charcoal samples: A. Elongated and fusciform cells, tangential section, vascular system with septa without points, own to gymnosperms (VS), simple perforation plates (PP), medullary radius (RM), intervascular pits (PI), fibers (F) and tracheids (TR); B. Tangential cut: intervascular pits (PI), simple perforation plates (PP), medullary radius (RM), fibers (F), and xylem (X). C. Woody vascular system (VS), showing woody tracheid (TR), axial parenchyma (PA); B. Fragment of charred wood.

Interestingly, the cultural layer is sealed by a significant, uninterrupted deposit of volcanic ash reaching 85 centimeters in thickness. The features discovered, as well as the artifacts' angles of deposition suggest that this ashfall occurred while living activity at Papayita was ongoing. In other words, the site had not been abandoned at the moment the ashfall event began. The evidence of human activity after the ashfall is minimal and there is, so far, no indication of further human occupation until modern times. The mineralogical and geochemical data coincide with the geochronological outcome of the charcoal which yielded an age of 3530 ±30 years, identical to the 3560 ±70 years BP, 3540 ±30 years BP and 3549 ±30 years BP ages of previous studies (Zeidler, 1994; Zeidler, 2016; Robin *et al.*, 2008; Robin *et al*., 2010). The fossilized wood fragments collected in Papayita, were identified, thanks to their perfectly preserved anatomical structure, as a plant from the Gymnosperm group, of the Podocarpaceae family, being vegetation from temperate or cold climates in the foothills of the Andes (Páez-Barrera et al., 2024).

Conclusion

A dome collapse of the Pululahua caldera and dome complex some 10k ago, was able to cover and preserve an ancient fluvio-lagunar environment. Based on this volcanic event, it has been possible to identify several dozens of microorganisms, such as plants, diatomens, fungi and bacteria allowing to reconstruct the paleo-environment shortly after glaciation and just prior human settlements.

The species belonging to the Podocarp family inhabit temperate and cold areas of the Andes with an altitudinal distribution range between 1900 and 3800 m a.s.l., meaning that the volcanic activity of the PVC transported Podocarpus wood from a cloud forest of the high Andean zone to the Papayita site located in a coastal environment near the sea level where it was preserved. The vast ashfall and the subsequent charcoal-laden ash layer, coupled with the ensuing environmental disturbances, were probable key contributors to the ending of human occupation at the Papayita settlement and may have played a part in the termination or final metamorphosis of the Valdivia cultural tradition in this region ~3500 years ago.

References

Andrade, S. D., Müller, A. V., Vasconez, F. J., Beate, B., Aguilar, J., & Santamaría, S. (2021). Pululahua dome complex, Ecuador: eruptive history, total magma output and potential hazards. Journal of South American Earth Sciences, 106, 103046.

Ayala-Usma, D. A., Lozano-Gutiérrez, R., Orejuela, C., Pérez-Ángel, L. C., Montes, C., & González-Arango, C. (2024). Exceptionally preserved subfossil woods from late Pleistocene volcanic deposits from the Northern Andes of Colombia. Review of Palaeobotany and Palynology, 324, 105090.

Cadena, E. A., & Román-Carrión, J. L. (2018). A review of the fossil record of Ecuador, with insights about its challenges and future development. Ameghiniana, 55(5), 571-591.

Monzier, M., Samaniego, P., Robin, C., Beate, B., Cotten, J., Hall, M. L., ... & Toulkeridis, T. (2002, September). Evolution of the Pichincha volcanic complex (Ecuador). In Proceedings of fifth international symposium on Andean geodynamics, Toulouse (pp. 429-432).

Páez-Barrera, G. T., Vizuete, K., Ortiz-Aguilu, J. J., Castro, G., Debut, A., & Toulkeridis, T. (2024). Characterization and chronology of charcoal found in the volcanic ashfall that impacted a late Valdivia community in coastal Ecuador. Acta Palaeobotanica, 35-50.

Robin, C., Samaniego, P., Le Pennec, J.L., Mothes, P., Van Der Plicht, J., 2008. Late Holocene phases of dome growth and Plinian activity at Guagua Pichincha volcano (Ecuador). Journal of Volcanol- ogy and Geothermal Research 176(1), 7–15.

Robin, C., Samaniego, P., Le Pennec, J. L., Fornari, M., Mothes, P., & van Der Plicht, J. (2010). New radiometric and petrological constraints on the evolution of the Pichincha volcanic complex (Ecuador). Bulletin of volcanology, 72, 1109-1129.

Svoboda, J., Krejčí, O., Krejčí, V., Dohnalová, A., Sázelová, S., Wilczyński, J., & Wojtal, P. (2019). Pleistocene landslides and mammoth bone deposits: The case of Dolní Věstonice II, Czech Republic. Geoarchaeology, 34(6), 745-758.

Toulkeridis, T., & Zach, I. (2017). Wind directions of volcanic ash-charged clouds in Ecuador–implications for the public and flight safety. Geomatics, Natural Hazards and Risk, 8(2), 242-256.

Ukraintseva, N., Leibman, M., Streletskaya, I., & Mikhaylova, T. (2014). Geochemistry of plant-soil-permafrost system on landslide-affected slopes, Yamal, Russia as an indicator of landslide age. Landslides in cold regions in the context of climate change, 107-131.

Vallé, F., Morelli, C., Krainer, K., Roghi, G., & Kustatscher, E. (2024). Depositional environments and plant communities in the exceptional context of the Kungurian megacaldera of the Athesian Volcanic Group (Southern Alps, N-Italy). Review of Palaeobotany and Palynology, 324, 105083.

Zeidler, J.A., 2016. Modeling cultural responses to volcanic disaster in the ancient Jama–Coaque tradition, coastal Ecuador: A case study in cultural collapse and social resilience. Quaternary International 394, 79–97.

Zeidler, J., 1994. Archaeological Testing in the Middle Jama Valley. In: Zeidler, J., Pearsall, D. (eds), Regional Archaeology in Northern Manabí, Ecuador, Volume 1: Environment, Cultural Chronology, and Prehistoric Subsistence in the Jama River Valley. University of Pittsburgh Memoirs in Latin American Archaeology 8, pp. 71–98. Ediciones Libri Mundi.

17th INTERNATIONAL CONGRESS of the Geological Society of Greece

BULLETIN OF THE GEOLOGICAL SOCIETY OF GREECE, SP. PUBL.

EXTENDED ABSTRACT 235

Foreshock-aftershock discrimination in real-time during the 2025 seismic cluster near Santorini volcano, Greece, based on earthquake statistics and complex networks theory

Papadopoulos G.A.[1], Triantafyllou I.[2], Siettos C.[3], Spiliotis K.[4]

(1) Hellenic Mediterranean University, 71410 Heraklion, Greece, gerassimospapadopoulos2@gmail.com (2) Institute of Physics of the Earth's Interior and Geohazards, Hellenic Mediterranean University Research Center, 73133 Chania, Greece, ioannatriantafyllou@hmu.gr (3) Dipartimento di Matematica e Applicazioni "Renato Caccioppoli", Università degli Studi di Napoli "Federico II", Naples, Italy, constantinos.siettos@unina.it (4) School of Civil Engineering, Democritus University of Thrace, Greece, spiliotiskos@gmail.com

Introduction / Background

Foreshocks, aftershocks and swarms are the most common types of space-time seismicity clusters (Mogi, 1963). The real-time discrimination between foreshocks and other types of clusters is of great importance for the short-term hazard assessment but it is a challenging issue. Therefore, only *a posteriori* solutions have been proposed. During January-March 2025 a space-time seismicity cluster was recorded between Santorini and Amorgos islands, South Aegean, with the largest earthquake (M_L=5.3) occurring on 10 February 2025. This case offered a good opportunity to decipher the type of the ongoing seismic cluster based on the daily re-evaluation of the seismicity state. We utilized tools from the earthquake statistics and the complex networks theory and were able to discriminate beforehand the foreshock-aftershock nature of the ongoing cluster. Our findings were documented on time with internal reports as well as with public reports and statements.

Methods

The real-time characterization of the type of the ongoing seismicity cluster near Santorini was based on the daily monitoring of the 3D seismicity changes, i.e. in the dimensions of space, time and magnitude. Real-time means that the evaluation of a data set retrieved from the earthquake catalogue up to time t, was completed at time t+1 days. The onset of the cluster has been considered to occur on 30 January 2025 which corresponds to t=1 day. The 3D changes detected were compared with the 3D state of background seismicity (BS) in the same area in the time interval from January 2015 to January 2025. This procedure was followed up to 12 March 2025 when we realized that the cluster activity was already at very low level. The implementation of our method has been made possible thanks to the open availability of earthquake data by the Institute of Geodynamics of the National Observatory of Athens (https://bbnet.gein.noa.gr/HL/seismicity/real-time-seismicity/last-24-hours), which provides real-time updating of the national earthquake catalogue.

In the magnitude domain the monitoring of the seismicity state was performed by calculating the variation of the critical geophysical parameter b, which is the slope of the straight line in the Frequency Magnitude Distribution (FMD) well-known as G-R law expressed by (1) (Gutenberg and Richter, 1944):

$$\log N = a - b\,M \qquad (1)$$

N is the discrete or cumulative number of events of magnitude $\geq M \pm \Delta M$, and a, b are parameters determined by the data. For global seismicity b is about 1 (e.g., Schorlemmer *et al.*, 2005). However, in regional and local seismic zones the b-value is sensitive in many factors the most important being the stress loading conditions (Mogi, 1963) and the crustal heterogeneity (e.g., Abercrombie and Mori, 1996). Therefore, the b-value has been considered as a stress-meter within the crustal material (e.g., Schorlemmer *et al.,* 2005). The methods of Maximum Curvature and of Fixed-M_c, both incorporated in the z-map toolbox (Wiemer, 2001), were utilized to calculate the completeness magnitude threshold, M_c, and the b-value during the BS as well as during the 2025 cluster. The significance of the b-value changes was tested with the test of Utsu (1966).

In the domain of space, we were based on the spatial distribution of the betweeness centrality (BC), which is a topological metric that quantifies the number of times a node (surface patch or earthquake epicenter) acts as a bridge along the shortest path between two other nodes. Bridging nodes that connect disparate parts of the network often have high BC value. Such nodes greatly participate in the flow of information in the network. In earthquake processes high BC indicates persistent seismic activity. From the first few days of the cluster it became obvious that the earthquake epicenters gradually migrated from SW to NE, which is the direction of the main tectonic faults in the area. Since M_c=2.9 was found for the first days of the cluster, for the monitoring of the seismicity migration we considered as zero point the epicenter of the first earthquake of $M_L \geq 2.9$ at time t=1 day. Then we measured from

that point the mean distance, D, of epicenters of the subsequent earthquakes with an ensemble of 100 earthquakes in each measurement step. In the domain of time we analyzed the seismicity rate, r, in terms of r=n/T or r=N/T, where n=discrete number of earthquakes, N=cumulative number of earthquakes and T is a constant time interval.

Results

At time t=4 days (2 February 2025) after the initiation of the seismic cluster, we were able to recognize that the cluster was characterized by the basic properties of the foreshock sequences, i.e. acceleration of the seismicity rate, r, gradual increase of the earthquake magnitudes and significant drop of the b-value as time goes on towards the mainshock occurrence (Jones and Molnar, 1979, Papadopoulos and Minadakis, 2017). This pattern was evident until the largest earthquake (M_L=5.3) on 10 February 2025. The earthquake epicenters migrated from SW to NE towards the epicentral area of the M_L=5.3 mainshock. The maximum distance of D~25 km was found for the mainshock epicentral area. The foreshock move towards the mainshock epicenter has also been observed in other foreshock sequences. The maximum migration velocity was on the order of 3 km/day. On the 13th February we detected important drop in both the number and the magnitudes of the earthquakes. The gradual decrease of r followed power-law and was consistent with the well-known Omori aftershock decay. At the same time, a gradual increase of the b-value was detected, which was an additional evidence of aftershock activity. On the other hand, the betweeness centrality (BC) metric showed that during the stage of background seismicity although the activity was important and persistent in the Santorini-Amorgos area only weak seismicity hubs were detected in the Nea Kammeni (Santorini) and the Kolumbo volcanoes. From the first days of the 2025 seismic cluster the BC metric became quite strong in the Santorini-Amorgos seismic cluster but no seismicity hubs appeared in the two volcanic centers. This picture did not change until 12 March 2025.

During the seismic cluster in Santorini-Amorgos our findings were periodically transmitted by one of us (GP) to the competent state authorities, i.e. the Ministry for Climate Change and Civil Protection, including the Earthquake Planning and Protection Organization, and were communicated through reports (Triantafyllou and Papadopoulos, 2025) and statements in mass and social media, thus documenting beforehand the real-time foreshock-aftershock discrimination during the ongoing cluster.

Conclusions

The 2025 seismic cluster in Santorini-Amorgos area is a good example of real-time discrimination between foreshocks, aftershocks and swarms. The foreshock nature of the cluster was detected as early as the 4th day of the cluster and was verified by daily seismicity monitoring until the occurrence of the mainshock (M_L=5.3) on 10 February 2025. A few days later the aftershock sequence following the mainshock was also detected. These results disfavor the interpretation of the 2025 seismicity cluster as a swarm case. The gradual migration of epicenters with maximum velocity of ~3 km/day does not account for hydraulic diffusion and favors a cascade failure process. The findings of our analysis were documented in many ways beforehand during the ongoing seismic cluster. The area between Santorini and Amorgos acts as a long-term seismicity hub and stress concentrator.

References

Abercrombie, R. E., Mori, J., 1996. Occurrence patterns of foreshocks to large earthquakes in the western United States. Nature 381, 303–307.

Jones, L.M., Molnar, P., 1979 Some characteristics of foreshocks and their possible relationship to earthquake prediction and premonitory slip on faults. J. Geophys. Res. 84, 3596–3608.

Mogi, K., 1963. Some discussion on aftershocks, foreshocks and earthquake swarms – the fracture of a semi-infinite body caused by an inner stress origin and its relation to the earthquake phenomena (3rd paper). Bull. Earthq. Res. Inst. Univ. Tokyo 41, 615–658.

Gutenberg, B. and Richter, C.,1944. Frequency of earthquakes in California. Bull. Seism. Soc. Am. 34, 185–188.

Papadopoulos, G.A., Minadakis, G., 2016. Foreshock Patterns Preceding Great Earthquakes in the Subduction Zone of Chile. Pure Appl. Geophys., https://doi.org/10.1007/978-3-319-51529-8_3.

Schorlemmer, D., Wiemer, S., Wyss, M., 2005. Variations in earthquake-size distribution across different stress regimes. Nature 437, 539–542.

Triantafyllou, I., Papadopoulos, G.A., 2025. A unique seismic cluster near Santorini, Greece, foreshadows a strong earthquake? https://www.emsc.eu/Special_reports/, 3 p. (uploaded on 6 February 2025).

Utsu, T., 1966. A statistical test of the difference in b-value between two earthquake groups. J. Physics Earth 14, 37–40.

Wiemer, S., 2001. A software package to analyze seismicity: ZMAP. Seismol. Res. Lett. 72, 374-383.

17th INTERNATIONAL CONGRESS of the Geological Society of Greece

BULLETIN OF THE GEOLOGICAL SOCIETY OF GREECE, SP. PUBL.

EXTENDED ABSTRACT 236

Image-based grain size analysis of coastal sediments

Papadopoulos Th.[1], Pechlivanidou S.[1], Foumelis M.[1], Pennos Ch.[1]

(1) Department of Physical & Environmental Geography, School of Geology, Aristotle University of Thessaloniki, Thessaloniki, Greece

Abstract

In this study we show that image-based grain size analysis, could under appropriate conditions, replace the traditional grain size analysis in the laboratory, providing reliable results, especially for coarse-grained samples.

Coasts are dynamic systems affected both by natural and anthropogenic factors. Over the last few decades, the impact of climate change in coastal areas has become increasingly evident, with accelerated erosion significantly altering shorelines, threatening ecosystems, and endangering human settlements. Grain size analysis of coarse sediments (i.e. coarser than silt) traditionally held with the sieving method, remains one of the basic tools for studying coastal processes. However, this approach can be time-consuming and requires strategic sampling, particularly in extensive areas, along with a thorough understanding of geological principles. New methods, such as the use of satellite imagery and high-resolution photographs from drones or smartphones, provide faster solutions, although they often require further validation and comparison with laboratory-based grain size analysis to ensure accuracy.

Here, we investigate the effectiveness and accuracy of Buscombe's (2013) code in photographic grain size analysis techniques, both on-site and in the laboratory. We compare the grain size results obtained from this method with those from traditional sieving to draw reliable conclusions, while assessing the technical specifications and external factors affecting the accuracy of the method. The aim is to save time and resources to improve coastal zone research.

Buscombe's code is a Python algorithm that speeds up grain size analysis using sediment photos (Buscombe, 2013). It relies on Morlet wavelet to estimate the grain size distribution, by analyzing selected regions of the image to reduce computational load. This algorithm identifies patterns and frequencies in the image that correspond to different grain sizes. The results are presented as Power Spectrum Density (PSD) and, through interpolation, a complete grain size distribution is generated, eliminating the need for further adjustments.

Sampling took place in the coastal area of Kalamaria, Thessaloniki, Greece. The site was carefully selected to avoid interference from swimmers or municipal equipment. Sediment samples were collected from six different locations, based on visual observation of grain size distribution. The samples were first dried in the oven at 100°C and then sieved using 0.5Φ sieves in the Sedimentology Laboratory, at the Aristotle University of Thessaloniki. Processing of the grain size results performed using Gradistat software (Blott & Pye, 2001) following Folk and Ward method (Folk & Ward, 1957).

To evaluate the accuracy of the method for obtaining automated grain size results, we took high-resolution photographs (12MP and 108MP) of the samples in the laboratory using a Xiaomi Redmi Note 11S smartphone. Photographs were processed using the Buscombe's code and the results were compared with those from sieving. The comparison included the whole sediment samples as well as specific grain size fractions (i.e., 0 Φ).

After testing the accuracy of the code on laboratory photographs, we applied the same approach to photographs taken in the field, where external factors, such as lighting and shadows, could influence the results. Field photographs were taken of three samples (i.e., samples ΝΟΘ-201, ΝΟΘ-202, and ΝΟΘ-203) in the afternoon under mild natural lighting with some shadows, and two samples (i.e., samples ΝΟΘ-301 and ΝΟΘ-302) at noon with strong natural lighting with minimal shadows. The grain size results from field photographs were then compared to those of the same samples photographed in the laboratory.

Table 1. Grain size results using the Buscombe's code (2013) for sediment samples sieved at 0 Φ (1 mm)

Sample	Mean grain size (mm) using Buscombe's with 108MP camera resolution	% Difference	Mean grain size (mm) using Buscombe's with 12MP camera resolution	% Difference
ΝΟΘ-2P	0.61	39%	0.69	31%
ΝΟΘ-3P	0.89	11%	0.89	11%
ΝΟΘ-4P	0.94	6%	0.82	18%
ΝΟΘ-5P	0.91	9%	0.92	8%
ΝΟΘ-6P	0.98	2%	0.87	13%

Table 1 shows the mean grain size results for the 0 Φ fractions using the Buscombe code on photographs with 108MP and 12MP resolution. The percentage deviations range from 2% to 39% with the 108MP resolution photos and from 8% to 31% with the 12MP ones, indicating that higher resolution provides slightly more accurate results. The ΝΟΘ-6P sample displays the smallest deviation (2%), while the ΝΟΘ-2P sample demonstrates the largest (39% for the 108MP resolution photos and 31% for the 12MP resolution photos). Overall, both analyses yield comparable results, with the 108MP resolution offering a slight advantage in precision.

Table 2. Grain size results using the Buscombe's code (2013) for the whole sediment samples

Sample	Camera Analysis	Mean grain size (mm) using Buscombe code	Grain Size results from sieving (mm)	% Difference
ΝΟΘ-1P	12MP	1.19	0.38	213%
ΝΟΘ-1P	108MP	1.14	0.38	202%
ΝΟΘ-3P	12MP	1.78	0.98	82%
ΝΟΘ-3P	108MP	1.57	0.98	59%

Table 2 presents the mean grain size results for whole sediment samples analyzed using Buscombe's code, along with the differences compared to sieving results. For the fine-grained sample ΝΟΘ-1P (i.e., 0.38 mm), discrepancies are substantial, reaching 213% with 12MP resolution photos and 202% with108MP resolution photos. In contrast, for the coarser-grained ΝΟΘ-3P sample (i.e., 0.98 mm), discrepancies decrease significantly to 82% with 12MP resolution photos and 59% with 108MP resolution photos. These results suggest that the accuracy of the Buscombe code improves with higher resolution images and coarser-grained samples are used, while it exhibits greater errors with finer-grained samples.

Table 3. Comparison of the grain size results using the Buscombe's code (2013) on lab and field photos

Sample	Grain Size (mm) Lab	Grain Size (mm) Field	% Difference
ΝΟΘ – 201	1.08	2.36	118%
ΝΟΘ – 202	1.14	2.68	135%
ΝΟΘ – 203	1.15	2.76	141%
ΝΟΘ – 301	0.99	1.74	76%
ΝΟΘ – 302	1.09	1.17	8%

Table 3 highlights variations in grain size between laboratory and field photographs, which range from 8% to 141%. Samples ΝΟΘ-201, ΝΟΘ-202 and ΝΟΘ-203, photographed under less favorable lighting conditions and shadows, show the largest differences, ranging from 118% to 141%. Conversely, samples ΝΟΘ-301 and ΝΟΘ-302, captured under more favorable conditions with adequate lighting, show significantly smaller discrepancies, with ΝΟΘ-302 having the smallest difference at just 8%. These findings indicate that the shooting conditions play a crucial role in the accuracy of the particle size analysis. Despite these variations, sediment classifications based on the Wentworth chart (Wentworth, 1922) differ by only one class. For samples ΝΟΘ-201, ΝΟΘ-202, and ΝΟΘ-203, results from the field photos are classified as very fine gravel, while results from the lab photos as classified as very coarse sand. Similarly, samples ΝΟΘ-301 and ΝΟΘ-302, show even smaller discrepancies, with samples being classified as very coarse sand in both field and lab photos.
Our results show that the application of the Buscombe code to 0 Φ grain size fraction has satisfactory accuracy, when compared to the sieving data. However, in the whole sediment samples, the deviations are higher, especially in the finer grain sizes, reaching up to 200%, highlighting the need for method optimization. In the coarse grain sizes, the discrepancies decreased, with the use of high-resolution (108MP) photographs enhancing accuracy. Overall, the code proved to be effective for larger grain sizes, while its accuracy is significantly affected by the resolution of the photograph and the homogeneity of the sample.
Comparison of field and laboratory photographs highlighted the importance of external factors, such as lighting and shadows. Field photographs under good lighting conditions showed smaller differences compared to photos taken under unfavorable conditions. Coarse-grained samples showed better convergence between methods, while the use of high-resolution photographs improved the results.

Acknowledgements
Sincere gratitude is extended to the doctoral candidates, surveyors Ion and Kostas, for dedicating their valuable time to ensure the accurate and scientific acquisition of field photographs.

References

Blott, S.J. and Pye, K., 2001. GRADISTAT: a grain size distribution and statistics package for the analysis of unconsolidated sediments. Earth Surface Processes and Landforms, 26(11), pp.1237-1248.

Buscombe, D., 2013. Transferable wavelet method for grain□size distribution from images of sediment surfaces and thin sections, and other natural granular patterns. Sedimentology, 60(7), pp.1709-1732.

Folk, R.L. and Ward, W.C., 1957. Brazos River bar [Texas]; a study in the significance of grain size parameters. Journal of Sedimentary Research, 27(1), pp.3-26.

Wentworth, C.K., 1922. A scale of grade and class terms for clastic sediments. *The Journal of Geology*, 30(5), pp.377-392.

17th INTERNATIONAL CONGRESS of the Geological Society of Greece

BULLETIN OF THE GEOLOGICAL SOCIETY OF GREECE, SP. PUBL.

EXTENDED ABSTRACT 237

Development of a cartographic web application for monitoring the Corinth Canal using UAV data

Papadopoulou Ermioni Eirini[1], Proestakis Stavros[2], Anagnostopoulos Christos Nikolaos[3], Soulakellis Nikolaos[2]

(1) Department of Civil Engineering and Geomatics, School of Engineering and Technology, Cyprus University of Technology, Lemesos 3603, Cyprus, e.papadopoulou@cut.ac.cy

(2) Department of Geography, University of the Aegean, 81100 Mytilene, Greece

(3) Department of Cultural Technology, University of the Aegean, 81100 Mytilene, Greece

Introduction / Background

The Corinth Canal is a landmark of immense historical, cultural, and industrial significance, bridging the Saronic and Corinthian gulfs. It serves as a symbol of engineering ingenuity and a vital transportation route (Manolopoulou, 2024). The Corinth Canal cuts through the isthmus of Corinth, a geologically dynamic area characterized by sedimentary rock formations, tectonic activity, and steep slopes (Anagnostopoulos et al., 1991). The canal, approximately 6.4km long and 25m wide, exposes a cross-section of the region's stratigraphy, offering a unique opportunity for geological study. However, its steep walls, composed primarily of loose conglomerates and marls, are prone to erosion, landslides, and structural instability. These risks are compounded by the area's seismic activity, necessitating continuous monitoring and management. The Corinth Canal has been mapped using modern 3D mapping techniques, such as UAVs data processing and Structure-from-Motion (SfM) photogrammetry, enabling the creation of highly accurate 3D models and orthomosaics (Saroglou et al., 2019). Additionally, the canal's deformation is being monitored using SBAS (Small Baseline Subset) Interferometric Synthetic Aperture Radar (InSAR) and GNSS (Global Navigation Satellite Systems) techniques (Yaragunda and Oikonomou, 2024). These techniques have been applied to recent landslides, providing valuable insights into slope geometry, stability analysis, and risk assessment. Despite the advanced mapping efforts, a dedicated online platform for aggregating and unifying the mapping data has not yet been developed. This presents a significant opportunity to create a unified web-based mapping application that would enhance access to and utilization of these data by the scientific community and relevant stakeholders. To address these needs, this study, in collaboration with Corinth Canal S.A (A.E.DI.K) aimed to create a detailed geospatial archive of the canal through advanced UAV (Unmanned Aerial Vehicle) technologies. The initiative combined cutting-edge data collection techniques and a robust flight planning strategy to support sustainable management, promote its historical value, and enable continuous monitoring of its condition.

Objectives.

The study had three interlinked objectives:

i. **Developing high-resolution geospatial data products**: These included 3D point clouds, textured models, orthomosaics, and digital elevation models (DEMs), capable of capturing the canal's intricate details with spatial resolutions of 10-20 cm.

ii. **Implementing precise flight planning for optimized data acquisition**: A systematic and carefully designed flight plan was crucial to ensure comprehensive coverage, minimize data gaps, and maintain high geometric accuracy.

iii. **Creating a web-based mapping platform**: This platform integrates the collected datasets, enabling spatiotemporal monitoring of the canal's slopes, assessing structural stability, and supporting effective management strategies.

Methods

The data collection process between October 23-29, 2023, utilized UAVs equipped with RGB cameras, thermal sensors, and GNSS receivers. To ensure systematic coverage, the canal was divided into nine segments. Each segment was mapped using three meticulously planned flight patterns: vertical (nadir), east-west oblique, and north-south oblique. This design minimized data voids and ensured optimal image overlap (90% frontal and 80% lateral). Flight paths were pre-designed using DJI's Pilot 2 software, considering terrain variability, safety parameters, and the need for uniform data quality. The flights captured high-resolution imagery at height of flights ranging from 120 meters for general mapping, to 3-10 meters for detailed thermal scans and panoramic images at specific points of interest. Between October 23 and 29, 2023, UAV flights systematically captured high-resolution geospatial data of the

Corinth Canal. Employing UAV models such as the Mavic 3E and Matrice 300, the project utilized RGB and thermal sensors for diverse imaging needs. Each flight was executed with specific gimbal angles—typically -90° for vertical (nadir) and -70° for oblique imagery—ensuring precise coverage and minimizing data voids. The captured images featured resolutions ranging from 3.22 to 3.45 cm/pixel for general mapping to less than 1 cm/pixel for specific locations. This meticulous planning facilitated the creation of comprehensive datasets, later integrated into a web-based cartographic platform to enhance monitoring and management efforts.

Table 1: Characteristics of Flights Conducted for the 3D Mapping of the Corinth Canal

Date	**October 23, 2023**	**October 24, 2023**	**October 25, 2023**	**October 28, 2023**	**October 29, 2023**
Number of Flights	6	14	7	4	3
UAV Model	Mavic 3E	Mavic 3E	Mavic 3E	Mavic 3E	Matrice 300
Sensor Type	RGB Camera	RGB Camera	RGB Camera	RGB Camera	RGB + Thermal Sensors
Gimbal Angle	-90° (vertical), -70° (oblique)	-90° (vertical), -70° (oblique)	-90° (vertical), -70° (oblique)	360° Panoramic	Various
Image Resolution	3.22–3.45 cm/pixel	3.22–3.45 cm/pixel	3.22–3.45 cm/pixel		5–10 cm/pixel
Flight Patterns	Vertical (nadir), oblique east-west	Vertical (nadir), oblique east-west	Vertical (nadir), oblique east-west	Panoramic and detailed imaging	Vertical, oblique imaging

The collected data were processed using photogrammetric algorithms such as Structure from Motion (SfM) and Multi-View Stereo (MVS) (Westoby et al., 2012), producing dense point clouds, DEMs, and orthomosaics. Geometric accuracy was further validated by comparing the results with existing topographic diagrams. The photogrammetric outputs were then enhanced with thermal data to supporting the identification of potential structural vulnerabilities.

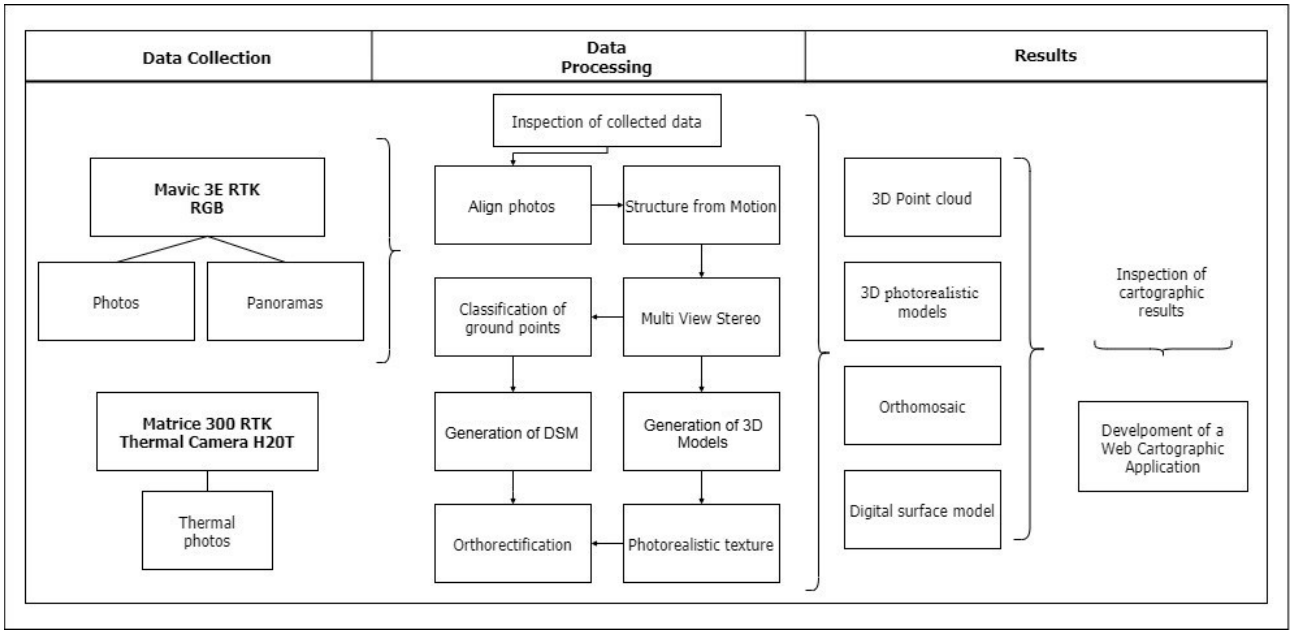

Figure 1. Flow diagram of the methodology

A key aspect of the study was the development of the “Corinth Canal” web mapping platform. This platform integrates all spatial datasets into a user-friendly interface, enabling stakeholders to visualize and interact with the canal’s digital representation. The platform was developed using GIS-based tools, such as ArcGIS Online and customized web applications, to provide functionalities including spatial analysis (distance, area, and slope measurement), thematic comparisons, and annotation capabilities. Special emphasis was placed on supporting multitemporal monitoring of the canal’s slopes, with tools designed to track changes over time, enabling early detection of risks such as landslides or structural instability.

Results

The study successfully delivered a comprehensive suite of geospatial products that offer detailed insights into the Corinth Canal's current condition. Seven georeferenced 3D models and point clouds were created, covering the entire canal and its individual segments, alongside high-resolution orthophotos, digital elevation models (DEMs), and thermal imagery. The results demonstrated high accuracy, with spatial resolutions ranging from 10-20 cm, and were validated through comparisons with existing topographic diagrams. This process confirmed the reliability of UAV-based data collection as a highly precise and efficient method for documenting such complex structures.

The integration of thermal imagery further enriched the dataset, enabling the identification of potential structural vulnerabilities, such as hotspots indicative of material stress or instability. These thermal findings, combined with detailed 3D models and DEMs, provide critical information for assessing the canal's geotechnical and structural health.

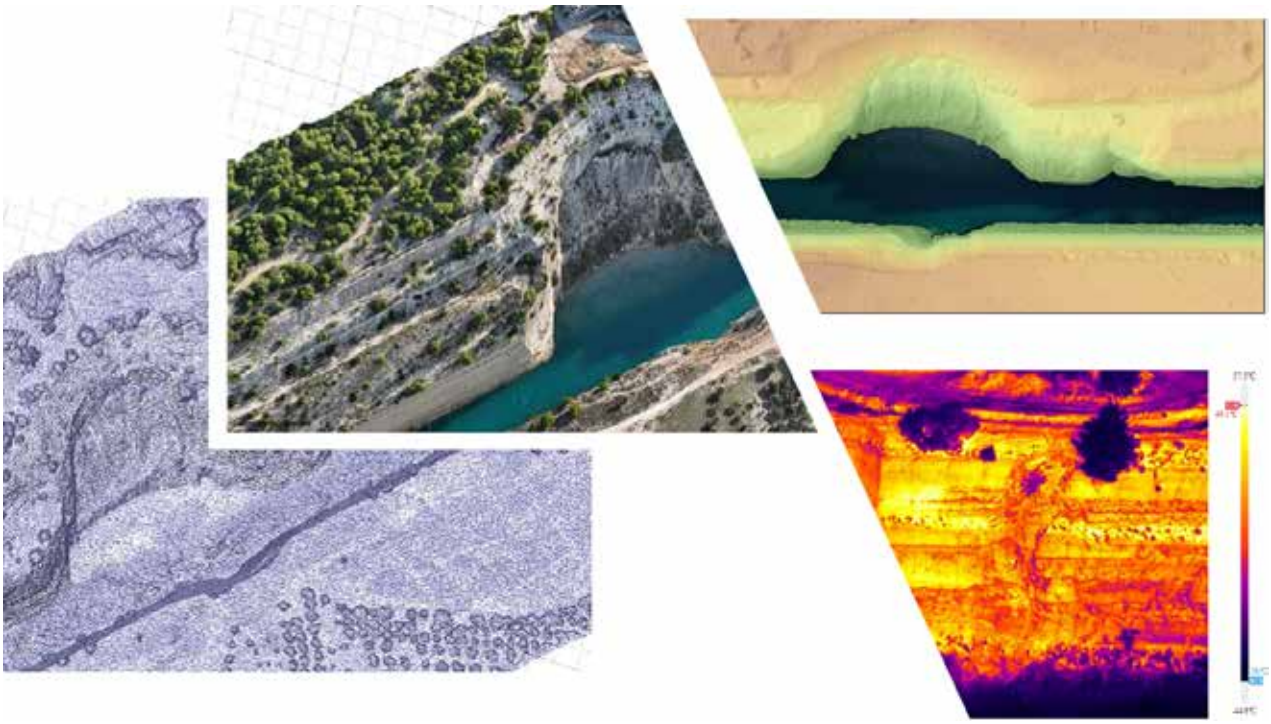

Figure 2. 3D photorealistic model, mesh of an irregular triangular network, DEM and a thermal photo of the 4th section of the Corinth Canal.

A significant outcome of the study was the development of the cartographic web application named "Corinth Canal". This interactive tool consolidates all spatial datasets, offering a user-friendly interface for visualizing and analyzing the canal's digital representation. The platform includes a variety of tools tailored to the needs of stakeholders:

- **Measurement Tools**: Users can perform distance, area, and slope calculations directly within the platform, enabling precise spatial analysis for maintenance and planning activities.
- **Thematic Comparisons**: Layers such as thermal imagery, 3D models, and orthophotos can be overlaid and compared, facilitating the identification of changes or inconsistencies over time.
- **Annotation and Note-Taking**: Users can add annotations and comments to specific areas, enhancing communication among teams and stakeholders involved in the canal's management.

The platform's design emphasizes accessibility and ease of use, ensuring that both technical and non-technical users can interact effectively with the data. Moreover, it enhances operational workflows by providing centralized access to critical geospatial information, streamlining decision-making processes. By bridging advanced UAV-based data collection with modern GIS technology, this study has laid the foundation for a sustainable, data-driven approach to the monitoring and management of the Corinth Canal. The web application not only supports day-to-day operations but also contributes to long-term preservation efforts, offering a scalable model for similar cultural and industrial heritage sites worldwide.

Figure 3: "Corinth Canal" cartographic web application.

Conclusions

The development of the "Corinth Canal" web mapping platform stands as a pivotal achievement in this study, offering an innovative and user-friendly tool for visualizing and managing the canal's digital representation. By integrating high-resolution spatial datasets—including 3D models, orthomosaics, DEMs, and thermal imagery—the platform provides stakeholders with the capability to monitor and assess the canal's structural stability in a dynamic and accessible manner. Designed with tools for distance and area measurement, thematic comparisons, and annotation, the platform supports multitemporal analysis, enabling early detection of risks such as landslides or structural instability. This interactive application not only streamlines operational workflows but also serves as a scalable model for preserving and monitoring similar cultural/industrial heritage sites or critical infrastructures worldwide.

This study underscores the transformative potential of UAV technologies in cultural heritage management. By employing precise flight planning and advanced photogrammetric methods, we achieved a comprehensive and high-resolution geospatial archive of the Corinth Canal. The integration of thermal data enriched the analysis, enabling the identification of structural vulnerabilities such as material stress and instability. UAV-based mapping it is considered a reliable and efficient method for documenting complex geological and structural settings, with centimeter-level accuracy that surpasses traditional methods in both speed and cost-effectiveness.

Future work could focus on integrating machine learning algorithms with the collected UAV data to automate the detection of structural vulnerabilities, such as cracks or erosion patterns, along the canal's slopes. Additionally, expanding the monitoring system to include real-time data acquisition using UAVs equipped with advanced sensors (e.g., LiDAR or hyperspectral imaging) could enhance the multitemporal analysis of geological and structural changes. Finally, collaborative efforts could explore creating a shared digital twin of the canal, enabling global access for research, education, and cultural preservation initiatives.

Acknowledgements

This work was supported by the sub-contract action "3D Geometric Documentation of the Corinth Canal and Digitization of the Cultural Content of the Corinth Canal Museum," which is part of the project "Promotion and Exploitation of the History and Cultural Value of the Corinth Canal and Digital Promotion of the Industrial Museum," under the OPERATIONAL PROGRAMME COMPETITIVENESS, ENTREPRENEURSHIP, AND INNOVATION 2014-2020 framework, funded by Greece and the EU.

Special thanks are extended to George Zouglis, General Manager of Corinth Canal S.A. (A.E.DI.K), and Dimitrios Roussis for their continuous support, collaboration, and technical assistance

References

Anagnostopoulos, A.G., Kalteziotis, N., Tsiambaos, G.K., Kavvadas, M., 1991. Geotechnical properties of the Corinth Canal marls. Geotech. Geol. Eng. 9, 1–26. https://doi.org/10.1007/BF00880981

Manolopoulou, A.-R., 2024. Museum of the Isthmus of Corinth--History with a view. Technische Universität Wien.

Saroglou, C., Kallimogiannis, V., Bar, N., Manousakis, G., Zekkos, D., 2019. Analysis of slope instabilities in the Corinth canal using UAV-enabled mapping. Proc. Int. Conf. Nat. Hazards Infrastruct.

Westoby, M.J., Brasington, J., Glasser, N.F., Hambrey, M.J., Reynolds, J.M., 2012. “Structure-from-Motion” photogrammetry: A low-cost, effective tool for geoscience applications. Geomorphology. https://doi.org/10.1016/j.geomorph.2012.08.021

Yaragunda, V.R., Oikonomou, E., 2024. Monitoring the Los (Line of Sight) Deformation of the Corinth Canal, Greece Using SBAS and GNSS Techniques. IGARSS 2024 - 2024 IEEE Int. Geosci. Remote Sens. Symp. 11056–11061. https://doi.org/10.1109/igarss53475.2024.10642704

17th INTERNATIONAL CONGRESS of the Geological Society of Greece

BULLETIN OF THE GEOLOGICAL SOCIETY OF GREECE, SP. PUBL.

EXTENDED ABSTRACT 238

An integrated approach using Remote Sensing and the Environmental Seismic Intensity Scale ESI 2007 for three major earthquakes in the Aegean region

Papadopoulou E.[1], Chatzipetros A.[1]

(1) Department of Structural, Historical and Applied Geology, School of Geology, Aristotle University of Thessaloniki, Greece, epapadoas@geo.auth.gr

Introduction / Background

The study of earthquake impacts on the environment is important for understanding seismic hazards and reducing associated risks. Remote sensing, particularly through Sentinel-1 satellite imagery, offers an effective method for detecting ground displacement and mapping fault systems. The Environmental Seismic Intensity Scale (ESI 2007) provides a robust framework for evaluating earthquake effects on the environment (Michetti et al., 2007) with high precision (Papanikolaou & Melaki, 2017). This study combines Sentinel-1 remote sensing techniques with the ESI 2007 scale to assess seismic hazards and disaster potential by analysing recent seismic events in the Aegean region, focusing on the Kozani-Grevena 1995, Lesvos 2017 and Samos 2020 earthquakes. On 1995 May 13, Kozani and Grevena were struck by an Ms = 6.6 (Mw 6.5) earthquake, causing extensive damage. Meyer et al. (1996) reported surface ruptures over 8 km comprising open fissures and scarps on the pre-existing Palaeochori Fault striking N70◦E. It was preceded by foreshocks, causing significant impacts to buildings, and triggered environmental effects such as rockfalls, landslides, liquefaction, and surface ruptures (Meyer et al., 1998, Hatzfeld et al. 1995, Pavlides et al. 1995, Chatzipetros 1998). On June 12, 2017, a Mw 6.3 earthquake struck southeastern Lesvos Island, causing disasters to the natural environment, buildings, and infrastructure, particularly in southeastern Lesvos. The earthquake's epicentre was offshore, with a depth of ~13 km, and was associated with a NW-SE striking (Papadimitriou et al., 2017), SW-dipping normal fault along the northern margin of the offshore Lesvos basin (Chatzipetros, et. al, 2013). It triggered secondary earthquake environmental effects (EEE) (Lekkas et al., 2017) such as ground cracks, slope movements, and a tsunami in Plomari port, likely caused by offshore landslides (Karamvasis et al., 2017 Vlachakis et al., 2020). The 2020 Samos earthquake, with a magnitude of 7.0, struck the eastern Aegean Sea on October 30th, significantly impacting Samos Island, Greece, and Izmir, Turkey. Caused by normal faulting along the North Aegean Trough, it triggered substantial ground deformation (Mavroulis et al., 2020), including co-seismic uplifts and displacements and produced surface ruptures, landslides, liquefaction, coastal changes, and hydrological anomalies (Foumelis et al., 2021, Ganas et al., 2021, Sakkas, 2021). The Samos earthquake serves as a focal point in such studies.

Methods

The methodology integrates advanced remote sensing techniques and field-based analyses to investigate ground displacement and environmental effects caused by seismic events. Sentinel-1 Synthetic Aperture Radar (SAR) data were utilized for pre- and post- seismic periods, with differential interferometric SAR (DInSAR) processing, employed to measure co-seismic deformation. The analysis involved co-registering SAR images, removing the topographic phase using Shuttle Radar Topographic Mission (SRTM) data, unwrapping phase data using SNAP Desktop software. Vertical (up-down) displacement component was calculated from ascending and descending LOS data and was visualized within a GIS environment. Using published and field information about the distribution and magnitude of surface effects and the ESI 2007 scale, the study evaluates environmental impact, such as uplifts, surface ruptures, slope failures, and liquefaction, by mapping and digitizing these data in GIS, producing isoseismal maps with the method of kriging that illustrate intensity patterns. The final step involves an analysis of remote sensing data and traditional field measurements to validate their consistency and potential data overlap.

Results and Conclusions

The analysis of ascending Sentinel-1 data (Fig. 1 and Fig. 3) and descending Sentinel-1 SAR data (Fig. 2 and Fig. 4) for the Lesvos and Samos earthquakes demonstrated significant ground displacement, accurately captured through interferometric synthetic aperture radar (InSAR). Moreover, the ascending and descending Sentinel-1 data showed similar results for both seismic events. Field measurements used for the ESI 2007 scale and the seismic intensities ranged from IV to IX, which are broadly in agreement with other studies (Lekkas et al., 2017, Papanikolaou & Melaki, 2017, Mavroulis et al., 2021), reflecting the widespread impacts of all three events. Moreover, the use of the Environmental Seismic Intensity (ESI-07) scale demonstrated its effectiveness in evaluating primary and secondary earthquake environmental effects (EEEs), such as slope failures, liquefaction, and ground cracks, particularly in inaccessible areas.

The maps (Fig. 1, 2, 3, 4) of surface co-seismic deformation fields obtained by analysis of interferometric synthetic aperture radar (InSAR) images have significantly improved the description of earthquake effects. The seismic intensity was visualized in isoseismal maps to illustrate the spatial distribution of impacts for the Kozani-Grevena (for which no InSAR data was available Fig. 5), Lesvos (Fig. 6) and Samos (Fig. 7) earthquakes present the spatial distribution of seismic intensity and highlighted areas

of heightened risk, enhancing seismic hazard assessment and disaster preparedness for future applications. This integrated approach offered valuable insights into the environmental impacts of seismic events and improved hazard assessment. It also emphasized the complementary roles of remote sensing in covering inaccessible areas and field data for high-resolution, localized studies. The multidisciplinary response shown in these studies demonstrates the growing integration of advanced geospatial technologies, field observations, and historical data in seismic risk assessment.

In conclusion, this study underscores the effectiveness of combining Sentinel-1 SAR imagery with the ESI 2007 scale to assess environmental impacts of strong earthquakes. It enhances our understanding of seismic risks by detecting concealed faults and quantifying ground displacement, especially in remote or inaccessible areas. The findings contribute to the ESI 2007 database and highlight the critical role of remote sensing in earthquake research. This integrated framework has the potential to strengthen disaster preparedness and response strategies, providing a foundation for future advancements in seismic risk assessment.

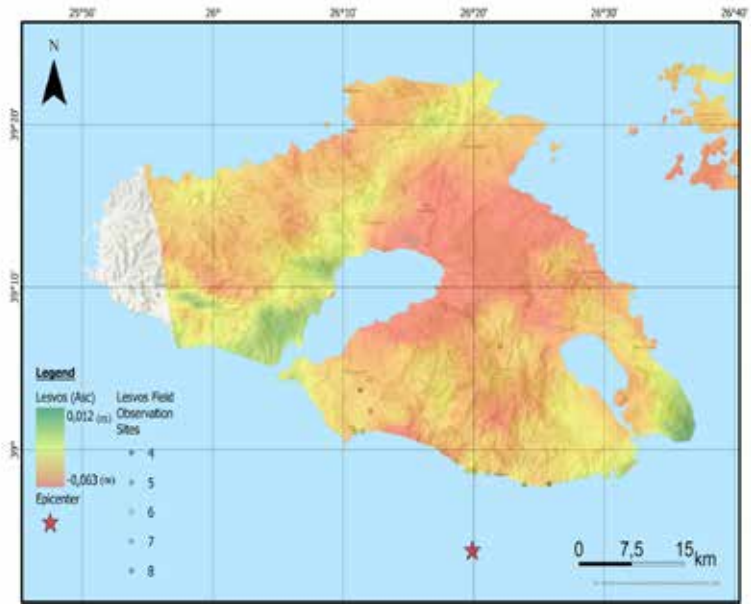

Figure 1. Ground displacement map in meters after the Lesvos earthquake in 2017 using Ascending Sentinel-1 orbit data.

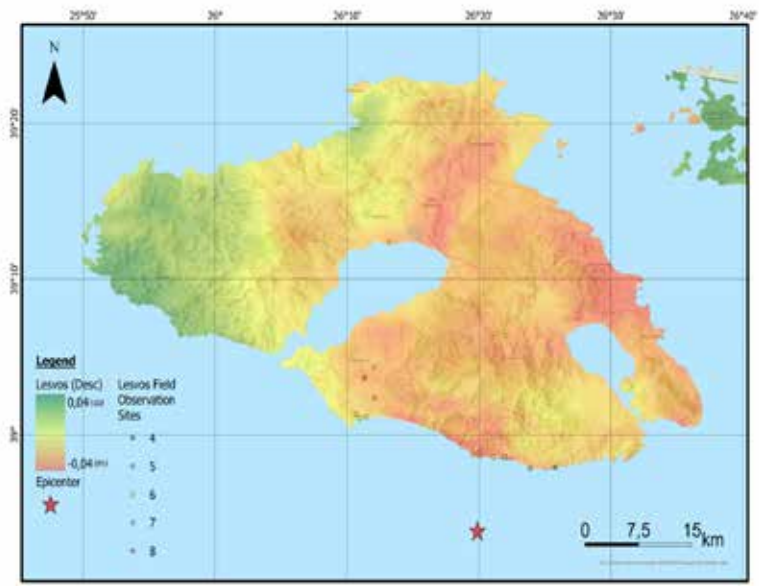

Figure 2. Ground displacement map in meters after the Lesvos earthquake in 2017, using Descending Sentinel-1 orbit data.

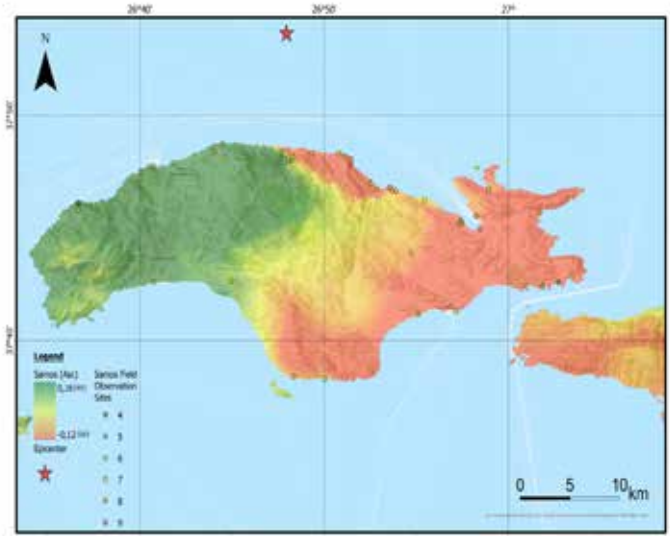

Figure 3. Ground displacement map in meters after the Samos earthquake in 2020, using Ascending Sentinel-1 orbit data.

Figure 4. Ground displacement map in meters after the Samos earthquake in 2020, using Descending Sentinel-1 orbit data.

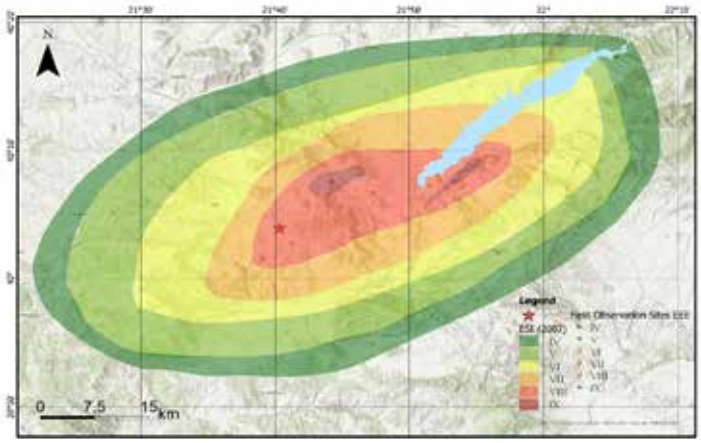

Figure 5. Isoseismal map of the Kozani-Grevena earthquake in 1995, using field survey data.

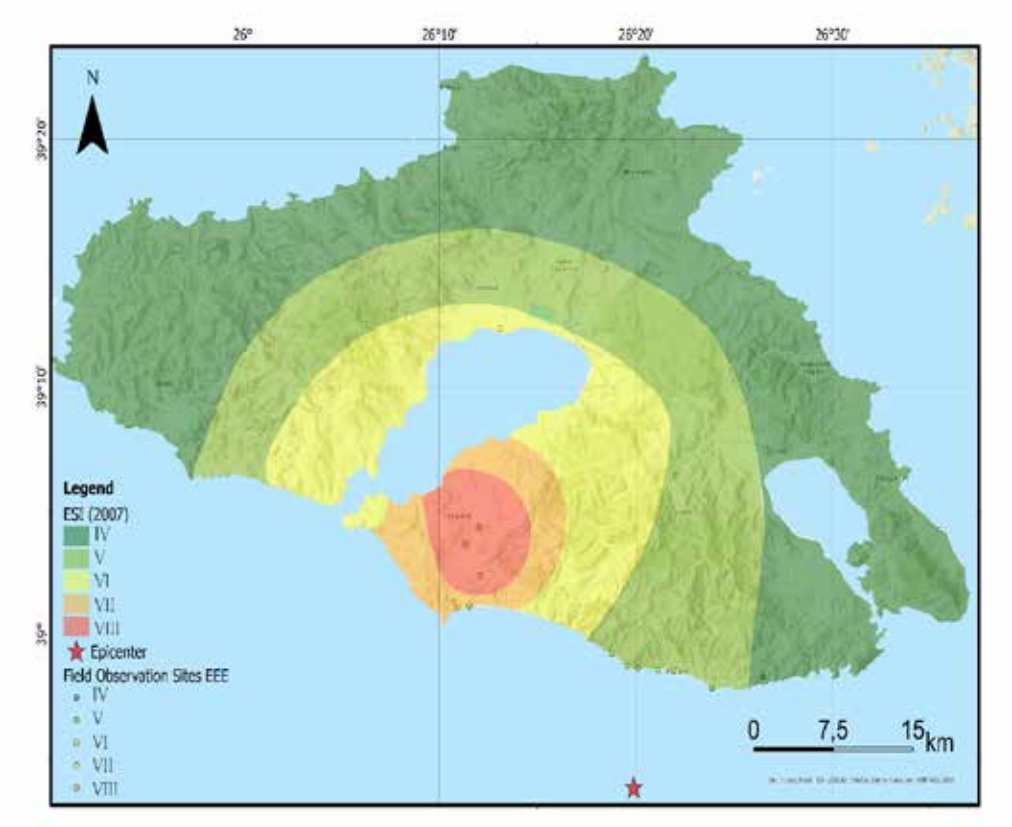

Figure 6. Isoseismal map of the Lesvos earthquake in 2017, using field survey data.

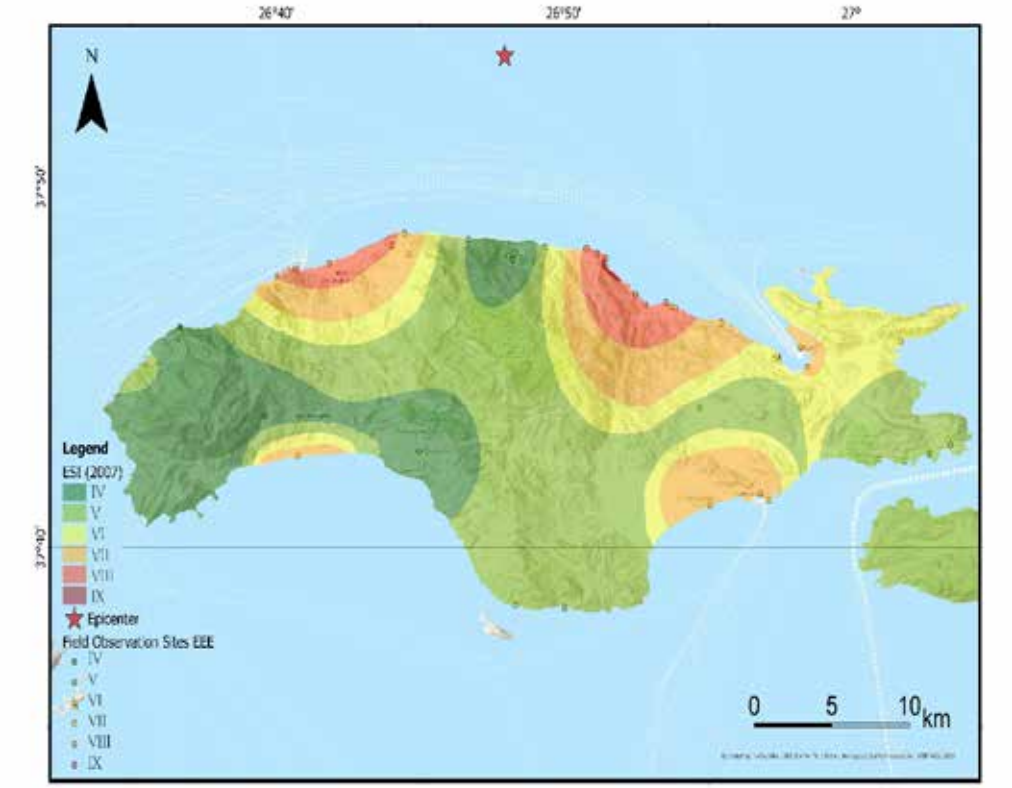

Figure 7. Isoseismal map of the Samos earthquake in 2020, using field survey data.

Acknowledgements

The authors would like to express thank to ESA and Copernicus for providing access to SAR images. The figures were created using SNAP Desktop and ArcGIS Pro Geographic Information System.

References

Chatzipetros, A.A., 1998. Palaeoseismological and Morphotectonic Study and Mechanical Behavior of Active Fault Systems in Mygdonia, Eastern Chalkidiki, Kozani - Grevena. Ph.D. Dissertation, Department of Geology, Aristotle University of Thessaloniki, Thessaloniki, Greece.

Chatzipetros, A., Kiratzi, A., Sboras, S., Zouros, N., Pavlides, S. 2013. Active faulting in the north-eastern Aegean Sea Islands. Tectonophysics 597-598, 106-122.

Foumelis, M., Papazachos, C., Papadimitriou, E., Karakostas, V., Ampatzidis, D., Moschopoulos, G., Kostoglou, A., Ilieva, M., Minos-Minopoulos, D., Mouratidis, A. and Kkallas, C., 2021. On rapid multidisciplinary response aspects for Samos 2020 M7. 0 earthquake. Acta Geophysica, 69, pp.1025-1048.

Ganas, A., Elias, P., Briole, P., Valkaniotis, S., Escartin, J., Tsironi, V., Karasante, I. and Kosma, C., 2021. Co-seismic and post-seismic deformation, field observations and fault model of the 30 October 2020 Mw= 7.0 Samos earthquake, Aegean Sea. Acta Geophysica, 69(3), pp.999-1024.

Hatzfeld, D., Nord, J., Paul, A., Guiguet, R., Briole, P., Ruegg, J.-C., Cattin, R., Armijo, R., Meyer, B., Hubert, A., Bernard, P., Karakostas, V., Papaioannou, C., Papanastassiou, D., Veis, G., 1995. The Kozani-Grevena (Greece) earthquake of May 13, 1995, Mw = 6.6: Preliminary results of a field multidisciplinary survey. Seismological Research Letters 66, 61–70.

Karamvasis, K. and Karathanassi, V., 2017. Deformation effects of dams on coastal regions using sentinel-1 iw tops time series: The west Lesvos, Greece case. The International Archives of the Photogrammetry, Remote Sensing and Spatial Information Sciences, 42, pp.91-96.

Lekkas, E., Mavroulis, S., Skourtsos, E., Andreadakis, E., Antoniou, V., Kranis, C., Soukis, K., Lozios, S., Alexoudi, V., 2017. Earthquake environmental effects induced by the 2017 June 12, Mw 6.3 Lesvos (North Aegean Sea, Greece) earthquake. Department of Dynamic Tectonic Applied Geology, Faculty of Geology and Geoenvironment, School of Sciences, National and Kapodistrian University of Athens, Athens, Greece.

Mavroulis, S., Triantafyllou, I., Karavias, A., Gogou, M., Katsetsiadou, K.N., Lekkas, E., Papadopoulos, G.A. and Parcharidis, I., 2021. Primary and secondary environmental effects triggered by the 30 October 2020, Mw= 7.0, Samos (Eastern Aegean Sea, Greece) earthquake based on post-event field surveys and InSAR analysis. Applied Sciences, 11(7), p.3281.

Meyer, B. et al., 1996. The 1995 Grevena (Northern Greece) earthquake: fault model constrained with tectonic observations and SAR interferometry, Geophys. Res. Lett., 23, 2677–2680.

Meyer, B., Armijo, R., Massonnet, D., de Chabalier, J.B., Delacourt, C., Ruegg, J.C., Achache, J. & Papanastassiou, D., 1998. Comment on 'Geodetic investigation of the 13 May Kozani-Grevena (Greece) earthquake' by Clarke et al., Geophys. Res. Lett., 25, 129–l30.

Michetti, A.L.E.S.S.A.N.D.R.O., Audemard, F., Azuma, T., Clague, J., Comerci, V., Esposito, E., Guerrieri, L., Grpinar, A., McCalpin, J., Mohammadioun, B. and Mrner, N.A., 2007. Environmental Seismic Intensity Scale 2007-ESI 2007.

Papadimitriou, P., Tselentis, G.A., Voulgaris, N., Kouskouna, V., Lagios, E., Kassaras, I., Kaviris, G., Pavlou, K., Sakkas, V., Moumoulidou, A. and Karakonstantis, A., 2017. Preliminary report on the Lesvos 12 June 2017 Mw= 6.3 earthquake. Euro-Med Seismological Centre (EMSC).

Papanikolaou, I. and Melaki, M., 2017. The Environmental Seismic Intensity Scale (ESI 2007) in Greece, addition of new events and its relationship with magnitude in Greece and the Mediterranean; preliminary attenuation relationships. Quaternary International, 451, pp.37-55.

Pavlides, S.B., Mountrakis, D.M., Chatzipetros, A.A., Zouros, N.C., Kostopoulos, D.S., 1995. The Grevena - Kozani (May 13, 1995) earthquake, western Macedonia, Greece: seismogenic faulting in an "aseismic" area. Department of Geology and Physical Geography, Aristotle University of Thessaloniki, GR-54006, Thessaloniki, Greece.

Sakkas, V., 2021. Ground deformation modelling of the 2020 Mw6. 9 Samos earthquake (Greece) based on InSAR and GNSS data. Remote Sensing, 13(9), p.1665.

17th INTERNATIONAL CONGRESS of the Geological Society of Greece

BULLETIN OF THE GEOLOGICAL SOCIETY OF GREECE, SP. PUBL.

EXTENDED ABSTRACT 239

Expertise on Specifications – Evaluation Criteria and Design of a Special Label for Local Agrotourism Products and Services: a cooperation for the benefit of four Greek UNESCO Global Geoparks!

Papadopoulou P.[1], Fassoulas, Ch.[2], Iliopoulos, G.[1,3], Kitsaki, G.[4], Kolendrianou, M.[2], Mikroulea, E.[5], Papaioannou, Ch.[4], Pattakos, D.[6], Perakis, V.[7], Tsoni, M.[3], Tsimpri, I.[8]

(1)Laboratory of Palaeontology and Stratigraphy, Geology Department, University of Patras, Patras, Greece, penelpapadop@upatras.gr (2) Psiloritis UNESCO Global Geopark, Anogia, Greece (3) Management Unit of Chelmos - Vouraikos National Park and Protected Areas of Northern Peloponnese, Natural Environment and Climate Change Organization, Chelmos Vouraikos UNESCO Global Geopark, Kalavryta, Greece (4) Epirus Developmental S.A., Vikos-Aoos UNESCO Global Geopark, Ioannina, Greece (5) Lassithi Developmental S.A., Agios Nikolaos, Lasithi, Greece (6) Psiloritis Developmental S.A., Anogia, Greece (7) Sitia UNESCO Global Geopark, Sitia, Greece (8) Achaia S.A., Kalavryta, Greece

Introduction

The purpose of this work is to study the specifications required for developing or improving a quality label for products and services offered by businesses in the regions of the four collaborating geoparks (Vikos-Aoos UNESCO Global Geopark, Sitia UNESCO Global Geopark, Chelmos Vouraikos UNESCO Global Geopark, Psiloritis UNESCO Global Geopark).

The project involves the design of a special label for local agrotourism products and services in the cooperating areas, based on global market quality standards and UNESCO principles for Global Geoparks. Additionally, it includes the design of the specifications and evaluation criteria for the products and services of each region, which will carry this special label, in alignment with UNESCO's principles for Global Geoparks.

This expertise is conducted within the framework of the Interterritorial Cooperation Plan entitled "EMPOWERMENT, PROMOTION, AND NETWORKING OF UNESCO GEOPARKS" and, more specifically, as part of the project "Expertise on Specifications – Evaluation Criteria and Design of a Special Label for Local Agrotourism Products and Services."

Fig.1: Presentation of the project partners

The Interterritorial Cooperation Plan is implemented under the local CLLD/LEADER program, Submeasure 19.3 of Measure 19 of the Rural Development Program (RDP) 2014–2020, by the coordinating Local Action Group (LAG) ACHAIA S.A. – DEVELOPMENTAL ANONYMOUS COMPANY OF LOCAL AUTHORITIES, in collaboration with the following participating partners: EPIRUS DEVELOPMENTAL S.A. – Developmental Organization of Local Authorities, LASSITHI DEVELOPMENTAL S.A. – Developmental Organization of Local Authorities, AKOMM – PSILORITIS DEVELOPMENTAL S.A. – Developmental Organization of Local Authorities (Fig.1).

Methodology

The design of the quality label and the proposals for improving the existing ones (Psiloritis and Sitia UGGps) were based on several aspects:

- Study of Criteria and Application of 1st Generation Quality Labels: Examination of standards like AGRO (Hellenic Agricultural Organization–DIMITRA) and the EU's Eco-Label for environmental certification of products and services.

- Study of 2nd Generation Quality Labels: Investigation on labels such as the certification for the Samaria National Park, the "CRETE" quality label, local cultural support agreements like the Epirus Ancient Theaters Cultural Route, the PINDOS quality pact (no longer in effect), and the Special Quality Label for Greek Cuisine (E.S.P.E.K.).
- Study of Quality Labels for Geoparks: Analysis of existing labels from participating geoparks (Sitia and Psiloritis) and international geopark labels such as "Naturtejo Geopark Geoproduct," "Qualità parco" from Adamello Brenta Geopark, and "Naturally Tasty" from Beigua Geopark.
- Study of GEOfood Label Standards: Inspection of the guidelines and specifications of the GEOfood label.
- Review of Literature including research on the history and philosophy of quality label development, as well as other public surveys (e.g. Ilbery and Kneafsey, 1998; Henchion and McIntyre, 2000; Eckardt, 2007; Marques, 2007; Carpenter and Larceneux, 2008; Lorenzini, 2011; Ramos and Garrido, 2014; Košičiarová Kajima et al., 2016; 2017; Hutagalung et al., 2024 and other).
- Discussions with Project Partners and Geopark Representatives Five online meetings were held, including one kickoff meeting and four individual meetings with each partner. These meetings focused on expectations and challenges regarding quality label use.
- Online meeting with Lassithi Developmental S.A., Sitia Geopark, and Local Businesses: Local businesses shared their experiences, challenges, benefits, and suggestions for improving the label's operation. A survey conducted by the Psiloritis Geopark also provided insights from businesses using its quality label.
- Contractor's experience and discussions with local businesses and geopark representatives
- Designing of a customized questionnaire (Google Forms) aiming on a) obtaining general information about the participating businesses, information about the promotion methods and sustainable practices they use and information about their level of knowledge about geoparks and quality labels in general and b) in assessing the intentions of geoparks that do not implement certification as well as to evaluate the experiences of already certified businesses. The questionnaire was distributed to relevant businesses in all four areas and the results were analysed and validated.

An analysis of the needs of the co-operating partners was also conducted.

Results

The research resulted in proposals regarding the improvement of the already existing quality labels and the drafting of a regulation which sets out the conditions that must be followed by beneficiaries who wish to use this quality mark. The aim of granting this quality mark is to certify the suitability of the product-service to represent the geopark area as a genuine expression of its identity.

Additional objectives for applying the quality mark to products and businesses are:

- To certify the locality of the product-service
- To create added value to the product-service by providing or enriching the identity of the region and leveraging participation in the UNESCO Global Geoparks Network
- To connect the products-services with the geodiversity elements of the geopark area
- To provide differentiation to the products-services in relation to similar products by leveraging the uniqueness of the region and the experiences provided
- To enhance the credibility of the product/service
- To promote local products-services at a national and international level
- To strengthen relationships between producers, entrepreneurs and other interested parties
- To ultimately strengthen the local economy either directly or indirectly.
- To enhance the feeling of "belonging" in the collaborating businesses

The quality mark is aimed at businesses related to agro tourism, agriculture and rural tourism.

Eligibility criteria

The eligibility criteria are divided into general criteria, specific criteria and proportional coverage criteria. The general criteria are applied in their entirety to all enterprises and regard the legality, locality and mode of operation of the enterprise. The specific criteria are applied per type of enterprise (catering and accommodation businesses, manufacturing businesses -inside or outside the geopark area-, tourist-ecotourism offices, use of organic products etc.). The proportional coverage criteria constitute a set of criteria, the application of which can substantially contribute to the achievement of the objectives of the certification but are more specialized and difficult to apply practices (e.g. ISO or other certifications, minimizing the consumption of natural resources and waste in at least one way etc). For this reason, it is not recommended to cover all of these criteria, but it is required to cover at least 5 of them.

The coverage of the required criteria is confirmed by the presentation of the corresponding supporting documents.

Code of conduct

The "identity" of a region is not shaped solely by measurable characteristics, and for this reason, granting the current certification requires, in addition to meeting specific criteria by the interested businesses, a commitment to a set of **ethical rules**. This involves a collection of principles and rules that the parties involved must fully adopt as a way of life. These cannot function as criteria because their evaluation by individuals is inherently subjective. The signing of a **Code of Conduct** is proposed as a way to operate with integrity and commit to common values.

The proposed quality label regulation also determines obligations of both the participating businesses and geoparks, as well as of the certification process (application, evaluation, inspections and audit, issuance and monitoring) and proposes actions in order to maximize the impact of the quality label.

Discussion and Conclusions

The establishment of a quality label for geopark products and services represents a significant step towards promoting sustainable development and the responsible management of natural and cultural resources. Through this initiative, the high quality of offered products and services is ensured, while simultaneously the visibility of geoparks as exemplary areas that integrate tourism, education, and environmental protection os enhanced.

The implementation of the quality label can make a crucial contribution to the economic development of local communities by offering incentives for innovation while protecting and showcasing the unique natural wealth of geoparks. Strict adherence to the criteria established for the quality label will guarantee its reliability and strengthen the trust of visitors and consumers.

Finally, collaboration among various stakeholders—such as local communities, producers, management bodies, and educational institutions—serves as the foundation for the successful implementation and continuous improvement of the quality label. This will enhance the sustainability and uniqueness of geoparks in the long term.

References

Carpenter, M., Larceneux, F., 2008. Label equity and the effectiveness of values-based labels: an experiment with two French Protected Geographic Indication labels. International Journal of Consumer Studies, 32(5), pp.499-507.

Eckardt, C., 2007. Creating economic benefit by regional and international networking in the Global and European Geopark Bergstrasse-Odenwald, Germany. Abstracts of 7th European Geopark Network Open Conference, NW Highlands Geopark 10,

Henchion, M., McIntyre, B., 2000. Regional Imagery and Quality Products: the Irish Experience. British Food Journal, 102(8), 630-644,

Hutagalung, P.M., Nasution, Z., Ginting, N., 2024. The role of geological relationship and brand of geoproduct on regional development in Samosir Island of Geopark Caldera Toba with mediating method. GeoJournal of Tourism & Geosites, 52(1),

Ilbery, B., Kneafsey, M., 1998. Promoting Quality Products and Services in the Lagging Rural Regions of the European Union. European Urban and Regional Studies, 5(4), 329-341.

Kajima, S., Tanaka, Y., Uchiyama, Y., 2017. Japanese sake and tea as place-based products: a comparison of regional certifications of globally important agricultural heritage systems, geopark, biosphere reserves, and geographical indication at product level certification. Journal of Ethnic Foods, 4(2), 80-87.

Košičiarová, I., Nagyová, Ľ., Holienčinová, M., Rybanská, J., 2016. Quality Label as the Guarantee of Higher Quality of Food–A Case Study of Slovak Food Market. Procedia-Social and Behavioral Sciences, 220, pp.200-209.

Lorenzini, E., 2011. Territory branding as a strategy for rural development: experiences from Italy.

Marques, R. T., 2007. Sustainable tourism and certification in Geopark Naturtejo: A case study. Paper presented at 7th European Geopark Network Open Conference, HighLands Geopark, NW.

Ramos, E., Garrido, D., 2014. Towards a" 2nd Generation" of Quality Labels: a Proposal for the Evaluation of Territorial Quality Marks. Cuadernos de desarrollo rural, 11(74), pp.101-123.

17th INTERNATIONAL CONGRESS of the Geological Society of Greece

BULLETIN OF THE GEOLOGICAL SOCIETY OF GREECE, SP. PUBL.

EXTENDED ABSTRACT 240

West Akrocheiras section: a pilot multi-proxy palaeoenvironmental analysis

Papadopoulou P.[1], Iliopoulos, G[1], Bendle, J.[2], Christanis, K.[1], Kalaitzidis, S.[1], Liapi, E.[3], Perleros, K.[1], Soulakelis, N.[3], Tzortzi, M.[1], Zouros, N.[3,4]

(1) Department of Geology, University of Patras, Patras, Greece, penelpapadop@upatras.gr (2) School of Geography, Earth and Environmental Sciences, University of Birmingham, Birmingham, UK (3) Department of Geography, University of the Aegean, Mytilene, Greece (4) Natural History Museum of the Lesvos Petrified Forest, Sigri, Greece

Introduction / Background

The Lesvos Petrified Forest is a geological heritage site of global significance, featuring silicified tree trunks, fossil leaves and volcanic deposits dated back to the lower Miocene. Initially brought to scientific attention in 1844, it gained broader recognition in late 19th and early 20th centuries, with pivotal research in the 1990s elucidating its formation processes (e.g. Velitzelos & Zouros, 1997). Designated as one of the first European Geoparks in 2000, and Global Geopark in 2004, the Lesvos Petrified Forest is the main geological heritage area of international significance for the recognition of Lesvos island as an UNESCO Global Geopark in 2015 (https://www.lesvosmuseum.gr/en/node). Recognized as one of the first 100 IUGS geological heritage sites in 2022, the Lesvos Petrified Forest is a hub for research, education, and sustainable tourism.

Recent construction works of the Kalloni-Sigri road brought to the light new fossiliferous localities hosting thousands of fossils including fossilized trees and leaves (Zouros et al., 2022). The road cuts at the new fossiliferous sites enable detailed stratigraphic analysis of the Sigri pyroclastic rocks and a reevaluation of the area's stratigraphy and palaeoenvironmental evolution. This study focuses on the analysis of West Akroheiras section (39.230107°, 25.905465°, 320 m section length, Fig. 1) following a pilot multi-proxy approach and aiming to establish the most effective methods for palaeoenvironmental reconstruction of the Lesvos Petrified Forest monument.

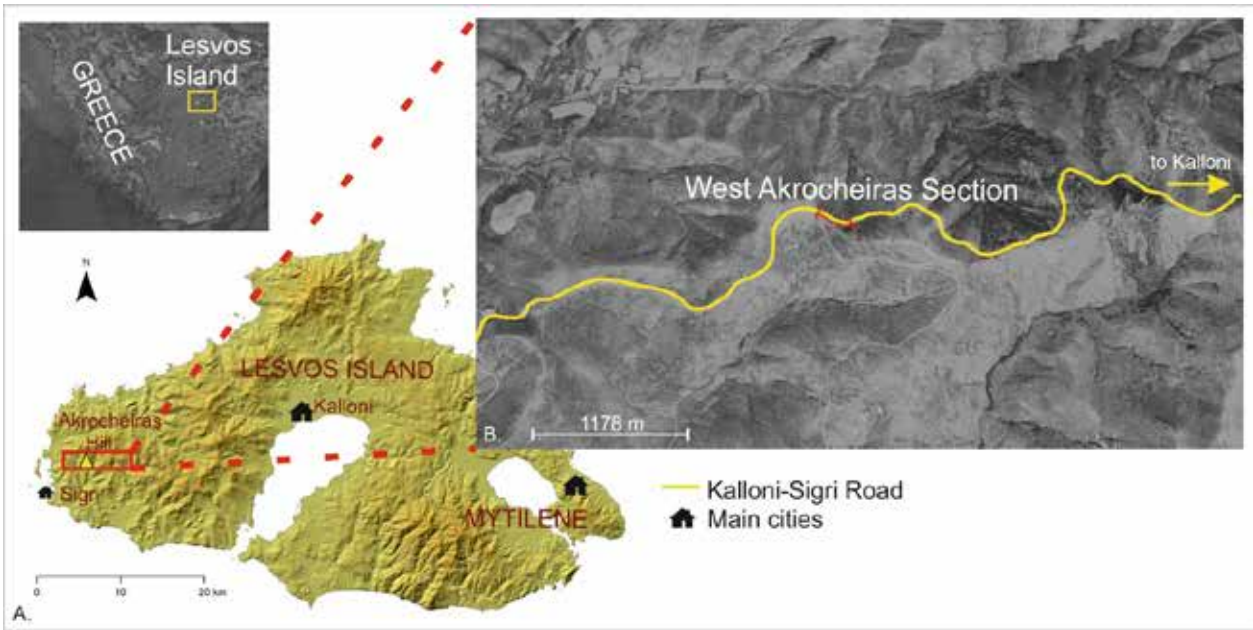

Fig. 1: A. DEM image of Lesvos Island. Main cities and main points of interest are noted. The study area is noted with the red rectangle. B. Satellite image of the study area, where the studied section (red line) is noted.

Geological setting

The volcanic rocks of Lesvos have been extensively studied and mapped, with notable contributions from researchers such as Hecht (1972, 1974a,b), Pe-Piper (1978, 1980) and Pe-Piper et al. (2019), who established the stratigraphic framework and identified key volcanic structures. These formations lie at the top of Permian schists (Katsikatsos et

al., 1982) and marbles, and include the Sigri Pyroclastic Formation, which features pyroclastic and volcaniclastic deposits rich in silicified tree trunks and fossilized leaves (Velitzelos & Zouros, 1997, Zouros, 2021). The Sigri pyroclastics derived from an early Miocene stratovolcano chain (Hecht, 1972; 1974a, b; Pe□Piper, 1980), dating between 21.5 and 18.4 Ma ago (Pe-Piper et al., 2019), with stratigraphic divisions inferred from adjacent geological formations. The volcanic chain follows a NNE-SSW orientation influenced by the dextral strike-slip tectonic regime of the Aegean-Anatolian microplate (Yilmaz et al., 2000). Over geological time, this regime evolved, giving rise to various fault systems, including dextral, sinistral and normal faults during Neogene and Quaternary times. These findings highlight the complex tectonic and volcanic history of the island, contributing to a deeper understanding of its geological evolution.

Material and Methods

Stratigraphic logging was performed in several places of the studied section as the lateral continuity of the layers was interrupted by faults, in addition to the many lateral changes in the nature of the pyroclastic material. The lithological characterisation of the pyroclastic rocks followed Fisher & Schmincke (1984) and Francis & Oppenheimer (2003). The most prominent fallen or standing tree trunks and fossil leaf horizons were noted along with basic sedimentological characteristics. Taphonomic observations of the fossil leaves were made in situ. Bed by bed sampling was also conducted.

Generalised stratigraphic cross sections containing the most important features (characteristic horizons, major faults etc.) were compiled and photos were taken. The sections were digitised later on (using CorelDRAW Graphics Suite), and the respective stratigraphic columns were drawn (using Strater 5 software) (Figs 2 and 3) and correlated. Moreover, very high-resolution Images acquired through Unmanned Aerial Vehicles were used to generate: i. a 2D orthophotomap and ii. 3D textured model, both used for digital stratigraphic measurements (e.g. layer thickness).

A number of rock samples were picked up for selected pilot analysis methods (XRD, organic petrography, micropalaeontologic analyses, and organic geochemistry, as well as systematics and taphonomy of fossil leaves). Powder XRD analysis was conducted on three palaeosoil samples (B6, B13, B23; Fig. 2) in the Department of Geology, University of Patras. Organic petrographical analysis was conducted on five samples (B3, B6 and B12; Fig. 2) also at the Department of Geology, University of Patras. Micropalaeontological analysis for aquatic organism remains (e.g. ostracods, diatoms) was conducted in fifteen samples (A1, A2, A3, A4, A5, B1, B2, B9, B10, B12, B13, D1, D2, Fig. 2) (Department of Geology, University of Patras). Samples B1, B6, B9, B12, B13, B19, B20 and D1 (Fig. 2) were subjected to organic geochemistry analysis at the Birmingham University. The systematic classification of the fossil leaves was based on their macro-morphological characteristics and was performed at the Natural History Museum of the Lesvos Petrified Forest.

Results

West Akrocheiras section consists mainly of coarse tuffs, lapilli tuffs and less of tuff breccia layers intercalated with palaeosoil horizons, with a total thickness of 22 m (Figs 2 and 3, columns C8.1-C8.13). Volcaniclastic layers are also included. Several strike slip faults exist with vertical displacements < 2 m, uplifting the western parts of the section. After correlating the stratigraphic data from the combined study of several sections along the Akrocheiras Hill roadcuts, seven palaeosoil horizons have been recorded in this section (Figs. 2 and 3, PS8.1-PS8.7), separating it in eight units (Units 8.1-8.8, Figs 2 and 3).

Standing fossil trunks were recorded in three palaeosoil horizons (Figs. 2 and 4 - PS8.3, Fig. 3 - PS8.5 and PS8.6). Fossil leaves were recorded in great numbers in many horizons throughout this section (units U8.1, U8.3 and U8.4), both as leaf litter between different layers and also oriented in different directions, mixed with the pyroclastic materials. The lower part of the section (units U8.1-U8.4) exhibits intense volcaniclastic characteristics (conglomerate lenses mostly at the western part).

Unit U8.2 possibly represents deposition of volcaniclastic material in a water body, as implied by the massive unconsolidated pyroclastic coarse ash layer with thickness around 1 m (column C8.1, Fig. 2). In this unit transported coal were found (column C8.2). Unit U8.4 bears a series of pyroclastic flows with leaf litter in at least five horizons (columns C8.2 and C8.3).

XRD analysis in the soil samples revealed that they consist mostly of crystalline intermediate feldspars and clay minerals or/and zeolites. Amorphous inorganic or/and organic material is also included.

Maceral analysis of sample B3 (unit 8.2) obtained from the 1-m-thick coarse pyroclastic ash layer at the bottom of the sequence, proved containing partially charred biomass derived from fresh and/or slightly peatified organic matter, probably of arboreal origin. Several organic fragments display a gelified texture and are heat-affected, as the relatively high mean random vitrinite reflectance values (0.47-2.0%) and the cracks indicate. These partially or totally-

carbonised peaty, and woody fragments may be air-borne transported from the surroundings and deposited there. Sample B6 (unit 8.2) represents a thin black layer, which contains charred particles (semifusinite and degradofusinite) with plasticized edges and displays a mean reflectance of 0.85%. In the same strata, charred particles with thin cell walls (pyrofusinite) are also common, with reflectance values ranging up to 1.4%. Interestingly, several particles display a pre-charring gelification, whereas the in-situ growth of the precursor plants is evident by the included charred corpohuminite particles. Sample B12 (unit 8.3) is characterized as a carbonaceous or sapropelic coaly layer (i.e. elevated liptinite content), with limited thermal affection and VR of 0.5%; the mode of deposition seems to be in a short-lasted water-logged limnic/limnotelmatic environment; an epigenetic thermal influence is evident only by some cracks.

All the samples that were micropalaeontologically examined, were barren. This implies either a non-aquatic environment, unfavorable life conditions (e.g. anoxic) or/and unfavorable preservation conditions (e.g. low pH values).

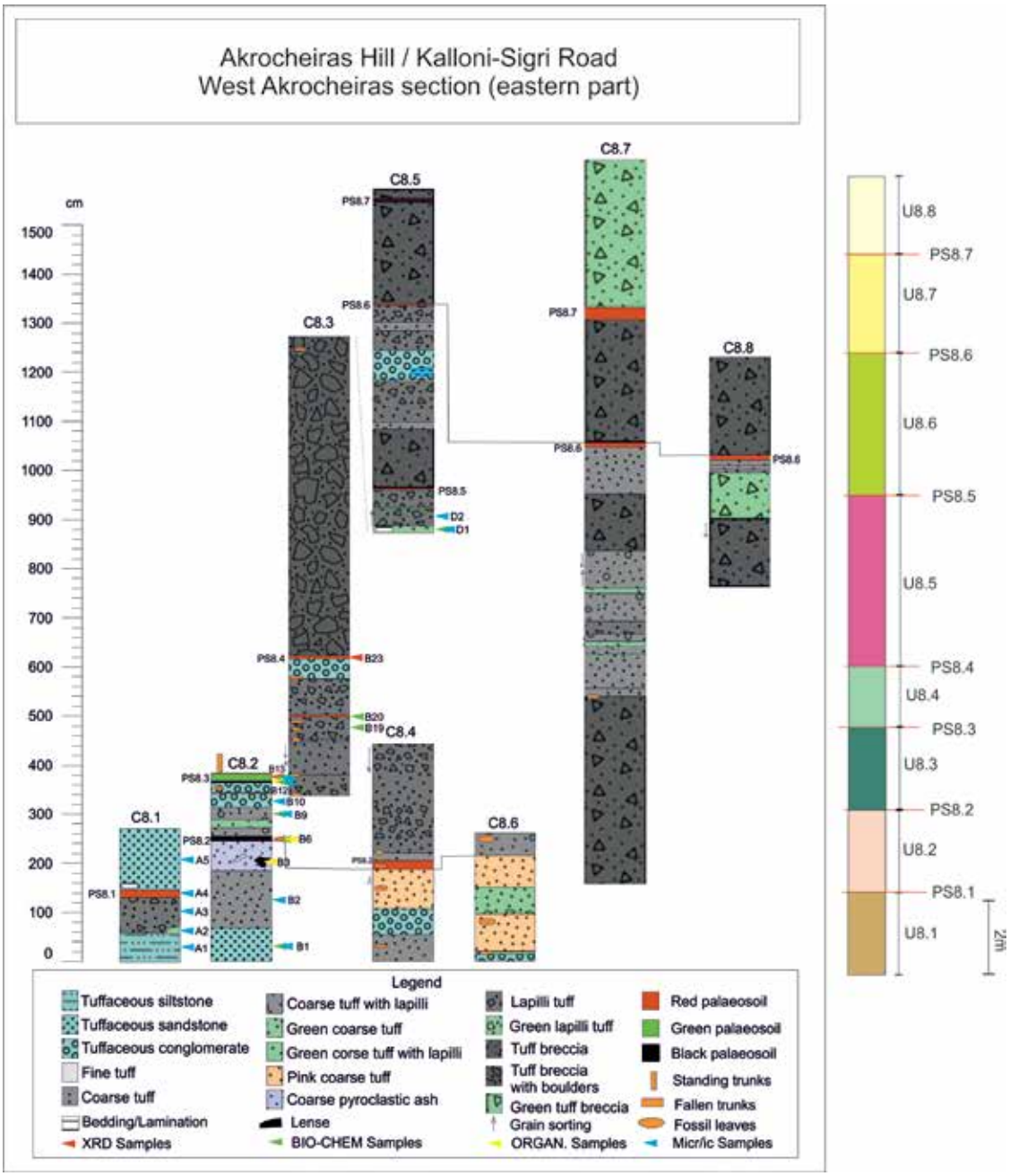

Fig. 2: Stratigraphic columns presenting the logged sequences from the eastern part of West Akrocheiras section. On the right, the units are schematically presented.

Pilot biomarker analyses of the eight samples revealed that the majority of them have plant wax n-alkanes in with only one showing an absence of these compounds. Some samples show some signs of thermal/diagenetic impact (B1), but overall the samples show high potential for organic geochemical work, including sufficient concentrations for compound specific isotope analyses. Some samples appear exquisitely well preserved, comparable with extract leaf matter of modern or very recent age (Holocene). Alkane response varies from 0-91% (samples D1 and B1/B20, respectively). Total Lipid content (TLE) varies from 0.6 mg (sample B19) to 5.8 mg (sample B9). No correlation was found between TLE and the abundance of n-alkanes in the samples. Sample B20 shows a very distinctive pattern where alkanes are persistent but a cluster of broad peaks is observed around C26-C29 alkane response time.
To date, the systematic taxonomy of the fossil leaves has revealed more than 55 plant taxa from West Akrocheiras. The palaeoflora consist of bryophytes, ferns and several angiosperms (including herbaceous and woody monocots, dicots). Among the identified plant taxa, *Daphnogene polymorpha* (A. Braun) Ettingshausen, *Laurophyllum* sp., *Phoenicites* sp., *Rosa* sp., *Nerium* sp., *Myrtophyllum* sp., *Pungiphyllum cruciatum* (A.Braun) Frankenhäuser & V.Wilde and members of Fagaceae family are abundant floristic elements.

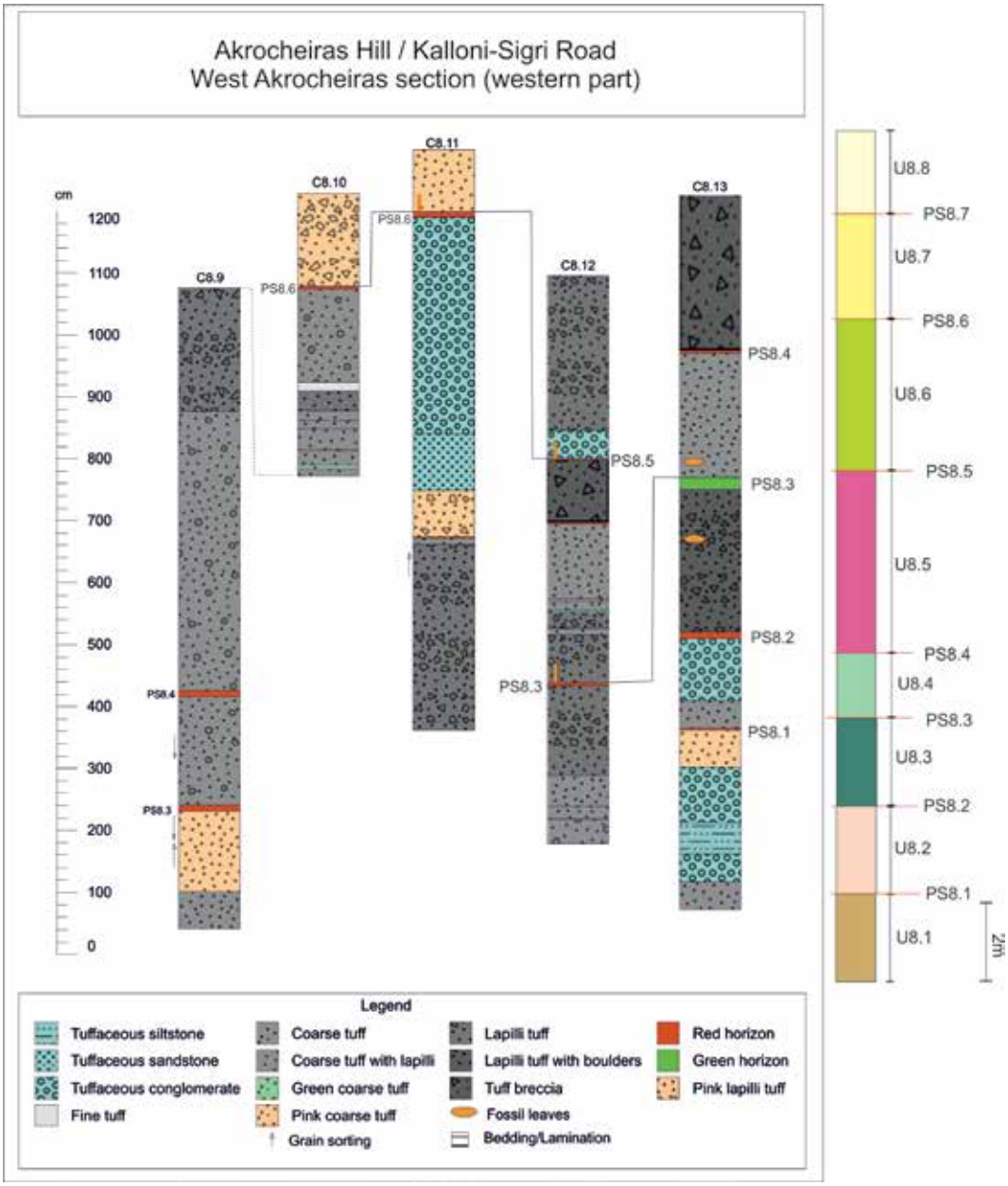

Fig. 3: Stratigraphic columns presenting the logged sequences from the western part of West Akrocheiras section. On the right the units are schematically presented.

Discussion

Palaeosoil horizons were examined in order to distinguish the different eruption phases. In West Acroheiras section at least 8 different eruption phases have been recognized corresponding to units U8.1- U8.8 (Figs 2 and 3).

The pilot studies on the palaeoenvironmental evolution of West Acroheiras section gave encouraging results. The lithology of some layers of the lower part (units 8.1 and 8.2) provides evidence of a water body (layer of samples B1-B2), nevertheless, the micropalaeontological analysis gave no results implying unfavorable life or preservation conditions. The organic geochemical analysis of sample B1 revealed high content of thermally matured organic matter, possibly rapidly deposited under anoxic conditions. Thus, if there was a water body there, then a hot pyroclastic flow must have entered it. This is in agreement with the results of the organic petrography analysis for sample B3, which reveals organic matter charred in various degrees, representing roots and arboreal plants, possibly deriving from a nearby peat-forming environment. The combined analysis of sample B6 from palaeosoil horizon PS8.2 (which marks the end of unit 8.2) reveals a palaeoenvironment with high organic matter content, partially affected by thermal alteration and buried rapidly under anoxic conditions. The very good preservation conditions of alkanes can be also attributed to clay minerals as was shown by the XRD analysis of the same sample.

Unit 8.3 shows volcaniclastic lithological characteristics. The fossil leaves scattered in the layer, reveal the deposition of transported material. Both organic petrography and organic geochemistry analyses of palaeosoil horizon PS8.3 show preservation of organic material (samples B12/B23). The palaeoenvironment is characterized as water-logged with limited thermal affection. On this palaeosoil horizon a remarkable fossilized standing tree trunk has been preserved (possibly a giant *Sequoia* tree, typically thriving on soils with good moisture retention). It is worth mentioning that the layers of units 1-3 show limited lateral continuity.

Fig. 4: Fossil giant *Sequoia* trunk standing on palaeosoil horizon PS8.3 in West Akrocheiras section.

Unit 8.4 bears a lot of fossiliferous layers. Fossilized leaf litter (fossil leaves laid on fine-grained horizons) were found at various levels along with transported fossilized leaves and trunks scattered in the pyroclastic material. Organic geochemical analysis of sample B19, deriving from a lapilli tuff layer with scattered fossilized leaves and trunks, gave low values of alkane response and TLE relatively to samples from palaeosoil horizons such as sample B20 but still includes organic remains. According to Retallack (1984), the preservation of leaves and wood in non-calcareous environments is only possible in water-logged environments with 0<Eh<200 mV and pH 2-5. Thus, the pyroclastic flow that generated this specific layer contained a sufficient amount of acidic water for the preservation of fossilized plant material and thus the depositional environment was anoxic. Sample B20, from a small palaeosoil horizon, gave evidence for a dry climate and a terrestrial environment (where waxy coatings on plants were more prominent) possibly consisted of vascular plants, trees, shrubs and herbaceous elements.

The systematic taxonomy of fossil leaves indicates a rich flora dominating different habitats such as riparian and mesophytic forests in the lowlands and adjacent surroundings. Several plant taxa including ferns, diverse palms (e.g, *Phoenicites* sp.), *Daphnogene polymorpha* suggest proximity to a water source, while others such as *Laurophyllum* sp., *Nerium* sp. and Fagaceae spp. are indicative of well-drained soils.

Units 8.5 to 8.8 present more thick and coarse-grained, organic matter-lean layers.

Conclusions

- The stratigraphic analysis of West Akroheiras section allowed the identification of at least eight different eruption phases recorded in the layers of this section (units 8.1-8.8). Based on standing fossil trunks at

least three forests had developed on some of the palaeosoil horizons of this section. Detailed stratigraphic analysis of the volcaniclastic sequence serves as a basis for the synthesis of the results from all methods and for palaeoenvironmental reconstruction.

- The taxonomy of the fossil leaves so far has revealed a mosaic of habitats such as riparian and mesophytic forests occurring in the broader area. The high alkane response and/or TLE implies decomposition and chemical transformation of organic matter (plants, algae or/and microrganisms) and favourable conditions for organic matter preservation (e.g. anoxic conditions, rapid burial and presence of clay minerals).
- The preservation of leaves and wood in non-calcareous environments is only possible in water-logged environments with 0<Eh<200 mV and pH 2-5 (acidic environments). Thus, evidence for the physicochemical conditions of the water-saturated layers is provided.
- Organic petrography on palaeosoil horizons gave evidence for water-logged environments amongst others.

The diverse methods revealed that there is a great potential in clarifying the Miocene palaeoclimatic and palaeoenvironmental conditions of the Lesvos Petrified Forest and this potential is multiplied when these methods are applied in combination. In the future more systematic and detailed analyses are needed in order to fully unravel the history of the area, its palaeoclimatic and palaeoenvironmental evolution.

Acknowledgements
We would like to sincerely thank Ass. Prof. Lambropoulou Paraskevi for the XRD analysis.

References

Fischer, R., Schmincke, H.U., 1984. Pyroclastic Rocks, Springer-Verlag Berlin Heidelberg.
Francis, P., Oppenheimer, C., 2003. Volcanoes. Oxford University Press.
Hecht, J.,1972: Geological map Plomari-Mytilene sheet. 1:50000. IGME, Athens.
Hecht, J., 1974a: Geological map Mithimna sheet. 1:50000. IGME, Athens
Hecht, J., 1974b: Geological map Polychnitos sheet. 1:50000. IGME, Athens.
Katsikatsos, G., Mataragas, D., Migiros, G., Triandafillou, E., 1982. Geological study of Lesbos island, Special Report, IGME, Athens.
Pe-Piper, G., 1978. The Cenozoic volcanic rocks of Lesbos (Greece), unpublished readership thesis, University of Patras.
Pe- Piper, G., 1980. The Cenozoic Volcanic Sequence of Lesvos, Greece. Z. dt. geol. Ges., 131, 889- 901.
Pe-Piper, G., Piper, J.W.D., Zouros, N., Anastasakis, G., 2019. Age, stratigraphy, sedimentology and tectonic setting of the Sigri Pyroclastic Formation and its fossil forests, Early Miocene, Lesbos, Greece. Basin Research 2019, DOI: 10.1111/bre.12365.
Retallack, G., 1984. Completeness of the rock and fossil record: some estimates using fossil soils. Paleobiology, 10(1), pp.59-78.
Velitzelos, E., Zouros, N., 1997. The petrified forest of Lesvos–Protected natural monument. Proc. Internat. Sympos. On Engineering Geology and the Environment, Athens, 3037-304.
Yılmaz, Y., Genç, Ş. C., Gürer, F., Bozcu, M., Yılmaz, K., Karacik, Z., … Elmas, A., 2000. When did the western Anatolian grabens begin to develop? Geological Society, London, Special Publication, 173, 353–384. https://doi.org/10.1144/GSL.SP.2000.173.01.17.
Zouros, N.C., 2021. The Miocene petrified forest of Lesvos, Greece: Research and geoconservation activities. Geoconservation Research. 4(2), 635–649.
Zouros,N., Soulakellis,N.,Valiakos,I., Bentana,K., Theodorou,E., Zgournios,E., Antonakis,E. and Lamprakopoulos,A.: Enhancement and promotion of the new fossiliferous sites along the new Kalloni Sigri road.-An example of good practice in geoconservation in Lesvos Isl. UNESCO Global Geopark Greece. Bulletin of Geological Society of Greece Sp. Publ. 10, pp. 849-850.

17th INTERNATIONAL CONGRESS of the Geological Society of Greece

BULLETIN OF THE GEOLOGICAL SOCIETY OF GREECE, SP. PUBL.

EXTENDED ABSTRACT 241

Comparing broadband and strong-motion data using collocated sensors in the HP network, Greece

Papageorgiou A.[1,2], Ktenidou O.-J.[1], Pikoulis E.-V.[1], Sokos E.[2]

[1] *National Observatory of Athens, Greece*

[2] *University of Patras, Greece*

Introduction and motivation

High-quality seismic data is of great importance in a wide range of seismological applications and studies, whether focusing on the source, path or site effect. Errors related to the sensors (calibration, orientation, or installation issues) or erroneous metadata may produce unreliable data that do not reflect true ground motion, either in all or in part of the frequency range of interest. We select stations of the Hellenic Unified Seismic Network (HUSN), and in particular the two networks that possess a significant number of co-located broadband and strong-motion sensors, namely HL (National Observatory of Athens; DOI:10.7914/SN/HL) with 24 co-located stations, and HP (University of Patras, DOI:10.7914/SN/HP) with 11 co-located stations. Our aim is to scrutinize their data over their frequency band during all periods of joint operation, in order to understand to what extent, the data from the two sensors agree and investigate potential discrepancies. In the abstract at hand, we focus on the HP network (Figure 1. black diamonds represent the collocated stations of HP network).

Figure 1. Map of collocated stations in Greece. HP stations appear as black diamonds.

Methodology

To perform a detailed analysis, we developed a targeted in-house code for data processing. We compiled a dataset of more than 1000 recordings from a total of 11 collocated sensors for the time period 2012-2023. Our records are of events with magnitudes M4 or larger, out to distances depending on magnitude. Our starting point was the NGA-West2 and NGA-East processing protocols by PEER, UC Berkeley (Kishida et al 2016) and the recent automated processes of Cauzzi et al. (2022). After inspecting the raw waveforms and identifying clipped data, we manually process them in the time and frequency domain, considering both horizontal components per event.

First, in the time domain we: perform visual inspection and detect issues such as lags (Figure 2. left) or amplitude discrepancies (Figure 2. right) in the time domain, manually pick P and S arrivals to select signal and noise windows, calculate peak-to-peak ratios (Figure 2. bottom) and inspect them with time. After that, in the frequency domain we perform visual inspection of S-wave and noise FAS (Fourier Amplitude Spectrum) of acceleration, examine the usable bandwidths, and calculate FAS ratios (Figure 3.).

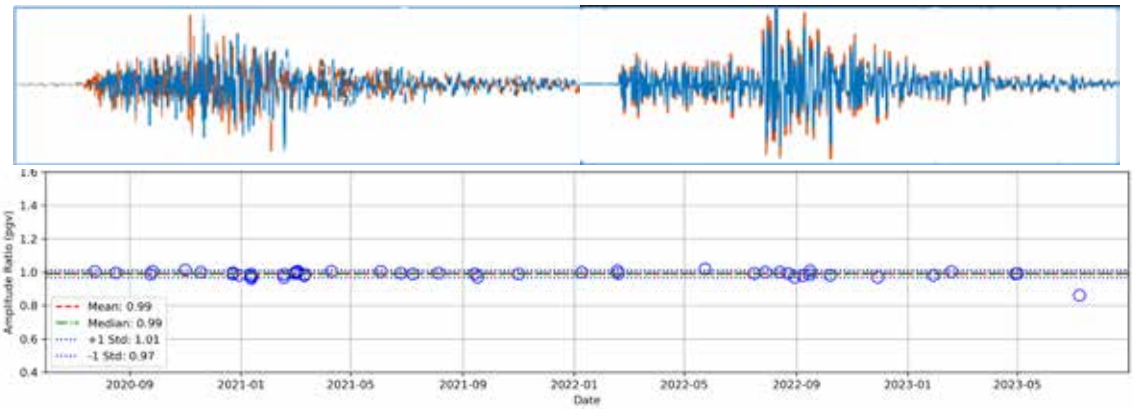

Figure 2. Top: Comparison of waveforms and problem detection in time (left) and amplitude (right). Bottom: peak amplitude ratio for a single component with time: no discrepancy observed.

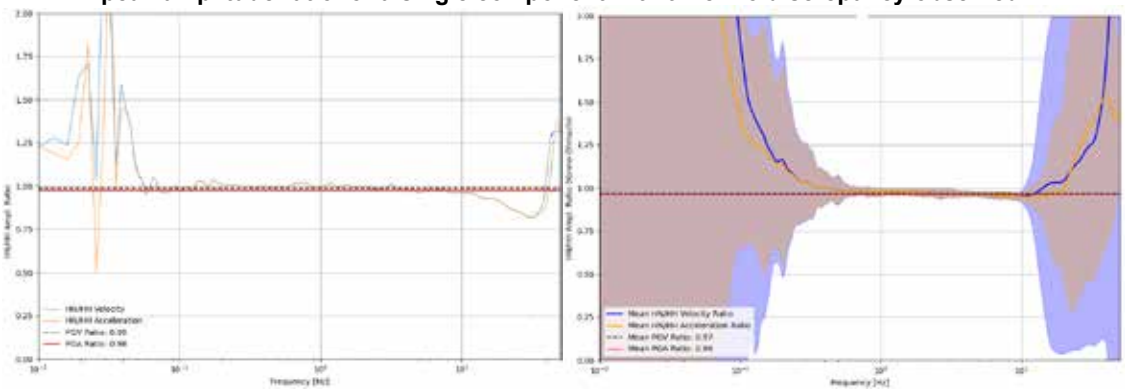

Figure 3. FAS ratios (SM/BB) for a single event (left) and average ratios for a station (right).

Results and conclusions

In this work we attempted a careful visual inspection of data from the collocated stations of the HP network in both the time and frequency domain, with the aim of compiling parameters that describe and assess data usability. By examining the observed discrepancies, we identify and amend certain underlying errors in sensor response. We compare the usable frequency between channels, per station, and assess data reliability and usability in the frequency domain. We calculate peak amplitude ratios for the 2 sensors per component and investigate if this deviates from unity, either persistently or sporadically. We identified GPS problems (time lags), component errors (amplitude discrepancies due to hardware), and metadata issues. Issues detected are fed back to the operator, so these findings contribute to network health monitoring and highlight potential for system improvement. Studies such as this one can help underline the potential impact that amplitude or time issues may have on several methods, including event location, tomographic studies, source analysis (moment tensor, slip inversion, etc.), as well as strong-motion applications, shakemaps, and dynamic analyses of structures.

References

Cauzzi C., Bindi D., Buscetti M., Cambaz D., Carrilho F., Custodio S., Clinton J., Felicetta C., Evangelidis Ch., Kalafat D. and Gallovic F. (2022). Comparison of Velocity and Acceleration Earthquake Records as a Quality Assessment Tool for European Co-Located Seismic Stations. 3rd European Conference on Earthquake Engineering & Seismology, Bucharest, Romania, 2022.

Kishida T., Ktenidou O-J., Darragh R.B. and Silva W.J. (2016). Semi- Automated Procedure for Windowing Time Series and Computing Fourier Amplitude Spectra for the NGA-West2 Database. PEER Report, Pacific Earthquake Engineering Research Center, UC Berkeley

17th INTERNATIONAL CONGRESS of the Geological Society of Greece

BULLETIN OF THE GEOLOGICAL SOCIETY OF GREECE, SP. PUBL.

EXTENDED ABSTRACT 242

Groundwater changes and induced seismicity influencing surface deformation in post-mining landscapes

Papageorgiou E.[1], Foumelis M.[1], Dominique P.[2], Bonatis P.[1], Raucoules D.[2], De Michele M.[2], Papadimitriou E.[1]

(1) Aristotle University of Thessaloniki, Thessaloniki, Greece, elenpapageo@geo.auth.gr (2) French Geological Survey (BRGM), Orléans, France

Introduction

In this study, we employed advanced interferometric time series analysis to explore the relationship between water level variability, seismicity, and induced surface motion over the Gardanne coalfield (Figure 1), while also accounting for potential long-term contributions. A spatio-temporal investigation of surface motion measurements was therefore conducted using data from the Copernicus Sentinel-1 mission, ultimately aiming to attribute the observed motion to a deformation mechanism.

The Gardanne coalfield, located in southern France between Marseille and Aix-en-Provence, was mined from the 17th century until 2003. Different techniques were employed along the basin with the deepest exploitation reaching up to 1300 m depth to the west of the basin (Dominique *et al*., 2022). The gradual progression of the mine workings to the west of the basin was affected by groundwater flow and pumping was considered essential to lower the water level and allow access to deeper levels. After mining ceased in 2003, the ending of pumping led to the flooding of the mine, with groundwater levels stabilizing around 2010. Since then, water level is relatively stable by pumping, with annual fluctuations of about twenty meters (Dominique, 2016).

With the gradual rise of the underground water level microseismicity was felt by the population in 2010 and a strong seismic swarm occurred in November 2012. Since then, swarming seismic activity lasting a few days has been re-appearing periodically in the same area, especially in November 2012, December 2014, November 2016 - March 2017 and August 2017. Prior analysis of seismic data revealed apparent connection of seismic activity with seasonal changes of underground water level in the mine, as well as with pumping rates (Dominique, 2016). Further analysis showed that swarming activity is related to the reactivation of minor fault segments being favorably oriented with respect to the local tectonic stress field (Dominique *et al*., 2022). However, no impact on the surface has been observed in post mining period that would indicate collapses of underground mining works (Namjesnik *et al*. 2022).

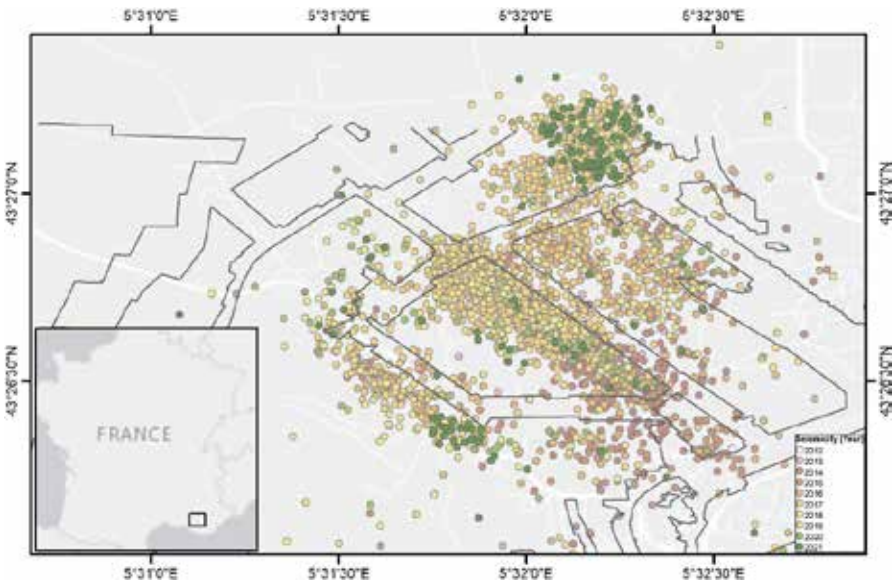

Figure 1. Gardanne coal mine area with observed seismicity (Ineris, BRGM). In the background the coal mine workings are depicted with black lines.

Methods / Results

Post-mining surface deformation detected from multi-temporal interferometric processing for the period from April 2015 to December 2022 via the SNAPPING service (Foumelis *et al*., 2022) revealed deformation patterns spatially correlated with the epicentral area of the 2016-2017 Gardanne micro-seismic activity (Figure 2). The temporal evolution of surface motion shows a signal attributed to induced seismicity, evidenced by a clear change in the displacement time series during this specific period.

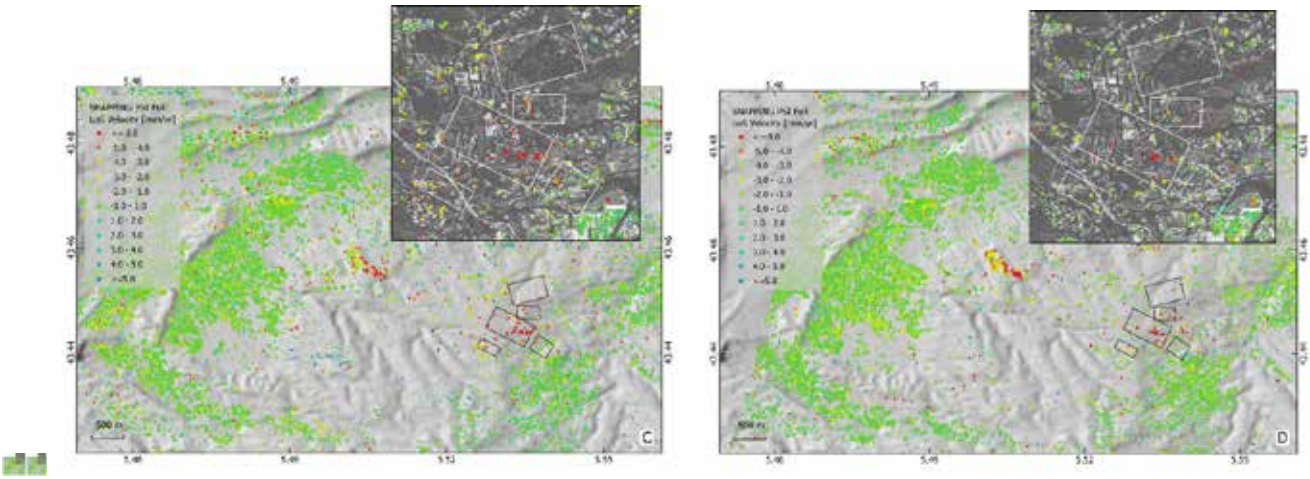

Figure 2. Surface motion rate along the LoS considering the period 2015-2022 and SNAPPING PSI processing schemes for ascending (a) and descending (b) satellite tracks. The rectangles outline the clusters of seismicity.

Geometric decomposition of the ascending and descending LoS measurements confirms the above observation, showing prevailing vertical motion with a negligible E-W component. This is also consistent with the focal mechanisms of major recorded events, which indicate normal faulting, typical of post-mining sites.

To investigate the relationship between seismicity locations and observed surface motion, we performed spatial clustering of micro-seismicity using the k-means algorithm. This process resulted in 5 distinct clusters (Figure 2), which accounted for ~80% of the total number of events in the catalogue within the epicentral area. It is apparent that seismic activity increased after each pumping phase, with a notable correlation between the magnitude of water table lowering and the frequency of seismic events. The consecutive drops in the water table during 2015 and 2016 contributed to the largest seismic swarm of late 2016 - early 2017, also coincided with the largest surface motion signal. An overall consistency was observed between the timing of micro-seismic events and the occurrence of surface displacements across the various seismic clusters.

Although the interpretation of the measurements until early 2017 is straightforward, it becomes more complex when examining the seismic activity and related surface motion for the August 2017 swarm. This signal seems to extend well beyond the main epicentral region, representing a seasonal subsidence component observed in the inter-annual displacement time series from 2015 to 2022. This seasonal signal might mask the maximum motion, potentially impacting the assessment of deformation caused by post-mining seismic activity during this period.

Conclusions

Our findings suggest that the observed surface motion is likely a result of energy released by both seismicity and aseismic motion caused by fluctuations of the mine's water table. The onset and variability of surface motion may also be controlled by the heterogeneity of the mine workings, such as differences in the gallery dimensions and the lithological composition of the overlying lithology.

Acknowledgements

This work is a contribution to the Research Fund for Coal and Steel (RFCS 2019) by the European Commission -Directorate - General for Research and Innovation under the Grant agreement (899192) – PostMinQuake and to Research Fund for Coal and Steel (RFCS 2023) by the European Commission -Directorate - General for Research and Innovation under the Grant agreement (101157400) - SIRIMA

References

Dominique, P., 2016. Microseismicity in a mining context-The Gardanne coal basin (Bouches-du-Rhône), 1280–1287. JNGG_Nancy_2016_miscrosismicite_Gard.pdf Accessed 2025–01–25 [in French]

Dominique, P., Aochi, H., Morel, J., 2022. Triggered seismicity in a flooded former coal mining Basin (Gardanne Area France). Mine Water Environ 41(2):1–18.

Foumelis, M., Delgado Blasco, J.M., Brito, F., Pacini, F., Papageorgiou, E., Pishehvar, P., Bally, P., 2022. SNAPPING Services on the Geohazards Exploitation Platform for Copernicus Sentinel-1 Surface Motion Mapping. Remote Sens., 14, 6075. https://doi.org/10.3390/rs14236075.

Namjesnik, D., Kinscher, J., Contrucci, I., Klein, E., 2022. Impact of past mining on public safety: seismicity in area of flooded abandoned coal Gardanne mine, France. Int J Coal Sci Technol 9, 90. https://doi.org/10.1007/s40789-022-00558-1.

17th INTERNATIONAL CONGRESS of the Geological Society of Greece

BULLETIN OF THE GEOLOGICAL SOCIETY OF GREECE, SP. PUBL.

EXTENDED ABSTRACT 243

Hydrochemical characterization of multi-layer porous aquifer of Larissos system, Peloponnese

Papailiopoulou Maria., Apostolopoulou P., Stavropoulou V., Pouliaris C., Kazakis N. and Zagana E.
(1) University of Patras, Faculty of Natural Sciences, Department of Geology, Greece; m.papailiopoulou@ac.upatras.gr; up1065363@ac.upatras.gr; vstavropoulou@ac.upatras.gr; christospouliaris@gmail.com; nkazakis@upatras.gr; zagana@upatras.gr
**Correspondence: m.papailiopoulou@ac.upatras.gr*

Introduction

The groundwater system of Larissos has poor chemical status due to human activities in the area. Due to the high-water needs of the population, aquifers have been underused for many years and have degraded the quality and quantity of groundwater. As a result, aquifers have been in a state of over pumping for decades, which has led to a reduction in the water table, which has reached negative absolute altitudes, and to the occurrence of seawater intrusion, particularly in the northern and north-eastern part of the region. In addition, the aquifers are also affected by the agricultural activity taking place in the study area, resulting in locally elevated nitrate (NO_3^-) values. Through sampling and chemical analyses carried out in the laboratory, these phenomena of seawater intrusion and increased nitrate values are observed and are shown in the graphs. Chemical analyses were carried out for the determination of major cations (Ca^{2+}, Mg^{2+}, Na^+ and K^+ and major anions (HCO_3^-, SO_4^{-2}, Cl^-, NO_3^-, NO_2^-, NH^{4+} and PO_4^{2-}). In the Laboratory of Hydrogeology of the Department of Geology at the University of Patras, all analyses were carried out in accordance with the suggested procedures and standards. The Na^+, K^+, Ca^{2+}, Mg^{2+} were measured using a Perkin Elmer atom absorption spectrometer. The HCO_3^- were determined by indicator H_2SO_4 titration. The other main anions were measured by a Hach® DR 4000 spectrophotometer.

Study Area

The study area is located in northwestern Peloponnese, and specifically in the prefecture of Achaia, and occupies an area of approximately 163 km^2. The main river in the study area is the Larissos river. The main riverbed of Larissos is 19,5 km long, originating from mountain Movri and emptying into the Prokopou lagoon. It is one of the most important sources of surface runoff in the area and collects water from various streams along its course. In addition, the river also receives overflows and excess water from the irrigation ditch from the Pinios river. The Larissos groundwater system is mainly developed in deposits dating back to the Neogene and Quaternary periods.

According to data from the "River basin management plan", the groundwater system of Larissos is estimated to have an average annual supply of approximately $26 \cdot 10^6$ m^3/y and the total annual water withdrawal is $33 \cdot 10^6$ m^3/y. These quantities are used to fill the supply needs of irrigation and water supply. Furthermore, the hydraulic characteristics of the system, such as hydraulic conductivity and storage coefficient, also have been calculated and equal $3{,}5 \cdot 10^{-5}$m/sec και 5-8% respectively.

Geology

The Larissos groundwater system is structured by rock formations of the tectonostratigraphic zone of Ionian and is mostly covered by sediments dating back to Neogene and Quaternary periods. In particular, the Ionian zone includes limestones of Upper Jurassic to Palaeocene age and Eocene flysch. The postalpine sediments include sands, screes, recent cones of scree, eluvial formations, terrestrial and torrential deposits and alluvial deposits dating from Quaternary period and friable sandstones, sandy clays and yellowish to grey clayey marls from the Neogene (Figure 1). Geomorphologically, the study area is divided into flat zone (79,23%), semi-mountainous zone (13,42%), hilly zones (4,95%) and lagoons (2,40%). It is observed that the transition from flat to the hilly and mountainous zones is gentle and smooth (Stavropoulos, X., 1992).

Hydrogeology

In the study area there are two types of aquifers, the first is found in carbonate rocks and the second in sediments that are dating in Neogene and Quaternary periods (Stavropoulos, X., 1992). The hydropermeability of geological formations depends on the porosity, the size, the shape and the distribution of the grains. The geological formations of the area are classified into three categories based on their hydro-lithological behavior. The first category concerns hydropermeable formations which allow water to penetrate and circulate and include formations of the Holocene age such as scree, recent cones of scree and alluvial deposits. The second category includes semi-hydropermeable formations which have low permeability and can store and allow water to flow but at a low rate. These include formations dating from the Pleistocene and contain pebbles, sandstones, clays and clay marls. The third category includes impermeable formations, such as flysch, which do not allow the flow of water.

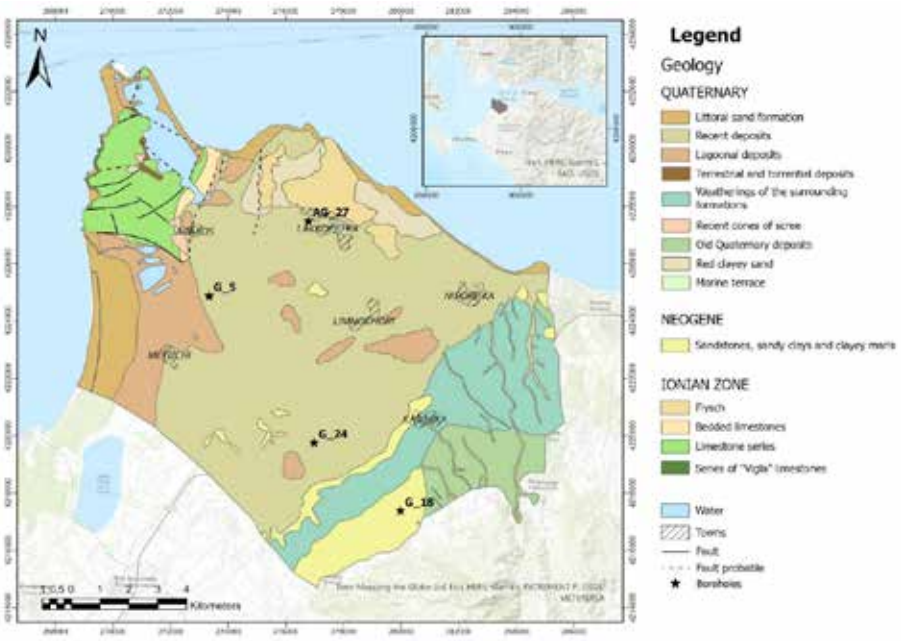

Figure 1. Geological map of study area (modified from I.G.M.E., 1977-1980)

Results and Discussion

Characteristics of groundwater hydrochemistry

Table 1 indicates the physicochemical characteristics of water samples. Especially, the electrical conductivity depends on the temperature and the amount of dissolved salts in the water. When high values of electrical conductivity occur then there is likely to be water pollution (Kazakis N., 2013). It is observed by Figure 2 that in boreholes G_24, G_5 and G_18 the values of electrical conductivity range from 630 μS/cm to 1600 μS/cm, while in borehole AG_27 the values are very high and exceed 2000 μS/cm. The pH expresses the concentration of hydroxide cations (H3O+) in an aqueous solution. The solution is neutral when pH = 7, acidic when pH < 7 and alkaline when pH > 7. It is observed that in boreholes G_24, G_5 and G_18 the pH values increase with depth and the water solution can be classified from acidic to alkaline, while in borehole AG_27 there is a decrease in pH values. The Oxidation Reduction Potential (ORP) gives information about the oxidation state of the elements in an aqueous solution. The water is called reductive when the values are negative and oxidative when it shows positive values (Mandhlaras, D., 2005). It is observed that borehole G_24 shows negative values, borehole G_5 has both positive and negative values and boreholes G_18 and AG_27 have positive values. Dissolved Oxygen (DO) provides informations on the exposure of groundwater to atmospheric air. When the values are zero or very low then the water is old and non-renewable. It is observed that all boreholes have low values ranging from 1.5 mg/l to 5.8 mg/l. The total dissolved solids are a parameter that related to electrical conductivity and depends on the type of rock through which the water and its flow velocity. For values of TDS<1000 mg/l the water is classified as fresh (Davis – DeWiest, 1966). It is observed that in boreholes G_24, G_5 and G_18 the values of TDS range from 270 to 575 mg/l, while in borehole AG_27 the values reach 857 mg/l. The increase in calcium ions is associated with the initial stages of salinization where cations are exchanged as Ca^{+2} is released and Na^{+}, Mg^{+} and K^{+} are absorbed from seawater (Walraevens et al. 1993). It is observed that all boreholes show high values and in borehole AG_27 the values reach 310 mg/l. Sodium ions are associated with the infiltration of seawater and its mixing with fresh water. The concentration of Na^{+} increases with the continuous pumping of aquifers. It is observed that boreholes G_24 and G_18 have values ranging between 20 mg/l and 32 mg/l, while boreholes G_5 and AG_27 have higher values up to 134 mg/l (Figure 3). Cloride ions are associated with seawater infiltration and their high value indicates high pumping conditions. It is observed that in boreholes G_5 and AG_27 the values are >100 mg/l and in boreholes G_24 and G_18 they range between 40 mg/l and 51 mg/l (Figure 4). Nitrate ions in groundwater are associated with agricultural activities that cause contamination of the aquifer (Figure 5). It is observed that all boreholes have high nitrate values while boreholes G_18 and AG_27 have the highest. The Revelle factor is a parameter for the identification of salinization. For seawater it takes values >150 and for good water the index has values <1 (Kalergis, G., 2000). It is observed that the water of boreholes G_24, G_18 and AG_27 is good while the water of borehole G_5 is slightly contaminated.

	Sampling date	Sampling depths (m)	EC (μS/cm)	T (ºC)	pH	ORP	DO (mg/l)	TDS (mg/l)	Ca^{+2} (mg/l)	Mg^{+2} (mg/l)	Na^{+} (mg/l)	K^{+} (mg/l)	HCO_3^- (mg/l)	SO_4^{-2} (mg/l)	Cl^- (mg/l)	NO_3^- (mg/l)	NO_2^- (mg/l)	NH_4^+ (mg/l)	PO_4^{-3} (mg/l)	F^- (mg/l)
G_24	14/11/2024	46	840	19.1	7.08	-155.9	1.58	457	86	13.90	30	3.7	298.9	0	44.3	51.2	0		0	0
		49	831	19.1	6.86	-142.3	2.38	312	84.8	15.61	24	3.6	381.86	0	42.4	49.3	0.028		0.11	0
		52	641	19.1	7.25	-162	2.28	314	72	13.66	20	3.9	336.72	1	41.7	48.8	0		0.12	0.11
G_5	14/11/2024	30	697	20	7.39	-38.4	3.38	294	58.4	17.56	58	3.3	145.18	6	98.8	48.6	0.021	0.742	0.15	0.24
		45	697	19.9	7.48	-8.4	3.1	269	56	16.58	54	3.2	186.66	5	97.7	47.8	0	0.911	0.15	0.31
		60	700	19.9	7.61	9.5	3.2	272	58.8	14.39	58	3.2	197.64	4	102	48.4	0.003	0.574	0.14	0.28
		75	1512	19.9	7.47	98.4	3.94	569	94	41.22	108	7.4	185.44	21	339	48.3	0.054	1.72	0.16	0.42
		90	1505	19.9	7.49	174.2	3.54	575	90.4	48.05	112	8.4	219.6	19	351	49	0.062	1.867	0.09	0.38
		105	1467	20	7.5	16.5	2.92	567	91.6	47.56	116	8.4	176.9	19	352	16.8	0.002	1.914	0.05	0.47
G_18	14/11/2024	40	1034	18.9	7.4	102.8	4.36	396	159.2	3.17	30	0.6	392.84	81.3	49.4	83.4	0.017	0.032	0.44	0
		50	1038	18.8	7.43	161.1	5.36	394	130.4	14.15	30	0.6	363.56	82.8	50.9	184.4	0.021	0.13	0	0.05
		60	1042	18.7	7.43	158.3	4.39	407	131.2	13.66	32	0.6	372.1	84.7	50.8	127	0.03	0.042	0.11	0.07
AG_27	14/11/2024	20.7	2010	19.7	7.04	243.2	4.83	839	310.4	10.73	126	1.5	397.72	500	156	108	0.026	0.047	0.09	0.51
		21.9	2018	22.4	7.02	221.6	5.78	857	282.4	22.93	134	1.5	384.3	540	162	96.4	0.033	1.23	0.04	0.71

Table 1. Physicochemical characteristics of water samples

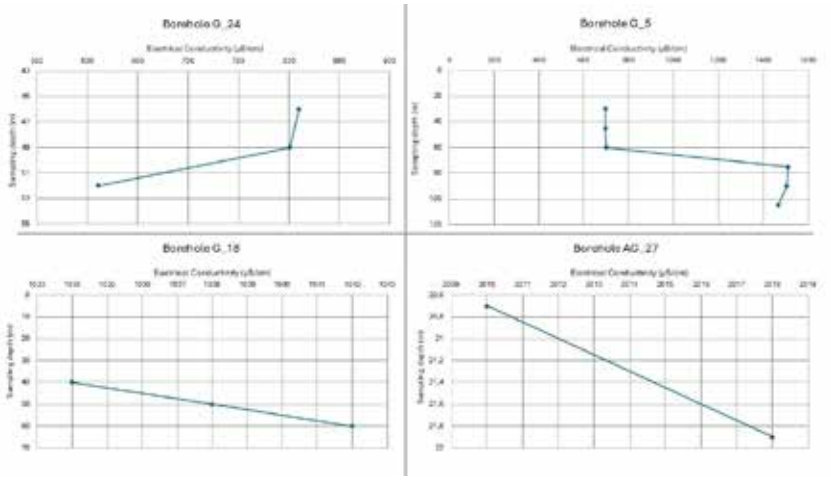

Figure 2. Profiling of EC (μS/cm) in the four boreholes of study area

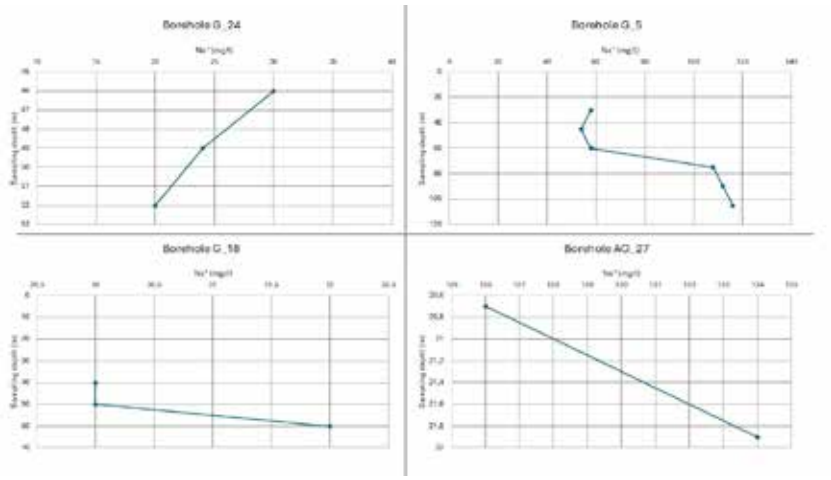

Figure 3. Profiling of Na^+ in the four boreholes of study area

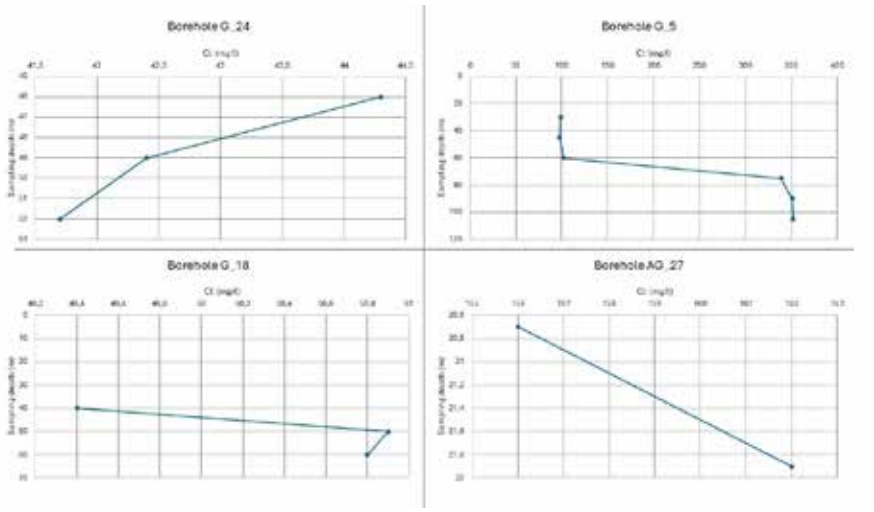

Figure 4. Profiling of Cl^- in the four boreholes of study area

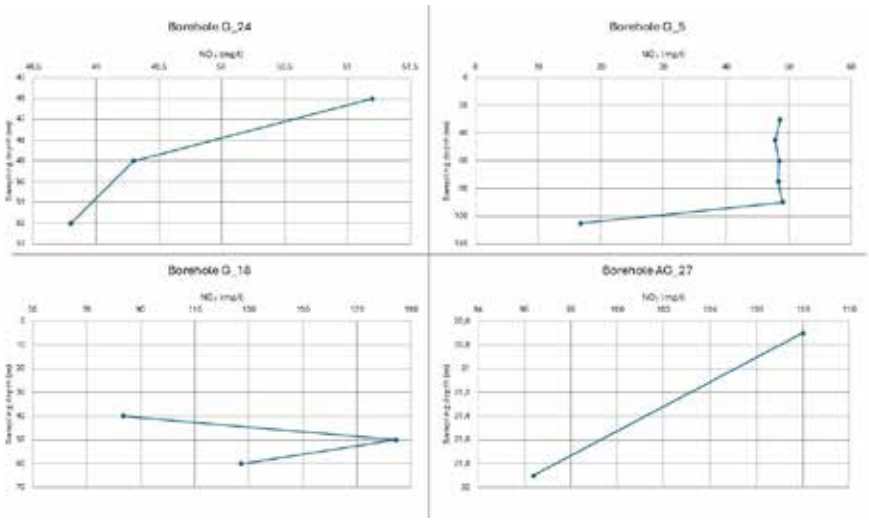

Figure 5. Profiling of NO_3^- in the four boreholes of study area

Study of hydrochemical facies

With respect to the main cations and anions in solution, it was determined that the hydrochemical facies changed from the low salinity Ca^{2+}-HCO_3^- type to the Na^+-Cl^- type as salinity increased (Mahlknecht et al., 2017). Typically, samples with higher salinity have been identified close to the coast or in areas that had been severely affected by the hydraulic gradient inversion, while samples with lower salinity were found further from the coast (Tamez-Meléndez et al., 2016). The Piper diagram at Figure 6 (a) shows the two main water chemical types of Ca-HCO_3 and Ca-Mg-Cl. Also, the samples from boreholes G_18 and three samples from G_5 is mainly dominated by type Ca-Mg-HCO_3 or types of Mg-Ca-HCO_3. The samples from boreholes AG_27 and the other samples from G5 appear to be enriched in Cl. According to the results figure 6 (b) shows the Schoeller Berkaloff diagram. This diagram shows the groundwater samples in different depths of mains cations and anions respectively. Moreover, in the Schoeller diagram the water samples show high concentrations of Ca, Na, Cl, and NO_3 in relation to low concentrations of SO_4 and Mg. For borehole G_24 the diagram shows that with increasing depth the concentrations of the elements decrease. Also, in borehole G_5 the lines of the samples in depths 30, 45 and 60 m appear almost parallel. In addition, in relation to the next three sampling depths 75, 90 and 105 m the samples are enriched in all elements. Regarding borehole G_18, the concentrations of the elements are low at the depth of 40 m compared to the next two depths, and specifically the NO_3 at the depth of 50 m are increased compared to the depth of 60 m. In addition, all major ions except nitrate increase with increasing depth.

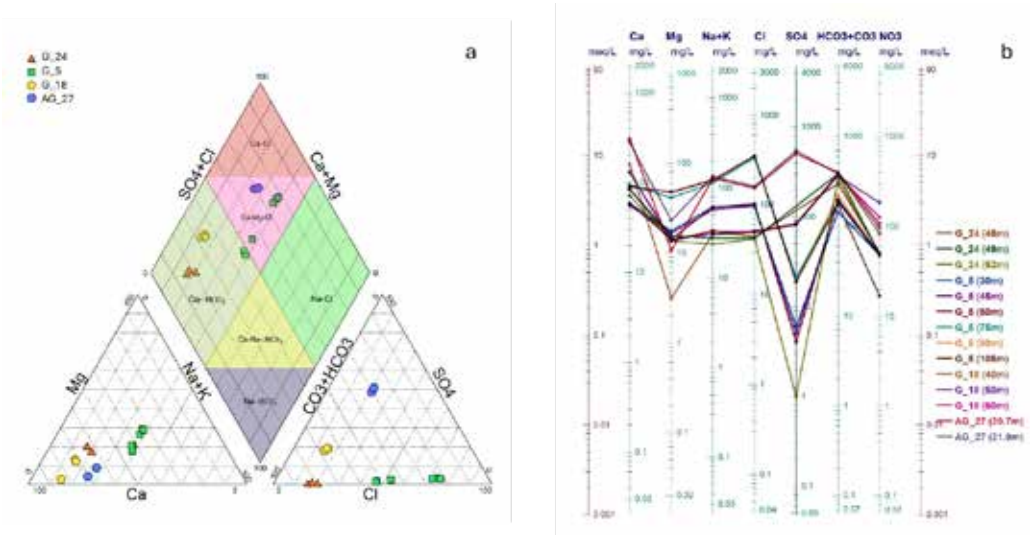

Figure 6. (a) Piper diagram showing the water type; (b) Schoeller Berkaloff diagram

Conclusions

The samples were collected from different depths and analyzed for physicochemical parameters, major cations, and anions. The interpretation was carried out using Piper and Schoeller–Berkaloff diagrams. During the cation exchange phenomena with seawater intrusion, the hydrochemical facies of groundwater evolves from Ca–HCO_3 to Na–Cl. Ion exchange is one of the fundamental geochemical processes occurring during the salinization of groundwater. The seawater intrusion leads to an increase in Na^+, Mg^{2+}, and SO_4^{2-} concentrations due to ion exchange. The geochemical processes controlling groundwater chemistry in the research area include ion exchange, carbonate production, mineral precipitation, and seawater intrusion (Salem and Osman, 2017). Moreover, the dissolution of gypsum in coastal aquifers containing gypsum beds results in more complex water–rock interactions when freshwater mixes with saline fluids or seawater (Campana and Fidelibus, 2015). Two groups of groundwater were identified on the Larissos groundwater system of Ca-HCO_3 and Ca-Mg-Cl according to Piper diagram. As the above results show that the borehole AG_27 faces the most serious problem regarding seawater intrusion. The borehole AG_27 exhibited high electrical conductivity values, with elevated concentrations of Na^+, Cl^-, and SO_4^{2-}, indicating possible influence from seawater intrusion or interaction with evaporate formations. In contrast, borehole G_5 showed dominance of Ca^{2+} and HCO_3^-, classifying it as a Ca–HCO_3 type, particularly at lower depths. At greater depths, however, an evolution toward a mixed Ca–Mg–Cl type was observed. The gradual increase in ion concentrations with depth in borehole G_5 can be attributed to the fact that deeper groundwater has a longer residence time within the aquifer and comes into contact with rock formations richer in soluble components, leading to ion enrichment in the water. The sudden decrease in electrical conductivity was created at lower depths in G_24. Borehole G_24 exhibits stable physicochemical parameters, with minor variations among the samples collected at depths of 46, 49, and 52 meters. The major ions show consistent concentrations, with a dominance of Ca^{2+} and HCO_3^-, classifying the water as Ca–HCO_3 type. The concentrations of Na^+, Cl^-, and SO_4^{2-} are low, with no indication of seawater intrusion. Moreover, in all boreholes, the concentration of NO_3 decreases with respect to the depth, except for the borehole G_18, where at the intermediate depth their concentration is increased. In addition, the concentration of Cl increases in relation to the depth of the borehole, and in particular the boreholes which are located near to the coast have high concentrations of Cl. Consequently, the borehole sample logging helps to find out the interactions of freshwater and saltwater in coastal areas. This strategy is expected to support a much wider range of coastal aquifer research. The study highlighted the importance of vertical sampling and multiparametric analysis in understanding the qualitative evolution of aquifers and identifying zones of contamination or salinization. The results contribute to the management of groundwater resources in areas with complex geological and hydrogeological conditions.

Acknowledgments

The present work was financially supported by the «Andreas Mentzelopoulos Foundation»

References

Campana, C., Fidelibus, M.D., 2015. Reactive-transport modelling of gypsum dissolution in a coastal karst aquifer in Puglia, southern Italy. Hydrogeol J 23, 1381–1398. https://doi.org/10.1007/s10040-015-1290-x.

Davis, S.N., DeWiest, R.J.M., 1966 : Hydrogeology . 2nd edition, Wiley, New York, pp.463.

I.G.M.E., 1978 - 1980. Geological Map of Greece, Scale 1:50.000. Nea Manolas and Patrai, Sheets.

Kalergis, G., 2000. Applied – Environmental Hydrogeology. 2nd edition, volume B, Techical Chamber of Greece, Athens.

Kazakis, N., 2013. Assessment of the risk of external groundwater pollution: Application to the Anthemounta river basin. PhD Dissertation, Department of Geology, Aristotle University of Thessaloniki, Greece.

Mandhlaras, D., 2005. Environmental – hydrogeological research in the Glafkos basin. University of Patras, Department of Geology, Division of Applied Geology and Geophysics, Laboratory of Hydrogeology – Technical Geology.

Salem, Z.E.-S., Osman, O.M., 2017. Use of major ions to evaluate the hydrogeochemistry of groundwater influenced by reclamation and seawater intrusion, West Nile Delta, Egypt. Environ Sci Pollut Res 24, 3675–3704. https://doi.org/10.1007/s11356-016-8056-4.

Specific Secretariat for Water, 2013. River Basin Management Plan. Management Plan for the River Basins of North Peloponnese River Basin District.

Stavropoulos, X., 1992. Hydrogeological conditions of a wide area of Kato Achaia – Manolados (NW Peloponnese). PhD Dissertation, Department of Mining and Metallurgical Engineering, National Technical University of Athens.

Warlaevens, K., Lebbe, L., Ceukelaire, M.D., Houtte, E.V., Greuck, W.D., (1993): Influence on groundwater quality of the Paleozoic Brabant Massif in Belgium due to overexploitation. Groundwater Quality Management (Proceedings of the GQM 93 Conference held at Tallinn, September 1993). IAHS Publ. no. 220, 1994.

17th INTERNATIONAL CONGRESS of the Geological Society of Greece

BULLETIN OF THE GEOLOGICAL SOCIETY OF GREECE, SP. PUBL.

EXTENDED ABSTRACT 244

Assessment of the groundwater vulnerability using DRASTIC method in Larissos watershed, Greece

Papailiopoulou Maria., Chrisanthakopoulou K., Stavropoulou V., Pouliaris, C., Kazakis, N. and Zagana, E.

(1) Faculty of Natural Sciences, Department of Geology, University of Patras, Greece

Introduction

Especially in the world's arid areas, groundwater provides the only source of water because of its extensive supply, low sensitivity to pollution compared to surface water, and storage capacity (Zghibi et al., 2016). In addition, as groundwater is the primary supply of drinking water, it is crucial to determine how vulnerable it is to anthropogenic contamination (Iqbal et al., 2015). Therefore, nitrate contamination of groundwater due to agricultural practices and an important increase in the use of fertilizers is becoming an increasingly serious problem (Zghibi et al., 2016). The probability with which a contaminant introduced into the ground surface might enter and spread throughout groundwater due to human activity is known as inherent vulnerability having consideration given to the region under research's natural geological, hydrological, hydrogeological, and hydrogeochemical characteristics (Zghibi et al., 2016). In most parts of the world, groundwater reservoirs are the only supply of water that is drinkable, yet they are rapidly transforming into a resource that is not renewable (Udosen et al., 2024). Aquifer vulnerability has been evaluated using DRASTIC, a reliable and validated vulnerability model (Aller, n.d.) (Kazakis and Voudouris, 2015). The acronym DRASTIC originates from the parameters that the model is intended to assess: depth to groundwater (D), net recharge rate (R), aquifer media (A), soil media (S), topography (T), impact of vadose zone (I) and hydraulic conductivity rating (C). The study proposes to develop and carry out an assessment tool that uses a geographic information system (GIS) and the DRASTIC model to control the groundwater vulnerability of the watershed of Larissos in Greece. Assessing the relative importance of the DRASTIC criteria for determining aquifer vulnerability is an additional objective of this study.

Study area

The study area is located in the north-west part of Peloponnese, which is located in Greece (Fig.1). The mean annual precipitation is approximately 781 mm, and the temperature it is observed in the months of July and August reaches approximately 27.4°C, while the minimum is placed at month of January with rising around 10.2°C is 10.2 °C these values were estimated based on five years of records (2020–2024) which collected in the study area. The study area is characterized to numerous rivers, from east to west with the main river being the Larissos. Characteristic of the Ionian series in the Lower Cretaceous is the plunge of the watershed that originated due to the taphrogenesis and the deposition along it of Vigla limestones-rich in planktonic organisms-due to the high rate of sedimentation (Karakitsios, 1995). Also, the overlay of "Pantokrator" limestones is found from the Vigla limestones, a fact attributed to a large extent erosion of the stratigraphic sequence. In the deposition phase of limestones of the Upper Senonian, the conditions of carbonate sedimentation they are homogenous until the Eocene, with characteristic features the low rate of sedimentation and the partial supply of material from the Pro-Apulias to the west and Gavrovou-Tripoli to the east, favorable for him formation of micro-breccia and micro-conglomerate limestones with Nummulitidae. Finally, like any sequence, likewise the sequence of Ionia Zone ends with the presence of the flysch. These are clay exchanges, marls, sandstones, siltstones and conglomerates, starting from their deposition in the Eocene, which also reflects its change sedimentation from carbonate to clastic (appearance of Pliocene deposits and Quaternary deposits). It is observed that a wide range of faults in its northwestern and southeastern parts of study area with dominant directions W-E, N-S and SW-NE respectively. The majority of faults occurring within the boundaries of our study area are recorded in the carbonate series and in alluvial deposits.

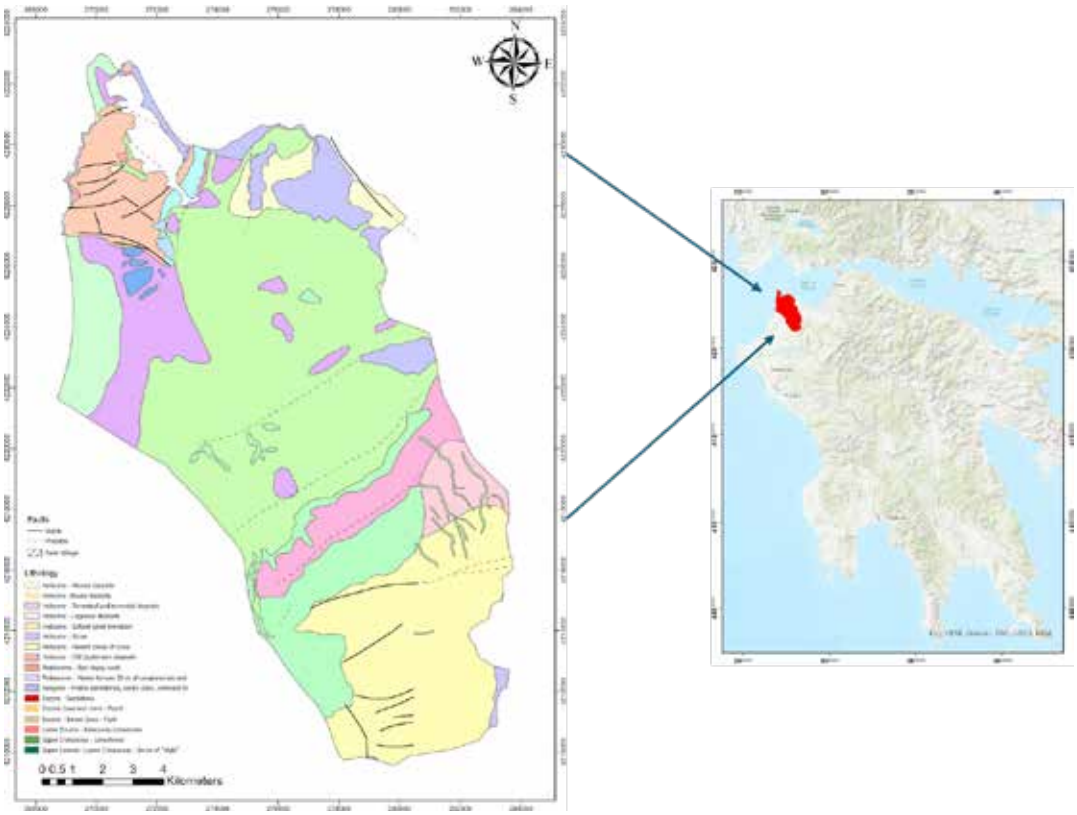

Figure 1. Geological map of study area (modified from I.G.M.E., 1977-1980)

Materials and methods

This is one of the most important parameters in the methodology DRASTIC (Table 1) as it determines the time required until the pollutant reaches the aquifer. Great depth of groundwater indicates a long-time transport interval of the contaminant in the groundwater and sufficient thickness of it unsaturated zone resulting in the weakening of the pollutant and the greater aquifer protection. The hydrological parameters that are widely used for the application of the method in areas with granular formations is seven in number and are also the acronyms of the term DRASTIC and are as follows:

The DRASTIC index is calculated as follows:

DI=DrDw+RrRw+ArAw+SrSw+TrTw+IrIw+CrCw

r index is the value of the parameter

w index is the weight of each parameter

Table 1. DRASTIC weighting and ratings for every DRASTIC parameter (Aller et al., 1987)

Parameters	Interval	Rating	Weight
D (m)	0-1,5	10	5
	1,5-4,5	9	
	4,5-9	7	
	9-15	5	
	15-23	3	
	23-30,5	2	
	>30,5	1	
R (mm/year)	>254	9	4
	178-254	8	
	102-178	6	
	51-102	3	
	0-51	1	

A	Massive shale	2	3
	Metamorphic/Igneous Weathered	3	
	Metamorphic/Igneous Glacial Till	4	
	Bedded Sandstone	5	
	Limestone and Shale sequences	6	
	Massive Sandstone	6	
	Massive Limestone	6	
	Sand and Gravel	8	
	Basalt	9	
	Karst Limestone	10	
S	Thin or absent	10	5
	Gravel	10	
	Sand	9	
	Laterite / peat	8	
	Shrinking and/ or aggregated clay	7	
	Sandy loam	6	
	Loam	5	
	Silty Loam	4	
	Clay Loam	3	
	Muck	2	
	Non-shrinking and non-aggregated clay	1	
T (%)	0-2	10	3
	2–6	9	
	6–12	5	
	12–18	3	
	>18	1	
I	Karstified limestone	10	3
	Βασάλτης	9	
	Sand and gravel	8	
	Άμμοι και χαλίκια με σημαντικό ποσοστό ιλύος και αργίλου	6	
	Στρωματώδης ασβεστόλιθος, ψαμμίτης σχιστή άργιλος	6	
	Sandstone	6	
	Limestones	6	
	Μεταμορφωμένα/ Πυριγενή	4	
	Σχιστή άργιλος	3	
	Clay	2	
	Confined aquifer	1	
C (m/day)	>81,6	10	2
	40,8-81,6	8	
	28,56-40,8	6	
	12,24-28,56	4	
	4,08-12,24	2	
	0,04-4,08	1	

Results and discussion

This work analyzed the DRASTIC model to accurately and effectively assess groundwater vulnerability (Ozegin et al., 2024). The primary factor influencing aquifer vulnerability is water table depth, which is the height between the thickness of subsurface earth components and the water level (Rahman, 2008). The distribution of the parameter in the bounded area differs from point to point, as seen in the groundwater depth thematic map (fig. 2a). Low values of the depth are observed in the NE part of the area, while the high values of this dominate the SW side of the watershed. Moreover, high recharge indicates a higher

vulnerability to contamination. This is due to the fact that increased internal water movement could transport more pollutants (Jesiya and Gopinath, 2019). High values of recharge dominate in the NW part of the watershed, on both sides the lagoon Kalogria, characterized by gentle slopes and the heavy rains (fig. 2b). Conversely, low values of R occur in the NE, NW and N part of the study area, with its prevailing large slopes and small amounts of rain. Aquifer media are different kinds of geological formations that serve as pathways for the transmission and storage of water. The aquifer's media shows a lower vulnerability to groundwater when the grain size is smaller (Saha and Alam, 2014). The distribution map of parameter A the prevailing type of aquifer in the study area is lithological consisting of sand and gravels (fig. 2c). As most of the area consists of the specific combination of materials, the study area calibrated mainly with 8. However, the study area indicates different aquifer material. In the NW part of the watershed karstified limestone and sandstone layers are noted and limestones with layers of clay in the southern part of it. The study area at these positions is rated with 10 and 6 respectively. The soil media affect the area's replenishment and have a greater impact on the movement of contaminants across the geologic layers (Bhuvaneswaran and Ganesh, 2019). In the case of this parameter, the data is not sufficient and consequently the map of soil cannot be carried out. An inclined gradient angle increases the intensity of water discharge and reduces pollution susceptibility, but a small slope angle supports significant contaminat migration with water, which is absorbed through a vertical channel (Ozegin et al., 2024). According to the map of the T parameter the study area in almost its entire extent is represented by gradients >18%, so it is rated as 10 (fig. 2d). However, the distribution of slopes it is different in the NW and SE part of the watershed and in a limited part of that in the NE, because of the increase in altitude. Also, with the territory of gentle slopes favoring active infiltration. The domain that extends before the water table and is an aeration zone is known as the vadose zone (Ahmed et al., 2015). For the study area, in the case where clay minerals dominate in the unsaturated zone and its thickness is large, the length of time the contaminant remains in the unsaturated zone increases and this results in its weakening and preventing the infiltration to the groundwater. According to the results are observed 3 different lithologies (fig. 2e). Almost completely the unsaturated zone in the watershed of Larissos consists of sand and gravel with significant percentage of silt and clay. Also at the center of it are places where the unsaturated zone consists of sand and gravel and the value of parameter is 8. On the contrary, to the west of the watershed is observed the value 3, indicating that the material of the unsaturated zone is detailed. By indicating the aquifer's capacity to transport water, C affects the rate at which contaminated material moves through the groundwater system (Aller et al., 1987). In addition, the size of an unconsolidated aquifer's pores and the interconnected of its intergranular void spaces affect its hydraulic conductivity. As particle size increases, hydraulic conductivity decreases (Ozegin et al., 2024). High water values hydraulic conductivity corresponds to high values of water permeability. The different calibration of values is shown in while the distribution of the parameter in the watershed is shown with the distribution map (fig. f).

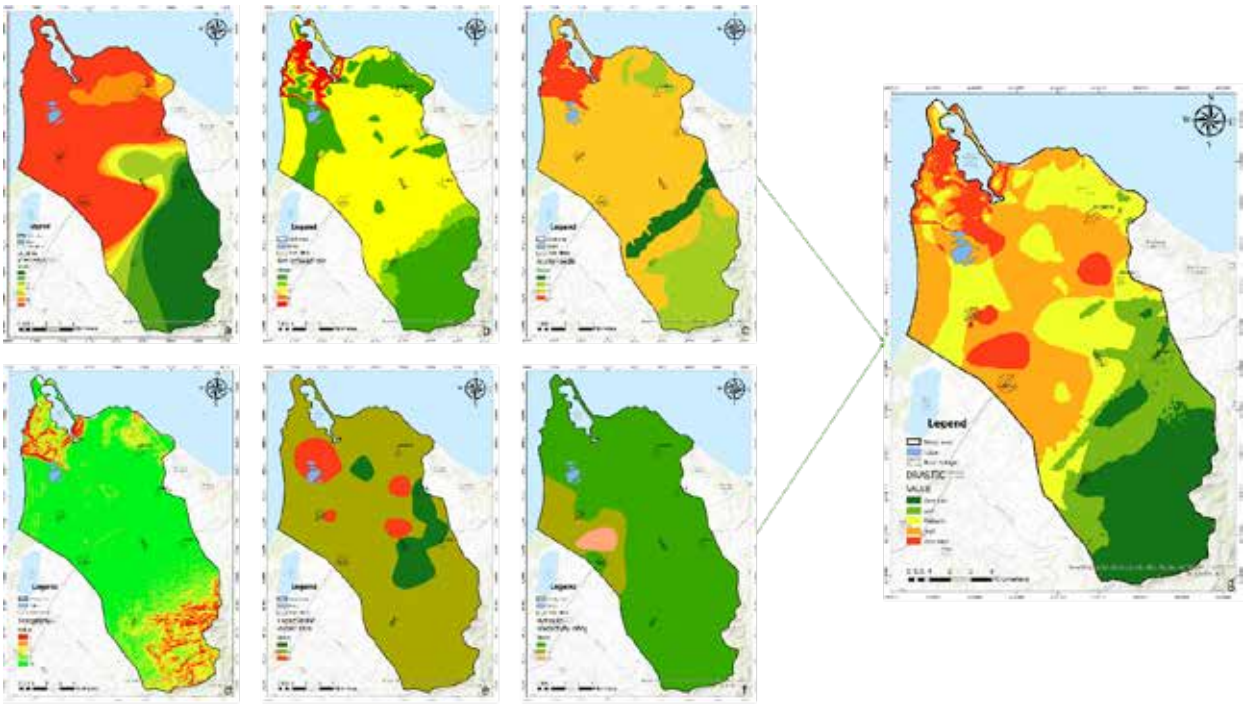

Figure 2. (a) Map of depth to groundwater; (b) Map of net recharge rate; (c) Map of aquifer media; (d) Map of topography; (e) Map of impact of the vadose zone; (f) hydraulic conductivity rating; (g) Map of DRASTIC method

Conclusions

It is crucial and necessary for investigation into the vulnerability of aquifers, which are groundwater resource systems. Throughout the research area, aquifer formations are still in risk from pollutants that are both naturally occurring and caused by humans. The results of six distribution maps, which correspond to the six parameters of the DRASTIC methodology contributed to the drafting of the final DRASTIC map (fig. 1g) that indicates the distribution of its vulnerabilities study area in terms of external pollutant. The maps were produced using the ArcGIS Pro program as well as the value of the gravity of each parameter. According to the final vulnerability map almost completely the SW part of the watershed it appears in green as the least sensitive part of the study area. This is reasonably explained as this section characterized by a large depth of the aquifer, high slopes, low rainfall and clay material that is impermeable, preventing the infiltration of the pollutant. Instead, highly vulnerable positions within it defined area are in red in the NW part of it, on both sides of the Kalogria lagoon, and in some places in the central part of the basin, which are characterized by gentle slopes, shallow depth of groundwater, intense rainfall and the presence of karstic limestone. The above features favor active recharge and the infiltration of pollutants. Finally, the other areas in the central and NW extent of the study area are characterized by high to moderate vulnerabilities as well present intermediate characteristics. Due to its ability to adapt to specific hydrogeology and human (land use) factors, this model-based technique can be used to study and manage groundwater resources. The pollution hazard map provides the data sets and model predictions required for land use and water resource management and strategic planning.

References

Ahmed, I., Nazzal, Y., Zaidi, F.K., Al-Arifi, N.S.N., Ghrefat, H., Naeem, M., 2015. Hydrogeological vulnerability and pollution risk mapping of the Saq and overlying aquifers using the DRASTIC model and GIS techniques, NW Saudi Arabia. Environ Earth Sci 74, 1303–1318. https://doi.org/10.1007/s12665-015-4120-5

Aller, L., n.d. DRASTIC: A STANDARDIZED SYSTEM FOR EVALUATING GROUND WATER POLLUTION POTENTIAL USING HYDROGEOLOGIC SETTINGS.

Aller, L., Lehr, J.H., Petty, R., Bennett, T., 1987. Drastic: A Standardized System to Evaluate Groundwater Pollution Potential using Hydrogeologic Setting. Journal Geological Society of India 29, 23–37. https://doi.org/10.17491/jgsi/1987/290112

Bhuvaneswaran, C., Ganesh, A., 2019. Spatial assessment of groundwater vulnerability using DRASTIC model with GIS in Uppar odai sub-watershed, Nandiyar, Cauvery Basin, Tamil Nadu. Groundwater for Sustainable Development 9, 100270. https://doi.org/10.1016/j.gsd.2019.100270

Iqbal, J., Gorai, A.K., Katpatal, Y.B., Pathak, G., 2015. Development of GIS-based fuzzy pattern recognition model (modified DRASTIC model) for groundwater vulnerability to pollution assessment. Int. J. Environ. Sci. Technol. 12, 3161–3174. https://doi.org/10.1007/s13762-014-0693-x

Jesiya, N.P., Gopinath, G., 2019. A Customized FuzzyAHP - GIS based DRASTIC-L model for intrinsic groundwater vulnerability assessment of urban and peri urban phreatic aquifer clusters. Groundwater for Sustainable Development 8, 654–666. https://doi.org/10.1016/j.gsd.2019.03.005

Kazakis, N., Voudouris, K.S., 2015. Groundwater vulnerability and pollution risk assessment of porous aquifers to nitrate: Modifying the DRASTIC method using quantitative parameters. Journal of Hydrology 525, 13–25. https://doi.org/10.1016/j.jhydrol.2015.03.035

Ozegin, K.O., Ilugbo, S.O., Adebo, B., 2024. Spatial evaluation of groundwater vulnerability using the DRASTIC-L model with the analytic hierarchy process (AHP) and GIS approaches in Edo State, Nigeria. Physics and Chemistry of the Earth, Parts A/B/C 134, 103562. https://doi.org/10.1016/j.pce.2024.103562

Rahman, A., 2008. A GIS based DRASTIC model for assessing groundwater vulnerability in shallow aquifer in Aligarh, India. Applied Geography 28, 32–53. https://doi.org/10.1016/j.apgeog.2007.07.008

Saha, D., Alam, F., 2014. Groundwater vulnerability assessment using DRASTIC and Pesticide DRASTIC models in intense agriculture area of the Gangetic plains, India. Environ Monit Assess 186, 8741–8763. https://doi.org/10.1007/s10661-014-4041-x

Udosen, N.I., George, N.J., Ekanem, A.M., 2024. Aquifer vulnerability valorization via DRASTIC index-based assessment within litho-facies of a coastal environment. Results in Earth Sciences 2, 100033. https://doi.org/10.1016/j.rines.2024.100033

Zghibi, A., Merzougui, A., Chenini, I., Ergaieg, K., Zouhri, L., Tarhouni, J., 2016. Groundwater vulnerability analysis of Tunisian coastal aquifer: An application of DRASTIC index method in GIS environment. Groundwater for Sustainable Development 2–3, 169–181. https://doi.org/10.1016/j.gsd.2016.10.001

17th INTERNATIONAL CONGRESS of the Geological Society of Greece

BULLETIN OF THE GEOLOGICAL SOCIETY OF GREECE, SP. PUBL.

EXTENDED ABSTRACT 245

RescueME, a Research Action that focuses on the enhancement of the resilience of coastal cultural landscapes in Europe. The case study of Psiloritis UGGp, Crete, Greece

C.Papailiou[1], M. Kolendrianou[2] C. Fassoulas[1,3]

(1) Psiloritis UGGp, Crete, Greece, cpapailiou@psiloritisgeopark.gr , (2) Psiloritis UGGp, Crete, Greece, info@psiloritisgeopark.gr , (3) Natural History Museum, Univ. of Crete, Crete, Greece, bfassoulas@gmail.com

Research highlights

How can we protect European cultural heritage from climate change, natural hazards and other stressors such as pollution and over-tourism?

Introduction

RescueME (Resilient Cultural Landscapes) is a Research project funded by the Horizon Europe programme where five Resilience Landscape Laboratories (R-labscapes) are working with 12 consortium research and technology partners to create new approaches of protecting coastal cultural heritage and landscapes, implementing innovative resilience solutions and culture-focused strategies. The project started in February 1st, 2023, lasts for 42 months and focuses on the enhancement of the resilience of coastal cultural landscapes (CLs) in Europe.

The five case studies (Psiloritis UGGp in Greece, the island of Neuwerk in Germany, Portovenere, Cinque Terre & the Islands in Italy, L'Horta in Spain, and the city of Zadar in Croatia) have been selected carefully as complementary representatives of European coastal landscapes. They act as resilience landscape laboratories (R-labscapes) to validate the results and ensure their replicability. For these five target areas, RescueME is going to produce digital tools and innovative solutions for climate change adaptation and natural disaster risk management.

Regarding Psiloritis UGGp located at the island of Crete, Greece, planned actions focus on shielding of its northern coast (parts of the Municipalities of Mylopotamos & Rethymnon) from the impacts of extreme weather phenomena such as heatwaves, droughts, water shortages and, secondarily, floods. Also, Psiloritis UGGp has set as priority to enhance heritage resilience, raise awareness among local stakeholders and make RescueME project results actionable in the local framework.

Common heritage is a central element of our communities and economies, and a principal but vulnerable dimension of our common identity as Europeans. It has been proven that cultural heritage contributes to well-being, social cohesion, identity, local economy, territorial attractiveness, and environmental sustainability (European Commission, 2021), but the climate crisis and natural hazards threaten this heritage. RescueME is going to take immediate action to demonstrate how an innovative data-driven, community-based and heritage-centric actionable landscape approach for resilience enhancement can protect our cultural heritage and landscapes, while supporting the transition toward a green society and economy that sustains resilient, cohesive, nature-connected communities. RescueME proposes a call for broadening the scope, triggering actions, untapping and mobilizing resources, engaging actors, and facilitating the decision making and the implantation of co-created just resilience solutions to protect our common heritage.

RescueME is developing, testing and demonstrating the effectiveness of an Actionable Framework based on the Resilient Historical Landscape approach (RHL) complemented by data, models, methods, and tools able to assess risks and opportunities, co-develop inclusive and just resilience strategies and innovative solutions to protect European cultural heritage and cultural landscapes from climate change, disaster risk, as well as other stressors (such as pollution and over-tourism) with special focus on European coastal landscapes (FUNDACION TECNALIA RESEARCH & INNOVATION, 2023).

Methodology

Figure 1: Map of RescueME area. This area applies to the semi-mountainous and lowland part of the Municipality of Mylopotamos as well as part of the old Municipality of Arkadi of the current Municipality of Rethymno.

For project implementation, the study area of Psiloritis UGGp (Figure 1) has been determined as well as the main hazards the area faces due to climate change, while stakeholder task forces have been set. These, comprise of local CCSIs (Creative & Cultural Sectors and Industries) and other businesses, experts with local knowledge, researchers as well as civil society, and participate in the co-creation process of the project that entails the collaborative engagement of diverse local stakeholders in the development of resilience measures and strategies in the R-labscape.

For the purpose of co-creation of local measures and solutions, these local stakeholders have already been engaged in an intensive Resilience Baseline Assessment for a better understanding of the local knowledge/awareness. The assessment has been conducted via a questionnaire of 78 quantitative and qualitative questions which was distributed amongst targeted users as well as stakeholders based on the RescueME indicator approach. This approach implements a GLOCAL (global and local) strategy blending global and local factors alongside top-down and bottom-up approaches, as well as the adoption of the concepts of Socio-Ecological Systems (SES) and a landscape approach, as described in the Deliverable “Actionable framework for resilient historic landscapes”. By this way, weak spots and strong points have been identified in Psiloritis R-labscape and the most appropriate approach is going to inform the co-creation of resilience measures.

Stakeholders have also participated in two “impact chain” workshops (Impact Chains) to address the impacts from heatwaves and temperature rise and possible adaptive measures, on the sectors of agriculture and tourism. At a first step, these impact chains identified first the main hazards that threat the R-labscape, analyzed the potential capitals (build, natural, cultural, economic, social etc.) that might be affected, and determined the specific impacts that might occur. In a second step, the focus was concentrated on the impacts in tourism and agricultural activities, identifying the vulnerabilities, the weaknesses and the potential drivers for enhancing local resilience.

Based on the Impact Chains, a predictive impact model which is going to be defined to model and quantify the impacts of the considered hazards and stressors, specifically addressing the aspects of ecosystems services and local heritage values. Especially in Psiloritis UGGp, the model is going to focus on the impact of changes in temperature and precipitation patterns on agriculture and tourism. As a start, a Multiscale risk and resilience assessment of the

R-labscape has been developed through a questionnaire and bilateral meetings with the R-labscape in order to analyze the possibilities of the development of the final model. Following, local quantitative data have been selected, such as the population number of the area, tourism turnover in euros and agricultural area in m^2 etc., in order to have a selection of indicators for the spatial analysis of the impact model.
After thorough analysis of the results obtained by the Impact Chains, the Resilience Baseline Assessment and the Multiscale risk and resilience assessment a long list of issues and common findings between them was created by the relevant work package leaders which were categorized in capitals and key elements according to the SES Framework. This list was validated by the R-labscape in order to understand what matters most and what needs to be addressed urgently to enhance resilience. Currently, resilience issues have been further categorized in a reduced list and prioritized via a prioritization exercise by assessing their impact on resilience, complexity and effort required to address them. By this way, the Psiloritis UGGp focuses on the most critical issues when co-creating resilience measures and solutions.
Moreover, a RescueME resilience meta-repository as well as local policy tools have been created which show existing knowledge and solutions on community- or system-based resilience in order to define measures, solutions and conditions to guide Cultural Landscapes in building their transformative resilience strategies. Also, RescueME research partners are starting the development of the first steps of a social innovation and co-creation tool, the Resilient Landscapes Serious Game for resilience strategy development. By this way, compatible solutions are going to be adapted in a local context with in-person workshops with local stakeholders. Currently, the structure of the game Board mock-up game, game steps, resilience strategy objectives and possible scenarios are being built.
RescueME aims, also, to deliver a set of advanced digital solutions, easily accessible through a single application portal (RescueME One-stop Shop). The design and development of all foreseen digital solutions will follow a human-centred approach, based on a common set of definitions, including a comprehensive multi-scale data model. The digital solutions will include a geospatial and interoperable Data Lake, a geospatial Data Intelligent Platform for heterogeneous data aggregation, processing, and visualization, and a set of AI-based tools and solutions (crowdsourcing, satellite mapping, AR app). Currently, in order to deliver a set of advanced digital solutions, social media posts are being analyzed and available local actionable data sources are being gathered to be inserted in a Data Lake of AI based tools. Also, already calculated by Psiloritis UGGp geographical, demographic and, economic data at the Multiscale risk and resilience assessment phase, are going to be selected and displayed through the Geospatial Data Intelligent Platform, to allow the users further use of such data sources if necessary.
Last but not least, the project is going to produce a digital One-Stop-Shop (OSS) that will include advanced tools for the protection and promotion of coastal cultural landscapes of Europe.

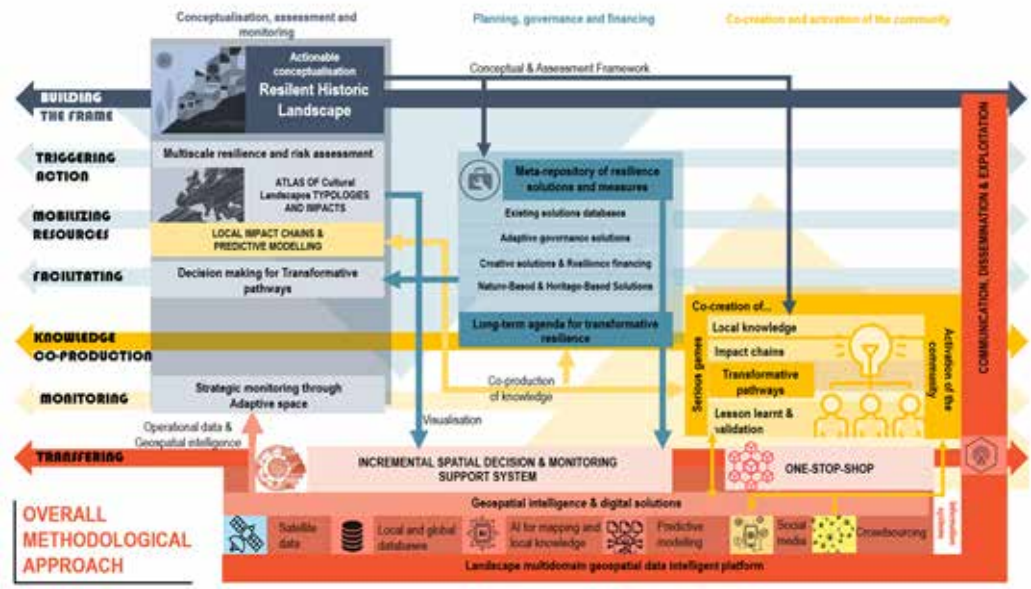

Figure 2: RescueME methological approach

For all the above, the RescueME methodological approach (Figure 2) interconnects the conceptualisation of approaches and quantification of values and impacts with the development of resilience solutions and measures to create long-term transformative strategies. From a bottom-up approach, these strategies are being co-created with the R-labscapes and for the top-down approach, they are implemented in the decision-making tools to facilitate the transference.

Results

Key conclusions have been drawn by the local stakeholders at the two local Impact Chains. In specific, on 11th October 2023, at the 1st Impact Chain, 13 local stakeholders from the public and private sector gathered at Panormos in Crete in an interactive group session to discuss how they perceive the existing and potential future climate-related hazards in the region. The workshop's results revealed how the selected area's climate-related hazards, such as the rise of winter temperatures, may cause impacts on agriculture, culture, ecosystems, infrastructure, people, tourism and Crete's economy. At the same time, the participants' discussions explored how the impacts are affected by exposed elements of the Cultural Landscape, apparent sensitivities and capacities in these sectors. Therefore, the workshop concluded in an effort by the stakeholders to propose potential adaptation measures. For instance, the rise of winter temperatures may cause diseases that affect both livestock and agricultural production as well as public health. As a sub-effect, less products are available on the market, the income is getting lower, the welfare state gets weakened and rural communities are being abandoned. At the same time, there is an apparent sensitivity: the lack of civic engagement and participation of citizens in planning & implementation. Workshops/seminars were, therefore, proposed for good practice exchange at the local level.

On 2nd February 2024, at Aggeliana in Crete, a deeper review and analysis of the same topic was made by 12 different local stakeholders from targeted sectors. This time, the focus of 2nd Impact Chain was only on agriculture and tourism, since these are the main driving forces in the economy of Crete. At that workshop, new adaptation measures were also addressed. For instance, climate related hazards such as heat waves may increase the time spent inside hotel units, the energy and water consumption but also reduce travel agencies income due to the lack of tourist mobility. The promotion of off-season alternative tourism could be one of the adaptation measures.

Figure 3: Impact Chain Workshop 2

This task supported the next steps of the project along with the results obtained by the Resilience Baseline Assessment and the Multiscale risk and resilience assessment developing the list of all related resilience issues. As a result, the prioritized list of issues has been created in order to focus on the issues which are most critical for the co-creation of resilience measures and solutions, having in mind the main co-creation aims of Psiloritis UGGp (enhancing heritage resilience, raising awareness among stakeholders and making RescueME project results actionable in the local framework). Examples of those issues include the lack of agricultural training which may pose challenges in terms of implementing sustainable farming practices, adopting modern agricultural techniques and ensuring the long-term viability of traditional farming methods. This is of relatively high impact but also feasible to address. Also, climate impacts on crop productivity and water resources may pose concerns regarding water availability and management, highlighting vulnerabilities to drought and over-pumping with significant risks to agricultural productivity and livelihoods, a challenge highly complex but also with a high impact if addressed. Lastly, facing the reduced attractiveness of the destination for tourists due to the impacts of natural hazards on the cultural landscape (e.g. coastal erosion), human health (heatwaves) and recreational outdoor activities, may become a "Big Project" having relatively high impact, requiring also to address quite intensive resource efforts.

All these actions are part of a long co-creation and decision-making process that is taking place with the collaboration of project partners and local actors in order to enhance the common heritage resilience from climate change, natural hazards and other stressors.

Acknowledgements

This study is funded under the EU's Horizon Europe, key funding programme for research and innovation, with title: "Equitable RESilience solutions to strengthen the link between CUltural landscapEs and coMmunitiEs", Grant agreement ID: 101094978. We would like to thank all those technical and research partners of the project who make a vast contribution for the success of this on-going research.

References

European Commission, 2021, Culture and the Sustainable Development Goals: Challenges and Opportunities [Voices of Culture Brainstorming Report]

FUNDACION TECNALIA RESEARCH & INNOVATION, 2023, "Equitable RESilience solutions to strengthen the link between CUltural landscapEs and coMmunitiEs", Grant Agreement ID: 101094978, – RescueME - Part B – 7 [Research Project under EU's Horizon Europe funding programme]

17th INTERNATIONAL CONGRESS of the Geological Society of Greece

BULLETIN OF THE GEOLOGICAL SOCIETY OF GREECE, SP. PUBL.

EXTENDED ABSTRACT 246

Innovative Efforts in Geotourism: The Vikos-Aoos UNESCO Global Geopark

Haritakis Papaioannou[1], Christos Stergiou[2], Spiros Staridas[1], Aristotelis Stagkikas[1], *Georgia Kitsaki[1]*

[1]Vikos-Aoos UGGP – Development Agency of Epirus S.A. (EPIRUS S.A.), 45332, Ioannina, Greece, h.papaioannou@epirussa.gr; [2]School of Geology, Aristotle University of Thessaloniki, 54124, Thessaloniki, Greeece

Introduction

To enhance geotourism and public awareness, the Vikos-Aoos Geopark launched the "Enhancement of Geosites and Geological Formations" project (2022–2024). This initiative integrates modern technology and infrastructure to improve visitor experience and promote sustainable tourism. Key components include a mobile app offering interactive geological and cultural content, visitor centers providing in-depth interpretation, and outdoor viewing platforms showcasing geosites through strategic placements and aerial imagery. Additionally, a visitor tracking system at eight major sites has provided valuable data on geotourism trends. These efforts strengthen conservation-focused tourism and serve as a model for balancing heritage preservation with visitor engagement.

Methods

The Vikos-Aoos Geopark, in collaboration with the Hellenic Ministry of Environment and Energy, has undertaken a comprehensive initiative to enhance geotourism, visitor engagement, and public awareness of its geological heritage. This project, titled "Enhancement of Geosites and Geological Formations and Evaluation of Visitability of Geosites and Landscapes of High Aesthetic Value in Vikos-Aoos UNESCO Global Geopark", is funded by the Natural Environment & Climate Change Agency (N.E.C.C.A.) under the framework of a cooperation memorandum signed between N.E.C.C.A. and the Hellenic UNESCO Global Geoparks Forum in 2022. Spanning from 2022 to 2024, the project implements a strategic, multi-faceted approach to improving visitor services and sustainable tourism development.

The first major action (Action 1) of the project focused on enhancing information and geosite interpretation services through the development of a web-based digital mapping application. Designed for use both within visitor centers and on mobile devices, this platform allows for interactive exploration of the Geopark's geological, environmental, and cultural heritage. The application provides dynamic, user-friendly access to geosite data, enabling visitors to engage with scientific information through maps, multimedia content, and interactive tools.

The second action (Action 2) centered on the installation of Outdoor Viewing Spots (OVS) at carefully selected locations within the Geopark. These platforms were strategically placed to highlight key geosites and landscapes of high aesthetic value, offering visitors enhanced vantage points to appreciate and understand the region's unique geomorphology. This intervention not only improves the geotourism experience but also reinforces the Geopark's educational mission by making significant geological formations more accessible and visually interpretable.

The third action (Action 3) involved the installation and operation of a visitor counting system, aimed at collecting real-time data on tourist activity within the Geopark. By monitoring visitor numbers across key sites, this system provides valuable insights into seasonal tourism trends, site popularity, and the overall impact of geotourism initiatives. The collected data supports future planning efforts, ensuring that conservation strategies align with sustainable tourism growth. Together, these actions contribute to a more immersive and informative visitor experience while supporting the long-term management and conservation goals of the Vikos-Aoos UNESCO Global Geopark.

Results

Action 1 was titled "Improvement of Information and Geosite Interpretation Services" and was implemented to enhance the educational and awareness-raising capacity of the Vikos-Aoos Geopark, two modern Information Centers were established (Action 1.1) in the municipalities of Zagori (Vitsa) and Konitsa. These centers serve as key hubs for visitors, providing structured insights into the Geopark's geological, environmental, and cultural heritage. Their design prioritizes accessibility and engagement, utilizing modern technology to improve visitor interaction with geosite information. By centralizing interpretive resources, these centers strengthen the Geopark's role as an educational destination, promoting geotourism and fostering appreciation for natural landscapes.

A web-based digital mapping application was developed (Action 1.2) to complement the Information Centers and extend accessibility to geosite data (Figure 1a-d). This interactive platform presents the entirety of the Geopark's

geological, cultural, and environmental assets through a user-friendly, two-dimensional map. Accessible via web browsers on desktop and mobile devices, the application allows users to navigate geosites, explore categorized information on geoheritage, culture, and geotourism, and interact with multimedia content. Developed in collaboration with geologists, biologists, and historians, the platform ensures scientifically accurate and engaging content delivery. Its digital format modernizes geosite interpretation, allowing visitors to plan their routes, visualize geodiversity, and interact with the Geopark's rich heritage beyond the physical boundaries of the information centers.

To maximize the effectiveness of these digital tools, specialized IT equipment was installed (Action 1.3) at both Information Centers (Figure 1a,b). In Konitsa, a digital presentation screen wall system, an interactive info kiosk, and a dedicated computer provide visitors with dynamic, on-demand access to geosite information (Figure 1a,b). Similarly, the Vitsa Information Center features a digital screen wall system, a smart interactive table, and a computer, fostering an immersive educational experience (Figure 1c,d). These installations modernize the visitor experience by integrating smart technology into geotourism services, enabling real-time exploration of geological data and supporting sustainable tourism development in the Geopark.

Figure 1. Examples of the specialized IT equipment installed in the Informations Centers at Konitsa and Vitsa. a, b. The digital screen wall systems installed at Konitsa projecting the web-based digital mapping application developed for the Vikos-Aoos Geopark. c. Top view of the smart interactive table at Vitsa. d. The smart interactive table during installation at Vitsa.

To enhance visitor engagement and raise awareness about the geological and geomorphological features of the Vikos-Aoos Geopark, a series of outdoor viewing areas were installed at carefully selected locations, under Action 2: "Installation of Outdoor Viewing Areas at Significant Geosites in Landscapes of High Aesthetic Value". These viewing platforms were designed to provide strategic vantage points where visitors could appreciate geosites, geological formations, and landscapes of exceptional beauty while simultaneously accessing educational interpretative panels. The primary goal of this initiative was to merge the aesthetic appreciation of these landscapes with scientific knowledge, helping visitors understand the forces that shaped the region.

Each outdoor viewing area features a specialized prefabricated canopy structure equipped with exhibit panels that highlight key geological, environmental, and cultural aspects of the surrounding landscape. The structures maintain a uniform design, but the content of each panel is tailored to the specific geosite, ensuring site-specific interpretation. The panels, measuring three meters in length, present information in both Greek and English and include photographs, diagrams, and explanatory texts. The selection of these locations was based on their scientific, educational, and touristic value, ensuring that visitors have access to some of the most iconic geological features within the Geopark. Three major outdoor viewing areas were established at critical geosites, two in the eastern-southern section of the Geopark (Municipality of Zagori) and one in the western-northern section (Municipality of Konitsa). Each location was selected to showcase significant geological formations, offering visitors an immersive experience that blends scenic beauty with

scientific exploration.
The first outdoor viewing area, located at Kapesovo fault (geosite 12) and the Stone Stairway of Vradeto, provides a remarkable perspective of the Kapessovo fault and its role in shaping the regional geomorphology. The mountainous landscape of Tymfi, composed primarily of limestone formations dating from 145 to 15 million years ago, is revealed through aerial photographs and diagrams. The interpretative panel at this site highlights nine distinct geological features, including the effects of glacial activity during the Pleistocene epoch, which sculpted the area's characteristic U-shaped valleys (Telbisz *et al.,* 2019). Visitors can gain insight into the tectonic and erosional forces that shaped the terrain while admiring the rugged beauty of the surrounding cliffs and gorges.
The second viewing area, is related to the Voïdomatis river Valley and Astraka Fault (geosite 9), offers a spectacular panoramic view of the Vikos Gorge and the surrounding mountain formations. The Towers of Papigo, a striking set of vertical limestone formations, dominate the landscape, shaped by the Astraka fault and karstic erosion processes (Chatzipetros *et al.,* 2024). This site also provides insight into the hydrological system of the Voidomatis river, which emerges from the karst springs of Mount Tymfi before flowing towards its confluence with the Aoos river. The exhibit panel at this location presents nine key geological features, allowing visitors to explore the interplay between faulting, river dynamics, and mountain-building processes.
The third viewing area, positioned at Prophet Elias Hill (1071 m) near Konitsa fault (geosite 8), provides an unparalleled panoramic view of the Konitsa plain and the surrounding mountain ranges. This location offers vistas of Lapatos, Trapezitsa, Gamila, and Astraka, with the Aoos river flowing through the valley, shaping the landscape through continuous erosion and sediment deposition. Visitors can trace the 24-km long Konitsa fault and learn about the structural features of this active seismogenic fault (Chatzipetros *et al.,* 2024). Furthermore, they can explore the sedimentary processes of the Aoos river, learn about the sulfur caves of Sarantaporos river valley and admire the Smolikas (2497 m) and Gamila (2497 m) peaks (Lazaridis *et al.,* 2024). The panel here showcases seven distinct geological features, explaining how the tectonic forces responsible for the formation of the Konitsa fault have influenced the region's topography. From this vantage point, visitors can also observe the Nemerçika mountain range, marking the natural border between Greece and Albania, as well as the ophiolite peaks of Smolikas (2637 m), Greece's second highest mountain.
These outdoor viewing areas provide an unparalleled opportunity to connect with the geological past while enjoying breathtaking landscapes. Visitors gain a deeper appreciation of the region's dynamic geological history, from ancient fault movements and glacial sculpting to modern river systems and ongoing erosional processes. By merging scientific interpretation with stunning natural beauty, these installations reinforce the Geopark's mission of education, conservation, and sustainable geotourism, offering an immersive and enriching outdoor experience.
The third action implemented under this project was tilted "Installation and Operation of a Visitor Counting System at Geosites". Its scope was to effectively manage visitor traffic and ensure sustainable tourism in the Vikos-Aoos Geopark. A visitor counting system was installed at key geosites and geomorphological formations (Figure 3a-c). This system aims to collect data on the number of hikers in specific areas, such as the Vikos and Aoos Gorges and the Dragon Lakes of Tymfi and Smolikas. By analyzing visitor numbers and movement patterns, park authorities can develop informed strategies for conservation, infrastructure planning, and visitor experience enhancement. The system utilizes passive infrared sensors to count visitors discreetly. Counters were placed at eight strategic locations along major hiking trails, ensuring coverage of high-traffic areas like the Vikos Gorge and its branches, the Aoos Gorge, and popular scenic viewpoints such as the Oxya (Stone Forest) in Monodendri. These bidirectional sensors not only track the number of hikers but also identify their direction of movement (Figure 4a). Additionally, the counting data can be co-evaluated in relation with real time weather and extract information on how weather may affect or not visitor traffic (Figure 4b). The collected data is transmitted to a central unit, where it is processed using specialized software for further analysis. The placement of the sensors was carefully designed to minimize their visual impact on the natural landscape while maintaining accurate and reliable data collection (Figure 3a,c).
A significant example of the system's effectiveness is the monitoring of visitor numbers at the Agkastromeni Spring (geosite 4), located at the exit of the Vikos Gorge (Figure 4a). This site marks the main springs of the Tymfi karst system, where water emerges from limestone and dolomitic limestone formations with black chert. The spring, formed due to the Astraka fault, has an intermittent flow that varies with seasonal water availability. Nearby, an 18th-century church, once a monastery, serves as a cultural landmark and a resting point for hikers. The results from the counter at this site indicate that approximately 16,000 visitors pass through annually, with a steady flow throughout the year. The highest visitor numbers occur on weekends and holidays, peaking during the summer and early autumn months, particularly in August, when around 4,000 hikers visit the site.
The implementation of the visitor counting system provides invaluable insights into hiking trends and seasonal variations in visitor traffic. This data will help park managers maintain a balance between accessibility and conservation, ensuring the long-term protection of the geopark's natural and cultural heritage while enhancing the visitor experience.

Figure 2. a. The interpretive panel at viewpoint located opposite to the Kapesovo fault and the participants of the Vikos-Aoos Geopark re-evaluation (July, 2024).

Figure 3. a. Detail of the counting system that was installed at key geosites and geomorphological formations. b. Field work photograph during the installation of the system. c. Detail of the rugged case protecting the logging-transmitting digital apparatus.

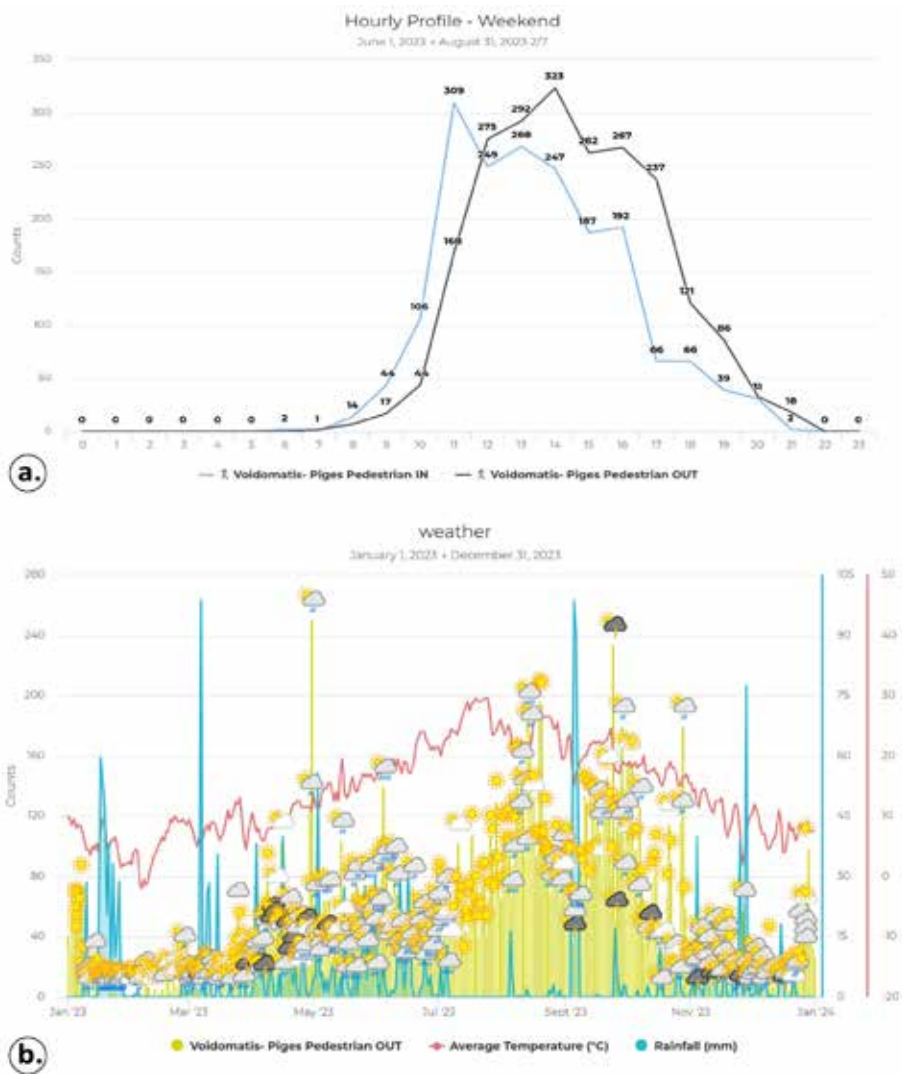

Figure 4. a. Diagram showing the hourly allocation of incoming and out coming visitors to the Agkastromeni spring of Voidomatis river. b. Visitors counts coupled with weather conditions from January 2023 to January 2024.

Conclusions

The implemented actions in the Vikos-Aoos Geopark enhance visitor experience while promoting geoconservation and awareness. The outdoor viewing areas provide panoramic insights into key geosites, while the new interpretation panels educate visitors on geological processes shaping the landscape. Additionally, the visitor counting system enables sustainable management by monitoring foot traffic across major trails. These efforts contribute to preserving the park's natural and cultural heritage while fostering appreciation for its geological significance. Through these initiatives, the Geopark strengthens its role as a model for responsible geotourism and environmental stewardship.

Acknowledgements

Authors would like to thank the Natural Environment and Climate Change Agency (NECCA) for founding the project.

References

Chatzipetros, A., Stergiou, C.L., Papaioannou, H., 2024. Seismic hazard in an actively uplifting area: the case of Vikos-Aoos UNESCO Global Geopark, NW Greece, in: Pellicer, M.X., Aytac, A., Amorfini, A., Delaby, S. (Eds.), Geohazards in European Geoparks, Akademisyen Yayınevi Kitabevi, Ankara, Turkey, pp.150-153.

Lazaridis, G.T., Melfos, V., Papadopoulou, L., Onac, B.P., Stergiou, C.L., Maravelis, A.G., Voudouris, P., Dora, D., Fitros, M., Papaioannou, H., Vouvalidis, K., 2024. Sulfuric acid speleogenesis in Greece. Acta Carsologica 53, 127–144.

Telbisz, T., Stergiou, C.L., Mindszenty, A., Chatzipetros, A., 2019. Karst features and related social processes in the region of the Vikos Gorge and Tymphi Mountain (Northern Pindos National Park, Greece), Acta Carsologica 48, 29-42.

17th INTERNATIONAL CONGRESS of the Geological Society of Greece

BULLETIN OF THE GEOLOGICAL SOCIETY OF GREECE, SP. PUBL.

EXTENDED ABSTRACT 247

Volcanism and the metamorphic core complexes of Rhodope and Cyclades

Papanikolaou D.[1], Nomikou P.[1] & Lambridou D.[1]

(1) Department of Geology and Geoenvironment, National and Kapodistrian University of Athens, Greece

The four active volcanic centres of the Aegean arc and another ten inactive volcanic centres, activated during Oligocene – Middle Pleistocene, following its southward migration are described with emphasis on their tectonic signature. They are all localized within tectonic grabens, resulting from the back-arc extension of the Hellenic arc throughout its Late Eocene – Present evolution. Our study was based on geological maps and the transverse tectonic profiles both onshore and offshore. The material presented is either from our own publications (usually modified) or new. The orientation of the tectonic grabens depends on the extensional stress field of each period and region. The existence of Late Miocene granitic rocks in the Cyclades without outcrops of Late Miocene volcanics is probably due to the considerable uplift of the Cycladic metamorphic core complex that has denudated the upper geological formations together with the volcanic rocks. The volcanic activity is observed within the arc parallel marine molasse of the North Aegean – Rhodope back arc basin during Oligocene – Early Miocene and within the Plio-Quaternary marine arc parallel tectonic grabens/basins of the South Aegean. Middle-Late Miocene volcanic rocks are observed within continental tectonic grabens/basins only in the lateral margins of the Cycladic metamorphic tectonic window.

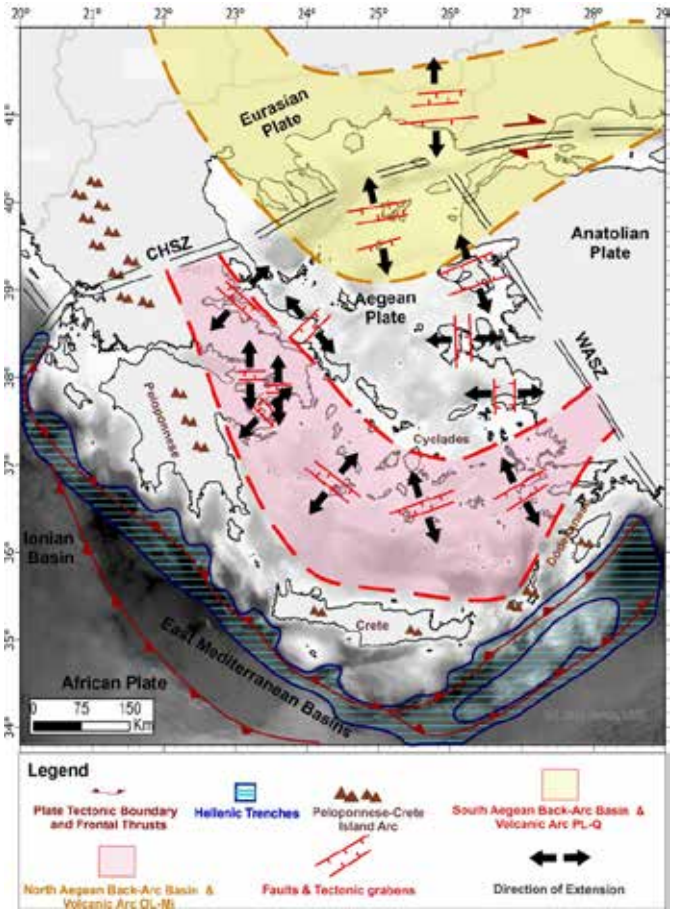

Fig. 1. Map showing the dominant tectonic trend and stress orientation in the 14 volcanic fields studied in this paper. The volcanism during Oligocene – early Miocene is observed within the molassic back arc basin of Rhodope – North Aegean Sea (No 11, No 12, No 13, No 14) whereas the Plio-Quaternary volcanism is observed in marginal marine basins along the northern border of the present back arc Cretan Basin (No 1, No 2, No 3, No 4, No 6). Exceptions are observed in the eastern Aegean islands (No 8, No 9) with N-S tectonic trend during the Middle – Late Miocene and W. Attica-Corinth (No 5, No 7) with E-W tectonic trend during Late Pliocene – Early Pleistocene.

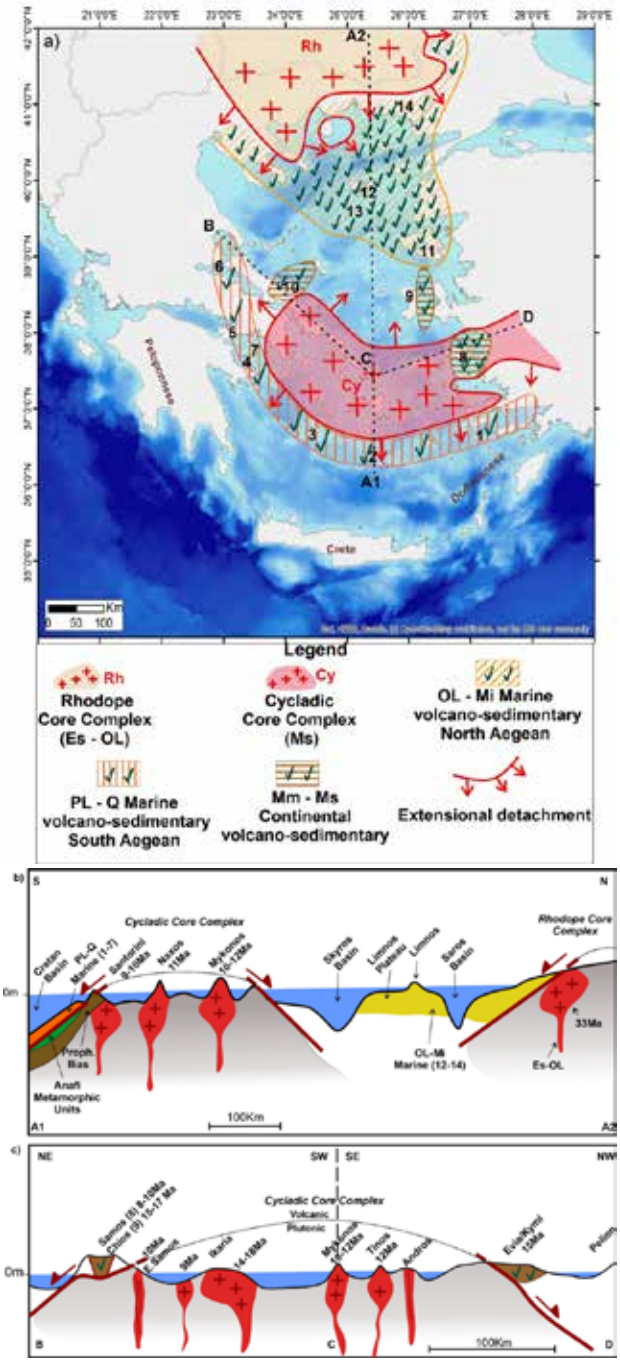

Fig. 2. a) The location of the 14 studied volcanic outcrops of the Hellenic arc within the Aegean tectonic structure. The volcanic outcrops are related to the Rhodope and Cycladic metamorphic core complexes with marine outcrops in the molassic basin of the North Aegean during Oligocene – Early Miocene and marine outcrops during Late Pliocene - Quaternary along the southern border of the Cycladic belt. Middle – Late Miocene continental outcrops are observed at the margins of the Cycladic core complex in Evia and Samos-Chios. b) N- S- schematic cross section A1-A2 through the Aegean Sea showing the volcanic outcrops in relation to the two metamorphic core complexes. Miocene granites of the Cyclades are indicated in Mykonos, Naxos and Santorini. c) Longitudinal schematic section B-C-D along the Cycladic core complex from Pelion – Northern Evia to Samos. The Miocene granitic rocks are shown within the core complex (Samos, Ikaria, Mykonos, Tinos) and the volcanic rocks within Miocene continental sedimentary basins at the two margins (Evia/Kymi and Samos, Chios).

Conclusions

In conclusion, almost all volcanic outcrops of the evolving Hellenic arc throughout the Late Eocene – Present are related to extensional tectonic graben structures associated with sedimentary basins, either marine or continental. Exceptions to this rule are very few, such as the Skyros andesite of Middle Miocene age about 15 Ma (Fytikas et al., 1980), which intruded the Alpine basement rocks of marbles, tectonically emplaced ophiolites and Cretaceous limestones. The role of the metamorphic core complexes in the distribution of the magmatic and volcanic products of the evolving Hellenic arc is documented and it is shown that the overall image of the upwelling magmas can be obtained only by combining the plutonic with the volcanic products.

References

Papanikolaou, D., Nomikou, P. & Lambridou, D. 2024. Tectonic grabens and volcanism in the Aegean, Greece. Geological Society of London, Special Publications, accepted.

17th INTERNATIONAL CONGRESS of the Geological Society of Greece

BULLETIN OF THE GEOLOGICAL SOCIETY OF GREECE, SP. PUBL.

EXTENDED ABSTRACT 248

The influence of stratigraphy for the generation of surface evidence of liquefaction phenomena; case study Piniada, Greece

Papathanassiou G.[1], Valkaniotis S.[1], Taftsoglou M.[2]
(1) School of Geology, Aristotle University of Thessaloniki, Greece, gpapatha@geo.auth.gr
(2) Department of Earth Science, University of Ferrara, Italy

Introduction / Background

The present study focuses on the assessment of liquefaction potential in an area where numerous liquefaction phenomena were triggered by the 2021 Damasi, Greece, earthquake. The liquefaction features were reported during a field survey conducted few hours after the event along the Piniada Valley (Papathanassiou et al. 2022). They were classified as i) sand craters, as singular features as well as aligned ones, ii) ground fissures, from where a mixture of water and fine sandy and silty material was ejected, and iii) lateral spreading phenomena. According to eyewitnesses, the phenomena occurred during the March 3rd mainshock, locally caused mixed fluid fountaining as high as 1 m from the topographic surface. The total area covered by the ejected material (sand blow) at Piniada Valley was estimated as 0.0325 km^2, approximately 0.5% of the zone that is delimited by the village Piniada, to the north, and the present-day river channel of river Pinios, to the south (Papathanassiou et al. 2022).

This area is covered by Holocene sediments deposited along the meandering fluvial system of Pinios. The characteristic evolution of Pinios River dictates the depositional process of the sediments and contributed to the lateral and vertical heterogeneity of the surficial soil material. That was clearly shown during the 2021 event since liquefaction phenomena preferred to concentrate in specific location forming clusters of liquefaction-induced ground disruption such as sand boils, craters and ground fissures (Valkaniotis et al. 2024). In addition, it is highlighted that within a short distance, the severity of ejecta was totally different.

Methodology

For the purposes of this research, we investigated the role of the stratification of soil deposits for the generation (or not) of liquefaction-induced surface evidence and to the relevant ejecta severity. In order to achieve this, we used data derived by six CPTu tests conducted on an area where liquefaction phenomena were mapped. The liquefaction potential at each site was estimated following the method proposed by Hutabarat and Bray (2022), who concluded that the layer stratification can lead to not producing ejecta.

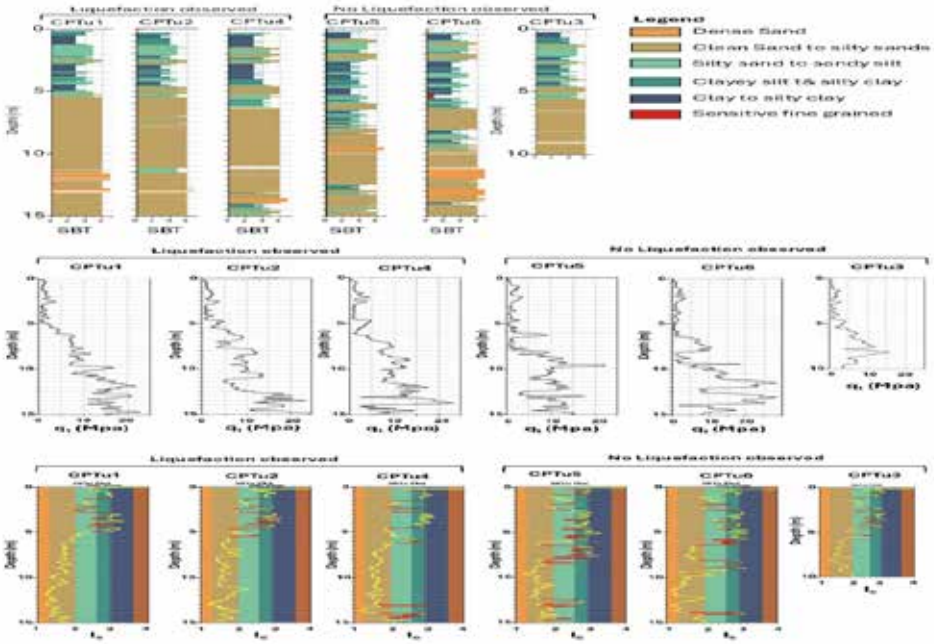

Figure 1. Soil stratigraphy of investigated sites, classified as liquefaction and non-liquefaction ones (Papathanassiou et al. 2025)

Thus, they developed a methodology aiming to address the prediction of the liquefaction-induced ejecta severity by quantifying two new factors: the liquefaction ejecta demand (L_D) and the crust layer resistance (C_R). The former considers the soil layer beneath the crust layer that may contribute to ejecta production and captures the hydraulic conductivity contrast, while the latter one (C_R) is related to the non-liquefiable crust layer that prevents liquefied material to eject and is estimated by taking into account the shear strength and thickness of this surficial stratum. According to Hutabarat and Bray (2022), this new method considers the system response of the soil column and captures the liquefaction-induced upward seepage that can erode the crust layer resulting in the generation of ejecta.

Conclusions

The outcome arisen by our study is that partially or highly stratified soil deposits are not expected to generate artesian flow pressure capable of producing liquefaction surface evidence, i.e. ejecta. This is due to the fact that i) the thickness of liquefiable sand-like layers is usually too small to produce large value of excess hydraulic head h_{exc}, while ii) in case this happens, the interbedded low-k_v soil layers impede the upward seepage. On the other hand, soil deposits where thick continuous sand-like material is encountered, are expected to produce excess hydraulic head that can lead the soil-water mixture onto the surface, i.e., ejecta. It is pointed out that this type of soil deposit can produce ejecta even when the thickness of the crust layer is larger than 4 m.

Acknowledgements

This study was financially supported by the Research Committee of Aristotle University of Thessaloniki. We would like to thank Dr. John Ioannidis for providing the software CLiq 3.0, the GEOT.ER. DIDASKALOU S.P. for conducting the in-situ tests (CPTu), the residents of Piniada village for their contribution and support, and especially Themistoklis Raptis and Christos Giannakos for permitting access to their properties during the geotechnical and geophysical surveys.

References

Hutabarat D, Bray JD (2022) Estimating the severity of liquefaction ejecta using the cone penetration test. J Geotech Geoenviron Eng 148(3):04021195. https://doi.org/10.1061/(ASCE)GT.1943-5606.0002744

Papathanassiou G, Valkaniotis S, Ganas A, Stampolidis A, Rapti D, Caputo R (2022) Floodplain evolution and its influence on liquefaction clustering: the case study of March 2021 Thessaly, Greece, seismic sequence. Eng Geol 298:106542. https://doi.org/10.1016/j.enggeo.2022.106542

Papathanassiou G., Fikos Il., Valkaniotis S., Stampolidis Al., Rapti D., Taftsoglou M., Caputo R. (2025). Response of stratified soil deposits to the severity of liquefaction phenomena: the Piniada Valley, Greece, case study, Bulletin of Engineering Geology and the Environment, under review

Valkaniotis, S., Rapti, D., Taftsoglou, M., Papathanassiou G., Caputo R. (2024). Geomorphological mapping for liquefaction likelihood: the Piniada Valley case study (central Greece). Bull Earthquake Eng 22, 5451–5474 (2024). https://doi.org/10.1007/s10518-024-01993-y

17th INTERNATIONAL CONGRESS of the Geological Society of Greece

BULLETIN OF THE GEOLOGICAL SOCIETY OF GREECE, SP. PUBL.

EXTENDED ABSTRACT 249

Monitoring the Santorini Volcano for 3 decades (1995-2025) by ISMOSAV and its role for the early detection of the 2011-2012 and 2024-2025 intra-caldera unrests

C. Papazachos[1], G. Vougioukalakis[3], S. Bitharis[2], Ch. Pikridas[2], M. Foumelis[1], Ch. Ventouzi[1], Ch. Kkallas[1], E. Karagianni[1], D. Vamvakaris[1], and E. Papageorgiou[1]

(1) Aristotle University of Thessaloniki, School of Geology, Thessaloniki, Greece (kpapaza@geo.auth.gr)

(2) Aristotle University of Thessaloniki, School of Rural and Surveying Engineering, Thessaloniki, Greece

(3) Institute for the Study and Monitoring of Santorini Volcano, Santorini, Greece

Introduction

The Institute for the Study and Monitoring of Santorini Volcano (ISMOSAV) was established in 1995 as a non-profit entity, with the main purpose of continuing the operation of the Volcanological Observatory and the volcano monitoring networks (seismological, geodetic, geophysical and geochemical) in 1993 in the framework of a European research program. A secondary objective of ISMOSAV was to promote volcanological research in Santorini, contributing significantly to the improved assessment of volcanic hazard and improving the ability to predict any volcanic activity or unrest in a timely manner. In this way, ISMOSAV has filled the gap left by the lack of a public body in Greece (e.g. research institute, etc.) that is responsible for the study and management of volcanic hazard, striving to protect Santorini by maintaining a reliable monitoring system that increases the likelihood of early warning of the volcano's reactivation, while also refuting, when necessary, any unfounded rumors and/or speculation. As a result, over the past 30 years and mainly with the support of the island's local authorities, ISMOSAV has managed to overcome several problems related to the lack of permanent research infrastructure on the island, maintaining and upgrading installed networks, replacing obsolete equipment, and processing real-time and near-real time information.

We present information on the early detection of the 2011-2012 and 2024-2025 volcano-tectonic intra-caldera unrests in Santorini. The presented results verify the critical role of ISMOSAV for the identification of these unrests, as well as on the measures that were taken to handle them. Moreover, they strongly suggest the need to establish the first permanent Volcanological Observatory on the island, operated by a local or other state authority, that will rely on and "assimilate" the existing ISMOSAV infrastructure, as well as monitoring sensors operated by other institutes, allowing to continue and expand on the ISMOSAV's 30-year legacy.

Data and Analysis

During the first 15 years of operation, ISMOSAV mainly relied on monitoring microseismicity to assess volcanic activity. This was mainly performed in collaboration with the Seismological Station of the Aristotle University of Thessaloniki (AUTh), gradually evolving and improving on the initial network of 5 analogue seismological stations. The recordings of the first analogue seismological network, initially recorded on paper in a local acquisition facility in Profitis Ilias, where later locally digitized and transmitted via the internet to AUTh. Until 2010 (Figures 1) these data showed continuous but relatively low seismic activity, mainly in the area of the submarine volcano of Koloumbo, as well as in several tectonic faults to the north and northeast of Santorini (e.g., an **M**5.1 sequence in June 2009), but also along the active tectonic line Koloumbos-Anydro-Amorgos area (e.g., Dimitriadis et al., 2005). These results, which showed little variability between 1995 and 2010, were in agreement with the findings of local seismological networks periodically installed on the island, as well as in the broader Santorini area (e.g. Bohnhoff et al., 2006; Dimitriadis et al., 2009).

As a result of this monitoring, ISMOSAV was able to detect the 2011-2012 volcanic unrest as early as February 2011. Figure (2) depicts the very early intra-caldera seismicity distribution, as presented in a confidential report submitted to the Earthquake Planning and Protection Organization in March 2011. From

this map, it was evident that the seismic activity began in January 2011 on the NE coast of Nea Kameni and expanded towards the NE (and less towards the SW) in February, continuing both to the northeast (Firostefani-Imerovigli) and southwest (Palaia-Nea Kameni area) in March 2011. From these early results it was evident that the activity was mainly concentrated at depths of 2-6 km, with shallower depths (2-4 km) in Palaia and Nea Kameni, increasing towards the mainland (Firostefani). The small hypocentral errors (0.7 km and 1.4 km for the horizontal and vertical coordinates) showed that this unusual seismicity was a reliable feature. This unrest was further supported by the temporal evolution of this low magnitude seismicity (Figure 3), that showed clear indications of significant temporal variations, increasing in late February 2011, as well as independent data (sea temperature increase, sea level changes, etc.).

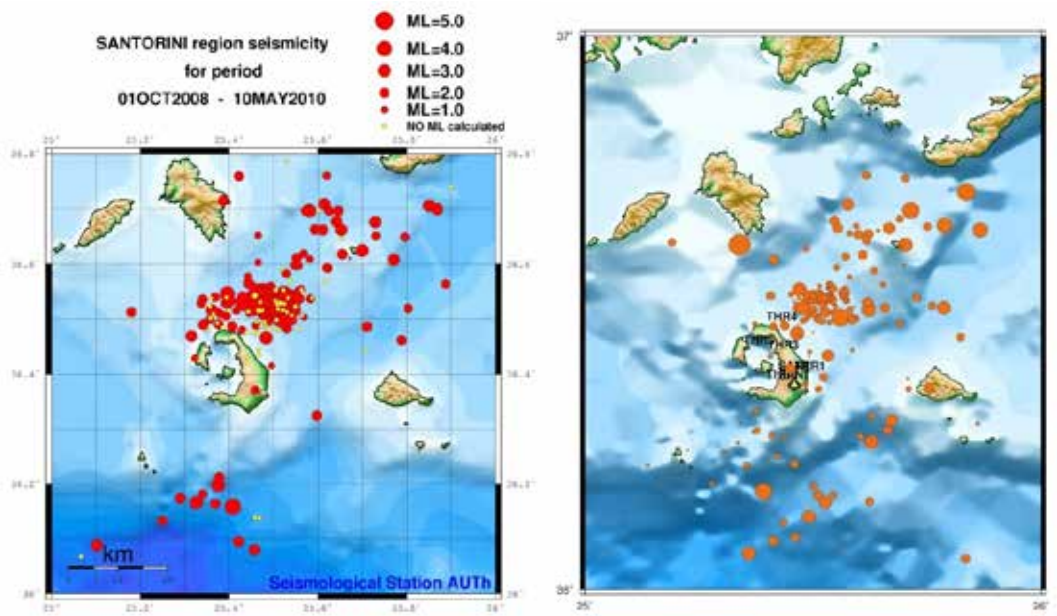

Figure 1. Seismic activity in the volcanic center of Santorini between October 2008 and May 2010 (left) and January 2006 and October 2008 (right).

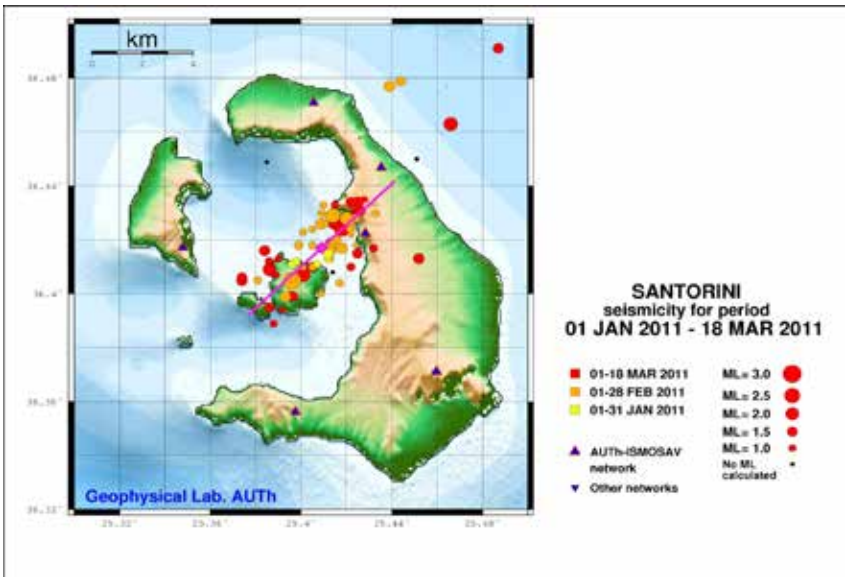

Figure 2. Seismic activity in the volcanic center of Santorini between January 9 and March 18, 2011, as originally reported in March 2011.

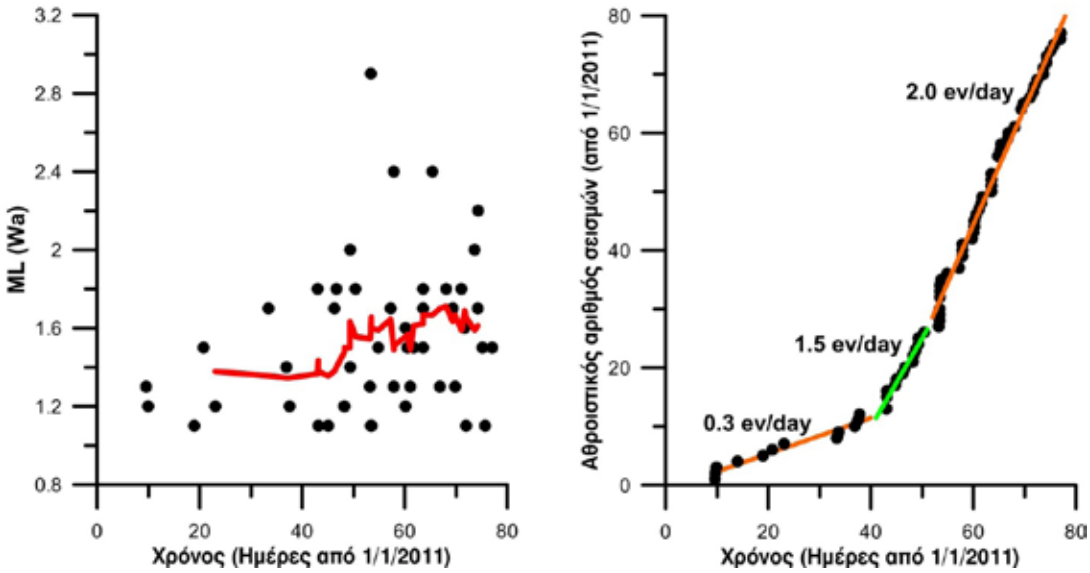

Figure 3. Temporal variation of the local earthquake magnitude for events with M_L>1.1 (left) and cumulative number of earthquakes (right) for the seismic sequence shown in Fig. 2. The moving average is shown by a red line for the left figure, while colored lines depict the rate (number of events per day) in the right figure.

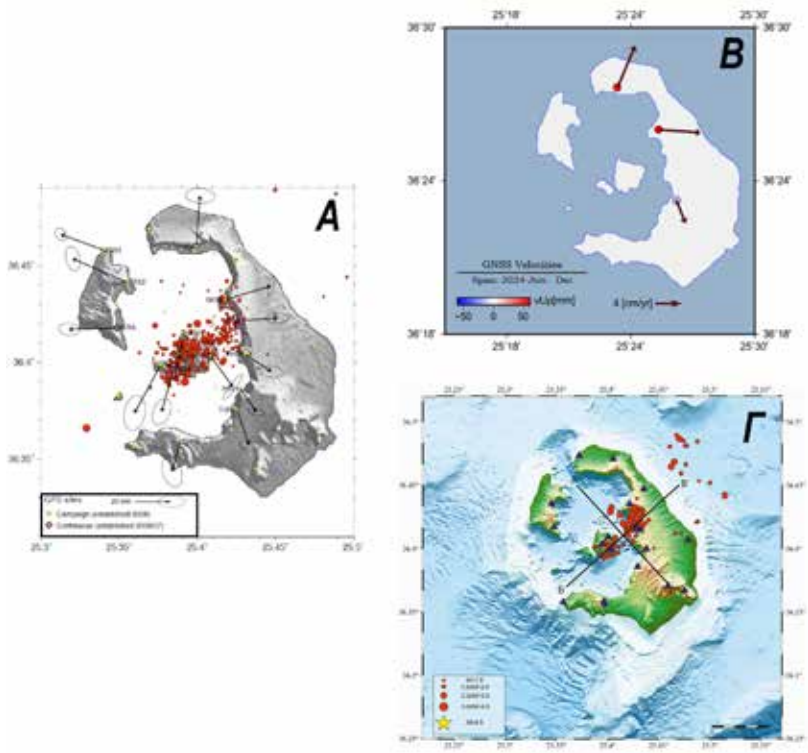

Figure 4. A) Earthquakes (red circles) in the Kameni fault and related displacements from GPS data in the Santorini caldera during the 2011–2012 seismic–volcanic crisis (Newman et al., 2012). B) Relative movements in the Santorini caldera from late June to early December 2024 for the three real-time GPS stations of ISMOSAV. Γ) Best located epicenters of earthquakes with magnitude M_L≥1.1 in the Santorini caldera during the second half of 2024 (mid-September-19 Dec. 2024).

While the 2011-2012 unrest was later extensively studied using a combination of earthquake, GPS, InSAR and geochemical data (e.g. Newman et al., 2012; Foumelis et al., 2013; Parks et al., 2012, 2013, 2015; Saltogianni et al., 2014; Tassi et al., 2013, Papadimitriou et al., 2015 among others), and while a large number of instruments were additionally installed during the unrest, within a few years the monitoring of the island returned to its previous state, with a small number of permanent seismographs and a single GPS station operating in real-time after 2016. To handle this situation, ISMOSAV installed three new GNSS receivers along with the corresponding ancillary equipment in October 2919, establishing a new modern geodetic network to monitor changes in the Earth's relief caused by possible volcanic activity. Furthermore, it continued to monitor seismicity, improving the network coverage and quality. Finally, it also relied on the use of the SNAPPING PSI operational service for InSAR data to further monitor surface deformation. This platform is integrated into ESA's Geohazards Exploitation Platform (GEP) and has been used for automated updates at regular intervals, providing an additional monitoring option for the volcano.

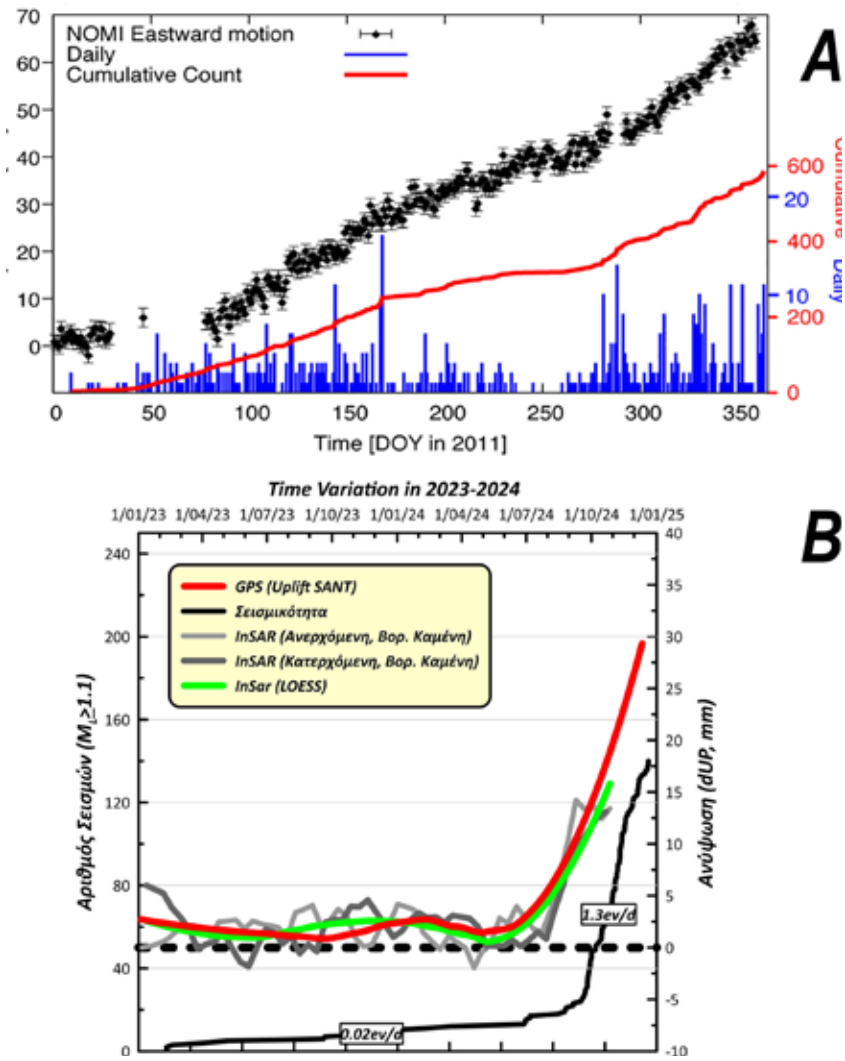

Figure 5. A) Eastward motion of GPS station NOMI station (black circles) and seismicity at the Santorini caldera from the 2011-2012 earthquake-volcanic crisis (Newman et al., 2012). B) Relative elevations at GNSS station SANT station and the northern segment of Nea Kameni (InSAR data) and seismicity rate at the Santorini caldera since January 2023, as originally reported by ISMOSAV. The island's caldera uplift is evident from June 2024 and seismicity has increased by almost 2 orders of magnitude during the period September-December 2024.

This persistent and systematic monitoring has allowed ISMOSAV to detect and inform the Greek government (Civil Protection, Earthquake Planning and Protection Organization) on January 2, 2025, for the on-going (at the time) intra-caldera unrest, as this was identified by seismicity, GNSS and InSAR data (Figures 4 and 5). More specifically, the ISMOSAV network detected since mid-September 2024 an anomalous seismic activity on the central fault of Kameni (Figure 4Γ). Analysis of geodetic data (Figure 4B) confirmed that this activity was accompanied by strong deformation, which started earlier (end of June 2024). This activity was almost identical to the 2011-2012 unrest, where more than 15 million cubic meters of magma rose to a depth of ~3-4 km, north of Nea Kameni. As shown by Figure 4, the displacements detected in northern Santorini and the relative seismic activity from mid-September 2024 were almost identical to the corresponding 2011-12 activity. This was verified by Figure (5), which presents the variation of seismic activity and relative deformation from GPS and InSAR data, as well as its comparison with similar data from the 2011-2012 crisis. From these figures it became evident that from the end of June 2024 (for deformation) and from mid-September 2024 (for seismicity) an unrest very similar to the 2011-12 phenomenon was evolving in Santorini.

Discussion and Conclusions

It is worth noticing that the continuous (for more than 3 decades) monitoring of the Santorini volcano by ISMOSAV did not only lead to the identification of the important 2011-2012 and 2024-2025 unrests, which had a significant impact on the island, but also led to important developments in volcanic risk management in Greece. These developments involved the publication of the TALOS Civil Protection plan for volcanic hazard in Santorini, as well as the creation of a Permanent Scientific Committee for the monitoring of the Greek Volcanic Arc under the auspices of the Earthquake Planning and Protection Organization, both motivated and realized after the 2011-2012 unrest. It is evident that the recent 2024-2025 caldera unrest should also be used as a platform to further strengthen and support the development of the necessary volcanic hazard policy in Greece. As noted in the Jan 2, 2025, letter of ISMOSAV to the Civil Protection and EPPO, this can be realized by adopting several measures, such as:

a) Strengthening of the role of the Permanent Scientific Committee for the Monitoring of the Greek Volcanic Arc of EPPO by creating permanent working research groups, with appropriate support for the volcanic arc monitoring and evaluation.

B) The allocation of the necessary resources (financial and other) for the permanent improvement (upgrading) and densification of the monitoring networks in Santorini, to improve the scientific and operational response, especially if there is an adverse evolution of tecto-volcanic activity.

C) The review and refinement of the TALOS plan, especially with respect to other volcanic centers (Koloumbo), as well as regarding the possible actions that will be required for the residents and visitors of Santorini in case of unrest or eruption.

D) Establishment of a permanent Volcanological Observatory of Santorini supported by the state. This observatory, for which a suitable site has been already selected and allocated by the Municipality of Thera, could “assimilate” existing monitoring networks to provide continuous volcano monitoring and reliable assessment of the associated volcanic hazard and risk, especially in periods of unrest.

Acknowledgements

The authors would like to acknowledge the help of Geothira MAE, the Municipality of Thera, EPPO, Greek Civil Protection, as well as ISMOSAV members and Santorini locals for their continuous support during the 30+ years of Santorini volcano monitoring by ISMOSAV. We would also like to thank a) Metrica SA for the donation of 3 GNSS stations that are permanently installed on Santorini, b) the Research Committee of the Aristotle Univ. Thessaloniki for partly funding 4 wide-band seismological and 1 GNSS stations, that are also permanently installed on Santorini, c) the IRIS technical company operating in Santorini, for providing valuable assistance regarding the permanent ISMOSAV network maintenance during the last 10+ years.

References

Bohnhoff, M., Rische, M., Meier, T., Becker, D., Stavrakakis, G., Harjes, H., (2006). Microseismic activity in the Hellenic Volcanic Arc, Greece , with emphasis on the seismotectonic setting of the Santorini – Amorgos zone. Tectonophysics, 423, 17–33

Dimitriadis, I. M., Panagiotopoulos, D. G., Papazachos, C. B., Hatzidimitriou, P. M., Karagianni, E. E., & Kane, I. (2005). Recent seismic activity (1994-2002) of the Santorini volcano using data from local seismological network. In: Developments in Volcanology (Vol. 7, pp. 185-203), Elsevier.

Dimitriadis, I., Karagianni, E., Panagiotopoulos, D., Papazachos, C., Hatzidimitriou, P., Bohnhoff, M., ... & Meier, T., (2009). Seismicity and active tectonics at Coloumbo Reef (Aegean Sea, Greece): Monitoring an active volcano at Santorini Volcanic Center using a temporary seismic network. Tectonophysics, 465(1-4), 136-149.

Foumelis, M., Trasatti, E., Papageorgiou, E., Stramondo, S., & Parcharidis, I. (2013), Monitoring Santorini volcano (Greece) breathing from space, Geoph. J. Int., 193(1), 161-170, https://doi.org/10.1093/gji/ggs135

Newman, A.V., Stiros, S., Feng, L., Psimoulis, P., Moschas, F., Saltogianni, V., Jiang, Y., Papazachos, C., Panagiotopoulos, D., Karagianni, E., & Vamvakaris, D. (2012), Recent geodetic unrest at Santorini Caldera, Greece. Geophys. Res. Lett., 39, L06309.

Papadimitriou, P., Kapetanidis, V., Karakonstantis, A., Kaviris, G., Voulgaris, N., & Makropoulos, K. (2015). The Santorini Volcanic Complex: A detailed multi-parameter seismological approach with emphasis on the 2011–2012 unrest period. J. Geodyn., 85, 32-57, https://doi.org/10.1016/j.jog.2014.12.004

Parks, M. M., Biggs, J., England, P., Mather, T. A., Nomikou, P., Palamartchouk, K., ... & Zacharis, V. (2012), Evolution of Santorini Volcano dominated by episodic and rapid fluxes of melt from depth. Nature Geoscience, 5(10), 749-754.

Parks, M.M., S Caliro, G Chiodini, DM Pyle, TA Mather, K Berlo, M Edmonds, J Biggs, P Nomikou, & C Raptakis, (2013). Distinguishing contributions to diffuse CO2 emissions in volcanic areas from magmatic degassing and thermal decarbonation using soil gas 222Rn-δ13C systematics: application to Santorini volcano, Greece. Earth and Planetary Science Letters, 377-378, 180-190, https://doi.org/10.1016/j.epsl.2013.06.046

Parks, M. M., Moore, J. D., Papanikolaou, X., Biggs, J., Mather, T. A., Pyle, D. M., ... & Nomikou, P. (2015). From quiescence to unrest: 20 years of satellite geodetic measurements at Santorini volcano, Greece. J. Geoph. Res.: Solid Earth, 120(2), 1309-1328.

Saltogianni, V., Stiros, S.C., Newman, A.V., Flanagan, K., & Moschas, F (2014), Time-space modeling of the dynamics of Santorini volcano (Greece) during the 2011-2012 unrest, Journal of Geophysical Research, 119, 8517-8537, https://doi.org/10.1002/2014JB011409

Tassi, F., Vaselli, O., Papazachos, C.B., Giannini, L., Chiodini, G., Vougioukalakis, G.E., Karagianni, E., Vamvakaris, D., & Panagiotopoulos, D., (2013). Geochemical and isotopic changes in the fumarolic and submerged gas discharges during the 2011-2012 unrest at Santorini caldera (Greece). Bull. Volcanol., 75, 711, https://doi.org/10.1007/s00445-013-0711-8

17th INTERNATIONAL CONGRESS of the Geological Society of Greece

BULLETIN OF THE GEOLOGICAL SOCIETY OF GREECE, SP. PUBL.

EXTENDED ABSTRACT 250

Effects of boiling and seawater mixing on hyper-enrichment of antimony in active polymetallic seafloor massive sulfide hydrothermal diffusers at the Aegean Kolumbo volcano

Papoutsa A.[1], Kilias S.[1], Zegkinoglou N.[1], Pletsas V.[1], Avoukatou R.[1], Nomikou P.[1], Polymenakou P. [2], Somogyi A.[3], Ahmad Q.[4]

(1) National and Kapodistrian University of Athens, Athens, Greece, angpapou@geol.uoa.gr
(2) Hellenic Centre for Marine Research, Heraklion Crete, Greece
(3) Synchrotron Soleil, Saint-Aubin, Gif-sur-Yvette, France
(4) Centre de Recherches Petrographiques et Geochimiques (CRPG), Universite de Lorraine, Nancy, France

Highlights

Coupled to magmatic degassing of metal (loid)- and volatile-rich fluids, boiling, and fluid-seawater mixing mechanisms are responsible for Sb hyper-enrichment in the Kolumbo SMS mineralization. Our results raise the possibility of (sub) seafloor Sb-rich mineralization at Kolumbo and other submarine volcanoes along the 500 km of the Hellenic Volcanic Arc.

Introduction / Background

Antimony (Sb) is a metalloid of Critical Raw Materials (CRMs) that are both of great economic importance for the EU and of high supply risk (European Commission, 2023). Therefore, its sustainable supply greatly depends on understanding the Sb-ore precipitation mechanisms, especially stibnite (Sb_2S_3), the worldwide major source of Sb. A target setting to secure sustainable access to CRMs, including Sb and related metal(loid)s (Au, Ag, Ga, Ge, Te), is sea-floor massive sulfide (SMS) deposits worldwide. Recent advances in understanding Sb solubility and transportation in hydrothermal ore-fluids on land, showed mainly aqueous species of thioantimonite ($H_2Sb_2S_4$) and hydroxothioantimonite [$Sb_2S_2(OH)_2$], while vein-type stibnite precipitation was controlled by: boiling-related solubility reduction of $H_2Sb_2S_4$, and subsequent cooling-induced solubility decrease of $Sb_2S_2(OH)_2$ (Yu *et al*., 2023). Recently, Kodera *et al.* (2024), and Kaufmann *et al.* (2024), have suggested that hydrothermal fluid temperature decrease has been the main mechanism for stibnite precipitation in vein-type epithermal deposits on land (Slovakia). However, whether these phenomena can cause Sb mineralization (i.e., stibnite and Sb-bearing sulfosalts) in submarine hydrothermal systems, remains incompletely known. To our knowledge only Dekov *et al*. (2022) have dealt with the physicochemical conditions of stibnite precipitation at the Daiyon-Yonaguni Knoll (Okinawa Trough) hydrothermal barite deposits, and suggested that precipitation at ~80°C, low $\log_{10}a$ of $Sb_2S_4^{2-}$ and Eh<0), from sub-seafloor phase separated fluids. Driven by the scarce knowledge on Sb enrichment (i.e., stibnite, Sb-sulfosalts) processes at seafloor hydrothermal conditions, we investigated the Sb-rich, polymetallic, SMS mineralization of modern CO_2-degassing, SMS diffuser vents, of Kolumbo submarine volcano, Hellenic volcanic arc [hereafter "Kolumbo CO_2 diffusers" ("KCO_2Ds")]. These rare actively forming Sb- and Au-rich polymetallic (As, Ag, Tl, Pb, Zn, Hg) SMS SMS deposits comprising pyrite, marcasite, sphalerite, chalcopyrite, galena, Pb-Sb sulfosalts, stibnite, orpiment/realgar and barite (Kilias *et al*., 2013). The KCO_2Ds display a distinct mineral zonation, grading from a pyrite-dominated, barite-polymetallic sulfide inner part (ISSC), through a thin sphalerite-dominated sulfide zone, to a barite-sulfide outer layer, and finally to an orpiment-dominated exterior (OAsL) locally covered by $Fe3^+$-(hydrated)-oxyhydroxides (SFeC) (Kilias *et al*. 2013). Importantly, pyrite occurs erratically within, and throughout, the KCO_2Ds, and occurs as compositionally zoned colloform pyrite 1 (Py1) that is overgrown by aggregated anhedral pyrite 2 (Py2), and coarse-grained euhedral pyrite 3 (Py3) (see Fig. 1 and Kilias *et al*., 2022). Samples came from KCO_2Ds that vent nearly pure CO_2 boiling fluids at 265°C (Kilias *et al.*, 2013; Zegkinoglou *et al.*, 2023). Hence, the Kolumbo system represents an optimum natural laboratory to decipher the effect of boiling and cooling due to fluid-seawater mixing, on stibnite composition, and Sb hyper-enrichment associated with SMS mineralization.

Materials and Methods

- **Sampling**

Sulfide samples were retrieved with Remotely Operated Vehicles (ROVs) from the northern part of the Kolumbo crater. Detailed descriptions on sampling and preparation methods are presented in Kilias *et al*. (2013) and in HCMR's "SeaBioTech Report 2013".

- **Optical microscopy and Mineral Analyses**

All samples were petrographically examined via transmitted and reflected light microscopy. The quantitative analyses of the main sulfide-sulfosalt phases were conducted by Energy Dispersive Spectroscopy (EPMA-EDS) using a JEOL JXA-8600 Superprobe. The S contents were determined by EPMA analysis. Trace element analysis was performed by laser ablation-inductively coupled plasma-mass spectrometry (LA-ICP-MS) using a New Wave Research-ESI 213 nm laser unit attached to a ThermoScientific ICAP-Q quadrupole ICP-MS. Analytical precision and accuracy were monitored by the repeated analysis of FeS-1 and MASS-1 (United States Geological Survey-USGS). Trace element concentrations were processed by the Iolite software package (https://iolite-software.com).

- **Raman spectroscopy**

Raman spectroscopy was performed using a Renishaw inVia Raman confocal microscope. Spectra were obtained using the 785 nm laser and a grating of 1200 groves per mm, with a power range between 0.5 and 0.05 mW, due to the varying stability and fluorescence of the analysis spots. Samples were exposed to the laser through a long-focal distance, 50X objective lens with 0.55 numerical aperture, and with the measured spectral range extended from 100 to 3200 cm-1. The obtained spectra were then processed by the WiRE software for Windows. Background noise was reduced by the subtraction of a polynomial baseline, and cosmic ray removal corrections were performed for all spectra.

- **Synchrotron X-ray fluorescence (μ-XRF)**

Polished thin sections of selected representative samples were analyzed using scanning μ-XRF at the Nanoscopium hard X-ray CX3-scanning spectromicroscopy beamline of Synchrotron Soleil (France). A monochromatic X-ray beam, with an energy range of 11.8–20 keV, was focused on the sample area using a Kirkpatrick–Baez nano-focusing mirror. To achieve micrometer resolution in elemental mapping of mm²-sized sample areas, the fast-continuous scanning (FLYSCAN) technique was employed.

Results

- **Mineralogy, textures and paragenesis of stibnite (Sb_2S_3) and Sb-sulfosalts**

Antimony phases include thin, needle-like stibnite crystals mainly in the OBL (Fig. 1A) and OAsL and individual Sb-bearing sulfosalt phases, such as semseyite and meneghinite, throughout the KCO_2Ds (see below and Kilias *et al*., 2022). Sb-bearing sulfosalts, relatively abundant in the ISSC, mostly occur as dendritic fishbone-like crystals (Figs. 1B, C), as intergrowths with barite rimming pyrite successions (Fig. 1D), and as overgrowths on Py1 (Fig. 1E). Sb-bearing sulfosalts may also occur as colloform-like phases (Fig. 1F) rimming As-sulphides, such as orpiment. Replacement of Sb-bearing sulfosalts by orpiment has also been observed, resulting in a porous and inclusion-rich (Pb-Sb sus) As-sulphide. The As-sulfide overgrowth precipitates from hydrothermal solution, indicating boiling-induced Coupled Dissolution Reprecipitation (CDR) processes (Fig. 1G). Moreover, a progressive transition of Pb-Sb sulfosalts to orpiment-like As-sulfides resembling frutexites-like microstomatolites with branching and outgrowths formed by cyclic growth has also been detected. The alternating banding consists of Pb-Sb sulfosalts progressively transitioning to orpiment-like As-sulphides (Fig. 1H). Rare stibnite occurs as independent needle-like crystals in open space, as inclusions in prismatic barite, or as intergrowths with Pb-Sb sulfosalts and orpiment of the OAsL (Figs. 1I, J, K respectively). Stibnite has also been found as a tube-like core in orpiment filamentous structures (Fig. 1L).

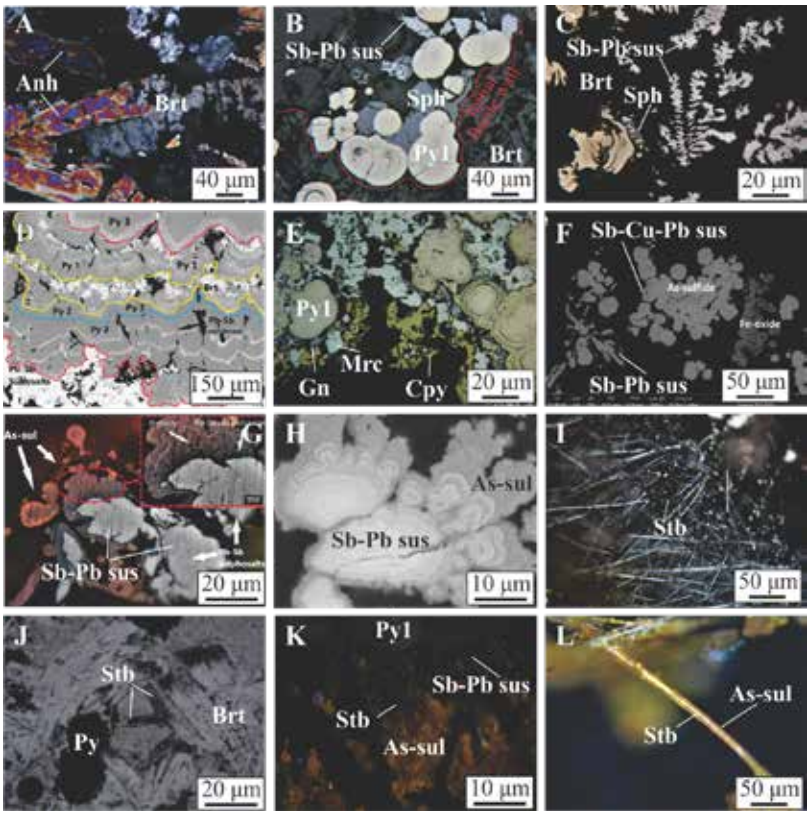

Figure 1. Reflected photomicrographs (A, B, C, F, I, G, K, L) and BSE images (D, G, H), showing textural features of stibnite, semseyite and meneghinite and other KCO2Ds minerals. (A) Replacement of anhydrite (Anh) by barite. (Brt) Colloform Py1 intergrown with sphalerite (Sph) and semseyire (Pb-Sb sus) on pore space of the barite "mound". (C) Dendritic texture of semseyite, with pyrite and sphalerite on barite substrate. (D) Repeated cycles (separated by colored dotted lines) of successive and subparallel colloform-crustiform micronscale bands of Py1, 2, and 3, interbanded with barite; semseyite is intergrown with barite (lower left). (E) Chalcopyrite lining channel edge, with marcasite, galena and Py1; (F) Colloform meneghinite (Sb-Cu-Pb sus) intergrown with As-sulfides, associated with semseyite and Fe oxyhydroxides. (G) Semseyite (Pb-Sb sus) sulfosalt partially replaced by orpiment (As-sul) with trace metal(loid)-rich Pb-Sb sulfosalt inclusions, indicating CDR processes; (H) Frutexites-like stromatolitic structure showing a CDR reaction of fine Pb-Sb sulfosalt laminae alternating with, and gradually replaced by As-sulfide laminae. (I) Needle-like, radiating stibnite (Stb) crystals, filling cavities and covering barite surface. (J) Radial and random needle-like stibnite crystals within transparent crystals of barite; (K) Intergrowth of barite, pyrite 1, semseyite (Sb-Pb sus), stibnite (Stb) and orpiment (As-sul). (L) Core-shell filamentous structure including core of stibnite and shell of orpiment.

- **Spectral characterization of Sb-bearing phases**

The majority of the obtained Raman spectra indicate that the dominant Sb-bearing phases in the KCO_2Ds are stibnite (Sb_2S_3) and semseyite ($Pb_9Sb_8S_{21}$). Stibnite exhibits sharp, characteristic Raman peaks, with decreasing intensity, at 312, 283, 240, 192, 156 and 129 cm^{-1}. Semseyite, presents a dominant Raman peak at 217 cm-1, with a broad shoulder at 176 cm^{-1}. Raman peaks of lesser intensity are present at 335, and 120 cm^{-1}. A less abundant, Sb-bearing sulfosalt that has been identified through Raman spectroscopy is meneghinite ($Pb_{13}CuSb_7S_{24}$), presenting a dominant Raman peak at 212 cm^{-1} with a shouldering peak at 248 cm^{-1}, and a secondary but intense peak at 328 cm^{-1}.

- **Mineral chemistry and Sb enrichment (LA-ICP-MS)**

LA-ICP-MS spot analyses show a unique enrichment in Sb in all the mineral phases present at the KCO_2Ds (Fig. 2). Galena exhibits a strong Sb enrichment with maximum concentration of 98000 ppm. Py1 is the most common sulfide mineral in the system and displays high Sb concentrations, up to 111192 ppm. The concentration of Sb in Py2 reaches up to 36100 ppm, whereas Py3 is the most depleted generation of pyrite, with maximum concentration of 79000. Sphalerite is also highly enriched in Sb concentration, reaching up to 98000 ppm. Marcasite and chalcopyrite are moderately enriched in Sb ranging up to 7730 ppm, and 16100 ppm, respectively. Lastly, the Sb concentration in orpiment is measured up to 16100 ppm.

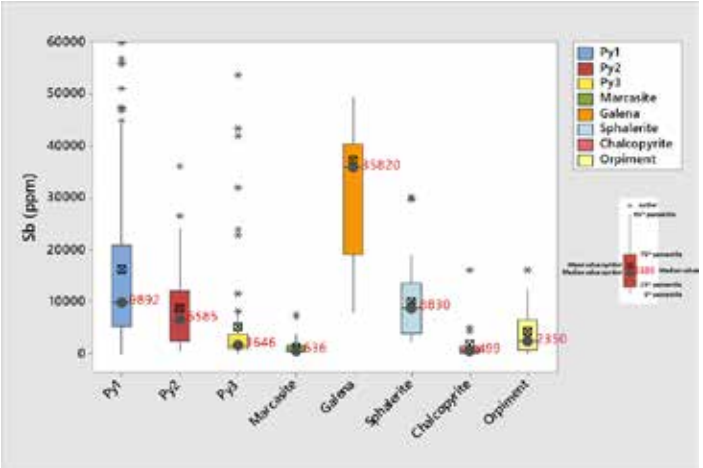

Figure 2. Box and whisker plots of Sb concentration in sulfide minerals present at the KCO2Ds analyzed by LA-ICP-MS. Mean values (black squares) are calculated using the entire dataset (including outliers), and might plot outside the respective box, whereas median values (gray dots, red numbers) are based solely on data within the box (25th to 75th percentile).

To better understand the sequestration of trace metals and especially Sb, in the main mineral phases, LA-ICP-MS depth profiles were thoroughly examined. The smooth parts of LA-ICP-MS time resolved spectra indicate structurally bound metal(loid)s while the irregular and spiky parts of the profiles signify the presence of micro/nanoparticles in the structure (George *et al*., 2019). The LA-ICP-MS depth profiles in stibnite display irregular parts for most trace elements (Zn, Ag, Au, Tl) implying that these elements are incorporated as nanoparticles in the structure of stibnite (Fig. 3A, 3B). The depth profiles for Sb in pyrite exhibit both smooth and spiky parts indicating that Sb precipitates both as nanoparticles along with other metal(loid)s and as lattice bounded in the structure of pyrite (Fig. 3C). Pb-Sb sulfosalts depth profiles appear spiky with respect to As, Cu, Ag, Zn and Au suggesting the incorporation of those metal(loid)s as inclusions (Fig. 3D).

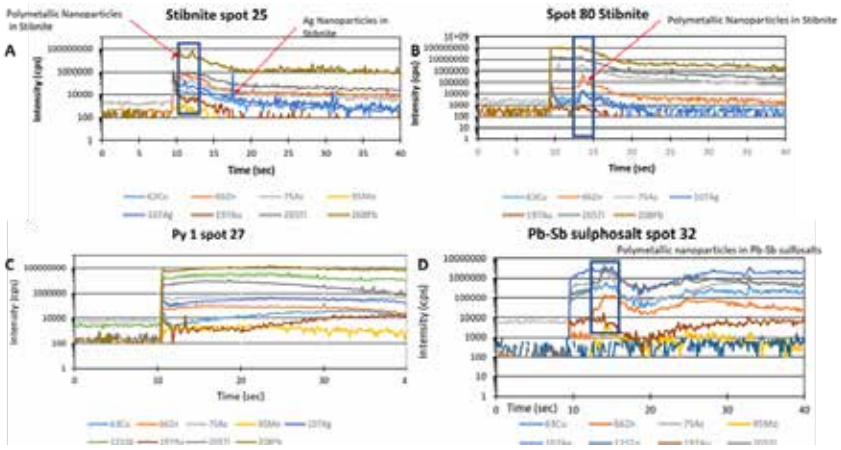

Figure 3. Time resolved spectra of metal(loid)s in pyrite and stibnite. A., B. LA-ICP-MS irregular depth profiles in stibnite. Note the presence of spikes in the same wavenumber for different trace elements, indicating the existence of polymetallic inclusions in stibnite. C. Smooth Sb LA-ICP-MS depth profile in Py1, signifying the sequestration of antimony in solid solution. D. Spiky depth profiles in Pb-Sb sulfosalts exhibiting polymetallic inclusions.

- **Synchrotron X□ray fluorescence (μ□XRF)**

Multi-scale length elemental maps on Py1 demonstrate that metal(loids) do not exhibit a homogeneous distribution, but rather a concentric chemical zoning. Elements such as Fe and Pb exhibit oscillatory chemical zoning at the inner part of the pyrite (Fig. 4A, E), whereas Zn, Cu, and As tend to enrich the outer zones of the crystal (Fig. 4B, C, F). Antimony, on the other hand (Fig. 4D) demonstrates oscillatory zoning rimwards. Core-to-rim traverse on Py1 indicates that the Sb, Pb and Tl concentrations have been affected predominately by boiling processes (Fig, 5A). The spatial distribution of Sb/Pb ratios with values less than 0.5, which are characteristic of boiling-induced precipitation (Falkenberg *et al*.,

2021) demonstrate an alternation of boiling-dominated, and likely seawater mixing-dominated regions (Fig. 5B), that coincide with the oscillatory chemical zoning of Sb (Fig, 4D).

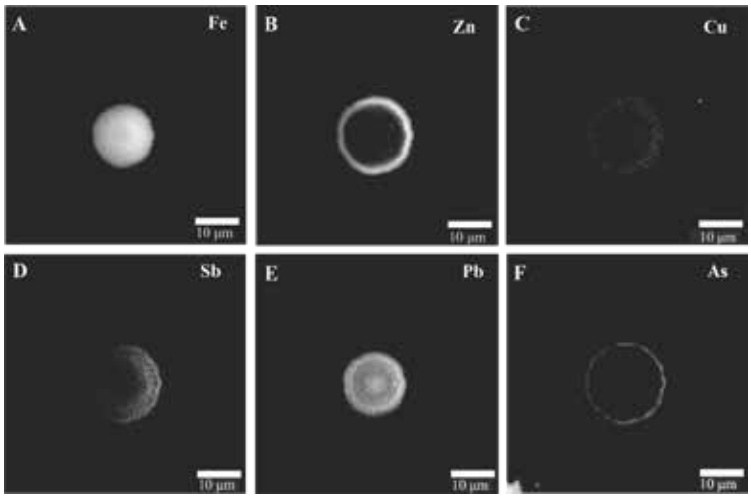

Figure 4. Synchrotron µ-XRF elemental maps of spheroidal pyrite from KCO_2Ds, illustrating the spatial distribution patterns of A) Fe, B) Zn, C) Cu, D) Sb, E) Pb, F) As.

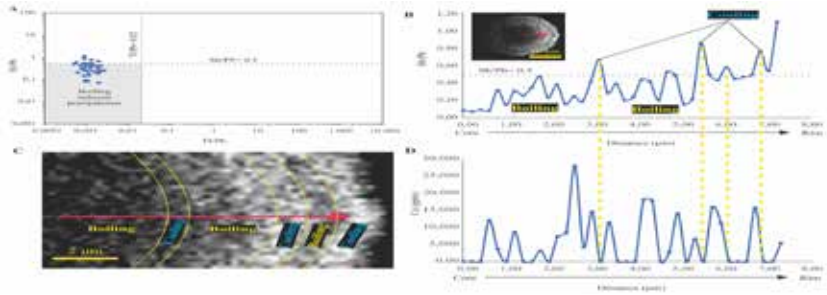

Figure 5. Synchrotron-obtained data from Py1 showing: (A) Sb/Pb vs. Tl/Pb (modified from Falkenberg et al., 2021) demonstrating boiling-induced precipitation, (B) a core-to-rim traverse in Py1 showing the alternation of boiling-dominated and likely non-boiling or fluid-seawater mixing (cooling) dominated regions

Discussion and Conclusions

Kolumbo is a submarine arc volcano that hosts a complex and dynamic magmatic-hydrothermal system with constantly evolving fluid chemistry through space and time (Zegkinoglou *et al.*, 2023; Patten *et al.*, 2024; Hector *et al.*, 2024. Geochemical and micro-textural evidence shows that the Kolumbo SMS mineralization has been formed by fluids undergoing multiple recurrent intense boiling and/or flashing or gentle and/or non-boiling events (Fig. 5); moreover, the high contents of Sb, along with As, Hg, and Tl in the KCO_2 Ds (Figs. 2 and 3) support boiling and zone refining processes, as these metal(loid)s are easily mobilized in the vapor phase (see Zegkinoglou *et al.*, 2023). The Kolumbo pyrite has recorded critical information related to boiling vs. non-boiling: The features displayed by Py1(±Py2) that occurs erratically distributed within the KCO_2Ds, reflect multiple episodes of vigorous boiling to flashing, whereas Py2 that occurs mostly in the inner KCO_2D parts, it is spatially concurrent with chalcopyrite lining narrow channels (Fig. 1E), has features that suggest precipitation from hot (>250°C) gently boiling to non-boiling fluids (Zegkinoglou *et al.*, 2023). Thus, pyrite can provide key information for the interpretation of associated Sb mineralization (stibnite, semseyite and meneghinite) forming conditions, and conditions of Sb incorporation in pyrite, during the 3-stage KCO_2Ds growth model (Berkenbosch *et al.*, 2012; Zegkinoglou *et al.*, 2023; Roman *et al.*, 2019; Falkenberg *et al.*, 2021). Vigorous boiling events have coincided with periods of intense magmatic degassing of volatiles and metal(loid)s (i.e., Cu, Au, Sb), and increase of the proportion of magmatic fluids into the Kolumbo hydrothermal system. In addition, the evolving Kolumbo magmatic-hydrothermal system could include periods of magmatic quiescence that results in a seawater-dominated hydrothermal fluid (Zegkinoglou *et al.*, 2023; Hector *et al.*, 2024).

At Kolumbo, textural (Fig. 1) and chemical variations of multiple pyrite (colloform, microcrystalline, crustiform banding, euhedral), chalcopyrite (linings), Pb-Sb sulfosalt (semseyite, meneghinite) (dendrites, colloform and subhedral crystals)

generations, are indicative for sulfide-sulfosalt precipitation during repeated cycles of progression from a young low-temperature <150–200°C) seawater-dominated, to a more "refined" system with a higher temperature (up to 300-350°C) upwelling of phase separated liquid-, or vapor-, dominated fluid flux and less seawater mixing (Falkenberg *et al.*, 2021). The close association of dendritic semseyite ($Pb_9Sb_8S_{21}$) (Fig. 1C), with adjacent concentrically layered colloform Py1, and anhedral sphalerite, occupying pore space of the Stage 1 barite substrate (Fig. 1B), suggests an early semseyite formation due to rapid precipitation and undercooling at temperatures <150–200°C, due to mixing of upwelling boiling, liquid- or vapor-dominated fluids, with seawater, in seawater-dominated inner KCO_2Ds (ISSC) zones (Berkenbosch *et al*., 2012; Falkenberg *et al*., 2021). In addition, semseyite that is interbanded with barite layers associated with colloform-crustiform banded Py1 (Fig. 1D), suggests that semseyite was synchronous with the development of barite and Py banding, and resulted from rapid precipitation due to boiled off hydrothermal fluid-seawater mixing-cooling cycles (Berkenbosch *et al*., 2012; Roman *et al*., 2019). Similarly, semseyite associated with orpiment [highly enriched in Sb (≤1.23 wt%)-unpublished data)] (Fig. 1F,G,H), on the outer chimney wall (OBL, OAsL), indicates a genetic linkage to low-temperature (≤100 °C) As and Sb-rich boiled off vapor input and vapor-seawater mixing (Dekov *et al*., 2013). The replacement and recrystallization of massive, or stromatolite-like, semseyite to colloform As-sulfides (i.e., orpiment) (Figs. 1G, H) probably represent a low-temperature (100 to 150°C) overprint and coupled dissolution and reprecipitation (CDR) processes based on zone refining (Berkenbosch *et al*., 2012; Falkenberg *et al*., 2021).
The trace element incorporation mechanisms in the Kolumbo stibnite, semseyite, and pyrite, also depends on variable degrees of fluid-seawater mixing and fluid boiling precipitation. For example, intensity spikes in time-integrated LA-ICP-MS spectra (Fig. 3D) are likely related to microscale polymetallic inclusions in stibnite and semseyite (Fig. 3A,B). Such inclusions may well reflect hydrothermal fluid supersaturation in Cu, Ag, Sb, and Pb, caused either by abrupt cooling because of abundant fluid-seawater mixing, or boiling that caused destabilization of metal(loid) complexes (Falkenberg *et al.*, 2021). These notions are supported by chemically zoned Py1 spheroids that exhibit low Sb/Pb and Tl/Pb ratios, and decoupled zoning between trace metal(loids), indicating boiling-induced precipitation (Fig. 5A). In this paper, we have documented that additional to magmatic volatile degassing, boiling- and seawater mixing-induced processes, may be responsible for hyper-enrichment of Sb in the Kolumbo SMS mineralization.

Acknowledgements
We thank Daniel Smith (University of Leicester) and Manuel Keith (Friedrich-Alexander-Universitat) for their assistance in the LA-ICP-MS analyses.

References

Berkenbosch H. A., de Ronde C. E. J., Gemmell J. B., McNeill A. W., Goemann K., 2012. Mineralogy and Formation of Black Smoker Chimneys from Brothers Submarine Volcano, Kermadec Arc. Economic Geology 107, 1613–1633.
Falkenberg, J.J., Keith, M., Haase, K.M., Bach, W., Klemd, R., Strauss, H., Yeo, I.A., Rubin, K.H., Storch, B., Anderson, M.O., 2021. Effects of fluid boiling on Au and volatile element enrichment in submarine arc-related hydrothermal systems. Geochimica et Cosmochimica Acta 307, 105-132.
Hector, S., Patten, C.G., Beranoaguirre, A., Lanari, P., Kilias, S., Nomikou, P., Peillod, A., Eiche, E., Kolb, J., 2024. Magmatic evolution of the Kolumbo submarine volcano and its implication to seafloor massive sulfide formation. Mineralium Deposita 59, 1229-1248.
George, L.L., Biagioni, C., Lepore, G.O., Lacalamita, M., Agrosi, G., Capitani, G.C., Bonaccorsi, E., d'Acapito, F., 2019 The speciation of thallium on (Tl,Sb,As)-rich pyrite. Ore Geology Reviews 107, 364-380.
Kaufmann, A.B., Lazarov, M., Weyer, S., Števko, M., Kiefer, S., Majzlan, J., 2024. Changes in antimony isotopic composition as a tracer of hydrothermal fluid evolution at the Sb deposits in Pezinok (Slovakia). Mineralium Deposita 59(3), 559-575.
Koděra, P., Mathur, R., Zhai, D., Milovský, R., Bačo, P. and Majzlan, J., 2024. Coupled antimony and sulfur isotopic composition of stibnite as a window to the origin of Sb mineralization in epithermal systems (examples from the Kremnica and Zlatá Baňa deposits, Slovakia). Mineralium Deposita, pp.1-17.
Patten, C.G.C., Hector, S., Kilias, S., Ulrich, M., Peillod, A., Beranoaguirre, A., Nomikou, P., Eiche, E., Kolb, J., 2024. Transfer of sulfur and chalcophile metals via sulfide-volatile compound drops in the Christiana-Santorini-Kolumbo volcanic field. Nature Communications, 15(1), 4968.
Roman N., Reich M., Leisen M., Morata D., Barra F., Deditius A. P., 2019. Geochemical and micro-textural fingerprints of boiling in pyrite. Geochimica et Cosmochimica Acta 246, 60–85.
Yu, H.C., Qiu, K.F., Simon, A.C., Wang, D., Mathur, R., Wan, R.Q., Jiang, X.Y., Deng, J., 2023. Telescoped boiling and cooling mechanisms triggered hydrothermal stibnite precipitation: Insights from the world's largest antimony deposit in Xikuangshan China. American Mineralogist, 108(7), 1213-1223.
Zegkinoglou, N.N., Ryan, M., Kilias, S.P., Godfrey, L., Pletsas, V., Nomikou, P., Zaronikola, N., 2023, Boiling-induced extreme Cu isotope fractionation in sulfide minerals forming by active hydrothermal diffusers at the Aegean Kolumbo volcano: Evidence from in situ isotope analysis. Geology 51,1072–1076.

17th INTERNATIONAL CONGRESS of the Geological Society of Greece

BULLETIN OF THE GEOLOGICAL SOCIETY OF GREECE, SP. PUBL.

EXTENDED ABSTRACT 251

V_{S30} Estimation from P-Wave Seismograms: Exploring a Frequency-Domain Approach for Stations Located in Sedimentary Basins

Pappa E[1]., Papazachos C[1]., Chatzis N[1].

[1]*Geophysical Laboratory, Aristotle University of Thessaloniki, P.O. Box 352-1, GR-54124, Thessaloniki, GREECE*

Introduction

Earthquakes are natural phenomena, often with significant impacts on the human infrastructure. Understanding the factors that influence seismic motion at a specific location is crucial for reducing earthquake risk. These factors include the earthquake source (e.g., magnitude and rupture mechanism), the propagation path (e.g., geometrical spreading and anelastic attenuation), as well as local site effects.

The later factor, local site effects, can play a critical role, as they can amplify seismic motion and significantly influence the level of ground shaking. One of the most common approaches to assess local site effects involves calculating the time-averaged shear wave velocity down to 30 meters, V_{S30}, (e.g., EN1998-1, NEHRP97, etc.). However, reliably estimating V_{S30} is not always straightforward. Traditional methods such as borehole drilling, or geophysical measurements, including refraction, MASW (Multichannel Analysis of Surface Waves), and microtremor measurements (e.g., Chatzis et al., 2018, Chatzis et al., 2022), require significant time, human resources, and funding. Meanwhile, proxy methods, like those based on slope or terrain (e.g., Wald and Allen, 1997) often introduce significant errors. This highlights the need for simple, cost-effective, and reliable methodologies.

Ni et al. (2014) proposed a promising approach, the P-wave seismogram method, to estimate the time-averaged shear wave velocity down to a depth z (V_{SZ}) at a station's location using seismic records. This methodology has been extensively validated using small to moderate magnitude earthquakes (**M**2–4) across various regions, including Central and Eastern North America (Kim et al., 2016), Texas, Oklahoma, and Kansas (Zalachoris et al., 2017), California (Li and Rathje, 2023), Japan (Miao et al., 2018, Kang et al., 2020), and Korea (Kim et al., 2020). It has also been applied to larger earthquakes (**M**4.0–5.5) near the Anchorage Basin in Alaska (Skarlatoudis et al., 2022) and microearthquakes ($-1.1 \leq M_L \leq 1.7$) in the Pohang Basin, South Korea (Lee et al., 2022). In all cases, the method demonstrated a good correlation between estimated and reference (*in situ*) V_{S30} values, verifying its potential as a reliable tool.

Greece, one of Europe's most seismically active countries, has a dense seismic network covering both inhabited and remote areas. However, reliable V_{S30} data is unavailable for many of the stations' locations, making it a critical area of study. Pappa et al. (2025) applied the P-wave seismogram method to two accelerometric arrays in Greece and found a strong correlation with reference values, after employing a standard bandpass filter (0.2–40 Hz) and making appropriate corrections for the effect of the ray parameter and earthquake magnitude on V_{SZ}. In this study, we applied the same methodology to test its applicability at seven stations, those with the most extensive datasets, from the arrays already used by Pappa et al. (2025). However, we deliberately chose not to apply the bandpass filter to assess whether the method performs reliably without it. Our findings revealed that the results were not satisfactory, with all stations showing a bias with respect to reference values, typically exceeding 50%, especially in basin areas (low V_{S30} sites). To address this issue, we explored an alternative approach, by considering the same data in the frequency domain instead of the time domain. This modification significantly reduced the method errors, offering a potential pathway to improve the reliability of the P-wave seismogram method in estimating V_{S30} values for noisy sites, especially for stations located in basin sites.

The P-wave seismogram Method and its Frequency Domain Adapting

Most earthquakes originate within the crust, where seismic waves travel with relatively high velocities. In contrast, seismic stations are often located on near surface, lower-velocity media. Due to Snell's law, the incident angle of incoming P and SV waves at the free surface is smaller than their takeoff angle at the source. This phenomenon results in a stronger P wave on the vertical component and a weaker P wave on the radial component (Figure 1a). The softer the medium, the weaker the P wave contribution to the radial component. Consequently, the ratio of the radial to vertical component amplitudes increases as the soil becomes stiffer. Conversely, the SV reflections from an surface impinging P-wave are generally stronger on the radial component, even in softer sites, as the SV polarization is perpendicular to the ray path. Theoretical arguments (Aki and Richards, 2002; Ni et al., 2014) have shown that the amplitude ratio of the radial (U_R) to vertical (U_Z) components of the incident P wave is reliable indicator of the near surface shear-wave velocity (Vs):

$$\frac{U_R}{U_Z} = \frac{-2V_s\, p\, cosj U_R}{1-2p^2{V_S}^2\, U_Z} = \frac{-2V_s\, p\, cosj}{1-2p^2{V_S}^2} \quad (1)$$

Where, p, is the ray parameter for plane waves:

$$p = \frac{\sin j}{V_S} \left(= \frac{\sin i}{V_P}\right) \quad (2)$$

By combining equations (1) and (2) to eliminate the angle j, the time-averaged shear wave velocity down to a depth z, V_{SZ}, can be estimated as a function of U_R/U_Z and p (Li et al. 2014):

$$V_{SZ} = \frac{1}{\sqrt{2}p}\left[1 - \left(\frac{1}{1+(\frac{U_R}{U_Z})^2}\right)^{\frac{1}{2}}\right]^{\frac{1}{2}} \quad (3)$$

The depth z to which the estimated V_{SZ} corresponds is roughly equal to the dominant wavelength of the S-wave:

$$z = \tau_p V_{SZ}^{Pseis} \quad (4)$$

where τ_p is the duration of the source time function, e.g. duration of the P-wave pulse.

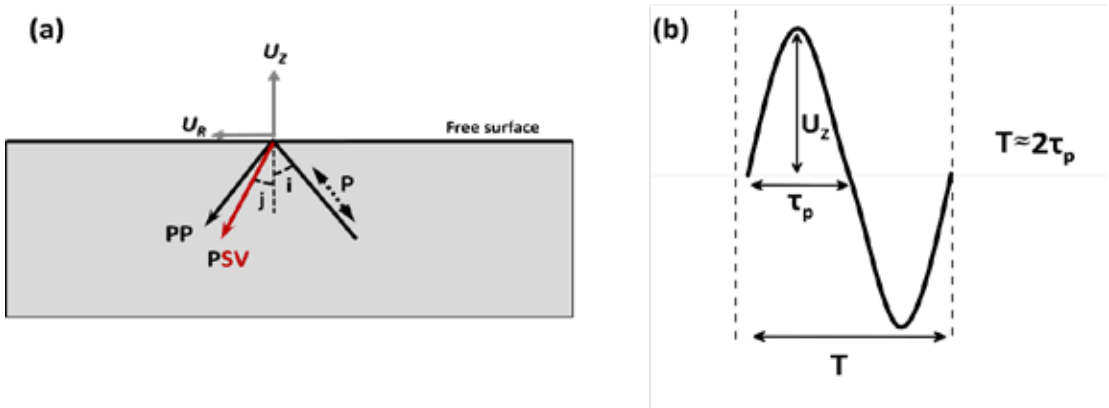

Figure 1. (a) Interaction between an incident P wave and a free surface. The vertical and horizontal components of the P wave result from the superposition of the incident P wave, the reflected P wave, and the S wave generated at the free surface. (b) Schematic representation of a simplified single wave time series, illustrating the source time function (τ_p), the period (T), and their durations.

The application of Fast Fourier Transform (FFT) analysis for the U_R/U_Z estimation section offers several advantages over traditional time-domain analysis, allowing for a more detailed investigation of signal characteristics. In the frequency domain, a signal is represented by independent frequency components, whereas in the time domain, the signal is described by a single waveform that contains the sum of all frequency-dependent contributions.
Figure (1b) presents a schematic first P wave pulse. The source time function used in equation (4) corresponds to the duration of the first pulse, τ_P. If we consider that this waveform is dominated by a characteristic frequency, the duration of this wavetrain should correspond to this dominant wave period. Thus, the period of the first P wave should be approximately twice the source time function, τ_P. The Discrete Fourier Transform (DFT) of the signal shown in Fig.1b includes a minimum (first) frequency component after the zero-frequency, which is determined by the duration of the signal, since this first frequency component is the inverse of the total signal duration. By analyzing the DFT amplitudes, we can better understand the characteristics of the seismic signal, which may be less evident in the time domain. Additionally, this approach allows us to identify and retain only the records where the signal in both components (R and Z) is above the noise level.

Site Selection and Data Processing

Several previous studies have applied the P-wave method using hundreds of stations, with or without reliable reference velocity profiles. In contrast, we focused in two specific arrays and a total of seven stations, selecting those with the most extensive dataset. These arrays are located in sedimentary basins, which are of particular interest due to the significant amplification of seismic motion often observed in such areas. Additionally, the arrays are situated in earthquake-prone regions with well-established velocity profiles (Raptakis et al., 2000; Theodoulidis et al., 2018,

Cushing et al., 2020), making them ideal for testing the methodology.
The first array, EUROSEISTEST, is located in the epicentral area of the 1978 **M**6.5 earthquake in the Mygdonia Basin, which caused severe damage in the neighboring city of Thessaloniki (Papazachos and Papazachou, 2003). The basin spans 5.5 km in the NNW-SSE direction and consists of Quaternary deposits, with a maximum bedrock depth of 200 m, where gneiss was identified (Raptakis et al., 2000). The second array, ARGONET, is located in the Koutavos Basin on the island of Cephalonia, near the Cephalonia Transform Fault Zone (CTFZ). This array was established as part of the SINAPS project (Berg-Thierry et al., 2017). The basin consists of a range of geological formations, including Cretaceous limestones (below 90 m depth, as indicated by borehole data), Upper Pliocene marly sandy limestones and claystones, Pleistocene lithological clays, and Holocene clays and silty sands (Theodoulidis et al., 2018).
From the EUROSEISTEST array, we selected five stations (BUT, GRA, PRO, STC, TST), while from the ARGONET array two surface stations (CK0, CKWP) were chosen for further processing. Among these seven stations chosen, CKWP and PRO are located on bedrock sites, while the others are situated on soft sediments. We utilized all available data, i.e. records of regional earthquakes recorded by the two networks, spanning from 1994 to 2020. The only restriction applied to the dataset was to reject data with ray parameter values p<0.1s/km, as Pappa et al. (2025) demonstrated that the use of smaller p values leads to a systematic bias of the near-surface velocity results.
For the first P-arrival we manually picked the maximum amplitudes of both the radial and vertical components. We opted not to rely on automatic pickers, even though they could expedite the process, as they can introduce errors, especially in noisy signals. We also chose not to apply any filters (highpass, lowpass, or bandpass) in order to preserve the original information contained in the initial P-wave arrivals and examine the method robustness to noise, since we aimed to test the method without applying any a priori filtering. For each waveform, we performed baseline corrections and identified the maximum values of the initial P-wave pulse (indicated between the red dotted lines in Figures 2a and 2b) in both radial and vertical components to calculate the U_R/U_Z ratio.

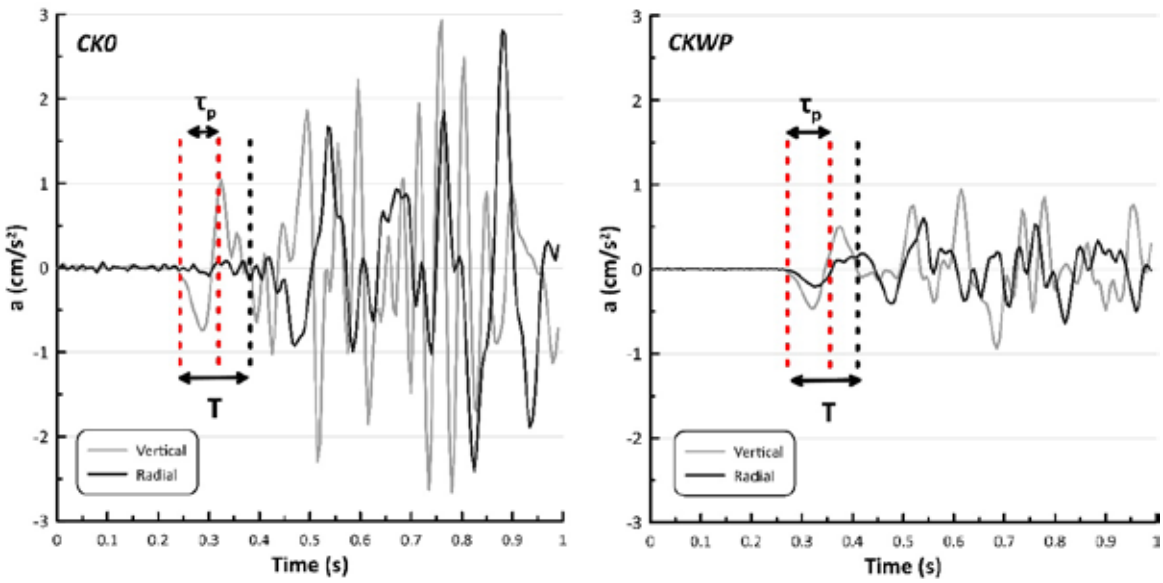

Figure 2. Example of a record at (a) CK0 and (b) CKWP stations for the arrival of the first P wave from the same local earthquake. The source time function, τ_P, and the duration, T, of the corresponding first period are also depicted.

We also extracted the arrival time of the earthquake at the station, the ending time of the first pulse, as well as the end time of the first period (see examples in Figures 2a and 2b). Figure 2a shows a waveform from station CK0, located in soft sediments, where the vertical component is much larger than the radial component. Figure 2b, from station CKWP (located on bedrock), shows a smaller difference between the radial and vertical components, which is attributed to the higher velocity of the near-surface structure.
Once the U_R/U_Z was estimated, we proceeded with the p estimation for each waveform using the TauP toolkit (Crotwell et al., 1999), implemented in ObsPy (Beyreuther et al., 2010). We used the epicentral distance, focal depth, and a local 1D P and S velocity model for each station, derived from the 3D tomographic model of Papazachos and Nolet (1997). As already mentioned, we kept only data with a ray parameter p≥0.1s/km. Since U_R/U_Z and p are known, we applied Equation (3) to estimate V_{SZ} for each record. However, since V_{S30} values are most widely used, we used the V_{SZ}-to-V_{S30} conversion equations from Boore et al. (2011) to assess V_{S30} values for each recording station. To apply

these equations, we first estimated the depth z corresponding to each V_{SZ} value using Equation (4). The duration of the first P-wave pulse was used as τ_p. Unlike Lee et al. (2022), who used an average value for τ_p, we opted to use the specific τ_p for each record to more accurately estimate the correspnding depth samples by the P-pulse wavetrain. The corresponding median V_{S30} values, noted as $V_{S30}^{Original}$, showed significant deviations, involving values with a ~ 50% relative bias (BUT, GRA, PRO, STC, TST) compared to the reference values, increasing to over 80% for stations CK0 and CKWP.

In an attempt to improve these results, we tested the possibility of computing the U_R/U_Z in the frequency domain, where we could more easily identify frequencies where the signal was above the noise level. This approach appears to be promising, especially since most of the stations used in this study were located in soft soil sediments, for which the radial components are more prone to noise compared to rock sites, potentially leading to erroneously larger U_R/U_Z values. For this reason, we applied the Fast Fourier Transform (DFT) to each waveform with a duration equal to the dominant period, T, and selected only those with an SNR in the radial component greater than or equal to 1.2 for the first (lower) frequency. This SNR threshold was applied to the radial component because stations in soft soil often exhibit weak P-wave arrivals, making them susceptible to noise. In the frequency domain, the U_R/U_Z ratio was calculated as the amplitude of the radial component divided by the amplitude of the vertical component at the first frequency. Figures 3a and 3b show examples of how the picking was done in the frequency domain for indicative records from the CK0 and CKWP stations, respectively. The subsequent processing steps, namely from the ray parameter estimation up to the V_{S30} calculation, noted as V_{S30}^{FFT} for this application, remained the same as in case of U_R/U_Z processing in time domain.

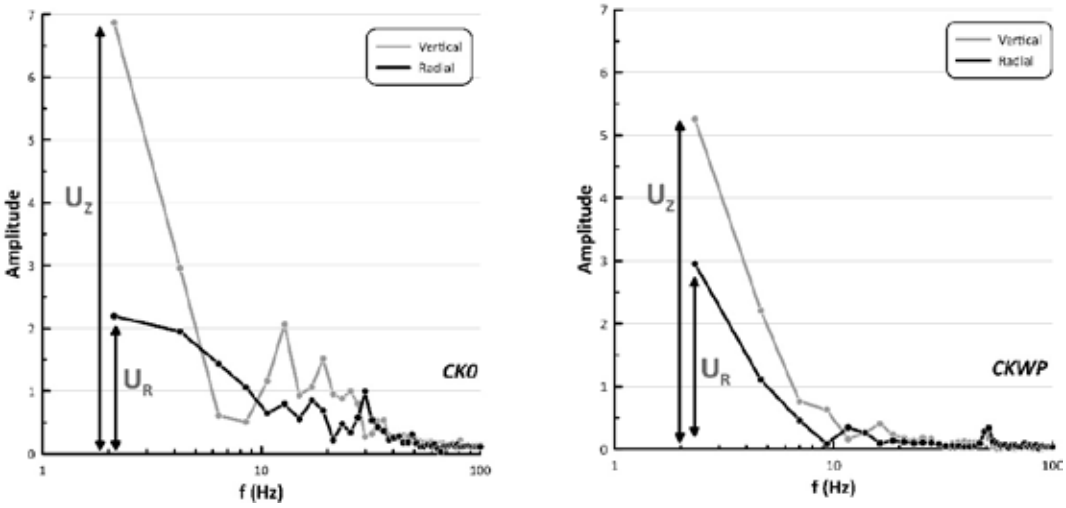

Figure 3. Example of waveform amplitude spectra at (a) CK0 and (b) CKWP stations for the first P wave and a duration equal to the dominant period (see Fig.2). The amplitude of the two components, used for U_R/U_Z estimation, is also depicted.

Results

The results of the V_{S30} estimations using both the time-domain and frequency-domain (FFT) approaches are summarized in Table 1. For stations CK0 and CKWP, the time-domain methodology ($V_{S30}^{Original}$) produced significantly overestimated values, with CK0 showing the largest deviation from the reference values (V_{S30}^{ref}). Applying the FFT-based approach reduced the overestimation across all stations, yielding lower V_{S30}^{FFT} values that were closer to the reference ones. Despite this improvement, all stations still exhibited some degree of overestimation with the FFT approach, except for station GRA, where the methodology failed to provide an improvement. The exclusion of waveforms due to low signal-to-noise ratio (SNR < 1.2) in the radial component has a different impact, depending on the recording station. CK0 had the highest exclusion rate (21%), while PRO and CKWP had no data rejections. Other stations, such as STC (2%), BUT (5.7%), and TST (6.7%), had minimal rejection rates, reflecting the overall improved data quality in the FFT-based analysis.

Figure 4 illustrates these findings: in Figure 4a we present the comparison of time-domain results with reference V_{S30} values, showing a pronounced overestimation compared to the reference, with most points lying far from the 1:1 line. On the contrary, the FFT-based results (Figure 4b) demonstrate a much better agreement with the reference values.

Table 1. V_{S30} median values, estimated from the P-wave Seismogram method with a time domain U_R/U_Z picking procedure, $V_{S30}^{Original}$, and frequency domain approach V_{S30}^{FFT} for SNR in the radial component greater than 1.2. For comparison, we also present the reference V_{S30}^{ref} values from local velocity profiles estimated from active and passive seismic methods.

Station	$V_{S30}^{Original}$ (km/s)	V_{S30}^{FFT} (km/s)	V_{S30}^{ref} (km/s)
CK0	1.05	0.48	0.24
CKWP	1.44	0.87	0.79
BUT	0.43	0.29	0.26
GRA	0.4	0.46	0.23
PRO	1.24	1.23	0.83
STC	0.54	0.52	0.35
TST	0.35	0.32	0.22

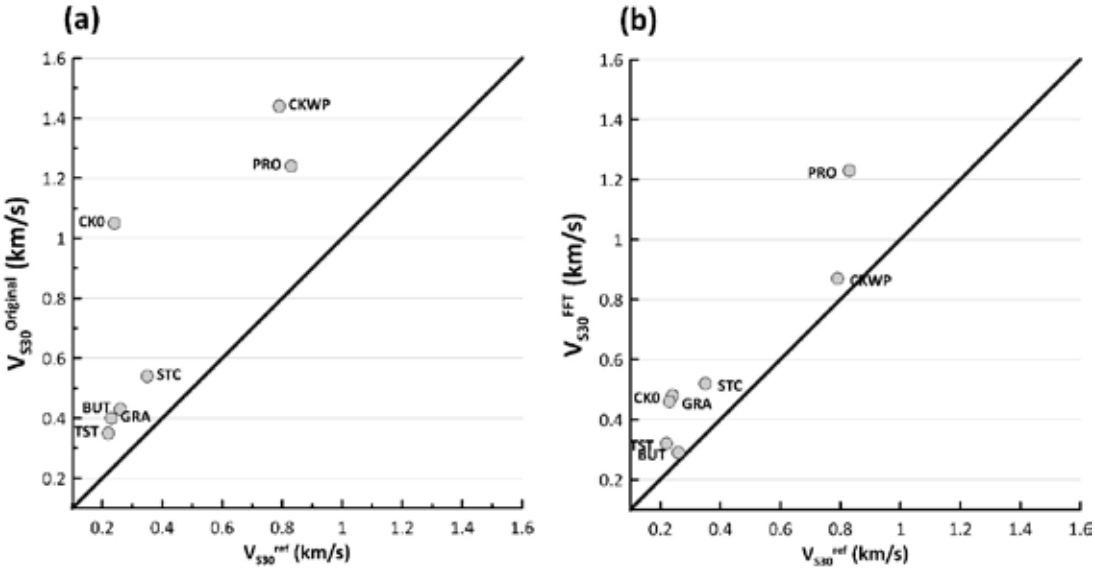

Figure 4. Plot of (a) $V_{S30}^{Original}$ and (b) V_{S30}^{FFT} as a function of V_{S30}^{ref} of each station, estimated from various active and passive seismic methods. The 1:1 line is also presented.

Conclusions

We have processed seven selected stations from two seismic arrays (EUROSEISTEST and ARGONET) located in sedimentary basins with well-documented velocity profiles and a large number of seismic records from regional earthquakes. These stations were chosen to test and refine the P-wave seismogram method for estimating V_{S30} values, focusing on both time-domain and frequency-domain approaches. Specifically, the use of FFT and imposing an SNR threshold on the radial component significantly reduced errors for most stations, bringing the estimated V_{S30}^{FFT} values closer to the reference values. However, the station GRA remains an exception, with noisy waveforms likely contributing to larger errors. This highlights the critical role of the picking process, which is particularly sensitive to noise, especially for stations in soft-soil conditions.

CK0, one of the noisiest stations, presented challenges in the time-domain approach, where its U_R/U_Z ratio was highly exaggerated. After applying the frequency-domain methodology, only 78 waveforms (less than 50% of the total dataset) were retained due to the SNR filter, leading to much better results. Similarly, other stations, especially those in ARGONET, benefited significantly from the frequency-domain approach, with notable improvements in V_{S30} estimates. The results also suggest that the softer the formation at a station's location, the lower the U_R/U_Z ratio tends to be, consistent with theoretical expectations. Stations such as BUT, which have a reference V_{S30}^{ref} value close to the V_{S30}^{FFT}, exhibited a median U_R/U_Z of ~0.11, whereas GRA, with noisier data, showed a higher median U_R/U_Z of ~0.16.

In conclusion, the proposed frequency-domain approach can enhance the reliability of V_{S30} estimations, particularly in noisy environments or soft-soil conditions. However, challenges are still present regarding the handling of noisy data, such as at GRA, where an additional refinement of the proposed approach may be necessary. The findings underscore the potential of frequency-domain analysis to improve site condition assessment, but additional investigation is needed to address the remaining discrepancies and optimize the approach for broader applications.

Acknowledgements
We would like to thank D. M. Boore for sharing with us the unpublished coefficients for V_{SZ} to V_{S30} conversion equations.

References

Aki, K., and P. G. Richards, (2002). Quantitative Seismology, University Science Books, Sausalito CA, 700.
Aristotle University of Thessaloniki. (1993). EUROSEISTEST Strong Motion Network [Data set]. International Federation of Digital Seismograph Networks. https://doi.org/10.7914/SN/EG
Berge-Thierry, C., A. Svay, A. Laurendeau, T. Chartier, V. Perron, C. Guyonnet-Benaize, E. Kishta, R. Cottereau, F. Lopez-Caballero, F.Hollender, B. Richard, F. Ragueneau, F. Voldoire, F. Banci, I. Zentner, N. Moussallam, M. Lancieri, P. Y. Bard, S. Grange, S. Erlicher and N. Theodoulidis (2017). Toward an integrated seismic risk assessment for nuclear safety improving current French methodologies through the SINAPS@ research project, Nucl. Eng. Des. 323 185–201.
Beyreuther, M., R. Barsch, L. Krischer, T. Megies, Y. Behr, and J. Wassermann (2010). ObsPy: A Python toolbox for seismology SRL 81 530–533.
Boore, D. M., E. M. Thompson, and H. Cadet (2011). Regional correlations of VS30 and velocities averaged over depths less than and greater than 30 meters, Bull. Seism. Soc. Am. 101 3046–3059.
Chatzis N., C. Papazachos, N. Theodoulidis, N. Klimis, M. Anthymidis (2018). 1D VS MODELS BY SINGLE-STATION NOISE DATA INVERSION AND JOINT INTERPRETATION WITH INDEPENDENT DATA, 16th European conference on earthquake engineering, Thessaloniki 18-21 June.
Chatzis N., C. Papazachos, N. Theodoulidis, P. Hatzidimitriou, G. Vougioukalakis, M. Paulatto, B. Heath, E. Hooft, D. Troomey, M. Anthymidis, C. Ventouzi (2022). Metamorphic bedrock geometry of Santorini using HVSR information and geophysical modeling of ambient noise and active-source surface-wave data. J. Volcanol. Geotherm. Res. 432 107692.
Crotwell, H. P., and T. J. Owens (1999). The TauP Toolkit: Flexible Seismic Travel-Time and Raypath Utilities, SRL 70 154–160.
Cushing, E. M., F. Hollender, D. Moiriat, C. Guyonnet-Benaize, N. Theodoulidis, E. Pons-Branchu, S. Sépulcre, P. Y. Bard, C. Cornou, A. Dechamp, A Mariscal, and Z. Roumelioti (2020). Building a three dimensional model of the active Plio-Quaternary basin of Argostoli (Cephalonia Island, Greece): An integrated geophysical and geological approach, Eng. Geol. 2265 105441
EN 1998-1 (2004). Eurocode 8: Design of structures for earthquake resistance – Part 1: General rules, seismic actions and rules for buildings, European Union Regulation 305/2011, Directive 98/34/EC, Directive 2004/18/EC
Kang, S., B. Kim, H. J. Park, and J. Lee. (2020). Automated procedure for estimating VS30 utilizing P-wave seismograms and its application to Japan, Eng. Geol. 264 105388.
Kim, B., Y. M. A. Hashash, E. M. Rathje, J. P. Stewart, S. Ni, P. G. Somerville, A. R. Kottke, W. J. Silva, and K. W. Cambell (2016). Sub-surface shear wave velocity characterization using P-wave seismograms in Central and Eastern North America, Earthq. Spectra 32 143–169.
Kim, J., B. Kim, and H. Cho (2020). Shear Wave Velocity Estimation in Korea Using P-Wave Seismograms, KSCE J. Civ. Eng. 24 3650–3658. J. Seismol
Lee, J., K. H. Kim, S. Y. Kang, M. Son, & B. Kim. (2022). Shear-wave velocity map for Pohang Basin, South Korea, based on the P-wave seismogram method, Earthq. Spectra 38 2162–2182.
Li, Z., S. Ni, & P. Somerville (2014). Resolving shallow shear-wave velocity structure beneath station CBN by waveform modeling of the Mw 5.8 mineral, Virginia, earthquake sequence, Bull. Seism. Soc. Am. 104 944–952.
Li, M., and E. M. Rathje (2023). Evaluation of the P-wave seismogram approach to estimate VS30 in California, Earthq. Spectra 39 454-477.
Miao, Y., Y. Shi, and S. Y. Wanga (2018). Estimating near-surface shear wave velocity using the p-wave seismograms method in Japan, Earthq. Spectra 34 1955–1971.
NEHRP (1997). Recommended Provisions for Seismic Regulations for New Buildings (FEMA 273), Washington, DC, Federal Emergency Management Agency.
Ni, S., Z. Li, and P. Somerville (2014). Estimating subsurface shear velocity with radial to vertical ratio of local P Waves, SRL 85 82–90.
Papazachos, B. C., and C. Papazachou (2003). The earthquakes of Greece, Ziti Editions (3rd Edition), 288.
Papazachos, C., and G. Nolet (1997). P and S deep velocity structure of the Hellenic area obtained by robust nonlinear inversion of travel times, J. Geophys. Res. Solid Earth 102 8349–8367.
Pappa, E., C. Papazachos, N. Chatzis, I. Grendas, N. Theodoulidis, and P. Triantafyllidis (2025). Analyzing the stability of P-wave Seismogram method for estimating VS30: Insights from two accelerometer arrays in Greece, BSSA (accepted for publication).
Raptakis, D., F. J. Chávez-García, K. Makra, and K. Pitilakis (2000). Site effects at Euroseistest-I. Determination of the valley structure and confrontation of observations with 1D analysis, Soil Dyn. Earthq. Eng. 19 1-22.
Skarlatoudis, A. A., H. K. Thio, and P. G. Somerville (2022). Estimating shallow shear-wave velocity profiles in Alaska using the initial portion of P waves from local earthquakes, Earthq. Spectra 38 1076–1102.
Theodoulidis, N., F. Hollender, A. Mariscal, D. Moiriat, P. Y. Bard, A. Konidaris, M. Cushing, K. Konstantinidou, and Z. Roumelioti. (2018). The ARGONET (Greece) seismic observatory: An accelerometric vertical array and its data, SRL 89 1555–1565.
Wald, D. J., and T. I. Allen (2007). Topographic slope as a proxy for seismic site conditions and amplification, Bull. Seismol. Soc. Am. 97 1379–1395.
Zalachoris, G., E. M. Rathje, and J. G. Paine (2017). VS30 Characterization of Texas, Oklahoma, and Kansas using the P-wave seismogram method, Earthq. Spectra 33 943–961.

17th INTERNATIONAL CONGRESS of the Geological Society of Greece

BULLETIN OF THE GEOLOGICAL SOCIETY OF GREECE, SP. PUBL.

EXTENDED ABSTRACT 252

Preliminary results of High-Resolution Microgravity Monitoring During the 2025 Santorini Unrest

Paraskevas M.[1,2], Katsafados I.[1,2], Anastasiou D.[1], Tsakiri M[1]., Nomikou P[3]., Synolakis C[4].

(1) Hellenic Military Geographical Service, john.katsafados@gmail.com
(2) National Technical University of Athens
(3) National and Kapodistrian University of Athens
(4) University of Southern California and Academy of Athens

Research Highlights

- Gravity changes during early 2025 suggest renewed subsurface activity in Santorini.
-Integrated microgravity and GNSS monitoring reveal localized mass redistributions.

Introduction

The Santorini volcanic complex is well known around the globe, largely due to the catastrophic Bronze Age eruption (~1600 BCE), possibly contributing to the collapse of the Minoan civilization (Bruins et al 2008, Friedrich 2000; Pyle 1990). The last eruption occurred in 1950, after which the volcano remained dormant. Between January 2011 and February 2012, significant unrest was recorded, characterized by seismicity, ground uplift of approximately 14 cm, and changes in fumarolic gas compositions (Newman et al. 2012; Parks et al. 2012; Tassi et al. 2013; Tarchini et al. 2019). After this unrest period, gravity surveys were conducted by the National Technical University of Athens (NTUA) in 2012 and 2014. The processing of these datasets indicated the injection of approximately 330 billion kg of basaltic magma at a depth of ~3 km, north of Nea Kameni, and highlighted concurrent changes in the hydrothermal regime (Paraskevas et al, 2023).

Beginning in August 2024, preliminary GNSS and InSAR observations indicated renewed ground uplift, marking the onset of a new phase of geophysical unrest (Paraskevas et al. 2023). Since late January 2025, Santorini has experienced a significant seismic swarm, centered primarily offshore between Santorini and Amorgos islands. Over 50,000 earthquakes have been recorded from January 31, 2025 to April 8, 2025 (Margarita Segou, British Geological Survey, pers. comm) , several exceeding magnitudes 4.0, with the largest event reaching M 5.3 on February 10, 2025(National Observation of Athens). These developments triggered a targeted gravity survey conducted from 7 to 13 February 2025.

Methods

Between February 7 and 13, 2025, a high-resolution gravity survey was carried out at Santorini, during which a total of 865 gravity measurements were collected at 137 established stations distributed across Santorini (96 stations), Nea Kameni (18 stations), Thirasia (8 stations), and Anydros (15 stations). All measurements were referenced to a fixed base station (ID 2000) located in Santorini, with a calibrated absolute gravity value of 979992.9261 mGal. Data processing was conducted using a least squares adjustment approach, incorporating 677 gravity observations to resolve 137 unknown station values, resulting in 540 degrees of freedom. The initial variance factor (σ^2) of 0.225 and the maximum residual of 0.0394 mGal indicated an overestimation of the observational errors. Consequently, a rescaling of weights and standard deviations was applied, yielding robust absolute gravity values for each of the 137 stations referenced to the Santorini base station. Following the derivation of these absolute gravity values, Free-Air and Complete Bouguer anomaly maps were produced according to the methodology thoroughly detailed by Paraskevas et al. (2024). Subsequently, offshore gravity measurements from the PROTEUS project (Hooft et al. 2015) were integrated with the new onshore data, enabling the generation of updated and comprehensive Free-Air and Complete Bouguer gravity anomaly maps for the Santorini volcanic complex and its surroundings

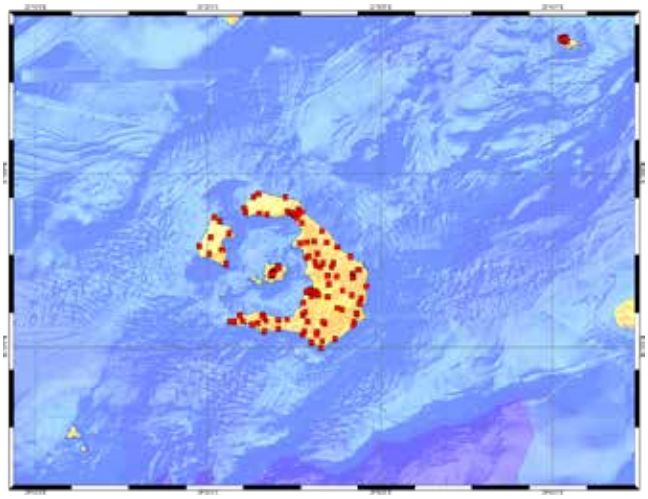

Figure 1 – 137 Gravity stations measured from 7 to 13 Feb 25

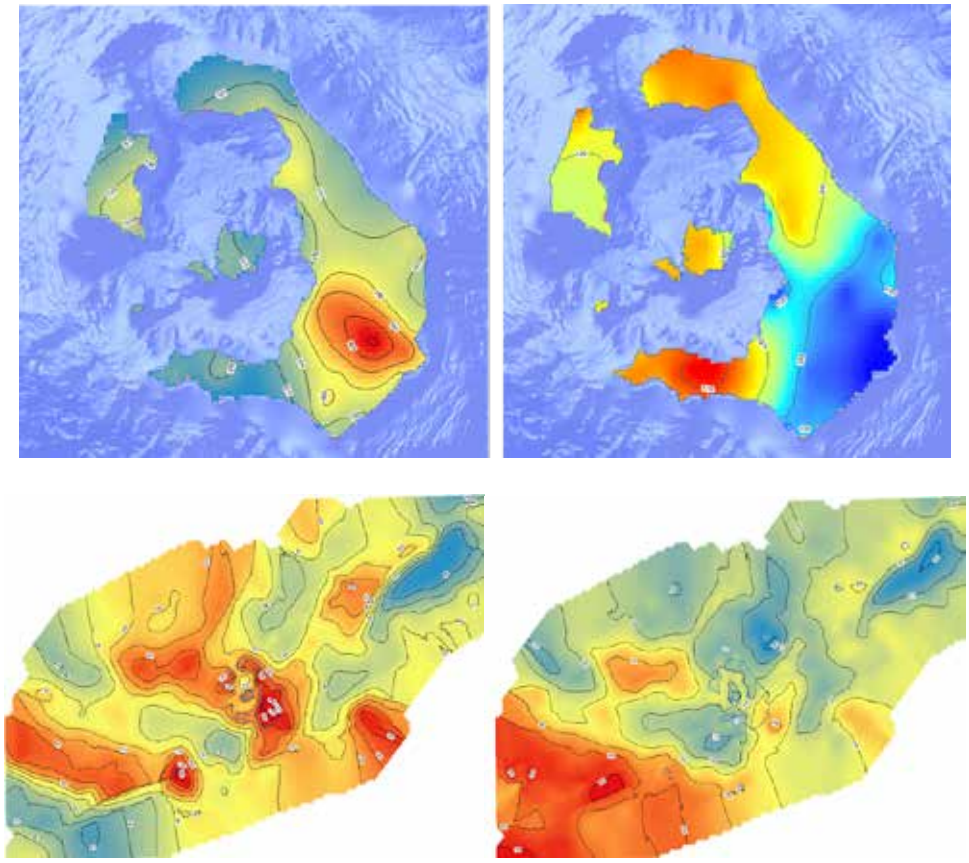

Data Analysis

Out of the 137 stations surveyed in 2025, 93 stations had previously been measured in either 2012 or 2014, providing a baseline for temporal gravity comparisons. At these 93 stations, absolute gravity values from the current study were directly compared with those earlier measurements. Subsequently, gravity effects associated with ground deformation were isolated and removed using GNSS and InSar-derived displacement data, allowing for the calculation of residual spatiotemporal gravity variations within the study area. The results of this comparative analysis are illustrated in Figure 4. These preliminary results indicate the presence of a subsurface mass deficit beneath the Santorini volcanic system during the period of measurements, primarily focused in the area of Nea Kameni and extending northwestward towards Kolumbo. Additionally, statistically significant gravity variations highlight a notable subsurface mass redistribution within the broader Santorini volcanic complex.

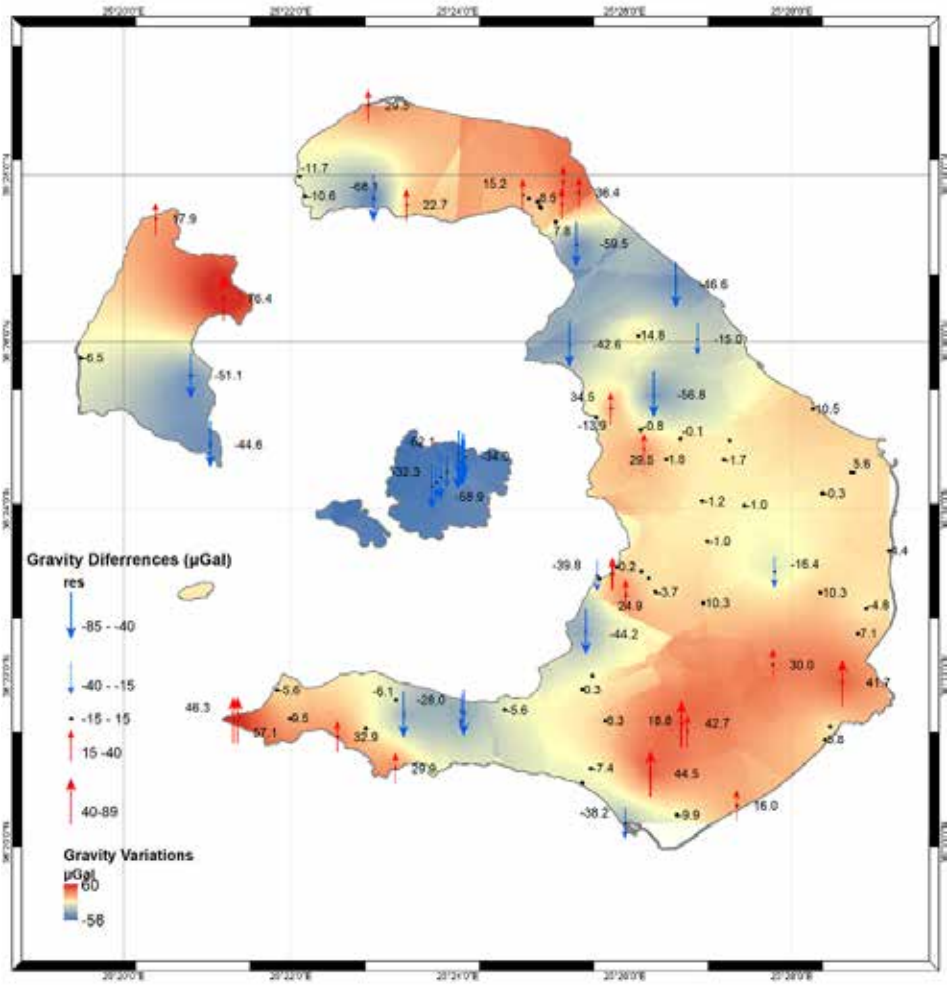

Figure 4 – Spatiotemporal Gravity changes from 2025 to 2012 or 2014

Conclusions

The high-resolution microgravity measurements conducted between February 7 and 13, 2025, provide critical insights into the ongoing geophysical unrest at the Santorini volcanic complex. The comparative analysis of gravity data collected in 2025 against previous measurements from 2012 and 2014 reveals statistically significant spatiotemporal gravity variations, indicative of substantial subsurface mass redistribution processes. The observed mass deficit, predominantly beneath Nea Kameni and extending northwest toward Kolumbo, strongly suggests changes in the volcanic and hydrothermal systems. These preliminary findings highlight the importance of integrating gravity monitoring with GNSS and InSAR deformation analyses, underscoring their collective capability to enhance our understanding and monitoring of volcanic unrest. Continued monitoring and multidisciplinary analyses are recommended to refine interpretations and provide timely updates on potential volcanic hazards.

References

Bruins H.J., MacGillivray, J.A., Synolakis C.E., Benjamini C., Keller J., Kisch H.J, Klugel A, van der Plicht, J., 2008, Geoarchaeological tsunami deposits at Palaikastro (Crete) and the Late Minoan IA eruption of Santorini, Journal of Archeological Sciences 35 , 191– 212, doi:10.1016/j.jas.2007.08.017.

Friedrich, W.L. 2000. Fire in the Sea: The Santorini Volcano and the Lost Atlantis. Cambridge University Press, Cambridge.

Hooft E. E. E., ToomeyD. Nomikou P., 2015: PROTEUS: Plumb in reservoirs of the Earth under Santorini.MGL1521Cruise report 2015,website:https://pages.uoregon.edu/emilie/PROTEUS/

Newman, A.V., Stiros, S., Feng, L., Psimoulis, P., Moschas, F., Saltogianni, V., Jiang, Y.,Papazachos, C., Panagiotopoulos, D.G., Karagianni, E. and Vamvakaris, D., 2012. Recent geodetic unrest at Santorini Caldera, Greece, Geophys. Res. Lett., 39, L06309, doi:10.1029/2012GL051286..

Paraskevas M.,Paradissis D., Raptakis C., Nomikou P., Hooft, E., Bejelou K. (2021). Gravity observations on Santorini island (Greece): Historical and recent campaigns. Contributions to Geophysics and Geodesy. 51. 24. 10.31577/congeo.2021.51.1.1.

Paraskevas M. (2024). Πεδίο Βαρύτητας Ελλαδικού Χώρου με έμφαση στην περιοχή της Σαντορίνης, Μάρτιος 2024, PhD Thesis(in Greek). http://dx.doi.org/10.13140/RG.2.2.11448.76807

Paraskevas M., Paradissis D., Hooft E., Nomikou P., Spatiotemporal gravity changes at the Santorini Volcanic complex and their interpretation, Quaternary Science Advances, Volume 13,2024, 100140, ISSN 2666-0334, https://doi.org/10.1016/j.qsa.2023.100140.

Parks, M.M., Moore, J., Papanikolaou, X., Biggs, J., Mather, T.A., Pyle, D.M., Raptakis, C., Paradissis, D., Hooper, A., Parsons, B. and Nomikou, P., 2015. From quiescence to unrest - 20 years of satellite geodetic measurements at Santorini volcano, Greece, Journal of Geophysical Research (Solid Earth), 120, 1309-1328, doi: 10.1002/2014JB011540.

Pyle, D.M. and Elliott, J.R., 2006. Quantitative morphology, recent evolution and future activity of the Kameni islands volcano, Santorini, Greece, Geosphere 2, 253-268

Tarchini, L., Carapezza, M.L., Ranaldi, M. 2019. Fluid geochemistry contribution to the interpretation of the 2011–2012 unrest of Santorini, Greece. Tectonics 38, no. 2: 552–575.

Tassi, F., Vaselli, O., Papazachos, C.B., Giannini, L., Chiodini, G., Vougioukalakis, G.E., Panagiotopoulos, D. 2013. Geochemical and isotopic changes in fumarolic and submerged gas discharges during the 2011–2012 unrest at Santorini caldera (Greece). Bulletin of Volcanology 75: 711.

17th INTERNATIONAL CONGRESS of the Geological Society of Greece

BULLETIN OF THE GEOLOGICAL SOCIETY OF GREECE, SP. PUBL.

EXTENDED ABSTRACT 253

Stone bridges. Resilience to catastrophic phenomena

Paschos Panagiotis
Dr Geologist
Hellenic Survey of Geology and Mineral Exploration (H.S.G.M.E.), Regional Branch of Epirus, Eleonas, 48100 Preveza. Greece

Introduction / Background

Epirus, being an integral part of Greece with the complex geodynamic evolution that remains active until today, is characterized by the diversity of relief elements, featuring a set of successive mountain ranges with rapid and abrupt altitude changes and a dense hydrographic network.

Numerous settlements, endowed with abundant natural resources (water, food) and protected throughout history, evolved within this environment. Due to the mountainous nature of the area, the construction of bridges was of paramount significance, as it facilitated the free movement of inhabitants from one place to another.

This presentation describes the results of the project: Recording stone bridges in the Region of Epirus that face problems from catastrophic phenomena. The project is implemented by EAGME, with funding from the Public Investment Program.

In the Region of Epirus, there are several stone bridges as a result of the intense relief and the multifaceted dissection of the hydrographic network. These bridges are architectural monuments of exceptional aesthetics and are part of the cultural identity of the region. However, the action of catastrophic phenomena (earthquakes, floods, landslides) but in some cases also human intervention result in the deterioration of these monuments. The fact of the collapse of the Plaka Bridge is an example to avoid similar incidents.

The bridges were constructed from blocks of limestone and sandstone, which are common building materials in the area.

The bridges' foundation positions were chosen so as to ensure their stability and durability against the flooding phenomena of the streams and rivers.

They were located at narrow passages where the cross-section of the stream was confined.

Stone bridges receive the entire volume of water during flood conditions, as well as large quantities of accumulated debris from mud, stones and wood, along with all sorts of objects/materials that were discarded on the slopes and the beds of torrents and rivers.

The hydraulic restriction regarding the amount of water that has to pass only through the bridges' arches creates an increase in water velocity that is accompanied, in some cases, by erosion of the riverbed and damage to the bridge pedestal.

High rainfall is a frequently occurring phenomenon in the area of Epirus. Sometimes recorded extremely high rainfall that takes place in the region

Considering that due to the lithology of the catchment area (flyschic background with limited infiltration) all these quantities of water accumulate abruptly and flow downstream, forming flood conditions.

With this specific project, the bridges that have been affected and are at risk from the ongoing action of the destructive phenomena are recorded in cooperation with Municipalities of Epirus and in collaboration with the Service of Modern Monuments and Technical Works of Epirus, North Ionian and West Macedonia.

The identification, prevention and minimization of the corrosive processes affecting the foundation platforms, especially during flooding conditions, as well as the submission of proposals for their mitigation, constitute determining factors as far as the bridges' protection is concerned.

The procedures and actions that will be launched, after the completion of the project, to remove the risk and restore the possible damage to the bridges, will require combined interventions and collaborations of several scientific specialties and specialized technicians. This will create, in addition to preservation, a turnover and the creation of jobs. Through this project, knowledge will be enriched for minimizing the consequences of the action of the destructive phenomena.

Stone bridges constitute part of the cultural heritage of Greece and most of them have been designated, by legislative regulations, as protected monuments. Responsible for their protection is the Service of Modern Monuments and Technical Works of Epirus, North Ionian and West Macedonia, whereas the local authorities play a crucial role in the implementation of protection measures and monitoring.

Figure 1. Panoramic view of the bridge. Damage from vegetation and erosion to the foundation can be seen.

Figure 2. Detail of erosion in the foundation pedestal.

References

Αράπογλου Μιχάλης, 1981. Γεφύρια του Ζαγορίσιου χώρου, Δελτίο Κέντρου Ερευνών Ζαγορίου, τεύχος 1,

Βλαχοστέργιος Ι., Λύτρα Α., Παπαχριστοδούλου Γ., 2013. Τα πετρογέφυρα της Ηπείρου, Φωτογραφικό άλμπουμ, ΥΝΜ&ΤΕ Ηπείρου, 213 σελ.

Γκράσσος Γεώργιος,2007. Τα πέτρινα τοξωτά γεφύρια της Ελλάδας, Κέντρο Περιβαλλοντικής Εκπαίδευσης Μακρινίτσας, ISBN: 978-960-98043-9-4

Μαντάς Σπύρος, 2020. Γεφυρογραφία της Πίνδου και των Όμορων περιοχών, 5 Τόμοι, Περιφερειακό ταμείο Ανάπτυξης Ηπείρου. Αρχείο γεφυριών Ηπειρωτικών. Ιωάννινα.

Τσομπανάκης Δ., Δημουβγία Α. 2019. Καταγραφή και μελέτη των πέτρινων γεφυριών της Περιφερειακής ενότητας Κοζάνης, Διεύθυνση τεχνικών έργων ΠΕ Κοζάνης, 48 σελ.

17th INTERNATIONAL CONGRESS of the Geological Society of Greece

BULLETIN OF THE GEOLOGICAL SOCIETY OF GREECE, SP. PUBL.

EXTENDED ABSTRACT 254

Mineralogy and Geochemistry of the polymetallic nodules of the Clarion Clipperton Zone, NE Pacific.

Passali N[1]., Sakellaris G.A. [1], Melfou M[1]., Papadopoulou L. [1], Kantiranis N. [1]
(1) Faculty of Geology, Aristotle University of Thessaloniki, 54124 Thessaloniki, Greece, npassali@geo.auth.gr

Abstract
The Clarion Clipperton Zone (CCZ), located in the Northeast Pacific Ocean between the Hawaii islands and Mexico, is a region known for its polymetallic nodules. These nodules are iron and manganese-rich concretions formed of concentric layers of hydroxides and are found on the ocean floor, at depths ranging from 3500 to 6500 meters. They contain valuable metals such as nickel, copper, cobalt, and rare earth elements, making them a potential resource for various high-tech applications. This study focuses on the mineralogical and geochemical analysis of polymetallic nodules collected from the eastern part of the CCZ. X-ray Diffraction (XRD) and Scanning Electron Microscopy (SEM) with EDS techniques were used to investigate the mineral composition, morphology and textures of these nodules. Special attention is given to key minerals such as manganese oxides, todorokite, and birnessite, which serve as indicators of growth processes as well as concentric layering patterns and compositions to identify the specific environmental and geochemical conditions under which these formed.

Introduction

The existence of manganese (Mn) or polymetallic nodules has been known since the early 19th century but it was during the Challenger expedition of 1873–1876 that they were recognized for their significance as metal resources. It was only after World War II that the nodules became focus of detailed research, due to their unique ability to absorb important metals from seawater and form valuable ore deposits. However, the exploration and interest in their potential economic use diminished, due to technical, economic and environmental challenges. In recent years, the interest in the polymetallic nodules has revived, as they can be important source of nickel, copper, cobalt, and rare earth metals. These elements are essential for the continuous advancement of high technologies, the transition to green energy systems, and the development of efficient energy storage systems.

Manganese, ferromanganese and polymetallic nodules are metal-rich concretions found on the deep ocean floor, in depths ranging from 3500 to 6500 meters. Their size ranges from a few millimeters to several centimeters and exhibit irregular shapes. Structurally they consist of multiple, concentric micron-thick layers that form around a core, growing in an extremely slow rate over millions of years. The central core, may either be of biogenetic origin such as shark tooth, or of sedimentary origin such as sand grains, and rock fragments.

Manganese nodules form over millions of years through two main processes: hydrogenetic and diagenetic growth. In the hydrogenetic growth process, the minerals precipitate directly from oxic seawater and their mineralogy is dominated by vernadite (δ-MnO□) and amorphous δ-FeOOH phase (Halbach et. al., 1988). Their composition is characterized by low Mn/Fe ratio (≤3) and relatively low concentrations of Ni and Cu. Hydrogenetic nodules are found commonly in seamounts and on their slopes. When nodules grow diagenetically, the metals precipitate from the sediment pore water under oxic conditions. The Mn/Fe ratio is between 3 and 10 and Ni and Cu concentrations are significantly higher. Todorokite, -a phyllomanganate mineral, and birnessite are the most common Mn-minerals. Nodules that form through the influence of both processes are named as mixed-type nodules and are characteristic of the CCZ (Halbach et al., 1981).

This research work investigates several polymetallic nodules from the CCZ with focus on their internal structures, mineralogy and mineralogical textures in micron-scale. The primary objective is to classify the nodules based on their formation processes (hydrogenic or diagenetic).

Geological Setting of the Clarion Clipperton Zone

The Clarion Clipperton zone is a vast segment of the Pacific Oceanic Plate located in the northeastern Pacific Ocean. It covers an area of approximately 5 million square kilometers, which is equivalent to the size of continental Europe.

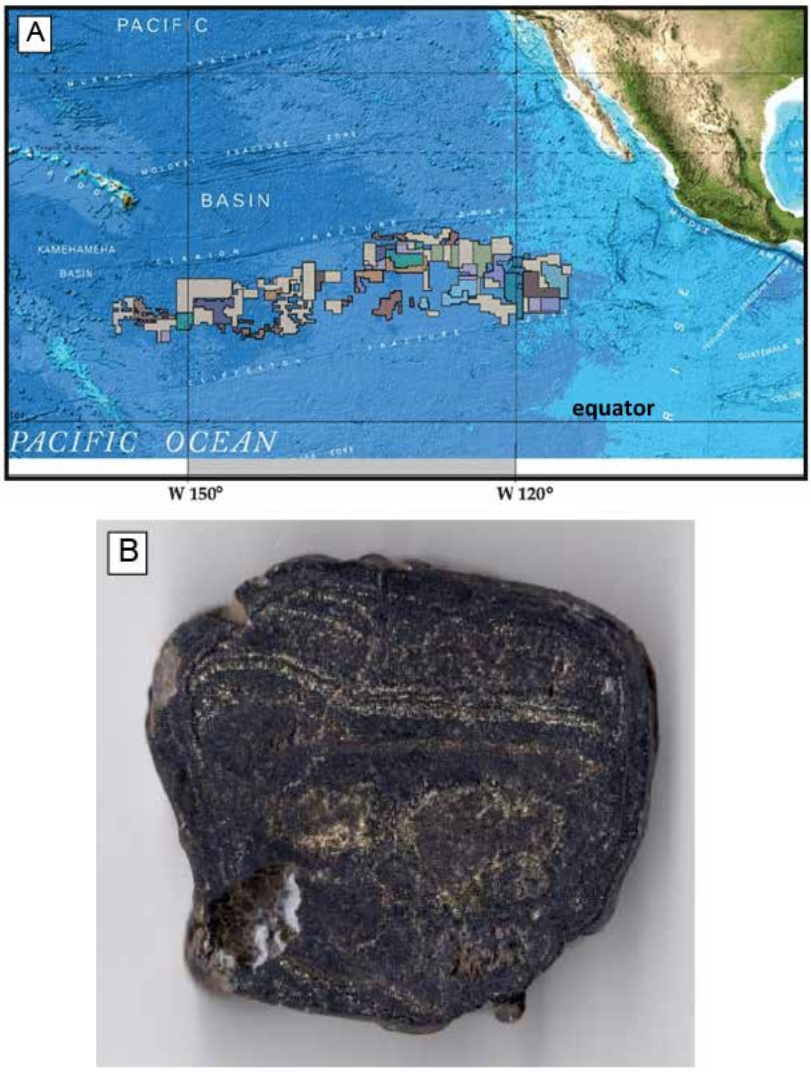

Figure 1. A) Map showing the location of the Clarion Clipperton Zone and the numerous exploration areas (Abramowski et al., 2021). B) Polished slab of a typical polymetallic nodule from the CCZ studied in this work.

The depth is relatively uniform and ranges from 4000 meters to the southeast up to 5000 meters in the northwest. The CCZ lies between of two major fracture zones: The Clarion to the north and the Clipperton to the south. The seabed of the CCZ is predominately composed of basaltic abyssal hills covered by layers of siliceous and calcareous sediments (Parianos et al., 2021). The abyssal hills are the result of normal faulting at mid-ocean ridges, that formed horst and graben structures, indicative of the extensional tectonic regime during opening of the Pacific Ocean. Other occurring geomorphological features include volcanic knolls, seamounts, and lava outcrops.

Samples and Methodology

Approximately 3 kilograms of individual polymetallic nodules were made available for this study by the AllSeas Group S.A. X-ray Diffraction (XRD) was used for the identification and characterization of mineral phases based on their crystallographic structure. The nodules were first heated at 140ºC for 24h and then crushed powdered in homogenous samples and finally pressed into holders. The X-ray Diffractometer used is D8 ADVANCE BRUKER. Polished thin sections were prepared for microscopic examination using a Zeiss Axioscope 40 Pol, and by backscattered electron imaging with a JEOL JSM-6390LV scanning electron microscope (SEM) equipped with INCA 300 energy-dispersive X-ray Spectroscopy (EDS). All sample preparation and analytical procedures were carried out in the laboratory facilities of the Mineralogy-Petrology-Economic Geology at the Department of Geology, Aristotle University of Thessaloniki.

Results

Nodule mineralogy: The XRD analysis revealed that the main mineral phases found in most samples are a) todorokite $Mn_6O_{12}(H_2O)_4$, b) birnessite $MnO_2(H_2O)$, c) manganese dioxide MnO_2 or vernadite (and/or hydroxide), d) goethite FeO(OH), e) quartz SiO_2, f) baryte $BaSO_4$, and, g) ilmenite $FeTiO_3$ (Figure 2). Other aluminosilicates observed are illite $(K,H_3O)(Al,Mg,Fe)_2(Si,Al)_4O_{10}(OH)_2\ nH_2O$, smectite (and probably zeolite), and detrital anorthite $(Ca,Na)_x(Al,Si)_xSi_2O_8$.

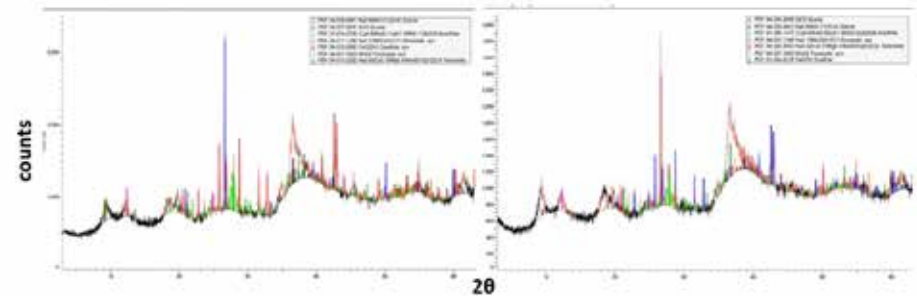

Figure 2. Typical X-ray powder diffractograms from two samples (No.205, No.104). Peak positions indicate the main minerals identified as listed in the legend box.

Manganoan mineral textures and chemistry:

a) MnO_2 and $Mn(OH)_2$: In BSE imaging vernadite is the brightest mineral after barite and ilmenite found as finely crystalline, botryoidal, or in dendritic structures (Figure 3, 4). It contains > 70 wt % MnO_2 and significant amounts of Fe, Ni and Cu as well as impurities of Si, Al, Na and Mg.

b) Todorokite and Birnessite: These form concentric zones where todorokite is slightly brighter than birnessite because it incorporates higher levels of heavier metal cations (Ni, Cu) in its structure. However, these are difficult to distinguish because of the incorporation of various amounts (or impurities) of clay minerals. They both contain commonly more than 40% MnO_2, Fe, Ni and Cu up to 10% in total (oxides), and locally very high amounts of Si and Al.

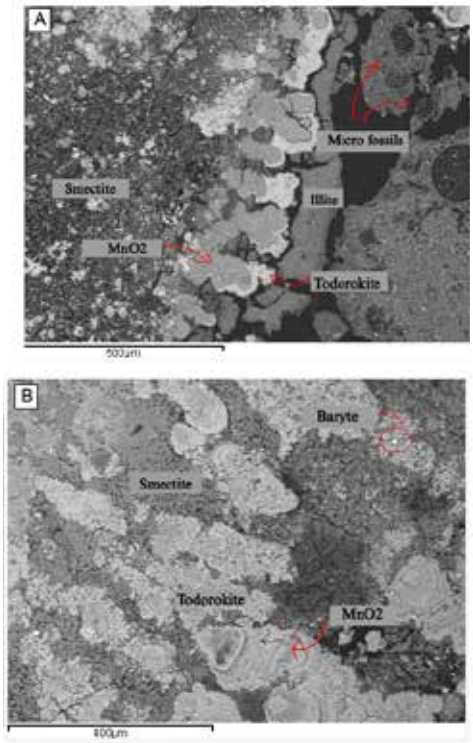

Figure 3. BSE high resolution images of: A) sample CCZ101 showing the different layers and microfossils (possibly radiolaria). B) sample CCZ206 showing the dendritic structures of the manganoan oxides, bright white are baryte crystals.

SEM analyses revealed three distinct types of layers based on texture and composition (labeled as 1-3):
Layer Type 1: These layers exhibit low reflectivity and appear dense with columnar growth. Energy Dispersive Spectroscopy (EDS) spot analyses show Mn/Fe ratios ranging from 0.53 to 4.24, and Ni+Cu contents between 0.16 and 2.55 wt %. These layers are indicative of the hydrogenetic growth process.
Layer Type 2: These layers show high reflectivity and are the most dominant in the nodules, with characteristic dendritic, porous growth patterns. These dendritic zones contribute to the high porosity of the nodules. EDS spot analyses reveal Mn/Fe ratios ranging from 1 to 30, with Ni+Cu contents averaging 3.9 wt %, reaching a maximum of 6.5 wt %. These layers are characteristic of the diagenetic growth process.
Mixed Layer Type 3: These layers have low reflectivity and a columnar growth pattern, with Mn/Fe ratios ranging from 3 to 11 and Ni+Cu contents ranging from 1 to 4.6 wt %. These layers represent a transitional type from Layer Type 1 to Layer Type 2.

Elemental Distribution:
The element map shown in Figure 4 illustrates the distribution of the critical metals in different layers of the nodule. Iron, Ni, Cu, and Mg show a similar distribution pattern to Mn, indicating that these metals are absorbed by the layered and tubular structure of the phyllomanganate minerals, such as birnessite and todorokite, respectively. Areas enriched with Si and Al correspond to the non-crystalline aluminosilicates (e.g., smectite).

Aluminosilicates:
The chemical composition of the aluminosilicates in the nodules varies widely, including smectites, illite, and their manganous varieties. These aluminosilicates are primarily deposited directly on the seafloor or form through early diagenetic processes.

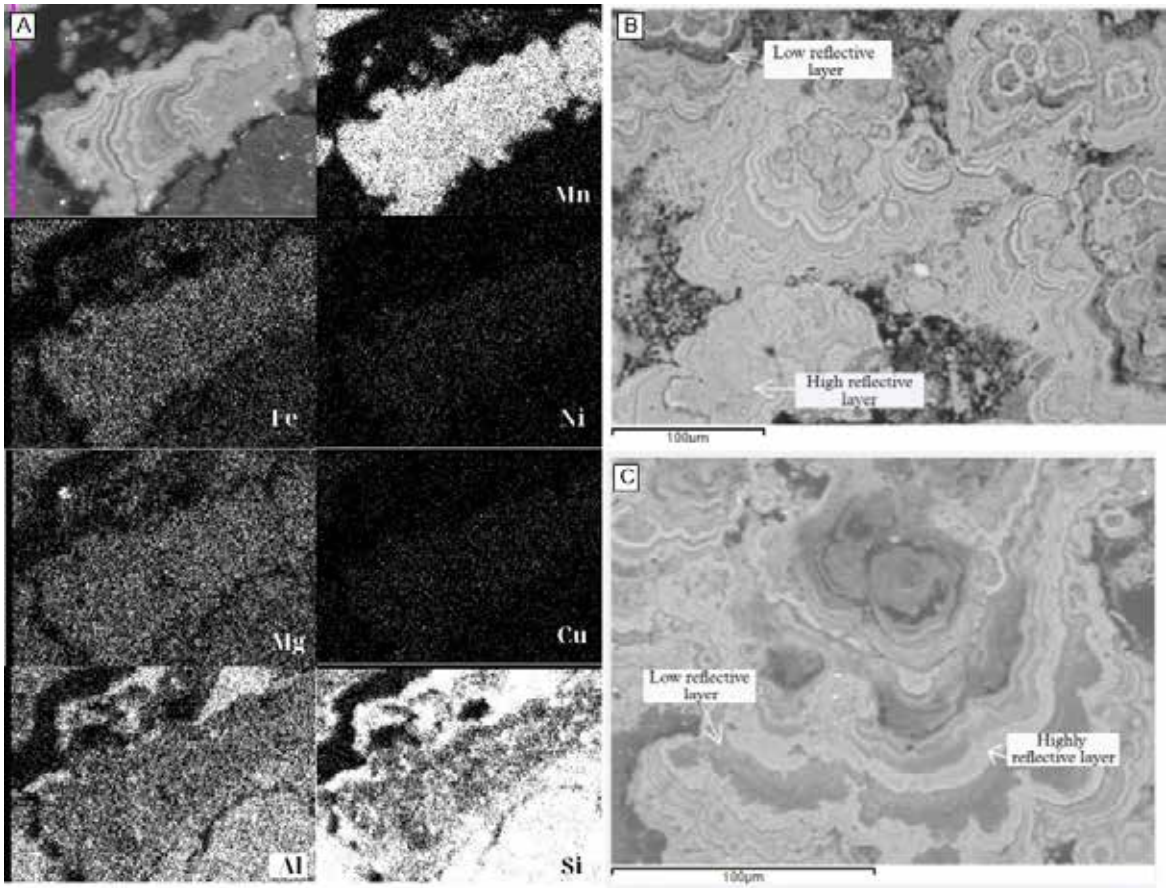

Figure 4. A) SEM-EDS elemental mapping images showing the distribution of metals in the high-manganese layers (sample CCZ203). B) BSE images of concentric layers of types 1 to 3. The higher the reflectivity intensity, the greater the manganese content.

Discussion and conclusions

The polymetallic manganese nodules of the Clarion-Clipperton Zone (CCZ) consist of macroscopically distinguishable layers, which include fine-grained, partially crystallized clays (e.g., smectite, illite) containing detrital quartz, plagioclase, ilmenite, and abundant visible microfossils. These layers alternate with metal-rich layers primarily composed of vernadite, todorokite, and birnessite. Baryte, in the form of small acicular crystals, is a common accessory mineral.

The phyllomanganates are not present as pure phases; rather, they incorporate significant amounts of substituted cations such as Fe, Ni, Mg, and Cu, as well as impurities from surrounding sediments. These impurities result in elevated concentrations of SiO□, Al□O□, and trace metals (e.g., Ti), contributing to the complex compositions of the manganese minerals. Additionally, manganese-rich clays, most likely Mn-smectite (e.g., Mn-nontronite), were identified in the nodules.

These aluminosilicates are typical clay minerals, primarily deposited directly on the seafloor (e.g., smectite) or formed through early diagenetic processes (e.g., illite). The detrital material, such as quartz and ilmenite, accumulated from the erosion of basaltic rocks and was transported by deep ocean currents. Based on the mineralogy and textures observed, the manganese minerals in the nodules formed through both hydrogenetic and diagenetic growth processes. The presence of dendritic todorokite, enriched in Ni, Cu, and Mg, suggests these metals are concentrated within its tunnel structure, while the higher Mn/Fe ratios (compared to birnessite) indicate a diagenetic origin. The Ni, Cu, and Mn metals may have originated from multiple sources, including terrestrial influx and hydrothermal activity associated with the East Pacific Rise (Piper et al., 1981).

Minerals such as vernadite (MnO□) and birnessite, which contain higher Fe, Ca, and Na, likely precipitated directly from oxic seawater during hydrogenetic growth due to their layered structure. The presence of baryte in the nodules further supports the diagenetic processes involved, likely precipitating from sulfate-rich pore waters enriched in barium released from biogenic material (e.g., radiolarians) or organic degradation. Baryte formation may have occurred alongside todorokite. In conclusion, the nodules from this part of the CCZ exhibit a mixed-type hydrogenetic-diagenetic growth pattern, consistent with the observations of Halbach et al. (1981).

Acknowledgements

We express our sincere gratitude to AllSeas S.A. and particularly Mr. Wouter Duijnstee for their generous provision of the samples used in this study.

References

Abramowski T., Urbanek M., 3 Baláž P. (2021). Structural Economic Assessment of Polymetallic Nodules Mining Project with Updates to Present Market Conditions, Minerals 2021, 11(3), 311.

Baturin, G. N. (1987). The Geochemistry of Manganese and Manganese Nodules in the Ocean. In G. N. Baturin (Ed.), *Sedimentology and Petroleum Geology* (pp. 1–166). Dordrecht: D. Reidel Publishing Company.

Dekov, V. M., Rouxel, O., Gu´eguen, B., Wegorzewski, A. V., Khripounoff, A., & Menot, L. (2021). Mn-micronodules from the sediments of the Clarion-Clipperton zone (Pacific Ocean): Origin, elemental source, and Fe-Cu-Zn-isotope composition. *Chemical Geology*, *580*, 120388. [Journal Article]

Halbach, P. (1986). Processes controlling the heavy metal distribution in Pacific ferromanganese nodules and crusts. *Geologische Rundschau*, *75*(1), 235–247.

Halbach, P., Friedrich, G., & Stackelberg, U. (1988). *The Manganese Nodule Belt of the Pacific*. Stuttgart: Enke Verlag.

Hein, J.R. (2016). Manganese Nodules. In J. Harff, M. Meschede, S. Petersen, & J. Thiede (Eds.), *Encyclopedia of Marine Geosciences* (pp. 408–412).

Hüneke, H., & Mulder, T. (Eds.) (2011). *Deep-sea sediments* (Developments in Sedimentology, 63). Amsterdam: Elsevier.

Parianos, J., & Madureira, P. (2021). Geomorphology of the Clarion Clipperton Zone, tropical North Pacific Ocean. *Journal of Maps*, *17*(2), 901–909.

Piper, D.Z., & Williamson, M.E. (1981). Mineralogy and Composition of Concentric Layers Within a Manganese Nodule from the North Pacific Ocean. *Marine Geology*, *40*, 255–268. [Journal Article]

Wegorzewski, A. V. (2015). *Geochemical and mineralogical investigations of fine growth structures of ferromanganese nodules from the Clarion and Clipperton Zone, Pacific Ocean* [Dissertation]. Gottfried Wilhelm Leibniz Universität Hannover.

17th INTERNATIONAL CONGRESS of the Geological Society of Greece

BULLETIN OF THE GEOLOGICAL SOCIETY OF GREECE, SP. PUBL.

EXTENDED ABSTRACT 255

A Pilot Study of Erosion in the Mavro Lithari Beach, part of the Highly Urbanized Coastal Zone of the Eastern Saronic Gulf, through the use of drone technology

Paschali Patouchi Adamantia[1], Ioannis P. Panagiotopoulos[1], Dimitrios Vandarakis[2]

(1) Faculty of Geology and Geoenvironment, School of Science, National and Kapodistrian University of Athens, University Campus, Zografou, Greece, adama_paschali_patouhi@yahoo.com

(2) Hellenic Centre for Marine Research, Institute of Oceanography, Anavyssos, Greece

Introduction

On the basis of aerial photographs collected from seasonal drone flights between May and November 2023, a shoreline retreat of 1-2 m in the central part of Mavro Lithari beach was observed, which can be characterized not very significant in comparison to other places of the Saronic Gulf.

Beaches are dynamic geomorphic systems that are in constant evolution and can be affected by a number of human and natural factors leading to erosion. Specifically, the increase in coastal population, combined with climate change, have disturbed the annual balance of erosive and reserve processes (it has become negative in the majority of cases), so that erosion is now a permanent regime even within an annual cycle of beach evolution, especially when human populations occupy the active part of the beach and create conditions of 'coastal squeeze'. Such conditions are now the norm in highly urbanized coastal areas.

In Greece, coastal erosion threatens more than 30% of its coastlines, making it one of the country's most important environmental problems. In particular, the coastal areas of Attica face significant environmental and aesthetic degradation due to excessive urbanization, due to the artificial transport of sediment from the hinterland to the coast (with the transported sediment subject to erosion) and due to the development of facilities and structures to serve tourism and trade (Belibassakis and Karathanasi, 2017). Human interventions and coastal erosion lead to ecosystem degradation and the destruction of shorelines that are important paleo-indicators of a beach's changes while protecting it from further erosion (Koutsomichou et al, 2009).

Regarding the Saronic Gulf and the phenomenon of its coastal erosion, this seems to be linked to human interventions, to climatic factors, to the change in sea level and at the same time to the tectonics that characterizes the Gulf. The Gulf is characterized by moderate seismicity, with the northern and western Gulf margins exhibiting high magnitude historical and recent earthquakes, associated with the presently active N-S extensional tectonic regime (Foutrakis and Anastasakis, 2020). The basin of the Gulf forms a complex neotectonic structure in the NW edge of the inner, modern, Hellenic volcanic arc, while a relatively shallow underwater ridge at its central portion demarcates the eastern from the western part of the basin (Kolaiti and Mourtzas, 2016). This central platform implies the existence of a NNE–SSW trending rupture zone, which is probably the offshore extension of a large thrust belt dominating the adjacent onshore areas (Drakatos et al., 2005).

For the study of erosion and the short- and long-term assessment of changes in a coastline, drone technology has become particularly effective. According to Joyce et al. (2023), drone technology is well suited to providing data in coastal environments and offers flexible timeframes that sequentially cover continuous changes in coastal dynamics; it can be applied to a variety of data types while offering better spatial resolution than that offered by other modes of survey (such as aircraft and satellites), as drones move at lower altitudes and therefore closer to the area of interest. In addition, their data can be combined with free satellite data to produce high fidelity images, which can then be used to build digital terrain models (DEMs and DTMs) and surface models (DSMs). Of course, drone technology presents its own challenges when using it in research, a topic that is beyond the scope of this research.

Objectives

The aim of this research is to investigate, using drone technology, the extent of erosive processes in the highly urbanized coastal zone of the Eastern Saronic Gulf, by determining the extent of horizontal shoreline displacement at the touristic beach of Mavro Lithari within two consecutive seasons - spring and autumn - of 2023. Understanding the size and dynamics of the active part of a beach is crucial for the sustainable environmental management of the wider coastal zone, although each beach due to its particular physiographic features may show smaller or larger deviations from the general morphological trend of the wider coastal area.

Methods

The collection of high-resolution images from the beach of Mavro Lithari in the two different seasons of 2023 (spring and autumn) was carried out using a rotor-wing UAS, the 'DJI Matrice 210 RTK' model series (Figure 1). This drone is one of the most suitable for coastal monitoring, and thanks to its RTK antenna equipment it shows great stability in flight, even in conditions with strong winds. Moreover, this type of drone can support different types of sensors and, therefore, can be applied in a variety of research fields (Vandarakis et all., 2016). At the same time, 14 Ground Control Points (GCPs) were selected for the georeferencing of the

collected aerial photographs, 7 points for the flight that took place in the spring season and additional 7 points for the autumn flight. In general, the use of GCPs (these are black and white targets of 25 cm × 25 cm., see Figure 1) plays an important role in maximizing the positional accuracy of the collected aerial photographs.
Therefore, the methodology followed was based on the use of drone technology for the collection of high-resolution aerial photographs and their processing through the Pix4D Mapper software in order to compose two orthophoto maps, one for the spring period (early May 2023) and one for the autumn period (late November 2023). Thus, the overall processing of the recorded data, led to the conversion of the orthophotomosaic into a format of two maps with all the necessary elements (such as orientation, scale, background and description of details), using ArcGIS Pro software. At the end, a combined, also, map was created that included both seasonal orthophotos in order to achieve a comparison of the results of the two flights performed (Figure 2).

Figure 1: The DJI Matrice 210 RTK drone and one of the seven GCPs

Results

Based on the acquisition and processing of the data collected, the orthophotos and the corresponding maps that were produced, the combined map showed the shoreline change between the two seasons (Figure 2). The comparison of the two seasonal orthophoto maps indicated an obvious shoreline retreat in the central part of Mavro Lithari beach, by the end of autumn, of 1-2 m. This calculation has not been influenced by the negligible error values (absolute and relevant), as showed in the comparative data of Table 1. The retreat of 1-2 m is an expected seasonal (probably) temporary retreat of the shoreline, as the physiography of the Saronic Gulf does not favor the development of frequent extreme wave conditions, while Mavro Lithari beach has not been subject to much human intervention in the active sedimentation zone, as the case is in other coastal areas of the Saronic Gulf (e.g. Ormos Faliros, Alimos, Glyfada), which present much more significant erosion processes.

Absolute camera position and orientation uncertainties (sigma) for the May 2023 orthophotomosaic

	X(m)	Y(m)	Z(m)	Omega(degrees)	Phi(degrees)	Kappa(degrees)
Mean	0,064	0,046	0,123	0,034	0,033	0,009
Sigma	0,013	0,016	0,011	0,014	0,010	0,002

Relevant camera position and orientation uncertainties (sigma) for the May 2023 orthophotomosaic

	X(m)	Y(m)	Z(m)	Omega(degrees)	Phi(degrees)	Kappa(degrees)
Mean	0,022	0,023	0,031	0,060	0,032	0,011
Sigma	0,005	0,008	0,015	0,026	0,013	0,002

Absolute camera position and orientation uncertainties (sigma) for the November 2023 orthophotomosaic

	X(m)	Y(m)	Z(m)	Omega(degrees)	Phi(degrees)	Kappa(degrees)
Mean	0,343	0,364	0,577	0,176	0,169	0,155
Sigma	0,054	0,071	0,034	0,008	0,005	0,003

Relevant camera position and orientation uncertainties (sigma) for the November 2023 orthophotomosaic

	X(m)	Y(m)	Z(m)	Omega(degrees)	Phi(degrees)	Kappa(degrees)
Mean	0,020	0,022	0,027	0,062	0,031	0,012
Sigma	0,004	0,006	0,012	0,025	0,013	0,003

Table 1. Absolute and relevant camera position and orientation uncertainties

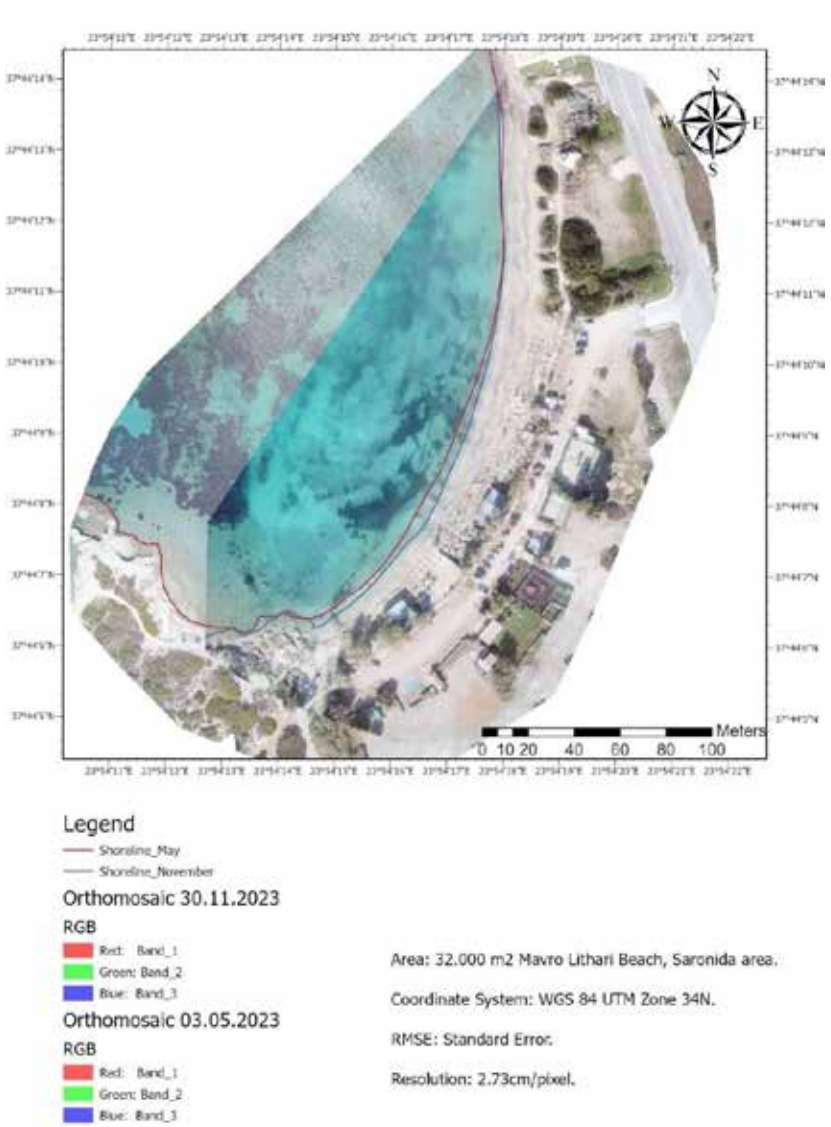

Figure 2: Combination of the two seasonal orthophotomosaics for the beach of Mavro Lithari

Discussion and Conclusions

The orthophotos produced by the two flights of the DJI Matrice 210 RTK drone showed that the shoreline in the central part of the study area receded by 1-2 m. It is considered that this shoreline shift probably represents a seasonal, temporary situation, as the beach of Mavro Lithari has not been subjected to significant human interventions (which are an erosional factor), while at the same time it is part of a bay whose general physiography favors only a small frequency of extreme wave conditions. Regarding the uncertainties of the determined erosion amplitude at Mavro Lithari beach, as calculated by the relevant Pix4D software of the two flights, they show very low error values, so the 1-2 m shoreline retreat is realistic and indicative of the degree of receding of a natural beach in the Eastern Saronic Gulf, albeit probably seasonally.

These results seem particularly interesting if we compare them with other studies for the Saronic Gulf. For example, Skilodimou et al. (2021) state that in the last 76 years the coastline has been enhanced by 40% in terms of extension (e.g. through earth filings, technical works, artificial structures) and the 60% of its total length is artificial, 29% includes rocky shores and the remaining part consists of beaches. The largest interventions have been made in Ormos Faliro (287%), Alimos (256%) and Glyfada (194%), areas with a higher coastal erosion. For comparative purposes, Figure 3 shows the artificial extension (tens to hundreds of meters) of various shorelines in the Eastern Saronic Gulf, which is the main factor of coastal erosion in the region. In our case, with the measurements showing a much smaller erosive area compared to the above-mentioned areas of the Saronic Gulf, this can be interpreted due to the physiography of the Mavro Lithari beach and the fewer human interventions (or absence of them).

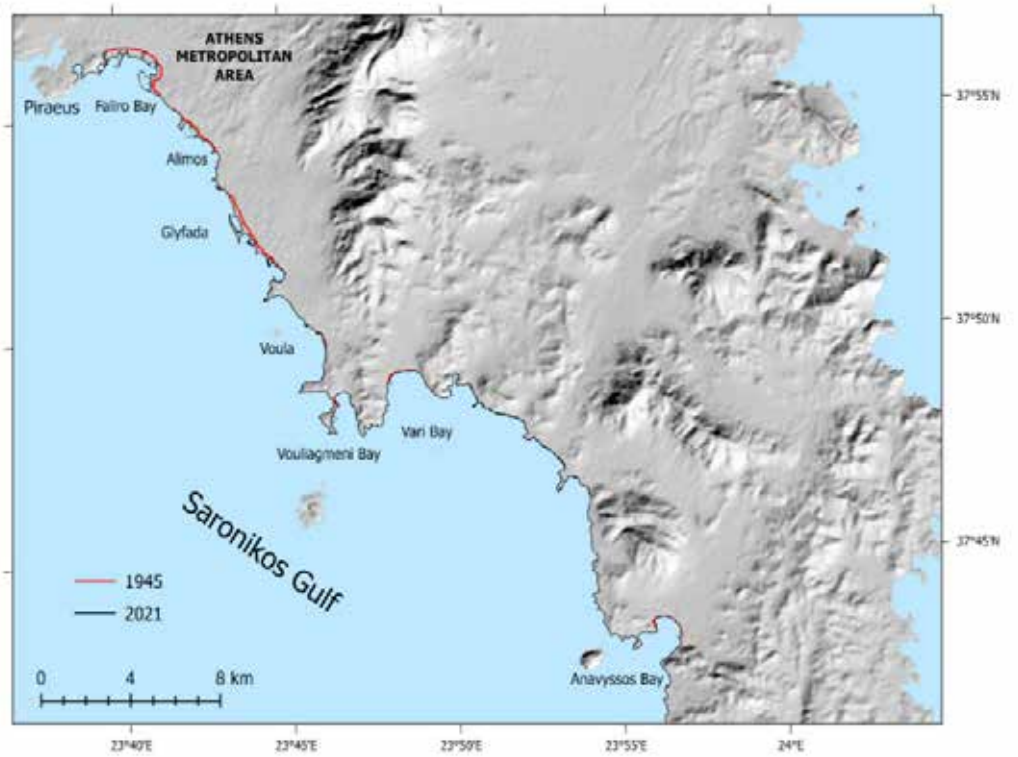

Figure 3: Shoreline changes in the northwest of the studied beach of Black Lithari (red arrow) which has undergone intense changes over the last decades (from Skilodimou et al., 2021)

The results of the research also highlight that drone technology is a very useful and versatile tool, which can produce very high resolution orthophotos and thus accurately capture the changes of coastlines in different regions of the planet at regular intervals, thus contributing significantly to the study of the phenomenon of coastal erosion, which is critical for humanity.
To conclude the discussion, our research has some limitations: a) the measurements were made between 3 May and 30 November 2023, so they cannot capture inter-annual changes; b) the research would be more complete if there were data related to the quality of sediments and rocks in the area as well as wave and wind data.

References

Belibassakis, K.A., Karathanasi, F.E., 2017. Modelling nearshore hydrodynamics and circulation under the impact of high waves at the coast of Vakia in Saronic-Athens Gulf. Oceanologia 59, 350-364.

Drakatos, G., Karastathis, V., Makris, J., Papoulia, J., Stavrakakis, G., 2005. 3D crustal structure in the neotectonic basin of the Gulf of Saronikos (Greece). Tectonophysics 400, 55–65.

Foutrakis, M.P., Anastasakis, G., 2020. Quaternary continental shelf basins of Saronikos Gulf, Aegean Sea. Geo-Marine Letters, 40, 629–647.

Guerrera, F., Martín-Martín, M., Tramontana, M., Nimon, B., Kpémoua K.E., 2021. Shoreline changes and coastal erosion: The case study of the Coast of Togo (Bight of Benin, West Africa Margin). Geosciences 11, Article No 40.

Joyce, K.E., Fickas, K.C., Kalamandeen, M., 2023. The unique value proposition for using drones to map coastal ecosystems. Cambridge Prisms: Coastal Futures 1, e6, 1-10.

Kolaiti, E., Mourtzas, N.D., 2016. Upper Holocene sea level changes in the West Saronic Gulf, Greece, Quantenary International, 401, 71-90.

Koutsomichou, I., Poulos, S., Evelpidou, N., Anagnostou, C., Chionis, G., Vassilopoulos, A., 2009. The role of beachrock formations in the evolution of embayed coastal zones of Attica (Greece) in relation to sea level rise. The case of Kalyvia beach zone. Geografia Fisica e Dinamica Quaternaria 32, 49-56.

Skilodimou, D.H., Antoniou, V., Bathrellos, D.G, Tsami, E., 2021. Mapping of coastline changes in Athens Riviera over the past 76 years' measurements. Water 13, Article No 2135.

Vandarakis, D., Pavlopoulos, K., Kapsimalis, V., 2016. Coastal geomorphological features and geoarchaeological potential of Kavouri Bay, Attica, Greece. 14th International Conference of the Geological Society of Greece, Thessaloniki, 25-27 May, Bulletin of the Geological Society of Greece, vol. L, pp. 265-273.

17th INTERNATIONAL CONGRESS of the Geological Society of Greece

BULLETIN OF THE GEOLOGICAL SOCIETY OF GREECE, SP. PUBL.

EXTENDED ABSTRACT 256

Active Faulting in Santorini and the recent intra-caldera (2024-2025) seismic activity along the Kameni-Fira Fault line

Pavlides S.[1], Karastathis V.[2], Mouzakiotis E.[2], Sboras S.[2], Chatzipetros A.[1], Lazos I.[1]
(1) School of Geology, Aristotle University of Thessaloniki, Greece, pavlides@geo.auth.gr
(2) Institute of Geodynamics, National Observatory of Athens, Greece

This paper presents certain elements of the neotectonic and active structure of the Santorini island complex. The active structures consist of sets of primarily normal fault systems with right-lateral component in an *en échelon* pattern, trending at or around N30°E (Mountrakis et al., 1998). Another important and common feature on Santorini is the feeder dykes that are related with those faults. Along the major Columbo fault line, which appears to start at the southernmost tip of Therassia Island (Cape Trypiti) and stretch up to the Columbo submarine volcano and Anhydros Islet, they are primarily concentrated on the northern narrow part of the island, north of Mikros Prophitis Elias ridge.

The Fira normal fault is another active structure that is visible in the caldera walls. Significant tectonic evidence of recent activity may be seen on the Yialos Caldera cliff, including fractured and tilted late Quaternary volcanic layers, as well as new on-land tectonic scarps. A syn-depositional normal fault, it is a significant structure that deforms various volcanic lava layers, scoria, and pyroclastic flows. As evidenced by the microseismic activity during the 2011–2012 crisis and the one ongoing since the end of 2024, this fault is classified as active.

A large scarp of the same strike affects the relief along the fault-line and continues farther to the northeast on the island, even though volcanic material near the topmost part of the fault appears undeformed. It is thought to be a longer, seismically hazardous structure that follows the tectonic line of the Kameni volcano. The fault was modelled by using data from a UAV campaign, that allowed for the construction of a precise DTM (Figure 1, Pavlides & Chatzipetros, 2018). It shows that fault throw episodically declines upward on the caldera's highly steep inner escarpment, from 22 m at sea level to nearly 2 m at the highest point (Pavlides et al., 2025, this volume).

Two extensional contemporary stress phases have been documented, implying that the first is attributed to the tectonic stresses related to the well-established Aegean motion towards SSW, whereas the second, which gives rise to recent microseismicity of the area, is a local stress regime attributed to buoyancy forces relating to magmatic processes of the area (Pavlides & Tranos 2014). Therefore, the combination of these two stress regimes reflects the competition between the tectonic (lithospheric) and magmatic (local volcano-tectonic) forces, in a fault-dynamic regime that could be characterized as extensional-transtentional field.

During the 2024-2025 volcano-seismotectonic crisis, the Fira fault ("Kameni line") is activated producing a shallow sequence which slowly initiated in the beginning of late September 2024 and is still in progress. More than 200 eventst were recorded within the study region for this period and their hypocentres were calculated using the NonLinLoc earthquake location algorithm (Lomax et al., 2000) along with the local 1D velocity model proposed for the region by Dimitriadis et al. (2009). The NonLinLoc algorithm utilizes the equal-differential-time (EDT) likelihood function (Zhou, 1994; Font et al., 2004), which uses travel-time differences between observed and synthetic travel times for pairs of stations, resulting to a more robust calculation of the optimal hypocentral location, due to the fact that the 4-D problem (x,y,z, t) is reduced to a 3-D search over space (x,y,z). Furthermore, mispicked phase data can be identified by the methodology and excluded from the solution. Due to the large number of local seismographic stations at a very close proximity to the sequence, for most of the located events the horizontal error was as low as 0.5km, whereas the vertical (depth) error was between 0.8-1.2 km. The majority of the sequence's hypocentres is located at shallow depths (3-8 km). The strongest earthquake (ML 3.6) occurred on January 25, 2025. The moderately linear horizontal trend of the epicentres is main the characteristic of the sequence.

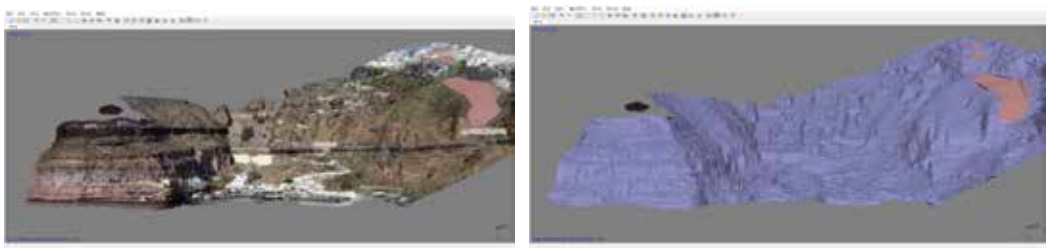

Figure 1. Digital Terrain Model of the Yialos cliff face, where the Fira fault is observed deforming the layers of lavas and pyroclastics. It was obtained through a targeted UAV campaign (Pavlides & Chatzipetros, 2018). Left image shows the outcrop photomosaic draped over the 3D model, which is shown at the right one.

The majority of earthquakes are thought to be caused solely by tectonic forces, specifically the Fira fault. If we additionally consider the estimation of the volume and depth of the magma intrusion, some of them are most likely caused by the volcanotectonic activity. More specifically, the Fira fault likely both facilitates the magma chamber's upward progress and marks it off to the south.

All evidence, both geological and seismological, indicate that the Fira fault is an active tectonic structure. Its activated length is estimated to about 6-8 km, corresponding to a moderate expected earthquake magnitude of Mw 5.5-6.0, as calculated from known empirical relationships (Wells & Coppersmith, 1994). The fault probably extends bilaterally, i.e. toward the NE, as shown by the seismic activity of the beginning of 2025, and toward the SW as well. Northward onward intracaldera tectonic structures formation example elucidates a swelling of the volcanic edifice.

References

Dimitriadis, I., Karagianni, E., Panagiotopoulos, D., Papazachos, C., Hatzidimitriou, P., Bohnhoff, M., ... & Meier, T. (2009). Seismicity and active tectonics at Coloumbo Reef (Aegean Sea, Greece): Monitoring an active volcano at Santorini Volcanic Center using a temporary seismic network. Tectonophysics, 465(1-4), 136-149.

Font, Y., Kao, H., Lallemand, S., Liu, C. S., & Chiao, L. Y. (2004). Hypocentre determination offshore of eastern Taiwan using the Maximum Intersection method. Geophysical Journal International, 158(2), 655-675.

Lomax, A., Virieux, J., Volant, P., & Berge-Thierry, C. (2000). Probabilistic earthquake location in 3D and layered models: Introduction of a Metropolis-Gibbs method and comparison with linear locations. Advances in seismic event location, 101-134.

Mountrakis, D., Pavlides, S., Chatzipetros, A., Meletlidis, S., Tranos, M., Vougioukalakis, G., & Kilias, A., 1998. Active deformation of Santorini. In: Casale et al. (Eds), The European laboratory volcanoes, European Commission, EUR 18161 EN, 13-22.

Pavlides, S. & Chatzipetros, A. (2018). The Fira fault (Santorini, Greece) from the French "Expédition de Morée (1829□38)" to modern scientific approach, *In:* Koukousioura, O. & Chatzipetros, A. *(Eds.),* Proceedings of the 9th International INQUA Workshop on Paleoseismology, Active Tectonics and Archeoseismology, Possidi, Greece, 25-27 June 2018, 218-220.

Pavlides, S. & Tranos, M. (2012). Fault geometry and kinematics of the broader Santorini area in relation to seismic activity and volcanism. Abst. VOLSAM2012.

PavlidesS., Sboras S., LazosI., Mouzakiotis E., & Karastathis V. (2025). The Fira fault, Santorini (Thera): morphotectonic, geomorphological and seismological evidence of fault activity, 17th International Congress of the Geological Society of Greece, Mytilene, Greece.

Zhou, H.W. (1994). Rapid three□dimensional hypocentral determination using a master station method. Journal of Geophysical Research: Solid Earth, 99(B8), 15439-15455.

17th INTERNATIONAL CONGRESS of the Geological Society of Greece

BULLETIN OF THE GEOLOGICAL SOCIETY OF GREECE, SP. PUBL.

EXTENDED ABSTRACT 257

The Fira fault, Santorini (Thera): morphotectonic, geomorphological and seismological evidence of fault activity

Pavlides S.[1], Sboras S.[2], Lazos I.[2], Mouzakiotis E.[2], Karastathis V.[2]

(1) School of Geology, Aristotle University of Thessaloniki, Thessaloniki, Greece, pavlides@auth.gr (2) Institute of Geodynamics, National Observatory of Athens, Athens, Greece

Introduction

The volcanic island of Santorini, *aka* Th(i)era, is located in the central part of the Hellenic Arc (or Hellenic Subduction Zone), in the South Aegean Sea, where the Nubian (African) and Eurasian tectonic plates converge (Figure 1; Pavlides *et al*., 2024 and references there in). Santorini has a rich geological history including recent tectonic and volcanic activity, particularly in the last century. The Fira Fault (*aka* Phera) is one of the most prominent active faults in Santorini (Figure 2). It outcrops on the eastern rim of the Caldera crossing the capital town of the island, in a NE-SW direction. Santorini's fault system includes numerous faults and fractures that contribute to its seismic activity, particularly around the caldera, which has been the focus of volcanic activity for thousands of years. The Fira Fault plays a key role in the ongoing geodynamic processes of the island. In addition to this fault, there are several other active faults around the caldera, including the "Kulumbo (or Columbo) line" and the "Kamenes line" (Pfeiffer, 2001), and others that create a complex tectonic pattern in the region (Figure 2; Mountrakis *et al*., 1998; see also Nomikou *et al*., 2021; Sakellariou *et al*., 2021).

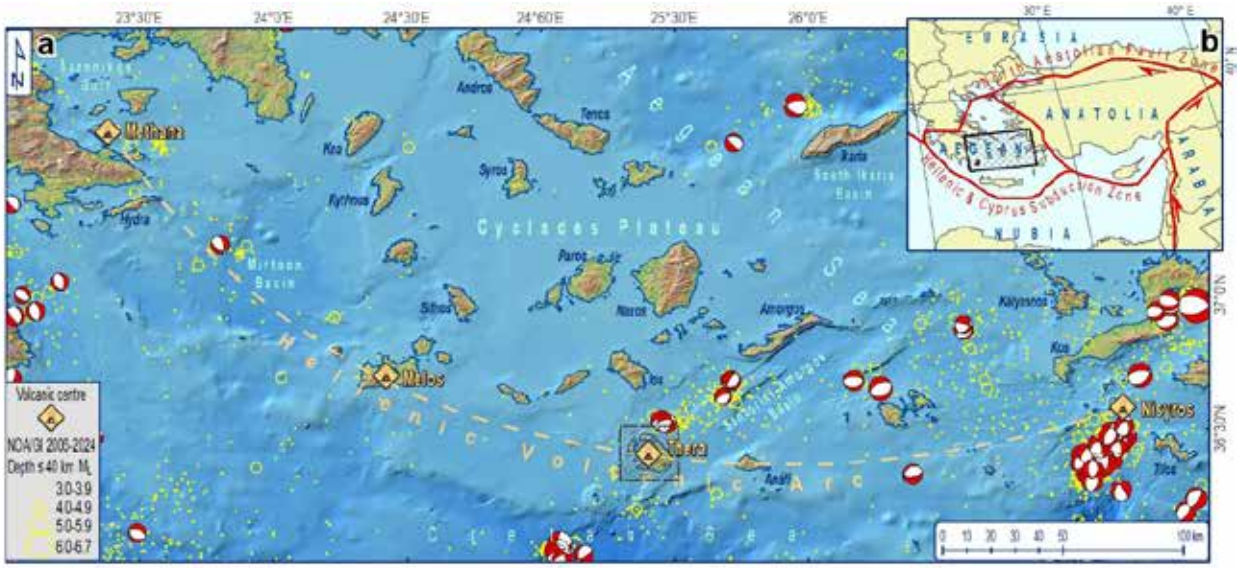

Figure 1. (a) Map of the South Aegean Sea showing seismicity (yellow circles; NOA/GI revised catalogue since 2006 for depths ≤ 40 km) and RCMT's focal mechanisms for depths ≤ 40 km (Pondrelli, 2002). The Hellenic Volcanic Arc is marked by an orange dashed line. Hatched frame indicates location of Thera as shown in Figure 2. (b) The tectonic plates boundaries in eastern Mediterranean Sea according to Bird (2003). Hatched frame indicates position of map (a).

Geodynamic & seismotectonic setting

The recent tectonic regime of the Aegean Sea is characterized by a regional extension deriving from the subducting slab's roll-back and retreat as the Hellenic Arc has been migrating southwards during the last 80 Myr (*e.g.* Le Pichon & Angelier, 1979; 1981; Jolivet *et al*., 2013; Barbot & Weiss, 2021; van der Stoel *et al*., 2024). This extension generates normal faults in the upper crust and rifting in the shallower part of the lithosphere (Jolivet *et al*., 2013). The extensional thinning of the crust facilitates the magma intrusion from the melting of the subducting slab and the emergence of the Methana, Melos, Santorini, Kolumbo and Nisyros volcanic centres which comprise the volcanic arc. The Santorini–Amorgos offshore basin is a crustal weakness zone in an overall right-lateral oblique-slip transtensional regime, representing a major structural boundary *(e.g.* Sakellariou & Tsampouraki-Kraounaki, 2019; Tsampouraki-Kraounaki *et al*., 2021).

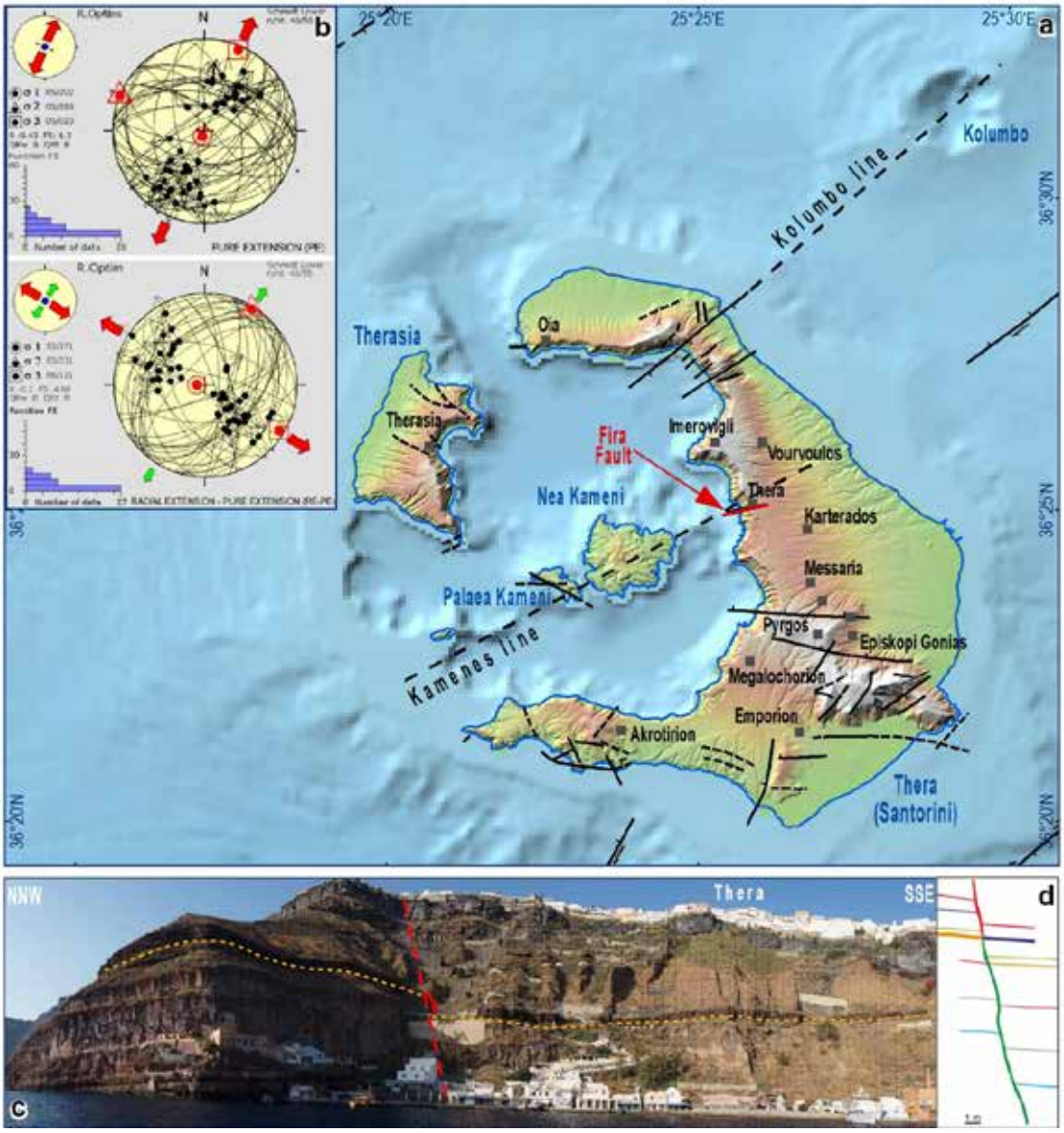

Figure 2. (a) Morphotectonic map of Santorini Island after Mountrakis *et al*. (1998). The "Kulumbo line" and "Kamenes Line" are modified from Pfeiffer (2001). (b) Meso-structural analysis of active faults on Santorini and surroundings showing two co-existing extensional stress fields: one (upper) due to pure tectonic forces (typical of the Aegean back-arc), and the other (lower) probably due to magmatic (local volcano-tectonic) forces (more radial extension). (c) Snapshot of a 3D image obtained from UAV depicting the inner caldera flank and the Fira fault cutting and downthrowing toward the SSE the lava layers (the most distinguishable layer is marked by a dashed orange line). (d) Sketch of the Fira fault and the displaced lava layers as shown in (c).

Santorini Island is an emergent remnant on the central and eastern flanks of a collapsed caldera. Its summit is preserved with over 50 active tectonic structures of the Middle Pleistocene to Holocene. Seafloor topography and subsurface fault data show a complex system of faulting from Christiana island to Amorgos island, with mainly NE trending normal and oblique faults in a right-stepping en echelon arrangement. A tectonic model demonstrating the occurrence of the volcanic centers at the fault segment boundaries is presented. In the case of Santorini – Amorgos Fault System, volcanic centers of Christiana Island, Thera – Kammeni and the submarine crater of Columbo are positioned in the boundaries of the right-stepping en echelon segments of normal and oblique faults. Fault segment boundaries comprise low strength multi-fractured parts of the upper crust, enabling insertion and ascendance of magma dykes. Possible interaction between volcanic activity and fault activation is also investigated based on the

early 20th century eruption activity in Kammeni islands and the 1956 double-earthquake event, as well as the 2011-12 volcanotectonic crisis. Dykes and fault swarms are the two main modes of brittle tectonics in the area. The active tectonic structures mainly consist of normal fault systems often in an *en-échelon* pattern. Reverse and right-lateral, or oblique-slip, faulting also occur in the area. Meso-structural analysis reveals the three main stress axes acting on Santorini and surrounding islets (Tranos & Pavlides, 2012; see also Tranos 2012): σ_1 in a NE–SW direction, σ_3 in a normal direction, and σ_2 in the third leading σ_2 direction. Santorini's tectonic structures are then probably the result of this stress field (Manning *et al*., 2020). Basaltic dykes, associated with neotectonic faulting, are another common feature in Santorini. They are aligned along the axial zone of the submarine caldera and are exposed on the marine cliffs, forming up to a 100-m wide rail on the caldera wall, concentrated on the northern narrow part of the island. The N30°E-trending arc (?) of Santorini and its orientation guide the spatial correlation in the dyke-fault system. This system is expected to be connected at depth because tensional fracturing is expected to occur in fissure eruptions and in the effects of ascending magma within the surrounding rocks (Mountrakis *et al*., 1998; Ruch *et al*., 2016). The orientation of the N30°E-striking structures, comprising mostly of normal and a few reverse faults restricted in the alpine basement, represent the local σ_3 axis. Northward, in the inner flank of the caldera, tectonic structures document a swelling of the volcanic edifice. The neotectonic map of Santorini in Figure 2 (Mountrakis *et al*., 1998) indicates the more recent tectonic structures and the active processes shaping the island's landscape. It shows the fault systems, including the Fira Fault and other fractures, which have been active in recent geologic and historical times. This map also highlights the zones of volcanic activity and deformation, which are critical for understanding the island's seismic hazards.
The faults that control the eruptive history of Santorini and changes of the magmatic chamber produce characteristic earthquake swarms. The 2011-2012 seismic crisis on Santorini is a typical example.

Morphotectonic study of the Fira fault

Neotectonic field studies on Santorini started in 1992-94 and were completed during 2016-22 (Figure 2; see Mountrakis *et al*., 1998; Pavlides & Chatzipetros, 2018). Among the on land mapped faults, the less studied is the Fira fault, named after the capital town of the Island. The fault has been a prominent feature of Fira cliff (Yalos harbour), and it has been described as a simple tectonic structure since the early French "Expédition de Morée (1829□38)". New airborne (UAV) and terrestrial (LiDAR) images were used to produce 2D and 3D photomosaics with photogrammetric methods so as to detect the location and map the Fira fault.
Meso-structural analyses, where the fault outcrops in accessible locations, indicate a normal dip-slip sense of movement with a right-lateral strike-slip component on an ENE-WSW (N60°E to70°E) striking fault. According to our 3D terrain model obtained from UAV images, on the very steep inner escarpment of the caldera, fault throw episodically decreases from 22 m at the sea level down to almost 2 m at the highest elevation where the Nomikos Conference Centre is built (Figure 2). At this point, the uppermost lava layer is affected suggesting a syn-depositional normal fault that deforms even the most recent volcanic lava layers and pyroclastic flow strata. This lava layer, which is also the last, 40-60 ka old, volcanic flow, documenting typical cooling fractures and tectonic open joints outcrop, has been vertically displaced. The episodic pattern of displacement can be interpreted as intermittent periods of possibly volcano-tectonic activity rather than simply tectonic. A non-typical fault scarp affecting the volcanics is detected in the urban area of Fira running subparallel to *i)* a longer "fault zone" which includes the known volcanic centres of Kamenes (Kamenes line), and *ii)* the large Amorgos-Thera seismic fault which produced the 1956 M7.5 earthquake (Kolumbo line). Due to its proximity to the "Kamenes line", the Fira fault can be considered as part of this line.
The Fira fault is classified as active, as it is documented not only from field observations, but also from the microseismic activity during the 2011□2012 volcano-tectonic crisis. Its activated length has estimated about 6 km, corresponding to moderate earthquake Ms 5.5 +_ , as calculated from known empirical relationships, while it is possibly extended both towards NE and SW.

Seismic Activity and the Volcanic Crisis of 2011-2012

During the 2011-2012 volcano-seismotectonic crisis, the Fira fault of the "Kamenes line" was activated producing a shallow sequence which slowly initiated in the beginning of late February 2011 and outburst in October of the same year (Kaviris et al., 2015). The strongest earthquake (M_L3.3) occurred on January 9, 2012; Five (5) earthquakes with $M_L \geq 3.0$ preceded and one followed the strongest shock.
The local seismicity for the period of interest was accurately located with the use of a local 1D velocity model proposed for the region by Dimitriadis *et al*. (2009), by applying the NonLinLoc -linear location algorithm (Lomax *et al*., 2000). The NonLinLoc algorithm utilizes the equal-differential-time (EDT) likelihood function (Zhou, 1994; Font *et al*., 2004),

which uses travel-time differences between observed and synthetic travel times for pairs of stations, resulting to a more robust calculation of the optimal hypocentral location, due to the fact that the 4-D problem (x,y,z, t) is reduced to a 3-D search over space (x,y,z). Furthermore, mispicked phase data can be identified by the methodology and excluded from the solution.

The majority of the sequence's hypocentres is concentrated at very shallow depths (2-6 km). The spatial distribution shows a quite well-formed cluster (cluster A in Figure 3 *left*) on the SW continuation of the Fira fault which moderately aligned along a NE-SW axis, *i.e.* parallel to the fault's strike. Two transverse profiles show the vertical extent of the sequence from ca. 1 km to 12 km depth (Figure 3 *right*). However, the density differs in the two profiles (Figure 3 *right*): in the profile B-B' it is much more concentrated than in profile A-A'. This also explains the moderately linear horizontal trend of the epicentres. In profile B-B', the density of hypocentres is much higher at depths shallower than 6 km. From this depth and deeper (down to 12 km), a much more linear, SSE steeply dipping trend can be observed, the upward continuation of which also marks the southern limit of the cluster. Thus, two sub-clusters can be distinguished: the shallow one, cluster A_1, down to the depth of 6 km, and the deeper one, cluster A_2, at depths between 6 and 12 km. Cluster A_2 is attributed to purely tectonic causes, and more particularly to the Fira fault. Cluster A_1 is probably due to the combined tectonic and volcanic (magmatic) activity if we also take into account the estimation of both volume and depth of the magma intrusion (Newman *et al*., 2012; Feuillet, 2013; Parks *et al*., 2012; 2015; Druitt *et al*., 2016). In more detail, the Fira fault probably restrains the magma chamber to the south and, at the same time, facilitates it movement.

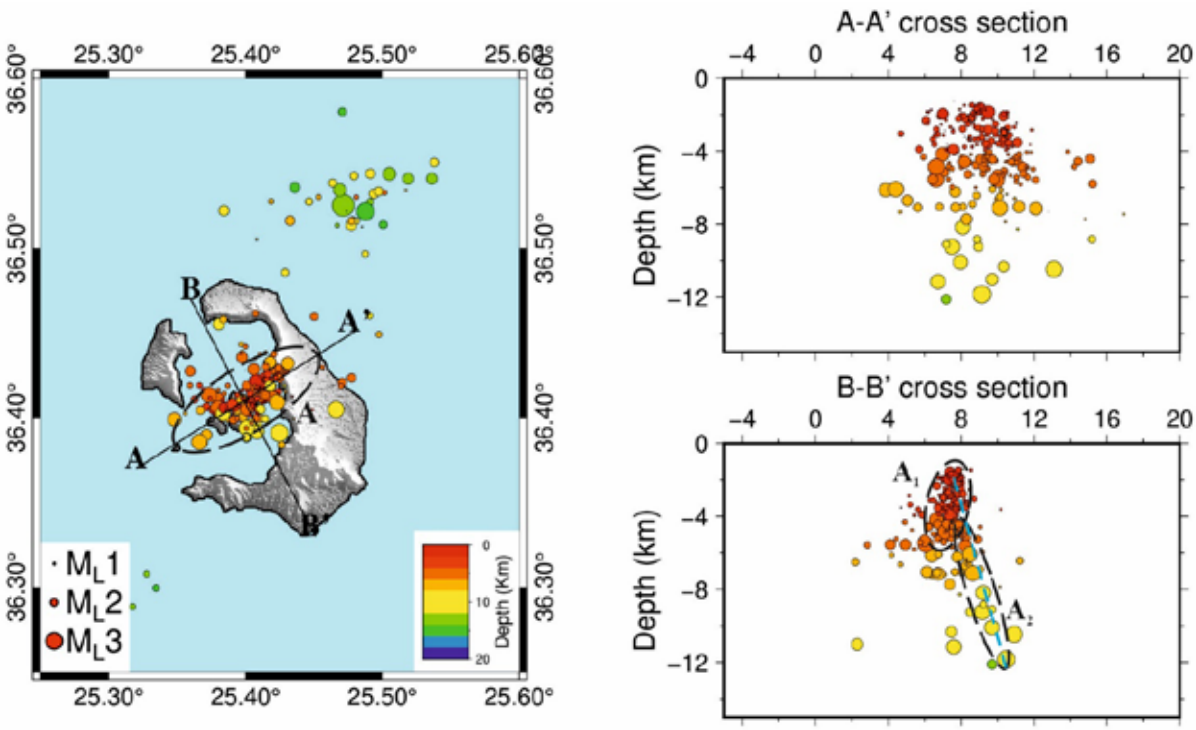

Figure 3. (Left) Relocated epicentres of the 2011-2012 crisis. The main cluster A is marked by a dashed ellipsis. A sparse concentration NE of Santorini Island is located under the Kolumbo submarine volcano. (Right) Vertical profiles of the 2011-2012 main cluster which is divided into two more sub-clusters (A_1 and A_2). The blue dashed line represents the Fira fault. The profile traces are shown on the left map.

The 2011-2012 volcanic crisis in Santorini was marked by increased seismic activity, volcanic unrest, and noticeable ground deformation. This period of volcanic crisis also involved:

- Ground deformation: There were reports of ground uplift, which is often associated with magma intrusion or movement beneath the surface (e.g. ISMOSAV, 2013). GPS measurements and InSAR images show both lateral extension and uplift, clearly suggesting inflation (Newman *et al*., 2012; Foumelis *et al*., 2013; Papoutsis *et al*., 2013; Saltogianni *et al*., 2014). This is typical in volcanic regions where magma rises and causes the earth's crust to stretch or deform.
- Magma intrusion: A magma intrusion of 10–25 million m^3 is estimated (Newman *et al*., 2012; Parks *et al*., 2012;

2015) at a depth of ca. 4 km (Druitt *et al*., 2016). This magma is suspected to be linked to the dyke systems beneath the island, contributing to the seismic events. A dyke system refers to a network of vertical or steeply inclined fractures filled with magma, often causing crustal deformation and triggering earthquakes.

Conclusions

The Fira normal fault shows significant tectonic evidence of recent activity such as fresh scarps and faulted and tilted late Quaternary volcanic strata. It has not been studied in depth.

- The Fira fault is a typical normal tectonic structure trending ENE-WSW, with a right-lateral oblique-slip sense of movement. It shows decreasing downthrow from the sea level to the top lava layer, indicating a syn-volcanic deposition fault growth.
- It is an active fault in the western part of the Santorini caldera rim, contributing to seismic hazard.
- It is a “segment” of sub-parallel, left stepping faults belonging to the larger fault zone of “Kamenes line”, including the known volcanic centers. It is also subparallel to the 1956 earthquake great Amorgos-Thera fault. Its internal structure is complex (under investigation).
- The 2011-2012 volcanotectonic crisis was characterized by increased seismicity and ground deformation, linked to magma intrusion and fault activity, associated with the Fira fault. It was a segment of 6 km that was activated by a series of small-magnitude earthquakes, along the Kamenes volcanic line. It is believed to be longer.
- This known fault length corresponds to a minor or moderate earthquake.

Understanding these elements is crucial for monitoring and assessing the potential volcanic and seismic hazards in the region.

Acknowledgements

Bathymetric DTM data used in figures are obtained from the EMODnet Bathymetry (2022). On land DEM data derive from ALOS World 3D, 30-m DEM, v3.2 (Japan Aerospace Exploration Agency, 2021) and the National Cadastre and Mapping Agency S.A. (5-m resolution).

References

Barbot, S., Weiss, J. R., 2021. Connecting subduction, extension and shear localization across the Aegean Sea and Anatolia. Geophysical Journal International, 226(1), 422-445.

Bird, P., 2003. An updated digital model of plate boundaries. Geochemistry, Geophysics, Geosystems, 4(3), 1027.

Dimitriadis, I., Karagianni, E., Panagiotopoulos, D., Papazachos, C., Hatzidimitriou, P., Bohnhoff, M.,..., Meier, T., 2009. Seismicity and active tectonics at Coloumbo Reef (Aegean Sea, Greece): Monitoring an active volcano at Santorini Volcanic Center using a temporary seismic network. Tectonophysics, 465(1-4), 136-149.

Druitt, T. H., Mercier, M., Florentin, L., Deloule, E., Cluzel, N., Flaherty, T., Médard, E., Cadoux, A., 2016. Magma storage and extraction associated with plinian and interplinian activity at Santorini Caldera (Greece). Journal of Petrology, 57(3), 461-494.

Feuillet, N., 2013. The 2011–2012 unrest at Santorini rift: Stress interaction between active faulting and volcanism. Geophysical Research Letters, 40, 3532-3537.

Font, Y., Kao, H., Lallemand, S., Liu, C. S., & Chiao, L. Y., 2004. Hypocentre determination offshore of eastern Taiwan using the Maximum Intersection method. Geophysical Journal International, 158(2), 655-675.

Foumelis, M., Trasatti, E., Papageorgiou, E., Stramondo, S., Parcharidis, I., 2013. Monitoring Santorini volcano (Greece) breathing from space. Geophysical Journal International, 193(1), 161-170.

ISMOSAV - Institute for the Study and Monitoring of the Santorini Volcano, 2013. Current status of the volcano and proposal for monitoring continuation of the Santorini volcano during the year 2014. Final report of ISMOSAV for the 2013 Santorini volcano monitoring, 34 pp.

Kaviris, G., Papadimitriou, P., Kravvariti, Ph., Kapetanidis, V., Karakonstantis, A., Voulgaris, N., Makropoulos, K., 2015. A detailed seismic anisotropy study during the 2011–2012 unrest period in the Santorini Volcanic Complex. Physics of the Earth and Planetary Interiors, 238, 51-88.

Jolivet, L., Faccenna, C., Huet, B., Labrousse, L., Le Pourhiet, L., Lacombe, O.,…, Driussi, O., 2013. Aegean tectonics: Strain localisation, slab tearing and trench retreat. Tectonophysics, 597, 1-33.

Le Pichon, X., & Angelier, J., 1979. The Hellenic arc and trench system: a key to the neotectonic evolution of the eastern Mediterranean area. Tectonophysics, 60(1-2), 1-42.

Le Pichon, X., & Angelier, J., 1981. The Aegean Sea. Philosophical Transactions of the Royal Society of London, Series A, Mathematical and Physical Sciences, 300(1454), 357-372.

Lomax, A., Virieux, J., Volant, P., Berge-Thierry, C., 2000. Probabilistic earthquake location in 3D and layered models: Introduction of a Metropolis-Gibbs method and comparison with linear locations. Advances in seismic event location, 101-134.

Manning, S. W., Wacker, L., Büntgen, U., Bronk Ramsey, C., Dee, M. W., Kromer, B., Lorentzen, B., Tegel, W., 2020.

Radiocarbon offsets and old world chronology as relevant to Mesopotamia, Egypt, Anatolia and Thera (Santorini). Scientific Reports, 10(1), 13785.

Mountrakis, D., Pavlides, S., Chatzipetros, A., Meletlidis, S., Tranos, M., Vougioukalakis, G., Kilias, A., 1998. Active deformation of Santorini. In: Casale et al. (Eds), The European laboratory volcanoes, European Commission, EUR 18161 EN, 13-22.

Newman, A. V., Stiros, S., Feng, L., Psimoulis, P., Moschas, F., Saltogianni, V., Jiang, Y., Papazachos, C., Panagiotopoulos, D., Karagianni, E., Vamvakaris, D., 2012. Recent geodetic unrest at Santorini caldera, Greece. Geophysical Research Letters, 39(6), L06309.

Nomikou, P., Krassakis, P., Kazana, S., Papanikolaou, D., Koukouzas, N., 2021. The Volcanic Relief within the Kos-Nisyros-Tilos Tectonic Graben at the Eastern Edge of the Aegean Volcanic Arc, Greece and Geohazard Implication. Geosciences, 11(6), 231.

Papoutsis, I., Papanikolaou, X., Floyd, M., Ji, K. H., Kontoes, C., Paradissis, D., Zacharis, V., 2013. Mapping inflation at Santorini volcano, Greece, using GPS and InSAR. Geophysical Research Letters, 40(2), 267-272.

Parks, M. M., Biggs, J., England, P., Mather, T. A., Nomikou, P., Palamartchouk, K., Papanikolaou, X., Paradissis, D., Parsons, B., Pyle, D.M., Raptakis, C., Zacharis, V., 2012. Evolution of Santorini Volcano dominated by episodic and rapid fluxes of melt from depth. Nature Geoscience, 5(10), 749-754.

Parks, M. M., Moore, J. D., Papanikolaou, X., Biggs, J., Mather, T. A., Pyle, D. M., Raptakis, C., Paradissis, D., Hooper, A., Parsons, B., Nomikou, P., 2015. From quiescence to unrest: 20 years of satellite geodetic measurements at Santorini volcano, Greece. Journal of Geophysical Research: Solid Earth, 120(2), 1309-1328.

Pavlides, S., Chatzipetros, A., 2018. The Fira fault (Santorini, Greece) from the French “Expédition de Morée (1829□38)” to modern scientific approach. Proceedings of the 9th International INQUA Meeting on Paleoseismology, Active Tectonics and Archeoseismology (PATA), Possidi, Greece, 25-27 June 2018, 218-220.

Pavlides, S., Drakatos, G., Zouros, N., 2024. Active Tectonics and Seismicity in Greece. In: Darques, R., Sidiropoulos, G., Kalabokidis, K. (eds), The Geography of Greece. World Regional Geography Book Series, Springer, Cham, 431-444.

Pavlides, S. Tranos, M. 2012. Fault geometry and kinematics of the broader Santorini area in relation to seismic activity and volcanism. Abst. VOLSAM2012.

Pfeiffer, T., 2001. Vent development during the Minoan eruption (1640 BC) of Santorini, Greece, as suggested by ballistic blocks. Journal of Volcanology and Geothermal Research, 106 (3-4), 229-242

Pondrelli, S., 2002. European-Mediterranean Regional Centroid-Moment Tensors Catalog (RCMT) [Data set]. Istituto Nazionale di Geofisica e Vulcanologia (INGV).

Ruch, J., Wang, T., Xu, W., Hensch, M., Jónsson, S., 2016. Oblique rift opening revealed by reoccurring magma injection in central Iceland. Nature Communications, 7, 12352.

Sakellariou, D., Rousakis, G., Drakopoulou, P., Tsampouraki-Kraounaki, K., Morfis, I., Panagiotopoulos, I., Livanos, I., Loukaidi, V., Kyriakidou, C., Manta M., Lykousis, V., 2021. Geomorphology, Geological Structure, Active Tectonics, and Basin Formation in the Aegean Sea. In: Anagnostou, C.L., Kostianoy, A.G., Mariolakos, I.D., Panayotidis, P., Soilemezidou, M., Tsaltas, G. (eds) The Aegean Sea Environment. The Handbook of Environmental Chemistry, vol 127. Springer, Cham., 49-69.

Sakellariou, D., Tsampouraki-Kraounaki, K., 2019. Plio-Quaternary extension and strike-slip tectonics in the Aegean. In: Duarte, J. C. (ed), Transform plate boundaries and fracture zones, Elsevier, 339-374.

Saltogianni, V., Stiros, S. C., Newman, A. V., Flanagan, K., Moschas, F., 2014. Time□space modeling of the dynamics of Santorini volcano (Greece) during the 2011–2012 unrest. Journal of Geophysical Research: Solid Earth, 119(11), 8517-8537.

Tranos, M.D. 2012. Slip preference on pre-existing faults: a guide tool for the separation of heterogeneous fault-slip data in extensional stress regimes. Tectonophysics, 544-545, 60–74.

Tsampouraki-Kraounaki, K., Sakellariou, D., Rousakis, G., Morfis, I., Panagiotopoulos, I., Livanos, I., Manta, K., Paraschos, F., Papatheodorou, G., 2021. The Santorini-Amorgos Shear Zone: Evidence for Dextral Transtension in the South Aegean Back-Arc Region, Greece. Geosciences, 11(5), 216.

van der Stoel, J. M., Strak, V., Schellart, W. P., 2024. The role of subduction and gravitational collapse in driving extension in the Aegean Sea. Tectonophysics, 872, 230206.

Zhou, H. W., 1994. Rapid three□dimensional hypocentral determination using a master station method. Journal of Geophysical Research: Solid Earth, 99(B8), 15439-15455.

17th INTERNATIONAL CONGRESS of the Geological Society of Greece

BULLETIN OF THE GEOLOGICAL SOCIETY OF GREECE, SP. PUBL.

EXTENDED ABSTRACT 258

Geological routes on Ammouliani Island, northern Greece

Pegioudi E.[1], Chatzipetros A.[2]

(1) University of the Aegean, Mytilene, Greece, pegiou@hotmail.com (2) Department of Structural, Historical and Applied Geology, School of Geology, Aristotle University of Thessaloniki, Greece, ac@geo.auth.gr

Introduction

The study area is an island located west of Agio Oros (Mt. Athos) peninsula. It consists of basement rocks of Kerdilia and Vertiskos Units (Kockel et al., 1977), intruded by younger magmatic products. Ammouliani Unit is suggested as a new Unit, between Kerdilia and Vertiskos Units (Plougarlis & Tranos, 2015). Published geological maps featuring the island are: (1) Geological Map of Chalkidiki peninsula and the surrounding region, scale 1:100,000 (Kockel et al., 1977), (2) Geological Map of Greece, Ierissos Sheet. Scale 1:50,000 (Kockel et al., 1978), (3) Geology of Ammouliani Island (Northern Greece), scale 1:10,000 (Plougarlis & Tranos, 2015), (4) Geological Map of Greece, scale 1:500,000 (IGME). The pre-alpine basement rocks are characterized by a general ENE-WSW strike and generally intermediate to large angles of dip, mainly towards the WNW. The northern part of Ammouliani is characterized by the rocks of Kerdilia , Vertiskos, and Ammouliani Units. The southern part of the island consists of Ammouliani's granitoid, which is considered to be part of the Sithonia/Ouranoupoli-type granite (Papapavlou, 2021).

Objectives

The aim of this paper is to propose georoutes on Ammouliani Island, targeted to both the scientific community, as well as the general public. This enhances the potential of an alternative form of tourism in this area and suggests a different approach to the economic and cultural development of the island. It promotes geology as a multidisciplinary scientific field accessible to everyone. It encourages people to become familiar with this science and cultivate curiosity for their surroundings. The island's geology contributes to its unique character and beauty, which has been valued by tourists and the scientific community.

Methods

Pre-existing studies of the island and the wider area were collected and, their description of general geology was unified. Also, this work utilizes the 1:12.000 topographic map of the area from the Ierissos Sheet (1:50,000) of the Hellenic Army Geographical Service using the Quantum Geographical Information System (QGIS). A detailed geological study was carried out and confirmed the evidence of previous researchers who studied this island. Based on the most recent 1:10,000 scale map (Plougarlis & Tranos, 2015), the geological sections of the same scale, and visitor accessibility, decisions were made about possible geopaths that could be mapped and documented. Fieldwork along these geopaths was conducted and original structural data were acquired. They were exported and analyzed using the appropriate software for each product. A digital topographic map of the area and a Digital Elevation Model (DEM) were created, as well as digitized detailed geological maps. All data, as well as the results of the quantitative structural analysis of faults, folds, schistocity etc., were incorporated into an integrated GIS database, of which any query can produce various outcomes. Three geological trails were selected for presentation, the technical information of which is shown in Table 1. Their profile is generally gentle, with occasional small irregularities (Fig. 1). They are shown in the summary map of Fig. 2.

Table 1. Technical details of georoutes

Georoute	Max Altitude	Average Duration	Max Incline	Average Incline	Existing Road
1.1-1.5	74 m	1:05 h	32.6%	7%	Yes (1.1-1.2), No (1.2-1.6)
1.7-1.11	23 m	1:15 h	22.5%	6.2%	Yes
2	67 m	2:00 h	31.1%	7.3%	Yes
3	65 m	2:30 h	31.5%	7.4%	Yes

Figure 1. Georoutes elevation graph.

The purpose was to cover the geology of the entire island, showcasing specific sites, and ensuring convenient visitor access to existing roads. The rocks mentioned in each area are based on the already existing geological map of 1:10,000 scale (Plougarlis & Tranos, 2015). An effort was made to categorize them in geotopes according to the geology they highlighted.

Results and Conclusions

Georoute 1 focuses on Sithonia-type granite intrusions into the existing bedrock. Georoute 2 refers to the gneisses of the Kerdilia and Ammouliani Units. Georoute 3 focuses on the biotite-mica gneiss of the Vertiskos Unit, however, geosites of the Ammouliani Unit have also been chosen to be presented, so a comparison of the two types of lithology and their characteristics is achieved. Additionally, two locations of structural interest have been selected as Geosites 4.1 and 4.2 on Karagatsia Beach. The study refers to all the rocks mapped on the previously mentioned 1:10,000 scale geological map, except for the marbles of the Kerdilia Unit, which had limited outcrops in areas that are currently under building construction.

Georoute 1 (Fig. 3)

This route is 4.5 km long, crosses Ammouliani's gneissic granite and is divided into two branches in the middle of the hiking path, southeast of Agionissi Resort. The first branch (Georoute 1.1) passes from the southernmost part of the island and moves along Psili Rachi, reaches 74 m altitude, and ends before Turkolimano beach. The second branch (Georoute 1.2) continues the road in the northern part starting from Agionisi Resort, reaches an altitude of 24 m and has direction to the north-east part of the Island. The granite of this area is mentioned by Plougarlis (2011) as the Eocene granitoid of Ouranoupolis and Sithonia.

The route starts from Ormos Glastri (location 1.1). In this location, the separation of the granite body, which is a typical plutonite structure, is evident. The granitic bodies are produced by magma in its cooling stages. The exposure of a granitic body at its surface causes corrosion, disintegration, and deformation associated with the creation of the plutonite. The structure that develops in the igneous masses is shaped during its cooling conditions and the process of intrusion of the magmatic body from the moment it is finally consolidated. These later forms non-tectonic rock separations (Vidal Romaní, 2008). Those form outcrop along Georoute 1.1. At Georoute 1.2 the fault and the crustal-deformation phenomena are firstly presented at Plougarlis & Tranos (2015) map.

Georoute 2 (Fig. 4)

Georoute 2 is approximately 3.7 km long and crosses the rocks of the Kerdilia Unit, including the plagioclase-microcline gneiss, and the Ammouliani Unit. It represents an attempt to trace the path along cross section A-A', as outlined by the most recent geological mapping (Plougarlis & Tranos, 2015).

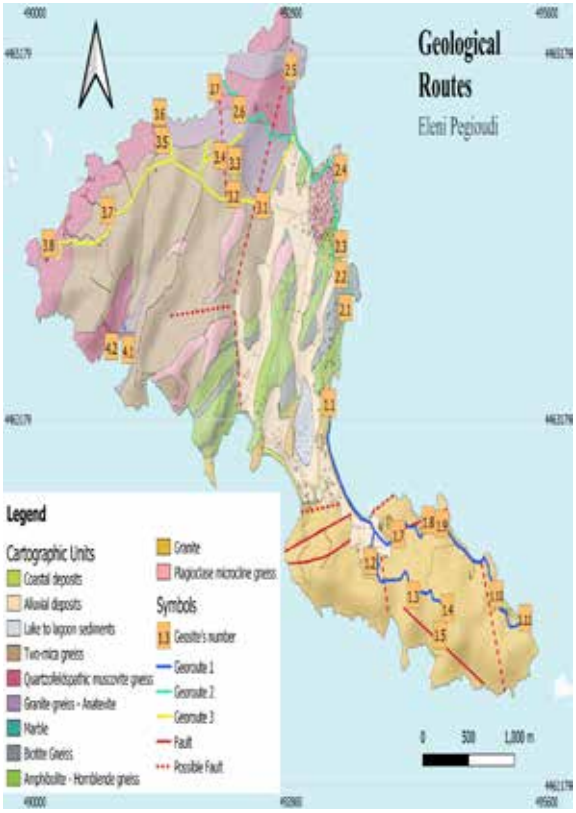

Figure 2. Geological Map of Ammouliani Island (modified from Plougarlis & Tranos, 2015) with the proposed georoutes and geosites

Figure 3. Georoute 1 at the southern side of the Island. Photos show a selection of geosites along the georoutes as well as the viewing orientation

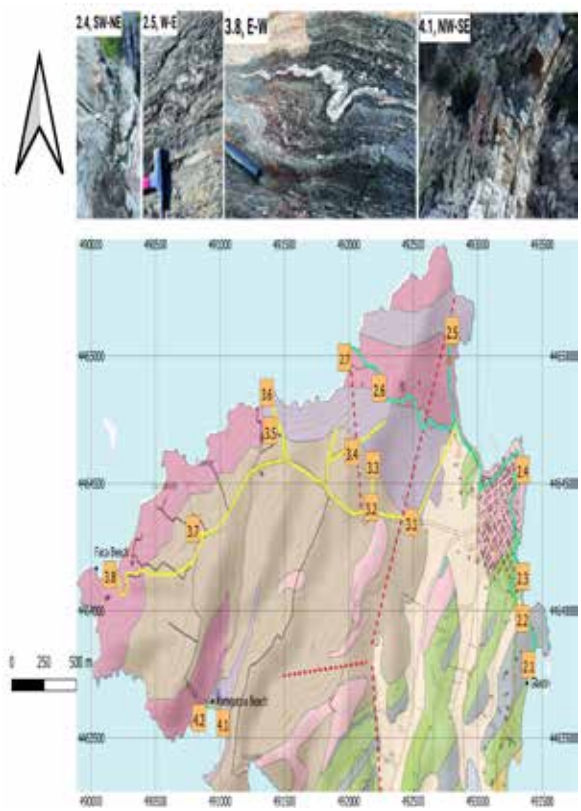

Figure 4. Georoutes 2,3,4 at the northern side of Ammouliani Island. Photos show a selection of geosites along the georoutes, as well as the viewing orientation.

Georoute 3 (Fig. 4)

This geological route is 5.2 km long and primarily features two-mica gneiss and its geological contacts with the Ammouliani Unit. The brownish two-mica gneiss belongs to the Vertiskos Unit and consists of quartz, plagioclase, muscovite, and biotite, with rare garnet, chlorite, and epidote occurrences. These gneisses are often interbedded with quartzofeldspathic muscovite gneiss of light brown-beige color, consisting of quartz, plagioclase, and muscovite. Additionally, muscovite-garnet gneisses appear as layers a few meters thick within the two-mica and quartzofeldspathic muscovite gneiss. Within the two-mica and quartzofeldspathic muscovite gneiss, augen gneisses with a variety of thickness that extending for several kilometers are observed, often showing features of intense shearing and mylonitization. Mineralogically, they consist of quartz, plagioclase, K-feldspar, muscovite, biotite, and in smaller amounts, hornblende and epidote.

Georoute 4 (Fig. 3)

An attempt was also made to trace two additional geological routes in the northwest part of the island; however, the flat geomorphology, the road network, cultivated olive groves, and vegetation inhibited exposure of rocks. However, there is information about Karagatsia Beach, which could be an interesting geological site, as its rocks belong to the Ammouliani Unit and are in contact with the Vertiskos Unit.

Discussion

The island, despite its small area, presents a variety of structures and lithological types. A multitude of kinematic indicators characterizes its entire range, while at the same time, it varies petrologically. Various types of rock deformation, such as faults, are quite new. Further studies of it may contribute to the disciplines of petrology, structural geology, stratigraphy, and neotectonics. Its small area and rich geology are suitable for developing geotourism for interested parties. Routes are easy to use for educational purposes, as they are short, have good accessibility, and are not physically demanding.

Acknowledgments

The first author would like to thank her family and friends for fieldwork assistance and georoute validation. The authors would like to thank an anonymous reviewer for their comments.

Reference

Kockel, F., Mollat. H. and Walther, H.W., 1977. Erlauterungen zur Geologischen Karte der Chalkidiki und angrenzender Gebiete 1:100.000 (Nord-Griechenland). Bundesanstalt fur Geowissenschaften und Rohstoffe, Hannover 119 pp

Kockel F, Mollat H and Antoniadis P (1978) Geological Map of Greece, Ierissos Sheet. Scale 1:50.000. Athens: Institute of Geology and Mineral Exploration of Greece.

Neofotistos, P. G., Tranos, M. D., & Heilbronner, R. (2020). Geology and deformation of the Serbo-Macedonian massif in the northern part of the Athos Peninsula, Northern Greece: Insights from two detailed cross-sections. Bulletin of the Geological Society of Greece, 56(1), 167. https://doi.org/10.12681/bgsg.22529

Papapavlou, K. (2021). Zircon U–Pb–Hf snapshots on the crustal evolution of the Serbo-Macedonian massif: new insights from Ammouliani island (Northern Greece). Geological Magazine, 158(11), 2079–2086. https://doi.org/10.1017/S0016756821000698

Papathanasoglou A. and Sagias I. (2017). Institutional Framework for Geosite Protection [in Greek], Environment and Law, 2017/4,628-636

Pazaras, G. (2016). Petrographic Study of metapelite from the Island Ammouliani, S. Chalkidiki [in Greek]. Bsc. Thesis, School of Geology, Aristotle University of Thessaloniki. http://geolib.geo.auth.gr/digeo/index.php/grelit/article/view/11270

Plougarlis, A. (2011). Geological and tectonic structure of Ammouliani Island (Peninsula Chalkidiki). Digital Library "Theofrastos", School of Geology, Aristotle University of Thessaloniki, 0(0). DOI 10.26262/heal.auth.ir.126766, https://ikee.lib.auth.gr/record/126766/

Plougarlis, A. P., & Tranos, M. D. (2015). Geology of Ammouliani Island (Northern Greece) – implications for the tectono-magmatic evolution of the Serbo-Macedonian Massif. Journal of Maps, 11(4), 552–560. https://doi.org/10.1080/17445647.2014.948504

Tranos, M., Kilias, A., & Mountrakis, D. (1993). Emplacement and deformation of the Sithonia granitoid pluton (Macedonia, Hellas). Bulletin of the Geological Society of Greece, 28, 195–210.

Vidal Romaní, J. R. (2008). Forms and structural fabric in granite rocks. Cadernos Do Laboratorio Xeoloxico de Laxe, 33.

Shapefile of coastlines for DEM creation in Global Mapper:
http://geodata.gov.gr/maps/?package=d59c2895-49c0-416f-a77e-122459cc8cac&resource=eb718a13-6e4a-45d6-9f9d-b3439d92a668&locale=en

Maps and other digital sources:

Army Geographical Service. (1970). Ierissos Sheet (Topographical Map). 1:50.000 Army Geographical Service.

Geological Map of Greece, scale 1:500,000 EAGME

17th INTERNATIONAL CONGRESS of the Geological Society of Greece

BULLETIN OF THE GEOLOGICAL SOCIETY OF GREECE, SP. PUBL.

EXTENDED ABSTRACT 259

Assessing Microplastic Pollution in Atzinolakas caves, Crete: Implications for Remote Karst Aquifers

Christos Pennos[1,2], Maria Perraki[3], Sofia Pechlivanidou[1], Rannveig Øvrevik Skoglund[4], Christos Salmas[4], Eleni Vasileiou[3], Yorgos Sotiriadis[5], Markos Vaxevanopoulos[6]

(1) School of Geology, Department of Physical Geography, Aristotle University of Thessaloniki, 54636 Thessaloniki, Greece cpennos@auth.gr

(2) Emil Racoviță Institute of Speleology, Romanian Academy, 400006 Cluj-Napoca, Romania

(3) School of Mining and Metallurgical Engineering, National Technical University of Athens, 15780 Zografou Campus-Athens, Greece

(4) Mineralogy-Geology Laboratory, Department of Natural Resources Management and Agricultural Engineering, Agricultural University of Athens, 11855 Athens, Greece

(4) Department of Geography, University of Bergen, Fosswinckels gt. 6, 5007 Bergen, Norway

(5) Proteas caving club, 54636 Thessaloniki, Greece

(6) Department Of History, Archaeology and Social Anthropology, University of Thessaly, Greece

Introduction

Over the last decade, microplastics (MPs) have increasingly attracted the attention of both the scientific community and the public. Microplastics are usually defined as plastic particles <1 mm but in a broader sense as all particles < 5 mm. A large proportion of MPs form unintentionally, for instance through the decomposition of larger pieces of plastic waste (i.e., secondary MPs). However, tiny fragments of synthetic or chemically modified natural polymers are also produced to be used as such or added to products (i.e., primary MPs). In 2022, the European Chemical Agency (ECHA) estimated that more than 42,000 tons of intentionally present microplastics are eventually released into the environment each year. The widespread presence of MPs, both in the terrestrial and marine environments, also in surface and groundwater has only been recently demonstrated (e.g., Yu et al., 2020, Drummond et al., 2022, Perraki et al, 2024), Microplastics have also been detected in the food chain, and eventually enter humans (De-la-Torre, 2020), highlighting their pervasive impact. In this study, we analyze water samples collected from two caves at the Atzinolakkas area of Lefka Ori in Crete, a uniquely remote location, to determine whether the water is contaminated by (MPs). We performed water sampling at three locations using glass vials to minimize contamination from external sources such as equipment or clothing. The sampling sites were selected to ensure maximum spatial coverage of the caves.

Setting

Our study area is in Atzinolakas (or Atzines), on the northern side of the Lefka Mountains in the Chania Prefecture of Crete (fig.1), approximately 2 km east of the Agio Pneuma summit (2262 m). The broader area hosts more than 1000 caves (Adamopoulos, 2013) including the two deepest caves in Greece, the Gourgouthakas and the Lion caves namely. These caves are part of a larger hydrological system that composes the recharge area of the Koiliaris drainage area (Lili et al, 2020) and that most probably discharges at the Stylos spring.

The karst system of the White Mountains comprises an autochthonous geotectonic unit (Plattenkalk nappe) and two allochthonous units: the Western Crete unit (Trypali limestones and phyllites) and the Arna unit (metamorphic schists). Within the alpine nappes, the Plattenkalk nappe exhibits a stratigraphic sequence, from base to top, as follows: a)karstified unbedded dolomites, b) dolomitic marbles, c) thinly bedded calcitic marbles intercalated with chert layers and nodules, d) metamarls and limeschists.

Although the geological composition of the area appears to be quite uniform, it shows both spatial and deep changes. Based on the observations made during the visits to the cave, black dolomites with brecciated textures are predominant in the wider region, especially south-west of the entrance to the Gourgouthakas cave. Surrounding the Gourgouthakas cave entrance, partially recrystallized and locally brecciated white limestones are observed. This lithological unit persists within the cave to a depth of 522 m below the cave entrance, where transitions to thick bedded to platy limestones occurs, the same succession continues to 850 m below the entrance. Between 646 and 670 meters, interbeds of green schist are encountered.

In climatic terms, the western part of Crete, and particularly the Lefka Ori, is characterized by significant winter precipitation, estimated at around 2331 mm (Agou et al, 2019). The winter low pressure associated with the North Atlantic Oscillation (NAO) typically originates in the Atlantic near the Strait of Gibraltar. These systems exhibit a

northeastward trajectory, generally skirting the Adriatic Sea. Consequently, significant rainfall is primarily confined to western Greece. As these frontal systems approach Greece from the west, they induce predominantly southwest winds over the Ionian and Aegean Sea, thereby advecting maritime air masses eastward (e.g. Pennos et al., 2018).

Figure 1. Topographic map of the broader study area. Red rectangle highlights the Atzinolakas caves (basemap: Google satellite; GGRS87).

Methods

The water samples were collected at three different locations in Gourgouthakas, Lion Cave and LO23 cave systems in August 2024 Gourgouthakas-Liontari caving expedition. Glass vials of 30 ml were used as sampling containers. To minimise the risk of contamination from external sources such as equipment or clothing the sampling group performed the sampling in the beginning of the expedition. In the Gourgouthakas Cave, the Marcel Waterfall was designated as the sampling site (fig.3a&e). In Lion Cave, dripwater was collected (fig. 3b&d) from a location situated above the first hotspot, minimizing the potential for external contamination. In LO23 Cave, the spring utilized to supply the expedition's water requirements served as the sampling point and a small stream with continuous flow was selected (fig.3c). Unfortunately, the sample obtained from Lion Cave was lost during transport as the vial broke. Concurrently with the MP sampling, in situ measurements of the electrical conductivity (EC) were carried out on water samples from the same sampling sites.

Samples were filtered using a filtration device, a mechanical pump (-100kbar) and filter membranes (Macherey-Nagel, 47 Ø and 0.45 μm pore size, REF: 65300045047). Before filtering the samples, we performed a cleaning round with double filtered de-ionized water, to ensure that the apparatus was cleaned to proceed with blank samples. A negative blank sample (BL1) was prepared prior to analysis. All filters were covered with glass Petri dishes and stored in a controlled environment in a closed laminar flow hood for 24h to dry. After filtration a second negative blank (BL2) was prepared and intentionally left uncovered to measure possible air contamination inside the laminar flow hood. Each surface was cleaned with 95% ethanol prior to analysis and cotton labware, and glassware were used during the whole procedure. No pretreatment protocol was applied.

Particles were quantified using a Leica Ivesta 3 stereoscope (x40-x63 optics) with a Leica Flexacam C3 attached at the Laboratory of Mineralogy and Geology, Department of Natural Resources Management and Agricultural Engineering, Agricultural University of Athens. The material was sorted based on its visual characteristics (size, color, shape, degradation degree) (Hidalgo-Ruiz et al., 2012) and classified as potential microplastics using the LASX image analysis software. The particle size was estimated based on the Feret min diameter.

Subsequently, μ-Raman analysis was performed on 10 suspect particles (24%) without further treatment, using a Renishaw inVia Reflex micro-Raman at the School of Mining and Metallurgical Engineering of the Technical University of Athens, Greece. The spectra were excited at room temperature with the 532 nm excitation wavelength of a diode laser, in the spectral range from 200 cm^{-1} to 2000 cm^{-1}. Spectra acquisition time was set to 10s, 1 accumulation cycle and laser power at 1%. The spectra were processed with the WIRE 3.4 software.

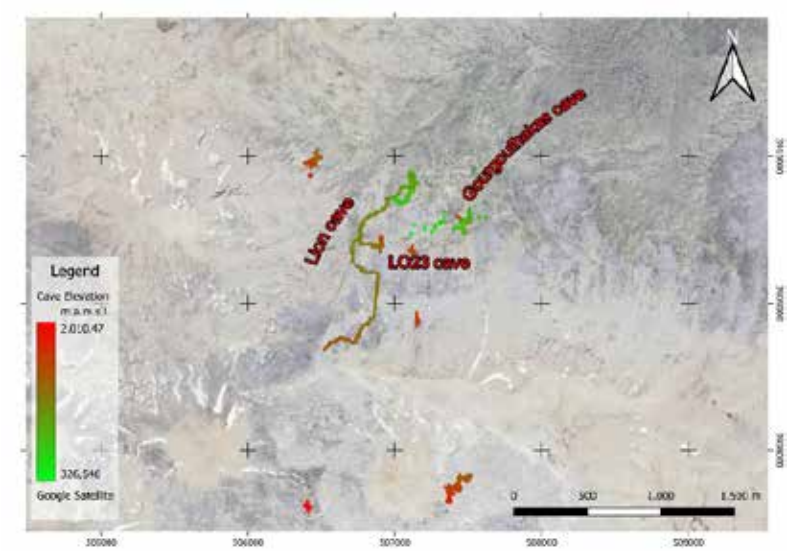

Figure 2. Map of the broader area with interpolated plan view of the caves. The color on the cave surveys represents the absolute elevation of the cave (cave data shared by Adamopoulos K.; GGRS87).

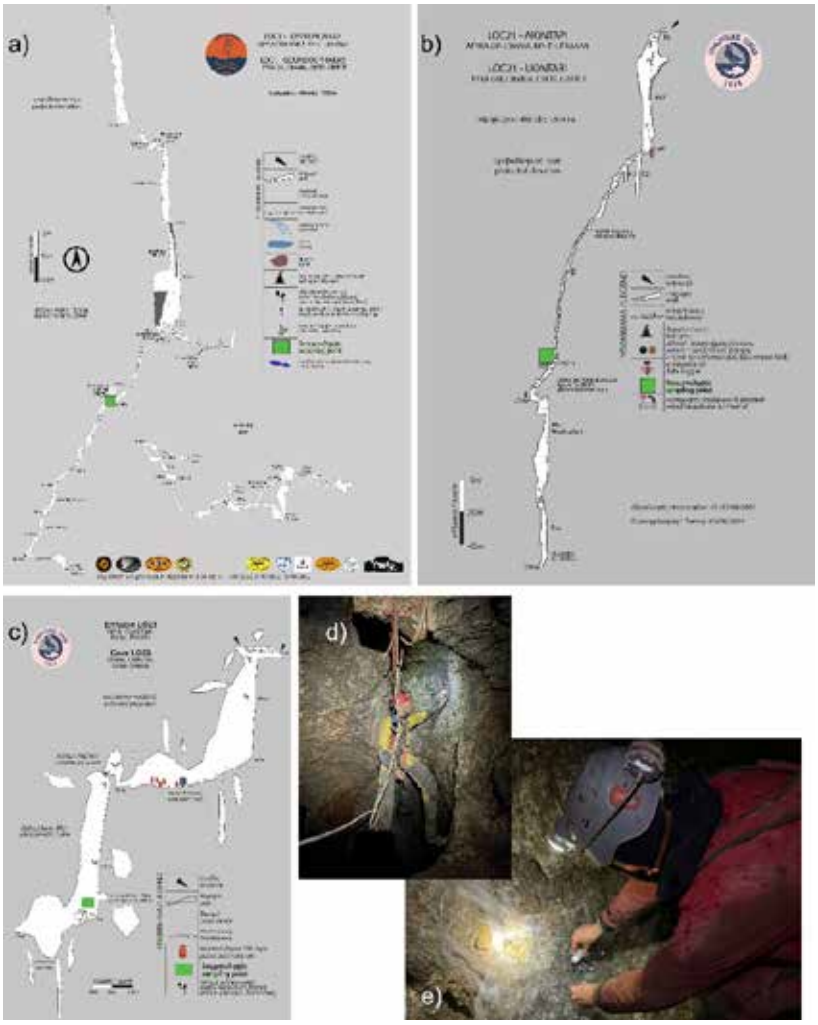

Figure 3. Extended projection of caves. a) Gourgouthakas cave, b) Lion cave, c) LO23 cave. d&e) collecting water samples in Lion and Gourgouthakas, respectively. Cave surveys are courtesy of Gourgouthakas expeditions.

Results

A total of 42 particles in the form of fibers and fragments were visually identified and classified as potential microplastics. Sample LOC1 contained 16 fibers and 4 fragments (fig.4). The predominant fiber color was blue (56.25%) followed by transparent (31.25%) and red (12.5%) (fig.5). Irregular fragments were only found in red color (100%). Regarding size, fibers in the LOC1 sample were distributed in 3 size classes namely, <500 μm (37.5%), 501-1000 μm (31.25%), > 1001 μm (31.25%), indicating a relative size homogeneity in their distribution. On the other hand, all fragments were measured with a size of <50 μm (100%). In the LO23 sample, a total of 22 particles were identified divided into 14 fibers and 8 fragments (fig. 6). Fibers were mostly transparent (71.43%) followed by blue (21.43%) and red (7.14%). Fragments were mainly blue (62.50%) but red, black and white colors were observed (12.5% each). Fibers were distributed in 3 size classes namely, <500 μm (50%), 501-1000 μm (35.7%), > 1001 μm (14.28%), with the <500 μm size class occupying 50% of the total fibrous material. Fragments were measured to be <50 μm (37.5%) and >51 (62.5%). Blank samples were also visually observed. BL1 had 2 fibers (transparent and black) and BL2 (opened Petri dish) had 2 white fragments and 1 blue fiber. Contamination was neither classified nor considered in the results. Raman spectroscopy of selected microplastic particles, revealed a very strong overlap of the MP peaks with the pigment peaks and in particular the indigo blue [547(s), 599(s), 939, 1010, 1147, 1252(s), 1297, 1310, 1365(vs), 1462, 1484, 1579(s), 1585, 1609, 1697 cm-1 (s)] and the copper phthalocyanine blue [peaks at 484, 594, 681(s), 748, 954(s), 1342(s), 1452(s) and 1529 cm-1 (vs)]. Besides, Raman peaks of polyethylene oxide (850, 1283, 1374cm-1) were also identified.

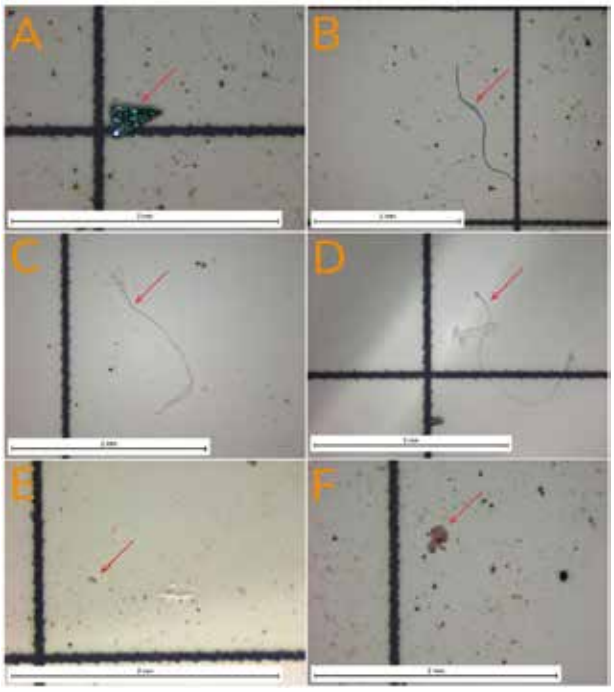

Figure 4. Particles identified as potential microplastics under the stereoscope in both samples: (A) black fragment, (B) blue fiber, (C, D) transparent fibers, (E, F) red fragments.

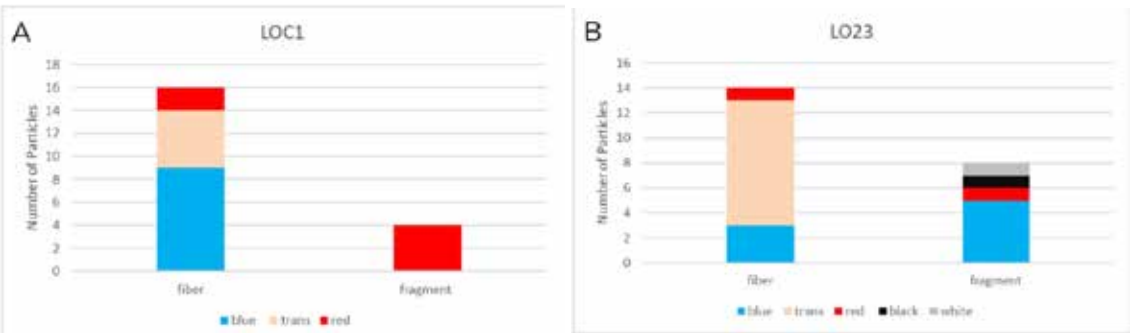

Figure 5. Total particle number of LOC1 (A) and LO23 (B) samples sorted by particle type and color, based on stereoscopical observations.

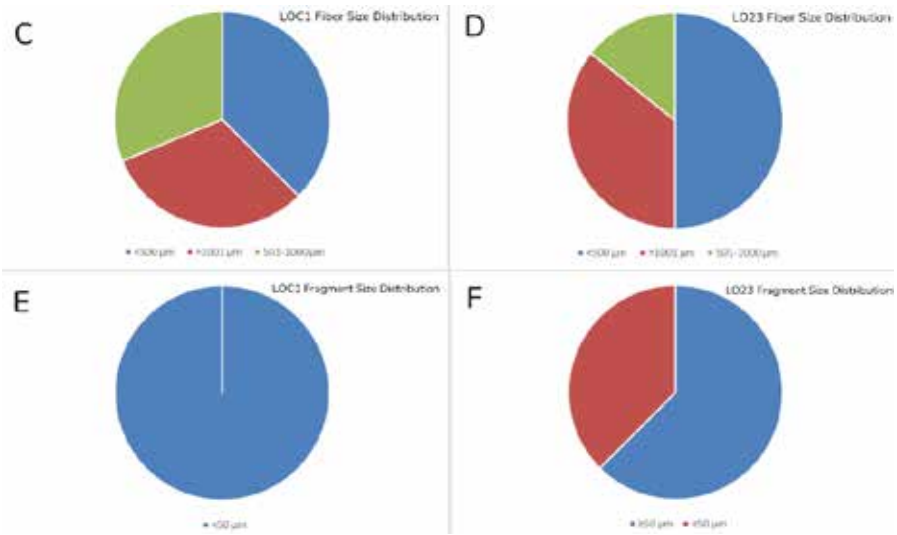

Figure 6: Distribution of fibers and fragments in LOC1 (C, E) and LO23 samples (D, F) based on stereoscopical observations.

The measurements on each sampling site showed similar EC values. In detail, in Gourgouthakas cave at the Marcel waterfall site the EC was 196 μS/cm at 9.6 °C, in Lion cave the EC of the drip water was 188 μS/cm at 9.3 °C. Finaly, the sample from LO23 exhibits EC of 180 μS/cm.

Discussion

Electrical conductivity measurements of the cave water samples exhibited values below the average reported for Greek karstic springs (Li Vigni et al., 2023). These low values of EC suggest a relatively short residence time within the karst aquifer and the recharge from the meteoric water. Despite the deep location of the sampling points within the karst massif, the observed low conductivity indicates rapid water percolation. This rapid flow likely occurs through high-permeability pathways, enabling swift infiltration and limited interaction with the limestone bedrock. Furthermore, the low water temperature recorded during mid-summer in the northern hemisphere strongly suggests a significant contribution from snowmelt, likely to originate from residual snow patches within the catchment area.

The presence of microplastics (MPs) in the collected samples suggests that it was transported to the sampling sites with infiltrating water. Given the remote location of the area above the caves and the minimal anthropogenic activities, a plausible transport mechanism for the MPs is proposed. Aeolian transport by westerly winds may have carried MPs from regions west of Crete, similar evidence was recorded recently to Mt. Tymfi's Alpine Lake (Salmas et al, 2024). These MPs could have subsequently precipitated snowfall during winter months. During summer, snowmelt would have introduced the MPs into the karst system, facilitating their rapid transport to the sampling points (fig. 7).

While this interpretation is based on limited data, it highlights the potential environmental hazard posed by aeolian-transported MPs and warrants further investigation.

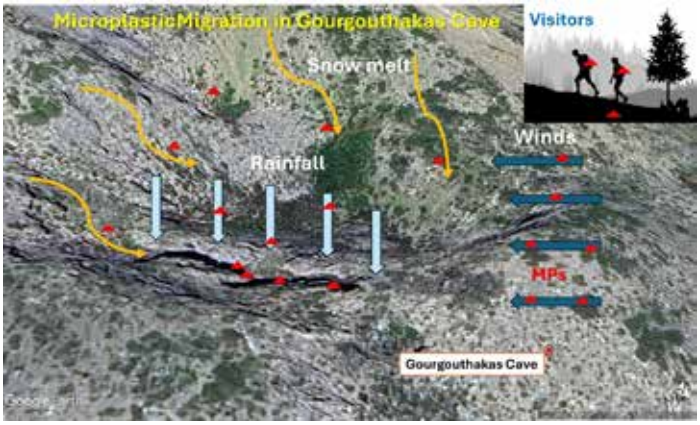

Figure 7: A schematic representation of the possible migration mechanism of microplastics in the Gourgouthakas cave.

Acknowledgements
The authors would like to thank the members of the Gourgouthakas – Liontari 2024 speleological expedition for helping us during our fieldwork and facilitating our stay. Keith Chatteraton is gratefully thanked for sacrificing his pair of clean socks to extract safely to surface the sample from Gourgouthakas cave. CP has been supported by the project titled "MP-Karst, Development of a methodological approach to detect Microplastics in Karstic environments" (code ΥΠ2ΤΑ-0554154) funded in the context of the call "Visiting Professors/Visiting Researchers" by the European Union - Next Generation EU. SP and RØS acknowledge support from the project "Comprehensive Assessment of Microplastics in Karst Environments / CAVE-MP" (MIS5224501) funded by EEA financial Mechanism for Bilateral funds 2014-2021.

References

Adamopoulos, K. 2013. 1000 and 1 caves in "Lefka Ori" massif, on Crete, Greece. 16th International congress of Speleology, Czech Republic, Brno.

Agou, V.D., Varouchakis, E.A. & Hristopulos, D.T. Geostatistical analysis of precipitation in the island of Crete (Greece) based on a sparse monitoring network. *Environ Monit Assess* **191**, 353 (2019). https://doi.org/10.1007/s10661-019-7462-8

Background Document to Committee for Risk Assessment (RAC) and Committee for Socio-economic Analysis (SEAC) Opinions on the on intentionally added microplastics, 10 December 2022

Drummond, J. D., Schneidewind, U., Li, A., Hoellein, T. J., Krause, S., & Packman, A. I. (2022). Microplastic accumulation in riverbed sediment via hyporheic exchange from headwaters to mainstems. Sci Adv, 8(2), eabi9305. https://doi.org/10.1126/sciadv.abi9305 Gabriel Enrique De-la-Torre, 2020. Microplastics: an emerging threat to food security and human health. J Food Sci Technol, 57(5):1601–1608

Hidalgo-Ruz, V., Gutow, L., Thompson, R. C., & Thiel, M. (2012). Microplastics in the Marine Environment: A Review of the Methods Used for Identification and Quantification. Environmental Science & Technology, 46(6), 3060–3075. https://doi.org/10.1021/es2031505

Li Vigni, L., Daskalopoulou, K., Calabrese, S., Brusca, L., Bellomo, S., Cardellini, C., Kyriakopoulos, K., Brugnone, F., Parello, F., & D'Alessandro, W. 2023. Hellenic karst waters: geogenic and anthropogenic processes affecting their geochemistry and quality. Sci Rep, 13(1), 11191. https://doi.org/10.1038/s41598-023-38349-6

Lilli, M. A., Efstathiou, D., Moraetis, D., Schuite, J., Nerantzaki, S. D., & Nikolaidis, N. P. 2020. A Multi-Disciplinary Approach to Understand Hydrologic and Geochemical Processes at Koiliaris Critical Zone Observatory. Water, 12(9). https://doi.org/10.3390/w12092474

Pennos, C., Styllas, M., Sotiriadis, Y., & Vaxevanopoulos, M. 2018. Ice Caves in Greece. In A. Persoiu & S. E. Lauritzen (Eds.), Ice Caves (pp. 385-397). Elsevier. https://doi.org/10.1016/b978-0-12-811739-2.00018-8

Yu, Q., Hu, X., Yang, B., Zhang, G., Wang, J., Ling, W., 2020. Distribution, abundance and risks of microplastics in the environment. Chemosphere Chemosphere 249, 126059.

Perraki, M.; Skliros, V.; Mecaj, P.; Vasileiou, E.; Salmas, C.; Papanikolaou, I.; Stamatis, G. Identification of Microplastics Using μ-Raman Spectroscopy in Surface and Groundwater Bodies of SE Attica, Greece. *Water* **2024**, *16*, 843. https://doi.org/10.3390/w16060843

Salmas, C., Alexopoulos, K., Kaspar, B., Skliros, V., Mecaj, P., Vasileiou, E., Papanikolaou, I., Perraki, M. & Papaioannou, H. First Evidence of Microplastics in Mt. Tymfi's Alpine Lake (Dragonlake) in Greece, Using μ-Raman Spectroscopy. Extended abstract, 16th International GeoRAMAN Conference 24-27 September 2024, Rhodes, Greece

17th INTERNATIONAL CONGRESS of the Geological Society of Greece

BULLETIN OF THE GEOLOGICAL SOCIETY OF GREECE, SP. PUBL.

EXTENDED ABSTRACT 260

Investigating the failure characteristics of certain rock types using the Acoustic Emission technique.

D. Pepas[1], V. Marinos[1], P. Nomikos[2], C. Saroglou[1]
(1) School of Civil Engineering (NTUA), Athens, Greece, dimitris.pepas99@gmail.com
(2) School of Mining and Metallurgical Engineering (NTUA), Athens, Greece

Introduction / Background

In recent years, the Acoustic Emission (AE) method has seen significant advancement and usage in the field of rock mechanics for monitoring the gradual fracturing process and stress-induced damage due to crystal or grain sliding, crack growth and coalescence. The AE technique has been used both in laboratory and in-situ applications, especially in tunnels for studying the elastic wave propagation characteristics and acquiring parameters that can reflect the rock fabric and damage evolution process before the macroscopic rock failure. Acoustic Emissions consist of elastic sound waves that are transmitted from the interior of a localized source (etc. rock sample) during crack development. These elastic waves are the result of stored accumulated energy that suddenly releases during external loading. The resulting AE waves propagate through the rock and then captured from specialized surface piezoelectric sensors. The sensors convert the mechanical waves into electrical signals and record them as AE events (Hits) in specialized acquisition programs. Several parameters can be extracted from the raw data such as hits, amplitude, frequency, duration and energy of the AE signals.
According to literature, the AE method has been used in the laboratory for the determination of various values and factors such as (1) the AE activity regions (Boyce et al., 1981) and their connection with the main cracking stages, namely the crack coalescence (σ_{cc}), the crack initiation (σ_{ci}) and the crack damage (σ_{cd}) stages in the stress-strain diagram (Martin C.D., 1993), (2) the B-value factor whose reduction during the loading process provides insight on the gradual failure and the stability of the rock (C. H. Scholz, 1968) and has been used as a risk assessment tool in various civil projects (Gerd Manthei et al., 2018) and (3) the Felicity ratio (FR) after several loading cycles that can be used as a rock's quality index (Kallimogiannis, 2023). Outside the laboratory scale and into the deep tunnel construction, the already complex in-situ stress environment is redistributed during excavation causing microcrack and later macrocrack generation if the crack initiation load is exceeded. As such, AE monitoring has been utilized together with numerical simulations and laboratory AE tests in several underground mining and tunneling projects to examine the size of the excavation-disturbed zone (EDZ) (Stephen D. et. al., 1996), determine the rock mass strength parameters through back-analysis (M. Cai et. al., 2006) and predict hazards such as rockbursts (A. Hirata et. al., 2006), thermal induced dilation (J Hesser et. al., 2015) and ruptures of not-persistent joints (Shuting Miao et. al., 2024).
The failure mechanism and consequently the acoustic emission (AE) activity is strongly influenced by the rock's texture, mineralogical composition, and formation history (Gramberg, 1989). In particular, fine-grained monomineralic rocks tend to fail abruptly as σ_{cd} and σ_c almost occur simultaneously. In contrast, more ductile or plastic rocks exhibit lower AE activity, partly due to the deformability of clay minerals. Additionally, factors such as porosity and lamination significantly affect the microcrack development mechanism.

Objectives

In this study, the AE method was implemented during Uniaxial Compressive and Cyclic loading laboratory tests* in several rock types such as a Limestone both in intact and karst form from Revithousa island, a tectonized Mudshale from South Crete and a Trachyandesite from Poros island. The scope of this study is to examine if the determination of the above factors with the Acoustic Emission method can be utilized as a basic monitoring tool both inside the laboratory and in underground construction projects, providing greater insight into the rockmass behavior from the standard rock mechanic tests.
*All the tests were executed according to the ISRM standards in the laboratory of Engineering geology and Rock-mechanics (NTUA) in the School of Civil Engineering

Physical parameters

Before proceeding with the Uniaxial Compression Tests (UCS), itis necessary to obtain the rocks' physical parameters. Particularly, the density (pd, psat) and porosity (n%) of every rock type was determined using the saturation and caliper technique in at least three specimens. The results are given in **Table 1**. Some noteworthy findings include 1) the high density (2.77) and the inversely proportional low porosity (< 1%) of the intact Limestone indicative of its very high strength (Koukis et al., 1998) and 2) the high porosity (n=19%) of Trachyandesite which depicts the vesicular, but otherwise homogenous texture with albite, anorthite and biotite phenocrystals. These rocks' characteristics were also confirmed by measuring the primary-P and secondary- S ultrasonic wave velocity. In general, higher rock density facilitates faster propagation of sound waves. Finally, petrographic (via stereoscope) and if necessary XRD- analysis was conducted to derive the exact mineralogical composition of every rock.

Table 1. Physical properties (density and porosity) and ultrasonic wave velocity of every rock type.

Rock type	pdry	psat	ps	γdry	γsat	n	VP	VS
	*10^3 kg/m^3			kN/m^3		%	m/s	
Limestone (L)	**2.77**	2.77	2.79	27.2	27.2	**0.63**	6549	3945
Karstified Limestone (KL)	**2.53**	2.59	2.68	24.9	25.4	**5.49**	4197	2328
Trachyandesite (A)	**1.99**	2.18	2.45	19.5	21.4	**19.00**	3033	1769
Mudshale (S)	**2.62**	2.63	2.66	25.7	25.8	**1.57**	3749	2228

Experimental set-up for UCT tests

A servo-hydraulic load frame with a built-in load cell was used for loading the specimens under a constant stress rate (MPa/s). Axial and circumferential strain gauge extensometers were used for the strain measurement. The AE activity was recorded by two AE sensors connected via a signal pre-amplifier in the specialized AE data acquisition system. Full contact between the specimen and sensors was achieved using an ultrasonic gel couplant. Finally, HRC58 steel discs were positioned between specimen and load platens for minimizing the friction's influence in the AE signal. The exact sensor arrangement is presented in **Figure 1**.

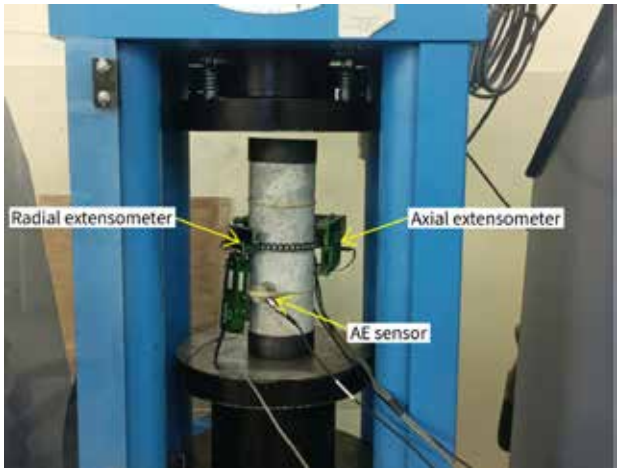

Figure 1. Experimental setup for the UCT-AE laboratory tests

Uniaxial Compressive Test with AE measurement (UCT-AE)

Before further examination, the first UCT results including strength, Young modulus and Poisson's ratio for every rock are presented in **Table 2**. Two sets of parameters (⊥ and //) were derived for Mudshale, based on the orientation of laminas with respect to the loading axis. The resulting stress-strain curves were divided into four microcracking stages, as presented in **Figure 2** (Martin CD et. al., 2001).

Table 2. Average values of strength and elastic parameters for every rock type.

Rock type	Limestone	Karstified Limestone	Trachyandesite	Mudshale (⊥ and //)	
σc (MPa)	106.5	31.0	20.2	54.6	23.8
E (GPa)	79.2	30.3	8.0	23.3	13.6
v	0.15	0.28	0.24	0.10	0.13

The brittle behavior of limestone is evident, as the elastic stage covers most of the loading range and is difficult to distinguish from the stable cracking stage. Also, the unstable cracking stage is presented just before failure within the final 5% and there is no post- failure stage. Karstified Limestone behaved similarly with a limestone breccia. The loading curve presents a clear distinction between the elastic and stable cracking stages, but from there the rock presents two different stages of severe cracking, the first one at around at 75% and the second at 98% of the total strength just before ultimate failure. In Trachyandesite, the microcrack coalescence was favored by the high porosity. Moreover, all failure stages are clearly visible. The Mudshale underwent the most significant deformation and failed by shearing along its laminations.

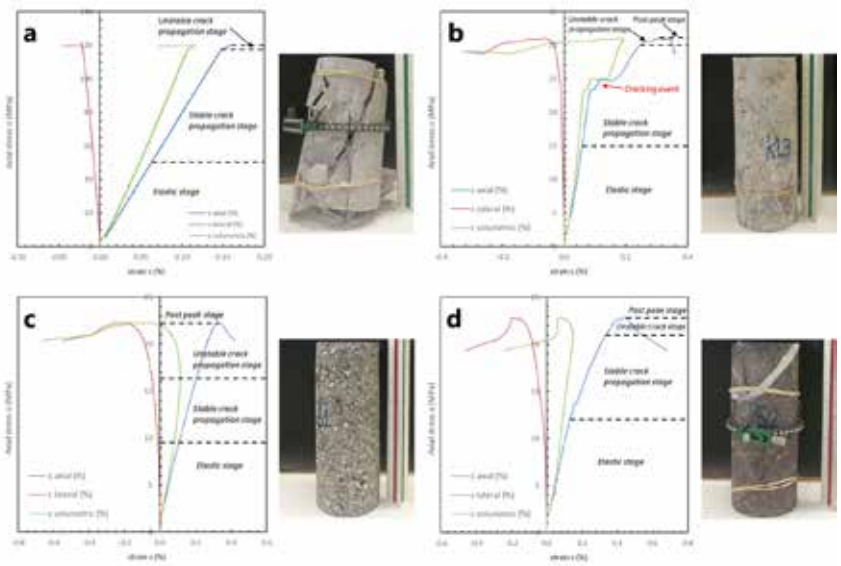

Figure 2. Distinction of microcracking stages along the stress–strain curve for every rock type. a) Limestone, b) karstified Limestone, c) Trachyandesite and d) Mudshale.

Microcracking stages determination with the AE method

Both microcracking stages (σci and σcd) were determined from the AE data by plotting the graph of the cumulative acoustic emission hits versus the axial stress (**see Figure 3**). Particularly, the microcracking stages correspond to the points of abrupt AE hit generation (i.e., where the slope of the curve suddenly increases). If the curve displays a continuous concave-up trend, precise determination becomes difficult. Therefore, the AE hit rate was employed as an alternative (Kallimogiannis, 2016). Moreover, AE activity is strongly influenced by the presence of pre-existing weak surfaces within each rock (e.g., veins, discontinuities). As such, it should be noted that the selection of the following values is subjective and relies on the user's experience.

Based on the results, the standard deviation for σ_{ci} is much lower (**see Table 3**), so it can be considered a more appropriate value for characterizing the mechanical behavior of the rock. The σ_{cd} is very close to the ultimate failure in the brittle rocks. On the other hand, the unstable cracking stage comes earlier in the porous or semi-plastic rocks, as they are slowly losing the ability to bear increasing loads. This microcrack generation and propagation is accompanied by increasing deformation (both axial and radial) and dilation.

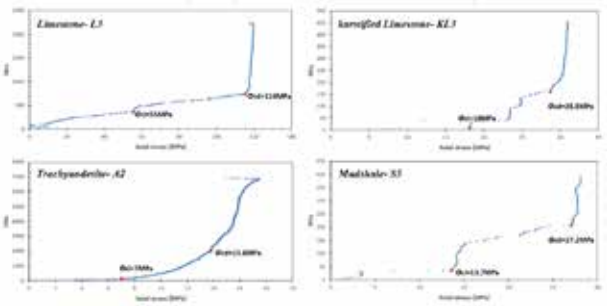

Figure 3. Examples of the produced AE hits vs stress curve for every rock type. The σ_{ci} and σ_{cd} values have been marked.

Table 3. Average values, % ultimate strength and St. deviation of the microcracking stages for every rock type.

Rock type (I.D)	σ_{ci}			σ_{cd}			σ_c	
	μ	% σ_c	St.dev	μ	% σ_c	St.dev	μ	St.dev
Limestone	55.7	52	9.0	97.8	92	29.8	106.5	37.9
Karstified Limestone	18.0	58	-	28.8	93	-	31.0	
Trachyandesite	9.5	47	2.3	15.5	77	2.1	20.2	2.5
Mudshale	15.9	49	3.6	27.5	84	11.7	32.8	18.9

B-value

Unlike the number of hits-stress relationship, the B- value accounts for the intensity of the AE waves (Hardy RH., 2003) and particularly it represents the relative proportion between weak and strong acoustic emission events that are produced under a specific load. B- values lower than one are indicative of intensive AE events that produce large-scale microfractures as the rock approaches failure. B- values larger than one mean that small-scale microfractures are dominant, so the rock has not experienced significant damage (Kallimogiannis, 2023).

All rocks display similar behavior (**see Figure 4**). Particularly, under low stress conditions, any microcracking event produce AE waveforms of low amplitude, resulting in higher B-values, ranging from 1.5 to 4. As the stress increases, crack propagation and coalescence occur, producing higher amplitude waves and therefore decreasing the B- value below one. The B- value decrement is more evident after the σci and σcd stresses are exceeded close to failure.

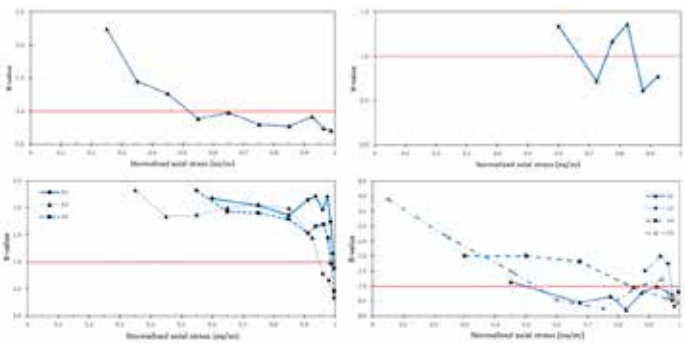

Figure 4. The B-value vs axial stress curve for every rock type. Notice that the B-value reduces after the main microcrack events. Limestone (top left), karstified Limestone (top right), Trachyandesite (below left), Mudshale (below right).

Cyclic Uniaxial Compressive Test with AE measurement. (CUCT-AE)

The rock specimens were repeatedly loaded, each cycle corresponding to a 10-20% increment towards the expected peak strength. The main objective was to study the rock damage accumulation in a damage "controlled" environment

(Eberhardt E. et. al., 1999). The results demonstrate that both axial and lateral strain curves move incrementally after each cycle (**see Figure 5**).

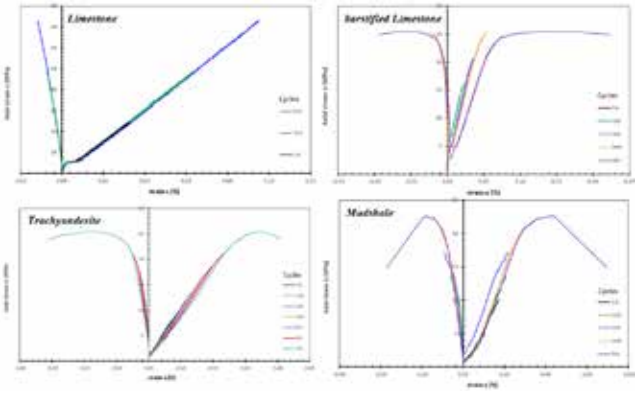

Figure 5. Combined stress–strain curves for every loading cycle.

This shift becomes more obvious as the stress approaches the σc and can be explained by microstructural damage accumulation. In particular, when microcracks generate in a preceding loading cycle, they partially close upon unloading. As such, during the following reloading phase, they extend at considerably lower stress level. Moreover, as most tensile microcracks generate along the specimen's length, lateral extension is the dominant deformation mechanism. The only exception belongs to Limestone in which the elastic phase has not yet passed, so no severe microcracking has yet occurred.

The acoustic emission (AE) method is employed in cyclic loading tests through the Felicity ratio. FR less than unity depicts the transition from the Kaiser effect (absence of AE events until the previously experienced stress on the material is exceeded (Lavrov, 2002) to the Felicity effect (presence of AE events before the previous cycle's peak stress) from which point, the damage that has been accumulated is irreversible. The Felicity ratio was calculated by dividing the stress in which the first AE activity was recorded, namely the AE onset stress with the maximum stress of the previous cycle. As illustrated in **Figure 6**, the FS value exhibits a gradual decline with increasing stress across all rock types.

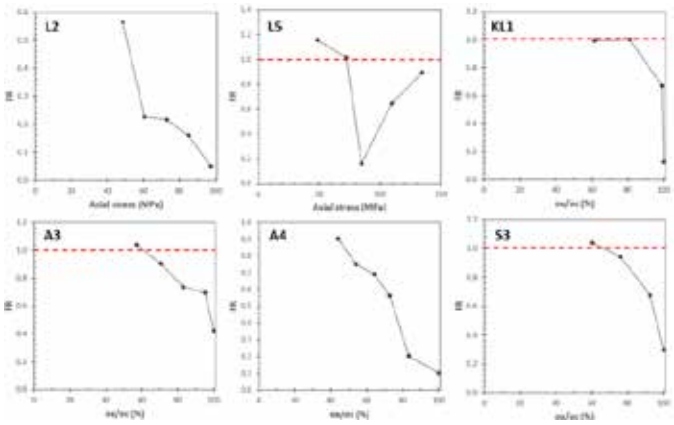

Figure 6. FR vs stress curve for every specimen. The red line marks the transition from the Kaiser to the Felicity effect.

Conclusions

This study highlights the application of acoustic emission (AE) monitoring across four different lithologies. Specifically, it was found that the crack initiation (σ_{ci}) and crack damage stress (σ_{cd}) occur earlier in porous and semi-plastic rocks and later in brittle rocks, relative to the unconfined compressive strength (UCS). Notably, σ_{ci} exhibits significantly lower variability, indicating its potential for use in estimating a more representative UCS through inverse analysis. Moreover, sudden reduction in the B-value reflects the intensity of microcracking activity which peaks near failure.

In damage-controlled UCS tests, the reactivation of microcracks is reflected in the progressive increase of deformation, irreversible strain and Poisson's ratio after each loading cycle. Furthermore, the Felicity Ratio (FR) emerges as a promising parameter for identifying both the onset and evolution of internal damage within the rockmass.
Consequently, the physical properties of rocks significantly influence both their failure behavior and their AE response. High-density rocks exhibit well-defined phases of intense microcracking, accompanied by elevated AE activity, while highly porous rocks tend to show continuous but less intense AE signals, indicative of a more distributed damage mechanism. In contrast, argillaceous rocks display limited AE activity, primarily due to the ductile behavior of their clay minerals, which inhibits microcrack formation. Collectively, these findings highlight the potential of the AE method to enhance understanding of rock failure processes and improve predictive modeling in geotechnical engineering.

Acknowledgements

The authors would like to thank the geotechnical company GeoTerra for providing the rock samples from various geotechnical projects in Greece and their support throughout the entire duration of the study. Special thanks to Geologists Tzivolias Efstratios, Varvadakis Manolis and Antoniou Anastasios.

References

A. Hirata, Y. Kameoka, and T. Hirano, 2006. Safety Management Based on Detection of Possible Rock Bursts by AE Monitoring during Tunnel Excavation. Rock Mech. Rock mechanics and Rock engineering 40 (6), 563–576. **[Journal Article]**

A. Lavrov, 2002. The Kaiser effect in rocks: Principles and stress estimation techniques. International Journal of Rock Mechanics & Mining Sciences 40, 151–171. **[Journal article]**

Boyce, 1981. Acoustic Emission Signatures of Various Rock Types in Unconfined Compression. **[Symposia paper, ASTM article]**

C. H. Scholz, 1968. The frequency-magnitude relation of microfracturing in rock and its relation to earthquakes. **[Book Chapter]**

Eberhardt, E., Stead, D., Stimpson, B., 1999. Quantifying progressive pre-peak brittle fracture damage in rock during uniaxial compression. Int. J. Rock Mech. Min. Sci., 36, 361–380. **[Journal article]**

Gerd Manthei, Katrin Plenkers, 2018. Review on In Situ Acoustic Emission Monitoring in the Context of Structural Health Monitoring in Mines. **[Journal Article]**

Hardy RH (2003), Acoustic Emission/ Microseismic Activity. Volume 1: Principles, Techniques and Geotechnical Applications, A.A. Balkema, The Netherlands. **[Book]**

ISRM. Suggested methods for Rock Characterization, Testing and Monitoring (1974-2006). **[Book]**

ISRM. Suggested methods for Rock Characterization, Testing and Monitoring (2006-1014). **[Book]**

J Hesser et. al., 2015. Measurements of Acoustic Emission and Deformation in a Repository of Nuclear Waste in Salt Rock, p. 551. **[Book chapter]**

J. Gramberg, 1989. A Non-Conventional View on Rock Mechanics and Fracture Mechanics. **[Book]**

Kallimogiannis V., 2016. Laboratory investigation on the impact of the fracturing degree on rock's wave velocity. **[MSc Thesis]**

Kallimogiannis V., 2023. Investigation of the mechanical properties and classification of weak carbonate fault rocks with application in western Lefkada island, Greece. **[Ph.D. thesis]**

Koukis G., Sabatakakis N, Tsiambaos G, 1998. ''Geotechnical properties of Greek limestones''. Proc. 8th Intern. Congress of IAEF, Vancouver, pp. 2883-2888. **[Symposia paper]**

M. Caia, , H. Moriokab, P.K. Kaisera, Y. Tasakac, et. al., 2006. Back-analysis of rock mass strength parameters using AE monitoring data. International Journal of Rock Mechanics & Mining Sciences 44, 538–549. **[Journal article]**

Martin C.D., 1993. Strength of Massive Lac du Bonnet Granite Around Underground Openings'. Ph.D. thesis, Department of Civil and Geological Engineering, University of Manitoba, Winnipeg, p. 278. **[PhD thesis]**

Martin CD, Christiansson R, Soderhall J, 2001. Rock stability considerations for siting and constructing a KBS-3 repository. Based on Experiences from .Aspo HRL, AECL's URL, Tunneling and Mining. **[Journal article]**

Shuting Miao et. al., 2024. Shear band evolution and acoustic emission characteristics of sandstone containing non-persistent flaws **[Journal Article]**

Stephen D. Falls et. al., 1996. Acoustic emission and ultrasonic-velocity methods used to characterize the excavation disturbance associated with deep tunnels in hard rock. **[Journal Article]**

Tsuyoshi Ishida, Joseph F. Labuz, Gerd Manthei, Philip G. Meredith, M.H.B. Nasseri, Koichi Shin, Tatsuya Yokoyama, Arno Zang, 2017. ISRM Suggested Method for Laboratory Acoustic Emission Monitoring **[Journal Article]**

X. Chang et. al., 2015. Acoustic Emission Technique to Detect Micro Cracking During Uniaxial Compression of Brittle Rocks, p. 465. **[Book chapter]**

17th INTERNATIONAL CONGRESS of the Geological Society of Greece

BULLETIN OF THE GEOLOGICAL SOCIETY OF GREECE, SP. PUBL.

EXTENDED ABSTRACT 261

Coal and Asbestos Mining-Induced Pulmonary Pathologies: Radiological Diagnosis and Associated Challenges

Argyrios Periferakis[1,2,3], Lamprini Troumpata[1], Aristodemos-Theodoros Periferakis[1,3], Konstantinos Periferakis[2,4]

(1) Department of Physiology, The "Carol Davila" University of Medicine and Pharmacy, 050474 Bucharest, Romania; (2) Akadimia of Ancient Greek and Traditional Chinese Medicine, 16675 Athens, Greece; (3) Elkyda, Research & Education Centre of Charismatheia, 17675 Athens, Greece; (4) Pan-Hellenic Organization of Educational Programs (P.O.E.P), 17236 Athens, Greece

Introduction

The majority of the first tools devised by Prehistoric men were made of stone; while it is reasonable to assume that a great many of these tools where made from rocks found lying around, at some point it seems inevitable that our ancestors would have to go about actively procuring the materials for their rudimentary tools and implements (Coulson, 2012). The oldest mine yet discovered is, most probably, that of Lion Cave in Swaziland, Africa, which is estimated to be about 30.000 years old (Dart & Beaumont, 1969). The first quarrying operation discovered is even older, and it is located in the Nile Valley, where numerous evidence for Palaeolithic flint and chert extraction is present (Vermeersch *et al.*, 1990). These are then the origins of mining and quarrying, an activity which grew steadily from the Bronze Age onwards (Coulson, 2012), and has influenced the course of history and civilisations (Periferakis *et al.*, 2019; Periferakis, 2021), being regarded as an integral part of the local heritage in certain places (Periferakis *et al.*, 2022).

However, neither mining nor quarrying are easy and danger-free tasks; in fact, they are rather laborious and potentially dangerous, especially in more primitive conditions. The recognition that mining is associated with specific pulmonary diseases has been made since the 16th century by Agricola (Ross & Murray, 2004). Since then, and especially after the 19th century, a systematic documentation of mining- and quarrying-related and induced occupational diseases is underway, revealing an ever-increasing number of pathologies and their associated mechanisms. Aside from increased awareness and potential of diagnostic techniques to identify such pathologies, the massive increase of the global mining and quarrying activities in the last two decades (Jasansky *et al.*, 2023) brings this problem even more to the foreground. Given that such occupational diseases represent a diverse and multifaceted issue, from the point of view of pathogenicity, diagnosis, and treatment, here we will focus on a brief overview of the radiographic evidence of pulmonary pathologies associated with coal and asbestos mining, and the associated diagnostic challenges. We have chosen coal and asbestos mining, as a wealth of data exist on the subject, and the relevant pathologies are associated specifically with these materials and are not generically caused by the mining conditions themselves.

Coal Miners' Pneumoconiosis (Black Lung Disease) and Other Pulmonary Pathologies

Coal deposits occur in coal-bearing strata, which can be found today in numerous locations worldwide. The Eurasia-China and the North America coal belts existing today were formed in the ancient supercontinent of Laurasia, while a third coal belt has formed across regions which were originally part of Gondwana. While coal from the Devonian age has been found, the majority of currently known deposits has formed during the Permian and Carboniferous ages; younger coal deposits from the Mesozoic and Cenozoic eras exist but there are fewer in number and less widespread (Wagner, 2020).

Ever since the industrial revolution, coal has been perhaps the most important source of energy, followed by oil as the 20th century progressed. Today, the major coal producing countries are China, the US, Australia, Indonesia and India, with a number of other countries also having significant resources (Wagner, 2020). Pneumoconiosis is most probably the oldest occupational disease, especially given the importance of mining and quarrying from a very early stage in human prehistory, as presented above. It is also the most prevalent occupational disease at a worldwide level (Wang et al., 2023). Coal mining-related pneumoconiosis has been identified since the 1830s, when miners presented with black sputa, breathlessness and coughing, and in autopsies, the lungs had a black pigmentation (Ronsmans & Nemery, 2022).

Pneumoconiosis is defined as a form of interstitial lung disease induced by particle inhalation, which leads to scarring and progressively diminished breathing capacity (Shekarian *et al.*, 2021). Regarding the pathophysiology of pneumoconiosis, this is determined by the interaction and deposition of the inhaled particles at the different levels of the respiratory system. As such, the smaller the particle, the more it will penetrate into the respiratory system, with

nanoparticles being the most dangerous and pathogenic

In coal mining the prolonged exposure to coal dust can lead to a particular form of pneumoconiosis, called coal workers' pneumoconiosis due to exposure to both coal and silica dust. The relevant forms of pneumoconiosis are anthracosis, silicosis and anthracosilicosis. In this context, particles with a 1-100 μm are characterised as dust, while particles below 1 μm are classified as the nano-sized fraction and are also damaging to the lungs when inhaled (Pan *et al.*, 2021); it is estimated that in mining enterprises, about 3% of the mined material will be converted to dust in the extraction process. About 40% to over 90% of dust in coal mines, at any moment, is pure coal. The particular characteristics of such dust and its relative pathogenicity depend both on the characteristics of the coal itself and on the mining methods and equipment used.

From a diagnostic perspective, the radiographic findings between the three forms are similar, with milder forms of the disease being confined to the upper parts of the lungs and presenting as small (< 1 cm) rounded opacities. The coalescence of these opacities into more massive forms is indicative of progressive massive fibrosis, a more severe form of this disease. Interestingly, in miners which are already suffering from rheumatoid arthritis, Caplan syndrome, i.e., rheumatoid pneumoconiosis, may occur. This presents as well-defined rounded nodules in the lung periphery, resembling rheumatoid nodules (Schreiber *et al.*, 2010). Anthracosis, in its mild and moderate forms, has COPD-like symptoms and a similar treatment scheme (Mirsadraee, 2014). Compared to asbestosis, it is usually less severe in the absence of comorbidities.

Other pulmonary pathologies, associated with dust inhalation in the context of coal mining are dust-related diffuse fibrosis, and some diseases of the airways such as emphysema and chronic bronchitis. Dust-related diffuse fibrosis is also, like pneumoconiosis, an interstitial lung disease, but radiographically appears as irregular opacities and presents difficulties in the differential diagnosis with idiopathic pulmonary fibrosis if an exposure history is not available (Petsonk *et al.*, 2013); it is more frequent in long-tenured coal miners compared to idiopathic pulmonary fibrosis prevalence in the general population (Laney & Weissman, 2014).

Notably, since the 1970s, due to legislation regulating the amounts of maximum permissible coal dust in mines, in major coal-producing countries, such as the US, and Australia, coal miners' pneumoconiosis incidence begun to decline. However, during the last decade, there has been an apparently unexplained increased in incidence, despite the improvement of working conditions and safety standards (Wang *et al.*, 2023). In the US, there also has been a constant incidence increase since the 1990s. In this resurgence, silica particles are implicated more than coal particles, and this may be attributable to a shift in mining methods as well as the stricter control of maximum allowed coal dust in mines compared to silica dust (Go *et al.*, 2023), although more research is required on this matter.

Pulmonary Pathologies Associated with Asbestos Exposure

The term asbestos is used to describe a group of silicate minerals, which form elongate thin fibers. These will release numerous microscopic fibers when tampered with or crashed. Their usual diameter is less than 1 μm and their length may range from several to hundreds of micrometres. Remarkably, even though the peak for asbestos demand is associated with the onset of the industrial age, such minerals have been known and used for over 5000 years (Ross & Nolan, 2003). Asbestos fibres have a number of very positive physicochemical properties, are especially durable to fire, and are very good insulators (Ross & Virta, 2001). From a mining and use perspective, chrysotile asbestos represents over 90% of the total mined asbestos (Ross & Virta, 2001).

From a mineralogical perspective, the term "asbestos" is used to refer to a family of fibrous silicate minerals, which occur in igneous and metamorphic settings. The asbestiform minerals can either be amphiboles or seprentines. The former group comprise grunerite$[(Fe_2^{2+})(Fe_5^{2+})(Si_8O_{22})(OH)_2]$, cummingtonite and its dimorph anthophyllite$[(Mg_2)(Mg_5)(Si_8O_{22})(OH)_2]$, crocidolite$[(Na_2)(Z_3^{2+}Fe_2^{3+})(Si_8O_{22})(OH,F,Cl)_2]$, tremolite, and actinolite $[Ca_2(Mg_{4.5-2.5}Fe_{0.5-2.5}(Si_8O_{22})(OH)_2)]$; anthophyllite is also known as amosite. About 90% of the total production of asbestos corresponds to crocidolite, with the rest comprising mostly chrysotile $[Mg_3(Si_2O_5)(OH)_4]$and amosite. All commercially exploitable asbestos minerals share a number of physical properties, i.e., (1) they occur as fibrous bundles, (2) these fibres have high tensile strength, (3) they have a high aspect (length:width) ratio, (4) they are flexible enough to be coiled. Due to their chemical composition, they are very stable in a variety of environments, have high thermal resistance, are not very biodegradable and are poor conductors of electricity. Other minerals which exhibit an asbestiform habit but do not exhibit all such properties are not classified as asbestos (Campbell *et al.*, 1977; Ross *et al.*, 1984; Hodgson, 1986; Skinner *et al.*, 1988).

Even though mining and use of asbestos have decreased in recent years, while safety standards and protective measures have gradually improved, there is a notable and quantifiable risk of development of asbestos-related diseases. A factor compounding the problem of correlating such pathologies with the original asbestos exposure is

the notable time lag between exposure and the manifestation of the pathology. This lag is commonly between 15 and 40 years (Luus, 2007). Exposure to asbestos can occur through a number of ways, via skin contact, ingestion, and inhalation; the first two are relatively harmless, or at least there is no significant evidence of severe asbestos-related pathologies in relation to these routes. Inhalation is the most dangerous avenue of exposure, being associated with severe pathologies (Luus, 2007).

Asbestos fibers, when inhaled, exhibit irritative, genotoxic and immunosuppressive properties. Respiratory mucosa irritation by asbestos fibers will lead to scar tissue formation, and finally benign fibrosis, effusions and plaques in the lung cavities (Pedley, 1930). Amphibole fibers are far more dangerous in that aspect given their chemical stability; chrysotile fibers can be removed relatively quickly while amphiboles may remain forever in their place of deposition (Bernstein & Hoskins, 2006). The induction of autoimmunity by asbestos fibers is not fully understood, although there is evidence indicating that they can suppress the activity of natural killer and pulmonary parenchymal cells, thus potentially leading to lung cancer (Sider *et al.*, 1987; Tsang *et al.*, 1988). Asbestos has also been found to damage the DNA and alter gene transcription and protein production (Sider *et al.*, 1987; Berry *et al.*, 2000); it seems that the genotoxic properties of asbestos fibers are proportional to their length, with the chrysotile fibers being longer and thus more dangerous (Keane *et al.*, 1999).

It is therefore clear that asbestos fibers can cause both benign and malignant lung pathologies. Regarding benign pathologies, there are asbestosis, effusions and plaques (Luus, 2007). Asbestosis represents one of the most characteristic pathologies associated with asbestos exposure and is, essentially, a bilateral interstitial pulmonary fibrosis, which preferentially affects the base of the lungs (Mossman & Churg, 1998). Amphibole fibers are the principal culprits in this case (Hessel *et al.*, 2005). The localization of asbestos-related fibrosis in specific lung regions leads to the development of plaques, which gradually limit lung functionality (Goldsmith, 1982; Cudgell & Kamp, 2004). The plaques themselves are benign but are associated with an increased cancer incidence (Sprince *et al.*, 1991). Effusions, i.e., lung collections in the lungs, which occur in association with asbestosis, plaque development and mesothelioma, can be either acute or chronic (Davies *et al.*, 1991) and can be potentially deadly. Amphibole fibers are again more responsible for this pathological aspect compared to chrysotile fibers (Davies *et al.*, 1991).

Clinical features of asbestosis comprise cough and dyspnea, while common signs are diminished breath sounds, limited chest expansion, finger clubbing, and cyanosis. The most severe complication and the usual cause of mortality is cor pulmonale (Kleinfeld, 1966). Localized fibrotic plaques may or may not impact lung function depending on a number of factors (Kerper *et al.*, 2015). In addition, the presentation of clinical effusions may vary from asymptomatic to difficulty in breathing, depending on its size and other comorbidities (Iyer *et al.*, 2019).

Mesothelioma is a type of cancer of the cell lining of the lungs and abdomen. It is often misdiagnosed as pneumonia (Peto *et al.*, 1999). Radiographically, mesothelioma presents as plaque-like or nodular pleural thickenings, which are concentric and unilateral. They may be associated with pleural effusions, with the tumor frequently extending into the lung fissures. Even though a simple chest radiograph is not enough to conclusively diagnose mesothelioma, it is highly suggestive in patients with a previous exposure history (Aziz, 2009). From a clinical perspective, most cases of mesothelioma present with chest pain and dyspnea; even with treatment, the prognosis is usually very poor (Berzenji & Van Schil, 2018). Asbestosis can subsequently lead to bronchogenic lung cancer (Luus, 2007). Bronchogenic carcinoma is the most frequently diagnosed pulmonary cancer and comprises a number of histopathological patterns. For its staging, a CT scan is necessary (Reddy & Reddy, 2022).

Discussion

As has been presented, both asbestos and coal mining are associated with a number of potentially severe pulmonary pathologies, which are mostly irreversible. While anthracosis and related pathologies are generally less severe than asbestosis and mesothelioma, they nevertheless correspond to a notable burden of disease (Lu *et al.*, 2021), especially given the prominence of coal mining relative to asbestos mining. The mortality and morbidity of such diseases is compounded by a frequent late diagnosis or misdiagnosis, especially if occupational exposure is not taken into account by medical personnel.

The diagnosis of occupational diseases associated with mining and quarrying, and their causative connection to these activities, is also important from a socioeconomic perspective, i.e., the possibility of workers to both demand safer working conditions and to claim compensation for such diseases from the owners of the enterprises where they work. While this may seem self-evident, it is not always the case. On one hand, in third world the countries working conditions in mines and quarries are not constrained by modern safety regulations and compensatory policies. But even in countries of the western world, there can be situations where the actual dangers are discounted. For example, in Britain in the early 20th century, anthracosis was considered eradicated in miners, thus leading to laxer safety regulations and the inability to claim compensation for this particular pathology; initial compensatory policies

of the period, both in the US and Britain were considered relevant only for miners suffering from silicosis (Ronsmans & Nemery, 2022). In the case of asbestos, exposure has rapidly decreased in countries where it has been banned, and it is only relevant in non-mining related contexts. In the EU, the first measures for reducing asbestos exposure were taken in the 1980s (Belackova *et al.*, 2022). Legislation to that effect has also been discussed and gradually implemented in the US around that time (Cohen, 1991). Even so, in spite of the known dangers inherent in asbestos mining and use, the global asbestos industry continues to thrive in certain countries, although globally the demand for asbestos has dropped after 2000 (Frank & Joshi, 2014).

For mesothelioma, a simple chest X-ray is a good screening test, but its non-specific findings may be confused with cases of lymphomas and metastatic carcinomas, or even benign asbestosis. Both CT and MRI scans are more useful in determining the disease and its extend, but the definitive diagnosis is always made after a biopsy (Aziz, 2009). A CT scan is also necessary for the staging of bronchogenic carcinoma (Reddy & Reddy, 2022), which in a chest X-ray usually appears as a peripheral mass (Sider, 1990). Likewise, screening for diseases associated with coal mining may be performed by radiography, although the fact that they may initially not manifest via specific signs and symptoms will most likely be associated with a delayed patient presentation, and thus diagnosis.

Even though coal miners' pneumoconiosis and asbestosis have histological differences, they both present as fibrotic pneumoconioses, and the differential diagnosis on imaging is not always simple. In principle, in pneumoconiosis we can identify diffusely distributed granular micronodules with a perilymphatic pattern, which may present central calcifications; these are often accompanied by hilar or mediastinal lymph node enlargement and may also associate emphysema. Conversely, in asbestosis we encounter dot-like opacities which are usually distributed to the inferior lobes with a reticular centrilobular pattern; it is usually associated with pleural effusions and plaques, as well as traction bronchiectasis and honeycomb fibrosis (Chong *et al.*, 2006).

Based on the aforementioned evidence, the particularities of coal mining and asbestos mining-related pulmonary pathologies, from a diagnostic perspective, have been briefly outlined. In considering the associated morbidity and mortality, and thus decrease in quality of life, it is evident that they represent a matter not only of medical, but also of socioeconomic significance (Yokoyama *et al.*, 2013; Deng *et al.*, 2022). Such aspects are highlighted also in other mining and quarrying-associated occupational diseases in scientific literature (Mandel *et al.*, 2016; Periferakis, 2020; Bonilla *et al.*, 2024). It is for these reasons that adequate enforcement of workplace regulations is necessary, along with the implementation of novel measures and technologies aimed at further improving the safety and hygiene of these occupational environments. Social support and financial assistance aimed at improving of the quality of life of affected miners must also be implemented, especially in communities where a significant part of the workforce is thus occupied. But, first and foremost, there is the need of timely diagnosis, of accurate and efficient screening methods, which will enable prompt diagnosis, therefore improving patient prognosis. Hopefully, future developments in imaging, surgical techniques and biomaterials (Nedelea *et al.*, 2024; Periferakis *et al.*, 2024) will improve care and treatment standards for such patients.

References

Aziz, F., 2009. Radiological Findings in a case of Advance staged Mesothelioma. Journal of Thoracic Disease, 1, 46-47.

Belackova, L., Verbeek, J.H., Hoving, J.L., van der Molen, D.G., Curti, S., Hulshof, C.T.J., Scheepers, P.T.J., Marinaccio, A., 2022. Legal banning of asbestos for preventing asbestos exposure. Cochrane Database of Systematic Reviews 2022, CD015106.

Bernstein, D.M., Hoskins, J.A., 2006. The health effects of chrysotile: current perspective based upon recent data. Regulatory toxicology and Pharmacology 45, 252-264.

Berry, G., Newhouse, M.L., Wagner, J.C., 2000. Mortality from all cancers of asbestos factory workers in east London 1933-80. Occupational and Environmental Medicine 57, 782-785.

Berzenji, L., Van Schil, P., 2018. Multimodality treatment of malignant pleural mesothelioma. F1000 Research 7, 1681.

Bonilla, J.S., Idrovo, A.J., Figueroa, H.H., 2024. Intoxication in a Colombian mercury mine: Aranzazu, 1948-1975. História, Ciências, Saúde-Manguinhos 31, e2024048.

Campbell, W.J., Blake, R.L., Brown, L.L., Cather, E.E., Sjoberg, J.J., 1977. Selected Silicate Minerals and Their Asbestiform Varieties. Mineralogical Definitions, Identification and Characterisation. U.S. Bureau of Mines.

Chong, S., Lee, K.S., Chung, M.J., Han, J., Kwon, O.J., Kim, T.S., 2006. Pneumoconiosis: Comparison of Imaging and Pathologic Findings. Radiographics 26, 59-77.

Cohen N., 1991. Regulation of in-place asbestos-containing material. Environmental Research 55, 97-106.

Coulson, M., 2012. The history of mining: The events, technology and people involved in the industry that forged the modern world. Harriman House Limited.

Cudgell, D.W., 2004. Kamp DW. Asbestos and Pleura. Chest 125,1103-1117.

Dart, R.A., Beaumont, P., 1969. Evidence of iron ore mining in Southern Africa in the Middle Stone Age. Current Anthropology 10, 127-128.

Davies, D., Andrews, M.I., Jones, J.S., 1991. Asbestos induced pericardial effusion and constrictive pericarditis. Thorax 46, 429-432.
Deng, Z., Tao, T.Y., Qiao, Q., 2022. Socioeconomic Status, Occupational Disease, and Psychological Well-Being: Evidence from People with Pneumoconiosis in China. Social Sciences 11, 28.
Frank, A.L., Joshi, T.K., 2014. The global spread of asbestos. Annals of Global Health 80, 257-262.
Go, L.H., Rose, C.S., Zell-Baran, L.M., Almberg, K.S., Iwaniuk, C., Clingerman, S., Richardson, D.L., Abraham, J.L., Cool, C.D., Franko, A.D., Green, F.H., 2023. Historical shift in pathological type of progressive massive fibrosis among coal miners in the USA. Occupational and Environmental Medicine 80, 425-430.
Goldsmith, J.R., 1982. Asbestos as a systemic carcinogen: the evidence from eleven cohorts. American Journal of Industrial Medicine 3, 341-348.
Hessel, P.A., Gamble, J.F., McDonald, J.C., 2005. Asbestos, asbestosis, and lung cancer: a critical assessment of the epidemiological evidence. Thorax 60, 433-436.
Hodgson, A.A., 1986. Scientific Advances in Asbestos, 1967 to 1985. Anjalena Publications.
Iyer, N.P., Reddy, C.B., Wahidi, M.M., Lewis, S.Z., Diekemper, R.L., Feller-Kopman, D., Gould, M.K., Balekian, A.A., 2019. Indwelling Pleural Catheter versus Pleurodesis for Malignant Pleural Effusions. A Systematic Review and Meta-Analysis. Annals of the American Thoracic Society 16, 124-131.
Jasansky, S., Lieber, M., Giljum, S., Maus, V., 2023. An open database on global coal and metal mine production. Scientific data 10, 52.
Keane, M.J., Stephens, J.W., Zhong, B.Z., Miller, W.E., Ong, T.M., Wallace, W.E., 1999. A study of the effect of chrysotile fiber surface composition on genotoxicity in vitro. Journal of Toxicology and Environmental Health Part A 57, 529-541.
Kerper, L.E., Lynch, H.N., Zu, K., Tao, G., Utell, M.J., Goodman, J.E., 2015. Systematic review of pleural plaques and lung function. Inhalation Toxicology 27, 15-44.
Kleinfeld, M., Messite, J., Shapiro, J., 1966. Clinical, radiological, and physiological findings in asbestosis. Archives of Internal Medicine 117, 813-819.
Laney, A.S., Weissman, D.N., 2014. Respiratory diseases caused by coal mine dust. Journal of Occupational and Environmental Medicine 56, S18-22.
Lu, C., Dasgupta, P., Cameron, J., Fritschi, L., Baade, P., 2021. A systematic review and meta-analysis on international studies of prevalence, mortality and survival due to coal mine dust lung disease. PLoS One 16, e0255617.
Luus, K., 2007. Asbestos: mining exposure, health effects and policy implications. McGill Journal of Medicine 10, 121-126.
Mandel, J.H., Alexander, B.H., Ramachandran, G., 2016. A review of mortality associated with elongate mineral particle (EMP) exposure in occupational epidemiology studies of gold, talc, and taconite mining. American Journal of Industrial Medicine 59, 1047-1060
Mirsadraee, M., 2014. Anthracosis of the Lungs: Etiology, Clinical Manifestations and Diagnosis: A Review. Tanaffos 13, 1-13.
Mossman, B.T., Churg, A., 1998. Mechanisms in the pathogenesis of asbestosis and silicosis. American Journal of Respiratory and Critical Care Medicine 157, 1666-1680.
Nedelea, D.G., Vulpe, D.E., Viscopoleanu, G., Radulescu, A.C., Mihailescu, A.A., Gradinaru, S., Orghidan, M., Scheau, C., Cergan, R., Dragosloveanu, S., 2024. Progressive Thoracolumbar Tuberculosis in a Young Male: Diagnostic, Therapeutic, and Surgical Insights. Infectious Disease Reports 16(5), 1005-1016.
Pan, L., Golden, S., Assemi, S., Sime, M.F., Wang, X., Gao, Y., Miller, J., 2021. Characterization of Particle Size and Composition of Respirable Coal Mine Dust. Minerals, 11, 276.
Pedley, F.G., 1930. Industrial Hygiene: Asbestosis. Canadian Public Health Journal 21, 576-577.
Periferakis, A., 2020. The Keramos Antimonite Mines in Chios Island, Greece: Mining History and Current Situation. News on Minerals 35, 5-21.
Periferakis, A., 2021. The emery of Naxos: A multidisciplinary study of the effects of mining at a local and national context. JournalNX: A Multidisciplinary Peer Reviewed Journal 7, 93-115.
Periferakis, A., Paresoglou, I., Paresoglou, N., 2019. The significance of the Lavrion mines in Greek and European Geoheritage. European Geologist 48, 24-27.
Periferakis, A., Periferakis, A.-T., Troumpata, L., Dragosloveanu, S., Timofticiuc, I.A., Georgatos-Garcia, S., Scheau, A.-E., Periferakis K., Caruntu, A., Badarau, I.A., Scheau, C., 2024. Use of Biomaterials in 3D Printing as a Solution to Microbial Infections in Arthroplasty and Osseous Reconstruction. Biomimetics 9, 154.
Periferakis, A., Periferakis, K., Periferakis, A.-T., 2022. The Geoheritage of Malta from Prehistory to the Present Day. Proceedings of the 16th International Congress of the Geological Society of Greece, Patra, Greece, p. 816-817.
Peto, J., Decarli, A., La Vecchia, C., Levi, F., Negri, E., 1999. The European mesothelioma epidemic. British Journal of Cancer 79, 666-672.
Petsonk, E.L., Rose, C., Cohen, R., 2013. Coal mine dust lung disease. New lessons from an old exposure. American Journal of Respiratory and Critical Care Medicine 187, 1178-1185.
Reddy, R., Reddy, S., 2022. Trends in Imaging Patterns of Bronchogenic Carcinoma: Reality or a Statistical Variation? A Single-Center Cross-Sectional Analysis of Outcomes. Medical Principles and Practice 31, 480-485.
Ronsmans, S., Nemery. B., 2022. Pneumoconiosis in Coal Miners: Anthracosilicosis after All?. Annals of the American Thoracic Society 19, 1451-1452.
Ross, M., Nolan, R.P., 2003. History of asbestos discovery and use and asbestos-related disease in context with the

occurrence of asbestos within ophiolite complexes, in: Dilek, Y., Newcomb, S., (Eds.), Ophiolite Concept and the Evolution of Geological Thought, 447-470.

Ross, M., Virta, R.L., 2001. Occurrence, production and uses of asbestos, in: Nolan, R.P., Langer, A.M., Ross, M., Wicks, F. J., Martin, R.F., (Eds.), The health effects of chrysotile asbestos—Contribution of science to risk-management decisions, 79-88.

Ross, M.H., Murray, J., 2004. Occupational respiratory disease in mining. Occupational Medicine (London) 54, 304-310.

Ross, M., Kuntze, R.A., Clifton, R.A., 1984. A Definition for Asbestos, in: B. Levadie, B. (Ed.), Definition for Asbestos and Other Health Related Silicates: A Symposium, 139-147.

Schreiber, J., Koschel, D., Kekow, J., Waldburg, N., Goette, A., Merget, R., 2010. Rheumatoid pneumoconiosis (Caplan's syndrome). European Journal of Internal Medicine 21, 168-172.

Shekarian, Y., Rahimi, E., Rezaee, M., Su, W.-C., Roghanchi, P., 2021. Respirable Coal Mine Dust: A Review of Respiratory Deposition, Regulations, and Characterization. Minerals 11, 696.

Sider, L., 1990. Radiographic manifestations of primary bronchogenic carcinoma. Radiologic Clinics of North America 28, 583-597.

Sider, L., Holland, E.A., Davis Jr, T.M., Cugell, D.W., 1987. Changes on radiographs of wives of workers exposed to asbestos. Radiology 164, 723-726.

Skinner, H.C.W., Ross, M., Frondel, C., 1988. Asbestos and Other Fibrous Materials, Oxford Press.

Sprince, N.L., Oliver, L.C., McLoud, T.C., Eisen, E.A., Christiani, D.C., Ginns, L.C., 1991. Asbestos exposure and asbestos-related pleural and parenchymal disease. American Review of Respiratory Disease 143, 822-828.

Tsang, P.H., Chu, F.N., Fischbein, A., Bekesi, J.G., 1988. Impairments in functional subsets of T-suppressor (CD8) lymphocytes, monocytes, and natural killer cells among asbestos-exposed workers. Clinical Immunology and Immunopathology 47, 323-332.

Vermeersch, P.M., Paulissen, E., Van Peer, P., 1990. Palaeolithic chert exploitation in the limestone stretch of the Egyptian Nile Valley. African Archaeological Review 8, 77-102.

Wagner, N.J., 2020. Geology of Coal, in: Alderton, D., Elias, S.A. (Eds.)., Encyclopedia of Geology, 2nd ed., vol. 5, 745-761.

Wang, H., Ye, Q., Chen, Y., Li, T., 2023. Epidemiology of coal miners' pneumoconiosis and its social determinants: An ecological study from 1949 to 2021 in China. Chinese Medical Journal Pulmonary and Critical Care Medicine 1, 46-55.]

Yokoyama, K., Iijima, S., Ito, H., Kan, M., 2013. The socio-economic impact of occupational diseases and injuries. Industrial Health 51, 459-461.

17th INTERNATIONAL CONGRESS of the Geological Society of Greece

BULLETIN OF THE GEOLOGICAL SOCIETY OF GREECE, SP. PUBL.

EXTENDED ABSTRACT 262

Mineralogical composition and mineral chemistry of the listvenite-hosted mineralization in Kato Vyrsini area, Thrace, Greece

Peristeridou E.[1], Melfos V.[1], Voudouris P.[2], Papapodoulou L.[1], Pršek J.[3], Kantiranis N.[1]

(1) School of Geology, Aristotle University of Thessaloniki, Thessaloniki, Greece, peristee@geo.auth.gr

(2) School of Geology and Geoenvironment, National and Kapodistrian University of Athens, Athens, Greece

(3) Faculty of Geology, Geophysics, and Environmental Protection, AGH UST University of Science and Technology, Kraków, Poland

Research highlights:

The study focuses on Ni-Co sulfides and arsenides, highlighting their association with hydrothermal processes and ultramafic protolith alteration in the listvenite-hosted mineralization of the Rhodope massif.

Introduction / Background

Hydrothermal alteration of peridotites or serpentinites from ophiolite complexes, remnants of the Neotethys oceanic lithosphere has formed listvenites either mineralized or non-mineralized in many places, including Kosovo, Greece, Turkey, Oman, and Iran. In Greece, listvenites have been reported in Tinos Island, Mount Oeta in Central Greece, Gerakini and Vavdos at Chalkidiki, and in Vyrsini at Komotini (Iliadis, 2006, Hinsken et al., 2017 and references therein). The term listvenitization is used to describe the range of carbonization processes, from carbonate-rich to silica-rich phases, caused by hydrothermal fluids enriched in CO_2. These rocks are typically composed of quartz, Ca-Fe-Mg carbonates, fuchsite, serpentine, talc, chlorite, relics of chromite, magnetite, sulfides, and arsenides (Boskabadi et al., 2020). They commonly occur in shear or fault zones that serve as pathways for hydrothermal fluids, facilitating CO_2 infiltration and subsequent metasomatism. Listvenites are important since they are commonly associated with lode gold mineralization, as well as enrichment in other precious and critical metals, such as Ag, Hg, Co, Ni, As, and Sb that have been formed under low temperature conditions (Boskabadi et al., 2020).

The transformation of peridotite to listvenite involves multiple stages, beginning with hydration to form serpentinite, followed by carbonation and metasomatism through the influx of CO_2 rich fluids (Boskabadi et al., 2020). This transition is gradual, evolving with increasing CO□, and involves intermediate stages characterized by the progressive replacement of serpentine or talc, leading to quartz-carbonate assemblages. Based on the modal proportions of quartz and carbonate, three types of listvenite lithologies can be classified: carbonate listvenites, silica-carbonate listvenites, and silica listvenites (Boskabadi et al., 2020).

The objective of this study is to present preliminary data on the mineral composition of the listvenite occurrences in the Kato Vyrsini region in the Rhodope massif, and to document the mineralization they host, which has not been studied in detail so far.

Geology

The study area is part of the Kechros metamorphic core complex, which belongs to the Rhodope Massif in northeastern Greece. The Kechros complex is the lowermost tectonic unit of the Rhodope domain, exhumed against the Kimi complex by extensional deformation of the low-angle Kechros detachment fault during Early Eocene (36-32 Ma) (Mposkos et al. 2013, Kounov et al., 2024). This terrain consists of both continental and oceanic lithologies, represented by orthogneisses, pelitic gneisses, and high-alumina metapelites, intercalated with schists, amphibolites, boudins of eclogites, and scarce marbles. The oceanic affinity lithologies are tectonically intercalated and comprise serpentinized peridotites with dykes of gabbroic pegmatites, diabases, rodingitic gabbros, and blocks of trondjemites (Iliadis 2006, Mposkos et al. 2013). The antigorite serpentinite at Vyrsini spans approximately 95 km^2 and is considered one of the largest ultramafic bodies in the Greek Rhodopes. Its boundaries are defined by two major tectonic structures: the Smigada dip slip fault, and the Ragada-Esochi low-angle fault in the northern and southern parts, respectively. Over a large area, these rocks have undergone intense serpentinization and subsequent silica-carbonate alteration forming the listvenite zones. The largest listvenite body in the region extends from NW of the Kato Vyrsini village to Akritas occupying an area of approximately 2.5 km^2 (Fig. 1).

Methods

A preliminary investigation of the mineralization hosted in the listvenites of the Kato Vyrsini region was carried out on polished and thin sections. Observations were made using a Leitz LaborLux 11 Pol dual reflected-transmitted light polarizing microscope equipped with a Levenhuk M base series digital camera. The analysis was complemented by SEM back-scattered electron imaging, and the chemical composition of the ore minerals was determined by JEOL JSM- 6390LV scanning electron microscope (SEM) (JEOL Ltd., Tokyo, Japan) equipped with an OXFORD INCA 300 energy dispersive system (EDS). All the analyses were performed in the School of Geology at Aristotle University of Thessaloniki.

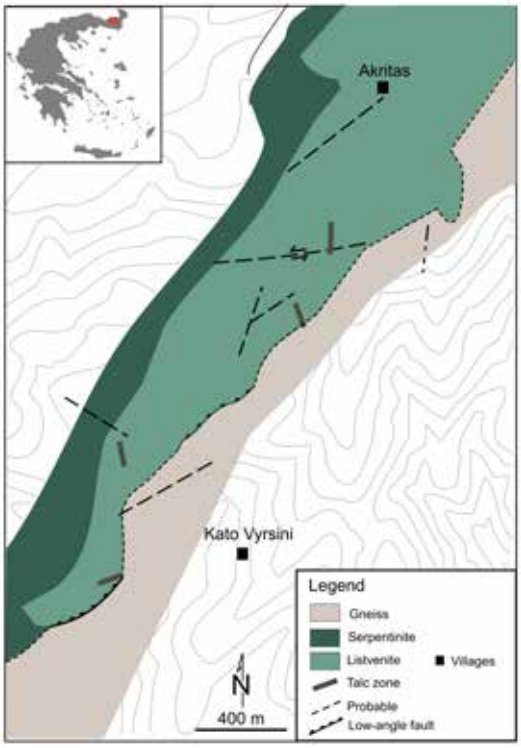

Figure 1. Simplified geological map of the area between Kato Vyrsini and Akritas (modified after Iliadis et al., 2006 and Kounov et al., 2024)

Results

In Kato Vyrsini, the listvenitization of serpentinite has resulted in the formation of three different rock types, each differing in mineralogy and the degree of metasomatism. These rock types include transitional rocks (Type I), carbonate-rich listvenite (Type II) and silica-rich listvenite (Type III) (Fig. 2a-c). Transitional rock types occur as lenses within the serpentinite body. They exhibit a greyish green color (Fig. 2a) and are characterized as magnesite-bearing serpentinite that contains over 70% serpentine along with magnesite and minor talc, chromite, magnetite, and hematite (Fig. 3a). Commonly, magnetite destabilized into hematite. Carbonate-rich listvenite is found adjacent to shear zones and is characterized by a green color (Fig. 2b). Its mineralogical composition is dominated by carbonate minerals, mainly dolomite, magnesite, with rare calcite, as well as quartz (Fig. 3b). It also contains chromite, which is often thinly rimmed by magnetite or ferri-chromite, and minor amounts of pyrite. Silica-rich listvenite, commonly referred to as “birbirite”, is formed along fault planes, indicating brittle deformation (Fig. 2c). It consists of a silicified mass with fine-grained quartz (Fig. 3c) and disseminated chromite, pyrite, marcasite, a Ni-sulfarsenide (gersdorffite), Ni-sulfides (vaesite, violarite), and minor rutile.

Figure 2. Hand specimen of different types of listvenite (a) Transition rock type (Type I), (b) Carbonate-rich listvenite (Type II), (c) Silica-rich listvenite (Type III) with mineralization

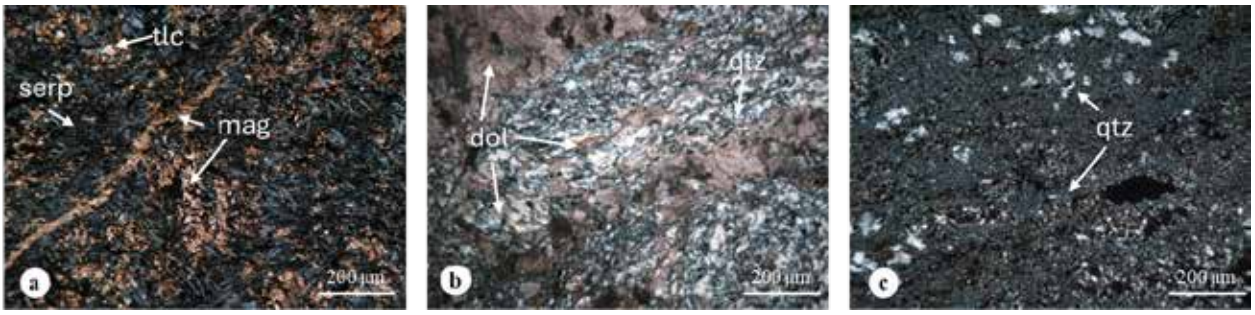

Figure 3. Microphotographs with closed-polarized light, of the different listvenite types (Type I-III) (a) Magnesite with fine-grained talc within a serpentine groundmass in Type I listvenite, (b) Dolomite with quartz in Type II listvenite, (c) Coarse- and fine-grained quartz in type III listvenite. Abbreviations: serp=serpentine, tlc=talc, mag=magnesite, dol=dolomite, qtz=quartz

Chromite appears with intense cataclastic texture in all listvenite types, with a decreasing extent from type I to type III, reaching sizes of up to 500 μm. In types I and II, chromite occurs within the carbonate mass and is commonly rimmed by magnetite or ferri-chromite (Figure 4a). In type III, it occurs as disseminated subhedral grains within the fine-grained matrix and appears more homogenous, without zoning. The chemical composition of chromite differs between the types II and III. When it is hosted in carbonate listvenites, it exhibits higher Cr_2O_3 contents, which decrease from the core to the outer rims, ranging from 45.98 to 49.56 wt.%. Similarly, MgO follows this trend, demonstrating contents of 6.67 wt.% in the core and 4.34 wt.% towards the rim. Conversely, Al_2O_3 ranges between 14.83 and 17.67 wt.% and increases towards the rims of the chromite crystals. Minor amounts of SiO_2 (up to 0.88 wt.%), V_2O_3 (up to 0.53 wt.%), ZnO (up to 0.96 wt.%) and NiO (up to 0.74 wt.%) are also present. Chromite in the silica-rich listvenites exhibits Fe content ranging from 24.6 to 52.01 wt.%, while Cr_2O_3 concentrations are lower compared to those in carbonate-rich listvenites, ranging from 40.74 to 44.05 wt.%. Additionally, there are minor contents in Al_2O_3 (0.7-0.91 wt.%) and MgO (0.66-1.16 wt.%). These chromites also contain TiO_2 ranging from 2.68-3.59 wt.%. Overall, the analyzed chromite grains in type III are characterized by a high chromite component, with a Cr# [Cr/(Cr+Al)] of 0.97, whereas those in Type II listvenites have a lower average Cr# of 0.67. Similarly, the average Fe# [$(Fe^{+2} / (Mg + Fe^{+2})$] value is 0.95 for chromites in silica listvenites and 0.72 for chromites in carbonate listvenites.

The abundance of magnetite decreases as the silica metasomatism increases, similar to chromite. Magnetite occurs as coarse- and fine-grained euhedral and subhedral grains, disseminated or massive, within the transitional listvenite and carbonate-rich listvenite. It commonly forms rims around chromite and occasionally it alters to hematite. It contains inclusions of Ni-bearing phases, such as violarite ($FeNi_2S_4$) (Fig. 4b). Variations in composition are observed within the same grains. In the cores, Fe content is lower and Cr decreases, while Ni is omnipresent (0.58–1.17 wt.%).

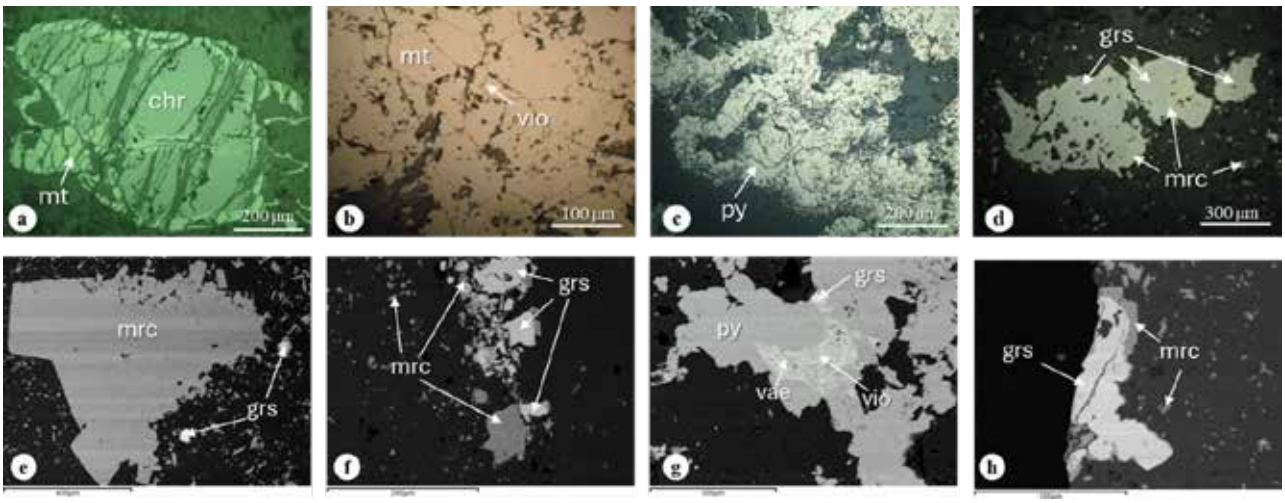

Figure 4. Microphotographs (a-d) and BSE images (e-h) of ore minerals in different listvenite types. (a) Chromite rimmed by magnetite. The microcracks are filled by serpentine (Type I listvenite), (b) Massive magnetite with violarite inclusion in Type II listvenite, (c) Oscillatory coarse-zoned pyrite in Type III listvenite, (d) Gersdorffite rimmed by marcasite in Type III, (e) Marcasite and gersdorffite with rims of marcasite in Type III listvenite, (f) Gersdorffite intergrown with marcasite in Type III listvenite, (g) Pyrite intergrown with Ni-phases (violarite and vaesite) in type III listvenite, (h) Gersdorffite with marcasite rim in Type III listvenite. Abbreviations: mt= magnetite, chr=chromite, vio=violarite, py=pyrite, grs=gersdorffite, mrc= marcasite, vae= vaesite.

Pyrite is present in listvenites of type II and III at Kato Vyrsini. Pyrite hosted within the carbonate-rich listvenites, exhibits a cataclastic texture and occurs as small subhedral to euhedral crystals, up to 20 μm in size. It is often oxidized to goethite while retaining the hexahedron crystal shape. In contrast, pyrite in the silica-rich listvenites forms significantly larger aggregates and is often associated with marcasite (Fig. 4c). The chemical composition of pyrite varies, with notable element concentrations. It contains up to 5.91 wt.% Ni, up to 1.91 wt.% As, up to 1.03 wt.% Ag and Zn, up to 0.87 wt.% Ti, up to 0.59 wt.% Sb, up to 0.47 wt.% Cu and up to 0.23 wt. % Co, many of which may be associated with micro-inclusions of other minerals. Iron content ranges from 35.48 to 43.09 wt.%, while S content ranges 54.82-59.16 wt.%. The average chemical composition can be expressed as $Fe_{0.87}Ni_{0.01}S_{2.11}$.
Gersdorffite is distributed within silicified listvenite (Type III) and occur as euhedral crystals up to 200 μm in size. These grains are often rimmed by marcasite or pyrite (Fig. 4d-h). Gersdorffite is the most widespread Ni-bearing phase of listvenites at Kato Vyrsini. The general chemical composition is NiAsS, with significant amounts of Fe and Co that can substitute for Ni, and minor amounts of Sb that can replace As. Gersdorffite from Kato Vyrsini contains 42.53-46.92 wt.% As and 27.89-36.01 wt.% Ni, 1.74-5.40 wt.% Fe, up to 3.28 wt.% Sb, 0.08-2.77 wt.% Co, and up to 0.53 wt.% Cu (Table 1). The average chemical formula is $(Ni_{0.9}Fe_{0.09}Co_{0.03})_{1.02}As_{0.99}S_{0.99}$.
Nickel sulfides are present in lower abundances and are represented by violarite and vaesite. Vaesite appears as anhedral grains interstitial to pyrite, alongside to violarite and gersdorffite in the silicified listvenites (Fig. 4g). Violarite is found in small grains associated with magnetite in the carbonate-rich listvenites. The average chemical composition of vaesite is $Fe_{0.2}Ni_{0.77}As_{0.02}S_2$, while violarite has a composition of $Fe_{0.99}Co_{0.01}Ni_{1.89}As_{0.03}S_4$. Violarite grains coexisting with magnetite are slightly richer in Ni and Co, contain no As, and exhibit a mean composition of $Fe_{0.75}Co_{0.06}Ni_{2.19}S_4$.

Table 1. Representative microanalyses (wt %) and calculated formulae of gersdorffite (1-6), vaesite (7-8), violarite (9-10) and pyrite (11-12) of the Kato Vyrsini listvenites

	1	**2**	**3**	**4**	**5**	**6**	**7**	**8**	**9**	**10**	**11**	**12**
Sb	0.33	0.9	bdl[1]	bdl	3.28	bdl	bdl	bdl	bdl	0.00	0.00	bdl
As	43.18	43.68	42.53	43.1	44.59	45.91	2.37	bdl	0.00	0.00	0.68	0.86
Zn	0.00	0.00	0.00	0.00	0.00	0.00	0.00	0.00	0.00	0.00	bdl	0.69
Ni	34.92	32.17	36.01	35.35	31.01	31.17	29.96	44.29	42.97	41.82	6.57	0.43
Co	0.49	0.53	0.19	0.08	0.47	1.62	0.16	bdl	1.25	1.08	bdl	0.15
Fe	2.81	4.15	1.92	2.32	1.88	2.4	15.13	3.25	13.19	14.51	39.42	45.55
S	19.19	18.86	19.47	19.71	18.90	19.15	52.52	52.35	42.35	42.42	53.44	53.24
Total	100.93	100.29	100.12	100.56	100.14	100.25	100.14	99.89	99.76	99.83	100.10	100.92
Chemical formula												
Sb	-	0.01	-	-	0.05	-	-	-	-	-	-	-
As	0.94	0.97	0.93	0.94	1.00	1.01	0.04	-	-	-	0.01	0.01
Zn	-	-	-	-	-	-	-	-	-	-	-	0.01
Ni	0.97	0.91	1.01	0.98	0.89	0.88	0.62	0.93	2.22	2.16	0.13	0.01
Co	0.01	0.01	0.01	-	0.01	0.05	-	-	0.06	0.06	-	-
Fe	0.08	0.12	0.06	0.07	0.06	0.07	0.33	0.07	0.72	0.79	0.85	0.98
S	0.98	0.97	1.00	1.00	0.99	0.99	2.00	2.00	4.00	4.00	2.01	1.99
Total	3.00	3.00	3.00	3.00	3.00	3.00	3.00	3.00	7.00	7.00	3.00	3.00

1: bdl: below detection limit

Discussion and Conclusions

The study of listvenites in the Kato Vyrsini area provides significant insights into their classification, mineralogical composition, and the associated mineralization processes. Based on mineralogical investigations, distinct types of listvenite were identified, differentiated by their dominant mineral assemblages. Serpentinization precedes listvenitization, as evidenced by the remnants of serpentine within the listvenite bodies, forming a transitional rock type (Type I). Type II (Carbonate-Rich Listvenites) forms during a subsequent phase of carbonation, characterized by the development of carbonate-dominated assemblages. Type III (Silica-Rich Listvenites) represents the most advanced stage, marked by intense silicification forming quartz-rich assemblages with disseminated Fe-Ni-S mineralization.
Most listvenites at Kato Vyrsini formed within or at the borders of serpentinized ultramafic rocks, along major tectonic zones (i.e. low-angle faults zones), which acted as pathways for hydrothermal fluids. However, some occurrences are associated with second order structures, such a small-scale cracks and high-angle faults, and also related to the porosity of highly altered serpentinized zones. A key aspect of listvenite-hosted ore formation in the study area is the role of a potential tectonic reactivation. Early-stage Mesozoic thrust faults were reactivated during Cenozoic

extension, and created low-angle detachment faults, enhancing fluid mobility and contributing to extensive alteration and mineralization, consistent with the tectonic regime observed in the Rhodope Massif (Melfos and Voudouris, 2017, Kounov et al., 2024). However, on the absence of age data, any genetic relationship between specific types of alteration and mineralization in the studied listvenites cannot be yet proven. We suggest here a scenario, where detachment faults facilitated deep circulation of CO_2-rich fluids, initiating carbonation reactions in the ultramafic protolith forming the transitional listvenite (Type I). As the system was uplifted the carbonate-rich fluids were substituted by silica-rich fluids and formed the carbonate-rich listvenite (Type II) and the silica-rich listvenite (Type III).
Chromite and magnetite occur in the least altered meta-ultramafic rocks. During listvenitization, these minerals are progressively replaced by newly formed mineral assemblages, especially sulfides, Ni-sulfarsenides, and Ni-arsenides. Pyrite and marcasite are the dominant sulfides, occurring in all types, and are accompanied by Ni-minerals, including gersdorffite, vaesite and violarite enriched in cobalt. The source of Ni and Co is attributed to the ultramafic protoliths, where they are hosted in silicates (primarily olivine or serpentine) or in magmatic sulfides that were destroyed during serpentinization and the subsequent hydrothermal alteration facilitated their leaching and mobilization (Kiefer et al., 2023). Although earlier studies in the Kato Vyrsini listvenites do not mention the presence of nickel minerals, they note attempts to explore nickel mineralization in the 1960s (Iliadis, 2006). This research shows that nickel mineralization is fairly common in the mineralization of the broader area.

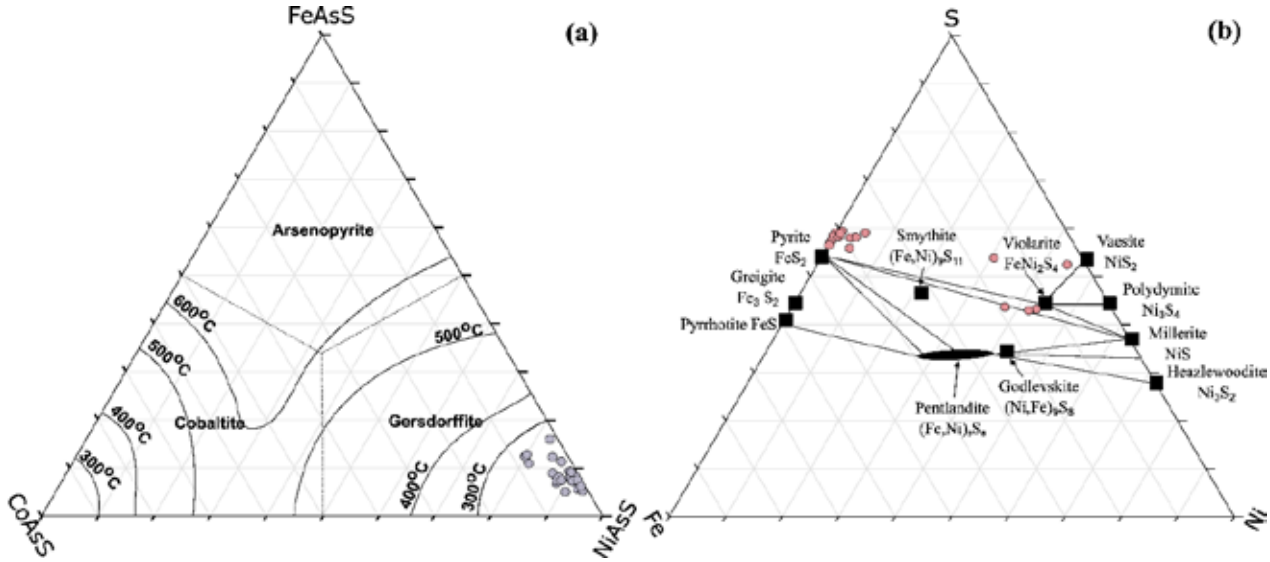

Figure 5. (a) Composition of gersdorffite in the FeAsS-CoAsS-NiAsS system. The solid lines contour the compositional fields of solid solutions in the system FeAsS-CoAsS-NiAsS at the specified temperatures (after Klemm, 1966), (b) Mineral stabilities in the ternary diagram Fe–Ni–S (after Schwarzenbach et al., 2014).

The ternary plot of gersdorffite analyses on the FeAsS-CoAsS-NiAsS system indicates formation temperatures between ~220-280 °C (Klemm, 1966, Mederski et al., 2021). Antimony, although not a common component of gersdorffite, was observed in grains coexisting with residual chromite within the listvenite mass. Correlation diagrams reveal a strong relationship (R^2=0.99) between Ni+Co+Fe and S+As+Sb (Fig. 6a), indicating that the elements behave in a coupled manner during mineral formation, transitioning to the gersdorffite-ullmannite series. Additionally, the substitution of Ni by Co is evident from the negative correlation between these elements in Fig. 6b. Iron, however, exhibits limited substitution for nickel (Fig. 6c), possibly due to the presence of a Fe-bearing phase intergrown with gersdorffite on a sub-microscopic scale, or due to the pyrite-marcasite rims around gersdorffite grains, creating observed irregularities. Figure 6d presents the correlation of R^2=0.67 of the couple substitution between Ni by Co and Fe.
Vaesite is intergrown with pyrite, gersdorffite and violarite. It typically forms at low temperatures through the replacement or remobilization of earlier Ni- and Co-bearing minerals. Vaesite is generally associated with the listvenitization of ultramafic rocks, where disulfides replace or overgrow older assemblages of sulfides (Schwarzenbach et al., 2014). Co- and Fe-bearing vaesite also contains more arsenic, while pyrite associated with vaesite exhibits higher cobalt concentrations. The same behavior is observed by the associated violarite. Violarite also forms intergrowths in magnetite with notable Ni and Co contents, suggesting formation at higher temperatures. Chemical analyses of vaesite and violarite indicate formation temperatures of ~230 °C consistent with phase relations in the Fe-S-Ni system (Fig. 5b) (Schwarzenbach et al., 2014).

The results of this study indicate that the Kato Vyrsini listvenites formed through complex processes involving hydrothermal fluids and tectonic activity. Further investigation is required to a more precise determination of the conditions that influenced their formation and mineralogical evolution.

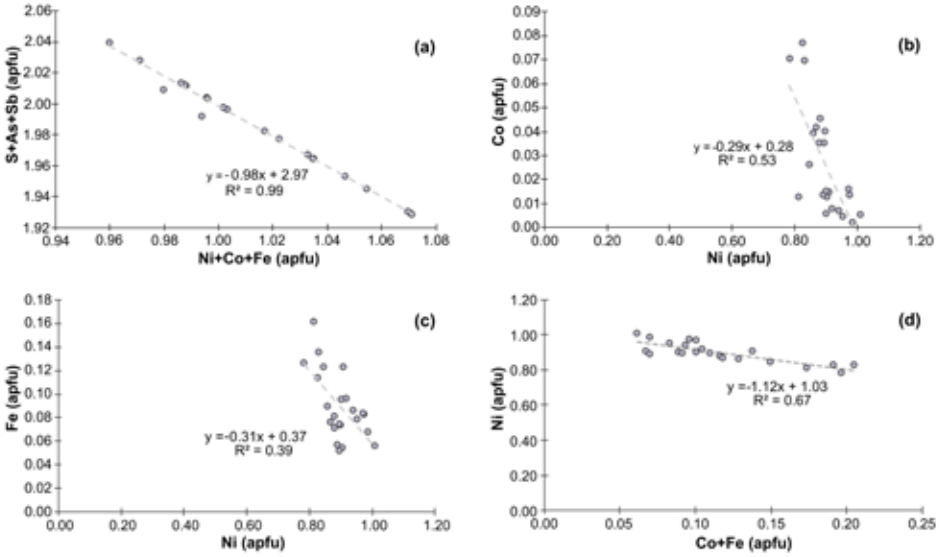

Figure 6. Plots showing substitution mechanisms in gersdorffite lattice: (a) S+As+Sb vs Ni+Co+Fe, (b) Co vs Ni, (c) Fe vs Ni, and (d) Ni vs Co+Fe

Acknowledgements

E. Peristeridou received a scholarship of excellence for PhD Candidates of the School of Sciences of Aristotle University of Thessaloniki, through the Special Account for Research Grants (S.A.R.G.) A.U.Th. in the context of the project 50186, No 673429-Excellence Scholarships for the Schools: Faculty of Engineering, School of Sciences, School of Agriculture – 2023. In addition, the research was funded by the Society of Economic Geologists Foundation (SEGF) and the SEG Canada Foundation (SEGCF) through the Student Research Grant Awards of 2024.

References

Boskabadi, A., Pitcairn, I. K., Leybourne, M. I., Teagle, D. A., Cooper, M. J., Hadizadeh, H., Bezenjani, R. N., & Bagherzadeh, R. M., 2020. Carbonation of ophiolitic ultramafic rocks: Listvenite formation in the Late Cretaceous ophiolites of eastern Iran. Lithos, 352, 105307.

Hinsken, T., Bröcker, M., Strauss, H., & Bulle, F., 2017. Geochemical, isotopic and geochronological characterization of listvenite from the Upper Unit on Tinos, Cyclades, Greece. Lithos, 282, 281-297.

Iliadis, A., 2006. Study of the ultrabasic rocks of Ano Vyrsini (Geology–Petrology–Metallogeny). PhD Thesis, National Technical University of Athens, Athens, 249p.

Kiefer, S., Ivan, P., Kaufmann, A. B., VĎAČNÝ, M., & Majzlan, J., 2023. Remobilization of Ni–Co–As and platinum-group elements by carbonate metasomatic alteration (listvenitization) of metaultramafic rocks from Dobšiná, Slovakia. Geologica Carpathica, 74(2), 139-153.

Klemm, D. D., 1966. Synthesen und Analysen in den Dreickdiagrammen FeAsS-CoAsS-NiAsS und FeS_2-CoS_2-NiS_2. Neues Jahrb. Mineral. Abh., 103, 205-255.

Kounov, A., & Gerdjikov, I., 2024. On the Rhodopean protoliths and their Middle Jurassic to Early Cretaceous evolution. A review. Geologica Balcanica, 53(1).

Mederski, S., Wojslaw, M., Prsek, S., Majzlan, J., Kiefer, S., & Asllani, B., 2021. A geochemical study of gersdorffite from the Trepça Mineral Belt, Vardar Zone, Kosovo. Journal of Geosciences, 66(2), 97-115.

Melfos, V., & Voudouris, P., 2017. Cenozoic metallogeny of Greece and potential for precious, critical and rare metals exploration. *Ore Geology Reviews*, *89*, 1030-1057.

Mposkos, E., Baziotis, I., Leontakianakos, G., & Barry, P. H.,2013. The metamorphic evolution of the high-pressure Kechros complex in East Rhodope (NE Greece): Implications from Na–Al-rich leucocratic rocks within antigorite serpentinites. *Lithos*, *177*, 17-33.

Schwarzenbach, E. M., Gazel, E., & Caddick, M. J., 2014. Hydrothermal processes in partially serpentinized peridotites from Costa Rica: evidence from native copper and complex sulfide assemblages. Contributions to Mineralogy and Petrology, 168, 1-21.

17th INTERNATIONAL CONGRESS of the Geological Society of Greece

BULLETIN OF THE GEOLOGICAL SOCIETY OF GREECE, SP. PUBL.

EXTENDED ABSTRACT 263

The geological structure of the Myrtoan Sea islets

Photiades A. [1], Kampolis I.[1,2], Vakalas I.[1,2], Deligiannakis G.[1,3]

(1) Hellenic Survey of Geology & Mineral Exploration, Acharnes, Greece, afotiadis@eagme.gr (2) National Technical University of Athens, Zografou, Greece (3) Agricultural University of Athens, Athens, Greece

Research Highlights

The previously unexplored geological structure of the Myrtoan Sea islets is briefly presented.

Myrtoan Sea stretches north to south between Spetses and Kithira Islands and east to west between Laconia Peninsula and Milos Island, comprising a subdivision of the Aegean Sea. It hosts a number of small islands (Antimilos, Ananes, Paximadi, Falconera and Velopoula) scattered on its marine territory, documenting the interesting, surficial geological structure of the area. With the scope of recording this local geology, the personnel of the Hellenic Survey of Geology and Mineral Exploration (HSGME) surveyed and mapped these islets in the framework of the project "Islets and rocky islets of the Aegean Sea" (2021-2025), supported by the National Funds Programme (NFP). This project attempted to shed light on the previously unexplored geological stratigraphy of the islets within the Myrtoan Sea, and place them in the context of the Hellenides belts.

The geology of the respective region can be distinguished in: a) the recent processes that took part at the northwestern segment of the active volcanic system of the South Aegean volcanic arc, b) the Mesozoic metamorphic basement of the Attic-Cycladic metamorphic complex and c) the Pelagonian realm. Each of these environments can be traced on the individual islets of the area. In the following sections, the stratigraphy description for each islet is given, starting from the most recent geological events and moving backwards in time.

Antimilos and Ananes Islets

Antimilos is situated almost 9 km northwest of Milos Island, whereas Ananes lies 22 km southwest of it. Both islets are part of the northwestern segment of the active South Aegean volcanic arc. The latter is comprised of a series of volcanic centers in a chain arrangement, that have produced a range of edifice-rich domes and lava flows with pyroclastic ejecta. The volcanic rocks vary from basaltic, through andesitic and dacitic, to rhyolitic compositions. They bear a typical calc-alkaline chemical composition associated with the active volcanic arc, triggered by the convergence of the African and Aegean plates. The volcanic activity initiated 3 million years ago (Ma) and remains active (Innocenti *et al.,* 1981). The tectonic regime of the area is characterized by a compressional phase during the Middle Miocene, followed by intense extensional stresses in the Pliocene (Angelier, 1979).

Antimilos Islet (Fig. 1) represents a large cone-shaped stratovolcano with steep-sided slopes, formed by an alternation of lava flow layers, composed mainly of dacite lava domes and subordinate andesite (Marinos, 1961) as well as pyroclastics. This volcano is characterized by explosive eruptions due to the high viscosity of the lava, suggesting a rhyolitic, dacitic and andesitic composition for the latter. The Antimilos rhyolitic activity (0.32 ± 0.05 Ma; Fytikas *et al.*, 1986) is coeval with the most recent eruptive phase on Milos.

Ananes Islets (Fig. 2) comprise a six-islet group, with the largest recording an altitude of 82 m, the intermediate 42 m, and the smallest ranging from 9 to a few meters. They consist mainly of highly-altered porphyritic andesitic lava flows, developed in dome structures, and their explosive and extrusive activities belong to the Milos Volcanic Field, dating back from 3.5 to 1.6 Ma (Late Pliocene-Early Pleistocene) (Fytikas *et al.,* 1986).

Paximadi Islet

Paximadi Islet is located 1,5 km southwest of Milos Island and consists of alpine and post-alpine lithologies. More particularly, Paximadi hosts the pre-volcanic metamorphic basement of the Attic-Cycladic Metamorphic Complex and on top of it, Neogene sediments lie unconformably. The metamorphic rock consists mainly of glaucophanitic schist and partly green schist, phyllite, metabasalt and quartz veins. It has undergone high-pressure (HP-LT) metamorphic facies in the Eocene and low-pressure (LP-LT) facies in the middle to late Miocene. Thus, it constitutes part of the Cyclades Blueschist unit (Grasemann *et al.,* 2018), and is identical to that of Milos Island.

Additionally, the Blueschist unit is subject to pervasive ductile deformation, possibly during the Paleocene-Eocene period, with a shearing direction towards south to southwest.

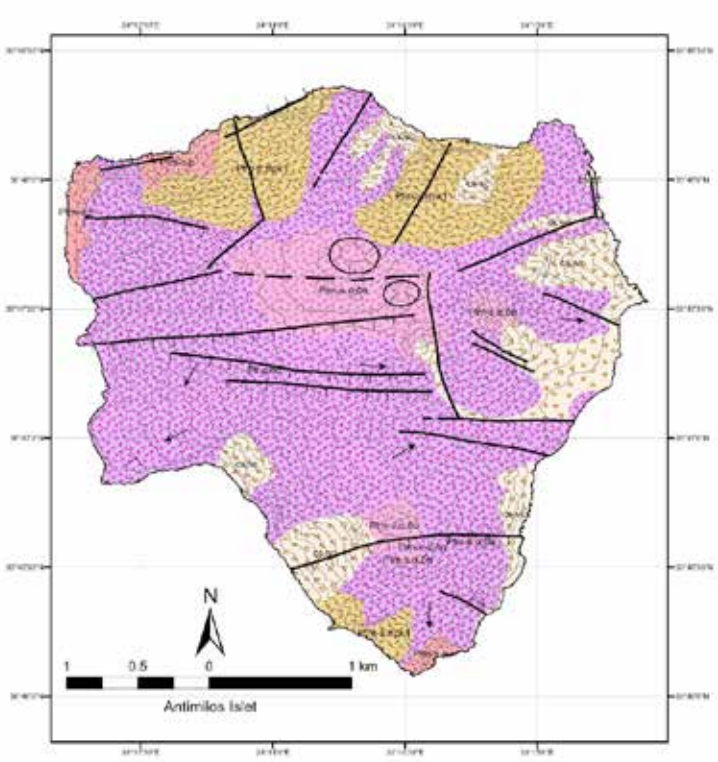

Figure 1. Geological map of Antimilos Islet. **cs,sc**: recent scree, **Pt_{m-s}.p**: pyroclastic-rhyolitic lavas, **Pt_{m-s}.πρκ1**: pyroclastic cones, **Pt_{m-s}.αδα**: mainly andesitic lavas , **Pt_{l}.α.δα**: mainly dacitic lavas.

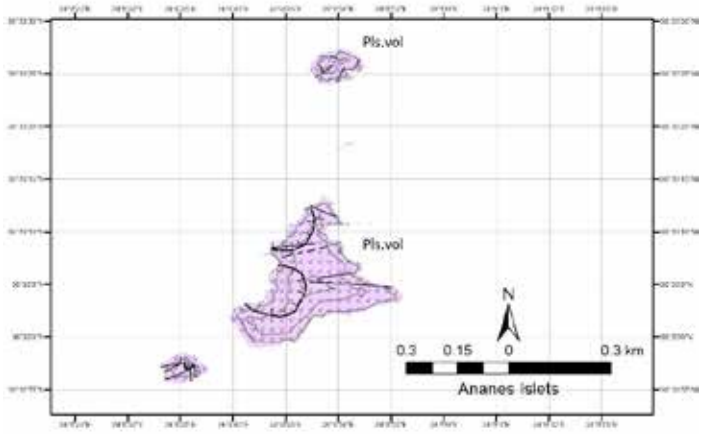

Figure 2. Geological map of Ananes Islet. **Pl_{s}.vol**: highly hydrothermally-altered volcanite.

Falconera, Velopoula and Karavia Islets

Falconera, Velopoula and Karavia Islets occupy the southeastern sector of the Pelagonian sensus lato (s.l.) geotectonic unit. Karavia comprises two islets where the larger one is delimited by faulted surfaces trending NW-SE and NE-SW, resulting in steeper and more vertical cliffs compared to the smaller one, lying southwestwards. It consists of limestone rich in Upper Permian-age fossils (determination by J. Bizon in Tataris 1988).

The main characteristic of the larger islets of Falconera and Velopoula is the outcropping of the ophiolitic unit that could be palaeotectonically related to a back-arc environment, as the ophiolitic and flyschoidal materials that fed the mélange of the Argolis tectonic units (Photiades *et al.,* 2024a). Moreover, the ophiolitic unit can be regarded as representative of a back-arc basin opening during the Middle to Late Jurassic (?), analogous to that of Guevgeli and

Skra ophiolite complexes that occur to the east of the Paikon volcanic arc (Saccani *et al.,* 2008).

Falconera resembles an elongated Z in shape (Fig. 3) and has a steep coastline controlled by NW-SE and NE-SW trending faults. Its name derives from the "Black Hawk" due to the dark color of its surface owing to the lithological composition of gabbro. The ophiolitic complex of Falconera consists of the crustal section of the ophiolitic sequence, lacking the mantle rock remnants, probably due to the sequence's emplacement onto the continental margin, as in the case of the post-flysch Upper Tectonic Unit with serpentinite mélange in Argolis (Photiades *et al.,* 2024a). Therefore, it only includes (from base to top): a) the lower members of the ophiolitic complex that outcrop towards the NW basal part of the islet and they are magmatically characterized by a basic cumulate sequence consisting of stratified-layered gabbro, b) an isotropic massive gabbro, dominated by cumulate intrusive coarse-grained rocks of hornblende-bearing gabbro, c) a sheeted dyke diabase complex system which is interconnected and magmatically overlain by a submarine extrusion lava cover, without any presence of red radiolarian chert. The lava cover comprises horizons of massive vesicular to porphyritic lava flows with acidic volcanic veins, which are successively derived from multiple underlying feeder veins (see geological section in Fig. 3).

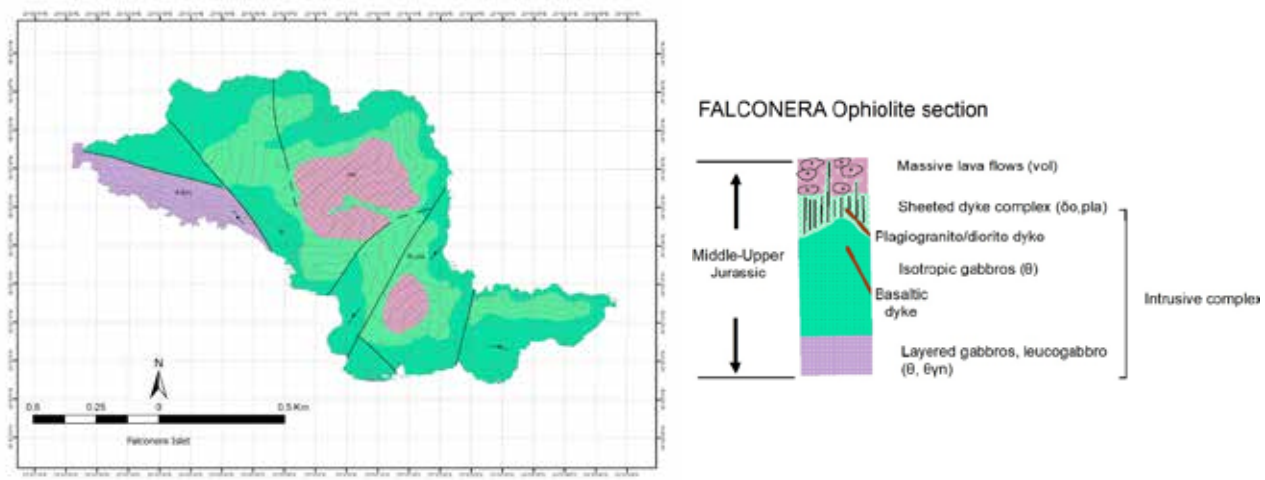

Figure 3. Geological map of Falconera Islet with its respective schematic stratigraphic column.

Velopoula is a 3-km long islet, bearing an elongated NW-SE steep ridge (Fig. 4). The presence of NW-trending faults contributes to the formation of its steep and weathered coasts. Ktenas (1924) mentions the outcropping of tuff, diorite, thick red jasper and Mesozoic carbonate at this islet.

Tectono-stratigraphically, Velopoula constitutes a nappe pile of the ophiolitic unit, thrusted on the Pelagonian continental margin, resulting from the compressional tectonic activity during the paleohellenic (eohellenic) phase as well as the post-flysch phase. The latter successively affected the neighboring Argolis Peninsula, too. Thus, from top to base, it comprises isotropic gabbro and tectonic slices of diabase intruded successively by quartz diorite, sub-ophiolitic mélange, red jasper succession, the carbonate platform and a basal volcano-sedimentary formation of Permo-Triassic age. Lithologically, the ophiolitic unit is homologous to the Falconera rocks. In general, Velopoula has undergone brittle deformation and low-grade, greenschist metamorphic conditions with recrystallizations.

The geological mapping of the above islets extending in the Myrtoan Sea between the Peloponnese and the Cyclades highlighted the following points: 1) The Upper Permian carbonate within the Karavia islets occurs as isolated blocks both in the Adheres-Argolis flyschoidal mélange of the internal Hellenides and in the imbricated Tertiary mélange unit between the Tripolis and Pindos Units in Peloponnese; 2) the Falconera and Velopoula ophiolite units can be regarded as representative as back-arc basin opening during the Middle to Late Jurassic (?), analogous to that of Guevgeli and Skra ophiolite complexes that obducted during late Jurassic-early Cretaceous times the continental margin of the internal Hellenides. Later, they were implicated by the post-Eocene continental collision of the Hellenides, leading to a non-metamorphic upper Cycladic Unit via a Miocene detachment over the Cycladic Blueschist Unit; and 3) Antimilos and Ananes volcanoes erupted during the Late Pliocene-Early Pleistocene, characterizing the Milos Volcanic Field on that subbasement.

The abovementioned geology of the islets at the Myrtoan Sea has been included in the geological sheet of Greece "Myrtoan Sea Islets", in scale 1:25000, edited by the HSGME (Photiades *et al.,* 2024b).

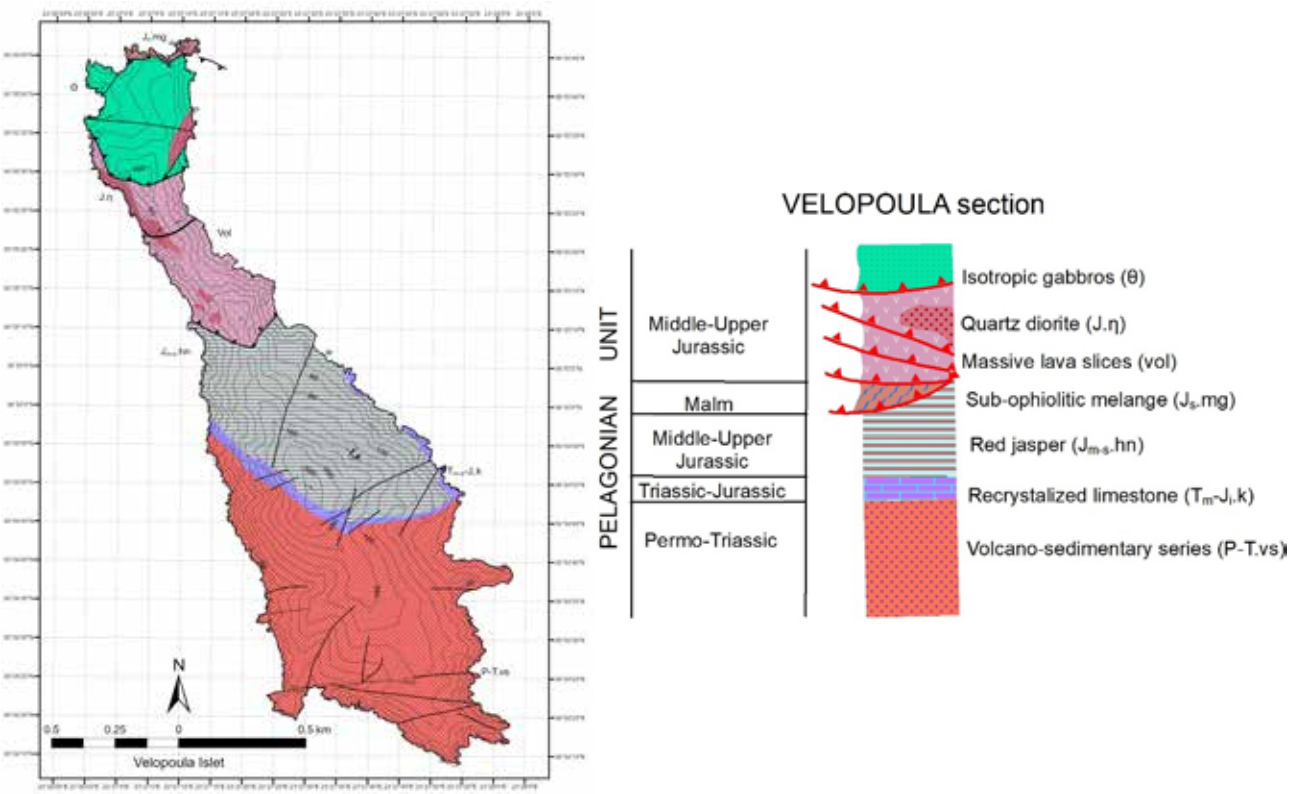

Figure 4. Geological map of Velopoula Islet with its respective schematic stratigraphic column.

Acknowledgements

The current work was carried out in the frame of the project “Islets and rocky islets of the Aegean Sea” (2021-2025), supported by the NFP.

References

Angelier, J., 1979. Recent Quaternary Tectonics in the Hellenic Arc: Examples of geological Observation on Lands. Tectonophysics, 52, 267-275.

Fytikas, M., Innocenti, F., Kolios, N., Manetti, P., Mazzuoli, R., Poli, G., Villari, L.,1986. Volcanology and petrology of volcanic products from the island of Milos and neighbouring islets. Journal of Volcanology and Geothermal Research, 28, 3–4, 297–317.

Grasemann, B., Huet, B., Schneider, D. A., Rice, A. H. N., Lemonnier, N., Tschegg, C., 2018. Miocene post-orogenic extension of the Eocene synorogenic imbricated Hellenic subduction channel: New constraints from Milos (Cyclades, Greece). GSA Bulletin, 130 (1–2), 238–262.

Innocenti, F., Manetti, P., Peccerillo, A., Poli, G., 1981. South Aegean Volcanic Arc: Geochemical Variations and Geotectonic Implications. Bulletin of Volcanology, Vol. 44-3, 377-391.

Ktenas, K., 1924. L’île de Bélopoula entre le Péloponnèse et les Cyclades. Société Géologique de France, séance 28 avril 1924, p.13-14.

Marinos, G.,1961. The Antimilos volcano in Aegean Sea. Bulletin of the Geological Society of Greece IV 1, 38-50.

Photiades, A., Deligiannakis, G., Vakalas, I., Carras, N., 2024a. Geological map of “TROIZINA sheet” in scale 1:50.000. Edited by HSGME, Athens.

Photiades, A., Kampolis, I., Vakalas, I., Deligiannakis, G., 2024b. Geological map of “MYRTOAN SEA ISLETS sheet” in scale 1:25.000. Edited by HSGME, Athens.

Saccani E., Bortolotti, V., Marroni, M., Pandolfi, L., Photiades, A., Principi, G., 2008. The Jurassic association of back-arc basin ophiolites and calk-alcaline volcanics in the Guevgueli complex (Northern Greece: implication for the evolution of the Vardar Zone). Ofioliti, 33, 2, 209-227.

Tataris, A., 1988. The Paleozoic of the Karavia islets, east of Lakonia (Aegean Sea). Bulletin of the Geological Society of Greece, 20, 2, 21-38.

17th INTERNATIONAL CONGRESS of the Geological Society of Greece

BULLETIN OF THE GEOLOGICAL SOCIETY OF GREECE, SP. PUBL.

EXTENDED ABSTRACT 264

Assessment of the exposure of coastal sectors of the Greek Mainland to hazards induced by climate change, using the Coastal Hazard Wheel

Poulos S.E.[1], Alexandrakis[2] G., Karditsa[3] S. Lesioti[1], F. Markozanes[1], Katritsis[1] I., and A. Kampanis[2] N.

(1) Laboratory of Physical Geography, Section of Geography and Climatology, Department of Geology and Geoenvironment, Panepistimioupolis-Zografou 15784, Attiki, Greece.

(2) Coastal & Marine Research Laboratory, Institute of Applied and Computational Mathematics, Foundation for Research and Technology-Hellas, 70013 Heraklion, Crete, Greece

(3) Department of Port Management and Shipping, National and Kapodistrian University of Athens, Psahcna, Evia, Greece

Introduction

Low-lying coasts such as beaches and lagoons are vulnerable to erosion and/or coastal flooding due to sea storms. A tool for the evaluation of the vulnerability of the coasts is the (CHW: Coastal Hazard Wheel), that is a universal coastal management framework (extended landwards to 200 m) for coastal classification, hazard information and adaptation guidance (Rosendahl Appelquist 2012; Appelquist & Halsnæs, 2015).

The coastal classification system is based on the bio geophysical components that are considered most important for the characteristics of a particular generic coastal environment; these are: (1) geological layout, (2) wave exposure, (3) tidal range, (4) flora/fauna, (5) sediment balance and (6) storm climate. Obviously, each generic coastal environment has a specific combination of these variables (Appelquist, 2012).)

The inherent hazard levels are defined as the hazards being an inherent part of the bio-geophysical properties of a coastal environment when exposed to the predicted changes in global climate over the coming decades. The inherent hazards covered by the CHW system are:

(a) ecosystem disruption that describes the possibility of a disruption of the current state of the coastal ecosystems under a changing climate

(b) gradual inundation, which describes the possibility of a gradual submergence of a coastal environment under a changing climate.

(c) salt water intrusion that describes the possibility of salty sea water penetrating into coastal surface waters and groundwater aquifers under a changing climate

(d) erosion and flooding, which describes the possibility of a sudden, abrupt and often dramatic inundation of a coastal environment caused by a short term increase in water level due to storm surge and extreme tides, under a changing climate

The purpose of the present study is to investigate the exposure of beach sectors from 4 different coastal areas of the Greek mainland The Kotychi lagoon, the Alfios River deltaic coast (north Kyparissiakos), the beach/dunes in the central Kyparissiakos coast and central part of the north coast of the Messiniakos Gulf, and four beaches from the coast of Attika (Figure 1).

Figure 1. Beaches under investigation (a: West and Southwest Peloponnese, b: West Attica Coast)

Methodology

The application of CHW requires quantification/categorization of the bio-geo-physical components, as it is described below (Mangor, 2004).

The geological layout categories include (i) sedimentary plain; (ii) barrier; (iii) delta/low estuary island; (iv) sloping soft rock coast; (v) flat hard rock coast; (vi) sloping hard rock coast; (vii) coral island; (viii) tidal inlet/sand; and (ix) spit/river mouth (e.g., Davis and Fitzgerald, 2004).

Regarding wave exposure, coasts are classified as: (i) Exposed Coasts when fetches >100 km, (ii) moderately exposed, when fetches are 10–100 km and (iii) protected costs when fetches <10 km, but can also be seen along larger waterbodies with shallow nearshore zones or mild onshore wind climates (Mangor 2004).

The effect of tidal range includes 3 main categories: (i) microtidal <2 m; (ii) meso-tidal 2-4 m; and (iii) macro-tidal >4 m (Masselink and Hughes, 2003).

The flora/fauna component includes nine different categories; (i) intermittent marsh; (ii) intermittent mangrove; (iii) marsh/tidal flat; (iv) mangrove; (v) marsh/mangrove; (vi) vegetated; (vii) not vegetated; (viii) coral and (ix) any. Moreover, the vegetated category is applied when more than 25 % of the sloping soft rock coast is covered with vegetation while the not vegetated category is used when less than 25 % is vegetated (Appelquist & Halsnæs, 2015).

The sediment balance includes the two main categories: (i) balance/deficit; and (ii) surplus for the low-lying ssoft coasts and other two special categories (i) no beach and (ii) beach that applies to the hard rock coastlines (Haslett, 2009).

Storm climate differentiates between locations (i) with and (ii) without tropical cyclone activity, irrespective of their frequency. In areas identified as being under tropical cyclone influence (i.e., 5°–15°N and 5°–15°S), the classification system assigns a “yes” to tropical cyclone activity, while it assigns a “no” to locations outside these regions. (Appelquist, 2012).

The CHW hazard levels are divided into four categories ranging from 1 (low hazard) to 4 (high hazard). (Rosendahl Appelquist & Halsnæs, 2015). Each generic coastal environment is assigned a specific inherent hazard level for each hazard type. In the CHW, this information is presented using a combined number and color code, providing users with a clear and comprehensive overview of the hazard profile for a given coastal environment (Figure 2).

Results and Discussion

The results refer to: (1) The coastal zone of Kotyki, which extends in front of the homonymous lagoon, (2) The deltaic coastline of the Alphios River, (3) The coastal zones of the Central Kyparissia Gulf and the central part of the Messinian Gulf coastline, which include dunes and develop in front of a coastal lowland plain and (4) Four pocket beaches along the coast of the Athinaiki Riviera.

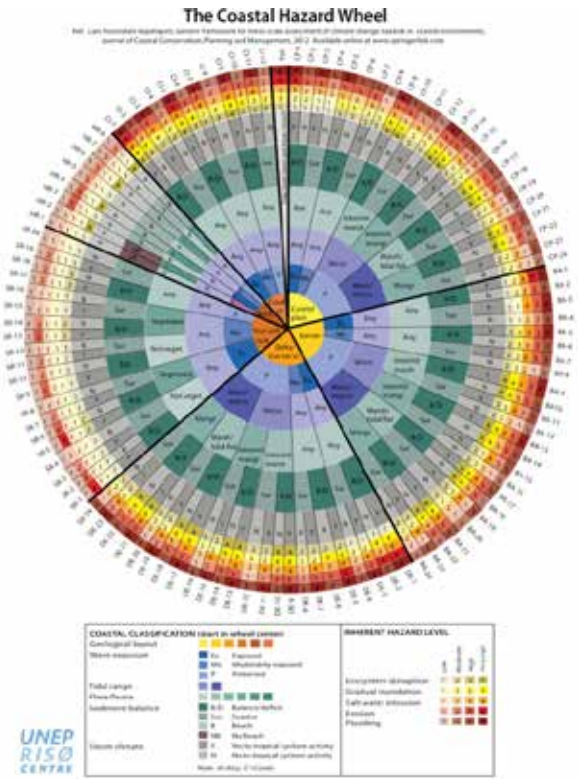

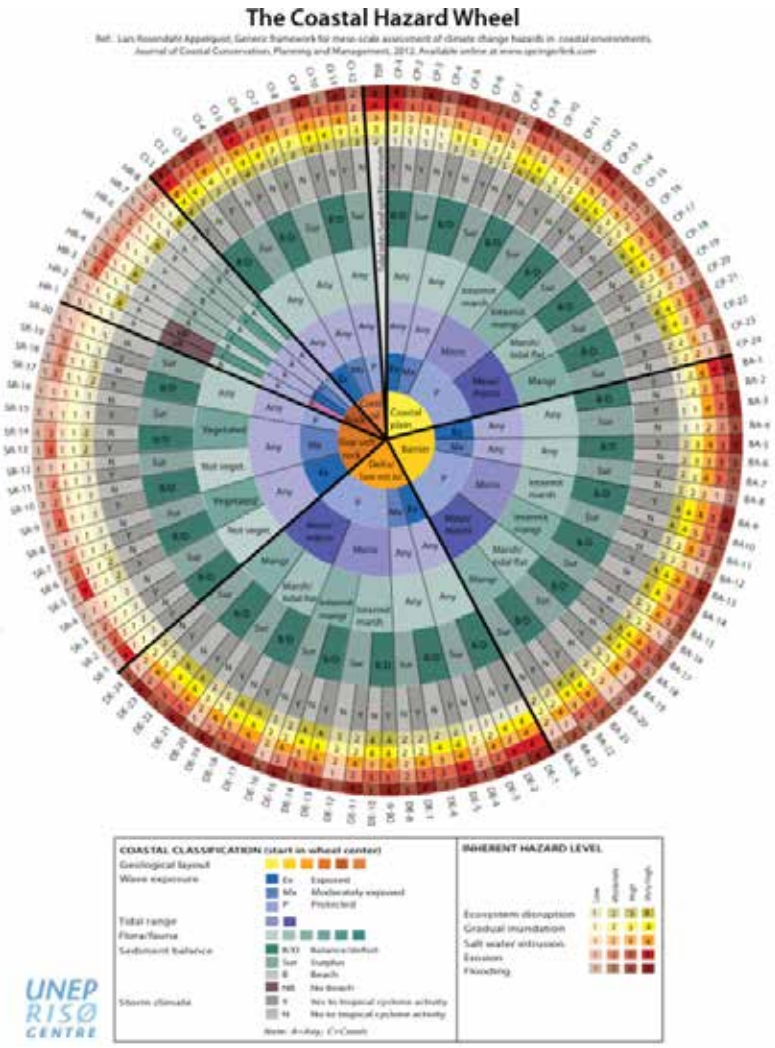

Figure 2. Coastal classification Wheel (abstracted from Rosendahl Appelquist & Halsnæs, 2015.

.

A. Kotychi Laggoon

Geological layout	Beach barrier	BA-5 (2-3-4-3-4)
Wave exposure	Moderate	Ecosystem disruption = Moderate (2)
Tidal range	Micro-tidal	Gradual inudation= High (3)
Flora/fauna	Swampy /not continous	Salt water intrusion= Very High (4)
Sediment balance	Deficit, beach presence	Erosion = High (3)
Storm (tropical) climate	No	Flooding= Very high (4)

B Alfios Delta

Geological layout	Delta	DE-2 (1-4-3-4-3)
Wave exposure	High	Ecosystem disruption = Small (1)
Tidal range	Micro-tidal	Gradual inudation= Very High (4)
Flora/fauna	Any	Salt water intrusion = High (3)
Sediment balance	Deficit, beach presence	Διαβρωση = Very High (4)
Storm (tropical) climate	No	Flooding= High (3)

C Central Kyparissiakos and Central Messiniakos Beaches (with dunes)

Geological layout	Coastal plain	CP-2 (1-2-2-3-3)
Wave exposure	High	Ecosystem disruption = Small (1)
Tidal range	Micro-tidal	Gradual inudation = Moderate (2)
Flora/fauna	Any	Salt water intrusion = Moderate (2)
Sediment balance	Balance	Erosion = High (3)
Storm (tropical) climate	No	Flooding= High (3)

D. Athinaiki Riviera

D.1. Kavouri and Anavyssos beaches

Geological layout	Coastal plain	CP-6 (2-3-2-3-3)
Wave exposure	Moderate	Ecosystem disruption = Moderate (2)
Tidal range	Micro-tidal	Gradual inudation = High (3)
Flora/fauna	Any	Salt water intrusion = Moderate (2)
Sediment balance	Balance	Erosion = High (3)
Storm (tropical) climate	No	Flooding= High (3)

D.2. Vouliagmeni and Varkiza beaches

Geological layout	Coastal plain	CP-2 (1-2-2-3-3)
Wave exposure	High	Ecosystem disruption = Small (1)
Tidal range	Micro-tidal	Gradual inudation = Moderate (2)
Flora/fauna	Any	Salt water intrusion = Moderate (2)
Sediment balance	Balance	Erosion = High (3)
Storm (tropical) climate	No	Flooding= High (3)

Discussion and Conclusions

According to the results on biodiversity threat, the threat is low (category 1) for groups B and C, and moderate (category 2) for groups A and D1. In the micro-tidal environment of Greece, the gradual inundation is moderate (category 2) for group C (dune beaches) and D2 (pocket beaches not exposed to high waves), high (category 3) for group B (deltaic coast) and D2 (pocket beaches exposed to high waves), and very high (category 4) for group A (coastal barrier in front of a lagoon). Regarding saltwater intrusion, it was assessed as moderate (category 3) for groups B, C, and D, and high for group A. The risk of erosion is high (category 3) in groups A, C, and D, and very high (category 4) in group B. Finally, the risk of coastal (marine) flooding is high (category 3) in groups B, C, and D, and very high (category 4) in group A. Therefore, the main factors controlling the variability of exposure to coastal hazards appear to be primarily related to the geological layout and exposure to wave activity, followed by sediment balance and the type of flora and fauna.

Acknowledgements

The authors S. Poulos, A. Karditsa, S. Lesioti, F. Markozanes acknowledge the project ATHINAIKI RIVIERA (P4-0325990) entitled: “Study for the development of smart infrastructure along the coastal front of Southwest Attica, with emphasis on the promotion of the natural and cultural reserve for the enhancement of tourist services”, Attica Regional Programme (2014-2020).

References

Appelquist, L. R. (2013). Generic framework for meso-scale assessment of climate change hazards in coastal environments. Journal of Coastal Conservation, 59-74.

Davis RA Jr, Fitzgerald DM (2004) Beaches and coasts. Blackwell Publishing

Haslett SK (2009) Coastal systems. Routledge Rosendahl

Mangor, K. (2004). Shoreline Management Guidelines.” DHI Water and Environment, 294p

Rosendahl Appelquist, L., & Halsnæs, K. (2015). The Coastal Hazard Wheel system for coastal multi-hazard assessment & management in a changing climate. Journal of coastal conservation, 19, 157-179.

17th INTERNATIONAL CONGRESS of the Geological Society of Greece

BULLETIN OF THE GEOLOGICAL SOCIETY OF GREECE, SP. PUBL.

EXTENDED ABSTRACT 265

Hydrogeological and hydrochemical investigations of Selinous basin region

Pyrgakis D. [1], Stavropoulou V.[1], Kaskani E.[1], Papailiopoulou M.[1], Pouliaris C. [1], Lampropoulou D.[2], Zagana E.[1], Chalikakis K.[3], Kazakis N.[1]

(1) University of Patras, Department of Geology, Laboratory of Hydrogeology, Patra, Greece, dpyrgakis@upatras.gr, vstavropoulou@ac.upatras.gr , up1074001@upatras.gr, m.papailiopoulou@ac.upatras.gr, christospouliaris@gmail.com, zagana@upatras.gr, kazakis@upatras.gr ,

(2) Aristotle University of Thessaloniki, Department of Chemistry, Environmental Pollution Control Laboratory, Thessaloniki, Greece, dlambro@chem.auth.gr

(3) UMR 1114 EMMAH (AU-INRAE), Avignon Université, 84029 Avignon, France; konstantinos.chalikakis@univavignon.fr

Introduction

Rock weathering constitute a major factor controlling the hydrochemical evolution of river basins (Wang et al., 2022; Zhou et al., 2021; M. Zhu et al., 2021). Carbonate weathering is typically the main source of ions, followed by silicate weathering (Wang et al., 2020; Zhou et al., 2021). Land use and land cover changes in the river basin can have a direct influence on the hydrological realm and water quality (Lima et al., 2014; Raj and Azeez, 2010; Wang et al., 2022). Deforestation and agricultural expansion can lead to changes in the water balance, water availability, and water quality (Lima et al., 2014; Wang et al., 2022). Conversely, afforestation can increase the buffering capacity and pH of streams (Burgess-Conforti et al., 2022).

River basins are dynamic systems shaped by diverse factors, including geology, land use, and human activities, all of which can significantly influence the hydrochemical properties of both surface water and groundwater. In karst regions, characterized by soluble rock formations such as limestone and dolomite, the interaction between surface water and groundwater is particularly intricate. This complexity arises from the unique hydrological pathways and chemical processes inherent to these environments, where water movement and composition are heavily influenced by the dissolution of the surrounding rock (Xiao et al., 2021). Kazakis et al. (2018) point out that a holistic approach combining hydrodynamic analysis, vulnerability assessment, and integrated management strategies is essential for the sustainable exploration, protection, and management of Greece's karst aquifers, ensuring their long-term viability as critical water resources.

Karst aquifers are renowned for their heterogeneity and rapid flow dynamics, which contribute to significant variations in water quality and chemical composition. Research indicates that the dominant hydrochemical type of karst groundwater typically features bicarbonate and sulfate ions, reflecting the dissolution of carbonate minerals and the impact of surrounding geological formations (Yu et al., 2023; H. Zhu et al., 2021). The hydrochemical facies of karst groundwater are influenced by factors such as recharge mechanisms, land use practices, and pollution sources. These complexities underscore the need for comprehensive hydrochemical analyses to better understand the interactions within these aquifer systems (Kshetrimayum, 2015). Karst aquifers are highly vulnerable to contamination due to their unique hydrological characteristics, such as well-developed conduit systems, which allow rapid pollutant transport with minimal natural filtration (Kazakis et al., 2015).

In summary, hydrochemical investigations in river basins and karst groundwater systems are important for evaluating water quality, understanding hydrological processes, and managing water resources effectively. The integration of hydrochemical analyses of main and trace elements provides a comprehensive framework for unraveling the complexities of these aquatic systems (Pacheco Castro et al., 2018).

Study area

The study area is located in northwest Peloponnese in western Greece. The NW Peloponnese region has been the focus of numerous geological and tectonic studies, shedding light on the area's rock formations and their evolution (Doutsos & Poulimenos, 1992; Poulimenos et al., 1993; Flotte et al., 2005; Ghisetti & Vezzani, 2005; Trikolas, 2008; Backert et al., 2010; Ford et al., 2016). Geologically, the rocks in this region are classified as part of the External Hellenides (Koukouvelas, 2019, and references therein), specifically including formations from the Pindos and Tripolis Units.

From a paleogeographic perspective, the sequences of the Pindos and Tripolis Units were deposited along the eastern passive margin of the Apulian microplate. This margin was bounded to the east by the Pindos Ocean. The External Hellenides were formed during the Tertiary period as a result of the closure of the Pindos Ocean and the subsequent continental collision between the Apulian and Pelagonian microplates during the Alpine orogeny. A significant portion of the broader study area is now covered by post-Alpine Neogene and Quaternary formations, including modern alluvial deposits linked to the opening of the Corinth Rift.

The Pindos Unit occupies the largest part of the study area and comprises Mesozoic deep-sea carbonate and siliceous sedimentary rocks with a total thickness of approximately 1200 meters. These rocks are overlain by a clastic flysch sequence of Paleocene–Oligocene age (Degnan & Robertson, 1998). Structurally, the Pindos Unit is composed of distinct formations arranged from lower to higher levels. At the base lies the Triassic Clastic Formation, characterized by alternating sandstones, clays, and argillaceous layers interbedded with tuffs, granites, and gabbros, reaching a total thickness of about 100 meters. Above this, the Drymos Limestone Formation consists of hemipelagic limestones interbedded with cherts and clays, with a maximum thickness of 300 meters. This is followed by the Radiolarite Formation, a sequence of glassy cherts, clayey horizons, and pink limestones dated to the Jurassic–Lower Cretaceous, with a maximum thickness of 350 meters.

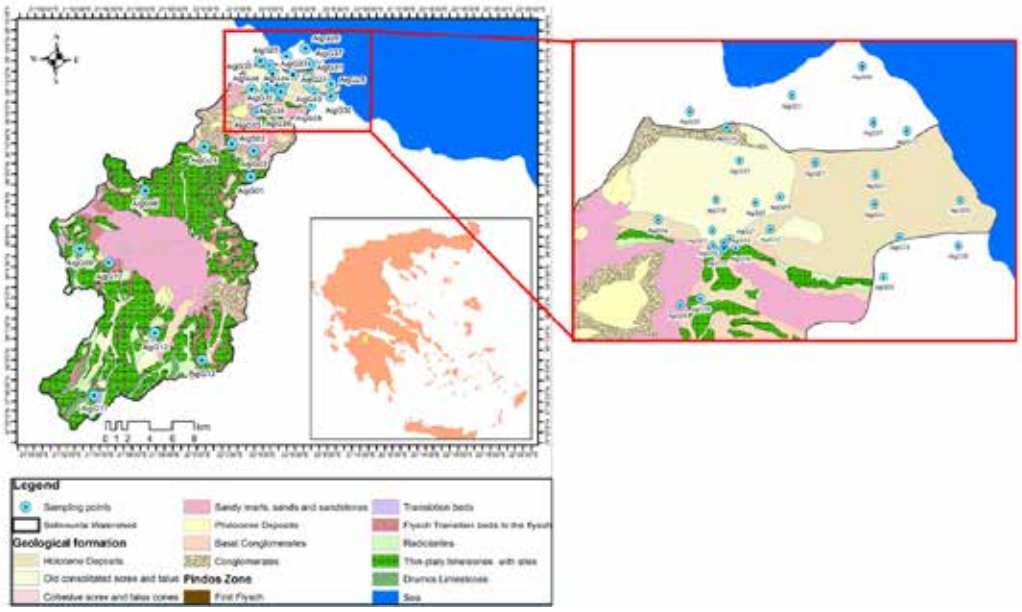

Figure 1: Geological map of the study area (modified by IGME geological maps)

The sequence continues with the Clastic Horizon, also known as the First Flysch, consisting of alternating sandstones and clays from the Lower Cretaceous, approximately 50 meters thick. Above this horizon lie the Upper Cretaceous Thin-Plated Limestones, containing cherts and reaching a thickness of 400 meters. Finally, the unit transitions into flysch deposits, including Transitional Flysch Layers and the Pindos Flysch Formation, composed of alternating sandstones, clays, and argillaceous layers of Paleocene–Oligocene age.

The Tripolis Unit, which underlies the Pindos Unit, has limited surface exposure within the broader study area. Its stratigraphy begins with a volcanic-sedimentary sequence of variable thickness, up to 400 meters, of Middle Triassic age, referred to as the “Tyros Beds.” Overlying this sequence is a thick carbonate succession, ranging from 3000 to 3500 meters, dating from the Triassic to the Eocene. This carbonate sequence is followed by a flysch sequence of Oligocene–Miocene age, which can be up to 1800 meters thick (Fleury, 1980; Jacobshagen, 1986). The Tripolis Unit includes dolomites and dolomitized limestones of Middle Triassic–Lower Jurassic age, neritic limestones with occasional dolomitic intercalations from the Upper Jurassic–Upper Cretaceous, and massive limestones rich in foraminifera of Paleocene–Middle Eocene age. These formations are capped by the flysch deposits of Oligocene–Lower Miocene age.

Hydrogeology

The flow of groundwater in porous media is influenced by the presence of faults (Knipe, 1997), which create boundaries with convergent and divergent flows, forming zones of drainage and recharge, respectively. Additionally, the depth of groundwater is a critical parameter for its protection. Greater depth offers a higher degree of protection from surface-originating pollutants, as contaminants must travel a longer distance to reach the saturated zone.

In the study area, groundwater level measurements were conducted to determine the direction of groundwater flow. Results indicate that groundwater flows in a southwest-northeast direction, from the mountainous region toward the coastal area. The highest hydraulic heads (64.87 m) are observed in the karstic aquifer, while the lowest are found in the coastal granular aquifer. Notably, no negative hydraulic heads were recorded in the study area.

Methodology

In this study, 40 water samples were collected from distinct sites, which included 7 springs, 2 surface water and 31 boreholes. From each sampling site, three separate water samples were collected and stored in thoroughly cleaned polyethylene bottles that had been acid-washed and rinsed. The first sample, with a volume of 1 liter, was designated for the analysis of anions, including (NO_3^-, NO_2^-, SO_4^{2-}, Cl^-, and F^-) and cations (Ca^{2+}, K^+, Mg^{2+}, and Na^+). The second sample, measuring 0.1 liters, was filtered using a Whatman 0.45 μm cellulose membrane and treated with 0.5 mL of ultrapure HNO_3 to analyze trace elements concentrations. Chemical calculations, such as the determination of saturation indices, were performed using PHREEQC version 3.0 (Appelo and Postma, 2004). The accuracy of the major element analyses was checked by using charge mass balance, and analyses were considered as acceptable when charge mass balance was less than 5%.

Results and Discussions

In Table 1 are presented the descriptive statistical parameters of the physicochemical characteristics, major elements, and trace elements for the 40 samples collected in the study area. Additionally, hydrochemical diagrams such as Piper and Durov were constructed for all samples collected during the investigation.

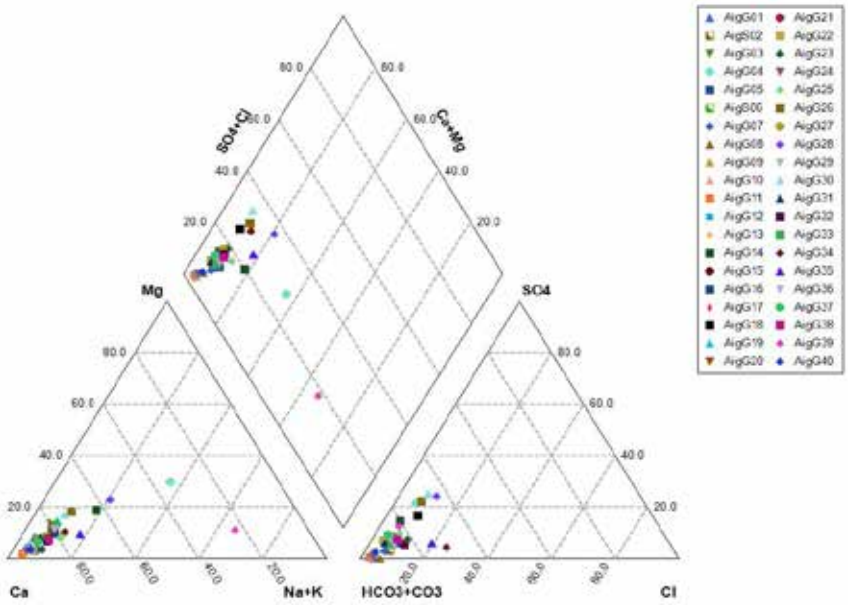

Figure 2. Piper diagram of samples in the study area

Piper diagram facilitates the identification of geochemical processes within a group of groundwater samples. The data from Selinountas river basin are shown in Figure 2. The results of ion exchange are particularly evident; when cation exchange occurs, the data points are projected parallel to the outer side of the diamond-shaped diagram. In contrast, when other reactions occur, the points deviate from the outer side. The dissolution of calcium carbonate is reflected in the movement of data points toward the calcium (Ca^{2+}) and bicarbonate (HCO_3^-) corners. The reduction of sulfate (SO_4^{2-}) shifts the points parallel to the anion axis, while the precipitation of calcium carbonate ($CaCO_3$) directs the points toward the sodium (Na^+), sulfate (SO_4^{2-}), and chloride (Cl^-) corners. The hydrochemical type Ca-HCO_3 represents the majority of the samples, and their chemical composition indicates rapid and shallow interactions with the geological formations of the area. Most waters in this category, primarily natural springs, exhibit low temperatures (Tw <20°C), although several boreholes show higher temperatures (Tw >20°C). Ca^{2+} concentrations range from 34.0 mg/L to 152.0 mg/L, with an average of 84.3 mg/L. Chloride (Cl^-) concentrations vary between 3.5 mg/L and 54.0 mg/L, with an average of 14.5 mg/L, which is typical for the study area.

The Mg^{2+}/Ca^{2+} ratio provides insights into the origin of water, the dissolution of subsurface minerals, and the geochemical processes that have occurred. In the study area, this ratio ranges from 0.017 to 0.86, with an average value of 0.14. All samples are associated with limestone and dolomitic aquifers. Specifically, the borehole samples AigG15 and AigG16 exhibit Mg^{2+}/Ca^{2+} values of 0.17 and 0.12, respectively. In regions dominated by limestone or dolomitic rocks, the Ca^{2+}/Cl^- ratio is typically high, as limestone contributes significant amounts of calcium to the water. Typical values may range from 0.5 to 10 or more, depending on the chloride concentration. In the study area, the samples show Ca^{2+}/Cl^- ratios ranging from 3.31 to 37.64, indicating calcium dominance resulting from the dissolution of carbonate rocks.

Table 1. Statistical parameters of chemical composition.

	Min	Max	Average	Std. Division
pH	7,37	8,05	7,76	0,16
T(°C)	14,20	27,80	20,75	2,89
ORP	-9,30	170,00	120,10	34,05
E.C (T°C)	213,00	1080,00	460,80	217,73
E.C (25°C)	239,00	1109,00	496,10	220,24
Ca^{2+}	34,00	152,00	84,34	28,71
Mg^{2+}	0,73	32,68	6,75	6,99
Na^{+}	2,60	110,00	14,40	20,16
K^{+}	0,30	5,00	1,47	1,04
HCO_3^{-}	134,20	446,52	269,28	87,67
SO_4^{2-}	0,00	132,00	24,15	32,26
F^{-}	0,00	1,51	0,16	0,28
Cl^{-}	3,50	54,00	14,52	12,02
NO_3^{-}	0,70	49,50	9,54	9,35
NO_2^{-}	0,00	0,04	0,01	0,01
NH_4^{+}	0,00	0,55	0,06	0,13
PO_4^{3-}	0,03	4,30	0,26	0,73
Li (μg/L)	0,54	43,55	4,69	7,99
B (μg/L)	0,00	327,57	15,01	65,70
Cr (μg/L)	0,00	3,5	1,2	0,7
Mn (μg/L)	0,29	599,82	20,33	94,13
Fe (μg/L)	9,60	720,51	46,71	110,61
Zn (μg/L)	0,00	217,66	21,32	38,47
Co (μg/L)	0,04	0,53	0,18	0,10
Cu (μg/L)	0,19	7,09	1,64	1,41
Sr (μg/L)	113,84	2261,52	434,01	398,41
Ba (μg/L)	9,59	114,46	61,30	21,63
U (μg/L)	0,03	0,85	0,22	0,14

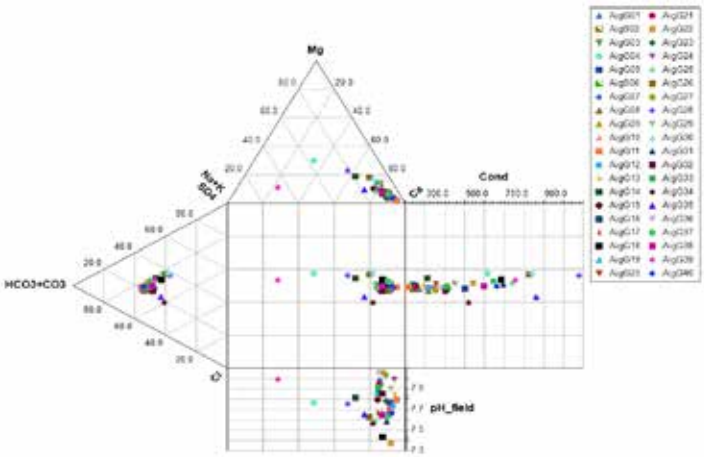

Figure 3. Durov diagram of samples in the study area.

The lithium (Li) concentrations of samples range from 0.5 to 43.5 μg/L, with an average value of 4.7 μg/L. The highest concentrations were recorded in boreholes AigG04 (43.5 μg/L), AigG28 (30.7 μg/L), and AigG39 (13.9 μg/L), while the remaining samples showed values between 0.5 μg/L and 5.9 μg/L. Boreholes Coca Cola AigG15 and AigG16 reported lithium concentrations of 3.8 μg/L and 4.1 μg/L, respectively. Chromium (Cr) concentrations range from 0.0 μg/L to 3.5 μg/L, which are below the drinking water limit (25.0 μg/L). Arsenic (As) concentrations were below the drinking water limit in all groundwater samples from the study area. Strontium (Sr) is found in natural waters at concentrations that depend on the geology of the area, with typical values reaching up to 2000 μg/L. In the analyzed samples, strontium concentrations range from 113.8 μg/L to 2261.5 μg/L, with the highest value recorded in sample AigG04. The average concentration is 434.0 μg/L. Generally, higher strontium concentrations are observed in waters that flow through limestone or dolomitic rocks, as well as in areas with geology rich in celestite ($SrSO_4$) or strontianite ($SrCO_3$) (Banner, 1995).

Iron (Fe) can be released to groundwater under specific conditions from minerals such as amphiboles, pyroxenes, ferromagnesian micas, iron sulfides, sandstones with oxides, carbonates, and clay minerals. The concentrations of Fe range from 9.6 μg/L to 720.5 μg/L, while the highest concentration occurs in sample AigG26 which was the only sample with concentration above drinking limit. Manganese (Mn) typically occurs alongside iron, enriching groundwater in acidic environments. Its sources include soils, sediments, and metamorphic rocks rich in micas and amphiboles. The drinking water limit for manganese is 50 μg/L, and samples from boreholes AigG26 and AigG29 exceed this limit.

Conclusion

In conclusion, the hydrochemical analysis of 40 water samples from the study area has provided significant insights into the quality and characteristics of the region's groundwater resources. The Ca-HCO□ hydrochemical type dominates in the water samples. The hydrochemical pattern of the samples suggests quick and shallow interactions with the region's geological formations. The parameters with concentration above the drinking limit are two (Fe and Mn), however the excess is limited only to two samples (AigG26 and AigG29).

Such concentrations might pose potential risks to human health. These results underscore the critical role of hydrogeological variability which shapes groundwater hydrochemical regime in river basins.

Acknowledgement

This paper is a part of Pyrgakis' PhD.

References

Appelo, C.A.J., Postma, D., 2004. Geochemistry, Groundwater and Pollution, 2nd ed. CRC Press, London. https://doi.org/10.1201/9781439833544

Banner, Jay.L., 1995. Application of the trace element and isotope geochemistry of strontium to studies of carbonate diagenesis. Sedimentology 42, 805–824. https://doi.org/10.1111/j.1365-3091.1995.tb00410.x

Burgess-Conforti, J.R., Moore Jr, P.A., Owens, P.R., Miller, D.M., Ashworth, A.J., Hays, P.D., Evans-White, M.A., Anderson, K.R., 2022. Relationships between land use and stream chemistry in the Mulberry River basin, Arkansas. River Research and Applications 38, 1031–1040. https://doi.org/10.1002/rra.3970

Degnan, P. J., Roberston, A.H.F. 1998. Mesozoic- Early Tertiary passive margin evolution of the Pindos Ocean (NW Peloponnese, Greece). Sedimentary Geology, 117, 33–70.

Dercourt, J. 1964. Contribution à l'étude géologique d'un secteur du Peloponnèse septentrional. Annales Géologiques des Pays Helléniques, 15, 1–418.

Doutsos, T., Poulimenos, G. 1992. Geometry and Kinematics of active faults and their seismotectonic significance in the Western Corinth-Patras rift (Greece). J. Struct. Geol., 14(6), 689-699.

Fleury, J. 1980. Les zones de Gavrovo-Tripolitza et du Pinde-Olonos (Grèce continentale et Péloponnèse du Nord). Evolution d'une plateforme et d'un bassin dans leur cadre alpin. (p. 651). France: Annales de la Société Géologique du Nord, 4.

Flotté, N. 2003. Caracterisation structurale et cinematique d'un rift sur detachement: Le rift de Corinthe-Patras, Grece. Thesis 197 pp., Universite de Paris-Sud.

Flotté, N., Sorel, D., Müller, C., Tensi, J. 2005. Along strike changes in the structural evolution over a brittle detachment fault: example of the Pleistocene Corinth–Patras rift (Greece). Tectonophysics, 403, 77–94, http://doi.org/10.1016/j.tecto.2005.03.015

Ford, M., Hemelsdael, R., Mancini, M., Palyvos, N. 2016. Rift migration and lateral propagation: evolution of normal faults and sediment-routing systems of the western Corinth rift (Greece). In: The Geometry of Normal Faults (Ed. by C. Childs, R.E. Holdsworth, C.A-L. Jackson, T. Manzocchi, J.J. Walsh, G. Yielding), Geol. Soc. London, Spec. Publ., 439.

Freeze, A., Cherry, J.A (1979). Groundwater. Prentice Hall, Englewood Cliffs.

Gawthorpe, R. L., Leeder, M. R., Kranis, H., Skourtsos, E., Andrews, J. E., Henstra, G. A., Mack, G, Muravchik, M., Turner, J., Stamatakis, M. 2018. Tectono-sedimentary evolution of the Plio-Pleistocene Corinth rift, Greece. Basin Research, 30, 448-479.

Ghisetti, F., Vezzani, L. 2005. Inherited structural controls on normal fault architecture in the Gulf of Corinth (Greece). Tectonics, 24, TC4016 doi: 10.1029/2004TC001696.

Jacobshagen, V. 1986. Geologie von Griechenland (p. 363). Berlin: Gebruder Borntraeger.

Kazakis, N., Oikonomidis, D. & Voudouris, K.S. (2015) Groundwater vulnerability and pollution risk assessment with disparate models in karstic, porous, and fissured rock aquifers using remote sensing techniques and GIS in Anthemountas basin, Greece. Environ Earth Sci 74, 6199–6209. https://doi.org/10.1007/s12665-015-4641-y

Kazakis, N., Chalikakis, K., Mazzilli, N., Ollivier, C., Manakos, A., & Voudouris, K. (2018). Management and research strategies of karst aquifers in Greece: Literature overview and exemplification based on hydrodynamic modelling and vulnerability assessment of a strategic karst aquifer. Science of the Total Environment, 643, 592-609.

Knipe, R.J., (1997) Juxtaposition and seal diagrams to help analyze fault seals in hydrocarbon reservoirs. American Association of Petroleum Geologists Bulletin 87, 185-197.

Kshetrimayum, K.S., 2015. Hydrochemical evaluation of shallow groundwater aquifers: a case study from a semiarid Himalayan foothill river basin, northwest India. Environ Earth Sci 74, 7187–7200. https://doi.org/10.1007/s12665-015-4697-8

Lima, Letícia S., Coe, M.T., Soares Filho, B.S., Cuadra, S.V., Dias, L.C.P., Costa, M.H., Lima, Leandro S., Rodrigues, H.O., 2014. Feedbacks between deforestation, climate, and hydrology in the Southwestern Amazon: implications for the provision of ecosystem services. Landscape Ecol 29, 261–274. https://doi.org/10.1007/s10980-013-9962-1

Pacheco Castro, R., Pacheco Ávila, J., Ye, M., Cabrera Sansores, A., 2018. Groundwater Quality: Analysis of Its Temporal and Spatial Variability in a Karst Aquifer. Groundwater 56, 62–72. https://doi.org/10.1111/gwat.12546

Poulimenos, G., Zelilidis, A., Kontopoulos, N., Doutsos, T. 1993. Geometry of trapezoidal fan deltas and their relationship to extensional faulting along the south-western active margins of the Corinth rift. Basin Res., 5, 179–192.

Raj, P.P.N., Azeez, P.A., 2010. Land Use and Land Cover Changes in a Tropical River Basin: A Case from Bharathapuzha River Basin, Southern India. Journal of Geographic Information System 02, 185. https://doi.org/10.4236/jgis.2010.24026

Wang, Q., Dong, S., Wang, H., Yang, J., Huang, H., Dong, X., Yu, B., 2020. Hydrogeochemical processes and groundwater quality assessment for different aquifers in the Caojiatan coal mine of Ordos Basin, northwestern China. Environ Earth Sci 79, 199. https://doi.org/10.1007/s12665-020-08942-3

Wang, Wanrui, Chen, Y., Wang, Weihua, Yang, Y., Hou, Y., Zhang, S., Zhu, Z., 2022. Assessing the Influences of Land Use Change on Groundwater Hydrochemistry in an Oasis-Desert Region of Central Asia. Water 14, 651. https://doi.org/10.3390/w14040651

Xiao, S., Zeng, C., Lan, J., Di, Y., He, J., Xiao, H., Wang, J., 2021. Hydrochemical Characteristics and Controlling Factors of Typical Dolomite Karst Basin in Humid Subtropical Zone. Geofluids 2021, 8816097. https://doi.org/10.1155/2021/8816097

Yu, D., Yu, J., Wu, D., Han, Y., Sun, B., Zheng, L., Chen, H., Liu, R., 2023. Isotopic and Hydrochemical Characteristics of the Changqing-Xiaolipu Water Resource, Jinan, Eastern China: Implications for Water Resources in the Yellow River Basin. Sustainability 15, 2439. https://doi.org/10.3390/su15032439

Zhou, B., Wang, H., Zhang, Q., 2021. Assessment of the Evolution of Groundwater Chemistry and Its Controlling Factors in the Huangshui River Basin of Northwestern China, Using Hydrochemistry and Multivariate Statistical Techniques. IJERPH 18, 7551. https://doi.org/10.3390/ijerph18147551

Zhu, H., Zhou, J., Liu, Z., Yang, L., Liu, Y., 2021. Hydrogeochemistry Evidence for Impacts of Chemical Acidic Wastewater on Karst Aquifer in Dawu Water Source Area, Northern China. International Journal of Environmental Research and Public Health 18, 8478. https://doi.org/10.3390/ijerph18168478

Zhu, M., Kuang, X., Feng, Y., Hao, Y., He, Q., Zhou, H., Chen, J., Zou, Y., Zheng, C., 2021. Hydrochemistry of the Lhasa River, Tibetan Plateau: Spatiotemporal Variations of Major Ions Compositions and Controlling Factors Using Multivariate Statistical Approaches. Water 13, 3660. https://doi.org/10.3390/w13243660

17th INTERNATIONAL CONGRESS of the Geological Society of Greece

BULLETIN OF THE GEOLOGICAL SOCIETY OF GREECE, SP. PUBL.

EXTENDED ABSTRACT 266

Assessment of natural and anthropogenic contamination of the sediments in the Sacca di Goro lagoon (Po river delta, northern Italy)

Rapti D.[1,2]

(1) University of Ferrara, Department of Chemical, Pharmaceutical and Agricultural Sciences, cpr@unife.it (2) New Energies And environment, spinoff company of Ferrara University, Ferrara, Italy

Abstract

The definition of heavy metal content in lagoon sediments plays a critical role in distinguishing between natural contamination (geohazard) and anthropogenic impact, and is essential for assessing the risk posed by these pollutants in the aquatic environment.

In particular, the Sacca di Goro lagoon, located in the Po River delta (Northern Italy), represents a significant area of interest due to its natural and economic value. Spanning an area of approximately 20 km², with an average depth of 1.5 meters and salinity levels of 29‰, the lagoon is not only crucial for its biodiversity but also plays a pivotal role in regional aquaculture, particularly for mussels and clams (Figure 1).

In this unique lagoon system, understanding the quality of the sea-bottom sediments is fundamental not only for the health and growth of cultivated species but also in addressing potential bioaccumulation problems of heavy metals that may impact both wildlife and human health. By evaluating the qualitative status of the sediments, we can develop effective strategies for sustainable environmental management and safeguard productive aquaculture activities while minimizing risks to the ecosystem.

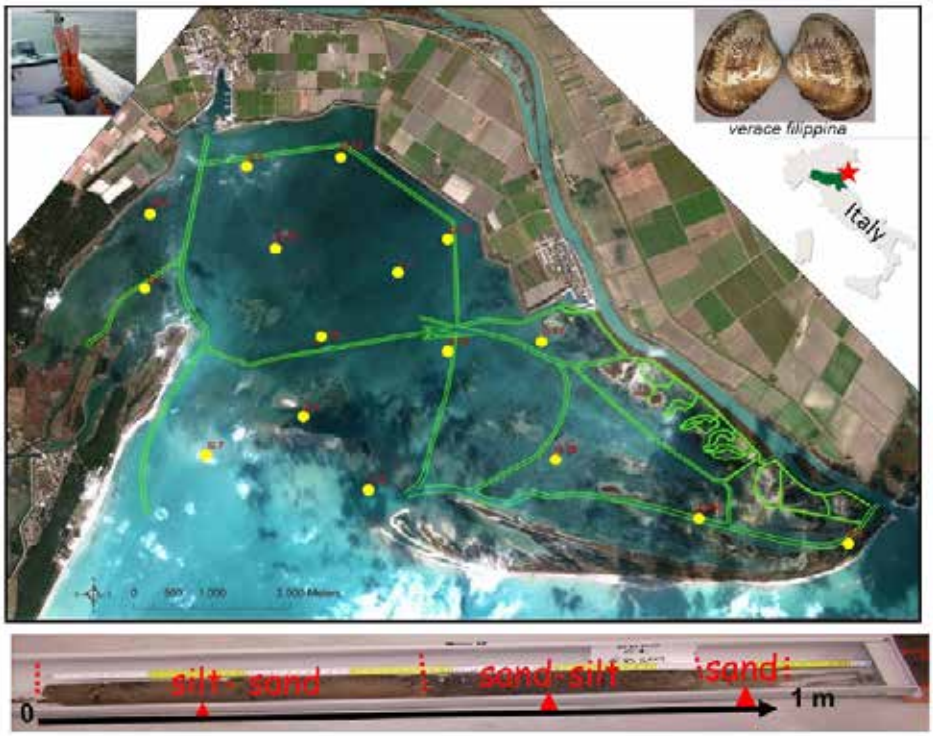

Figure 1: Location of the Sacca di Goro lagoon. The yellow circles represent the sampling points. Below, an example of a continuous core drilling. The green lines represent the sub-lagoon channels.

In the present study, fifteen continuous core drilling surveys were conducted, with depths ranging from 100 to 200 cm, distributed evenly across the lagoon area. A total of 70 sediment samples were collected and analyzed for grain size composition, organic matter content, and concentrations of various elements such as SiO_2, TiO_2, Al_2O_3, Fe_2O3, MgO, MnO, CaO, Na_2O, K_2O, P_2O_5, Ba, Ce, Co, Cr, La, Nb, Ni, Pb, Rb, Sr, Th, V, Y, Zn, Cu, Ga, Nd, S, and Sr. Furthermore, in selected samples, sediment toxicity was evaluated using the bacterial bioluminescence toxicity assay, which provides insight into the potential biological impact of the sediments.

The comprehensive dataset obtained from these analyses enabled us to achieve several important goals: i) defining the overall environmental quality of the sediments, ii) identifying areas with the highest contamination risks, iii) establishing a relationship between grain size distribution and chemical concentrations (Figure 2), and iv) emphasizing the local occurrence of natural pollution phenomena linked to metals such as chromium (> 50 ppm) and nickel (> 30 ppm), as well as human-induced contamination from lead (> 30 ppm) and copper (> 60 ppm).. Additionally, the toxicity results from the bioluminescence assay further clarified the potential harmful effects of these sediments on marine life.

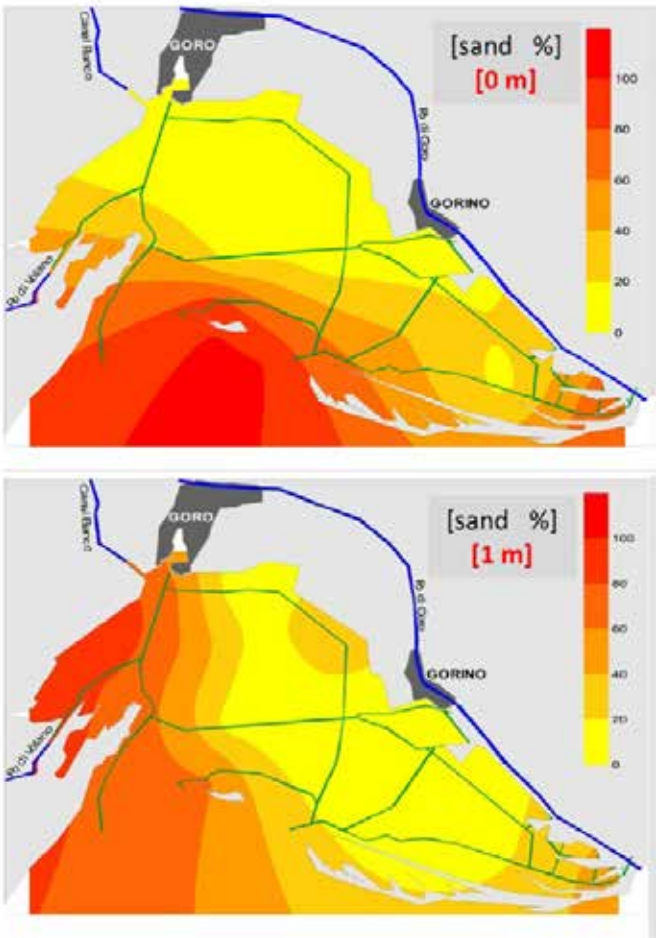

Figure 2: Example of the spatial distribution of sand content in the sediments at depths of 0 cm (lagoon bottom) and 100 cm.

This study provides valuable information for the formulation of effective management policies that can mitigate the risks posed by both natural and anthropogenic pollution, while ensuring the sustainable development of the aquaculture industry and the protection of the broader ecosystem in the Po River delta.

17th INTERNATIONAL CONGRESS of the Geological Society of Greece

BULLETIN OF THE GEOLOGICAL SOCIETY OF GREECE, SP. PUBL.

EXTENDED ABSTRACT 267

The role of hydrogeology in the sustainable exploration of shallow geothermal resources

Rapti D.[1,2]

(1) University of Ferrara, Department of Chemical, Pharmaceutical and Agricultural Sciences, Italy cpr@unife.it (2) New Energies And environment, spinoff company of Ferrara University, Ferrara, Italy

Abstract

Climate change, the diffusion of micropollutants in the atmosphere, as well as European energy and environmental policies, are driving the research and use of renewable and eco-sustainable energy resources to support the energy transition process.

The optimization of a geothermal exchange system requires a holistic approach that takes into account both the energy needs of the building and the hydrogeological, chemical, and thermophysical characteristics of the subsoil, as well as the presence of natural and legislative constraints.

In this context, a new dynamic closed-loop heat? exchanger designed for the exploitation of shallow geothermal resources has been installed at a test site in the alluvial Po plain (northern Italy). By means of *in situ* and laboratory tests, we collected data on:

a) sedimentary sequences and grain size, obtained through continuous core drilling and laboratory tests;

b) hydrogeological conditions and the local conceptual hydrogeological model up to a depth of 80 meters, assessed via pumping tests, measurement, and analysis of hydrodynamic data;

c) hydrochemical characteristics of the aquifer systems, determined through chemical and isotopic analyses (oxygen, deuterium, strontium);

d) thermo-physical monitoring, conducted via the implementation of a Distributed Thermal Response Test and laboratory measurements of thermal conductivity. Additionally, a monitoring system based on Distributed Fibre-Optic Temperature-Sensing (DTS) has been installed to better define underground temperature profiles under both natural and thermal solicitation conditions (Fig. 1).

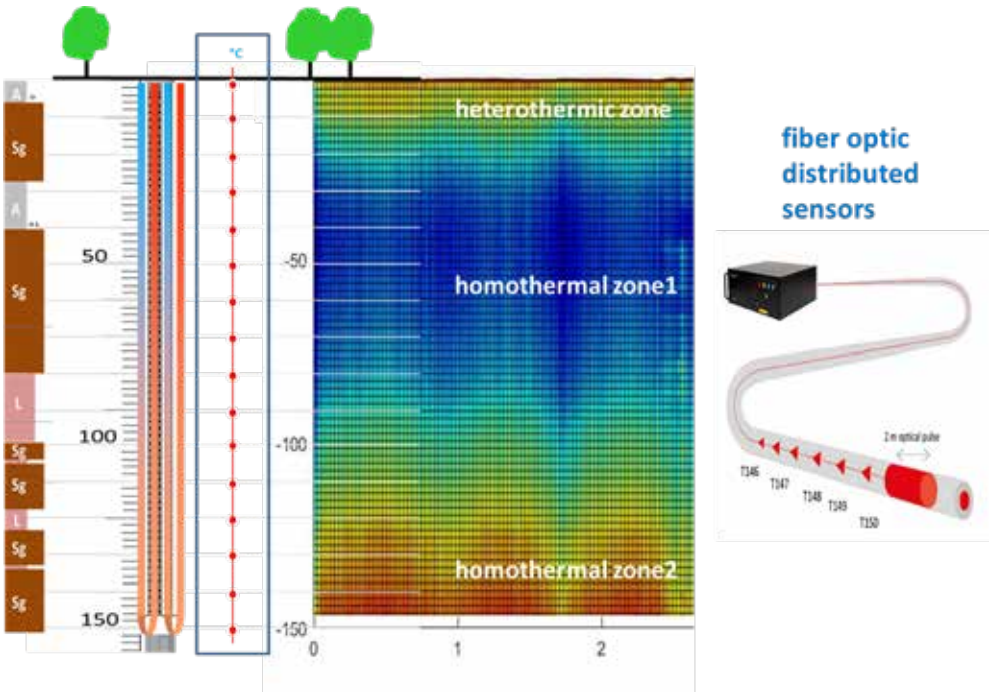

Figure 1. Results of the Distributed Fibre-Optic Temperature-Sensing (depth in meters; A: clay; Sg: sandy; L: silt).

By employing a comprehensive and holistic methodology, the integrated analysis of various data sets facilitated a rigorous characterization of the hydrodynamic and thermo-physical properties of the local aquifers. This characterization was further enhanced through the utilization of advanced numerical simulation models. Additionally,

the study assessed the subsoil's responses to the thermal stresses that could potentially be induced by a low-enthalpy geothermal plant with an approximate capacity of 350 kW. Finally, this analysis enabled us to assess the energy and environmental sustainability of these innovative dynamic closed-loop heat exchangers.

17th INTERNATIONAL CONGRESS of the Geological Society of Greece

BULLETIN OF THE GEOLOGICAL SOCIETY OF GREECE, SP. PUBL.

EXTENDED ABSTRACT 268

Liquefaction susceptibility in delta environments: the case of the Po delta area (northern Italy)

Rapti D.[1] Papathanassiou G.[2], Valkaniotis S.[2], Taftsoglou M.[3], Caputo R.[3]

(1) University of Ferrara, Department of Chemical, Pharmaceutical and Agricultural Sciences, Ferrara, Italy cpr@unife.it.

(2) Aristotle University of Thessaloniki, School of Geology, Thessaloniki, Greece

(3) University of Ferrara, Department of Physics and Earth Sciences, Ferrara, Italy.

Abstract

We know that, during a seismic event, liquefaction phenomena are not randomly distributed over an active or recent floodplain but are strongly dependent on the depositional evolution of the area like grain size of the sediments, depositional age shallow layering, and depth of the groundwater level. Recent unconsolidated sediments (Holocene age), deposited by fluvial or wave action, such as those found in paleo-channels and point bars in coastal areas, generally exhibit a higher frequency of liquefaction compared to sediments deposited under different conditions within the same floodplain and/or coastal zone.

Based on these considerations, Youd and Perkins (1978) proposed the division of geological units into four classes of liquefaction susceptibility: low, moderate, high, and very high. They also emphasized that water-saturated geological formations, such as river channels, floodplains, deltaic regions, and dunes, are generally characterized by a high to very high susceptibility to liquefaction.

The reliability of a liquefaction susceptibility map is heavily influenced by the investigation scale, as well as the density and accuracy of the geological, geomorphological, and hydrogeological data.

In this paper, an area of about 560 km², situated in the eastern sector of the Po River plain (northern Italy) within the Po River delta, including part of the modern delta, has been considered and analyzed in detail to examine the likelihood of geological units to liquefaction. To achieve this, a large variety of data has been considered. Lithological, chronological (14C data), geomorphological, hydrological, hydrogeological data, satellite imagery, modern and historical topographic maps, as well as historical and archaeological evidence, were integrated with data from continuous core drilling and penetrometer tests (Figure 1).

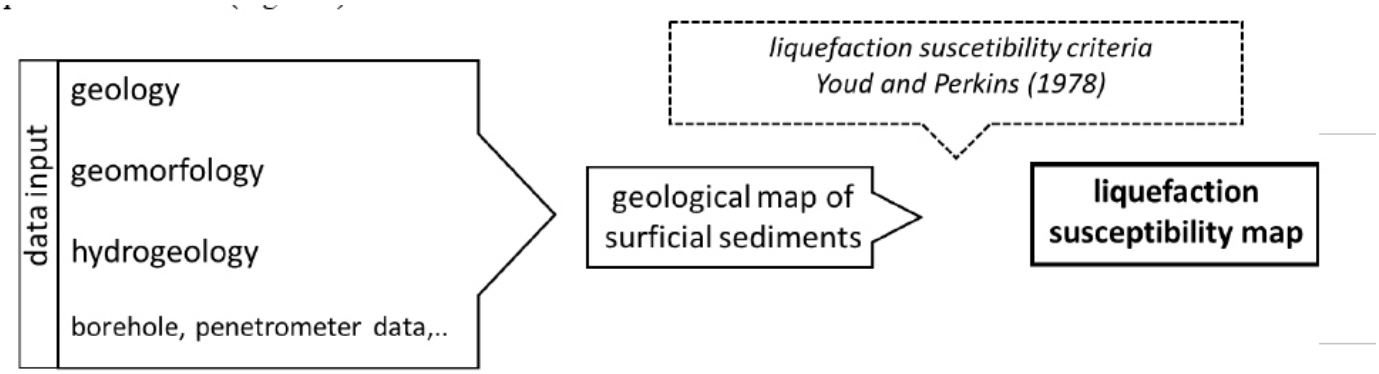

Figure 1. Flowchart showing the phases of the method applied in this study.

This integrated data analysis allowed us to define the liquefaction susceptibility map. Specifically, four classes were identified, corresponding to the following susceptibility levels:

a) *very high*, in the portion of the territory occupied by the floodplain of the main Po channel, which accounts for 4% of the overall area;

b) *high*, corresponding to 26% of the area, found in geological formations such as floodplains, channels, crevasse splays, abandoned channels, and coastal dunes;

c) *moderate*, covering approximately 20% of the territory, mainly characterized by beach barrier formations;

d) *non-susceptible features*, representing 50% of the territory, including marshes of interdistributary areas and brackish marshes and lagoons of the front delta plain, since they are fully infilled by clays, silty clays, and silts.

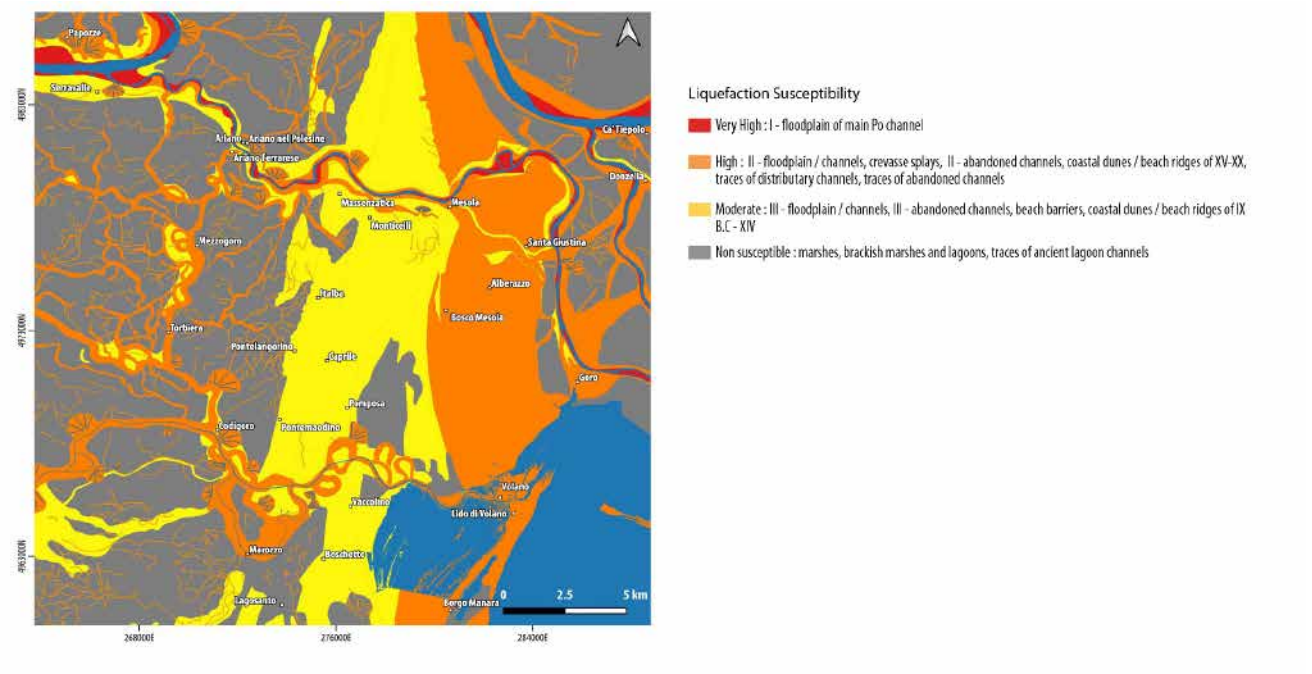

Figure 2. Liquefaction Susceptibility map of Po delta plain, based on the proposed refined classification of Youd and Perkins criteria (1978).

The obtained data could be used by public authorities to implement strategies and governance measures aimed at the sustainable management of the territory, considering the significant natural (a large portion of the area is included in the Natura 2000 protected areas network), environmental, cultural, and economic value of the Po Delta area.

References

Youd T.L., Perkins D.M., 1978. Mapping of Liquefaction induced Ground Failure Potential, J. Geotech. Eng. Div., 104, 433-446.

17th INTERNATIONAL CONGRESS of the Geological Society of Greece

BULLETIN OF THE GEOLOGICAL SOCIETY OF GREECE, SP. PUBL.

EXTENDED ABSTRACT 269

Investigation of legislation and tools for coastline demarcation: the coastline along the Kalamas delta in Thesprotia as a case study

Rapti Georgia[1], Tzoraki Ourania[2]

1 University of the Aegean, Mytilene, Greece, grapti@hotmail.com, 2 University of the AegeanMytilene, Greece

Introduction / Background

The purpose of this study is first to investigate the Greek legislation regarding the delimitation of the coastline and second compare the delimitation tools used internationally. In addition, the question arises whether the automatic coastline extraction tool SAET is feasible to be used for the delimitation of coastlines by a simple user.The region of Thesprotia was chosen as a case study, and specifically, a part of the coastline along the Kalamas River delta.
For the Greek state, in 21.06.1837 was the first time that the definition of the coastline was established and it was defined its common use (Skandali G. D.,2010). Since then, many laws have used for the definition, protection and the exploitation of the coastline and the shoreline. The table below attempts to summarize the differences between the basic laws regarding the definition and mapping of the coastline.

Table 1. Differences of the basic Greek laws regarding the determination and mapping of the coastline

Low	Coast-beach width	Determination of the coast	Mapping -drawing of the coastline	Scale	Comments
L.2344/1940	20m	Testimonies of witnesses and without appropriate tools	Topographic and elevation chart and relevant report	Not specified	
L. 2971/2001	50m	Drawn after anon siteinspection or as interpreted from aerial photographs by the committee as a polygonal line closest to the actual natural line, based on the country's trigonometric network	Drawing on a cadastral-elevational chart based on the country's trigonometric network, referring to a coastline of at least 500 m	1:1000	In case of error redefinition is allowed
Amendments to Law 2971/2001	50m	Photographic captures 2008-2009, Digitized Coastline using photo interpretative methods, with a minimum cartographic unit of 2m. (Cadastre s.a.)	Precision Digital ColorOrthophoto Maps withaltitudeinformation ina Digital Terrain Model (DTM) (inraster grid format) with,points dependenton the HellenicGeodetic Reference System 1987Drawing of thePreliminary CoastalBorderline(POA) based on ten thematic categoriesof boundary lines drawingcriteria.	1:1000	
L. 5092/2024	50m	From the orthophotographic backgrounds kept in the Greek Land Registry and in site inspection		1:1000	In overall the previous procedure is not modified

(F.E.K. – National Printing House,1940, F.E.K. – National Printing House,2001, F.E.K. – Joint Ministerial Decision 1089532/P.E./8205P.E./2005, 2005, National Printing House,2024)

With the help of the bibliographic review and the PRISMA Statement 2020 protocol,documents were extracted from the international bibliography Scopus, based on keywords.regarding the tools used for the delimitation of coastlines. A total number of 328studieswere selected, mainly published articles and conference proceedings, between the years 2000-2024 with the year 2022 presenting the largest number of studies. India appeared the country with the biggest involvement in studies and research on coastline detection and demarcation tools and also hadthe largest network of cooperation with other countries, followed by China and Italy.In almost half of the

studies, the coastline was demarcated due to integrated beach management because erosion and deposition had been observed. A large percentage concerned integrated management and monitoring. Other reasons were the detection of the coast, themonitoring of changes due to anthropogenic factors, or due to storms or for reasons of governance, or changes in the coastline due to tsunamis and due to changes in land use.Regarding the size, type and land use near the coasts, in numerous studiesthey were not mention but the next highest percentage involves small sandy beaches with multiple uses and close to urban areas.Most of the studies used a combination of data sources, followed by those that used Landsat, Sentinel and generally satellite images. In some of the studies the date source was not stated, while in others were used synthetic aperture radar, UAV/UAS or images from videos, cameras and mobile phones. Some chose SPOT, LIDAR, bathymetry. Among the less used are Global Navigation Satellite system (GNSS), Pléiades, QuickBird.

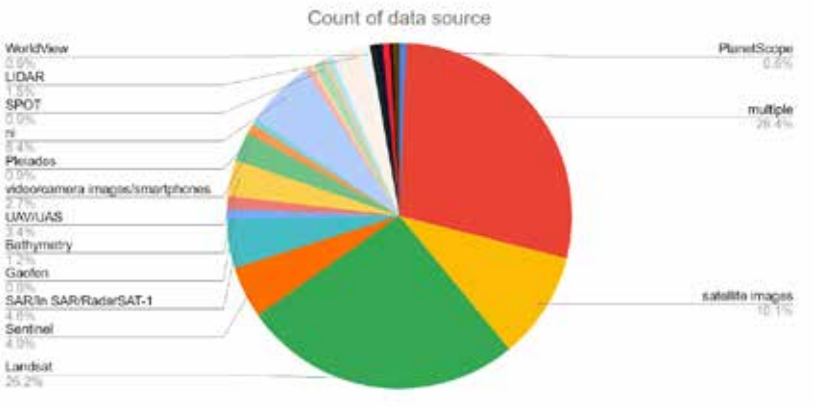

Figure 1. Data source used

Regarding the tools for coastline delineation in most studies, more than one tool was used, with the Digital Shoreline Analysis System (DSAS) and GIS being chosen quite often.In the table below we observe that the dominant tool for coastline delineation is the Digital Shoreline Analysis System (DSAS), while GIS is generally mentioned as a tool, some of the studies seems to have used some kind of model or an algorithm. Others used ENVI software, SAET, ERDAS and Convolutional Neural Networks, Google Earth Engine (GEE). Numerus studies used more than one coastal delineation tool, while SELI, AMBUR, SHOREX. CoastSat, CoastSnap, CLAHE, MATLAB, Pix4dMapper, Beachmeter, AgisoftPhotoscan, CET, ODSAS, Cliff DelineaTool, ArcMapCASSIE are also presented (Figure 2.)

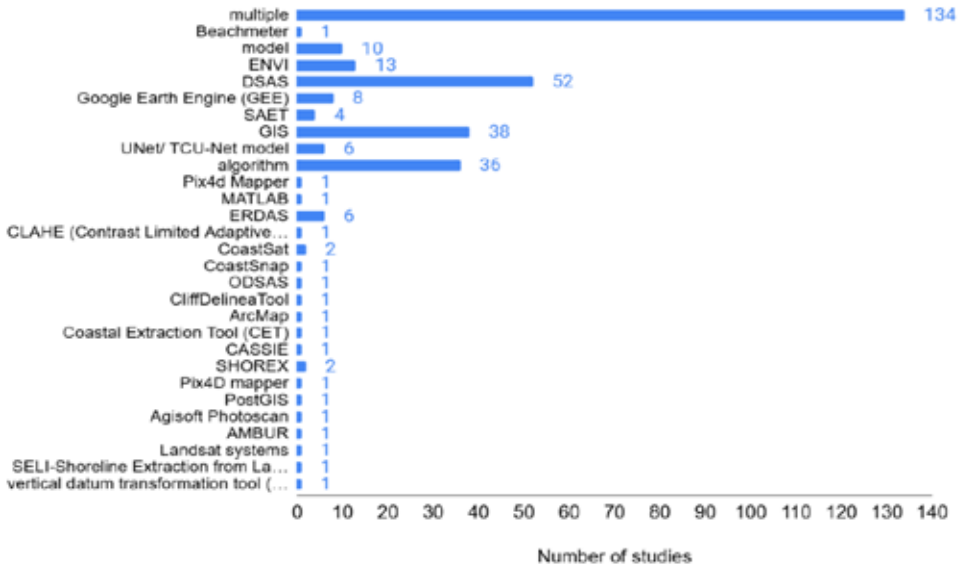

Figure 2. Shoreline extraction tools

In most studies, not just one coastal delineation method was chosen, but multiple, followed bythe segmentation and classification method.

Study area and storm events

The Kalamas River Delta is located on the coast of the Ionian Sea, in the region of Thesprotia (Epirus, northwestern Greece) and is one of the most important wetlands of western Greece. It has an area of approximately 85 km², and its shape corresponds to an “arc-shaped” delta and consists of two different mouths: one anthropogenic, active today, and the other located less than 10 km south (old estuary), which is now inactive and sheltered behind sandy beaches. In general, the front consists of sandy beaches and large sandy “tongues”. The construction of the dam in 1962 upstream of the delta as well as several works aimed at draining the land to facilitate cultivation and the construction of a river channel in 1951, have significantly changed the appearance of the delta. It should also be noted that the Kalamas River delta developed in the straits of Corfu, so it is protected from the strong currents that prevail in the Ionian Sea. (Chabrol et al., 2022, Epirus Water Resources Authority - EL05, (n.d.))

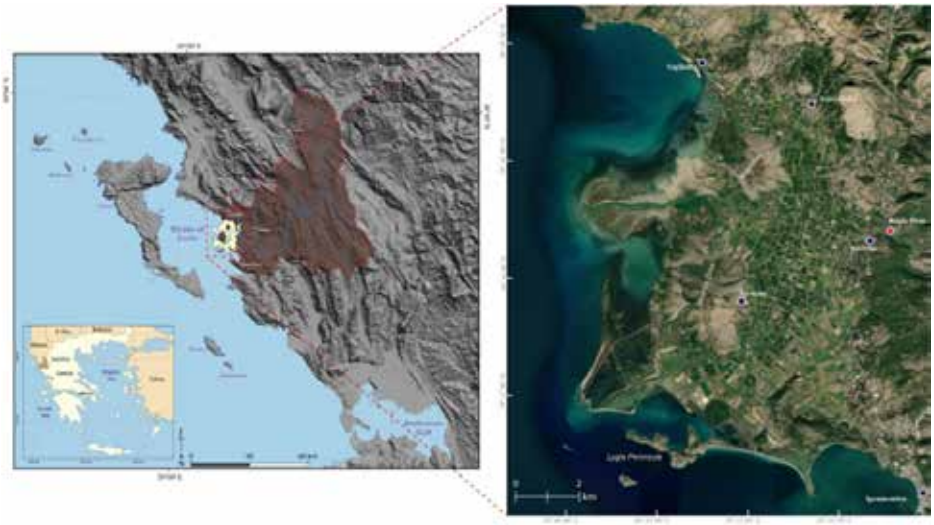

Figure 3. Study area (Chabrol et al., 2022)

Figure 4. Damage caused by the storm on 11/12/2021, (photos by author)

Figure 5. Damage caused by the storm on 06/01/2024 (photos by author)

Three storm events were selected because of the reported problems (erosion and flooding) in the area. The first one occurred 10-12 December 2021, the second one 6-7 January 2024 and the third 5-6 October 2024 (Cassandra storm). (meteo.gr, https://meteo.gr/article_view.cfm, https://www.cnn.gr/ellada/story/442473/kakokairia-cassandra-plimmyrisan-spitia-kai-katastimata-stin-ipeiro-xoris-reyma-stous-filiates.). In all three storm events strong southerly winds and a fairly high percentage of precipitation were the main characteristics. (https://www.in.gr/2024/01/06/greece/synagermos-gia-tin-kakokairia-ekspres-neo-ektakto-deltio-deite-xartes/, https://www.cnn.gr/ellada/story/442056/allazei-o-kairos-apo-paraskevi-me-tin-kakokairia-cassandra-na-xtypa-kerkyra-kai-ipeiro, meteo.gr)

Methodology

The Shoreline Analysis and Extraction Tool (SAET) software was developed within the framework of the European project ECFAS (European Coastal Flood Awareness System), with the aim of providing a solution to enhance the resilience of coasts to climate change and reduce the exposure of the population and infrastructure to risk.It was developed by the Geo-Environmental Cartography and Remote Sensing group of the University of Valencia (UniversitatPolitècnica de València, Spain) and is the work of Jesús Palomar Vázquez, Jaime Almonacid Caballer, Josep E. and is the intellectual property of the university SAET is a software developed in Python and focuses on the automatic extraction of coastlines from optical satellite images (Sentinel-2, Landsat-8 and Landsat-9). The main algorithm is based on the subpixel coastline detection approach, allowing the acquisition of the coastline before and after the storm, enabling comparison and the identification of the impact of storm erosion on beaches.(Palomar-Vázquez et al., 2023).

The first step for coastline delineation is the collection of satellite images, based on their coverage and acquisition date in relation to the storm. In our case, the study area is covered by a single Landsat scene and a Sentinel-2 tile. We then searched for the closest satellite images before and after the storm peak date (11/12/2021) by running SAET in “search only” mode and selected the images with the highest spatial resolution between (Landsat and Sentinel-2), so two Sentinel-2 images before and after the storm (12 November and 17 December) were selected, according to the criteria of the lowest possible cloud cover (up to 10%), the closest storm peak date (11 December). These two images were used as input to run SAET again, butthis time, in the “acquire” mode, and then in the “process” modeusing the AWEInsh water index for the segmentation method.Thus, two Sentinel-2 images were processed, resulting in the extractedcoastline.(Figure 6)The same procedure was followed for the following storms, for the one on January 6, 2024, Landsat images were selected, on 12/28/2023 and on 01/29/2004 (Figure 7) Finally, in the case of the Kassandra storm that hit the area on October 4,2024, 2 Landsat images were used on 09/01/2024 and 10/27/2024.(Figure 8)

Figure 6. Satellite-Derived Shorelines before and after the storm 11/12/2021 The coastline in green is the shoreline before the storm and the coastline in red is the shoreline after the storm.

Figure 7. Satellite-Derived Shorelines before and after the storm 06/01/2024 The coastline in green is the shoreline before the storm and the coastline in red is the shoreline after the storm.

Figure 8. Satellite-Derived Shorelines before and after the storm 04/10/2024 The coastline in green is the shoreline before the storm and the coastline in red is the shoreline after the storm.

Results

The analysis of the extracted coastlines for all three cases was done through the QGIS program, on a coastline length of approximately 2 kilometers, for each one separately. A single section of the coastline was selected in order to reduce the number of points to be compared of the coastlines obtained from SAET in order to make their analysis easier.These were then divided into 10 sections each.In the first storm in 2021, maximum erosion was observed at nine meters in some points but also deposition in some others with a maximum of eleven meters. It should be noted that erosion occurred on the largest part of the coastline. (Figure 9) In the second storm in January 2024(Figure 10), the greatest erosion observed was 15 meters, while the deposition reached 20 meters. In this case, the coastline, according to the analysis, showed total deposition after the storm.Finally, in the storm of October 2024 (Figure 11), the greatest erosion reached 15 meters, while the maximum deposition was 24 meters. In general, the storm left the coastline with erosion in most of its part.In some sections, the same phenomenon is observed in all 3 cases, which also agree with the damages that had been reported. The first two cases seem to have more similarities, while in the case concerning the storm Kassandra, the analysis also shows sections in which, while they showed deposition in the previous storms, after “Kassandra” they were eroded and vice versa.

Figure 9. Analysis of SDS before and after the storm in December2021 Dark blue indicates maximum erosion and yellow indicates maximum deposition.

Figure 10. Analysis of SDS before and after the storm in January 2024. Dark blue indicates maximum erosion and yellow indicates maximum deposition.

Figure 11 Analysis of SDS before and after the storm in October 2024. Dark blue indicates maximum erosion and yellow indicates maximum deposition.

Uncertainties

In the original SAET file, the area of interest is divided into 3 smaller beaches with a different code each, so the largest one was selected, with the code 2127.The beach areas were taken from the European zone dataset provided by the Earth Observation Service. Copernicus. Also, when applying the software in the “download” mode in order

toreceive satellite images from Sentinel, the error “Access token” occurred and it was not possible to overcome it by the specific user, while a request was made tobecome “online” again.In addition, it was not possible to produce SDS close to the dates of the events andin the three cases the time period before and after exceeds one month, while ideallyit should have been one day before and one day after the storm, we believe that this alsoaffected the results.It shouldbe noted that the cases selected for examination did not involve majorstorms.

Conclusions

Comparing the results, we observe that in all three cases, in most sections, the same phenomenon is observed, erosion or deposition, which is in agreement with the damages caused. The first two cases seem to have more similarities, while in the case of the storm Kassandra, the analysis also shows sections in which, while they presented deposition in the previous storms, after˙Kassandra˙they were eroded and vice versa.

The delineation of a coastline is now achieved:in a short time, almost automatically which reduces the error rate from the userand at low cost, since much of the data is freely available with a fairly high resolutionFor a given section of coastline after a coastal storm, SAET facilitates the selection of the closest satellite images in time to the analyzed events, ensures a sufficient level of coverage for the analysis of the coastline change, and automatically ‘downloads’ the images from the official satellite repositories, processes them and exports them to the location of the coastline.

SAET: performs a tool for studying the impact and recovery of beach morphology in a coastal storm, but also in the case of anthropogenic interventions and long-term SDS, thus contributing to the effort to address and mitigate the effects of coastal and not only storms and to finding the most appropriate measures for their timely response.

References

Chabrol, A., Gonnet, A., Fouache, E., Pavlopoulos, K., &Lecoeur, C. (2022). Geomorphology of the Kalamas river delta (Epirus, Greece). Journal of Maps, 18(2), 276–287.

Palomar-Vázquez, J., Almonacid-Caballer, J., Eliseu Pardo-Pascual, J., & Sánchez-García, E. (2018).Proceedings of the 7 th International Conference on the Application of Physical Modelling in Coastaland Port Engineering and Science (Coastlab18) SHOREX: A NEW TOOL FOR AUTOMATIC ANDMASSIVE EXTRACTION OF SHORELINES FROM LANDSAT AND SENTINEL 2 IMAGERY.

Palomar-Vázquez, J., Pardo-Pascual, J. E., Almonacid-Caballer, J., & Cabezas-Rabadán, C. (2023).Shoreline Analysis and Extraction Tool (SAET): A New Tool for the Automatic Extraction ofSatellite-Derived Shorelines with Subpixel Accuracy. Remote Sensing 2023, Vol. 15, Page 3198,15(12), 3198.

Athanasakopoulou, M. (2019). Coastal zone. National legislative framework for coastal zone management. Coastal protection projects against erosion - The case of the Kalamaki region, Western Achaia. Faculty of Engineering Project Management (DCHT), MSc Thesis, Hellenic Open University, Patra.

Petrelis V. N. (2012 Investigating the estimation models of the coastline displacement, Faculty of Agricultural and Surveying Engineering, Ph.D. Thesis, National Technical university of Athens.

Skandali G. D. (2010). Development of a knowledge base in an object-oriented analysis environment of digital telescopic data for the purpose of automatic delineation of the coastal coastal zone, Faculty of Agricultural and Surveying Engineering, National Technical university of Athens.

Coastal Vulnerability and Shoreline Mapping - ECFAS. (n.d.). Retrieved September 26, 2024, from, https://www.ecfas.eu/public-deliverables/coastal-vulnerability-and-shoreline-mapping/.

meteo.gr: Severe weather until Sunday 12 December 2021. (n.d.-a). Retrieved December 18,2024, from https://meteo.gr/article_view.cfm?entryID=2041.

meteo.gr: New wave of bad weather until Friday 10 December. (n.d.). Retrieved December 18,2024, from https://meteo.gr/article_view.cfm?entryID=2040.

The weather changes from Friday with the bad weather Cassandra hitting Corfu and Epirus -CNN.gr. (n.d.). Retrieved January 16, 2025, from https://www.cnn.gr/ellada/story/442056/allazei-o-kairos-apo-paraskevi-me-tin-kakokairia-cassandra-na-xtypa-kerkyra-kai-ipeiro.

Epirus Water Resources Authority - EL05 – Flood Risk Management Plans. (n.d.). Retrieved September 29, 2024,from https://floods.ypeka.gr/sdkp-lap/maps-1round/sdkp-el05-1round/.

Storm «Cassandra»: Houses and shops flooded in Epirus - No electricity in Filiates - CNN.gr. (n.d.). Retrieved December 18, 2024, fromhttps://www.cnn.gr/ellada/story/442473/kakokairia-cassandra-plimmyrisan-spitia-kai-katastimata-stin-ipeiro-xoris-reyma-stous-filiates.

Bad weather alert - express: New emergency bulletin [maps] | in.gr. (n.d.). RetrievedDecember 18, 2024, from https://www.in.gr/2024/01/06/greece/synagermos-gia-tin-kakokairia-ekspres-neo-ektakto-deltio-deite-xartes/.

EMY - Home.. (n.d.). Retrieved December 18, 2024, from https://www.emy.gr/?area=forecast.

Joint Ministerial Decision 1089532/P.E./8205P.E./2005 - FEKB-595/4-5-2005 - AIGIALOS -PARALIA. (n.d.).

BANK OF LEGAL INFORMATION OF THE STATE ADMINISTRATION. (1946).

F.E.K. –National Printing House. (1940). https://search.et.gr/el/fek/?fekId=653170

F.E.K. – National Printing House. (2001). https://search.et.gr/el/fek/?fekId=230027

F.E.K. – National Printing House (2024). https://search.et.gr/el/fek/?fekId=763363

17th INTERNATIONAL CONGRESS of the Geological Society of Greece

BULLETIN OF THE GEOLOGICAL SOCIETY OF GREECE, SP. PUBL.

EXTENDED ABSTRACT 270

Remnants of oceanic crust of Edessa ophiolite (North Greece): Petrographic and geochemical characteristics

Rogkala A.[1], Petrounias P.[1], Giannakopoulou P.P.[1], Koutsovitis P.[1], Kalpogiannaki M.[2], Lampropoulou, P.[1], Tsikos H.[1]

(1) Department of Geology, University of Patras, Patras, Greece, krogkala@upatras.gr (2) Department of Geology and Geoenvironment, National and Kapodistrian University of Athens, Athens, Greece

Introduction

Ophiolites are fragments of oceanic lithosphere that have been tectonically emplaced along the continental margins in accretionary prisms during orogenic processes providing important insights regarding the petrogenetic activity within the oceanic lithospheric mantle beneath spreading centers in mid-ocean ridge (MOR) and suprasubduction zone (SSZ) settings (Dilek and Furnes, 2011, Ahmed, 2013, Dai *et al.*, 2013).These tectonic settings include oceanic spreading centres, hot spots, backarc and forearc basins (supra-subduction zone environments) as well as arcs and other extensional magmatic settings including those in association with plumes. Furthermore, they provide information about the magmatic, metamorphic and geotectonic processes that occurred in the oceanic crust and the upper mantle (Arai *et al.*, 2006, Uysal *et al.*, 2007). The mantle-derived ophiolites provide significant information for paleotectonic evolution of the oceanic lithosphere, partial melting processes, melt-rock interaction and melt fractionation of the uppermost mantle (Singh *et al.*, 2016). Specifically, the abyssal peridotites represent mantle residues produced by partial melting beneath MOR settings, whereas the highly depleted SSZ peridotites experience intense partial melting above a subduction zone.

The aim of the present study is to provide new petrographic and geochemical data of mafic rocks from the Edessa ophiolite complex, in order to shed light on their petrogenesis.

Geological setting

The ophiolitic complex of Edessa, comprises a series of oceanic crust and mantle fragments linking the Veria-Naousa ophiolite (Rogkala *et al.*, 2017) in the south with the Guevgeuli ophiolite (Giannakopoulou *et al.*, 2018) in the northeast (Figure 1). It represents remnants of oceanic lithosphere that was thrust out of one or more ocean basins during Upper Jurassic to Lower Cretaceous time (Michailidis, 1990).

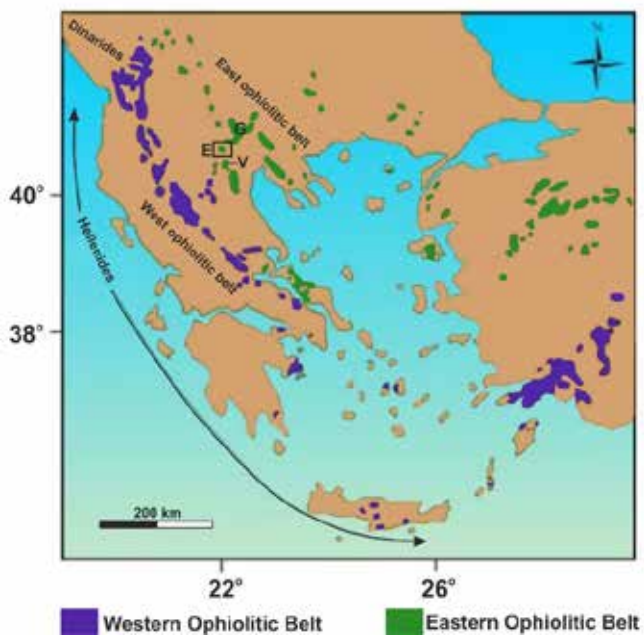

Figure 1. Distribution of ophiolites in the southernmost part of the Balkan Peninsula and Turkey (Rogkala *et al.*, 2019). Key to lettering: E = Edessa (also marked by the open square), G: Guevgeuli, V: Veria-Naousa.

The ophiolitic complex has been significantly affected by tectonically related emplacement mechanisms and it consists of several tectonic units (Pe-Piper and Piper, 2002, Saccani *et al.*, 2008). It includes lherzolites, serpentinised harzburgites

with high degree of serpentinisation, gabbros, diorites, diabasic sheeted dykes and pillow basalts. The serpentinised harzburgite is the dominant rock type amongst the ultramafics and encloses chromitites (Rogkala *et al.*, 2019). A sparse network of gabbroic and dioritic dykes crosscuts the serpentinised harzburgite. Massive diabase and basalt are thrust over serpentinised harzburgite and pass upwards into basaltic pillow-lava flows (Figure 2). A sparse network of rodingite dykes within the highly serpentinised harzburgites has also been identified. The ophiolitic rocks are unconformably overlain by Middle-Upper Cretaceous to Paleocene transgressive sediments (conglomeritic limestone, flysch).Other, non-ophiolitic volcanic rocks crop out to the eastern part of the ophiolite occurrence and they belong to the Almopias subzone (Vougioukalakis, 2002).

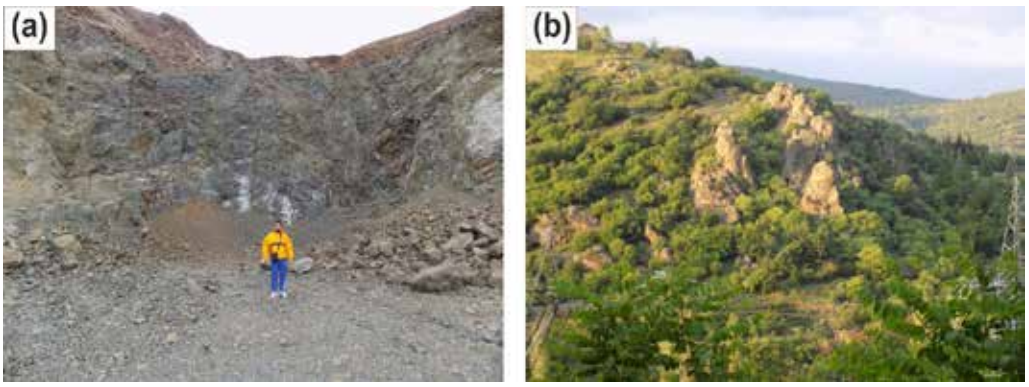

Figure 2. Mafic rocks from Edessa ophiolites: (a) Diabase, (b) Basalt.

Analytical methods

The textural characteristics of the samples were studied in polished-thin sections in a polarising microscope (Leitz Ortholux II POL-BK Ltd., Midland, ON, Canada) at the Department of Geology and scanning electron microscope (SEM) at the Laboratory of Electron Microscopy and Microanalysis, University of Patras. Whole-rock chemical analysis for major and trace elements was performed at Bureau Veritas Mineral Laboratories at Vancouver (Canada). Major element analysis was carried out using an XRF spectrometer and a sequential spectrometer (ICP-ES). Trace elements and rare earth elements were determined in totally digested samples by inductively coupled plasma-mass spectrometry (ICP-MS) in the same laboratory. Detection limits for major and trace elements range from 0.01 wt.% to 0.04 wt.% and from 0.01 ppm to 10 ppm, respectively. The analytical precision calculated by replicate analyses is better than 3% for most major elements and better than 5% for trace elements.

Results

Petrographic features

The Edessa mafic rocks comprise gabbroic (gabbros and less frequent diorites) and volcanics rocks (diabases and basalts). Diorites are moderately altered and they are fine to medium-grained rocks (Figure 3a). Their texture is granular but locally becomes porphyritic with subhedral to euhedral plagioclase phenocrysts. Sporadic, euhedral hornblende grains are enclosed within larger plagioclase crystals forming poikilitic textures. Gabbros are mainly comprised of clinopyroxene and plagioclase (Figure 3b). Ilmenite, magnetite, titanite and zircon are present in small amounts, less than 5% of the mode. Primary textures have been obliterated by alteration.

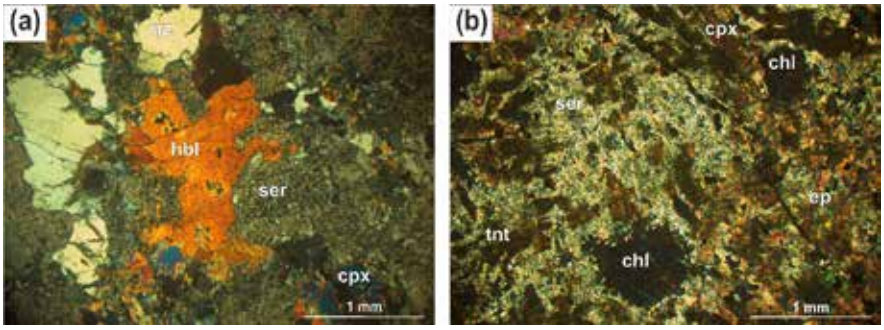

Figure 3. Photomicrographs of:(a) hornblende (hbl) crystal with irregular shape surrounded by sericitised (ser) plagioclase, quartz (qz) and clinopyroxene (cpx) in diorite, (b) subophitc texture in altered gabbro showing seriticised plagioclase (ser), clinopyroxene (cpx), chlorite (chl), epidote (ep) and titanite (tnt).

Diabase samples exhibit porphyritic, ophitic and subophitic textures. The mineral assemblage is similar to that of gabbros including clinopyroxene and subhedral plagioclase. In some cases the plagioclase is partially to completely altered to sericite (Figure 4a). Basalts display interwoven, porphyritic and microlitic textures (Figure 4b). Their primary assemblage includes plagioclase, clinopyroxene, magnetite, ilmenite and accessory zircon. They have suffered by a low-grade, oceanic alteration episode and by the development of quartz, epidote, chlorite, calcite and titanite, occurring in the groundmass and within joints or amygdules.

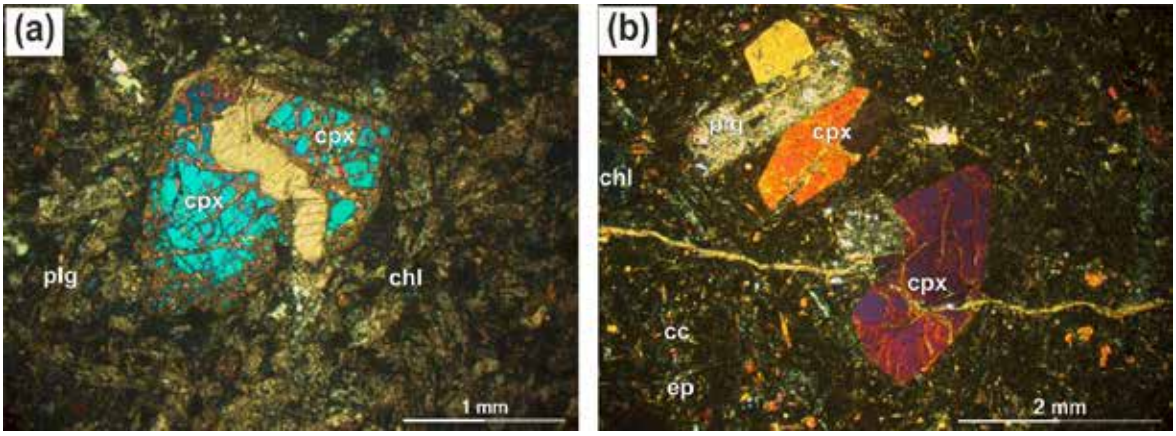

Figure 4. Photomicrographs of: (a) clinopyroxene (cpx) porphyroclast cross cutting by calcite (cc) and surrounding by plagioclase (plg), sericite (ser) and chlorite (chl) in diabase, (b) porphyritic texture in basalt showing clinopyroxene (cpx), plagioclase (plg), chlorite (chl), epidote (ep) and calcite veinlet.

Geochemical features

All the investigated mafic rock samples were moderately affected by alteration, resulting in the mobility of the large ion lithophile (LIL) elements (such as Na, K, Ca, Rb, Ba, Sr, Pb) and thus their measured values may not be able to define these rocks (Shervais, 1982). Therefore, we use only high field strength (HFS) elements (Ti, Nb, Y, Zr, Hf, Ta, REE) and transition elements (such as Y, V, Ni, Cu) for interpretation, as these elements are considered immobile during alteration and can effectively be used to describe the primary chemical features of rocks. Immobile-element ratios such as Zr/Ti and Nb/Y are commonly used to identify mafic, intermediate and acid rocks that they might have been variably altered (Winchester and Floyd, 1977, Pearce, 1996). In order to clarify the nature of the environment of mafic rocks, we have applied the Zr-Nb-Y diagram in the analyzed results. In this diagram, gabbro, basalt and diabase, except one sample (ED.110), are plotted in gabbro field, whereas the diorite clusters in the tonalite, a fact that supports the mafic character of the investigated samples (Figure 5).

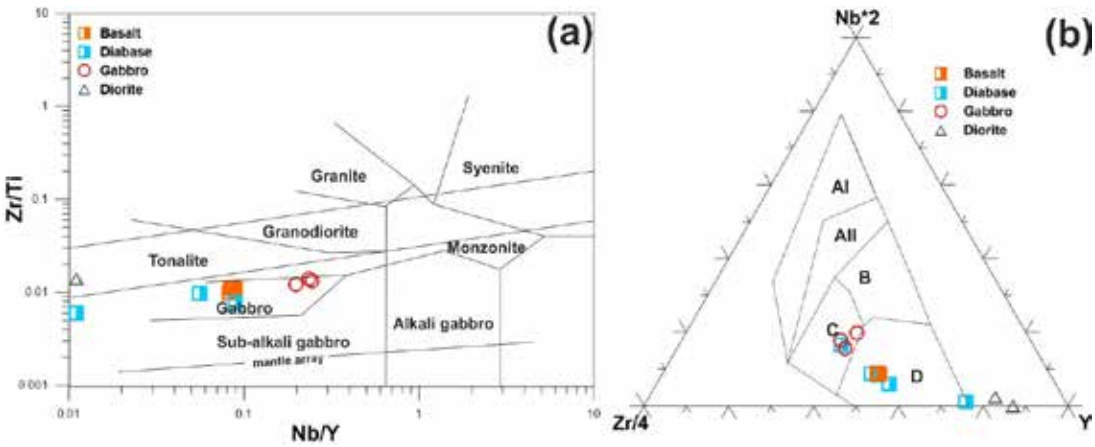

Figure 5. a. Binary classification diagram of Zr/Ti versus Nb/Y for the mafic rocks of Edessa ophiolites (Winchester and Floyd 1977; modified by Pearce 1996). b. Discrimination Nb-Zr-Y diagram (Meschede, 1986) (fields: Al = within-plate alkali basalts, All = within-plate alkali basalts and within-plate tholeiites, B = E-type MORB, C = within-plate tholeiites and volcanic basalts, D = N-type and volcanic-arc basalts).

Basalts show remarkably high Ti and REE concentrations than the other mafic rock samples. The chondrite normalised REE patterns for diorite, gabbro, diabase and basalt are plotted individually and they show four distinct REE patterns (Figure 6). Though all studied samples show almost flat HREE pattern, gabbro shows highly fractionated LREE patterns relative to the HREE, with positive Eu anomalies, which implies plagioclase accumulation. These patterns are similar to E-MORB type represented from many ophiolitic complexes. Diabases present two subgroups. The first is enriched in LREE and depleted in HREE, similar to OIB-like lavas. The second is depleted in LREE and enriched in HREE, similar to the SSZ type. Basalt exhibits almost flat REE pattern without any LREE enrichment relative to HREE, which is similar to N-MORB type. Diorite shows totally depleted LREE pattern (SSZ type) with negative Eu anomaly, which implies removal of plagioclase.

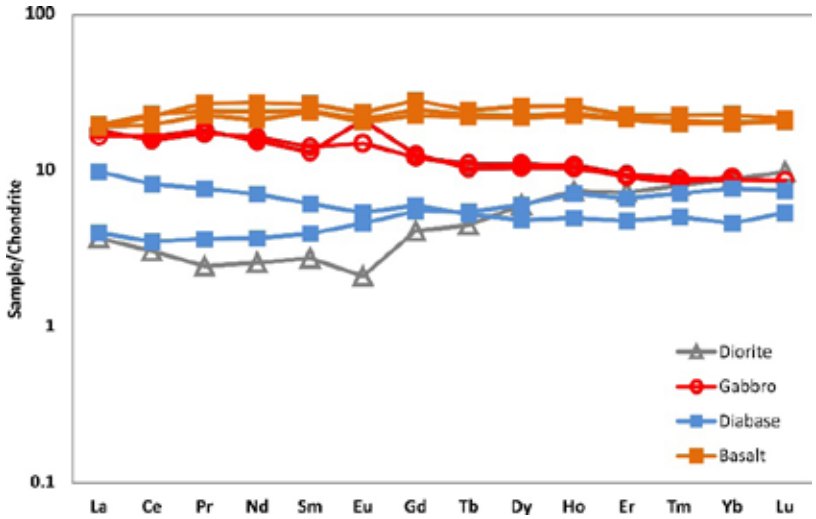

Figure 6. Chondrite-normalised REE patterns of the mafic rocks from the Edessa ophiolite. Normalising values are from McDonough and Sun (1995).

Conclusions

Based on these geological, petrographic and geochemical evidences, we suggest that mid ocean ridge (MOR) type mafic rocks (basalt and gabbro) from the Edessa ophiolite represent the section of older oceanic crust which was generated during the opening of the Axios Ocean. Conversely, diorite and partially diabase represent the younger oceanic crust which was formed at the forearc region by partial melting of the depleted mantle wedge modified by hydrous fluids released from the subducting oceanic slab.

Acknowledgements

We kindly thank Dr. A.K. Seferlis of the Laboratory of Electron Microscopy and Microanalysis, University of Patras for his assistance with the microanalyses and SEM micrographs. We kindly thank Dr. K. Hatzipanagiotou and Dr. B. Tsikoura for their assistance in the fieldwork, in the interpretation of the results and for their whole contribution of this study.

References

Ahmed, A.H., 2013. Highly depleted harzburgite-dunite-chromitite complexes from the Neoproterozoic ophiolite, south Eastern Desert, Egypt: a possible recycled upper mantle lithosphere. Precambrian Research 233, 173-192.

Arai, S., Kadoshima, K., Moeishita, T., 2006. Widespread arc-related melting in the mantle section of the northern Oman ophiolite as inferred from detrital chromian spinels. Journal of the Geological Society of London 163, 869-879.

Dai, J., Wang, C., Polat, A., Santosh, M., Li, Y., Ge, Y., 2013. Rapid forearc spreading between 130 and 120 Ma: evidence from geochronology and geochemistry of the Xigaze ophiolite, southern Tibet. Lithos 172-173, 1-16.

Dilek, Y., Furnes, H., 2011. Ophiolite genesis and global tectonics: geochemical and tectonic fingerprinting of ancient oceanic lithosphere. Geological Society of American Bulletin 123, 387-411.

Giannakopoulou, P.P., Petrounias, P., Tsikouras, B., Kalaitzidis, S., Rogkala, A., Hatzipanagiotou, K., Tombros, S.F., 2018. Using Factor Analysis to Determine the Interrelationships between the Engineering Properties of Aggregates from Igneous Rocks in Greece. Minerals 8, 580.

McDonough, W.F., Sun, S.S., 1995. The composition of the Earth. Chemical Geology 120, 223-253.

Meschede, M., 1986. A method of discriminating between different types of mid-ocean ridge basalts and continental tholeiites with the Nb-Zr-Y diagram. Chemical Geology 56, 207-218.

Michailidis, K.M., 1990. Zoned chromites with high Mn-contents in the Fe-Ni-Cr-laterite ore deposits from the Edessa area in

Northern Greece. Mineralium Deposita 25, 190–197.
Pearce, J.A., 1996. A user's guide to basalt discrimination diagrams. In: Wyman, D.A. (Ed.), Trace element Geochemistry of Volcanic Rocks: Applications for Massive Sulphide Exploration Geological Association of Canada, 12. Short Course Notes, 79-113.
Pe-Piper, G.; Piper, D.J.W., 2002. The Igneous Rocks of Greece: The Anatomy of an Orogen; Gebrueder Borntraeger: Berlin/Stuttgart, Germany.
Rogkala, A., Petrounias, P., Tsikouras, B., Giannakopoulou, P. P., & Hatzipanagiotou, K., 2019. Mineralogical Evidence for Partial Melting and Melt-Rock Interaction Processes in the Mantle Peridotites of Edessa Ophiolite (North Greece). Minerals 9(2), 120.
Rogkala, A., Petrounias, P., Tsikouras, B., Hatzipanagiotou, K., 2017. New Occurrence of Pyroxenites in the Veria-Naousa Ophiolite (North Greece): Implications on Their Origin and Petrogenetic Evolution. Geosciences 7(4), 92.
Saccani, E., Photiades, A., Santato, A., Zeda, O., 2008. New evidence for supra-subduction zone ophiolites in the Vardar zone of northern Greece: implications for the tectonomagmatic evolution of the Vardar oceanic basin. Ofioliti 33, 65–85.
Shervais, J.W., 1982. Ti-V plots and the petrogenesis of modern and ophiolitic lavas. Earth and Planetary Science Letters 59 (1), 101-118.
Singh, A.K., Nayak, R., Khogenkumar, S., Subramanyam, K.S.V., Thakur, S.S., Singh, R.K.B., Satyanarayanan, M., 2016. Genesis and tectonic implications of cumulate pyroxenites and tectonite peridotites from the Nagaland-Manipur ophiolites, Northeast India: constraints from mineralogical and geochemical characteristics. Geological Journal DOI: 10.1002/gj.2769.
Uysal, I., Kaliwoda, M., Karsli, O., Tarkian, M., Sadiklar, M.B., Ottley, C.J., 2007. Compositional variations as a result of partial melting and melt-peridotites interaction in an upper mantle section from the Ortaca area, southwestern Turkey. Canadian Mineralogist 45, 1791-1813.
Vougioukalakis, G., 2002. Petrological, Geochemical and Volcanological Study of the Almopias Pliocene Volcanic Formations and their Correlation with the Geothermal Manifestations in the area. PhD thesis, Aristotle Univ. of Thessaloniki, Thessaloniki, 303pp.
Winchester, J.A., Floyd, P.A., 1977. Geochemical discrimination of different magma series and their differentiation products using immobile elements. Chemical Geology 20, 325-343.

17th INTERNATIONAL CONGRESS of the Geological Society of Greece

BULLETIN OF THE GEOLOGICAL SOCIETY OF GREECE, SP. PUBL.

EXTENDED ABSTRACT 271

Shallow Depth P-wave Velocity Profiling Using Seismic Interferometry: The CORSSA Site

Roumelioti Z.[1], Katsaitis N.[1]
(1) Department of Geology, University of Patras, Patras, Greece, zroumelioti@upatras.gr

Abstract

We apply the method of seismic interferometry by deconvolution to analyze vertical accelerometer array data from the CORSSA site in Greece and determine P-wave velocities (VP) at shallow depths. We show that in the case of the CORSSA site, the method is able to overcome the challenges of resolving the much faster P-wave travel times and provide statistically robust mean velocity values for different depth ranges. Thus, we propose a V_P velocity model for the studied site to complement the previously proposed V_S models. We also compare the interferometry inferred V_PV_S values with independent results and find them to be realistic and consistent with empirical relationships based on rich data sets from different parts of the world. Within the nearly 10 years that the studied dataset spans, we observe a significant temporal variation of V_P, mostly in the shallower depth ranges studied, which appears to be longer in duration than the seasonal variation previously reported for V_S at this site. However, the lack of temporal continuity in our dataset does not allow a detailed analysis of this variation.

Background and objectives

Changes in the ratio of P-wave to S-wave velocity, V_P/V_S, in soft sediments often reveal variations in fluid content, sediment compaction, material composition, and stress conditions. Monitoring these changes is critical for both geotechnical and geophysical applications. Historically, the method of seismic interferometry by deconvolution has been applied to horizontal recordings of vertical accelerometer array data sets to monitor temporal variations of V_S at shallow depths (e.g., Nakata and Snieder, 2011; Chandra et al., 2016; Gueguen, 2016; Roumelioti et al., 2020, Qin et al., 2022). The vertical component is usually not exploited in the specific method, primarily because the much faster travel times of P-waves are difficult to resolve.

The CORSSA vertical accelerometer array (e.g., Kassaras et al., 2016) was installed in the coastal area of the city of Aigio (northern Peloponnese, western Gulf of Corinth) a few years after the catastrophic 1995 M6.5 Aigio earthquake. The primary goal of this infrastructure was to collect strong motion records to be used in studies of site effects and soil response. To understand the changes in the seismic wavefield as it propagates from the bedrock to the ground surface, four stations were installed inside boreholes at different depths (14, 31, 57 and 178 m) and one station was installed on the surface inside a lightweight protective structure. The infrastructure operated in trigger mode for several years, although with several interruptions due to technical problems, and its data for the period 2022-2012 have been organized and published as a database (http://corssa.gr/; Kassaras et al., 2016).

The CORSSA dataset has been analyzed by seismic interferometry by deconvolution with respect to the horizontal recordings and associated Vs (Roumelioti et al., 2018), revealing a seasonal variation of V_S in shallow layers that decreases with depth and becomes undetectable below ~30m. In this work, we extend the analysis to the vertical components of the earthquake records in the CORSSA database, with the aim of determining the V_P profile for the CORSSA site and investigating the V_P values with respect to previously published V_S in terms of their ratio, V_P/V_S, and its change with depth.

Methods and Data

Seismic interferometry by deconvolution on an array of sensors comprises the division of the spectral representation of one trace at one receiver by that of another. Assuming that the distance between a specific earthquake source and the array is many times larger than the array inter-station distances, the spectral division is expected to remove any source-specific imprints and common path propagation effects, yielding the transfer function of the medium between the two involved stations, which resembles a pulse signal. This transfer function is the inverse Fourier transform of:

$$D_{j-i}(\omega) = \frac{A_j(\omega)A_i^*(\omega)}{|A_i(\omega)|^2+\varepsilon} \quad (1)$$

where $A_j(\omega)$ and $A_i(\omega)$ represent the Fourier transforms of the recordings at the *j*-th and *i*-th (reference) receivers, respectively, and ε the water-level parameter, introduced to stabilize the deconvolution at very low denominator values (Clayton and Wiggins, 1976). By measuring the travel times of the resulting pulses and knowing the exact distances between stations in the array, it is possible to compute wave velocities in the between the two stations propagating medium.

For this study, the seismic interferometry by deconvolution was applied to the vertical components of recordings from four CORSSA borehole stations, using the surface station as a reference. In total, we analyzed records of 709 earthquakes at each

station. Some characteristics of the dataset, such as the distribution of magnitudes (local magnitude, M_L) in magnitude bins, the distribution of magnitude with epicentral distance, and the distribution of peak ground acceleration (PGA) with distance, are shown graphically in Figure 1.

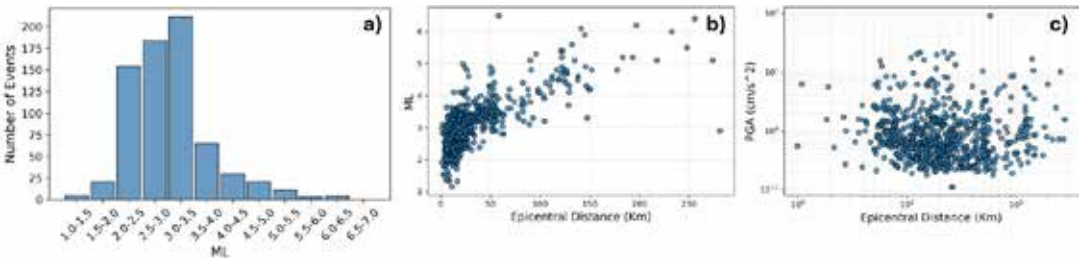

Figure 1. Brief description of the processed dataset: a) Distribution of earthquake records in the dataset in magnitude (M_L) bins, b) M_L occurrences and c) PGA (east-west component of the surface CORSSA station) with respect to the epicentral distance of the earthquakes from the CORSSA site.

We set ε=10% and resampled the inverse Fourier transform of $D_{i-i}(\omega)\,D_{i-i}(\omega)$ with a step 100 times smaller than the original. In this way, we artificially densified the pulse-like transfer functions to improve the accuracy of the picking of the travel time of the pulse (e.g., Roumelioti et al., 2020; Qin et al., 2023). Figure 2 shows a sample output from the application of the described method to the vertical recordings of a M_L3.5 earthquake at 14 km distance. The subplots show the results of the interferometry at different depth intervals and include an upward propagating pulse. We use the top of this pulse as a characteristic point to follow its propagation and measure its travel times from one sensor depth to the other. At the 14m subplot in Figure 2, two pulses appear, one on the negative side of the time axis and one on its positive side. This means that there is significant wave energy that has been reflected at the surface and propagated downward, but it does not affect our results, which are based solely on time measurements on the negative side. In recordings richer in low frequencies, or as V_P increases, the two pulses may move closer together and become inseparable, making it impossible to measure V_P.

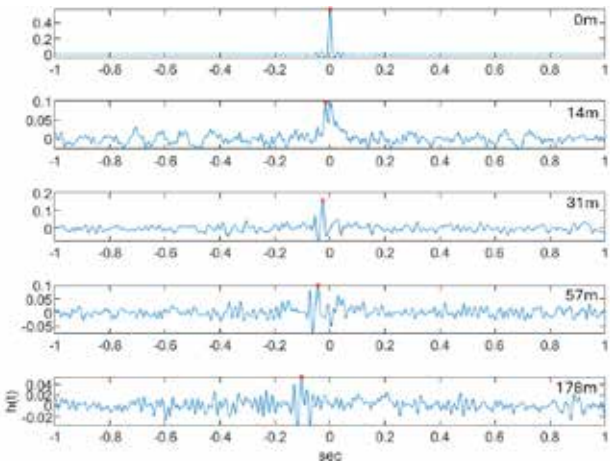

Figure 2. Example output of the interferometry by deconvolution on the vertical components of a record (29/12/2011, 15:19UTM, M_L3.5, R14km) at the CORSSA site. Each subplot shows the deconvolution of a waveform at the depth marked on the top right with respect to the waveform at the surface. A propagating pulse appears on the negative side of the x-axis and its top is marked (red dot) as a characteristic point to measure time differences (i.e., travel times).

V_P from seismic interferometry by deconvolution

We have applied seismic interferometry by deconvolution to resolve P-wave velocities in the depth intervals 0-14 m, 0-31 m, 0-57 m, 0-178 m, 14-31 m, 31-57 m, and 57-178 m. As noted above, there are inherent difficulties in applying the method to the much faster P-waves. The first is the sampling rate commonly used for ground acceleration monitoring, which is low for resolving very small changes in the propagation time of the impulse response of soft soils. In our case (sampling rate of 200 s/s), we limit this restriction to some extent by resampling the interferometric result at a higher rate, allowing a more accurate measurement of the travel times. The second major difficulty is the very high velocities of the P-waves, even in soft sediments, which in combination with the often small distances between the stations result

in extremely short travel times that cannot be resolved. A third difficulty is that the wavelengths of interest change as we attempt to define velocities at different depth intervals, and not all recordings have the necessary frequency content to provide an unambiguous time reading. As a result, the efficiency of the method at a particular location and depth interval may not always be known a priori, but only through trial and error. Furthermore, even if the method is successful but V_P increases with time, it may fail above a certain level of increase.

For all of the above reasons, in our application at the CORSSA site although we had many stable results, we also had numerous "outliers", which we define in the following. To isolate and work with the most populated concentrations of resulting V_P values, we applied a two-step interquartile range (IQR) outlier removal. First, we removed V_P values that were outside 3 times the IQR (Q3-Q1) of the overall distribution. These "extreme" outliers were also manually checked and were found to be related to poor quality waveforms or to the events with the richest low-frequency signal, resulting in broad pulses with an almost flat top (i.e., the area where we usually expect a sharp peak to be used for travel time measurement). In the second step, we performed a standard removal of values outside 1.5 times the IQR. The procedure is shown graphically in Figure 3 for the example case of the 0-14m depth interval. The IQR, i.e., the area where 75% of the computed values are concentrated, is shown in purple and the lighter color marks the 1.5×IQR area. Everything that falls within these two areas is included in the subsequent analysis, and values outside these areas are considered outliers. Figure 3 also marks the mean of the finally considered values ± 1 standard deviation (s.d.).

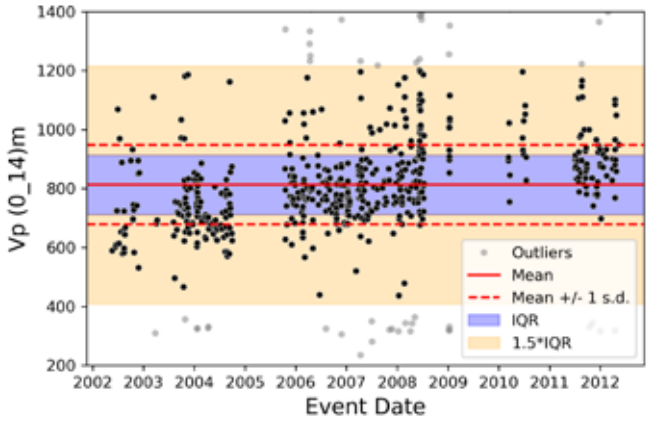

Figure 3. Graphical description of the outlier removal procedure for the example case of V_P estimates for the depth interval 0-14m. Gray points, lying beyond 1.5 times the interquartile range (IQR) (orange shaded area), are considered as outliers and are not being used in the estimate of the mean V_P value.

The results of the interferometry by deconvolution for all depth intervals examined are summarized in Table 1. More specifically, Table 1 lists percentage of final data points and outliers with respect to the initial dataset of 709 earthquake records for each depth interval, the mean V_P ± 1 s.d. and the corresponding information for the two horizontal components (from Roumelioti et al., 2018), east-west (V_{Se}) and north-south (V_{Sn}), for comparison. The agreement of the results of the two V_S is remarkable, as well as the amount of data finally considered for V_P despite the difficulties mentioned above. The depth interval with the largest number of outliers, for both V_P and V_S computations is the 0-178m interval. This is a rather unsurprising result considering the very weak character of most of the waveforms in the dataset (Kassaras et al., 2016) (Figure 1c). An interesting finding was the high mean V_P in the 14-31m depth interval, quite higher than the underlying examined "layer", most likely indicating an increased presence of groundwater.

Table 1. Mean V_P and V_P/V_S values inferred from interferometry for the CORRSA site and percentages of determined values and outliers with respect to the starting dataset. Depth intervals are defined by the downhole sensors' installation depths. V_S values for the two horizontal components of Roumelioti et al. (2018) are included for comparison.

Depth Interval (m)	Data/Outliers (%) for V_P	V_P (± 1s.d.) (m/sec)	Data/Outliers (%) for V_{Se}	V_{Se} (± 1s.d.) (m/sec)	Data/Outliers (%) for V_{Sn}	V_{Sn} (± 1s.d.) (m/sec)	V_P/V_{Se}	V_P/V_{Sn}
0-14	76/24	813 (135)	97/3	208 (7)	97/3	214 (8)	3.9	3.8
0-31	93/7	1135 (107)	99/1	240 (6)	98/2	240 (6)	4.7	4.7
0-57	77/23	1224 (96)	96/4	268 (4)	94/6	268 (4)	4.6	4.6
0-178	67/33	1710 (59)	63/37	430 (4)	61/39	424 (15)	4.0	4.0
14-31	76/24	1754 (233)	93/7	277 (7)	86/14	271 (11)	6.3	6.5
31-57	81/19	1382 (46)	91/9	308 (3)	93/7	314 (4)	4.5	4.4
57-178	87/13	2140 (32)	71/29	602 (5)	60/40	583 (11)	3.6	3.7

Figures 4 and 5 show the results graphically, Figure 4 for interferometry results with respect to the surface station and Figure 5 for pairs where both stations were in boreholes. Each row of the subplots corresponds to a different depth interval (i.e., station pair in the interferometry), while the columns from left to right include: the V_P values derived in this study, the V_{Se} and V_{Sn} values computed by Roumelioti et al. (2018) using the same method. In all subplots, the mean velocity ± 1 s.d. (i.e., the values included in Table 1) is also marked. Although our dataset is not continuous in time, it is clear that there is a temporal variation in both V_P and V_S values that increases in amplitude with depth. Although the left column in Figure 4 may suggest some seasonal variation, it is certainly not as clear as for V_S, and the temporal discontinuity of the dataset examined, as well as the variability of V_P make any identification even more difficult. It is possible that the temporal variation of V_P is longer in period than an expected seasonal one. This can be seen very clearly in the upper left subplot of Figure 4, where V_P values in 2003-2004 are mostly clustered around 700m/s, whereas in 2006-2008 they are around 800m/s. Reasons for such slower changes could be, for example, multi-year changes in groundwater, or sudden compaction of sediments after shaking caused even by relatively distant strong earthquakes.

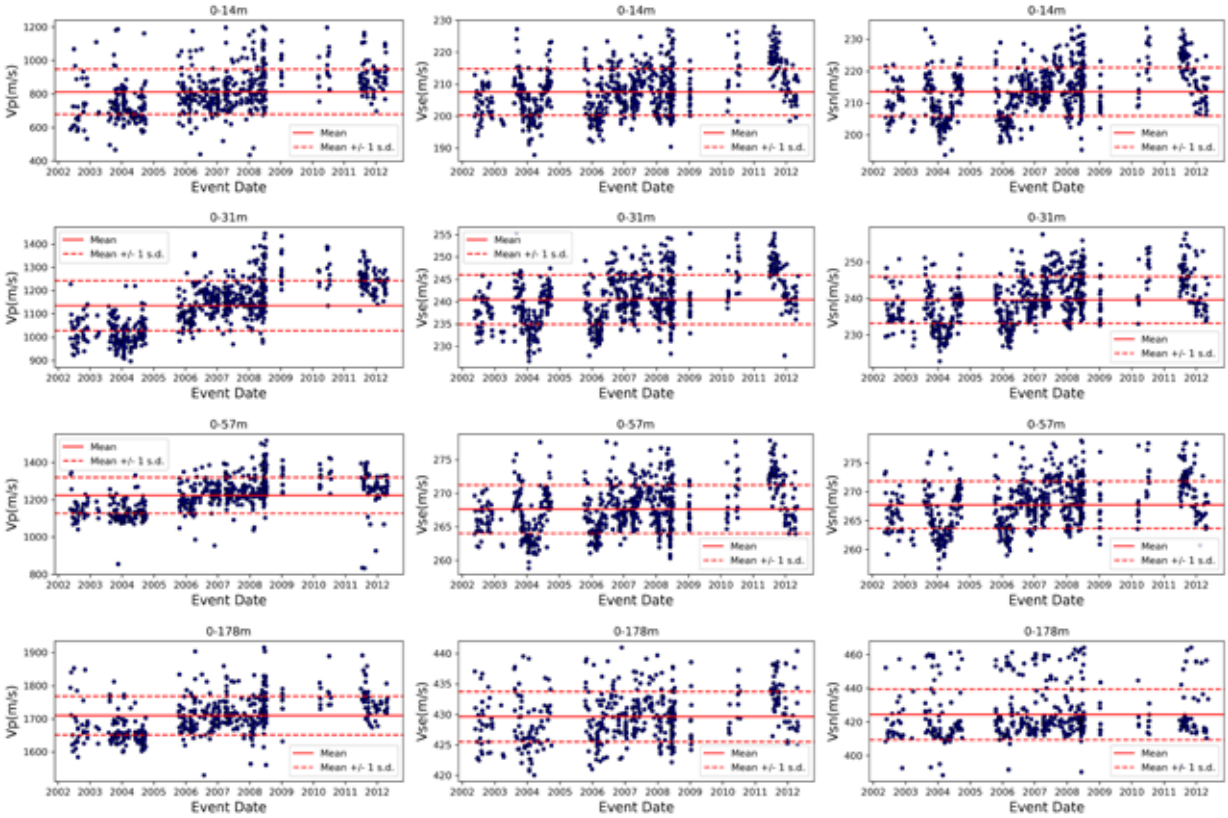

Figure 4. Velocity variation with time for depth intervals noted at the top of each subplot (0-14m, 0-31m, 0-57m, 0-178m from top to bottom. The left column contains the V_P values, the middle the V_S in the east-west component (V_{Se}) and the right column the V_S in the north-south component (V_{Sn}). V_S values are taken from Roumelioti et al. (2018).

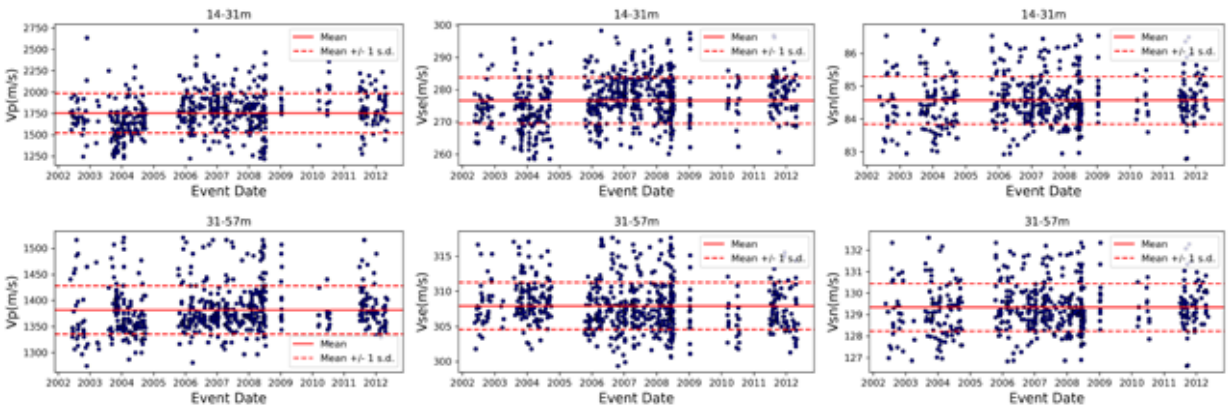

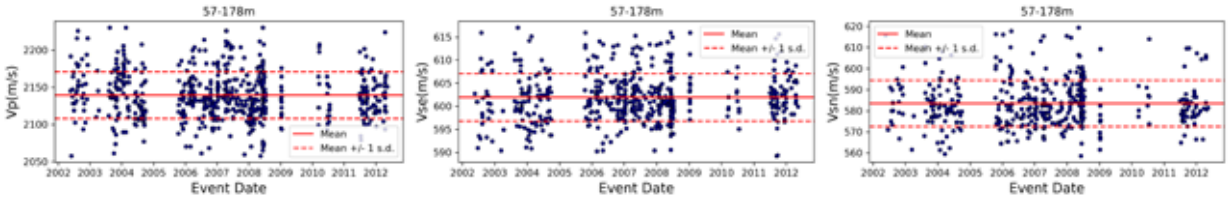

Figure 5. As in Figure 5, but for the intermediate depth intervals (from top to bottom) of 14-31m, 31-57m, and 57-178m.

V_P profile at the CORSSA site

The mean VP values derived for the depth intervals 0-14m, 14-31m, 31-57m and 57-178m are plotted in Figure 6 in the form of a velocity profile, along with previously proposed VS profiles (CORSSA, 2002; Roumelioti et al., 2018). Although the applied method provides well-constrained mean VP values directly at the site and from actual ground motio data, a shortcoming is that the interferometric "layer" thicknesses in Figure 6 have no physical or geological meaning and are defined by the depths of the sensors in the accelerometer array.

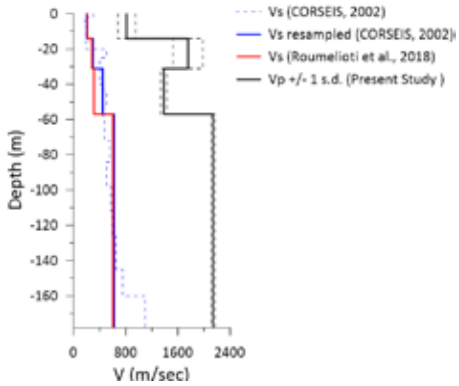

Figure 6. Seismic wave velocity profiles at CORSSA. The V_P profile is a result of this study and "layers" thicknesses are enforced by the depths of the borehole array sensors. The V_S profiles are from Roumelioti et al. (2018) and include the information from the European project "CORSEIS" (2002) as originally provided and resampled at the depth intervals of the CORSSA array.

V_P/V_S ratio

The last two columns in Table 1 show the V_P/V_S using the mean velocity values for each depth interval examined. The results using the mean V_S values in the two horizontal components show insignificant differences. V_P/V_S has values <4 in the shallowest (0-14m) and deepest (57-178m) depth ranges and well >4 in the 14-31m and 31-57m intervals. Figure 6 shows how these values compare to previously published V_P-V_S relations. We chose to compare the CORSSA values to the empirical relation of Brocher (2005), who has incorporated many northern California profiles that are more representative of younger tectonic terranes such as the one examined in this study. We also compare our values with two relations proposed in a more recent study by Nagashima and Kawase (2021), which is based on a very large number of KiK-net and K-NET station sites in Japan. Nagashima and Kawase (2021) found an abrupt increase in V_P around 4m depth and attributed it to the transition from unsaturated to saturated soil formations. As a result, they proposed two different V_P-V_S relationships. The CORSSA values for the three deepest ranges investigated compare well with the Brocher (2005) relation and the saturated soil version of Nagashima and Kawase (2021). The 0-14m appears to be more compatible with the unsaturated version of the Nagashima and Kawase (2021) relationship, suggesting that the top 14m at CORSSA is mostly unsaturated. This is also supported by the absolute value of the mean V_P for this layer, ~ 800m/s, which is much lower than the speed of P-waves in water (1200 to >1400 m/s, also depending on the salinity).

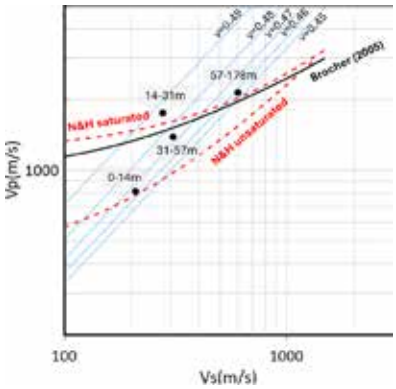

Figure 6. Mean V_P versus mean V_S for the examined depth intervals at the CORSSA site. Blue straight lines mark the V_P, V_S relation for Poisson's ratios (v) of 0.45-0.49. Previously published pertinent relations are also shown for comparison; black curve for Brocher (2005) and red dashed curves for Nagashima and Kawase (2021; N&H) for saturated and unsaturated soils.

Conclusions/Discussion

We applied the method of seismic interferometry by deconvolution to the vertical components of a dataset of 709 earthquake records at the CORSSA borehole array. We examined the four borehole stations of the array (at depths of 14, 31, 57 and 178m) with respect to the surface station, as well as station pairs at 14-31m, 31-57m, and 57-178m, and computed V_P velocities for the corresponding depth intervals. Due to the high velocities of the P-waves, the short distances examined and the weak character of most of the waveforms in the dataset, the results included several unrealistically high or low V_P values, many of which were removed as outliers using a two-step interquartile outlier removal approach. The outliers for the V_P computation were in the range of 7-33% of the initial number of data points, which is considered rather small considering the previously mentioned difficulties in measuring V_P. Based on the final data points, we computed the mean $V_P \pm 1$ s.d. for each depth interval examined and we provided a V_P velocity model for the site of the CORSSA infrastructure. We used our V_P values and the V_S values of Roumelioti et al. (2018) to compute V_P/V_S ratios for the different depth intervals examined, but also to demonstrate that continuous monitoring of this quantity is feasible with the applied method.

Acknowledgements

The study was carried out in the framework of the research project "UNMASK", supported by the Hellenic Foundation for Research and Innovation (H.F.R.I.) under the "2nd Call for H.F.R.I. Research Projects to support Faculty Members & Researchers" (Project Number: 2724).

References

Brocher, T.M., 2005. Empirical relations between elastic wave speeds and density in the earth's crust. Bull. seism. Soc. Am. 95, 2081–2092.

Chandra, J., Guéguen, Ph., Bonilla, L.F., 2016. PGA-PGV/VS considered as a stress-strain proxy for predicting nolinear soil response. Soil Dynamics and Earthquake Engineering 85, 146-160.

Clayton, R.W., Wiggins, R.A., 1976. Source shape estimation and deconvolution of teleseismic bodywaves. The Geophys. J. of the Royal Astronomy Soc. 47, 151-177.

CORSSA, 2002. Project Final Report, available in hard copy from the Research Unit of Soil Dynamics and Earthquake Engineering of the Department of Civil Engineering of the Aristotle University of Thessaloniki (personal communication with M. Manakou).

Guéguen, Ph., 2016. Predicting nonlinear site response using spectral acceleration VS PGV/VS30: A case history using the Volvi-Test site. Pure Appl. Geophys. 173(6), 2047-2063.

Kassaras, I., Roumelioti, Z., Ktenidou, O.-J., Pitilakis, K., Voulgaris, N., Makropoulos, K., 2016. Accelerometric data and web portal for the vertical Corinth Gulf soft soil array (CORSSA). Bulletin of the Geological Society of Greece, 50(2), 1081–1090.

Nagashima, F., Kawase, H., 2021. The relationship between V_S, V_P, density and depth based on PS-logging data at K-NET and KiK-net sites. Geophys. J. Int. 225, 1467 – 1491.

Nakata, N., Snieder, R., 2012. Estimating near-surface shear wave velocities in Japan by applying seismic interferometry to KiK-net data. J. Geophys. Res. 117 B01308, 1-13.

Qin, L., Steidl, J.H., Qiu, H., Nakata, N., Ben-Zion, Y., 2022. Monitoring Seasonal Shear Wave Velocity Changes in the Top 6 m at Garner Valley in Southern California with Borehole Data. Geophys. Res. Lett. 49.

Roumelioti, Z., Hollender, F., Gueguen, Ph., 2018. Shear wave velocity variations at the CORSSA (Central Greece) vertical array. 16th European Conference on Earthquake Engineering, Thessaloniki, Greece, p. 12.

Roumelioti, Z., Hollender, F., Guéguen, P., 2020. Rainfall-induced variation of seismic waves velocity in soil and implications for soil response: What the Argonet (Cephalonia, Greece) vertical array data reveal. Bull. Seismol. Soc. Am. 110, 441–451.

17th INTERNATIONAL CONGRESS of the Geological Society of Greece

BULLETIN OF THE GEOLOGICAL SOCIETY OF GREECE, SP. PUBL.

EXTENDED ABSTRACT 272

Establishing the soil geochemical mapping in Lesvos Island, Greece

Roussos A.[1], Kelepertzis E.[1], Kypritidou Z.[1], Aivatzidis, E.[1], Drougas C.[1], Vassilakis, E.[1], Voudouris, P.[1], Zouros N.[2]

(1) Department of Geology and Geoenvironment, National and Kapodistrian University of Athens, Panepistimioupolis, Zografou, 15784, Athens, Greece

(2) Geography Department, University of the Aegean, Mytilene, 81100, Lesvos, Greece

Research Highlights

- Effect of different lithological types on the chemical composition of the soil.
- Application of multivariate analysis and G.I.S. techniques to determine controlling factors on soil geochemistry.

Abstract

Geochemical mapping is commonly applied by geoscientists to document the spatial distribution of elemental concentration levels in materials occurring at the Earth's surface, such as soil. Here, we present the applied methodology for establishing the soil geochemical mapping in the unique island of Lesvos that exhibits a complex geological structure with different rocks occurring on island surface. A total of 74 surface (0-20 cm depth) soil samples were collected from 66 locations on a 5 km x 5 km grid extending across the whole island. Preliminary results in terms of distribution of major and trace element concentrations and interpretations based on geology and mineralization will be presented.

Introduction / Background and Objectives

Geochemical mapping is a technique rooted in mineral exploration but has now found worldwide application in environmental studies. Geochemical mapping has a crucial role, nowadays, not only for mineral exploration, but also for studies about environment and human health (Kirkwood et al., 2016). Officially, International Geochemical Mapping Project was accepted by UNESCO/IUGS just in 1988 and technical – regional committees, which include scientists and organizations from all over the world, coordinated the project with aim to resolve scientific and technical issues. For example, many surveys have a huge number of samples that have been analyzed for different groups of elements by a variety of analytical methods, with uncertain quality control (Darnley, 1990). Another problem is the sampling density and the map scale that should be followed, but these depend on the objectives of each project (Demetriades et al., 2022). By definition the geochemical maps are based on the concentrations of chemical elements from samples of surface media such as soil, water or stream sediments (e.g. Salminen et al., 1998).

In this project, Lesvos Island is the study area and soil samples were collected in order to produce geochemical maps of elements across the whole island. The samples were collected during July 2024 and the aim was to contribute new knowledge in terms of the geochemical characterization of the island. The density of soil sampling followed a 5 km x 5 km grid in order to produce a comprehensive geochemical mapping of the island's soils.

The diverse geological formations that occur on the island, the various types of mineralizations found in the northeastern Aegean, but also the limited research on the geochemistry of the island's soils, motivated us to carry out this research. The main objective is the accomplishment of the soil geochemical mapping in terms of major and trace elements with the aim to determine the effect of local geology on soil geochemistry. On the island of Lesvos, geological mapping has been carried out previously (Hecht, 1972; Katsikatsos et al., 1986; Thomaidou, 2009), but extensive geochemical mapping of soils on the island has not been carried out.

Description of the study area

Lesbos is the third largest island in Greece, covering an area of 1,630 km² and is located in the northeastern part of the Aegean Sea, very close to the Anatolian coast. Regarding the geomorphology of Lesbos, two large, enclosed bays dominate the southern part of the island: Kalloni Bay and Geras Bay, which are clearly related to the tectonic evolution of the broader northern Aegean area and especially to the neotectonic activity. Two large mountain masses, Mount Lepetymnos (968 m) at the northern part and Mount Olympus (967 m) at the southern part of Lesbos, between the two bays, stand out on the overall mountainous island of Lesbos. In general, the topography of Lesbos is varied, showing abrupt changes and is quite pronounced in other areas as well, such as the Amali Peninsula (527 m) and especially in the western part, where Mount Ordymnos (589 m) dominates, creating a very impressive landscape with steep transitions toward the island's western coast (Thomaidou, 2009).

Lesbos Island, located in the northeastern Aegean Sea, is known for its unique geological features, diverse

rock formations, and significant tectonic activity. The island's geology offers a fascinating glimpse into the Earth's geological processes, particularly with respect to its volcanic history, the presence of numerous mineral deposits, and its tectonic setting along the boundary of the Eurasian and African plates (Apostolopoulos et al., 2009).

Lesbos has a rich volcanic history. Volcanic activity is responsible for much of the island's landscape, with lava flows, volcanic ash deposits, and geothermal activity still visible in several locations. The island's most famous volcanic area is near Molyvos, where extensive basaltic lava flows have been found. Sigri, on the western part of the island, is another significant volcanic site, with large volcanic deposits and fossilized lava formations (Georgiadis, 2001).

Obviously, the geological structure and composition of Lesvos played a key role in the geomorphology of the island. The western and northern parts are mostly covered by volcanic rocks and there are the important volcanic centers of the island. This is one more element that contributes to the morphology, with the existence of large calderas (e.g. the caldera of Vatoussa), but also the presence of important dykes (e.g. the dome of Ypsilos) that characteristically elevate the morphology of the island, creating large differences in altitude with rounded mountain ranges without vegetation (Papadopoulos et al., 1991).

On the contrary, the south-east part of Lesvos, i.e. the areas of Mount Olympus, the village of Agiasos up to the town of Plomari, as well as the area around the Gulf of Gera and the peninsula of Amalis, have a mountainous landscape but smoothed by erosion and with significant vegetation cover (Papadopoulos et al., 1991).

However, it is mainly neotectonic activity that has played a decisive role in shaping the morphology of Lesbos, as it is responsible for the large depressions of height and the strong transitions that occur (Apostolopoulos et al., 2009), as Turkey's microplate moves to the SW and pushes the Aegean area, forcing it to make an expansion in the same direction. The wider tectonic field in the NE Aegean region is dominated by the action of large clockwise horizontal displacement faults, on which the region is mainly moving and which, together with normal-moving fault surfaces, form the lacy-looking Asia Minor coastline (Georgiadis, 2001).

At Western Lesbos volcanic rocks dominate, mainly basalts and andesites, along with pyroclastic deposits (tuffs and tephra). Central and Eastern Lesbos are characterized by the occurrence of predominantly sedimentary rocks, including limestone, marl, conglomerates and sandstones. Also, at specific regions, north and at the center of the island, metamorphic rocks are observed, such as schists and gneisses. In the western region of the island, Sigri, fossil-rich sedimentary rocks are observed (Papanikolaou, 2005) and of course geothermal deposits, such as silica, appeared in some regions of the island linked to geothermal springs (Georgiadis, 2001).

The rest of Lesvos, i.e. the northern, western and central parts of the island around the Gulf of Kalloni, is occupied by Neogene volcanic formations (Figure 2) and other mineral deposits covering the pre-alpine and alpine rocks universally. Exceptions are the small outcrops of alpine and pre-alpine rocks in the north-western edge of Lesvos in the areas of Sigri and Gavathas and some isolated micro-outcrops of the same rocks in the area of Eressos. These small occurrences are exposed beneath the surrounding Neogene volcanic formations in the form of island (Thomaidou, 2009).

Lesbos Island's mineral deposits are mostly associated with its volcanic history and hydrothermal activity. Although the island is not renowned for large-scale mining operations, there are localized mineral occurrences worth noting. For example, silica was deposited through hydrothermal processes during and after volcanic activity in the Miocene epoch and was found in hydrothermal veins and as silicified material in the Petrified Forest. The fossilized trees in the Petrified Forest are a result of extensive silicification, making silica the most visually striking mineral deposit on the island. Sulfide minerals, such as Chalcopyrite ($CuFeS_2$) and Galena (PbS) are scattered and often localized to hydrothermal zones near volcanic centers. Clay Minerals, such as Kaolinite and Montmorillonite formed through the hydrothermal alteration of volcanic rocks and found in areas with extensive weathering and hydrothermal influence. Also, there have been occasional reports of minor occurrences of Gold (Au) associated with hydrothermal quartz veins, though in trace amounts, and Copper (Cu) linked to chalcopyrite in volcanic and hydrothermal systems.

The island's land use is characterized by extensive olive cultivation, significant forested areas, agricultural zones, and protected natural habitats (Figure 1). The most esteemed olives are harvested between Plomari and Agiasos from November to December. Lesbos features diverse forested regions, including pine and oak forests, as well as Mediterranean maquis vegetation. The island's varied habitats support a rich array of plant species, contributing to its impressive biodiversity. Beyond olive groves, Lesbos maintains areas dedicated to vineyards, pastures, and other agricultural activities. Livestock farming, particularly sheep and goats, is also prevalent, supporting the production of traditional cheeses.

Also, recognizing its ecological significance, several areas of Lesbos are designated under the Natura 2000 network, aiming to preserve valuable and endangered species and habitats. Notable protected regions include:

- Kalloni Bay: A vital wetland area supporting diverse bird species.

- Gera Bay – Mount Olympus: An area encompassing significant ecological elements.
- Western Lesbian Peninsula: A region with unique ecological features.

These protected areas underscore Lesbos's commitment to conserving its unique natural environment.

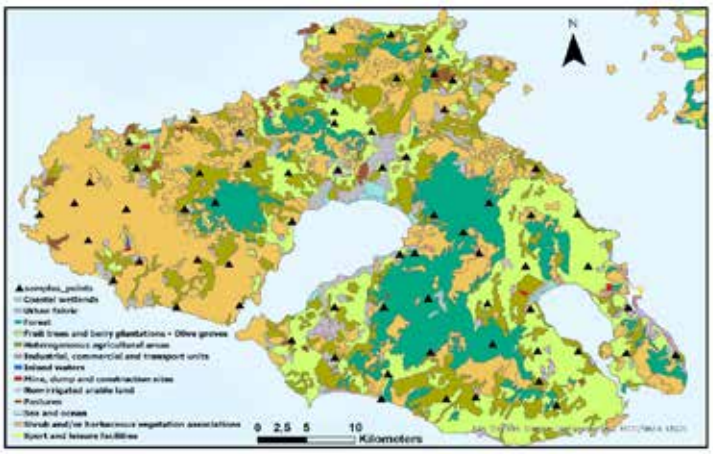

Figure 1: Land use map of the study area in Lesvos Island, showing sampling points on the Corine Land Cover (CLC) map (Heymann et al., 1994).

Sampling and Analysis

A total number of 74 soil samples (0 – 20 cm depth), from 66 locations, were collected from all over the island (Figure 2). The sampling procedure was common for the collection of 66 soil samples, as well as for the 8 randomly selected duplicate samples. All soil samples were collected at distance at least 200 m from main roads and away from tree roots, recent crops and rubble. To collect the soil sample, it was necessary to create a square with a side of 20 cm and digging to a depth of 10-20 cm (Demetriades et al., 2022). Approximately 1.5 - 2 kg of sample was collected, and the duplicate samples were spaced 3 m apart from each other (Demetriades et al., 2022). After daily collection of soil samples, the bags of these samples were left open in order to release the soil moisture. Upon return to the laboratory, they were placed in a drying oven at 40°C for 48 hours to remove the volatile components of the soil.

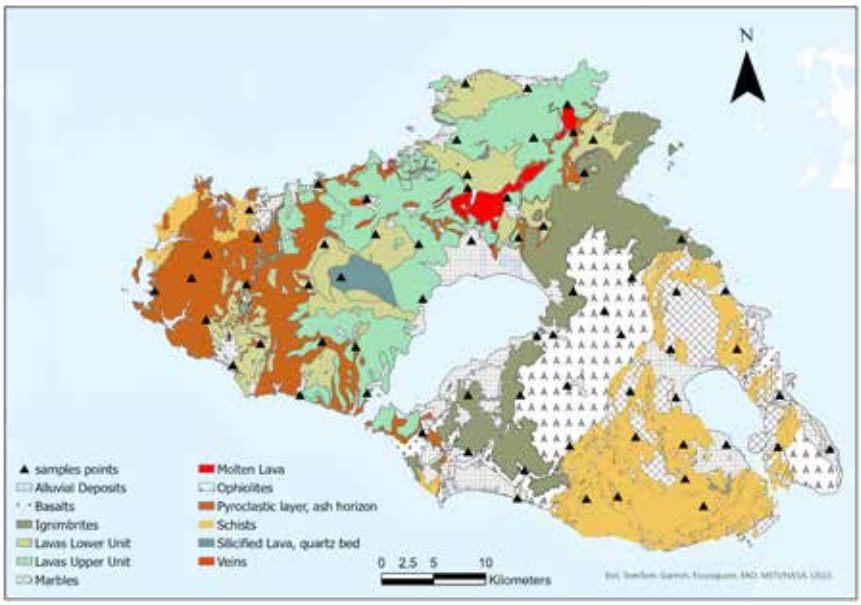

Figure 2: Geology (Hecht, 1972) and sampling points of the soil samples in Lesvos Island.

Sample preparation included disaggregation, during which each soil sample was disaggregated in a porcelain mortar

and sieved through a 2 mm sieve. Between the samples, the mortar and sieve were thoroughly cleaned with air and acetone. A portion of the 2mm fraction of the soil samples was mechanically pulverized in an automatic agate mortar to obtain a particle size of <0.063 mm. Initially, the soil samples were homogenized and divided in four quarters. Two of the diagonal quarters of the soil sample were selected to be pulverized. This step is repeated (3 times in total) to obtain approximately 100 ml of soil sample of less than 200 μm in size. Between the samples, the mortar was also cleaned with 30 ml of cristobalite to avoid cross contamination. The mortar and the tools used (spoon, beakers, brushes) were thoroughly cleaned with air and acetone (where necessary) after the end of the powdering of each sample.

The analysis will be carried out with aqua regia for soils and the samples will be analyzed by ICP-MS for trace elements (e.g. As, Cd, Zn, Pb, Cu, Cr, Ni) and by ICP-OES for major elements (e.g. K, Na, Ca, Fe, Al, Mg).

Results and Discussion

The analytical data will be processed in terms of quality control and the elemental concentrations will be compared with the island's geology.

Acknowledgements

Geochemical analyses and fieldwork were supported by the Natural History of the Lesvos Petrified Forest and the Special Account for Research Grants, NKUA (MSc programme: Earth Sciences and Environment, Department of Geology & Geoenvironment, National and Kapodistrian University of Athens).

References

Apostolopoulos, G., & Dimitriadis, A., 2009. Geology of the Aegean Sea: Contributions to the tectonic evolution of the eastern Mediterranean. Springer.

Darnley, A.G., 1990. International geochemical mapping: a new global project. Journal Geochemical Exploration 39. 1–13.

Demetriades, A., Johnson, C.C., Smith, D.B., Ladenberger, A., Adánez Sanjuan, P., Argyraki, A., Stouraiti, C., Patrice de Caritat, Knights K.V., Rincón G.P., Simubali, G.N., 2022. International Union of Geological Sciences Manual of Standard Methods for Establishing the Global Geochemical Reference Network. The International Union of Geological Sciences (IUGS).

Georgiadis, S., 2001. Volcanic and Geothermal Features of Lesbos Island. Hellenic Geological Society, Athens.

Hecht, J., 1972. Geological map "Plomari-Mytilini" sheet, scale 1:50.000. I.G.M.E.

Heymann, Y., Steenmans, Ch, Croissille, G., Bossard, M., 1994. Corine Land Cover. Technical Guide, EUR12585. Office for Official Publications of the European Communities, Luxembourg.

Katsikatsos, G., Migiros, G., Triantaphyllis, M. and Mettos, A., 1986. Geological structure of the internal Hellenides (E. Thessaly - SW. Macedonia, Euboea - Attica - Northern Cyclades Islands and Lesvos). I.G.M.E. Geological and Geophysical Research. Special Issue, 191-212.

Kirkwood, C., Cave, M., Beamish, D., Grebby, S., Ferreira, A., 2016. A machine learning approach to geochemical mapping. Journal of Geochemical Exploration 167. 49–61.

Papadopoulos, G., & Papanikolaou, D. (1991). The Geology of the Island of Lesbos. Bulletin of the Geological Society of Greece, 25(2), 287–297.

Papanikolaou, D., 2005. Pleistocene Fossils and Stratigraphy of Lesbos Island. Journal of the Geological Society, 162(2), 253-265. .

Salminen, R., Tarvainen, T., Demetriades, A., Duris, M., Fordyce, F., Gregorauskiene, V., Kahelin, H., Kivisilla, J., Klaver, G., Klein, H., 1998. FOREGS Geochemical Mapping Field Manual.

Thomaidou, E., 2009. The geological structure of the island of Lesvos.

17th INTERNATIONAL CONGRESS of the Geological Society of Greece

BULLETIN OF THE GEOLOGICAL SOCIETY OF GREECE, SP. PUBL.

EXTENDED ABSTRACT 273

Pluto is lost!

Rozi A.[1] , Papadimitriou Z.[2]

(1) 3rd Junior High-school of Glyfada , Athens, Greece, rosi_corina@yahoo.gr (2) 3rd Junior High-school of Glyfada , Athens, Greece

Abstract

This paper examines the integration of drama and science as an innovative approach to teaching scientific concepts, focusing on the educational theatrical production *Pluto is Lost!*, created and performed by students at the 3rd Junior High School of Glyfada, Athens, Greece. The initiative aimed to introduce students to the Solar System and environmental science—subjects often overlooked in the Greek compulsory school curriculum—while fostering creativity, teamwork, and critical thinking. The project was implemented within the framework of the "Learning Science Through Theatre" program, which promotes interdisciplinary learning by merging science education with artistic expression.

Through a project-based learning model, students engaged in five phases: defining goals, designing, executing tasks, presenting results, and evaluating outcomes. They humanized astronomical and environmental concepts by creating a storyline where celestial bodies and Earth's ecosystems were personified, and the dynamics of the Solar System and environmental sustainability were explored through imaginative narratives. The embodied learning process enabled students to express scientific ideas through gestures, movements, and emotional engagement, enhancing comprehension and retention.

The production also addressed contemporary challenges, such as climate change, environmental conservation, and societal issues, connecting science to real-world contexts. Dissemination efforts included performances in collaboration with local institutions and recognition through multiple awards, including the "Learning Science Through Theatre" award for best theatrical and musical performance, the EPI2 award from the Athens Science Festival, and presentations at COSPAR 2022 (Athens, Greece) with the latter receiving a full grant.

The study concludes that combining science and theatre effectively engages students, promotes scientific literacy, and encourages creative exploration of complex topics. This initiative highlights the potential of arts-based methods in science education, offering a replicable model for fostering interdisciplinary learning and inspiring passion for STEAM fields.

Figure 1. Asteroids Dancing

Acknowledgements

The authors would like to express their gratitude to Mr. Menelaos Sotiriou, Dr. Zacharoula Smyrnaiou, and Science View for their invaluable support and guidance throughout this project.

References

Aikenhead G. (2006) *Science education for everyday life: Evidence-based practice* (New York and London, Teachers' College Press).

Alexopoulos I., Sotiriou S., Smyrnaiou Z., Sotiriou M., Bogner F (2016) *Developing an Engaging Science Classroom* Available online at https://www.researchgate.net/publication/312176004_Developing_an_Engaging_Science_Classroom (accessed 11 July

2022).

Braund M. (2010) *Talk in science: Forgotten corner of the constructivist classroom?,* in: D. Mogari, A. Mji, F. Mundalamo, U. Ogbonnaya (Eds) *Proceedings of the ISTE international conference on mathematics, science and technology education: towards effective teaching and meaningful learning in mathematics, science and technology education*. Mopani Camp, Kruger National Park, South Africa, 18–21 October 2010 (Pretoria, University of South Africa (UNISA) Press), 287–301.

Braund, M. (2013) *Drama and learning science: An empty space?* Available online at https://www.researchgate.net/publication/260410840_Drama_and_learning_science_An_empty_space (accessed 11 July 2022)

Brinder, K., Anuj, S.(2004) *S & T Communication through pupperty – A case study (India)* Available online at https://www.academia.edu/48647908/S_and_T_Communication_Through_Puppetry_a_Case_Study_India_(accessed 11 July 2022)

Musacchio, G, Lanza, T, D'Addezio(2015) *An Experience of Science Theatre to Introduce Earth Interior and Natural Hazards to Children* Available online at https://www.ccsenet.org/journal/index.php/jel/article/view/43677 (accessed 11 July 2022)

Ødegaard, M. (2003) Dramatic science. A critical review of drama in science education, *Studies inScience Education*, 39(1), 75–101.

Smyrnaiou, Z., Georgakopoulou, E., Sotiriou, M., Sotiriou, S. (2018). Constructing Scientific Notions: Students' Conceptual Change through a Re-sponsible Research and Innovation Initiative. Co-Create ! - Co-creation of curricula, tools and educational scenarios for building softcompetences for personal development and employability (Multi-conference on Responsible Research and Innovation in Science, Innovation and Society m-rrisis 2018). Tartu, Estonia, 17-19 Septembre

Smyrnaiou Z., Georgakopoulou E., Sotiriou M., Sotiriou S. (2017). The Learning Science Through Theatre initiative in the context of Responsible Research and Innovation. Proceedings of The 10th International Multi-Conference on Society, Cybernetics and Informatics: IMSCI 2017

Toonders, W., Verhoeff, R.P., Zwart, H.A.E.(2016) *Performing the future: on the use of drama in philosophy courses for science students* Available online at https://repository.ubn.ru.nl/handle/2066/161707 (accessed 11 July 2022)

17th INTERNATIONAL CONGRESS of the Geological Society of Greece

BULLETIN OF THE GEOLOGICAL SOCIETY OF GREECE, SP. PUBL.

EXTENDED ABSTRACT 274

Rheological behaviour along the Hellenic Subduction Zone and the Adria-Eurasia continental collision

Russo D.[1,2], Caputo R.[1,2]

(1) Department of Physiscs and Earth Sciences, University of Ferrara, Ferrara, Italy, davide.russo@unife.it (2) Centro Interuniversitario per La Sismotettonica Tridimensionale, CRUST-UR Ferrara, Italy

Based on the approach and workflow of the recently proposed 3D thermo-rheological model of the broader Aegean Region (Maggini et al., 2023), the present work focuses on the rheological properties corresponding to both the slab interface of the Hellenic Subduction Zone (HSZ) and the basal thrust of the Adriatic-Eurasian Continental Collision Zone (CCZ). For the purpose of this note, the geometry of the interfaces (Figure 1) was mainly reconstructed on the basis of the results of Bocchini et al. (2018), especially for the HSZ sector, and Halpaap et al. (2018) for the continental collision zone. For the Montenegro sector of the CCZ, the results of Schmitz et al. (2020) were also considered.

The aforementioned 3D model is based on a simplified approach: two main rheological behaviours have been assumed to occur at depth within the study area, namely the brittle and the ductile, described by the constitutive equations for frictional sliding (e.g. Sibson, 1977; Scholz, 1988; Ranalli, 1995) and power-law creep (e.g. Brace and Kohlstedt, 1980; Sibson, 1983; Ranalli, 1995) deformational mechanisms, respectively.

The calculations required to reproduce the thermo-rheological features of the considered area have been performed through purposely written MATLAB scripts (Maggini, 2020; Maggini and Caputo, 2020a; 2020b; 2021). The first output obtained is a number of 1D rheological profiles or “strength envelopes” (e.g. Sibson, 1977; Goetze and Evans, 1979; Brace and Kohlstedt, 1980; Scholz, 1988), which reconstruct the vertical rheological behaviour and the geothermal gradient of the investigated rock volumes in correspondence of the nodes of a regular horizontal grid (115 x 115 pixels). Among the input parameters, a considerable influence was attributed to the heat flow; derived merging and smoothing, applying a Gaussian filter in order to remove outliers, local-scale (e.g. Fytikas and Kolios, 1979; Taktikos, 2001) and regional scale (e.g. Hurter and Haenel, 2002; Cloetingh et al., 2010) measurements. The adopted strain rate was based on weighted and averaged available maps mainly derived from GPS measurements (e.g. Kahle et al., 1998; Hollenstein et al., 2008; Floyd et al., 2010; Kreemer et al., 2014; Chousianitis et al., 2015; England et al., 2016). Considering the results of Byerlee (1968) a standard value (0.6) was attributed to the internal friction coefficient; however, in correspondence of major the seismogenic sources (from GreDaSS 2.0; Caputo and Pavlides, 2013) this value was reduced to 0.5. This choice was motivated by the presence of well-defined shear zones in these crustal volumes, characterized by wearing processes that cause a significant reduction in the friction coefficient values (e.g. Viti et al., 2018; Collettini et al., 2019). For the frictional sliding equation, the Skempton coefficient (e.g. Skempton, 1954; Wang, 2000) was taken equal to 0.4, basically assuming, as a first approximation, a hydrostatic fluid pressure (e.g. Ranalli and Murphy, 1987; Ranalli, 1995). Both the upper and lower plates were modelled considering four vertical litho-mechanical layers (i.e. sedimentary cover, upper crust, lower crust and upper mantle), each one associated to a representative lithology and the related thermo-rheological parameters given by the considered constitutive equations (see Maggini, 2020 for a more detailed description and references).

The thickness of the considered layers was reconstructed from the depth of the top of the crystalline basement, the Moho discontinuity and the Lithosphere-Asthenosphere Boundary (LAB). The first two were strongly influenced by the work of Makris et al. (2013), while the LAB from the work of Sodoudi et al. (2006).

The selected pixel size for the 3D model is 10 x 10 km with vertical steps each 100 m. All the input parameters, have been accordingly averaged using standard GIS tools. In order to provide the 3D cover for the Aegean Region, the 1D logs were then interpolated to reconstruct a pseudo 3D model.

Following the general results of Maggini et al. (2023), and for the purpose of the present note, we examined a 500 m thick volume on each side of the modelled plate boundary (Figure 1), in both the continental-continental and oceanic-continental lithosphere domains, north and south of the Cephalonia Transform Fault Zone, respectively. In particular, we analysed the rheological behaviour of the lowermost part of the upper plate (i.e. Eurasian or Aegean) and the uppermost part of the lower plate (i.e. African or Nubian in the oceanic subduction zone and Adriatic block in the continental collision zone). Although in principle four different combinations, or “rheological contrasts”, of brittle *versus* ductile and upper *versus* lower plate could occur, the results emphasise the predominance of three conditions, each one uniformly and regularly covering wide sectors of the investigated interface zones (Figure 2).

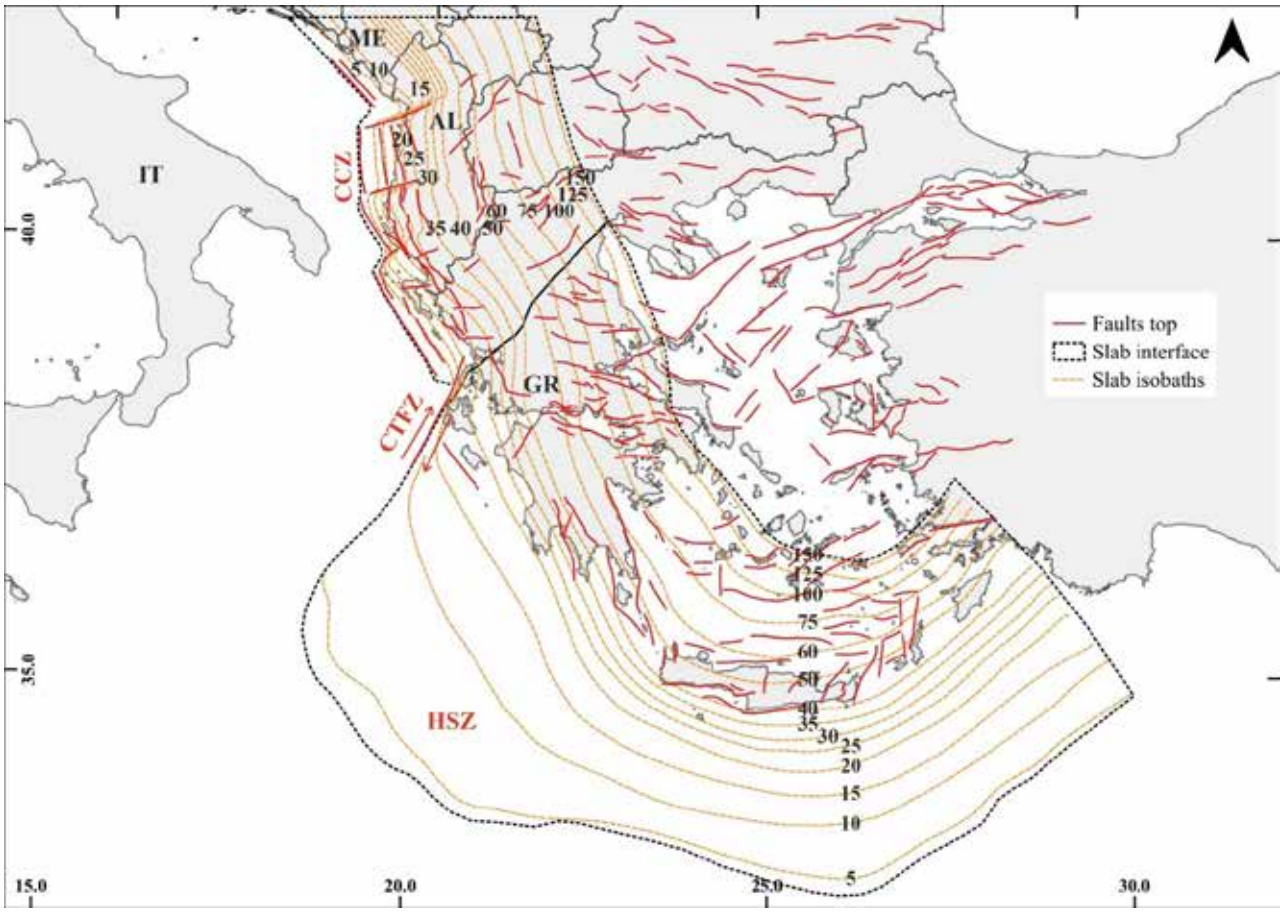

Figure 1. Modelled geometries of the Hellenic Subduction Zone (HSZ) and the Adria-Eurasia Continental Collision Zone (CCZ) based on Bocchini et al. (2018) and Halpaap et al. (2018). Black dotted polygons represent the projection of the slab interface; black solid line is the separation between continental collision and oceanic subduction domains. CTFZ = Cephalonia Transform Fault Zone. Slab isobaths expressed in km (orange dashed). Red solid represents the seismogenic sources top lines from GreDaSS 3.0 (Caputo et al., 2025; submitted to this congress).

Based on these results, five different 'rheological zones' were reconstructed in the continental collision area and in the vicinity of the basal thrust. The first emphasises a predominant brittle behaviour in both the Adria microplate and the European plate (Figure 2, blue) and extends down to a depth of ca. 25 km, except in the Montenegro sector where its limit is shallower at ca. 15 km. The second modelled zone, developing down to a depth of ca. 30 km (25 km in Montenegro), exhibits brittle behaviour in the upper plate and ductile behaviour in the lower one (Figure 2, green). The same brittle-on-ductile conditions have been recognised between 40 and 75 km-depth, but geometrically separated by an interposed sector, between 30 and 40 km, characterised by a ductile-on-ductile behaviour (Figure 2, magenta). Finally, at depths greater than 75 km, the conditions in the investigated area show again a ductile-on-ductile setting.

As concerns the HSZ, only three major sectors have been recognised along the interface; the outermost and shallower one (Figure 2), roughly at the base of the sedimentary accretionary wedge, shows a predominant brittle behaviour both above and below the slab interface. This condition persists down to a depth of ca. 50 km, although this limit is not homogeneous, being at ca. 45 km in the western sector of the HSZ, at ca. 50 km in the central sector and at ca. 40 km on the eastern side (Figure 2). The second zone, modelled continuously to a depth of about 100 km, is characterised by a predominance of brittle behaviour at the base of the overlying plate facing a ductile behaviour at the top of the lower plate (Figure 2, green). Deeper than 100 km, the interpolate shear zone shows predominant ductile properties on both sides of the interface (Figure 2, magenta). Finally, in a small sector of the HSZ at a depth of 35 and 40 km in correspondence of Aetolo-Akarnania and northern Peloponnesus, the results of the rheological model show that the interface is characterised by predominantly ductile behaviour in the upper plate and brittle characteristics in the lower plate (Figure 2, yellow).

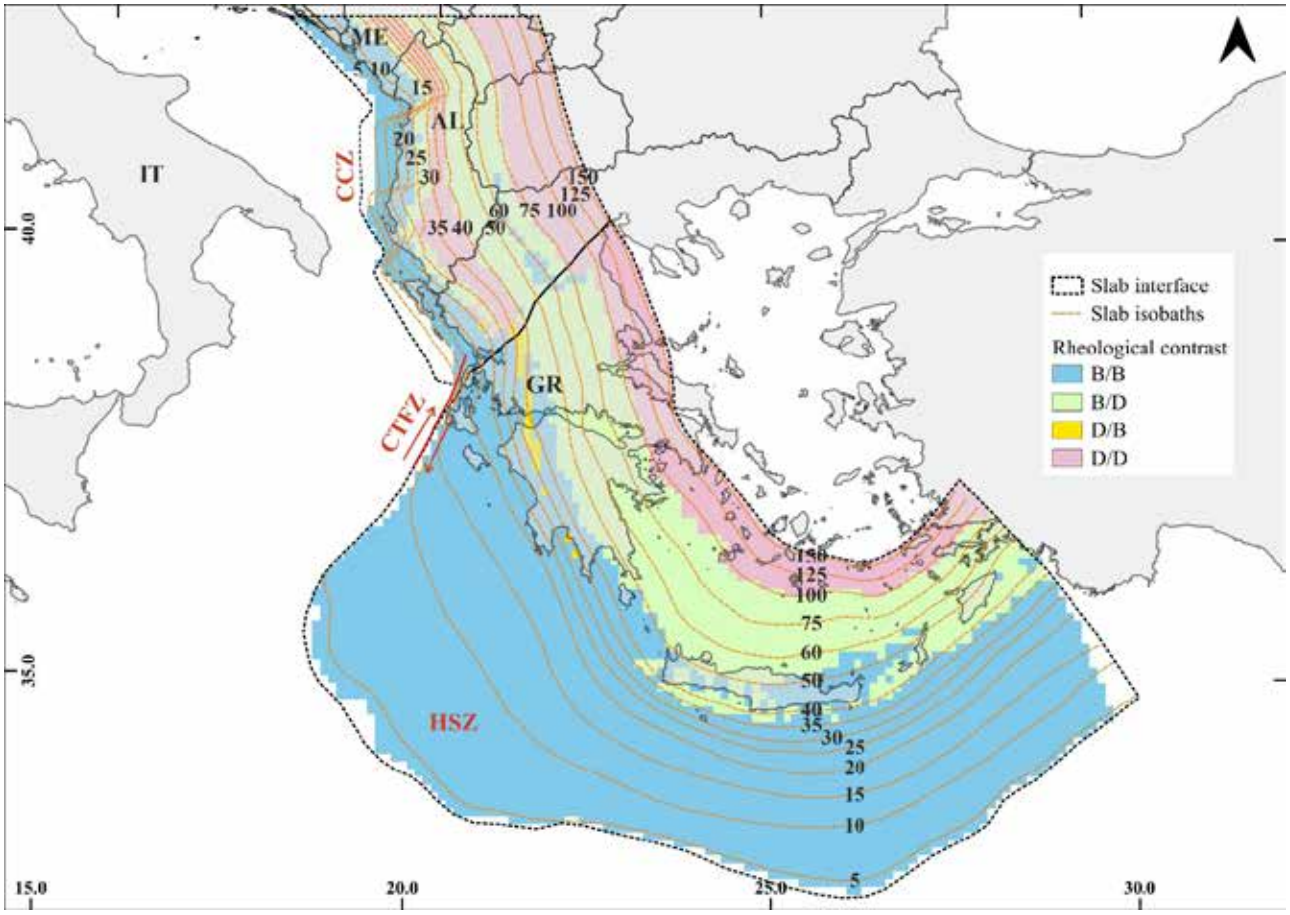

Figure 2. Same as Figure 1; coloured areas represent the recognised rheological behaviours (B/B = brittle/brittle; B/D = brittle/ductile; D/B = ductile/brittle; D/D = ductile/ductile) in correspondence of the slab interface (orange dashed).

Based on these results and considering both the overall geometry of the interplate surface and the associated seismicity (Bocchini et al. 2018), as a preliminary major conclusion the possible maximum down-dip extension of the seismogenic portion (i.e. the Wadati-Benioff zone) along the Hellenic subduction could be constrained at ca. 100 km-depth. Indeed, at greater depths, where at least 1 km-thick rock volume embedding the interplate shear zone has been modelled to behave ductilely, seismogenesis is not expected to occur. Accordingly, deeper recorded seismicity should likely occur within the subducting slab and not along the plate interface. These latter considerations are supported by literature; in Meier et al. (2004), for example, the relocated interplate seismicity plotted on the reconstructed profile across the Aegean generally does not exceed 60 km-depth, with only a few events between 80 km and 100 km. Halpaap et al. (2018), who tomographically imaged the Hellenic Wadati-Benioff zone, identified earthquake clusters characterised by inter-slab seismicity between 40 km and 60 km, while in Bocchini et al. (2018), the interface seismicity is imaged at depths systematically shallower than 100 km.
As a final comment, it should be noted that geometrical models of the interface surface slightly differing from the selected one used in the performed exercise would not likely impact on the overall obtained results especially in terms of the distribution of the contrast in terms of rheological contrast between upper and lower plate.

References

Bocchini, G. M., Brüstle, A., Becker, D., Meier, T., van Keken, P. E., Ruscic, M., Papadopoulos, G. A., Rische, M., Friederich, W., 2018. Tearing, segmentation, and backstepping of subduction in the Aegean: New insights from seismicity. Tectonophysics, 734–735, 96–118.

Brace, W. F., Kohlstedt, D. L., 1980. Limits on lithospheric stress imposed by laboratory experiments. Journal of Geophysical Research: Solid Earth, 85(B11), 6248–6252.

Byerlee, J. D, 1968. Brittle-ductile transition in rocks. Journal of Geophysical Research (1896-1977), 73(14), 4741–4750.

Caputo, R., Pavlides, S., 2013. The Greek Database of Seismogenic Sources (GreDaSS), version 2.0. 0: A compilation of potential

seismogenic sources (Mw> 5.5) in the Aegean Region.

Caputo, R., Koukouvelas, I., Papathanassiou, G., Russo, D., Taftsoglou, M., Tarabusi, G., Valkaniotis, S., 2025. The Greek Database of Seismogenic Sources (GreDaSS) version 3.0. A compilation of potential seismogenic sources (Mw> 5.5) in the Aegean Region. 17th International Congress of the Geological Society of Greece, Mytilene, Greece, (this volume).

Cloetingh, S., van Wees, J. D., Ziegler, P. A., Lenkey, L., Beekman, F., Tesauro, M., Förster, A., Norden, B., Kaban, M., Hardebol, N., Bonté, D., Genter, A., Guillou-Frottier, L., Ter Voorde, M., Sokoutis, D., Willingshofer, E., Cornu, T., Worum, G., 2010. Lithosphere tectonics and thermo-mechanical properties: An integrated modelling approach for Enhanced Geothermal Systems exploration in Europe. Earth-Science Reviews, 102(3), 159–206.

Collettini, C., Tesei, T., Scuderi, M. M., Carpenter, B. M., Viti, C., 2019. Beyond Byerlee friction, weak faults and implications for slip behavior. Earth and Planetary Science Letters, 519, 245–263.

Floyd, M. A., Billiris, H., Paradissis, D., Veis, G., Avallone, A., Briole, P., McClusky, S., Nocquet, J.-M., Palamartchouk, K., Parsons, B., England, P. C., 2010. A new velocity field for Greece: Implications for the kinematics and dynamics of the Aegean. Journal of Geophysical Research: Solid Earth, 115(B10).

Fytikas, M. D., Kolios, N. P., 1979. Preliminary Heat Flow Map of Greece, in V. Čermák & L. Rybach (Eds.), Terrestrial Heat Flow in Europe, 197–205. Springer Berlin Heidelberg.

Goetze, C., Evans, B., 1979. Stress and temperature in the bending lithosphere as constrained by experimental rock mechanics. Geophysical Journal International, 59(3), 463–478.

Halpaap, F., Rondenay, S., Ottemöller, L., 2018. Seismicity, Deformation, and Metamorphism in the Western Hellenic Subduction Zone: New Constraints From Tomography. Journal of Geophysical Research: Solid Earth, 123(4), 3000–3026.

Hollenstein, Ch., Müller, M. D., Geiger, A., Kahle, H.-G., 2008. Crustal motion and deformation in Greece from a decade of GPS measurements, 1993–2003. Tectonophysics, 449(1), 17–40.

Hurter, S., Haenel, R. (Eds.), 2002. *Atlas of geothermal resources in Europe*. European Commission Office for Official Publications of the European Communities.

Kahle, H.-G., Cocard, M., Peter, Y., Geiger, A., Reilinger, R., Barka, A., Veis, G., 2000. GPS-derived strain rate field within the boundary zones of the Eurasian, African, and Arabian Plates. Journal of Geophysical Research: Solid Earth, 105(B10), 23353–23370.

Maggini, M., 2020. 3D rheological modelling in the Aegean Region and its importance for the seismotectonics of the area. PhD Thesis, University of Ferrara, Italy, 268 pp.

Maggini, M., Caputo, R., 2020a. Rheological behaviour in continental and oceanic subduction: Inferences for the seismotectonics of the Aegean Region. Turkish Journal of Earth Sciences, 29(3), 381–405.

Maggini, M., Caputo, R., 2020b. Sensitivity analysis for crustal rheological profiles: Examples from the Aegean region. Annals of Geophysics, 63(3), GT334–GT334.

Maggini, M., Caputo, R., 2021. Seismological data versus rheological modelling: Comparisons across the Aegean Region for improving the seismic hazard assessment. Journal of Structural Geology, 145, 104312.

Maggini, M., Russo, D., Caputo, R., 2023. A 3D rheological model for the Aegean Region: Mechanical layering and seismotectonic implications. Journal of Structural Geology, 175, 104956.

Makris, J., Papoulia, J., Yegorova, T., 2013. A 3-D density model of Greece constrained by gravity and seismic data. Geophysical Journal International, 194(1), 1–17.

Meier, T., Dietrich, K., Stöckhert, B., Harjes, H.-P., 2004. One-dimensional models of shear wave velocity for the eastern Mediterranean obtained from the inversion of Rayleigh wave phase velocities and tectonic implications. Geophysical Journal International, 156(1), 45–58.

Ranalli, G., 1995. Rheology of the Earth. Springer Science & Business Media.

Ranalli, G., Murphy, D. C., 1987. Rheological stratification of the lithosphere. Tectonophysics, 132(4), 281–295.

Scholz, C. H., 1988. The brittle-plastic transition and the depth of seismic faulting. Geologische Rundschau, 77(1), 319–328.

Sibson, R. H., 1977. Fault rocks and fault mechanisms. Journal of the Geological Society, 133(3), 191–213.

Sibson, R. H., 1983. Continental fault structure and the shallow earthquake source. Journal of the Geological Society, 140(5), 741–767.

Sodoudi, F., Kind, R., Hatzfeld, D., Priestley, K., Hanka, W., Wylegalla, K., Stavrakakis, G., Vafidis, A., Harjes, H.-P., Bohnhoff, M., 2006. Lithospheric structure of the Aegean obtained from P and S receiver functions. Journal of Geophysical Research: Solid Earth, 111(B12), 1-23.

Taktikos, S., 2001. Heat flow–Underground temperatures of Greece. Institute of Geology and Mineral Exploration.

Viti, C., Collettini, C., Tesei, T., Tarling, M. S., Smith, S. A. F. , 2018. Deformation Processes, Textural Evolution and Weakening in Retrograde Serpentinites. Minerals, 8(6), 241, 1-20.

Wang, H., 2000. Theory of linear poroelasticity with applications to geomechanics and hydrogeology (Vol. 2). Princeton university press.

17th INTERNATIONAL CONGRESS of the Geological Society of Greece

BULLETIN OF THE GEOLOGICAL SOCIETY OF GREECE, SP. PUBL.

EXTENDED ABSTRACT 275

Marine geological-geophysical data may contribute to the understanding of the early 2025 seismic activity in the Santorini-Amorgos Zone

Sakellariou D.[1], Morfis I.[1], Livanos I.[1], Varesis A.[1], Petrakis S.[1], Kapsimalis V.[1]
(1) Institute of Oceanography, Hellenic Centre for Marine Research, Anavyssos, Greece, sakell@hcmr.gr

Introduction

The late 2024 earthquake activity below the Caldera of Santorini and the early 2025 seismic crisis between Santorini and Amorgos, in particular below Anydros Ridge, renewed the interest on the tectonic / volcanic / magmatic structure and the active geodynamic processes that control the evolution of the area. Here below we re-evaluate existing data along with new marine geological-geophysical data obtained in February 2025 with the aim to contribute to the understanding of the processes that led to the recent earthquake activity and their relationship with the long-term deformation of Santorini-Amorgos Zone.

The Santorini-Amorgos Zone is a complex morphological feature (Fig. 1) composed of seven NE-SW trending, spindle-shaped or elongated basins: Anydros, Anafi, Amorgos South, Amorgos North, Kinairos, Astypalea North and Astypalea South Basins. Two uplifted, shallow ridges, Anydros and Astypalea, separate the aforementioned basins. Two more, smaller ridges, Akrotiri and Anafi, occur south and southwest of Santorini (Tsampouraki-Kraounaki et al. (2021). Akrotiri Ridge marks the SW-ward prolongation of the southern part of Thera where the metamorphic alpine basement outcrops. Anafi Ridge extends WSW of Anafi Island.

Mascle & Martin (1990) proposed NE-SW strike-slip faulting in the area and Papadopoulos & Pavlides (1992) characterized Amorgos Fault as oblique-normal with significant right-lateral component. Piper & Perissoratis (2003) and Piper et al (2007) have suggested that the NE-SW faulting, the narrow basement ridges and the basin inversions in the area are evidence of strike-slip regime. Sakellariou et al. (2010) proposed that both Thera and Kolumbo volcanic centers occur within the NE-SW-trending Anydros graben, which constitutes a negative flower structure related to a 40 km long, possibly dextral, strike-slip zone, the Kameni-Kolumbo strike-slip, which can be extended SW-wards to the Christiana volcanic island. Sakellariou & Tsampouraki-Kraounaki (2019) and Tsampouraki-Kraounaki et al. (2021) suggest that the NE-SW-trending Santorini-Amorgos Shear Zone undergoes dextral transtensional deformation accommodated by NE-SW strike-slip to oblique faults and E-W normal step-over faults (Fig. 2). This is compatible with the microseismicity data observed by Bohnhoff et al. (2006), the results of Papadimitriou et al. (2015) on the seismic activity in the caldera of Santorini and the dextral transtensional movement of 4.5 mm yr-1 between Amorgos and Astypalea islands observed by Briole et al. (2021). Nomikou et al. (2016, 2018), Hooft et al. (2017) and others propose normal NE-SW trending faulting as the main deformation mechanism that forms the geomorphological features of the area with secondary, steep faults probably indicating strike-slip component. Finally, Tzanis et al (2020) studied the kinematic regime of the Santorini area by using gravity, magnetotelluric and DGPS data and suggested that Santorini-Amorgos area is characterized by NW-SE dextral strike slip faults and NE-SW normal to sinistral faults.

Data

Swath bathymetry, airgun seismic profiles, deep-towed side scan and chirp subbottom profiles and sediment cores have been collected during various cruises of HCMR's research vessel AEGAEO in the broader area around Santorini, between Santorini, Anafi, Astypalea, Amorgos, Kinairos and Kos (Fig. 1). New swath bathymetry data and high resolution sparker subbottom profiles were collected during the recent cruise of R/V AEGAEO (12-17 Febr. 2025) in the area around Anydros Island (Fig. 3) and between Santorini and Kolumbo.

Results & Discussion

Seismic profiles studied and interpreted by Tsampouraki-Krounaki et al. (2021) show that the northwestern steep flank of Akrotiri Ridge is controlled by the NE-SW striking, NW-dipping Akrotiri Fault (AF) (Fig. 2). The possible prolongation of AF to the NE coincides with the southeastern wall of Santorini Caldera as well as with the boundary between the alpine basement (that outcrops in Athinios and Profitis Ilias Mt.) to the South and the volcanic formations to the North. The Profile 1 of Fig. 6 shows a schematic NW-SE cross section across the Caldera with the NW-dipping inferred prolongation of AF. The recent earthquake activity in the Caldera occurred at shallow depths below the Nea and Palaia Kameni Islands and Fira, along the NE-SW striking "Kameni Line". "Kameni Line" strikes parallel to the prolongation of AF. It is proposed here that the "Kameni Line" represents the linear distribution of earthquake epicenters that, at depth, occur on the NW-dipping, steep Akrotiri Fault. If so, Akrotiri Fault may be considered as the southern boundary of the volcanic activity that has shaped Santorini throughout Quaternary.

Geodetic data obtained during the seismic activity showed fast movement of the northern part of Santorini toward

NE (unpublished data of EPPO Seismic Hazard Committee, M. Foumelis courtesy). That motion occurred roughly in the first half of February 2025, it affected mainly the northern part of Thera and the island of Therasia while the southeastern part of Thera remained almost unaffected. In other words, the NE-ward movement affected mostly the volcanic part of Santorini on the hanging-wall of Akrotiri Fault, while the foot-wall of the fault (the basement) remained more or less stable.

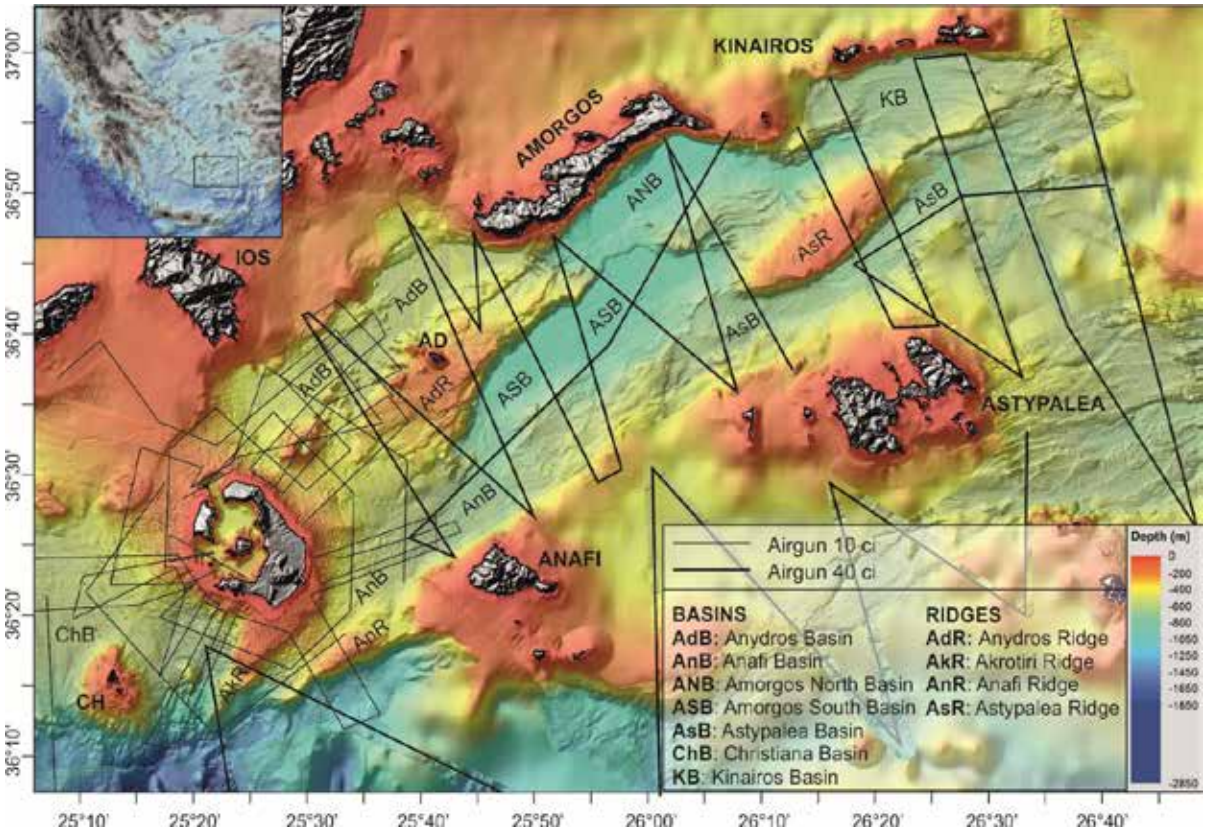

Figure 1. Shaded relief map of the Santorini-Amorgos Zone modified after Tsampouraki-Kraounaki et al (2021).

Anydros Ridge is a shallow, positive, SW-NE trending morphological feature that has been uplifted between the 400 m deep Anydros Basin to the NW from the 700 m Amorgos South Basin to the SE (Fig. 2, 3). It displays a rather complicate shape controlled by SW-NE and E-W striking faults. Morphological and seismic/subbottom profiling data indicate a mean, gentle, NW-ward tilting of Anydros Ridge seafloor by 0.5°-1.5° (Fig. 4, 5). Astypalea Ridge along with Amorgos and the Kinairos-Levitha Islands display similar, NW- / N-ward tilting, with steep, high SW- / S-ward facing slopes and gently sloping northwestern / northern flanks (Fig. 2, 3). Several faults crosscut the top of Anydros Ridge, they have led to local subsidence and the creation of small depressions filled with sedimentary deposits with up to 80 msecs thickness on top of the alpine basement of the ridge (Fig. 4, 5). Two geometrical unconformities U1 and U2 within the seismic stratigraphy of the sedimented depressions display gentle NW-ward dip direction, following the tilting of the ridge.
Geodetic data obtained during the seismic activity showed significant NW-ward tilting of Anydros Island (unpublished data of EPPO Seismic Hazard Committee, M. Foumelis courtesy) roughly in the first half of February 2025. The sense of the tilting of Anydros Island coincides with the tilting of the entire Anydros Ridge as described above.
The mostly linear and steep SE slope of the ridge has developed along the SE-dipping Anydros Ridge South Fault Zone (AdRSFZ). The NW limit of the ridge is rather irregular and less well defined and is largely controlled by multiple segments of the NW-dipping Anydros Ridge North Fault Zone (AdRNFZ) (Fig. 2, 3).
The sparker subbottom profile of Fig. 4 provides a high-resolution imaging of the shallow sub-seafloor structure across Anydros Ridge and at short distance southwest of Anydros Island. Three NW-dipping fault splays of AdRNFZ offset the seafloor (Fig. 4B). The northern one displays minimum cumulative offset of 50 msecs, extends further to the NE and outcrops on Anydros island (Fig. 3). On site measurements of the geometric and kinematic data on Anydros (unpublished data of EPPO Seismic Hazard Committee, D. Galanakis courtesy) show a steep, NW-dipping oblique normal fault with significant dextral horizontal component.

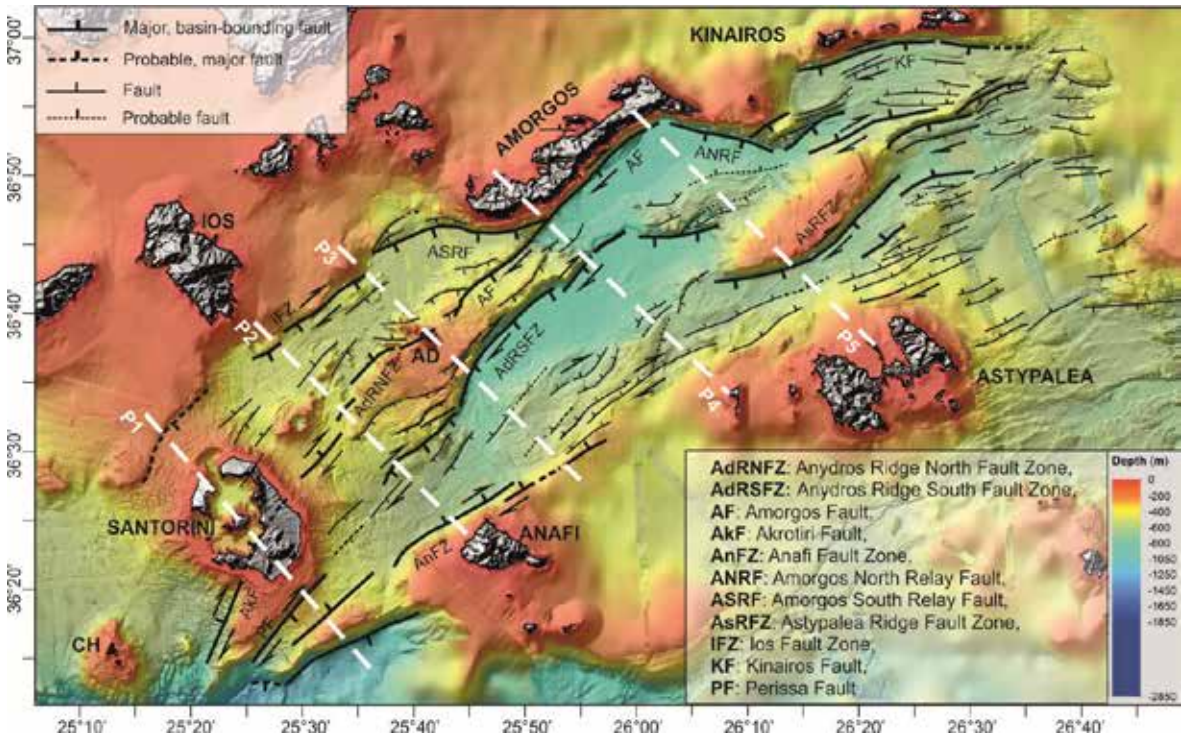

Figure 2. Shaded relief map and fault network of the Santorini-Amorgos Zone modified after Tsampouraki-Kraounaki et al (2021). White dashed lines P1 – P5 indicate the location of the geological profiles shown on Figure 6.

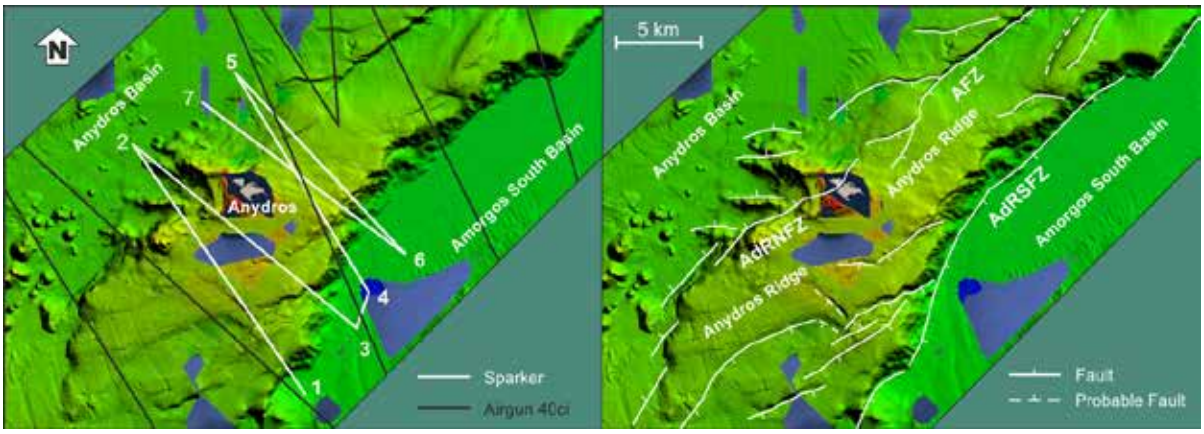

Figure 3. Shaded relief map, airgun and sparker profiles (left map) and fault network (right map) of Anydros Ridge.

The trace of the NW-dipping AdRNFZ terminates at a short distance north-northeast of Anydros Island. Further to the NE the structure of Anydros Ridge is controlled by the SE dipping Amorgos Fault Zone (AFZ). The sparker subbottom profile of Fig. 5 provides a high-resolution imaging of the shallow sub-seafloor structure across Anydros Ridge and at a few kilometers distance northeast of Anydros Island. Fig. 5B and C shows the SE-dipping fault splays of AFZ that offset the seafloor and unconformity U2 by up to 50 msecs or less.

The northeastern termination of the NW-dipping AdRNFZ and the southwestern termination of the SE-dipping AFZ are only a couple of kilometers apart (Fig. 3). The reversal of the tectonic polarity between them is not well understood.

Re-exploitation of the pre-2025 data along with the analysis of the new swath bathymetry and seismic profiling data provide insights into the geological and tectonic structure of the Santorini-Amorgos Zone. The five profiles shown on Fig. 6 aim to provide a schematic visualization of the here proposed structure of the upper crust at up to 10 km depth. Under the light of the new knowledge and information derived from the multiple datasets obtained during the recent seismic activity, they may be used as a first draft scheme that may certainly need corrections or improvements and can contribute to the understanding of the longterm processes that controlled the evolution of Santorini-Amorgos Zone and the processes that led to the 2025 seismic activity.

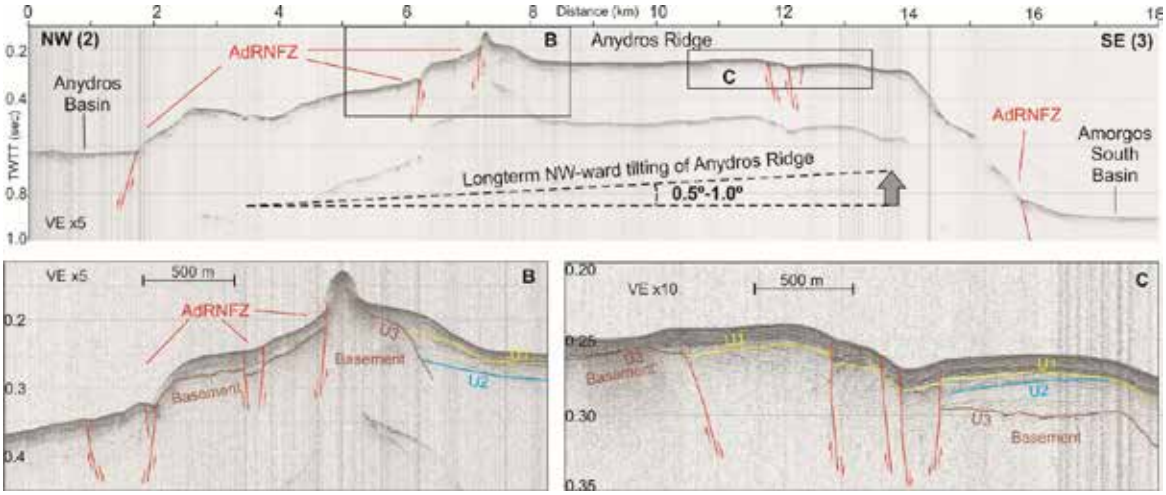

Figure 4. Sparker Subbottom Profile 2-3 across Anydros Ridge. See Figure 3 for location.

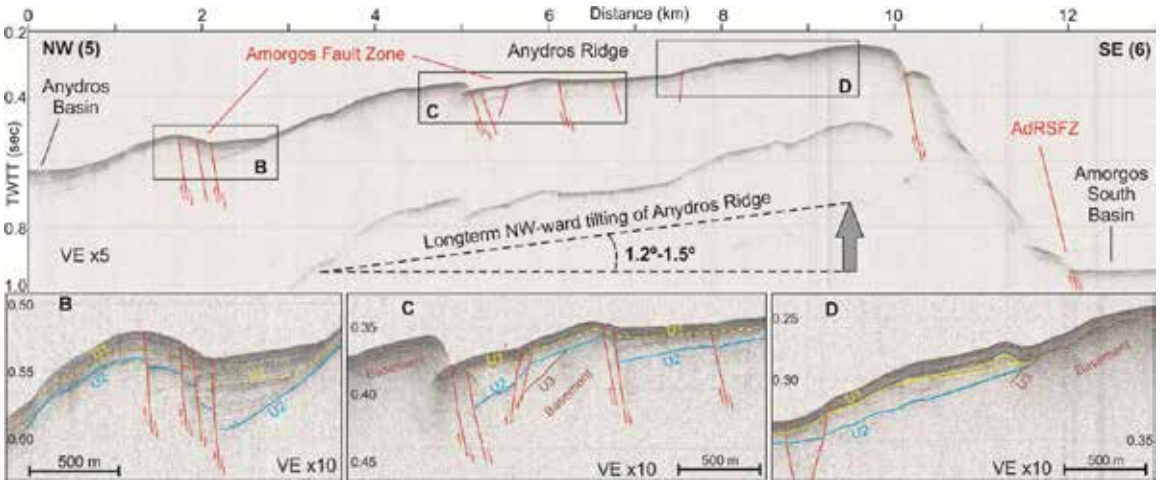

Figure 5. Sparker Subbottom Profile 5-6 across Anydros Ridge. See Figure 3 for location.

Profile 1 (Fig. 6), across Therasia, Caldera/Kameni, Thera, Anafi Basin and Anafi Ridge, proposes that magmatic and volcanic activity of Santorini is confined between Ios FZ and Akrotiri FZ. The latter marks the boundary between the alpine basement and the volcanic formations of Santorini. The late 2024 – early 2025 earthquake activity in the Caldera occurred at shallow depths below the Nea and Palaia Kameni Islands and Fira, along the NE-SW striking "Kameni Line". It is possible that the earthquakes were triggered by magma flow on the NW-dipping Akrotiri Fault.
Profile 2 (Fig. 6), across Anydros Basin, Anydros Ridge and Anafi Basin, proposes that magmatic and volcanic activity of the Kolumbo volcanic chain is confined below Anydros Basin, between Ios FZ and AdRNFZ.
Profile 3 (Fig. 6), across Anydros Basin, Anydros Ridge, Anydros Island, Amorgos South Basin and Anafi Basin, shows the transtensional Anydros and Amorgos South Basins separated by the uplifted Anydros Ridge. Anydros Basin displays symmetrical geometry while Amorgos South Basin exhibits enhanced subsidence along its NW margin. The eastern termination of Anafi Basin displays SE-ward asymmetry. Preliminary location of the earthquake hypocenters indicates that the 2025 seismic activity occurred predominantly below Anydros Ridge between AdRNFZ and AdRSFZ.
Profile 4 (Fig. 6), across Amorgos Island, Amorgos North Basin, Amorgos South Basin and Astypalea Basin, displays NW-ward asymmetry of the Amorgos North and South Basins and SE-ward asymmetry of the Astypalea Basin.
Profile 5 (Fig. 6), across Amorgos Island, Amorgos North Basin, Astypalea Ridge, Astpalea Basin and Astypalea Island, displays NW-ward asymmetry of the Amorgos North Basin and NW-ward tilting of Astypalea Ridge.
All major faults drawn on the above profiles are considered as oblique normal faults with significant component of dextral lateral slip. It is proposed here that lateral slip on some of the faults may exceed vertical slip.
The entire Santorini-Amorgos Zone is considered here as a transtensional feature or dextral oblique rift that has evolved during Quaternary.

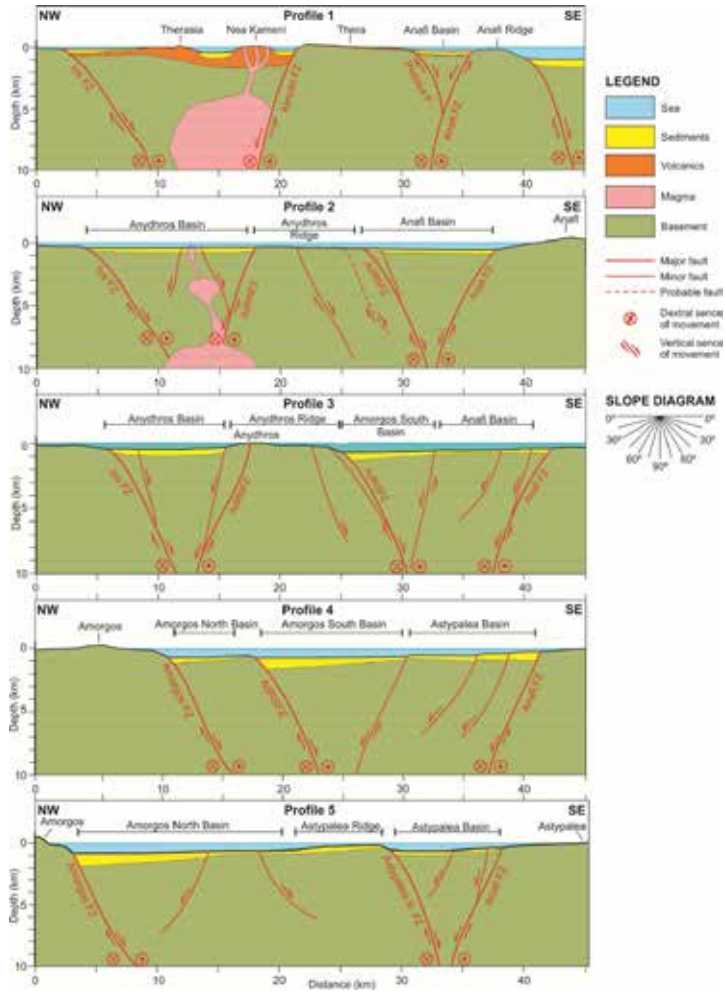

Figure 6. Schematic cross-sections across the Santorini-Amorgos Zone. The location of the five profiles is shown on the map of Figure 2. No vertical exaggeration. Abbreviations and names shown on the profiles are as in Fig. 1 & 2.

Conclusions

Re-exploitation of the pre-2025 data along with the analysis of the recently collected swath bathymetry and seismic profiles provide the following conclusions on the geological and tectonic structure of the Santorini-Amorgos Zone that can contribute to the understanding of the longterm processes controlling its evolution and the processes that led to the 2025 seismic activity:

- The “Kameni Line” represents the linear distribution of earthquake epicenters that, at depth, are probably associated with the NW-dipping, steep Akrotiri Fault.
- The geodetically observed NE-ward movement of Santorini that occurred in the first half of February 2025 affected the hanging-wall of Akrotiri Fault, while the foot-wall of the fault (the basement) remained more or less stable.
- The significant NW-ward tilting of Anydros Island observed on geodetic data during the seismic activity coincides with the long-term tilting of the entire Anydros Ridge observed on swath bathymetry and seismic profiling data.
- The NW-dipping Anydros Ridge North Fault Zone (AdRNFZ) controls the NW flank of Anydros Ridge and crosscuts the island of Anydros. Geometric and kinematic data of this fault measured on Anydros show a steep, NW-dipping oblique normal fault with significant dextral horizontal component.
- The trace of NW-dipping AdRNFZ is followed laterally towards northeast by the trace of the SE-dipping Amorgos Fault Zone (AFZ). The reversal of the tectonic polarity between these two fault zones is not well understood.
- Earthquake activity and ground deformation observed during the early 2025 seismic crisis are compatible with the long-term deformation of Santorini-Amorgos Zone.

Acknowledgements

This work uses swath bathymetry and seismic profiling data acquired during several cruises of R/V AEGAEO between 2001 and 2017 and funded partly by THERA (2006) and Eurofleets2 LGT-AMORGOS-56 international projects and partly by national (HCMR) funds. The February 2025 cruise of R/V ARGAEO was implemented within the “Athena vs. Egeladus” project funded by the Hellenic Foundation for Research & Innovation (HFRI). The authors are grateful to the colleagues and technicians who contributed to the acquisition of the data during all mentioned cruise. The crew and the captain of R/V AEGAEO are particularly acknowledged for their continuous support and smooth collaboration.

References

Bohnhoff, M., Rische, M., Meier, T., Becker, D., Stavrakakis, G., Harjes, H., 2006. Microseismic activity in the Hellenic Volcanic Arc, Greece , with emphasis on the seismotectonic setting of the Santorini – Amorgos zone. Tectonophysics **2006**, 423, 17–33

Briole, P., Ganas, A., Elias, P., Dimitrov, D., 2012. The GPS velocity field of the Aegean. New observations, contribution of the earthquakes, crustal blocks model. Geophysical Journal International, ggab089, https://doi.org/10.1093/gji/ggab089

Hooft, E.E.E., Nomikou, P., Toomey, D.R., Lampridou, D., Getz, C., Christopoulou, M.-E., O’Hara, D., Arnoux, G.M., Bodmer, M., Gray, M., Heath, B.A., VanderBeek, B.P., 2017. Backarc tectonism, volcanism, and mass wasting shape seafloor morphology in the Santorini-Christiana-Amorgos region of the Hellenic Volcanic Arc. Tectonophysics, 712-713, 396-414.

Mascle, J., Martin, L., 1990. Shallow structure and recent evolution of the Aegean Sea: A synthesis based on continuous reflection profiles. Mar. Geol., 94, 271–299

Nomikou, P., Hűbscher, C., Ruhnau, M., Bejelou, K., 2016. Tectono-stratigraphic evolution through successive extensional events of the Anydros Basin, hosting Kolumbo volcanic field at the Aegean Sea, Greece. Tectonophysics**,** 671, 202–217, doi:10.1016/j.tecto.2016.01.021.

Nomikou, P., Hübscher, C., Papanikolaou, D., Farangitakis, G.P., Ruhnau, M., Lampridou, D., 2018. Expanding extension, subsidence and lateral segmentation within the Santorini - Amorgos basins during Quaternary: Implications for the 1956 Amorgos events, central - south Aegean Sea, Greece. Tectonophysics, 722, 138–153

Papadimitriou, P., Kapetanidis, V., Karakonstantis, A., Kaviris, G., Voulgaris, N., Makropoulos, K., 2015. The Santorini Volcanic Complex: A detailed multi-parameter seismological approach with emphasis on the 2011 – 2012 unrest period. J. Geodyn.**,** 85, 32–57

Papadopoulos, G.A., Pavlides, S.B., 1992. The large 1956 earthquake in the South Aegean: Macroseismic field configuration, faulting, and neotectonics of Amorgos Island. Earth Planet. Sci. Lett.**,** 113, 383–396

Piper, D.J.W., Perissoratis, C., 2003. Quaternary neotectonics of the South Aegean arc. Mar. Geol., 198, 259–288

Piper, D.J.W., Pe-Piper, G., Perissoratis, C., Anastasakis, G., 2007. Distribution and chronology of submarine volcanic rocks around Santorini and their relationship to faulting. Geol. Soc. Lond. Spec. Publ.**,** 291, 99–111

Sakellariou, D., Sigurdsson, H., Alexandri, M., Carey, S., Rousakis, G., Nomikou, P., Georgiou, P., Ballas, D., 2010. Active tectonics in the hellenic volcanic arc: the Kolumbo submarine volcanic zone. Bull. Geol. Soc. Greece**,** 43, 1056–1063.

Sakellariou, D., Tsampouraki-Kraounaki, K., 2019. Plio-Quaternary extension and strike-slip tectonics in the Aegean. In: J. Duarte (Ed.): Transform Plate Boundaries and Fracture Zones, Chapter 14, **2018**, p. 339-374, https://doi.org/10.1016/B978-0-12-812064-4.00014-1, ELSEVIER, 2019.

Tsampouraki-Kraounaki, K., Sakellariou, D., Rousakis, G., Morfis, I., Panagiotopoulos, I., Livanos, I., Manta, K., Paraschos, F., Papatheodorou, G., 2021. The Santorini-Amorgos Shear Zone: Evidence for Dextral Transtension in the South Aegean Back-Arc Region, Greece. Geosciences 2021, 11, 216, https://doi.org/10.3390/geosciences11050216

Tzanis, A., Chailas, S., Sakkas, V., Lagios, E., 2020. Tectonic deformation in the Santorini volcanic complex (Greece) as inferred by joint analysis of gravity, magnetotelluric and DGPS observations. Geophys. J. Int.**,** 220, 461–489

17th INTERNATIONAL CONGRESS of the Geological Society of Greece

BULLETIN OF THE GEOLOGICAL SOCIETY OF GREECE, SP. PUBL.

EXTENDED ABSTRACT 276

Airborne and marine survey of the 8th June 2023 earthquake-triggered coastal collapse at Mylos Gialtron, North Evia: Contribution to the understanding of coastal zone vulnerability

Sakellariou D., Morfis I., Vandarakis D., Livanos I., Kourliaftis I.
Institute of Oceanography, Hellenic Centre for Marine Research, 19013 Anavyssos, Greece, sakell@hcmr.gr

Introduction

An earthquake with magnitude Mw:4.9 occurred on June 8th 2023, 10 km southwest of Atalanti, at 9 km depth (https://bbnet.gein.noa.gr/HL/seismicity/mts , 2023-06-08, 12:33:53.52, Lat: 38.5635°, Long.:22.9209°) (Fig. 1A). The tremor was felt in North Evia and triggered a landslide on the coastal zone of Mylos Gialtron (Fig. 1B). A 20 m long by 10 m wide part of the sandy beach in front of Mylos collapsed into the sea and created local turbulence of the seawater.
One week after the earthquake, on June 15th 2023, the Inst. Of Oceanography of HCMR undertook airborne mapping and documentation of the coastal collapse at Mylos Gialtron with a drone. Two weeks after the earthquake, on June 22nd and 23rd, a marine survey was implemented using a multibeam echosounder on board the research vessel Alkyon of HCMR. The results of the airborne and marine surveys on the coastal slide at Mylos Gialtron are presented here below and provide insights into the vulnerability of the Greek shoreline to co-seismic and non-seismic coastal slides.

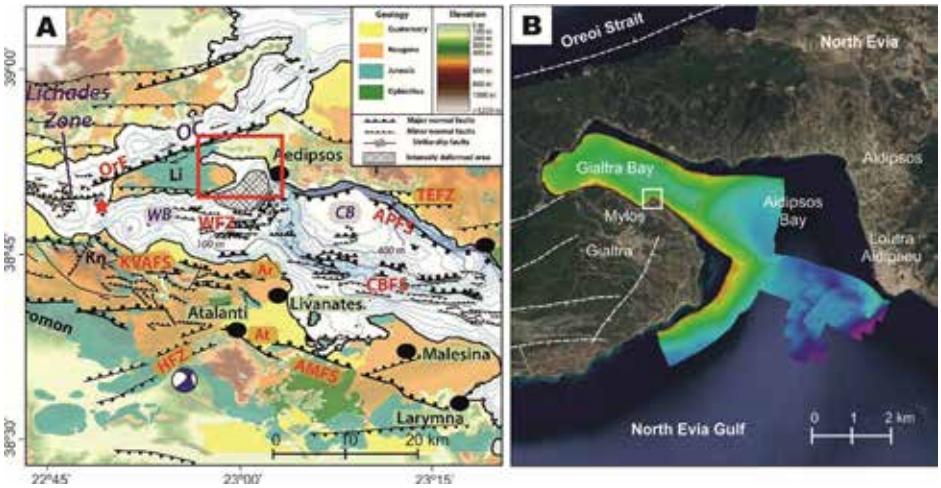

Figure 1. A: Geological and tectonic map of the broader North Evia Gulf (modified after Caroir et al., 2024). Red box: Fig. 1B. Blue-white beachball: Epicenter and moment tensor solution of the 8th June 2023 earthquake. B: Google Earth image with location of Mylos Gialtron (white box) and swath bathymetry coverage during the survey on board R/V Alkyon. White dashed lines: Faults after Galanakis et al. (1998) and Caroir et al. (2024).

Tectonic and Geographic Setting

Active neotectonics of the broader area of Eastern Central Greece, North Evia Gulf, North Evia and Oreoi Strait is dominated by E-W, SW-NE and NW-SE striking normal, oblique and dextral/sinistral strike-slip faults (Galanakis et al., 1998; Kranis, 2007; Sakellariou et al., 2007; Ganas et al., 2016; Caroir et al., 2024 and references therein). The two nodal planes observed by the moment tensor solution (https://bbnet.gein.noa.gr/HL/seismicity/mts) of the 8 June 2023 Mw 4.9 earthquake are compatible with the local tectonic pattern (Fig. 1A).
The sandy beach of Mylos (windmill) is located in North Evia, north of the village of Gialtra and west of Loutra Aidipsou, roughly 30 km north of the epicenter of the 8th June 2023 earthquake. It is a small, flat, triangular cape on the southern shoreline of Gialtra Bay that has been formed by the deposition of alluvial deposits due to the local coastal marine currents. The onshore area adjacent to Mylos is built mostly of carbonates and schists and displays rough relief.

Methods

In this study, a DJI Matrice 210 RTK Unmanned Aerial Vehicle (UAV) was used for the airborne mapping of the coastal

and shore morphology and the documentation of the shallow coastal collapse (Casella et al., 2020; Papakonstantinou et al., 2016). The UAV was equipped with a Zenmuse X5S sensor and RTK technology. Six (6) Ground Control Points (GCPs) were implemented to achieve geolocation accuracy of ±2 cm. The flight plan consisted in nine (9) N-S and eight (8) E-W oriented tracks (Fig. 2 A) (Trajkovski et al., 2020; Zhou et al., 2024). In total, 185 photos were taken from 120m Above Ground Level (AGL), the front and side overlap were at 80% and the Ground Sampling Distance (GSD) was at 2.69 cm/pixel. The achieved Root Mean Square Error (RMSE) of accuracy of the resulted Orthomosaic, Digital Surface Model (DSM) and Digital Terrain Model (DTM) was about 0.012 m (Fig. 2B). The Pix4d mapping software was used for the construction of the maps. The total area covered was 377 X 319 m and the coordinate system used was GCS_GGRS_1987. Based on the height of the drone flight the DSM and Orthomosaic resolution was fixed at 2.69cm/pixel. Noise and surface filters were implemented to eliminate potential errors during the processing. The Inverse Distance Weighting Method was used for the construction of the DSM (and DTM) raster.
A Teledyne/RESON SEABAT T50-R, 200 – 400 kHz multibeam echosounder hull-mounted on HCMR's Research vessel Alkyon was used for the acquisition of swath bathymetry data in the Aidipsos and Gialtra Bay. T50-R multibeam echosounder emits up to 1024 beams arranged in iso-distance or iso-angle mode at 165° across the vessel's track and offers maximum swath equal to up to 5 times the current water depth. A Sea Bird Electronics SeaCat 19 Profiler CTD (Conductivity – Temperature – Depth) was used for the sound velocity profile of the water column during the survey. The resulted swath bathymetry of 13.5 km^2 in Gialtra and Aidipsos Bays has been processed at 1 m spatial resolution.

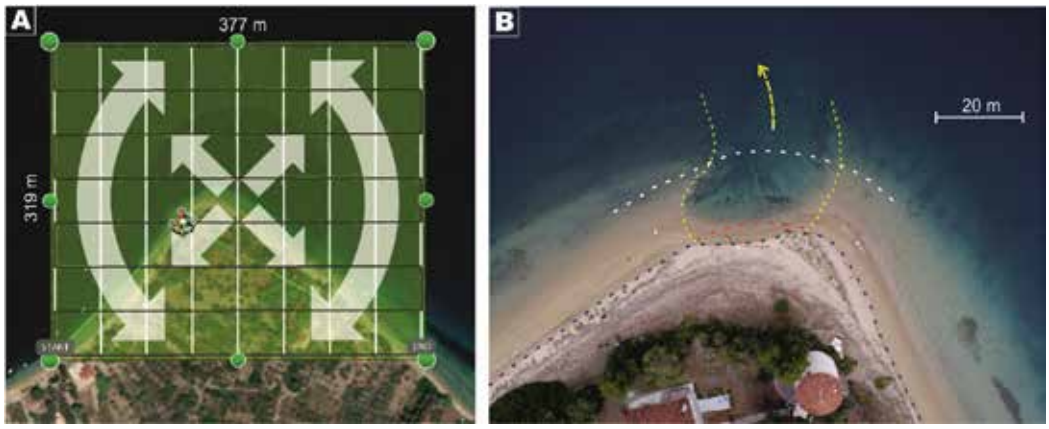

Figure 2. A: Flight plan of the drone over the area of Mylos Gialtron. B: Airphoto of the coastal collapse at the tip of Mylos Gialtron sandy beach taken from the drone on June 15, 2023. Blue dashed line: post-earthquake shoreline. Red dashed line: pre-earthquake shoreline. White dashed line: pre-earthquake 4 m depth contour (approximately).

Results

The swath bathymetry data showed that Gialtra Bay is a flat, 35-40 m shallow embayment with a large number of a few meters high mounds of probable biogenic origin (Fig. 3). The up to 50% steep littoral slope connects the southern, narrow coastal zone with the flat bottom of the Bay. The northern side displays gentler slope value. A 30 m shallow, NE-SW trending sediment ridge (Barrier in Fig. 3) separates the shallow seafloor of Gialtra Bay to the East from the deeper Aidipsos Bay. The latter is characterized by rather flat seafloor that deepens smoothly to 55 m depth towards the center. Aidipsos Bay is open to the South to the North Evia Gulf. A prominent, >5 m deep valley incises the 50 m shallow, flat seabed between Gialtra and Loutra Aidipsou and connects the 55 m deep seafloor of Aidipsos Bay with the 440 m deep Central Basin of the North Evia Gulf.
Three areas with slope failures have been identified on the seafloor (Fig. 3). An amphitheatric scar occurs east of Gialtra at depths between 20 and 30 m and marks a submarine landslide that took place not very long ago, possibly not earlier than 5-6 kyrs before present, when the area was already drowned by the last sea-level rise. Multiple evidence of recent coastal slides and mass transport deposits have been observed off the shoreline of Mylos Gialtron (Fig. 4 & 5) and will be described below. Finally, evidence of composite on- and offshore slope failure and rock falls have been found at the southwestern part of Gialtra Bay coastal zone (Fig. 6).

The Mylos Gialtron coastal collapse(s)

The airborne DTM and orthophotomosaic of Mylos Gialtron provide a precise documentation of the onshore coastal plain, the sandy beach and the shallow seafloor up to roughly 9 to 10 m depth (Fig. 4). The western slope is steeper than the eastern one and show evidence of slope failures at shallow depth. The scar created by the coastal collapse

of 8th June 2023 at the northern tip of the shoreline has been mapped in detail up to the depth of 4.5 m (Fig. 4 & 2B). The airphoto of Fig. 2B shows the coastal zone at the tip of Mylos Gialtron one week after the earthquake-triggered collapse of 8th June 2023. A 20 m long by up to 10 m wide part of the sandy beach and its offshore continuation are missing because they collapsed northwards and slid downslope leaving behind an amphitheatric scar. The dashed red line shows the shoreline prior to the collapse. The white dashed line shows the approximate location of the 4 m depth contour prior to the collapse. Note that the 4 m depth contour is less than 20 m away from the shoreline indicating a minimum mean coastal slope value of 25%. The two yellow dashed lines mark the edges and the yellow arrow shows the direction of the slide.

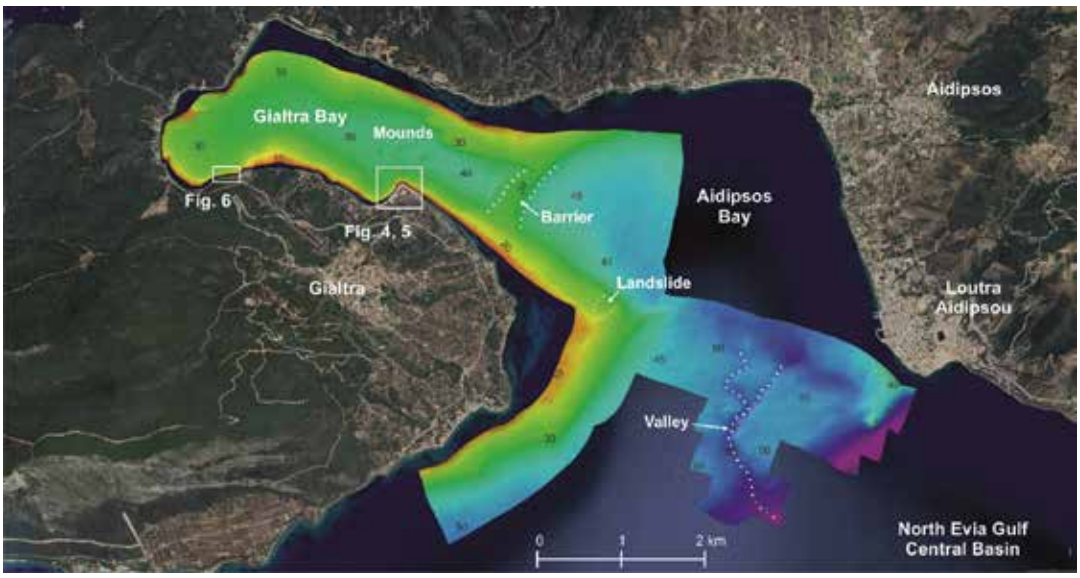

Figure 3. Swath bathymetry of the Aidipsos and Gialtra Bay acquired on board R/V Alkyon on June 22-23, 2023.

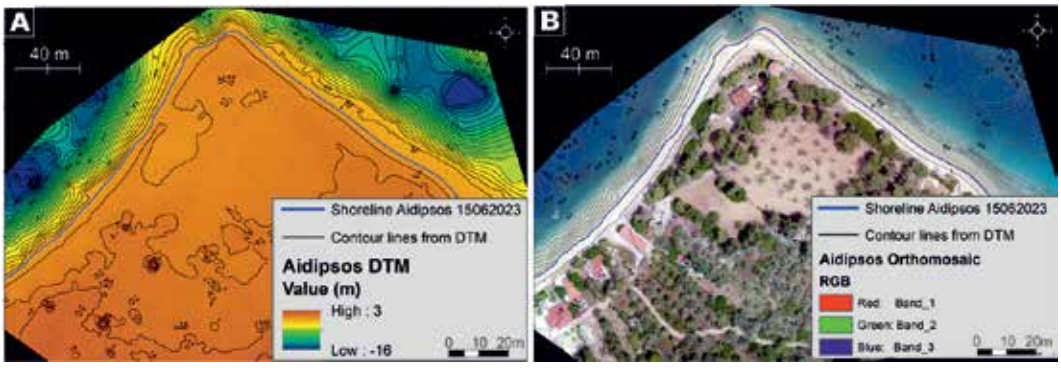

Figure 4. DTM (A) and Orthophotomosaic (B) derived from the airborne survey at Mylos Gialtron on June 15, 2023.

The swath bathymetry acquired with R/V Alkyon complemented the airborne mapping of the seafloor off Mylos Gialtron. Thanks to the crew of R/V Alkyon, the vessel navigated at very short distance from the shoreline during the marine survey in order to achieve sufficient complementarity, without gaps between the airborne and the marine coverage.

Multiple shallow slope failures are evident off the western shoreline of Mylos (Fig. 5A). The toe of the slope deposits reaches 30 m depth. No scar has been identified on the airborne and marine data indicating that these failures may have taken place at least some tens of years ago, sufficient time for the dynamic coastal zone environment to heal the failure scars.

The coastal scar at the northern tip of the sandy beach continues downslope toward north-northwest (Fig. 5B). A 15 m wide and 3-4 m deep gully incises the slope down to roughly 15-20 m depth and is followed by the depositional lobe. The lobe widens to reach a diameter of at least 50 to 60 m and extends up to the 30 m depth contour. Assuming a mean thickness of 2 m for the depositional lobe, the estimated volume of the slide is calculated to >7,000 m^3. Local witnesses reported extensive turbulence of the seawater in front of the sandy beach when the collapse took place. This indicates that the collapse and the slide evolved abruptly and at high velocity, however, no tsunami was reported.

At least one more, older, depositional lobe is evident on the seafloor. The white dashed line on the map of Fig. 5A outlines the morphological expression of an older lobe that is located further off the slide deposits of 8th June 2023. This older lobe extends off the 35 m depth contour, at roughly 150-200 m distance from the shoreline and has the shape of a wide, flat mound with its highest surface 2-3 m higher than the surrounding seafloor. The shape and orientation of this depositional lobe strongly indicates that it is the result of a coastal slide similar to but two times larger than the one of June 2023. Local witnesses reported to the survey team that a coastal collapse similar to the one of 8th June 2023 occurred at the time of the 9th July 1980, M:6.3 Almyros earthquake. It has not been possible to verify this information, however it is reasonable to assume that the older slide may have been triggered by an earthquake in the recent past.

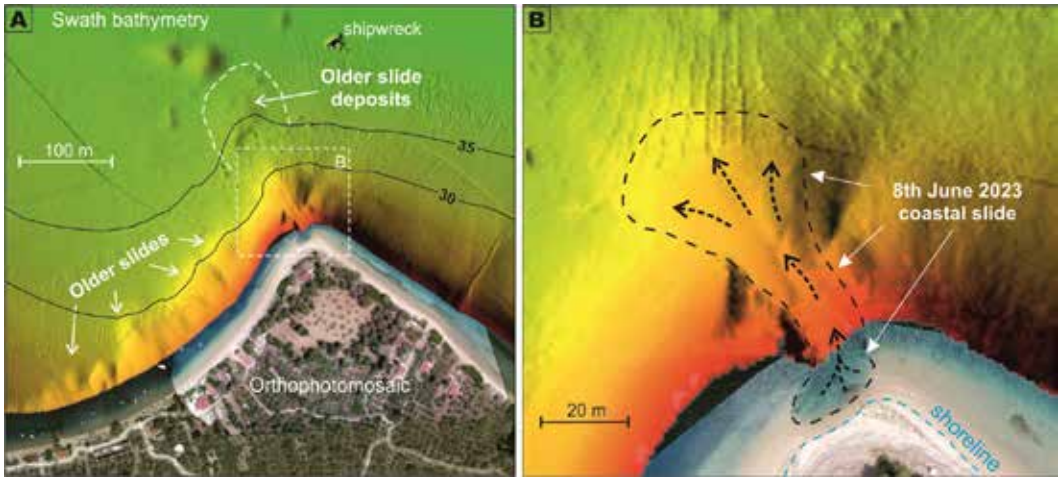

Figure 5. A: Orthophotomosaic and shaded bathymetry of the coastal and offshore Mylos Gialtron area. White arrows point to landslide deposits before the 8th of June 2023. Black thin lines are depth contours B: Detail of previous image showing the 8th June 2023 co-seismic coastal collapse and slide deposits off the sandy beach of Mylos Gialtron.

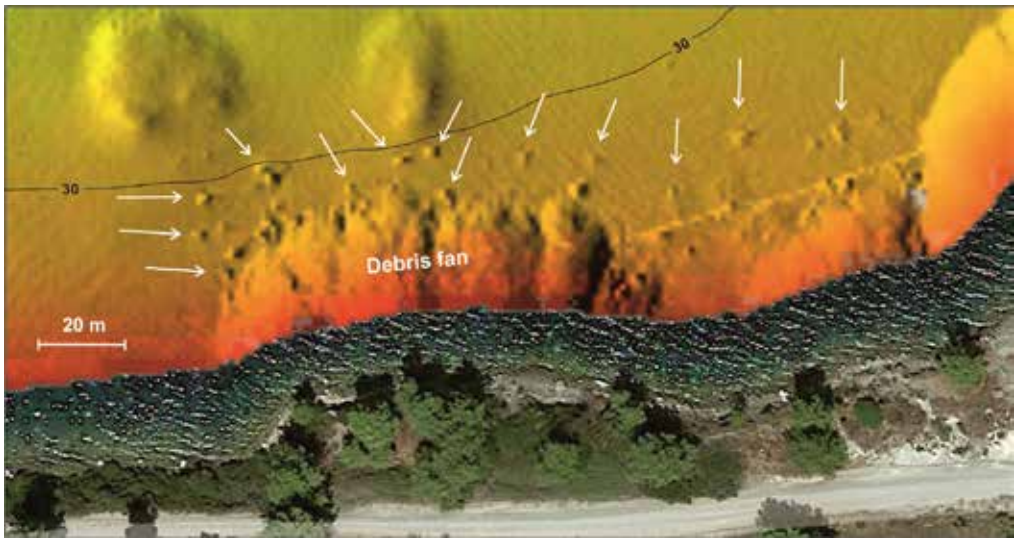

Figure 6. Shaded swath bathymetry off the southern shoreline of Gialtra Bay (see Fig. 3 for location) showing a submarine debris fan and multiple boulders (arrows) fallen from the nearby onshore rocky cliff. Thin black line: 30 m depth contour.

Evidence of coastal slope failure has been found on the seafloor at the southwestern margin of Gialtra Bay (Fig. 6). The shaded relief of the seafloor shows a 100 m wide submarine fan. The fan has evolved off and parallel to the convex-shaped shoreline and is incised by several small gullies. The foot of the debris fan is at 25-28 m depth and is surrounded by multiple, small positive features (pointed with arrows on Fig. 6). Based on their shape, dimensions and context they are interpreted as rock boulders with diameter up to roughly 2 meters. Both the debris fan and the boulders may have derived from a landslide on the nearby onshore, north-facing, mountain flank. The available data

provide no constraints on the possible age of the landslide that is responsible for the creation of the debris fan and the rock falls.

Discussion

The co-seismic coastal collapse and submarine landslide of 8th June 2023 is probably the first one in Greece that has been documented right after its occurrence with the use of airborne and marine survey techniques. The results presented above highlight two main critical factors that favor the development of slide events in the coastal zone once a proper triggering mechanism (e.g. earthquake) is activated (Fig. 7A & B).

The first factor is the presence of a coastal sedimentary prism built and thickened by fast accumulation of non-coherent sediments, e.g. the loose deposits that accumulate along the shoreline and build the sandy beaches and the dynamically changing, on- and offshore coastal zone. The second factor is the presence of a relatively steep slope on the seafloor at short distance off the shoreline. In the case of Mylos Gialtron the submarine slope starts at 10-15 m off the shoreline and displays dipping value >25% basinwards. Certainly, the initial, driving factor for the collapse is the magnitude of the seismic acceleration that will or will not destabilize the non-coherent coastal deposits.

The schematic drawing shown on Fig. 7 visualizes in a simplified way the main factors described above as well as the evolution of the coastal collapse to a submarine landslide. Fig. 7A shows the structure of the coastal zone before the event. The red, dashed line marks the sliding plane of the imminent slide. The area highlighted in yellow indicates the sedimentary material (evacuation zone) to be involved into the coastal collapse and slide. The red line in Fig. 7B marks the slide scar and the red half arrow points the pathway of the sliding mass. The yellow lobe on the deep seafloor visualizes the deposition lobe of the landslide.

The structural and morphological characteristics as presented above for Mylos Gialtron and visualized in Fig. 7 are fairly common along the Greek shoreline. Large or smaller segments of the coastal zone of the Ionian Islands, the Gulf of Corinth, the islands of the Hellenic Arc (Crete, Kasos, Karpathos, Rhodes), the eastern Peloponnese to the Argolikos Gulf and Myrtoon Sea, the coast of Evia to the Aegean Sea and the North Evia Gulf, the Sporadhes Islands are some of the areas along the Greek coastline that (a) display structural and morphological characteristics similar to the ones described above and (b) are characterized by frequent, high earthquake activity.

These areas need to be systematically surveyed with the aim to document precisely the structure and morphology of the coastal zone, estimate and understand their vulnerability to coastal landslides similar to or even larger than the recent one at Mylos Gialtron and design measures for the mitigation of their impact on the coastal societies.

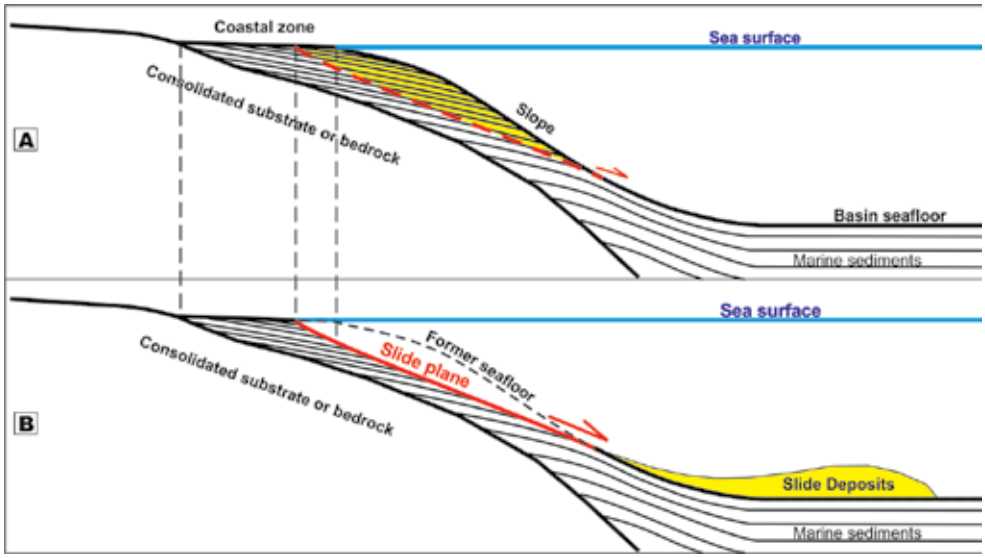

Figure 7. Schematic visualization of the coastal collapse and submarine landslide of 8th June 2023 at the sandy beach of Mylos Gialtron. See text for description.

Conclusions

The coastal collapse at Mylos Gialtron, southern shoreline of Gialtra Bay in North Evia was triggered by the Mw:4.9 magnitude earthquake of June 8th 2023, 10 km southwest of Atalanti. Airborne orthophotomosaic, digital terrain and surface models (DTM, DSM) of the coastal zone combined with swath bathymetry mapping of Gialtra and Aidipsos Bays provided detailed documentation of the coastal collapse and showed that it evolved as submarine landslide.

Gialtra Bay is characterized by flat, 35-40 m shallow seafloor with an up to 50% steep southern slope and gentler sloping northern margin. It is separated from the deeper Aidipsos Bay by a 30 m shallow, NE-SW trending sediment ridge. Aidipsos Bay displays rather flat, up to 55 m deep seafloor and is open to the South to the North Evia Gulf. A prominent, submarine valley incises the 50 m shallow, flat seabed between Gialtra and Loutra Aidipsou and connects Aidipsos Bay with the 440 m deep Central Basin of the North Evia Gulf.

A 20 m long by up to 10 m wide part of the sandy beach at Mylos Gialtron and its offshore continuation collapsed and slid downslope, toward the 35-40 m deep flat seafloor of Gialtra Bay, leaving behind an amphitheatric scar. The sliding mass created a 15 m wide by 3-4 m deep gully on the slope down to roughly 15-20 m depth. The gully is followed by the 50 to 60 m in diameter depositional lobe that extends up to the 30 m depth contour. Assuming a mean thickness of 2 m for the depositional lobe, the estimated total volume of the slide is calculated to >7,000 m^3.

One more, older, larger depositional lobe is found on the seafloor. It extends beyond the 35 m depth contour, at roughly 150-200 m distance from the shoreline and has the shape of a wide, 2-3 m high, flat mound. The shape and orientation of this depositional lobe strongly indicates that it is the result of a coastal slide similar to but two times larger than the one of June 2023. According to local witnesses, a coastal collapse at the same spot was triggered by the 9th July 1980, M:6.3 Almyros earthquake, 43 years before the recent coastal collapse. This collapse may be associated with the older slide.

Further evidence of extensive on/offshore landslide, debris flow and rock falls has been found at the southwestern margin of Gialtra Bay. According to the bathymetric and morphological data this slope failure is relatively recent, however no precise age constraints are available.

Certain, larger or smaller segments of Greece's coastal zone (e.g. Ionian Islands, Gulf of Corinth, Hellenic Arc islands, Eastern Peloponnese etc.) display structural and morphological characteristics similar to the ones of Mylos Gialtron coastal zone and are characterized by frequent, moderate to high earthquake activity. These areas need to be systematically surveyed with the aim to understand their vulnerability to coastal landslides similar to or even larger than the recent one at Mylos Gialtron and design measures for the mitigation of their impact on the coastal societies. Detailed geological mapping along the broader, on- /offshore coastal zones is of outmost importance for the understanding of their morphology and sedimentary structure and the assessment of coastal landslide vulnerability.

Acknowledgements

The implementation of this two-phase survey has been possible thanks to the internal funding by the Institute of Oceanography of the Hellenic Centre for Marine Research and the assistance of the Major of Istiaia-Aidipsos Municipality and the Master of Aidipsos Harbor. Our colleagues M. Moschides and N. Nicolis, captain and engineer of R/V Alkyon, are greatly acknowledged for their continuous support and assistance during the marine survey.

References

Caroir, F., Chanier, F., Gaullier, V., Sakellariou, D., Bailleul, J., Maillard, A., Paquet, F., Watremez, L., Averbuch, O., Graveleau, F., Ferriere, J., 2024. Late Quaternary deformation in the western extension of the North Anatolian Fault (North Evia, Greece): Insights from very high-resolution seismic data (WATER surveys). Tectonophysics 870 (2024) 230138.

Casella, E., Drechsel, J., Winter, C., Benninghoff, M., Rovere, A. (2020). Accuracy of sand beach topography surveying by drones and photogrammetry. In Geo-Marine Letters (Vol. 40, Issue 2). Geo-Marine Letters. doi: 10.1007/s00367-020-00638-8

Galanakis, D., Pavlides, S., Moundrakis, D. [1998] Recent brittle tectonic in Almyros-Pagasiticos, Maliakos, N. Euboea and Pilio. Bulletin of the Geological Society of Greece, 32, 263-273.

Ganas, A., Mouzakiotis, E., Moshou, A., Karastathis, V., 2016. Left-lateral shear inside the North Gulf of Evia Rift, Central Greece, evidenced by relocated earthquake sequences and moment tensor inversion. Tectonophysics 682, 237–248. https://doi. org/10.1016/j.tecto.2016.05.031.

Kranis, H., 2007. Neotectonic Basin evolution in Central-Eastern mainland Greece: an overview. Bull. Geol. Soc. Greece 37, 1–14. https://doi.org/10.12681/bgsg.16621.

Papakonstantinou, A., Topouzelis, K., Pavlogeorgatos, G. (2016). Coastline zones identification and 3D coastal mapping using UAV spatial data. In ISPRS International Journal of Geo-Information (Vol. 5, Issue 6). doi: 10.3390/ijgi5060075

Sakellariou, D., Rousakis, G., Kaberi, H., Kapsimalis, V., Georgiou, P., Kanellopoulos, Th., Lykousis, V., 2007. Tectono-sedimentary structure and late Quaternary evolution of the North Evia Gulf basin, Central Greece: preliminary results. Bull. Geol. Soc. Greece 40, 1–12. https://doi.org/10.12681/bgsg.16644.

Trajkovski, K. K., Grigillo, D., Petrovič, D. (2020). Optimization of UAV flight missions in steep terrain. Remote Sensing, 12(8), 1–20.

Zhou, X., Zhu, Q., Zhang, Q., & Du, Y. (2024). The full-field displacement intelligent measurement of retaining structures using UAV and 3D reconstruction. Measurement, 227, 114311.

17th INTERNATIONAL CONGRESS of the Geological Society of Greece

BULLETIN OF THE GEOLOGICAL SOCIETY OF GREECE, SP. PUBL.

EXTENDED ABSTRACT 277

Continuous GNSS Geodetic Networks. A Powerful Tool for Monitoring and Understanding Complex Volcanic Environments: The Case of Santorini Volcano During the Seismic Crisis of 2024-2025

Sakkas V.[1], Pikridas C.[2], Ganas, A.[3], Anastasiou D.[4], Elias P.[5], Bitharis S.[2], Chousianitis K.[3], Raptakis K.[4], Kapetanidis V.[1], Kaviris G.[1], Liadopoulos S.[3], Voulgaris N.[1], Alexopoulos J.[1], Lagios E.[1]

(1) National and Kapodistrian University of Athens, Laboratory of Geophysics, Laboratory of Seismology, Greece (vsakkas@geol.uoa.gr)

(2) Aristotle University of Thessaloniki, School of Rural and Surveying Engineering, Thessaloniki, Greece

(3) National Observatory of Athens, Institute of Geodynamics, Athens, Greece

(4) National Technical University of Athens, School of Rural, Surveying and Geoinformatics Engineering, Athens, Greecde

(5) University of Patras, Department of Geology, Patra, Greece

Abstract

Late summer of 2024 an unusual raise of the seismic activity was observed inside the Caldera of Santorini Volcanic Complex. This was the first time since the 2011-2012 unrest period that increased seismicity was recorded inside the Santorini Caldera. Together with the raise of the seismicity, daily GNSS data from a permanent station in Imerovigli (station SANT) as well as two other operating stations in Santorini, exhibited change on the kinematic behavior of the Island. The typical SE directional motion of the SANT station (with respect to ITRF2014) observed the last decade was altered to a strong ENE motion. Moreover, increased uplift started taking place in the SANT station with a rate of almost 80mm/yr, an order of amplitude higher than the typical of 2-3 mm/yr of the last years. This kinematic motion could be explained by volcanic activity inside the caldera, modeled as a typical Mogi point source.

However, at the end of January 2025, almost 6 months after the initiation of the activity inside the caldera, there was an abrupt migration of the seismicity NE of Santorini, in the marine area between Thira and Amorgos Islands. During a period of almost a month (February 2025) intense seismic activity was recorded in the marine area around the islet of Anydros, located ~25km NE of Thira. Several seismic events of M>3 were recorded almost every day, during that period, with the larger event to be of M5.3. This intense seismicity was accompanied by strong ground deformation on the broad area of South Aegean. As was expected, the most intense ground deformation was observed in Thira Island and in Anydros Islet. However, the type of motion in SANT cGNSS station was of completely different type compare to the previous period (while the seismicity was located inside the Caldera). The SANT station showed a strong North motional component and intense subsidence. It has to be noticed that the daily amplitude of the ground deformation reached values up to 10mm/day during the peak of the seismic crisis (10-15 of February). Moreover, GNSS data from the surrounding islands, as is Ios and Naxos to the North of Thira exhibited changes in their kinematic behavior, highlighting the intense activity that was taking place in the marine area of Anydros Islet.

The strong ground deformation decreased around the end of February 2025, almost a month after its initiation. Since then, it appears that the rate of ground deformation has significantly decreased in both horizontal and vertical component. The decrease of ground displacement coincided with the decrease in the seismicity, that has been expressed not only with smaller number of events per day, but also and of smaller amplitude, with the events of ~M3 to be less than the previous one month long period.

A major issue during this crisis was the identification of the seismic activity; it was of volcanic or tectonic character / origin? In the complex environment of South Aegean, where the Santorini Volcanic complex is located, there is not an easy or unique answer to such issues. Major tectonic zones, as is the Amorgos area (with a history of strong earthquakes), volcanic centers as is the Kameni Islet and the submarine Kolubo volcano, create an extremely complex geological environment that requires a multidisciplinary approach in order to comprehend it. To better understand, explain and monitor the ongoing processes in the broad area of south Aegean the geodetic and seismological academic and research community of Greece took action establishing a dense network of continuous GNSS stations, as well as seismological stations. In this common effort several institutes from abroad also collaborate and joint efforts with the Greek institutes. The main scope of this effort is to achieve a better spatial coverage of the area, with permanent operating stations, and be able not only to monitor the daily progress of the deformation and seismological crisis but also to foresee its evolution. As result of this joint effort, it was the establishment, and/or

re-start of more the 20 permanent GNSS stations in the broad area of South Aegean Sea. The new GNSS stations that were established in the island of Thira, Thirasia, Ios, Amorgos, Anafi, Sikinos, and in the islets of Anydros and Christiana, together with the existing stations in the surrounding islands that were operated by other private entities (Hellenic Cadastre HEPOS, Metrica SA, JGC SA, TreeCompany SA,), together with new sites that were established by other international institutes in collaboration with the Greek ones (ie, CNRS - École Normale Supérieure - PSL, France, INGV, Instituto Nazionale di Geofisica e Vulcanologia, Italy) and with the support of Earthquake Planning and Protection Organization of Greece (EPPO) will provide on a continuous base all the necessary data in order to monitor this vital area of Greece, will help to better protect the local community and will also provide valuable insight on the geological processes that are taking place in the complex environment of Santorini Volcano, the broad area of South Aegean, as well as along the Hellenic Volcanic Arc. The daily GNSS data from all the operating stations are processed on a near real-time basis, using advanced algorithms, from all the participating institutions providing solutions and information not only for scientific use but also for operational use on the framework of the civil protection actions.

Acknowledgements

The authors would like to acknowledge the organization efforts of Dr. S. Lalexos on behalf of Earthquake Planning and Protection Organization of Greece. Daily GNSS raw (RINEX) data were contributed by: (1) The “Institute for the Study and Monitoring of Santorini Volcano” IMOSAV providing data from several GNSS stations in Thira, Thirasia and Nea Kameni (https://ismosav.gr/en/home/); (2) The Hellenic Positioning System (HEPOS) provides data from five stations in the south Aegean free of charge by the Hellenic Cadastre (www.ktimatologio.gr); (3) METRICA S.A. provides GNSS data from several stations located in the broad area of South Aegean (https://gr-sbc.nrtk.eu); (4) JGC Geoinformation Systems S.A. offers data from one permanent station in Thira (https://www.jgc.gr/jgc-net/) (5) TreeCompany and its GNSS network URANUS provides data from one station in Thira (https://uranus.gr/). Also, the authors acknowledge the contribution of Dr. P. Briole (from CNRS France) in order to establish new GNSS stations in the South Aegean area, as well as the establishment of GNSS sites from INGV (Instituto Nazionale di Geofisica e Vulcanologia, Italy).

17th INTERNATIONAL CONGRESS of the Geological Society of Greece

BULLETIN OF THE GEOLOGICAL SOCIETY OF GREECE, SP. PUBL.

EXTENDED ABSTRACT 278

Ground Deformation in Nisyros Volcano (Greece) Determined by GPS and SAR Interferometric Techniques

Sakkas V.[1], Tzanis A.[1], Lagios E.[1]
(1) Geophysics Laboratory, Department of Geology and Geoenvironment, National and Kapodistrian University of Athens, Greece, vsakkas@geol.uoa.gr

Introduction

The southeastern part of the Hellenic Volcanic Arc (HVA), including Kos, Yali and Nisyros islands, is geodynamically very active (Figure 1). Intense seismic activity occurred on Nisyros Island during 1996-1998, accompanied with strong ground deformation and temperature increase of the fumaroles. Nisyros Island lies above a basement of Mesozoic limestone (Geotermica Italiana 1983; 1984). The exposed rocks are Quaternary volcanics. The evolution of Nisyros Volcano during the past 160,000 years, together with the succession of calc-alkaline lavas and pyroclastic rocks, has been studied in detail by various authors (ie Hardimann 1999; Tibaldi et al. 2008).
Major fault systems have been identified within the volcanic edifices of the Kos-Yali-Nisyros Volcanic Field (Figure 1) on the basis of structural and geological investigations (ie Papanikolaou and Nomikou 2001; Nomikou and Papanikolaou 2011). The caldera's rim and its accompanying cone-shaped local faults are entirely volcanic structures, which are a result of the collapsing of the caldera after the last Plinian eruptions.

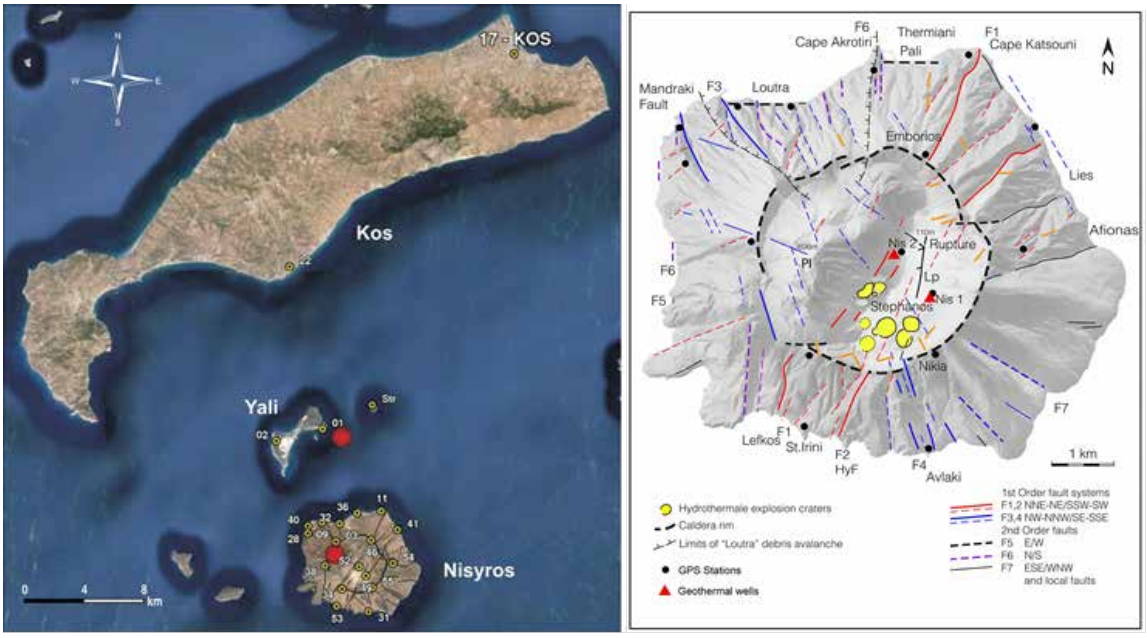

Figure 1. Left part: Distribution of stations of the GPS network of the Kos-Yali-Nisyros Volcanic Field. Solid red circles represent the two modelled Mogi point sources. Str stands for the station established on Strongyli Islet). Right part: Fault pattern of major faulting systems (F1 to F7), location of hydrothermal explosion craters and other significant features superimposed on a digital elevation model of Nisyros Island. Abbreviations of locations; Pl: Prophitis Elias, Lp: Lakki Plain.

Earthquakes have been described throughout historical times as has been reported in detail since 1830 (Gorceix 1873a, b and c; Stiros and Vougioukalakis 1996). Their origin may be a result of regional tectonic processes, magma ascent, degassing phenomena of deep crustal magma and steam explosions within the hydrothermal system. The Mandraki Fault (Figure 1) that comprises a branch of the F3 fault system was reactivated in 1996 (Lagios et al. 2005) and caused damage to buildings and other structures within Mandraki (Ioannidis 1998). Tectonic processes expressed by the latest seismicity indicate tensional fracturing (Makris and Chonia 1999) which could reduce the lithostatic pressure and trigger explosive volcanic phenomena, such as those reported in 1871 and 1873 by Gorceix (1873a). The most recent seismic activity in the area was in 2017 with a strong earthquake (Mw6.2; Jul. 20, 2017) taking place NE of Kos Island (Ganas et al., 2019). Moreover, increased seismicity occurred during Jun-August 2021, in the marine area SW of Nisyros. Both these bursts of seismicity were of tectonic character and have not been

associated with volcanic activity.
Efforts for studying the ground deformation on Nisyros started after the outbreak of the seismic activity in 1996 and have involved GPS observations and SAR interferometric analysis (e.g. Lagios et al. 2005;). This study presents the ground deformation on Nisyros up to 2023 and addresses its evolution during the years 2002-2023 on the basis of combined GPS/GNSS and advanced SAR interferometric techniques.

GPS/GNSS Measurements

A geodetic GPS network (Figure1) was established in the broader area of Nisyros in June 1997 in order to study ground deformation. It initially consisted of 21 stations and included a local reference station (17-Kos) at the northeastern part of Kos Island (Lagios et al. 2005). Another station (benchmark) was installed on Strongyli Islet in 2013. Moreover, a continuous operating GNSS station was established in Mandraki in November 2016, as well two more continuous station were established in 2023 in Nikia and Yali. Campaign measurements were performed in periodic times, with the last measuring period to be December 2023. All campaigns were made in the static mode using tripods cantered above the permanently installed benchmark at a given station. Post-processing was performed using the Bernese GNSS Software, versions 5.2 (Dach et al. 2015), together with post-computed satellite orbits (available through the International GNSS Service) to improve the error estimation. Accuracies of 2 to 5mm and 4 to 8 mm were achieved for the horizontal and vertical components, respectively.
The GPS measurements during the active period (1997-1999) showed that the amplitude of the horizontal deformation ranged from 20 to 60 mm. The maximum horizontal displacement occurred between 1997 and 1998 during the peaking (1997) and subsequent high level (1998) of seismic activity. The period 1999-2002 Nisyros entered a different mode of deformation with a clear westward in-crease of the horizontal component in almost all its western part for the period 2001-2002. Vertical deformation in the sense of a general uplift of the whole island occurred over almost the entire active period of observation up to 2002, and in particular the majority of stations exhibited uplifts of 40 to 60 mm between 1997 and 1998. Greater values of uplift were measured at stations installed on the western uplifted side of the activated Mandraki Fault.
The GPS network on Nisyros after 2002 was remeasured in August 2012, which was a decade after its establishment. Through this decade (2002-2012), there was no significant seismic activity in the broader area, nor was there any other type of volcanic activity as would be detected via temperature increase in the fumaroles. It may thus be assumed that the ground deformation that occurred in the island was of an almost linear character without any strong fluctuations. After 2012, the network was re-measured more often, in total eight times up to 2023, deducing a more accurate velocity field of the area (Figure 2).

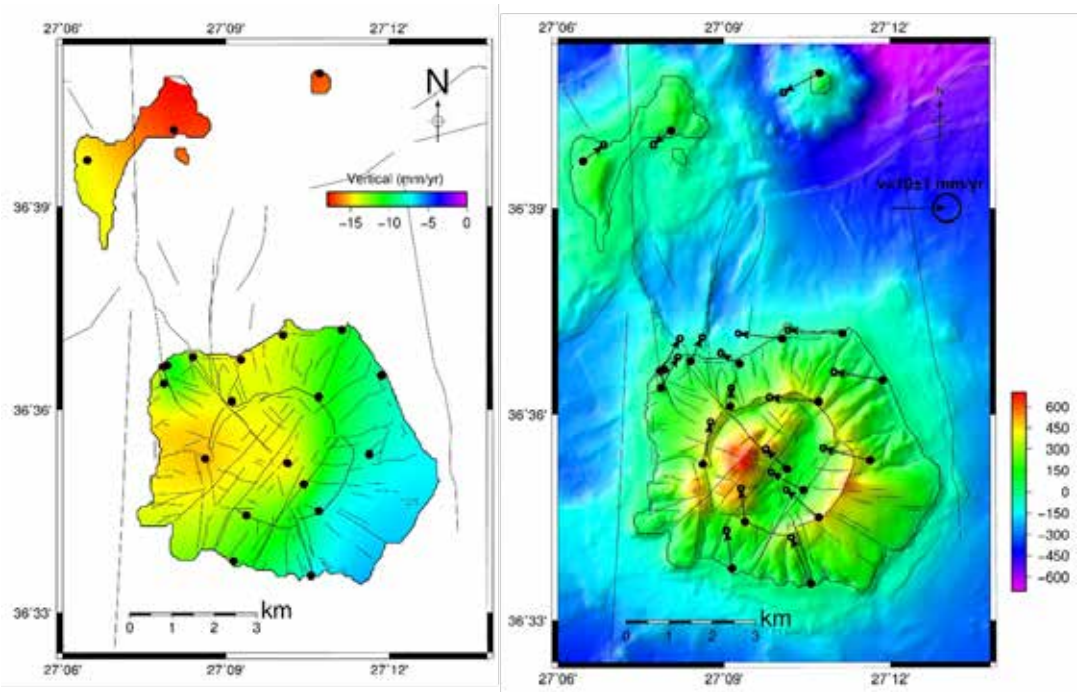

Figure 2. Vertical (left panel) and horizontal (right panel) deformation on Yali-Nisyros for the period 2002-2023 (relative to ITRF2014 reference frame, subtracting the regional motion of the area).

As can be seen on the velocity map for the period 2002-2023 (Figure 2), the most prominent aspect of ground deformation is the subsidence that took place in Nisyros and Yali during this ,ore than 20 years period. The subsidence reached values of more than 10mm/yr in the northern part of Nisyros, but with smaller values (~3-5 mm/yr.) in the southern and eastern parts. The horizontal velocity vectors of the stations located on the NE had motion to the SW, while the stations on the NW exhibited motion to the ENE. The amplitudes of the horizontal velocity vectors are slightly higher for the stations at the northeastern part (~9 mm/yr.) as compared to the northwestern part (~5 mm/yr.). The two GPS stations located in Lakki Plain also subsided. Generally, it should be noticed that the stations located outside the caldera's rim had exhibited stronger deformation as compared to those located inside the rim for both horizontal and vertical components. The nearly opposite direction of horizontal motion that is observed for the stations located at the eastern and western parts of Nisyros may be due to the strong subsidence which had taken place at its northern and central parts during this period, thus forcing the facing eastern and western flanks of the island to 'collapse' towards its centre which produced the observed westward and eastward horizontal motions, respectively.
Significant subsidence (~8 mm/yr.) had also occurred in Yali islet. The horizontal velocity components of the two stations, located on the extreme eastern and western parts, have similar amplitudes (~8 mm/yr.) and clearly point towards the central area of the islet. It is concluded that strong subsidence likely occurred in the region between Yali and Nisyros which caused the two edges of the islet to converge toward this area, consistent with the deformational pattern observed at those two stations.

SAR Interferometry

Conventional Synthetic Aperture Radar (SAR) Interferometry (InSAR) and GPS measurements are the most widely used techniques to measure the ground deformation in volcanoes. For the period 2003-2010 ASAR ENVISAT images were processed in ascending and descending orbital geometry using the SqueeSAR™ Technique. Based on this technique Line of Sight (LOS) velocity maps were produced (Figure 3).

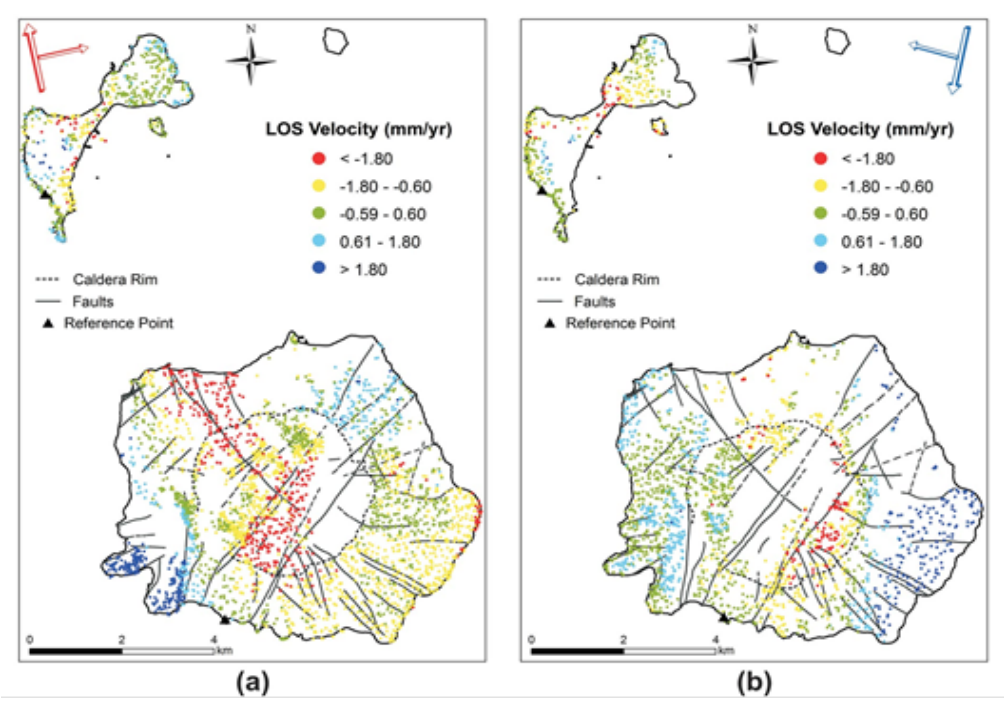

Figure 3. LOS Velocity Field deduced from the SqueeSARTM for Ascending (left panel), and Descending (right panel) orbital geometries, for the period 2003-2010. Red and blue arrows indicate the orbit and acquisition directions for the ascending and the descending data sets, respectively.

Greater negative LOS velocities (~2.5 mm/yr) are observed along the F3 faulting system and between F1 and F2 faulting zones inside the caldera in the ascending image. These values are not observed in the descending image. The western part of Nisyros and west of the caldera's rim show similar velocities for both images, ranging from relatively stable to slightly positive values (~1.5 mm/yr). The greatest LOS velocities (1.8 to 3.0 mm/yr) are observed in the ascending image near the two small peninsulas at the extreme southwestern part, bounded by F1 and F6 faulting systems. The southeastern part of Nisyros shows small negative LOS velocities (~-1.5 mm/yr) in the ascending

image and positive values (up to 2 mm/yr) in the descending image, indicating an eastward component of ground deformation during 2003-2010. The northeastern part of Nisyros has positive LOS velocities (0.6 to 1.8 mm/yr) on both images, with an inconsistent pattern of ground deformation in the northern part due to dense vegetation. The Yali islet shows no consistent deformation pattern between acquisition geometries, except in the northeastern part with relatively stable to small negative LOS velocities. Differential motion between the northeastern and southwestern parts may be due to differing geological characteristics: obsidian in the northeast and pumices in the southwest.
For the period 2018-2022 interferometric results were obtained by the European Ground Motion Service (EGMS, https://egms.land.copernicus.eu/). The data of Ascending and Descending orbital geometries were initially calibrated using the permanent station in Mandraki, and then decomposed on East-West and Vertical component (Figure 4).
To perform the calibration of the InSAR data in the island the velocity vector of the continuous operating GNSS station NISY has been taken into consideration. Initially, the GNSS velocity vector was estimated for the time period that the EGMS product covered, and it was projected into the LOS direction, for both ascending and descending orbital geometries. As a second step, from the EGMS products the LOS velocity vector in both geometries for the “Data Points” located close to GNSS station were compared to the GNSS projected LOS vector, and the difference between the GNSS LOS projected vector and the InSAR LOS vector was estimated. Finally, the difference was “added” to the rest of the “Data Points” to obtain the GNSS calibrated LOS velocity fields. The new calibrated LOS velocity maps on both geometries were combined in order to decompose the LOS vector into the Vertical and the East-West components.

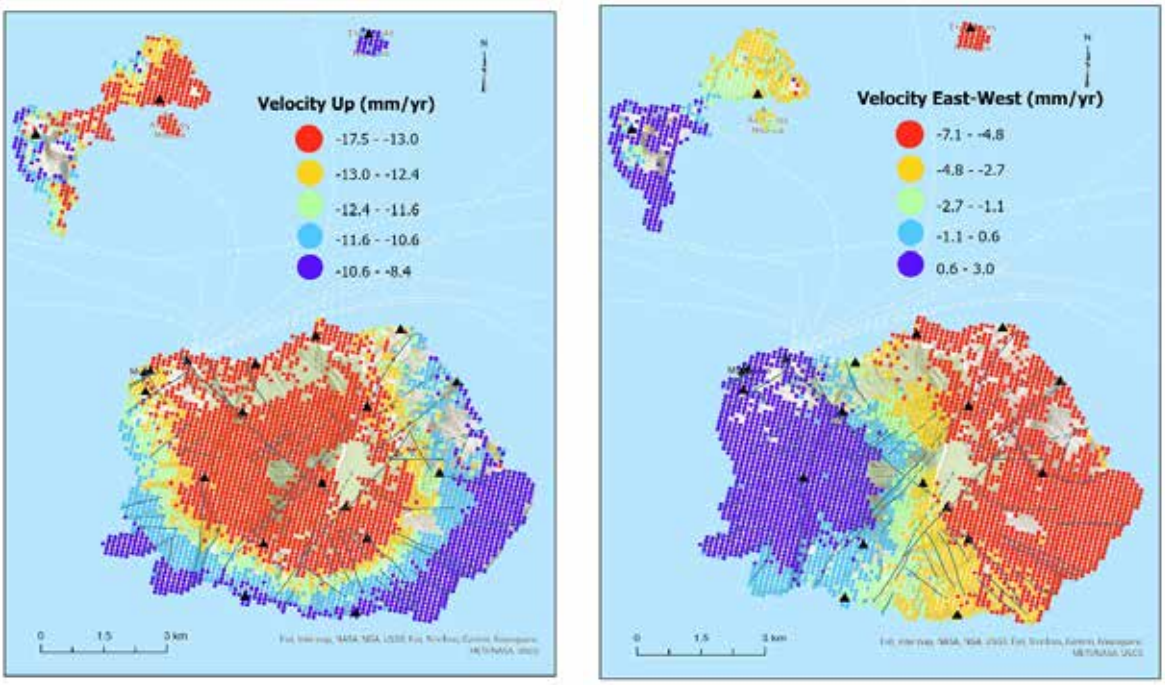

Figure 4. Vertical (left panel) and East-West (right panel) velocity field calibrated using the continuous GNSS station in Mandraki area.

The local calibrated and decomposed EGMS interferometric product show small velocities values for both components, indicative of linear type of deformation. The vertical velocity field highlights and confirm the velocity field deduced by the GPS technique, showing intense subsiding motion in the central and northern part of island (up to -17 mm/yr), but smaller subsidence in the southern Nisyros. The East-West component also clearly depicts the diametrical opposition between the eastern and western part of Nisyros and Yali. The western part exhibits positive velocity values, consistent to eastward motion, while the eastern flanks show negative velocities, indicative of westward motions. A feature that rises observing the East-West velocity field is that changes on the sign of motion coincide with the main tectonic zones that cross-cut the island.

Discussion

During the “unrest” period from 1996 to 2000, strong ground non-linear deformation was observed, which was explained using a model that included two MOGI Point Sources: one offshore and one inland. Interferometric results

(SqueeSAR™) for the subsequent period from 2003 to 2010 showed linear deformation along major faulting zones that cross-cut the island. This deformation included a significant vertical component (subsidence) mainly in the central and northern parts, and a considerable horizontal component in the eastern, western, and southeastern parts. Differential GPS measurements for the period from 2002 to 2023, and interferometric products for the period 2018-2022 indicated intense subsidence at all stations, with a horizontal component pointing towards the central part of Nisyros. The observed deformation may be explained as a result of combined volcanic and tectonic activity, including a decrease in pressure in the possible magma chambers beneath and offshore of Nisyros Island, and possible tectonic motions along the trough offshore north of Nisyros and south of Yali Islet. Notably, there was an absence of any significant shallow seismic activity during the period from 2002 to 2023 in the vicinity of Nisyros.

Acknowledgements

SqueeSAR™ processing was performed by TRE company. Part of this research was supported by the project “Provision of services regarding the implementation of an integrated solution for the continuous and necessary microseismic monitoring of the island of Nisyros, with emphasis on the area of Agia Irini, highlighting the parameters required for geothermal projects” funded by the Public Power Corporation Renewables SA (PPCR) (Special Account for Research Grants of NKUA, project).

References

Ganas A., Elias P., Kapetanidis V., Valkaniotis S., Briole P., Kassaras I., Argyrakis P., Barberopoulou A., Moshou A., 2019. The July 20, 2017 M6.6 Kos Earthquake: Seismic and Geodetic Evidence for an Active North-Dipping Normal Fault at the Western End of the Gulf of Gökova (SE Aegean Sea) (2019), 176 (10), pp. 4177 – 4211.

Geotermica Italiana. 1984. Nisyros 2 geothermal well. PPC EEC report: 1-44.

Geothermica Italiana. 1983. Nisyros 1 geothermal well. PPC EEC report:1-106.

Gorceix MH, 1873a. Sur d’´etat du volcan de Nisyros au mois de mars 1873. C.R. Acad. Sci. (Paris) 77: 597–601

Gorceix MH, 1873b.Sur la r´ecente ´eruption de Nisyros. C.R. Acad. Sci. (Paris) 77: 1039

Gorceix MH, 1873c. Sur l’´eruption boueuse de Nisyros. C.R. Acad. Sci. (Paris) 77: 1474–1477

Hardimann JC, 1999. Deep sea tephra from Nisyros Island, Eastern Aegean Sea, Greece. In Firth, C.R. & McGuire W.J. (eds.) Volcanoes in the Quaternary. Geol. Soc. (London), Spec. Publ. 161: 69-88.

Ioannidis K.,1998. Nisyros Island: Observed damages to buildings in Mandraki. Newsletter, European Center for Prevention & Forecast Earthquakes 2: 33–353

Lagios E, Sakkas V, Parcharidis I, Dietrich V., 2005. Ground deformation of Nisyros Volcano (Greece) for the period 1995-2002: Results from DInSAR and DGPS observations. Bull. Volcanology 68: 201-214

Makris J, Chonia T., 1999. Active and Passive Seismic studies of Nisyros Volcano, East Aegean Sea. In: Jacob BAW, Bean CJ, Jacob STF (eds), Active and Passive Seismic Techniques Reviewed, Proc. 1999 CCSS Workshop Dublin, Ireland: pp 9–12

Nomikou P, Papanikolaou D., 2011. Extension of active fault zones on Nisyros Volcano across the Yali-Nisyros Channel based on onshore and offshore data. Mar. Geophys. Res. 32: 181-192

Papanikolaou D, Nomikou P., 2001. Tectonic structure and volcanic centres at the eastern edge of the Aegean Volcanic Arc around Nisyros Island. Bull. Geol. Soc. Greece XXXIV: 1289–296

Stiros SC, Vougioukalakis G., 1996. The 1970 Yali (SE edge of the Aegean Volcanic Arc) earthquake swarm: Surface faulting associated with a small earthquake. Ann. Tecton. X: 20–30

Tibaldi A, Pasquare, FA, Papanikolaou D, Nomikou P.,2008. Tectonics of Nisyros Island, Greece, by field and offshore data, and analogue modelling. J. Structural Geol. 30: 1489-1506

17th INTERNATIONAL CONGRESS of the Geological Society of Greece

BULLETIN OF THE GEOLOGICAL SOCIETY OF GREECE, SP. PUBL.

EXTENDED ABSTRACT 279

Comparison of dermal bioaccessibility of Cu, Pb, and Hg between modern and ancient cosmetics

Samothraki M-I.[1], Kypritidou Z.[1], Argyraki A.[1]

(1) Department of Geology and Geoenvironment, National and Kapodistrian University of Athens, Panepistimiopolis, Zographou, 15784, Athens, Greece

Introduction

This research highlights the severe health risk that the ancient populations faced by applying raw minerals as cosmetics on a daily basis, following the risk assessment methodology used in modern cosmetics.

In each century, facial cosmetics fulfilled a specific purpose. Since ancient times, the use of cosmetics has been a way of making a statement, an element of culture, as well as an example of scientific development in the field of health. Both men and women in ancient Egypt, Greece and Rome (14th century BCE) used cosmetics not only during religious rituals, but as a daily-care routine to show their social status and prestige. Black-coloured eyeliners were the most common facial cosmetics, which were produced by grinding galena or stibnite (Murube J., 2013, Perez-Arantegui J., 2021). Green, grey, white, red and bluish eyeshadows were prepared by malachite, galena, cerussite, and chryssocolla powders, respectively (Murube J., 2013). Red ochre, cinnabar and minium were used to blush their cheeks. Cerussite and white marl were often used as skin whiteners.

It is reported that cerussite and cinnabar were used until the 16th century BCE by royalty as skin whiteners, lipsticks, and blush (McMullen & Dell'Acqua, 2023; Welcomme *et al*., 2006). However, these natural cosmetics consist of highly toxic elements such as Pb, Sb, Cu, As and Hg, causing serious health effects in ancient populations (Olson K., 2009). Anemia, neurological disorders, kidney failure, liver damage, miscarriage and cancer, are some of the health impacts induced upon ingestion or inhalation of mineral dust containing the above elements. However, references regarding the effects of dermal exposure to these elements (except for exema) and their bioaccessibility through the skin, are scarce.

The aim of this study was the comparison of the potential dermal bioaccessibility of Pb, Cu and Hg contained in ore minerals (such as those used in antiquity) and modern cosmetics. The specific objectives of the study were the determination of: (a) the pseudo-total and sweat extractable elemental concentration, (b) the bioaccessible metal content, and (c) the examination of the systematic exposure and hazard from these elements, in both minerals and cosmetics.

Materials and Methods

Four minerals and the respective commercial cosmetics were selected and studied for their dermal bioaccessible content of toxic elements. The selected minerals include galena, cerussite, malachite, and cinnabar, which were used as eyeliner, foundation, eyeshadow, and blush respectively. By analogy to these minerals, the respective modern cosmetics include foundation, blush, eyeliner, and eyeshadow, purchased from local stores (Table 1). The mineralogical composition of the samples (minerals and cosmetics) was examined through X-ray Diffraction spectroscopy in randomly oriented mounts, from 3-65° 2-theta, with a scanning rate 1°/min (Cuka radiation, 40kV, 40mA, SIEMENS D5000).

Table 1. The associated minerals and cosmetics, and the respective analyzed element of the current study

Mineral	Modern cosmetics	Associated element
Galena	Eyeliner	Pb
Cerussite	Foundation	Pb
Malachite	Eyeshadow	Cu
Cinnabar	Blush	Hg

The pseudo-total elemental composition of minerals and cosmetics was identified by aqua regia digestion. Specifically, about 0.1g of mineral or 1g of cosmetic powders were digested in 1:3.5 HNO3:HCl mixture, for 2hrs in a sandbath (~110°C) following the procedure as described by Irfan *et al.* (2022). The dermal bioaccessible elemental concentrations were determined by extracting the solids with an artificial sweat solution. The extraction solution was composed of 0.5% NaCl, 0.1% urea and 0.1% lactic acid according to EN 1811:2023. The pH 6.5 was adjusted by drops of NH_3. About 0.4g of solid was dispersed in 40ml solution following the assumption that the solid/sweat ratio that is deposited on the face daily is 1mg/0.1ml per skin surface area (Anselm et al., 2022). The suspensions were mixed for 2 hours in the thermal chamber under the constant temperature of 37 Celsius (similar to the human body). Then, followed centrifugation for 5 minutes. Due to the high concentrations level, the aqua regia samples were diluted by 1: 10 ml ratio of sample and 2% HNO_3, whereas, dermal samples were diluted by 1:10 ml ratio of dermal sample and half of the amount of sweat solution with 2% HNO_3. Each sample (mineral and cosmetic) was analyzed in dublicates, and the mean and relative percent difference were calculated. Blanks were also included in each analytical batch. The

extracted solutions were stored at 4°C prior to analysis with F-AAS and ICP-MS, for Pb, Cu, and Hg.
The dermal bioaccessibility of Pb, Cu, and Hg (D_{dermal}, %) from each mineral and/or cosmetic was calculated by dividing the sweat extracted concentration (C_{sweat}, mg/kg) with the pseudo-total concentration (C_{AR}, mg/kg) obtained by aqua regia digestion (Eq 1):

$$D_{dermal}(\%) = \frac{C_{sweat}}{C_{AR}} \times 100 \qquad \text{(Eq. 1)}$$

The systematic exposure dose (SED, mg/kg bw/d) of each element from minerals and cosmetics was calculated according to the European Scientific Committee on Consumer Safety (SCCS, 2023) (Eq. 2):

$$SED = \frac{E_{prod}}{BW} \times \frac{C}{100} \times \frac{D_{abs}}{100} \qquad \text{(Eq. 2)}$$

where E_{prod} is the effective exposure per product (mg/kg/d), BW is the body weight of the consumer (60 kg), C is the elemental concentration (%wt) in the product, and Dabs is the dermal absorption factor (%). E_{prod} values were 0.005 for galena/eyeliner, 0.51 for cerussite/foundation, 0.02 for malachite/eyeshadow and cinnabar/blush, and 0.4 for orpiment/waxing cream respectively (SCCS, 2023).
The risk to human health by application of minerals and modern cosmetics onto the skin on a daily basis, was assessed by calculating the Hazard Quotent (HQ) for each element as (Eq. 3):

$$HQ = \frac{SED}{RfD} \qquad \text{(Eq. 3)}$$

Where RfD is the reference dermal dose for each element. The established RfD for Pb, Cu, and Hg are $1.6*10^{-4}$, $5*10^{-1}$, and $2.3*10^{-4}$ mg/kg bw (Irfan *et al.*, 2022). The sum of HQ for minerals and cosmetics defines the Hazard Index (HI), with an accepted value less than one, when no hazard is induced.

Results & Discussion

The mineralogical analysis of minerals revealed that cerussite and malachite were free of impurities, whereas cinnabar contained minor quartz and galena traces of wurtzite (Fig. 1a). The examined cosmetics (blush, foundation, eyeshadow) consisted mainly of talc, kaolinite and micas. Blush contained also chlorite, smectite and anorthite, whereas the foundation contained zincite and anatase (Fig. 1b).
The pseudo-total elemental concentrations in minerals range from 11.3% wt Hg in cinnabar to 47%wt Pb in cerussite (Fig. 2a), exceeding by far the EU limits for metals in cosmetics (2 mg/kg Pb and 0.1 mg/kg Hg). The respective concentrations in cosmetics range from 6.4 mg/kg Hg in blush to 134 mg/kg Pb in eyeliner, also exceeding the regulatory values.

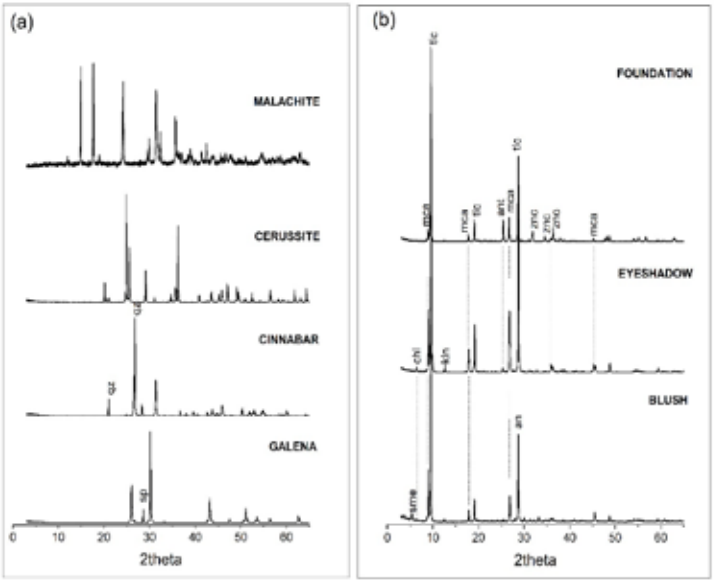

Figure 1. XRD patterns of minerals and cosmetics. The non-annotated peaks in (a) are assigned to the corresponding main mineral phases (i.e. galena, cerussite, cinnabar and malachite). Mineral symbols after IMA (Warr, 2021) (anorthite (an), anatase (ant), chlorite (chl), kaolinite (kln), mica (mca), talc (tlc), quartz (qz), smectite (sme), sphalerite (sp), zincite (znc))

The elemental concentrations extracted by the artificial sweat are much lower in minerals, showing a relative stability to dissolution (Fig. 2b). Particularly, the sweat-extracted concentrations range from 78 mg/kg Hg in cinnabar to 2299 mg/kg Pb in cerussite. The dermal bioaccessibility of minerals is less than 2%. The respective sweat-extracted concentrations in cosmetics range between 0.5 mg/kg Hg in blush and 108 mg/kg Pb in eyeliner. However, the dermal bioaccessibility of the elements is high, following the order: Cu (eyeshadow, 100%)> Pb (eyeliner, 81%)>Pb (foundation, 67%)>Hg (blush, 7%). This shows that, although the sweat extracted concentrations in cosmetics are much lower compared to minerals, they are readily bioaccessible. This is explained by the fact that these elements are bound onto the clay surfaces of cosmetics (smectite, micas) and are easily exchanged by sodium (the major cation in sweat solution).

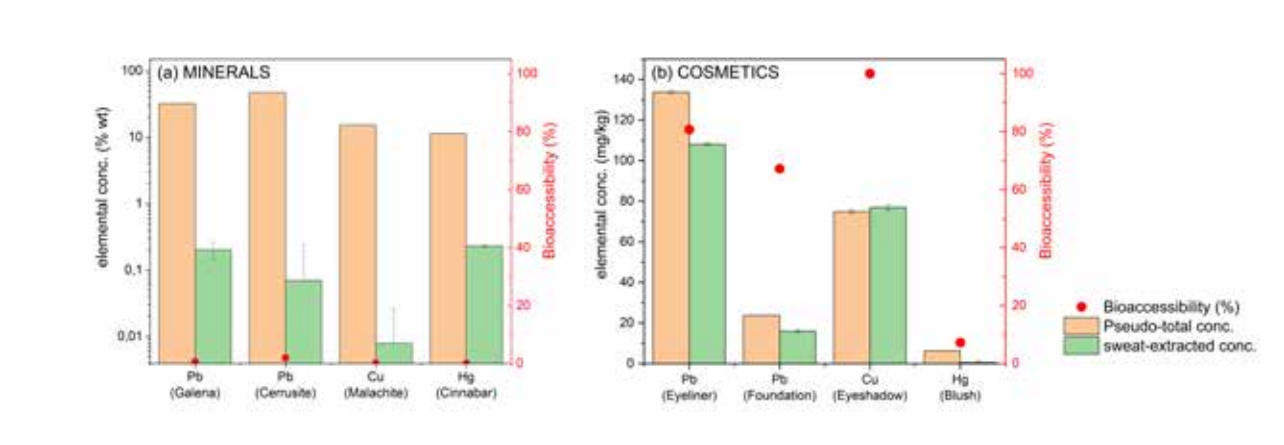

Figure 2. Pseudo-total and sweat extracted concentrations of Pb, Cu, Hg and As from (a) minerals and (b) cosmetics, and their bioaccesibilities

The exposure of consumers to various ingredients contained in cosmetics is assessed based on the systematic exposure dose (SED) as established by SCCS (2023). The SED values for Pb, Cu and Hg were calculated for both minerals and cosmetics, by examining two bioaccessibility scenarios. The first (worst case) scenario assumed that 100% of the pseudo-total concentration of each element is bioaccessible (D_{abs}=100%), whereas the second scenario assumed that only the sweat-extracted elemental concentrations are bioaccessible (D_{abs}=D_{dermal}%). The obtained SED values are given in Table 2.

Table 2. SED values (mg/kg bw/d) as calculated for each element contained in minerals and cosmetics for the two bioaccessibility scenarios

Element	Mineral	D_{abs}=100%	D_{abs}=D_{dermal}%
Pb	Galena	$2,68*10^{-2}$	$1,68*10^{-4}$
Pb	Cerussite	$9,61*10^{-1}$	$1,95*10^{-2}$
Cu	Malachite	$1,57*10^{-1}$	$2,32*10^{-4}$
Hg	Cinnabar	$5,09*10^{-2}$	$2,62*10^{-5}$

Element	Cosmetic	D_{abs}=100%	D_{abs}=D_{dermal}%
Pb	Eyeliner	$1,12*10^{-5}$	$9,00*10^{-6}$
Pb	Foundation	$2,02*10^{-4}$	$1,36*10^{-4}$
Cu	Eyeshadow	$2,49*10^{-5}$	$2,57*10^{-5}$
Hg	Blush	$2,13*10^{-6}$	$1,67*10^{-7}$

As expected, the SED values elements in minerals are much higher than those in cosmetics. The 100% bioaccessibility scenario gives the highest SED values especially for minerals. However, these cosmetics (ancient and modern ones) are applied together onto the face skin on a daily basis, therefore a cumulative systematic exposure should also be calculated. The cumulative SED value ranged from 0.02 to 1.2 mg/kg bw/d in minerals, and $1.7*10^{-4}$ to $2.4*10^{-4}$ mg/kg

bw/d in cosmetics. It is evident that the ancient populations were systematically exposed in high metal concentrations compared to today on a daily basis by applying the raw minerals onto their faces.
The Hazard Quotent and the Hazard Index (HI) for minerals and cosmetics were also calculated for each element in each bioaccessibility scenario. Specifically, at the 100% bioaccessibility scenario the HI for minerals is 2700, whereas for cosmetics 0.16. Additionally, when the dermal bioaccessibility is considered as the exposure scenario, the HI for minerals is 6.22 and for cosmetics 0.05. In either case the HI values of minerals is much higher than 1, implying that the high hazard due to application of ancient cosmetics.
In the 100% bioaccessibility scenario, Hg is the most hazardous element, contributing 63.7% and 89.8% to the total hazard in ancient and modern cosmetics respectively (Fig. 3). On the contrary, when dermal bioaccessibility is considered, Pb is the more hazardous element, contributing over 70% in total HI. This shows that, although Hg is more toxic and carcinogenous, it is less hazardous due to its lower penetration through the skin. It is documented that, among the mercuric substances, cinnabar is insoluble in water with low oral bioaccessibility (~0.2%) (Liu et al., 2009). Moreover, studies on dermal contact between cinnabar-rich sands and workers, showed that Hg was not bioaccessible through skin (Cegolon et al., 2022). However, Pb has high bioaccessibility, explaining the various health effects induced during ancient times. Among lead compounds, lead released from cerussite is more bioavailable than from galena, due to its higher solubility. Considering that cerussite is more easily dissolved and applied as a foundation in a larger surface area, the expected health impacts are more severe, compared to the other elements.

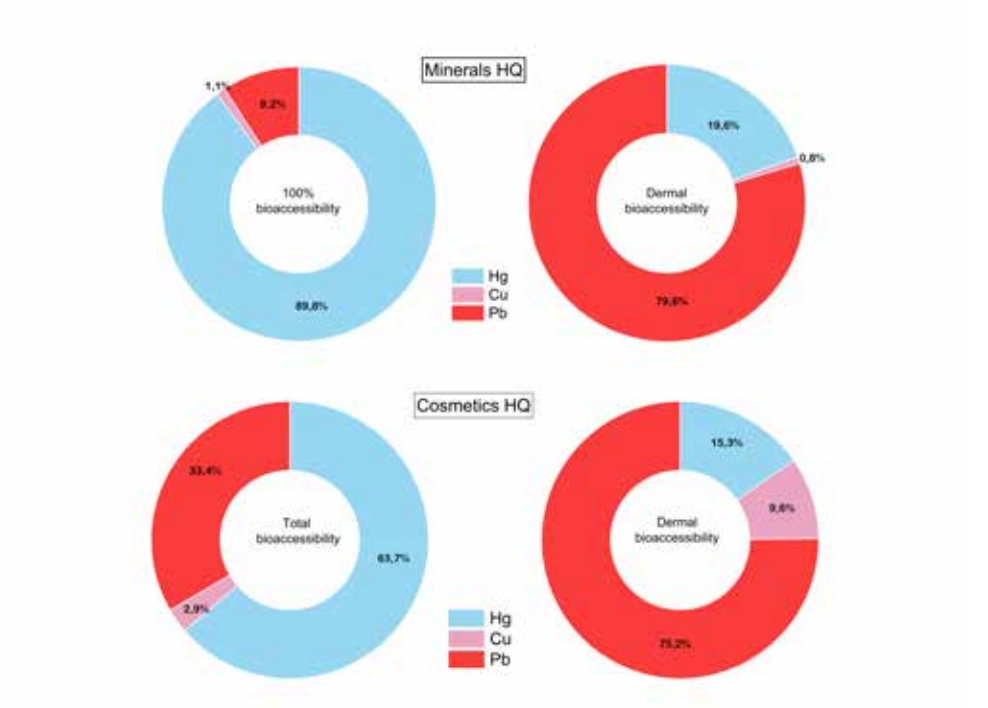

Figure 3. Contribution of each element to the total HI obtained by applying minerals and modern cosmetics, in the two bioaccessibility scenarios

Conclusions

Minerals have been extensively used as cosmetics from ancient times since the 16th century BCE, due to their variety of colours, such as galena, cerussite, cinnabar and malachite. However, these phases are primary ore minerals for the extraction of Pb, Cu and Hg, elements of high toxicity for living organisms. Although numerous in vitro and in vivo toxicological studies have been carried out regarding the bioaccessibility of these elements, most of them involve artificial organic compounds (mostly present in commercial products) with different physicochemical properties compared to natural mineral phases. Moreover, these studies refer to bioaccessibility due to inhalation and/or ingestion of these compounds, which is much higher compared to the penetration through skin. In this study we tried to assess the bioaccessibility of elements contained in ancient cosmetics following the risk assessment procedure of modern cosmetics. The results indicate that the ancient populations were exposed to severe health risk due to the application of raw minerals onto their skin on a daily basis.

References

Anselm, O.H., Davidson, C.M., Oyeyiola, A.O., Oluseyi, T.O., 2022. Effects of Artificial Sweat Formulation and Extraction Temperature on Estimation of the Dermal Bioaccessibility of Potentially Toxic Elements in a Contaminated Soil from an E-Waste Recycling Site. Geosciences 12, 31.

Cegolon, L., Mastrangelo, G., Covelli, S., Petranich, E., Pavoni, E., Filon, F.L., 2022. Occupational exposure to mercury from cinnabar enriched sand in workers of Grado Beach, Gulf of Trieste (North-eastern Italy, upper Adriatic Sea). Marine Pollution Bulletin 184, 114057

European Committee for Standardization, 2023. EN 1811:2023 Reference test method for release of nickel from all post assemblies which are inserted into pierced parts of the human body and articles intended to come into direct and prolonged contact with the skin, p.29

Irfan, M., Shafeeq, A., Siddiq, U., Bashir, F., Ahmad, T., Athar, M., Butt, M.T., Ullah, S., Mukhtar, A., Hussien, M., Lam, A.S., 2022. A mechanistic approach for toxicity and risk assessment of heavy metals, hydroquinone and microorganisms in cosmetic creams. Journal of Hazardous Materials 433, 128806

Liu, J., Shi, J-Z., Yu, L-M., Goyer, R.A., Waalkes, P., 2008. Mercury in traditional medicines: Is cinnabar toxicologically similar to common mercurial? Exp Biol Med (Maywood) 233(7), 810–817

Murube, J., 2013. Ocular cosmetics in Ancient Times. The Ocular Surface, 11 (1), 2-7.

Olson, K., 2009. Cosmetics in Roman Antiquity: Substance, Remedy, Poison. The Classical World 102, 3, 291-310

Perez-Arantegui, J. 2021. Not only wall paintings—pigments for cosmetics. Archaeological and Anthropological Sciences 13, 189

SCCS (Scientific Committee on Consumer Safety), 2023. The SCCS notes of guidance for the testing of cosmetic ingredients and their safety evaluation, 12th revision, p.199

Warr L.N. 2021. IMA-CNMNC approved mineral symbols. Mineralogical Magazine 85, 291–320

17th INTERNATIONAL CONGRESS of the Geological Society of Greece

BULLETIN OF THE GEOLOGICAL SOCIETY OF GREECE, SP. PUBL.

EXTENDED ABSTRACT 280

Result of an inventory program (SAMY) of boreholes of various uses and their contribution to the water balances of groundwater systems.

P. Sabatakakis[1], M. Theodoropoulou, M. Tzima, C. Christidis.
[1]*Hellenic Survey of Geology and Mineral Exploration (H.S.G.M.E) 1 Spirou Loui St., 13677 Acharne, Greece, psampatakakis@eagme.gr*

Research Highlights

This project constitutes the first systematic documentation of Greece's water resources, with a focus on both qualitative and quantitative groundwater characteristics.

The project data, combined with the Daniel storm in the Thessaly Region, demonstrated its contribution to aquifer management in the affected area and to mitigating the impacts of severe weather.

Introduction

Water is a heritage that must be protected. Both internationally and in Greece, the pressures on water resources are increasing, because of the growing demand from various users for sufficient quantity and quality of water.

Boreholes constitute a critical parameter in the management of water resources, particularly groundwater. The large number of boreholes as well as uncontrolled abstractions have created and accumulated several problems of mismanagement, either in the form of salinization of coastal aquifers or depletion of aquifers. The extensive operation of boreholes in Greece, many of which remain undeclared, significantly affects water balance calculations, the quantitative assessment of groundwater systems, and the evaluation of water usage and needs.

The SAMY Project is carried out by the Hellenic Survey of Geology and Mineral Exploration (H.S.G.M.E.). Project main activities in Greek Territory are: (a) borehole inventory by recording drilling technical data and on-line measurements, (b) database production based to all recorded data and (c) groundwater abstraction related to groundwater resources in ground water bodies. During fieldwork, data recording includes geographical coordinates, operational status, and technical borehole characteristics (depth, drill hole diameter, casing diameter, and pump type). Also, borehole usage such as irrigation, drinking water, stock farming are basic features of recording data with details of pumping.

Based on inventory data final reports are drawn up for all Ground Water Systems in the field including also geomorphological, geological, hydrogeological conditions, land use area, statistics with processing of all recording raw data, drawing water estimation and aquifer water balance.

The result of the inventory program with the systematic counting of boreholes in all the Ground Water Systems (GWS) and the recording of the extractable quantities of water, contributed to the effective implementation of the Water Framework Directive 60/2000, but also to the formulation, implementation and control of policies (water saving, programs of measures, etc.) concerning the rational management of water resources.

The annual volume of groundwater which is used from an aquifer system is one of the two basic factors of the 'equation' required to achieve its rational exploitation in each case. The other factor concerns the recording and mapping of the hydrogeological and hydrological characteristics of a groundwater table, some of which require a "one-time" recording and mapping, such as geological and hydrolithological structures. The establishment of such an information platform, alongside the development of an institutional mechanism for continuous data updating, is essential for effective groundwater management.

Materials and Methods

This study represents the first systematic documentation of water resources in Greece. The program created an extensive database far beyond that of the hydrogeological management of the country's groundwater systems, such as: irrigation needs in different areas for the same crops, energy costs for the same pumping quantities but from different depths in the various rural areas, etc.

A total of 108,092 boreholes of various uses were inventoried and the information collected for this project is:

- geographical and topographic data of the project location
- data of the owner and user of the project
- data of the use of the project (duration, water supplies, type of use)
- hydrological data (average precipitation of at least 20 years, and evapotranspiration), utilizing the information of the 3rd Community Support Framework (CSF) Program of the H.S.G.M.E, which was implemented in all water compartments simultaneously during the period 2006-2012)

- on-site data of the technical characteristics of the boreholes, in particular with regard to the depth of borehole and extraction, duration of extraction / year, yields / hour
- physicochemical data of water (conductivity, temperature, pH)

The high density of collected data, particularly in plains with a significant number of boreholes, facilitated both precise estimations of annual and peak-period water consumption and the detailed analysis of specific hydrogeological parameters. The detailed mapping whose information may be useful beyond hydrogeology.

The methodology for processing large-scale aquifer data included: (a) aquifer system delineation based on Management Plan boundaries, (b) assessment of infiltration and evapotranspiration parameters, and (c) analysis of meteorological data spanning at least 20 years.

For the compilation of the maps, the same methodology was followed in terms of processing the measurements in “non-pumping” conditions and not in dynamic conditions. This is because, as is known, for example, both the level and the conductivity can vary significantly in pumping conditions, resulting in the mapping presenting irregular local variations.

The collection of annual groundwater consumption data and withdrawal rates facilitated not only the total volume estimation but also the assessment of the groundwater systems’ overall transfer capacity during the same period. The Project provided important hydrogeological information regarding the supply capacities of a groundwater system or a large part of it is under universal intensive exploitation, as occurs during the period when irrigation is at its peak. During this period and in whatever groundwater systems the inventory work was in progress, it became possible to capture the dynamic salinization conditions in coastal groundwater systems with an “open” hydraulic front to the sea, as well as the overall dynamic retreat of the hydrostatic level.

Results and discussion

The project’s results support the General Directorate of Water of the Ministry of Environment & Energy in strengthening national water policy, ensuring both water quality and quantity while aligning with EU Directives (60/2000/EC, 118/2006/EC, and 91/676/EEC).

The total number of recorded boreholes is 108,092. Also, the technical reports include statistical analysis and processing to draw conclusions on all basic parameters as they arise from the registration of the inventory forms, the recording of all parameters on thematic maps and the assessment of the water balance components with the characterization of the Ground Water System (G.W.S.) as Surplus or Deficit. From the preparation of the Technical Reports, it emerged that the large G.W.S. that concentrate the largest number of active boreholes are characterized as deficient.

Figure 1. The total of boreholes in Greece by SAMY Project.

SAMY and DANIEL storm

Following the devastating DANIEL storm, the SAMY Project played a key role in identifying water points within the flooded areas and monitoring underground aquifers in the Thessaly Region. During the SAMY Project, more than 21,894 boreholes have been recorded in Thessaly Region.

Based on the boundaries of the flooded areas of the DANIEL storm (as produced by the Copernicus program - 11/09/2023) and the data of the SAMY, the following results emerge:

- Within the boundaries of the flooded areas, 4,452 boreholes are located, which correspond to approximately 20% of the total boreholes in Region Thessaly.
- More specifically, within the flooded areas, the rate of 87.1% (3,876 boreholes) are active and main use for irrigation, 12.1% (539 boreholes) are inactive/unexploded, 0.5% (22 boreholes) for domestic water 0.3% (15 boreholes) for livestock water and 297 abandoned boreholes have been inventoried.
-

Table 1. Number of boreholes in Thessaly Region

Municipality	Boreholes	Flood zone	Boreholes
Sofades	1,160	Larisa- Stefanovikeio	843
Palama	1,060		
Larisa	383	Trikala – Karditsa - Palamas	3,617
Trikaion	345		
Farsala	299		
Kileler	281		
Farkadonas	186		
Tirnavos	183		
Tempi	181		
Dokomos	173		
Riga Feraioy	61		
Mouzaki	120		
Karditsa	20		

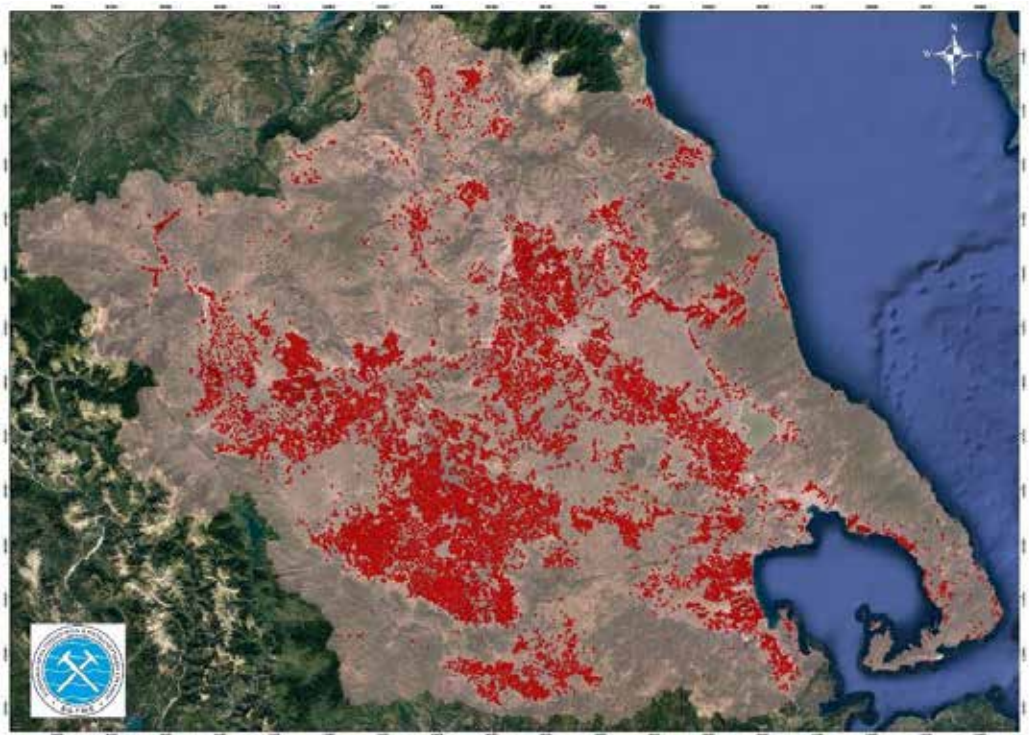

Figure 2. Boreholes in Thessaly aquifer

The functionality of the boreholes located within the flooded areas may have been affected to a very large extent due to the reverse infiltration of water and the subsequent deposition of fine clay material (mud) within the permanent piping of the boreholes, resulting in the non-functionality of the filter pipes and submersible pumping units due to blockage (clogging). Extensive damage is also expected to the accompanying facilities such as sheds, electrical supply panels, pumping units, etc.

Table 2. Number of each use and operational function of boreholes in Thessaly Region

Operational function	Boreholes	Main Use	Boreholes
Active	3,921	Irrigation	3,876
Unexploited	297	Domestic water	22
Inactive	242	Livestock uses	15
		Industrial use	8

Also, from the total available quantities in the entire Water District of Thessaly, it emerged that approximately 90% is used to cover irrigation needs, 6.7% for livestock farming, 1.6% for water supply and 1.7% for industrial and other use.

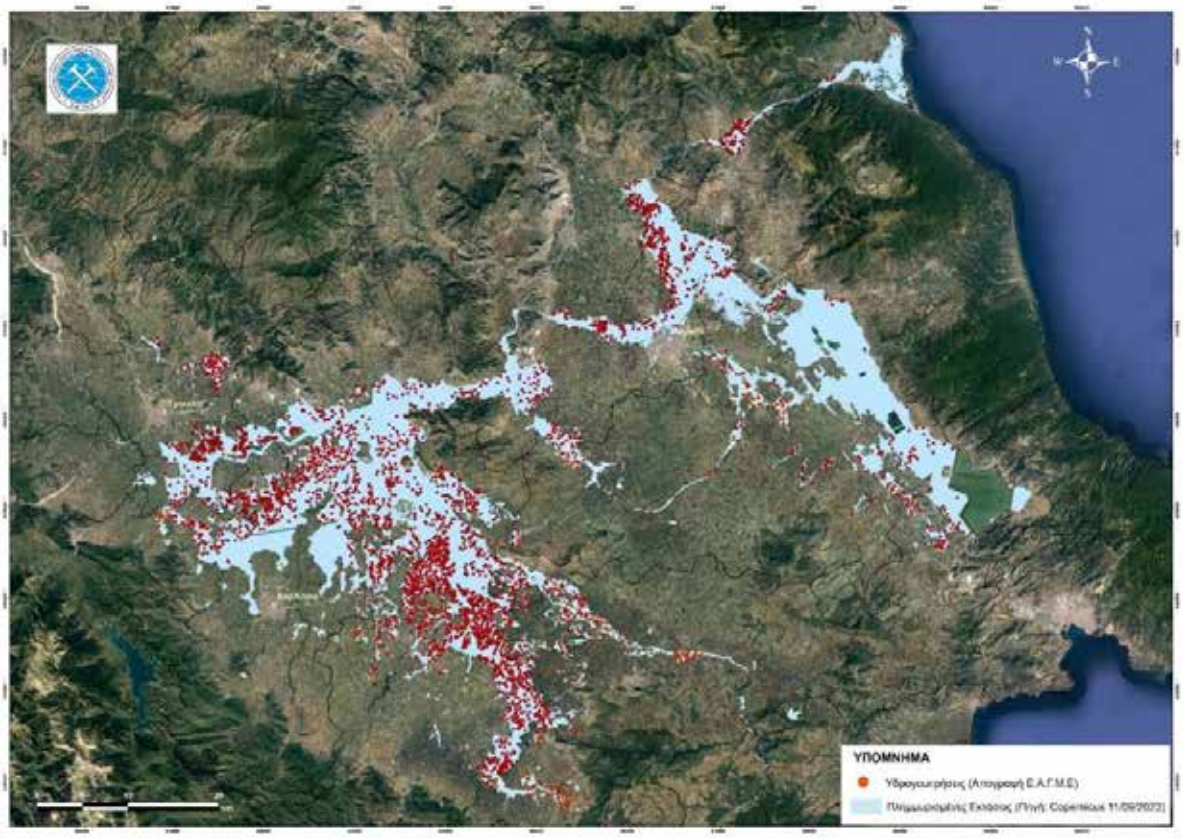

Figure 3. Borehole distribution and flooded areas in the Thessaly Region

Conclusions

This study presents an overview of Greece's water resources. The SAMY Project is a key tool in the effective management of water abstraction and the protection of groundwater systems from over-pumping. The volume of water abstraction is an important parameter for the calculation of water balances, helping to assess the status of Groundwater Systems and the pressures they are exposed to take appropriate measures, as well as to achieve the goal of their rational management. For the first time, we integrate temporal and spatial groundwater data with geological, hydrogeological, land use, and other relevant information to provide a comprehensive analysis. Our key findings are:

- Rational management of the country's water resources and thereby ensuring sustainable development,

benefiting the entire population of the country. This will significantly contribute to the correct decision-making on water resources management by the competent decision-making centers.

- Achieving social consensus and citizen support, allowing them to understand the importance of the entire project by helping to collect data, as well as the benefits that will arise with a direct impact on productive and social life.
- Informing local communities, through a mechanism that will promote dialogue, to learn about the possibilities of the Aquifer System from which they are supplied and thus have knowledge about the possibilities of its exploitation, or even the need to contain and protect the reserves. In both cases there is a social benefit for the integrated and sustainable management of water systems.
- Approval of a strategic plan for the exploitation of the country's water resources by implementing specific actions, to ensure the needs of society and the economy for sustainable water, while at the same time raising awareness among citizens and making them stakeholders in the rational management of available water resources.
- Provision of the National Water Abstraction Register with points/data that will result from the implementation of this project in accordance with Directives 60/2000/EC, 118/2006/EC & 676/91/EEC.

Finally, the continuous update and integration of groundwater data are fundamental for sustainable management in Greece. Furthermore, establishing a Strategic Water Policy will be crucial in addressing future demands and mitigating climate change impacts. The establishment and operation of an Entity, that will utilize the experience and data of the SAMY Project. Also, it ensures the continuation of the flow of this information is the only way for the rational management of water resources.

Acknowledgements

We acknowledge the Hellenic Survey of Geology and Mineral Exploration (H.S.G.M.E.) for their invaluable support in providing data and technical information essential to this research.

References

Copernicus, (2024). Copernicus program - 11/09/2023 data.

H.S.G.M.E., (2024). Results from the hydro-census work and water balance calculation of all groundwater system in Greece. Technical Report. (in Greek).

H.S.G.M.E., (2024). 3rd Community Support Framework (CSF) Program for the period 2006-2012.

Ministry of Environment and Energy (2024). Watershed Management Plans (WMP). Available online: https://wfdver.ypeka.gr/el/management-plans-gr/2revision-approved-management-plans-gr/

17th INTERNATIONAL CONGRESS of the Geological Society of Greece

BULLETIN OF THE GEOLOGICAL SOCIETY OF GREECE, SP. PUBL.

EXTENDED ABSTRACT 281

The 2025 Santorini Swarm: Spatiotemporal Distribution and Coulomb Stress Changes. Preliminary Results

Sardeli E.[1], Pavlou K.[1], Karakonstantis A.[1,2], Athanasopoulos A.[1], Pappas S.[1], Vallianatos F.[1,3]

(1) Section of Geophysics-Geothermics, Department of Geology and Geoenvironment, National and Kapodistrian University of Athens, 15784 Athens, Greece, eirsard@geol.uoa.gr

(2) University of Patras, Patra, Greece

(3) Institute of Physics of Earth's Interior and Geohazards, UNESCO Chair on Solid Earth Physics and Geohazards Risk Reduction, Hellenic Mediterranean University Research & Innovation Center, 73133 Chania, Greece

Introduction

Santorini Island is located in the central part of the Hellenic Volcanic Arc, which lies in the back-arc region of the Hellenic subduction zone. The majority of identified faults in Santorini exhibit a SW-NE orientation (Heiken & McCoy, 1984). Similarly, Santorini's main volcanic centers, including the Christiana Islands and the submarine volcano Columbo (located 7 km northeast of Santorini), are aligned along two seismic fault lines: the Kameni Line and the Columbo Line. These lines intersect the caldera in a northwest-southeast direction. Santorini is predominantly composed of volcanic rocks, except for a pre-volcanic substratum in the southeastern region, consisting of Mesozoic and Cenozoic metamorphic limestones and schists (Nicholls, 1971; Druitt et al., 1989).

The most significant eruption of the Santorini volcano, known as the Minoan eruption, occurred approximately in 1600 BC. In 1650, Santorini Island suffered significantly from the explosive eruption of the Columbo submarine volcano, The last recorded eruption occurred in 1950. The most intense seismic activity in this region has been observed along the NE–SW trending Santorini–Columbo volcano-tectonic line (Druitt et al., 1999).

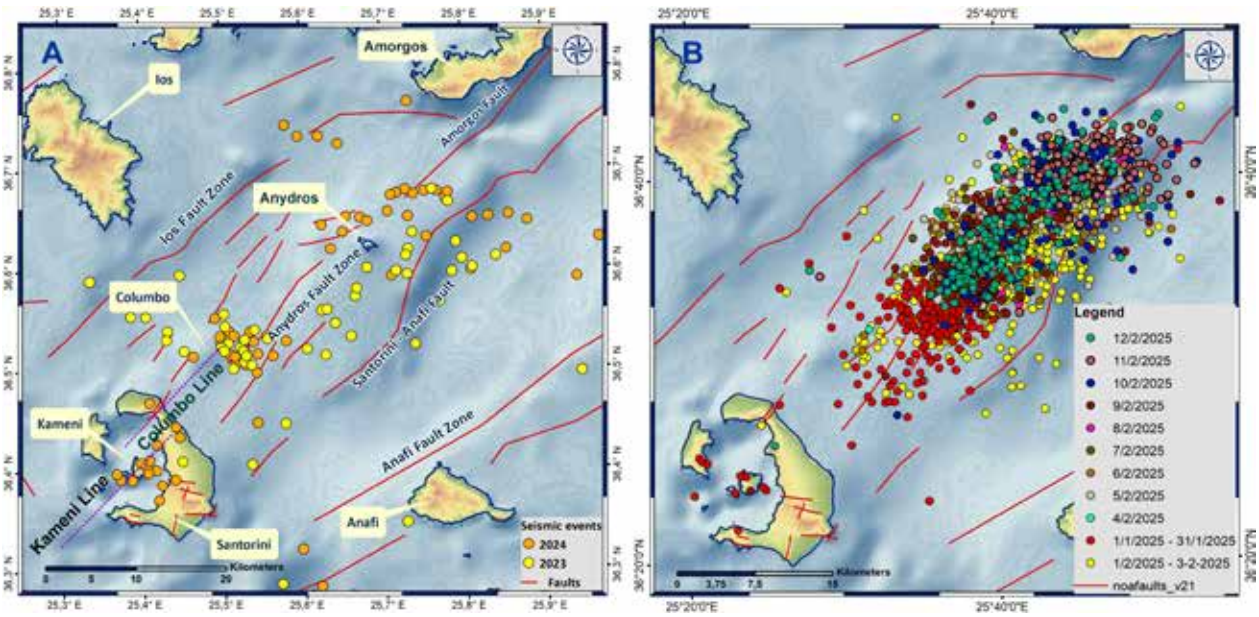

Figure 1. (A) Seismicity in the broader area of Santorini Island during the period 2023-2024. (B) Spatiotemporal distribution of the earthquake swarm during the first period of temporal distribution.

Since January 2025, weak to moderate earthquakes have occurred north – east of Santorini (Figure 1A). However, in early 2025, Santorini Island experienced a significant seismic swarm, recording over 4,000 earthquakes (Figure 1B). The largest earthquake had a local magnitude of M_L 5.3 on February 10, 2025. This seismic activity initiated in the caldera area of Santorini and progressively migrated northeast, offshore the island, between Santorini and Amorgos. In this study, we examine the spatiotemporal distribution and the computed Coulomb stress changes resulting from each earthquake of moment magnitude $M_w \geq 4.7$ that occurred during the 2025 Santorini - Amorgos swarm. Additionally, we determined the Coulomb stress changes at each focus of the following significant earthquakes, defined as those of moment magnitude $M_w \geq 4.7$. Finally, a modified Wadati method was used to determine the average V_p/V_s ratio for the Santorini-Amorgos area.

Seismic Data and Methodology

To investigate the spatiotemporal distribution and the computed Coulomb stress changes during the 2025 Santorini earthquake swarm, we used data such as the earthquake catalog from January 1, 2025, to February 28, 2025, and the available CMT (Centroid Moment Tensor) focal mechanism solutions from the National Observatory of Athens (https://bbnet.gein.noa.gr/HL/seismicity/mts). The earthquakes that were selected for the period from February 3rd to 18th have a moment magnitude M_w greater than or equal to 4.7 (Table 1).

Numerous studies on major earthquakes have demonstrated a strong correlation between positive Coulomb stress changes and the spatial evolution of seismic events (King et al., 1994; Vallianatos & Pavlou, 2021). Research has shown that Coulomb failure stress changes (ΔCFS) triggered by large earthquakes can either accelerate or delay the occurrence of subsequent seismic events. Additionally, these Coulomb stress changes can influence and control their temporal and spatial distribution (Stein, 1999; Kilb et al., 2002). Specifically, a positive ΔCFS transfer to a receiver fault brings it closer to failure, whereas a negative ΔCFS indicates a delay in failure.

The calculation of Coulomb Failure Stress changes (ΔCFS) under undrained rock conditions is based on the Coulomb failure criterion, which quantifies the proximity to failure. It is expressed by the following equation (Scholz, 2019):

$$\Delta CFS = \Delta_T - \mu' \Delta_\sigma$$

where Δ_T represents the changes in static shear stress, Δ_σ denotes the changes in effective normal stress, and $\mu\mu$' is the coefficient of friction (Cocco, 2002).

The ΔCFS changes were calculated using the Coulomb 3.3 software (Toda et al., 2011) in an elastic half-space, assuming a uniform slip on the rupture planar surfaces that imposes an "ideal" stress redistribution around the seismic faults. The software was used to model the Coulomb failure stress changes (ΔCFS) with a mean friction coefficient of μ' = 0.4. Additionally, the empirical relations of Wells and Coppersmith (1994) were employed to determine the width and length of the subsurface faults for each modeled earthquake (Lin & Stein, 2004; Toda et al., 2005).

Table 1. The most significant 2025 Santorini seismic events

No	Date -Time	Latitude	Longitude	Depth	Mw	Strike	Dip	Rake
1	3/2/2025 9:29	36.5854	25,7364	13,7	4,8	41	52	-117
2	3/2/2025 12:17	36,6389	25,7478	10,5	4,8	50	55	-86
3	3/2/2025 20:19	36,6289	25,6975	13,9	4,8	14	78	-161
4	4/2/2025 2:46	36,6197	25,7066	14,3	4,7	44	51	-97
5	4/2/2025 13:04	36,6167	25,727	5,0	5,0	44	48	-98
6	5/2/2025 19:09	36,6582	25,7213	11,2	5,0	45	48	-80
7	7/2/2025 7:16	36,5664	25,7278	7,0	4,7	19	56	-127
8	8/2/2025 9:00	36,5799	25,7439	5,0	4,7	35	55	-118
9	9/2/2025 19:05	36,6454	25,6544	11,2	5,1	26	62	-133
10	10/2/2025 11:23	36,6602	25,8546	10,0	4,7	15	79	-172
11	10/2/2025 20:16	36,6538	25,7456	5,0	5,2	207	66	-154
12	10/2/2025 22:37	36,6255	25,787	10,0	4,9	50	45	-92
13	11/2/2025 5:58	36,6952	25,8178	5,0	4,7	192	79	179
14	12/2/2025 8:29	36,4071	25,9418	5,0	4,8	221	85	-164
15	12/2/2025 9:15	36,5977	25,6425	8,8	4,7	247	37	-57
16	17/2/2025 7:49	36,599	25,7047	5,1	4,8	233	43	-82
17	18/2/2025 4:46	36,6199	25,8577	5,0	4,9	39	46	-110

Furthermore, the present study used the best-located hypocentral solutions (~1600 earthquakes) to improve hypocentre depth estimates. This subset of events was recorded in stations with both P- and S-wave arrival time picks at epicentral distances <200 km. An average $V_p/V_s V_p/V_s$ ratio was determined for the Santorini-Amorgos area using a modified Wadati method (Chatelain, 1978). This method is based on the differences in body wave arrival times P_i and P_j and S_i and S_j for an event k recorded by two stations (i, j) at hypocentral distances x_i and x_j, respectively, $DT_p = P_i - P_j = (x_i - x_j)/V_p$ and $DT_s = S_i - S_j = (x_i - x_j)/V_s$. Thus, $DT_s/DT_p = V_p/V_s$, and a plot of versus DT_p indicates a V_p/V_s ratio of 1.76 for the broader region (Figure 2). Konstantinou et al. (2013) estimated the Vp/Vs ratio between February 2011 and June 2012 at Santorini caldera. The average Vp/Vs ratio was 1.54 ± 0.17, much lower than the regional background value of 1.77. This led the authors to conclude that the involvement of gases was the

main factor that influenced the evolution of that swarm. On the contrary, Andinisari et al. (2021) estimated that Vp/Vs ratios varied from 1.74 to 1.91 during the 2011 to 2019 time period.

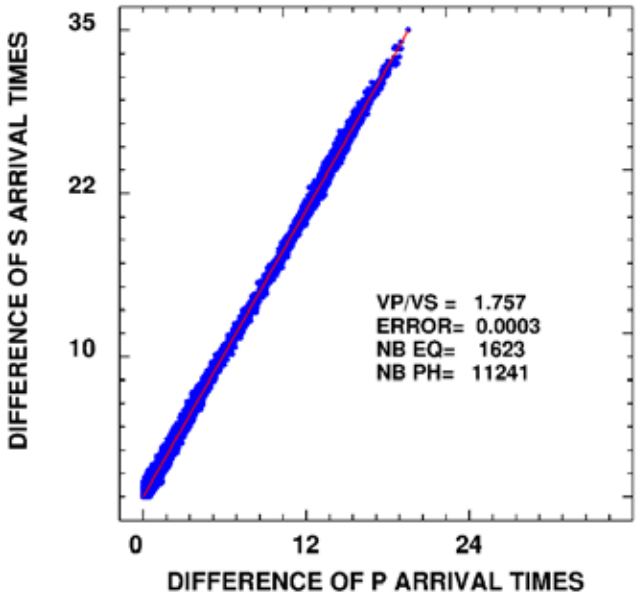

Figure 2: Vp/Vs ratio in the Santorini-Amorgos area using a modified Wadati diagram.

In the same study, the authors estimated the Vp/Vs ratio between 1.77 and 1.86 in the area to the NE, between Santorini and Amorgos, near the region that was activated in this period that we have examined.

Results and Discussion

The seismic swarm began with small seismic events in January 2025. However, on February 3, 2025, three earthquakes of magnitude M_w 4.8 occurred. In the following days, specifically until February 18, 2025, another 15 seismic events of a magnitude M_w greater than 4.7 took place in the Santorini-Amorgos area. Hence, to understand the evolution of the earthquake sequence, the co-seismic static Coulomb stress changes for each of these earthquakes, which occurred at depths ranging from 5 to 15 km (Table 1), were calculated.

Figure 3 depicts the first two significant earthquakes on February 3, 2025, at 9:25 and 12:17, both of a magnitude M_w 4.8 and at depths 13.7 km and 10.5 km, respectively. The spatial distribution of the ΔCFS reveals a stress decrease towards the NW and SE and a stress increase towards the NE and SW. Earthquakes that occurred up to February 18, 2025, are represented by white dots, and their spatial distribution follows the fault strike with a significant concentration in positive lobes. Cross-section AB, which illustrates the seismic events in the seismically activated area, shows that the subsequent events following the mainshock occur in regions with positive values of Coulomb stress changes (red lobe). These positive values indicate that the transfer of Coulomb stress changes due to the occurrence of the first strong event may have triggered the following events.

Additionally, the ΔCFS values at the hypocenters of the following seismic events were estimated. The results indicate a stress increase of +1.425 bar from the earthquake on February 4, 2025, at 13:04 to February 17, 2025, +0.314 bar from the earthquake on February 4, 2025, at 13:04 to February 10, 2025, at 20:16, +0.196 bar from the earthquake on February 4, 2025 at 13:04 to February 7, 2025, and +0.173 bar from the earthquake on February 9, 2025 to February 12, 2025 at 9:15. It is worth noting that while the co-seismic Coulomb stress changes were modeled assuming pure double-couple (DC) sources, recent studies (Zahradnik et al., 2025) have shown that several events within the 2025 Santorini–Amorgos swarm exhibit significant non-double-couple components. These components may locally alter the stress field beyond what is captured by DC-only modeling.

The spatial distribution of the static Coulomb stress changes for earthquakes with a magnitude greater than or equal to M_w 4.7 reveals a stress increase towards NE and SW. The migration of seismicity in the Santorini-Amorgos region closely aligns with the Coulomb stress transfer results, confirming that stress redistribution played a crucial role in triggering subsequent earthquakes. The initial scattered seismicity in late January intensified in early February, with a clear NE migration until February 5. This pattern corresponds to areas of increased Coulomb Failure Stress (ΔCFS), indicating that the stress changes induced by earlier earthquakes facilitated the activation of nearby faults.

The return of seismicity to the broader Anydros region after February 6 and the secondary NE shift on February 10–11 further support the influence of stress transfer on the sequence's evolution. These findings underscore the strong correlation between seismic migration and Coulomb stress changes, highlighting the importance of stress redistribution in controlling the evolution of the sequence.

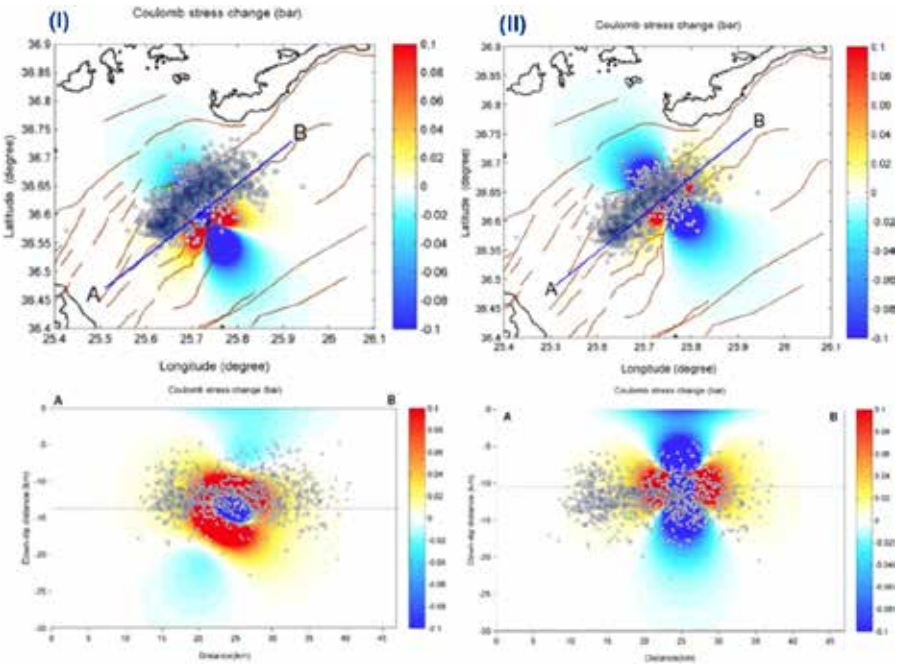

Figure 3: Coseismic Coulomb stress change distributions resulting from (I) the M_w 4.8 earthquake on February 3, 2025, at 9:29 and (II) the M_w 4.8 earthquake on February 3, 2025, at 12:17, with centroid depths of 13.7 km and 10.5 km, respectively. The white circles represent the hypocenters of the swarm until February 18, 2025. Cross-sections AB illustrate the changes in Coulomb stress (ΔCFS) relative to depth related to these seismic events.

Acknowledgements

The research work of S.E was supported by the Hellenic Foundation for Research and Innovation (HFRI) under the 5th Call for HFRI PhD Fellowships (Fellowship Number: 20518).

References

Andinisari, R., K.I. Konstantinou, and P. Ranjan (2021). Seismicity along the Santorini-Amorgos zone and its relationship with active tectonics and fluid distribution, Physics of the Earth and Planetary Interiors, 312, 106660, https://doi.org/10.1016/j.pepi.2021.106660

Cocco, M. 2002. Pore pressure and poroelasticity effects in Coulomb stress analysis of earthquake interactions. Journal of Geophysical Research, 107(B2), 2030. DOI: 10.1029/2000JB000138

Druitt T. H., Davies M. S., et al., 1999. The Santorini Volcano. (Geological Society Special Memoir, 19), Geological Society Pub House, London. ISBN 1 86239 048 7

Druitt, T. H., Mellors, R.A., Pyle, D.M., and Sparks, R.S.J., 1989. "Explosive volcanism on Santorini, Greece." GEOLOGICAL MAGAZINE, Vol. 126, No. 2, p. 95-126. DOI:10.1017/S0016756800006270. [Journal Article]

Heiken, G., McCoy, F., 1984. Caldera Development during the Minoan Eruption, Thira, Cyclades, Greece. Journal of Geophysical Research, 89, 8441-8462. https://doi.org/10.1029/JB089iB10p08441

Kilb, D., Gomberg, J., Bodin, P., 2002. Triggering of earthquake aftershocks by dynamic stresses. Nature 408,570–574. DOI: 10.1038/35046046

King, G. C., Stein, R. S., Lin, J., 1994. Static stress changes and the triggering of earthquakes: Bulletin of the Seismological Society of America, 84(3),935-953. https://doi.org/10.1785/BSSA0840030935

Konstantinou, K.I., Evangelidis, C.P., Liang, W.-T., Melis, N.S., Kalogeras, I., 2013. Seismicity, Vp/Vs and shear wave anisotropy variations during the 2011 unrest at Santorini caldera, southern Aegean. J. Volcanol. Geotherm. Res. 267, 57–67. https://doi.org/10.1016/j.jvolgeores.2013.10.001

Lin, J., & Stein, R. S., 2004. Stress triggering in thrust and subduction earthquakes and stress interaction between the southern San Andreas and nearby thrust and strike-slip faults: STRESS TRIGGERING AND FAULT INTERACTION. Journal of Geophysical Research: Solid Earth, 109(B2). https://doi.org/10.1029/2003JB002607

Nicholls, I. A., 1971. Petrology of Santorini Volcano, Cyclades, Greece. J. Petrol. 12 (1), 67–119. https://doi.org/10.1093/petrology/12.1.67

Scholz, C.H., 2019. The Mechanics of Earthquakes and Faulting (3rd ed.). Cambridge University Press. https://doi.org/10.1017/9781316681473

Stein, R. S., 1999. The role of stress transfer in earthquake occurrence. Nature, 402(6762), 605-609. https://doi.org/10.1038/45144

Toda, S., 2005. Forecasting the evolution of seismicity in southern California: Animations built on earthquake stress transfer. Journal of Geophysical Research, 110(B5), B05S16. https://doi.org/10.1029/2004JB003415

Toda, S., Stein, R.S., Sevilgen, V., Lin, J., (2011). Coulomb 3.3 Graphic□rich deformation and stress□change software for earthquake, tectonic, and volcano research and teaching□user guide. U.S. Geological Survey Open□File Report 2011□1060, 63.

Vallianatos, F., Pavlou, K., 2021. Scaling properties of the Mw7.0 Samos (Greece), 2020 aftershock sequence. Acta Geophysica, 69(3), 1067–1084. https://doi.org/10.1007/s11600-021-00579-5

Wells, D.L., & Coppersmith, K.J., 1994. New empirical relationships among magnitude, rupture length, rupture width rupture area, and surface displacement. Bull Seismol Soc Am 84(4), 974–1002. https://doi.org/10.1785/BSSA0840040974

Zahradnik, J., Sokos, E., Roumelioti, Z., & Turhan, F. (2025). Positive isotropic components of the 2025 Santorini-Amorgos earthquakes. https://doi.org/10.31223/X5RD9S

17th INTERNATIONAL CONGRESS of the Geological Society of Greece

BULLETIN OF THE GEOLOGICAL SOCIETY OF GREECE, SP. PUBL.

EXTENDED ABSTRACT 282

Stabilisation of volcanic rock slopes in traditional settlements. The case of Petra, Lesvos Island

Saroglou C. [1], Kallimogiannis V.[2], Tsirogianni A.[3], Klironomou G.[4]

(1) National Technical University Athens, Greece, saroglou@central.ntua.gr (2) Civil Engineer, MSc, PhD NTUA (3) Civil Engineer, MSc, (4) Civil Engineer.

Introduction

Rock slope instabilities pose a significant problem to cultural heritage sites in Greece (Saroglou, 2012a and Saroglou *et al*., 2012b). The paper presents the assessment of rock slope stability of the volcanic rock cliff in the village of Petra in Lesvos Island, on which the Church of the Koimisi of Theotokos is founded (Figure 1). The rock cliff has almost vertical slopes with height up to 40 m and is formed by an andesitic rockmass, fractured by four discontinuity sets. The predominant kinematic instability is wedge or toppling failures of medium-sized rock blocks. The problem of potential rock instability of the volcanic slope in Petra has been investigated in the past (Apostolopoulos & Koukis, 1979) and rock fall episodes have occurred mainly triggered by intense rainfall. Due to the weathering and deterioration of the andesitic rockmass, the risk of rock instability has increased in the last two decades and it was deemed necessary to protect the foundation of the monument as well as the surrounding settlement and visitors from potential rockfalls. Stabilisation measures were proposed to minimize the risk of rockfalls and protect the foundation of the Church.

Similar problems of rock instabilities have been identified in many sites in Greece (Saroglou, 2019) but also near the study area at Mythimna Castle (Marinos *et al*, 2002). Saroglou (2012a) has studied the engineering geological behaviour of the volcanic formations in the northern part of Lesvos Island and highlighted the controlling factors of different types of slope instabilities, including landslides and rockfalls. The properties of the volcanic formations and their long-term behaviour in slopes are strongly controlled by the degree of weathering and the mineralogy of clay components when totally weathered (Irfan, 1999).

Figure 1. Volcanic rock cliff of Church of the Koimisi of Theotokos, Lesvos Island

Geological setting

Geologically the northern part of Lesvos Island consists of 400 m thick Neogene volcanic formations, formed by the Upper Miocene to the Middle Pliocene volcanic activity in the northeast Aegean Sea. These formations can be further distinguished in an upper lava unit and lower lava unit of Stypsi (Pe-Piper,1978). The upper lava unit consists of rhyodacitic, latitic and latiandesitic lavas, which are strong and hard formations, usually highly fractured, characterized by the magmatic pseudolayering, and intensely altered at places (kaolinitized) due to hydrothermal

activity. Two fault zones exist in the wider area, the main one with a WNW-ESE strike forming the tectonic graben of Petra and the secondary one with a NE-SW strike. As a result of compressive strains, the structure of rhyodacitic and latiandesitic lavas is characterized by two perpendicular joint systems which are vertical and intersect the pseudo bedding of lavas, thus forming orthogonal rock blocks. The rock cliff consists of rhyodacitic and latiandesitic lavas of the upper lava unit.

Rockmass conditions

The rock slopes surrounding the cliff were divided into eight distinct areas and the kinematic analysis of each area was analysed separately according to the discontinuity geometry and properties and the prevailing mechanism of failure (Figure 2). The volcanic rock appears massive in most places but locally is intensely fractured with a dense discontinuity network which forms wedges and rock pillars. The rockmass of the southern cliff appears extensively fractured and highly weathered, resulting in cavities. Due to the inaccessibility of the cliff, the rock slopes were mapped with UAV and LiDAR survey producing a point cloud and digital terrain model was created for the entire study site (Figure 3).

Figure 2. Plan view of the study site with designated slope areas

The discontinuity geometry was assessed using Discontinuity Set Extractor (Riquelme, 2015) which processes the point cloud data and then classifies points into planes (discontinuities) with similar orientation (dip/dip direction). The rockmass is intersected by three main discontinuity sets, as presented in Figure 4. The joint spacing was calculated as less than 1m (ranging from 0.3 to 0.7m), thus most blocks have a maximum volume of 0.5m^3.

Kinematic stability and rockfall analysis

Based on the mechanism of kinematic analysis (planar sliding, wedge sliding or toppling) in each area of the cliff, stability analysis was carried out for all the slope sections to define the factor of safety against each type of failure and determine the appropriate stabilisation measures. The analysis was performed in static conditions, with presence of water pressure in joints and under seismic loading.

The principal failure type is rockfall due to toppling, mainly in areas where large cavities are formed by the combined effect of weathering of the volcanic rock and the presence of discontinuities. Secondly, there are planar and wedge sliding failures in specific slope areas. The slope angle ranges between 55° and 88° and the steepest slopes are found in Areas 3,4 and 7, while the slope height ranges from 7 to 18m, with the highest slopes found in Areas 1, 3 and 4.

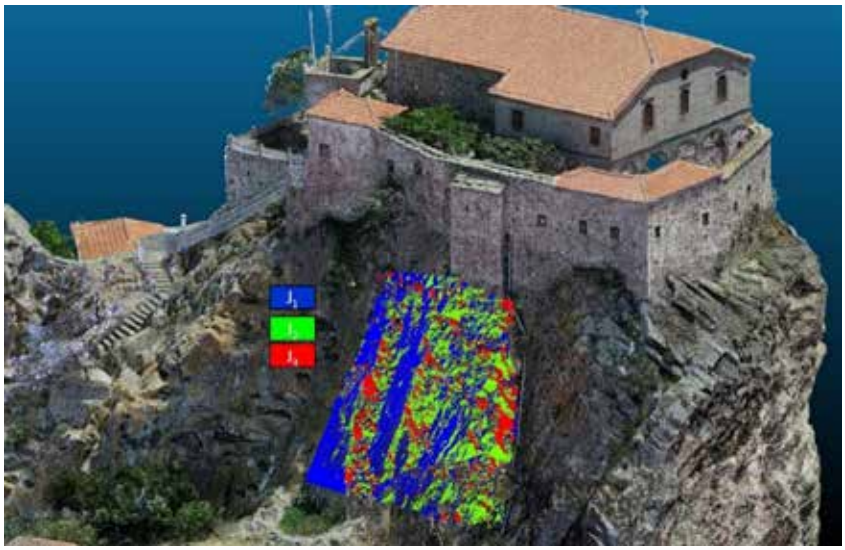

Figure 3. Digital terrain model and discontinuity mapping in the south side of the cliff

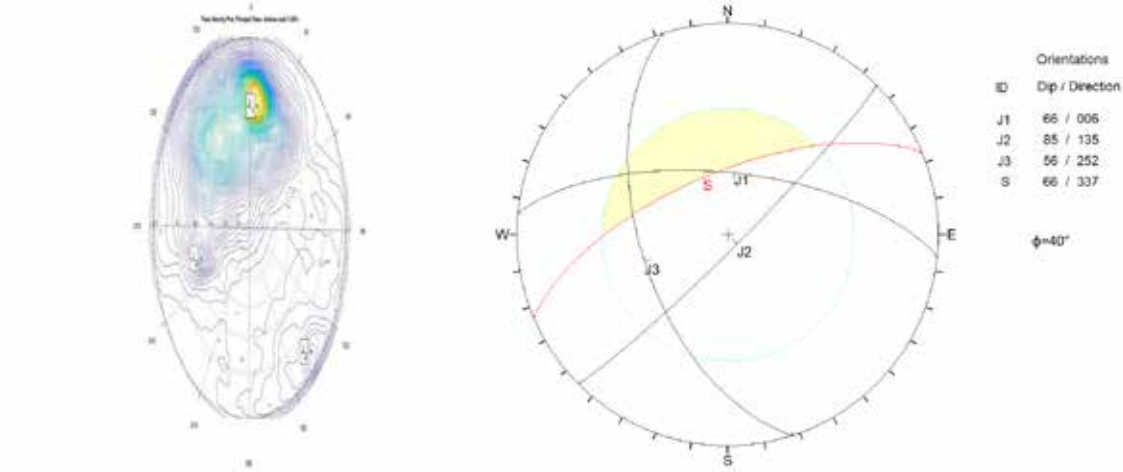

Figure 4. a) discontinuity pole density (from DSE), b) Stereographic plots with main sets in south cliff side.

In Area 1 (south side), toppling failure prevails due to a discontinuity set with NE-SW strike, as presented in Figure 4. In Area 2, planar sliding could occur along a discontinuity set with NW-SE strike. In Area 3, potential wedges are formed by the intersection of discontinuity sets of NW-SE and WE strike. In Areas 4 and 5, no systematic presence of discontinuity sets was observed. In Area 6, toppling failure prevails due to a discontinuity set with NNW-SSE strike, while in Area 7 toppling failure prevails due to a discontinuity set with N-S strike. In Area 8, planar sliding could occur along a discontinuity set with N-S direction and wedge failures could occur with a conjugate joint system. The determined factors of safety were not acceptable in many cases and therefore installation of rock bolts was considered necessary.

Rockfall analyses were performed for certain slope sections under different loading conditions. The critical locations of potential detached blocks were selected based on in-situ observations and the 3D terrain model of the slope and were used in the rockfall analysis performed in RocFall (Rocscience Ltd). The normal and tangential coefficients of restitution for the andesitic slope surfaces were taken equal to 0.45 and 0.85, respectively, based on experience from previous studies (Saroglou et al.,2012). The height of block detachment was defined in the range of 17 to 29 m above the slope base, with a maximum of 29 m in Area 1 (Figure 5a). The analysis shows that Areas 1, 4 and 5 are the most critical sections due to impact of falling rocks on houses and on the street which is around the cliff. In Area 1, the majority of falling blocks impact the houses with a maximum kinetic energy of 110 kJ. In Area 4 certain blocks reach the houses with a maximum kinetic energy of 160 kJ (Figure 5b). In Area 5 most falling blocks reach directly the residential zone with a maximum kinetic energy of 90 kJ and significant bouncing heights. On the contrary, there

are areas that are considered as lower risk, such as Area 2, where falling blocks stop at a plateau located near the base of the slope and Area 3 where most rocks reach the base of the slope with a maximum kinetic energy of 80kJ.

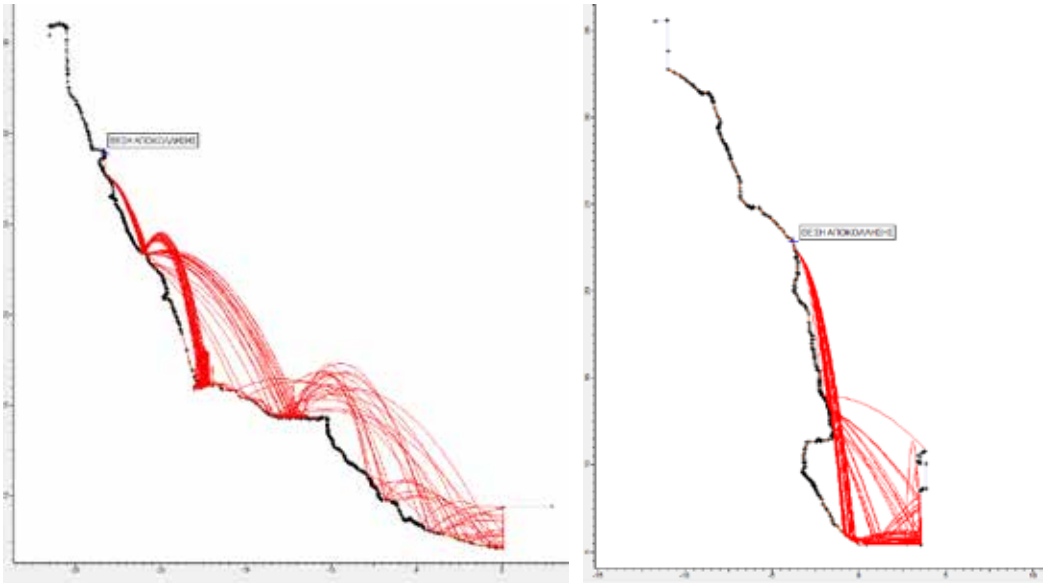

Figure 5. a) Rockfall analysis in Area 1 (south cliff) and b) in Area 4 (north cliff)

Stabilisation measures

Based on the stability analyses it was considered necessary that active support measures (rock bolts, anchored wire mesh) are installed to minimise the risk of rock blocks falling from the upper parts of the slopes, instead of installing passive measures (rockfall barriers). The option of installing rockfall barriers on the slope was not acceptable to due to achieve the minimum impact on the cultural heritage site.

The proposed rock stabilization works aimed to enhance the overall stability and reduce the risk of further rock falls. The stabilization measures are summarised below, and an example is presented in Figure 6.

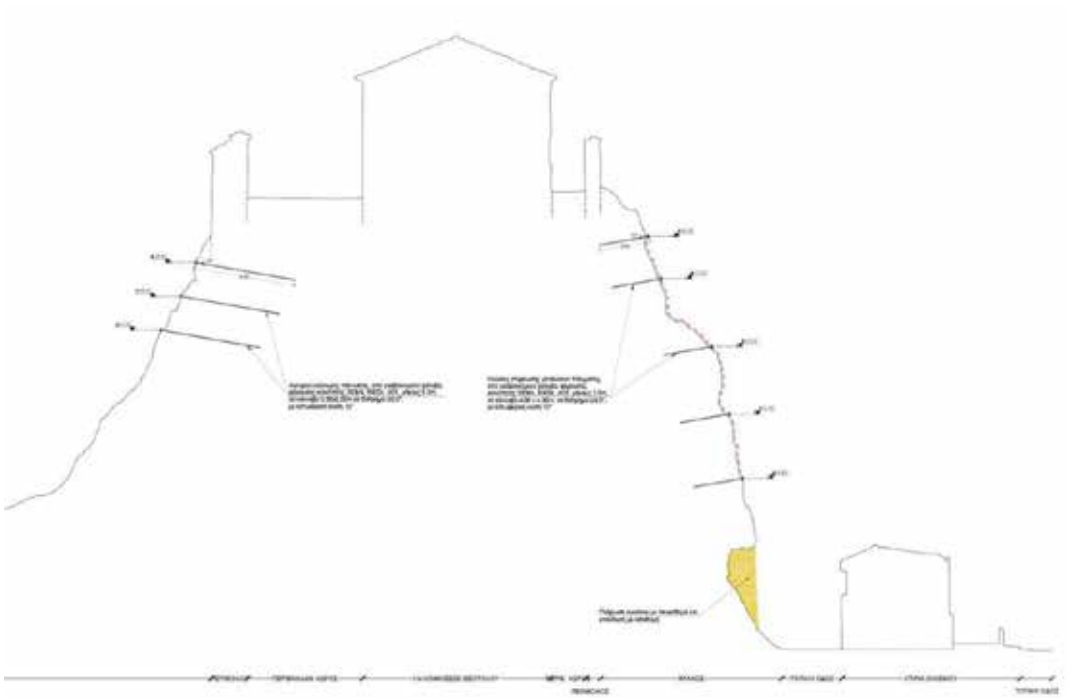

Figure 6. Section with proposed stabilisation measures in Area 1 (south) and Area 4 (north)

The main measures were:
1. Installation of spot bolts for anchoring individual relatively small rock blocks and pattern bolting for anchoring of larger blocks. The aim of this measure was to support potentially unstable blocks and improve the stability conditions of the upper part of the cliff below the foundation of the Church.
2. Installation of a steel wire rope net, anchored with fully grouted bolts in order to control further loosening of the rock mass in areas where it is fractured.
3. Filling of voids in specific locations with sprayed concrete or reinforced concrete, depending on their location, geometry and size. The intention was to minimise the enlargement of voids due to weathering and support the overhangs of rocks.

Conclusions

The stabilisation of steep rock slopes in areas where human activities are impacted is a very challenging task. The case of Church of the Koimisi of Theotokos in Petra is such an example, which demonstrates the difficulty to stabilise a rock slope in inhabited area, while at the same time respecting the cultural heritage character of the monument.
In this study, a methodology was presented which is based on identifying the engineering geological behavior of the volcanic rock formations and determining the prevailing failure mechanisms in different sections of the slope to propose the appropriate stabilisation measures. The advantage of technologies, such as UAV and LiDAR and use of software for automatic detection of discontinuities was demonstrated to enhance the assessment of kinematic stability analysis and protection of the monument.

Acknowledgements

The authors acknowledge the support of the Ministry of Culture for funding the present research and would like to thank Emeritus Prof. C. Spyrakos for the collaboration.

References

Andronopoulos B. and Koukis G. 1979. Geological, Microtectonic and Geotechnical Study in the NW part of the Lesbos Island. Unpublished report, Institute of Geological and Mining Research, Engineering Geology Investigations No. 8, 41 p., Athens.
Irfan, T.Y., 1999. Characterization of weathered volcanic rocks in Hong Kong. Quaternary Journal Engineering Geololgy, 32, 317–348.
Marinos P., Kavvadas M., Tsiambaos G., Saroglou H., 2002. Rock slope stabilization in Mythimna castle, Lesvos Island, Greece. 1st European conference on landslides, Balkema, ed: Rybar Stemberk & Wagner, Prague, p. 635-639.
Pe-Piper G, 1978. The Cenozoic volcanic rocks of Lesvos Island. Ph.D.Thesis. University of Patras.
Riquelme AJ, Abellan A, Tomas R., 2015. Discontinuity spacing analysis in rock masses using 3D point clouds. Engineering Geology, 195,185–195.
Rocscience Ltd. 2022. Rocfall user's manual.
Saroglou, H. 2012a. Engineering geological behaviour of volcanic formations. References to instability phenomena and town planning in Lesvos Island, Greece. Bulletin of the Geological Society of Greece, 46, 108-122.
Saroglou H., Marinos V., Marinos P., Tsiambaos G., 2012b. Rockfall hazard and risk assessment: an example from a high promontory at the historical site of Monemvasia, Greece. Natural Hazards and Earth System Sciences, 12, 1823–1836.
Saroglou C., 2019. GIS-based rockfall susceptibility in Greece. Geosciences, 9, 163.

17th INTERNATIONAL CONGRESS of the Geological Society of Greece

BULLETIN OF THE GEOLOGICAL SOCIETY OF GREECE, SP. PUBL.

EXTENDED ABSTRACT 283

Mapping pyroclastic formations at the Lesvos Petrified Forest, Greece the Akrocheiras hill pyroclastic sequence

Savvelos L.[1, 2] and Zouros N.[1, 2]
(1) Natural History Museum of the Lesvos Petrified Forest
(2) Department of Geography, University of the Aegean, Greece

Introduction

The Lesvos Petrified Forest is a unique natural monument located in western Lesvos. It is the geological heritage treasure with international significance of the Lesvos Island UNESCO Global Geopark. It is also included in the 100 first Geological Heritage sites of the International Union of Geological Sciences (IUGS). The Lesvos Petrified Forest includes massive assemblages of silicified tree trunks located in situ within the Sigri pyroclastic formation of Lower Miocene (Velitzelos and Zouros 1997, 1998, Pe-Piper et al. 2019, Zouros 2021).The Natural History Museum of the Lesvos Petrified Forest is conducting scientific research, excavation and conservation works in the Lesvos Petrified Forest during the last 30 years. Excavations in the Lesvos Petrified Forest reveled a large number of standing and lying silicified tree trunks, root systems, brunches, leaves and cones that belong to conifer and angiosperm tree species. The composition of the forest ecosystem represents subtropical climatic conditions (Velitzelos and Zouros 1997, 1998, Pe-Piper et al. 2019).

Silicification of the Lesvos Petrified Forest is related with the volcanic activity in Lesvos during Lower Miocene (Pe-Piper et al. 2019b, 2024). The perfect preservation of the fossils is due to the circulation of hydrothermal fluids rich in silicon dioxide SiO_2, (Pe-Piper et al. 2019b).

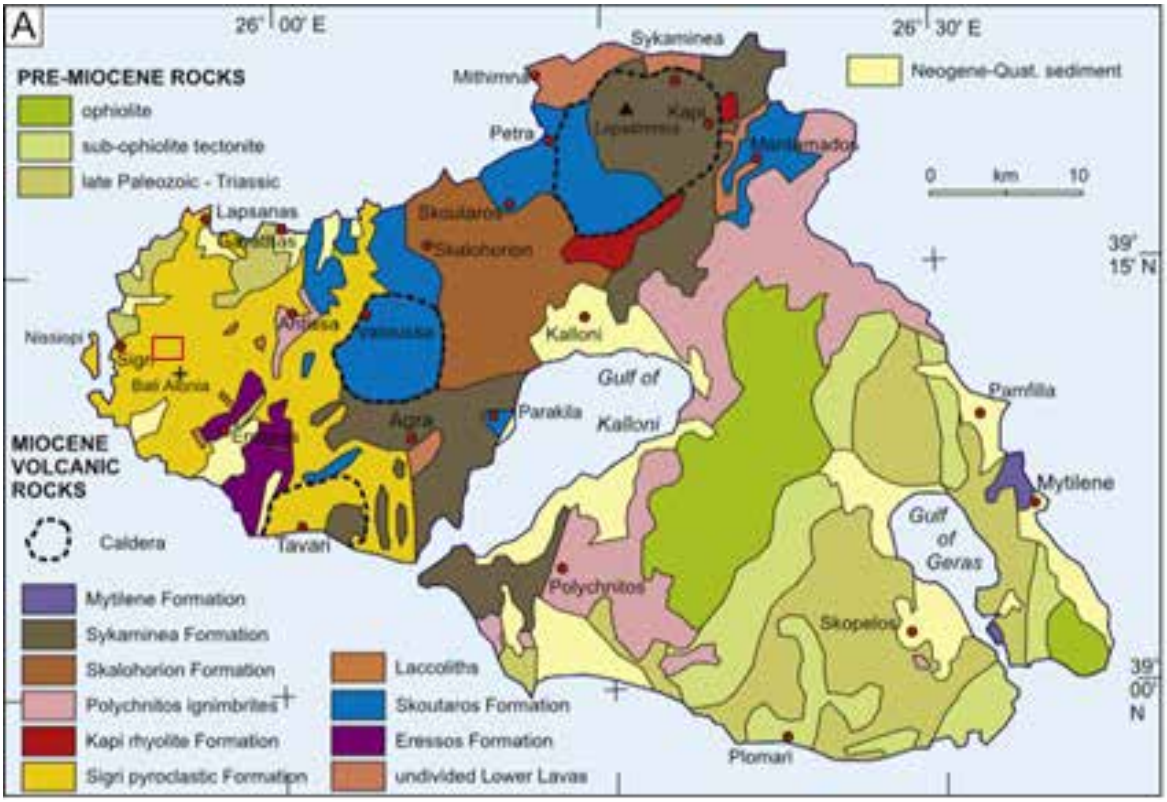

Figure 1: Geological Map of Lesvos Based on Hecht (1972-1976), modified by Pe-Piper (1992). Red rectangle indicating the study area of current research

Since 2014 extensive rescue excavation works were carried out by the Natural History Museum of the Lesvos Petrified Forest due to the construction of the Kalloni - Sigri, road crossing the protected area of the Lesvos Petrified Forest. As a result large amounts of new data in a number of significant fossil sites were collected (Zouros et al. 2015, Zouros 2021, Pe-Piper et al. 2019b, 2024).

As several significant fossil sites are located on the northern flanks of the Akrocheiras hill, a detailed mapping project in the area of Akrocheiras hill was carried out, in order to archive a better understanding of the stratigraphy of the pyroclastic sequence. Therefore the main objective of the current study is the identification and mapping of successive fossiliferous horizons associated with different volcanic eruptions that led to the preservation of the fossilized forests

Study Area

The protected area of the Petrified Forest of Lesvos spans at the western peninsula of the island covering 15.000 ha. Throughout the area, silicified trunks can be found at various depths. Akrocheiras hill lies in the center of the protected area, 7 km east of Sigri village (Fig. 2), reaching an altitude of 370 meters above sea level and covering an area of approximately 1.2 km². Recent rescue excavations conducted in the area along the Kalloni-Sigri road uncovered thousands of petrified trunks along the road, which were showcased and preserved in situ through the efforts and acts of the Natural History Museum of the Lesvos Petrified Forest. Additionally, hundreds of fossils were uncovered and preserved on the hilltop, due to rescue excavations for the re-construction of the Sigri windmill farm, where the longest fallen petrified trunks were excavated, along with a large number of standing in-situ and lying silicified tree trunks.

The study area is entirely covered by the Sigri pyroclastic formation (Figure 1), featuring a variety of volcanic deposits that covered and preserved fossiliferous horizons (Pe-Piper et al., 2019b). The Sigri pyroclastic formation is several hundred meters thick and consists of tuffs and coarse-grained volcanic materials. Stratigraphically, it overlies the Gavathas and Eresos formations and underlies the younger Skoutaros formation (Pe-Piper et al., 2019b).

Following the deposition of this formation, the intrusion of the Moni Ipsilou dome occurred, dated to approximately 17.9 million years ago. The Sigri pyroclastic formation in several sites is covered by recent deposits.

This description highlights the geological complexity and significance of the area, particularly in the context of preserving the fossilized forest and understanding its volcanic history.

Methodology

To achieve the identification of successive fossiliferous horizons associated with different volcanic eruptions and the evaluation of volcanic episodes that preserved fossilized forests, detailed mapping was conducted in the study area (Fig. 5). The mapping included fossil sites with standing in-situ petrified tree trunks, root systems, and fallen petrified tree trunks in direct contact with pyroclastic material, as well as occurrences of volcanic sequence of pyroclastic formations marking the onset of deposition from a volcanic eruption (Fig. 5).

The standing petrified tree trunks (Fig. 2, Fig. 4), being fossilized in their original position, serve as significant evidence to define a fossiliferous horizon. When the root system of the trunk is a marker of the original layer where a dense subtropical forest once thrived.

The fallen petrified trunks are displaced from their original position by pyroclastic flows. The composition of the clasts and orientation of the fallen trunks provide significant information on the origin of the pyroclastic flows involved in the silicification of the trees.

Coarse-grained horizons of volcanic conglomerates with clasts of diameter <2m are found throughout the area(Fig. 3a). These usually contain polygenetic volcanic pebbles, consisting of flows—volcanic conglomerates or debris flows—and appear to have been formed by water-driven flows that filled a complex network of paleo-river channels of that time (Pe-Piper et al., 2019b). This formation was created during a relatively calm period, meaning it was not driven by eruptions, unlike the tuffs found in the area. This feature provides insights into how the region's morphology developed between eruptions.

Therefore, the fine-grained pyroclastic horizons, the tuffs, whose creation and deposition are processes closely linked to the various volcanic eruptions, are expected to appear in the field as stratigraphically overlying on the previously formed substrate of the area—in this case, the debris flow. Thus the fine-grained formations simultaneously act as markers of deposition from a volcanic eruption.

Vitric tuff (Figure 3b) is a volcanic tuff primarily composed of fragments of volcanic glass that have undergone alteration (Pe-Piper et al., 2019b). It forms during an eruption and the rapid cooling of magma (Sparks & Walker, 1977; Pe-Piper et al., 1980). The binding material of the tuff consists of volcanic ash and contains fragments of pumice and small pieces of lava ejected during the eruption (pumice-lithic lapilli) (Pe-Piper et al., 2019b). It is deposited from the air (Sparks & Walker, 1977) directly onto already formed substrate of the area and serves as a strong indicator of the onset of deposits from a volcanic eruption.

Lithic tuff is pyroclastic sediment (Figure 3c). It consists of a primary binding material (matrix) made of volcanic ash with a grain size of ~2 mm and fragments of andesitic-dacitic lava <64 mm, which are shattered from pre-existing surrounding rocks and spread during the eruption (Pe-Piper et al., 2019a).

Figure 2 a, b, c, d: Standing in situ petrified trunks at the north and south flanks of Akrocheiras

Its deposition is closely linked to the volcanic eruption. It usually exhibits variability in the distribution of clasts due to the varying intensity of the eruption that caused its deposition (Pe-Piper et al., 2019a). Additionally, the deposition of this formation usually in the most cases succeeds that of Vitric tuff. In many cases though, in the field the two formations are found together, with lithic tuff being the base and vitric tuff overlying on top, directly on the already formed substrate (Pe-Piper et al., 2019a). Consequently, lithic tuff also serves as an important indicator for the onset of deposits from a volcanic eruption.

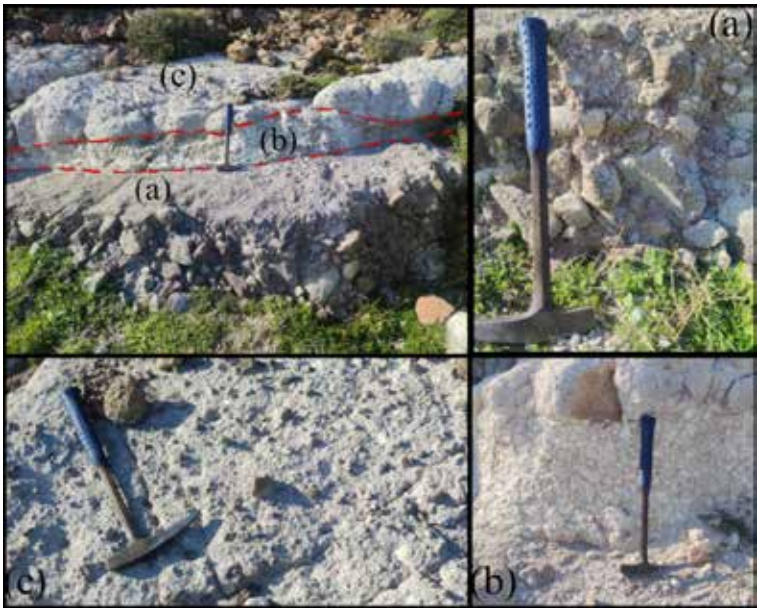

Figure 3: Appearance of the main sequence marking the deposition of a new volcanic eruption, where: a: Coarse-grained pyroclastic flow (Debris flow). b: Vitric tuff, deposited directly from the air; the vitric tuff forms during the eruption due to the rapid cooling of magma and serves as a critical marker indicating the onset of a new volcanic sequence. c: Lithic tuff, a pyroclastic sediment containing volcanic tuff and andesitic-dacitic clasts.

The formations mentioned above (debris flow, vitric tuff, lithic tuff) constitute a representative stratigraphic volcanic sequence (Figure 3), which is observed in the field and marks the onset of deposits from a volcanic eruption. The identification of locations where the whole sequence or parts of it appear is crucial for understanding and evaluating

the fossiliferous horizons and volcanic episodes hosted by Akrocheiras.
The occurrence of the primary volcanic sequence or parts of it containing vitric and lithic tuff, and the extent to which it repeats upstream on the slopes of Akrocheiras is the key element distinguishing fossiliferous horizons from one another, as well as different volcanic episodes.
The main and primary indicator is vitric tuff, as mentioned earlier, since it forms during the rapid cooling of magma during a volcanic eruption. It is deposited from the air directly onto the already formed topography of the ground surface, which supports a subtropical forest. Therefore, it is expected that the vitric tuff horizons represent the main fossiliferous horizons.
In the field, petrified trunks and root systems that protrude directly from vitric tuff (Fig. 4) are encountered, and in such cases, the recognition of the fossiliferous horizon is facilitated. However, even in cases where the formation is found without the presence of fossils, this does not mean that fossils are absent, they simply do not happen to be visible at the specific location.

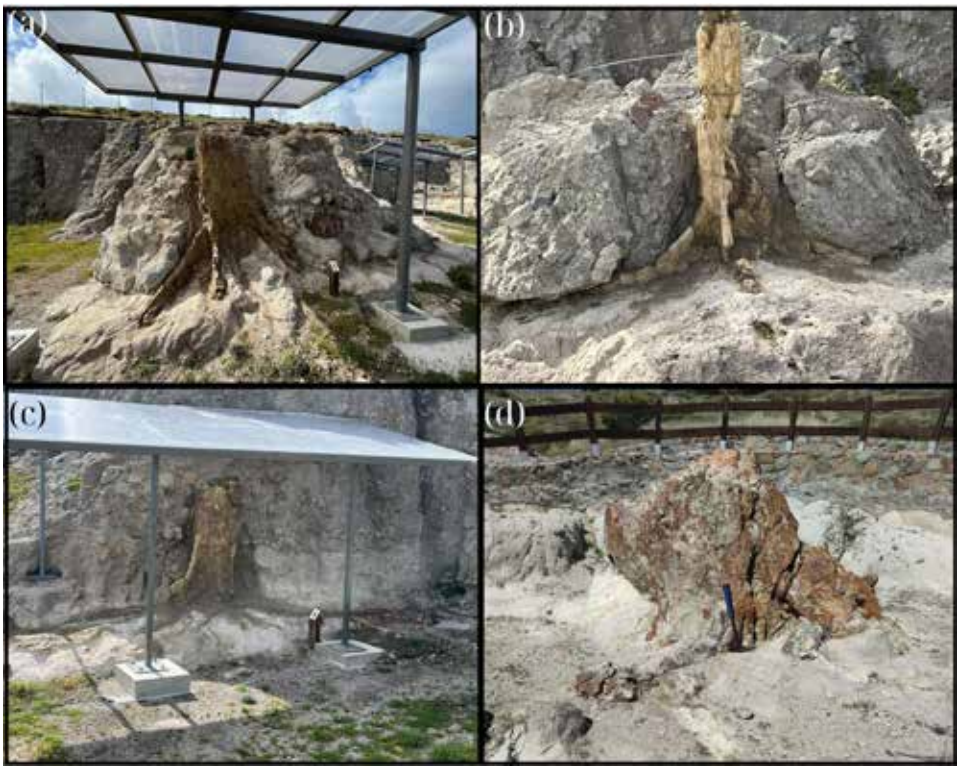

Figure 4 a, b, c, d: Standing in situ petrified trunks at the broader area of Akrocheiras illustrated with their roots systems spreading in the air fall vitric tuff and a, b, c also covered by coarse-grained volcanic conglomerates.

Results
The primary objective of this study is the identification and evaluation of successive fossiliferous horizons associated with different volcanic eruptions, as well as the assessment of volcanic episodes that preserved fossilized forests.
By combining the locations of standing petrified trunks that display their root systems, along with the occurrences of the entire volcanic sequence or parts of it featuring vitric tuff or lithic tuff, the following map is produced (Figure 5).
Documented locations (Figure 5) indicate that the Akrocheiras hill hosts at least 11 successive fossiliferous horizons associated with different volcanic eruptions. This represents the minimum number that can be established based on the evidence and their respective locations.
Conclusions-Discussion
Akrocheiras hill is covered by the Quaternary deposits and low vegetation, which makes the mapping effort very challenging. Detailed mapping curried out in Akrocheiras hill provide evidence for the presence of at least 11 successive pyroclastic horizons representing successive volcanic eruptions.
If we consider that only in the “Ioannis Toumpelekis Park”, at the northeastern edge of the Akrocheiras Hill, where the soil horizon has been removed and the volcanic formations are fully exposed, at least 8 fossiliferous horizons have been documented, it becomes evident that the Akrocheiras hill hosts dozens of petrified forests.

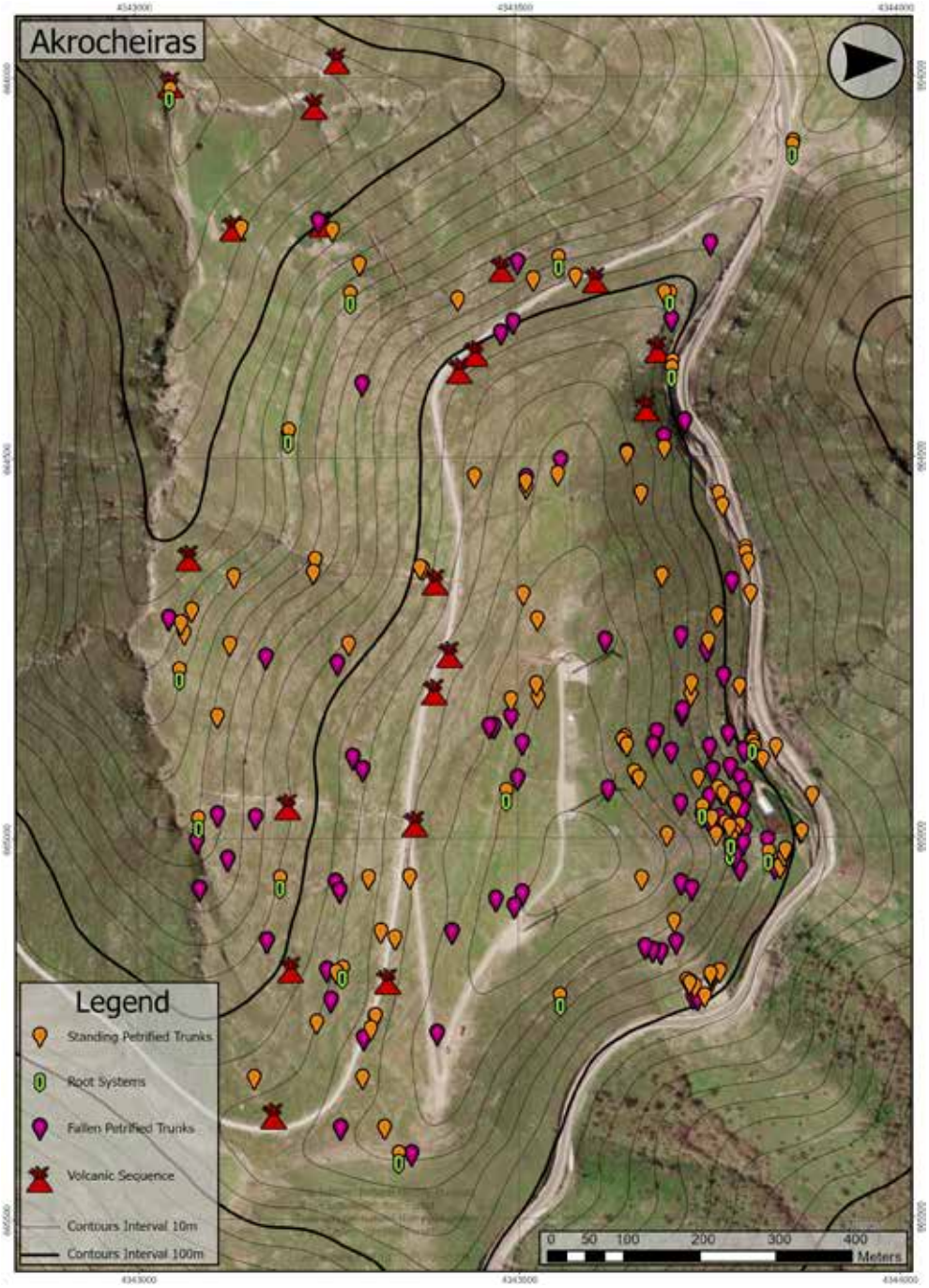

Figure 5: Result of the mapping of the plant fossils (standing, petrified tree trunks, lying petrified tree trunks , root systems) and volcanic horizon contacts conducted in the Akrocheiras area, within the protected area of the Lesvos Petrified Forest.

Additionally, the fact that the volcanic sequence in the northern part of the hill, along with the significantly higher density of fossil concentrations (see Figure 6), are phenomena that require further scientific investigation. These are possibly directly linked to the geomorphology of the area during the deposition of the Sigri pyroclastic formation. Finally, the primary objective of this study is a topic that requires much more research. This initial approach and estimation open a significant scientific discussion regarding the minimum number of successive fossiliferous horizons associated with different volcanic eruptions and the assessment of volcanic episodes that preserved fossilized forests, initially for the Akrocheiras hill and, by extension, for the broader recognized area of the Petrified Forest of Lesvos.

References

Pe-Piper, G., 1980: Geochemistry of Miocene Shoshonites, Lesbos, Greece. Contributions to Mineralogy and Petrology 72, 387-396.

Pe-Piper, G., Piper, D. J.W., Zouros, N.C., Anastasakis, G., 2019: Age, Stratigraphy, Sedimentology and Tectonic Setting of the Sigri Pyroclastic Formation and its Fossil Forests, Early Miocene, Lesbos, Greece. Basin Reasearch 31, 1178-1197.

Pe-Piper, G., Imperial, A., Piper, D. J.W., Zouros, N.C., Anastasakis, G., 2019: Nature of the hydrothermal alteration of the Miocene Sigri Petrified Forest and host pyroclastic rocks, western Lesbos, Greece. Journal of Volcanology and Geothermal Research 369, 172-187.

Pe-Piper, G., Piper, D. J.W., Anastasakis, G., Zouros, N.C., Lyras, G., 2024: Variability in mineralization of the petrified forests in the UNESCO Global Geopark of Lesvos, Greece. Marine and Petroleum Geology 167, Article 106990.

Sparks, R.S.J. & Walker, G.P.L., 1977: The Significance of Vitric-Enriched Air-Fall Ashes Associated With Crystal-Enriched Ignimbrites. Journal of Volcanology and Geothermal Reasearch 2 329-341.

Velitzelos, E., & Zouros, N. (1998). New results on the petrified forest of Lesvos. *Bulletin of theGeological Society of Greece*, *32*(2), 133–142.

Zouros, N.C., 2021. The Miocene petrified forest of Lesvos, Greece: Research and geoconservation activities. Conservation Research 4 (2), 635–649.

Zouros,N., Soulakellis,N.,Valiakos,I., Bentana,K., Theodorou,E., Zgournios,E., Antonakis,E. and Lamprakopoulos,A. 2022: Enhancement and promotion of the new fossiliferous sites along the new Kalloni Sigri road.-An example of good practice in geoconservation in Lesvos Isl. UNESCO Global Geopark Greece. Bulletin of Geological Society of Greece Sp. Publ. 10, pp. 849-850.

17th INTERNATIONAL CONGRESS of the Geological Society of Greece

BULLETIN OF THE GEOLOGICAL SOCIETY OF GREECE, SP. PUBL.

EXTENDED ABSTRACT 284

Mapping petrified tree trunks and pyroclastic formations at the Lesvos Petrified Forest, Greece, case study of the Bali Alonia area

Savvelos L.1, 2 and Zouros N.1, 2
(1) Natural History Museum of the Lesvos Petrified Forest
(2) Department of Geography, University of the Aegean, Greece

Introduction / Background

The Lesvos Petrified Forest constitutes a distinctive natural monument situated in the western region of Lesvos. It represents a geological heritage asset of considerable international importance within the Lesvos Island UNESCO Global Geopark. Additionally, it is recognized among the first 100 Geological Heritage sites designated by the International Union of Geological Sciences (IUGS). The Lesvos Petrified Forest encompasses extensive assemblages of silicified tree trunks that remain in situ within the Sigri pyroclastic formation, dating back to the Lower Miocene epoch (Velitzelos & Zouros 1997, 1998; Pe-Piper et al. 2019; Zouros 2021). The Natural History Museum of the Lesvos Petrified Forest has been engaged in scientific research, excavation, and conservation efforts within the Lesvos Petrified Forest for the past 30 years. Excavations conducted in the Lesvos Petrified Forest have unveiled a substantial quantity of both standing and fallen silicified tree trunks, root systems, branches, leaves, and cones attributable to coniferous and angiosperm tree species. The composition of the forest ecosystem reflects subtropical climatic conditions (Velitzelos & Zouros 1997, 1998; Pe-Piper et al. 2019).

The silicification process of the Lesvos Petrified Forest is intricately associated with the volcanic activity that transpired in Lesvos during the Lower Miocene epoch (Pe-Piper et al. 2024). The exceptional preservation of the fossils is attributed to the circulation of hydrothermal fluids that were enriched in silicon dioxide (SiO2) (Pe-Piper et al. 2019).

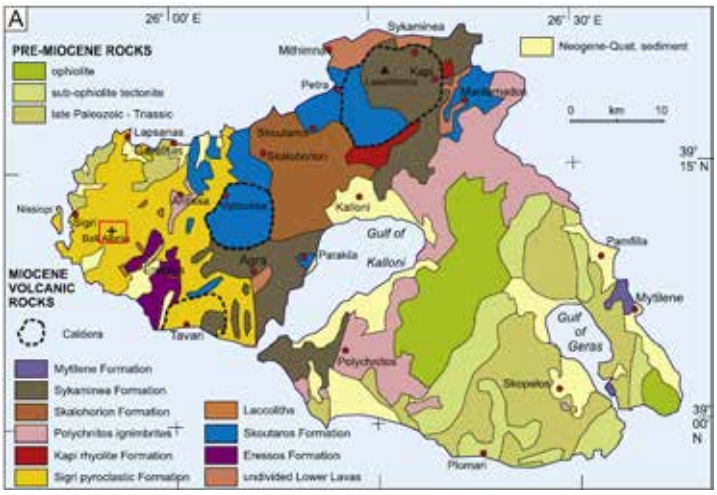

Figure 1: Geological Map of Lesvos Based on Hecht (1972-1976), modified by Pe-Piper (1992). Red rectangle indicating the study area, Bali Alonia broader area.

Since 2014, extensive rescue excavation initiatives have been conducted by the Natural History Museum of the Lesvos Petrified Forest in response to the construction of the Kalloni - Sigri road, which crosses the designated protected area of the Lesvos Petrified Forest. Therefore, a considerable amount of new information has been collected from various notable fossil locations (Zouros 2021; Pe-Piper et al. 2024).

Due to the presence of several prominent fossil sites inside the fenced area of “Bali Alonia Park”, an extensive mapping initiative was conducted within this region to meticulously identify and document fossil-bearing locations. Consequently, the primary aim of the present investigation is the identification and cartographic representation of standing tree trunks, fallen tree trunks, root systems, as well as vitric and lithic tuffs. By determining the precise locations of these fossils, we can more effectively safeguard and analyze the Petrified Forest. The mapping effort has also facilitated an enhanced comprehension of the stratigraphy associated with the pyroclastic formations.

Study Area

The Petrified Forest of Lesvos spans an area on the western edge of the island of Lesvos. Within this area, with the efforts of the Natural History Museum, accessible parks have been established where visitors can view the in situ petrified tree trunks. Approximately 10 km away from the settlement of Sigri lays the area of Bali Alonia (Fig. 2). Historically, this is where the first petrified tree trunks were protected and showcased. Subsequently, a section of the area was fenced and protected, leading to the creation of the first park of the Petrified Forest, named the Main Fossil area or the Bali Alonia Park. Fossilized in situ trunks can be found both within the fenced section and in the broader area of Bali Alonia

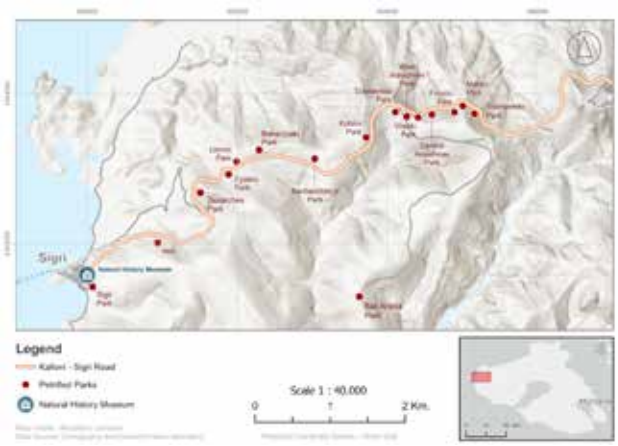

Fig 2: Regional map indicating locations of significant fossil parks along the Kalloni-Sigri road, also the main fossil area petrified forest park Bali Alonia.

For the purposes of this specific study, the broader area, covering approximately 7 km², was designated as the study area (Fig. 1). From the lowest point at an elevation of ~60 meters to the highest point of the study area at ~300 meters above sea level, standing tree trunks, fallen tree trunks, root systems and vitric and lithic tuffs are distributed.

The geographical region under investigation is comprehensively enveloped by the pyroclastic formation of Sigri (Fig. 1), which is distinguished by a diverse array of volcanic deposits that have effectively covered and preserved petrified forests in different strata (Pe-Piper et al. 2018). The Sigri pyroclastic formation exhibits a thickness of several hundred meters and is composed of tuffs alongside coarse-grained volcanic materials. From a stratigraphic perspective, it is situated above the Gavathas and Eresos formations while being positioned beneath the more recent Skoutaros formation.

Subsequent to the deposition of this geological formation, the intrusion of the Moni Ipsilou dome transpired, with a temporal attribution of approximately 17.9 million years ago. The majority of the Sigri pyroclastic formation is obscured by more recent deposits, with only the coarse-grained materials, lava flows, and volcanic domes emerging above these overlying layers. In select regions, tuffs are also present, exhibiting formations characterized by grain sizes of less than 2 mm (Pe-Piper et al. 2018).This exposition emphasizes the intricate geological attributes and importance of the region, especially concerning the conservation of the petrified forest**s** and the comprehension of its volcanic past.

Coarse-grained materials characterized by clasts with a diameter of less than 2 meters are prevalent throughout the region. These formations are typically distributed, consisting of overcompressed flows—specifically volcanic conglomerates or debris flows (Fig. 5a)—and appear to have originated from water-induced flows that infiltrated a complex network of paleo-river channels from that period (Pe-Piper et al. 2018). This formation emerged during a relatively tranquil epoch, between volcanic episodes, indicating that it was not a result of volcanic eruptions, in contrast to the tuffs present in the vicinity. This characteristic offers valuable insights into the morphological evolution of the region between volcanic events.

Consequently, the finely textured pyroclastic materials known as tuffs, whose formation and deposition are definitely associated with volcanic eruptions, are anticipated to be found in the field as stratigraphically overlying layers on top

the pre-existing substrate of the region—in this instance, the debris flow or volcanic conglomerate. Therefore these layers concurrently function as indicators of deposition resulting from a volcanic episode.
Vitric tuff is a type of volcanic tuff that is predominantly contains volcanic glass fragments that have experienced alteration (Fig. 5b) (Pe-Piper et al. 2019). It is generated during an eruption and the quick cooling of magma (Sparks & Walker 1988; Pe-Piper et al. 1980). The matrix of the tuff comprises volcanic ash and includes fragments of pumice and small lava pieces expelled during the eruption (pumice-lithic lapilli) (Pe-Piper et al. 2018). It is deposited as air fall formation (Sparks & Walker 1977) directly onto the pre-existing substrate of the region and serves as a main indicator of the initiation of deposits resulting from a volcanic eruption.

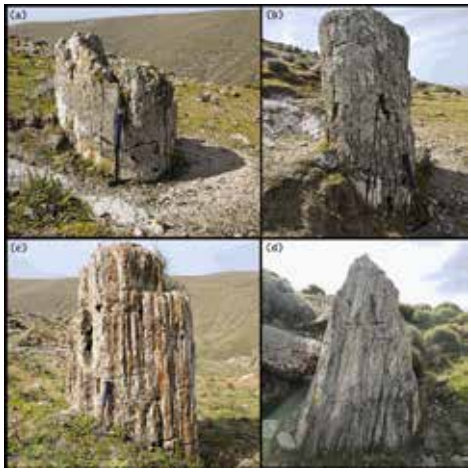

Figure 3 a,b,c,d: Standing in situ petrified trunks stable in their original position. . a: 663,737.98E 4,340,605.91N m, b: 663,709.15E 4,340,596.20N m, c: 663,617.72E 4,340,502.68N m, d: 663,692.56E 4,340,621.39N m,

Lithic tuff is classified as pyroclastic sediment. It comprises a primary binding material (matrix) consisting of volcanic ash with a grain size of approximately 2 mm, along with fragments of andesitic-dacitic lava measuring less than 64 mm, which are fragmented from pre-existing surrounding rocks and disseminated during the eruption (Fig. 5c) (Pe-Piper et al. 2018). The process of its deposition is intricately associated with volcanic eruptions. Typically, it displays variability in clasts distribution, a consequence of the differing intensities of the eruptions responsible for its deposition (Pe-Piper et al. 2018). Moreover, the deposition of this formation generally follows, on top, that of Vitric tuff. Nevertheless, in numerous instances, both formations are observed in situ, with Lithic tuff acting as the substrate and Vitric tuff overlaying it directly upon the pre-existing substrate (Pe-Piper et al. 2018). Consequently, lithic tuff serves as a significant indicator of the initiation of deposits resulting from a volcanic eruption.
This description highlights the geological complexity and significance of the area, particularly in the context of preserving the fossilized forest and understanding its volcanic history.

Methodology

The research encompassed a thorough cartographic endeavor within the specified study region, employing a methodical field survey methodology. The principal objective was to precisely identify and document fossiliferous sites, including both upright and fallen petrified tree trunks. To achieve this, we also delineated the stratigraphy of the pyroclastic deposits, with particular focus on the tuff horizons (both vitric and lithic tuff).
Field investigations were executed utilizing the FieldMove Clino Version 3.0.6 application, which afforded precise geospatial coordinates and enabled real-time data recording. In advance of data acquisition, the application underwent calibration in accordance with the manufacturer's specifications to guarantee measurement precision and dependability. Special attention was directed towards mapping regions where tuffs were exposed, particularly along the stream valleys that define the study area.
Subsequent to the identification of each relevant site, positional data was systematically documented through the

FieldMove Clino application, along with further site-specific observations recorded manually. These observations encompassed geological and geomorphological attributes. Data points were collected at locations deliberately selected during the mapping process to maximize spatial resolution and reliability.
The KMZ file format was chosen for its intuitive usability and compatibility with ArcGIS Pro, coupled with its ability to include location-specific images, thus considerably improving the data processing and interpretative phases. Data accuracy and consistency assessments were conducted to ensure the quality of the gathered dataset.
The standing petrified tree trunks (Fig. 3, Fig. 4), being fossilized in their original position, serve as significant evidence to define a fossiliferous horizon. The root systems of these trunks are markers of the original layers where a dense

Figure 4 a, b, c, d: Standing in situ petrified trunks at the broader area of Akrocheiras illustrated with their roots systems spreading in the air fall vitric tuff and a, b, c also covered by coarse-grained volcanic conglomerates. a: 663,805.18E 4,341,410.44N m located in the Park Bali Alonia, b: 663 770,269E 4,343,366,122N m, c: 663 777,896E 4,343,388,585N m, d: 664,396.99E 4,343,703.54N m. Trunks b, c, located at the Park Kotsini and d located at the Park Vrysaki.

Figure 5: Appearance of the main sequence marking the deposition of a new volcanic eruption, where: a: Coarse-grained pyroclastic flow (Debris flow). b: Vitric tuff, deposited directly from the air; the vitric tuff forms during the eruption due to the rapid cooling of magma and serves as a critical marker indicating the onset of a new volcanic sequence. c: Lithic tuff, a pyroclastic sediment containing volcanic tuff and andesitic-dacitic clasts. Coordinates of the locality: 664,134.57E 4,341,600.77N m

Figure 4 illustrates the distinctive geological formations of the Bali Alonia region previously discussed (debris flow, vitric tuff, lithic tuff) that have been observed in situ and signify the commencement of deposits resulting from volcanic activity. The discernment of sites where the interrelationship among the pyroclastic layers is evident is essential for comprehensively understanding and assessing the fossiliferous stratas and volcanic episodes present in the broader area of Bali Alonia.

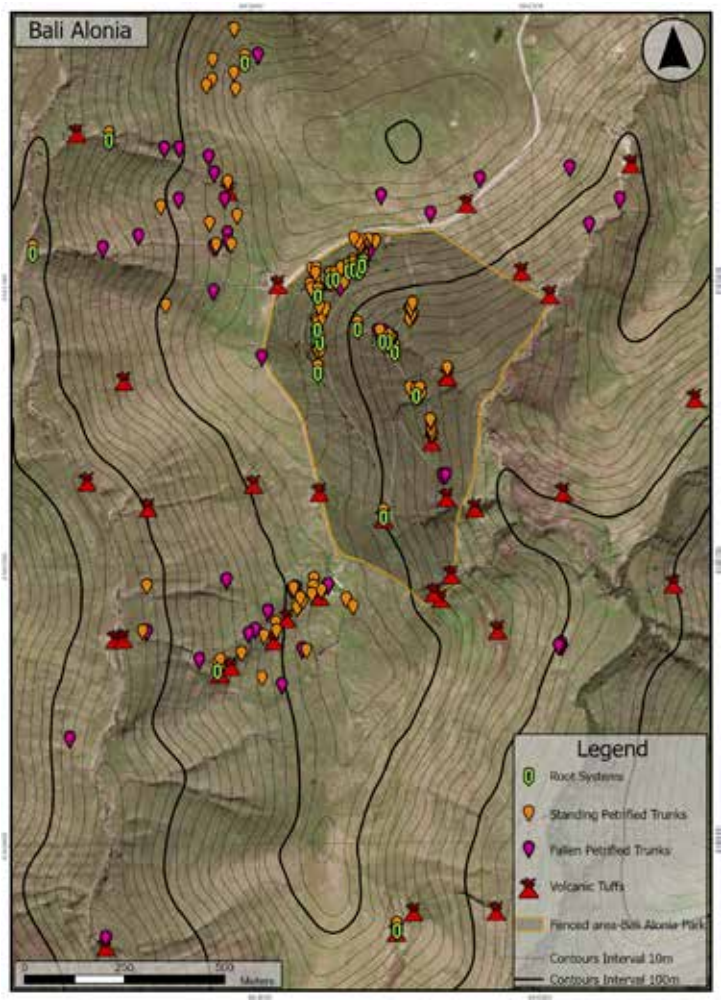

Figure 6: Result of the mapping of the plant fossils (standing, petrified tree trunks, lying petrified tree trunks , root systems) and volcanic horizon contacts conducted in the Bali Alonia area, within the protected area of the Lesvos Petrified Forest.

Results

The principal aim of this research is to identify and delineate standing tree trunks, fallen tree trunks, root systems, also vitric and lithic tuffs, which are instrumental in pinpointing successive fossiliferous horizons linked to distinct volcanic eruptions. By integrating the geographical coordinates of upright petrified trunks that exhibit their root systems, in conjunction with the occurrences of vitric tuff or lithic tuff, the resultant map was generated (Fig. 6).

The recorded locations (Fig. 6) suggest that the Bali Alonia region contains multiple successive fossiliferous horizons corresponding to various volcanic eruptions.

Discussion

Bali Alonia broader area is characterized by its coverage of quaternary deposits and sparse vegetation, which complicates the mapping endeavors significantly. Comprehensive mapping conducted on Bali Alonia region has furnished substantial evidence for the existence of multiple successive pyroclastic layers that

signify a series of volcanic eruptions.
The excavation activities undertaken by the Natural History Museum of the Lesvos Petrified Forest have resulted in the removal of quaternary deposits and soil profiles, thereby fully exposing the volcanic formations at the excavation sites along the Kalloni Sigri thoroughfare. It is noteworthy that within the confines of "Ioannis Toumpelekis Park" located at the northeastern periphery of Akrocheiras Hill, a minimum of 8 fossiliferous layers have been documented. This finding underscores the notion that the study area is home to numerous successive fossiliferous horizons.
Empirical observations reveal that petrified tree trunks that have fallen are predominantly located at lower elevations, embedded within debris flow deposits, while standing trunks with visible root systems are typically found protruding from tuff layers at higher altitudes. This observed distribution implies that the occurrence of fallen trunks within debris flow deposits does not directly correlate with volcanic eruptions. Rather, these trunks likely represent fragments of previously standing trees that were displaced and subsequently deposited during debris flow events. These flows, influenced by hydrological factors during non-eruptive intervals, transported tree remnants alongside volcanic materials, embedding them within coarse-grained deposits. The consistent vertical and spatial arrangement of standing trunks above fallen trunks is recurrently observed along Bali Alonia broader Area. Consequently, the distribution of fallen trunks in these instances is indicative of prolonged natural transport mechanisms rather than direct volcanism; however, this pattern does not universally apply across the entirety of the study area, as in other locations the distribution of fallen trunks is directly associated with volcanic activity.
Furthermore, the instant correlation of the petrified trunks hosted in the fenced area, the Bali Alonia Park at the West side of the hill, with the numerous trunks at the East of the hill (Fig. 6), it is a subject that demands furthermore research. These occurrences are potentially directly associated with the geomorphological characteristics of the region during the deposition of the Sigri pyroclastic formation and of course will provide very important additional information to the main objective of the current study.
Ultimately, the principal aim of this research represents a subject that warrants extensive further investigation. This preliminary analysis and assessment catalyze a substantial academic discourse concerning the distribution of petrified tree trunks and volcanic tuffs, which contribute to the identification of successive fossiliferous horizons correlated with diverse volcanic eruptions and the evaluation of volcanic episodes that have preserved fossilized forests, initially focusing on Akrocheiras hill and subsequently extending to the broader recognized expanse of the Petrified Forest of Lesvos.

References

Pe-Piper, G. (1980). Geochemistry of Miocene shoshonites, Lesbos, Greece. *Contributions to Mineralogy and Petrology, 72*(4), 387–396. https://doi.org/10.1007/BF00371346

Pe-Piper, G., Piper, D. J. W., Zouros, N. C., & Anastasakis, G. (2019). Age, stratigraphy, sedimentology and tectonic setting of the Sigri Pyroclastic Formation and its fossil forests, Early Miocene, Lesbos, Greece. *Basin Research, 31*(6), 1178–1197. https://doi.org/10.1111/bre.12365.

Pe-Piper, G., Imperial, A., Piper, D. J. W., Zouros, N. C., & Anastasakis, G. (2019). Nature of the hydrothermal alteration of the Miocene Sigri Petrified Forest and host pyroclastic rocks, western Lesbos, Greece. *Journal of Volcanology and Geothermal Research, 369*, 172–187. https://doi.org/10.1016/j.jvolgeores.2018.11.018.

Pe-Piper, G., Piper, D. J. W., Anastasakis, G., Zouros, N. C., & Lyras, G. (2024). Variability in mineralization of the petrified forests in the UNESCO Global Geopark of Lesvos, Greece. *Marine and Petroleum Geology, 167*, Article 106990. https://doi.org/10.1016/j.marpetgeo.2024.106990

Sparks, R. S. J., & Walker, G. P. L. (1977). The significance of vitric-enriched air-fall ashes associated with crystal-enriched ignimbrites. *Journal of Volcanology and Geothermal Research, 2*(4), 329–341. https://doi.org/10.1016/0377-0273(77)90019-1

Velitzelos, E., & Zouros, N.C. 1998. New results on the petrified forest of Lesvos. *Bulletin of theGeological Society of Greece*, *32*(2), 133–142.

Zouros, N. C. (2021). The Miocene petrified forest of Lesvos, Greece: Research and geoconservation activities. *Geoconservation Research, 4*(2), 635–649. https://doi.org/10.30486/gcr.2021.1927340.1090

17th INTERNATIONAL CONGRESS of the Geological Society of Greece

BULLETIN OF THE GEOLOGICAL SOCIETY OF GREECE, SP. PUBL.

EXTENDED ABSTRACT 285

Travertine deposits of Greece, a mineralogical and geochemical study

Schifano V.[1], Li Vigni L.[1], Randazzo L.[1,2], Brusca L.[2], Bellomo S.[2], Calabrese S.[1,2], D'Alessandro W[2]

(1) Department of Earth and Marine Sciences, University of Palermo, Palermo, Italy, vanessa.schifano@community.unipa.it; (2) National Institute of Geophysics and Volcanology, Palermo, Italy

Research Highlights

- Greek travertines are dominated by calcite with aragonite, hydromagnesite, hematite and clay minerals;
- Chemical composition of travertines shows high concentrations of some potentially toxic elements (e.g. As, Ba, Cu, Cr, Ni, Pb, V).

Introduction

Travertine, also known as *Lapis Tiburtinus* by ancient Romans, is a type of "chemically precipitated continental limestone" which consists of calcite or aragonite minerals. (Pentecost, 2005). The precipitation of carbonate minerals occurs primarily through the degassing of carbon dioxide from a groundwater source, resulting in calcium carbonate supersaturation (Pentecost, 2005). The occurrence of travertine deposits has been observed around both cold springs (i.e. tufa or meteogene travertine) and warm-hot springs (i.e. travertine or thermogene travertine), suggesting two distinct origins of travertine. The distinction between these two types of deposit can be determined based on features of parent waters and on the source of CO_2 (e.g. Pentecost and Viles, 1994; Ford and Pedley, 1996). Meteogene travertines are formed from parent waters that are characterized by lower temperature and neutral pH values (7-8). CO_2 has a meteoric and/or biogenic origin and shows carbon isotope compositions that range mostly from about -11 to 0 ‰, reflecting the depleted ^{13}C of soil CO_2 (Deines, 1980). On the other hand, thermogene travertines form from parent waters with high temperatures and lower pH values. The CO_2 in this case has mostly a geogenic source, with a $\delta^{13}C$ range of -4 to +8 ‰ (Pentecost and Viles, 1994), resulting from the interaction between host rocks and deep CO_2-rich fluids, such as mantle fluids or metamorphic decarbonation reactions (Ohmoto and Rye, 1979). In addition, while meteogene travertines display low deposition rates (<10 mmol cm^{-2} a^{-1}), thermogene travertine show very high deposition rate of hundreds of mmol cm^{-2} a^{-1} (D'Alessandro *et al.*, 2007).

An increased interest in studying travertine deposits is driven by their potential applications in paleoclimatic and paleoenvironmental studies, as well as in hydrogeological studies, rock and oil exploitation. Thermogenic travertine deposits also allow for the evaluation of any endogenic processes. Additionally, travertine deposits facilitate the estimation of paleo CO_2 fluxes associated with their deposition (Mancini *et al.*, 2019).

Travertine deposits are widespread in Greece, with the most studied being found in Northern Euboea and Eastern Central Greece. These areas are characterised by a high geothermal gradient, which leads to the presence of several thermal springs. In some of these thermal springs are depositing thermogene travertine, as a result of the cooling and degassing of thermal waters, leading to the rapid precipitation of calcium carbonate (Kanellopoulos *et al.*, 2017 and references therein).

In this research, we present data about the mineralogical and geochemical compositions of 39 travertine samples collected along the whole Hellenic territory from thermal, cold–gas-rich, acidic and hyperalkaline springs, in order to better investigate the possible differences between different type of parent waters.

Methods

Thirty-nine travertine samples were collected along the whole Hellenic territory (Fig.1 and Table 1) from a variety of springs, including thermal, cold–gas-rich, acidic and hyperalkaline springs. Samples were analysed for their mineralogical and geochemical composition. Information on the physico-chemical parameters and the chemical composition of the parent waters were taken from (Li Vigni *et al.*, 2022, 2023).

Samples were, firstly, pulverised in an agate mortar and then, subdivided in two aliquots. The first aliquot was used for the investigation of mineralogical composition by X-ray powder diffraction (XRPD). The XRPD analysis was being carried out at the laboratories of the Department of Earth and Marine Sciences of the University of Palermo, using a PANanalytical X'PERT PRO diffractometer. The second aliquot was mineralized to obtain the chemical composition of the samples. About 100 mg of dried sample were dissolved in a polypropylene bottle with a solution of 1 mL of ultrapure HCl (37%), 0.5 mL of ultrapure HNO_3 (65%) and 50 mL of milliQ water. The obtained solutions were analysed for major cations (Ca, K, Mg, Na, P, S, Si) by Inductively Coupled Plasma Optical Emission Spectrometry

(ICP-OES; Jobin Yvon Ultima 2), whilst 26 trace elements (Li, Be, B, Al, Ti, V, Cr, Mn, Fe, Co, Ni, Cu, Zn, As, Se, Rb, Sr, Mo, Cd, Sn, Sb, Cs, Ba, Tl, Pb, and U) were analysed by Inductively Coupled Plasma Mass Spectrometry (ICP-MS; Agilent 7800). Results are expressed as μg g^{-1} of solid. Pre-treatment procedures were carried out at the laboratories of the Department of Earth and Marine Sciences of the University of Palermo, and analysis were carried out at laboratories of the Istituto Nazionale di Geofisica e Vulcanologia (INGV-Palermo).

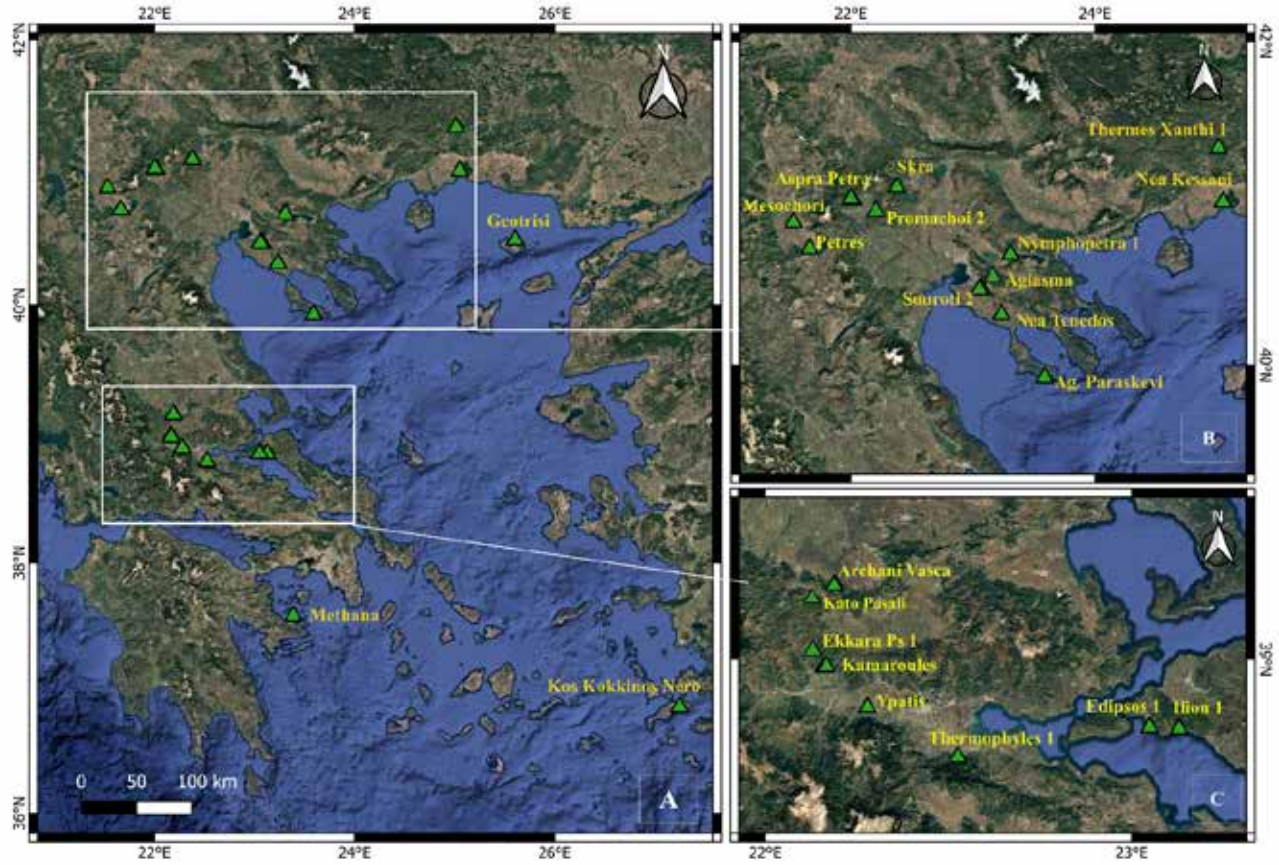

Figure 1. Geographic distribution of sampling sites of travertine deposits. Map was created using the QGIS software, version 3.28.6. Basemap by ESRI maps.

Table 1. Identification number and geographical coordinates of travertine samples. Type of parent waters are also indicated.

ID	Name	Type waters	Date	Latitude	Longitude
GR 01	Mesochori	Thermal	22/05/2016	40.89119	21.53241
GR 02	Geotrisi	Thermal	23/05/2016	40.49705	25.603
GR 03	Archani Vasca	Hyperalkaline	05/10/2017	38.98339	22.16155
GR 04	Skra	Gas-rich cold	03/03/2020	41.10575	22.37831
GR 05	Ekkara Ps	Hyperalkaline	05/09/2017	39.15805	22.18965
GR 06	Ekkara Ps 2	Hyperalkaline	05/09/2017	39.15805	22.18965
GR 07	Nea Kessani	Thermal	18/05/2016	41.01707	25.05148
GR 08	Pareskevi	Thermal	28/05/2016	39.92402	23.59009
GR 09	Kos Kokkino Ner	Acidic	30/09/2016	36.85501	27.24797
GR 10	Ypatis	Thermal	07/10/2016	38.89774	22.2789
GR 11	Kamaroules	Hyperalkaline	07/10/2016	38.98465	22.16633
GR 12	Geotrisi	Thermal	20/03/2017	40.49705	25.603
GR 13	Thermes Xanthi 1	Thermal	22/03/2017	41.34762	25.01361
GR 14	Thermes Xanthi 2	Thermal	22/03/2017	41.34762	25.01361

GR 15	Thermes Xanthi 3	Thermal	22/03/2017	41.34762	25.01361
GR 16	Nymphopetra 1	Thermal	23/03/2017	40.69157	23.30884
GR 17	Nymphopetra 2	Thermal	23/03/2017	40.69157	23.30884
GR 18	Nymphopetra 3	Thermal	23/03/2017	40.69157	23.30884
GR 19	Kato Pasali	Hyperalkaline	09/05/2017	39.15659	22.18749
GR 20	Archani 159	Hyperalkaline	10/05/2017	38.98319	22.16115
GR 21	Archani 160 fuori	Hyperalkaline	10/05/2017	38.98317	22.16124
GR 22	Archani 160	Hyperalkaline	10/05/2017	38.98317	22.16124
GR 23	Thermopyles 1	Thermal	11/05/2017	38.79254	22.52572
GR 24	Thermopyles 2	Thermal	11/05/2017	38.79254	22.52572
GR 25	Thermopyles 3	Thermal	11/05/2017	38.79254	22.52572
GR 26	Ilion 1	Thermal	23/06/2018	38.85212	23.12909
GR 27	Ilion 2	Thermal	23/06/2018	38.85212	23.12909
GR 28	Promachoi 1	Thermal	14/10/2018	41.02973	22.0195
GR 29	Promachoi 2	Thermal	14/10/2018	41.02973	22.0195
GR 30	Promachoi 3	Thermal	14/10/2018	41.02973	22.0195
GR 31	Aspra Petra	Gas-rich cold	27/07/2021	41.03720	22.00308
GR 32	Petres	Gas-rich cold	30/04/2023	40.72604	21.66508
GR 33	Nea Tenedos	Thermal	03/05/2023	40.3178	23.2343
GR 34	Agiasma	Gas-rich cold	03/05/2023	40.47342	23.0551
GR 35	Souroti	Gas-rich cold	03/05/2023	40.4733	23.07653
GR 36	Methana	Thermal	/	37.57744	23.38702
GR 37	Edipsos	Thermal	/	38.85514	23.04845
GR 38	Edipsos	Thermal	/	38.85514	23.04845
GR 39	Archani incrostazioni	Hyperalkaline	10/05/2017	38.98339	22.16155

Results

X-ray diffraction analyses were carried out on 13 travertine samples. The analysis revealed that the main mineral phases show close similarities. The samples are predominantly composed of calcite (Fig. 2), with a very low percentage of aragonite in few samples. Traces of halite and hydromagnesite were also found. Further investigations are underway to verify their presence. Moreover, traces of hematite were found in travertine samples of Mesochori (GR01) and Giotrisi (GR02), whereas traces of clay minerals were found in Archani (GR20).

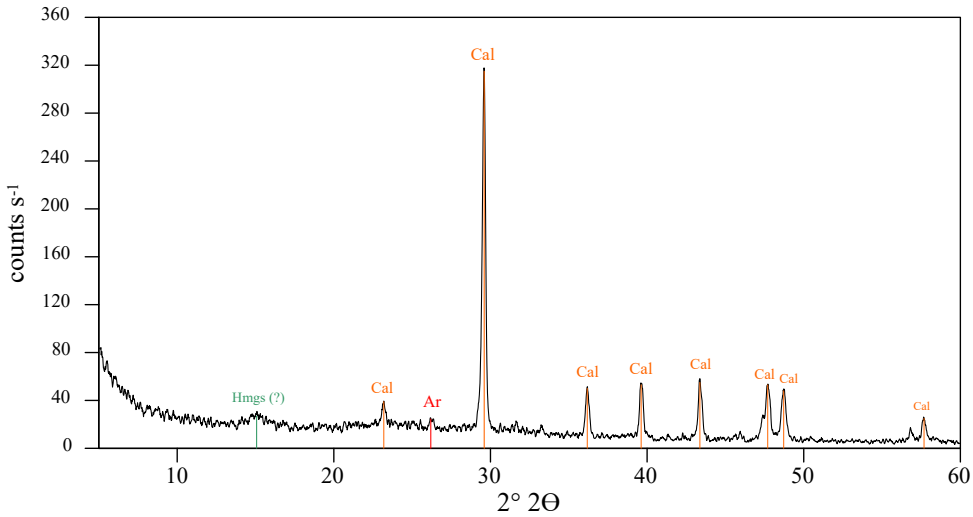

Figure 2. X-ray diffractogram of the travertine sample of Nea Kessani. Hmgs = Hydromagnesite; Cal = Calcite; Ar = Aragonite.

The results of the geochemical analyses are summarised in the boxplot in figure 3, which shows a wide range of concentration, generally, exceeding three orders of magnitude. Calcium is the dominant cation in all the samples,

with concentrations ranging from 94,800 μg g^{-1} to 462,000 μg g^{-1}. The elements can be categorized, based on their median concentrations, into minor elements (Mg, S, Na, Fe, Sr, Si), which show a median values between 1% and 0.1%, and into trace elements (Mn, Ba, P, B, Zn, As, Li, Ti, Ni, Cr, Cu, V, Pb, Rb, Co, Be, U, Cs, Sb, Mo, Se, Cd, Sn, Tl) with median concentrations below to 0.1%.

Thermogene travertine samples of Thermopyles (GR23, GR24, GR25), Ilion (GR26, GR27) and Edipsos (GR37, GR38) have been compared with literature data (Kanellopoulous et al., 2017), showing a similar composition. Elements such as Fe (Thermopyles up to 265 μg g^{-1}, Ilion up to 285,800 μg g^{-1}, Edipsos up to 9280 μg g^{-1}) and As (Thermopyles up to 156 μg g^{-1}, Ilion up to 15,360 μg g^{-1}, Edipsos up to 90.6 μg g^{-1}) displayed concentrations within the range reported by the same authors. According to them, the lithogeochemistry of these ore-bearing travertines reflects the geochemical composition of the parent hydrothermal fluids, which are enriched in Fe and As, particularly in the case of Ilion. The presence of metal(loid)s in thermogenic travertine can be attributed to a primary magmatic source and to reduced and low-sulfidation state of the hydrothermal fluids (Kanellopoulous *et al.*, 2017). However, other travertine samples exhibit enrichment in some metal(loid)s, including Mesochori (GR01), Giotrisi (GR02, GR12) and Skra (GR04).

All these trace elements may be incorporated in the mineral structure of the carbonates substituting for Ca or precipitate as constituents of secondary minerals or be adsorbed onto the surface of the forming crystals or amorphous phases. Therefore, further studies are required to ascertain both the origin and water-rock interaction processes, such as the precipitation of secondary minerals, that took place.

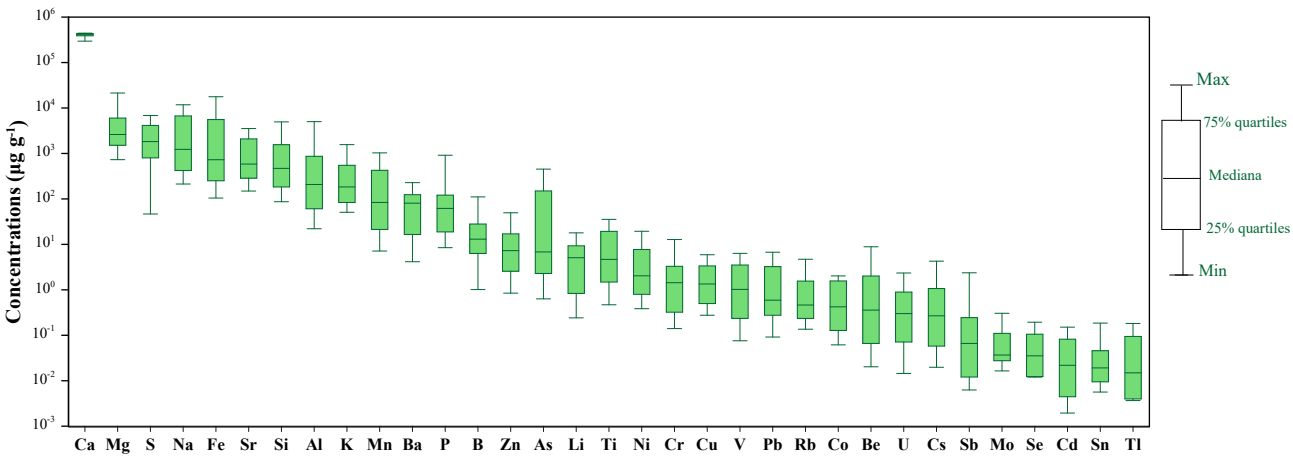

Figure 3. Boxplot of major ions and trace elements of collected travertine samples.

Conclusions

Despite the widespread presence of travertine in Greece, few studies can be found in the scientific literature. Their geochemical and mineralogical characterization may provide important information on water-rock interaction processes, dissolution and precipitation patterns, the origin of CO_2 and the genesis of travertines themselves. These preliminary data show both their mineralogical phases associated dominantly with calcite although traces of aragonite, hydromagnesite, hematite and clay minerals are sometimes found. From a geochemical perspective, calcium is the predominant element. Nonetheless, their chemical composition comprises a large number of trace metals, including some potentially toxic elements (e.g. As, Ba, Cu, Cr, Ni, Pb, V) and some strategical industrial elements like Li and B. Further steps of this preliminary study will be to investigate the relationship between travertine samples and their parent waters in order to better understand water-rock interaction processes.

References

D'Alessandro, W., Giammanco, S., Bellomo, S., Parello, F., 2007. Geochemistry and mineralogy of travertine deposits of the SW flank of Mt. Etna (Italy): Relationships with past volcanic and degassing activity. Journal of Volcanology and Geothermal Research, 165, 64–70.

Deines, P., 1980. The isotopic composition of reduced carbon, in: Fritz, P., and Fontes, J.C. (Eds.), Environmental Isotope Geochemistry, 329-407.

Ford, T.D., Pedley, H.M., 1996. A review of tufa and travertine deposits of the world. Earth-Science Reviews 41, 117–175.

Kanellopoulos, C., Mitropoulos, P., Valsami-Jones, E., Voudouris, P., 2017. A new terrestrial active mineralizing hydrothermal system associated with ore-bearing travertines in Greece (northern Euboea Island and Sperchios area). Journal of

Geochemical Exploration, 179, 9-24https://doi.org/10.1016/j.gexplo.2017.05.003

Li Vigni, L., Daskalopoulou, K., Calabrese, S., Parello, F., Brugnone, F., D'Alessandro, W., 2022. Geochemical characterization of the thermo-mineral waters of Greece. Environmental Geochemistry and Health, 44, 2111-2133. https://doi.org/10.1007/s10653-021-01001-1

Li Vigni, L., Daskalopoulou, K., Calabrese, S., Kyriakopoulos, K., Bellomo, S., Brusca, L., Brugnone, F., D'Alessandro, W., 2023. Characterization of trace elements in thermal and mineral waters of Greece. Environmental Science and Pollution Research, 30, 78376–78393. https://doi.org/10.1007/s11356-023-27829-x

Mancini, A., Frondini, F., Capezzuoli, E., Galvez Mejia, E., Lezzi, G., Matarazzi, D., Brogi, A., Swennen, R., 2019. Evaluating the geogenic CO_2 flux from geothermal areas by analysing quaternary travertine masses. New data from western central Italy and review of previous CO_2 flux data. Quaternary Science Reviews, 215, 132-143. https://doi.org/10.1016/j.quascirev.2019.04.030.

Ohmoto, H. and Rye, R.O. 1979. Isotopes of sulfur and carbon, in: Barnes, H.L. (Eds.), Geochemistry of Hydrothermal Ore Deposits, 509-567.

Pentecost, A., Viles, H., 1994. A review and reassessment of travertine classification. Géographie Physique et Quaternaire, 48, 305–314

Pentecost, A., 2005. Travertine, Springer, Berlin.

17th INTERNATIONAL CONGRESS of the Geological Society of Greece

BULLETIN OF THE GEOLOGICAL SOCIETY OF GREECE, SP. PUBL.

EXTENDED ABSTRACT 286

The Upper Devonian sequence of the Noravank and Ertych geosites in Armenia: stratigraphy and geotouristic potential

Serobyan V.[1], Danelian T.[2], Grigoryan A.[1]

(1) Institute of Geological Sciences of the National Academy of Sciences of the Republic of Armenia, 24A, Marshal Baghramyan Avenue, Yerevan 0019, Republic of Armenia, (2) University of Lille, CNRS, UMR 8198- Evo-Eco-Paleo, F-59000 Lille, France

Introduction / Background

Upper Devonian sequences crop out in the southern part of central Armenia (Fig. 1). They are relatively thick and rich in fossils, especially brachiopods, a fact that has been acknowledged since mid-19th century, at the time of the first geological expeditions in the region by Hermann Abich, considered as "the Father of Caucasian Geology". Interest on these sequences and their brachiopods was revived after the end of World War II, when at the time of the Soviet Union, extensive stratigraphic and mapping efforts were conducted by the Institute of Geological Sciences of the National Academy of Sciences of the Republic of Armenia. The rich brachiopod fauna was studied by Abrahamyan (1957); it allowed her to recognize a number of stratigraphically succeeding brachiopod assemblages that served as a foundation for the stratigraphic understanding and mapping of the Upper Devonian and Lower Carboniferous sequences of Armenia (Arakelyan, 1964). Following this phase of extensive mapping the sequences were considered as relatively well known. In the framework of the preparation of the IGCP n° 491 meeting (*Devonian Vertebrates of the Continental Margins*), held at Yerevan in May 2005, some identifiable conodonts and chondrichthyan microremains were found in limestones processed by Araiyk Grigoryan (Ginter *et al.*, 2011). However, comprehensive and systematic studies of these Upper Devonian sequences in Armenia, with deployment of modern approaches and techniques, only began in earnest with the launch of the co-tutorial PhD work of Vahram Serobyan, which focused on a revision of the taxonomy and biostratigraphy of the Brachiopods recovered from the Frasnian and lower Famennian sequences of Armenia (Serobyan, 2021).

Previous studies conducted in Armenia and Nakhichevan would suggest that some of the Upper Devonian outcrops could include sedimentary sequences deposited during the late Frasnian and early Famennian interval; however, detailed stratigraphic studies were missing. The Frasnian–Famennian transitional interval bears a particular significance for the evolution of marine ecosystems, since the diversity of the marine biosphere was affected profoundly during the Kelwasser mass extinction event. Although the study of Serobyan (2021) was mainly focused on the brachiopods, it allowed to clarify stratigraphic relationships of the Noravank section, which takes its name from the presence of the famous Noravank monastery constructed on top of the Upper Devonian sequence (Fig. 2). This section was correlated with the better-exposed Ertych section (Fig. 1). The correlations established by Serobyan (2021) were based not only on revised brachiopod assemblages, but also on lithostratigraphy. His PhD study confirmed the interest of these sequences as potentially containing the transition between the Frasnian and the Famennian stages, with the possibility of documenting a regional record of the Kelwasser mass extinction in the Lesser Caucasus. This latter part is currently one of the objectives of the ongoing GREATPAL project (*Deciphering the Global vs Regional record of Environmental chAnges in The PALeozoic mountains of Armenia*), funded by the Higher Education and Science Committee of Armenia. We here present recent biostratigraphic results obtained in the framework of this project and discuss the potential of these sections to become geotouristic destinations in Armenia, especially the Noravank geosite, given that the Noravank monastery is one of the most visited touristic attractions in Armenia.

Stratigraphic and palaeogeographic setting

The Upper Devonian sedimentary sequences in Armenia are over 1,000 m-thick; they represent the earliest part of the depositionary history of the Paleozoic sediments that are present in the region. These sedimentary sequences accumulated in a tropical shallow-water platform that was positioned on the northern margin of Gondwana, facing the Paleotethys to the North. This part of Gondwana was individualized afterwards, during the Triassic, as the South-Armenian Block, after it started migrating northwards as a result of the opening of Neotethys further to its South.

In Armenia, the known Frasnian–Famennian sequences crop out essentially on the flanks of a deep valley that has been formed along the Gnishik river, where the Noravank monastery is located, and on the southern bank of the Arpa river, ca. 8.5 Km east of the village of Areni, near the ruins of the ancient village Ertych (Fig. 1). Both sections display a similar lithostratigraphic succession (Fig. 3) and can be subdivided into four lithostratigraphic intervals. The lower and upper parts of the sections are represented by two distinct carbonate intervals that are composed essentially of marly/sandy limestones. The older (lower) carbonate interval is rich in brachiopods characteristic of the *Ripidiorhynchus gnishikensis–Angustisulcispirifer arakelyani* assemblage zone, which have been directly correlated with the latest early

to late Frasnian interval, based on conodonts characteristic of the *transitans* to late *rhenana* conodont zones (Serobyan *et al.*, 2023). It is stratigraphically overlain by an interval dominated by black shales that are intercalated by relatively thin sandstone beds. They are in their turn overlain by thick mature sandstones, in which we may find occasionally some intercalations of shales. Finally, the younger (upper) limestone interval is also rich in brachiopods characteristic of the *Aramazdospirifer orbelianus–Tornitospirifer armenicus* brachiopod assemblage. Conodonts identified by Ginter et al. (2011) in this limestone interval correspond to the lower Famennian *Palmatolepis crepida* conodont zone.

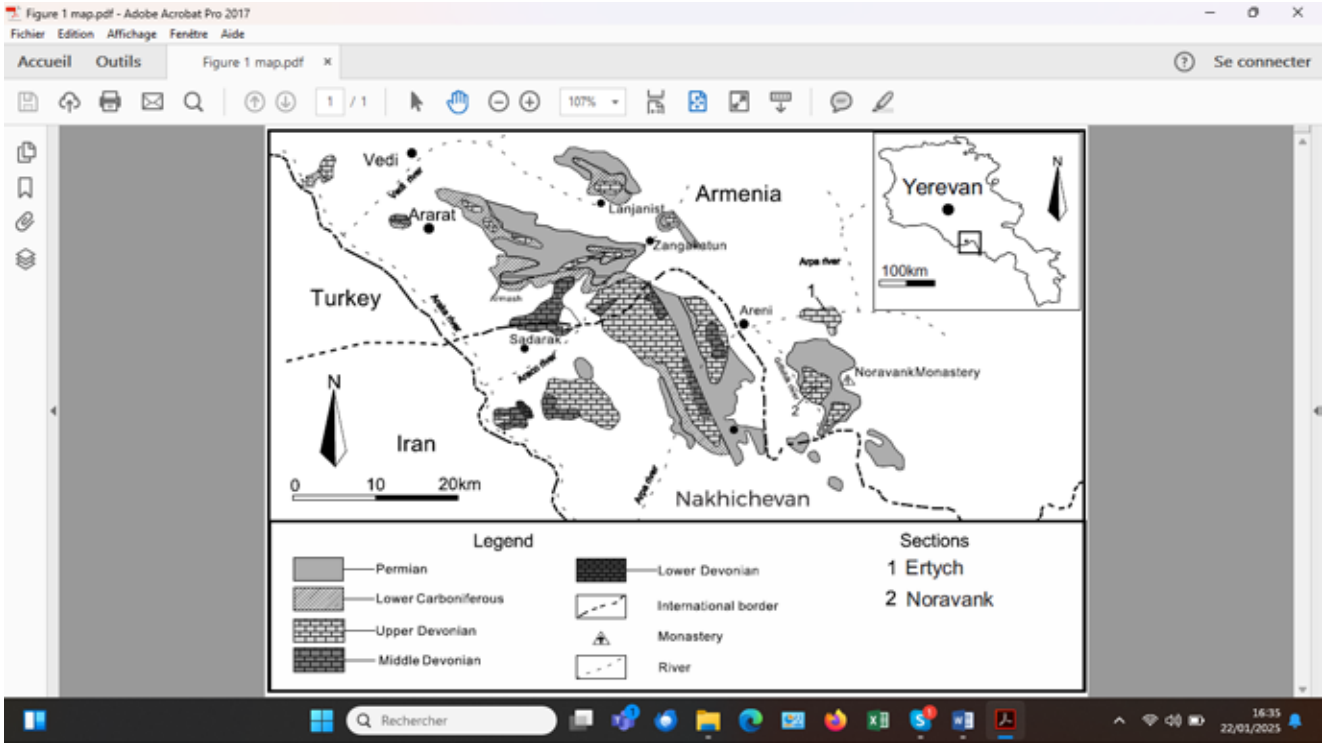

Figure 1. Schematic geological map of the Middle-Upper Palaeozoic sequences in the Lesser Caucasus (Central Armenia and Nakhichevan), with localization of the Noravank and Ertych sections discussed in this study.

Stratigraphy: recent palynological results and correlations

The Upper Devonian sequences of Armenia are indeed rich in fossils; more particularly, they contain a diverse and well-preserved brachiopod fauna (Serobyan *et al.*, 2023). However, they also contain chondrichtyan microremains and conodonts (Ginter *et al.*, 2011), tentaculitides (Vinn *et al.*, 2025), rare bryozoans (Ernst *et al.*, 2024), corals and trilobites (unpublished data). However, since terrigenous siliciclastic sediments, devoid of any carbonate beds, are intercalated between the lower and the upper limestones, the critical Frasnian–Famennian transitional interval has largely remained unzoned. Nevertheless, major biostratigraphic progress has recently been achieved for this interval thanks to the initiation of palynological studies. Indeed, Khachatryan *et al.* (2025) discovered abundant and diverse palynomorphs from the entire terrigenous interval. These authors document for the first time miospore assemblages recovered from eleven samples of the Ertych section. The presence of the miospore species *Teichertospora torquata*, found present in most of the examined samples, suggests that the entire terrigenous siliciclastic interval should be attributed to the *torquata-gracilis* miospore zone, indicating a late Frasnian to early Famennian age. Interestingly, this terrigenous interval contains also the species *Acinosporites lindlarensis*, which corresponds to the spores of the herbaceous lycophyte *Leclerquia*, for which it is well established that it went extinct at the end of the Frasnian. Thus, the miospore record suggests that the age of the black shales and mature sandstones should be limited only to the late Frasnian. In addition, acritarchs, prasinophytes and chitinozoans are also found in the same samples, which establishes that these terrigenous sediments were accumulated in a marine depositional environment (Yeghiazaryan *et al.*, 2025).

Geotouristic potential: where history meets palaeontology, stratigraphy and the topic of mass extinctions

Noravank has an immense historical and touristic significance for Armenia. The geosite hosts a monastery that is composed of a church built initially during the 9th and 10th century. The existing church was re-built during the 12th, 13th and 14th centuries to become the mausoleum of the Orbelian royal family, as it represents one of the most notable monasteries constructed by the Orbelian dynasty.

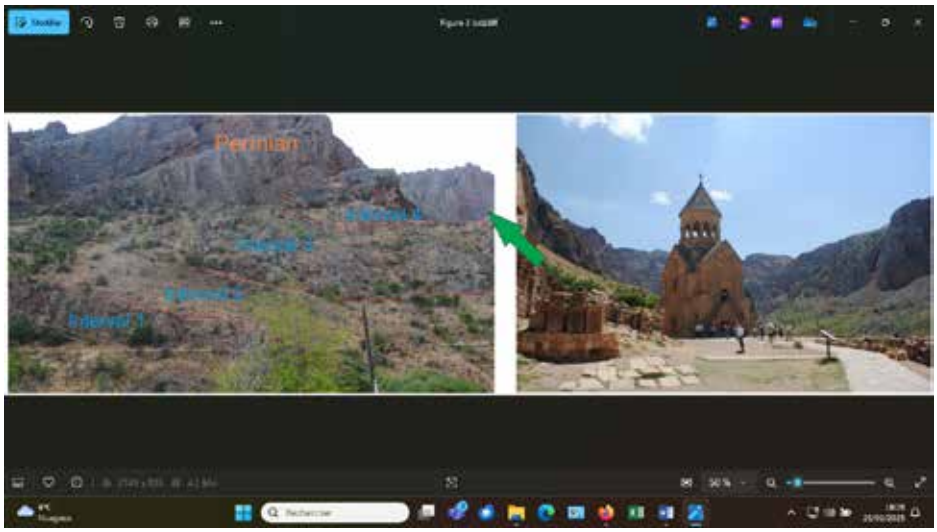

Figure 2. Left: Field photograph of the Noravank section. Right: the Noravank monastery.

The area surrounding the Noravank geosite has been studied since the 19th century by Abich (1858). Born and educated in Germany, he spent most of the time of his life in Russia. He travelled for 30 years different regions of the Lesser Caucasus and more particularly in the current and historic Armenia.

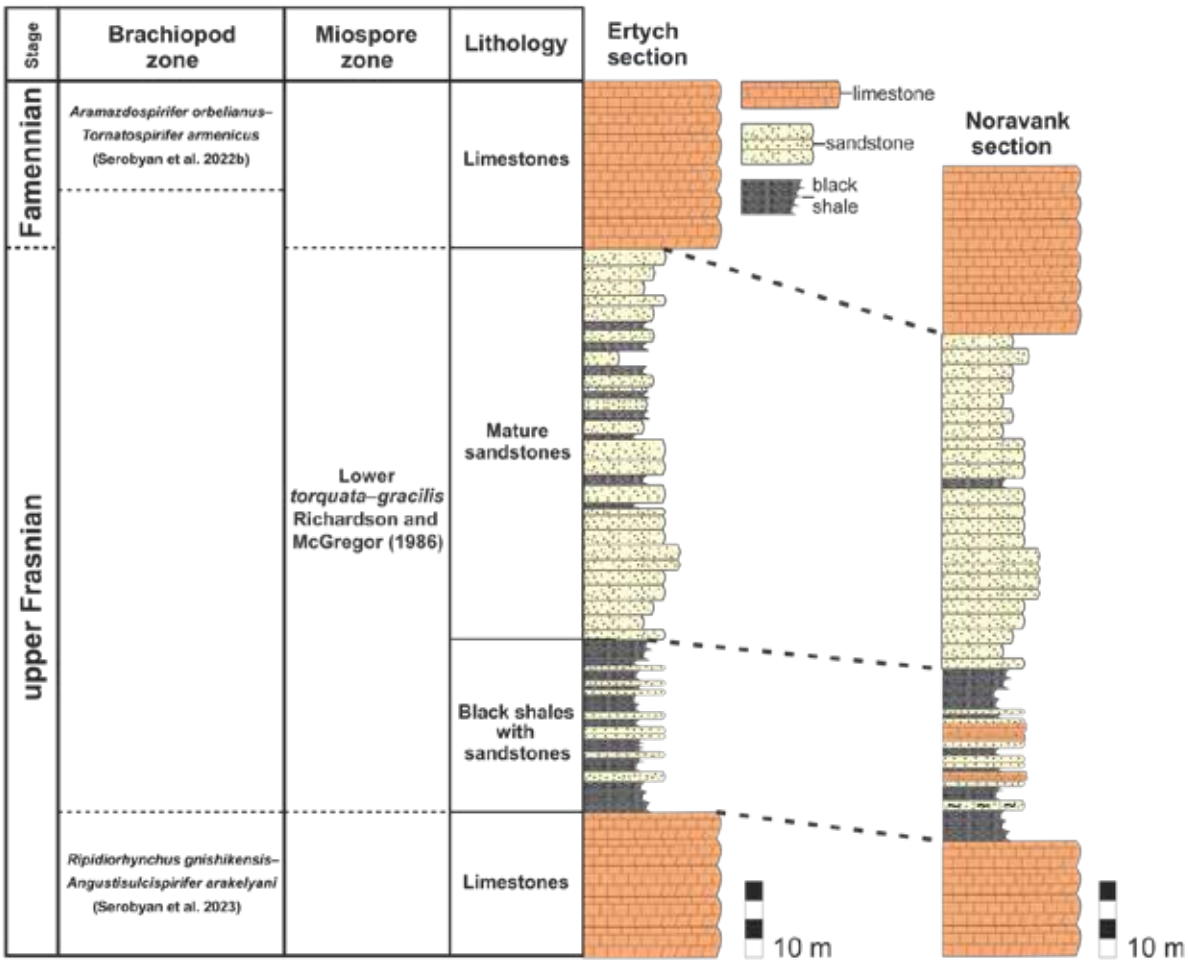

Figure 3. Lithostratigraphic columns and biochronostratigraphic framework of the Upper Frasnian–lower Fammenian sedimentary sequences of the Ertych and Noravank sections.

At Noravank, he found a new brachiopod species, which he dedicated to the Orbelian dynasty, one of the most prominent in medieval Armenia; he named it *Spirifer orbelianus* Abich, 1858. The Orbelian family has had a long-lasting political influence in Armenia and this has been materialized in numerous inscriptions found in different constructions throughout southern Armenia, namely the Vayotz Dzor and Syunik regions. Although Abich did not explicitly mention where exactly he had found the holotype of this species, we believe that it was found in the lower Famennian marly limestones cropping out just below the Noravank monastery (see Serobyan *et al.*, 2022, for more details). During his PhD, V. Serobyan re-examined new specimens of this species (Fig. 4), which he collected from the type locality (the Noravank section). He studied the internal structure of this brachiopod species based on numerous serial thin sections. He found out that this species should be assigned to a new genus, which he introduced under the genus name *Aramazdospirifer*, in honor of Aramazd, the chief god in pre-Christian Armenian mythology. It is obvious that all these palaeontological and stratigraphic elements are of great potential interest for a touristic visit. The Noravank, but also Ertych geosites, may be considered as open-air geological museums for tourists interested in geoeducation.

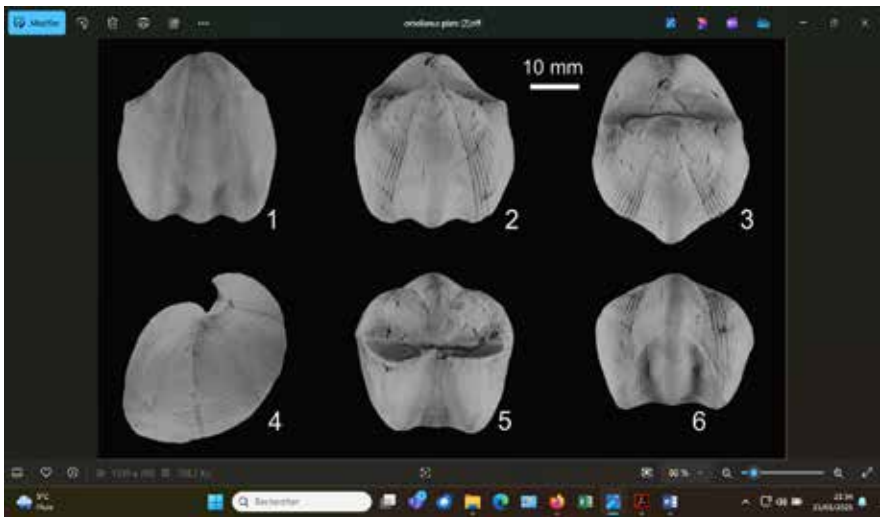

Fig. 4: Microphotographs of a single specimen of *Aramazdospirifer orbelianus* (Abich, 1858) collected from the lower Famennian limestones of the Noravank section. ventral (1), dorsal (2), posterodorsal (3), lateral (4), posterior (5) and anterior (6) views (deposited at the Institute of Geological Science, Yerevan, collection n° IGSNASRAGM 3897/AB97/48; neotype).

Acknowledgements

The research of this extended abstract was supported by the Higher Education and Science Committee of the Ministry of Education, Science, Culture, and Sports of the Republic of Armenia (Research project 22RL-016).

References

Abich, H., 1858, Vergleichende geologische Grundzüge der Kaukasischen, Armenischen und Nordpersischen Gebirge: Prodromus einer Geologie der Kaukasischen Länder: Mémoires de l'Académie impériale des Sciences de Saint-Pétersbourg, 6ème série, Sciences mathémathiques et physiques, v. 7, p. 359–534.

Abrahamyan, M.S., 1957, Brakhiopody verkhnefamenskikh i etrenskikh otlozheniy yugo-zapadnoy Armenii: Yerevan, Izdatelstvo Akademii Nauk Armyanskoy SSR, 142 p. [in Russian]

Arakelyan, R.A., 1964, Devon, *in* Mkrtchian, S.S., Vardaniants, L.A., Gabrielian, A.A., Maghakian, I.G., and Paffenholz, C.N., eds., Geologiya Armyanskoy SSR: Yerevan, Akademiya Nauk Armyanskoy SSR, v. 2, p. 46–96. [in Russian]

Ernst., A., Serobyan, V., Danelian, T., 2024. Biostratigraphic, palaeoenvironmental and palaeobiogeographic implications of bryozoan fauna from the Upper Devonian sequences of Armenia. Geobios 85, 10–18.

Ginter, M., Hairapetian, V., and Grigorian, A, 2011, Chondrichthyan microfossils from the Famennian and Tournaisian of Armenia: Acta Geologica Polonica, v. 61, p.153–173.

Khachatryan S., Cascales-Miñana B., Danelian T., Breuer P., Steemans P., Grigoryan A., Gabrielyan I., Hairapetian V., Regnier S.,

Kroeck D.M., Serobyan V. 2025. First palynological evidence from the Upper Devonian of Armenia (northern Gondwanan margin): biostratigraphic implications. Palaeoworld v. 34, 100879.

Serobyan, V., 2021. Upper Devonian brachiopods and sedimentary sequences from Armenia; biodiversity, stratigraphy and paleobiogeography. Co-tutorial Ph.D. Thesis, University of Lille and Institute fo Geological Sciences of Armenia, Lille/ Yerevan, 280 p.

Serobyan, V., Danelian, T., Crônier, C., Grigoryan, A., Mottequin, B. 2022a. *Aramazdospirifer*, a new cyrtospiriferid genus (Brachiopoda) from the lower Famennian (Upper Devonian) of the Gondwanan South-Armenian Block. Comptes Rendus PalEvol v. 21, 145–156.

Serobyan, V., Danelian, T., Hairapetian, V., Grigoryan, A., Crônier, C., Randon, C., Mottequin, B., 2023. Frasnian (Upper Devonian) brachiopods from Armenia: Biostratigraphic & Palaeobiogeographic Implications. Rivista Italiana di Paleontologia e Stratigrafia v. 129, 373-409.

Vinn, O., Hambardzumyan, T., Temereva, E., Grigoryan, A., Tsatryan, M., Harutyunyan, L., Asatryan, K., Serobyan, V., 2025. Fossilized soft tissues in tentaculitids from the Upper Devonian of Armenia: Towards solving the mystery of their phylogenetic affinities. Palaeoworld 34, 100888.

Yeghiazaryan, M., Kroeck D.M., Danelian T., Grigoryan A., Regnier S., Serobyan V. 2025. Acritarchs and prasinophytes from the Upper Devonian of Armenia: biostratigraphical and palaeobiogeographical implications. Palynology, https://doi.org/10.1080/01916122.2024.2445040

17th INTERNATIONAL CONGRESS of the Geological Society of Greece

BULLETIN OF THE GEOLOGICAL SOCIETY OF GREECE, SP. PUBL.

EXTENDED ABSTRACT 287

Marble as an educational fabric interweaving cultural and geological heritage, the case study of ancient Philippi site rock art, Kavala, Greece

Sideridis A.[1], Koutsoumpis E.[1], Mytakidou K.[2], Boumpouka M.[3], Anevlavi V.[4], Rousopoulos P.[5]

(1) Krinides Gymnasium, Kavala, Greece, alkisside@sch.gr (2) 4th Gymnasium of Kavala, Kavala, Greece (3) 1st elementary school of Nea Peramos, Kavala, Greece (4) Austrian Archaeological Institute, Austrian Academy of Sciences, Vienna, Austria (5) Kupa Ceramics, Kavala, Greece

Introduction

The educational system is dealing with ever-changing classrooms in constant need of contemporary teaching methodologies. Due to technological advancements and changes in the perception of the world, students are not efficiently responding to traditional teaching methods. Most prefectures in Greece combine both interesting Geology and Archaeology and these make up for great educational tools, especially when combined with alternative teaching methods and an interdisciplinary approach. As detailed below, the paradigm of the ancient Philippi site will be presented.

Geology of Ancient Philippi site

The area around the Philippi site belongs to the Rhodope massif and, more specifically, to the lower tectonic unit (Pangaion unit). The latter consists of marbles, gneisses, schists and amphibolites of upper greenschist-lower amphibolite metamorphic facies (Eleftheriadis and Koroneos, 2003; Papanikolaou and Panagopoulos, 1981) and later underwent retrograde greenschist metamorphism (Mposkos and Liati, 1993). NE of the archaeological site (Figure 1A, B, C), small occurrences of the Philippi middle Oligocene granitoid intrude in marbles and gneisses of the Pangeon unit (Tranos et al., 2009), inducing local contact metamorphism. The Philippi Plain comprises quaternary sediments. Local geo-materials such as clay, granite and coarse-grained marble were used in the ancient Philippi site. Marbles from Thasos and ophicalcite from Larissa have also been used.

Historical background

Philippi's inclusion on the UNESCO World Heritage list in 2016 underscores the site's cultural and archaeological significance (Delev, 2018). These monuments, comprising relief images, etchings, inscriptions, and niches, have historically been documented on the acropolis slopes (Figure 1C, D). The predominant depiction among these carvings is a youthful huntress, commonly identified as Artemis/Diana (Figure 1D), which suggests an emphasis on themes of popular religion from the Roman era (Graml et al., 2024). The origins of these carvings, however, extend beyond the Roman period. Some are attributed to the Thracian Hedones tribe, dating from the Late Bronze Age to the Early Iron Age (Dimitriadis, 2008). Despite the rise of Christianity in the region, many of these pagan carvings persisted, reflecting the endurance of earlier religious traditions (Abrahamsen, 1988).

Educational methods and results

Regarding the subject of Geology-Geography in public Greek schools, this is only being taught sparsely in primary schools and for two years in middle school, a time not sufficient to ingrain basic geoscience concepts with the current educational form. Considering the needs of a classroom consisting of Generation Z and Alpha students (born between 2012-2018) the following methods have been adapted: a) Interdisciplinary education (subjects of technology, arts, history), b) Education Through Art and Storytelling, c) Nature-Culture Trails and d) Working groups and reverse classroom (Politis, 2019). This methodology is based on the environmental projects of the Philippi Centre of Environmental and Sustainability Education and was modified to meet the needs of the students. A trail was planned leading to the site. Along the way, students were introduced to the local geology, identifying lithologies and understanding their physical properties and potential uses. Reaching the site and the rock art monuments, students either etched or photographed the carvings and listened to stories related to rock art. Moreover, they tried to identify the lithologies within the Philippi site and discuss rock-provenance and uses. In the classroom, students working in teams tried to interpret the carvings and produce their own rock art on pieces of clay, inspired by their everyday life. The questionnaire results demonstrate that students were able to better grasp the geological and local history and make links between the local geology and other disciplines such as technology, commerce, and architecture. More importantly, they developed their environmental consciousness through the environmental trail and interaction with nature. Art proved to be an effective method for increasing student engagement while nurturing fine motor skills.

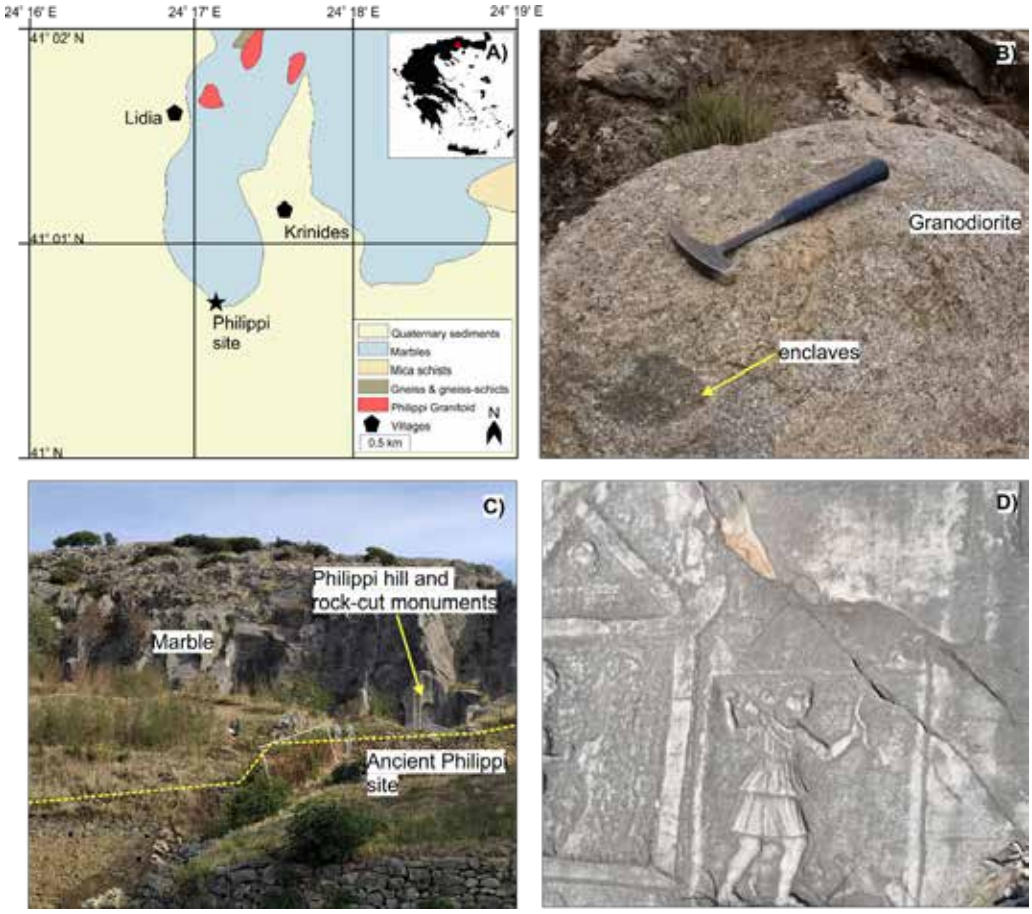

Figure 1 A) Simplified geological map of the studied area; B) Granodiorite occurrence adjacent to the site of Philippi; C) 'Contact' between the natural environment and the ancient Philippi site; D) relief image of hunting Artemis.

Conclusions

To conclude teaching of geosciences can make use of the following methods: a) Interdisciplinary education, b) Education Through Art and Storytelling, c) Nature-Cultural Trails and d) Working groups and reverse classroom. Better engagement, interdisciplinary and syllogistic reasoning, introduction to sustainability and differentiated expression through art are a few of the outcomes. The adapted plan is especially feasible for schools in the Greek countryside that have archaeological sites in their vicinities.

References

Abrahamsen, V., 1988. Christianity and the Rock Reliefs at Philippi. Biblic Archaeol 51, 46–56. https://doi.org/10.2307/3210038

Delev, P., 2018. The History of Philippi. Classical Rev 68, 543–545. https://doi.org/10.1017/S0009840X18001439

Dimitriadis, G., 2008. Hellenic Rock Art-State of Art, Open Questions and New Paradigms. Man India 88, 449–458.

Eleftheriadis, G., Koroneos, A., 2003. Geochemistry and Petrogenesis of Post-Collision Pangeon Granitoids in Central Macedonia, Northern Greece. Geochemistry 63, 364–389. https://doi.org/10.1078/0009-2819-00024

Graml, C., Diosono, F., Hunziker, M., 2024. Rock-Cut Monuments at Macedonian Philippi – Taking Image Analysis to the Religioscape. Open Archaeology 10. https://doi.org/10.1515/opar-2024-0018

Mposkos, E., Liati, A., 1993. Metamorphic evolution of metapelites in the high-pressure terrane of the Rhodope Zone, northern Greece. The Canadian Mineralogist 31, 401–424. https://doi.org/10.3749/1499-1276-31.2.401

Papanikolaou, D., Panagopoulos, A., 1981. Observations on the structural style of the Southern Rhodope. Geologica Balcanica 11, 12–22.

Politis, I., 2019. The Value of the "Environmental Trail" as a Holistic Experiential Approach in Reenforcing the Educational Role for the Environment and Sustainability of Nature Centres Through the Beliefs of their Staff - Problems and Adversities. Hellenic Open University, Athens.

Tranos, M.D., Eleftheriadis, G.E., Kilias, A.A., 2009. Philippi granitoid as a proxy for the Oligocene and Miocene crustal deformation in the Rhodope Massif (Eastern Macedonia, Greece). Geotectonic Research 96, 69–85. https://doi.org/10.1127/1864-5658/09/96-0069

17th INTERNATIONAL CONGRESS of the Geological Society of Greece

BULLETIN OF THE GEOLOGICAL SOCIETY OF GREECE, SP. PUBL.

EXTENDED ABSTRACT 288

First record of pockmarks in the North Aegean Trough

Sklavounaki P.[1], Tzafaridi V.[1], Hasiotis T.[1], Missias S.[2], Paleokrassas A.[2]
(1) Department of Marine Sciences, University of the Aegean, Mytilene, Greece, mar21053@marine.aegean.gr, (2) Akti Engineering, Piraeus, Greece

Research Highlights

Discovery of small depressions in the North Aegean Trough that probably contribute to the Limnos oil seep cluster

Introduction

Pockmarks are crater-like depressions of the seafloor where underlying fluids in the sediment pores escape to the water column. They have been discovered in numerous environments all around the world: in shallow areas, along continental margins, and in deep environments (Judd and Hovland, 2007), even in lakes (i.e., Toker and Tur, 2021). The records of pockmarks in Greece are numerous as well (Papatheodorou *et al.*, 1993), mostly found in shallow areas, like the pockmark fields in Patra and Corinth gulfs (Christodoulou *et al.*, 2003). During a marine survey for the laying of a power cable between Thrace and Limnos Island, numerous small depressions resembling pockmarks were discovered along a narrow corridor in the North Aegean Trough (NAT) (Figure 1a,b). NAT is a main geotectonic and morphological feature in the North Aegean Sea. It has a complex bathymetry containing three main basins (Limnos, Athos and Sporades). The tipping point of the most important fault system that characterizes the region, the dextral strike-slip fault known as the North Anatolian Fault (NAF), is differentiating the SW part of the NAT (Sporades and Athos basins) from the NE part of the NAT (Limnos basin) (Sakellariou *et al.*, 2016). The basins have small dimensions and steep slopes, and they are isolated and separated from each other by bathymetric highs (Roussakis *et al.*, 2004). The bathymetric high between Athos and Limnos Basins is the area under consideration for this study. Recently, Jatiault *et al.* (2024) discovered numerous oil seeps in the wider NAT region probably related to leakage from the broader fault system (Figure 1b). The western part of NAT (to the west of north Limnos), including the survey area, was mapped by Papanikolaou *et al.* (2002), however, pockmarks were not discerned. Thus, the objective of this study is to describe the distribution, morphology, size and density of the observed depressions and examine their potential relation with the oil seeps reported by Jatiault *et al.* (2024).

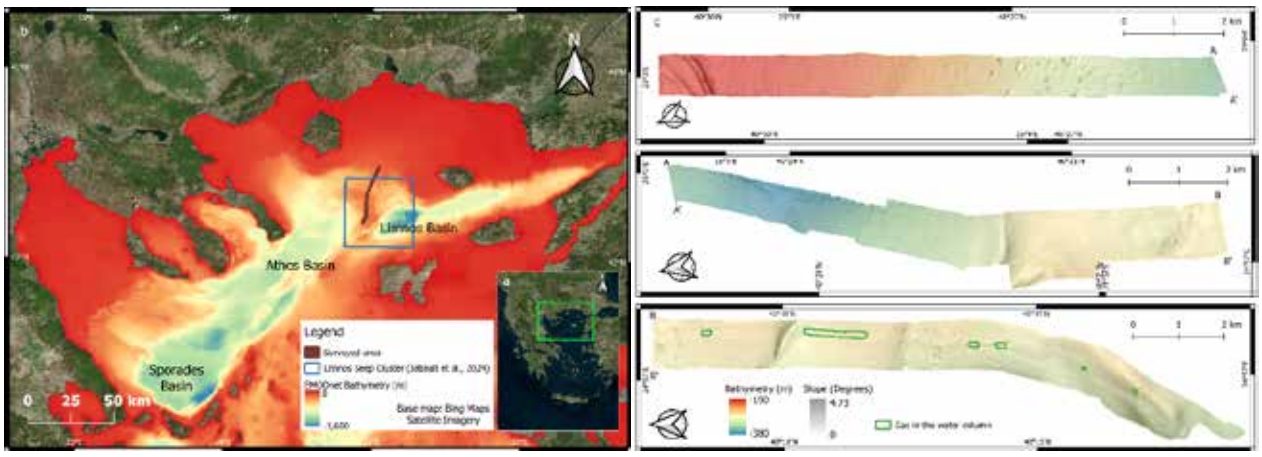

Figure 1. (a) Location of the broader study area (in green), (b) general bathymetric map of the North Aegean and location of the surveyed area (brown line) and of the Limnos seep cluster (blue box) studied by Jatiault *et al.* (2024), (c) bathymetry of the surveyed area overlaid by slope (selected layer transparency: 40%), clipped to 3 subregions for better visualization.

Methods

The survey was conducted during June 2024, along a corridor that was pre-selected by the Independent Power Transmission Operator (IPTO) of Greece, to pass along a bathymetric high in-between Limnos and Athos basins, so as to limit the depth of cable laying and burial. The distance between the survey lines was approximately 250 m. For bathymetry an R2Sonic 2026 (170-450 kHz) multibeam echosounder (MBES) was used. A Valeport Midas profiler was utilized for sound velocity profiles. Data acquisition was performed using the NaviScan and R2Sonic controller software packages. For the morphological survey, an EdgeTech 2050 Side Scan Sonar (SSS) was deployed, able to

scan simultaneously the seafloor with a lower (230 kHz) and a higher frequency (540 kHz). A Sonardyne Ranger-2 USBL system was used for the towfish position. Survey speed was maintained at approximately 3-4 knots. Subbottom profiler records and sediment cores were also collected but are not presented in this study. MBES processing was performed utilizing EIVA, whilst for the SSS data processing and analysis and the production of high-resolution georeferenced sonar mosaics (pixel size of 0.25 m), the Chesapeake Technology SonarWiz software was used. QGIS was used for (i) mapping purposes (bathymetry cell size of 1 m), (ii) the descriptive measurements of the depressions, (iii) slope extraction and (iv) the creation of shaded relief imagery.

Results

Water depths in the study area range between 194 and 373 m. The northernmost part of the surveyed area is relatively shallow but gradually towards the south, the depth increases, reaching its maximum value (Figure 1c) with the deepest region occupying only a small part of the corridor. After this area and towards the southernmost part of the surveyed area, the depth is maintained at approximately 260 m. Slopes gradients are mild, not exceeding ~4.5°.

Throughout the surveyed area, numerous depressions were easily observed. Most of the pockmarks appear in the northern and southern parts of the surveyed zone, whilst along the deepest part depressions rarely occur. A total of 136 depressions were recognized and mapped (Table 1). Although relatively small (average spatial extent of ~1830 m^2) and shallow (1-3 m deep) they appear in a variety of shapes, and they were categorized following the definitions of Judd and Hovland, (2007) for pockmark morphologies. 90 resemble “asymmetrical pockmarks”, lacking a well-defined rim, something that made their recognition difficult in the bathymetric maps. 40 were categorized as “well-defined circular”, and 6 appeared as “composite pockmarks”, implying merging of two or more smaller depressions.

Table 1. Summary of pockmarks’ main characteristics.

	Minimum	Maximum	Average
Occurrence water depth (m)	197	370	282.4
Pockmark depth (m)	1	3	1.3
Perimeter (m)	15.8	675.8	149.9
Area (m^2)	16.6	21414.9	1831.2

The SSS records revealed a uniformly low reflectivity seabed, which indicates the presence of fine-grained sediments. Abundant crossing longitudinal marks suggest intense trawling fishing creating sharp scars on the soft seabed. Upon comparing the pockmarks detected in the bathymetric data with the SSS observations, it was evident that numerous depressions observed in the bathymetrical survey were not observed in the morphological survey, and SSS navigation errors produced discrepancies in the pockmark positions. Thus, unlike the bathymetric data, the SSS images discerned only 104 pockmarks, 28 in both SSS frequencies, 53 only in the low frequency, 11 only in the high frequency, whilst for 12 only low-frequency data were available, thus they could not be compared with the higher frequency information that was missing. Also, along specific areas towards the southern part of the surveyed area, anomalous reflections were recognized in the water column of the SSS records, probably due to fluid seepage (Figure 1c).

Jatiault *et al.*, (2024) studying Sentinel-1 data, reported oil seepage on topographic highs located west of Limnos trough and close to the NAF that coincides with the area under consideration. Fluid leakage was attributed to upward fluid migration through the local fault zone that displaces the shallow sedimentary structure.

Discussion and Conclusions

The study area is located within a topographic high of NAT, separating Limnos and Athos basins and has depths that do not exceed 370 m. The observed pockmarks are so far the deepest observed in the Greek maritime region, even if they have small dimensions. It must be mentioned that since the surveyed corridor spreads only for 1.1-1.2 km, pockmarks are obviously expected to occur in the wider area. This is also supported by the fact that the Limnos oil seep cluster (Jatiault *et al.*, 2024) extends over ~40 km, in water depths ranging from 140 to 1200 m. Leakage in the water column is fueled through faults from deeper sedimentary strata, however, fluid seepage may also take place through pockmarks, and this process might have likewise contributed to their formation. Yet, the fact that leaking fluids in the water column, as observed in the SSS images, were not detected over the entirety of the pockmark field, possibly indicates that seeping activity through pockmarks is sporadic, and that probably only some of the observed pockmarks contribute to the fluid leakage in lower concentrations. Although the wider area is characterized by relatively high sedimentation rates (Roussakis *et al.*, 2004) the topographic high where pockmarks occur probably corresponds to an area of lower sediment accumulation rates, thus ensuring the more stable conditions also needed for pockmark formation (Judd and Hovland, 2007). Finally, at least the surficial sediments are fine-grained, as observed in SSS images, a fact that contributes to the variety of pockmark morphologies that can be found in certain fields (Judd and Hovland, 2007).

References

Christodoulou, D., Papatheodorou, G., Ferentinos, G., Masson, M., 2003. Active seepage in two contrasting pockmark fields in the Patras and Corinth gulfs, Greece. Geo-Mar Letters 23, 194-199.

Jatiault, R., Henry, P., Loncke, L., Sadaoui, M., Sakellariou, D., 2024. Natural oil seep systems in the Aegean Sea. Marine and Petroleum Geology 163, 106754.

Judd, A., Hovland, M., 2007. Seabed Fluid Flow: The Impact on Geology, Biology, and the Marine Environment, 1st ed. Cambridge University Press.

Papanikolaou, D., Alexandri, M., Nomikou, P., Ballas, D., 2002. Morphotectonic structure of the western part of the North Aegean Basin based on swath bathymetry. Marine Geology 190, 465-492.

Papatheodorou, G., Hasiotis, T., Ferentinos, G., 1993. Gas charged sediments in the Aegean and Ionian Seas, Greece. Marine Geology 112, 171-184.

Roussakis, G., Karageorgis, A.P., Conispoliatis, N., Lykousis, V., 2004. Last glacial–Holocene sediment sequences in N. Aegean basins: structure, accumulation rates and clay mineral distribution. Geo-Mar Letters 24, 97-111.

Sakellariou, D., Rousakis, G., Vougioukalakis, G., Ioakim, C., Panagiotopoulos, I., Morfis, I., Zimianitis, E., Athanasoulis, K., Tsampouraki-Kraounaki, K., Mpardis, D., Karageorgis, A.P., 2016. Deformation pattern in the western North Aegean trough: preliminary results. Bulletin of the Geological Society of Greece 50 (1), 124-133.

Toker, M., Tur, H., 2021. Shallow seismic characteristics and distribution of gas in lacustrine sediments at Lake Erçek, Eastern Anatolia, Turkey, from high-resolution seismic data. Environmental Earth Sciences 80, 727.

17th INTERNATIONAL CONGRESS of the Geological Society of Greece

BULLETIN OF THE GEOLOGICAL SOCIETY OF GREECE, SP. PUBL.

EXTENDED ABSTRACT 289

Mineralogical and petrographic characterization of different limestones used as raw materials in cement production

Skontovolou L.[1], Lampropoulou P.[1], Baskoutas I.[2], Raptopoulou C.[2], Giannakopoulou P.P.[1], Rogkala A.[1], Kareli A.[1], Savvatis P.[1], Petrounias P.[1]

(1) Department of Geology, University of Patras, 265 04 Patras, Greece, loukiaskontovolou@gmail.com (2) Titan Cement Company S.A., Drepano Plant, Patras, Greece

Introduction

Nowadays, global environmental regulations require industrial production to align according to principles of sustainable development. In cement industry it consists of priority, since optimizing raw material use and energy efficiency are crucial for reducing environmental impact. Limestone is a key raw material in cement production, primarily serving as a source of calcium carbonate ($CaCO_3$) for clinker formation. Its mineralogical composition and structural characteristics significantly influence both grinding efficiency and thermal behavior during calcination (Nuhu et al., 2020).

This preliminary study focuses on the petrographic characteristics of different limestone types and their effects on the critical stages of grinding, calcination and clinker formation. A deeper understanding of these variations enables a more targeted selection and design of the initial raw material mixture, improving grinding and calcination efficiency as well as ensuring a stable, high-quality clinker product. Such improvements can lead to reduced production costs, lower energy consumption, and enhanced process control, all contributing to a more sustainable cement manufacturing process.

Materials and methods

This study consists of part of a project in progress in cooperation with TITAN Cement Company S.A. (Drepano plant, Patras, Greece). Under this project rrepresentative limestone samples were collected from the quarries of the company in Drepano, Achaia. These samples, were delivered from TITAN to the Department of Geology, University of Patras, in order to be studied regarding their mineralogical and petrographic characteristics.

The characterization of the samples was conducted by the following techniques and methodology:

- XRD (X-ray diffraction)

The mineralogical analyses of the studied samples were carried out by an X-ray diffractometer, Bruker D8 Advance type, equipped with a copper cathode with nickel filter and fast, high-resolution detector (Lynxye). The scan area was in the range of 2–70o 2ϑ, with a resolution step of 0.3 s / 0.015o. Before the analyses, the powdered samples placed in the special container and flattened by a glass in order to ensure uniform surface. Identification of these phases was done using DIFFRACplus EVA12® software (Bruker-AXS) and the accompany ICDD Powder Diffraction, PDF- 2 2006, EVA database, which compares the data to a database of known crystal phases. The semi-quantitative analysis was performed using the TOPAS 4.0® software (TOPAS MC Inc., Oakland, CA, USA), based on the Rietveld method. Finally, ccorrections of the semi-quantitative results were performed by chemical analyses.

- Petrographic microscope

A Leitz Ortholux polarized light petrographic microscope was used for the petrographic study of the samples, while thin sections of representative samples were prepared for observation.

- SEM (Scanning electron microscope)

A JEOL 6300 SEM was used to observe the microstructure and perform microanalyses. The microscope is equipped with an X-ray Energy Dispersive Spectrometer (EDS), which was utilized for elemental analysis. The analyses were performed on carbon-coated thin sections.

Results and discussion

Mineralogical study

During the analyses of limestone samples using XRD, the amount of calcite ranges from 88% (sample 3) to 97% (sample 4), (Figure 1, Table 1). Additionally, small amounts of quartz (max of 8% in sample 3) were detected, along with low amounts of clay minerals and opaque in the detection limit of technique (max 4% in sample 3), (Figure 1, Table 1)

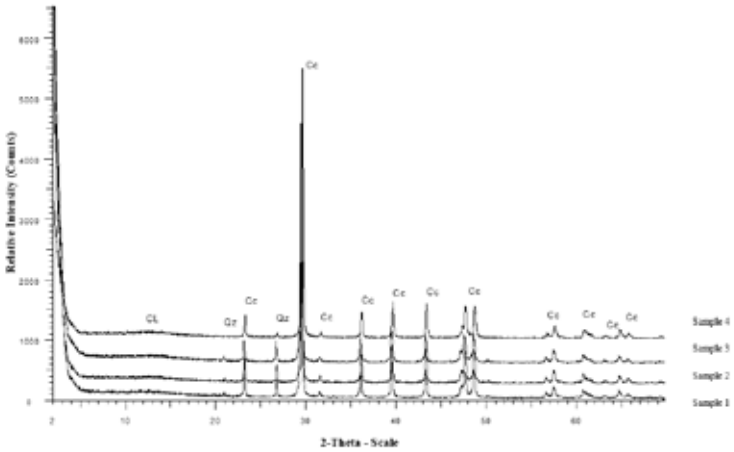

Figure 1. X-ray diffractogram of limestone samples.
Abbreviations: Cc: Calcite, CL: Clay, Qz: Quartz.

Table 1. Qualitative and semi-quantitative phase analysis results obtained through Rietveld refinement, with corrections based on chemical analyses, for the analyzed limestone samples. GOF Good of Fitness (GOF) is 1.25 and error is below 1%.

Mineral phases	**Samples**	**Sample 1**	**Sample 2**	**Sample 3**	**Sample 4**
Calcite	**$CaCO_3$**	91%	93%	88%	97%
Quartz	**SiO_2**	6%	4%	8%	2%
Clay/Opaque	**Al-Si minerals/ Fe oxides or hydroxides**	3%	3%	4%	tr*

Abbreviation: tr: traces

Overall, considering the results and the potential impact of impurities in the primary limestone material, such as silicate, clay minerals and opaque, sample 4 exhibits the purest calcite composition in contrasts to sample 3, which contains the highest percentage of quartz and opaque minerals (such as oxides and hydroxides, see Table 1), is the least favorable raw material for cement.

Petrographic study

Examination of the samples under a petrographic microscope proves that these are sedimentary rocks classified as biochemical limestones.

Figure 2. The analyzed limestone samples (Sample 1, Sample 2, Sample 3, Sample 4).

Sample 1 shows micritic to microsparitic and locally oolitic texture (Figure 3). Carbonate veins with sparitic material

are sometimes partially oriented. Also, porosity is low in the form of mostly individual pores. The shape of the crystals is hypidiomorphic to anhedral. Minerals that prevail in this sample are calcite with accompanying minerals of quartz, muscovite or other clay minerals and opaque (as iron oxides/hydroxides) in low percentages.

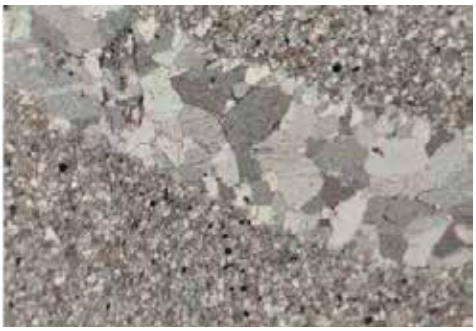

Figure 3. Microstructure in the polarizing microscope of sample 1 (Nicols vertical with magnificence 100x). Sparitic vein with isometrical calcite crystals developed in a mainly micritic microstructure.

Sample 2 exhibits micritic to locally oolitic texture. Moreover, sparitic veins and microveinlets filled with hypidiomorphic to adhedral grains occur (Figure 4). Porosity is low and sometimes capillary channels (i.e. microcracks) appear. The primary mineral in this sample is calcite, and it coexists with minor amounts of quartz, muscovite and plagioclase.

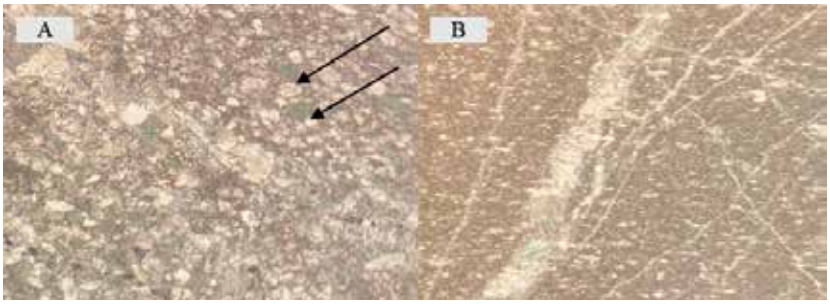

Figure 4. Microstructure in the polarizing microscope of sample 2 (Nicols vertical with magnificence 100x). A. Locally oolitic texture (spheroidal shaped grains). B. Micro veinlets filled with carbonate material of sparitic texture within a micritic main mass.

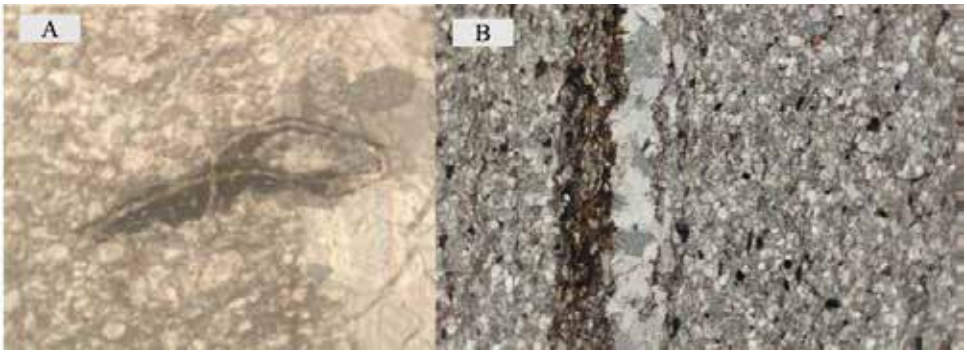

Figure 6. Microstructure in the polarizing microscope of sample 3 (Nicols vertical with magnificence 100x). A. Presence of fossil material. B. Sparite vein composed of calcite and opaque minerals. Polarization colors range from brown and red-brown to black, corresponding to calcite, clay minerals, and opaque phases. Gray coloration is associated with silicate minerals, including quartz and feldspars.

Sample 3 is characterized by micritic texture, locally oolitic, with the presence of scattered veins (Figure 5). The porosity forms capillary-shaped or even larger channels. The presence of opaque minerals, partially in an oriented distribution, is common. The primary minerals of this sample are calcite, while feldspars, microcrystalline quartz and muscovite appear more often than in the other samples. Opaque, most iron oxides and some fossils are observed too (Fiure 6).

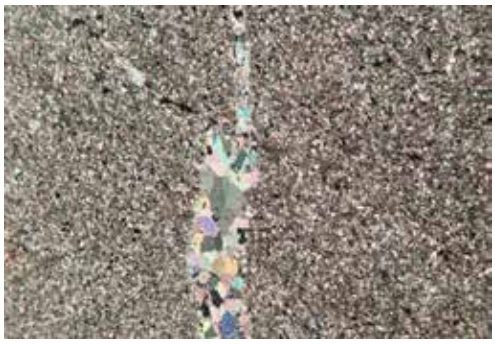

Figure 5. Microstructure in the polarizing microscope of sample 3 (Nicols vertical with magnificence 100x). Presence of sparitic vein in a micritic mass with calcite.

Sample 4 appears a more homogeneous mineral composition and microstructure compared to the others. Specifically, it is appeared fine-grained with a micritic to locally oolitic texture and low porosity. The mineralogical composition consists of calcite and low amounts of quartz. However, micro-areas filled with carbonate material and veins of various sizes and orientations were identified.

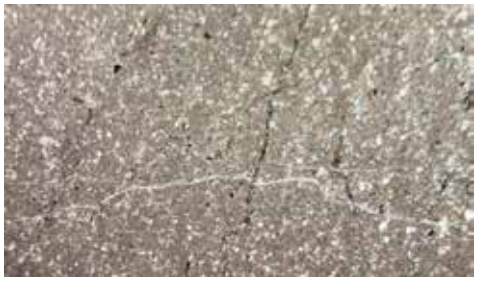

Figure 7. Microstructure in the polarizing microscope of sample 4 (Nicols vertical with magnificence 100x). Homogeneous microstructure with micritic texture.

Influence of petrographic characteristics of limestone to the grinding and calcination processes

Grinding and calcination are critical processes in cement production and are significantly influenced by the physical and mineralogical characteristics of raw materials (Soltan & Serry, 2011). Understanding these characteristics is essential for the optimizing processes in cement production regarding the energy cost, environmental impact in accompany with the quality of final product. The main mineralogical and petrographic features of the limestones, along with their potential effects on the two crucial parameters mentioned above, are summarized in the table below (Sousa, 2021).

The desired characteristics for grinding are:

- **Micritic texture**: It is the fine-grained texture of the calcite material, which facilitates the milling process, as the smaller and uniform crystal sizes require less milling time.
- **Reduced number of veins:** Micro micritic veins contribute less to the inhomogeneity of the structure than the larger ones or/ with the occurrence of veins filled with sparite (He et al., 2022).
- **Homogeneous structure and mineralogical composition:** A uniform distribution of fine-grained structure and minerals are expected to promote the efficient of grinding. Moreover, homogeneity would positively influence some crucial parameters such as hardness and plasticity. Minor amounts of quartz, opaque minerals, feldspars, and soft phyllosilicates are not expected to affect significantly the process.

Likewise, for calcination:

- **Micritic texture – microcrystalline:** Having a fine-grained and microcrystalline texture facilitates uniform heating and consistent sintering performance.
- **Reduced number of veins:** The reduced presence of veins limits the possibility of uneven heating and the occurrence of failures in the material during the firing process (He et al., 2022).
- **Homogeneous structure and mineralogical composition:** The stable structure and uniformity in mineral composition ensure isomeric heating and predictable reactions, which is critical to creating high-quality end products.
- **Fossils:** The presence of fossils of a non-calcic composition is not desirable because it can affect the thermal behavior of the material and lead to inhomogeneities or to the formation of undesirable by-products during firing.
- **Porous in the form of channels:** Having pores in the form of channels can favor heating as it facilitates air circulation, improving calcination efficiency (Freire-Gormaly et al., 2015).
- **Impurities of other minerals:** Low percentages of quartz and opaque minerals could have a positive or neutral effect during

the firing process (Sandström et al., 2024).

Based on the above characteristics, the analyzed samples are categorized and presented in Table 2. In particular, the sample 4 presents the smallest grain size, the most suitable mineralogical composition and high homogeneity of microstructure. Micro veinlets, porosity or even fossils are sometimes present in the microstructure but they do not alter significantly the prevalence of the micritic texture.

Sample 1 exhibits the desired characteristics in terms of grain size, mineralogical composition and homogeneity, although it falls slightly short compared to sample 4. The micritic texture is satisfactorily developed. It has high porosity and a small percentage of veins, but the presence of fossils is more rare compared to that in sample 4.

Sample 2 has a relatively fine grain size but exhibits significant heterogeneity, which may cause issues during processing. The predominance of sparitic texture makes it less desirable, as its involvement in the formation of new phases is expected to be delayed. Its relatively high porosity may contribute to improved combustion efficiency.

Sample 3 has characteristics that place it lower in the overall evaluation. Even it exhibits the lowest porosity and contains few fossils, it is the most heterogeneous in terms of grain size and mineralogical composition. Although it displays veins less frequently than the other samples, the larger grain size of its mass may prolong the heating time or potentially cause inhomogeneity during calcination.

Table 2. Summary table including the most favorable characteristics for cement production observed for each limestone sample.

Grain Size	Mineralogical Composition	Homogeneity	Micrite-Sparite	Veins	Porosity	Fossils
Samples	4, 1, 2, 3	4, 1, 2, 3	4, 1, 3, 2	4, 1, 3, 2	3, 1, 4, 2	3, 4, 2, 1

Conclusions

- Sample 4 is the purest compositionally with the most homogenous structure of predominantly micritic character, while porosity channels and veins of carbonate material are present in its structure.
- Sample 3 is the most mineralogically inhomogeneous with microsparitic main texture. In addition, it presents the highest percentage of quartz, opaque minerals and porosity in the form of channels.
- Samples 1 and 2 appear an intermediate mineralogical composition compared to the above, low porosity in the form of isolated pores and microsparitic-micritic oolitic texture.
- Sample 4 is considered as the most favorable material, as it gathers the most desirable characteristics. It is followed by samples 1, 2 and 3 in terms of suitability.

Although no significant differences were observed in the suitability of the different limestone types for cement production, variations in their grinding and calcination behavior could impact energy consumption, cost, and time during production, as well as clinker phase formation. More homogeneous raw materials, in terms of texture and mineral composition, are expected to facilitate grinding and reduce energy and time consumption. These characteristics also promote sintering, enabling more efficient phase formation.

Despite their general suitability, micro-scale differences in the limestones may influence the final material properties and should be considered. Ongoing experiments on clinker production from different raw materials and grinding processes will further optimize raw material mixtures and process parameters, with results to be presented in a future work.

Acknowledgements

Special thanks to TITAN Cement Company S.A., Drepano plant, Patras, Greece for our collaboration, support and funding of this project.

References

Freire-Gormaly et al., 2015. Pore Structure Characterization of Limestones.

He, J., Li, T., Zheng, B., Mao, T., Wu, Y., Li, S., & Li, X. 2022. Effect of calcite veins on the mechanical behavior and fracture propagation of carboniferous limestone. Engineering Geology, 300, 106592.

Nuhu, S., Ladan, S., Muhammad, A. U., Cao, A. F., 2020. Effects and control of chemical composition of clinker for cement production. International Journal of Control Science and Engineering, 10(1), 16-21.

Sandström, K., Carlborg, M., Eriksson, M., Broström, M., 2024. Characterization of Limestone Surface Impurities and Resulting Quicklime Quality. Minerals 14(6), 608.

Soltan, A. M. M., & Serry, M. A., 2011. Impact of limestone microstructure on calcination activation energy. Advances in Applied Ceramics 110(7), 409-416.

Sousa, L., Menningen, J., López-Doncel, R., Siegesmund, S., 2021. Petrophysical properties of limestones: influence on behaviour under different environmental conditions and applications. Environmental Earth Sciences 80(24), 814.

17th INTERNATIONAL CONGRESS of the Geological Society of Greece

BULLETIN OF THE GEOLOGICAL SOCIETY OF GREECE, SP. PUBL.

EXTENDED ABSTRACT 290

The role of the epikarst zone in the influx of water and the manifestation of humidity at the Holy Monastery of Kleiston, Mount Parnitha, Attica, Greece

Skourtsos E[1], Filis, C.[1], Vassilakis, E.[1], Konsolaki, A.[1], Kotsi E.[1], Lekkas, E.[1]
(1) National and Kapodistrian University of Athens, Department of Geology and Geoenvironment, Athens, Greece
eskourt@geol.uoa.gr

Introduction

The epikarst zone represents an essential facet of karst landscapes, positioned at the boundary between the soil and the underlying bedrock. This area, distinguished by its high porosity, plays a significant role in the hydrology and ecology of karst systems.

Originally defined by Mangin (1974), the term “epikarst” has undergone a nuanced evolution in its interpretation. Williams (1983) characterized it as “subcutaneous”, highlighting its importance as the karst morphology of the rock layer directly beneath the soil. As noted by Bakalowicz (2004), the epikarst can be envisioned as the “skin” of the karst system, implying its function as a protective and interactive layer that governs water infiltration, drainage, and the overarching dynamics of the karst environment.

At the Holy Monastery of Kleiston which is situated on Mount Parnitha in Attica, localized points of water and humidity intrusion manifest in several buildings and functional spaces, particularly during the winter months and following rainfall of considerable intensity and/or prolonged duration, as well as snowfalls. The issues of humidity display greater persistence, even becoming evident in the summer months. The localized sites of water and humidity intrusion include the following:

- The Catholicon of the Holy Monastery of Kleiston (Holy Monastery of the Dormition of the Theotokos).
- The storage facility of the Holy Monastery of Kleiston, located within a cavern (to the north of the Catholicon).
- The building of the cells situated immediately before the entrance to the Catholicon (to the south of the Catholicon).
- The edifice housing the old cells of the Fathers, in addition to various common areas (the reception hall, the dining room, the kitchens, etc.) (to the east of the Catholicon).
- The Church of the Holy Cross.

This work outlines the epikarst in the region of the Holy Monastery of Kleiston, and analyzes its role in the aforementioned phenomena of water and humidity intrusion.

Morphology and Geological Setting

The Holy Monastery of Kleiston is situated within the gorge of the Giannoulas stream, which divides the mountainous mass of Strati to the west from the peaks of Korifoula, Koromilia, and Alogorachi to the east. The gorge has an average orientation from north to south and features steep slopes primarily composed of carbonate rocks. These steep to nearly vertical slopes attain heights of up to 400 m. The Monastery is founded on the edge of a narrow “terrace” on the western slope of the valley, at an elevation of 450 m, rising approximately 80 m above the valley floor.

The region of Monastery is composed of geological formations belonging to the Sub-Pelagonian or unmetamorphosed Pelagonian Unit (Dounas, 1971; Katsikatsos et al., 1986). Specifically, it comprises clastic and volcanic rocks from the Upper Paleozoic to the Lower Triassic (P-Ti.tf), as well as limestones and dolomites dated Lower Triassic to Lower Jurassic (Ti-Ji.k,d).

The lower stratigraphically volcanosedimentary formation exhibits an elongated outcrop that originates to the north of the Monastery, passes west of it, and is observable along the road leading to it. This consists of keratophyres and keratophyric tuffs, sandstones, and argillaceous schists. The thickness of the formation varies from 10 m near the Church of the Holy Cross and reaches 50 to 60 m to the north and south of the Monastery.

The carbonate rocks consist of platy to thick-bedded, locally massive limestones dolomitic limestones and dolomites. The upper strata are mainly thin-bedded to platy carbonates with intercalations and nodules of chert.

To the north-northwest of the Monastery, the appearance of the volcanosedimentary formation is obscured by debris and scree (H.cs,sc) composed of breccias and carbonate blocks of various sizes. This formation originates from the overlying limestones, where carbonate fragments were dislodged from their original positions-potentially due to erosion-and subsequently rolled downstream.

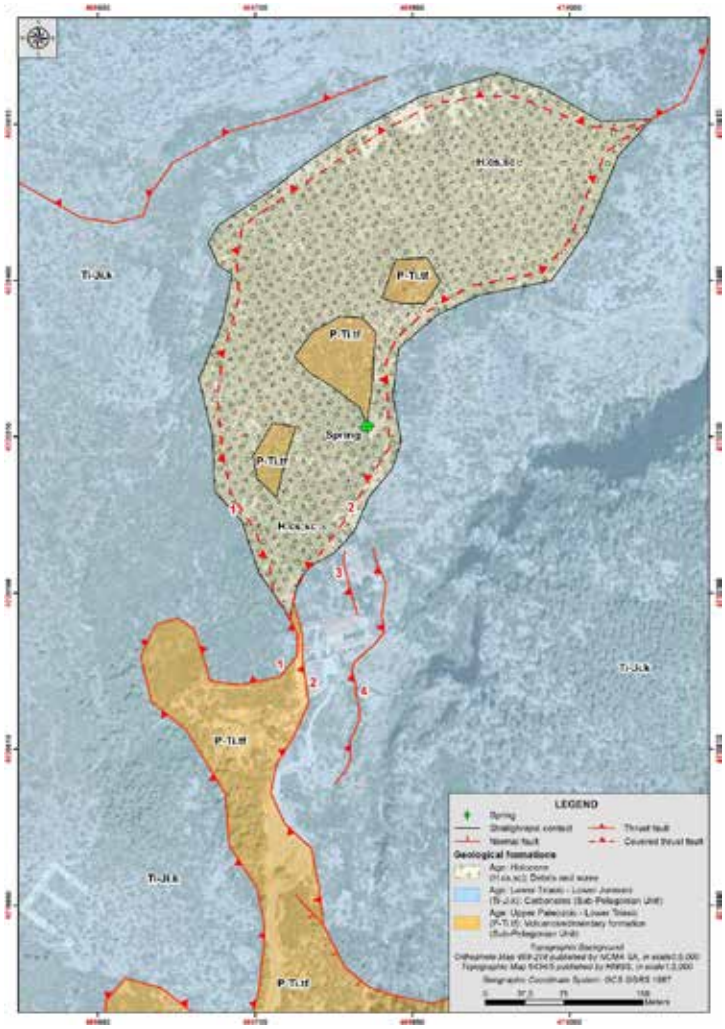

Figure 1. Geological map of the area of the Holy Monastery of Kleiston.

The formations of the Sub-Pelagonian Unit are in contact with one another via reverse faulting (thrusts) and steep normal faults, resulting in the lower clastic formations being thrust upon and overlain by the carbonate rocks. This deformation can be attributed to at least two tectonic episodes, one during the Middle Jurassic to Lower Cretaceous and another during the Middle Eocene to Lower Miocene. Subsequently, steeply dipping normal to oblique-normal faults led to the fragmentation of the earlier structures, constituting a third tectonic episode, which remains active in the broader region to this day (e.g., the Fili earthquake).

Through detailed mapping in the vicinity of the Holy Monastery of Kleiston, the following tectonic contacts were identified:

- Upper thrust (No 1, Figure 1 & Figure 2), which places the carbonate rocks above the volcanosedimentary rocks. This tectonic contact is characterized by a gentle slope, generally dipping towards the south-southwest, as the elevation of the contact gradually decreases in that direction.
- Lower thrust (No 2, Figure 1 & Figure 2), which positions the volcanosedimentary formation upon the carbonate rocks. The trace of this fault is sub-parallel to the upper thrust. The lithologies of the overlying volcanosedimentary formation along the tectonic contact are markedly faulted, brecciated and schistose.

Within the footwall of the lower thrust and within the carbonate rocks, successive tectonic surfaces can be observed, many of which have developed along or sub-parallel to the bedding of the carbonates. These are sub-horizontal to gently and moderately dipping surfaces, occasionally flat but also slightly undulating, anastomosed surfaces that primarily incline towards the north-northwest and southwest, though locally they may trend in other directions.

In the vicinity of the Monastery, two primary low-angle fault surfaces can be observed:

- An upper low-angle fault surface (No 3, Figure 1, Figure 2 & Figure 3, left), located at the main foundation level of the Monastery, which is the minor of the two.

- A lower and larger low-angle fault surface (No 4, Figure 1, Figure 2 & Figure 3, right), situated at lower elevation than the main foundation level of the Monastery.
-

Figure 2. UAV image showing the synthetic depiction of the tectonic contacts at the Holy Monastery of Kleiston. 1: Upper thrust which places the carbonate rocks above the volcanosedimentary rocks. 2: Lower thrust which positions the volcanosedimentary formation upon the carbonate rocks. 3: Upper low-angle fault surface located at the main foundation level of the Monastery. 4: Lower low-angle fault surface situated at lower elevation than the main foundation level of the Monastery. 5: Carbonate fragment.

Figure 3. View of the upper low-angle fault surface (No 3, Figure 1 & Figure 2) which forms the roof of the Catholicon (left). View of the lower low-angle fault surface (No 4, Figure 1 & Figure 2), situated at lower elevation than the main foundation level of the Monastery, where minor caves and undermining have formed (right).

The measurements conducted on the discontinuities at the Holy Monastery of Kleiston revealed two principal systems, with average strike of north-northwest to south-southeast and northeast to southwest, inclined primarily towards the northeast and southeast, respectively. Other secondary systems of discontinuities include northeast-southwest and northwest-southeast, which dip towards the north to north-northwest and southwest, respectively.
Overall, the discontinuities are represented by planar, curved, and open joints, as well as fractures or faults. When classified as open, the gaps range from 1 to 2 centimeters up to 0.30 m. They are frequently infilled with reddish soil and carbonate breccias. Along the open joints, root systems from trees and shrubs that have flourished in the area have penetrated. The depth of this penetration is not easily discoverable but exceeds 2 to 3 m, and in certain instances, it has been found to surpass 5 to 7 m. This phenomenon is evidenced by the presence of roots extending all the way to the Catholicon and the storage rooms.

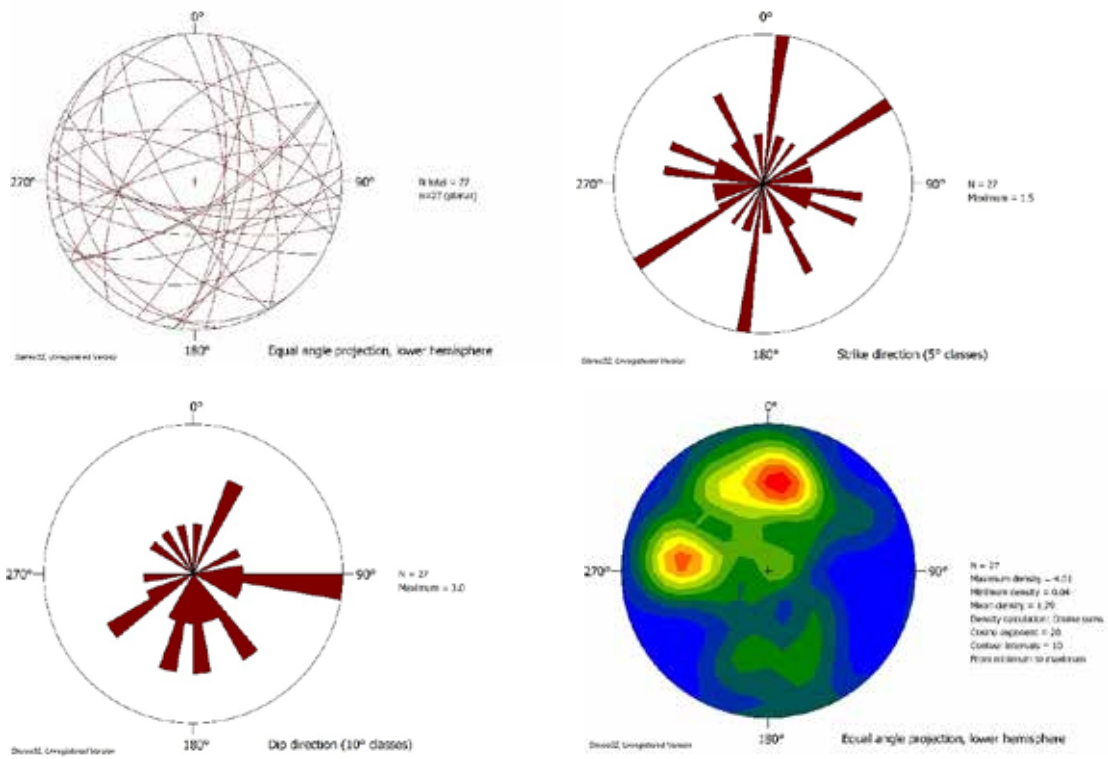

Figure 4. Stereographic projection (up, left), rose diagrams of direction (up, right) and dip direction (down, left) of maximum inclination, and pole density chart (down, right) for all measured discontinuities in the vicinity of the Holy Monastery of Kleiston.

Hydrogeological Conditions

The geological formations within the Holy Monastery of Kleiston fall into the following categories, according to the standards of the International Association of Hydrogeologists (Struckmeier & Margat, 1995; Nikas et al., 2010):

- Debris and scree (H.cs,sc): They develop local and thin aquifers with high yield or extensive aquifers with moderate yield (Subclass 1b).
- Carbonate formation of the Lower Triassic to Lower Jurassic (Ti-Ji.k,d): This formation generates extensive aquifers with high yield (Subclass 2a).
- Volcanosedimentary formation of the Upper Paleozoic to Lower Triassic (P-Ti.tf): This formation develops aquifers of little practical significance or non-aquifer formations (Subclass 3b).

The Holy Monastery of Kleiston is supplied by a spring located 150 m to its north. Improvement work has been performed in the spring, which operates year-round. This spring discharges from the weathered mantle of the volcanosedimentary formation, which is likely fed upstream by the overlying carbonate formations.

In the underlying carbonate formation, a deep karst aquifer of significant capacity has developed. This carbonate formation appears to be highly fragmented and fissured, displaying two primary systems of joints, alongside additional secondary systems that exhibit pronounced karstification.

Epikarst zone

The surface layer of the lower carbonates is characterized by the development of an extensive epikarst zone of high permeability, resulting from significant secondary porosity, with thickness exceeding 10 m in certain locations. The epikarst zone forms a locally saturated zone or an aquifer near the surface, occurring almost exclusively during the winter months when precipitation levels are elevated.

The recharge of the epikarst zone, upstream from the Holy Monastery of Kleiston, occurs through:

- Direct inputs from precipitation.
- Contribution from the overlying granular aquifer developed in the debris and scree, due to hydraulic communication. Notably, upstream there is localized lateral recharge to the granular aquifer from the upper karst aquifer, facilitated by the fractured volcanosedimentary formation at the base of the upper nappe.

The groundwater of the epikarst zone partially infiltrates the underlying rapid flow karst system developed within the

lower carbonates and partially discharges into fronts of epikarst springs that manifest at both the upper and lower fault surfaces of the lower carbonate rocks.
The front of the epikarst springs that emerges at the upper low-angle fault surface discharges in the area encompassing the Catholicon of the Holy Monastery as well as the adjacent buildings and functional spaces, including:

- The cell building located immediately prior to the entrance of the Catholicon (south of the Catholicon).
- The storage facility situated within a cave (north of the Catholicon).
- The small cave (north of the Catholicon).
- The building of the old cells of the Fathers and other common areas (east of the Catholicon).

1.

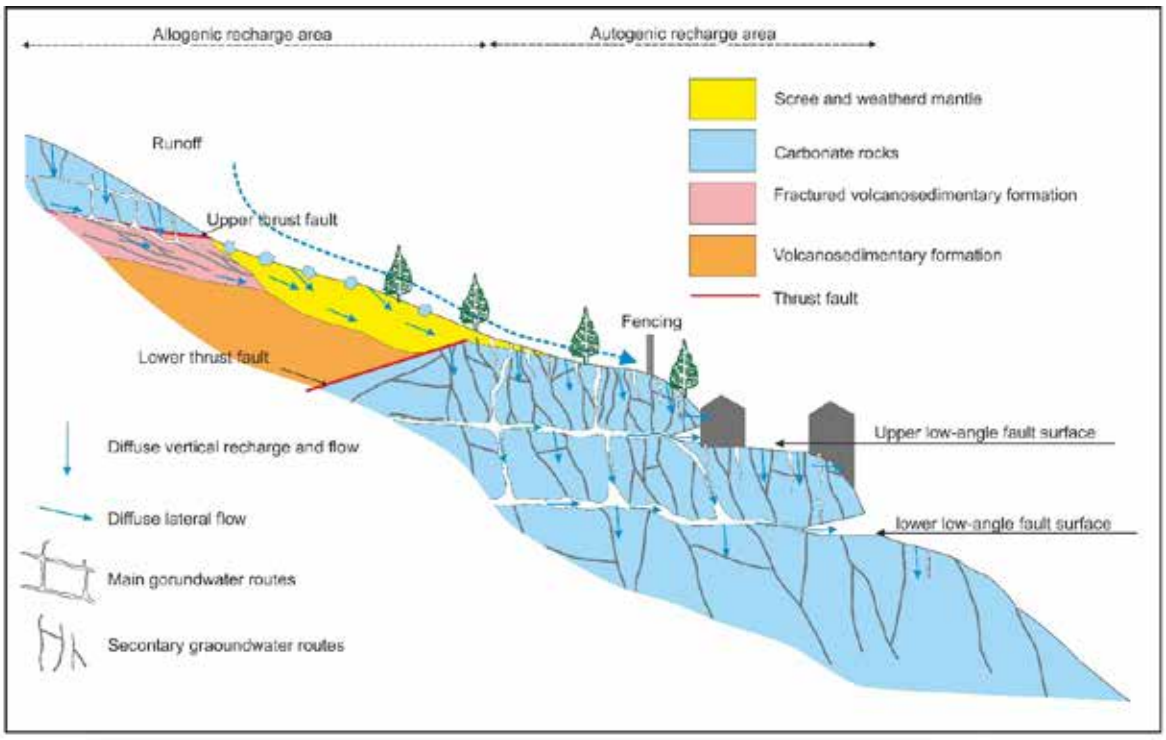

Figure 5. Sketch of the geological and hydrogeological conditions in the vicinity of the Holy Monastery of Kleiston. The various hydrogeological units and the main tectonic elements of the area, the main and secondary routes of the groundwater and the location of the main building infrastructure of the monastery are distinguished.

The front of the epikarst springs that appear at the lower low-angle fault surface discharges into minor caves beneath the foundation of several retaining walls along the northeastern and southeastern perimeter of the Monastery as well as the building containing the old cells of the Fathers and other communal spaces.
The building housing the old cells of the Fathers and other communal spaces is situated between the two discharge fronts of the epikarst springs, yet it is primarily influenced by the upper front and secondarily by the lower front, particularly following prolonged and continuous periods of intense rainfall and snowfall.
Given that the thickness of the overlying carbonate formation upstream of the Catholicon of the Monastery does not exceed 5-6 meters, this facilitates the direct infiltration of rainwater. This is further exacerbated by the significantly fractured and fissured nature of the rock mass, which is compounded by the presence of trees whose root systems have penetrated the rock's discontinuities, leading to further enlargement of these openings. Water intrusion thus extends into the interior of the Catholicon and the adjacent buildings and functional spaces.
In the vicinity of the Church of the Holy Cross, both the upper and lower carbonate series are observed in very close proximity, in places not exceeding 5 meters apart, resulting in highly deformed of the volcanosedimentary formation, which is entirely fissured.
The upper nappe of the carbonates upon the practically impermeable volcanosedimentary formation dips southeast, resulting in this carbonate formation discharging at a front of springs on the artificially constructed slope west of the Sanctuary of the Church. As water flows downstream, the path leading to Gkoura, which runs behind the Sanctuary, transforms into a small and ephemeral stream, with quantities of water infiltrating the interior of the Church through the foundation base (floor).

Discussion - Conclusions

The epikarst zone in the vicinity of the Holy Monastery of Kleiston constitutes a surface horizon of the lower carbonate formations, approximately 10 meters in thickness, characterized by high porosity and permeability. This significant porosity arises not only from the dissolution of carbonate rocks by CO_2-rich water but also from the presence of two main systems and at least two smaller groups of fractures and joints, as well as the existence of two low-angle fault surfaces. The lower of the two fault surfaces governs the base of the epikarst zone.

The epikarst is recharged by precipitation and laterally through the scree and the weathered mantle of the volcanosedimentary formation. These two formations, in turn, are fed by the upper carbonates. These conditions indicate that the recharge of the epikarst is dual in nature, both allogenic and autogenic.

During the wet season, rainwater and meltwater infiltrate the epikarst zone through discontinuities and percolate deeper into the horizons of the carbonate rocks. However, a portion of the infiltrating water remains within the voids and fractures of the epikarst zone, forming an epikarst aquifer where the presence of two low-angle fault surfaces enables the lateral flow of groundwater and the discharge of the epikarst aquifer into springs within caves observed along those two fault surfaces.

This discharge is the cause of water influx and the manifestation of moisture within many of the buildings of the Holy Monastery of Kleiston. The presence of vegetation cover in the epikarst zone helps retain soil moisture, minimizing evaporation and enhancing humidity in the areas surrounding the Monastery.

This study highlights the overall importance of the epikarst zone in the collection and flow of water infiltrating karst formations, particularly emphasizing its critical role in the hydrogeological conditions of the area surrounding the Holy Monastery of Kleiston. Its impact on water influx and the manifestation of humidity is complex and is influenced by morphological, lithostratigraphic, tectonic, and climatic factors.

Acknowledgements

The research team extends its most heartfelt gratitude to the Monks of the Holy Monastery of Kleiston, particularly to the Abbess Mariam, for the time they dedicated and their invaluable assistance during the fieldwork both within and beyond the Monastery. Additionally, we express our appreciation to Mayor Mr. Christos Pappous, the elected officials, and the staff of the Municipality of Fili for their collaboration and the generous provision of support.

References

Bakalowicz, M., 2004. The epikarst. The skin of karst. In: Jones, W.K., Culver, D.C. & Herman, J.S. (Eds.). Epikarst. Special Publication 9. Charles Town, WV: Karst Waters Institute: 16-22.

Dounas, A., 1971. The geology between Megara and the Red area. PhD thesis. Athens. Geological and Geophysical Research, 15/2, 250p.

Katsikatsos, G., Mettos, A., Vidakis, M., Dounas, A.,1986. Geological map of Greece, sheet “Athens – Elefsis”, scale 1:50,000, I.G.M.E. Publications, Athens.

Mangin, A., 1975. Contribution a` l’e´tude hydrodynamique des aquiferes karstiques, Ph.D. Thesis, Univ. de Dijon, Dijon, France, 124p.

Nikas, K, Antonakos, A, Kallergis, G, Kounis, G., 2010. International Hydrogeological Map of Europe: Sheet D6 “Athina”. Proceedings of the 12th International Congress, Patras, 2010 Bulletin of the Geological Society of Greece, Volume XLIII No 4, pages 1821-1830.

Struckmeier, W.F., Margat, J., 1995. Hydrogeological maps: a guide and a standard legend (Vol. 17). Hannover: Heise.

Williams, P.W., 1983. The role of the subcutaneous zone in karst hydrology, J. Hydrol., 61, 45-67.

17th INTERNATIONAL CONGRESS of the Geological Society of Greece

BULLETIN OF THE GEOLOGICAL SOCIETY OF GREECE, SP. PUBL.

EXTENDED ABSTRACT 291

Composition and physicochemical properties of muds from the Evros river delta, Thrace district (Northern Greece) and their potential use in pelotherapy

Sofianska E.[1], Athanassoulis K.[1], Tarenides D.[1], Gkagka M.[1]

(1) Hellenic Survey of Geology and Mineral Exploration, 1 S. Louis st., 13677, Acharnes, Athens, Greece, esofianska@eagme.gr

Abstract

Mud samples from the Evros river deltaic sediments (ERDS) Thrace district (Northern Greece) were analyzed by several physicochemical techniques: grain size distribution, X-ray diffraction, optical microscopy, chemical composition (major and trace elements), cation exchange capacity (CEC) and plasticity index (PI), at an effort to evaluate their potential use in pelotherapy. Results showed that in terms of granulometry ERDS are characterized as loam-silts and silts, with silt-clay fractions varying from 69.8% to 97.72%. Non clay minerals include quartz, feldspars, amphiboles, calcite, sphene, rutile, magnetite, ilmenite, hematite, and pyrite. Main clay minerals present are illite (15-20 wt%), kaolinite (14-18 wt%), smectite (4-9 wt%), micas (6-8 wt%), and chlorite (5-7 wt%), and constituting 49 to 59 wt% of the mud samples. Among the analyzed potentially toxic elements (PTEs) average values of V, Cr, Ni, Cu, Zn, As and Pb exceed the Earth's crust content. Cation exchange capacity and PI range from 19.32 to 23.22 meq/100g and 18 to 32%, respectively. The measured properties of the studied Evros muds are comparable to those of peloids commonly used in SPA centers and, therefore, render them potentially suitable for pelotherapy. However, a sieving process of the muds is recommended to enhance the silt-clay size fraction particles and consequently to further improve the CEC and PI values, which are the more favorable properties for peloids in pelotherapy.

Key words: Clay minerals, physicochemical properties, pelotherapy, Evros river muds, Greece.

Introduction

Mud therapy or pelotherapy is the topical application of thermal muds (peloids) on the human body for medical or cosmetic purposes, and it is known since ancient times (Veniale et al., 2007). These applications are carried out either at natural sites or in thermal centers (SPAs) for the treatment of muscle, bone, skin pathologies, or for beauty therapy (Rebelo et al., 2010, Barthoumi et al., 2018). Peloids are defined as "matured muds composed of a complex mixture of fine-grained geological materials, mineral water or sea/lake water and very often organic compounds from biological metabolic activity" (Gomes et al., 2013, Maraver et al., 2021).

The growing interest in human health and welfare has increased the scientific investigation on the selection of potentially suitable materials for the formulation of thermal muds to be used in pelotherapy. To this direction a five years research project (2018-2023) has been performed by the Hellenic Survey of Geology and Mineral Exploration (HSGME) on many areas of Greece to localize natural occurrences of suitable muds for pelotherapy (Sofianska et al., 2019, 2022). Natural occurrences of thermal muds, which are empirically used for therapeutic, aesthetic, and pharmaceutical purposes exist in Greece (Kamitsou et al., 2017, Sofianska et al., 2019).

The suitability of a geologic material for pelotherapy can be defined on the basis of its mineralogy and chemistry, along with some physical and technological properties like granulometry, CEC, pH, organic matter content, adsorption capacity, plasticity, rheological and thermal behavior (Carretero et al., 2014).

With regard to chemical composition of muds in pelotherapy it is important to know the concentration of elements either beneficial (Ca, Mg, Na, K, Fe among others) or PTEs (Hg, As, Cu, Cr, Pb, Zn, Co, Sb, Ba, V, U) since both pass through the skin of the patient during treatment (Veniale et al., 2007, Carretero et al., 2014).

In the present investigation the texture, mineralogy, chemistry and some physicochemical characteristics of representative mud samples from the Evros river deltaic sediments (Thrace district, Northern Greece) were studied, at an effort to evaluate their potential use as raw material for peloids in pelotherapy.

Materials and methods

Mud samples collected in June of 2020 from the Evros river delta shore were used in this investigation. Four samples were collected from the sea bottom offshore and one from a river lagoon (AL-DE-05). The sampling points were randomly distributed, and their spatial site was recorded using a handhold positioning system (GPS). Collection of mud samples was carried out using a plastic pipe (3 m long and 2.5" ⌀) pressed on the bottom deposits. The raw material was collected in plastic boxes. Besides, depth, temperature and pH of water column were measured in each

sampling point. Mud samples collected were dried for 7 days and stored in polyethylene bags for further analytical work. Portions of the samples were used for grain size, mineralogical and geochemical analyses, as well as for the evaluation of physicochemical properties. Grain size distribution was performed in two stage processes. Firstly, the samples were wet sieved to separate the coarser particles (>74μm) in accordance with the ASTM D422-63. The fractions <74 μm were measured by means of a Laser granulometer Microtrac S 3500.
Optical microscopy and X-ray powder diffraction (XRD) analysis were used for the study of the mineralogical composition of the samples. Bulk samples and the separated clay fraction (<2 μm) in oriented, glycolized and heated to 550°C were X-rayed using a X'Pert PRO X-ray diffractometer equipped with graphite-filtered CuKα radiation.
Semiquantitative mineralogical composition of ERDS was found by analysis of the XRD patterns using the X'Pert PRO program.
The chemical composition of the samples (major and minor elements) was determined by X-ray fluorescence analysis (XRF), using the S4 PIONEER equipment of the BRUKER AXS. The concentration of PTEs were found by Inductively coupled plasma mass spectrometry (ICP-MS) using the PE SCIEX ELAN 6100 equipment.
Cation exchange capacity (CEC) was estimated by using the barium chloride solution method (ISO 11260:1994).
Plasticity index was calculated using Atteberg limit in the Casagrande test.
Chemical results were compared with the composition of the Earth's upper crust (Rudnick and Gao, 2003) and with peloids applied in pelotherapy in Spain (Carretero et al., 2014), Turkey (Karakaya et al., 2010) and Slovenia (Glavas et al., 2017).
All the analytical work was conducted at the Laboratories of the Hellenic Survey of Geology and Mineral Exploration (HSGME).

Results and discussion

In Table 1 the coordinates of the mud samples sites, along with some physicochemical parameters of sea water column are given.

Table 1. Coordinates of mud sampling sites and physicochemical parameters of water column.

Sample	X	Y	Depth of sea water	T °C of sea water	pH of sea water
AL-DE-01	670273,61	4517556,74	1.5	28.7	8.6
AL-DE-02	671573,00	4514546,00	2.0	28.3	8.6
AL-DE-03	670426,07	4518083,25	1.0	28.7	8.6
AL-DE-04	669227,00	4519268,00	2.0	28.2	8.6
AL-DE-05 lagoon	670731,06	4518477,55	0.1	34.1	8.4

Textural analyses showed that the ERDS are composed of 17.61 (2.28-30.19%) sand, 76.86% (64.92-92.86%) silt and 5.54% (4.89-5.92%) clay, with the silt and clay average fractions exceeding 82.49% (Table 2) and they are plotted in the silt and silt loam fields (Curtis, 2005) of the ternary discrimination diagram (Fig. 1).
In terms of granulometry best peloids should contain a high percentage of the clay fraction or a high silt and clay fraction as stated for the Spanish peloids (Carretero et al., 2014) and the Turkish thermal muds (Karakaya et al., 2010). Large clay fraction content creates a pleasant sensation, when applied to the skin and enhances ion exchange capacity through mud/skin interface (Veniale et al. 2004, 2007, Rebelo et al., 2010). Therefore, a sieving process to remove sand fraction is needed to improve the granulometry of the studied samples and their quality as raw material for peloid formulation.
Optical microscope study showed a polymineralic composition of the samples, including mainly detrital grains of quartz, feldspars, amphiboles, calcite, chlorite, mica, epidote, with minor amounts of sphene and rutile. Opaque minerals include magnetite, ilmenite, hematite and pyrite (single microcrystals and framboids). Calcite is present in the form of detrital grains, as well as biogenic in fossil shells. Non clay minerals match to 41-51wt%.
X-ray diffraction analyses showed that the clay minerals present are mainly illite (17.6 wt%), kaolinite (16.2 wt%), smectite (6.8 wt%), mica (7.4), chlorite (5.8%), and in one sample interstratified chlorite-smectite (3 wt%) (Table 2). The clay mineral content (mainly smectite) is relevant to therapy and of great importance, determining properties like high water absorption, CEC and specific heat (Cara et al., 2000).
Regarding the chemical composition of the studied muds, only TiO_2, MnO, MgO and F_2O_3 were found increased compared to the Earth's crust (Table 3, Fig. 2). Among the analyzed PTEs (values in mg/kg) (Table 3) V (98-125),

Cr (100-180), Ni (55-93), Cu (38-59), Zn (84-160), Pb (38-92) and As (6-13) were found to exceed significantly the composition of the Earth's upper crust (Rudnick and Gao, 2003). However, many examples of peloids applied in pelotherapy are referred to contain similar or even higher levels of these elements (Quintela et al., 2012, Carretero et al., 2014). Clayey materials selected for peloid applications must be safe. Therefore, elements like Cd, Pb and As known to be toxic to human and environmentally hazardous must be absent. European directives and USA regulations state that heavy metal concentrations in cosmetic products must be avoided if they exceed 10 mg/kg in case of Pb, 3 mg/kg for Cd and As (Rebelo et al., 2010). Besides, Mo, Ni, V, Cr and Cu, been reported to have less toxicity than previously mentioned elements must be limited in pharmaceutical formulations (Berthoumi et al., 2019). It is worth noting that the bioavailability and the potential enter of the PTEs in to the patient's body is more important than their concentration in the peloid constituents (Carreretero et al., 2014).

The analyzed SO_3 content of the Evros area muds was found varying between 1.04% and 2.01 wt% and comes most probably from pyrite. Sulfur content could influence therapeutic action as sulfur shows a keratolytic effect, analgetic influence on the pain receptors and inhibition of the immune response and has a bactericidal and antifungal effect (Baricz et al., 2021).

The CEC is controlled by the clay size fraction content, the kind of clay minerals, and the presence of organic matter (Baricz et al.,2021). The CEC of the muds studied are relatively low, ranging from 19.32 to 23.33meq/100g (average 21.54), and reflecting the clay minerals contents. Enhance CEC values in the studied muds are most probably related to both higher content of smectite and organic matter (Table 2).

Table 2. Main physical and chemical characteristics of the Evros area muds

Sample	Particle size (%)			CEC meq/100g	Clay mineral content (%)						Non clay min. (%)	LL (%)	PI (%)	Org. matt. (%)
	Sand	Silt	Clay		Ilt	Kln	Sme	Chl	Chl/ Smc	Mca				
AL-DE-01	11.82	82.45	5.73	20.47	19	18	7	5	-	8	43	57	30	6.31
AL-DE-02	24.17	70.52	5.31	19.32	15	14	4	6	3	8	50	43	18	4.56
AL-DE-03	2.28	91.86	5.86	23.22	20	18	8	5	-	6	43	63	32	7.76
AL-DE-04	19.56	74.52	5.92	21.41	15	15	6	6	-	7	51	51	24	6.78
AL-DE-05	30.19	64.92	4.89	23.76	19	16	9	7	-	8	41	51	23	9.09
Average	17.60	76.85	5.54	21.63	17.6	16.2	6.8	5.8	0.8	7.4	45.6	53	25	6.9

Ilt – Illite, Kln – Kaolinite, Sme – Smectite, Chl – Chlorite, Mca – Mica.

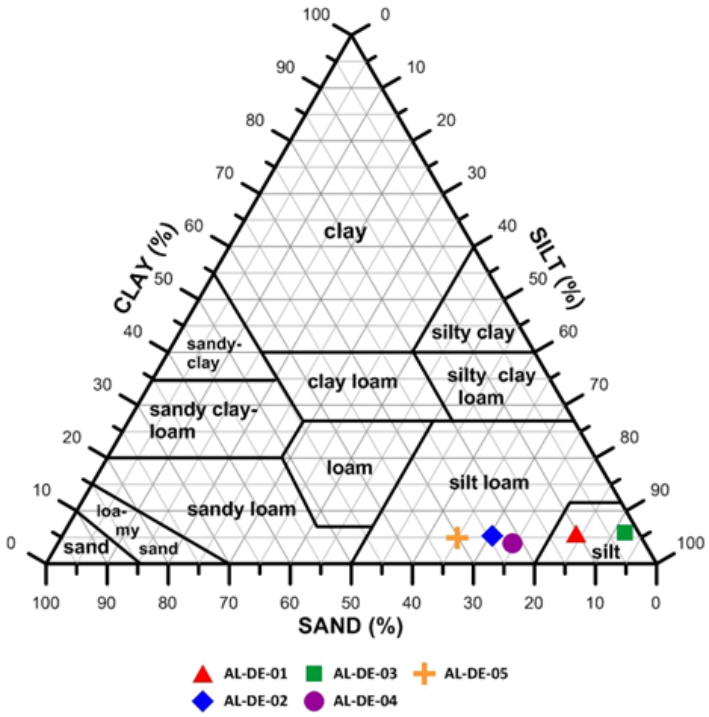

Figure 1. Ternary discrimination diagram of the studied muds.

Table 3. Chemical composition of the ERDS (major and minor elements as oxides, trace elements in mg/kg), upper continental crust, range of variability of Spanish (Carretero et al., 2010), Turkish peloids (Karakaya et al., 2010) and Sečovlje healing saline mud (Glavas et al., 2017).

Element	AL-DE-01	AL-DE-02	AL-DE-03	AL-DE-04	AL-DE-05	Average.	UCC	Spanish peloids range	Turkish peloids range	1*
wt%										
SiO_2	53.18	57.97	52.30	55.13	48.79	53.53	65.89	18.41 - 51.12	28.56 - 50.79	38.68
TiO_2	0.74	0.62	0.71	0.65	0.65	0.66	0.50	0.22 - 0.55	0.35 - 0.66	0.46
Al_2O_3	15.59	15.55	15.39	14.68	14.42	15.03	15.17	3.58 - 12.24	6.24 - 13.34	8.27
MnO	0.06	0.07	0.08	0.08	0.19	0.10	0.07	0.02 - 0.61	0.05 - 0.19	0.05
MgO	3.43	3.26	3.52	3.02	3.72	3.38	2.20	0.98 - 22.35	1.65 - 9.95	3.30
CaO	1.61	2.11	1.71	2.43	2.74	2.22	4.19	2.27 - 26.48	5.9 - 29.69	12.30
Na_2O	3.16	2.74	3.35	3.43	3.82	3.33	3.89	0.3 - 4.34	0.53 - 3.39	4.21
K_2O	2.85	2.97	2.79	2.72	2.77	2.81	3.39	0.57 - 2.57	0.97 - 2.93	1.84
P_2O_5	0.14	0.18	0.15	0.16	0.18	0.17	0.20	-	0.06 - 0.2	0.07
Fe_2O^3T	5.63	5.21	6.12	5.35	5.63	5.38	4.49	1.7 - 5.24	3.1 - 5.49	3.69
SO_3^T	1.75	1.04	1.22	1.65	2.01	1.49		0.15 - 5.92	0.15 - 1.82	
LOI	11.61	8.21	12.7	10.67	15.12	11.67		13.95 - 53.84	18.3 - 27.1	
mg/kg										
V	105	98	125	115	125	113.6	107	31.6 - 90.9	55 - 95	
Cr	120	180	145	110	110	133.0	85	14.6 - 68.2	61.6 - 547.4	85
Co	15	13	16	14	19	15.4	17	4 - 16.8	9.1 - 54.5	11
Ni	67	93	74	55	72	72.2	44	3.4 - 50.8	27 - 671	64
Cu	59	40	52	38	46	47.0	25	11.5 - 52.3	12.4 - 32.2	29
Zn	115	84	155	92	160	121.2	71	33.1 - 160.4	33 - 56	78
As	13	6	11	12	11	10.6	1.5	4.4 - 29.6	5.1 - 62.6	9
Se	<1	<1	<1	<1	<1	<1	0.05	<1 - 1.6	<0.5 - 0.7	
Rb	32	38	42	24	38	34.8	112	35.5 - 120.5	38.7 - 175.1	
Sr	3	31	39	24	52	29.8	350	87.3 - 1879	214.3 - 1540.4	530
Mo	1	3	2	2	1	1.8	1.5	<1 - 4.4	0.2 - 1.2	4
Cd	<1	<1	<1	<1	<1	<1	0.098	<10	0.1 - 0.2	0
Ba	97	67	95	46	110	83	550	147.7 - 799	110 - 1153	138
Pb	65	39	81	38	92	63	17	10.9 - 37.5	6.9 - 38.2	23
U	2	1	1	1	3	1.6	2.8	<1.20 - 18.4	1 - 6.3	
Bi	2	1	1	1	1	1.2				0.3
Ag	2	1	1	1	1	1.2	50	<6	<0.1 - 0.1	0.1

UCC Upper Continental Crust (Rudnick and Gao 2003) 1* Average composition of Sečovlje healing saline mud (Glavas et al., 2017).

Similar CEC values are, however, referred for Spanish peloids (Pozo et al., 2013). As stated by Matike et al. (2011) at high CEC values (>15 meq/100g) ions exchange from the skin to the clay minerals mixture and release of ions to the skin can occur during application of peloid, facilitating skin cleansing and providing a refreshing sensation. CEC of clay mineral particles is significantly affecting ion exchange between peloid and the skin of the patient and thus contributes to a cleansing process (Tateo et al., 2009).

The liquid limit measured values and the plasticity indices found are varying between 43 and 63 (average 53) and 18 to 32% (average 25), respectively (Table 2), classifying the muds into the high plasticity clays in the Casagrande chart (Fig. 3) (except the AL-DE-02 sample). The liquid limit values >50% reflect the relative smectite content of the studied muds.

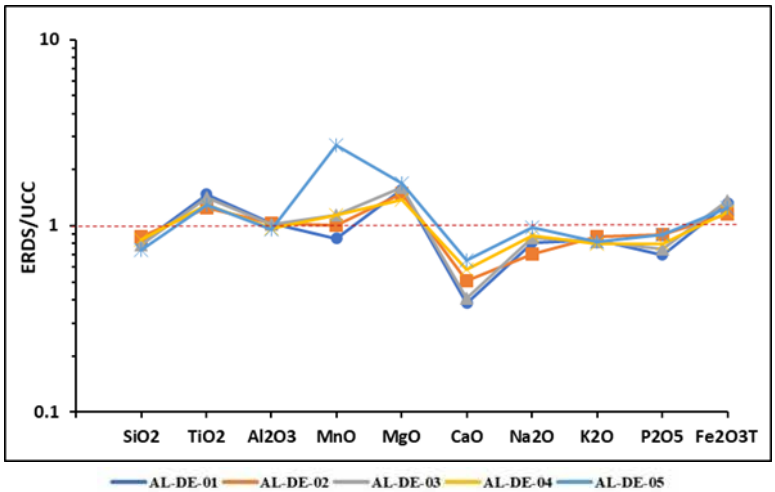

Figure 2. Earth's upper crust normalized composition of the Evros area muds.

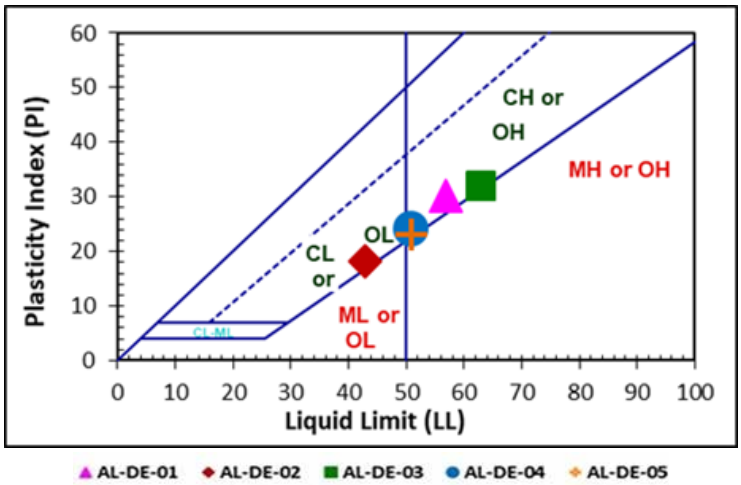

Figure 3. Projection of plasticity indices (PI) and liquid limits (LL)%values of the Evros delta muds in the Casagrande chart (C-clay, M-silt, O- organic, L- Low plasticity, H-High plasticity).

Conclusions

Mud samples from the Evros delta area were characterized in terms of different physicochemical (granulometry, mineralogy geochemistry, CEC and plasticity) properties.

Particle size, clay mineral content, CEC and PI found render the investigated mud samples from the Evros river delta potentially suitable for use as peloids in pelotherapy. Potentially toxic elements (PTEs) concentrations, although were found exceeding the Earth's crust composition, are considered acceptable because their concentrations are within the ranges referred for peloids applied in pelotherapy.

A sieving process is recommended to enhance the clay-size fraction particles of them and consequently improve their CEC and plasticity. Moreover, a further investigation is needed to study the technical properties of a derivative peloid formed from the mixture of the Evros muds with a medical mineralized water or sea water, after a maturation process.

Acknowledgements

This work was financed by the Project: Characterization of muds and volcanic rocks for therapeutic uses, H.S.G.M.E., N.S.R.F. (National Strategic Reference Framework) 2014-2020 / Operational Programme «Competitiveness and Entrepreneurship» / Project "ACTIONS FOR THE RATIONALE AND SUSTAINABLE USE OF GEOTHERMAL ENERGY" Athens 2023.

Thanks are also due to the anonymous reviewer who helped to improve the present manuscript.

References

American Society for Testing and Material ASTM D422 – 63, 1997 (second edition). Standard Test Method for Particle-Size Analysis of Soils, In: Annual book of ASTM Standards: Soil and rock, p. 1026.

Baricz A, Levei EA, Șenilă M, Pînzaru SC, Aluaş M, Vulpoi A, Filip C, Tripon C, Dădârlat D, Buda DM, Dulf FV, Pintea A, Cristea A, Muntean V, Keresztes ZG, Alexe M, Banciu HL., 2021. Comprehensive mineralogical and physicochemical characterization of recent sapropels from Romanian saline lakes for potential use in pelotherapy. Sci Rep. 2021 Sep 20;11(1):18633. doi: 10.1038/s41598-021-97904-1. PMID: 34545115; PMCID: PMC8452724.

Barhoumi, T., Bekri-Abbes, I., Srasra, E., 2019. Physicochemical characteristics and suitability of curative pastes made of Tunisian clay minerals and thermal waters for use in pelotherapy. C. R. Chimie 22, 126–131.

Cara, S., Carcangiu, G., Padalino, G., Palomba, M., Tamanini, M., 2000. The bentonites in pelotherapy: Chemical, mineralogical and technological properties of materials from Sardinia deposits (Italy). Applied Clay Science, 16, 117–124.

Carretero, M., Pozo, M., Martín-Rubí, J., Pozo, E., Maraver, F., 2010. Mobility of elements in interaction between artificial sweat and peloids used in Spanish spas. Applied Clay Science, 48, 506–515.

Carretero, M. I., Pozo, M., Legido, J. L., Fernández-González, M. V., Delgado, R., Gómez, I., Armijo, F., Maraver, F., 2014. Assessment of three Spanish clays for their use in pelotherapy. Applied Clay Science, 99, 131–143.

Curtis, J.O., 2005. Electromagnetic Poser Attenuation in Soils. ERDC/EL TR-05-5. Vicksburg, MS: U.S. Army Engineer Research and Development Center.

Glavas, N., Mourelle, M.L., Gómez, C.P., Legido, J.L., Smuc, N.R., Dolenec, M., Kovac, N., 2017. The mineralogical, geochemical, and thermophysical characterization of healing saline mud for use in pelotherapy. Appl. Clay Sci. 135, 119–128.

Gomes, C., Carretero, M. I., Pozo, M., Maraver, F., Cantista, P., Armijo, F., Legido, J., Texeira, F., Rautureau, M., Delgado, R., 2013. Peloids and pelotherapy: Historical evolution, classification and glossary. Applied Clay Science, 75-76, 28–38.

ISO 11260, 1994. Soil quality – Determination of effective cation exchange capacity and base saturation level using barium chloride solution.

Kamitsou, M.D., Sygouni, V., Kanellopoulou, D.G., Gardikis, K., Koutsoukos, K.P.G., 2018. Physicochemical characterization of sterilized muds for pharmaceutics/cosmetics applications. Environ. Geochem. Health 40, 1449–1464.

Karakaya, M.C., Karakaya, N., Sarıoğlan, S., Koral, M., 2010. Some properties of thermal muds of some spas in Turkey. Applied Clay Science, 48, 531–537.

Li, YH.A., 2009. A compendium of geochemistry. Princeton: Princeton University Press.

Maraver, F., Armijo F., Fernández-Toran, M.A., Armijo, O., Ejeda J.M., Vazquez, I., Corvillo I., Torres-Piles, S., 2021. Peloids as thermotherapeutic agents. International Journal of Environmental Research and Public Health, 18 (4), 1-17.

Matike, D. M. E., Ekosse, G. I. E., Ngole, V. M., 2011. Physico-chemical properties of clayey soils used traditionally for cosmetics in Eastern Cape, South Africa. International Journal of the Physical Sciences, 6(33), 7557–7566.

Pozo, M, Carretero, M.I, Maraver, F, Pozo, E, Gómez, I, Armijo, F, Martín-Rubí, JA, 2013. Composition and physico-chemical properties of peloids used in Spanish spas: a comparative study. Applied Clay Science, 83–84, 270–279.

Quintela, A., Terroso, D., Da Silva, E. F., Rocha, F., 2012. Certification and quality criteria of peloids used for therapeutic purposes. Clay Minerals, 47, 441–451.

Rebelo, M., Viseras C., Lopez Galindo, A., Rocha F., Fereira da Silva, E., 2011. Characterization of Portugese geological materials to be used in medical hydrology. Applied Clay Science 51, 258-66.

Rizo, O.D., Rudnikas, A.G., Rodrigues, K.D., Padila, D.B., 2000. Assessment of historical heavy metal content in healing muds from San Diego (Cuba) using nuclear analytical techniques. Nucleaus 53, 19-23.

Rudnick, R. & Gao, S., 2003. Composition of the Continental Crust. Treatise on Geochemistry, 3, 1–64.

Sofianska E., Athanassoulis, K., Tarenides, D., Gaga M., 2022. Assessment of marl samples from Kefalonia Island (western Greece) for their potential use in pelotherapy. 16th International Congress of the Geological Society of Greece, 17-19 October, 2022 - Patras, Greece, Bulletin of the Geological Society of Greece, Sp. Publ., Ext. Abs. ID 106.

Sofianska E., Athanassoulis, K., Tarenides, D., Xirokostas, N., Gaga M., 2019. Textural, Mineralogical and Geochemical Assessment of the Pikrolimni Lake Sediments (Kilkis district, Northern Greece) and suitability for use in pelotherapy, Bulletin of the Geological Society of Greece 55 (1), 170. DOI: 10.12681/bgsg.21080.

Tateo, F., Ravaglioli, A., Andreoli, C., Bonina, F., Coiro, V., Degetto, S., Giaretta, A., Menconi Orsini, A., Puglia, C., Summa, V., 2009. The in-vitro percutaneous migration of chemical elements from a thermal mud for healing use. Applied Clay Science, 44, 83–94.

Veniale, F Battero, A., Jobstraibizer, P.G., Setti M., 2007. Thermal muds: Perspectives of innovations. Applied clay science, 36, 141-147.

Veniale, F., Barberis, E., Carcangiu, G., Morandi, N., Setti, M., Tamanini, M., Tessier, D., 2004. Formulation of muds for pelotherapy: Effects of “maturation” by different mineral waters. Applied Clay Science, 25, 135–148.

17th INTERNATIONAL CONGRESS of the Geological Society of Greece

BULLETIN OF THE GEOLOGICAL SOCIETY OF GREECE, SP. PUBL.

EXTENDED ABSTRACT 292

REE distribution in the b1 bauxite strata of the Parnassos–Giona Unit, Greece

Sofis N.[1], Ntouros E.[1], Kalaitzidis S.[1*]

(1) Laboratory of Economic Geology, Department of Geology, University of Patras, Rio, Greece, skalait@upatras.gr

Research Highlights

The REE distribution in b1 bauxite strata of the Parnassos-Giona Unit points to variable forming conditions
The content of REE is moderate and strongly depended on the lithologies
REE bearing minerals were identified for the first time in b1 bauxite strata

Introduction

The Mesozoic carbonate sequence of Parnassos-Giona Unit extends over the mountainous areas of Oiti, Giona, Parnassos and Helicon. The neritic carbonate sedimentation began at the Upper Triassic and ceased at the beginning of Paleocene. The Unit hosts three major karstic-type bauxite strata namely b1, b2, b3, which were deposited between Middle Jurassic and Upper Cretaceous times (Papastamatiou, 1960; Celet 1962). The allochthonous karst-type bauxite deposits of the Parnassos-Giona Unit are part of the Mediterranean bauxite zone, and have been the subject of research by numerous researchers (e.g. Valeton 1972; Bárdossy 1982; Valeton *et al*. 1987).

The lower bauxite strata (b1) hasn't been studied extensively in the past decades, as it occurs sporadically (mainly in the east and northeast parts of the Parnassos-Giona Unit), with limited quantities and low grade in terms of Al.

In this study, seven sampling sites were examined in order to assess their main mineralogical, geochemical and mineral-chemical characteristics, with emphasis on the REE distribution. The aim of this study is to investigate the REE mode of occurrence in the bauxite samples in the lower bauxite strata of the Parnassos-Giona Unit (Fig. 1).

Figure 1: The PL2 section, in which the overlying Upper Jurassic limestones and the b1 bauxite strata are outcropping.

Methods

The main objective of this study is the assessment of the geochemical distribution of rare earth elements in the studied geological sites. In order to achieve this, geochemical analysis was applied on representative bauxite samples and transitional lithologies (in total 39 samples), including X-Ray Fluorescence (XRF) and Inductively Coupled Plasma Mass Spectrometry (ICP-MS), as well as Scanning Electron Microscopy to determine mineralogical chemistry. Furthermore, X-Ray Diffraction was applied to the total amount of samples to determine the mineralogical assemblage of each sample (Fig. 2A). Optical observation was performed using optical microscope of polarized white light for describing the petrographic characteristics and main morphological features.

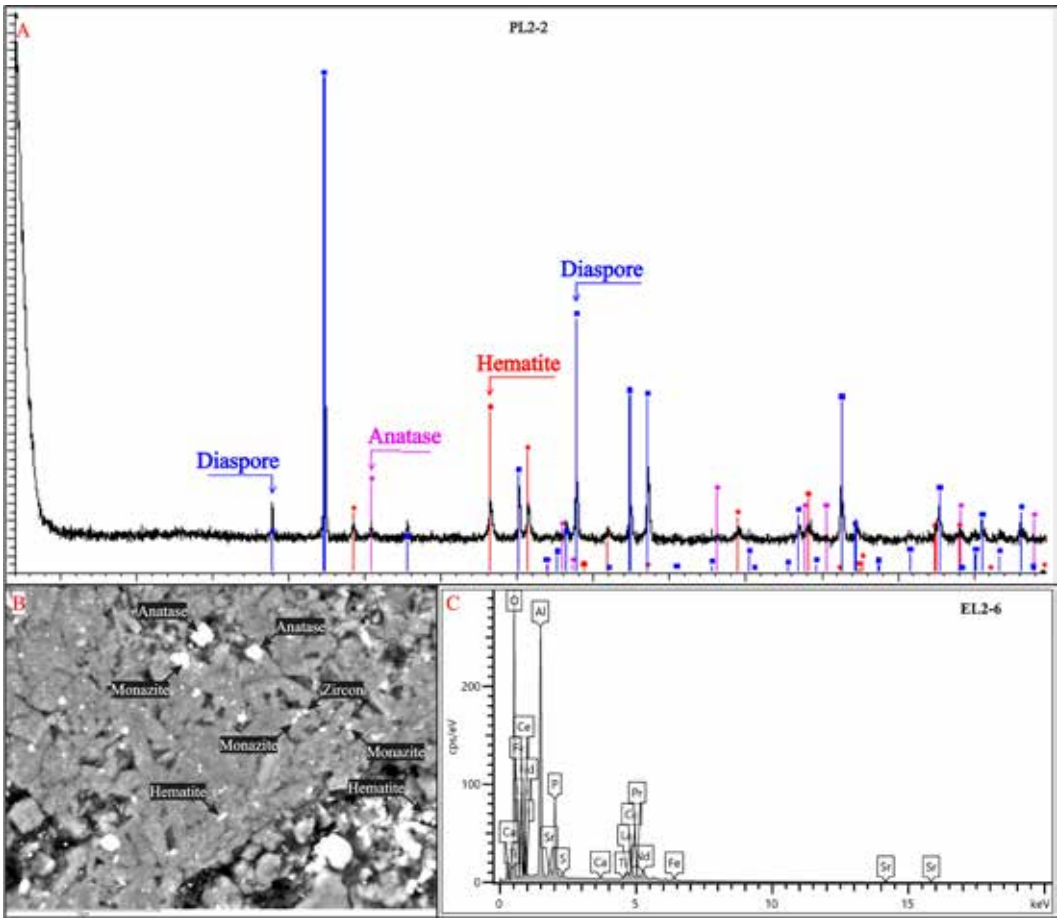

Figure 2: A) Evaluated PL2-2 X ray diffractogram, B) Back Scattered Electron image of the EL2-6 bauxite sample showing the presence of REE bearing mineral monazite, C) scanning electron microscopy (SEM) spectrum of monazite in sample EL2-6 bauxite sample.

Results

The geochemical data reveal an average Al_2O_3 content of 42.73 wt.-% in the bauxite samples, 58.08 wt.-% of CaO in the limestone samples, and 35.86 wt.-% of Fe_2O_3 in the bauxite samples and transitional lithologies. The SiO_2 and TiO_2 average value the studied lithologies are 6.77 and 2.24 wt.-%, respectively. The mean value of the ΣREE in bauxite samples is 565.4 mg/kg, while the ΣLREE and the ΣHREE are 433.06 mg/kg and 132.33 mg/kg respectively. The SEM analysis provided the mineral chemistry of the representative bauxite samples, as well as the presence of REE-bearing and REE minerals, e.g. cerianite and monazite (Fig. 2B and 2C).

Discussion

According to REE/Chondrite normalized patterns of the studied bauxite samples per sampling site, a positive anomaly is observed for Ce, Er, and Tm, while Eu, Dy and Ho show a negative one. Furthermore, the ratio Eu/Eu* ranges from 0.56 to 0.69, whereas the Ce/Ce* fluctuates from 0.41 to 7.43.

Variations on the total content of the REE depending on the lithological facies were observed. Generally, the bauxite samples seem to be more enriched (ΣREE = 565.4 mg/kg) than the transitional lithologies (ΣREE = 404.97 mg/kg). The Eu/Eu* fluctuates from 0.56 to 0.69, which based on published data regarding the parental rocks of the bauxites of the Parnassos-Giona region (Mameli et al., 2007; Mongelli et al., 2014; Mondillo et al., 2022) indicates that igneous rocks with intermediate to basic affinity were the parental rocks of the b1 bauxite.

According to Ellahi et al. (2016), positive La/Y anomalies indicate alkaline conditions during bauxitization, whereas the negative ones acidic. At the PR1, PR2, PL2, EL2, EL3A and EL4 profiles alkaline conditions prevailed, whereas at EL3 acidic ones. The positive Ce/Ce* anomaly indicates oxic conditions during bauxitization, whereas the negative ones show reduced conditions. At PR1, PR2, EL2, EL3A and EL4 bauxite profiles, most probably oxic conditions prevailed, while at PL2 and EL3 reduced ones.

Conclusions

The lower bauxitic strata b1 at Parnassos-Giona Unit shows a relative enrichment in rare earth elements, which seem to concentrate at the pure bauxite samples in comparison to the transitional lithologies. In most sampling sites alkaline and oxic conditions prevailed during the bauxitic mud deposition. Most probably, igneous rocks with intermediate to basic affinity were the parental rocks of the b1 lenses confirming previous studies in the area.

References

Bardossy, G., 1982. Karst Bauxites, Bauxite Deposits on Carbonate Rocks, Developments in Economic Geology, Elsevier, Amsterdam, Vol. 14, 441 p.

Celet, P. 1962. Contribution a l' etude geologique du Parnaasse-Kiona et d' une partie des regions meridionales de la Grece continentale. Ann. Geol. Pays Hellen. 7, 1-358

Ellahi, S.S.; Taghipour, B.; Zarasvandi, A.; Bird, M.I.; Somarin, A.K., 2016. Mineralogy, geochemistry and stable isotope. studies of the dopolan bauxite deposit, Zagros Mountain, Iran. Minerals, 6, 11.

Mameli, P., Mongelli, G., Oggiano, G., Dinelli, E., 2007. Geological, geochemical and mineralogical features of some bauxite deposits from Nurra (western Sardinia, Italy): Insights on conditions of formation and parental affinity. Int. J. Earth Sci., 96 (5), 887-902.

Mondillo, N., Di Nuzzo, M., Kalaitzidis, S., Boni, M., Santoro, L., Balassone, G., 2022. Petrographic and geochemical features of the B3 bauxite horizon (Cenomanian-Turonian) in the Parnassos-Ghiona area: A contribution towards the genesis of the Greek karst bauxites. Ore Geology Reviews, 143, 104759.

Mongelli, G., Boni, M., Buccione, R., Sinisi, R., 2014. Geochemistry of the Apulian karst bauxites (southern Italy): chemical fractionation and parental affinities. Ore Geol. Rev. 63, 9-21.

Papastamatiou, J., 1960. La géologie de la région montagneuse du Parnasse Kiona Oeta. Bull. Soc. Géol. Fr., (7), 11, 398-409, Paris.

Valeton, I., 1972. Bauxites. Elsevier Publishing Company, Amsterdam, 226 pp.

Valeton, I., Biermann, M., Reche, R., Rosenberg, F., 1987. Genesis of nickel laterites and bauxites in Greece during the Jurassic and Cretaceous, and their relation to ultrabasic parent rocks. Ore Geol. Rev., 2, 359-404.

17th INTERNATIONAL CONGRESS of the Geological Society of Greece

BULLETIN OF THE GEOLOGICAL SOCIETY OF GREECE, SP. PUBL.

EXTENDED ABSTRACT 293

Plio-Quaternary tectonics and evolution of Southeastern Lesvos Island and Lesvos Basin, Greece: Transtensional deformation and relationship with the July 2017 earthquake activity

Sotiropoulou S.[1,2], Kalaitzis M.[1,2], Skourtsos E.[1], Sakellariou D.[2], Kranis H.[1]

1 Department of Geology & Geoenvironment, National and Kapodistrian University of Athens, 15784, Zografou, Greece

2 Institute of Oceanography, Hellenic Centre for Marine Research, 19013, Anavyssos, Greece

Introduction

The Aegean domain is regarded as a distinct, deforming microplate situated between the converging Eurasian (to the north) and African (to the south) tectonic plates, alongside the westward advancing Anatolian block (to the east) and Apulia (to the west) (Le Pichon & Angelier, 1979, 1981; Dewey & Şengör, 1979; Mascle & Martin, 1990; Armijo et al. 1996, 1999;). It is delineated to the north by the dextral, NE-SW strike-slip North Anatolian Fault (NAF), to the west by the NNE-SSW striking dextral strike-slip Kefallonia Fault, and to the southeast by the sinistral strike-slip fault zones of Strabo and Pliny. The region is characterized by a south-southwest directional extension, with a velocity of 40-50 mm per year relative to Eurasia, and experiences intricate extensional and strike-slip deformation influenced by the retreat of the Hellenic Subduction and the pressure exerted by the movement of the Anatolian Block along the NAF and its southern branches.

The present study concentrates on the northeastern margin of the North Aegean Sea, specifically on the southern part of Lesvos Island, encompassing the area that stretches from the eastern edge of the Gulf of Kalloni to the region further east of Vatera. The objective of this research is to provide insights into how the fault patterns of the study area are connected to the Lesvos Basin through geological mapping, conducting geological and structural observations, and integrating these findings with recent onshore data, particularly elucidating their significance in relation to the seismicity of the larger region.

Methodology

The present study employed a multifaceted approach to interpret the tectonic regime and fault network of the study area. A thorough examination of existing literature and research findings served as a foundational element in the development of this study's methodologies and framework. Between 2019 and 2021, a series of extensive field campaigns were conducted to comprehensively map the fault network governing the region. These expeditions enabled the possession of crucial geometric and kinematic data necessary for decoding the tectonic characteristics of the area. To supplement the field data, high-resolution topographic maps were utilized to establish the hydrographic network and identify potential fault zones of significance. The integration of geospatial techniques facilitated a more nuanced understanding of the tectonic landscape.

Tectonic Setting of NE Aegean and Lesvos Island

Most of the research conducted in the broader region predominantly relies on geological and geophysical data, focusing on earthquake mechanisms (e.g. Koukouvelas et al., 2002; Kiratzi et al., 2018, Papadimitriou et al., 2018). Seismic activity dates back to ancient time highlighted by a significant seismic event of magnitude 7.0 in 1867 along the Agia Paraskevi – Kalloni dextral strike – slip fault zone (Poumelioti and Kiratzi 2010; Chatzipetros et al., 2013). This activity persists today (Papazachos et al. 1997; Papazachos and Papazachou 2003; Taymaz et al. 1991, 2007), with a notable seismic event occurring in June 2017 featuring a mainshock of magnitude 6.3, characterized by a WNW-ESE normal fault, dipping 45º to the SSE. It was followed by two main aftershocks of magnitudes 5.2 and 5.0 on two NW-SE sub – vertical faults showing strike – slip motion (Nomikou et al., 2021; Papadimitriou et al., 2017; Kiratzi 2018).

The main fault structures in Lesvos can be categorized into three groups based on their strike. These consist of (i) NNE-SSW striking faults, which are mainly characterized as clockwise strike – slip faults, such as the Agia Paraskevi Fault Zone (APFZ), (ii) WNW-ESE striking faults which are represented mostly of normal faults with significant counterclockwise strike – slip component., (iii) E-W striking which is usually represented by normal faults, which act as "relay ramps" connecting the aforementioned strike-slip faults (Chatzipetros et al., 2013; Papadimitriou et al., 2018).

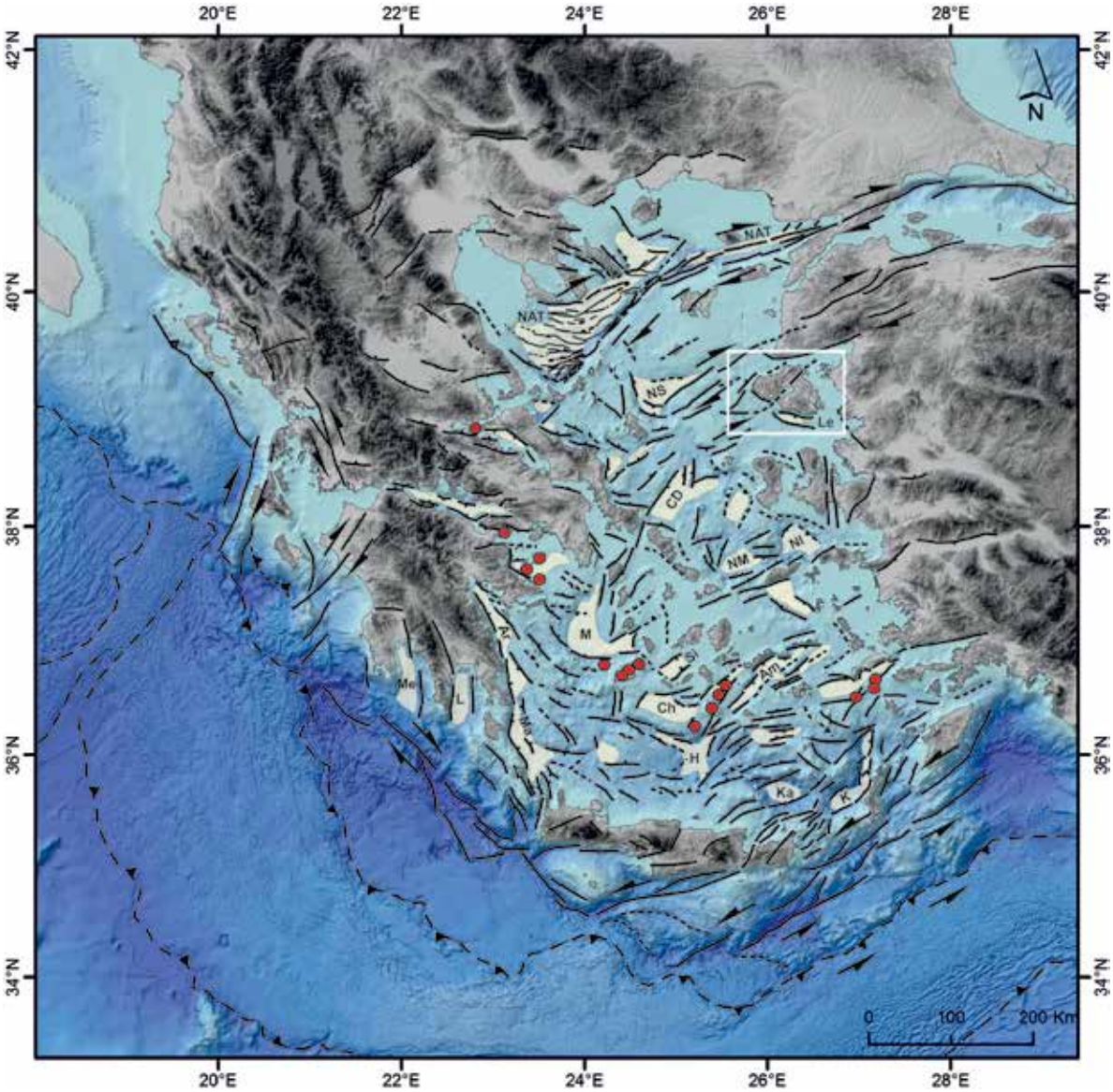

Figure 1. Active fault network and distribution of Plio-Quaternary basins in the Aegean. Red dots show the main volcanoes of the Volcanic Arc. Yellow areas indicate Plio-Quaternary basins with sediment thickness >500 m. Black lines show active faults, dashed black lines indicate possible/inferred faults. Ticks on the faults mark the hangingwall. Half arrows show the sense of strike-slip motion. Basins: Am; Amorgos, Ar: Argolikos, CD: Cavo Doro, Ch: Christiana, H: Heraklion, K: Karpathos, Ka: Kamilonisi, L; Lakonikos, Le: Lesvos, M: Myrtoon, Me: Messiniakos, NAT: North Aegean Trough, NI: North Ikarian, NM: North Mykonos, NS: North Skyros, Si: Sikinos (Sakellariou & Tsampouraki – Kraounaki, 2019). The white box marks the island of Lesvos and the broader study area.

Geology and fault geometry of the SE Lesvos

The principal geological structure within the study area is the asymmetrical Vatera Basin, characterized by its triangular shape, bordered to the north by a series of hills that rise to altitudes of up to 350 meters, and to the south by the coastline. At the base of the southern slopes of this hill range lies the Vrisa Fault (VFZ), extending approximately 13 km from the Gulf of Kalloni to the west, passing south of the village of Polichnitos, north of the settlement of Vrisa, and reaching eastward to the settlement of Drota, while its trace terminates at the coastline, with a likely offshore extension further eastward. Vacchi et al. (2012) refer to this fault as the Vatera Fault, while Chatzipetros et al. (2013) and Papadimitriou et al. (2018) identify it as the Plomari-Polichnitos Fault. The fault exhibits a WNW-ESE strike with high-angle dips to the NNW. Kinematically, it displays counterclockwise strike-slip motion with a notable normal slip component, although normal characteristics were also observed through slickensides identified in its central segment. The thickness of the damage zone exceeds 1 m.

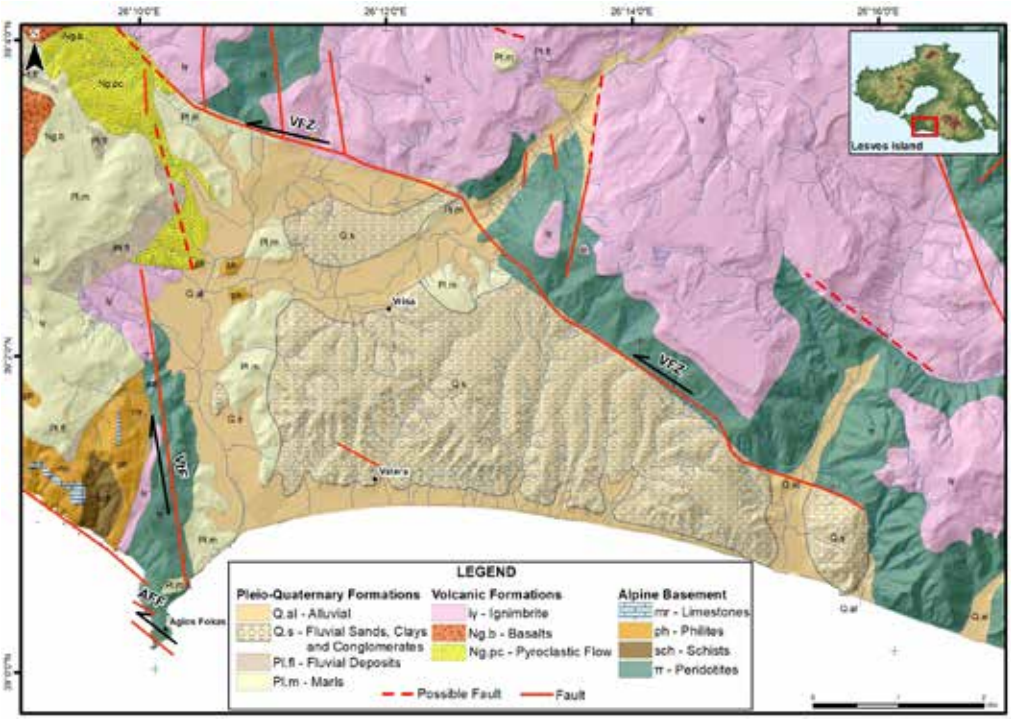

Figure 2. Geological and tectonic map of the study area, based on IGME maps (POLYCHNITOS and PLOMARI Sheets), showing the major fault zones described in this study. AFF: Agios Fokas Fault, VtF: Vatera Fault, VFZ: Vrisa Fault Zone.

The hill range constitutes the footwall of the fault and is composed of ophiolitic rocks, upon which beds of ignimbrites have been deposited. Above the fault block lies a thick sequence of Pleistocene fluvial conglomerates that comprises the central and eastern parts of the basin; beneath this, a Pliocene sequence primarily consisting of alternating marls and conglomerates, is distinguished in the western part. The size of the gravels in the upper sequence decreases from east to west, indicating a source of sediments from the northeast. The lower marly sequence exhibits eastern dips, while the overlying conglomeratic sequence dips southwest, although near the fault, it tends to tilt towards it.
During the June 2017 earthquake, surface ruptures were observed along the fault on the dirt roadway intersecting it. These ruptures measured 50 m in length and 1 cm in width without accompanying displacements. Additionally, large fragments of the fractured ophiolitic rock detached from the fault scarp and tumbled downward, while pre-existing ruptures within the fault's damage zone were widened (Mavroulis et al., 2018).

Figure 3. Fault scarps with the striations of the AFF (left image) and VFZ (right image). The geometry of the slickensides in AFF is 01º/122º and for VFZ is 112º/30º in a fault which dips towards SW.

Agios Fokas Fault Zone (AFFZ) is situated in the central south-southwestern region of the study area and predominantly extends parallel to the coastline, with its most notable onshore manifestation found at the eponymous cape. The AFFZ follows a NW-SE orientation, almost parallel to the VFZ, is a steep fault and consists of numerous

fault segments arranged in an en-échelon pattern. The footwall of the fault is built by old alpine formations, such as phyllites, crystalline limestones, green schists and metabasalts, on which Miocene volcanic rocks and finally Pliocene marls of the lower series of the Vatera basin have been deposited. Kinematical this fault zone is mainly characterized by strike-slip motion as indicated by the slickenlines observed on its fault surfaces. However, the presence of beachrocks above sea level on its footwall may suggest uplift attributable to this fault zone, potentially implying the coexistence of a normal component of shear. These kinematic features match those on the VFZ.
The faults situated in the NNW-SSE/N-S strike tend to play a subordinate role in the main fault zones outlined above (VFZ and AFFZ), serving as the structural connections between them. Notably, the steep Vatera Fault Zone (VtFZ), located in the central portion of the study area, is characterized by an almost N-S to NNW-SSE orientation, with a primary dip to the ENE. This fault zone extends from the VFZ to the north, terminating at the cape of Agios Fokas to the south. The existence of VtFZ is corroborated by the presence of distinct successive fault scarps arranged in an en échelon pattern, as well as geomorphological observations. In kinematic terms, VtFZ predominantly exhibits a clockwise component of slip, although its normal component holds substantial importance, as it significantly influences the hydrographic network of the region, causing it to shift towards the southwest and forming an asymmetry in its drainage basin. This asymmetry arises from the pronounced elevation of the western footwall of VtFZ relative to the eastern hanging wall. This relative vertical motion is further substantiated by the presence of Pleistocene conglomerates exclusively in the eastern part of the Vatera Basin.

Levos Basin

South of the study area, geomorphological analysis of the offshore morphology south of the Lesvos Island and seismic analysis results, highlight the existence of a depression, which is called the Lesvos Basin (LB) formed in Pliocene (Mascle & Martin, 1990). It is an asymmetric depression of about 700 m deep and of NW-SE strike which is characterized by a thick sedimentation (Sakellariou & Tsampouraki – Kraounaki, 2019). The results from a series of transverse Parasound profiles in the N-S direction, showed that the eastern part of LB is WNW-ESE basin, running parallel to the southeastern Lesvos coastline, with a length of more than 30km, maximum depth of 703m and its axis located at 5-6 km from the coast. Its northern margin is controlled by a WNW-ESE marginal fault of the Lesvos Basin with steep slopes forming a steep submarine escarpment more than 600 m height (Mascle & Martin, 1990; Sakellariou & Tsampouraki – Kraounaki, 2019; Nomikou et al., 2021). The eastern segment of the fault, located south of the town of Plomari, exhibits a WNW-ESE strike and is situated in the southeastern extension of the VFZ. Further west, south of the Vatera coastline, the marginal fault shifts slightly in strike, transitioning to a nearly E-W orientation. The earthquake of June 2017, along with its seismic aftershocks, aligns in a WNW-ESE direction within the LB, and it has been proposed that it resulted from the activation of the marginal fault associated with the basin, which corresponds to its eastern segment (Papadimitriou et al., 2018).
South of Agios Fokas Cape an abrupt change of the bathymetry of the LB is observed with a shallow-water platform around 300–400 m depth formed westwards. The change from the main basin occurs along a N-S boundary zone (Nomikou et al., 2021). According to the authors, a similar structure is evident in the eastern margin of the basin, where it has been proposed by them that this zone corresponds to a sinistral strike-slip fault. The western zone is in the submarine extension of the VtFZ. Thus, it can be suggested that this zone is also tectonically shaped by a strike-slip fault.

Discussion and conclusions

Various studies, (e.g. Sakellariou & Tsampouraki-Kraounaki, 2019; Beniest et al.,2016), indicate that certain faults in NE Aegean form transtensional and transpressional structures, especially where faults change strike. The Plio-Quaternary basins formed in a transtensional regime—such as releasing bends and pull-apart basins, or at the junction of NE-SW dextral and NW-SE sinistral strike-slip faults—are entirely controlled by those faults.
We have established that the VFZ is a NW-SE to NNW-SSE, sinistral strike-slip fault zone that exhibits a notable normal component. The kinematic characteristics of this fault align with the proposed models for the Northern Aegean, which support for this type of slip across all faults of similar strike (Sakellariou & Tsampouraki-Kraounaki, 2019). The characteristics of the VFZ are also corroborated by the tilting of conglomerates in the eastern part of the VB, indicating local extension. Furthermore, the VFZ is regarded as the onshore extension of the offshore eastern segment of the marginal fault of the LB (Vacchi et al., 2012; Papadimitriou et al., 2018), as both faults share comparable strike and dip orientations, as well as analogous kinematic behaviors.
The data presented above indicates the following possible scenario of basin evolution in the study area.
In Pliocene, a large basin was formed in the area of Southern Lesvos Island and the present LB. It was characterized by the deposition of (lacustrine?) marls and was bounded to the north-northeast by the VFZ and to the west by the NE-SW striking prolongation of the dextral Agia Paraskevi – Kalloni FZ (APFZ).

In Early Quaternary, enhanced uplift and erosion of the footwall of VFZ led to deposition of massive fluvial conglomerate deposits in the hanging wall of the fault, on VFZ hanging wall and possibly further east and south. At the same time two new faults initiate: the WNW-ESE striking Lesvos Fault (LF) and the NNW-SSE striking Vatera Fault (VtF). The latter marks the new western margin of the basin while the former leads to enhanced subsidence of its hanging wall (Lesvos Basin). Initiation of the Agios Fokas Fault (AFF) may also have taken place in Early Quaternary.
In Late Quaternary, activity on Lesvos Fault leads to uplift of the area of Vatera (Vatera Basin, conglomerate deposits) and enhanced subsidence of Lesvos Basin. The latter is bounded to the west by the offshore possible prolongation of Vatera Fault (VtF).
From Late Quaternary until present day, the morphology of the study area has changed a lot. The most important change concerns the uplift of the study area, which is now exposed to the surface conditions on land. The main reason for this relative uplift was the intense activity of the now offshore, normal, LF, which causes uplift of the NNE onshore part of the LB, and further subsides its NW part.

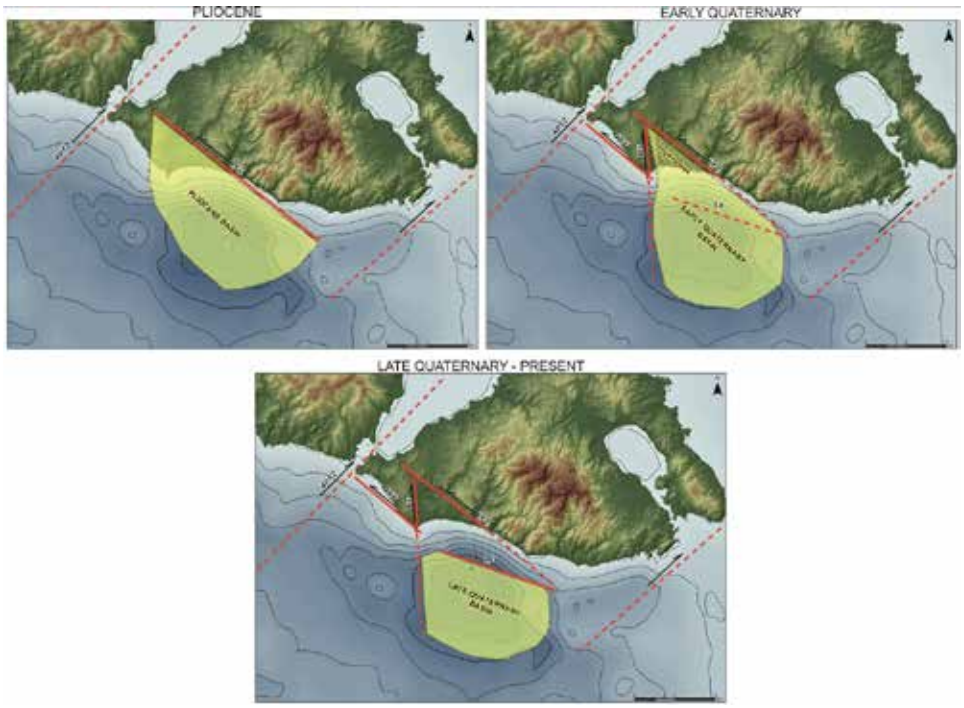

Figure 4. Proposed paleogeographic evolution of the basin in the study area. APFZ: Agia Paraskevi Fault Zone, VFZ: Vrisa Fault Zone, AFF: Agios Fokas Fault, VtF: Vatera Fault.

As regards the offshore LF, although the so far acquired data show a predominant normal slip character, it is considered quite possible for it to simulate the kinematic characteristics of almost all the fault zones mentioned in this study and act both as a normal and a strike – slip fault, which from the Pliocene until the present day, has greatly shifted the morphology of the study area.
The activity of the above structure is confirmed by the recent earthquake of June 2017 (Mw 6.3), with the seismic sequence taking place within the basin, in the hanging wall of the boundary fault (Kiratzi et al., 2018; Papadimitriou et al, 2018) and the focal mechanisms showing normal sense of shear (Kiratzi et al., 2018; Papadimitriou et al., 2018). According to the morphological data provided, this newly formed, offshore basin is probably delimited to the west by the offshore prolongation of the VtFZ, as the direction of both zones is similar.
In conclusion, it is noteworthy that both the VFZ and the AFFZ are regarded as segments or splays of the LF, collectively forming a comprehensive fault zone that governs the entire southern boundary of Lesvos Island and significantly contributes to the geological evolution of its southern region. It is evident that the strike orientations and kinematic characteristics of the mentioned fault zones, both onshore and offshore, align perfectly with the findings from prior research conducted in the North Aegean. Therefore, the kinematics of the fault network in the study area oscillates between strike-slip and extension, epitomizing a distinctly transtensional regime. This observation parallels the broader deformation occurring in the North Aegean region, attributable to the North Anatolian Fault and its extension into the Aegean Sea through its associated strands.

References

Armijo, R., Meyer, B., King, G. C. P., Rigo, A. & Papanastassiou, D. 1996. Quaternary evolution of the Corinth rift and its implications for the Late Cenozoic evolution of the Aegean. Geophysical Journal International 126:11-53.

Armijo, R., Meyer, B., Hubert, A., Barka, A., 1999. Westward propagation of the north Anatolian into the northern Aegean: timing and kinematics. Geology 27 (3), 267–270.

Beniest, A., Brun, J.P., Gorini, C., Crombez, V., Deschamps, R., Hamon, Y., Smit, J., 2016. Interaction between trench retreat and Anatolian escape as recorded by neogene basins in the northern Aegean Sea. Mar. Pet. Geol. 77, 30–42. https://doi.org/10.1016/j.marpetgeo.2016.05.011

Chatzipetros, A., Kiratzi, A., Sboras, S., Zouros, N., Pavlides, S., 2013. Active faulting in the north-eastern Aegean Sea Islands. Tectonophysics 597–598, 106–122. https://doi.org/10.1016/j.tecto.2012.11.026

Dewey, J. F. & Şengör, A. M. C. 1979. Aegean and surrounding regions: Complex multiplate and continuum tectonics in a convergent zone. Geological Society of America Bulletin 90:84-92.

Hecht, J., 1972. Geological map of Greece 1:50000, Sheet Plomari - Mytilene. I.G.M.E.

Hecht, J., 1974b. Geological map of Greece 1:50000, sheet Polychnitos. I.G.M.E.

Nomikou, P., Papanikolaou, D., Lampridou, D., 2021. The active tectonic structures along the southern margin of Lesvos Island, related to the seismic activity of July 2017, Aegean Sea, Greece. Geo-Mar Lett 41, 49 https://doi.org/10.1007/s00367-021-00723-6

Katsikatsos, G., Migiros, G., Triantaphyllis, M., Mettos, A., 1986. Geological structure of the internal Hellenides (East Thessaly - Southwest Macedonia, Eubea - Attica - Northern Cyclades islands and Lesvos). Geol. Geophys. Res. 191–212.

Kiratzi, A., 2018. The 12 June 2017 Mw 6.3 Lesvos Island (Aegean Sea) earthquake: Slip model and directivity estimated with finite-fault inversion. Tectonophysics 724–725, 1–10. https://doi.org/10.1016/j.tecto.2018.01.003

Koukouvelas, I.K., Aydin, A., 2002. Fault structure and related basins of the North Aegean Sea and its surroundings. Tectonics 21. https://doi.org/10.1029/2001TC901037.

Le Pichon, X., Angelier, J., 1979. The Hellenic arc and trench system: a key to the neotectonic evolution of the eastern Mediterranean area. Tectonophysics 60, 1–42.

Le Pichon, X., Angelier, J., 1981. The Aegean Sea. Philosophical Transactions of the Royal Society of London 300, 357–372.

Mascle, J., Martin, L., 1990. Shallow structure and recent evolution of the Aegean Sea: A synthesis based on continuous reflection profiles. Mar. Geol. 94, 271–299. https://doi.org/10.1016/0025-3227(90)90060-W

Papadimitriou, P., Kassaras, I., Kaviris, G., Tselentis, G.A., Voulgaris, N., Lekkas, E., Chouliaras, G., Evangelidis, C., Pavlou, K., Kapetanidis, V., Karakonstantis, A., Kazantzidou-Firtinidou, D., Fountoulakis, I., Millas, C., Spingos, I., Aspiotis, T., Moumoulidou, A., Skourtsos, E., Antoniou, V., Andreadakis, E., Mavroulis, S., Kleanthi, M., 2018. The 12th June 2017 Mw = 6.3 Lesvos earthquake from detailed seismological observations. J. Geodyn. 115, 23–42. https://doi.org/10.1016/j.jog.2018.01.009

Papazachos, B. C., Kiratzi, A. A., & Karacostas, B. G., 1997. Toward a homogeneous moment-magnitude determination for earthquakes in Greece and the surrounding area. Bulletin of the Seismological Society of America, 87(2), 474–483.

Pe-Piper, G., Piper, D.J.W., 1992. Geochemical variation with time in the Cenozoic high-k volcanic rocks of the island of Lesbos, Greece: significance for shoshonite petrogenesis. J. Volcanol. Geotherm. Res. 53, 371–387. https://doi.org/10.1016/0377-0273(92)90092-R

Pe-Piper, G., Piper, D.J.W., Zouros, N., Anastasakis, G., 2019. Age, stratigraphy, sedimentology and tectonic setting of the Sigri Pyroclastic Formation and its fossil forests, Early Miocene, Lesbos, Greece. Basin Res. 31, 1178–1197. https://doi.org/10.1111/bre.12365

Sakellariou, D., Tsampouraki-Kraounaki, K., 2019. Plio-quaternary extension and strike-slip tectonics in the aegean, Transform Plate Boundaries and Fracture Zones. Elsevier Inc. https://doi.org/10.1016/B978-0-12-812064-4.00014-1

Taymaz, T., Jackson, J., McKenzie, D., 1991. Active tectonics of the north and central Aegean Sea. Geophys. J. Int. 106, 433–490. https://doi.org/10.1111/j.1365-246X.1991.tb03906.x

Vacchi, M., Rovere, A., Zouros, N., Desruelles, S., Caron, V., Firpo, M., 2012. Spatial distribution of sea-level markers on Lesvos Island (NE Aegean Sea): Evidence of differential relative sea-level changes and the neotectonic implications. Geomorphology 159–160, 50–62. https://doi.org/10.1016/j.geomorph.2012.03.004

17th INTERNATIONAL CONGRESS of the Geological Society of Greece

BULLETIN OF THE GEOLOGICAL SOCIETY OF GREECE, SP. PUBL.

EXTENDED ABSTRACT 294

Discovering the geoheritage of Skiathos Island (Northern Sporades, Greece)

Soultanis K.[1], Soukis K.[1], Triantaphyllou M.V.[1]
(1) National and Kapodistrian University of Athens, Athens Greece, kimonasofficial@gmail.com

This paper attempts to probe and highlight the geoenvironmental attractions of Skiathos Island and to propose friendly geo-routes and accessible geo-locations that could appeal to visitors.

Skiathos Island belongs to the Northern Sporades located in north Aegean, Greece. It has an irregular, NE-SW elongated shape, stretching approximately 12 km in length and 6 km in width, with a hilly and undulating terrain. The highest peak, Mount Karafiltzanaka (433 m), and other smaller hills form a central spine running through the island, gradually sloping towards the coast. The island's northern part is steeper and more mountainous, with cliffs dropping sharply into the sea, while the southern part has gentler slopes and is more developed, with sandy beaches and natural harbors. The presence of weathered rock formations and thin soil layers supports dense pine forests and small seasonal streams that contribute to its lush, green environment. Skiathos features a well-developed coastal zone with numerous bays, peninsulas, small capes, and sandy shores formed by sediment transport and coastal processes.

Skiathos is situated in the back-arc area of the Hellenic Arc and comprises rocks belonging to the Pelagonian domain, a continental lithospheric block considered part of the Cimmerian ribbon continent, affected by the Late Jurassic - Early Cretaceous closure of the Vardar Ocean and the early Cenozoic Alpine deformation. The lower part includes late Paleozoic augen gneisses, para- and orthogneisses, amphibolites, and schists, occupying the central and western part, overlain by a Triassic-Jurassic marble and late Jurassic calc phyllites and slates, observed at the eastern and northern parts. The upper part is made of a transgressive late Cretaceous limestone observed at the central and northern parts of the island. (Ferentinos 1973; Jacobshagen and Wallbrecher 1986; Mountrakis 1986; Papanikolaou 2021)

We have identified and classified several key locations across the island, comprising distinct geosites that combine natural geoscientific monuments with aesthetic, naturalistic, cultural, historical, touristic and educational values (Figure 1). All included geosites have been assessed based on the criteria applied by Skentos (2012). The outcome of this assessment enabled the development of sustainable geo-routes (e.g., Spyrou et al., 2002; Triantaphyllou et al., 2023).

Figure 1. Geo-routes and geo-locations of Skiathos Island and the surrounding islets (Basemap: Esri Worldmap Imagery).

These sites exhibit significant geomorphological, mineralogical, tectonic, and historical interest. While primarily of local significance, they serve as an essential introduction for visitors and residents to engage with the island's diverse geoenvironment.

Beyond their scientific and educational value, these locations play a crucial role in advocating for the preservation of Skiathos' rich geological heritage. Some of these geosites form well-defined geo-routes, accessible by foot or vehicle, allowing visitors to immerse themselves in the island's breathtaking landscapes while exploring its geological diversity (Figure 2a-c). Others, more secluded and reachable only by sea, offer a unique opportunity to experience the island's untouched, rugged terrain, making them ideal destinations for daily excursions to remote and pristine coastal areas.

Figure 2a-c. a) Augen gneisses of the prealpine Pelagonian basement. b) Crenulation cleavage in the Late Jurassic calc phyllites. c) View of the narrow canal of the Strofilia lagoon.

References

Jacobshagen, V. and Wallbrecher, E., 1984. Pre-Neogene nappe structure and metamorphism of the North Sporades and the southern Pelion peninsula. Geological Society, London, Special Publications, 17(1), pp.591-602.

Manda, A.K., Horsman, E., 2015. Fracturesis Jointitis: Causes, Symptoms, and Treatment in Groundwater Communities. Groundwater 53(6), pp.836-840.

Ferentinos, G. C. 1973. The geology-petrology of the island of Skiathos. Bull. Geol. Soc. Greece, 10, 323-358.

Mountrakis, D., 1986. The Pelagonian zone in Greece: A polyphase-deformed fragment of the Cimmerian continent and its role in the geotectonic evolution of the eastern Mediterranean. The Journal of Geology, 94(3), pp.335-347.

Papanikolaou, D.I., 2021. Regional Geology Reviews The geology of Greece. Springer Nature.

Skentos, A. 2012. Geosites of Greece: Record, Schematic, Geological Regime and Geotouristic Assessment; National and Kapodistrian University of Athens: Athens, Greece.

Spyrou, E., Triantaphyllou, M.V., Tsourou, T., Vassilakis, E., Asimakopoulos, C., Konsolaki, A., Markakis, D., Marketou-Galari, D. and Skentos, A., 2022. Assessment of geological heritage sites and their significance for geotouristic exploitation: The case of Lefkas, Meganisi, Kefalonia and Ithaki Islands, Ionian Sea, Greece. Geosciences, 12(2), p.55.

Triantaphyllou, M.V., Firkasis, N., Tsourou, T.; Vassilakis, E., Spyrou, E., Koukousioura, O., Oikonomou, A., Skentos, A., 2023. "Geo-Archaeo-Routes" on the Island of Lemnos: The "Nalture" Experience as a Holistic Geotouristic Approach within the Geoethical Perspective», Geosciences 13, 143.

17th INTERNATIONAL CONGRESS of the Geological Society of Greece

BULLETIN OF THE GEOLOGICAL SOCIETY OF GREECE, SP. PUBL.

EXTENDED ABSTRACT 295

Cyclone Daniel's Impact: A Study of Geohazards in Meteora, Greece

Natalia Spanou[1]
(1) Hellenic Survey of Geology and Mineral Exploration (HSGME), Athens, Greece

Research Highlights

- Extreme weather events, such as Cyclone Daniel, significantly impact slope stability and increase the occurrence of geohazards, such as landslides, erosion, and flood-induced deposition of eroded materials.
- Understanding the mechanisms of geohazards can enhance risk mitigation strategies for affected communities.
- Evaluation of existing landslide susceptibility maps highlights the need for improved predictive tools in vulnerable regions.
-

Introduction/ Background

Cyclone Daniel, a severe weather event in September 2023, triggered extensive flooding, landslides, and associated phenomena across Central Greece. This event provides a unique case study for examining the link between extreme weather and the occurrence of geohazards. This analysis specifically focuses on the Meteora municipality, particularly the Municipal Units of Kleinovos, Kastania, and Aspropotamos, an area heavily impacted by landslide phenomena.

Detailed data on the geohazards that occurred in Meteora, meticulously collected through in-situ investigations, are analyzed. These data include the location, size, and characteristics of the geohazards. By examining these data, researchers aim to understand how the intensity of the cyclone and precipitation patterns affected slope stability in this region.

Existing landslide susceptibility maps for Greece are evaluated for the Meteora region. By comparing these maps with the actual landslide distribution, their effectiveness for the municipality is assessed, revealing areas that require adjustments.

Objectives

This study aims to achieve the following key objectives:

- Decipher Triggering Mechanisms: Identify specific meteorological factors associated with Cyclone Daniel that contributed to geohazards occurrences within the Meteora municipality.
- Inform Mitigation Strategies: Develop recommendations for improved geohazards risk mitigation strategies specific to Meteora, with potential applicability to other vulnerable municipalities.
- Validate Susceptibility Maps: Assess the accuracy of existing susceptibility maps in predicting landslide locations during the extreme weather event.
-

Methods

The detailed data on geohazard occurrences in Meteora, triggered by Cyclone Daniel, have been subjected to meticulous in-situ investigation and subsequent analysis. The dataset includes information on the location, dimensions, and characteristics of these phenomena. A total of 114 geohazard events were documented within the municipal boundaries of Meteora (Fig.1). These phenomena encompass a variety of processes, including rotational and translational slides, as well as soil and debris flows. Erosion in stream beds is also a common occurrence. Additionally, the accumulation of transported materials from the high sediment supply of the streams is another notable phenomenon (Spanou, 2024; Spanou, 2025a; Spanou 2025b).

The objective of this analysis is to assess the impact of the cyclone's intensity and precipitation patterns on slope stability within the region (Fig. 2). Additionally, recommendations for improved geohazard risk mitigation strategies specific to Meteora—with potential applicability to other vulnerable municipalities—are developed. Furthermore, the effectiveness of existing landslide susceptibility maps for the Meteora region has been evaluated. A comparison of these maps with the actual landslide distribution allows for an estimation of their accuracy for the municipality and identifies areas that may require adjustments (Apostolidis *et al.*, 2023).

Results

This study aimed to elucidate the mechanisms that precipitate geohazards in the Meteora municipality, which was significantly impacted by Cyclone Daniel. The specific meteorological factors triggering geohazard events within the municipality have been identified. Additionally, recommendations for enhanced geohazard risk mitigation strategies—tailored to Meteora and potentially applicable to other vulnerable municipalities—have been put forth. Finally, the accuracy of existing susceptibility maps in predicting landslide locations during extreme weather events was assessed (Spanou *et al.*, 2024).

Conclusions

Following the study, the most effective protection and mitigation measures were identified as follows:

- Surface and Subsurface Water Management: Implementation of surface water settlement projects and underground water drainage systems.
- Landslide-Specific Approaches: Adopting a case-by-case approach for selecting appropriate support works for landslides.
- Risk Demarcation: Conducting detailed demarcation studies to accurately identify and delineate areas already affected or at risk.
- Infrastructure Maintenance: Ensuring ongoing maintenance and repair of infrastructure along the road network—encompassing technical components, bridges, and other structures—to guarantee continued functionality and safety.

These measures provide a comprehensive framework for mitigating geohazard risks and enhancing public safety in vulnerable regions.

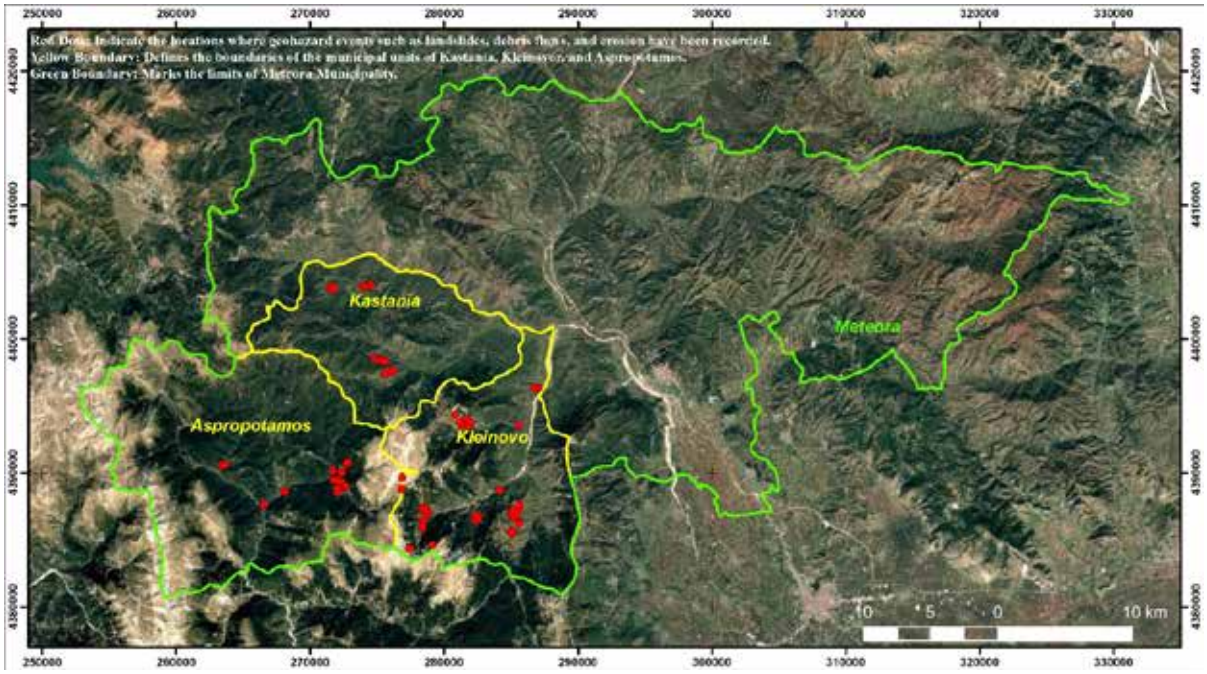

Figure 1. A total of 114 geohazard events were recorded in Meteora Municipality following Cyclone Daniel.

Figure 2. A few of the impacts of geohazards triggered by Cyclone Daniel in the Meteora Municipality.

References

Apostolidis, E., Spanou, N., Kavoura, K., Panagiotidou, F., Ieronymakis, V., Kokkali, P. 2023. Assessment of Landslide Susceptibility in Greece. Unpublished Report HSGME, T – 3273, Athens.

Spanou, N., 2024. Geotechnical Survey of Landslide Phenomena in the Municipal Communities of Krania, Kallirroi, Katafyto, and Chaliki of the Aspropotamos Municipal Unit of Meteora Municipality, Trikala Prefecture. Unpublished Report HSGME, T – 3296, Athens.

Spanou, N., Kavoura, K., Nikolaou, N., 2024. Cyclone Daniel's scars: a landslide analysis in Meteora, Greece. EUROENGEO 2024 - 4th European Regional Conference of IAEG, Dubrovnik, Croatia.

Spanou, N., 2025a. Geotechnical Survey of Landslide Phenomena in the Municipal Communities of Kastania, Amarantos, Ampelochori, and Matoneri of the Kastania Municipal Unit of Meteora Municipality, Trikala Prefecture. Unpublished Report HSGME, T – 3297, Athens.

Spanou, N., 2025b. Geotechnical Survey of Landslide Phenomena in the Municipal Communities of Ampelia, Kleino, Aidona, and Chrysomilia of the Kleinovo Municipal Unit of Meteora Municipality, Trikala Prefecture. Unpublished Report HSGME, T – 3298, Athens.

17th INTERNATIONAL CONGRESS of the Geological Society of Greece

BULLETIN OF THE GEOLOGICAL SOCIETY OF GREECE, SP. PUBL.

EXTENDED ABSTRACT 296

Combining Ground and UAV Mapping for GIS-Based Assessment of Flash Flood Impact Severity: Application of the FFISS to the 2009 and 2020 Evia (Greece) Floods

Nafsika Ioanna Spyrou [1], Michalis Diakakis [2], Spyridon Mavroulis [1], Georgios Deligiannakis [3], Emmanuel Andreadakis [1], Christos Filis [1], Evelina Kotsi [1], Zacharias Antoniadis [1], Maria Melaki [1], Marilia Gogou [1], Katerina-Navsika Katsetsiadou [1], Eirini-Spyridoula Stanota [1], Emmanuel Skourtsos [1], Emmanuel Vassilakis [2], and Efthymios Lekkas [1]

1 Department of Dynamic, Tectonic, Applied Geology, Faculty of Geology and Geoenvironment, School of Sci-ences, National and Kapodistrian University of Athens, 15784 Athens, Greece; nspyrou@geol.uoa.gr (N.I.S.); smavroulis@geol.uoa.gr (S.M.); eandreadk@geol.uoa.gr (E.A.); chfilis@geol.uoa.gr (.C.F.); ekotsi@geol.uoa.gr (E.K.); zaxarias@gmail.com (A.Z.); mariamelaki@gmail.com (M.M.); mgogou@geol.uoa.gr (M.G.); knavsi-ka@geol.uoa.gr (K.N.K.); estanota@geol.uoa.gr (E-S.S.); eskourt@geol.uoa.gr (E.S.); elekkas@geol.uoa.gr (E.L)
2 Department of Geography and Climatology, Faculty of Geology and Geoenvironment, School of Sciences, National and Kapodistrian University of Athens, 15784 Athens, Greece; diakakism@geol.uoa.gr (M.D.); evassilak@geol.uoa.gr (E.V.)
3 Department of Natural Resources Management and Agricultural Engineering, Agricultural University of Athens, 10447Athens, Greece; gdeligian@aua.gr (G.D.)

1. ntroduction

Flash floods are among the most destructive natural hazards, causing loss of life, infrastructure damage, and environmental harm, impacts expected to worsen with climate change, especially in the Mediterranean. Their sudden and localized nature makes systematic assessment difficult, particularly in urban and large-scale events (Merz et al., 2010; Petersen, 2001; Diakakis et al., 2017). The variability of impacts across different areas hinders the development of a standardized evaluation method. Existing approaches often target specific sectors, limiting a holistic understanding. A simple, multi-criteria system is needed to assess flash flood severity across events. (Marchi et al. 2023; Gourley et al., 2013; Boudou et al., 2016; Sîli et al., 2020). Lack of systematic impact data limits flood risk identification, relying on history and local knowledge. This weakens future predictions and mitigation efforts due to poor understanding of flood impacts. Using the Flash Flood Impact Severity Scale (FFISS), the study compares 2009 and 2020 floods to analyze severity patterns and improve preparedness (Schroeder et al., 2026; Boudou, 2016; Calianno et al., 2013; Diakakis et al., 2020).

2. Study area and flood events

The Lilas River catchment covers 249 km² in Evia Island (Greece), within two municipalities (Figure 1). It includes Vassiliko and nearby settlements, with a total population of about 16,500 residents (Hellenic Statistical Authority, 2021). Most of the area is forested, while the mid and lower sections support significant agriculture. The fertile Lilas Plain near the outlet has held historic agricultural and strategic importance. The Lilas catchment collects water from the southern and southwestern slopes of Mount Dirfi (1,743 m a.s.l.) and the surrounding Messapios mountains. Initially, the terrain is steep and rugged, but as the elevation decreases, the slopes become more gradual. Covering an area of 259.19 km², the drainage network is denser in the upper reaches, while in the lower elevations, the floodplain and main river channel have experienced flooding in the past (Figure 2).

2.1. The 2009 Flood

The 2009 flood in central Evia was triggered by intense rainfall, with 376.8 mm recorded in 18 hours at Steni. It caused major damage to infrastructure, homes, and vegetation, including roof collapse and severe erosion. Sediment deposition altered the river's flow, uprooted vegetation worsened flooding, and vehicles were swept away. The event underscored the need for better flood management, infrastructure upgrades, and ecosystem restoration (Meteo, n.d.).

2.2. The 2020 Flood

On August 8, 2020, a persistent storm system brought extreme rainfall to central Evia, with 300 mm recorded at Steni. The flood devastated the Lilas catchment resulting in damage to homes, roads, bridges, and farms and five fatalities. Infrastructure failures disrupted emergency response, while erosion reshaped riverbanks and reduced water capacity. The event revealed the need for resilient infrastructure, ecological restoration, and better flood preparedness (Lekkas et al., 2020; Mavroulis et al., 2021).

Figure 1. Map of the Evia Island in the eastern part of Mainland Greece. The red frame indicates the study area affected by flash floods in 2009 and 2020.

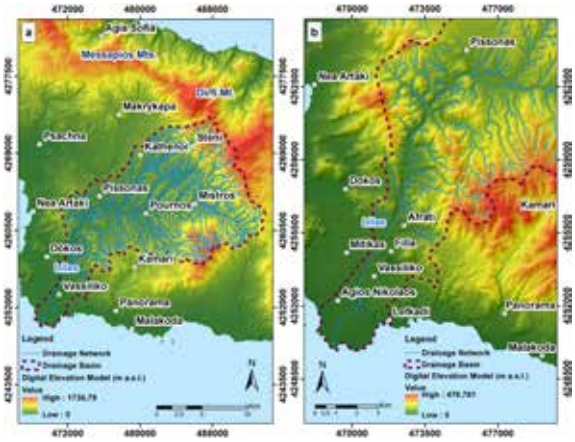

Figure 2. (a) Map showing the flood-affected Lilas catchment along with its drainage network and the elevation reaching over 1,730 m a.s.l. in the wider mountainous area comprising Messapios and Dirfi Mts located north of Lilas. (b) Map illustrating the lower part of the Lilas catchment, which was mainly affected by the 2009 and 2020 flash floods.

3. Methodology

3.1. Flash Flood Impact Data Collection

Flood impact data were gathered from official reports and media sources, alongside field surveys by the authors. These surveys used drones (DJI Mavic 2) and on-ground methods to capture high-resolution images and videos. UAS technology helped assess damage in areas too large or inaccessible for traditional methods. Geo-tagged data documented the location, type, and scale of damage with high spatial accuracy. Combining aerial and ground surveys ensured a complete picture of both widespread and localized impacts. Using the Unique Flood Impact Elements (UFIEs) enabled structured analysis, supporting better flood response and long-term planning (Spyrou et al., 2020; Spyrou et al., 2025; Andreadakis et al., 2020).

3.2. FFISS application

Flood impact data from both events were added in a GIS geo-database, with each entry (UFIE) mapped as a point and described by type, severity, and damage using FFISS (Diakakis et al. 2020). FFISS includes four impact categories:

(i) Built environment – damage to structures and infrastructure, from minor flooding to collapse or dam failure.

(ii) Mobile objects – displacement of items from lightweight to large vehicles.

(iii) Natural environment – effects on geomorphology, vegetation, agriculture, and pollution, from debris to severe contamination.

(iv) Population – from minor disruptions to fatalities. The scale consists of ten classes (Class I–X) to differentiate flood impact severity and avoid saturation seen in other models. It was developed through a global review of flash flood impacts, ensuring comprehensive coverage of diverse effects (Musson & Cecić, 2012; Diakakis et al., 2020).

3.3. Data processing and uncertainties

Only UFIEs with precise locations were used. Data lacking exact coordinates were excluded from analysis. Field data were GPS-logged with 3 m accuracy, while official records were mapped using building centroids or multiple points if needed. Visible pollution signs marked contamination, and with a 100 m grid, minor placement errors were acceptable unless exceeding cell size. (Diakakis et al., 2020; Spyrou et al., 2025).

4. Results

4.1. Application of the FFISS scale in the study area

According to the FFISS scale, the impacts of the 2009 Lilas River flood were systematically recorded and mapped across several affected areas, including Vassiliko, Afrati, and critical road networks. The transportation infrastructure experienced a range of damage severity, from road inundation and asphalt degradation to embankment erosion. Notably, partial and complete bridge failures led to the temporary isolation of entire communities during the peak of the flooding event (Figure 3). Varying levels of impact severity were recorded in the built environment, particularly at the level of individual buildings. In many inundated areas, flooding affected gardens, yards, pilotis, ground floors, and basements of both residential and commercial properties, significantly disrupting daily life. Structural damages ranged from collapsed fences to partial building failures, necessitating urgent search, rescue, and evacuation operations (Figure 4). The impact severity on mobile objects ranged from minor incidents, such as lightweight items and flower pots being displaced, to more significant cases like large waste bins carried by floodwaters. The severity escalated considerably with the displacement of vehicles, including cars and trucks swept into the sea, posing

serious risks to human life, particularly if occupants were present during the event (Figure 5). Finally, the observed impact severity in the natural environment included the uprooting and transport of low vegetation to riverbeds, roads, bridges, and residential areas, along with the flooding of higher ground plants. Severity increased with the uprooting of trees over 3 meters and significant geomorphological changes, such as soil erosion and deposition exceeding 3 meters in depth, which altered the morphology of the riverbed and delta (Figure 6).

Figure 3. Different flash flood impact severity classes on transportation. (a, b) Inundation of road surface in Vassiliko village (a) and Afrati settlement (b) (Class I). (c, d) Damages to the asphalt surface and levees scoured on the road Afrati – Pissonas (c) and in the Afrati settlement (d) (Class V). (e, f, g) Bridges suffered from structural damages and partial collapses in Vassiliko (e), Filla (f) and Afrati (g) (Class VII). (h) Bridge suffered from complete collapse in the settlement of Mistros (Class VIII).

Figure 4. Different flash flood impact severity classes on buildings. (a, b) Garden and pilotis had flooded in Lefkadi beach (Class I). (c) Yard walls and fences suffered from structural damages including total collapse in Vassiliko (Class IV). (d) House suffered from structural damages including failure of supporting elements in Vassiliko (Class VI).

Figure 5. Different flash flood impact severity classes on mobile objects. (a) Very light and small objects were transported at the beach of Agios Nikolaos (Class I). (b) Flower pots transported by floodwaters at Agios Nikolaos beach (Class II). (c) Large trash bins were carried away by floodwaters at Agios Nikolaos beach (Class III). (d, e, f), Cars were carried away during the flood in Vassiliko (Class IV). (g, h) Large tracks were transported by floodwaters in Afrati (Class VIII).

Figure 6. Different impact severity classes on the natural environment including (a, b) low vegetation uprooted and transported in the riverbed in Vassiliko (a) and on the bridge of Afrati (b) (Class II), (c) higher ground plants are affected by the flood in Vassiliko village (Class III), (d) tree smaller than 3 meters uprooted and carried away in the riverbed in Vassiliko (Class V), (e) large tree over 3 meters uprooted and destroyed on the riverbank in the village of Vassiliko (Class VI), (f, g) deposited material with a thickness of less than 3 meters in the riverbed downstream of Vassiliko village (f) and upstream of Afrati settlement (g) (Class VI), (h, i) eroded material with a thickness of more than 3 meters on the riverbank along the street of Afrati - Pissonas (h) and in Afrati (i) (Class VII).

Overall, 886 unique flood impact elements (UFIEs) were identified. We identified 187 and 699 UFIEs for the 2009 and the 2020 events, respectively. The frequency distribution across severity classes, highlighting key trends in the built and natural environments for the years 2009 and 2020. In the built environment, 2020 exhibited the highest frequency in Class III, with 104 events, indicating a notable concentration of lower-impact occurrences, while 2009 showed a peak in Class V with 15 events, reflecting more severe impacts. In the natural environment, both years recorded the highest frequency in Class IV. However, 2020 had a significantly higher count (116 events) compared to 2009 (57 events). This consistent dominance of Class IV, despite differing magnitudes, reveals a recurring vulnerability in the natural environment over time. Also, the highest frequency of severity for mobile objects was observed in Class IV, with 27 recorded events, indicating a notable concentration of impacts within this

class. Similarly, the human population sector showed the highest frequency in Class III, with 48 events, reflecting a moderate level of impact during the 2020 flood. No impact data were recorded for either sector in 2009, likely due to the absence of precise georeferenced information during that period.

4.2. Comparison of flood impact severity between 2009 and 2020

A comparison of impact severity between the two events shows both similarities and differences, influenced by environmental factors, land use changes, and discharge magnitude. In the built environment near the Lilas delta, the 2020 event showed lower severity than the 2009 one, largely due to post-2009 riverbed widening and the removal of damaged structures. However, in areas like Vassiliko, Filla, and Afrati, 2020 recorded higher severity, driven by greater discharge, erosion, and resulting structural damage to bridges. These findings underline the role of river morphology and infrastructure changes in shaping flood impact severity (Figures 7, 8).

Figure 7. Depiction of the morphological changes and the riverbed widening from the 2020 flood.

Figure 8. Illustration of the riverbed and estuary morphology of the Lilas River before the 2009 flood (above), as well as the destroyed buildings during the 2009 flood due to the widening of the riverbed (below).

The 2020 flood event resulted in a marked increase in impact severity in the area extending from Agios Nikolaos to Afrati and along the Afrati-Pissonas road. Elevated water levels and increased discharge significantly affected the river's geomorphology, leading to substantial sediment deposition within the riverbed and pronounced erosion along the riverbanks, phenomena not observed during the 2009 flood, which was characterized by lower discharge levels. This contrast in hydrological intensity and geomorphological outcomes is illustrated in Figure 9. Furthermore, no impact data concerning mobile objects or the human population were recorded during the 2009 event, although the absence of fatalities implies a lower severity level. Consequently, all relevant data and observations pertain exclusively to the 2020 flood. Notably, near the Afrati Bridge, high severity was recorded due to the floodwaters sweeping away heavy trucks and bulldozers from a nearby business (Figure 10).

Figure 9. A downstream view of the Vassiliko bridge, illustrating the estimated maximum water levels during the 2009 and 2020 flood events (indicated by white and yellow lines), based on high-water marks identified during post-flood surveys. The blue arrow indicates the river flow direction.

Figure 10. Illustration of the Afrati Bridge featuring bulldozers and large trucks that were carried away by the floodwaters. The yellow arrow indicates the river flow direction.

Across the entire impacted region and within all sectors of flood impact, the 2020 flood event was characterized by high-severity classifications in areas upstream of Agios Nikolaos, extending toward the settlement of Pissonas. In contrast, the 2009 flood exhibited lower-intensity classifications overall, with the notable exception of the Lilas River delta. This variation is primarily attributed to the fact that, in 2009, the built environment in the delta area suffered extensive damage, as several structures that

existed at the time were destroyed, thereby elevating the severity levels. By 2020, these structures had been removed, leading to a notable reduction in impact severity.

In addition, elevated severity classes (Classes V to VIII) were recorded in 2020 along the stretch from Agios Nikolaos to Afrati, due to extensive geomorphological alterations, significant damage to the built environment, particularly bridges, and the displacement of large mobile objects. Conversely, in 2009, no impact severity was documented in the areas of Agios Nikolaos and Lefkandi. Downstream of Pissonas, higher severity classifications (Class VIII) were also recorded in 2020 compared to 2009, mainly due to pronounced geomorphological changes and widespread vegetation disturbance caused by increased surface runoff. As for the Lilas River delta, severity classifications in 2020 were generally lower (Classes II–V) than those recorded in 2009 (Classes V–VIII) (Figure 11).

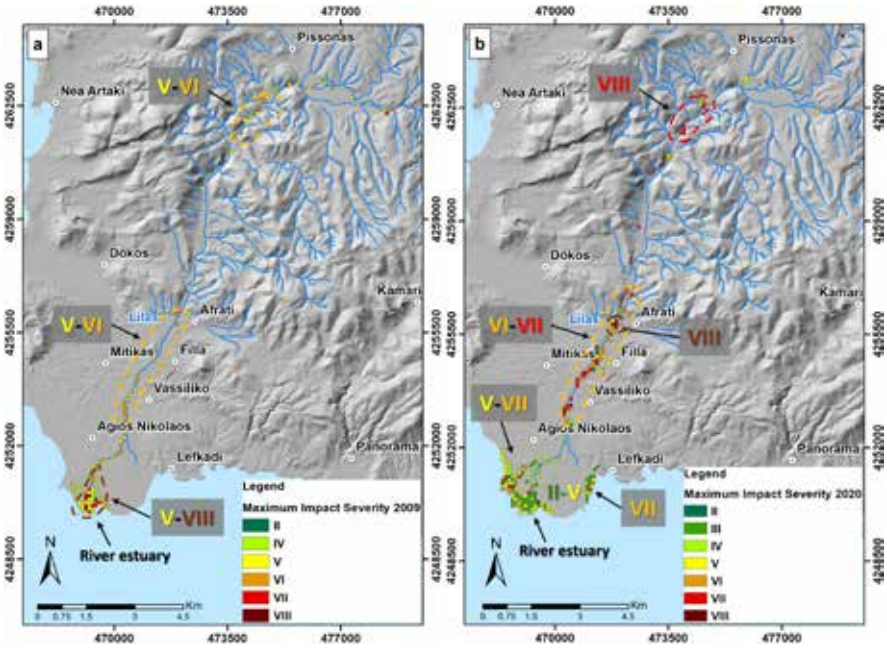

Figure 11. Comparison of maximum flash flood impact severity in the affected area of 2009 (a) and 2020 (b). The zones of impact concentration are divided as follows: at the estuary of the Lilas River, upstream of the Vassiliko bridge and downstream of Filla, in Afrati, and along the road Afrati-Pissonas.

5. Conclusions

This study applied the FFISS scale with four categories (built environment, natural environment, mobile objects, and population) and ten severity classes to assess two flood events in 2009 and 2020. Advanced technologies, including drones and ground-based observations, were used to capture high-resolution imagery and data across the affected areas. The FFISS scale allowed for a detailed comparison of both events, revealing a range of severity from classes II to VIII. While the 2009 flood had higher severity near the Lilas River delta, the 2020 flood impacted a wider area, including regions near the Vassiliko bridge and Pissonas. The 2020 flood was more intense, with increased discharge, higher flow velocities, and severe impacts such as sediment deposition, bank erosion, and bridge collapse. In 2009, riverbed widening near the delta affected the built environment, increasing the severity, but the absence of these structures in 2020 reduced impacts. The study demonstrated that the FFISS scale is useful even without geo-referenced data, as seen in the 2009 flood's movable objects and population sectors. The 2020 flood, however, involved significant displacement of large vehicles and fatalities, highlighting increased risks. The findings suggest that riverbed widening and flood mitigation measures, including hydraulic structures and retention measures upstream, are essential to reduce future flood risks.

References

Andreadakis, E.; Dakakis, M.; Vassilakis, E.; Deligiannakis, G.; Antoniadis, A.; Andriopoulos, P.; Spyrou, N-I.; Nikolopoulos, E. Unmanned aerial systems-aided post-flood peak discharge estimation in ephemeral streams. Journal of Remote Sensing. 2020, 12, 24, 4183. https://doi.org/10.3390/rs12244183

Boudou, M. Approche multidisciplinaire pour la caractérisation d'inondations remarquables: Enseignements tirés de neuf évènements en France (1910-2010). Environnement et Société. Université Paul-Valéry Montpellier III 2016.

Boudou, M.; Lang, M.; Vinet, F.; Coeur, D. Comparative hazard analysis of processes leading to remarkable flash floods (France, 1930–1999). J. Hydrol. 2016, 541, 533–552. https://doi.org/10.1016/j.jhydrol.2016.05.032

Calianno, M.; Ruin, I.; Gourley, J.J. Supplementing flash flood reports with impact classifications. J. Hydrol. 2013, 477, 1–16. https://doi.

org/10.1016/j.jhydrol.2012.09.036

Diakakis, M;Andreadakis, E.; Nikolopoulos, E.I.; Spyrou, N.I., Gogou, M.E.; Deligiannakis, G.; Katsetsiadou, N.K.;Antoniadia, Z.; Melaki, M.; Georgakopoulos, A.; Tsaprouni, K.; kalogiros, J.; Lekkas, E. An integrated approach of ground and aerial observations in flash flood disaster investigations. The case of the 2017 Mandra flash flood in Greece. International Journal of Disaster Risk Reduction, Elsevier 2019, 33, 290-309. https://doi.org/10.1016/j.ijdrr.2018.10.015

Diakakis, M.; Deligiannakis, G.; Antoniadis, Z.; Melaki, M.; Katsetsiadou, N.K.; Andreadakis, E.; Spyrou, N.I., Gogou, M. Proposal of a flash flood impact severity scale for the classification and mapping of flash flood impacts. Journal of Hydrology 2020, 590, 125452, ISSN 0022-1694. https://doi.org/10.1016/j.jhydrol.2020.125452

Gourley, J.J.; Hong, Y.; Flamig, Z.L.; Arthur, A.; Clark, R.; Calianno, M.; Ruin, I.; Ortel, T.; Wieczorek, M.E.; Kirstetter, P.E.; Clark, E.; Krajewski, W.F. A unified flash flood database across the United States. Bull. Am. Meteorol. Soc. 2013, 94, 799–805. https://doi.org/10.1175/BAMS-D-12-00198.1

Lekkas, E.; Spyrou, N.I.; Kotsi, E.; Filis, C.; Diakakis, M.; Cartalis, C.; Vassilakis, E.; Mavrakou, T.; Sartabakos, P.; Gogou, G.; Katsetsiadou, K.N.; Barsaki, V.; Lagouvardos, K.; Kotroni, V.; Karagiannidis, A.; Dafnis, S.; Parcharidis, I.; Karavias, A.; Bafi, D.; Gougoustamos, I. (2020). The August 9, 2020 Evia (Central Greece) Flood. Preliminary Report: National and Kapodistrian University of Athens 2020, ISSN 2653-9454. https://edcm.edu.gr/images/docs/newsletters/Newsletter_19_2020_Evia_flood.pdf.

Marchi, L.; Borga, M.; Preciso, E.; Gaume; E. Characterisation of selected extreme flash floods in Europe and implications for flood risk management. J. Hydrol. 2010, 394, 118–133. https://doi.org/10.1016/j.jhydrol.2010.07.017

Mavroulis, S.; Mavrouli, M.; Lekkas, E. Geological and hydrometeorological hazards and related disasters amid COVID-19 pandemic in Greece: Post-disaster trends and factors affecting the COVID-19 evolution in affected areas. Safety Science 2021, 138, 105236. ISSN 0925-7535. https://doi.org/10.1016/j.ssci.2021.105236

Meteo, n.d. Available online: https://www.meteo.gr/gmap.cfm (last accessed on 12 December 2024).

Merz, B.; Kreibich, H.; Schwarze, R.; Thieken, A. Review article “assessment of economic flood damage”. Nat. Hazards Earth Syst. Sci. 2010, 10, 1697–1724. https://doi.org/10.5194/nhess-10-1697-2010

Merz, B.; Kreibich, H.; Schwarze, R.; Thieken, A. Review article “assessment of economic flood damage”. Nat. Hazards Earth Syst. Sci. 2010, 10, 1697–1724. https://doi.org/10.5194/nhess-10-1697-2010

Musson, R.; Cecić, I. Intensity and Intensity Scales, in: Bormann, P. (Ed.). New Manual of Seismological Observatory Practice 2. IASPEI, GFZ German Research Centre for Geosciences, Potsdam 2012, 1–41. https://doi.org/10.2312/GFZ.NMSOP-2

Hellenic Statistical Authority (HAS), 2021. Available online: https://unece.org/fileadmin/DAM/stats/documents/ece/ces/ge.41/2000/files/Greece/Presentation%20of%20the%20census%202001.pdf (last accessed on 12 December 2024).

Petersen, M.S. Impacts of Flash Floods. In: Gruntfest, E., Handmer, J. (eds) Coping with Flash Floods. NATO Science Series, Springer 2001, 77. https://doi.org/10.1007/978-94-010-0918-8_2

Spyrou, N.I.; Stanota, E.S.; Diakakis, M.; Andreadakis, E.; Lekkas, E.; Vassilakis, E. Estimation of Flow Velocity During Flash Floods with the synergy of Unmanned Aerial Systems (UAS) data and Ground Observations: The Case of 2017 Mandra Flash Flood, Greece. EGU 2020 International Conference 4-8 May, Vienna 2020. https://doi.org/10.5194/egusphere-egu2020-17845

Spyrou, N. I., Diakakis, M., Mavroulis, S., Deligiannakis, G., Andreadakis, E., Filis, C., Kotsi, E., Antoniadis, Z., Melaki, M., Gogou, M., Katsetsiadou, K.-N., Stanota, E.-S., Skourtsos, E., Vassilakis, E., & Lekkas, E. (2025). Integrating Ground and UAV Mapping for GIS-Based Application of the Flash Flood Impact Severity Scale (FFISS) for the 2009 and 2020 Evia (Greece) Flash Floods. Applied Sciences, 15(3), 1100. https://doi.org/10.3390/app15031100

Schroeder, A.J.; Gourley, J.J.; Hardy, J.; Henderson, J.J.; Parhi, P.; Rahmani, V.; Reed, K.A.; Schumacher, R.S.; Smith, B.K.; Taraldsen, M.J. The development of a flash flood severity index. J. Hydrol. 2016, 541, 523–532. https://doi.org/10.1016/j. jhydrol.2016.04.005

Sîli, N.; Apostu, I.; Faur, F. Floods and their effects on agricultural productivity. Research Journal of Agricultural Science 2020, 52, 4.

Meteo, n.d. Available online: https://www.meteo.gr/gmap.cfm (last accessed on 12 December 2024).

17th INTERNATIONAL CONGRESS of the Geological Society of Greece

BULLETIN OF THE GEOLOGICAL SOCIETY OF GREECE, SP. PUBL.

EXTENDED ABSTRACT 297

Evaluating Airborne LiDAR and RGB Imagery for Accurate Shoreline Detection

Panagiotis Stamatis[1*], Michaela Doukari[1], Kostas Topouzelis[1]

(1) Department of Marine Sciences, School of the Environment, University of the Aegean, University Hill, 81100 Mytilene, Greece.

** Correspondence: p.stamatis@aegean.gr*

Abstract

Understanding and monitoring shoreline changes is critical for effective coastal zone management, particularly in regions experiencing dynamic erosion and accretion. This study evaluates the effectiveness of airborne LiDAR and RGB imagery acquired via Unmanned Aerial Systems (UAS) for accurate shoreline detection, focusing on Gavathas Beach, Lesvos Island, Greece. Both technologies were utilized to generate high-resolution Digital Elevation Models (DEMs) and orthophotographs, enabling precise delineation of the shoreline. The LiDAR data, collected using the YellowScan VX-15 system mounted on a DJI Matrice 600 Pro, provided dense 3D point clouds with centimeter-level accuracy. Simultaneously, RGB imagery was captured using a Sony Alpha 6000 camera synchronized with the LiDAR system. The RGB-derived orthophotographs facilitated visual interpretation and supported the identification of shoreline features under varying environmental conditions.

Digital Shoreline Analysis System (DSAS) was employed to quantify shoreline changes by comparing the extracted shorelines with reference data collected using a Differential GPS (DGPS) system. The results demonstrated that LiDAR-derived shorelines exhibited superior accuracy, with mean deviations of less than 0.5 meters from the reference data. RGB-derived shorelines showed slightly higher deviations due to challenges in image contrast and environmental lighting conditions but remained within acceptable thresholds for practical applications. This comparative analysis highlights the potential of integrating airborne LiDAR and RGB imagery for efficient and reliable shoreline mapping. The findings emphasize the advantages of LiDAR for its high spatial resolution and robust performance in complex coastal environments, while RGB imagery offers a cost-effective and operationally flexible alternative for areas with clear land-water boundaries. These insights contribute to the optimization of coastal monitoring practices and inform future applications of remote sensing technologies in shoreline management.

Keywords: LiDAR, UAV, 3D point cloud, Erosion, Remote Sensing

Introduction

Coastline mapping is an essential practice for understanding and managing coastal dynamics. Coastal zones worldwide are subject to significant changes due to natural and anthropogenic factors, including sediment transport, sea-level rise, and human intervention (Boak and Turner 2005). Monitoring these changes is critical for mitigating the risks associated with coastal erosion, flooding, and habitat loss (Klemas 2011). Traditional methods of monitoring, such as aerial photography and satellite imagery, have provided valuable insights into large-scale patterns but often lack the spatial resolution required for detailed shoreline mapping (Ford 2013; Kaichang Di, Jue Wang, Ruijin Ma et al. 2003). Measurement sensors deployed along coastlines, such as geodetic instruments and soil pressure gauges, also offer systematic data but are constrained by limited coverage and resource-intensive operations (El-Raey et al. 1999).

Over recent decades, advancements in remote sensing technologies have transformed coastal monitoring practices. Unmanned Aerial Systems (UAS) equipped with LiDAR sensors and RGB cameras now enable high-resolution, cost-effective data collection in dynamic and inaccessible coastal environments. Airborne LiDAR, in particular, is recognized for its ability to produce detailed Digital Elevation Models (DEMs) with high vertical and horizontal accuracy, making it an indispensable tool for analyzing complex topographies (Fiedler et al. 2021; Wozencraft and Millar 2005). For example, Wozencraft and Millar (2005) emphasized the critical role of LiDAR in capturing high-resolution elevation data for developing accurate DEMs, which significantly enhance shoreline delineation and coastal management practices.

Complementary to LiDAR, RGB imagery offers a more affordable and operationally flexible approach to shoreline mapping, particularly in areas with clear visual contrast between land and water. Gómez-Gutiérrez et al. (2024) demonstrated the effectiveness of combining RGB photogrammetry with LiDAR to generate accurate 3D models, even in the absence of ground control points (GCPs) (Lin et al. 2019). This integration highlights the growing potential of combining LiDAR and RGB technologies for coastal applications, as it balances precision and cost-efficiency.

In this study, we leverage the capabilities of airborne LiDAR and RGB imagery to evaluate their performance in shoreline mapping at Gavathas Beach, Lesvos Island, Greece. This site, characterized by its diverse coastal features—including sandy beaches, rocky outcrops, and vegetated dunes—offers a robust testing ground for these technologies. By employing Differential GPS (DGPS) as ground-truth data, we assess the accuracy of LiDAR- and RGB-derived shorelines and provide a comparative analysis of their strengths and limitations. The findings aim to contribute to the optimization of remote sensing methods for coastal monitoring and to inform sustainable coastal management strategies.

Materials and Methods

Study Area

The study area is Gavathas Beach, situated on the northwest coast of Lesvos Island, Greece. This location was selected for its diverse coastal morphology, characterized by a gently sloping sandy shoreline bordered by rocky outcrops and vegetated dunes. Gavathas Beach experiences minimal tidal variation, with a microtidal range typically less than 0.5 meters, providing stable conditions for data collection. The wave energy is generally low to moderate, influenced by the northwest orientation of the beach, which shelters it from prevailing winds and swells. This relatively undisturbed environment, with limited human activity, was ideal for uninterrupted data collection and minimized interference with the deployed equipment. The study focused on a 200-meter segment of the eastern beach, where the combination of sandy and rocky sections offered a valuable testing ground for evaluating the performance of airborne LiDAR and RGB imagery in shoreline mapping. The data collection was conducted on June 8, 2023, under clear skies and light winds, ensuring optimal conditions for aerial surveys.

Field data

The data collection process involved the coordinated use of airborne LiDAR and RGB imagery systems. A DJI Matrice 600 Pro Unmanned Aerial System (UAS) was employed as the platform for both sensors. The YellowScan VX-15 LiDAR system was mounted on the UAS to capture high-resolution 3D point clouds, providing detailed elevation data with centimeter-level accuracy. This system integrates a LiDAR sensor with advanced GNSS and IMU systems, ensuring precise georeferencing of the collected data. The TopCON Hiper VR GNSS system was utilized to achieve precise georeferencing and real-time measurement capabilities. Supporting multiple GNSS constellations (GPS, GLONASS, Galileo, BeiDou), it provided exceptional accuracy, reaching up to 8 mm in horizontal and 15 mm in vertical measurements under optimal conditions. This system ensured the reliable alignment of the airborne LiDAR data. Ground control points (GCPs) were established using the Hiper VR rover, which also measured the reference coastline for subsequent shoreline change analysis. Simultaneously, a Sony Alpha 6000 camera was mounted and synchronized with the LiDAR system to capture high-resolution RGB imagery. The camera underwent professional calibration to ensure optimal alignment with the LiDAR system, enabling seamless integration of image and elevation data during post-processing. The RGB images were used to create orthophotographs, which provided additional context for shoreline delineation. The data acquisition was conducted early in the morning to ensure stable environmental conditions and minimize potential disturbances. Ground control points (GCPs) were established using a Differential GPS (DGPS) system to provide accurate georeferencing for both LiDAR and RGB datasets. The UAV followed a pre-programmed flight path, capturing overlapping data to ensure complete coverage of the study area. This coordinated approach ensured the collection of high-quality datasets for subsequent analysis of shoreline changes.

Methodological framework

The methodological framework for this study integrates data acquisition, processing, and analysis to evaluate the accuracy of shoreline delineation using airborne LiDAR and RGB imagery, as shown in **figure 1**. The workflow began with field data collection, as described above, followed by pre-processing of the datasets. LiDAR data were first georeferenced and processed using Applanix's POSPac Mobile Mapping Suite to correct trajectory data and align the LiDAR point clouds accurately. The refined point clouds were imported into YellowScan's CloudStation software for visualization, noise filtering, and delineation of the study area. Key processes included the removal of redundant points, outliers, and the selection of the region of interest for analysis. The data were then exported in LAS format for compatibility with GIS software and further processing. The RGB imagery underwent a structured photogrammetric workflow using Agisoft Metashape. The process started with image alignment, where overlapping images were analyzed to generate a sparse point cloud. This was followed by the creation of a dense point cloud, which provided high-resolution 3D spatial data. An orthophotograph was subsequently generated, ensuring accurate representation of the study area. Ground control points were used to enhance the spatial accuracy of the outputs, and the resulting orthophotographs were exported in GeoTIFF format for integration into GIS platforms.

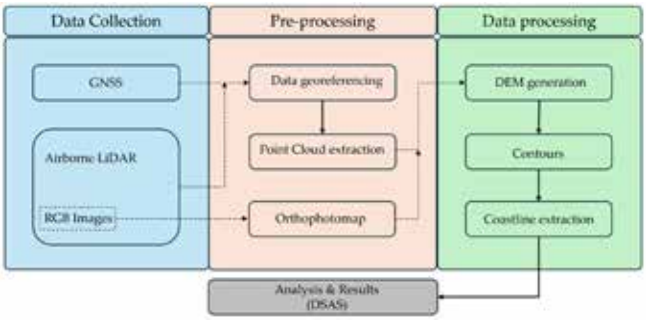

Figure 1. Methodology flowchart.

The data processing workflow involved generating high-resolution Digital Elevation Models (DEMs), extracting elevation contours, and analyzing shoreline changes using the Digital Shoreline Analysis System (DSAS). Initially, LAS files derived from LiDAR pre-processing were imported into ArcGIS Pro for further analysis. These georeferenced point clouds were visualized using the LAS Dataset Layer tool, enabling a detailed overlay of elevation data on basemaps of the study area. The creation of DEMs utilized the LAS Dataset to Raster tool in ArcGIS Pro, which transformed the elevation points into a continuous raster format. The interpolation method was configured to Binning (Natural Neighbor), and a cell size of 0.5 meters was selected to balance high resolution with computational efficiency. The Z-values from the LAS files represented elevation data, and the resulting raster was exported as a GeoTIFF file, capturing the intricate topography of the coastal zone. From these DEMs, elevation contours were extracted using the Contour tool in ArcGIS Pro. Contours provided a vectorized representation of elevation data, simplifying the interpretation of topographic variations. The contour interval was set to 0.5 meters, reflecting fine-scale changes in coastal morphology, and the base contour value was aligned with the minimum elevation within the DEM. The resulting contours were saved in ESRI Shapefile format, ensuring compatibility with spatial analysis tools. These contours served as a critical reference for shoreline delineation by identifying the contour line closest to the mean sea level (MSL). The integration of DEMs and contours enabled a comprehensive examination of the coastal environment, providing precise inputs for shoreline extraction and subsequent DSAS analysis. This systematic approach ensured that the spatial data maintained high accuracy and reliability, supporting detailed assessments of coastal dynamics and morphological changes.
The Digital Shoreline Analysis System (DSAS) was utilized within ArcGIS to quantify shoreline changes and assess accuracy. Baselines were manually digitized landward of the shorelines to serve as references. Transects were generated perpendicular to the baselines at regular intervals to measure deviations between LiDAR, RGB-derived shorelines, and the DGPS reference data. Metrics such as Net Shoreline Movement (NSM) and End Point Rate (EPR) were computed to evaluate temporal and spatial changes. Visual outputs, including charts and maps, were created to illustrate deviations and shoreline dynamics.

Results

For the evaluation of different mapping technologies, this study utilized data from airborne LiDAR and RGB imagery, which were processed to generate high-resolution Digital Elevation Models (DEMs) and elevation contours. These data were georeferenced using a GNSS base station, a GPS rover, and ground control points strategically placed within the study area to ensure accuracy. Additionally, on the day of data acquisition, the shoreline was recorded using DGPS as a reference line, serving as the benchmark for validating results from the airborne sensors. Table 1 summarizes the detected shorelines from DGPS, RGB imagery, and airborne LiDAR, focusing on their ability to delineate features such as the Instantaneous Shoreline, Intermediate Shoreline, and Wave Runup.

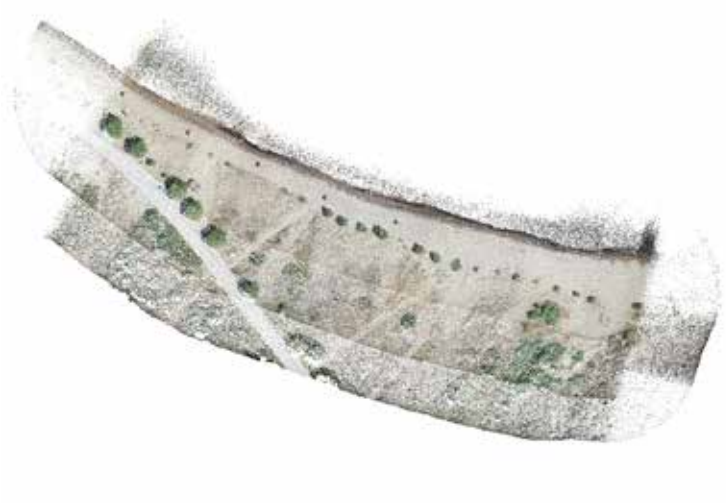

Figure 2. Results of airborne LiDAR: Colorized point cloud.

Airborne LiDAR showcased outstanding capability in shoreline mapping, delivering high spatial resolution and accuracy across extensive coastal areas. The method excelled in identifying key shoreline features, including the instantaneous shoreline, wave runup, and intermediate shoreline, with minimal deviations. Its deployment on a UAV platform enabled rapid data acquisition with consistent coverage, even in complex and dynamic coastal environments. The coastline derived from LiDAR data demonstrated

a mean deviation of just 0.5 meters when compared to the DGPS reference, emphasizing its precision. Moreover, the wave runup and intermediate shoreline were accurately captured, reflecting the system's ability to resolve fine-scale topographic variations. **Figure 2** highlights the outcomes of LiDAR data processing, showcasing the raw point cloud colored with aerial RGB imagery and **figure 3** shows the corresponding Digital Elevation Model (DEM) with extracted contours on the right, which were used to delineate the final shoreline.

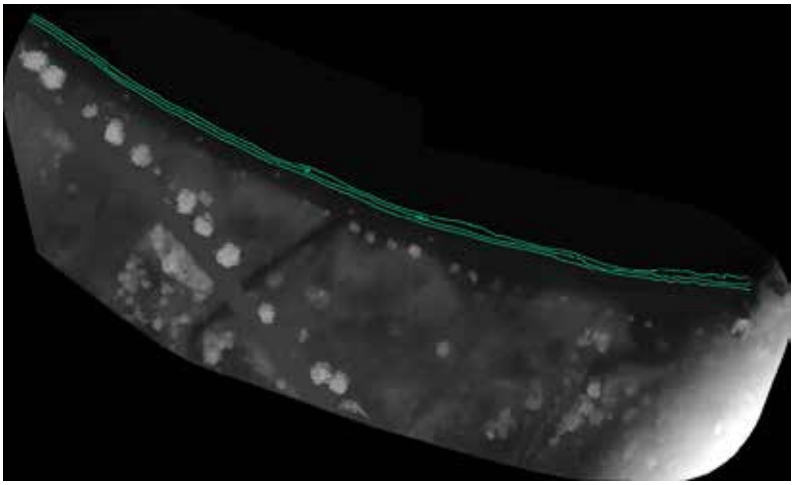

Figure 3. Results of airborne LiDAR: Digital Elevation Model (DEM) and elevation contours.

The RGB imagery captured by the mounted Sony Alpha 6000 camera on the UAV proved effective in generating a high-resolution orthophotomap, providing a visual reference for shoreline extraction, as shown in **figure 4**. However, this method was more prone to errors influenced by lighting conditions and image contrast. The approach performed best in areas with distinct land-water boundaries, where photogrammetric techniques delivered accurate results. Nevertheless, the shoreline derived from the RGB orthophotomap exhibited a larger deviation from the DGPS reference, with a mean offset of approximately 1.5 meters. This discrepancy was primarily attributed to difficulties in identifying clear shoreline boundaries in regions with low contrast. **Figure 5** presents the Digital Elevation Model (DEM) and the extracted elevation contours are shown, which were employed for precise coastline delineation.

Figure 4. RGB imagery results: Orthophotomap.

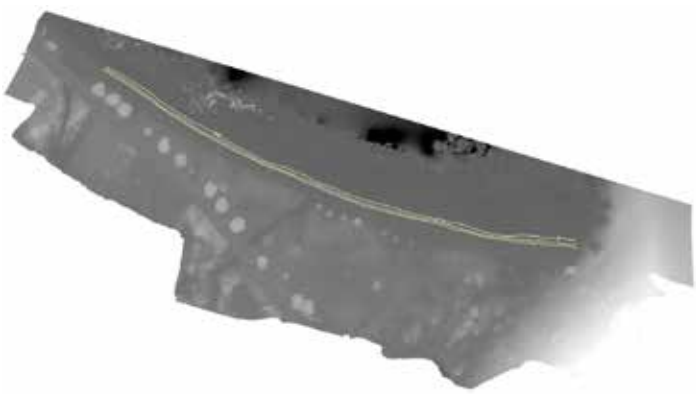

Figure 5. RGB imagery results: Digital Elevation Model (DEM) and elevation contours.

The analysis results demonstrate that airborne LiDAR provides superior accuracy and precision in delineating coastal features compared to the RGB imagery. LiDAR data achieved a mean deviation of only 0.5 meters from the DGPS reference coastline, showcasing its exceptional capability in capturing fine-scale topographic details. This accuracy is particularly evident in the identification of critical shoreline features, such as the instantaneous shoreline, wave runup, and intermediate shoreline. The ability of the LiDAR system to generate high-resolution Digital Elevation Models (DEMs) and extract detailed elevation contours further highlights its effectiveness in coastal monitoring. In contrast, the RGB-derived orthophotomap, while offering valuable visual context, exhibited a larger deviation from the DGPS reference. The mean offset of approximately 1.5 meters was primarily attributed to limitations in photogrammetric processing, especially in areas with low contrast or ambiguous land-water boundaries.

These challenges were particularly evident in vegetated or shadowed regions, where the RGB imagery struggled to distinguish the shoreline accurately. Despite these limitations, the RGB orthophotomap proved to be a cost-effective and operationally flexible alternative for areas with well-defined shoreline features. In **figure 6**, we can observe the coastlines detected using the RGB sensor (on the left) and airborne LiDAR (on the right).

Figure 6. Results of coastline detection: (Left) Coastlines from Orthophotomap; (Right) Coastlines from airborne LiDAR.

The DSAS analysis revealed consistent trends between the LiDAR and RGB-derived shorelines, with LiDAR consistently outperforming RGB in terms of accuracy. The transects generated across the study area showed that the maximum deviation between the LiDAR and RGB-derived shorelines reached up to 2.1 meters in areas with complex coastal features, such as rocky outcrops or densely vegetated dunes. However, in regions with clear visual contrast between land and water, the RGB orthophotomap aligned closely with the LiDAR data, demonstrating its potential for efficient shoreline mapping in less challenging environments. **Figure 7** illustrates the results of the DSAS analysis. The baseline and transects used for measuring deviations between the LiDAR- and RGB-derived shorelines are displayed, providing an overview of the study area. **Figure 8** demonstrates a close-up section that highlights the alignment of the shorelines, clearly showing the areas where deviations are most pronounced. The LiDAR data precision in capturing subtle elevation changes is evident in its ability to detect features such as the wave runup and intermediate shoreline, which are less distinct in the RGB-derived data.

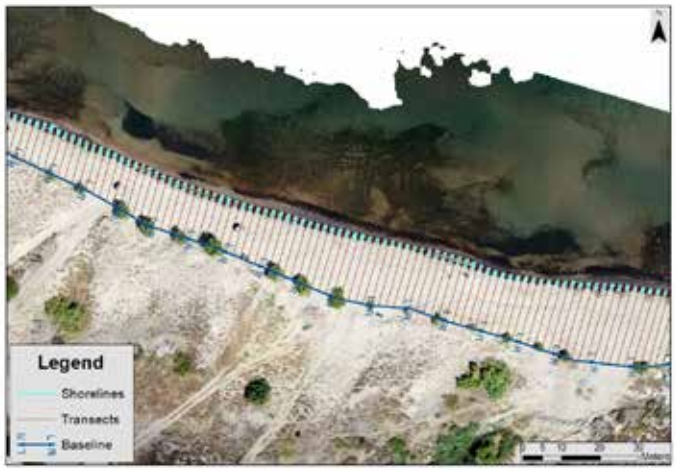

Figure 7. Results of the DSAS analysis: The entire study area, showing the baseline, transects, and shorelines.

In addition to accuracy, the efficiency of data collection and processing was another significant advantage of the airborne LiDAR system. The LiDAR system required only 7 minutes of flight time and approximately 30 minutes of preparation to complete the survey, compared to the longer photogrammetric processing time required for the RGB data. Moreover, LiDAR's elevated perspective and dense point cloud generation minimized the influence of environmental factors, such as lighting conditions or vegetation movement, which significantly impacted the RGB results.

Figure 8. Results of the DSAS analysis: A portion of the study area, highlighting the difference between the shorelines.

While both methods have their strengths, the comparative analysis underscores the superior performance of airborne LiDAR in terms of accuracy, efficiency, and versatility. However, the RGB orthophotomap remains a valuable tool for providing supplementary visual information and serves as a practical alternative for mapping in areas where LiDAR deployment may be constrained by budget or logistical challenges. These findings contribute to the ongoing development of integrated approaches for coastal monitoring, combining the strengths of both technologies to optimize shoreline detection and analysis.

Conclusions

The outcomes of this study confirm the efficacy and unique characteristics of airborne LiDAR and RGB imaging in coastal mapping applications. Airborne LiDAR demonstrated unparalleled accuracy and spatial coverage, closely aligning with the reference coastline captured via DGPS. Its ability to precisely capture dynamic shoreline features, such as the instantaneous shoreline, wave runup, and intermediate shoreline, highlights its suitability for complex coastal environments. The dense 3D point clouds generated by the LiDAR system enabled the creation of high-resolution Digital Elevation Models (DEMs) and detailed elevation contours, which are essential for understanding subtle topographic variations and monitoring morphological changes over time.

In contrast, RGB imaging, while a cost-effective and flexible alternative, exhibited greater sensitivity to environmental factors, including lighting conditions and surface contrast. These challenges resulted in slightly lower precision, with deviations from the reference coastline averaging 1.5 meters. Nevertheless, RGB orthophotomaps provided valuable visual context, particularly in areas with distinct land-water boundaries, and offered an operationally efficient method for shoreline delineation in less dynamic environments.

This comparative analysis underscores the importance of selecting the appropriate technology based on specific project needs. Airborne LiDAR excels in applications requiring high accuracy, extensive spatial coverage, and the ability to capture fine-scale details in dynamic coastal settings. Meanwhile, RGB imaging serves as a practical alternative for budget-constrained projects or areas where logistical challenges limit the deployment of LiDAR systems.

The integration of Differential GPS (DGPS) data as ground truth further validated the performance of both methods, providing a reliable benchmark for assessing their accuracy. Additionally, the use of the Digital Shoreline Analysis System (DSAS) enabled a comprehensive evaluation of shoreline changes, quantifying spatial discrepancies and providing insights into the dynamic processes shaping coastal environments. The ability to combine LiDAR and RGB data into an integrated analysis framework enhances our understanding of shoreline dynamics and supports the development of more robust coastal monitoring practices.

The broader implications of this research highlight the growing need for innovative and hybrid approaches to coastal management. As demonstrated, the complementary strengths of airborne LiDAR and RGB imaging can significantly improve the precision and reliability of coastal assessments. By leveraging these technologies in tandem, researchers and policymakers can better address the challenges posed by coastal erosion, sea-level rise, and other environmental changes.

This study contributes to the advancement of coastal monitoring methodologies by offering a detailed comparative framework for evaluating remote sensing technologies. The findings emphasize the importance of tailoring the choice of technology to the specific requirements of each project, ensuring the optimal balance between accuracy, cost, and operational feasibility. As environmental changes accelerate, integrating cutting-edge remote sensing tools will be crucial for sustainable coastal development and the implementation of effective erosion mitigation strategies.

Acknowledgments: We would like to express our gratitude to Professor Christos-Nikolaos Anagnostopoulos from the Department of Cultural Technology and Communication at the University of the Aegean for providing the Terrestrial Laser Scanner (TLS) used in this study. We also extend our thanks to the team from the Cartography & Geoinformatics Laboratory at the Department of Geography, University of the Aegean,

for their valuable assistance in the TLS data collection process. Special thanks go to Argyris Moustakas and Apostolos Papakonstantinou for their significant contributions during the fieldwork operations.

References

Boak, Elizabeth H., and Ian L. Turner. 2005. "Shoreline Definition and Detection: A Review." Journal of Coastal Research 21(4): 688–703.

El-Raey, M., S. H. Sharaf El-Din, A. A. Khafagy, and A. I. Abozed. 1999. "Remote Sensing of Beach Erosion /Accretion Patterns along Damietta-Port Said Shoreline, Egypt." International Journal of Remote Sensing 20(6): 1087–1106.

Fiedler, Julia W. et al. 2021. "Enhanced Surf Zone and Wave Runup Observations with Hovering Drone-Mounted Lidar." Journal of Atmospheric and Oceanic Technology 38(11): 1967–78.

Ford, Murray. 2013. "Shoreline Changes Interpreted from Multi-Temporal Aerial Photographs and High Resolution Satellite Images: Wotje Atoll, Marshall Islands." Remote Sensing of Environment 135: 130–40.

Kaichang Di, Jue Wang, Ruijin Ma, Ron Li et al. 2003. "Automatic Shoreline Extraction from Highresolution IKONOS Satellite Imagery." ASPRS 2003 Annual Conference Proceedings 130(May): 1–4.

Klemas, Victor. 2011. "Remote Sensing Techniques for Studying Coastal Ecosystems: An Overview." Journal of Coastal Research 27(1): 2–17.

Lin, Yi Chun et al. 2019. "Evaluation of UAV LiDAR for Mapping Coastal Environments." Remote Sensing 11(24): 1–32.

Wozencraft, Jennifer, and David Millar. 2005. "Airborne Lidar and Integrated Technologies for Coastal Mapping and Nautical Charting." Marine Technology Society Journal 39(3): 27–35.

17th INTERNATIONAL CONGRESS of the Geological Society of Greece

BULLETIN OF THE GEOLOGICAL SOCIETY OF GREECE, SP. PUBL.

EXTENDED ABSTRACT 298

Domestic Rainwater Harvesting Tanks´ Sizing under Climate Change Conditions in Nisyros Island

Stavropoulos T., Feloni E.
Department of Surveying and Geoinformatics Engineering, University of West Attica, 28 Ag. Spiridonos, 12243 Egaleo, Athens, Greece; tstavropoulos@uniwa.gr; efeloni@uniwa.gr

Introduction

The Mediterranean region has long been recognized as a climate change hotspot by numerous studies and researchers (e.g., Giorgi, 2006; Zittis et al., 2022). Arid and semi-arid areas, such as the Greek islands (Pnevmatikos and Katsoulis, 2006), face heightened challenges due to their unique climatic conditions (Köppen, 1936), which make them particularly susceptible to extreme heat, droughts, and water scarcity. Additionally, the growing influx of tourists, even on smaller islands like those in the Aegean Sea, further strains local water resources. This evolving reality underscores the urgent need for stakeholders to implement cost-effective strategies to ensure water security. In this context, the present study examines the performance of a rainwater harvesting system (RWHS) on Nisyros, a small island in the southeastern Aegean Sea, Greece, with a population of 1,048. Nisyros is renowned for its unique geological history and volcanic origin and is currently a candidate for UNESCO Global Geopark designation (Nomikou et al., 2023).

Aligned with Sustainable Development Goals 9 and 11, enhancing resilience in local communities and ensuring sustainable water management solutions are critical for the years ahead (UNDESA, 2024). Rainwater harvesting (RWH) is explored as a viable domestic-scale approach to supplement water needs for non-potable uses, reducing reliance on conventional freshwater sources. RWH is an economically feasible and relatively simple method to implement (Farreny et al., 2011) and has been widely utilized for centuries, dating back to ancient civilizations (Valdez et al., 2016). Depending on the level of treatment, RWHS can provide both potable and non-potable water for household and agricultural applications (Londra et al., 2015).

Methodology

This study employs a daily water balance model to evaluate the efficiency of an urban RWHS (Figure 1) using rooftop collection. The model is designed to determine the optimal rainwater tank dimensions necessary to store the collected rainwater while meeting a targeted percentage of household water demand, excluding drinking water. In this study, the household water consumption was determined to be 150 liters per capita per day. This value represents the average prescribed limits according to Government Gazette Issue B 174/1991, which sets a minimum consumption of 100 liters per day per person and a maximum of 200 liters per day per person. Additionally, according to the official data from ELSTAT (2011), most households consist of 1 to 3 members (Ncap). Therefore, scenarios are applied for Ncap = 1, Ncap = 2, and Ncap = 3.

The simulation tracks the daily water balance in the tank, considering both inflow from rainfall and outflow for domestic use, providing insights into the system's overall efficiency.

Daily rainfall data from the National Meteorological Service station on Nisyros were used for the available period from 2017 to 2023, spanning six hydrological years. This timeframe aligns with the German standard DIN 1989-1 (2002), which recommends a minimum of 5 to 10 years of rainfall data for RWHS dimensioning. The rainfall station was selected based on data availability, completeness, and geographic relevance, ensuring accuracy in tank sizing calculations.

The water balance equation applied in this study is:

$$S_t = S_{t-1} + R_t - D_t, 0 \leq S_{t-1} \leq V_{tank}$$

where: St is the stored volume at the end of t day (m^3); St-1 is the stored volume at the beginning of t day (m^3); Rt is the daily harvested (added) rainwater volume at the end of t day (m^3); Dt is the daily water demand at the end of t day (m^3); and Vtank the capacity of the rainwater harvesting tank (m^3).

To enhance the accuracy of the system's spatial assessment, mapping tools such as ArcGIS and Google Earth Pro were utilized to calculate the available rooftop catchment area of buildings (Durgasrilakshmi et al., 2018). This approach ensures that the estimated collection areas reflect real-world conditions.

Additionally, future climate projections were incorporated to assess RWHS performance under climate change conditions. Two Representative Concentration Pathways (RCPs) were examined: RCP 4.5 (moderate emissions scenario) and RCP 8.5 (high emissions scenario). Future rainfall data for the period 2026–2060 were obtained from the DEAR Clima database (DEAR-Clima-2024).

Three main scenarios were investigated, varying in household size and catchment area:

- A single-person household with a rainwater collection area of 20–120 m².
- A two-person household with a rainwater collection area of 20–120 m².
- A three-person household with a rainwater collection area of 20–120 m².

These scenarios provide a comprehensive evaluation of RWHS effectiveness under different household and climate conditions, offering valuable insights for sustainable water management on Nisyros.

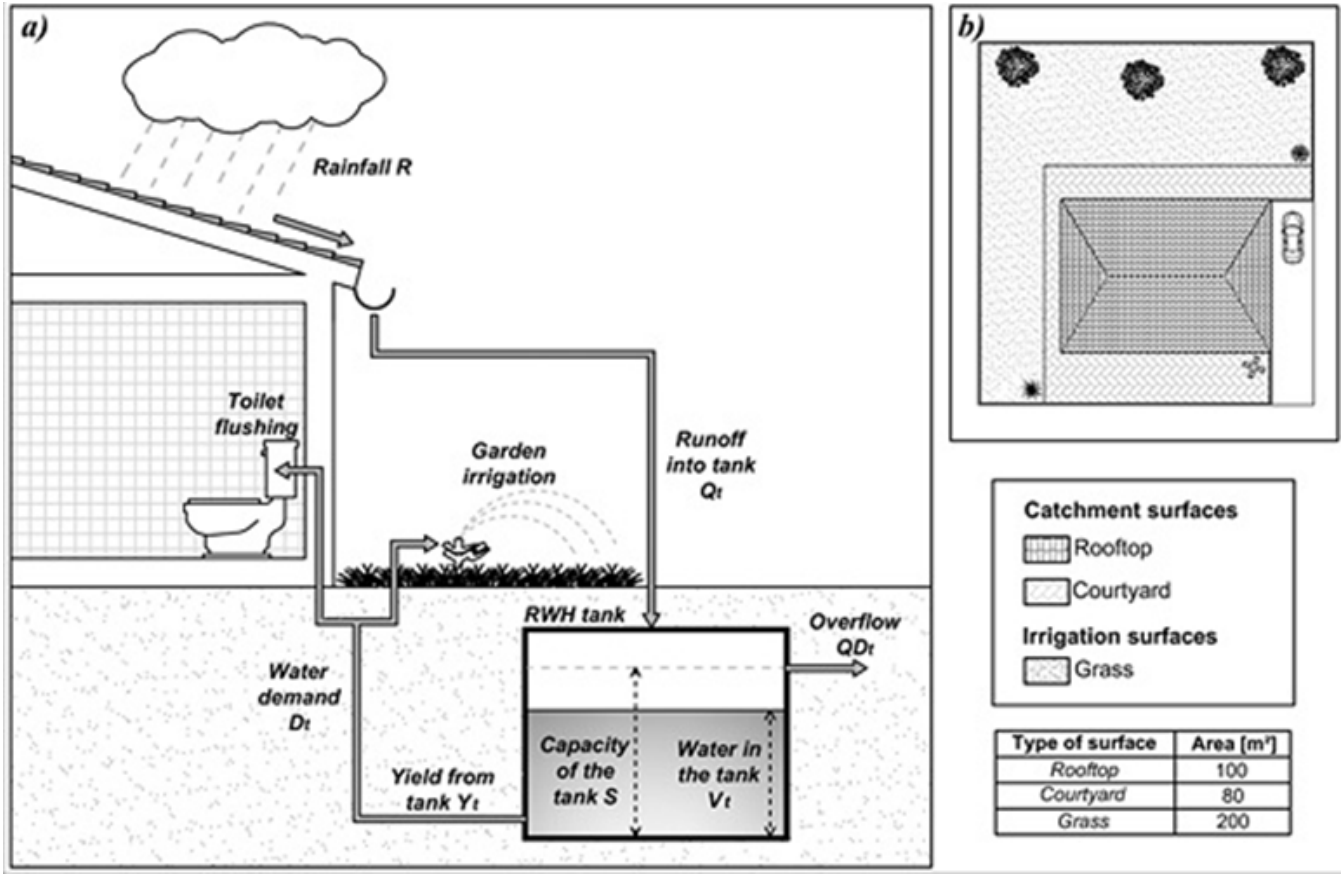

Figure 1: RWHS scheme (Source: Liuzzo et al., 2016)

Results

A. Results for historical timeseries

Figure 2 illustrates the results for the first scenario (single-person household), showing that system reliability ranges from 38% to 100%. The smallest rainwater collection area that ensures 100% reliability is 40m², with a tank capacity of 30m³. Additionally, the smallest tank volume that achieves full reliability is 5m³ when paired with a 60m² collection area. In general, for collection areas between 60 and 120m², the system consistently reaches 100% reliability for a single-person household, with tank volumes (Vtank) varying from 5 to 30m³. Notably, a significant shift in system performance is observed for collection areas between 20 and 40m², while at 20m², full reliability is not attained.

For the second scenario (Figure 3), which considers a two-person household, system reliability ranges from 14% to 100%. Compared to the first scenario, minimum efficiency is notably reduced due to the increased water demand. A sharp transition in system efficiency occurs for collection areas between 20 and 100m². Full reliability is achieved for households with collection areas of 100m² and 120m², with tank capacities between 10 and 30m³. The table below details the combinations of tank volume and collection area that ensure full reliability.

In the third scenario (Figure 4), representing a household with three members, reliability values range from 6% to 82%. Unlike the previous cases, full reliability is not achieved under any configuration. Additionally, a pronounced shift in system reliability is observed across collection areas ranging from 20 to 120m².

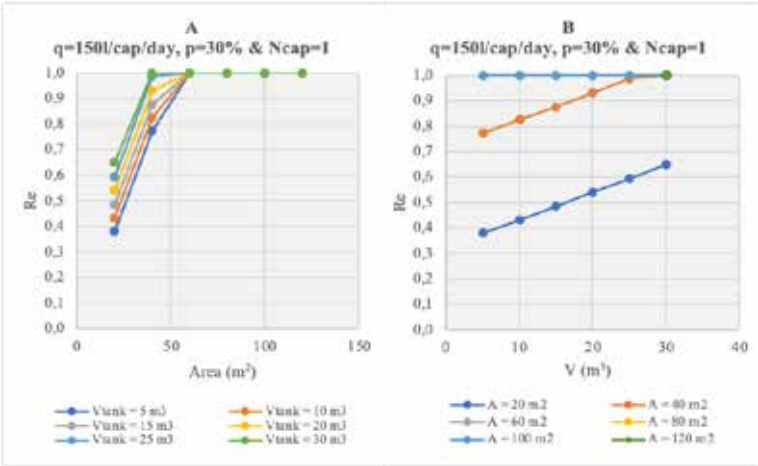

Figure 2. Reliability of demand coverage by the studied rainwater harvesting system for an average daily demand of q=150 l/cap/day, a demand coverage percentage of p=30%, and Ncap=1, with water collection areas ranging from 20 to 120 m². A: Reliability as a function of collection area range. B: Reliability as a function of tank volume.

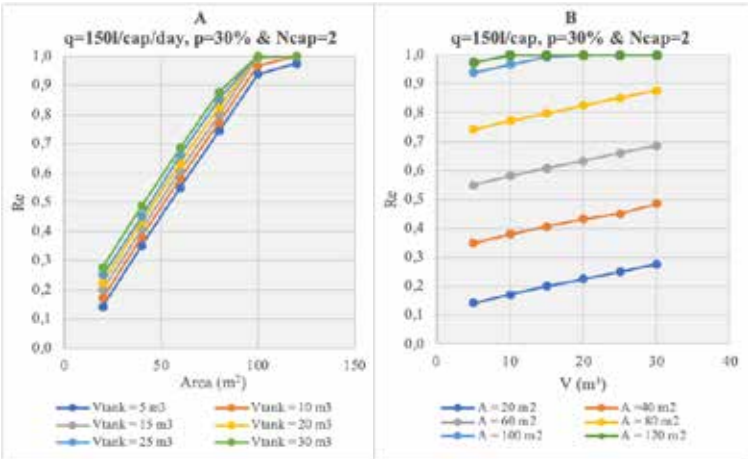

Figure 3. Reliability of demand coverage by the studied rainwater harvesting system for an average daily demand of q=150 l/cap/day, a demand coverage percentage of p=30%, and Ncap=2, with water collection areas ranging from 20 to 120 m². A: Reliability as a function of collection area range. B: Reliability as a function of tank volume.

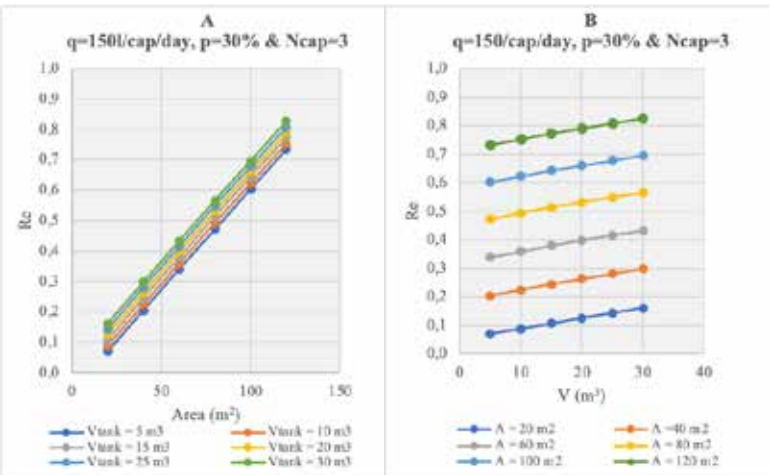

Figure 4. Reliability of demand coverage by the studied rainwater harvesting system for an average daily demand of q=150 l/cap/day, a demand coverage percentage of p=30%, and Ncap=3, with water collection areas ranging from 20 to 120 m². A: Reliability as a function of collection area range. B: Reliability as a function of tank volume.

B. Results for future climatic scenarios

In most scenarios involving a two-person household, the system successfully meets the target of supplying 30% of the total water demand. The water collection area (A) is identified as a critical factor, with smaller collection areas leading to lower reliability. Regarding the rainwater tank volume (Vtank), increasing the storage capacity results in only a marginal improvement in system reliability.

For households with three members, full reliability is achieved in certain cases under the RCP 4.5 climate scenario. However, under the RCP 8.5 scenario, a slight decline in reliability is observed compared to RCP 4.5, which is in accordance with the negative trends of rainfall patterns, indicating a potential impact of future climate conditions on system performance.

Table 1: Combinations of minimum rainwater collection areas and rainwater tank volumes for full system efficiency under the scenario Ncap=2.

	A (m^2)	Vtank (m^3)
Historic Time Series	100	20
RCP 4.5	60	5
RCP 8.5	60	5

Table 2: Combinations of minimum rainwater collection areas and rainwater tank volumes for full system efficiency under the scenario Ncap=3.

	A (m^2)	Vtank (m^3)
Historic Time Series	-	-
RCP 4.5	80	5
RCP 8.5	80	10

Conclusions

The study demonstrated that the reliability of the rainwater harvesting system is highly sensitive to both the collection surface area and tank volume. For the historical rainfall time series (2017–2023), reliability increased with larger collection areas and storage capacities. A single-person household achieved full reliability with a 40m² collection surface and a 30m³ tank, while the smallest volume ensuring 100% reliability was 5m³ with a 60m² surface. In the two-person household scenario, full reliability was reached at 100m² with a 20m³ tank, with the minimum tank volume ensuring complete reliability being 10m³ for a 120m² surface. However, for three-member households, full reliability was not achieved due to higher water demands. Regarding future climate projections (2026–2060), the system generally showed improved reliability under the RCP 4.5 and RCP 8.5 scenarios compared to historical data, except for the SMHI-RCA4_IPSL-IPSL-CM5A-MR dataset, which exhibited lower reliability. The system's reliability appears to improve, likely due to an increase in daily rainfall values within the upper 20% of the distribution, as observed in future scenarios compared to historical data. Most projections also indicate a reduction in wet days, though the duration of the longest drought periods does not appear to be significantly affected. Although RCP 8.5 led to a slight decline in system performance compared to RCP 4.5, it still outperformed the historical series. However, due to the limited timespan of the available historical data, the reliability of these estimates remains uncertain. For two-member households, full reliability was first achieved with a 60m² collection surface and a 5m³ tank in both RCP scenarios, while in the three-person household scenario, full reliability was obtained at 80m² with a 5m³ tank under RCP 4.5 and at 80m² with a 10m³ tank under RCP 8.5. Further research could provide valuable insights by assessing the system's performance under a broader range of climate projections and exploring the relationship between reliability and changing water consumption.

References

Data Extraction Application for Regional Climate (DEAR-Clima); Web Application Tool. Available online: http://meteo3.geo.auth.gr:3838/ (accessed on 5 February 2024).

DIN 1989-1, 2002. Rainwater harvesting systems. German Institute for Standardisation.

Durgasrilakshmi Hari et al., (2018). Assessment of rainwater harvesting potential using GIS. IOP Conf. Ser.: Mater. Sci. Eng.

Farreny, R.; Gabarrell Durany, X.; Rieradevall, J., 2011. Cost-Efficiency of Rainwater Harvesting Strategies in Dense Mediterranean Neighbourhoods. Resour. Conserv. Recycl. 55, 686–694

Giorgi, F. (2006) Climate change hot-spots. Geophysical Research Letters, 33.

Köppen, W. (1936) Das Geographische System der Klimate.In: W. K ¨oppen and R. Geiger (eds), Handbuch derKlimatologie 3. Berlin: Gebrueder Borntaeger, 46 pp

Liuzzo, L.; Notaro, V.; Freni, G. A Reliability, 2016. Analysis of a Rainfall Harvesting System in Southern Italy. Water, 8, 18.

Londra P.A., Theoharis A.T., Baltas E. and Tsihrintzis V.A. (2015), Optimal sizing of sainwater harvesting tanks for domestic use in Greece, Water Resources Management, 29, 4357-4377.

Nomikou, P.; Panousis, D.; Nikoli, E.; Antoniou, V.; Emmanouloudis, D.; Pehlivanides, G.; Agiomavritis, M.; Nastos, P.; Cieslak-Jones, E.; Batis, A., 2023. Nisyros Aspiring UNESCO Global Geopark: Crucial Steps for Promoting the Volcanic Landscape's Unique Geodiversity. Geosciences 2023, 13, 70.

Pnevmatikos, J.D. and Katsoulis, B.D. (2006), The changing rainfall regime in Greece and its impact on climatological means. Met. Apps, 13: 331-345

UNDESA, 2024. The Sustainable Development Goals Report 2024 – June 2024. New York, USA: UN DESA. © UN DESA. https://unstats.un.org/sdgs/report/2024/.

Valdez C.M., Adler I., Barrett M., Ochoa R. and Pérez A. (2016), The water-energy-carbon nexus: optimizing rainwater harvesting in mexico city, Environmental Processes, 3, 307-323.

Zittis, G., Almazroui, M., Alpert, P., Ciais, P., Cramer, W., Dahdal, Y. et al. (2022) Climate change and weather extremes in the Eastern Mediterranean and Middle East. Reviews of Geophysics, 60,

17th INTERNATIONAL CONGRESS of the Geological Society of Greece

BULLETIN OF THE GEOLOGICAL SOCIETY OF GREECE, SP. PUBL.

EXTENDED ABSTRACT 299

Numerical modeling of fault genesis in the Santorini-Amorgos basin: an interplay of tectonic forces and magmatism

M Stavropoulou[1] G. Soukis K,[1] Kranis H.[1] Skourtsos Em.[1] Exadaktylos[2]

(1) National and Kapodistrian University of Athens, Athens, Greece, mstavrop@geol.uoa.gr, (2) National Technical University of Athens, Athens, Greece

Research Highlights

The structure and evolution of the Santorini-Amogos basin can be reproduced by applying a plane-strain numerical model.

The Santorini-Amorgos basin (SE Cycladic plateau) is the stage of a complex interaction between active faulting and magmatism, causing the January- March 2025 swarm-type earthquake sequence.

Introduction

The Aegean Sea (Greece), in its present configuration, was formed as a response to the retreat of the Hellenic subduction zone, a retreat that was accelerated since the Middle Miocene, leading to the exhumation of lower and middle crustal rocks that were previously subducted to great depths (Jolivet and Brun, 2010; Ring et al., 2010). Active faulting is restricted along narrow zones with strike-slip and oblique-normal sense of motion, where shallow-intermediate depth seismicity also manifests (Kokkalas et al., 2006).

The Attic Cycladic Crystalline Complex (ACCC, Figure 1) is one such area where the central part is generally aseismic, and major active faults and earthquake activity are located along the north and especially the southern margin, where the modern volcanic arc has been established since the Pliocene (Pe-Piper and Piper 2002 and references therein; Papanikolaou 2021). At the southeastern margin, the Santorini – Amorgos basin is characterized by NE-SW faults creating a complex horst and graben pattern with sediments exceeding 1000m thickness (Figure 2a-b, Nomikou et al., 2016, 2018; Sakellariou and Tsampouraki 2019; Tsampouraki et al., 2021). From January to March 2025, swarm-type earthquakes of magnitudes in the range 1≤M≤5.2 were recorded, having epicenters at depths mainly from 15 km up to 4 km concentrated along a narrow zone extending offshore Santorini near the Columbo volcanic center towards NE, south of Amorgos island (Figure 2c, seismicity catalog of the National Observatory of Athens available in http://www.gein.noa.gr). Whether this sequence could result just from tectonic forces or the combined effect of tectonic forces and magmatic activity is debated.

In this paper, we investigate the structural evolution of the region by virtue of a numerical model, starting from a pure continuum brittle crust due to combined tectonic forces and magmatism. Given that the studied region of the south Cyclades plateau is a major volcanic center and driven from knowledge of hydraulic fracturing processes in deep reservoirs, we examine the hypothesis that the swarm-type of earthquakes is that of magma injections in chambers or dykes lying along this narrow zone.

Geological Framework

The Hellenides represent a segment of the Alpine-Himalayan orogeny, characterized by the convergence between the Eurasian and African plates since the Jurassic (Jolivet and Brun, 2010; Papanikolaou 2021). The Attic-Cycladic Crystalline Complex (ACCC) in the central Aegean comprises scattered relics of the Upper Cycladic Nappe (UCN), which overlies the Cycladic Blueschist unit (CBU), the Cycladic Basement (CB), and the Basal Unit. The lower units experienced Eocene-Oligocene high-pressure metamorphism and then were exhumed to the surface first synorogenically within the subduction zone and then post-orogenically during the Neogene through low-angle crustal-scale detachment systems (Figure 1), rooting in the brittle-ductile transition, as a result of subduction zone retreat (Jolivet and Brun 2010; Jolivet et al., 2010; Ring et al., 2010; Grasemann et al., 2012). The southeastern part of the Cycladic plateau was exhumed from the top-to-SE Santorini Detachment system (Schneider et al., 2018; Grasemann et al., 2022; Laskari et al., 2024; Roche et al., 2024). High-angle faults that succeeded the low-angle faulting further contributed to the exhumation of the metamorphic rocks since the Pliocene and facilitated the ascent of melts that formed, among others, the Santorini volcanic center with the adjacent Christiana and Columbo volcanoes (Kokkalas et al., 2006; Kokkalas and Aydin 2013). The Santorini – Amorgos Fault Zone comprises NE-SW faults with NW-SE direction of extension and a significant dextral sense of motion in the same area where the 1956 Amorgos >7Mw earthquake took place (Nomikou et al., 2018; Sakellariou and Tsampouraki 2019; Tsampouraki et al., 2021).

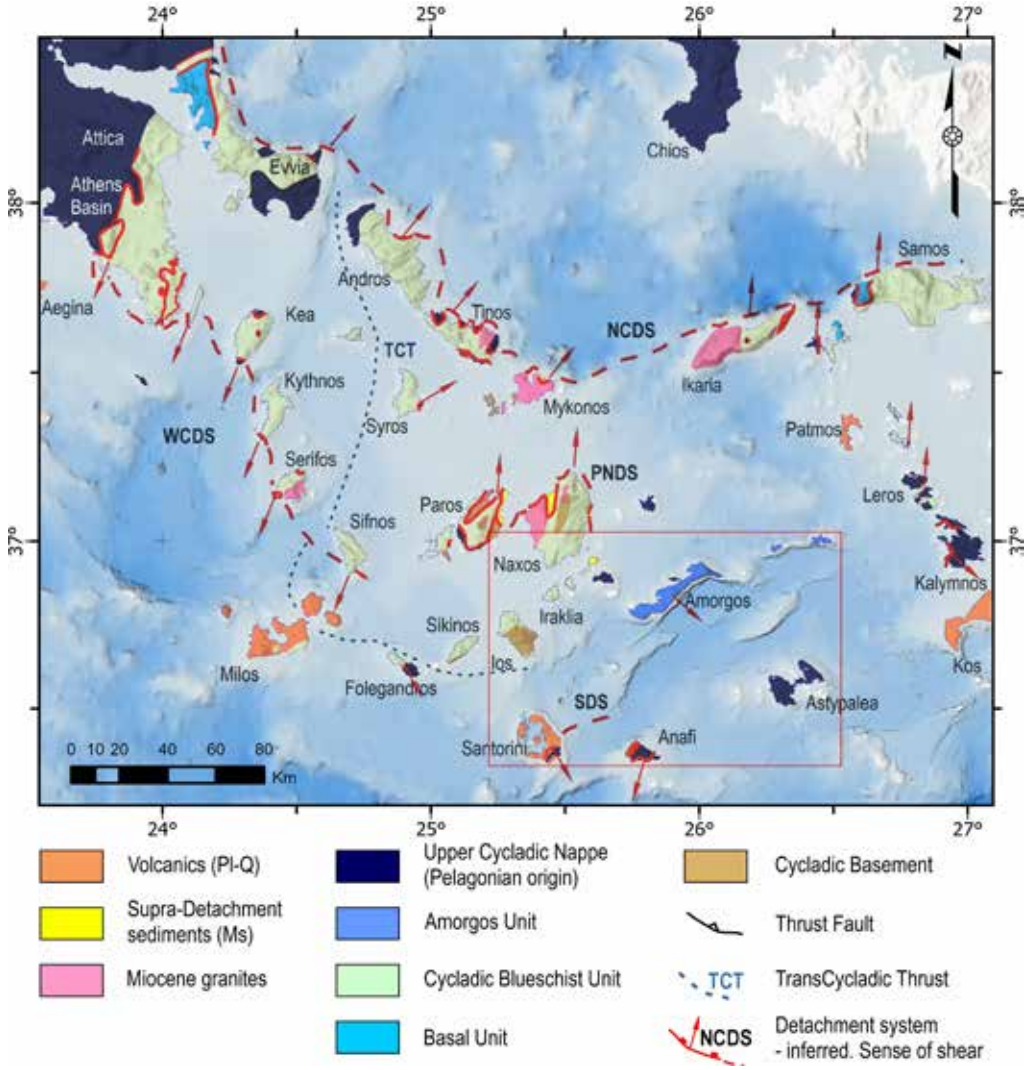

Figure 1. Geotectonic map of the Attic-Cycladic Crystalline Complex (modified after Laskari et al., 2024 and references therein). (Rectangle indicates the study area shown in detail in Figure 2a).

Model Parameters

As mentioned, the first objective is to reproduce the structural features of the Santorini-Amorgos basin associated with the NW-SE extension direction, and the second is to introduce magmatic activity. The sedimentation in the basin is ignored for simplification reasons. To this purpose, a plane strain numerical model corresponding to the NW-SE section of Figure 2a-b was constructed (Figure 3). The model comprises two regions above and below a mechanical decoupling zone 1-2-3 dipping SE (detachment zone) between the upper and the lower crust, corresponding to the brittle-ductile transition for silicate-dominated rocks. The upper region (A) corresponds to the upper crust and is occupied by brittle material, whereas the lower (K) corresponds to the lower crust and is occupied by ductile material. The rock material of the upper crust (A) is modeled as an elastoplastic (e-p) Mohr-Coulomb material, whereas the material of the lower crust (K) is considered a rigid body (r-b).

Simulations were performed with FLAC, a large-strain finite difference software, and an explicit time-marching solution of the full equations of motion (including inertia terms). The finite difference grid is shown in Figure 3. The top surface is stress-free, whereas we assume H_M=10km; thus, the depth of the upper crust at the right end of the model is approximately $2H_M$. Each simulation was conducted in two stages: an initial stage to establish initial equilibrium under the influence of gravitational body forces and boundary restraints, followed by a stage during which the kinematic or static boundary conditions were applied. The extensional loading of the continuum model was simulated by imposing a constant displacement velocity *v* along the right-vertical boundary and the segment 2-3 of the detachment zone.

In the sequel, we assume the formation of a magmatic chamber due to the injection of magma in the weakest region between the two half-grabens between points 1 and 2 of the model. We assume a hemispherical shape of the chamber with the center at the detachment zone and its apex at a depth of 5 km, given that the dip angle of the detachment zone is δ_M=12°. To obtain new shear bands after a few simulation steps, we have applied constant pressure *p/E=1/1000* where E denotes Young's modulus of the upper crust. We do not consider infiltration of magma in the crust; hence, all new cracks are not propagating due to hydraulic fracturing but due to stresses created by the constant applied pressure. This is a reasonable assumption, provided that the viscosity of the fluids is large, and the cracks are tortuous.

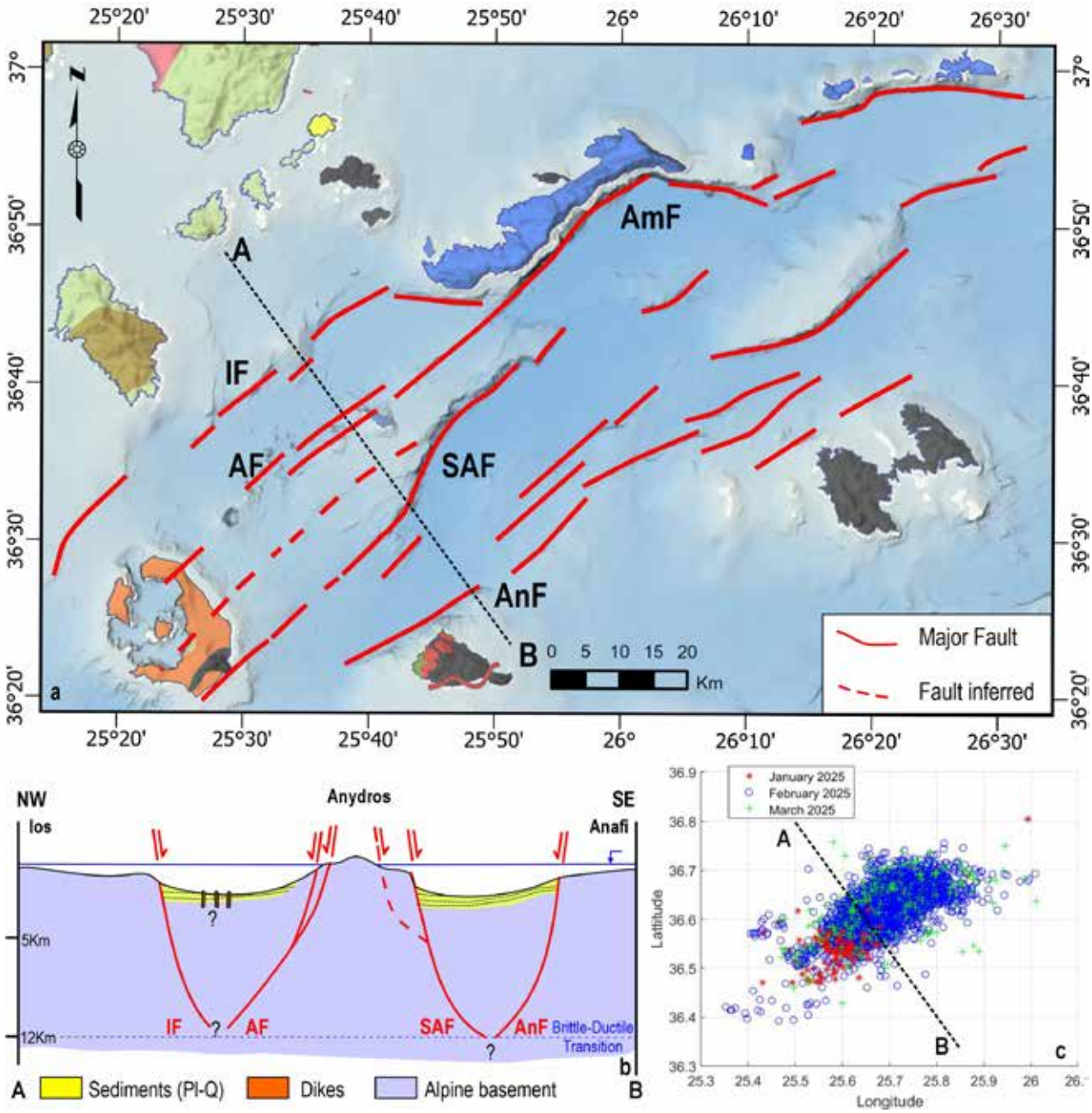

Figure 2a-c. a) Detail of Figure 1 showing the Santorini-Amorgos basin and the main faults (compiled after Nomikou et al., 2018; Sakellariou and Tsampouraki 2019; Tsampouraki et al., 2021), IF: Ios Fault, AF: Anydros Fault, SAF: South Anydros Fault, AnF: Anafi Fault b) Schematic NW-SE cross-section AB (not to scale) c) Projection of the swarm-type earthquake sequence of January-March 2025 (Seismic catalog. of the National Observatory of Athens http://www.gein.noa.gr)

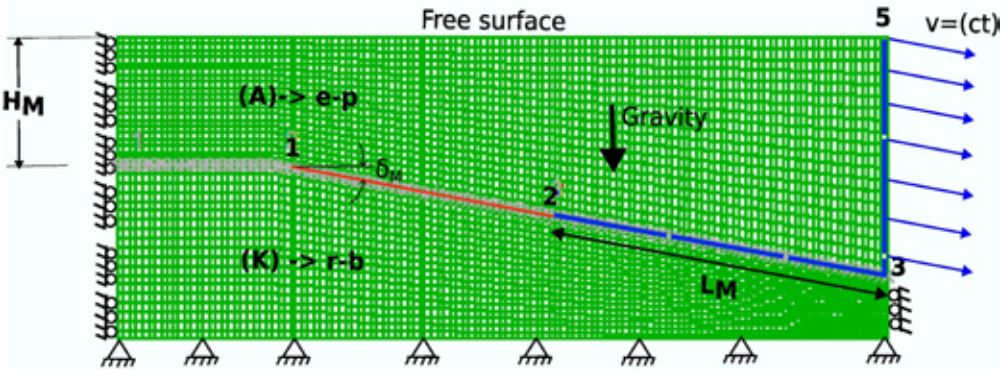

Figure 3. Vertical section of the discretized model and boundary conditions, along the AB cross-section of Figure 2a.

Results

The first stage of the simulation depicts the obtained structural configuration without the interference of magmatic activity. In this first stage, a decoupling zone is assumed at a depth of ~10-12 kilometers. Seismic reflection surveys in the Cycladic plateau estimate the upper and lower crust boundary at ~15 Km (Sachpazi et al., 1997). Since the area is adjacent to the Santorini volcanic center, e.g., within the volcanic arc domain, the geothermal gradient is probably elevated, and it is reasonable to assume that it is close to ~25-30°C/Km. Accordingly, at 10-12 Km depth, the temperature is ~300°C, roughly corresponding to the brittle-ductile transition zone. This zone corresponds to the level of the crust where deformation is localized.

Figure 4a depicts the contours of the maximum shear strain rate after a certain amount of sliding along the detachment zone. These contours indicate strain localization in shear bands (faults). Inside the band, the stress is lower than immediately outside. This stress drop at a newly formed shear band (fault) segment during the upward propagation of the normal fault creates an earthquake. Four sets of contours are formed in the final configuration, e.g., four fault zones, creating alternating horst and graben structures. Our model predicts that the southeast-dipping faults are the main faults and the northwest dipping are antithetic. The dip of the main fault (South Anydros Fault, SAF) of the right half-graben is greater (~70°) compared to the dip values of the rest of the normal faults (Ios Fault IF →60°, Anydros Fault AF →50°, Anafi Fault AnF→50°). It is also evident from the subsidence profile of the surface that the antithetic fault AnF has reached the surface like the rest of the faults.

Figure 4b shows the results of the second stage, where the effect of magmatic activity on the structural configuration obtained in the first stage is depicted. The application of pressure causes the creation of new faults starting at the chamber wall and propagating upwards. These could correspond to earthquakes clustering at 4-6Km depth. Some shallow faults are created due to the bending of the surface. New radially propagating faults are confined in the ridge between Anydros Fault (AF) and the main fault of South Anydros Fault (SAF). Shear strain also accumulates at the base of the fault zones, along the detachment zone, which could correspond to the second group of earthquakes clustering around 12Km depth.

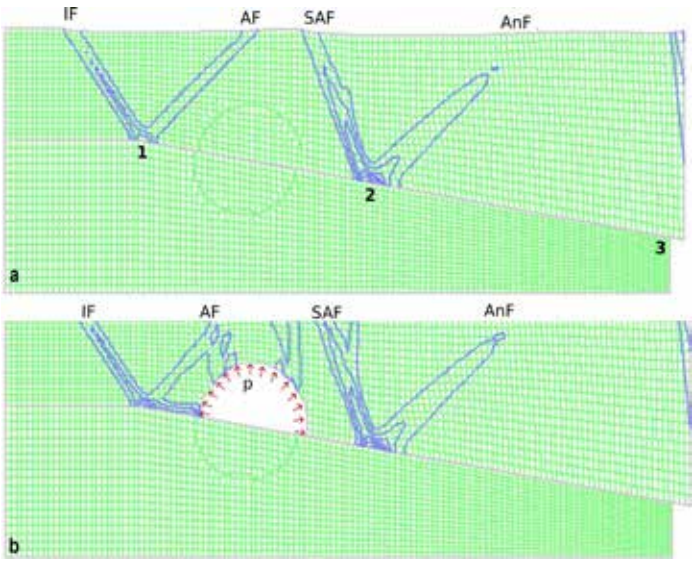

Figure 4a-b. a) Final graben structure of the modeled region at the end of the first simulation phase b) Second simulation phase: applied constant pressure at the wall of the magmatic chamber leads to initiation and propagation of shear bands in the ridge between AF and SAF faults.

Conclusions

- The application of a plane strain numerical model can simulate the structural configuration of the Santorini Amorgos basin and the January-March 2025 swarm-type earthquakes.
- The proposed model is based on the localization of deformation and differential sliding along a decoupling zone at a depth of 10-12Km, corresponding to the brittle-ductile transition.
- The complex geometry of the basin with alternating horst and graben segments results from successive NE-SW faults perpendicular to the local direction of extension.
- The shallow part of the structural configuration obtained from the first step of the simulation is at least in accordance with shallow seismic reflection data in the region.
- The injection of magma strike increases shear strain and creates new faults starting at the magma chamber wall and propagating upwards. The occurrences of new faults are confined in the Anydros ridge, between the AF and SAF.
- The Santorini-Amorgos basin is in the stage of a complex interaction between active faulting and magmatism, causing the January- March 2025 swarm-type earthquake sequence.

Acknowledgements

Field work was supported by grants from the National and Kapodistrian University of Athens ELKE to K. Soukis, H. Kranis and Em Skourtsos.

References

Grasemann, B., Schneider, D.A., Stockli, D.F., and Iglseder, C. 2012. Miocene bivergent crustal extension in the Aegean: Evidence from the western Cyclades (Greece). Lithosphere, 4(1), 23-39.

Grasemann, B., Schneider, D.A., Soukis, K., Roche, V. and Hubmann, B., 2022. Paleogeographic position of the central Dodecanese Islands, southeastern Greece: The push-pull of Pelagonia. Bulletin, 134(5-6), pp.1506-1528.

Jolivet, L., and Brun, J.P. 2010. Cenozoic geodynamic evolution of the Aegean. Int. J. Earth Sci., (Geol. Rundsch.), 99(1), 109–138.

Jolivet, L., Lecomte, E., Huet, B., Denèle, Y., Lacombe, O., Labrousse, L., Le Pourhiet, L., Mehl, C. 2010. The North Cycladic detachment system. Earth Planet. Sci. Lett., 289, 87–104.

Kokkalas, S., Xypolias, P., Koukouvelas, I., and Doutsos, T., 2006, Postcollisional contractional and extensional deformation in the Aegean region. In: Dilek, Y., and Pavlides, S., (Eds.), Postcollisional tectonics and magmatism in the Mediterranean region and Asia: Geological Society of America Special Paper 409, p. 97–123.

Kokkalas, S. and Aydin, A., 2013. Is there a link between faulting and magmatism in the south-central Aegean Sea?. Geological Magazine, 150(2), pp.193-224.

Laskari, S., Soukis, K., Lozios, S. and Stockli, D.F., 2024. Switching from the top-NW backthrusting to top-SE post-orogenic deformation in the Aegean domain: Insights from the calcite microfabric and siliciclastic rocks of the Amorgos Unit (SE Cyclades, Greece). Journal of Structural Geology, 178, p.105011.

Nomikou, P., Hübscher, C., Ruhnau, M. and Bejelou, K., 2016. Tectono-stratigraphic evolution through successive extensional events of the Anydros Basin, hosting Kolumbo volcanic field at the Aegean Sea, Greece. Tectonophysics, 671, pp.202-217.

Nomikou, P., Hübscher, C., Papanikolaou, D., Farangitakis, G.P., Ruhnau, M. and Lampridou, D., 2018. Expanding extension, subsidence and lateral segmentation within the Santorini-Amorgos basins during Quaternary: Implications for the 1956 Amorgos events, central-south Aegean Sea, Greece. Tectonophysics, 722, pp.138-153.

Papanikolaou, D.I. 2021. The Geology of Greece. 345pp, Springer Nature.

Pe-Piper, G., and Piper, D.J.W. 2002. The igneous rocks of Greece. The anatomy of an orogen. Gebr. Borntraeger, Berlin, pp 1–573.

Ring, U., Glodny, J., Will, T., and Thomson, S. 2010. The Hellenic Subduction System: High-Pressure Metamorphism, Exhumation, Normal Faulting, and Large-Scale Extension. Ann. Rev. Earth Planet. Sci., 38(1), 45–76.

Roche, V., Grasemann, B., Schneider, D., Soukis, K. and Pichler, M., 2024. Cold tectonics of Kos, central Dodecanese: Oligocene bivergent extension of the Pelagonian domain. Tectonics, 43(12), p.e2024TC008355.

Sachpazi, M., Hirn, A., Nercessian, A., Avedik, F., Mc Bride, J., Loucoyannakis, M. and Nicolich, R.I.N.A.L.D.O., 1997. A first coincident normal-incidence and wide-angle approach to studying the extending Aegean crust. Tectonophysics, 270(3-4), pp.301-312.

Sakellariou, D., & Tsampouraki-Kraounaki, K. 2019. Plio-Quaternary Extension and Strike-Slip Tectonics in the Aegean. In: J. Duarte (ed). Transform Plate Boundaries and Fracture Zones, 339–374.

Schneider, D.A., Grasemann, B., Lion, A., Soukis, K., Draganits, E. 2018. Geodynamic significance of the Santorini Detachment System (Cyclades, Greece). Terra Nova 30, 414–422.

Tsampouraki-Kraounaki, K., Sakellariou, D., Rousakis, G., Morfis, I., Panagiotopoulos, I., Livanos, I., Manta, K., Paraschos, F. and Papatheodorou, G., 2021. The Santorini-Amorgos shear zone: Evidence for dextral transtension in the south Aegean back-arc region, Greece. Geosciences, 11(5), p.216.

17th INTERNATIONAL CONGRESS of the Geological Society of Greece

BULLETIN OF THE GEOLOGICAL SOCIETY OF GREECE, SP. PUBL.

EXTENDED ABSTRACT 300

Sedimentary, Metamorphic, and Igneous Rocks in Harmony: Unveiling the rocky microcosm of the Vikos-Aoos UNESCO Global Geopark

Stergiou C.L.[1], Papaioannou H.[2], Dimou G.V.[1], Peristeridou E.[1], Melfou M.[1], Stamatiadis A.G.[1], Melfos V.[1], Koukousioura O.[1], Kitsaki G.[2]

(1) School of Geology, Aristotle University of Thessaloniki (AUTH), 54124 Thessaloniki, Greece (2) Vikos-Aoos UNESCO Global Geopark - Development Agency of Epirus S.A. (EPIRUS S.A.), Ioannina, Greece

Research Highlights

Laboratory and field investigations held for a rock and mineral exhibition of the Vikos-Aoos UNESCO Global Geopark revealed new intersections between geoheritage and cultural heritage, indicating significant links between specific rocks, minerals and cultural features.

Introduction

Geodiversity forms the basis of geoheritage and geoconservation, representing the variety of geological, geomorphological, pedological, and hydrological features of Earth. Geoheritage refers to geodiversity elements deemed significant for conservation due to their cultural, scientific, and educational value (Wolniewicz, 2021). It supports the preservation of unique geological sites and provides essential resources like raw materials, water, and energy. Rocks, minerals, and fossils are key components, revealing the dynamic history of the Earth (Pereira, 2023). The growing connection between geoheritage and cultural heritage enhances the value of geoheritage sites by linking them to social identity, history, and art (Pijet-Migón & Migón, 2022). In Greece, this extraordinary geodiversity is exemplified by the Vikos-Aoos UNESCO Global Geopark, where ophiolites, igneous and metamorphic rocks, and fossil-rich sedimentary formations narrate the story of the evolving landscapes of the Earth. UNESCO Global Geoparks like Vikos-Aoos play a vital role in fostering education, conservation, and sustainable tourism, offering a platform to explore the deep connections between geology, culture, and society.

In this context, the Development Agency of Epirus S.A. (EPIRUS S.A.), the managing organization of the Vikos-Aoos UNESCO Global Geopark, organized the exhibition "The Rocks of the Vikos-Aoos UNESCO Global Geopark Under the Microscope: Aspects of Their Microcosm" to highlight the geoheritage of the region. The exhibition was curated by members of the School of Geology, Aristotle University of Thessaloniki, and was first presented in Ioannina from 7th to 10th June 2023, and later traveled to Konitsa and Aristi village in Zagori. The exhibition welcomed hundreds of visitors, which had the opportunity to explore the geology of the geopark and the intricate world hidden within its rocks, through large-scale photomicrographs taken under a petrographic microscope. The exhibition featured hands-on rock and mineral samples, and a microscope allowed attendees, especially younger visitors, to examine thin sections of rocks. Informational material and volunteers helped explain the mineral microcosm, complemented by maps and field photographs, encouraging further exploration of the geopark.

The research conducted for the preparation of the exhibition further expanded the existing knowledge on the mineralogy, petrology, and micropaleontology of the geopark, while also exploring new aspects where geoheritage and cultural heritage intersect. This has led to the development of new research fields and geoeducational potential. In this publication, we briefly present the exhibition and highlight two major findings from the ongoing research that link specific rock types and minerals to cultural aspects and processes and are related to the large spherical concretions of Gamila peak and the Oxya ophiolites.

Geology of the Vikos-Aoos Geopark

The Vikos-Aoos UNESCO Global Geopark, located in the Pindos mountain range in NW Greece, spans 1200 sq. km and presents a geological history that exceeds 200 million years. Rock units belonging to the Ionian Unit, the Pindos Unit and the ophiolitic nappe of Pindos Unit build up the geopark. The Ionian Zone encompasses extensive formations of carbonate rocks and flysch (Figure 1). Upper Jurassic-Lower Cretaceous dolomites and limestones of Vigla Formation, "Senonian limestones" with rudist fossils, and Paleocene-Eocene limestones rich in planktonic microfossils constitute a continuous, collectively over 2200 m thick, calcareous marine stratigraphy, deeply exposed within the Vikos and Aoos Gorges through karstification (Perrier *et al.,* 1968). Overlying the Paleocene-Eocene limestones the Oligocene to Lower Miocene flysch formation is found, including an 1,800 m thick, turbiditic sequence of sandstones and marlstones, which dominates the eastern Zagori region and parts of Konitsa (Perrier *et al.,* 1968, Figure 1).

Pindos Unit underpins almost half of the regional geology covering the eastern part of the geopark (Figure 1). It is represented by Upper Cretaceous limestones and the overlying Paleocene to Eocene flysch formation (Mavridis & Manakos, 1987). The flysch, over 1250 m thick, consists of silty marlstones, fine-grained sandstones, limestones and conglomerates with ophiolitic clasts. Ophiolitic rocks are found obducted on the Pindos flysch and constitute fragments of the old Tethyan oceanic sediments,

crust and upper mantle that were obducted on Pindos Unit forming a now appearing fragmented ophiolitic nappe. The ophiolite components date back to the Lower Jurassic, and consist of ultramafic to mafic igneous rocks that have undergone extensive serpentinization. These include harzburgite, dunite, pyroxenite, gabbro, and diabase veins (i.e. igneous rocks), alongside large occurrences of serpentinite (i.e. metamorphic rocks, Mavridis & Manakos, 1987). The thickness of the ophiolitic thrust sheets reaches 1000 m at their most prominent and complex exposure found at Mount Smolikas (Figure 1). Locally, small outcrops of Jurassic schists, red cherts and limestones intercalated with cherts occur, representing Tethyan deep sea and hemipelagic sedimentation respectively (Mavridis & Manakos, 1987). These outcrops are typically less than 100 m thick and are often bounded by tectonic contacts (Figure 1). This complex geology combined with faulting and folding, documents the tectonic evolution of the region, which transitioned from passive margin sedimentation to compressional orogenesis during the Alpine orogeny.

The Pleistocene-Quaternary deposits include glacial moraines, prominent in the Tymfi and Smolikas mountains, and Holocene alluvial sediments along the Voidomatis, Aoos, and Sarantaporos rivers (Perrier *et al.,* 1968, Figure 1). Glacial deposits often loosely cemented and landslide-prone, contrast with the sands, clays, cobbles, and angular fragments of alluvial terraces elevated above current river flows (Perrier *et al.,* 1968, Figure 1).

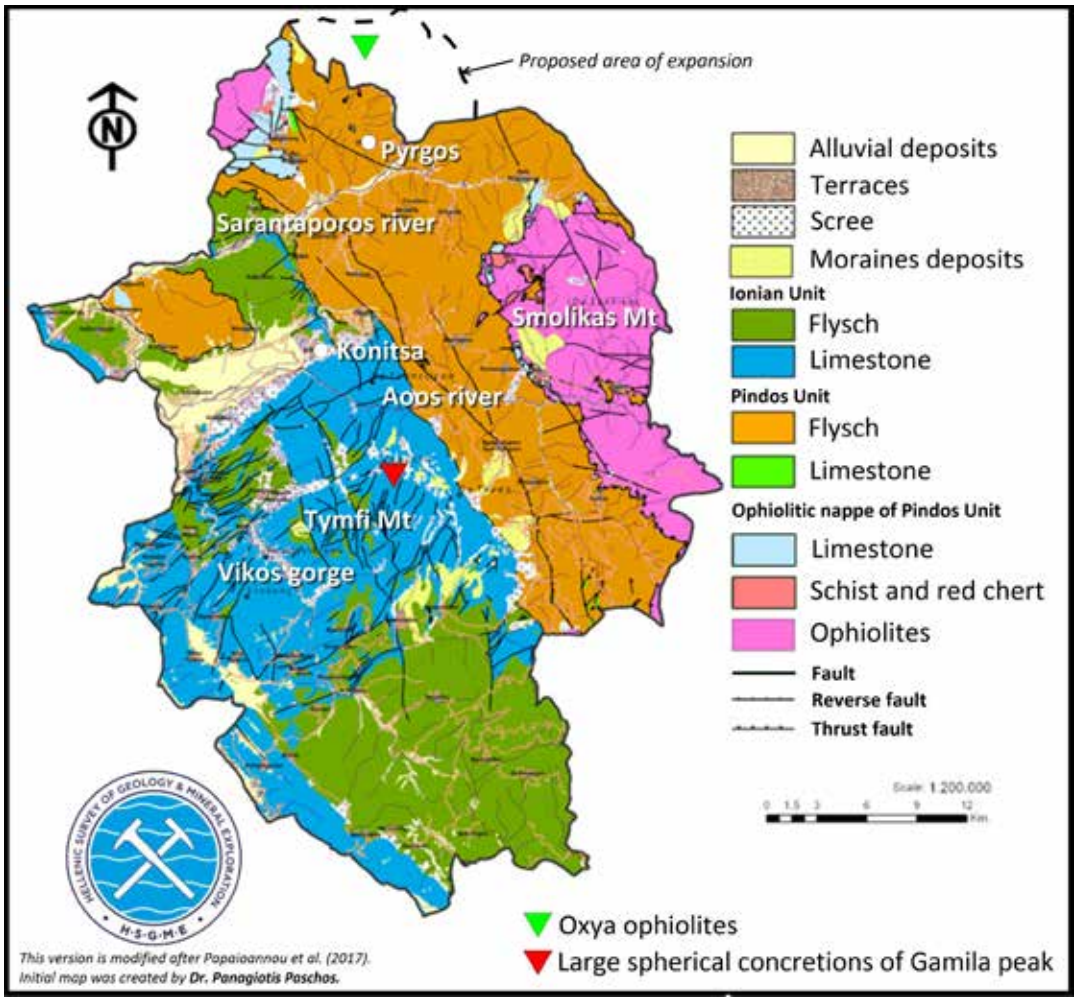

Figure 1. Simplified geological map of the Vikos-Aoos UNESCO Global Geopark. Main rock units and faults are shown. The Ionian limestone sequence is presented unified for clarity (modified after Papaioannou *et al.* (2017), initial map was created by Dr. Panagiotis Paschos).

Methods

Forty one samples were collected from primary outcrops and secondary sources, such as alluvial deposits, representing all the rock units of Vikos-Aoos Geopark, as well as special geological features (e.g. concretions, ore minerals, calcite masses). Rock samples were collected from outcrops close to the 51 recognized geosites and to the additional 30 sites of special

geological interest, which represent the geodiversity and geoheritage of the geopark. The collection sites were documented photographically using appropriate scales, and GPS data were collected for future reference. Thirty one of these samples were selected to be studied under the microscope. Thus, twenty six thin sections and 5 polished sections were produced and studied under a ZEISS Axioskop 40 dual reflected-transmitted light polarizing microscope coupled with a Canon Powershot A640 digital camera at the Department of Mineralogy-Petrology-Economic Geology, School of Geology, Faculty of Sciences, Aristotle University of Thessaloniki. The acquired micro-photographs were saved and logged. The digital enhancement of the micro-photographs and the preparation of the exhibition materials were carried out using the software Adobe Photoshop and Adobe Illustrator. For the exhibition needs twenty one micro-photographs were printed on 70 cm X 50 cm foam boards to cover the needs of the photographic exhibition. Following the exhibition, EPIRUS S.A. decided to publish a special volume dedicated to the mineral microcosm of the Vikos-Aoos UGGp in an effort to extend the impact of the exhibition and to ensure that the educative content and the aesthetics captured in the photographs will continue to inspire and engage audiences and forward the education on geoheritage and cultural heritage intersections (see Figure 4 below).

The Oxya ophiolites

The ophiolitic occurrence (N40.243086°, E20.804622°) at Oxya village, Konitsa, lies just outside the northern periphery of the geopark in a proposed area of expansion, and is one of the 30 designated sites of special geological interest (Figures 1, 2a). It is part of the ophiolitic cover of Pindos Unit, which appears thrusted on the flysch of Pindos Unit. These outcrops were first studied and reported back in the 1950s by Marinos *et al.* (1957) during the post-World War II efforts to support the economic development for Epirus. The ophiolitic assemblage includes gabbros and diabases intruding into basalts and pillow lavas, surrounded by serpentinites and scattered serpentinized dunites. Within the diabases, disseminations and minor stockworks of metallic mineralization occur, comprising pyrite, magnetite, and minor pyrrhotite, chalcopyrite, galena and ilmenite. In contrast, the pillow lavas host mainly pyrite and minor magnetite (Figure 2b,c), which, in surface samples, is heavily oxidized to form yellowish brown to red encrustations of goethite and hematite (Figure 2b).

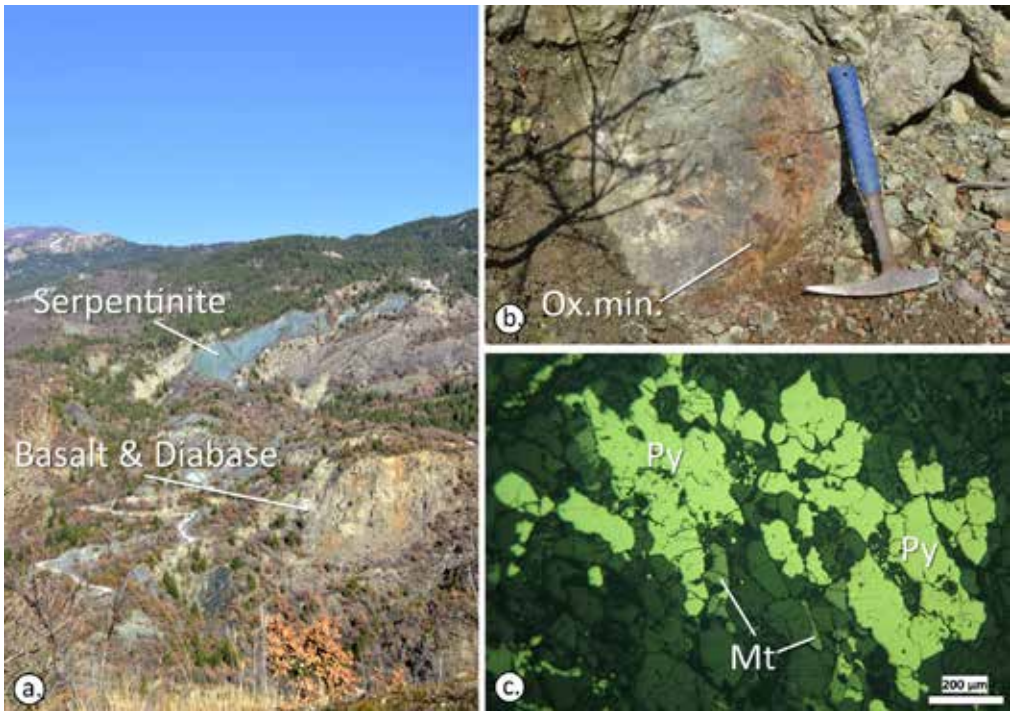

Figure 2. a. Field photograph of the Oxya ophiolites, characteristic outcrops of serpentinite, basalt and diabase are highlighted. Rocky cliffs appear yellowish brown due to the extent encrustations of goethite and hematite. b. Oxidized mineralization (Ox.min.) in diabase. c. Photomicrograph under plane reflected light (Nichols //) of the pyrite (Py) and magnetite (Mt) mineralization hosted in basalt.

Local reports support that pieces of the oxidized pyrite mineralization collected as ochre have historically been utilized as pigments for coloring by the famous Chioniadites painters, demonstrating an intersection of geological and cultural significance. Chioniades village is located NW of the Oxya ophiolites at 1150 m on the eastern slopes of Mount Grammos, and is where the Chioniadites School of painters had thrived between 18th and 20th centuries. Religious and popular creations of this school of painters are found from Albania and Epirus to Macedonia and Thessaly (Tsiodoulos, 2009). The artistic tradition of the village dates back to 1747 as is documented by the signed depiction of Saint George in the church of Koimisi Theotokou at Vourbiani

village, attributed to Konstas of Chionades (Tsiodoulos, 2009). The Chioniadites School of painters does not exhibit any characteristic painting style but follows the aesthetic standards of each time period (Stergiou 2024). Anastasios Papakostas-Marinas (1856) and his sons Christodoulos (1857-1932) and Thomas (1864-1930), are among the last and most famous painters of the Chioniadites School of painters (Stergiou 2024).

South of the Chioniades and Oxya villages, near Pyrgos village, another smaller ophiolitic outcrop (N40.164892°, E20.785197°) is found thrusted on the flysch of Pindos Unit (Figure 1). There, the local tradition narrates the extraction of a hard stone, locally called "gretzia," derived from the local term "grentzos" (meaning rough, coarse, uneven on the surface), which in turn comes from the Italian greggio/grezzo (meaning raw, unprocessed, unshaped) for the production of millstones. Hard, fine grained volcanic rocks like diabase or basalt have been traditionally used across Greece for the production of millstones (Melfos *et al.,* 2014), and this could also be the case at Pyrgos village.

The Large Spherical Concretions of Gamila Peak

The Gamila Peak spherical concretions (N39.97753°, E20.79079°), is another remarkable geological feature of the Vikos-Aoos Geopark, first described by Telbisz *et al.* (2019). Found at approximately 2,100 m a.s.l. along the trail to Gamila Peak (2,497 m a.s.l., Figure 1), these formations are observed in limestone boulders or as individual concretions within collapsed rocky scraps. The Paleocene-Eocene limestone formation of the Ionian Zone is the host rock of the concretions. The concretions exhibit spherical to elongated elliptical shapes, ranging usually from 0.1 to 1 m in diameter, and exhibit distinctive concentric layering (Figure 3a). Locally, large concretions form discontinuous layers reaching or exceeding 20 m in length (Figure 3b). The concentric layers that build up the concretions, alternate between fine-grained carbonate material and varying amounts of siliceous and carbonate cement, and contain abundant bioclastic material (Figure 4). The mixed cement suggests a diagenetic process involving early, incomplete carbonate cementation coupled with substantial SiO_2 precipitation in the intergranular spaces. The silicification likely resulted from the dissolution of siliceous bioclasts, though contributions from external SiO_2-enriched fluids cannot be excluded. The microscopic study revealed that the concretions retain embedded microfossils of *Nummulites*, *Alveolina* and orthophragmines. The size of the microfossils in some cases exceeds 3 mm in length (Figure 4). These microorganisms, part of the Large Benthic Foraminifera group, lived in shallow marine environments during the Middle Eocene (47 to 41 My ago), in depths up to 40 m according to the total recorded assemblage. Their presence, along with the intricate mineralogical composition of the concretions, underscores the complex diagenetic and paleoenvironmental history preserved within this extraordinary natural feature. A smaller outcrop of spherical concretions is found at the northern foundation (N39.862341°, E20.775298°) of the Noutsos (or Kokkoris) arch-stone bridge near Kipoi village, Zagori. Mapping and documentation of all outcrops with such concretions on Mount Tymfi is essential for reconstructing the paleoenvironment and understanding its geological history.

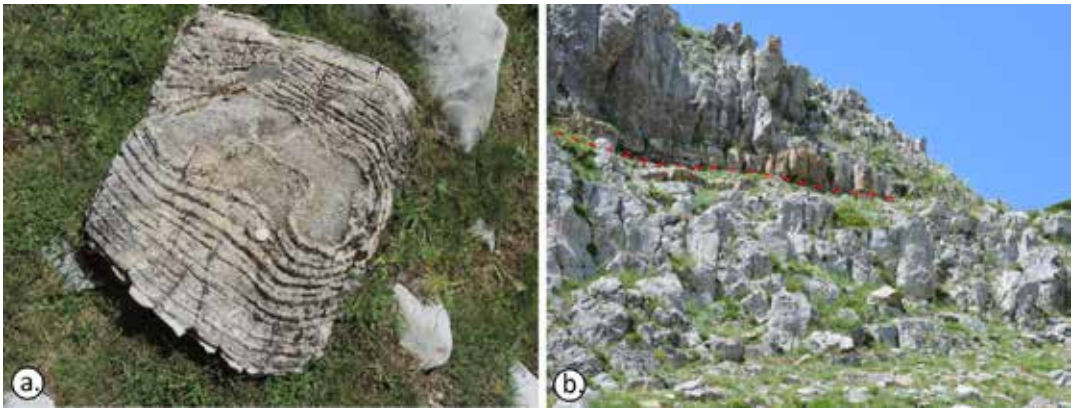

Figure 3. Field photographs of the large spherical concretions appearing as a fragmented boulder (a) and a discontinuous layer (red dashed line) of such large spherical concretions at a cliff close to Gamila peak, Mount Tymfi.

Recent field research at the villages of Megalo Papigo, Zagori, held by Christos L. Stergiou and Haritakis Papaioannou, documented another case of intersection between the geoheritage and cultural heritage of the Vikos-Aoos Geopark. Concentric concretions, texturally identically to those found near the Gamila peak but of smaller size (<40 cm in width) have been documented being embedded as stone carvings on traditional house facades that were mainly built along the 19th century (Figure 5a,b). These stone carvings are called hologlyphs and typically depict relief representations of anthropomorphic or dragon-like heads and were often embedded in churches, houses, fountains, and bridges in the Epirus region. They served a protective and apotropaic role, supported by three main characteristics: their grotesque appearance, the expression of the eyes, and the locations where they were placed (Tsoupi, 2006).

Figure 4. Sample layout from the upcoming special volume of the Vikos-Aoos UNESCO Global Geopark, showcasing rocks and minerals under the microscope alongside stories highlighting the intersection of geoheritage and cultural heritage. This example presents the geological significance and mineralogical composition of spherical concretions through macro-photographs and photomicrographs.

Figure 5. Photographs of the apotropaic hologlyphs installed on the facade of a traditional house at Megalo Papigo village build at 1876. Both are made of small spherical concretions. a. A roaring dragon-like. b. An anthropomorphic figure with a critical and stern gaze.

Conclusions

The Vikos-Aoos UNESCO Global Geopark, nestled in the geologically diverse terrain of the Pindos Mountains, exemplifies the intricate interplay between geology, culture, and nature. This research has highlighted key geological features within the geopark, such as the ophiolitic occurrences in Oxya and Pyrgos, the Gamila Peak

spherical concretions, and their connections to cultural heritage. The Oxya ophiolitic outcrops, part of Pindos Unit, host metallic mineralization, which were historically used by the Chioniadites painters as pigments. Similarly, the "gretzia" stone from Pyrgos village, likely derived from local diabases or basalts, showcases the traditional use of volcanic rocks for millstone production.

The spherical concretions at Gamila Peak, with their concentric layers and microfossil inclusions, offer insights into the Paleocene-Eocene shallow marine habitats and diagenetic processes that shaped the region. These concretions not only reveal vital biostratigraphic and paleoenvironmental data but also intersect with cultural heritage through their use as decorative carvings in traditional architecture. The hologlyphs embedded in house facades and other structures across the region serve as powerful symbols of the protective and artistic traditions of Zagori and Epirus. By uncovering these connections between geoheritage and cultural heritage, this ongoing research deepens our understanding of the geological and cultural history and enhances the geotourism and educational potential of the Vikos-Aoos Geopark.

Acknowledgements

Eleni Tsirigoti is acknowledged for handling the graphic production of the exhibition and the handbook under development. Region of Epirus, Municipality of Konitsa and the Ioannis Saralis Foundation are thanked for supporting the exhibitions held at Ioannina, Konitsa and Aristi, Zagori, respectively. The Development Agency of Epirus S.A. (EPIRUS S.A.) funded the thin and polished sections preparation of the collected rock samples, and covered the printing costs for the photographs and the informative material of the exhibition. Furthermore, EPIRUS S.A. is acknowledged for undertaking the publication of the album on the minerals and rocks of the geopark.

References

Marinos, G., Andronopoylos, B., Melidonis, N. 1957. Geology and mineral deposits of Epirus. Institute of Geology and Subsurface Research.

Mavridis, A., Manakos, K. 1987. Geological map sheet Konitsa, 1:50.000. Institute of Geology and Mineral Exlporation, Athens.

Melfos V., Papacharalampou C., Voudouris P.Ch., Kaiafa A., Voudouris, K. 2014. Raw materials used for the millstones production in ancient Greece: Examples from Macedonia and Thrace, in: Kalavrouziotis, I.K., Angelakis, A.N. (Eds.), Proceedings of the 4th IWA Regional Symposium on Water, Wastewater and Environment: Traditions and Culture, 773-783.

Papaioannou, H., Paschos, P., Nikolaou, E., Kitsaki, G. 2017. Vikos-Aoos Geopark. Visitor's Guide. Region of Epirus. Epirus SA – Development Agency, Ioannina, pp. 120.

Pereira, D. 2023. The value of Natural stones to Gain in the Cultural and Geological Diversity of our global Heritage. Heritage 6(6), 4542-4556.

Perrier, R., Koukouzas, K., Bizon, J.J., Bizon, G. 1968. Geological map sheet Doliana, 1:50.000. Institute of Geology and Mineral Exlporation, Athens.

Pijet-Migón E., Migón, P. 2022. Geoheritage and Cultural Heritage - A Review of Recurrent and Interlinked Themes. Geosciences 12, 98.

Stergiou, G. 2024. Conservation and restoration of a double-sided ecclesiastical banner from Saint Nicholas church, Molista, Ioannina, Greece, in: Karydis, C., Oikonomou, A., Kouloumpi, E., Vasilev, I., Stanev, S. (Eds.), The 2nd International Meeting for Conservation & Documentation of Ecclesiastical Artefacts (IMCDEA), Balkan Heritage Foundation, Sofia, Bulgaria, pp. 197-201.

Telbisz, T., Stergiou, C.L., Mindszenty, A., Chatzipetros, A. 2019. Karst features and related social processes in the region of the Vikos gorge and Tymphi mountain (Northern Pindos National Park, Greece). Acta Carsologica 48(1), 29-42.

Tsiodoulos, S. 2009. The Painted Decoration of the Houses in Zagori, Late 18th– early 20thCentury: A Historical and Cultural Approach, 1st edition. Rizareio Idryma.

Tsoupi, M. 2006. Epirotic Stone Carvings: Art and Society - Tracing in Zagori, 1st ediiton. Gefyra publications.

Ziogas, T.V. 2013. Place Names & Settlements of the Stone Mason Villages of Konitsa, 1st edition. Self publication.

Wolniewicz, P. 2021. Beyond geodiversity sites: exploring the educational potential of widespread geological features (rocks, minerals and fossils). Geoheritage 13(2), 34.

17th INTERNATIONAL CONGRESS of the Geological Society of Greece

BULLETIN OF THE GEOLOGICAL SOCIETY OF GREECE, SP. PUBL.

EXTENDED ABSTRACT 301

Insights from the mineralogy and mineral chemistry of the antimony mineralization at Philadelphio, Vertiskos Unit, Northern Greece

Stergiou C.L.[1,2], Sakellaris G.A.[2], Melfou M.[2], Melfos V.[2], Papadopoulou L.[2], Stefanou C.[2]

(1) Chemical Process & Energy Resources Institute (CPERI), Centre for Research and Technology Hellas (CERTH), 50200 Ptolemaida, Greece (2) School of Geology, Aristotle University of Thessaloniki (AUTH), 54124 Thessaloniki, Greece

Research Highlights

Preliminary results on the mineralogy and chemistry of Sb-mineralization at Philadelphio emphasize the mineral intergrowths and inclusions within stibnite, as observed through SEM-EDS analysis. Discussed with data from Rizana and Gerakario, these findings provide insights into the mineralization processes, with ongoing EPMA and LA-ICP-MS analyses focused on refining the genetic model and investigating key metal compositions.

Introduction

Antimony (Sb), a critical metalloid, has a long history of use, from early cosmetics to modern applications in flame retardants, aerospace, and defense. Primarily occurring in stibnite (Sb_2S_3), it is associated with over 100 minerals, including sulfosalts like tetrahedrite. Major Sb deposits are found in diverse geological settings, such as orogenic, Carlin-type, volcanogenic seafloor, and epithermal environments (Kanellopoulos et al., 2024). Stibnite often contains micro- to nano-scale inclusions of minerals that contain critical metals, underscoring its economic and geochemical significance.

The Serbo-Macedonian Metallogenic Belt (SMMB), spanning from Serbia to northern Greece, is a Pb–Zn–Ag district with notable Au resources and polymetallic Sb deposits. In northern Greece, the SMMB includes the Kilkis ore district within the Vertiskos Unit, hosting porphyry, epithermal, and carbonate-replacement deposits formed during Oligocene-Miocene magmatic-hydrothermal processes (Melfos and Voudouris, 2017; Stergiou *et al.,* 2018; Voudouris *et al.,* 2019). Mineralized veins along shear zones in metamorphic rocks contain Cu-As-Pb-Bi-Au-Te polymetallic and Sb-rich varieties (Stergiou et al., 2023). These mineralizations are linked to concealed magmatic intrusions and magmatic-hydrothermal processes along shear zones under retrograde greenschist facies conditions (Stergiou et al., 2023).

Major Sb mineralizations in the Vertiskos Unit include Rizana and Philadelphio, and minor Sb mineralization at Gerakario (Stergiou et al., 2023, Kanellopoulos et al., 2024). This study presents preliminary findings on the mineralogy and chemistry of Sb-mineralization at Philadelphio, based on optical microscopy and scanning electron microscopy and energy dispersive X-ray spectroscopy (SEM-EDS) analysis. The results, combined with data from Rizana and Gerakario, enable a comparison of the three mineralizations. As part of ongoing research, electron probe microanalysis (EPMA) and laser ablation inductively-coupled plasma mass spectrometry (LA-ICP-MS) analyses are being used to refine the genetic model, examine critical metal compositions, and compare with similar studies in the region.

Geological setting

The Vertiskos Unit is a northwest-trending geotectonic zone with a complex polytectonic and polymetamorphic history, extending from the Greek-North Macedonian border to the Chalkidiki peninsula (Brun & Sokoutis, 2018). It consists primarily of gneisses, schists, amphibolites, Paleozoic to Triassic metagabbros, metadiabases, and A-type granites, alongside Cenozoic I-type plutonic, sub-volcanic, and volcanic rocks from four magmatic episodes (Late Paleocene to Pliocene) with calc-alkaline, high-K calc-alkaline, and shoshonitic affinities (Stergiou et al., 2023, Figure 1).

Mineralized intrusions from the Oligocene-Miocene are prominent in the Kilkis and northeastern Chalkidiki ore districts, linked to structural controls from the Eocene-Oligocene Kerdylion and Miocene Strymon detachment faults. These faults, part of an extensional regime active from the Late Cretaceous to the Miocene, facilitated the south-southwest-directed collapse of the Vertiskos Unit, with shear zones, normal to oblique faults, and strike-slip faults influencing the region's magmatic activity and mineralization (Stergiou et al., 2023).

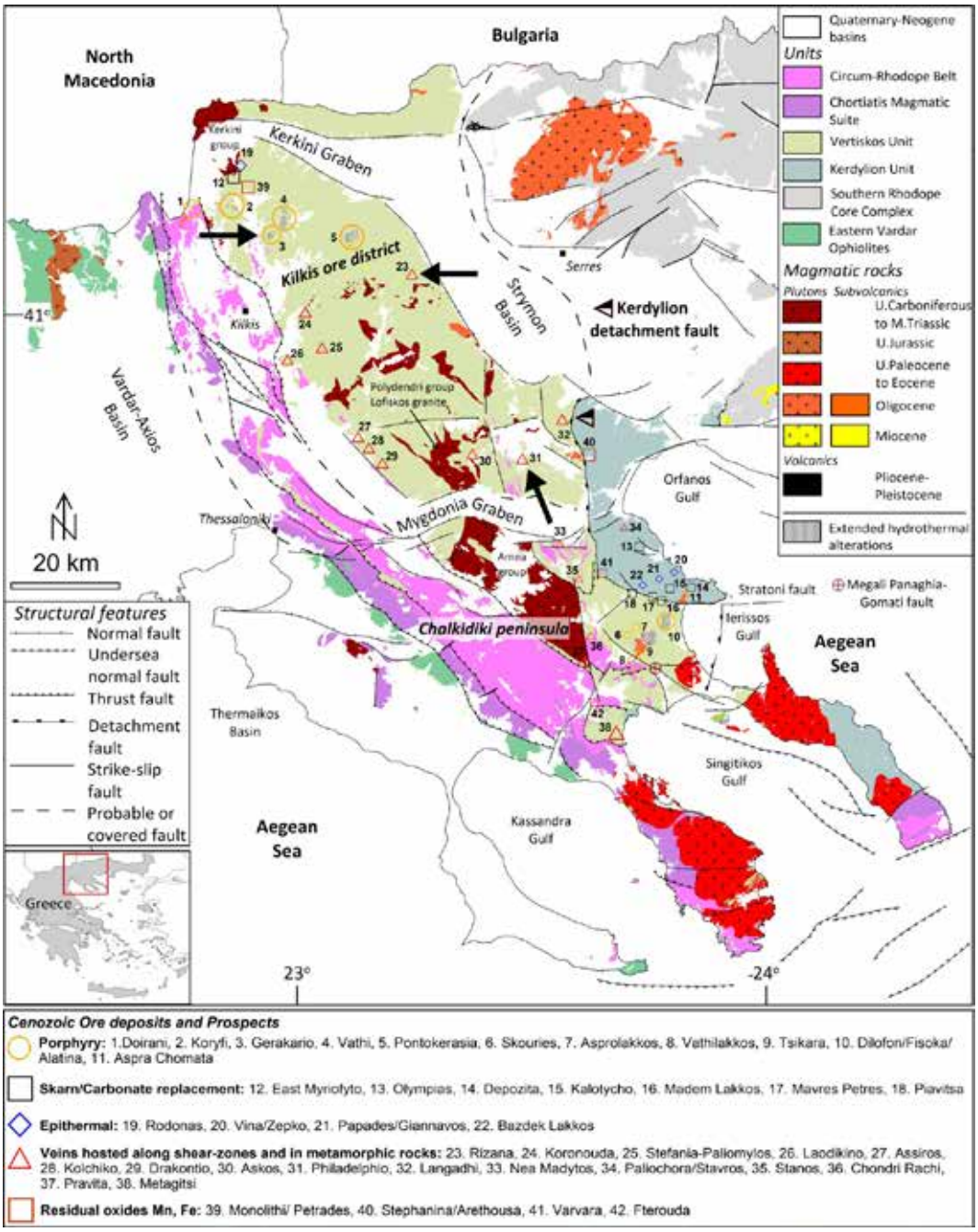

Figure 1. Geological map of Cenozoic magmatism and Oligocene-Miocene mineralization in the Vertiskos and Kerdylion Units (modified from Stergiou *et al.,* 2023), with black arrows marking ore deposits at Philadelphio, Rizana, and Gerakario.

Antimony occurrences at Philadephio, Rizana and Gerakario

The Philadelphio (or Philadelpia) Sb-mineralization has experienced historical mining during the early 20th century. Indicative resources are estimated at 10.08 Mt of ore, with an average grade of 3.36 wt.% Sb (Kanellopoulos *et al.,* 2024; Figures 1 & 2a-c). The mineralization is hosted in a shear zone cutting amphibolite, gneiss and schist of the Vertiskos Unit. Cenozoic magmatic rocks are absent from the region, but geothermal manifestations are found (Kanellopoulos *et al.,* 2024). The ore texture includes massive and discordant quartz veins, set along faults (<1 m wide). The main hydrothermal alteration is silicification and chloritization (Figure 2c). Ore related faults strike in average N30°W and dip 80°NE. Mineralization occurred in two stages: an early Zn-Fe-As-Cu-Au-enriched phase, and a later Sb-dominated. Metallic, gangue and alteration minerals are presented in Table 1.

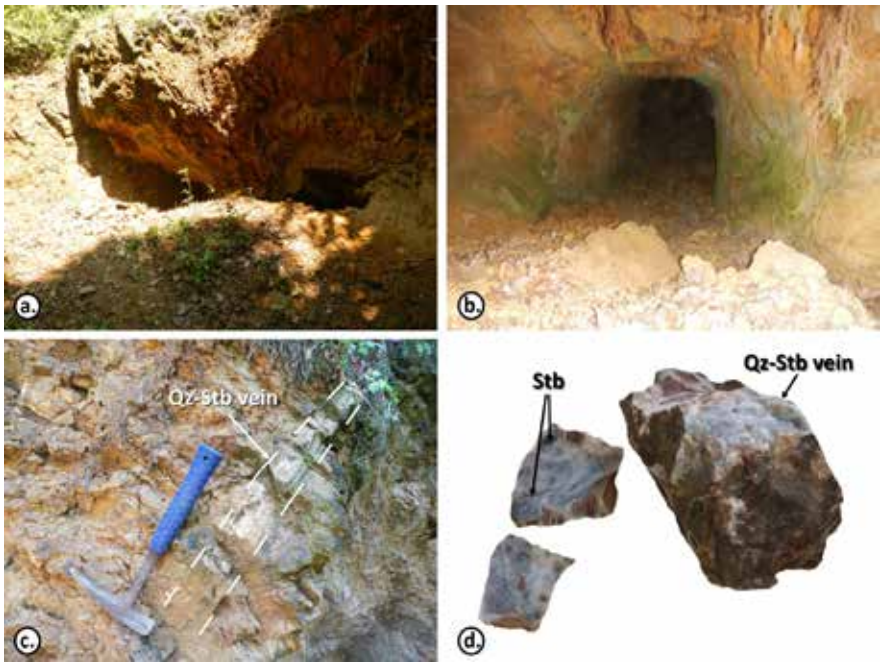

Figure 2. Field photographs (a-c) and macroscopic photograph (d) of the sampled ore from Philadelphio. a. Entrances to the underground workings. b. The interior of a gallery. c. A quartz (Qz)-stibnite (Stb) vein cutting the gneiss. d. Cuttings of a quartz (Qz)-stibnite (Stb) vein indicative of the ore texture in these veins.

The Rizana (or Lachanas) mineralization hosts the most significant Sb-ore deposits in Greece, with historical mining efforts dating back to pre-1930. Between the 1930s and 1950s, approximately 9000 metric tons of stibnite ore were extracted; averaging 40% Sb content (Stergiou *et al.,* 2023 and references there in; Figure 1). At "Tas-Kapou" location, the mineralization occurs within NE–SW-oriented brittle shear zones intersecting two-mica and augen gneiss of the Vertiskos Unit (Stergiou *et al.,* 2023). The Rizana rhyodacite is found close to the mineralization; it is hydrothermally altered (sericitic alteration) and contains pyrite disseminations (Stergiou *et al.,* 2023). The mineralized fault zones strike in average N30°E and dips 80°NW. Ore bodies are found as veins and discordant lodes with brecciated and massive textures, surrounded by hydrothermal halos marked by sericitization and silicification, predominantly affecting the two-mica gneiss (Stergiou *et al.,* 2023; Table 1). The metallic assemblage includes mainly stibnite, berthierite, pyrite, sphalerite, and chalcopyrite, (Dimou, 1989, Stergiou *et al.,* 2023; Table 1). In close proximity to the Sb-mineralization at Rizana a wolframite mineralization also occurs. At "Pilaf-Tepe," 1 km southeast of the Rizana rhyodacite, W-mineralization occurs in a silicified fault zone, featuring Fe-wolframite and stibnite with supergene oxidation products like tungstite, cervantite, and stibiconite, while minor Pb-Zn veins are found at the margins of the W-Sb mineralization and near the rhyodacite (Vasilatos et al., 2001). According to Stergiou *et al.,* (2023), the Rizana Sb-mineralization shows enrichments mainly in As, as well as Mn, Cu, Zn, Ni, Pb, Mo, Au and Ag.

The Sb-mineralization at Gerakario constitutes a minor prospect that has experienced random historical exploration and possibly exploitation probably between the 19th and early 20th century (Figure 1). Resources estimates are not available. It is found at the periphery of the Gerakario Cu-Au porphyry deposit (Stergiou *et al.,* 2022), which is related to Cenozoic plutonic and subvolcanic rocks, including silica-saturated granodiorite (34 ± 0.5 Ma) and syenite (22 ± 0.8 Ma) with calc-alkaline to slightly alkaline affinities (Stergiou *et al.,* 2022). Potassic, propylitic, and sericitic hydrothermal assemblages are superimposed on both magmatic and surrounding metamorphic rocks. The porphyry-style mineralization, associated with syenite, is characterized by pyrite-chalcopyrite disseminations, A- and D-type veins, and extensive oxidation near the surface (Stergiou *et al.,* 2022). The structurally controlled (N45°E/75°NW in average) epithermal quartz-stibnite veins, intersect the hydrothermally altered two-mica gneiss, and accommodate mainly stibnite, berthierite, native antimony, pyrite, arsenopyrite (Stergiou *et al.,* 2022, Table 1). The geochemistry of the mineralization reveals poor enrichments in trace elements, mainly including Co, Ag, Ga and Au (Stergiou *et al.,* 2022).

The formation of these Sb-mineralizations is associated with the Cenozoic (Neogene-Quaternary) structural framework and magmatic-hydrothermal activity of the Vertiskos Unit. At Rizana the mineralization occurred in two stages: tungsten-rich fluids forming wolframite and arsenopyrite, followed by antimony-rich fluids forming stibnite under low salinities

(6.6–8.1 wt.% NaCl) and moderate temperatures (217–254°C) (Stergiou et al., 2023). At Gerakario, fluid boiling in A-type veins generated high-salinity fluids (35.7–45.6 wt.% NaCl equiv.) at 380–460°C and pressures of 100–580 bar, later mixing with meteoric water to form lower salinity fluids (8–10 wt.% NaCl equiv.) associated with epithermal mineralization at 280–320°C (Stergiou et al., 2022). Although microthermometric data are unavailable for Philadelpeio, the comparable structural controls and regional geothermal activity strongly suggest analogous formation conditions (Kanellopoulos et al., 2022).

Table 1. Summary table of the metallic, gangue, alteration and oxidation assemblages of the Sb-mineralizations at Philadelphio, Rizana, and Gerakario (Dimou, 1989, Stergiou et al., 2022, 2023, Kanellopoulos *et al.,* 2024, this study).

Locality	Alteration style	Metallic assemblage	Gangue and alteration assemblage	Oxidation assemblage
Philadelphio	Silicification + chloritization	1st stage: Sph + Py + Apy + Cpy + Au, 2nd stage: Stb + Sb + Sph + Py + Ccsb + Ttr + Mln + Wf + Zkn ± Bth ± Mrc ± Po ± Bou	Qtz + Ser + Chl + Rt	Kem ± Sbc ± Cpm ± Sfz ± Cov ± See
Rizana	Silicification + Sericitization	Stb + Bth + Sph + Py + Cpy + Sb ± Wf ± Gn ± Ttr ± Mrc ± Po ± Apy ± Rlg ± As ± Au	Qtz + Brt + Ank + Ser	Vln ± Gth ± Cld
Gerakario	Sericitization	Stb + Bth + Sb + Py + Apy ± Mrc ± Po ± Cpy ± Lo ± Au	Qtz + Cal + Ser	Vln

Abbreviations: Apy = arsenopyrite, As = native arsenic, Au = native gold, Bou = boulangerite, Bth = berthierite, Ccsb = chalcostibite, Cov = covellite, Cld = claudetite, Cpm = chapmanite, Cpy = chalcopyrite, Gth = goethite, Kem = kermesite, Lo = löllingite, Mln = melnikovite, Mrc = marcasite, Po = pyrrhotite, Pn = pentlandite, Py = pyrite, Rlg = realgar, Sb = native antimony, Sbc = stibiconite, See = seelite, Sfz = schafarzikite, Stb = stibnite, Sph = sphalerite, Ttr = tetrahedrite, Rt = rutile, Vln = valentinite, Wf = wolframite, Zkn = zinkenite.

Methods

Optical microscopy and SEM-EDS analysis was focused on Sb-mineralized samples from Philadelphio. Six polished and thin-polished sections were studied under a ZEISS Axioskop 40 dual reflected-transmitted light polarizing microscope at the Faculty of Geology, AUTH. Scanning electron microscope (SEM) studies were conducted at the Faculty of Sciences, AUTH, using a JEOL JSM-6390LV SEM equipped with an OXFORD INCA 300 EDS (Oxford Instruments Ltd., Abingdon, UK). Set in the back-scattering electron (BSE) mode, the operating conditions were: 20 kV accelerating voltage, 0.4 mA probe current, 80 s analysis time, and a beam diameter of ≈1 μm. The SEM–EDS micro-analyses were targeted on mineral texture and chemistry of stibnite and sphalerite. The results were examined after univariate statistical analysis (minimum, maximum, standard deviation, and average) for comparison with previously shared SEM-EDS results for stibnite and related minerals from Rizana and Gerakario (Stergiou *et al.,* 2022, 2023).

Results & Discussion

The Sb-mineralization at Philadelphio, linked to the 2nd mineralizing stage, includes stibnite, native antimony, sphalerite, pyrite, chalcostibite, tetrahedrite, wolframite, zinkenite, berthierite, marcasite, pyrrhotite, and boulangerite (Table 1). Stibnite shows bireflectance, pressure lamellae, and forms massive or disseminated textures in quartz or cavity fillings. Sphalerite, berthierite, and pyrite (<700 μm) occur in massive stibnite or at stibnite-quartz boundaries, while euhedral pyrite (<200 μm) is also found in quartz (Figure 3a-d). Boulangerite and native antimony occur as inclusions in stibnite. Supergene oxidation resulted in the oxidation of stibnite to stibiconite ($Sb^{3+}Sb^{5+}{}_2O_6(OH)$), chapmanite ($Fe2^{3+}Sb^{3+}(Si_2O_5)O_3(OH)$), schafarzikite ($Fe^{2+}Sb^{3+}{}_2O_4$) and kermesite ($Sb_2S_2O$), with dimensions below 50 μm (Figure 3a-d).
Chemically, stibnite contains impurities of trace elements including Ag, As, Cu and Fe. The standard deviation values for impurities in stibnite indicate a consistent but slightly variable incorporation of elements. Silver shows a maximum concentration of 3.00 wt.% with a relatively low standard deviation (STDEV: 0.71 wt.%), suggesting a stable distribution across the samples (Table 2). Arsenic with a maximum content of 1.36 wt.% and a STDEV of 0.32 wt.%, also exhibits moderate stability. Cu and Fe show slightly higher variability, with STDEV of 0.33 wt.% and 0.35 wt.%, respectively, relative to their maximum values of 1.05 wt.% and 0.95 wt.%, respectively (Table 2). This suggests localized or irregular incorporation, possibly influenced by varying mineralization conditions. Overall, these trends indicate that trace metals incorporation in stibnite is not entirely random but influenced by geochemical and structural factors.
Sphalerite, identified through SEM-EDS analysis, is the predominant Zn phase in the studied samples. It occurs in

association with quartz, where it fills interstices (<400 μm in width) and occasionally contains stibnite inclusions (<40 μm in width). Sphalerite also forms intergrowths with stibnite, suggesting co-precipitation or later infiltration. Trace metals in sphalerite include As, Cd, Fe, Mn, Sb, Sn and Te displaying low averages (<0.2 wt.%) but relatively high standard deviations (<0.52 wt.%), suggesting heterogeneous incorporation, potentially due to variable fluid conditions during formation (Table 2). The standard deviation values of impurities in sphalerite suggest moderate variability in their incorporation during mineral formation. Iron (STDEV: 0.34 wt.%), Mn (STDEV: 0.23 wt.%), and Sn (STDEV: 0.49 wt.%) show relatively low but noticeable variations, indicating a consistent yet slightly heterogeneous inclusion process (Table 2). Conversely, elements like Sb (STDEV: 0.40 wt.%) and Te (STDEV: 0.52 wt.%) exhibit slightly higher standard deviation values despite their low average concentrations (<0.15 wt.%, Table 2). These observations highlight that the mineralization environment for sphalerite was relatively stable overall but subject to minor compositional variability, likely due to dynamic changes in fluid chemistry or temperature during its formation.
Quartz, the dominant gangue mineral associated with the mineralization, exhibits a range of textures from semi-transparent to polycrystalline. Quartz veins display features such as lamellar and brecciated textures, reflecting intense hydrothermal brecciation that caused significant fragmentation and grain size reduction. These veins often contain a mix of angular and rounded quartz fragments.

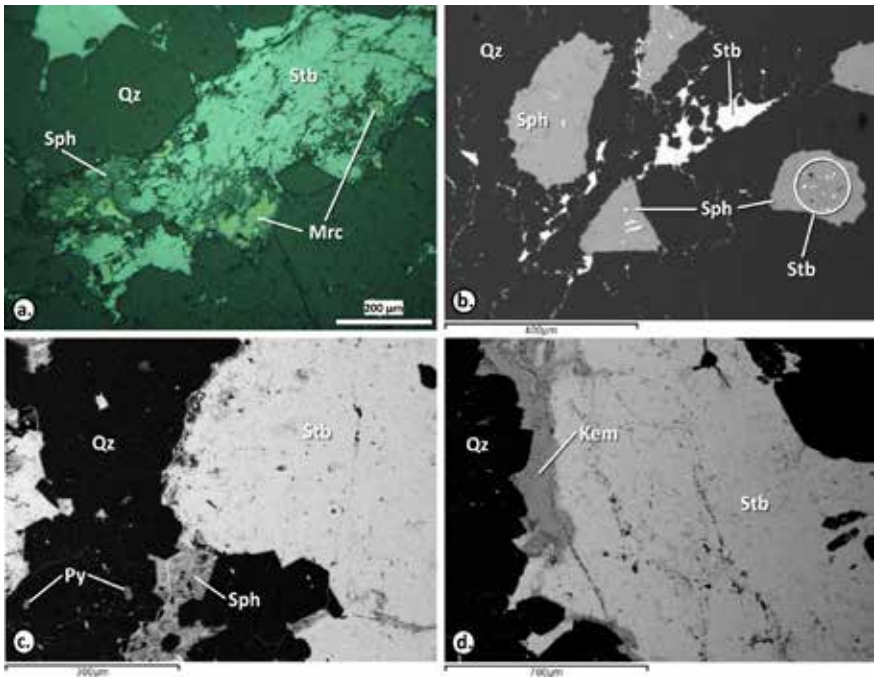

Figure 3. Micro-photograph (a) from Philadelphio under plane reflected light (Nichols //) and SEM back-scattered electron images (b-d): a. Stibnite (Stb), sphalerite (Sph) and marcasite (Mrc) cementing euhedral quartz (Qz). b. Stibnite (Stb) and sphalerite (Sph) with stibnite replacements (white cycle) filling cavities in quartz (Qz). c. Stibnite (Stb) and sphalerite (Sph) cementing quartz (Qz) including euhedral pyrite (Py). d. Stibnite (Stb) rimmed by kermesite (Kem) cementing quartz (Qz).

The stibnite from the Philadelphio mineralization after SEM-EDS analysis indicate a more complex and variable mineral chemistry compared to the stibnite from Rizana and Gerakario (Stergiou *et al.,* 2022, 2023). The trace impurities in Philadelphio stibnite, such as Ag, As, Cu, and Fe, display moderate to significant variability, while at Rizana trace impurities, are present at low levels and show minimal variability. At Rizana, Fe shows the highest variability (STDEV: 0.33 wt.%), with concentrations reaching up to 0.95 wt.%, which may suggest localized substitutions or inclusions (Stergiou *et al.,* 2023). Copper (Cu) also exhibits notable variability (STDEV: 0.21 wt.%), while Ag, As, and Zn display minimal influence on the overall composition, with low concentrations and STDEV values (Stergiou *et al.,* 2023). Trace element incorporation in Gerakario stibnite is more pronounced than in Rizana, with Ag concentrations reaching up to 1.33% and showing significant variability (STDEV: 0.57 wt.%). Other impurities, such as Cu, Zn, and As, occur at lower levels but exhibit moderate variability. Iron is present at up to 0.18 wt.% and shows limited variation, with a STDEV of 0.08 wt.% (Stergiou *et al.,* 2022).

Table 2. Mineral chemistry and formulas of stibnite and sphalerite from Philadelphio as calculated for MIN, MAX, and AVG values after SEM-EDS micro-analysis. Values are in weight percent (wt.%).

	Stibnite (n = 13)				Stibnite with impurities (n = 18)				Sphalerite (n = 16)			
Element	**MIN**	**MAX**	**STDEV**	**AVG**	**MIN**	**MAX**	**STDEV**	**AVG**	**MIN**	**MAX**	**STDEV**	**AVG**
Sb	70.03	75.16	1.51	71.92	24.84	29.97	1.36	28.27	b.d.l.	1.54	0.40	0.11
Ag	b.d.l.	b.d.l.	-	-	b.d.l.	3.00	0.71	0.17	b.d.l.	b.d.l.	-	-
As	b.d.l.	b.d.l.	-	-	b.d.l.	1.36	0.32	0.08	b.d.l.	1.46	0.45	0.17
Zn	b.d.l.	b.d.l.	-	-	b.d.l.	b.d.l.	-	-	58.48	62.53	1.29	60.65
Cu	b.d.l.	b.d.l.	-	-	b.d.l.	1.05	0.33	0.11	b.d.l.	b.d.l.	-	-
Mn	b.d.l.	b.d.l.	-	-	b.d.l.	b.d.l.	-	-	b.d.l.	0.61	0.23	0.11
Cd	b.d.l.	b.d.l.	-	-	b.d.l.	b.d.l.	-	-	b.d.l.	1.05	0.27	0.07
Sn	b.d.l.	b.d.l.	-	-	b.d.l.	b.d.l.	-	-	b.d.l.	1.49	0.49	0.19
Te	b.d.l.	b.d.l.	-	-	b.d.l.	b.d.l.	-	-	b.d.l.	2.03	0.52	0.14
Fe	b.d.l.	b.d.l.	-	-	b.d.l.	0.95	0.35	0.15	b.d.l.	0.94	0.34	0.19
S	24.84	29.97	1.51	28.08	67.54	75.16	1.82	71.22	35.29	40.39	1.46	38.37
Total	100.00	100.00	0.00	100.00	100.00	100.00	0.00	100.00	100.00	100.00	0.00	100.00
Mineral	**Mineral formulas**											
Stb	MIN: $Sb_{2.13}S_{2.87}$ – MAX: $Sb_{1.99}S_{3.01}$ – AVG: $Sb_{2.01}S_{2.99}$											
Stb imp.	MIN: $Sb_{0.44}S_{4.56}$ – MAX: $Sb_{0.46}Ag_{0.05}As_{0.03}Cu_{0.03}Fe_{0.03}S_{4.39}$ – AVG: $Sb_{0.47}Fe_{0.01}S_{4.51}$											
Sph	MIN: $Zn_{0.90}S_{1.10}$ – MAX: $Zn_{0.87}As_{0.02}Cd_{0.01}Fe_{0.01}Mn_{0.01}Sb_{0.01}Sn_{0.01}Te_{0.01}S_{1.12}$ – AVG: $Zn_{0.87}S_{1.12}$											

Abbreviations: AVG = average value, b.d.l. = below detection limit, MIN = minimum value, MAX = maximum value, Sph = sphalerite, Stb = stibnite, Stb imp. = stibnite with impurities, STDEV = standard deviation.

Conclusions

The stibnite from the Philadelphio mineralization displays specific mineralogical and geochemical characteristics. Microscopically, it exhibits strong bireflectance, pressure lamellae, and quartz intergrowths, indicating a complex crystallization history. Trace metals such as Ag, As, Cu, and Fe, along with minor phases like sphalerite, berthierite, and pyrite, highlight the heterogeneity of the mineralization. Compared to Rizana and Gerakario, the stibnite at Philadelphio shows greater trace element enrichment, suggesting more enriched mineralizing fluids and varied formation conditions.

Acknowledgements

Authors would like to acknowledge the “Programme for the Promotion of the Exchange and Scientific Cooperation Between Greece and Germany - IKYDA2022” for funding the field work visits to Philadelpio. The authors would like to acknowledge Aristeidis Stamatiadis for the preparation of the thin-polished and polished sections.

References

Brun, J.P., Sokoutis, D. 2018. Core complex segmentation in North Aegean, a dynamic view. Tectonics 37, 1797-1830.

Dimou, E. 1989. Native minerals in rocks and mineralizations of Greece and their significance. Bulletin of the Geological Society of Greece 23, 207–223.

Melfos, V., Voudouris, P. 2017. Cenozoic metallogeny of Greece and potential for precious, critical and rare metals exploration. Ore Geology Reviews 89, 1030–1057.

Stergiou, C.L., Melfos, V., Voudouris, P. 2018. A review on the critical and rare metals distribution throughout the Vertiskos Unit, N.Greece, Proceedings of the 1st International Electronic Conference on Mineral Science, MDPI, Basel, Switzerland.

Stergiou, C.L., Melfos, V., Voudouris, P., Papadopoulou, L., Spry, P.G., Peytcheva, I., Dimitrova, D., Stefanova, E. 2022. A Fluid Inclusion and Critical/Rare Metal Study of Epithermal Quartz-Stibnite Veins Associated with the Gerakario Porphyry Deposit, Northern Greece. Applied Sciences 12, 909.

Stergiou, C.L., Sakellaris, G.A., Melfos, V., Voudouris, P., Papadopoulou, L., Kantiranis, N., Skoupras, E. 2023, Mineralogy, Geochemistry and Fluid Inclusion Study of the Stibnite Vein-Type Mineralization at Rizana, Northern Greece. Geosciences 13(2), 61.

Kanellopoulos, C., Sboras, S., Voudouris, P., Soukis, K., Moritz, R. 2024. Antimony’s Significance as a Critical Metal: The Global Perspective and the Greek Deposits. Minerals 14, 121.

Vasilatos, C., Barlas, K., Stamatakis, M., Tsivilis, S. 2001, Wolframite-stibnite mineral assemblages from Rizana Lachanas, Macedonia, Greece and their possible use as flux agent in the manufacturing of clinker. Bulletin of the Geological Society of Greece 34, 827–834.

Voudouris, P., Mavrogonatos, C., Spry, P.G., Baker, T., Melfos, V., Klemd, R., Haase, K., Repstock, A., Djiba, A., Bismayer, U., Tarantola, A., Scheffer, C., Moritz, R., Kouzmanov, K., Alfieris, D., Papavassiliou, K., Schaarschmidt, A., Galanopoulos, E., Galanos, E., Kolodziejczyk, J., Stergiou C., Melfou, M. 2019. Porphyry and epithermal deposits in Greece: an overview, new discoveries, and mineralogical constraints on their genesis. Ore Geology Reviews 107, 654-691.

17th INTERNATIONAL CONGRESS of the Geological Society of Greece

BULLETIN OF THE GEOLOGICAL SOCIETY OF GREECE, SP. PUBL.

EXTENDED ABSTRACT 302

Threshold Value Analysis in Geochemical Mapping for Gold-Only Vein-Type Mineralization

Strongylis S.[1], Sakellaris G.A.[1], Kantiranis N.[1], Chatzipetros A.[2]

(1)Department of Mineralogy-Petrology-Economic Geology, School of Geology, Aristotle University of Thessaloniki, 54124, Greece, email: Spyroslis.spyros@gmail.com, (2)Department of Structural, Historical and Applied Geology, School of Geology, Aristotle University of Thessaloniki, 54124, Greece

Introduction

Gold-only vein deposits such as these of the orogenic-gold type are among the most significant sources of gold worldwide, but their exploration has several challenges. Besides their weak physical properties and commonly deep burial depth, orogenic-gold deposits often exhibit weak geochemical signatures and/or subtle surface gold anomalies, especially in regions with thick overburden or significant weathering. In addition, gold concentrations within the quartz veins or soil cover, can deviate significantly from the statistical normal distribution, commonly showing extreme positive skewness and nugget effect, complicating anomaly detection.

The fundamental task when using surface geochemical data for mineral exploration is to identify and delineate geochemical anomalies within the various occurring lithologies. This is realized by calculating the threshold value (Garrett, 1991) above the background levels (Hawkes and Webb, 1962) and by applying interpolation to the anomaly (point) data to produce a continuous anomaly map. The latter can act as a single predictive layer or queried in a mineral prospectivity mapping technique, to indicate potential drilling locations.

Exploratory Data Analysis (EDA) is a robust technique that leverages both statistical and graphical methods in order to identify patterns, anomalies, and relationships in the exploration geochemical datasets (Tukey, 1977; Kürzl, 1988).

In this work, the accuracy and efficiency of four different threshold estimation techniques are tested, which can be applied in areas with unexposed bedrock and thick soil cover. High-resolution gold-concentration distributions in thick soil cover are investigated and visualized, collected during brownfields exploration campaign for orogenic-gold. Finally, through spatial analysis and zonal statistics the degree of element (gold) dispersion is evaluated.

The case study area is the southern segment of the Archaean Hattu orogenic-gold district in Eastern Finland (Hattu Schist Belt - HSB), which is part of the Ilomantsi greenstone belt and covers an area of 6 km in length with width 3 km. The main rock types of the belt consist of the Hattu supracrustal rocks, which include sedimentary-metasedimentary rocks (e.g., greywacke, schist, tuff), intruded by the plutonic rock units (tonalitic and granodioritic compositions). The belt has been progressively deformed, characterized by steeply dipping, upward-facing structures with transpressional N-NE trending dextral shear systems, and intensely hydrothermally altered due to large-scale fluids under greenschist to lower amphibolite-facies conditions peaking at 500-600°C at 4-6 kbars (O'Brien et al., 1993; Kojonen et al., 1993; Sorjonen-Ward et al., 2015). The Archean bedrock of the area is entirely covered by ~5-meter-thick glacial till, and the gold mineralization exact locations are depicted solely by drill core data.

Database and Software

The surface geochemical dataset contained gold concentrations from 936 basal till samples, collected and analysed by Endomines Oy. The company used Fire Assay for analysis of the gold content, which is measured in mg/kg, with a detection limit of 1 μg/kg. The classification of the soil samples, as well as their locations relative to the southern segment of the HSB, can be seen in Figure 1.

The lithological formations and their boundaries that occur in the area were first digitized and further classified according to the two main lithologies of the belt. After projecting drill core data (lithological and geochemical) the main mineralization zone is traced on the map (Figure 4).

For statistical analysis, IBM SPSS Statistics 27.0 was used, and for geochemical data processing and visualization, ArcMap 10.8.1 GIS software with the Spatial Analyst tool was utilized under academic license.

Methodology

The flowchart in Figure 1 illustrates the methodology used for threshold estimation and the generation of gold anomaly map for the HSB area. Briefly includes:

1) Descriptive statistics for measuring mean, median, skewness and kurtosis to understand the central tendency and spread of element concentrations. This phase also includes the examination of the dataset regarding censored and extreme values.

2) EDA graphical tools such as histograms and boxplots for visualization of data distribution, assessing the frequency of gold concentrations, and identifying outliers that may signify anomalies or errors in the dataset.

3) Logarithmic transformation (Miesch and Chapman, 1977) to manage the highly skewed data.
4) Geochemical anomaly detection to identify the threshold values for gold and delineate the anomalous zone. Four different threshold estimation techniques were applied, namely the:
i) Mean +2Standard Deviation (SD)
ii) Upper Whisker (UW)
iii) Median + 2Median Absolute Deviation (MAD)
iv) Percentiles
5) Application of the straightforward Inverse Distance Weighting (IDW) interpolation method (Shepard, 1968) to generate continuous geochemical anomaly surface maps and contribute to the comparison of the threshold techniques.
6) Validation of the results through the GIS-diagnostics (Mean Error - ME, Root Mean Square Error - RMSE), to assess whether geochemical anomaly mapping provided a reliable anomaly map with a rational threshold.
7) Interpretation and evaluation of the gold anomaly zones. Spatial and zonal statistics analysis to further correlate gold concentrations with other types of geological information.

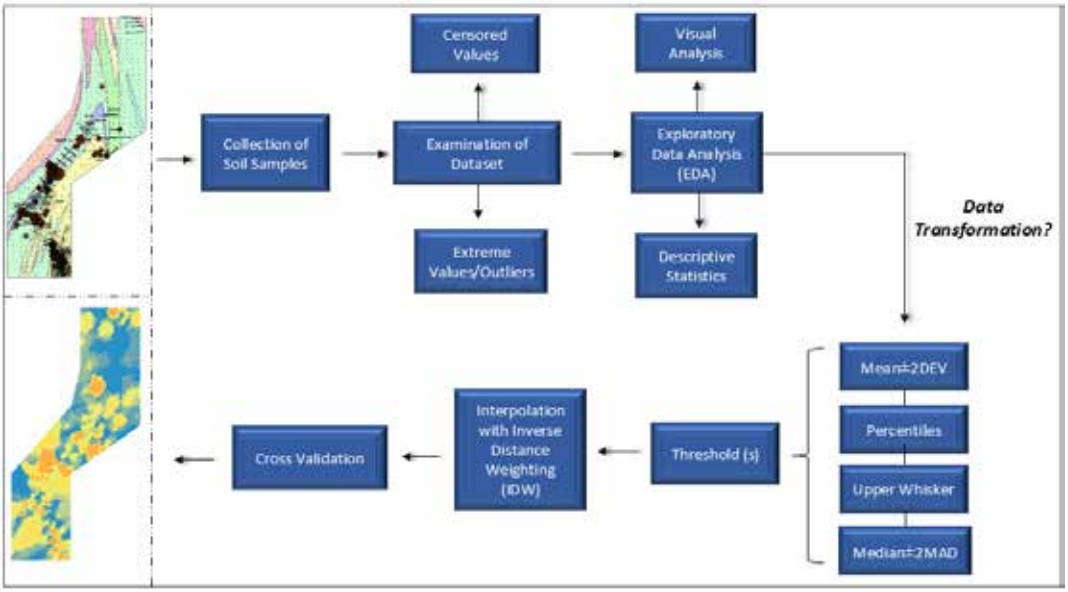

Figure 1. Overall methodology for threshold estimation and gold anomaly mapping for the southern segment of the HSB.

Results

Histograms and boxplots revealed positive extreme values and outliers. Since the number is too small and have minimal effect on the mean values, no top-cut was applied.

Table 1. Descriptive statistics of the datasets related to the threshold methods

Au in till (mg/kg)	Raw dataset	Transformed dataset
Mean	0.046	-3.88
Standard Deviation (SD)	0.13	0.96
Median	0.014	-4.26
Median Absolute Deviation (MAD)	0.04	0.34
Percentile90 (P90)	0.07	-2.55
Skewness	9.73	1.77
Kurtosis	136.86	3.28
Max	9.00	2.19

As shown in Figures. 2a and 2b the data are extremely positive-skewed and did not conform to normal or near-normal distribution model. The data were first logarithmically transformed and then an inverse transformation was applied to estimate reliable positive thresholds for each method and ensure that the final thresholds are meaningful to the original dataset. The transformed dataset demonstrated improved symmetry, reducing the impact of outliers (Figures 2c, 2d).

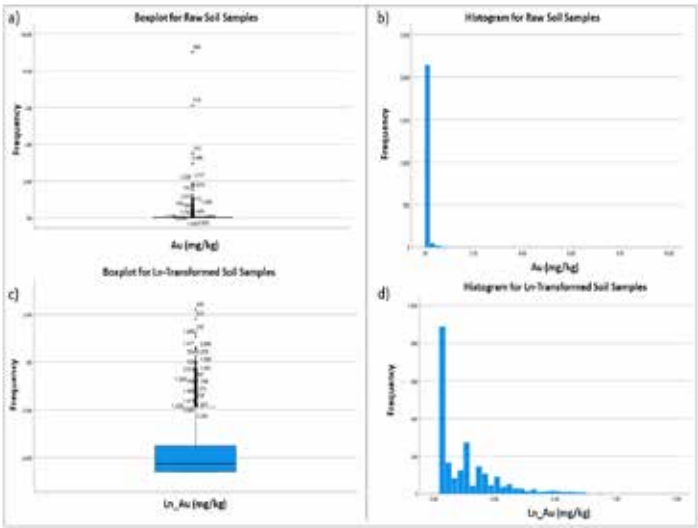

Figure 2. The figures (a, b) at the top present the boxplot and histogram for the raw soil dataset with their ID's, while figures (c, d) below display the boxplot and histogram after applying the natural logarithm transformation.

Table 2 shows the threshold values calculated using the four different methods. A comparison between them shows that the median +2MAD produces the lowest threshold for the soil samples, followed by the percentiles, the mean +2SD, and the upper whisker method.

Table 2. Overview of the threshold values

Au (mg/kg) in till	**Mean + 2 SD**	**Median + 2 MAD**	**Upper Whisker**	**Percentile (P90)**
Threshold	0.14	0.027	0.15	0.07

Figure 3 shows the geochemical gold-anomaly maps produced using the threshold values as calculated by each method. The parameters of IDW interpolation were carefully evaluated and tested to minimize the diagnostics of ME and RMSE and are summarized in Table 3.

Table 3. Parameters for IDW interpolation for soil samples

IDW Analysis	**Soil Parameters**
Neighbourhood Type	Standard
Power Parameter	1
Maximum Neighbours	5
Minimum Neighbours	2
Sector Type	One Sector
Angle	30°

Cross-validation (Table 4) of IDW indicated that the ME is close to zero, implying high accuracy in the prediction. The RMSE values are similarly near zero, further confirming the reliability of the interpolation method (Johnston et al., 2003). Finally, the location of the known gold occurrences of the south segment, revealed through drill core data, attests the accuracy of the prediction.

Table 4. Cross validation diagnostics for IDW in GIS.

Diagnostics	**Soil Validation Statistics**
Mean Error (ME)	0.03
Root Mean Square Error (RMSE)	0.15

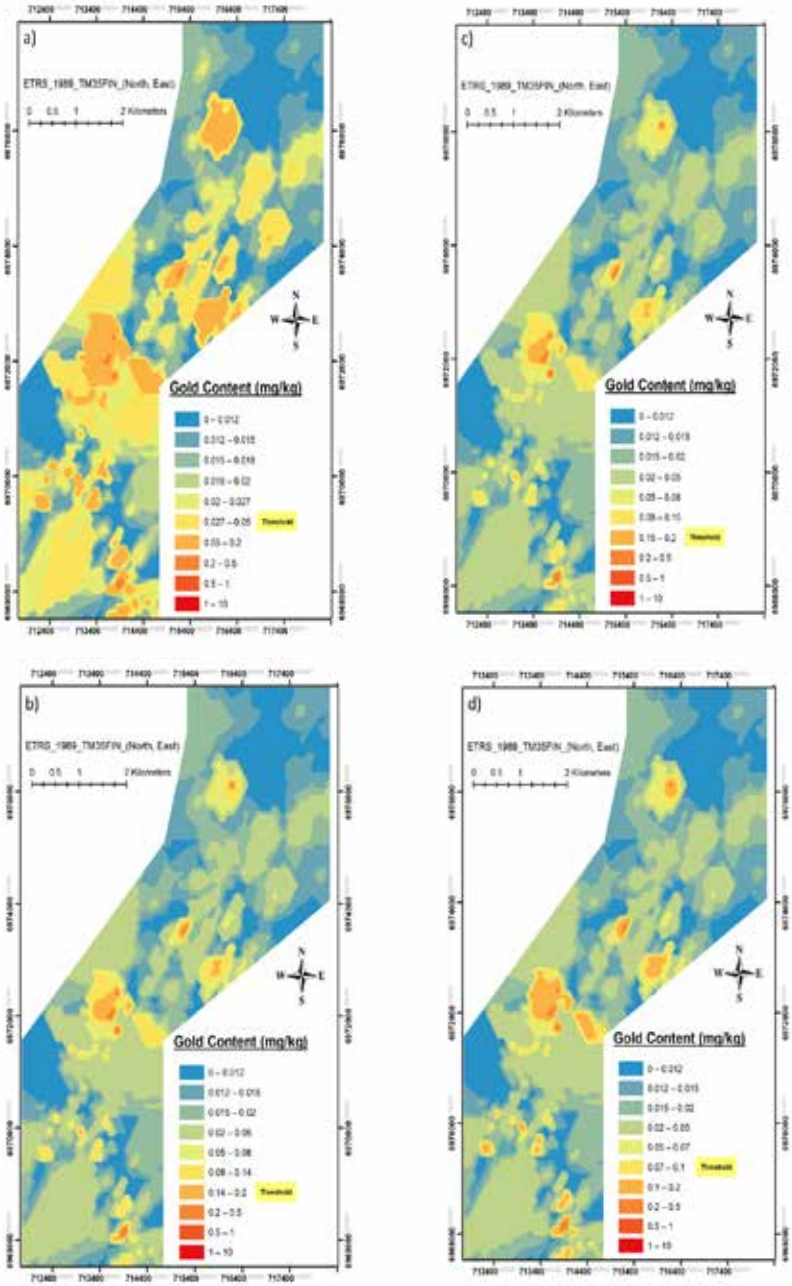

Figure 3. Gold geochemical distribution maps for soil, of the south HSB segment. The maps were generated with the IDW interpolation method using the different threshold in each case: (a) Median + 2MAD, (b) Mean + 2SD, (c) Upper Whisker, and (d) Percentiles.

Discussion and Conclusions

The soil geochemical dataset in this study represents a typical orogenic gold district, characterized by a predominance of low gold concentrations ranging from 0.01 to 0.5 mg/kg, along with a few exceptionally high gold values (up to 9 mg/kg). Like most gold deposits, including orogenic gold deposits, these geochemical concentrations deviate significantly from a Gaussian (normal) or near-normal distribution. Due to high skewness even after logarithmic transformation, the distribution remained non-Gaussian. Any multimodal distribution was not observed which implies a uniform dataset, not affected by secondary or complex geological processes.

The median +2MAD method detects the greatest number of geochemical anomalies, followed by the percentile method. Due to the dataset's extreme positive skewness, mean ±2SD was unreliable. The outliers exceed 10% giving similar threshold to the mean ±2SD. The median +2MAD, provided lower, more suitable threshold (0.027 mg/

kg), selected as more reliable in this work for mapping. This value corresponds to the thresholds (0.02 – 0.06 mg/kg) used in gold exploration programs worldwide as well as in previous HSB studies (Xuejing and Xueqiu, 1991; Hartikainen and Nurmi, 1993).

Validation and evaluation of the derived gold geochemical map based on spatial analysis and zonal statistics show an average geochemical anomaly value of 0.04 mg/kg across the mineralization zone, which is above the calculated 0.027 mg/kg threshold. In some areas, there is a weak association with geochemical anomalies falling below the threshold, even reaching zero gold concentration. The highest anomaly within the ore-body reaches 0.23 mg/kg confirming the geochemical anomaly mapping analysis and highlights these areas, among others, as promising zones for further exploration.

The total area of geochemical mapping aligning with the mineralization covers 1,046,328 square meters. The most significant gold anomalies (>0.027 mg/kg) which align with the well-defined mineralization line covers 634,427 square meters, which corresponds to approximately 60.7% of the total surface area (Figure 4). This indicates that threshold analysis with EDA and geochemical mapping has been very successful in tracing the bedrock mineralization.

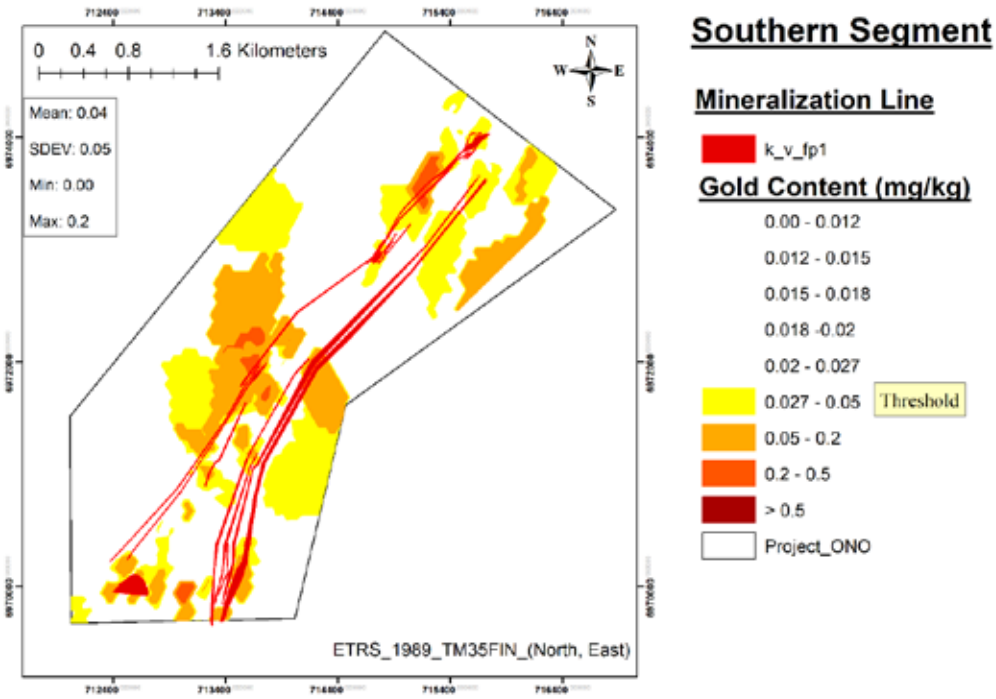

Figure 4. Geochemical anomalies that exceed the given threshold of the median+2MAD method, classified as the most promising gold anomalies in the southern HSB area, and their spatial relationship to the known bedrock mineralization zone depicted in red (drill core data).

Concluding, the independence of median +2MAD method from Gaussian distribution and transformations provides a powerful tool for estimating thresholds, thus geochemical anomalies in soil. The presented methodology can contribute to the development of cost-effective and efficient exploration strategies both in greenfields and brownfields settings.

Acknowledgements

We express our sincere gratitude to Endomines Oy company for their generous provision of the geochemical data set. The anonymous reviewers are especially thanked for their constructive comments and revisions, which greatly improved the initial manuscript.

References

Garrett, R. G. (1991). The Management, Analysis and Display of Exploration Geochemical Data, Exploration Geochemistry Workshop. Geological Survey of Canada Open File 2390, Paper 9, 9-1 to 9-4.

Hartikainen, A., & Nurmi, P. A. (1993). Till geochemistry in gold exploration in the Late Archean Hattu schist belt, Ilomantsi, eastern Finland. Geological Survey of Finland, Special Paper, 17, 323-352.

Hawkes, H.E., & Webb, J.S. (1962) Geochemistry in Mineral Exploration. (pp. 1–415). New York: Harper & Row.

Johnston, K., Ver Hoef, J.M., Krivoruchko, K., & Lucas, N. (2003). The principles of geostatistical analysis, Using ArcGIS geostatistical Anal., ESRI, Redlands, CA pp. 4980.

Kojonen, K., Johanson, B., O'Brien, H. E., & Pakkanen, L. (1993). Mineralogy of gold occurrences in the late Archean Hattu schist belt, Ilomantsi, eastern Finland. Geological Survey of Finland, Special paper, 17, 233-271.

Kürzl, H. (1988). Exploratory data analysis: recent advances for the interpretation of geochemical data. Journal of Geochemical Exploration 30(1-3): 309-322.

Miesch, A. T., & Chapman, R. P. (1977). Log transformations in geochemistry. Journal of the International Association for Mathematical Geology, 9, 191-198.

O'Brien, H. E., Nurmi, P. A., & Karhu, J. A. (1993). Oxygen, hydrogen and strontium isotopic compositions of gold mineralization in the Late Archean Hattu schist belt, Ilomantsi, eastern Finland. Geological Survey of Finland, Special Paper, 17, 291-306.

Shepard, D. (1968). A two-dimensional interpolation function for irregularly-spaced data. In Proceedings of the 1968 23rd ACM national conference (pp. 517-524).

Sorjonen-Ward, P. B., Hartikainen, A., Nurmi, P. A., Rasilainen, K., Schaubs, P., Zhang, Y., & Liikanen, J. (2015). Exploration targeting and geological context of gold mineralization in the Neoarchean Ilomantsi greenstone belt in eastern Finland. Mineral Deposits of Finland, 435-466.

Tukey, J.W. (1977). Exploratory Data Analysis (Vol. 2, pp. 131-160). Addison-Wesley, Reading.

Xuejing, X., & Xueqiu, W. (1991). Geochemical exploration for gold: a new approach to an old problem. Journal of Geochemical Exploration, 40(1-3), 25-48.

17th INTERNATIONAL CONGRESS of the Geological Society of Greece

BULLETIN OF THE GEOLOGICAL SOCIETY OF GREECE, SP. PUBL.

EXTENDED ABSTRACT 303

Liquefaction risk assessment of airport infrastructure using geological data and remote sensing techniques

Taftsoglou M.[1], Valkaniotis S.[2], Papathanassiou G.[3], Argyroudis S.[4]

(1) Department of Earth and Marine Science, University of Ferrara, Italy, tftmra@unife.it , (2) Department of Civil Engineering, Democritus University of Thrace, Greece , (3) Department of Geology, Aristotle University of Thessaloniki, Greece , (4) Department of Civil and Environmental Engineering, Brunel University of London, UK

Abstract

This research serves toward safeguarding airport infrastructure in liquefaction-prone regions. Although airports contribute to the socioeconomic vitality of a region and serve as emergency means in cases of seismic events, their functionality remains vulnerable to disruption caused by secondary earthquake effects such as soil liquefaction. Hence, the risk and vulnerability assessment of airport facilities is crucial for their functionality and preparedness during and after the liquefaction events. This study introduces a practical and rapid assessment tool for the preliminary identification of areas prone to liquefaction and the risk analysis of airport infrastructure on a regional scale. As region of research was selected the Nestos delta in Greece, where the critical infrastructure of Kavala International Airport is placed (KVA). According to the results, a significant section of KVA's runway and taxiways are located on highly susceptible soils of abandoned meanders. Aiming to quantify the impacts of liquefaction in the susceptible areas, FEMA's HAZUS (FEMA, 2022) methodology is applied, estimating values of 20% of liquefaction probability and 3.1-12.3 cm of expected ground settlements for the class of very high susceptible units. The results of the liquefaction hazard analysis are used for the risk assessment of the airport infrastructure, estimating a total direct loss of €5 million. Validation of the proposed methodology was achieved using datasets from three international airports that sustained extensive seismic damage in the past.

Introduction

As it was concluded in the aftermath of major seismic events such as the Loma Prieta in 1989, the Northridge in 1994, the Kobe in 1994, the Nisqually in 2001 and the Türkiye-Syria in 2023, a significant part of the damage induced to airport facilities is correlated with the earthquake secondary effects of liquefaction. Highly correlated with the hydrogeological conditions and the depositional history of sediments, liquefaction is generally induced in fluvial and coastal environments and filled land areas that contain shallow layers of young, saturated, low density, granular sediments (Youd and Hoose, 1978; Holzer, 1998; Tinsley et al., 1985). As a result, liquefaction-related phenomena of ground settlement and cracking, lateral spreading and foundation failure can occur affecting airport's runways, air control towers, terminal buildings, power and communications and fuel systems. Therefore, it is crucial to have a comprehensive understanding of liquefaction mechanisms and their impacts on airport environments, to ensure that efficient mitigation measures are taken.

This paper presents a practical and quick tool for the regional assessment of airport susceptibility and risk to liquefaction events. Focusing on the critical infrastructure of Kavala International Airport (KVA) in the northern Greece, a geomorphological map is initially developed using remote sensing data and geological information. Based on this map, the susceptibility of the critical infrastructure's formations to liquefaction is assessed resulting to a related liquefaction susceptibility map, which is utilized to estimate the permanent ground displacement (PGD); caused by liquefaction; in the form of ground settlements. Subsequently, PGD is used as the intensity measure for the risk analysis of the infrastructure. The liquefaction susceptibility and vulnerability assessment are validated using datasets from Oakland, King County (USA) and Hatay.

Methodology

The proposed methodology is divided into two main phases of 7 individual steps. "Phase I" is based on a workflow described by Taftsoglou et al. (2022) and focuses on assessing the susceptibility of the investigation area following the four steps of: (1) data input and processing, (2) mapping geomorphological features, (3) classification of susceptible to liquefaction surficial geological units, (4) liquefaction susceptibility map of surficial geological features. On the other hand, "Phase II" aims to analyze the risk of the critical infrastructure located in the same region and is consisted by four additional steps of: (5) estimation of the probability to liquefaction phenomena, (6) estimation of permanent ground displacement (PGD), (7) Vulnerability and loss.

In step 1 geological and historical maps of the area, orthophotos and satellite images were collected in order to

examine the geological formations and the geomorphological evolution of the plain. Tracing geomorphological features such as abandoned stream/meanders, point bars, oxbow lakes, dunes and lagoons through processing of multi-temporal and historical layers in correlation with the local topography (DEM) was performed in step 2, resulting in a geomorphological map. In the 3rd step, the age of the delineated surficial geological units and their classification to susceptibility classes were assessed, with the latter conducted based on the criteria proposed by Youd and Perkins (1978). In step 4, a liquefaction susceptibility map was compiled, including four classes (Low, Moderate, High and Very High), where coastal and fluvial deposits were classified as high to very high susceptible units.
Having estimated the liquefaction susceptibility on a regional scale, "Phase II" with steps 5 to 8 took place to evaluate the related risk of these critical facilities. Specifically, HAZUS (FEMA, 2022) methodology was applied in step 5, according to which, a seismic scenario was selected, based on SHARE and GreDaaS databases of seismogenic sources (Caputo et al, 2012; Giardini et al, 2013). Taking into consideration the parameters of the susceptibility categories, a moment magnitude value of Mw 6.3, a ground shaking of PGA=0.36g and a groundwater depth of 6m, the probability of liquefaction according to HAZUS method was determined for the airport location, classifying the area into four probability classes. Therefore, based on the estimated probability in correlation with the ground settlement amplitude proposed by HAZUS, the expected ground settlement was assessed for each susceptibility class in step 6. Through the last step of this workflow, vulnerability and expected losses of airport facilities are estimated, following the fragility functions that are included in HAZUS methodology.

Results

Based on the spatial distribution of surficial geological units proposed by this study, application of Youd and Perkins criteria classified KVA area into four liquefaction susceptibility classes. According to the resulted liquefaction susceptibility map, 300m of the northwestern runway limit, 2.7 km of the adjacent taxiway and 78m^2 of the apron area are constructed in the very high susceptible zone of an abandoned Nestos River branch, while the rest of the facilities are located on regions of moderate susceptibility.
Application of FEMA's HAZUS methodology (FEMA, 2002) estimated 0.2 probability values for the zone of KVA classified as very high susceptible and 0.08 for the moderate one, while the corresponding average ground settlements values (PGD) for these classes were assessed as 6.1 cm (3.1 – 12.3 cm) and 0.4 cm (0.2 – 0.8 cm). As the critical facilities of runway, taxiway and apron are in moderate and very high susceptible zones, the estimated PGD values for these classes were used for the evaluation of the average loss ratios. Finally, multiplication of these values with the reconstruction cost and extent of its facility, resulted in direct losses of € 0,37 million for the case of runway, € 2,5 million for the taxiway and € 2 million for the apron and consequently a total loss of €5 million.

Validation

The liquefaction susceptibility assessment and risk analysis for the KVA airport are validated in the case studies of Oakland (OAK), Hatay (HTY) and King County (BFI) International airports, where the most extended liquefaction-related damages occurred to the runway's areas. A comparison of results estimated according to HAZUS methodology revealed that the observed damages of liquefaction after the earthquakes of Loma Prietta (1989), Turkey-Syria (2023) and Nisqually (2001) in the three airport locations align with the estimated ones, as all the records were detected in areas characterized as very high susceptible to these phenomena.
Particularly, 900 m of the northwestern runway in the OAK airport was damaged by sand boils, as well as by buckling and cracking of the pavement, while cracks were also detected in the adjacent taxiway (Holzer, 1998; Seed et al. 1991). Application of the proposed methodology shown consistency with these observations as according to it OAK is located predominantly in the zone of very high susceptibility, with probability of 0.22 for liquefaction occurrences and expected PGD values of 3.4 – 13.6 cm. Similarly, after the Nisqually earthquake, extensive liquefaction was recorded in the eastern runway of BFI airport (Nisqually Earthquake Clearinghouse Group, 2001; Bray and others, 2001), where application of the proposed method resulted in the classification of this region as very high susceptible and the estimation of probability and PGD values of 0.17 and 2.5 – 10.2 cm respectively. Moreover, the projection of liquefaction occurrences in HTY airport shown consistency with the maps obtained from the proposed methodology, since the entire airport infrastructure is characterized as highly susceptible to liquefaction, with a probability of 0.24 of observation of liquefaction phenomena and predicted PGD values ranging from 3.6 to 14.4 cm. However, it should be noted that the availability and the quality of the recorded data resulted in more qualitative comparisons between the observed and predicted values, since the extent of the observed failures is considerably more localized than anticipated.

Conclusions

This paper presents an efficient and rapid evaluation tool for assessing the risk of airport infrastructure located in

liquefaction-prone areas, using geological and remote sensing data. As the area of interest was selected International Airport of Kavala (KVA), built in the Nestos delta in Greece. Application of the proposed methodology initially resulted in a liquefaction susceptibility map of the study area. Afterwards the probability of liquefaction and the expected ground settlements were estimated according to a representative seismic event. The direct losses for the runway, taxiways and apron are estimated to €5 million. The methodology is validated using three cases study airports which sustained damage due to liquefaction. According to the application of the proposed approach, the observed damaged areas of these infrastructures align closely with the estimations of the expected ones, confirming the accurate identification of the areas susceptible to liquefaction phenomena.
The proposed methodology provides a useful guide to reducing the risk of liquefaction phenomena specifically affecting airport facilities, highlighting areas more susceptible to these processes and, through targeted prevention, reducing possible service interruptions due to seismic events.

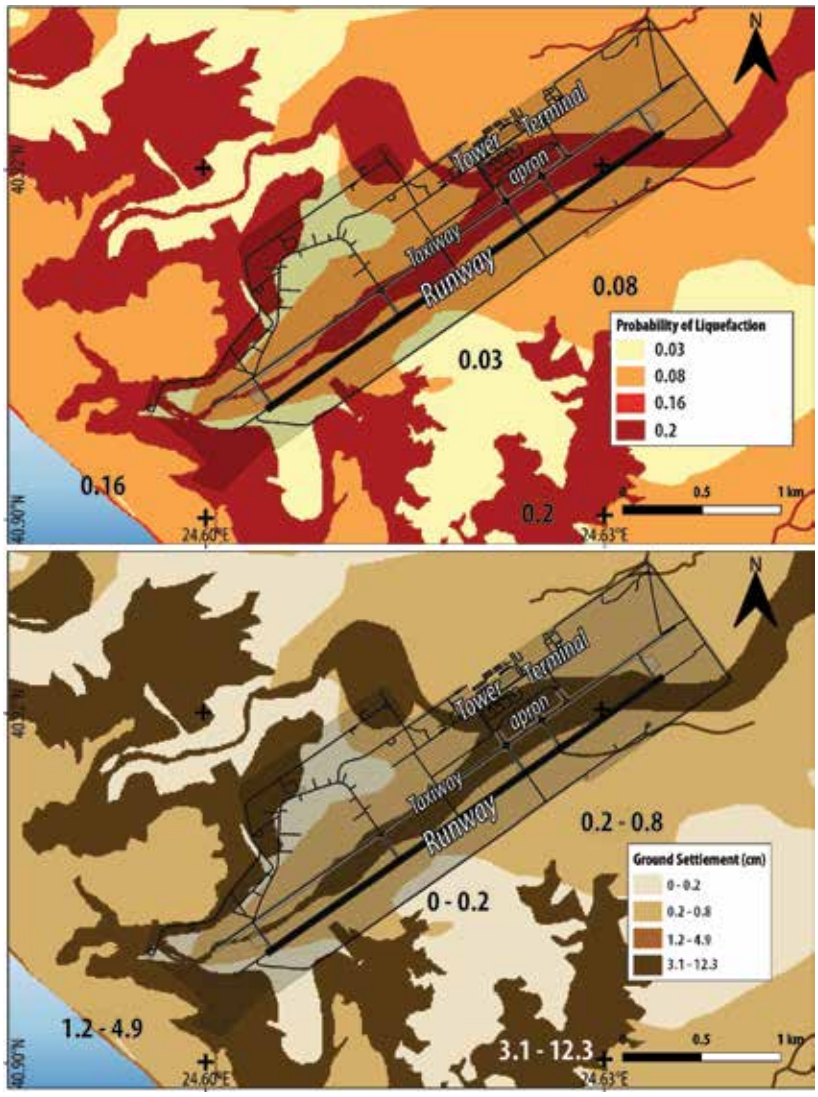

Figure 1. Probability of liquefaction and expected ground settlements in KVA area.

References

Bray, J.D., et al. (2001). Some observations of geotechnical aspects of the February 28, 2001, Nisqually earthquake in Olympia, South Seattle, and Tacoma, Washington, A NSF-PEER sponsored reconnaissance effort: http://peer.berkeley.edu/nisqually/geotech/.

Caputo, R., Chatzipetros, A., Pavlides, S., Sboras, S., 2012. The Greek Database of Seismogenic Sources (GreDaSS): state-of-the-art for northern Greece. Annals of Geophysics, 55(5), 859-894.

FEMA., 2022. Hazus Earthquake Model Technical Manual, Hazus 5.1, FEMA US.

Giardini et al., 2013. Seismic Hazard Harmonization in Europe (SHARE): Online Data Resource, doi: 10.12686/SED-00000001-SHARE.

Holzer, T.L., 1998. The Loma Prieta, California, Earthquake of October 17, 1989 - Liquefaction: U.S. GSPP 1551-B, 314.

Nisqually Earthquake Clearinghouse Group (2001). The Nisqually, Washington, earthquake of February 28, 2001: EERI, 2001-01, 26 p.

Seed, R.B., Riemer, M., Dickenson, S.E., 1991. Liquefaction of Soils in the 1989 Loma Prieta Earthquake. International Conferences on Recent Advances in Geotechnical Earthquake Engineering and Soil Dynamics. 9.

Taftsoglou, M., Valkaniotis, S., Papathanassiou, G., Klimis, N., Dokas I., 2022. A Detailed Liquefaction Susceptibility Map of Nestos River Delta, Thrace, Greece Based on Surficial Geology and Geomorphology. Geosciences. 2022; 12(10).

Tinsley, J.C., Youd, T.L., Perkins, D.M. and Chen, A.T.F., 1985. Evaluating liquefaction potential. Evaluating earthquake hazards in the Los Angeles region—An earth science perspective: US Geological Survey Professional Paper, 1360, pp.263-316.

Youd, T.L., Hoose, S.N., 1978. Historic ground failures in Northern California triggered by earthquakes: U.S. GSPP 993.

Youd, T.L., Perkins, D.M., 1978. Mapping of liquefaction induced ground failure potential. Geotechnical Engineering Division 104, 433–446.

17th INTERNATIONAL CONGRESS of the Geological Society of Greece

BULLETIN OF THE GEOLOGICAL SOCIETY OF GREECE, SP. PUBL.

EXTENDED ABSTRACT 304

A correlation of liquefaction phenomena with the surficial geology of point bar deposits; case studies 2021 Damasi, Greece, 2023 Kahramanmaraş, Türkiye and 2010-2011 Christchurch, New Zealand

Taftsoglou M.[1], Valkaniotis S.[2], Papathanassiou G.[3], Ntouvartzis V.[3], Rapti D.[4], Caputo R.[1]

(1) Department of Earth and Marine Science, University of Ferrara, Italy, tftmra@unife.it, (2) Department of Civil Engineering, Democritus University of Thrace, Greece, (3) Department of Geology, Aristotle University of Thessaloniki, Greece, (4) Department of Chemical, Pharmaceutical and Agricultural Sciences, Ferrara University, Italy

Abstract

After the seismic sequences of 2021 in Damasi (Greece), 2023 in Kahramanmaraş (Türkiye) and 2010-2011 in Christchurch (New Zealand), extensive liquefaction phenomena were induced in the floodplain and point bars of the associated meandering rivers. As the identification of paleoenvironmental features plays a pivotal role in the assessment of the liquefaction susceptibility of an area, this research aims to statistically investigate the spatial distribution of liquefaction phenomena within point bar formations. By combining historical and remote sensing data, reconstruction of the evolution of each meandering fluvial system took place to delineate the different types of lithofacies encountered in point bars. Afterwards, correlation of the density of liquefaction manifestations (ejecta and lateral spreading) with sand- and mud-prone sediments occurred, based on a relationship proposed in this study. The outcome that arose from this procedure resulted in the attribution of weight values for each heterogeneity type, according to which, most of the liquefaction phenomena are correlated with the sandy sediments deposited on the upstream flow direction.

Introduction

During the last decade and especially following some major earthquakes associated with widespread secondary seismic effects, researchers started realizing that the triggering of liquefaction clustering phenomena tend to follow distinct patterns. This preferential behavior of the sediments to produce liquefaction manifestations has been extensively studied in notable events occurred in New Zealand, Italy, Greece and Turkey (Wotherspoon *et al*. 2012; Di Manna *et al*. 2012; Galli *et al*. 2012; Bastin *et al*. 2015; Papathanassiou *et al*. 2012, 2015, 2022; Civico *et al*. 2015; Taftsoglou *et al*. 2023; Abayo *et al*. 2023). In several cases, it was concluded that specific geomorphological areas within fluvial meandering systems such as old/abandoned channels, point bars and oxbow lakes favored the occurrences of liquefaction phenomena, showing a higher liquefaction density compared to other sectors of the same floodplain. Consequently, the reliability of a liquefaction susceptibility map is highly dependent on the scale and accuracy of the geological and geomorphological mapping of a floodplain.

Following this approach, this research focuses on the valleys of Piniada in Thessaly (Greece), Orontes in Hatay (Türkiye) and Avon in Christchurch (New Zealand) where the mainshocks of Mw=6.3 (March 2021), Mw=7.7 (February 2023) Mw =7.1 (September 2010) and Mw =6.2 (February 2011) occurred respectively. Covered mostly by Quaternary fluvial deposits, our study focused on the inner part of the meandering systems, i.e. point bars, where liquefaction manifestations were recorded after these seismic sequences. Considering the heterogeneity of the noncohesive material accumulated on the inner part of the meander (point bars), correlation between the distribution of liquefaction sites and sand- and mud-prone sediments was examined. To achieve this, the method introduced by Russel (2017) applied in the first step, resulted in the delineation of different types of lithofacies. In order to correlate the density of liquefaction phenomena with the different types of lithofacies, a relationship was proposed afterwards, which resulted in the attribution of weight indexes to each heterogeneity type.

Methodology

For the purposes of this study, the methodology proposed by Russell (2017) was applied to analyze point-bar formations in the Piniada, Avon and Orontes Valleys. According to this method, point-bar deposits are characterized by lateral discontinuity (Allen, 1965) and a complex distribution of lithofacies of sandstone and mudstone beds (Thomas, 1987, Tye, 2004, Miall, 2006, Durkin *et al*., 2015), while their sedimentation is influenced by the meander system evolution and its associated variations in channel geometry and deposition patterns. Moreover, grain size distribution within these formations reflects the flow direction and speed of a meander, with finer materials predominating downstream and coarser deposits upstream (Jackson, 1976, Fustic *et al*., 2012, Nardin *et al*., 2013).

Based on Russell's (2017) methodology during the first step meander shapes were classified according to their geometric shapes into the four groups of open asymmetric, angular, bulbous, and open symmetric. Afterwards, utilization of high-resolution satellite images and historical aerial imagery for each case took place in order to map meander's thalweg lines and apexes as well as the inflection points, which indicate the transitional zones between sand- to mud-prone sediments (Smith et al., 2009). Combination of sediment deposition patterns with meander geometry resulted in a map classifying the meander heterogeneity into four types of Sand-I, Sand-II, Mud-I, and Mud-II.
Having compiled this map, the liquefaction areas (polygons) of ejecta phenomena for Piniada, Avon and Orontes valleys and lateral spreading for the last two were projected in order to examine their distribution to each type of sediment. Particularly, based on the factors of (a) density of liquefaction manifestations per heterogeneity type (DenseHT) and (b) the total density of liquefaction sites in point bar formations (DensePB), a relationship is proposed expressed by the equation:

$$\text{Weight HT} = \ln(\text{DenseHT} / \text{DensePB})$$

Application of this relationship for each case study and for the different categories of liquefaction phenomena (ejecta, lateral spreading) resulted in the estimation of four total weight indexes attributed to the heterogeneity types of Sand-I, Sand-II, Mud-I and Mud-II.

Results
In order to examine the correlation between the density of liquefaction phenomena and the distribution of sand and mud rich deposits, we initially delineated the different lithofacies on selected point bars in Piniada, Avon and Orontes Valleys.
Specifically, 4.7km^2, 1.57 km^2 and 6.9 km^2 of point bar formations were examined for each case respectively and characterized according to their meander shape into the four groups of open asymmetric, angular, bulbous, and open symmetric. Based on the high resolution satellite images and the historical aerial imagery, geometrical characteristics of the meander evolution, such as thalweg lines, apexes, inflection points and scroll bar formation were detected resulting in the mapping of the four heterogeneity types. Projection of the liquefaction phenomena of ejecta in the case of Piniada Valley, shown that 81% of the total records covered the coarser deposits of the upstream limb, while in Orontes Valley 57% were observed in Sand-II type. Similarly, liquefaction phenomena triggered by the Christchurch major events of September 2010 and February 2011 indicated that most of the ejecta occurred in the Sand-II type, covering 60% of these deposits. Regarding the lateral spreading manifestations in Orontes and Avon Valleys, most of them were detected in sandy types I and II, with 70% coverage in the case of Orontes and more than 85% in Avon.

Conclusion
The spatial distribution of liquefaction phenomena in Piniada, Orontes and Avon Valleys clearly indicate that one of the most susceptible to liquefaction geomorphological features are the point bars formations. As these features are characterized by different heterogeneity types with alterations between the ratio of coarse and fine materials, a detailed mapping of the different lithofacies is considered in order to analyze the preferential behavior of the areas more or less susceptible to liquefaction phenomena.
For the purposes of this study, point bar features were traced and classified into four heterogeneity classes of Sand-I, Sand-II, Mud-I and Mud-II, based on geological, geomorphological and remote sensing. Comparison between the spatial distribution of different lithofacies with liquefaction manifestations indicated that most of the effects were triggered in deposits mainly consisted of sandy materials.
Based on the density of ejecta and lateral spreading phenomena per heterogeneity type and their total density in point bar formations, a relationship is proposed according to which different weight values were attributed for Sand-I, Sand-II, Mud-I and Mud-II deposits. The outcome that arose from this procedure resulted in weight values of 0.13 and 0.10 for Sand-I and Sand-II types respectively, while for the lateral spreading phenomena, the attributed coefficients for the same types are -0.19 (Sand-I) and -0.09 (Sand-II).

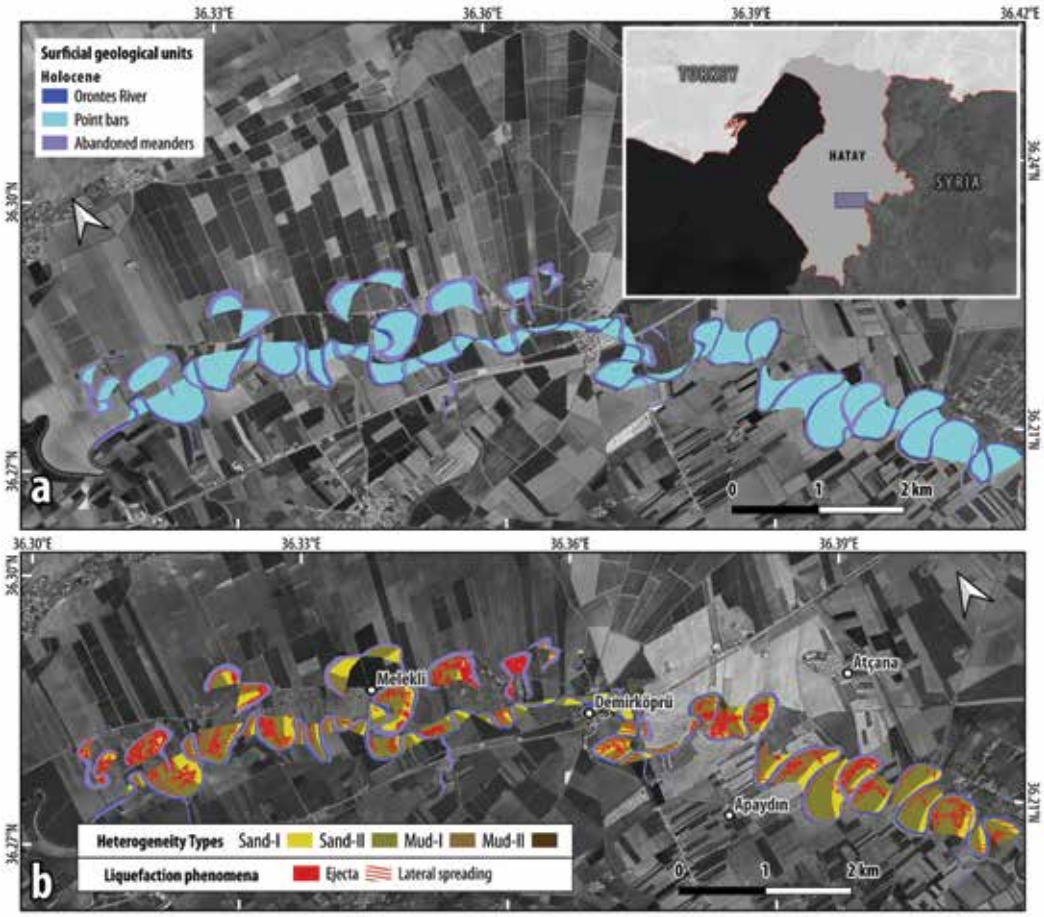

Figure 1. Liquefaction phenomena in Orontes valley triggered by the 2023 Kahramanmaraş earthquake in Turkey. (a) Map of surficial geological units of Orontes River, point bars and abandoned meanders. (b) Heterogeneity types of point bars in Orontes meanders in correlation with the liquefaction phenomena (ejecta and lateral spreading). The Index map on the right corner illustrates the study area (blue box) located in the province of Hatay.

References

Abayo NI.; Caba AC.; Chamberlin E.; Montoya B., 2023. Fluvial geomorphic factors affecting liquefaction induced lateral spreading. Earthquake Spectra. 39(4), 2518-2547.

Allen J.R.L., 1965. A review of the origin and characteristics of recent alluvial sediments. Sedimentology 5, 89-191.

Bastin S.; Quigley M. and Bassett K., 2015. Paleoliquefaction in easter Christchurch, New Zealand. Geological Society of America bulletin. 12, 1348-1365.

Civico, R.; Brunori, C.A.; De Martini, P.M.; Pucci, S.; Cinti, F.R.; Pantosti, D., 2015. Liquefaction susceptibility assessment in fluvial plains using airborne lidar: The case of the 2012 Emilia earthquake sequence area (Italy). Natural Hazard Earth System Sciences. 15, 2473–2483.

Di Manna P.; Guerrieri L.; Piccardi L.; Vittori E.; Castaldini D.; Berlusconi A.; Bonadeo L.; ComercibV.; Ferrario F.; Gambillara R.; Livio F.; Lucarini M. and Michetti A.M., 2012. Ground effects induced by theb2012 seismic sequence in Emilia: implications for seismic hazard assessment in the Po Plain. Annales geophysicae. 55(4), 697-703.

Durkin P.R.; Hubbard S.M.; Boyd R.L. and Leckie D.A.., 2015. Stratigraphic expression of intra-point-bar erosion and rotation. Journal of sedimentary research, 2015. 85, 1238-1257..

Fustic M.; Bennett B.; Huang H. and Larter S., 2012. Differential entrapment of charged oil - new insights on McMurray Formation oil trapping mechanisms. Marine and Petroleum Geology. 36(1), 50-69.

Galli P, Castenetti S, Peronace E., 201. May 2012 Emilia earthquakes (Mw 6, northern Italy): macroseismic effects distribution and seismotectonic implications. Alpine and Mediterranean Quaternary 25(2):105–123.

Jackson R.G., 1976. Sedimentological and fluid-dynamic implications of the turbulent bursting phenomenon in geophysical flows. Journal of Fluid Mechanics 77(3), 531-560.

Miall A.D., 2006. Reconstructing the architecture and sequence stratigraphy of the preserved fluvial record as a tool for reservoir development: a reality check. AAPG Bulletin. 90, 989-1002.

Nardin T.R.; Howard R.F. and Carter B.J.,2013. Stratigraphic architecture of a large-scale point-bar complex in the McMurray

Formation: light detection and ranging and subsurface data integration at Syncrude's Mildred Lake Mine, Alberta, Canada. In: Hein F.J., Leckie D.A. and Suter J.R. (Eds), Heavy oil and oil sand petroleum systems in Alberta and Beyond. AAPG Bulletin 64, 273-311.

Papathanassiou G.; Caputo R. and Rapti-Caputo D., 2012. Liquefaction phenomena along the paleo-Reno River caused by the May 20, 2012, Emilia (northern Italy) earthquake. Annales geophysicae 55(4), 735- 742.

Papathanassiou G.; Mantovani A.; Tarabusi G.; Rapti D. and Caputo R.,2015. Assessment of liquefaction potential for two liquefaction prone area considering the May 20, 2012 Emilia (Italy) earthquake. Engineering Geology 189, 1-16.

Papathanassiou G.; Valkaniotis S.; Ganas A.; Stampolidis A.; Rapti D. and Caputo R., 2022. Floodplain evolution and its influence on liquefaction clustering: the case study of March 2021 Thessaly, Greece, seismic sequence. Engineering Geology 298, 1-18

Russell C.E. 2017. Prediction of sedimentary architecture and lithological heterogeneity in fluvial point-bar deposits. PhD thesis, University of Leeds, Leeds, UK.

Smith, D.G., Hubbard, S.M., Leckie, D.A. and Fustic, M. (2009) Counter Point Bar Deposits: Lithofacies and Reservoir Significance in the Meandering Modern Peace River and Ancient McMurray Formation, Alberta, Canada. Sedimentology, 56, 1655–1669.

Taftsoglou M.; Valkaniotis S.; Papathanassiou G.; Karantanellis, E., 2023. Satellite Imagery for Rapid Detection of Liquefaction Surface Manifestations: The Case Study of Türkiye–Syria 2023 Earthquakes. Remote Sensing. 15, 4190.

Thomas R.G.; Smith D.G.; Wood J.M.; Visser J.; Calverley-Range E.A. and Koster E.H., 1987. Inclined Heterolithic Stratification-terminology, Description, Interpretation and Significance. Sedimentary Geology 53, 123-179.

Tye R.S., 2004. Geomorphology: An approach to determining subsurface reservoir dimensions. AAPG Bulletin 88(8), 1123-1147

Wotherspoon L.; Pender M. and Orense R.,2012. Relationship between observed liquefaction at Kaiapoi following the 2010 Darfield earthquake and former channels of the Waimakariri River. Engineering Geology.125, 45-55

17th INTERNATIONAL CONGRESS of the Geological Society of Greece

BULLETIN OF THE GEOLOGICAL SOCIETY OF GREECE, SP. PUBL.

EXTENDED ABSTRACT 305

Earthquake hazard implications for Lesvos (Midilli) and the surrounding region

Tan O.[1], Karagöz Ö.[2]

(1) İstanbul University-Cerrahpaşa, Faculty of Engineering, Department of Geophysical Engineering, İstanbul, Türkiye. onur.tan@iuc.edu.tr, (2) Çanakkale Onsekiz Mart University, Faculty of Engineering, Department of Geophysical Engineering, Çanakkale, Türkiye.

Introduction

The most recent seismic activities around Lesvos Island and the coastal area of western Turkey show that the potential for earthquake hazards is evident. The shallow soil structure beneath an urban area is more dominant than the source features for earthquake damage.

The western part of the Türkiye and the Greek islands in the east of the Aegean Sea have suffered from destructive earthquakes throughout history. The 1912 Mürefte (Mw 7.3), 1944 Edremit (Ms 6.8), 1953 Yenice-Gönen (Ms 7.2) and 1964 Manyas (Ms 6.9) earthquakes shake the NW Türkiye in the 20th century. There were three significant events in the coastal areas of in the eastern Aegean Sea. In south, the 20 July 2017 Kos (Mw 6.6) earthquakes shake the island and city of Bodrum. In north, the Ayvacık swarm in February and the Lesvos (Midilli) earthquake (Mw 6.3) in June were strongly felt in the region and moderately damaged the villages. Then, the most recent 2020 Samos (Mw 7.0) earthquake affected the Samos Island and city of Izmir. The mainshock, which generated high damage especially in the Bornova Basin (Izmir), showed that the importance of the effect of deep basin structure and building quality in urban areas. The effect of the recent earthquakes broadly in the eastern Mediterranean region indicate that the knowledge of earthquake sources, seismic wave propagations and characteristics of ground motions is critical for urban hazard mitigation and planning in active seismic zones.

In this study, the earthquake hazard of Lesvos Island and the western coast of Türkiye where contain high populated cities, historic heritage and important touristic destinations were investigated considering (1) faulting and rupture features of the 12.06.2017 Lesvos mainshock, (2) numerical waveform simulations with regional 1D velocity structure and shallow soil amplification, (3) relocated earthquakes and (4) cumulative crustal Coulomb stress change due to the destructive earthquakes in the region. The inversion algorithm by Kikuchi and Kanamori (1991) for the teleseismic body waveforms is used to obtain the mainshock's focal mechanism parameters and the rupture propagation. Different from the routine approach in seismological studies, we compared the rupture models of the mainshock using numerical waveform simulations (Karagoz et al., 2018). For this aim, the synthetic seismograms were generated utilizing the discrete wavenumber method with a characterized source model, 1D velocity model between event and stations and amplification of shallow soil beneath stations. The simulation let us not only validate the source model and 1D regional velocity structures but also understand the high damage in the region. We also relocated the earthquakes in the study area with the double-difference inversion method (Waldhauser and Ellsworth, 2000) to understand the seismicity with reliable horizontal and vertical uncertainties. Finally, Coulomb stress change analyses (Lin and Stein, 2004) are performed to calculate the static stress loading areas where the next destructive earthquake may occur.

Results and Conclusions

We invert teleseismic waveforms to determine fault plane solution and rupture propagation of the mainshock. The fault plane parameters are 127°, 47° and -97° for the strike, dip and rake angles, respectively. The finite fault slip model indicates that the rupture propagates circularly from the focal in the first 2-3 s with maximum energy release. Then, it moves to the surface in the next 7-8 s. The maximum slip is 1.8 m, and the average stress drop is 3.6 MPa. The aftershock activity (Papadimitriou et al., 2018) is low in the high-slip patch on the rupture area and vice versa, as observed in the recent 2020 Samos and 2023 Kahramanmaraş destructive earthquakes.

The numerical waveform simulation considering the local soil information is applied to the Lesvos stations to understand the reason for the structural damage on the island. The frequency of the synthetic waveforms with the highest horizontal amplitude (PGV, PGA) is around 3 Hz in Vrissa, which agrees with the fundamental frequency determined from the reported shallow soil Vs model for the region (Figure 1). This frequency match may generate a resonance phenomenon in the soil-covered western part of Vrissa. Thus, we can conclude that the damage in Vrissa is caused mainly by site effects of soil structure, not rupture propagation of the mainshock.

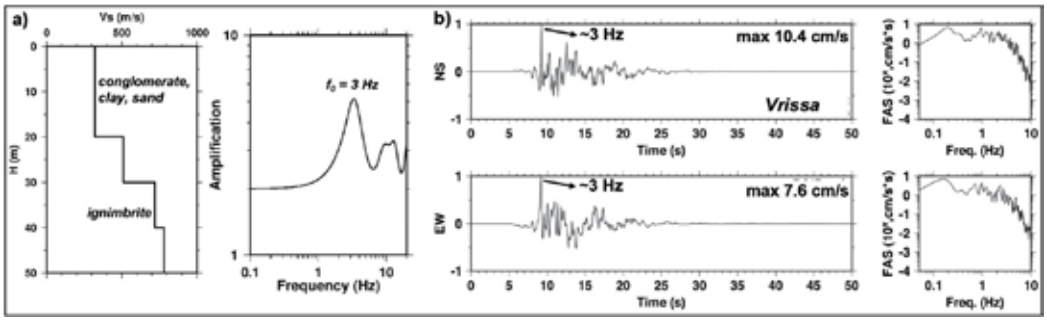

Figure 1. a) Shallow S-wave velocity (Vs) model near Vrissa (Karastathis et al., 2020) and its calculated SH soil amplification. The fundamental frequency is about 3 Hz. b) Synthetic velocity seismograms (normalized) in Vrissa. The wave phase with the maximum peak has a frequency of 3 Hz.

The relocated earthquakes with the double-difference inversion method show the detail of the seismic activity in the region (Figure 2). The 2019 (ML 5.0) and 2024 (ML 4.9) earthquakes in Ayvacık are on the southwest of the right-lateral Evciler Fault, and their oblique focal mechanism solutions indicate that the strike-slip motion extends to Ayvacık. However, the 2017 Ayvacık swarm has a NW-SE normal faulting mechanism. Different characteristics of these earthquakes indicate a complex tectonic structure in a small area on the Biga Peninsula (NW Türkiye). One of the important observations in this study is that the two notable clusters in 2021 and 2023 are at the two ends of the Agia-Paraskevi Fault. Each cluster has more than 300 events appearing in a limited period and has a right-lateral strike-slip mechanism. The spatio-temporal characteristics of seismicity show that there are several earthquake clusters in the region, and they show a high activation rate in a short period, like in different regions in western Türkiye. We consider that the Psara-Lesvos and Agia-Paraskevi faults are the principal displacement zone of a SW-NE right-lateral strike-slip shear zone (SW continuation of the southern branch of the North Anatolian Fault Zone), and the 2021 and 2023 earthquake clusters are on its right-lateral synthetic shears (R).

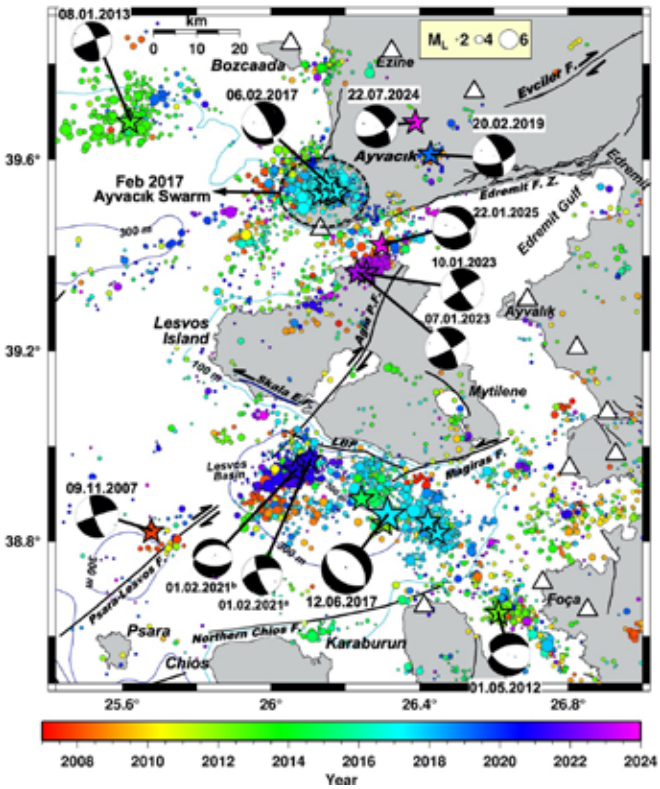

Figure 2. Relocated earthquakes with the double-difference algorithm in the study area. The color scale shows the event date. Stars are events with $M_L \geq 5.0$. Triangles are the seismological stations. The bathymetry contours are from the GEBCO databases.

The Coulomb stress change analyses utilizing the well-known destructive earthquakes in the last 150 years argue that the final stress loading stage on the faults infers continuity of earthquake hazard possibility for Lesvos Island and its surroundings. The cumulative stress change calculations for the events on optimal normal and strike-slip faults are shown in Figure 3. In general, positive and negative stress lobs for both fault types are similar; there is no important difference. The stress load in the region and the most recent 22.01.2025 earthquake are evidence of the future earthquake hazard for the study area.

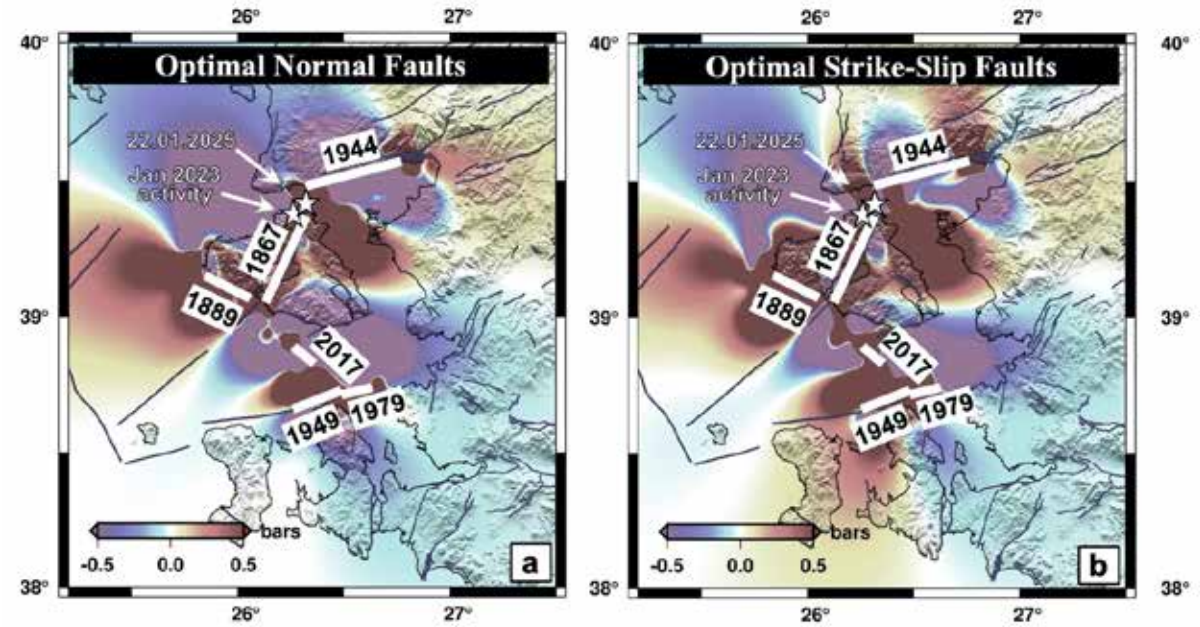

Figure 3. Coulomb stress changes on optimal normal (a) and strike-slip (b) faults for large earthquakes since 1867. The January 2023 and the latest 22 January 2025 (Mw 5.3) activities are shown with small stars.

Acknowledgments
We gratefully thank George Karviris and Vassilis Karakostas for sharing aftershock data of the 2017 Lesvos earthquake.

References
Karagoz, O., Chimoto, K., Yamanaka, H., Ozel, O., Citak, S., 2018. Broadband ground-motion simulation of the 24 May 24 Gokceada (North Aegean Sea) earthquake (Mw 6.9) in NW Turkey considering local soil effects. Bull Earthquake Eng., 16, 23–43.

Karastathis, V., Novikova, T., Mouzakiotis, E., Tselentis, G.A., 2020. Seismic response of the soil with thermo fluids: Case study of 12 June 2017 earthquake in Lesvos Island (NE Aegean, Greece). Soil Dynamics and Earthquake Engineering, 129, 105942.

Kikuchi, M., Kanamori, H., 1991. Inversion of complex body waves—III. Bulletin of the Seismological Society of America, 81(6), 2335-2350.

Lin, J., Stein, R.S., 2004. Stress triggering in thrust and subduction earthquakes and stress interaction between the southern San Andreas and nearby thrust and strike-slip faults. Journal of Geophysical Research: Solid Earth, 109(B2).

Papadimitriou, P., Kassaras, I., Kaviris, G., Tselentis, G. A., Voulgaris, N., Lekkas, E., Kleanthi, M., 2018. The 12th June 2017 Mw = 6.3 Lesvos earthquake from detailed seismological observations. Journal of Geodynamics, 115, 23-42.

Waldhauser, F., Ellsworth, W.L., 2000. A double-difference earthquake location algorithm: Method and application to the northern Hayward fault, California. Bulletin of the Seismological Society of America, 90(6), 1353-1368.

17th INTERNATIONAL CONGRESS of the Geological Society of Greece

BULLETIN OF THE GEOLOGICAL SOCIETY OF GREECE, SP. PUBL.

EXTENDED ABSTRACT 306

The Megala Therma-Katsilemonas gold-silver mineralization, Lesvos island, Greece: a new alkalic-type epithermal deposit in Greece?

Tektonidou D.[1], Voudouris P.[1,11], Mavrogonatos C.[2], Zaccarini F.[3], Melfos V.[4], Soulamidis G.[1,11], Georgatou A.A.[1,11], Serfa E.[1,11], Zhai D.[6], Keith M.[7], Tarantola A.[8], Tombros S.[5], Alfieris D.[9], Melfou M[4], Zygouri E[1,11], Kanellopoulos C.[10]

(1) Faculty of Geology and Geoenvironment, NKUA, Athens, Greece, despoina.tektonidou@gmail.com; voudouris@geol.uoa.gr; gsoulamidis@geol.uoa.gr; a.georgatou@geol.uoa.gr; tzeniserfa5@gmail.com; ezygouri@geol.uoa.gr (2) Department of Earth Sciences, University of Pisa, Pisa, Italy, konstantinos.mavrogonatos@unipi.it (3) Geosciences Programme, Faculty of Science, University Brunei Darussalam, Jalan Tungku Link, Gadong, Brunei; federicazaccarinigaruti@gmail.com (4) Faculty of Geology, Aristotle University of Thessaloniki, Thessaloniki 54124, Greece, melfosv@geo.auth.gr; melfoumv@geo.auth.gr (5) Department of Materials Science, University of Patras, Rio, Greece, stel@upatras.gr (6) School of Earth Sciences and Mineral Resources, China University of Geosciences, Beijing, China, dgzhai@cugb.edu.cn (7) GeoZentrum Nordbayern, Friedrich-Alexander-Universität (FAU) Erlangen-Nürnberg, Erlangen, Germany; manuel.keith@fau.de (8) GeoRessources Laboratory (UMR 7359), University of Lorraine-CNRS, France, alexandre.tarantola@univ-lorraine.fr (9) Transforming Data into Business Strategy, dimitrisal@hotmail.com (10) Hellenic Survey of Geology and Mineral Exploration (HSGME), Attiki, Greece, ckanellopoulos@eagme.gr (11) Mineralogy-Petrology Museum, NKUA, Athens, Greece

Introduction

Epithermal gold ± silver deposits are major commodities for precious and critical metals (i.e. Au, Ag, Te, Se, Sn, Bi, In, Ga, Ge) (John et al. 2018). They are subdivided in three categories based on the sulfur fugacity of the mineralizing fluids: low- (LS), intermediate- (IS), and high-sulfidation (HS), following the classification schemes of Hedenquist *et al.* (2000) and Einaudi *et al.* (2003). Among the low-sulfidation class, the so-called alkalic-type gold deposits are spatially associated with alkaline igneous rocks and display specific mineralogical and geochemical characteristics, as for example, the presence of tellurides, fluorite and the vanadium-bearing mica roscoelite (Jensen and Barton, 2000; Cook *et al.*, 2009; Kelley and Spry, 2016; Kelley *et al.*, 2020; Keith *et al.*, 2020).

Northeastern Greece (Western Thrace and the Greek Aegean islands of Limnos and Lesvos) hosts a variety of porphyry-epithermal systems enriched in tellurides (i.e.,Pagoni Rachi-St Philippos, Pefka, Fakos and Stypsi-Megala Therma), which are spatially and genetically associated with Oligocene to Miocene, high-K calc-alkaline to shoshonitic magmatic rocks (Arikas and Voudouris, 1998; Voudouris and Alfieris, 2005; Voudouris *et al.*, 2013,2019a,b,2022; Fornadel *et al.*, 2012; Melfos and Voudouris, 2012,2017, Mavrogonatos *et al.*, 2020; Börner *et al.*, 2022). Thus, it emerges as one of the most favorable exploration provinces in Europe for precious, critical and energy-transition elements. On Lesvos island, the Megala Therma-Katsilemonas (i.e., Argenos-Mythimna) epithermal mineralization was mined during Antiquity for silver, gold and lead, which is located about 5 km to the north of the Stypsi porphyry Cu-Mo-Re-Au prospect (Kontis *et al.*, 1994; Voudouris *et al.*, 2019b). The mineralization was suggested to be a fossil equivalent to active geothermal systems in northern Lesvos, as evidenced by hot springs in the Megala Therma area (Kontis *et al.* 1994). This work expands on previous work by Kontis *et al.* (1994), Vamvoukakis (2009) and Voudouris *et al.* (2018, 2019b) and presents new mineralogical, geochemical and geological information of the Megala Therma-Katsilemonas deposit. Here, we present new metallic phases from Megala Therma, a revised paragenetic sequence, and new bulk ore analyses for the mineralization. Based on existing geothermometric data, we constrain the physicochemical conditions of ore formation. We compare the data with the adjacent mineralization at the Biga Peninsula and we discuss similarities between Megala Therma-Katsilemonas and other epithermal-style mineralization hosted in alkaline igneous rocks with implications for similar settings in the Aegean alkaline igneous provinces.

Methods

Fourteen polished-thin sections and fourty five polished blocks of surface samples of host-rocks and sulfide mineralization were studied by optical microscopy and a JEOL JSM 5600 scanning electron microscope, equipped with back-scattered imaging capabilities, at the Department of Mineralogy and Petrology, National and Kapodistrian University of Athens (NKUA). The chemical composition of sulfides, sulfosalts, tellurides and native elements were carried out using a JEOL JXA 8200 Superprobe electron-microprobe at the "Eugen F. Stumpfl" Laboratory, Leoben University, Leoben, Austria. The operating conditions were an accelerating voltage of 20 kV, a beam current of 10 nA and a beam size of 1 μm. Counting times were 20s on the peak and 10s on the backgrounds for major elements. The counting times were increased to 60s and 30s for peak and background measurements, respectively, when analyzing trace elements. The following X-ray lines were used: AsLα, AuLα, SeLα, BiMα, TeLα, CuKα, FeKα, PbMα, SKα, SbLα, NiKα, CoKα, and ZnKa. The following standards and their detection limits included synthetic GaAs for As (350 ppm), synthetic electrum for Au (100 ppm), synthetic AgBiSe2 for Se (200 ppm) and Bi (200 ppm), Bi_2Te_3 for Te (150 ppm) cinnabar for Hg (400 ppm), chalcopyrite for Cu (150 ppm), pyrite for S and Fe (150 ppm), galena for Pb (700 ppm), stibnite for Sb (350 ppm), skutterudite for Co (150 ppm), millerite for Ni (150 ppm), and sphalerite for

Zn (400 ppm). In addition, bulk mineralized samples were analyzed for their trace element composition by 1:1:1 Aqua Regia digestion by ultra-trace ICP-MS analysis at ACME analytical laboratories (Vancouver, Canada).

Results

Geology and Mineralization

Lesvos island comprises early to middle Miocene volcanic to subvolcanic rocks of shoshonitic to calc-alkaline affinity (Pe-Piper and Piper 1993) that overlie the metamorphic Paleozoic-Mesozoic basement, which belongs to the Sakarya Zone of the Rhodope-Pontide Fragment (Pe-Piper *et al.*, 2001). The volcanic rocks occur in a series of stratovolcanoes, which extend SW–NE across the center of the island (Pe-Piper and Piper 1993). The early volcanism (~21.5 Ma) as calc-alkaline, while the main shoshonitic phase occurred from 17.3 to 18.4 Ma and was followed by minor calc-alkaline volcanism at about ~16.5 Ma based on K-Ar and Ar-Ar geochronology (whole rock, hornblende and biotite; Borsi *et al.*, 1972; Pe-Piper and Piper, 1993; Voudouris *et al.*, 2019b).

The Megala Therma-Katsilemonas deposit, in the northern part of the island, consists of NNE-, NNW, NE- and NW-trending epithermal quartz veins and stockworks, hosted in propylitic, to sericite-adularia altered trachyandesitic lavas (21-18 Ma) of the lower lava unit (Kontis *et al.*, 1994; Voudouris *et al.*, 2018, 2019b). The veins that are up to 5 m wide and up to hundreds m in length are crustified, colloform banded and brecciated (Fig. 1). Other textures such as cockade, drusy, comb and quartz pseudomorphs after bladed calcite, were observed. The total amount of sulfide minerals in veins does not exceed 10 vol%, with more sulfide-rich zones being locally developed. Gangue minerals include quartz (e.g., amethyst), chalcedony, carbonates, adularia, chlorite, barite and fluorite (Kontis *et al.*, 1994; Voudouris *et al.*, 2018). The ore assemblage comprises pyrite, marcasite, sphalerite, chalcopyrite, galena, tetrahedrite–tennantite, polybasite–pearceite, famatinite, argentite, native gold, electrum, and the telluride altaite. Paragenetic relationships indicate early deposition of pyrite, followed by sphalerite and chalcopyrite, and then by Ag-Te bearing phases, such as Sb-As-Cu sulfosalts, argentite and altaite, and finally by galena and native gold/electrum (Figs 1 and 2).

Ore mineralogy and mineral-chemistry

Pyrite forms euhedral to subhedral crystals, which contain small amounts of As (up to 0.96 wt%), Co (up to 0.44 wt%), and Au (up to 0.07 wt%). Sphalerite is characterized by chalcopyrite disease and contains minor Mn (up to 0.20 wt%) and Cd (up to 0.47 wt%). Iron reaches concentrations of up to 5.53 wt%, which corresponds to 10.43 mol% FeS. Chalcopyrite contains up to 0.10 wt% Au and up to 0.07 wt% Ag. Galena is the major ore phase at Megala Therma (Fig. 2). It includes Ag-bearing sulfides/sulfosalts, tellurides and native gold/electrum (Fig. 2). Galena is Ag-free, but contains up to 0.20 wt% Te, up to 0.36 wt% Bi, and up to 0.18 wt% Hg. A positive correlation between Bi and Te probably suggests the presence of submicroscopic bismuth-telluride inclusions in galena. Tellurium-Cu-bearing argentite forms small grains (up to 10 μm) hosted by galena Fig. 2a). Concentrations of up to 5.7 wt% Cu and up to 5.1 wt% Te were found (Table 1). Tellurium-bearing polybasite and pearceite are Ag-rich sulfosalts with the general formula $[(Ag,Cu)_6M_2S_7][Ag_9CuS_4]$ with M = Sb (i.e. polybasite) and As (i.e. perceite) (Bindi et al. 2007). A Te-rich variety of polybasite has also been reported from the Kalianou deposit, Evia island, Greece (Bindi *et al.*, 2013; Tombros *et al.*, 2021), where Te partially substitutes for S. At Megala Therma deposit polybasite-perceite solid solution forms small grains (up to 40 μm length and ~ 10 μm width) hosted in galena (Fig. 2b). The studied polybasite contains up to 4.12 wt% Te (up to 0.719 apfu), thus corresponding to at Te-rich polybasite, similar to the occurrence of Kallianou, which is the second occurrence in Greece (Table 1). Tetrahedrite group minerals are minor but ubiquitous constituents within the deposit. At Megala Therma, both tetrahedrite and tennantite occur, and are associated with galena and chalcopyrite (Fig. 2c). Silver-rich (up to 10.2 wt% Ag, Table 1) zincian tetrahedrite is present as subhedral grains inside galena, chalcopyrite and sometimes pyrite. Zincian tennantite occurs at the margins of galena crystals. Selenium, Te, Bi and Hg are below the detection limit in both tetrahedrite and tennantite. Altaite (PbTe) is present as small grains hosted in galena (Fig. 2d). Native gold and electrum are mainly found as isolated grains in gangue quartz (Kontis *et al.*, 1994) and/or as inclusions in galena (Figs 2e,f, this study). Silver substituting for Au ranges from 7.74 to 28.9 wt% (Table 1). Native gold and electrum contain up to 0.50 wt% Bi, and up to 0.05 wt% Hg. Most of the analyzed grains are electrum as they contain between 60 and 75 atomic % Au. Few native gold grains with ~90 atomic % Au occur disseminated in the gangue quartz.

Bulk Ore Analyses

Results of multi-element analyses for selected (n=14) samples indicate that the mineralization is enriched in the so-called epithermal suite of elements as follows: Bi up to 396 ppm, Co up to 320 ppm, Ag > 100 ppm, Se up to 80 ppm, Au up to 26 ppm, Te up to 7 ppm, Mo up to 8 ppm, and Pd up to 77 ppb. In addition, Pb reaches values > 1wt%, Zn up to 0.7 wt%, Cu up to 0.65 wt%, As up to 69 ppm, Sb up to 99 ppm, Ga up to 2.7 ppm, Sn up to 1.2 ppm, and Hg up to 155 ppb.

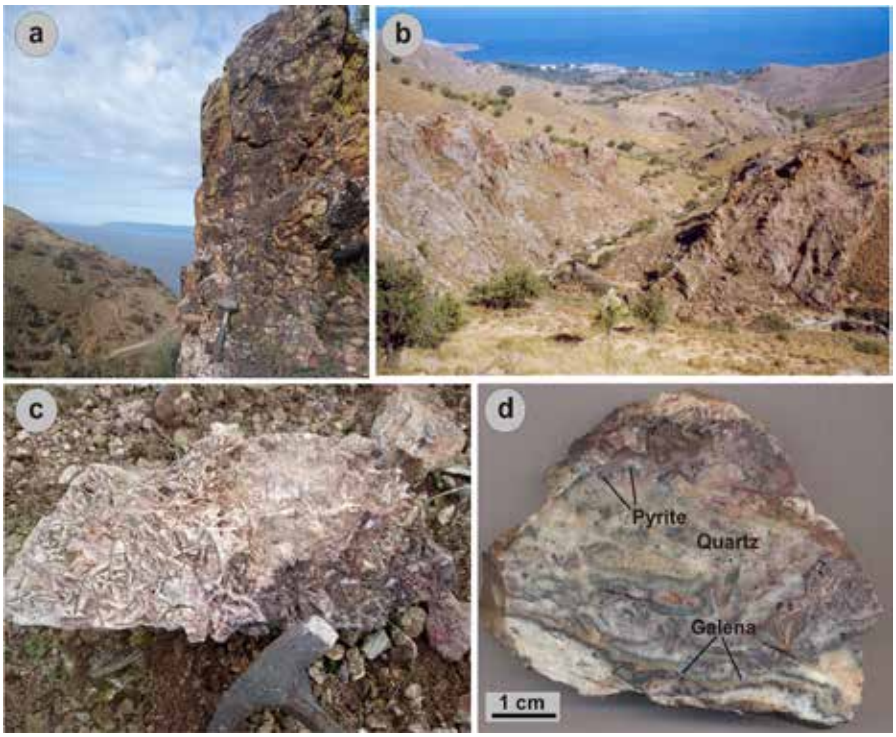

Figure 1. Field photographs (a,b) and hand specimens (c,d) from the Megala Therma-Katsilemonas mineralization. (a) Brecciated quartz vein crosscutting propylitic altered lavas at Megala Therma. Biga Peninsula is seen in the background; (b) Katsilemonas quartz-fluorite veins (view from S to N); (c) Quartz pseudomorph after bladed calcite at Megala Therma; (d) Crustiform/colloform banded quartz/chalcedony vein with minor galena from Megala Therma.

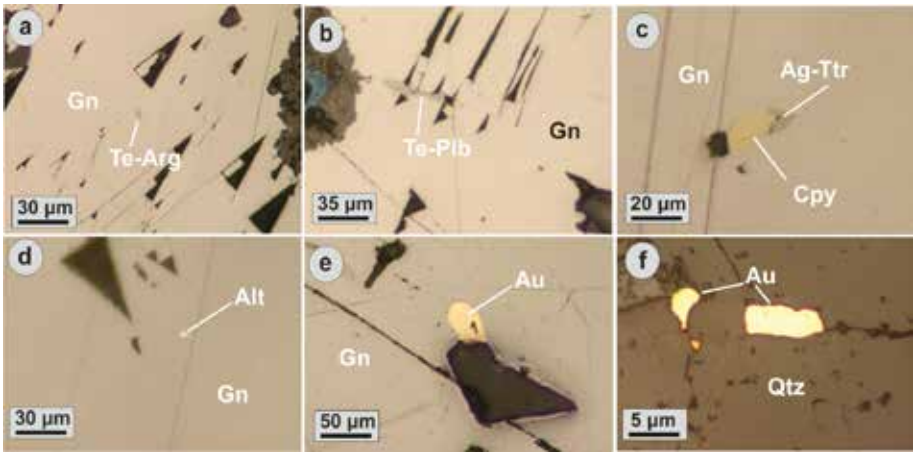

Figure 2. Photomicrographs (reflected light) showing Au, Ag and Te-bearing phases at Megala Therma deposit. (a) Te-bearing argentite (Te-Arg) included in galena (Gn); (b) Te-bearing polybasite (Te-Plb) included in galena; (c) Ag-bearing tetrahedrite-(Zn) included in galena and associated with chalcopyrite (Cpy); (d) Altaite (Alt) included in galena; (e) Native gold (Au) included in galena; (f) Native gold included in quartz (Qtz).

Table 1. Representative electron probe microanalyses (EPMA) of Ag, Au, Bi and Te bearing phases at Megala Therma

Sample	Cu	S	As	Zn	Sb	Fe	Ag	Au	Pb	Se	Te	Bi	Total
wt%													
1	40.21	27.60	18.66	7.69	1.64	3.36	1.15	na	0.16	0.17	0.05	0.17	100.86
2	34.80	24.72	0.83	7.04	29.33	0.16	3.74	na	0.19	0.00	0.00	0.00	100.83
3	31.70	24.60	0.73	5.83	26.56	0.61	10.19	na	0.24	0.00	0.00	0.00	100.50
4	5.91	13.88	0.03	0.02	0.00	0.00	75.74	na	0.46	0.00	3.00	0.03	99.07
5	3.25	14.29	0.77	0.00	0.00	0.00	74.38	na	0.21	0.00	5.08	0.08	98.07
6	4.23	13.85	2.10	0.00	6.33	0.00	69.63	na	0.00	0.00	3.96	0.00	100.09

7	bd	na	na	na	na	na	7.74	92.93	na	na	na	0.41	101.08
8	bd	na	na	na	na	na	28.88	71.51	na	na	na	0.37	100.76
9	bd	na	na	na	na	na	20.06	80.65	na	na	na	0.25	100.96
						Structural formula							**apfu**
1	9.416	12.810	3.707	1.750	0.201	0.896	0.159	na	0.011	0.032	0.006	0.012	29
2	9.250	13.024	0.188	1.819	4.069	0.048	0.585	na	0.016	0.000	0.000	0.000	29
3	8.561	13.166	0.167	1.530	3.744	0.188	1.621	na	0.020	0.000	0.000	0.000	29
4	0.222	1.034	0.001	0.001	0.000	0.000	1.679	na	0.005	0.000	0.056	0.000	3
5	0.124	1.080	0.025	0.000	0.000	0.000	1.671	na	0.002	0.000	0.096	0.009	3
6	1.537	9.979	0.649	0.000	1.201	0.000	14.921	na	0.000	0.000	0.719	0.000	29
7	0.000	na	na	na	na	na	0.132	0.865	na	na	na	0.004	1
8	0.000	na	na	na	na	na	0.423	0.574	na	na	na	0.003	1
9	0.000	na	na	na	na	na	0.312	0.686	na	na	na	0.002	1

1: Tennantite; 2, 3: Tetrahedrite; 4,5: Cu-Te bearing Argentite; 6: Te-bearing polybasite; 7: Native gold; 8,9: Electrum. Abbreviations: na = not analyzed, bd = below detection limit

Discussion and Conclusions

The Megala Therma-Katsilemonas mineralization occurs at the northern flank of the Stypsi caldera, and resembles intermediate- to low-sulfidation quartz-calcite veins overprinting the Stypsi porphyry Cu-Mo±Re±Au mineralization, exposed about 5 km to south within the caldera (Voudouris and Alfieris, 2005; Voudouris *et al.*, 2019b). Previous fluid inclusion studies at Megala Therma indicated that the mineralization formed at temperatures between 244 and 315 ˚C by hydrothermal fluids of low salinity (<3.7 wt % eq. NaCl) (Kontis *et al.*, 1994; Vamvoukakis, 2009). These authors suggested boiling and fluid mixing as potential mechanisms for ore deposition. Voudouris et al. (2018) indicated for amethystine quartz-carbonate veins in the broader area that the homogenization temperatures range between 211 and 250 ˚C, with a mode at 230 ˚C. The salinity of the fluid inclusions in amethystine quartz range from 3.1 to 4.8 wt% NaCl equiv., according to previous results (i.e., Kontis *et al.*, 1994; Vamvoukakis, 2009). Here we used, the sulfide/sulfosalt and telluride mineralogy, the composition of sphalerite (1.1-10.5 mole% FeS), as well as the published fluid inclusion data, to determine fTe_2 and fS_2 values of the hydrothermal solutions in the Megala Therma prospect (Fig. 3). Telluride stabilities were calculated for an average temperature of 250 ˚C. For the tetrahedrite/tennantite-chalcopyrite assemblage, maximum $logfTe_2$ values can be defined by the calaverite-native gold boundary at about –9.1. The presence of native gold suggests that the $logfTe_2$ values did not exceed the calaverite-native gold boundary. The minimum $logfTe_2$ values can be defined by the hessite (Ag_2Te) - argentite (Ag_2S) boundary at about –15. The minor presence of altaite in galena, suggests that the mineralization also took place at conditions along the galena-altaite boundary at $logfTe_2$ values of about –10.5. The $logfS_2$ values calculated from sphalerite composition vary between –10.78 and –12.78 (Fig. 3).

The studied mineralization occurs in the western extension of the Biga and Bergama metallogenic districts, located in the northeastern sector of the Aegean extensional province (Sanchez *et al.*, 2016; Rabayol *et al.*, 2019). Continental extension in the Biga and Bergama areas resulted in E-W to NNW-SSE back-arc extensional sedimentary basins, and Miocene magmatism on Lesvos can be further traced eastwards to western Anatolia (e.g. southern Biga Peninsula and Menderes massif) (Yigit, 2012; Sánchez *et al.*, 2016). Although most porphyry and epithermal prospects in Biga are associated with Late Eocene-Oligocene magmatism (Yigit, 2012; Sanchez *et al.*, 2016), some low-sulfidation epithermal deposits (e.g. Kisacik, Küçükdere and Çoraklık Tepe, Karadere) are located within lower-middle Miocene volcanic rocks (Yilmaz *et al.*, 2007; Yigit, 2012; Oyman, 2019), similar in age to that of Megala Therma. In addition, the low-sulfidation epithermal Ovacik (Au-Ag) deposit, located in the Menderes massif on the mainland of Turkey to the west of Lesvos island is a quartz-carbonate vein system with mineralized E-trending and NW-trending veins hosted in Early Miocene (19.76 ± 0.14 Ma) andesites (Yilmaz *et al.*, 2007). Epithermal-style mineralization at Megala Therma cannot be classified as typical low-sulfidation mineralization, but rather as a low- to intermediate sulfidation transitional style, a feature also described from several Mexican deposits, where the low- and intermediate sulfidation veins coexist in an extensional environment (Camprubí and Albinson, 2007). These authors suggested that a process of progressive neutralization and/or sulfur consumption may result to low-sulfidation styles of mineralization as a natural evolutionary consequence of neutralizing intermediate-sulfidation-type fluids. According to Menant *et al.* (2018), the progressive north-south shift of the magmatic and hydrothermal activity in northeastern Aegean (i.e. Lesvos island) and western Anatolia was coeval with the southward migration of back-arc extension and the associated Kazdağ and Menderes metamorphic core complex exhumation.

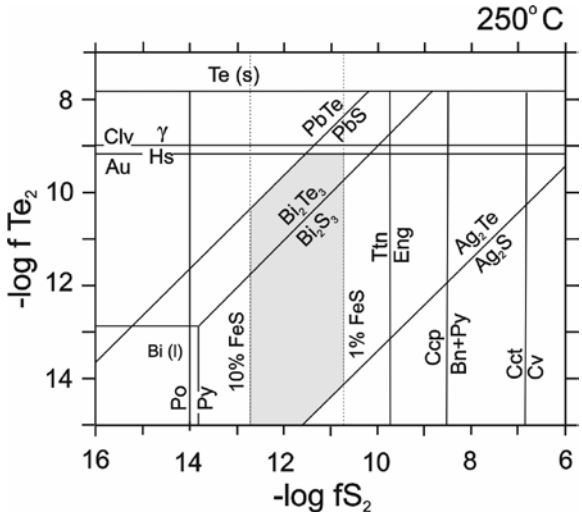

Figure 3. Log*f*Te$_2$-log*f*S$_2$ diagrams indicating equilibria between tellurides and sulfides at 250 °C. The shaded area indicates approximate conditions of gold deposition at Megala Therma, calculated from the composition of sphalerite and observed mineral assemblages. Thermodynamic data for sulfides and tellurides used for calculating fTe$_2$ and fS$_2$ were derived from Barton and Skinner (1979) and Afifi et al. (1988). Abbreviations: (Clv) calaverite, (Hs) hessite, (Tnt) tennantite, (En) enargite, (Ccp) chalcopyrite, (Bn) bornite, (Py) pyrite, (Po) pyrrhotite, (Cct) chalcocite, (Cv) covellite.

The Megala Therma-Katsilemonas deposit also shares some characteristics with alkalic-type epithermal gold deposits. These include the presence of fluorite and tellurides, and the elevated Pd content in the mineralization (Kelley and Spry, 2016; Kelley *et al.,* 2020). It is suggested that Megala Therma-Katsilemonas mineralization represents a transitional LS-IS Au-Ag-Pb-Cu mineralization with affinities to the alkalic-type epithermal Au deposits. Similarly, Fornadel et al. (2012); Kelley *et al.* (2020; Börner *et al.* (2022) characterized the Lower Miocene epithermal type Au-Te deposit in the Fakos area of Limnos Island as alkalic-type. This system consists of polymetallic quartz veins including tetrahedrite/tennantite, Au-Ag tellurides, altaite, native gold and electrum, similar to Megala Therma. However, also some calc-alkaline related mineralization with mineralogical characteristics of alkalic-type porphyry-epithermal systems exist. An example is the Oligocene Pagoni Rachi porphyry-epithermal deposit, which contains fluorite, Pd anomalies and abundant tellurides, in both porphyry and sub-epithermal ores (Voudouris *et al.*, 2013). Based on the less attention given to the alkalic-class of epithermal Au deposits in Greece, we emphasize here that Miocene magmatic belts in the Aegean domain are prospective for alkalic-type low-sulfidation precious and critical metal mineralization.

References

Afifi, A.M., Kelly, W.C., Essene, J.E., 1988. Phase relations among tellurides, sulfides, and oxides; I, Thermochemical data and calculated equilibria. Economic Geology 83 (2), 377–394.

Arikas, K., Voudouris, P., 1998. Hydrothermal alterations and mineralizations of magmatic rocks in the southeastern Rhodope massif. Acta Vulcanologica 10, 353-365.

Barton, P.B.Jr, Skinner, B.J., 1979. Sulfide mineral stabilities. In: H.L. Barnes (Ed.), Geochemistry of Hydrothermal Ore Deposits (2nd edition), Wiley Interscience, New York (1979), pp. 278-403.

Bindi, L., Evain, M., Spry, P., Menchetti, S., 2007. The pearceite-polybasite group of minerals: Crystal chemistry and new nomenclature rules. American Mineralogist 92, 918–925.

Bindi, L., Voudouris, P., Spry, G., 2013. Structural role of tellurium in the minerals of the pearceite-polybasite group. Mineralogical Magazine 77, 419–428.

Börner, F., Keith M., Buecker J.L., Voudouris, P., Klemd R., Haase K.M., Kutzschbach, M, Schiperski, F., 2022. In-situ trace element and S isotope systematics in porphyry-epithermal pyrite, Limnos Island, Greece. Frontiers in Earth Science 10, 916107.

Borsi, S., Ferrara, G., Innocenti, F., Mazzuoli, R., 1972. Geochronology and petrology of recent volcanics in the Eastern Aegean Sea (West Anatolia and Lesvos Island). Bulletin of Volcanology 3, 473–496.

Camprubí, A., Albinson, T., 2007. Epithermal deposits in Mexico – update of current knowledge, and an empirical reclassification. Geological Society of America Special Publication 422, pp. 377-415.

Cook, N., Ciobanu, C., Spry, P., Voudouris, P., 2009. Understanding gold-(silver)-telluride-(selenide) mineral deposits. Episodes 32, 4, 249-263

Einaudi, M., Hedenquist, W.J., Inan, E., 2003. Sulfidation State of Fluids in Active and Extinct Hydrothermal Systems: Transitions from Porphyry to Epithermal Environments, In Press: Giggenbach Volume, Society of Economic Geologists and Geochemical Society, Special Publication 10.

Fornadel, A., Voudouris, P., Spry, P., Melfos, V., 2012. Mineralogical, stable isotope, and fluid inclusion studies of spatialy related porphyry

Cu and epithermal Au-Te mineralization, Fakos Peninsula, Limnos Island, Greece, Mineralogy and Petrology 105, 85-111.
Hedenquist, J.W., Arribas, A.Jr., Urien-Gonzalez, E., 2000. Exploration for epithermal gold deposits. Reviews in Economic Geology, 13, 245–277.
Jensen, E.P., Barton, M.D., 2000. Gold deposits related to alkaline magmatism, Reviews in Economic Geology 13, 279-314.
John, D.A., Vikre, P.G., du Bray, E.A., Blakely, R.J., Fey, D.L., Rockwell, B.W., Mauk, J.L., Anderson, E.D., and Graybeal, F.T., 2018. Descriptive models for epithermal gold-silver deposits: U.S. Geological Survey Scientific Investigations Report 2010–5070–Q, 247 p. [Also available at https://doi.org/ 10.3133/ sir20105070Q.]
Keith, M., Smith, D.J., Doyle, K., Holwell, D.A., Jenkin, G.R.T., Barry, T.L., Becker, J., Rampe, J., 2020. Pyrite chemistry: A new window into Au-Te ore-forming processes in alkaline epithermal districts, Cripple Creek, Colorado. Geochimica et Cosmochimica Acta 274, 172–191.
Kelley H. and Spry P., 2016. Critical elements in alkaline igneous rock-related epithermal gold deposits. Economic Geology 18, 195-216.
Kelley, K.D., Spry, P.G., McLemore, V., Fey, D.L., Anderson, E., 2020. Alkalic-type epithermal gold 696 deposit model: Chapter R of Mineral Deposit Models for Resource Assessment. U.S. Geol. Surv. Rep. 697 2010–5070-R.
Kontis, E., Kelepertsis, A. Skounakis, S., 1994. Geochemistry and Alteration Facies Associated with Epithermal Precious Metal Mineralization in an Active Geothermal System, Northern Lesvos, Greece. Mineralium Deposita 29, 430-433.
Mavrogonatos, C., Voudouris, P., Zaccarini, F., Klemme, S., Berndt, J., Tarantola, A., Melfos, V., Spry, P.G., 2020. Multi-stage introduction of precious and critical metals in pyrite: A case study from the Konos Hill and Pagoni Rachi porphyry/epithermal prospects, NE Greece. Minerals 10, 784. https://doi.org/10.3390/min10090784
Melfos, V., Voudouris, P., 2012. Geological, mineralogical and geochemical aspects for critical and rare metals in Greece. Minerals 2, 300-317, https://doi.org/10.3390/min2040300
Melfos, V., Voudouris, P., 2017. Cenozoic metallogeny of Greece and potential for precious, critical and rare metals exploration, Ore Geology Reviews 59, 1030-1057.
Menant, A., Jolivet, L., Tuduri, J., Loiselet, C., Bertrand, G., Guillou-Frottier, L., 2018. 3D subduction dynamics: A first-order parameter of the transition from copper- to gold-rich deposits in the eastern Mediterranean region. Ore Geology Reviews 94, 118–135.
Oyman, T., 2019. Epithermal Deposits of Turkey, in Pirajno et al. (Eds) Mineral Resourcs of Turkey, Springer, vol 16, p. 159-223.
Pe-Piper, G., Piper, D., 1993. Revised stratigraphy of the Miocene volcanic rocks of Lesbos, Greece. Neues Jahrbuch für Geologie und Paläontologie / Monatshefte 97–110.
Pe-Piper, G., Piper, D., Matarangas, D., Varti-Matarangas, M., 2001. The sub-ophiolithic melange of the island of Lesbos, Greece. Neues Jahrbuch für Mineralogie, Monatshefte, 241–260.
Rabayrol, F., Hart, C.J.R., Creaser, R.A., 2019. Tectonic triggers for postsubduction magmatic-hydrothermal gold metallogeny in the Late Cenozoic Anatolian Metallogenic Trend, Turkey. Economic Geology 114,1339–1363
Sanchez, M.G., McClay, K., King, A., 2016. Crustal extension and its relationship to porphyry Cu-Au and epithermal Au mineralization in the Biga Peninsula, NW Turkey, Society of Economic Geologists Special Publication 19, 113–156.
Tombros, S.F., Kokkalas, S., Seymour, K.St., Voudouris, P., Williams-Jones, A.E., Zhai, D., Liu, J., Fitros, M.G. 2021. The Kallianos Au-Ag-Te mineralization, Evia Island, Greece: A detachment-related distal hydrothermal deposit of the Attico-Cycladic Metallogenetic Massif. Mineralium Deposita, 56, 665–684.
Vamvoukakis, C., 2009. Epithermal Ore Deposit in Lesvos Island, PhD Thesis, University of Patras, Patra [in Greek].
Voudouris, P., Alfieris, D., 2005. New porphyry - Cu±Mo occurrences in the north-eastern Aegean, Greece: Ore mineralogy and epithermal relationships. In: Mao, J., Bierlein, F.P. (eds) Mineral Deposit Research: Meeting the Global Challenge. Springer, Berlin, Heidelberg. https://doi.org/10.1007/3-540-27946-6_123.
Voudouris, P., Melfos, V., Spry, P.G., Kartal, T., Schleicher, H., Moritz, R., Ortelli, M., 2013. The Pagoni Rachi/Kirki Cu-Mo±Re±Au deposit, Northern Greece: Mineralogical and fluid inclusion constrains on the evolution of a telescoped porphyry-epithermal system, Canadian Mineralogist, 51, 411-442.
Voudouris, P., Melfos, V., Mavrogonatos, C., Tarantola, A., Götze J., Alfieris, D., Maneta, V., Psimis, J., 2018. Amethyst occurrences in Tertiary volcanic rocks of Greece: Mineralogical, fluid inclusion and oxygen isotope constraints on theis genesis. Minerals, 8, 324, 1-26, doi: 10.3390/min8080328.
Voudouris, P., Mavrogonatos, C., Spry, G., Baker, T., Melfos, V., Klemd, R., Haase, K., Repstock, A., Djiba, A., Bismayer, U., Tarantola, A., Scheffer, C., Moritz, R., Kouzmanov, K., Alfieris, D., Papavassiliou, K., Schaarschmidt, A., Galanopoulos, A., Galanos, E., Kołodziejczyk, J., Stergiou, C., Melfou, M., 2019a. Porphyry and epithermal deposits in Greece: An overview, new discoveries, and mineralogical constraints on their genesis. Ore Geology Reviews, 107.
Voudouris P., Mavrogonatos C., Melfos V., Spry G., Magganas A., Alfieris D., Soukis K., Tarantola A., Periferakis A., Kolodziejczyk J., Scheffer C., Repstock A., Zeug M., 2019b. The geology and mineralogy of the Stypsi porphyry Cu-Mo-Au-Re prospect, Lesvos Island, Aegean Sea, Greece. Ore Geology Reviews, 112, 103023, https://doi.org/10.1016/j.oregeorev.2019.103023.
Voudouris, P, Repstock, A, Spry, P.G., Frenzel, M., Mavrogonatos, C., Keith, M., Tarantola, A., Melfos, V., Tombros, S., Zhai, D., Cook, N.J., Ciobanu, C.L., Schaarschmidt, A., Rieck, B., Kolitsch, U., Falkenberg, J., 2022. Physicochemical constraints on indium-, tin-, germanium-, gallium-, gold-, and tellurium-bearing mineralizations in the Pefka and St Philippos polymetallic vein- and breccia-type deposits, Greece. Ore Geology Reviews, 140, 104348.
Yigit, O., 2012. A prospective sector in the Tethyan Metallogenic Belt: Geology and geochronology of mineral deposits in the Biga Peninsula, NW Turkey. Ore Geology Reviews, 46, 118–148.
Yilmaz., H., Oyman, T., Arehart, G., Colakoglu, A., Billor, Z., 2007. Low-sulfidation type Au-Ag mineralization at Bergama, Izmir, Turkey. Ore Geology Reviews, 32, 81-124.

17th INTERNATIONAL CONGRESS of the Geological Society of Greece

BULLETIN OF THE GEOLOGICAL SOCIETY OF GREECE, SP. PUBL.

EXTENDED ABSTRACT 307

Source rock potentiality of the late Miocene sapropelic layers of Gavdos Island, Greece, based on geochemical and stratigraphic data

Telemenis D.[1,2], Bellas S.[2], Vavouranakis E.[1], Manoutsoglou E.[1]

(1) School of Mineral Resources Engineering, Technical University of Crete, Chania, Greece, (2) Institute of GeoEnergy, Foundation for Research and Technology (IG/FORTH), Chania, Greece, dtelemenis@ig.forth.gr

Introduction / Background

The island of Gavdos is the southernmost part of Greece and at the same time represents the southernmost island of whole Europe. It is located in the eastern part of central Mediterranean Sea, south of the western Crete Island (Figure 1, left). It is rather considered a small island with an overall size of ca. 33 km^2. Based on the general geological framework, the island is directly connected to the subduction of the African lithospheric plate beneath the European one, precisely the Aegean microplate. It is placed right at the north of the Hellenic trench, that is developed due to the subduction, with a peculiar position, where the latter bends from a NNW-SSE to a NNE-SSW direction. Gavdos may have been related to the late N-S shortening that followed the N-S extension and graben formation and created the accretionary wedge of the Mediterranean ridge commencing by 11 Ma (Ring and Yngwe, 2018).

Mesozoic limestones, Eocene flysch, a few ophiolites (Sarakiniko Bay, located at the north-northwest) and Neogene to recent carbonate to clastic deposits build the island. The limestones occur at the south, southwestern part of the island, and are developing along a NNW-SSE direction, parallel to the general Hellenides trend of western Greece and Peloponnesus, while flysch is present in spot locations.

The Neogene unconformably overlies the pre-Neogene rocks and covers most of the central and northern part of the island, while a Pleistocenic marly limestone marine terrace (detailed literature review in Antonarakou, 2001; Tsaparas, 2005) and recent-subrecent aeolianites are among the youngest strata of the island. According to Anastasakis *et al.* (1995) in (Antonarakou, 2001), the Neogene deposits consist of two formations, namely these of Potamos and Metochia. Based on biostratigraphic data, Potamos Fm represents the oldest strata of Middle Serravallian to lower Tortonian age, while sedimentation in Metochia developed from the Middle/Lower Tortonian and ranged up to the Messinian (Triantaphyllou *et al.*, 1999) in (Antonarakou, 2001). The Metochia section was initially studied by (Postma *et al.*, 1993: Metochia-B), (Krijgsman *et al.,* 1995: Metochia-B/C) and (Postma and Ten Veen, 1999: Metochia-B/C). Based on the mostly regular alternations of brownish, organic rich layers and grey to blue hemipelagic marlstone, they first recognized consistent sedimentary cycling of late Miocene, and connected them to the Earth's orbit, and more precisely to the precession cycles, while by applying magnetostratigraphy they assigned an age of 9.642 Ma to the sections' basal strata. Initially, fifty-eight (58) such sapropelic layers (i.e. successive cycles) were distinguished in Metochia-B (56 in Krijgsman *et al.*, 1995), while additional forty (40) cycles were documented in Metochia-C, which represents the upper part of the section (Krijgsman *et al.,* 1995). Based on the later author's samples from the Metochia sections, Schenau *et al.* (1999) investigated the mechanism of formation for specific sapropelic layers, while Köhler *et al.* (2008) studied provenance changes of the material during the late Miocene The later authors concluded on changes a) from arid to more humid conditions (paleoclimatic) and b) from terrigenous input material to marine dominated (base to top of the section, respectively). By studying paleoflora from Gavdos locations of Tortonian age, Mantzouka *et al.* (2015) suggested that rather the paleogeographical setting than (paleo-)temperature changes affected the island during that time. Recently, Zachariasse and Lourens (2021), by studying the uppermost part of Metochia section (namely part D) concluded that the intercalated limestones are evaporitic, and that their formation onset is placed at 6.00 Ma, indicating abrupt sedimentation changes and a distinct rise in salinity, which in turn is connected to the MSC onset.

Objectives

By using Rock-Eval pyrolysis, this study focuses on the geochemical analysis of two sets of sapropelic layers from Gavdos Island (Figure 1, right): a) The first set correlates to the lowermost eight of those (L1-L8) described by Postma *et al.* (1993) and represents the lateral equivalent of the basal part of Metochia-B (compare Pyliotis *et al.*, 2013), and b) the second sampling set comes from the uppermost part of these sapropelic successions, located just below the sandstones of the MSC, which has never been geochemically studied up to now. The aim is to unravel the hydrocarbon generation potentiality of the late Miocene sapropelic deposits of the eastern Mediterranean, closing the gap between the basal (Tortonian) and the top sapropelic layers deposition (Messinian) of Gavdos and further to investigate the development of lateral continuity or differentiation of the geochemical properties of these strata relevant to gas prospectivity south and southwest of Crete, that is currently under way in two major offshore blocks southwest and south of Crete.

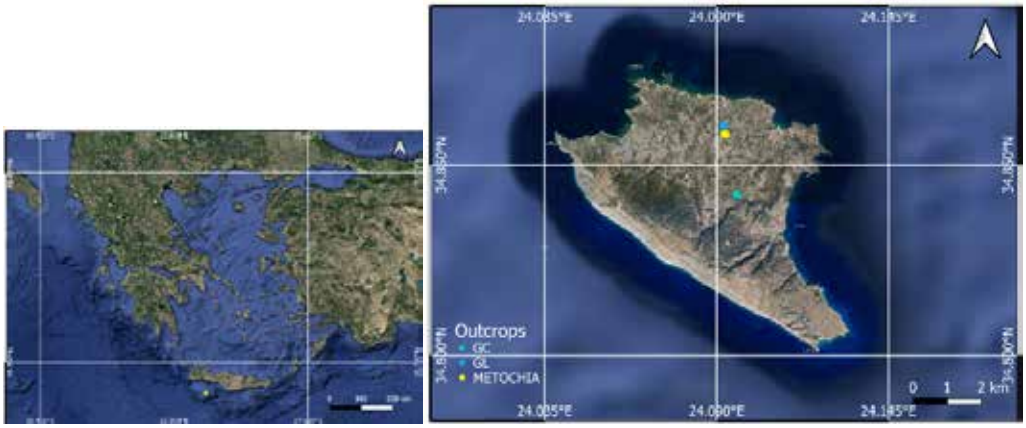

Figure 1. Gavdos Island with the investigated outcrops position.

Material and Methods

Two outcrops were investigated for this study. The first one is GL# outcrop and is located north of the main Metochia-B outcrop (Postma *et al.,* 1993). It consists of alternations of sapropelic layers and marlstones (silty mudstones) and specifically 8 levels/ intervals of sapropels (approximately 7 m thick). In the basal part of the outcrop, a 2.4 m marly sandstone prevails and underneath of it, a 1-m-thick, grey to green muddy siltstone (GL#1 and GL#2 samples) was monitored, with noticing oxidations occasionally. As we proceed to the uppermost levels, thick sandstones (over 5 m) close the section. Regarding the second section, which is named GC#, it is situated south-east from Metochia section near the buildings of University of Crete. The total thickness of the outcrop is almost 16.5 m. Its bottom part (GC#0 sample) is a few meters eastern from the main body of the section and is considered as its base. Furthermore, a 12-m-thick section with similar alternations of sapropelic levels and marls is observed. The main issue in this section is the presence of oxidation levels in some of the intervals, which renders the distinction of the lithologies more difficult. Proceeding to the top part, bioclastic sandstones over 2.5 m thick close the outcrop.

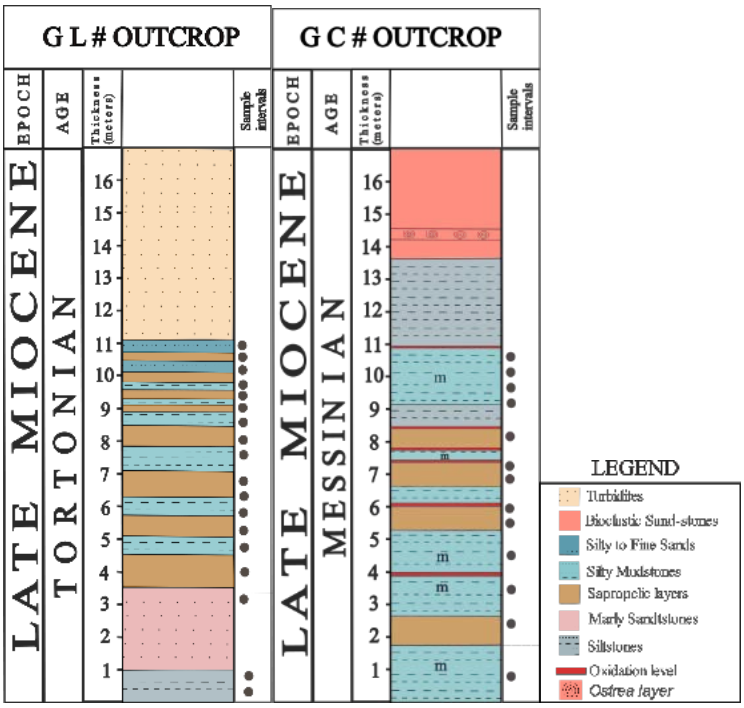

Figure 2. Lithostratigraphy of the studied GL and GC outcrops from Gavdos Island.

Bulk sampling was carried out in both outcrops. The total number of samples is fifty-nine (59). Thirty-five (35) come from the GL# outcrop and twenty-four (24) from the GC# outcrop. Both sapropelic layers and marlstones (mudstones, siltstones etc.) were collected. Rock-Eval pyrolysis was conducted to those samples, utilizing a Rock-Eval VI® (RE6) anhydrous open system pyrolyzer (Vinci Technologies; Lafargue *et al.,*1998) following the standard organic matter (OM) analysis setup (Behar *et al.*, 2001).

Samples, finely ground (<250 μm or 60 mesh) and dried at 60°C (overnight drying), were subjected to sequential pyrolysis and oxidation (Espitalie *et al.,* 1984). Various authors have provided analytical details of the RE VI methodology and interpretations of the resultant data (Behar *et al.,* 2001; Lafargue *et al.,* 1998, and other researchers). The volatile hydrocarbons produced were identified and quantified using a flame ionization detector (FID). Pyrolysis was conducted isothermally, commencing at 300 ◦C and escalating with a gradient of 25 ◦C/min until reaching a peak of 650 ◦C. Subsequent to pyrolysis, oxidation was performed from 300 to 850 ◦C at a heating rate of 20 ◦C/min. Consequently, key parameters such as S1 (mg HC/g rock), S2 (mg HC/g rock), S3 (mgCO_2/g rock), Tmax (◦C), TOC [(total organic carbon content) (%wt)], Hydrogen Index [(HI) (mg HC/g TOC)], and Oxygen Index [(OI) (mgCO_2/g TOC)] were determined (Espitalie *et al.*, 1984; Lafargue *et al.*, 1998). The evaluation of the data relied upon the studies by Tissot and Welte, (1984) and other researchers.

Results and Discussion

Based on the Rock-Eval pyrolysis data (RE-VI), all important parameters that measured and calculated, such as TOC, S2, HI and OI are presented in Figures 3 and 4 (for the studied outcrops GL# and GC#, respectively), from bottom to the top, according to the stratigraphic development of the deposits from older to younger.

A. GL# outcrop (lateral equivalent to the lower part of Metochia-B).
   The TOC content of the sapropelic layers fluctuates from 0.06%wt (GL#8b) up to 0.5%wt (GL#14). The rest lithologies' samples (silty mudstones, siltstones and sandstones) provide similar TOC results with a minimum of 0.03%wt (GL#5) and a maximum of 0.44%wt (GL#9). The average TOC content of this studied section is 0.24%wt with maximum S2 value of 0.52 mg HC/g rock at the basal samples. Additionally, the HI and OI values range between 0-130 mg HC/g TOC and 133-917 mg CO_2/g TOC.
B. GC# outcrop (uppermost part of Metochia-C).
   The TOC content varies from 0.13%wt (GC#7) to 0.43%wt (GC#4b) with an average value of 0.28%wt for the whole studied section. The HI and OI values found to range between 6-115mg HC/g TOC and 365- >1000 mg CO_2/g TOC.

Considering all above values distribution for both studied outcrops of the late Miocene (Tortonian and Messinian) of Gavdos Island, it can be concluded that they are indicative of a rather poor to fair H/C potential generation.

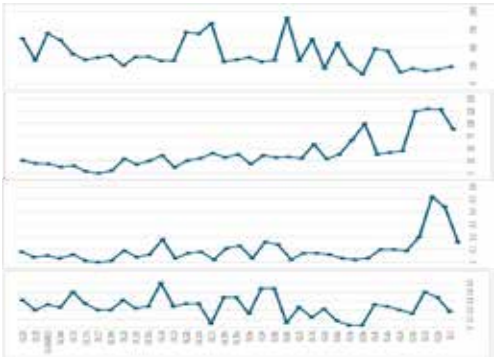

Figure 3. GL# outcrop; Vertical distribution of the main Rock-Eval VI parameters that have been recorded. Shaded intervals correspond to the sampled sapropelic layers.

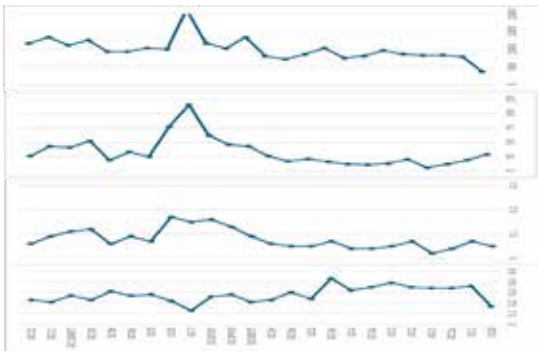

Figure 4. GC# outcrop; Vertical distribution of the main Rock-Eval VI parameters that have been recorded. Shaded intervals correspond to the sampling positions of the sapropelic layers.

Following the laboratory analysis and based on all RE-VI pyrolysis data, and in order to evaluate the maturity and hydrocarbon potentiality of the samples, a number of XY-diagrams were created, where all values obtained have been plotted. In the present work only two of them are presented, namely a) the HI vs Tmax diagram and b) the TOC (log) vs S2 (log) diagram.
The first one (Fig. 5, left), is representative of the kerogen types of the analyzed samples. As it is clearly shown, the majority of the plotted samples' values reveal a Type IV kerogen, while a small amount of them tends to a Type III kerogen and a possible gas-prone source rock.
The second diagram (Fig. 5, right) indicates the hydrocarbon generation potential of the rocks. All values are plotted in the lower left quadrate of the diagram, therefore, as we mentioned before, the analyzed samples exhibited a poor to fair H/C potential generation for both outcrops. A slightly poorer indication is apparent for the GC#, which represents the Messinian samples, where a number of oxidized layers occurred at various stratigraphic levels (Fig. 2: GC#). Despite the careful sampling procedure, being conducted to minimize the effects of weathering and oxidation, it is highly likely that the analyzed samples could display more favorable organic geochemical signatures.

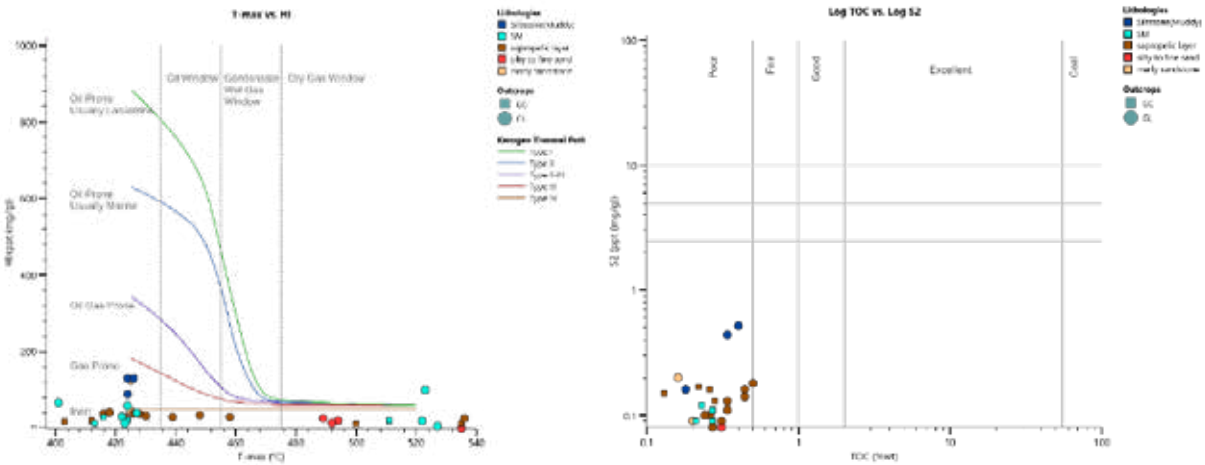

Figure 5. At the left: HI (mg HC/g TOC) versus Tmax (°T) showing idealized kerogen types and thermal maturity of the studied samples and (at the right) Logarithmic plot of TOC (%wt.) versus S2 (mg HC/g rock) illustrating the source-rock potential. As in the legend, squares represent samples of the GC# outcrop, while circles the GL#.

This study completes previous research for the organic-rich layers of Metochia [(Schenau *et al.*, 1999); who studied particularly three sapropelic layers of the basal section: L5-L7], the source rock potentiality of Gavdos (Pyliotis *et al.*, 2013), as well as the review work for the organic geochemistry signature of various Crete Neogene sediments of (Maravelis *et al.,* 2022) by contributing additional data to compare the geochemical analysis of the Gavdos Metochia-B lower part section with its lateral equivalent (GL#). The first set of samples of the present work (GL#), represents the sapropelic/mudstones interval that stratigraphically is situated below the turbiditic sequence (Krijgsman *et al.*, 1995). Furthermore, by extending this type of analysis to locations that have not yet undergone geochemical investigation (Metochia-C), the gap with the analysis of samples from the GC# outcrop is closed. The latter appears to correlate with the upper cycles of the Metochia-C section (M92-M96) as an equivalent. Gaining a comprehensive understanding of the entire area through its stratigraphic evolution is crucial for its paleogeographic development prior to the Messinian Salinity Crisis, and at the same time for the hydrocarbons exploration that is currently underway.

Conclusions

A geochemical analysis has been conducted on samples obtained from outrcrops on Gavdos Island to reveal new potential source rocks. Fifty-nine samples of two outcrops (GL# and GC#) have been studied by using RE-VI pyrolysis. These samples included mainly sets of sapropelic layers and mustones/siltstones alternations. GL# samples are of Tortonian age, while GC# samples are of Messinian age (Metochia-C, upper part).

1) The RE-VI results have shown that hydrocarbons generation potential varies from poor to fair in both studied outcrops.
2) The lateral equivalent GL# outcrop (to Metochia-B, basal part, cycles L1-L7/L8) provided lower values in relation to data from previous authors, indicating that the outcrop was located at a more marginal sector of the sedimentary basin.

3) Samples of the GC# outcrop, proved of poor H/C potential generation, indicating that locally, the productivity was rather decreased approaching the onset of the Messinian Salinity Crisis (MSC).
4) By studying these two outcrops, a research "gap" is partially covered, particularly in relation to the Messinian record (GC# outcrop samples). However, more analyses need to be conducted to get a better and more detailed understanding of the maturation of these rocks under proper burial conditions.
5) These analyses and their findings have enriched the hydrocarbon map of the Eastern Mediterranean and made an additional contribution to the energy sector, which should expect enhanced results moving to the offshore area, due to better organic matter preservation.

Acknowledgements
Financial support was partly provided by the HelleniQ Energy (Upstream Sector), through a project assignment to Dr. S. Bellas (PI). N. Pasadakis (Professor of TUC) is acknowledged for his support throughout the work, while providing older samples and raw geochemical data for correlation to present ones.

References
Antonarakou, A., 2001. Biostratigraphic and Paleoenvironmental Interpretation in Miocene Sediments of the Eastern Mediterranean (Gavdos Island). PhD Thesis, National and Kapodistrian University of Athens, Department of Geology and Geoenvironment, Athens, 176 p. (in Greek).
Behar, F., Beaumont, V., Penteado, H.L. De B., 2001. Rock-Eval 6 Technology: Performances and Developments. Oil & Gas Science and Technology-Rev. IFP 56(2), 111–34.
Espitalie, J., Marquis, F., Barsony, I., 1984. Geochemical Logging, in: Voorhees, K.J. (ed.) Analytical Pyrolysis: Techniques and Applications, 276–304.
Köhler, C.M., Heslop, D., Dekkers, M.J., Krijgsman, W., Van Hinsbergen, D.J.J., Von Dobeneck, T., 2008. Tracking Provenance Change during the Late Miocene in the Eastern Mediterranean Using Geochemical and Environmental Magnetic Parameters. Geochemistry, Geophysics, Geosystems 9(12), 1–14.
Krijgsman, W., Hilgen, F.J., Langereis, C.G., Santarelli, A., Zachariasse, W.J., 1995. Late Miocene Magnetostratigraphy, Biostratigraphy and Cyclostratigraphy in the Mediterranean. EPSL Earth and Planetary Science Letters 136, 475–494.
Lafargue, E., Marquis, F., Pillot D., 1998. Rock-Eval 6 Applications in Hydrocarbon Exploration, Production, and Soil Contamination Studies. Revue de l'Institut Français Du Pétrole 53(4), 421–37.
Mantzouka, D., Kvaček, Z., Teodoridis, V., Utescher, T., Tsaparas, N., Karakitsios, V., 2015. A New Late Miocene (Tortonian) Flora from Gavdos Island in Southernmost Greece Evaluated in the Context of Vegetation and Climate in the Eastern Mediterranean. Neues Jahrbuch für Geologie und Paläontologie - Abhandlungen 275(1), 47–81.
Maravelis, A., Kontakiotis G., Bellas, S., Antonarakou, A., Botziolis, C., Janjuhah, H.T., Makri, P., Moissette, P., Cornée, J.J., Pasadakis, N., Manoutsoglou, E., Zelilidis, A., Karakitsios, V., 2022. Organic Geochemical Signatures of the Upper Miocene (Tortonian—Messinian) Sedimentary Succession Onshore Crete Island, Greece: Implications for Hydrocarbon Prospectivity. Journal of Marine Science and Engineering 10(1323), 1-17.
Postma, G., Hilgen, F.J., Zachariasse, W.J., 1993. Precession□punctuated Growth of a Late Miocene Submarine□fan Lobe on Gavdos (Greece). Terra Nova 5(5), 438–44.
Postma, G., Ten Veen, J.H., 1999. Astronomically and Tectonically Linked Variations in Gamma-Ray Intensity in Late Miocene Hemipelagic Successions of the Eastern Mediterranean Basin. Sedimentary Geology 128, 1–12.
Pyliotis, I., Zelilidis, A., Pasadakis, N., Panagopoulos, G., Manoutsoglou. E., 2013. Source Rock Potential of the Late Miocene Metochia Formation of Gavdos Island, Greece. Bulletin of the Geological Society of Greece 47(2), 871–79.
Ring, U., Yngwe, F., 2018. To Be, or Not to Be, That Is the Question' - The Cretan Extensional Detachment, Greece. Tectonics 37(9), 3069–3084.
Schenau, S.J., Antonarakou, A., Hilgen, F.J., Lourens, L.J., Nijenhuis, I.A., Van Der Weijden, C.H., Zachariasse, W.J., 1999. Organic-Rich Layers in the Metochia Section (Gavdos, Greece): Evidence for a Single Mechanism of Sapropel Formation during the Past 10 My. Marine Geology 153, 117–35.
Tissot B.P., Welte D.H., 1984. Petroleum Formation and Occurrence. 2nd ed. Springer-Verlag Berlin Heidelberg New York Tokyo.
Tsaparas, N., 2005. Contribution to the Sedimentation History of Marine Formations of Upper Cenozoic of Gavdos Island. PhD Thesis, National and Kapodistrian University of Athens, Department of Geology and Geoenvironment. Athens, 210 p. (in Greek).
Zachariasse, W.J., Lourens. L.J., 2021. The Messinian on Gavdos (Greece) and the Status of Currently Used Ages for the Onset of the MSC and Gypsum Precipitation. Newsletters on Stratigraphy 55(3), 333–60.

17th INTERNATIONAL CONGRESS of the Geological Society of Greece

BULLETIN OF THE GEOLOGICAL SOCIETY OF GREECE, SP. PUBL.

EXTENDED ABSTRACT 308

Study of "Corundum" Samples from the Collection of the Mineralogical – Petrological Museum at Aristotle University of Thessaloniki, Greece

Theocharaki A.[1], Nikopoulou M.[1], Karampelas S.[1,2], Kantiranis N.[1], Oikonomidis S.[1] and Papadopoulou L.[1]

(1) Department of Mineralogy, Petrology, Economic Geology, School of Geology, Aristotle University of Thessaloniki 54124, Thessaloniki, Greece, alexitheoc@geo.auth.gr , (2) Laboratoire Français de Gemmologie (LFG), 30 rue de la Victoire, 75009 Paris, France

Introduction

This study focuses on the mineralogical and chemical characterization of four unknown samples from the Mineralogical and Petrological Museum in School of Geology at Aristotle University of Thessaloniki. According to the museum's records, three samples with pinkish red color are referred as rubies, while the fourth, which exhibits a blue color, is classified as a blue sapphire; both primary gem varieties of corundum (Al_2O_3). The most significant chromophore of corundum is Cr^{3+} and Fe^{2+}-Ti^{4+} intervalence charge transfer pair is responsible for the blue color in blue sapphire (Fritsch & Rossman 1988; Dubinsky et al., 2020). In gemology, corundum holds a prominent position due to its exceptional optical and physical properties, making it highly valued in the jewelry industry. For this reason, many corundum crystals undergo heat treatment to enhance their color and transparency (Nassau, 1981). Additionally, synthetic rubies and sapphires are produced using various methods, including the Verneuil process, the flux growth method, and the Czochralski method. The identification of corundum, including its treatments and whether it is natural or synthetic, requires specialized gemological techniques. such as UV fluorescence analysis and microscopic examination of inclusions (Hughes et al., 1997).

For the analysis of these samples, mineralogical techniques were utilized, including Scanning Electron Microscopy (SEM), Energy Dispersive X-ray Fluorescence spectroscopy (EDXRF) along with Visible-Near Infrared (Vis-NIR), Raman and Photoluminescence (PL) spectroscopies. The aim of this study is to highlight the significance of non-destructive minerals and gemstones analyses with museum and collector value, ensuring their precise scientific documentation and mineralogical characterization.

Materials & Methods

For this study 4 samples (Fig. 1) from the Mineralogical – Petrological Museum of AUTh were studied with advanced spectroscopic and analytical methods. Raman and Photoluminescence (PL) spectra were obtained by using a micro-Raman Renishaw inVia spectrometer, coupled with an optical microscope and with a 514 nm laser excitation (diode-pumped solid-state laser). Raman spectra from 100 to 2000 cm^{-1} region were obtained with 10 accumulation and 15 s exposure time with laser power at 100%. PL spectra (520–900 nm) were acquired with 10 s of exposure time, 1 accumulation and 0.1% laser power. A diamond was used for the calibration of the Raman spectrometer by considering its 1331.8 cm^{-1} Raman peak. For the Visible-Near Infrared (Vis-NIR) spectra (from 400 to 1000 nm), a mobile spectrometer was used, equipped with an integrating sphere, and with an acquisition time of 0.05–0.50 s and 20 accumulations. Raman and Vis-NIR experiments were conducted in the Laboratoire Français de Gemmologie (LFG).

The chemical analyses were conducted using a Scanning Electron Microscope (SEM). In order to obtain conductivity, the samples were carbon coated. The scanning electron microscope is equipped with an Energy Dispersive Spectrometer (EDS), specifically a JEOL JSM-6390LV (Tokyo, Japan) and using an EDXRF, model S4-Pioneer (Bruker-AMS, Germany), at the Interdepartmental Laboratory of the School of Sciences at Aristotle University of Thessaloniki (AUTh). For the optical observation of the samples a ZEISS Stemi 2000-C microscope was used and reaction under 3 W longwave ultraviolet (LWUV) emitting at 365 nm.

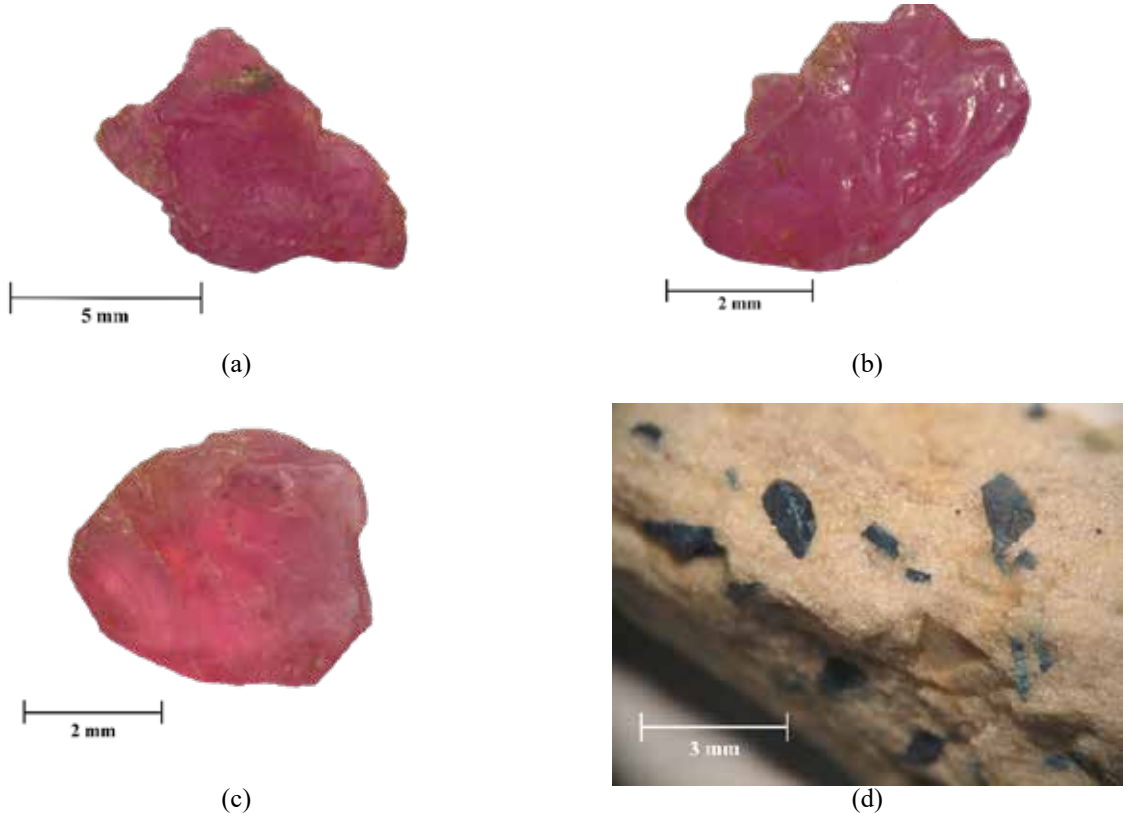

Figure 1: Macroscopic pictures of the studied samples. (a) 89A, (b) 89B, (c) 89C, (d) 89D.

Results

All samples were tested under a UV-lamp (3 Watt) of 365 nm. The 89A and 89B samples presented red fluorescence of medium intensity. The rest samples were inert under UV light. Both 89A and 89B samples presented similar spectroscopic and chemical results. PL spectra exhibit absorption peaks at 693 and 694 nm, (Fig.2a) which are characteristic to the presence of chromium ions (Cr^{+3}) in corundum (Hughes et al., 1997). These peaks are related to the red color in ruby. Vis-NIR spectra revealed characteristic absorption peaks of chromium at around 420 and 550 nm Additionally, they exhibit a characteristic negative chromium peak at 694 nm in the Vis-NIR spectra (Emmett et al., 2017) confirming that both 89A and 89B samples can be determined as rubies (Fig.2b). Under optical microscope, the samples present a foggy appearance due to numerous particles; no indication of treatment is observed.

In the case of the 89C sample, the PL spectra (Fig. 3a) presents a main peak at 685 nm and a lower peak at 686 nm which are characteristic of Cr^{3+} impurities in spinel structure and responsible for its red color (Fritsch & Rossman, 1987). The examined spinel also exhibits characteristic Cr^{3+} absorption bands at 392, 415, and 538 nm in the visible absorption spectrum (Chankhantha et al., 2020). Absorption spectra in the Visible-Near Infrared region recorded two Cr^{3+} absorption peaks at 400 nm and 536 nm respectively, which are also the characteristic to red spinel (Bootkul et al., 2016; Chankhantha et al., 2020; Zhang et al., 2023) The position and the width (FWHM) of the main PL bands at 695 – 700 nm confirm that the studied spinel sample is unheated (Widmer et al., 2015; Bootkul et al., 2016). Under optical microscope numerous inclusions are observed.

Raman spectroscopy was performed only for the 89D sample because neither Vis-NIR spectroscopy nor PL spectroscopy provided a clear result. The sample 89D exhibited one peak at 413 cm^{-1} due to H_2PO_4 bending modes and two large peaks at 1030 and 1060 cm^{-1} attributed to PO stretching vibrations (Fig. 4). According to Frost et al. (2013), the Raman the above peaks are related to the mineral lazulite. Lazulite is a mineral with a deep blue color and the chemical composition $(Mg, Fe)Al_2(PO_4)_2 \cdot (OH)_2$. The blue color is related to its chemical composition, and it is not attributed to any chromophore such as in the case of blue sapphire (Frost et al., 2013).

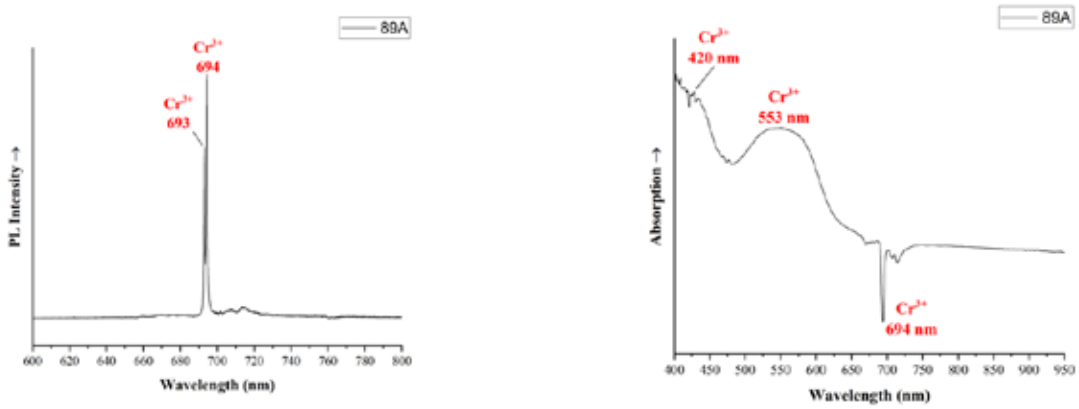

(a) (b)

Figure 2: Representative spectra of the 89A sample. (a) Photoluminescence (PL) spectra, (b) Vis-NIR absorption spectra.

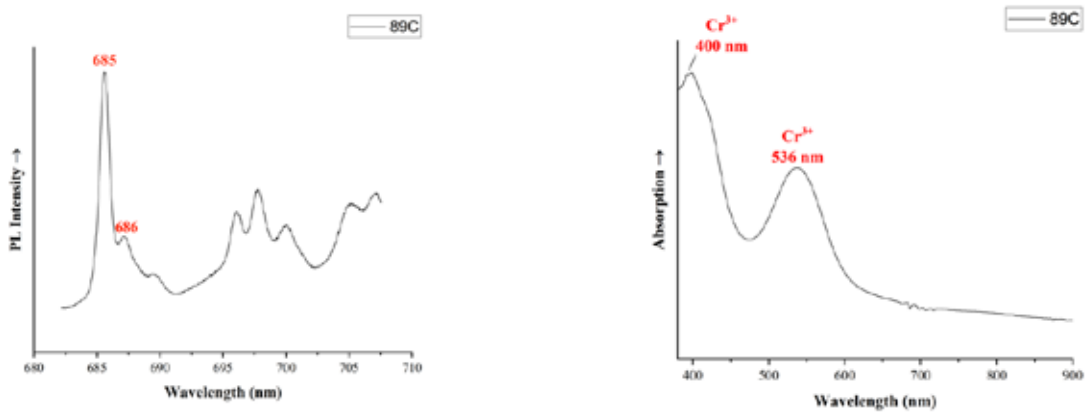

(a) (b)

Figure 3: Representative spectra of the 89C sample. (a) Photoluminescence (PL) spectra, (b) Vis-NIR absorption spectra.

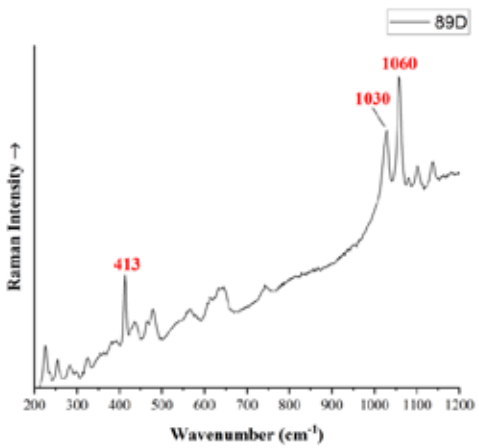

Figure 4: Raman absorption spectra of the 89D sample.

In the Scanning Electron Microscope (SEM), samples 89A, 89B, 89C, and 89D exhibited the results shown respectively in Table 1, Table 2 and Table 3. It is observed that samples 89A and 89B exhibit similar results. Both samples have an average Al_2O_3 content of 97.41 wt.% and 96.18 wt.%, respectively, a composition consistent with corundum. In both samples, the presence of Cr□O□, V□O_5, FeO, and TiO□ were confirmed, with average concentrations below 1 wt.%, Additionally, the chemical composition of the ruby samples is presented in Table 1.

Table 1: Results of microanalyses on samples 89A and 89B.

Oxides (wt.%)	89A			89B			
	Spot 1	Spot 2	Spot 3	Spot 1	Spot 2	Spot 3	Spot 4
Al_2O_3	99.23	98.66	99,06	99.28	99.43	99.64	99.64
Cr_2O_3	0.43	0.24	0.62	0.40	0.15	bdl	0.23
V_2O_5	bdl	0.64	bdl	0.31	0.17	0.03	bdl
FeO	0.03	0.41	0.25	0.01	0.24	0.33	Bdl
TiO_2	0.31	0.05	0.07	Bdl	bdl	bdl	0.13
Total	100	100	100	100	100	100	100
bdl: below detection limits							

In contrast, sample 89C shows a variation in the results. The Al_2O_3 content ranges from 61.79 to 70.04 wt.%, MgO from 24.65 to 28.01 wt.%, while FeO varies between 0.37 and 1.84 wt.%, Additionally, the chemical formula of the sample 89C is presented with distribution based on 4 O ions in Table 2.

Table 2: Results of microanalyses of sample 89Γ (in weight %) and calculation of the chemical formula of spinel based on 4 O ions.

Oxides (wt.%)	1	2	3	4	5	6	7
TiO_2	0.13	0.42				0.34	
Al_2O_3	69.90	66.22	70.27	61.42	70.42	70.66	70.46
FeO	0.37	0..60	0.57	1.84		1.04	1.11
MnO	0.07			0.45	0.76		
MgO	26.31	27.69	28.07	27.82	27.24	25.15	27.24
Cr_2O_3	2.23	2.14	0.66	0.52	0.65	1.36	0.28
V_2O_5	0.54	0.55	0.30		0.75	1.10	0.67
Distribution based on 4 O ions							
Ti	0.002	0.008				0.006	
Al	1.977	1.935	1.977	1.963	1.983	1.998	1.986
Fe^{2+}	0.007	0.010	0.001	0.001		0.021	0.022
Mn	0.001			0.009	0.016		
Mg	0.941	0.993	0.998	0.995	0.970	0.899	0.971
Cr	0.042	0.041	0.012	0.001	0.012	0.026	0.005
V	0.010	0.011	0.006		0.015	0.021	0.013
Total	2.983	2.999	3.003	3.014	2.996	2.971	2.998

Finally, sample 89D exhibits high concentrations of P_2O_5 (46.28 - 46.48 wt.%) and Al_2O_3 content (from 33.15 to 33.78 wt.%), with lower contents of MgO (from 11.09 to 11.94 wt.%), and FeO (from 3.02 to 3.71 wt.%). The chemical analysis does not point to a sapphire but rather to another mineral that was considered as such. Additionally, the chemical formula of the sample 89C is presented with distribution based on 2 P ions (Table 3).

Table 3: Results of microanalyses of sample 89D (in weight %) and calculation of the chemical formula of lazulite based on 2 P ions.

Oxides (% wt.)	1	2	3	4	5	6	7
MgO	11.60	11.94	11.46	11.52	11.13	11.06	11.09
Al_2O_3	33.15	32.78	33.28	33.22	33.23	33.21	33.22
FeO	3.02	3.03	3.17	3.09	366	3.64	3.71
P_2O_5	46.39	46.48	46.46	46.45	46.39	46.28	46.33
Total	94.15	94.23	94.37	94.28	94.41	94.19	94.35
Distribution based on 2 P ions							
P	2.000	2.000	2.000	2.000	2.000	2.000	2.000
Al	1.990	1.963	1.995	1.992	1.995	1.998	1.996

Mg	0.881	0.905	0.869	0.873	0.845	0.842	0.843
Fe	0.129	0.129	0.135	0.131	0.156	0.155	0.158
A	2.999	2.997	2.998	2.996	2.996	2.995	2.997
Sum of cations	4.999	4.997	4.998	4.996	4.996	4.995	4.997
Mg/(Mg+Fe)	0.889	0.935	0.872	0.877	0.846	0.839	0.844

XRF analyses of the samples 89A and 89B showed concentrations of Cr_2O_3 from 0.34 wt.% to 0.85 wt.%, FeO from 0.21 wt.% to 0.72 wt.%, and Ga_2O_3 at around 0.04 wt.% for both samples. The sample 89C revealed Al_2O_3 at around 67.40 wt.%, Cr_2O_3 at 1.72 wt.% and FeO at 0.59 wt.%. The 89D sample was not examined by the XRF method due to its small size. Based on observations with optical microscope, as well as both SEM-EDS and XRF results, the studied ruby samples contain V and Ga impurities revealing their natural origin in contrast to synthetic rubies which do not contain measurable amounts of these trace elements (Muhlmeister et al., 1998; Dele et al., 1997). They also contain relatively high amounts of Fe (over 300 ppm). Therefore, they can be characterized as high-iron rubies (Palke et al., 2019) probably originating from amphibolite or basalt related rocks. Main high-iron ruby deposits can be found in Cambodia, Thailand, Madagascar and Mozambique as well as Sri Lanka for pink to pinkish-red samples.

Conclusions

This study utilized a combination of spectroscopic and analytical techniques to characterize four gem samples from the Mineralogical - Petrological Museum of Aristotle University of Thessaloniki. The samples provided valuable insights into their mineralogical composition and gemological properties. Samples 89A and 89B were confirmed as natural rubies, based on their high Al_2O_3 content (over 97 wt.%) and the presence of Cr_2O_3 (<1 wt.%), responsible for their red coloration. Their PL and Vis-NIR spectra exhibited the characteristic chromium bands which further support their classification. The presence of V and Ga impurities, detected through SEM-EDS and XRF analyses, indicates their natural origin and distinguishes them from synthetic counterparts. Sample 89C, initially presumed to be a ruby, was identified as a red spinel. Its high MgO and Al_2O_3 are inconsistent with corundum but align with the composition of spinel. PL and Vis-NIR spectroscopy revealed absorption peaks at 400 nm and 536 nm, characteristic of natural, untreated red spinel. These findings underscore the importance of advanced spectroscopic techniques in accurately distinguishing between visually similar gemstones.

Sample 89D, initially classified as a blue sapphire, was determined to be lazulite. Its high P_2O_5 content and Raman absorption peaks at 413 cm^{-1} and 1060 cm^{-1} confirmed this identification. Unlike blue sapphire, whose coloration is attributed to chromophore elements like Fe^{2+} and Ti^{4+}, lazulite derives its blue color from its intrinsic chemical composition. These findings highlight the critical role of multi-technique analytical approaches in gemstone identification.

Acknowledgements

The authors wish to thank Laboratoire Français de Gemmologie (LFG) for providing the micro-Raman and Vis- NIR spectrometers for this study.

References

Bootkul, D., Tengchaisri, T., Tippawan, U., & Intarasiri, S. (2016). Analysis and modification of natural red spinel by ion beam techniques for jewelry applications. Surface and Coatings Technology, 306, 211–217.

Chankhantha, C., Amphon, R., Rehman, H. U., & Shen, A. H. (2020). Characterisation of Pink-to-Red Spinel from Four Important Localities. *Journal of Gemmology*, *37*(4).

Dele, M. L., Dhamelincourt, P., Poirot, J. P., Dereppe, J. M., & Moreaux, C. (1997). Use of spectroscopic techniques for the study of natural and synthetic gems: application to rubies. Journal of Raman Spectroscopy, 28(9), 673–676.

Dubinsky, E. V., Stone-Sundberg, J., & Emmett, J. L. (2020). A quantitative description of the causes of color in corundum. *Gems Gemol*, *56*(1), 1-27.

Emmett, J.L., Dubinsky, E.V., Hughes, R.W. and Scarratt, K. (2017). Color, Spectra & Luminescence. In: Hughes, R. (ed) Ruby & Sapphire: A Gemmologist's guide. RWH Publishing, 90-148.

Fritsch, E., & Rossman, G. R. (1987). An Update on Color in Gems. Part 1: Introduction and Colors Caused by Dispersed Metal Ions. Gems & Gemology, 23(3), 126–139.

Fritsch, E., & Rossman, G. R. (1988). An Update on Color in Gems. Part 2: Colors Involving Multiple Atoms and Color Centers. Gems & Gemology, 24(1), 3–15.

Frost, R. L., Xi, Y., Beganovic, M., Belotti, F. M., & Scholz, R. (2013). Vibrational spectroscopy of the phosphate mineral lazulite (Mg, Fe) Al2 (PO4) 2·(OH) 2 found in the Minas Gerais, Brazil. *Spectrochimica Acta Part A: Molecular and Biomolecular Spectroscopy*, *107*, 241-247.

Giuliani, G., Groat, L. A., Fallick, A. E., Pignatelli, I., & Pardieu, V. (2020). Ruby deposits: A review and geological classification. *Minerals*, *10*(7),

597.
Hughes, R. W. (1997). Ruby & Sapphire RWH publishing. *Boulder, USA.*
Muhlmeister, S., Fritsch, E., Shigley, J. E., Devouard, B., & Laurs, B. M. (1998). Separating Natural and Synthetic Rubies on the Basis of Trace-Element Chemistry. Gems & Gemology, 34(2), 80–101.
Nassau, K. (1981). Heat Treating Ruby and Sapphire: Technical Aspects. Gems & Gemology, 17 (3), 121-131.
Palke, A. C., Saeseaw, S., Renfro, N. D., Sun, Z., & McClure, S. F. (2019). Geographic Origin Determination of Ruby. Gems & Gemology, 55(4).
Widmer, R., Malsy, A. K., & Armbruster, T. (2015). Effects of heat treatment on red gemstone spinel: single-crystal X-ray, Raman, and photoluminescence study. *Physics and chemistry of minerals*, *42*, 251-260.
Zhang, L., He, K., & Guo, Q. (2023). Spectroscopic Characteristics and Coloring Mechanisms of Different Colored Spinels from Myanmar. *Crystals*, *13*(4), 575.

17th INTERNATIONAL CONGRESS of the Geological Society of Greece

BULLETIN OF THE GEOLOGICAL SOCIETY OF GREECE, SP. PUBL.

EXTENDED ABSTRACT 309

Climatic Variability and Wind Pattern Shifts in Alexandria: Twenty Years of Data to Guide Coastal Resilience in Northern Egypt

Tonbol K.M.[1],

(1) Arab Academy for Science, Technology & Maritime Transport (AASTMT), ktonbol@aast.edu

For the monitoring of the climate and assessing the risks related to the coast in port cities, it is important to track the meteorological variability over longer time periods.

This research examines the weather patterns of Alexandria in Egypt by using twenty years of observational data (2007-2025) from weather stations located around Alexandria Port. The main variables studied are: temperature, wind speed and direction, humidity, precipitation, and atmospheric pressure.

The work has shown that by applying the methods of statistical trend analysis and seasonal decomposition, there are significant changes in the climatic characteristics of Alexandria such as the growth of the mean annual temperature. Of particular concern is the shift in the seasonal wind circulation. The findings also confirm the Eastern Mediterranean climate change projections, which increases the concern about the coast's climate vulnerability. This study does not analyze the operational data from the ports; however, it's motivated by the need for continuous local meteorological observations in support of port climate adaptation strategies in maritime regions. These observations are essential for urban designers, climate change researchers, and decision-makers to strengthen the policies and frameworks aimed at developing warning networks for coastal infrastructure in the northern coastal region of Egypt.

17th INTERNATIONAL CONGRESS of the Geological Society of Greece

BULLETIN OF THE GEOLOGICAL SOCIETY OF GREECE, SP. PUBL.

EXTENDED ABSTRACT 310

The effect of microorganisms in the fossilization of skeletal material

Toska A.[1], Stathopoulou E.[2]

(1) School of Geology, Aristotle University of Thessaloniki, 54124, Thessaloniki, Greece, aris_toska@outlook.com

(2) Department of Geology & Geoenvironment, National and Kapodistrian University of Athens, Athens, Greece.

Research Highlights

Secondary bone microstructures are identified and correlated with specific microorganisms (bacteria, cyanobacteria, fungi, etc.).

The presence of these micro-organisms are correlated to specific geochemical conditions and specific environments of activity (terrestrial or aquatic).

Introduction / Background

Microorganisms play a profound role in bone diagenesis, affecting the preservation, mineralization, and structural integrity of fossilized remains across various environments (Jans *et al*., 2004). The action of microorganisms in bones, referred to as microbial activity or MFD (microbial focal destruction) influences the survival of bone through time and causes collagen hydrolysis, deterioration of bone microstructure and an increase of macroporosity. It is believed that bacteria follow the orientation of the collagen fibres and exploit planes of weakness in bones e.g. fractures, breakages (Turner-Walker, 2008), while the different sizes and morphologies of microbial activity, are the result of one or more, closely related species of bacteria and their interaction with bone microarchitecture and the local hydrologic flow (Kendall *et al*., 2018). MFD is controlled by the local physicochemical conditions of the burial microenvironment (Hackett, 1981; Turner-Walker, 2008). Cyanobacteria occur in aquatic environments, both marine and freshwater, including lacustrine and waterlogged sediments (Kendall *et al.*, 2018).

On the other hand, the possibility that microbes themselves may be mineralized and thus preserved through geological time has also been reported, often in detail with surface ornamentation, including spines, substrate mycelia and aerial hyphae appearing in or close to their original growth positions (Jones, 2009).

Objective

This study concerns the geobiological dimension of the influence of microorganisms on skeletal elements in relation to the fossilization/conservation environment. Our first aim is the identification of microstructures and their correlation with specific microorganisms (bacteria, cyanobacteria, fungi, etc.). The second aim is to correlate the presence of micro-organisms to specific geochemical conditions and to specific environment of activity (terrestrial or aquatic). However, it is also important to determine the exogenous or endogenous origin of microorganisms.

Materials

The skeletal material studied, comes from the prehistoric settlement of Dispilio (on the southern shore of Lake Orestias, in Kastoria, Northern Greece), the only lake settlement in Greece to have undergone systematic investigation (Hourmouziadis, 2002).

The samples were selected to cover the different microenvironments of the site. Some excavation squares are in purely terrestrial zones, while others are in aquatic environments. Another criterion was the origin of the bone fragments (mammals/fish). A total of 28 fish bone samples and 16 mammal bone samples were chosen for this study. Additionally, the color of the samples played an important role, with both light-colored and dark-colored bones being carefully studied. According to Stathopoulou *et al.,* (2013) the bone samples at the site can be classified based on their discoloration into 7 color types, from red dark (1) to yellow (7). The bones selected belong to colour groups 3, 5 and 6,7.

Methodology

To study the bone tissue histology of the selected samples, small compact bone fragments from all specimens were manually extracted, mounted on stubs using conductive carbon cement, and coated with Au-Pd. They were then examined using a JEOL JSM – 6390 Scanning Electron Microscope.

Results-Conclusions

The bone microstructure of our samples does not seem to have been heavily affected. The histological structural features that characterize mammal and fish bone are well preserved in most samples. Their observation under the

SEM indicated restricted microbial activity. Only three mammal samples suggested possible MFD, at a very initial stage. Also, only six of the fish bone samples exhibited MFD, recognized as spongiform porosity with a diameter of micropores of around 1 μm. Bone was found to be affected around the vascular canals and along the periosteal/outer margins. In some cases, though microbial activity expanded towards the inner surface. In most cases the affected areas were surrounded by a halo which delineated them from healthy bone surface and filled the space between the micropores. This halo appears bright under the BSE mode and is associated with the dissolution and reprecipitation of Hydroxylapatite (Hap). It is worth mentioning that we also observed such local hypermineralized areas without the co-presence of micropores.

The fact that most of the studied bones did not exhibit MFD means that they were probably preserved in conditions that did not allow for such an activity throughout their diagenetic history. Microbial activity was detected mainly in fish bones. Fish bone is characterized by a higher macroporosity, a lack of mineralization and less tightly packed collagen fibrils. This may provide additional opportunities for microbial degradation of bone.

This type of microstructural destruction can be attributed to the action of bacteria (Jackes et al., 2001). Bacterial activity in our samples is very restricted and seems to have stopped before it could develop more extensively. The latter could mean that these samples were initially buried under geochemical conditions that allowed for such activity (relatively humid aerobic terrestrial environments with high temperature and a pH: 4–9) but an undetermined event led to the modification of the conditions of the burial site. From then on, a low–temperature and/or anoxic local burial microenvironment can be deduced (Child et al., 1993). Bacteria seem to prefer open-air environments and do not affect sites that are constantly under water or in a very wet/extremely dry environment. A possible change from an open-air site to a waterlogged site for example, could explain the above. Or a change of geochemical conditions due to climatic fluctuations. Anoxic (oxygen-deprived) burial conditions can significantly slow down or halt the process of bodily putrefaction and are consistently noted for preventing bacterial bioerosion in bone microstructures (Hollund et al, 2012).

On the other hand, meandering tunnels with a diameter of about 10–15 μm along the outer surface of the bone were observed in a sample. In addition, some of these tunnels were found to host spherical grains whose semi-quantitative analysis did not show a differentiation from the analysis of the surrounding surface of unaffected bone. These can be attributed to cyanobacteria, that create tunnels that do not align with the bone's micro-architecture and show ragged, branched tunnels, differing from terrestrial bacterial degradation (Davis, 1997). Cyanobacteria, found in tidal or estuarine deposits, exhibit a different attack pattern, moving from the periosteal surface inward.

Alongside organisms such as fungi, green and red algae, and sponges, cyanobacteria are also known to exhibit a euendolithic lifestyle, meaning they penetrate and live within substrates like rocks (Gleason *et al.,* 2017). In this study we managed to observe such structures that are most likely made by cyanobacteria and euendolithic microorganisms such as actinobacteria.

In many of our samples, both mammal and fish, the presence of microbes themselves were observed. The question is whether these microbes have been mineralized and thus preserved through geological time or if they have developed recently due to storage conditions of the skeletal material. Evidence of their occurrence includes substrate mycelia and aerial hyphae appearing in or close to their original growth positions, microbial mats, spores and chains often in detail with surface ornamentation such as spines etc. Various morphotypes of each category were observed. It appears that most of these occurrences can be attributed to Actinobacteria, which are filamentous Gram-positive bacteria, classified within the phylum Actinobacteria and the order Actinomycetales (Segaran *et al*., 2017). They are predominantly aerobic, but some are facultative anaerobes or obligate anaerobes. These bacteria produce mycelium and often reproduce by sporulation, resembling filamentous fungi in this aspect.

In many of our samples, various purely aquatic species of diatoms were also observed, often in large numbers, indicating that the specific bone samples have at some time been deposited in the lake.

Clearly, the taphonomic pathway followed by the samples is largely reflected in the findings observed through the electron microscope. The structures and microorganisms identified can be correlated with the environment in which they were found. For example, the presence of microstructures from cyanobacteria indicates the bones' residence in an aquatic environment, at a depth and clarity that allows photosynthesis. Equally significant is the presence of diatoms, which could be associated with a longer residence in a deeper environment as well as an extended period of time for the samples. All the above is considered in relation to the archaeological context of the site and the characteristic features of the different parts (terrestrial and waterlogged). The discolouration of the skeletal material by Mn and Fe can also be correlated to the microbial activity, but also to the post depositional organic environment that enhances the discolouration as well as the migration of Mn to the bones (Marin Arroyo *et al.,* 2008).

References

Child, A., Gillard, R., Pollard, A., 1993. Microbially-induced promotion of amino acid racemization in bone: isolation of microorganisms and the detection of their enzymes. Journal of Archaeological Science 20, 159–168.

Davis, P.G., 1997. The bioerosion of bird bones. International Journal of Osteoarcheology 7: 388-401.

Hackett, C.J., 1981. Microscopical focal destruction (Tunnels) in exhumed human bones. Medicne, Science and the Law 21 (4), 243–265.

Hollund, H.I., Jans, M.M.E., Collins, M.J., Kars, H., Joosten, I., Kars, S.M., 2012. What happened here? Bone histology as a tool in decoding the postmortem histories of archaeological bone from Castricum, The Netherlands. International Journal of Osteoarcheology 22, 537-548.

Hourmouziadis, G.H., 2002. Dispilio. 7500 Years After. University Studio Press, Thessaloniki (In Greek).

Jackes, M., Sherburne, R., Lubell, D., Barker, C., Waymen, M., 2001. Destruction of microstructure in archaeological bone: a case study from Portugal. International Journal of Osteoarcheology 11, 415–432.

Jans, M., Nielsen-Marsh, CM., Smith, C., Collins, M., Kars, H.,2004. Characterisation of microbial attack on archaeological bone. Journal of Archaeological Science 31, 87-95.

Jones, B., 2009. Phosphatic precipitates associated with actinomycetes in speleothems from Grand Cayman, British West Indies. Sedimentary Geology 219 (1–4), 302-317.

Kendall, C., Hoier Eriksen, A.M., Kontopoulos, I., Collins, M.J., Turner-Walker, G., 2018. Diagenesis of archaeological bone and tooth. Paleogeography, Palaeoclimatology, Palaeoecology 491, 21–37.

Marin Arroyo, A.B., Landete Ruiz, M.D., Vidal Bernabeu, G., Seva Román, R., González Morales, M.R., Straus, L.G., 2008. Archaeological implications of human-derived manganese coatings: a study of blackened bones in El Mirón cave, Cantabrian Spain. Journal of Archaeological Science 35, 801–813.

Mergelov, N., Mueller, C.W., Prater, I., 2018. Alteration of rocks by endolithic organisms is one of the pathways for the beginning of soils on Earth. Scientific reports 8, 3367.

Segaran, Gayathri & Dhevi Vs, Ranjitha & Settu, Sugashini & Shankar, Saranya & Sathiavelu, Mythili. (2017). A Review on Endophytic Actinomycetes and their Applications. Journal of Chemical and Pharmaceutical Research. 9. 7.

Stathopoulou, E.T., Theodoropoulou, T., Phoca-Cosmetatou, N., 2013. Black fish bones in waterlogged deposits: the case of the Neolithic Lake settlement of Dispilio, Greece. Archaeofauna 22, 51–74.

Turner-Walker, G., 2008. The chemical and microbial degradation of bones and teeth, in: Pinhasi, R., Mays, S. (Eds.), Advances in Human Palaeopathology. John Wiley & Sons, Ltd.

17th INTERNATIONAL CONGRESS of the Geological Society of Greece

BULLETIN OF THE GEOLOGICAL SOCIETY OF GREECE, SP. PUBL.

EXTENDED ABSTRACT 311

Ecuadorian candidates for the World Natural Heritage List - The Triple Volcano and Tayos caves

Theofilos Toulkeridis[1,2], Aaron Addison[3], Silviu Constantin[4], Grace Tatiana Páez-Barrera[5]

(1) Aristotle University of Thessaloniki, Thessaloniki, Greece (2) Universidad UDET, Quito Ecuador (3) Fellow Cave Research Foundation, Fellow National Speleological Society, Fellow Explorer's Club, USA (4) "Emil Racoviţă" Institute of Speleology, Dept. of Geospeleology and Paleontology, Frumoasă 31, Bucharest, Romania (5) Universidad de las Fuerzas Armadas ESPE, Sangolquí, Ecuador

Research Highlights

Two significant subterranean environments in Ecuador have been chosen as proposed candidates for the UNESCO World Heritage List. These are the Tayos cave in the Amazonian basin, and the Triple Volcano Cave in the Galapagos, because both sites represent a unique beauty and meet several criteria of the UNESCO conditions to be considered exceptional Natural Heritage.

Introduction / Background

Since 1978, there have been a variety of sites in Ecuador that have been declared as Natural and Cultural Heritage of Humanity by the UNESCO Organization. This list includes Quito, the capital of Ecuador, with its colonial center, rich history and architecture, which is the largest historical center in the Americas. Next in line is the Galapagos as a Biosphere Reserve in 1978 and Cuenca, the "Athens of Ecuador" for its buildings and natural environment in 1999. Other Ecuadorian icons on this list include the Sangay National Park, the Zárapa language, the traditional weaving of the Ecuadorian straw hat, also known as the Panama Hat and, finally, the Qhapaq Ñan (Inca Trail, in Quechua), a masterful road communication network, with its 6,000 km from south to north covering and crossing the countries of Argentina, Chile, Bolivia, Peru, Ecuador and Colombia.

UNESCO is the global organization responsible for including exceptional and extraordinary sites for protection or preservation for humanity. The criteria for inclusion on the World Heritage List are explained in the Operational Guidelines for the Implementation of the World Heritage Convention which, in addition to the text of the Convention, is the main working tool on World Heritage. Among the ten criteria for inclusion on the World Heritage List are that they must (a) Contain superlative natural phenomena or areas of outstanding natural beauty and aesthetic importance; (b) Be eminently representative examples of major stages in the history of the earth, including testimony to life and significant ongoing geological processes in the development of landforms, or significant geomorphic or physiographic features; (c) Be eminently representative examples of significant ongoing ecological and biological processes in the evolution and development of terrestrial, aquatic, coastal and marine plants and animal communities; and (d) To contain the most representative and important natural habitats for the in situ conservation of biological diversity, including those containing endangered species of outstanding universal value from an aesthetic or scientific point of view.

To be included on the World Heritage List, sites must have universal value and meet at least one of the ten selection criteria. The List includes 962 properties that are part of the cultural and natural heritage that the World Heritage Committee considers having outstanding universal value. Among the 962 properties, it is noted that the great majority are located in the developed regions of the world, especially in Europe. Among the 188 natural sites, there are 14 caves, of which 6 are in Europe, 5 in Asia, 2 in the USA and one in Mexico.

There are no caves located in South America on the list. Our research of the last two decades with an interdisciplinary group included several dozen selected caves, which are carefully mapped (geology, geography etc.) and investigated for their biological content (bacteria, insects, mammals etc.). We have aimed to find some caves of karst origin in the Amazon or volcanic origin in the Galapagos, which meet one of the World Heritage Committee's selection criteria for inclusion on the World Heritage List.

Thus, based on several investigations during dozens of explorations, workshops and symposia in Ecuador by a multidisciplinary group together with a wide variety of national experts and from several other countries, interesting discoveries have been realized which are in international focus. Based on these investigations, two objectively spectacular natural sites are proposed to be included as candidates for the World Heritage List, being the Tayos cave in the Province of Morona Santiago in the Ecuadorian Amazon and Triple Volcano cave on the Sierra Negra volcano on Isabela Island, Galapagos (Toulkeridis and Angermeyer, 2019).

Previous and recent speleological studies in Ecuador and the Galapagos

Very little is known about the cartographic part of the caves in the Amazonian part of Ecuador, except for a few maps from a French expedition in the last century (Besson *et al.*, 1982) and from two Belgian and Spanish campaigns in the Galapagos

in the seventies and early nineties respectively (Hernandez *et al.,* 1991 and references within this study). Entomological and paleontological studies have recorded only a few species in the Galapagos. Recent studies of our research group include a variety of findings of worldwide interest, including new species and an unusual behavior of a wall-climbing catfish (Constantin *et al.*, 2019; Miller *et al.*, 2020; Katz *et al.*, 2016; Kempe *et al.*, 2021; Espinasa *et al.*, 2018; Martin-Solano *et al.*, 2016; Hoese *et al.*, 2015; Basantes *et al.*, 2017; Zambrano *et al.*, 2017). Additionally, there has been the production of a variety of cinematographic arts, including documentaries especially about the Tayos cave, by known producers such Expedition Unknown of the Travel Channel (Hunt for the Metal Library), Discovery Channel, National Geographic and Disney+.

The Tayos Cave in the Ecuadorian Amazon

The Tayos cave is located within the geological formation called Santiago, which extends from the beginning of the Late Triassic to near the end of the Liassic. This same formation is visible exclusively in the Cutucú Mountain Range and is composed of a sequence of non-metamorphosed marine sediments such as gray siliceous limestone, calcareous sandstone (turbidite in parts) and black slate and volcano-sediments towards the upper part. There are correlations towards the north of Ecuador with the Sacha Formation of continental environment which forms with the Santiago Formation a syn-tectonic cycle recording the opening of a “Rift”.

The Tayos cave is formed in a set of limestone layers, interspersed with dolomites, argillites and sandstones. Due to the geodynamics, the layers have been lifted from the depths of the crust, outcropping today near the surface. Due to these tectonic movements, folds and geological faults were formed. Both structural processes can be observed in the cave where there is a slight dip (5-15º) in the western part of the cave and another more steeply inclined one (~70º) in the eastern part of the cavity, while rectangular dislocations of rocks and deposits expressed in fissures or vertical fractures are noted. The general direction of the cave with its passages is SW-NE and it has an extension of just under 5 km in total. The cave has a series of enormous chambers. The main entrance is a doline with a depth of about 70 meters, but there is a deeper doline where most of the unique Tayos birds are found in the western part of the main entrance. Next to the sinkholes are impressive sites of stalagmites and stalactites, waterfalls, an amphitheater, a dome and smooth, flat walls called the “Portal of Moricz”. The entire length of the known part of the cave is almost 5 km, while at least 3 km are still unmapped.

Figure 1. Resting spot within the “Cathedral” of the Tayos cave.

There are numerous myths about this emblematic Ecuadorian cave. In popular culture, these myths revolve around the arrival and existence of extraterrestrials and intraterrestrials, the supposed discovery of metal plates or books and various other treasures, such as golden statues, hieroglyphs and prehistoric antiquities unknown to mankind and much more. These tales originated primarily with Hungarian-Argentine Juan Moricz, the first speleologist who promoted the cave since 1969 and Erich von Däniken, a pseudoscientist and pseudohistorian. Erich von Däniken, known for his frauds, published in 1973 the book entitled “The Gold of the Gods” without ever visiting this site or Ecuador itself. In this book, which has sold millions of copies, it was claimed “A gigantic system of tunnels, thousands of miles long and built by unknown persons at an unknown date, lies hidden deep beneath the South American continent.” The Tayos cave is truly spectacular, apart from the lies and myths surrounding it. The formations of the geological deposits, the limestone structures in speleothems, stalagmites and stalactites as well as the endemic flora and fauna attracted by the surrounding forests make this site unique, and surely in the whole continent. The real treasures are the information that is yet to be discovered, such as what is recorded in paleontology, paleoclimatology, paleoceanography, bacteria, gases, minerals, animal behavior (Tayos birds, bats, rats, frogs, snakes etc.), entomological life, ethnology, archaeology alongside other natural and social sciences.

Figure 2. Left "Portal of Moricz; right "Skylight" doline, one of the two entrances of the Tayos cave.

Figure 3. Part of the Stalagmite-forest of the Tayos cave.

The Triple Volcano in the Galapagos

Volcanic caves are found on all islands of the Galapagos, which have been formed in almost all the same way with a few exceptions. Island caves are the product of low-viscosity and very fluid lava flows, sometimes with enormous proportions or volumes, which harden at their edges when in contact with air or water and thus allow the conservation of heat and fluidity in their interior. As the molten lava continues to flow and seeps beneath the crust it leaves behind a void in the flow, which is known as a lava tube or cave. Some lava tubes are only a few centimeters high while others are so large or high that many people can walk on or inside them simultaneously. Lava caves can be several kilometers long and partially flooded, others may be dry and some have sometimes collapsed. Most are very shallow, but some older tubes are partially buried by younger tubes and extend deep into the ground. A few exceptions of volcanic caves have been formed in very curious ways. In the midst of volcanic activity in a parasitic volcanic cone above the huge shield volcanoes, the explosions abruptly stop, and the volcano's conduit is left open. These caverns are characterized by their verticality and depth. These sites are excellent environments to study the interior of a frozen and preserved magma chamber of a volcano.

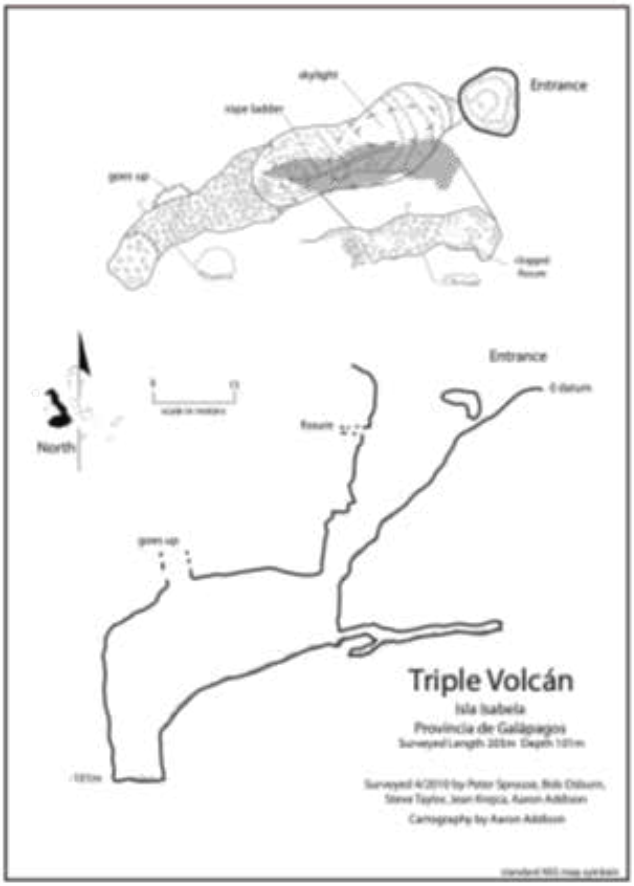

Figure 4. Map of the Triple Volcano.

Figure 5. Insight image of the Triple Volcano´s magma chamber

The Cave called "Triple Volcano" meets all of the above and is precisely the cave that represents a fossilized magma chamber with its intact conduct towards the surface. This cave is located on the southern flank of the Sierra Negra volcano on Isabela Island. Its maximum depth is 101 meters below the entrance (Addison, 2011; Addison *et al.*, 2013). The colors of the internal formations of this cave leave even speleologists with decades of experience with their mouths open. There is no color missing, a complete rainbow. These colors are represented by various crystallizations, mainly of zeolites, in the inner part of the magma chamber reflecting different volcanic processes during times of activity (Debut *et al.*, 2021). Furthermore, at the bottom of the cave there are other witnesses of the varied and complex past history of this underground site such as fossils, bacteria and insects, still unknown to the scientific world.

Conclusion

Both Ecuadorian caves, Tayos and Triple Volcano, have difficult access and entrances, but therefore these sites remained isolated from natural processes existing on their upper part and in general surroundings. However, both caves meet several criteria proposed by UNESCO to be considered candidates for the List of Natural World Heritage Sites. Therefore, both sites will be soon proposed, after few complementary studies, as the next Ecuadorian icons on the UNESCO List of World Heritage Sites.

Acknowledgements

The authors are grateful to different organizations that sponsored our research in various ways, The Galapagos National Park, the Army Special Forces, the Iwia School, the Ecuadorian Scientific Society of Speleology - ECUCAVE, the Military Geographic Institute, the Pan-American Center for Geographic Research - CEPEIGE, the National Speleological Society and the communities in eastern Ecuador the Cave Research Foundation and the many researchers with specialized skills needed to property document these world class resources.

References

Addison A., 2011. Gálapagos – Caving the Equator, National Speleological Society News 69: 8–18.

Addison, A., Toulkeridis, T., Taylor, S., Osburn, G., Hoese, G., & Delgado, V. (2013, July). Recent investigations in the Galápagos Islands, Ecuador. In *16th International Congress of Speleology*.

Basantes, J., Godoy, L., Carvajal, T., Castro, R., Toulkeridis, T., Fuertes, W., ... & Addison, A. (2017, October). Capture and processing of geospatial data with laser scanner system for 3D modeling and virtual reality of Amazonian Caves. In *2017 IEEE Second Ecuador Technical Chapters Meeting (ETCM)* (pp. 1-5). IEEE.

Besson JP, Lera, D, Valicourt, E. de, 1982. Ecuador 82 Expedition Speleologique De La S.S.P.P.O. Pages 69–88.

Constantin, S., Toulkeridis, T., Moldovan, O. T., Villacís, M., & Addison, A. (2019). Caves and karst of Ecuador–state-of-the-art and research perspectives. *Physical Geography*, *40*(1), 28-51.

Debut, A., Toulkeridis, T., Vaca, A. V., & Arroyo, C. R. (2021). Origin of color variations of thin, nano-sized layers of volcanic cinder from the Sierra Negra Volcano of the Galapagos Islands. *Uniciencia*, *35*(2), 210-222.

Espinasa, L., Robinson, J., Soares, D., Hoese, G., Toulkeridis, T., & Toomey III, R. (2018). Troglomorphic features of Astroblepus pholeter, a cavefish from Ecuador, and possible introgressive hybridization. *Subterranean Biology 27: 17–29*.

Hernández JJ, Izquierdo, Oromi P, 1991. Contribution to the vulcanospeleogy of the Gálapagos Islands. Pages 204–220. 6th International Symposium on Vulcanospeleology.

Hoese, G., Addison, A., Toulkeridis, T., & Toomey III, R. (2015). Observation of the catfish Chaetostoma microps climbing in a cave in Tena, Ecuador. *Subterranean Biology*, *15*, 29-35.

Katz, A. D., Taylor, S. J., Soto-Adames, F. N., Addison, A., Hoese, G. B., Sutton, M. R., & Toulkeridis, T. (2016). New records and new species of springtails (Collembola: Entomobryidae, Paronellidae) from lava tubes of the Galápagos Islands (Ecuador). *Subterranean Biology*, *17*, 77-120.

Kempe, S., Middleton, G., Addison, A., Toulkeridis, T., and Hoese, G., 2021: New Insights into the Genesis of Pyroducts of the Galápagos Islands, Ecuador. *Acta Carsologica*, 50(1), 53-73.

Martin-Solano, S., Toulkeridis, T., Addison, A., & Pozo-Rivera, W. E. (2016). Predation of Desmodus rotundus Geoffroy, 1810 (Phyllostomidae, Chiroptera) by Epicrates cenchria (Linnaeus, 1758) (Boidae, Reptilia) in an Ecuadorian Cave. *Subterranean Biology*, *19*, 41-50.

Miller, A. Z., García-Sánchez, A. M., L. Coutinho, M., Costa Pereira, M. F., Gázquez, F., Calaforra, J. M., ... & Saiz-Jimenez, C. (2020). Colored microbial coatings in show caves from the Galapagos Islands (Ecuador): first microbiological approach. *Coatings*, *10*(11), 1134.

Toulkeridis, T. and Angermeyer, H., 2019: Volcanoes of the Galapagos. 2nd Edition, Abad Offest, Guayaquil, Ecuador: 324pp

Zambrano, A., Padilla, O., Toulkeridis, T., Zapata, J., Ordoñez, E., & Mato, F. (2017, November). Software constraints for caves' virtual environments modeling. In *2017 IEEE Symposium Series on Computational Intelligence (SSCI)* (pp. 1-5). IEEE.

17th INTERNATIONAL CONGRESS of the Geological Society of Greece

BULLETIN OF THE GEOLOGICAL SOCIETY OF GREECE, SP. PUBL.

EXTENDED ABSTRACT 312

A review of calcareous nannofossil biostratigraphic studies in the Hellenic territory (Greece): the contribution of the Micropaleontology Collection of the Laboratory of Historical Geology and Biogeosciences (NKUA)

Triantaphyllou M.V.[1], Skampa E.[1], Dimou V.-G.[2]

(1) National and Kapodistrian University of Athens, Department of Geology and Geoenvironment, Athens, Greece, mtriant@geol.uoa.gr (2) Aristotle University of Thessaloniki, School of Geology, Thessaloniki, Greece

Introduction

The calcareous nannofossil biostratigraphy is widely based on the standard zonal schemes of Martini (1971), Okada and Bukry (1980), Bown (1998), Burnett (1998) and the updated schemes of e.g., Backman *et al.* (2012) and Agnini *et al.* (2017). In the marginal Mediterranean basin, the fragmentation of the geological record, together with the strong diachroneity of zonal boundary events and/or the absence or extreme rareness of primary marker species, does not allow easily the application of the standard nannofossil zonations. Therefore, regional zonal schemes were developed (e.g., Theodoridis, 1984; Rio *et al.*, 1990; Fornaciari & Rio 1996).

In this study, an extended dataset concerning the investigated locations of the Hellenic territory (alpine, flysch, mollasic and post-alpine deposits) and the available published calcareous nannofossil biostratigraphic results, has been constructed, aiming to standardize the available data and provide realistic biochronologic estimations, according to the magnetobiochronology of Berggren *et al.* (1995) and the more recent astrobiochronological approaches of e.g., Lourens *et al.* (2004), Raffi *et al.* (2006), Backman *et al.* (2012), Agnini *et al.* (2017). In addition, a series of new locations with their unpublished calcareous nannofossil biostratigraphic determinations (e.g., Triantaphyllou, 2017), are incorporated to the dataset, providing a useful framework for correlations in the eastern Mediterranean and beyond. The geographical distribution of all the available data is presented in a series of geological maps arranged per each nannofossil biozone.

A big part of the micropaleontological/geological material associated with the constructed calcareous nannofossil biostratigraphy dataset, is already incorporated into the Micropaleontology Collection at the Laboratory of Historical Geology and Biogeosciences (HG-BioGeoSci), National and Kapodistrian University of Athens (NKUA).

The curation of this Collection undergoes the auspices of the newly introduced international MSc Programme “Industrial and Environmental Applications in Micropaleontology” (IdEA-M, https://idea-m.com/) at the Department of Geology and Geoenvironment (NKUA) and the Interinstitutional MSc Programme “Paleontology-Geobiology” directed by the Aristotle University of Thessaloniki. Our aim is to create a free access database of all micropaleontological objects stored in the HG-BioGeoSci, not only for educational purposes but also benefiting all interested parties to visit and study the collections.

Materials and Methods

The calcareous nannofossils Collection concerns microscope slides, mounted SEM stubs and filtered water samples. The majority of the items comes from the Greek territory and the broader Mediterranean area as well as from other locations worldwide, including samples collected by the global deep-sea drilling programs (DSDP, ODP, IODP etc.).

Except for the microfossil content, the raw material comprising rock samples, marine core records, boreholes and drillings, surface sediments, sediment traps, as well as sample residues are also recorded in a digital database.

The database displays a 2-level classification where all different types of microfossils are documented, labeled with a unique Laboratory code and linked to all available data, i.e., lithology/material type, sampling date and methods, preparation date and analysis techniques, biozone/ biostratigraphic assignment, applied biozonal scheme, age, paleoenvironment type, owner, analyst, references list, repository and notes (e.g., field notes, photos, original drawings, derived publications etc.).

The nannofossil biostratigraphy has been accomplished through qualitative, semiquantitative and quantitative analyses.

Results and Conclusions

The presented calcareous nannofossil biostratigraphy dataset contributes to a better understanding of the spatiotemporal impact on calcareous nannofossil biostratigraphic assignments of the different geological-geotectonic origin deposits in the Hellenic territory and of the factors limiting the distribution and controlling the presence of the widely used nannofossil biostratigraphic indices (examples in Figures 1, 2).

The effort to synthesize and critically evaluate all available biostratigraphic data based on calcareous nannofossil analysis contributes to e.g., defining the age of alpine carbonates, the onset of clastic sedimentation in the various geotectonic units, the stratigraphic age of the different flysch and post-alpine deposits, etc.

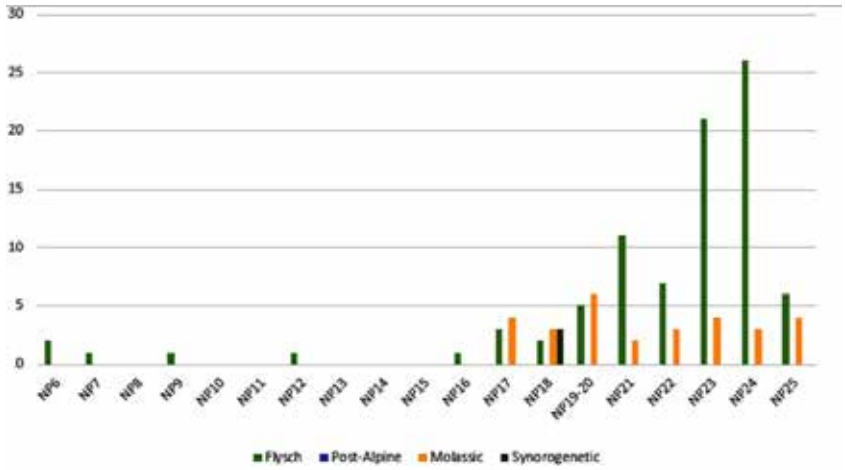

Figure 1. Example of the distribution of calcareous nannofossil Paleogene biozones in the Hellenic territory clastic deposits.

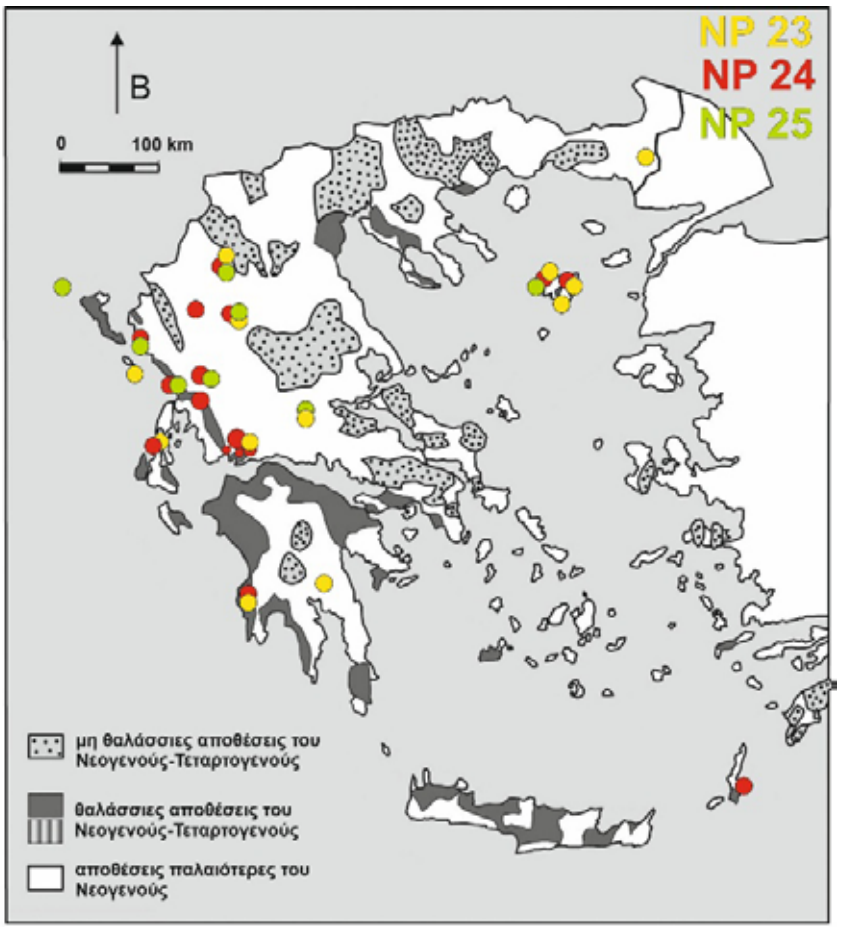

Figure 2. The presence of the Paleogene biozones NP23-NP25 in the clastic deposits.

More than 8.000 available calcareous nannoplankton preparations have been entered in the HG-BioGeoSci Micropaleontology Collection database, associated with more than 20.000 entries of sample residues and raw samples. The aforementioned material derived from more than 100 sites, has been introduced in the digital database and demonstrated in Figure 3. Most sites are distributed in the Mediterranean area; nevertheless, data from North and South Atlantic Ocean, Gulf of Mexico, Gulf of Aden, Laccadive Sea, etc. are also included, offering a worldwide record.

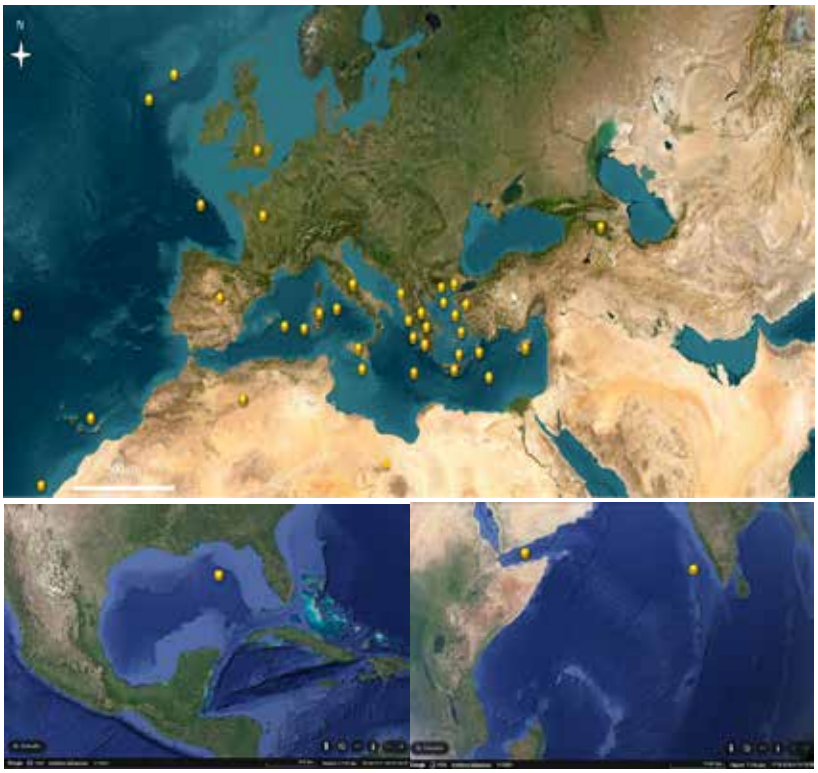

Figure 3. Overview map of the up-to-date calcareous nannofossil entities in the HG-BioGeoSci Micropaleontology Collection.

Up to now, the calcareous nannofossil HG-BioGeoSci Micropaleontology Collection (Figure 4) exhibits mostly Neogene (46%) entities, followed by Quaternary and Paleogene (18% and 17%, respectively). Modern coccolithophore records (water column filtered samples and sediment trap timeseries) are also well represented (13%).

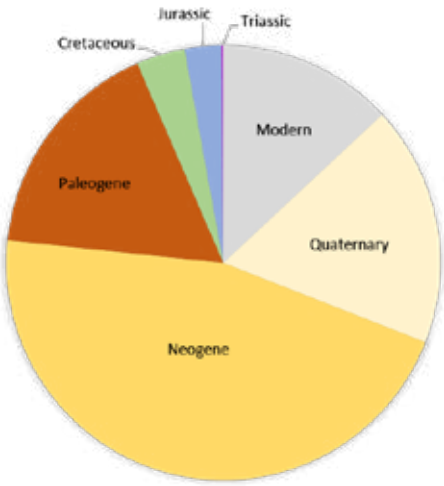

Figure 4. Pie chart showing the abundances of various time periods in respect of the up-to-date record of biostratigraphic entities.

The digitization, archiving and storage of calcareous nannofossil and coccolithophore dataset together with (paleo) environmental data are expected to allow us the understanding of long-term (paleo)ecosystem and ecological dynamics mainly in the Mediterranean area in comparison to the worldwide record. This information is crucial in predicting long-term human-induced environmental and climatic changes.

References

Agnini, C., Monechi, S., Raffi, I., 2017. Calcareous nannofossil biostratigraphy: historical background and application in Cenozoic chronostratigraphy. Lethaia, 50, 447–463.

Backman, J., Raffi, I., Rio, D., Fornaciari, E., Pälike, H., 2012. Biozonation and biochronology of Miocene through Pleistocene calcareous nannofossils from low and middle latitudes. Newsletters on Stratigraphy, 45, 221–244.

Berggren, W. A., Kent, D.V., Swisher, C. C. III, Aubry, M.-P., 1995. A revised Cenozoic geochronology and chronostratigraphy. In: Berggren, W. A., Kent, D.V., Aubry, M.-P., Hardenbol, J., Geochronology, time scales and global stratigraphic correlation: A unified temporal framework for an historical geology. Spec. Publ. Soc. Econ. Paleontol. Mineral., 54, 29–212.

Bown, P.R., 1998. Triassic. In, Bown, P. R. (ed.) Calcareous Nannofossil Biostratigraphy. British Micropalaeontological Society Publication Series, 29–33.

Burnett, J.A., 1998. Upper Cretaceous. In, Bown, P. R. (ed.) Calcareous Nannofossil Biostratigraphy. British Micropalaeontological Society Publication Series, 132–199.

Fornaciari, E., Rio, D., 1996. Latest Oligocene to early Middle Miocene quantitative Calcareous Nannofossil Biostratigraphy in the Mediterranean region. Micropaleontology 42 (1), 1–36.

Lourens, L.J., Hilgen, F.J., Shackleton, N.J., Laskar, J., Wilson, D., 2004. The Neogene Period. In: Gradstein, F. M., Ogg, J. G., Smith, A. G. (Eds.), A Geological Time Scale 2004. Cambridge University Press, Cambridge, 409–440.

Martini, E., 1971. Standard Tertiary and Quaternary calcareous nannoplankton zonation. In Farinacci, A. (ed.): Proceedings of the Second Planktonic Conference Roma 1970, 2, Edizioni Tecnoscienza, Rome, p. 739–785.

Okada, H., Bukry, D., 1980. Supplementary modification and introduction of code numbers to the low-latitude coccolith biostratigraphic zonation (Bukry, 1973; 1975). Marine Micropaleontology, 5, 321–325.

Raffi, I., Backman, J., Fornaciari, E., Pälike, H., Rio, D., Lourens, L., Hilgen, F., 2006. A review of calcareous nannofossil astrobiochronology encompassing the past 25 million years. Quaternary Science Reviews, 25, 3113–3137.

Rio, D., Raffi, I., Villa, G., 1990. Pliocene–Pleistocene calcareous nannofossil distribution patterns in the western Mediterranean. In: Kastens, K. A., Mascle, J., et al., Proceedings ODP, Scientific Results, 107, 513–533.

Theodoridis, S., 1984. Calcareous nannofossil biozonation of the Miocene and revision of the helicoliths and discoasters. Utrecht Micropaleontological Bulletins, 32, 1–271.

Triantaphyllou, M.V., 2017. A review of Cenozoic calcareous nannofossil biostratigraphic studies in the Hellenic territory (Greece): achievements and limitations. INA16 Athens Sept. 2017, Journal of Nannoplankton Research, 37,127.

17th INTERNATIONAL CONGRESS of the Geological Society of Greece

BULLETIN OF THE GEOLOGICAL SOCIETY OF GREECE, SP. PUBL.

EXTENDED ABSTRACT 313

Assessing Future Climate Change Risk to Cultural Heritage of Greece: A Case Study of Mycenae and Delos

Tringa E.[1], Tolika K.[1]

(1) Department of Meteorology and Climatology, School of Geology, Aristotle University of Thessaloniki, Thessaloniki, 54124 Greece

Research Highlights

Assessing the risk of damage to cultural heritage due to climate change.

Future projections using the up-to-date regional climate model (RCM) RegCM4 for two Greek cultural heritage sites.

Introduction

Cultural heritage sites have historically been, and will continue to be, affected by environmental factors such as weathering processes. However, climate change presents significant new challenges, accelerating deterioration processes and amplifying the vulnerability of these non-renewable heritages. Changes in temperature, precipitation, air pollution, wind intensity, and the frequency and severity of extreme weather events—such as droughts, floods, and landslides—along with sea level rise (SLR) and the interaction between climate change and air pollution, have significant impacts on cultural heritage (Sesana et al. (2021)). These factors have been recognized by UNESCO as serious threats to cultural heritage (UNESCO World Heritage Centre, (2008)). Climate change can intensify physical, chemical, and biological mechanisms of degradation, affecting the structure and composition of materials. The destructive effects of climate change are particularly evident in regions like the Mediterranean, which include monuments that remain actively used long after their original construction. Outdoor cultural heritage, such as ancient Greek theaters, which form an integral part of Mediterranean culture, provides a prime example of how monuments are impacted by climate change and other contributing factors. These include the natural deterioration of materials over time, the increasing frequency and intensity of extreme weather events, and degradation caused by continued human use of the monuments and their surroundings. Researchers have recognized the risks posed by climate change to cultural heritage sites and have approached the issue in various ways. Ioannidis et al. (2024) studied the impacts of climate change on European cultural heritage sites from 1970 to 2020, highlighting the increased heat stress on elements made from stone and marble, thereby increasing the risk of damage. Kapsomenakis et al. (2023) evaluated the impacts of climate change on multiple UNESCO cultural and natural heritage sites in the Mediterranean, revealing that as global warming progresses, the risks to most of the sites studied intensify. In our previous work (Tringa and Tolika (2023)), we explored the impacts of climate change on Thessaloniki and Delphi, showing that the risk of damage to inorganic materials is expected to increase with temperature fluctuations. Despite the growing body of research on the effects of climate change on cultural heritage, the need for quantitative data and projections remains critical for developing effective adaptation and mitigation strategies, as emphasized by Bonazza and Sardella (2023).

Research aims

Awareness of the significant social and economic value of cultural monuments to the country, along with recognition of the potentially negative impacts of climate change on them, served as the motivation for this research. The aim of this work is to assess the future heritage microclimate risk due to climate change and to quantify the predicted risk of damage to the construction materials of monuments at two Greek cultural heritage sites. Future simulations will provide valuable insights into how climate change could affect the monuments of these sites, offering a basis for informed decision-making in the management and conservation of cultural heritage. This work will contribute to the development of adaptive strategies to safeguard cultural monuments, ensuring their resilience in the face of climate-related challenges.

Data and Methods

This work examines the impacts of climate change on cultural heritage at two Greek sites: Mycenae and Delos. Using the Heritage Outdoor Microclimate Risk (HMR_{out}) and Predicted Risk of Damage (PRD) indices, this study quantifies potential damage to inorganic materials due to long-term changes in temperature and relative humidity (RH). The analysis was carried out for three different time periods, the period 1980–2000 and the future periods 2039–2059 and 2079–2099. Climate projections are based on the up-to-date regional climate model RCM RegCM4 with the fine spatial resolution of 10x10km, providing detailed simulations of the climate parameters in Greece. The model's output is based on the updated "medium" emission scenario, Representative Concentration Pathway (RCP4.5).

Discussion

The results of this study indicate that climate change poses an increasing threat to the preservation of cultural heritage at both Mycenae and Delos. The long-term analysis, which covers both the present and future climate projections, highlights the potential for accelerated material degradation due to the combination of increased heat stress and relative humidity fluctuations. By using indices such as HMR_{out} and PRD, this study provides valuable insights into the potential future threats faced by the case study sites, offering a scientific basis for conservation efforts and the development of adaptive strategies. Furthermore, the high spatial resolution of the RegCM4 model enables more accurate projections of climate conditions at specific heritage sites, which is essential for developing targeted, site-specific conservation strategies. Finally, as climate change continues to affect both environmental and cultural sites, it is essential for decision-makers and heritage conservationists to incorporate climate change projections into their strategies.

References

Sesana, E., Gagnon, A.S., Ciantelli, C., Cassar, J., Hughes, J.J., 2021. Climate Change Impacts on Cultural Heritage: A Literature Review. WIREs Clim. Chang. 12, e710.

UNESCO World Heritage Centre. Policy Document on the Impacts of Climate Change on World Heritage Properties; London, UK, 2008.

Ioannidis, C., Verykokou, S., Soile, S., Istrati, D., Spyrakos, C., Sarris, A., Akritidis, D., Feidas, H., Georgoulias, A.K., Tringa, E., et al., 2004. Safeguarding Our Heritage—The TRIQUETRA Project Approach. Heritage 7, 758–793, doi:10.3390/heritage7020037.

Kapsomenakis, J., Douvis, C., Poupkou, A., Zerefos, S., Solomos, S., Stavraka, T., Melis, N.S., Kyriakidis, E., Kremlis, G., Zerefos, C., 2023. Climate Change Threats to Cultural and Natural Heritage UNESCO Sites in the Mediterranean. Environ. Dev. Sustain. 25, 14519–14544, doi:10.1007/s10668-022-02677-w.

Tringa, E., Tolika, K., 2023. Analysis of the Outdoor Microclimate and the Effects on Greek Cultural Heritage Using the Heritage Microclimate Risk (HMR) and Predicted Risk of Damage (PRD) Indices: Present and Future Simulations. Atmosphere 14, 663, doi:10.3390/atmos14040663.

Bonazza, A., Sardella, A., 2023. Climate Change and Cultural Heritage: Methods and Approaches for Damage and Risk Assessment Addressed to a Practical Application. Heritage 6, 3578–3589, doi:10.3390/heritage6040190.

17th INTERNATIONAL CONGRESS of the Geological Society of Greece

BULLETIN OF THE GEOLOGICAL SOCIETY OF GREECE, SP. PUBL.

EXTENDED ABSTRACT 314

Preliminary results of GEM concentration in interstitial soil and free gases from Mt. Etna, Sicily

Tripodi F.[1], Brugnone F.[1], D'Alessandro W.[2], Parello F.[1], Pecoraino G.[2], Giammanco S.[3], Stagno V.[2,4], Calabrese S.[1, 2]

(1) Università degli Studi di Palermo, Dipartimento di Scienze della Terra e del Mare (DiSTeM), Palermo, Italia. francesco.tripodi01@unipa.it (2) Istituto Nazionale di Geofisica e Vulcanologia (INGV), Sezione di Palermo, Palermo, Italia (3) Istituto Nazionale di Geofisica e Vulcanologia – Osservatorio Etneo (INGV-OE), Catania, Italia (4) Sapienza Università di Roma, Dipartimento di Scienze della Terra, Roma, Italia.

Introduction

Mercury (Hg) is one of the most hazardous elements released into the atmosphere from both natural and human-made sources. It exists in three oxidation states: gaseous elemental mercury (GEM), monovalent mercury, and divalent mercury. Volcanic emissions represent a significant natural source of mercury to the environment and over the last 40 years several studies have been focused on estimating mercury fluxes (Varekamp & Buseck, 1986; Pyle & Mather, 2003; Nriagu & Becker, 2003). Understanding the pathways of mercury once it is released into the atmosphere is crucial, given its potential toxicity and long atmospheric residence time (approximately one year) that allows for efficient global distribution compared to many other volcanogenic elements. This research focuses on the biogeochemical study of mercury at Mt. Etna volcano, where both passive degassing and volcanic eruptions represent important sources of Hg input into the environment, with total annual fluxes between 2.1 to 27.3 t yr^{-1} (Bagnato *et al.*, 2007; Edwards *et al.*, 2021; Ferrara *et al.*, 2000; Ferrara & Maserti, 1990; Dedeurwaerder *et al.*, 1982; Buat-Ménard & Arnold, 1978). The specific objectives are: (i) to determine the concentrations of mercury in soils and interstitial gases within these soils; (ii) to characterize the microbiota associated with the mercury cycle in the soils; (iii) to quantify the mercury emissions from the volcano's peripheral sources; and (iv) to measure the atmospheric deposition fluxes of mercury. Our preliminary results focused on the gaseous elemental mercury concentrations both in free and in soil interstitial gases on Mt. Etna.

Methods

The levels of gaseous elemental mercury (GEM) were measured in real-time using the Lumex RA-915M, an atomic absorption spectrometer that utilizes the Zeeman effect and high-frequency modulation of light polarization (ZAAS-HFMLP). This instrument isolates spectral lines at a wavelength of 254 nm with the help of a permanent external magnetic field, using a mercury (Hg) lamp as the radiation source. It operates at a flow rate of 10 L min^{-1} and has a detection limit of 0.5 ng m^{-3}, with an accuracy of 20% for concentrations ranging from 2 to 50,000 ng m^{-3}. During several field campaigns, we measured GEM at different sites of Mt. Etna (Fig. 1) in atmosphere, in diffuse degassing areas and in the interstitial soil gases. To determine GEM in interstitial soil gases, gas samples were collected from the soil at a depth of approximately 50 cm using a rigid Teflon tube embedded in the ground, connected with a 100 mL syringe and then injected into the instrument's gas inlet (Tassi *et al.*, 2016). In case of free gases (fumaroles and bubbling pools), GEM was collected using a three-way valve connected to an inverted funnel placed inside the degassing pools.

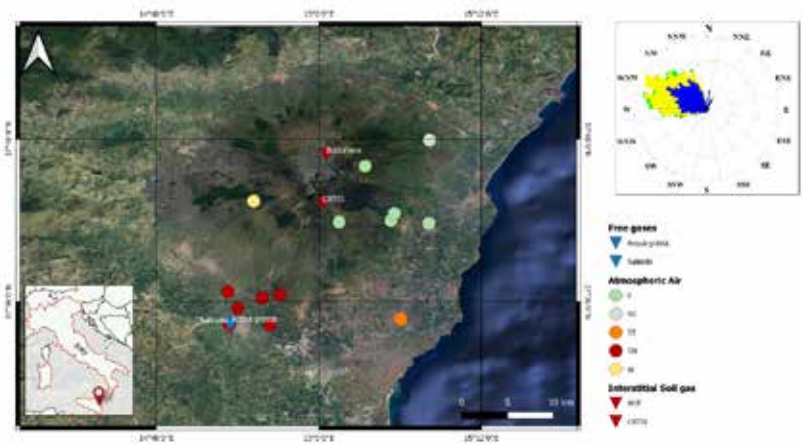

Figure 1. a: The study area; b: Wind rose diagram.

Results

Atmospheric gaseous elemental mercury (GEM) concentrations were measured at various locations around Mt. Etna (Fig. 1). The results revealed concentrations ranging from 0.5 to 5 ng m^{-3}. Our preliminary findings indicate that the median Hg concentration at sampling points in the east, northeast, west, southwest, and southeast sectors aligns with the global background level of 2 ng m^{-3} (Fig. 2a). Based on this data, it appears that the volcanic plume does not significantly deliver Hg at downwind sites, at least at ground level. In contrast, in some degassing areas on the volcano's flanks (e.g. low-temperature fumaroles or degassing bubbling pools) high Hg levels were measured, ranging from 2 to 200 ng m^{-3}. In particular, at the Aqua Grassa site GEM concentrations exceeded 1,000 ng m^{-3}, which is the WHO average annual concentration limit for mercury vapor inhalation (Fig. 2b).

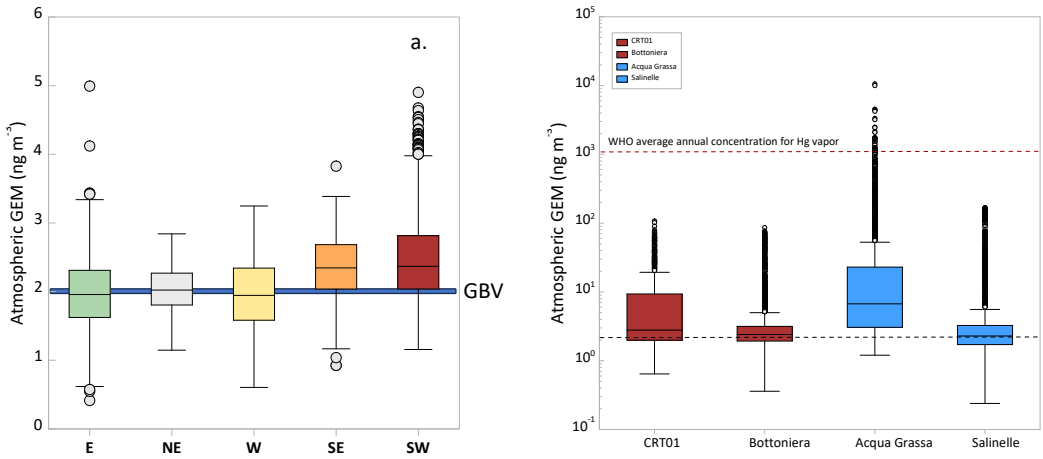

Figure 2- a. Box plot of GEM in atmospheric air; b. Box plot of GEM measured in the free gases and low-temperature fumaroles.

In addition to atmospheric GEM measurements, interstitial soil GEM concentrations were measured. GEM concentrations were recalculated considering the dimensions of the areas of the Hg-spikes in the instrumental output, with respect to the standard. The sampling points were located near low-temperature fumaroles, namely CRT1 and BOT sites, where soil temperature varied from 29.5 to 59 °C and from 12.5 to 90.2 °C, respectively. At the CRT01 site, the measured mercury (Hg) concentrations ranged from 146 to 9615 ng m^{-3}, indicating significant variations in Hg levels across the study area. Meanwhile, the BOT site showed a gaseous elemental mercury (GEM) concentration ranging from 114 to 3109 ng m^{-3}. The binary diagrams of Figure 3 demonstrated a strong correlation between GEM concentration and soil temperature at the BOT site (R^2 = 0.68). In contrast, no correlation was observed at the CRT01 site (R^2 = 0.05).

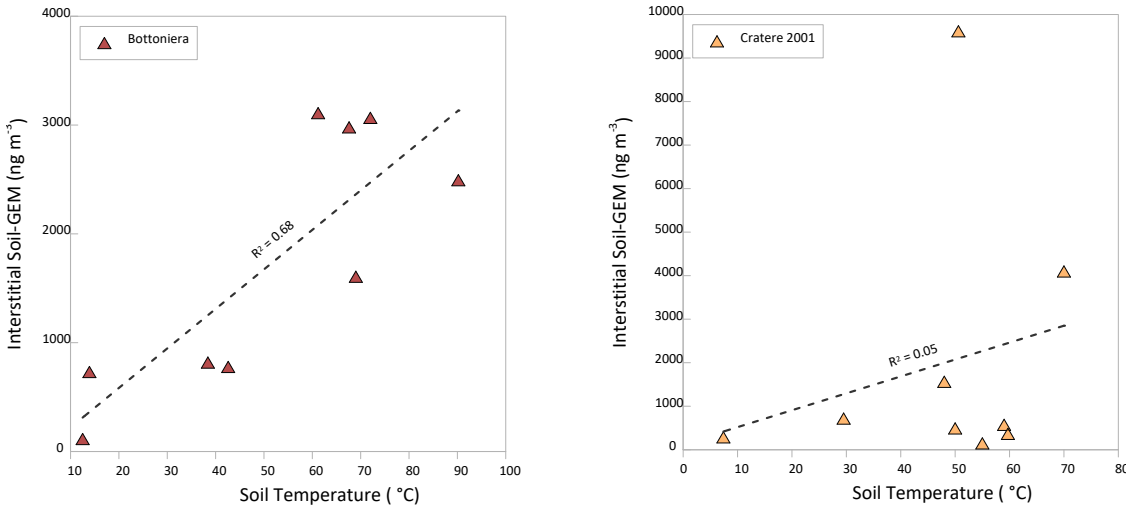

Figure 3. Binary diagram of Interstitial Soil-GEM *vs* Soil Temperature.

Conclusions

This study highlights that peripheral volcanic emissions significantly contribute to atmospheric mercury levels. Field measurements at Mt. Etna and its surrounding areas demonstrated substantial outgassing of mercury, with GEM concentrations far exceeding median global atmospheric levels. Free gas emissions (e.g. fumaroles, bubbling pools), as well as interstitial soil gases, can reach high concentrations of mercury, thus underscoring the importance of volcanic sources of mercury. Notably, GEM concentrations had a strong correlation with soil temperature at certain sites, like BOT, but not uniformly across all locations, such as CRT01. These preliminary findings emphasize the necessity of further research to better understand the biogeochemical cycles of mercury, especially regarding its peripheral emissions, and their broader environmental impact.

References

Bagnato, E., Aiuppa, A., Parello, F., Calabrese, S., D'Alessandro, W., Mather, T.A., McGonigle, A.J.S., Pyle, D.M., Wängberg, I., 2007. Degassing of gaseous (elemental and reactive) and particulate mercury from Mount Etna volcano (Southern Italy). [Atmospheric Environment 41(35), 7377–7388. https://doi.org/10.1016/j.atmosenv.2007.05.060].

Buat-Ménard, P., Arnold, M., 1978. The heavy metal chemistry of atmospheric rarticulate matter emitted by Mount Etna Volcano. [Geophysical Research Letters 5(4), 245–248. https://doi.org/10.1029/GL005i004p00245].

Dedeurwaerder, H., Decadt, G., Baeyens, W., 1982. Estimations of mercury fluxes emitted by Mount Etna Volcano. [Bulletin Volcanologique 45(3), 191–196. https://doi.org/10.1007/BF02597729].

Edwards, B.A., Skye Kushner, D., Outridge, P.M., Wang, F., 2021. Fifty years of volcanic mercury emission research: Knowledge gaps and future directions. Science of The Total Environment 757, 143800. https://doi.org/10.1016/j.scitotenv.2020.143800.

Ferrara, R., Maserti, B.E., 1990. Atmospheric mercury levels in the mount ETNA volcanic area after an eruptive phase. [Environmental Technology 11(1), 51–56. https://doi.org/10.1080/09593339009384838].

Ferrara, R., Mazzolai, B., Lanzillotta, E., Nucaro, E., Pirrone, N., 2000. Volcanoes as emission sources of atmospheric mercury in the Mediterranean basin. Science of The Total Environment 259(1), 115–121. https://doi.org/10.1016/S0048-9697(00)00558-1.

Nriagu, J., Becker, C., 2003. Volcanic emissions of mercury to the atmosphere: global and regional inventories. [Science of The Total Environment 304(1), 3–12. https://doi.org/10.1016/S0048-9697(02)00552-1].

Pyle, D.M., Mather, T.A., 2003. The importance of volcanic emissions for the global atmospheric mercury cycle. [Atmospheric Environment 37(36), 5115–5124. https://doi.org/10.1016/j.atmosenv.2003.07.011].

Tassi, F., Cabassi, J., Calabrese, S., Nisi, B., Venturi, S., Capecchiacci, F., Giannini, L., Vaselli, O., 2016. Diffuse soil gas emissions of gaseous elemental mercury (GEM) from hydrothermal-volcanic systems: An innovative approach by using the static closed-chamber method. [Applied Geochemistry 66, 234–241. https://doi.org/10.1016/j.apgeochem.2016.01.002].

Varekamp, J.C., Buseck, P.R., 1986. Global mercury flux from volcanic and geothermal sources. [Applied Geochemistry 1(1), 65–73. https://doi.org/10.1016/0883-2927(86)90038-7].

17th INTERNATIONAL CONGRESS of the Geological Society of Greece

BULLETIN OF THE GEOLOGICAL SOCIETY OF GREECE, SP. PUBL.

EXTENDED ABSTRACT 315

"Unfolding the Fold"- An Introduction to the Geology of Greece Through a Museum Kit by the Natural History Museum of Arsakeia Schools

Tripolitsiotou F[1], Argyraki A[2], Drinia H[2]

(1) Natural History Museum of Society for Promoting Education and Learning (Arsakeia Schools), Athens, Greece
(2), Department of Geology and Geoenvironment, Athens, Greece

Abstract:
This study aims to highlight Natural History Museums as suitable educational spaces for teaching geosciences to High school students. Specifically, it presents the design and practical use of a museum kit inspired by the geology of Greece. Museum kits are innovative educational tools that combine experiential learning with environmental education. This study examines the design, development, and application of a museum kit that connects the exhibits of the Natural History Museum of Arsakeia Schools with the teaching of Geology-Geography, as outlined in the curriculum for 2nd and 3rd High School grades This educational tool focuses on familiarizing students with the geological history of Greece. It includes geological maps, rocks, minerals, fossils, and activities designed to help students understand the unique geotectonic structure of the region. The museum kit was piloted with 90 students, yielding highly positive results.

Keywords: Museum Kit, Natural History Museums, Geology of Greece, Teaching Geology

Introduction

The education of natural sciences takes place through various formal and informal approaches. Learning opportunities extend beyond the classroom and can be organized in other school spaces or even outside the school premises. One of the most significant educational spaces is the Natural History Museum (Kokkotas, 2004). Museums, in general, play an educational role by creating interactive materials where learning occurs through exhibits, collections, and specially designed educational programs (Tripolitsiotou, 2020). Educational programs are considered a modern approach to exploring the natural and cultural environment within museums (Kaloforidis, 2015). These programs align with the curricula of primary and secondary education, as defined by the Ministry of Education, and are adapted to meet the cognitive needs of each class and group visiting the museum (Tripolitsiotou, 2023). Active teaching methods are utilized to familiarize visitors with the museum space, turning their visit into both an educational and entertaining experience (Tziaferi, 2005).

Description of the museum kit

The Natural History Museum of Arsakeia Schools is located within the school complex of Arsakeia Schools in Psychiko, allowing students frequent access to this unique space and participation in museum-based educational interventions. The primary criterion for selecting the topic of this educational program was the experiential approach to the chapter on the geology of Greece, part of the Geology-Geography curriculum of High School.
The program was designed based on the principles of constructivist and mediated, inquiry-based learning. It follows the educational model of Allard & Boucher and Paquin and incorporates cooperative teaching methods. It primarily targets high school students, especially 2nd graders, without excluding other grade levels.
The materials included in the program are as follows:

- The printed Geological Map of Greece (Bornovas and Rondogianni-Tsiambaou, 1983) at scale 1:500000, published by the Institute of Geology and Mineral Exploration and printed in dimensions 200 x 140 cm.
- Interactive material simulating geological processes
- Authentic specimens of minerals and rocks characteristic of Greece's geological formations
- Fossils providing insights into the paleoenvironment of various regions
- A 6-meter-long geological time tape, an educational model designed by the Natural History Museum of Arsakeia Schools for teaching geological time
- Worksheets

The educational program was piloted with 90 2nd grade students over 2-3 teaching hours.
Initially, through an interactive presentation, students are introduced to the convergence of lithospheric plates, specifically the African plate and the Eurasian plate, and the results of this convergence (e.g., trench formation, orogenesis, and the creation of a volcanic arc).
Next, a brief description of the Tethys Ocean and the role of Alpine orogenesis in shaping the Greek region over

geological time is provided, based on the overall geodynamic and paleogeographic evolution of the Hellenides as described by Pananikolaou (2021). Examples include the formation of the Pindos mountain range, volcanic activity in the Rhodope region, the present-day volcanic arc, and the creation of the Ionian Islands. As noted by Papanikolaou (2021), explaining the Geology of Greece is a complex and rather challenging task, incorporating a Late Paleozoic—Early Cenozoic orogenic history of a Tethyan segment and an active subduction and orogenic arc in the Eastern Mediterranean. Thus, teaching by using typical "by the book" methodologies, combined with the limited prescribed time allowed in order to explain complex concepts and theories, becomes difficult for students and science teachers alike.
The aim of the program is to enable participants to understand, through cognitive, psychomotor, and emotional objectives, that:
a. The geological structure of Greece was not always as it is today over geological time.
b. The geological structure did not form simultaneously across its entire extent but rather evolved gradually over a vast timescale, requiring millions of years.
c. The current landscape is not final; the process is dynamic and continues to evolve over time.
d. There is a significant difference between geological and historical time.

Students explore the geological history of Greece through hands-on interaction with rocks and fossils found in the region. The activity begins with the printed geological map laid on the floor, where students gather to place labeled rock and fossil specimens according to their geographical origin. As they work, the characteristics and geological history of each specimen are explained. In the second part of the activity, students reconstruct the formation of the Hellenic orogen. Starting with the youngest specimens, they progressively "unfold" the tectonic structures as well as the geological timeline by placing the rocks and fossils on a 6-meter-long time tape arranged next to the map, corresponding to their age of formation.
By the end of the activity, students gain a deeper understanding of the spatial and temporal dimensions of the geological processes that have shaped Greece over time.

The evaluation was conducted using worksheets and questionnaires. The program's success inspired the idea of expanding it into a museum kit that could travel to schools nationwide. Museum kits are innovative tools in museum education, enabling knowledge dissemination in diverse cultural and educational settings. This broader reach enriches feedback and contributes to the continuous improvement of this educational material.

Conclusions
Museum educational programs and kits provide students with opportunities to actively participate, develop initiatives, and cultivate scientific processes and skills. Specifically, students:

- Engage with real objects
- Gain a better understanding of geological phenomena and their connection to the Greek environment
- Actively participate in discovering knowledge through pedagogically designed activities
- Learn about nature and its creations
- Develop critical thinking skills
- Practice scientific processes (observation, classification, recording, comparison, communication)

Moreover, the museum's role proves particularly significant in linking informal education with formal education by:

- Creating interactive educational materials
- Utilizing collections and exhibits in teaching
- Designing learning conditions through tailored educational programs and museum kits aligned with the national curriculum

This approach transforms curriculum content from mere information into knowledge through experiential learning, offering students the joy and satisfaction of participating in the educational process.

References
Bornovas, J. and Rondogianni-Tsiambaou, Th. (1983) The Geological Map of Greece, Scale 1:500000. 2nd Edition, Institute of Geology and Mineral Exploration, Athens.
Kokotas, P. (2004) Teaching of Natural Sciences. Athens: Self-published.
Kaloforidis, V. (2015). The Educational Role of the Museum in the Contemporary Social and Cultural Environment. e-jst.teiath.gr
Papanikolaou, D.I. (2021) The Geology of Greece. Regional Geology Reviews (R. Oberhänsli, M.J. de Wit, F.M. Roure Eds.),

Springer, Cham, Switzerland, ISSN 2364-6446.

Tziaferi, S. (2005). The Modern Museum in Greek Education Through the Example of Educational Programs. Kyriakidis, Thessaloniki.

Tripolitsiotou, F. (2020). *Inside the Museum… I Want to See the Treasures of Lands and Seas: An Educational Program Utilizing the 3D Sandbox.* In: Proceedings of the 11th Panhellenic Conference, *Natural Sciences in Early Childhood Education: Mapping the New Twenty-Year Period of Research and Teaching Practice* (e-book), pp. 1232-1242

Tripolitsiotou, F. (2023). With the Compass and the Map: An Educational Program of the Museum of Natural History of the Arsakeia Schools. In: Proceedings of the 16th National Cartography Conference, Cartography in the Contemporary Multidisciplinary World.

17th INTERNATIONAL CONGRESS of the Geological Society of Greece

BULLETIN OF THE GEOLOGICAL SOCIETY OF GREECE, SP. PUBL.

EXTENDED ABSTRACT 316

Exploring Urban Geotourism Through Geomythology: A Geotrail from Faliro Bay to Vouliagmeni Peninsula, Attiki Region, Greece

Tripolitsiotou F[1], Drinia H[1], Argyraki A[1]
(1) Department of Geology and Geoenvironment, Athens, Greece

Introduction

Urban geotourism is a growing field that focuses on the exploration and appreciation of geological features and geocultural heritage within urban environments. It bridges the natural and human-made worlds by highlighting the geological significance of urban landscapes while incorporating historical, cultural, and mythological narratives. As Del Lama (2018) defines, urban geotourism involves visiting sites within city boundaries that are connected to geological concepts and features, whether these are purely natural formations or modified by human intervention. Geotrails play a central role in this context by offering structured routes that connect points of geological, cultural, and historical interest.

On the other hand, geomythology, the study of how natural geological phenomena inspires myths and legends, provides a fascinating lens through which to explore the relationship between human culture and the Earth's dynamic processes. By examining the interplay of geological events and ancient narratives, geomythology offers insights into how early civilizations interpreted and mythologized their environments. In the context of urban geotourism, geomythology enriches the exploration of geosites by connecting scientific interpretations with cultural heritage.

The purpose of this study is to create a geotrail in order to promote awareness and appreciation of the geological and cultural heritage of the Attiki Region, highlighting the connections between natural processes and human history. It aims to present geological concepts in an accessible and engaging manner, fostering environmental awareness and encouraging sustainable tourism practices. The geotrail also offers an alternative perspective on Athens' urban and natural landscapes, combining geological diversity, historical narratives, and geomythological interpretations.

Study Area

Athens, the capital of Greece, is a city where history, culture, and geology converge in a unique urban landscape (Drinia et al., 2022). Nestled in the Attiki Region, Athens boasts a geological heritage shaped by millions of years of dynamic processes. The Attica Basin features a diverse lithology, including Pliocene marine deposits, Pleistocene clays, and rocks from the Alpine orogenic cycle, such as the famous marbles of Pendeli, used in ancient architecture. The study area extends along the southern coastline of the Attiki Region, from Faliro Bay to the peninsula of Vouliagmeni, covering approximately 20 kilometers. This coastal zone, situated southwest of Athens, serves as a natural outlet of the Attiki Basin into the Saronic Gulf. Rich in geological and cultural features, the area includes key sites such as the Ilissos River estuary, ancient ports, beach rock formations, and fossilized remains. The route traverses diverse lithologies and landscapes, from urbanized waterfronts to the striking natural beauty of Vouliagmeni, making it an ideal setting for exploring the interplay of geology, history, and urban development within the framework of urban geotourism. (fig.1)

Figure 1. Depiction of the geotrail with the selected geocities of the study area

Methodology

The development of this geotrail involved identifying and studying geological, cultural, and historical points of interest along the route. Specific attention was paid to sites with geomythological significance, where natural features and processes inspired ancient myths. Scientific literature, field observations, and geomorphological mapping were combined to document the area's geological formations and their interactions with cultural heritage.

The trail highlights nine key points of interest, beginning at the mouth of the Ilisos River and culminating at the Church of Saint Nicholas on the Vouliagmeni Peninsula. Along this route, sites were selected for their geological diversity, cultural relevance, and accessibility. These include areas that host ancient ports, beach rocks, ancient saline lakes (lagoons), fossils, and unique geomorphological features.

Results

The geotrail showcases the geological and cultural richness of the Faliro to Vouliagmeni route. The journey begins at Faliro Bay, specifically at the mouth of the Ilisos River, one of the few wetlands on the western coast of Attica. Although the Ilisos River has been largely transformed into an artificial structure, it remains a significant geosite, reflecting the region's dynamic interaction between natural and urban development.

Key points along the route include:

Trocadero (the small chapel of Saint George), Pani Hill (a geological and cultural landmark), Elliniko Beach (featuring beach rocks and other coastal formations), Voula Beach (known for its proximity to the Town Hall and fossilized

remains), Great Kavouri (a site of unique geological interest), Vouliagmeni Peninsula (the endpoint of the trail, where visitors encounter the Church of Saint Nicholas, constructed from local rocks and pebbles).
The lithology of the region reveals significant variations, including clays, silts, breccias, sandy marls, conglomerates, and cohesive breccio-conglomerates. These formations reflect the coastal depositional environment and offer a window into the paleoenvironment during the mythological period (Charalambakis, 1952; Papanikolaou et al., 2004).
The geotrail provides visitors with a structured, immersive journey into the geological and cultural history of Attica, combining scientific insights with cultural narratives to foster a deeper appreciation of this unique urban landscape.

Discussion - Conclusion

The geotrail from Faliro Bay to Vouliagmeni Peninsula highlights the unique interplay of geology, culture, and urban development in the southern Attiki Region. By combining geomythological narratives with geological observations, the trail offers an innovative approach to urban geotourism that engages visitors in exploring the region's natural and cultural heritage. The study illustrates how geological features have influenced both the environment and human activity, shaping the myths, legends, and history of the area.
This geotrail serves multiple purposes: it fosters environmental awareness, promotes sustainable tourism, and showcases the scientific and cultural significance of geosites within urban settings. Additionally, it emphasizes the importance of integrating urban development with the preservation of natural and cultural resources. By connecting the scientific understanding of geological formations with the myths that arose from them, the geotrail bridges the gap between science and culture, offering a holistic perspective on the dynamic relationship between humans and their environment.
The creation of such trails not only enhances public appreciation of geology but also demonstrates the potential for urban geotourism to contribute to sustainable urban planning and development. Future initiatives could further expand on this approach by incorporating digital tools, guided tours, and community engagement to enhance the visitor experience while ensuring the long-term conservation of these valuable geosites**.**

References

Del Lama, E. A. (2018). Urban geotourism with an emphasis on the city of São Paulo, Brazil. In *Handbook of geotourism* (pp. 210-220). Edward Elgar Publishing.

Drinia, H., Tripolitsiotou, F., Cheila, T., & Zafeiropoulos, G. (2022). The geosites of the sacred rock of acropolis (UNESCO world heritage, athens, greece): cultural and geological heritage integrated. *Geosciences*, *12*(9), 330.

Charalambakis, S. (1952). Contribution to the knowledge of Neogene of Attica. In *Annales Géologiques des Pays Helléniques* (Vol. 4, pp. 1-156).

Papanikolaou, D., Bassi, E. K., Kranis, H., & Danamos, G. (2004). Paleogeographic evolution of the Athens Basin from the Upper Miocene to the present. Bulletin of the Geological Society of Greece, 36(2), 816-825

17th INTERNATIONAL CONGRESS of the Geological Society of Greece

BULLETIN OF THE GEOLOGICAL SOCIETY OF GREECE, SP. PUBL.

EXTENDED ABSTRACT 317

Exploring Social Perceptions of Water Scarcity and Local Water Resource Management in Greece: Insights from a National Survey.

Troupakis A , Feloni E. , Kalogeropoulos K., Tsatsaris A.
Department of Surveying and Geoinformatics Engineering, University of West Attica, 28 Ag. Spiridonos, 12243 Egaleo, Athens, Greece; efeloni@uniwa.gr

Abstract

Water scarcity has emerged as a critical challenge in Greece, particularly following the extreme drought of summer 2024, which led to significant shortages in multiple regions. In response, a nationwide survey was conducted to examine public perceptions of water scarcity and local water resource management. The survey, structured into seven sections, explored awareness levels, personal conservation habits, policy perspectives, and regional disparities in water availability and governance.

Beyond assessing public opinion, this study investigates spatial patterns that may reveal connections between perceived water scarcity and local limitations in water resources or management strategies. Findings indicate notable regional variations in concern levels, conservation efforts, and trust in governmental responses. Notably, areas that experienced more severe shortages demonstrated heightened awareness and a stronger inclination toward water-saving behaviors. Additionally, a significant majority of respondents expressed the need for environmental education programs in schools, recognizing their potential to cultivate long-term sustainable practices.

By integrating public perceptions with spatial insights, this study provides valuable input for policymakers to develop targeted, region-specific strategies for sustainable water management. The findings underscore the necessity of both technical improvements in water governance and widespread educational initiatives to foster a culture of water conservation in Greece.

Keywords: Water scarcity, Greece, drought 2024, public perception, water management, spatial analysis, environmental education, conservation policies

Introduction

Community engagement plays a crucial role in shaping effective policies for sustainable water management, particularly in the face of increasing water scarcity. Public perception surveys serve as an essential tool in this process, enabling policymakers to assess awareness, attitudes, and behavioral patterns related to water resources, water use and management (Dolnicar et al., 2011; Willis et al., 2011; Fielding et al., 2012; Garcia-Cuerva et al., 2016). Understanding social perceptions not only facilitates informed decision-making but also enhances public trust and participation in conservation initiatives. Given the unprecedented drought conditions that affected Greece during the summer of 2024, leading to severe shortages in multiple regions (keeptalkinggreece.com), the necessity of examining public opinion on water scarcity has become more pressing than ever.

Water scarcity is a multidimensional issue influenced by climatic variability, infrastructure resilience, and governance strategies. While technical and economic interventions are critical in addressing supply challenges, social acceptance and engagement significantly impact the success of water conservation efforts. Previous studies have investigated public perceptions of water-related issues in various contexts, highlighting regional variations in awareness and acceptance of solutions. For instance, research conducted by Pathiranage et al. (2024) explored public attitudes toward water reuse in the Southeastern United States, demonstrating that public perception plays a key role in shaping water policies and acceptance of alternative water sources. Similarly, a growing body of literature underscores the importance of understanding regional and demographic variations in perceptions to design effective, localized interventions (e.g., Dolnicar et al., 2011; Willis et al., 2011; Fielding et al., 2012).

Building upon this foundation, the present study aims to provide a comprehensive analysis of public perceptions regarding water scarcity and local water resource management in Greece. Through a structured nationwide survey with 500 participants, the study examines levels of awareness, personal conservation behaviors, policy preferences, and spatial patterns in attitudes toward water governance. The findings offer valuable insights into the relationship between water scarcity experiences and public response, with implications for both short-term crisis management and long-term sustainability strategies, while the majority of participants believe that comprehensive educational initiatives are essential for fostering a culture of water conservation, as also evidenced by Heath and Gifford (2006).

Materials and Methods

A. Survey design

The survey was designed to assess public perceptions of water scarcity in Greece, particularly following the extreme drought of summer 2024. It was structured into seven sections, covering key aspects of awareness, attitudes, and potential solutions. The questionnaire included a mix of multiple-choice and open-ended questions to capture both quantitative and qualitative insights.

The first section gathered demographic data, including age, gender, education level, and geographic location, enabling spatial analysis of responses. Subsequent sections explored awareness levels, personal experiences with water shortages, and perceptions of the main causes of water scarcity. Respondents were also asked about their water conservation behaviors and their views on governmental measures to address the issue. A key objective of the survey was to identify regional patterns in perceptions and examine whether attitudes toward water management varied based on local water resource availability. Additionally, the survey assessed public support for various policy interventions, such as infrastructure investments, regulatory measures, and environmental education programs in schools. The structured yet flexible design allowed for a comprehensive understanding of public sentiment, providing valuable insights for policymakers seeking to implement targeted, region-specific water management strategies.

B. Platform

The survey was designed and implemented using the Microsoft Forms platform, a widely used digital tool for collecting and analyzing survey responses. Microsoft Forms ensures participant anonymity by allowing responses to be recorded without collecting personal identifiers, aligning with General Data Protection Regulation (GDPR) requirements. The platform provides secure data encryption and access controls, ensuring that responses remain confidential and are used solely for research purposes. By leveraging Microsoft Forms, the study adhered to ethical guidelines for data protection and privacy, maintaining participant trust while facilitating an efficient and compliant survey process. The questionnaire can be accessed in Greek through the link: https://bit.ly/42p4IDG.

Results

A. Participants

The survey on water scarcity in Greece gathered responses from a diverse group of participants across various demographic categories. The majority of respondents were between the ages of 25 and 54, representing a balanced mix of young professionals and middle-aged individuals. Gender distribution was relatively even, with a slight predominance of female participants. In terms of educational background, a significant portion held university degrees, reflecting a well-educated sample group. Geographically, responses were collected from multiple regions across Greece, with a notable concentration in urban centers such as Athens and Thessaloniki, but also including perspectives from rural areas affected by last summer's severe drought. This diverse representation provides valuable insights into public perceptions of water scarcity across different social and geographic contexts.

B. Overall perception

Public Awareness of Water Scarcity: The survey results indicate varying levels of public awareness regarding water scarcity in Greece. A significant portion of respondents, totaling 212 individuals, consider themselves "moderately informed" on the issue, while 140 participants stated they were "slightly informed." In contrast, only 116 respondents reported being "well-informed." These findings suggest that although some awareness exists, there remains a considerable knowledge gap among the public. This highlights the need for more effective awareness campaigns to enhance public understanding of water scarcity issues and their long-term consequences.

Perceived Causes of Water Scarcity: When asked about the primary causes of water scarcity, respondents identified several key factors. The most commonly cited reason was climate change, with 207 responses highlighting its impact on water availability. Additionally, 141 respondents attributed the problem to aging infrastructure and water network losses, emphasizing the role of outdated systems in exacerbating water shortages. Overconsumption of water resources was another major concern, noted by 107 participants. While fewer respondents pointed to water pollution as a significant factor, many acknowledged that multiple causes contribute to the issue. This underscores the complexity of water scarcity and the necessity of a holistic water management strategy that addresses both environmental and infrastructural challenges.

Perception of Water Scarcity as a Serious Issue: The vast majority of survey participants, perceive water scarcity as a very serious problem in Greece (Figure 1). This overwhelming consensus indicates widespread public concern, likely influenced by the extreme drought of summer 2024. The severity of recent water shortages appears to have heightened awareness of the issue, reinforcing the need for urgent and comprehensive policy responses to ensure sustainable water management.

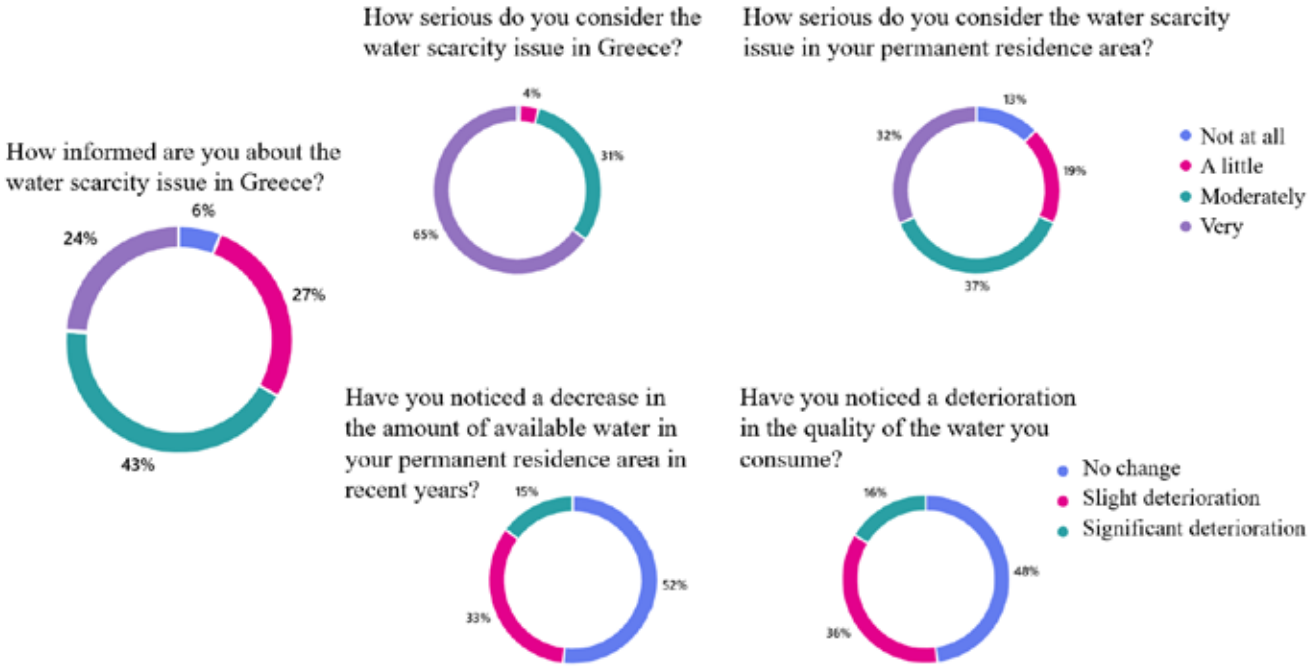

Figure 1. Aggregated responses to general questions about water scarcity

Policy Preferences for Addressing Water Scarcity: In terms of policy measures, respondents expressed strong preferences for actions that enhance water security. Among the most favored solutions were increased investment in water infrastructure, including supply and sewage systems, as well as the promotion of water-saving technologies. Many participants also supported the establishment of a central government authority dedicated to managing water resources. These responses indicate a clear recognition of the need for both governmental intervention and technological advancements in addressing the country's water challenges.

Preference for Water Conservation Measures: The survey also explored public attitudes toward water conservation strategies. A large number of respondents advocated for the mandatory implementation of water-saving technologies in buildings, recognizing their potential to reduce excessive water consumption. Similarly, there was strong support for initiatives promoting the recycling and reuse of water. These preferences align with the broader call for infrastructure investments and highlight a willingness among the public to embrace regulatory measures aimed at long-term water conservation.

Regional Disparities in Water Scarcity Perception: Geographic differences in the perception of water scarcity were also evident in the survey results. The majority of participants (329) reside in Attica, followed by Central Greece and the South Aegean. While national concern over water scarcity remains high, regions with historically strained water resources—such as island communities and agricultural areas—expressed greater dissatisfaction with current water management policies. This suggests that regional disparities must be taken into account when designing policies to address water scarcity, ensuring that the most affected areas receive targeted interventions.

Support for Environmental Education in Schools: One of the most notable findings of the survey is the strong public endorsement of environmental education programs in schools. A large majority of respondents emphasized the importance of integrating water conservation topics into the curriculum, believing that such initiatives could foster long-term behavioral changes. This suggests that beyond immediate policy interventions, efforts should also focus on educating future generations about sustainable water use. By embedding environmental awareness into school programs, policymakers can contribute to a more informed and proactive society in the years to come.

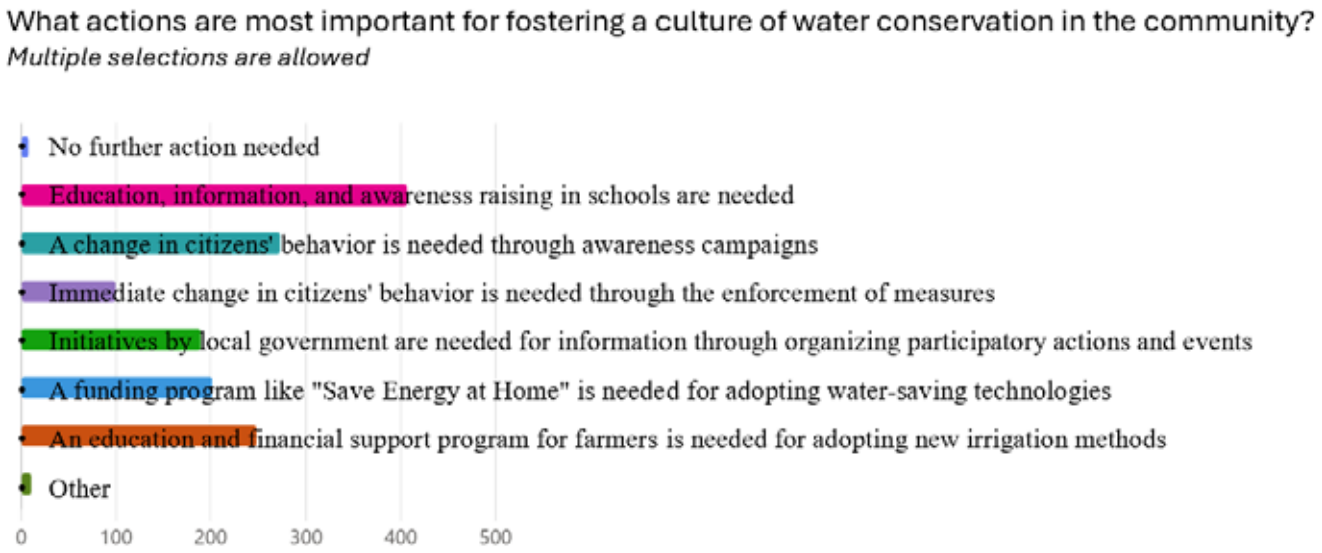

Figure 2. Question on actions that may help foster a culture of water conservation in the community

Concluding Remarks

In conclusion, the study highlights widespread public concern about water scarcity in Greece, particularly following the severe drought of 2024. The findings reveal that while many individuals are aware of the issue, there is still a significant knowledge gap, indicating the need for more effective awareness campaigns. Climate change, aging infrastructure, and overconsumption are commonly cited as the main causes of water shortages.

Furthermore, the study underscores the importance of regional strategies to address water scarcity, with areas facing more severe water shortages expressing greater dissatisfaction with current management efforts. There is strong public backing for government action, particularly in improving infrastructure and promoting water-saving technologies. Moreover, there is significant support for incorporating environmental education into school curricula to encourage long-term changes in water conservation behavior. These findings offer valuable guidance for creating targeted policies to achieve sustainable water management in Greece.

References

Dolnicar, S., Hurlimann, A. and Grün, B., 2011. What affects public acceptance of recycled and desalinated water?. Water research, 45(2), pp.933-943.

Fielding, K.S., Russell, S., Spinks, A. and Mankad, A., 2012. Determinants of household water conservation: The role of demographic, infrastructure, behavior, and psychosocial variables. Water Resources Research, 48(10).

Garcia-Cuerva, L., Berglund, E.Z. and Binder, A.R., 2016. Public perceptions of water shortages, conservation behaviors, and support for water reuse in the US. Resources, Conservation and Recycling, 113, pp.106-115.

Heath, Y. and Gifford, R., 2006. Free-market ideology and environmental degradation: The case of belief in global climate change. Environment and behavior, 38(1), pp.48-71.

keeptalkinggreece.com, 2024. Water scarcity threatens Greece's islands, agriculture and wildlife. Available online: https://www.keeptalkinggreece.com/2024/07/25/water-scarcity-threatens-greeces-islands-agriculture-and-wildlife/#comments (Last accessed: 10/12/2024).

Pathiranage, W.B., Bray, L., Jones, K., Redwine, N., Saralvarez, J. and D'Alessio, M., 2024. Perception and acceptance towards water reuse in the Southeast United States: A public survey. Science of The Total Environment, 908, p.168224

Willis, R.M., Stewart, R.A., Panuwatwanich, K., Williams, P.R. and Hollingsworth, A.L., 2011. Quantifying the influence of environmental and water conservation attitudes on household end use water consumption. Journal of environmental management, 92(8), pp.1996-2009.

17th INTERNATIONAL CONGRESS of the Geological Society of Greece

BULLETIN OF THE GEOLOGICAL SOCIETY OF GREECE, SP. PUBL.

EXTENDED ABSTRACT 318

Contribution of Engineering Geology to the rescuing and enhancing of cultural works and constructions. Case study: The fountain at the Antaeus and Gennaios Kolokotronis streets' junction in the Amalia Merkouri Square in Petralona

Tsagkas D.[1], Chalkiopoulou F.[2], Kanakidis G.[3], Charmalia A.[4]

(1) Dr. Geologist - Engineering Geologist, Former Director General IGME-HSGME, Managing Director of Consultant Office "Geoenvironment", Ilioupoli Athens, geoenv@tee.gr, (2) Mining Engineer IGME-HSGME, (3) Msc Geologist at Consultant Office "Geoenvironment", (4) Geologist at Consultant Office "Geoenvironment"

Introduction

Different types of Engineering Geology research works and studies have already become not only necessary but in fact obligatory steps for the permitting of new construction projects. Furthermore, it is recognized amongst related scientists that Engineering Geology can contribute to the rescuing and enhancing of even small-scale cultural works effectively. This article presents how the major findings of the geological – geotechnical engineering study of the ancient Antaeus Fountain environment can be used for the Fountain's protection and enhancement. The close co-operation among geologists and the other scientists involved like archaeologists constitutes key component for the successful implementation of the research results.

Background

The archaeological site of the Fountain is located at the Antaeus and Gennaios Kolokotronis streets' junction in the Amalia Merkouri Square in Ano Petralona. It was discovered by the archaeologist Olga Dakoura – Vogiatzoglou during excavations in July 1976 (Fig.1).

The Ano Petralona district is well known for its remarkable historical and archaeological character. Based on published documents (Kontopanagou & Spamoudi, 2013), this area was a ceramic craftsmen district characterized by the abundant presence of ceramic craftwork places in the years between the latter half of the 4th Century BC and the beginning of the 5th Century BC.

The study area is very close (less than 1km distance to the east and north east) to a number of limestone hills of high historical importance, linked to the social, political and religious setting of Ancient Athens. More specifically, these are the well-known Hill of the Nymphs (+105.38m), the Hill of the Pnyx (+104.67m) and the Hill of the Muses – Filopappou (+147.23m). Eastern to the above, one can see the sacred rock of Athens, the Acropolis (+159.56m), the most magnificent monument of Athens, the Parthenon, which is devoted to Athena, the patron goddess of the city (Fig.2).

Figure 1. Western view of the Antaeus Fountain, photo from the pavement of Gennaios Kolokotronis Street.

Figure 2. The Hillsides in the neighborhood of the study area (Extract from the 2016 Land Registry orthophoto map).

The three historic hills and the Sacred Rock of the Acropolis are a single, integral and living part of an important civilization that first laid its foundations, developed and spread to the ends of the Earth, around these rocky outcrops. Their historical relationship is more than obvious and self-evident, but this is also due to the specificity of the geological background of the Athens basin. The Parthenon was founded on the limestone rock of the Acropolis, the meetings of the Church of the Municipality were also held on the limestone rock of the hill of the Pnyx and the remains of the sanctuary of the Nymphs were found on the

top of the homonymous hill of limestone composition. The common geological history of the limestone outcrops begins in the Upper Cretaceous 100 million years ago, where the allochthonous series of Athens was tectonically emplaced on top of the autochthonous series of the Sub-Pelagonian zone. The allochthonous series consists mainly of limestones of the neritic and pelagic phase, in which clastic turbiditic formations are intercalated. The 'footprints' of this geotectonic unit are evident in a series of hilly rocky outcrops scattered throughout the Athens basin (Turkovounia, Lycabettus, Strefi Hill, Ardittos Hill, etc.).
The immediate proximity of the district of Petralona with the hills upstream, as well as with the Sacred Rock of the Acropolis, make this district an active historical part of the civilization that developed during the ancient times in the area of Athens. This character has been preserved to this day in the specific district, under the concerted efforts of the State, the competent Ephorate of Antiquities and the residents, who are resisting the violent tourist homogenisation and commercialisation of their city.
The Fountain construction was placed at a strategic point between the Long Walls, perhaps outside the Western Gate of the Walls of Themistocles, where the Street of Koilis passed, and could be characterized as the "Fountain of Koilis" (Fig.1). It should be noted here that the fall in the water table of Athens during the 4th century BC and the need to find water at greater depths led to public concern for the provision of this precious commodity, with the construction of fountains. The office of 'curator of fountains' is mentioned, responsible for the supervision, proper operation and repair of fountains and pipelines. The Fountain probably forms part of this programme of public works in the second half of the 4th century BC (Kontopanagou & Spamoudi, 2013). Water entered the fountain's water collection tank through two pairs of holes formed in the natural rock (Fig.3). Then through a socket, where a marble vault had been carved, the hydria for water collection was placed (Fig.4).

Figure 3. Artificial holes, carved within the rock formation to feed the Fountain, through the main hydro-amalgamated surface conduit developed in a general N-S direction.

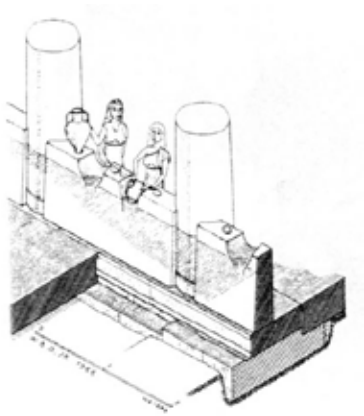

Figure 4. Schematic typical representation of groove for the reception of urn to a fountain.

As mentioned above, the geomorphology and geology of the area played an important role in the choice of the location of the Fountain, constituting a "capable and necessary condition" for its exploitation by the inhabitants of ancient Athens, where, with the use of the available mechanical means and the know-how of the time, it was transformed into a reservoir for water collection and distribution.
Specifically, in the case of the fountain in question, it is a partly natural semi-rocky - rocky cavity, in which weak soil zones are interspersed. In particular, this cavity is located in a brecciated limestone, which is mainly the natural roof of the Fountain. This limestone eventually and in the front part of the cavity develops into a calcareous breccia, which is directly related to the tectonic processes of the wider area. The opening of the enclosure (i.e. the chamber of the Fountain) is about 5-6m and bears in its front part, which is also the entrance, two natural pillars of the same calcareous breccia, thus forming three rudimentary arches, a wider one in the center and two smaller ones on either side of it (Fig.1).
The sophisticated location of the monument consists in the fact, that it is developed on the foothills of the limestone complex of hillsides (Hill of the Nymphs, Hill of the Pnyx and Hill of the Muses-Philopappou), constituting a natural recipient of small water tributaries which start from the upstream hills and pass through the location of the study area. These streams, may have been natural tributaries of the Ilissos River, according to historical maps (Curtius & Kaupert, 1903). Ilissos was the main source of the hydrographic network in the study area at the time, with its active bed located 400m south of the ancient Petralona Fountain, where a characteristic meandering development is observed. Today, the River Ilissos is mostly enclosed and flows for a large part underground, usually under main roads.

Objectives

The physical condition of the archaeological monument as a whole, is judged today as relatively moderate, considering also its age. Factors that contributed significantly to its preservation are the construction materials and the architectural design. Moreover, the continuous and intense urbanisation changed the hydrological regime with the gradual disappearance of natural streams and their conversion into underground rainwater pipes. This fact along with the particular geomorphological configuration of the Fountain (namely a cavity protected from the climatic conditions), indirectly acted as a brake on the deterioration of the Monument.

However, the passage of time, past and present man-made interventions, certain vandalism and the need for prevention to avoid future disasters from extreme weather events and potential geohazards, make it imperative to protect the Monument immediately. In particular, the objective of the Geological - Geotechnical Study performed included the following: a) the investigation of the geological - geotechnical conditions prevailing in the immediate area of the project; b) the detection of the paleogeographic evolution of the area; c) the determination of the seismic risk; d) the assessment of the physical and mechanical characteristics of the rock formations occurring in the environment of the Fountain; e) the collection and analysis of tectonic discontinuities in order to identify kinematically unstable surfaces; f) the classification of rock masses according to international standards and regulations. Summarizing, the accomplishment of the above investigations and studies was considered necessary in order to be able to propose and design the appropriate support measures in the area of the Fountain, with the aim of its conservation and enhancement.

Methods

Within this framework, extensive literature review was carried out regarding the climatic, geomorphological, geological-hydrogeological, tectonic and seismological conditions in the broader project area. Furthermore, this review was completed with fieldwork that was carried out in order to gain a more complete understanding of the geological-techno-geological conditions and to determine important geotechnical parameters.

During the geological mapping, the occurring alpine and meta-alpine geological formations and their geological boundaries were identified. Also, typical slopes and directions of the maximum slope of discontinuities (joints), as well as the erosion degree of the formations were recorded. The 1:75 scale geological map of the wider Fountain area (Fig.6), including a generated view and cross-sectional images of the narrow area (Fig.7 & 8) are given below.

During the fieldwork, the existence of a sparse network of tectonic discontinuities was recognised, which were recorded despite the small height of the shaped slope on the face of the monument (<3.0m), the intense weathering and erosion of the rocky ledges, the coating with artificial lime mortar of the entire interior of the cave and the base of the rocky pillars. The geometrical characteristics (dip/dip direction) of the three observed groups of tectonic disconuities, as well as those of the slope are J1: 03/087, J2: 75/260, J3: 35/178 and S: 88/220.

Subsequently, the existing technical-geological status of the formations that make up the archaeological site of Fountain was assessed and the rock mass classification was estimated using the international empirical classification system GSI. From a geotechnical point of view, the georesearch programme carried out - included:

- A series of measurements at selected locations using a Schmidt rebound hammer to determine the strength of the rock mass (non-destructive tests).
- The surface sampling of three (3) pieces of detached rock mass, for the formation of prismatic samples in a certified laboratory of soil mechanics - rock mechanics, in order to determine their physical and mechanical characteristics.
-

Results

The Petralona Fountain is part of an area with the lowest precipitation levels in Greece. However, due to the fact that the archaeological monument is a naturally formed cave with special morphological and tectonic characteristics and taking into account the existence of two different floor levels with an altitude difference of about 3.00m in the cave, it is considered possible that in the future a concentration of rainwater may be observed on the floor of the archaeological site, in extreme rainfall events. Based on the results of the geological mapping and the on-site macroscopic geological observations, the geological substratum in the immediate project area is composed of Quaternary formations (artificial deposits, backfill materials and alluvial deposits) and Upper Cretaceous formations (Breccia Limestone – Lim_{br}, Calcareous Breccia II - Br_{lim}II and Calcareous Breccia I - Br_{lim}I). The major findings for the formations in the Fountain environment are as follows:

- The backfill materials (loamy sand and gravel, crushed stone) come mainly from the roadbed support works on Antaiou Street. The formation in question is located on the northern flank of the fenced area of the archaeological site, with a maximum height of about 2.00m and a width of about 4.40m. A small-scale ground failure is evident, with a portion of the formation having slide across the floor of the Fountain construction. Contributing to this has been the limited presence of water, manifested in the form of moisture in the lower parts of the formation. The roof of the formation is underlain by the 7cm thick asphalt material of the road surface of Antaiou Street, which has collapsed in some parts. From a technical-geological point of view, this

formation consists of loosely unbound roadwork materials and is characterised by poor mechanical properties. Furthermore, it is an uneven formation and, in combination with its steep slope, it is generally considered to be prone to soil failure and erosion. The above is also evidenced by a small-scale flat ground slip observed within the archaeological site, a fact to which the weak hydrology found in the form of moisture in the lower parts of the formation has also contributed.

- Alluvial deposits (al): This formation may be of small thickness and consists of medium cohesive – cohesive dark brown clay and gravels. They entirely occupy the floor of the ancient Fountain, on which the marble slabs that formed the courtyard of the Fountain construction are placed. The deposits are covered by the characteristic low herbaceous vegetation (wild grass, periwinkle, etc.), which covers part of the floor. As known, alluvial deposits are the youngest geological formation, have poor mechanical characteristics and are susceptible to all types of soil failure and erosion. However, because of their position on the floor of the archaeological site and in small residual deposits in the upper part of the archaeological site, they do not affect the structure and stability of the monument.
- Breccia Limestone (Lim_{br}): It is a white to off-white, in places sub-ashy un-stratified limestone. It appears mildly karstified with superficial presence of small-scale cavities. Dark brown and reddish-brown marly intercalations were observed within the rock's mass. The formation occurs in the upper parts of the Fountain pillars, possibly occupying a large area of the cavity roof, as revealed in places where the Fountain internal construction mortar has deteriorated. The formation also occurs at the entrance to the archaeological site near the metal door, and in an adjacent south-eastern plot. In the parts of the cavity that have not been coated with mortar, there is a very sparse network of discontinuities. The formation presents a visible thickness ranging from 0.50-0.90m and is slightly weathered (degree of weathering: IB-II), while its susceptibility to erosion and all kinds of failures is estimated to be low. An isolated occurrence of potential failure of wedge-shaped detachment of significant volume was noticed in the cross-section of three (3) levels of tectonic discontinuities.
- Calcareous Breccia II (Br_{lim}II): It is an un-stratified calcareous gravel and nodules breccia with angular sub-white to sub-ash gravels Dmax≈7cm, bound together by a matrix of reddish-brown calcareous-marly material. The presence of soil zones, strongly weathered (pulverized) within this formation, suggests the potential existence of tectonism. The formation has a thickness ranging from 0.20-1.00m. It is located in the central parts of the pillars, part of the cave roof and in the northern part of the site. The formation is highly inhomogeneous and due to the presence of fragmented zones it exhibits poor to moderate cohesiveness and appears moderately to highly weathered (degree of weathering: III-IV). Unstable conditions are expected in its contacts with the neighbor formations, revealed in the form of soil and/or rock slides and the presence of natural gaps.
- Calcareous Breccia I (Br_{lim}I): It is an un-stratified formation, with maximum visible thickness of about 0.70m, mainly found at the base of the fountain pillars and at the edges of the Backfill Materials (M.M.M.) on the north side. It consists of ash-white-coloured angular gravels (Dmax≈15cm) and pebbles, bound by a matrix of reddish-brown calcareous marly material. There were not noticed any discontinuities in the formation, which represents moderately to well-connected materials with satisfactory mechanical behavior and appears slight to moderate weathering (degree of weathering: II-III). Though it should be noted that even if the formation is relatively homogeneous and shows partial susceptibility to erosion and all kinds of failures, in the event of heavy rainfall and seismic loading, its mechanical behaviour may be impaired.

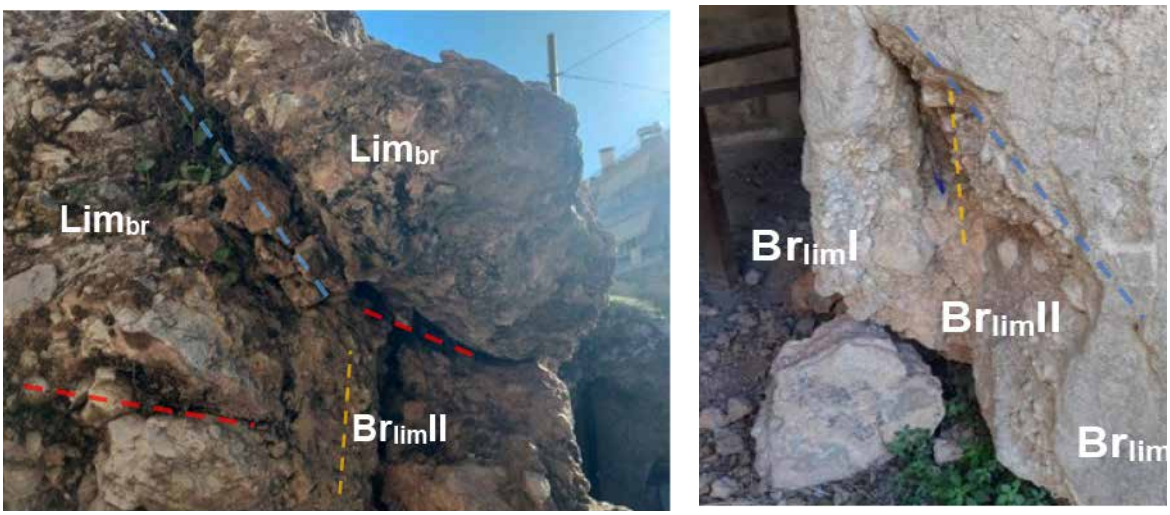

Fig. 5. On the left: Precarious equilibrium conditions in overhanging fractures of the Lim_{br} Limestone and the Br_{lim}II Calcareous Breccia on the northern pillar, due to the cross-sectional plane of tectonic discontinuities. On the Right: Detachment of rock fragment from the base of the southern pillar - creation of a local undercrop. The failure occurred at the contact of the Calcareous Breccia II (Br_{lim}II) and the Calcareous Breccia I (Br_{lim}I), along discontinuities J2 and J3.

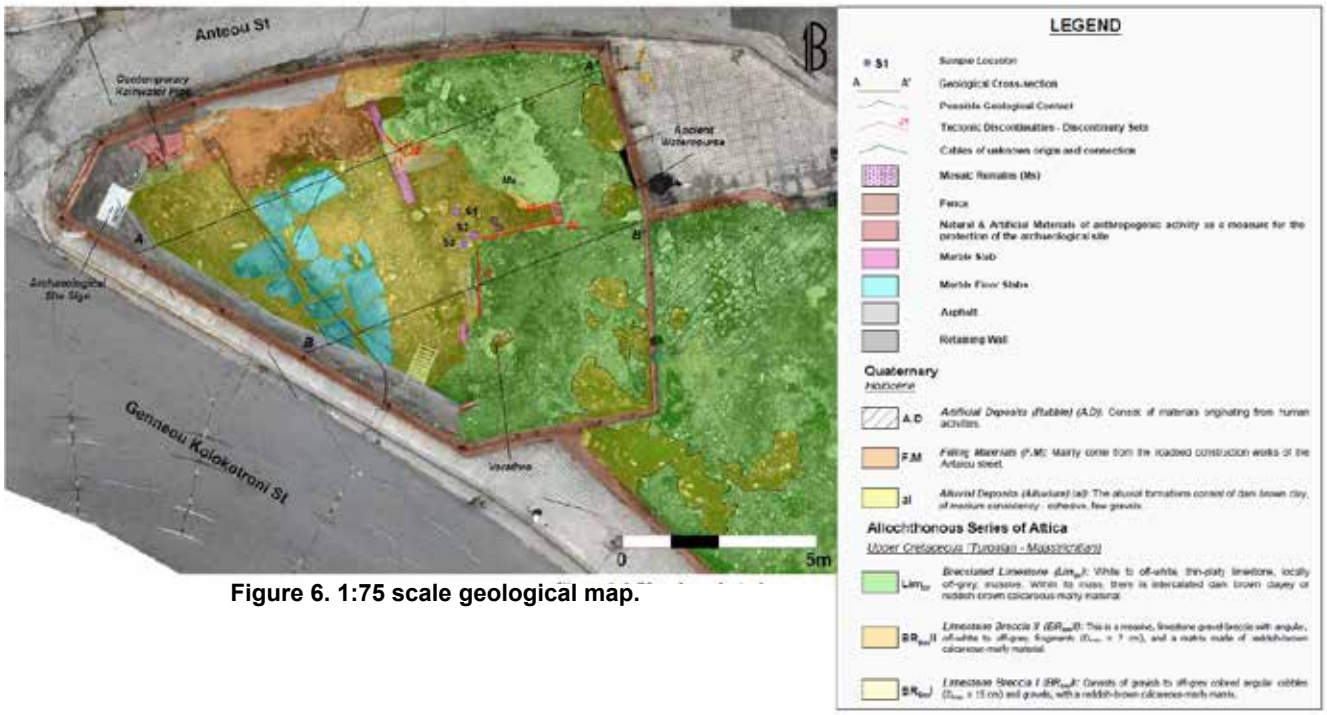

Figure 6. 1:75 scale geological map.

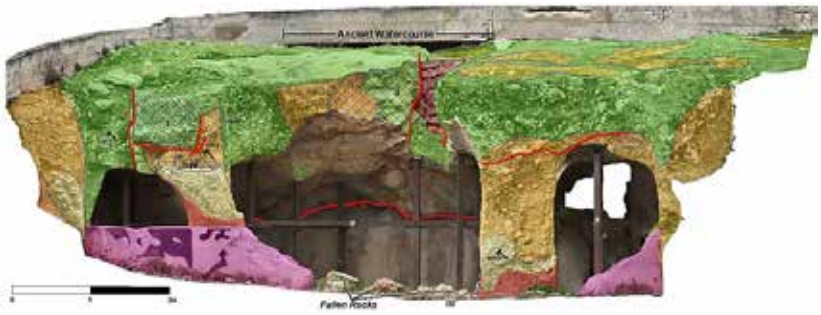

Figure 7. Output image following the geological mapping (facade).

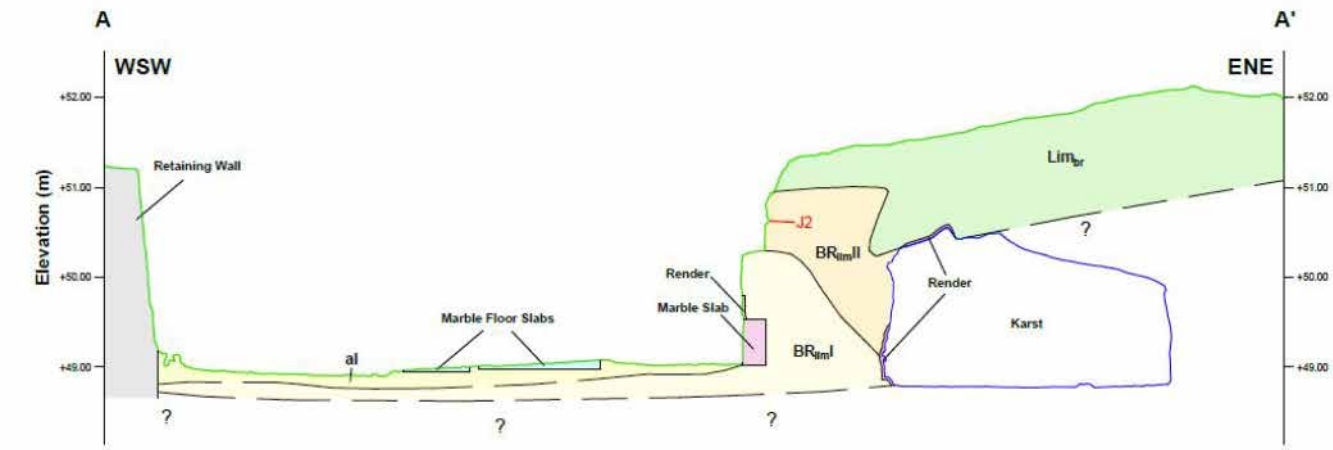

Figure 8. Output image following the geological mapping (cross-section).

Conclusions

The city of Athens is one of the driest places in Greece and the streams and rivers that cross it are of short length and

have a strong seasonal flow. The anxiety and care of the ancient inhabitants of the city for the provision, management and distribution of water is strongly reflected in a series of works that dominated the city (aqueducts, baths, fountains, wells, reservoirs, rainwater and sewage pipes).

The fact that concentration of considerable amounts of rainwater may be observed on the floor of the archaeological site during extreme rainfall phenomena, combined with the fact that no flood forecasting works (overflow) are provisioned leads to the conclusion that measures may be required for the management of rainwater in order to protect the Monument from future flooding phenomena. It is also proposed to consider the necessity of erecting a metal roof to in order to protect the Fountain from rainwater.

In case of intense rainfall and/or possible seismic loading, the technical-geological characteristics of the loose formations (backfill materials) that occur in the environment of the Fountain may be degraded. It is therefore estimated that some type of intervention should be needed in the future, in order to stabilise these formations.

Precaution stabilization measures are proposed to be taken (e.g. wire rope fencing, either filling of the discontinuities or scaling by simple mechanical means) regarding the northern pillar of the Fountain, where a wedge-shaped detachment of a significant volume of the Breccia Limestone (Lim_{br}) limestone was noticed in the cross-section of three (3) levels of tectonic discontinuities.

In the event of heavy rainfall and seismic loading, the mechanical behaviour both of the Breccia Limestone (Lim_{br}) and the Calcareous Breccia II (Br_{lim}II) formations may be impaired. It is underlined that the latter is found in the central parts of the pillars, in part of the roof of the cave and in the northern part of the fountain's plot creating precarious conditions for the integrity of the Monument. As far as the Calcareous Breccia I (Br_{lim}I) is concerned, which is mainly found at the base of the Fountain pillars and at the edges of the Backfill Materials (M.E.) on the north side, it has satisfactory mechanical behaviour.

Finally, in the context of the present investigation, the rock failures noticed or/and the potential rock slides due to unstable conditions found along specific tectonic discontinuities, should be taken into account for the design and planning of retaining works and roof support of the Fountain rock environment and construction correspondingly (Fig.5).

Acknowledgements

We thank the Ephorate of Antiquities of Athens City for their cooperation.

References

Arvantikaki, A., 2025: Preparation of studies for the restoration, protection and enhancement of the fountain at the intersection of Anteou and Genneou Kolokotroni streets at Amalias Merkouri square in Petralona.**]**

Curtius, E., Kaupert, J. A., 1903. Karten von AttiKa. Athen-Hymettos & Athen-Peiraieus map sheets. Dietrich Reimer Publications, Berlin.

Dimou, E., Papatrecha, C., Perdikatsi, V., Economou, G., 1995. Results of Mineralogical Analysis of Building Materials from the Ancient Petralona Fountain. EPET II Project: Development of New Materials for the Structural-Surface Conservation of Monuments Based on Construction Materials and Wear Mechanisms.

Kontopanagou, M., Spamoudi, A., 2013. The archaeological character of Upper Petralona. Archaeological Contributions, Volume B Attica, 316-317.

Koukis, C.G., Sabatakakis, S.N., 2019. Technical Geology. 2nd ed. Papasotiriou Publications, Athens.

Tsagkas, D., 2024. Preparation of studies for the restoration, protection and enhancement of the fountain at the intersection of Anteou and Genneou Kolokotroni Streets at Amalias Merkouri Square in Petralona.

17th INTERNATIONAL CONGRESS of the Geological Society of Greece

BULLETIN OF THE GEOLOGICAL SOCIETY OF GREECE, SP. PUBL.

EXTENDED ABSTRACT 319

Preliminary results on the mapping of uplifted marine terraces in the Laconic Peninsula, SE Peloponnese, Greece

Tsanakas K.[1], Sorrentino A.[2], Mattei G.[2], Aucelli P.P.C.[2], Karymbalis E.[1]

(1) Department of Geography, Harokopio University of Athens, Athens, Greece, ktsanakas@hua.gr,

(2) Department of Science and Technology, Parthenope University of Naples, Naples, Italy.

Introduction

Coastal regions located above subduction zones are useful to understanding the complex tectonic processes occurring at convergent plate boundaries. They are particularly significant when they contain geomorphic markers, which offer information into the deformation of the upper plate. Such markers enable researchers to quantify tectonic activity, making these areas a focus of scientific investigation (e.g., Lajoie, 1986; Marquardt et al., 2004; Pedoja et al., 2011).

Palaeoshoreline markers—including beachrocks, marine notches, benches, marine terraces, and palaeostrandlines—serve as indicators of past shoreline positions and are essential tools for assessing long-term tectonic movements, particularly in terms of rock uplift rates and tilting patterns in tectonically active regions. By providing a record of crustal deformation over geological timescales, these features allow researchers to reconstruct the interaction between tectonics, sea-level changes, and coastal processes (Merritts and Bull, 1989; Mouslopoulou et al., 2015).

Among these indicators, marine terraces are particularly noteworthy. Marine terraces form in areas where tectonic uplift elevates former coastal platforms above sea level. They generally consist of two distinct elements: an abrasion platform, a relatively flat surface that slopes seaward, shaped by wave action; and an inland-facing sea cliff, which forms at a stable angle of repose due to coastal erosion. The junction between the flat palaeoplatform and the inland palaeocliff is called the palaeoshoreline angle, or the inner edge of the platform. This angle is often preserved as a wave-cut notch, providing a direct indicator of the sea level at the time of terrace formation (Burbank and Anderson, 2007).

The palaeoshoreline angle is of particular importance because it closely approximates the elevation of the sea level during its formation, typically corresponding to periods of highstand when sea levels were stable. As a result, it serves as a critical palaeo-horizontal marker that allows researchers to analyze tectonic tilting and to map vertical movement of the Earth's crust. These analyses can help to identify tectonic activity over extended timeframes (Lajoie, 1986; Scott and Pinter, 2003).

In Greece, marine terraces provide compelling evidence of tectonic uplift and are widely observed along the southern coastline of the Gulf of Corinth (the Corinth Rift) and throughout the forearc of the Hellenic Subduction Zone. This includes areas such as the south- and southwestern Peloponnese and the islands of Cephalonia, Kythera, Crete, Karpathos, and Rhodes. (Armijo et al., 1996; Gaki-Papanastassiou et al., 2011; Strobl et al., 2014; Karymbalis et al., 2013;2022; Tsanakas et al., 2022).

The aim of this study is to identify and map the uplifted marine terraces along the western and eastern coasts of the Laconic peninsula, SE Peloponnese, through digital elevation model analysis utilizing GIS techniques and extensive field work.

Study area

The study area is located along the western and eastern coasts of the Laconic Peninsula (Fig. 1a). The alpine rocks of the study area belong to two tectonic units (Fig. 1b). The lower one is the high-pressure metamorphic unit called Phyllites-Quartzites (PQ) Unit while the upper one is the non-metamorphic Tripolis Unit (Lekkas et al., 1997; I.G.M.E, 1999). The PQ Unit consists of mica schists and quartzites and have suffered at least four deformation phases. The upper Tripolis Unit consists of a volcanosedimentary sequence of Permio-Triassic age (Tyros Beds) followed by a thick carbonate sequence of limestones and dolomites of Mesozoic to Lower Tertiary age (Lekkas et al., 1997; I.G.M.E, 1999). The Pelagonian unit crops out in a very small part and consists of limestones (mainly biosparites) of the Upper Cretaceous age (I.G.M.E, 1999). The occurrence of Pliocene-Pleistocene sedimentary sequences of marine origin up to ~180 m above present-day sea level is the most evident consequence of the widespread Quaternary uplift due to the proximity to the Hellenic Subduction Zone. Pliocene formations are composed of marine deposits occasionaly including gypsum layers and Pleistocene formations consist of marine deposits mainly marls, clays, sands and conglomerates (I.G.M.E, 1999). The Holocene deposits consist of talus cones, scree and unconsolidated alluvial deposits.

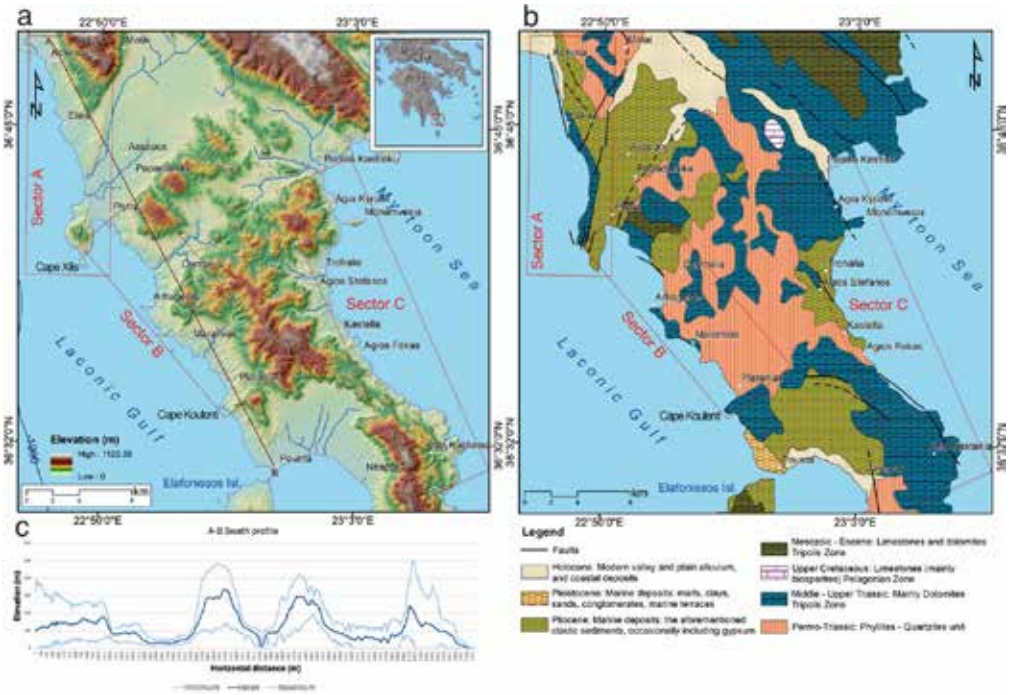

Figure 1. a) Map showing the Laconic Peninsula's location in Greece, the three study sectors, and the region's topography based on a digital elevation model (DEM). b) Geological map of the study area (IGME, 1999). c) Swat Profile along A-B line.

The study area is tectonically very active since it is situated approximately 60-80 km E-NE of the Hellenic subduction zone where the African tectonic plate is subducting beneath the Eurasian plate at a rate of ~36 mm a^{-1} (Reilinger et al., 2006). The Hellenic subduction zone is the largest and most seismically active subduction zone in the Mediterranean as revealed by earthquakes, seismic tomography and seismic reflection data (e.g. Wortel and Spakman, 2000). Rates of crustal motion offshore the Peloponnese and the Island of Crete, estimated from GPS measurements, are up to ~40 mm a^{-1} (Kahle et al., 2000). It is obvious that the geodynamic processes in the study area are also related to the active convergent plate boundary hence it provides a first-order example of actively deforming continental crust situated in the forearc of a subduction zone.

Specific focus was given in three sectors within the Laconic Peninsula (Fig. 1a). Sectors A and B are situated on the western coast of the Maleas Peninsula (eastern Laconic Gulf), between Kokinia and Cape Xilis and between Plytra and Cape Koulenti respectively. The bathymetry of the Laconic gulf shows an asymmetric basin, elongated in the N-S direction with the axis of the basin running close to the eastern coastline (Papanikolaou et al, 2001). The asymmetry is marked by the difference in the slope morphology, which shows abrupt slopes along the eastern margin as opposed to more gentle slopes along the western margin of the gulf (Papanikolaou et al, 2001). The basin is bounded by N-S marginal normal faults which control the geometry of the basin by producing subsidence (of more than 1000 m) (Papanikolaou et al, 2001) at its central part and uplift at the margins.

Sector C is located on the eastern part of the Laconic Peninsula, between Paralia Kastraki and Kato Kastania. The coastal morphology of sector C is steep enough due to recent fault activity (Lapas et al, 2011).

Data and methods

The detailed mapping of the distinct marine terrace surfaces and their inner edges has been carried out using both Geographic Information System (GIS) analyses and field techniques (Tsanakas et al., 2019). Data for the GIS analyses included a 5m cell size DEM obtained from National Cadastre & Mapping Agency S.A., the geological maps of the study area, at 1:50,000 scale, published by the Institute of Geology and Mineral Exploration of Greece, and the neotectonic map of Gythio, Neapolis and Elafonisos (Scale 1:100.000) published by the Earthquake Planning and Protection Organization and the European Center on Prevention and Forecasting of Earthquakes.

For the delineation and mapping of the marine terraces and their corresponding inner edges, a Red Relied Image Map was produced. This method is based on multi-layered topographic information computed from three - dimensional data (DEM). The basic concept is the multiplication of three element layers, topographic slope, positive and negative openness (Chiba et al., 2008). Positive and negative openness were defined by (Yokoyama et al., 2002). Negative openness represents concavities of surfaces and takes higher values on landforms such as valleys, gorges, or the inside parts of craters (Figure 2a). On the other hand, positive openness represents convexities and is ideal for mapping crests, ridges, scarps etc (Figure 2b). In this way the Red Relief Image Map can visualize not only topographic slopes, but also concavities and convexities at the same time.

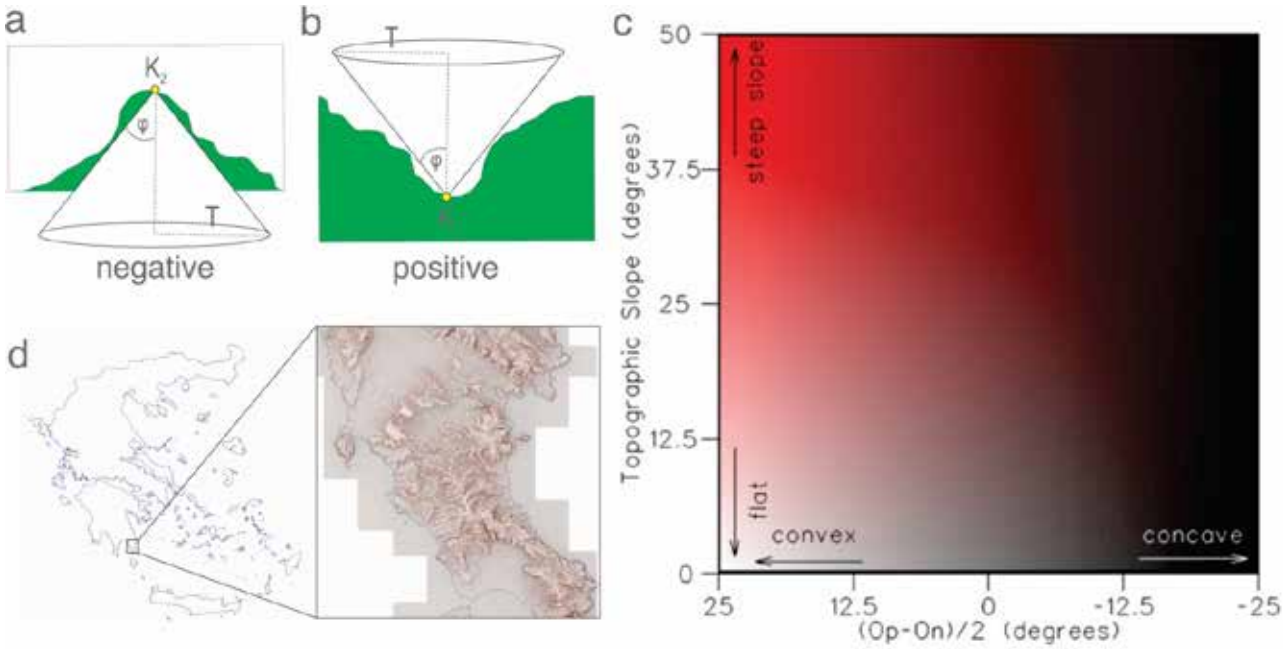

Figure 2. Conceptual diagram of positive openness (a) and negative openness (b), modified by (Yokoyama et al., 2002). c) Colour diagram of RRIM. Topographic slope is showed as chroma value of red (y axis) and (Op-On)/2 is showed as brightness (x axis) (Chiba et al., 2008). d) Red Relief Image Map (RRIM) of part of the Laconic Peninsula. The visualization emphasizes topographic details such as ridges, valleys, and escarpments and flat surfaces.

The generation of the RRIM is based primarily on the calculation of the Ridge and Valley Index (RVi) (Chiba et al., 2008) as shown below:

$$\mathrm{RVi} = \frac{\mathrm{Op}-\mathrm{On}}{2} \qquad \text{(i)}$$

where Op is the positive openness and On is the negative openness as defined by Yokoyama et al, (2002). The RVi overcomes the dependency on incident light direction, unlike shaded relief images, while capturing both convexity and concavity. It assigns high values to convex features and low values to concave ones. In RRIM, this information is displayed using a grayscale layer for topographic expression and a red layer for slope (Figure 2c).

The derivative mentioned above, along with imagery from Google Earth and UAVs, was visually analyzed and interpreted to create an initial morphographic sketch of the study area, highlighting marine terrace surfaces and their inner edges. Comprehensive fieldwork was essential for validating this preliminary sketch and producing the final map of the uplifted marine terraces.

The field survey primarily focused on examining the spatial distribution of the uplifted terraces and verifying the accuracy of inner edge elevations at specific points. Field validation was crucial for refining and confirming the maps and sketches derived from the DEM analysis, as well as the Google Earth and UAV imagery interpretation. The entire study area was thoroughly examined to verify most of the uplifted marine terraces identified during the earlier stages. A handheld Topcon GMS-2 differential GPS (DGPS) was used to record precise waypoints marking the locations of inner edges, which correspond to former shorelines. During the post-field mapping phase, the collected GPS data was integrated into the existing GIS database. A comparison of field-based observations and remote sensing data was conducted to validate the preliminary marine terrace map and facilitate the creation of final maps.

The resulting maps illustrate a sequence of well-defined marine terrace surfaces, categorized based on the elevation ranges of their inner edges.

Results

The GIS procedures combined with field survey identified sequences of uplifted marine terraces in sectors A and B along the western coast of the Laconic peninsula and in sector C along the eastern coast (Fig. 3).

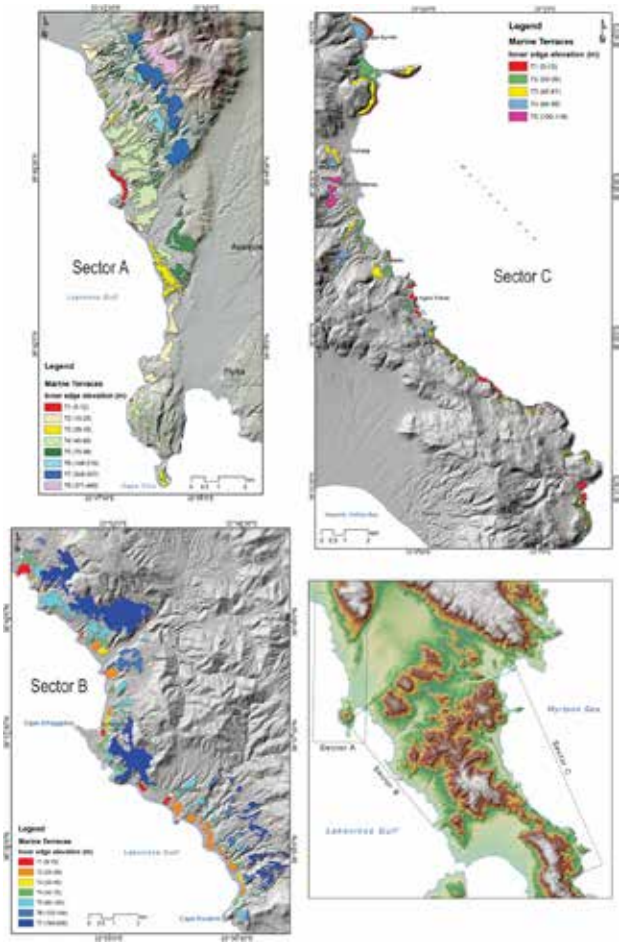

Figure 3. Map of the uplifted marine terraces in sectors A, B and C in the Laconic Peninsula.

Sector A

A sequence of eight uplifted marine terraces has been identified and mapped in sector A, between Kokkinia and Cape Xilis (Fig 3a). In most locations, these terraces are characterized by well-preserved wave-cut surfaces interrupted by landward palaeocliffs. The inner edge elevations range from 5 to 12 m above sea level for the lowest terrace and from 371 to 460 m above sea level for the highest one. Terraces T_1, T_2, T_3, T_4, T_5, and T_6 are primarily cut into Mesozoic-Eocene limestones and dolomites of the Tripolis Zone, as well as Middle to Upper Triassic dolomites of the same geotectonic zone. The highest terraces, T_7 and T_8, are cut into Permo-Triassic phyllites and quartzites. In some locations, the T_2 and T_4 terraces are overlain by well-cemented sediments, forming a prominent cap-rock. Terraces T_2, T_4, T_5, T_6, T7, and T_8 can be traced across a large part of sector A but are not laterally continuous due to intense fluvial incision. The T_1 terrace has been identified mainly in the Elaia area.

Sector B

In sector B, located between Plytra and Cape Koulenti (Fig. 3b), a sequence of seven uplifted marine terraces has been identified and mapped. Compared to those in sector A, these terraces are less well-preserved. Their elevations range from 9 to 15 m above sea level asl for the lowest terrace and from 160 to 200 m asl for the highest one. The terraces have been incised into Mesozoic-Eocene limestones and dolomites and Middle to Upper Triassic dolomites of the Tripolis Zone, as well as into Permo-Triassic phyllites and quartzites. The extensive fluvial incision within this sector has disrupted their lateral continuity. Terraces T_1 and T_3 are highly fragmented, with only isolated remnants preserved in a few locations. In contrast, Terrace T_5 exhibits more extensive preservation and can be traced at multiple sites across sector B. The most prominent feature is Terrace T_7, which appears particularly extensive in the central and northern portions of the sector. Its relatively broad morphology suggests it may represent a well-developed rasa surface, indicative of prolonged erosional processes and subsequent tectonic uplift.

Sector C

In the eastern part of the Laconic peninsula (sector C), a well-preserved sequence of five uplifted marine terraces has been identified, forming a distinct flight of emerged abrasion platforms (Fig 3c). These terraces exhibit inner edges ranging from 5 to 15 m above sea level for the lowest terrace (T_1), up to 100 to 118 m asl for the highest terrace (T_5). The terraces are primarily

carved into Mesozoic-Eocene limestones and dolomites, Middle to Upper Triassic dolomites of the Tripolis Zone, and Permo-Triassic phyllites and quartzites. Compared to sectors A and B, the terraces in sector C exhibit greater lateral continuity. This continuity is likely attributed to the reduced density of drainage networks and the smaller size of drainage basins in this area, resulting in minimal fluvial incision and better terrace preservation.

Discussion

The study of marine terraces in the Laconic Peninsula provides information into the tectonic and geomorphological evolution of the region during the Late Pleistocene. Our findings, supported also by previous research, suggest that the broader area has experienced tectonic uplift during the late Pleistocene, likely driven by its proximity to the Hellenic subduction zone.

Marine terrace analysis revealed notable spatial variations between sectors A, B, and C, which can be attributed to tectonic deformation and differential uplift rates. In sector A, eight distinct marine terraces were identified, and they were found at higher elevations compared to the seven terraces in sector B. This pattern can be explained by the presence of the Molai normal fault, which separates the two sectors (Fig 1b). Sector A is situated on the footwall of this fault, resulting in a higher degree of uplift compared to sector B, which lies on the hanging wall.The vertical displacement of marine terraces between sectors A and B further supports the tectonic influence of the Molai fault. The lack of consistent terrace elevations between these sectors further enhances the role of fault-related deformation in shaping the landscape.

The T_1 marine terrace in sector B can be traced in the broader area of Neapolis, Profitis Ilias, and Agia Marina (Kelletat et al., 1976; Tsartsidou et al., 2002; Karymbalis et al., 2022). Previous research by Karymbalis et al (2022) linked this terrace to Marine Isotope Stage (MIS) 5a. The dating conducted in this study in the nearby Neapoli Bay region provided an uplift rate of 0.36 ± 0.11 mm a^{-1} over the last 215 ± 5.5 ka. Given the geomorphological similarities, it is reasonable to apply this uplift rate to sector B. However, this uplift rate is unlikely to be uniform across the entire Laconic Peninsula due to the presence of local faults, which create differential uplift patterns between sectors A and B. The localized tectonic deformation necessitates caution when extrapolating uplift rates across different sectors. Absolute dating of terraces in both sectors A and B is necessary to accurately correlate terraces between these sectors and to draw conclusions regarding the activity of the faults.

Sector C displayed significantly fewer marine terraces (five) and at much lower elevations compared to sectors A and B. This sector is situated farther from the influence of the Hellenic subduction zone, resulting in reduced tectonic activity and a correspondingly lower rate of uplift.

Conclusions

The distribution and elevation of marine terraces across the Laconic Peninsula are clear indicators of differential tectonic uplift driven by proximity to the Hellenic subduction zone and the influence of local faults. The higher number and elevation of terraces in sector A compared to sector B reflect the footwall-hanging wall relationship imposed by the Molai normal fault, while the reduced number and elevation of terraces in sector C suggest the diminishing tectonic influence with distance from the subduction zone. These findings contribute to a better comprehension of the tectonic evolution of the Laconic Peninsula and emphasize the need for localized geomorphological assessments when interpreting uplift rates and landscape development. Further detailed geochronological studies are recommended to refine the age constraints of the marine terraces and improve our understanding of tectonic activity in the region.

References

Armijo, R., Meyer, B., King, G., Rigo, A., Papanastassiou, D., 1996. Quaternary evolution of the Corinth Rift and its implications for the Late Cenozoic evolution of the Aegean. Geophysical Journal International, 126, 11-53.

Burbank, D.W., Anderson, R.S., 2011. Tectonic Geomorphology, 2nd ed. Wiley-Blackwell, Chelsea, UK. Gaki-Papanastassiou, K., Karymbalis, E., Papanastassiou, D., Maroukian, H., 2009. Quaternary marine terraces as indicators of neotectonic activity of the Ierapetra normal fault SE Crete (Greece). Geomorphology, 104, 38-46.

Chiba, T. atsuro, Kaneta, Shin-ichi, & Suzuki, Yusuke., 2008. Red Relief Image Map: New visualization method for three dimensional data. The International Archives of the Photogrammetry, Remote Sensing and Spatial Information Sciences., XXXVII.

Gaki-Papanastassiou, K., Maroukian, H., Kourbanian, V., 2011. The morphotectonic evolution of the southern half of Kythera Island, Ionian Sea, Greece, during the Quaternary. Prace Geograficzne, 127, 49–60.

I.G.M.E., 1999. Geological Map of Greece (Scale 1:50,000) Sheet Neapolis-Ag. Nikolaos; Institute of Geology and Mineral Exploration of Greece: Athens, Greece.

Kahle, H., Cocard, M., Peter, Y., Geiger, A., Reilinger, R., Barka, A., Veis, G., 2000. GPS-derived strain rate field with the boundary zones of the Eurasian, African and Arabian Plates. J. Journal of Geophysical Research, 105(B10), 23353–23370.

Karymbalis, E., Papanastassiou, D., Gaki-Papanastassiou, K., Tsanakas, K., Maroukian, H., 2013. Geomorphological study of Cephalonia Island, Ionian Sea, Western Greece. Journal of Maps, 9(1), 121-134.

Karymbalis, E., Tsanakas, K., Tsodoulos, I., Gaki-Papanastassiou, K., Papanastassiou, D., Batzakis, D.-V., Stamoulis, K.

(2022) Late Quaternary Marine Terraces and Tectonic Uplift Rates of the Broader Neapolis Area (SE Peloponnese, Greece). Journal of Marine Science and Engineering, 10(1), 99, https://doi.org/10.3390/jmse10010099

Kelletat, D., Kowalczyk, G., Schroder, B., Winter, K.P., 1976. A synoptic view on the neotectonic development of the Peloponnesian coastal region. Zeitchrift der Deutchen Geologischen Gesellschaft, 127, 447-465.

Lajoie, K.R., 1986. Coastal tectonics, in: Wallace, R. (Ed.), Active Tectonics-Geophysics Series, National Academy Press, Washington, D.C., U.S.A., 95–124.

Lappas, I., Sabatakakis, P., Stefouli, M., 2011. The hydrodynamic behaviour of the coastal karst aquifer system of Zarakas-Parnon (Southeastern Peloponnesus). In: Lambrakis, N., Stournaras, G., Katsanou, K. (Eds.), Advances in the Research of Aquatic Environment. Environmental Earth Sciences. Springer, Berlin, Heidelberg.

Lekkas, S.; Alexopoulos, A.; Danamos, G., 1997. Neotectonic Map of Greece: Gythio, Neapolis, Elafonisos Sheets, Scale 1/100,000; Earthquake Planning and Protection Organization (EPPO) and the European Center on Prevention and Forecasting of Earthquakes (ECPFE): Athens, Greece.

Marquardt, C., Lavenu, A., Ortlieb, L., Godoy, E., Comte, D., 2004. Coastal neotectonics in Southern Central Andes: uplift and deformation of marine terraces in Northern Chile (27 S). Tectonophysics, 394, 193–219.

Merritts, D., Bull, W.B., 1989. Interpreting Quaternary uplift rates at the Mendocino triple junction, northern California, from uplifted marine terraces. Geology, 17, 1020–1024.

Mouslopoulou, V., Begg, J., Nicol, A., Oncken, O., Prior, C., 2015. Formation of Late Quaternary paleoshorelines in Crete, Eastern Mediterranean. Earth and Planetary Science Letters, 431, 294–307.

Papanikolaou, D., Metaxas, C., Chronis, G., 2001. Neotectonic structure of the Lakonikos Gulf. Bulletin of the Geological Society of Greece 34 (1), 297–302.

Pedoja, K., Husson, L., Regard, V., Cobbold, P.R., Ostanciaux, E., Johnson, M.E., Kershaw, S., Saillard, M., Martinod, J., Furgerot, L., Weill, P., Delcaillau, B., 2011. Relative sea-level fall since the last interglacial stage: are coasts uplifting worldwide? Earth Science Reviews, 108, 1–15.

Reilinger, R., McClusky, S., Vernant, P., Lawrence, S., Ergintav, S., Cakmak, R., Ozener, H., Kadirov, F., Guliev, I., Stepanyan, R., Nadariya, M., Hahubia, G., Mahmoud, S., Sakr, K., ArRajehi, A., Paradissis, D., Al-Aydrus, A., Prilepin, M., Guseva, T., Evren, E., Dmitrotsa, A., Filikov, S.V., Gomez, F., Al-Ghazzi, R., Karam, G., 2006. GPS constraints on continental deformation in the Africa–Arabia–Eurasia continental collision zone and implications for the dynamics of plate interactions. Journal of Geophysical Research, Solid Earth, 111, 26.

Scott, A., Pinter, N., 2003. Extraction of Coastal Terraces and Shoreline-Angle Elevations from Digital Terrain Models, Santa Cruz and Anacapa Islands, California. Physical Geography, 24, 271–294.

Strobl, M., Hetzel, R., Fassoulas, C., Kubik, P.W., 2014. A long-term uplift rate for eastern Crete and geodynamic implications for the Hellenic subduction zone. Journal of Geodynamics, 78, 21-31.

Tsanakas, K., Karymbalis, E., Gaki-Papanastassiou, K., Maroukian, H., 2019. Geomorphology of the Pieria Mtns, Northen Greece. Journal of Maps, 15(2), 499-508.

Tsanakas, K., Saitis, G., Evelpidou, N., Karymbalis, E., Karkani, A., 2022. Late Pleistocene geomorphic evolution of Cephalonia Island, Western Greece, inferred from uplifted marine terraces. Quaternary 5(3), 35 https://doi.org/10.3390/quat5030035

Tsartsidou, G., Gaki-Papanastasiou, K., Maroukian, H., 2002. Coastal evolution of the inner Lakonic Gulf in the late Pleistocene-Holocene period. In: Proceedings of the 6th Pan-Hellenic Geographical Conference of the Hellenic Geographical Society, Thessaloniki, Greece, pp. 380 387.

Wortel, M.J.R., Spakman, W., 2000. Subduction and slab detachment in the Mediterranean–Carpathian region. Science, 290, 1910–1917.

Yokoyama, R., Shirasawa, Michio, & Pike, R. J., 2002. Visualizing Topography by Openness:A New Application of Image Processing to Digital Elevation Models. Photogrammetric Engineering & Remote Sensing, 68(3), 257–265.

17th INTERNATIONAL CONGRESS of the Geological Society of Greece

BULLETIN OF THE GEOLOGICAL SOCIETY OF GREECE, SP. PUBL.

EXTENDED ABSTRACT 320

Applications of satellite data analysis in the exploration of geothermal systems: The case of the Methana Peninsula, Greece

Panagiota-Elpida Tsekoura[1], Marianthi Stefouli[2], Ioannis Vakalas[3], Eleni Vasileiou[3], Maria Perraki[3]
(1) School of Civil Engineering, National Technical University of Athens, 5 Iroon Polytechniou St., 15780 Zografou, Greece, nota.elpida.tsekoura@gmail.com, (2) Consultant Geospatial Tech & Applications KLEOS S.A., 22 Vas. Konstantinou Avenue, 11635 Greece, (3) School of Mining and Metallurgical Engineering, Division of Geo-Sciences, National Technical University of Athens, 9 Heroon Polytechniou St., 15773 Zografou, Greece

Introduction / Background

Satellite data may have a decisive contribution to the preliminary exploration of geothermal fields, enabling large-scale investigations of target areas in a cost-effective manner, while providing access to otherwise inaccessible locations (Abubakar et al., 2017; Silvestri et al., 2020). The use of satellite data in hydrology is increasing due to the availability of high-resolution data for monitoring parameters such as soil moisture, precipitation, evapotranspiration, irrigation water use, and reservoir water volumes. Soil moisture data is also employed in slope stability, flooding, and landslides investigation (Brocca et al., 2023). Satellite-based detection of thermal anomalies in geothermal regions has been explored in previous studies (Silvestri et al., 2020). Different categories of satellite data can be applied in geothermal research, including thermal data to identify water discharges, tectonic data to assess structural features, and land cover data for land-use analysis.

The Thermal Infrared Remote Sensing (TIRS) method, registers electromagnetic radiation based on surface temperatures. Thermal infrared radiation penetrates the Earth's atmosphere efficiently in two wavelength ranges, 3.5–5 μm and 8.0–14.0 μm, enabling thermal imaging acquisition during both day and night. This data is primarily used to map thermal anomalies and detect submarine thermal water discharges in offshore areas (Abubakar et al., 2017; Meijerink et al., 2007). Thermal and quantitative variations of the water draining into the sea can complicate the detection of thermal discharges. Evapotranspiration can also be estimated by combining thermal and meteorological data.

Satellite data can also be used for tectonic analysis in geothermal fields, facilitating the detection of thermal fluid pathways across fault structures in reservoir rocks. The use of data from Synthetic Aperture Radar (SAR) and other remote sensing techniques, enables the investigation of the subsurface dynamics in geothermal fields and the characterization of structural discontinuities (Abubakar et al., 2017; Ali et al., 2016; Saepuloh et al., 2015). Satellite data are useful for mapping tectonic structures, providing critical insights into the geological framework and the evolution of geothermal areas. These datasets serve as a valuable tool for assessing the impact of tectonic activity in the study area (Silvestri et al., 2020)for example, following the evolution of thermal anomalies, which may represent a modification of the current state of the geothermal field and a possible hazard for both the population and industrial assets. Here, we show the results obtained in three field campaigns during which the simultaneous acquisition of Landsat 8 satellite and UAV (FlyBit octocopter, IDS, Rome, Italy.

Although land cover is not directly related to geothermal processes, satellite-derived land use data can be a valuable support for preliminary studies on geothermal fields. Such information could help in identifying surface features that indicate ongoing geothermal activity, such as altered vegetation of arid land, as well as in assessing accessibility for future field work and infrastructure development. The data from the Sentinel-2 satellite offers significant advantages for land use monitoring, as it has a high spatial and temporal resolutions of 10 meters and revisiting capability of 5 days, and also includes red-edge bands. The integration of Sentinel-2 data with other remote sensing datasets offers enhanced analysis of land cover mapping and provides valuable observations in the development of crops, forests and urban areas. Satellite data for land use are also used to monitor water resources and natural hazards. Sentinel-2 data monitoring capability can be reduced due to cloud cover, but shows high compatibility with other satellite data, such as Landsat thermal imagery, which helps to mitigate the effects of cloud interference (Phiri et al., 2020).

This study emphasizes the crucial contribution of remote sensing in geothermal field research by providing valuable insights in advance of field research. It provides recommendations on how satellite data can be used in geothermal studies and serves as a methodology that can be applied in future research in geothermal regions. Using the geothermal field of the Methana peninsula as a case study, we present here a methodology that integrates different satellite data from multiple satellite systems and demonstrate its applicability to other geothermal systems.

Geological setting

The geological structure of Argolis, encompassing the Methana peninsula, is complex and remains partially interpreted. The region (Photiades & Deligiannakis, 2022; Suesskoch et al., 1974) includes three main geological units: (a) Post-Alpine Formations comprising Quaternary alluvial deposits, colluvial sediments, debris cones, and Pliocene-Pleistocene conglomerates, marls, and sandstones of the Porto Heli-Kranidi Unit; (b) Post-Alpine Volcanic Formations of Methana-Poros, dated to the Middle-Upper

Pleistocene; and (c) Alpine Formations, subdivided into the Didyma Unit (Sub-Pelagonian) with schists, sandstones, cherts, ophiolites, and limestones, and the Complex Upper Tectonic Unit of Southern Argolis, including the Adheres flysch, Cretaceous carbonates, and ultrabasic serpentinites. The Methana peninsula (Fig. 1) is predominantly volcanic, with Cretaceous limestones and conglomeratic formations exposed at its southern tip, and alluvial deposits and debris cones observed in coastal areas and stream channels. The peninsula's volcanic rocks include: a) Loose Reworked Volcanic Materials characterized by poor stratification, b) Pyroclastic deposits identified in the Kameno Vouno complex and Paleokastro dome, consisting primarily by black tuffs with scoria layers and xenoliths of metamorphosed limestones. c) Breccias that represent dome collapse and pyroclastic flows. d) Dacites (SiO_2: 63–70%) structured in domes and lava flows with zoned plagioclase, hornblende, orthopyroxene, and biotite. Quartz and magnetite are common, with signs of magmatic corrosion. e) Andesites that are subdivided into: Basaltic Andesites (SiO_2: 52–56%) with porphyritic textures, zoned plagioclase, pyroxenes, magnetite, and sporadic olivine and hornblende; and andesites (SiO_2: 56–63%) with similar textures, abundant hornblende, dispersed biotite, magnetite, and quartz with reaction rims. Regarding the tectonic regime according to Tzanis et al., (2018, 2020), the ascent of magmatic material that fuels volcanic eruptions in the broader Methana region occurs through major fault structures mapped in the area. These fault and fracture zones are oriented along NW-SE, NE-SW, and WNW-ESE directions. Radiometric K-Ar dating places volcanic activity between 0.75 and 0.32 Ma. The youngest volcanic dome dates to 258 BC in the Kameni area, while the last recorded eruption occurred in AD 1700 at the submarine "Pausanias" volcano, north-northwest of Kameni. Detailed documentation of the latter was provided by Foutrakis and Anastasakis, (2018).

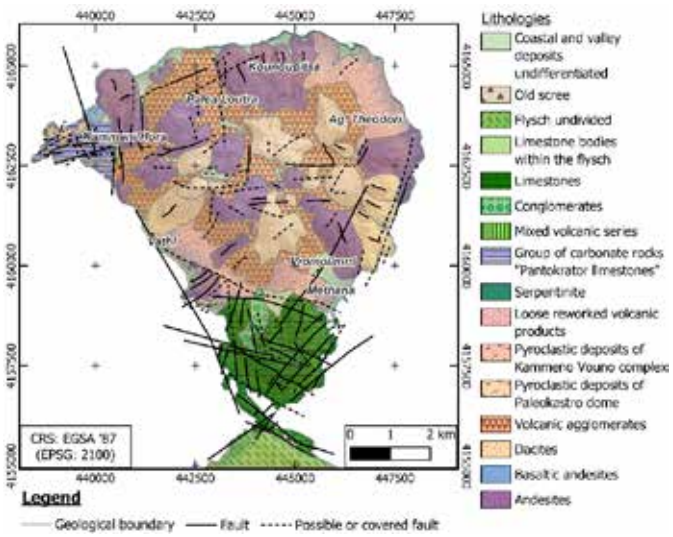

Figure 1. Geological map of Methana.

Methodology

The first step of the study was to digitize the geological map of the Methana peninsula using to identify the geological factors that influence groundwater circulation. This process was implemented using the Quantum GIS (QGIS) software and was based on the geological sheet provided by the Hellenic Authority for Geological and Mineral Exploration (EAGME), illustrating the geological formations and fault structures and the onshore tectonic discontinuities in the study area mapped by Tzanis et al., (2020) (Fig. 1). The satellite data analysis is implemented according to the following six consecutive phases: a) collection and evaluation of available data, b) field survey to address gaps, including periodical water level measurements, c) establishment of GIS-linked databases, d) testing aquifer responses to scenarios of the future plans, e) implementation of a remote sensing technique to refine the geological map and create a lineaments map, and f) employment of satellite images to identify land cover / agricultural practices and generate a regional land-use map.

For the purposes of this study, satellite data were acquired from the Sentinel 2 and Landsat 9 satellites. To ensure the acquisition of high-quality data, cloud coverage threshold was adjusted to 10–20% during data selection, allowing an uninterrupted view of the peninsula and its surrounding area. These datasets provide critical information on thermal discharges, land cover, and fault structures. Digital Elevation Model (DEM) derived from the Hellenic National Cadastral authority was employed to analyze key hydrological and topographical parameters within the study area. It was utilized to delineate flow paths, watershed boundaries, and drainage basins. Furthermore, DEM enabled the estimation of stream order, elevation changes, slope, and upstream and downstream flow distances, providing insights into the geomorphological characteristics of the region. The collected data were synthesized and subsequently processed using the Quantum GIS (QGIS) and Datum Workstation software programs.

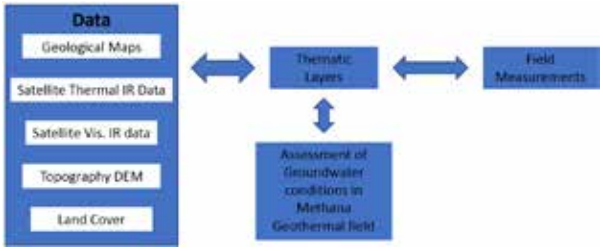

Figure 2: Methodology flow chart for satellite data analysis in geothermal field assessment.

Figure 2 presents the flow chart that describes the methodology followed in the terms of the present research, aiming in the deployment of satellite data in the examination of geothermal fields. Every step of the flow chart is serving a specific purpose. The next step in the process involved the analysis of Thermal Infrared Sensor (TIRS) data from the Landsat satellite to generate a map of surface coastal water outflows, enabling the identification and visualization of areas with elevated groundwater discharge potential. The detection of thermal discharges was initiated with the creation of a buffer zone, enabling the selection of the desired portion of each satellite image. This buffer zone was defined to extend 2 km from the coastline, directed outward toward the sea. The selected satellite images were acquired from the Bands 10 and 11 of Landsat 9. Subsequently, the parts of the satellite images within the buffer zone were extracted and the geospatial analysis was performed using Datum Workstation.
In the following phase, satellite images were employed to illustrate geological features, such as lithological units, tectonic discontinuities, lineaments, and land cover on a map. This analysis provides valuable insights into the factors that affect the overall conditions of groundwater. All thematic maps were validated through field confirmation, including in situ measurements in water samples.

Results and Discussion

The analysis of the acquired remote sensing data resulted in the generation of detailed images of the Methana peninsula that illustrate several key geophysical and environmental phenomena. Some of these images depict the thermal discharges from geothermal waters into the surrounding sea, offering insight into the heat exchange processes occurring at the coastline. Data revealing mineral degradation processes resulting from the flow of hydrothermal fluids through rock formations was also acquired. This information was utilized to identify alterations in the surface materials. Land uses were also depicted using satellite records, providing a comprehensive view of the spatial distribution of vegetation across the peninsula.
Thermal satellite data from Landsat 9 provide significant insights into the water discharges of the Methana peninsula, during the summer (Fig. 3a) and winter (Figs. 3b and 3c) periods. Surface runoff was computed using a 5-meter spatial resolution DEM, producing the hydrographic network of the study area, also illustrated in Figure 3. Stream classification was based on the Strahler system. During the summer period (Fig. 3a), thermal discharges from the peninsula to the sea are undetectable due to high seawater temperatures, obscuring the required thermal differentiation for their identification. In winter (Figs. 3b and 3c), thermal discharges are clearly revealed, marked with yellow circles, particularly in the southeastern part of the peninsula, as well as in the northern region. These areas correspond to the well-known thermal springs of Methana's baths, Agios Nikolaos and Pausanias. Field measurements confirmed the presence of thermal discharges, recording temperatures in thermal waters up to 35.7°C and a maximum electrical conductivity of 62,354 mS/cm (Tsekoura, 2024). It is observed that several higher-order Strahler branches of the Strahler classification converge in the areas with thermal discharges (N and SE), enhancing water flow from the peninsula to the sea.

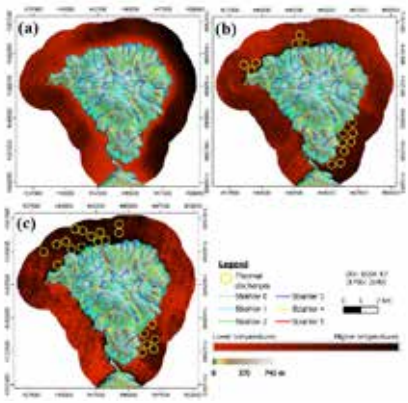

Figure 3. Digital Elevation map of Methana featuring the submarine thermal discharges in the summer and winter periods, based on thermal satellite records from Landsat 9 on (a) 25/07/2024, (b) 09/11/2022 and (c) 04/01/2023. The hydrographic network is displayed with Strahler stream order system.

Figure 4 was generated based on satellite data and highlights tectonic structures and mineral alteration zones in the Methana peninsula. The combination of geological and remote sensing data reveals the relationship between the tectonic evolution of the region and oxidation processes caused by the hydrothermal fluid flow within the volcanic and carbonate rocks of Methana. The bands utilized for the development of Figure 4 represent hydroxyl-bearing minerals (red) that are considered indicators of geothermal activity, along with iron oxides (green) that indicate oxidation processes and ferrous iron oxides (blue) that can be linked in specific mineral compositions. In this case, andesites and dacites (lithologies δα, α1 and α2) appear mineralogically differentiated, as indicated by their blue and green colors. A particularly characteristic occurrence of andesites is present in the NW part of the region, probably due to their elevated content in iron oxides. At this site, the volcanic rocks are originating from the most recent volcanic activity on the peninsula, which took place approximately 2,200 years ago, during historic times (D'Alessandro et al., 2017; Dotsika et al., 2010; Tzanis et al., 2020).

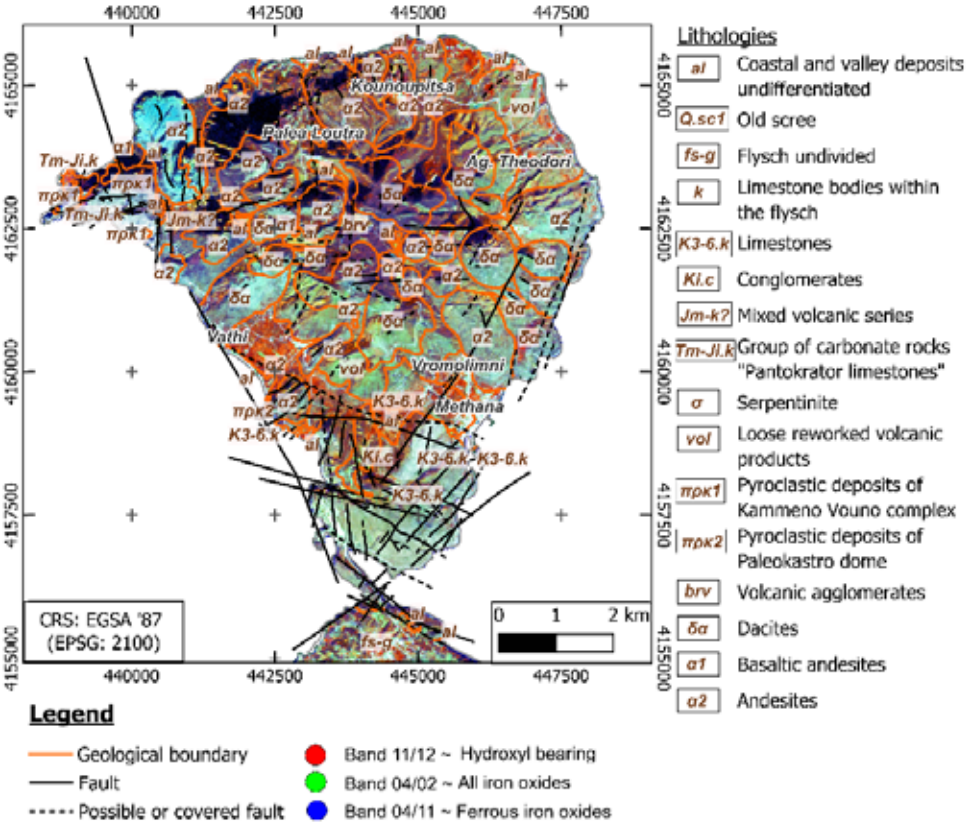

Figure 4. Geological map of Methana with tectonic elements and alteration zones using satellite-derived band combinations.

Figure 5 was generated using data from Sentinel-2 Bands 2, 3, and 4, providing a true-color visualization of vegetation and rock formations for enhanced readability. Digital optimization improved clarity and ensured a realistic representation of surface features. Visual processing of the satellite data revealed previously unmapped tectonic discontinuities, highlighted as dashed orange lines. The overlay of fault systems of Methana indicates terrain morphology and facilitates the identification of vegetation disruptions linked to fault activity, particularly in the W-E oriented faults in the southern region. The concurrent presentation of thermal discharges creates a synthetic visual presentation of the interaction between tectonic discontinuities and hydrothermal fluid flow on the peninsula.

The analysis of tectonic discontinuities in Methana (Fig. 5) provides insights into the region's volcanic evolution and geothermal potential. Faults alignment around the central and northwestern regions indicates a radial flow of andesitic and dacitic lavas toward the coast (Megalovasilis, 2014). In contrast, the southeastern fault systems are more linear and attributed to regional tectonic stress rather than volcanic activity. Identifying tectonic discontinuities, including potential covered faults, is crucial for assessing both seismic risks and their impact on the geothermal system. Furthermore, the development of the fracture network in a geothermal field is essential for identifying potential conduits for hydrothermal fluids. In this context, the NW-SE oriented possible faults of Methana should be mentioned, which appear to extend along the terrestrial corridor between the thermal discharges, linking the Pausanias hot spring in the north with the Agios Nikolaos and Methana hot springs in the southeastern part of the peninsula. Such insights are particularly valuable for the potential exploitation of geothermal resources.

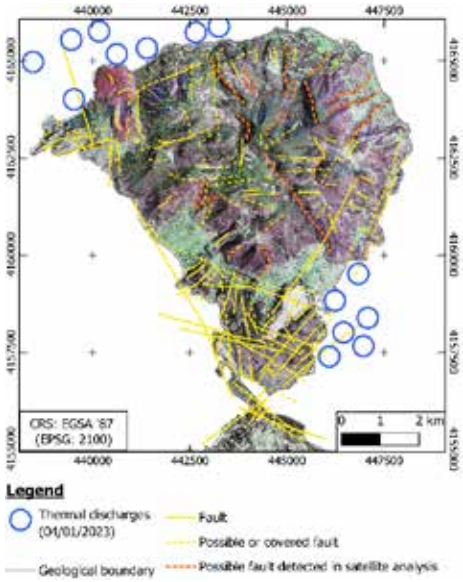

Figure 5. Digitally enhanced Sentinel-2 image in natural colors (RGB: 4/3/2), featuring the landscape of Methana, tectonic discontinuities and thermal discharges.

The Normalized Difference Vegetation Index (NDVI) and classified land cover map of Methana were created based on Sentinel 2 data (Fig. 6). Combining these maps provides a comprehensive view of the regional land use. The Corine land cover classification aligns closely with the NDVI values scaled to 100, confirming the extent of agricultural land and uncultivated areas. Forested areas and natural grasslands dominate the central, northern and NW parts of the peninsula. Agricultural zones, including olive groves and vineyards are more prominent in the NE and the southern areas. Higher NDVI values correspond well with the cultivated lands from the Corine map, whereas low NDVI values are associated with urban zones and barren lands, where the majority of volcanic rocks is located.

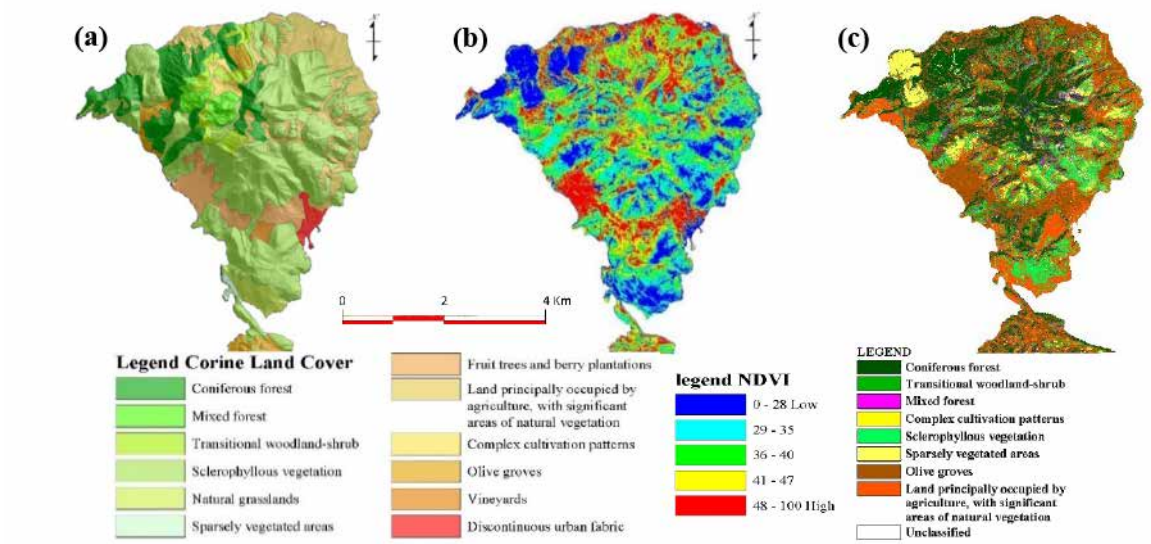

Figure 6. Land uses using Sentinel 2 data - L2A 19/01/2025, (a) Corine land cover map, (b) Map of the NDVI of bands 8 and 4 at 10 m resolution, (c) Land cover classification using Mahalanobis distance classifier bands 2 to 8 at 10 m resolution.

Conclusions

The conducted study revealed the potential of satellite imagery in the preliminary exploration of active geothermal fields, which also enables access in inaccessible areas. The methodology that is presented can be adapted to any active geothermal field,

providing valuable information regarding its potential. The identification of thermal discharges is among the primary benefits, for coastal geothermal systems, since it enables the detection of hot springs. It allows the early detection of geothermal resources, attracting potential investing interest for the exploitation of the geothermal resources of the region. The integration of geological information, including lithologies and fault systems, along with the spatial visualization of chemical components associated with hydrothermal discharges, facilitates the recognition of geological formations impacted by hydrothermal fluids within the study area. This approach improves the detection of fluid flowing paths within the reservoir rocks and surrounding formations. The utilization of digitally enhanced natural color maps generated from remotely sensed data may also enable the detection of non-mapped tectonic discontinuities, along with the identification of alterations in the local vegetation. Evaluating the land uses is equally important, since it provides valuable insights on the distribution of cultivated and arid areas. Land cover analysis is especially beneficial in order to evaluate the optimal method of utilizing geothermal energy to fulfill the existing needs of the region and support its further development. The use of remotely sensed data in the initial stages of evaluating and exploring active geothermal fields offers significant benefits. However, it is important to note that the analysis of satellite images can provide valuable insights, without fully substituting in-situ investigations of geothermal fields. Satellite analysis is subject to crucial limitations, the most significant of which include cloud coverage, which may hinder the acquisition of high-quality data, and spatial resolution constraints, which may prevent the detection of finer geological features. The presented approach requires limited financial resources and time, consisting an efficient and cost-effective methodology for utilizing satellite imagery as an initial step in the investigation of geothermal fields.

References

Abubakar, A. J., Hashim, M., Pour, A. B., & Shehu, K. (2017). A review of geothermal mapping techniques using remotely sensed data. *Science World Journal*, *12*(4).

Ali, S. T., Akerley, J., Baluyut, E. C., Cardiff, M., Davatzes, N. C., Feigl, K. L., Foxall, W., Fratta, D., Mellors, R. J., Spielman, P., Wang, H. F., & Zemach, E. (2016). Time-series analysis of surface deformation at Brady Hot Springs geothermal field (Nevada) using interferometric synthetic aperture radar. *Geothermics*, *61*, 114–120. https://doi.org/10.1016/j.geothermics.2016.01.008

Brocca, L., Zhao, W., & Lu, H. (2023). High-resolution observations from space to address new applications in hydrology. *The Innovation*, *4*(3). https://doi.org/10.1016/j.xinn.2023.100437

D'Alessandro, W., Bellomo, S., Brusca, L., Kyriakopoulos, K., Calabrese, S., & Daskalopoulou, K. (2017). The impact of natural and anthropogenic factors on groundwater quality in an active volcanic/geothermal system under semi-arid climatic conditions: The case study of Methana peninsula (Greece). *Journal of Geochemical Exploration*, *175*, 110–119. https://doi.org/10.1016/j.gexplo.2017.01.003

Dotsika, E., Poutoukis, D., & Raco, B. (2010). Fluid geochemistry of the Methana Peninsula and Loutraki geothermal area, Greece. *Journal of Geochemical Exploration*, *104*(3), 97–104. https://doi.org/10.1016/j.gexplo.2010.01.001

Foutrakis, P. M., & Anastasakis, G. (2018). The active submarine NW termination of the South Aegean Active Volcanic Arc: The Submarine Pausanias Volcanic Field. *Journal of Volcanology and Geothermal Research*, *357*, 399–417. https://doi.org/10.1016/j.jvolgeores.2018.05.008

Megalovasilis, P. (2014). Partition Geochemistry of Hydrothermal Precipitates from Submarine Hydrothermal Fields in the Hellenic Volcanic Island Arc. *Geochemistry International*, *52*(11), 992–1010. https://doi.org/10.1134/S0016702914110044

Meijerink, A. M. J., Bannert, D., Batelaan, O., Lubczynski, M. W., & Pointet, T. (2007). *Remote sensing applications to groundwater (Vol. 16). Paris: Unesco.* United Nations Educational, Scientific and Cultural Organization (UNESCO).

Phiri, D., Simwanda, M., Salekin, S., Nyirenda, V. R., Murayama, Y., & Ranagalage, M. (2020). Sentinel-2 Data for Land Cover/Use Mapping: A Review. *Remote Sensing*, *12*(14). https://doi.org/10.3390/rs12142291

Photiades, A., & Deligiannakis, G. (2022). The flyschoidal mélange unit of the Adheres massif (SE Argolis), in relation to the geological mapping of Trizina sheet at a scale of 1: 50,000. *16th International Congress of the Geological Society of Greece*, *Ext. Abs. GSG2022-260*.

Saepuloh, A., Susanto, A., Sumintadireja, P., & Suparka, E. (2015, April). Characterizing surface manifestation of geothermal system under Torrid Zone using Synthetic Aperture Radar (SAR) data. *Proceedings of the World Geothermal Congress*. World Geothermal Congress (WGC) 2015, Melbourne, Australia. https://www.academia.edu/download/81059750/11051.pdf

Silvestri, M., Marotta, E., Buongiorno, M. F., Avvisati, G., Belviso, P., Bellucci Sessa, E., Caputo, T., Longo, V., De Leo, V., & Teggi, S. (2020). Monitoring of Surface Temperature on Parco delle Biancane (Italian Geothermal Area) Using Optical Satellite Data, UAV and Field Campaigns. *Remote Sensing*, *12*(12). https://doi.org/10.3390/rs12122018

Suesskoch, H., Bannert, D., Kalkreuth, W., Walliner, P., Strauss, M., & Jacobshagen, V. (1974). *Geological Map Sheet "Methana"* [Map]. Institute of Geological and Mineral Exploration, Greece.

Tsekoura, P. E. (2024). *The Hydrochemical Characteristics of Groundwater and Surface Water in Active Geothermal Fields: The Case of Methana (in Greek)*. National Technical University of Athens.

Tzanis, A., Efstathiou, A., Chailas, S., Lagios, E., & Stamatakis, M. (2020). The Methana Volcano – Geothermal Resource, Greece, and its relationship to regional tectonics. *Journal of Volcanology and Geothermal Research*, *404*, 107035. https://doi.org/10.1016/j.jvolgeores.2020.107035

Tzanis, A., Efstathiou, A., Chailas, S., & Stamatakis, M. (2018). Evidence of recent plutonic magmatism beneath Northeast Peloponnesus (Greece) and its relationship to regional tectonics. *Geophysical Journal International*, *212*(3), 1600–1626. https://doi.org/10.1093/gji/ggx486

17th INTERNATIONAL CONGRESS of the Geological Society of Greece

BULLETIN OF THE GEOLOGICAL SOCIETY OF GREECE, SP. PUBL.

EXTENDED ABSTRACT 321

The influence of mineralogy on the non-dilatant friction angle of rock fractures

Tsikrikis A.[1], Marinos V.[2], Papaliangas T.[3]

(1) Aristotle University, Department of Geology, Thessaloniki, Greece, tsikrika@geo.auth.gr

(2) National Technical University, Department of Civil Engineering, Athens, Greece

(3) International Hellenic University, Department of Environmental Engineering, Thessaloniki, Greece.

Research Highlights

Laboratory results of direct shear tests on fresh tension-induced fractures of natural rocks are presented. The results indicate a clear influence of mineralogy on the non-dilatant sliding friction angle, with the values that correspond to fractures in carbonate rocks being distinctly higher than those of silicate ones.

Background

The shear strength of rock joints controls the mechanical behaviour of rock masses. The main factors affecting the shear strength of an unfilled joint are the mineral composition, the magnitude of the normal stress on the joint, the roughness and size of the joint, the degree of weathering, the joint wall strength, moisture and water pressure (Kulatilake, 1995).

The shear strength of a rock surface arises from three sources (e.g. Paterson and Wong 2005): (1) shearing of welded contacts and plastic flow (basic friction), (2) riding over topographic highs (dilation) and (3) local brittle fracture (asperity failure). At low normal stresses the asperity failure component can be ignored (Olsson and Barton 2001; Barton *et al*. 2023). In these cases, such as in slope stability problems, the other two shear strength components (basic friction and dilation) can be determined separately from direct shear tests, also referred to as sliding friction tests (Muralha *et al*. 2014). The dilation can be directly measured from normal and shear displacement diagrams and the sliding friction angle is determined easily and reliably, under conditions of non-dilatant shearing (i.e. dilation is zero) as the difference between the peak friction angle and the dilation angle (Hencher and Richards 1989, 2015).

Objectives

The objective of this laboratory-based study is (a) to examine the effect of mineralogy on the sliding friction angle of essentially flat surfaces with their natural texture retained and (b) to demonstrate that the shear strength of a rock joint can be considered to consist of two components: the first component is due to dilation (dilatant component), which depends on surface roughness, and the second is due to the frictional properties of the rock surface (non-dilatant component).

Methods

Blocks from ten rock types (six silicates and four carbonates) with porosities ranging from 0.15% to 4.29%, including three igneous (diorite, granodiorite and metadolerite), four metamorphic (amphibolite and 3 types of marble) and three sedimentary (2 types of sandstone and one limestone), were collected from natural outcrops, stone and marble quarries and tested in the laboratory. The samples of nine of the investigated rocks were collected from quarries and natural exposures in Greece. The tenth rock was Carrara marble from Italy, which was selected as a standard calcite rock material often used for laboratory tests. The petrophysical properties and the modal analysis of the ten rocks used in the study are depicted in Table 1.

The specimens used in the direct shear tests were rough artificial tension joints, created by inducing bending fractures in rectangular prismatic blocks. The rectangular shear surfaces of these specimens had average dimensions of 120 ± 16 mm in length and 80 ± 11 mm in width.

The tests were conducted using a custom-designed direct shear testing apparatus capable of accommodating samples of varying sizes and shapes and applying both shear and normal loads up to 100 kN. Shear forces were applied using a mechanical gear-driven actuator without closed-loop control, while a hydraulic actuator, connected to a constant-pressure pump, was used to maintain constant the selected normal load.

Shear displacement was monitored with a 25 mm linear variable differential transducer (LVDT) attached to the movable lower shear box, while dilation was measured using two additional 25 mm LVDTs positioned symmetrically, 1 cm from the edges of the specimen's upper half. The LVDTs offered an accuracy of 0.01 mm.

Table 1. Petrophysical properties and the modal analysis of the investigated rocks (Tsikrikis *et al*., 2024)

a/a	Rock name	Mean grain diameter (μm)	Dry density (kg/m³)	Open porosity (%)	Modal Analysis (%)
1	Rhodope Sandstone 1 (RS1)	134	2517	3.88	Q 56, K 18, Pl 22, M 4
2	Rhodope Sandstone 2 (RS2)	411	2513	4.29	Q 67, K 14, Pl 14, M 3, Kaol 2
3	Giannitsa Limestone (GL)	8	2682	0.75	C 99, Q 1
4	Tranovaltos Marble (TM)	146	2717	0.15	C 95, Do 3, Q 2
5	Thasos Krystallina Marble (TKM)	1433	2709	0.32	C 98, Do 1, Q 1
6	Carrara Marble (CM)	187	2710	0.35	C 99, Q 1
7	Terpni Amphibolite (TA)	143	3010	1.27	Am 55, Pl 33, Chl 12
8	Terpni Diorite (TDR)	510	2745	3.11	Q 19, Pl 27, Am 17, Chl 35, M 2
9	Sithonia Granodiorite (SG)	1072	2621	1.79	Q 30, K 11, Pl 36, Bt 21, Chl 1, C 1
10	Mikrokleisoura Metadolerite (MD)	62	2761	1.13	Q 10, Pl 45, Chl 20, Op 20, Am 5

Q: Quartz, K: K-Felspar, M: Muscovite, Bt: Biotite, Pl: Plagioclase, Kaol: Kaolinite, Am: Amphibole, Chl: Chlorite, C: Calcite, Op: Opaque mineral, Do: Dolomite

All tests were performed under constant normal load (CNL) conditions, with normal stresses ranging from 5 kPa to 2.0 MPa. The multistage shear testing method was employed, with the joint repositioned to its original position before each shear stage, as described by Muralha *et al*. (2014). Repositioning during multi-stage tests significantly enhances accuracy compared to procedures without repositioning (MacDonald *et al.,* 2023).

Normal and shear stresses were computed by dividing the respective forces by the nominal area of the sample. The total relative shear displacement during testing was at least 5% of the specimen's length. Special care was taken to accurately record the normal displacement, which was subsequently used to calculate the dilation angle. This dilation angle enabled the separation of the total shear strength into two components: the geometric contribution due to dilation and the sliding frictional (non-dilatant) contribution.

The procedure followed for the determination of the non-dilatant friction angle from direct shear tests with detailed records of stress and dilation is described by Hencher and Richards (1989, 2015). The method is based on the assumption that shearing of a dilating joint (Figure 1i) is equivalent to a shear movement along an inclined plane (Figure 1ii), with a slope angle equal to the instantaneous dilation angle and involves resolving stresses with respect to the actual plane of sliding using the following equations:

$$\tau_i = (\tau\cos\psi - \sigma_n\sin\psi)\cos\psi \quad (1)$$

$$\sigma_i = (\sigma_n\cos\psi + \tau\sin\psi)\cos\psi \quad (2)$$

where

τ is the measured shear stress,

σ_n is the measured normal stress,

τ_i is the shear stress along the actual plane of sliding

σ_i is the normal stress along the actual plane of sliding and

ψ is the instantaneous dilation angle

An indicative diagram of measured and non-dilatant stresses is shown in Figure 1 (iii).

The direct shear test results were analyzed using the non-linear peak shear strength criterion for rock joints proposed by Papaliangas *et al.* (1995), which uses the non-dilatant friction angle as the basic frictional parameter. The criterion is described by equations (3) and (4):

$$\tau_p = \sigma_n\tan(\varphi_{nd} + \psi) \quad (3)$$

$$\tan\psi = \tan\psi_o(\log_{10}\frac{\sigma_{nt}}{\sigma_n})/(\log_{10}\frac{\sigma_{nt}}{\sigma_{no}}) \quad (4)$$

where

τ_p is the peak shear stress

σ_n is the normal stress

φ_{nd} is the sliding friction angle of a frictional, non-dilatant rock surface with zero tensile strength and cohesion
ψ is the dilation angle at the instant of peak shear strength, under effective normal stress σ_n
ψ_o is the peak dilation angle under a normal stress σ_{no} which causes negligible asperity deformation and
σ_{nt} is the transitional effective normal stress under which the normal dilation is completely suppressed.

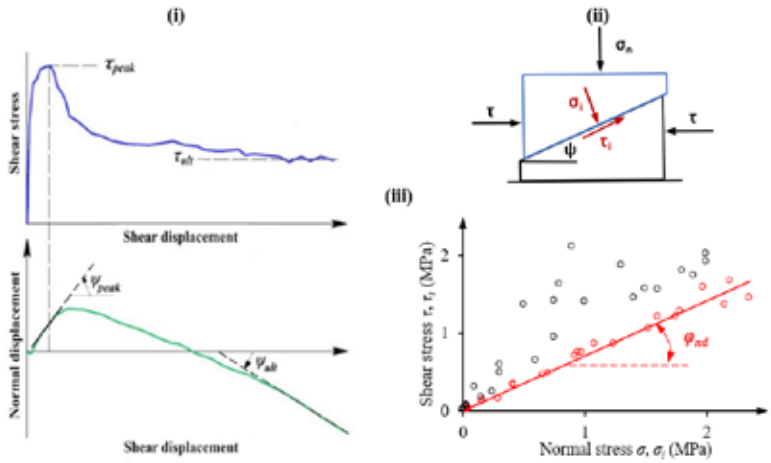

Figure 1. (i) Representative plots from a rock joint shear test conducted under constant normal stress conditions, following the ISRM recommended methodology.
(ii) Decomposition of applied stresses (σ_n, τ) into components acting on the sliding plane (σ_i, τ_i).
(iii) Peak shear stress (black) and non-dilatant shear stress (red) recorded during the tests (Tsikrikis *et al.*, 2024).

It is noted that both the sliding friction angle φ_{nd} and the maximum surface angle ψ_o (a three-dimensional roughness parameter) have clear physical meanings and are easily measurable in the laboratory.
When determined from direct shear tests of natural surfaces, the effect of various surface conditions like weathering, alteration, surface coating etc. is incorporated in the value of φ_{nd}.

Results

A total of 42 fresh, tension-induced joint specimens with prismatic geometry were prepared and subjected to direct shears testing, yielding 286 individual shear runs. The non-dilatant friction angle, a key parameter in the non-linear peak shear strength criterion proposed by Papaliangas *et al.* (1995), was employed to interpret the results, that are shown in Figure 2 for silicate rock samples and Figure 3 for carbonate ones.
For each pair of measured shear (τ) and normal (σ) stresses, the corresponding shear and normal stresses on the sliding plane (τ_i and σ_i) were calculated using the instantaneous dilation angle ψ. These stresses (τ_i and σ_i) represent conditions where shearing occurs without dilation along a naturally textured surface. In essence, they reflect stress states during non-dilatant shearing, where dilation is absent, and the granular texture of the surface exhibits no macroscopic roughness that could induce interlocking or dilation during sliding.
The non-dilatant friction angle (φ_{nd}) was derived from the slope of the regression line in the τ_i versus σ_i plot, as depicted in red in Figures 2 and 3. Peak shear strength envelopes, including an upper and lower bound, were fitted to the data using Papaliangas' criterion (Papaliangas *et al.*, 1995). The parameters φ_{nd}, ψ_o, and σ_{nt} are provided in the respective graphs.
The non-dilatant friction angles of the ten investigated rocks ranged from 32.7° to 40.2°, revealing a clear distinction between carbonate rocks (range 34.1°–40.2°) and silicate rocks (range 32.7°–36.3°). When categorized by origin (igneous, metamorphic and sedimentary) and mineralogy (silicates and carbonates), the following five subgroups emerged with the indicated values of φ_{nd}:
Igneous rocks:
Silicate (SG, TDR): 32.8º – 34.6º
Sedimentary rocks:
a. Silicate (RS1, RS2): 35.3º – 35.6º
b. Carbonate (GL): 34.1º
Metamorphic rocks:
a. Silicate (MD, TA): 32.7º–36.3º

b. Carbonate (TM, TKM, CM): 39.3º – 40.2º

The values of φ_{nd} correspond to the sliding friction angle of essentially flat surfaces with their natural texture retained and may be different (usually higher) from those of the corresponding values of saw-cut surfaces, that is attributed to the removal of the original rock texture caused by saw-cutting.

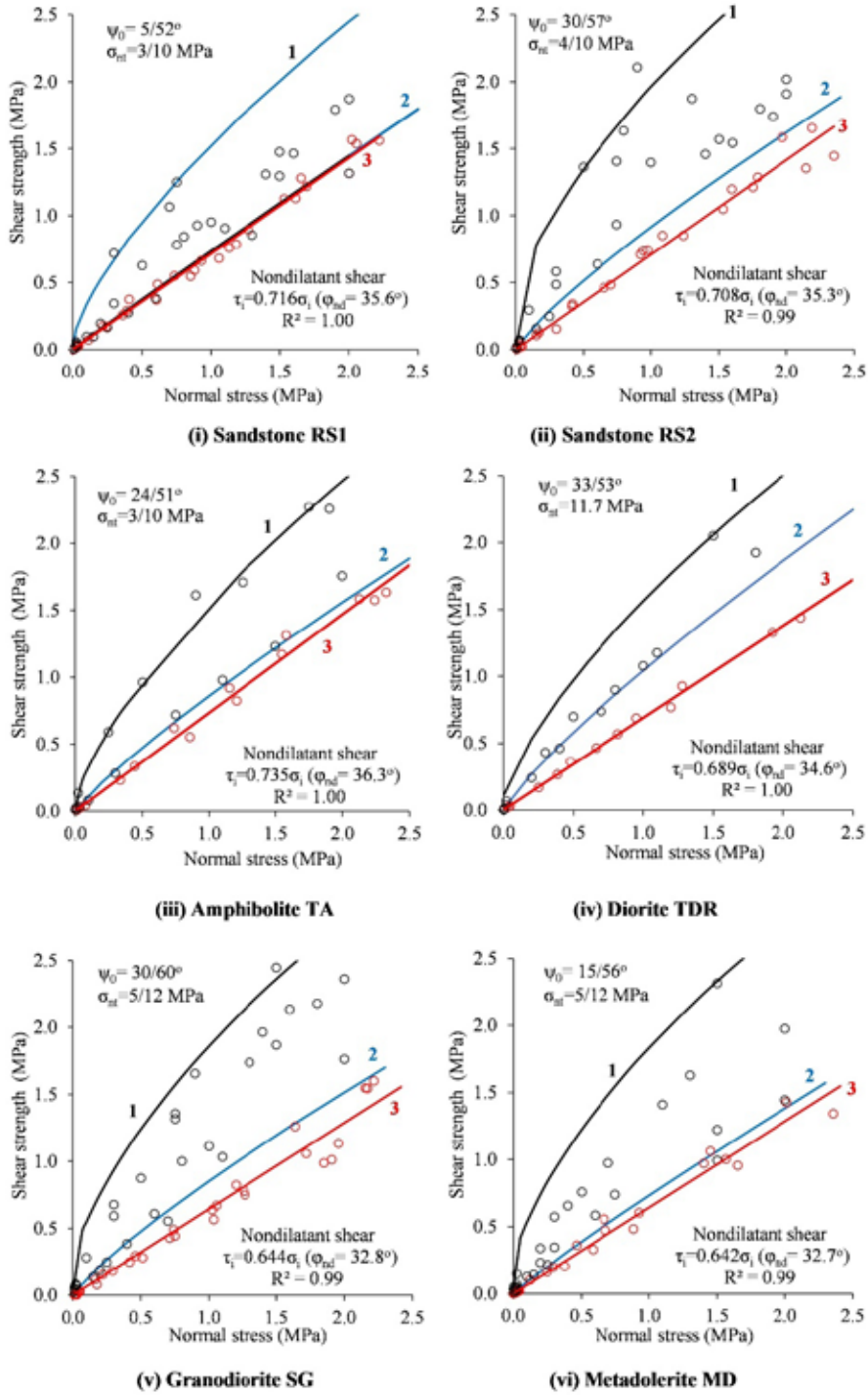

Figure 2. Fitted peak shear strength envelopes and the non-dilatant shear strength best-fit line for silicate rock induced tension joints. Curve 1 (black) and Curve 2 (blue) correspond to the upper and lower bounds of peak shear strength, respectively, as predicted by Papaliangas' criterion, with the parameters φ_{nd}, ψ_o, and σ_{nt} displayed on the diagram. Line 3 (red) denotes the non-dilatant shear strength (Tsikrikis *et al.*, 2024).

According to our results, the sliding friction angles for the studied rocks, are lower than those predicted from Byerlee's (1978) friction law $\tau = 0.85\sigma_n$ that provides an upper bound of our obtained values.
From the experimental results shown in Figures 2 and 3 it becomes evident that despite variations in peak shear strength across the tested rock types, the individual best-fit regression lines between normal stress and non-dilatant shear strength were well-defined. These linear relationships held consistently across the applied normal stress range (0–2 MPa), irrespective of mineralogy, grain size, porosity and joint surface roughness. This consistency highlights that non-dilatant shear strength is fundamentally frictional, as it is proportional to the applied normal stress.

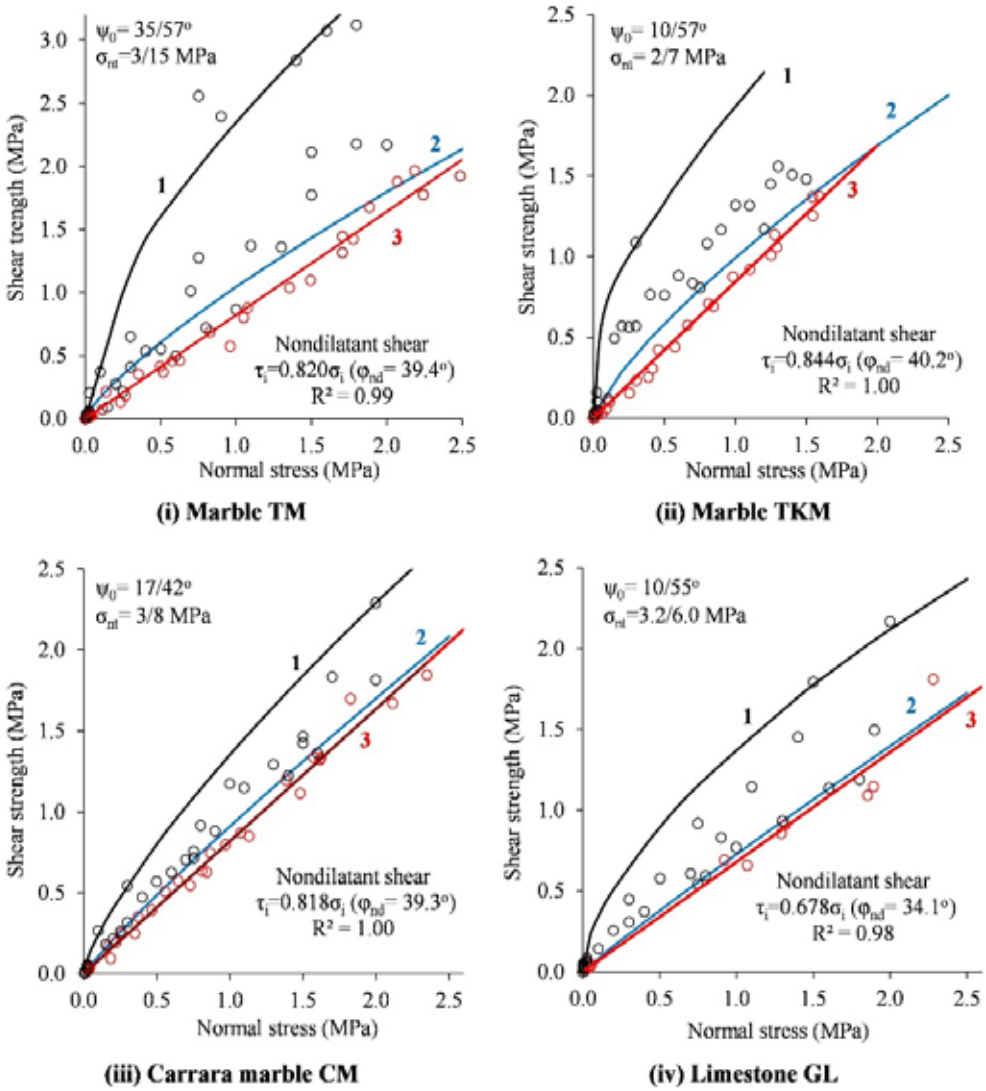

Figure 3. Fitted envelopes representing the peak shear strength and the non-dilatant shear strength best-fit line for carbonate rock induced tension joints tested in direct shear. Notations and methodology are consistent with Figure 2 (Tsikrikis *et al.*, 2024).

Accordingly, the shear strength can be divided into two components: a) a dilatant component, attributed to surface dilation, b) a non-dilatant component, stemming from the frictional properties of the rock surface.
Since the non-dilatant friction angle is derived from direct shear tests on natural surfaces, it inherently accounts for various surface conditions, including weathering, alterations and coatings. Importantly, both the sliding friction angle (φ_{nd}) of a naturally textured surface and the maximum surface angle (ψ_o), a three-dimensional roughness parameter, have clear physical significance and are easily measurable in the laboratory.

Conclusions

In this paper, several fresh induced tension fractures with different surface roughness from ten rock types (six silicates and four carbonates) tested dry in direct shear. The main conclusions resulted from 286 peak shear strength (τ_p) - normal stress (σ_n) - peak dilation angle (ψ) data sets are:

1) Although variations were observed in the peak shear strength across joints from the ten rock types tested, the sliding friction shear strength determined under conditions of non-dilatant shearing of each rock type was found to be proportional to the applied normal stress. This indicates that it is fundamentally frictional in nature. This proportionality holds across the applied normal stress range (0–2 MPa), regardless of mineralogy, grain size, or surface roughness. Consequently, the shear strength can be divided into two components: (a) a sliding friction component (non-dilatant component), and (b) a dilation component.
2) The values of the non-dilatant sliding friction angle φ_{nd} ranged from 32.7° to 40.2°, with weaker and more ductile carbonate rocks showing distinctly higher values (34.1°–40.2°) compared to the stronger and more brittle silicate rocks (32.7°–36.3°).

References

Barton N, Wang C, Yong R. (2023) Advances in joint roughness coefficient (JRC) and its engineering applications. J Rock Mech Geotech Eng 15 (12): pp. 3352-3379. https://doi.org/10.1016/j.jrmge.2023.02.002

Byerlee J.D., 1978. Friction of rocks. PAGEOPH 116:615–626. https:// doi. org/ 10. 1007/ BF008 76528.

Hencher, S.R. and Richards, L.R., 1989. Laboratory direct shear testing of rock discontinuities. Ground Engng 22:24-31.

Hencher, S. R. and L. R. Richards., 2015. Assessing the Shear Strength of Rock Discontinuities at Laboratory and Field Scales. Rock Mechanics and Rock Engineering 48 (3): 883–905. https://doi.org/10.1007/s00603-014-0633-6

Kulatilake P.H.S.W., Shou G., Huang T.H., Morgan R.M., 1995. New peak shear strength criteria for anisotropic rock joints. Int Rock Mech Min Sci Geomech Abstr 32(7):673–697. https://doi.org/10.1016/0148-9062(95)00022-9

MacDonald N.R., Packulak T.R.M., Day J.J., 2023) A Critical Review of Current States of Practice in Direct Shear Testing of Unfilled Rock Fractures Focused on Multi-Stage and Boundary Conditions. Geosciences (Switzerland), 13 (6), art. no. 172, DOI: 10.3390/geosciences13060172

Muralha, J., Grasselli, G., Tatone, B., Blümel, M., Chryssanthakis P., Yujing, J., 2014. ISRM Suggested Method for Laboratory Determination of the Shear Strength of Rock Joints: Revised Version. Rock Mechanics and Rock Engineering 47 (1): 291–302. https://doi.org/10.1007/s00603-013-0519-z.

Olsson R, Barton N (2001) An improved model for hydro-mechanical coupling during shearing of rock joints Int J Rock Mech Min Sci 38:317-329

Paterson MS, Wong T-F (2005) Experimental Rock Deformation - The Brittle Field. Experimental Rock Deformation - The Brittle Field. https://doi.org/10.1007/b137431

Papaliangas, T. T., Hencher, S.R., Lumsden, A.C.,1995. A comprehensive peak shear strength criterion for rock joints. In T.Fuji (ed.) Proc. 8th Int. Congress ISRM, Tokyo, Vol. 1, pp. 359-366. Rotterdam: Balkema

Tsikrikis, A., Marinos, V, Papaliangas, T., 2024. Relation between the sliding friction angle of rock joints and the friction angle of intact cores at the brittle-ductile transition: An experimental study. Bull Eng Geol Environ 83, 500. https://doi.org/10.1007/s10064-024-03966-6.

17th INTERNATIONAL CONGRESS of the Geological Society of Greece

BULLETIN OF THE GEOLOGICAL SOCIETY OF GREECE, SP. PUBL.

EXTENDED ABSTRACT 322

Exploring Participant Experiences in a Geoconservation Program in Apano Meria, Syros island, Greece

Tsipra Th.[1], Drinia H.[1]

(1) National and Kapodistrian University of Athens, Department of Geology and Paleontology, Panepistimiopolis 15784, Athens, Greece, ttsipra@geol.uoa.gr; cntrinia@geol.uoa.gr

Introduction

The purpose of this paper is to highlight the benefits the public gains from educational programs centered on the geocultural wealth of Greece. For this purpose, the study focuses on Apano Meria in Syros Island, South Aegean Sea, presenting an educational program designed to raise awareness about geoheritage and geoenvironmental awareness (Figure 1). Syros Island, with its remarkable petrological and tectonic history, provides an ideal backdrop for such an initiative. Its unparalleled preservation of mineral parageneses and tectonic structures—arising from a geotectonic environment associated with subduction—offers invaluable insights into the processes and evolution of our planet. These unique geological features have made Syros a global attraction for research geologists and an exemplary site for geoconservation and geoeducational efforts.

Learning in informal educational settings, such as field trips to geosites, museums, or natural parks, has proven to be one of the most effective methods of integrating theory with practice. Outdoor environments not only enhance children's ability to perceive and focus on natural phenomena but also provide a naturalistic, experiential approach to scientific learning. Wells (2000) emphasizes that daily exposure to natural settings significantly improves this process. In Syros, the exceptional and well-preserved rock formations offer an ideal environment for structured outdoor learning, allowing participants to engage directly with geological phenomena and processes.

The proposed educational program aligns with the island's candidacy for inclusion in the UNESCO Global Geoparks Network, as suggested by Drinia et al. (2021) and Tsipra and Drinia (2022). It underscores the island's potential as a platform for raising awareness about geoheritage and fostering sustainable behaviors through hands-on, outdoor learning experiences. This paper evaluates participants' experiences with the program to explore its educational value and effectiveness in promoting geoconservation and environmental awareness.

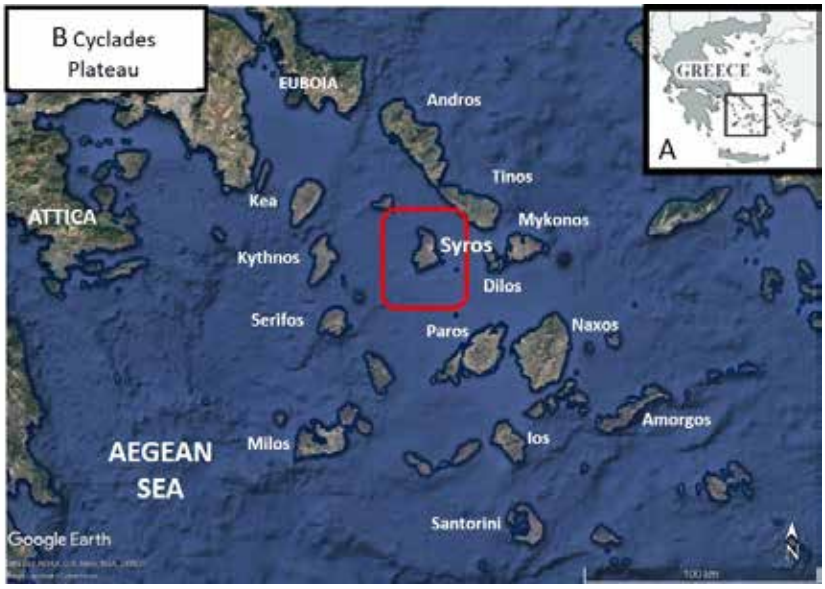

Figure 1. A. Sketch map of Greece indicating the location of Cyclades Plateau, B. Satellite photo of the Cyclades plateau, indicating the location of Syros island.

Methodology

The educational program is inspired by the geological evidence of the Apano Meria region in Syros. It introduces participants to the unique mineral rocks of the area in an engaging and enjoyable manner, while emphasizing the cultural and environmental significance of Geoparks. Designed according to principles of "learning by doing" and

teamwork, the program is structured based on Bloom's taxonomy (knowledge, comprehension, application, analysis, synthesis, and evaluation). A mystery game format resembling a treasure hunt forms the core of the program. Participants collaborate to follow clues, solve problems, and discover a "blue diamond," providing insights into geological processes and the formation of the island's unique rock formations. Creative activities were also integrated to help participants understand the historical formation of rocks and their connections to geocultural heritage.

The program has been tailored to different audiences and implemented in various settings. For postgraduate students, it was delivered as part of the "Museum Studies" program at the University of Athens during the "Museum Education" course. This included lectures on ecomuseums and a mini-workshop addressing age-group characteristics in educational planning. The program was also implemented with primary and secondary school students at the Aerolithos eclogite site on Syros Island (Figure 2). For public engagement, it featured an interactive exhibit at the Athens Science Festival, including augmented reality videos showcasing the geological and cultural heritage of Syros.

The evaluation process involved collecting qualitative and quantitative feedback through surveys. Thematic coding and word cloud visualizations highlighted recurring themes, while pie charts and graphs summarized satisfaction levels, willingness to reengage, and demographic information.

Figure 2. Eclogitic monolith locally known as "aerolithos", in Apano Meria, north Syros island

Results

Participants identified key elements of the program that resonated with them, including the significance of the geological area and natural heritage. Enjoyable aspects included walking routes, nature immersion, team activities, and problem-solving exercises. Challenges revolved around physical exertion, puzzle-solving, and environmental conditions, but most participants expressed no desire for significant changes. Emotional responses to the program were overwhelmingly positive, with terms such as "happy," "good," and "relaxed". A majority of participants (57) indicated they would participate in a similar program, emphasizing its perceived value. Demographically, the group was almost evenly split between female (34) and male (31) participants, with one individual identifying as a non-binary gender.

Discussion - Conclusions

The findings underline the program's success in creating an engaging and educational experience that highlights the importance of geoconservation. The interactive and nature-focused activities fostered positive emotions and a sense of community among participants. The challenges reported were minor and did not significantly detract from participants' overall enjoyment. The high percentage of participants willing to re-engage in similar programs demonstrates the potential for such initiatives to build long-term interest in geodiversity and sustainability. These insights provide a foundation for refining future programs, ensuring they remain inclusive, accessible, and impactful for diverse audiences...

Acknowledgements
The authors extend their heartfelt thanks to the organizing committee of the 17th International Congress of the Geological Society of Greece and the anonymous reviewers for their thorough consideration of this extended abstract.

References

Drinia, H., Tsipra, T., Panagiaris, G., Patsoules, M., Papantoniou, C., & Magganas, A. (2021). Geological Heritage of Syros Island, Cyclades Complex, Greece: An Assessment and Geotourism Perspectives. Geosciences, 11(3), 138. https://doi.org/10.3390/geosciences11030138

Tsipra, T., & Drinia, H. (2022). Geocultural Landscape and Sustainable Development at Apano Meria in Syros Island, Central Aegean Sea, Greece: An Ecomuseological Approach for the Promotion of Geological Heritage. Heritage, 5(3), 2160-2180. https://doi.org/10.3390/heritage5030113

Wells, N. M. (2000). At home with nature: Effects of “greenness” on children’s cognitive functioning. Environment and behavior, 32(6), 775-795.

17th INTERNATIONAL CONGRESS of the Geological Society of Greece

BULLETIN OF THE GEOLOGICAL SOCIETY OF GREECE, SP. PUBL.

EXTENDED ABSTRACT 323

Crustal Block Kinematics in Western Greece using geodetic data

Tsironi V.[1], Nocquet J-M.[2,3], Ganas Ath.[1], Sokos Eth.[4], Koukouvelas I.[4]

(1) Institute of Geodynamics, National Observatory of Athens, 11810 Athens, Greece, vtsironi@noa.gr , (2) Université Côte d'Azur, IRD, CNRS, Observatoire de la Côte d'Azur, Géoazur, 06560 Valbonne, France, (3) Université Paris Cité, Institut de Physique du Globe de Paris, 75005 Paris, France, (4) Department of Geology, University of Patras, Rio 26504, Greece

Introduction

Western Greece (Fig. 1), a tectonically active region, is marking a North to South shift between collision to subduction, driven by the interaction between the Apulian platform, the oceanic subduction beneath the central and south Ionian Sea, and surrounding micro-blocks on the overriding plate. This region exhibits complex fault interactions and significant seismicity due to broader active faulting and the convergence of the Nubian and Eurasian plates (Perouse et al. 2012; Pearce et al. 2012). The area's tectonics are dominated by the Cephalonia Transform Fault Zone (CTF), a series of right-lateral fault segments, which mediates the transition from continental collision in the north to oceanic subduction in the south (Louvari et al., 1999; Ganas et al., 2016). This study leverages geodetic data (GNSS observations) to develop an elastic block model that elucidates fault geometries, block rotations, and slip rates, improving understanding of seismic hazards and regional deformation.

Study Area and Tectonic Setting

Western Greece encompasses the Ionian Islands, the western Peloponnese, and mainland areas such as Epirus and Aitoloakarnania. The CTF delineates a significant tectonic boundary between the Apulian-Ionian block and northwestern Greece (Briole et al., 2021; Vassilakis et al., 2011; Perouse et al., 2017). In addition, extensional grabens, including the Gulf of Amvrakikos (GoA Fig. 1), Gulf of Patras (GoP), and Gulf of Corinth (GoC), mark Plio-Quaternary active fault systems linked to slab retreat. Strike-slip faulting along two major continental faults is taking place along the Katouna-Stamna Fault (KSF) and the Movri Fault Zone (MFZ) which is located in the northwestern Peloponnese (Perouse et al., 2017; Gallovic et al., 2009; Ganas et al., 2009).

Methodology

Using geodetic data from 92 published GNSS stations spanning Greece and southern Italy, this study applies an elastic block model to analyze horizontal velocity fields (Hollenstein et al., 2008, Briole et al., 2021, Serpelloni et al., 2022). The model estimates block rotations, fault slip rates, and strain accumulation, integrating seismic, geological, and geodetic data. Euler poles and velocity residuals were employed to validate fault activity and block boundaries. Key fault segments and their kinematics were characterized based on observed velocity gradients and published geological and seismological data.

Model Results and Block Kinematics

The best-fitting model identifies five major tectonic blocks in Western Greece (Fig. 1b):

1. **Apulian Block (APUL):** Encompasses the central Ionian Sea and parts of the Italian peninsula.
2. **Ionian-Akarnania Block (IAB):** Bounded by the CTF, GoA graben, and Katouna-Stamna Fault (KSF).
3. **Central Greece Block (CGRE):** Defined by faults along the GoC and GoP.
4. **Peloponnese Block (PELOP):** Southern boundary influenced by the Movri Fault Zone (MFZ) and offshore structures.
5. **South Aitolia Block (SAB):** Proposed as a micro-block between the GoT and GoP.

Key Findings:

1. **Cephalonia Transform Fault (CTF):**
   - The CTF exhibits a right-lateral strike-slip motion (~16 mm/yr) with a reverse component (~5 mm/yr). The fault's slip rates align with previous studies, confirming its role as a boundary accommodating significant crustal deformation.
2. **Extensional Grabens:**
   - The GoA shows rapid extension (~10 mm/yr), with indications of left-lateral shear consistent with the KSF's westward continuation. The GoC and GoP are characterized by northward and southward fault-dipping systems.

3. **Katouna-Stamna Fault (KSF):**
   - This NW-SE striking fault displays left-lateral slip (~12 mm/yr) with low locking depths, suggesting aseismic creep along segments.
4. **Movri Fault Zone (MFZ):**
   - The MFZ demonstrates right-lateral motion (~8 mm/yr) with a possible tensional component. It likely contributes to the southern boundary of the IAB.
5. **Triple Junctions:**
   - Two triple junctions were identified -one near the western GoC (Rio area) and another near the GoA (offshore Preveza)- and define zones of complex deformation and intense seismicity. The GoP is a site of interaction between strike-slip and extensional faults.

Validation and Model Performance

The model achieves a high data variance reduction (99.4%) and a weighted root mean square error (wrms) of 0.94 mm/yr. Residual analysis highlights minor localized mismatches in areas with complex secondary faults or diffuse deformation zones. Slip vectors from earthquake focal mechanisms align well with predicted fault motions (see Fig. 1a), validating the model's accuracy.

Conclusions

This study underscores the utility of elastic block modeling in delineating the kinematics of fault systems and tectonic blocks using tectonic velocities from high-quality GNSS data. Western Greece's tectonics are dominated by crustal block interactions of the overriding Aegean plate along major faults such as the CTF, KSF, and MFZ, as well as active grabens. The findings include new data on fault slip rates and locking depths and highlight critical areas for seismic hazard assessment, such as the GoA and GoP, where significant strain accumulation and potential fault creep are observed. Further integration of subduction processes and secondary faults into models could refine predictions of regional seismic risks.

Acknowledgements

This research was supported by the Hellenic Foundation for Research and Innovation (HFRI) under the 3rd Call for HFRI PhD Fellowships (Fellowship Number: 05176). Also, this work is supported in part by funds from the Erasmus+ Internships.

References

Briole, P., Ganas, A., Elias, P., & Dimitrov, D. (2021). The GPS velocity field of the Aegean. New observations, contribution of the earthquakes, crustal blocks model. Geophysical Journal International, 226(1), 468–492. https://doi.org/10.1093/gji/ggab089

Dziewonski, A. M., Chou, T.-A., & Woodhouse, J. H. (1981). Determination of earthquake source parameters from waveform data for studies of global and regional seismicity. Journal of Geophysical Research: Solid Earth, 86(B4), 2825–2852. https://doi.org/10.1029/JB086iB04p02825

Ekström, G., Nettles, M., & Dziewoński, A. (2012). The global cmt project 2004–2010: Centroid-moment tensors for 13,017 earthquakes. Physics of the Earth and Planetary Interiors, 200-201, 1–9. https://doi.org/10.1016/j.pepi.2012.04.002

Gallovic, F., Zahradn´ık, J., Kˇr´ıˇzov´a, D., Plicka, V., Sokos, E., Serpetsidaki, A., & Tselentis, G.-A. (2009). From earthquake centroid to spatial-temporal rupture evolution: Mw 6.3 movri mountain earthquake, June 8, 2008, Greece. Geophysical Research Letters, 36 (21). https://doi.org/10.1029/2009GL040283942

Ganas, A., Tsironi, V., Efstathiou, E., Konstantakopoulou, E., Andritsou, N., Georgakopoulos, V., Tsimi, C., Fokaefs, A., & Madonis, N. (2023). The National Observatory of Athens active faults of Greece database (NOAFaults), version 2023. Past Earthquakes and Advances in Seismology for Informed Risk Decision-Making, Book of Abstracts, Proceedings of the 8th International Colloquium on Historical Earthquakes, Palaeo—Macroseismology and Seismotectonics, 36–38.

Ganas A., Briole P., Bozionelos G., Barberopoulou A., Elias P., Tsironi V., Valkaniotis S., Moshou A., Mintourakis I., 2020. The 25 October 2018 Mw= 6.7 Zakynthos earthquake (Ionian Sea, Greece): a low-angle fault model based on GNSS data, relocated seismicity, small tsunami and implications for the seismic hazard in the west Hellenic Arc, Journal of Geodynamics doi: https://doi.org/10.1016/j.jog.2020.101731

Ganas, A., Tsironi, V., Kollia, E., Delagas, M., Tsimi, C., & Oikonomou, A. (2018). Recent upgrades of the NOA database of active faults in Greece (NOAFaults). Proceedings of the 19th General Assembly of WEGENER, Grenoble, France, 10–13.

Ganas, A., Elias, P., Bozionelos, G., Papathanassiou, G., Avallone, A., Papastergios, A., Valkaniotis, S., Parcharidis, I., & Briole, P. (2016). Coseismic deformation, field observations and seismic fault of the 17 November 2015m=6.5, Lefkada island, Greece earthquake. Tectonophysics, 687, 210–222. https://doi.org/https://doi.org/10. 10931016/j.tecto.2016.08.012 1094

Ganas, A., Serpelloni, E., Drakatos, G., Kolligri, I., M. Adamis, Tsimi, C., & Batsi, E. (2009). The mw 6.4 SW Achaia (western Greece) earthquake of 8 June 2008: Seismological, field, gps observations, and stress modeling. Journal of Earthquake

Engineering, 13 (8), 1101-1124. doi: 10.1080/13632460902933899960

Halpaap, F., Rondenay, S., & Ottemöller, L. (2018). Seismicity, deformation, and metamorphism in the western hellenic subduction zone: New constraints from tomography. Journal of Geophysical Research: Solid Earth, 123(4), 3000–3026. https://doi.org/10.1002/2017JB015154

Hollenstein, C., Müller, M., Geiger, A., & Kahle, H.-G. (2008). Crustal motion and deformation in Greece from a decade of gps measurements, 1993–2003. Tectonophysics, 449(1), 17–40. https://doi.org/10.1016/j.tecto.2007.12.006

Louvari, E., Kiratzi, A., & Papazachos, B. (1999). The Cephalonia transform fault and its extension to western Lefkada island (Greece). Tectonophysics, 308(1), 223–236. https://doi.org/https://doi.org/10.1016/S0040-1951(99)00078-5

Makropoulos, K., Kaviris, G., & Kouskouna, V. (2012). An updated and extended earthquake catalogue for Greece and adjacent areas since 1900. Natural Hazards and Earth System Sciences, 12(5), 1425–1430. https://doi.org/10.5194/nhess-12-14252012

Pearce, F. D., Rondenay, S., Sachpazi, M., Charalampakis, M., & Royden, L. H. (2012). Seismic investigation of the transition from continental to oceanic subduction along the western hellenic subduction zone. Journal of Geophysical Research: Solid Earth, 117(B7). https://doi.org/https://doi.org/10.1029/2011JB009023

Pérouse, E., Chamot-Rooke, N., Rabaute, A., Briole, P., Jouanne, F., Georgiev, I., & Dimitrov, D. (2012). Bridging onshore and offshore present-day kinematics of central and eastern mediterranean: Implications for crustal dynamics and mantle flow. Geochemistry, Geophysics, Geosystems, 13(9). https://doi.org/https://doi.org/10.1029/2012GC004289

Pérouse, E., Sébrier, M., Braucher, R., Chamot-Rooke, N., Bourlès, D., Briole, P., Sorel, D., Dimitrov, D., & Arsenikos, S. (2017). Transition from collision to subduction in western Greece: The Katouna–Stamna active fault system and regional kinematics. International Journal of Earth Sciences, 106, 967–989. https://doi.org/10.1007/s00531-016-1345-9

Serpelloni, E., Cavaliere, A., Martelli, L., Pintori, F., Anderlini, L., Borghi, A., Randazzo, D., Bruni, S., Devoti, R., Perfetti, P., et al. (2022). Surface velocities and strain-rates in the euro-mediterranean region from massive gps data processing. Frontiers in Earth Science, 10, 907897. https://doi.org/10.3389/feart.2022.907897

Triantafyllis, N., Venetis, I. E., Fountoulakis, I., Pikoulis, E.-V., Sokos, E., & Evangelidis, C. P. (2021). Gisola: A High-Performance Computing Application for Real-Time Moment Tensor Inversion. Seismological Research Letters, 93(2A), 957–966. https://doi.org/10.1785/0220210153

Vassilakis, E., Royden, L., & Papanikolaou, D. (2011). Kinematic links between subduction along the Hellenic trench and extension in the gulf of corinth, greece: A multidisciplinary analysis. Earth and Planetary Science Letters, 303 (1), 108-120. https://doi.org/10.1016/j.epsl.2010.12.0541176

17th INTERNATIONAL CONGRESS of the Geological Society of Greece

BULLETIN OF THE GEOLOGICAL SOCIETY OF GREECE, SP. PUBL.

EXTENDED ABSTRACT 324

Optically stimulated luminescence (OSL) dating of a shell midden layer at Umhlanga Rocks, Natal North Coast, South Africa

Tsodoulos I.[1], Karymbalis E.[1], Ferentinou M.[2], Green A.[3], Stamoulis K.[4], Gallousi C.[1]

(1) Department of Geography, Harokopio University, Athens, Greece, Karymbalis@hua.gr (2) School of Civil Engineering and Built Environment, Faculty of Engineering and Technology, John Moores University, Liverpool, United Kingdom (3) School of Agricultural, Earth and Environmental Sciences, University of Kwazulu-Natal, Durban, South Africa (4) Department of Physics, University of Ioannina, Ioannina, Greece

Introduction

Shell middens are anthropogenic deposits containing significant amounts of shell material (Campbell, 2005). They form in areas where human communities - whether hunter-gatherers, horticulturalists, agriculturalists or industrial societies - intensively harvest shellfish, extract and process the meat for consumption, or repurpose the shells as raw materials. The resulting shell debris accumulates at habitation or processing sites, where shells dominate the matrix. Shell middens are believed to have formed rapidly, with shell deposition rates exceeding those of sediments (Marean, 2014).

Shell middens are widespread in coastal regions worldwide, spanning environments from subarctic to tropical zones (Stratham, 1892, Álvarez *et al.*, 2011, Rabett *et al.*, 2011, Cardoso, 2015). Coastal shell middens can be found as exposed layers of shell in dunes, cliff faces, coastal scrub, and wetlands or as scattered shell deposits on eroded surfaces. These middens may consist of a single, thin layer or develop into thick, stratified deposits with multiple layers. Their size varies greatly ranging from small shell concentrations just a few meters across to extensive formations covering many hundreds of meters.

Research on shell midden began in the 1800s and gained significant momentum in the late 19th and early 20th centuries (Rick, 2024). The study of these deposits has been crucial in archaeological research, providing valuable insights into the relationship between humans and aquatic habitats, and revealing the significance of marine environments in human evolution and ecology (Wurz *et al.*, 2022, Rick, 2024).

Shell middens are among the most prominent archaeological sites along the entire coast of South Africa (Jerardino, 2010). The Stone Age shell middens of South Africa offer the richest and longest record of coastal adaptations, while shell middens of Early Iron Age are a critical archive for understanding past human activities in the region. However, the eastern Indian Ocean coast in South Africa has received less attention than the south coast, despite clear evidence of sustained coastal resource use there as well (Will *et al.*, 2022).

In this study, we present the results of optically stimulated luminescence (OSL) dating of five sediment samples collected from sand layers developed below and above a coastal shell midden outcrop approximately 80 m from the shore at Umhlanga Rocks on the Natal north coast.

Previous excavations from the nearby sites of Emberton Way and Umhlanga Rocks (Davies & MacDonald, 1978) revealed approximately 1.5 m of stratified sands containing ceramics, stone artifacts, shells and shell fragments. It is currently impossible to assess the original extent of the midden layer due to extensive disturbance in the surrounding area, primarily caused by urban development, one of the major causes of midden damage worldwide (Ceci, 1984). The midden must have been extensive, as in 1974 it was recorded as being 19 m long and 2 m thick at its deepest exposure with compacted *Perna perna* (brown mussel) layers, hearths and numerous ashy layers.

Study Area

The study area is located on the east coast of South Africa, along the north coast of KwaZulu Natal (north coast) (Figure 1). Along most of the KwaZulu-Natal coastline, a series of large, coast-parallel dune complexes, mainly of Cenozoic age, occur. The site of the stratigraphic section studied on the southern end of the Ohlanga Estuary, approximately 20 km north-northeast of Durban (Figure 1). The 2.3 m thick stratigraphic section is located about 80 m from the present-day shoreline and is part of the face of a low foredune cliff. The bulk of the studied deposit appears to remain undisturbed, despite evidence of large-scale disturbances to the immediate surroundings of the midden and the uppermost surface of the foredune cliff face.

Figure 1. A relief map showing the location of Umhlanga in KwaZulu Natal, South Africa.

Methodology

The stratigraphy of the sediment layers in the section containing the shell midden were identified and described in detail. To achieve this, the face of the low dune cliff was carefully excavated and cleaned (Figure 2). The chronostratigraphy of the section was established using five samples collected from selected sedimentary layers below and above the shell midden layer, dated through OSL.

Figure 2. Photographs of the stratigraphic units exposed in the coastal natural outcrop at Umhlanga Rocks, Natal north coast, South Africa, along with the locations of luminescence sampling points.

OSL sample preparation was conducted in the Physical Geography laboratory of Harokopio University of Athens, Greece, while the OSL signal measurements were performed at the Nuclear Physics laboratory of the University of Ioannina, Greece.

Quartz grains (150-250 μm) were extracted through wet sieving and acid treatment (HCl, H_2O_2, HF), under subdued red-light conditions. The purity of the quartz extract was verified using the OSL-IR depletion ratio (Duller, 2003). The Single-Aliquot Regenerative-dose (SAR) protocol of Murray and Wintle (2000), was used to determine all equivalent doses (De).

All measurements were performed on an automated Risø TL/OSL-DA-20 reader equipped with a $^{90}Sr/^{90}Y$ beta radiation source. Quartz OSL signals were obtained by stimulating with blue LEDs (470 nm, ~47 mW/cm^2) and the signals were detected using a 7 mm Hoya U-340 optical filter. Environmental dose rates were calculated from radionuclide concentrations measured by high-resolution gamma spectrometry, applying the conversion factors of Liritzis *et al*. (2013).

Results

The stratigraphy of the site revealed deposits approximately 2.3 m thick (Figure 3), with six distinct layers identified and described:

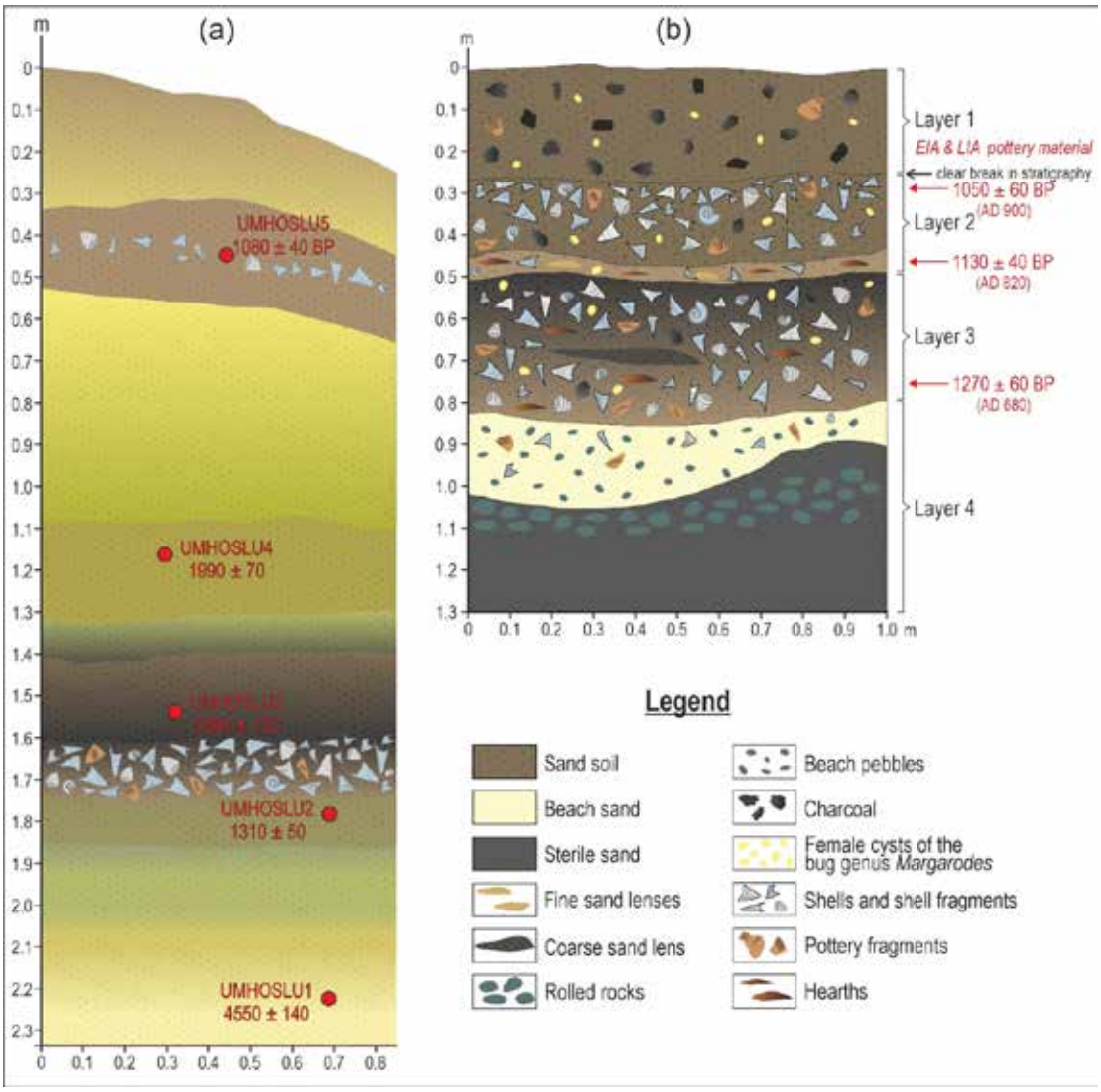

Figure 3. (a) Simplified stratigraphy exposed in the coastal natural outcrop located at Umhlanga Rocks, Natal north coast, South Africa. OSL sample points are shown and their corresponding OSL ages are provided. The stratigraphy revealed deposits up to 2.3 m deep, with six distinct layers identified and described. (b) Simplified stratigraphic log from a previous excavation at Emberton Way, Natal north coast (modified from Horwitz *et al*., 1991). The obtained radiocarbon ages are also provided. EIA: Early Iron Age, LIA: Late Iron Age.

The uppermost layer (Layer 1) is approximately 30 cm thick and consists of light brown, well-sorted sandy soil with root remnants. The sand appears to originate from the most recently active dune adjacent to the beach. Beneath it lies Layer 2, which is 18 cm thick and composed of brown sandy soil rich in humic material, with occasionally fragmented shell. The interface between Layers 1 and 2 is marked by a break in stratigraphy. A sample (UMHOSLU5) for OSL dating was collected from the middle of this layer. Layer 3, which underlies Layer 2, is 85 cm thick and incorporates three stratigraphic features. It consists of aeolian sands that range in color from olive green to dark green. A distinct stratigraphic break separates Layers 2 and 3. A sample (UMHOSLU4) for OSL dating was taken from the lower part of this layer. Layer 4, which is 20 cm thick, comprises dark brown, well-sorted sandy soil that becomes slightly lighter towards the upper contact. This layer is the upper part of the shell midden. A sample (UMHOSLU3) for OSL dating was collected near the contact between this sandy soil layer and the underlying shell midden. Layer 5 is the main shell midden, with a thickness of 12 cm. It is dark in color, likely due to a higher soil fraction, and contains a dense concentration of mollusk shells (including a variety of closely packed shells). Pottery sherds were also scattered throughout the layer. The lowermost layer, Layer 6, is 60 cm thick and composed of aeolian, well-sorted sandy sediments. The sediment color transitions from dark green at the top to light yellow at the base. Two samples (UMHOSLU2 and UMHOSLU1) for OSL dating were collected from the upper and the lower part of this layer, respectively (Figure 3).

The environmental dose rates calculated from radionuclide concentrations measured using high-resolution gamma spectrometry are presented in Table 1. A typical dose-response curve for sample UMHOSLU2, along with a natural OSL signal decay curve, is illustrated in Figure 4. The decay curve indicates that the signal is dominated by the fast component. The results of the preheat plateau test conducted at different preheat temperatures are displayed in Figure 5. Based on these results, a preheat temperature of 240 °C for 10s was selected for all subsequent measurements. Furthermore, a dose recovery test was performed on all samples. Statistical analysis of the doses recovered yielded a mean and standard deviation of 1.01 ± 0.06 relative to the given laboratory dose, confirming the suitability of the chosen SAR protocol for these samples. The De estimates and the corresponding ages are summarized in Table 1.

Table 1. Sample information and a summary of dosimetry and equivalent doses (De) measurements. Quartz OSL ages were calculated using the Central Age Model (CAM).

No	Sample ID	Water content (%)	Total dose rate (Gy/ka)	n	CAM De (Gy)	CAM age (ka)
1	UMHOSLU1	2.6	1.15±0.02	23	5.25±0.12	4.55±0.14
2	UMHOSLU2	3.4	4.58±0.06	23	6.01±0.2	1.31±0.05
3	UMHOSLU3	3.9	2.83±0.04	23	11.28±0.39	3.99±0.15
4	UMHOSLU4	4.1	3.56±0.05	23	7.08±0.23	1.99±0.07
5	UMHOSLU5	3.4	4.44±0.06	23	4.81±0.17	1.08±0.04

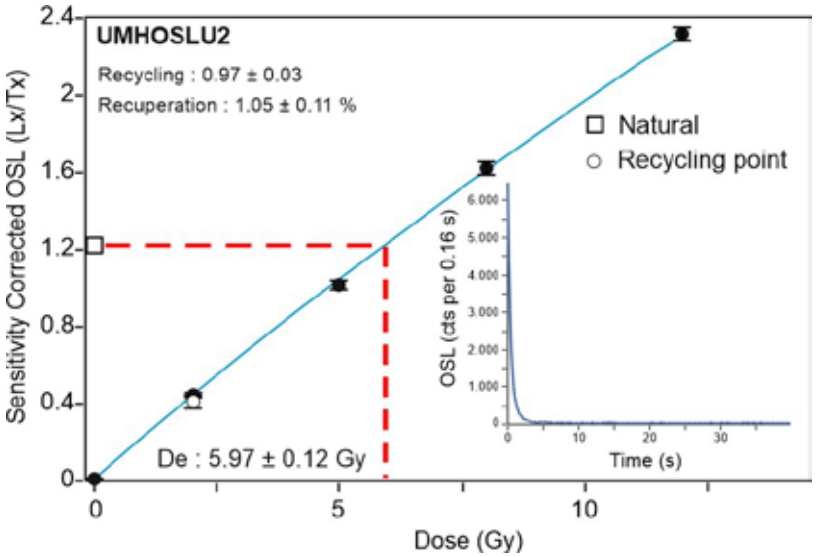

Figure 4. Typical dose-response curve with the natural OSL signal decay curve shown as an inset for sample UMHOSLU2.

The OSL age results for the collected samples, derived using the central age model, range from 4.55±0.14 ka to 1.08±0.04 ka, and are in stratigraphic order, with one exception. A comparison of the estimated OSL ages with radiocarbon dating results obtained from charcoal samples during a previous shell midden excavation at Emberton Way (Horwitz *et al*., 1991), approximately 20 km north-northeast of the stratigraphic section site studied here, reveals agreement between the OSL ages and the independent radiocarbon age controls. The archaeological findings from the excavation of the Emberton Way shell midden suggest a connection between large beachfront shell midden deposits and substantial inland village sites during the Msuluzi-Ntshekane period. Named after key archaeological sites, such as Msuluzi and Ntshekane, this period spans the 7th to 9th centuries AD and represents cultural phases within the Early Iron Age in South Africa (Whitelaw, 2019). This era is marked by the emergence of settled agricultural communities, the introduction of metallurgy, and significant cultural transformations.

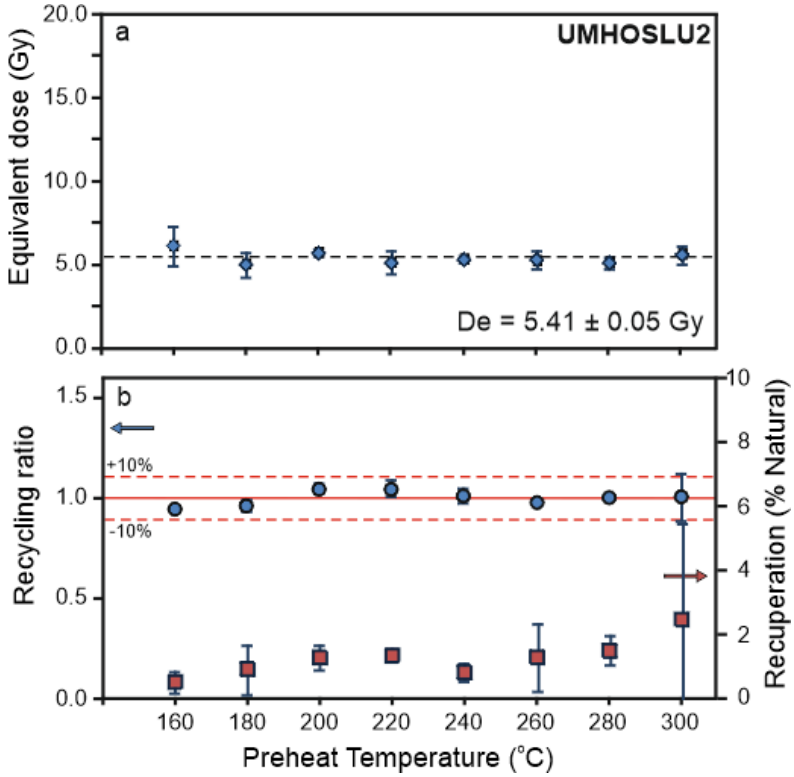

Figure 5. Preheat plateau test results show no dependence of the equivalent dose (a), recycling ratio and recuperation (b) on preheat temperature for sample UMHOSLU2. The cut heat temperature was 160°C, and the test dose was 2 Gy. Each point represents the average results from three aliquots.

Concluding Remarks

This study led to the following conclusions:

- The OSL dating of sedimentary layers within the stratigraphic section yielded ages ranging from 4.55±0.14 ka to 1.08±0.04 ka. With one notable exception, these results exhibit a coherent stratigraphic progression and demonstrate strong concordance with independent chronological benchmarks established through radiocarbon dating of Emberton Way site samples, as documented by Howitz *et al.* (1991).
- This study is the first to demonstrate that OSL dating using quartz has significant potential in this region. It proves to be a reliable method for establishing precise chronologies for coastal sediments along the Natal north coast.
- Findings from the archaeological excavation of the Emberton Way midden, located near the stratigraphic section studied here, suggest a connection between large beachfront shell midden deposits and substantial inland village sites during the Msuluzi-Ntshekane period.
- The limited range of resources exploited from the middens, as documented by previous researchers (Howitz *et al*., 1991), along with the distinctive Early Iron Age (dating from around AD 200 to AD 900) ceramics, strongly supports an agriculturist attribution for these sites. This evidence contradicts the earlier hypothesis of residual hunter-gatherer origin.

References

Álvarez, M., Godino, I.B., Balbo, A., Madella, M., 2011. Shell middens as archives of past environments, human dispersal, and specialized resource management. Quaternary International 239, 1–7.

Campbell, S.K., 2005. Shell Middens, in: Schwartz, M.L. (Ed.), Encyclopedia of Coastal Science, 870–873.

Cardoso, J.L., 2015. Carlos Ribeiro and Francisco António Pereira da Costa: Dawn of Mesolithic shell middens of Muge (Salvaterra de Magos), in: Bicho, N., Detry, C., Price, T. D., Cunha, E. (Eds.), Muge 150th: The 150th Anniversary of the Discovery of Mesolithic Shell middens, Vol. 1, 1–18.

Ceci, L., 1984. Shell midden deposits as coastal resources. World Archaeology 16, 62–74.

Davies., O., MacDonald, J., 1978. Excavation of a shell-midden at Umhlanga Rocks, Natal. Annals of the Natal Museum 23 (2), 461-464.

Duller, G.A.T., 2003. Distinguishing quartz and feldspar in single grain luminescence measurements. Radiation Measurements 37, 161–165.

Horwitz, L., Maggs, T., Ward, V., 1991. Two shell middens as indicators of shellfish exploitation patterns during the first millennium AD on the Natal north coast. Natal Museum Journal of Humanities 3, 1–28.

Jerardino, A., 2010. Large shell middens in Lamberts Bay, South Africa: a case of hunter-gatherer resource intensification. Journal of Archaeological Science 37, 2291–2302.

Liritzis, I., Stamoulis, K., Papachristodoulou, C., Ioannides, K., 2013. A re-evaluation of radiation dose-rate conversion factors. Mediterranean Archaeology and Archaeometry 13, 1–15.

Marean, C.W., 2014. The origins and significance of coastal resource use in Africa and western Eurasia. Journal of Human Evolution 77, 17–40.

Murray, A.S., Wintle, A.G., 2000. Luminescence dating of quartz using an improved single-aliquot regenerative-dose protocol. Radiation Measurements 32, 57–73.

Rabett, R., Appleby, J., Blyth, A., Farr, L., Gallou, A., Griffiths, T., Hawkes, J., Marcus, D., Marlow, L., Morley, M., Cao Tan, N., Van Son, N., Penkman, K., Reynolds, T., Stimpson, C., Szabo, K., 2011. Inland shell midden site-formation: Investigation into a late Pleistocene to early Holocene midden Tràng An, Northern Vietnam. Quaternary International 239, 153–169.

Rick, T., 2024. Shell midden archaeology: Current trends and future directions. Journal of Archaeological Research 32, 309–366.

Stratham, E.J., 1892. Observations on shell-heaps and shell-beds. Journal of the Royal Society of New South Wales 26, 304–314.

Whitelaw, G., 2019. Ntshekane and the end of the Early Iron Age in Kwazulu-Natal. The Digging Stick 37(2), 1–4.

Will, M., Bader, G., Sommer, C., Cooper, A., Green, A., 2022. Coastal adaptations on the eastern seaboard of South Africa during the Pleistocene and Holocene? Current evidence and future perspectives from archaeology and marine geology. Frontiers in Earth Science, 10:964423.

Wurz, S., Pickering, R., Mentzer, S., 2022. U-Th dating, taphonomy, and taxonomy of shell middens at Klasies River main site indicate stable and systematic coastal exploitation by MIS 5c-d. Frontiers in Earth Science, 10:1001370.

17th INTERNATIONAL CONGRESS of the Geological Society of Greece

BULLETIN OF THE GEOLOGICAL SOCIETY OF GREECE, SP. PUBL.

EXTENDED ABSTRACT 325

Chelmos- Vouraikos Unesco Global Geopark 2024: Advancing Conservation, Education, and Community Engagement

Tsoni M.[1], Koumoutsou E.[1], Iliopoulos G.[2]

(1) Management Unit of Chelmos - Vouraikos National Park and Protected Areas of Northern Peloponnese, Natural Environment and Climate Change Organization, Chelmos Vouraikos UNESCO Global Geopark, Kalavryta, Greece, m.tsoni@necca.gov.gr , (2) Laboratory of Palaeontology and Stratigraphy, Geology Department, University of Patras, Patras, Greece

Introduction

The Chelmos-Vouraikos UNESCO Global Geopark has continued to demonstrate its unwavering commitment to conservation, education, and community engagement through a series of impactful actions during 2024. These initiatives highlight the Geopark's dedication to preserving natural and cultural heritage, while fostering sustainable development in close collaboration with local communities, national organizations, and international stakeholders.

Engaging with Society

Throughout the year, the Geopark got actively engaged with society through various events and initiatives that bridged cultural, environmental, and recreational themes. The organization of the 5th UNESCO Global Geoparks Conference of Greece and Cyprus, in Kalavryta, by Chelmos-Vouraikos Geopark, provided an international platform to showcase the Geopark's efforts in conservation and sustainable tourism. Publications such as the new geodiversity and plant guides and leaflets about freshwater fish fauna and the endemic plants of the geopark have been produced and distributed to educate visitors about the region's unique biodiversity (fig.1). Additionally, the new Geopark's Information Center (fig.2), which serves as a hub for visitor orientation and education, commenced its operation last year, offering an enhanced experience for visitors to learn about the area's natural and cultural heritage.

Promoting Sustainable Tourism and Regional Identity

Events like Oinoxeneia highlighted local gastronomy and traditions, fostering a deeper connection between the Geopark and its communities. Digital and physical tools, including info kiosks and a dedicated Geopark mobile application, enhanced visitor experiences and accessibility. Recreational activities such as the 44th Annual Vouraikos Gorge Crossing, the 1st Helmos Enduro 2024, and the 2nd Helmos Mountain Festival (fig.3), which took place in the past year, were organized by local entities within the Geopark, such as the Kalavryta Mountaineering Club and the Kalavryta Ski Center. These events were always accompanied by collaboration and parallel actions from the Chelmos-Vouraikos Geopark, emphasizing the strong partnership in promoting sustainable tourism and outdoor recreation within the region. Cultural collaborations, including the Ziria Festival and TEDx Patras, which were organized outside the Geopark, further underscored the Geopark's role in promoting regional identity. Despite being external events, these initiatives involved collaboration with the Chelmos-Vouraikos Geopark, highlighting its active role in supporting and enhancing regional cultural efforts. Additionally, the annual meeting of Trekking Hellas Achaia emphasized sustainable trekking practices and eco-tourism, while the participation of handball federation athletes in the Vouraikos Gorge connected sports with natural heritage under the organization of Chelmos- Vouraikos Geopark. The Aigio Mountaineering Club hosted a symposium entitled "On the Mountain's Paths," featuring a presentation on "Biodiversity Conservation: Linking with Mountaineering," which was delivered by staff members of the Chelmos-Vouraikos Geopark. This presentation highlighted the Geopark's efforts in promoting the connection between mountaineering and biodiversity conservation. Historical significance was also honored through the event commemorating the 20-year anniversary of the Holocaust Museum. This two-day event, organized by the Kalavryta Holocaust Museum, featured a presentation on the protected area, and participants of the seminar were given a guided tour of the Geopark's Information Center. These activities further highlighted the importance of conservation and the Geopark's role in preserving the region's natural and cultural heritage, reinforcing the ongoing collaboration between the Geopark and the Museum. This partnership has been strengthened through joint initiatives, such as the seminar on climate change co-organized the previous year as part of the International Museum Day celebrations. Environment Day this year was celebrated in three distinct ways: with a hike on Mount Panachaiko, a volunteer cleanup of Kastria stream, and a planting initiative with students from the Special School of Kalavryta. These activities highlighted the community's commitment to environmental stewardship and provided an opportunity for collaboration

with local schools and organizations.

Inspiring Education and Academic Research

Educational activities with schools and universities played a pivotal role in inspiring the next generation and supporting academic research. Collaborative efforts with the Special School of Kalavryta under the GRECABAT program integrated hands-on activities that connected biodiversity with education. On International Mountain Day, a presentation and interactive games at Diakopto Primary School raised awareness about mountain ecosystems. At Arsakeio School of Patras, a presentation titled “Natural Disasters and UNESCO Global Geoparks” emphasized the role of Geoparks in disaster risk reduction. Activities at Rodea Camp included an informational session and guided hike, fostering environmental awareness among participants. The European Bird Day celebration at Lake Doxa highlighted the importance of avian biodiversity and was celebrated in collaboration with the Primary, Secondary, and High School of Kleitoria. The event featured birdwatching activities and games, providing students with a hands-on learning experience about local wildlife and the significance of bird conservation. Field trips with Harokopio University provided students with the opportunity to conduct research in Vouraikos Gorge, focusing on topics such as fluvial geomorphology, ecosystem services and environmental cartography. The Geopark also welcomed annual visits from international researchers studying glacial formations, showcasing its global scientific relevance.

Advancing Research and Conservation Management

Research and management activities within the Geopark have been equally robust, aiming to enhance conservation and sustainable development. Efforts to protect rare and endemic species were supported through the establishment of micro-reserves. Biodiversity studies focusing on otters, dormice, and ichthyofauna enriched the understanding of local ecosystems. A monitoring station in Vouraikos River provides essential data for conservation strategies by measuring parameters such as water temperature, water level, conductivity, pH, dissolved oxygen, and turbidity. This data plays a crucial role in the proper management of the Vouraikos River, ensuring the health of the ecosystem and supporting sustainable tourism development through informed decision-making. The renowned Cave of the Lakes was the subject of a comprehensive management study to protect its geological and ecological features. Additionally, the development of a quality label study aligned local products and services with sustainable practices. The conservation program for *Silene conglomeratica*, a critically endangered endemic species within the Chelmos-Vouraikos UNESCO Global Geopark, highlights the essential link between geodiversity and biodiversity. Moreover, a carrying capacity study for Mount Helmos is currently underway, emphasizing the importance of regulating visitor numbers to balance tourism promotion with the preservation of the area’s natural environment.

Conclusions

Through these comprehensive actions, the Chelmos-Vouraikos UNESCO Global Geopark continues to exemplify its role as a leading stakeholder in conservation, education, and community collaboration. These efforts contribute significantly to the global mission of UNESCO Global Geoparks, ensuring a sustainable future for the region’s natural and cultural heritage.

Figure 1. The new Geodiversity and Plant Guidebooks of Chelmos- Vouraikos UNESCO Global Geopark

Figure 2. Photo from the interior of the new Geopark's Information Center

Figure 3. A sketch of the view from Chelmos mountain, created by a visitor during the 2nd Chelmos Mountain Festival, as part of the Geopark's educational activities.

17th INTERNATIONAL CONGRESS of the Geological Society of Greece

BULLETIN OF THE GEOLOGICAL SOCIETY OF GREECE, SP. PUBL.

EXTENDED ABSTRACT 326

Deep sea agglutinated foraminifera from the surface sediments of NE Mediterranean Sea

Tsourou Th.[1], Markoglou E.A. [1,2], Danelian T. [3], Parinos C [4], Gogou A.[4], Triantaphyllou M.V.[1]
(1) National and Kapodistrian University of Athens, Department of Geology and Geoenvironment, Athens, Greece, ttsourou@geol.uoa.gr, (2) University of Thessaloniki, Department of Geology and Palaeontology, Faculty of Geology, Thessaloniki Greece, (3) Universite de Lille, CNRS, UMR 8198- Unite Evo-Eco-Paleo, Lille, France, (4) Hellenic Centre for Marine Research, Institute of Oceanography, Attiki, Greece

The purpose of this study is to record and present the deep sea benthic foraminiferal assemblages, focusing on the agglutinated forms, retrieved from the surface sediments of the central and southern Aegean Sea and the NW Levantine Basin (Figure 1a). There are several previous studies about agglutinated foraminifera from the broader area mainly from Marmara Sea (e.g., Frontalini et al., 2011; Chatelet et al., 2013) and Saros Bay (NE Aegean; e.g., Frontalini et al., 2014; 2018), referring mostly to shallower regimes.
The southern Aegean is connected to the Levantine Basin and the Ionian Sea through the eastern (Kassos) and western (Antikithira-Kithira) Cretan Straits, respectively. The various subbasin gyre patterns namely the Cretan Cyclonic Gyre, the West Cretan Anticyclone, the Myrtoan West Cretan Cyclone, and the Pelops Gyre affect the circulation of the area (Theocharis et al., 1999). Additionally, the surface water circulation is influenced by the presence of low-salinity Modified Atlantic Waters (MAW), which primarily enter the Cretan Sea through the Antikithira Strait and occasionally through the Kassos Strait. Warm and saline Levantine Waters (LW) enter the Aegean through the eastern Cretan Straits and travel north along the eastern Aegean Sea (Zervakis et al., 2005).
Micropaleontological analysis was performed in eight surface sediments samples. The samples were recovered with a box corer during R/V Aegaeo MSFD cruise in March 2019, from relatively shallow to bathyal environments from 8 sampling stations (Figure 1b). In particular, the three shallower stations are located in the Cyclades plateau (2MSFD11), the broader area of Myrtoan Basin (2MSFD8) and the central-eastern Aegean (2MSFD12), while the deeper stations are located in the Cretan Sea (2MSFD9 and 2MSFD10) and off Crete and Rhodes islands towards the Levantine (2MSFD5, 2MSFD6 and 2MSFD7). The position and depth distribution of the sampling stations is presented in Figure 1b. The collected sediment was stored in an ethanol-Rose Benghal mixture. In the laboratory the samples were carefully wet sieved through 63 μm and 125 μm sieves, oven dried at 50°C, and the sediment fraction >125 μm was examined for the micropaleontological content.

Figure 1. a. Location map of the study area. b. The study area and the sampling stations during R/V Aegaeo MSFD cruise in March 2019.

The biogenic content of the analyzed samples consisted mainly of pteropods planktonic and benthic foraminifera, as well as rare ostracods and otoliths. Benthic foraminiferal assemblages presented the higher diversity and abundance among all the other groups of benthic organisms and their assemblages were composed of calcareous (hyaline) and agglutinated taxa. Calcareous foraminifera and agglutinated foraminifera present an inversely proportional relation with agglutinated foraminifera being more abundant in the samples from the lower bathyal stations.

The agglutinated foraminiferal assemblages demonstrate higher diversity in the samples from the shallower basins (e.g., stations 8, 11, 12), which decreases towards the deep lower bathyal environments (e.g., stations 9, 10). This pattern is in accordance with other studies such as the one of Hyams-Kaphzan et al. (2018) from the Levantine basin. A total of 13 genera and 15 species of agglutinated foraminifera have been so far identified. Their assemblages were composed mainly of arborescent/tubular taxa and globular forms. The most common taxon is the arborescent/tubular species *Saccorhiza ramosa* (Brady, 1879) which is the present in all the samples and displays the higher participation rates (11-84% of the agglutinated fauna). Its wall is made of mineral grains, coccoliths and sponge spicules, while in certain samples spumellarian radiolaria and pteropods are also incorporated in the test structure (Figure 2). Other common arborescent/tubular species are *Rhabdamminella cylindrica* (Brady, 1882) (present in stations 5, 8, 9, 10, 11; 0.2-12.5%); *Rhizammina algaeformis*, Brady, 1879 (present in stations 5, 6, 9, 10, 11; 1-26%), being coarsely agglutinated, beside inorganic grains, with planktonic foraminifera, radiolaria and pteropods and *Psammosiphonella* spp. (present in stations 5, 6, 8, 9, 10 11, 12; 0.44-63%). The most abundant globular taxon is *Glomospira* spp. (present in stations 5, 6, 7, 9, 10; 1-57%). Other taxa with scarce presence in the studied samples are *Psammosphaera fusca* Schulze, 1875 and species of *Bathysiphon*, *Marsipella*, *Hyperammina*, *Reophax*, *Cribrostomoides*, *Ammoscalaria* and *Ammodiscus*.

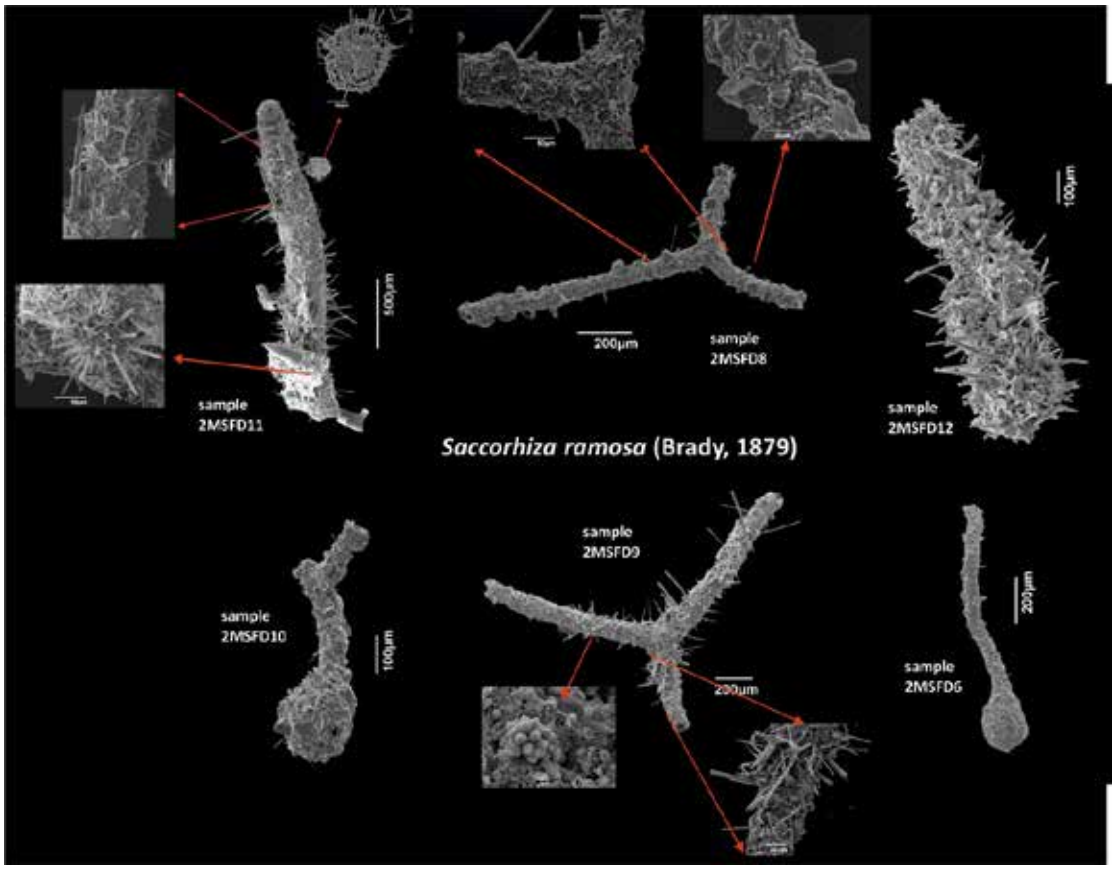

Figure 2. a. The most abundant species of agglutinated foraminifera in the studied samples and details of the test with several different biogenic particles.

The arborescent/tubular taxa *S. ramosa, R. cylindrica, R. algaeformis, Bathysiphon*, *Hyperammina, Psammosiphonella, Marsipella* belong to Morphogroup 1 (M1) of Kaminski and Gradstein (2005) and they are epifaunal forms, suspension feeders, preferring quite, bathyal-abyssal, oligotrophic environments. Generally, all the identified taxa, besides *Reophax* (infaunal, deposit feeders, preferring increased organic matter flux), are considered epifaunal forms indicating oligotrophic conditions (Kaminski and Gradstein, 2005). Especially *S. ramosa* seems to have developed the skill to survive for long time without food, benefiting from episodic sedimentation events e.g. in canyon environments (Koho et al., 2007). *Reophax* is present in all the samples from the shallower stations (8, 11, 12), demonstrating its higher participation rates (4-9.2%). Overall, the composition of the assemblages in the study area is in accordance with the oligotrophic character of the South Aegean Sea and eastern Mediterranean.

References

Chatelet E.A., Armynot R., Roumazeilles V., Coccioni R., Frontalini F., Guillot F., Kaminski M. A., Recourt P., Riboulleau A., Trentesaux A., Tribovillard N., Ventalon S., 2013. Environmental control on shell structure and composition of agglutinated foraminifera along a proximal–distal transect in the Marmara Sea. Marine Geology 335, 114-128.

Frontalini F., Kaminski M.A., Coccioni R., Bucci C., Asku A., 2011. 1. Bathymetry distribution and ecological characterization of agglutinated foraminifera along an inner neritic to upper bathyal transect in the Marmara Sea. In: Kaminski, M. A. and Filipescu, S., Eds., Proceedings of the Eighth International Workshop on Agglutinated Foraminifera, 37-52. Krakow: Grzybowski Foundation. Special Publication 16.

Frontalini F., Chatelet E. A., Kaminski M.A., Coccioni R., Mikellidou I., Yasar D., Asku A.E., 2014. Distribution of modern agglutinated foraminifera along an inner neritic- to mid-bathyal transect in Saros Bay (northern Aegean Sea). Micropaleontology 60, 1, in, Advances in agglutinated foraminiferal research: The Ninth International Workshop on Agglutinated Foraminifera, IWAF-9 (2014), pp. 27-42 Published by: The Micropaleontology Project., Inc.

Frontalini F., Kaminski M.A., Coccioni R., Kowalewwsk M., 2018. Agglutinated vs. calcareous foraminiferal assemblages as bathymetric proxies. Source: Micropaleontology 64, 5/6, 403-415.

Hyams-Kaphzan, O., Lubinevsky, H., Crouvi, O., Harlavan, Y., Herut, B., Kanari, M., Tom, M., Almogi-Labin, A., 2018. Live and dead deep-sea benthic foraminiferal macrofauna of the Levantine basin (SE Mediterranean) and their ecological characteristics. Deep-Sea Res. Part I Oceanogr. Res. Pap. 136, 72–83. doi.org/10.1016/j.dsr.2018.04.004.

Kaminski, M. A., Gradstein, F. M., 2005. Atlas of Paleogene cosmopolitan deep-water agglutinated foraminifera. Krakow: Grzbowski Foundation. Special Publication 10, 547 pp.

Koho, K. A., Kouwenhoven, T. J., De Stigter, H. C., van der Zwaan, G. J., 2007. Benthic foraminifera in the Nazaré Canyon, Portuguese continental margin: sedimentary environments and disturbance. Marine Micropaleontology, 66, 27.

Theocharis, A., Balopoulos, E., Kioroglou, S., Kontoyiannis, H., Iona, A., 1999. A synthesis of the circulation and hydrography of the South Aegean Sea and the Straits of the Cretan Arc (March 1994–January 1995). Progress in Oceanography, 44(4), 469–509. https://doi.org/10.1016/S0079-6611(99)00041-5

Zervakis, V., Theocharis, A., Georgopoulos, D., 2005. Circulation and hydrography of the open seas (pp. 104–110).

17th INTERNATIONAL CONGRESS of the Geological Society of Greece

BULLETIN OF THE GEOLOGICAL SOCIETY OF GREECE, SP. PUBL.

EXTENDED ABSTRACT 327

Stratigraphic assignment of the Mesozoic shallow carbonate succession of Epos Mountain, Chios Island, Greece

Tsourou Th.[1], Sakoulas N.[1], Paraskevopoulou A. [1], Perraki I.[1], Triantaphyllou M.V.[1]
(1) National and Kapodistrian University of Athens, Department of Geology and Geoenvironment, Athens, Greece, ttsourou@geol.uoa.gr

According to Besenecker *et al.* (1968;1971) the geology of Chios comprises, in general, two tectonostratigraphic units: the lower, Autochthonous Unit overthrusted by the upper, Allochthonous Unit. The Autochthonous Unit consists of a Paleozoic chaotic flysch type complex, including four olisthostromes of Permian age (Papanikolaou and Sideris 1983), which is transgressed by a Triassic basal conglomerate and an overlying carbonate succession of Triassic to Early Jurassic age (Figure 1b). This carbonate sequence corresponds to the internal platform of the "Sub-Pelagonian" Unit (Papanikolaou, 2021), in other words the easternmost part of the Pelagonian domain (e.g., Jacobshagen, 1986; Meinhold et al., 2007).
The study area includes Epos Mountain, in the central-eastern part of Chios Island (Figure 1a). Epos Mt is built up of thick carbonates, related to the upper part of the Mesozoic carbonate sequence of the Autochthonous Unit. The aim of this study is the micropaleontological analysis and paleoenvironmental interpretation of the shallow water carbonates of Epos Mountain. Furthermore, the results are compared to those from previous studies for the same stratigraphic interval in other regions of Greece.

Figure 1. a. Location of the study area. b. Chios autochthonous unit: general view of the internal carbonate platform (Triassic-Lower Jurassic) overlying the volcano-sedimentary complex (Upper Paleozoic–Lower Triassic).

Several samples of limestones and dolomitic limestones were collected following the road from the base of the mountain towards the top and along the Epos plateau. More than 50 samples have been collected from the stratigraphic sequence; twenty-four of them have been selected and prepared at the Laboratory of Historical Geology and BioGeosciences (National and Kapodistrian University of Athens) for the purposes of the current study.
At the lower part of the sequence, the microfacies consist mainly of grainstones/packstones with peloids, ooids, benthic foraminifera, bivalves, gastropods and ostracods representing an internal platform (FZ8; Flügel, 2004), subtidal environment,. These microfacies alternate with facies with fenestral voids pointing to supratidal environments (FZ9; Flügel, 2004). The micropalaeontological content of the samples is characterized by the presence of benthic foraminifera with Duostominidae and Involutinidae (mainly of the genus *Aulotortus*) being the most abundant specimens, pointing to a Late Triassic age, in particular, Norian-Rhaetian.
Upwards, the succession becomes shallower presenting distinct lofer cycles (Figure 2a). Open space structures such as fenestral pores, birdseyes and karst dissolution cavities indicate a supratidal environment and subaerial exposure. The micropaleontological content is poor, with the subtidal layers of the loferitic facies bearing few ostracods, bivalves and gastropods. In some cases, these layers present rare benthic foraminifera and algae.

Figure 2. a. Loferitic horizons. b-c. Subtidal beds with gastropods (b) and bivalves (c).

The micropaleontological and microfacies analysis of the studied material reveals clear similarities of the Late Triassic Epos succession to the sequences described from the Pelagonian domain in mainland Greece; e.g., Argolis peninsula, Corinthia, central Greece, as well as Euboea Island (Varti-Mataranga and Matarangas, 1991; Pomoni-Papaioannou, 2008; Scherreiks *et al.*, 2010; Kostopoulou, 2018).

References

Besenecker, H., Durr, S., Herget, G., Jacobshagen, V., Kauffman, G., Ludtke, G., Roth, W, Tietze, K.V., 1968. Geologie von Chios (Agais). Geologica et Palaeontologica 2, 121-150.

Besenecker, H., Durr, S., Herget, G., Kauffman, G., Ludtke, G., Roth, W, Tietze, K.V., 1971. Chios (2 sheets: Northern and Southern). Geological map of Greece , Chios, 1:50,000, I.G.S.R., Athens.

Flügel, E. 2004. Microfacies of carbonate rocks: Analysis, interpretation and application. Springer.

Papanikolaou, D. I., 2021. Regional Geology Reviews The Geology of Greece. http://www.springer.com/series/8643.

Papanikolaou, D., Sideris, Ch. 1983. Le Paléozoique de l' autochtone de Chios: Une formation à blocs de type wildflysch d' âge Permien (pro parte). C. R. Acad. Sc.Paris, 297, 603–606.

Kostopoulou, V. 2018. Lofer cycles in the Upper Triassic-Lower Jurassic carbonate platform of the Eastern Greece zone. Ph.D. Thesis, National & Kapodistrian University of Athens, Athens, 362 p.

Pomoni-Papaioannou, F. 2008. Facies analysis of Lofer cycles (Upper Triassic), in the Argolis Peninsula (Greece). Sedimentary Geology, 208, 79-87. https://doi.org/10.1016/j.sedgeo.2008.04.005

Scherreiks, R., Bosence, D., BouDagher-Fadel, M. *et al.*, 2010. Evolution of the Pelagonian carbonate platform complex and the adjacent oceanic realm in response to plate tectonic forcing (Late Triassic and Jurassic), Evvoia, Greece. Int J Earth Sci (Geol Rundsch) 99, 1317–1334. https://doi.org/10.1007/s00531-009-0461-1

Varti-Mataranga, M., Matarangas, D. 1991. Depositional facies and diagenetic phenomena in "Pantokrator Limestones" of Argolis Peninsula (Tasoulaika-Karnazaiika area). Bulletin Geological Society Greece, XXXV/I, 339–354.

17th INTERNATIONAL CONGRESS of the Geological Society of Greece

BULLETIN OF THE GEOLOGICAL SOCIETY OF GREECE, SP. PUBL.

EXTENDED ABSTRACT 328

The geothermal prospect of the NW Lesvos Island, Greece: Three-dimensional magnetotelluric and gravity exploration

Tzanis A.[1], Chailas S.[1], Spyridonos E.[2]

(1) Section of Geophysics and Geothermy, Department of Geology and the Geo-environment, National and Kapodistrian University of Athens; atzanis@geol.uoa.gr. , (2) PPC Renewables S.M.S.A, 3 Kapodistriou st., Agia Paraskevi, GR-153 43.

Introduction

Lesvos has been part of a broader area of volcanic activity in the Miocene. This has bequeathed the NW sector of the modern island with an intermediate to high-temperature hydrothermal system and field, which has been the target of significant geothermal exploration efforts during the past few decades. Herein, we attempt to re-interpret with modern 3-D inversion tools, legacy magnetotelluric data acquired in the year 2000 by the private sector company Geosystem Srl. on behalf of PPC Renewables S.M.S.A., and to jointly appraise the resulting geoelectric model with Bouguer gravity anomaly data extracted from the databank of the Department of Geophysics and Geothermy of the National and Kapodistrian University of Athens (Lagios *et al.*, 1996). As will be seen below, the results point toward a complex and potentially productive hydrothermal system with several distributed shallow reservoirs, set up by past (Miocene) tectonic activity and still controlled by its legacy to the present.

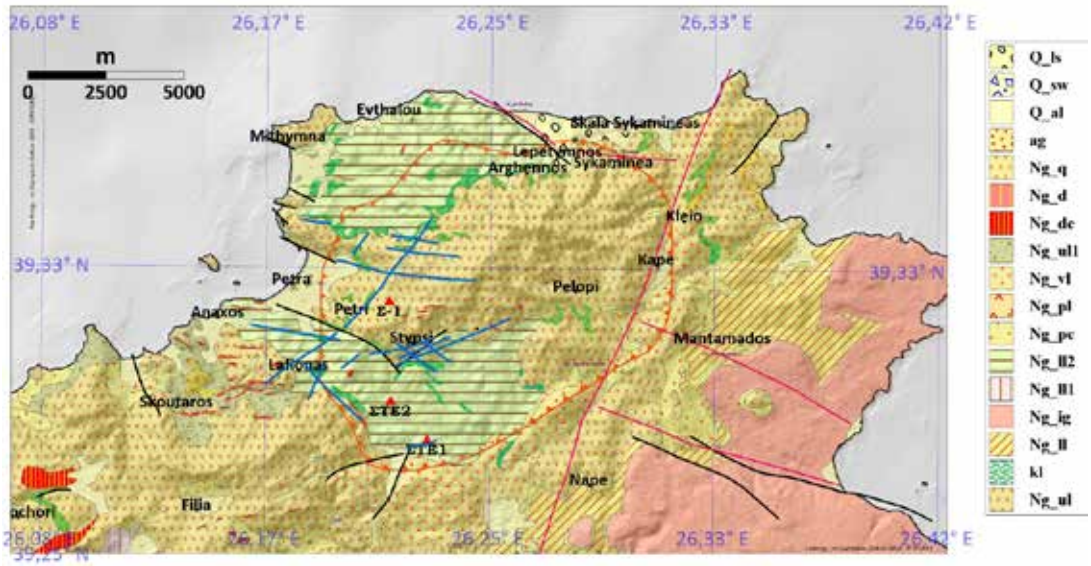

Figure 1. Geological Map of NW Lesvos. Q-ls: Sliding Scree; Q-sw: Slope wash; Q-al: Alluvial Plains; ag: Magmatic conglomerates and breccia; Ng_q: Silicified lava; Ng-d: dykes; Ng-dc: Coarse-grain phanero-dacite; Ng_ul1: Lowermost parts of Upper Lava; Ng_pl: Perlite; NG-pc: Pyroclastic layer; Ng_ll2: Lower lava unit of the Stypsi and Vatoussa areas; Ng_ll1: Uppermost layer of the lower lava unit; Ng_ig: Ignimbrite layer; Ng_ll: Lower lava unit of the Agia Paraskevi area; kl: Kaolinized dyke; Ng_ul: Upper lava unit. The toothed red line outlines the Lepetymnos Caldera. Coloured lines are faults (various sources).

Volcanic Background

Lesvos, along with the region of the north-central Aegean, belongs to a wider field of past volcanism that extends to northwestern Turkey and was part of the volcanic arc that operated since the Upper Oligocene-Middle Miocene period. The volcanic rocks occupy the entire central and western parts of Lesvos. The pre-alpine and alpine (Carboniferous to Triassic) basement outcrops mainly in southeastern Lesvos, with only minor occurrences in its western extremities. Volcanic activity lasted for almost 6.0 Ma with rocks of mainly shoshonitic composition, while a few calcareous andesites were emplaced at the beginning (Eressos area, 21.5Ma) and the end (Mytilene area, 16.5Ma) of the volcanism. The ensuing history of volcanic activity is based on Pe-Piper *et al.* (2019). At 21.6 ± 0.5 Ma, with new radiometric dating suggesting 23.3 ± 0.5 Ma, andesite□dacite domes intruded through and covered the metamorphic basement, spreading the area of Eressos, western Lesbos (Eressos Formation). This, together with the Gavathas formation, was overlaid

by the Sigri Pyroclastics of several hundred metres in thickness, which mainly consists of tuffs. A prominent welded ignimbrite approximately 25 m thick is interbedded with the upper stratum of the Sigri Pyroclastics west of Antissa. In turn, the Sigri Pyroclastics are covered by the Skoutaros Formation comprising basaltic and andesitic flows palaeomagnetically dated to 17.6–17.9 Ma. Some younger andesites and dacites are also included in the formation. The Polychnitos Ignimbrite Formation consists of seven widespread welded ignimbrite units in eastern Lesbos, each of 30–50 m thickness. It appears to be contemporary with the upper part of the Skoutaros Formation and may have originated in a caldera near Lepetymnos (older units), or in the caldera of Vatoussa (youngest units deposited in the southeast of the Gulf of Kalloni). The Skalohorion (eastern Lesvos) and Sykaminea (northern Lesvos) formations consist of younger andesitic and dacitic lavas palaeomagnetically dated to 17.0 – 17.6 Ma. These were followed by the younger (16.8Ma) basalts and andesites of the Mytilene Formation. Several ensembles of dykes of different ages run in different directions through the above formations. A significant stage in the geological evolution of western Lesvos is the main volcanic phase dated to about 17 Ma, during which the intensity of volcanism increases and culminates with the eruption of the Polychnitos ignimbrites and the formation of the Lepetymnos and Vatoussa calderas.
Our investigation essentially focuses on the area of the Lepetymnos caldera (according to Pe-Piper *et al.*, 2019, see Fig. 1), which has been subject to intense hydrothermal activity during and after its formation. As will be seen in the following, this has resulted in intense alteration along fault zones (which comprise significant fluid transportation and circulation conduits) and has begotten a hydrothermal geothermal system that is still active today.

Data and Methods

The magnetotelluric data used herein was produced by the private sector company Geosystem Srl. in the year 2000 (Geosystem, 2000), on behalf of PPC Renewables S.M.S.A. A total of 52 measurements (stations) were conducted, distributed as in Fig. 2. The original (time series) data were acquired with the Metronix ADU-06 system with GPS synchronization, EMI induction coils and $Pb/PbCl_2$ electrodes. Impedance tensors were then computed with the robust processing method of Larsen *et al.* (1996). For reasons unspecified, the observed (measured) impedance tensors were made available to PPC Renewables only in hardcopy and in the form of physical diagrams. The tensors were rotated (anti-diagonalized) to their intrinsic coordinate frames, and the diagrams displayed the principal apparent resistivities and phases together with their associated rotation angles. The physical diagrams were converted (scanned) to high-resolution digital images, which were rectified to correct distortions and subsequently digitized with custom-built software. In a final step, the principal apparent resistivities and phases were converted to principal impedances, which were subsequently rewound (inverse rotated) to recover as faithful as possible models of the observed impedance tensors.

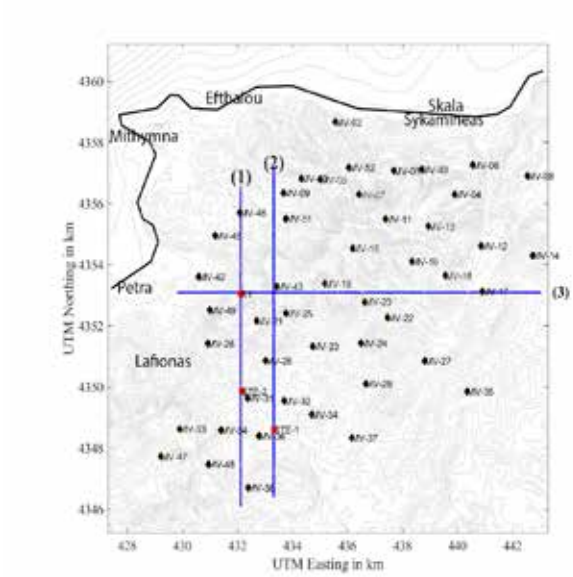

Figure 2. The distribution of the magnetotelluric measurements. The numbered blue lines indicate the locations of the three vertical resistivity cross-sections displayed in Fig. 5, 6 and 7.

The recovered impedance tensors were inverted to resistivity using the three-dimensional **Mod**ular system for **E**lectro-**M**agnetics (ModEM) software of Egbert and Kelbert (2012) and Kelbert *et al.* (2014). The resistivity (geoelectric) struc-

ture of the study area is approximated by a cuboid discretized into a grid of rectangular cells with dimensions 54 (N-S) × 54 (E-W) × 50 (vertically) and *includes* the topography and bathymetry of the study area (initial model). The coordinate system used in the inversion is the Universal Transverse Mercator (UTM) projection, zone 35S The physical dimensions of each cell in the horizontal plane are fixed to 300 m × 300 m; in the vertical direction, cell dimensions are variable with discretization being finer toward the surface of the earth and progressively becoming coarser with increasing depth. The initial resistivity values of cells representing 'the solid Earth' were set to 100 Ωm and were allowed to vary during the inversion. The resistivity values of cells representing 'air' and 'sea water' were respectively fixed to 10^6 Ωm and 0.3 Ωm and were *not* allowed to vary during the inversion. The *final* geoelectric model presented herein is based on the inversion of the *off-diagonal* elements (Z_{xy}, Z_{yx}) of the impedance tensor; it is the *best* of a set of alternative models and was obtained after a long series of trials (conducted by tuning the parameters controlling the inversion). The final RMS error was 1,65 and the final χ^2 metric was 349 with an expected value of 1824. Technically, this is a *very satisfactory* result.
The Bouguer gravity anomaly map of Lesvos was compiled on the basis of the Gravity Data Bank of the Department of Geophysics and Geothermy, National and Kapodistrian University of Athens (Lagios *et al.*, 1996). In the area of Lesvos, gravity stations are distributed evenly, with a spatial density of approx. 2 per 5 square kilometres; this allows for the generation of gravity anomaly grids with 1km spacing and enables the study of geological structures with scales comparable to the distances between stations (a handful of kilometres), including the major fault zones.

Results and Conclusions

Figures 3 and 4 display two horizontal resistivity sections at depths of 0.5 and 1.0 km below mean sea level. Fig. 2 shows the locations of two N-S oriented vertical resistivity cross-sections, of which the western (No. 1) passes through the locations of wells ΣΤΕ-2 and Σ-1 and the eastern (No. 2) through well ΣΤΕ-1. It also shows the location of an E-W cross-section through well Σ-1 (No. 3); finally, Figs 5, 6 and 7 display the resistivity cross-sections 1, 2 and 3, respectively.

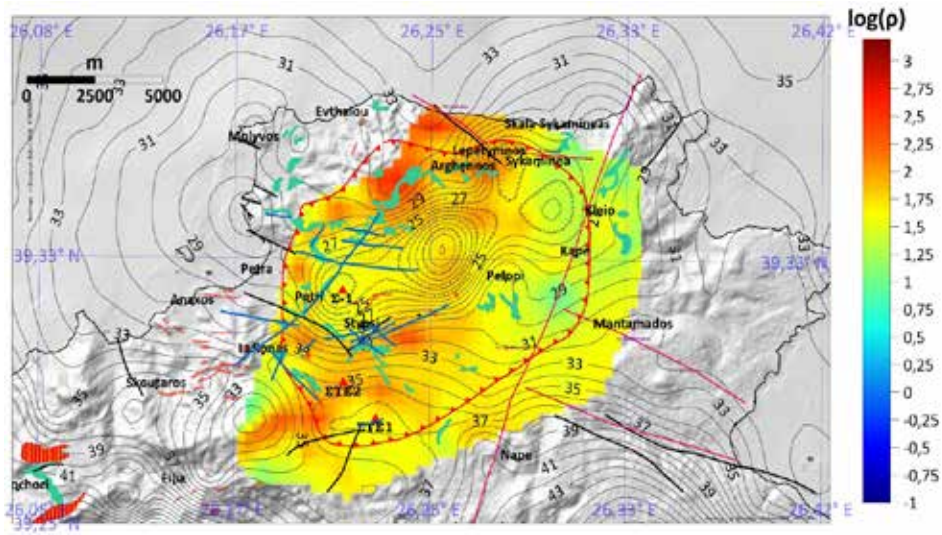

Figure 3. Horizontal resistivity section at the depth of 0.5 km bmsl, including known (mapped) faults and other geological features – see text for details.

In Figs 3 and 4, the general outlook of the geoelectric structure is that of a "mosaic" in which intersecting NE-SW and NW-SE bands of relatively high resistivity (ρ > 200 Ωm) engulf zones of relative conductors (100 Ωm < ρ < 5 Ωm). Resistivity is *noticeably* lower at 500m bmsl, where the relative conductors appear to diffuse laterally to all directions; it increases with depth so that the relative conductors progressively wedge into the resistive basement and vanish at depths greater than 2 km bmsl.
Such a configuration of the geoelectric structure is remarkably consistent with that of known (mapped) faulting features of the area. Therefore, it is consistent with the hypothesis that the relative conductors are collocated with intersecting faulting zones of NE-SW and NW-SE orientation, which generate a system of permeable structures capable of storing thermal fluids that ascend and laterally diffuse through the same faulting zones. Although not shown here, it was observed that at sea level the thermal fluid mixes with sea water intruding through the same fault zones and diffusing through the altered/porous near-surface lithological formations.
This interpretation is consistent with the configuration of the faulting zones relative to the geoelectric conductors mapped in the Petra – Stypsi zone of the study area and the findings of well Σ-1 in particular (Fig. 5 and 7). The geoelectric

model is apparently paradoxical in the vicinity of well ΣTE-2, where a column of resistive material is featured below the surface of the Earth although abundant thermal fluids were found there (Fig. 5). However, ΣTE-2 is located at the boundaries of significant conductors and possibly in the neighbourhood of intersecting faults (see below). Both of these features may explain the presence of fluids as a result of circulation/lateral diffusion from nearby sources.

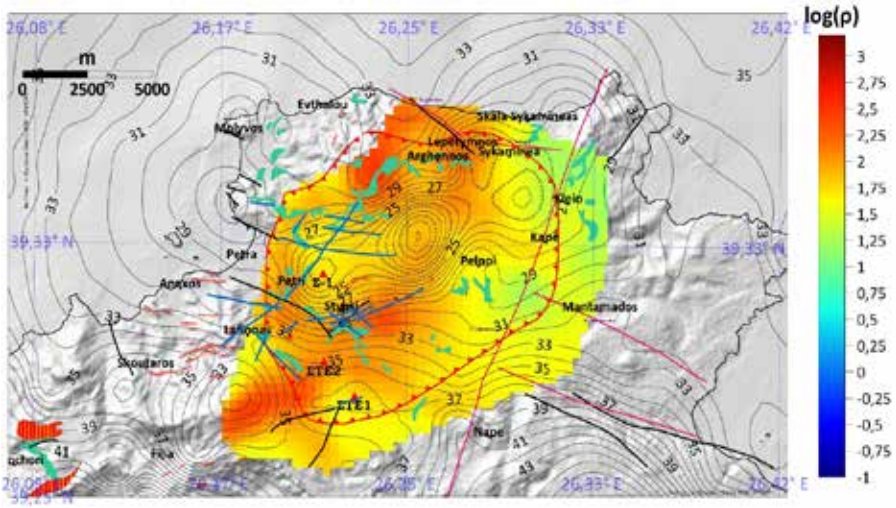

Figure 4. Horizontal resistivity section at the depth of 1 km bmsl, including known (mapped) faults and other geological features – see text for details.

At the southern boundary of the study area, in the neighbourhood of well STE-1, the model is consistent with the findings at the well ΣTE-1, where abundant thermal fluids were observed through and through (Fig. 6). However, the geoelectric structure cannot be adequately constrained in the N-S direction due to one-sided coverage with magnetotelluric measurements. Nevertheless, because the model is consistent with the findings of the drilling exercise, the same conclusions as above can be (tentatively) drawn.

Comparative analysis of resistivity and Bouguer anomaly data

Figures 3 and 4 also display the Bouguer anomaly map of the broader study area and enable its joint evaluation with the 3-D electrical resistivity model. In addition to the gravity and electrical resistivity information, they include: **a)** traces of known faults (mapped by Hecht, 1972-1976) illustrated with black and broken red lines; **b)** traces of known faults mapped by researchers of the Department of Geography of the University of the Aegean (2022) illustrated with blue lines; **c)** the perimeter of the Lepetymnos caldera as per Pe-Piper *et al.*, (2019); **d)** the kaolinization zones mapped by Pe-Piper *et al.*, (2019), illustrated as green patches (also see Fig. 1) and, **e)** the rhyo-dacitic dykes mapped by Hecht (1972-1976), illustrated as elongate orange patches (also see Fig. 1).

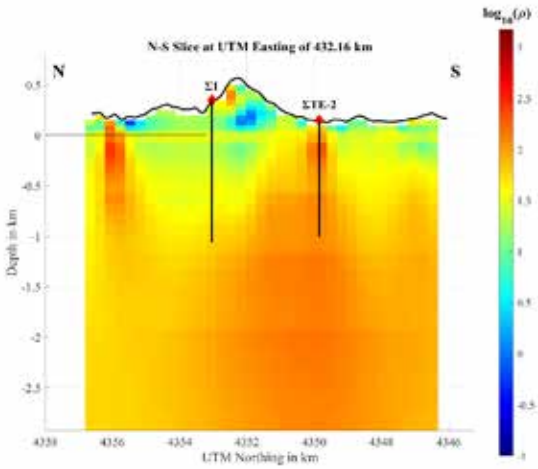

Figure 5. The N-S resistivity cross-section No. 1 through wells Σ1 and ΣTE-2. South is to the right and North is to the left.

The most prominent and characteristic feature is an approximately N70° - N80° alignment of collocated gravity and electrical resistivity lows between the broader areas of Stypsi – Petra and Lepetymnos – Sykaminea towns. Low Bouguer anomalies indicate low-density material beneath the surface and low resistivity values indicate the presence of water. Their coincidence indicates the presence of low-density rock filled with water and, in the geological setting of the study area, alteration/argillization of volcanic rocks due to hydrothermal activity.

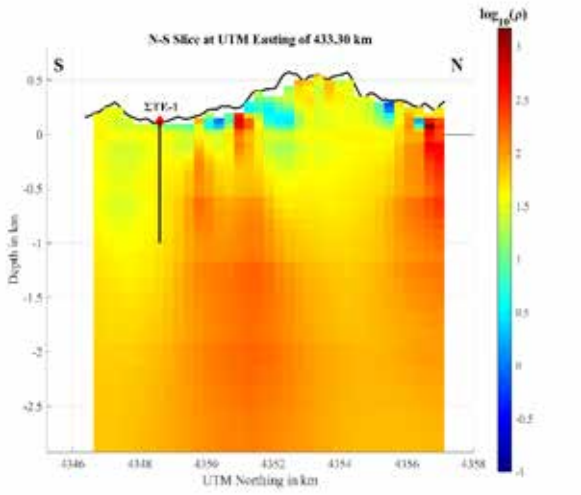

Figure 6. The vertical N-S resistivity cross-section No. 2 through well ΣTE-1. South is to the left and North is to the right.

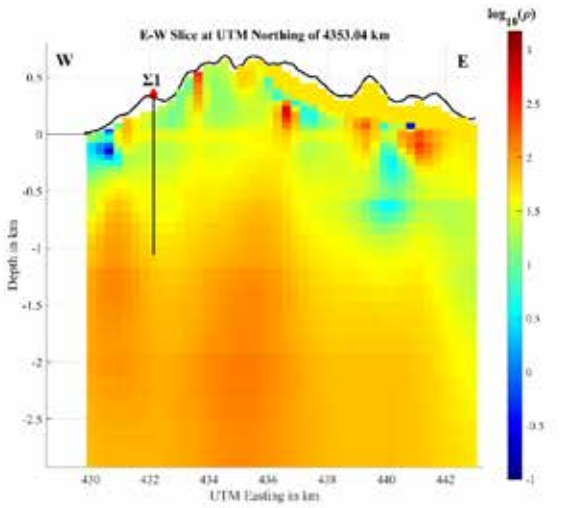

Figure 7. The vertical W – E resistivity cross-section No. 3 through well Σ1.

In the broader area of Stypsi, this low-gravity – low resistivity alignment is also collocated with traces of faults with approximately N70° - N80° orientation. Another very interesting observation is that between Stypsi and Skoutaros, there is a series of outcropping parallel, N80° oriented rhyo-dacitic dykes arranged in a manner suggestive of a direct (genetic) relationship with said faults. If so, the observed fault – dyke configuration would imply that the dykes were emplaced through an N70°-N80° oriented (*oblique–normal*?) fault zone during a *localized* event of syn-tectonic extrusive magmatism. A further (and possibly corroborating) observation is that in the same area, but *near* the Anaxos – Petra coast, the rhyo-dacitic dykes outcrop with an N330° orientation, parallel to the short fault strands of similar orientation mapped at Petra. This may indicate that the syn-tectonic extrusive event took place at, or near the intersection of two associated fault zones. Furthermore, kaolinization zones are produced by hydrothermal activity; if they are elongated and coincide with fault zones, as evident in Figs 3 and 4, then it is safe to conclude that kaolinization is an effect of thermal fluid circulation in faults.

Accordingly, the collocated gravity and resistivity lows may be epiphenomenal to the action of faulting due to which the circulation/transportation of (thermal) fluids depresses the electrical resistivity (epiphenomenon 1) and, hydrothermal alteration/argillization and bleaching of the heavier elements depress the density of the host rocks (epiphenomenon 2). Given the broader tectonic setting of the study area, the above observations indicate the presence of N80° and N330° fault zones, which have established well-defined circulation zones that are operational today, although it is yet difficult to infer the possibility of these faults being tectonically active at present.

Acknowledgements
This work was supported by the contract PO77000646 between the National and Kapodistrian University of Athens and PPC Renewables S.M.S.A.

References

Egbert, G.D. and Kelbert, A., 2012. Computational recipes for electromagnetic inverse problems, Geophys. J. Int., 189, 251-267, doi: 10.1111/j.1365-246X.2011.05347.x

Geosystem Srl., 2000. Electromagnetic Surveys. Lesvos, Greece, Final Report. Public Power Corporation of Greece, Contract DEME 9916019, 217 pp.

Hecht, J. (1972–1976). Geological map of Greece, Scale 1□50,000: Sheets of Plomari-Mytilene, Hagia Paraskevi, Mithymna, Polychnitos and Eresos. Institute of Geological and Mining Research (IGME), Athens, Greece.

Kelbert, A., Meqbel, N., Egbert G.D. and Tandonet, K., 2014. ModEM: A modular system for inversion of electromagnetic geophysical data, Computers & Geosciences, 66, 40-53, doi: 10.1016/j.cageo.2014.01.010

Lagios E., Chailas, S. and Hipkin R.., 2007. Gravity and topographic data banks of Greece. Geophysical Journal International. 126, 287 – 290, doi: 10.1111/j.1365-246X.1996.tb05287.x.

Larsen, J., Mackie, R.L., Manzella, A., Fordelisi, A., and Rieven, S., 1996). Robust smooth magnetotelluric transfer functions, *Geophysical Journal International,* 124, 801-819.

Pe□Piper G., Piper D.J.W., Zouros N. and Anastasakis G., 2019. Age, stratigraphy, sedimentology and tectonic setting of the Sigri Pyroclastic Formation and its fossil forests, Early Miocene, Lesbos, Greece, Basin Res., **31,** 1178–1197, doi: 10.1111/bre.12365.

University of the Aegean, 2022. Stipsi Geothermal Field Tectonic Study. Unsigned Technical Report, Mytilini, August 2022, 213pp.

17th INTERNATIONAL CONGRESS of the Geological Society of Greece

BULLETIN OF THE GEOLOGICAL SOCIETY OF GREECE, SP. PUBL.

EXTENDED ABSTRACT 329

Tracking mobility of Late Pleistocene ruminants using enamel strontium isotope analysis of teeth from Melitzia Cave, Mani Peninsula (Greece)

Tzortzi M.[1], Lugli F.[2], Tütken T.[3], Golfinopoulos V.[1], Iliopoulos G.[1], Darlas A.[4]

(1) Department of Geology, University of Patras, Patras, Greece, mtzortzi@upatras.gr (2) Department of Chemical and Geological Sciences, University of Modena and Reggio Emilia, Modena, Italy (3) Institute of Geosciences, Johannes Gutenberg University of Mainz, Mainz, Germany (4) Ephorate of Palaeoanthropology-Speleology, Hellenic Ministry of Culture, Athens, Greece

Research Highlights:

Strontium isotope analysis ($^{87}Sr/^{86}Sr$) of enamel from Late Pleistocene ungulate teeth reveals a predominant local habitat range of these ruminants within the Mani Peninsula with only minimal migration. Results reveal insights into human subsistence strategies, with hunting focused on fauna from nearby areas.

Introduction

Determining the mobility and provenance of Late Pleistocene fauna are crucial for understanding past ecosystems, predator-prey dynamics, and human-animal interactions. Among geochemical methods, strontium isotope analysis ($^{87}Sr/^{86}Sr$) has proven to be a powerful tool, offering the ability to trace geographic origins and movement patterns through the isotope composition of tooth enamel (Bentley, 2006; Britton and Guiry, 2020). The bioavailable $^{87}Sr/^{86}Sr$, which varies with composition and age of the underlying bedrock geology, enters the food chain through soil, water, and vegetation and is subsequently recorded in the biological (hard) tissues of consumers of higher order (Ericson, 1985).

This study examines the $^{87}Sr/^{86}Sr$ in tooth enamel of ruminant species excavated from the Melitzia Cave in Mani Peninsula, Greece. The faunal assemblage includes species such as *Cervus elaphus* (red deer), *Capra ibex* (ibex), and *Dama dama* (fallow deer), these species were hunted and consumed by the cave's occupants (*Homo sapiens*) during Upper Pleistocene (Darlas and Psathi, 2016), who lived in the numerus cave sites of Mani Peninsula. By comparing $^{87}Sr/^{86}Sr$ in tooth enamel of archaeological faunal remains to a bioavailable baseline derived from modern plant samples, this research aims to establish provenance and assess the habitat use and mobility of the human prey animals. It also seeks to contextualize these findings within the broader palaeoecological and geological framework of Mani Peninsula.

Material and Methods

To construct the bioavailable strontium (BASr) baseline, modern plant samples were collected systematically across 13 geological formations in the Mani Peninsula. A total of 36 leave samples, representing 12 different species of shrubs and trees, were processed. The sampling design accounted for variations in altitude, geology, and vegetation type. The spatial strontium distribution map was created by the Inverse Distance Weight (IDW) method in ArcGIS.

Isolated third and second molars from three ruminant taxa were analyzed to investigate animal mobility. In total, 42 bulk enamel samples were analyzed, and 13 of these teeth were also sequentially sampled to assess seasonal habitat changes.

The Sr isotope analyses were conducted at the Department of Chemical and Geological Sciences of the University of Modena and Reggio Emilia. The samples were prepared according to the protocol described by Lugli et al. (2017). For tooth enamel, 5–10 mg of powder was used, and the modern plants were mixed per sampling site and burned to ash at 500 □ and 15 mg of these ashes were analysed. Sr isotope ratios were determined using the dissolution method MC-ICP-MS by means of a Neptune MC-ICP-MS, housed at the Centro Interdipartimentale Grandi Strumenti (CIGS) of the University of Modena and Reggio Emilia.

Results and discussion

The $^{87}Sr/^{86}Sr$ from plant samples, ranging from 0.70801 to 0.71749, were used to create an isoscape map representing the spatial distribution of bioavailable $^{87}Sr/^{86}Sr$ across the region (Figure 1). Enamel $^{87}Sr/^{86}Sr$ of ruminant teeth from the cave deposits range from 0.70852 to 0.71014 and nearly all of them fall within the range of the Upper Cretaceous to upper Eocene marine limestones (in which Melitzia cave formed) and modern seawater (i.e., sea spray effects) (Figure 2). The average $^{87}Sr/^{86}Sr$ of the enamel samples vary for *C. ibex* between 0.70852 and 0.70861 (mean: 0.70871, 0.000006 SD), for *C. elaphus* between 0.70860 and 0.70911 (mean: 0.70878, 0.0001 SD) and for *D. dama* between 0.70856 and 0.71014 (mean: 0.70894, 0.0005 SD). The lowest ratio occurs in *C. ibex* and the highest in *D. dama* although most of the enamel ratios lie within the narrow $^{87}Sr/^{86}Sr$ range of the limestone rocks in which the cave formed, except for one *D. dama* individual (0.71014) that lies outside of this range. This suggests that most of these animals likely spend their early lives (i.e., the time of tooth mineralization) in the vicinity of the cave. The identification of one individual with a higher $^{87}Sr/^{86}Sr$ value, indicates a short-term migration, suggesting that the individual possibly moved across different geological formations during its lifetime. This non-local value likely fits to $^{87}Sr/^{86}Sr$ of a region

with metamorphic bedrocks, that are exposed in the peninsula's north-eastern part. The findings suggest that this animal either migrated into the area or was hunted there and then transported to the site by predators. Altogether, the enamel $^{87}Sr/^{86}Sr$ range indicates that humans hunted mainly in the surroundings of the Melitzia Cave and do not show any spatial niche partitioning. *C. ibex* exhibited the least isotopic variability, consistent with its narrow ecological niche, its preference for rugged, steep terrains likely restricted its movement to local areas. While *C. elaphus* and *D. dama* show slightly broader variations in their $^{87}Sr/^{86}Sr$ isotope ratios compared to *C. ibex*, the variations show still a narrow range. This indicates that their movement was limited to areas with isotopically similar bedrock.

By integrating strontium isotope analysis with palaeoecological investigation, this study sheds light on the movement and habitat use of Late Pleistocene ruminants in Mani Peninsula. It underscores the utility of isotopic methods in unravelling past faunal behaviours and contributes to broader discussions of human-animal interactions and ecological stability in Upper Pleistocene Mediterranean ecosystems.

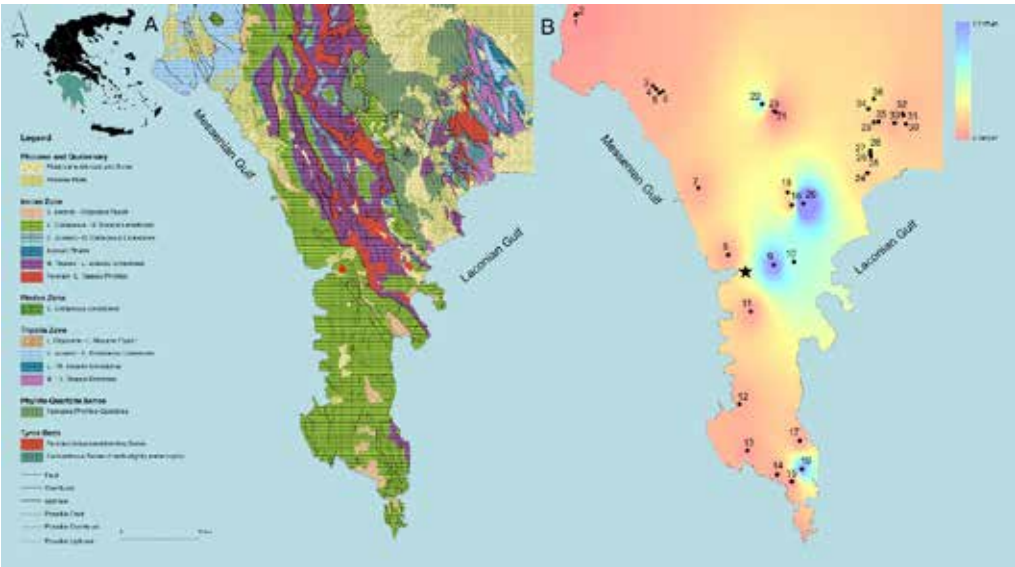

Figure 1. Geological map of Mani Peninsula (modified by Latsoudas, 1984) (A) and BASr baseline for the Mani Peninsula, with the locations of the modern plant sampling sites (B). Numbers on the BASr baseline map indicate sampling sites, while star on each map represents the position of Melitzia Cave. At the top left, corner map of Greece highlighting the Peloponnesus and the study area.

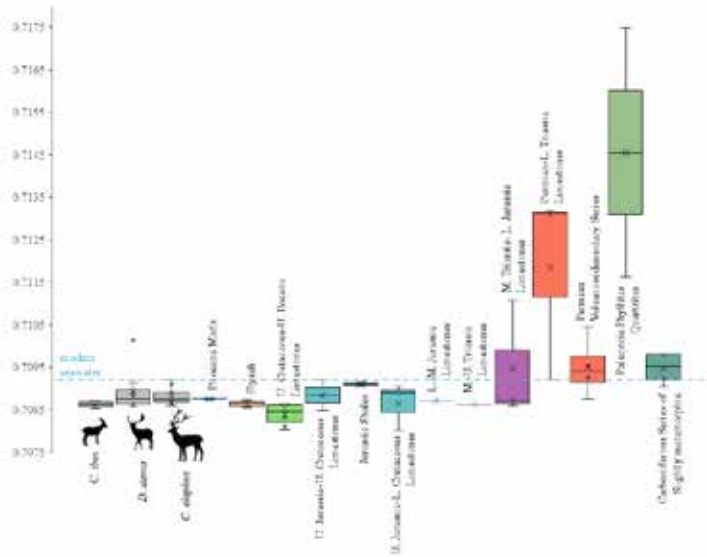

Figure 2. $^{87}Sr/^{86}Sr$ ratio of tooth enamel from the analysed fossil ruminant teeth from Melitzia Cave and the bioavailable $^{87}Sr/^{86}Sr$ from the analysed plant samples from different bedrock substrates across the Mani Peninsula. Boxplots are ordered according to stratigraphic age and colours are based on the geological map.

Acknowledgements

The authors extend their gratitude the Ephorate of Palaeoanthropology-Speleology of the Hellenic Ministry of Culture and Sports and all the colleagues who contributed to the 2009–2016 Melitzia Cave excavations. This research was part of a PhD Thesis and the implementation of the doctoral thesis was co-financed by Greece and the European Union (European Social Fund-ESF) through the Operational programme «Human Resources Development, Education and Lifelong Learning» in the context of the Act "Enhancing Human Resources Research Potential by undertaking a Doctoral Research" Sub-action 2: IKY Scholarship Programme for PhD candidates in the Greek Universities.

References

Bentley, R. A., 2006. Strontium Isotopes from the Earth to the Archaeological Skeleton: A Review. Journal of Archaeological Method and Theory, 13, 135–187.

Britton, K., Guiry, E., 2020. Isotope bioarchaeology in historical archaeology, in: Orser, C., Zarankin, A., Funari, P.P., Lawrence, S., Symonds J. (Eds.), The Routledge Handbook of Global Historical Archaeology, pp. 423–442.

Darlas, A., Psathi, E., 2016. The Middle and Upper Paleolithic on the Western Coast of the Mani Peninsula (Southern Greece), in: Harvati K., Roksandic M. (Eds.), Paleoanthropology of the Balkans and Anatolia: Human Evolution and its Context, 95–118.

Ericson, J. E., 1985. Strontium isotope characterization in the study of prehistoric human ecology. Journal of Human Evolution, 14, 503–514.

Lugli, F., Cipriani, A., Peretto, C., Mazzucchelli, M., Brunelli, D., 2017. In situ high spatial resolution $^{87}Sr/^{86}Sr$ ratio determination of two Middle Pleistocene (c.a. 580ka) *Stephanorhinus hundsheimensis* teeth by LA–MC–ICP–MS. *International Journal of Mass Spectrometry,* 412, 38-48.

17th INTERNATIONAL CONGRESS of the Geological Society of Greece

BULLETIN OF THE GEOLOGICAL SOCIETY OF GREECE, SP. PUBL.

EXTENDED ABSTRACT 330

Application of UAVs in Rockfall Hazard Assessment and Mitigation Measures in the Vrachon Theatre, Byron Area, Greece

Vagionakis N., Andreadakis E., Diamantis K., Stavropoulou M.
Department of Geology and Geoenviroment, Sector of Dynamic, Tectonic and Applied Geology, National and Kapodistrian University of Athens, Athens, Greece

Abstract
The analysis of rockfall hazard on rocky slopes is of vital importance for the safety of engineering works and the protection of human lives, being the subject of numerous scientific studies. Advances in technology, with the use of unmanned aerial vehicles (UAVs) combined with photogrammetric techniques, allow the creation of high accuracy 3D models for rockfall mapping, even in inaccessible areas. Although internationally these methods are widely applied, in Greece the relevant studies are limited. In the area of the Vrachon Theatre in the Municipality of Byron, UAV was used to collect 500 aerial photographs, which were processed with Pix4DMapper. Using AutoCAD and ArcGISPro, a topographic map and cross-sections were created, while RocFall was used for falling simulations. The objective was to assess the hazard, suggest mitigation measures and generate a hazard map.

Introduction
Generally, the study of the hazard and risk assesment of rocky slopes is crucial for engineering projects, for ensuring social security and is the subject of many geotechnical and other studies. Depending on its magnitude, can cause serious damage to structures and threaten human lives. The need to predict and prevent the phenomenon has led many scientists to address it (Budetta, 2004; Lioni, 2010; Ferrari et al., 2016; Hussain, 2018; Wang et al., 2020; Papavasilis, 2020; Vassou, 2022 et al.). Developments in technology have led to new methods and tools that facilitate low-cost data collection and capture. Combining these with remote sensing systems enhances data collection, even in inaccessible areas with difficult morphology. A typical example is the use of unmanned aerial vehicles (UAVs) in combination with photogrammetric techniques, which allows the creation of high accuracy 3D digital elevation models for mapping and subsidence at any scale. For this reason, efforts have been made in recent years to apply these methodologies (Kim et al., 2020; Konstantinidis et al., 2021; Longhui Zhao et al., 2024 etc.). However, few of them have taken place in Greece (Thomopoulos, 2009; Stanota, 2019; Zucher El Azouz, 2020 et al.).
In our study area, i.e. the Vrachon Theatre of the Municipality of Byron (Prefecture of Attica), only one study was carried out (Andrakako and Zacharaki, 2020), in which, however, remote sensing methods and remote applications were not used. In this study 500 aerial photographs were taken through the use of UAV, which were imported into Pix4DMapper software, processed and thus the Digital Surface Model (DSM), Orthomosaic and Digital Terrain Model (DTM) of the study area were constructed. Also, AutoCAD software, in combination with ArcGISPro, was used to create the topographic map, divide the slope into 5 sub-slopes and construct their respective cross-sections, based on which the simulations of possible collapses were carried out using RocFall software. The aim of this work is to assess the rockfall hazard in the area of the Vrachon Theatre, to propose mitigation measures and to construct the hazard map.

Study Area
The Vrachon Theatre is located west of Mount Hymettus, ANA of the Attica basin (Fig.1) and is one of the many quarries that used to operate in Attica. This area has now been exploited by the Municipality of Byron, but also by the Municipality of Daphne-Ymittos, as a place of entertainment for the residents. The intense morphological features, which were exacerbated by its earlier use as a quarry, have stimulated interest in the forthcoming analysis of the hazard of rockfall phenomena in the study area.
Based on the geological map of the I.G.M.E. (today's E.A.G.M.E.) and specifically the sheet Koropi-Plaka, by Latsouda (2003) and at a scale of 1:50. 000, the formations surrounding the Vrachon Theatre are Alpine and belong to the upper tectonic cover of the Aleppouvouni unit, which consists mainly of carbonate, sedimentary rocks and more specifically of Upper Cretaceous limestones. Thus, the study area consists of white to tephra and brownish limestones.

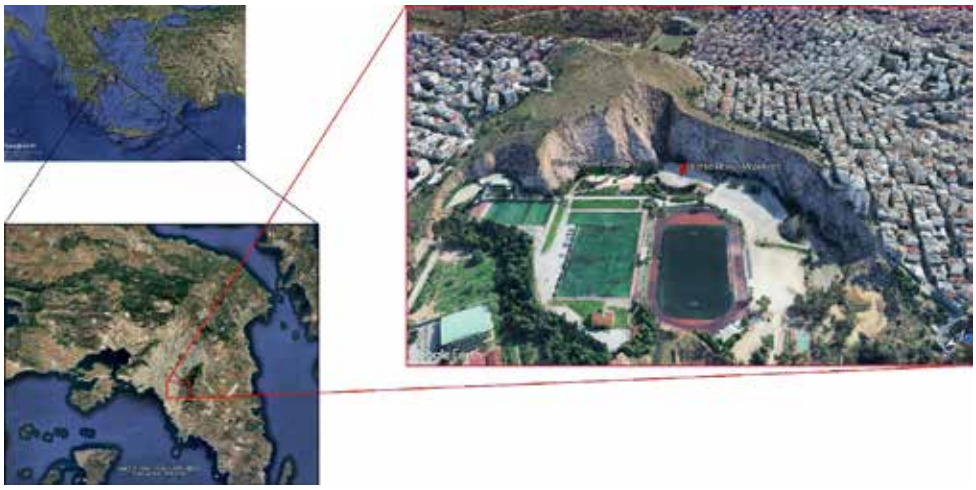

Figure 1. Display and labelling of the study area

The average inclination of morphological slopes observed in the study area is 65° and the altitude ranges from 120 to 260 meters. From a hydrogeological point of view, it is observed that mostly porous formations are encountered, as well as karstic formations, such as limestones. The Municipality of Byron belongs to Seismic Risk Zone I (Greek Seismic Regulation, 2000) and is characterized as an area of very low seismicity. Furthermore, an analysis of seismic events in Greece (1900-2024) shows that no earthquakes have occurred near the area. However, in the stability analyses (RocFall software) we included seismic activity using the relevant index to approximate as closely as possible the stability of the rocky slopes in our study area.

Methodology

The methodology of the research process started with the aerial mapping of the rocky slopes, through the use of unmanned aerial vehicle (UAV) and subsequently, the DSM, the DTM, as well as the orthomosaic of the area were constructed through the Pix4Dmapper program, in order to achieve a more accurate analysis of the research area. Then, with the contribution of the above images, the man-made structures of the area were captured and, through the digitization process, the rock masses of the entire rocky slopes were mapped (Fig. 2).

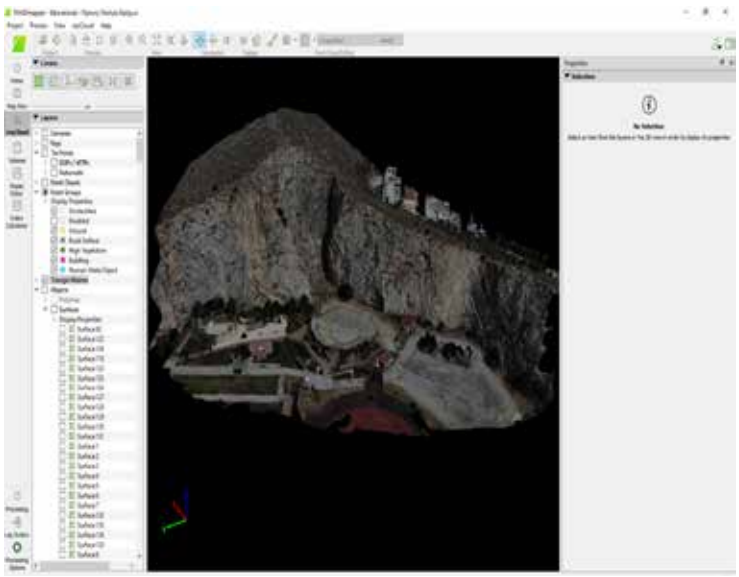

Figure 2. Illustration of the digitized 3D model of the area

The single slope around the Vrachon Theatre was divided into 5 individual slopes, according to their morphological variations, through the 3D model of the area in AutoCAD software (Fig. 3a). An additional element resulting from the combination of Pix4DMapper, AutoCAD and ArcGISPro software was the visualization of the contour curves. Cross-sections were thereafter drawn with AutoCAD, the 13 most precarious ones were selected and a mileage measurement was performed along the study

area (Fig. 3b). In addition, Figure 4 illustrates the above elements, as well as the different materials encountered in each cross-section (Google Earth Pro).

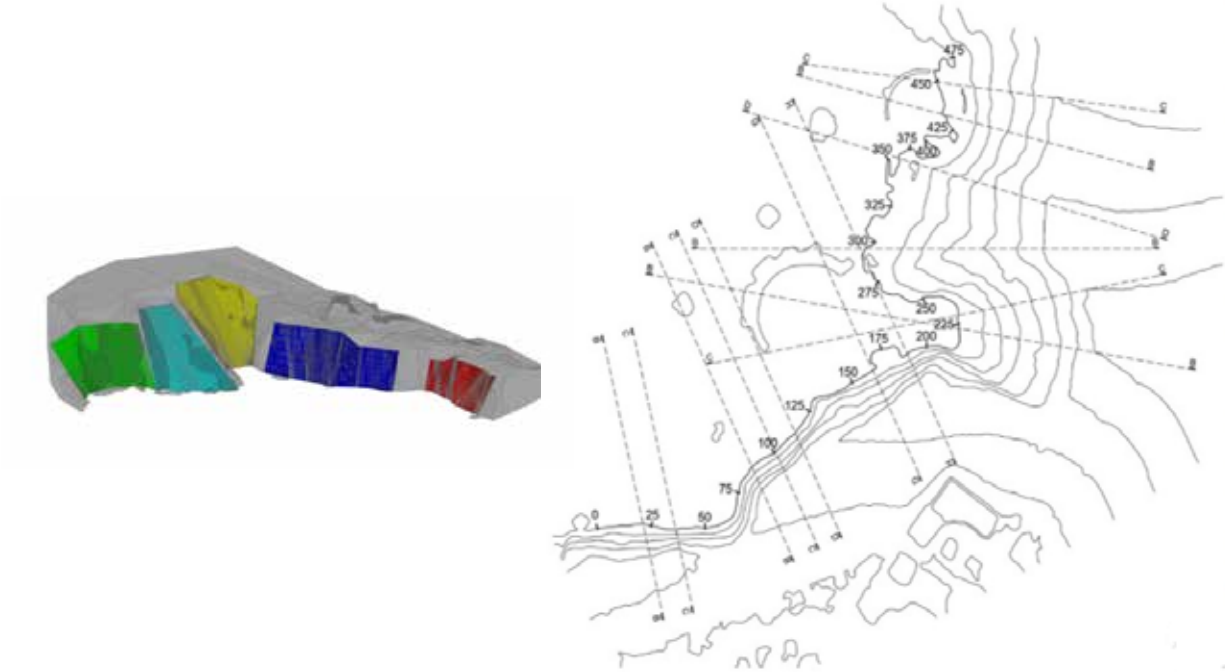

Figure 3. a) 3D solid representation of the 5 slopes, b) topographic map with the 13 high risk locations

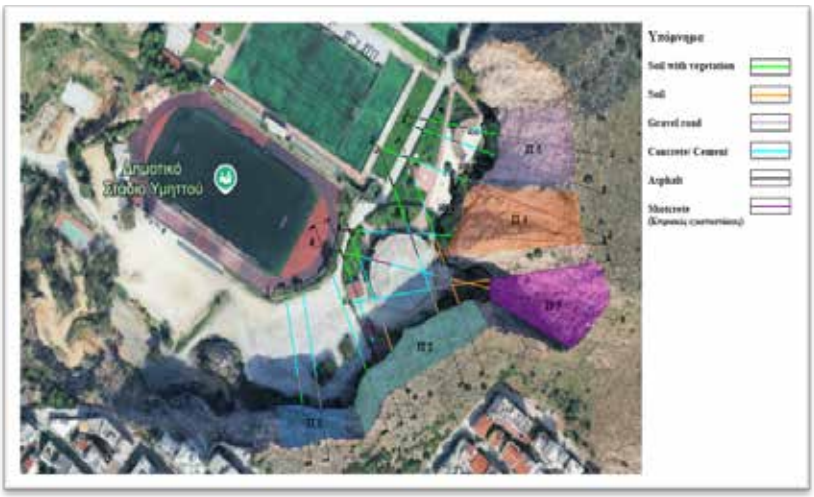

Figure 4. Visualization of the high risk locations through the cross-sections and their corresponding materials in Google Earth Pro

Subsequently, the determination of the rock block weight was implemented, based on which the relevant simulations of their possible paths were carried out. So, taking into consideration the dimensioned ones, we concluded that the majority of them approach the value of 450 kg. The next step carried out was the defining of the seeding positions (seeders) of the potential rock fragments to include all possible cases of fragments taking place near the crest of the slope, which is the worst-case scenario.

Survey results

Figure 5 shows the analyses of the BB cross-section of the first slope, for which the line seeder was initially placed in the area between the two points, with respective heights of 35.504 m and 40 m from the base of the slope, the simulation was configured and the diagrams were drawn showing the final potential positions of the fragments, their total kinetic energy per measurement position, as well as the bounce height.

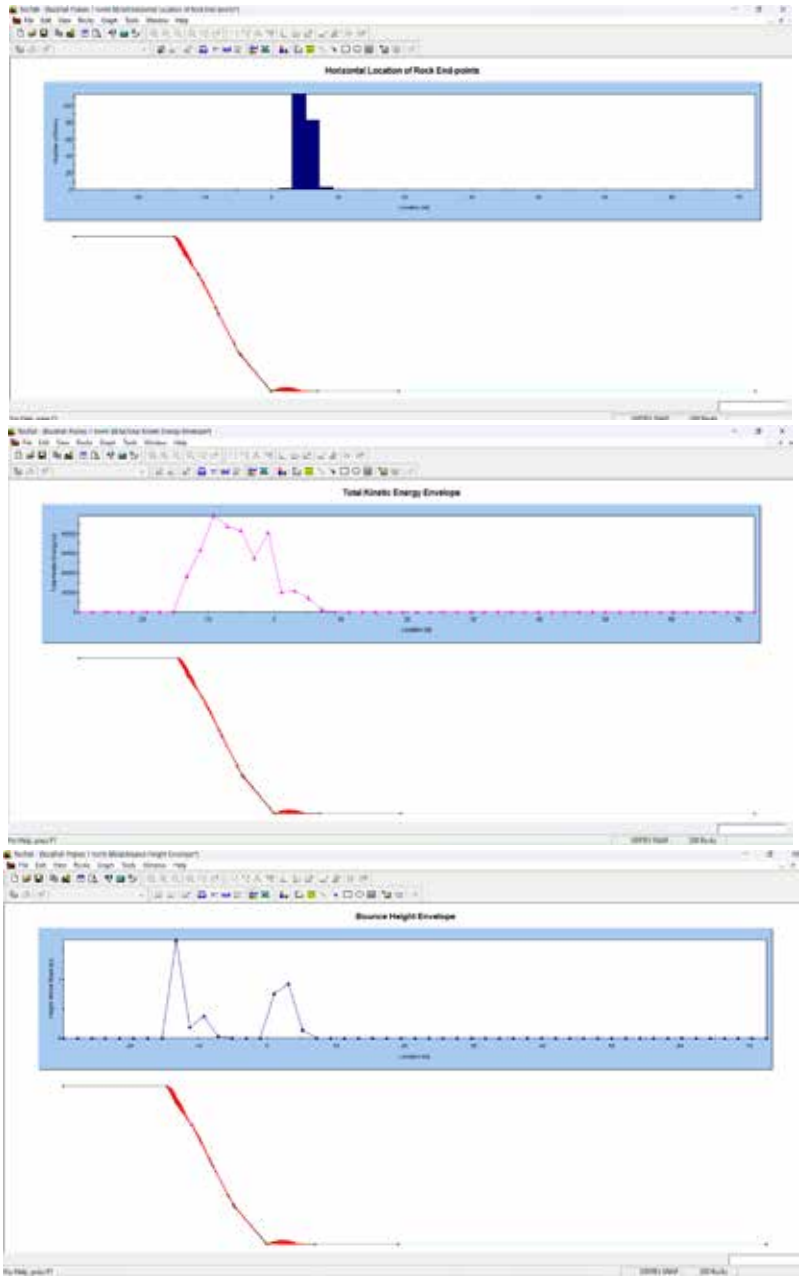

Figure 5. Diagrams of rock fragments of section BB: a) with their horizontal end positions, b) their total kinetic energy and c) their bounce height

According to the above, the decision was made to place or not a suitable retaining fence (barrier) and what characteristics it will fulfill. The fence should therefore be placed in a position where it stops the path of all the fragments and at the same time in this position the kinetic energy should be the minimum possible. Thus, the proposed position is illustrated below, in which the value of the total kinetic energy is distinguished (Fig. 6a).

Subsequently, the simulation was repeated in order to check the energy capacity of the barrier. Figure 6b shows the corresponding diagram of the expected final positions of the fragments, where in this case all of them will be stopped and trapped before the barrier.

We worked in the same way for the sections of the other 4 slopes. Based on the whole analysis above and according to the aggregated results of all the sections, the hazard map (Fig. 7) was constructed, where the planned hazard zones (High Hazardous Zone and Very High Hazardous Zone), as well as the development of a related fencing wall, are marked. Therefore, as can be observed, Slope 2 is the most precarious slope.

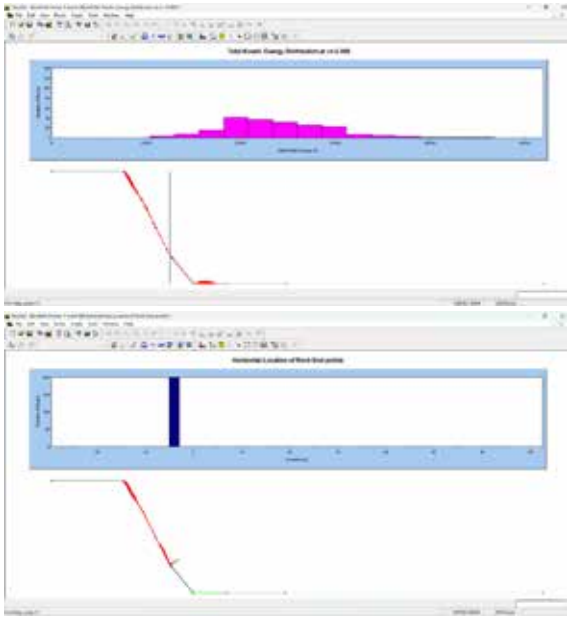

Figure 6. a) Proposed location of the barrier and the distribution of the total kinetic energy of the fragments, and b) final potential end positions of the fragments on it

Conclusions

In this paper we dealt with the rockfall hazard and mitigation measures evaluation of the rocky slopes surrounding the Vrachon Theatre of the Municipality of Byron. An aerial survey of the slopes was carried out using UAVs and 500 aerial images were obtained. These were processed in Pix4DMapper software and produced the 3D digital model of the area, the digital elevation model, the digital terrain model and the orthomosaic of the study area. Based on the above, the topographic map was constructed, where the 13 cross-sections of the most high risk locations were selected using AutoCAD software. Then, according to these, the simulations of the potential rock falls of 450 kg rock fragments were carried out and the relevant diagrams of the potential end positions, total kinetic energy as well as the bounce height were generated. Subsequently, the placement of an interception barrier was proposed, on the basis of which the potential fragments were finally excavated and trapped in it. Finally, the final hazard map was produced, distinguishing the so-called high hazardous Zone, based on the maximum potential end positions of a small number of individual fragments, the very high hazardous Zone, which in turn is based on the maximum end positions of the majority of these fragments, and the corresponding perimeter wall delimiting these two zones, marked in black. Based on all of the above, it was determined that the most precarious and critical slope is Π2.

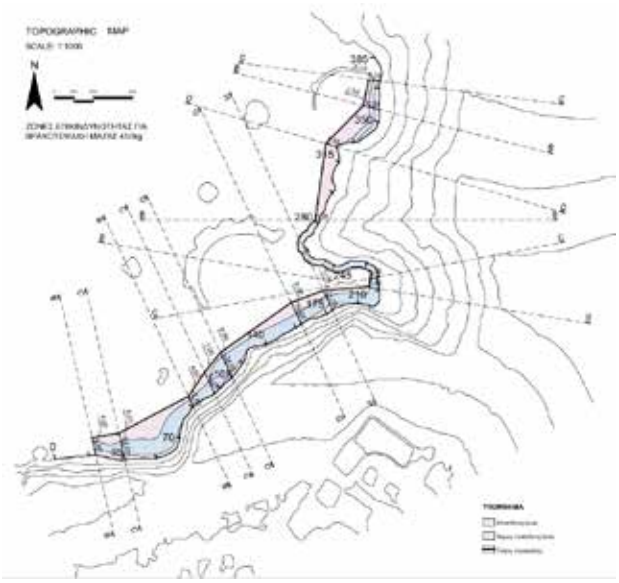

Figure 7. Illustration of the topographic map of the study area showing the potential high hazardous zone, the very high hazardous zone, and the proposed fencing wall

References

Andrakakos, A. and Zacharakis, Z., 2020. Rock Stability and Risk Prevention Capabilities of Rockfall Risk at the "Ergani" Quarry (Vrachon Theatre Quarry) in the area of Byron. Diploma Thesis, National Technical University of Athens, School of Mining and Metallurgical Engineering, Department of Geological Sciences, Athens.

Budetta, P., 2004. Assessment of rockfall risk along roads. Natural Hazards and Earth System Sciences 4: 71–81, SRef-ID: 1684-9981/nhess/2004-4-71, European Geosciences Union, Part of Special Issue "Landslide and flood hazards assessment".

Ferrari, F. et al., 2016. Qualitative Rockfall Hazard Assessment: A Comprehensive Review of Current Practices. Rock Mech Rock Eng, DOI 10.1007/s00603-016-0918-z, Springer-Verlag Wien.

Greek Earthquake Regulation (2000). https://oasp.gr/userfiles/EAK2000.pdf

Hussain, A., 2018. Investigation of the Stability Conditions and Design of Containment Works in Rocky Prairie of the Turkovounia Hill. Postgraduate Diploma Thesis, National Technical University of Athens, Athens, Greece.

Kim, S.S. et al., 2020. RISK ASSESSMENT OF STEEP SLOPE USING DRONE MAPPING AND TERRESTRIAL LiDAR IN KOREA. Commission IV, The International Archives of the Photogrammetry, Remote Sensing and Spatial Information Sciences, Volume XLIV-3/W1-2020, 2020 Gi4DM 2020 – 13th GeoInformation for Disaster Management conference, 30 November–4 December 2020, Sydney, Australia (online). https://doi.org/10.5194/isprs-archives-XLIV-3-W1-2020-81-202.

Konstantinidis, I.; Marinos, V.; Papathanassiou, G. UAV-Based Evaluation of Rockfall Hazard in the Cultural Heritage Area of Kipinas Monastery, Greece. Appl. Sci. 2021, 11, 8946. https://doi.org/10.3390/ app11198946.

Latsouda, Ch., 2003. Geological Map of Greece at a scale of 1:50.000. Sheet "Koropi - Plaka". Published by IGME.

Lionis, Ch., 2010. "Risk of Falls and Slides against Rock Slope Failure in Residential Areas". Diploma Thesis, Harokopio University of Athens, Department of Geography, Athens, Greece.

Longhui, Z. et al., 2024. Rockfall mapping and susceptibility evaluation based on UAV high-resolution imagery and support vector machine method. Open Geosciences 2024; 16: 20220692, published by De Gruyter. https://doi.org/10.1515/geo-2022-0692.

Papavasilis, N., 2020. Rock mechanics and rockfalls. Diploma Thesis, Aristotle University of Thessaloniki, Faculty of Engineering, Department of Civil Engineering, Geotechnical Engineering, Technical Geology Laboratory, Thessaloniki, Greece.

Stanota, Irini - Spyridoula C., 2019. Unmanned Aircraft Systems (UAS) in geological mapping and tectonic analysis in quarries in the areas of Kaisariani Ymittos and Volakas Drama. Diploma Thesis, National and Kapodistrian University of Athens, School of Sciences, Department of Geology and Geoenvironment, Department of Dynamics, Tectonics and Applied Geology, Athens.

Thomopoulos, A., 2009. Stability Conditions of the Symbol Tunnel in the Asprovalta - Kavala Section of the Egnatia Highway at the Construction Stage. Dissertation, Aristotle University of Thessaloniki, Faculty of Sciences, Department of Geology, Geology, Laboratory of Technical Geology and Hydrogeology, Thessaloniki.

Vassou, A., 2022. "Technicogeological evaluation and analysis of rockfall event in a road trench of the provincial road Karpenisi - Prousos, location Karitsa". Postgraduate Diploma Thesis, Aristotle University of Thessaloniki, Department of Geology, Thessaloniki, Greece.

Wang, X. et al., 2020. Dynamic rockfall risk analysis. Engineering Geology 272 105622, 0013-7952/ © 2020 Elsevier B.V.

Zucher El Azouz, K., 2020. Applications of SEM in the design and modelling of marble quarries. M.Sc. thesis, National and Kapodistrian University of Athens, School of Sciences, Department of Geology and Geoenvironment, Athens, Greece.

17th INTERNATIONAL CONGRESS of the Geological Society of Greece

BULLETIN OF THE GEOLOGICAL SOCIETY OF GREECE, SP. PUBL.

EXTENDED ABSTRACT 331

Boosting Cave Ostracods Biodiversity: A case study from the Cave of the Lakes (Chelmos Vouraikos UNESCO Global Geopark, Peloponnese, Greece) with report of a new species of *Trapezicandona*

Dimitra Valavani[1], Penelope Papadopoulou[1], Peter Frenzel[2], Mauro Alivernini[3], Maria Tsoni[4], Maria Groumpou[1], Theodora Tsourou[5], Silvia Kolomaznik[2], Magdalena Kreuzheck[2] & George Iliopoulos[1]

(1) Laboratory of Palaeontology and Stratigraphy, Geology Department, University of Patras, Patra, Greece, dimval833@gmail.com (2) Institute of Geosciences, Friedrich Schiller University, Jena, Germany (3) Thüringen Inselsberg - Drei Gleichen UNESCO Global Geopark, Germany (4) Chelmos Vouraikos UNESCO Global Geopark, Kalavryta, Greece (5) Department of Geology and Geoenvironment, National & Kapodistrian University of Athens, Athens, Greece

Research Highlights

Palaeoecological study in sediments from one of the most touristic caves in Greece (the Cave of the Lakes, Peloponnese) and the discovery of a new species of Ostracod.

Introduction

Karst landscapes are characterized by a variety of features formed from water-soluble rocks (Scheffers et al., 2015). They showcase a diverse mix of environmental and climatic conditions, including sinking streams, sinkholes, large spring caves, and enclosed depressions. This environmental heterogeneity, combined with local climate effects and geographic isolation, fosters remarkable biological diversity, including many endemic species. Especially caves, are vital for biodiversity as they provide unique and stable habitats that support a wide variety of life, including many rare and specialized species (Howarth and Moldovan, 2018).

Ostracods, due to their sensitivity to environmental variations, have emerged as valuable model organisms for investigating climate and ecosystem changes (Holmes & Chivas, 2002). They inhabit almost every aquatic ecosystem, including freshwater, brackish, and saline waters—from oceans to streams, and even groundwater and caves—demonstrating their widespread distribution and ecological diversity and high endemism (Martens et al., 2008). This extensive habitat range makes them excellent indicators of physical and chemical conditions in aquatic environments. For central Europe, information regarding cave ostracods has already been provided (e.g. Meisch,2000). In Greece the related works seem to be significantly reduced when it comes to subterranean species (e.g. Karanovic, 2003) and almost absent when it comes to cave environments. The only extensively known work to date is that of Popa et al., (2019) from Melissotrypa Cave in central Greece. However, Karanovic (2003) has highlighted the high ostracod endemism in the Greek karstic system and the need for further studies due to the high possibility of undescribed taxa existence. Therefore, the study of cave ostracods presents a promising frontier for new discoveries.

This work aims on presenting the results of the ostracod analysis conducted on surface samples from a touristic cave (Cave of the Lakes), located in Northern Peloponnese, Greece. The ostracod taphocoenosis revealed new data on the cave biodiversity and depositional environment. Furthermore, a new species is introduced adding valuable information for the little studied cave ostracods of Greece.

Study area-The Cave of the Lakes

The study area lies in Northern Peloponnese, Greece. The Cave of the Lakes is located in Mount Amolinitsa near Kastria, Kalavryta (Fig.1). It is one of the most emblematic geosites of the Chelmos Vouraikos UNESCO Global Geopark (https://chelmosvouraikosgeopark.necca.gov.gr) and receives thousands of visitors each year. Discovered in 1963, the cave extends over 1,980 meters and features rich and impressive speleothems and 13 interconnected lakes located at different levels. It is also an important palaeontological and archaeological site (Sampson, 1997). The cave extends partly within the Cretaceous limestones of the Tripolis geotectonic zone and partly within the Late Cretaceous thin-bedded limestones of the Pindos zone (Fig.2). It has developed along the northwest-directed fault and is characterized by a long, narrow passage with a comparatively high roof. The 1st part is divided from the 2nd one by a small fault. Both parts are developed in the limestones of Tripolis zone. The intensive rock falls that can be seen in the third part are the result of tectonism of the thin platted Pindos limestones.

Figure 1. Location of the study area.

Material and Methods

Sampling in the Cave of the Lakes took place during October 2022, resulting in seven surface sediment samples (CL1–CL7) (Fig.2). Sampling was conducted only along the touristic part of the cave. Samples from dry areas were collected using a small shovel, while those from the lake were obtained using a box corer. Water samples from the lakes were also retrieved. Samples were stored and processed at the Laboratory of Palaeontology and Stratigraphy, University of Patras.
After inspection for living populations with negative results, approximately 300 gr from each sample were dried and treated with 5% H□O□ for at least 24 h, with the solution heated to 90 °C when necessary. Residues were wet-sieved through 125 μm and 63 μm sieves and then oven-dried at 70 °C. Identification and data on the ecology and distribution of ostracod species are primarily derived from Meisch (2000) and Karanovic (2012). The ostracods were photographed, and morphological details were examined using Leica MZ16 stereomicroscope with a Jenoptik Gryphax Altair digital camera and scanning electron microscope Jeol JSM 6390 (Laboratory of Historical Geology-BioGeoSciences, Faculty of Geology and Geoenvironment, National and Kapodistrian University of Athens).
The taphonomic index Adult/Juvenile (Belis et al., 1997) was calculated at the family level as an indicator of environmental energy.

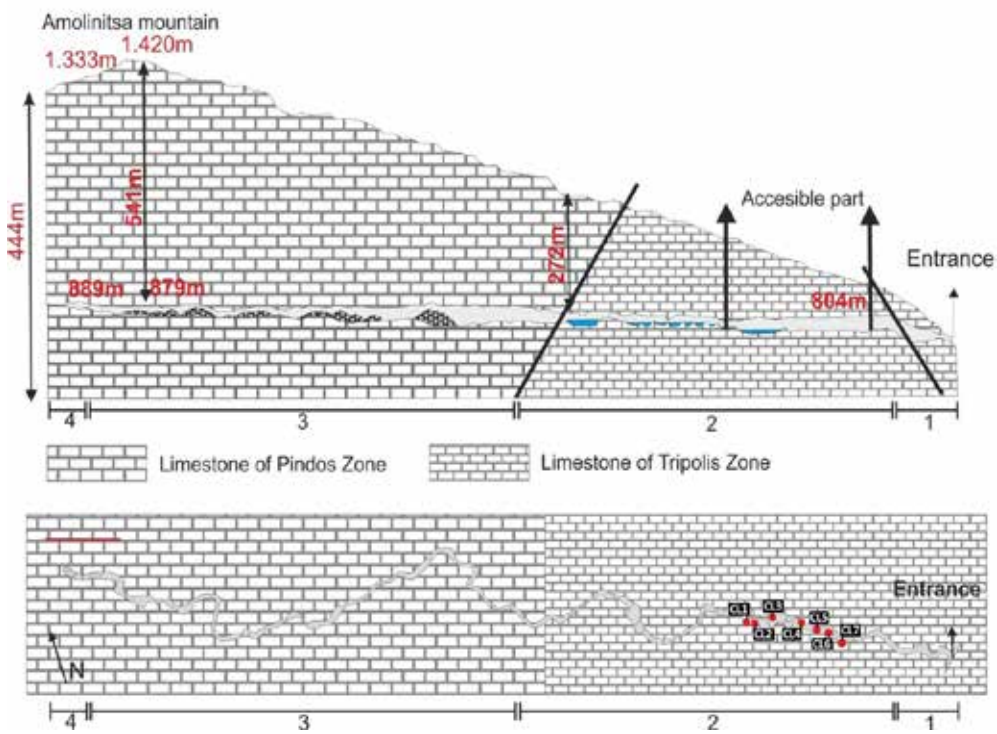

Figure 2. Cross section of Mount Amolinitsa and the Cave of the Lakes. The sampling points are marked in red.

Results

The results of the ostracod analysis revealed low diversity (taxa number 1 in sample CL7 to 3 in samples CL2, CL4, CL5 and CL6) and varying frequency assemblages (7 valves/gr in sample CL7 to 665 valves/gr in sample CL1). More specifically, three taxa were identified.

Neglecandona vernalis dominated the assemblages in all samples (except sample CL7) (maximum number of valves in sample CL4). *N. vernalis* in Germany has been found in small water bodies that dry up temporarily especially meadow puddles and ditches.

A new species of *Trapezicandona* accompanied the taphocoenosis (except sample CL1) with lower frequency (from 1 valve in sample CL2 to 59 valves in samples CL6). Genus *Trapezicandona* is a holarctic hypogean taxon and it is very common in Italy and Spain. Nevertheless, it is the first time that is mentioned from Greece. Detailed morphological study of the studied herein valves revealed that it consists of a new species.

Schellencandona sp. has been found with low numbers (1 in samples CL6 and CL2 to 9 in sample CL1) except samples CL3 and CL7 where it was absent. It is a clearly hypogean stygobite taxon (Meisch, 2000). However, the high endemism of the genus and the low number of valves did not allow its identification to the species level.

The A/J ratio revealed that most of the samples were deposited in situ. More specifically, samples CL1 (A/J ratio: 0.16), CL3 (0.14) and CL5 (0.24) were deposited in situ implying a depositional environment of very low energy. Samples CL4 (0.60), CL6 (1.09) and CL7 (1.73) were deposited in situ, but with taphonomic removal of juvenile valves implying a relatively higher energy depositional environment. The A/J ratio calculated for sample CL2 revealed transported juvenile valves in a low energy depositional environment or a mass death event.

Moreover, in samples CL3, CL5, CL6 and CL7 gastropods of the Hydrobiidae family were also recorded (with very high frequency in sample CL6). Samples CL1, CL6 and CL7 contained a high number of microplastics indicating severe anthropogenic impact.

Conclusions

The ostracod study of seven surface samples deriving from the Cave of the Lakes, Peloponnese, Greece revealed a unique ostracod taphocoenosis. Among them a new stygobiote species is described (*Trapezicandona* n. sp.) contributing to the list of identified cave ostracod species worldwide. Especially for Greece this is a pioneering work since no other detailed works have been published yet. Moreover, the depositional environment inside the cave is inferred as temporal freshwater with no or low transportation energy, uniform in all studied parts of the cave. The high presence of organic material (bat guano) is certain.

The current work is showcasing the perspective of the ostracod research in caves. More scientific work must be done in the cave of the lakes in different directions since a lot of questions arise such as the synthesis of the ostracod assemblage in the other 11 lakes, the search for living populations, the correlation and the possible connection of the subterranean assemblages with the surface ones and the evolution of the lakes' palaeoenvironment through time and its response to climatic effects and the anthropogenic impact.

Acknowledgements

This project was implented in the frame of the "PROGRAMME FOR THE PROMOTION OF THE EXCHANGE AND SCIENTIFIC COOPERATION BETWEEN GREECE AND GERMANY, IKYDA 2022: Cave ostracoda from Greece and Germany: a pilot study for (palaeo)ecological and biogeographical collaboration.

References

Belis, C. A., 1997. Palaeoenvironmental Reconstruction of Lago di Albano (Central Italy) during the Late Pleistocene using fossil ostracod assemblages. Wat. Air Soil Poll. 99: 593–600.

Holmes, J. A. & Chivas, A. R. 2002: Ostracod shell chemistry overview. In Holmes, J. A. & Chivas, A. R. (eds.): The Ostracoda: Applications in QuaternaryResearch, 185–204. American Geophysical Union Geophysical Monograph 131.

Howarth, F.G. and Moldovan, O.T., 2018. The ecological classification of cave animals and their adaptations. Cave ecology, pp.41-67.

Karanovic, T. (2003). First representative of the genus Allocyclops Kiefer, 1932 (Crustacea, Copepoda, Cyclopoida) from the Australian subterranean waters. Annales de Limnologie 39: 141-149.

Karanovic I. 2012. Recent Freshwater Ostracods of the World, Crustacea, Ostracoda, Podocopida. Springer, Heidelberg/Dordrecht/London/New York.

Martens, K., Schön, I., Meisch, C., Horne, D.J., 2008. Global diversity of ostracods (Ostracoda, Crustacea) in freshwater. *Freshwater animal diversity assessment*, pp.185-193.

Meisch, C., 2000. Freshwater Ostracoda of Western and Central Europe. Spektrum Akademischer Verlag.

Popa, I.; Brad, T., Vaxevanopoulos, M., Giurginca, A., Baba, S.C., Iepure, S., Plaiasu, R., Sarbu, S. Rich and Diverse

Subterranean Invertebrate Communities Inhabiting Melissotrypa Cave in Central Greece. *Trav. Inst. Spéol. «Émile Racovitza»* 2019, *58*, 65–78.

Sampson, A., 1997. *The Cave of the Lakes in Kastria Kalavryta*. [In Greek: Το Σπήλαιο των λιμνών στα Καστριά Καλαβρύτων]. Society of Peloponnesian studies,7, Athens. ISSN:1107-96-81

Scheffers, A.M., May, S.M., Kelletat, D.H., Scheffers, A.M., May, S.M. and Kelletat, D.H., 2015. Karst Landscapes: Topographies Sculptured by Dissolution of Rock. *Landforms of the World with Google Earth: Understanding our Environment*, pp.147-161.

17th INTERNATIONAL CONGRESS of the Geological Society of Greece

BULLETIN OF THE GEOLOGICAL SOCIETY OF GREECE, SP. PUBL.

EXTENDED ABSTRACT 332

Overview of Legislation and Tools for Stream Flood Risk Assessment

Valavani Eleni[1], Siarkos Ilias[2], Tzoraki Ourania[2]

1 Directorate of Technical Works of the North Aegean Region, Greece, valavani_eleni@yahoo.gr, 2. epartment of Civil Engineering, Democritus University of Thrace, 3 Marine Sciences Department, University of the Aegean

Abstract

There is a growing need to manage flood risks, particularly in the context of urban expansion, climate change, land desertification, and deforestation. Due to rapid rainfall and geographical variability, many regions in Greece are prone to flash floods. Infrastructure works such as hydraulic projects, dam construction, and river diversions are essential for mitigating the impacts of flooding. Although multiple laws and regulations exist (e.g., EU Directive 2007/60/EC), the current legal framework remains fragmented and is often inadequately enforced. Public misunderstanding and the lack of centralized data further exacerbate the problem. This study explores the complex issue of flood risk assessment in Greece, with a specific focus on the town of Petra in Lesvos. A hydrological and hydraulic analysis of the local stream was conducted using: a) the Rational Method for peak flow estimation, and b) HEC-RAS software for hydraulic simulation under return periods of 50, 100, and 1000 years. The analysis revealed that the stream in Petra fails to accommodate floodwaters even for the 50-year return period, with many cross-sections experiencing overflow. Contributing factors include narrow channels, riverbank erosion, and inadequate maintenance. The study highlights the urgent need for regular cleaning, implementation of protective measures, and reforestation. While existing tools such as the Rational Method and HEC-RAS are useful, they should be applied cautiously due to their simplifying assumptions. Ultimately, there is a critical need for improved legislative frameworks and technical tools to manage flood risks effectively, especially given Greece's climatic variability and hydrological challenges.

17th INTERNATIONAL CONGRESS of the Geological Society of Greece

BULLETIN OF THE GEOLOGICAL SOCIETY OF GREECE, SP. PUBL.

EXTENDED ABSTRACT 333

Conservation and Interpretation of Fossiliferous Sites in the Lesvos Island UNESCO Global Geopark

Valiakos I.[1,2], Bentana K.[1,2], Zouros N.[1,2]
(1) Natural History Museum of the Lesvos Petrified Forest, Mytilini, Greece, ivaliakos@yahoo.gr (2) University of the Aegean, Mytilini, Greece

Introduction / Background

The Lesvos Petrified Forest stands as the hallmark of the Lesvos Island UNESCO Global Geopark, representing a unique natural monument celebrated for its remarkable fossilized trees. These fossils provide invaluable insight into the region's geological history. Preserving and interpreting these fossil-rich sites is essential for advancing scientific research, promoting public education, and fostering sustainable tourism. This paper examines key strategies for conserving and interpreting the newly excavated sites within the Geopark framework.

Formed approximately 20 million years ago due to intense volcanic activity in the northeastern Aegean, the Lesvos Petrified Forest is a geological treasure of international significance. It played a crucial role in Lesvos Island's recognition as a UNESCO Global Geopark. Covering an area of 15,000 hectares in the island's western region, the protected area of the Lesvos Petrified Forest offers a rich window into past ecosystems and geological processes.

The Natural History Museum of the Lesvos Petrified Forest serves as the public institution dedicated to the protection and sustainable management of this extraordinary heritage. The Museum also conducts rescue excavations within the protected area when fossils are discovered during public or private construction projects, ensuring their preservation and proper study.

Challenges in Fossiliferous Site Conservation

While fossils may appear robust and enduring, they are, in reality, highly susceptible to various environmental factors that can lead to significant mechanical and chemical deterioration. Elements such as humidity, temperature fluctuations, and exposure to biological agents, including plant roots, lichens and fungi, contribute to their gradual decay. Additionally, human activities such as vandalism and unauthorized fossil collection pose substantial threats to their preservation (Kyriazi, et al. 2008)

Fossiliferous sites face multiple threats that jeopardize their preservation. Natural processes such as erosion and weathering progressively degrade these sites over time. Human activities exacerbate these risks, including uncontrolled tourism, which can physically damage delicate fossils, illegal excavations that disrupt the geological context, and infrastructure development that may permanently destroy valuable paleontological resources. Furthermore, climate change compounds these challenges, as increasing temperatures and the rising frequency of extreme weather events accelerate the deterioration of fossils and their surrounding environments.

Consequently, conservation efforts must extend beyond the fossils themselves to include the broader geological and ecological contexts in which they are embedded. Protective measures such as erosion control, vegetation management, and site stabilization are essential to ensuring the long-term integrity of fossiliferous sites. By maintaining these sites, researchers and educators can continue to derive scientific and educational value from them, benefiting future generations.

Efforts to protect and sustainably manage Earth's heritage and geodiversity are being advanced in UNESCO Global Geoparks. These initiatives align with international frameworks, including Agenda 21 and the Agenda of Science for Environment and Development, which were adopted at the United Nations Conference on Environment and Development (UNCED) in Rio de Janeiro (1992) and reaffirmed at the World Summit on Sustainable Development in Johannesburg (2002). Geology, geomorphology, and landscapes have profoundly shaped human societies, civilizations, and cultural diversity.

The Lesvos Island UNESCO Global Geopark initiative enhances the objectives of the 1972 Convention on

the Protection of the World Cultural and Natural Heritage by emphasizing the interconnectedness of socio-economic development, cultural heritage, and the conservation of natural environments.

Conservation Strategies

Effective site protection involves the establishment and enforcement of protected areas around fossiliferous sites, the implementation of erosion control measures such as soil stabilization and drainage systems, and continuous monitoring and surveillance to deter illegal activities.

Scientific research is indispensable, requiring ongoing palaeontological and geological investigations to deepen our understanding of a site's significance. This includes systematic data collection and analysis on site conditions, microclimate variations, and visitor impact to inform conservation strategies (Velitzelos et.al. 1997).

Geoconservation techniques play a vital role in preserving these valuable resources. Wherever feasible, in situ preservation should be prioritized to maintain the original context of fossils. The construction of protective structures, such as shelters, helps shield fossils from weathering, while fences and designated safe pathways limit human impact without compromising fossil integrity. These paths should be strategically designed with materials that blend with the natural landscape, ensuring accessibility while safeguarding the site's geological and palaeontological features. Additionally, visitor education and guided tours serve as essential tools in fostering public awareness and reducing inadvertent damage to fossil sites.

Figure 1: Emblematic fossilized tree trunk in the main park of the Lesvos Petrified Forest "Kyria Apolithomeni" during and after the conservation works

Controlled excavations, accompanied by meticulous documentation and secure storage of recovered fossils, are critical for scientific research and the preservation of palaeontological heritage. Advanced digital documentation methods, including 3D scanning and photogrammetry, can aid in creating precise and non-invasive records of fossil sites. Moreover, fostering collaboration with local communities, policymakers, and conservation organizations strengthens long-term protection efforts by integrating traditional knowledge with sustainable conservation practices.

By adopting a comprehensive approach that integrates scientific research, infrastructure development,

community engagement, and stringent policy enforcement, fossiliferous sites can be effectively conserved for future generations (Fig. 1). These measures ensure that these invaluable scientific and natural resources remain accessible for research, education, and public appreciation while maintaining their geological and ecological integrity.

Protection measures

A series of protection and enhancement works have been implemented to improve the accessibility, interpretation, and promotion of the fossiliferous sites within the Geopark. These interventions include:

- Protective measures for the preservation and promotion of fossiliferous sites including shelters and protective stone constructions for the control of erosion (fig. 2).
- Infrastructure improvements to facilitate safe visitor access, ensuring accessibility for all, including individuals with disabilities.
- Signage and interpretative projects that provide information on the fossils that appear in the fossiliferous sites, along with awareness campaigns and educational programs for schools and universities.
- Initiatives to promote alternative forms of tourism, particularly environmental and cultural tourism, through targeted promotional and publicity campaigns.

Figure 2. Shelters protecting petrified tree trunks and their extensive root systems

By integrating scientific research with innovative interpretation strategies, the Lesvos Island UNESCO Global Geopark serves as a model for fossiliferous site conservation worldwide. Its comprehensive approach highlights the balance between conservation, education, and sustainable development, ensuring that the palaeontological heritage of the region is preserved and appreciated by future generations.

Interpretation and Public Engagement

The Lesvos Island UNESCO Global Geopark plays a crucial role in conserving and interpreting fossiliferous sites. As a designated UNESCO site, it has a responsibility to balance the needs of conservation with the socio-economic development of the region, support scientific research and promote public education about the geological and palaeontological significance of the area, engage local communities in the management and interpretation of heritage sites, and share best practices and lessons learned with other geoparks worldwide.

The Lesvos Petrified Forest is an outstanding example of a fossiliferous site that combines conservation,

education, and sustainable tourism. The interpretation of fossiliferous sites within the Geopark is a crucial aspect of its management, aiming to enhance public understanding of the geological heritage and promote geotourism.

Interpretation efforts include well-designed information panels, and guided tours that provide insight into the region's palaeontological significance. Interactive exhibits, 3D models, and digital reconstructions allow visitors to visualize the past ecosystems that existed 20 million years ago. Moreover, on-site interpretation through signage and designated trails ensures that visitors can explore the fossiliferous sites without causing damage to delicate specimens.

Figure 3. VR and QR digital tools help the public understand the geological processes that formed Lesvos Island landscape, landforms and led to the creation of the Lesvos Petrified Forest

The Natural History Museum of the Lesvos Petrified Forest employs modern technology, such as augmented reality (AR) applications and virtual reality (VR) experiences, to engage visitors and present scientific information in an accessible and compelling manner. Additionally, educational and outreach programs involving schools, universities, the local communities and visitors foster a deeper appreciation for the importance of geoconservation and the need to protect fossiliferous sites (fig. 3).

Conclusions

The conservation and interpretation of fossiliferous sites in the Lesvos Petrified Forest UNESCO Global Geopark demonstrate the significance of integrating scientific research, infrastructure development, community engagement, and policy enforcement to ensure the long-term preservation of this invaluable natural heritage. The Geopark serves as a model for sustainable management, balancing the protection of fossiliferous sites with public education and regional socio-economic development.

Effective conservation strategies have been implemented to mitigate environmental and human-induced threats, including erosion control, site stabilization, and protective infrastructure. In situ preservation remains a priority, ensuring that fossils retain their original geological context while minimizing damage from external factors. The application of geoconservation techniques, such as the construction of shelters, designated visitor pathways, and fencing, has proven effective in reducing human impact while maintaining site accessibility and visitor engagement (Zouros 2021).

Public interpretation and engagement play a crucial role in fostering awareness and appreciation of fossiliferous sites. The Geopark has invested in comprehensive educational programs, guided tours, interpretative signage, and innovative digital tools, such as augmented and virtual reality applications, to enhance visitor experiences and scientific outreach. These efforts not only improve public understanding of geological heritage but also promote geotourism as a sustainable economic activity for the region.

The series of enhancement projects within the Geopark—ranging from improving accessibility for all

visitors, including individuals with disabilities, to promoting alternative tourism models—illustrates a holistic approach to conservation and interpretation. By integrating cutting-edge scientific documentation methods like 3D scanning and photogrammetry with traditional conservation practices, the Geopark ensures the meticulous recording and preservation of fossiliferous sites for future research and educational initiatives. Moreover, the collaborative efforts between the Natural History Museum of the Lesvos Petrified Forest, the University of the Aegean, local communities, and policymakers highlight the importance of interdisciplinary cooperation in geoconservation. The involvement of local stakeholders strengthens conservation efforts, fosters a sense of ownership, and enhances the sustainable development of the region.

Ultimately, the Lesvos Petrified Forest UNESCO Global Geopark exemplifies best practices in fossiliferous site conservation by maintaining a delicate balance between scientific study, heritage protection, and responsible tourism. Its comprehensive approach ensures that these palaeontological treasures continue to contribute to global scientific knowledge, public education, and sustainable economic growth, while preserving their ecological and geological integrity for future generations.

References

Kyriazi, E., Zouros, N. 2008. Conserving the Lesvos Petrified Forest. Studies in Conservation, 53(sup1), 141–145. https://doi.org/10.1179/sic.2008.53. Supplement-1.141

Velitzelos, E., Zouros, N., 1997. The petrified forest of Lesvos–Protected natural monument. Proc. Internat. Sympos. On Engineering Geology and the Environment, Athens, 303-304.

Velitzelos, E., Zouros, N., 1998. New results on the petrified forest of Lesvos. Bulletin of the Geological Society of Greece, 32(2), 133–142.

Zouros, N.C., 2021. The Miocene petrified forest of Lesvos, Greece: Research and geoconservation activities. Geoconservation Research. 4(2), 635–649.

17th INTERNATIONAL CONGRESS of the Geological Society of Greece

BULLETIN OF THE GEOLOGICAL SOCIETY OF GREECE, SP. PUBL.

EXTENDED ABSTRACT 334

Geomorphological mapping and lithological heterogeneity as tools for the assessment of liquefaction likelihood: Piniada Valley case study (central Greece)

Valkaniotis S.[1], Rapti D.[2], Taftsoglou M.[3], Papathanassiou G.[1], and Caputo R.[3]

(1) School of Geology, Aristotle University of Thessaloniki, Greece, valkaniotis@yahoo.com , (2) Department of Chemical, Pharmaceutical & Agricultural Sciences, University of Ferrara, Italy, (3) Department of Earth Sciences, University of Ferrara, Italy

Introduction

Assessment of liquefaction susceptibility of Holocene sediments in alluvial plains is one of the first step for regional planning, hazard mitigation, and land use management in seismically active regions. Subtle geomorphological features resulting from recent depositional processes can significantly improve mapping liquefaction likelihood since they also express the lithology and distribution of Holocene sediments. Widespread liquefaction phenomena were triggered by the 2021 Mw 6.,3, Damasi, Larisa earthquake over Piniada Valley (Ganas, *et al.,* 2021; Papathanassiou, *et al.,* 2022), a narrow section of Pinios river course in central Thessaly (Figure 1). As we compiled a detailed geomorphological/geological map for the purposes of this investigation and correlated it to the spatial distribution of the earthquake-induced liquefaction phenomena, we observed that liquefaction surface occurrences (ejecta, craters. ground fissures, lateral spreading) are highly correlated to point bars and abandoned river channels formed during the last century (Figure 1 & 2). Both geomorphological units consist of mainly sand, with the common occurrence of a thin clayey cap layer if abandoned.

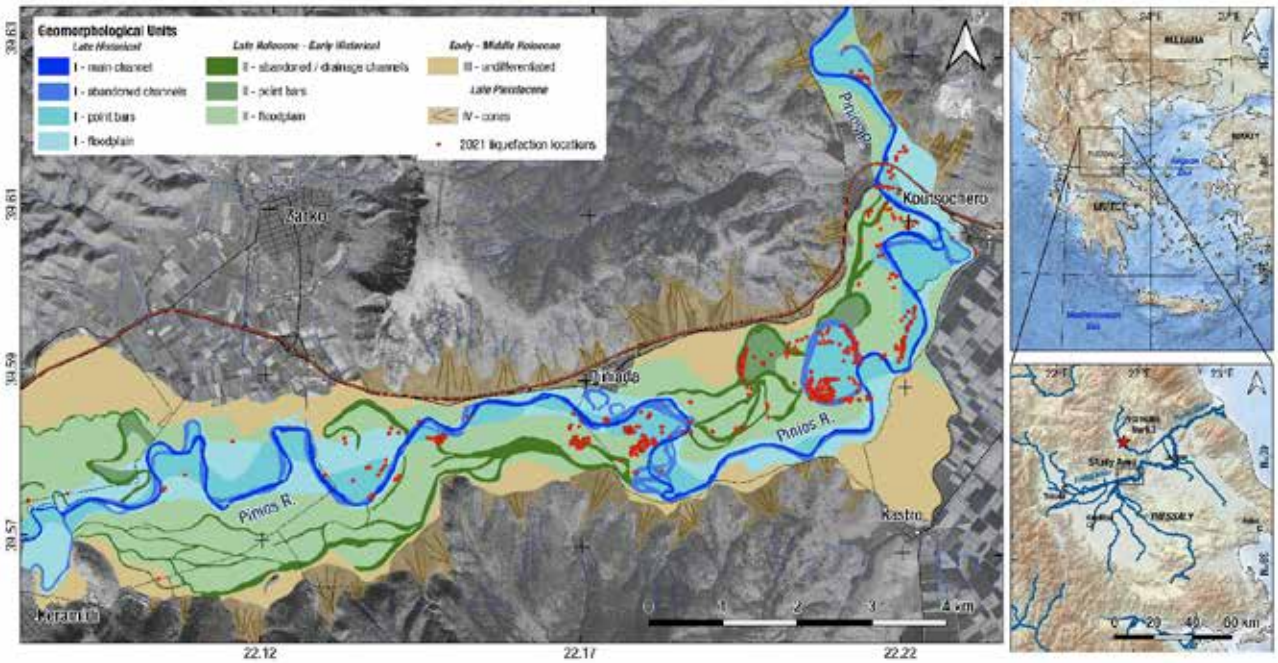

Figure 1. Geomorphological map of the Piniada Valley after Caputo et al. (2021) and Valkaniotis et al. (2024). Liquefaction surface manifestations mapped after the 2021 earthquake (Papathanassiou et al. 2022) are shown as red dots. Inset maps show the location of Piniada valley in central Greece.

Methods/Results

Piniada valley is a narrow section of Pinios river, where Late Pleistocene and Holocene fluvial sediments deposited by the Pinios river meander dominate the valley form (Caputo, *et al.,* 2021; Valkaniotis, *et al.,* 2024). Liquefaction manifestations after the 2021 M_w 6.3 earthquake were mapped in detail using a combination of field, UAS and satellite data (Papathanassiou, *et al.,* 2022). Remote sensing data (optical and radar satellite data) can significantly improve rapid mapping after an earthquake event, and can guide and focus field mapping over large regions (Taftsoglou, *et al.,*

2023). Published geologic map sheets show little variation in Quaternary sediment mapped formations, with only few general groups present as undifferentiated alluvial sediments and terrace deposits along Pinios river. We developed a detailed mapping of the late Upper Pleistocene and mainly Holocene deposits outcropping along the Piniada Valley that was largely based on the field and remote sensing observation of geomorphological features. Using historical topographic maps, detailed digital surface models and remote sensing data (historical aerial imagery and satellite imagery), allows us to improve surficial geological mapping (Taftoglou, *et al.,* 2022; Valkaniotis, *et al.,* 2024). During moderate-to-strong seismic events, such maps could better resolve the distribution and the characteristics of the surficial deposits and hence the potential location of earthquake-induced liquefaction phenomena. At this regard, the behavior of the subsoil layer and the occurrence of liquefaction are basically dictated by the type of predominant material, the general stratigraphic succession and the depth of water table.

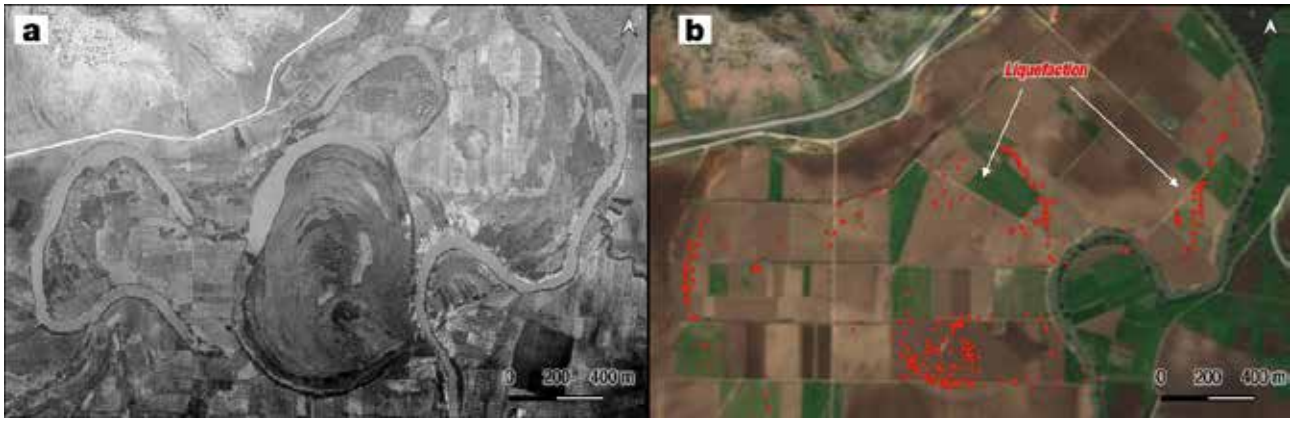

Figure 2. a) Historical aerial imagery from 1935 showing abandoned meander channels and point bars in Piniada valley. b) Liquefaction surface features (red dots) of the 2021 earthquake (Papathanassiou et al. 2022). Liquefaction manifestations correlate with recently abandoned meanders and point bar formations.

Point bars deposits are developed on meandering fluvial systems where the depositional process is strongly influenced by the river channel. Although the prevailing grain size is represented by sand, the lateral heterogeneity (Russel, *et al.,* 2018) plays a crucial role in determining the liquefaction susceptibility and its potential. In order to verify and apply this concept to the Piniada Valley case study, we separated sand and mud prone zones within point bar features and compared their spatial distribution with the occurrence of liquefaction cases during the 2021 Damasi earthquake. Results indicates that most liquefaction phenomena occurred in sand rich shallow deposits. Thus, it is confirmed that in point bars settings, it is feasible to further detect distinct zones with different liquefaction likelihood. If only regional scale geological maps are available, distinguishing or even simply recognizing the different fluvial sedimentary facies is quite challenging; for this reason, a detail mapping should become essential for large geotechnical surveys and a very good proxy of surficial and shallow lithology that can guide the proposed locations of boreholes and/or penetrometric tests. Statistical results from Piniada Valley, highlight that a refinement of existing liquefaction susceptibility classifications (e.g. Youd, *et al.,* 1978) is required. It is proposed to include point bars as a distinct class characterized by a very high susceptibility to liquefaction for material recently deposited, especially of age younger than ~100 years (Valkaniotis, *et al.,* 2024).

Acknowledgements
We acknowledge the contribution and support of Themistoklis Raptis, Christos Giannakos and other Piniada residents during the post-seismic and later field work.

References

Caputo, R., Helly, B., Rapti, D. and Valkaniotis, S., 2021. Late Quaternary hydrographic evolution in Thessaly (Central Greece): The crucial role of the Piniada Valley. Quat. Int., 635, 3-19, https://doi.org/10.1016/j.quaint.2021.02.013

Ganas, A., Valkaniotis, S., Briole, P., Serpetisdaki, A., Kapetanidis, V., Karasante, I., Kassaras, I., Papathanassiou, G., Karamitros, I., Tsironi, V., Elias, P., Sarhosis, V., Karakonstantis, A., Konstantakopoulou, E., Papadimitriou, P., and Sokos, E., 2021. Domino-style earthquakes along normal faults in Northern Thessaly (Greece): Kinematic evidence from field observations, seismology, SAR interferometry and GNSS. Bull. Geol. Soc.

Greece https://doi.org/10.12681/bgsg.27102

Papathanassiou, G., Valkaniotis, S., Ganas, A., Stampolidis, A., Rapti, D. and Caputo, R., 2022. Floodplain evolution and its influence on liquefaction clustering: the case study of March 2021 Thessaly, Greece, seismic sequence. Eng. Geol., 298, 1-18, https://doi.org/10.1016/j.enggeo.2022.106542

Russell, C.E., Mountney, N.P., Hodgson, D.M. and Colombera, L., 2018. A novel approach for prediction of lithological heterogeneity in fluvial point-bar deposits from analysis of meander morphology and scroll-bar pattern, in: Ghinassi, M., Colombera, L., Mountney N.P., Reesink, A.J.H. and Bateman, M. (Eds), Fluvial meanders and their sedimentary products in the rock record. Wiley, https://doi.org/10.1002/9781119424437.ch15

Taftsoglou, M., Valkaniotis, S., Papathanassiou, G., Klimis, N. and Dokas, I.A., 2022. Detailed Liquefaction Susceptibility Map of Nestos River Delta, Thrace, Greece Based on Surficial Geology and Geomorphology. Geosciences, 12, 361, https://doi.org/10.3390/geosciences12100361

Taftsoglou, M., Valkaniotis, S., Papathanassiou, G., Karantanellis, E., 2023. Satellite Imagery for Rapid Detection of Liquefaction Surface Manifestations: The Case Study of Türkiye–Syria 2023 Earthquakes. Remote Sensing, 15 (17), 4190 https://doi.org/10.3390/rs15174190

Valkaniotis, S., Rapti, D., Taftsoglou, M., Papathanassiou, G., Caputo, R. 2024. Geomorphological mapping for liquefaction likelihood: the Piniada Valley case study (central Greece). Bull. Earthquake Engineering, 22, 5451-5474 https://doi.org/10.1007/s10518-024-01993-y

Youd, T.L. and Perkins, D.M., 1978. Mapping of Liquefaction induced Ground Failure Potential, J. Geotech. Eng. Div., 104, 433-446 https://doi.org/10.1061/AJGEB6.0000612

17th INTERNATIONAL CONGRESS of the Geological Society of Greece

BULLETIN OF THE GEOLOGICAL SOCIETY OF GREECE, SP. PUBL.

EXTENDED ABSTRACT 335

Development of a Medicane-induced landslide inventory with field and remote sensing data; 2023 Storm Daniel, central Greece

Valkaniotis S.[1], Taftsoglou M.[2], Samara, D.[1], Papathanassiou, G[1], Tolika, K.[1], Zei C.[3] and Chatzitheodosiou T.[4]

(1) School of Geology, Aristotle University of Thessaloniki, Greece, valkaniotis@yahoo.com
(2) Department of Earth Sciences, University of Ferrara, Italy
(3) National Institute of Geophysics and Volcanology - INGV, Italy
(4) School of Civil Engineering, National Technical University of Athens, Greece

Introduction

Severe meteorological phenomena such as storms, hurricanes and cyclones have devastating impact on the population, infrastructure but also the natural environment. Apart from flooding, these events usually trigger numerous landslides along the impacted areas. Mapping and studying of these landslides are necessary steps towards understanding and mitigating these types of natural disasters.

Medicanes (Mediterranean hurricanes), a concatenation of Mediterranean Sea with hurricanes, resemble tropical cyclones but present certain differences like much shorter expected lifespan. Medicane Ianos (September 2020) was the first devastating event that led to extensive destruction in Greece, including flooding, serious damages to infrastructure and numerous landslides (Lekkas, *et al.,* 2020; Zekkos, *et al.,* 2020).

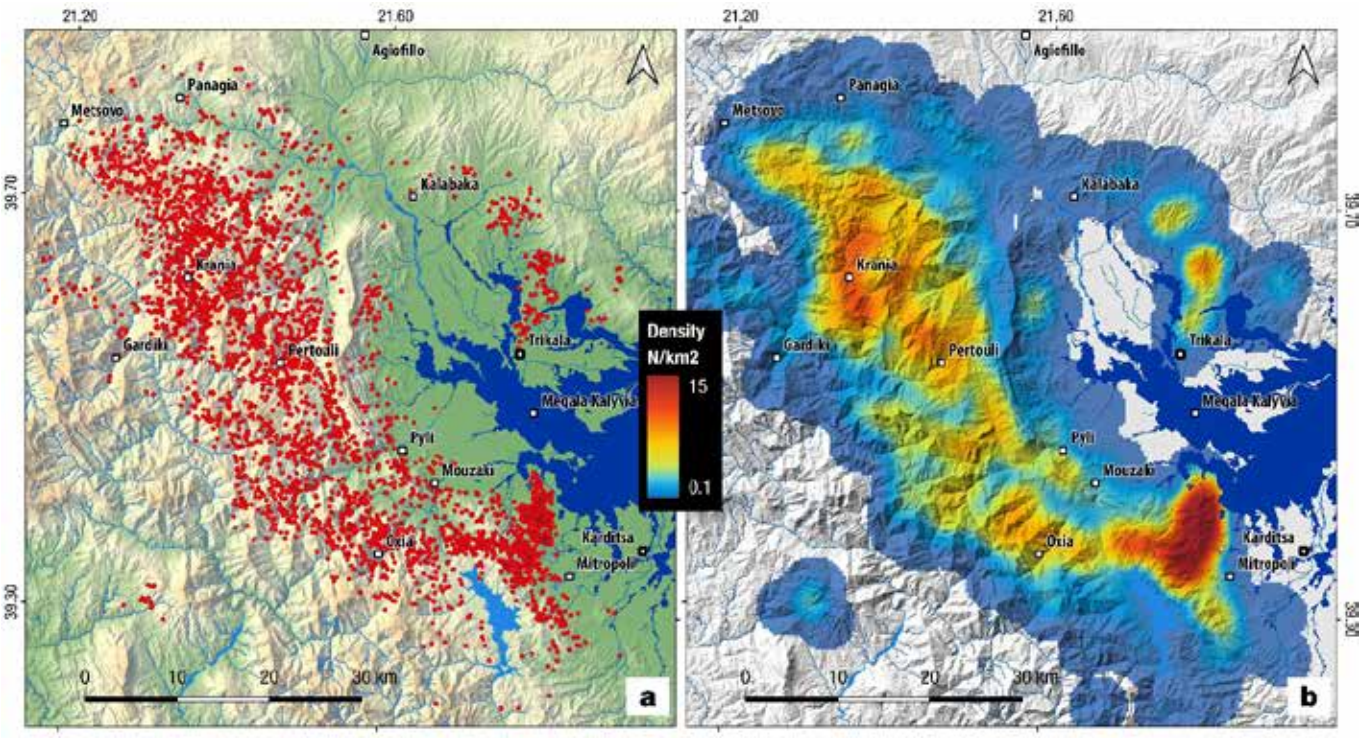

Figure 1. Landslide inventory of Storm Daniel (September 4-8 2023) in western Thessaly (a) and landslide density (b). Red dots show the location of landslide polygons mapped from satellite imagery. Dark blue shows areas on Thessaly plain that were flooded during Storm Daniel.

A large number (>2000) of landslides were triggered by Ianos in the mountainous area of western Thessaly (Valkaniotis, *et al.,* 2022). Storm (Medicane) Daniel, three years after Ianos, landed on Greece in September 2023. From September 4 up to September 7 2023, central Greece and especially Thessaly region, experienced severe rainfall exceeding 1000 mm at places. More than 1400 km^2 of Thessaly were flooded during this event. Debris flows and floods in mountainous watersheds and torrents led to serious damages of property and infrastructure in most parts of Thessaly. Southern Pilio mountain and the mountainous area of western Thessaly (Pindos Mountain range) experienced thousands of

landslides triggered by Cyclone Daniel (Lekkas, *et al.,* 2023; Valkaniotis, *et al.,* 2024). We focused on the landslides triggered in the western Thessaly region, in order to develop an event-based landslide inventory.

Methods/Results

We acquired all available USGS Landsat 8/9 (15 meters ground resolution) and Copernicus Sentinel-2 (10 meters ground resolution) satellite imagery after the event, covering the dates of September 8 up to September 15 2023. Additional frames of Planet imagery (3-4 meters ground resolution) were acquired over the study area of western Thessaly for multiple dates (September 8 – September 14). Parts of the study area were covered by early post-event very high resolution (<2 meters ground resolution) satellite imagery (WorldView-3, SPOT, GeoEye-1) that were acquired through Copernicus Data Archive. A series of post-event field surveys in the study area (Trikala – Karditsa, Thessaly) were performed in the days following the event (Figure 2). During these surveys, satellite imagery rapid mapping was verified and checked in the field. In more than 15 locations, UAS photogrammetric surveys were executed in sites where major landslides occurred.

Figure 2. a) Large complex landslide (rotational-flow) on Triggia mountain range, Trikala. b) Numerous small landslides along forest roads. Pyli municipality, Trikala. c) Multiple landslides along the road slopes of the road Morfovouni-Kanalia (Karditsa).

A preliminary landslide inventory of 3200 landslides was compiled using high resolution Copernicus Sentinel-2 multispectral imagery ten days after the event (Valkaniotis, *et al.,* 2024). Landslides were mapped using visual inspection, with comparison of pre- and post-event images. Manual process was assisted by using semi-automatic methods, such as normalized band differencing, and Google Earth Engine codes for change detection (Valkaniotis, *et al.,* 2022). After the development of the preliminary rapid mapping landslide inventory, we proceeded with the final event inventory, using Planet and VHR satellite imagery for more detailed mapping of landslide locations and polygons. UAS orthophotos and digital elevation models of major deep-seated landslides were also used for detailed delineation. One of the largest landslides with length exceeding 500m was triggered at the Pindos Mountain range, near Pyrra settlement, Trikala region, and created a small landslide dam lake that persists up to this date (Valkaniotis, *et al.,* 2024).

The Daniel landslide inventory of 5446 landslides is presented in Figure 1. Most of the landslides are found along the Pindos Mountain range, with additional concentrations in the hilly areas north of Trikala and near Mouzaki. Studying the distribution of landslides, we can estimate the area of peak rainfall (more than 400-500 mm) on the mountainous part of the affected region as the one that encloses most of the landslides. A comparison with the Medicane Ianos inventory (Figure 3) shows the more severe intensity of the Daniel event in comparison to Ianos, that led to more landslides in the same region but also triggered a large number of rockslides and large deep-seated landslides that were quite uncommon for the Ianos inventory. Distribution and density of landslides shows correlation with geological formations susceptible to landslides, but also with local rainfall amount and rain intensity during Storm Daniel.

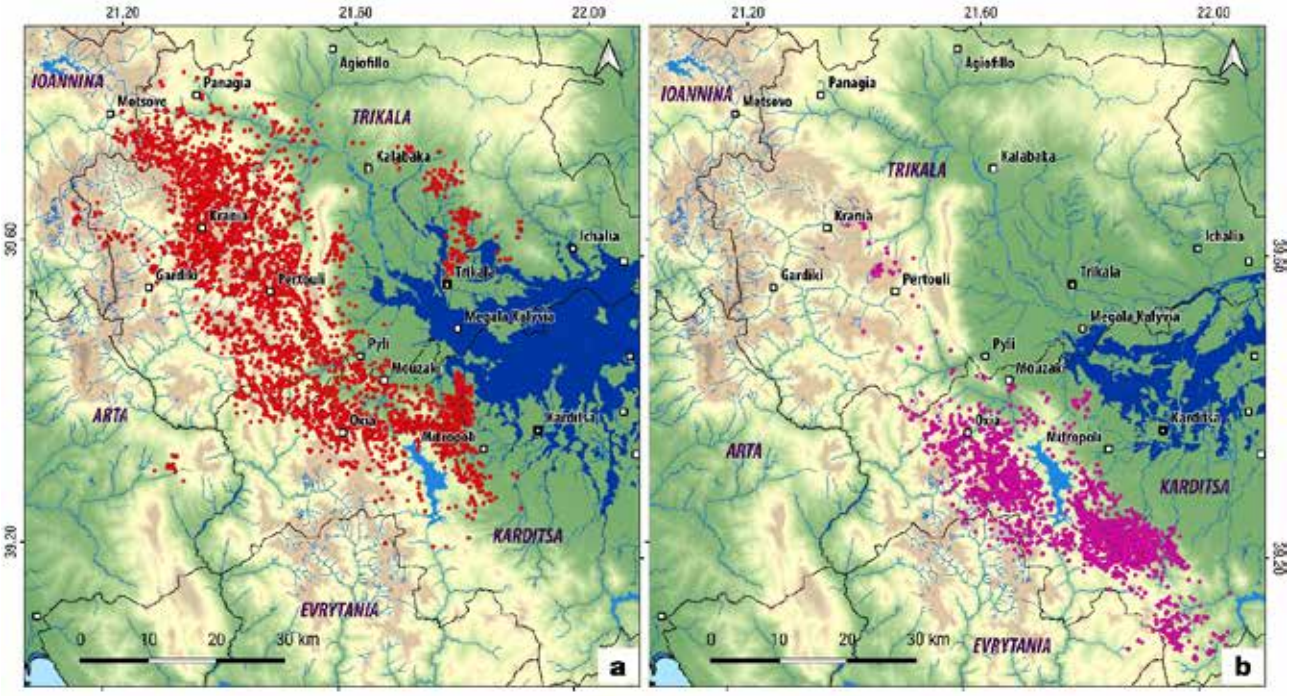

Figure 3. Comparison of Daniel (a) and Ianos (b) landslide inventories. Ianos landslide inventory updated from Zekkos et al. (2020) and Valkaniotis et al. (2022). Dark blue areas mark the location of flooding during Medicane Daniel (a) and Ianos (b) respectively.

Acknowledgements

Planetscope imagery was provided by Planet Team (2023); Planet Application Program Interface, In Space for Life on Earth. San Francisco, CA. https://api.planet.com/Planet (Planet Labs, Inc., San Francisco, CA, USA). Copernicus Sentinel-2 imagery was accessed through Copernicus Data Space Ecosystem (https://browser.dataspace.copernicus.eu). We thank Copernicus Data Archive for providing access to post-event VHR imagery acquisitions.

References

Lekkas, E., Nastos, P., Cartalis, C., Diakakis, M., Gogou, M., Mavroulis, S., Spyrou, N.-I., Kotsi, E., Vassilakis, E., Katsetsiadou, K.-N., Skourtsos, E., Andreadakis, E., Kapourani, E., Soukis, K., Theodorakatou, D., Tsironis, A., Lekka, C., Moraitis, S., Stamati, E., Psaris, D., Lagouvardos, K., Kotroni, V., Dafis, S., Karagiannidis, A., Parcharidis, I., Falaras, T., Karavias, A., Mourampetzis, A., Foumelis, M., Ganas, A., Valkaniotis, S., 2020. Impact of medicane "IANOS" (September 2020) on Cephalonia and Ithaki Islands. In Newsletter of Environmental, Disaster and Crises Management Strategies, National Capodistrian University of Athens: Athens, Greece, 2020, ISSN 2653-9454

Lekkas, E., Diakakis, M., Mavroulis, S., Filis, C., Bantekas, Y., Gogou, M., Katsetsiadou, K.-N., Mavrouli, M., Giannopoulos, V., Sarantopoulou, A., Nastos, P., Vassilakis, E., Konsolaki, A., Kotsi, E., Carydis, P., Parcharidis, I., Tounta, S., Falaras, T. , Skourtsos, E., Bakopoulou, A., Korkovelos, A., Ronzi, L., Speis, D.-P., Lekka, Ch., Stamati, E., Moraitis, S., 2023. The early September 2023 Daniel storm in Thessaly region (central Greece). In Newsletter of Environmental, Disaster and Crises Management Strategies, National Capodistrian University of Athens: Athens, Greece, 2023, ISSN 2653-9454

Valkaniotis, S., Papathanassiou, G., Marinos, V., Saroglou, C., Zekkos, D., Kallimogiannis, V., Karantanellis, E., Farmakis, I., Zalachoris, G., Manousakis, J., Ktenidou, O-J. 2022. Landslides Triggered by Medicane Ianos in Greece, September 2020: Rapid Satellite Mapping and Field Survey. Geosciences, 12(23), 12443, https://doi.org/10.3390/app122312443

Valkaniotis, S., Taftsoglou, M., Papathanassiou, G., Samara, D., Zei, C., Chatzitheodosiou, Th. 2024. Development of a Medicane-induced Landslide Inventory; Case Study of 2023 Cyclone Daniel, Central Greece. Procceedings of 4th European Regional Conference of IAEG. Dubrovnik, 08-12 October 2024, Croatia. p. 128-134. https://doi.org/10.5592/CO/EUROENGEO.2024.163

Zekkos, D., Zalachoris, G., Alvertos, A.E., Amatya, P.M., Blunts, P., Clark, M., Dafis, S., Farmakis, I., Ganas, A., Hille, M., Kalimogiannis, V., Karagiannidis, A., Karantanellis, E., Khan, K., Kirshbaum, D., Kourkoulis, R., Kotroni, V., Ktenidou, O.-J., Lagouvardos K., Loli, M., Makrinikas, A., Marinos, V., Manousakis, J., Nikas, K., Panousis, D., Papathanassiou, G., Saroglou, C., Simopoulos, A., Stanley, T., Tsavalas, A., Valkaniotis, S. 2020. The September 18–20 2020 Medicane Iaonos Impact on Greece—Phase I Reconnaissance Report, Geotechnical Extreme Events Report–Reconnaissance Report, GEER-068, GEER Association: San Francisco, CA, USA, 2020 https://doi.org/10.18118/G6MT1T

17th INTERNATIONAL CONGRESS of the Geological Society of Greece

BULLETIN OF THE GEOLOGICAL SOCIETY OF GREECE, SP. PUBL.

EXTENDED ABSTRACT 336

Investigating the interaction between Flood Hazard and Soil Erosion in Northern Evia Island, Greece, using GIS Morphometric Analysis

Kanella Valkanou [1], Efthimios Karymbalis [2], Konstantinos Tsanakas [3]
1, 2, 3 Department of Geography, Harokopio University, Athens, Greece, kvalkanou@hua.gr

Introduction

Among all hydrometeorological events, floods are widely considered the most dangerous to human life, causing both immediate destruction and long-term impacts (Wang et al., 2022). Despite extensive efforts to mitigate flood risks, the frequency and severity of these events continue to rise globally. Recent studies indicate a significant increase in both the economic damage and fatalities caused by floods, with millions of people affected each year worldwide (UNDRR, 2023). In this context, flood hazard mapping plays a crucial role in early warning systems and emergency preparedness, by helping to identify areas at risk by their physical characteristics and vulnerability to flooding (Hagos et al., 2022). The goal is the timely implementation of preventive and preparedness measures to manage flood risk and eliminate the negative impacts of these events.

Effective flood risk mitigation requires among other, identifying watersheds most vulnerable to erosion. Morphometric analysis and quantitative evaluation serve as essential tools for comprehensively understanding and characterizing drainage basins and their systems. These methods provide insights into the development processes of drainage networks and the complex interactions between various soil erosion processes (Bashir and Alsalman, 2023). Recognizing watersheds highly prone to soil erosion provides policymakers, researchers, and planners with valuable insights for developing targeted strategies and implementing mitigation measures.

The objective of this research is to explore the interplay between flooding and erosion. Specifically, the study aims to assess and map flood hazard in the study area by employing Fuzzy Analytical Hierarchy Process (FAHP) method using six (6) flooding hazard factors and to prioritize erosion-prone drainage basins through the application of a composite index based on eight (8) morphometric parameters. This integrated approach facilitates a comprehensive evaluation of the study area's vulnerability, contributing to a deeper understanding of the synergistic effects of these hazards. While much research has focused on flood hazard or soil erosion individually, the combined assessment of these hazards is still limited. This study aims to fill this gap by exploring the interactions of these factors in Northern Evia Island.

Study area

The study area is located in the northern part of Evia Island, in Central Greece, and covers 1842.3 km2 (Figure 1). It consists of one hundred eighty-nine (189) drainage basins, whereas the total channel length of the drainage networks is approximately 3745.6 km (Figure 2) (Valkanou et al., 2022). A significant role in the evolution and shaping of the morphological features of the area is played by the northern Evia Gulf. The fault structures of the study area correspond to two submarine opposing zones of normal faults, oriented NW-SE, which define the mountainous relief of the northern part of the island and separate it from the northern Evia Gulf to the west and the Aegean Sea to the east (Leeder and Jackson, 1993). The submarine fault zones along the eastern and western coasts are responsible for the development of the relief in the study area (Figure 1). Lithologically the study area consists of carbonate rocks, ophiolites, schists, cherts, marls, and sandstones, while alluvial deposits occur along the major channels of the drainage networks as well as at the mouth of the rivers.

Methods

The flood hazard has been calculated using Fuzzy Analytic Hierarchy Process (FAHP) and GIS, which is an advanced extension of the classical method. The weighting coefficients were calculated alongside the fuzzy utility of the alternatives, providing better representation of judgments and uncertainty. The triangular membership function (l, m, u) was used. The parameters were ranked and compared in pairs, resulting in fuzzy weights that were normalized. The results were verified using the consistency ratio, and in the final stage, the parameters were combined through a weighted linear combination to produce the flood hazard map. Six criteria were considered (determined by literature review): slope, elevation, precipitation, lithology, hydrographic density, and land use (Ogato et al., 2020). The natural breaks classification method was used to categorize the watersheds into four classes of flood hazard: very high, high, moderate and low/very low.

The second part of the study evaluates and prioritizes 189 drainage basins by calculating a compound parameter derived from eight morphometric indices within a GIS environment. Linear parameters (bifurcation ratio, drainage density, stream frequency, and texture ratio) and shape parameters (circularity ratio, form factor, elongation ratio, and compactness ratio) were used to assess erosion susceptibility (Gajbhiye et al., 2014). Based on the values of these morphometric parameters the drainage basins were classified into soil erosion susceptibility categories. After the priority ranking, a compound parameter which corresponds

to the average of the ranked values, was calculated. The compound parameter was finally ranked based on the parameters' priorities (small numbers correspond to higher priority). The natural breaks classification method was then used to categorize the watersheds into four classes of soil erosion susceptibility: very high, high, moderate and low/very low.

Figure 1. DEM and main tectonics of the study area

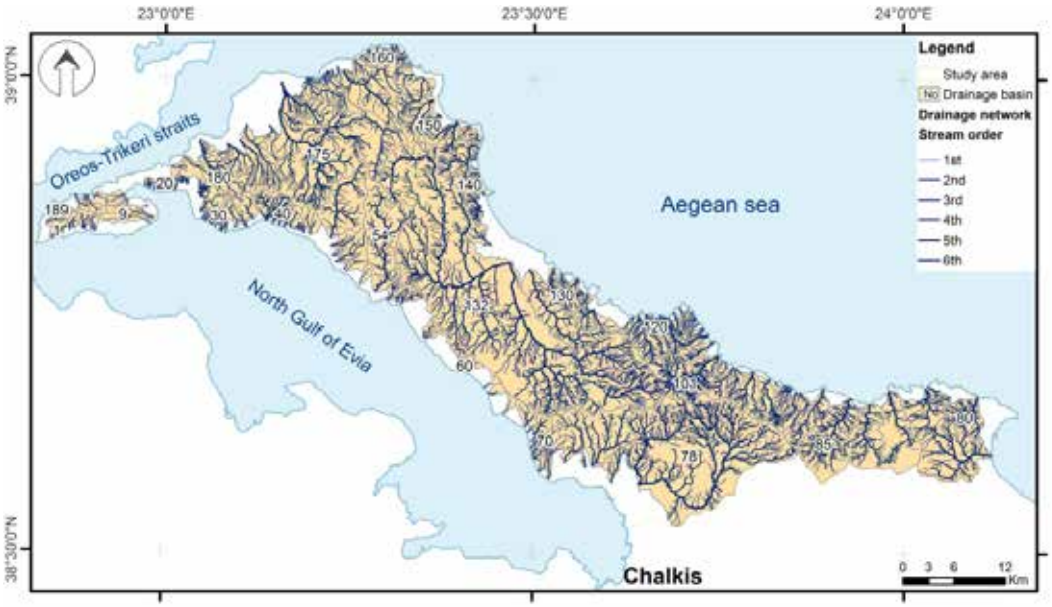

Figure 2. The drainage networks of the study area and their corresponding catchments.

Results

Based on the above mentioned methodology, a ranking table for flood hazard contributing factors and a weighted comparison table were prepared. A summary of the information applied to generate the flooding hazard map, the factors, their weights and rankings, are listed in Table 1. The ranking of each reclassified factor was determined through a comprehensive literature review, with factors of highest influence assigned a rank of 5 and those with the lowest influence assigned a rank of 1.

The flood hazard assessment classified the study area into four hazard categories, as depicted in Figure 4. The results indicate that approximately 30% of the area falls under the "very high hazard" category, 11.8% under "high hazard," 11.2% under "moderate hazard" and 47% under the "low hazard" category. Subsequently, the drainage

basins were prioritized based on the values of the estimated morphometric parameters. The final priority ranking and the composite parameter are presented in Table 2 while the spatial distribution of the prioritized basins is illustrated in Figure 5. Drainage basins No1-37 which are the most prone to erosion, are classified as having a very high priority, covering 16.4% of the study area. Drainage basins No 38-75 follow with high priority, encompassing 46.4% of the area. Finally drainage basins 76-113 are characterized as moderate priority covering 26.8% of the study area. Particularly, specific drainage basins No 40-41, 130-131 and 181 (located south of Mantoudi and north of Rovies) require the highest level of soil erosion management, covering an area of 251km^2. In contrast, drainage basins 63-64, 13-14 and 145, exhibit lower level of degradation and therefore require a lower level of soil erosion priority.

Maps resulting from the two analyses, flood hazard and prioritization, were overlaid, and it was observed that 52.8% of the basins' areas, which were classified as more susceptible to erosion, fall within a very high to moderate flood hazard zone. These zones are located up to 200 m and correspond to low and gentle slopes in the northern part of the study area, while in the western and southeastern parts of the study area, these zones are found at higher elevations and steeper slopes (Figure 3).

The analysis identified areas of very high to high flood hazard, covering 58.2% of the study area, and prioritized the drainage basins based on the compound parameter values, highlighting 113 basins as being most susceptible to erosion (categorized as very high to moderate hazard). Geological factors, including Neogene and Quaternary formations, intense neotectonic deformation in the northern and eastern part of the island, and high precipitation levels, may contribute to increased sediment supply and amplify erosion. This study highlights the critical need for soil conservation measures, particularly in the high priority basins that have the highest erosion risk, to mitigate potential environmental and socio-economic impacts of further soil degradation.

Historical flood events and existing flood hazard maps (YPEN, 2023) align with these findings, confirming the vulnerability of the identified areas. To further validate the results, two additional prioritization methods, based on morphometric parameters (as proposed by Singh et al., 2021, and Kadam et al., 2021), were applied. The results from these methods were in strong agreement with the findings of the present study.

Table 1. Weighted flood hazard ranking.

Parameters	Weight	Reclassified Parameter	Ranking	Parameters	Weight	Reclassified Parameter	Ranking
Land cover	0.36	Coniferous forest, mixed forest and broadleaf forest	1	Rainfall (mm)	0.11	400-500	1
		Land occupied by agriculture/natural vegetation	2			500.001-600	2
		Natural Pastures, grasslands and shrubs	3			600.001-700	3
		Scattered urban development, beaches etc	4			700.001-1.100	4
Slope (degree)	0.27	27.28-68.84	1	Drainage density (km/km^2)	0.05	2.97-4.52	1
		16.48-27.27	2			2.09-2.96	2
		7.3-16.47	3			1.2-2.08	3
		0-7.29	4			0-1.19	4
Lithology	0.18	Group 1 (alluvial deposits, recent talus cones and scree)	1	Elevation (meters)	0.03	743.77-1733.18	1
		Group 4 (limestones, dolomites, greywackes)	2			443.54-743.76	2
		Group 2 (marls, sandstones, schists, cherts, and travertines)	3			204.72-443.53	3
		Group 3 (schists and phyllites)	4			0-204.71	4

Figure 3. Field photos

Figure 4. Flooding hazard map of the study area

Table 2. Watershed prioritization analysis results based on the morphometric parameters (the blue colour indicates the morphometric parameters which are directly related to soil erodibility, while the pink colour corresponds to the morphometric parameters that are inversely related to soil erodibility)

Watershed No	Bifurcation ratio Rb	Drainage density Dd	Stream frequency Df	Circularity ratio Rc	Form factor Rf	Elongation ratio Re	Drainage texture T	Compactness coefficient Cc	Compound parameter	Priority rank
1	14	156	151	138	116	116	121	67	109.88	142
2	148	157	143	76	62	62	144	112	113.00	148
3	144	174	139	142	96	96	138	113	130.25	172
4	125	170	123	53	155	155	112	75	121.00	161
5	133	77	28	128	100	100	99	168	104.13	134
6		47	84	106	76	76	152	180	103.00	131
7	46	137	134	119	58	58	122	86	95.00	105
⋮	⋮	⋮	⋮	⋮	⋮	⋮	⋮	⋮	⋮	⋮
182	53	187	182	78	117	117	162	36	116.50	153
183	47	172	161	171	157	157	129	65	132.38	174
184	153	180	177	64	85	84	167	70	122.50	163
185		44	98	79	64	64	158	178	97.86	117
186		81	74	143	126	126	148	181	125.57	169
187	50	135	136	34	88	88	135	94	95.00	106
188	45	128	108	56	40	40	118	109	80.50	56
189	4	136	156	102	74	75	123	61	91.38	91

Figure 5. Prioritized Ranks Map of Erosion-Prone Drainage Basins Based on Geomorphometric Analysis

Conclusions

A quantitative geomorphological analysis, which forms the basis for assessing flood hazard and prioritizing watersheds according to erosion susceptibility, is the first step in identifying catchments that require flood and erosion management interventions. In this study, land use/land cover, elevation, slope, drainage density, soil, and rainfall were considered critical factors for assessing flood hazard (Figure 4). Drainage basins were then prioritized based on their linear and shape parameters (Figure 5).

The flood hazard mapping identified three (3) main extended areas under the high flood hazard category, near Istiaia (Sarantaporos River), near Psachna (Messapios River) and near Mantoudi (Voudoros River). Smaller areas under the moderate flood hazard category were identified near Aedipsos, Rovies, and Psaropouli. Most high and moderate flood hazard areas are distributed across relatively low and gentle terrain within the study area.

In contrast, the prioritization analysis revealed that 113 of 189 drainage basins, including the two (2) largest watersheds, fall under the very high to moderate erosion susceptibility category. These basins are distributed across the study area, rather than concentrated in specific regions, although areas classified as high flood hazard zones correspond to prioritized erosion-prone drainage basins. This correlation highlights that flooding is strongly linked to increased sediment supply from surface runoff on steep hillsides and areas with high slope gradients. Sediment discharged into the lower reaches increases flood hazard.

It is important to note that not all sediments are deposited in the lower reaches, as demonstrated by patterns observed in the eastern part of the study area. The Dirfis Fault Zone plays a crucial role, as the uplifted footwall is not under high flood hazard, even though the drainage basins in this area are prone to erosion. In contrast, the Telethrio Fault Zone has a synergistic effect on soil erosion and flooding. It crosses the area near Rovies, at the fan apex, converting and maintaining the hanging wall as a sediment deposition zone. This process significantly increases the flooding hazard in the region.

These findings highlight the need for an integrated strategy in flood and erosion management, emphasizing the importance of focused interventions in high-risk areas and promoting a holistic framework for disaster risk reduction. Future studies could explore the impacts of climate change on flood and erosion dynamics in the region, as well as investigate the potential effects of human activities such as deforestation and urbanization on these hazards.

Acknowledgements

We would like to thank the Organizing Committee of the Congress and the Geological Society of Greece.

References

Wang, Y., Hong, H., Chen, W., Li, S., Panahi, M., Khosravi, K., Shirzadi, A., Shahabi, H., Panahi, S., Costache, R., 2019. Flood susceptibility mapping in Dingnan County (China) using adaptive neuro-fuzzy inference system with biogeography-based optimization and imperialistic competitive algorithm. J. Environ. Manag. 247, 712–729. https://doi.org/10.1016/j.jenvman.2019.06.102.

UNDRR, 2023. Global flood impact and trends: Annual disaster report. United Nations Office for Disaster Risk Reduction.

Hagos, Y.G., Andualem, T.G., Yibeltal, M., Mengie, M.A., 2022. Flood hazard assessment and mapping using GIS integrated with multi-criteria decision analysis in upper Awash River basin, Ethiopia. Appl. Water Sci. 12 (7), 148. https://doi.org/10.1007/s13201-022-01674-8

Bashir, B., & Alsalman, A., 2023. Geospatial Analysis for Tectonic Assessment and Soil Erosion Prioritization: A Case Study of Wadi Al-Lith, Red Sea Coast, Saudi Arabia. Applied Sciences, 13(22), 12523. https://doi.org/10.3390/app132212523

Valkanou, K., Karymbalis, E., Bathrellos, G.D., Skilodimou, H.D., Tsanakas, K., Papanastassiou, D., Gaki-Papanastassiou, K., 2022. Soil Loss Potential Assessment for Natural and Post-fire Condition in Evia Island, Greece. Geosciences, 12 (10): 367. https://doi.org/10.3390/geosciences12100367

Leeder, M.R., and Jackson, J.A., 1993. The Interaction between normal faulting and drainage in active extensional basins, with examples from the Western United States and Central Greece. November 2007 Basin Research 5(2):79 – 102 DOI: 10.1111/j.1365-2117.1993.tb00059.x

Ogato, G.S., Bantider, A., Abebe, K., Geneletti, D., 2020. Geographic information system (GIS)-Based multicriteria analysis of flooding hazard and risk in Ambo Town and its watershed, West shoa zone, oromia regional State, Ethiopia. J. Hydrol. Reg. Stud. 27, 100659 https://doi.org/10.1016/j.ejrh.2019.100659.

Gajbhiye, S., Mishra, S.K., & Pandey, A., 2014. Prioritizing erosion-prone areas through morphometric analysis: An RS and GIS perspective. Applied Water Science, 4, 51–61. https://doi.org/10.1007/s13201-013-0129-7.

YPEN - Ministry of Environment and Energy, 2023. 1st Revision of Flood Risk Management Plans for River Basin Districts of Attica (EL06), Eastern Central Greece (EL07), and Aegean Islands (EL14), Deliverable 5: “Flood Hazard Maps, Technical Report”.

Singh, W. R., Barman, S., & Tirkey, G., 2021. Morphometric analysis and watershed prioritization in relation to soil erosion in Dudhnai Watershed. Applied Water Science, 11(151). https://doi.org/10.1007/s13201-021-01483-5

Kadam, A. K., Jaweed, T. H., Kale, S. S., Umrikar, B. N., & Sankhua, R. N., 2019. Identification of erosion-prone areas using modified morphometric prioritization method and sediment production rate: A remote sensing and GIS approach. Geomatics, Natural Hazards and Risk, 10(1), 986–1006. https://doi.org/10.1080/19475705.2018.1555189

17th INTERNATIONAL CONGRESS of the Geological Society of Greece

BULLETIN OF THE GEOLOGICAL SOCIETY OF GREECE, SP. PUBL.

EXTENDED ABSTRACT 337

Preliminary results on geological and hydrogeological conditions in Vilia, Attica, Greece

Vardava A. [1], Kyriakopoulos V. [1], Skourtsos E. [1], Filis C. [1]

(1) Department of Geology and Geoenvironment, National and Kapodistrian University of Athens, Athens, Greece, eskourt@geol.uoa.gr

Introduction

The factors that influence the occurrence of a spring are analogous to those that govern the formation of aquifers. In addition to climatic conditions, these include morphology, lithology, and tectonic structures. Therefore, an understanding of the geological setting of the area under study is essential to ensure that the hydrogeological conclusions drawn are accurate, especially when these springs are utilized for the water supply of the local population.

This study focuses on the eastern sector of Mount Kithairon in Western Attica, particularly the hill known as Malliaras or Lestori, situated north of the residential area of Vilia. The objective of the research is to identify the geological and hydrogeological conditions of the region, to interpret the emergence of springs observed on the slopes of the hill, to define the margins of the hydrogeological basin of the springs, and to assess the expected water reserves therein.

Morphology and Geological Setting

The Malliaras hill, which constitutes the area of research, is located on the southern slopes of the eastern section of Mount Kithairon, north of the settlement of Vilia. The hill displays an average orientation of northwest to southeast, extending approximately 2 km in length and 1 km in width, rising from an elevation of 550 m in the vicinity of the settlement to 986 m at its highest southeastern peak.

Geologically, the broader region is comprised of alpine rocks that belong to the Sub-Pelagonian or unmetamorphosed Pelagonian Unit. Within the research area, only the Upper Paleozoic and Triassic formations of this unit are present, represented primarily by a Permian-Triassic mainly clastic formation and an overlying Triassic carbonate sequence. Tectonically, the area is characterized by two thrust sheets, which are separated by two thrust faults, tectonically overlying a comparatively autochthonous carbonate series (Figure 1).

The Lower to Middle Triassic formation is comprised of thin-bedded to bedded limestones of the Hallstatt facies, intercalated with cherts, sandstones, clay shales, and tuffs. This formation in the research area exhibits a small outcrop on the southeastern slopes of the hill, uphill of the Church of Panagia Gkouras, at the base of the upper thrust sheet.

The Middle to Upper Triassic carbonate formations consist of thick-bedded to bedded limestones, dolomitic limestones, and dolomites. In contrast, those of the Upper Triassic are composed of ash-gray to black, thin-bedded to bedded, laminated limestones and dolomitic limestones featuring thin intercalations and nodules of chert. Together, these two formations constitute both the relatively autochthonous series and the upper thrust sheet of the study area.

Thin alluvial deposits are found along the streams surrounding the hill. In contrast, scree and colluviums occupy a significant expanse, covering a considerable portion of the southwestern and eastern slopes of the hill.

The structure of the overlapping thrust sheets has been disrupted by more recent normal faults striking E-W which define the Malliara hill to the north and south and dip to the south. More significant is the large high-angle normal fault distinguished along the base of the southern slopes of the hill, on the northern periphery of the Vilia settlement.

Precipitation

Table 1 presents the monthly precipitation data for the years 2012 to 2023 at the Vilia Station in Attica, of the National Observatory of Athens (N.O.A.). In certain months, there are no precipitation records, as the station was not operational during that time. The months highlighted in gray contain precipitation records, yet these do not accurately reflect the overall precipitation, as the station's data for that specific month was incomplete (possibly due to being non-operational for several days or having sustained some form of damage).

From this table, it is evident that the precipitation in the region varies between 618 mm and 961.2 mm, with an average value of 742 mm over the aforementioned years.

Hydrogeological Classification of Geological Formations

The formation of the Upper Paleozoic – Lower Triassic is considered practically impermeable. The thin interlayers of thin-bedded, marly limestones and of the sandstones do not constitute significant aquifers.

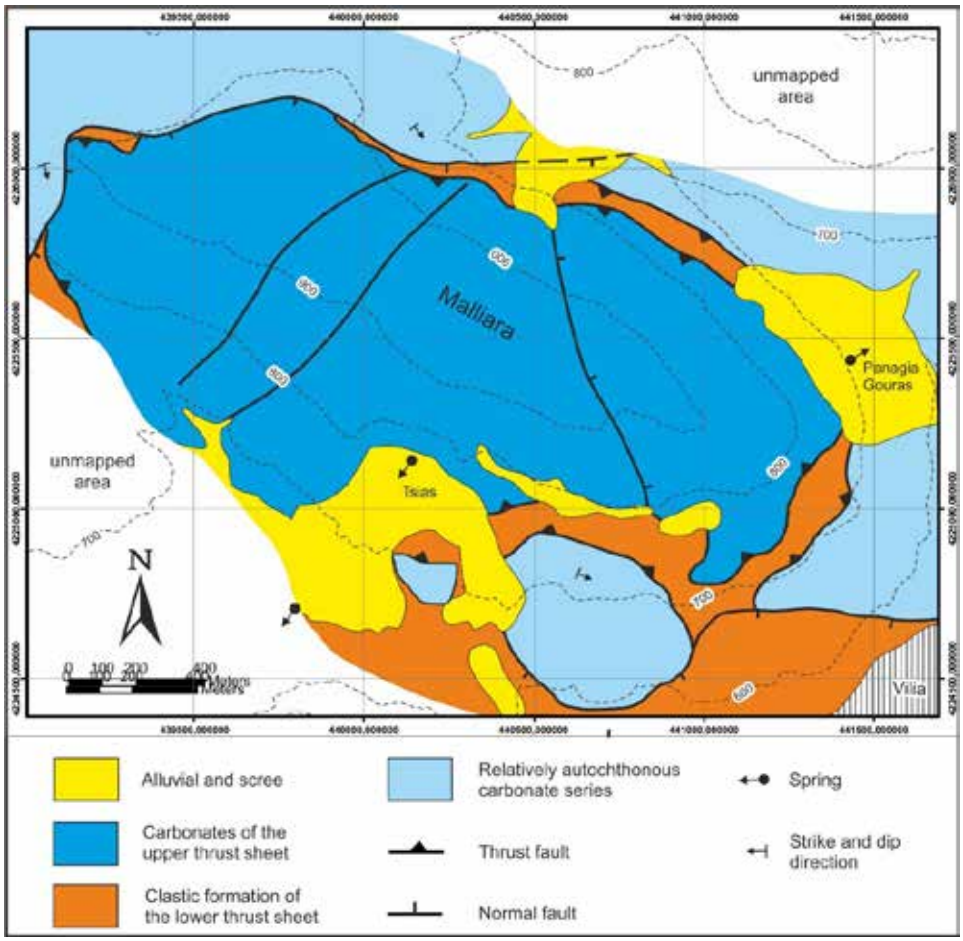

Figure 1. Geological map of the study area.

The carbonates of the Lower - Middle Triassic are wedged between the two thrust sheets. Their thickness is merely around 10 m, essentially forming a cohesive aquifer with the overlying carbonates of the upper thrust sheet.

Table 1. Precipitation records (mm) for the period 2012-2013 at the Vilia Station of the N.O.A.

Year	1	2	3	4	5	6	7	8	9	10	11	12	Annual
2012	51.4	129.8	32.0	85.8	20.6	0.0	0.0	3.8	24.2	63.8	64.8	168.8	645.0
2013	109.2	188.8	30.4	12.6	14.4	24.8	1.0	0.0	0.4	47.6	192.4	91.4	713.0
2014	60.2	22.0	146.0	69.2	1.2	18.0	3.2	5.8	34.0	69.6	58.4	187.6	675.2
2015	41.2	126.2	169.0	25.8	16.2	18.6	4.6	7.6	83.8	163.8	48.8	17.6	723.2
2016	94.4	72.2	94.0	0.0	15.0	6.0						49.6	331.2
2017	74.8	30.6	133.2	13.2	108.2	132.4	36.4	0.0	30.6	10.6	194.0	28.0	792.0
2018	153.6	119.4	13.0	5.2	88.4	57.6	56.0	42.0	175.2	13.2	87.2	127.2	938.0
2019	281.8	159.4	85.8	69.4	9.4	5.8	7.2	0.2	25.6	38.8	185.6	92.2	961.2
2020	86.6	98.4	70.4	129.4	20.8	50.8	0.2	17.0	16.0	26.4	55.0	208.4	779.4
2021	106.6	26.0	63.6	33.4	2.4	44.4	0.0	4.4	8.6	75.4	74.6	175.4	614.8
2022	127.2	83.0	39.2	18.0	53.2	22.2	10.2	28.8	18.6	44.2	89.6	83.8	618
2023	97.6	44.0	72.6	46.4	50.2	73.4	0.0	5.0	105.0	3.8	47.2	152.0	697.2

The carbonates of the Middle - Upper Triassic that comprise the eastern sector of the upper thrust sheet are characterized by significant fracturing and dense fissuring, which has led to considerable karstification. The carbonates of the Upper Triassic, which form the central and western sectors of the upper thrust sheet as well as the lower comparatively autochthonous series, are characterized by their thin-bedded texture with intercalations of cherts and are frequently dolomitized. However, they are also highly folded, densely fractured, and exhibit surface indications of

karstification. These two carbonate formations present a satisfactory coefficient of permeability.
The alluvial deposits, in practice, show no significant groundwater presence. In contrast, the scree formation demonstrates greater surface distribution and thickness. This formation consists of highly permeable materials and harbors groundwater during the wet seasons.

Aquifers and springs

The presence of groundwater in the research area was identified within the upper thrust sheet and the scree. The groundwater within those formations is discharged from two main springs, along with several considerably smaller ones.
The two main springs are discharged from the upper thrust sheet. The more prominent of the two is in the courtyard of the Church of Panagia Goura, situated at the southeastern edge of the hill and at an elevation of 697 m. This spring has formed at the tectonic contact of the carbonates of the upper thrust sheet and the impermeable clastic rocks of the lower one. Notably, however, the spring appears within a small cavern, situated a few meters lower in elevation than the tectonic contact, encompassed by fallen carbonate masses and scree that have obscured the tectonic contact.

Figure 2. The Panagia Gouras Spring is located in the courtyard of the church within a small cavern. A wall with a metal door has been constructed to isolate the spring, while next to it there is a tank for collecting the outflowing water.

According to an earlier report from EAGME (Gintoni et al., 2021), the discharge rate of the spring in January 2021, which falls midway through the wet season, was recorded at 35 m³/h, whereas in November 2020, marking the onset of the wet season, it measured 25 m³/h.
The second spring is located in the southwestern slopes of the hill, also at the tectonic contact between the two thrust sheets and is referred to as the Tsias Spring. This spring exhibits a relatively lower discharge rate than its

counterpart. The water flows within the limestones, where a small collection basin has been constructed, open at the top, from which the water is conveyed through pipes to a reservoir situated approximately one kilometer west of the Vilia settlement, adjacent to the Church of Panagia Zoodochou Pigi.
On the southwestern slopes of the hill, there are lateral debris of considerable thickness and sliding limestone blocks of various sizes, forming a cover overlying the formation of the lower thrust sheet, which extends to the base of the hill. Through this cover, during wet periods significant quantities of water are transported that are discharged from small contact springs at the base of the hill, near the Church of Panagia Zoodochou Pigi.
The occurrence of the two springs is due to the geometry of the fault between the two thrust sheets. This fault contact has the shape of a turtle shell, simulating the morphology of the hill on which it is observed. This geometry results in the formation of an underground drainage axis of approximately N-S strike that is almost identical to the position of a N-S fault crossing the upper nappe. Thus, two separate hydrogeological basins are formed, the largest one is discharged at the spring of Panagia Goura and the other at the smaller Tsias Spring.
The area of the hydrogeological basin of the Panagia Gkouras Spring is estimated to be 0.6 km². According to Table 1, the average annual precipitation over the past decade amounts to 742 mm; thus, the volume of precipitation is calculated to be 445,200 m³. Adopting an infiltration rate between 0.45 and 0.5 for the limestones (e.g., Dounas, 1971; Hatoupis, 2004), the volume of water that infiltrates ranges from 222,600 m³ to 200,340 m³, respectively.
The area of the hydrological basin of the Tsias Spring is estimated to be approximately 0.48 km², resulting in a precipitation volume of 356,160 m³ and an infiltration volume ranging between 178,080 m³ and 160,272 m³.
The recharge of the carbonates of the upper thrust sheet occurs exclusively through precipitation, and consequently, the discharge of the springs is directly dependent upon those inputs. As observed during the field investigation in early summer of 2024, all the small springs had run dry, while the two main springs exhibited a significantly reduced flow compared to the measurements recorded two years prior.
The relatively autochthonous series composed of carbonate rocks does not manifest any springs within the research area. Furthermore, the depth at which an underlying impermeable substrate may be encountered, as well as the geometry of their interface, remains unknown. Along the shores of the cove of Porto Germeno, approximately 9 km west of the study area, submarine springs are observed, which discharge corresponding carbonate formations (Dounas, 1971).
Upon conducting hydrochemical analyses of the springs, the water is found to be bicarbonate and magnesium-rich, which is understandable given that the aquifer is composed of carbonate formations.

Conclusions

The research area is part of the unmetamorphosed Pelagonian Unit, characterized by Upper Paleozoic and Triassic formations. These formations form two superimposed thrust sheets that overlie the relatively autochthonous series. The upper thrust sheet and the relatively autochthonous series comprise carbonate rocks that are identified as aquifer formations and exhibit karstification. These two carbonate sequences are separated by an impermeable layer composed of Permian-Triassic clastic rocks.
The aquifer of the upper carbonates is discharged by two springs observed at the tectonic contact between the two thrust sheets. Their formation is due to the geometry of the thrust fault, which is reconstructed in the form of a turtle shell, thus forming two small hydrogeological basins. The recharge of those springs is directly dependent on precipitation.
The carbonate formations of the relatively autochthonous series constitute a very good target for the investigation of the existence of groundwater in the area to further meet the water supply and irrigation needs of the area.

Acknowledgements

We thank Dr Sabatakakis P., hydrogeologist of EAGME for the help he offered to Aikaterini and Vasilis during their diploma thesis.

References

Gintoni E., Sabatakakis P., Tzima M., 2021. Proposed hydrological works for the improvement of water supply conditions in the Western district of Villia in the municipality of Mandra-Idyllia, Attica. Technical Report, EAGME, 22 p.
Dounas, A. G. 1971. The geology of the area between Megara and Erithrai village (Attica). Geological and Geophysical Research, 15/2, 250p.
Hatoupis, T., 2003. Geological research into the possibility of artificial enrichment of the karst aquifer of Northern Parnitha (SE basin of Boeoticos Asopos). Master Thesis, Department of Geology, National and Kapodistrian University of Athens, Athens, 295 p.

17th INTERNATIONAL CONGRESS of the Geological Society of Greece

BULLETIN OF THE GEOLOGICAL SOCIETY OF GREECE, SP. PUBL.

EXTENDED ABSTRACT 338

Contribution of Electrical Resistivity Tomography to the investigation of landslide conditions on slopes

Vargemezis G. [1], Tsourlos P.[1], Fikos I.[1], Amanatidou E. [1], Louvaris P. [1] and Tzima E. [1]

(1) Dept. of Geophysics, Aristotle's University of Thessaloniki, Thessaloniki, Greece, varge@geo.auth.gr

Introduction / Background

A key characteristic of flysch as a geological formation is its heterogeneity, a property that is generated by its composition, since it is composed of various rocks (clays, sandstones, marls, limestones and conglomerates). The alternation of these layers, especially if they are relatively thin and the clay layers predominate, creates a favorable environment for the development of interfaces in which landslides can occur. These conditions, especially on steep slopes, are aggravated by the presence of groundwater and under particular tectonic conditions.

The usual slope exploration methods, in addition to surface mapping, are enhanced by the digging of trenches and the drilling of geotechnical exploration boreholes. A characteristic of these methods is that they constitute point information and in locations that are most often dictated by local access conditions (vegetation, road network, soil conditions).

Geophysical methods that largely address these problems, such as geoelectric, seismic and ground radar, are called upon to contribute to this problem. Among them, we distinguish geoelectric tomography, as the most suitable for its application in difficult geomorphological environments but also in its ability to provide information with significant resolution for stratigraphy and the presence of groundwater.

This paper presents examples of geoelectric tomography carried out on slopes of a mountainous area dominated by the Pindos flysch consisting of alternations of sandstones, calcitic sandstones and clay shales. The data of the geophysical survey were correlated with those of the trenches and drillings carried out in the area.

From the interpretation carried out, it emerged that geoelectric tomographies have a special contribution in identifying locations where conditions favor landslides and in formulating proposals to prevent the development of landslide phenomena.

Geology geomorphology of the study area

The Flysch of the Pindus zone is found in the research area, which consists of alternations of sandstones and clayey schists with lenticular layers of conglomerates of varying lithological composition and thickness. It has undergone intense tectonics and exhibits a significant thickness that in places exceeds 1000 meters (Geological map of the Hellenic Geological Survey, 1984). With an area of approximately 500 acres, it exhibits an average slope of 17°.

Landslides have been observed in the wider area, which led to the geotechnical investigation of the area under investigation.

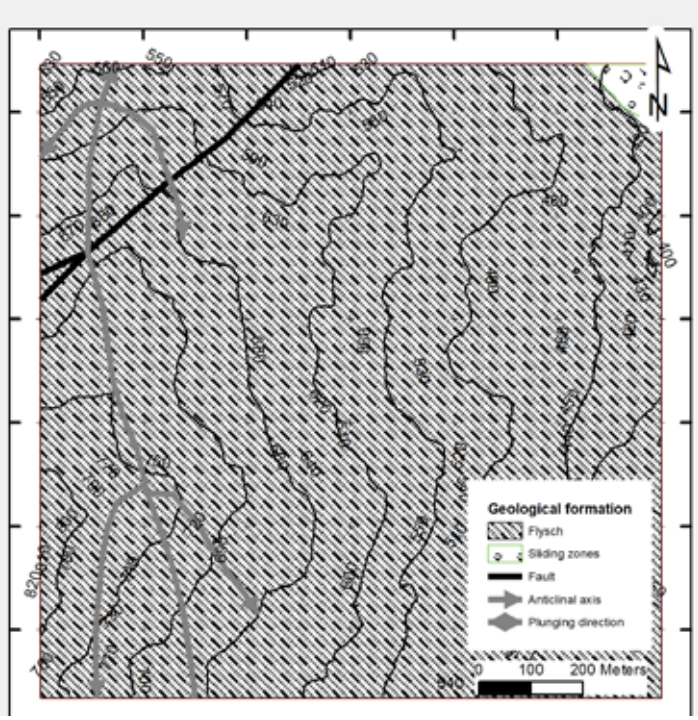

Figure 1. Geological map of the study area.

Geophysical methods for landslides investigation

Geophysical commonly used to the investigation of landslides are Electrical Resistivity Tomography (ERT), Shallow Seismic Refraction (SSR) and Ground Penetrating Radar (GPR) (Taborik *et al.*, 2017). The main target of geophysical investigation is the detection of the possible failure interfaces, taking advantage of the geophysical contrast between different lithological layers. A major role in the activation of such an interface and thus, the provocation of a landslide, is the groundwater content within the layer affected by slide processes.

Both targets are mostly covered by electrical and electromagnetic methods. Especially, geoelectrical tomography can provide accurate and reliable geoelectrical 2D and 3D models of the stratigraphy of an area under investigation along with the detection of groundwater, since the water content has a significant impact to the resistivity of the geological layer.

According to Pilecki (2017), the main advantages of the geophysical methods are the efficiency, the non-invasion, the multi-information, the penetration depth and the resolution they provide. Among the disadvantages of geophysical methods, is the ambiguity of the results of geophysical interpretations which is stronger in case of malicious data or limited resolution to the depth. To overcome this issue, more than one geophysical method is better to be used, and/or geophysical results need to be correlated with geotechnical information.

Case study: Field data acquisition, processing and results

Forty (40) geoelectrical tomographies were measured in the survey area. At each line, 24 electrodes were used at an inner distance of 2, 3 and 4 meters, depending on the desired depth of investigation and the local conditions. Dipole-Dipole and Multi Gradient arrays were measured, allowing the combination of the two data sets for the final inversion calculated in DC2dPro software (Kim, 2009).

Geophysical data were correlated with geological information provided by geotechnical drillings and pits. In five boreholes full core sampling has been done while in five boreholes piezometers have been installed. For the investigation of the weathering zone, twenty pits were dug, at 4 meters depth.

Below are presented typical examples from the combined interpretation of geophysical and geotechnical data.

ERT R24- BH 1

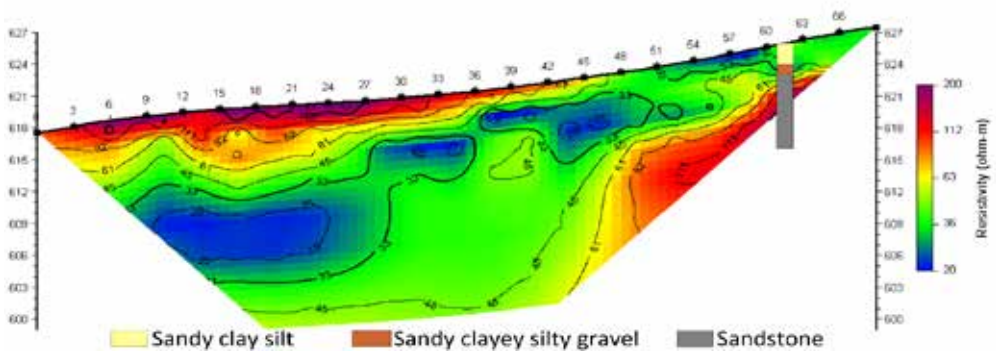

Figure 2. Borehole 1 superimposed to ERT 24 (from South to the North).

In Figure 2, we can see the resistivity model ion ERT 24 where the findings of the BH1 are sown. The first layer is 2 meters thick, and it is described as ashy - ash-yellow, very cohesive sandy clay loam of medium plasticity (decomposed flysch). The thin layer below is described as medium density clayey sandy gravels and the deeper formation (2.5 to 7.3m) is attributed to ashy sandstone.

The correspondence with resistivity values is shown in the next table.

Table 1. Correspondence of geological layers and resistivity values

Geological description	Resistivity (Ωm)
Ashy - ash-yellow, very cohesive sandy clay loam of medium plasticity (decomposed flysch)	25-32
Medium density clayey sandy gravels	33-45
Sandstone	80-110

In the first place, we can notice the very well correspondence between the resistivity model and the observations in the borehole samples.
The most important fact, however, is the lateral change of the geological structure just a few meters far from the location of the borehole. The first jump of 4 meters of the sandstone is noticed just 3 meters to the south (beginning of the ERT) and the second of more than 12 meters, in the next 11 meters. The more clayey formation (blue lenses) seems also to have water content (resistivity values in the range of 33 to 45 Ωm).
In this case we can notice that, even the borehole met the sandstone -which is considered to be the stable formation in the area- at the depth of 2.5 meters, just several meters away, a fault makes the area possible to slide in certain conditions.
ERT R33- BH 2

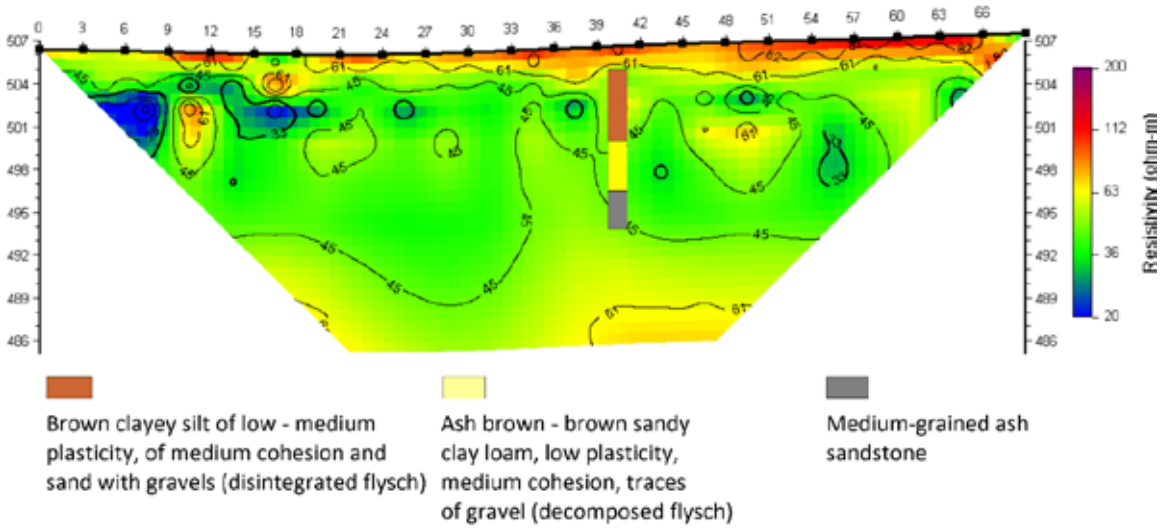

Figure 3. Borehole 2 superimposed to ERT 33 (from South to the North).

The borehole was drilled 10 meters to the east of the line and at the elevation of 505 meters. We can see that the most conductive resistivity layer corresponds to the green area (resistivity values between 45 and 33 Ωm) with less gravel than the overlying layer. The deeper layer is described as medium grained sandstone, while at the area between 6.5 and 7 meters, ash blue disintegrated flysch with indications of possible sliding (slickensided).

ERT R17- BH 4

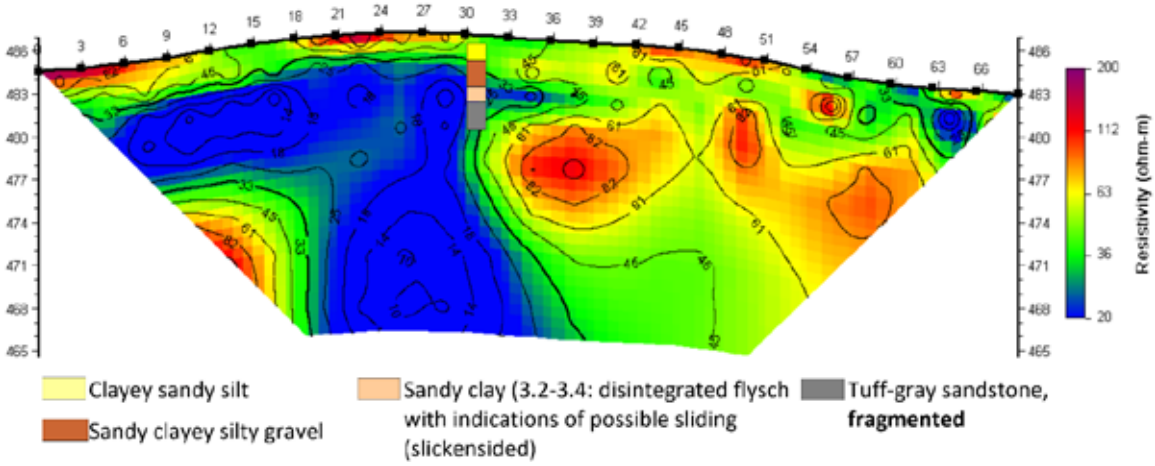

Figure 4. Borehole 4 superimposed to ERT 17 (from North to the South).

This is probably the most indicative example of the ERT contribution to the geotechnical evaluation of a slope. Surficial layers correspond to clayey sandy silt and sandy clayey silty gravel, followed by a thin layer which is described as

possible sliding and at the bottom (of the borehole) the fragmented sandstone.
The borehole is in total agreement with the resistivity model which shows that the borehole is drilled exactly on the fault. The formation at the northern half part of the resistivity model is very clayey showing the disintegrated of flysch, probably decomposed clay shale. The most important information arising from this example is that the model is entirely a 2D model and the borehole information is not enough to reveal this structure.

Concluding remarks

Investigation of slopes, geologically constructed by flysch formation, aiming to the detection of possible failure surfaces, is very difficult, because of the high inhomogeneity of the structure.
Information from boreholes, even is a direct and indisputable, is still a point one. This is an important disadvantage for the investigation plan since, in addition, the amount of boreholes that can be drilled is limited because of access problems and the high cost of geotechnical, full core sampling drillings.
In this article, the contribution of the Electrical Resistivity Tomography method aiming to combined interpretation with geotechnical data is suggested.
Especially in large areas, where flysch is met and inclination of the slope(s) is high, electrical resistivity tomography is suggested among other geophysical methods that could be used. The main reason for this suggestion is that, except for the fact that it can be easily adapted to rough terrains, it can provide reliable information about the presence of groundwater in 2 and 3D complicated geological models.

References

IGME, 1984. Geological map of Greece. Sheet Mouzaki.
Taborik, P., Lenart, J., Blecha, V., Vilhelm, J., Tursky, O., 2017. Geophysical anatomy of counter-slope scarps in sedimentary flysch rocks (Outer Western Carpathians), Geomorphology 276, 59-70.
Pilecki, Z., 2017. Basic principles for the identification of landslides using geophysical methods. AG 2017 - 3rd International Conference on Applied Geophysics, E3S Web of Conferences 24, 01001.
Kim, J.H., 2009. DC2DPro-2D Interpretation System of DC Resistivity Tomography. User's Manual and Theory, Publisher: KIGAM, S. Korea.

17th INTERNATIONAL CONGRESS of the Geological Society of Greece

BULLETIN OF THE GEOLOGICAL SOCIETY OF GREECE, SP. PUBL.

EXTENDED ABSTRACT 339

Mineralogical and Petrographic study of Hellenistic stamped transport amphorae from the area of Aigion, NW Peloponnese, Greece.

Athanasios Varotsos[(1)], Konstantinos Filis[(2)], Vayia Xanthopoulou[(1,3)], and Ioannis Iliopoulos, I.[(1,4)]
(1) KERAMOS Research Group, Department of Geology, University of Patras, University Campus, 26504 Patras, Greece, avarotsos@ac.upatras.gr, (2) Hellenic Ministry of Culture, Ephorate of Antiquities of Chalcidice and Mount Athos Ippodromiou square 7, 546 22 Thessaloniki , (3) Laboratory of Electron Microscopy and Microanalysis, School of Natural Sciences, University of Patras, 26504 Patras, Greece, (4) Institut d'Arqueologia, Universitat de Barcelona (IAUB), c/ Montalegre 6-8, Soterrani 08001 Barcelona, Spain

Introduction

During the Hellenistic period (323–32 BC), the city of Aigion, in the NW Peloponnese, Greece, was a prominent city-state and served as the capital of the Achaean League. The population of the city grew rapidly during this period, and the city also experienced economic growth. After the defeat of the Achaean League by the Romans in 146 BC, Aigion gradually lost its political importance and primacy on the see routes to Patras, the main gateway for the Romans to and from the Italian peninsula. The city flourished again in the 1st century BC, when Italian merchants were settled there. By the end of that century, the population had increased again and economic vitality had been established. After extensive archaeological research kilns, waste pits, workshops and probably a site associated with ancient Agora have been discovered in the city. Located in the northwestern Peloponnese, the area in which the city is situated, is geologically part of the Pindos geotectonic unit, which is a sequence of carbonate and silicate rocks, with a total thickness of 1050m. This sequence is overlain by the syntectonic classical sequence of the Pindian flysch. The Upper Triassic-Jurassic formations and Jurassic-Lower Cretaceous age have been identified in this unit. The Upper Triassic-Jurassic formations consist mainly of sandstones and marls alternations with limestone intercalations, while the upper strata consist of stratified limestones. Similarly, the Jurassic-Lower Cretaceous formations which consist of thin red siltstones and chert alternations (Xanthopoulou, 2019), underlie the Cretaceous pelagic limestones.
This paper, part of the research activities of the KERAMOS Research Group at the Department of Geology, University of Patras, Greece, investigates the mineralogical and petrographic characteristics of Greek transport amphorae and two fragments of tiles discovered in the Trapeza Aigion area in northwestern Peloponnese, where Ancient Rypes was located.
The study aims to shed light on ceramic technology in the region during the Hellenistic – Early Roman period by analyzing this ceramic assemblage. Specifically, it explores the origins of the raw materials used in their production (Amphoras types I, II and III), the ceramic manufacturing processes, and the technical expertise of the potters. Additionally, the study examines trade aspects and production techniques of the era, offering a comprehensive framework for understanding the economy and society of the period.

Methods

A sample set of 27 specimens were carefully selected among the studied repertoire of the amphoras assemblage considering the representativeness of the three main amphoras typologies (I, II, and III). In more detail, amphorae of type I (A5, A7, A9, A10, A11, A15, A16, A17, A18, A19, A20, A21, A22, A23, A24; n=15) have a height of 64 cm, with a rim diameter of about 12 cm, a base diameter of 3.5 cm, a maximum body diameter of approximately 40 cm, and with a capacity of approximately 38 litres (Filis, 2019). The rim is usually beak-shaped, rarely oval in cross-section and quite thin (Filis, 2019). The neck of the amphoras of type I is mainly cylindrical, relatively narrow and short, and in some cases has slightly inwardly sloping walls (Filis, 2019). The amphora has a broad oval shaped body with an extremely narrow knob type base and its outline is curved (Filis, 2019). The handles of the amphorae, are thin and oval in cross-section, are slightly upwards and then curve sharply (Filis, 2019). In some cases, on their outer surface two or three vertical grooves can be observed, while they can also be rolled (bifid) handles, similar to the Koan type amphorae (Filis, 2019). Often only one of the handles has a rectangular banded stamp, measuring approximately 7x1.8 cm, with the name of the potter - fabricant engraved on it (Filis, 2019). Type II (A1, A4, A6, A8, A12, A13, A14, A25; n=8) is similar to the so called Greek Brindisian amphorae type, which is characterized by a high, vertical or outwardly sloping, thick rim, with a curve on its upper surface and two characteristic plastic bands, the upper one being larger than the lower one, placed on the upper part of the short neck (Filis, 2019). At the height of the band, solid, coarse handles of circular or almost circular cross-section are attached (Filis, 2019). These take at the upper part of the neck and then arch to the shoulder (Filis, 2019). One handle bears a rectangular banded type stamp, with names probably associated with ceramic workshop owner or the fabricant. In the type III amphorae (A2, A3; n=2), the rim is thick, quite high, with an angular outline and a maximum outer diameter ranging from 13.3 to 14.8 cm. The neck is low and has conical-shape, surrounded by two similar horizontal plastic ridges (Filis, 2019). It is estimated that the body of the type III amphorae was broadly ovoid, while the knob type base is small hemispherical (Filis, 2019). The han-

dles are solid, fairly robust, circular cross-section, with curves and more often without stamps (Filis, 2019). Two tile samples were also included, potentially playing the role of reference material.

The selected specimens were thin sectioned and grinded to powder using an agate mortar in the Minerals and Rocks Research Laboratory of the Department of Geology at the University of Patras. The thin sections prepared were examined using a Zeiss AxioScope A.1 polarizing microscope aiming to describe their mineralogical and petrographic characteristics which comprise the composition and the textural characteristics of the groundmass, the mineralogy of the non-plastic inclusions according to the methodology proposed by Whitbread (1995). Representative photomicrographs both under plane polarized light (PPL) and in crossed polars (XP) were captured employing a Jenoptik ProgRes C3 videocamera attached to the microscope and processed with ProgRes Capture Pro 2.5 software. The X-ray powder diffraction (XRPD) of the prepared powders was performed using the Bruker D8 Advance diffractometer of the Research, Minerals and Rocks Laboratory of the Department of Geology, University of Patras. This diffractometer has a Ni-Cu filter for Ka radiation and operates at 40kV/40mA conditions and is equipped with the Bruker LynxEye high-speed silicon strip detector. The scan range covered was 2°-70° 2θ with an interval of 0.015^{o} every 0.1s. The qualitative analysis of the XRPD patterns obtained was performed using the DIFFRACplus EVA software (Bruker-AXS, Madison, WI, USA) based on the ICDD Powder Diffraction File (2006 version). The XRPD analysis has permitted us to study the mineralogical composition of the analyzed samples for further confirmation of the petrographic results and in addition for obtaining information about the newly formed mineral phases, which are indicative of the firing conditions during the manufacturing process.

The information obtained from the petrographic analysis is important for identifying the source of the raw materials, for determining the composition of each sample and subsequently for understanding how it was produced, while information on the firing temperature of each sample and on the source of the raw materials can be obtained from the XRPD analysis in combination with the results of the petrographic analysis.

Results and Discussion

The examination of the thin sections under the polarizing microscope has led us to identify four petrographic fabric groups based upon the similarity of their textural and compositional characteristics. The EG1 group contains ferro-micaceous micromass with a wide variation in grain size (Figure 1A), the EG2 group, where the two tiles are classified, is characterized by the presence of micritic calcite and monocrystalline quartz (Figure 1B), the EG3 group by the presence of ferro-calcareous micromass and the absence of silt class in the finer paste (Figure 1C) and the EG4 group by the presence of ferro-calcareous micromass with pores (Figure 1D). The micromass of each group is ferrous-calcareous, excluding the group EG-1 which has a ferrous composition. Additionally, the clay paste of the EG-1 group has a micaceous composition, while the others have a calcareous one. Moreover, the use of grog seems to be a common practice as it is observed in all petrographic groups except from the group EG-2.

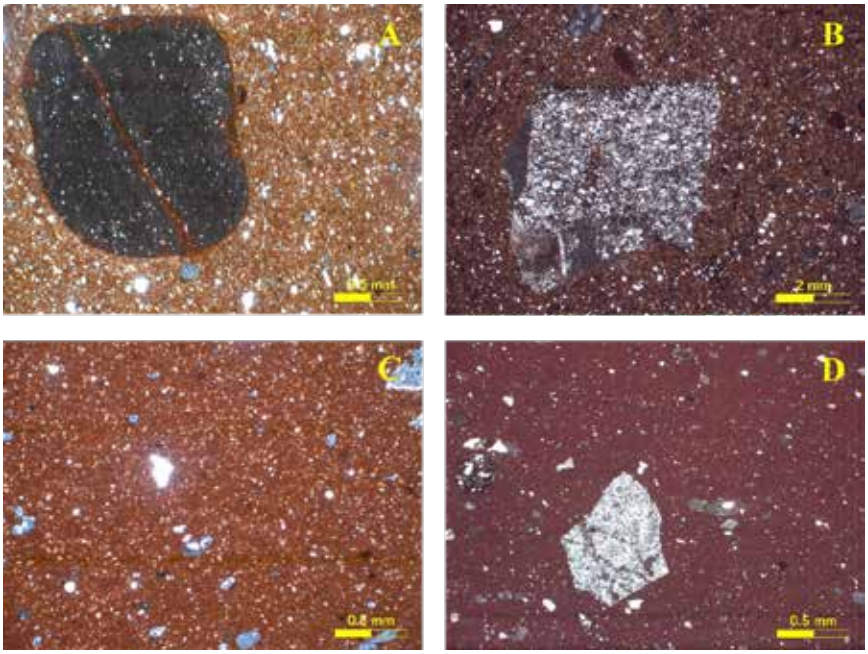

Figure 1: Representative photomicrographs of the petrographic fabric groups established during the present study. A. EG1 (sample A7); B. EG2 (sample A27); C. EG3 (sample A15); D. EG4 (sample A23). All pictures are taken in XP

In more detail, the EG1 group includes 12 samples (A1, A4, A6, A7, A8, A9, A12, A13, A19, A21, A24 and A25). The micromass appears optically inactive, with an olive-greenish brown color when observed under plane-polarized light (PPL) and light brown color under crossed polars (XP). In samples A1 and A8, mottled areas are observed due to the presence of secondary calcite and only these areas are optically active. Samples A1, A6, A7, A8, A9, A12, A13, A19, contain chert fragments in contrast to the remaining samples in this group. Sandstone fragments were also observed in samples A1, A6 and A8, while samples A6 and A19 also include fragments of reused pottery (grog). Regarding the plastic material, clay pellets are observed in sample A7 and characteristic clay striation lines are identified in samples A12 and A13. Finally, the predominant mineralogical component of the fine-grained micromass is white mica.

As for EG2, this group consists of 5 samples (A2, A3, A18, A26 and A27) with an optically inactive micromass with a brown color in plain polarized light (PPL) while in crossed Nicols (XP) the color is reddish brown. The dominant minerals of this group comprise monocrystalline quartz as well as micritic calcite. Moreover, opaque minerals are also observed in the samples and the micromass is impregnated by secondary microsparite. Finally, sample A18 contains brown mica and siltstone.

The EG3 group consists of 8 samples (A5, A10, A11, A15, A16, A17, A20 and A22) with an optically inactive micromass with a dark brown color in observation in the plain polarized light (PPL), while in the crossed Nicols (XP) it is reddish brown. The dominant mineral is monocrystalline quartz, whereas grog and secondary calcite are observed in most samples. In addition, in samples A5, A11, A17, chert fragments are present, with A17 containing siltstone fragments. Moreover, in samples A5, A10, A11, A15 and A16, striation lines are observed.

The EG4 group consists of 2 samples (A14 and A23) with an optically inactive ferro-calcareous micromass with many voids while quartz is the dominant mineral and grog is also present. Finally, in most of the samples the clay treatment is very good, which suggests very good know-how of the potters, especially as regards the addition and mixing of the clay with those materials that could give their ceramics the particular properties they wanted.

According to the evaluation of the XRPD patterns the samples studied were classified based on their common qualitative and semi-quantitative mineralogical characteristics into three mineralogical classes. The Class I includes 5 samples A11, A16, A21, A25, A26 (tile), which comprise quartz, calcite, plagioclase, illite, and only few quantities of diopside hematite and ± gehlenite. The presence of these minerals indicates that these samples were fired at moderate temperatures, and more specifically below or very close to 850°C (Gliozzo, 2020a). The class II is represented by 6 samples A1, A2, A3, A19, A20, A24 which consist of quartz, calcite, plagioclase, diopside, hematite, and ±gehlenite. The presence of these minerals indicates a firing temperature between 850°C-900°C, possibly reaching even higher temperatures (950°C) in some of the samples (Gliozzo, 2020a). The class III consists of 16 samples A4-9, A10, A12, A13 A14, A15, A17 A18, A22, A23, A27 (tile). The samples of this class consist of quartz, plagioclase, diopside, hematite, ±calcite and ±gehlenite. The presence of these minerals indicates a firing temperature above 900-950°C (Gliozzo, 2020a). It should be noted that the presence of calcite in the latter two classes (II and III) is due to the secondary formation of this mineral due to the burial condition, as was also verified by the petrographic evidence.

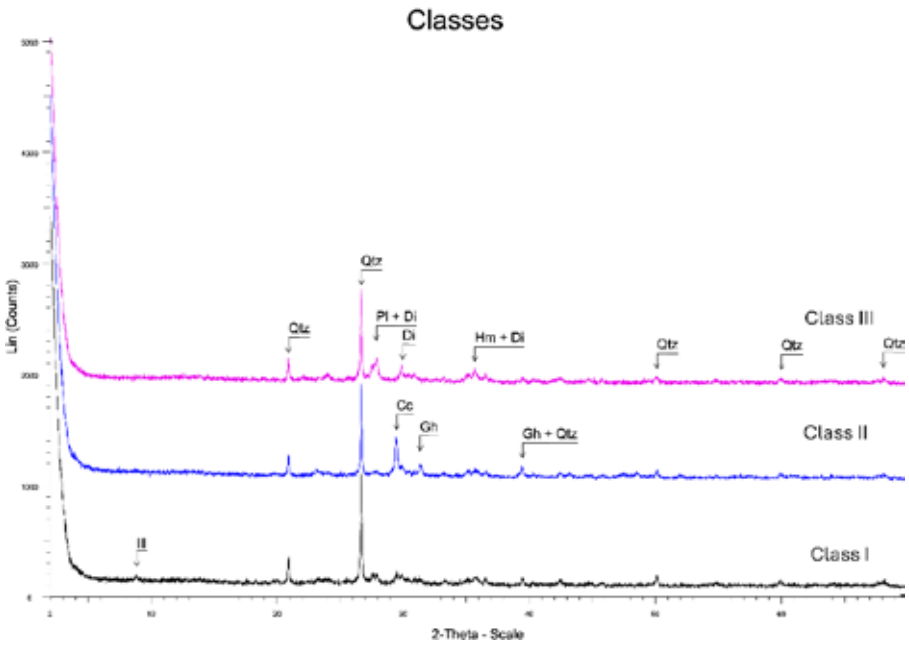

Figure 2: Representative diffractograms of the main mineralogical classes identified in the present study through XRPD. Qtz: Quartz, Pl: Plagioclase, Hm: Hematite, Gh: Gehlenite, Dio: Diopside, Cc: Calcite, Ill: illite

The correspondence between the data obtained from the petrographic analysis of the thin sections through the polarizing microscope and the XRPD analysis is presented in Table 1. With the exception of the samples classified in petrographic fabric group EG-4, which are fired in temperatures above 950°C, no specific firing pattern is emerging for the samples assigned to the rest of the fabric groups (ie. EG-1, EG-2 and EG-3).

Table 1: Comparative table of mineralogical classes and petrographic groups

Mineralogical classes XRPD	**Petrographic fabric groups**			
	EG-1	**EG-2**	**EG-3**	**EG-4**
Class I EFT< 850 °C	A21, A25	A26	A11, A16	-
Class II 850 °C <EFT< 950 °C	A1, A19, A24	A2, A3	A20	-
Class III EFT> 950 °C	A4, A6-A9, A12, A13	A18, A27	A5, A10, A15, A17, A22	A14, A23

The petrographic results showed that all the fabric groups are compositionally correlated with the local lithogeology and are differentiated in terms of technological choices of the potters and probably the use of different sources of the raw materials.

The results were correlated with the mineralogical composition of the sediments in the surrounding area. More specifically, according to Filis, 2019 the clay source of the Hellenistic transport amphorae could be either the Selinous River or the region of Neratzies Aigialia to the west of Aigion, close to the river Salmeniko. The Selinous river catchement is richer in chert material compared to the one of Neratzies (Filis, 2019). Moreover, Xanthopoulou (2019), collected calcareous sand samples, comprising mainly fragments of micritic limestone and subordinate to rare sparitic calcite, from the Selinous River. These sands are also rich in radiolarian chert and mudstone. Xanthopoulou also collected samples from sandy marls, sands and sandstones and clay layers formations cropping out in the area. Some of these also contain siltstone fragments. Lastly, the clayey raw material from the same area studied by Xanthopoulou (2019) are of illitic-chloritic composition and contain mixed-phases which include mainly illite-smectite, chlorite-smectite, chlorite-vermiculite and to a lesser extent mica-vermiculite (Xanthopoulou, 2019). Another possible source could be the area around Kerinitis River where, based on Xanthopoulou (2019), clays have a similar composition to those studied in proximity to the Selinous River.

Conclusion

This paper analyzed samples of Hellenistic-Early Roman stamped transport amphorae from the area of Aigion. The above samples were analyzed mineralogically and petrographically using optical X-ray diffractometry and optical microscopy respectively. The identified mineralogical phases indicate that the majority of the ceramics were fired at temperatures above 950°C. Furthermore, a comparison of the composition of the samples with the local geology of the area (Xanthopoulou, 2019) suggests that the raw materials for the production of the stamped amphorae could originate from the wider Aigio area, possibly from the Selinous River catchment (Filis, 2012, Filis, 2019). Finally, there is a very high level of homogeneity in the production of pottery, with a high level of expertise among the potters.

Acknowledgements

We would like to thank Mr Panagiotis Mpalasis for the preparation of the thin sections as well as Dr Paraskevi Lampropoulou for performing the XRPD analysis of the samples.

References

Filis, K. (2019). The Ovoid Amphorae from Aigion, in the NW Peloponnese. The Connection with Corinth and Brindisi, στο E. Garcia Vargas, R. Roberto de Almeida, H. Gonzalez Cesteros, A. M. Saez Romero (eds.), A Familiy Business: The Ovoid Amphorae in the Central and Western Mediterranean. Between the Last Two Centuries of the Republic and the Early Days of the Roman Empire, University of Seville / San Fernando, 10–11 December 2015, Oxford 2019, 3-34

Filis, K. (2012). «Ενσφράγιστοι εμπορικοί αμφορείς από το Αίγιο», στο Θ' Επιστημονική Συνάντηση για την Ελληνιστική Κεραμική. Θεσσαλονίκη, 5-9 Δεκεμβρίου 2012, Πρακτικά Ι, Αθήνα 2018, 407-421.

Gliozzo, E. (2020a). Ceramic technology. How to reconstruct the firing process. Archaeological and Anthropological Sciences, 12(11), 260. https://doi.org/10.1007/s12520-020-01133-y

Gliozzo, E. (2020b). Ceramics investigation: research questions and sampling criteria. *Archaeological and Anthropological Sciences*, *12*(8), 202. https://doi.org/10.1007/s12520-020-01128-9

Rathossi, C., 2005. Ancient ceramics from NW Peloponnese and the provenance of their raw materials: a petrographic, mineralogical, geochemical and archaeometric approach. PhD Dissertation, University of Patras, Greece.

Whitbread, I. K. (1995). Greek Transport Amphorae: A Petrological and Archaeological Study. Athens: Fitch Laboratory Occasional Paper 4.

Xanthopoulou, V., Iliopoulos, I. An Insight into the Suitability of Clayey Raw Materials: The Ceramic Provinces of the Northern Peloponnese and South Epirus, Greece. *Buildings* 2023, *13*, 473. https://doi.org/10.3390/buildings13020473

Xanthopoulou, V., Iliopoulos, I., and Liritzis, I., (2020). Characterization techniques of clays for the archaeometric study of ancient ceramics: a review. Scientific Culture, 6(2): 73-86. https://doi.org/10.5281/zenodo.3724849

Xanthopoulou V. (2019): Assessment of clayey raw material suitability for ceramic production in northern Peloponnese: an archaeometric approach, PHD thesis

17th INTERNATIONAL CONGRESS of the Geological Society of Greece

BULLETIN OF THE GEOLOGICAL SOCIETY OF GREECE, SP. PUBL.

EXTENDED ABSTRACT 340

Morphotectonic Analysis and Geohazard Implications of the Messiniakos Gulf

Varotsou E.[1,*], Nomikou P.[1], Papanikolaou D.[1], Poulos S.[1], Asteriou I.[2], Tsernotopoulos N.[2], Tsaparas Y.[2], Koliopanos I.[2], Petroulia M.[2]

(1) Department of Geology and Geoenvironment, National and Kapodistrian University of Athens, Panepistimioupoli Zografou, 15784 Athens, Greece, effrosynivar@geol.uoa.gr (2) Hellenic Navy Hydrographic Service, Mesogeion 229, TGN 1040, 15661 Athens, Greece

Introduction / Background

Research Highlights

The 1986 Kalamata earthquake (Mw 6.0) in Messiniakos Gulf (SW Peloponnese, Greece) triggered underwater landslides or slumping, leading to the movement and redistribution of sediment in shallow waters.

The submarine canyons, main fault zones controlling the evolution of the gulf, and areas of tectonic uplift, which are crucial for geohazard assessment, although investigated with advanced methods, were found to be, more or less, in agreement with previous key findings (Pavlakis et al., 1989)

Background

Marine and coastal environments often face significant geohazards, including earthquakes, submarine landslides, and rapid morphological changes (Chiocci et al. 2011). The Messiniakos Gulf, located in southwestern Peloponnese at the western part of the Aegean arc system, close to the Hellenic Trench, exemplifies such dynamic environments (Papanikolaou et al., 1988a). Intense seismic activity, the prevalence of normal faulting, and notable crustal uplift are among the key geodynamic processes that dominate the region's evolution due to the subduction of the African plate beneath the Eurasian plate (Figure 1). The region is a complex multi-fractured neotectonic macrostructure, characterized by the presence of large grabens and horsts bounded by wide fault zones, trending approximately NNW-SSE and E-W (Mariolakos and Papanikolaou, 1981, 1987; Mariolakos et al., 1985; Fountoulis, 1994; Mariolakos et al. 2004; Fountoulis and Mariolakos, 2008; Fountoulis et al., 2014).

Previous studies have highlighted the role of active faulting in shaping the Gulf's geomorphology and emphasized its vulnerability to seismic events (Papanikolaou et al. 1988b; Papoulia et al., 2001; Papoulia and Makris et al., 2004). The seismicity of the area, exemplified by the 1986 Kalamata earthquake (Mw 6.0), highlights the importance of assessing geohazard risks in this region. This earthquake, caused by an NNE-SSW striking normal fault, not only led to extensive damage in the Kalamata region but also revealed instability in terms of bottom surface sediment and sliding phenomena, situated in the northeastern corner of the gulf and other geomorphic changes in the Gulf. Co-seismic uplift of shorelines at the northeastern coast of the Messiniakos Gulf during the Holocene was observed by tens of meters, particularly adjacent to significant marginal faults (Pavlakis et al., 1989). This event, combined with the region's ongoing tectonic activity, served as the primary motivation for this research.

The present research highlights the complex relationship between tectonics and geomorphology in the Messiniakos Gulf (Varotsou 2024).

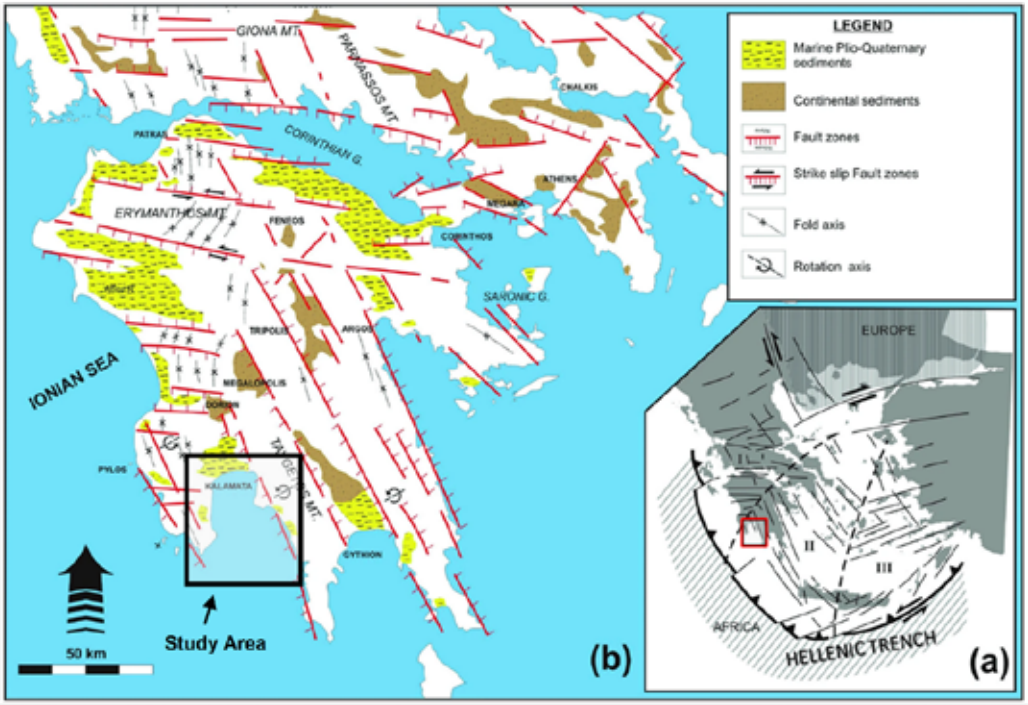

Figure 1. (a) Inset map displaying the three morpho-neotectonic regions and the 3 sectors of the Hellenic arc. (b) The neotectonic map with the main marginal fault zones of the post-Alpine basins in southern continental Greece, highlighting the location of the study area (Black frame) (modified from Papanikolaou 2021a, b).

Objectives

The general objective of this study is to explore the morphotectonic features of Messiniakos Gulf using high-resolution multibeam bathymetry data. By integrating recently acquired bathymetric data through GIS-based analysis, this study aims to provide a comprehensive evaluation of the Gulf's morphotectonic characteristics and their implications for geohazard risks. By producing a detailed bathymetric map and analyzing the morphotectonic map, morphological changes that reflect a landscape influenced by significant tectonic activity may be revealed.

Methods

Bathymetric data were obtained in the course of four different hydrographic surveys conducted by the Hellenic Navy Hydrographic Service in 2006, 2015, 2017, and 2023, using both single-beam and multibeam echosounders. During the 2006, 2017 and 2023 cruises, multibeam data were acquired onboard the Hydrographic - Oceanographic Vessel NAFTILOS, and on board the Hydrographic Vessel LAUNCH 14 in 2015.

During the 2006 cruise, bathymetric data were acquired using the Kongsberg EM1002 multibeam, which generates 111 beams at a 95 kHz frequency, with an operational depth up to 1000 meters. During the 2015 cruise, the Teledyne RESON SeaBat 7125 multibeam echosounder was used, operating at either 200 or 400 kHz, with a depth range of 1–500 meters. Swath data from the 2023 cruise were obtained with the hull-mounted RESON SeaBat 7160, which operates at 44 KHz nominal frequency, with equidistant beam spacing mode, forming 512 beams per swath. Single-beam data were collected using Atlas Deso-25 echosounder during the 2006 and 2017 cruises on board the Hydrographic / Oceanographic Vessel NAFTILOS, as well as during the 2015 cruise on board the Hydrographic Vessel STRAVON.

The processing of multibeam data utilizing QPS QIMERA software involved multiple steps, including sound velocity corrections, removal of erroneous beams, filtering noise, and adjustments of navigation data. The bathymetric datasets were then merged to create a Digital Terrain Model (DTM) with a consistent grid of 20 m spatial resolution, supplemented in areas not covered with swath data, by additional data sources (EMODNET, https://emodnet.ec.europa.eu/en/bathymetry).

The morphotectonic analysis focused on primary and secondary morphometric parameters like slope and curvature. Slope maps were created to show slope gradients and identify, map, and characterize major tectonic structures. A

drainage analysis using ArcGIS tools mapped drainage pathways and basins, illustrating the impact of topography on hydrology.

Results and Conclusion

The study culminated in a simplified morphotectonic map displaying significant morphotectonic features in the area derived from the analysis of the detailed bathymetric map and morphological slope map (Figure 2, Figure 3). It emphasizes the importance of high-resolution data for understanding the geomorphology and tectonics of the Messiniakos Gulf.

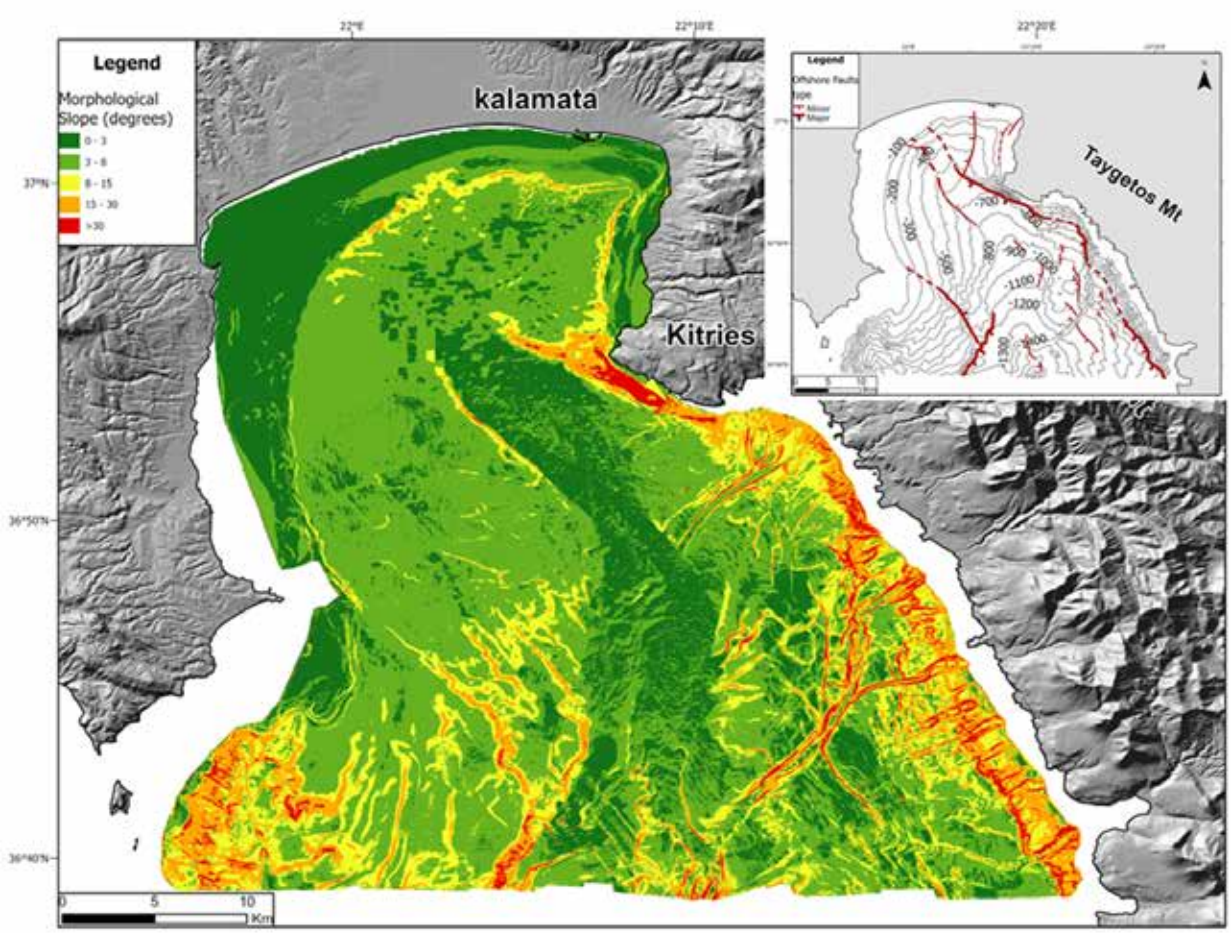

Figure 2. Morphological Slope Map of the area studied. The inset tectonic sketch map demonstrates Major- indicated by the high slopes and Minor morphological discontinuities. The degree of slope steepness is illustrated by green to red colors – flat surfaces as deep green, flat to shallow slopes as light green to yellow, shallow to moderate slopes as light orange, and steep slopes as red.

The analysis revealed an asymmetric, oriented NNW-SSE basin, characterized by steep slopes up to 40° along its eastern margin. This forms a distinct NW-SE narrow geometric zone, approximately 1.5 km wide, striking parallel to the Kitries coastline and extending southward with NNW-SSE orientation. This steep slope zone corresponds to the major active normal fault zone bordering the eastern part of the half-graben structure of the Messiniakos Basin to the southwest, where the maximum thickness of Plio-Quaternary sediments has been deposited, as it has been verified by lithoseismic profiling (Papanikolaou et al. 1988b). In contrast, the non-deformed western margin is rather homogeneous represented by consistent gradients (2-5 °) and a shallow area indicating the extended continental shelf.

Submarine canyons were discovered for the first time, aligned NE-SW and N-S, extending from the continental shelf to depths exceeding 1,400 m. The edge of the continental shelf aligns with the horizontal plane of the Holocene transgressive unconformity, formed by the global sea level rise following the last glacial period. By examining the interplay between eustatic sea-level changes and tectonic activity, driven by fault slip rates, this study identifies a

significantly higher uplift rate in the northeastern part of the Gulf. Notably, the edge of the continental shelf is traced all along the Messiniakos Gulf (Figure 3), except on the northeastern coast of the gulf where it has been partly buried and distorted, due to fault throw rates and the sliding phenomena.
Thus, since the Holocene transgression, the total uplift has been measured at 4–31 m, determined by the change in depth of the shelf break, compared to the findings of Palvakis et. al., (1989).

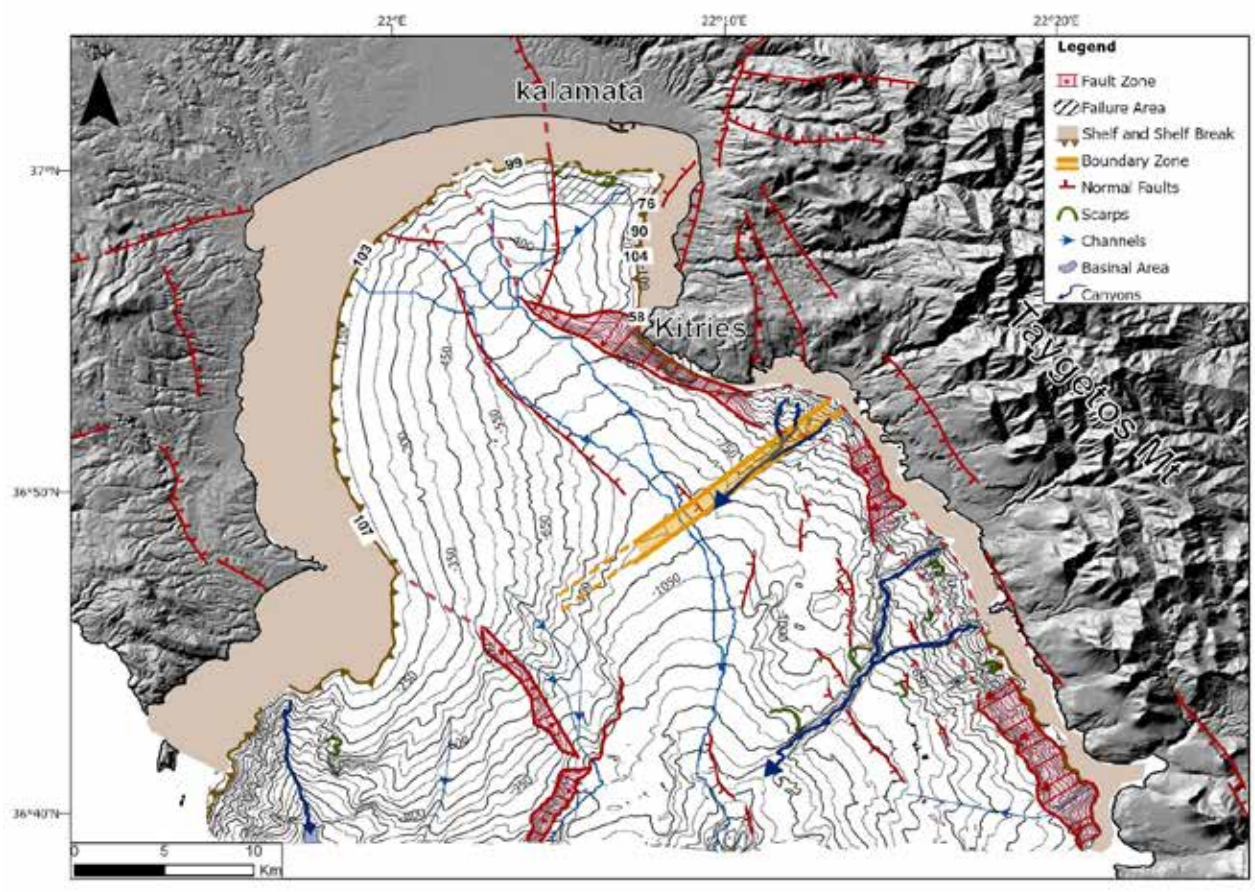

Figure 3. Simplified Morphotectonic Map of Messiniakos Gulf. The continental shelf is extended up to 6 km mainly along the western part of the Messiniakos Gulf, whereas the marginal NNW-SSE fault dominates the eastern part with a narrow shelf of 1 km. Onshore faults are denoted with red solid lines (after Ganas et al. 2013).

The morphotectonic synthesis highlights the interplay between tectonic uplift, sediment deposition, and erosion in shaping the Messiniakos Gulf. Active fault zones along the eastern margin likely influence canyon development and drainage patterns. The spatial correlation of seismicity with geomorphic features suggests that fault activity remains a primary driver of landscape evolution. The absence of extensive submarine fans indicates limited sediment transport from the shelf to the deeper basin, possibly constrained by fault-controlled topography. Submarine drainage analyses revealed a dendritic pattern, with prominent channels guiding sediment flows to the deepest parts of the Gulf.
The analysis of high-resolution bathymetric data, following the interpretation of previously published single-channel seismic reflection data (Papanikolaou et al., 1988b; Palvakis et al., 1989), has revealed seafloor primary as well as secondary scarps and signs of active deformation. These features suggest slope failures that completely distort the continental shelf and indicate mass transport towards the southwest (Figure 3). This activity is associated with the Kalamata earthquake (Mw 5.7) that struck on September 13, 1986, just a few kilometers south of Kalamata Harbor. More specifically, the resulting microfracture zone coincides with the northern edge of the previously described N-S fault zone. This zone, recorded shortly after the earthquake, aligns with the event's NNW-SSE fault plane solution, reinforcing the correlation between seismic activity and observed seafloor instability. All these findings emphasize the dynamic nature of the Gulf's geomorphology and highlight areas with a heightened potential for geological hazards.
In conclusion, this study underlines the importance of integrating high-resolution bathymetric data with GIS tools to effectively map geohazards. The findings contribute to a refined understanding of the Messiniakos Gulf's active tectonic regime and provide a framework for assessing future geohazard risks in the region. Continued monitoring

and advanced modeling are recommended to quantify fault dynamics and associated risks to coastal and submarine infrastructures.

Acknowledgments
We would like to acknowledge the Hellenic Navy Hydrographic Service for the provision of the bathymetric data used in this paper and the excellent cooperation.

References

Chiocci, F.L., Cattaneo, A. and Urgeles, R., 2011. Seafloor mapping for geohazard assessment: state of the art. Marine Geophysical Research, 32, pp.1-11.
Fountoulis I.; 1994. Neotectonic evolution of the central-western Peloponnese. PhD Thesis, Faculty of Geology, Department of Dynamic Tectonic Applied Geology, University of Athens, Greece, GAIA 7, 386 pp. (in Greek).
Fountoulis I. and Mariolakos I., 2008. Neotectonic folds in the central-western Peloponnese, Greece. Z. Dtsch. Ges. Geowiss., 159, 485-494.
Fountoulis, I., Mariolakos, I. and Ladas, I., 2014. Quaternary basin sedimentation and geodynamics in SW Peloponnese (Greece) and late stage uplift of Taygetos Mt. Bollettino di Geofisica Teorica ed Applicata, 55(2).
Ganas, A., Oikonomou, I. A., Tsimi, C., 2013. NOAfaults: a digital database for active faults in Greece. Bulletin of the Geological Society of Greece, 47(2), 518–530.
Mariolakos, I., Papanikolaou, D., 1981. The Neogene basins of the Aegean arc from the paleogeographic and the geodynamic point of view, International Symposium on the Hellenic Arc and Trench System, Natl. Tech. Univ. of Athens, Athens.
Mariolakos I. and Papanikolaou D., 1987. Deformation pattern and relation between deformation and seismicity in the Hellenic arc. Bull. Geol. Soc. Greece, 19, 59-76 (in Greek).
Mariolakos I., Papanikolaou D. and Lagios E., 1985. A neotectonic geodynamic model of Peloponnesus based on: morphotectonics, repeated gravity measurements and seismicity. Geol. Jb., B50, 3-17
Mariolakos I., Zagorchev I., Fountoulis I. and Ivanov M., 2004. Neotectonic Transect Moesia Apulia. In: 32nd Int. Geol. Congress, Florence, Italy, Field Trip B26, 72 pp. and Greek route B26 (appendix) 25 pp.
Papanikolaou, D. I., 2021a. The Geology of Greece. Springer Nature, Basel, Switzerland; ISBN 9783319761015.
Papanikolaou, D.I., 2021b. Neotectonics and Recent Paleogeography. In: The Geology of Greece. Regional Geology Reviews. Springer, Cham. https://doi.org/10.1007/978-3-030-60731-9_11
Papanikolaou, D., Lykousis, V., Chronis, G., & Pavlakis, P., 1988a. A comparative study of neotectonic basins across the Hellenic arc: the Messiniakos, Argolikos, Saronikos and Southern Evoikos Gulfs. Basin Research, 1(3), 167-176.
Papanikolaou, D., Chronis, G., Pavlakis, P., Lykoussis, B., Roussakis, G. & Syskakis, D., 1988b. Submarine Neotectonic Map of Ano Messiniakos Gulf. Scale 1/100,000, Earthquake Planning & Protection Organization, National Centre Marine Research, University of Athens
Papoulia, J., & Makris, J., 2004. Microseismicity and active deformation of Messinia, SW Greece. Journal of seismology, 8, 439-451.
Papoulia, J., Stavrakakis, G., & Papanikolaou, D., 2001. Bayesian estimation of strong earthquakes in the Inner Messiniakos fault zone, southern Greece, based on seismological and geological data. Journal of Seismology, 5(2), 233-242.
Pavlakis P., Papanikolaou D., Chronis G., Lykoussis B. and Anagnostou E., 1989. Geological structure of inner Messiniakos gulf. Bull. Geol. Soc. Greece, 23, 333-347.
Varotsou E., 2024. Morphotectonic analysis based on swath bathymetry and associated geohazards: Case of Messiniakos Gulf. MSc. Thesis, Faculty of Geology and Geoenvironment NKUA.

17th INTERNATIONAL CONGRESS of the Geological Society of Greece

BULLETIN OF THE GEOLOGICAL SOCIETY OF GREECE, SP. PUBL.

EXTENDED ABSTRACT 341

Assessment of Geo-environmental Status of Trichonis Lake, Greece: Mineralogy, Sedimentology, and Chemistry

Vasilatos C.[1], Megremi I.[1], Gkioka Z.[1], Theori N.[2], Cuida Lopez E.[3], Stoica A.I.[3], Economou-Amilli A.[2]
(1) Faculty of Geology & Geoenvironment, National and Kapodistrian University of Athens, Athens, Greece, vasilatos@geol.uoa.gr (2) Faculty of Biology, National and Kapodistrian University of Athens, Athens, Greece (3) Department of Landscape, Water and Infrastructure, University of Natural Resources and Life Sciences, Vienna

Research Highlights

Sediments of Trichonis Lake are dominated by quartz and calcite, reflecting the lithological influence of surrounding limestone and flysch formations.

Reduced nutrient levels in lake water since the late 1990s highlight the positive ecological impact of decreased agricultural pressures, providing a foundation for sustainable lake management strategies.

Introduction / Background

European Union countries have evaluated all freshwater habitats larger than 50 hectares to comply with the Water Framework Directive 2000 (European Commission, 2000). To support biological, hydromorphological, and physico-chemical monitoring, a range of indicators and multimetric indices has been developed. These include factors such as morphology, hydrology, nutrient levels, thermal conditions, salinity, pollutants, and priority substances. Geochemical indicators such as pH, sediment mineralogy, and the concentrations of ions, nutrients, and potential pollutants in soil and water, are normally used to assess habitat quality and quantify the environmental stress affecting ecosystems (ecological status) (e.g. Vasilatos et al., 2019).

Trichonis Lake, located in western Greece, is the largest and one of the deepest natural freshwater lakes in Greece, with a maximum depth of 58 m and a surface area of approximately 98 km² (Figure 1). On the northeastern side of the lake the steep slope of Panaitoliko Mountain is visible, while the southwestern side is bounded by the ridge of Arakinthos Mountain. The wider "Trichonis basin" is a neo-tectonic graben approximately 30 km in length and 10 km in width (Doutsos et al., 1987); its hydrological basin extends to an area of 402 km^2 (Koutsoyiannis et al., 2008) and its southern boundary is defined by a prominent WNW-ESE trending normal fault. Geologically, the area belongs to the External Hellenides, specifically the Pindos and Gavrovo geotectonic units (Figure 2). Trichonis Lake occupies the eastern margin of a fractured tectonic trough at a semi-circular shape. This trough was formed primarily due to the intense tectonic activity of the region and partially by the collapse of limestone masses into existing underground caverns, which constitute an extensive karstic network. These karsts are continually enlarged by the erosive and solvent action of water, leading to the collapse of overlying layers and contributing to ongoing changes in the morphology of the region (Evangelidis et al., 2008; Kiratzi et al., 2008, Benekos et al., 2013). Trichonis Lake main geomorphological characteristics are summarized in Table 1.

Table 1. Geomorphological characteristics of Trichonis Lake (cf. Tafas et al., 1997).

Max. length	18.2 km
Max. width	7.5 km
Max. depth	58 m
Mean depth	30.45 m
Lake volume	2.99 x 10^9 m^3
Shore length	52.1 km
Surface area	98.2 km^2
Drainage area	215 km^2

The water level of the lake is artificially controlled by a dam being constructed to regulate its discharge at an average altitude of 15.5 m with a fluctuation of ±1 m. This dam communicates by means of a 2.8 km long Trichonis-Lysimachia Unifying Trench with Lysimachia Lake, to which its excess water potential is channeled.

The lake is recognized for its rich biodiversity, including endemic fish (e.g. Vardakas et al. 2022), freshwater hydrobiids

(e.g. Radea et al. 2017), and algae species (Economou-Amilli 1979, 1982); and generally, for the presence of unique aquatic plants, as well as its role in local hydrology and as a water source for nearby communities. However, like many freshwater ecosystems globally, Trichonis faces environmental pressures due to agricultural activities, urban runoff, and sedimentation processes, potentially threatening the health of its ecosystem. In previous studies (e.g., Kehayias & Doulka, 2014; Overbeck et al., 1982; Tafas et al., 1997) due to its limnological and biological characteristics Trichonis was classified as a carbonate-type, low-conductivity lake ("class II, low salinity" warm lake) with an oligotrophic to mesotrophic ecosystem. Furthermore, Kehayias & Doulka (2014), using zooplankton as a biotic indicator, suggested that Trichonis Lake is undergoing a transitional shift toward a eutrophic state, emphasizing the need for continuous monitoring and inspection of the ecosystem.

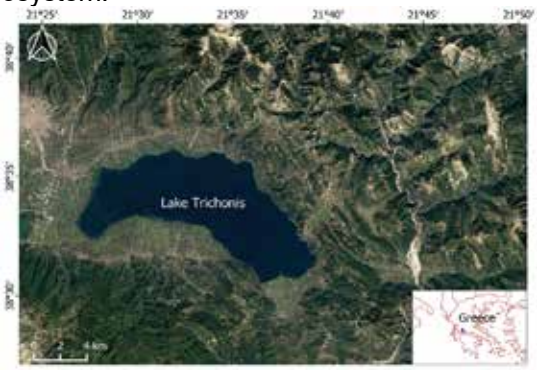

Figure 1. Location map of the study area (Perivolioti et al., 2021).

Objectives

The objective of this study is to assess the geo-environmental status of Trichonis Lake by analyzing the mineralogical and sedimentological characteristics of its sediments along with the physicochemical parameters of lake water. This analysis aims to identify changes in sediment composition, assess nutrients concentrations, and evaluate the impact of anthropogenic activities, offering a comprehensive assessment of current environmental condition of the lake and helping guide future management efforts.

Methods

Study Area and Sampling Sites

Bottom sediment and water samples were collected from various sites throughout Trichonis Lake in September 27-28, 2024, to capture a representative profile of the lake's sedimentary environment (Figure 2). Sampling sites were selected to encompass areas near potential pollution sources, such as agricultural runoff zones and areas adjacent to urban settlements, as well as deeper, central lake locations to account for natural sediment deposition.

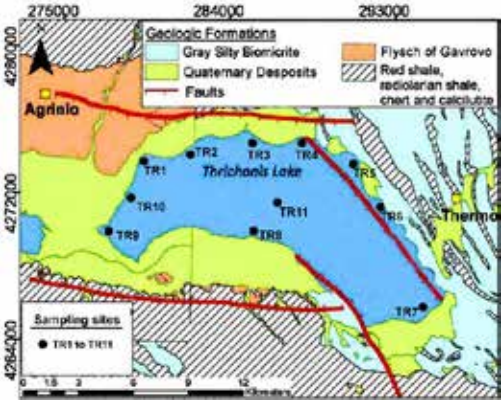

Figure 2. Simplified geological map of the study area (modified after Benekos et al., 2013) with the sampling sites.

Sediment Sampling, Preparation and Analysis

Sediment was retrieved from each site using a stainless-steel dredge bottom sludge sediment grab sampler

(Figure 3). Sediment samples were collected in 2 L plastic bags. Before the experimental procedure, the coarse organic matter was removed from the samples. In the laboratory they were air-dried, homogenized, and sieved to remove particles larger than 2 mm. Fine fractions were preserved for further mineralogical, sedimentological, and chemical analyses. The granulometric characterization was conducted according to Folk's methodology and classification (Folk, 1974). Mineralogical analysis was carried out by using an X-Ray Siemens D 5005 Diffractometer, equipped with a Cu tube and a graphite monochromator, in combination with the DIFFRACplus software package at NKUA, Department of Geology and Geoenvironment. The organic matter (OM) content was determined using dry combustion, involving drying at 105°C for 24 hours and combustion at 380°C for 6 hours in a muffle furnace (Vasilatos et al., 2019). The $CaCO_3$ (%) content was estimated by combusting the above samples at 950°C for 1 hour.

Figure 3. Sampling in Trichonis Lake. Photographs have been captured from sampling site TR4 (Figure 2).

Water Sampling, Preparation and Analysis

pH, redox potential (Eh), conductivity, total dissolved solids (TDS) and dissolved oxygen (DO) measurements were performed *in situ*, using a portable Multiparameter Analyzer (CyberScan Series 600, EUTECH). Water samples (Figure 3) were filtered through 0.45 μm membrane filters, collected and stored in polyethylaine containers. They were divided into two groups; the first group was persevered for the measurements of anions while the second was acidified by addition of concentrated HNO_3 for the measurements of cations. Then they were all stored at cooling conditions (~ 4°C) into a portable refrigerator.

Chemical analyses for NO_2^-, NO_3^-, NH_4^+, PO_4^{3-} and SO_4^{2-} were performed using a HACH DR/2400 spectrometer. The detection limits of the methods were 0.007 mg·L^{-1}, 0.05 mg·L^{-1}, 0.013 mg·L^{-1}, 0.01 mg·L^{-1}, and 3 mg·L^{-1}, respectively.

Results and Discussion

Sedimentology

Particle size data (Figure 4) can reveal sediment transport patterns and indicate environmental conditions impacting sedimentation, such as changes in water flow or anthropogenic disturbances.

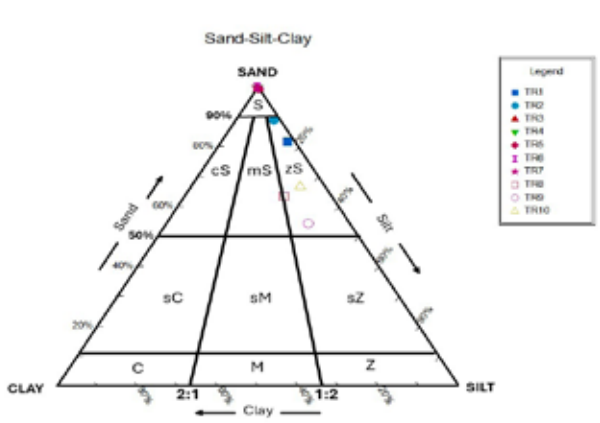

S: sand
s: sandy
Z: silt
z: silty
C: clay
c: clayey
M: mud
m: muddy

Figure 4. Bottom sediments granulometry according to Folk's (1974) classification scheme.

Sedimentological analysis indicated that sites near limestone formations are classified as sand while samples nearby flysch formations are silty sand, dominated by finer sediment fractions (Figure 4). This distribution suggests that sedimentation processes in the lake are controlled by the mineralogical composition of the adjacent lithologies and rock erosion.

Sediments Mineralogy and Chemistry

Quartz and calcite were confirmed in all samples originated from the surrounding flysch and limestone formations (Table 2). Clay minerals (chlorite and muscovite) and feldspars have been identified in samples adjacent to the flysch and related Quaternary deposits (Figure 2). These findings align with typical mineral assemblages expected in freshwater lake sediments within flysch and limestone-rich areas.

Table 2. Mineralogical composition of the bottom sediments (qualitative).

	TR1	TR2	TR3	TR4	TR5	TR6	TR7	TR8	TR9	TR10
Quartz	+	+	+	+	+	+	+	+	+	+
Calcite	+	+	+	+	+	+	+	+	+	+
Aragonite								+		
Orthoclase		+					+			
Albite	+	+						+	+	+
Anorthite		+						+		
Muscovite	+	+						+	+	+
Chlorite	+	+						+	+	+

+ referring to the presence of the mineral phase

The organic matter content in the bottom sediments ranged from 0.1% to 6.2% (Table 3). The maximum value (6.2%) was observed at sampling site TR9, located near the opening of the Trichonis-Lysimachia Unifying Trench, pointing out the ecological importance of this trench. The high value of organic matter content at that site is a strong indicator of ecological processes like increased biological productivity or enhanced sediment accumulation. Samples with the lowest organic matter content showed the highest quartz content based on their X-ray diffraction (XRD) patterns

Table 3. Quantitative analysis of the Organic Matter and $CaCO_3$ content of the samples.

	TR1	TR2	TR3	TR4	TR5	TR6	TR7	TR8	TR9	TR10
Organic Matter (%)	1.7%	1.2%	1.0%	0.1%	1.2%	0.6%	1.0%	5.3%	6.2%	2.6%
$CaCO_3$ (%)	19.4%	23.0%	39.0%	39.8%	11.6%	69.4%	19.3%	52.4%	67.3%	42.3%

Water Chemistry

Physicochemical parameters, concentration and chemical composition of the major anions of water samples from Trichonis Lake are presented in Table 4. All measured water parameters comply with the standards for water intended for human consumption (European Commission, 2000).

The measured pH values range from 6.52 to 7.90, falling within the typical range for lake water associated with limestone or flysch lithologies. The observed high concentrations of NH_4^+, NO_3^-, and PO_4^{2-} in the sample TR8, as well as of NO_3^-, NO_2^-, and PO_4^{2-} in the sample TR4 suggest a tangible impact of agricultural and urban runoff on Trichonis Lake. The consistent SO_4^{2-} levels (27.1–28.4 mg/L) across sampling sites indicate minimal influence from human activities, which would cause greater variability near potential sources. Instead, these concentrations may stem from natural processes, such as the presence of evaporitic formations in the wider area.

Nutrient levels are much lower than in 1980–1997 (Koutsoyiannis et al., 2008) but similar to 2000–2002 (Koutsoyiannis et al., 2008) presumably due to the late-1990s abandonment of extensive tobacco cultivation around the lake, which had caused ecological strain.

Table 4. Measurements of the water physical and chemical parameters.

	Units	TR1	TR2	TR3	TR4	TR5	TR6	TR7	TR8	TR9	TR10	TR11
pH		7.83	7.83	7.35	6.52	7.74	7.64	7.13	7.13	7.89	7.90	7.16
Eh	mV	113	117.4	107	92.2	129.8	105.9	115.8	162.7	90.7	79.4	154.5
DO	mg/l	5.68	6.91	5.72	7.99	6.67	5.4	6.69	6.69	7.02	6.39	6.88
EC	μS/cm	347	334	312	323	324	318	289	334	298	310	330
TDS	mg/l	232.49	223.78	209.04	216.41	217.08	213.06	193.63	223.78	199.66	207.7	221.1
NH_4^+	mg/l	<0.013	<0.013	0.030	<0.013	0.040	0.013	0.040	0.050	<0.013	0.030	0.064
NO_3^-	mg/l	0.886	4.43	1.77	11.96	3.54	5.32	1.33	14.61	5.76	0.87	0.89
NO_2^-	mg/l	<0.007	<0.007	0.01	0.06	0.02	<0.007	0.033	0.01	0.023	0.016	0.009
PO_4^{3-}	mg/l	0.03	0.03	0.03	0.06	0.07	0.01	0.06	0.04	0.01	0.06	0.04
SO_4^{2-}	mg/l	27.7	27.7	27.9	28.4	27.1	28.3	27.9	28.3	27.3	27.2	26.3

Comparison with Other Mediterranean Lakes

Even though Trichonis Lake has been classified as a typical warm lake, it resembles more closely to temperate lakes than tropical ones (Tafas et al., 1997) exhibiting shallow metalimnia that characterize lakes of higher latitudes.

The bottom sediments of Trichonis Lake are primarily composed of quartz, calcite, and clay minerals such as chlorite and muscovite, reflecting the geological influence of surrounding flysch and limestone formations. This composition is characteristic of carbonate-type lakes in limestone-dominated regions (Tafas et al., 1997; Kehayias & Doulka, 2014). In contrast, many Mediterranean lakes exhibit more diverse sediment compositions depending on local geology, including higher proportions of volcanic materials (e.g., in volcanic lake basins) or organic-rich sediments in eutrophic systems (Karathanasis & Hajek, 1993; Gkenas et al., 2012; Michaloudi et al., 2013; Köprücü & Polat, 2017).

The relatively low organic matter content (ranging from 0.1% to 6.2%) in Trichonis sediments aligns with its oligotrophic to mesotrophic status, whereas highly eutrophic Mediterranean lakes often exhibit significantly higher organic matter concentrations due to increased biological productivity and nutrient input (Overbeck et al., 1982; Tafas et al., 1997; Kehayias & Doulka, 2014). The high $CaCO_3$ content (up to 69.4%) further distinguishes Trichonis as a carbonate-rich system, a feature not universally observed in Mediterranean lakes, where sediment composition varies widely.

Nutrient levels (e.g., NH_4^+, NO_3^-, and PO_4^{3-}) in Trichonis Lake water are relatively low compared to heavily impacted Mediterranean lakes, although localized agricultural and urban runoff has resulted in elevated nutrient concentrations in specific sites, indicating ongoing anthropogenic pressure (Petaloti et al., 2004). When compared to other Mediterranean lakes, Trichonis exhibits nutrient levels and chemical parameters indicative of a transitional ecosystem, less impacted by eutrophication than many lakes in the region.

Conclusions

Comprehensive assessment of the geo-environmental status in Trichonis Lake revealed insights into its sedimentological, mineralogical, and chemical characteristics, as well as into the impact of natural and anthropogenic factors.

Key conclusions include:

- The sediments are predominantly composed of quartz and calcite, reflecting a lithological influence of the surrounding flysch and limestone formations. Variations in sediment texture, ranging from sand to silty sand, highlight localized sediment transport and deposition processes.
- Organic matter content ranged from 0.1% to 6.2%, with higher values near areas of enhanced biological productivity, such as at the Trichonis-Lysimachia trench. This differentiation signifies the ecological importance of sedimentary organic matter accumulation in assessing ecosystem “health”.
- Physicochemical parameters, including pH, Eh, and TDS, are consistent with those expected in freshwater systems influenced by limestone and flysch. Elevated nutrient levels at specific sites point to agricultural runoff and urban influences, although the overall nutrient concentrations declined since the late 1990s, likely due to reduced agricultural pressures, including the cessation of tobacco cultivation.
- While some localized contamination is evident, such as elevated NH_4^+, NO_3^-, and PO_4^{3-} levels near agricultural areas, the consistent SO_4^{2-} levels across sites suggest limited anthropogenic influence on this parameter. The mineralogical composition of the lake sediments also emphasizes the dominance of natural geochemical processes in shaping its chemistry.
- Overall, Trichonis Lake shares some commonalities with other Mediterranean lakes in terms of its sensitivity to anthropogenic impacts and nutrient dynamics. However, its distinct carbonate-rich sediment composition and relatively stable water chemistry highlight its unique geological and ecological context. This underscores the importance of tailored conservation efforts to preserve the lake’s ecological balance amidst regional anthropogenic pressures.

This study provides a baseline for understanding the geo-environmental dynamics of Trichonis Lake and offers valuable guidance for future conservation and management strategies aimed at maintaining the health of this vital

freshwater ecosystem. Findings underscore the need for continued monitoring and sustainable land-use practices to mitigate anthropogenic pressures and preserve the ecological integrity of the lake.

Acknowledgements

This work was supported by the EU frame of HORIZON-MISS-2023-OCEAN-01 “Integrated emerging approaches for joint protection and restoration of Natural Lakes in the spirit of European life heritage support (ProCleanLakes)”.
The presentation of this work was funded by the Special Account for Research Grants, National and Kapodistrian University of Athens.

References

Benekos, G., Parcharidis, I., Foumelis, M., & Ganas, A. 2013. Ground deformation measurements over Lake Trichonis based on SAR interferometry. Bulletin of the Geological Society of Greece, 47(3), 1071–1080. https://doi.org/10.12681/bgsg.10951

Doutsos, T., Kontopoulos, N., Frydas, D. 1987. Neotectonic evolution of northwestern continental Greece. Geol. Rdsch., 76, 433-450. https://doi.org/10.1007/BF01821085

Economou-Amilli, A. 1979. Two new taxa of *Cyclotella* Kützing from Lake Trichonis, Greece. Nova Hedwigia, 31, 467-477.

Economou-Amilli, A. 1982. SEM-Studies on *Cyclotella trichonidea* (Bacillariophyceae). Arch. Hydrobiol. Suppl. 63,1, Algological Studies, 30, 25-34.

European Commission. Directive 2000/60/EC, EU Water Framework Directive, 2000; pp. 72.

Evangelidis, C.P., Konstantinou, K.I., Melis, N.S., Charalambakis, M., Stavrakakis, G.N. 2008. Waveform relocation and focal mechanism analysis of an earthquakeswarm in Trichonis Lake, Western Greece. Bull. Seismol. Soc. Am. 98, 804–811, http://dx.doi.org/10.1785/0120070185.

Folk, R.L. 1974. Petrology of Sedimentary Rocks. Hemphill Publishing Co, Austin, Texas.

Gkenas, C., Gkelis, S., Leonardos, I. 2012. Temporal patterns of phytoplankton community in a newly reconstructed shallow lake in Greece. Knowledge and Management of Aquatic Ecosystems, 406, 07. DOI: 10.1051/kmae/2012026

Karathanasis, A.D., Hajek, B.F. 1993. Soil development in volcanic ash and alluvium derived sediments in relation to hydrological conditions. Geoderma, 57(3–4), 207–230. DOI: 10.1016/0016-7061(93)90009-G

Kehayias, G., Doulka, E. 2014. Trophic State Evaluation of a Large Mediterranean Lake Utilizing Abiotic and Biotic Elements. Journal of Environmental Protection, 5, 17-28. https://doi.org/10.4236/jep.2014.51003.

Kiratzi, A., Sokos, E., Ganas, A., Tselentis, A., Benetatos, C., Roumelioti, Z., Serpetsi-daki, A., Andriopoulos, G., Galanis, O., Petrou, P. 2008. The April 2007 earthquakes. The April 2007 earthquake swarm near Lake Trichonis and implications for active tectonics in western Greece. Tectonophysics 452, 51–65.

Köprücü, K., Polat, A. 2017. The impacts of agricultural runoff on the water quality of Lake Beyşehir in Turkey. Environmental Science and Pollution Research, 24, 14908–14917. DOI: 10.1007/s11356-017-9084-3

Koutsoyiannis, D., Andreadakis, A., Mavrodimou, R., Christofides, A., Mamassis, N., Efstratiadis, A., Koukouvinos, A., Karavokiros, G., Kozanis, S., Mamais, D. and Noutsopoulos, K. 2008. National Programme for the Management and Protection of Water Resources, Support on the compilation of the national programme for water resources management and preservation, https://doi.org/10.13140/RG.2.2.25384.62727, Department of Water Resources and Environmental Engineering – National Technical University of Athens, Athens, 748 p.

Michaloudi, E., Bobori, D.C., Kallimanis, A. 2013. Lake Kerkini: A Balkan hotspot of biodiversity under anthropogenic stressors. Water Science and Technology: Water Supply, 13(5), 1317–1324. DOI: 10.2166/ws.2013.140

Overbeck, J., Anagnostidis K., Economou-Amilli, A. 1982. A limnological survey of three Greek lakes: Trichonis, Lyssimachia and Amvrakia. Arch. Hydrobiol. 95: 365–394.

Petaloti, C., Voutsa, D., Samara, C., Sofoniou, M., Stratis, I., Kouimtzis, T. 2004. Nutrient dynamics in shallow lakes of Northern Greece. Environ Sci & Pollut Res 11, 11–17. https://doi.org/10.1065/espr2003.06.156

Perivolioti, T.M., Mouratidis, A., Terzopoulos, D., Kalaitzis, P., Ampatzidis, D., Tušer, M., Frouzova, J., Bobori, D. 2021. Production, Validation and Morphometric Analysis of a Digital Terrain Model for Lake Trichonis Using Geospatial Technologies and Hydroacoustics. ISPRS Int. J. Geo-Inf., 10, 91. https://doi.org/10.3390/ijgi10020091.

Radea, C., Louvrou, I., Bakolitsas, K., & Economou-Amilli, A. 2017. Local endemic and threatened freshwater hydrobiids of western Greece: elucidation of anatomy and new records. Folia Malacologica, 25(1). https://doi.org/10.12657/folmal.025.001

Tafas, T., Danielidis, D., Overbeck, J., Economou-Amilli, A. 1997. Limnological Survey of the Warm Monomictic Lake Trichonis (Central Western Greece). I. The Physical and Chemical Environment. Hydrobiologia, 344(1-3), 129-139.

Vardakas, L., Koutsikos, N., Perdikaris, C., Petriki, O., Bobori, D., Zogaris, S. & Economou, A. 2022. The fish fauna in lentic ecosystems of Greece. Mediterranean Marine Science, 23(1), 223-265.

Vasilatos, C., Anastasatou, M., Alexopoulos, J., Vassilakis, E., Dilalos, S., Antonopoulou, S., Petrakis, S., Delipetrou, P., Georghiou, K., & Stamatakis, M. 2019. Assessment of the Geo-Environmental Status of European Union Priority Habitat Type “Mediterranean Temporary Ponds” in Mt. Oiti, Greece. Water, 11(8), 1627. https://doi.org/10.3390/w11081627

17th INTERNATIONAL CONGRESS of the Geological Society of Greece

BULLETIN OF THE GEOLOGICAL SOCIETY OF GREECE, SP. PUBL.

EXTENDED ABSTRACT 342

Rockfall Source Identification and Risk Assessment at the Caldera of Santorini Island, Greece, based on Aerial LiDAR Data

Vassilakis E.[1], Lekkas, E.[1], Antonarakou, A.[1], Nastos P.[1], Konsolaki, A.[1], Kotsi, E.[1], Lialiaris, J.[2] Foumelis, M.[3]

(1) National and Kapodistrian University of Athens, Department of Geology and Geoenvironment, Athens, Greece evasilak@geol.uoa.gr , (2) Geodesign PPC, 12134, Peristeri, Greece, (3) Aristotle University of Thessaloniki, Department of Geology

Research Highlights

- Aerial LiDAR point cloud acquisitions provide exceptionally high-quality basemap data for rockfall simulations.
- Detailed mapping of the Santorini caldera slopes offers valuable insights for rockfall risk assessment.

Introduction / Background and Objectives

Rockfalls are among the most common and hazardous types of landslides, posing significant risks to human activities (Notti *et al.,* 2021). They can cause extensive damage to infrastructure, including buildings, roads, and railways, and may even result in loss of life. As tourism continues to expand around the Santorini caldera, attracting millions of visitors each year, assessing rockfall risks becomes increasingly essential (Vassilakis *et al.,* 2024). However, the unpredictability of rockfalls, the complexity of their triggering mechanisms, and the numerous factors influencing their paths make their analysis particularly challenging (Westoby *et al.,* 2020), especially in the aftermath of the seismic sequence in February 2025. Effective rockfall risk assessment necessitates comprehensive data collection and interdisciplinary approaches for detailed analysis and accurate interpretation (Lim *et al.,* 2010). The precision of these interpretations is secured by employing datasets gathered from Light Detection and Range (LiDAR) sensors mounted on aerial platforms, such as unmanned aerial vehicles (UAVs).

On Santorini Island, where tourism is closely linked to the steep slopes of the caldera, the need to analyse highly localized rockfall phenomena has led to a growing demand for extremely high-resolution topographic data, within a relatively short time frame (Jiang *et al.,* 2021). The contemporary technology enables the rapid acquisition of high-density elevation data across large and inaccessible areas, capturing fine-scale topographic details of the caldera cliffs with high slope inclinations, and surface roughness. Consequently, the generation of ultra-high-density point clouds -integrating elevation information and surface colour data- has become essential for developing Digital Surface Models (DSMs) and ortho-photo-mosaics which are essential for simulating rockfall trajectories, determining impact zones, and identifying unstable rock masses. To address this need, we utilized close-range remote sensing data from UAVs alongside high-resolution satellite imagery, both of which have been widely applied in hazard mapping and risk assessment for floods, forest fires, soil erosion, and large-scale landslides, among other hazardous phenomena. In this context, this work aims to tackle the challenges of rockfall assessment, with a particular focus on five locations placed on the steep coastal cliffs of the Santorini Island volcanic complex (Fig. 1a). These are: (i) Ammoudi bay, (ii) Armeni bay, (iii) Thira Old Harbour, (iv) Athinios New Harbour and (v) Korfos bay at Therasia Island.

Methods

During the Santorini-Anydros paroxysmal seismic earthquake sequence of February 2025, during which more than 20,000 earthquakes were recorded, several LiDAR point clouds were collected by a laser scanning system deployed on an Unmanned Aerial Vehicle flying at various altitudes and flight plans, above the steep slopes of Santorini caldera, at the aforementioned locations (Table 1).

A LiDAR sensor employs advanced laser echo technologies to penetrate ground vegetation, regardless of lighting conditions. LiDAR has a natural advantage in surveying regions covered with vegetation since it can partially penetrate the canopy to acquire information about the earth's surface itself. Due to this LiDAR specification, this type of sensor is ideal for outcrops covered by medium density vegetation and therefore essential for not confusing the canopy of small bushes and trees with fallen boulders. By utilizing several filtering algorithms, it accurately detects and classifies ground features, producing extremely precise elevation data. This makes LiDAR point cloud acquisition an essential technique for determining the exact location and key characteristics of rockfalls -among other earth surface deformations- especially for rockfall back analysis, as well as for change detection through multi-temporal surveys (Esposito *et al.,* 2017; Mora *et al.,* 2018; Bernard *et al.,* 2021; Konsolaki *et al.,* 2024).

Figure 1. Index map of Thira volcanic complex with the areas of interest marked with red rectangles (a) and the equipment involved with the LiDAR sensor mounted on the UAV (b).

However, UAV LiDAR surveys have certain limitations, including Network-RTK signal loss (Panagiotopoulou *et al.,* 2022), which can cause decrease of the UAV accurate location during the data acquisition, not to mention increased sensitivity to meteorological conditions, which can cause laser beam scattering. Both of the above could result much difficultness in acquiring accurate target data. Until very recently, the high cost of these highly precise devices also restricted the widespread use of LiDAR for landslide monitoring, in general. Unlike ground-based LiDAR systems, the aerial ones are not limited by terrain constraints and can generate highly accurate data within a short timeframe (Lague *et al.,* 2013; Farmakis *et al.,* 2020).

Table 1. Information and specifications of the 5 flights that were carried out during the study.

Area	Take off altitude (m ASL[1])	Flying altitude (m AGL[2])	Aerial Photos	Points of cloud	Point Density (poi/m^2)	DSM Resolution (cm)	Ortho-Image Resolution (cm)	XY Error (mm)	Z Error (mm)
Ammoudi	113	30	802	71,350,599	557	5	2.53	9.07	8.13
Armeni	113	50	325	46,464,874	391	5	2.98	14.99	16.13
Old Harbour	265	45	1,577	223,600,457	568	5	5.18	7.51	6.64
Athinios	263	70	1,223	181,596,313	258	5	5.96	7.36	10.45
Korfos	173	50	1,367	98,342,420	381	5	3.79	7.51	6.64

1: Above Sea Level in GGRS'87, 2: Above Ground Level

The equipment we used during this study included a Zenmuse L2 LiDAR sensor mounted on a DJI Matrice 350 RTK UAV (Fig. 1b). On average, the point clouds density reached about 500 data points per square meter. The points were acquired simultaneously with high resolution aerial photographs, which were used for coloring each point of the cloud and produce seamless ortho-photo-mosaics, after photogrammetric processing.

The raw data was processed to remove outliers and noise and used also to generate surface 3D models that were used to inspect previous rockfalls in the study area (Fig. 2). Point cloud classification, Digital Surface Model (DSM) and ortho-photo-mosaic generation for each one of the areas of interest, were performed using DJI-Terra software (v.4.4). The statistics of the processing results show that there was an absolute vertical accuracy of 12.94 mm and a horizontal accuracy of 9.29 mm (root mean square error).

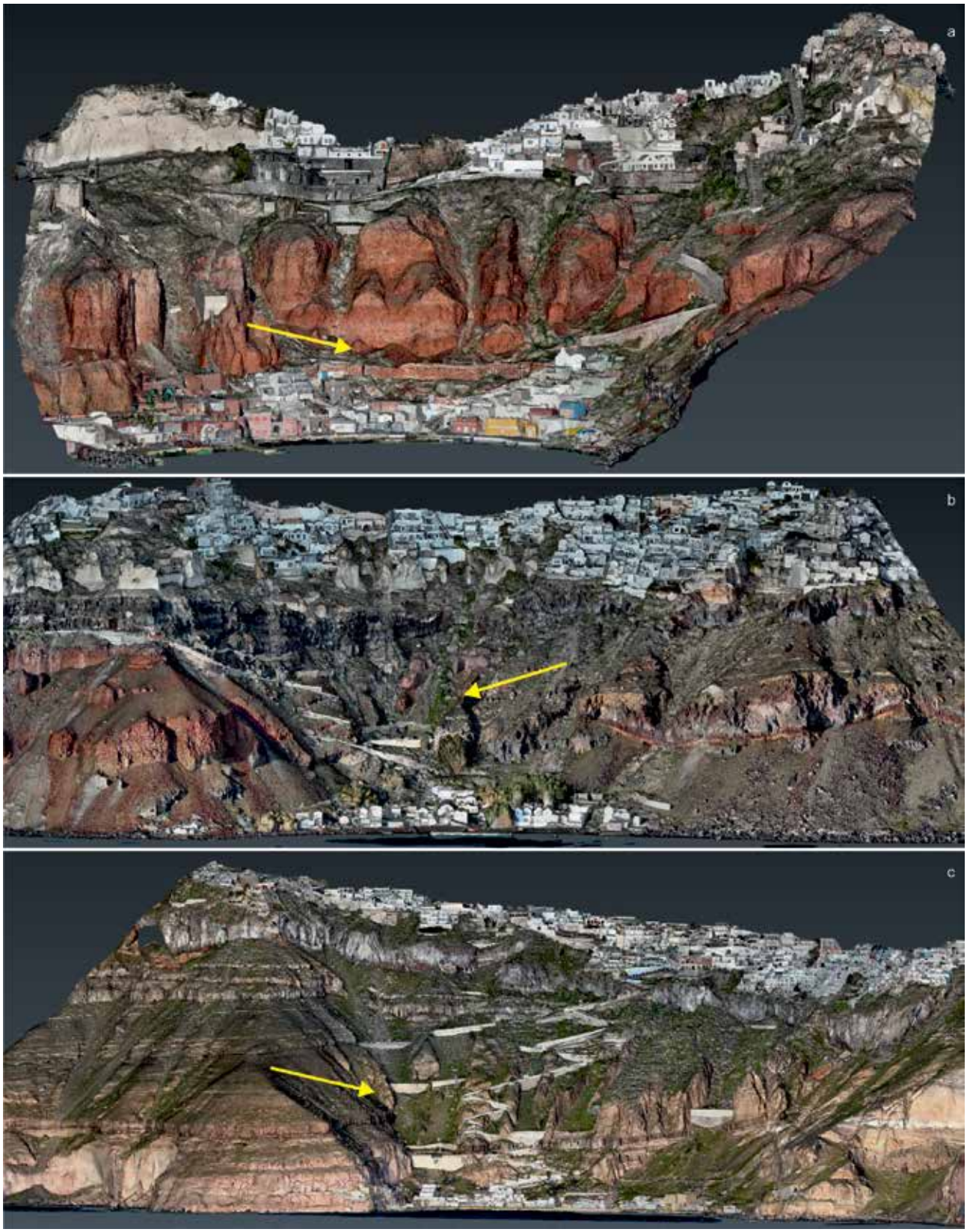
a
b
c

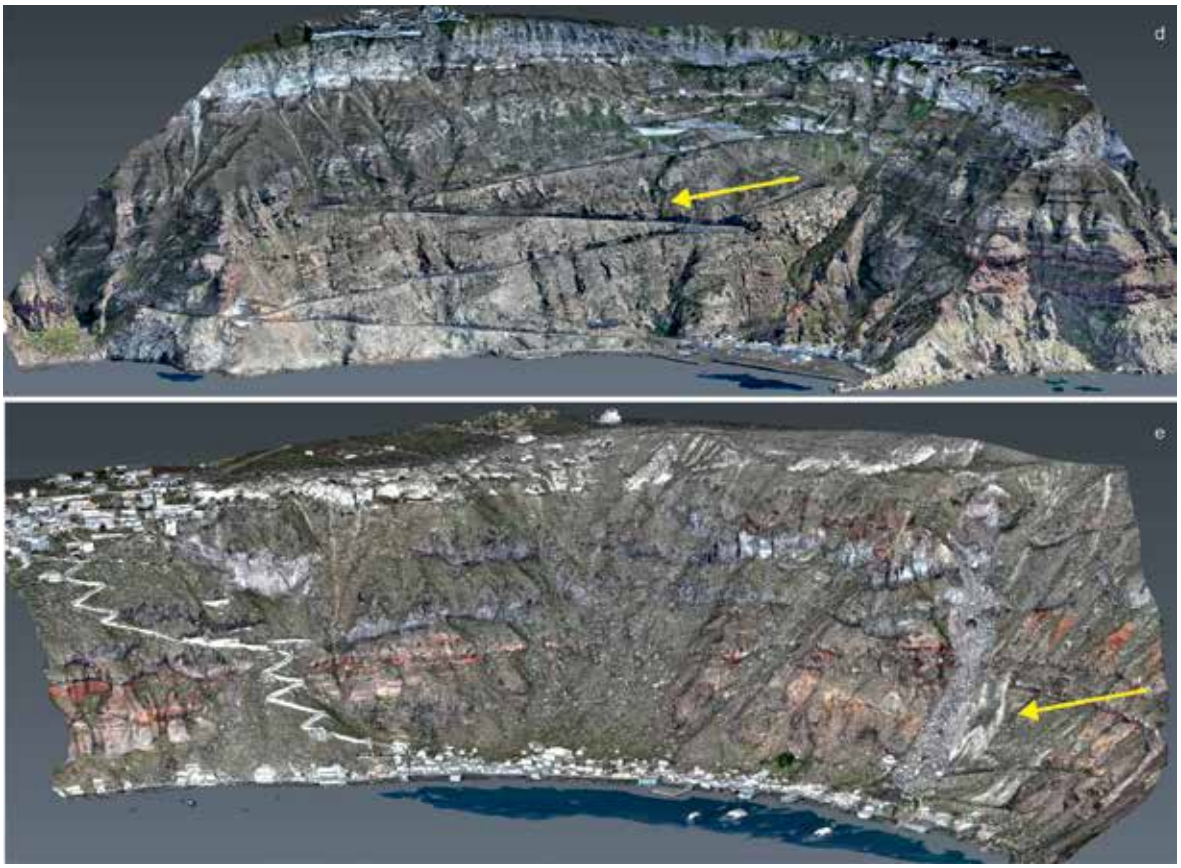

Figure 2. The processing of the acquired point clouds resulted in the construction of five photorealistic 3D models for Ammoudi (a), Armeni (b), Old Harbour (c), Athinios (d) and Korfos (e). Yellow arrows show the enlarged images from the models in Figure 3.

Results – Risk Assessment

The derived datasets were in turn used for the inspection of rock block stability at each one of the five areas, studied within this project. In particular, the geotechnical analysis for the determination of potentially unsafe rock masses was focused on the high-detailed mapping of every single rockfall that happened the recent years. Furthermore, specialized software was used for the simulation of rockfalls in three dimensions, using the constructed 3D models as basal datasets, on which the examination of wedge and plane sliding could be possible and would initiate rock falls at the caldera. The analysis revealed every single rockfall that happened the recent years. Additionally, the efficiency of the already installed measures was examined, and it was rather clear that in most cases they were successfully designed and constructed.

The application of the described methodology, covering the five onshore areas of the island that seem to delineate its most vulnerable parts to rockfalls, proved to be a valuable tool for integrated rockfall simulations and consequently led the way for designing additional reliable safety measures (Toe *et al.,* 2018). Conventional methods, such as mesh and cable nets, as well as barriers -already installed at high-risk locations- could be upgraded or enhanced in certain cases, particularly where recent rockfalls have altered the slope morphology. Furthermore, proposals for new installations have been submitted to local authorities to further mitigate risks in highly frequented areas while maintaining respect for the local environment and simultaneously prevent rocks from reaching manmade constructions.

Conclusions

Understanding rockfall behaviour and evaluating the potential for reactivation necessitate a detailed analysis of the movement patterns of surface materials. As real-scene 3D technology continues to evolve, its applications are expanding across diverse fields, driving a growing demand for greater precision and higher-quality 3D models. In disciplines such as geomorphology and geology, especially in rockfall risk assessment, there is a critical need to develop highly accurate real-scene 3D models.

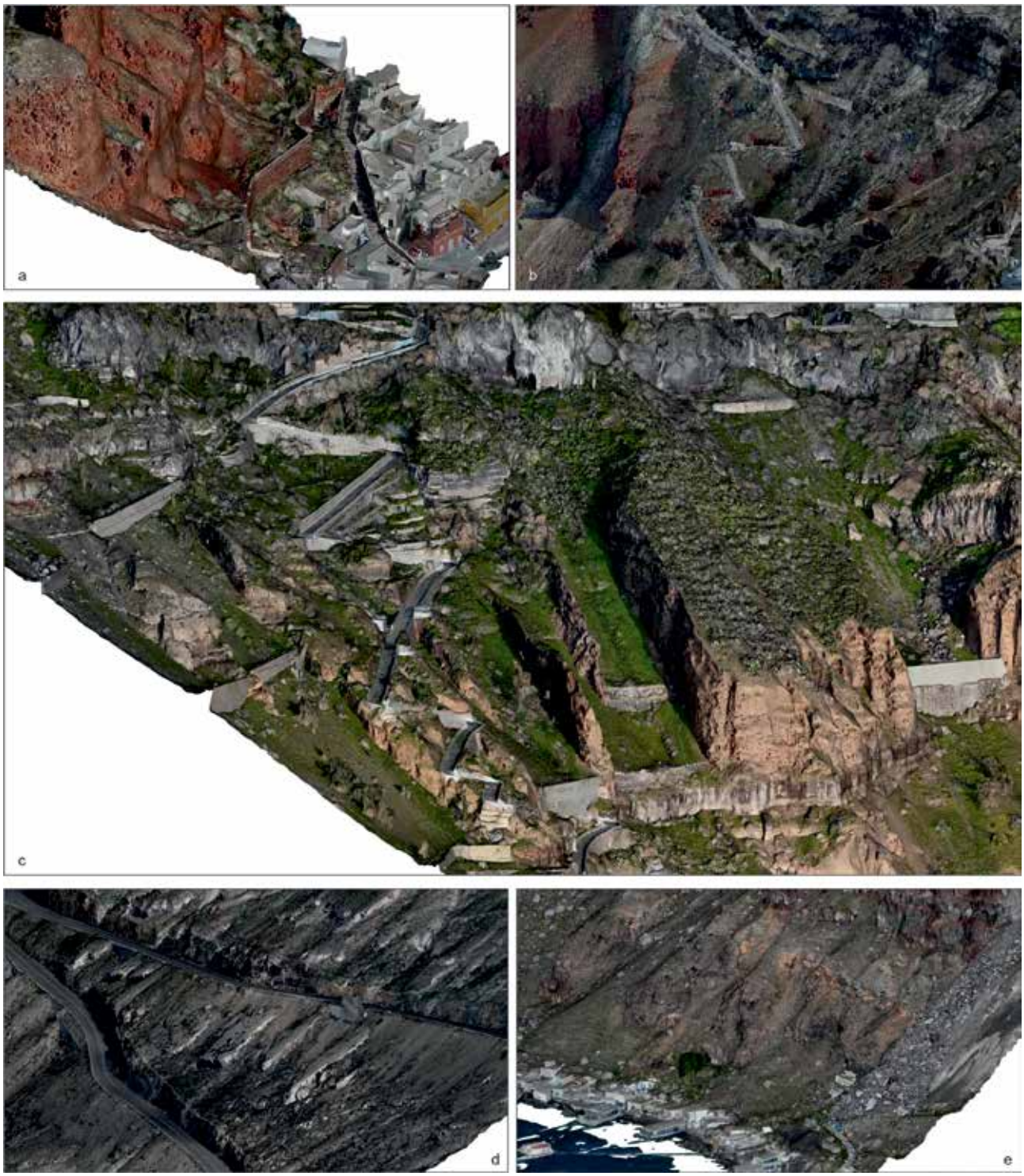

Figure 3. Enlarged images of the five photorealistic 3D models for retaining walls at Ammoudi filled with debris (a), barriers along the path at Armeni (b), retaining walls partially filled with debris below the cable car and other locations upstream the Old Harbour (c), barriers along the road to Athinios (d) and debris upstream Korfos village without any precaution measures (e).

This study presents a novel approach that combines UAV photogrammetry with LiDAR data to achieve high-precision hazard mapping. The proposed methodology follows a streamlined workflow, beginning with field data acquisition using UAV mounted sensors, followed by data fusion that optimally leverages each sensor's capabilities in capturing terrain features. While UAV photogrammetry has limitations in detecting surfaces obscured by dense vegetation

but also confused small trees and bushes with boulders, the processing of LiDAR data that can partially penetrate foliage, can make their integration particularly advantageous. For the selected active rockfall locations, LiDAR and photogrammetric raster images were combined based on terrain characteristics, including vegetation coverage and anthropogenic elements.

The results highlight that integrating data from both sensors enables highly accurate mapping by utilizing the most appropriate technology for each terrain condition, thereby enhancing the analysis of rockfall dynamics and kinematics. The insights gained from this study underscore the necessity of integrating geospatial techniques in steep slopes monitoring. This approach is not only effective in detecting immediate changes but also holds potential for long-term predictions of slope instability. As the Santorini caldera cliffs face increasing environmental and anthropogenic stressors, methodologies like the ones applied in this study would become crucial for proactive hazard management and mitigation efforts. Despite the effectiveness of the proposed method, challenges remain in the semi-automated zoning process, emphasizing the need for advanced machine learning techniques to improve automation and better distinguish between bare ground and vegetation. Future research will focus on refining this approach and conducting continuous, long-term monitoring of the study area, which will continue suffer from rockfalls due to the volcanic lithologies.

In conclusion, the methodology developed here offers a robust framework for future studies and can be adapted to other regions facing similar risks. Ongoing monitoring and refinement of these techniques are essential for improving the predictive capabilities and ensuring the safety of vulnerable touristic environments.

Acknowledgements

The authors would like to express their gratitude to the local authorities (Thira Municipality, Coast Guard, Santorini Cable Car) for their assistance during the field work and E.P.P.O. for providing financial support for the field work of this project.

References

Bernard, T.G., Lague, D., Steer, P., 2021. Beyond 2D landslide inventories and their rollover: synoptic 3D inventories and volume from repeat lidar data. Earth Surf. Dynam., 9, 1013-1044.

Esposito, G., Salvini, R., Matano, F., Sacchi, M., Danzi, M., Somma, R., Troise, C., 2017 Multitemporal monitoring of a coastal landslide through SfM-derived point cloud comparison. The Photogrammetric Record, 32, 459-479.

Farmakis, I., Marinos, V., Papathanassiou, G., Karantanellis, E., 2020. Automated 3D Jointed Rock Mass Structural Analysis and Characterization Using LiDAR Terrestrial Laser Scanner for Rockfall Susceptibility Assessment: Perissa Area Case (Santorini). Geotechnical and Geological Engineering, 38, 3007-3024.

Jiang, N., Li, H., Zhou, J., 2021. Quantitative hazard analysis and mitigation measures of rockfall in a high-frequency rockfall region. Bulletin of Engineering Geology and the Environment, 80, 3439-3456.

Konsolaki, A., Karantanellis, E., Vassilakis, E., Kotsi, E., Lekkas, E., 2024. Multitemporal Monitoring for Cliff Failure Potential Using Close-Range Remote Sensing Techniques at Navagio Beach, Greece. Remote Sensing, 16, 4610.

Lague, D., Brodu, N., Leroux, J., 2013. Accurate 3D comparison of complex topography with terrestrial laser scanner: Application to the Rangitikei canyon (N-Z). ISPRS Journal of Photogrammetry and Remote Sensing, 82, 10-26.

Lim, M., Rosser, N.J., Allison, R.J., Petley, D.N., 2010. Erosional processes in the hard rock coastal cliffs at Staithes, North Yorkshire. Geomorphology, 114, 12-21,

Mora, O.E., Lenzano, M.G., Toth, C.K., Grejner-Brzezinska, D.A., Fayne, J.V., 2018. Landslide Change Detection Based on Multi-Temporal Airborne LiDAR-Derived DEMs. Geosciences, 8, 23.

Notti, D., Guenzi, D., Lasaponara, R., Giordan, D., 2022. Merging Historical Archives with Remote Sensing Data: A Methodology to Improve Rockfall Mitigation Strategy for Small Communities. Land, 11, 1951.

Panagiotopoulou, S., Erkeki, A., Grigorakakis, P., Vassilakis, E., 2022. The use of UAS imagery equipped with multispectral camera for Precision Agriculture applications. 1st Workshop on Data Science for GNSS Remote Sensing, Potsdam, Germany, p. 1.

Toe, D., Mentani, A., Govoni, L., Bourrier, F., Gottardi, G., Lambert, S., 2018. Introducing Meta-models for a More Efficient Hazard Mitigation Strategy with Rockfall Protection Barriers. Rock Mechanics and Rock Engineering, 51, 1097-1109.

Vassilakis, E., Konsolaki, A., Soukis, K., Laskari, S., Kotsi, E., Lialiaris, J., Lekkas, E., 2024. Rockfall Mapping and Monitoring Across the Kalymnos Sport Rock Climbing Sites, Based on Ultra-High-Resolution Remote Sensing Data and Integrated Simulations. Land, 13, 1873.

Westoby, M., Lim, M., Hogg, M., Dunlop, L., Pound, M., Strzelecki, M., Woodward, J., 2020. Decoding Complex Erosion Responses for the Mitigation of Coastal Rockfall Hazards Using Repeat Terrestrial LiDAR. Remote Sensing, 12, 2620.

17th INTERNATIONAL CONGRESS of the Geological Society of Greece

BULLETIN OF THE GEOLOGICAL SOCIETY OF GREECE, SP. PUBL.

EXTENDED ABSTRACT 343

Scaling Relations Between Earthquake Magnitude and Source Duration with Applications to Greece

N. Vavlas[1], A. Kiratzi[1]

(1) Aristotle University of Thessaloniki, Thessaloniki, Greece, navavlas@geo.auth.gr; kiratzi@geo.auth.gr

Research Highlights

The engineering significance of earthquake source duration lies in its direct impact on the design and safety of structures, earthquake engineering, and seismic hazard assessment. This research, while focusing on global datasets, provides essential insights into how seismic source parameters can be scaled and interpreted across varying depths and faulting mechanisms.

Introduction

Earthquake magnitude is commonly linked to parameters describing fault geometry (rupture length, width and area) by empirically obtained scaling relations (Papazachos *et al*., 2004; Somerville, 2021; Thingbaijam *et al*., 2017; Wells and Coppersmith, 1994). They are fundamental for estimating rupture dimensions from earthquake magnitudes, or conversely, predicting the maximum potential magnitude based on fault characteristics. Such estimates are vital for seismic hazard assessment and engineering applications.

Here we focus on the connection between moment magnitude (M_w) and the source duration (t_d) of an earthquake (e.g., Courboulex *et al*., 2016; Ekström *et al*., 1992; Ekström and Engdahl, 1989; Furumoto and Nakanishi, 1983; Kanamori and Given, 1981; Singh *et al*., 2000; Somerville *et al*., 1999). The source duration of an earthquake refers to the time over which seismic energy is released by the fault rupture. A longer source duration typically correlates with sustained ground shaking, which can influence the way buildings and infrastructure respond to the earthquake, specifically in the near field. In engineering terms, a longer shaking duration can result in: (a) increased structural damage, as structures may suffer more extensive damage if the shaking lasts longer, particularly those with resonant frequencies close to the earthquake's frequency content and (b) Nonlinear behaviour: Prolonged shaking increases the likelihood of materials undergoing nonlinear deformations, such as cracking or liquefaction, which can undermine the structural integrity of buildings and infrastructure.

In terms of seismic hazard models, the contribution of having relations to calculate the source duration from the magnitude is significant, because the likelihood of ground motion over an extended period, can be critical for critical infrastructure as hospitals, bridges, dams, storage sites, schools, pipelines among others. Moreover, longer duration shaking in soft soils can lead to amplified ground motion and increase the likelihood of structural damage. In areas where induced seismicity is a concern, such as regions with Carbon Capture and Storage (CCS) or hydraulic fracturing activities, source duration provides insight into the potential for long-duration events that may affect infrastructure over extended periods and helps inform the monitoring and management of such activities.

It is often suggested that source duration scales with seismic moment as $t_d \propto (M_0)^{1/3}$, assuming constant static stress drop (Δ_σ), and constant rupture velocity (V_R) (e.g., Duputel *et al*., 2012; Ekström *et al*., 2005; Furumoto and Nakanishi, 1983; Kanamori and Brodsky, 2004; Singh *et al*., 2000). The above studies have also indicated that the ratio between td and $(M_0)^{1/3}$ can vary with seismogenic region or when different global datasets are used. The satisfaction of the above with invariant Δ_σ and V_R implies that there is source similarity, that is to say, a predictable scale-invariant pattern exists for all earthquakes. However, the question of whether earthquakes truly scale self-similarly remains open as several studies (e.g., Mayeda *et al*., 2007; Malagnini *et al*., 2008; Mayeda and Malagnini 2010; Denolle and Shearer 2016; Poli and Prieto 2016; Morasca *et al*., 2019) challenge this and suggest that earthquakes may not always follow a self-similar behavior.

Data and Methods

Two empirical approaches were used to relate M_w to t_d were adopted. The first one utilizes centroid time-delays as proxies for source durations (t_d), following the methodology established by Duputel *et al*. (2013). The global dataset of the authors as reported in their original paper was used, consisting of 798 global earthquakes from 1991 to 2012 with magnitudes ranging from 6.3 to 9.2, and depths up to ~650km (top panels of Figure 1).

The second dataset includes directly measured t_d values from the global Source Time Function (STF) database of SCARDEC (from Seismic source ChAracteristics Retrieved from DEConvolvolving teleseismic body waves; Vallée and Douet, 2016). It includes 3,950 earthquakes from the period 1992 to 2022, with magnitudes ranging from approximately 5.5 to 9.0, spanning all depths and faulting styles lower panels of Figure 1).

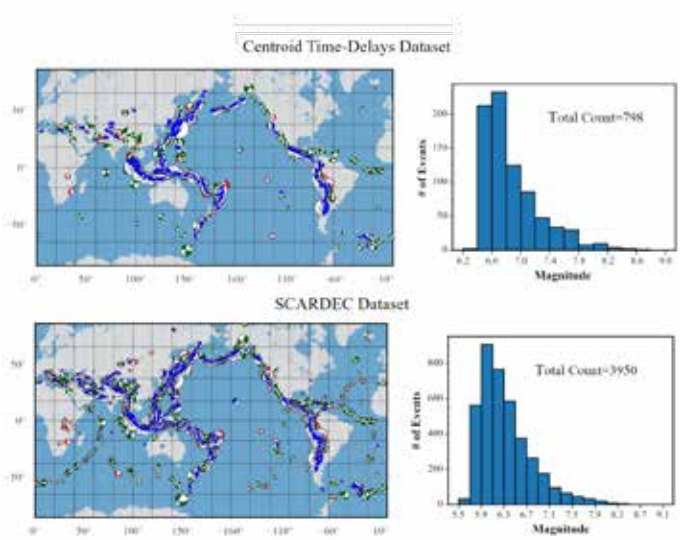

Figure 1. The two global datasets utilized in this work: Top panels show the focal mechanism dataset of Duputel *et al*., (2013), with faulting type percentages of 44% for reverse, 42% for strike-slip, and 15% for normal faulting. Bottom panels show the SCARDEC database of source time functions, with color-coded focal mechanism beachballs in map view. The colors represent the faulting types: green for reverse faulting (46%), blue for strike slip faulting (36%), and red for normal faulting (18%).

Source Durations from Centroid Time-Delays

Centroid time-delay (τ_c) is defined as the time difference between the earthquake's hypocenter origin time (t_o), and the centroid time (t_c), which represents the point in time when the best-fitting point source is located, thus ($\tau_c = t_c - t_o$). Centroid time, t_c is routinely calculated during Global Centroid Moment Tensor (GCMT) inversion, which also determines the centroid's geographical coordinates and depth.

In the GCMT inversion, the Source Time Function (STF) of an earthquake is modeled as a symmetric triangular function (Figure 2[a]). The centroid time (t_c) corresponds to the peak of this triangle, while the half-duration (t_h) is derived from an empirical relationship with respect to seismic moment (M_0). Therefore, τ_c is more reliably constrained compared to t_h, and doubling it leads to a reasonable proxy for the source duration (t_d):

$$t_d \approx 2\tau_c \quad (1)$$

The examined dataset of Duputel *et al*. (2013) includes centroid time-delays from both the GCMT inversion and the W-phase source inversion algorithm (WCMT). The geometric mean of these two values was computed, resulting in data pairs of M_w and t_d that were later used in a regression scheme.

Source Durations from the SCARDEC Source Time Function Database

The SCARDEC database estimates the source time function (STF) of an earthquake using teleseismic body-wave deconvolution. For each event, it reports both average and optimal STFs. The "apparent" STF is derived by deconvolving synthetic point-source waveforms from observed recordings, reflecting the azimuthal dependence of the STF. It is influenced by the varying radiation of seismic energy to different stations, which may incorporate effects from both the source process and wave propagation through the Earth.

The average STF represents an aggregation of high-quality P-wave apparent STFs, providing a global perspective of the earthquake source. This averaging minimizes biases in the overall shape of the STF, as directivity effects are generally modest for teleseismic P waves. However, this process may smooth out high-frequency details that are significant in spectral analyses. To address this, an optimal STF is chosen for its similarity to the average STF and its ability to produce a good fit between synthetic and observed waveforms when convolved with point-source synthetics. Using the average STFs, the start and end times of moment release were determined (Figure 2[b]). The time difference between these two instances was used to estimate the source duration, t_d which in combination with the M_w values reported in the database, produced (t_d, M_w) regression pairs.

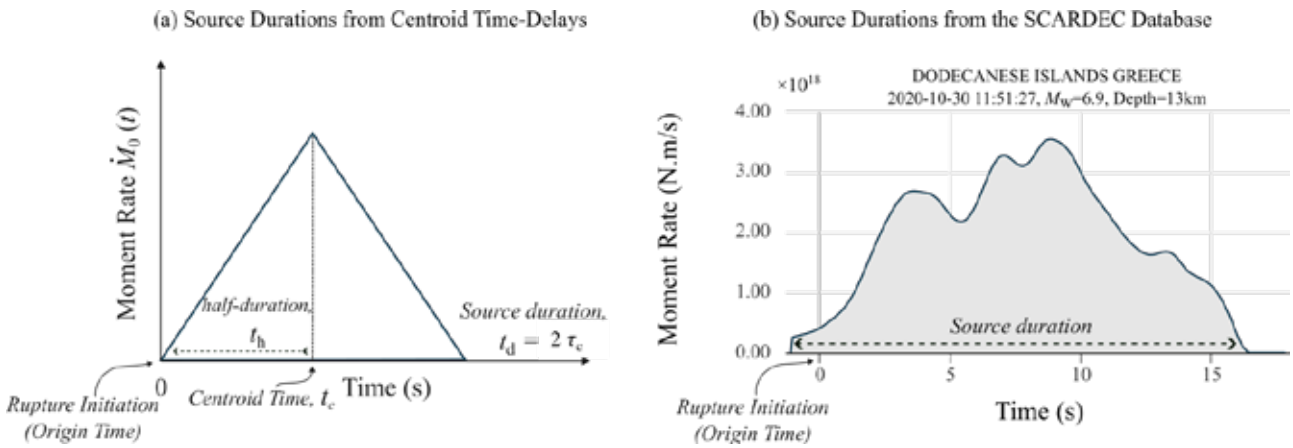

Figure 2. Source duration (t_d) of earthquakes as obtained from: (a) the isosceles triangular Source Time Function (STF) used in the GCMT inversion. The centroid time, t_c, is defined as the point in time where the peak of the STF is observed (clearly coincides with the top vertex of the triangle) and expresses the point in time where the best fitting centroid is located. Since the source is assumed to have a symmetrical STF, doubling the centroid time-delay (τ_c) yields the total source duration t_d. (Duputel *et al.*, 2013). (b) The source duration as obtained from the STFs included in the SCARDEC database, where t_d can directly be measured (an example is shown here).

Results: Analysis of Scaling Relationships

To investigate the scaling relationship between earthquake magnitude and source duration, we performed linear regression analyses on two key datasets: the centroid-time delays dataset for half-durations (τc) and the SCARDEC Source Time Function (STF) dataset for source durations (td). These datasets were further segmented based on faulting mechanisms and seismic depth to explore regional and structural variability in scaling behavior.

Separate regressions for shallow (≤60 km) and deep (>60 km) events, as shown in Figure 3, reveal a clear distinction between the two depth categories. Deep earthquakes exhibit shorter source durations, consistent with theoretical models like the Brune circular crack model (1970, 1971), which predicts faster moment release for deeper events. Specifically, shallow events have a longer mean duration of 14.3 seconds and higher intercepts, while deep events show a shorter mean duration of 6.7 seconds. This trend supports the hypothesis that deeper earthquakes, experiencing higher stress conditions at depth, release seismic moment more rapidly than their shallow counterparts.

A comprehensive analysis of potential variations in scaling relationships based on faulting mechanisms (e.g., strike-slip, normal, or reverse) revealed no significant dependence on these parameters. This suggests that, regardless of faulting style, the scaling between moment magnitude (Mw) and source duration (td) holds consistent, providing a robust method for estimating earthquake source durations based on magnitude alone. Such relationships are critical for improving seismic hazard models, as they allow for more accurate predictions of ground shaking in regions with limited seismic data.

Furthermore, we examined the regional applicability of the centroid-time delays dataset by focusing on a subset of Global Centroid Moment Tensor (GCMT) data for Greece (19°–30°E, 33.5°–42.5°N), which included 667 earthquakes from 1976 to 2020, with magnitudes ranging from 4.6 to 7.6 and depths extending to 160 km. The Greek dataset exhibited substantial scatter, particularly for earthquakes with magnitudes smaller than Mw 6.5. This scatter is likely attributed to the limited range of magnitudes, coupled with the smaller number of larger magnitude events, which hindered the development of a reliable scaling relationship within this subset alone.

To improve the analysis, the Greek dataset was supplemented with larger magnitude events from global datasets. This inclusion resulted in a more discernible trend with a high linear correlation coefficient of 0.81, suggesting that a broader dataset improves the robustness of the scaling relationship. However, the applicability of this scaling behaviour to smaller magnitude events within this specific region remains uncertain. The higher variability observed in lower-magnitude events could be due to increased uncertainty in the origin time and centroid time estimates, as well as the absence of stronger (Mw ≥ 6.3) earthquakes that might help better define the scaling trend.

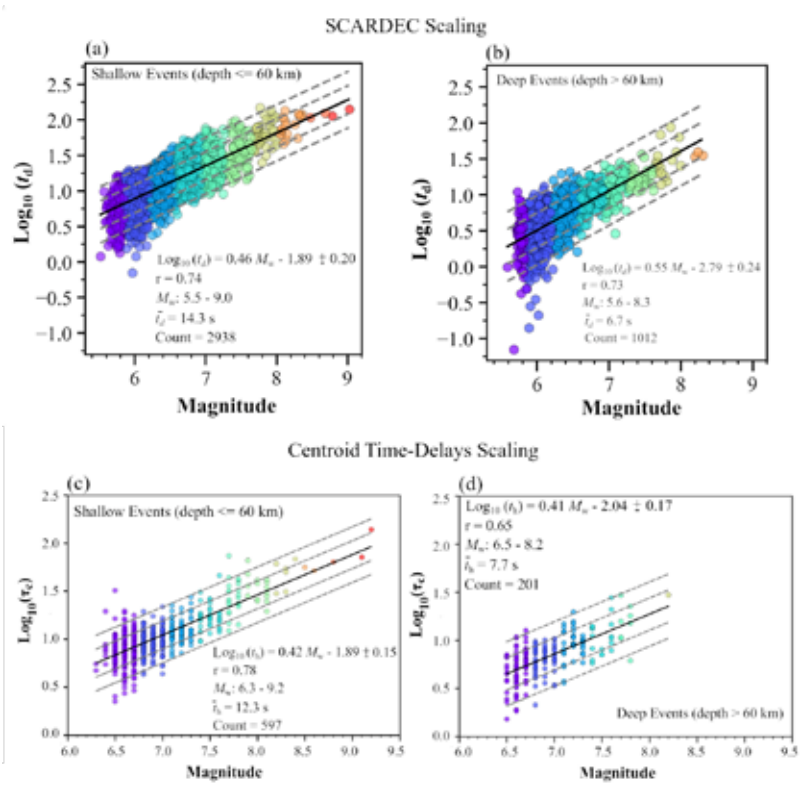

Figure 3. Linear regression between earthquake magnitude and the logarithm of source duration based on source time functions from the SCARDEC database for shallow (a) and deep events (b). (c, d) Show analogous regressions for earthquake half-duration, using the centroid time-delay dataset.

Discussion and Conclusions

In this work, the scaling between earthquake moment magnitude, M_w and source duration, t_d, was examined, using two distinct datasets, to assess variability across depths and focal mechanisms. While for different faulting styles, slight differences were noted among normal, reverse, and strike-slip faulting (not presented herein), notable differences were observed across earthquake depths, with deeper earthquakes exhibiting shorter source durations across both datasets, implying more rapid moment release.

Using the herein obtained scaling relations, for the generic cases (no constraints on focal mechanism or focal depth), we created a catalog of source durations for earthquakes in the Greek region, for both historical and instrumental events (Figure 4), to gain an overview on their spatial distribution and their statistical distribution. Note that these two distributions are not equivalent, as the relationships were applied only within their valid applicability range.

Table 1 summarizes the scaling coefficients and regression parameters for all the scaling relationships presented in this work. The regression formula is given by:

$$log_{10}(t_d) = b M_w + a \pm \sigma, \quad (2)$$

where a and b are the regression coefficients and σ represents the regression error.

Table 1. Coefficients from linear regressions (Eq. 2) between source duration (t_d) and moment magnitude (M_w). For the centroid time-delay datasets, regressions presented below were conducted for double the half-duration ($2\tau_c$) which equates to the source duration (t_d) and allows a direct comparison between the relationships.

Dataset	b	a	σ	r	Mag. Range	Count
Centroid Time-Delays (Generic)	0.42	-1.61	0.17	0.71	6.3–9.2	798
Centroid Time-Delays (Shallow)	0.42	-1.59	0.15	0.78	6.3–9.2	597
Centroid Time-Delays (Deep)	0.41	-1.74	0.17	0.65	6.5–8.2	201
SCARDEC (Generic)	0.48	-2.11	0.26	0.66	5.5–9.0	3950
SCARDEC (Shallow)	0.46	-1.89	0.20	0.74	5.5–9.0	2938
SCARDEC (Deep)	0.55	-2.79	0.24	0.73	5.6 – 8.3	1012

*Note: *Generic scaling relationships involve no constraints on depth; shallow refers to depth ≤ 60 km; deep refers to depth > 60 km.*

The scaling relationships derived in this study enable the retrospective prediction of source durations for historical earthquakes. For instance, the source durations for the very strong earthquakes of 365 and 1303 CE, shown in Figure 4, were estimated based on the established scaling relations. This predictive capability holds particular significance for earthquake early warning systems. Building upon previous work (Vavlas *et al*., 2021), we demonstrate how these scaling relationships can be utilized to estimate early warning timelines for hypothetical earthquake scenarios. These estimations rely on the symmetry often present in Source Time Functions (STFs) and account for factors such as the spatial density of monitoring networks, rates of ground motion attenuation, and other relevant theoretical considerations.

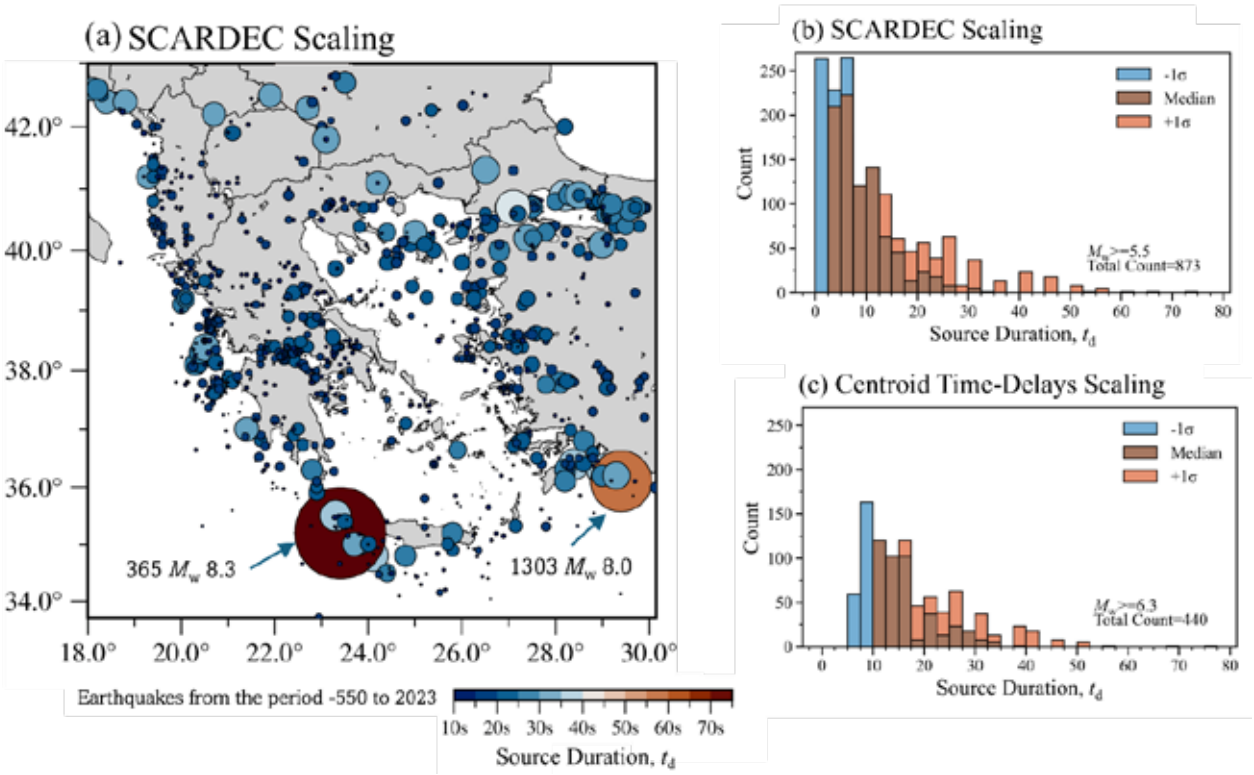

Figure 4. Spatial and Statistical Distribution of Source Durations. (a): Distribution of source durations of historical and instrumental strong earthquakes derived using the generic scaling relationship from the SCARDEC STFs. The map shows earthquake epicenters color-coded by source duration (t_d) and circle-size proportional to magnitude. (b) Frequency distribution of source durations (t_d) based on the median prediction of the scaling relationship, including a range of values corresponding to one standard deviation above and below the median. (c) Similar (b) but derived from the generic scaling relationship of centroid time-delays. All calculations were made for earthquakes with magnitudes above the lower applicability limit of each scaling relationship and adopting the generic regression case, i.e., no constraints on depth or faulting mechanisms.

This workflow allows the estimation of early warning timelines for customized scenario earthquakes, considering the spatial density of monitoring networks, the attenuation of ground motion with distance, among other theoretical factors. The above processes have been containerized and can be applied to provide warning timelines for critical infrastructure from scenario earthquakes from induced seismicity or from scenario earthquakes from seismic hazard disaggregation.

Acknowledgements

Partial funding from the European Union's HE Research and Innovation programme (Project COREu under grant agreement No 101136217) is gratefully acknowledged.

References

Courboulex, F., Vallée, M., Causse, M., & Chounet, A. (2016). Stress□Drop Variability of Shallow Earthquakes Extracted from a Global Database of Source Time Functions. Seismological Research Letters, 87(4), 912–918. https://doi.org/10.1785/0220150283

Denolle, M. A., & Shearer, P. M. (2016). New perspectives on self-similarity for shallow thrust earthquakes. Journal of Geophysical Research: Solid Earth, 121(9), 6533–6565.

Duputel, Z., Rivera, L., Kanamori, H., & Hayes, G. (2012). W phase source inversion for moderate to large earthquakes (1990–2010). Geophysical Journal International, 189(2), 1125–1147.

Duputel, Z., Tsai, V. C., Rivera, L., & Kanamori, H. (2013). Using centroid time-delays to characterize source durations and identify earthquakes with unique characteristics. Earth and Planetary Science Letters, 374, 92–100.

Ekström, G., & Engdahl, E. (1989). Earthquake source parameters and stress distribution in the Adak Island region of the central Aleutian Islands, Alaska. Journal of Geophysical Research: Solid Earth, 94(B11), 15499–15519.

Ekström, G., Stein, R. S., Eaton, J., & Eberhart-Phillips, D. (1992). Seismicity and geometry of a 110-km-long blind thrust fault 1. The 1985 Kettleman Hills, California, earthquake. Journal of Geophysical Research: Solid Earth, 97(B4), 4843–4864.

Ekström, G., Dziewoński, A., Maternovskaya, N., & Nettles, M. (2005). Global seismicity of 2003: centroid–moment-tensor solutions for 1087 earthquakes. Physics of the Earth and Planetary Interiors, 148(2–4), 327–351.

Furumoto, M., & Nakanishi, I. (1983). Source times and scaling relations of large earthquakes. Journal of Geophysical Research: Solid Earth, 88(B3), 2191–2198.

Hwang, R.-D., Ho, C.-Y., Lin, T.-W., Chang, W.-Y., Huang, Y.-L., Lin, C.-Y., & Lin, C.-Y. (2020). Relationship between seismic moment and source duration for seismogenic earthquakes in Taiwan: Implications for the product of static stress drop and the cube of rupture velocity. Pure and Applied Geophysics, 177, 3191–3203.

Kanamori, H., & Brodsky, E. E. (2004). The physics of earthquakes. Reports on Progress in Physics, 67(8), 1429.

Kanamori, H., & Given, J. W. (1981). Use of long-period surface waves for rapid determination of earthquake-source parameters. Physics of the Earth and Planetary Interiors, 27(1), 8–31.

Kikuchi, M., & Ishida, M. (1993). Source retrieval for deep local earthquakes with broadband records. Bulletin of the Seismological Society of America, 83(6), 1855–1870.

Kostka, F., Zahradník, J., Sokos, E., & Gallovič, F. (2022). Assessing the role of selected constraints in Bayesian dynamic source inversion: Application to the 2017 M w 6.3 Lesvos earthquake. Geophysical Journal International, 228(1), 711–727.

Malagnini, L., Scognamiglio, L., Mercuri, A., Akinci, A., & Mayeda, K. (2008). Strong evidence for non-similar earthquake source scaling in central Italy. Geophysical Research Letters, 35(17).

Mayeda, K., & Malagnini, L. (2010). Source radiation invariant property of local and near-regional shear-wave coda: Application to source scaling for the Mw 5.9 Wells, Nevada sequence. Geophysical Research Letters, 37(7).

Mayeda, K., Malagnini, L., & Walter, W. R. (2007). A new spectral ratio method using narrow band coda envelopes: Evidence for non□self□similarity in the Hector Mine sequence. Geophysical Research Letters, 34(11).

Morasca, P., Walter, W. R., Mayeda, K., & Massa, M. (2019). Evaluation of earthquake stress parameters and its scaling during the 2016-2017 Amatrice-Norcia-Visso sequence—Part I. Geophysical Journal International, 218(1), 446–455.

Papazachos, B., Scordilis, E., Panagiotopoulos, D., Papazachos, C., & Karakaisis, G. (2004). Global relations between seismic fault parameters and moment magnitude of earthquakes. Bulletin of the Geological Society of Greece, 36(3), 1482–1489.

Poli, P., & Prieto, G. A. (2016). Global rupture parameters for deep and intermediate-depth earthquakes. Journal of Geophysical Research: Solid Earth, 121(12), 8871–8887.

Sawade, L., Beller, S., Lei, W., & Tromp, J. (2022). Global centroid moment tensor solutions in a heterogeneous earth: the CMT3D catalogue. Geophysical Journal International, 231(3), 1727–1738. https://doi.org/10.1093/gji/ggac280

Singh, S., Pacheco, J., Ordaz, M., & Kostoglodov, V. (2000). Source time function and duration of Mexican earthquakes. Bulletin of the Seismological Society of America, 90(2), 468–482.

Sokos, E, Zahradník, J., Gallovič, F., Serpetsidaki, A., Plicka, V., & Kiratzi, A. (2016). Asperity break after 12 years: the Mw6. 4 2015 Lefkada (Greece) earthquake. Geophysical Research Letters, 43(12), 6137–6145.

Sokos, Efthimios, Gallovič, F., Evangelidis, C. P., Serpetsidaki, A., Plicka, V., Kostelecký, J., & Zahradník, J. (2020). The 2018 M w 6.8 Zakynthos, Greece, earthquake: Dominant strike-slip faulting near subducting slab. Seismological Research Letters, 91(2A), 721–732.

Somerville, P. (2021). Scaling relations between seismic moment and rupture area of earthquakes in stable continental regions. Earthquake Spectra, 37(1_suppl), 1534–1549.

Somerville, P., Irikura, K., Graves, R., Sawada, S., Wald, D., Abrahamson, N., et al. (1999). Characterizing crustal earthquake slip models for the prediction of strong ground motion. Seismological Research Letters, 70(1), 59–80.

Thingbaijam, K. K. S., Martin Mai, P., & Goda, K. (2017). New Empirical Earthquake Source-Scaling Laws. Bulletin of the Seismological Society of America, 107(5), 2225–2246. https://doi.org/10.1785/0120170017

Vallée, M., & Douet, V. (2016). A new database of source time functions (STFs) extracted from the SCARDEC method. Physics of the Earth and Planetary Interiors, 257, 149–157.

Vallée, M., Charléty, J., Ferreira, A. M., Delouis, B., & Vergoz, J. (2011). SCARDEC: a new technique for the rapid determination of seismic moment magnitude, focal mechanism and source time functions for large earthquakes using body-wave deconvolution. Geophysical Journal International, 184(1), 338–358.

Wells, D. L., & Coppersmith, K. J. (1994). New empirical relationships among magnitude, rupture length, rupture width, rupture area, and surface displacement. Bulletin of the Seismological Society of America, 84(4), 974–1002.

17th INTERNATIONAL CONGRESS of the Geological Society of Greece

BULLETIN OF THE GEOLOGICAL SOCIETY OF GREECE, SP. PUBL.

EXTENDED ABSTRACT 344

Microseismicity Monitoring of the Broader Stypsi Geothermal Field Area (Northern Lesvos Island, Greece) Using a Local Seismological Network

Ventouzi Ch.[1], Papazachos C.[1], Kkallas Ch.[1], Spyridonos, E.[2]

(1) Aristotle University of Thessaloniki, Thessaloniki, Greece, xrusven@geo.auth.gr, (2)PPC Renewables S.M.S.A., Athens, Greece

Introduction

The broader Stypsi region, located in NW Lesvos, Greece, has attracted significant interest as an area of high geothermal potential. Understanding the microseismicity of geothermal areas is crucial for the evaluation of their geotectonic setting and associated active stress field prior to any resource exploitation. Moreover, there have been cases where induced seismicity has been attributed to geothermal energy exploitation (e.g. Woo et al., 2019). As a result, the monitoring of microseismicity in such areas has attracted the attention of both industry and society.

The present study focuses on the installation and operation of a dense local seismic network in the previously mentioned area of particular interest. Data from this local, as well as permanent seismological networks are employed and processed with recently developed machine learning methods, to enhance the resolution of seismicity analysis. The results verify that the current permanent network of seismological stations (Hellenic Unified Seismological Network, HUSN) is not able to detect the background microseismic activity, as well as the seismic sequences generated by relatively small magnitude earthquakes. This is clearly demonstrated in the present study, where for the operation time of the local network only 1/10 of the manually located events were identified by HUSN, even though the same detection algorithm was employed. The obtained results are in agreement with the dominant trans-tensional seismotectonic regime of Lesvos, with most events being associated to normal and strike-slip faults, revealing a roughly N-S extension. We also present results from the use of a deep learning model (SEISBENCH toolbox), which managed to detect a very large number of events (~6000 events-initial determination) that were missed by the conventional STA/LTA detection algorithms of the acquisition software currently used (Seiscomp). The results suggest that the combination of dense local network of seismological stations, with novel machine learning techniques can provide significantly improved results regarding microseismicity monitoring in similar environments.

Figure 1. Map of the current N Lesvos (FDSN code 4H) local network (yellow squares). Station LES5 has been relocated to LES5N. The region of interest for possible future geothermal exploration is depicted by two (2) polygons.

Data and method

A surface network of five (5) high-sensitivity 24-bit mid-range (10s-98Hz) seismographs was installed in October 2023, as depicted in the map of Figure 1. The FDSN code 4H (2023) has been assigned to this network for future reference (see https://www.fdsn.org/networks/detail/4H_2023/). Since October 16, 2023, all data for these seismological stations are collected on a dedicated server, using the Seiscomp software (https://www.seiscomp.de/). This open-source software has become the “golden” standard for similar work, used by almost all European networks, as well as the Hellenic Unified

Seismological Network. The software and its tools allow easy data visualization, as well as the necessary data processing and event analysis. It provides automatic and interactive seismological data acquisition, processing, and data exchange over the internet by using the SeedLink transmission protocol. Since the database creation is performed, seismic events within ~15km from the area of interest were identified using an automatic detection algorithm employed by Seiscomp, for event identification and preliminary relocation. After the initial automated determination of earthquake epicenters, a manual analysis of all seismic events has been conducted by manually picking P and S phases. This was initially performed using the advanced NonLinLoc location code (http://alomax.free.fr/nlloc/, (Lomax *et al.*, 2000) embedded in Seiscomp, as well as a 1D velocity model extracted from the 3D tomographic model of Papazachos and Nolet (1997). To discriminate local events from regional seismicity, a large number of real-time regional neighboring stations from the Hellenic Unified Seismological Network (HUSN), as well as from Turkish stations (Kandili Observatory) have been included in the acquisition. Magnitudes for all recorded events were estimated using the local magnitude M_L, as calculated using the Hutton and Boore (1987) relationship, which uses the maximum trace amplitudes recorded on standard Wood-Anderson horizontal seismometers. For events with larger magnitudes (eg. $M_L \geq 1.9$), if the first motions of P waves were clearly recorded by more than 4 stations (typically more, using regional stations), a focal mechanism of the earthquake was also calculated using the approach offered by the Seiscomp software.

From the beginning of the network operation (October 16, 2023) until January 10, 2025, 1044 events have been manually picked and relocated within the broader region of the study area. Figure 2 presents a map of the local seismicity recorded by the N. Lesvos local monitoring network, as well as from the Hellenic Unified Seismological Network (HUSN) and Turkish stations (Kandili Observatory). Events with $M_L<1.0$ are shown as black dots, while yellow circles show events with magnitudes $1.0 \leq M_L<2.0$ and light green circles represent earthquakes with magnitudes $2.0 \leq M_L<3.0$. In the legend red circles illustrate events with magnitude $3.0 \leq M_L<4.0$ and white star events with $M_L \geq 4.0$. While such magnitude events were not recorded during the operation of the Lesvos local monitoring network (maximum recording magnitude of $M_L=3.9$), on January 21, 2025, a $M_L=5.1$ earthquake occurred in the coastal area of Efthalou and Sikaminea. In Fig. 2 we also present information (black lines) for all known active faults in the broader Stypsi area, as provided by the tectonic map of Stypsi-Lesvos by the Department of Geography of the University of the Aegean (compiled by Prof. Zouros and colleagues), while the light-green ones depict possible faults. The regions of interest for possible geothermal exploration are depicted by two (2) polygons, while green squares and blue triangles depict existing boreholes performed by the Greek PPC Renewables. We also show the seismological stations of the local N. Lesvos monitoring network. The dashed circle indicates a region with a radius of 15km centered around the network area, where quantitative calculations (i.e., Gutenberg-Richter distribution) were performed for the study area. Figure 3 presents the seismicity recorded over the 15-month operational period of the network, during which only 155 earthquakes were located by HUSN (Combined earthquake catalog generated from the online catalogues of the Aristotle University of Thessaloniki and the National Observatory of Athens, Institute of Geodynamics, Athens).

As can be seen from the map of Figure 2, the majority of the events is clustered in the Northern part of Lesvos, mainly in the areas of Efthalou, Lepetymnos and Sikaminea, with magnitudes $2.0 \leq M_L<3.0$, roughly at a 6km distance to the NE from the Areas of Interest (AoI). In this area we observed a prolonged seismic excitation (seismic swarm), lasting several hours, on the 19th of August 2024, starting from about 02:00PM until 13:00 AM (GMT). 118 events from this swarm have been relocated, revealing an almost E-W trend for the corresponding seismicity distribution. A second seismic sequence was recorded in the same area of the previous excitation, where a $M_L=3.9$ earthquake occurred on 27 October 2024 16:56:01 local time, ~1km North of Argennos and to the NNW of Lepetymnos village. This event corresponds to the largest one recorded since the beginning of the operation of the local network. This led to a sequence requiring the manual relocation of almost twice the number of the events located since the beginning of the network operation, since in the previous trimester the number of the events of the catalog was ~600 and this number increased to ~1050 until January 10th of 2025. In just two days after the $M_L=3.9$ earthquake, 204 earthquakes were manually picked and relocated in the same area. After the third day, the number of the events recorded returned to “normal” (background) levels. The spatial distribution of the events located by the October 27-30, 2024, seismic sequence indicates a WNW-ESE trend, similar to the August 19th excitation. In the marine area of Stypsi gulf, a few kilometers (~5km) to the east of the areas of interest, a few lower magnitude events $1.0 \leq M_L<2.0$ occurred. In the same region, the second largest event recorded to date had magnitude $M_L=3.3$ occurred on 2024-09-15. For the whole area of interest, only one event with magnitude $M_L<2.0$ has been recorded within 15 months since the deployment of the local network, while only two earthquakes with magnitude $2.0 \leq M_L<3.0$ have occurred nearly ~2km outside of the area of interest (on land). Almost ~2.3km to the NNW, in the marine area of Mythimna, three earthquakes with magnitudes $2.0 \leq M_L<3.0$ have occurred, and several others with lower magnitude for the last 3-month period. The difference in the number of earthquakes recorded by the local network compared to those identified by the permanent seismograph network is striking. This difference is mostly pronounced for earthquakes with M<2.0, underlining the necessity of the installation of local networks in areas of special interest.

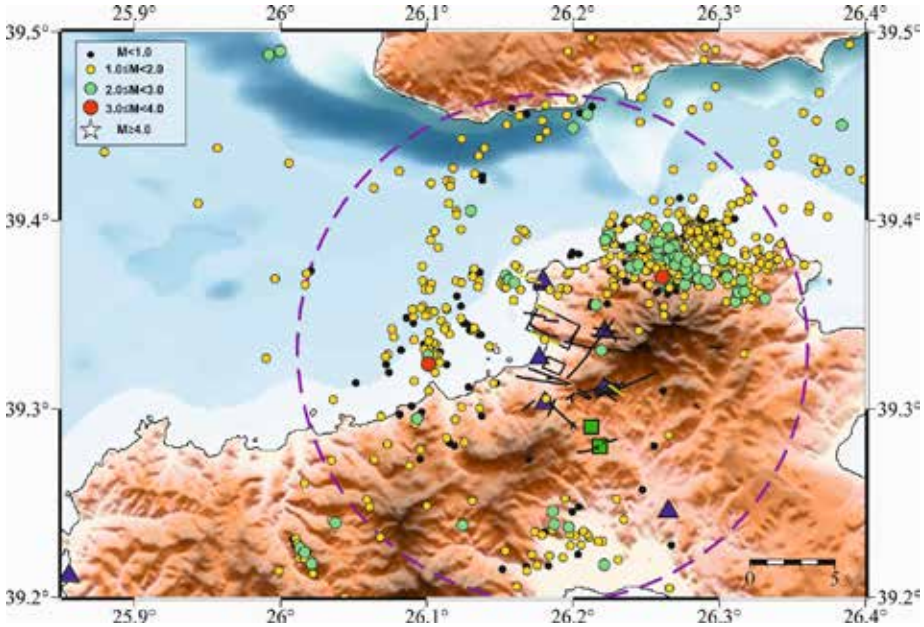

Figure 2. Map of the recorded seismicity for the study area of N. Lesvos for the period of 16 October 2023-10 January 2025 (15 months of local network operation). Blue triangles indicate the operating seismological stations of the N. Lesvos local monitoring network, as well as regional stations (PRK and SIGR), while green squares depict exploration boreholes performed by PPC Renewables. The two black polygons indicate the regions of interest for possible geothermal exploration. Black and light green lines show the active faults and the possible faults, respectively. The dashed circle indicates the area of 15km radius, for which the quantitative seismicity assessment was performed.

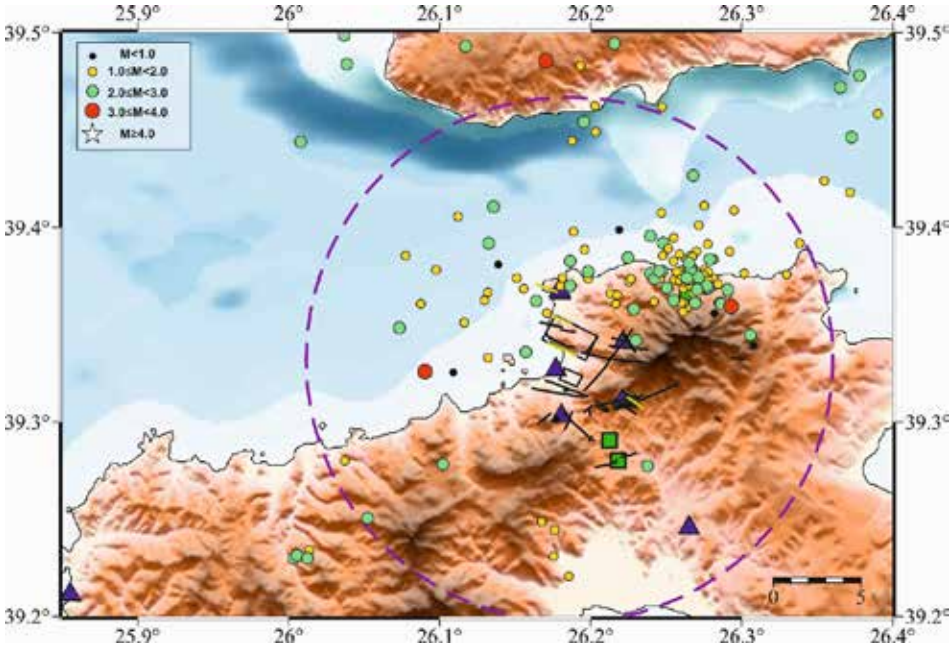

Figure 3. Same as figure 2, depicting the seismicity recorded for the study area by the Hellenic Unified Seismological Network (HUSN).

Figure 4 presents the focal mechanisms which were calculated, whenever possible (clear first motions of P-waves), for earthquakes with magnitudes $M_L \geq 1.9$. Black beach balls represent focal mechanisms associated with normal faults, red beach balls represent focal mechanisms of strike slip faults, while blue beach balls represent focal mechanisms of thrust faulting. The regions of Lepetymnos and Sikaminea are dominated by strike-slip focal mechanisms, while the Efthalou region shows mostly normal focal mechanisms. Focal mechanisms for earthquakes with magnitudes $M_L < 1.9$ were also calculated in some cases but are not shown in the map of Figure 4, as they were prone to very large errors. The largest event recorded with magnitude $M_L = 3.9$, shows a strike-slip fault plane solution, as depicted in the map of Figure 2.3 with the largest red “beach-ball”.

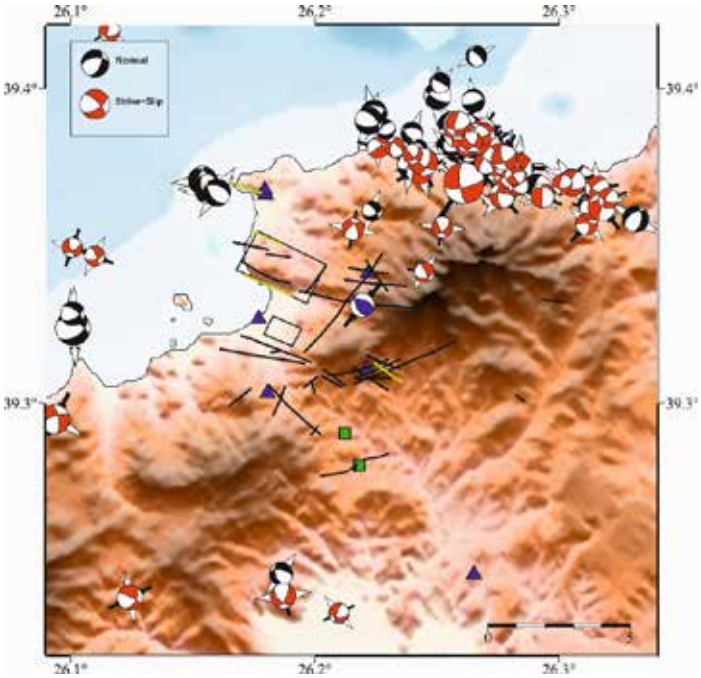

Figure 4. **Focal mechanisms calculated for the study area for the 15-month operational period for earthquakes with magnitude $M_L \geq 1.9$. Black beach balls depict normal focal mechanisms, blue ones correspond to thrust mechanisms, while red ones indicate strike slip focal mechanisms. All other symbols are the same as in Figure 2.**

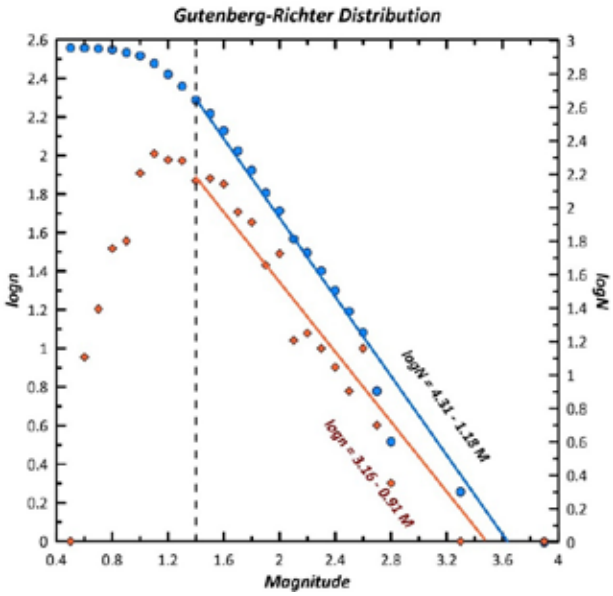

Figure 5. **Magnitude distribution of the earthquakes recorded by the local N. Lesvos network within 15km radius from the areas of interest for the time period of 16 October 2023 to 10 January 2025. Red symbols and best-fit line are derived from the number of events recorded at the time period with the corresponding magnitude, M_L, while blue symbols and line depict the cumulative number of earthquakes with magnitude equal or larger than M_L that occurred in the same area. The dashed line indicates the completeness magnitude of the catalogue for the study region (M_L~1.4), while the b value is determined to be ~0.91 (red fonts equation for the number of earthquakes, n, with magnitude, M).**

To quantitatively describe the distribution of earthquake magnitudes in this region, the Gutenberg and Richter (1944) distribution was calculated in order to obtain a frequency-magnitude relation of the form:

$$\log N_t = a_t - bM \qquad (1)$$

where N_t is the number of events with magnitude M or larger that occurred in a t-years period of time within the examined seismogenic region. a_t and b parameters are calculated by the data, provided that they are homogeneous and complete. We have estimated the Gutenberg-Richter distribution for the 15-month operational period, within a radius of 15km around the areas of interest. Figure 5 presents the G-R graph for the cumulative number of events in N. Lesvos, where $\log N_t$ is plotted against the local earthquake magnitude, M_L. We also present the distribution of **n**, which indicates the number of earthquakes with the same magnitude (rounded to 0.1 magnitude units). The dashed line shows the indicative completeness magnitude for the study area of the 15km radius, which is $M_L \simeq 1.4$. Both considered relationships correspond to equation (1), with the red solid line in Figure 5 denoting the number of earthquakes against magnitude and the black one depicting the cumulative number of earthquakes against magnitude.
Since in our case, no earthquakes of magnitudes larger than M_L=3.9 have occurred, affecting the cumulative magnitude distribution, we consider as more reliable the relationship derived by logn, which is not suffering from the lack of larger events in the (relatively small) time-period examined. For the study area, the b value of the G-R distribution is 0.91 as shown in red in Figure 5 below. This b value is larger than the b value determined by Papazachos (1999) from regional 20th century instrumental data, who calculated a value of b ~0.75-0.83 for the North Aegean region. While b-value variations are often prone to over-interpretation, we believe that thus bias is probably due to the absence of strong seismicity in the study area during the recording period.

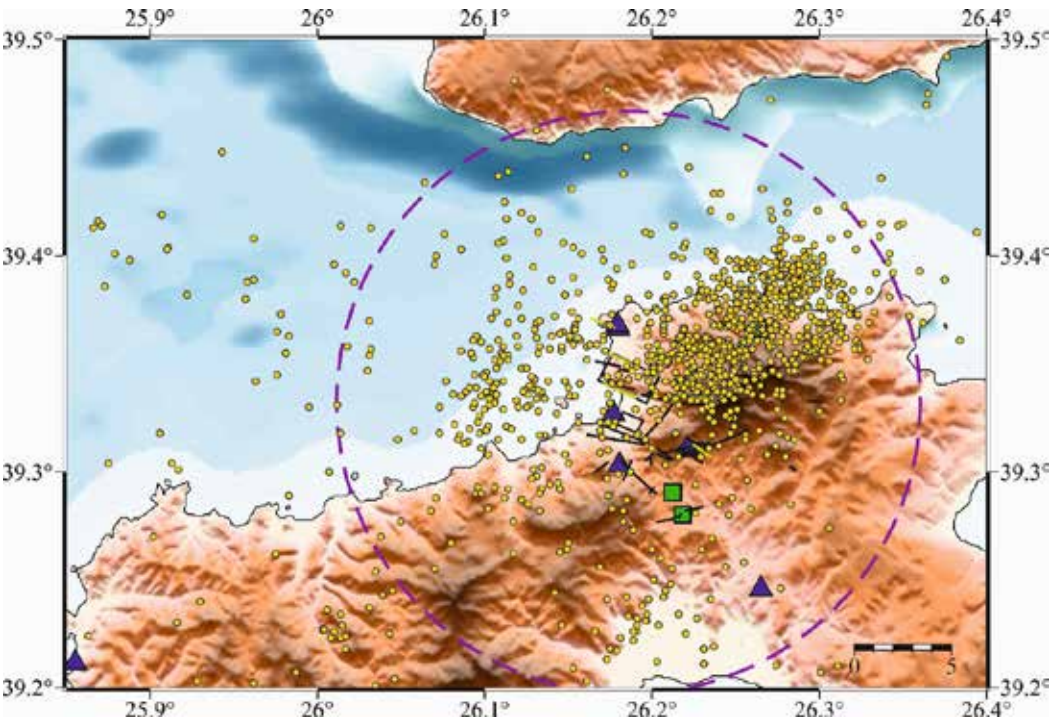

Figure 6. **Seismicity distribution using SeisBench toolbox with EQTransformer. Only events with RMS<0.35, ERH<5km and ERZ<10km are shown.**

To improve the network detectability, we also employed the SeisBench software, which is an open-source Python toolbox designed to facilitate machine-learning applications in seismology. The interface provided by SeisBench toolbox for accessing seismic datasets and deploying machine learning models makes it easier to integrate advanced algorithms into the seismic analysis workflow (Woollam *et al.*, 2022). More specifically, we have employed EQTransformer, a deep learning model available in SeisBench toolbox, well known for its effectiveness in earthquake detection and phase picking. With an architecture based on a deep neural network with an attention mechanism, EQTransformer has been trained on the global seismic data, to enable detection and picking arrival times simultaneously and efficiently (Mousavi *et al.*, 2020). We modified SeisBench toolbox to include data recorded by the local network and HUSN stations and defined new a seismic event when a minimum number of 10 seismic phases was identified as belonging to the same earthquake. The detected phases were then processed using the HypoInverse (Klein, 2002) software, using the same

local velocity model used in the manual analysis. This process has produced an initial catalog of 6680 seismic events. To ensure improved accuracy, we filtered out the events recorded by fewer than seven stations, with RMS relocation errors larger than 0.35 sec, horizontal location errors (ERH) larger than 5.0 km and vertical location errors (ERZ) more than 10.0 km. After this filtering, the catalogue was reduced to 1214 events. The resulting seismicity distribution is shown in Figure 6. It is interesting to notice that the areas of high seismic activity identified by the manual analysis (Fig. 2), are very similar to the results provided by the SeisBench automated algorithm, which is an encouraging result for both the quality of manual relocations, as well as for the potential to employ automated relocation tools for microseismicity analysis.

Conclusions

In the present study, we demonstrate the critical role of combining dense local seismic networks with modern machine learning techniques for the detailed monitoring microseismic activity. By deploying a local network of high-sensitivity seismographs in the Stypsi geothermal field area, we significantly enhanced the detection and analysis of seismic events compared to regional networks. This underscores the importance of local networks for identifying low-magnitude seismicity, which is essential for understanding the geotectonic setting, as well as studying related phenomena (e.g. induced seismicity events). Integration with SeisBench and EQTransformer allowed the detection of thousands of additional events; however, after applying quality filtering criteria, we obtained a significantly reduced number of events (~20% of the initial automatically located dataset), in good agreement with the spatial pattern of the manually relocated seismicity. This correlation highlights the potential of using machine-learning approaches as supplementing methods to traditional seismic analysis. The spatial and temporal distribution of seismicity, focal mechanisms, and Gutenberg-Richter analysis have provided valuable insight into the stress field and active faulting of the area. These findings underscore the importance of integrating localized seismic monitoring networks, with modern computational techniques for efforts towards mitigating seismic hazard for safe and sustainable exploitation of geothermal resources.

Acknowledgements

The network installation and data analysis were realized within the context of the project “Continuous Microseismic Monitoring of Lesvos” funded by PPC Renewables (contracts PO77001033 and PO77001833). The authors would like to acknowledge the assistance and support of Dr. Nikos Germenis and Geobit SA who provided the instrumentation and assisted in the local network installation.

References

Aristotle University of Thessaloniki, 1981. Aristotle University of Thessaloniki Seismological Network. https://doi.org/10.7914/SN/HT

Gutenberg, B., Richter, C.F., 1944. Frequency of earthquakes in California*. *Bull. Seismol. Soc. Am.* **34**, 185–188. https://doi.org/10.1785/BSSA0340040185

Hutton, L.K., Boore, D.M., 1987. The Ml Scale in Southern California. *Bull. Seismol. Soc. Am.* **77**, 2074–2094.

Klein, F.W., 2002. User’s Guide to HYPOINVERSE-2000, a Fortran Program to Solve for Earthquake Locations and Magnitudes. *U.S. Geol. Surv. Open File Rep. 02-171* 123 pp.

Lomax, A., Virieux, J., Volant, P., Berge-Thierry, C., 2000. Probabilistic Earthquake Location in 3D and Layered Models BT - Advances in Seismic Event Location, in: Thurber, C.H., Rabinowitz, N. (Eds.), . Springer Netherlands, Dordrecht, pp. 101–134. https://doi.org/10.1007/978-94-015-9536-0_5

Mousavi, S.M., Ellsworth, W.L., Zhu, W., Chuang, L.Y., Beroza, G.C., 2020. Earthquake transformer—an attentive deep-learning model for simultaneous earthquake detection and phase picking. *Nat. Commun.* **11**, 1–12. https://doi.org/10.1038/s41467-020-17591-w

National Observatory of Athens, Institute of Geodynamics, Athens, 1975. National Observatory of Athens Seismic Network. https://doi.org/10.7914/SN/HL

Papazachos, C., 1999. An alternative method for a reliable estimation of seismicity with an application in Greece and the surrounding area. *Bull. Seismol. Soc. Am.* **89**, 111–119. https://doi.org/10.1785/BSSA0890010111

Papazachos, C., Nolet, G., 1997. P and S deep velocity structure of the Hellenic area obtained by robust nonlinear inversion of travel times. *J. Geophys. Res.* **102**, 8349–8367.

Helmholtz-Centre Potsdam - GFZ German Research Centre for Geosciences and gempa GmbH, 2008. The SeisComP seismological software package. GFZ Data Services. doi: 10.5880/GFZ.2.4.2020.003.

Woo, J.U., Kim, M., Sheen, D.H., Kang, T.S., Rhie, J., Grigoli, F., Ellsworth, W.L. and Giardini, D. An in□depth seismological analysis revealing a causal link between the 2017 MW 5.5 Pohang earthquake and EGS project. Journal of Geophysical Research: Solid Earth, 124(12), 13060-13078, 2019.

Woollam, J., Münchmeyer, J., Tilmann, F., Rietbrock, A., Lange, D., Bornstein, T., Diehl, T., Giunchi, C., Haslinger, F., Jozinović, D., Michelini, A., Saul, J., Soto, H., 2022. SeisBench—A Toolbox for Machine Learning in Seismology. *Seismol. Res. Lett.* **93**, 1695–1709. https://doi.org/10.1785/0220210324

17th INTERNATIONAL CONGRESS of the Geological Society of Greece

BULLETIN OF THE GEOLOGICAL SOCIETY OF GREECE, SP. PUBL.

EXTENDED ABSTRACT 345

Preliminary results on the interseismic deformation of the Argolis Peninsula, Greece

Viger, Amélie[1], Kranis, Haralambos[1], Ganas, Athanassios[2], Whittaker, Alex[3]
(1) National and Kapodistrian University of Athens, Athens, Greece; email: amelievig@geol.uoa.gr.
(2) National Observatory of Athens, Athens, Greece.
(3) Imperial College, London, United Kingdom.

Introduction

Ongoing research highlights that the present-day deformation in eastern part of the onshore areas around the Gulf of Corinth (Corinth area, Perachora Peninsula) is characterized by an average rate of 1 mm/yr, induced by the Corinth rift extension (Evelpidou et al., 2023). Notably, though, the northwest of the Perachora peninsula presents a clear displacement pattern (subsidence), related to the active Pissia fault, according to recent study by Mildon et al. (2024), while the Argolis peninsula displays an overall subsidence pattern. Subsidence patterns are also observed locally, at the area between Kiato and Melissi at the NE coast of the Peloponnese

The inception and evolution of the Corinth rift, since c. 4-3.5 Ma, is associated with the development of the Central Hellenic Shear Zone (Papanikolaou and Royden, 2007) and the roll-back and geometry of the subducting African slab. The rapid N-S extension of the Corinth rift, in the order of 10-15 mm/yr (Briole et al., 2000), is accommodated by E-W normal faults, which provided the depocenters for syn-rift hemi-pelagic sedimentation and extended, massive deltas along its southern margin, which migrated northwards through time (e.g.: Nixon et al., 2016; Gawthorpe et al., 2018). Quaternary uplift of the northern Peloponnese is testified by uplifted flights of marine terraces along the NE coast of the Peloponnese, lying on the hanging-wall of E-W, north-dipping normal faults (Armijo et al., 1996).

The Argolis Peninsula is built of several tectonic units that belong to the Pelagonian and Sub-Pelagonian domains, forming the inherited alpine backbone of the area (Bortolotti et al., 2003). The current deformation in the Argolis Peninsula is influenced by the three neighboring extensional structures, namely the Saronic Gulf, the Argos Gulf, and the Gulf of Corinth. The structure of the Argolis Peninsula that comprises mainly NW-SE normal faults is associated with back-arc extension that started in the Late Miocene, including the Cretan basin (Saronic Gulf and Argos Gulf), induced by the southwestward roll-back of the Hellenic subduction.

Combining fault identification (field reconnaissance, combined with geomorphological and drainage analysis) and geodetic data allows us to understand whether some onshore structures in the Argolis Peninsula are still active, affecting present-day deformation.

Methods

In this preliminary study, we use the Permanent-Scatterer InSAR of the ORTHO dataset from the European Ground Motion Service (EGMS; https://land.copernicus.eu/en/products/european-ground-motion-service) acquired by Sentinel-1 in ascending and descending orbit, during 2019-2023. The time-series provide by the EGMS website cover 2019 to 2023 period. We also use Global Navigation Satellite System (GNSS) data from Briole et al. (2021) with a vertical reference of the ITRF2016 (Altimimi et al., 2016). The permanent GNSS stations in the Argolis Peninsula show a vertical velocity consistent with that of the PS-InSAR data (Fig.1).

Here, we mainly use the vertical component of the available geodesic dataset to identify the present-day deformation of the Argolis Peninsula. The East component from EGMS is similar throughout the study area and the InSAR acquisition method from EGMS does not detect the North component by the line-of-sight (LOS).

The interseismic vertical deformation is compared with the geology and structures of the area. The onshore faults in Argolis Peninsula are determined by geomorphological analysis, then adjusted according to the literature, such as Bortolotti et al. (2003) and Wicker et al. (2024), and the NOAFaults v6.0 dataset. The offshore faults are based on Nixon et al. (2016) for the Gulf of Corinth, Foutrakis and Anastasakis (2020) for the Saronic Gulf, and Papanikolaou et al. (1988) for the Gulf of Argos.

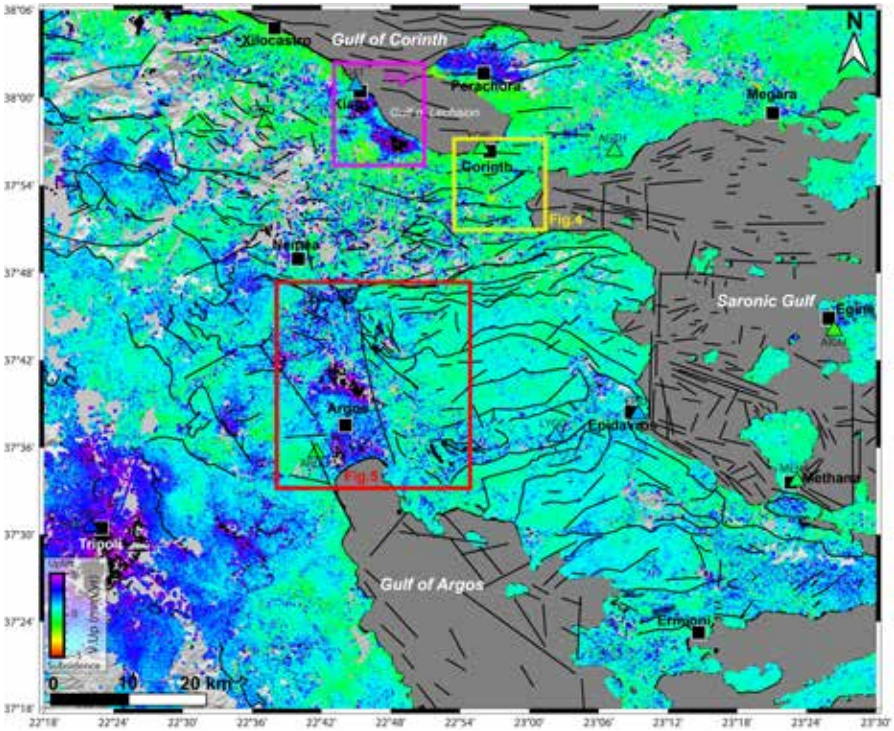

Figure 1: Map of the vertical velocities of Permanent-Scatterer InSAR data (2019-2023) from EGMS (https://land.copernicus.eu/en/products/european-ground-motion-service) and GNSS data from Briole et al. (2021) (represented by triangle) in the Argolis Peninsula.

Results

The PS-InSAR and GNSS data show that the whole of the Argolis Peninsula subsides with an average velocity of -1 ± 0.4 mm/yr for PS-InSAR and -0.5 ± 1 mm/yr for GNSS data inherited with the Corinth rift expansion, even if the Gulf of Lechaion is considered inactive currently. However, we could see at shorter wavelengths that some parts of the peninsula subside or uplift more than the trend of the Argolis Peninsula (Fig.1). Unlike the East component of the PS-InSAR only shows a westward trend averaging -16 ± 0.5 mm/yr at long wavelengths, and the corrected horizontal components from Briole et al. (2021), show a southwestward trend of the Argolis Peninsula for a stable Eurasia plate, averaging -8 ± 0.4 mm/yr for the East component and -12 ± 0.4 mm/yr for the North component (Fig.2).

Subsidence pattern between Kiato and Corinth

At the short-wavelength signal, we observe subsidence with an average of ~3.5 ± 0.3 mm/yr between Kiato and Assos, reaching -10 mm/yr in Assos (Fig.3). We also observe a minor uplift of ~1mm/yr further south of the Assos pattern. Besides, the deformation in Assos and Kiato-Nerantza presents an interesting PS-InSAR time series showing the subsidence increase since April 2021 (Fig. 3a and b). We also observe the same deformation for the slower subsidence, at ~1.5 ± 0.3 mm/yr, between Assos and Nerantza (in pink, Fig.3b). Time-series shows an uplift of 1.4 ± 0.3 mm/yr for the PS-InSAR stacked between Kiato and Nerantza (in red, Fig.3c), and a subsidence of -0.9 ± 0.3 mm/yr for the region of Assos before April 2021 (in yellow, Fig.3a). We also observed the subsidence increases westward since August 2022 (Fig. 3a, b, and c).

This area is a flat alluvial plain with extensive agricultural activity and geographically corresponds to the “gap” of marine terraces in the Northeastern Peloponnese (Armijo et al., 2016). No seismic event is recorded in April 2021 or August 2022. The uplift area corresponds to the New Corinth (49 ka) marine terrace documented by Armijo et al. (2016). Although no faults are known in this location, the uplift could be explained by the general uplift observed on the northeastern coast of the Peloponnese, induced by the E-W normal faults of the Corinth rift. Hence, the subsidence pattern observed could be attributed to sediment compaction, induced by lowering of the water table, which could explain the subsidence range of 3 to 10 ± 0.3 mm/yr, or more if the subsidence is added to the uplift of the northeastern coast.

Uplift pattern in Xilokeriza

At Corinth, the KORI GNSS station and the PS-InSAR show an uplift of ~1 mm/yr related to the Corinth rift extension

(Fig.4). At Xilokeriza, we observe a focused uplift of 1.4 ± 0.4 mm/yr in 1 km of diameter (Fig.4d). The four-year period covered by the PS-InSAR dataset shows a clear seasonality in this area (amplitude of 1 mm), with maximum uplift in spring and maximum subsidence in autumn, related to the local hydrological conditions, which overprints a clear upward trend (Fig.4d). Besides, the area undergoing uplift lies at the possible south-western tip of a presumed NE-SW fault that was identified through geomorphological analysis, but we do not observe any subsidence in the north-dipping hanging-wall of this fault, but an uplift of 1 mm/yr. The time-series of Xilokeriza reveals an uplift of 1.8 mm/yr between August 2019 to August 2020, then a subsidence of -1.7 ±0.4 mm/yr since November 2022. We could also observe a signal between January and August 2019, decreasing at around +0.5 to -2 mm for around eight months, estimating a subsidence of ~1.8 ± 0.4 mm/yr. It is possible that in Xilokeriza there is a seasonal and multi-annual effect, of ± 1.8 mm/yr recorded by PS-InSAR. It is worth noting that uplifted area at Xilokeriza coincides with a marl outcrop surrounded by alluvial deposits.
Further south, we observe subsidence in the hanging-wall of the E-W active Kenchreai normal fault with N-dipping (Koukouvelas et al. 2017), also identified by geomorphological analysis, representing the northern boundary of a Pelagonian Unit faulted block (Fig.4). This fault could extend into the Saronic Gulf according to the seismic reflection analysis of Foutrakis and Anastasakis (2020). However, the other faults in the southern boundary of the horst does not show any deformation. The subsidence between Kiras Vrisa and Corinth corresponds to the highway.

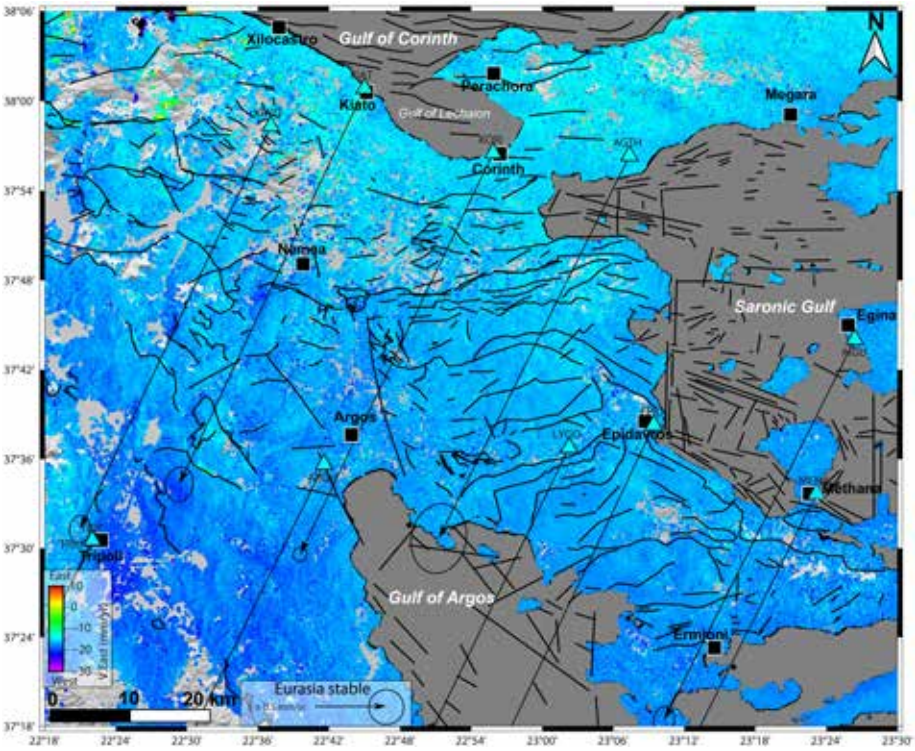

Figure 2: Map of the East-West component of Permanent-Scatterer InSAR data (2019-2023) from EGMS (https://land.copernicus.eu/en/products/european-ground-motion-service) and the horizontal component of GNSS data (represented by triangle) with the Eurasia stable from Briole et al. (2021).

Argos basin

Deformation in the Argos and Nafplion regions may correspond to the main, basin-bounding faults (Fig.5). Indeed, the subsidence is higher along the hanging-wall of NW-SE normal faults formed by the opening of the Cretan Sea and the Gulf of Argos. The PS-InSAR data reveals that the Argos basin has a higher subsidence rate than the whole peninsula, which is in the order of ~2 ± 0.4 mm/yr, reaching a subsidence of -7.5 ± 0.4 mm/yr in the northern part of the basin (Fig.5h). The seasonal variation, common to alluvial plains, is clearly detectable, as well (Fig.5h).
We could identify a difference in PS-InSAR of -1 ± 0.4 mm/yr in the footwall and -2 ± 0.4 mm/yr in the hanging-wall of the southeast-dipping SW-NE normal fault inferred by geomorphological analysis, which marks the boundary between the Pindos unit and the alluvial deposits. The interseismic deformation appears also to be influenced by the overall geological structure, with the Pelagonian and Pindos nappes subsiding slower than the syn/post-rift

sediments.

The northern part of the Argos basin shows an interesting deformation pattern, as the subsidence trend of the basin is ~2 ± 0.4 mm/yr except the southern part of it, which subsides at a rate of ~0.5 ± 0.4 mm/yr, while all the area is characterized by the same post-alpine sediments (conglomerates). Geomorphological analysis in this area, postulates the occurrence of E-W normal faults, with the same geometry as the Mykines fault. These faults may be related to the deposition of conglomerates to the north (potentially a delta in Argos), with the northernmost fault being the more active one. Consequently, the E-W fault delineating the -0.5 ± 0.4 mm/yr subsidence pattern to the north may not have been responsible for the uplift in the footwall, causing a decrease of subsidence.

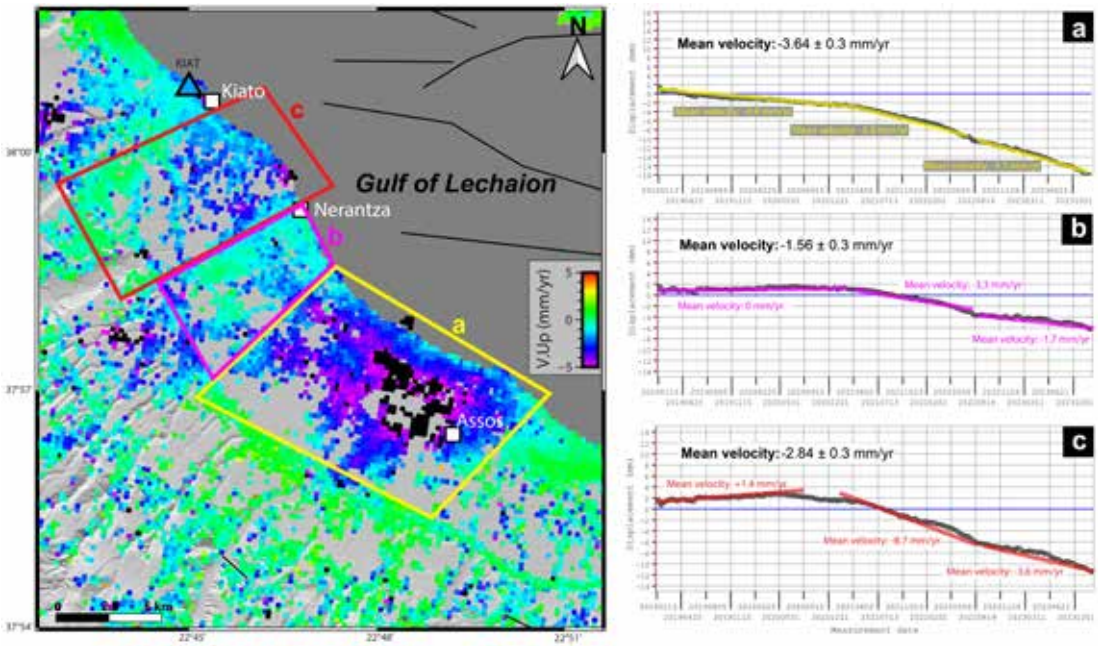

Figure 3: Map of the vertical velocities of Permanent-Scatterer InSAR data (2019-2023) from EGMS and GNSS data (represented by triangle) from Briole et al. (2021). Time-serie of PS-InSAR (2019-2023) from EGMS for a) Assos area (yellow box), b) Nerantza area (pink box), and c) Kiato-Nerantza area (red box) with the mean velocity of each area (in black), and the mean velocity of trend observed in the area (color associated of the area).

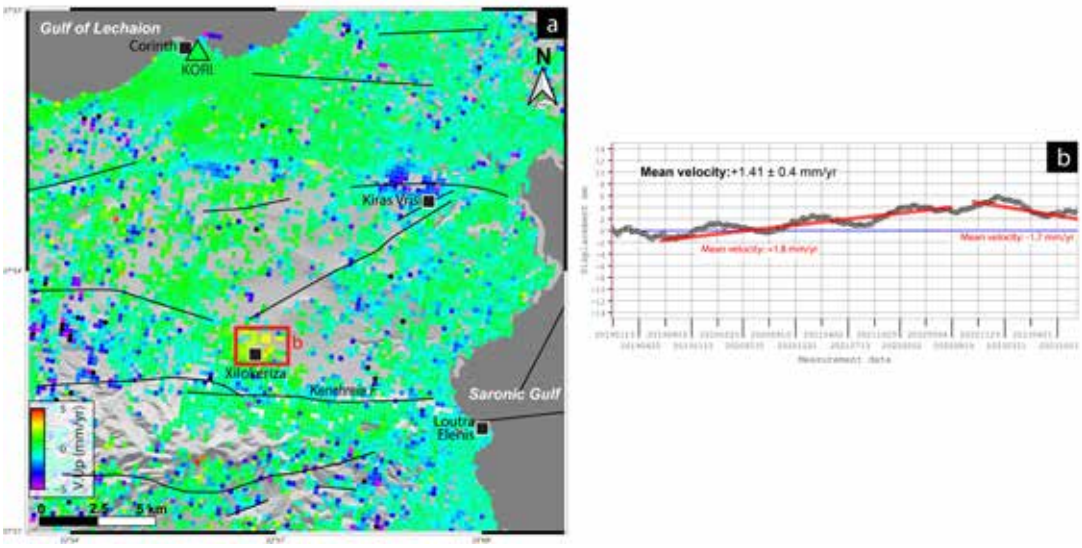

Figure 4: Map of the vertical velocities of Permanent-Scatterer InSAR data (2019-2023) from EGMS and GNSS data (represented by triangle) from Briole et al. (2021). d) Time-series (2019-2023) of PS-InSAR from EGMS of the Xilokeriza area (red rectangle) with the mean velocity of the area (in black), and the mean velocity of trend observed in the area (in red).

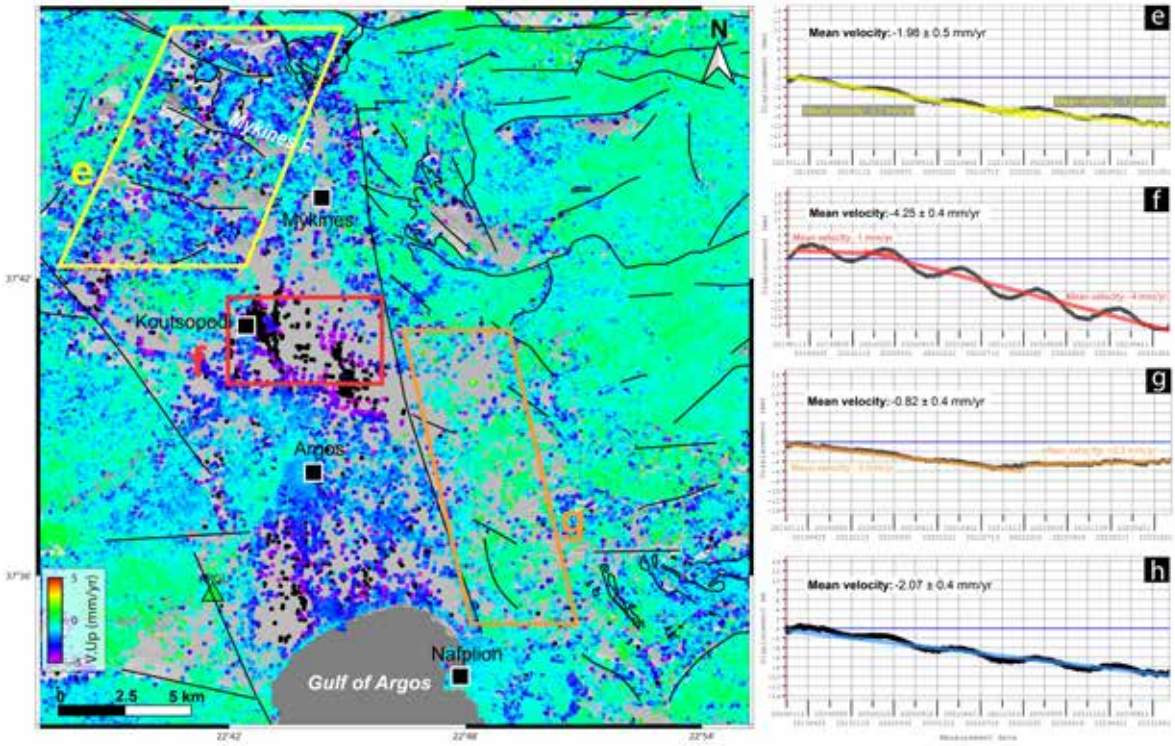

Figure 5: Map of the vertical velocities of Permanent-Scatterer InSAR data (2019-2023) from EGMS and GNSS data (represented by triangle) from Briole et al. (2021) of the Argos Basin. Time-series of vertical velocities of PS-InSAR data (2019-2023) from EGMS of the e) west part of Mykines, f) region of Koutsopodi, g) east part of the eastern boundary of the Argos basin with the mean velocity of each area (in black), and the mean velocity of trend observed in the area (color associated of the area or boxes), and h) whole of Argos basin with a mean velocity represented in black.

We observe three different areas that have different time series in the whole Argos basin, which have a trend with subsidence of ~2 ± 0.4 mm/yr, during the PS-InSAR period from 2019 to 2023 (fig.5g). We observe that the subsidence recorded in western Mykines (~2.7 ± 0.5 mm/yr) becomes less pronounced (-1.5 ± 0.5 mm/yr), since October 2021 (Fig.5e). This area corresponds to the outcrops of conglomerates discussed above.
On the contrary, near Koutsopodi we observe an increase in the subsidence. The time-series of this area shows a subsidence of 1 ± 0.4 mm/yr after an initial uplift until the beginning of the 2020, followed by an average subsidence an of 4 ± 0.4 mm/yr (Fig.5f). Besides, the seasonal effect in this area is important, in the order of 4 mm amplitude, with maximum subsidence in autumn and maximum uplift in spring. The seasonal effect in the Koutsopodi region is higher than that observed in the whole Argos basin or in the eastern part of Mykines that displays a ~1 mm in amplitude. Locally, the Koutsopodi area may have different sediments beneath the alluvium of the Argos Basin that are more influenced by hydrological conditions, explaining this strong seasonal effect, as observed in Xilokeriza.
On the east part of the Argos basin boundary, we observed a -2 ± 0.4 mm/yr subsidence, common in the Argos basin, until October 2021, followed by an uplift of 0.5 ± 0.4 mm/yr (Fig.5g). This area is composed of alluvium, as in the region of Koutsopodi, but the seasonal effect is low (at 0.5 mm in amplitude.) This area lies in the footwall of the west-dipping, NW-SE normal fault dipping and the uplift observed could be explained by a seismic event, but no earthquake was recorded in October 2021. It is worth noting that the 1788 seismic event of M6.2 in Nafplion (NOAFaults v6.0) could be associated with the activity of this NW-SE normal fault.

Conclusions

The present-day deformation of the Argolis Peninsula calls for more investigation, with the view to identifying the deformation observed in the Argos basin, Corinth-Xilokeriza, and Kiato-Assos areas. It will be interesting to investigate the various deformation patterns observed in the Argolis Peninsula, such as the regional subsidence in the Adheres unit (southeastern of Argolis Peninsula, near Methana), the subsidence in northern Ermioni, and the subsidence close to Epidavros. Further work on this, besides detailed structural mapping, includes the comparison of the GNSS dataset and EGMS dataset with another Permanent Scatter approach (Surface motioN mAPPING method

https://docs.terradue.com/geohazards-tep/tutorials/Snapping.html), and the NSBAS approach (Flatsim computation led by the CNES https://flatsim.cnes.fr) which involves using the existing permanent GNSS stations combined with displacement time-series computed from Sentinel-1 satellite data.

Acknowledgements

This research is part of the European-based Marie Skłodowska-Curie Actions Doctoral Network TALENTS (https://www.talents-dn.eu), Horizon 2022 project. We are thankful for the Geo-INQUIRE Personalised Training Programme, part of the Horizon 2020 Europe project, that fund collaboration with Lyon University (LGL-TPE) for the post-processing of the Flatsim dataset.

References

Altamimi, Z., Rebischung, P., Métivier, L., and Collilieux, X., 2016. ITRF2014: A New Release of the International Terrestrial Reference Frame Modeling Nonlinear Station Motions. J. Geophys. Res. Solid Earth, 121, 6109–6131, https://doi.org/10.1002/2016JB013098.

Bortolotti, V., Carras, N., Chiari, M., Fazzuoli, M., Marcucci, M., and Principi, G., 2003. The Argolis Peninsula in the paleogeographic and geodynamic frame of the Hellenides. Ofioliti, 28, 79-94.

Briole, P., Rigo, A., Lyon-Caen, H., Ruegg, J. C., Papazissi, K., Mitsakaki, C., Baltodimou, A., Veis, G. and Deschamps, A., 2000. Active deformation of the Corith rift, Greece: Results from repeated Global Positioning System surveyd between 1990–995. J. Geophys. Res., 105, 25,605–25,625.

Briole, P., Ganas, A., Elias, P., and Dimitrov, D., 2021. The GPS velocity field of the Aegean. New observations, contribution of the earthquakes, crustal blocks model, Geophysical Journal International, Volume 226, Issue 1, Pages 468–492, https://doi.org/10.1093/gji/ggab089.

Evelpidou N., Ganas A., Karkani A., Spyrou E., and Saitis G., 2023. Late Quaternary Relative Sea-Level Changes and Vertical GNSS Motions in the Gulf of Corinth: The Asymmetric Localization of Deformation Inside an Active Half-Graben. Geosciences, 13(11):329. https://doi.org/10.3390/geosciences13110329.

Foutrakis, P. M., and Anastasakis, G., 2020. Quaternary continental shelf basins of Saronikos Gulf, Aegean Sea, Geo-Marine Letters, 40(5), 629-647, doi:10.1007/s00367-020-00653-9.

Gawthorpe, R., Leeder, M., Kranis, H., Skourtsos, E., Andrews, J., Henstra, G., Mack, G., Muravchik, M., Turner, J. and Stamatakis, M., 2017. Tectono-sedimentary evolution of the Plio-Pleistocene Corinth rift, Greece. Basin Research. 30. https://doi.org/10.1111/bre.12260.

Koukouvelas, I. K., Zygouri, V., Papadopoulos, G. A., and Verroios, S., 2017. Holocene record of slip-predictable earthquakes on the Kenchreai Fault, Gulf of Corinth, Greece, J. Struct. Geol., 94, 258-274, doi:https://doi.org/10.1016/j.jsg.2016.12.001.

Mildon, Z. K., Diercks, M., Roberts, G. P., Faure Walker, J. P., Ganas, A., Papanikolaou, I., Sakas, V., Robertson, J., Sgambato, C., and Mitchell, S., 2024. Transient aseismic vertical deformation across the steeply-dipping Pisia-Skinos normal fault (Gulf of Corinth, Greece). *Tectonics*, 43, e2024TC008276. https://doi.org/10.1029/2024TC008276

Nixon, C., Mcneill, L.C., Bull, J., Bell, R., Gawthorpe, R.L., Henstock, T., Christodoulou, D., Ford, M., Taylor, B., Sakellariou, D., Ferentinos, G., Papatheodorou, G., Leeder, M.R., Collier, R., Goodliffe, A., Sachpazi, M., and Kranis, H., 2016. Rapid spatiotemporal variations in rift structure during development of the Corinth Rift, central Greece. Tectonics. 35.

Papanikolaou, D., and Royden, L., 2007. Disruption of the Hellenic arc: Late Miocene extensional detachment faults and steep PlioceneQuaternary normal faults—or what happened at Corinth? Tectonics, 26.

Papanikolaou, D., Lykousis, V., Chronis, G., and Pavlakis, P., 1988. A comparative study of neotectonic basins across the Hellenic arc: the Messiniakos, Argolikos, Saronikos and Southern Evoikos Gulfs. *Basin Research*, *1*(3), 167-176.

17th INTERNATIONAL CONGRESS of the Geological Society of Greece

BULLETIN OF THE GEOLOGICAL SOCIETY OF GREECE, SP. PUBL.

EXTENDED ABSTRACT 346

Spatial distribution and deformation of columnar calcite occurred in the high-pressure marbles of Cycladic Massif (Hellenides)

P. Xypolias, N. Gerogiannis, E. Aravadinou, K.A. Tsourtis
Department of Geology, University of Patras, 26500 Patras, Greece; p.xypolias@upatras.gr

Research Highlights

High-pressure (HP) marbles in the Cycladic Massif bear a columnar-shaped calcite microstructure that represents a powerful marker of deformation.

Detailed structural analysis of the columnar calcite microstructure can further refine our knowledge about the exhumation processes of HP terranes.

Objectives

Calcite marbles constitute large parts of the Alpine orogenic system and thus they can be used to study the structural evolution and exhumation processes of HP rocks within subduction zones (e.g., Molli *et al*., 2000; Spanos *et al*., 2015). The presence of a columnar calcite microstructure within marbles of several HP terranes, including the Cycladic Massif of Internal Hellenides, has been reported (Fig. 1a) (Brady *et al*., 2004; Seaton *et al*., 2009; Zulauf *et al*., 2018; Gerogiannis *et al*., 2021, Aravadinou *et al*., 2022; Potočný *et al*., 2023). This microstructure is thought to be formed at static conditions within the stability field of aragonite at the deep subduction levels (HP conditions). The resulted microstructure, after exhumation of the rocks to shallow crustal levels, is interpreted as calcite pseudomorph after aragonite and is defined by coarse-grained calcite crystals oriented at high angles to the pre-existing foliation (e.g., Brady *et al*., 2004; Gerogiannis *et al*., 2021). The columnar microstructure has been used as a marker for the record and quantification of the deformation of rocks within the subduction channel as well as for the identification of spatiotemporal variations in deformation intensity of distinct events during the subduction-exhumation cycle (e.g., Seaton *et al*., 2009; Gerogiannis *et al*., 2021, 2022; Aravadinou *et al*., 2022).

In this work, we combine new and published (Gerogiannis *et al*., 2021, 2022; Aravadinou *et al*., 2022) data about the occurrence and deformation of the columnar calcite microstructure in different areas and structural positions of the Cycladic Massif (Fig. 1b; Basal Unit, Evia Island; Cycladic Blueschist Unit, Evia, Syros, and Ios islands) highlighting their importance on the study of the structural evolution of HP terranes such as the Cyclades area. We show that the columnar calcite microstructure is present in several exposures of HP marbles of the Basal Unit and Cycladic Blueschist Unit, whereas the observed variation in the extent of its preservation/modification indicates that the deformation was highly heterogeneous in space and time within the subduction channel during the exhumation of the HP rocks.

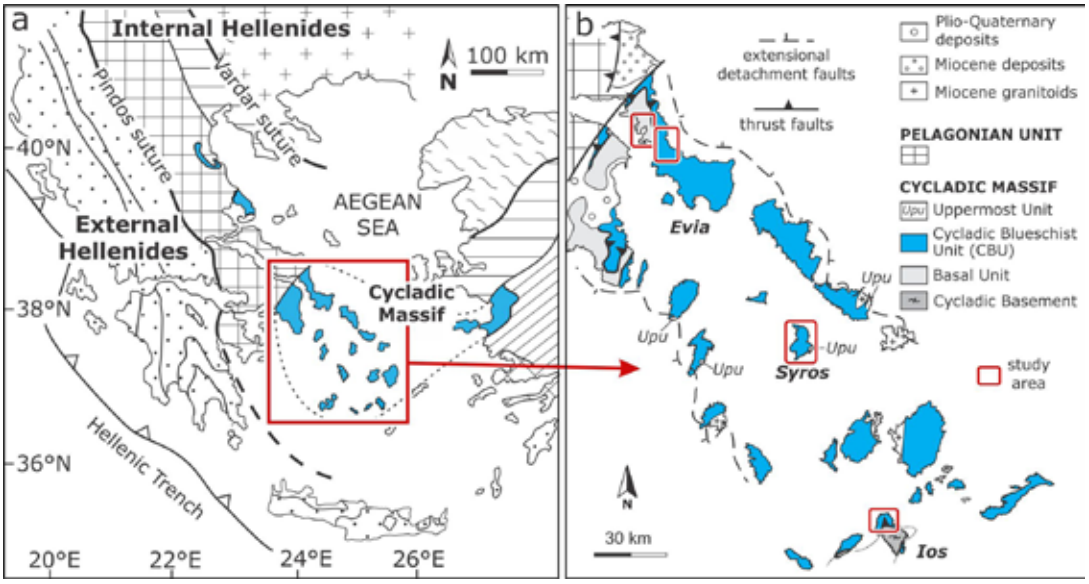

Figure 1. (a) Geological map of the Aegean region showing the position of the Cycladic Massif in the Internal Hellenides. (b) Simplified geological map of the Cycladic Massif indicating the study areas.

Geological framework

The Cycladic Massif is part of the Internal Hellenides and is represented by four metamorphosed units stacked within an Eocene-Oligocene subduction channel during the Hellenides formation (Fig. 1a; Dürr *et al*., 1978). The Cycladic Massif is divided into the Uppermost Unit, the intermediate Cycladic Blueschist Unit (CBU), and the structurally deeper Cycladic Basement and Basal Unit (Fig. 1b). The rarely exposed Uppermost Unit mainly comprises Permo-Mesozoic crystalline rocks, which have not been affected by the Alpine HP/LT metamorphism. The CBU consists of a metamorphosed Mesozoic succession of meta-sedimentary rocks and metabasic bodies, that underwent blueschist to eclogite facies metamorphism during early Eocene. Exhumation initiated under blueschist facies conditions and progressively continued at greenschist facies conditions during Oligocene-Miocene. In south Evia, the CBU subdivided from the lower to upper structural levels into three nappes: a) the Tsaki nappe including various schists with marble intercalations and serpentinitic blocks; b) the Styra nappe, which represents a marble-schist sequence; and c) the Ochi nappe consisting of a meta-volcano-sedimentary sequence interleaved with slices of metaophiolitic rocks. In Syros Island, the CBU is generally composed of marbles, schists, metabasites (blueschists and eclogites) and paragneisses, whereas in Ios Island, it is made up of a marble-schist sequence. The Cycladic Basement crops out on the central and southern Cyclades and comprises mostly deformed Paleozoic granitoids and schists sharing a common metamorphic history with the rocks of the CBU during the Alpine orogeny. Finally, the Basal Unit consists mainly of a Mesozoic carbonate sequence that was affected by HP/LT metamorphism during post-middle Eocene times. In Evia Island, the Basal Unit consists of a thick sequence of Triassic to middle Eocene marbles with local intercalations of schists. The marbles transition upwards to a sequence of quartzites and metapelites (metaflysch).

Results

Microstructural observations in the marbles of Cycladic Massif revealed the presence of columnar calcite in all studied areas (Fig. 2a, b). However, the extent of their preservation and deformation differs from one area to another. Generally, observed calcite microstructure can be subdivided into four groups based on the recrystallization mechanism, grain size, shape, and distribution. The first microstructure (m1) is represented by large columnar calcite (grain size 800 – >3000 μm and aspect ratio >3) with a strong shape preferred orientation (SPO) that forms an angle >60° with the macroscopic foliation. These columnar grains typically present columnar subgrains and associated recrystallized grains indicating recrystallization by subgrain rotation (SGR). The second microstructure (m2) is characterized by inequant (aspect ratios 2–3) calcite grains, with sizes between 200 and 600 μm. These grains display a strong SPO that marks the original columnar calcite forming angles of 30°–60° with macroscopic foliation. All microstructural features indicate that these grains originated by the SGR recrystallization of the larger columnar grains. The third microstructure (m3) is characterized by (sub)equant calcite grains with sizes ranging between ~50 and 500 μm and a weak to well-developed SPO. These grains are typically associated with the presence of subgrains of similar size and shape implying recrystallization through SGR. The fourth microstructure (m4) is represented by small (<70 μm) (sub)equant to elongated calcite grains that have originated by SGR and bulging recrystallization. These grains are typically localized within bands that vary in thickness from <1mm to several centimeters. The density of these bands also varies from meter to millimeter scale.

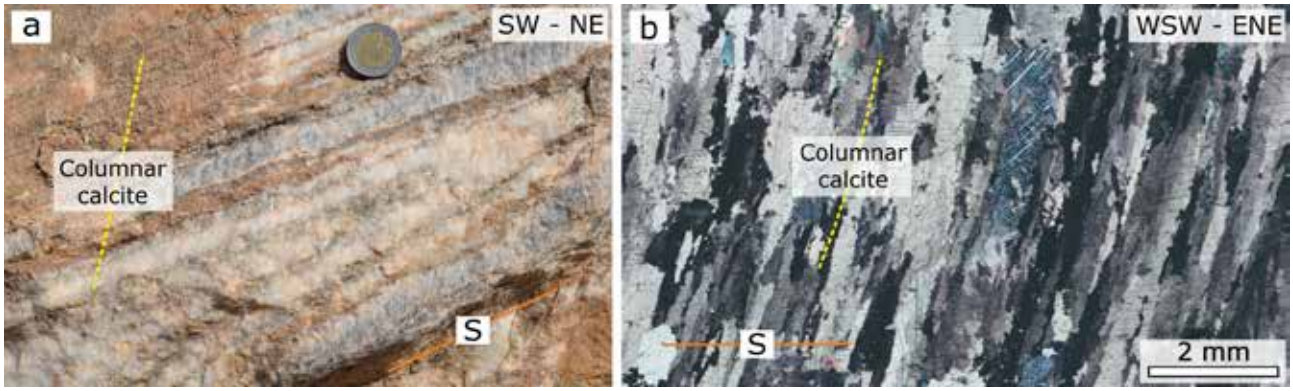

Figure 2. Columnar calcite oriented at high angles to the macroscopic foliation was recorded in outcrop- (a) and micro- (b) scale (a: CBU, Syros Island; b: Basal Unit, Evia Island). S, macroscopic foliation.

In the Basal Unit exposed in Evia Island, m2 is typically the dominant microstructural group within the marbles located

in the eastern part of the unit. However, in several marble outcrops exposed in this area, m1 is present. In turn, in the western part of the unit, and structurally upwards, the marbles are usually characterized by m3, whereas m4 is recorded in specific zones within m3 that are aligned with map-scale shear zones. In the marbles of the CBU (Styra nappe) that overlies the Basal Unit, m2 typically characterizes the marbles that are located in the structurally lower positions of the nappe near the contact with the marbles of the Basal Unit. In these structural levels, m1 was also observed in several marble outcrops. Moving structurally upwards within the Styra nappe (eastwards), marbles are typically associated with the development of m3. Here, m3 is represented by calcite grains with a well-developed SPO.

In marbles of the CBU exposed in Syros Island, the observed microstructures also present a spatial variation. Specifically, in the north part of the island, marbles are clearly dominated by the development of m1. Locally within m1, individual thin bands characterized by m4 are recorded. In turn, in the south part of the island, and moving structurally downwards, the main calcite microstructure recorded within marbles is m3. In this case, m3 is characterized by calcite grains with a weak SPO. Although m3 is dominant in this part of the island, the other three microstructural groups (m1, m2, m4) are also recorded in several marble outcrops.

In the CBU exposed in northern Ios, m1 is recorded in only some marble outcrops located in the northwest part of the island, relatively close to the contact with the underlying Cycaldic Basement. The main calcite microstructural group recorded in the marbles of northern Ios is m3. This microstructure is typically observed near the contact with the Cycladic Basement and generally in the lower structural positions of the CBU. In several outcrops, thin bands characterized by m4 are observed within m3. The marbles located in structurally upper positions of the CBU, near the north coastline of the island, are typically characterized by the presence of m4, that is developed within thick (several centimeters to meter) bands.

Conclusions

HP marbles of the CBU and Basal Unit that belong to the Cycladic Massif of Hellenides are characterized by the occurrence of coarse-grained columnar calcite that is oriented at high angles to the mesoscopic foliation. This columnar calcite microstructure should be formed at deep subduction levels where HP metamorphism was active. The degree of preservation or obliteration of this microstructure in specific positions of the subduction channel provides information about the spatiotemporal variations in deformation conditions during exhumation of the HP rocks.

Combination of new and published data about the occurrence and deformation of the columnar calcite microstructure in the marbles of the CBU and Basal Unit within the Cycladic Massif, showed that this microstructure was initially formed within the marbles of all study areas (i.e., Basal Unit, Evia Island; Blueschist Unit, Evia, Syros, and Ios islands). However, the degree of preservation of this microstructure varies from one area to another. It is noted that preservation and modification / obliteration of the columnar microstructure are linked with absent /weak and intense deformation during exhumation, respectively. Well-preserved columnar microstructure is extensively presented in the marbles of the CBU exposed in northern Syros (upper structural levels). Moreover, well-preserved to partly modified columnar microstructure is observed in the lower structural levels of the Basal Unit and CBU in south Evia. In turn, the columnar microstructure is highly modified or obliterated in the upper structural levels of Basal Unit and CBU in south Evia, as well as in the CBU exposed in south Syros and Ios Island. These results indicate that the intensity of deformation was highly heterogeneous in space and time within the subduction channel during the exhumation of the HP rocks.

Acknowledgements

Parts of this research are co-financed by Greece and the European Union (European Social Fund-ESF) through the Operational Programme «Human Resources Development, Education and Lifelong Learning» in the context of the project “Reinforcement of Postdoctoral Researchers - 2nd Cycle” (MIS-5033021), implemented by the State Scholarships Foundation (IKY) (awarded to N. Gerogiannis), and by the “Andreas Mentzelopoulos Foundation” (awarded to K.A. Tsourtis). Part of the field investigation was supported by Grant E045 (awarded to P. Xypolias) from the Research Committee of the University of Patras (Programme K. Karatheodori).

References

Aravadinou, E., Gerogiannis, N., Xypolias, P., 2022. Development and passive exhumation of high-pressure shear zones (Blueschist Unit, Syros): Insights from quartz and columnar calcite microstructures. Journal of Structural Geology 159, 104607.

Brady, J.B., Markley, M.J., Schumacher, J.C., Cheney, J.T., Bianciardi, G.A., 2004. Aragonite pseudomorphs in high-pressure marbles of Syros, Greece. Journal of Structural Geology 26, 3-9.

Dürr, S., Altherr, R., Keller, J., Okrusch, M., Seidel, E., 1978. The Median Aegean Crystalline belt: stratigraphy, structure, metamorphism, magmatism, in: Closs, H., Roeder, D., Schmidt, K. (Eds.), Alps, Apennines, Hellenides. Inter-Union

Commission on Geodynamics, Scientific report 38, 455-476.
Gerogiannis, N., Aravadinou, E., Chatzaras, V., Xypolias, P., 2021. Calcite pseudomorphs after aragonite: a tool to unravel the structural history of high-pressure marbles (Evia Island, Greece). Journal of Structural Geology 148, 104373.
Gerogiannis, N., Chatzaras, V., Aravadinou, E., Gürer, D., Xypolias, P., 2022. Microstructural and textural modification of columnar calcite under increasing shear strain (Evia Island, Greece), Journal of Structural Geology 160, 104632.
Molli, G., Conti, P., Giorgetti, G., Meccheri, M., Oesterling, N., 2000. Microfabric study on the deformational and thermal history of the Alpi Apuane marbles (Carrara marbles), Italy. Journal of Structural Geology 22, 1809-1825.
Potočný, T., Jeřábek, P., Plašienka, D., 2023. Subduction–exhumation cycle recorded by calcite deformation microstructures: blueschist-facies metacarbonates and kinematic implications for deformation of the Meliata Unit (Western Carpathians). International Journal of Earth Sciences 112, 2097-2117.
Seaton, N.C., Whitney, D.L., Teyssier, C., Toraman, E., Heizler, M.T., 2009. Recrystallization of high-pressure marble (Sivrihisar, Turkey). Tectonophysics 479, 241-253.
Spanos, D., Xypolias, P., Koukouvelas, I., 2015. Vorticity analysis in calcite tectonites: an example from the Attico-Cycladic massif (Attica, Greece). Journal of Structural Geology 80, 120-132.
Zulauf, G., Dörr, W., Marko, L., Krahl, J., 2018. The late Eo-Cimmerian evolution of the external Hellenides: constraints from microfabrics and U–Pb detrital zircon ages of upper Triassic (meta)sediments (Crete, Greece). International Journal of Earth Sciences 107, 2859-2894.

17th INTERNATIONAL CONGRESS of the Geological Society of Greece

BULLETIN OF THE GEOLOGICAL SOCIETY OF GREECE, SP. PUBL.

EXTENDED ABSTRACT 347

Preliminary findings from expedition DY190 to the Christiana-Santorini-Kolumbo volcanic field in March 2025

Yeo I. A.[1], Nomikou P.[2], Clare M. A.[1], Jamieson J.[3], Bayrakci G.[1], Lichtschlag A.[1], Gregory E.[1], Portlock G.[4], Dela Sala S.[5], Hopkins A.[6], Nash J.[1], Favela J.[7], Adamczyk K.[7], Bethell E.[8], Spalding J.[8], Katsigera K.[2] Hölz S.[9], Reeck K.[9], Wollatz-Vogt M.[9], Zimmer H.[9], Tan J.[9], Kwasnitchka T.[9]

(1) National Oceanography Centre, Southampton, UK, i.yeo@noc.ac.uk (2) National and Kapodistrian University of Athens, Athens, Greece (3) Memorial University of Newfoundland, St. John's, Canada (4) University of Southampton, Southampton, UK (5) University of Oxford, Oxford, UK (6) University of Leeds, Leeds, UK (7) United States Geological Survey, California, USA (8) University of Ottawa, Ottawa, Canada (9) GEOMAR Helmholtz Institute for Ocean Research Kiel, Kiel, Germany

Introduction

Expedition DY190 onboard the Royal Research Ship (RRS) Discovery explored the Christiana-Santorini-Kolumbo volcanic field between the 3rd and the 28th March 2025. The primary aim of the expedition was to study the interaction between caldera volcanoes and their hydrothermal systems, to understand the role they play in increasing or decreasing the explosivity of eruptions. However, the expedition was serendipitously scheduled a month after the start of the "Seismic Crisis" in the region and hence provided a unique opportunity to assist in efforts to understand and monitor this seismicity and to assess its impact on both Santorini and Kolumbo volcanoes.

Methods

The data presented here was primarily collected by the Remotely Operated Vehicle (ROV) Isis, during 22 different dives to Santorini and Kolumbo. The ROV is a deep-diving robotic submersible designed for scientific research and exploration owned and operated by the National Oceanography Centre, Southampton (UK) and is capable of diving to depths of 6,500 m. During the expedition the ROV conducted high-definition imaging including detailed underwater video and photography, sample collection of rocks, sediments, seawater and hydrothermal fluids, and operated heat flow and temperature probes.

Additionally, during the expedition an array of 12 broad-band ocean bottom seismometers (OBS) from Dublin Institute of Advance Sciences (DIAS) and 13 ocean bottom nodes (OBX) from the National Oceanography Centre were deployed for a duration of 3 weeks to monitor seismicity and noise associated with hydrothermal circulation. OBSs were manufactured by K.U.M. and feature a120 s broadband seismometer housed in a titanium pressure tube, along with a 100 s hydrophone. Titanium tube also contains the K.U.M. 6D6 four-channel datalogger and batteries. Each tube is integrated within a syntactic foam flotation unit and equipped with a flasher, radio beacon, signal flag, anchor and acoustic release. OBXs were manufactured by Geospace and are equipped with three orthogonal geophones (15 Hz cut off frequency) and one hydrophone (4 Hz cut off frequency) and a tilt sensor. These instruments do not have a floatation or anchoring and are relatively small, which allows for the deployment and recovery by the ROV.

Measurements of CSEM were carried out with two different systems with different depths of investigation: using the transient electromagnetic coincident loop system MARTEMIS, with a shallow investigation depth of several 10s of meters and a relatively localized footprint and a dual dipole transmitter system named CAGEM, which in combination with OBEM receivers offers an investigation depth of up to 500 m below the seafloor.

Gravity cores were collected with a gravity corer (GC), collecting the upper 2 m of the sediment. The GCs were equipped with USBL transponder attached to the winch cable (50 m above the gravity corer) for more precise positioning during deployment. The speed of the final drop of the gravity corer was up to 1.2 m/s.

The deployment locations of all equipment are shown in Figure 1. The expedition also deployed and collected two OBS for GEOMAR, which will extend their array (installed to December) and deployed and recovered instruments for the SANTORY observatory at Kolumbo (Nomikou et al., 2022).

Preliminary observations of the volcanic systems in the wake of the seismic crisis

During the expedition we did not observe evidence of major changes from pre-existing data that could clearly be attributed to the seismic unrest in February and March. We did not observe major bathymetric changes (e.g. associated with landslides, volcanic inflation/deflation, or fault

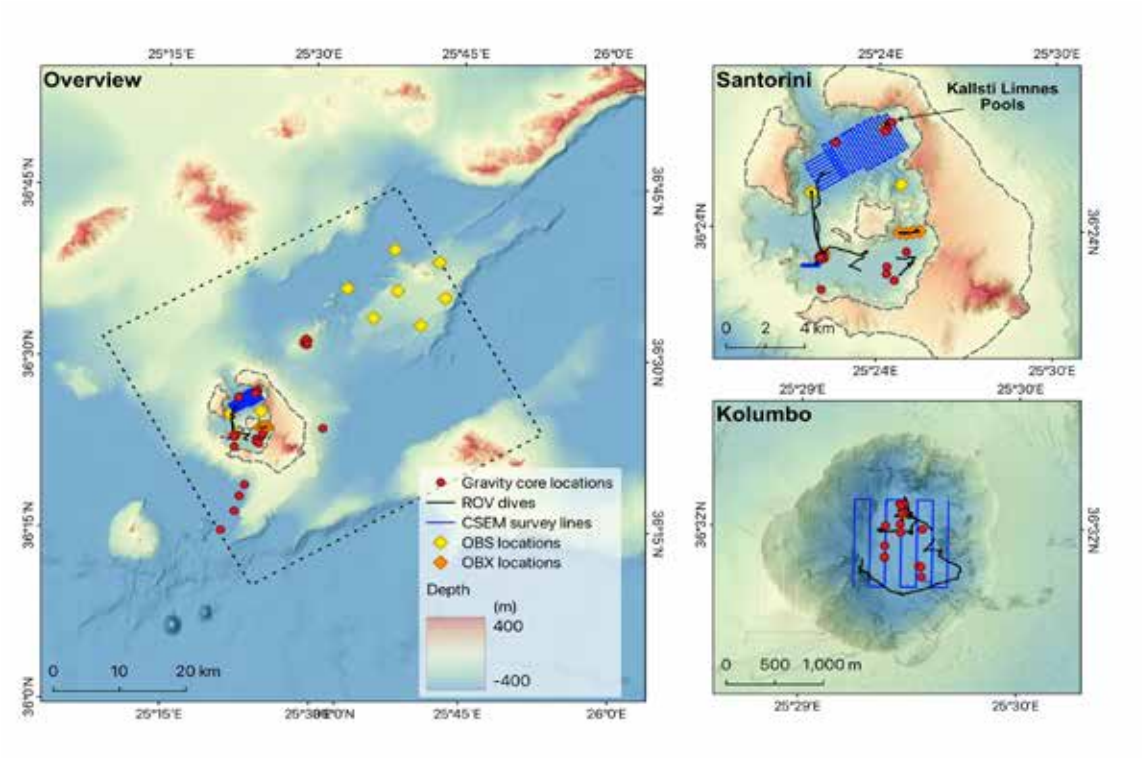

Figure 1. Deployment locations of equipment during expedition DY190.

displacements), however the data remain mostly unprocessed at the time of writing the report, so smaller changes in the bathymetry may exist but be undiscernible from the current unprocessed datasets. We did not find evidence of major landsliding at either Santorini or Kolumbo, nor did we observe evidence of recent turbidity currents in the upper sediments of the cores collected. We did not observe major new cracking or fracturing in the seafloor in the regions we surveyed and we did not find new vent fields in either Santorini or Kolumbo, though we did not cover the entirety of either caldera. Thus, we conclude there is no evidence in the data we collected and have currently analysed for major volcanic unrest or change at either system.

However, there may well be subtler changes in these systems that could be attributed to the seismic unrest, and which might become clearer with further analysis. For example, there may be changes in vent fluid compositions, temperatures and fluxes that will only become apparent with full analysis of the datasets and comparison with previous studies. More detailed processing and interpretation of the bathymetry may highlight smaller changes that are not currently visible. Comparison of the underway measurements made by the ROV may highlight changes in the water column and deep-water properties that are not initially apparent.

There are two differences between our collected data and previous work that we believe can be reliably observed. These are:

1. *Changes in the bacterial coverage in the bottom waters at Kolumbo*

The entire floor of the Kolumbo Caldera was covered in bacterial mats to an extent that had not been previously observed and the turbidity in the water column was very high at depth below 250 m (Figure 1). Professor Nomikou, who has worked inside the Kolumbo caldera many times, observed that both the turbidity and bacterial coverage on the floor of the caldera were higher than she had observed on previous visits, and that these two observations are likely related (the bacteria was extremely light and floccy and easily kicked up into the water column taking a very long time to settle). It is unclear what this means in practice. For example, it may indicate enhanced venting of CO_2 that has accumulated at or near to the seafloor, encouraging the bacterial growth, or increased seeping across the floor of the caldera (though we observe no evidence for this). We highlight, however, that Kolumbo is and will remain

a potentially very dangerous volcano. Measurements of temperatures in the sediments were consistently high in the northern area, and in the venting regions to the east of the main field (so high in one region that we melted the base of a push core, indicating temperatures >100ºC at a depth of just 30-40 cm. Further work is recommended to compare our measurements and observations at Kolumbo with those from previous expeditions, in order to create a time series of data that would make changes and increases in activity clearer than the snapshot measurements presented herein.

2. *Changes in the Kallisti Limnes Pools since December 2024*

Photogrammetric data acquired over the Kallisti Limnes (Pools) in December 2024 was provided by Dr Tom Kwasnitchka at GEOMAR Helmholtz Institute for Ocean Research Kiel, to aid with planning and assessment of the Kallisti Limnes (Pools). This dataset provided an opportunity to assess changes in the degree to which the Kallisti pools were "full" (i.e., amount of cloudy blue fluid within these pools) between December 2024 and March 2025 by comparing the photogrammetry images to ROV dive video. This was accomplished by plotting the ROV dive tracks on the photogrammetry dataset, and identifying pools along the dive track that could also be clearly identified in the photogrammetry. The results of this analysis indicated that, of 22 pools observed in the ROV dives that could also be unambiguously identified in the photogrammetry, only 4 that contained cloudy fluid in December 2024 also contained cloudy fluid in March 2025. The remaining 18 pools that appear full in the photogrammetry did not contain any noticeable cloudy fluid in the ROV video footage. Of the 4 pools that were "full" in both datasets, for at least 1 of the pools, the amount of fluid appears to have diminished since December 2024. Overall, there is a clear reduction in the amount of cloudy fluid that is stored in the pools between December 2024 and March 2025. It is unclear from the datasets if any of the pools that were found to contain cloudy fluid in March were empty in December. It is therefore unclear whether this is a result of the seismic crisis or normal behaviour for the Kallisti Limnes (Pools), as it is currently unknown on what timescales pools fill and empty.

Acknowledgements

We thank the officers and crew or the RRS Discovery for their professionalism and dedication to achieving this expedition. We thank the ROV team, Dave Turner, Russ Locke, Emre Mutlu, Martin Yeomans, Andrea Afonso, Antonio Caldero, Bruno Ramos, and scientific technical team, Dean Cheeseman and Josue Rivero, for their hard work and expertise without which none of the expedition objectives could have been completed. We unreservedly thank the Government and authorities in Greece for allowing us to work in their waters and for their logistical support of activities. We thank the Natural Environmental Research Council (NERC, UK) for funding this research under grant number NE/X01519X/1 and the National Oceanography RISC Scheme for providing the funding for the OBS.

References

Nomikou, P., Polymenakou, P.N., Rizzo, A.L., Petersen, S., Hannington, M., Kilias, S.P., Papanikolaou, D., Escartin, J., Karantzalos, K., Mertzimekis, T.J. and Antoniou, V., 2022. SANTORY: SANTORini's seafloor volcanic ObservatorY. Frontiers in Marine Science, 9, p.796376.

17th INTERNATIONAL CONGRESS of the Geological Society of Greece

BULLETIN OF THE GEOLOGICAL SOCIETY OF GREECE, SP. PUBL.

EXTENDED ABSTRACT 348

Non-shear faulting of the 2025 Santorini-Amorgos (Anydros) earthquakes

Zahradník J.[1], Sokos E.[2], Roumelioti Z.[2], Turhan F.[3],

(1) Faculty of Mathematics and Physics, Charles University, Prague, Czech Republic (jiri.zahradnik@matfyz.cuni.cz) (2) Department of Geology, University of Patras, Patras, Greece (3) Kandilli Observatory and Earthquake Research Institute (KOERI), Regional Earthquake-Tsunami Monitoring Center (RETMC), Boğaziçi University, Istanbul, Türkiye.

Data, Method, and Results

The 2025 seismic activity near Anydros Island contributes to understanding the relative roles of tectonic and volcanic processes in the Santorini-Amorgos zone (Andinisari et al., 2021a; Heath et al., 2019). Here we report on non-double-couple (non-DC) components of the full moment tensor (MT) analyzed in a probabilistic Bayesian framework. This is a continuation of the study preliminarily reported to EMSC and EarthArXiv in mid-February, during the crisis (Zahradník et al., 2025a). The non-DC components are isotropic ISO (= volumetric, VOL), and compensated-linear-vector-dipole CLVD. Absolute values of these two, and the always positive DC component, sum up to 100%. The six-parameter MT allows for mixed signs of ISO and CLVD in an event. The shear-tensile/compressional model, hereafter STC (Vavryčuk, 2011), allows only the same sign of ISO and CLVD in an event. The STC model enables a phenomenological interpretation of the MT in terms of shear faulting part (strike/dip/rake angles) and angular deviation of the slip vector from the fault plane, ranging from 0° to 90°/-90° for crack opening/closing, respectively. Further, the ISO and CLVD values in the STC model imply the Vp/Vs ratio in the source region which may differ from the values measured from travel times.

We use a semi-automatic station selection, starting from the deviatoric moment-tensor calculation of the Institute of Geodynamics, National Observatory of Athens (NOA) with the software GISOLA (Triantafyllis et al., 2016 and 2022), http://orfeus.gein.noa.gr/gisola/realtime/2025/, and we adopt their pre-processed instrumentally corrected full waveforms. A typical set consists of ~ 8-15 stations of the Hellenic Unified Seismological Network (HUSN; Evangelidis et al. 2021) at epicentral distances from ~40 to ~300 km. Further, we use the manually revised epicenter location by NOA and set the trial source positions below the epicenter. We perform a linear least-squares inversion for the full MT while centroid position and time are grid searched. Four 1D velocity models were tested, i.e., Novotný et al. (2001), Brüstle (2012), Dimitriadis et al. (2010), and a combination of the latter two by Fountoulakis (personal communication). All the tested models provide qualitatively the same results in the typical frequency range of 0.03-0.06 Hz. Results for the latter velocity model are presented below. The full moment tensor was calculated with the ISOLA2024 software (Zahradník and Sokos, 2018 and 2025) and its newer Bayesian bootstrap version (not yet published). By bootstrapping station weights, the method yields a posterior probability density of model parameters, thus enabling calculation of confidence intervals. An example of the processing for two events is shown in Fig. 1, where we demonstrate histograms of source depth, ISO, and CLVD. A suite of ISO-CLVD values of an event, almost equally well-fitting observed waveforms, provides quantification of the uncertainty of the source type (green circles in Hudson's plot of Fig. 1); for reference purposes, each event is also characterized by the median MT (blue circle in Fig. 1). We emphasize a relatively large uncertainty, see Table 1; thus, the representation of an event with confidence intervals is more reliable than with median. Since the non-DC components partly tradeoff with depth (Zahradník et al, 2025a), the optimum solutions are those for which an independent depth constraint is available. Using the NLL-SSST-coherence location results of Lomax (2025), followed by our HypoDD relocation (Waldhauser, 2001; Waldhauser and Ellsworth, 2000), we constrained solutions to depths 7-20 km for events 1-19, while the shallower events 20-25 were inverted in the range of 1-20 km (step 1 km).

Results for the 25 events are presented in Tables 1 and 2 and in Fig. 2. Each blue circle in Fig. 2 is a median MT of an event, analogical to the blue circle in Fig. 1; medians are highlighted in bold in Table 1. As demonstrated in Fig. 2, the waveform inversion unambiguously provides the full MTs with ISO > 0 and CLVD > 0 for most of the investigated events. Note also that blue circles are tightly clustered in Fig. 2. This indicates robustly resolved non-shear faulting, stable across the events. The positive signs of ISO and CLVD point to the shear-tensile source process, i.e., crack opening. Two events (shallower, numbered 20 and 21 in Table 1) represent a shear-compressional process, i.e., crack closing (ISO < 0, CLVD < 0). The DC-part of focal mechanisms of all analyzed events is mostly normal faulting, but strike-slip events were also found.

Discussion

Geodetic measurements indicated a possible dike volume of 3 x 10^6 m^3 (Briole, 2025; Ganas and Tsironi, 2025). We found a typical volume change of a single magnitude 5 event to be 10^5 m^3. An effective model corresponding to the 10^5 m^3 volume change can be, for example, a 1 km x 100 m x 1 m co-seismically opened space (filled with a fluid). Since the MT inversion was performed at low frequencies (shear wavelengths greater than 50 km), a more realistic scenario for this activity would involve a series of smaller, interconnected cracks whose spatial details are not resolvable here. Typical positive ISO and CLVD values of Table 1 and the STC model indicate an opening angle of about 10°-20°. The inferred non-shear faulting in the region is

consistent with submarine volcanism, diffuse seismicity and magmatic intrusions indicated in this region by tomography (Health et al., 2019). Significant ISO and CLVD components have been previously reported near Anydros Island (Fig. 5 of Andinisari et al., 2021b), although with more variability across events than in our study, and without uncertainty assessment. Elevated Vp/Vs ratios 1.77–1.86 calculated from seismic travel times by Andinisari et al. (2021a) were interpreted by them in terms of crack density and fluid saturation.

We used ~60 focal mechanisms of Andinisari et al. (2021b) to calculate the stress field in the region (Vavryčuk, 2014) and obtained a normal friction coefficient ~0.7. Interestingly, when we applied the same approach to the 50 focal mechanisms of NOA retrieved via EMSC for the 2025 Anydros activity, we obtained a much lower friction of ~ 0.2. This is shown in Fig. 2, where all events are cumulating at the top of the Mohr's diagram, and may indicate a co-seismic stress change. Faulting under near-zero friction (Tresca's failure criterion) has been laboratory observed (Rutter et al., 2013), yet it remains debated for real faults.

While non-zero isotropic components have been observed globally, their sign and relation to the tectonic-volcanic process remain ambiguous. Some observations in Iceland, at depths of 2-5 km, reported ISO < 0 for normal events and ISO > 0 for reverse ones (Hrubcová et al., 2021), while others observed ISO > 0 for strike-slip events there (Büyükakpınar et al., 2025). The latter has been interpreted as "an interaction between magmatic intrusions and the derived magmatic gases with shear fractures in the dike damage zone". Cyclic surface motions and seismic activity in Iceland have been explained as due to the migration of deep magmatic fluids and gases (of mantle origin) into upper crustal hydrothermal systems (Flóvenz et al., 2022). Normal faulting correlating with ISO > 0 has been found near injection wells in The Geysers geothermal reservoir, interpreted as tensile opening due to lower differential stresses than in reverse faulting (Martínez-Garzón et al., 2017). Slow magma flow can coexist with the fast spread of earthquakes during the crisis. Fluid-filled cracks do not necessarily need to be created during earthquakes; they may exist in the region and be activated by injections. A fast horizontal expansion of a magma-filled dike can occur, with just a small opening over the dike surface, effectively producing a large ISO > 0 (Dahm and Brandsdóttir, 1997). As a subvertical dike overpressure yields expansion increasing horizontal stress, thus possibly activating nearby reverse faults, subhorizontal sills may possibly trigger nearby normal faults in our transtensional region. Distinguishing between sill-like and pluton-like magma chambers may be difficult under existing measurement errors of geodetic data (Fialko et al., 2001). A 3D finite-element modeling can illuminate the interaction between stress fields due to over-pressurized sills/dikes and tectonic faults in the region (Zhan et al., 2022). Non-DC components represent sensitive parameters, less robust than strike, dip, rake, and moment. We already mentioned a possible tradeoff with depth. Other well-known factors possibly creating wrong non-DC estimates, even under low-noise conditions, are velocity models, station distributions, etc. Here we emphasize the danger of the MT inversion under the deviatoric constraint (assuming ISO=0). This assumption is applied in routine MT calculations by many agencies, e.g. GCMT and NOA. For event No. 1 of this paper, 2025/02/04 13:04:14.56, GCMT reported CLVD = 1%, i.e., DC= 99 %, an almost pure shear faulting. In other words, if an earthquake contains a significant ISO component, and is inverted as deviatoric, it may result in an erroneous CLVD. Thus, under the deviatoric assumption, the detection of non-shear-faulting may completely fail. This issue has been explained through synthetic tests accompanying the previous calculations of non-DC in Santorini region (Křížová et al., 2013 and 2016). That is why we intend to help update the current GISOLA at NOA toward reporting full MTs with uncertainty based on Bayesian bootstrap.

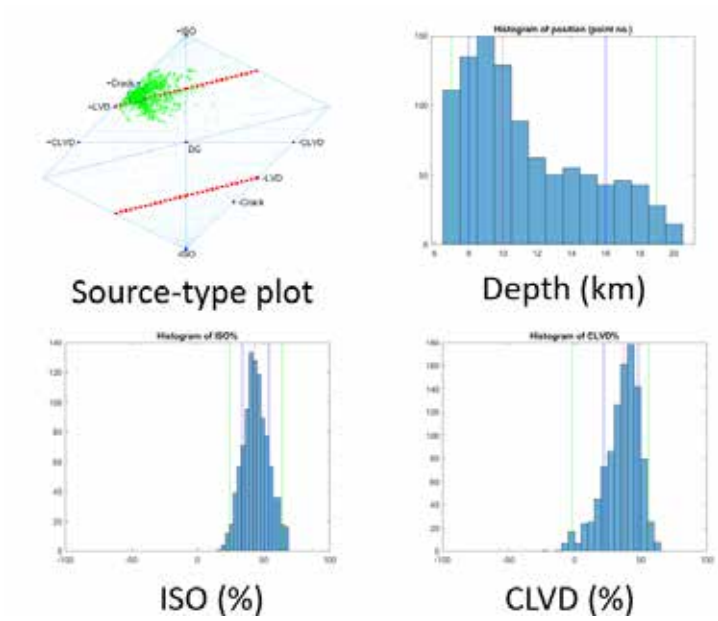

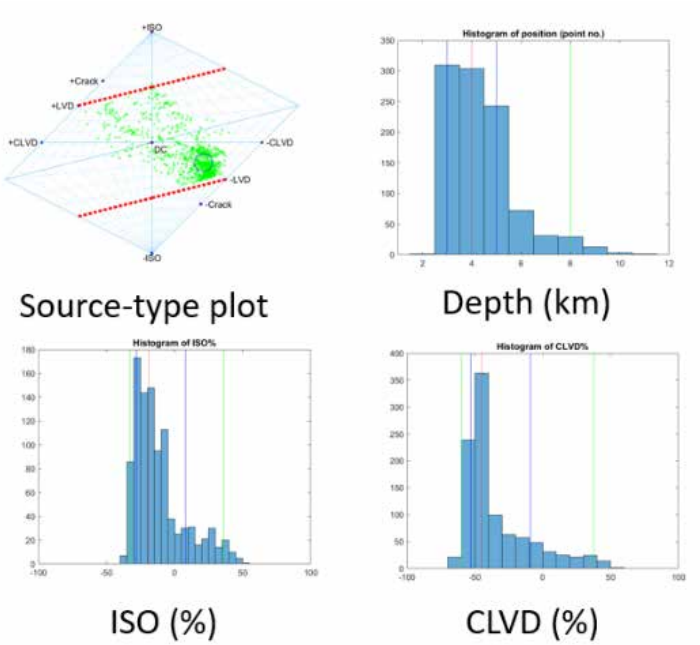

Figure 1. Example of the Bayesian analysis of two earthquakes: (top) No19 of Table 1, 2025/02/11 11:43:54.22, an opening crack, and (bottom) No20 of Table 1, 2025/02/12 01:14:54.63, a closing crack. Percentiles are shown in histograms by vertical lines (median in red).

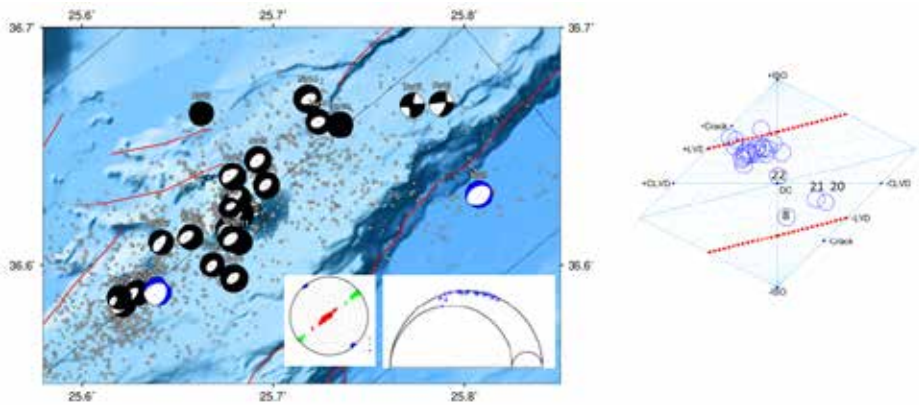

Figure 2. Left: Regional map with "beachballs" for the herein derived full moment tensors. Faults (red lines) are from the NOAFAULTS v5.0 database (Ganas, 2023). In the two insets, the principal stress axes (s_1 red, s_2 green, and s_3 blue) and the Mohr's diagram are shown. Right: Hudson's source type plot of the 25 analyzed earthquakes. No 8 is a poorly resolved event.

Table 1. ISO, CLVD and depth are given with their 15.87%, 50% (median; in bold), and 84.13% percentiles. Mw, and strike/dip/rake angles refer to the median MT. "No" is an internal numbering of events in this study. CLVD with question mark (?) is a value modified by a few percent to have the same sign as ISO, as required in the STC model. Events 1-19 were inverted in depths 7-20 km (step 1 km), events 20-25 in depths 1-20 km (step 1 km). Shaded No. 8 is a poorly resolved event. Shown in red are the two shear-compressional events; all the others are shear-tensional.

Date	Mw	ISO (%)			CLVD (%)			Depth (km)			Strike Dip Rake (°)		
No01 2025/02/04 13:04:14.56	5.25	24	**36**	46	-1	**16**	27	9	**11**	13	235	39	-81
No02 2025/02/05 19:09:38.62	5.05	18	**29**	42	9	**29**	39	7	**9**	10	241	35	-69
No03 2025/02/03 09:29:42.49	4.95	19	**39**	58	-41	**3?**	19	7	**9**	14	250	40	-52

No04 2025/02/03 20:19:39.39	4.77	15	**29**	42	3	**21**	42	7	**9**	11	255	43	-49
No05 2025/02/08 16:30:00.76	4.02	19	**35**	51	-6	**17**	35	7	**9**	14	205	52	-126
No06 2025/02/08 09:00:41.37	4.83	15	**27**	42	13	**26**	37	7	**8**	11	263	44	-40
No07 2025/02/07 07:16:13.66	4.77	12	**25**	44	16	**36**	50	7	**9**	13	243	31	-59
No08 2025/02/02 23:54:41.58	4.18	-43	**-26**	-1	-38	**6**	56	7	**9**	17	253	69	-79
No09 2025/02/09 19:05:39.41	5.13	16	**26**	34	22	**29**	37	7	**8**	10	244	40	-73
No10 2025/02/05 17:47:28.04	4.67	43	**51**	60	-4	**8**	28	7	**8**	10	266	76	-19
No11 2025/02/04 02:46:06.98	4.86	18	**33**	45	-1	**17**	32	8	**10**	12	244	38	-67
No12 2025/02/03 12:17:40.53	4.92	18	**34**	46	-5	**14**	27	9	**11**	13	230	37	-87
No13 2025/02/02 17:45:44.99	4.62	19	**35**	49	-12	**8**	24	7	**9**	10	230	39	-78
No14 2025/02/10 20:16:29.37	5.24	16	**33**	45	-10	**7**	21	7	**9**	11	238	45	-94
No15 2025/02/10 22:37:25.55	5.08	13	**28**	43	-13	**6**	20	8	**9**	11	238	43	-81
No16 2025/02/10 11:23:17.71	4.68	8	**17**	26	19	**32**	42	10	**12**	14	279	71	-25
No17 2025/02/11 05:58:44.81	4.68	17	**23**	32	18	**32**	45	10	**11**	13	191	84	-177
No18 2025/02/11 07:17:19.00	4.67	8	**29**	45	-19	**1?**	15	8	**10**	12	251	48	-88
No19 2025/02/11 11:43:54.22	4.88	34	**43**	54	22	**37**	48	8	**10**	16	206	55	-144
No20 2025/02/12 01:14:54.63	5.18	-28	**-19**	8	-53	**-45**	-9	3	**4**	5	259	43	-58
No21 2025/02/18 04:46:52.13	5.05	-31	**-15**	26	-49	**-35**	-11	4	**5**	7	247	40	-80
No22 2025/02/12 08:29:48.29	4.72	14	**7**	26	-28	**3?**	21	3	**6**	8	265	35	-49
No23 2025/02/12 09:15:07.42	4.65	8	**31**	39	4	**26**	36	5	**8**	14	254	38	-48
No24 2025/02/17 07:49:51.04	4.94	5	**29**	45	-16	**15**	43	6	**8**	11	237	38	-77
No25 2025/02/18 06:08:08.96	4.64	24	**38**	50	12	**28**	42	4	**5**	7	254	44	-37

Table 2. Median full MTs (Nm), in Harvard notation (spherical coordinates r-radial, t-theta, p-phi). Event numbering as in Table 1. Shaded No. 8 is a poorly resolved event.

	Mrr	Mtt	Mpp	Mrt	Mrp	Mtp
1	-2.07E+16	7.47E+16	6.21E+16	-7.94E+15	-1.31E+16	4.11E+16
2	-1.14E+16	3.26E+16	2.86E+16	-6.81E+15	-1.29E+16	2.39E+16
3	-3.15E+15	2.51E+16	2.33E+16	3.01E+14	-1.14E+16	1.35E+16
4	-3.77E+15	1.22E+16	9.86E+15	-2.88E+14	-5.43E+15	9.83E+15
5	-6.35E+13	1.04E+15	7.76E+14	-8.86E+13	1.37E+14	7.39E+14

6	-3.31E+15	1.55E+16	9.85E+15	-9.26E+14	-7.79E+15	1.18E+16
7	-3.75E+15	9.25E+15	1.04E+16	-3.37E+15	-7.16E+15	8.84E+15
8	-2.06E+15	-3.93E+13	-5.09E+14	1.27E+15	2.22E+14	5.26E+14
9	-2.11E+16	4.75E+16	3.04E+16	-5.05E+15	-1.13E+16	3.14E+16
10	5.68E+15	8.12E+15	8.65E+15	1.41E+15	-9.03E+14	5.91E+15
11	-5.47E+15	1.86E+16	1.56E+16	-1.96E+15	-6.17E+15	1.13E+16
12	-7.60E+15	2.33E+16	2.10E+16	-4.19E+15	-4.64E+15	1.25E+16
13	-2.97E+15	7.29E+15	8.30E+15	-4.64E+14	-1.88E+15	4.49E+15
14	-3.01E+16	8.72E+16	4.77E+16	-1.19E+15	3.00E+15	3.18E+16
15	-2.18E+16	4.14E+16	3.10E+16	-3.02E+14	-5.08E+15	2.25E+16
16	-1.74E+15	9.27E+15	2.39E+14	2.43E+15	-2.35E+15	8.76E+15
17	8.81E+14	8.84E+15	1.18E+15	-8.90E+14	3.57E+14	9.86E+15
18	-5.86E+15	1.26E+16	5.59E+15	1.04E+15	1.98E+14	3.11E+15
19	5.26E+15	2.53E+16	1.16E+16	-2.00E+15	4.97E+14	1.09E+16
20	-7.11E+16	2.38E+16	1.36E+15	6.11E+15	-3.17E+16	1.69E+16
21	-5.13E+16	2.03E+16	6.75E+15	-3.59E+15	-9.27E+15	1.06E+16
22	-8.58E+15	9.61E+15	2.08E+15	-2.63E+15	-7.31E+15	5.76E+15
23	-1.33E+15	7.99E+15	7.00E+15	-1.15E+15	-4.12E+15	6.05E+15
24	-1.11E+16	2.37E+16	2.04E+16	-3.17E+15	-6.61E+15	1.51E+16
25	1.97E+15	6.98E+15	8.76E+15	-7.86E+14	-2.75E+15	5.51E+15

Data and Resources

Regional waveform data used in this study were obtained from the Hellenic Unified Seismic Network (HUSN) networks, HL, DOI:10.7914/SN/HL, HC, DOI:10.7914/SN/HC, HP, DOI:10.7914/SN/HP and HA, DOI:10.7914/SN/HA. Data from the HL, HC, HP, and HA networks can be accessed through the National Observatory of Athens (NOA) EIDA node https://eida.gein.noa.gr/ (Evangelidis et al., 2021). The data set of full moment tensors of the present study is archived in Zahradník et al. (2025b). The ISOLA software can be downloaded from https://geo.mff.cuni.cz/~jz/for_ISOLAnews/ and https://github.com/esokos/isola/tree/master (archived in Zahradník et al., 2025c). For Stressinverse code of Vavryčuk (2014), see https://www.ig.cas.cz/en/stress-inverse/. The maps were generated using the Generic Mapping Tools v.6, https://www.generic-mapping-tools.org/download/.

Acknowledgements

The authors would like to thank I. Fountoulakis and C. Evangelidis for valuable discussions and for providing the crustal velocity model. We also thank A. Lomax for sharing his location results. Special thanks to all the Greek colleagues who maintained networks, deployed new and processed all sorts of data during this remarkable sequence. The code sti2MT.m for the STC model and related routines written by V. Vavryčuk were used. J.Z. was supported by the Czech Science Foundation (grant 23-06345S). E.S. was supported by the "TowaRds AdvaNced multidiSciplinary Fault ObseRvatory systeMs²" (TRANSFORM²) project, (101188365 HORIZON-INFRA-2024-DEV-01-01.

References

Andinisari, R., Konstantinou, K.I., Ranjan, P., 2021a. Seismicity along the Santorini-Amorgos zone and its relationship with active tectonics and fluid distribution, *Phys. Earth Planet. Int.*, 312, 106660, https://doi.org/10.1016/j.pepi.2021.106660.

Andinisari, R., Konstantinou, K.I. , Ranjan, P., 2021b. Moment tensor inversion of microearthquakes along the Santorini-Amorgos zone: Tensile faulting and emerging volcanism in an extensional setting, *J. Volcanol. Geotherm. Res.*, 420, 107394, ISSN 0377-0273, https://doi.org/10.1016/j.jvolgeores.2021.107394.

Briole, P., 2025. Santorini seismo-volcanic event: GNSS time series and preliminary models. Report to EMSC, https://www.emsc-csem.org/Files/event/1765158/20250213b-santorini-seismo-volcanic-crisis-gnss.pdf

Brüstle, A. (2012). Seismicity of the eastern Hellenic Subduction Zone. *Ph.D. thesis*. Ruhr University, Bochum.

Büyükakpınar, P., Isken, M. P., Heimann, S., Dahm, T., Kuhn, D., Starke, J., et al., 2025. Understanding the seismic signature of transtensional opening in the Reykjanes Peninsula Rift Zone, SW Iceland. *J. Geophys. Res.: Solid Earth*, *130*, e2024JB029566. https://doi.org/10.1029/2024JB029566.

Dahm, T., Brandsdóttir, B., 1997. Moment tensors of microearthquakes from the Eyjafjallajokull volcano in South Iceland. *Geophys. J. Int.*, *130*(1), 183–192. https://doi.org/10.1111/j.1365-246X.1997.tb00997.x.

Dimitriadis, I., Papazachos, C., Panagiotopoulos, D., Hatzidimitriou, P., Bohnhoff, M., Rische, M., Meier, T., 2010. P and S velocity structures of the Santorini-Coloumbo volcanic system (Aegean Sea, Greece) obtained by non-linear inversion of travel times and its tectonic implications. *J. Volcanol. Geotherm. Res.* 195 (1), 13–30.

Evangelidis, C. P., N. Triantafyllis, M. Samios, K. Boukouras, K. Kontakos, O. J. Ktenidou, I. Fountoulakis, I. Kalogeras, N. S. Melis, O. Galanis, *et al.,* 2021. Seismic Waveform Data from Greece and Cyprus: Integration, Archival, and Open Access, *Seismol. Res. Lett.* **92**, no. 3, 1672–1684, doi: 10.1785/0220200408.

Fialko, Y., Khazan, Y., Simons, M., 2001. Deformation due to a pressurized horizontal circular crack in an elastic half-space, with applications to volcano geodesy, *Geophys. J. Int.*, 146, 181–190, https://doi.org/10.1046/j.1365-246X.2001.00452.x.

Flóvenz, O. G., Wang, R., Hersir, G. P., Dahm, T., Hainzl, S., Vassileva, M., et al., 2022. Cyclical geothermal unrest as a precursor to Iceland's 2021 Fagradalsfjall eruption. *Nature Geoscience*, *15*(5), 397–404. https://doi.org/10.1038/s41561□022□00930□5.

Ganas., A., 2023. NOAFAULTS KMZ layer Version 5.0 (V5.0) [Data set]. Zenodo. https://doi.org/10.5281/zenodo.8075517.

Ganas, A., Tsironi, V., 2025. 2024-2025 Deformation of the Santorini Caldera: InSAR time-series data from the S1A satellite of the European Space Agency. Report to EMSC, https://www.emsc-csem.org/Files/event/1765158/report_English_InSAR_V2.pdf.

Heath, B. A., Hooft, E. E. E., Toomey, D. R., Papazachos, C. B., Nomikou, P., Paulatto, M., et al., 2019. Tectonism and its relation to magmatism around Santorini volcano from upper crustal *P* wave velocity. *J. Geophys. Res.: Solid Earth*, 124, 10610–10629. https://doi.org/10.1029/2019JB017699.

Hrubcová, P., Doubravová J., Vavryčuk, V., 2021. Non-double-couple earthquakes in 2017 swarm in Reykjanes Peninsula, SW Iceland: Sensitive indicator of volcano-tectonic movements at slow-spreading rift. *Earth Planet. Sci. Lett.*, *563*, 116875. https://doi.org/10.1016/j.epsl.2021.116875.

Křížová, D., Zahradník, J., Kiratzi, A., 2013. Resolvability of isotropic component in regional seismic moment tensor inversion, *Bull. Seis. Soc. Am.* 103, no. 4, 2460–2473, doi: 10.1785/0120120097.

Křížová, D., Zahradník, J., Kiratzi, A., 2016. Possible Indicator of a Strong Isotropic Earthquake Component: Example of Two Shallow Earthquakes in Greece. *Bull. Seis. Soc. Am.,* 106 (6), 2784–2795, https://doi.org/10.1785/0120160086.

Lomax, A. (2025). NLL-SSST-coherence high-precision earthquake location catalog for the 2025 Santorini-Amorgos earthquake swarm (v1.0) [Data set]. Zenodo. https://doi.org/10.5281/zenodo.14956645.

Martínez-Garzón, P., G. Kwiatek, M. Bohnhoff, G. Dresen, 2017. Volumetric components in the earthquake source related to fluid injection and stress state, *Geophys. Res. Lett.*, 44, 800–809, doi:10.1002/2016GL071963.

Novotný, O., Zahradník, J., Tselentis, G. A., 2001. Northwestern Turkey earthquakes and the crustal structure inferred from surface waves observed in Western Greece, *Bull. Seis. Soc. Am.* **91**, no. 4, 875–879, doi: 10.1785/0120000116.

Rutter, E.H. , A.J. Hackston, E. Yeatman, K.H. Brodie, J. Mecklenburgh, S.E. May, 2013. Reduction of friction on geological faults by weak-phase smearing, *J. Struct. Geol.*, 51, 52-60, https://doi.org/10.1016/j.jsg.2013.03.008.

Triantafyllis, N., Sokos, E., Ilias, A., Zahradník, J., 2016. Scisola: Automatic moment tensor solution for SeisComP3, *Seismol. Res. Lett.* **87**, no. 1, 157–163, doi: 10.1785/0220150065.

Triantafyllis, N., Venetis, I. E., Fountoulakis, I., Pikoulis, V., Sokos, E., Evangelidis, C. P., 2022. Gisola: A High-Performance Computing Application for Real-Time Moment Tensor Inversion, *Seismol. Res. Lett.* **93**, no. 2A, 957–966, doi: 10.1785/0220210153.

Vavryčuk, V., 2011. Tensile earthquakes: theory, modeling, and inversion. *J. Geophys. Res.* 116, B12320, doi:10.1029/2011JB008770.

Vavryčuk, V., 2014. Iterative joint inversion for stress and fault orientations from focal mechanisms. *Geoph. J. Int.* 199(1), 69–77. https://doi.org/10.1093/gji/ggu224.

Waldhauser, F., 2001. HypoDD: A computer program to compute double-difference earthquake locations, *USGS Open File Rep.,* 01-113, 2001.

Waldhauser F. , Ellsworth, W.L., 2000. A double-difference earthquake location algorithm: Method and application to the northern Hayward fault, *Bull. Seism. Soc. Am.*, 90, 1353-1368.

Zahradník, J., Sokos, E., 2018. ISOLA code for multiple-point source modeling –review, in *Moment Tensor Solutions - A Useful Tool for Seismotectonics*, S. D'Amico (Ed.), Springer Natural Hazards, 1–28, doi: 10.1007/978-3-319-77359-9.

Zahradník, J., Sokos, E., 2025. ISOLA2024 – assessing and understanding uncertainties of full moment-tensors. *Seis. Res. Lett.,* https://doi.org/10.1785/0220240420.

Zahradník, J., Sokos, E., Roumelioti, Z., Turhan, F., 2025a. Positive isotropic components of the 2025 Santorini-Amorgos earthquakes. Non-peer reviewed report, EarthArXiv, https://doi.org/10.31223/X5RD9S.

Zahradník, J., Sokos, E., Roumelioti, Z., Turhan, F., 2025b. Full moment tensors of the 2025 Santorini-Amorgos earthquakes [Data set]. Zenodo. https://doi.org/10.5281/zenodo.14995537.

Zahradník, J., Sokos, E., Plicka, V. (2025c). Supplementary software for JGR paper Liu et al. (2025). [Software]. Zenodo. https://doi.org/10.5281/zenodo.14923691.

Zhan, Y., Roman, D. C., Le Mével, H., Power, J. A., 2022. Earthquakes indicated stress field change during the 2006 unrest of Augustine Volcano, Alaska. *Geoph.Res. Lett.*, *49*, e2022GL097958. https://doi.org/10.1029/2022GL097958.

17th INTERNATIONAL CONGRESS of the Geological Society of Greece

BULLETIN OF THE GEOLOGICAL SOCIETY OF GREECE, SP. PUBL.

EXTENDED ABSTRACT 349

Integrating micropalaeontological, geotechnical and sedimentological data to reconstruct the palaeoenvironmental evolution of Mesolongi Lagoon

Zanai F. Tz.[1], Papadopoulou P.[2], Depountis N.[2] Pelekis P.[3], Iliopoulos G.[2]

(1) Aristotle University of Thessaloniki, Department of Geology, Thessaloniki, Greece, tzanai@geo.auth.gr , (2) University of Patras, Department of Geology, Patras, Greece , (3) University of Patras, Department of Civil Engineering, Patras, Greece

Research Highlights

- Reconstruct the environmental evolution of the Mesolongi lagoon, revealing transitions between freshwater-influenced, brackish, and marine-dominated systems over time.
- Integrated micropaleontological, sedimentological, and geotechnical analysis to uncover ecological dynamics and depositional changes.

Background and Objectives

Coastal lagoons such as Mesolongi lagoon are critical ecosystems that record environmental and climatic changes through their sedimentary archives (Khadraoui et al., 2019). Foraminifera and ostracods, as sensitive bioindicators, provide key insights into these transformations due to their responsiveness to palaeoenvironmental factors such as salinity, oxygen, and sedimentary conditions (Frenzel & Boomer, 2005; Milker et al., 2009; Murray, 2006). This study examines a 21-meter borehole core to reconstruct the Mesolongi lagoon's paleoenvironmental history and identify factors driving its ecological and depositional changes. Geotechnical parameters are also examined to check whether these are affected by ecological and depositional changes and if there is any correlation with micropaleontological parameters.

Figure 1. General satellite view of the study area, showing the borehole sampling exact location, in respect to Mesolongi lagoon, Klisova Lagoon and the Gulf of Patras.

Methods

A multiproxy approach was employed, integrating sedimentological, micropaleontological, and geotechnical analysis. Sedimentological studies characterized lithological variability of the studied sequence, while geotechnical parameters—including plasticity index (PI), undrained shear strength (S_u or q_u), natural moisture content (w), and consolidation parameters—were assessed to interpret substrate physical properties and deformation values. Micropaleontological analysis identified and quantified foraminiferal and ostracod assemblages, with diversity

indices (e.g., species richness, dominance, and evenness) calculated to track ecological shifts. Data was analyzed using Past4.03 software and visualized with Tilia, allowing for stratigraphic interpretation and paleoenvironmental reconstruction.

Results/Discuss

Four stratigraphic units were identified, reflecting distinct environmental phases:

Unit A: Freshwater-Influenced Brackish Lagoon (20.9–15.4 m):

- Dominated by *Ammonia tepida* and *Cyprideis torosa*, indicative of brackish conditions (Altınsaçlı et al., 2015; Debenay et al., 1998; Murray, 2006). However, the presence of freshwater ostracods, such as *Candona* spp., *Fabaeformiscandona* spp., and *Potamocypris fulva*, provides evidence of freshwater inputs influencing the lagoon environment (Altınsaçlı et al., 2015; Frenzel & Boomer, 2005).
- Geotechnical properties revealed a soft to stiff silty-clayey material (CL, ML) with moderate plasticity and undrained shear strength (qu) values which characterize normal consolidated substrate in the depositional environment.

Unit B: Transitional Brackish-Marine Environment (15.4–9.4 m):

- Subunit B1 (15.4–12.8 m): Characterized by an increase in planktonic foraminifera, indicating a stronger marine influence and enhanced water exchange with open sea environments. The dominance of these microfauna reflects a clear shift away from the brackish conditions observed in Unit A.
- Subunit B2 (12.8–9.4 m): Features the notable presence of epiphytic species such as *Rosalina globularis* and *Triloculina trigonula* (Triantaphyllou et al., 2005; Wilson, 2007), which thrive in well-oxygenated environments with vegetation. This subunit also includes localized occurrences of organic material and shells, further suggesting a dynamic interaction between marine and lagoonal conditions.
- Across Unit B, the non-plastic behavior and the decreasing plasticity index (PI) highlight a transition to sandier, less cohesive deposits, such as silty sands (SM) with low oedometric modulus of deformation (Es). These changes correspond to a depositional environment influenced by stronger marine incursions, resulting in reduced clay content and greater permeability.

Unit C: Marine-Dominated Lagoon (9.4–6.1 m):

- This unit reflects a significant marine influence, as evidenced by the high abundance of planktonic foraminifera. The presence of terrestrial material at a depth of 9 meters strongly suggests a washover event, likely caused by storm surges or high-energy waves breaching the lagoon's barrier. This event would have introduced marine water and sediments into the lagoon, altering its ecological and sedimentological dynamics.
- The geotechnical profile highlights the impact of this shift. In the lower part of Unit C, PI and w are relatively low, while Pc (pre-consolidation pressure) and σ'v (effective vertical stress) are moderately high. These characteristics suggest compacted, coarse-grained sediments such as sands and silty sands, deposited under moderately high-energy conditions, likely linked to washover events or barrier breaches introducing marine sediments. In the upper part, a slight increase in PI and w, along with a moderate decrease in Pc and σ'v, indicates a gradual transition to finer-grained, less compacted sediments like silts or clays. This shift reflects reduced depositional energy and overburden stress, corresponding to a more stable and calmer environment as high-energy marine influences diminished overtime.

Unit D: Evolved Lagoonal System (6.1–2.2 m):

Subunit D1 (6.1–4.5 m):

- Represents a stable brackish lagoonal phase, dominated by *Ammonia tepida* and *Cyprideis torosa*, with consistent representation of brackish foraminifera like *Haynesina germanica* and *Quinqueloculina seminulum* (Murray, 2006).
- Geotechnical properties, including moderate PI (Plasticity Index) and w (natural moisture content), reflect cohesive silty clay deposition under stable, moderate-energy conditions that supported a diverse ecosystem.

Subunit D2 (4.5–2.2 m):

- The sharp increase in *Loxoconcha elliptica*, combined with a decline in miliolids, indicates a transition from stable to more stressful environmental conditions. The high abundance of *L. elliptica* suggests the presence of detritus-rich substrates, which support this species (Altınsaçlı et al., 2015). Additionally, the small but notable occurrence of low-oxygen foraminifera points to declining oxygen levels, further reflecting a shift toward environmental stress. These faunal patterns suggest a lagoonal environment experiencing salinity fluctuations, oxygen depletion, and seasonal variations, contributing to ecological instability.
- Increasing PI (Plasticity Index), w (natural moisture content) and eo (voids ratio), alongside decreasing γb (bulk density) and very low oedometric modulus of deformation (Es), indicate the deposition of softer, organic-rich silty clays under lower-energy conditions. These changes in sediment characteristics align with the faunal evidence of a more dynamic and stressful lagoonal phase.

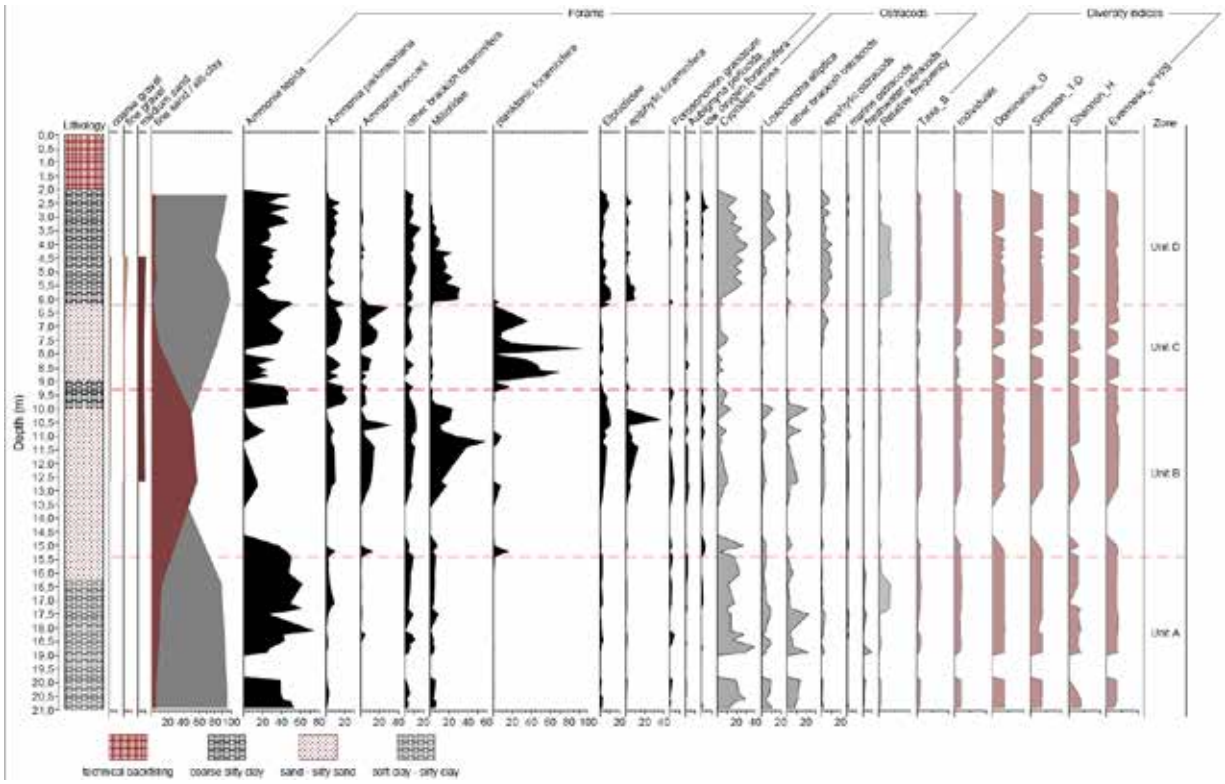

Figure 2. Relative abundances (%) of the identified foraminiferal and ostracod taxa in the samples, alongside log-transformed relative frequency (taxa/g) and diversity indices, integrated with lithology and granulometry.

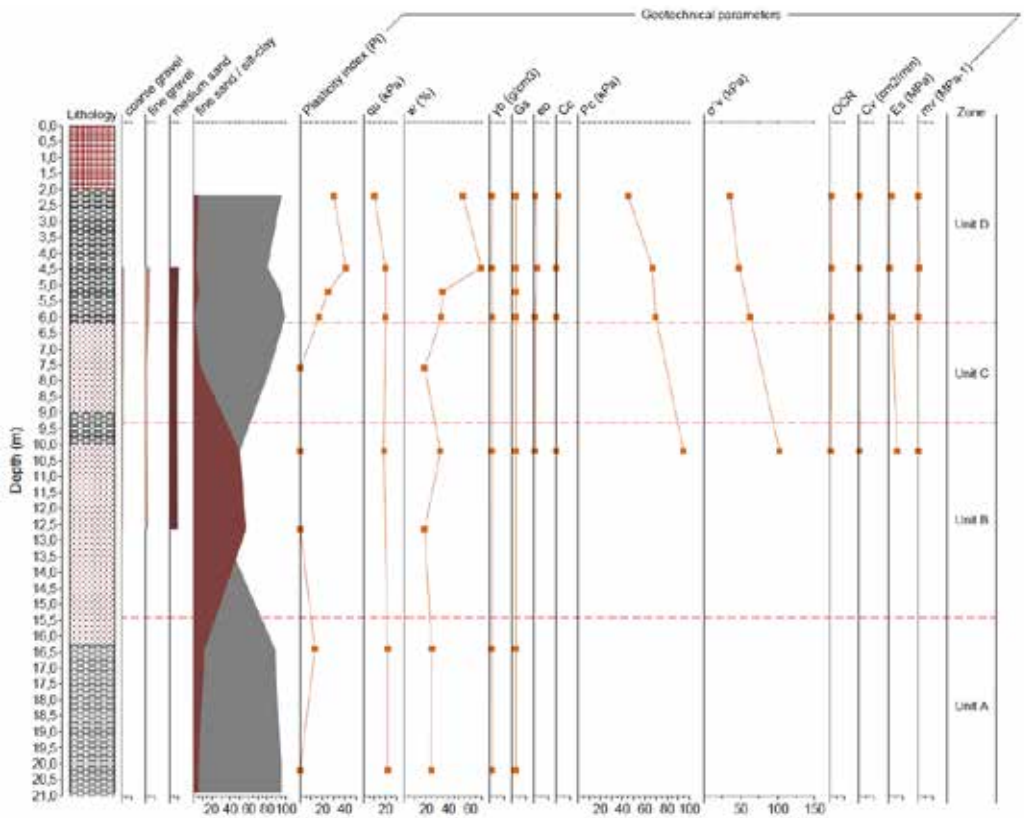

Figure 3. Figure 3 presents the values of the geotechnical parameters throughout the stratigraphic column, except for the consolidation parameters (σ´v, OCR, Cv, Es,mv), which were examined only within the first 10 meters.

Conclusion

This study demonstrates the integration of sedimentological, micropalaeontological, and geotechnical analyses to reconstruct the palaeoenvironmental evolution of the Mesolongi Lagoon and provides an interesting and rather uncommon correlation between the different datasets. The findings highlight the utility of foraminifera and ostracods as bioindicators for interpreting environmental changes and sediment dynamics. By examining geotechnical parameters throughout the stratigraphic column, alongside lithological and granulometric data, this research provides critical insights into the lagoon's historical environmental conditions and resilience. Further exploration of consolidation parameters in deeper strata could enhance the understanding of sediment behavior and coastal processes in similar lagoon systems. Interestingly, micropalaeontological data and palaeoecological interpretations correlate well with geotechnical data.

References

Altınsaçlı, S., Altınsaçlı, S., & Perçin Paçal, F. (2015). International Journal of Fisheries and Aquatic Studies 2015; 3(2): 374-390 Diversity, species composition and habitat preferences of Ostracoda (Crustacea) in seven karstic springs of varying salinity in Milas (Muğla, Turkey). *IJFAS*, *3*(2). www.fisheriesjournal.com

Debenay, J.-P., Bénéteau, E., Zhang, J., Stouff, V., Geslin, E., Redois, F., & Fernandez-Gonzalez, M. (1998). Ammonia beccarii and Ammonia tepida (Foraminifera): morphofunctional arguments for their distinction. In *Marine Micropaleontology* (Vol. 34).

Frenzel, P., & Boomer, I. (2005). The use of ostracods from marginal marine, brackish waters as bioindicators of modern and Quaternary environmental change. *Palaeogeography, Palaeoclimatology, Palaeoecology*, *225*(1–4), 68–92. https://doi.org/10.1016/j.palaeo.2004.02.051

Khadraoui, A., Zaïbi, C., Carbonel, P., Bonnin, J., & Kamoun, F. (2019). Ostracods and mollusks in northern Sfax coast: reconstruction of Holocene paleoenvironmental changes and associated forcing. *Geo-Marine Letters*, *39*(4), 313–336. https://doi.org/10.1007/s00367-019-00576-0

Milker, Y., Schmiedl, G., Betzler, C., Römer, M., Jaramillo-Vogel, D., & Siccha, M. (2009). Distribution of recent benthic foraminifera in shelf carbonate environments of the Western Mediterranean Sea. *Marine Micropaleontology*, *73*(3–4), 207–225. https://doi.org/10.1016/j.marmicro.2009.10.003

Murray, J. W. . (2006). *Ecology and applications of benthic foraminifera*. Cambridge University Press.

Triantaphyllou, M. V., Tsourou, T., Koukousioura, O., & Dermitzakis, M. D. (2005). Foraminiferal and ostracod ecological patterns in coastal environments of SE Andros Island (Middle Aegean Sea, Greece). *Revue de Micropaleontologie*, *48*(4), 279–302. https://doi.org/10.1016/j.revmic.2005.09.003

Wilson, B. (2007). Guilds among epiphytal foraminifera on fibrous substrates, Nevis, West Indies. *Marine Micropaleontology*, *63*(1–2), 1–18. https://doi.org/10.1016/j.marmicro.2006.10.001

17th INTERNATIONAL CONGRESS of the Geological Society of Greece

BULLETIN OF THE GEOLOGICAL SOCIETY OF GREECE, SP. PUBL.

EXTENDED ABSTRACT 350

The presence of nappes, in SW Peloponnesus peninsula, and the strongly metamorphic Plattenkalk series, in central south Peloponnesus and Crete Island, change the dynamic evolution of west and south Greece

Zelilidis A.[1], Iliopoulos G.[2], Maravelis A.G.[3], Bourli N.[4]

1 Department of Geology, University of Patras, 26504 Rion, Greece. a.zelilidis@upatras.gr

2 Department of Geology, University of Patras, 26504 Rion, Greece.

3 Department of Geology, Aristotle University of Thessaloniki, 54124 Thessaloniki, Greece.

4 Department of Geology, University of Patras, 26504 Rion, Greece.

Abstract

Southeast Mediterranean is characterized by the presence of nappes that overthrusted the authochonous Plattenkalk series, during Oligocene to early Miocene. South of Crete, the Hellenic Trench (HT) and the Mediterranean Ridge (MR) were developed during the late Miocene. By Messinian time, most of the MR had been already formed and rose above the neighboring abyssal plains. On the elevated portion of the MR, where fields of mud diapirs (volcanoes) have been discovered, the Messinian layer is significantly thinner than on its deeper southern flank. The comparison of western Greece and western Ionian basin with Gythion/Sparta and Crete Island regions with the Plattenkalk series, showed the same depositional conditions, introducing equivalent depositional conditions between Ionian Basin (western part) and the Plattenkalk series, in south Peloponnesus and Crete Island. Therefore, Crete Island could represents the Ionian basin whereas the HT could be the equivalent of the Apulian Platform Margins (APM); whereas the MR could represents a platform, equivalent to the Apulian Platform (AP). During the Oligocene compressional regime, the Crete Island represents the wedge top area, the Hellenic trench the foredeep area and the area of Mediterranean ridge could be the fore bulge area. Later and during the late Miocene migration of compressional regime southwards the MR represents the wedge top, northwards the HT the extensional backstop areas (e.g. Gavdos Trench), and southwards the Sirte abyssal plain the new foredeep. The presence of nappes in SW Peloponnesus, only in Pylos area, shows how the strike-slip faults influence the nappes development. Furthermore, the presence of reefs, according EDDEY in 2018 announcements, reefs must be developed on the MR. The question is if the nappes overstepped the HT (when they were the APM) and covered the MR (when they were the AP)? or the nappes filled up only the HT and therefore the MR now is without any nappe?

Keywords: *Mediterranean Ridge, Apulian Platform, Ionian Basin, Plattenkalk Series, Nappes*

Introduction

Over the last 80 Myr, the Alpine-Himalayan belt represents the most spectacular result of the relative motion between the African and Eurasian plates (Olivet et al., 1982). The MR, which arises from the same plate motion (at a rate in the order of 10 mm/yr), can also be considered as a direct consequence of this plate kinematics (Jackson et al., 1992).

The MR, the principal structure in the Eastern Mediterranean, stretches from the Calabrian Rise in the west to the Florence Rise in the east, a distance of 1500 km. Its width changes from about 150 to 300 km, and it has an arcuate southward convex shape, almost parallel to the Hellenic Arc. The average water depth on the MR is about 2.1–2.2 km, varying between 1,200 m and more than 3,000 m. The MR rises 1–2 km above the surrounding seafloor, but because of its large width the general slope, angles rarely exceed 20°. The Ridge is bordered on the north by a number of deep and narrow trenches forming the Hellenic Trench (HT) system (Le Pichon et al., 1982) (Figure 1).

Between the Hellenic trench system to the north and the MR crustal domain (chiefly west of the Matapan Trench), a wide area known as the “flat inner zone” (Truffert et al., 1993) extends at 2500–3000 m water depth. South of Crete, particularly south of the island of Gavdos, this flat domain becomes progressively narrower towards the east and the MR central domains appear almost in contact with the Poseidon and Strabo trenches (Leite and Mascle, 1982). The southern boundary of the MR is delineated by a chain of flat abyssal plains adjoin to the African margin. Their depths decrease in general from west to east and they consist of the Messina (Ionian) (4,140 m), the Sirte (4,149 m), and the Herodotus A.P. (3,225 m) abyssal plains. The ridge topography is generally dominated by small, closely spaced depressions and ridges, with a relief of 50–100 m and a wavelength 0.5–2 km, that are mostly parallel to the Ridge trend. These features were attributed both to tectonic deformations displayed in the seafloor relief and to karst forms resulting from dissolution of the shallow lying Messinian evaporites (Belderson et al., 1978). This relief creates hummocky hyperbolic acoustic reflections when using conventional echo sounding devices, and is known as “cobblestone topography “(Hersey, 1965).

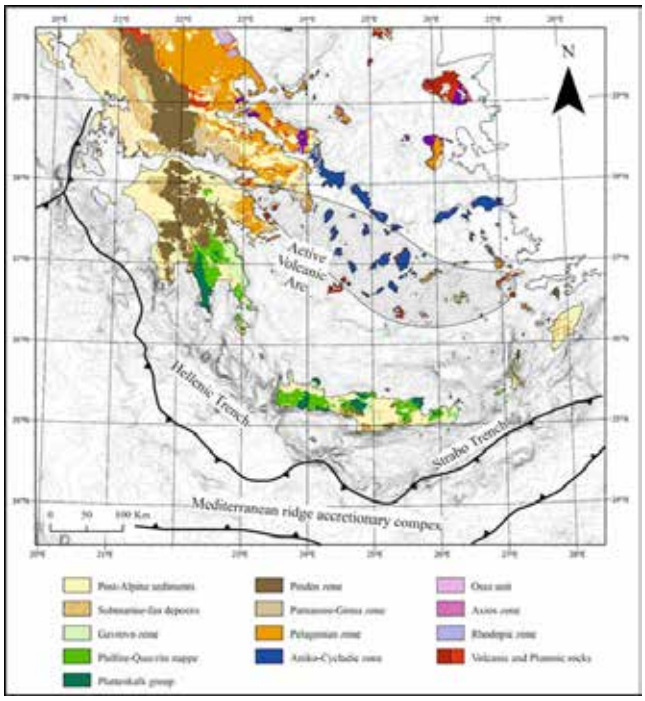

Figure 1. Geological map of southern Greece showing the geotectonic zones and especially the Plattenkalk series, Hellenic Trench and the Mediterranean Ridge (Maravelis et al., 2022).

The MR is characterized by mud diapirs, with the first Mud volcano (MV) identified on the Ridge was named Prometheus and is located southwest of Peloponnesus. MV and mud cones have since been identified and cored (Cita et al., 1989) in three other areas (Prometheus-2; Olimpi, and Pan di Zucchero) also located in the Inner portion of the crustal area of the M.R. accretionary complex. Seismic refraction data and expanding spread seismic reflection experiments, as well as gravity modeling, indicate that the MR consists of a thick (up to 10 km) pile of sediments (Truffert et al., 1993) representing a huge sedimentary accreted wedge (Kastens et al., 1992).

The subduction in the Hellenic trench is complex: in the west, where a frontal subduction takes place in the trench, only the lower level of the sedimentary cover is subducted while the upper one is scrapped off and accumulated in the giant accretionary prism, the M.R., which is under a strong compressional stress. East of 25°E the movement at the plate boundary becomes more of a left lateral displacement. The Pliny Trench, which is also a sinistral shear zone, is treated as the trace of an earlier stage of the subduction zone. Such a pattern of compressional and shear stresses defines the step-like plan shape of the H.T.S. (Huchon et al., 1982). The subduction began about 13 Ma ago in the Late Serravallian (Le Pichon and Angelier, 1979), and as a result, the residual Tethys oceanic basin has been closed completely between Crete and Cyrenaica. M.R. is a large sedimentary wedge involving the upper 4 km of the sedimentary basins. It has also been proposed that the present backstop had been formed in Middle Miocene time by the outward migration of the Hellenic nappes between 20 and 15 Ma (Le Pichon et al., 1982).

The aim of this study is to analyze the geological characteristics of this accretionary wedge system in order to reveal its possibility to be equivalent to the Apulian Platform and to become an important hydrocarbon province and to suggest parts for further research. Undoubtedly, information given in this study is a preliminary approach and further, in-depth research is required to define the petroleum prospectivity of this spectacular feature. Remote sensing, seismic and wireline log data, as well as cores and fluid samples from wells should be integrated to define the exact thickness and lateral extent of the possible seal, reservoir and source rocks, and the trap style.

Geological Setting

Southeast Mediterranean, from Crete Island as far as Libya territory, is characterized by the presence of nappes that overthrusted the authochonous Plattenkalk series, during Oligocene to early Miocene. South of Crete, the Hellenic Trench (HT) and the Mediterranean Ridge (MR) were developed during late Miocene. The MR accretion started at the same time as the HT system subduction began. By Messinian time, most of the MR had been formed already and rose above the neighboring abyssal plains. On the elevated portion of the MR, where fields of mud diapirs (volcanoes) have been discovered, the Messinian layer is significantly thinner than on its deeper southern flank.

The Plattenkalk series represent the autochthonous or para-autochthonous series outcropping in Gythion-Sparta region, south Peloponnesus, and along the Crete Island, and is considered as the equivalent to the Ionian zone. The PS is characterized as

high-pressure low temperature metamorphic series deposits, and comprise generally a carbonate sequence up to 5km thick that deposited in a period of about 300 m.y. The stratigraphy of the Ionian Basin (IB) in western Greece, and especially for the part of upper Triassic to lower Jurassic, consist of Triassic evaporites that pass upwards to Triassic breccia and the Foustapidima limestones and finally to Pantokrator limestones. Under the Triassic evaporites there are the Paleozoic deposits, but they don't outcrop in western Greece. According the literature it seems that the evaporitic breccia and Foustapidima limestones could be or could represent source rocks whereas the Pantokrator limestones represent the reservoirs.

In Gythion-Sparta region, PS consists of dolomites, crystalline limestones and massive marbles, up to 500m thick. These deposits are compared with Pantokrator limestones of western Greece, and rest unconformably over Permian? to lower Triassic Phyllite basement, with up to 500m thick outcropped deposits. The characteristic event for this region is 1. The absence of Triassic evaporites, and 2. The unconformably overlying of upper Triassic to lower Jurassic deposits to Paleozoic (Permian) deposits.

In Crete Island, PS consist of upper Carboniferous-lower Permian to Eocene age deposits. Metamorphic conditions took place during Oligocene to upper Miocene in HP-LT conditions. There are differences from west to east and from north to south. In detail Plattenkalk series consist of dolomites and dolomitic limestones with an outcropped thickness up to 800m (Iraklion and Rethymnon geological sheets). In middle Crete (Perama and Vrisses sheets) of dolomities and dolomitic limestones of upper Triassic to lower Jurassic, with up to 300m thickness, and banded recrystallized dolomitic stromatolites of middle Triassic, up to 150m thick (Perama sheet) or of recrystallized limestones to marbles and dolomites up to 100m thick (Vrysses sheet). In western Crete (Palaeohora sheet) of Upper Triassic variegated formation of schists, recrystallized limestones and quartzite, up to 100m thick, recrystallized limestones and dolomites, up to 300m thick, and Evaporites, with an outcropped thickness up to 300m. The characteristic regime in Crete is the High-pressure low temperature metamorphism of the entire rocks. This metamorphic conditions reduced from west to east of the Island. In Crete Island, there are two different assemblages, the autochthonous Ionian Basin deposits (Plattenkalk series and Phyllite-Quartzite series) and the allochthonous nappes of Tripolitsa, Pindos and Pelagonian zones. The Ionian Basin (IB) comprises Triassic clastic rocks overlain by Mesozoic limestone and late Eocene to Miocene flysch (~35–10 Ma) (Jacobshagen, 1986). The two main nappes making up the Ionian Basin are the P-Q and the underlying Plattenkalk, both of which constitute the high-P belt of the External Hellenides on the Peloponnese and Crete (e.g., Jolivet et al.; Marsellos et al., 2010; Papanikolaou & Vassilakis, 2010). The Cretan Detachment tectonically separates the non-high-P nappes from the underlying, 24–21 Ma high-P rocks of the Ionian Unit (Fassoulas et al., 1994; Jolivet et al., 1996; Kilias et al., 1994; Thomson et al., 1998).

The entire nappe pile has been thrust over the Mediterranean Ridge Accretionary Complex, which started to form at or before 19 Ma and was and still is being underthrust beneath Crete at the leading edge of the overriding plate (Kokinou et al., 2012; Kopf et al., 2003). The present crustal thickness of western Crete is ~ 40–50 km and the bottom 20–30 km of this crust are interpreted to be newly accreted sediments (Knapmeyer & Harjes, 2000). This suggests that high-P rocks are currently forming beneath Crete. Due to its enormous size, M.R. cannot be structured by a unique and stable stratigraphy. It is characterized by the absence of Triassic evaporites in contrast to the external Hellenides.

Several trap styles may be present within the potential M.R. petroleum province, including both structural and stratigraphic traps. Structural Traps may include traps formed by (1) compressive tectonic processes and (2) diapiric processes. Compressive tectonic processes commonly lead to the development of large-scale contractional folds and thrusts. Such contractions are common in convergent plate boundaries (e.g., M.R.) leading to the development of major trap anticlines. Diapiric processes lead to upward movement of both salt and mud can create anticlinal structures that could form petroleum traps. Stratigraphic Traps referred to the Messinian evaporites within the M.R. overly, either directly or unconformably, typical basinal, hemipelagic, pelagic, and turbiditic sediments can lead to the creation of truly massive traps (Maravelis et al., 2015).

Microfacies analysis

From both regions (Sparta-Gythion and Crete) has been selected thirty samples (eighteen samples from Sparta-Gythion and twelve samples from Crete) for micropaleontological analysis. The general description of the thin sections is that the samples are crystalline and metamorphosed and therefore no facies zone identification could be made. Specifically, only two samples from Crete Island have been recognized as evaporitic of brackish and Platform-margin sand shoals facies zones.

Facies analysis showed a platform environment within the Plattenkalk-Ionian basin. Although the evolution of the Ionian basin during the rift stage showed the presence of grabens and highs, until now we have not found any sample showing the platform environment in west Greece. Our explanation is that as normal faults, with east dipping direction, re-activated as thrust faults the platforms overstepped by the accretionally prisms, of the above thrusts, and now are lying under the pelagic limestones of the grabens.

Rock eval analysis

Total selected samples two hundred and five (205) for TOC analysis. Results organized into three different areas: Western Greece, Southwestern Peloponnese and Crete Island. All samples are organized into three-age time span: Paleozoic, Upper Triassic-Lower Jurassic (below Pantokrator limestones) and Upper Jurassic-Eocene.

These results showed in general that samples are poor in TOC content, but taking into account the fact that the Plattenkalk series

is strongly metamorphosed, the presence of at least twenty samples with high TOC content in specific areas lead us to study in detail the above areas.

Approaching the basin evolution

In light of our results two scenarios were build up, the first scenario that is proposed consider that the PS deposits further to the west and south of the Crete Island, if exist, could represent a potentially new source rocks, due to the burial history differences, and furthermore in metamorphic conditions. Hellenic Trench could be the equivalent of the Apulian Platform Margins; whereas Mediterranean Ridge could be a platform, equivalent to the Apulian Platform.

Therefore, the areas west of Sparta-Gythion region and south of Crete Island could represent the equivalent to APM in western Greece, and as a result, the nappes could wedged out or partly overstepped the Platform Margins. The above fact shows different elevation indicating lower metamorphic conditions in the Hellenic Trench and probably without metamorphic conditions in the Mediterranean Ridge.

According to Palamakumbura, et al. (2012), who deals with the Geochemical, sedimentary and micropaleontological evidence for a Late Maastrichtian oceanic seamount within the Pindos Ocean (Arvi Unit, S Crete, Greece), the presence of Apulian Plate is shown south of the existing Ionian Basin (mentioned as Ida-Ionian through) during Cretaceous time.

In the same sense, Accordi et al. (2014) presented in their figure 1a the presence of the African plate west of the Hellenic arc.

Therefore, for this first scenario, the indicated models for deformation – movements presented in figure 2 are: A: for West Greece, B: for Peloponnesus (Pylos area) and C: for west Crete Island).

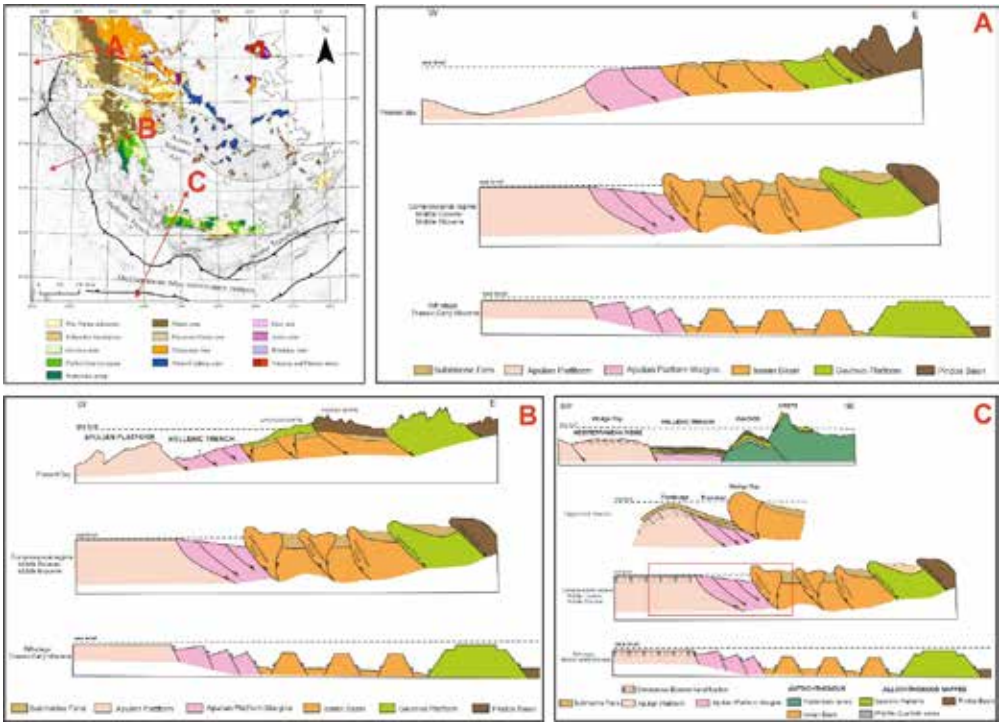

Figure 2. Indicated models for the deformation – nappes movements: A. for West Greece, B for Peloponnesus (Pylos area) and C for west Crete Island).

The application of this scenario for the Pylos region (Figure 3) introduce that parts from Gavrovo platform Pindos unit, must be nappes that moved from east to west and rest now unconformably over the Ionian basin.

The second scenario, supported from few evidences, is that Mediterranean Ridge could corresponds to the external Ionian sub-basin, as this presented for west Greece, and Crete Island the middle Ionian sub-basin (there are not data for Sparta-Gythion areas).

The facts that support this idea are: Crete Island was uplifted during Oligocene as the accretionally prism of a thrust fault, equivalent with middle Ionian sub-basin in western Greece. Therefore, the nowadays-Hellenic Trench could be the foreland basin of the middle Ionian thrust. Later and as the subduction migrated southwards during middle Miocene the MR representing the accretionary prism of this subduction could be equivalent to the external Ionian sub-basin in the west Greece.

The second scenario, supported from few evidences, is that Mediterranean Ridge could corresponds to the external Ionian sub-basin, as this presented for west Greece, and Crete Island the middle Ionian sub-basin (there are not data for Sparta-Gythion

areas).
The facts that support this idea are: Crete Island was uplifted during Oligocene as the accretionally prism of a thrust fault, equivalent with middle Ionian sub-basin in western Greece. Therefore, the nowadays-Hellenic Trench could be the foreland basin of the middle Ionian thrust. Later and as the subduction migrated southwards during middle Miocene the MR representing the accretionary prism of this subduction could be equivalent to the external Ionian sub-basin in the west Greece.

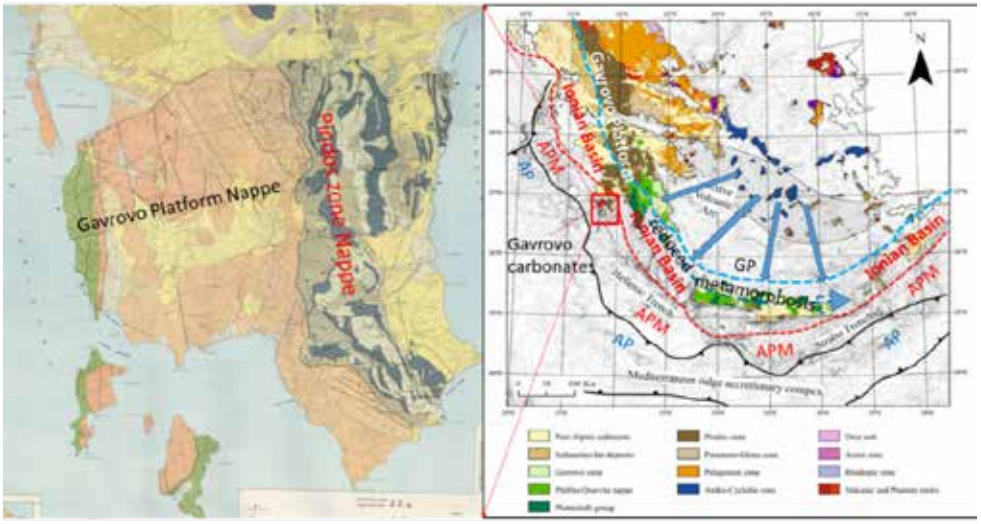

Figure 3. Geological of southwest Peloponnesus (Pylos region), where both Gavrovo and Pindos units overstepped the Ionian unit.

Support to this scenario is the fact that from the only two-studied thin section it seems that Crete Island Mesozoic sequence represents shallow water deposits and not deep-water conditions.
If this scenario will be acceptable then it is clear that:
1. The width of the Ionian basin was at least double in size in Crete in relation with the western Greece, and could be the original width of the Ionian basin.
2. The Ionian basin, during rifting stage was sub-divided into grabens and highs,
2. The nappes in Crete overstepped the Ionian basin without to shorten it and for this reason, some of the Ionian basin highs outcropped in Crete. The explanation of the highs absence in western Greece is that due to thrust activity the highs overstepped and now lies under the accretionary prism, beneath the mountains.

Conclusion.

A. Tethys during upper Triassic to lower Jurassic represent a shallow restricted basin, and analysis of the deposits from southern Peloponnesus and Crete Island, indicate that Tethys in the studied areas was very narrow. It seems that the above studied areas were very close to brackish conditions, where there was a high concentration of organic matter, and for this reason, it shows some differences in the bitumen content from the other areas. During upper Jurassic to Eocene, the basin is characterized by rifting with Ionian Basin sub-division into three sub-basins with characteristics of grabens and highs.
B. The Ionian basin width, in the area of nappe presence, is wider than in the western Greece where the basin shorted due to the compression of the Hellenic orogeny.
C. Plattenkalk series samples are strongly recrystallized, in all regions, although they present different metamorphic influences.
D. Rock-eval analysis, in all studied samples, organized into three different time spans: Paleozoic, Upper Triassic-Lower Jurassic, Jurassic-Eocene, could serve as source rocks. The underlying the metamorphic Plattenkalk series, the Paleozoic deposits, showed that there are many black horizons with high TOC content, in some of them. The fact that many black horizons are poor in TOC content could be related with the metamorphic conditions (high temperature values). The Upper Triassic-Lower Jurassic sequence (as far as Pantokrator limestones) was studied for Triassic breccia and Foustapidima limestones, and showed that there are quite interesting horizons in the studied areas. In detail, in Crete Island the richest deposits referred to the Triassic breccia, in the western part of the Island, and the Foustapidima limestones to the northern part of the Island. The Upper Jurassic-Eocene sequence, was studied for the Jurassic schists with Posidonia and the Cretaceous (Vigla shales), and showed that there are many rich horizons and especially in the areas of probably lower metamorphosis such as the eastern part of Southwestern Peloponnese and the Northern part of Crete Island, probably due to lower metamorphic conditions.
E. As the key points for the MR and the HT are their evolutionary conditions, during the compressional phases, it is very crucial for oil companies (in this case for EXXON and CHEVRON Oil Companies) to understand the depositional conditions of the HT

and MR, both during the syn-rift stage and the compressional phases. The question we tried to answer is about the nappes movements and the areas that they covered. The nappes overstepped the HT (when they were the APM) and covered the MR (when they were the AP) or the nappes stopped in the HT and never covered the MR.
F. Therefore the M.R. could be the equivalent Apulian Platform or could be the external Ionian sub-basin basement, and the Hellenic Trench could be equivalent with Apulian Platform Margins or represents the middle Ionian sub-basin foreland basin during Oligocene.

Acknowledgements
We would like to thank HEREMA for the research project economic support.

References

Accordi, G., Carbone, F., Di Carlo, M., Pignatti, J. 2014. Microfacies analysis of deep-water breccias clasts: A tool for interpreting shallow-vs. deep-ramp Paleogene sedimentation in Cephalonia and Zakynthos (Ionian Islands, Greece). Facies 60, 445–466.
Belderson, R. H., Kenyon, N. H., Stride, A. H. 1978. Local submarine salt-karst formation on the Hellenic Outer Ridge, eastern Mediterranean. Geology 6, 716–720.
Cita, M. B., Camerlenghi, A., Erba, E., McCoy, F. W., Castradori, D., Cazzani, A., Guasti, G., Giambastiani, M., Lucchi, R., Nolli, V., Pezzi, G., Redaelli, M., Rizzi, E., Torricelli, S., Violanti, D. 1989. Discovery of mud diapirism in the Mediterranean Ridge: A preliminary report. Boll. Soc. Geol. Ital. 108, 537−543.
Fassoulas. C. 2001. The tectonic development of a Neogene basin at the leading edge of the active European margin: the Heraklion basin, Crete, Greece, J. Geodynamics 31, 49-70.
Flügel, E. 2004. Microfacies Analysis of Carbonate Rocks. Springer: Berlin, Germany.
Hersey, J.B. 1965. Sedimentary basins of the Mediterranean Sea. 17th Symposium Colston Res. Sot. (Colston Pap., VII). Bristol, England: University of Bristol, pp. 75–91.
Huchon, Ph., Lyberis, N., Angelier, J., Le Pichon, X., Renard, V. 1982. Tectonics of the Hellenic Trench: A synthesis of the Sea-Beam and submersible observations. Tectonophysics 86, 69–112.
Jacobshagen V. 1986. Geologie Von Griechenland, Borntraeger, Berlin-Stuttgart.
Jackson, J.A., Haines, J.A., Holt, W.E. 1992. The horizontal velocity field in the deforming Aegean Sea region determined from the moment tensor of earthquakes. J. Geophys. Res. 97, 17657–17684.
Jolivet, L., Goffé, B., Monié, P., Truffert-Luxey, C., Patriat, M., Bonneau, M., 1996. Miocene detachment in Crete and exhumation P-T-t paths of high-pressure metamorphic rocks. Tectonics 15(6), 1129-1153.
Knapmeyer, M., Harjes, H-P., 2000. Imaging crustal discontinuities and the downgoing slab beneath western Crete. Geophysical Journal International 143(1), 1–21.
Kastens, K.A., Nancy, A.B., Cita, M.B., 1992. Progressive deformation of an evaporites-bearing accretionary complex: Sea-Marc I, Sea Beam and Piston core observations from the Mediterranean Ridge. Marine Geophys. Res. 14, 249–298.
Kilias, A., Fassoulas, C., Mountrakis, D., 1994. Tertiary extension of continental crust and uplift of Psiloritis metamorphic core complex in the central part of the Hellenic Arc (Crete, Greece). Geol Rundsch 83, 417 -430.
Kokinou, E., Kamberis, E., Vafidis, A., Monopolis, D., Ananiadis, G., Zelilidis, A., 2005. Deep seismic reflection data from offshore western Greece: a new crustal model for the Ionian Sea. Journal of Petroleum Geology 28, 185–202.
Kopf, A., Mascle, J., Klaeschen, D., 2003 The Mediterranean Ridge: A mass balance across the fastest growing accretionary complex on Earth. J. Geoph. Res. 108 (B8), pp.2372.
Leite, O., Mascle, J., 1982. Geological structure of the south Cretan continental margin and Hellenic trench. Marine Geol. 49, 199-223.
Le Pichon, X., Angelier, J., 1979. The Hellenic Arc and trench system: A key to the neotectonic evolution of the Eastern Mediterranean area. Tectonics 60, 1–42.
Le Pichon, X., Lybtris, N., Angelier, J., Renard, V., 1982. Strain distribution over the East Mediterranean Ridge: A synthesis incorporating new Sea-Beam data. Tectonophysics 86, 243–274.
Maravelis, A., Manutsoglou, E., Konstantopoulos, P., Pantopoulos, G., Makrodimitras, G., Zoumpoulis, E., Zelilidis, A., 2015. Hydrocarbon plays and prospectivity of the Mediterranean ridge. Energy Sources, Part A: Recovery, Utilization, and Environmental Effects 37, 347–355.
Maravelis, A.G., Kontakiotis, G., Bellas, S., Antonarakou, A., Botziolis, C., Janjuhah, H.T., Makri, P., Moissette, P., Cornée, J.-J., Pasadakis, N., Manoutsoglou, E., Zelilidis, A., Karakitsios, V. 2022. Organic Geochemical Signatures of the Upper Miocene (Tortonian— Messinian) Sedimentary Succession Onshore Crete Island, Greece: Implications for Hydrocarbon Prospectivity. J. Mar. Sci. Eng. 2022, 10, 1323.
Marsellos, A.E., Kidd, W.S.F., Garver, J.I., 2010. Extension and exhumation of the HP/LT rocks in the Hellenic forearc ridge. American Journal of Science 310(1), 1-36
Olivet, J.L., Bonnin, J., Beuzart, P., Auzende, J.M., 1982. Cinematique des plaques et paleogeographie: Une revue. Geol. Soc. France Bull. 24, 875–892.
Palamakumbura, R.N., Robertson, A.H.F., Dixon, J.E., 2013. Geochemical, sedimentary and micropaleontological evidence for a Late Maastrichtian oceanic seamount within the Pindos Ocean (Arvi Unit, S Crete, Greece). Tectonophysics V. 595–596, p. 250-262.
Papanikolaou, D., Vassilakis, E., 2010. Thrust faults and extensional detachment faults in Cretan tectono-stratigraphy: Implications for Middle Miocene extension. Tectonophysics 488, 233-247.
Truffert, C., Chamot-Rooke, N., Lallemant, S., De Voogd, B., Huchon, P., Le Pichon, X., 1993. The crust of the Western Mediterranean Ridge from deep seismic data and gravity modelling. Geophys. J. Int. 114, 360–372.
Thomson, S.N., Stockhert, B., Brix, M.R., 1998. Thermochronology of the high-pressure metamorphic rocks of Crete, Greece: Implications for the speed of tectonic processes. Geology 26(3), 259-262.

17th INTERNATIONAL CONGRESS of the Geological Society of Greece

BULLETIN OF THE GEOLOGICAL SOCIETY OF GREECE, SP. PUBL.

EXTENDED ABSTRACT 351

The trace fossil *Zoophycos* as an indicator for the Apulian Platform Margins evolution during Eocene in Lefkas Island

Zelilidis P.[1], Uchman A.[2], Iliopoulos G.[1], Dalgkitsi P.[3], and Bourli N.[3]

(1) University of Patras, Department of Geology, Laboratory of Paleontology and Stratigraphy 26504, Patras, Greece. zelilidis2001@gmail.com, (2) Faculty of Geography and Geology Institute of Geological Sciences, Jagiellonian University, Gronostajowa 3a, 30-387 Kraków, Poland., (3) University of Patras, Department of Geology, Laboratory of Sedimentology, 26504, Patras, Greece.

The Apulian Platform Margin (APM), situated between the Apulian Platform to the west and the Ionian Basin to the east, are outcropped in Lefkas Island, on the Ionian Sea, and are characterized by the presence of Jurassic to Eocene deposits. During the middle Miocene, the Ionian Thrust activity produced narrow foreland basins between the Ionian Basin and the Apulian Platform, where carbonate sub-marine fan deposits were accumulated. The APM representing the forebulge area of the Ionian foreland was strongly deformed. The studied section with a NE-SW direction is cross cut by many faults. Some of the faults showed synsedimentary activity and were responsible for the deformation within the outcrops. Bedding planes present an eastward dipping direction, up to 70° angle. In the studied Eocene carbonates, up to 400 m total thickness, the facies analysis showed the presence of four different types of deposits, i.e., pelagic calcilutites, calcarenites, and debris flow deposits. All of them accumulated in slope and toe of slope facies zones. Their microfacies point to deep sea conditions. Additionally, there are also breccia with angular clasts, indicating an active tectonics and very close source. The presence of siliceous concretions within the carbonates supports the above suggestion. Small lenses of red granule-size breccia, with abundant calcareous algae indicate also a proximity of a platform source. The trace fossils *Trichichnus*, ?Palaeophycus, *Zoophycos*, crinoids and nummulites in calcarenites were recognized. The *Zoophycos* appearance, with normal and reverse positions led to the sub-division of the sedimentary succession into two parts (both up to 200 m thick), the lower one with the normal position, and the upper one with the reverse position. The upper part probably reversed due to an intense giant slumping event during the sedimentation, indicating that the deformation of the APM started earlier than the middle Miocene, time of the Ionian Thrust activity. Although Eocene was characterized by deep-sea conditions, the normal fault activity produced many tectonic pulses with the development of slumps and slides, close to the Apulian Platform. Due to this fault activity, diverse sedimentary material (e.g., large foraminifers) was transported from the close extended platform to the slope or to the toe of the slope.

Key words: slope facies, carbonates, Eocene, Greece.

17th INTERNATIONAL CONGRESS of the Geological Society of Greece

BULLETIN OF THE GEOLOGICAL SOCIETY OF GREECE, SP. PUBL.

EXTENDED ABSTRACT 352

New results on the Miocene gymnosperm fossil wood of Lesvos Petrified Forest, Lesvos Island, Greece, and its palaeoenvironment significance

Yanbin Zhu[1], Yongdong Wang[2*], Nikolaos Zouros[3, 4*]

(1) Nanjing Center, China Geological Survey, Nanjing 210016, China, (2) Nanjing Institute of Geology and Palaeontology, Chinese Academy of Sciences, Nanjing 210008, China, (3) Department of Geography, University of the Aegean, Mytilene 81103, Greece, (4) Natural History Museum of the Lesvos Petrified Forest, Sigri, Lesvos 81103, Greece

Abstract

This paper briefly reports the new results on Miocene gymnosperm fossil wood assemblages from Lesvos, including two families and nine genera: Tsuga, Pseudotsuga, Keteleeria, Larix, Pinus, Lesbosoxylon (Pinaceae), Metasequoia, Sequoia, Taxodium (Cupressaceae). Among them, Pinaceae exhibits the highest taxonomic richness, Pseudotsuga, Keteleeria and Metasequoia were found in Greece for the first time. At present, the Lesvos fossil wood flora is one of the Miocene wood floras with highest diversity found in Greece and even in the Mediterranean, which enriches the fossil record of gymnosperms in the Miocene of Greece. The occurrence of abnormal growth rings and traumatic resin canals in Lesvos fossil woods reflects the short-term climate fluctuations, natural hazards or the interaction between plants and the associated organisms in the forest ecosystem. Further study of this fossil wood flora will provide important evidence for understanding the evolution and development history of modern gymnosperms in the Mediterranean as well as their palaeoenvironment and palaeoclimate background.

Key words: Lesvos Petrified Forest, Miocene, Fossil wood, Gymnosperm, Palaeoenvironment

1 Introduction

Plant fossils constitute exceptional archives for investigating terrestrial ecosystem dynamics and palaeoenvironmental evolution throughout geological history. As durable biogenic structures, they provide critical evidence for reconstructing palaeoclimatic parameters and vegetation responses to environmental shifts (Creber and Francis, 1999; Wang *et al*., 2017). Among various fossil plant remains, fossil wood plays a vital role in exploring the composition characteristics and evolutionary history of fossil floras (Creber and Francis, 1999).

The Lower Miocene petrified forest of Lesvos Island (39°12'N, 26°18'E) (Fig. 1A), preserved within pyroclastic deposits of the North Aegean volcanic province, represents one of the most extensive in situ fossil wood assemblages in the Mediterranean realm (Zouros *et al*., 2004, 2007, 2011; Pe-Piper *et al*., 2019; Zhu *et al*., 2021). This extraordinary preservation event resulted from the rapid burial of standing forests by volcanic ejecta during the Burdigalian (Pe-Piper *et al*., 2019), yielding three-dimensional specimens with intact cellular structures and root systems–a taphonomic phenomenon rarely observed in continental depositional settings.

This study presents a systematic analysis of conifer fossil wood from the new fossil sites along the Kalloni-Sigri road, aiming to: 1) establish taxonomic affinities through quantitative anatomical comparisons, 2) reconstruct the structural composition of Burdigalian forest communities.

2 Geological setting and stratigraphy

The Lesvos Petrified Forest, designated as one of the first 4 European Geoparks in 2000, and a Global Geopark since 2004 preserves one of the world's most remarkable examples of three-dimensional silicified forest ecosystems (Zouros, 2010, 2021). The Lesvos Petrified Forest is the main geological heritage monument of international significance that led to the recognition of Lesvos Island as an UNESCO Global Geopark in 2015. This palaeobotanical Lagerstätte is embedded within the Sigri Pyroclastic Formation (Lower Miocene, ~20–18 Ma), a volcaniclastic succession spanning over 200 m thick that records forest burial events across western Lesvos (i.e. Bali Alonia, Plaka, Nissiopi sites) (Fig. 1B) (Zouros *et al*., 2004, 2007; Zouros, 2004, 2010; Pe-Piper *et al*., 2019). Recent investigations along the Kalloni-Sigri transect have expanded the known spatial extent of fossiliferous outcrops, revealing nine new sublocalities with exceptional stem-root junction preservation (Zouros, 2021; Kafetzidou *et al*., 2022, Zhu, 2024). These discoveries confirm the Sigri Formation as containing the most extensive in situ fossil assemblages in the Aegean region.

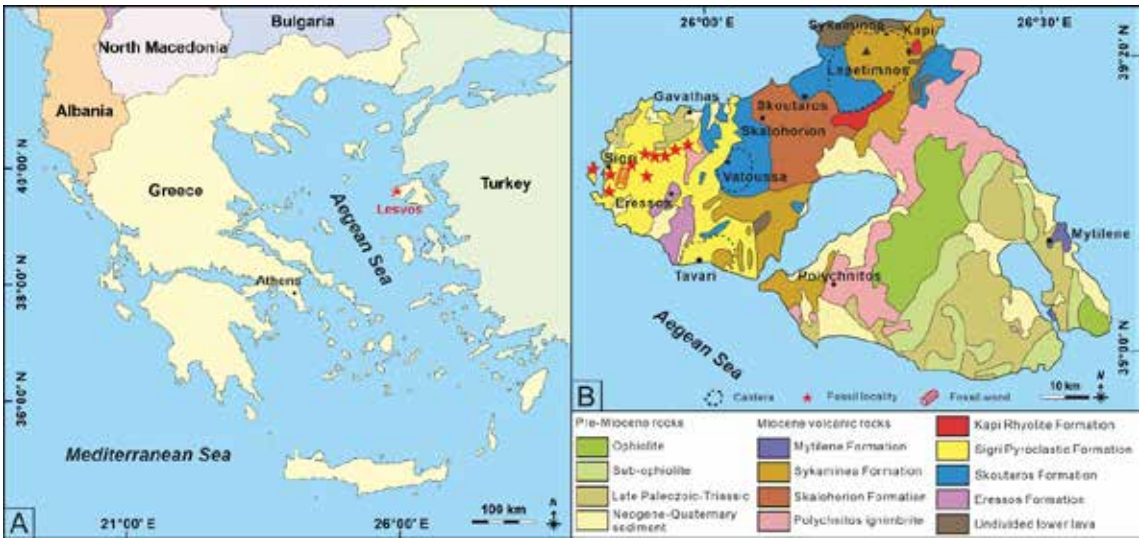

Figure 1. Geographical and geological maps of the fossil locality in Lesvos Island, Greece.
A. Map showing the specific fossil locality within Lesvos Island, Greece (Base map from d-maps (https://d-maps.com)); B. Geological map of the Lesvos Island (Base map modified from Pe-Piper *et al*., 2019).

3 Materials and methods

The fossil woods described in this study were preserved as permineralized wood. They were collected from the Lower Miocene Sigri Pyroclastic Formation in the Lesvos Petrified Forest, Greece. The thin sections in this study were processed by the Natural History Museum of the Lesvos Petrified Forest during the period from 2014 to 2021, and they consist mainly specimens from the fossiliferous sites along the newly excavated Kalloni-Sigri road, this investigation discusses and presents preliminary results for gymnosperms only. Transversely, radially, and tangentially cuts were applied to the investigated petrified wood specimens for preparing thin sections (Hass and Rowe, 1999; Zheng *et al*., 2008). Thin sections were examined under an optical microscope, and photographs were captured based on OPTIKA P20 Pro camera and OPTIKA LITEVIEW software attached to the OPTIKA B-510POL-1 microscope. Anatomical characteristics and geological maps were illustrated and organized with CorelDRAW 2019. All fossil wood and thin sections are housed at the Natural History Museum of the Lesvos Petrified Forest, Lesvos Island, Greece. The descriptive terminology utilized in this study adheres to the recommendations of the International Association of Wood Anatomists (IAWA) Committee (2004).

4 Results

After identification, it can be concluded that the conifer fossil wood assemblages of the Lesvos Petrified Forest contain 9 genera of 2 families: *Tsuga*, *Pseudotsuga*, *Keteleeria*, *Larix*, *Pinus*, *Lesbosoxylon* of the Pinaceae, and *Metasequoia*, *Sequoia*, *Taxodium* of the Cupressaceae.

Systematic Palaeontology

Division: Gymnospermae Prantl, 1831

Family: **Pinaceae** Lindley, 1836

Genus: ***Tsuga*** Carrière, 1855

***Tsuga* sp.**

Description: Specimen number BPY061, Figure 2A–C. Growth ring is distinct, a sharp change from earlywood to latewood, a large number of continuous traumatic resin canals present in the latewood band (Fig. 2A), earlywood tracheids square and polygonal, the latewood band 8–20 cells wide, with a thick, oblong cell wall, with abundant axial parenchyma, tangentially zonate and marginal (Fig. 2A). Earlywood tracheid pitting in radial walls are uniseriate and biseriate, mostly biseriate opposite, crassulae present (Fig. 2B), cross-field pits are cupressoid, also pinoid, 4–6 pits per cross-field (Fig. 2B). Rays uniseriate, ray heights 1–25, mostly 5–18 (Fig. 2C), normal resin canals absent.

Genus: ***Pseudotsuga*** Carrière, 1867

***Pseudotsuga* sp.**

Description: Specimen number TX272, Figure 2D–F. Growth rings are weakly defined, tracheids of the early wood are large and polygonal and thin-walled, axial resin canals are present within the earlywood layer, displaying single distribution along with 8–12 thick-walled epithelial cells (Fig. 2D). The cross-field pit arrangement is piceoid type,

occasionally taxodioid type, the bordered pits on the tracheid walls belong to the abietinean type and are predominantly uniseriate and spaced at a distance (Fig. 2E). Furthermore, longitudinal tracheids show well-developed single and narrowly spaced helical thickenings, with a density of 150–200 coils per millimeter (Fig. 2D, 2E). Rays are uniseriate and fusiform, uniseriate rays in height from 1–13 cells (Fig. 2F).

Genus: ***Keteleeria*** Carrière, 1866

***Keteleeria* sp.**

Description: Specimen number TX302, Figure 2G–I. Growth ring is indistinct with extremely curved abnormal growth ring (Fig. 2G), axial resin canals are present within the earlywood layer, displaying single distribution (Fig. 2G). The cross-field pit arrangement is cupressoid type, occasionally taxodioid type, the bordered pits on the tracheid walls are indistinct (Fig. 2H). Rays are uniseriate in height from 1–30 cells, radial resin canals absent (Fig. 2I).

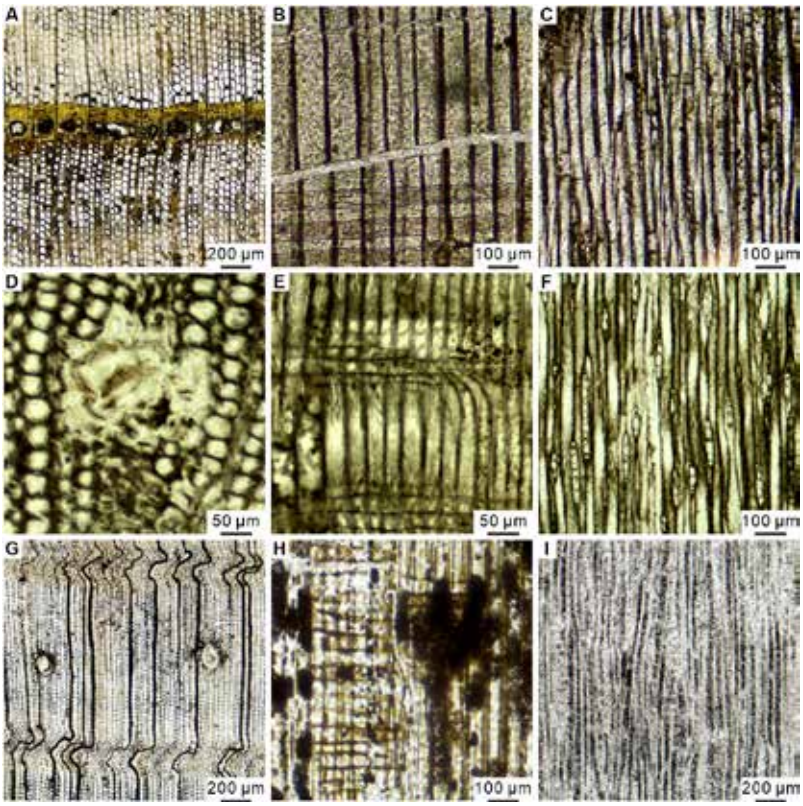

Figure 2. Anatomical characteristics of fossil wood *Tsuga* sp. (A–C, Specimen number BPY061), *Pseudotsuga* sp. (D–F, Specimen number TX272), and *Keteleeria* sp. (G–I, Specimen number TX302) from Lesvos Petrified Forest

Genus: ***Larix*** Miller, 1754

***Larix* sp.**

Description: Specimen number NBA155, Figure 3A–C. Growth rings are distinct, abrupt transition from earlywood to latewood, the presence of a large number of continuous axial resin canals in the latewood band (Fig. 3A), earlywood tracheids square and polygonal, the latewood band 4–8 cells wide, with a thick, oblong cell wall (Fig. 3A). Earlywood tracheid pitting in radial walls are uniseriate and biseriate, mostly biseriate opposite, crassulae present (Fig. 3B), cross-field pits are taxodioid and piceoid, 2–5 pits per cross-field (Fig. 3C). Tangential section absent.

Genus: ***Pinus*** Linné, 1753

***Pinus* sp.**

Description: Specimen number BPY062, Figure 3D–G. Growth rings are distinct, abrupt to gradual transition from earlywood to latewood, axial resin canals present in the latewood band (Fig. 3D), earlywood tracheids are polygonal, the latewood band 4–15 cells wide, with a thick, oblong cell wall (Fig. 3D). Earlywood tracheid pitting in radial walls are predominantly uniseriate, occasionally biseriate, crassulae absent (Fig. 3E, 3F), cross-field pits are window-like, 2–3 pits per cross-field (Fig. 3E). Rays are uniseriate and fusiform with radial resin canals (Fig. 3G).

Genus: ***Lesbosoxylon*** Süss *et* Velitzelos, 2010

***Lesbosoxylon* sp.**

Description: Specimen number TX022, Figure 3H–J. Growth ring is indistinct, earlywood tracheids square-oblong to

polygonal, axially normal resin canals present, resin canals mostly single rounded, scattered in earlywood band (Fig. 3H). Tracheid pitting in radial walls with uniseriate and biseriate, uniseriate detached rounded, biseriate opposite, cross-field pitting commonly pinoid occasionally taxodioid, with a common of 2–6 (2–4) pits per cross-field (Fig. 3I). Rays were mainly uniseriate, fusiform with enlarged secretory cells, and a few fusiform with resin canals (Fig. 3J).

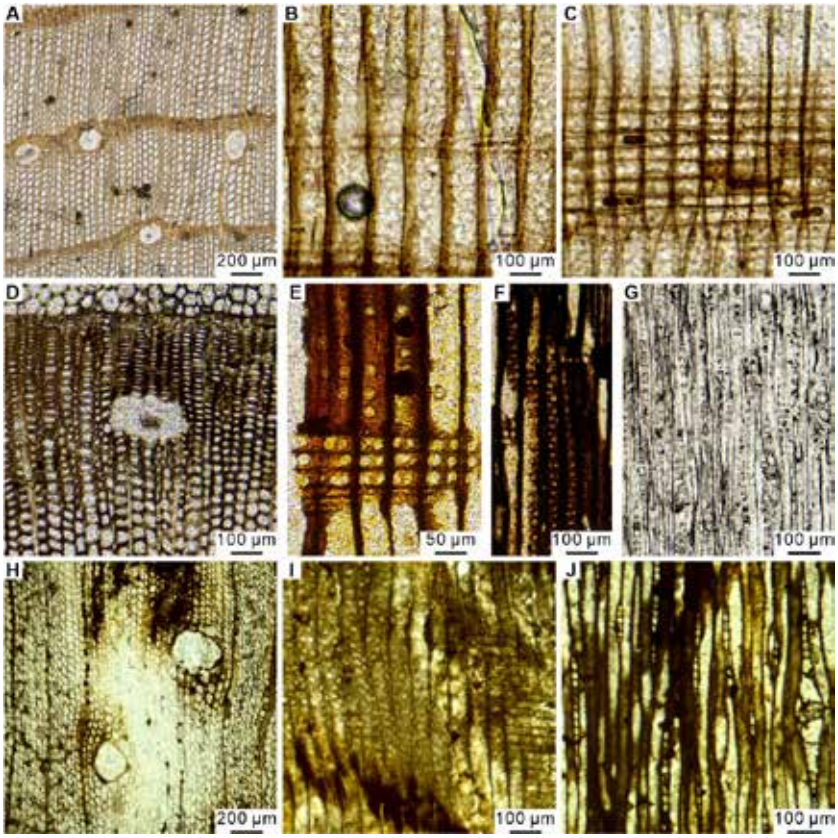

Figure 3. Anatomical characteristics of fossil wood *Larix* sp. (A–C, Specimen number NBA155), *Pinus* sp. (D–G, Specimen number BPY62), and *Lesbosoxylon* sp. (H–J, Specimen number TX022) from Lesvos Petrified Forest

Family: **Cupressaceae** Bartling, 1830

Genus: ***Metasequoia*** Miki ex Hu *et* Cheng, 1941

***Metasequoia* sp.**

Description: Specimen number TX024, Figure 4A–E. Growth ring is obvious and transition from earlywood to latewood is gradual (Fig. 4A). The early wood tracheids are mostly square polygonal, and no resin canals are observed, the late wood band is very narrow, only 1–3 tracheids wide (Fig. 4A). Cross-field pitting taxodioid, 1–6 (mostly 2–3) pits per cross-field (Fig. 4B). The bordered pits on the radial walls in 1–3 seriates, mostly opposite in 2–3 seriates (Fig. 4C, 4D). Rays are mostly uniseriate, 1–60 cells in height, mostly 6-30 cells high (Fig. 4E).

Genus: ***Sequoia*** (David Don) Endlicher, 1847

***Sequoia* sp.**

Description: Specimen number TX047, Figure 4F–I. Growth ring is evident and transition from earlywood to latewood is abrupt (Fig. 4F). The early wood tracheids are mostly square polygonal, axial parenchyma rare, traumatic resin canals present (Fig. 4F). Cross-field pitting is taxodioid, 2–4 pits per cross-field (Fig. 4G). The bordered pits on the radial walls in 1–3 seriates, mostly opposite in 2–3 seriates (Fig. 4H). Rays are mostly uniseriate, 1–50 cells in height, mostly 6-30 cells high, occasionally ray up to 12 cells wide (Fig. 4I).

Genus: ***Taxodium*** Richard, 1810

***Taxodium* sp.**

Description: Specimen number TX301, Figure 4J–M. Growth ring is distinct and transition from earlywood to latewood is abrupt, the early wood tracheids are mostly square and oblong, axial parenchyma abundant, diffuse, and tangentially zonate and marginal (Fig. 4J). Cross-field pitting is taxodioid and piceoid, 2–4 pits per cross-field (Fig. 4K). The bordered pits on the radial walls are uniseriate to triseriate, mostly opposite in 2–3 seriates (Fig. 4L). Rays are mostly uniseriate, 1–40 cells in height, mostly 3–20 cells high (Fig. 4M).

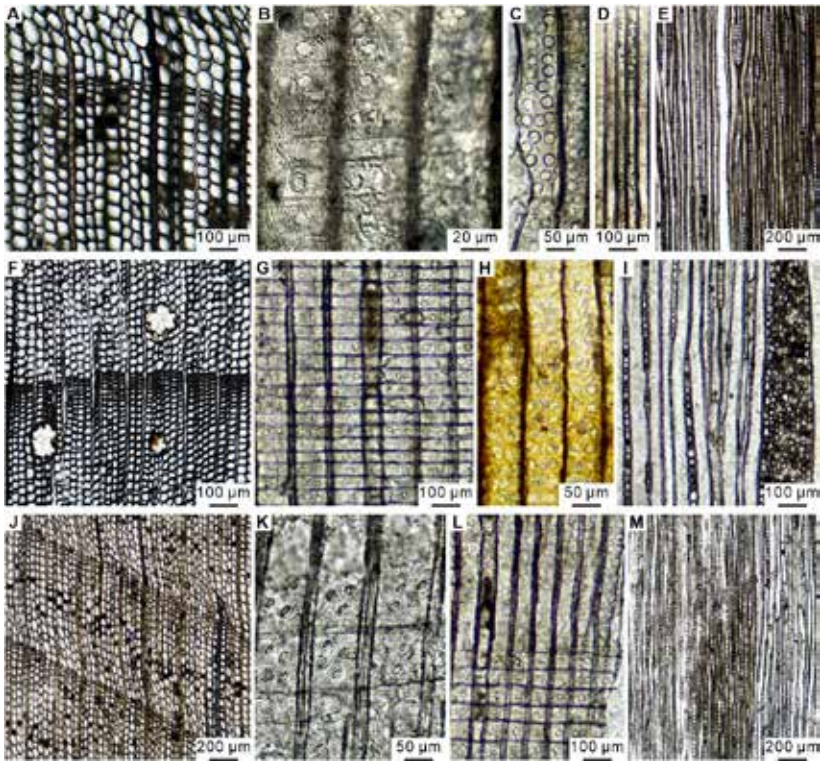

Figure 4. Anatomical characteristics of fossil wood *Metasequoia* sp. (A–E, Specimen number TX024), *Sequoia* sp. (F–I, Specimen number TX047), and *Taxodium* sp. (J–M, Specimen number TX031) from Lesvos Petrified Forest

5 Discussion

5.1 Palaeobiogeographic implications of gymnosperm diversification

The Mediterranean region is one of the Northern Hemisphere regions with the richest fossil records of Cenozoic gymnosperms. In this investigation in the Lesvos Petrified Forest, 9 genera from 2 families of gymnosperms fossil wood were identified, and among of them, *Pseudotsuga*, *Keteleeria*, and *Metasequoia* are first occurrences at Lesvos Petrified Forest. Today, *Pseudotsuga* is discontinuously distributed in western North America and East Asia (Farjon and Filer, 2013; Zhu *et al*., 2025), *Keteleeria* is endemic to East and Southeast Asia (Farjon and Filer, 2013), and *Metasequoia* is a relict genus, distributed only in southwestern China (Farjon and Filer, 2013). The fossil gymnosperm wood assemblage is similar to the modern flora of western North America (Farjon and Filer, 2013).

Current results not only further enrich the biodiversity of the fossil flora in the Petrified Forest of Lesvos, Greece, but also provides insights into the origin and evolutionary trend of the fossil flora. Additionally, it contributes to the fossil record and provides additional evidence for their palaeogeographical distribution range.

5.2 Growth rings of fossil wood and palaeoenvironment

Modern wood anatomy research shows that the appearance of abnormal growth rings is related to climate change and natural disasters (Gou and Feng, 2021; Cheng *et al*., 2023). For example, the occurrence of narrow or missing rings may be associated with wildfires that burn tree crowns and thus interrupt the radial growth of growth rings in the year that the fire occurred (Ortloff, 1996; Cheng *et al*., 2023). The occurrence of extreme drought or insect damage during the growth of trees can lead to the appearance of false growth rings (Creber *et al*., 1984; Cheng *et al*., 2023). Traumatic resin canals (Fig. 2A), abnormal growth rings (Fig. 2G) and traces of arthropod feeding (Fig. 4F) were observed in some fossil wood.

The above phenomenon reflects the impact of climate change, natural disasters, and arthropods in the forest on the growth process of plants during tree growth. This shows that Lesbos Island developed an extremely complicated environment during the Miocene Epoch.

6 Conclusion

Lesvos Petrified Forest is one of the richest Miocene fossil wood assemblages in Greece and even in the Mediterranean. This study enriches the Greek Cenozoic gymnosperm fossil record and provides important evidence for understanding the plant diversity in the Mediterranean region.

The abnormal growth rings, traumatic resin canals and arthropod feeding traces in this fossil wood group provide significant fossil evidence for understanding the palaeoclimate fluctuations, palaeoenvironment and the interaction between organisms in this forest ecosystem during the Miocene.

7 Acknowledgments

We express our gratitude to the Natural History Museum of the Lesvos Petrified Forest for the permission to conduct research activities in the new fossil sites of the Lesvos Petrified Forest, and for the study of the fossils and thin sections of the fossil wood. We also express our sincere thanks to the researchers and technical staff of the Natural History Museum of the Lesvos Petrified Forest for their support and collaboration in the field survey.

8 References

Cheng, Y., Wang, X., Chen, X., Liu, F., 2023.The Early Cretaceous woods in Yichun: Evidence for conifer diversity and Palaeoenvironment significance. Acta Geologica Sinica 97 (3), 661–671.

Creber, G.T., Chaloner, W.G., 1984. Environmental significance of wood structure in living and fossil trees. The Botanical Review 50, 357–448.

Creber, G.T., Francis, J.E., 1999. Fossil tree-ring analysis: Palaeodendrology. In: Jones, T.P., Rowe, N.P. (Eds.), Fossil Plants and Spores Modern Techniques. London: The Geological Society of London 245–250.

Farjon, A, Filer, D., 2013. An atlas of the world's conifers: An analysis of their distribution, biogeography, diversity and conservation status. Leiden: Brill, 218–220.

Gou, X., Feng, Z., 2021. Quantitative analysis of growth rings and their applications on fossil conifer wood. Acta Palaeontologica Sinica 60 (2), 299–313.

Hass, H., Rowe, N.P., 1999. Thin section and wafering. In: Jones, T.P., Rowe, N.P. (Eds.), Fossil plants and spores: modern technique. Geological Society of London, London, 76–81.

IAWA Committee, 2004. IAWA list of microscopic features for softwood identification. IAWA Journal 25, 1–70.

Kafetzidou, A., Kouli, K., Zidianakis, G., Kostopoulos, D., Zouros N., 2022. The early Miocene angiosperm flora of Akrocheiras in Lesvos Petrified Forest (North Aegean, Greece)–Preliminary results. Review of Palaeobotany and Palynology 296, 104559.

Ortloff W. 1996. Wood-anatomical evidence of fire seasonality, In: Dean, J.S., Meko, D.M., Swetnam, T.W. (Eds.), Tree Rings, Environment, and Humanity. Tucson: Radiocarbon, Department of Geosciences, The University of Arizona, 89–93.

Pe-Piper, G., Piper, D.J.W., Zouros, N., Anastasakis, G., 2019. Age, stratigraphy, sedimentology and tectonic setting of the Sigri Pyroclastic Formation and its fossil forests, Early Miocene, Lesbos, Greece. Basin Research 31, 1178–1197.

Wang, Y., Tian, N., Jiang, Z., Yang, X., Ding, Q., 2017. Recent advances in Mesozoic fossil wood studies in China: diversity variations and palaeoclimate implications. Earth Science Frontiers 24(1), 52–64 (in Chinese with English abstract).

Zheng, S., Li, Y., Zhang, W., Li, N., Wang, Y., Xi, J., Yi, T., Yang, J., Fu, X., 2008. Fossil woods of China (English Edition). China Forestry Press, Beijing.

Zhu, Y., 2024. Investigations on the fossil wood from the Miocene petrified forest in Lesvos Island, Greece—Systematics, fossil diversity and palaeoenvironmental significance. Ph.D. Thesis, University of Chinese Academy of Sciences, Beijing, 410p.

Zhu, Y., Zouros, N., Zhang, J., Wang, Y., Li, Y., Cui, Y., 2021. Progress in the study of Miocene petrified woods from Lesvos, Greece. Acta Palaeontologica Sinica 60(4), 594–615.

Zhu, Y., Li, Y., Zhang, J., Wang, Y., Zouros, N., 2025. A new species of *Pseudotsuga* (Pinaceae) from the lower Miocene of Lesvos, Greece, and its palaeogeographical and palaeoclimatic implications, Palaeoworld 34, 100852.

Zouros, N., 2004. The European Geoparks Network–Geological heritage protection and local development. Episodes 27, 165–171.

Zouros, N., 2010. The Petrified Forest of Lesvos. A Unique Natural Monument. In: Evelpidou, N., Figueiredo, T., Tecim V., Vassilipoulos A. (Eds.), Natural Heritage from East to West (2). Berlin, Heidelberg: Springer Berlin Heidelberg 15–26.

Zouros, N., 2021. The Miocene Petrified Forest of Lesvos, Greece: Research and Geoconservation Activities. Geoconservation Research 4(2), 635–649.

Zouros, N., Pavlides, S., Soulakellis, N., Chatzipetros, A., Vasileiadou, K., Valiakos, I., Mpentana, K., 2011. Using active fault studies for raising public awareness and sensitization on seismic hazard: a case study from Lesvos Petrified Forest Geopark NE Aegean Sea, Greece, Geoheritage 3, 317–327.

Zouros, N., Velitzelos, E., Valiakos, E., Ververis, K., 2004. Submarine petrified forest in Lesvos Greece. Proceedings of the 5th International Symposium on Eastern Mediterranean Geology, Thessaloniki 437–440.

Zouros, N., Velitzelos, E., Valiakos, I., Labaki, O., 2007. The Plaka petrified forest park in western Lesvos-Greece. Bulletin of the Geological Society of Greece 40, 1880–1891.

17th INTERNATIONAL CONGRESS of the Geological Society of Greece

BULLETIN OF THE GEOLOGICAL SOCIETY OF GREECE, SP. PUBL.

EXTENDED ABSTRACT 353

Utilizing ultrasound velocity measurements to estimate physicomechanical properties of carbonate ornamental rocks

Ziazopoulou K.[1], Loupasakis C.[1], Laskaridis K.[2], Patronis M.[2], Arapakou A.[2], Kouseris I.[2]

(1) Laboratory of Engineering Geology and Hydrogeology, School of Mining and Metallurgical Engineering, National Technical University of Athens, Athens, Greece, kziaz24@gmail.com, (2) "Lithos" ornamental stones quality control laboratory, Hellenic Survey of Geology & Mineral Exploration (HSGME), Athens, Greece

Research Highlights

High to very high correlation values have been achieved between the ultrasound velocity and many of the physicomechanical properties, providing substantial information on the application of fast, non-destructive methods for the quality control of the ornamental stones.

Introduction / Background

The quality control of ornamental stones requires the determination of numerous physical and mechanical properties and the conduction of expensive time-consuming tests. Therefore, the development of alternative methods for estimating these properties can be very attractive. This research was conducted to achieve a satisfactory correlation of ultrasound velocity with properties such as Uniaxial Compressive Strength, density, open porosity, water absorption, flexural strength and abrasion resistance of certain samples.

Methods

Thirty eight rock samples, the majority of them from northern Greece, have been tested to correlate the ultrasound velocity with the physicomechanical properties of the ornamental stones. The selected samples were calcitic marbles, dolomitic marbles and limestones. They were shaped cubic (7cm) following the European standards, in which most of the tests are carried out at the Laboratory of ornamental stones "Lithos".

For all the 38 samples, the P-wave and S-wave ultrasound velocity were measured, in all three dimensions, and the mean value was used for the correlations (Figure 1).

Figure 1. ***The ultrasonic velocity measurement procedure for all marble and limestone samples.***

Following, the Uniaxial Compressive Strength (UCS) of every sample was measured by applying the standard destructive method according to the European standard EN 1926 (Figure 2). The ultrasound velocities were measured in m/s and the Uniaxial Compressive Strength was measured in MPa.

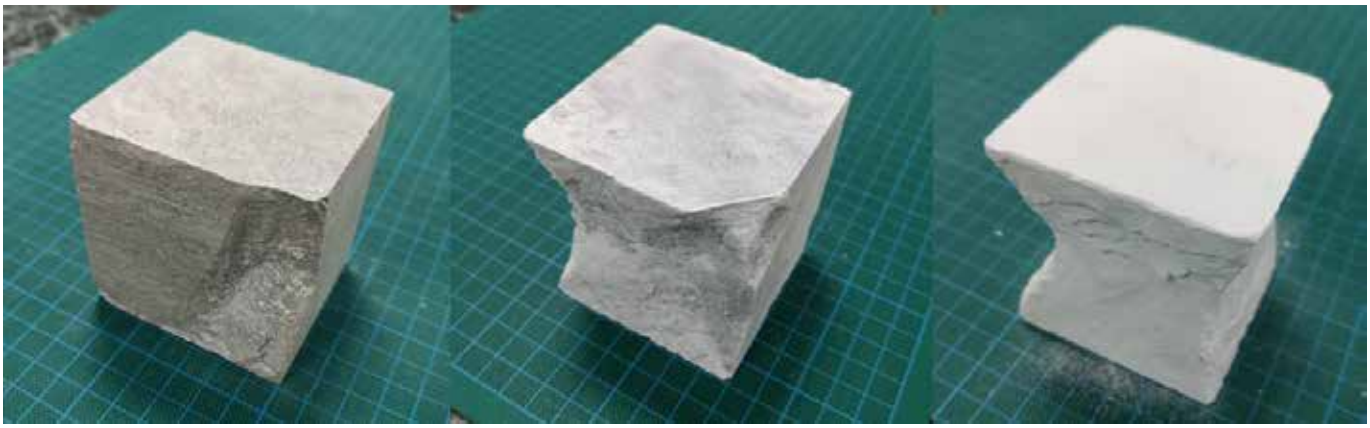

Figure 2. ***The differences of the samples of a limestone, a calcitic marble and a dolomitic marble (from left to right) after the measurement of their Uniaxial Compressive Strength.***

As expected, the correlation between the mean P-wave and S-wave velocity values was very high for all the samples, with a correlation coefficient reaching up to 99%.
The mean values for the density (European standard EN 1936, measured in kg/m^3), open porosity (European standard EN 1936, measured in percent % by volume), water absorption (European standard EN 13755, measured in percent % by mass), flexural strength (European standard EN 12372, measured in MPa) and abrasion resistance (European standard EN 14157, measured in cm^3/(50*cm^2)) were provided by the "Lithos" Laboratory. Following the European standards, those values were calculated by testing 10 samples of the same batch for every rock, within the framework of former contracted projects.

Results

Initially, primary importance was given in the correlation between P-wave velocity and Uniaxial Compressive Strength (UCS) which is, arguably, the most relevant parameter in most fields of applied geosciences, engineering and material science, as it establishes the mechanical response of material under unconfined conditions.
Subsequently, more properties were considered, yielding rewarding results. In particular, the highest correlation coefficients ($R^2 > 0.8$) were obtained for the following pairs of properties:

- P-wave velocity and density for limestones ($R^2 = 0,92$).
- P-wave velocity and flexural strength for limestones ($R^2 = 0,88$).
- P-wave velocity and open porosity for calcitic marbles ($R^2 = 0,86$).
- P-wave velocity and water absorption for all the samples ($R^2 = 0,86$).
- P-wave velocity and water absorption for limestones ($R^2 = 0,81$).
- P-wave velocity and water absorption for all the samples ($R^2 = 0,80$).

Furthermore, sufficient correlation coefficient values ($R^2 > 0,5$) were obtained for the following pairs of properties:

- P-wave velocity and density for all marbles ($R^2 = 0,68$).
- P-wave velocity and open porosity for all the samples ($R^2 = 0,61$).
- P-wave velocity and UCS for all marbles ($R^2 = 0,60$).
- P-wave velocity and open porosity for limestones ($R^2 = 0,60$).
- P-wave velocity and abrasion resistance for dolomitic marbles ($R^2 = 0,60$).
- P-wave velocity and density for all the samples ($R^2 = 0,58$).

In cases where no clear correlation can be established between the ultrasound velocity and the physical and mechanical properties, the datasets were further divided and analyzed considering the rock type. In those cases, the mean values of the physicomechanical properties were correlated with the rock type and the mean values of the ultrasonic velocities (Figure 3). Boxplots were also designed to provide clear information about the range of values, as well as the extreme values (Figure 4).

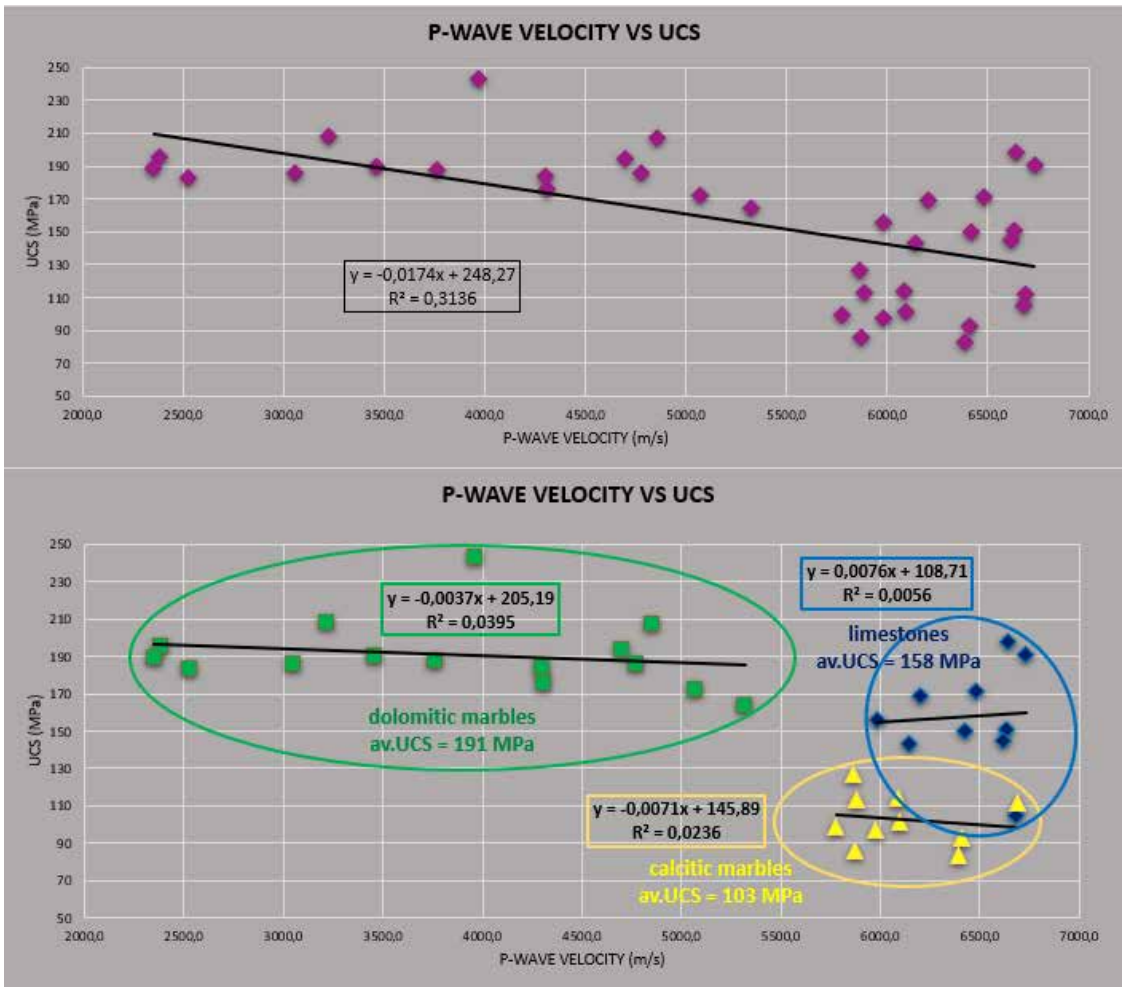

Figure 3. ***In the upper graph it is made clear that the correlation coefficient between P-wave velocity and UCS is not good enough. However, in the graph below, the point areas are showcasing that there can be other conclusions other than just a correlation.***

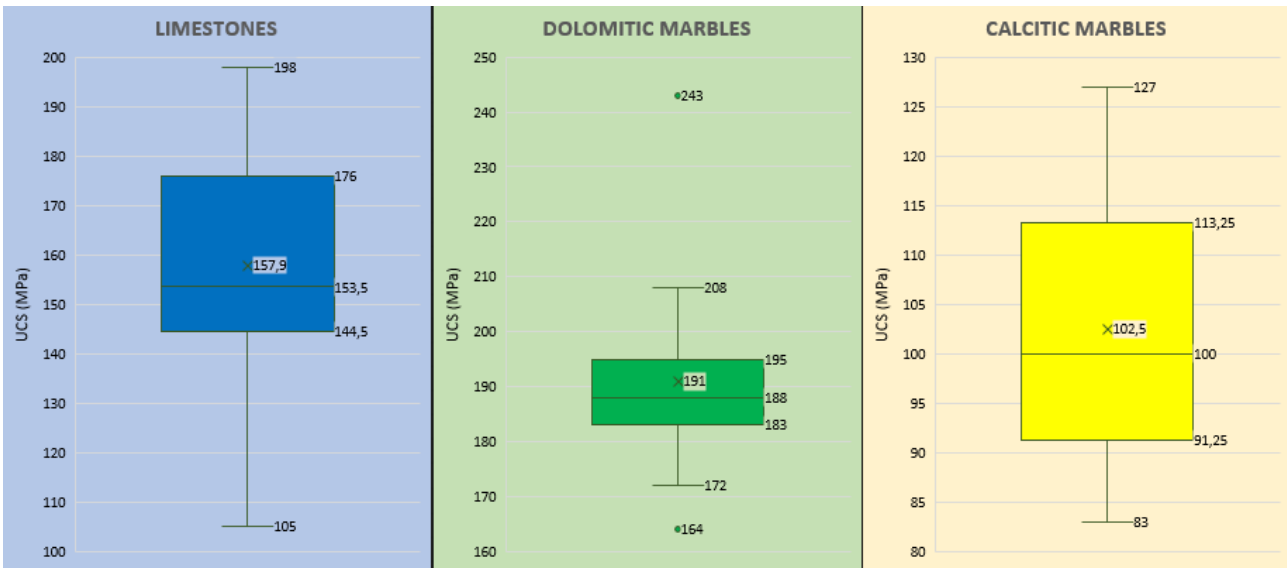

Figure 4. ***Boxplots providing the mean values, as well as the extreme values of the Uniaxial Compressive Strength (UCS) of the three categories of the samples.***

Conclusions

In conclusion, due to the high correlation coefficient values obtained, it seems possible to use ultrasonic velocity measurements as an alternate, non-destructive method to estimate various physical and mechanical properties of ornamental stones.

Acknowledgements
The authors acknowledge the “Lithos” ornamental stones quality control laboratory of the Hellenic Survey of Geology & Mineral Exploration (HSGME) for the provision of data and the use of the laboratory equipment.

References

David Benavente, Rafael Fort, Miguel Gomez-Heras, (2021). Improving uniaxial compressive strength estimation of carbonate sedimentary rocks by combining minimally invasive and non-destructive techniques.
EN 12372:2006 Natural stone test methods - Determination of flexural strength under concentrated load.
EN 13755:2008 Natural stone test methods - Determination of water absorption at atmospheric pressure.
EN 14157:2004 Natural stone test methods - Determination of the abrasion resistance.
EN 1926:2006 Natural stone test methods - Determination of uniaxial compressive strength.
EN 1936:2006 Natural stone test methods - Determination of real density and apparent density and of total and open porosity.
“Lithos” laboratory of ornamental stones, HSGME.
“Lithos” laboratory of ornamental stones, HSGME, Tests required to provide CE marking in final products from natural stones depending on the application.
Zhichun Fang, Jafar Qajar, Kosar Safari, Saeedeh Hosseini, Mohammad Khajehzadeh and Moncef L. Nehdi, (2023). Application of Non-Destructive Test Results to Estimate Rock Mechanical Characteristics—A Case Study.

17th INTERNATIONAL CONGRESS of the Geological Society of Greece

BULLETIN OF THE GEOLOGICAL SOCIETY OF GREECE, SP. PUBL.

EXTENDED ABSTRACT 354

Spatial distribution of trace elements in four water districts of Greece during the period 2018-2023. Results from National Groundwater Monitoring Network Program of Greece.

Zorapas V.[1] Chalkiadaki O.[2]

(1) Head of the Department of Hydrogeology and Hydrology, Division of Water Resources and Geothermal Energy, Hellenic Survey of Geology and Mineral Exploration, Athens, Greece, vzorapas@eagme.gr, (1) Department of Analytical Laboratories, Division of Water Resources and Geothermal Energy, Hellenic Survey of Geology and Mineral Exploration, Athens, Greece, ochalkiadaki@eagme.gr

Introduction / Background

According to Directives 2000/60/EC, 2006/118/EC, and 91/676/EEC, Member States are required to establish a National Water Monitoring Network to ensure the systematic monitoring of the qualitative and quantitative characteristics of inland surface, transitional, coastal, and groundwater bodies. The aim is to assess and classify their ecological and chemical status, as well as their quantitative status, and to evaluate long-term changes resulting from human activities, in conjunction with the implementation of the measures set out in River Basin Management Plans.

Given Greece's unique climatic, geological, and physiographic conditions, groundwater resources hold exceptional significance. Unlike Northern European countries that primarily rely on surface water, Greece's water needs are largely met by groundwater. Regions experiencing intensive groundwater use have reported significant quantitative and qualitative degradation, including salinization and nitrate pollution. Prolonged droughts and high temperatures exacerbate these issues, necessitating robust and systematic monitoring of groundwater conditions.

The National Monitoring Network for groundwater, as defined in Government Gazette Issue 5384/B/19-11-2021 "Revision of the National Monitoring Network for the quality and quantity of water with the determination of monitoring stations and the responsible bodies for their operation," consists of 1,896 monitoring stations and covers almost the entire Greek territory, including remote islands. The goal of the project is to provide a coherent and comprehensive overview of the qualitative and quantitative status of the country's groundwater systems. The Network contributes significantly to the rational management and protection of groundwater resources from degradation, as the country is highly dependent on these resources (water supply, irrigation, industry).

The Hellenic Survey of Geology and Mineral Exploration conducted the entire range of tasks (sampling, analysis, evaluation, and results reporting) in a comprehensive manner. A synchronized sampling campaign was conducted annually or semi-annually during the period 2018-2023 in each water district to collect groundwater samples for major and trace element analysis. At the same time, on-site measurements of physicochemical parameters, groundwater level and spring discharge rate, were performed. Water samples were analyzed in HSGME's analytical laboratories (Athens, Preveza, and Xanthi).

The monitoring included:

- Hydrometric measurements such as groundwater level and spring discharge rate.
- Physical – chemical field measurements (pH, electrical conductivity, water temperature, dissolved oxygen)
- Sampling and chemical analysis for major ions (Ca, Mg, Na, K, HCO_3, Cl, SO_4), nitrogenous and phosphorus compounds, trace elements (Cr, Fe, Mn, Hg, Cu, Pb, Zn, Al, Cd, Ni), organic compounds (solvents and pesticides)

The evaluation reports and analysis results were submitted to the Directorate General for Water, the designated national authority for overseeing water management, to inform relevant EU bodies and to be further utilized in the review of RBMPs and the development of management policies.

Groundwater trace element concentrations are governed by complex processes, reflecting the inherent chemical variability of groundwater itself (Farnham *et al*., 2003). Natural factors, including aquifer lithology, recharge water quality, and water-rock interactions, significantly influence trace element composition. However, human activities can disrupt these natural systems, leading to pollution or alterations in the hydrological cycle (Helena *et al*., 2000). Consequently, interpreting trace element data in groundwater necessitates sophisticated analytical techniques.

Study area

This study focuses on four water districts in eastern Greece: EL06 (Attica), EL07 (Eastern Sterea), EL08 (Thessaly), and EL10 (Central Macedonia). Despite their geographic proximity, these areas exhibit significant heterogeneity in terms of geology, anthropogenic pressures, and socio-economic development. Attica and Central Macedonia, hosting Athens and Thessaloniki cities, are characterized as highly urbanized environments with industrial activities, and high population density. In contrast, Eastern Sterea (EL07) is influenced by industrial activities and the geological presence of ophiolitic rocks. Thessaly (EL08), on the other hand, is predominantly an agricultural region. By examining these basins, our research aims to provide a comprehensive understanding of the spatial distribution of trace elements (Cr, Fe, Mn, Hg, Cu, Pb, Al, Cd, Ni) in groundwater, considering the interplay between natural and anthropogenic factors.

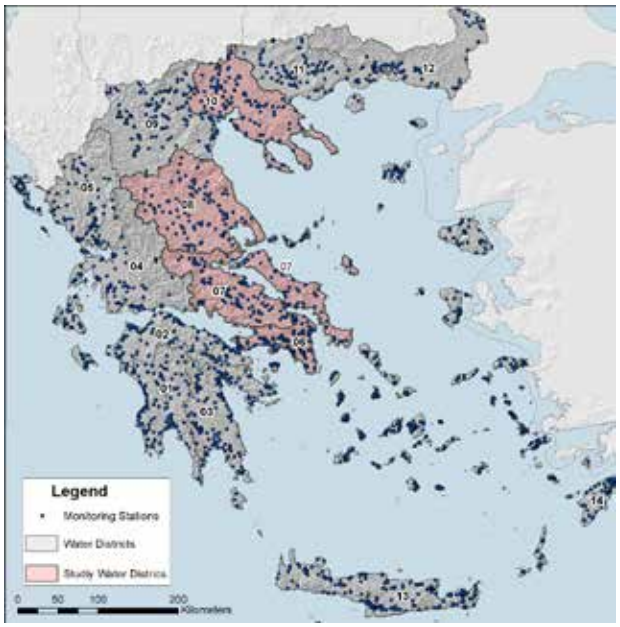

Figure 1. The monitoring network includes 1896 representative monitoring stations (boreholes, wells and springs). Study areas in light red color (Water Districts 06, 07, 08, 10)

Objectives

The objectives of the present work are:

- To investigate the spatial trends of selected trace elements in groundwater across four water districts of Greece, attempting to identify regional variations in groundwater quality and potential sources of contamination.
- To assess the potential impacts of human activities (e.g., agriculture, industry) and natural factors (e.g., geology, climate) on trace element concentrations, providing valuable insights into the factors driving groundwater contamination in different regions.
- To evaluate the effectiveness of existing water management measures in mitigating trace element contamination for future management strategies.
- To contribute to the scientific understanding of trace element occurrence and behavior in groundwater systems in Greece, enhancing the knowledge base for future research and monitoring efforts.

Methods

All groundwater samples were collected from four water districts in Greece (EL06-Attica, EL07-Eastern Sterea, EL08-Thessaly, and EL10-Central Macedonia), from February 2018 to December 2023. The groundwater samples collected using acid pre-washed polyethylene bottles according to the APHA methods (APHA, 2012). Sampling procedure and groundwater analysis followed the APHA guidelines and Mineral and Geosciences Department guidelines (APHA, 2012). Samplers or submersible pumps were used to pump the groundwater samples and the stagnant was removed in 15 to 30 minutes to eliminate the unnecessary substances during the sampling procedures (Appelo and Postma, 2005).

Conductivity and pH were measured upon their arrival at the Analytical Laboratories of HSGME. For trace elements all groundwater samples were filtered in field using Whatman cellulose Nylon-type Millipore filters with a pore size of 0.45 μm. After filtration, samples were acidified using SUPRAPUR® 65% nitric acid. Trace elements (Al, Cr, Mn, Ni, Cu, Fe, As, Cd, and Pb) were analyzed using inductively coupled plasma mass spectrometry (ICP-MS) model ELAN 6100, PE-SCIEX. Major ions (Na, K, Mg, and Ca) were analyzed using inductively coupled plasma optical emission mass spectrometry (ICP-OES) model OPTIMA 5300 DV, PerkinElmer. Bicarbonate and chloride were analyzed using the titration method that was conducted in the laboratory.

Statistical analysis

Multivariate statistical methods were performed using the computer Software SPSS 17.0 in order to investigate the relationships among the trace elements in each geographical area's samples. Correlation analysis was also performed between the trace and major elements and the physicochemical parameters at each of the four water districts in order to establish correlations between every two elements and to explore the strength of such correlations. Boxplots were used to depict the distributions of each of the parameters examined for all the stations of each water district.

Results

SPSS 17.0 was used to perform correlations of the 10 trace elements, and the major elements in all samples of each water district for the sampling period 2018-2023. The sample number analyzed and correlated for each trace element differs for each of the four water districts. For EL06, 509 samples were analyzed, while for EL07, 867 samples, for EL08, 595 samples and for EL10, 712 samples. The difference in trace element concentrations in groundwater is influenced by the activities and types of adjacent areas as well as the characteristics of the aquifer. The main findings are the following:

For Water District EL06:

- Fe: Ranged from 9.9 to 1390 μg/L (mean 62, median 21 μg/L). 31 values out of 509 were above the proposed quality threshold of 200 μg/L, while in 2 out of 93 stations (EL6110609 & EL6160602) the median Fe concentrations throughout the years exceeded the proposed threshold.
- Mn: Ranged from 5.0 to 390 μg/L (mean 15, median 5.0 μg/L). In 14 out of 93 stations one or more values of Mn exceeded the proposed quality threshold of 50 μg/L. In 5 out of 93 stations the median Mn concentrations throughout the years exceeded the proposed quality threshold of 50 μg/L.
- Cu: Ranged from 4.6 to 2500 μg/L (mean 7.6, median 5.0 μg/L). No values were above the National Guideline value, while 32 stations have constant measurements of Cu at LOQ 5μg/L.
- Cr: Ranged from 4.9 to 70 μg/L (mean 7.8, median 5.0 μg/L). Only 9 values were determined above the threshold of 50μg/L, while 14 values were between 25 μg/L (new threshold after 2036) and 50 μg/L. At 2 stations the overall median value throughout the years was equal or above 50 μg/L (EL6010604 and EL6050612)
- Ni: Ranged from 0.5 to 70 μg/L (mean 7.8, median 5.0 μg/L). 49 values out of 509 were measured above or equal to 20μg/L, while in 35 out of 93 stations one or more values of Ni exceeded the proposed limit of 20 μg/L. Moreover, in 2 out of 93 stations the median Ni concentrations throughout the years exceeded the proposed limit of 20μg/L.
- Pb: Ranged from 5.0 to 50 μg/L (mean 5.2, median 5.0 μg/L). Most measurements (501 out of 509) were equal to the LOQ of 5μg/L. In 3 out of 93 stations one or more values of Pb exceeded the proposed limit of 10 μg/L and in 2 stations the future legislative threshold after 2036 of 5 μg/L. There was 1 station (EL6170603, 186038) where the overall median Pb value throughout the years was above 10μg/L (min 16-50, median 23.5μg/L)
- Cd: Ranged from 0.5 to 30 μg/L (mean 0.6, median 0.5 μg/L). 6 values were equal to or above the limit of 5μg/L (in 6 stations) but no station where the overall median Cd value throughout the years was equal to or above 5μg/L. These values were measured in 2 of the systems (EL060806, EL060906) located in Aspropyrgos and Elefsina.
- As: Ranged from 0.5 to 50 μg/L (mean 6.4, median 5.0 μg/L). 46 values out of 509 were above the legislative threshold of 10μg/L. In 19 stations one or more cases the measurement of As exceeded the limit of 10μg/L, in 6 of them the overall median As value throughout the years also exceeded the limit. The water bodies with As with at least one value above the limit of 10μg/L were 11 and only in 1 the overall median As value throughout the years also exceeded the limit.
- Hg: Ranged from 0.5 to 11 μg/L (mean 0.6, median 5.0 μg/L). From the entire dataset of 509 values only 7 exceeded the 1μg/L legislative limit. 502 samples were at the LOQ of 0.5μg/L. The maximum values above 1μg/L were found in 3 stations located in Aspropyrgos.

For Water District EL07:

- Fe: Ranged from 5.0 to 10400 μg/L (mean 219, median 44 μg/L). 184 values out of 867 were above the proposed quality threshold of 200μg/L. In 25 out of 145 stations the median Fe concentrations throughout the years exceeded the proposed quality threshold.
- Mn: Ranged from 4.8 to 1100 μg/L (mean 20, median 5.0 μg/L). 67 out of 867 values were above the proposed quality threshold of 50μg/L, while in 9 out of 145 stations the median Mn concentrations throughout the years exceeded this threshold.
- Cu: Ranged from 1.8 to 630 μg/L (mean 9.9, median 5.0 μg/L). No values were above the National Guideline value, while some stations have constant measurements at LOQ 5μg/L.
- Cr: Ranged from 4.8 to 360 μg/L (mean 15, median 5.0 μg/L). 49 values were determined above the threshold of 50μg/L, while 14 values were between 25 μg/L (new threshold after 2036) and 50 μg/L. In 4 stations the overall median values throughout the years exceeded the limit of 50μg/L, while in 6 stations the overall median values throughout the years exceeded the limit of 25μg/L (threshold after 2036).
- Ni: Ranged from 1.0 to 1800 μg/L (mean 11, median 5.0 μg/L). 38 values out of 865 were measured above or equal to 20μg/L, while in 28 stations there is at least one Ni value above 20μg/L, and only in one of them (7180711) the overall median of all monitoring years is above 20μg/L.
- Pb: Ranged from 5.0 to 105 μg/L (mean 6.1, median 5.0 μg/L). Most measurements (782 out of 866) were equal to the LOQ of 5μg/L. In 51 stations there was at least one Pb value equal to or above 10μg/L and in 7 stations there was at least one Pb value above 5μg/L. There were 4 stations (7090703, 7090712, 7090714, 7320703) where the overall median Pb value throughout the years was equal to or above 10μg/L equal to or above 10μg/L.

- Cd: Ranged from 0.5 to 17 μg/L (mean 0.8, median 0.5 μg/L). 39 values were equal to or above the limit of 5μg/L (in 37 stations).
- As: Ranged from 5.0 to 51.8 μg/L (mean 5.0, median 5.8 μg/L). 38 values were equal to or above are above the legislative threshold of 10μg/L. In 25 stations one or more measurements of As was equal to or above the limit of 10μg/L. In 2 stations (EL7050706 and EL7150702) the overall median As values throughout the years was above 10μg/L.
- Hg: No measurable Hg values were determined. All values were at the LOQ (0.5μg/L).

For Water District EL08:

- Fe: Ranged from 10 to 27000 μg/L (mean 225, median 29 μg/L). 94 values out of 595 were above the proposed quality threshold of 200μg/L. In 55 out of 95 stations one or more values of Fe exceeded the proposed quality threshold. In 6 out of 95 stations the median Fe concentrations throughout the years exceeded 200 μg/L.
- Mn: Ranged from 3.0 to 3458 μg/L (mean 56, median 7.2 μg/L). 120 out of 595 values were above the proposed quality threshold of 50μg/L, while in 18 out of 95 stations the median Mn concentrations throughout the years exceeded this threshold.
- Cu: Ranged from 4.0 to 180 μg/L (mean 7.1, median 5.0 μg/L). No values were above the National Guideline value, while 27 stations have constant measurements at LOQ.
- Cr: Ranged from 4.5 to 75 μg/L (mean 7.3, median 5.0 μg/L). 65 stations have constant measurements of Cr at LOQ 5μg/L. There were 12 values above the future legislative threshold of 25μg/L (2036) and 12 values above the current limit of 50μg/L. In 2 stations the overall median Cr value throughout the years was above 50μg/L (EL8090802 range: 50-75, median 61.3, EL8110806 range: 5-67, median 58.2, Magnesia, Dimos R. Fereou).
- Ni: Ranged from 5.0 to 52 μg/L (mean 6.9, median 5.0 μg/L). 26 values out of 596 were measured above 20μg/L, while in 19 stations there is at least one Ni value above 20μg/L, and only in one of them the overall median of all monitoring years was above 20μg/L (EL8200803, 6 out of 7 values above 20μg/L, Fthiotida, Dimos Domokou, 16.4-39, median 23)
- Pb: Ranged from 0.7 to 690 μg/L (mean 6.5, median 5.0 μg/L). Most measurements (581 out of 596) were equal to the LOQ of 5μg/L. However, there were 8 values above the current legislative threshold of 10μg/L and 6 more values above 5μg/L (future legislative threshold after 2036). In 7 stations there was at least one Pb value equal to or above 10μg/L and in 5 stations there was at least one Pb value above 5μg/L but in none of these stations the overall median Pb value throughout the years did not exceed either limit.
- Cd: Ranged from 0.5 to 2.7 μg/L (mean 0.5, median 0.5 μg/L). Most values (591 out of 596) were measured at the LOQ (0.5μg/L). There were no values above or equal to 5μg/L.
- As: Ranged from 0.2 to 26 μg/L (mean 5.3, median 5.0 μg/L). Most values (558 out of 596, 75 stations) were measured at the LOQ (5μg/L). There were 14 values equal to or above the legislative threshold of 10μg/L. There are 7 stations where in one or more cases the measurement of As was equal to or above the limit of 10μg/L. In 1 station the overall median As values throughout the years were above 10μg/L (EL8280802, 3 out of 5 values, min 7, max 16, median 11.6).
- Hg: No measurable Hg values were determined. All values were at the LOQ (0.5μg/L).

For Water District EL10:

- Fe: Ranged from 6.0 to 23,000 μg/L (mean 495, median 50 μg/L). 153 values out of 712 were above the proposed quality threshold of 200μg/L. In 65 out of 114 stations one or more values of Fe exceeded the proposed quality threshold. In 18 out of 114 stations the median Fe concentrations throughout the years exceeded 200 μg/L.
- Mn: Ranged from 4.6 to 2,500 μg/L (mean 81, median 11 μg/L). 105 out of 712 values were above the proposed quality threshold of 50μg/L, while in 29 out of 114 stations the median Mn concentrations throughout the years exceeded this threshold.
- Cu: Ranged from 5.0 to 295 μg/L (mean 7.4, median 5.0 μg/L). No values were above the National Guideline value, while 49 stations have constant measurements at LOQ.
- Cr: Ranged from 0.5 to 62 μg/L (mean 15, median 5.0 μg/L). Only one value was above the threshold of 50μg/L.
- Ni: Ranged from 1.0 to 480 μg/L (mean 7.0, median 5.0 μg/L). 14 values out of 712 were measured above 20μg/L.
- Pb: Ranged from 0.5 to 25 μg/L (mean 5.0, median 5.0 μg/L). Most measurements were equal to the LOQ of 5μg/L. Only 6 values out of 712 were measured above 5μg/L (future legislative threshold after 2036) and 2 were above the current legislative threshold of 10μg/L.
- Cd: Ranged from 0.5 to 1.0 μg/L (mean 0.7, median 0.5 μg/L). There were no values above or equal to 5μg/L.
- As: Ranged from 0.5 to 390 μg/L (mean 24, median 5.0 μg/L). 94 values are above the legislative threshold of 10μg/L. The 26 stations where in one or more cases the measurement of As exceeded the limit of 10μg/L.
- Hg: Ranged from 0.5 to 5 μg/L (mean 0.5, median 0.5 μg/L). From the entire dataset of 712 values, only 5 exceeded the 1μg/L legislative limit. (702 samples at the LOQ 0.5).

Correlation analysis of trace elements for possible sources of pollution identification and geochemical relationships

Pearson's correlation matrix has been used to evaluate the association between major and trace metals of the groundwater of each water district and to find out the probable factors that control the distribution of trace elements. The positive correlation indicates the metals are from the same origin while the negative significant co-relationship means the sources of metals are different (Hoque *et al,* 2024). Level of significance was set at 0.01.

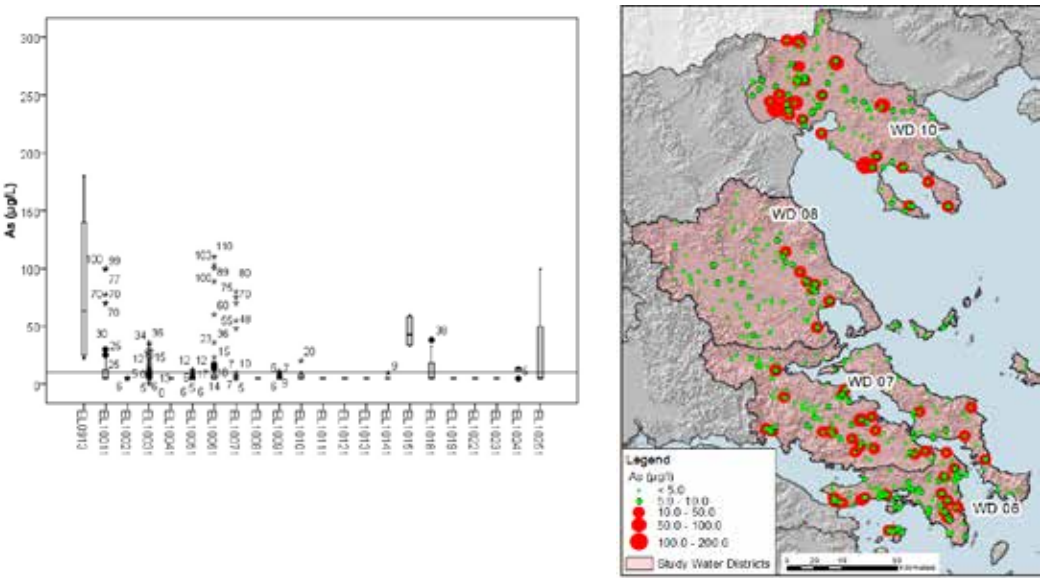

Figure 5. Variation of arsenic (As) boxplot in all groundwater bodies of Water District 10 (with thin line, the legislative limit is depicted) and spatial map of As in the study Water districts (right) showing the geographical distribution pattern of As in the sampling points (As Concentration above the legislative limit depicted in red color).

Table 1. Correlations of physicochemical parameters, major elements and trace elements in the four water districts (level of significance was set at 0.01)

Element	Water District 06	Water District 07	Water District 08	Water District 10
Fe	+: Mn, Al, Cond., Mg, Na, K, Cl -: Cr, Cd, Hg	+: Mn, Cu, Cr, Ni, pH, Cond., Mg, Na, Al, -: Cd, Pb	+: Mn, Cu, Al, As, Cond., Mg, Na, K, Cl -: pH	+: Mn, Cu, Ni, Al, Cond., Na, Cl -: Cd, Cr
Mn	+: Fe, Ni, Pb -: Cr, pH	+: Fe, Cu, Ni, Pb, Al, As	+: Fe, Cu, Ni, Al, Cond., Mg, Na, K -: Cr	+: Fe, Al, Cond., Na, Cl -: Cr
Cu	+: Ni, Pb, Cd, As, Cond, Ca, Mg, K, Na, Cl -: pH	+: Fe, Mn, Ni, Pb, Al, As, Cond., Ca, Mg, K, Na, Cl	+: Fe, Mn, Ni, Pb, As, Cond., Mg, Na	+: Fe, Ni, Al, As, Cond., Na, Cl
Cr	+: Cd, Hg, pH, Mg, HCO_3 -: Fe, Mn, Ni, Al, Ca	+: pH, Cond., Mg, Na, K Cl -: Fe, Al, Pb, Ca	+: Cond., Mg, Na -: Mn, Ca	+: Fe -: Pb, Mn
Ni	+: Mn, Cu, Al, As, Cond, Ca, Mg, Na, K, HCO_3, Cl -: Cr, Cd, pH	+: Fe, Mn, Cu, Pb, Cd, Al, As, Cond., Ca, Mg, Na, K, Cl -: pH	+: Mn, Cu, Pb, As, Cond., Ca, Mg, Na	+: Fe, Cu, Cd, Cond., Na, Cl
Pb	+: Mn, Cu	+: Mn, Cu, Ni, Cd, Al, As -: Fe, Cr, Cl	+: Cu, Ni, Al	no correlations
Cd	+: Cr, Hg -: Fe, Ni, Al and As	+: Ni, Pb, As, Ca -: Fe, Cr, pH, Na, Cl	no correlations	+: Ni, Pb, As, pH -: Fe, Cr
Al	+: Fe, Ni, As -: Cr, Cd	+: Fe, Mn, Cu, Cr, Ni, Pb, pH, Cond, Mg	+: Fe, Mn, Pb	+: Fe, Mn, Cu, Hg, pH, Na, Cl
As	+: Cu, Ni, Pb, Al, Cond., Ca, Mg, Na, K, Cl -: Cd	+: Mn, Cu, Ni, Pb, Cd, Cond., Mg, Na, K, Cl	+: Fe, Cu, Ni, Cond., Mg, Na, K	+: Cu, Hg, Cond., Na, Cl

Hg	+: Cd, Cond., Ca, Na, K, Cl	no correlations	no correlations	+: Al, As, pH, Na

+ Positive correlation, - Negative correlation

Common Correlations in all water districts:

- **Ca-Mg: This strong positive correlation across all water districts is expected, as these elements often occur together in minerals like calcite and dolomite.**
- **Conductivity - Major Ions: Conductivity is strongly correlated with most major ions (Ca, Mg, Na, K, Cl, HCO3) in all districts, as expected, since these ions contribute significantly to the electrical conductivity of the water.**
- **pH - Conductivity: A negative correlation between pH and Conductivity is observed in most districts, which is generally expected as higher pH values can lead to the precipitation of certain ions, reducing conductivity.**
- **pH - Ca, Mg, Na, K: Negative correlations between pH and these major cations are observed in many districts, suggesting that higher pH values may favor the precipitation of carbonate minerals.**
- **Fe-Mn:** Strong positive correlation observed in all water districts, suggesting a strong association between these elements, likely due to their similar geochemical behavior and common occurrence in iron-bearing minerals.
- **Cu-Ni:** Positive correlation observed in all basins, indicating a potential association between these elements, possibly due to their co-occurrence in sulfide minerals or their similar geochemical behavior.
- **Cu-As:** Positive correlation observed in all basins, suggesting a possible association between these elements, potentially related to their occurrence in organic matter or association with sulfide minerals.
- **Al-Fe:** Positive correlation observed in all basins, indicating a strong association between these elements, likely due to their common occurrence in aluminosilicate minerals.
- **Cr-Fe, Mn, Al:** Cr shows negative correlations with Fe, Mn, Ni, and Al in EL06 and with Fe and Mn in EL07 and EL10. This suggests that Cr may have a different geochemical behavior compared to these elements, possibly due to its redox sensitivity or association with different mineral phases.

Overall, the correlation analysis suggests that the distribution of trace elements in the groundwater of each water district is influenced by a combination of factors, including:

- **Mineralogy:** The presence of specific minerals, such as Fe-oxyhydroxides, sulfides, and clay minerals, can control the distribution of trace elements.
- **Redox conditions:** Redox conditions can influence the mobility and speciation of trace elements.
- **Organic matter:** Organic matter can play a role in the sorption and transport of trace elements.
- **Anthropogenic activities:** Human activities, such as agriculture and industrial processes, can contribute to the presence of trace elements in groundwater.

Conclusions

- The geochemical analysis of groundwater samples at four water districts in Greece revealed that the distribution of trace elements in the studied regions is primarily influenced by geological factors, such as the underlying bedrock and soil types. The presence of specific minerals, such as carbonates and sulfides, significantly influences the concentrations and associations of elements like Ca, Mg, Fe, and Cu.
- Anthropogenic activities, including agriculture and industrial processes, have introduced additional contaminants, leading to localized contamination.
- The presence of chromium, particularly in areas with ophiolitic rocks, suggests the influence of natural geochemical processes.
- The elevated concentrations of arsenic, often associated with volcanic rocks and agricultural practices, highlight the importance of geological and anthropogenic factors in determining groundwater quality.
- The strong correlation between calcium, magnesium, and bicarbonate ions indicates the dominance of carbonate weathering in these regions.
- A thorough understanding of the geological and hydrogeological setting of each basin is essential for a more comprehensive interpretation of the observed correlations.

Acknowledgements

The author gratefully acknowledge the valuable contribution of Ms Helen Gintoni, former Head of the Department of Analytical Laboratories, Hellenic Survey of Geology and Mineral Exploration, Athens, Greece, in the analysis of the samples and the timely delivery of the results, as well as the assistant Dr Vasiliki Paraskevopoulou (Laboratory Teaching Staff, Laboratory of Environmental Chemistry, National and Kapodistrian University of Athens, Department of Chemistry, Athens, Greece) for the statistical analysis of the dataset using SPSS 17.0.

References

APHA. 2012. Standard methods for the examination of water and wastewater, 22nd Edition. American Public Health Association, American Water Works Association, Water Environment Federation, Washington.

Appelo, C.A.J., Postma, D. 2005. Geochemistry, Groundwater and Pollution, 2nd Edition Balkema, Rotterdam.

Hoque, Md. M., Hossen, Md. A., Zuthi, Mst. F. R, Mullick, Md. R.A., Hasan, S.M. F., Khan, F., Das, T. 2024. Exploration of trace elements in groundwater and associated human health risk in Chattogram City of Bangladesh, Heliyon, Volume 10, Issue 15, e35738.

Rakib M.A., Quraishi S.B., Newaz M.A., 2022. Groundwater quality and human health risk assessment in selected coastal and floodplain areas of Bangladesh J. Contam. Hydrol., 249, Article 104041.

Farnham, I.M., Johannesson, K.H, Singh, A.K, Hodge, V.F, Stetzenbach, K.J, 2003. Factor analytical approaches for evaluating groundwater trace element chemistry data, Analytica Chimica Acta, Volume 490, Issues 1–2, Pages 123-138.

Helena, B., Pardo, R., Vega, M., Barrado, E., Fernandez, J.M., Fernandez, L., 2000. Temporal evolution of groundwater composition in an alluvial aquifer (Pisuerga River, Spain) by principal component analysis, Water Research, Volume 34, Issue 3, Pages 807-816, ISSN 0043-1354.

17th INTERNATIONAL CONGRESS of the Geological Society of Greece

BULLETIN OF THE GEOLOGICAL SOCIETY OF GREECE, SP. PUBL.

EXTENDED ABSTRACT 355

The actions of Kefalonia and Ithaca UGGp aiming at the promotion of the area through sustainable development

Zoumpouli E.[1,2], Bourli N.[1], Papadopoulou P.[1], Zelilidis A. [1,2], Iliopoulos G.[1], Xanthakis M.[2]

(1) Department of Geology, University of Patras, Greece, zoumpouel@gmail.com (2) Kefalonia Ithaca UNESCO Global Geopark, Management Unit of Zakynthos and Ainos National Parks and Protected Areas of the Ionian Islands, branch of Argostoli

Introduction

The Kefalonia-Ithaca UNESCO Global Geopark (UGGp) consists a distinct geographical area renowned for its remarkable geological features, valuable ecosystems, unique cultural identity, and traditional ways of life. The Kefalonia-Ithaca UGGp is characterised by its intense seismic activity due to its geotectonic setting, which is one of the most tectonically active regions in Europe. Another defining feature of the geopark is the pronounced karstification, caused by water dissolving the limestones that cover large surfaces along the two islands. This unique combination of widespread limestones, tectonic activity, and climatic conditions has led to the formation of numerous karstic features, both underground and surfacial, such as caves, sinkholes, dolines, and poljes. The richness of the natural and cultural heritage of the two islands due to their geological wealth makes the territory of Kefalonia-Ithaca UGGp a unique territory, whose structured approach will strengthen its knowledge, the importance of its functions, and its tourist, heritage, and cultural potential. Kephalonia-Ithaca UGGp constitutes a territory that promotes the sustainable development of its region by leveraging their unique geological heritage, natural landscapes, and cultural traditions.
Several actions are specifically designed to highlight the area's rich geological heritage, aligning closely with the United Nations Sustainable Development Goals (SDGs). Below there is an overview of the typical actions Kefalonia-Ithaca UGGp takes to achieve these goals:

Education and Awareness

One of the primary goals of the Kefalonia-Ithaca UGGp is to provide educational programs regarding the different aspects of the natural and anthropogenic environment, aiming to inform, raise awareness, and foster a deeper connection with the region. Particularly there are several educational programs specifically designed to showcase its rich geological heritage. These initiatives play a vital role in advancing the sustainable development of the region. Additionally, the curated exhibitions at the Koutavos Lagoon Information Center and in Anogi village serve as outstanding educational resources, offering engaging and informative experiences to visitors.
The educational programs (Figure 1), which focus on geological heritage, include the following:

- The Kefalonia-Ithaca UGGp has developed a school programme specifically for geodiversity, named "Identification and protection of the geological heritage of the Kefalonia-Ithaca Geopark" for all grade levels.
- A newly developed educational package concerning the fossils of the geoparks. This educational package presents to the children how life, landscapes, and climate have changed over time and how organisms responded/adapted to those changes. The educational package consists of a worksheet, educational games for children of different ages that can be played both indoors and outdoors plus other activities all included in a dedicated museum box containing also real fossils and replicas.
- Caves in Kefalonia-Ithaca UGGp.
- The links Between Biodiversity & Geodiversity in the Aenos National Park.
- Earthquakes in Kefalonia-Ithaca UGGp
- Finally, ten 3-minute videos have been created with the theme of the presentation and interpretation of geological phenomena and structures such as deltas, the geological evolution of Kefalonia, volcanoes, sinkholes, "menirs" (monoliths), earthquakes, caves, Poros gorge, Ithaca "Fjords" and Rudists.

The involvement of the local community is very important. Partnering with schools, universities, and community groups can help foster a deeper appreciation and understanding of local heritage. Such initiatives not only cultivate pride in the community but also strengthen social bonds and contribute to reducing emigration. The Educational programs of Kefalonia-Ithaca UGGp are very well developed. Especially, the high number of visits proves their success. In total, 2,708 pupils and 143 teachers have visited the two environmental centers of Kefalonia-Ithaca geopark, since 2022. The participation of schools and the local community in the educational excursions is also remarkable.

Figure 1 Educational programs in Kefalonia Ithaca UGGp

Research and Innovation

Kephalonia-Ithaca UGGp recognizes the importance of the collaboration with academic institutions for research on geology, biodiversity, and cultural history, in order to achieve the public awareness of understanding the Earth processes, as well as the links among all these themes. For all these reasons, the Geopark collaborates with the local institutions, universities, as well as with the Department of Geology of the University of Patras, in order to develop sustainable practices.

Recent projects have focused on studying and promoting the palaeontological heritage of the Geopark, enhancing scientific understanding and attracting geotourism. For this reason, the Department of Geology of the University of Patras implemented the project “Study and exploitation of the palaeontological heritage of the Geopark of Kefalonia and Ithaca” (Iliopoulos *et al.,* 2024). Another project that the University of Patras has taken over is “The Possibilities of exploitation of clay outcrops for mud therapy” (Botziolis *et a*l., 2024) (Figure 2). Additionally, the University of Patras implemented a geotechnical study on the “Restoration of the Mycenaean Cemeteries in Mazarakata – Lakithra” (Zelilidis *et al*., 2023). It is very important also that the results of the three projects have already been published in international scientific journals.

Another project implemented by the Kefalonia-Ithaca UGGp is “BIO-MEMORY”, a project about the “Memorial Olives and olive trees” including recording, imprinting, dating and promoting them as high valued ecosystems, funded by the Ionian Islands Region. Furthermore, “BIONIAN” is another project which includes actions to protect & promote biodiversity in the Ionian Islands Region, funded also by the Ionian Islands Region and by the Ionian University, supervised also by the Geopark. A different project, “LAERTIS”, consists of an innovative management system for natural disasters management in the Ionian Islands Region funded and implemented by the Ionian Islands Region, the Ionian University, the University of Athens and the Technical chamber and the Geopark. Finally, a recent project that the University of Patras is responsible for concerns the setting up of a proposal for the development of three caves as sheaves in the wider area of the Sami Municipality and their connection to the existing speleological park of the Municipality.

Figure 2 Opening ceremony of the "Palaeontological exhibition" and presentation of the project "The Possibilities of exploitation of outcrops of clay for mud therapy"

Promotion and Visibility actions

The Kephalonia-Ithaca UGGp recognizes the importance of enhancing its promotion and visibility. For this reason, it develops and implements targeted strategies to enhance awareness and visibility of the Kephalonia-Ithaca UGGp, including organisation of conferences and workshops (Figure 3), active participation in the Greek Geopark forum, EGN and GGN, partnerships with local and international stakeholders, and use social media to reach out broader audiences.

Additionally, Kephalonia-Ithaca UGGp develops innovative technologies and strategies to improve visitor experience, while ensuring sustainability. For example, the geopark has developed two visitor centers (one in Kefalonia and one in Ithaca), guided tours, and educational excursion on a systematic basis, which is a very important tool for studying climate change impacts on geological and ecological systems; and develop innovative geotourism strategies to enhance visitor experiences sustainably. Additionally, the Geopark provides presentations and facilitates meaningful discussions with visitors at its information centers.

Kefalonia-Ithaca UGGp has since 2021 organized several events. These events have variable subject topics and include the natural, cultural and intangible heritage of the geopark. The organization of these events avoids the depletion of natural resources, in order to keep an ecological balance that doesn't allow the quality of life of modern societies to decrease.

Some examples of these actions follow below:

- 10 new geosites and three new thematic georoutes to promote sustainable tourism and educate visitors about the importance of preserving natural and cultural heritage were created last year.
- International Festival of Environmental Arts "WE ARE NATURE" at the Ionian center of arts and culture and at Koutavos lagoon geosite
- Wild life photography workshop and bird watching event at Koutavos Lagoon geosite

- Annual informative trip about the aromatic and edible oregano plant in Aenos area
- Geofestival

Additionally, Kephalonia-Ithaca UGGp acknowledges the significance of cooperation by integrating people from local communities, in order to achieve its goals for sustainable development and prosperity, supporting peace and protecting our planet. For this reason, Kefalonia-Ithaca UGGp organizes voluntary actions of Geosites' maintenance as well as educational excursions on a systematic basis, with students of elementary schools in cooperation with Municipalities, in order to awaken ecological awareness.

Furthermore, during the last two years, Kefalonia-Ithaca UGGp in cooperation with the Municipality of Argostoli has created five walking routes for the public in areas where no cars exist. Also, in Ithaca 16 signalized paths that already exist have been added to the geoparks hiking routes. Until now, in Kefalonia-Ithaca UGGp there are almost 30 hiking routes, 13 thematic georoutes and 2 sea georoutes. All of them include geosites with combined value as well as cultural monuments and rich biodiversity.

Finally, the geopark is also responsible for the maintenance of the geosites and the paths in cooperation with the Municipalities of Kefalonia and Ithaca. Additionally, the geopark takes part regularly to the maintenance of several sites in cooperation with other public authorities and within celebration events of Special Days.

Figure 3 Some Examples of promotional events

Acknowledgements

Ionian Island Region, Touristic Committee of Municipality of Argostoli, Municipality of Lixouri, Mynicipality of Sami and Municipality of Ithaca.

References

Iliopoulos, G., Golfinopoulos, V., Kalampalika, A., Karanika,K., Kolendrianou, M., Papadopoulou, P., Tsacos, T., Tzortzi, M., Valavani, D., Zoumpouli, E., Bourli, N., and Zelilidis, A., 2024. From the Ground to the Public: Old and New Fossil Discoveries from Kefalonia–Ithaca UNESCO Global Geopark and Their Value in Research, Education, and Local

Palaeontological Heritage. Sustainability [doi.org/10.3390/su16062521]

Botziolis, C., Bourli N., Zoumpouli, E., Papadopoulou, P., Dimopoulos N., Kovani A., Zelilidis, P., Aspioti, D.C, Iliopoulos, G., and Zelilidis, A., 2024. The Knowledge and Application of Sedimentary Conditions of Shallow Marine and Tidal Waters of Ionian Islands, Greece: Implications for Therapeutic, Geosciences, [doi.org/10.3390/geosciences14020048]

Zelilidis, A., Zoumpouli, E., Papadopoulou, P., Bourli N., Zelilidis, P., Grigorakakis, G., Papafloratou, E., Iliopoulos, G., 2023. The Geological Knowledge and Its Contribution to the Development of Mycenaean Cemeteries in Argostoli Area, Kefalonia Greece. Journal of Anthropological and Archaeological Sciences Volume 7, Issue 4. [DOI: 10.32474/JAAS.2023.07.000268]

17th INTERNATIONAL CONGRESS of the Geological Society of Greece

BULLETIN OF THE GEOLOGICAL SOCIETY OF GREECE, SP. PUBL.

EXTENDED ABSTRACT 356

Excavations in the Lesvos Petrified Forest - A significant geo-conservation project alomg the Kalloni-Sigri road, in the Lesvos island UNESCO Global Geopark, Greece.

Zouros, Nikolaos,[1,2] Valiakos, Ilias,[1,2], Bentana, Konstantina,[1,2] Grimbilakos, George[2], Zgournios, Efstratios[1,2], Tsoukalas, Nikolaos[1], Michalis Georgitsis[1], Savvelos, Loukas, [12,] Agiasoti, Maria[1], Grammenopoulos, Nikolaos[1], Chorafas, Ioannis[1], Salamparchos, Nikolaos,[1]

(1) Natural History Museum of the Lesvos Petrified Forest, Sigri, Greece nzour@aegean.gr (2) Department of Geography, University of the Aegean, Mytilene, Greece

Introduction / Background

The Petrified Forest of Lesvos is a unique natural monument located in the western part of Lesvos Island, Greece. It was formed during the Lower Miocene due to intense volcanic activity in the North Eastern Aegean region.

The Lesvos Petrified Forest was declared a protected natural monument in 1985, and its protected area covers 15,000 hectares. In 2000, it became one of the first four European Geoparks. In 2004, it was a founding member of the Global Geoparks Network. Lesvos Island was designated a UNESCO Global Geopark in 2015 by the UNESCO General Conference. The Lesvos Petrified Forest is the primary geological heritage feature of international significance that led to the recognition of Lesvos Island as a UNESCO Global Geopark. Furthermore, it was recognized as one of the first 100 IUGS geological heritage sites by the International Union of Geological Sciences. Thus, the Lesvos Petrified Forest is one of the most important geological heritage sites for research, education, tourism, and sustainable development.

During the last decade, the new road connecting Kalloni with Sigri was constructed, traversing the western peninsula of Lesvos and specifically the protected area of the Lesvos Petrified Forest. During road construction, a large number of remarkable fossil sites with impressive fossilized tree trunks were unearthed, located along the roadside. Consequently, twelve fossiliferous localities along the Kalloni-Sigri road now constitute an open-air park, offering visitors a unique experience within the Lesvos Petrified Forest.

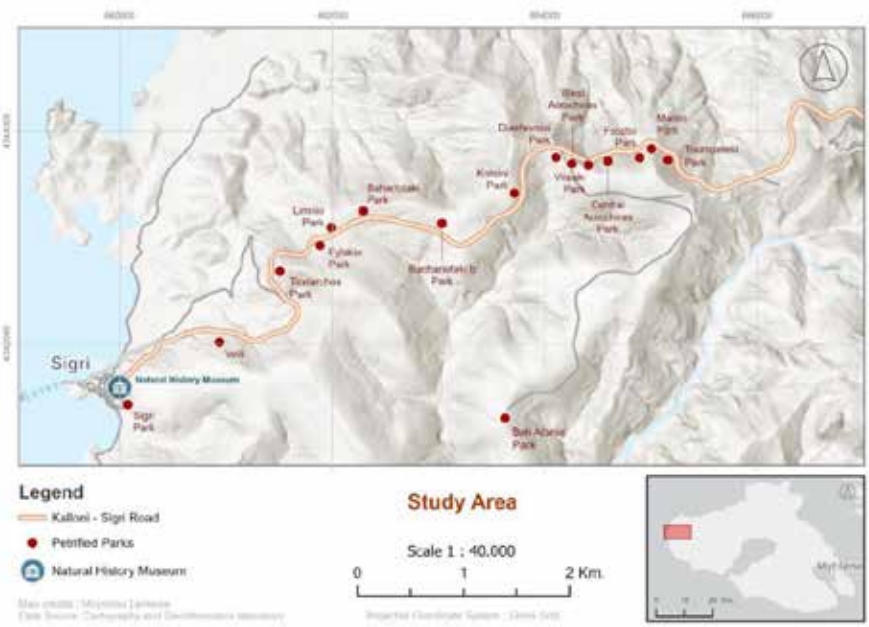

Fig. 1: Location map of the studied area within the Lesvos Island UNESCO Global Geopark, illustrating the 14 fossiliferous localities transformed into open-air parks along the Kalloni-Sigri road.

Geological setting

Lesvos Island is located in the northeastern Aegean Sea. Miocene volcanic rocks dominate western Lesvos and cover the metamorphic basement, which consists of schists and marbles principally of Permian age (Katsikatsos et al., 1982). The oldest Cenozoic rocks overlying the metamorphic basement are lacustrine marls, shales, sandstones, and lignites of the Gavathas Formation (Koufos et al., 2003). The Miocene volcanic sequence of Lesvos comprises andesite, dacite, and basalt lavas, ignimbrites, and a thick pyroclastic sequence (Pe-Piper, 1980; Pe-Piper & Piper, 1993, 2002), which hosts impressive numbers

of silicified tree trunks. The Sigri Pyroclastic Formation consists of several hundred meters of pyroclastic flow tuffs (unwelded ignimbrites) interbedded with fluvial conglomerate and volcaniclastic sandstone. The Sigri Pyroclastic Formation ranges in age from 21.5–22 Ma to younger than 18.4 Ma. Tuffs and fluvial conglomerates in the Sigri Pyroclastic Formation coarsen eastward. Fossiliferous localities with a large number of standing and lying petrified trees, as well as soil horizons, occur throughout the formation (Velitzelos & Zouros, 1997, 1998; Pe-Piper et al., 2019; Zouros et al., 2022).

Research, Excavations and Geoconservation activities in the Lesvos Petrified Forest

The Natural History Museum of the Lesvos Petrified Forest, established in 1995, is a public institution dedicated to the protection and sustainable management of the Lesvos Petrified Forest. Since 1997, the Museum has conducted research activities to identify and map fossiliferous localities in the western peninsula of Lesvos Island. These localities have been identified around Sigri village, in the Tsichliontas river valley, in the Akrocheiras hill range, in the areas of Gavathas and Lapsarna villages, the area north of the Tapsas river valley, the area of Skamiouda, and the area of Eressos village. Systematic excavations have been carried out in the area of Kyria Apolithomeni (Bali Alonia), owned by the Greek state, as well as in areas offered to the Museum by the Greek state, such as the Sigri, Plaka, and Nissiopi Parks (Velitzelos & Zouros, 1997; Zouros et al., 2007; Zouros, 2021). The Museum also conducts rescue excavations within the protected area of the Lesvos Petrified Forest in response to fossil findings during the construction of public and private works.

During the Kalloni-Sigri road construction, the Museum, with support from the Ministry of Public Works, implemented necessary measures, including revisions to the initial road plan, to ensure the protection of fossils and the preservation of significant fossil sites along the road (Zouros et al., 2022).

The Museum implemented a comprehensive geoconservation plan, which included significant challenges: conducting rescue excavations along the Kalloni-Sigri road during road construction, mapping and protecting the newly discovered fossil sites, collecting and conserving the vast number of unearthed fossils, transferring and storing the movable fossils, and protecting and preserving in situ the standing fossil trees and significant lying fossil tree assemblages. This rescue excavation project, which lasted ten years (2004-2014), represents the most extensive paleontological excavation in Greece.

The rescue excavation project was followed by a second project funded by the Operational Programme 2014-2020: North Aegean,.that included a series of interventions to improve accessibility to the fossiliferous sites, provide interpretation and information signage, and develop infrastructure for visitor services. The various fossiliferous sites along the Kalloni-Sigri road are now part of a new, globally unique open-air museum, offering Lesvos Geopark visitors a novel geotourism attraction. In addition to various awareness-raising activities, a new campaign entitled “Walk the Forest” introduces the new petrified forest parks to the public.

Material and Methods

The Museum’s research team monitored the construction work to detect and protect fossils along the new Kalloni-Sigri road. When a new fossiliferous location was encountered, construction work was halted, and the Museum’s excavation team, with the assistance of the Museum’s conservation team, uncovered the fossils from their pyroclastic cover. Detailed cleaning and conservation work took place in situ. Detailed information on the dimensions and stratigraphic location was recorded at 15 fossiliferous locations along the new Kalloni-Sigri road. For all fossils, detailed measurements and location data were taken. The main fossil assemblages, the most prominent fallen tree trunks, and the majority of the standing tree trunks were preserved in their original positions. The removed fossils were secured in plaster casts, and fossil fragments, as well as parts of the respective fossil leaf horizons, were stored in wooden boxes.

Results of the rescue excavations along the Kalloni - Sigri road

The Museum’s research team was monitoring the construction work to detect and protect fossils along the new Kalloni-Sigri road. Fifteen fossiliferous localities have been excavated, revealing numerous fossilized trees and leaves that offer new data on the creation and composition of the Lesvos Petrified Forest.

The **Taxiarchis** locality (Fig. 1) hosts two large conifer tree trunks rooted in tuffs and volcanic conglomerates of the Sigri Pyroclastic Formation, inclined towards the west. In the same locality, two other large conifer trees lie within the volcanic conglomerates, indicating a NNW-SSE tree fall direction.

The **Filakio** locality (Fig. 1) is a significant site hosting three successive paleosol horizons associated with standing tree trunks and extensive root systems. More than 31 standing and lying tree trunks are preserved in their original positions. In this location, six large and medium-sized conifer and angiosperm tree trunks lie within the pyroclastic horizons, indicating a N-S to NNW-SSE tree fall direction.

The **Bachariotaki** locality (Figs. 1, 2) features more than 35 lying and standing tree trunks preserved in their original positions. The majority of the lying tree trunks indicate a N-S to NNW-SSE tree fall direction.

The **Kotsini** locality (Figs. 1, 3) primarily hosts standing tree trunks covered by volcanic conglomerates overlying a very characteristic paleosol horizon. Two lying tree trunks indicate a N-S to NNW-SSE tree fall direction.

Fig. 2. General view of the Bachariotaki fossiliferous locality. N-S to NNW-SSE tree fall direction detected at the site, indicating the moving direction of the pyroclastic flow.

Fig. 3. Petrified tree trunk in Kotsini fossiliferous locality. The roots of the standing tree trunk are diveloped in the silicified paleosoil holizon dividing the lower tuffs with the upper pyroclastic conglomerate.

The **Diastavrosi** locality (Figs. 1, 4) features an intact petrified tree, 19 meters high, with its branches and roots unearthed. The tree was embedded and entombed by the cataclysmic volcanic eruptions of the Vatousa volcano, as the ESE-WNW tree fall direction indicates the moving direction of the pyroclastic flow that transported trees from their original growing location. This is a unique find worldwide. In the same location, two more fossilized trunks have been identified in their natural positions, along with five fossilized trunks, 30 parts of fossilized trunks, and 2,989 fragments of fossiliferous horizons with an abundance of fossilized leaves.
The **West Akrocheiras** locality (Fig. 1) exhibits seven successive paleosol horizons visible between the pyroclastic horizons. Five fossilized tree trunks are rooted in their natural positions. Additionally, 42 fossilized logs or parts of fossilized logs and 6,357 fragments of fossiliferous horizons with an abundance of fossilized leaves are present.
The **Vrysaki** locality (Fig. 1), a continuation of the previous site, also features successive paleosol horizons. Standing and lying tree trunks are embedded in the pyroclastic horizons, including a large standing conifer tree trunk. Ten fossilized trunks are found standing in their original positions. In the same locality, 30 lying fossilized trunks and 2,989 fragments of fossiliferous horizons with an abundance of fossilized leaves are present.

Fig. 4. General view of the Diastavrosi excavation site. 19 meters long tree found intact with its branches and roots with a fall direction towards 113°.

Fig. 5. General view of the Freation fossiliferous locality. E-W and NNW-SSE orientation of the tree fall direction indicate the moving direction of the pyroclastic flow that transported trees from their original site

Fig. 6. The western part of Freation fossiliferous locality. Several excavated tree trunks are covered by plaster cast to avoid damage during excavation works, while others are visible during excavation works

The **Central Akrocheiras** locality (Fig. 1) exhibits successive pyroclastic horizons. Six fossilized tree trunks are rooted in their natural positions. Additionally, 28 fossilized logs or parts of fossilized logs and 2,620 fragments of fossiliferous horizons with an abundance of fossilized leaves are present.

The **Freatio** locality (Figs. 1, 5, 6) is a significant site due to the exceptionally high number of fossilized trunks excavated and preserved on-site. In this locality, 400 silicified tree trunks have been excavated and remain in their excavation positions. Remnants of the trees are found embedded and entombed in pyroclastic flows created by cataclysmic volcanic eruptions from different volcanic centers located east and south of the excavation site. Successive horizons of tuffs are visible, with lying and standing tree trunks preserving evidence of large-scale mudflows. There are also 395 fossilized logs and parts of fossilized logs that have been removed to allow the excavation of the lower fossiliferous horizons. At the same location, 216 selected fragments of fossiliferous horizons with an abundance of fossilized leaves are present. Most of the fossil trunk fragments have been revealed from the Quaternary fluvial conglomerates overlying the pyroclastic tuffs. Three groups of fallen tree trunks are present. The lower group includes tree trunks in the N-S to NNE-SSW (180°-190°) direction, the middle group with an E-W direction (250°), including the longest tree trunks exceeding 25 meters, and the upper group with a NW-SE direction (140°).

Fig. 7: Panoramic view of the I. Toubelekis park fossiliferous locality, where five successive horizons of standing and rooted fossil trunks are visible

Table 1: Fossiliferus localities along the new Kalloni-Sigri road

A/A	Site name	Code	In situ fossils	Removed fossils	Fossil leaves
1	Veili	ΒΕΛ	1	655	
2	Taxiarchis	ΤΧ	2	31	
3	Fylakio	ΦΥ	31	88	
4	Limnio	ΜΡΤ	2	5	
5	Bachariotaki	ΜΠΤ	35	91	
6	Bachariotaki B	ΜΠΤ	4	3	
7	Kotsini	ΜΠΥ	20	2	55
8	Diastavrosi	ΔΜΠ	2	35	2.989
9	West Akrocheiras	ΑΚΥ	5	42	6.357
10	Vrysaki	ΒΡΥ	11	53	3.600
11	Central Akrocheiras	ΒΡΦ	6	28	2.620
12	Freatio	FRE	400	395	216
13	Mantri Toumpeleki	ΤΟΑ	243	0	281
14	I Toumpelekis	ΜΤΟ	127	75	236
15	Moni Ypsiloy	ΑΚΒ ΜΥΒ	2	6	
	Total		**909**	**1.491**	**16.354**

The **Mantri Toumbeleki** locality (Fig. 1) exhibits successive layers of tuffs with lying and standing tree trunks, preserving evidence of large-scale mudflows. The site hosts 243 lying and standing fossilized tree trunks. Additionally, 281 fragments of fossiliferous horizons with an abundance of fossilized leaves are present.
The **I. Toumbelekis** locality (Figs. 1, 7) is a significant site featuring successive layers of tuffs with lying and standing tree trunks. Five successive layers with standing and rooted fossil trunks are visible. The site hosts 127 lying and standing fossilized tree trunks. Furthermore, 395 fossilized logs and parts of fossilized logs have been transported from the site, and 236 fragments of fossiliferous horizons with a plethora of fossilized leaves are present.

Discussion

The excavated localities provide new data regarding the composition of the Lesvos Petrified Forest, its creation, and the stratigraphy of the Sigri Pyroclastic Formation (Zouros et al., 2015; Pe-Piper et al., 2019; Zouros, 2021; Papadopoulou et al., 2025). The vast amount of fossils recovered from the rescue excavation sites along the Kalloni-Sigri road, presented in Table 1, provides a unique archive with significant new data and research results on the composition of the flora, as already published (Zouros et al., 2015, 2022; Zouros, 2021; Kafetzidou et al., 2022; Liapi et al., 2022, 2024; Tsitsou et al., 2022; Zhu et al., 2024). The collected materials will yield further results as they are gradually studied in the coming years.
The rescue excavations along the Kalloni-Sigri road have demonstrated that the Petrified Forest of Lesvos is the result of successive cataclysmic volcanic eruptions that occurred during the period from 21 to 18 million years ago (Pe-Piper et al., 2019). The excavation sections revealed that the formation of the Lesvos Petrified Forest resulted from various eruptive events, leading to the presence of successive pyroclastic horizons hosting standing and rooted petrified trees, separated by paleosol horizons and erosional discontinuities. The collected data are consistent with the suggestion that the pyroclastic materials originated from a southeast-located volcanic center, possibly the one in Messotopos (Pe-Piper et al., 2019).

References

Katsikatsos, G., Mataragas, D., Migiros, G., Triandafillou, E., 1982. Geological study of Lesbos Island, Special Report, IGME, Athens.

Liapi, E., Zidianakis, G., Tsitsou, E., Iliopoulos, G., Zouros, N., 2022. New floristic data of the Early Miocene Lesvos Petrified Forest − Part A: Non-vascular plants, ferns and monocots from the West Akrocheiras outcrop. Bulletin of Geological Society of Greece Sp. Publ. 10, pp. 395–396.

Liapi, E., Iliopoulos, G., Zouros, N., 2024. Documenting the leaf flora of a new fossiliferous locality from the Lesvos Petrified Forest. Folia Musei rerum naturalium Bohemiae occidentalis - Geologica et Paleobiologica 58 (1), pp. 29–33.

Pe-Piper, G., 1978. The Cenozoic volcanic rocks of Lesbos (Greece), unpublished readership thesis, University of Patras.

Pe-Piper, G., 1980. The Cenozoic Volcanic Sequence of Lesvos, Greece. Z. dt. geol. Ges., 131, 889- 901.

Pe-Piper, G. & Piper, D.J.W. (1993) Revised stratigraphy of the Miocene volcanic rocks of Lesbos, Greece. Neues Jahrbuch für Geologie und Palaeontologie Monatshefte, 1993 (2),97–110.

Pe-Piper, G., Piper, J.W.D., Zouros, N., Anastasakis, G., 2019. Age, stratigraphy, sedimentology and tectonic setting of the Sigri Pyroclastic Formation and its fossil forests, Early Miocene, Lesbos, Greece. Basin Research 2019, DOI: 10.1111/bre.12365.

Pe-Piper, G., Imperial, A.M., Piper, D.J.W., Zouros, N.C. & Anastasakis, G. 2019. Nature of the hydrothermal alteration of the Miocene Sigri Petrified Forest and host pyroclastic rocks, western Lesbos, Greece. Journal of Volcanology and Geothermal Research, 369,172–187.

Tsitsou, E., Zidianakis, G., Liapi, E., Iliopoulos, G., Zouros, N., 2022. New floristic data of the Early Miocene Lesvos Petrified Forest − Part B: Dicotyledon taxa from the West Akrocheiras outcrop Bulletin of Geological Society of Greece Sp. Publ. 10, pp. 398–399.

Velitzelos, E., Zouros, N., 1997. The petrified forest of Lesvos–Protected natural monument. Proc. Internat. Sympos. On Engineering Geology and the Environment, Athens, 3037-304.

Velitzelos, E., Zouros, N., 1998. New results on the petrified forest of Lesvos. Bulletin of the Geological Society of Greece, 32(2), 133–142.

Zouros,N., I. Valiakos, G. Gribilakos, A. Plougarlis, K. Mpentana, V. Rozakis, M. Agiasoti, O. Tsalkitzi, 2015. *New fossil findings in the Petrified Forest of Lesvos along the new Kaloni-Sigri road. The forest under the road a new tarveling exhibition of the Lesvos Geopark.* 13th European Geoparks Conference, Rokua, Finland.

Zouros, N.C., 2021. The Miocene petrified forest of Lesvos, Greece: Research and geoconservation activities. Geoconservation Research. 4(2), 635–649.

Zouros,N., Soulakellis,N.,Valiakos,I., Bentana,K., Theodorou,E., Zgournios,E., Antonakis,E. and Lamprakopoulos,A. 2022: Enhancement and promotion of the new fossiliferous sites along the new Kalloni Sigri road.-An example of good practice in geoconservation in Lesvos Isl. UNESCO Global Geopark Greece. Bulletin of Geological Society of Greece Sp. Publ. 10, pp. 849-850.

17th INTERNATIONAL CONGRESS of the Geological Society of Greece

BULLETIN OF THE GEOLOGICAL SOCIETY OF GREECE, SP. PUBL.

EXTENDED ABSTRACT 357

UNESCO Global Geoparks and Global Geoparks Network : Protecting, promoting and managing Earth heritage - Building Sustainable Communities

Zouros, Nikolaos,[1,2]
(1) Department of Geography, University of the Aegean, Mytilene, Greece (2) Natural History Museum of the Lesvos Petrified Forest, Sigri, Greece nzour@aegean.gr

Introduction / Background

The Geopark concept was introduced at late 90's aiming to protect and promote Earth heritage sites through the sustainable local development of territories containing abiotic nature of significant value.

In June 2000 the first Geoparks Network was formed in Europe by four territories hosting geological heritage sites of international significance. The first four Geoparks in Europe were the Reserve Geologique Haute Provence - France, the VulkanEifer Geopark - Germany, the Petrified Forest of Lesvos - Greece and the Maestrazgo Cultural Park - Spain.

Geoparks adopted a bottom-up process involving all relevant local and regional stakeholders and authorities in the area (e.g. local authorities, heritage managing bodies, national/natural park managers, museums, landowners, community groups, tourism providers, community initiatives, indigenous people, and local associations). This process requires firm commitment by the local communities, a strong local multiple partnership, public and political support.

The European Geoparks Network (EGN) developed quickly including new territories from from the founding countries as well as from UK, Italy, Ireland and Austria offering a new model for the protection and sustainable management of the geological heritage monuments through the sustainable development of the local communities. Geoparks activities gain support of the United Nations Educational, Scientific and Cultural Organization (UNESCO) as part of it's official programme. UNESCO's Division of Earth Sciences supported the EGN development and signed a collaboration agreement in 2001. In 2004 the EGN included 17 members from 8 European countries.

Taking into account the success of the EGN as well as Geopark initiatives in China, UNESCO's Division of Earth Sciences started efforts for the creation of the Global Geoparks Network as a platform of cooperation between areas hosting and managing geological heritage of international significance.

The Global Geoparks Network (GGN) was established in 2004, under the umbrella of UNESCO, including 25 Global Geoparks from Europe and China. The GGN operated initially as an international voluntary network, bringing together protected geological heritage sites management bodies, government agencies, non-governmental organizations, scientists and experts from all countries around the world in a unique worldwide partnership.

Global Geoparks as members of GGN operate to share best practice and exchange know how on various aspects in order to protect, conserve and enhance the value of geological heritage sites, including landscapes and geological formations, which are key witnesses to the evolution of our planet and to promote the sustainable development of their territories through geo-tourism and education activities.

In 2014 after one decade of successful operation as a volunteer network the GGN gained legal personality in order to achieve a major goal, the recognition of the Geopark label, the officialization of it's relationship with UNESCO and the establishment of the third UNESCO site designation. The GGN General Assembly during the 6th International Geoparks Conference in Stonehammer Global Geopark, Canada agreed to the new GGN Statutes and the GGN became an international non-profit international association, subject to French legislation (the 1901 law on associations).

Thus the GGN became an International Association following the ICOM model, including institutional members - Global Geoparks and individual members - Global Geopark professionals. The GGN includes Regional Geopark Networks which foster international co-operation and promotion of the Geopark concept and activities at the regional level.

The 38th UNESCO General Conference on November 17th 2015, ratified the statutes of the new International Geoscience and Geoparks Programme and the UNESCO Global Geoparks Operational Guidelines, introducing the brand UNESCO Global Geopark as a label of excellence for areas that meet certain criteria. The GGN is maintaining formal relations with UNESCO and became the official partner for the operation of the UNESCO Global Geoparks programme under the umbrella of the International Geosciences and Geoparks Programme (IGGP).

21 years after its establishment the GGN includes 213 UNESCO Global Geoparks in 48 countries and during 2025 will add 16 new members, reaching 229 UNESCO Global Geoparks in 50 countries.

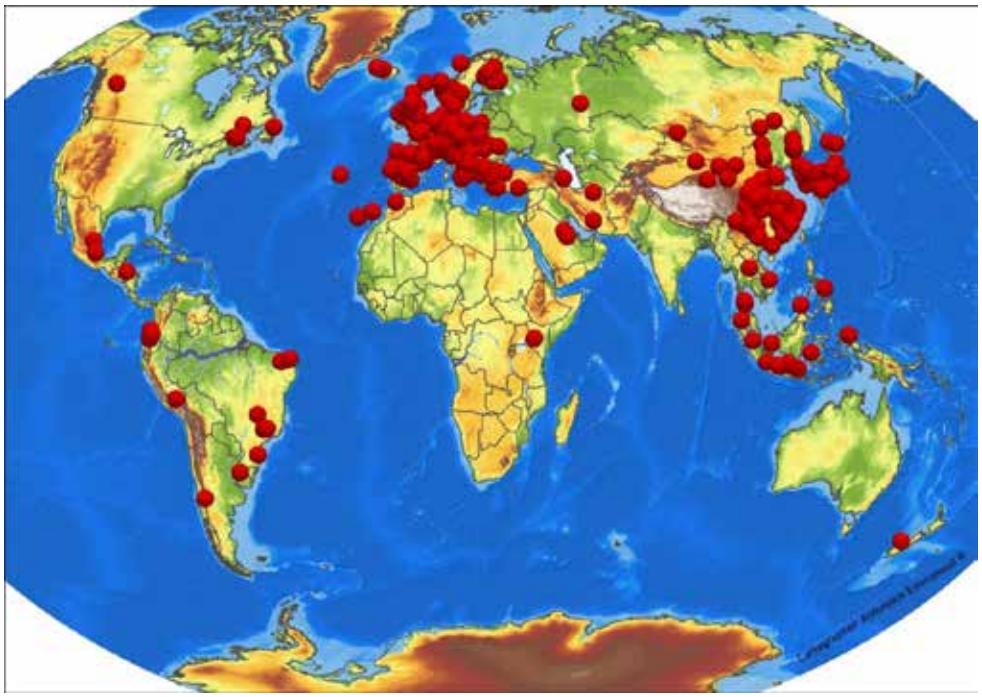

Fig. 1. The Global Geoparks Network includes 229 Geoparks in 50 Countries (2025). List of the UNESCO Global Geoparks at unesco.org

The UNESCO Global Geoparks

The UNESCO's decision introducing under the umbrella of the International Geosciences and Geoparks Programme (IGGP) the UNESCO Global Geoparks Programme (UGGp) together with the existing since 1972 International Geosciences Programme (IGCP) [originally termed the International Geological Correlation Programme], has legally establish the new UNESCO site designation "UNESCO Global Geopark" and endorsed the existing 120 Global Geoparks to become UNESCO Global Geoparks with immediate effect.

The UNESCO Global Geopark branding strongly contributed to raise UNESCO's visibility in Earth Sciences community but also to local communities around the globe in territories hosting exceptional geological heritage sites. The new Programme offer UNESCO a new field of activities and high-quality public outreach on sustainable development in rural territories linked with main global challenges such as the holistic environmental and heritage management, the geodiversity protection and conservation, the geo-hazards mitigation, the climate change adaptation and the sustainable use of natural resources.

Moreover it has been identified that this new UNESCO branding could also be of clear advantage for the development of Global Geoparks in those regions where none currently exist and will be the mechanism to assist countries in the development of Global Geoparks.

UNESCO Global Geoparks according to the Programmes statutes and operational guidelines should fulfill the following basic criteria (UNESCO, 2015):

i. UNESCO Global Geoparks must be single, unified geographical areas where sites and landscapes of international geological significance are managed with a holistic concept of protection, education and sustainable development. The geological heritage sites of international significance should be independently verified by scientific professionals.

ii. UNESCO Global Geoparks should use that heritage, in connection with all other aspects of that area's natural and cultural heritage, to promote awareness of key issues facing society in the context of the dynamic planet we all live on, in particular to increase knowledge and understanding of: geohazards; climate change; the need for the sustainable use of Earth's natural resources; and the empowerment of indigenous peoples.

iii. UNESCO Global Geoparks should be areas with a management body having legal personality recognised under national legislation. The management bodies should be appropriately equipped to adequately address the area of the UNESCO Global Geopark in its entirety.

iv. UNESCO Global Geopark status shall add value by being both independently branded and in synergy with the other designations.

v. UNESCO Global Geoparks should actively involve local communities and indigenous peoples as key stakeholders in the Geopark. In partnership with local communities, a co-management plan needs to be drafted and implemented

that provides for the social and economic needs of local populations, protects the landscape in which they live and conserves their cultural identity.

vi. UNESCO Global Geoparks are encouraged to share their experience and advice and to undertake joint projects within the GGN. Membership of GGN is obligatory.

vii. A UNESCO Global Geopark must respect local and national laws relating to the protection of geological heritage. The defining geological heritage sites within a UNESCO Global Geopark must be legally protected in advance of any application. At the same time, a UNESCO Global Geopark should be used as leverage for promoting the protection of geological heritage locally and nationally. The management body must not participate directly in the sale of geological objects within the UNESCO Global Geopark (regardless of their origin) and should actively discourage unsustainable trade in geological materials.

UNESCO Global Geoparks are evaluated during the initial application by an independent team composed of desk-top advisors and field evaluators.

The justification of the international significance for the geological heritage sites present in an applicant territory is made by experts nominated by the IUGS Geoheritage Commission, through a desk top examination of the geological heritage section of the application. The assessment follows the agreed methodology described by the document Guidelines for the assessment of the international significance of geological heritage in UNESCO Global Geopark applications, which was adopted by the UNESCO Global Geoparks Council. (https://unesdoc.unesco.org/ark:/48223/ pf0000386952)

The evaluation of the Geopark application is made by field evaluators, nominated by the UNESCO Global Geoparks Bureau. The evaluators verify the application in the field using the Checklist to define an aspiring UNESCO Global Geopark (aUGGp). (https://unesdoc.unesco.org/ark:/48223/pf0000383838). The evaluators are submitting their evaluation report and proposal to the UNESCO Global Geoparks Council.

The field evaluators are currying out also the re-validation of the Geoparks operation and activities, submitting their re-validation report and proposal of a green, yellow or red card to the UNESCO Global Geoparks Council. Re-validation missions take place every 4 years (or two years in case of a yellow card).

The UNESO Secretariat in conjunction with the GGN has established and maintains a roster of field evaluators who undertake field evaluations of new applications for aspiring UNESCO Global Geoparks and the revalidations of the already recognized UNESCO Global Geoparks.

The UNESCO Global Geoparks Council, composed by 12 experts and 4 representatives of international bodies supporting Geoparks, is the decision making body for new UNESCO Global Geopark applications and the revalidation of the already recognized Geoparks. The Council takes proposes the new UNESCO Global Geoparks to the UNESCO Executive Board which is the responsible for the nomination of the new UNESCO Global Geoparks. It is also responsible for advising the UNESCO's Director-General on the strategy planning and implementation of the Global Geoparks activity of the IGGP.

During the last 21 years hundreds of Geopark evaluation and re-validations missions have been curried out by Geopark experts. Due to UNESCO's international recognition through Geopark evaluation and revalidation missions outstanding geological heritage sites were protected, conserved and rationally managed.

The Global Geoparks Network

Since its foundation in 2004, the Global Geoparks Networks (GGN) mission is to influence, encourage and assist local communities all over the world to protect and conserve geological heritage sites of international significance, to enhance the integrity and diversity of abiotic and biotic nature and to support economic and cultural development of local communities through the valorisation of their unique heritage and identity.

The GGN established ethical standards which must be adopted and respected by Global Geoparks and Global Geopark professionals.

Every two years the GGN organizes the International Conference on UNESCO Global Geoparks which takes place each time in a different UNESCO Global Geopark selected after a public bid.

The operation of the Global Geoparks Network is based on the active participation of its members through networking at the international, regional, national and local level.

The GGN Members meet every two years at the GGN General Assembly which takes place during the International Conference on UNESCO Global Geoparks, to discuss the GGN activities during the previous years and adopt the strategic action plan for the next biennium. The GGN General Assembly elects the Executive Board which is the decision making body of the Network and responsible to implement the decisions of the General Assembly.

The GGN Advisory Committee consists of the representatives of all the National Geopark Networks and is responsible to advice the GGN on the strategic planning issues. GGN Advisory Committee meets 4 times a year to discuss the implementation of the GGN Strategic Action Plan and to define the GGN Long Term strategy as well as the biannual Strategic Action Plan.

Fig.2. The GGN General Assembly during the 10th International Conference on UNESCO Global Geoparks organized by the M'Goun UNESCO Global Geopark, in Marrakesh, Morocco, September 2023

The GGN Executive Board established several Thematic Working Groups with the participation of GGN Regional Network representatives and Geopark professionals to elaborate proposals and activities in the respected session. The themes of the GGN Working Groups are : a. Geohazards, b. Climate change adaptation, c. Geological heritage and Geodiversity, d. Geodiversity and Biodiversity, e. Sustainable Development Goals, f. Education, g.Tourism, h. Geopark Cultural Heritage, i. Indigenous people, j. Island and coastal areas / Waters / Ocean, k. Gastronomy, l. Communication, m. Geoparks as therapeutic landscapes and n. International Networking.

The GGN Executive Board in order to strengthen the GGN logo visibility and use in activities aiming the promotion of the Geoparks brand, took measures to register and protect the GGN Graphic logo, acronym and the name "Global Geoparks Network" and created a series of combined GGN logos to be used by the different GGN bodies and Regional and National Networks, in order to enhance consistency, efficiency, and flexibility in communication and promotion of the Geopark brand.

GGN Capacity building activities

The GGN advances and disseminates knowledge through capacity building activities organized in collaboration with the UNESCO Secretariat. Capacity building activities include training courses for Geopark managers and staff, on disciplines related to Geopark management, geo-heritage and geo-diversity, geo-conservation, geo-tourism, geo-education and sustainable local development.

The International Intensive Course on UNESCO Global Geoparks is organized every June in Lesvos since 2007 as a join initiative between GGN and UNESCO Secretariat. It is organized by the University of the Aegean and the Natural History Museum with field trips in Lesvos island UNESCO Global Geopark. Since 2001 the UNESCO Chair on Geoparks and the sustainable development of insular and coastal areas at the University of the Aegean is operator for the Course academic programme.

The annual International Training Course on UNESCO Global Geoparks Management and Development has been successfully operated by the China University of Geosciences (Beijing) since 2016. This Course receives full support of UNESCO Global Geoparks Secretariat and Global Geoparks Network, as well as Asia Pacific Geoparks Network and the University of the Aegean. With the close collaboration of Yanqing, Fangshan, Taishan, Songshan, Yimengshan, Zhangye and Xiangxi UNESCO Global Geoparks, the last seven sessions of this Course took place successively in these geoparks, starting with just field lectures and gradually turning into both indoor and field lectures in geoparks.

Fig 3. The international capacity building activities of the Global Geoparks Network in Lesvos, Greece and Beijing, China

The lecturers of the courses are top international Geopark experts and experienced geoscientists and managers from UNESCO Global Geoparks, UNESCO officials, members of the UNESCO Global Geoparks Council and the Global Geoparks Network Executive Board and academic institutions.

Global Geoparks Network facilitates Geopark networking and international collaboration

The GGN encourages and supports co-operation, twinning agreements and exchanges between UNESCO Global Geoparks through common projects, initiatives and activities.
The GGN encourages and supports geopark networking through Geopark conferences, workshops, meetings, common projects and common promotional activities but mainly through the operation of its Regional Geopark Networks and National Geopark Geopark Networks/For a, including all GGN members in each region or country.
The GGN structure includes five regional geopark networks in Europe, Asia Pacific, Latin America and Caribbean, North America and Africa. Regional Networks operate , Thematic Workshops, Meetings and Promotional activities.
Geopark networking facilitates the development and transfer of new methodologies and approaches for the management of Geoparks. The holistic geopark approach in territorial heritage management includes biotic and abiotic factors, landscapes and cultural heritage, holistic nature conservation strategies and action plans, sharing of know-how and new approaches to improve landscape interpretation, awareness raising and public sensitization and the development of educational and touristic activities.
Geopark cooperation provides excellent outcomes and help Geoparks to achieve an effective management and a high level of services and infrastructure. The quick development of Global Geoparks around the globe during the last two decades proves the success of the Geopark concept as a new tool for holistic nature conservation and sustainable rural development through geo-tourism.
The Global Geopark Network seek for international cooperation with other partners on common interests. GGN is a statutory partner of UNESCO for the operation of the UNESCO Global Geoparks programme. GGN has affiliation relationship with the International Union of Geological Sciences (IUGS) and longstanding cooperation with International Union for Nature Conservation (IUCN) to support the Geoparks development. The GGN signed a cooperation agreement with the World Tourism Organization (UNWTO) for the International Year of Sustainable Tourism.

UNESCO Global Geoparks protecting and managing Geological Heritage

A main field of operation for a Geopark is the protection and management of the geological heritage within the Geopark territory. Geopark activities include scientific research, identification and mapping of the geological heritage sites, creation and management of an inventory of geological sites, protection and conservation of geological heritage sites, operation of open air parks, thematic museums and interpretation centers, interpretation and promotion of geological heritage sites, organization of scientific and cultural events.
Through Geoparks operation important geological sites gain worldwide recognition and benefit through the exchange of knowledge, expertise, experience and staff among Geoparks. The new initiative of the IUGS for the first 100 IUGS Geological Heritage Sites (announced in 2022 in Zumaia, Spain) and second 100 IUGS Geological Heritage Sites (announced during the 37th IGC in Busan, Republic of Korea) includes 38 outstanding Geological monuments located in UNESCO Global Geoparks. Among them, the Amonite slab in Digne-les-Bains (Haute Provence Geopark) France, the Lesvos petrified forest, (Lesvos Geopark) Greece, the Holocene Ulmen Maar (Vulkaneifel Geopark) Germany, the alpine superposed buckle folds in Aliaga (Maestrazgo Geopark) Spain, the Dashanpu dinosaus fossil site (Zigong Geopark) China, the Cretaceus-Paleogene Stratigraphic section in Zumaia (Basque Coast Geopark) Spain, the Genbudocave (Sanin Kaigan Geopark) Japan, the Messel Pit fossil site (Bergstrasse-Odenwald Geopark) Germany, the Lower pillow lavas of Troodos ophiolites (Troodos Geopark) Cyprus, the Ngorongoro Crater (Ngorongoro-Lengai Geopark) Tanzania, Shilin Karst (Shilin Geopark) China and Monte Perdito Massif Tectonic structure (Sobrarbe Geopark) Spain.
This recognition shows the value of the geological heritage sites included in UNESCO Global Geoparks as well as the importance of the Geopark label for safeguarding outstanding geological heritage sites, lacking proper management and propmotion.

UNESCO Global Geopark activities and sustainable local development

A broad range of activities combines the main components of a UNESCO Global Geopark operation such as geoconservation, geoeducation, geotourism, and sustainable development.
Geoparks promote themselves as educational territories for sustainability. Geopark educational activities include

a vast range of programmes for all levels of education, from kindengrden and elementary schools, highschools, university students, master courses, vocational training and lifelong learning. Main target group for educational activities in Geoparks are schoolchildren and University students.
Geoparks also promote themselves as ideal destinations for geotourism. Geo-tourism in a form of tourism that sustains, or even enhances, the identity of a place, such as its environment, culture, heritage, and the well-being of its residents.
During the last years Geoparks following the provisions of their management plan implemented a range of actions aimed at the further improvement of its geotourism infrastructure, services, activities and promotion.
The results of the Geopark operation show a significant increase in the number of visitors, the enrichment of their geotourism offer and services to visitors and improvement in geological heritage protection and management..
An important component of the Geopark operation is the support of the local economy. Geoparks create links with local tourist enterprises, restaurants and small hotels in order to provide the necessary infrastructure to meet the needs of the increasing number of park visitors. The majority of visits to the Geopark occur during the summer period, but the aim is to extend the visiting period to the spring and autumn seasons. Geoparks present impressive results in this field. In some cases the number of “Bed and Breakfast” accommodations has doubled over the last few years in order to meet the increasing demand. More importantly, visitors have increased the duration of their visit to the Geopark area. As a result many new enterprises are connected with the activities of the Geopark.
Geoparks support local handicrafts making such as the production of fossil casts and souvenirs by local enterprises. These items are on sale in the Geopark shop along with a variety of other locally made products and the Geopark promotes these products to its visitors.
GGN promotes local gastronomy as an important factor of the Geopark’s identity. Food is reflecting the traditions, history, and values of a territory. In Geoparks, where the conservation of local heritage is paramount, gastronomy serves as a means of celebrating and safeguarding traditional culinary practices, recipes, and food products. By promoting Geopark Gastronomy as a quality brand, local communities can strengthen their cultural identity and promote a sense of pride and belonging among residents and visitors alike. Whether through traditional food festivals, farm-to-table dining experiences, or culinary workshops, Geoparks engage visitors in authentic gastronomic experiences that create lasting memories and foster a deeper connection to the destination. Geoparks collaborate closely with women’s agrotouristic cooperatives and local organic food producers to offer their visitors the opportunity to taste and buy local food products (pasta, organic vegetables, wine, liquors, traditional sweets and marmalades etc). The catering for all Geopark events (conferences, meetings etc.) is supplied using the local traditional food. The Geoparks organize agro-touristic festivals, which promotes quality local products, food and drinks. The event brings local producers and potential customers together. The Women’s agrotouristic cooperative found that this festival provided them with an excellent opportunity to promote their products and their success lead to the creation of similar cooperatives in other villages.

Conclusions

Geoparks contribute significantly to territorial development by directly and indirectly creating new jobs. But what is even more important for the employment in the area is the number of other job opportunities which are created in tourist enterprises, small hotels, guest houses, restaurants and other activities connected with the increase of tourist flow in the Geopark area.
For more than 20 years UNESCO Global Geoparks have campaigned for a holistic understanding of our planet and its evolution, for the protection of Earth heritage and for the sustainable development of their territories. With their initiatives, environmental education and awareness programmes and projects, they place a special emphasis on conveying these natural interrelationships and the impact Man has on these. UNESCO Global Geoparks have been actively pursuing the Global Agenda 2030 with the 17 SDGs for a number of years. Their bottom-up approach with community participation and capacity building, their sustainable regional development activities make the UNESCO Global Geoparks ideal places to understand the relevance of the SDGs and also the responsibility of their implementation. The GGN provides through networking the opportunity for exchanging ideas with partners around the world. Thus the UNESCO Global Geoparks provide ideal model territories for implementing the Agenda 2030. They form the decisive interface between international declarations of intent and concrete on-the-spot activities – which means the transformation from strategy to action.

References

IUGS 2022. The first 100 IUGS Geological Heritage Sites, ISBN 978-1-7923-9975-6
IUGS 2024. The second 100 IUGS Geological Heritage Sites, ISBN 979-8-218-45558-3

Global Geoparks Network 2014. Statutes of the Global Geoparks Network www.globalgeoparksnetwork.org
Global Geoparks Network Magazine Issues 1-7 Published by the Global Geoparks Network www.globalgeoparksnetwork.org
Mc Keever P. & Zouros N. 2005. Geoparks: Celebrating earth heritage, sustaining local communities. Episodes vol. 28, No 4, p. 274-278.
Mc Keever P., Zouros N., Patzak M. 2009. Global Network of National Geoparks. World Heritage No 52, 54-59.
UNESCO 2015. UNESCO Global Geoparks Operational Guidelines. www.unesco.org
Zouros N. 2004. The European Geoparks Network. Geological heritage protection and local development. Episodes vol 27, No 3, pp 165-171.
Zouros N., Mc Keever P. 2008. European Geoparks – Tools for earth heritage protection and sustainable local development, in: European Geoparks (N. Zouros ed.) Published by the European Geoparks Network, ISBN 9789607646910, p.15-30.
Zouros N. 2012 Measuring progress in European Geoparks: a contribution for a smart, sustainable and inclusive growth of Europe. 11th European Geoparks Conference. Arouca Geopark, Portugal. September 2012. Abstract volume.
Zouros N. 2013. European Geoparks: new challenges and innovative tools towards Earth heritage management and sustainable local development. 12th European Geoparks Conference, National Park of Cilento, Vallo di Diano and Alburni Geopark; 09/2013
Zouros, N. (2016). Global Geoparks Network and the new UNESCO Global Geoparks Programme. Bulletin of the Geological Society of Greece, 50(1), 284–292. https://doi.org/10.12681/bgsg.11729

17th INTERNATIONAL CONGRESS of the Geological Society of Greece

BULLETIN OF THE GEOLOGICAL SOCIETY OF GREECE, SP. PUBL.

EXTENDED ABSTRACT 358

Lemnos Island Geosites and their Geotourism and Education Potential

Zouros, Nikolaos,[1,2] Soulakellis Nikolaos [1,2], Valiakos Ilias. [1,2], Bentana, Konstantina,[1,2] Grimpylakos Giorgos, [2] Lamprakopoulos Aggelos. [1,2], Panidou Parthenopi, P[1,2]. Papadopoulou Ermioni-Eirini. [1] and Tataris Georgios. [1]
Aegean University, Department of Geography, Mytilene, Greece, nzour@aegean.gr
Natural History Museum of Lesvos Petrified Forest, Sigri of Lesvos, Greece,

Introduction / Background

Lemnos Island, located in the northeastern Aegean Sea, is an area rich in a wide variety of geological and geomorphological features, including fossiliferous sites, volcanic geosites, and impressive erosional landforms within sedimentary formations. These features are outstanding representatives of the island's geodiversity.

Geosites are protected under Greek environmental legislation (Law 1650/1986 and Law 3937/2011), as they serve as important witnesses to Earth's geological history. However, the geosites of Lemnos and their geotourism potential remain largely underexplored.

This paper presents the work undertaken to identify, map, and assess the geosites of Lemnos Island, with the aim of selecting the most representative ones—based primarily on their aesthetic value and potential for geotourism development.

The research team on geological heritage and geodiversity from the Department of Geography at the University of the Aegean, in collaboration with the Natural History Museum of the Lesvos Petrified Forest, initiated a project in 2012 to identify and map fossiliferous sites containing fossilized plants on Lemnos. As a result, the Lemnos Petrified Forest was declared a protected natural monument in 2013.

The research has since expanded to include the identification and mapping of a wider variety of geosites across the island. In line with the growing global interest in geotourism, the main objective has been to connect these geosites through thematic geotrails, linking them with other sites of ecological and cultural significance. This approach has the potential to foster greater community interest, engagement, and involvement in their sustainable management.

This initiative is supported by the North Aegean 2014–2020 Regional Operational Program through the action "Creation and Operation of Digital Applications for the Promotion of Geo-monuments of Lemnos." This project, implemented by the Natural History Museum of the Lesvos Petrified Forest in collaboration with the Municipality of Lemnos, focuses on promoting geological monuments, landscapes, and ecologically significant sites, with the aim of encouraging the development of alternative forms of tourism.

Geological setting

The island of Lemnos is the eighth-largest Greek island, covering an area of 476 km² and featuring a coastline of approximately 310 km. The island's morphology is generally smooth, with low relief on the eastern side, while the western part is more hilly. The highest point is Skopia (Vigla) in the northwest, reaching an elevation of 470 meters.

Lemnos lies on the southern margin of the North Aegean Trough, which is associated with the western extension of the North Anatolian Fault Zone. This 1,200 km-long dextral strike-slip fault and its branches that extend into the Aegean Sea facilitate the westward extrusion of the Anatolian Plate. The tectonic structures of Lemnos play a key role in understanding the recent geodynamic evolution of the broader region and the prevailing active transtensional stress regime (Pavlides et al., 1990).

The geological structure of Lemnos is relatively simple compared to other islands in the northeastern Aegean. It consists of two main units: a lower unit composed of sedimentary deposits dating from the Middle Eocene (Lutetian) to the Early Oligocene, and an upper unit of Lower Miocene volcanic rocks.

The lower sedimentary unit (Roussos et al., 1993; Innocenti et al., 1994) consists of conglomerates, sandstones, and claystones, which have been interpreted as deep-water deposits. Petrographic analysis of the sandstones indicates that the detritus is primarily composed of clasts from low- to medium-grade metamorphic and sedimentary rocks, sourced from the Rhodope Massif and the Circum-Rhodope Belt (Innocenti et al., 1994). During the Early Oligocene, these deposits were conformably overlain by shallow marine (shelf) sediments.

Volcanic activity began in the Early Miocene with the eruption of pyroclastic flows, followed by the emplacement of sills, lava flows, and domes. Three volcanic units, along with a small quartz-monzonite intrusion (the Fakos intrusion), cover much of the southwestern part of the island (Davis, 1959; Fytikas et al., 1980; Innocenti et al., 1994). These volcanic rocks include andesite, trachyandesite, trachyte, and dacite, featuring porphyritic plagioclase and alkali feldspar set in a microlitic groundmass composed of plagioclase, alkali feldspar, biotite, and quartz in varying proportions (Roussos et al., 1993).

Secondary mineral phases include micas, calcite, quartz, and clay minerals. Radiometric dating of these volcanic rocks yields ages ranging from 21 to 18.2 million years (Fytikas et al., 1984; Innocenti et al., 1994). The igneous rocks of Lemnos represent the earliest volcanic products in the North Aegean region, where volcanic activity ceased by the Middle Miocene.
The Miocene period concludes with the deposition of conglomerates, marls, and marly sandstones. Locally, Pleistocene porous calcareous and oolitic limestones occur, while Holocene alluvial deposits, coastal sediments, and dunes are also present.

Fig. 1: *Geotouristic map of Lemnos island*

Geosite identification and mapping
Fieldwork conducted between 2013 and 2020 led to the identification of 150 geosites distributed across the entire island of Lemnos.
These geosites were classified into the following categories:
a. fossiliferous sites,
b. volcanic sites,
c. stratigraphic–tectonic sites,
d. geomorphological sites (erosional and depositional),
e. other sites of interest.

The geosites were mapped using traditional field mapping methods. In parallel, Unmanned Aerial Systems (UASs) were employed, allowing for the creation of accurate, high-resolution 3D maps and models at various scales. The main objective of these maps was to promote the rich geological and geomorphological heritage of Lemnos and to effectively communicate geo-scientific concepts.
Additionally, 3D geovisualizations were developed using advanced multimedia techniques and technologies, including augmented reality, 360-degree panoramas, and ultra-high-resolution video.

Photo 1. The petrified tree trunk in Baros village. And Moudros area

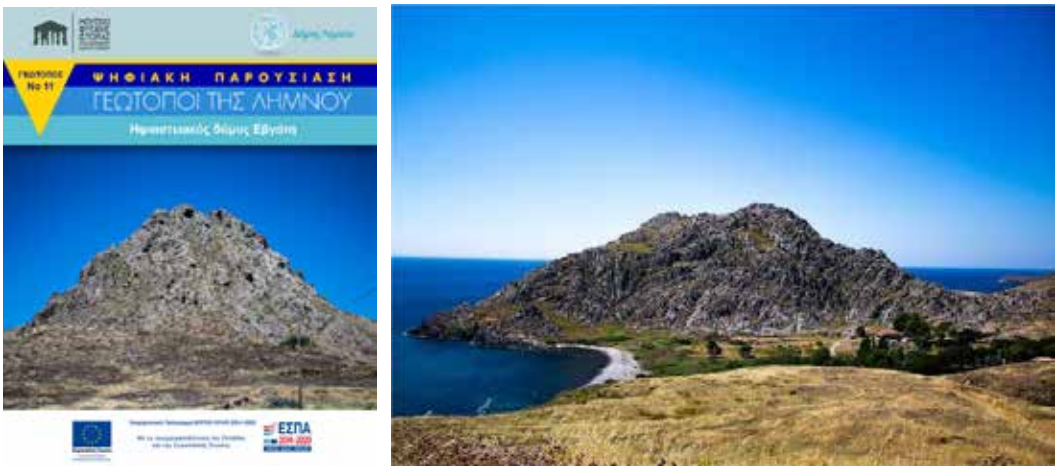

Photo 2 The volcanic domeσ of Evgatis and Agios Pavlos

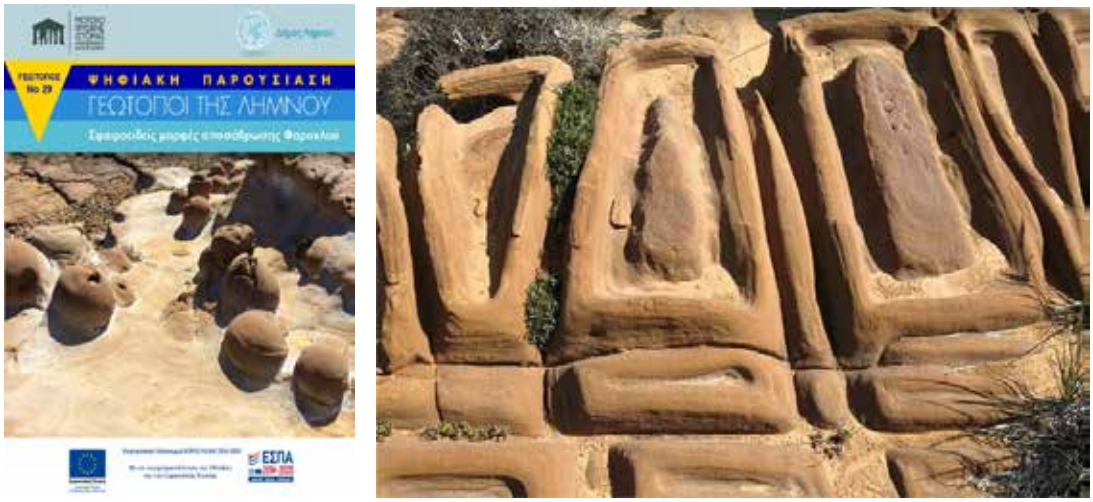

Photo 3 : The spheroidal geoforms at Farakla and Agios Ermolaos

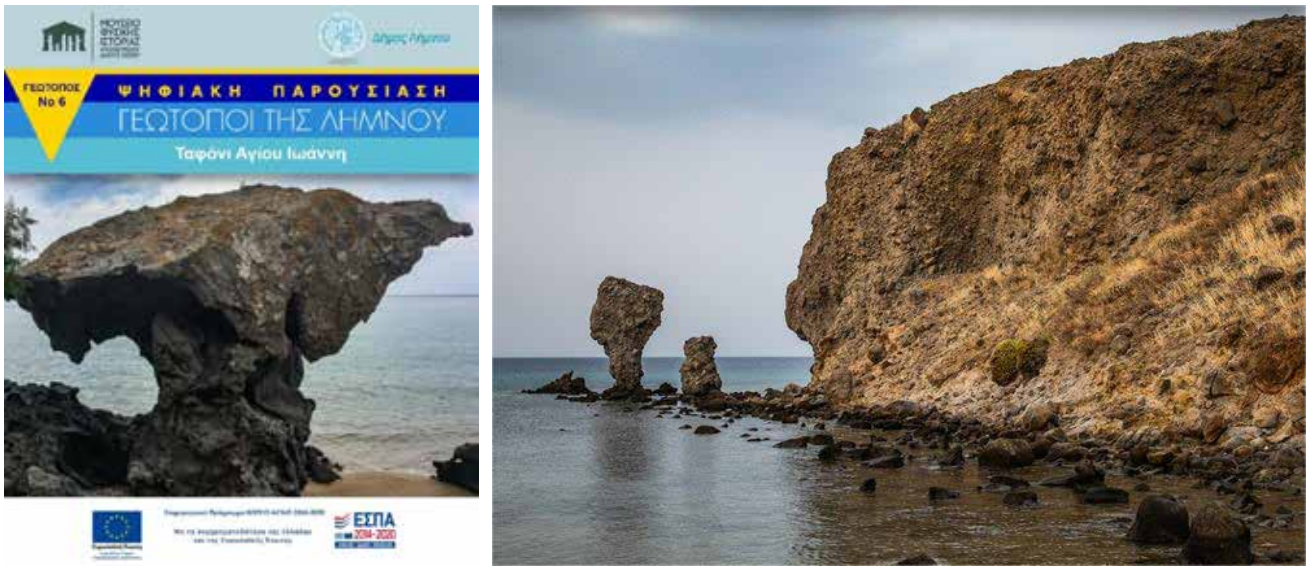

Photo 4 The Agios Ioanis tafoni structure and the sea stacks

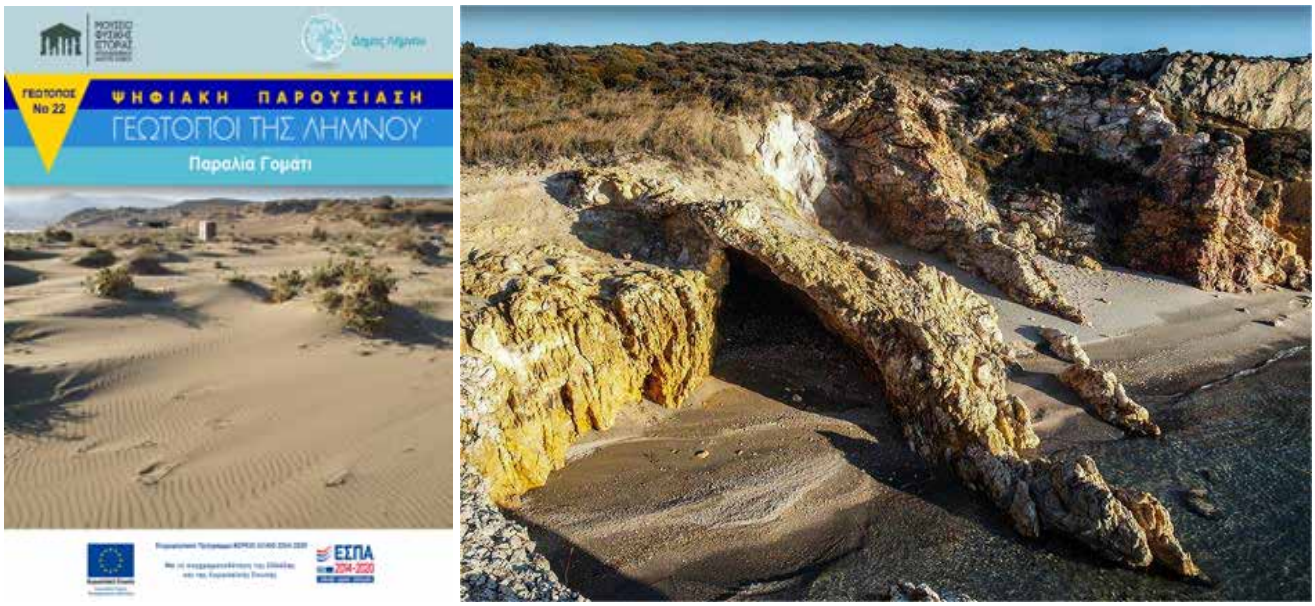

Photo 5 : The dunes at Gomati and the sea caves at Fanaraki

The geological and geomorphological heritage sites were assessed using the methodology proposed for the assessment of geomorphosites (Zouros 2007, 2009).
As a result the selection of the 50 representative geological and geomorphological heritage sites was made. The 50 geosites have been documented for their geoscientific significance. The information for these geosites are taken from field work and literature (Roussos et al., 1993, Innocenti et al.,1994, Maravelis et al. 2007, Chatzipetros et al., 2013). These geological and geomorphological heritage sites as well as sites of ecological and cultural value, form the basis for the creation of the interpretative geotouristic map of Lemnos island, presenting a balanced proportion of scientific and touristic information.
The sites will be linked alond thematic “geo-tails” which will introduce the visitor to the main geological and geomorphological processes that created the landscapes of Lesmnos.

Interpretation and promotion of the Lemnos geological heritage sites
The promotion of Lemnos’ geological heritage is supported by a variety of tools developed throughout the project.

The geotouristic map of Lemnos is designed to highlight the island's rich geological and geomorphological heritage and to communicate geoscientific themes to a non-specialist audience. It offers the public an opportunity to understand fossils and fossilization processes, geomorphological and geological phenomena, rock types, landforms, and landscapes.
The website www.lemnosgeomonuments.gr was created to consolidate all available information about the island's geological heritage sites. It serves both the general public and visitors to Lemnos, as well as educators in local schools and special interest groups looking to explore the island's natural treasures.
To enhance the on-site user experience, a mobile navigation application was developed for smartphones, featuring visual, audio, and augmented reality (AR) content.
All interpretation and promotional tools were developed using advanced technologies, with a strong focus on user-friendly design and long-term sustainability.
Moreover, the promotion and utilization of this material—when combined with broader efforts to highlight the geoenvironment—can provide a competitive advantage in the development of alternative and sustainable tourism.
Finally, a Digital Information Center for the Petrified Forest and Geosites of Lemnos was established in Roussopouli. This center also serves as an information hub for special forms of tourism, including hiking, rural, geological, agritourism, and educational tourism.

Educational activities

Educational activities on geological heritage sites were designed and implemented using the interpretation and promotional tools developed during the project. Educational programs were offered to students and teachers of primary and secondary schools on Lemnos, focusing on the geological heritage of the island and presenting the main geosites identified, mapped, and recorded by the Natural History Museum of the Lesvos Petrified Forest. These classroom programs were complemented by field visits to key geosites, helping students to deepen their understanding of the significance of Lemnos' geological heritage.
Students, teachers, and parents from the 2nd Primary School of Myrina, the Primary School of Atsiki, the Middle School of Moudros, and the General Lyceum of Moudros participated in these educational activities. Additionally, the principals of primary and secondary schools on Lemnos took part in an educational workshop organized in collaboration with the Regional Directorate of Primary and Secondary Education of the North Aegean, as part of the project "Creation – Operation of Digital Applications for the Promotion of the Geo-Monuments of Lemnos."
During the activities, students had the opportunity to explore the impressive geological monuments and the Petrified Forest of Lemnos, as well as to learn about the geological processes that led to their formation. The students participated actively and enthusiastically, asking insightful questions not only about the Petrified Forest and its origins but also about volcanic activity and volcanic structures on the island.
The students of the 2nd Primary School of Myrina also participated in a model educational activity using newly developed virtual reality (VR) applications, created within the same project by the Natural History Museum of the Petrified Forest of Lesvos.
In addition, special informational sessions were held for teachers of primary and secondary education on Lemnos regarding the possibility of organizing educational visits to Lesvos—recognized by UNESCO as a Global Geopark—and its renowned Petrified Forest. Through a detailed presentation of a proposed three-day educational program and rich photographic material, teachers became familiar with the educational activities available on Lesvos, emphasizing the island's geological, natural, and cultural heritage. Special interest was shown in the educational programs of the Natural History Museum of the Petrified Forest of Lesvos, which are conducted within the protected area of the forest.

Conclusions

The systematic identification, documentation, and promotion of geosites on Lemnos Island have revealed the island's significant geodiversity and its potential as a destination for geotourism and geoscience education. Through fieldwork, geosite mapping, and the development of interpretive materials, 150 geosites were classified and assessed, highlighting fossiliferous areas, volcanic features, tectonic structures, and diverse geomorphological landforms.
Fifty of these sites were selected as the most representative of Lemnos' geological and geomorphological heritage and were integrated into an interpretive geotouristic map. These sites form the foundation for thematic geotrails, aiming to connect geological heritage with ecological and cultural landmarks across the island.
The use of innovative digital tools—including Unmanned Aerial Systems (UASs), high-resolution 3D mapping, augmented reality applications, and virtual reality educational modules—has significantly enhanced the ability to communicate geoscientific information in an accessible and engaging manner. The website www.lemnosgeomonuments.gr, the smartphone navigation app, and the establishment of the Digital Information Center in Roussopouli have created a robust framework for both public engagement and sustainable tourism development.

The educational activities implemented as part of the project have demonstrated strong local interest and participation, fostering greater understanding and appreciation of Lemnos' geological heritage among students, educators, and the broader community. The collaboration with the Regional Directorate of Education and the integration of innovative learning technologies have proven effective in bridging scientific knowledge with experiential learning.

There is a strong potential of Lemnos Island to serve as a model for the promotion of geodiversity through geotourism and education. With continued investment in infrastructure, interpretation, and local engagement, Lemnos can enhance its position as a destination for alternative and sustainable tourism, while preserving and valorizing its unique geological heritage for future generations.

The geomonuments of Lemnos will be used to promote the island's rich geological and geomorphological heritage and to communicate geoscientific themes to a non-specialist audience, offering opportunities to understand fossils and fossilization processes, geomorphological and geological phenomena, rock formations, and the island's recent evolution and ongoing geodynamic processes.

References

Chatzipetros, A., Kiratzi, A., Sboras, S., Zouros, N. and Pavlides, S. (2013): Active faulting in the north-eastern Aegean Sea Islands. *Tectonophysics* 597–598 (2013) 106–122

Fytikas, M., Giuliani, O., Innocenti, F., Manetti, P., Mazzuoli, R., Peccerillo, A. & Villari, L. (1980) Neogene volcanism of the northern and central Aegean region. *Annales Geologiques des Pays Helleniques*, 30, 106–129.

Fytikas, M., Innocenti, F., Manetti, P., Mazzuoli, R., Peccerillo, A. & Villari, L. (1984) Tertiary to Quaternary evolution of volcanism in the Aegean region.. Pp. 687–699 in: *The Geological evolution of the Eastern Mediterranean* (Dixon, J.E. & Robertson, A.H.F., editors). Special Publication, 17, Geological Society, London.

Innocenti, F., Manetti, P., Mazzuoli, R., Pertusati, P., Fytikas, M. & Kolios, N. (1994) The geology and geodynamic significance of the island of Limnos, North Aegean sea, Greece. *Neues Jahrbuch für Geologie und Paläontologie, Monatshefte*, part 11, 661-691.

Innocenti F., Manetti P., Mazzuoli R., Pertusati P., Kolios N., Vougioukalakis G. and Androulakakis N. (2003). Geological Map (scale 1:50,000) of the Island of Limnos (Greece), Intern. Conf. The South Aegean Active Volcanic Arc: present knowledge and future perspectives, Milos Island (Greece), 17-20 September 2003, Book of Abstracts,38-39.

Koukouvelas, I.K. & Aydin, A. (2002) Fault structure and related basins of the North Aegean Sea and its surroundings. *Tectonics*, 21(5), 1046.

Maravelis, A., Konstantopoulos, P., Pantopoulos, G., and Zelilidis, A., (2007) North Aegean Sedimentary Basin Evolution During the Late Eocene to Early Oligocene Based on Sedimentological Studies on Lemnos Island (NE Greece), *Geologica Carpathica*, vol. 58, pp. 455□464.

Pavlides S., Mountrakis D., Kilias A. and Tranos, M. (1990). The role of strike-slip movements in the extensional area of Northern Aegean (Greece). A case of transtensional tectonics. Annales Tectonicae, 4, 196-211.

Pe-Piper, G. & Piper, D.J.W. (2002) *The Igneous Rocks of Greece. The Anatomy of an Orogen.* Gebrüder Borntraeger, Berlin, Stuttgart.

Pe-Piper, G., Piper, D.J.W., Koukouvelas, I., Dolansky, L.D., and Kokkalas, S. (2009) Postorogenic shoshonitic rocks and their origin by melting underplated basalts: The Miocene of Limnos, Greece. GSA Bulletin, 121, 39_54.

Rousssos, N., Katsaounis, A., Tsaila-Monopoli, S., Ioakeim X, Karadasi, S. & Davi, E. (1993) *Geological Map of Limnos Island.* IGME, Greece.

Zouros, N., (2007). Geomorphosite assessment and management in protected areas of Greece. Case study of the Lesvos Island – coastal geomorphosites. Geogr. Helv., 62, 169–180 p., 2007.

Zouros N. (2009) Geomorphosites within Geoparks. In Reynard E., Coratza P., Regolini-Bissig G. (eds.). Geomorphosites, München, Pfeil, 105-118. ISBN 978-3-89937-094-2

Zouros N. Soulakellis N. Valiakos I. Grimpylakos G, Rozakis V., Lamprakopoulos A. Panidou, P. Evangelou G. Papadopoulou E. and Tataris G. 2020. GEOLOGICAL AND GEOMORPHOLOGICAL HERITAGE SITES IN LEMNOS ISLAND, GREECE AND THEIR GEOTOURISM POTENTIAL Proceedings of the workshop "The role of geomorphology in modern society. Committee of Geomorphology and Environment of GSG. Harokopio University.

17th INTERNATIONAL CONGRESS
of the Geological Society of Greece

MYTILENE, LESVOS GREECE
28-31 MAY 2025
GSG2025

Bulletin of the Geological Society
Special Publication No. 15, 2025
Publisher: Geological Society of Greece
ISBN (print) 978-618-86841-6-4
ISBN (e-book) 978-618-86841-7-1